

Springer
Handbook *of*
**Crystal
Growth**



*Dhanaraj
Byrappa
Prasad
Dudley
Editors*



Springer

Springer Handbook of Crystal Growth

Springer Handbooks provide a concise compilation of approved key information on methods of research, general principles, and functional relationships in physical sciences and engineering. The world's leading experts in the fields of physics and engineering will be assigned by one or several renowned editors to write the chapters comprising each volume. The content is selected by these experts from Springer sources (books, journals, online content) and other systematic and approved recent publications of physical and technical information.

The volumes are designed to be useful as readable desk reference books to give a fast and comprehensive overview and easy retrieval of essential reliable key information, including tables, graphs, and bibliographies. References to extensive sources are provided.

Springer Handbook of Crystal Growth

Govindhan Dhanaraj, Kullaiah Byrappa,
Vishwanath Prasad, Michael Dudley (Eds.)

With DVD-ROM, 1320 Figures, 134 in four color and 124 Tables



Springer

Editors

Govindhan Dhanaraj
ARC Energy
18 Celina Avenue, Unit 17
Nashua, NH 03063, USA
dhanaraj@arc-energy.com

Kullaiah Byrappa
Department of Geology
University of Mysore
Manasagangotri
Mysore 570 006, India
kbyrappa@gmail.com

Vishwanath Prasad
University of North Texas
1155 Union Circle #310979
Denton, TX 76203-5017, USA
vish.prasad@unt.edu

Michael Dudley
Department of Materials Science & Engineering
Stony Brook University
Stony Brook, NY 11794-2275, USA
mdudley@notes.cc.sunysb.edu

ISBN: 978-3-540-74182-4 e-ISBN: 978-3-540-74761-1
DOI 10.1007/978-3-540-74761-1
Springer Heidelberg Dordrecht London New York

Library of Congress Control Number: 2008942133

© Springer-Verlag Berlin Heidelberg 2010

This work is subject to copyright. All rights are reserved, whether the whole or part of the material is concerned, specifically the rights of translation, reprinting, reuse of illustrations, recitation, broadcasting, reproduction on microfilm or in any other way, and storage in data banks. Duplication of this publication or parts thereof is permitted only under the provisions of the German Copyright Law of September 9, 1965, in its current version, and permission for use must always be obtained from Springer. Violations are liable to prosecution under the German Copyright Law.

The use of general descriptive names, registered names, trademarks, etc. in this publication does not imply, even in the absence of a specific statement, that such names are exempt from the relevant protective laws and regulations and therefore free for general use.

Production and typesetting: le-tex publishing services GmbH, Leipzig
Senior Manager Springer Handbook: Dr. W. Skolaut, Heidelberg
Typography and layout: schreiberVIS, Seeheim
Illustrations: Hippmann GbR, Schwarzenbruck
Cover design: eStudio Calamar Steinen, Barcelona
Cover production: WMXDesign GmbH, Heidelberg
Printing and binding: Stürtz GmbH, Würzburg

Printed on acid free paper

Springer is part of Springer Science+Business Media (www.springer.com)

57/3180/YL 5 4 3 2 1 0

Preface

Over the years, many successful attempts have been made to describe the art and science of crystal growth, and many review articles, monographs, symposium volumes, and handbooks have been published to present comprehensive reviews of the advances made in this field. These publications are testament to the growing interest in both bulk and thin-film crystals because of their electronic, optical, mechanical, microstructural, and other properties, and their diverse scientific and technological applications. Indeed, most modern advances in semiconductor and optical devices would not have been possible without the development of many elemental, binary, ternary, and other compound crystals of varying properties and large sizes. The literature devoted to basic understanding of growth mechanisms, defect formation, and growth processes as well as the design of growth systems is therefore vast.

The objective of this Springer Handbook is to present the state of the art of selected topical areas of both bulk and thin-film crystal growth. Our goal is to make readers understand the basics of the commonly employed growth processes, materials produced, and defects generated. To accomplish this, we have selected more than 50 leading scientists, researchers, and engineers, and their many collaborators from 22 different countries, to write chapters on the topics of their expertise. These authors have written 52 chapters on the fundamentals of crystal growth and defect formation; bulk growth from the melt, solution, and vapor; epitaxial growth; modeling of growth processes and defects; and techniques of defect characterization, as well as some contemporary special topics.

This Springer Handbook is divided into seven parts. Part A presents the fundamentals: an overview of the growth and characterization techniques, followed by the state of the art of nucleation at surfaces, morphology of crystals grown from solutions, nucleation of dislocation during growth, and defect formation and morphology.

Part B is devoted to bulk growth from the melt, a method critical to producing large-size crystals. The

chapters in this part describe the well-known processes such as Czochralski, Kyropoulos, Bridgman, and floating zone, and focus specifically on recent advances in improving these methodologies such as application of magnetic fields, orientation of the growth axis, introduction of a pedestal, and shaped growth. They also cover a wide range of materials from silicon and III–V compounds to oxides and fluorides.

The third part, Part C of the book, focuses on solution growth. The various aspects of hydrothermal growth are discussed in two chapters, while three other chapters present an overview of the nonlinear and laser crystals, *KTP* and *KDP*. The knowledge on the effect of gravity on solution growth is presented through a comparison of growth on Earth versus in a microgravity environment.

The topic of Part D is vapor growth. In addition to presenting an overview of vapor growth, this part also provides details on vapor growth of silicon carbide, gallium nitride, aluminum nitride, and organic semiconductors. This is followed by chapters on epitaxial growth and thin films in Part E. The topics range from chemical vapor deposition to liquid-phase epitaxy to pulsed laser and pulsed electron deposition.

Modeling of both growth processes and defect formation is presented in Part F. These chapters demonstrate the direct correlation between the process parameters and quality of the crystal produced, including the formation of defects. The subsequent Part G presents the techniques that have been developed for crystalline material characterization and analysis. The chapters in Parts F and G demonstrate how well predictive tools and analytical techniques have helped the design and control of growth processes for better-quality crystals of large sizes.

The final Part H is devoted to some selected contemporary topics in this field, such as protein crystal growth, crystallization from gels, in situ structural studies, growth of single-crystal scintillation materials, photovoltaic materials, and wire-saw slicing of large crystals to produce wafers.

We hope this Springer Handbook will be useful to graduate students studying crystal growth and to re-

searchers, scientists, and engineers from academia and industry who are conducting or intend to conduct research in this field as well as those who grow crystals.

We would like to express our sincere thanks to Dr. Claus Acheron and Dr. Werner Skolaut of Springer and Ms Anne Strohbach of le-tex for their extraordinary efforts without which this handbook would not have taken its final shape.

We thank our authors for writing comprehensive chapters and having patience with us during the publication of this Handbook. One of the editors (GD) would

like to thank his family members and Dr. Kedar Gupta (CEO of ARC Energy) for their generous support and encouragement during the entire course of editing this handbook. Acknowledgements are also due to Peter Rudolf, David Bliss, Ishwara Bhat, and Partha Dutta for their help in editing Parts A, B, E, and H, respectively.

Nashua, New Hampshire, April 2010	G. Dhanaraj
Mysore, India	K. Byrappa
Denton, Texas	V. Prasad
Stony Brook, New York	M. Dudley

About the Editors

Govindhan Dhanaraj is the Manager of Crystal Growth Technologies at Advanced Renewable Energy Company (ARC Energy) at Nashua, New Hampshire (USA) focusing on the growth of large size sapphire crystals for LED lighting applications, characterization and related crystal growth furnace development. He received his PhD from the Indian Institute of Science, Bangalore and his Master of Science from Anna University (India). Immediately after his doctoral degree, Dr. Dhanaraj joined a National Laboratory, presently known as Rajaramanna Center for Advanced Technology in India, where he established an advanced Crystal Growth Laboratory for the growth of optical and laser crystals. Prior to joining ARC Energy, Dr. Dhanaraj served as a Research Professor at the Department of Materials Science and Engineering, Stony Brook University, NY, and also held a position of Research Assistant Professor at Hampton University, VA. During his 25 years of focused expertise in crystal growth research, he has developed optical, laser and semiconductor bulk crystals and SiC epitaxial films using solution, flux, Czochralski, Bridgeman, gel and vapor methods, and characterized them using x-ray topography, synchrotron topography, chemical etching and optical and atomic force microscopic techniques. He co-organized a symposium on Industrial Crystal Growth under the 17th American Conference on Crystal Growth and Epitaxy in conjunction with the 14th US Biennial Workshop on Organometallic Vapor Phase Epitaxy held at Lake Geneva, WI in 2009. Dr. Dhanaraj has delivered invited lectures and also served as session chairman in many crystal growth and materials science meetings. He has published over 100 papers and his research articles have attracted over 250 rich citations.



Kullaiah Byrappa received his Doctor's degree in Crystal Growth from the Moscow State University, Moscow in 1981. He is Professor of Materials Science, Head of the Crystal Growth Laboratory, and Director of the Internal Quality Assurance Cell of the University of Mysore, India. His current research is in crystal engineering of polyscale materials through novel solution processing routes, particularly covering hydrothermal, solvothermal and supercritical methods. Professor Byrappa has co-authored the Handbook of Hydrothermal Technology, and edited 4 books as well as two special editions of Journal of Materials Science, and published 180 research papers including 26 invited reviews and book chapters on various aspects of novel routes of solution processing. Professor Byrappa has delivered over 60 keynote and invited lectures at International Conferences, and several hundreds of colloquia and seminars at various institutions around the world. He has also served as chair and co-chair for numerous international conferences. He is a Fellow of the World Academy of Ceramics. Professor Byrappa is serving in several international committees and commissions related to crystallography, crystal growth, and materials science. He is the Founder Secretary of the International Solvothermal and Hydrothermal Association. Professor Byrappa is a recipient of several awards such as the Sir C.V. Raman Award, Materials Research Society of India Medal, and the Golden Jubilee Award of the University of Mysore.



Vishwanath "Vish" Prasad is the Vice President for Research and Economic Development and Professor of Mechanical and Energy Engineering at the University of North Texas (UNT), one of the largest university in the state of Texas. He received his PhD from the University of Delaware (USA), his Masters of Technology from the Indian Institute of Technology, Kanpur, and his bachelor's from Patna University in India all in Mechanical Engineering. Prior to joining UNT in 2007, Dr. Prasad served as the Dean at Florida International University (FIU) in Miami, where he also held the position of Distinguished Professor of Engineering. Previously, he has served as a Leading Professor of Mechanical Engineering at Stony Brook University, New York, as an Associate Professor and Assistant Professor at Columbia University. He has received many special recognitions for his contributions to engineering education. Dr. Prasad's research interests include thermo-fluid sciences, energy systems, electronic materials, and computational materials processing. He has published over 200 articles, edited/co-edited several books and organized numerous conferences, symposia, and workshops. He serves as the lead editor of the Annual Review of Heat Transfer. In the past, he has served as an Associate Editor of the ASME Journal of Heat. Dr. Prasad is an elected Fellow of the American Society of Mechanical Engineers (ASME), and has served as a member of the USRA Microgravity Research Council. Dr. Prasad's research has focused on bulk growth of silicon, III-V compounds, and silicon carbide; growth of large diameter Si tube; design of crystal growth systems; and sputtering and chemical vapor deposition of thin films. He is also credited to initiate research on wire saw cutting of large crystals to produce wafers with much reduced material loss. Dr. Prasad's research has been well funded by US National Science Foundation (NSF), US Department of Defense, US Department of Energy, and industry.



Michael Dudley received his Doctoral Degree in Engineering from Warwick University, UK, in 1982. He is Professor and Chair of the Materials Science and Engineering Department at Stony Brook University, New York, USA. He is director of the Stony Brook Synchrotron Topography Facility at the National Synchrotron Light Source at Brookhaven National Laboratory, Upton New York. His current research focuses on crystal growth and characterization of defect structures in single crystals with a view to determining their origins. The primary technique used is synchrotron topography which enables analysis of defects and generalized strain fields in single crystals in general, with particular emphasis on semiconductor, optoelectronic, and optical crystals. Establishing the relationship between crystal growth conditions and resulting defect distributions is a particular thrust area of interest to Dudley, as is the correlation between electronic/optoelectronic device performance and defect distribution. Other techniques routinely used in such analysis include transmission electron microscopy, high resolution triple-axis x-ray diffraction, atomic force microscopy, scanning electron microscopy, Nomarski optical microscopy, conventional optical microscopy, IR microscopy and fluorescent laser scanning confocal microscopy. Dudley's group has played a prominent role in the development of SiC and AlN growth, characterizing crystals grown by many of the academic and commercial entities involved enabling optimization of crystal quality. He has co-authored some 315 refereed articles and 12 book chapters, and has edited 5 books. He is currently a member of the Editorial Board of Journal of Applied Physics and Applied Physics Letters and has served as Chair or Co-Chair for numerous international conferences.



List of Authors

Francesco Abbona

Università degli Studi di Torino
Dipartimento di Scienze Mineralogiche
e Petrologiche
via Valperga Caluso 35
10125 Torino, Italy
e-mail: francesco.abbona@unito.it

Mohan D. Aggarwal

Alabama A&M University
Department of Physics
Normal, AL 35762, USA
e-mail: mohan.aggarwal@aamu.edu

Marcello R.B. Andreeta

University of São Paulo
Crystal Growth and Ceramic Materials Laboratory,
Institute of Physics of São Carlos
Av. Trabalhador Sãocharlense, 400
São Carlos, SP 13560-970, Brazil
e-mail: marcello@if.sc.usp.br

Dino Aquilano

Università degli Studi di Torino
Facoltà di Scienze Matematiche, Fisiche e Naturali
via P. Giuria, 15
Torino, 10126, Italy
e-mail: dino.aquilano@unito.it

Roberto Arreguín-Espinosa

Universidad Nacional Autónoma de México
Instituto de Química
Circuito Exterior, C.U. s/n
Mexico City, 04510, Mexico
e-mail: arrespin@unam.mx

Jie Bai

Intel Corporation
RA3-402, 5200 NE Elam Young Parkway
Hillsboro, OR 97124-6497, USA
e-mail: jie.bai@intel.com

Stefan Balint

West University of Timisoara
Department of Computer Science
Blvd. V. Parvan 4
Timisoara, 300223, Romania
e-mail: balint@math.uvt.ro

Ashok K. Batra

Alabama A&M University
Department of Physics
4900 Meridian Street
Normal, AL 35762, USA
e-mail: ashok.batra@aamu.edu

Handady L. Bhat

Indian Institute of Science
Department of Physics
CV Raman Avenue
Bangalore, 560012, India
e-mail: hlbhat@physics.iisc.ernet.in

Ishwara B. Bhat

Rensselaer Polytechnic Institute
Electrical Computer
and Systems Engineering Department
110 8th Street, JEC 6031
Troy, NY 12180, USA
e-mail: bhati@rpi.edu

David F. Bliss

US Air Force Research Laboratory
Sensors Directorate Optoelectronic Technology
Branch
80 Scott Drive
Hanscom AFB, MA 01731, USA
e-mail: david.bliss@hanscom.af.mil

Mikhail A. Borik

Russian Academy of Sciences
Laser Materials and Technology Research Center,
A.M. Prokhorov General Physics Institute
Vavilov 38
Moscow, 119991, Russia
e-mail: borik@lst.gpi.ru

Liliana Braescu

West University of Timisoara
Department of Computer Science
Blvd. V. Parvan 4
Timisoara, 300223, Romania
e-mail: lilianabraescu@balint1.math.uvt.ro

Kullaiah Byrappa

University of Mysore
Department of Geology
Manasagangotri
Mysore, 570 006, India
e-mail: kbyrappa@gmail.com

Dang Cai

CVD Equipment Corporation
1860 Smithtown Ave.
Ronkonkoma, NY 11779, USA
e-mail: dcai@cvdequipment.com

Michael J. Callahan

GreenTech Solutions
92 Old Pine Drive
Hanson, MA 02341, USA
e-mail: mjcal37@yahoo.com

Joan J. Carvajal

Universitat Rovira i Virgili (URV)
Department of Physics and Crystallography
of Materials and Nanomaterials (FiCMA-FiCNA)
Campus Sescelades, C/ Marcel·lí Domingo, s/n
Tarragona 43007, Spain
e-mail: joanjosep.carvajal@urv.cat

Aaron J. Celestian

Western Kentucky University
Department of Geography and Geology
1906 College Heights Blvd.
Bowling Green, KY 42101, USA
e-mail: aaron.celestian@wku.edu

Qi-Sheng Chen

Chinese Academy of Sciences
Institute of Mechanics
15 Bei Si Huan Xi Road
Beijing, 100190, China
e-mail: qschen@imech.ac.cn

Chunhui Chung

Stony Brook University
Department of Mechanical Engineering
Stony Brook, NY 11794-2300, USA
e-mail: chuchung@ic.sunysb.edu

Ted Ciszek

Geolite/Siliconsultant
31843 Miwok Trl.
Evergreen, CO 80437, USA
e-mail: ted_ciszek@siliconsultant.com

Abraham Clearfield

Texas A&M University
Distinguished Professor of Chemistry
College Station, TX 77843-3255, USA
e-mail: clearfield@chem.tamu.edu

Hanna A. Dabkowska

Brockhouse Institute for Materials Research
Department of Physics and Astronomy
1280 Main Str W.
Hamilton, Ontario L8S 4M1, Canada
e-mail: dabkoh@mcmaster.ca

Antoni B. Dabkowski

McMaster University, BIMR
Brockhouse Institute for Materials Research,
Department of Physics and Astronomy
1280 Main Str W.
Hamilton, Ontario L8S 4M1, Canada
e-mail: dabko@mcmaster.ca

Rafael Dalmau

HexaTech Inc.
991 Aviation Pkwy Ste 800
Morrisville, NC 27560, USA
e-mail: rdalmau@hexatechinc.com

Govindhan Dhanaraj

ARC Energy
18 Celina Avenue, Unit 77
Nashua, NH 03063, USA
e-mail: ghanaraj@arc-energy.com

Ramasamy Dhanasekaran

Anna University Chennai
Crystal Growth Centre
Chennai, 600 025, India
e-mail: rdhanasekaran@annauniv.edu;
rdcgc@yahoo.com

Ernesto Diéguez

Universidad Autónoma de Madrid
 Department Física de Materiales
 Madrid 28049, Spain
 e-mail: ernesto.diequez@uam.es

Vijay K. Dixit

Raja Ramanna Center for Advance Technology
 Semiconductor Laser Section,
 Solid State Laser Division
 Rajendra Nagar, RRCAT.
 Indore, 452013, India
 e-mail: dixit@rrcat.gov.in

Sadik Dost

University of Victoria
 Crystal Growth Laboratory
 Victoria, BC V8W 3P6, Canada
 e-mail: sdost@me.uvic.ca

Michael Dudley

Stony Brook University
 Department of Materials Science and Engineering
 Stony Brook, NY 11794-2275, USA
 e-mail: mdudley@notes.cc.sunysb.edu

Partha S. Dutta

Rensselaer Polytechnic Institute
 Department of Electrical, Computer
 and Systems Engineering
 110 Eighth Street
 Troy, NY 12180, USA
 e-mail: duttap@rpi.edu

Francesc Díaz

Universitat Rovira i Virgili (URV)
 Department of Physics and Crystallography
 of Materials and Nanomaterials (FICMA-FICNA)
 Campus Sescelades, C/ Marcel·lí Domingo, s/n
 Tarragona 43007, Spain
 e-mail: f.diaz@urv.cat

Paul F. Fewster

PANalytical Research Centre,
 The Sussex Innovation Centre
 Research Department
 Falmer
 Brighton, BN1 9SB, UK
 e-mail: paul.fewster@panalytical.com

Donald O. Frazier

NASA Marshall Space Flight Center
 Engineering Technology Management Office
 Huntsville, AL 35812, USA
 e-mail: donald.o.frazier@nasa.gov

James W. Garland

EPIR Technologies, Inc.
 509 Territorial Drive, Ste. B
 Bolingbrook, IL 60440, USA
 e-mail: jgarland@epir.com

Thomas F. George

University of Missouri–St. Louis
 Center for Nanoscience,
 Department of Chemistry and Biochemistry,
 Department of Physics and Astronomy
 One University Boulevard
 St. Louis, MO 63121, USA
 e-mail: tfgeorge@umsl.edu

Andrea E. Gutiérrez-Quezada

Universidad Nacional Autónoma de México
 Instituto de Química
 Circuito Exterior, C.U. s/n
 Mexico City, 04510, Mexico
 e-mail: 30111390@escolar.unam.mx

Carl Hemmingsson

Linköping University
 Department of Physics, Chemistry
 and Biology (IFM)
 581 83 Linköping, Sweden
 e-mail: cah@ifm.liu.se

Antonio Carlos Hernandez

University of São Paulo
 Crystal Growth and Ceramic Materials Laboratory,
 Institute of Physics of São Carlos
 Av. Trabalhador São-carlense
 São Carlos, SP 13560-970, Brazil
 e-mail: hernandes@ifsc.usp.br

Koichi Kakimoto

Kyushu University
 Research Institute for Applied Mechanics
 6-1 Kasuga-kouen, Kasuga
 816-8580 Fukuoka, Japan
 e-mail: kakimoto@riam.kyushu-u.ac.jp

Imin Kao

State University of New York at Stony Brook
Department of Mechanical Engineering
Stony Brook, NY 11794-2300, USA
e-mail: imin.kao@stonybrook.edu

John J. Kelly

Utrecht University,
Debye Institute for Nanomaterials Science
Department of Chemistry
Princetonplein 5
3584 CC, Utrecht, The Netherlands
e-mail: j.j.kelly@uu.nl

Jeonggoo Kim

Neocera, LLC
10000 Virginia Manor Road #300
Beltsville, MD, USA
e-mail: kim@neocera.com

Helmut Klapper

Institut für Kristallographie
RWTH Aachen University
Aachen, Germany
e-mail: klapper@xtal.rwth-aachen.de;
helmut-klapper@web.de

Christine F. Klemenz Rivenbark

Krystal Engineering LLC
General Manager and Technical Director
1429 Chaffee Drive
Titusville, FL 32780, USA
e-mail: ckr@krystalengineering.com

Christian Kloc

Nanyang Technological University
School of Materials Science and Engineering
50 Nanyang Avenue
639798 Singapore
e-mail: ckloc@ntu.edu.sg

Solomon H. Kolagani

Neocera LLC
10000 Virginia Manor Road
Beltsville, MD 20705, USA
e-mail: harsh@neocera.com

Akinori Koukitu

Tokyo University of Agriculture and Technology
(TUAT)
Department of Applied Chemistry
2-24-16 Naka-cho, Koganei
184-8588 Tokyo, Japan
e-mail: koukitu@cc.tuat.ac.jp

Milind S. Kulkarni

MEMC Electronic Materials
Polysilicon and Quantitative Silicon Research
501 Pearl Drive
St. Peters, MO 63376, USA
e-mail: mkulkarni@memc.com

Yoshinao Kumagai

Tokyo University of Agriculture and Technology
Department of Applied Chemistry
2-24-16 Naka-cho, Koganei
184-8588 Tokyo, Japan
e-mail: 4470kuma@cc.tuat.ac.jp

Valentin V. Laguta

Institute of Physics of the ASCR
Department of Optical Materials
Cukrovarnicka 10
Prague, 162 53, Czech Republic
e-mail: laguta@fzu.cz

Ravindra B. Lal

Alabama Agricultural and Mechanical University
Physics Department
4900 Meridian Street
Normal, AL 35763, USA
e-mail: rbllal@comcast.net

Chung-Wen Lan

National Taiwan University
Department of Chemical Engineering
No. 1, Sec. 4, Roosevelt Rd.
Taipei, 106, Taiwan
e-mail: cwlan@ntu.edu.tw

Hongjun Li

Chinese Academy of Sciences
R & D Center of Synthetic Crystals,
Shanghai Institute of Ceramics
215 Chengbei Rd., Jiading District
Shanghai, 201800, China
e-mail: lh_li@mail.sic.ac.cn

Elena E. Lomonova

Russian Academy of Sciences
Laser Materials and Technology Research Center,
A.M. Prokhorov General Physics Institute
Vavilov 38
Moscow, 119991, Russia
e-mail: *lomonova@lst.gpi.ru*

Ivan V. Markov

Bulgarian Academy of Sciences
Institute of Physical Chemistry
Sofia, 1113, Bulgaria
e-mail: *imarkov@ipc.bas.bg*

Bo Monemar

Linköping University
Department of Physics, Chemistry and Biology
58183 Linköping, Sweden
e-mail: *bom@ifm.liu.se*

Abel Moreno

Universidad Nacional Autónoma de México
Instituto de Química
Circuito Exterior, C.U. s/n
Mexico City, 04510, Mexico
e-mail: *carcamo@unam.mx*

Roosevelt Moreno Rodriguez

State University of New York at Stony Brook
Department of Mechanical Engineering
Stony Brook, NY 11794-2300, USA
e-mail: *roosevelt@dove.eng.sunysb.edu*

S. Narayana Kalkura

Anna University Chennai
Crystal Growth Centre
Sardar Patel Road
Chennai, 600025, India
e-mail: *kalkura@annauniv.edu*

Mohan Narayanan

Reliance Industries Limited
1, Rich Branch court
Gaithersburg, MD 20878, USA
e-mail: *mohan.narayanan@ril.com*

Subramanian Natarajan

Madurai Kamaraj University
School of Physics
Palkalai Nagar
Madurai, India
e-mail: *s_natarajan50@yahoo.com*

Martin Nikl

Academy of Sciences of the Czech Republic (ASCR)
Department of Optical Crystals, Institute of Physics
Cukrovarnicka 10
Prague, 162 53, Czech Republic
e-mail: *nikl@fzu.cz*

Vyacheslav V. Osiko

Russian Academy of Sciences
Laser Materials and Technology Research Center,
A.M. Prokhorov General Physics Institute
Vavilov 38
Moscow, 119991, Russia
e-mail: *osiko@lst.gpi.ru*

John B. Parise

Stony Brook University
Chemistry Department
and Department of Geosciences
ESS Building
Stony Brook, NY 11794-2100, USA
e-mail: *john.parise@stonybrook.edu*

Srinivas Pendurti

ASE Technologies Inc.
11499, Chester Road
Cincinnati, OH 45246, USA
e-mail: *spendurti@asetech.com*

Benjamin G. Penn

NASA/George C. Marshall Space Flight Center
ISHM and Sensors Branch
Huntsville, AL 35812, USA
e-mail: *benjamin.g.penn@nasa.gov*

Jens Pflaum

Julius-Maximilians Universität Würzburg
Institute of Experimental Physics VI
Am Hubland
97078 Würzburg, Germany
e-mail: *jpflaum@physik.uni-wuerzburg.de*

Jose Luis Plaza

Universidad Autónoma de Madrid
Facultad de Ciencias,
Departamento de Física de Materiales
Madrid 28049, Spain
e-mail: joseluis.plaza@uam.es

Udo W. Pohl

Technische Universität Berlin
Institut für Festkörperphysik EW5-1
Hardenbergstr. 36
10623 Berlin, Germany
e-mail: pohl@physik.tu-berlin.de

Vishwanath (Vish) Prasad

University of North Texas
1155 Union Circle
Denton, TX 76203-5017, USA
e-mail: vish.prasad@unt.edu

Maria Cinta Pujol

Universitat Rovira i Virgili
Department of Physics and Crystallography
of Materials and Nanomaterials (FiCMA-FiCNA)
Campus Sescelades, C/ Marcel·lí Domingo
Tarragona 43007, Spain
e-mail: mariacinta.pujol@urv.cat

Balaji Raghothamachar

Stony Brook University
Department of Materials Science and Engineering
310 Engineering Building
Stony Brook, NY 11794-2275, USA
e-mail: braghoth@notes.cc.sunysb.edu

Michael Roth

The Hebrew University of Jerusalem
Department of Applied Physics
Bergman Bld., Rm 206, Givat Ram Campus
Jerusalem 91904, Israel
e-mail: mroth@vms.huji.ac.il

Peter Rudolph

Leibniz Institute for Crystal Growth
Technology Development
Max-Born-Str. 2
Berlin, 12489, Germany
e-mail: rudolph@ikz-berlin.de

Akira Sakai

Osaka University
Department of Systems Innovation
1-3 Machikaneyama-cho, Toyonaka-shi
560-8531 Osaka, Japan
e-mail: sakai@ee.es.osaka-u.ac.jp

Yasuhiro Shiraki

Tokyo City University
Advanced Research Laboratories,
Musashi Institute of Technology
8-15-1 Todoroki, Setagaya-ku
158-0082 Tokyo, Japan
e-mail: yshiraki@tcu.ac.jp

Theo Siegrist

Florida State University
Department of Chemical
and Biomedical Engineering
2525 Pottsdamer Street
Tallahassee, FL 32310, USA
e-mail: siegrist@eng.fsu.edu

Zlatko Sitar

North Carolina State University
Materials Science and Engineering
1001 Capability Dr.
Raleigh, NC 27695, USA
e-mail: sitar@ncsu.edu

Sivalingam Sivananthan

University of Illinois at Chicago
Department of Physics
845 W. Taylor St. M/C 273
Chicago, IL 60607-7059, USA
e-mail: siva@uic.edu; siva@epir.com

Mikhail D. Strikovski

Neocera LLC
10000 Virginia Manor Road, suite 300
Beltsville, MD 20705, USA
e-mail: strikovski@neocera.com

Xun Sun

Shandong University
Institute of Crystal Materials
Shanda Road
Jinan, 250100, China
e-mail: sunxun@icm.sdu.edu.cn

Ichiro Sunagawa

University Tohoku University (Emeritus)
 Kashiwa-cho 3-54-2, Tachikawa
 Tokyo, 190-0004, Japan
 e-mail: *i.sunagawa@nifty.com*

Xu-Tang Tao

Shandong University
 State Key Laboratory of Crystal Materials
 Shanda Nanlu 27, 250100
 Jinan, China
 e-mail: *txt@sdu.edu.cn*

Vitali A. Tatartchenko

Saint – Gobain, 23 Rue Louis Pouey
 92800 Puteaux, France
 e-mail: *vitali.tatartchenko@orange.fr*

Filip Tuomisto

Helsinki University of Technology
 Department of Applied Physics
 Otakaari 1 M
 Espoo TTK 02015, Finland
 e-mail: *filip.tuomisto@tkk.fi*

Anna Vedda

University of Milano-Bicocca
 Department of Materials Science
 Via Cozzi 53
 20125 Milano, Italy
 e-mail: *anna.vedda@unimib.it*

Lu-Min Wang

University of Michigan
 Department of Nuclear Engineering
 and Radiological Sciences
 2355 Bonisteel Blvd.
 Ann Arbor, MI 48109-2104, USA
 e-mail: *lmwang@umich.edu*

Sheng-Lai Wang

Shandong University
 Institute of Crystal Materials,
 State Key Laboratory of Crystal Materials
 Shanda Road No. 27
 Jinan, Shandong, 250100, China
 e-mail: *slwang@icm.sdu.edu.cn*

Shixin Wang

Micron Technology Inc.
 TEM Laboratory
 8000 S. Federal Way
 Boise, ID 83707, USA
 e-mail: *shixinwang@micron.com*

Jan L. Weyher

Polish Academy of Sciences Warsaw
 Institute of High Pressure Physics
 ul. Sokolowska 29/37
 01/142 Warsaw, Poland
 e-mail: *weyher@unipress.waw.pl*

Jun Xu

Chinese Academy of Sciences
 Shanghai Institute of Ceramics
 Shanghai, 201800, China
 e-mail: *xujun@mail.shcnc.ac.cn*

Hui Zhang

Tsinghua University
 Department of Engineering Physics
 Beijing, 100084, China
 e-mail: *zhhui@tsinghua.edu.cn*

Lili Zheng

Tsinghua University
 School of Aerospace
 Beijing, 100084, China
 e-mail: *zhenglili@tsinghua.edu.cn*

Mary E. Zvanut

University of Alabama at Birmingham
 Department of Physics
 1530 3rd Ave S
 Birmingham, AL 35294-1170, USA
 e-mail: *mezvanut@uab.edu*

Zbigniew R. Zytkiewicz

Polish Academy of Sciences
 Institute of Physics
 Al. Lotnikow 32/46
 02668 Warszawa, Poland
 e-mail: *zytkie@ifpan.edu.pl*

Contents

List of Abbreviations	XXXI
------------------------------------	-------------

Part A Fundamentals of Crystal Growth and Defect Formation

1 Crystal Growth Techniques and Characterization: An Overview	
<i>Govindhan Dhanaraj, Kullaiah Byrappa, Vishwanath (Vish) Prasad, Michael Dudley</i>	3
1.1 Historical Developments	3
1.2 Theories of Crystal Growth	4
1.3 Crystal Growth Techniques	6
1.4 Crystal Defects and Characterization	11
References	15
2 Nucleation at Surfaces	
<i>Ivan V. Markov</i>	17
2.1 Equilibrium Crystal–Ambient Phase	18
2.2 Work for Nucleus Formation	24
2.3 Rate of Nucleation	28
2.4 Saturation Nucleus Density	35
2.5 Second–Layer Nucleation in Homoepitaxy	38
2.6 Mechanism of Clustering in Heteroepitaxy	43
2.7 Effect of Surfactants on Nucleation	45
2.8 Conclusions and Outlook	48
References	48
3 Morphology of Crystals Grown from Solutions	
<i>Francesco Abbona, Dino Aquilano</i>	53
3.1 Equilibrium Shape	55
3.2 The Theoretical Growth Shape	64
3.3 Factors Influencing the Crystal Habit	71
3.4 Surface Structure	72
3.5 Crystal Defects	73
3.6 Supersaturation – Growth Kinetics	73
3.7 Solvent	75
3.8 Impurities	78
3.9 Other Factors	84
3.10 Evolution of Crystal Habit	85
3.11 A Short Conclusion	86
3.A Appendix	86
References	87

4 Generation and Propagation of Defects During Crystal Growth
Helmut Klapper 93

4.1 Overview 94

4.2 Inclusions 95

4.3 Striations and Growth Sectors 101

4.4 Dislocations 107

4.5 Twinning 120

4.6 Perfection of Crystals Grown Rapidly from Solution 125

References 127

5 Single Crystals Grown Under Unconstrained Conditions
Ichiro Sunagawa 133

5.1 Background 134

5.2 Smooth and Rough Interfaces: Growth Mechanism and Morphology 136

5.3 Surface Microtopography 139

5.4 Growth Forms of Polyhedral Crystals 143

5.5 Internal Morphology 146

5.6 Perfection of Single Crystals 152

References 156

6 Defect Formation During Crystal Growth from the Melt
Peter Rudolph 159

6.1 Overview 159

6.2 Point Defects 163

6.3 Dislocations 176

6.4 Second-Phase Particles 188

6.5 Faceting 191

6.6 Twinning 193

6.7 Summary 194

References 195

Part B Crystal Growth from Melt Techniques

7 Indium Phosphide: Crystal Growth and Defect Control by Applying Steady Magnetic Fields
David F. Bliss 205

7.1 Historical Overview 205

7.2 Magnetic Liquid-Encapsulated Growth 206

7.3 Magnetic Field Interactions with the Melt 209

7.4 Dislocation Density 216

7.5 Magnetic Field Effects on Impurity Segregation 220

7.6 Optical Characterization of InP:Fe 224

7.7 Summary 226

References 227

8 Czochralski Silicon Single Crystals for Semiconductor and Solar Cell Applications	
<i>Koichi Kakimoto</i>	231
8.1 Silicon Single Crystals for LSIs and Solar Applications	232
8.2 Control of Crystal Defects in Czochralski Silicon	237
8.3 Growth and Characterization of Silicon Multicrystal for Solar Cell Applications	239
8.4 Summary	240
References	241
9 Czochralski Growth of Oxide Photorefractive Crystals	
<i>Ernesto Diéguez, Jose Luis Plaza, Mohan D. Aggarwal, Ashok K. Batra</i>	245
9.1 Background	246
9.2 Crystal Growth	246
9.3 Design and Development of Czochralski Growth System	247
9.4 Growth of Lithium Niobate Crystals and Its Characteristics	252
9.5 Other Oxide Photorefractive Crystals	262
9.6 Growth of Sillenite Crystals and Its Characteristics	264
9.7 Conclusions	273
References	273
10 Bulk Crystal Growth of Ternary III–V Semiconductors	
<i>Partha S. Dutta</i>	281
10.1 III–V Ternary Semiconductors	282
10.2 Need for Ternary Substrates	283
10.3 Criteria for Device-Grade Ternary Substrates	284
10.4 Introduction to Bridgman Crystal Growth Techniques	286
10.5 Overview of III–V Binary Crystal Growth Technologies	292
10.6 Phase Equilibria for Ternary Compounds	300
10.7 Alloy Segregation in Ternary Semiconductors	302
10.8 Crack Formation in Ternary Crystals	304
10.9 Single-Crystalline Ternary Seed Generation Processes	308
10.10 Solute Feeding Processes for Homogeneous Alloy Growth	311
10.11 Role of Melt–Solid Interface Shapes	318
10.12 Conclusion	321
References	321
11 Growth and Characterization of Antimony-Based Narrow-Bandgap III–V Semiconductor Crystals for Infrared Detector Applications	
<i>Vijay K. Dixit, Handady L. Bhat</i>	327
11.1 Importance of Antimony-Based Semiconductors	329
11.2 Phase Diagrams	330
11.3 Crystal Structure and Bonding	331
11.4 Material Synthesis and Purification	333

11.5	Bulk Growth of InSb	334
11.6	Structural Properties of InSb, InAs _x Sb _{1-x} , and InBi _x Sb _{1-x}	340
11.7	Physical Properties of InSb, InAs _x Sb _{1-x} , and InBi _x Sb _{1-x}	346
11.8	Applications	357
11.9	Concluding Remarks and Future Outlook	359
	References	360
12	Crystal Growth of Oxides by Optical Floating Zone Technique	
	<i>Hanna A. Dabkowska, Antoni B. Dabkowski</i>	367
12.1	Historical Notes	367
12.2	Optical Floating Zone Technique – Application for Oxides	368
12.3	Optical Floating Zone and Traveling Solvent Crystal Growth Techniques	369
12.4	Advantages and Limitations of the Floating Zone Techniques	370
12.5	Optical Floating Zone Furnaces	371
12.6	Experimental Details of Ceramics and Rod Preparation for OFZT	372
12.7	Stable Growth of Congruently and Incongruently Melting Oxides	373
12.8	Constitutional Supercooling and Crystallization Front Stability	375
12.9	Crystal Growth Termination and Cooling	377
12.10	Characterization of Crystals Grown by the OFZ Technique	377
12.11	Determination of Defects in Crystals – The Experimental Approach ..	380
12.12	Details of Conditions for Growth of Selected Oxide Single Crystals by OFZ and TSFZ Methods	383
12.13	Conclusions	386
	References	386
13	Laser-Heated Pedestal Growth of Oxide Fibers	
	<i>Marcello R.B. Andreeta, Antonio Carlos Hernandes</i>	393
13.1	Fiber-Pulling Research	394
13.2	The Laser-Heated Pedestal Growth Technique	399
13.3	Fundamentals	402
13.4	Fiber Growth Aspects	409
13.5	Conclusions	418
	References	419
14	Synthesis of Refractory Materials by Skull Melting Technique	
	<i>Vyacheslav V. Osiko, Mikhail A. Borik, Elena E. Lomonova</i>	433
14.1	Overview	433
14.2	Techniques for Growth of Single Crystals in a Cold Crucible	435
14.3	Growth of Single Crystals Based on Zirconium Dioxide	443
14.4	Glass Synthesis by Skull Melting in a Cold Crucible	465
14.5	Conclusion	469
	References	469

15 Crystal Growth of Laser Host Fluorides and Oxides

<i>Hongjun Li, Jun Xu</i>	479
15.1 Crystal Growth of Laser Fluorides and Oxides from Melt	479
15.2 Laser Crystal Defects	487
15.3 Crystal Growth Techniques Characterization	501
References	503

16 Shaped Crystal Growth

<i>Vitali A. Tatartchenko</i>	509
16.1 Definitions and Scope of Discussion: SCG by CST	510
16.2 DSC – Basis of SCG by CST	512
16.3 SA and SCG by CZT	517
16.4 SA and SCG by VT	519
16.5 SA and SCG by FZT	522
16.6 TPS Capillary Shaping.....	522
16.7 TPS Sapphire Growth	539
16.8 TPS Silicon Growth	546
16.9 TPS Metals Growth	551
16.10 TPS Peculiarities	552
References	552

Part C Solution Growth of Crystals**17 Bulk Single Crystals Grown from Solution on Earth and in Microgravity**

<i>Mohan D. Aggarwal, Ashok K. Batra, Ravindra B. Lal, Benjamin G. Penn, Donald O. Frazier</i>	559
17.1 Crystallization: Nucleation and Growth Kinetics	561
17.2 Low-Temperature Solution Growth	566
17.3 Solution Growth by Temperature Lowering	567
17.4 Triglycine Sulfate Crystal Growth: A Case Study	574
17.5 Solution Growth of Triglycine Sulfate Crystals in Microgravity	582
17.6 Protein Crystal Growth	592
17.7 Concluding Remarks	594
References	594

18 Hydrothermal Growth of Polyscale Crystals

<i>Kullaiah Byrappa</i>	599
18.1 History of Hydrothermal Growth of Crystals	603
18.2 Thermodynamic Basis of the Hydrothermal Growth of Crystals	606
18.3 Apparatus Used in the Hydrothermal Growth of Crystals	615
18.4 Hydrothermal Growth of Some Selected Crystals.....	620
18.5 Hydrothermal Growth of Fine Crystals.....	634

18.6	Hydrothermal Growth of Nanocrystals	637
18.7	Concluding Remarks	640
18.A	Appendix	641
	References	646
19	Hydrothermal and Ammonothermal Growth of ZnO and GaN	
	<i>Michael J. Callahan, Qi-Sheng Chen</i>	655
19.1	Overview of Hydrothermal and Ammonothermal Growth of Large Crystals	657
19.2	Requirements for Growth of Large, Low-Defect Crystals	661
19.3	Physical and Mathematical Models	666
19.4	Process Simulations	669
19.5	Hydrothermal Growth of ZnO Crystals	674
19.6	Ammonothermal GaN	681
19.7	Conclusion	685
	References	685
20	Stoichiometry and Domain Structure of KTP-Type Nonlinear Optical Crystals	
	<i>Michael Roth</i>	691
20.1	Background	691
20.2	Stoichiometry and Ferroelectric Phase Transitions	697
20.3	Growth-Induced Ferroelectric Domains	703
20.4	Artificial Domain Structures	708
20.5	Nonlinear Optical Crystals	713
	References	716
21	High-Temperature Solution Growth: Application to Laser and Nonlinear Optical Crystals	
	<i>Joan J. Carvajal, Maria Cinta Pujol, Francesc Díaz</i>	725
21.1	Basics	726
21.2	High-Temperature Solution Growth	731
21.3	Growth of Bulk Laser and NLO Single Crystals by the TSSG Method	736
21.4	Liquid-Phase Epitaxy: Growth of Epitaxial Films of Laser and NLO Materials	746
	References	752
22	Growth and Characterization of KDP and Its Analogs	
	<i>Sheng-Lai Wang, Xun Sun, Xu-Tang Tao</i>	759
22.1	Background	759
22.2	Mechanism and Kinetics of Crystallization	761
22.3	Growth Techniques for Single Crystals	769
22.4	Effect of Growth Conditions on Defects of Crystals	776
22.5	Investigations on Crystal Quality	783
	References	789

Part D Crystal Growth from Vapor

23 Growth and Characterization of Silicon Carbide Crystals	
<i>Govindhan Dhanaraj, Balaji Raghothamachar, Michael Dudley</i>	797
23.1 Silicon Carbide – Background and History	797
23.2 Vapor Growth	799
23.3 High-Temperature Solution Growth	801
23.4 Industrial Bulk Growth by Seed Sublimation	802
23.5 Structural Defects and Their Configurations	805
23.6 Concluding Remarks	816
References	817
24 AlN Bulk Crystal Growth by Physical Vapor Transport	
<i>Rafael Dalmau, Zlatko Sitar</i>	821
24.1 PVT Crystal Growth	822
24.2 High-Temperature Materials Compatibility	825
24.3 Self-Seeded Growth of AlN Bulk Crystals	827
24.4 Seeded Growth of AlN Bulk Crystals	829
24.5 Characterization of High-Quality Bulk Crystals.....	832
24.6 Conclusions and Outlook.....	839
References	839
25 Growth of Single-Crystal Organic Semiconductors	
<i>Christian Kloc, Theo Siegrist, Jens Pflaum</i>	845
25.1 Basics	845
25.2 Theory of Nucleation and Crystal Growth	847
25.3 Organic Materials of Interest for Semiconducting Single Crystals	848
25.4 Pregrowth Purification.....	850
25.5 Crystal Growth.....	854
25.6 Quality of Organic Semiconducting Single Crystals	862
25.7 Organic Single-Crystalline Field-Effect Transistors	863
25.8 Conclusions.....	864
References	865
26 Growth of III-Nitrides with Halide Vapor Phase Epitaxy (HVPE)	
<i>Carl Hemmingsson, Bo Monemar, Yoshinao Kumagai, Akinori Koukitu</i>	869
26.1 Growth Chemistry and Thermodynamics	869
26.2 HVPE Growth Equipment.....	872
26.3 Substrates and Templates for Bulk GaN Growth.....	875
26.4 Substrate Removal Techniques	879
26.5 Doping Techniques for GaN in HVPE.....	882
26.6 Defect Densities, Dislocations, and Residual Impurities	883
26.7 Some Important Properties of HVPE-Grown Bulk GaN Material	887
26.8 Growth of AlN by HVPE: Some Preliminary Results	888
26.9 Growth of InN by HVPE: Some Preliminary Results	890
References	891

27 Growth of Semiconductor Single Crystals from Vapor Phase	
<i>Ramasamy Dhanasekaran</i>	897
27.1 Classifications of Vapor Growth	899
27.2 Chemical Vapor Transport – Transport Kinetics	901
27.3 Thermodynamic Considerations	905
27.4 Growth of II–VI Compound Semiconductors by CVT	912
27.5 Growth of Nanomaterial from Vapor Phase	916
27.6 Growth of I–III–VI ₂ Compounds	917
27.7 Growth of GaN by VPE	925
27.8 Conclusion	929
References	930

Part E Epitaxial Growth and Thin Films

28 Epitaxial Growth of Silicon Carbide by Chemical Vapor Deposition	
<i>Ishwara B. Bhat</i>	939
28.1 Polytypes of Silicon Carbide	941
28.2 Defects in SiC	942
28.3 Epitaxial Growth of Silicon Carbide	944
28.4 Epitaxial Growth on Patterned Substrates	952
28.5 Conclusions	961
References	961

29 Liquid-Phase Electroepitaxy of Semiconductors	
<i>Sadik Dost</i>	967
29.1 Background	967
29.2 Early Theoretical and Modeling Studies	971
29.3 Two-Dimensional Continuum Models	977
29.4 LPEE Growth Under a Stationary Magnetic Field	978
29.5 Three-Dimensional Simulations	981
29.6 High Growth Rates in LPEE: Electromagnetic Mobility	992
References	996

30 Epitaxial Lateral Overgrowth of Semiconductors	
<i>Zbigniew R. Zytewicz</i>	999
30.1 Overview	1000
30.2 Mechanism of Epitaxial Lateral Overgrowth from the Liquid Phase	1002
30.3 Dislocations in ELO Layers	1011
30.4 Strain in ELO Layers	1016
30.5 Recent Progress in Lateral Overgrowth of Semiconductor Structures	1026
30.6 Concluding Remarks	1034
References	1035

31 Liquid-Phase Epitaxy of Advanced Materials	
<i>Christine F. Klemenz Rivenbark</i>	1041
31.1 Historical Development of LPE	1042
31.2 Fundamentals of LPE and Solution Growth	1042
31.3 Requirements for Liquid-Phase Epitaxy	1044
31.4 Developing New Materials: On the Choice of the Epitaxial Deposition Method	1044
31.5 LPE of High-Temperature Superconductors	1046
31.6 LPE of Calcium Gallium Germanates.....	1055
31.7 Liquid-Phase Epitaxy of Nitrides	1059
31.8 Conclusions	1063
References	1064
32 Molecular-Beam Epitaxial Growth of HgCdTe	
<i>James W. Garland, Sivalingam Sivananthan</i>	1069
32.1 Overview	1070
32.2 Theory of MBE Growth	1073
32.3 Substrate Materials	1076
32.4 Design of the Growth Hardware	1088
32.5 In situ Characterization Tools for Monitoring and Controlling the Growth	1090
32.6 Nucleation and Growth Procedure.....	1101
32.7 Dopants and Dopant Activation.....	1104
32.8 Properties of HgCdTe Epilayers Grown by MBE	1107
32.9 HgTe/CdTe Superlattices	1112
32.10 Architectures of Advanced IR Detectors	1115
32.11 IR Focal-Plane Arrays (FPAs)	1118
32.12 Conclusions	1119
References	1121
33 Metalorganic Vapor-Phase Epitaxy of Diluted Nitrides and Arsenide Quantum Dots	
<i>Udo W. Pohl</i>	1133
33.1 Principle of MOVPE.....	1133
33.2 Diluted Nitride InGaAsN Quantum Wells	1137
33.3 InAs/GaAs Quantum Dots.....	1142
33.4 Concluding Remarks	1148
References	1148
34 Formation of SiGe Heterostructures and Their Properties	
<i>Yasuhiro Shiraki, Akira Sakai</i>	1153
34.1 Background	1153
34.2 Band Structures of Si/Ge Heterostructures	1154
34.3 Growth Technologies	1156
34.4 Surface Segregation	1157
34.5 Critical Thickness	1161
34.6 Mechanism of Strain Relaxation	1163

34.7	Formation of Relaxed SiGe Layers	1165
34.8	Formation of Quantum Wells, Superlattices, and Quantum Wires	1173
34.9	Dot Formation	1177
34.10	Concluding Remarks and Future Prospects	1184
	References	1184
35	Plasma Energetics in Pulsed Laser and Pulsed Electron Deposition	
	<i>Mikhail D. Strikovski, Jeonggoo Kim, Solomon H. Kolagani</i>	1193
35.1	Energetic Condensation in Thin Film Deposition	1193
35.2	PLD and PED Techniques	1194
35.3	Transformations of Atomic Energy in PLD and PED	1195
35.4	Optimization of Plasma Flux for Film Growth	1204
35.5	Conclusions	1208
	References	1209
 Part F Modeling in Crystal Growth and Defects		
36	Convection and Control in Melt Growth of Bulk Crystals	
	<i>Chung-Wen Lan</i>	1215
36.1	Physical Laws for Transport Processes	1217
36.2	Flow Structures in the Melt	1219
36.3	Flow Control by External Forces	1228
36.4	Outlook	1238
	References	1238
37	Vapor Growth of III Nitrides	
	<i>Dang Cai, Lili Zheng, Hui Zhang</i>	1243
37.1	Overview of Vapor Growth of III Nitrides	1244
37.2	Mathematical Models for AlN/GaN Vapor Deposition	1248
37.3	Characteristics of AlN/GaN Vapor Deposition	1251
37.4	Modeling of GaN IVPE Growth – A Case Study	1258
37.5	Surface Evolution of GaN/AlN Film Growth from Vapor	1274
37.6	Concluding Remarks	1275
	References	1276
38	Continuum-Scale Quantitative Defect Dynamics in Growing Czochralski Silicon Crystals	
	<i>Milind S. Kulkarni</i>	1281
38.1	The Discovery of Microdefects	1283
38.2	Defect Dynamics in the Absence of Impurities	1284
38.3	Czochralski Defect Dynamics in the Presence of Oxygen	1304
38.4	Czochralski Defect Dynamics in the Presence of Nitrogen	1313
38.5	The Lateral Incorporation of Vacancies in Czochralski Silicon Crystals	1321
38.6	Conclusions	1328
	References	1332

39 Models for Stress and Dislocation Generation in Melt Based Compound Crystal Growth

<i>Vishwanath (Vish) Prasad, Srinivas Pendurti</i>	1335
39.1 Overview	1335
39.2 Crystal Growth Processes	1336
39.3 Dislocations in Semiconductors Materials	1337
39.4 Models for Dislocation Generation	1339
39.5 Diamond Structure of the Crystal	1343
39.6 Deformation Behavior of Semiconductors	1346
39.7 Application of the Haasen Model to Crystal Growth	1350
39.8 An Alternative Model	1351
39.9 Model Summary and Numerical Implementation	1360
39.10 Numerical Results	1362
39.11 Summary	1374
References	1375

40 Mass and Heat Transport in BS and EFG Systems

<i>Thomas F. George, Stefan Balint, Liliana Braescu</i>	1379
40.1 Model-Based Prediction of the Impurity Distribution – Vertical BS System	1380
40.2 Model-Based Prediction of the Impurity Distribution – EFG System ..	1389
References	1400

Part G Defects Characterization and Techniques

41 Crystalline Layer Structures with X-Ray Diffractometry

<i>Paul F. Fewster</i>	1405
41.1 X-Ray Diffractometry	1406
41.2 Basic Direct X-Ray Diffraction Analysis from Layered Structures	1407
41.3 Instrumental and Theoretical Considerations	1412
41.4 Examples of Analysis from Low to High Complexity	1413
41.5 Rapid Analysis	1419
41.6 Wafer Micromapping	1420
41.7 The Future	1421
References	1422

42 X-Ray Topography Techniques for Defect Characterization of Crystals

<i>Balaji Raghothamachar, Michael Dudley, Govindhan Dhanaraj</i>	1425
42.1 Basic Principles of X-Ray Topography	1426
42.2 Historical Development of the X-Ray Topography Technique	1428
42.3 X-Ray Topography Techniques and Geometry	1430
42.4 Theoretical Background for X-Ray Topography	1435
42.5 Mechanisms for Contrast on X-Ray Topographs	1440

42.6	Analysis of Defects on X-Ray Topographs	1445
42.7	Current Application Status and Development	1449
	References	1450
 43 Defect-Selective Etching of Semiconductors		
	<i>Jan L. Weyher, John J. Kelly</i>	1453
43.1	Wet Etching of Semiconductors: Mechanisms	1454
43.2	Wet Etching of Semiconductors: Morphology and Defect Selectivity ..	1459
43.3	Defect-Selective Etching Methods	1461
	References	1473
 44 Transmission Electron Microscopy Characterization of Crystals		
	<i>Jie Bai, Shixin Wang, Lu-Min Wang, Michael Dudley</i>	1477
44.1	Theoretical Basis of TEM Characterization of Defects	1477
44.2	Selected Examples of Application of TEM to Semiconductor Systems ..	1493
44.3	Concluding Remarks: Current Application Status and Development ..	1514
	References	1515
 45 Electron Paramagnetic Resonance Characterization of Point Defects		
	<i>Mary E. Zvanut</i>	1521
45.1	Electronic Paramagnetic Resonance	1522
45.2	EPR Analysis	1524
45.3	Scope of EPR Technique	1534
45.4	Supplementary Instrumentation and Supportive Techniques	1538
45.5	Summary and Final Thoughts	1545
	References	1546
 46 Defect Characterization in Semiconductors with Positron Annihilation Spectroscopy		
	<i>Filip Tuomisto</i>	1551
46.1	Positron Annihilation Spectroscopy	1552
46.2	Identification of Point Defects and Their Charge States	1560
46.3	Defects, Doping, and Electrical Compensation	1565
46.4	Point Defects and Growth Conditions	1569
46.5	Summary	1576
	References	1576

Part H Special Topics in Crystal Growth

47 Protein Crystal Growth Methods		
	<i>Andrea E. Gutiérrez-Quezada, Roberto Arreguín-Espinosa, Abel Moreno</i>	1583
47.1	Properties of Biomacromolecular Solutions	1584
47.2	Transport Phenomena and Crystallization	1587
47.3	Classic Methods of Crystal Growth	1587
47.4	Protein Crystallization by Diffusion-Controlled Methods	1588

47.5	New Trends in Crystal Growth (Crystal Quality Enhancement)	1591
47.6	2-D Characterization via Atomic Force Microscopy (Case Study).....	1595
47.7	3-D Characterization via X-Ray Diffraction and Related Methods	1598
	References	1599

48 Crystallization from Gels

	<i>S. Narayana Kalkura, Subramanian Natarajan</i>	1607
48.1	Gel Growth in Crystal Deposition Diseases	1608
48.2	Experimental Methods	1609
48.3	Pattern Formation in Gel Systems	1610
48.4	Crystals Grown Using Gel Technique	1611
48.5	Application in Crystal Deposition Diseases	1614
48.6	Crystal-Deposition-Related Diseases	1616
48.7	Calcium Oxalate	1617
48.8	Calcium Phosphates	1619
48.9	Hydroxyapatite (HAP)	1620
48.10	Dicalcium Phosphate Dihydrate (DCPD)	1620
48.11	Calcium Sulfate	1623
48.12	Uric Acid and Monosodium Urate Monohydrate	1623
48.13	L-Cystine	1624
48.14	L-Tyrosine, Hippuric Acid, and Ciprofloxacin	1625
48.15	Atherosclerosis and Gallstones	1625
48.16	Crystallization of Hormones: Progesterone and Testosterone	1628
48.17	Pancreatitis	1628
48.18	Conclusions	1629
	References	1630

49 Crystal Growth and Ion Exchange in Titanium Silicates

	<i>Aaron J. Celestian, John B. Parise, Abraham Clearfield</i>	1637
49.1	X-Ray Methods	1637
49.2	Equipment for Time-Resolved Experiments	1642
49.3	Detectors	1642
49.4	Software	1644
49.5	Types of In Situ Cells	1645
49.6	In-Situ Studies of Titanium Silicates (Na-TS) with Sitinakite Topology	1649
49.7	Discussion of In Situ Studies	1658
49.8	Summary	1660
	References	1660

50 Single-Crystal Scintillation Materials

	<i>Martin Nikl, Anna Vedda, Valentin V. Laguta</i>	1663
50.1	Background	1663
50.2	Scintillation Materials	1670
50.3	Future Prospects	1689
50.4	Conclusions	1691
	References	1691

51 Silicon Solar Cells: Materials, Devices, and Manufacturing	
<i>Mohan Narayanan, Ted Cizek</i>	1701
51.1 Silicon Photovoltaics.....	1701
51.2 Crystal Growth Technologies for Silicon Photovoltaics	1704
51.3 Cell Fabrication Technologies	1711
51.4 Summary and Discussion	1715
References	1716
 52 Wafer Manufacturing and Slicing Using Wiresaw	
<i>Imin Kao, Chunhui Chung, Roosevelt Moreno Rodriguez</i>	1719
52.1 From Crystal Ingots to Prime Wafers	1721
52.2 Slicing: The First Postgrowth Process in Wafer Manufacturing	1726
52.3 Modern Wiresaw in Wafer Slicing	1730
52.4 Conclusions and Further Reading	1733
References	1733
 Acknowledgements	1737
About the Authors	1741
Detailed Contents	1759
Subject Index	1791

List of Abbreviations

μ -PD	micro-pulling-down
1S-ELO	one-step ELO structure
2-D	two-dimensional
2-DNG	two-dimensional nucleation growth
2S-ELO	double layer ELO
3-D	three-dimensional
4T	quaterthiophene
6T	sexithienyl
8MR	eight-membered ring
8T	hexathiophene

A

a-Si	amorphous silicon
A/D	analogue-to-digital
AA	additional absorption
AANP	2-adamantylamino-5-nitropyridine
AAS	atomic absorption spectroscopy
AB	Abrahams and Burocchi
ABES	absorption-edge spectroscopy
AC	alternate current
ACC	annular capillary channel
ACRT	accelerated crucible rotation technique
ADC	analog-to-digital converter
ADC	automatic diameter control
ADF	annular dark field
ADP	ammonium dihydrogen phosphate
AES	Auger electron spectroscopy
AFM	atomic force microscopy
ALE	arbitrary Lagrangian Eulerian
ALE	atomic layer epitaxy
ALUM	aluminum potassium sulfate
ANN	artificial neural network
AO	acoustooptic
AP	atmospheric pressure
APB	antiphase boundaries
APCF	advanced protein crystallization facility
APD	avalanche photodiode
APPLN	aperiodic poled LN
APS	Advanced Photon Source
AR	antireflection
AR	aspect ratio
ART	aspect ratio trapping
ATGSP	alanine doped triglycine sulfo-phosphate
AVT	angular vibration technique

B

BA	Born approximation
BAC	band anticrossing

BBO	BaB ₂ O ₄
BCF	Burton–Cabrera–Frank
BCT	Ba _{0.77} Ca _{0.23} TiO ₃
BCTi	Ba _{1-x} Ca _x TiO ₃
BE	bound exciton
BF	bright field
BFDH	Bravais–Friedel–Donnay–Harker
BGO	Bi ₁₂ GeO ₂₀
BIBO	BiB ₃ O ₆
BLIP	background-limited performance
BMO	Bi ₁₂ MO ₂₀
BN	boron nitride
BOE	buffered oxide etch
BPD	basal-plane dislocation
BPS	Burton–Prim–Slichter
BPT	bipolar transistor
BS	Bridgman–Stockbarger
BSCCO	Bi–Sr–Ca–Cu–O
BSF	bounding stacking fault
BSO	Bi ₂₀ SiO ₂₀
BTO	Bi ₁₂ TiO ₂₀
BU	building unit
BaREF	barium rare-earth fluoride
BiSCCO	Bi ₂ Sr ₂ CaCu ₂ O _n

C

C–V	capacitance–voltage
CALPHAD	calculation of phase diagram
CBED	convergent-beam electron diffraction
CC	cold crucible
CCC	central capillary channel
CCD	charge-coupled device
CCVT	contactless chemical vapor transport
CD	convection diffusion
CE	counterelectrode
CFD	computational fluid dynamics
CFD	cumulative failure distribution
CFMO	Ca ₂ FeMoO ₆
CFS	continuous filtration system
CGG	calcium gallium germanate
CIS	copper indium diselenide
CL	cathode-ray luminescence
CL	cathodoluminescence
CMM	coordinate measuring machine
CMO	CaMoO ₄
CMOS	complementary metal–oxide–semiconductor
CMP	chemical–mechanical polishing
CMP	chemomechanical polishing

COD	calcium oxalate dihydrate
COM	calcium oxalate-monohydrate
COP	crystal-originated particle
CP	critical point
CPU	central processing unit
CRSS	critical-resolved shear stress
CSMO	$\text{Ca}_{1-x}\text{Sr}_x\text{MoO}_3$
CST	capillary shaping technique
CST	crystalline silico titanate
CT	computer tomography
CTA	CsTiOAsO_4
CTE	coefficient of thermal expansion
CTF	contrast transfer function
CTR	crystal truncation rod
CV	Cabrera–Vermilyea
CVD	chemical vapor deposition
CVT	chemical vapor transport
CW	continuous wave
CZ	Czochralski
CZT	Czochralski technique

D

D/A	digital to analog
DBR	distributed Bragg reflector
DC	direct current
DCAM	diffusion-controlled crystallization apparatus for microgravity
DCCZ	double crucible CZ
DCPD	dicalcium-phosphate dihydrate
DCT	dichlorotetracene
DD	dislocation dynamics
DESY	Deutsches Elektronen Synchrotron
DF	dark field
DFT	density function theory
DFW	defect free width
DGS	diglycine sulfate
DI	deionized
DIA	diamond growth
DIC	differential interference contrast
DICM	differential interference contrast microscopy
DKDP	deuterated potassium dihydrogen phosphate
DLATGS	deuterated L-alanine-doped triglycine sulfate
DLTS	deep-level transient spectroscopy
DMS	discharge mass spectroscopy
DNA	deoxyribonucleic acid
DOE	Department of Energy
DOS	density of states
DPH-BDS	2,6-diphenylbenzo[1,2- <i>b</i> :4,5- <i>b'</i>]diselenophene
DPPH	2,2-diphenyl-1-picrylhydrazyl
DRS	dynamic reflectance spectroscopy

DS	directional solidification
DSC	differential scanning calorimetry
DSE	defect-selective etching
DSL	diluted Sirtl with light
DTA	differential thermal analysis
DTGS	deuterated triglycine sulfate
DVD	digital versatile disk
DWBA	distorted-wave Born approximation
DWELL	dot-in-a-well

E

EADM	extended atomic distance mismatch
EALFZ	electrical-assisted laser floating zone
EB	electron beam
EBIC	electron-beam-induced current
ECE	end chain energy
ECR	electron cyclotron resonance
EDAX	energy-dispersive x-ray analysis
EDMR	electrically detected magnetic resonance
EDS	energy-dispersive x-ray spectroscopy
EDT	ethylene dithiotetrathiafulvalene
EDTA	ethylene diamine tetraacetic acid
EELS	electron energy-loss spectroscopy
EFG	edge-defined film-fed growth
EFTEM	energy-filtered transmission electron microscopy
ELNES	energy-loss near-edge structure
ELO	epitaxial lateral overgrowth
EM	electromagnetic
EMA	effective medium theory
EMC	electromagnetic casting
EMCZ	electromagnetic Czochralski
EMF	electromotive force
ENDOR	electron nuclear double resonance
EO	electrooptic
EP	EaglePicher
EPD	etch pit density
EPMA	electron microprobe analysis
EPR	electron paramagnetic resonance
erfc	error function
ES	equilibrium shape
ESP	edge-supported pulling
ESR	electron spin resonance
EVA	ethyl vinyl acetate

F

F	flat
FAM	free abrasive machining
FAP	$\text{Ca}_5(\text{PO}_4)_3\text{F}$
FCA	free carrier absorption
fcc	face-centered cubic
FEC	full encapsulation Czochralski

FEM	finite element method
FES	fluid experiment system
FET	field-effect transistor
FFT	fast Fourier transform
FIB	focused ion beam
FOM	figure of merit
FPA	focal-plane array
FPE	Fokker–Planck equation
FSLI	femtosecond laser irradiation
FT	flux technique
FTIR	Fourier-transform infrared
FWHM	full width at half-maximum
FZ	floating zone
FZT	floating zone technique

G

GAME	gel acupuncture method
GDMS	glow-discharge mass spectrometry
GE	General Electric
GGG	gadolinium gallium garnet
GNB	geometrically necessary boundary
GPIB	general purpose interface bus
GPMD	geometric partial misfit dislocation
GRI	growth interruption
GRIIRA	green-radiation-induced infrared absorption
GS	growth sector
GSAS	general structure analysis software
GSGG	Gd ₃ Sc ₂ Ga ₃ O ₁₂
GSMBE	gas-source molecular-beam epitaxy
GSO	Gd ₂ SiO ₅
GU	growth unit

H

HA	hydroxyapatite
HAADF	high-angle annular dark field
HAADF-STEM	high-angle annular dark field in scanning transmission electron microscope
HAP	hydroxyapatite
HB	horizontal Bridgman
HBM	Hottinger Baldwin Messtechnik GmbH
HBT	heterostructure bipolar transistor
HBT	horizontal Bridgman technique
HDPCG	high-density protein crystal growth
HE	high energy
HEM	heat-exchanger method
HEMT	high-electron-mobility transistor
HF	hydrofluoric acid
HGF	horizontal gradient freezing
HH	heavy-hole
HH-PCAM	handheld protein crystallization apparatus for microgravity
HIV	human immunodeficiency virus

HIV-AIDS	human immunodeficiency virus–acquired immunodeficiency syndrome
HK	high potassium content
HLA	half-loop array
HLW	high-level waste
HMDS	hexamethyldisilane
HMT	hexamethylene tetramine
HNP	high nitrogen pressure
HOE	holographic optical element
HOLZ	higher-order Laue zone
HOMO	highest occupied molecular orbital
HOPG	highly oriented pyrolytic graphite
HOT	high operating temperature
HP	Hartman–Perdok
HPAT	high-pressure ammonothermal technique
HPHT	high-pressure high-temperature
HRTEM	high-resolution transmission electron microscopy
HRXRD	high-resolution x-ray diffraction
HSXPD	hemispherically scanned x-ray photoelectron diffraction
HT	hydrothermal
HTS	high-temperature solution
HTSC	high-temperature superconductor
HVPE	halide vapor-phase epitaxy
HVPE	hydride vapor-phase epitaxy
HWC	hot-wall Czochralski
HZM	horizontal ZM

I

IBAD	ion-beam-assisted deposition
IBE	ion beam etching
IC	integrated circuit
IC	ion chamber
ICF	inertial confinement fusion
ID	inner diameter
ID	inversion domain
IDB	incidental dislocation boundary
IDB	inversion domain boundary
IF	identification flat
IG	inert gas
IK	intermediate potassium content
ILHPG	indirect laser-heated pedestal growth
IML-1	International Microgravity Laboratory
IMPATT	impact ionization avalanche transit-time
IP	image plate
IPA	isopropyl alcohol
IR	infrared
IRFPA	infrared focal plane array
IS	interfacial structure
ISS	ion-scattering spectroscopy
ITO	indium-tin oxide
ITTFA	iterative target transform factor analysis
IVPE	iodine vapor-phase epitaxy

J		LGS	$\text{La}_3\text{Ga}_5\text{SiO}_{14}$
JDS	joint density of states	LGT	$\text{La}_3\text{Ga}_{5.5}\text{Ta}_{0.5}\text{O}_{14}$
JFET	junction FET	LH	light hole
K		LHFB	L-histidine tetrafluoroborate
K	kinked	LHPG	laser-heated pedestal growth
KAP	potassium hydrogen phthalate	LID	laser-induced damage
KDP	potassium dihydrogen phosphate	LK	low potassium content
KGW	$\text{KY}(\text{WO}_4)_2$	LLNL	Lawrence Livermore National Laboratory
KGdP	$\text{KGd}(\text{PO}_3)_4$	LLO	laser lift-off
KLYF	KLiYF_5	LLW	low-level waste
KM	Kubota–Mullin	LN	LiNbO_3
KMC	kinetic Monte Carlo	LP	low pressure
KN	KNbO_3	LPD	liquid-phase diffusion
KNP	$\text{KNd}(\text{PO}_3)_4$	LPE	liquid-phase epitaxy
KPZ	Kardar–Parisi–Zhang	LPEE	liquid-phase electroepitaxy
KREW	$\text{KRE}(\text{WO}_4)_2$	LPS	$\text{Lu}_2\text{Si}_2\text{O}_7$
KTA	potassium titanyl arsenate	LSO	Lu_2SiO_5
KTN	potassium niobium tantalate	LST	laser scattering tomography
KTP	potassium titanyl phosphate	LST	local shaping technique
KTa	KTaO_3	LT	low-temperature
KTaN	$\text{KTa}_{1-x}\text{Nb}_x\text{O}_3$	LTa	LiTaO_3
KYF	KYF_4	LUMO	lowest unoccupied molecular orbital
KYW	$\text{KY}(\text{WO}_4)_2$	LVM	local vibrational mode
L		LWIR	long-wavelength IR
LACBED	large-angle convergent-beam diffraction	LY	light yield
LAFB	L-arginine tetrafluoroborate	LiCAF	LiCaAlF_6
LAGB	low-angle grain boundary	LiSAF	lithium strontium aluminum fluoride
LAO	LiAlO_2	M	
LAP	L-arginine phosphate	M–S	melt–solid
LBIC	light-beam induced current	MAP	magnesium ammonium phosphate
LBIV	light-beam induced voltage	MASTRAPP	multizone adaptive scheme for transport and phase change processes
LBO	LiB_3O_5	MBE	molecular-beam epitaxy
LBO	LiBO_3	MBI	multiple-beam interferometry
LBS	laser-beam scanning	MC	multicrystalline
LBSM	laser-beam scanning microscope	MCD	magnetic circular dichroism
LBT	laser-beam tomography	MCT	HgCdTe
LCD	liquid-crystal display	MCZ	magnetic Czochralski
LD	laser diode	MD	misfit dislocation
LDT	laser-induced damage threshold	MD	molecular dynamics
LEC	liquid encapsulation Czochralski	ME	melt epitaxy
LED	light-emitting diode	ME	microelectronics
LEEBI	low-energy electron-beam irradiation	MEMS	microelectromechanical system
LEM	laser emission microanalysis	MESFET	metal-semiconductor field effect transistor
LEO	lateral epitaxial overgrowth	MHP	magnesium hydrogen phosphate-trihydrate
LES	large-eddy simulation	MI	morphological importance
LG	LiGaO_2	MIT	Massachusetts Institute of Technology
LGN	$\text{La}_3\text{Ga}_{5.5}\text{Nb}_{0.5}\text{O}_{14}$	ML	monolayer
LGO	LaGaO_3	MLEC	magnetic liquid-encapsulated Czochralski

MLEK	magnetically stabilized liquid-encapsulated Kyropoulos
MMIC	monolithic microwave integrated circuit
MNA	2-methyl-4-nitroaniline
MNSM	modified nonstationary model
MOCVD	metalorganic chemical vapor deposition
MOCVD	molecular chemical vapor deposition
MODFET	modulation-doped field-effect transistor
MOMBE	metalorganic MBE
MOS	metal–oxide–semiconductor
MOSFET	metal–oxide–semiconductor field-effect transistor
MOVPE	metalorganic vapor-phase epitaxy
mp	melting point
MPMS	mold-pushing melt-supplying
MQSSM	modified quasi-steady-state model
MQW	multiple quantum well
MR	melt replenishment
MRAM	magnetoresistive random-access memory
MRM	melt replenishment model
MSUM	monosodium urate monohydrate
MTDATA	metallurgical thermochemistry database
MTS	methyltrichlorosilane
MUX	multiplexor
MWIR	mid-wavelength infrared
MWRM	melt without replenishment model
MXRF	micro-area x-ray fluorescence

N

N	nucleus
N	nutrient
NASA	National Aeronautics and Space Administration
NBE	near-band-edge
NBE	near-bandgap emission
NCPM	noncritically phase matched
NCS	neighboring confinement structure
NGO	NdGaO ₃
NIF	National Ignition Facility
NIR	near-infrared
NIST	National Institute of Standards and Technology
NLO	nonlinear optic
NMR	nuclear magnetic resonance
NP	no-phonon
NPL	National Physical Laboratory
NREL	National Renewable Energy Laboratory
NS	Navier–Stokes
NSF	National Science Foundation
nSLN	nearly stoichiometric lithium niobate
NSLS	National Synchrotron Light Source
NSM	nonstationary model

NTRS	National Technology Roadmap for Semiconductors
NdBCO	NdBa ₂ Cu ₃ O _{7–x}

O

OCP	octacalcium phosphate
ODE	ordinary differential equation
ODLN	opposite domain LN
ODMR	optically detected magnetic resonance
OEIC	optoelectronic integrated circuit
OF	orientation flat
OFZ	optical floating zone
OLED	organic light-emitting diode
OMVPE	organometallic vapor-phase epitaxy
OPO	optical parametric oscillation
OSF	oxidation-induced stacking fault

P

PAMBE	photo-assisted MBE
PB	proportional band
PBC	periodic bond chain
pBN	pyrolytic boron nitride
PC	photoconductivity
PCAM	protein crystallization apparatus for microgravity
PCF	primary crystallization field
PCF	protein crystal growth facility
PCM	phase-contrast microscopy
PD	Peltier interface demarcation
PD	photodiode
PDE	partial differential equation
PDP	programmed data processor
PDS	periodic domain structure
PE	pendeo-epitaxy
PEBS	pulsed electron beam source
PEC	polyimide environmental cell
PECVD	plasma-enhanced chemical vapor deposition
PED	pulsed electron deposition
PEO	polyethylene oxide
PET	positron emission tomography
PID	proportional–integral–differential
PIN	positive intrinsic negative diode
PL	photoluminescence
PLD	pulsed laser deposition
PMNT	Pb(Mg, Nb) _{1–x} Ti _x O ₃
PPKTP	periodically poled KTP
PPLN	periodic poled LN
PPLN	periodic poling lithium niobate
ppy	polypyrrole
PR	photorefractive
PSD	position-sensitive detector
PSF	prismatic stacking fault

PSI	phase-shifting interferometry	RTV	room temperature vulcanizing
PSM	phase-shifting microscopy	R&D	research and development
PSP	pancreatic stone protein		
PSSM	pseudo-steady-state model	S	
PSZ	partly stabilized zirconium dioxide		
PT	pressure–temperature	S	stepped
PV	photovoltaic	SAD	selected area diffraction
PVA	polyvinyl alcohol	SAM	scanning Auger microprobe
PVD	physical vapor deposition	SAW	surface acoustical wave
PVE	photovoltaic efficiency	SBN	strontium barium niobate
PVT	physical vapor transport	SC	slow cooling
PWO	PbWO ₄	SCBG	slow-cooling bottom growth
PZNT	Pb(Zn, Nb) _{1–x} Ti _x O ₃	SCC	source-current-controlled
PZT	lead zirconium titanate	SCF	single-crystal fiber
		SCF	supercritical fluid technology
Q		SCN	succinonitrile
		SCW	supercritical water
QD	quantum dot	SD	screw dislocation
QDT	quantum dielectric theory	SE	spectroscopic ellipsometry
QE	quantum efficiency	SECeRTS	small environmental cell for real-time studies
QPM	quasi-phase-matched	SEG	selective epitaxial growth
QPMSHG	quasi-phase-matched second-harmonic generation	SEM	scanning electron microscope
QSSM	quasi-steady-state model	SEM	scanning electron microscopy
QW	quantum well	SEMATECH	Semiconductor Manufacturing Technology
QWIP	quantum-well infrared photodetector	SF	stacking fault
R		SFM	scanning force microscopy
		SGOI	SiGe-on-insulator
RAE	rotating analyzer ellipsometer	SH	second harmonic
RBM	rotatory Bridgman method	SHG	second-harmonic generation
RC	reverse current	SHM	submerged heater method
RCE	rotating compensator ellipsometer	SI	semi-insulating
RE	rare earth	SIA	Semiconductor Industry Association
RE	reference electrode	SIMS	secondary-ion mass spectrometry
REDG	recombination enhanced dislocation glide	SIOM	Shanghai Institute of Optics and Fine Mechanics
RELF	rare-earth lithium fluoride	SL	superlattice
RF	radiofrequency	SL-3	Spacelab-3
RGS	ribbon growth on substrate	SLI	solid–liquid interface
RHEED	reflection high-energy electron diffraction	SLN	stoichiometric LN
RI	refractive index	SM	skull melting
RIE	reactive ion etching	SMB	stacking mismatch boundary
RMS	root-mean-square	SMG	surfactant-mediated growth
RNA	ribonucleic acid	SMT	surface-mount technology
ROIC	readout integrated circuit	SNR	signal-to-noise ratio
RP	reduced pressure	SNT	sodium nonatitanate
RPI	Rensselaer Polytechnic Institute	SOI	silicon-on-insulator
RSM	reciprocal space map	SP	sputtering
RSS	resolved shear stress	sPC	scanning photocurrent
RT	room temperature	SPC	Scientific Production Company
RTA	RbTiOAsO ₄	SPC	statistical process control
RTA	rapid thermal annealing	SR	spreading resistance
RTCVD	rapid-thermal chemical vapor deposition	SRH	Shockley–Read–Hall
RTP	RbTiOPO ₄	SRL	strain-reducing layer
RTPL	room-temperature photoluminescence	SRS	stimulated Raman scattering
RTR	ribbon-to-ribbon		

SRXRD	spatially resolved XRD
SS	solution-stirring
SSL	solid-state laser
SSM	sublimation sandwich method
ST	synchrotron topography
STC	standard testing condition
STE	self-trapped exciton
STEM	scanning transmission electron microscopy
STM	scanning tunneling microscopy
STOS	sodium titanium oxide silicate
STP	stationary temperature profile
STS	space transportation system
SWBXT	synchrotron white beam x-ray topography
SWIR	short-wavelength IR
SXRT	synchrotron x-ray topography

T

TCE	trichloroethylene
TCNQ	tetracyanoquinodimethane
TCO	thin-film conducting oxide
TCP	tricalcium phosphate
TD	Tokyo Denpa
TD	threading dislocation
TDD	threading dislocation density
TDH	temperature-dependent Hall
TDMA	tridiagonal matrix algorithm
TED	threading edge dislocation
TEM	transmission electron microscopy
TFT-LCD	thin-film transistor liquid-crystal display
TGS	triglycine sulfate
TGT	temperature gradient technique
TGW	Thomson–Gibbs–Wulff
TGZM	temperature gradient zone melting
THM	traveling heater method
TMCZ	transverse magnetic-field-applied Czochralski
TMOS	tetramethoxysilane
TO	transverse optic
TPB	three-phase boundary
TPRE	twin-plane reentrant-edge effect
TPS	technique of pulling from shaper
TQM	total quality management
TRAPATT	trapped plasma avalanche-triggered transit
TRM	temperature-reduction method
TS	titanium silicate
TSC	thermally stimulated conductivity
TSD	threading screw dislocation
TSET	two shaping elements technique
TSFZ	traveling solvent floating zone
TSL	thermally stimulated luminescence
TSSG	top-seeded solution growth
TSSM	Tatarchenko steady-state model
TSZ	traveling solvent zone

TTV	total thickness variation
TV	television
TVM	three-vessel solution circulating method
TVTP	time-varying temperature profile
TWF	transmitted wavefront
TZM	titanium zirconium molybdenum
TZP	tetragonal phase

U

UC	universal compliant
UDLM	uniform-diffusion-layer model
UHPHT	ultrahigh-pressure high-temperature
UHV	ultrahigh-vacuum
ULSI	ultralarge-scale integrated circuit
UV	ultraviolet
UV-vis	ultraviolet–visible
UVB	ultraviolet B

V

VAS	void-assisted separation
VB	valence band
VB	vertical Bridgman
VBT	vertical Bridgman technique
VCA	virtual-crystal approximation
VCSEL	vertical-cavity surface-emitting laser
VCZ	vapor pressure controlled Czochralski
VDA	vapor diffusion apparatus
VGf	vertical gradient freeze
VLS	vapor–liquid–solid
VLSI	very large-scale integrated circuit
VLWIR	very long-wavelength infrared
VMCZ	vertical magnetic-field-applied Czochralski
VP	vapor phase
VPE	vapor-phase epitaxy
VST	variable shaping technique
VT	Verneuil technique
VTGT	vertical temperature gradient technique
VUV	vacuum ultraviolet

W

WBDF	weak-beam dark-field
WE	working electrode

X

XP	x-ray photoemission
XPS	x-ray photoelectron spectroscopy
XPS	x-ray photoemission spectroscopy
XRD	x-ray diffraction
XRPD	x-ray powder diffraction
XRT	x-ray topography

Y		YPS	(Y ₂)Si ₂ O ₇
		YSO	Y ₂ SiO ₅
		Z	
YAB	YAl ₃ (BO ₃) ₄	ZA	Al ₂ O ₃ -ZrO ₂ (Y ₂ O ₃)
YAG	yttrium aluminum garnet	ZLP	zero-loss peak
YAP	yttrium aluminum perovskite	ZM	zone-melting
YBCO	YBa ₂ Cu ₃ O _{7-x}	ZNT	ZN-Technologies
YIG	yttrium iron garnet	ZOLZ	zero-order Laue zone
YL	yellow luminescence		
YLF	LiYF ₄		
YOF	yttrium oxyfluoride		

Part A Fundamentals

Part A Fundamentals of Crystal Growth and Defect Formation

1 Crystal Growth Techniques and Characterization: An Overview

Govindhan Dhanaraj, Nashua, USA
Kullaiah Byrappa, Mysore, India
Vishwanath (Vish) Prasad, Denton, USA
Michael Dudley, Stony Brook, USA

2 Nucleation at Surfaces

Ivan V. Markov, Sofia, Bulgaria

3 Morphology of Crystals Grown from Solutions

Francesco Abbona, Torino, Italy
Dino Aquilano, Torino, Italy

4 Generation and Propagation of Defects During Crystal Growth

Helmut Klapper, Aachen, Germany

5 Single Crystals Grown Under Unconstrained Conditions

Ichiro Sunagawa, Tokyo, Japan

6 Defect Formation During Crystal Growth from the Melt

Peter Rudolph, Berlin, Germany

1. Crystal Growth Techniques and Characterization: An Overview

Govindhan Dhanaraj, Kullaiah Byrappa, Vishwanath (Vish) Prasad, Michael Dudley

A brief overview of crystal growth techniques and crystal analysis and characterization methods is presented here. This is a prelude to the details in subsequent chapters on fundamentals of growth phenomena, details of growth processes, types of defects, mechanisms of defect formation and distribution, and modeling and characterization tools that are being employed to study as-grown crystals and bring about process improvements for better-quality and large-size crystals.

1.1	Historical Developments	3	1.2	Theories of Crystal Growth	4
			1.2.1	Surface Energy Theory.....	5
			1.2.2	Diffusion Theory.....	5
			1.2.3	Adsorption Layer Theory.....	6
			1.2.4	Screw Dislocation Theory.....	6
			1.3	Crystal Growth Techniques	6
			1.3.1	Solid Growth.....	7
			1.3.2	Solution Growth.....	8
			1.3.3	Crystal Growth from Melt.....	9
			1.3.4	Vapor-Phase Growth.....	10
			1.4	Crystal Defects and Characterization	11
			1.4.1	Defects in Crystals.....	11
			1.4.2	Observation of Crystal Defects.....	12
			References		15

1.1 Historical Developments

Crystals are the unacknowledged pillars of the world of modern technology. They have attracted human civilization from prehistoric times owing to their beauty and rarity, but their large-scale applications for devices have been realized only in the last six decades. For a long time, crystal growth has been one of the most fascinating areas of research. Although systematic understanding of the subject of crystal growth began during the last quarter of the 19th century with Gibbs' phase equilibrium concept based on a thermodynamical treatment, man practiced crystal growth and or crystallization processes as early as 1500 BC in the form of salt and sugar crystallization. Thus, crystal growth can be treated as an ancient scientific activity. However, the scientific approach to the field of crystal growth started in 1611 when Kepler correlated crystal morphology and structure, followed by Nicolous Steno, who explained the origin of a variety of external forms. Since then crystal growth has evolved steadily to attain its present status. Several theories were proposed from the 1920s onwards. The current impetus in crys-

tal growth started during World War II. Prior to that, applications of crystals and crystal growth technology did not catch the attention of technologists. The growth of small or fine crystals in the early days, which involved uncontrolled or poorly controlled crystal growth parameters without much sophistication in instrumentation or crystal growth equipment, slowly led to the growth of large bulk crystals during World War II. With advancement in instrumentation technology, the attention of crystal growers focused on the quality of the grown crystals and understanding of their formation. Also, tailoring of crystal shape or morphology, size, and properties plays a key role in crystal growth science. In this context it is appropriate to mention nanocrystals, which exhibit desirable physicochemical characteristics. Similarly, the growth of thin films has emerged as a fascinating technology. Further crystal growth research is being carried out in microgravity or space conditions. There are various methods of evaluating the quality of grown crystals. Thus the growth of crystals with tailored physics and chemistry, characterization of crystals

with more advanced instrumentation, and their conversion into useful devices play vital roles in science and technology [1.1,2].

Crystal growth is a highly interdisciplinary subject that demands the collaboration of physicists, chemists, biologists, engineers, crystallographers, process engineers, materials scientists, and materials engineers. The significance of the beauty and rarity of crystals is now well knitted with their symmetry, molecular structure, and purity, and the physicochemical environment of their formation. These characteristics endow crystals with unique physical and chemical properties, which have transformed electronic industries for the benefit of human society. Prior to commercial growth or production of crystals, man depended only on the availability of natural crystals for both jewelry and devices. Today the list of uses of artificially grown crystals is growing exponentially for a variety of applications, such as electronics, electrooptics, crystal bubble memories, spintronics, magnetic devices, optics, nonlinear devices, oscillators, polarizers, transducers, radiation detectors, lasers, etc. Besides inorganic crystal growth, the world of organic, semiorganic, biological crystal growth is expanding greatly to make crystal growth activity more cost-effective. Today, the quality, purity, and defect-free nature of crystals is a prerequisite for their technological application. A reader can get useful information

on the history of crystal growth from the works of Scheel [1.3,4].

Crystal growth is basically a process of arranging atoms, ions, molecules or molecular assemblies into regular three-dimensional periodic arrays. However, real crystals are never perfect, mainly due to the presence of different kinds of local disorder and long-range imperfections such as dislocations. Moreover, they are often polycrystalline in nature. Hence, the ultimate aim of a crystal grower is to produce perfect single crystals of desired shape and size, and to characterize them in order to understand their purity and quality and perfection for end users. Accordingly, crystal growth techniques and characterization tools have advanced greatly in recent years. This has facilitated the growth and characterization of a large variety of technologically important single crystals. Crystal growth can be treated as an important branch of materials science leading to the formation of technologically important materials of different sizes. Hence, it covers crystals from bulk to small and even to fine, ultrafine, and nanoscale sizes. In this respect, crystal growth has a close relationship with crystal engineering, and also polyscale crystal growth is relevant. This concept becomes even more relevant with progress achieved in nanotechnology, wherein the size effect explains changes in the physical properties of crystalline materials with size.

1.2 Theories of Crystal Growth

Growth of single crystals can be regarded as a phase transformation into the solid state from the solid, liquid or vapor state. Solid–solid phase transformations are rarely employed to grow single crystals, except for certain metals and metal alloys, whereas liquid to solid and vapor to solid transformations are most important in crystal growth and have resulted in a great variety of experimental techniques. When a crystal is in dynamic equilibrium with its mother phase, the free energy is at a minimum and no growth can occur. This equilibrium has to be disturbed suitably for growth to occur. This may be done by an appropriate change in temperature, pressure, pH, chemical potential, electrochemical potential, strain, etc. The three basic steps involved in the formation of a crystal from an initially disordered phase are:

1. Achievement of supersaturation or supercooling
2. Nucleation

3. Growth of the nuclei into single crystals of distinct phases

The driving force for crystallization actually derives from supersaturation, supercooling of liquid or gas phase with respect to the component whose growth is required. Therefore steady-state supersaturation/supercooling needs to be maintained during crystal growth to obtain higher-quality results. Nucleation or crystallization centers are an important feature of crystal growth. Nucleation may occur either spontaneously due to the conditions prevailing in the parent phase or it may be induced artificially. Therefore, the study of nucleation forms an integral part of crystal growth process. Several theories to explain nucleation have been proposed from time to time. Perhaps Gibbs was the first to comprehend that the formation of small embryonic clusters of some critical size is a prerequisite for the development of a macroscopic crystal. The

Gibbs–Thomson equation is fundamental for nucleation events [1.5], expressed for a cluster inside a supercooled phase under equilibrium conditions inside a supersaturated/supercooled phase as

$$k_B T \ln \left(\frac{p}{p^*} \right) = \frac{2\sigma V}{r}, \quad (1.1)$$

where r is the radius of the cluster formed inside a vapor at temperature T , k_B is the Boltzmann constant, p is the vapor pressure outside the cluster, p^* is the saturated vapor pressure over a plane liquid surface, σ is the surface energy per unit area, and V is the volume of the growth units.

For nucleation from solution,

$$k_B T \ln \left(\frac{c}{c^*} \right) = \frac{2\sigma V}{r}. \quad (1.2)$$

Here, c is the actual concentration and c^* is the concentration of the solution with a crystal of infinite radius. The condition for nucleation from the melt is

$$\Delta H_m \left(\frac{T_m - T_r}{T_m} \right) = \frac{2\sigma V}{r}. \quad (1.3)$$

Here, T_r is the melting point of a crystal of radius r and T_m is the melting point of a large crystal. ΔH_m is the latent heat of fusion per molecule.

The Gibbs–Thomson equation, which gives the free energy change per unit volume for solution growth, is given by

$$\Delta G_v = \frac{2\sigma}{r} = -k_B T \ln \left(\frac{c}{c^*} \right) = -\frac{k_B}{V} \ln S, \quad (1.4)$$

where S is the degree of supersaturation and V is the molecular volume.

There are several theories to explain crystal growth, involving the mechanism and the rate of growth of crystals. The important crystal growth theories are the surface energy theory, diffusion theory, adsorption layer theory, and screw dislocation theory. Gibbs proposed the first theory of crystal growth, in which he assumed growth of crystals to be analogous to the growth of a water droplet from mist. Later *Kossel* and others explained the role of step and kink sites on the growth surface in promoting the growth process [1.6].

1.2.1 Surface Energy Theory

The surface energy theory is based on the thermodynamic treatment of equilibrium states put forward by Gibbs. He pointed out that the growing surface would assume that shape for which the surface energy is lowest. Many researchers later applied this idea. *Curie* [1.7]

worked out the shapes and morphologies of crystals in equilibrium with solution or vapor. Later, *Wulff* [1.8] deduced expressions for the growth rate at different faces and the surface free energies. According to him, the equilibrium is such that excess surface free energy $\sigma_{hkl} dA_{hkl}$ is minimum for crystal with its $\{hkl\}$ faces exposed. The value of σ_{hkl} determines the shape of a small crystal; for example, if σ is isotropic, the form of the crystal is spherical, provided the effect of gravity is negligible. *Marc* and *Ritzel* [1.9] considered the effect of surface tension and solution pressure (solubility) on the growth rate. In their opinion, different faces have different values of solubility. When the difference in solubility is small, growth is mainly under the influence of surface energy, and the change in the surface of one form takes place at the expense of the other. *Bravais* [1.10] proposed that the velocities of growth of the different faces of a crystal depend on the reticular density.

1.2.2 Diffusion Theory

The diffusion theory proposed by *Nernst* [1.11], *Noyes*, and *Whitney* [1.12] is based on the following two basic assumptions:

1. There is a concentration gradient in the neighborhood of the growing surface;
2. Crystal growth is the reverse process of dissolution.

Consequently, the amount of solute that will get deposited on a crystal growing in a supersaturated solution is given by

$$\frac{dm}{dt} = \left(\frac{D}{\delta} \right) A(c - c_0), \quad (1.5)$$

where dm is the mass of solute deposited in a small time interval dt over an area A of the crystal surface, D is the diffusion coefficient of the solute, c and c_0 are the actual and equilibrium concentrations of the solute, and δ is the thickness of the torpid layer adjacent to the solid surface.

The importance of surface discontinuities in providing nucleation sites during crystal growth was the main consideration of *Kossel* [1.6], *Stranski* [1.13], and *Volmer* [1.14]. *Volmer* suggested a growth mechanism by assuming the existence of an adsorbed layer of atoms or molecules of the growth units on crystal faces. Later, *Brandes* [1.15], *Stranski*, and *Kossel* modified this concept. *Volmer's* theory was based on thermodynamical reasoning. The units reaching a crystal face are not immediately attached to the lattice but migrate over the

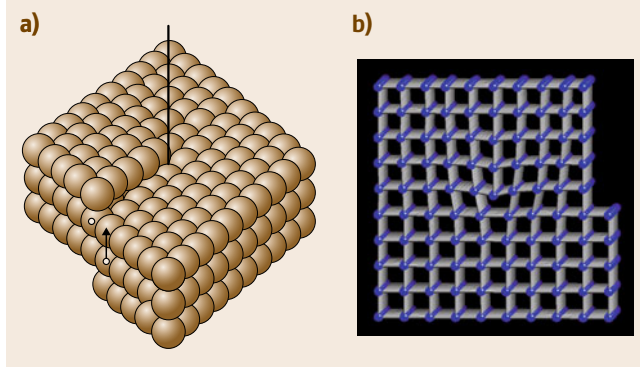


Fig. 1.1a,b Screw dislocation in a crystal (a); edge dislocation (b)

crystal face to find a suitable site for attachment. They form a loosely adsorbed layer at the interface, and soon a dynamic equilibrium is established between the layer and the bulk solution.

1.2.3 Adsorption Layer Theory

Kossel viewed crystal growth based on atomistic considerations. He assumed that crystal is in equilibrium with its solution when it is just saturated. Also, the attachment energy unit on growing surface is a simple function of distance only. The attachment energy is due to van der Waals forces if the crystal is homopolar, while it is due to electrostatic forces if the crystal is heteropolar (ionic). A growth unit arriving at a crystal surface finds attachment sites such as terraces, ledges, and kinks. The attachment energy of a growth unit can be considered to be the resultant of three mutually perpendicular components. The binding energy or attachment energy of an atom is maximum when it is incorporated into a kink site in a surface ledge, whilst at any point on the ledge it is greater than that for an atom attached to the flat surface (terrace). Hence, a growth unit reaching a crystal surface is not integrated into the lattice immediately. Instead

it migrates to a step and moves along it to a kink site, where it is finally incorporated. Based on this consideration of attachment, Kossel was able to determine the most favorable face for growth. According to the Kossel model, growth of a crystal is a discrete process and not continuous. Also, a new layer on a preferably flat face of a homopolar crystal will start growing from the interior of the face. For heteropolar crystals, the corners are the most favorable for growth, while mid-face is least favored. According to Stranski, the critical quantity that determines the growth process is the work necessary to detach a growth unit from its position on the crystal surface. Growth units with the greatest detachment energy are most favored for growth, and vice versa. The greatest attraction of atoms to the corners of ionic and metallic crystals often leads to more rapid growth along these directions, with the result that the crystal grows with many branches called dendrites radiating from a common core.

1.2.4 Screw Dislocation Theory

However, the Kossel, Stranski, and Volmer theory could not explain the moderately high growth rates observed in many cases at relatively low supersaturation, far below those needed to induce surface nucleation. *Frank* [1.16] proposed that a screw dislocation emerging at a point on the crystal surface could act as a continuous source of steps (surface ledges) which can propagate across the surface of the crystal and promote crystal growth. Growth takes place by rotation of the steps around the dislocation point (Fig. 1.1). *Burton et al.* [1.17] proposed the famous screw dislocation theory based on the relative supersaturation as the Burton–Cabrera–Frank (BCF) model determining the absolute value of growth rate depending upon the concentration. Frank's model could explain the experimental observations on the growth rate and spiral pattern mechanism.

1.3 Crystal Growth Techniques

Crystal growth is a heterogeneous or homogeneous chemical process involving solid or liquid or gas, whether individually or together, to form a homogeneous solid substance having three-dimensional atomic arrangement. Various techniques have been employed, depending upon the chemical process involved. All

crystal growth processes can be broadly classified according to the scheme presented in Table 1.1. The subject of crystal growth has therefore developed as an interdisciplinary subject covering various branches of science, and it is extremely difficult to discuss the entire subject in this overview chapter. However, the

Table 1.1 Classification of crystal growth processes [1.18]

1. Solid–Solid	Solid	\xrightarrow{T}	Solid Devitrification Strain annealing Polymorphic phase change Precipitation from solid solution
2. Liquid–Solid			
i) Melt growth	Molten material	$\xrightarrow{\text{Dec. } T}$	Crystal Bridgman–Stockbarger Kyropoulos Czochralski Zoning Verneuil
ii) Flux growth	Solid(s) + Flux agent(s)	$\xrightarrow{\text{Dec. } T}$	Crystal(s)
iii) Solution growth	Solid(s) + Solvent	$\xrightarrow{\text{Low } T}$	Crystal(s) Evaporation Slow cooling Boiling solutions
iv) Hydrothermal growth	Solid(s) + Solvent	$\xrightarrow[\text{High } p]{\text{High } T}$	Crystal(s) Hydrothermal sintering Hydrothermal reactions Normal temperature gradient Reversed temperature gradient
v) Gel growth	Solution + Gel medium	$\xrightarrow{\text{Low } T}$	Crystal Reaction Complex decomplex Chemical reduction Solubility reduction Counter-flow diffusion
	Solution	\longrightarrow	Crystal(s) + products
3. Gas–Solid	Vapor(s)	\longrightarrow	Solid Sublimation–condensation Sputtering Epitaxial processes Ion-implantation

present Handbook covers most important techniques adopted in modern crystal growth through the chapters authored by world authorities in their respective fields.

1.3.1 Solid Growth

The solid-state growth technique is basically controlled by atomic diffusion, which is usually very slow ex-

cept in the case of fast ionic conductors or superionic conductors. The commonly used solid-state growth techniques are annealing or sintering, strain annealing, heat treatment, deformation growth, polymorphic phase transitions, quenching, etc., and most of these are popularly used in metallurgical processes for tailoring material properties. In fact, gel growth is also considered as solid growth by some researchers. Solid growth is not covered in this Handbook.

1.3.2 Solution Growth

This is one of the oldest and most widely used crystal growth techniques compared with vapor-phase melt growth. Solution growth is used not only for growth of technologically important crystals but also for a variety of crystalline products for daily life such as the growth of foods, medicines, fertilizers, pesticides, dye stuffs, etc. Most crystallization processes of ionic salts are conducted in aqueous solutions or in some cases in solvents which are a mixture of miscible and organic solvents. Solution growth is used for substances that melt incongruently, decompose below the melting point, or have several high-temperature polymorphic modifications, and is also often efficient in the absence of such restrictions. The important advantage of solution growth is the control that it provides over the growth temperature, control of viscosity, simplicity of equipment, and the high degree of crystal perfection since the crystals grow at temperatures well below their melting point. We can divide solution growth into three types depending upon the temperature, the nature of the solvent, solute, and the pressure: low-temperature aqueous solution growth, superheated aqueous solution growth, and high-temperature solution growth. Aqueous solution growth has produced the largest crystals known to mankind, such as potassium dihydrogen phosphate (KDP), deuterated potassium dihydrogen phosphate (DKDP), etc. produced at the Lawrence Livermore Laboratory, USA.

For successful growth of a crystal from solution, it is essential to understand certain basic properties (physicochemical features) of the solution. The behavior of water with temperature and pressure; the critical, subcritical, and supercritical conditions; its structure, the variation in pH; viscosity; density; conductivity; dielectric constant; and coefficient of expansion are critical for successful crystal growth. Recently, a rational approach to the growth of a given crystal was carried out in order to: compute the thermodynamic equilibrium as a function of the processing variables, generate equilibrium (yield) diagrams to map the processing variable space for the phases of interest, design experiments to test and validate the computed diagrams, and utilize the results for mass production [1.19]. The change in ionic strength of the solution during crystal growth results in formation of defects, and variation in the crystal habit and even the phases, and therefore has to be maintained constant, often with the help of swamping-electrolyte solutions. Similarly, chelating agents are frequently used to sequester ions and form respective complexes,

which are later thermodynamically broken to release their cations very slowly into the solution, which helps in controlling the growth rate and crystal habit.

In the last decade crystal growth from solution under microgravity conditions has been studied extensively to grow a wide variety of crystals such as zeolites, compound semiconductors (InP, GaAs, GaP, AlP, etc.), triglycine sulfate, etc.

Crystal Growth from Low-Temperature Aqueous Solutions

The greatest advantages of crystal growth from low-temperature aqueous solutions are the proximity to ambient temperature, which helps to retain a high degree of control over the growth conditions, especially with reference to thermal shocks, and reduction of both equilibrium and nonequilibrium defects to a minimum (even close to zero). Solution growth can be classified into several groups according to the method by which supersaturation is achieved:

1. Crystallization by changing the solution temperature
2. Crystallization by changing the composition of the solution (solvent evaporation)
3. Crystallization by chemical reaction

Crystal Growth from Superheated Aqueous Solutions

This method is commonly known as the hydrothermal method and is highly suitable for crystal growth of compounds with very low solubility and phase transitions. When nonaqueous solvents are used in the system, it is called the solvothermal method. The largest known single crystal formed in nature (beryl crystal of > 1000 kg) is of hydrothermal origin, and similarly some of the largest quantities of single crystals produced in one experimental run (quartz single crystals of > 1000 kg) are based on the hydrothermal technique. The term “hydrothermal” refers to any heterogeneous (usually for bulk crystal growth) or homogeneous (for fine to nanocrystals) chemical reaction in the presence of aqueous solvents or mineralizers under high-pressure and high-temperature conditions to dissolve and recrystallize (recover) materials that are relatively insoluble under ordinary conditions [1.20]. The last decade has witnessed growing popularity of this technique, and a large variety of crystals and crystalline materials starting from native elements to the most complex coordinated compounds such as rare-earth silicates, germinates, phosphates, tungstates, etc. have been obtained. Also,

the method is becoming very popular among organic chemists dealing with synthesis of life-forming compounds and problems related to the origin of life. The method is discussed in great detail in Chap. 18.

Crystal Growth from High-Temperature Solutions

This is popularly known as flux growth and gained its importance for growing single crystals of a wide range of materials, especially complex multicomponent systems. In fact, this was one of the earliest methods employed for growing technologically important crystals, for example, single crystals of corundum at the end of the 19th century. The main advantage of this method is that crystals are grown below their melting temperature. If the material melts incongruently, i.e., decomposes before melting or exhibits a phase transition below the melting point or has very high vapor pressure at the melting point, one has indeed to look for growth temperatures lower than these phase transitions. The method is highly versatile for growth of single crystals as well as layers on single-crystal substrates (so-called liquid-phase epitaxy, **LPE**). The main disadvantages are that the growth rates are smaller than for melt growth or rapid aqueous solution growth, and the unavoidable presence of flux ions as impurities in the final crystals. Some of the important properties to be considered for successful flux growth of crystals are stability and solubility of the crystal to be grown, low melting point and lower vapor pressure of the flux, the lower viscosity of the melt (which should not attack the crucible), and also ease of separation [1.4,21]. The most commonly used fluxes are the basic oxides or fluorides: PbO, PbF₂, BaO, BaF, Bi₂O₃, Li₂O, Na₂O, K₂O, KF, B₂O₃, P₂O₅, V₂O₅, MoO₃, and in most cases a mixture consisting of two or three of them. The prime advantage of this method is that growth can be carried out either through spontaneous nucleation or crystallization on a seed. Supersaturation can be achieved through slow cooling, flux evaporation, and vertical temperature gradient transport methods. Also, during the growth, one can introduce rotation of the seed or crucible, or pulling of the seed, and so on. Accordingly, several versions of flux growth have been developed: slow cooling (**SC**), slow cooling bottom growth (**SCBG**), top-seeded solution growth (**TSSG**), the top-seeded vertical temperature gradient technique (**VTGT**), bottom growth with a nutrient, growth by traveling solvent zone (**TSZ**), flux evaporation, **LPE**, and so on.

The flux method has been popularly used especially for the growth of a large variety of garnets, and recently

for a wide range of laser crystals such as rare-earth borates, potassium titanyl phosphates, and so on. The reader can get valuable information from several interesting reviews on flux growth [1.22–24].

1.3.3 Crystal Growth from Melt

Melt growth of crystals is undoubtedly the most popular method of growing large single crystals at relatively high growth rates. In fact, more than half of technological crystals are currently obtained by this technique. The method has been popularly used for growth of elemental semiconductors and metals, oxides, halides, chalcogenides, etc. Melt growth requires that the material melts without decomposition, has no polymorphic transitions, and exhibits low chemical activity (or manageable vapor pressure at its melting point). The thermal decomposition of a substance and also chemical reactions in the melt can disturb the stoichiometry of the crystal and promote formation of physical or chemical defects. Similarly, the interaction between the melt and crucible, or the presence of a third component derived from the crystallization atmosphere, can affect melt growth. Usually, an oxygen-containing atmosphere is used for oxides, a fluorine-containing atmosphere for fluorides, a sulfur-containing atmosphere for sulfides, and so on. In melt growth, crystallization can be carried out in a vacuum, in a neutral atmosphere (helium, argon, nitrogen), or in a reducing atmosphere (air, oxygen). In a large melt volume, convective flows caused by the temperature gradient within the melt lead to several physical and chemical defects. In a small melt volume, transport is affected by diffusion.

Selection of a particular melt growth technique is done on the basis of the physical and chemical characteristics of the crystal to be grown. Metal single crystals with melting point < 1800 °C are grown by Stockbarger method, and those with melting point > 1800 °C by zone melting. Semiconducting crystals are grown chiefly by Czochralski method, and by zone melting. Single crystals of dielectrics with melting point < 1800 °C are usually grown by the Stockbarger or Czochralski methods, while higher-melting materials are produced by flame fusion (Verneuil method). If the physicochemical processes involved in crystallization are taken into account, it is possible to establish optimum growth conditions.

One of the earliest melt techniques used to grow large quantity of high-melting materials was the Verneuil method (flame fusion technique), first described by *Verneuil* in 1902 [1.25]. This marks the

beginning of commercial production of large quantities of high-melting crystals, which were essentially used as gems or for various mechanical applications. Today, the technique is popular for growth of a variety of high-quality crystals for laser devices and precision instruments, as well as substrates. The essential features are a seed crystal, the top of which is molten and is fed with molten drops of source material, usually as a powder through a flame or plasma. Following this, the Czochralski method, developed in 1917 and later modified by several researchers, became the most popular technique to grow large-size single crystals which were impossible to obtain by any other techniques in such large quantity. This technique has several advantages over the other related melt-growth technique, viz. the Kyropoulos method, which involves a gradual reduction in the melt temperature. In the Czochralski technique the melt temperature is kept constant and the crystal is slowly pulled out of the melt as it grows. This provides a virtually constant growth rate for the crystal. Several versions of Czochralski crystal pullers are commercially available. A large variety of semiconductor crystals such as Si, Ge, and several III–V compounds are being commercially produced using this technique. Besides, several other crystals of oxides, spinel, garnets, niobates, tantalates, and rare-earth gallates have been obtained by this method. The reader can find more valuable information on this method from the works of *Hurle and Cockayne* [1.26].

There are several other popularly used melt growth techniques that are feasible for commercial production of various crystals. Amongst them, the Bridgman–Stockbarger, zone melting, and floating zone methods are the most popular. The Bridgman technique is characterized by the relative translation of the crucible containing the melt to the axial temperature gradient in a vertical furnace. The Stockbarger method is a more sophisticated modification of the Bridgman method. There is a high-temperature zone, an adiabatic loss zone, and a low-temperature zone. The upper and lower temperature zones are generally independently controlled, and the loss zone is either unheated or poorly insulated.

1.3.4 Vapor-Phase Growth

Vapor-phase growth is particularly employed in mass production of crystals for electronic devices because of its proven low cost and high throughput, in addition to its capability to produce advanced epitaxial structures. The technique is especially suitable for growth of

semiconductors, despite the rather complex chemistry of the vapor-phase process. The fundamental reason for their success is the ease of dealing with low- and high-vapor-pressure elements. This is achieved by using specific chemical precursors in the form of vapor containing the desired elements. These precursors are introduced into the reactor by a suitable carrier gas and normally mix shortly before reaching the substrate, giving rise to the nutrient phase of the crystal growth process. The release of the elements necessary for construction of the crystalline layer may occur at the solid–gas interface or directly in the gas phase, depending on the type of precursors and on the thermodynamic conditions.

The advantage of vapor growth technique is that crystals tend to have a low concentration of point defects and low dislocation densities compared with crystals grown from the melt, as the temperatures employed are usually considerably lower than the melting temperature. Moreover, if the material undergoes a phase transformation or melts incongruently, vapor growth may be the only choice for the growth of single crystals. Although the method was initially used to grow bulk crystals, with the enormous importance of thin films in electronic and metallurgical applications, vapor growth is now widely used to grow thin films, epitaxial layers, and substrates in the field of semiconductor technology [1.27, 28].

Vapor-phase growth primarily involves three stages: vaporization, transport, and deposition. The vapor is formed by heating a solid or liquid to high temperatures. Transportation of vapor may occur through vacuum, driven by the kinetic energy of vaporization. Deposition of the vapor may occur by condensation or chemical reaction.

Various techniques exist in vapor-phase growth, differentiated by the nature of the source material and the means and mechanism by which it is transported to the growing crystal surface. Conceptually, the simplest technique is that of sublimation, where the source material is placed at one end of a sealed tube and heated so that it sublimates and is then transported to the cooler region of the tube, where it crystallizes.

Among vapor-phase growth techniques, vapor-phase epitaxy is the most popularly used, especially for the growth of p- and n-type semiconductor whose dimers and monomers are difficult to achieve by other methods (e.g., physical evaporation) or too stable to be reduced to the necessary atomic form. Furthermore, there are different variants such as metalorganic vapor-phase epitaxy (MOVPE), plasma-assisted mo-

Table 1.2 Main application fields of vapor-phase epitaxy techniques and the relevant classes of materials

Growth technique	Devices and semiconductor family			
	Si, Ge	II–VI	III–V	III–nitrides
Hydride VPE	SiGe alloys		LEDs and photodetectors (GaP, InGaP, GaAsP)	GaN thick layers
Chloride VPE MOVPE	Bipolar transistors, MOS	IR sensors (HgCdTe), LEDs and lasers (ZnCdSe, ZnSSe)	Solar cells (GaAs, AlGaAs, InGaP), transistors (AlGaAs, InGaAs), LEDs (AlGaAs), TC and CD lasers (InGaPAs, AlGaAs), photodetectors, LEDs and lasers (InGaPAs)	LEDs and lasers (GaN, InGaN, GaAlN)

molecular beam epitaxy (MBE), etc. to suit the growth of particular compounds. Table 1.2 summarizes the main

application fields of the VPE techniques and the relevant classes of materials [1.29].

1.4 Crystal Defects and Characterization

Characterization of crystals has become an integral part of crystal growth and process development. Crystal defects and their distribution together with composition and elemental purity determine most of their properties such as mechanical strength, electrical conductivity, photoconductivity luminescence, and optical absorption, and these properties influence their performance in applications. Therefore, investigating the origin, concentration, and distribution of imperfections in crystals is critical to controlling them and thereby the crystal properties influenced by these imperfections.

1.4.1 Defects in Crystals

Imperfections or defects can be broadly classified based on their dimensionality.

Point Defects

These zero-dimensional defects are vacancies, interstitials, and impurity atoms deliberately added to control the conductivity of the semiconductor, and impurities that are unintentionally incorporated as contaminants during material growth and processing. Electronic defects such as holes and electrons also constitute point defects. In compounds, point defects form disorders such as Frenkel, Schottky, and antistructure disorders.

Line Defects

Line defects consist of purely geometrical faults called dislocations. The concept of dislocations arose from

the crystallographic nature of plastic flow in crystalline materials. A dislocation is characterized by its line direction and Burgers vector \mathbf{b} , which is, as a rule, one of the shortest lattice translations. Dislocation lines may be straight or follow irregular curves or closed loops. Dislocations whose line segments are parallel to \mathbf{b} are called screw dislocations. Edge dislocations have their line segments perpendicular to the \mathbf{b} direction. In mixed dislocations, the line direction is inclined to \mathbf{b} and hence they have both screw and edge components.

Planar Defects

Planar defects include high- and low-angle boundaries, growth striations, growth-sector boundaries, twin boundaries, stacking faults, and antiphase boundaries. Growth striations are lattice perturbations that arise from local variations of the dopant/impurity concentration created by fluctuations in the growth conditions. Stacking faults are formed when there are errors in the normal stacking arrangement of the lattice planes in the crystal structure. These could be caused by plastic deformation or agglomeration of point defects. High- and low-angle boundaries consist of arrays of dislocations, and they separate regions of different orientations. In crystal growth, high-angle boundaries separate grains that have been nucleated independently, and hence misorientations are generally large. Low-angle grain boundaries are formed during cool down by stress-induced glide and climb of dislocations, leading to these energetically favorable configurations. Misorientations

in this case usually do not exceed more than 1° . Twin boundaries are planar defects that separate regions of the crystal whose orientations are related to each other in a definite, symmetrical way.

Volume Defects

Precipitates, inclusions, and voids or bubbles are volume defects, and these are formed when gases dissolved in the melt precipitate out after solidification. For example, in microgravity growth, the absence of buoyancy precludes degassing of the melt, resulting in the formation of voids. While undissolved foreign particles are generally classified as inclusions, a second type of inclusion is formed during growth from nonstoichiometric melt. Compound semiconductors generally sublime incongruently, thereby causing a slight excess of one of the components in a stoichiometric melt. On solidification, the excess component forms inclusions.

1.4.2 Observation of Crystal Defects

Techniques for observing dislocations and their complex structures have been described in detail by *Verma* [1.30] and *Amelincks* [1.31]. The commonly used techniques come under the categories:

1. Optical methods
2. X-ray methods
3. Preferential etching
4. Microscopy techniques
5. Other techniques

All these methods provide almost direct observation of defects. Their merit is limited by the resolution achievable and their versatility. Choice of a suitable technique will depend on several factors, such as:

1. The shape and size of the crystal under investigation
2. Cleaving, cutting, and polishing possibilities
3. Ability to use destructive techniques, and above all
4. The extent of the details required

Optical Methods

A common inspection method for the as-grown optical crystal boule is detailed observation by illuminating the boule using high-intensity white light or a laser beam. Probably, this is the first technique to be applied to assess the quality of as-grown crystal and can reveal bubbles, cavities, growth bands, and seed interfaces which depend on the growth parameters.

The conoscope is a simple optical tool for investigating optical inhomogeneity in very small crystals to

large-size boules. Conoscopic patterns are characteristic for every main crystallographic orientation, and this feature is also frequently used for orienting crystals [1.32]. This method shows the overall quality of the crystal. If the whole crystal has low dislocation density without any grain boundaries and block structures, a nice symmetrical circular pattern of dark and bright fringes with four segments and a cross at the center is observed. Figure 1.2a shows the conoscopic pattern of a sapphire ingot with dislocation density 10^2 – 10^3 /cm² and without any low-angle grain boundaries. Figure 1.2b shows the pattern for a sapphire ingot of the same size but with a dislocation density of the order of 10^3 – 10^4 /cm² and a few low-angle grain boundaries. The presence of a few grain boundaries alters the birefringence and distorts the fringes. The fringe thickness and spacing depend on the length of the crystal along the direction of inspection. Even though this technique does not reveal the dislocation density very precisely, it can reveal the presence of grain boundaries and higher-order, complex defects. The crystals are normally sliced perpendicular to the *c*-axis, polished, and inspected under a polarizer and analyzer. As-cut surfaces without polishing can also be observed with the application of suitable refractive-index-matched fluid. In general, this technique can reveal the misorientations, grain boundaries, block structures, and also the stress levels. Conoscopy can be used under a polarizing microscope to study thinner samples. A custom-made polarizer and analyzer with rotation features for the analyzer and sample support can be used to study large crystal boules. Alternatively, conoscopic fringes can be projected onto a screen using a laser beam, polarizer and analyzer, and beam diffuser. These fringes are more influenced by the birefringence inhomogeneity induced by defect structures than by variation in the thickness distribution of the boule itself.

X-Ray Methods

X-ray methods can be classified into:

1. High-resolution x-ray diffraction
2. X-ray topography
3. Synchrotron x-ray topography

High-Resolution X-Ray Diffraction. Diffraction for a given plane and wavelength takes place over a finite angular range about the exact Bragg condition, known as the rocking-curve width [1.33]. In x-ray diffractometry, the intensity of the diffracted beam and the angle in the vicinity of a Bragg peak are measured and repre-

sented as a full-width at half-maxima (FWHM) rocking curve. The double-axis rocking curve is obtained by scanning the specimen in small steps through the exact Bragg condition and recording the diffracted intensity. The peak width of a rocking curve can be affected by tilts and dilations in the sample, and by curvature. Tilts are regions in the sample where grains or subgrains are tilted with respect to each other, although the lattice parameter is the same in each region. Dilations are regions where the lattice planes are still parallel but the spacing is slightly different due to strain. Changes in lattice parameter also occur in alloyed crystals with nonhomogeneous composition distribution. The experimentally obtained rocking-curve width (FWHM) value is a measure of the crystalline quality of the sample, and it can be compared with a theoretically calculated value. It is possible to obtain a rocking-curve width less than 10 arcsec for a good crystalline sample. Additional information that can be obtained from double-axis rocking curves are substrate–epilayer mismatch, epilayer composition, substrate offcut and/or layer tilt, and layer thickness.

A limitation of double-axis diffraction is that it cannot distinguish between tilts and dilations. In triple-axis diffraction, a third axis is introduced in the form of an analyzer crystal, and tilts and strain can be separated; the rocking-curve width is still narrow. Double-axis rocking curve analysis is sufficient for studying substrates and epitaxial films. Triple-axis x-ray diffraction is used for obtaining finer details of the defect structure of the sample.

X-Ray Topography. Localized variations in intensity within any individual diffracted spot arise from structural nonuniformity in the lattice planes causing the spot, and this forms the basis for the x-ray topographic technique. This topographic contrast arises from differences in the intensity of the diffracted beam as a function of position inside the crystal. The difference between the intensities diffracted from one region of the crystal which diffracts kinematically to another which diffracts dynamically is one of the ways that dislocations can be rendered visible in topography [1.34].

Even though the first topographic image of a single crystal was recorded as early as 1931 [1.35], the real potential of the technique was understood only in 1958 when Lang [1.36] demonstrated imaging of individual dislocations in a silicon crystal. In general, there are three main types of x-ray topographic geometries for studying defects:

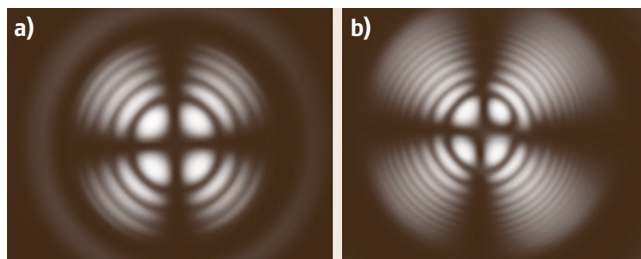


Fig. 1.2 (a) Conoscopic pattern of high-quality sapphire ingot. (b) Conoscopic pattern of sapphire ingot that has a few low-angle boundaries

1. The Berg–Barrett reflection technique [1.37]
2. The double-crystal technique [1.38]
3. The Lang technique [1.36] and its variant – the scanning oscillator technique [1.39]

Following Lang’s work [1.36, 40] in imaging of individual dislocations, x-ray topography has become an important quality-control tool for assessment of semiconductor wafers both before and after device fabrication. Using the scanning oscillator technique developed by Schwutke [1.39], it is possible to record transmission topographs of large-size wafers up to 150 mm in diameter, containing appreciable amounts of elastic and/or frozen-in strain.

Synchrotron X-Ray Topography. The advent of dedicated synchrotron radiation sources has enabled the development of a new field of x-ray topography known as synchrotron topography. Synchrotron radiation is especially suitable for x-ray topography because of the high brightness and low divergence of the x-ray beam. Due to the small source dimensions, low divergence angle, as well as the long source–specimen distance, extremely high resolution can be achieved using synchrotron radiation compared with conventional x-ray topography. For example, based on the geometrical factor, the theoretical resolution obtained can be as low as 0.06 μm . Also, it has numerous advantages over laboratory x-ray topography. One of the most important synchrotron topographic techniques developed is white-radiation topography [1.41]. In APS, the white beam is monochromatized by two cooled parallel Si(111) crystals, and the x-ray energy is tunable in the range 2.4–40 keV.

Crystals as large as 150 mm or even 300 mm in diameter can be imaged by using precision translation stages similar to those used in the Lang technique, and the exposure times are much shorter. If a single crystal is oriented in the beam, and the diffracted beams are

recorded on a photographic detector, each diffraction spot on the resultant Laue pattern will constitute a map of the diffracting power from a particular set of planes as a function of position in the crystal, with excellent point-to-point resolution. There are three common geometries for synchrotron x-ray topography [1.42]:

1. Transmission geometry, also called Laue geometry: In this mode, the x-ray beam passes through the sample and the topographs recorded reveal the bulk defect information of the crystal. Figure 1.3a shows typical transmission synchrotron topography of a 2-inch LED-grade wafer with a very low dislocation density of 10^2 – 10^3 /cm². The topograph shows the dislocation structure in the entire wafer, which shows the presence of basal dislocations.
2. Grazing-incidence reflection geometry: In this configuration, very small incident angle is used [in the case of SiC, typically 2° used and the (11 $\bar{2}$ 8) or (11 $\bar{2}$.12) are recorded]. Grazing incidence is used because of the low penetration depth of the x-ray beam, which is more suitable for studying epilayers.
3. Back-reflection geometry: In this mode, a large Bragg angle is used for basal plane reflection (000 l) (typically 80° for SiC). Screw dislocations along the c -axis and basal plane dislocations within the x-ray penetration depth can be clearly recorded. The wavelength satisfying Bragg condition is automatically selected in white-beam x-ray topography, while in monochromatic synchrotron x-ray topography (XRT), the energy of the x-ray beam has to be preset to satisfy the diffraction condition. Figure 1.3b shows individual screw dislocations and edge dislocation running almost perpendicular to the wafer.

X-ray topographs are typically recorded on Agfa Structurix D3-SC, Ilford L4 nuclear plate, or VRP-M holographic films, depending on the resolution needed.

Exposure time depends on the actual geometry and recording media and varies between a few seconds and 2 h.

Selective Etching

Selective etching is a simple and very sensitive tool for the characterization of single crystals. The usefulness of the etching technique lies in the formation of visible, sharp contrasting etch pits at dislocation sites. The power of etching has been reviewed by several workers [1.31, 43, 44]. The formation of etch pit can be explained as follows. The lattice is distorted for a distance of a few atoms around dislocations. As a result of the stress field generated by the deformation, the lattice elements dissolve more easily at the dislocation sites than in stress-free, undeformed areas. The etch pits are usually straight pyramids with polygonal bases, but other types of pyramids may also be found with various bases and heights. Etch pits can be formed only if certain conditions are satisfied, the most important of these being that the dissolution rate along the surface (V_t) must not greatly exceed the rate of dissolution perpendicular to the surfaces (V_n). The ratio (V_t/V_n) can be increased:

1. By increasing V_n , as has been done in the etchants of several metals
2. By decreasing V_t by adding an inhibitor such as in LiF
3. By varying the temperature to alter the activation energies of V_n and V_t

The etch pits are formed at the dislocation sites, which essentially reveal the emergent point of the dislocations in the surface; they therefore give a direct measure of dislocation density. Since they have certain depths, they also give information on the kind [1.45], configuration, and inclination of dislocations. Etching has also been used to study the stress-velocity rela-

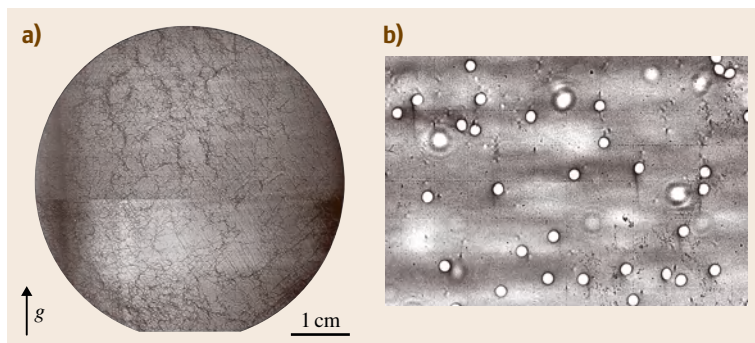


Fig. 1.3 (a) Transmission topograph of high-quality sapphire wafer. (b) Reflection topograph of SiC revealing individual threading screw dislocations running almost perpendicular to the wafer

tions for individual dislocations [1.46]. Movement of dislocations, deformation patterns like pile-up, origin of dislocations in as-grown crystals, polarity of the crystals, grain boundaries, and distribution of dislocations in crystals can be studied [1.44, 45] (Chap. 43). The greatest advantage of this technique is its simplicity and resolution ($0\text{--}10^{12}/\text{cm}^2$). This technique shows the defect density on small areas and hence requires averaging of values taken at a large number of locations. Also, this technique is not a nondestructive method and cannot show the basal plane dislocation when the sample is sliced exactly parallel to the c -axis. Figure 1.4 shows the presence of various defects such as threading edge dislocations, threading screw dislocations, and basal plane dislocations. During the development of SiC crystals, this technique has seen tremendous development and could reveal almost every type of dislocation [1.47].

Microscopy Techniques

Transmission electron microscopy (TEM) (Chap. 44) is a powerful tool to study dislocations when the sample has higher defect density. It is more commonly used for epitaxial films, where large numbers of dislocations originate due to the lattice misfit between the film and the substrate. This method requires tedious sample preparation and is not considered nondestructive.

Decoration is another important technique, where impurity atoms segregate and settle down along dislocation lines during annealing. The decorated dislocations can be observed easily under an optical microscope in transmission mode [1.31].

Growth spirals, which are true manifestations of screw dislocations, can be observed under optical microscopy, scanning electron microscopy (SEM), and atomic force microscopy (AFM). The presence of

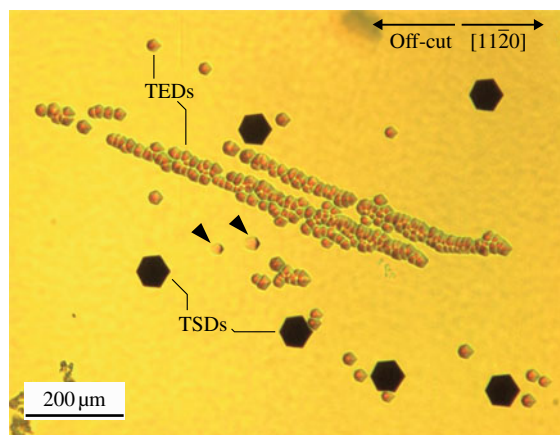


Fig. 1.4 Etch pit pattern of SiC wafer revealing threading edge dislocations (TEDs), threading screw dislocations (TSDs), and basal plane dislocations

growth spirals helps to understand the growth mechanism [1.30].

Infrared (IR) microscopy is similar to optical microscopy except for the fact that IR light is used for illumination, with a wavelength comparable to the bandgap of semiconductor materials. This technique is used to study inclusions, cavities, and even dislocations present in the sample [1.48, 49].

Other Techniques

Photoluminescence (PL) [1.50], electron paramagnetic resonance (EPR) (Chap. 45), positron annihilation (Chap. 46), and micro Raman spectroscopy [1.50] are also used to study semiconductor materials and show electronic defect states and the presence of impurities very successfully.

References

- 1.1 J. Kepler: *Strena seu de nive sexangula* (Tampach, Frankfurt 1611)
- 1.2 N. Steno: *De solido intra solidum naturaliter contento dissertationis prodromus* (Stella, Florence 1669), English translation by J.G. Winter (Hafner, New York 1968)
- 1.3 H.J. Scheel: Historical introduction. In: *Handbook of Crystal Growth*, Vol. 1a, ed. by D.T.J. Hurle (Elsevier, Amsterdam 1993) pp. 1–41, Chap. 1
- 1.4 D. Elwell, H.J. Scheel: *Crystal Growth from High Temperature Solution* (Academic, London 1975)
- 1.5 J.W. Gibbs: *On the Equilibrium of Heterogeneous Substances*, Collected Works (Longmans Green, New York 1928)
- 1.6 W. Kossel: Zur Theorie des Kristallwachstums, *Nachr. Ges. Wiss. Göttingen* **135**, 135–143 (1927)
- 1.7 P. Curie: Sur la formation des cristaux et sur les constantes capillaires de leurs différentes faces, *Bull. Soc. Franc. Mineral.* **8**, 145–150 (1885)
- 1.8 G. Wulff: Zur Frage der Geschwindigkeit des Wachstums und der Auflösung von Kristallflächen, *Z. Kristallogr.* **34**, 449 (1901)
- 1.9 R. Marc, A. Ritzel: Über die Faktoren, die den Kristallhabitus bedingen, *Z. Phys. Chem.* **76**, 584 (1911)
- 1.10 A. Bravais, A. Etudes: *Crystallographiques* (Gauthier Villers, Paris 1866)

- 1.11 W. Nernst: Theorie der Reaktionsgeschwindigkeit in heterogenen Systemen, *Z. Phys. Chem.* **47**(1), 52–55 (1904)
- 1.12 A.A. Noyes, W.R. Whitney: Über die Auflösungs-geschwindigkeit von festen Stoffen in ihren eigenen Lösungen, *Z. Phys. Chem.* **23**, 689–692 (1897)
- 1.13 I.N. Stranski: Zur Theorie des Kristallwachstums, *Z. Phys. Chem.* **136**, 259–278 (1928)
- 1.14 M. Volmer, A. Weber: Keimbildung in übersättigten Gebilden, *Z. Phys. Chem.* **119**, 277–301 (1926)
- 1.15 E.A. Brandes: *Smithells Reference Book* (Butterworths, London 1983)
- 1.16 F.C. Frank: The influence of dislocations on crystal growth, *Discuss. Faraday Soc.* **5**, 48–54 (1949)
- 1.17 W.K. Burton, N. Cabrera, F.C. Frank: The growth of crystals and the equilibrium structure of their surfaces, *Philos. Trans. R. Soc. London A* **243**, 299–358 (1951)
- 1.18 K. Byrappa, D.Y. Pushcharovsky: Crystal chemistry and its significance on the growth of technological materials, *Prog. Cryst. Growth Charact. Mater.* **24**, 269–350 (1992)
- 1.19 M.M. Lencka, R.E. Riman: Thermodynamics of the hydrothermal synthesis of calcium titanate with reference to other alkaline-earth titanates, *Chem. Mater.* **7**(1), 18–25 (1995)
- 1.20 K. Byrappa, M. Yoshimura: *Handbook of Hydrothermal Technology* (William Andrew Noyes, Norwich 2001)
- 1.21 W. Tolksdorf: Flux growth. In: *Handbook of Crystal Growth–Bulk Crystal Growth*, Vol. 2, ed. by D.T.J. Hurle (North-Holland, Amsterdam 1994) p. 563, Chap. 10
- 1.22 R.A. Laudise: *The Growth of Single Crystals* (Prentice Hall, Englewood Cliffs 1970)
- 1.23 B.M.R. Wanklyn: Practical aspects of flux growth by spontaneous nucleation. In: *Crystal Growth*, Vol. 1, ed. by B.R. Pamplin (Pergamon, Oxford 1974) pp. 217–288
- 1.24 V.V. Timofeeva: *Growth of Crystals from High Temperature Solutions* (Nauka, Moscow 1975)
- 1.25 A. Verneuil: Production artificielle du rubis par fusion, *C. R. Paris* **135**, 791–794 (1902)
- 1.26 D.T.J. Hurle, B. Cockayne: Czochralski growth. In: *Handbook of Crystal Growth*, Vol. 2a, ed. by D.T.J. Hurle (North Holland, Amsterdam 1994) pp. 99–212, Chap. 3
- 1.27 D.T.J. Hurle (Ed.): *Handbook of Crystal Growth* (North Holland, Amsterdam 1994)
- 1.28 G. Stringfellow: *Organometallic Vapor–Phase Epitaxy: Theory and Practice*, 2nd edn. (Academic, New York 1998)
- 1.29 R. Fornari: Vapor phase epitaxial growth and properties of III–Nitride materials. In: *Crystal Growth of Technologically Important Electronic Materials*, ed. by K. Byrappa, T. Ohachi, H. Klapper, R. Fornari (Allied Publishers, New Delhi 2003)
- 1.30 A.R. Verma: *Crystal Growth and Dislocations* (Butterworths, London 1953)
- 1.31 S. Amelinckx: The direct observation of dislocations. In: *Solid State Physics*, ed. by F. Seitz, D. Turnbull (Academic, New York 1964), Suppl. 6
- 1.32 E.A. Wood: *Crystals and Light* (Dover, New York 1977)
- 1.33 B.K. Tanner: High resolution x-ray diffraction and topography for crystal characterization, *J. Cryst. Growth* **99**, 1315 (1990)
- 1.34 B.K. Tanner: *X-ray Diffraction Topography* (Pergamon, Oxford 1976)
- 1.35 V.W. Berg: Über eine röntgenographische Methode zur Untersuchung von Gitterstörung an Kristallen, *Naturwissenschaften* **19**, 391–396 (1931)
- 1.36 A.R. Lang: Direct observation of individual dislocations, *J. Appl. Phys.* **29**, 597–598 (1958)
- 1.37 C.S. Barrett: A new microscopy and its potentialities, *Trans. AIME* **161**, 15–65 (1945)
- 1.38 W.L. Bond, J. Andrus: Structural imperfections in quartz crystals, *Am. Mineral.* **37**, 622–632 (1952)
- 1.39 G.H. Schwuttke: New x-ray diffraction microscopy technique for study of imperfections in semiconductor crystals, *J. Appl. Phys.* **36**, 2712–2714 (1965)
- 1.40 A.R. Lang: Point-by-point x-ray diffraction studies of imperfections in melt-grown crystals, *Acta Cryst.* **10**, 839 (1957)
- 1.41 J. Miltat: White beam synchrotron radiation. In: *Characterization of Crystal Growth Defects by X-ray Methods*, NATO ASI Ser. B, Vol. 63, ed. by B.K. Tanner, D.K. Bowen (Plenum, New York 1980) pp. 401–420
- 1.42 B. Ragothamachar, G. Dhanaraj, M. Dudley: Direct analysis in crystals using x-ray topography, *Microsc. Res. Tech.* **69**, 343 (2006)
- 1.43 A.J. Forty: Direct observations of dislocations in crystals, *Adv. Phys.* **3**, 1–25 (1954)
- 1.44 W.G. Johnson: Dislocations etchpits in nonmetallic crystals. In: *Progress in Ceramics*, Vol. 2, ed. by J.E. Burke (Pergamon, Oxford 1962) p. 1
- 1.45 K. Sangawal: *Etching of Crystals* (North-Holland, Amsterdam 1987)
- 1.46 J.J. Gilman, W.G. Johnston: Behaviour of individual dislocations in strain-hardened LiF crystals, *J. Appl. Phys.* **31**, 687–692 (1960)
- 1.47 W.J. Choyke, H. Matsunami, G. Pensl (Eds.): *Silicon Carbide: Recent Major Advances* (Springer, Berlin, Heidelberg 2004)
- 1.48 A. Hossain, A.E. Bolotnikov, G.S. Camarda, Y. Cui, G. Yang, K-H. Kim, R. Gul, L. Xu, R.B. James: Extended defects in CdZnTe crystals: Effects on device performance, *J. Cryst. Growth* (2010) in press (doi:10.1016/j.jcrysgro.2010.03.005)
- 1.49 U.N. Roy, S. Weler, J. Stein, A. Gueorguiev: Unseeded growth of CdZnTe: In by THM technique, *Proc. SPIE* **7449**, 74490U (2009)
- 1.50 J. Jimenez (Ed.): *Microprobe Characterization of Optoelectronic Materials* (Taylor Francis, New York 2003)

Nucleation at Surfaces

Ivan V. Markov

Part A | 2

This chapter deals with the thermodynamics and kinetics of nucleation on surfaces, which is essential to the growth of single crystals and thin epitaxial films. The starting point is the equilibrium of an *infinitely* large crystal and a crystal with a finite size with their ambient phase. When the system deviates from equilibrium density fluctuations or aggregates acquire the tendency to unlimited growth beyond some critical size – the nucleus of the new phase. The Gibbs free energy change of formation of the nuclei is calculated within the framework of the macroscopic thermodynamics and in terms of dangling bonds in the case of small clusters. In the case of nucleation from vapor the nuclei consist as a rule of very small number of atoms. That is why the rate of nucleation is also considered in the limit of high supersaturations. The effect of defect sites and overlapping of nucleation exclusion zones with reduced supersaturation formed around the growing nuclei is accounted for in determining the saturation nucleus density. The latter scales with the ratio of the surface diffusion coefficient and the atom arrival rate. The scaling exponent is a function of the critical nucleus size and depends on the process which controls the frequency of attachment of atoms to the critical nuclei to produce stable clusters, either the surface diffusion or the incorporation of atoms to the critical nuclei. The nucleation on top of two-dimensional (2-D) islands is considered as a reason for roughening in homoepitaxial growth. The mechanism of formation of three-dimensional (3-D) islands in heteroepitaxial growth is also addressed. The

2.1	Equilibrium Crystal–Ambient Phase	18
2.1.1	Equilibrium of Infinitely Large Phases	18
2.1.2	Equilibrium of Small Crystal with the Ambient Phase.....	20
2.1.3	Equilibrium Shape of Crystals.....	22
2.2	Work for Nucleus Formation	24
2.2.1	General Definition.....	24
2.2.2	Formation of 3-D Nuclei on Unlike Substrates.....	25
2.2.3	Work of Formation of 2-D Crystalline Nuclei on Unlike and Like Substrates.....	27
2.3	Rate of Nucleation	28
2.3.1	General Formulation	28
2.3.2	Rate of Nucleation on Single-Crystal Surfaces	30
2.3.3	Equilibrium Size Distribution of Clusters	31
2.3.4	Rate of Nucleation.....	32
2.4	Saturation Nucleus Density	35
2.5	Second-Layer Nucleation in Homoepitaxy	38
2.6	Mechanism of Clustering in Heteroepitaxy	43
2.7	Effect of Surfactants on Nucleation	45
2.8	Conclusions and Outlook	48
	References	48

effect of surface-active species on the rate of nucleation is explored.

Nucleation at surfaces plays a crucial role in the growth of crystals and epitaxial overlayers for the preparation of advanced materials with potential for technological

applications. In homoepitaxy of metal or semiconductor films the instability of planar growth against roughening depends on the kinetics of two-dimensional

nucleation [2.1]. The interplay of wetting and strain leads to clustering in overlayers growing under elastic stress in heteroepitaxy and determines the mechanism of growth and in turn the film morphology [2.2–4]. Smooth quantum wells or self-assembled quantum dots can be grown by varying the conditions of growth (temperature or growth rate) or by use of third species which change both the thermodynamics and kinetics of the processes involved [2.5]. The growth of thin epitaxial films in particular by molecular-beam epitaxy (MBE) usually occurs far from equilibrium. Thus, in addition to thermodynamics, one has to account for the kinetic processes taking place on the crystal surface [2.6]. The latter are responsible for the remarkable richness of patterns which are observed during growth [2.7].

This chapter gives the essential physics of the thermodynamics and kinetics of nucleation, both three- and two-dimensional, on like and unlike substrates as well as some later developments such as the Ehrlich–Schwoebel effect on second-layer nucleation and the effect of surface-active species on nucleation rate. The presentation is oriented more to the needs of experimentalists rather than going deeply into theoretical problems. The chapter is organized as follows. We start with problems of equilibrium of crystals and epitaxial overlayers with the parent phase (vapor, solution) in Sect. 2.1 and consider the equilibrium vapor pressure of infinitely large and finite-size crystals, the thermodynamic driving force for nucleation to occur, and the equilibrium shape of three-dimensional

(3-D) crystals on unlike surfaces. In Sect. 2.2 we define the work for nucleus formation in the most general way and consider the limiting cases of the classical (capillary) theory of nucleation at low or intermediate values of supersaturation and the atomistic approach at high supersaturations. We derive expressions for the work of formation of three-dimensional nuclei on like and unlike substrates. In Sect. 2.3 we give a general formulation of the nucleation rate and again derive expressions valid for high and low supersaturations. We consider further in Sect. 2.4 the saturation nucleus density accounting for the influence of defect (active) sites stimulating nucleation events and the overlapping of undersaturated nucleation exclusion zones around growing clusters. Making use of the rate equation approach we derive expressions for the saturation nucleus density in thin epitaxial films in diffusion and kinetic regimes of growth. In Sect. 2.5 we consider the effect of the step-edge Ehrlich–Schwoebel barrier on second-layer nucleation as a reason for the formation of mounds and thus roughening of surfaces in homoepitaxy. The mechanism of transformation of monolayer-high two-dimensional (2-D) islands into three-dimensional crystallites in Volmer–Weber and Stranski–Krastanov growth is addressed in Sect. 2.6. In Sect. 2.7 we explore the effect of surface-active species on the kinetics of nucleation. Some conclusions and outlook are given in Sect. 2.8.

2.1 Equilibrium Crystal–Ambient Phase

In treating the title problem we use the atomistic approach developed by *Kaischew* and *Stranski* [2.8]. It is based on the assumption of additivity of bond energies and accounts for the elementary processes taking place during growth and dissolution of the particles of the new phase. Although apparently old fashioned this approach is extremely instructive and informative for understanding the essential physics of the equilibrium of infinitely large phases and phases with finite size as well as of the deviation from equilibrium leading to transitions from one phase to another. Numerical studies of the stability of small clusters performed by making use of modern quantum-mechanical methods lead to the same conclusion that the closed atomic structures are most stable [2.9].

2.1.1 Equilibrium of Infinitely Large Phases

We consider for simplicity one-component system. The equilibrium between infinitely large phases (crystal, liquid or vapor) is determined by the equality of the respective chemical potentials. In 1927 *Kossel* and *Stranski* simultaneously developed an atomistic approach which is in fact identical to the definition of the macroscopic thermodynamics [2.10–12]. They considered the different sites that atoms can occupy on the crystal surface and found that there exists one particular site which plays a crucial role in crystal nucleation and growth. They introduced the concept of the *half-crystal position*, which turned out to be intimately connected with the chemical potential of an infinitely large crystal.

Consider the cubic face of a crystal with a simple cubic lattice (a Kossel crystal) containing a monatomic step (Fig. 2.1). Atoms can be located at different sites on the crystal surface. They can be built in the uppermost lattice plane or into the step edge, be adsorbed at the step edge or on the terrace, or can occupy the corner site (3) which has very peculiar properties. An atom in this position is connected with a half-atomic row, a half-crystal plane, and a half-crystal block. This is the reason the term half-crystal position (*Halbkristallage* or kink position) was coined for this particular site. Therefore, the work of separation of an atom from this position is exactly equal to the lattice energy of the crystal per building particle. Hence, the work of detachment of an atom from this position is given by

$$\varphi_{1/2} = \frac{1}{2}(Z_1\psi_1 + Z_2\psi_2 + Z_3\psi_3 \dots),$$

where Z_i are the numbers of neighbors of the consecutive coordination spheres and ψ_i are the respective bond energies.

Whereas atoms in other positions have different numbers of saturated and unsaturated (dangling) bonds, the atom in the kink position (3) has an equal number of saturated and dangling bonds. Therefore, the separation work from a half-crystal position serves as a specific reference with which the probabilities for elementary processes at other sites to take place can be compared. The detachment of an atom from the half-crystal position gives rise to the same position. It follows that, when an atom is detached from this position, the number of dangling bonds remains unchanged and in turn the surface energy does not change. Hence, the whole crystal (if it is large enough to avoid finite-size effects) can be built up or disintegrated into single atoms by repetitive attachment or detachment of atoms to and from this position.

In equilibrium with its vapor the probability of attachment of atoms to this position must be equal to the probability of their detachment. Hence the work of detachment of atoms from this position will determine the equilibrium vapor pressure and in turn its chemical potential. For simple crystals with monatomic vapor the latter will be given at zero temperature (the change of entropy is equal to zero) by

$$\mu_c^\infty = -\varphi_{1/2}, \quad (2.1)$$

where the superscript ∞ indicates an infinitely large crystal.

As seen the chemical potential of an infinitely large crystal is equal to the work of detachment of atoms from

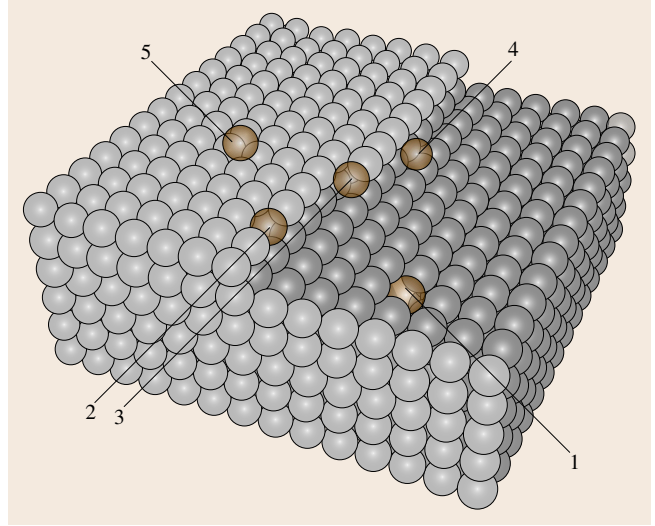


Fig. 2.1 The most important sites an atom can occupy on a crystal surface: 1 – atom embedded into the uppermost crystal plane, 2 – atom embedded into the step edge, 3 – atom in a half-crystal (kink) position, 4 – atom adsorbed at the step, 5 – atom adsorbed on the terrace

the half-crystal position taken with a negative sign. It is this property which makes this position unique in the theory of crystal nucleation and growth [2.13].

There is one more very important property of the half-crystal position. We can divide $\varphi_{1/2}$ into two parts: lateral interaction with the half-atomic row and the half-crystal plane, and the normal interaction with the half-crystal block underneath. If we replace the underlying crystal block by another block of different material and crystal lattice the lateral bonding will remain more or less unchanged if we assume additivity of bond energies. However, the normal bonding will change substantially owing to the difference in both chemical bonding and lattice strain. It is easy to show that the separation work from a kink position in this particular case can be written as

$$\varphi'_{1/2} = \varphi_{1/2} - (\psi - \psi'), \quad (2.2)$$

where ψ' is the energy of a bond between unlike atoms.

Having in mind (2.1), (2.2) can be written as

$$\mu'_c = \mu_c^\infty + (\psi - \psi'). \quad (2.3)$$

We now define the surface energy of a crystal by the following imaginary process. We cleave isothermally and reversibly the crystal into two halves and produce two surfaces with area S . We count the bonds we break

and divide the energy spent by $2S$. If we confine ourselves to nearest-neighbor bonds in the case of Kossel crystal we break one bond per atom and obtain ($S = a^2$)

$$\sigma = \frac{\psi}{2a^2}, \quad (2.4)$$

where a is the atomic diameter.

Using the above definition and the relation of Dupré [2.14]

$$\sigma_i = \sigma_A + \sigma_B - \beta, \quad (2.5)$$

which connects the specific interfacial energy σ_i between the unlike crystals A and B with the specific adhesion energy $\beta = \psi'/a^2$, (2.3) can be written as

$$\mu'_c = \mu_c^\infty + a^2(\sigma + \sigma_i - \sigma_s). \quad (2.6)$$

It is immediately seen that the term in the brackets $\Delta\sigma = \sigma + \sigma_i - \sigma_s$ is in fact the parameter that accounts for the wetting of the substrate (the half-crystal block underneath) by the overlayer in epitaxy of one material on the surface of another [2.15]. Thus, when $\Delta\sigma < 0$, or what is the same, $\psi < \psi'$ (complete wetting), the equilibrium vapor pressure of the first monolayer on the unlike substrate will be smaller than the equilibrium vapor pressure of the bulk crystal ($\mu = \mu_0 + k_B T \ln P$), i.e., $P'_\infty < P_\infty$. This means that at least the first monolayer can be deposited at a vapor pressure smaller than the equilibrium vapor pressure of the bulk crystal, or in other words, at undersaturation, $P'_\infty < P < P_\infty$ [2.16]. If the two crystals have different lattice parameters the growth should continue by formation of three-dimensional (3-D) islands. This is the famous Stranski–Krastanov mechanism of growth [2.17], in which the accumulation of strain energy with film thickness makes the planar film unstable against clustering. Obviously, if the lattice misfit is equal to zero the growth will continue layer by layer in the so-called Frank–van der Merwe mechanism of growth [2.18, 19]. In the opposite case of incomplete wetting ($\Delta\sigma > 0$), 3-D islanding will take place from the very beginning of deposition or Volmer–Weber growth, which requires supersaturation, $P > P_\infty$ [2.20]. We thus see that the separation work from a half-crystal position plays a fundamental role in determining the mechanism of epitaxial growth.

The lattice misfit increases the tendency for 3-D islanding by increasing the interfacial energy in (2.6) with the energy per unit area of misfit dislocations or elastic strain. Thus for heteroepitaxial growth the interfacial energy reads [2.21]

$$\sigma_i^* = \sigma_i + \varepsilon_m,$$

where ε_m is either the misfit dislocation energy or the energy of the homogeneous strain.

Thus the interfacial energy between misfitting crystals consists of two parts: a chemical part σ_i accounting for the difference in chemistry and strength of bonding, and a geometrical part ε_m accounting for the difference of lattices and lattice parameters. If the misfit in heteroepitaxy is accidentally or intentionally tailored to be equal to zero (particularly in binary or ternary alloys) $\varepsilon_m = 0$, but the chemical part σ_i remains different from zero and affects the mechanism of growth.

It should be noted that the misfit plays a decisive role for clustering only in Stranski–Krastanov growth, where it changes the sign of $\Delta\sigma$ from negative to positive beyond the so-called wetting layer. In Volmer–Weber growth $\Delta\sigma$ is positive and the strain energy makes a minor contribution with the same sign to it. Frank–van der Merwe growth takes place only in systems with zero misfit [2.22], which is why we will not take into consideration the effect of lattice misfit in nucleation.

2.1.2 Equilibrium of Small Crystal with the Ambient Phase

The separation work from the half-crystal position cannot determine the equilibrium of a crystal with finite size with its surrounding because the role of the crystal edges and corners cannot be ignored. The kink position is no longer a repetitive step for dissolution of the crystal. That is why Stranski and Kaischew suggested that the condition for a small crystal to be in equilibrium with the ambient phase is for the probability of building up a whole crystal plane to be equal to the probability of its dissolution. In this way the effect of the edge and corner atoms are accounted for in addition to the atoms in half-crystal positions. Obviously, the smaller the crystal, the greater will be the role of the corner and edge atoms, and vice versa. Thus they defined the *mean separation work* as the work per atom to disintegrate a whole crystal plane into single atoms. This quantity must have one and the same value for all crystal faces belonging to the equilibrium shape.

Consider for simplicity a small Kossel crystal with a shape of a cube with edge length $l_3 = an_3$, where n_3 is the number of atoms in the edge of the cube. Confining ourselves to nearest-neighbor bond energy ψ the energy for dissolution of a whole lattice plane into single atoms (by counting the bonds we break in the process of disintegration, Fig. 2.2) is $3n_3^2\psi - 2n_3\psi$. Dividing by the number of atoms n_3^2 the mean separation work

reads [2.8]

$$\bar{\varphi}_3 = 3\psi - \frac{2\psi}{n_3}, \quad (2.7)$$

or, bearing in mind that for a simple cubic lattice $3\psi = \varphi_{1/2}$,

$$\bar{\varphi}_3 = \varphi_{1/2} - \frac{2\psi}{n_3}.$$

It follows that the mean work of separation tends asymptotically to the work of separation from a half-crystal position as the crystal size is increased. We conclude that a crystal can be considered as small if $n_3 < 70$, or $l_3 < 2 \times 10^{-6}$ cm assuming $a \approx 3 \text{ \AA}$.

As $\bar{\varphi}_3$ determines the equilibrium vapor pressure of the small crystal and in turn its chemical potential we can write in analogy with (2.1) for $T = 0$

$$\mu_c = \mu_v = -\bar{\varphi}_3.$$

Then

$$\Delta\mu = \mu_v(P) - \mu_c^\infty(P) = \varphi_{1/2} - \bar{\varphi}_3 = \frac{2\psi}{n_3} \quad (2.8)$$

is the difference of the chemical potentials of the *infinitely large* vapor and crystal phases which represents the thermodynamic driving force for nucleation to occur, or the *supersaturation*.

The equilibrium of the vapor and the crystal takes place at some vapor pressure P_∞ (to stress the fact that the crystal is infinitely large) so that $\mu_v(P_\infty) = \mu_c(P_\infty)$. Then we can write (2.8) as

$$\Delta\mu = [\mu_v(P) - \mu_v(P_\infty)] - [\mu_c(P) - \mu_c(P_\infty)].$$

For small deviations from equilibrium the differences in the above equation can be replaced by derivatives and

$$\Delta\mu = \int_{P_\infty}^P \frac{\partial \mu_v}{\partial P} dP - \int_{P_\infty}^P \frac{\partial \mu_c}{\partial P} dP = \int_{P_\infty}^P (v_v - v_c) dP,$$

where v_v and v_c are the molecular volumes of the vapor and the crystal. As $v_v \gg v_c$ the above equation simplifies to

$$\Delta\mu = \int_{P_\infty}^P v_v dP.$$

Considering the vapor as an ideal gas ($v_v = k_B T / P$) gives upon integration

$$\Delta\mu = k_B T \ln\left(\frac{P}{P_\infty}\right). \quad (2.9)$$

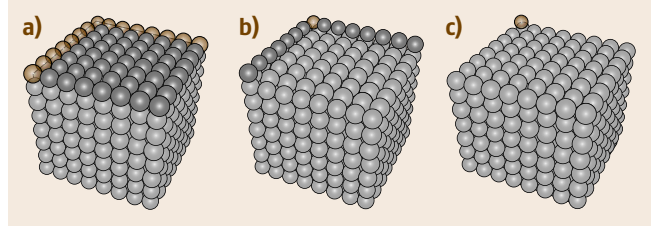


Fig. 2.2a–c Schematic for the evaluation of the mean separation work which determines the equilibrium of a small three-dimensional crystal with the supersaturated vapor phase. In stage (a) we detach $(n-1)^2$ atoms, breaking three bonds per atom, in stage (b) we detach $2(n-1)$ atoms, breaking two bonds per atom, and finally in (c) we detach the last atom, breaking a single bond

The supersaturation $\Delta\mu$ is usually very large in the case of nucleation from vapor, particularly in methods such as MBE. Let us evaluate it for the case of nucleation in MBE growth of Si(111). The supersaturation is given in terms of the ratio of the fluxes R/R_∞ , where $R = P/\sqrt{2\pi mk_B T}$, rather than in vapor pressures as in (2.9). Typical growth conditions are $T = 600$ K and $R = 1 \times 10^{13}$ atom/cm² s [2.23]. The equilibrium vapor pressure of Si at 600 K is $P_\infty = 1.3 \times 10^{-27}$ N/m². Then, $R_\infty \cong 6.5 \times 10^{-8}$ atom/cm² s and $\Delta\mu \cong 2.5$ eV. This means that the supersaturation is of the order of the enthalpy of evaporation of Si (≈ 4.5 eV). As we will see below this is why nuclei consist of a number of atoms of the order of unity.

Note that, with the approximation made, (2.9) is valid for very small deviations from equilibrium. If we repeat the above calculations at much higher temperature, say 1300 K, we find $\Delta\mu \cong 0.05$ eV. We can believe this value to be close to the real figure, but for low temperatures we can be sure only of the sign of the supersaturation (growth or evaporation) but not its numerical value.

Equation (2.8) represents the famous Thomson–Gibbs equation which gives the dependence of the equilibrium vapor pressure of a small crystal on its linear size. Using the definition of the specific surface energy (2.4) we obtain the Thomson–Gibbs equation in its form which is well known in the literature

$$\Delta\mu = \frac{4\sigma v_c}{l_3}. \quad (2.10)$$

We consider further the equilibrium with the vapor phase (and in turn with the dilute adlayer) of a small two-dimensional crystal with a monolayer height formed on the surface of a large three-dimensional crystal. Such an island grows or dissolves by attach-

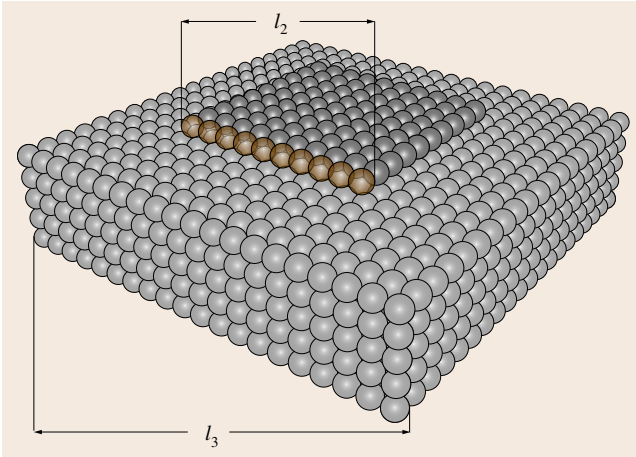


Fig. 2.3 Schematic for the evaluation of the mean separation work which determines the equilibrium of a small two-dimensional crystal with the supersaturated vapor phase. In equilibrium the probabilities of evaporation and building of a whole row of atoms (*black spheres*) are equal

ment or detachment of whole atomic rows. That is why *Kaischew* and *Stranski* suggested that the probability of building of a whole atomic row with length $l_2 = n_2 a$ is equal to the probability of its disintegration into single atoms [2.8]. The equilibrium 2-D island–vapor phase is now determined by the mean separation work $\bar{\varphi}_2$, which is equal to the energy per atom for evaporation of a whole edge row of atoms (Fig. 2.3). Assuming a square-shaped island with n_2 atoms in the edge the mean separation work reads

$$\bar{\varphi}_2 = 3\psi - \frac{\psi}{n_2} = \varphi_{1/2} - \frac{\psi}{n_2}.$$

The supersaturation necessary for the formation of a two-dimensional island with linear size l_2 then reads

$$\Delta\mu = \frac{\psi}{n_2}. \quad (2.11)$$

Note that in nucleation on surfaces the supersaturation can be expressed as a ratio of the real and the equilibrium adatom concentrations (in equilibrium the chemical potential of the vapor is equal to the chemical potential of the adlayer, which in turn depends on the adatom concentration)

$$\Delta\mu = k_B T \ln\left(\frac{N_1}{N_1^e}\right),$$

where [2.24]

$$N_1^e = N_0 \exp\left(-\frac{\Delta W}{k_B T}\right), \quad (2.12)$$

the difference $\Delta W = \varphi_{1/2} - E_{\text{des}}$ being the work to transfer an atom from a half-crystal position on the surface of a terrace, and N_0 is the atomic density of the crystal surface.

This is particularly true when the adatom concentration is determined by a dynamic adsorption–desorption equilibrium, i.e., when the atom arrival rate R is equal to the re-evaporation rate N_1/τ_s , where $\tau_s = \nu^{-1} \exp(E_{\text{des}}/k_B T)$ is the mean residence time of an atom on the surface before desorption.

We define now the specific edge energy in the same way that we defined the specific surface energy (2.4). We cleave an atomic plane into two halves and produce two edges with length L . We break one bond per atom and for the specific edge energy one obtains

$$\kappa = \frac{\psi}{2a}. \quad (2.13)$$

Combining (2.11) and (2.13) gives the Thomson–Gibbs equation for the two-dimensional case, or the supersaturation required to form an island with edge length l_2 , in its more familiar form [2.24]

$$\Delta\mu = \frac{2\kappa a^2}{l_2}. \quad (2.14)$$

Equations (2.10) and (2.14) can be derived by using the method of thermodynamic potentials introduced by Gibbs (for a review see [2.21]). However, contrary to the pure thermodynamics, the above *molecular-kinetic* or atomistic approach accounts in addition for the elementary processes of growth and dissolution of crystals. The growth of sufficiently large crystal takes place by attachment of building units to the half-crystal position. Once the atom is incorporated at this position we can say that it has joined the crystal lattice. Small three- and two-dimensional crystals grow and dissolve by building and dissolution of whole crystal planes or atomic rows, respectively.

2.1.3 Equilibrium Shape of Crystals

In 1878 *Gibbs* defined thermodynamically the problem of the equilibrium shape of crystals as the shape at which the crystal has a minimum surface energy at given constant volume [2.25]. This definition later acquired a geometric interpretation in the well-known Gibbs–Wulff theorem [2.26], according to which the distances h_n from an arbitrary (Wulff’s) point to the different crystal faces are proportional to the corre-

sponding specific surface energies σ_n of these faces

$$\frac{\sigma_n}{h_n} = \text{const.} \quad (2.15)$$

As a result the equilibrium shape represents a closed polyhedron consisting of the faces with the lowest specific surface energies. The areal extents of the crystal faces belonging to the equilibrium shape have one and the same value of chemical potential.

Half a century later *Kaischew* extended this approach to cover the case of a crystal on a foreign substrate and derived a relation known in the literature as the Wulff–Kaischew theorem [2.27]

$$\frac{\sigma_n}{h_n} = \frac{\sigma_i - \beta}{h_i} = \text{const.}, \quad (2.16)$$

where σ_i is the specific surface energy of the crystal face that is in contact with the substrate and h_i is the distance from the Wulff point to the plane of the contact (Fig. 2.4).

It is seen that the distance from the Wulff point to the contact plane is proportional to the difference $\sigma_i - \beta$. Therefore, when the catalytic potency of the substrate β is equal to zero, the distance h_i will have its value in the absence of a substrate. In this case we have *complete nonwetting*. At the other extreme $\beta = \sigma_A + \sigma_B = 2\sigma$ ($\sigma_A = \sigma_B = \sigma$) we have *complete wetting* and the three-dimensional crystal is reduced to a monolayer-high island. In the intermediate case $0 < \beta < 2\sigma$ we have *incomplete wetting* and the crystal height is smaller than its lateral extent.

The introduction of the separation work from half-crystal position and the mean separation works enabled Stranski and Kaischew to provide a new atomistic approach for determination of the equilibrium shape of crystals. The latter is necessary for calculation of the work of nucleus formation as it is assumed that the nuclei preserve the equilibrium shape as the lowest-energy shape. Thus the lowest-energy pathway of the crystallization process is ensured.

The basic idea is that atoms bound more weakly than an atom in the half-crystal position cannot belong to the equilibrium shape. We start from a sufficiently large crystal with a simple crystallographic form and remove in succession from its surface all atoms bound more weakly than in a half-crystal position. Precisely at that process all the faces of the equilibrium shape appear. Then the areas of the faces are varied by removal and addition of whole crystal planes up to the moment when the mean separation works of all crystal faces become equal. As the mean separation works are closely

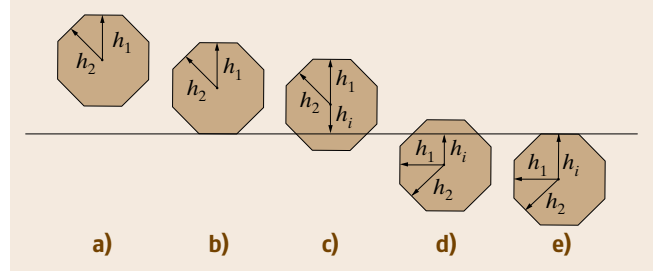


Fig. 2.4a–e Equilibrium shape of a crystal on an unlike substrate. The distances h_1 and h_2 in the free polyhedron (a) are proportional to the specific free energies σ_1 and σ_2 according to the Gibbs–Wulff theorem (2.15). In the presence of unlike substrate the distances to free surfaces remain the same as in the free polyhedron. The distance h_i to the plane of contact is determined by the difference $\sigma_i - \beta$ according to the Wulff–Kaischew theorem (2.16). (b) Complete nonwetting ($\beta = 0$); (c, d) different degrees of incomplete wetting (note that in the latter case the vector h_i is negative); (e) complete wetting ($\beta = 2\sigma$)

related to the chemical potentials the latter condition is equivalent to the definition of Gibbs. Thus, during the last operation of equating the mean separation works of all crystal faces, those which do not belong to the equilibrium shape disappear [2.28].

Therefore, the necessary and sufficient condition for the equilibrium shape of a crystal in the molecular-kinetic approach is equality of the mean separation works, or in other words, of the chemical potentials of all crystal faces. We use this condition to derive the equilibrium aspect ratio of a three-dimensional cubic crystal on the surface of an unlike crystal assuming incomplete wetting ($\Delta\sigma > 0$).

Consider a cubic crystal with a square base with edge length $l = na$ and height $h = n'a$, where n and n' are the number of atoms in the horizontal and vertical edges (Fig. 2.5). The mean separation work calculated

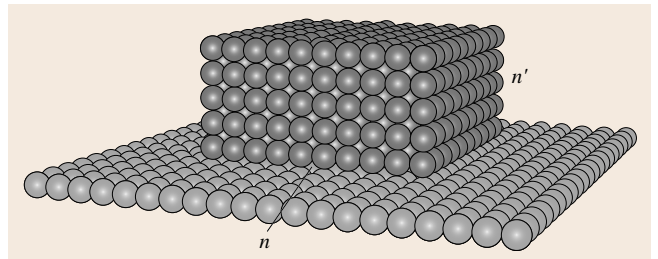


Fig. 2.5 A cubic crystal with n and n' atoms in the base and the height on the surface of an unlike crystal at incomplete wetting

from the side crystal face is

$$\bar{\varphi}'_3 = 3\psi - \frac{\psi - \psi'}{n'} - \frac{\psi}{n},$$

whereas the same quantity calculated for the upper base is given by (2.7). The condition $\bar{\varphi}_3 = \bar{\varphi}'_3$ gives

$$\frac{h}{l} = \frac{n'}{n} = \phi, \quad (2.17)$$

where

$$\phi = 1 - \frac{\psi'}{\psi}. \quad (2.18)$$

Substituting ψ and ψ' by the specific surface and adhesion energies and making use of the relation of

Dupré (2.5) gives ϕ in terms of surface energies

$$\phi = \frac{\sigma + \sigma_i - \sigma_s}{2\sigma}. \quad (2.19)$$

As seen, the equilibrium aspect ratio of the crystal is precisely equal to the familiar wetting condition (2.6) relative to 2σ . The parameter ϕ is known in the literature as the *wetting function*; it plays a crucial role in nucleation at surfaces and determines the mechanism of growth of thin epitaxial films [2.15, 29]. It can be shown that (2.19) can be derived by the classical thermodynamic condition of the minimum of the surface energy $\Phi = 4lh\sigma + l^2(\sigma + \sigma_i - \sigma_s)$ at constant volume $V = l^2h$ [2.15].

2.2 Work for Nucleus Formation

2.2.1 General Definition

The nuclei of the new phase represent local fluctuations of the density which can be considered as small molecular aggregates. If the phase is stable the density fluctuations increase the thermodynamic potential of the system. In this sense they are thermodynamically unfavorable. Their concentration is small and they cannot reach considerable size as the probability of decay is greater than the probability of growth. Thus they have no tendency to unlimited growth and can be considered as *lifeless*. Frenkel coined for them the term *homophase fluctuations* to emphasize the fact that they are well compatible with the stable state of aggregation [2.30]. As one approaches the phase equilibrium determined by the equality of the chemical potentials, their concentration increases and the maximum of the size distribution shifts to larger sizes. Once the chemical potential of the initial bulk phase (vapor or solution) becomes greater than that of the new, denser phase (liquid or crystal) the probability of growth becomes greater than the probability of decay and the tendency for growth of the density fluctuations prevails after exceeding some critical size. Frenkel referred to these as *heterophase fluctuations* to stress the fact that they are no longer compatible with the old, less dense phase. It is just these density fluctuations or clusters with a critical size which are called the *nuclei* of the new phase. In order to form such nuclei a free energy should be expended.

Consider a volume containing i_v molecules of a vapor with chemical potential μ_v at constant temperature T and pressure P . The thermodynamic potential

of this initial state is given by $G_1 = i_v\mu_v$. A small crystal with bulk chemical potential μ_c^∞ is formed from i molecules of the vapor phase and the thermodynamic potential of the final state reads $G_2 = (i_v - i)\mu_v + G(i)$, where $G(i)$ is the thermodynamic potential of a cluster consisting of i molecules. The work of formation of a cluster consisting of i molecules is given by the difference $\Delta G(i) = G_2 - G_1$ and [2.31]

$$\Delta G(i) = G(i) - i\mu_v. \quad (2.20)$$

As seen, the work of formation of the cluster represents the difference between the thermodynamic potential of the cluster and the thermodynamic potential of the same number of molecules but in the ambient phase (vapor, solution or melt). This is the most general definition of the work for nucleation. Taking different expressions for $G(i)$ we can approach different cases of nucleation, such as liquid or crystal nuclei, large or small clusters, clusters with or without equilibrium shape, nuclei on like and unlike surfaces, nuclei formed on small particles or ions, etc.

Equation (2.20) is usually illustrated with the simplest case, when the nucleus is a liquid droplet with the (equilibrium) shape of a sphere with radius r surrounded by its own vapor. We assume that the nucleus is sufficiently large that it can be described by macroscopic thermodynamic quantities. This is in fact the classical or capillary approach introduced by Gibbs. He considered nuclei as small liquid droplets, vapor bubbles or crystallites which, however, are sufficiently large to be described by their bulk properties. Although oversimplified, this approach was a significant step ahead

because, when phases with small linear sizes are involved, the surface-to-volume ratio is large.

The thermodynamic potential of the spherical droplet reads

$$G(r) = \frac{4\pi r^3}{3v_l} \mu_l^\infty + 4\pi r^2 \sigma ,$$

where $i = 4\pi r^3/3v_l$ is the number of atoms in the nucleus.

Writing the expression for $G(r)$ in this way we suppose that a cluster with radius r has the chemical potential μ_l^∞ of the infinitely large liquid phase. The second term accounts for the excess energy owing to the newly formed interface between the liquid droplet and the ambient vapor phase, to which we ascribe a specific energy σ that is characteristic of the bulk liquid phase.

The thermodynamic potential of a crystalline cluster with a cubic shape and lateral extent l in the capillary approximation is given by a similar expression

$$G(l) = -\frac{l^3}{v_c} \mu_c^\infty + 6l^2 \sigma . \quad (2.21)$$

Then for the work of nucleus formation in terms of the size l one obtains

$$\Delta G(l) = \frac{l^3}{v_c} \Delta\mu + 6l^2 \sigma , \quad (2.22)$$

where $i = l^3/v_c$, and $\Delta\mu = \mu_v - \mu_c^\infty$ is the supersaturation.

The dependence of $\Delta G(l)$ on the size l is plotted in Fig. 2.6. (Note that the growing cluster preserves its equilibrium shape of a cube with increasing linear size l .) As seen, $\Delta G(l)$ displays a maximum when the ambient phase is supersaturated ($\mu_c^\infty < \mu_v$) at some critical size

$$l^* = \frac{4\sigma v}{\Delta\mu} . \quad (2.23)$$

In the opposite case of undersaturated vapor ($\mu_c^\infty > \mu_v$) both terms in (2.22) are positive and the Gibbs free energy change goes to infinity as the density fluctuations are thermodynamically unfavorable.

Equation (2.23) is in fact the familiar equation (2.10) of Thomson–Gibbs. As discussed above the latter represents the condition of equilibrium of a small particle with its ambient phase. It is important to note that *this equilibrium is unstable*. When more atoms join the nucleus, its size increases and its equilibrium vapor pressure becomes smaller than that of the ambient phase. As a result the probability of growth becomes greater than the probability of decay and the nucleus

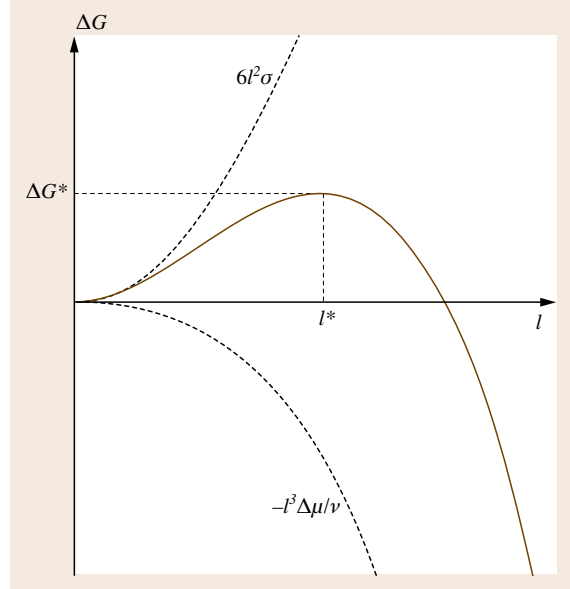


Fig. 2.6 Dependence on the crystal size l (or radius r) of the Gibbs free energy change connected with the formation of a crystalline (liquid) nucleus with a cubic (spherical) shape

will continue to grow. If several atoms detach from the nucleus, its equilibrium vapor pressure will increase and become higher than that of the ambient phase. The probability of decay will become dominant and the nucleus will decay further. In other words, any infinitesimal deviation of the size of the nucleus from the critical one leads to a decrease of the thermodynamical potential of the system.

Substituting l^* into (2.22) gives the value of the maximum, or in other words, the change of the Gibbs free energy to form the nucleus

$$\Delta G^* = \frac{32\sigma^3 v^2}{\Delta\mu^2} . \quad (2.24)$$

It is inversely proportional to the square of the supersaturation (a result which was obtained for the first time by Gibbs in 1878 [2.25]) and increases steeply when approaching the phase equilibrium, thus imposing great difficulties for crystallization to take place.

2.2.2 Formation of 3-D Nuclei on Unlike Substrates

Equation (2.21) gives the thermodynamic potential of a small crystallite with a cubic equilibrium shape whose

properties are described in terms of classical macroscopic thermodynamics. In order to relax this restriction Stranski suggested a new approach which can be used for both large crystals and arbitrarily small clusters with arbitrary shape. The thermodynamic potential is given in the more general form

$$G(i) = i\mu_c^\infty + \Phi, \quad (2.25)$$

where Φ plays the role of a surface energy.

The work for nucleus formation then reads

$$\Delta G(i) = -i\Delta\mu + \Phi. \quad (2.26)$$

According to the definition of *Stranski* the *surface* term is given by [2.32]

$$\Phi = i\varphi_{1/2} - U_i, \quad (2.27)$$

where $U_i > 0$ is the energy of disintegration of the whole crystal (or small cluster) into single atoms. In fact $-U_i$ is the potential (binding) energy of the cluster. In the approximation of additivity of bonds energies, U_i is equal to the number of bonds between the atoms of the cluster multiplied by the work ψ to break a single bond.

Equation (2.27) can be easily understood. The first term on the right-hand side gives the energy of the bonds as if all atoms are in the bulk of the crystal (recall that the separation work from the half-crystal position is equal to the lattice energy per atom). The second term gives the energy of the bonds between the atoms of the cluster. Therefore, the difference represents the number of unsaturated (dangling) bonds multiplied by the energy $\psi/2$ of a dangling bond. Obviously, if the cluster is sufficiently large, Φ can be expressed in terms of surface, edge, and apex energies, but as written above it is applicable to arbitrarily small clusters with arbitrary shape.

Combining (2.26) and (2.27) and substituting for $\Delta\mu$ from the Thomson–Gibbs equation (2.8) in atomistic terms in the resulting equation for the Gibbs free energy change for nucleus formation one obtains

$$\Delta G^* = i^* \bar{\varphi}_3 - U_{i^*}. \quad (2.28)$$

We can now calculate the work of formation of a nucleus with equilibrium shape shown in Fig. 2.5. In this case $i = n^2 n'$ and

$$U_i = 3n^2 n' \psi - 2nn' \psi - n^2 \psi \phi, \quad (2.29)$$

where ϕ is the familiar wetting function (2.17) which determines also the equilibrium shape of a crystal on an unlike substrate.

Combining (2.7), (2.28), and (2.29) gives

$$\Delta G^* = n^{*2} \psi \phi, \quad (2.30)$$

where n^* is the number of atoms in the lateral edge of the critical nucleus. Note that $l^* = an^*$ is the length of the edge of the homogeneously formed nucleus in the absence of a substrate or under the condition of complete nonwetting.

We show that (2.30) gives the work of formation of a complete cubic crystallite (2.24) multiplied by the wetting function (2.17), which is positive and smaller than unity in the case of incomplete wetting under study. For this purpose we substitute for n^* and ψ from (2.8) and (2.4), respectively, in (2.30) and obtain ($a^3 = v$)

$$\Delta G^* = \frac{32\sigma^3 v^2}{\Delta\mu^2} \frac{\sigma + \sigma_i - \sigma_s}{2\sigma}, \quad (2.31)$$

where the wetting function ϕ is given in terms of surface energies.

It follows that the work for nucleus formation at surfaces (heterogeneous nucleation) is equal to that of the homogeneously formed nuclei in the absence of a surface multiplied by the wetting function. Bearing in mind that

$$\phi = \frac{h}{l} = \frac{l^2 h}{l^3} = \frac{V}{V_0},$$

we conclude that the ratio of the works for heterogeneous and homogeneous nucleation is equal to the ratio of the respective volumes in the presence and absence of a substrate

$$\Delta G_{\text{het}}^* = \Delta G_{\text{hom}}^* \frac{V}{V_0}.$$

It is interesting to consider the case when a three-dimensional nucleus is formed in the concave edge of a *hill-and-valley* vicinal surface consisting of alternating low-index facets and which is often formed under the effect of adsorbed impurity atoms [2.33,34]. Assuming for simplicity a right angle of the concave edge we find that the nucleus has a prismatic equilibrium shape, having two edges with length $l' = n'a$ and one edge with a length $l = na$. Using the same procedure as before for ΔG^* one obtains

$$\Delta G^* = n^{*2} \psi \phi^2$$

or

$$\Delta G^* = \frac{32\sigma^3 v^2}{\Delta\mu^2} \left(\frac{\sigma + \sigma_i - \sigma_s}{2\sigma} \right)^2.$$

In the same way we find that the work of formation of a nucleus in a right-angle corner is proportional to the third degree of the wetting function ϕ , etc. As $\phi < 1$ we conclude that a rough surface containing concave edges and corners stimulates nucleation by decreasing the nucleus volume.

2.2.3 Work of Formation of 2-D Crystalline Nuclei on Unlike and Like Substrates

To solve this problem we apply the same procedure, bearing in mind that we have to account for the mean separation work for a two-dimensional square cluster. We consider first the more general case in which the 2-D nucleus is formed on an unlike substrate. Obviously, in order for the 2-D nucleus to be stable the wetting should be complete, although 2-D nuclei can be stable in incomplete wetting but only up to some critical size [2.35]. Beyond this size the monolayer islands become unstable against bilayer islands and should be rearranged into three-dimensional islands as required by the thermodynamics (Sect. 2.6).

The mean separation work calculated for a 2-D square nucleus consisting of $i = n^2$ atoms on unlike substrates reads

$$\bar{\varphi}'_2 = 3\psi - \frac{\psi}{n} - \psi\phi$$

and

$$\Delta\mu = \frac{\psi}{n} + \psi\phi. \quad (2.32)$$

The binding energy is $U_i = 3n^2\psi - 2n\psi - n^2\psi\phi$ and the Gibbs free energy change reads

$$\Delta G^* = n^*\psi. \quad (2.33)$$

Substituting for n^* from (2.32) and ψ from (2.13) in (2.33) gives

$$\Delta G^* = \frac{\psi^2}{\Delta\mu - \psi\phi} = \frac{4\kappa^2 a^2}{\Delta\mu - a^2(\sigma + \sigma_i - \sigma_s)}. \quad (2.34)$$

In the limiting case of a like substrate (nucleation on the surface of the same crystal) $\Delta\sigma = \sigma + \sigma_i - \sigma_s = 0$ and the Gibbs free energy change reads

$$\Delta G^* = \frac{\psi^2}{\Delta\mu} = \frac{4\kappa^2 a^2}{\Delta\mu}. \quad (2.35)$$

Substituting for ψ from the Thomson–Gibbs equation (2.32) in the case of complete wetting, $\phi = 0$, in (2.35) one obtains the very useful result that the work

for nucleus formation is precisely equal to the volume part of it

$$\Delta G^* = n^{*2} \Delta\mu = i^* \Delta\mu. \quad (2.36)$$

Equations (2.34) and (2.35) lead to some interesting conclusions. In the case of incomplete wetting ($\Delta\sigma > 0$) 2-D nucleation can take place only at supersaturation higher than $\Delta\mu_0 = a^2\Delta\sigma$, because when approaching the latter the work for nucleus formation goes to infinity. In the case of complete wetting ($\Delta\sigma < 0$) both terms in the denominator of (2.34) are positive and 2-D nucleation can take place even at undersaturation. As follows from (2.35) a 2-D nucleation event on the surface of the same crystal ($\Delta\sigma = 0$) can occur only at supersaturations higher than zero.

Equations (2.31) and (2.34) give another critical supersaturation $\Delta\mu_{cr} = 2\Delta\mu_0$ at which the 3-D nucleus is reduced to a 2-D nucleus with monolayer height. The reason is that, assuming a constant equilibrium aspect ratio $h/l < 1$, on decreasing the nucleus size with increasing supersaturation a moment comes when the thickness of the 3-D island becomes equal to one monolayer [2.36–38]. As a result three-dimensional nucleation should not take place at supersaturations larger than $\Delta\mu_{cr}$. The latter does not contradict the observed layer-by-layer growth of Pb on Ge(001) at 130 K [2.39].

In the end of this subsection we will briefly discuss the very interesting and important question of the existence and formation of one-dimensional nuclei. The latter can be considered as rows of atoms at the edge of a single height step. Using the approach of the mean separation works the equilibrium of a such row of atoms with the ambient phase will be given by the equality of the probabilities of attachment and detachment of atoms to the row's ends. However, the row's ends represent half-crystal positions, so the *mean separation work* reads $\bar{\varphi}_1 = 3\psi = \varphi_{1/2}$ and the supersaturation is $\Delta\mu = \varphi_{1/2} - \bar{\varphi}_1 = 0$. The latter means that a row of atoms has the same chemical potential as the bulk crystal, irrespective of its length. The potential energy of a row consisting of i atoms is $U_i = 3i\psi - \psi$, and the work of formation of a one-dimensional nucleus is $\Delta G_1^* = i\bar{\varphi}_1 - U_i = \psi$. As seen ΔG_1^* does not depend on the row's length, which means that a critical size as in 3-D and 2-D nucleation does not exist. All the above means that one cannot define thermodynamically one-dimensional nuclei. However, as pointed out by several authors, one-dimensional nuclei can be well defined kinetically [2.40–42]. It is in fact the formation of one-dimensional nuclei which allows the propagation of smooth steps, particularly at low temperatures.

We mention here only two cases of great practical importance: the advancement of S_A steps on the surface of Si(001) 2×1 [2.43, 44] and the growth of protein crystals [2.45]. We would like to stress once more that the one-dimensional nucleation is a purely kinetic process and a critical size cannot be defined thermodynamically.

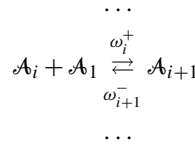
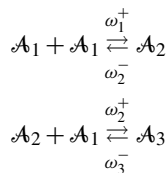
2.3 Rate of Nucleation

As discussed above the equilibrium of a small particle of the new phase with the supersaturated ambient phase is unstable. Accidental detachment of atoms from the critical nucleus can result in a decay of the cluster even to single atoms. Attachment of several atoms could lead to unlimited growth. It is not accidental that the exact solution of the time-dependent problem leads to a diffusion-type equation which reflects the random character of the processes of growth and decay around the critical size [2.30]. We can thus interpret the growth of the clusters as a *diffusion* in the space of the size. We conclude that nucleation is a random process. The steady-state rate of nucleation is a constant quantity which represents an average in time of randomly distributed events.

2.3.1 General Formulation

Becker and Döring advanced a purely kinetic approach which allowed them to derive a general expression for the steady-state nucleation rate making the assumptions of: (1) steady-state distribution of the heterophase fluctuations, (2) constant geometrical shape of the growing clusters which coincides with the equilibrium shape, and (3) constant supersaturation which is achieved by removal of clusters which are sufficiently large (much larger than the critical nucleus, $I \gg i^*$) from the system and then are returned back as single atoms [2.46]. The interested reader is referred to the excellent analysis of Christian [2.47]. Relaxing assumption 2 did not affect significantly the final result, whereas allowing variable supersaturation changed only the transient character of nucleation but not the steady-state nucleation rate [2.48]. It was in fact the first assumption which played the essential role in solving the problem.

Becker and Döring considered the nucleation process as a series of consecutive bimolecular reactions (a scheme proposed by Leo Szilard)



in which the growth and decay of the clusters take place by attachment and detachment of single atoms. Triple and multiple collisions are excluded as less probable. ω_i^+ and ω_i^- denote the rate constants of the direct and reverse reactions. Here \mathcal{A} is used as a chemical symbol.

Clusters consisting of i atoms are formed by the growth of clusters consisting of $i-1$ atoms and the decay of clusters of $i+1$ atoms (birth processes) and disappear by the growth and decay into clusters of $i+1$ and $i-1$ atoms (death processes), respectively. Then the change with time of the concentration $Z_i(t)$ of clusters consisting of i atoms is given by

$$\frac{dZ_i(t)}{dt} = J_i(t) - J_{i+1}(t),$$

where

$$J_i(t) = \omega_{i-1}^+ Z_{i-1}(t) - \omega_i^- Z_i(t) \quad (2.37)$$

is the net flux of clusters through the size i .

Assuming a steady-state concentration of the clusters in the system, $dZ_i(t)/dt = 0$, leads to

$$J_i(t) = J_{i+1}(t) = J_0,$$

where we denote by J_0 the time-averaged frequency of formation of clusters of any size. Therefore, J_0 is also equal to the frequency of formation of the clusters with the critical size i^* and thus is equal to the steady-state nucleation rate.

Applying a simple mathematical procedure to the system of rate equations which describe the scheme of Szilard for J_0 one obtains [2.49]

$$J_0 = Z_1 \sum_{i=1}^{I-1} \left(\frac{1}{\omega_i^+} \frac{\omega_2^- \omega_3^- \dots \omega_i^-}{\omega_1^+ \omega_2^+ \dots \omega_{i-1}^+} \right)^{-1}. \quad (2.38)$$

This is the most general expression for the steady-state rate of nucleation. It is applicable to any case of nucleation (homogeneous or heterogeneous, from

any ambient phase – vapor, solution or melt, three- or two-dimensional, etc.). It also allows the derivation of equations for the classical as well as the atomistic nucleation rate at small and high supersaturations as limiting cases. The only thing we should know in any particular case are the rate constants ω_i^+ and ω_i^- .

The analysis of (2.38) shows that every term in the sum is equal to $\exp(\Delta G(i)/k_B T)$, where $\Delta G(i)$ is the work to form a cluster consisting of i atoms [2.50]

$$\frac{\omega_2^- \omega_3^- \dots \omega_i^-}{\omega_1^+ \omega_2^+ \dots \omega_{i-1}^+} = \exp\left(\frac{\Delta G(i)}{k_B T}\right). \quad (2.39)$$

The condition of an imaginary equilibrium $J_0 = 0$ applied to (2.37) leads to an equation known in the literature as the equation of *detailed balance*

$$\frac{N_i}{N_{i-1}} = \frac{\omega_{i-1}^+}{\omega_i^-},$$

where N_i denotes the equilibrium concentration of clusters consisting of i atoms. Multiplying the ratios N_i/N_{i-1} from $i = 2$ to i gives an expression for the equilibrium concentration of clusters of size i

$$\frac{N_i}{N_1} = \prod_{n=2}^i \left(\frac{\omega_{n-1}^+}{\omega_n^-} \right) = \left(\frac{\omega_2^- \omega_3^- \dots \omega_i^-}{\omega_1^+ \omega_2^+ \dots \omega_{i-1}^+} \right)^{-1}. \quad (2.40)$$

Substituting (2.39) into (2.40) gives for the *equilibrium concentration of clusters of size i*

$$N_i = N_1 \exp\left(-\frac{\Delta G(i)}{k_B T}\right). \quad (2.41)$$

We recall that $\Delta G(i)$ displays a maximum at $i = i^*$. It follows that N_i should display a minimum at the critical size.

Substituting (2.39) into (2.38) and replacing the summation by integration valid for large critical nuclei one obtains

$$J_0 = \omega^* \Gamma N_{i^*},$$

where $\omega^* \equiv \omega_{i^*}$ is the frequency of attachment of atoms to the critical nucleus, $\Gamma = (\Delta G^*/3\pi k_B T i^{*2})^{1/2}$ is the so-called nonequilibrium Zeldovich factor which accounts for neglecting processes taking place far from the critical size, and N_{i^*} is given by (2.41) for the critical nucleus. It is assumed that the equilibrium monomer concentration N_1 is equal to the steady-state concentration Z_1 .

In the particular case of nucleation on surfaces we have to account for the configurational entropy of

distribution of clusters and single atoms among the adsorption sites of density N_0 ($\approx 1 \times 10^{15} \text{ cm}^{-2}$) which should be added to the Gibbs free energy changes (2.31), (2.34) or (2.35) [2.51]. Assuming that the density of clusters is negligible compared with that of single atoms the entropy correction reads

$$\Delta G_{\text{conf}} \approx -k_B T \ln\left(\frac{N_0}{N_1}\right).$$

Then for the steady-state nucleation rate on surfaces one obtains

$$J_0 = \omega^* \Gamma N_0 \exp\left(-\frac{\Delta G^*}{k_B T}\right), \quad (2.42)$$

where the frequency of attachment of atoms to the critical nucleus ω^* accounts only for the surface diffusion of atoms to the nucleus, the direct impingement from the vapor being neglected [2.52].

As discussed above the capillary nucleation theory is valid at supersaturations which are sufficiently low that the nuclei are large and can be described in terms of the classical thermodynamics. In order to find the limits of validity of (2.42), or in other words, the maximum value of the supersaturation at which the above equation is still valid, we have to find the values of the pre-exponential $K = \omega^* \Gamma N_0$ and ΔG^* and calculate the time τ elapsed from *switching on* the supersaturation to the appearance of the first nucleus. The latter is given by $\tau = 1/J_0 S$, where S is the area available for nucleation.

Consider for simplicity 2-D nucleation on the surface of the same crystal. The frequency of attachment of atoms to the critical nucleus ω^* is given by the product of the periphery of the nucleus and the flux of adatoms joining the nucleus. We assume that the nucleus consists of at least 49 atoms (a square of 7×7 atoms) in order for the classical theory to be valid. The flux of adatoms to the periphery is $j_s \approx D_s N_1 / a$, where $D_s = a^2 \nu \exp(-E_{sd}/k_B T)$ is the surface diffusion coefficient, and the adatom concentration is determined by a dynamic adsorption–desorption equilibrium and is given by $N_1 = R\tau_s$. The reason for using this definition is that it is supposed that the temperature is sufficiently high to ensure low supersaturation and the desorption flux N_1/τ_s is significant. Here ν is the attempt frequency and E_{sd} and E_{des} are the activation barriers for surface diffusion and desorption, respectively. Taking appropriate values for the parameters involved we find a value for the pre-exponential of the order of $10^{20} - 10^{25} \text{ cm}^{-2} \text{ s}^{-1}$ for nucleation from vapor. We can further evaluate the supersaturation by using (2.11).

Once we know the supersaturation we can easily evaluate ΔG^* by making use of (2.36).

We consider as an example nucleation on Si(001) at $T = 1500$ K and assume that $S = 1 \text{ cm}^2$, although a more realistic value could be determined from the width of the terraces on the crystal surface. From the enthalpy of evaporation we deduce the bond strength to be of the order of $2\text{--}2.2 \text{ eV}$. Then $\Delta\mu \approx 0.3 \text{ eV}$, $\Delta G^* = 15 \text{ eV}$, and $\tau \approx 1 \times 10^{15}$ millennia. This behavior of the classical nucleation rate was noticed by *Dash*, who noted that nucleation on defectless crystal surfaces according to the classical theory requires *astronomically* long times [2.53]. The reason for this behavior is that the pre-exponential in J_0 is a very weak function of the supersaturation compared with the exponential $\exp(-\Delta G^*/k_B T)$, which varies very

steeply with the latter. As a result there is a critical supersaturation below which the rate of nucleation is practically equal to zero and beyond which it takes values of many orders of magnitude (Fig. 2.7). We conclude that, in order for a nucleation event to take place on a laboratory scale of time, $\Delta G^*/k_B T$ should be smaller than ≈ 30 (in the case under consideration it is 4 times larger). This means that, for most materials at working temperatures between 600 and 1000 K, *the number of atoms in the critical nucleus should be of the order of unity*. This is why we will develop in more detail the atomistic theory of nucleation valid for nuclei consisting of very small number of atoms. It is important to note that a small value (usually not larger than ten) of the number of atoms in the critical nucleus should be expected also in the case of three-dimensional nucleation. A value of $i^* = 9$ was obtained in the case of nucleation of CoSi_2 from amorphous Co-Si alloy [2.54]. The reason for the comparatively larger size is due to the much greater value of the pre-exponential, which in this particular case is on the order of $10^{35}\text{--}10^{40} \text{ cm}^{-3} \text{ s}^{-1}$ [2.21].

2.3.2 Rate of Nucleation on Single-Crystal Surfaces

Single-crystal surfaces always represent vicinal surfaces consisting of terraces divided by steps due to the tilt of the surface by some small angle with respect to the low-index (singular) crystal face. Numerous processes can take place during deposition on the terraces (Fig. 2.8). We consider first the case of complete wetting. Atoms arrive from the vapor and accommodate thermally with the substrate [2.55], diffuse on the crystal surface, and re-evaporate if the temperature is sufficiently high. The atoms can also join pre-existing steps and diffuse along these steps to incorporate into kink sites. The reverse process of detachment of atoms from kink sites directly to the terrace or through the intermediate state of adsorption at the step edge can also take place. Thus when the temperature is sufficiently high the crystal grows by propagation of the pre-existing steps. If the temperature is low and the atom diffusivity is small the atoms cannot reach the steps and collide with other atoms to produce dimers. The dimers can grow further to produce trimers, tetramers, and finally large islands by attachment of new adatoms, or can decay into single atoms. Arriving atoms will preferably join the islands in a later stage of growth, the formation of new dimers being inhibited. Thus we can distinguish two

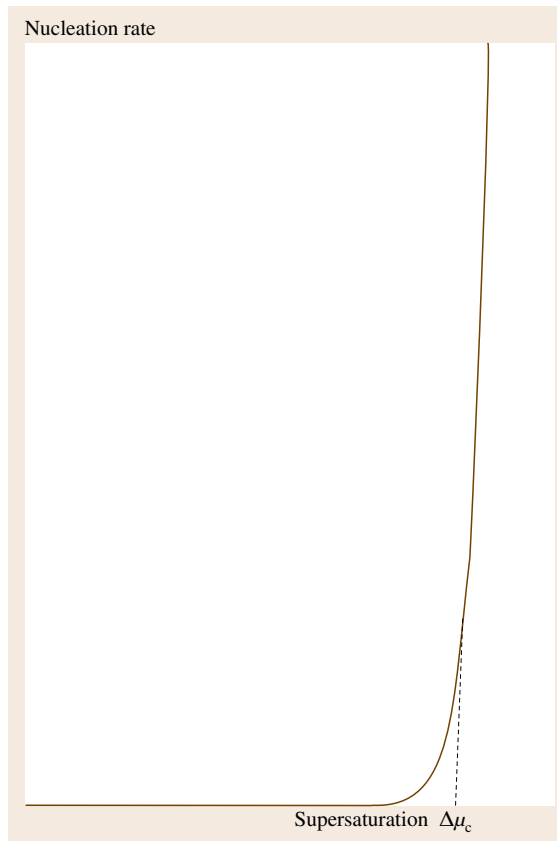


Fig. 2.7 Plot of the nucleation rate versus the supersaturation. The nucleation rate is practically equal to zero up to a critical supersaturation $\Delta\mu_c$. Beyond this value the rate of nucleation increases sharply by many orders of magnitude

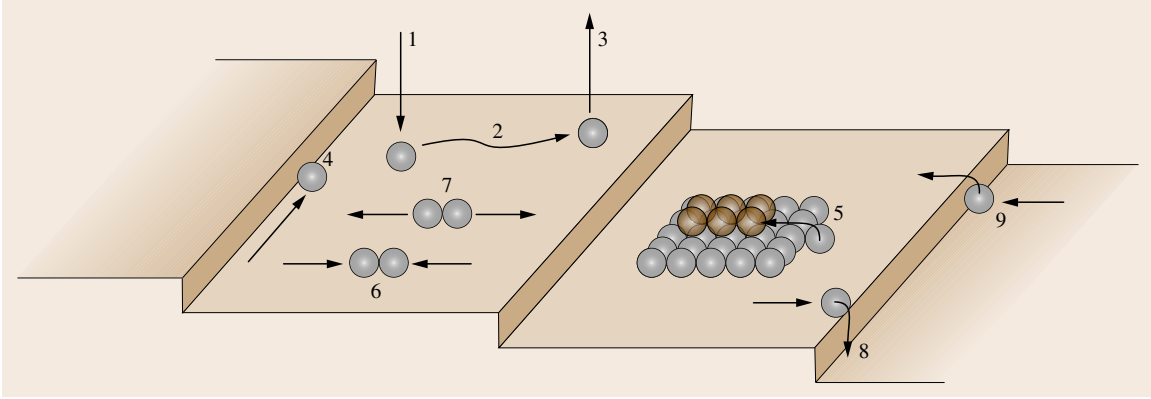


Fig. 2.8 Schematic representation of the different processes which can take place on surfaces during deposition on like and unlike substrates: 1 – adsorption, 2 – surface diffusion, 3 – desorption, 4 – edge diffusion, 5 – transformation of monolayer to bilayer island in heteroepitaxy, 6 – dimer formation, 7 – dimer decay, 8 – step-down hopping, 9 – step-up jump

regimes of growth: step flow growth at high temperatures and growth by two-dimensional nucleation at low temperatures.

In the case of incomplete wetting which favors three-dimensional clustering all the processes listed above remain the same with the exception that step flow growth does not take place (we consider the case of heteroepitaxy with $\psi > \psi'$); nucleation occurs at all temperatures. The mechanism of formation of 3-D clusters depends strongly on the wetting. In the extreme of very weak wetting (metals on alkali halides) visible clustering is observed from the very beginning of deposition. When the wetting is stronger as in the technologically important cases of metals on metals or semiconductors on semiconductors, two-dimensional islands are initially energetically favored but become unstable and transform beyond some critical size into 3-D clusters (Fig. 2.8) [2.35]. The same is observed in Stranski–Krastanov growth beyond the wetting layer [2.56, 57]. Thus in the beginning of deposition the overlayer can be considered as a population of molecules of different size, most of which are one atom high [2.58].

2.3.3 Equilibrium Size Distribution of Clusters

We calculate first the equilibrium concentration of the clusters of size i . The thermodynamic potential of the cluster of size i is given by (2.25), where i is an integer which can be arbitrarily small. Bearing in mind (2.26)

and (2.27) the work for nucleus formation reads

$$\Delta G(i) = G(i) - i\mu_v = i(\phi_{1/2} - \Delta\mu) - U_i. \quad (2.43)$$

Assuming the adlayer consisting of clusters of different size behaves as a two-dimensional ideal gas ($\sum_i N_i \ll N_0$) the thermodynamic potential of the population of clusters of size i will be [2.59]

$$\mathcal{G}(N_i) = N_i G(i) - k_B T \ln \frac{N_0!}{(N_0 - N_i)! N_i!}.$$

Then for the chemical potential of the two-dimensional ideal gas of clusters of size i one obtains

$$\mu_i = \frac{d\mathcal{G}(N_i)}{dN_i} = G(i) - k_B T \ln \left(\frac{N_0}{N_i} \right). \quad (2.44)$$

Suppose now that the pressure of the vapor is precisely equal to the equilibrium vapor pressure of the infinitely large crystal at the given temperature so that $\mu_i = i\mu_c^\infty$. The system is in a true equilibrium and the nucleation rate is precisely equal to zero. Rearranging (2.44) and inserting the above equality gives for the equilibrium concentration of i -atomic clusters

$$\frac{N_i^e}{N_0} = \exp \left(- \frac{G(i) - i\mu_c^\infty}{k_B T} \right).$$

Assume now that the vapor pressure is higher than the equilibrium vapor pressure so that $\mu_i = i\mu_v > i\mu_c^\infty$. The system will be supersaturated and the nucleation rate will differ from zero. We apply as before the artificial condition $J_0 = 0$, which determines a hypothetical equilibrium concentration of clusters of size i

$$\frac{N_i}{N_0} = \exp \left(- \frac{G(i) - i\mu_v}{k_B T} \right).$$

Substituting for $G(i)$ from (2.43) in the above equation gives

$$\frac{N_i}{N_0} = \exp\left(-\frac{i\varphi_{1/2} - i\Delta\mu - U_i}{k_B T}\right). \quad (2.45)$$

The condition $i = 1$ yields the density of monomers

$$\frac{N_1}{N_0} = \exp\left(-\frac{\varphi_{1/2} - \Delta\mu - U_1}{k_B T}\right),$$

the i -th power of which reads

$$\left(\frac{N_1}{N_0}\right)^i = \exp\left(-\frac{i\varphi_{1/2} - i\Delta\mu - iU_1}{k_B T}\right). \quad (2.46)$$

Dividing (2.45) and (2.46) gives for this hypothetical equilibrium concentration of clusters of size i [2.58]

$$\frac{N_i}{N_0} = \left(\frac{N_1}{N_0}\right)^i \exp\left(\frac{E_i}{k_B T}\right), \quad (2.47)$$

where $E_i = U_i - iU_1$ is the net energy gained to form an i -atom cluster from i single atoms. Bearing in mind that U_1 is, in fact, the adhesion energy ψ' , E_i is the potential (binding) energy of the lateral bonds in the cluster. The latter means that the value of E_i does not depend (within the framework of the approximation of the additivity of the bond energies) on the material of the substrate. It should be one and the same on like and unlike substrate crystals. Recall that we defined U_i as a positive quantity. This means that E_i is also positive. As $N_1/N_0 \ll 1$ the pre-exponential decreases whereas the exponential increases with i . It follows that (2.47) should display a minimum at some critical size or, in other words, will have the same qualitative behavior as the classical equilibrium size distribution (2.41).

2.3.4 Rate of Nucleation

An approximate expression for the nucleation rate can be obtained by multiplying (2.47) by the flux of atoms to the critical nucleus. Note, however, that in the case of small clusters the classical definition of a nucleus as a cluster with equal probabilities for growth and decay, each one equal to 0.5, is not valid. The nucleus should be defined as the cluster whose probability of growth is smaller than or equal to 0.5, but which after attachment of one more atom will have a probability of growth greater than or equal to 0.5 [2.58]. The latter is called the *smallest stable cluster*. Thus the nucleation rate is the rate at which clusters of critical size become *supercritical* or smallest stable clusters.

It is clear that for small clusters the requirement of constant geometrical shape required by the classical theory is violated. An analytical expression for i^* cannot be derived and the nucleus structure should be determined by a trial-and-error procedure by estimating the binding energy of the different configurations including the possibility of formation of three-dimensional structures. Let us consider as an example the formation of nuclei on the (111) surface of a face-centered cubic (fcc) metal (Fig. 2.9). At $\Delta\mu = 3.25\psi$ the critical nucleus consists of two atoms and the smallest stable cluster consists of three atoms (Fig. 2.10). The work required to decay the nucleus is equal to the work to break a single first-neighbor bond, whereas in order to detach an atom from the smallest stable cluster we have to break simultaneously two first-neighbor bonds. This means that the latter will be much more stable than the nucleus and a higher temperature is required to decay the three-atom cluster. The attachment of additional atoms up to $i = 6$ does not change the stability of the respective clusters. Then at $\Delta\mu = 2.75\psi$ the nucleus consists of six atoms and the smallest stable cluster represents

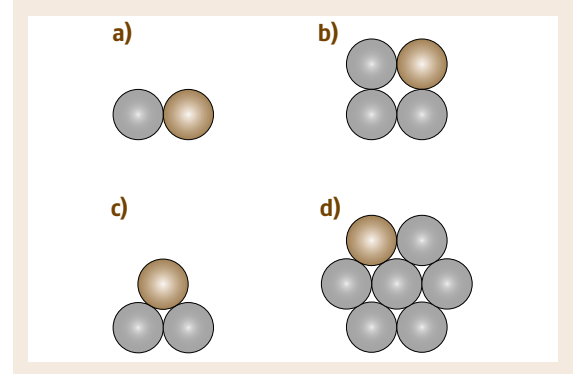


Fig. 2.9a–d Two-dimensional clusters on (001) and (111) surfaces of a crystal with a face-centered cubic lattice. The structure of the nuclei is given by the *gray circles*. The *black circles* denote the atoms that turn the critical nuclei into smallest stable clusters. **(a)** The nucleus consists of a single atom; the stable supercritical cluster is a dimer, which requires a single bond to be broken in order to decay. In **(b)** the nucleus consists of three atoms situated on the apexes of a rectangular triangle on (001) surface; the smallest stable cluster has a square shape. The decay of the latter requires the simultaneous breaking of two bonds. On (111) surface the nuclei consist of **(a)** one, **(c)** two, and **(d)** six atoms. The corresponding stable clusters consist of two, three, and seven atoms, respectively, which require breaking of one, two, and three bonds

a closed structure consisting of a complete ring of six atoms plus an atom in the middle. In order to detach an atom from the smallest stable cluster we have to break simultaneously three first-neighbor bonds. Obviously, such a cluster will be stable at much higher temperatures than a three-atom cluster.

Bearing in mind that every term in the sum of (2.38) is equal to $\exp(\Delta G(i)/k_B T)$ we study the behavior of the latter for small values of i (Fig. 2.10). It is seen that at extremely high supersaturations (low temperatures) $\Delta G(i)$ and $\exp(\Delta G(i)/k_B T)$ are represented by broken curves whereas at low supersaturations (large nuclei) the curve is smooth. Contrary to the classical case where the clusters in the vicinity of the critical size have values of $\exp(\Delta G(i)/k_B T)$ close to that of the nucleus, in the case of small clusters the contribution of $\exp(\Delta G(i^*)/k_B T)$ of the critical nucleus is the largest, all other terms in the sum of the denominator being negligible. Thus, instead of summing all the terms as in the classical theory, we can take the largest term and neglect all the others. For this purpose we write (2.38) in the form

$$J_0 = \omega_1^+ N_1 \left(1 + \frac{\omega_2^-}{\omega_2^+} + \frac{\omega_2^- \omega_3^-}{\omega_2^+ \omega_3^+} + \frac{\omega_2^- \omega_3^- \omega_4^-}{\omega_2^+ \omega_3^+ \omega_4^+} + \dots \right)^{-1} \quad (2.48)$$

and calculate the rate constants for the birth and death processes.

By analogy with the classical theory, where $\omega_i^+ \approx (P_i/a) D_s N_1$, P_i being the perimeter of the nucleus and P_i/a the number of the dangling bonds, in the atomistic approach [2.60]

$$\omega_i^+ = \alpha_i D_s N_1,$$

where α_i is the number of ways of attachment of an atom to a cluster of size i to produce a cluster of size $i+1$. Obviously, this parameter is proportional to the number of dangling bonds.

The decay constant reads

$$\omega_i^- = \beta_i \nu \exp\left(-\frac{E_i - E_{i-1} + E_{sd}}{k_B T}\right), \quad (2.49)$$

where E_i is the work to disintegrate a cluster of size i into single atoms, and $E_i - E_{i-1}$ is the work required to detach an atom from the cluster of size i . β_i is the number of ways of detachment of an atom from a cluster of size i . It is easy to show that there exists a one-to-one correspondence between the growth ($i \rightarrow i+1$) and decay ($i+1 \rightarrow i$) processes so that

$$\alpha_i = \beta_{i+1}.$$

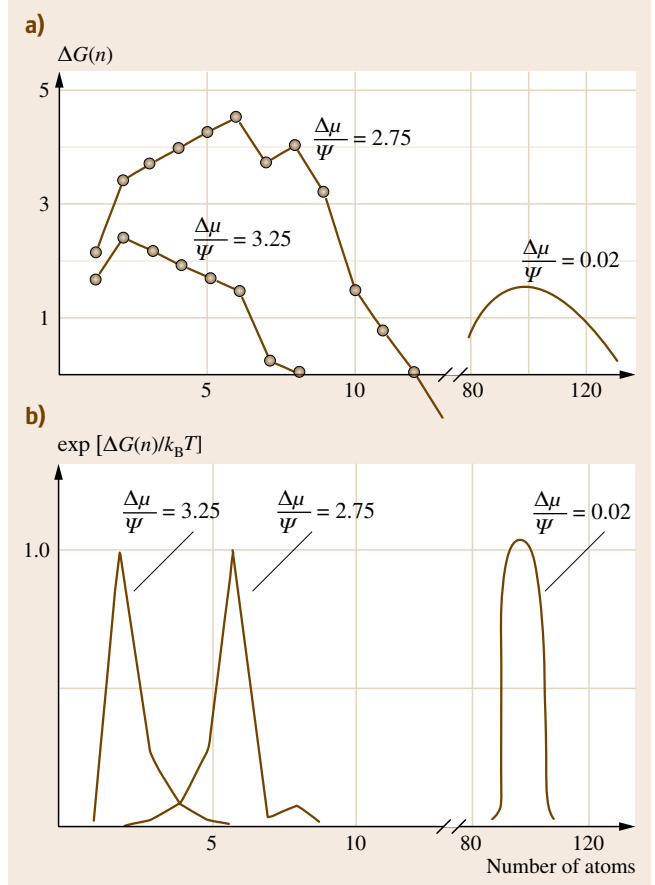


Fig. 2.10a,b Dependence of (a) the Gibbs free energy change $\Delta G(i)/\psi$ in units of the work ψ required to break a first-neighbor bond, and (b) $\exp(\Delta G(i)/k_B T)$ on the number of atoms i in the cluster at different values of the supersaturation. At small supersaturation ($\Delta\mu = 0.02\psi$) the cluster is large, the respective curves are smooth, and the summation can be replaced by integration. At very large supersaturations the curves are broken and the contribution of the critical nucleus is dominant

Recalling the expression for the diffusion coefficient $D_s = a^2 \nu \exp(-E_{sd}/k_B T)$ we can write (2.49) in the form

$$\omega_i^- = \beta_i D_s N_0 \exp\left(-\frac{E_i - E_{i-1}}{k_B T}\right),$$

where $N_0 \cong a^{-2}$.

The assumption that all terms in the denominator in (2.48) are smaller than unity means that $i^* = 1$

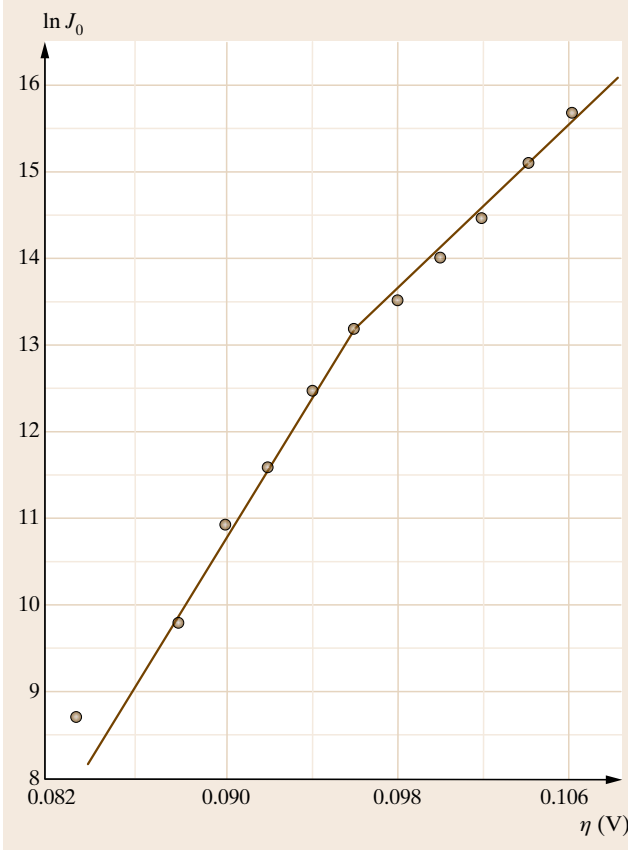


Fig. 2.11 Experimental data for the nucleation rate as a function of the overpotential η in the case of electrochemical nucleation of mercury on platinum single-crystal spheres (after [2.61]), in atomistic coordinates $\ln J_0 - \eta$, according to [2.62]. The number of atoms in the critical nucleus changes at about 0.096 V

($E_1 = 0$) and

$$J_0 = \omega_1^+ N_1 = \alpha_1 D_s N_1^2.$$

Assuming that the adatom concentration is determined by a dynamic adsorption–desorption equilibrium $N_1 = R\tau_s$ as before, for J_0 one obtains

$$J_0 = \alpha_1 \frac{R^2}{N_0 v} \exp\left(\frac{2E_{\text{des}} - E_{\text{sd}}}{k_B T}\right).$$

When the ratio ω_2^-/ω_2^+ is the largest term in the denominator of (2.48), $i^* = 2$ and

$$J_0 = \omega_1^+ N_1 \frac{\omega_2^+}{\omega_2^-} = \alpha_2 D_s^2 N_1^3 v^{-1} \exp\left(\frac{E_2 + E_{\text{sd}}}{k_B T}\right)$$

or

$$J_0 = \alpha_2 \frac{R^3}{N_0^2 v^2} \exp\left(\frac{E_2 + 3E_{\text{des}} - E_{\text{sd}}}{k_B T}\right).$$

In the general case

$$J_0 = \alpha^* R \left(\frac{R}{N_0 v}\right)^{i^*} \times \exp\left(\frac{E_{i^*} + (i^* + 1)E_{\text{des}} - E_{\text{sd}}}{k_B T}\right).$$

Very often the process of re-evaporation is negligible (complete condensation) and $N_1 \neq R\tau_s$. Then we can write J_0 in terms of the adatom concentration in the form

$$J_0 = \alpha^* D_s \frac{N_1^{i^*+1}}{N_0^{i^*-1}} \exp\left(\frac{E_{i^*}}{k_B T}\right), \quad (2.50)$$

which is very useful for solving various nucleation problems.

Whereas the attachment or detachment of atoms to and from a comparatively large liquid droplet or crystallite can be considered as a good approximation to a continuous process, this is impossible when the cluster consists of several atoms. In this case the general principles of the thermodynamics are violated, the best example of which is that the Thomson–Gibbs equation is not valid in its familiar form (2.10). The reason becomes obvious if we write it in terms of the number of atoms rather than the linear size of the crystallite

$$\frac{P_i}{P_\infty} = \exp\left(\frac{4\sigma v^{2/3}}{k_B T i^{1/3}}\right).$$

It is immediately seen that the vapor pressure in the left-hand side of the equation can be continuously varied whereas the right-hand side is a discrete function of the cluster size i . The latter means that to any particular size of the cluster corresponds a fixed value of the vapor pressure, but the opposite is not true; an integer number of atoms does not correspond to any arbitrary value of the vapor pressure. It follows that, contrary to the classical concept, a cluster with an integer number of atoms is stable in an interval of supersaturation (or vapor pressure) which becomes larger as the cluster size becomes smaller [2.63]. This interval is equal to $P_i - P_{i+1}$, where P_i is the fixed value of the vapor pressure corresponding to a cluster consisting of i atoms.

Substituting for ΔG^* from (2.26) with $i = i^*$ in (2.42) gives

$$J_0 = \omega^* \Gamma N_0 \exp\left(-\frac{\Phi}{k_B T}\right) \exp\left(i^* \frac{\Delta\mu}{k_B T}\right).$$

As the shape does not change at constant number of atoms the *surface* part Φ remains constant in the interval of stability of a given cluster size. Then the logarithm of the nucleation rate as a function of the supersaturation will represent a broken line when the supersaturation interval is sufficiently wide to cover the intervals of several cluster sizes. The slopes of the consecutive straight line parts will be equal to the respective number of atoms i^* of the critical nuclei. This is shown in Fig. 2.11, which represents experimental data for the nucleation rate in electrodeposition of mercury on platinum single-crystal spheres [2.61], interpreted in terms of the atomistic theory in [2.62] (see also [2.64]). The values $i^* = 6$ and 10 have been found from the slopes of the two parts of the plot. A clear evidence for a transition from

$i^* = 1$ to $i^* = 3$ has been reported by Müller et al. in the case of nucleation of Cu on Ni(001) [2.65]. Thus a single nucleus size is operative over a temperature (supersaturation) interval. The slopes of the consecutive intervals give a distinct series of consecutive numbers of atoms which depend on the crystallographic orientation of the substrate. Thus in the case of nucleation of (001) surface of fcc metals the numbers are one and three, whereas on (111) surface the numbers are one, two, and six. The corresponding smallest stable clusters ($i^* + 1 = 2, 3, 7$ on the fcc(111) surface) are often referred to as *magic* in the literature. The physics behind this magic is simple. In order to detach an atom from the corresponding smallest stable clusters we have to break simultaneously one, two or three bonds.

2.4 Saturation Nucleus Density

Measurements of the nucleus density as a function of time show that, after sufficiently long time, the nucleus density saturates; this means that the nucleation process ceases. Numerous factors can be responsible for this phenomenon. Preferred nucleation on defect sites, overlapping of zones with reduced supersaturation around growing islands, coalescence of neighboring islands, and growth of larger islands at the expense of smaller ones owing to the Thomson–Gibbs effect (Ostwald ripening) take place most frequently and are most studied [2.66].

Although the preparation of defectless single crystals is already a routine procedure, the complete absence of impurity particles, stacking faults, twin boundaries, emerging points of dislocations, etc. cannot be achieved. It is this presence of defects on the crystal surface which is one of the reasons for the observation of saturation of the nucleus density with time and this was the first to be studied. The defects represents sites on the crystal surface which stimulate nucleation by stronger wetting. Assume for simplicity that they have equal activity (wetting function). Nuclei can form on free active sites whose number is $N_d - N$ with a frequency J'_0 per site, N_d being the total number of active sites. Then the change with time t of the nucleus density reads [2.67]

$$\frac{dN}{dt} = J'_0(N_d - N).$$

Integration subject to the initial condition $N(0) = 0$ results in a simple exponential function

$$N(t) = N_d[1 - \exp(-J'_0 t)],$$

which tends with time to a saturation value equal to N_d . In the more realistic case of a certain activity distribution of the sites, increasing supersaturation will lead to inclusion of less-active sites in the process and increase of the saturation nucleus density [2.68].

Another reason for saturation of the nucleus density is the appearance of *locally undersaturated* zones around growing nuclei where the nucleation rate is reduced or even equal to zero owing to the consumption of the diffusing adatoms [2.69–71]. Sigsbee coined for these zones the term *nucleation exclusion zones* [2.72]. They are also known as *denuded* or *depleted* zones. Nuclei and in turn denuded zones around them are progressively formed and grow during film deposition. When the zones overlap and cover the whole substrate surface the process of nucleation is arrested and saturation of the nucleus density is reached. The radii of the nucleation exclusion zones are defined by the intersection of the gradient of the adatom concentration around the growing island and the critical adatom concentration (or supersaturation) for nucleation to occur (Fig. 2.12). A typical nucleation exclusion zone around a mercury droplet electrodeposited on a platinum single-crystal sphere is shown in Fig. 2.13 [2.73].

The problem of finding the nucleus density when the latter is limited by nucleation exclusion zones has been treated by many authors, such as Kolmogorov, Avrami, and Johnson and Mehl, and solutions for different cases have been found [2.74–78] (for a review see [2.47]). The simultaneous influence of both nucleation exclusion zones and active sites has also been

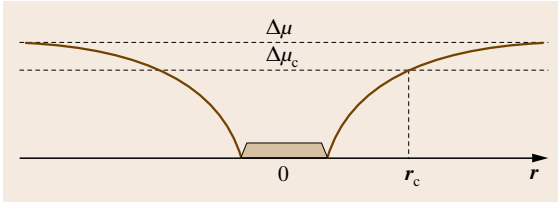


Fig. 2.12 The definition of nucleation exclusion zones. The radius of the latter is determined by the intersection of the gradient of the supersaturation and the critical supersaturation for noticeable nucleation to occur. Because of the very steep dependence of the nucleation rate on the supersaturation (Fig. 2.7) the nucleation rate inside the zone is assumed equal to zero

addressed [2.79,80]. The problem consists of finding the area $\Theta(t)$ uncovered by depleted zones and thus available for nucleation at a moment t . The number of nuclei is then given by

$$N = J_0 \int_0^t \Theta(\tau) d\tau.$$

The area $1 - \Theta(t)$ represents the sum of all nucleation exclusion zones accounting for the area where neighboring zones have overlapped. The latter is equal to the probability of finding an arbitrary point simultaneously in two or more nucleation exclusion zones [2.74]. Assuming that nuclei are formed on randomly distributed sites with a rate J_0 and that the zones grow with a velocity $v(t) = ck(t)$ the area $\Theta(t)$ is given by [2.74]

$$\Theta(t) = \exp \left(-J_0 \int_0^t S'(t') dt' \right),$$

where

$$S'(t', t) = \pi c^2 \left(\int_{t'}^t k(\tau - t') d\tau \right)^2$$

is the area of a nucleation exclusion zone at a moment t around a nucleus formed at a moment $t' < t$.

Assuming linear growth of the zones ($k(t) = 1$) gives for the nucleus density as a function of time

$$N(t) = J_0 \int_0^t \exp \left(-\frac{\pi}{3} J_0 c^2 t'^3 \right) dt'. \quad (2.51)$$

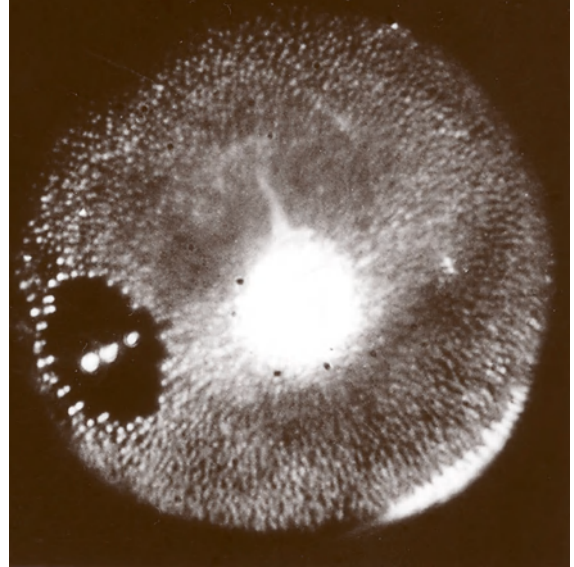


Fig. 2.13 Nucleation exclusion zone around a mercury droplet electrodeposited on a platinum single-crystal sphere. The droplet is practically invisible. Instead, three light reflections from the illuminating lamp are visible. The mercury droplet has been deposited by applying a short electric pulse followed by a lower overpotential in order to grow it to a predetermined size. Then a high electric pulse is applied to cover the whole surface with mercury with the exception of the area around the droplet (after [2.73])

The saturation nucleus density is obtained under the condition $t \rightarrow \infty$. Integrating (2.51) from zero to infinity gives

$$N_{\text{sat}} \cong 0.9 \left(\frac{J_0}{c} \right)^{2/3}.$$

Another approach was later developed, particularly for nucleation at surfaces, by using a system of kinetic rate equations. It was first introduced by Zinsmeister as a system of equations for the change with time of the concentrations of clusters dN_i/dt ($i = 1, 2, 3, \dots$) for each cluster size, beginning with that of single adatoms [2.81–84]. All birth and death processes were accounted for in dN_i/dt . In addition, the atom arrival rate and re-evaporation were taken into account in the equation of change of the monomers dN_1/dt . In order to solve quantitatively the above system of equations the attachment and detachment frequencies had to be determined. As a result a large amount of papers have been devoted to further elaborating the approach [2.85–92]. In the limit $i^* = 1$ (irreversible aggregation) the

detachment frequencies are equal to zero. The attachment frequencies (capture numbers) were considered by using different approximations, beginning from the mean-field approximation by assuming that the clusters are immersed and grow in a dilute adlayer with an average concentration that does not depend on the location of the clusters, to solutions of diffusion equation around the growing islands in terms of Bessel functions. The system was later greatly simplified by Venables et al. to a system of two equations which were sufficient to illustrate the essential physics [2.93].

We consider first the case of irreversible aggregation. The dimers are assumed to be stable (a third atom joins the dimer before the latter to decay) and immobile. The atoms arrive at the crystal surface, diffuse on it, and collide with each other to produce dimers. Atoms join the dimers and larger clusters upon striking without any obstacle of kinetic origin. This means that the growth of clusters is limited only by the surface diffusion. Coalescence of immobile clusters is ruled out. The detachment frequencies are equal to zero and the capture numbers are omitted for simplicity as they represent figures of the order of unity [2.93]. The system of equations is then reduced to

$$\frac{dN_1}{dt} = F - 2DN_1^2 - DN_1N_s, \quad (2.52a)$$

$$\frac{dN_s}{dt} = DN_1^2, \quad (2.52b)$$

where $F = R/N_0$ is the atom arrival rate in units of number of monolayers, $D = D_s/a^2 = v \exp(-E_{sd}/k_B T)$ is the diffusion (hopping) frequency, and N_s is the sum of all stable clusters

$$N_s = \sum_{i=2}^{\infty} N_i.$$

Single atoms arrive on the surface with frequency F and are consumed by the formation of dimers (the second term on the right-hand side of (2.52a)) and by incorporation into stable clusters (the third term on the right-hand side of (2.52a)). At the very beginning of deposition most of the adatoms are consumed by the formation of dimers. In a later stage of deposition the density of stable clusters increases and the arriving atoms preferentially join stable clusters rather than colliding with each other to produce dimers. Saturation (or very weak dependence on time) is reached and the consumption of atoms by formation of dimers $2DN_1^2$ is practically arrested and becomes negligible compared with the growth term DN_1N_s . A steady state is reached at this stage ($dN_1/dt = 0$) and $N_1 = F/DN_s$.

Substituting the latter into (2.52b) and carrying out the integration gives

$$N_s \propto \left(\frac{D}{F}\right)^{1/3}.$$

This result is easy to generalize for the case of *reversible aggregation*, assuming the critical nucleus consists of $i^* > 1$ atoms. Then one can write a system of two kinetic equations for the single adatoms and the sum of all clusters larger than i^* [2.93]

$$\frac{dN_1}{dt} = F - (i^* + 1)DN_1^{i^*+1} - DN_1N_s, \quad (2.53a)$$

$$\frac{dN_s}{dt} = \omega^* DN_1^{i^*+1}, \quad (2.53b)$$

where $\omega^* = \alpha^* \exp(E^*/k_B T)$ (see (2.50)).

Following the same procedure as above results in

$$N_s \propto \left(\frac{D}{F}\right)^{-\chi}, \quad (2.54)$$

where

$$\chi = \frac{i^*}{i^* + 2} \quad (2.55)$$

is the scaling exponent valid for the case of diffusion-limited nucleation and growth in the absence of any kinetic barrier inhibiting the attachment of atoms to the critical nucleus.

Later Kandel relaxed the condition for diffusion-limited regime of growth, assuming that a barrier exists which inhibits the attachment of atoms to any cluster including the critical nucleus [2.94]. Then the frequency ω^* for collision of atoms with the critical nucleus should contain the term $\exp(-E_b/k_B T)$, where E_b is the barrier concerned. He integrated (2.53b) taking for N_1 a value calculated by the solution of a diffusion equation from the radius R of the nucleus to half of the mean distance $L = 1/\sqrt{\pi N_s}$ between the nuclei and then averaged from R to L . As a result the average adatom concentration included two terms

$$N_1 = A \frac{F}{D} \frac{1}{N_s} + B \frac{F}{D} \frac{1 - \exp(-E_b/k_B T)}{\exp(-E_b/k_B T)} \frac{1}{\sqrt{N_s}},$$

where A and B are constants.

The first term is inversely proportional to N_s as before and does not include the cluster edge barrier E_b . The second term is inversely proportional to the square root of N_s and includes the barrier E_b . Obviously, when $E_b = 0$ the second term is equal to zero and the integration of (2.53b) naturally gives the scaling

exponent (2.55). In the other extreme of significant cluster edge barrier the second term dominates and the integration of (2.53b) gives the same power-law dependence (2.54) but with a scaling exponent

$$\chi = \frac{2i^*}{i^* + 3}, \quad (2.56)$$

which is valid for a kinetic regime of growth.

Equation (2.54) shows a simple power-law dependence of N_s on the ratio D/F of the frequency of surface diffusion to the frequency of atom arrival. While F represents the increase of atoms with time, D introduces the fluxes of disappearance of atoms due either to formation of nuclei or to the further growth of these nuclei. Physically this is the ratio of the flux of consumption of atoms on the crystal surface to the flux of their arrival. A constant ratio D/F means a constant adatom concentration or a constant supersaturation. The increase of D/F can be performed by either increasing the temperature or decreasing the atom arrival rate. The fact that the island density scales with D/F simply means that it depends on the supersaturation. The island density should have one and the same value at a given value of D/F , irrespective of whether it is a result of increasing (decreasing) of temperature or decreasing (increasing) of the atom arrival rate. Increasing D/F means decreasing the supersaturation, which in turn leads to an increase of the nucleus size i^* . Thus, at sufficiently low values of D/F of the order of 10^4 – 10^5 , i^* is expected to be equal to one, whereas at D/F of the order of 10^7 – 10^8 , i^* is expected to be equal to three on a square lattice [2.95]. Assuming a constant atom ar-

rival rate of the order of 10^{-2} monolayers per second, attempt frequency of the order of $1 \times 10^{13} \text{ s}^{-1}$, and a surface diffusion barrier of 0.75 eV an increase of D/F by four orders of magnitude is equivalent to a temperature increase of 200 K.

It should be noted that considering the size of the critical nucleus as an integer above which all clusters are stable is an approximation which strongly simplifies the mathematical treatment of the problem [2.95]. In fact there are never fully stable clusters. Atoms can always detach from them, particularly at high values of D/F or high temperatures. Things look better at low temperatures when bond breaking is strongly inhibited.

The scaling exponent (2.55) varies with i^* from $1/3$ to 1 , whereas (2.56) has values larger than unity already at $i^* > 2$. Thus, one can distinguish between diffusion and kinetic regimes of growth if χ is smaller or greater than unity. Examples of the scaling exponent (2.56) have been reported in surfactant-mediated epitaxial growth: homoepitaxy of Si on Sn-precovered surface of Si(111) [2.96], and of Ge on Pb-precovered surface of Si(111) [2.97]. In the former paper a value of $\chi = 1.76$ has been found from the plot of $\ln N_s$ versus $\ln F$. In the case of homoepitaxial growth of Si(111) under clean conditions a value of $\chi = 0.85$ has been obtained from the same plot of $\ln N$ versus $\ln F$ [2.98]. It could be concluded that the nucleation process takes place either in a diffusion regime with $i^* = 6$ or in a kinetic regime with $i^* = 2$. The latter seems more reasonable, bearing in mind the comparatively low temperature of growth ($< 700 \text{ K}$) and that Si is a very strongly bonded material.

2.5 Second-Layer Nucleation in Homoepitaxy

Growth of defectless low-index crystal surfaces takes place by formation and growth of 2-D nuclei with monolayer height. When the linear size L of the crystal face is small, in fact, smaller than $L_c = (v/J_0)^{1/3}$ [2.99], where v is the rate of lateral growth and J_0 is the nucleation rate, the growth proceeds by a periodic process of formation of a single nucleus followed by its growth to cover completely the crystal face. Thus, perfect layer-by-layer growth takes place.

When the surface area which is in contact with the supersaturated vapor is large, a large amount of nuclei are formed on the crystal surface on one and the same level. During the growth of the first layer nuclei, a certain size Λ can be reached at which second-layer nuclei

can form on top. The average time elapsed from the nucleation of the first-layer nucleus to the appearance of the second-layer nucleus is $\tau = \Lambda/v$. The latter should be inversely proportional to the frequency of nucleation on top of the first-layer nucleus $\bar{J}_0 = J_0 l^2$, or in other words, $\Lambda/v \cong 1/\bar{J}_0$. Thus we find that the critical size for second-layer nucleation is $\Lambda_c = (v/J_0)^{1/3}$ [2.99]. Obviously, when the surface coverage by first-layer nuclei is $\Lambda_c^2 N_s \ll 1$, where N_s is the saturation nucleus density, nuclei of the second, third, etc. layers can form before significant coalescence of the first-layer nuclei takes place. The crystal surface will be rough with many layers growing simultaneously. Multilayer growth takes place. The number N of simultaneously growing layers

depends on v and J_0 . If v is large or J_0 is small, Λ_c will be large and the surface roughness will be small, and vice versa.

In the above physical picture it is assumed that the probabilities of attachment of atoms to a step from both the upper and lower terrace are equal. In other words, it is accepted that the barrier which inhibits the incorporation of the atoms to the step and in turn leads to the kinetic regime discussed above is one and the same from both sides of the step. It was at the beginning of 1966 when Ehrlich and Hudda discovered that the above is completely incorrect [2.100]. They found with the help of field-ion microscopy (the first method which allowed the visualization of single atoms, invented by Erwin Müller in the early 1950s) [2.101], that an atom approaching the step from the upper terrace is repulsed by the step. The additional barrier E_{ES} , known now in the literature as the Ehrlich–Schwoebel barrier, was measured later by Wang and Tsong, who reported values of the order of 0.15–0.2 eV for Re, Ir, and W [2.102]. Much later Wang and Ehrlich reported that the steps attract the atoms approaching them from the lower terrace [2.103]. The same authors observed in the case of Ir(111) that the atoms, instead of being repelled from the descending step, were in fact attracted by it. Thus they found another, *push-out*, mechanism of step-down diffusion in which the second-level atom pushes out the edge atom and occupies the position of the latter rather than making a jump [2.104]. The atoms thus sample the potential profiles shown in Fig. 2.14a in the case of step-down jumping and in Fig. 2.14b in the case of the push-out mechanism.

The physics behind these effects are easy to understand if we compare interlayer diffusion with the same phenomenon on terraces. It is clear that an atom jumping down the step from the upper terrace will be less coordinated from the side of the lower terrace. On the contrary, an atom approaching the step from the lower terrace will be additionally attracted from the atoms belonging to the upper atomic plane. In the case of the push-out mechanism the atoms taking part in the process *respect a fundamental rule of chemistry – minimizing the breaking of bonds* [2.105].

Schwoebel immediately grasped the importance of the discovery of Ehrlich and Hudda and published later in the same year a paper dealing with the effect of the step-down diffusion barrier on the bunching of steps during evaporation [2.106, 107]. He went even further to foresee the push-out mechanism long before Ehrlich observed it experimentally [2.106].

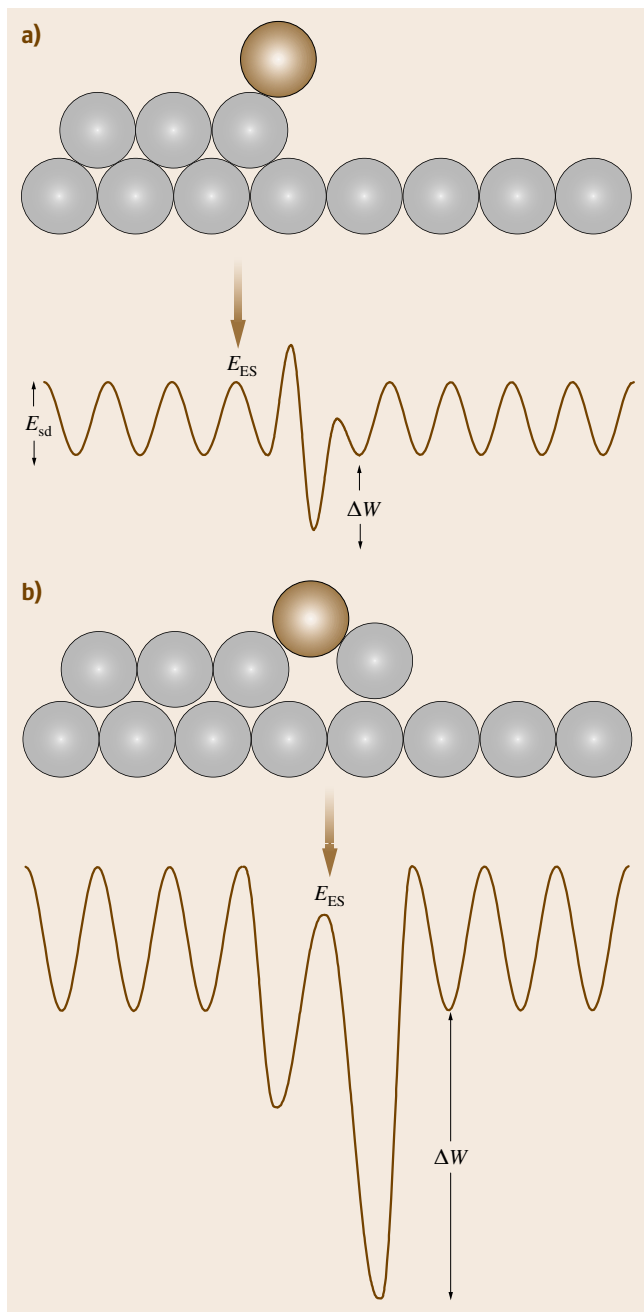


Fig. 2.14a,b Schematic potential diagrams for atoms moving toward ascending and descending steps. **(a)** Traditional view of the Ehrlich–Schwoebel barrier for atoms joining a descending step by a jump and short-range attractive behavior of the ascending step, **(b)** view of the potential sampled by an atom joining a descending step by a push-out mechanism

We consider in this chapter only the traditional Ehrlich–Schwoebel effect of repulsion of atoms from descending steps. The push-out mechanism together with an additional barrier from the lower terrace owing to the presence of surfactant atoms which have decorated the step (the reverse Ehrlich–Schwoebel effect) is considered in [2.108]. The additional ES barrier inhibits the flow of atoms from upper terraces downwards, thus enhancing the nucleation rate on upper terraces. This leads to formation of mounds consisting of concentric two-dimensional islands, one on top of the other, and thus to strong roughening of the surface, a phenomenon which was first predicted by Villain [2.109]. We will consider the same problem as above, defining the critical island size Δ for second-layer nucleation accounting for the ES barrier.

We define Δ in the same way as above but writing it in integral form

$$\int_0^{\Delta} \frac{\bar{J}_0(\rho)}{v(\rho)} d\rho = 1, \quad (2.57)$$

where

$$v(\rho) = \frac{d\rho}{dt} = \frac{R}{2\pi\rho N_s N_0} \quad (2.58)$$

is the rate of growth of the first-layer islands in the case of complete condensation before nuclei on their upper surfaces are formed.

The nucleation frequency \bar{J}_0 is defined as before as

$$\bar{J}_0 = 2\pi \int_0^{\rho} J_0(r, \rho) r dr, \quad (2.59)$$

where J_0 is the nucleation rate as given by (2.50). It is a function of the island's radius ρ through the adatom concentration on the upper surface of the island N_1 . The latter can be determined by solving the diffusion equation (in polar coordinates) in the absence of re-evaporation

$$\frac{d^2 N_1}{dr^2} + \frac{1}{r} \frac{dN_1}{dr} + \frac{R}{D_s} = 0. \quad (2.60)$$

The solution reads

$$N_1 = A - \frac{R}{4D_s} r^2, \quad (2.61)$$

where the integration constant should be determined by the boundary condition

$$j = -D_s \left(\frac{dN_1(r)}{dr} \right)_{r=\rho}, \quad (2.62)$$

where $j = j_+ - j_-$ is the net flux of atoms to the descending step which encloses the island, j_+ and j_- being the attachment and detachment fluxes.

Bearing in mind Fig. 2.14 j_+ and j_- read

$$j_+ = av N_{st} \exp\left(-\frac{E_{sd} + E_{ES}}{k_B T}\right),$$

$$j_- = av N_k \exp\left(-\frac{\Delta W + E_{sd} + E_{ES}}{k_B T}\right),$$

where N_{st} is the adatom concentration in the vicinity of the step, v is the attempt frequency, N_k is the concentration of atoms in a position (presumably kink position) for easy detachment from the step, and $\Delta W = \varphi_{1/2} - E_{des}$ is the energy to transfer an atom from a kink position onto the terrace.

The total flux j then reads

$$j = av(N_{st} - N_1^e) \exp\left(-\frac{E_{sd}}{k_B T}\right) \frac{1}{S}, \quad (2.63)$$

where $S = \exp(E_{ES}/k_B T)$, and $N_1^e = N_k \exp(-\Delta W/k_B T)$ is the equilibrium adatom concentration (see (2.12)).

Combining (2.62) and (2.63) and bearing in mind that $N_{st} = A - R\rho^2/4D_s$ yields [2.110]

$$N_1 = N_1^e + \frac{R}{4D_s} (\rho^2 + 2\rho a S - r^2). \quad (2.64)$$

As seen in the case of negligible ES barrier ($2aS/\rho \ll 1$), (2.64) turns into

$$N_1 = N_1^e + \frac{R}{4D_s} (\rho^2 - r^2). \quad (2.65)$$

The adatom concentration on top of the island surface has a profile of a dome with a maximum above the island's center ($r = 0$) and reaches its equilibrium value N_1^e near the island's edge ($r = \rho$). It follows that second-layer nucleation is favored around the middle of the island.

In the other extreme ($2aS/\rho \gg 1$) we neglect the difference $\rho^2 - r^2$ and obtain

$$N_1 \approx \frac{R}{2D_s} \rho a S.$$

This means that the adatom population on top of an island with repelling boundaries is uniformly distributed all over the surface of the island and a nucleation event can occur with equal probability at any point of it.

We substitute (2.64) into (2.50) and the latter into (2.59) to obtain after integration [2.110]

$$\bar{J}_0 = A[(\rho^2 + 2\rho a S)^{i^*+2} - (2\rho a S)^{i^*+2}], \quad (2.66)$$

where

$$A = \frac{\pi\alpha^*}{(i^*+2)} D_s N_0^2 \exp\left(\frac{E^*}{k_B T}\right) \left(\frac{R}{4D_s N_0}\right)^{i^*+1}.$$

As seen, a negligible ES barrier ($2aS \ll \rho$) turns (2.66) into

$$\bar{J}_0 = A \rho_1^{2(i^*+2)}. \quad (2.67)$$

The condition for layer-by-layer growth (formation of one nucleus for the time $T = R/N_0$ of deposition of a complete monolayer)

$$N = \int_0^T \bar{J}_0(\rho_1) dt = 1 \quad (2.68)$$

gives for the number of the growth pyramids the expression [2.111] (for a review see [2.21])

$$N_s = \frac{1}{4\pi} C^* N_0 \left(\frac{D}{F}\right)^{-\chi} \exp\left(\frac{E_{i^*}}{(i^*+2)k_B T}\right), \quad (2.69)$$

where C^* is a very weak function of i^* of the order of unity. The above equation is in fact (2.54) with the familiar scaling exponent (2.55).

In the other extreme ($2aS \gg \rho$) we take the last two terms of the expansion of the sum in (2.66) and the latter turns into

$$\bar{J}_0 = B \rho^{i^*+3}, \quad (2.70)$$

where

$$B = \pi\alpha^* D_s N_0^2 \exp\left(\frac{E^*}{k_B T}\right) \left(\frac{RaS}{2D_s N_0}\right)^{i^*+1}.$$

Following the above procedure gives for this case [2.112]

$$N_s = \frac{1}{\pi} C^* N_0 \left(\frac{D}{F}\right)^{-\chi} \exp\left(\frac{2[E_{i^*} + (i^*+1)E_b]}{(i^*+3)k_B T}\right), \quad (2.71)$$

where C^* is another very weak function of i^* of the order of unity. We again obtained (2.54) but the scaling exponent is given by (2.56).

We can now calculate the critical radii of the islands for second-layer nucleation in both cases of low (subscript “0”) and high (subscript “ES”) Ehrlich–Schwoebel barrier. Substituting (2.67), (2.70) and (2.58) into (2.57) gives after integration [2.110]

$$\Lambda_0 = aC_0 \left(\frac{D}{F}\right)^{i^*/2(i^*+3)}, \quad (2.72)$$

with

$$C_0 \cong \left(\frac{N_0 e^{-E^*/k_B T}}{\alpha^* N_s}\right)^{1/2(i^*+3)}, \quad (2.73)$$

for the case of negligible ES barrier, and

$$\Lambda_{ES} = aC_{ES} \left(\frac{D}{F}\right)^{i^*/(i^*+5)} S^{-(i^*+1)/(i^*+5)}, \quad (2.74)$$

with

$$C_{ES} \cong \left(\frac{N_0 e^{-E^*/k_B T}}{\alpha^* N_s}\right)^{1/(i^*+5)}, \quad (2.75)$$

for the other limiting case of a significant ES barrier.

Let us compare N_s and Λ in both cases. For this purpose we take typical values for the quantities involved: $N_0 = 1 \times 10^{15} \text{ cm}^{-2}$, $R = 1 \times 10^{13} \text{ cm}^{-2} \text{ s}^{-1}$, $F = R/N_0 = 1 \times 10^{-2} \text{ s}^{-1}$, $E_{sd} = 0.4 \text{ eV}$, $E_{ES} = 0.2 \text{ eV}$, $T = 400 \text{ K}$, $i^* = 1$, and $E^* = 0$. Then, in the case of $E_{ES} = 0$, $N_s \approx 6 \times 10^{10} \text{ cm}^{-2}$ and $\Lambda_0 \approx 180 \text{ \AA}$. In the other extreme, $N_s \approx 1 \times 10^{12} \text{ cm}^{-2}$ and $\Lambda_{ES} \approx 50 \text{ \AA}$ is 3 times smaller. We conclude that with a significant ES barrier a larger density of islands is formed which have much smaller critical size for second-layer nucleation. Mounding rather than planar growth is expected.

It is of interest to check the above theory. For this purpose we calculate the number n of atoms on the surface of the base island when its radius has just reached the critical value Λ . We integrate the adatom concentration (2.64) on the island's surface

$$n = 2\pi \int_0^\Lambda n_s(r, \Lambda) r dr$$

and find

$$n = \frac{\pi F}{8D} N_0^2 \Lambda^4 \left(1 + \frac{4aS}{\Lambda}\right).$$

We will consider as examples two surfaces of fcc crystals: (100) and (111). The reason is that the (100) surfaces are characterized by a large terrace diffusion barrier and a small step-edge barrier. This is the reason why, during growth, (100) surfaces demonstrate as a rule oscillations of the intensity of the specular beam, which are an indication of layer-by-layer growth. On the contrary, the smoother (111) surfaces are characterized with small intralayer diffusion barriers and large interlayer barriers. The result is a roughening of the crystal surface from the very beginning of deposition and a monotonous decrease of the intensity of the specular beam [2.112].

We consider first the case of Cu(001) [2.113]. The authors have measured the step kinetics of a pyramid consisting of 2-D islands, one on top of the other, and determined the critical radius $\Lambda \approx 3 \times 10^{-5}$ cm of the uppermost island at which the next layer nucleus is formed ($T = 400$ K, $F = 0.0075$ s $^{-1}$, $E_{sd} = 0.4$ eV, $a = 2.55 \times 10^{-8}$ cm, $N_0 = 1.53 \times 10^{15}$ cm $^{-2}$). Comparison with the theory produced the value $E_{ES} = 0.125$ eV. Then, by using the above formula we find for the number of atoms which gives rise to the new monolayer nucleus the value $n = 70$. Note that $aS/\Lambda \approx 0.03$, which confirms the above statement that the kinetics at fcc(001) surfaces is not dominated by the interlayer diffusion and the profile of the adatom concentration looks like a dome.

We consider next the case of Pt(111) [2.114]. Bott, Hohage, and Comsa observed by scanning tunneling microscopy (STM) the appearance of second-layer nuclei at surface coverages of 0.3 (425 K, $N_s = 3.37 \times 10^{10}$ cm $^{-2}$) and 0.8 (628 K, $N_s = 3.5 \times 10^9$ cm $^{-2}$) ($R = 5 \times 10^{12}$ cm $^{-2}$ s $^{-1}$). The activation energy for terrace diffusion is well known to be 0.25–0.26 eV [2.115, 116]. Values for E_{ES} varying from 0.12 eV (see [2.117]) to 0.44 eV have been estimated [2.118]. The average number of atoms on the island's surface as computed with the help of the above equation for n turned out to be of the order of 1×10^{-2} , i. e., much less than unity, which is unphysical. In fact n becomes greater than unity when $E_{ES} > 0.5$ eV, which means that the atoms at the island's periphery must overcome a total barrier of about 0.75 eV, which is too large to be believed. In contrast to the previous case, however, $aS/\Lambda \gg 1$, which means that it is interlayer diffusion that dominates the kinetics, and the adatom population on top of the island is spatially uniform.

Whereas the Cu(001) case is physically reasonable, the (111) case looks puzzling. In order to solve the problem of the high ES barrier Krug et al. accounted for the probabilistic nature of the main processes involved [2.117]. The authors have taken into account the fact that the atoms arrive randomly on the island's surface with an area $\pi\rho^2$ but not at equal intervals $\Delta t = 1/\pi\rho^2 R$ as is implicitly assumed in the model described above. Second, the time τ that the atoms reside on the island before rolling over and joining the descending edge is also a random quantity. The latter is directly proportional to the island's periphery $2\pi\rho$ and inversely proportional to the rate of step-down diffusion $\omega = av \exp[-(E_{sd} + E_{ES})/k_B T]$, i. e., $\tau \approx 2\pi\rho/\omega = 2\pi\rho aS/D_s$. We introduce further the time $\tau_{tr} = \pi\rho^2/D_s$ required for an atom to visit all sites of

the island. The condition $\tau/\tau_{tr} \gg 1$ is equivalent to $2aS/\rho \gg 1$, which is in fact the condition for nucleation kinetics dominated by step-down diffusion (see (2.70)). Assuming $i^* = 1$ (the dimers are stable and immobile) it is concluded that, as soon as two atoms are present simultaneously on the island's surface, their encounter is inevitable. Thus the necessary and sufficient condition for the atoms to meet each other and give rise to a stable cluster is $\tau_{tr} \ll \tau$. Then the probability of nucleation p_{nuc} is equal to the probability p_2 for two adatoms to be present simultaneously on the island. p_2 is determined by the condition that the time of arrival t_2 of the second atom be shorter than the time t_1 of departure of the first atom. Assuming that t_1 and t_2 are randomly distributed around the average values τ and Δt , respectively, one obtains after integration

$$p_{nuc} = \frac{1}{\tau \Delta t} \int_0^\infty dt_1 e^{-t_1/\tau} \int_0^{t_1} dt_2 e^{-t_2/\Delta t} = \frac{\tau}{\tau + \Delta t}.$$

Two limiting cases are possible. The case $\tau \gg \Delta t$ and $p_{nuc} \approx 1$ is trivial; it means that the ES barrier is infinitely high and there will always be at least one atom on top of the island. The physically interesting case is when $\Delta t \gg \tau$ and $p_{nuc} = \tau/\Delta t$. Then the nucleation frequency $\bar{J}_0 = \pi\rho^2 R p_{nuc}$ reads

$$\bar{J}_0 \propto \frac{aR^2\rho^5 S}{D_s}. \quad (2.76)$$

This equation should be compared with (2.70). With $i^* = 1$ the latter gives

$$\bar{J}_0 \propto \frac{a^2 R^2 \rho^4 S^2}{D_s}. \quad (2.77)$$

Comparing both formulae shows that the mean-field expression (2.77) is $aS/\rho \gg 1$ times larger than the probabilistic one (2.76). The explanation is simple. Equation (2.77) is based on the implicit assumption that on top of the island there is a time-averaged number (smaller than unity but constant) of atoms all the time. As shown above this is indicative of a large ES barrier whose mathematical expression is just $aS/\rho \gg 1$. In fact the island's surface is empty most of the time and is sometimes populated by a single atom, and it very rarely happens that during this time a second atom arrives. Once two atoms are simultaneously present on the island a nucleus is formed with a probability close to unity. That is why the authors coined for this model the term *the lonely adatom model*. The problem of second-layer nucleation has been intensively studied [2.119, 120]. It has been found that the mean-field

approach is applicable for critical nuclei consisting of more than three atoms. If this is not the case ($i^* = 1, 2$),

the random character of the processes involved becomes significant.

2.6 Mechanism of Clustering in Heteroepitaxy

Fig. 2.15 Plot of the binding energy per atom in units of the energy of a single first-neighbor bond ψ of monolayer, bilayer, and trilayer islands with simple cubic lattice as a function of the total number of atoms. The wetting parameter $\phi = 0.1$ (after [2.35]) ►

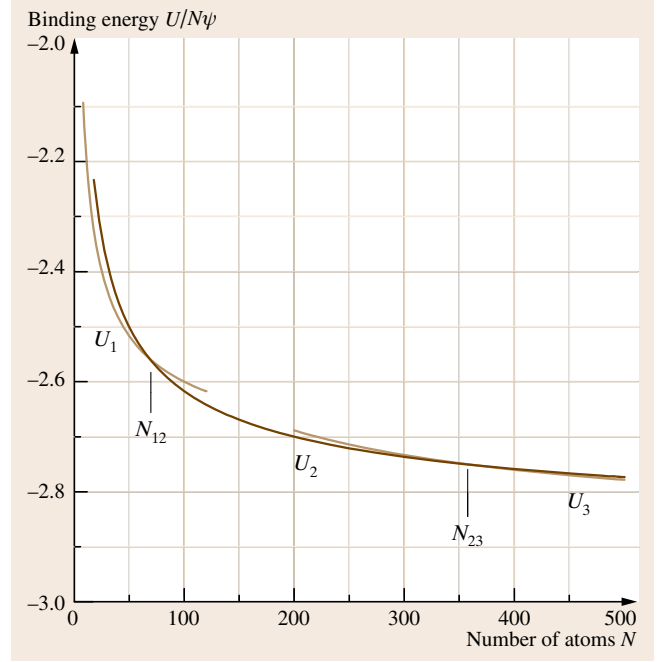
We consider first the growth of a heteroepitaxial thin film by the mechanism of Volmer–Weber. As the wetting is incomplete the thermodynamics requires 3-D islanding directly on top of the substrate. We study the stability of islands with different thickness beginning from one monolayer against their volume (or total number of atoms). In other words we study the behavior of the binding energy $-U_i$ in (2.27), which is equal to the surface energy term Φ up to a constant $i\phi_{1/2}$ [2.35].

We study for simplicity a Kossel crystal with (100) substrate orientation. The same result is obtained by using any other lattice and substrate orientation [2.35]. As a first approximation we omit the effect of the lattice misfit. As discussed above the strain energy makes as a rule a minor contribution with the same sign to the difference of the cohesive ψ and adhesive ψ' energies. As another approximation we consider our crystal in a *continuous* way, assuming that the shape remains a complete square irrespective of the number of atoms in it. We calculate first the binding energies of monolayer, bilayer, and trilayer islands with a square shape of the base and consisting of a total of N atoms. Restricting ourselves to nearest-neighbor bonds the energies read

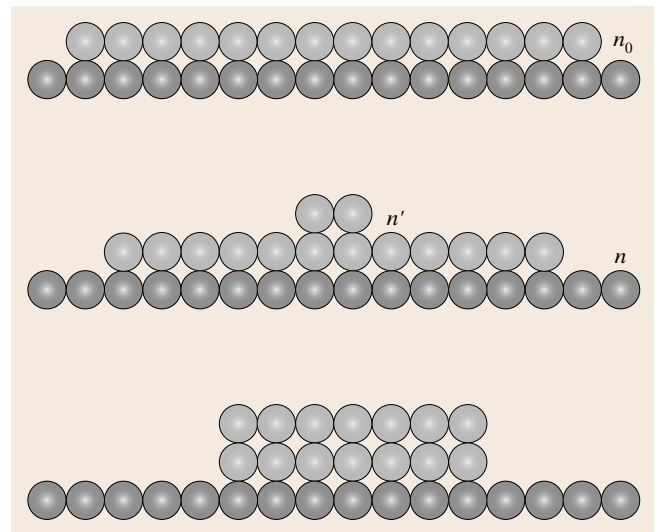
$$\begin{aligned}\frac{U_1}{N\psi} &= -3 + \phi + \frac{2}{\sqrt{N}}, \\ \frac{U_2}{N\psi} &= -3 + \frac{\phi}{2} + \frac{2\sqrt{2}}{\sqrt{N}}, \\ \frac{U_3}{N\psi} &= -3 + \frac{\phi}{3} + \frac{2\sqrt{3}}{\sqrt{N}},\end{aligned}$$

where ϕ is the wetting function (2.18).

Fig. 2.16 Schematic process for the evaluation of the activation energy of the mono–bilayer transformation. The initial state is a square monolayer island with n_0 atoms in the edge. The intermediate state is a monolayer island with n atoms in the edge plus a second level island with n' atoms in the edge so that $n^2 + n'^2 = n_0^2$. The final state is a complete bilayer island ►



We plot the above energies as a function of N and find that monolayer-high islands are stable against



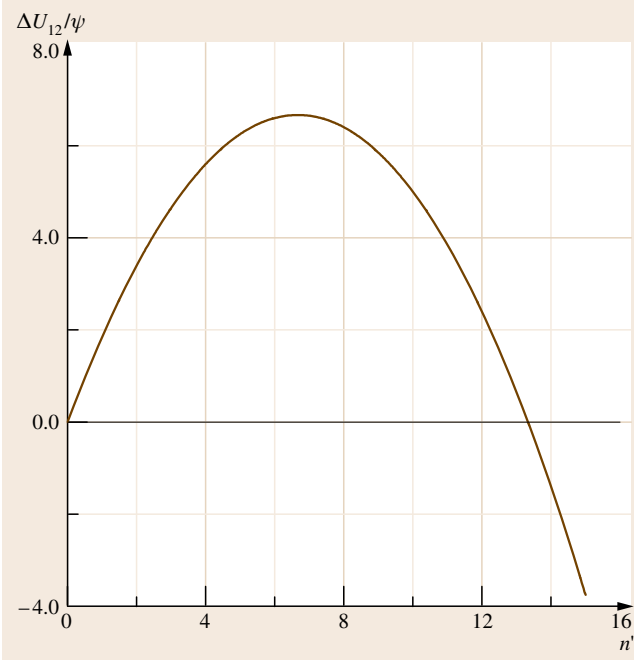


Fig. 2.17 The energy change which accompanies the mono–bilayer transformation in Volmer–Weber growth (after [2.35])

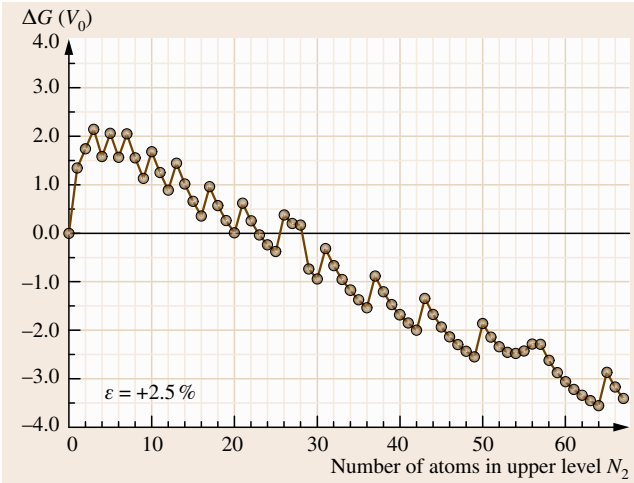


Fig. 2.18 Mono–bilayer transformation curve in Stranski–Krastanov growth representing the energy change in units of bond energy as a function of the number of atoms in the upper level. The lattice misfit is 2.5% (after [2.122])

bilayer islands up to a critical size denoted by N_{12} (Fig. 2.15). The bilayer islands are stable from this size up to a second critical size N_{23} , beyond which tri-

layer islands become stable, etc. These critical sizes are inversely proportional to the square of the wetting function and go to infinity when $\phi \rightarrow 0$. The latter means that, at $\phi = 0$, 3-D islands will not be able to form. Instead, layer-by-layer growth is expected according to the thermodynamics at complete wetting. At finite values of ϕ a mono–bilayer transformation should take place when $N > N_{12}$. A bi–trilayer transformation is expected to occur when $N > N_{23}$, etc. It is very important to note that *monolayer-high islands appear as necessary precursors for 3-D islands* [2.121].

We study further the mechanism of transformation of monolayer to bilayer islands, assuming the following imaginary process illustrated in Fig. 2.16 [2.35]. Atoms detach from the edges of the monolayer islands, which are larger than N_{12} and thus unstable against bilayer islands, diffuse on top of them, aggregate, and give rise to second-layer nuclei. The latter grow further at the expense of the atoms detached from the edges of the lower islands. The process continues up to the moment when the upper island completely covers the lower-level island. The energy change associated with the process of transformation at a particular stage is given by the difference between the energy of the incomplete bilayer island and that of the initial monolayer island

$$\frac{\Delta U_{12}(n')}{\psi} = -n^2\phi - \frac{n'^2}{n_0} + 2n', \quad (2.78)$$

where the approximation $n_0 + n = 2n_0$ is used in the beginning of the transformation, n_0 , n , and n' being the numbers of atoms in the edge of the initial monolayer island, in the lower edge of the incomplete bilayer island, and in the edge of the second-layer island, respectively (Fig. 2.16).

Equation (2.78) is plotted in Fig. 2.17. As seen, it displays a maximum at some critical size

$$n'^* = \frac{n_0}{1 + n_0\phi}. \quad (2.79)$$

The height of the maximum is given by

$$\Delta U_{12}^* = \frac{n_0}{1 + n_0\phi} \psi = n'^* \psi, \quad (2.80)$$

as should be expected by the classical consideration of the nucleation process (2.36). It follows that the mono–bilayer transformation is a nucleation process.

The same physics functions in the clustering during the Stranski–Krastanov growth of thin films beyond the wetting layer [2.122]. The Stranski–Krastanov growth represents a growth of A on strained A. The strained wetting layer of A is formed on the surface of another

crystal B with different lattice parameter. The 3-D islands which form on the wetting layer are fully strained in the middle but relaxed at the side-walls and edges. The atoms near the edges of the base are displaced from the positions they should occupy if the islands were completely strained to fit the wetting layer. As a result the adhesion of the atoms near the edges of the base to the substrate (the wetting layer) is weaker compared with the atoms in the middle of the island's base. Therefore, the average wetting is incomplete, $0 < \phi < 1$, which is the thermodynamic condition for clustering. The detachment of atoms from the edges and the formation of a cluster in the second level beyond some critical size is energetically favorable. The numerically calculated energy accompanying this process is shown in Fig. 2.18 [2.122]. The atoms interact through a pair potential of Morse type whose anharmonicity can be varied by adjusting two constants that govern separately the repulsive and attractive branches, respectively [2.123, 124]. The 3-D crystallites have fcc lattice and (100) surface orientation, thus possessing the shape of a truncated square pyramid. As seen, a critical nucleus consisting of three atoms is formed, beyond which the energy goes down as in an ordinary nucleation process. The misfit dependence of the critical size N_{12} , the nucleus size, and the work for nucleus formation are shown in Fig. 2.19 [2.122]. The nucleation character of the transformation is clearly observed. The energy barrier and the number of atoms in the cluster with highest energy increase steeply with decreasing lattice misfit, which in this case plays the role of the

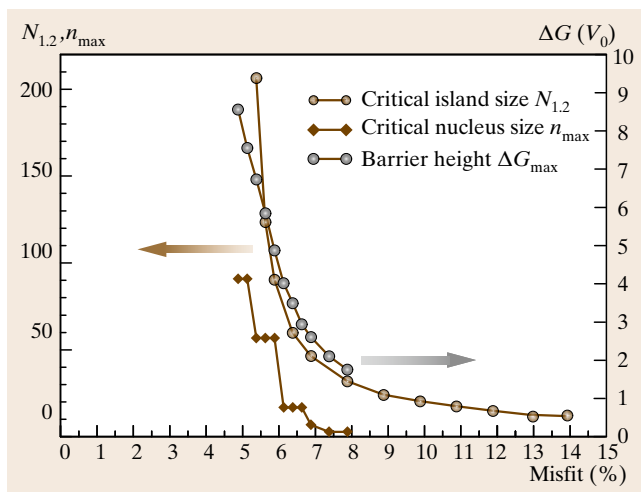


Fig. 2.19 Misfit dependence of the critical size N_{12} , the critical nucleus size (both expressed in number of atoms), and the nucleation barrier (in units of ψ) for compressed overlayers. The initial size of the monolayer island is 20×20 atoms (after [2.122])

supersaturation. The number N_{12} also goes to infinity, illustrating the critical behavior of the transition from monolayer (2-D) to bilayer (3-D) islands.

It should be pointed out that the mono-bilayer transformation of islands under tensile stress does not display a nucleation behavior, particularly at lower absolute values of the misfit. However, this problem is outside the scope of the present review and will not be discussed.

2.7 Effect of Surfactants on Nucleation

It was found long ago that very often epitaxial films grow in a layer-by-layer mode and show better quality when the vacuum is poor [2.125, 126]. Much later *Steigerwald* et al. found that intentionally adsorbed oxygen on Cu(001) suppresses agglomeration and interdiffusion upon deposition of Fe [2.127]. The significance of these observations was immediately grasped and the very next year *Copel* et al. reported that preadsorption of As drastically alters the mode of growth of Ge on Si(001) and of Si on Ge(001) by suppressing the clustering in the Stranski–Krastanov and Volmer–Weber modes of growth, respectively [2.128]. They suggested an interpretation of their observations in terms of the change of the wetting of the substrate by the overlayer due to the effect of the third element and

used the term *surfactant* to stress the thermodynamic nature of the phenomenon. Intensive studies and heated debate concerning the effect of the third elements on the thermodynamics and kinetics of the processes followed. It was shown that the surfactants change not only the thermodynamics but also the kinetics of the processes involved [2.5, 129]. Nevertheless, the term surfactant was widely accepted in the literature. We explore here the effect of surfactants on nucleation in the simpler case of homoepitaxy. Accounting for the unlike substrate requires only the inclusion of a term containing the wetting function (2.19) into the work of nucleus formation.

We calculate first the work for nucleus formation by using the following imaginary process

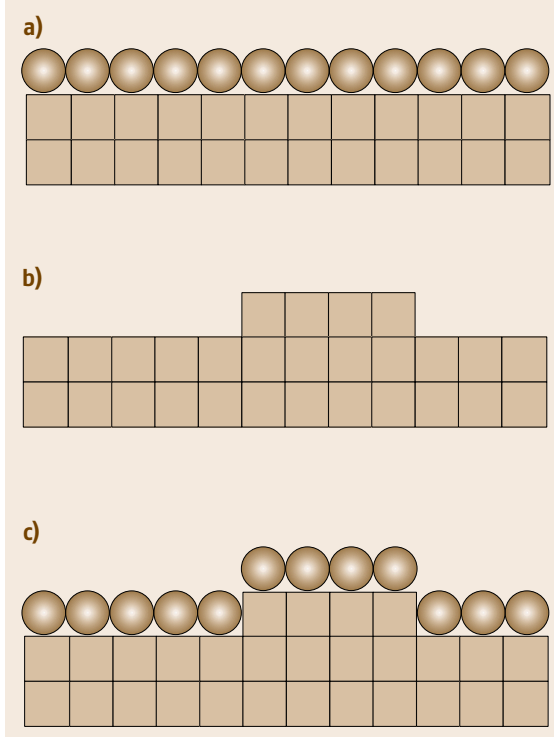


Fig. 2.20a–c Calculation of the Gibbs free energy change for nucleus formation on a surfactant-precovered surface. **(a)** The initial surface covered with a complete monolayer of surfactant atoms denoted by *filled circles*; **(b)** the surfactant layer is evaporated and a cluster consisting of i atoms is created; **(c)** the surfactant layer is condensed back and a cluster consisting of i surfactant atoms is formed on top (after [2.130])

(Fig. 2.20) [2.130]. In order to illustrate the essential physics for simplicity we first make use of the classical nucleation theory. The initial state is a surface of the crystal (C) covered by a complete monolayer of surfactant (S) atoms. We first evaporate reversibly and isothermally all S atoms. Then on the clean surface we produce a cluster consisting of i C atoms. Assuming a square shape with edge length l the work for cluster formation in absence of a surfactant reads

$$\Delta G_0 = -i\Delta\mu + 4l\kappa_c,$$

where κ_c is the specific edge energy.

We condense back the S atoms. We gain energy $-4ls\kappa_c$ due to saturation of the dangling bonds at the cluster periphery by the S atoms, and spend energy $4l\kappa_s$ to create the new step which surrounds the cluster con-

sisting of S atoms. The work for nucleus formation then reads [2.130]

$$\Delta G_s = \Delta G_0 - 4ls\kappa_c + 4l\kappa_s, \quad (2.81)$$

where κ_s is the specific edge energy of the S cluster and the parameter

$$s = 1 - \frac{\omega}{\omega_0}$$

accounts for the saturation of the dangling bonds by S atoms. It is a measure of the *surfactant efficiency*, as the quantities

$$\omega = \frac{1}{2}(\psi_{cc} + \psi_{ss}) - \psi_{sc} \quad (2.82)$$

and

$$\omega_0 = \frac{1}{2}\psi_{cc}$$

are the energies of the S-saturated and unsaturated dangling bonds, respectively. The subscripts “cc,” “ss,” and “sc” denote the bond energies C–C, S–S, and S–C, respectively.

Looking at (2.82) it becomes clear that it in fact represents the energetic parameter that determines the enthalpy of mixing of the two species C and S. It must be positive in order to allow the segregation of the surfactant. In the absence of a surfactant $\psi_{ss} = \psi_{sc} = 0$, $\omega = \omega_0$, and $s = 0$. In the other extreme, $\psi_{ss} + \psi_{cc} = 2\psi_{sc}$ and $s = 1$. Thus the parameter s varies from 0 at complete inefficiency to 1 at complete efficiency. (In general the parameter s can be greater than unity, which means $\omega < 0$. However, this means an alloying of the surfactant with the growing crystal, which will have deleterious consequences for the quality of the overlayer and should be avoided.)

It follows from (2.81) that, in the case of surfactant-mediated growth, the Gibbs free energy for nucleus formation contains two more terms that have opposite signs and thus compete with each other. The s -containing term accounts for the decrease of the edge energy of the cluster owing to the saturation of the dangling bonds by the surfactant atoms. The energy $4l\kappa_s$ of the dangling bonds of the periphery of the cluster, consisting of S atoms, which is unavoidably formed on top of the 2-D nucleus due to the segregation of the surfactant, increases the work of cluster formation.

Finding a solution for a small number of atoms in the critical nucleus in the atomistic extreme is straightforward. We make use of (2.27)

$$\Phi = i\phi_{1/2} - U_i$$

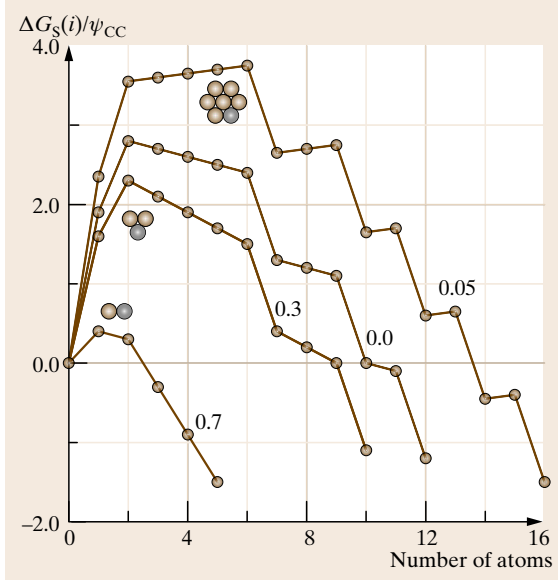


Fig. 2.21 Change of the Gibbs free energy for cluster formation relative to the work needed to disjoin two C atoms versus the number of atoms on the (111) surface of a fcc crystal. The value of the surfactant efficiency s is denoted by figures on each curve. The structure of the nucleus is given by the filled circles. The gray circles denote the atoms that turn the critical nuclei into smallest stable clusters (after [2.130])

for the edge energy of both clusters instead of using the capillary term for the edge energy κ .

The binding energy U_i can be divided into lateral energy E_i and desorption energy E_{des} (assuming additivity of the bond energies)

$$U_i = E_i + iE_{\text{des}},$$

and for Φ one obtains

$$\Phi = i\Delta W - E_i,$$

where $\Delta W = \varphi_{1/2} - E_{\text{des}}$ is the energy to transfer an atom from a kink position onto the terrace.

We then substitute Φ for $4l\kappa_c$ in (2.81) to obtain

$$\Delta G_s(i) = -i\Delta\mu + i(1-s)\Delta W - (1-s)E_i + \Phi_s, \quad (2.83)$$

where Φ_s has the meaning of the edge energy $4l\kappa_s$ of the surfactant cluster.

Figure 2.21 shows the dependence of $\Delta G_s(i)$ in units of the crystal bond strength, ψ_{cc} , on the cluster size i for the (111) surface of fcc metals ($\varphi_{1/2} = 6\psi_{cc}$,

$E_{\text{des}} = 3\psi_{cc}$, $\Delta W = 3\psi_{cc}$), with $\psi_{ss}/\psi_{cc} = 0.2$, constant supersaturation $\Delta\mu = 1.1\psi_{cc}$, and different values of s denoted by figures on each curve. As seen, $\Delta G_s(i)$ represents a broken line (as should be expected for a small number of atoms, cf. Fig. 2.10), displaying a maximum at $i = i^*$. Under clean conditions ($s = 0$) the critical nucleus consists of two atoms. When s is very small ($= 0.05$, the surfactant is almost inefficient), the number of atoms in the critical nucleus equals six due to the contribution of the edge energy of the surfactant cluster $4l\kappa_s$. The work of formation of the critical nucleus also increases. Increasing s to 0.3 due to decrease of the edge energy of the cluster leads to a decrease of the nucleation work and i^* becomes again equal to two. At some greater value of s ($= 0.7$), $i^* = 1$ and the aggregation becomes irreversible.

We see that the critical nucleus size differs under one and the same conditions (temperature, rate of deposition) in the absence and presence of a surfactant. In general, we should expect a decrease of the nucleus work and, in turn, a steep increase of the nucleation rate. As a result a larger density of smaller 2-D islands will form. The latter can coalesce and cover completely the surface before formation of nuclei of the upper layer. Thus surfactants can induce layer-by-layer growth by enhancing the nucleation rate [2.131, 132].

The rate of nucleation reads (see (2.42))

$$J_s = \omega_s^* \Gamma N_0 \exp\left(-\frac{\Delta G_s(i^*)}{k_B T}\right), \quad (2.84)$$

where ω_s^* is the flux of atoms to the critical nucleus in the presence of a surfactant, and $\Gamma \cong 1$ is the Zeldovich factor. $\Delta G_s(i^*)$ is given by (2.83) with $i = i^*$.

Bearing in mind that $\Delta\mu = k_B T \ln(N_1/N_1^e)$, where N_1 and N_1^e are the real and the equilibrium adatom concentrations, we can write

$$\Delta\mu = k_B T \ln\left(\frac{N_1}{N_0}\right) - k_B T \ln\left(\frac{N_1^e}{N_0}\right), \quad (2.85)$$

where N_1^e is given by (2.12).

Combining (2.83–2.85) and (2.12) gives

$$J_s = \omega_s^* \Gamma N_0 \left(\frac{N_1}{N_0}\right)^{i^*} \times \exp\left(\frac{i^* s \Delta W + (1-s)E^* - \Phi_s}{k_B T}\right). \quad (2.86)$$

In the absence of a surfactant, $s = 0$, we obtain the familiar expression (2.50) bearing in mind that $\omega_s^* = \omega^* = \alpha^* D_s N_1$.

Note that the presence of the surfactant is not accounted for only by the s -containing terms in the exponential. It is the flux ω_s^* that strongly depends on the mechanism of transport of crystal atoms to the critical nucleus [2.133, 134]. In the case when the transport of atoms to the critical nucleus takes place under the condition of reversible exchange/deexchange of S and C atoms (the time of de-exchange is much smaller than the time of deposition of complete monolayer and atoms have time to perform many exchange/de-exchange events) the nucleus density is given by [2.134] (see for more details [2.21])

$$N_S = N_{s,0} \exp\left(-\frac{\chi}{i^*} \frac{E_S}{k_B T}\right), \quad (2.87)$$

where $N_{s,0}$ and χ are given by (2.71) and (2.56), and E_S combines all energy contributions that depend on the presence of the surfactant. Within the framework of the classical nucleation theory the latter is given by

$$E_S = -4ls\kappa_c + 4l\kappa_s + E_{ex}^* - i^*[(E_{dex} - E_{ex}) - (E_{sd}^0 - E_{sd})], \quad (2.88)$$

where E_{ex} and E_{dex} are the barriers for exchange and de-exchange far from growing nuclei, E_{ex}^* is the barrier for exchange at the edge of the critical nucleus, and E_{sd}^0 and E_{sd} are the barriers for diffusion on clean surface and on top of the surface of the surfactant monolayer. As seen, the first two terms in E_S are of thermodynamic origin whereas the last two terms are of purely kinetic origin.

It follows that the exponential multiplying $N_{s,0}$ can be smaller or larger than unity depending on the sign of E_S . The latter in turn depends on the interplay of the energies involved. We consider in more detail the case of

Sb-mediated growth of Si(111) [2.98, 135]. For this case *Kandel* and *Kaxiras* computed the values $E_{dex} = 1.6$ eV, $E_{ex} = 0.8$ eV, and $E_{sd} = 0.5$ eV [2.136]. The value of $E_{sd}^0 = 0.75$ eV has been calculated from experimental data by *Voigtländer* et al. [2.98]. Thus a value of 0.55 eV was found for the difference $(E_{dex} - E_{ex}) - (E_{sd}^0 - E_{sd})$. We recall that $-4ls\kappa_c = sE^* - i^*s\Delta W$, where ΔW is of order of the half of the heat of evaporation, which for Si is equal to 4.72 eV [2.137]. It can be shown by inspection that $i^*\Delta W$ is always larger than E^* . Thus, when $i^* = 1$, $E^* = 0$ and $\Delta W \cong 2.3$ eV, and when $i^* = 2$, $E^* = 2.3$ eV and $i^*\Delta W \cong 4.6$ eV, etc. The value of s is close to unity as evaluated from the surface energies of Sb and Si available in the literature. It is thus concluded that it is the decrease of the edge energy of the nuclei $4ls\kappa_c$ due to the saturation of the dangling bonds with S atoms which plays the major role and determines the sign of E_S [2.21]. The latter explains the larger density of 2-D nuclei in surfactant-mediated growth of Si(111) compared with growth in clean conditions [2.98].

Kandel and *Kaxiras* assumed that the exchange/de-exchange processes influence the kinetics of nucleation by affecting the diffusivity of the atoms and derived an expression for an effective diffusion coefficient including the respective barriers [2.5]

$$D_{eff} \cong D_s^0 \exp\left(-\frac{(E_{dex} - E_{ex}) - (E_{sd}^0 - E_{sd})}{k_B T}\right),$$

and concluded that the atom diffusivity is inhibited due to $(E_{dex} - E_{ex}) > (E_{sd}^0 - E_{sd})$, which leads to increase of the nucleus density according to the scaling relation (2.54). As discussed above the more rigorous analysis shows that it is the thermodynamic term in (2.88) that controls the effect of the surfactant rather than the kinetic barriers.

2.8 Conclusions and Outlook

As shown above the nuclei of the new phase, particularly on surfaces, represent small clusters whose structure, shape, energy, and even size are still unclear. A large amount of work remains to be done

in order to study the stability of small clusters of materials with different chemical bonds and crystal lattices as a function of their structure, shape, and size.

References

- 2.1 T. Michely, J. Krug: *Islands, Mounds and Atoms: Patterns and Processes in Crystal Growth Far from Equilibrium* (Springer, Berlin Heidelberg 2003)
- 2.2 R. Kern, G. LeLay, J.J. Metois: Basic mechanisms in the early stages of epitaxy. In: *Current Topics in Materials Science*, Vol. 3, ed. by E. Kaldis (North-Holland, Amsterdam 1979) pp. 131–419

- 2.3 A. Pimpinelli, J. Villain: *Physics of Crystal Growth* (Cambridge Univ. Press, Cambridge 1998)
- 2.4 P. Politi, G. Grenet, A. Marty, A. Ponchet, J. Villain: Instabilities in crystal growth by atomic or molecular beams, *Phys. Rep.* **324**, 271–404 (2000)
- 2.5 D. Kandel, E. Kaxiras: The surfactant effect in semiconductor thin film growth, *Solid State Phys.* **54**, 219–257 (2000)
- 2.6 M. Zinke-Allmang, L.C. Feldman, M.H. Grabow: Clustering on surfaces, *Surf. Sci. Rep.* **16**, 377–463 (1992)
- 2.7 A.-L. Barabási, H.E. Stanley: *Fractal Concepts in Surface Growth* (Cambridge Univ. Press, Cambridge 1995)
- 2.8 R. Kaischew, I.N. Stranski: Über den Mechanismus des Gleichgewichts kleiner Kriställchen II, *Z. Phys. Chem.* **B26**, 114–116 (1934), in German
- 2.9 J.K. Nørskov, K.W. Jacobsen, P. Stoltze, L.B. Hansen: Many-atom interactions in metals, *Surf. Sci.* **283**, 277–282 (1993)
- 2.10 W. Kossel: Zur Energetik von Oberflächenvorgängen, *Nachrichten der Gesellschaft der Wissenschaften Göttingen, Mathematisch-Physikalische Klasse, Band 135* (1927), in German
- 2.11 I.N. Stranski: Über das Wachsen der Kristalle, *Ann. Sofia Univ.* **24**, 297–315 (1927), in Bulgarian
- 2.12 I.N. Stranski: Zur Theorie der Kristallwachstums, *Z. Phys. Chem.* **136**, 259–277 (1928), in German
- 2.13 R. Kaischew: On the history of the creation of the molecular-kinetic theory of crystal growth, *J. Cryst. Growth* **51**, 643–650 (1981)
- 2.14 A. Dupré: *Théorie Mécanique de la Chaleur* (Gauthier-Villard, Paris 1869) p. 369, in French
- 2.15 E. Bauer: Phänomenologische Theorie der Kristallabscheidung an Oberflächen I, *Z. Krist.* **110**, 372–394 (1958), in German
- 2.16 I.N. Stranski, K. Kulieliev: Beitrag zur isomorphen Fortwaschung von Ionenkristallen aufeinander, *Z. Phys. Chem. A* **142**, 467–476 (1929), in German
- 2.17 I.N. Stranski, L. Krastanov: Zur Theorie der orientierten Ausscheidung von Ionenkristallen aufeinander, *Monatsh. Chem.* **71**, 351–364 (1938), in German
- 2.18 F.C. Frank, J.H. van der Merwe: One-dimensional dislocations I. Static theory, *Proc. R. Soc. Lond. Ser. A* **198**, 205–216 (1949)
- 2.19 F.C. Frank, J.H. van der Merwe: One-dimensional dislocations II. Misfitting monolayers oriented overgrowth, *Proc. R. Soc. Lond. Ser. A* **198**, 216–225 (1949)
- 2.20 M. Volmer, A. Weber: Keimbildung in übersättigten Gebilden, *Z. Phys. Chem.* **119**, 277–301 (1926), in German
- 2.21 I. Markov: *Crystal Growth for Beginners*, 2nd edn. (World Scientific, New Jersey 2003)
- 2.22 M.H. Grabow, G.H. Gilmer: Thin film growth modes. Wetting and cluster nucleation, *Surf. Sci.* **194**, 333–346 (1988)
- 2.23 B. Voigtländer: Fundamental processes in Si/Si and Ge/Si epitaxy studied by scanning tunneling microscopy during growth, *Surf. Sci. Rep.* **43**, 127–254 (2001)
- 2.24 W.K. Burton, N. Cabrera, F.C. Frank: The growth of crystals and the equilibrium structure of their surfaces, *Philos. Trans. R. Soc. Lond. Ser. A* **243**, 299–358 (1951)
- 2.25 J.W. Gibbs: *On the Equilibrium of Heterogeneous Substances, Collected Works* (Longmans Green, New York 1928)
- 2.26 R.L. Dobrushin, R. Kotecky, S. Shlosman: *Wulff Construction: A Global Shape from Local Interactions* (American Mathematical Society, Providence 1993)
- 2.27 R. Kaischew: Equilibrium shape and work of formation of crystalline nuclei on substrates, *Commun. Bulg. Acad. Sci. (Phys.)* **1**, 100–133 (1950), in Bulgarian
- 2.28 I.N. Stranski, R. Kaischew: Gleichgewichtsformen homeopolarer Kristalle, *Z. Kristallogr.* **78**, 373–383 (1931), in German
- 2.29 R. Peierls: Clustering in adsorbed films, *Phys. Rev. B* **18**, 2013–2015 (1978)
- 2.30 Y.I. Frenkel: *Kinetic Theory of Liquids* (Dover, New York 1955)
- 2.31 R. Kaischew: On the thermodynamics of crystalline nuclei, *Commun. Bulg. Acad. Sci. (Phys.)* **2**, 191–202 (1951), in Bulgarian
- 2.32 I.N. Stranski: Zur Berechnung der spezifischen Oberflächen-, Kanten- und Eckenenergien an kleinen Kristallen, *Ann. Sofia Univ.* **30**, 367–375 (1936), in German
- 2.33 N. Cabrera, R.V. Coleman: Theory of crystal growth from the vapor. In: *The Art and Science of Growing Crystals*, ed. by J.J. Gilman (Wiley, New York 1963) pp. 3–28
- 2.34 H.-C. Jeong, E.D. Williams: Steps on surfaces: Experiment and theory, *Surf. Sci. Rep.* **34**, 171–294 (1999)
- 2.35 S. Stoyanov, I. Markov: On the 2D–3D transition in epitaxial thin film growth, *Surf. Sci.* **116**, 313–337 (1982)
- 2.36 S. Toshev, M. Paunov, R. Kaischew: On the question of formation of three-dimensional and two-dimensional nuclei in crystallization on substrates, *Commun. Dept. Chem. Bulg. Acad. Sci.* **1**, 119–129 (1968), in Bulgarian
- 2.37 I. Markov, R. Kaischew: Influence of the supersaturation on the mode of crystallization on crystalline substrates, *Thin Solid Films* **32**, 163–167 (1976)
- 2.38 I. Markov, R. Kaischew: Influence of the supersaturation on the mode of thin film growth, *Krist. Tech.* **11**, 685–697 (1976)
- 2.39 A. Crottini, D. Cvetko, L. Floreano, R. Gotter, A. Morgante, F. Tommasini: Step height oscillations during layer-by-layer growth of Pb on Ge(001), *Phys. Rev. Lett.* **79**, 1527–1530 (1997)
- 2.40 V.V. Voronkov: Movement of elementary step by formation of one-dimensional nuclei, *Sov. Phys. Crystallogr.* **15**, 13–19 (1970), in Russian

- 2.41 F.C. Frank: Nucleation-controlled growth on a one-dimensional growth of finite length, *J. Cryst. Growth* **22**, 233–236 (1974)
- 2.42 J. Zhang, G.H. Nancollas: Kink densities along a crystal surface step at low temperatures and under nonequilibrium conditions, *J. Cryst. Growth* **106**, 181–190 (1990)
- 2.43 S. Stoyanov: Formation of bilayer steps during growth and evaporation of Si(001) vicinal surfaces, *Europhys. Lett.* **11**, 361–366 (1990)
- 2.44 I. Markov: Kinetics of MBE growth of Si(001)1×1, *Surf. Sci.* **279**, L207–L212 (1992)
- 2.45 P. Vekilov: Kinetics and mechanisms of protein crystallization at the molecular level, *Methods Mol. Biol.* **300**, 15–52 (2005)
- 2.46 R. Becker, W. Döring: Kinetische Behandlung der Keimbildung in übersättigten Dämpfen, *Ann. Phys.* **24**, 719–752 (1935), in German
- 2.47 J.W. Christian: *The Theory of Transformations in Metals and Alloys*, 3rd edn. (Pergamon, New York 2002), Parts I and II
- 2.48 D. Kashchiev: *Nucleation* (Butterworths, Oxford 2000)
- 2.49 S.W. Benson: *The Foundations of Chemical Kinetics* (McGraw-Hill, New York 1960)
- 2.50 M. Volmer: *Kinetik der Phasenbildung* (Theodor Steinkopf, Dresden 1939), in German
- 2.51 J. Lothe, G.M. Pound: Reconsideration of nucleation theory, *J. Chem. Phys.* **36**, 2080–2085 (1962)
- 2.52 G.M. Pound, M.T. Simnad, L. Yang: Heterogeneous nucleation of crystals from vapor, *J. Chem. Phys.* **22**, 1215–1219 (1954)
- 2.53 J.G. Dash: Clustering and percolation transitions in helium and other thin films, *Phys. Rev. B* **15**, 3136–3146 (1977)
- 2.54 J.M. Liang, L.J. Chen, I. Markov, G.U. Singco, L.T. Shi, C. Farrell, K.N. Tu: Crystallization of amorphous CoSi₂ thin films I. Kinetics of nucleation and growth, *Mater. Chem. Phys.* **38**, 250–257 (1994)
- 2.55 J.P. Hirth, G.M. Pound: *Condensation and Evaporation, Progress in Materials Science* (MacMillan, New York 1963)
- 2.56 E. Korutcheva, A.M. Turiel, I. Markov: Coherent Stranski–Krastanov growth in 1+1 dimensions with anharmonic interactions: An equilibrium study, *Phys. Rev. B* **61**, 16890–16901 (2000)
- 2.57 J.E. Prieto, I. Markov: Thermodynamic driving force of formation of coherent three-dimensional islands in Stranski–Krastanov growth, *Phys. Rev. B* **66**, 073408 (2002)
- 2.58 D. Walton: Nucleation of vapor deposits, *J. Chem. Phys.* **37**, 2182–2188 (1962)
- 2.59 S. Stoyanov: Nucleation theory for high and low supersaturations. In: *Current Topics in Materials Science*, Vol. 3, ed. by E. Kaldis (North-Holland, Amsterdam 1979) pp. 421–462
- 2.60 S. Stoyanov: On the atomistic theory of nucleation rate, *Thin Solid Films* **18**, 91–98 (1973)
- 2.61 S. Toshev, I. Markov: An experimental study of nonsteady state nucleation, *Ber. Bunsenges. Phys. Chem.* **73**, 184–188 (1969)
- 2.62 A. Milchev, S. Stoyanov: Classical and atomistic models of electrolytic nucleation: comparison with experimental data, *J. Electroanal. Chem.* **72**, 33–43 (1976)
- 2.63 A. Milchev, J. Malinowski: Phase formation – Stability and nucleation kinetics of small clusters, *Surf. Sci.* **156**, 36–43 (1985)
- 2.64 D. Kashchiev: On the relation between nucleation, nucleus size and nucleation rate, *J. Chem. Phys.* **76**, 5098–5102 (1982)
- 2.65 B. Müller, L. Nedelmann, B. Fischer, H. Brune, K. Kern: Initial stages of Cu epitaxy on Ni(100): post-nucleation and a well-defined transition in critical island size, *Phys. Rev. B* **54**, 17858–17865 (1996)
- 2.66 J.A. Venables: *Introduction to Surface and Thin Film Processes* (Cambridge Univ. Press, Cambridge 2000)
- 2.67 J.L. Robins, T.N. Rhodin: Nucleation of metal clusters on ionic surfaces, *Surf. Sci.* **2**, 320–345 (1964)
- 2.68 R. Kaischew, B. Mutaftschiev: Über die elektrolytische Keimbildung des Quecksilbers, *Electrochim. Acta* **10**, 643–650 (1965), in German
- 2.69 B. Lewis, D. Campbell: Nucleation and initial growth behavior of thin film growth, *J. Vac. Sci. Technol.* **4**, 209–218 (1967)
- 2.70 M.J. Stowell: The dependence of saturation nucleus density on deposition rate and substrate temperature in the case of complete condensation, *Philos. Mag.* **21**, 125–136 (1970)
- 2.71 I. Markov: The influence of surface diffusion processes on the kinetics of heterogeneous nucleation, *Thin Solid Films* **8**, 281–292 (1971)
- 2.72 R.A. Sigsbee: Vapor to condensed-phase heterogeneous nucleation. In: *Nucleation*, ed. by A.C. Zettlemoyer (Marcel Dekker, New York 1969) pp. 151–224
- 2.73 I. Markov, A. Boynov, S. Toshev: Screening action and growth kinetics of electrodeposited mercury droplets, *Electrochim. Acta* **18**, 377–384 (1973)
- 2.74 A.N. Kolmogorov: Statistical theory of crystallization of metals, *Izv. Akad. Nauk USSR (Otd. Phys. Math. Nauk)* **3**, 355–359 (1937), in Russian
- 2.75 M. Avrami: Kinetics of phase change. I. General theory, *J. Chem. Phys.* **7**, 1103–1112 (1939)
- 2.76 M. Avrami: Kinetics of phase change. II. Transformation-time relations for random distribution of nuclei, *J. Chem. Phys.* **8**, 212–224 (1940)
- 2.77 M. Avrami: Kinetics of phase change III. Granulation, phase change and microstructure of phase change, *J. Chem. Phys.* **9**, 177–184 (1941)
- 2.78 W. Johnson, R. Mehl: Reaction kinetics in processes of nucleation and growth, *Trans. Am. Inst. Min. Metal. Eng.* **135**, 416–458 (1939)
- 2.79 I. Markov, D. Kashchiev: The role of active centers in the kinetics of new phase formation, *J. Cryst. Growth* **13/14**, 131–134 (1972)

- 2.80 I. Markov, D. Kashchiev: Nucleation on active centres I. General theory, *J. Cryst. Growth* **16**, 170–176 (1972)
- 2.81 G. Zinsmeister: A contribution to Frenkel's theory of condensation, *Vacuum* **16**, 529–535 (1966)
- 2.82 G. Zinsmeister: Theory of thin film condensation, Part b: Solution of the simplified condensation equations, *Thin Solid Films* **2**, 497–507 (1968)
- 2.83 G. Zinsmeister: Theory of thin film condensation, Part c: Aggregate size distribution in islands films, *Thin Solid Films* **4**, 363–386 (1969)
- 2.84 G. Zinsmeister: Theory of thin film condensation, Part d: Influence of variable collision factor, *Thin Solid Films* **7**, 51–75 (1971)
- 2.85 D.R. Frankl, J.A. Venables: Nucleation on substrates from the vapor phase, *Adv. Phys.* **19**, 409–456 (1970)
- 2.86 J.A. Venables: Rate equations approaches to thin film nucleation and growth, *Philos. Mag.* **27**, 697–738 (1973)
- 2.87 S. Stoyanov, D. Kashchiev: Thin film nucleation and growth theories: A confrontation with experiment. In: *Current Topics in Materials Science*, Vol. 7, ed. by E. Kaldis (North-Holland, Amsterdam 1981), pp. 69–141
- 2.88 G.S. Bales, D.C. Chrzan: Dynamics of irreversible island growth during submonolayer epitaxy, *Phys. Rev. B* **50**, 6057–6067 (1994)
- 2.89 G.S. Bales, A. Zangwill: Self-consistent rate theory of submonolayer homoepitaxy with attachment/detachment kinetics, *Phys. Rev. B* **55**, R1973–R1976 (1997)
- 2.90 J.G. Amar, F. Family, P.M. Lam: Dynamic scaling of the island-size distribution and percolation in a model of submonolayer molecular beam epitaxy, *Phys. Rev. B* **50**, 8781–8797 (1994)
- 2.91 J.G. Amar, F. Family: Critical cluster size: Island morphology and size distribution in submonolayer epitaxial growth, *Phys. Rev. Lett.* **74**, 2066–2069 (1995)
- 2.92 H. Brune, G.S. Bales, J. Jacobsen, C. Boragno, K. Kern: Measuring surface diffusion from nucleation island densities, *Phys. Rev. B* **60**, 5991–6006 (1999)
- 2.93 J.A. Venables, G.D.T. Spiller, M. Handbücken: Nucleation and growth of thin films, *Rep. Prog. Phys.* **47**, 399–460 (1984)
- 2.94 D. Kandel: Initial stages of thin film growth in the presence of island-edge barriers, *Phys. Rev. Lett.* **78**, 499–502 (1997)
- 2.95 C. Ratsch, P. Šmilauer, A. Zangwill, D.D. Vvedensky: Submonolayer epitaxy without a critical nucleus, *Surf. Sci.* **329**, L599–L604 (1995)
- 2.96 S. Iwanari, K. Takayanagi: Surfactant epitaxy of Si on Si(111) surface mediated by a Sn layer I. Reflection electron microscope observation of the growth with and without a Sn layer mediate the step flow, *J. Cryst. Growth* **119**, 229–240 (1992)
- 2.97 I.-S. Hwang, T.-C. Chang, T.T. Tsong: Exchange-barrier effect on nucleation and growth of surfactant mediated epitaxy, *Phys. Rev. Lett.* **80**, 4229–4232 (1998)
- 2.98 B. Voigtländer, A. Zinner, T. Weber, H.P. Bonzel: Modification of growth kinetics in surfactant mediated epitaxy, *Phys. Rev. B* **51**, 7583–7591 (1995)
- 2.99 A.A. Chernov: *Modern Crystallography III*, Springer Series in Solid State Sciences, Vol. 36 (Springer, Berlin 1984)
- 2.100 G. Ehrlich, F.G. Hudda: Atomic view of surface self-diffusion: tungsten on tungsten, *J. Chem. Phys.* **44**, 1039–1049 (1966)
- 2.101 E. Müller: Das Feldionenmikroskop, *Z. Phys.* **131**, 136–142 (1951), in German
- 2.102 S.C. Wang, T.T. Tsong: Measurements of the barrier height on the reflective W(110) plane boundaries in surface diffusion of single atoms, *Surf. Sci.* **121**, 85–97 (1982)
- 2.103 S.C. Wang, G. Ehrlich: Atom condensation at lattice steps and clusters, *Phys. Rev. Lett.* **71**, 4174–4177 (1993)
- 2.104 S.C. Wang, G. Ehrlich: Atom incorporation at surface clusters: an atomic view, *Phys. Rev. Lett.* **67**, 2509–2512 (1991)
- 2.105 P. Feibelman: Surface diffusion by concerted substitution, *Comments Condens. Matter. Phys.* **16**, 191–203 (1993)
- 2.106 R. Schwoebel, E.J. Shipsey: Step motion on crystal surfaces, *J. Appl. Phys.* **37**, 3682–3686 (1966)
- 2.107 R. Schwoebel: Step motion on crystal surfaces II, *J. Appl. Phys.* **40**, 614–618 (1966)
- 2.108 I. Markov: Kinetics of surfactant mediated epitaxial growth, *Phys. Rev. B* **50**, 11271 (1994)
- 2.109 J. Villain: Continuum models of crystal growth from atomic beams with and without desorption, *J. Phys. I France* **1**, 19–42 (1991)
- 2.110 J. Tersoff, A.W. Denier van der Gon, R.M. Tromp: Critical island size for layer-by-layer growth, *Phys. Rev. Lett.* **72**, 266–269 (1994)
- 2.111 S. Stoyanov: Layer growth of epitaxial films and superlattices, *Surf. Sci.* **199**, 226–242 (1988)
- 2.112 I. Markov: Surface energetics from the transition from step-flow growth to two-dimensional nucleation in metal homoepitaxy, *Phys. Rev. B* **56**, 12544–12552 (1997)
- 2.113 R. Gerlach, T. Maroutian, L. Douillard, D. Martinotti, H.-J. Ernst: A novel method to determine the Ehrlich–Schwoebel barrier, *Surf. Sci.* **480**, 97–102 (2001)
- 2.114 M. Bott, T. Hohage, G. Comsa: The homoepitaxial growth of Pt on Pt(111) studied by STM, *Surf. Sci.* **272**, 161–166 (1992)
- 2.115 P. Feibelman, J.S. Nelson, G.L. Kellogg: Energetics of Pt adsorption on Pt(111), *Phys. Rev. B* **49**, 10548–10556 (1994)
- 2.116 M. Bott, T. Hohage, M. Morgenstern, T. Michely, G. Comsa: New approach for determination of diffusion parameters of adatoms, *Phys. Rev. Lett.* **76**, 1304–1307 (1996)

- 2.117 J. Krug, P. Politi, T. Michely: Island nucleation in the presence of step-edge barriers: Theory and applications, *Phys. Rev. B* **61**, 14037–14046 (2000)
- 2.118 I. Markov: Method for evaluation of the Ehrlich-Schwoebel barrier to interlayer transport in metal homoepitaxy, *Phys. Rev. B* **54**, 17930–17937 (1996)
- 2.119 J. Rottler, P. Maass: Second layer nucleation in thin film growth, *Phys. Rev. Lett.* **83**, 3490–3493 (1999)
- 2.120 S. Heinrichs, J. Rottler, P. Maass: Nucleation on top of islands in epitaxial growth, *Phys. Rev. B* **62**, 8338–8359 (2000)
- 2.121 C. Priester, M. Lannoo: Origin of self-assembled quantum dots in highly mismatched heteroepitaxy, *Phys. Rev. Lett.* **75**, 93–96 (1995)
- 2.122 J.E. Prieto, I. Markov: Quantum dots nucleation in strained-layer epitaxy: Minimum energy pathway in the stress-driven two-dimensional to three-dimensional transformation, *Phys. Rev. B* **72**, 205412 (2005)
- 2.123 I. Markov, A. Trayanov: Epitaxial interfaces with realistic interatomic forces, *J. Phys. C* **21**, 2475–2493 (1988)
- 2.124 I. Markov: Static multikink solutions in a discrete Frenkel-Kontorova model with anharmonic interactions, *Phys. Rev. B* **48**, 14016–14019 (1993)
- 2.125 J.W. Matthews, E. Grünbaum: The need for contaminants in the epitaxial growth of gold on rock salt, *Appl. Phys. Lett.* **5**, 106–108 (1964)
- 2.126 E. Grünbaum: Epitaxial growth of single-crystal films, *Vacuum* **24**, 153–159 (1973)
- 2.127 D.A. Steigerwald, I. Jacob, W.F. Egelhoff Jr.: Structural study of the epitaxial growth of fcc-Fe films, sandwiches and superlattices on Cu(100), *Surf. Sci.* **202**, 472–492 (1988)
- 2.128 M. Copel, M.C. Reuter, E. Kaxiras, R.M. Tromp: Surfactants in epitaxial growth, *Phys. Rev. Lett.* **63**, 632–635 (1989)
- 2.129 I. Markov: Surfactants in semiconductor heteroepitaxy: thermodynamics and/or kinetics?. In: *NATO ASI Series: Collective Diffusion on Surfaces: Correlation Effects and Adatom Interactions*, ed. by M. Tringides, Z. Chvoj: (Kluwer, Dordrecht 2001) pp. 259–271
- 2.130 I. Markov: Kinetics of nucleation in surfactant-mediated epitaxy, *Phys. Rev. B* **53**, 4148–4155 (1996)
- 2.131 G. Rosenfeld, R. Servaty, C. Teichert, B. Poelsema, G. Comsa: Layer-by-layer growth of Ag on Ag(111) induced by enhanced nucleation: A model study for surfactant-mediated growth, *Phys. Rev. Lett.* **71**, 895–898 (1993)
- 2.132 H.A. van der Vegt, J. Vrijmoeth, R.J. Behm, E. Vlieg: Sb-enhanced nucleation in homoepitaxial growth of Ag(111), *Phys. Rev. B* **57**, 4127–4131 (1998)
- 2.133 I. Markov: Scaling behavior of the critical terrace width for step-flow growth, *Phys. Rev. B* **59**, 1689–1692 (1999)
- 2.134 I. Markov: Nucleation and step-flow growth in surfactant mediated homoepitaxy with exchange/de-exchange kinetics, *Surf. Sci.* **429**, 102–116 (1999)
- 2.135 M. Horn-von Hoegen, J. Falta, R. Tromp: Surfactants in Si(111) homoepitaxy, *Appl. Phys. Lett.* **66**, 487–489 (1995)
- 2.136 D. Kandel, E. Kaxiras: Surfactant mediated crystal growth of semiconductors, *Phys. Rev. Lett.* **75**, 2742–2745 (1995)
- 2.137 R. Hultgren, P.D. Desai, D.T. Hawkins, M. Gleiser, K.K. Kelley, D.D. Wagman: *Selected Values of the Thermodynamic Properties of the Elements* (American Society for Metals, Metals Park 1973)

3. Morphology of Crystals Grown from Solutions

Francesco Abbona, Dino Aquilano

Growth from solutions is widely used both in research laboratories and in many industrial fields. The control of crystal habit is a key point in solution growth as crystals may exhibit very different shapes according to the experimental conditions. In this chapter a concise review is given on this topic. First, the equilibrium shape is rather deeply developed due to its primary importance to understand crystal morphology, then the growth shape is treated and the main factors affecting the crystal habit are briefly illustrated and discussed. A rich literature completes the chapter.

Growth from solutions is widely used both in research laboratories and in many industrial fields. The control of crystal habit is a key point in solution growth as crystals may exhibit very different shapes according to the experimental conditions. In this chapter a concise review is given on this topic. First, the equilibrium shape is rather deeply developed due to its primary importance to understand crystal morphology, then the growth shape is treated and the main factors affecting the crystal habit are briefly illustrated and discussed. A rich literature completes the chapter.		3.4.2 Kinetic Roughening 72
		3.4.3 Polar Crystals 72
		3.4.4 Looking at Surfaces with AFM..... 73
		3.5 Crystal Defects 73
		3.6 Supersaturation – Growth Kinetics 73
		3.6.1 Growth Laws 74
		3.6.2 Some Experimental Results 74
		3.7 Solvent 75
		3.7.1 Choice of Solvent..... 76
		3.7.2 Change of Solvent 76
		3.7.3 Solvent–Solute 77
		3.7.4 Solvent–Crystal Surface 77
		3.7.5 Mechanisms of Action 77
		3.8 Impurities 78
		3.8.1 The Main Factors 78
		3.8.2 Kinetic Models 78
		3.8.3 Adsorption Sites 80
		3.8.4 Effect of Impurity Concentration and Supersaturation..... 80
		3.8.5 Effect of Impurity Size 82
		3.8.6 Composition of the Solution: pH 83
		3.9 Other Factors 84
		3.9.1 Temperature 84
		3.9.2 Magnetic Field 85
		3.9.3 Hydrodynamics 85
		3.10 Evolution of Crystal Habit 85
		3.11 A Short Conclusion 86
		3.A Appendix 86
		3.A.1 The Equilibrium Pressure of an Infinite Monoatomic Crystal with Its Own Vapor..... 86
		References 87
3.1	Equilibrium Shape 55	
3.1.1	The Atomistic Approach: The Kossel Crystal and the Kink Site 55	
3.1.2	Surface Sites and Character of the Faces 55	
3.1.3	The Equilibrium Crystal – Mother Phase: The Atomistic Point of View 57	
3.1.4	The Equilibrium Shape of a Crystal on a Solid Substrate 58	
3.1.5	The Stranski–Kaischew Criterion to Calculate the Equilibrium Shape. 60	
3.2	The Theoretical Growth Shape 64	
3.2.1	The Structural Approach 64	
3.2.2	Crystal Structure and Bond Energy: The Hartman–Perdok Theory 64	
3.2.3	The Effect of Foreign Adsorption on the Theoretical Growth Shape 66	
3.3	Factors Influencing the Crystal Habit 71	
3.4	Surface Structure 72	
3.4.1	The α -Factor and the Roughening Transition..... 72	

Interest in the crystal habit of minerals dates back a long time in the history of mankind. A detailed history on this topics and crystallization in general is given by *Scheel* [3.1]; here only a short account of crystal morphology is presented. Crystal habit, which attracted the interest of great scientists such as Kepler, Descartes, Hooke, and Huygens, is relevant from the scientific point of view, since it marks the beginning of crystallography as a science. Its birth can be dated to 1669 when the Danish scientist Niels Steensen, studying in Florence the quartz and hematite crystals from Elba island, suggested the first law of crystallography (constancy of the dihedral angle) and the mechanism of face growth (layer by layer). A century later this law was confirmed by Romé de l'Isle. At the end of the 18th century the study of calcite crystals led the French abbé René Just Haüy to enunciate the first theory on crystal structure and to discover the second law (rational indices). It is worth noticing that these early scholars met with great difficulty in studying crystal habit since, contrary to botany and zoology where each species has its own definite morphology, the crystal habit of minerals is strongly variable within the same species. In the first part of the 19th century the study of crystal habit led to the development of the concept of symmetry and the derivation of the 32 crystal classes. Bravais, by introducing the idea of the crystal lattice, was the first to try to relate crystal habit to internal structure (the Bravais law, saying that the crystal faces are lattice planes of high point density). At the end of the 19th century research on internal symmetry ended with the derivation of the 230 space groups. In this century research on crystallization, mainly from solution but also from melt, went on and interlaced with progress in other disciplines (chemistry, physics, thermodynamics, etc.). We should recall the important contributions by Gibbs (1878), Curie (1885), and Wulff (1901) on the equilibrium form of crystals, which was tackled later from an atomistic point of view by *Stranski* [3.2] and *Stranski* and *Kaischew* [3.3,4].

The relationship between morphology and internal structure (the Bravais law) was treated by *Niggli* [3.5] and developed by *Donnay* and *Harker* [3.6], who considered the space group instead of the Bravais lattice type as a factor conditioning the crystal morphology. From about 1950 onwards, interest in crystal growth in-

creased due to the role of crystals in all kinds of industry and the discovery of relevant properties of new crystalline compounds. Besides the technological progress, a milestone was the publication in 1951 of the first theory on growth mechanisms of flat crystal faces by *Burton*, *Cabrera*, and *Frank* (BCF) [3.7].

Also, the crystal habit was receiving growing attention due to theoretical interest and industrial needs. The Donnay–Harker principle is exclusively crystallographic. A chemical approach was adopted by Hartman and Perdok; looking at crystal structure as a network of periodic bond chains (PBC) they published in 1955 a method that is still fundamental to studies of theoretical crystal morphology [3.8–10]. The method, at first qualitative, was made quantitative through the calculation of the broken bond energy and, since about 1980, has been integrated with the statistical mechanical theory of Ising models which led to the integrated Hartman–Perdok roughening transition theory [3.11], later applied to modulated crystals [3.12]. These methods do not take into account the external habit-controlling factors, namely the effects of fluid composition and supersaturation, which are explicitly considered in the interfacial structure (IS) analysis [3.13]. An improvement in predicting morphology was represented by the application of ab initio calculations to the intermolecular interactions between tailor-made additives and crystal surface [3.14].

Computer facilities have promoted tremendous advances in all kinds of calculation necessary in the different sectors of crystal growth, enabling progress in theoretical approaches and sophisticated simulations which are now routine practice. A relevant instrumental advance was achieved when atomic force microscopy (AFM) was applied to study the features of crystal faces, giving new impulse to a topic that had always been the center of thorough research [3.15–18].

This chapter is devoted to the morphology of crystals grown from solution. In the first part, the theoretical equilibrium and growth shapes of crystals are treated from the thermodynamic and atomistic points of view. In the second part the factors affecting crystal habit will be considered with some specific examples. High-temperature solution growth, mass, and protein crystallization are excluded to limit the scope of the chapter.

3.1 Equilibrium Shape

When equilibrium is reached between a crystalline phase and its surroundings, the statistical amount of growth units exchanged between the two phases is the same and does not change with time. This implies that the crystallized volume remains constant, but nothing is specified about many important questions, such as:

1. The surface of the crystals, i. e., how large its extension is and which $\{hkl\}$ forms enter the equilibrium shape (ES).
2. The difference, if any, between the stable ES of a crystal immersed in either a finite or infinite mother phase and the unstable shape obtained when the activation energy for nucleation is reached.
3. How does the ES change when some adhesion is set up between the crystal and a solid substrate?
4. How can solvent and impurity concentrations affect the ES?

To address these questions, a few elementary concepts must be fixed to structure our language and a simple but effective crystal model adopted in the following.

3.1.1 The Atomistic Approach: The Kossel Crystal and the Kink Site

Let us consider a perfect monoatomic, isotropic, and infinite crystal. The work needed to separate an atom occupying a *mean lattice site* from all its n neighbors is $\varphi^{\text{sep}} = \sum_i^n \psi_i$, where ψ_i is the energy binding one atom to its i th neighbor. We will see later on that this peculiar site really exists and is termed a *kink*. The potential energy (per atom) of the crystal will be $\varepsilon_p^{\text{co}} = -(1/2)\varphi^{\text{sep}}$. The simplest model, valid for homopolar crystals, is due to *Kossel* [3.19]. Atoms are replaced by elementary cubes bounded by pair interactions, $\psi_1, \psi_2, \dots, \psi_n$: the separation work between the first, second, and n th neighbors, with the pair potential decreasing with distance, $\psi_1 > \psi_2 > \dots > \psi_n$ (Fig. 3.1a). In the first-neighbors approximation, the separation work for an atom lying in the crystal bulk is $\varphi^{\text{sep}} = 6\psi_1$. Thus, $\varepsilon_p^{\text{co}} = -3\psi_1$. On the other hand, $\varepsilon_p^{\text{co}}$ represents the variation of the potential energy that an atom undergoes when going from the vapor to a *mean lattice site*, which coincides with a well-defined surface site, as suggested by *Kossel* [3.19] and *Stran-ski* [3.2]. Once an atom has entered this special site, the potential energy variation of the considered system is equal to $-3\psi_1$ and so the separation work for

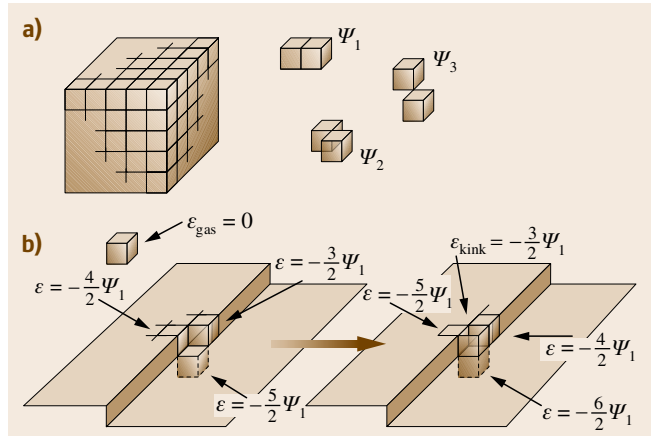


Fig. 3.1 (a) Kossel crystal; separation work between first (ψ_1), second (ψ_2), and third (ψ_3) neighbors. (b) When an atom enters a kink, there is a transition in the potential energy, the difference between final and initial stage being $-3\psi_1$ (first neighbors)

an atom occupying this site is $\varphi_{\text{co}} = 3\psi_1$ (Fig. 3.1b). A *kink* is the name adopted worldwide for this site, for practical reasons. Different historical names have been given: *repetitive step* [3.2, Z. Phys. Chem.] and *half-crystal position* [3.2, Annu. Univ. Sofia], both related to the physics of the site. In fact, deposition or evaporation of a growth unit onto/from a kink reproduces another kink, thus generating an equal probability for the two processes [3.20]. Moreover, the chemical potential (μ) of a unit in a kink is equal to that of the vapor. Hence, *kinks are crystal sites in a true (and not averaged) thermodynamic equilibrium*, as will be shown below.

3.1.2 Surface Sites and Character of the Faces

Flat (F) faces. A crystal surface, in equilibrium with its own vapor and far from absolute zero temperature, is populated by steps, adsorbed atoms, and holes. In the Kossel model all sites concerning the adsorption and the outermost lattice level are represented (Fig. 3.2). The percentage of corner and edge sites is negligible for an infinite crystal face, and hence we will confine our attention to the *adsorption and incorporation sites*. Crystal units can adsorb either on the surface terraces (ad_s) or on the steps (ad_l), with the same situation occurring for the incorporation sites (in_s, in_l).

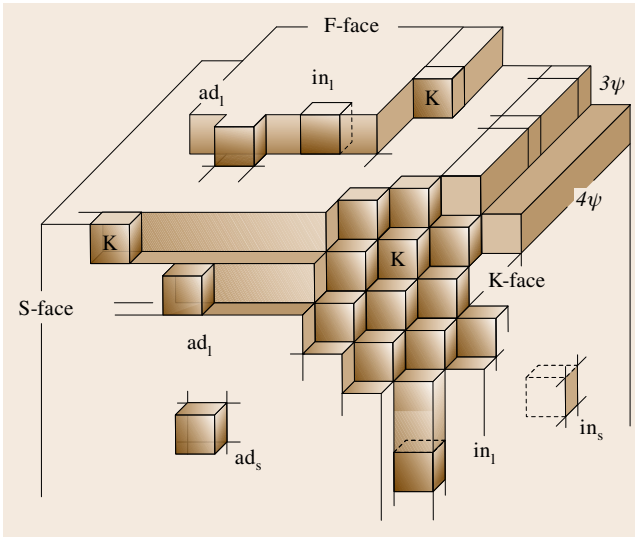


Fig. 3.2 The different types of faces of a Kossel crystal: {100}-F, {111}-K, and {110}-S faces. Adsorption (ad_s , ad_l) and incorporation (in_s , in_l) sites are shown on surfaces and steps. The uniqueness of the K (kink) site is also shown

The binding energies of *ad*-sites and *in*-sites are complementary to one another

$$\begin{aligned}\varphi_{ad_s} + \varphi_{in_s} &= \varphi_{ad_l} + \varphi_{in_l} \\ &= 2\varphi_{kink} \rightarrow \varphi_{ad} + \varphi_{in} = 2\varphi_{kink},\end{aligned}\quad (3.1)$$

which is generally valid since it depends neither on the type of face, nor on the crystal model, nor on the kind of lattice forces [3.21, p. 56]. The interaction of the unit in the kink with the crystal (φ_{kink}) consists of two parts. The first represents its *attachment energy* (φ_{att}) with all the *crystal substrate*, and coincides with that of an ad-unit, which implies

$$\varphi_{att} = \varphi_{ad}. \quad (3.2a)$$

The second is its *slice energy* (φ_{slice}), i.e., the interaction with the half of the outermost crystal slice, $\varphi_{slice} = (\omega/2)$, where ω is the interaction of the unit with all of its slice. Thus

$$\varphi_{in} = \varphi_{att} + \omega, \quad (3.2b)$$

and, from relation (3.1)

$$\varphi_{kink} = \varphi_{att} + \varphi_{slice}. \quad (3.2c)$$

Relation (3.2c) states that φ_{att} and φ_{slice} of a growth unit are complementary to one another. In fact, since

φ_{kink} is constant for a given crystal, the higher the lateral interaction of one unit, the lower its interaction with the subjacent crystal. This criterion is of the utmost importance for understanding the growth morphology of crystals. Moreover, the binding of a growth unit must fulfil the qualitative inequality: $\varphi_{ad} < \varphi_{kink} < \varphi_{in}$. The quantitative treatment was elegantly addressed by Kaischew [3.3, 4], who calculated the coverage degree (θ_i) and other related quantities for every *i*-site of the surface drawn in Fig. 3.2

$$\theta_i = \{1 + \exp[(\varphi_{kink} - \varphi_i)/(k_B T)]\}^{-1}, \quad (3.3)$$

where k_B is the Boltzmann constant. For a (001) Kossel surface and within the first-neighbors approximation, having assumed for the binding energy the standard value $\psi_1 = 4k_B T$ (valid for Au crystals not far from the melting point), the set of results shown in Table 3.1 was obtained.

From Table 3.1 it follows that:

1. Kinks are the only sites in thermodynamic equilibrium, being half filled and half empty at the same time.
2. Ad-units form a very dilute layer (row) which moves randomly on the surface (step edge) and hence cannot belong to the crystal.
3. In-units belong to the crystal, from which they may escape, generating a temporary hole, with a very low exchange frequency with respect to the other sites.

Looking at the face as a whole, the face profile can neither advance nor move backwards: hence, the face is in *macroscopic equilibrium*. Fluctuations around the equilibrium cannot change its flatness since the lifetime of the growth units in the ad-sites is very short and the vacancies generated among the in-sites are filled again in

Table 3.1 Coverage degree (3.3) and exchange frequency of growth units in the main surface sites of the (001) face of a Kossel crystal, assuming $\psi_1 = 4k_B T$ (after [3.21]). The exchange frequency is the reciprocal of the mean time between two successive evaporation (or condensation) events on the same *i*-site (i.e. s^{-1} indicates the number of exchanges per unit time in a given site)

Type of surface site	Separation work	Coverage degree θ_i	Exchange frequency (s^{-1})
$ad_{surface}$	ψ_1	0.0003	3.06×10^7
ad_{ledge}	$2\psi_1$	0.0180	3.02×10^7
kink	$3\psi_1$	1/2	1.54×10^7
in_{ledge}	$4\psi_1$	0.9820	5.55×10^6
$in_{surface}$	$5\psi_1$	0.9997	1.03×10^4

even shorter time. So, this kind of *equilibrium face* has been named an F-type (flat) face.

Kinked (K) and Stepped (S) Faces. The uniqueness of F-faces is even more evident when considering the behavior of the {111} form of a Kossel crystal, near the equilibrium. Only kinks can be found on this surface and hence only one type of binding exists ($3\psi_1$) among growth units, within the first neighbors. Since in this case no units exhibit bonds in their slice, $\omega = 0$, which implies: $\varphi_{ad} = \varphi_{kink} = \varphi_{in}$. With every ad-unit transforming into an in-unit, the surface profile is not constrained and hence fluctuates, with the mother phase, around the equilibrium. This interface is diffuse and the corresponding faces are termed K (kinked) faces.

The behavior of the {110} form may be thought of as midway between that of F- and K-faces, since only ledge-type sites exist, apart from the kinks. Any fluctuation near the equilibrium can lead either to the evaporation of an entire [100] step or to the growth of a new one. In the first case, it is sufficient that a unit leaves an in-ledge site to promote step evaporation, while in the second case the formation of an ad-ledge site automatically generates two kinks, allowing the filling of a new step. Both processes are not correlated, even for contiguous steps, since there are no lateral bonds ($\omega = 0$) in the outermost (110) slice; thus, steps can form (or disappear) independently of each other and may bunch, giving rise to an undulating profile around the zone axis. Parallel steps being the feature of this kind of surface, the corresponding faces are termed S-type (stepped) faces.

3.1.3 The Equilibrium Crystal – Mother Phase: The Atomistic Point of View

Here we will deal with the equilibrium between a crystal and its vapor; however, *our conclusions can be basically applied to solutions and melts as well*. Let us consider a Kossel crystal built by n^3 units (each having mass m and vibration frequency ν). Since the work to separate two first neighbors is ψ , the mean evaporation energy of the n -sized crystal is easily calculated

$$\langle \Delta H \rangle_{cn} = 3\psi[1 - (1/n)] = \varphi_{cn} . \quad (3.4a)$$

Then, for an infinite-sized crystal,

$$\langle \Delta H \rangle_{c\infty} = 3\psi = \varphi_{c\infty} = \text{const} . \quad (3.4b)$$

This means that the *units belonging to the crystal surface* reduce the value of the mean evaporation energy

and so they *cannot be neglected when dealing with finite crystals*.

An Infinite Crystal and Its Mother Phase

As shown in Appendix 3.A, the equilibrium pressure (p_{eq}^∞) between a monoatomic vapor and its infinite crystalline phase decreases with its evaporation work $\varphi_{c\infty} = (\varepsilon_v - \varepsilon_{c\infty})$, according to

$$p_\infty^{eq} = [(2\pi m)^{3/2} (k_B T)^{-1/2} \nu^3] \exp(-\varphi_{c\infty}/(k_B T)) , \quad (3.5a)$$

ε_v and $\varepsilon_{c\infty}$ being the potential energy of a unit in the vapor and in the infinite crystal, respectively. The term $p dV$ can be neglected in $\langle \Delta H \rangle_{c\infty}$ with respect to the term (dU). Assuming, as a reference level, $\varepsilon_v = 0$, it is easy to show that $\langle \Delta H \rangle_{c\infty} = \varphi_{c\infty} = -\varepsilon_{c\infty}$.

The Finite Crystal – The Link to the Thermodynamic Supersaturation

When dealing with finite crystals (3.5a) transforms simply by changing $\varepsilon_{c\infty}$ with ε_{cn} , which is the potential energy of a unit in the finite crystal. It ensues that $\varphi_{cn} = (\varepsilon_v - \varepsilon_{cn})$. The frequency (ν) does not vary from large to small crystal size, so

$$p_n^{eq} = (2\pi m)^{3/2} (k_B T)^{-1/2} \nu^3 \exp(-\varphi_{cn}/(k_B T)) . \quad (3.5b)$$

From (3.5a) and (3.5b) the following fundamental relation is obtained:

$$p_n^{eq} = p_\infty^{eq} \exp[(\varphi_{c\infty} - \varphi_{cn})/(k_B T)] . \quad (3.5c)$$

Since $\varphi_\infty > \varphi_n$, (3.5c) shows that *the equilibrium pressure for finite crystals is higher than that for infinite ones*. This can also be written

$$\varphi_{c\infty} - \varphi_{cn} = k_B T \ln (p_n^{eq}/p_\infty^{eq}) = k_B T \ln \beta , \quad (3.6)$$

where $\beta = p_n^{eq}/p_\infty^{eq} = (p_\infty^{eq} + \Delta p)/p_\infty^{eq} = 1 + \sigma$ is the *supersaturation ratio* of the vapor with respect to the finite crystal. The (percentage) distance from equilibrium is $\sigma = (\Delta p/p_\infty^{eq})$, the exceeding pressure being $\Delta p = p_n^{eq} - p_\infty^{eq}$.

Equilibrium can also be viewed in terms of chemical potentials. Using the Helmholtz free energy, the chemical potentials, per unit, of the infinite and finite crystal read: $\mu_{c\infty} = -\varphi_{c\infty} - Ts_{c\infty}$ and $\mu_{cn} = -\varphi_{cn} - Ts_{cn}$. The vibrational entropies per unit, $s_{c\infty}$ and s_{cn} , are very close. Thus $\varphi_{c\infty} - \varphi_{cn} = \mu_{cn} - \mu_{c\infty} = \Delta\mu$ (Fig. 3.3). Hence, the following master equation for the equilibrium is obtained:

$$\Delta\mu = k_B T \ln \beta , \quad (3.7)$$

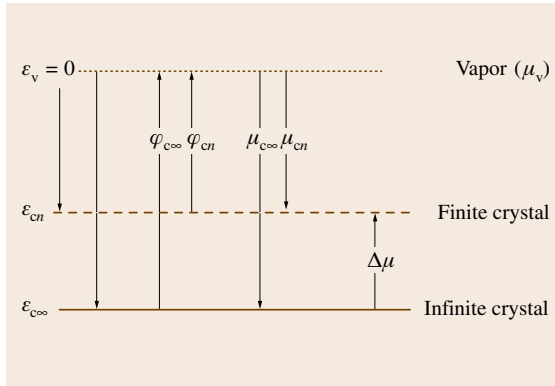


Fig. 3.3 Potential energy ε , evaporation work φ , and chemical potential μ of a growth unit in the vacuum, in a *mean site* of both finite and infinite crystal. $\Delta\mu = \mu_{cn} - \mu_{c\infty}$ is the thermodynamic supersaturation

where $\Delta\mu$ is the *thermodynamic supersaturation*. In heterogeneous systems a unit spontaneously goes from the higher chemical potential (μ') to the lower one (μ''). During the transition a chemical work ($\mu'' - \mu'$) = $-\Delta\mu$ is gained, per growth unit.

The equilibrium between a finite crystal and its surroundings is analogous to the equilibrium of a spherical liquid drop of radius r (finite condensed phase 2) immersed in its own vapor (infinite dispersed phase 1). The phenomenological treatment is detailed in [3.21], where the two different equilibria are compared in the same way as we dealt with the atomistic treatment. Hence, one obtains the Thomson–Gibbs formula for droplets

$$\Delta\mu = k_B T \ln(p/p_{eq}) = \Omega_2 p_\gamma = 2\Omega_2(\gamma/r), \quad (3.8)$$

where:

1. p_{eq} is the pressure of the vapor in equilibrium with a flat liquid surface
2. γ and Ω_2 are the surface tension at the drop–vapor interface and the molecular volume of the drop, respectively
3. The capillarity pressure p_γ at the drop interface defined by Laplace's relation ($p_\gamma = 2\gamma/r$) equilibrates the difference between the internal pressure of the drop (p_r) and the actual vapor pressure (p): $p_\gamma = (p_r - p)$.

The ratio (p/p_{eq}) is nothing else than β . When working with ideal or nonideal solutions, β is expressed by the concentrations (c/c_{eq}) or by the activities (a/a_{eq}), respectively. When a crystal is considered instead of a liquid drop, the system is no longer isotropic and then

the radius r represents only the *size* of the crystal, as we will see later on. Nevertheless, the Thomson–Gibbs formula continues to be valid and expresses the relation among the deviation $\Delta\mu$ of the solution from saturation, the tension γ_{cs} of the crystal–solution interface, and the size of the crystals in equilibrium with the solution.

3.1.4 The Equilibrium Shape of a Crystal on a Solid Substrate

This topics has been deeply treated by Kern [3.22], who considered simultaneously both mechanical (capillary) and chemical (thermodynamic) equilibrium to obtain the ES of a crystal nucleating on a substrate from a dispersed phase. In preceding treatments, the Curie–Wulff condition and the Wulff theorem [3.23] only took into account the minimum of the crystal surface energy, the crystal volume remaining constant. According to [3.22], when n_A units of a phase A (each having volume Ω) condense under a driving force $\Delta\mu$ on a solid substrate B (heterogeneous nucleation) to form a three-dimensional (3-D) crystal (Fig. 3.4), the corresponding variation of the free Gibbs energy reads

$$\Delta G_{\text{hetero}}^{3-D} = -n_A \times \Delta\mu + (\gamma_i^A - \beta_{\text{adh}})S_{AB} + \sum_j \gamma_j^A S_j^A, \quad (3.9)$$

where the second and the third term represent the work needed to generate the new crystal–substrate interface of area S_{AB} and the free crystal surfaces (of surface tension γ_j^A and area S_j^A), respectively.

The term $(\gamma_i^A - \beta_{\text{adh}})S_{AB}$ comes from the balance between the surface work lost ($-\gamma_B \times S_{AB}$) and gained ($\gamma_{AB} \times S_{AB}$) during nucleation. It is obtained from Dupré's formula: $\gamma_{AB} = \gamma_B + \gamma_i^A - \beta_{\text{adh}}$, where γ_{AB} is the crystal/substrate tension, γ_B is the surface tension of the substrate, γ_i^A is the surface tension of

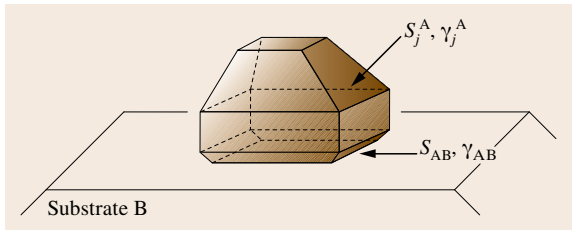


Fig. 3.4 Surface parameters involved in the balance of the free Gibbs energy variation when n_A units of a phase A condense on a solid substrate B to form a 3-D crystal (heterogeneous nucleation)

the i -face of the A crystal (when considered not in contact with the substrate), and β_{adh} stands for the specific crystal/substrate adhesion energy. At the (unstable) equilibrium of the nucleation any variation of $\Delta G_{\text{hetero}}^{3-D}$ must vanish. Then, under the reasonable assumption that also the specific surface tensions do not vary for infinitesimal changes of the crystal size,

$$d(\Delta G_{\text{hetero}}^{3-D}) = -dn_A \times \Delta\mu + (\gamma_i^A - \beta_{\text{adh}}) dS_{AB} + \sum_j \gamma_j^A dS_j^A = 0. \quad (3.10)$$

The fluctuation dn_A is related to those of the face areas (dS_j^A and dS_{AB}) and to their distances (h_j and h_s) with respect to the crystal center. Then, (3.10) may be written in terms of dS_j^A and dS_{AB} . Its solution is a continuous proportion between the energies of the faces and their h_j and h_s values

$$\begin{aligned} \frac{\gamma_1^A}{h_1} = \frac{\gamma_2^A}{h_2} = \dots = \frac{\gamma_j^A}{h_j} = \frac{\gamma_i^A - \beta_{\text{adh}}}{h_s} \\ = \text{const} = \frac{\Delta\mu}{2\Omega}. \end{aligned} \quad (3.11)$$

This is the *unified Thomson–Gibbs–Wulff (TGW) equation*, which provides the ES of a crystal nucleated on a solid substrate:

1. The ES is a polyhedron limited by faces whose distances from the center are as shorter as lower their γ values.
2. The distance of the face in contact with the substrate will depend not only on the γ value of the lattice plane parallel to it, but also on its adhesion energy.
3. The faces entering the ES will be only those limiting the *most inner* polyhedron, its size being determined once $\Delta\mu$ and one out of the γ values are known.

The analogy between the crystal ES and that of a liquid drop on solid substrates is striking. It is useful to recall Young's relation for the mechanical equilibrium of a liquid drop on a substrate (Fig. 3.5)

$$\gamma_{\text{sl}} = \gamma_{\text{lv}} \cos \alpha + \gamma_{\text{sv}}, \quad (3.12a)$$

where α is the contact angle and γ_{sl} , γ_{lv} , and γ_{sv} are the surface energies of the substrate–liquid, liquid–vapor, and substrate–vapor interfaces, respectively. Besides, from Dupré's relation one obtains

$$\gamma_{\text{sl}} = \gamma_{\text{sv}} + \gamma_{\text{lv}} - \beta_{\text{adh}}. \quad (3.12b)$$

Since $-1 \leq \cos \alpha \leq 1$, the range of the adhesion energy (wetting) must fulfil the condition

$$2\gamma_{\text{lv}} \geq \beta_{\text{adh}} \geq 0. \quad (3.12c)$$

Adhesion values affect the sign of the numerator in the term $(\gamma_i^A - \beta_{\text{adh}})/h_s$ (3.11).

The ES of the crystal is a nontruncated polyhedron when the crystal/substrate adhesion is null, as occurs for homogeneous nucleation. However, as the adhesion increases, the truncation increases as well, reaching its maximum when $\beta_{\text{adh}} = \gamma_i^A$. If the wetting

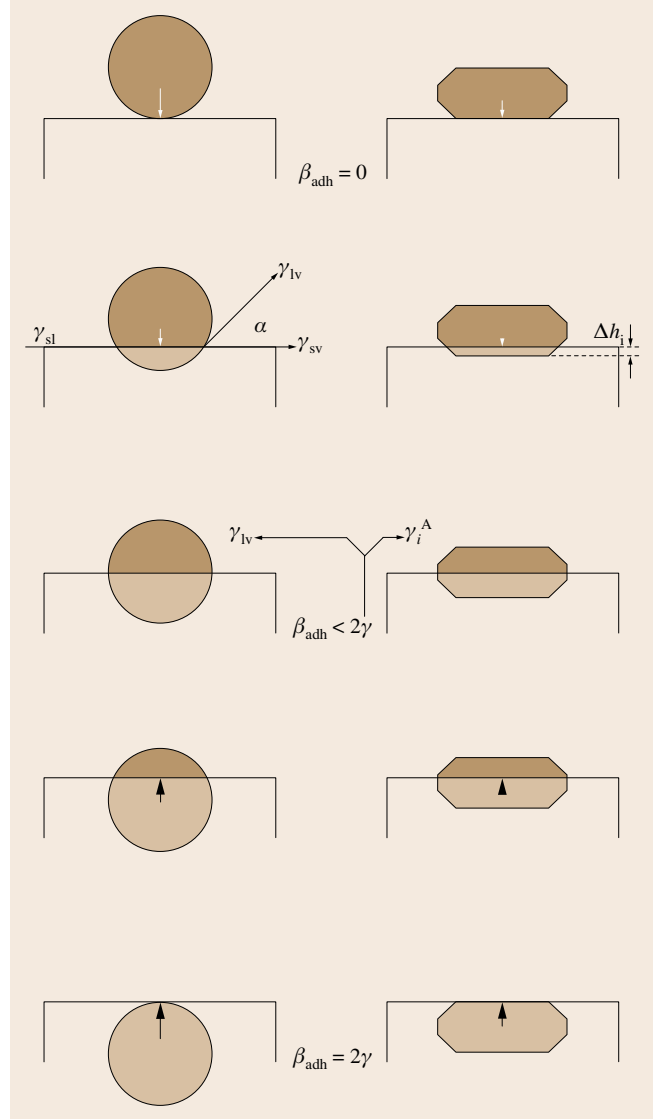


Fig. 3.5 Analogy between the equilibrium shape of a liquid drop on a solid substrate and that of a crystal, both heterogeneously nucleated. The adhesion energy β_{adh} rules both the contact angle of the drop with the substrate and the *crystal truncation*

further increases the truncation decreases, along with the thickness of the crystal cup. When β_{adh} reaches its extreme value, $2\gamma_i^A$, the crystal thickness reduces to a *monomolecular* layer.

The Equilibrium Shape of a Finite Crystal in Its Finite Mother Phase

Microscopic crystals can form in fluid inclusions captured in a solid, as occurs in minerals [3.25], especially from solution growth under not low supersaturation and flow. If the system fluctuates around its equilibrium temperature, the crystal faces can exchange matter among them and with their surroundings: then crystals will reach their *ES*, after a given time. *Bienfait* and *Kern* [3.24], starting from an inspired guess by *Klija* and *Lemlein* [3.26], first observed the *ES* of NH_4Cl , NaCl , and KI crystals grown in small spherical inclusions (10–100 μm) filled by aqueous solution (Fig. 3.6). The crystals contained in each inclusion (initially dendrites) evolve towards a single convex polyhedron and the time to attain the *ES* is reasonable only for microscopic crystals and for droplet diameter of a few millimeters. The *ES* so obtained did not correspond to

the maximum of the free energy (unstable equilibrium) but to its minimum, and then to a stable equilibrium. Finally, it was shown that both unstable and stable *ESs* are homothetic but with different sizes.

3.1.5 The Stranski–Kaischew Criterion to Calculate the Equilibrium Shape

Without Foreign Adsorption

In the preceding sections, the surface tensions of the $\{hkl\}$ forms have been considered to be independent of crystal size. This is true when the crystal exceeds microscopic dimensions, but is no longer valid for those sizes which are very interesting both in the early stages of nucleation and in the wide field of nanosciences. In these cases, it should be reasonable to drop the use of the surface tension values, which are macroscopic quantities, to predict the equilibrium shape of micro- and nano-crystals. To face this problem, it is useful to recall the brilliant path proposed by *Stranski* and *Kaischew* [3.21, p. 170]. Their method, named the *criterion of the mean separation works*, is based on the idea that the mean chemical potential $\langle\mu\rangle_{c,m} = (1/m) \sum_{j=1}^m \mu_{j,c}$ averaged over all m units building the outermost layer of a finite facet, must be constant over all the facets, once the phase equilibrium is achieved. The chemical potential of a unit in a kink (Appendix 3.A) is

$$\mu_{c\infty} = -\varphi_{\text{kink}} - k_B T \ln \Omega_c + \mu^0, \quad (3.13a)$$

and, by analogy, in a j -site of the surface

$$\mu_{j,c} = -\varphi_{j,c} - k_B T \ln \Omega_j + \mu^0. \quad (3.13b)$$

The mean vibrational volumes being the same for every crystal sites, one can write for a generic site and especially at low temperature

$$\mu_{j,c} \approx -\varphi_{j,c} + \text{const}. \quad (3.14)$$

At equilibrium between a small crystal and its vapor: $\mu^{\text{gas}} = \langle\mu\rangle_{c,m}$. Subtracting the equality which represents the equilibrium between an infinite crystal and its saturated vapor ($\mu_{\text{saturated}}^{\text{gas}} = \mu_{c\infty}$) and applying relation (3.14), one can finally obtain

$$\begin{aligned} \Delta\mu &= \mu^{\text{gas}} - \mu_{\text{saturated}}^{\text{gas}} = \langle\mu\rangle_{c,m} - \mu_{c\infty} \\ &\approx \varphi_{\text{kink}} - \langle\varphi\rangle_{c,m}. \end{aligned}$$

That represents the *Thomson–Gibbs formula*, valid for every face of small-sized crystals

$$\varphi_{\text{kink}} - \langle\varphi\rangle_{c,m} \approx \Delta\mu = k_B T \ln \beta, \quad (3.15)$$

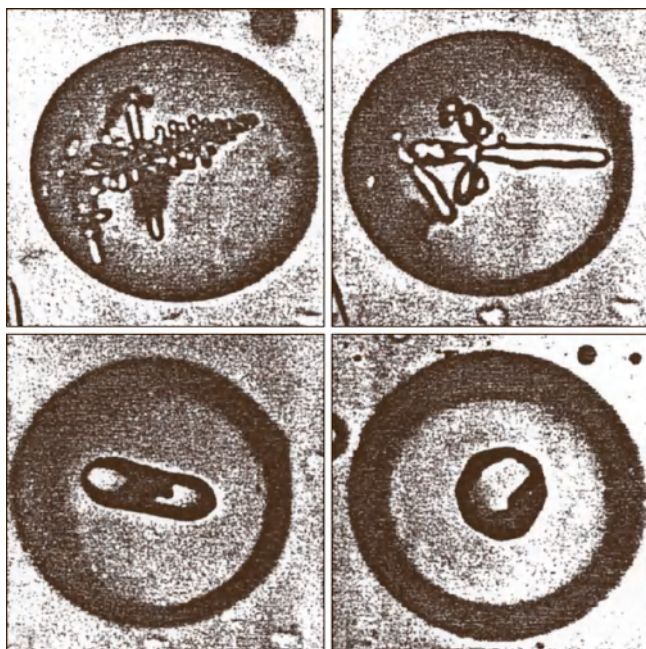


Fig. 3.6 The evolution towards equilibrium of NH_4Cl dendrites formed in an aqueous solution droplet (closed system) (after [3.24]). The total surface energy is minimized in passing from the dendritic mass to a single convex polyhedron at constant volume and T (equilibrium shape). Droplet size: 100 μm

which allows one to determine the β value at which a unit (lying on a given face) can belong to the ES. Using (3.15), the ES can be determined without using the γ values of the different faces.

Let n_{01} and n_{11} be the number (not known a priori) of units in the most external $\langle 01 \rangle$ and $\langle 11 \rangle$ rows of a 2-D Kossel crystal (Fig. 3.7). Within the second neighbors, the mean separation works for these rows are

$$\begin{aligned} \langle \varphi \rangle_{01} &= (1/n_{01})[2\psi_1(n_{01} - 1) + \psi_1 + 2\psi_2 n_{01}] \\ &= 2\psi_1 + 2\psi_2 - (\psi_1/n_{01}), \end{aligned} \quad (3.16a)$$

$$\begin{aligned} \langle \varphi \rangle_{11} &= (1/n_{11})[2\psi_2(n_{11} - 1) + \psi_2 + 2\psi_1 n_{11}] \\ &= 2\psi_1 + 2\psi_2 - (\psi_2/n_{11}). \end{aligned} \quad (3.16b)$$

The separation work from the kink is $\varphi_{\text{kink}} = 2\psi_1 + 2\psi_2$ and hence from (3.15) it ensues that

$$\begin{aligned} \Delta\mu &= \varphi_{\text{kink}} - \langle \varphi \rangle_{01} = \varphi_{\text{kink}} - \langle \varphi \rangle_{11} \\ &= (\psi_1/n_{01}) = (\psi_2/n_{11}), \end{aligned} \quad (3.16c)$$

which represents both the phase equilibrium and the ES of the 2-D crystal. In fact the ratio between the lengths of the most external rows is obtained as

$$(n_{01}/n_{11}) = (\psi_1/\psi_2). \quad (3.17)$$

Equation (3.17) is nothing other than Wulff's condition $(h_{01}/h_{11}) = (\gamma_{01}/\gamma_{11})$ applied to this small crystal (3.11) [3.21, p. 172].

The criterion of the mean separation work can also answer a question fundamental to both equilibrium and growth morphology: how can we predict whether a unit is stable or not in a given lattice site? Let us consider, as an example, the unit lying at corner X of the 2-D Kossel crystal (Fig. 3.7). Its separation work, within the second neighbors, reads $\varphi_X = 2\psi_1 + \psi_2$. Stability will occur only if the separation work of the unit X is higher than the mean separation work of its own row, i.e., $\varphi_X \geq \langle \varphi \rangle_{01}$ and hence, from (3.16c), $\varphi_X \geq \varphi_{\text{kink}} - \Delta\mu$. It ensues that $2\psi_1 + \psi_2 \geq 2\psi_1 + 2\psi_2 - \Delta\mu$. Finally, one obtains $\Delta\mu = k_B T \ln \beta \geq \psi_2$, which transforms to

$$\beta \geq \beta^* = \exp(\psi_2/k_B T). \quad (3.18)$$

This means that, when β is lower than the critical β^* value, the unit must escape from the site X, thus generating an ES which is no longer a square, owing to the beginning of the $\langle 11 \rangle$ row. In other words, the absolute size (n_{01}, n_{11}) of the crystal homothetically decreases with increasing β (ψ_1 and ψ_2 being constant), as ensues from (3.16c). Since $\psi_1 > \psi_2$, $n_{01} > n_{11}$ and the ES will assume an octagonal shape dominated by the four equivalent $\langle 01 \rangle$ sides, the octagon reducing to the square

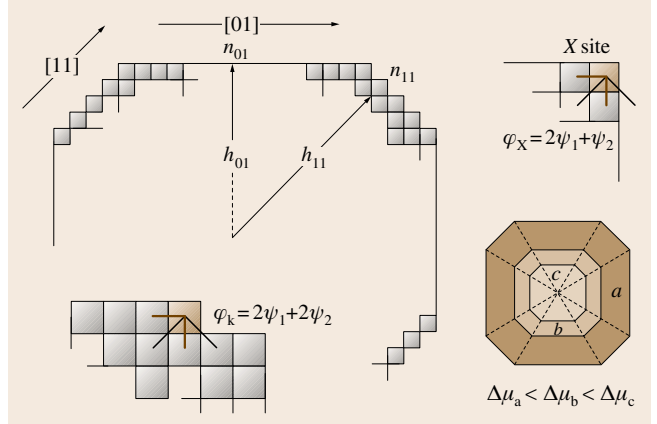


Fig. 3.7 To derive the equilibrium shape of a 2-D Kossel crystal by the criterion of the mean separation work, only the 1st, 2nd, ..., n -th-neighbors interactions are needed. The figure illustrates the scheme for the second-nearest neighbors approximation, the kink energy (φ_{kink}), the stability criterion for a unit X occupying a corner site and, finally, the 2-D equilibrium shape and size for $(\psi_1/\psi_2) = 1.5$ and for increasing supersaturation ($\Delta\mu$) values

when the number of units along the $\langle 11 \rangle$ sides is reduced to $n_{11} = 1$. As $\Delta\mu = (\psi_2/n_{11})$, this occurs when $\Delta\mu = \psi_2$, which exactly reproduces what we have just found in (3.18).

With Foreign Adsorption

In growth from solution a second component (the solvent) intervenes in the interfacial processes, since its molecules interact strongly with the crystallizing solute. Here we are interested in studying how the ES of a crystal is affected by the presence of a foreign component. Two approaches exist in order to give a full answer to this problem:

1. The *thermodynamic* approach, which allows one to forecast the variation $d\gamma$ of the surface tension γ of a face due to the variation $d\mu_i$ of the chemical potential of component i of the system, when it is adsorbed. To calculate $d\gamma$ for a flat face one has to apply Gibbs' theorem [3.22, p. 171]

$$d\gamma = -s^{(s)} dT - \sum_i \Gamma_i d\mu_i, \quad (3.19)$$

where $s^{(s)}$ is the specific surface entropy and $\Gamma_i = -(\partial\gamma/\partial\mu_i)_{T,s,\mu_{j \neq i}}$ corresponds to the excess of the surface concentration of component i . Solving (3.19) is not simple, even at constant T , since one has to know the functional dependence of Γ_i on

μ_i and hence on the activity a_i of component i . This means that one has to know Γ_i , which ultimately represents the adsorption isotherm of component i on a given face.

2. The approach grounded on the *atomistic view of equilibrium* proposed by Stranski [3.27, 28]. This model is based on the simplifying assumptions that foreign ad-units have the same size as those building the adsorbing surface (Kossel model) and that only first-neighbor interactions are formed between ad-units and the substrate. Three types of adsorption site are defined (Fig. 3.8), each of them having its own binding energy.

From (3.19) it ensues that adsorption generally lowers the surface tension of the substrate ($\Delta\gamma < 0$), so γ increases when an adsorption layer is reversibly desorbed. Let us denote the desorption work by $w = -\Delta\gamma \times a$, representing the increase per ad-site of the surface tension of the substrate (where a is the mean area occupied by an ad-unit) [3.29–31]. Thermodynamics allows to evaluate w , according to the type of adsorption isotherm [3.21, p. 175]

$$w = -k_B T \ln(1 - \theta) - (\omega/2)\theta^2 \quad \text{(Frumkin–Fowler type)}, \quad (3.20a)$$

$$w = -k_B T \ln(1 - \theta) \quad \text{(Langmuir type)}, \quad (3.20b)$$

valid when ω , the lateral interaction of the ad-unit with the surrounding, vanishes and

$$w = -k_B T \times \theta \quad \text{(Henry type)}, \quad (3.20c)$$

when the coverage degree in ad-units is low ($\theta \ll 1$). In the last case one can compare the θ values of the different sites remembering that, at given bulk concentration of foreign units, the coverage degree for an isolated ad-unit behaves as $\theta \propto \exp(\varphi_{\text{ads}}/(k_B T))$. Here, φ_{ads} is the

binding energy of the ad-unit with the substrate. From (3.20c) one can write

$$\frac{w_i}{w_j} = \frac{\theta_i}{\theta_j} = \exp \frac{(\varphi_{\text{ads}}^i - \varphi_{\text{ads}}^j)}{k_B T}, \quad (3.21)$$

which shows that the difference in the desorption works is very sensitive to the φ_{ads} value. This can be verified by applying (3.21) to the three sites in Fig. 3.8a of a cubic Kossel crystal and remembering that, in this case, φ_{ads} is equal to ψ_{ads} , $2\psi_{\text{ads}}$, and $3\psi_{\text{ads}}$, where $\psi_{\text{ads}} = k_B T$, $2 \times k_B T$, $3 \times k_B T, \dots$ is the energy of one adsorption bond. An important consequence of this reasoning is that *the chemical potential of an infinite crystal (and hence its solubility) is not changed by the adsorption of impurities on its surfaces*, as is proved by the balance detailed in Fig. 3.8b, which represents the initial and final stages of the desorption of a foreign unit from a kink site.

Let us now evaluate how the ES of a finite crystal changes, by applying the criterion of the mean separation works to the mentioned Stranski adsorption model. The stability of a unit in the corner site X when adsorption occurs (Fig. 3.9a) can be compared with that obtained without adsorption (3.18). The separation work of a unit in X is $\varphi_X^{\text{ads}} = 2\psi_1 + \psi_2 + 2w_1 - w_2$, where w_1 and w_2 are the desorption works for the two ad-sites, respectively.

The stability criterion requires $\varphi_X^{\text{ads}} \geq \langle \varphi \rangle_{01}$ and hence, from (3.16c), $\varphi_X^{\text{ads}} \geq \varphi_{\text{kink}} - \Delta\mu$.

Since $\varphi_{\text{kink}} = 2\psi_1 + 2\psi_2$, stability occurs only when $\Delta\mu \geq \psi_2 - (2w_1 - w_2)$. This implies

$$\beta_{\text{ads}}^* \geq \exp\{[\psi_2 - (2w_1 - w_2)]/(k_B T)\}. \quad (3.22)$$

Comparing (3.22) with (3.18) it turns out that the stability of the corner unit occurs at lower β value ($\beta_{\text{ads}}^* < \beta^*$) if $w_2 < 2w_1$. This means that, if the impurity fulfils the inequality $w_2 < 2w_1$, the ES is a pure square crystal at a β value lower than that predicted in pure growth medium. The $\langle 11 \rangle$ edges begin to appear when the corner units can escape from the crystal (instability of the X -site), i. e., if $\beta < \beta_{\text{ads}}^*$. On the contrary, if $w_2 > 2w_1$ the impurity adsorption does not favor the stability of the corner unit and an octagonal ES forms at a β value lower than that found in pure growth medium. Figure 3.9b illustrates how the smoothing of a 2-D K-face can be obtained with foreign adsorption [3.21, pp. 178–189]. The energy difference between the final and initial stages is that which we obtained for the X -site, so the conclusions are obviously those fulfilling (3.22). Figure 3.9c concerns the stability of an ad-unit (site A) on

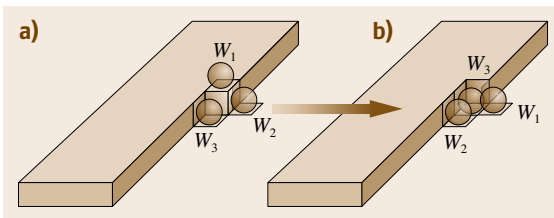


Fig. 3.8 (a) The three types of adsorption sites on a Kossel crystal (only 1st neighbors interaction). Each ad-site has its binding energy: $w_1 < w_2 < w_3$. (b) Energy balance representing the initial a) and the final b) stage of the desorption of a foreign unit from a kink-site. The binding energy does not vary on the adsorbance (after [3.21])

the $\langle 10 \rangle$ edges in the presence of foreign adsorption. The separation work of a unit at A is $\varphi_A^{\text{ads}} = \psi_1 + 2\psi_2 + 2(w_2 - w_1)$. The stability criterion for this site requires

$$\beta_{\text{ads}}^* \geq \exp\{[\psi_1 - 2(w_2 - w_1)]/(k_B T)\}, \quad (3.23)$$

while, in analogy with (3.18), the stability criterion without impurities reads

$$\beta^* \geq \exp\left(\frac{\psi_1}{k_B T}\right). \quad (3.24)$$

Thus, the foreign adsorption favors the stability of the growth units at site A if $\beta_{\text{ads}}^* < \beta^*$ and hence if $w_2 > w_1$. If this occurs, $\langle 10 \rangle$ edges transform from flat to rough owing to the random accumulation of ad-units.

Transferring these results from 2-D to 3-D crystals, the conditions expressed by (3.22) and (3.23), respectively, rule the transition of character K \rightarrow F and F \rightarrow K due to foreign adsorption.

The changes in the ES when adsorption occurs can now be calculated, according to the Stranski–Kaischew principle of the *mean separation work*. This means that, when an entire $\langle 10 \rangle$ or $\langle 11 \rangle$ row is removed from a 2-D crystal in the presence of adsorbed impurities, the mean separation works must fulfil the condition $\langle \varphi \rangle_{01}^{\text{ads}} = \langle \varphi \rangle_{11}^{\text{ads}}$, in analogy with (3.16a) and (3.16b). From calculation it ensues that

$$\left(\frac{n_{01}}{n_{11}}\right)_{\text{ads}} = \frac{\psi_1 - 2(w_2 - w_1)}{\psi_2 - (2w_1 - w_2)}, \quad (3.25)$$

which can be compared with the analogous expression (3.17) obtained without foreign adsorption

$$\begin{aligned} \left(\frac{n_{01}}{n_{11}}\right)_{\text{ads}} : \left(\frac{n_{01}}{n_{11}}\right) &= \frac{\psi_1 - 2(w_2 - w_1)}{\psi_2 - (2w_1 - w_2)} : \frac{\psi_1}{\psi_2} \\ &= \frac{\psi_1 \psi_2 - \psi_2 \times 2(w_2 - w_1)}{\psi_1 \psi_2 - \psi_1 \times (2w_1 - w_2)}. \end{aligned} \quad (3.26)$$

Hence the importance of the $\langle 10 \rangle$ edges in the ES increases to the detriment of the $\langle 11 \rangle$ edges, if the condition $2(w_2 - w_1)/(2w_1 - w_2) < \psi_1/\psi_2$ is fulfilled. A simpler solution is obtained within the first-neighbors approximation ($\psi_2 = 0$, $\psi_1 = \psi$). Remembering that, without foreign adsorption, the ES is a pure square, in the presence of impurities some changes should occur. In this case, expression (3.25) reduces to $(n_{01}/n_{11})_{\text{ads}}^{\text{1st}} = (\psi - 2(w_2 - w_1))/(w_2 - 2w_1)$.

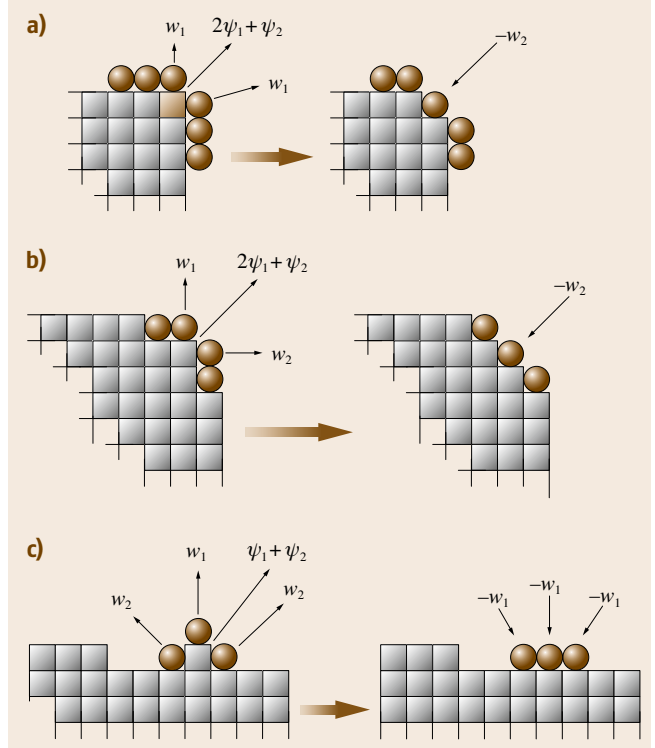


Fig. 3.9a–c The criterion of the mean separation works applied to the Stranski adsorption model in the second-neighbors approximation. (a) The first balance corresponds to the stability of the X site (*corner*) in the presence of foreign adsorption. (b) The second balance shows that the $\langle 11 \rangle$ row becomes smooth with foreign adsorption if $w_2 > 2w_1$. (c) The third balance describe the energies involved in calculating the stability of an ad-unit (site A) on the $\langle 10 \rangle$ edges in the presence of foreign adsorption. The figure has been inspired by [3.21]

The $\langle 11 \rangle$ row will exist if $n_{11} > 0$. Taking into account that necessarily $n_{10} > 0$, one must have simultaneously that $\psi > 2\psi(w_2 - w_1)$ and $w_2 > 2w_1$. The first inequality is verified by (3.23) since the ES of a finite crystal needs a supersaturated mother phase ($\beta_{\text{ads}}^* > 1$), so the only way for the $\langle 11 \rangle$ row to exist is for the second inequality also to be true, as found above. Summing up, the method of the *mean separation work* is a powerful tool to predict both qualitatively and quantitatively the ES of crystals, with and without foreign adsorption, without an a priori knowledge of the surface tension of their faces.

3.2 The Theoretical Growth Shape

When working with solution growth one usually has to deal with crystals having complex structures and/or low symmetry. In this case neither the Kossel model nor simple lattices, such as those related to the packing of rigid spheres, can be used to predict the most probable surface profiles. On the other hand, these profiles are needed both to evaluate the **ES** of crystals and for understanding the kinetics of a face. To do this, structural and energetic approaches have been developed.

3.2.1 The Structural Approach

The first works on theoretical growth morphology were grounded on structural considerations only and led to the formulation of the Bravais–Friedel–Donnay–Harker (BFDH) law [3.5, 6, 32]; see [3.33] for a recent review. According to this law, the larger the lattice distance d_{hkl} , the larger the morphological importance (**MI**) of the corresponding $\{hkl\}$ form

$$d_{h_1k_1l_1} > d_{h_2k_2l_2} \rightarrow \text{MI}(h_1k_1l_1) > \text{MI}(h_2k_2l_2), \quad (3.27)$$

$\text{MI}(hkl)$ being the relative size of a $\{hkl\}$ form with respect to the whole morphology. The inequality may also be viewed as the relative measure of the growth rate of a given form

$$R_{hkl} \propto (1/d_{hkl}) \quad (3.28)$$

once the *effective* d_{hkl} distances, due to the systematic extinction rules, are taken into account. Thus, the BFDH theoretical growth shape of a crystal can be obtained simply by drawing a closed convex polyhedron limited by $\{hkl\}$ faces whose distances from an arbitrary center are proportional to the reciprocal of the corresponding d_{hkl} values [3.5, 6]. The BFDH rule was improved [3.32], considering that many crystal structures show pseudosymmetries (pseudoperiods or subperiods), leading to extra splitting of the d_{hkl} distances, and hence to sublayers of thickness $(1/n) \times d_{hkl}$.

A typical example is that of the NaCl-like structures in which, according to the space group $Fm\bar{3}m$, the list of d_{hkl} values should be $d_{111} > d_{200} > d_{220}$, etc. Vapor-grown crystals show that the cube is the only growth form, while $\{111\}$ and $\{110\}$ forms can appear when crystals grow from aqueous solutions (both pure and in the presence of specific additives) [3.34]. This was explained [3.32] considering that the face-centered structural 3-D cell can also be thought of as a pseudo

unit cell (i.e., a neutral octopole) which, being primitive, leads to the cube as the theoretical growth shape.

The $R_{hkl} \propto (1/d_{hkl})$ structural rule works rather well since it implies an *energetic concept*. In fact, looking at the advancement of a crystal face as a layer-by-layer deposition, the energy released (per growth unit) when a d_{hkl} layer deposits on a fresh face is lower than that released by a sublayer since the interaction of the growth units slows down with their distance from the underlying face. Thus, the rule $R_{hkl} \propto (1/d_{hkl})$ is reasonable under the hypothesis that the face rate is proportional to the energy released when a growth unit attaches to it: $R_{hkl} \propto \text{probability of attachment}$. Nevertheless, this is a crude approximation, because neither the lateral interactions of the growth units nor the fact that only the flat faces can grow by lateral mechanism (i.e., layer by layer, as shown in Sect. 3.2.2) are considered.

3.2.2 Crystal Structure and Bond Energy: The Hartman–Perdok Theory

To go beyond these limitations, Hartman and Perdok (HP) looked at crystals as a 3-D arrays of bond chains building straight edges parallel to important $[uvw]$ lattice rows. Thus, *units* of the growth medium (**GU**) bind among themselves (through bonds in the first coordination sphere), forming more complex units that build, in turn, the crystal and reflect its chemical composition. These *building units* (**BU**) repeat according to the crystal periodicity, thus giving rise to *periodic bond chains* (**PBCs**). An example of a **PBC** is the set of equivalent **PBCs** running along the edges of the cleavage rhombohedron of calcite; these **PBCs** can be represented by the sequence shown in Fig. 3.10, where Ca^{2+} and CO_3^{2-} ions are the **GUs** assumed to exist in solution, the group CaCO_3 is the crystal **BU**, and the vector $\frac{1}{3}[\bar{4}41]$ is the period of the $[\bar{4}41]$ **PBC**. This **PBC** is stable, since the

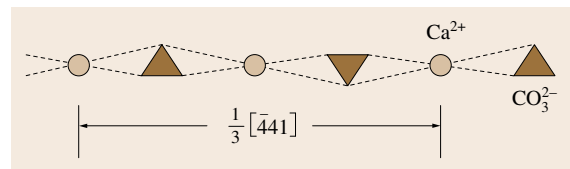


Fig. 3.10 Schematic drawing of the **PBC** running along the $[\bar{4}41]$ edges of calcite crystal. (○) calcium, (Δ) carbonate ions. The **PBC** is stoichiometric; the repeat period is shown. The dipole moments, perpendicular to the chain axis, cancel each other

resultant dipole moment cancels out perpendicular to its development axis.

When applying the **HP** method to analyze a crystal structure, one must look, first of all, at the effective d_{hkl} spacing. Then, one has to search for the number of different **PBCs** that can be found within a slice of thickness d_{hkl} . Three kinds of faces can be distinguished, according to the number n of **PBCs** running within the d_{hkl} slice ($n \geq 2$, 1 or 0). Looking at the most interesting case ($n \geq 2$), the **PBCs** contained in this kind of slice have to cross each other, so allowing one to define:

1. An area A_{hkl} of the cell resulting from the intersection of the **PBCs** in the d_{hkl} slice
2. The *slice energy* (E_{sl}), which is half of the energy released when an infinite d_{hkl} slice is formed; its value is obtained by calculating the interaction energy (per **BU**) between the content of the A_{hkl} area and the half of the surrounding slice
3. The *attachment energy* (E_{att}), i.e., the interaction energy (per **BU**) between the content of the area A_{hkl} and the semi-infinite crystal underlying it.

The **BUs** within the area A_{hkl} are strongly laterally bonded, since they form (at least) two bonds with the end of the two semi-infinite chains (Fig. 3.11). This implies that a **BU** forming on this kind of faces is likely to be incorporated at the end of the chains, thus contributing to the advancement of the face in (at least) two directions, parallel to the face itself. Hence, the characteristic of these faces will maintain their flat profile, since they advance laterally until their outermost slice is filled. In analogy with what we obtained within the frame of the Kossel crystal model, these are F-faces. Moreover, their E_{sl} is a relevant quantity with respect to their E_{att} , due to the prevailing lateral interactions within the slice. From Fig. 3.11 it ensues that the energy

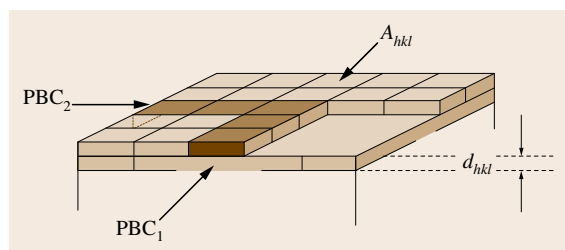


Fig. 3.11 Two **PBCs** within the slice d_{hkl} intersect in an elementary cell of area A_{hkl} , which occupies a kink site. The interaction of its content with half of the d_{hkl} slice gives the slice energy (E_{sl}); the interaction with all the crystal substrate gives its attachment energy (E_{att})

released (per **BU**) when the A_{hkl} content definitely belongs to the crystal is the crystallization energy (E_{cr}), which is a constant for a given crystal and hence for all crystal faces [3.35, p. 379]

$$E_{cr} = E_{att}^{hkl} + E_{sl}^{hkl} \quad (3.29)$$

This relation is of greatest importance to predict the growth shape of crystals, as can be understood when looking at the *kinetic meaning* of E_{att}^{hkl} . In fact, the central **HP** hypothesis is that, the higher the E_{att}^{hkl} value, the higher the probability that a **BU** will remain fixed to the (hkl) face, and thus of belonging to the crystal. It ensues that the E_{att}^{hkl} value becomes a relative measure of the normal growth rate of the $\{hkl\}$ form [3.36]

$$R_{hkl} \propto E_{att}^{hkl} \quad (3.30)$$

From (3.29) and (3.30) it follows that, as E_{sl} increases, both the attachment energy and the advancement rate of the face decrease. Examples par excellence can be found in layered crystal species such as the normal paraffins (C_nH_{2n+2}) and micas. Both cases are characterized by similar packing; in fact, in paraffin crystals, long-chain molecules are strongly laterally bonded within d_{00l} slices, while the interaction between successive slices is very weak; in micas, T-O-T sheets are built by strong covalent and ionic bonds whilst the interaction between them is ruled mainly by weak ionic forces. The best example is calcite, in which the E_{sl} of the $\{10\bar{1}4\}$ rhombohedron reaches 92% of the crystallization energy value and E_{att} reduces to account for the remaining 8%. This striking anisotropy explains, from one hand, the well-known cleavage properties of calcite and, on the other hand, the slowest growing of the $\{10\bar{1}4\}$ form, within a large β range and in the absence of impurities in the mother solution.

It is worth outlining the *similarity between the relation (3.2c) ruling the kink energy and the relation (3.29) defining the crystallization energy*

$$\varphi_{kink} = \varphi_{att} + \varphi_{slice} \rightarrow E_{cr} = E_{att}^{hkl} + E_{sl}^{hkl} \quad (3.31)$$

Both relationships can be expressed in energy/**BU**: the first relation concerns a single **GU** (atom, ion or molecule), while the second one is extended to a unit cell compatible with the d_{hkl} thickness allowed by the systematic extinction rules. This means that **HP theory permits one to predict the growth morphology of any complex crystal, through a brilliant extension of the kink properties to the unit cell of the outermost crystal layers.**

The example shown in Fig. 3.12a concerns the **PBC** analysis applied to the lithium carbonate structure

(space group $C2/c$). [001] PBCs are found along with another kind of PBC, running along the equivalent set of $\langle 110 \rangle$ directions. From this it ensues that the $\{110\}$ form has F-character, since two kinds of PBCs run within the allowed slice of d_{110} thickness. On the contrary, both $\{100\}$ and $\{010\}$ are S-forms, as no bond can be found between successive [001] PBCs within the slices of allowed thickness d_{200} and d_{020} , respectively. Figure 3.12b shows that only the $\{110\}$ prism exists in the [001] zone of a Li_2CO_3 crystal grown from pure aqueous solution, thus proving that the prediction obtained through the HP method is valid.

The choice of the BU is strategic for predicting both growth and equilibrium shapes. With reference to the preceding example, four different BUs can be found in Li_2CO_3 crystal, due to the distorted fourfold Li^+ coordination. Each of these BUs determines a different profile of the crystal faces and, consequently, different γ and E_{att} values. Hence, one has to search for all possible surface configurations and then calculate their corresponding γ and E_{att} values in order to choose those fulfilling the minimum-energy requirement.

Concerning methods to find PBCs and face characters, one has to carry out many procedures, ranging from the original visual method to computer methods, which began to be applied about 30 years ago and

reached their highest level of sophistication in elementary graph theory [3.11, 37–40], in which crystallizing GUs are considered as points and bonds between them as lines. A different computer method to find the surface profile with minimum energy was developed by Dowty [3.41], who searched for the plane parallel to a given (hkl) face cutting the minimum number of bonds per unit area, irrespective of the face character. This method has proved interesting as a preliminary step for calculating both equilibrium and growth crystal shapes. In the last 50 years, a lot of papers have been produced in which the theoretical growth morphology has been predicted for a wide variety of crystals exhibiting different types of bonds. The reader is invited to consult authoritative reviews on this subject [3.35, 42] and to proceed with caution in accepting predicted morphologies because there is a certain tendency to confuse, in practice, equilibrium and growth morphology.

3.2.3 The Effect of Foreign Adsorption on the Theoretical Growth Shape

In the original HP method, E_{att} is evaluated without considering either the temperature effect or the influence of the growth medium. Neglecting temperature does not imply a crude approximation on the predicted

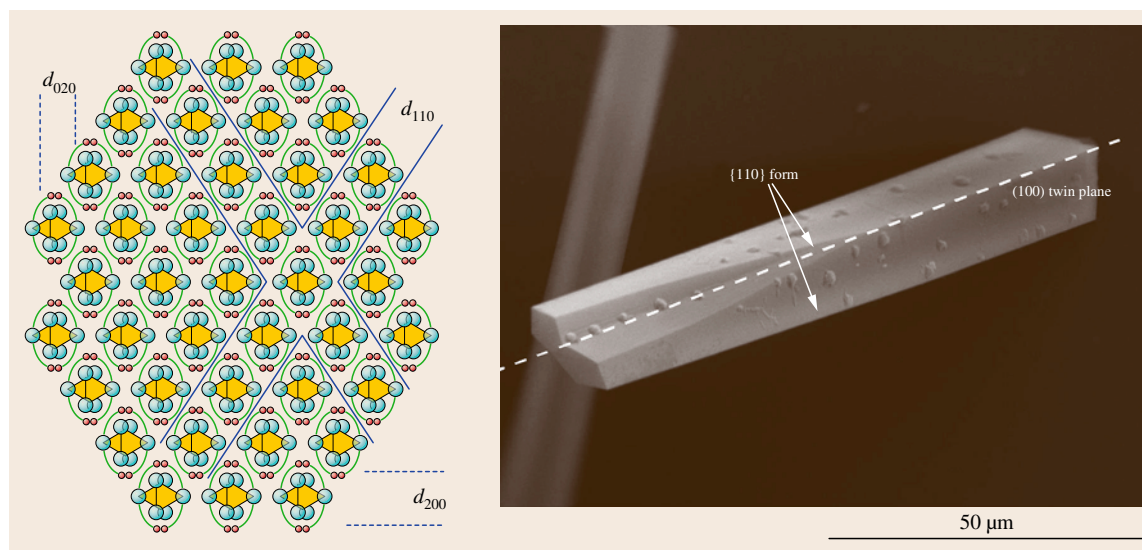


Fig. 3.12a,b Comparison between the experimental morphology, in the [001] zone, of lithium carbonate crystal and the theoretical one (HP method). (a) [001] PBCs are seen up-down with bonds among them, within the d_{110} slices. The $\{110\}$ prism is an F-form; the $\{100\}$ and $\{010\}$ are S-forms (no bonds within the slices of d_{200} and d_{020} , respectively). (b) Scanning electron microscopy (SEM) image of Li_2CO_3 twinned crystal grown from aqueous solution, showing the dominance of the $\{110\}$ prism. The 100 twin plane is indicated

equilibrium and growth shape, when dealing with low-temperature solution growth. In fact both γ and E_{att} values are not particularly affected by the entropic term, in this case. On the contrary, a condensed phase around the crystal (the solvent) and/or specific added impurities can deeply modify the behavior of the crystal faces.

The Role of the Solvent

This topic has been carefully examined, first with the aim of predicting *qualitatively* how the crystal–solution interface is modified by the solvent, and then which the slow-growing faces are likely to be. To do this, the roughness of the interface has been quantified in terms of the so-called α -factor [3.43, 44] which defines the enthalpy changes taking place when a flat interface roughens. This factor, originally conceived for crystal–melt interface, has been modified for solution growth and is commonly expressed in two ways

$$\alpha = \xi_{hkl} \frac{\Delta H_s}{RT} \quad \text{or} \quad \alpha = \xi_{hkl} \left[\frac{\Delta H_f}{RT_m} - \ln X_s(T) \right], \quad (3.32a)$$

where ΔH_s represents the heat of solution at saturation, ΔH_f the heat of fusion, X_s the solubility, T_m the temperature of fusion, and ξ_{hkl} is a factor describing the anisotropy of the surface under consideration [3.44]. ξ_{hkl} is evaluated by means of HP analysis, since it is strictly related to the slice energy of the $\{hkl\}$ form

$$\xi_{hkl} = \frac{E_{hkl}^{\text{slice}}}{E_{\text{cr}}}. \quad (3.32b)$$

Three different situations occur, according to the α value:

1. When $\alpha \leq 3$, the interface is rough and the face behaves as a K- or S-face.
2. If $3 \leq \alpha \leq 5$, the interface is smoother (F-face) and the creation of steps on the surface becomes a limiting factor at low β -values (birth and spread of 2-D nuclei).
3. When $\alpha > 5$ the growth at low β is only possible with the aid of screw dislocations since the barrier for 2-D nucleation is too high.

Equations (3.32a) and (3.32b) clearly show that different $\{hkl\}$ forms should have different α -factor values, not only owing to the ξ_{hkl} anisotropy, but also because of the solubility and of the heat of solution. Thus, the crystal morphology will also be dependent on the growth solvent.

As mentioned above, the evaluation of the α -factor is useful for predicting if a crystal form can survive

against competition with other forms, but nothing can be deduced on the relative growth rates of the surviving forms. To overcome this drawback, solvent interaction with crystal surfaces was considered quantitatively by Berkovitch-Yellin [3.14, 45] who calculated the electrostatic maps of certain faces and identified the most likely faces for adsorption.

A clear example of the role played by the solvent is that concerning the theoretical equilibrium and growth forms of sucrose. We will not consider here its polar $\{hkl\}$ forms to avoid the complications due to the coupling of adsorption and polarity; rather we will confine our attention to the nonpolar $\{h0l\}$ forms. HP analysis shows that the theoretical growth morphology of sucrose agrees with the experimental one, obtained from pure aqueous solution, with the only exception of the $\{101\}$ form [3.46]. In fact, the $[010]$ PBCs are not connected by strong bonds (H-bonds in this case) within the d_{101} slice (Fig. 3.13a) and then $\{101\}$ should behave as an S-form. Nevertheless, the S-character does not agree with its high occurrence frequency ($\approx 35\%$), rather unusual for a stepped form. The way to get out of this discrepancy is composed of two paths.

First, *one has to carry out a quantitative HP analysis* considering the strength of the PBCs running within the d_{101} slice. The energies released when a molecule deposits on the top of different molecular chains (i.e., the end chain energy, ECE) have been calculated. It results that $\text{ECE}[010] = -0.525 \times 10^{-12}$ and $\text{ECE}[10\bar{1}] = -0.077 \times 10^{-12}$ erg/molecule. These interactions being attractive, two PBCs really exist in the d_{101} slice and $\{101\}$ is a F-form, contrarily to what was concluded through qualitative application of the HP method. However, its F-character is weak, due to the strong anisotropy between the two PBCs and its E_{att} value being too high with respect to those of the other $\{h0l\}$ forms, so that the $\{101\}$ form cannot belong to the growth shape of the crystal (Table 3.2 and Fig. 3.13b).

Secondly, one has to *consider the specificity of water adsorption* on the $\{101\}$ surfaces. In fact, even if H-bonds do not exist within a d_{101} slice at the crystal–solution interface, water adsorption can occur between two consecutive $[010]$ chains by means of two strongly adsorbed water molecules over a $[010]$ period. Then, a new $[11\bar{1}]$ PBC forms and the PBC $[10\bar{1}]$ results stronger on the outermost crystal layer than in the crystal bulk. Consequently, the F-character of the face is greatly enhanced. This kind of water adsorption is specific to this form, as all other faces in the $\{h0l\}$ zone are built by $[010]$ PBCs strongly bonded among them, without allowing free sites for bonding of interchain wa-

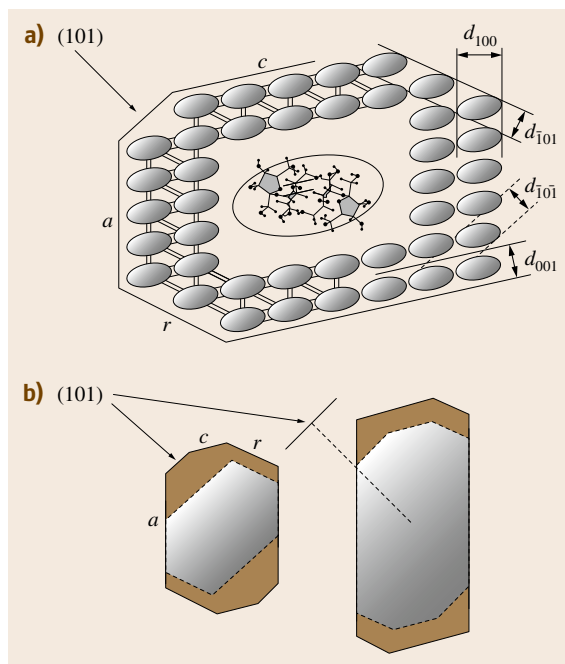


Fig. 3.13 (a) Projection along the [010] PBC of the sucrose structure. Each ellipse, containing two sucrose molecules, fixes the boundaries of a PBC. No bond can be found between two consecutive PBCs within a slice d_{101} , whilst bonds occur within the other $\{h0l\}$ forms. (b) Theoretical equilibrium and growth shapes of sucrose in the [010] zone, calculated without (full line) and with water adsorption (dotted line) (after [3.46])

ter molecules. New equilibrium and growth shapes are obtained (Fig. 3.13b), remembering that γ_{hkl} can be obtained from E_{att}^{hkl} through the relationship holding for molecular crystals [3.36], where the second-neighbors interactions are weak

$$E_{\text{att}}^{hkl} \cong \gamma_{hkl} \times 2A_{2D}^{hkl} / z, \quad (3.33)$$

where A_{2D}^{hkl} is the area of the unit cell related to the d_{hkl} slice and z are the molecules within it. Growth isotherms showed that the {101} form can grow by a spiral mechanism, thus proving its F-character, and that water desorption is the rate-determining process of its kinetics. Moreover, and for the first time, the idea of E_{att} was also successfully extended to the spiral steps running on the {101} surfaces, thus proving that the attachment energy at the spiral steps determines the growth shape of spirals, especially at low supersaturation values [3.47].

Table 3.2 Calculated surface (γ_{h0l} : erg cm⁻²) and attachment energies (E_{att}^{h0l} : 10⁻¹² erg/molecule) for the $\{h0l\}$ zone of sucrose crystal, in the crystal-vacuum system at $T = 0$ K

Form	{100}	{101}	{001}	{10 $\bar{1}$ }
γ_{h0l}	143	201	206	198
E_{att}^{h0l}	0.96	2.50	1.92	2.01

PBC analysis has been used, in recent times, as a preliminary step for predicting growth morphology in the presence of the solvent. A general and powerful kinetic model was elaborated by the *Bennema* school [3.13] in which growth mechanisms of the faces are considered, that is, spiral growth at low β -values and 2-D polynucleation at high β -values. Furthermore, to analyze the influence of the fluid phase on the crystal morphology, an interfacial analysis has been developed within the framework of inhomogeneous cell models [3.48, 49]. However, this model suffers from some limitations, since it is assumed that in solution growth the solute incorporation into the steps is governed by direct diffusion of molecules into the kinks. Experiments show that this is not always the case. Good examples are those of the growth isotherms obtained by the Boistelle group in Marseille for the normal paraffins. Surface diffusion is the rate-determining step for the {110} form of octacosane (C₂₈H₅₈) crystals [3.50], while coupled volume and surface diffusion effects dominate the growth rate of {001} form of hexatriacontane (C₃₆H₇₄) crystals growing from heptane solution [3.51, 52]. Another interesting case is that represented by the complementary {110} and {1 $\bar{1}$ 0} F-forms of sucrose crystals, which are ruled by volume and surface diffusion, respectively, when growing from pure aqueous solution between 30 and 40 °C [3.53, 54].

The modifications induced on E_{att} by the solvent have been evaluated theoretically by considering the relationship (3.33) holding for molecular crystals and obtaining a new expression for E_{att} , where the maximum number (n_s) of solvent molecules interacting with the surface unit cell (S_{hkl}) and their interaction energy (E_{hkl}^i) is taken into account [3.55]

$$\begin{aligned} E_{\text{att}}^{hkl} (\text{solvent modified}) \\ = E_{\text{att}}^{hkl} - [n_s E_{hkl}^i - N_A S_{hkl} \gamma_s] \times Z^{-1}, \end{aligned} \quad (3.34)$$

Z and N_A being the number of molecules in the unit cell and the Avogadro number, respectively. Expression (3.34) can be also easily adapted to the adsorption of an additive, treated as a medium, once the adhesion

energy of the solvent has been adequately replaced by that of the additive. This solvent-effect approach was successfully applied to the growth of the α -polymorph of glycine from aqueous solution, since a bi-univocal correspondence was found among the theoretical and experimentally observed F-faces. Moreover, this model explained as well the replacement of the most important {110} form of γ -aminobutyric acid in vacuo by the {120} form in water, and the flattening of the {001} form when a cationic or H-bonding additive is used [3.56].

The most complex and up-to-date method for predicting the growth morphology from solution was proposed by the Bennema school. Two interesting examples will be illustrated here.

In a first paper [3.57] it was shown that both 3-D and surface morphologies of tetragonal lysozyme crystals could be explained by a connected net analysis based on three different bond types corresponding to those used in the Monte Carlo growth simulation. Besides, the E_{att} of the different forms were estimated, along with their step energies. Furthermore, the significant β dependence of the relative growth rates of the {110} and the {101} forms, experimentally observed, was coherently explained on the basis of the multiple connected net analysis. More recently [3.58] a comparison was made between the E_{att} method and Monte Carlo simulations applied to all faces occurring in the growth morphology, with both approaches based on the connected net analysis. This was done considering that the E_{att} method cannot, intrinsically, take into account T , β , and growth mechanisms, while the simulation [3.59] can not only do this, but can also predict growth with or without the presence of a screw dislocation. The comparison was applied to solution growth of the monoclinic polymorph of paracetamol, using four different force fields [3.58]. It resulted that:

- The force field has only a small effect on the morphology obtained by the E_{att} method.
- The morphology so predicted does not resemble the experimentally ones for any of the β regimes.

Monte Carlo simulation gave different results, even under the limiting assumption that surface diffusion could be neglected: the {110}, {201}, and {100} forms have for all crystal graphs approximately the same growth curves, while all graphs show very different growth behaviors for the other two forms, {001} and {011}, owing to the differences of their step energies. Moreover, the {100} form is the theoretically fastest-growing form, according to the experimental observations. Finally, from the overall comparison between Monte Carlo simu-

lated and experimental morphologies, it emerged that the simulated results were poorer in form, even if the β effect was accounted for. This discrepancy is due to the {201} faces, which grow too slowly in the simulations and then assume too large an importance when compared with the other forms.

The Effect of Impurity Adsorption on the Theoretical Growth Shape

A large body of research on this topic is that carried out on NaCl-like crystals when specific ions are added to pure aqueous mother solutions. In the NaCl structure there are strong PBCs, in the equivalent $\langle 100 \rangle$ directions, determining the F-character of the cube- $\{100\}$ form. Other zigzag $\cdots \text{Na}^+ - \text{Cl}^- - \text{Na}^+ - \text{Cl}^- \cdots$ chains run along the $\langle 110 \rangle$ directions, within slices of thickness d_{111} , but they are polar chains and thus cannot be considered PBCs. Consequently, the {111} octahedron has K-character and is electrically unstable, being built by faces consisting of alternating planes containing either Na^+ or Cl^- ions. Stability can be achieved by removing 3/4 of the ions of the outermost layer and 1/4 of the subjacent one: thus, the new unit cell of the crystal, a cubic $4 \times [\text{Na}^+ \text{Cl}^-]$ octopole, has no dipole moment. Nonetheless, the *reconstructed octahedron maintains its K-character* and cannot appear either at equilibrium or in the theoretical growth shape of the crystal, owing to the too high values of $\gamma_{111}^{\text{NaCl}}$ and $E_{\text{att}}^{111(\text{NaCl})}$ with respect to $\gamma_{100}^{\text{NaCl}}$ and $E_{\text{att}}^{100(\text{NaCl})}$, respectively [3.60, 61]. Evidence of this behavior was shown by annealing {111} faces of NaCl crystals, near equilibrium with their vapor, and proving that they were structurally similar to those predicted by the reconstructed model [3.62].

A widely different situation emerges when NaCl-like crystals grow in solution in the presence of minor amounts of species such as Cd^{2+} , Mn^{2+} , Pb^{2+} , urea ($\text{CO}(\text{NH}_2)_2$), Mg^{2+} , and CO_3^{2-} . The most complete contribution on this subject is that of the Kern school [3.63–67]. Apart from the influence of β on the growth shape, Cd^{2+} is the most effective impurity, as even a small concentration gives rise to the habit change $\{100\} \rightarrow \{100\} + \{111\}$, as observed by optical microscopy. This change is not due to the random adsorption of Cd^{2+} ions on the {111} surfaces; it was attributed first to 2-D epitaxial layers of CdCl_2 , which can form matching the {111} surface lattice even if the mother solution is unsaturated with respect to the 3-D crystal phase of CdCl_2 [3.66]. Later on, and after measurements of adsorption isotherms, another interpretation was proposed [3.67]: the adsorption 2-D

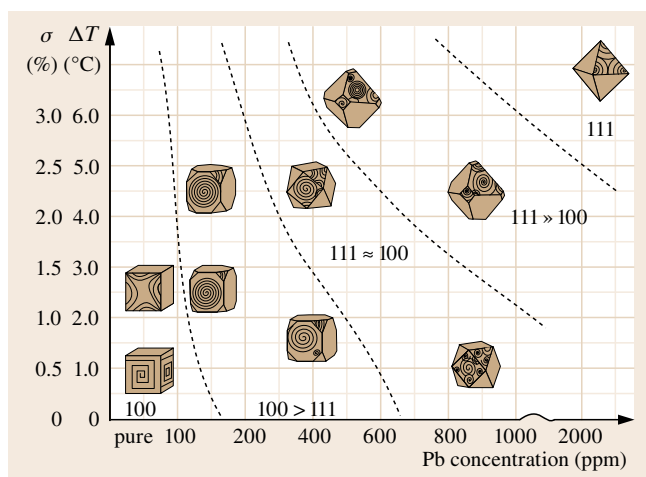


Fig. 3.14 Morphodrome showing the change $\{100\} \rightarrow \{100\} + \{111\}$ of crystal habit of KCl crystals with supersaturation excess ($\sigma = \beta - 1$) and impurity (Pb^{2+} ion) concentration. Surface patterns are also drawn (after [3.71])

epitaxial layer assumes the structure of the mixed salt $\text{CdCl}_2 \cdot 2\text{NaCl} \cdot 3\text{H}_2\text{O}$ once the isotherm has reached its saturation value. This hypothesis was supported by the finding, at supersaturation, of 3-D crystallites of the mixed salt epitaxially grown on $\{111\}$ surfaces. However, the existence of the 2-D epitaxial adsorption layer was not proved experimentally. More modern and recent research, based on optical observations, AFM measurements, and in situ surface x-ray diffraction [3.68–70] led to the conclusion that the polar $\{111\}$ surface should be stabilized by a mixed monolayer of Cd^{2+} (occupancy 0.25) and water (occupancy 0.75) in direct contact with the top Cl^- layers of $\{111\}$ NaCl underneath.

Summarizing, the evidence that emerges from this long-debated topic is that: when the surface of the growing crystal undergoes some intrinsic structural instability, such as surface polarity, and the growth medium contains some suitable impurities, *more or less ordered and layered structures form at the interface*, lending stability to the surface structure.

Since supersaturation plays a fundamental role in habit change, a sound and practical method was proposed [3.34] to represent the crystal habit as a function of both supersaturation (β) and impurity concentration. This drawing was called a *morphodrome*, as illustrated in Fig. 3.14, showing the changes of crystal habits of

KCl crystals with β and impurity (Pb^{2+} ion) concentration [3.71].

A behavior similar to that of NaCl-like crystals is shown by calcite (CaCO_3) crystals growing in the presence of Li^+ ions, which generate the $\{10\bar{1}4\} \rightarrow \{10\bar{1}4\} + \{0001\}$ morphological change [3.72]. Also in this case the formation of a 2-D epitaxial layer of the monoclinic Li_2CO_3 seems to be the most reasonable way of stabilizing the $\{0001\}$ form. In fact, AFM observations prove that lithium promotes the generation of quasiperiodic layer growth on the $\{0001\}$ surfaces ($\text{K} \rightarrow \text{F}$ character transition), while structural calculation indicates that Li^+ ions coming from the mother phase can perfectly take the place of calcium ions missing in the outermost reconstructed calcite layers. The credibility of this epitaxial model is enhanced by ab initio calculation [3.73] showing that the relaxed CO_3^{2-} ions, belonging to the d_{002} slice of Li_2CO_3 at the calcite/ Li_2CO_3 interface, entail the best coupling with the relaxed position of the outermost CO_3^{2-} ions of the reconstructed calcite crystal.

Certainly, the search for an epitaxial model for solution growth is most intriguing when one can both predict and interpret the effect of an impurity on the crystal habit, especially when the solvent may favor the formation of a structured crystal–solution interface. Nevertheless, there are other ways of assessing the impurity effects. One of these is to consider the modifications introduced by the impurity on the *energetics* of the elementary cell of the crystal in its outermost layer. This is the case for *disruptive tailor-made additives* [3.74], which are generally smaller than the host system but with a high degree of molecular similarity (e.g., benzamide/benzoic acid), which can adsorb on specific surface sites and thus influence the attachment energy value associated with the adsorption of subsequent growth layers. On the other hand, the *blocker type of molecular additive*, which is structurally similar but usually larger than the host material, has an end group which differs significantly and hence can be accepted at specific sites on some crystal faces. Thus, the end group (the blocker) prevents incoming molecules getting into their rightful positions at the surface. In fact, in the naphthalene–biphenyl host–additive system the E_{att} values of the different $\{hkl\}$ forms are selectively modified by the blocker additive. Steric repulsion resulting from the atoms of the blocker residing close to, or actually in, the same physical space in the crystal as atoms of the adjacent host molecules, both lowers the corre-

sponding E_{att} value and prevents host molecules from adsorbing, due to the blocking of surface sites [3.75]. Summarizing, the effects of solvent and impurities were

globally considered by calculating, through an ad hoc program, modified attachment energy terms, leading to simulated modified morphologies [3.76].

3.3 Factors Influencing the Crystal Habit

It is convenient to state some definitions. By *morphology* we mean the set of $\{hkl\}$ crystal forms occurring in a crystal independent of the surface areas, which is taken into consideration in the *crystal shape*. *Crystal habit* has to do with the dominant external appearance and is related to growth conditions. In the following only crystal habit is considered.

Crystals of the same phase can exhibit a great variety of crystal habits. This was one of the major difficulties in the beginning of crystal study and partly still remains, notwithstanding the enormous theoretical and experimental progress. This subject has both scientific and applied relevance. In many industrial sectors, crystal habit change is necessary to prevent crystal caking, filter crystal precipitates, obtain more convenient crystal products (in terms of shape, size, size repartition, purity, quality, etc.), simplify storage and package, etc. Empiricism played an important role in industrial crystallization in the past, but has been progressively supported and replaced by knowledge of crystal growth mechanisms and phenomenological rules.

Experiments show that crystal faces generally grow layer by layer, as already noticed by Niels Steensen. They move at different rates, and the fast-growing ones are destined to disappear. Therefore the habit of a crystal is determined by the faces having the slowest growth rates. Crystal habit may change either through the relative development of already existing $\{hkl\}$ forms or the appearance of new $\{h'k'l'\}$ forms.

The procedures to study the crystal habit change are well established: experimental crystal habits, grown from different solvents, are compared to the theoretical one, which may be obtained by calculations with different available methods (BFDH, PBC-attachment energy-connected nets, IS analysis) or by growing the crystal from the vapor phase, in which the fluid–solid and fluid–fluid interactions are negligible. Indeed, a complete study should involve the growth kinetics of each face, in order to determine its growth mechanism and the roles of the specific solvent and/or impurity.

As the crystal–solution interface is the critical site for face growth and crystal habit, all available approaches are applied to the study of this surface. A list is given in Chap. 5. The factors influencing the crystal habit are numerous and have different effects, which explains the great habit variability. They are usually classified into two main categories:

1. Internal factors: the crystal structure, on which the surface structures (i. e., the profiles) of the faces depend, and crystal defects
2. External factors, which act from the *outside*: supersaturation, the nature of the solvent, solution composition, impurities, physical conditions (temperature, solution flow, electric and magnetic fields, microgravity, ultrasound, etc.).

There are also mixed factors, such as the free energy of crystal surfaces and edges, which depend on both crystal surface structure (an internal factor) and the growth environment (an external factor). The most important ones are considered separately in the following, even if it is necessary to look at the crystal growth as a whole, complex process, in which a change in one parameter (temperature, solubility, solvent, supersaturation) influences all the others, so that they together affect crystal growth and habit. Let us consider a polymorphic system made of two phases: A and B. Changing, for example, the solvent at constant temperature and concentration, both surface free energy (γ) and supersaturation (β) are changed. If these variations are small, changes concern only the crystal habit of one polymorph (e.g., A). If the variations are large, the nucleation frequencies of the two polymorphs can be so affected that a change in crystal phase occurs and the B polymorph may nucleate. The same considerations apply to the temperature change, which promotes variations in solubility, surface tension, and supersaturation, especially in highly soluble compounds.

3.4 Surface Structure

Each crystal face has a specific surface structure, which controls its growth mechanism. As the crystal habit is limited by the faces having the slowest growth rates, i. e., the F-faces, in the following only the F-faces will be considered. The surface of an F-face is not perfectly flat and smooth, but is covered by steps and other features (hillocks), which condition the growth rate of the face and its development. Indeed, layer growth is possible when the edge energy of a 2-D nucleus is positive [3.2, 27]. The growing steps may be inclined with respect to the surface, forming an acute and obtuse angle which advance at two different velocities, as observed on the {001} face of monoclinic paraffins [3.77]. Surface features (dislocation activity, step bunching) and parameters (step speed, hillock slope) are sensitive to supersaturation and impurities and behave in different ways at low and high supersaturation, with linear and nonlinear dependence [3.78]. Connected to these factors is the morphological instability of steps and surfaces, which is enhanced or prevented by shear flow, depending on the flow direction [3.78–83]. Great theoretical, experimental, and technical contributions to the study of surface phenomena are due to Russian [3.78–81], Dutch [3.82–85], and Japanese [3.15, 16, 86] groups as well as to other researchers [3.87–92] and to those quoted in all these papers. Surface phenomena and morphology have been recently reviewed [3.15–18]. AFM has enormously enlarged this research field, as it allows the observation of the surface features of the growing faces both ex situ and in situ at a molecular level. This new technique is providing a growing number of new data and observations, and at the same time renewing and stimulating interest in surface phenomena and processes, especially step kinetics, impurity effects, edge fluctuations, and stability.

3.4.1 The α -Factor and the Roughening Transition

In Sect. 3.2.2 the concept of α -factor was introduced as a measure of the roughness of a surface and its probable growth mechanism. Knowledge of α is mostly useful; however, it may be not sufficient, as noticed for several alkanes, which show the same α value in different solvents, yet have different growth mechanisms [3.93], and also for the {010} and {001} faces of succinic acid grown from water and isopropyl alcohol (IPA). Each face has the same α -value in both solvents; nevertheless the growth rates are appreciably lower in IPA

than in water, owing to different efficiency of hydrogen bonding with IPA and water molecules [3.45]. With increasing temperature (3.32a) the α -factor decreases and may reach values lower than 3.2. In that case the surface loses its flatness, becomes rough, and grows by a continuous mechanism. This transition occurs at a definite roughening temperature which is characteristic for each face. For example, the {110} faces of paraffin $C_{23}H_{48}$ growing from hexane has a roughening temperature of $T^R = 10.20 \pm 0.5$. Below T^R the faces are straight, whereas above it they become rounded even if supersaturation is very low [3.11].

3.4.2 Kinetic Roughening

Beside thermal roughening, a surface may undergo kinetic roughening, which occurs below the roughening temperature when the supersaturation exceeds a critical value. In this case the sticking fraction on the surface is so high and the critical two-dimensional nucleus so small that the surface becomes rough and grows through a continuous mechanism. This behavior was observed on the {100} faces of NaCl in aqueous solutions [3.94] and in naphthalene crystals, which become fully rounded when σ attains 1.47% in toluene solvent. The same does not occur with hexane, due to structural dissimilarity of hexane molecules with respect to naphthalene [3.11]. Four criteria used to identify the beginning of kinetic roughening have been studied by Monte Carlo simulations on a Kossel (100) surface, leading to different values of the critical driving force [3.95].

3.4.3 Polar Crystals

In polar crystals a d_{hkl} slice may present a dipole moment. In that case a correction term, E_{corr} , should be added to the expression for E_{att} to maintain the value of E_{cr} constant [3.35, 36] (Sect. 3.2.2, (3.29)), i. e.,

$$E_{\text{cr}} = E_{\text{att}} + E_{\text{slice}} + E_{\text{corr}}, \quad (3.35)$$

with $E_{\text{corr}} = 2\pi\mu^2/V$, where V is the volume of the primitive cell and μ the dipolar moment of the slice (per formula unit) [3.96]. The surfaces of the two opposite faces (hkl) and ($\bar{h}\bar{k}\bar{l}$), being structurally complementary, interact in a selective way with the solvent and impurity molecules. The final result is a different development of these faces, which may lead to the occurrence of only one form, as observed in the case

of the $(011)/(0\bar{1}\bar{1})$ faces of $\text{N}(\text{C}_2\text{H}_5)_4\text{I}$ [3.97] and the $\{100\}$, $\{\bar{1}\bar{1}\bar{1}\}$, $\{0\bar{1}\bar{1}\}$, and $\{1\bar{1}0\}$ faces of $\text{ASO}_3 \cdot 6\text{H}_2\text{O}$ ($\text{A} = \text{Co}^{2+}$, Ni^{2+} , Mg^{2+}). In this case the water molecules are selectively adsorbed on the opposite faces since they have a different surface distribution of sulfite ions and $\text{A}(\text{H}_2\text{O})_6^{2+}$ groups [3.98]. The structural differences can be so great that the two opposite faces may grow with a different mechanism, as experimentally shown for the $\{110\}$ and $\{1\bar{1}0\}$ faces of sucrose crystals: the former by volume diffusion with $\Delta G_{\text{cr}} = 10 \text{ kcal/mol}$ and the latter by surface diffusion with $\Delta G_{\text{cr}} = 21 \text{ kcal/mol}$ [3.54].

3.4.4 Looking at Surfaces with AFM

AFM is becoming a routine technique in growth laboratories. Most experiments are carried out in static conditions, some in the dynamic regime. One of the most studied compounds, besides proteins, is calcite. The $\{10\bar{1}4\}$ cleavage form grows via monomolecular

steps, which are differently affected by anion and cation impurities [3.99]. AFM has been used to assess the stability of the $\{111\}$ faces of NaCl in pure and impure aqueous solutions and to attempt to solve the problem of surface reconstruction [3.70, 71]. Through AFM investigation of the $\{100\}$ faces of potassium dihydrogen phosphate KDP, the dependence of macrosteps and hillocks on β was measured and new values of the step edge energy, kinetic coefficients, and activation energies for the step motion were calculated, confirming the models of Chernov and van der Eerden and Müller-Krumbhaar [3.100]. In studying the influence of organic dyes on potassium sulfate the link between the surface features at the nanoscale level and the macroscopic habit change was proved [3.101]. To sum up, AFM analysis enables local details of surface structure and their evolution in real time to be captured, yielding a lot of information, but has the drawback that it does not permit large-scale views of the face, so it has to be integrated with other instrumental (optical and x-ray) techniques.

3.5 Crystal Defects

Defects easily and usually occur in crystals. It is not necessary to emphasize the role of screw dislocations in crystal growth. As concerns edge dislocations, they could affect the growth rate since a strain energy is associated with the Burgers vector and then increases the growth rate. Combined research on the effect of dislocations on crystal growth with in situ x-ray topography was done on ammonium dihydrogen phosphate ADP crystal [3.78]. Edge dislocations were proved to be inactive in step generation on the ADP (010) face, whereas screw dislocations were active. When a dislocation line emerges on a given (hkl) F-face, the face grows at higher rate than the other equivalent ones and therefore decreases its morphological importance with respect to the others. In crystals with cubic symmetry the habit may change from cubic to tetragonal prism or square tablet. When a screw dislocation crosses an edge, it becomes inactive [3.78]. Contrary to the current opinion that increasing the growth rate leads to a higher defect density, as supported by Monte Carlo simulations [3.102], large crystals with a high de-

gree of structural perfection can be obtained with the method of *rapid growth*, which consists of overheating a supersaturated solution, inserting a seed conveniently shaped, and strongly stirring the solution submitted to a temperature gradient. The method, applied for the first time in the 1990s, allows the preparation in short time of very large crystals of technologically important compounds such as KDP and deuterated potassium dihydrogen phosphate DKDP up to 90 cm long and nearly free of dislocations. The crystal habit, bounded by $\{101\}$ and/or $\{110\}$ faces, may be controlled by creating dislocation structures during the seed regeneration and changing the seed orientation [3.103, 104]. Crystals grown with the traditional method at low temperature are smaller and rich in striations and dislocations, originated by liquid inclusions. Large perfect crystals can also be quickly grown from highly concentrated boiling water solutions. The method has been successfully applied to some compounds, such as KDP, $\text{Pb}(\text{NO}_3)_2$, and $\text{K}_2\text{Cr}_2\text{O}_7$. Due to the high growth rates and β values, the crystal habit becomes equidimensional [3.105].

3.6 Supersaturation – Growth Kinetics

The effect of supersaturation on growth morphology is well known, but not yet well understood, since

when a system becomes supersaturated, other parameters change in turn, especially in solutions of poorly

soluble compounds (phosphates, sulfates, etc.). In this case a change in β involves variations in solution composition, chemical species, and related phenomena (ion coordination, diffusion, etc.) [3.106]. First of all, β is important in controlling both the size and shape of the 3-D and 2-D critical nucleus (3.11) and in determining the growth kinetics. The growth rates of S- and K-faces are linear functions of β . For an F-face the dependence is more complicated, being related to the growth mechanism. The dependence law for R_{hkl} versus β may be parabolic, linear (in the case of a spiral mechanism), exponential (for two-dimensional nucleation) or again linear (when the face grows by a continuous mechanism at high β values). Spectacular habit changes are observed with increasing β . At high β values, first hopper crystals, then twins, then dendrites, and finally spherulites may form [3.107]. All possible cases are gathered in the diagram of R_{hkl} versus σ proposed by Sunagawa [3.108] (Chap. 5). The basic kinetic laws for growth controlled by surface diffusion, i.e., in the kinetic regime, are summarized here.

3.6.1 Growth Laws

For the spiral mechanism (BCF theory [3.7]) the growth rate of a (hkl) face is given by

$$R_{hkl} = \frac{v_{\infty} d_{hkl}}{y_0}, \quad (3.36)$$

where v_{∞} is the step velocity, d_{hkl} is the interplanar distance, and y_0 is the equidistance between the spiral steps. The step velocity for growth from solution [3.109] is given by

$$v_{\infty} = \beta_k c_0 D_s n_{s0} f_0 \frac{\sigma}{x_s} \tanh \frac{y_0}{2x_s}, \quad (3.37)$$

where β_k is a retarding factor for the entry of a growth unit (GU) in the kink, $c_0 = \frac{x_s}{x_0} \ln(2x_s/(1.78a))$ valid for $x_s \ll x_0$ (when $x_s \gg x_0$, $c_0 = 1$), x_s is the mean displacement of the GUs on the surface, x_0 is the mean distance between kinks in the steps, D_s is the diffusion constant of GUs in the adsorption layer, n_{s0} is the number of GUs in the adsorption layer per cm^2 at equilibrium, f_0 is the area of one GU on the surface, and $\sigma = (X - X_s)/X_s$ is the relative supersaturation (where X and X_s are the actual and equilibrium molar fraction, respectively). The step equidistance y_0 is given for low supersaturation by

$$y_0 = fr^* = \frac{f \rho a}{k_B T \ln \beta} \cong \frac{f \rho a}{k_B T \sigma}, \quad (3.38)$$

being f a shape factor, r^* the critical radius of the 2-D nucleus, ρ the edge free energy (erg/cm), and a the

shortest distance between GUs in the crystal. The relationship is simplified if the supersaturation β is low, in which case $\ln \beta \cong \beta - 1 = \sigma$.

Then (3.36) may be written as

$$R_{hkl} = C \frac{\sigma^2}{\sigma_1} \tanh \frac{\sigma_1}{\sigma}, \quad (3.39)$$

where C and σ_1 are constants:

$$C = \frac{\beta_k c_0 D_s n_{s0} \Omega}{x_s^2},$$

$$\sigma_1 = \frac{9.5 \rho a}{\varepsilon k_B T x_s},$$

where Ω is the volume of growth unit and ε is related to the number of interacting growth spirals.

When $\sigma \ll \sigma_1$ (i.e. $y_0 \gg x_s$)

$$R = C \frac{\sigma^2}{\sigma_1} \quad (\text{parabolic law}),$$

When $\sigma \gg \sigma_1$ (i.e. $y_0 \ll x_s$)

$$R = C \sigma \quad (\text{linear law}).$$

Other relationships were found by Chernov for direct integration in the kink [3.110] and by Gilmer et al. [3.111] for coupled volume and surface diffusion.

For the two-dimensional nucleation mechanism

$$\text{mononuclear mechanism } R_{hkl} = K_m J_{2D}, \quad (3.40)$$

$$\text{polynuclear mechanism } R_{hkl} = K_p v^{2/3} J_{2D}^{1/3}, \quad (3.41)$$

where K_m and K_p are the kinetic constants for the two types of mechanism, v is the step speed, J_{2D} is the 2-D nucleation frequency, which is given by

$$J_{2D} = K \exp\left(-\frac{f \rho^2 a^2}{(k_B T)^2 \ln \beta}\right), \quad (3.42)$$

where K and f are the kinetic and shape factors, respectively. Equation (3.42), formerly derived for growth from vapor state, is usually applied to growth from solution.

There is also a general empirical law

$$R_{hkl} = K' \sigma^n, \quad (3.43)$$

where K' is a kinetic temperature-dependent constant; the value of n is related to the mechanism.

3.6.2 Some Experimental Results

As $R_F < R_S < R_K$, in the growth form at a given β only F-faces can occur, although not necessarily all of

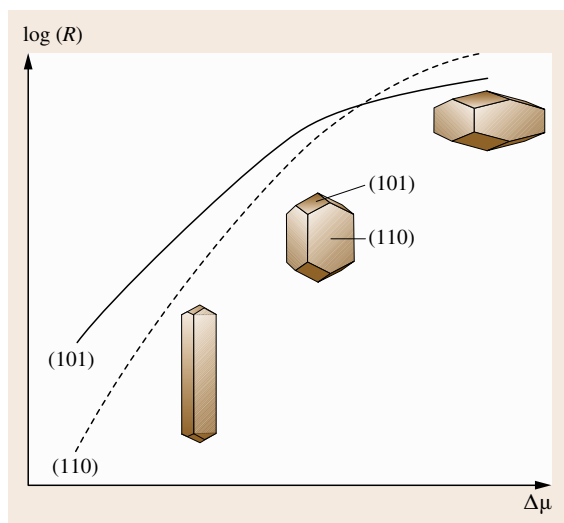


Fig. 3.15 Crossover of the growth rates versus thermodynamic supersaturation for the {110} and {101} faces of tetragonal lysozyme with change in crystal habit (after [3.57])

them. The faces of the same crystal may show a different dependence of R_{hkl} on β and then a crystal habit change can occur. The first static observations were made on NaCl, KCl, CsCl, KI, and many other ionic salts. When a crystal habit is made of F-faces, a higher critical supersaturation is needed for the S- or K-faces to appear [3.63, 112] (Sect. 3.2.2). When an F-face is replaced by another F-face at high supersaturation, the change is progressive. Kinetic measurements of crystal growth reveal that in most cases there is a supersaturation *dead zone* in which no growth occurs, and a critical supersaturation β^* should be reached for growth to start. Changes in relative face size and crystal habit are usually observed with increasing β [3.47, 53]. In *n*-paraffins the growth rate was found to be dependent also on the platelet thickness [3.93]. When a crossover in the relative growth rates of faces occurs, even radi-

cal changes in morphology are observed, as in the case of γ -aminobutyric acid [3.113] and lysozyme crystals (Fig. 3.15) [3.57, 114].

To explain the habit change, a variation in the crystal-solvent interaction is admitted, as for NaCl, CsCl, $M(H_2O)_6 \cdot SiF_6$, and CaF_2 [3.42]. In other cases the effect of supersaturation is attributed to the desolvation kinetics of the solute, as shown for KI, KBr, and KCl [3.115].

Supersaturation also causes changes in surface features, as seen on the {100} faces of $NH_4H_2PO_4$ (ADP), where there are no growth layers below a given β , and elliptical and then parallel layers appear with increasing β [3.116]. Supersaturation affects the activity of dislocation source [3.78]. The intensive studies of surfaces of ADP, KDP, and DKDP reveal that the step speeds on these faces and the hillock slopes may be nonlinear functions of β [3.78, 117]. This nonlinearity has been explained in terms of a complex dislocation step source [3.78], impurity adsorption [3.118], and the generation of kinks at growth steps [3.119]. Not only the step rates but also the kinetic coefficients can depend on β , which enhances the morphological instability [3.87]. It should be noted that, even in the kinetic regime, supersaturation is not constant along the growing face [3.78]. Small fluctuations in β may cause rapid change in the evolution of faces forming small interfacial angles, with the disappearance and reappearance of faces, as observed with potassium dichromate [3.120].

High supersaturation can determine phase transition, as shown in polymorph systems such as calcium carbonate, L-glutamic acid, and L-histidine [3.121]. Interest is also practical: from 2-propanol solutions it is possible through supersaturation to isolate the stable form of stavudine, an antiviral drug used for the treatment of human immunodeficiency virus-acquired immunodeficiency syndrome (HIV-AIDS) [3.122]. However resorting to high supersaturation in order to change the crystal habit is rarely used in industrial crystallization, as there is a risk of unwanted nucleation.

3.7 Solvent

Research into solvent effects on crystal growth and habit is relatively recent. In the years 1940–1967 a few studies were published, as summarized in two surveys papers [3.44, 123]. In the 1960s the first interpretations were geometric-structural [3.124]. The effect of the solvent in determining the mechanism of crystal

growth was evaluated through the entropic α -factor and the growth kinetics [3.44, 123]. Since then, interest in this topic has been increasing, also due to the mounting needs of industrial crystallization. Research was then successfully extended to tailor-made additives [3.14, 125] (see also Sect. 3.2.3). Molecu-

lar dynamics (MD) simulations are also extensively applied to study the solvent–surface interaction. The solvent itself acts as an impurity; however, due to its importance (e.g., concentration), it is treated separately.

3.7.1 Choice of Solvent

The first essential step for crystallization is the choice of solvent. Knowledge of solubility and of its change with temperature is required. The most common solvent is water, which exerts its influence even in traces in the vapor and liquid phase. When lead molybdate is grown in dry air, it crystallizes as needles, but as platelets in moisturized air [3.127]. Small amounts of water added to organic solvents markedly increase the yield and growth rate of the target polymorph of pharmaceutical compounds [3.128]. Growth in aqueous systems is a complex process. Water molecules are coordinated by cations and anions in solution; in addition, they can be

selectively adsorbed at the different sites on the growing faces (Fig. 3.16) [3.109, 126].

Dehydration and desolvation should then occur, besides diffusion, involving the respective activation energies [3.109]. It should be noted that solvent molecules (and possible impurities) are also involved in surface adsorption processes, with an ensuing competition between the corresponding energies (or relaxation times) of growth units. The bonds engaged may be ionic, hydrogen bond, and van der Waals, with energies of about 15 kcal/mol (for the $\text{H}_2\text{O}-\text{Na}^+$ bond), 5 kcal/mol in organic solutions with hydrogen bonds, whereas for the van der Waals bond the strength is one or more orders of magnitude smaller than that of the ionic one. Many other solvents, mostly organic and tailor-made, are nowadays used in the chemical industry. They differ from water in some molecular properties (dielectric constant, dipole moment, size, etc.) and are classified into three main classes: protic (hydrogen donors, e.g., methanol), dipolar aprotic (e.g., acetonitrile), and non-polar aprotic (e.g., hexane) [3.129].

3.7.2 Change of Solvent

Use is often made of different solvents in crystal growth. Solvent change has several correlated effects (on solubility and supersaturation, interactions with solute and crystal faces, surface free energy, etc.), and modifying the α -factor may change the growth mechanism. If a compound is grown from two different solvents, A and B, there are two values of α , which are related by [3.130]

$$\begin{aligned}\alpha_A &= \alpha_B + 4(\Phi_{B,\text{sf}} - \Phi_{A,\text{sf}})/(k_B T) \\ &\quad + 2(\Phi_{A,\text{ff}} - \Phi_{B,\text{ff}})/(k_B T) \\ &\approx \alpha_B + 4(\Phi_{B,\text{sf}} - \Phi_{A,\text{sf}})/(k_B T) .\end{aligned}\quad (3.44)$$

Let $\Phi_{A,\text{ff}} \approx \Phi_{B,\text{ff}}$. If the solute–solvent interaction energy $\Phi_{B,\text{sf}}$ is higher than $\Phi_{A,\text{sf}}$, then $\alpha_A > \alpha_B$. For example, the {110} faces of hexamethylene tetramine (HMT) grown in aqueous solution show $\alpha < 2.5$, whereas in ethanolic solutions the value is $\alpha = 3.2\text{--}5.4$ [3.130]. The growth mechanisms predicted by these values were confirmed by the growth kinetics [3.131]. Changing the solvent allows one to understand the role of the solvents and the bonds involved, as shown by *m*-nitroaniline. Grown from a nonpolar solvent, the crystal habit matches the theoretical one, based on the sole van der Waals bonds, whereas in polar solvents the electrostatic interactions play a great role [3.132]. By comparing steroid crystals grown from acetone and

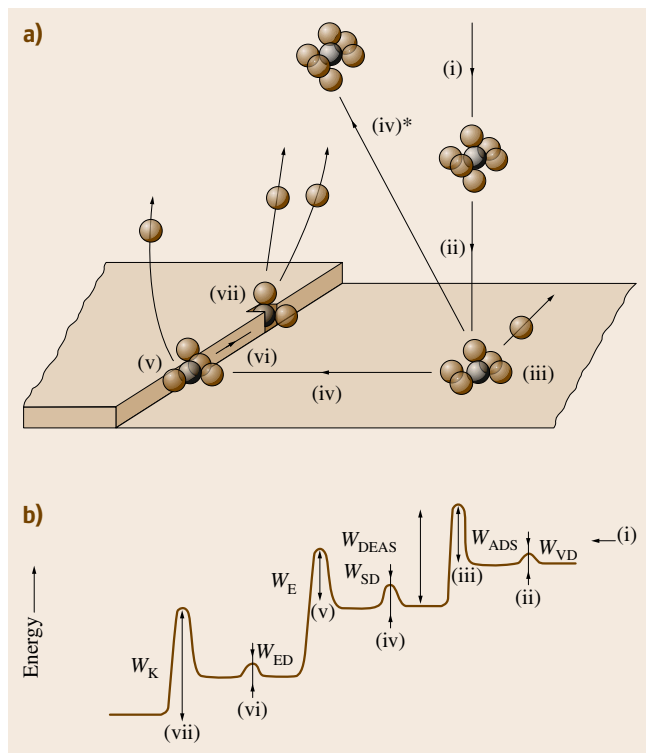


Fig. 3.16a,b The events leading to crystal growth: diffusion in the volume, on the surface, along the step, to the kink with integration; desolvation; and desorption. To each of these processes corresponds an activation energy of different magnitude (after [3.126])

methanol solutions and performing MD simulations of the solvent–surface interactions, it is found that the contributions of Coulomb and van der Waals bonds are more important than hydrogen bonding in determining the crystals habit [3.133]. Solvents may affect surface roughness [3.129] and the roughening transition of faces, with a change in the transition order too [3.134]. Mixtures of solvents are often used. They can show higher solubility than separate solvents, as happens with L-pyrogutamic acid, which is more soluble in a water–ethanol mixture than in pure water or pure methanol, with a strong change of crystal habit [3.135]. On the other hand, mixtures of water and isopropoxethanol, in which NaNO_3 is less soluble, do not affect the shape of the NaNO_3 crystals [3.136], whilst adding water to an ethanol–water solution saturated with benzoic acid reduces the solubility of the latter and causes its crystallization with habit change (the drowning-out technique) [3.137]. Solvent can also stabilize polymorphs, as shown with CaCO_3 precipitated from water or ethanol solutions [3.138], and promote the formation of twins as well [3.125].

3.7.3 Solvent–Solute

Molecules of solvent and solute always interact, affecting the growth kinetics according to the energy involved. The interaction is more pronounced in supersaturated solutions [3.106]. In aqueous solutions of ionic salts, solute clusters which have the lattice structure of the crystal surface can form [3.139]. In aqueous solutions of hexamethylene tetramine (HMT), each HMT molecule coordinates four water molecules, whereas in alcoholic solutions there is no coordination, with consequences for the growth mechanisms [3.123]. Solute dimers may form, and tetramers, octamers, and even larger -mers were also detected in lysozyme solutions at high supersaturation [3.57]. The strong morphological difference of alizarin crystals grown from alcoholic and other organic solvents is attributed to the partial deprotonation of the alizarin molecules occurring in alcohol solutions, which blocks the needle growth of the side faces, leading to a totally different habit [3.140].

3.7.4 Solvent–Crystal Surface

The approach to the problem of the role played by solvent–crystal interactions is different according to the system being studied and theoretical assumptions.

A relevant role is attributed to the α -factor [3.123, 130] with some reservations on its general validity [3.129]. Another way of looking at the solvent–crystal interactions is by considering adsorption of solvent molecules on the surface sites, as shown between the [010] PBCs on {101} faces of sucrose [3.47]. The role of solvents in terms of surface roughening and surface adsorption on crystal morphology is reviewed in [3.44]. A protic solvent can determine both the polymorph and crystal habit, as shown for stavudine, in the molecule of which one N atom is a very strong H-bonding donor and two O atoms are strong H-bonding acceptors. The crystal surfaces interact in different ways with polar and nonpolar solvents [3.122]. The effect of α -butyrolactone as a solvent on cyclotrimethylene trinitramine (RDX) crystals has been explained by invoking a third region between the crystal and solution bulk, i.e., a boundary layer. MD simulations show that the average energy of solvent molecules near the surface is higher than the average energy of the same molecules in the bulk, therefore the potential energy change per unit area can be chosen as a good parameter to use in explaining solvent effects on the crystal habit [3.141].

3.7.5 Mechanisms of Action

Solvent molecules are temporally adsorbed at the various sites of surface: ledges, steps, and kinks, with different lifetimes, which has an effect on growth rates. The formation of surface complexes was suggested for $\text{Hg}(\text{CN})_2$ crystals grown from methanol [3.142]. As solutions of *n*-paraffins in petrol ether behave as a melt, a structural model was proposed, which considers the paraffin crystal as a Kossel crystal and the solvent molecules as in the Ising model, so that they easily adhere by adsorption to steps [3.143]. In polar crystals the complementary forms $\{hkl\}$ and $\{\bar{h}\bar{k}\bar{l}\}$ exhibiting different surface structures selectively interact with the solvent molecules, as in $\text{N}(\text{C}_2\text{H}_5)_4\text{I}$ crystals grown from four solvents, which being differently adsorbed onto {011} and $\{0\bar{1}\bar{1}\}$ faces, invert the morphological importance of these faces [3.97]. The morphological difference is relevant for industrial crystallization: the analgesic ibuprofen grown from ethanol shows a pseudohexagonal tabular habit but thin elongated platelets from ethyl acetate, owing to the interactions between ethyl acetate molecules and ibuprofen carboxylic groups emerging at the surface of {100} and {002} faces of the crystal [3.144].

3.8 Impurities

The literature dealing with the effects of impurities on growth kinetics and crystal habit is enormous and increasing. After the publication in 1951 of the BCF theory [3.7] and of Buckley's book on crystal growth [3.145], the advance has been impressive. Fourteen years later a whole book was devoted to the relationships between adsorption, crystal growth, and morphology [3.146]. In Russia this topic has been widely studied, as evident from the series of volumes on crystal growth. The role of impurity is also a specific object of the proceedings of periodic symposia on industrial crystallization. Indeed, a strong impulse to research in this field is provided by mounting industrial demands. Many cases are given and discussed in some review papers [3.83, 147–149] and a summary with a nearly exhaustive literature is found in Sangwal's monograph [3.150]. In recent years, interest has focused on additives and other large molecules used as habit modifiers. A synthetic view is tentatively presented in the following. Admitting a hydrodynamic regime, the role of volume diffusion is neglected as impurities only influence the surface processes.

3.8.1 The Main Factors

Impurities influence both thermodynamic and kinetic factors. Addition of an impurity to a solution may change the surface free energy γ , the edge free energy ρ , and the solubility. Even if an increase of average surface energy is possible, it is usually admitted that ρ decreases with the concentration of the adsorbed impurity C_i . By assuming a Langmuir-type isotherm and equilibrium between the impurities adsorbed on the step and in the bulk, the resulting edge free energy (expressed in ergs, for the sake of simplicity) is given by [3.151]

$$\rho_i = \rho - k_B T \ln C_i. \quad (3.45)$$

Similarly, a positive adsorption produces a reduction in the specific free surface energy. It follows that, since ρ_i decreases with impurity concentration C_i , the growth rate of the face should increase.

The effect on solubility depends on C_i . If C_i is low or very low, of the order of ppm, the influence on solubility is negligible. If C_i is higher, of the order of mg/l or g/l, the solubility may change. In the case of solubility increase, the resulting effect is usually an increase in step velocity and the growth rate of faces [3.150]. Solubility and growth rate of ionic crystals may be increased by changing the pH or increasing the ionic strength

through addition of soluble salts, e.g., adding NaCl to $\text{CaSO}_4 \cdot 2\text{H}_2\text{O}$ solutions [3.151].

The growth rate depends on the kinetic constant C (3.39) and the step velocity v (3.37). Impurities adsorbed on the surface will cause a decrease of C and hinder the advances of steps by mechanisms that depend on the adsorption site. The retardation factor (3.37) of the steps becomes [3.83]

$$\beta_{\text{st}} \cong \beta_{\text{st}}^0 \left(1 - \frac{4d}{(\kappa^*)^2} \right). \quad (3.46)$$

where β_{st}^0 is the retardation factor without adsorption at the step, d is the density of adsorbed impurity (cm^{-2}), and κ^* the critical curvature of the step (cm^{-1}).

As a general result, the growth rate is decreased.

Impurities may therefore have two opposite effects on crystal growth. The final result depends on the supersaturation and impurity concentration, as shown in the classical experiment of $\text{Pb}(\text{NO}_3)_2$ grown in the presence of methyl blue [3.150]. The increase of the growth rate at low supersaturation and low impurity concentration (the so-called catalytic effect) is attributed to the prevailing thermodynamic factor and a low density of kinks. At higher impurity concentration the resulting effect is a decrease of growth rate due to the dominance of kinetic factors. Similar behaviors were found in other cases [3.150].

3.8.2 Kinetic Models

Various models have been proposed to relate the step velocity to the effect of impurity adsorption. One of the first contributions is due to Bliznakow [3.152], who assumes that impurities are adsorbed on some of the active sites on the surface and derives a quantitative relationship between the step velocity and the kink site adsorption

$$v = v_0 - (v_0 - v_m)\theta_{\text{eq}}, \quad (3.47)$$

in which v_0 is the step velocity without adsorption in the kink; $\theta_{\text{eq}} \leq 1$ is the coverage degree, in impurity, of the surface, and v_m is the limiting step velocity in impure solution, when all the surface is covered by impurities (i.e., $\theta_{\text{eq}} = 1$). If a Langmuir isotherm is valid, then

$$v = v_0 - (v_0 - v_m) \frac{KC_i}{(1 + KC_i)}. \quad (3.48)$$

The model was satisfactorily applied to experiments reported by the same author and others [3.146] chiefly on

inorganic compounds and confirmed by curves of R versus C_i and the heat of adsorption measured at different temperatures [3.112].

Cabrera and Vermilyea (CV) [3.153] proposed a different model, in which the impurities are assumed to be immobile, adsorbed on ledges ahead of steps, where they form a two-dimensional (2-D) lattice. The steps move with average velocity v

$$v = v_0[1 - 2r^*/(d^{-1/2})]^{1/2}, \quad (3.49)$$

where r^* is the critical radius of the 2-D nucleus, and d is the average density of impurities, corresponding to a mean distance $s = d^{-1/2}$. The density of impurities d can also be expressed by the coverage degree of impurity (θ) times the maximum number (n_{\max}) of sites available for adsorption per unit area: $d = n_{\max}\theta$. From (3.49) it follows that when $s < 2r^*$, the step will stop; when $s > 2r^*$, it squeezes between the two adjacent impurities. At equilibrium between impurities adsorbed on the surface and solution, and if the coverage degree θ is given by a Langmuir isotherm, then

$$\theta = \frac{KC_i}{1 + KC_i}, \quad (3.50)$$

where K is the Langmuir constant. If $v \propto R_{hkl}$ and introducing the relative growth rate η , we have

$$\eta = \frac{v}{v_0} = \frac{R_{hkl}}{R_0}. \quad (3.51)$$

Rearranging (3.49)

$$\frac{1}{(1 - \eta^2)^2} = \frac{1}{4(r^*)^2 n_{\max}} + \frac{1}{4(r^*)^2 n_{\max} K} \frac{1}{C_i}. \quad (3.52)$$

If the CV model is valid, then the previous relation should be satisfied and allows one to obtain n_{\max} .

Since r^* is related to the critical supersaturation β^* (3.38), when $KC_i \gg 1$ (i.e. $\theta \rightarrow 1$), then

$$\frac{1}{(\ln \sigma^*)^2} = \frac{1}{(\ln \sigma_{\max}^*)^2} \left(1 + \frac{1}{K_1 C_i} \right). \quad (3.53)$$

When $KC_i \ll 1$, then

$$\ln \sigma^* = \ln \sigma_{\max}^* (KC_i)^{1/2}, \quad (3.54)$$

i.e., the critical σ^* necessary for a step to move increases with increasing C_i , which has been experimentally confirmed.

The validity of the CV mechanism has been verified in many experiments, mainly with organic impurities

and tailor-made additives, for example, in the growth of $C_{36}H_{74}$ from petroleum ether [3.93] and also in the growth of {101} faces of ADP under low supersaturation [3.118]. It may happen that strongly bound impurities may become incorporated in the crystal.

Sears [3.154], observing that 10^{-5} – 10^{-6} molal concentration of FeF_3 was sufficient to poison LiF in aqueous solution, postulated a complete monostep adsorption at the growth steps. He calculated the fractional change of 2-D nucleation rate, which for low step coverage is proportional to the C_i change, and recognized that two opposite effects operate, one tending to increase the growth rate, the other to decrease it.

Albon and Dunning [3.155], studying the growth of sucrose in the presence of raffinose, admit adsorption of impurity at kinks, which lowers the step rate. When the impurity distance is less than the diameter d^* of the critical nucleus (measured as an integer number of molecular spacings), the advancing step is blocked. If $p = (1 - C_i)$ is the probability of finding a free site along a step, then the step speed is given by

$$v = v_0[d^* - (1 - C_i)d^* + (1 - C_i)](1 - C_i)^{d^*}. \quad (3.55)$$

This model gives also a good description of the effects of Cr^{3+} on the growth of the {100} faces of ADP for $C_i > 1.0 \times 10^{-2}$ kg/m³ [3.156].

Davey and Mullin [3.91] assumed that the rate-determining process is the surface diffusion, which is reduced by impurities absorbed on the ledge, and that the number of absorbed growth units is proportional to the fraction of free surface sites at equilibrium $n_i = n(1 - \theta)$. They derived the relation

$$v/v_0 = 1 - \theta_{eq}. \quad (3.56)$$

By expressing θ_{eq} in terms of Langmuir isotherm, the equation becomes

$$\frac{v_0}{v_0 - v} = 1 + \frac{1}{KC_i}. \quad (3.57)$$

This relation was shown to be valid, for example, for layer velocities in the [001] direction for the {100} faces of ADP in the presence of some ppm of $AlCl_3$, $FeCl_3$, and $CrCl_3$.

Since complete coverage ($\theta_{eq} = 1$) is not a necessary condition to stop crystal growth, *Kubota and Mullin (KM)* [3.157, 158] introduced in the Davey–Mullin equation an effectiveness factor α given by

$$\alpha = \frac{r^*}{L} = \frac{\rho a}{k_B T \sigma L}, \quad (3.58)$$

where L is the distance between two adsorption sites and a is the surface area of a growth unit. It follows that, depending on the ratio r^*/L , the factor α may be greater than, equal to, or less than 1. In their model a linear arrangement of adsorption sites is assumed to occur along the step, so that one-dimensional (1-D) coverage is combined with an adsorption isotherm. So we have

$$v/v_0 = 1 - a\theta_{\text{eq}}. \quad (3.59)$$

Relating the relative velocity η to C_i by a Langmuir isotherm, we have

$$\frac{1}{1-\eta} = \frac{1}{\alpha K} \frac{1}{C_i} + \frac{1}{\alpha}. \quad (3.60)$$

From this relationship it is possible to evaluate the critical supersaturation necessary to overcome the dead zone

$$\beta^* = \frac{\rho \alpha K C_i}{k_B T L (1 + K C_i)}, \quad (3.61)$$

which can be rearranged as: $1/\beta^* = (C_1/C_i) + C_2$ (where C_1 and C_2 are two constants) [3.158].

The authors provide a number of examples, drawn from the literature, of the validity of their model for growth systems showing different α effectiveness factors [3.157]. The KM model was successively applied to crystal growth of other systems. Very recently, in studying the growth kinetics of the four main F-faces of sucrose in the presence of raffinose, both CV and KM models associated with Langmuir isotherms were tested. The agreement was better with the KM model than with CV, which means that adsorption occurs at kink sites and a spiral growth mechanism operates. The α effectiveness coefficient seems to be a very good parameter to predict the raffinose effects [3.159].

3.8.3 Adsorption Sites

Impurities act through adsorption, as apparent from the above kinetics models, onto the crystal surfaces, at steps and kinks. Adsorption occurs in this order, but only one process is considered determinant in the reaction path. They can be distinguished on the basis of some parameters (adsorption heat, activation energy, lifetime of the adsorbed state). A detailed description of adsorption at the three kinds of growth sites is given in some surveys papers [3.150, 160, 161]. The overall effect on the crystal habit depends on the effect on growth rates of faces.

Adsorption of impurities at *kinks* reduces the number of kinks available for growth. As growth proceeds through integration at kinks, the step velocity and

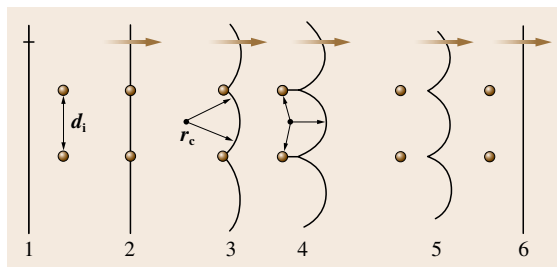


Fig. 3.17 The barrier presented by immobile impurities at the step motion on a ledge. The layer overcomes the impurities at a reduced rate if their distance is higher than the diameter of the critical nucleus

growth rate are decreased and eventually stopped. Examples and lists of experiments on kink adsorption are given in many papers [3.91, 149, 150, 156, 159–161]. Adsorption in kinks, by increasing x_0 , the mean distance between kinks, may cause polygonization of growth steps [3.160].

Impurities adsorbed at *steps* represent a steric barrier to diffusion of growth units along the step and to their entry into the kinks (Fig. 3.17). The step can move at a reduced rate only if the distance between two adsorbed impurities along the step is $s > 2r^*$; otherwise they are stopped.

Adsorption at steps is found to have occurred in many experiments [3.155, 156, 158, 160].

Besides the above kinds of adsorption, another possibility arises when the impurity concentration is high and strong lateral interactions occur among the molecules. A 2-D adsorption layer may form which has structural similarity with the growing face, as discussed in Sect. 3.2.3. The formation of the adsorption layer is easier with large molecules. The existence of an adsorbed solution layer, strongly structured at the interface, was suggested by Sipyagin and Chernov, who found that the layer may be disturbed by the addition of alcohol, which increases the growth rate [3.93].

3.8.4 Effect of Impurity Concentration and Supersaturation

The impurity effectiveness is very variable. To affect crystal habit, some g/l may be necessary (e.g., Na_2SO_4 for NaCl) or ppm are already sufficient (e.g., $\text{Na}_2\text{Fe}(\text{CN})_6$ for NaCl). A low or very low impurity concentration (C_i) may increase the growth rate due to its influence on the edge free energy, but higher C_i affecting the kinetic parameters may cause a sharp decrease. This effect is selective, as only some spe-

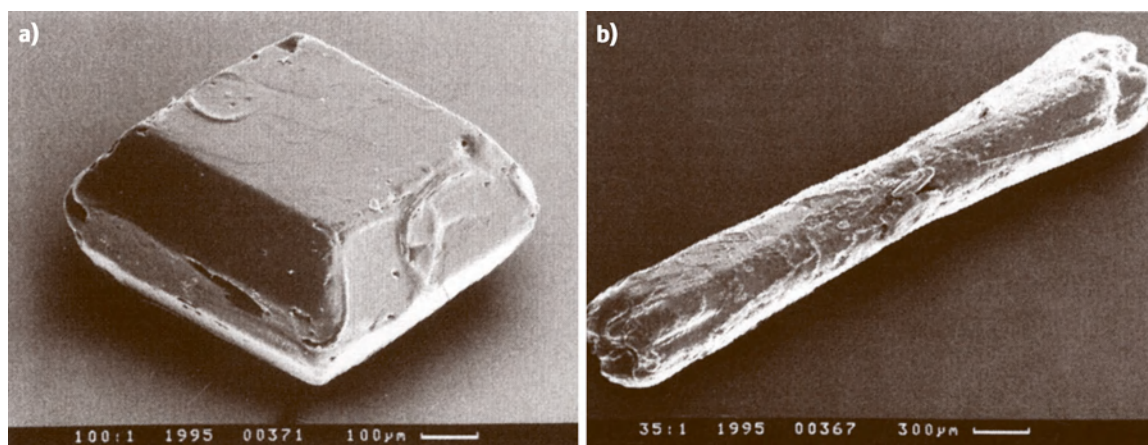


Fig. 3.18 (a) Ammonium sulfate crystals grown from pure solution and (b) in presence of 100 ppm Al^{3+} (after [3.163])

cific faces of a given crystal are concerned, and the crystal habit is modified. This occurs with organic and inorganic impurities (Fig. 3.18). For example, the growth rate of the {101} faces of **KDP** slowly increases, then decreases with increasing C_i of Fe^{3+} and Cr^{3+} , whereas it is not affected by Co^{2+} and Ni^{2+} [3.162]. Some ppm of Cr^{3+} are able to increase the step bunch spacing on the {100} faces of **ADP**, and some more to stop the formation of bunches [3.160].

Coupling of supersaturation and impurity concentration can have strong effects. Impurities are usually more efficient at low than at high supersaturation, where competition favors the adsorption kinetics of growth units with respect to that of impurities. For any impurity concentration there is a critical supersaturation σ^* below which growth is stopped (dead zone); the value of σ^* increases with C_i . A distinction is made between regular and irregular growth, according to whether an impurity changes the growth mechanism or

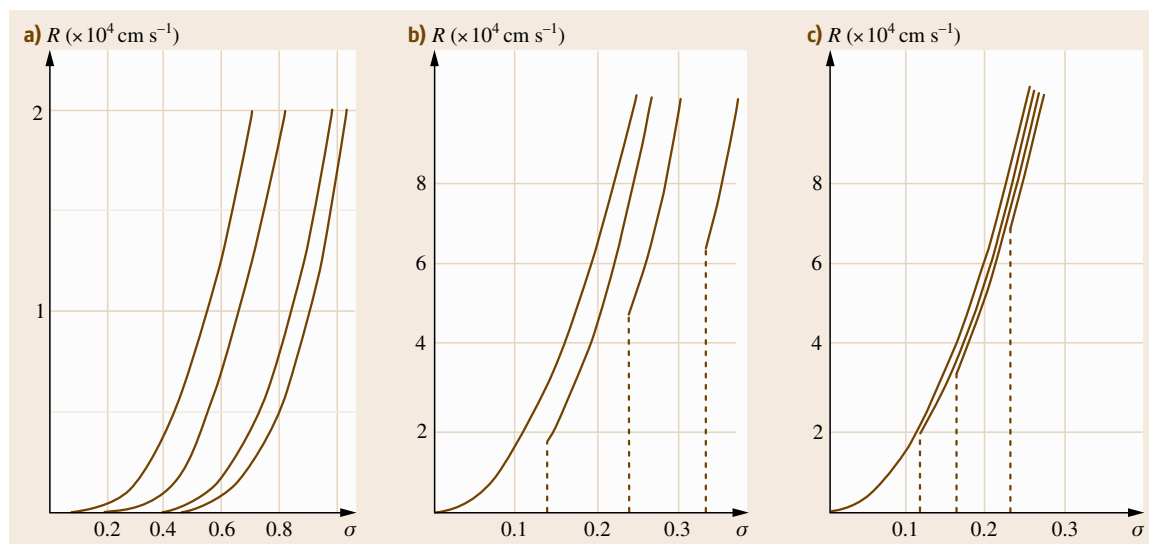


Fig. 3.19a–c Growth curves (R_{hkl} versus σ) for regular (a) and irregular (b,c) growth of different crystals in the presence of small and large impurity molecules, respectively, at increasing impurity concentrations. (a,b) (110) faces of $\text{C}_{36}\text{H}_{74}$ in the presence of an amine and a copolymer, respectively; (c) different faces of sodium perborate crystals. For a detailed description see [3.93, 150, 161]

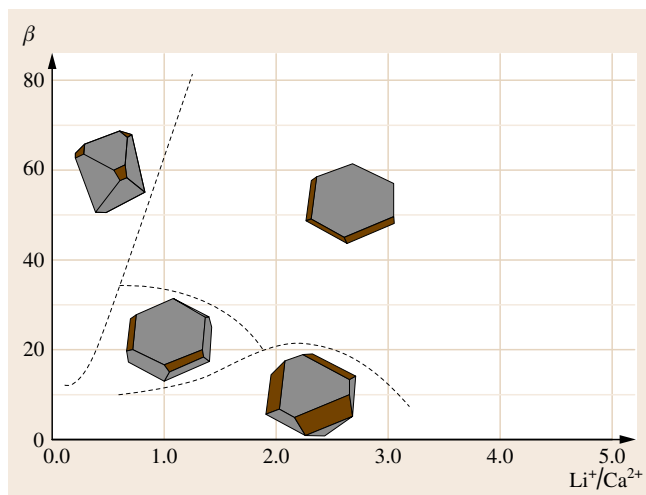


Fig. 3.20 Morphodrome (β versus $\text{Li}^+/\text{Ca}^{2+}$) of calcite crystals grown in the presence of Li^+ as impurity (after [3.72])

not, as can be seen from the curves for R_{hkl} versus β (Fig. 3.19).

In regular growth, the curves for impure solutions run parallel to that of pure solution, suggesting an unchanged growth mechanism, whereas in irregular growth the growth rate is stopped at low supersaturation, but starts at higher σ values. In this case impurities adsorbed on crystal surface promote step bunching and originate an irregular crystal morphology [3.93]. Growth rate fluctuations were observed in both static and kinetic regimes [3.78]. Many examples of the effects of supersaturation and impurity concentration are reported in [3.158, 160, 161]. These effects may be represented through morphodromes (Figs. 3.14 and 3.20) (Sect. 3.2.3).

Effects of impurities on 2-D islands lying on the (001) surface of a Kossel crystal have been simulated and a morphodrome calculated in which, due to the roles of edge diffusion and kink poisoning, an initial square crystal changes to a diamond with increasing β and C_i , in qualitative agreement with experimental observations [3.164].

3.8.5 Effect of Impurity Size

Three kinds of impurities are usually distinguished: ions and small molecules, polyelectrolytes, and tailor-made additives, the molecular weights of which are on the order of about 10^2 , 10^3 , and 10^4 , respectively [3.147]. The former may be mobile or immobile, while the two

latter types are nearly immobile with great effect on crystal habit and incorporation in the surface layers. A fourth class could be added, the amphiphiles (dyes, surfactants).

Ions

In crystal growth from aqueous solutions ions are often present as impurities. Their interaction with the crystal surface depends on their charge and size and on the structural properties of the crystal faces. For example, the divalent (Co^{2+} , Ni^{2+} , Ba^{2+}) cations generate greater local strains and surface change than the trivalent (Fe^{3+} , Cr^{3+}) ones on the surface of KDP faces due to the incorporation of the former and adsorption of the latter on the surface layer [3.162]. Interactions of divalent (Cd^{2+} , Ni^{2+}) and trivalent (Al^{3+} , Cr^{3+} , Fe^{3+} , La^{3+} , Ce^{3+}) cations with some inorganic crystals (gypsum, KDP, potassium hydrogen phthalate (KAP), etc.) are reported in [3.147]. Ions can be selectively incorporated into the different faces, such as Cr^{3+} and Fe^{3+} more easily included into {100} than into {101} faces, and also into different slopes of a vicinal hillock [3.103]. It is difficult to predict the influence of ionic impurities. For example, a number of divalent cations and anions have no significant effect on the crystal habit of gibbsite, which conversely undergoes dramatic changes in the presence of alkali ions (K^+ , Cs^+) [3.165]. The Ba^{2+} and Pb^{2+} cations have opposite effects on the growth of the {111} and {100} faces of $\text{Sr}(\text{NO}_3)_2$ [3.166]. There is no general criteria to interpret the effect of ions on crystal habit, although a guideline may be the hypothesis of the formation of an ordered adsorption layer at the interface. When an ion is incorporated to form a solid solution, it distributes between the crystal (c) and the solution (s) according to a partition coefficient $K_{eq} = C_c/C_s$. The surface acts as a source or sink for the ion depending on whether K_{eq} is less than or greater than 1. The role of inclusions of isomorphous impurities during crystal growth is widely discussed in a review paper [3.167].

Polyelectrolytes

Polyelectrolytes, which include soluble polymers, proteins, and polysaccharides, are all characterized by an array of polar groups on an open long chain, by which they may be effective at a ppm level. Summarizing the interaction between polyelectrolytes and sparingly soluble salts, two principles were enunciated: the dimensional fit between the functional groups of the impurities and the interionic distance on the surface, and the achievement of stereochemical constraints [3.168].

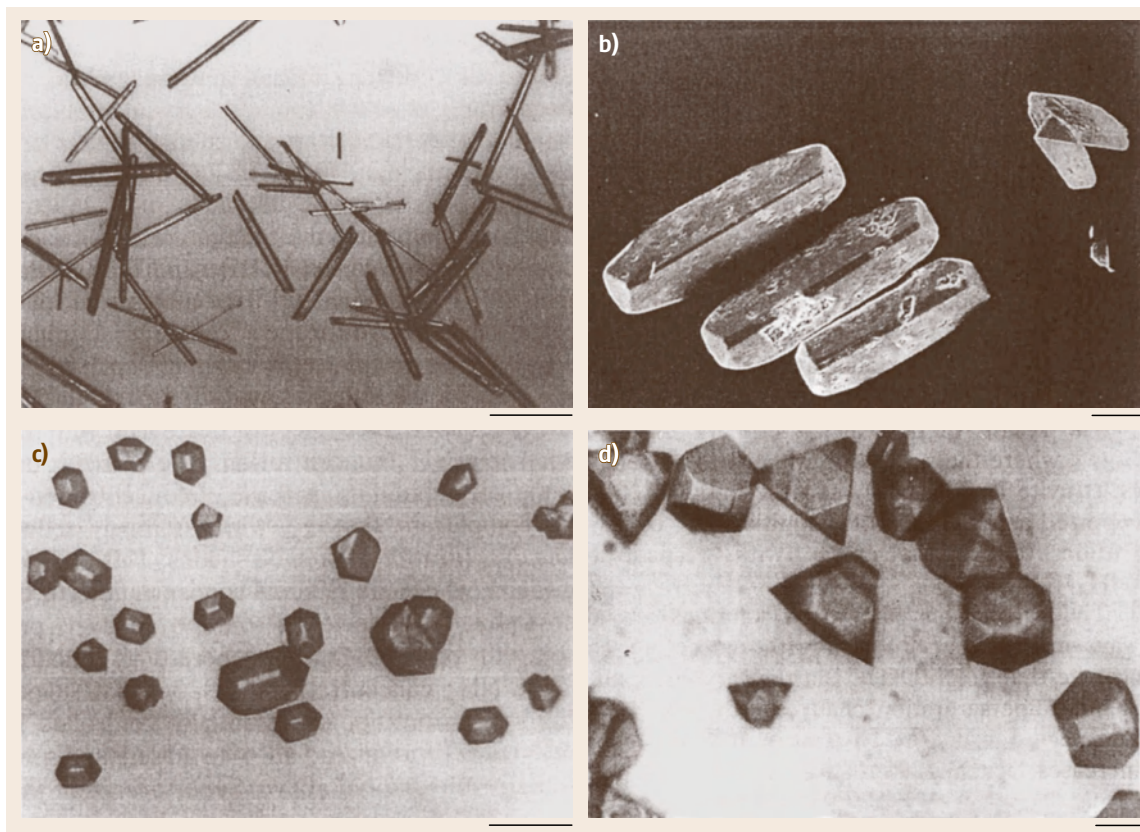


Fig. 3.21a–d Crystals of $\text{Ni}(\text{NH}_4)\text{PO}_4 \cdot 6\text{H}_2\text{O}$ grown in the presence of increasing ammonia excess. The crystals are elongated along $[100]$ in **(d)** and along $[010]$ in **(a–c)**. Bars: $40\ \mu\text{m}$ (after [3.170])

Any macromolecule may function selectively as a retardant or promoter, depending on specific conditions. A lot of research has been carried out on the influence of polyelectrolytes and biopolymers on the crystallization of biominerals, such as calcium carbonate and other mineral compounds (gypsum, fluorite, barite) [3.147, 154] and calcium oxalates, components of lithiasis [3.169].

Tailor-Made Additives

A special case of impurities is represented by tailor-made additives, which are used in organic crystallization to change habit. Their main characteristic is the partial resemblance of their molecular structure to that of the crystal molecules (Sect. 3.2.3). A wide list of experiments on tailor-made additives is given in the monograph [3.14]. Normal-paraffins that are used as solvents for the growth of lower and higher homologous can be considered as tailor-made additives [3.93, 129].

Molecules with long and rigid chains are easily adsorbed at the interfaces, whereas molecules with too long chains tend to fold, forming a 2-D heterogeneous nucleus on the surface, which promotes crystal growth [3.48]. To simulate the morphological change due to additives, the built-in approach and the surface docking approach were applied. The former works only if the intermolecular bonding is anisotropic, whereas the latter can be applied to both isotropic and anisotropic bonding [3.171].

3.8.6 Composition of the Solution: pH

In an ionic impurity-free solution, change of habit may occur when there is an excess of either cation or anion or when pH is changed:

1. The former case is presented by calcite, which assumes an elongated habit in the presence of

an excess of Ca^{2+} and becomes tabular when CO_3^{2-} ions are in excess [3.172]. Many other cases are known; we quote silver bromide, which crystallizes as a cube from stoichiometric solution, but as an octahedron in excess bromide [3.173]. $\text{Ni}(\text{NH}_4)\text{PO}_4 \cdot 6\text{H}_2\text{O}$ crystals grown in excess ammonia change from a needle-like habit to a pseudocubic symmetry due to $\text{Ni}(\text{NH}_3)_x(\text{H}_2\text{O})_{6-x}$ complexes selectively adsorbed at the surfaces (Fig. 3.21) [3.170]. A detailed analysis of the chemical aspects of the impurity effects is given in the paper [3.174].

- The effect of pH on crystal shape has been studied for a long time, especially for **ADP** and **KDP** by Russian researchers [3.175]. The change in pH modifies the concentration ratios of the chemical species in solution, especially of polyprotic acids. The growth rates of the $\{101\}$ and $\{100\}$ faces of **ADP** are differently affected by pH with change in crystal elongation, attributed to the role played by either hydration of NH_4^+ , H_2PO_4^- or $\text{NH}_4\text{PO}_4^{2-}$ ions or the concentration of hydroxonium ions $[\text{H}_3\text{O}(\text{H}_2\text{O})_3]^+$

in solution [3.115]. Addition of Fe^{3+} and Cr^{3+} causes crystal tapering, which is a function of pH. Change in pH does not affect the growth rate of $\{101\}$ faces of **KDP**, but when pH differs from the value corresponding to solution stoichiometry, the $\{100\}$ faces increase in size and crystals become more isometric. This effect is related to the change with pH of surface parameters (step velocity and hillock slope) on the two faces [3.176]. A small pH decrease causes a dramatic increase in growth rate in the $[001]$ direction and a decrease in the $[010]$ direction on L(+)-glutamic acid hydrochloride due to the formation of dimers at low pH, which selectively interact with the two directions [3.177]. The role of pH in crystal growth is fundamental in the presence of amino acids. Glycine exists in aqueous solution as zwitterions ($\text{H}_3\text{N}^+\text{CH}_2\text{COO}^-$) in a definite range of pH, in which the critical supersaturation necessary to obtain the $\{110\}$ form of NaCl attains its minimum value. The effect is explained by admitting adsorption of zwitterions along the $[001]$ directions on the $\{110\}$ faces [3.65].

3.9 Other Factors

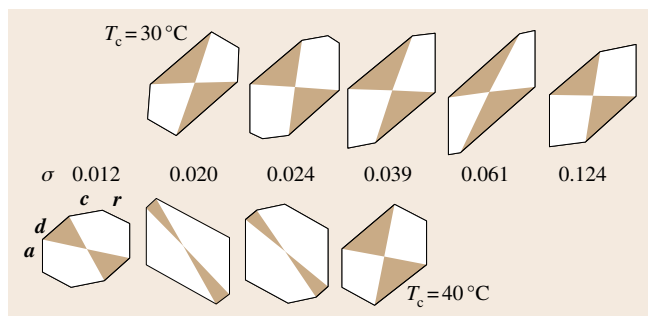
Crystal habit can be affected by (not less important) factors other than those mentioned above. Some of these are briefly considered below, while some (electric field, ultrasound, pressure, microgravity) are neglected.

3.9.1 Temperature

The influence of temperature on crystal growth is multifaceted. Not only does it directly promote growth, as results from the growth rate formulas, but it also affects

other factors that act on the growth rates: solubility, surface roughness, solvent/solute-interface interactions, and chemical equilibria. Since these factors work in a selective way on different faces, a change in temperature may cause relevant changes in crystal habit, as shown in experiments since the beginning of the 20th century. Some cases are quoted in [3.115, 126, 178]. Clear anomalies were detected in curves of R versus T for some salts (KCl, NaClO_3 , and KClO_3). Sipya-gin, Chernov, and Punin, quoted in [3.93], found that at definite temperatures the adsorbed layer at the crystal surface undergoes structural change, which suggests the occurrence of a third step between volume diffusion and surface diffusion. Significant changes were observed in sucrose crystals, in which the $\{101\}$ form dominates the other $\{h0l\}$ forms at 30°C , rendering crystals elongated, whereas at 40°C it becomes less important and crystals appear isometric. Growth sectors occur at any T and σ (Fig. 3.22) [3.46].

Fig. 3.22 Crystal habit of sucrose seen along $[010]$, grown at 30 and 40°C and at increasing σ values (after [3.46]) ◀



3.9.2 Magnetic Field

Research on the effects of a magnetic field on crystal growth started with the magnetic treatment of hard water in order to prevent scale formation. The number of papers on this topic is increasing due to its practical importance and criticism of results and reproducibility. A magnetic field has been recognized as affecting nucleation and crystal growth rate, polymorphism, and colloidal stability, and is now being applied to crystal growth of proteins and other compounds. In research on many poorly soluble inorganic salts a marked effect was only found for diamagnetic salts of weak acids (carbonates and phosphates): a magnetic field (0.27 T) increased their nucleation and growth rates. No effect on paramagnetic salts was recorded. These results are attributed to faster proton transfer from H-carbonate and H-phosphate ions to water molecules, due to proton spin inversion in the external field [3.179]. Also surface features are sensitive to the effects of magnetic field, as observed in the shape of etch pits and the shift of dislocations on paracetamol crystals [3.180]. Applying a strong magnetic field (10 T) to a lysozyme solution increases its viscosity and birefringence, which suggests molecular ordering with the formation of interconnected network, i. e., gel phase [3.181]. Experiments are also being carried out in gels, where magnetic field orientates PbBr_2 nanocrystallites and markedly increases their size [3.182]. Notwithstanding the amount of research in this area, the observed effects are as yet not adequately explained and no definite theory has been presented; indeed this is a new field of research.

3.9.3 Hydrodynamics

Crystal growth can take place under static or dynamic conditions. In the former case, which occurs in solution at rest and in gels, volume diffusion plays a decisive role in the growth kinetics. The latter condition is realized by stirring or shear flow. In this case the growth rate progressively increases with stirring or flow rate up to a limiting value which depends on the supersaturation. Beyond this value, the volume diffusion process does not influence the growth rate and surface diffusion becomes dominant [3.183]. The effects on crystal habit are different. Under static conditions concentration gradients are set up in solution and at the crystal surface, where they promote 2-D nucleation and the formation of hollow crystals and dendrites, depending on the supersaturation. Even in a solution at rest or zero gravity the crystal growth itself engenders convection, which influences morphological stability [3.184]. In a suitable stirred solution there are no concentration gradients except in the boundary layer, which is admittedly covering the crystal surface, and all the crystal faces are in contact with a homogeneous solution. Indeed, supersaturation is not constant along the face even in the kinetic regime [3.78], which may cause inclusions during growth. When a shear flow is applied, there are effects on crystal habit and surface features. The face on which flow is direct grows faster than the opposite face which is fed by a less supersaturated solution. In addition, a shear flow in the direction of step motion favors instability, whereas flow in the opposite direction enhances stability [3.87, 89].

3.10 Evolution of Crystal Habit

When a crystal with a given growth shape is left in contact with its mother solution, reaching saturation, rearrangements occur at the crystal–solution interface in order to achieve the minimum surface energy. A classical example is represented by NH_4Cl dendrites, which when grown in a small drop transform into a single crystal that corresponds to the equilibrium form (Fig. 3.6). Crystal habit evolution can also be observed in the growth from supersaturated solutions of poorly soluble compounds. In Fig. 3.23 the change with time of growth forms of $\text{MgHPO}_4 \cdot 3\text{H}_2\text{O}$, precipitated from solutions

of different concentration, is shown. There is a progressive decrease of supersaturation, which goes together with the habit change, which continues even when the solution has become saturated. The general trend, independent of the initial concentrations, is towards the same crystal shape [3.185].

Another kind of evolution takes place when a crystal, grown in a given solvent, is transferred to a supersaturated solution of another solvent. The original faces are slowly replaced by others that are stable in the new solution, as observed for mercuric iodide crystals

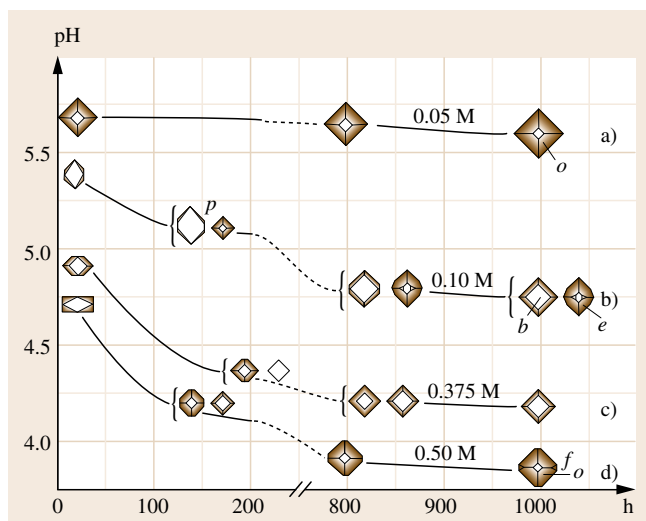


Fig. 3.23 Change of pH and crystal habit versus time of $\text{MgHPO}_4 \cdot 3\text{H}_2\text{O}$ crystals precipitated from equimolar solutions of different initial concentration. Dominant final forms: $o\{111\}$; $b\{010\}$ (after [3.184]) ◀

grown in aqueous solutions and subsequently inserted into methanol solutions [3.142]. A more drastic change occurs when several crystal phases may form from a supersaturated solution, as in the case of Ca-phosphate solutions. The normally stable phase is hydroxyapatite, which is the less soluble phosphate, but, obeying Ostwald's step rule, other more soluble phases nucleate first, even an amorphous phosphate at high pH. These phases are not stable, since the solution is still supersaturated with respect to the less soluble ones. A long process of chemical reactions starts in solution, which involves the nucleation of the more stable crystal phase and the dissolution of the first one [3.186].

3.11 A Short Conclusion

At the end of this concise review it is apparent that the crystal morphology is the result of the complex interaction of several factors – structural, thermodynamic and kinetic –, which make difficult and yet fascinating the study of this field. The great variability of the shape and size of crystals grown from solutions is mainly due to the capability of the crystalline structure of a compound to show different interfaces as a response to the variations introduced by the environment (solvent, impurity,...). The interaction of these inter-

faces with kinetic factors (such as supersaturation) give rise to the different morphologies and habits for the same crystal phase. On the contrary the shape, size and development of the living organisms are controlled by a genetic program which gives the same pattern to all individuals of a given species. An interesting field of combined research is bio-mineralization, where to the interplay of crystal structure and environment it is necessary to add the biological activity of the living organisms.

3.A Appendix

3.A.1 The Equilibrium Pressure of an Infinite Monoatomic Crystal with Its Own Vapor

From statistical thermodynamics the chemical potential of a molecule in a perfect gas reads

$$\mu^g = \varepsilon_p^g - k_B T \ln \Omega_g + \mu^0. \quad (3.A1)$$

The first term, ε_p^g , is the potential energy of the gas molecule, while the two last terms represent the entropy of dilution and the thermal entropy, respectively. Ω_g is the mean volume occupied in the gas phase, and $\mu^0 = k_B T \ln[h^3(2\pi mk_B T)^{3/2}]$ depends only on the mass of the molecule and on T . In a perfect monoatomic and infinite Einstein crystal (fulfilling the condition

$T \gg (h/k_B)\nu_E$, where ν_E represents the unique vibration frequency) the chemical potential of one atom occupying a mean volume Ω_c is

$$\mu_{c\infty} = \varepsilon_p^{c\infty} - k_B T \ln \Omega_c + \mu^0, \quad (3.A2)$$

where $\varepsilon_p^{c\infty}$ is the potential energy of the atom in any lattice site. At crystal–vapor equilibrium the chemical potentials of the two phases are the same, which implies

$$\varepsilon_p^g - \varepsilon_p^{c\infty} = k_B T \ln \left(\frac{\Omega_g}{\Omega_c} \right).$$

At equilibrium,

$$\Omega_g = k_B T / p_{\infty}^{\text{eq}} \quad \text{while} \quad \Omega_c = (k_B T / 2\pi m)^{3/2} \nu_E^{-3}.$$

Being necessarily $\varepsilon_p^g > \varepsilon_p^{c\infty}$, we can define the extraction work of an atom from a mean lattice site (kink) to

the vapor $\varphi_{c\infty} = \varepsilon_p^g - \varepsilon_p^c \infty > 0$ and then, from the preceding relation, one obtains the equilibrium pressure of a perfect monoatomic and infinite Einstein crystal

$$p_{\infty}^{\text{eq}} = \left[(2\pi m)^{\frac{3}{2}} (k_B T)^{-\frac{1}{2}} v_E^3 \right] \exp(-\varphi_{c\infty}/k_B T). \quad (3.A3)$$

References

- 3.1 H.J. Scheel: Historical introduction. In: *Handbook of Crystal Growth. 1a. Fundamentals*, ed. by D.T.J. Hurle (North-Holland/Elsevier, Amsterdam 1993) pp. 1–42
- 3.2 I.N. Stranski: Zur Theorie des Kristallwachstums, *Z. Phys. Chem.* **136**, 259–278 (1927), in German (see also *Annu. Univ. Sofia* **24**, 297 (1927))
- 3.3 I.N. Stranski, R. Kaischew: Gleichgewichtsform und Wachstumsform der Kristalle, *Ann. Phys.* **415**(4), 330–338 (1935)
- 3.4 I.N. Stranski, R. Kaischew: Kristallwachstum und Kristallbildung, *Phys. Z.* **36**, 393–403 (1935), in German
- 3.5 P. Niggli: *Geometrische Kristallographie des Diskontinuums* (Borntraeger, Leipzig 1919), in German
- 3.6 J.D.H. Donnay, D. Harker: A new law of crystal morphology extending the law of Bravais, *Am. Mineral.* **22**, 446–467 (1937)
- 3.7 W.K. Burton, N. Cabrera, F.C. Frank: The growth of crystals and the equilibrium structure of their surfaces, *Philos. Trans. R. Soc. Lond. A* **243**, 299–358 (1951)
- 3.8 P. Hartman, W.G. Perdok: On the relation between structure and morphology of crystals. I, *Acta Cryst.* **8**, 49–52 (1955)
- 3.9 P. Hartman, W.G. Perdok: On the relation between structure and morphology of crystals. II, *Acta Cryst.* **8**, 521–524 (1955)
- 3.10 P. Hartman, W.G. Perdok: On the relation between structure and morphology of crystals. III, *Acta Cryst.* **8**, 525–529 (1955)
- 3.11 P. Bennema: Growth and morphology of crystals: integration of theories of roughening and Hartman–Perdok theory. In: *Handbook of Crystal Growth. 1a. Fundamentals*, ed. by D.T.J. Hurle (North-Holland/Elsevier, Amsterdam 1993) pp. 477–581
- 3.12 P. Bennema: On the crystallographic and statistical mechanical foundations of the forty-years old Hartman–Perdok theory, *J. Cryst. Growth* **166**, 17–28 (1996)
- 3.13 X.Y. Liu, P. Bennema: Prediction of the growth morphology of crystals, *J. Cryst. Growth* **166**, 117–123 (1996)
- 3.14 Z. Berkovitch-Yellin, I. Weissbuck, L. Leiserowitz: Ab initio derivation of crystal morphology. In: *Morphology and Growth Unit of Crystals*, ed. by I. Sunagawa (Terra Scientific, Tokyo 1989) pp. 247–278
- 3.15 I. Sunagawa: Surface microtopography of crystal faces. In: *Morphology of Crystals*, ed. by I. Sunagawa (Terra Scientific, Tokyo 1987) pp. 321–365
- 3.16 I. Sunagawa: *Crystals, Growth, Morphology and Perfection* (Cambridge Univ. Press, Cambridge 2005)
- 3.17 W.A. Tiller: *The Science of Crystallization: Microscopic Interfacial Phenomena* (Cambridge Univ. Press, Cambridge 1991)
- 3.18 K. Sangwal, R. Rodriguez-Clemente: *Surface Morphology of Crystalline Solids* (Trans Tech, Zurich 1991)
- 3.19 W. Kossel: Zur Theorie des Kristallwachstums, *Nachr. Ges. Wiss. Göttingen Math.-Phys. Kl.* **1927**, 135–143 (1927), in German
- 3.20 M. Polanyi, E. Wigner: The interference of characteristic vibrations as the cause of energy fluctuations and chemical change, *Z. Phys. Chem.* **139**, 439 (1928), quoted in [3.21] pp. 49–51
- 3.21 B. Mutaftschiev: *The Atomistic Nature of Crystal Growth* (Springer, Berlin 2001)
- 3.22 R. Kern: The equilibrium form of a crystal. In: *Morphology of Crystals. Part A*, ed. by I. Sunagawa (Terra Scientific, Tokyo 1987) pp. 77–206
- 3.23 S. Toshev: Equilibrium forms. In: *Crystal Growth: An Introduction*, ed. by P. Hartman (North-Holland, Amsterdam 1973) pp. 328–341
- 3.24 M. Bienfait, R. Kern: Etablissement de la forme d'équilibre d'un cristal par la méthode de Lemmlein–Klija, *Bull. Soc. Fr. Minér. Crist.* **87**, 604–613 (1964)
- 3.25 E. Rodder, P.H. Ribbe (Ed.): *Fluid Inclusions*, Vol. 12 (Mineral. Soc. America, Chelsea 1984)
- 3.26 G.G. Lemmlein: About the equilibrium form of crystals, *Dokl. Akad. Nauk. SSSR* **98**, 973–975 (1954), in Russian
- 3.27 I.N. Stranski: Propriétés des surfaces des cristaux, *Bull. Soc. Fr. Minér. Crist.* **79**, 359–382 (1956)
- 3.28 O. Knacke, I.N. Stranski: Kristalltracht und Adsorption, *Z. Elektrochem.* **60**, 816–822 (1956), in German
- 3.29 R. Lacmann: Methoden zur Ermittlung der Gleichgewichts- und Wachstumsflächen von homöopolaren Kristallen bei der Adsorption von Fremdstoffen, *Z. Krist.* **112**, 169–187 (1959), in German
- 3.30 R. Kaischew, B. Mutaftschiev: *Bull. Chem. Dept. Bulg. Acad. Sci.* **7**, (1959), quoted in [3.21]
- 3.31 B. Honigmann: Gleichgewichtsformen von Kristallen und spontane Vergrößerungen. In: *Adsorption et Croissance Cristalline* (CNRS, Paris 1965) pp. 141–169

- 3.32 J.D.H. Donnay, G. Donnay: Structural hints from crystal morphology, 20th Annu. Diffr. Conf. (Pittsburg 1962)
- 3.33 J. Prywer: Explanation of some peculiarities of crystal morphology deduced from the BFDH law, *J. Cryst. Growth* **270**, 699–710 (2004)
- 3.34 R. Kern: Etude du faciès de quelques cristaux ioniques à structure simple. A. Le changement de faciès en milieu pur, *Bull. Soc. Fr. Minéral. Crist.* **76**, 325–364 (1953)
- 3.35 P. Hartman: Structure and Morphology. In: *Crystal Growth: An Introduction*, ed. by P. Hartman (North Holland, Amsterdam 1973) pp. 367–402
- 3.36 P. Hartman, P. Bennema: The attachment energy as a habit controlling factor. I. Theoretical considerations, *J. Cryst. Growth* **49**, 145–156 (1980)
- 3.37 F. Harary: *Graph Theory* (Addison Wesley, Reading 1969)
- 3.38 C.S. Strom: Finding F faces by direct chain generation, *Z. Krist.* **172**, 11–24 (1985)
- 3.39 R.F.P. Grimbergen, H. Meekes, P. Bennema, C.S. Strom, L.J.P. Vogels: On the prediction of crystal morphology. I. The Hartman–Perdok theory revisited, *Acta Cryst. A* **54**, 491–500 (1998)
- 3.40 S.X.M. Boerrigter, R.F.P. Grimbergen, H. Meekes: *FACELIFT-2.50, a Program for Connected Net Analysis* (Department of Solid State Chemistry University of Nijmegen, Nijmegen 2001)
- 3.41 E. Dowty: Crystal structure and crystal growth: I. The influence of internal structure on morphology, *Am. Mineral.* **61**, 448–459 (1976)
- 3.42 P. Hartman: Modern PBC theory. In: *Morphology of Crystals. Part A*, ed. by I. Sunagawa (Terra Scientific, Tokyo 1987) pp. 269–319
- 3.43 K.A. Jackson: *Liquid Metals and Solidification* (Am. Soc. Metals, Cleveland 1958) p. 174
- 3.44 R.J. Davey: The role of the solvent in crystal growth from solution, *J. Cryst. Growth* **76**, 637–644 (1986)
- 3.45 Z. Berkovitch–Yellin: Towards the ab initio determination of crystal morphology, *J. Am. Chem. Soc.* **107**, 8239–8253 (1985)
- 3.46 D. Aquilano, M. Rubbo, G. Mantovani, G. Sgualdino, G. Vaccari: Equilibrium and growth forms of sucrose crystals in the $\{h0l\}$ zone. I. Theoretical treatment of $\{101\}$ –d form, *J. Cryst. Growth* **74**, 10–20 (1986)
- 3.47 D. Aquilano, M. Rubbo, G. Mantovani, G. Sgualdino, G. Vaccari: Equilibrium and growth forms of sucrose crystals in the $\{h0l\}$ zone. II. Growth kinetics of the $\{101\}$ –d form, *J. Cryst. Growth* **83**, 77–83 (1987)
- 3.48 X.Y. Liu: Interfacial structure analysis for the prediction of morphology of crystals and implications for the design of tailor-made additives, *J. Cryst. Growth* **174**, 380–385 (1997)
- 3.49 X.Y. Liu, E.S. Boek, W.J. Briels, P. Bennema: Analysis of morphology of crystals based on identification of interfacial structure, *J. Chem. Phys.* **103**(9), 3747–3754 (1995)
- 3.50 R. Boistelle, A. Doussoulin: Spiral growth mechanisms of the $\{110\}$ faces of octacosane crystals in solution, *J. Cryst. Growth* **33**, 335–352 (1976)
- 3.51 M. Rubbo: Méthodes de mesure et cinétique de croissance et dissolution des faces $\{001\}$ de l'hexatriacontane en solution. Ph.D. Thesis (Univ. Aix-Marseille III, 1978), in French
- 3.52 M. Rubbo, R. Boistelle: Dissolution and growth kinetics of the $\{001\}$ faces of n-hexatriacontane crystals grown from heptane, *J. Cryst. Growth* **51**, 480–488 (1981)
- 3.53 D. Aquilano, M. Rubbo, G. Vaccari, G. Mantovani, G. Sgualdino: Growth mechanisms of sucrose from face-by-face kinetics and crystal habit modifications from impurities effect. In: *Industrial Crystallization 84*, ed. by S.J. Jančić, E.J. de Jong (Elsevier, Amsterdam 1984) pp. 91–96
- 3.54 D. Aquilano, M. Rubbo, G. Mantovani, G. Vaccari, G. Sgualdino: Sucrose crystal growth. Theory, experiments and industrial applications. In: *Crystallization as a Separation Process*, ed. by A.S. Myerson, K. Toyokura (ACS Symp. Ser., Washington 1990) pp. 72–84
- 3.55 C.H. Lin, N. Gabas, J.P. Canselier, G. Pèpe: Prediction of the growth morphology of aminoacid crystals in solution. I. α -Glycine, *J. Cryst. Growth* **191**, 791–802 (1998)
- 3.56 C.H. Lin, N. Gabas, J.P. Canselier: Prediction of the growth morphology of aminoacid crystals in solution. II. γ -Aminobutyric acid, *J. Cryst. Growth* **191**, 803–810 (1998)
- 3.57 R.F.P. Grimbergen, E.S. Boek, H. Meekes, P. Bennema: Explanation of the supersaturation dependence of the morphology of lysozyme crystals, *J. Cryst. Growth* **207**, 112–121 (1999)
- 3.58 H.M. Cuppen, G.M. Day, P. Verwer, H. Meekes: Sensitivity of morphology prediction to the force field: Paracetamol as an example, *Cryst. Growth Des.* **4**, 1341–1349 (2004)
- 3.59 S.X.M. Boerrigter, G.P.H. Josten, J. van der Streek, F.F.A. Hollander, J. Los, H.M. Cuppen, P. Bennema, H. Meekes: MONTY: Monte Carlo crystal growth on any crystal structure in any crystallographic orientation; application to fats, *J. Phys. Chem. A* **108**, 5894–5902 (2004)
- 3.60 C.S. Strom, P. Hartman: Comparison between Gaussian and exponential charge distributions in Ewald surface potentials and fields: NaCl, aragonite, phlogopite, *Acta Cryst.* **A45**, 371–380 (1989)
- 3.61 D. Aquilano, L. Pastero, M. Bruno, M. Rubbo: $\{100\}$ and $\{111\}$ forms of the NaCl crystals coexisting in growth from pure aqueous solution, *J. Cryst. Growth* **311**, 399–403 (2009)
- 3.62 D. Knoppik, A. Lösch: Surface structure and degree of coarsening of $\{111\}$ NaCl surfaces near the thermodynamic equilibrium between crystal and vapour, *J. Cryst. Growth* **34**, 332–336 (1976)

- 3.63 R. Kern: Etude du faciès de quelques cristaux ioniques à structure simple. B. Influence des compagnons de cristallisation sur le faciès des cristaux, Bull. Soc. Fr. Minér. Crist. **76**, 391–414 (1953)
- 3.64 R. Boistelle: Contribution à la connaissance des formes de croissance du chlorure de sodium, Ph.D. Thesis (Nancy, 1966)
- 3.65 M. Bienfait, R. Boistelle, R. Kern: Le morphodrome de NaCl en solution et l'adsorption d'ions étrangers. In: *Adsorption et Croissance Cristalline* (CNRS, Paris 1965) pp. 577–594
- 3.66 R. Boistelle, B. Simon: Epitaxies de $\text{CdCl}_2 \cdot 2\text{NaCl} \cdot 3\text{H}_2\text{O}$ sur les faces (100), (110) et (111) des cristaux de chlorure de sodium, J. Cryst. Growth **26**, 140–146 (1974)
- 3.67 R. Boistelle, M. Mathieu, B. Simon: Adsorption in solution of cadmium ions on {100} and {111} of NaCl. In: *Growth of Crystals*, ed. by A.A. Chernov (Consultants Bureau, New York 1984), vol 12, pp. 99–102
- 3.68 N. Radenović, W.J.P. van Enckewort, D. Kaminski, M. Heijna, E. Vlieg: Structure of the {111}NaCl crystal surfaces grown from solution in the presence of CdCl_2 , Surf. Sci. **599**, 196–206 (2005)
- 3.69 N. Radenović, W.J.P. van Enckewort, P. Verwer, E. Vlieg: Growth and characteristics of the {111}NaCl crystal surface grown from solution, Surf. Sci. **523**, 307–315 (2003)
- 3.70 N. Radenović: The Role of Impurities on the Morphology of NaCl Crystals. An Atomic Scale View. Ph.D. Thesis (Radboud Univ., Nijmegen 2006)
- 3.71 L. Li, K. Tsukamoto, I. Sunagawa: Impurity adsorption and habit changes in aqueous solution grown KCl crystals, J. Cryst. Growth **99**, 150–155 (1990)
- 3.72 L. Pastero, E. Costa, M. Bruno, M. Rubbo, G. Sgualdino, D. Aquilano: Morphology of calcite (CaCO_3) crystals growing from aqueous solutions in the presence of Li^+ ions. Surface behavior of the {0001} form, Cryst. Growth Des. **4**, 485–490 (2004)
- 3.73 M. Bruno, M. Prencipe: Ab-initio quantum-mechanical modeling of the (001), ($\bar{1}01$) and (110) surfaces of zabuyelite (Li_2CO_3), Surf. Sci. **601**, 3012–3019 (2007)
- 3.74 G. Clydesdale, K.J. Roberts, R. Docherty: Modelling the morphology of molecular crystals in the presence of disruptive tailor-made additives, J. Cryst. Growth **135**, 331–340 (1994)
- 3.75 G. Clydesdale, K.J. Roberts, K. Lewtas, R. Docherty: Modelling the morphology of molecular crystals in the presence of blocking tailor-made additives, J. Cryst. Growth **141**, 443–450 (1994)
- 3.76 G. Clydesdale, K.J. Roberts, R. Docherty: HABIT 95 – A program for predicting the morphology of molecular crystals as a function of the growth environment, J. Cryst. Growth **166**, 78–83 (1996)
- 3.77 D. Aquilano: Complex growth polytypism and periodic polysynthetic twins on octacosane crystals ($n\text{-C}_{28}\text{H}_{58}$), J. Cryst. Growth **37**, 215–228 (1977)
- 3.78 A.A. Chernov: Morphology and kinetics of crystal growth from aqueous solutions. In: *Morphology and Growth Unit of Crystals*, ed. by I. Sunagawa (Terra Scientific, Tokyo 1989) pp. 391–417
- 3.79 A.A. Chernov, T. Nishinaga: Growth shapes and their stability at anisotropic interface kinetics: theoretical aspects for solution growth. In: *Morphology of Crystals. Part A*, ed. by I. Sunagawa (Terra Scientific, Tokyo 1987) pp. 207–267
- 3.80 S.Y. Potapenko: Moving of steps through impurity fence, J. Cryst. Growth **133**, 147–154 (1993)
- 3.81 V.V. Voronkov, L.N. Rashkovich: Step kinetics in the presence of mobile adsorbed impurity, J. Cryst. Growth **144**, 107–115 (1994)
- 3.82 J.P. van der Eerden, H. Müller-Krumbhaar: Step bunching due to impurity adsorption: a new theory. In: *Morphology and Growth Unit of Crystals*, ed. by I. Sunagawa (Terra Scientific, Tokyo 1989) pp. 133–138
- 3.83 J.P. van der Eerden: Crystal growth mechanisms. In: *Handbook of Crystal Growth. Ia. Fundamentals*, ed. by D.T.J. Hurle (North-Holland, Amsterdam 1993) pp. 307–475
- 3.84 A.J. Derksen, W.J.P. van Enckewort, M.S. Couto: Behaviour of steps on the (001) face of $\text{K}_2\text{Cr}_2\text{O}_7$ crystals, J. Phys. D: Appl. Phys. **27**, 2580–2591 (1994)
- 3.85 H.M. Cuppen, H. Meekes, E. van Veenendaal, W.J.P. van Enckewort, P. Bennema, M.F. Reedijk, J. Arsic, E. Vlieg: Kink density and propagation velocity of the [010] step on the Kossel (100) surface, Surf. Sci. **506**, 183–195 (2002)
- 3.86 K. Tsukamoto: In situ observations of monomolecular steps on crystal growing in aqueous solution, J. Cryst. Growth **61**, 199–209 (1983)
- 3.87 S.R. Coriell, A.A. Chernov, B.T. Murray, G.B. McFadden: Step bunching: generalized kinetics, J. Cryst. Growth **183**, 669–682 (1998)
- 3.88 B.T. Murray, S.R. Coriell, A.A. Chernov, G.B. McFadden: The effect of oscillatory shear flow on step bunching, J. Cryst. Growth **218**, 434–446 (2000)
- 3.89 S.R. Coriell, G.B. McFadden: Applications of morphological stability theory, J. Cryst. Growth **237–239**, 8–13 (2002)
- 3.90 R. Ghez, S.S. Iyer: The kinetics of fast steps on crystal surfaces and its application to the molecular beam epitaxy of silicon, IBM J. Res. Dev. **32**, 804–818 (1988)
- 3.91 R.J. Davey, J.W. Mullin: Growth of the {100} faces of ammonium dihydrogen phosphate crystals in the presence of ionic species, J. Cryst. Growth **26**, 45–51 (1974)
- 3.92 M. Rubbo: Surface processes and kinetic interaction of growth steps, J. Cryst. Growth **291**, 512–520 (2006)
- 3.93 B. Simon, R. Boistelle: Crystal growth from low temperature solutions, J. Cryst. Growth **52**, 779–788 (1981)
- 3.94 M. Bienfait, R. Boistelle, R. Kern: Formes de croissance des halogénures alcalins dans un solvant polaire. In: *Adsorption et Croissance Cristalline* (CNRS, Paris 1965) pp. 515–531, in French

- 3.95 E. van Veenendaal, P.J.C.M. van Hoof, J. van Suchtelen, W.J.P. van Enckevort, P. Bennema: Kinetic roughening of the Kossel (100) surface, *J. Cryst. Growth* **198**, 22–26 (1999)
- 3.96 P. Hartman: The calculation of the electrostatic lattice energy of polar crystals by slice-wise summation, with an application to BeO, *Z. Krist.* **161**, 259–263 (1982)
- 3.97 R. Cadoret, J.C. Monier: Influence de l'adsorption des molécules de solvant sur la vitesse normale de croissance des faces opposées appartenant aux formes méridiennes complémentaires $\{hkl\}$ et $\{\bar{h}\bar{k}\bar{l}\}$ d'un cristal non centrosymétrique. In: *Adsorption et Croissance Cristalline* (CNRS, Paris 1965) pp. 559–573
- 3.98 E. van der Voort, P. Hartman: Morphology of polar $ASO_3 \cdot 6H_2O$ crystals ($A = Ni, Co, Mg$) and solvent interactions, *J. Cryst. Growth* **106**, 622–628 (1990)
- 3.99 A.J. Gratz, P.E. Hillner: Poisoning of calcite growth viewed in the atomic force microscope (AFM), *J. Cryst. Growth* **129**, 789–793 (1993)
- 3.100 T.N. Thomas, T.A. Land, T. Martin, W.H. Casey, J.J. DeYoreo: AFM investigation of the step kinetics and hillock morphology of the $\{100\}$ face of KDP, *J. Cryst. Growth* **260**, 566–579 (2004)
- 3.101 M. Moret: Influence of organic dyes on potassium sulphate crystal growth: A joint morphological and atomic force microscopy analysis, *Mater. Chem. Phys.* **66**, 177–188 (2000)
- 3.102 E. Haitema, J.P. van der Eerden: Defect formation during crystal growth, *J. Cryst. Growth* **166**, 141–145 (1996)
- 3.103 N. Zaitseva, L. Carman, I. Smolsky, R. Torres, M. Yan: The effect of impurities and supersaturation on the rapid growth of KDP crystals, *J. Cryst. Growth* **204**, 512–524 (1999)
- 3.104 N. Zaitseva, L. Carman, I. Smolsky: Habit control during rapid growth of KDP and DKDP crystals, *J. Cryst. Growth* **241**, 363–373 (2002)
- 3.105 R. Rodriguez-Clemente, S. Veintemillas-Verdaguer, F. Rull-Perez: Mechanism of crystal growth from boiling water solutions of soluble inorganic salts, mainly KDP. In: *Morphology and Growth Unit of Crystals*, ed. by I. Sunagawa (Terra Scientific, Tokyo 1989) pp. 479–512
- 3.106 A.S. Myerson, A.F. Izmailov: The structure of supersaturated solutions. In: *Handbook of Crystal Growth. 1a Fundamentals*, ed. by D.T.J. Hurle (North-Holland/Elsevier, Amsterdam 1993) pp. 249–306
- 3.107 F. Abbona, R. Boistelle: Nucleation of struvite ($MgNH_4PO_4 \cdot 6H_2O$) single crystals and aggregates, *Cryst. Res. Technol.* **20**, 133–140 (1985)
- 3.108 I. Sunagawa: Morphology of minerals. In: *Morphology of Crystals. Part B*, ed. by I. Sunagawa (Terra Scientific, Tokyo 1987) pp. 509–587
- 3.109 P. Bennema: Analysis of crystal growth models for slightly supersaturated solutions, *J. Cryst. Growth* **1**, 278–286 (1967)
- 3.110 A.A. Chernov: The spiral growth of crystals, *Sov. Phys. Usp.* **4**, 116–148 (1961)
- 3.111 G.H. Gilmer, R. Ghez, N. Cabrera: An analysis of combined surface and volume diffusion processes in crystal growth, *J. Cryst. Growth* **8**, 79–93 (1971)
- 3.112 R. Kern: Crystal growth and adsorption. In: *Growth of Crystals*, Vol. 8, ed. by N.N. Sheftal (Consultant Bureau, New York 1969) pp. 3–23
- 3.113 C.H. Lin, N. Gabas, J.P. Canselier, N. Hiquily: Influence of additives on the growth morphology of γ -aminobutyric acid, *J. Cryst. Growth* **166**, 104–108 (1996)
- 3.114 S.D. Durbin, G. Feher: Simulation of lysozyme crystal growth by the Monte Carlo method, *J. Cryst. Growth* **110**, 41–51 (1991)
- 3.115 R. Boistelle: Survey of crystal habit modification in solution. In: *Industrial Crystallization*, ed. by J.W. Mullin (Plenum, New York 1975) pp. 203–214
- 3.116 R.J. Davey, J.W. Mullin: The effect of supersaturation on growth features on the $\{100\}$ faces of ammonium dihydrogen phosphate crystals, *J. Cryst. Growth* **29**, 45–48 (1975)
- 3.117 A.A. Chernov, L.N. Rashkovic, A.A. Mkrtchyan: Solution growth kinetics and mechanism: Prismatic face of ADP, *J. Cryst. Growth* **74**, 101–112 (1986)
- 3.118 A.A. Chernov, A.I. Malkin: Regular and irregular growth and dissolution of $\{101\}$ faces under low supersaturation, *J. Cryst. Growth* **92**, 432–444 (1988)
- 3.119 K. Sangwal: On the mechanism of crystal growth from solutions, *J. Cryst. Growth* **192**, 200–214 (1998)
- 3.120 J. Prywer: Effect of supersaturation on evolution of crystal faces – Theoretical analysis, *J. Cryst. Growth* **289**, 630–638 (2006)
- 3.121 M. Kitamura: Controlling factor of polymorphism in crystallization process, *J. Cryst. Growth* **237–239**, 2205–2214 (2002)
- 3.122 M. Mirmehrabi, S. Rohani: Polymorphic behaviour and crystal habit of an anti-viral/HIV drug: Stavudine, *Cryst. Growth Des.* **6**, 141–149 (2006)
- 3.123 R. Bourne, R.J. Davey: The role of solvent-solute interactions in determining crystal growth mechanisms from solution. I. The surface entropy factor, *J. Cryst. Growth* **36**, 278–286 (1976)
- 3.124 P. Hartman: Le côté cristallographique de l'adsorption vu par le changement de faciès. In: *Adsorption et Croissance Cristalline* (CNRS, Paris 1965) pp. 479–506, in French
- 3.125 M. Lahav, L. Leiserowitz: The effect of solvent on crystal growth and morphology, *Chem. Eng. Sci.* **56**, 2245–2258 (2001)
- 3.126 S.D. Ewell, H.J. Scheel: *Crystal Growth from High-Temperature Solutions* (Academic, London 1975)
- 3.127 H.C. Zeng, L.C. Lim, H. Kumagai, M. Hirano: Effect of ambient water on crystal morphology and coloration of lead molybdate, *J. Cryst. Growth* **171**, 493–500 (1997)
- 3.128 J. Wang, C. Loose, J. Baxter, D. Cai, Y. Wang, J. Tom, J. Lepore: Growth promotion by H_2O in organic

- solvent-selective isolation of a target polymorph, *J. Cryst. Growth* **283**, 469–478 (2005)
- 3.129 R. Boistelle: Crystal growth from non aqueous solutions. In: *Interfacial Analysis of Phase Transformations*, ed. by B. Mutaftschiev (Reidel, Dordrecht 1982) pp. 531–557
- 3.130 B. Bourne, R.J. Davey: Solvent effects in the growth of hexamethylene tetramine crystals. In: *Industrial Crystallization*, ed. by J.W. Mullin (Plenum, New York 1975) pp. 223–237
- 3.131 J.R. Bourne, R.J. Davey: The role of solvent-solute interactions in determining crystal growth mechanisms from solution. II. The growth kinetics of hexamethylene tetramine, *J. Cryst. Growth* **36**, 287–296 (1976)
- 3.132 H.-X. Cang, W.-D. Huang, Y.-U. Zhou: Effects of organic solvents on the morphology of the meta-nitroaniline crystal, *J. Cryst. Growth* **192**, 236–242 (1998)
- 3.133 C. Stoica, P. Verwer, H. Meekes, P.J.C.M. van Hoof, F.M. Karspersen, E. Vlieg: Understanding the effect of a solvent on the crystal habit, *Cryst. Growth Des.* **4**, 765–768 (2004)
- 3.134 P.J.C.M. van Hoof, M. Schoutsen, P. Bennema: Solvent effect on the roughening transition and wetting of n-paraffin crystals, *J. Cryst. Growth* **192**, 307–317 (1998)
- 3.135 W.S. Wang, M.D. Aggarwal, J. Choi, T. Gebre, A.D. Shields, B.G. Penn, D.O. Frazier: Solvent effects and polymorphic transformation of organic nonlinear optical crystal L-pyrogutamic acid in solution growth process. I. Solvent effects and growth morphology, *J. Cryst. Growth* **198/199**, 578–582 (1999)
- 3.136 H. Oosterhof, R.M. Geertman, G.J. Witkamp, G.M. van Rosmalen: The growth of sodium nitrate from mixtures of water and isopropoxyethanol, *J. Cryst. Growth* **198/199**, 754–759 (1999)
- 3.137 X. Holmbäck, Å.C. Rasmuson: Size and morphology of benzoic acid crystals produced by drowning-out crystallization, *J. Cryst. Growth* **198/199**, 780–788 (1999)
- 3.138 K.-S. Seo, C. Han, J.-H. Wee, J.-K. Park, J.-W. Ahn: Synthesis of calcium carbonate in a pure ethanol and aqueous ethanol solution as the solvent, *J. Cryst. Growth* **276**, 680–687 (2005)
- 3.139 W. Polak, K. Sangwal: Modelling the formation of solute clusters in aqueous solutions of ionic salts, *J. Cryst. Growth* **152**, 182–190 (1995)
- 3.140 R.E. Aigra, W.S. Graswinckel, W.J.P. van Enckevort, E. Vlieg: Alizarin crystals: An extreme case of solvent induced morphology change, *J. Cryst. Growth* **285**, 168–177 (2005)
- 3.141 J.H. ter Horst, R.M. Geertman, G.M. van Rosmalen: The effect of solvent on crystal morphology, *J. Cryst. Growth* **230**, 277–284 (2001)
- 3.142 M. Ledésert, J.C. Monier: Modification du faciès des cristaux de cyanure mercurique par adsorption spécifique de molécules CH_3OH . In: *Adsorption et Croissance Cristalline* (CNRS, Paris 1965) pp. 537–554, in French
- 3.143 B. Simon, A. Grassi, R. Boistelle: Cinétique de croissance de la face (110) de la paraffine $\text{C}_{36}\text{H}_{74}$ en solution. I. Croissance en milieu pur, *J. Cryst. Growth* **26**, 77–89 (1974), in French
- 3.144 H. Cano, N. Gabas, J.P. Canselier: Experimental study on the ibuprofen crystal growth morphology in solution, *J. Cryst. Growth* **224**, 335–341 (2001)
- 3.145 E. Buckley: *Crystal Growth* (Wiley, New York 1951) pp. 330–385
- 3.146 *Adsorption et Croissance Cristalline*, Colloques Internationaux du CNRS, No. 152 (CNRS, Paris 1965), in French
- 3.147 G.M. Van Rosmalen, P. Bennema: Characterization of additive performance on crystallization: Habit modification, *J. Cryst. Growth* **99**, 1053–1060 (1990)
- 3.148 S. Sarig: Fundamentals of aqueous solution growth. In: *Handbook of Crystal Growth*. 2b, ed. by D.T.J. Hurle (North-Holland/Elsevier, Amsterdam 1994) pp. 1217–1269
- 3.149 K. Sangwal: Effect of impurities on the processes of crystal growth, *J. Cryst. Growth* **128**, 1236–1244 (1993)
- 3.150 K. Sangwal: Effects of impurities on crystal growth processes, *Prog. Cryst. Growth Charact. Mater.* **32**, 3–43 (1996)
- 3.151 R.J. Davey: The control of crystal habit. In: *Industrial Crystallization*, ed. by E.J. de Jong, S.J. Jančić (North-Holland, Amsterdam 1979) pp. 169–183
- 3.152 G. Bliznakow: Die Kristalltracht und die Adsorption fremder Beimischungen, *Fortschr. Min.* **36**, 149–191 (1958), in German
- 3.153 N. Cabrera, D.A. Vermileya: The growth of crystals from solutions. In: *Growth and Perfection of Crystals*, ed. by R.H. Doremus, B.W. Roberts, D. Turnbull (Wiley, New York 1958) pp. 393–408
- 3.154 G.W. Sears: The effect of poisons on crystal growth. In: *Growth and Perfection of Crystals*, ed. by R.H. Doremus, B.W. Roberts, D. Turnbull (Wiley, New York 1958) pp. 441–444
- 3.155 N. Albon, W.J. Dunning: Growth of sucrose crystals: determination of edge energy from the effect of added impurity on rate of step advance, *Acta Cryst.* **15**, 474–478 (1962)
- 3.156 R.J. Davey: Adsorption of impurities at growth steps, *J. Cryst. Growth* **29**, 212–214 (1975)
- 3.157 N. Kubota, J.W. Mullin: A kinetic model for crystal growth from aqueous solution in the presence of impurity, *J. Cryst. Growth* **152**, 203–220 (1995)
- 3.158 N. Kubota, M. Yokota, J.W. Mullin: Supersaturation dependence of crystal growth in solutions in the presence of impurity, *J. Cryst. Growth* **182**, 86–94 (1997)
- 3.159 G. Sgualdino, D. Aquilano, A. Cincotti, L. Pastero, G. Vaccari: Face-by-face growth of sucrose crystals from aqueous solutions in the presence of raffinose. I. Experiments and kinetic-adsorption model, *J. Cryst. Growth* **292**, 92–103 (2006)

- 3.160 R.J. Davey: The effect of impurity adsorption on the kinetics of crystal growth from solution, *J. Cryst. Growth* **34**, 109–119 (1976)
- 3.161 R. Boistelle: Impurity adsorption in crystal growth from solution. In: *Interfacial Analysis of Phase Transformations*, ed. by B. Mutaftschiev (Reidel, Dordrecht 1982) pp. 621–638
- 3.162 T.A. Eremina, N.N. Eremin, V.A. Kuznetsov, T.M. Okhrimenko, N.G. Furmanova, E.P. Efremova, V.S. Urusov: Characterization of defects generated by di- and trivalent cations in the potassium-dihydrophosphate structure and their influence on growth kinetics and face morphology, *Crystallogr. Rep.* **47**, 576–585 (2002)
- 3.163 M. Rauls, K. Bartosch, M. Kind, S. Kuch, R. Lacmann, A. Mersmann: The influence of impurities on crystallization kinetics – A case study on ammonium sulphate, *J. Cryst. Growth* **213**, 116–128 (2000)
- 3.164 L.N. Balykov, M. Kitamura, I.L. Maksimov: Effect of kink contamination on habit of two-dimensional crystal during growth with edge diffusion, *J. Cryst. Growth* **275**, 617–623 (2005)
- 3.165 C. Sweegers, H.C. de Coninck, H. Meekes, W.J.P. van Enckevort, I.D.K. Hiralai, A. Rijkeboer: Morphology, evolution and other characteristic of gibbsite crystals grown from pure and impure aqueous sodium aluminate solutions, *J. Cryst. Growth* **233**, 567–582 (2001)
- 3.166 C. Li, L. Wu, W. Chen: The impurity effects on growth and physical properties of strontium nitrate crystals, *Int. J. Mod. Phys. B* **16**, 114–121 (2002)
- 3.167 E. Kirkova, M. Djarova, B. Donkova: Inclusion of isomorphous impurities during crystallization from solutions, *Prog. Growth Charact. Mater.* **32**, 111–134 (1996)
- 3.168 H. Füredi-Milhofer, S. Sarig: Interactions between polyelectrolytes and sparingly soluble salts, *Prog. Growth Charact. Mater.* **32**, 45–74 (1996)
- 3.169 T. Jung, W.-S. Kim, C.K. Chou: Crystal structure and morphology control of calcium oxalate using biopolymeric additives in crystallization, *J. Cryst. Growth* **279**, 154–162 (2005)
- 3.170 F. Abbona, M. Angela-Franchini, C. Croni-Bono, H.E. Lundager Madsen: Effect of ammonia excess on the crystal habit of $\text{NiNH}_4\text{PO}_4 \cdot 6\text{H}_2\text{O}$ (Ni-struvite), *J. Cryst. Growth* **43**, 256–260 (1994)
- 3.171 J.J. Lu, J. Ulrich: An improved prediction model of morphological modification of organic crystals induced by additives, *Cryst. Res. Technol.* **38**, 63–73 (2003)
- 3.172 G.K. Kirov, I. Vesselinov, Z. Cherneva: Condition of formation of calcite crystals of tabular and acute rhombohedral habits, *Krist. Tech.* **7**, 497–509 (1972)
- 3.173 A. Millan, P. Bennema, A. Verbeeck, D. Bollen: Morphology of silver bromide crystals from $\text{KBr-AgBr-DMSO-water}$ systems, *J. Cryst. Growth* **192**, 215–224 (1998)
- 3.174 S. Veintemillas-Verdaguer: Chemical aspects of the effect of impurities in crystal growth, *Prog. Cryst. Charact. Mater.* **32**, 75–109 (1996)
- 3.175 I.M. Byteva: Effects of pH and crystal holder speed on the growth of crystals of ammonium dihydrogen phosphate. In: *Growth of Crystals*, Vol. 3, ed. by A.V. Shubnikov, N.N. Sheftal (Consultants Bureau, New York 1962) pp. 213–216
- 3.176 L.N. Rashkovic, G.T. Moldazhanova: Growth kinetics and morphology of potassium phosphate crystal faces in solutions of varying acidity, *J. Cryst. Growth* **151**, 145–152 (1995)
- 3.177 M. Delfino, J.P. Dougherty, W.K. Zwicker, M.M. Choy: Solution growth and characterization of L(+) glutamic acid hydrochloride single crystals, *J. Cryst. Growth* **36**, 267–272 (1976)
- 3.178 E.V. Khamskii: Some problems of crystal habit modification. In: *Industrial Crystallization*, ed. by J.W. Mullin (Plenum, New York 1975) pp. 215–221
- 3.179 H.E. Lundager Madsen: Influence of magnetic field on the precipitation of some inorganic salts, *J. Cryst. Growth* **152**, 94–100 (1995)
- 3.180 V.E. Ivashchenko, V.V. Boldyrev, Y.A. Zakharov, T.P. Shakhshneider, A.E. Ermakov, V.I. Krasheninina: The effect of magnetic field on the shape of etch pits of paracetamol crystals, *Mater. Res. Innov.* **5**, 214–218 (2002)
- 3.181 C. Zhong, L. Wang, N.I. Wakayama: Effect of a high magnetic field on protein crystal growth-magnetic field induced order in aqueous protein solutions, *J. Cryst. Growth* **233**, 561–566 (2001)
- 3.182 T. Kaito, S. Yanagiya, A. Mori, M. Kurumada, C. Kaito, T. Inoue: Effects of magnetic field on the gel growth of PbBr_2 , *J. Cryst. Growth* **289**, 275–277 (2006)
- 3.183 J. Garside: Kinetics of crystallization from solution. In: *Crystal Growth and Materials*, ed. by E. Kaldis, H.J. Scheel (Elsevier, Amsterdam 1978) pp. 483–513
- 3.184 W.R. Wilcox: Influence of convection on the growth of crystals from solution, *J. Cryst. Growth* **65**, 133–142 (1983)
- 3.185 R. Boistelle, F. Abbona: Morphology, habit and growth of newberyite crystals ($\text{MgHPO}_4 \cdot 3\text{H}_2\text{O}$), *J. Cryst. Growth* **54**, 275–277 (1981)
- 3.186 F. Abbona, M. Franchini-Angela: Crystallization of calcium and magnesium phosphates from solution of low concentration, *J. Cryst. Growth* **104**, 661–671 (1990)

4. Generation and Propagation of Defects During Crystal Growth

Helmut Klapper

This chapter presents a review of the typical growth defects of crystals fully grown on (planar) habit faces, i. e., of crystals grown in all kinds of solutions, in supercooled melt (mainly low-melting organics) and in the vapor phase. To a smaller extent growth on rounded faces from the melt is also considered when this seems appropriate to bring out analogies or discuss results in a more general context. The origins and typical configurations of defects developing *during* growth and *after* growth are illustrated by a series of selected x-ray diffraction topographs (Lang technique) and, in a few cases, by optical photographs.

After an overview (Sect. 4.1) the review starts with the formation of inclusions (Sect. 4.2), which are the main origin of other growth defects such as dislocations and twins. Three kinds of inclusions are treated: foreign particles, liquid inclusions (of nutrient solution), and solute precipitates. Particular attention is directed to the regeneration of seed crystals into a fully faceted shape (*capping*), and inclusion formation due to improper hydrodynamics in the solution, especially for potassium dihydrogen phosphate (KDP).

Section 4.3 deals briefly with striations (treated in more detail in Chap. 6 of this Handbook) and more comprehensively with the different kinds of crystal regions grown on different growth faces: growth sectors, vicinal sectors, and facet sectors. These regions are usually differently perfect and possess more or less different physical properties, and the boundaries between them are frequently faulted internal surfaces of the crystal. Two subsections treat the optical anomalies of growth and vicinal sectors and the determination of the relative growth rates of neighboring growth faces from the orientation of their common sector boundary.

In Sect. 4.4 distinction is made between dislocations connected to and propagating with the growth interface (*growth dislocations*), and

dislocations generated *behind* the growth front by plastic glide due to stress relaxation. The main sources of both types of dislocations are inclusions. In crystals grown on planar faces, growth dislocations are usually straight-lined and follow (frequently noncrystallographic) preferred directions depending on the Burgers vector, the growth direction, and the elastic constants of the crystal. These directions are explained by a minimum of the dislocation line energy per growth length, or equivalently by zero force exerted by the growth surface on the dislocation. Calculations based on anisotropic linear elasticity of a continuum confirm this approach. The influence of the discrete lattice structure and core energy on dislocation directions is discussed. Further subsections deal with Burgers vector determination by preferred directions, postgrowth movement of grown-in dislocations, generation of postgrowth dislocations, and the growth-promoting effect of edge dislocations.

Section 4.5 presents *twinning*, the main characteristics of twins and their boundaries, their generation by nucleation and by inclusions, their propagation with the growth front, and their growth-promoting effect. Postgrowth formation of twins by phase transitions and ferroelastic (mechanical) switching is briefly outlined. Finally, Sect. 4.6 compares the perfection of crystals (KDP and ammonium dihydrogen phosphate (ADP)) slowly and rapidly grown from solutions. It shows that the optical and structural quality of rapidly grown crystals is not inferior to that of slowly grown crystals, if particular precautions and growth conditions are met.

4.1 Overview	94
4.2 Inclusions	95
4.2.1 Foreign Particles	95
4.2.2 Solvent Inclusions	96
4.2.3 Solute Precipitates	99

4.3	Striations and Growth Sectors	101	4.4.6	Postgrowth Dislocations	118
4.3.1	Striations	101	4.4.7	The Growth-Promoting Role of <i>Edge</i> Dislocations	119
4.3.2	Growth Sectors.....	102	4.5	Twinning	120
4.3.3	Vicinal Sectors.....	103	4.5.1	Introductory Notes	120
4.3.4	Facet Sectors.....	104	4.5.2	Twin Boundaries	121
4.3.5	Optical Anomalies of Growth Sectors	105	4.5.3	Formation of Twins During Growth	122
4.3.6	Growth-Sector Boundaries and Relative Growth Rates	105	4.5.4	Growth-Promoting Effect of Twin Boundaries	124
4.4	Dislocations	107	4.5.5	Formation of Twins after Growth....	125
4.4.1	Growth Dislocations and Postgrowth Dislocations.....	107	4.6	Perfection of Crystals Grown Rapidly from Solution	125
4.4.2	Sources of Growth Dislocations	107	References	127
4.4.3	Burgers Vectors, Dislocation Dipoles	109			
4.4.4	Propagation of Growth Dislocations	110			
4.4.5	Postgrowth Movement and Reactions of Dislocations	116			

4.1 Overview

The present chapter mainly deals with growth defects in crystals fully grown on (planar) habit faces. To a smaller extent crystals grown on rounded faces from the melt are also considered when this seems to be appropriate to bring out analogies or discuss results in a more general context. Crystals grow on habit faces in solutions, supercooled melts, and vapor. A special feature of this growth method is that there is practically no temperature gradient inside the crystal, provided that facet growth occurs freely on the whole surface of the crystal (without contact with a container wall). This is also the case for growth in the supercooled melt: the crystallization heat released at the growing habit faces keeps these at the crystallization temperature – or at least close to it [4.1]. The absence of a temperature gradient, and thus of thermal stress, inside the crystal allows the development of defect structures according to first thermodynamical principles and their preservation in their as-grown geometries, unless thermal gradients are introduced by improper cooling to room temperature after growth. This particularly concerns dislocations in crystals growing in their plastic state. Dislocations are the essential elements of stress relaxation by plastic glide: they are generated, moved, and multiplied by stress. Thus – in the presence of thermal stress – it makes an essential difference whether crystals are grown in their brittle or their plastic state. From solution, crystals grow in the brittle or in the plastic state (depending on the specific mechanical properties at the growth temperature); from the melt, however, crystals *always* grow in the

plastic state, because each material has a more or less extended plastic zone below its melting point. It will be shown that growth dislocations develop the same geometrical features in crystals grown on habit faces from solution in the brittle state and from supercooled melts in the plastic state, provided that thermal gradients are absent.

In this review the generation of defects at the interface and their propagation with the advancing growth front are considered separately. This is because certain defects formed by a growth disturbance (e.g., by inclusions) may *heal out* and do not continue into the further growing crystal, whereas other defects (dislocations, twins, and grain boundaries), once initiated, are *forced* to proceed with the interface despite growth under optimal conditions. These defects can only be eliminated by growing out at the sides of the crystal, e.g., during Czochralski pulling on interfaces which are convex toward the melt. Moreover, distinction is made between *defects always connected to the interface (growth defects, especially growth dislocations)* and *defects generated “behind” the growth front (postgrowth defects)*. The latter defects may be formed already during the growth run, either by thermal stress or by precipitation. Furthermore, defect configurations may be preserved in their *as-grown* geometry or changed after growth (e.g., by *postgrowth* movement of dislocations).

Many experimental results and the majority of photographs presented in this review were obtained by growth experiments and x-ray topographic studies

(Lang technique) in the author's laboratories in Aachen and Bonn. Crystals were grown from aqueous and organic solutions, from supercooled melts (organics), and by Czochralski pulling (organics). The organic crystals were considered as low-melting *model substances* (melting points below 100 °C), chosen with the primary aim of studying the generation and propagation of growth defects in dependence on growth methods

and varying growth conditions. The main characterization method, x-ray diffraction topography, is not treated here; the reader is referred to the reviews [4.2–5] in the literature and to Chap. 42 in this Handbook. More specialized x-ray topographic treatments are given for twinned crystals [4.6] and for organic crystals [4.7]. Earlier reviews on the generation and propagation of growth defects were published by the author [4.8–11].

4.2 Inclusions

Two categories of inclusions are distinguished according to their origin [4.12, 13]: *primary inclusions* are associated with the growth front, i. e., they arise during growth, whereas *secondary inclusions* are formed after growth. Primary inclusions are *key defects* because they are the source of other defects (dislocations, twins) which propagate with the growth front into the further growing crystal. Inclusions of both categories may form stress centers which give rise to dislocation loops or half-loops by plastic glide (stress relaxation). Among the primary inclusions, three kinds are distinguished:

- Foreign particles
- Solvent (liquid) inclusions in crystals grown from solutions
- Solute precipitations in crystals grown from impure or doped melts.

Secondary inclusions are precipitates of solute impurities (dopants) formed after growth in the solid state during slow cooling, annealing or processing of crystals which are grown at high temperatures. They are due to the supersaturation of solutes at temperatures below the temperature at which the crystal was grown. These solutes precipitate if their diffusion mobility is sufficiently high and not frozen-in (as is usually the case at room temperature). In the same way vacancies and self-interstitials may condense into dislocation loops and stacking faults, e.g., during processing silicon crystals for electronic applications (*swirl defects*, e.g., [4.14]).

Here we treat only primary inclusions. A very detailed theoretical and experimental treatment of the capture of inclusions during crystal growth is presented by Chernov and Temkin [4.15]. A similar study with particular consideration of crystallization pressure is reported by Khaimov-Mal'kov [4.16].

4.2.1 Foreign Particles

Foreign particles preexisting in the nutrient (solution, melt) increase the risk of (heterogeneous) nucleation. Their incorporation into the growing crystal, however, is often considered as not very critical due to the crystallization pressure [4.16] (*disjoining force* after Chernov and Temkin [4.15]) which repulses foreign particles from the growth interface. Nevertheless, particles coming into contact with the growth face may be incorporated, depending on the size and chemical/physical nature of the particles and on growth conditions such as stirring, growth rate, and supersaturation [4.15]. For example, potassium alum crystals can be grown inclusion free (as assessed by optical inspection and x-ray topography) from *old* (i. e., repeatedly used) unfiltered aqueous solutions containing many floating dust particles, provided that growth conditions (temperature control, stirring) are stable enough to avoid the formation of liquid inclusions (see below). On the other hand in crystals of benzil grown in *old* (repeatedly filled up) supercooled melts ($T_m = 96\text{ °C}$), flocks of solid decomposition products floating in the melt are quite readily incorporated (unpublished observation by the author). In contrast to the solution growth of potassium alum, such benzil melts were not stirred, but thermal convection occurred due to the release of crystallization heat at the crystal surface [4.1]. In the latter case the incorporation seems to be favored by the higher viscosity and the lower agitation of the nutrient phase, and probably also by the chemical similarity (carbon) of the particles to the growing crystal.

Foreign solid inclusions are very common in minerals. In laboratory and industrial crystal growth they usually play a minor role because they are easily avoided by filtering of the nutrient before growth. If solid inclusions appear during the growth run, e.g.,

as abrasives of the stirring device, continuous filtering is advised. This has been demonstrated by Zaitseva et al. [4.17] for the rapid growth of huge potassium dihydrogen phosphate (KDP) and deuterated potassium dihydrogen phosphate (DKDP) crystals with linear sizes up to 55 cm: continuous filtering during the whole growth run considerably increased the optical quality and laser damage threshold of these crystals.

The intentional incorporation of particle inclusions for the study of the generation of dislocations is reported in Sect. 4.4.2. The intentional inclusion of oil drops during crystallization from solutions was studied by Kliia and Sokolova [4.18].

4.2.2 Solvent Inclusions

Solvent inclusions are very common in crystals grown by all variants of solution growth (aqueous and organic solvents, flux). Two origins are distinguished.

Faceting (Capping) of Rounded Surfaces

In general crystals grow from solutions with planar faces (habit faces), whereby faces with low surface energy grow slowly and determine the final morphology of the crystal (*Wulff theorem* [4.19]). If surfaces are rounded, (e.g., of the seed crystal or after redissolution), during first growth, facets of habit faces and (between them) terraces of these faces are formed. The facets become larger and the terraced regions grow out until a single edge between the two habit faces engaged is formed, as shown in Fig. 4.1 (*theorem of Herring* [4.20–23]; see also *growth on spheres* [4.24] and [4.25, p.130]). The *healed-out* regions often have the shape of caps (*capping region*). The growth on terraced surfaces favors the entrapment of solvent inclusions, which may lead in extreme cases to a spongy structure of the capping region. This usually happens during first growth on seed crystals which were rounded

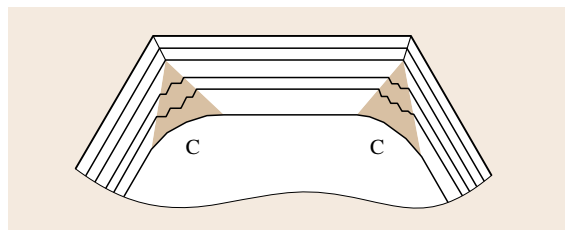


Fig. 4.1 Faceting and *capping* on rounded crystal surfaces. The shaded regions of terraced growth favor entrapment of liquid inclusions. They grow out and finally form the growth-sector boundary between the main habit faces



Fig. 4.2 A KDP crystal (length 45 mm) with {011} capping pyramid on a {001} seed plate

during a final etching (which is necessary in order to remove surface impurities and defects) before seeding-in. Therefore the zone of first growth around the seed crystals is usually more or less disturbed by liquid inclusions. These inclusions, however, can be largely avoided by a very slow (and thus time-consuming) growth under low supersaturation during the seed-faceting period.

A conspicuous example of capping is provided by potassium dihydrogen phosphate (KDP) grown in aqueous solution on {001} seed plates (Fig. 4.2). KDP develops habit faces {100} (tetragonal prism) and {011} (tetragonal dipyrmaid), but {001} is not a habit face. Thus in the first stage of growth on a {001} seed plate a spongy capping zone in the form of a tetragonal pyramid {011} over the seed plate as basis is formed, followed by clear further growth on {011} pyramid faces (Fig. 4.2). Detailed descriptions of this {001} capping process in KDP and ammonium dihydrogen phosphate (ADP) crystal growth are presented by Zerkoss and Slawson [4.12] and Janssen-van Rosmalen et al. [4.26].

Fluctuation of Growth Conditions (Growth Accidents)

A sufficiently strong change of growth condition (e.g., of supersaturation, stirring rate, stirring direction) may introduce – due to local variations of supersaturation – a (temporary) instability of growth faces: regions of retarded and promoted growth occur, leading to elevations

and depressions on the growth face. Overhanging layers then spread over the depressions and close them, thus trapping nutrient solution. Usually a group of inclusions arranged in a plane parallel to the growth face is formed (*zonal inclusions*, Fig. 4.3). If all growth faces of the crystal are affected by the same growth disturbance, inclusions are formed on all faces. After stabilization of growth conditions and further clear growth the inclusions, which are visible by scattered light (if the crystal is transparent), reveal the shape of the crystal at the instant of the disturbance (*phantom crystal* in mineralogy). This is often observed when, after an accidental (or intentional) temporary redissolution, the crystal is rounded, so that during further growth refaceting with increased tendency for inclusion trapping occurs. Due to the capping effect, these inclusions are concentrated and most visible in the edge regions of the crystal [4.27] (Fig. 4.1).

The tendency to form solvent inclusions may strongly depend on the type of growth face $\{hkl\}$. In general the formation of solvent inclusions is fa-

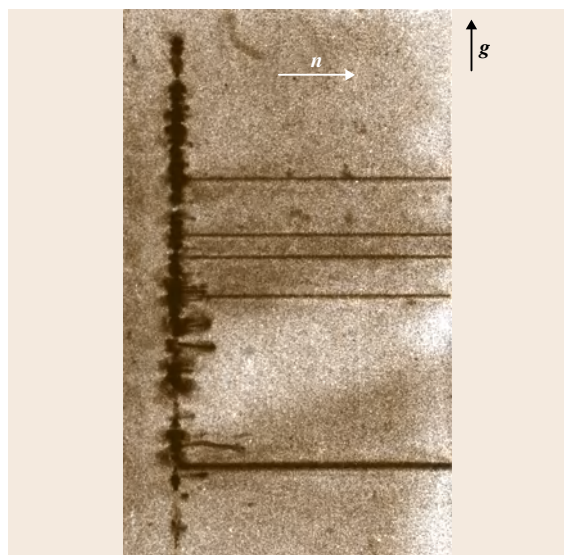


Fig. 4.3 Liquid (*zonal*) inclusions in solution-grown potassium alum (water), triggered on a $\{110\}$ face by intentionally introduced redissolution due to a temporary increase of the solution by 1°C . The original temperature (about 40°C) was restored after a slight rounding of the crystal edges had appeared. Arrow *n*: growth direction. A few edge dislocations originate from the inclusions. Section ($6 \times 12\text{ mm}^2$) of an x-ray topograph of a 0.9 mm -thick $\{001\}$ plate. Diffraction vector $\mathbf{g}(2\bar{2}0)$, MoK_α radiation

vored on faces with high surface (attachment) energy, and thus high growth rate. An instructive example is provided by potassium alum growing from aqueous solution: fluctuations of growth conditions lead to pronounced liquid-inclusion entrapment on the smaller and fast-growing cube faces $\{100\}$, whereas the slow and morphologically dominant octahedron faces $\{111\}$ resist the formation of inclusions even for strong changes of growth parameters [4.27]. There are also crystals for which certain growth faces trap tiny liquid inclusions despite controlled growth conditions. An example is shown in Fig. 4.4: The two pinacoid growth sectors of the crystal appear milky due to light scattering at solvent inclusions, whereas sectors of other faces are optically clear. The reason for the preferred inclusions trapping on certain growth faces is their specific surface structure, which favors the incorporation of solvent molecules and the formation of solvent bubbles. This phenomenon is known as *hourglass inclusions*, of which two types are distinguished: (1) face-specific preferential formation of liquid bubbles (which is the case in Fig. 4.4), and (2) preferential absorption of solvent and other foreign molecules as solid solution in the host crystal (without the formation of bubbles or solid precipitates). A well-known and frequently studied example of *hourglass inclusions* of type 2 is provided by potassium sulfate (e.g., Buckley [4.25, p. 415–420], Vetter et al. [4.28]; see also *dyeing crystals* [4.29, 30]). It is also repeatedly referred to in Sect. 4.3 of this chap-

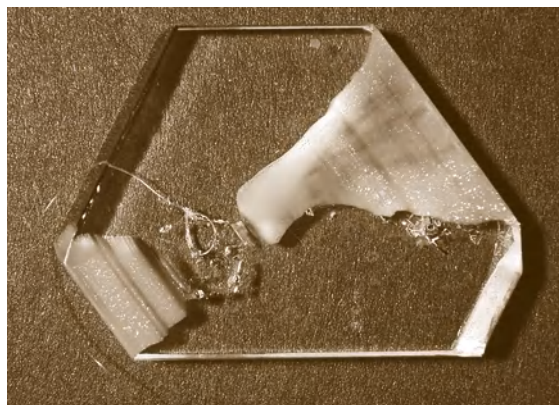


Fig. 4.4 Preferred liquid-inclusion entrapment in the $\{201\}$ pinacoid growth sectors of monoclinic Tutton salt $\text{K}_2\text{Zn}(\text{SO}_4)_2 \cdot 6\text{H}_2\text{O}$ grown from aqueous solution under well-controlled conditions (horizontal diameter 35 mm). The crystal plate, cut from a bulk crystal, contains the seed crystal with the nylon thread for suspension in the solution

ter. Often the preferred formation of liquid inclusions on certain growth faces can be largely suppressed by a proper pH value.

The hydrodynamics of the solution flow around the growing crystal may also play a significant role in the formation of liquid inclusions (e.g., Chernov et al. [4.31]). A particularly interesting example of this influence for the growth of KDP crystals is reported by Janssen-Van Rosmalen and Bennema [4.32], Janssen-van Rosmalen et al. [4.26], and van Enckevort

et al. [4.33]. In their experiments the KDP crystals (shape: tetragonal prism $\{100\}$ terminated on both side by dipyrmaid $\{011\}$) were mounted on a *tree* which rotated in the solution. The solution was flowing toward one (front) and away from the other (rear) pyramid. On pyramid faces on the trailing side, solvent inclusions are often formed in a quasiperiodic sequence (Fig. 4.5), whereas on the front side inclusions do not appear. This phenomenon is explained by the hydrodynamic situation at the rear-side pyramid face: in the wake *behind* the crystal a swirling region with no or strongly reduced liquid exchange with the bulk mother solution is formed. Thus the saturation decreases locally and growth is retarded compared with regions neighboring edges of the growth face. This leads to a depression in the growth face. After some distance of further growth this cavity is overgrown, forming a solvent inclusion. As shown in Fig. 4.5, this process is repeated several times in a quasiperiodic manner. A detailed study of this effect, including flow simulation experiments in a model system, is presented by Janssen-Van Rosmalen et al. [4.26], Janssen-Van Rosmalen and Bennema [4.32], and van Enckevort et al. [4.33], who also report that the formation of these inclusions is avoided by stronger stirring, in their experiment by faster rotation of the crystal tree. In any case, strong stirring smoothes out supersaturation differences on the growth face and thus may largely avoid interface instabilities. This is particularly significant in the solution growth of very large crystals where high saturation differences between the edge regions and the center of a growth face may occur. For the *rapid growth* of KDP (e.g., [4.34–36]) and other crystals very strong stirring is a prerequisite for inclusion-free growth.

Finally a special type of liquid inclusions, so-called *hair inclusions*, is mentioned. These were, for example, observed by Smolsky et al. [4.37] in rapidly grown KDP; they consist of long hair-thin channels or strings of tiny bubbles filled with mother liquor. These pipes and strings are not arranged along the instantaneous growth front but form a more or less large angle with it, which indicates that they have proceeded with the growth front. Their origin is unclear for the most part, but in the case of KDP [4.37] it was shown by in situ atomic force microscopy of the growth face that at least some of them are triggered by tiny solid inclusions. As was shown by x-ray diffraction topography [4.37], these *hairs* are not correlated with dislocations. Thus they are different from the so-called *micropipes* (channels), frequently observed along the hexagonal axis of



Fig. 4.5 X-ray diffraction topograph of a (100) -plate (about 1.5 mm thick, about 50 mm high), cut from the rear side of a KDP crystal moved by rotation through the solution. Due to a closed wake of solution with reduced supersaturation behind the $(0\bar{1}1)$ growth face, liquid inclusions were repeatedly formed. They are the origin of numerous dislocations which grow out of the crystal at the side because the $\{010\}$ prism faces practically do not grow. The dislocations in the triangular region above the capping zone belong to one of the growth sectors (101) or $(\bar{1}01)$. They are inclined and emerge out of the plate at their top ends. Diffraction vector $g(020)$, $\text{AgK}\alpha$ radiation

beryl [4.38] and silicon carbide [4.39–41]. These channels are the hollow cores of screw dislocations with large Burgers vectors.

Liquid inclusions play a significant role in mineralogy because they allow the reconstruction of the conditions of mineral formation. A comprehensive review is given by Roedder [4.43].

4.2.3 Solute Precipitates

A critical parameter in the growth of crystals from melts containing solute impurities or dopants is the effective distribution (segregation) coefficient k_{eff} of the impurity (dopant) between melt and crystal (see Chap. 6 in this Handbook). If $k_{\text{eff}} < 1$ (which is mostly the case), the solutes are rejected by the growing crystal, which leads to a higher solute concentration in the melt in front of the growth interface. The excess solute diffuses away from the interface. For high growth rates, however, the solute concentration may become supersaturated, leading to the precipitation of the solute and incorporation into the crystal during further growth. Thus the solute precipitation is an interplay between k_{eff} , the characteristic time scale of solute diffusion in the melt, and the growth rate.

If a solute precipitation is triggered by a short temporary increase of the growth rate, a solitary sheet of precipitations, marking the instantaneous growth front, will be formed. If, however, the high growth rate is permanent, the precipitations extend in the growth direction and form so-called *solute trails* (e.g., [4.44]). In more extreme development they lead to constitutional supercooling with cellular and dendritic growth (see Chap. 6 in this Handbook).

As examples the formation of solute inclusions during melt growth of organic crystals is shown in Figs. 4.6 and 4.7. The melts of organic materials contain considerable amounts of solute atmospheric gas which is precipitated as small bubbles. Figure 4.6 shows bubble precipitation in Czochralski crystals of benzophenone [$(\text{C}_6\text{H}_5)_2\text{CO}$, $T_m = 48^\circ\text{C}$] induced by intentionally introduced changes of the growth conditions [4.42]. In the example of Fig. 4.6a, the pulling rate was temporarily increased from 0.4 to 0.6 mm/h, the other parameters remaining constant. This instantaneously led to bubble precipitation and reduction of the crystal diameter. The shape of the growth front at the instant of the intervention and its changes during further growth are clearly visible in dark-field light illumination. Note that the bubbles are also arranged in strings normal to the growth interfaces, corresponding to solute trails. After

about 2 h the pulling rate was again reduced to its former value of 0.4 mm/h. Then the crystal adopted its former width and the bubble precipitation stopped. Figure 4.6b shows the effect of an intentionally introduced transition from Czochralski growth to supercooled-melt growth by lowering the temperature of the melt from about 1.5°C above to about 1°C below $T_m = 48^\circ\text{C}$ and stopping the pull (but retaining the crystal rotation). The bubble precipitations reveal the transition of the concave (towards the melt) interface to a convex one. After the growth rate fell below the critical value, the bubble precipitation stopped. The crystal grew into the now supercooled melt and adopted a fully faceted shape at its end [4.42]. We have also observed that the (internal) surface of gas bubbles, precipitated in old and impure melts, were often covered with a layer of brownish material. This indicates that nongaseous impurities of the melt have been precipitated together with the solute gas.

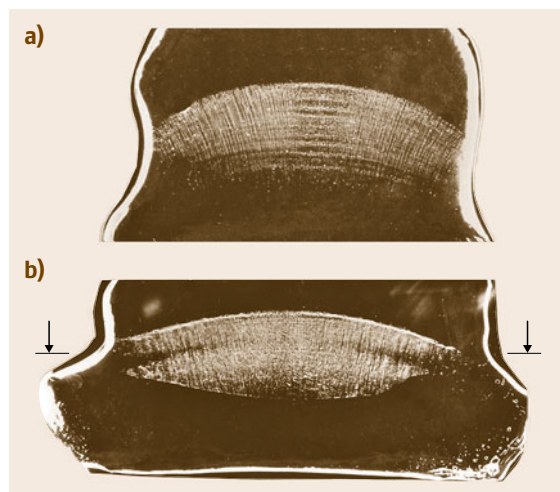


Fig. 4.6a,b Bubble precipitation in Czochralski benzophenone ($T_m = 48^\circ\text{C}$) by an intentionally introduced change of growth parameters. Optical dark-field photographs of about 1.6 mm-thick plates. **(a)** Temporary increase of the pulling rate from 0.4 to 0.6 mm/h without change of other growth parameters. The diameter of the crystal is temporarily reduced from about 11 to 10 mm. **(b)** Transition from Czochralski growth to growth from supercooled melt by lowering the temperature from about 1.5°C above to about 1°C below T_m and stopping the pulling while retaining the rotation. The crystal grew into the now supercooled melt and became fully faceted. The arrows indicate the level of the melt after stopping the pulling (after [4.42])

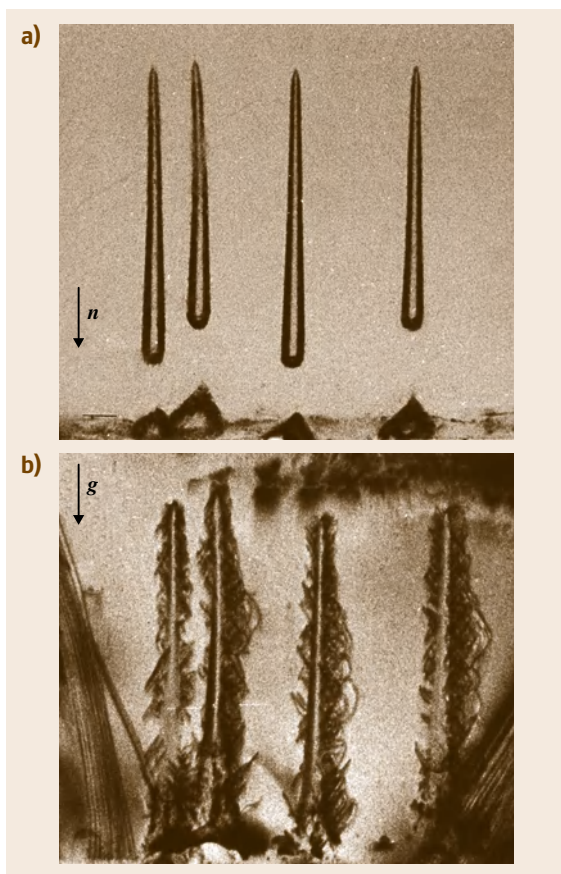


Fig. 4.7a,b Bubble channels filled with gas in a prism growth sector of trigonal benzil ($T_m = 96^\circ\text{C}$) grown from supercooled melt ($5.6 \times 5.1 \text{ mm}^2$ section of a 2.2 mm-thick (0001) plate cut from the bulk crystal). Growth direction vertically downward. **(a)** Optical photograph. The channels originate from four gas bubbles sticking to the seed surface when starting growth. They have partially been filled by recrystallization within about 6 months after growth (see text). **(b)** X-ray topograph taken before the channels were closed. Note the glide-dislocation half-loops emitted from the channels (after [4.1]). Diffraction vector $\mathbf{g}(2\bar{2}00)$, $\text{CuK}\alpha_1$ radiation

Another instructive example is provided by Fig. 4.7, which shows a section of a benzil crystal ($(\text{C}_6\text{H}_5\text{CO})_2$, $T_m = 96^\circ\text{C}$) grown from slightly supercooled melt (ΔT about 1°C) with four gas inclusions elongated normal to the planar growth face (i. e., in the growth direction) [4.1]. The inclusions started from small bubbles sticking to the bottom side of the seed crystal already

during the seeding-in procedure. During further growth the growth rate was always below the critical rate for gas precipitation. Nevertheless, the bubbles advanced with the growth front and elongated and became even wider by collecting gas from the gas-rich zone in front of the growth face, thus leaving behind a gas-filled channel.

The photograph in Fig. 4.7a was taken about half a year after growth [4.1]. During this period the channels were partially filled by recrystallization, as can be recognized by the funnels in the surface at the bottom, indicating the former channel openings. Optically the recrystallized regions appear homogeneous except for a string of tiny scatterers (bubbles) aligned along the central axis of the former channel, revealed by optical dark-field observation. The mechanism of this recrystallization is not clear, but it probably occurred via sublimation, since the vapor pressure of benzil is relatively high, and the crystal was welded between two gastight plastic foils and, thus, stored in his own vapor.

Figure 4.7b shows an x-ray diffraction topograph taken shortly after growth was finished, when the channels were still open [4.1]. Numerous glide dislocations in the shape of half-loops emitted from the channel surface have formed (cf. also Sect. 4.4.6).

The entrapment of gas bubbles and their elongation into channels has been studied in detail by *Chernov* and *Temkin* [4.15], *Khaimov-Mal'kov* [4.16], and *Gegusin* and *Dziyuba* [4.45].

The relatively high concentration of solute gas in organic melts significantly limits the growth rate allowing bubble-free growth. Comparative growth experiments in outgassed supercooled melts under their own vapor showed that the growth rate for visually perfect growth could be increased by a factor of about three [4.46] compared with growth in gas-rich melts. In these experiments the growth rate (i. e., the supercooling), however, cannot be increased too much, because strong thermal upward convection in the melt (induced by the high release rate of heat of crystallization at crystal surfaces) leads to turbulent melt flow and serious defects (ragged growth) at the top end of the crystals.

Precipitation of solutes is a serious problem in melt growth of doped and mixed crystals. A detailed treatment is given in Chap. 6 in this Handbook. An instructive investigation of this effect, including an x-ray topographic study of dislocations formed around the precipitations, is reported by *Bardsley* et al. [4.44].

4.3 Striations and Growth Sectors

4.3.1 Striations

Striations are local variations of the impurity (dopant) concentration or of the crystal stoichiometry. They arise from fluctuations of growth conditions, such as changes of temperature, cooling rate, pressure, or convection in the solution or melt. These fluctuations lead to temporary changes in the growth rate, and thus to changes of the impurity incorporation. As a rule, they affect the whole growth front and thus form inhomogeneous layers parallel to the interface. The term *striations* is usually applied when the impurity layers appear in a (quasi)periodic sequence (Fig. 4.8a). If there are isolated layers, due to sporadic changes of growth conditions, often the term *growth bands* is used. In mineralogy, the term *growth zoning* is common. In crystals

grown under rotation, strictly periodic *rotational striations*, correlated with the rotation rate, may occur. They are due to a nonuniform radial temperature distribution around the rotation axis, leading to slight changes of growth conditions (even with remelting) within a rotation period.

The impurities may be contaminants of the solution or of the melt, or incorporated solvent components. Striations are also formed by dopants intentionally introduced with the aim of tailoring specific physical properties of the crystals. The rate of incorporation depends on the impurity (dopant) species and is governed by their distribution (segregation) coefficient with regard to the crystal to be grown.

The regions of different impurities/dopants form layers coinciding with the instantaneous growth front. In crystals grown on habit faces (from solution or supercooled melt) they are planar, as shown in Figs. 4.8a and 4.9. The *intensity* of the striations, i. e., the concentration of impurities, may be considerably different in distinct growth sectors (Sect. 4.3.2). This is due to different surface structures of different growth faces which may facilitate or impede impurity capture. Symmetrically equivalent growth sectors show the same *intensity* of striations unless the growth conditions (e.g., solution

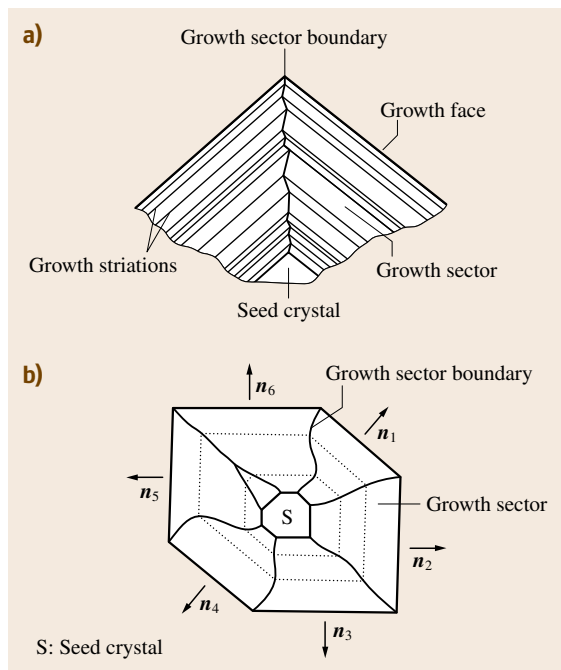


Fig. 4.8 (a) Growth striations and growth-sector boundary in a crystal grown on planar (habit) faces. The sector boundary is an internal surface formed by the movement of the edge joining the two faces during growth. It separates regions of different growth directions. (b) Division of a fully faceted crystal into growth sectors. The vectors n_i indicate the growth directions. *Dashed lines*: contours of the crystal at different stages of growth. One of the growth sectors has *grown out*

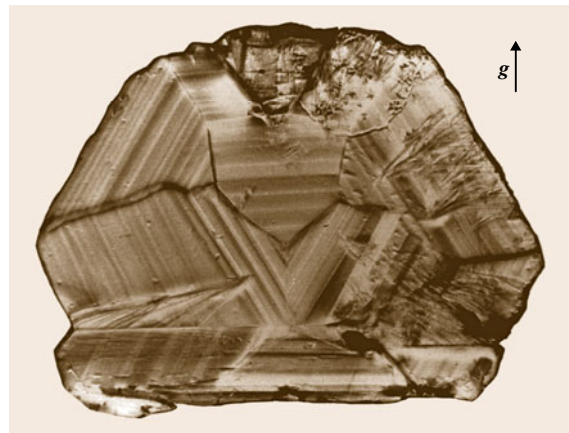


Fig. 4.9 X-ray topograph of a (0001) plate (about 8 mm diameter, 0.35 mm thick) cut out of a quartz-homeotypic gallium phosphate GaPO_4 crystal grown from high-temperature solution in phosphoric/sulfuric acid (after [4.47]), showing the triangular arrangement of growth sectors with pronounced striations. Growth-sector boundaries are visible by topographic contrast or by bends of the striations. Diffraction vector $g(10\bar{1}0)$, AgK_α radiation

flow) at the corresponding growth faces are different. Conspicuous examples are the so-called hourglass growth patterns of crystals stained with organic dyes. *Staining of crystals* has been thoroughly studied by Kahr and Guerny [4.29] and Kahr and Vasquez [4.30]. Striations are often modified by growth hillocks (*vicinal pyramids*) as discussed in Sect. 4.3.3. An x-ray topographic study of the striation formation in the presence of vicinal pyramids in rapidly grown KDP crystals is presented by Smolsky et al. [4.48].

Crystals grown on rounded interfaces exhibit curved striations. An example of striations accompanied by tiny gas bubbles in a Czochralski crystal is shown in Fig. 4.10. Facets formed on rounded interfaces lead to regions (*facet sectors*, Sect. 4.3.4) with planar striations. The occurrence and *intensity* of these striations may be quite different from those of striations formed along

curved interfaces. This is due to distinct growth modes with different distribution coefficients for rough growth on curved interfaces and growth on facets from supercooled melt (cf. Chap. 6 of this Handbook).

In general, growth striations lead to local changes of physical properties (e.g., electric conductivity, optical birefringence). This is a major problem in the growth of doped crystals for sophisticated electronic and optical solid-state devices. This can be encountered by suppression of melt convection, e.g., by growth under microgravity [4.49] or by growth in magnetic fields [4.50, 51], which are treated in Chaps. 7 and 17 of this Handbook. An extensive treatment of the origin of striations and of recipes to largely avoid them is presented by Scheel [4.52].

4.3.2 Growth Sectors

Bulk crystals grow in all directions of space. Due to their structural and physical anisotropy, the types, distribution, and geometry of growth defects are distinct for different growth directions. This is pronounced in crystals grown from solutions and supercooled melts, which develop planar growth (*habit*) faces, and thus consist of regions (*growth sectors*) grown in discrete directions defined by the normals of the growth faces involved (Fig. 4.8b). Among all habit faces that are possible in principle, the *final* crystal usually exhibits only those faces which possess low surface (attachment) energies and thus – according to Wulff's theorem [4.19–21] – have low growth velocities. *Fast* faces with higher attachment energy grow out and vanish from the external morphology (cf. *Wulff–Herring construction* [4.20–23]). Thus the crystal may contain more growth sectors, usually in close neighborhood of the seed crystal, than are recognized from its final outward morphology (Fig. 4.8b).

Growth sectors are separated by growth-sector boundaries. These boundaries are internal surfaces over which the edges between neighboring faces have swept during growth. They are surfaces generated by the parallel movement of a straight line. When projected parallel to the edge (zone axis) of the two faces 1 and 2 involved, the boundary appears as a straight or somewhat curved line, the (local) direction of which depends on the (instantaneous) relative growth velocity v_1/v_2 of these faces (Sect. 4.3.6 and Fig. 4.14). If v_1/v_2 is constant, the line is straight (i.e., the boundary is planar); if v_1/v_2 fluctuates, the line is irregular, often zigzag-like, as sketched in Fig. 4.8a (i.e., the boundary is an irregularly waved internal surface).



Fig. 4.10 Plate cut from the center of a Czochralski boule of orthorhombic salol ($T_m = 42^\circ\text{C}$), about 1.3 mm thick; imaged length is about 40 mm. The growth striations marking the interface at different stages of growth contain tiny gas bubbles, many of which are sources of growth dislocations. Due to the concave interface the dislocations are focused toward the center of the boule. Due to this effect many dislocations enter the plate from above through the plate surface. Diffraction vector $g(002)$, $\text{CuK}\alpha_1$ radiation

Growth-sector boundaries and their surroundings may be perfect crystal regions. In many cases, however, they are fault surfaces which can be observed by etching, optical birefringence, and x-ray diffraction topography. The fault may be due to increased local impurity incorporation when growth layers on neighboring faces meet at their common edge, or due to slightly different lattice parameters in both sectors. The latter lead to a transition zone along the boundary with lattice distortions which can be detected by the methods mentioned above. An example of this case is shown in Fig. 4.11. Lattice distortions preferentially occur along boundaries between symmetrically nonequivalent faces, due to different incorporation of impurities which leads to slight differences of their

d -values. Boundaries between symmetrically *equivalent* sectors are often strain free, but may be visible by the sharp bends of growth striations (if present), see Fig. 4.9. An illustrative example of the extraordinarily rich growth sectoring of natural beryl, revealed by x-ray topographic imaging of sector boundaries and striations, is presented by Herres and Lang [4.53]. For x-ray topographic characterization of faulted growth-sector boundaries as shift or tilt boundaries, see Klapper [4.7, 8, 54].

The different incorporation of additives in different growth sectors is strikingly demonstrated in the so-called *dyeing of crystals* which goes back to Sénarmont (1808–1862) and was extensively studied in the last two decades by Kahr and coworkers (e.g., [4.29, 30]). They grew crystals from solutions with organic dye molecules as additives. The distinct incorporation of these molecules on different growth faces is conspicuously apparent from the different coloring of their growth sectors (see also Sect. 4.3.5). A similar study of coloring of the growth sectors of KDP with organic dyes is reported by Maeda et al. [4.55].

4.3.3 Vicinal Sectors

Another, less pronounced kind of sectoring frequently arises within the growth sectors treated above, due to growth hillocks (growth pyramids). These very flat *vicinal* pyramids, which are caused by dislocations emerging at their apex, often exhibit facets (*vicinal facets*) deviating by only very small angles from the main growth face. The facets are formed by terraces of growth layers, and their slopes depend on the step height and the widths of the terraces. On facets with different slope angles the incorporation of impurities is different. This leads to slightly distinct d -values of the regions grown on different vicinal facets (*vicinal sectors*). In analogy to growth sectors, the ridges of vicinal pyramids are termed *vicinal-sector boundaries*, which may be faulted surfaces. This also holds for the *valleys* between neighboring vicinal pyramids.

A detailed x-ray topographic study of vicinal sectors and their boundaries formed on {011} dipyrmaid faces and {100} prism faces of KDP and ADP was published by Smolsky et al. [4.56] and Smolsky and Zaitseva [4.57], who also coined the term *vicinal sector*. Atomic force microscope in situ investigation of the step structures of vicinal hillocks in relation to the Burgers vectors of unit and multiple unit height of the dislocations generating the hillocks is presented by De Yoreo et al. [4.58]. Pronounced triangular vicinal pyramids are

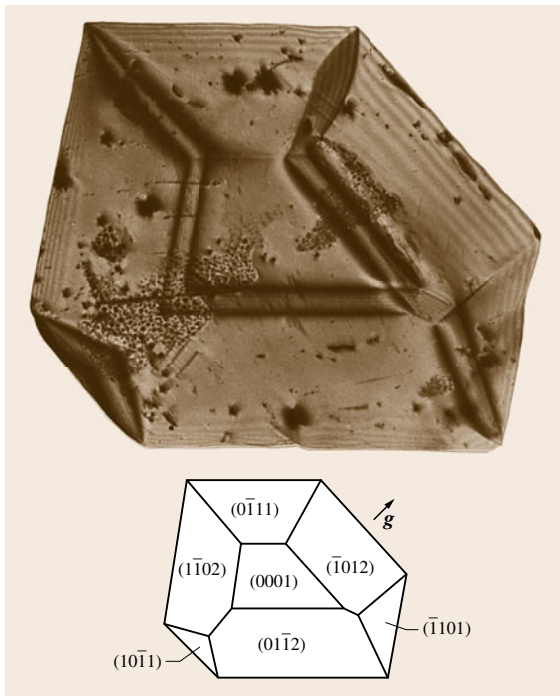


Fig. 4.11 (0001) Plate (about 14 mm diameter, 1 mm thick) of benzil grown from solution in xylene, containing faulted boundaries between the growth sectors shown in the drawing. The boundaries are inclined to the plate normal and appear as contrast bands with increased intensity at their emergence from the surface (increased strain due to stress relaxation at the surface). Some boundaries are invisible in the x-ray reflection used here. The plate tapers toward its edges, thus giving rise to *pendellösung* fringes. Some contrasts are due to surface damages. Diffraction vector $g(2020)$, $\text{CuK}\alpha_1$ radiation

observed on $\{111\}$ octahedron faces of potassium alum (cf. the optical and x-ray topographic study by *Shtukenberg* et al. [4.59] and *Klapper* et al. [4.60]). Tetragonal vicinal pyramids generating faulted sector boundaries on $\{001\}$ faces of tetragonal nickel sulfate hexahydrate have been studied by *van Enkevort* and *Klapper* [4.61]. Impurity incorporation on different slopes of vicinal hillocks on $\{111\}$ faces of synthetic diamond has been investigated by *Kanda* et al. [4.62].

Vicinal sectors are usually accompanied by optical inhomogeneities (variation of refractive index, stress birefringence) which can be visualized by sensitive optical polarization means. These inhomogeneities, although usually small, can reduce the threshold for laser damage in high-power optical applications, e.g., in **KDP** crystals used for laser applications [4.63, 64]. Another method of optical visualizing vicinal sectors, by staining with organic dyes (chromophores), was studied in **KDP** by *Zaitseva* et al. [4.65]. The staining was

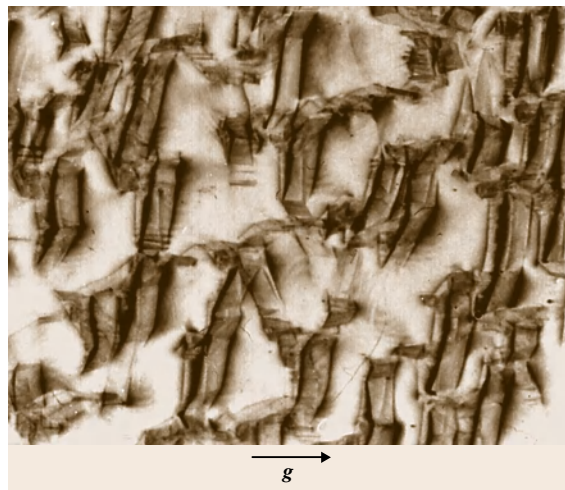


Fig. 4.12 X-ray topograph of a Z-plate of synthetic quartz cut from the growth sector of a strongly cobbled (0001) face (imaged section about $20 \times 25 \text{ mm}^2$, about 1 mm thick, diffraction vector $g(10\bar{1}1)$, MoK_α radiation). The cobble mounds exhibited a small $\{10\bar{1}1\}$ rhombohedron facet at their steepest side. The planar defects shown in the topograph are formed by the trajectory, during growth, of the groove segments between the hills attached to the facets, and result from increased impurity entrapment. The topographic contrast is stronger at the outcrops of these faults at the plate surfaces (increased strain due to stress relaxation at the surface). Since always the same facet of the three symmetrically equivalent ones was formed, all faults have the same orientation

due to different incorporation of the dye molecules on the distinct slopes of vicinal pyramids: the corresponding sectors appear with coloring of different strengths. A similar study is presented by *Bullard* et al. [4.66], who doped vicinal slopes of potassium hydrogen phthalate during growth from aqueous solution with luminescent organic molecules (fluorophores) and observed the slope pattern by luminescence microscopy. This staining and doping, however, develops during growth and is therefore not applicable to already grown crystals. It is also *destructive* insofar as it increases the degree of imperfection by addition of impurities (see also Sect. 4.3.5).

In this context another similar phenomenon, the very particular growth-cell formation on $\{0001\}$ growth faces of synthetic (hydrothermal) quartz, is noteworthy. The (0001) face is not a habit face according to the Wulff theorem (therefore it never appears on natural crystals), but it is forced to appear when large (0001) seed plates are used in synthetic growth. During growth these faces usually develop a pronounced *cobble* texture (*Lang* and *Miuskov* [4.67]), consisting of rounded hills, which define conical or columnar regions inside the grown crystal. The boundaries between these sectors, defined by the trajectory of the grooves between the *cobbles* during growth, are mostly faulted due to the increased incorporation of impurities. This is particularly the case when habit facets appear on the side of the cobble hill (Fig. 4.12). Moreover, dislocations are trapped into the groove, and thus form part of these boundaries. X-ray topographic studies of these *impurity cell walls* in synthetic quartz, containing dislocations, are presented by *Lang* and *Miuskov* [4.68].

4.3.4 Facet Sectors

These sectors, formed during melt growth on rounded interfaces, are analogous to the growth sectors described above. They arise at the segments of the interface whose orientation coincides with that of a pronounced habit face. This habit face then appears as a planar facet. When growth proceeds, this facet defines inside the crystal a conical or cylindrical region (*facet sector*) whose perfection usually differs considerably from that of the crystal regions grown on the rounded interface (rough growth). This is due to the different modes of growth on rounded and planar interfaces: growth on the latter proceeds from supercooled melt and thus exhibits different (usually higher) incorporation of impurities (dopants) compared with growth on rounded interfaces. This is apparent from the usually much more

pronounced striations in the facet sectors and the lattice distortions along their boundaries.

A favorite method to observe facet sectors and their perfection, in particular in garnets, is by polarized light (stress birefringence), e.g., *Schmidt and Weiss* [4.70] and *Cockayne et al.* [4.71]. An x-ray topography study is given by *Stacy* [4.72]. For a more detailed review on faceting, see Chap. 6 in this Handbook.

4.3.5 Optical Anomalies of Growth Sectors

As discussed above, different growth sectors usually contain different concentrations of impurities, or different deviations from stoichiometry, or – in mixed crystals – different compositional ordering. As a consequence, the physical properties are also – more or less – differ-

ent in different growth sectors. This is conspicuously apparent from the staining of crystals with organic dyes ([4.29,30], and the end of Sect. 4.3.2). In symmetrically equivalent growth sectors the *magnitude* of the property changes is essentially the same, unless the growth conditions at the corresponding faces are different (e.g., due to different hydrodynamics). The different growth directions of equivalent faces, however, lead to different *orientations* of the growth-induced (additional) anisotropies of the properties also for equivalent sectors. This effect can be considered as the reduction of the symmetry of the basic crystal by superposition with the symmetry of the external influence of *crystal growth*, which is represented by a rotational symmetry with polar axis along the growth normal (*Curie principle*, e.g., [4.73, Chap. 3.2]). This *dissymmetry* influences, in principle, all properties, but it is very pronounced for optical refraction due to the high sensitivity of the refractive index to compositional variations and stress. An instructive example is presented in Fig. 4.13, showing the optical anomaly of a (K,NH₄)-alum mixed crystal which is basically cubic, and thus should be optically isotropic [4.59,69]. Here the growth-induced birefringence (*optical anomaly*) is due to a partial ordering of K and NH₄ ions in the {111} sectors [4.59,73].

Optical anomalies of crystals had already been observed and investigated in the early 19th century, as documented in the review by *von Brauns* (1891) [4.74]. A richly illustrated survey, including a historical overview, is presented by *Kahr and McBride* [4.75]. Very recently a monograph has been published by *Shtukenberg et al.* [4.73]. Finally it is mentioned that optical anomalies also occur in vicinal sectors and facet sectors. An interesting example of the former is given by *Zaitseva et al.* [4.65] for large-scale KDP crystals.

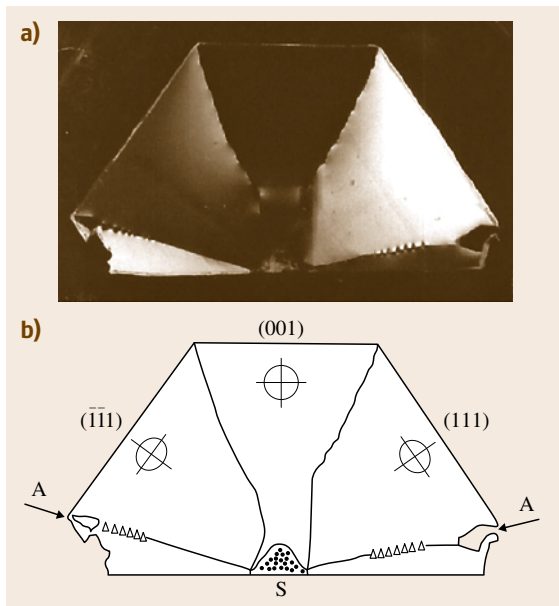


Fig. 4.13 (a) Optical anomaly of a cubic mixed (K,NH₄)-alum crystal grown from aqueous solution, as revealed by polarized light (crossed polarizers): (110) plate, 1 mm thick, horizontal width about 4 cm. (b) Sketch of growth sectors and their boundaries of the plate shown in (a). The {111} growth sectors are optically negative and approximately uniaxial, with their optic axes parallel to their growth directions $\langle 111 \rangle$ (after [4.59]). The (001) sector is nearly isotropic. Along the boundaries A between {111} sectors, small {110} growth sectors (resulting from small periodically appearing {110} facets) have formed during growth. S: seed crystal. After *Hahn and Klapper* [4.69, p. 393] (© 2003 IUCr)

4.3.6 Growth-Sector Boundaries and Relative Growth Rates

As mentioned above, the orientation of the growth-sector boundary is dependent on the relative growth velocity of the two neighboring faces involved. This is illustrated in Fig. 4.14, from which the relation

$$v_1/v_2 = \cos \beta_1 / \cos \beta_2, \quad \text{with } \beta_1 + \beta_2 = \alpha,$$

is easily derived, where α is the angle between the growth directions \mathbf{n}_1 and \mathbf{n}_2 , and β_1 and β_2 are the angles between \mathbf{n}_1 and \mathbf{n}_2 and the growth-sector boundary. The boundary is straight when the relative growth rate is constant; it is curved when it changes. In the latter case the *local* relative growth velocity is derived

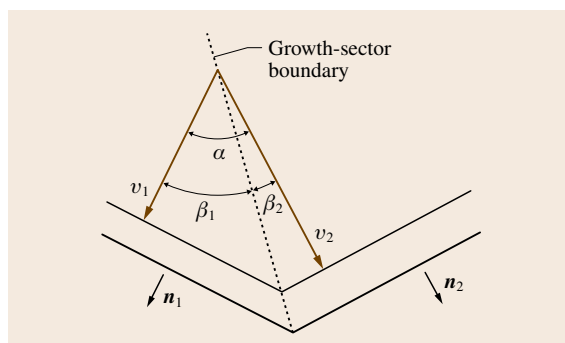


Fig. 4.14 Relation between growth velocities v_1 and v_2 of neighboring growth faces (growth directions n_1 and n_2) and the direction of the growth-sector boundary (dotted line)

from the angles β_1 and β_2 between n_1 and n_2 and the tangent plane to the sector boundary in the corresponding growth stage. Thus, the relative growth rates are easily reconstructed if the growth-sector boundary is visible.

An illustrative example, showing the strong changes of the growth velocities (*growth-rate dispersion*) due to fluctuations of growth conditions and defects is presented in Fig. 4.15a,b [4.60, 76], which shows x-ray topographs of a (110) plate cut from a potassium alum crystal (grown from aqueous solution by temperature lowering) which was subjected to temporary redissolution by a temporary temperature increase of about 1 °C [4.27]. The two boundaries between the central cube sector (001) and the two neighboring octahedron sectors ($\bar{1}11$) and ($1\bar{1}1$) are clearly depicted by kinematical contrast due to lattice distortions. (For the contrast variations in different x-ray reflections, see Chap. 42 in this Handbook.) Figure 4.15c outlines the shape of the crystal in different stages of growth, reconstructed from the course of the growth-sector boundaries (dotted line). Four regions (1–4) of different relative growth rates can be distinguished. In the first period, after seeding-in, the crystal was grown by continuous temperature decrease of about 0.3 °C/day until it reached the shape outlined by A–A–A–A. At this stage the temperature of the growth chamber was increased in one step by 1 °C. Due to the slow transfer of the temperature jump into the solution, redissolution started about half an hour later, recognized by the rounding of the crystal edges. Now the previous temperature and decrease rate were restored and growth continued as before. Due to this disturbance a layer of liquid inclusions covering a part of the (001) facet was formed, and its growth rate, rel-

ative to the neighboring {111} faces (the growth rate of which remained constant during the whole experiment), was strongly increased in region 2; in regions 3 and 4 it decreased again. From the angles β_1 and β_2 ($\alpha = 35.26^\circ$) the relative growth rates were determined as

$$v(001)/v(111) = 1.0/5.6/1.7/0.8$$

in growth intervals 1/2/3/4

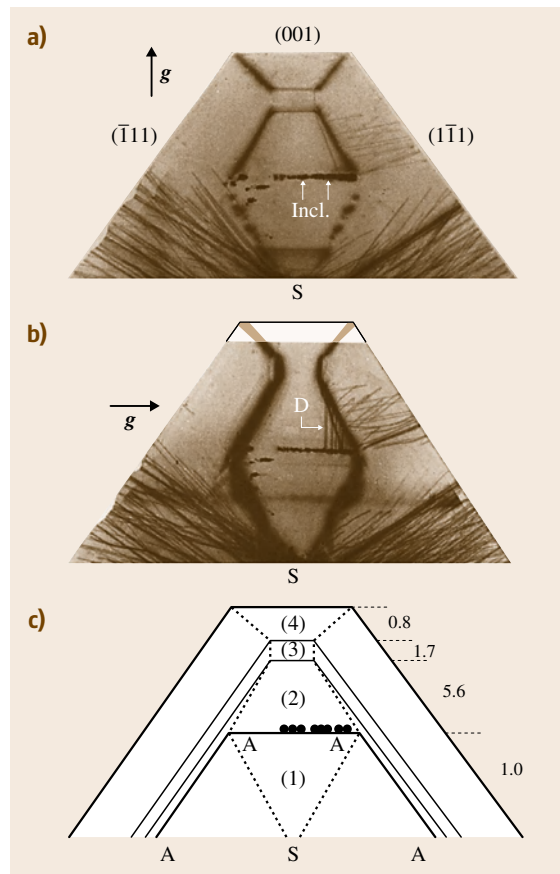


Fig. 4.15a–c Sections of topographs of a (110) plate cut from a potassium alum crystal subjected to a temporary redissolution (vertical extent 12 mm, reflections 004 (a) and 220 (b)). S: location of the seed (outside the section); Incl.: liquid inclusions; D: edge dislocations. (c) Illustration of the development of the crystal shape and of growth-sector boundaries (dotted lines) during growth. Contour A–A–A–A outlines the shape of the crystal at the time of redissolution. At the right side the relative growth rates $v(001)/v(111)$ of growth intervals 1–4 are given (after [4.76])

(averaged over the nearly equal left- and right-hand sides). The drastic increase in period 2 is obviously due to the dislocations D originating from the inclusions, and the retardation in periods 3 and 4 may arise from the elimination of these dislocation from the (001) face by bending at the growth-sector boundary into the (111) sector. Note that only part of the dislocations involved in this process is visible in the topographs (Fig. 4.15a,b) of the 1.4-mm-thick crystal cut, since the larger part

of the (001) sector (with a basis of about $8 \times 8 \text{ mm}^2$ in growth stage A–A–A–A) is outside the cut and thus not recorded. In this context reference is made to similar and more detailed studies on dislocation-dependent growth rate dispersion of {100} and {110} growth faces of potassium alum by Sherwood and Shiripathi [4.77], Bhat et al. [4.78], and Ristic et al. [4.79]. An interesting output of their investigations is evidence for the growth-promoting role of pure edge dislocations (Sect. 4.4.7).

4.4 Dislocations

4.4.1 Growth Dislocations and Postgrowth Dislocations

Dislocations are generated during crystal growth, by plastic deformation and by the condensation of self-interstitials and vacancies. In the study of crystal growth defects it is useful to distinguish between two categories of dislocations:

1. Dislocations which are connected with the growth front and proceed with it during growth (*growth dislocations* or *grown-in dislocations*)
2. Dislocations which are generated *behind* the growth front, either still during the growth run or during cooling to room temperature (*postgrowth dislocations*), or later during processing or by improper handling.

The final arrangement of dislocations in a crystal at room temperature results from growth dislocations, postgrowth dislocations, and the movement, multiplication, and reactions of both after growth. Crystals grown at low temperatures (e.g., from aqueous solution) and in their brittle state usually contain dislocations in their original *as-grown* configuration, whereas in crystals grown at high temperatures, the original dislocation configurations may be drastically altered by dislocation movement, dislocation multiplication, and dislocation reactions. These processes, which may occur during the growth run (*behind* the growth front), are induced by thermal stress due to temperature gradients and, particularly in crystals grown at very high temperatures, by the absorption of interstitials and vacancies (*dislocation climb*).

In this chapter the formation and propagation of dislocations in crystals grown at low temperatures (below 100°C) under zero or only low thermal gradients are treated. The development of dislocation configurations

during growth from melt under high thermal gradients or during processing at elevated temperatures has been experimentally and theoretically studied by various authors (e.g., [4.80–83]) and is reviewed in Chap. 6 of this Handbook.

4.4.2 Sources of Growth Dislocations

For topological reasons dislocation lines cannot start or end in the interior of a perfect crystal. They either form closed loops, or they start from external and internal surfaces (e.g., grain boundaries), or from other defects with a *break* of the crystal lattice. In crystal growth, such defects may arise from all kinds of inclusions (e.g., foreign particles, liquid inclusions, bubbles, solute precipitates). When inclusions are overgrown and *closed* by growth layers, *lattice closure errors* may occur. These errors are the origin of growth dislocations which are connected to the growth front and propagate with it during further growth.

It is a very common observation that inclusions are the source of growth dislocations. Examples are shown in Figs. 4.3, 4.5, 4.10, etc. The appearance of dislocations *behind* an inclusion (viewed in the direction of growth) is correlated with its size: small inclusions emit only a few dislocations or are often dislocation free. Large inclusions ($> 50 \mu\text{m}$) usually emit bundles of dislocations. In some cases, however, large inclusions (several millimeters in diameter) of mother solutions *without* dislocation generation have been observed (e.g., in the capping zone of KDP [4.84, 85]).

The generation of growth dislocations by foreign-particle inclusions has been experimentally studied by Neuroth [4.86] in crystals growing in aqueous solution (potassium alum) and in supercooled melt (benzophenone $(\text{C}_6\text{H}_5)_2\text{CO}$, $T_m = 48^\circ\text{C}$; salol $\text{C}_{13}\text{H}_{10}\text{O}_3$, $T_m = 42^\circ\text{C}$). A seed crystal is fixed to a support in

such an orientation that a dominant growth face [octahedron (111) for cubic potassium alum, prism (110) for orthorhombic benzophenone, pinacoid (100) for orthorhombic salol] develops horizontally. After a sufficiently long distance of (visually) perfect growth, a small ball of solder (0.3–0.5 mm) is placed on the horizontal growth face, and growth continued without change of conditions. During the whole experiment the growth surface was observed with a microscope (long focal distance) in reflected light or by Michelson interferometry, both with videotape recording. After the deposition of the ball the face grows slowly as before without additional surface features as long as the ball is not covered by growth layers. During this period the crystal seems to *sink* into the growing crystal. In the moment when the ball is covered by growth layers, a conspicuous, fast extending growth hillock appears, emitting macrosteps from its apex. After some time of growth the originally single hillock splits into a group of diverging hillocks. This indicates that a bundle of dislocations, fanning out during growth, has been created by the ball inclusion (Fig. 4.16).

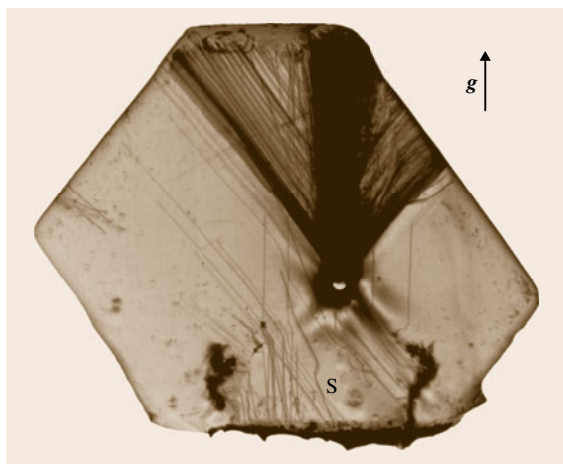


Fig. 4.16 X-ray topograph of a (010) plate (about 1.5 mm thick, width 21 mm) cut from a crystal of orthorhombic salol grown in supercooled melt. It contains a solder ball (diameter about 0.4 mm) dropped on a perfectly growing (100) facet (directed upward). Numerous dislocations were generated *behind* the ball. Dislocations of the fan propagating to the left are pure screw and exactly parallel to one of the prominent $\langle 101 \rangle$ edges which dominate the shape of the crystal (cf. *Deviations from Calculated Directions* (i) in Sect. 4.4.4 and Fig. 4.22). The (unresolved) dislocations of the vertical bundle have Burgers vectors $[100]$ and $[001]$. Diffraction vector $g(200)$, $\text{CuK}\alpha_1$

For the study of the dislocations associated with the inclusions, a plate containing the ball and the region *behind* it was cut out of the crystal and subjected to x-ray topography. Figure 4.16 shows that – in accordance with the observed surface pattern – numerous dislocations originate from the *back side* of the ball. Their density is partially too high to be resolved by this imaging method.

Similar experiments have been performed with mechanical in situ violation (puncturing, scratching) of an interface perfectly and steadily growing in solution, supercooled melt, and by Czochralski pulling [4.86]. Again, bundles of dislocations originate from these damages, which in solution growth frequently give rise to liquid inclusions. In plastic crystals (always the case in melt growth) the mechanical impact generates glide dislocations which emerge at the growth front and continue as growth dislocations. Similar experiments are reported by Forty ([4.87, esp. p. 23]). His review presents a rich collection of photographs of growth spirals and other surface patterns on growth faces of various crystals.

The formation of screw dislocations in thin plates of organic crystals during growth from solution and from the vapor has been studied in situ by Russian authors using (polarized) light microscopy with film recording [4.88–90]. Screw dislocations arise at reentrant corners between branches of dendrites [4.88] and by growth around intentionally introduced particles [4.89, 90]. In these cases the dislocations run through the lamellae and do not end inside the crystal. The mechanism of formation of lattice closure errors and of dislocations *behind* an inclusion on the nanometer scale is not yet fully understood, although simple models have been derived. An example is presented by Dudley et al. [4.91].

As pointed out in Sect. 4.4.2, in habit-face crystals inclusions preferentially arise in the regeneration zone of growth on rounded interfaces, in particular in the zone of first growth on a seed crystal. Moreover, dislocations and other defects (grain boundaries, twins) preexisting in the seed will continue into the growing crystal. Thus, the perfection of the seed as well as the seeding-in process are most crucial for the growth of perfect crystals. This holds for all methods of seeded growth, not only for habit-face crystals. That the regeneration zone around the seed crystal is the main source of dislocations is apparent from several topographs shown in this chapter (e.g. Figs. 4.19, 4.21 and 4.24). It is stressed that inclusions and dislocations can largely be avoided by very slow (and thus time-consuming)

growth during the regeneration period of first growth on a perfect seed.

Finally it is emphasized that inclusions can also block already existing dislocations. This has been observed several times by the author, and reported in the literature. It frequently happens to dislocations in the seed crystal which are blocked by inclusions formed in the regeneration zone (*capping*) of first growth and do not enter the growing crystal [4.84,85]. Thus provoking a capping zone by an intentionally introduced deviation of the seed surface from a habit face may be helpful for reducing the number of dislocations coming from the seed, but it implies also a considerable risk of generating *new* dislocations behind the inclusions. The blocking of growth dislocations by closed inclusions must obey the conservation law of Burgers vectors, as discussed below in Sect. 4.4.3.

4.4.3 Burgers Vectors, Dislocation Dipoles

The sum of the Burgers vectors of all dislocations originating from an inclusion fully embedded in an otherwise perfect crystal is zero [4.84]. This directly follows from Frank's conservation law of Burgers vectors (see textbooks on dislocations, e.g., [4.92–94]), which states that the sum of Burgers vectors \mathbf{b}_i of all dislocation lines going into a dislocation node (i. e., with line direction *into* the node) is zero $\sum \mathbf{b}_i = 0$ (analogous to Kirchhoff's law of electrical currents). Another proof may be given via the Burgers-circuit definition of Burgers vectors (e.g., [4.92–94]): imagine a Burgers circuit parallel to the growth face in the perfect crystal region grown before the inclusion was formed. Now shift the circuit stepwise in the growth direction over the inclusion and the dislocation bundle behind it. No closure error of the circuit, which now encircles all dislocations, will arise during this (virtual) procedure: $\sum \mathbf{b}_i = 0$.

From this it immediately follows that a *single* dislocation cannot originate from an inclusion. If dislocations are formed, there must be at least two of them, with opposite Burgers vectors. This is often observed when the inclusions are very small. Two slightly diverging dislocation lines emanating from small, x-ray topographically invisible or nearly invisible inclusions were observed in KDP by Fishman [4.84]. Examples are presented in Fig. 4.19 (label A) for salol grown from supercooled melt. A few pairs of slightly diverging dislocations, starting from a point, can also be recognized in Fig. 4.10 of a Czochralski salol specimen. There are, however, many x-ray topographic observations of apparently only one dislocation line arising from an in-

clusion (e.g., in Fig. 4.3, where only one wider contrast line indicates the presence of more than one dislocation). In all these cases the single lines must represent pairs of two closely neighboring (x-ray topographically unresolvable) parallel dislocations with opposite Burgers vectors: a dislocation dipole. Such a dipole can alternatively also be considered as a single dislocation in the shape of a narrow hairpin with its (virtual) bend in the inclusion. In this approach the two branches of the *hairpin* have the same Burgers vector, but opposite directional line sense. Examples of a pure-screw and two pure-edge dislocation dipoles are shown in Fig. 4.17. The two branches of the dipoles attract each other and may annihilate if they come close enough together. This annihilation is possible for screw dislocation dipoles, and for edge dipoles if both edge dislocations of the latter are on the same glide plane. If they are located on

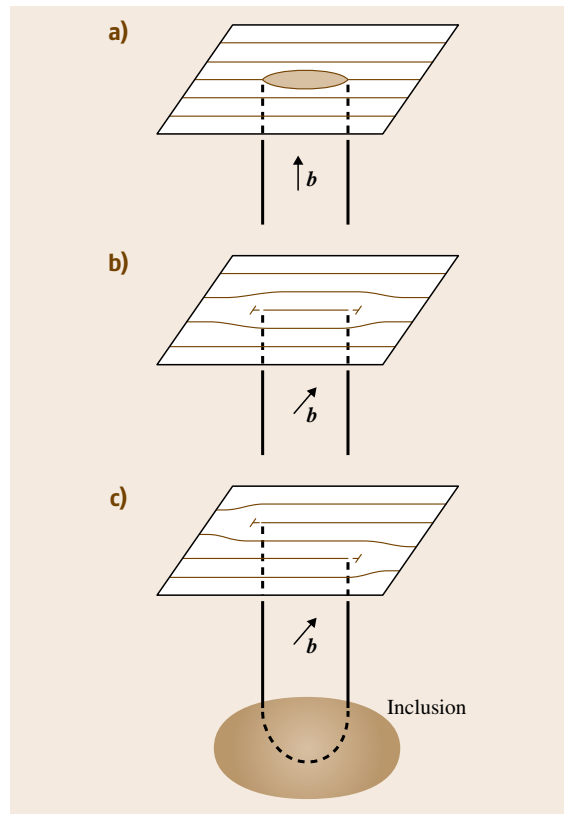


Fig. 4.17a–c Sketches of dislocation dipoles originating from an inclusion. Here a dipole is considered a single (hairpin) dislocation with Burgers vector \mathbf{b} but opposite line direction sense of the two branches. (a) Pure-screw dipole; (b,c): pure-edge dipoles

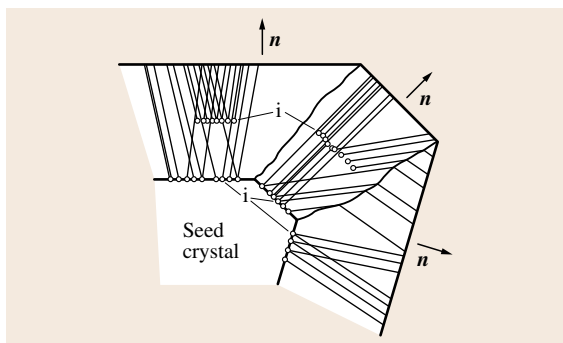


Fig. 4.18 Typical geometry of growth dislocations in crystals grown on habit faces. The different preferred directions of dislocations lines within one growth sector result from different Burgers vectors. These directions abruptly change their directions when they penetrate a growth-sector boundary, i. e., when, during growth, their outcrops shift over the edge from one face to the other (i: Inclusions)

different glide planes, the two dislocations can approach each other to a minimum separation, where they have prismatic character and form the edges of stripes of inserted or missing lattice planes (Fig. 4.17b). A model of the formation of a screw dislocation *behind* an inclusion is presented by Dudley et al. [4.91].

During x-ray topographic studies of growth dislocations it is often observed that *only one* contrast line originates from an inclusion, indicating – at first sight – a single dislocation (Fig. 4.3). Here the question arises, how by x-ray topography a dislocation dipole can be distinguished from a single dislocation with the same Burgers vector. If the dipole dislocations are sufficiently separated, they are resolved as two lines or appear as a broader contrast line. However, since the strain fields of the two dislocation have opposite signs and subtract each other, the resultant strain may also be smaller and less extended, if the separation of the two dislocations is small. Thus a dipole may appear on x-ray topographs with similar or even narrower contrast than a single dislocation with the same Burgers vector, and distinction of the two is often not immediately possible. An example is given by van Enkevort and Klapper [4.61, Fig. 11a], where a single contrast line represents a screw dislocation dipole in nickel sulfate hexahydrate, as is proven by the bulge of one of the two dipole arms. In the same crystal the presence of two closely neighboring etch pits at the apices of growth pyramids and slip traces, indicating the escape of one of the two screw dislocations from the hillock center, has been observed. Dislocation dipoles are also formed

during plastic flow of crystals, when the movement of glide dislocations is locally blocked by obstacles (inclusions, jogs; [4.95]). Examples are given in Sect. 4.4.5 (Figs. 4.25 and 4.26).

4.4.4 Propagation of Growth Dislocations

Characteristic Configurations, Theory of Preferred Direction

A dislocation line ending on a growth face will proceed with that face [4.7, 8, 96]. Its direction depends on the shape and orientation of the growth face and its Burgers vector. As shown in Sect. 4.3.2 and Fig. 4.8b, crystal growing on planar (habit) faces consist of growth sectors belonging to different growth faces (different growth directions \mathbf{n}). This leads – under ideal conditions (i. e., stress-free growth) – to a characteristic configuration of growth dislocations which is illustrated in Fig. 4.18. The dislocations start from inclusions and propagate as straight lines with directions \mathbf{l} usually close to, and frequently parallel to, the growth direction of the sector in which they lie. They usually exhibit sharply defined, often *noncrystallographically preferred*, directions \mathbf{l}_0 which depend on the growth direction \mathbf{n} and the Burgers vector \mathbf{b} : $\mathbf{l}_0 = \mathbf{l}_0(\mathbf{n}, \mathbf{b})$. The dependence of the preferred direction \mathbf{l}_0 on the growth direction \mathbf{n} becomes strikingly apparent when the dislocations penetrate growth-sector boundaries. This implies an abrupt change of the growth direction: the dislocation lines undergo an abrupt change of their preferred direction \mathbf{l}_0 (*refraction* of dislocation lines). An example is shown in Fig. 4.19.

These preferred direction of growth dislocations are explained by two approaches [4.7, 8, 96]:

1. *Minimum-energy theorem* (Fig. 4.20a). The dislocation lines adopt a direction \mathbf{l} (unit vector) for which its energy within any growth layer is a minimum. For a growth layer of unit thickness $d = 1$ this can be expressed as

$$E / \cos \alpha = \text{minimum},$$

where $E = E(\mathbf{l}, \mathbf{b}, c_{ij})$ is the elastic energy (strain energy) per unit length of the dislocation line (c_{ij} are the elastic constants of the crystal) and α is the angle between \mathbf{n} and \mathbf{l} . The factor $1 / \cos \alpha$ accounts for the length of the dislocation line in the layer.

2. *Zero-force theorem* (Fig. 4.20b). A dislocation line emerging at the surface experiences an *image* force $d\mathbf{F}$ which depends on the angle α between the dislocation direction \mathbf{l} and the surface normal \mathbf{n} , and on its distance r from the surface. At the surface this

force is infinitely large. According to *Lothe* [4.97] there exists always a direction l_0 for which this force is zero for the dislocation line segments at any depth below the surface. It is plausible that, during growth, a dislocation emerging at the growth face follows this direction of zero force.

Using the formula

$$dF = -\frac{1}{r} \left(\frac{\partial E}{\partial \alpha} + E \tan \alpha \right) dl$$

(*Lothe* theorem [4.97]), it can be shown that both approaches lead to the same preferred directions.

Verification of the Minimum-Energy Approach

The strain energy [4.7,8,96] per unit length of a straight dislocation line is given by (see textbooks on disloca-

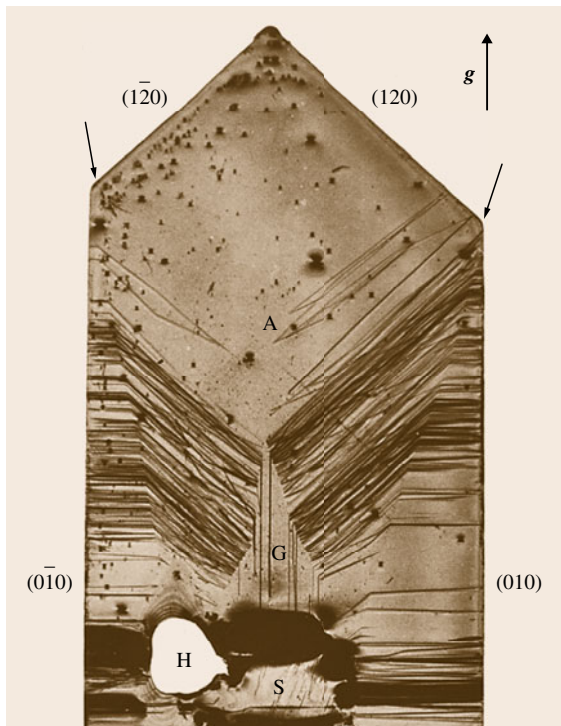


Fig. 4.19 Section of a (001) plate (horizontal width about 26 mm, thickness 1.5 mm) cut from a salol crystal grown from supercooled melt. The dislocation lines change their preferred directions when they penetrate the boundaries (arrows) from the {120} sectors into the {010} growth sectors (*refraction* of dislocation lines). A: Dislocation pairs originating from tiny inclusions. Dots: surface damages. Diffraction vector $g(200)$, $\text{CuK}\alpha$

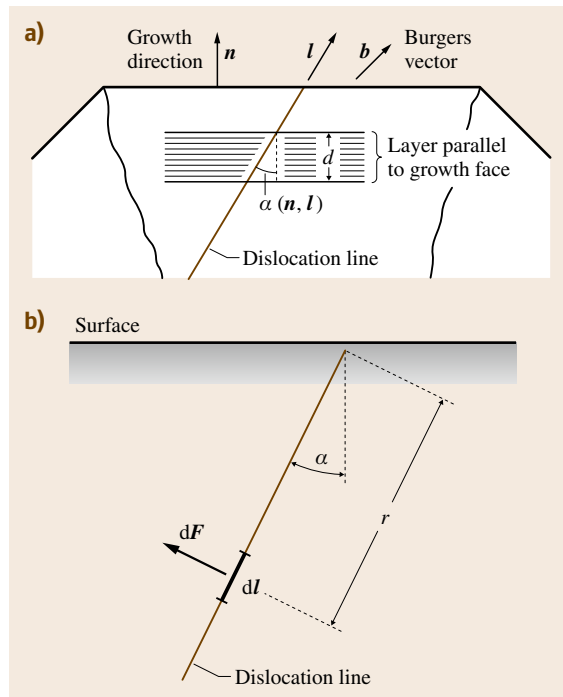


Fig. 4.20 (a) Derivation of the energy of a straight dislocation line within a layer parallel to the growth face. (b) Illustration of the force dF exerted by the crystal surface on a line segment dl of a straight dislocation line emerging at the surface (theorem of *Lothe* [4.97])

tions, e.g., [4.92–94])

$$E = \frac{Kb^2}{4\pi} \ln \left(\frac{R}{r_0} \right),$$

with $K = K(l, l_b, c_{ij})$ the so-called *energy factor* of a straight dislocation line, R the outer cutoff radius, r_0 the inner cutoff radius, and b the modulus of the Burgers vector b . The energy factor K describes the variation of the strain energy with the direction l of the dislocation line. It also depends on the Burgers vector direction l_b and on the elastic constants c_{ij} of the crystal. The inner cutoff radius defines the limit until which the linear elasticity theory is applicable, and it corresponds to the radius of the dislocation core.

Since the logarithmic term and the core energy are, in general, not accessible to a numerical calculation, the variation of strain energy E of a given dislocation with Burgers vector b with direction l is – in a certain approximation – considered as proportional to the energy factor $K(l, l_b, c_{ij})$, assuming the logarithmic term to be independent of l . The energy factor has been cal-

culated using the theory of dislocations in elastically anisotropic crystals developed by Eshelby et al. [4.98]. Since, in general, analytic solutions are not possible, numerical calculations have been performed using the program DISLOC, accounting for the elastic anisotropy of any symmetry down to the triclinic case [4.96]. Figure 4.21a,b shows a comparison of observed and

calculated preferred directions of dislocations with four different Burgers vectors in the (011) growth sector of KDP [4.99]. The agreement is excellent with deviations of 3–6°, except for dislocation 4, the observed directions of which scatter by $\pm 5^\circ$ around a direction deviating by about 20° from the calculated one. This may be due to the very flat minimum of K , which makes the minimum-energy directions more subject to other influences such as surface features and core-energy variations (see *Deviations from Calculated Directions*). Similar comparisons have been carried out for various crystals grown on planar faces from solutions and supercooled melts: benzil, $(\text{C}_6\text{H}_5\text{CO})_2$ [4.54, 100]; thiourea, $(\text{NH}_2)_2\text{CS}$ [4.101]; lithium formate monohydrate $\text{HCOOLi} \cdot \text{H}_2\text{O}$ [4.102]; ammonium hydrogen oxalate hemihydrate, $\text{NH}_4\text{HC}_2\text{O}_4 \cdot \frac{1}{2}\text{H}_2\text{O}$ [4.103]; and zinc oxide, ZnO [4.96]. In general, the agreement of observed and calculated directions is satisfactory and confirms the validity of the above theorems. It is pointed out that the preferred directions are independent of the growth method, provided that the growth faces (growth sectors) are the same. This has been demonstrated for benzil grown *in solution* in xylene and *in supercooled melt* ([4.1], [4.7, p. 138, Fig. 17]). Moreover, basal growth dislocations (Burgers vectors $\mathbf{b} = \langle 100 \rangle$) in prism sectors of hydrothermally grown hexagonal (wurtzite-type) ZnO crystals [4.104] show the same minimum-energy configuration as the corresponding growth dislocations in the prism sectors of benzil [4.96]. This similarity is due to the hexagonal lattice, the same prism growth sector, and

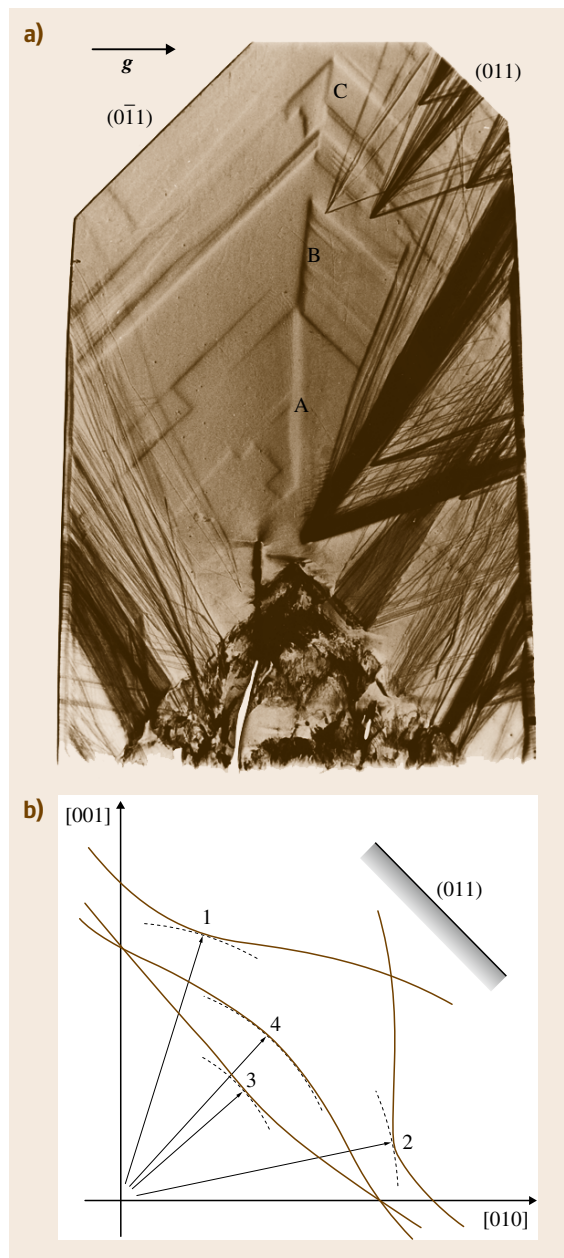


Fig. 4.21 (a) X-ray topograph ($g(020)$, Ag K_α radiation) of a KDP (100) plate (horizontal width ≈ 28 mm, thickness ≈ 1.5 mm), showing bundles of dislocations with noncrystallographically preferred directions emanating from small liquid inclusions (especially in the right-hand (011) growth sector) and from the capping region. The Burgers vectors of these dislocations can be recognized from their preferred directions. In addition, growth bands and features due to vicinal effects are visible. ABC: Boundary between (011) and $(0\bar{1}1)$ growth sectors. (b) Plots of calculated energies $E/\cos \alpha$ (arbitrary units) of dislocations with Burgers vectors $\mathbf{b} = [001]$ (1), $\mathbf{b} = [100]$ (2), $\mathbf{b} = [011]$ (3), and $\mathbf{b} = [0\bar{1}1]$ (4) in growth sector (011) of KDP (polar coordinates: the energies are given by the length of the radius vector to the curves). The preferred directions of minimum $E/\cos \alpha$ are represented by arrows. The dashed lines are circles with radii equal to the minimum values of $E/\cos \alpha$. Note the close coincidence to observed (a) and calculated (b) dislocation line directions ◀

the same Burgers vectors of the dislocations in both cases.

An interesting experimental study of preferred dislocation directions in synthetic quartz is presented by Alter and Voigt [4.105]. They cut (0001) plates (Z-plates) out of different growth sectors of previously grown highly perfect quartz crystals and used them as seed plates for further growth experiments. The seed plates contained growth dislocations following the preferred directions typical for the sector from which they were cut. Since growth now proceeded on the (0001) face, the dislocations of the seed continued into the growing crystals with preferred directions typical of the Z-sector, exhibiting sharp bends of up to 90° at their transition from the seed into the grown crystal. This is instructively shown by x-ray topography [4.105].

On account of the factor $1/\cos\alpha$ in the energy term above, the preferred directions of growth dislocations are mostly normal or nearly normal to the (local) growth face. In some cases of planar interfaces, however, deviations from the growth normal of up to 30° have been observed, in agreement with the calculations.

For interfaces with convex curvature (e.g., in Czochralski growth) the dislocation lines, propagating more or less normal to the growth front, diverge and grow out of the crystal boule through its side faces. For concave interfaces the dislocation lines are focused into the center of the crystal boule (Fig. 4.10). Trajectories of growth dislocations in Czochralski gadolinium gallium garnet (GGG) have been calculated and compared with observed ones by Schmidt and Weiss [4.70]. The curvature of the interface has been taken into account by performing the calculations stepwise in small increments, leading to curved dislocation trajectories. Again the agreement is satisfactory. Moreover, this allowed assignment of Burgers vectors to the different dislocation trajectories which were observed optically with polarized light.

In 1997 and following years, preferred dislocation directions and their bending when penetrating a growth-sector boundary were observed by transmission electron microscopy in GaN grown by metalorganic vapor-phase epitaxy (MOVPE) using the epitaxial lateral overgrowth (ELO) technique [4.106–110]. The GaN hexagonal pyramids {1122} growing through the windows in the mask are in the first stage topped by the (0001) basal plane, which during further growth becomes smaller and finally vanishes. Thus growth dislocations propagating normal to the (0001) facet penetrate the boundary to a {1122} sector and are bent by about 90° into the preferred direction in this sector [4.109]. By this pro-

cess the number of *threading* dislocations is drastically reduced. Very recently the bending of dislocations in growth-sector boundaries has also been used for the elimination of threading dislocations by *aspect-ratio trapping* in Ge selectively grown in submicron trenches on Si substrates [4.111]. Similarly, dislocations are eliminated from prism growth sectors of rapidly grown KDP crystals ([4.112, cf. Fig. 4]).

The above theory of preferred dislocation directions does not allow a dislocation line to proceed along a growth-sector boundary, as is sometimes discussed: the line would emerge on the edge constituting the boundary and thus be in a labile position. If, however, the edge is a narrow facet, the dislocation line can lie in its sector and appear to proceed along the boundary, but the probability of *breaking out* into one of the adjacent sectors would be high. Ester and Halfpenny [4.113] and Ester et al. [4.114] have observed in potassium hydrogen phthalate V-shaped pairs of dislocations originating from growth-sector boundaries, with the two arms of the V, following sharply defined directions, in the two adjacent sectors. This is in accordance with the minimum-energy concept.

Deviations from Calculated Directions

Although the agreement of observed and calculated directions of growth dislocations is in general satisfactory, frequently discrepancies are found. The reasons for this may be insufficient approximation in the model on which the calculations are based, or by influences of other defects or particular surface relief. The above calculations are based on linear anisotropic elasticity of the continuum and do not account for the discrete structure of the crystals, the dislocation core energy or (in piezoelectric crystals) for electrical contributions.

The following three causes have been found to affect preferred directions:

i. Discrete lattice structure of the crystals and the neglect of the core energy

It is frequently observed that growth dislocations are exactly parallel to a low-index lattice direction (mostly a symmetry direction), although calculations suggest another (usually noncrystallographic) direction. This seems to happen in cases of pronounced Peierls energies, where the dislocations tend to align along the Peierls *energy valleys* (see textbooks on dislocations, e.g., [4.92–94]). It is plausible that dislocations will favor directions parallel to closed-packed directions, strong bond chains, structural channels, and planes of

pronounced cleavage. A dislocation line inclined to such a direction will consist of line segments along this direction, (i.e., lie in the Peierls valley) and kinks or jog across the Peierls potential barrier [4.93, pp. 229–234]. This strongly affects the core energy, which varies considerably with direction, particularly in the neighborhood of the structurally pronounced directions, for which it has a minimum. This is the same effect that leads to those favored directions of, for example, 60° dislocations in diamond- and sphalerite-structure crystals.

An example of the influence of the lattice structure in organic salol grown in supercooled melt and by Czochralski pulling is given in Figs. 4.16 and 4.22, where dislocations with Burgers vectors $\mathbf{b} = \langle 101 \rangle$ align along directions parallel to the prominent crystal edges $\langle 101 \rangle$, independent of the growth directions. A detailed discussion of the competing influences of core energy and elastic

strain-field energy on dislocation directions, based on observations in solution-grown orthorhombic ammonium hydrogen oxalate hemihydrate, is presented by Klapper and Küppers [4.103].

ii. *Long-range stress*

Long-range stress arising near the growth face, e.g., due to other growth disturbances (neighboring inclusions, impurity layers), exerts forces on a dislocation and may locally change the zero-force direction, thus leading to curved dislocations lines.

iii. *Surface relief of the growth face*

Macrosteps sweeping over the dislocation outcrops lead to macroscopic (rounded) kinks in the dislocation lines. A particular influence is exerted by growth hillocks (vicinal pyramids, Sect. 4.3.3), the slopes of which possess an orientation somewhat different from that of the main face. Dislocations emerging from the vicinal slopes exhibit preferred directions different from those outcropping on the main face. Similar to the *refraction* of dislocation lines at growth-sector boundaries (Fig. 4.19), dislocation lines change their directions when they pass through an intervicinal boundary, i.e., when their outcrops shift from one vicinal facet to another. The influence of the surface relief, in particular of vicinal slopes, on the course of dislocations has been studied by Smolsky and Rudneva [4.116] and Smolsky et al. [4.48].

An example of the influence of vicinal pyramids on the course of growth dislocation lines is presented in Fig. 4.23. Here the dislocation lines in the right and left $\{011\}$ sectors of KDP change their directions when they pass through the boundaries appearing in the topograph as dark and white contrast bands roughly parallel to the traces of the $\{011\}$ faces. These boundaries are assumed to result from the competition of different growth pyramids. A dominating vicinal pyramid may be *overrun* by another pyramid which now takes over the dominating role. Since this overflowing of one growth pyramid over another can take place within a short growth period, the boundaries between regions grown on one or the other pyramid are practically parallel to the *main* growth face. Due to the different inclinations of the pyramid facets, the preferred directions of dislocations ending on these slopes are different.

Determination of Burgers Vectors

In x-ray topography, Burgers vectors are usually determined with the aid of the $\mathbf{g} \cdot \mathbf{b}$ criterion (*visibility rules*, see Chap. 42 of this Handbook). This requires

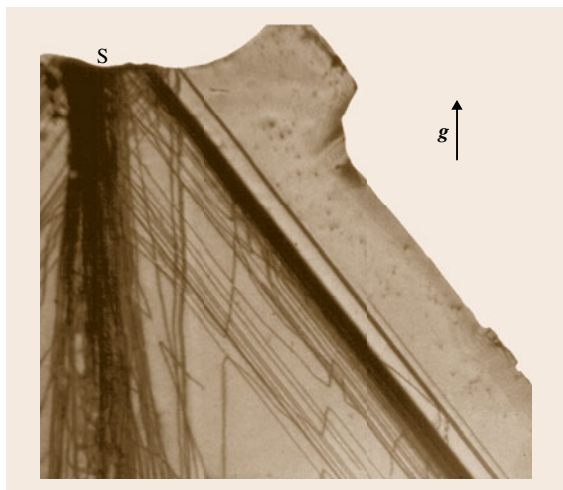


Fig. 4.22 Section (about $11 \times 11 \text{ mm}^2$) of a (010) plate (about 1.3 mm thick) cut from the cone region of a Czochralski salol crystal (pulling direction $[100]$ upward; S: seed crystal, broken off). The topograph shows many straight dislocation lines ($\mathbf{b} = \langle 101 \rangle$) exactly parallel to $\langle 101 \rangle$, which is the most prominent morphological edge of the crystal (Fig. 4.16). This direction is enforced by the discrete lattice structure, because the minimum-energy continuum approach suggests directions close to the normal to the concave interface. Furthermore, reactions (segment-wise annihilation) with a few *vertical* dislocations are recognized (after [4.115]). Diffraction vector $\mathbf{g}(200)$, $\text{CuK}\alpha_1$

the imaging of dislocations in several, at least two, different reflections, and sometimes an unambiguous determination is not possible with this method. Since the preferred directions of dislocation lines in a growth sector are characteristic of the Burgers vector, the observation of such directions may provide information on the Burgers vector direction. This should be particularly successful in cases where the dislocations penetrate a sector boundary, so that preferred directions of the same dislocation in different growth sectors are observed.

Depending on the knowledge of the elastic constants and the availability of a computer program the following three options are considered:

- a) If in a crystal the Burgers vectors and corresponding preferential directions of dislocations in a growth sector have been determined by application of the

visibility rules, then in further x-ray topographic studies of the same crystal species the Burgers vectors of these dislocations can be identified by their preferred direction \mathbf{l}_0 without necessarily taking exposures in different reflections.

- b) If the elastic constants of the crystal under investigation are known and if a computer program is available, the directions \mathbf{l}_0 may be calculated for various Burgers vectors and growth sectors and compared with the observed ones. This may be particularly helpful in cases where unambiguous identification of the Burgers vector direction by the visibility rules is not possible.
- c) Apart from these possibilities, the following three general statements, derived under the assumption that the energy factor K_s of a pure-screw dislocation is minimal and that K_e of a pure-edge dislocation is maximal (which is usually the case), may be useful [4.103]:

1. If $\mathbf{b} \parallel \mathbf{n}$, then $\mathbf{l}_0 \parallel \mathbf{n}$ (pure-screw dislocation normal to the growth face)
2. If $\mathbf{b} \perp \mathbf{n}$, then $\mathbf{l}_0 \parallel \mathbf{n}$ (pure-edge dislocation normal to the growth face)
3. If \mathbf{b} is inclined to \mathbf{n} , then \mathbf{l}_0 lies between \mathbf{n} and \mathbf{b} .

In case 1 the energy per unit growth length $E = K / \cos \alpha$ (see *Characteristic Configurations, Theory of Preferred Direction*) has a steep minimum, because both K and $1 / \cos \alpha$ (i. e., the length of the dislocation line in the unit growth layer) have a minimum along \mathbf{n} , whereas in case 2 K is maximal and $1 / \cos \alpha$ is minimal. In the latter case \mathbf{l}_0 is parallel to \mathbf{n} only if the decrease of K with increasing α is overcompensated by the increase of the length $1 / \cos \alpha$ (which is mostly the case), leading to a flat minimum of E along \mathbf{n} . In case 3 the minima of K (along \mathbf{b}) and of $1 / \cos \alpha$ (along \mathbf{n}) have different directions, thus the minimum direction \mathbf{l}_0 of E lies between them (i. e., it deviates from the growth direction \mathbf{n} towards the Burgers vector \mathbf{b}).

These three rules have proved to be obeyed in most cases studied [4.54, 99–103]. Exceptions are provided by those dislocations whose directions are predominantly influenced by the discrete lattice structure. An application and detailed discussion of these rules for Burgers vectors of dislocations in orthorhombic ammonium hydrogen oxalate hemihydrate is reported in [4.103, p. 502].



Fig. 4.23 X-ray topograph ($g(020)$, $\text{AgK}\alpha$ radiation) of a (100) plate of KDP (horizontal width 26 mm, about 2 mm thick) showing growth dislocations in two {011} growth sectors. The preferred directions are modified by the varying vicinal surface relief on the {011} growth faces

4.4.5 Postgrowth Movement and Reactions of Dislocations

The as-grown geometry of dislocations with preferential directions, described in the previous sections, may be more or less drastically changed by thermal stress during cooling to room temperature [4.7–11]. Crystals grown in their brittle state from solution are rather in-

sensitive in this respect. An example is benzil grown at about 40 °C from a solution in xylene by slow solvent evaporation (Fig. 4.24a): its growth dislocations are sharply straight-lined with preferred directions [4.7, 54, 100]. Even the thermal stress, which occurred by uncontrolled cooling and which induced a crack, did not change the grown-in dislocation configuration.

Crystals growing from their melt are always in the plastic state, and therefore their dislocations are subject to plastic glide even under small stress. As already mentioned in Sect. 4.1, gradient-free growth is possible from supercooled melt [4.1], and grown-in dislocation configurations can be preserved if the crystal is cooled very slowly to room temperature. This has been shown for benzil grown from slightly supercooled melt ($T_m = 96^\circ\text{C}$) and carefully cooled through its plastic zone into its brittle state: the grown-in dislocations are straight-lined and exhibit essentially the same geometry as that in crystals grown from solution ([4.1] and [4.7, Fig. 17]).

If stress arises during growth from the melt or during cooling through the plastic zone, the grown-in dislocations move and adopt a more or less irregular arrangement. This is shown in Fig. 4.24b, which presents a topograph of benzil grown from the melt with supercooling of about 0.5 °C. It shows numerous growth dislocations originating from the strongly disturbed zone of first growth on the seed crystal. Many of them follow irregular courses. They often exhibit straight-line segments along directions $\langle 100 \rangle$ (which are twofold-symmetry axes in the basal plane (0001) of the trigonal crystal), indicating the influence of the discrete lattice structure, and pinning points where dislocation movement was locally stopped by obstacles. Line elements parallel to the growth faces are also present. They cannot have formed in this orientation at the growth face, because the strong force at the surface would have pushed parallel segments out of the crystal or rotated them into an orientation of low or zero force (see the Lothe theorem above). This argues that the growth dislocations must have changed their course after growth, probably when the crystal was taken out of the melt. For this procedure the growth chamber was shortly opened whereby cool air flowed against the crystal. There are, however, also straight dislocations (pure-edge) normal to the growth faces, still following the preferred directions suggested by the minimum-energy theory.

Figure 4.25 shows, among others, four growth dislocations (arrows a) in orthorhombic benzophenone, grown in supercooled melt, which exhibit line segments with sharply defined noncrystallographic preferred di-

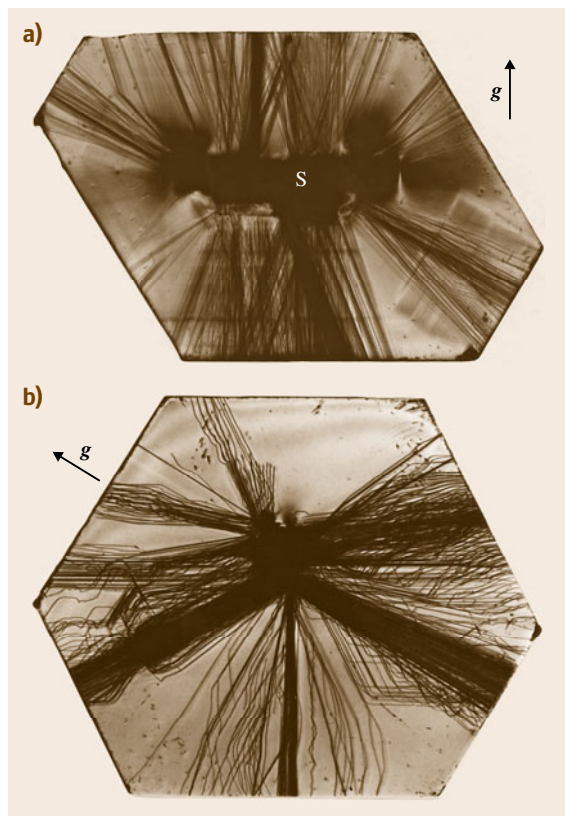


Fig. 4.24 (a) (0001) Plate (horizontal width 28 mm, thickness 1.2 mm) cut from a trigonal benzil crystal grown in its brittle state at about 40 °C from a solution in xylene by solvent evaporation. S: seed crystal, containing a crack which was formed at the end of the growth run. (The crack tips on the right and left sides of the seed induce extended long-range strain.) All dislocations are straight-lined with preferred directions. Diffraction vector $g(2020)$, $\text{CuK}\alpha_1$. (b) (0001) Plate (horizontal width about 35 mm, thickness 1.2 mm) cut from a crystal grown in its plastic state from a supercooled melt ($T_m = 96^\circ\text{C}$). Numerous growth dislocations start from the surface of the rather strongly disturbed seed S, and many of them show post-growth movement. $g(02\bar{2}0)$, $\text{CuK}\alpha_1$

rection (mainly screw character, Burgers vector $[001]$ vertical) and segments subjected to postgrowth movement. The latter consist of several bows generated by dislocation movement which was locally hindered by pinning points. The horizontal line segments d are pure-edge dislocation dipoles (Sect. 4.4.3). Note that these dipole segments, consisting of two closely neighboring edge dislocations with opposite Burgers vectors, exhibit mostly about the same and in some cases wider and stronger x-ray topographic contrast, compared with the single dislocation lines. Similar observations of postgrowth movement of growth dislocations with pinning points forming dipoles were made for sodium chlorate

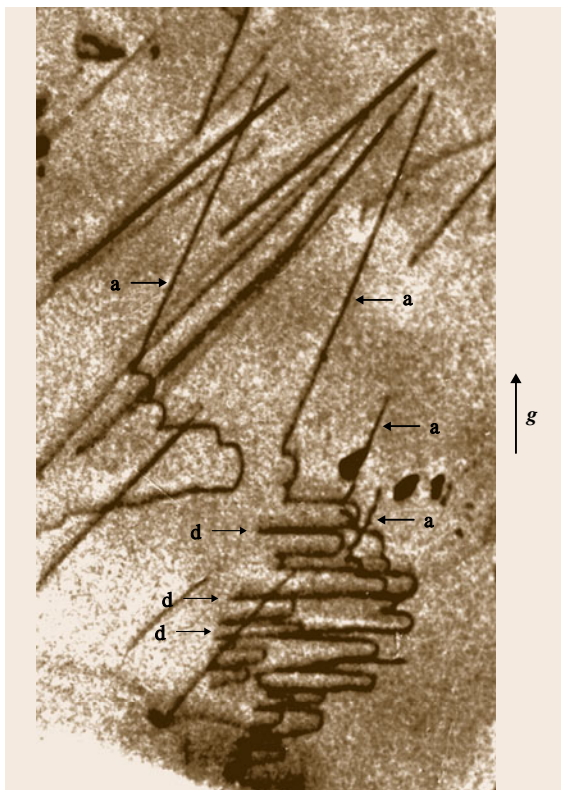


Fig. 4.25 Section (about $4 \times 7 \text{ mm}^2$) of a (110) plate (about 1.5 mm thick) of benzophenone grown from supercooled melt. The arrows a mark four growth dislocation in a (111) sector showing sharply defined noncrystallographically preferred directions (predominantly screw character) in their upper, and postgrowth movement with pinning stops in their lower, parts. Burgers vector $b = [001]$ vertical. The horizontal segments are pure-edge and form a few dislocation dipoles (arrows d). The dislocations emerge through the plate surfaces. $g(002)$, $\text{CuK}\alpha_1$

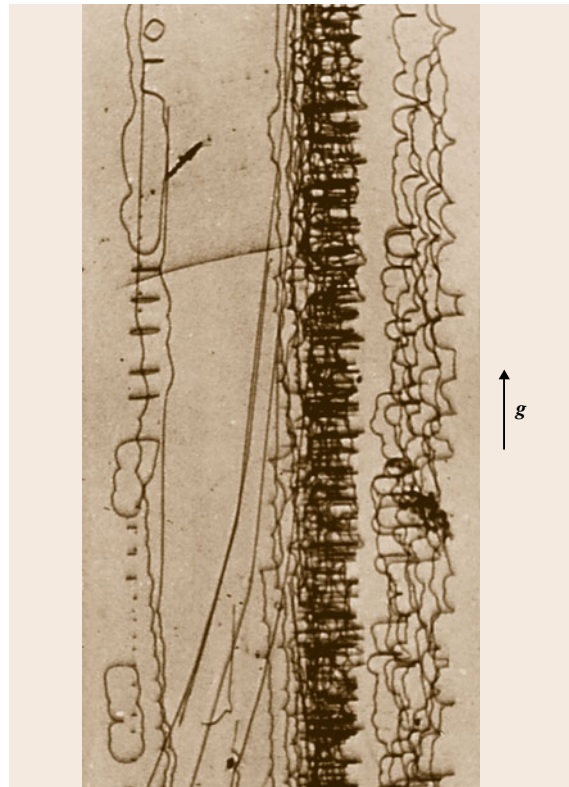


Fig. 4.26 Section ($3.8 \times 8.0 \text{ mm}^2$) of a plate (thickness about 1.2 mm) cut from a Czochralski crystal (pulling direction upward) of benzophenone ($T_m = 48^\circ\text{C}$), showing growth dislocation after postgrowth movement. The pinning points of one of the dislocations at the right-hand side mark its originally straight course. At the left side some dislocations have partially annihilated and formed closed loops. $g(002)$, $\text{CuK}\alpha_1$

NaClO_3 and lithium ammonium sulfate LiNH_4SO_4 . This finding is remarkable insofar as these two crystals appear, by microhardness indentations, as highly brittle, forming cracks even under lowest indentation loads. This indicates that in these crystals fast plastic flow is impeded by high friction but slow dislocation movement (creep) is possible.

An even more drastic change of growth dislocations is presented in Fig. 4.26, which shows a section of a plate cut out of the center of a Czochralski-grown benzophenone crystal (temperature of the melt about 1.5°C above $T_m = 48^\circ\text{C}$, pulling rate 20 mm/day). During pulling the crystal was cooled by blowing air of about 35°C against the rotating crystal in order to obtain a crystal diameter of 25 mm [4.42]. The topo-

graph shows growth dislocations which originate from the zone of first growth on the seed crystal (outside the top of the figure). A few of the dislocations have retained their original course (straight or slightly curved lines), but most of them have suffered postgrowth movement (which may have occurred already during the pulling process): they consist of a series of bow-shaped segments connected at pinning points (right-hand side of Fig. 4.26). The pinning points are aligned along straight lines marking the original position of the dislocations. On the left-hand side of Fig. 4.26 the changes are even more drastic: some dislocations have partially annihilated, leaving behind only a few large and several small dislocation loops. Postgrowth reactions of growth dislocations forming dislocation nodes in Czochralski salol have been studied by *Neuroth and Klapper* [4.115].

Interestingly, the dislocations in the Czochralski salol of Fig. 4.10 have preserved their growth configuration with straight lines roughly normal to the growth front, despite the thermal stress which is always present in this growth technique. This may be due to the low growth temperature ($T_m = 42^\circ\text{C}$) and the narrow plastic zone of salol below the melting point.

4.4.6 Postgrowth Dislocations

Dislocations formed in the interior of already grown crystal without connection to the growth front or other surfaces must be closed loops [4.7–11]. It is practically impossible to generate closed loops in a perfect crystal by stress, since the stress required for such processes would be extremely high. Inclusions, however, usually represent stress centers and form internal surfaces in the crystal. The stress in the crystal around the inclusions is relieved by the emission of concentric dislocations loops or – more frequently – of dislocation half-loops. The half-loops are – strictly speaking – also closed loops with a virtual closing line element inside the inclusion. Half-loops can also generate growth dislocations: if stress is built up around an inclusion just incorporated and still close to the growth front, half-loops emitted from the inclusion may *break through* to the growth interface, whereby each half-loop forms two separate dislocation lines with opposite Burgers vectors propagating with the growth front. Dislocation half-loops emitted from bubble inclusions and from decomposition particles in benzil grown from supercooled melt are shown in Fig. 4.27a,b. Examples of half-loops in solution-grown crystals, revealed by x-ray topography, are given in [4.9] (sodium chlorate)

and [4.117] (tetraoxane). The latter study shows the successive emission of half-loops from inclusions and their splitting into two separate dislocations when reaching the crystal surface. A very peculiar kind of dislocations loops is found in octadecanol crystals grown from xy-

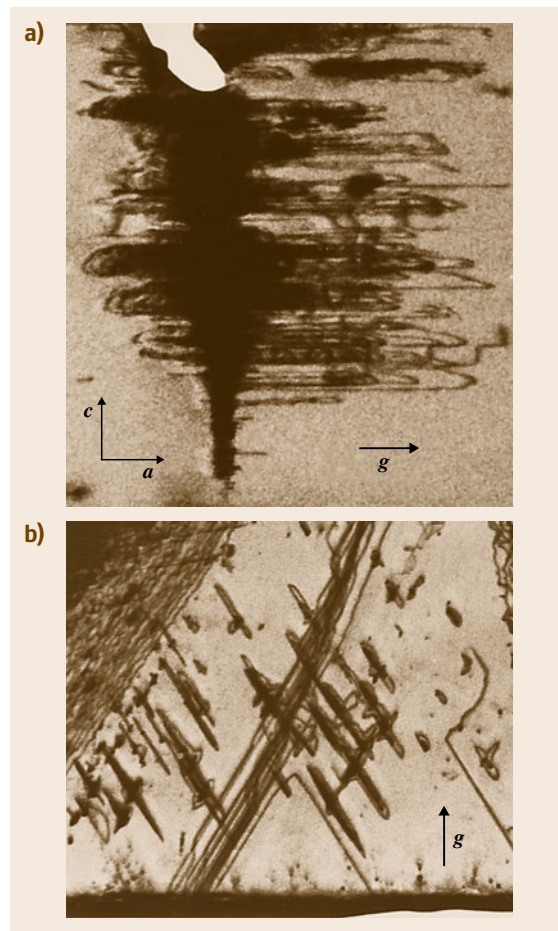


Fig. 4.27 (a) Postgrowth dislocation half-loops in benzil (grown from supercooled melt) emitted from a trail of bubbles. Section $4.5 \times 5 \text{ mm}^2$ of a $(01\bar{1}0)$ plate (after [4.1]). The dislocations belong to the $\{01\bar{1}0\}\langle 100 \rangle$ glide system and are pure-screw in their horizontal segments. $g(20\bar{2}0)$, $\text{CuK}\alpha_1$. (b) Section (about $9.5 \times 8 \text{ mm}^2$) of a (0001) plate of benzil grown from supercooled melt, showing dislocation loops of glide system $(0001)\langle 100 \rangle$ emitted from small inclusions. The loops are elongated in the direction of their (symmetrically equivalent) Burgers vectors $b = [100]$ and $[110]$; the loops with the third equivalent Burgers vector $[010]$ are x-ray topographically *extinct* in the reflection used. $g(02\bar{2}0)$, $\text{CuK}\alpha_1$

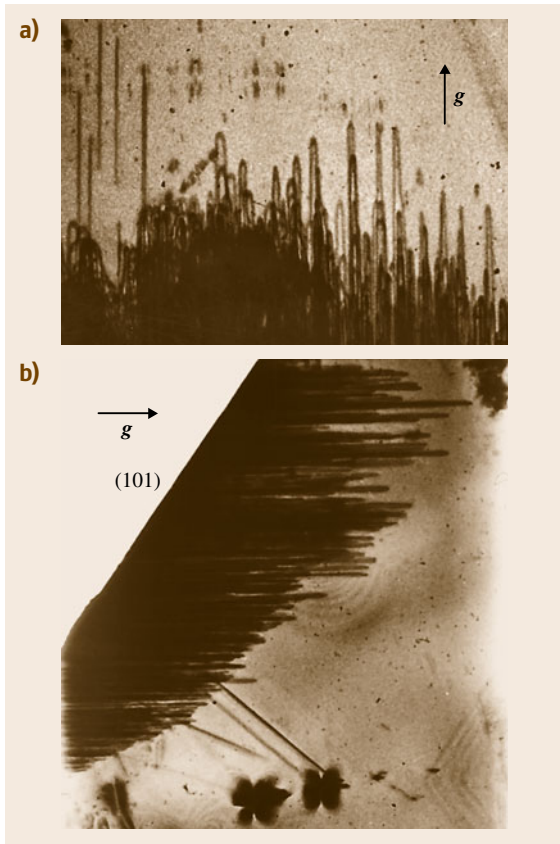


Fig. 4.28a,b Forests of hairpin dislocations (screw dipoles) of the easy glide system $(100)[001]$ of orthorhombic thiourea, $(\text{NH}_2)_2\text{CS}$, grown from a water-methanol solution [4.119]. The *hairpins* have invaded the crystal through the $\{101\}$ growth faces due to improper handling after growth. Both topographs $g(001)$, MoK_α . **(a)** Plate (section about $4 \times 6 \text{ mm}^2$) parallel to glide plane (100) , Burgers vector $[001]$ vertical. *Upper-left corner*: growth dislocations penetrating the plate. **(b)** (010) Plate ($7 \times 9 \text{ mm}^2$); the *hairpins* are projected edge-on. *Bottom*: three growth dislocations, liquid inclusions

lene solution: columns of prismatic loops are punched out from inclusions [4.118].

Postgrowth dislocations may also arise from the (external) crystal surface. This is common for growth in contact with a container wall (e.g., Bridgman melt growth). Dislocations are generated by stress due to the different thermal expansion of crystal and container wall or by sticking of the crystal to the wall. An illustrative example is presented in [4.7, Figs. 32 and 33]: it shows numerous glide dislocations in cleav-

age lamellae of 2,3-dimethylnaphthalene (grown by the Bridgman method), which arise from the seed region, from the contact with the growth ampoule, from internal stress centers, and from the point of the cleavage impact. In crystals which are plastic at room temperature glide dislocations may invade through the surface by improper handling after growth, e.g., by mechanical impacts (mechanical polishing, scratches). This is illustrated in Fig. 4.28a,b for orthorhombic thiourea grown from a water-methanol solution. Numerous hairpin dislocations (dipoles) with pure-screw character of their long branches originate from surface damages and extend a few millimeters on the main glide plane (which is also a pronounced cleavage plane) into previously perfect crystal regions [4.119]. In Fig. 4.28b these *hairpins* are projected *edge-on*. The invasion of glide dislocations from the specimen surface into the bulk quite frequently occurs during high-temperature processing of crystals for solid-state electronics and optics (e.g., [4.82]).

4.4.7 The Growth-Promoting Role of Edge Dislocations

Since the pioneering works of *Frank* [4.120, 121] and *Burton, Cabrera, and Frank* (BCF theory) [4.122] it is well established that screw dislocations play a decisive role in growth at low supersaturations by forming persistent step sources in the form of spirals or concentric loops. The latter are generated by pairs of screw dislocations of *opposite* Burgers vectors (screw dislocation dipoles), which separately form spiral hills of *opposite handedness*. These hills fuse into a single growth pyramid with self-perpetuating concentric steps, emitted from the dislocation pair, if the distance between the two dislocations is larger than the critical radius ρ_c of the two-dimensional nucleus for stable growth. For a distance smaller than ρ_c a growth-promoting pyramid is not formed. In contrast to this, a group of N screw dislocations with the *same sign* of Burgers vectors (*same handedness* of growth spirals) increases the growth activity of the face on which they terminate by a factor up to N , if these dislocations are separated by distances smaller than ρ_c (*cooperating spirals*). For distances larger than ρ_c the growth activity corresponds to that of a single screw dislocation (*noncooperating spirals*). These findings hold for all dislocations, normal or inclined to the growth surface, which possess a screw component normal to the growth face [4.122].

Later it was recognized that pure-edge dislocations are capable of generating growth spirals also,

e.g., a pure-edge dislocation, emerging at an angle of about 45° in such a way that its Burgers vector also forms an angle of 45° with the surface, will generate a growth spiral. This has been shown in models by *Strunk* [4.123] and *Ming* [4.124]. In their reasoning, dislocations with Burgers vector *parallel* to the growth surface, e.g., edge dislocations *emerging perpendicularly* from the growth face, were expected *not* to form persistent growth centers promoting growth. There is, however, much experimental evidence proving the opposite. For example, pure-edge dislocations generated by inclusions on {100} cube faces of potassium alum, growing from aqueous solution, drastically increase the growth rate of the {100} face (from which they perpendicularly emerge) in the moment of their appearance. The {100} growth rate is reduced again, when the edge dislocations shift during growth over a crystal edge on a neighboring {111} face (i.e., when they penetrate the boundary into the {111} growth sector [4.76–79], cf. Sect. 4.3.6 and Fig. 4.15). Detailed studies of this growth-promoting effect of edge dislocations in potassium alum are reported in [4.77–79].

The above results show that the term *screw dislocation mechanism* for the formation of growth spirals is not adequate. *Bauser* and *Strunk* [4.125] introduced the terms *longitudinal step source* for growth centers with a Burgers vector component normal to the growth face, and *transverse step source* for growth centers with zero component normal to the growth face. *Frank* [4.126] suggests the terms *rampant step source* and *couchant step source*, respectively, but a final choice of terms has not emerged in this matter.

The probably first demonstration of the growth-promoting effect of *transverse step sources*, based

on a reliable Burgers vector determination, was provided by *Bauser* and *Strunk* [4.125]. They observed, by liquid-phase epitaxial growth on a (100) facet of GaAs, step patterns with well-defined growth centers. High-voltage transmission electron microscopy (TEM) showed that each of these centers was associated with a single dislocation. Burgers vector analysis revealed that, besides hill dislocations *with* Burgers vector components normal to the growth face (*longitudinal* step centers), also those *without* a normal component (*transverse* step centers) occur. Though a statistical analysis is lacking, both types of growth centers seem – in this case – to occur with comparable frequency and activity. *Frank* [4.126] expects that the *transverse growth center* is active only for increased supersaturation approaching the critical value necessary for two-dimensional nucleation, whereas the *longitudinal center* works already for very low supersaturations.

The origin of the activity of transverse step sources is not yet clear. *Bauser* and *Strunk* ([4.125] and references therein) assume that the dislocation is split into two partials (spanning a stacking fault) with a surface step formed between their endpoints on the surface. The growth-promoting activity of this defect arrangement has been demonstrated by *Ming* [4.124]. This approach, however, can only hold for crystals capable of stacking faults. *Frank* [4.126] suggests that surface stress around the dislocation outcrop leads to increased local adsorption of atoms, and *Giling* and *Dam* [4.127] postulate a local roughening of the surface with increased growth, forming a hill which emits from its periphery concentric step rings over the otherwise flat growth face.

4.5 Twinning

4.5.1 Introductory Notes

A twin is a frequently occurring aggregate or intergrowth of two or more crystals of the same species (same chemical composition and crystal structure) with a defined *crystallographic orientation relation* (determining the *orientation states* of the *twin components*), which in mineralogy is called the *twin law*. Besides the twin law, the boundary between twin domains (the *contact relation*) plays a decisive role: twins occur in those crystals in which boundaries of low energy can be formed. This has been proven quantitatively by

Gottschalk et al. [4.128], who showed that the ease and frequency of the formation of (111) spinel twins in the sphalerite (zincblende) structure of III–V semiconductor compounds (GaAs, InP, etc.) is correlated to the (111) stacking-fault (twin-boundary) energy (see also [4.69, p. 422]). There is, however, also a theory which states that the boundary energy is of minor importance and that kinetic influences play a decisive role in the formation of twins [4.129]. This approach, however, is critically discussed [4.130, 131].

Historically, the concept of twinning was developed in mineralogy due to the rich occurrence of morpholog-

ically prominent twins in minerals. In the 1920s another approach, independent of mineralogy, was developed in physics with the investigation of ferroelectricity and ferroelasticity. The spontaneous electric polarization and spontaneous mechanical strain occurring in these *ferroic* crystals lead to ferroelectric and ferroelastic domains which are twin domains as defined in mineralogy. Though the concepts of *twinning* and *domain structures* (as the physical approach is now called) deal with the same phenomenon, there are (apart from a different nomenclature) certain differences: in contrast to *twinning*, the *domain structure* approach requires a (real or hypothetical) *crystallographic parent symmetry* (supergroup), from which the *orientation states* can be derived by a real or hypothetical phase transition. Therefore, this approach cannot be applied to many growth and deformation twins. A comparison of the concepts of *twinning* and of *domain structures* is given by Janovec et al. [4.132] and Janovec and Přívratská [4.133].

Twins are mainly classified by morphological features (dovetail, contact, penetration, sector, polysynthetic twins, etc.), by their genetic origin (growth, transformation, mechanical or deformation twins) and by their lattice coincidence features: *merohedral* twins (full, three-dimensional lattice coincidence), which are also called *twins with parallel axes*, and *nonmerohedral* twins (two or one-dimensional lattice coincidence), also called *twins with inclined axes*. Reviews on twinning are presented in many textbooks of mineralogy and crystallography (e.g., [4.134, 135]). A comprehensive treatment is provided by Hahn and Klapper [4.69, especially section *Growth twinning* p. 412–414]. A survey on x-ray topographic characterization of twinned crystals is given by Klapper [4.6]. In the present section only growth twins and twins generated in the cooling period after growth (postgrowth twins) are treated, whereby emphasis is placed on crystals grown from solutions on habit faces. A treatment of twinning in crystals grown from the melt is presented by in Chap. 6 of this Handbook.

4.5.2 Twin Boundaries

The shape and arrangement of twin domains is essentially governed by the twin boundaries and their preferred orientations. As mentioned in the previous subsection, twin boundaries are contact faces with good structural fit of the twin partners involved, i. e., they are internal surfaces of low energy. Accordingly they are, as a rule, low-index and structurally densely packed lattice planes common to both twin partners. For re-

flection twins and twins by a twofold axis, the twin mirror plane or the plane normal to the twofold twin axis is always an energetically favored contact plane because along this boundary the corresponding lattice planes of the two partners match perfectly. There is, however, a basic difference between *twins with parallel axes* (three-dimensional lattice coincidence: *merohedral* twins) and *twins with inclined axes* (two- or one-dimensional lattice coincidence: *nonmerohedral* twins [4.69, p. 422] [4.132, 133]). In the first case the lattices of the twin components match perfectly along any twin boundary for any twin law. In the latter case the boundary along the common lattice plane of perfect matching is usually strictly adopted. Deviations from strict planarity of these boundaries may occur by steps which form the *twinning dislocations*. These dislocations play an important role in the plastic deformation of crystals by twin formation.

For twins with parallel axes (full lattice coincidence, e.g., for inversion twins) the lattices of the twin components match perfectly along any arbitrary (also curved) boundary. Thus, from this lattice aspect alone, arbitrarily oriented boundaries are expected to occur. A prominent example is the Dauphiné twinning of quartz, which occurs as growth as well as transformation and mechanical (ferrobielastic) twinning: Dauphiné twin boundaries usually follow (at least macroscopically) arbitrary and curved surfaces, whereby low-index boundary segments sometimes also occur [4.136, pp. 75–99]. As a rule, however, low-index twin contact planes are favored also in twins with full lattice coincidence (merohedral twins). An example is given by quartz: Brazil twins (twin law: inversion), which are exclusively growth twins, develop boundaries along low-index planes, preferably parallel to prism and rhombohedron faces [4.136, Fig. 61].

A special case is given by the spinel twins of cubic crystals with twin law *reflection plane* ($\{111\}$) or *twofold axis along* $[111]$. They occur as growth twins in technologically significant crystals with diamond structure (Si, Ge), sphalerite (zincblende) structure (e.g., ZnS, GaAs, InP, and CdTe [4.128, 137]), and sodium chloride structure (photographic materials AgCl and AgBr [4.138–142]). They are characterized by a partial lattice coincidence of $1/3$ of the lattice points (so-called $\Sigma 3$ twins), which form a hexagonal sublattice of the cubic lattice, with the hexagonal axis along the threefold axis $[111]$ common to both twin components. Preferred twin boundaries are planes $\{111\}$ and $\{11\bar{2}\}$ (Fig. 4.29), which are twin reflection planes (in centrosymmetric crystals such as diamond, Si, Ge, AgBr) or planes

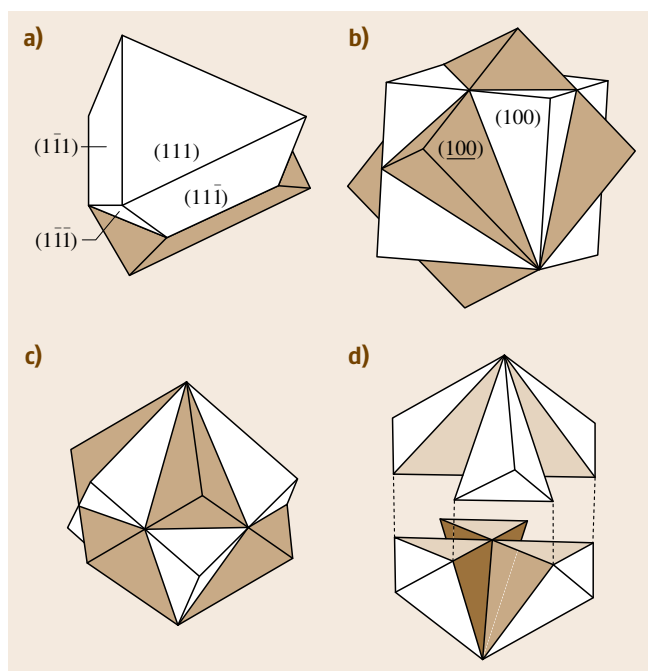


Fig. 4.29a–d Spinel twin of cubic crystals with twin mirror plane (111) or twofold twin axis $[111]$ (or alternatively $\pm 60^\circ$ rotation around $[111]$). The domains of the two orientation states are shown *white* and *shaded*. **(a)** Contact twin with (111) contact plane (two twin components). **(b), (c)** penetration twin (idealized) with one (111) and three $\{112\}$ contact planes (12 twin components, 6 of each orientation state) in two different views: **(b)** with one $[001]$ axis vertical, **(c)** with the threefold-symmetry axis $[111]$ common to the two orientation states and coinciding with the twofold twin axis vertical. **(d)** Skeleton of the six components (exploded along $[111]$) of the *shaded* orientation state of **(c)**. The components are connected along one $[111]$ and three $\langle 110 \rangle$ edges meeting in the center

normal to twofold twin axes (in noncentrosymmetric crystals of sphalerite structure, e.g., ZnS, GaAs).

4.5.3 Formation of Twins During Growth

Formation During Nucleation of the Crystal

In many cases, twins are formed already during the first stage of spontaneous nucleation, possibly before the subcritical nucleus reaches the critical size necessary for stable growth. This formation is strongly evidenced for penetration and sector twins, where all domains are of similar size and originate from one common, well-defined *point* in the center of the twinned crystal, which marks the location of the spontaneous nucleus (Figs. 4.29 and 4.30). Other prominent examples are

the penetration twins (two orientation states) in quartz-homeotypic gallium orthophosphate (GaPO_4 [4.47]) and in rhombohedral crystals such as corundum (sapphire, Al_2O_3 [4.143]) or iron borate (FeBO_3 , calcite structure [4.6, p. 390]), and sector twins of pseudo-hexagonal crystals such as lithium ammonium sulfate (Fig. 4.30), potassium sulfate [4.69, p. 408], and aragonite CaCO_3 (Fig. 4.31), which all form twins with three orientation states. The origin of twinning by nucleation must also be assumed for contact twins (Fig. 4.29a), if both partners of the twin have roughly the same size, or

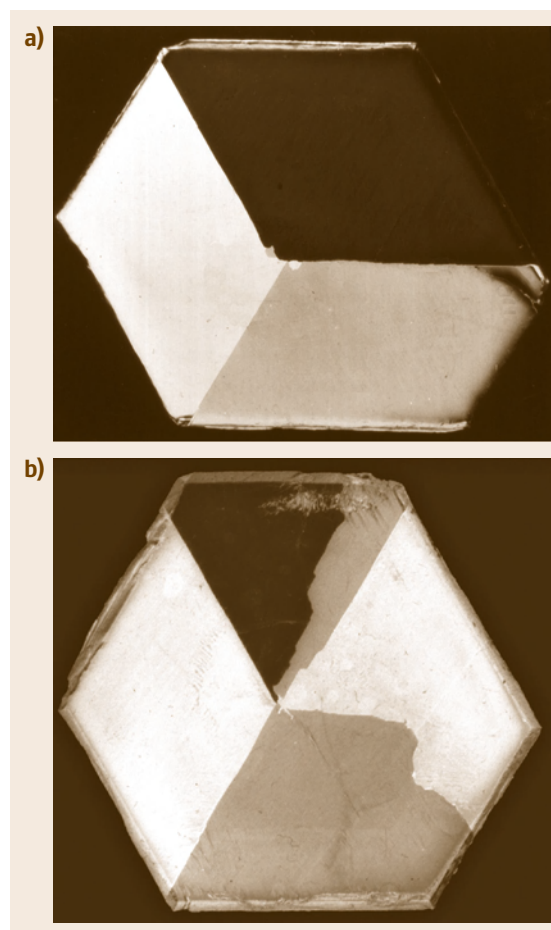


Fig. 4.30a,b Photographs of (001) plates (about 20 mm diameter, about 1 mm thick) of orthorhombic pseudo-hexagonal LiNH_4SO_4 between crossed polarizers, showing sector growth twins. **(a)** Nearly regular threefold sector twin (three orientation states, three twin components). **(b)** Irregular sector twin (three orientation states, but five twin components). After [4.69, p. 413]

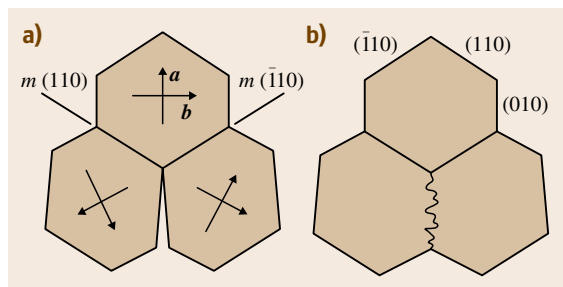


Fig. 4.31 (a) Triple growth twin of orthorhombic pseudo-hexagonal aragonite, CaCO_3 . The three twin components are related by two symmetrically equivalent mirror planes (110) and $(\bar{1}10)$. Due to a relatively high deviation from the hexagonal metrics, a gap of 11.4° should be formed. In actual crystal the gap is usually closed, as shown in (b), leading to a strongly disturbed irregular twin boundary

if all spontaneously nucleated crystals in one batch are twinned. For example, *all* crystals of monoclinic lithium hydrogen succinate precipitated from aqueous solution are, without exception, dove-tail contact twins.

An approach to twin formation during crystal nucleation has been advanced by *Senechal* [4.144]. She proposes that the crystal nucleus first formed has a symmetry which is not compatible with the lattice of the (macroscopic) crystal. This symmetry may even be non-crystallographic. It is assumed that, after the nucleus has reached a critical size beyond which the translation symmetry becomes decisive, the nucleus collapses into a twinned crystal with domains of lower symmetry and continues to grow as a twin. This idea of twin formation from noncrystallographic nuclei has been substantiated experimentally by high-resolution TEM (HRTEM) investigations of nanocrystalline diamond-type and face-centered cubic (fcc) crystals, such as Ge, Ag, and Ni [4.145].

Twin Formation by Inclusions

As they are for dislocations (Sect. 4.4.2), inclusions are frequently sources of twins. It is assumed that a nucleus in twinned orientation forms at the inclusion and proceeds in this orientation during further growth. An instructive experimental key study of this process is presented by *Sunagawa* et al. [4.146] for Dauphiné and Brazil twins in synthetic amethyst quartz. Amethyst quartz contains much more Dauphiné and, to a still higher extent, Brazil growth twins than normal (colorless) quartz. The higher frequency of twin formation is doubtlessly due to its relatively high content of iron [4.147]. *Sunagawa* et al. [4.146, and references

therein] grew amethyst quartz hydrothermally in various solutions containing ferric iron, on amethyst seed plates of various orientations. They studied the twinning on as-grown faces, on etched growth faces, and on cut surfaces by light-microscopic methods. In all cases the Dauphiné and Brazil twins originated from solid inclusions containing iron (probably as goethite, FeOOH). In some cases the Brazil twins are associated with dislocations originating from the same inclusion.

A twin component originating from an inclusion may have the following shapes, depending on the preferred orientation of the twin boundary:

- It forms a conical (pyramidal) insert, embedded in the *mother* crystal, with its apex in the inclusion and widening in the growth direction. This shape occurs, e.g., in quartz for Dauphiné as well as Brazil growth twins, whereby the surface of the twin inserts (i.e., the twin boundary) is rounded for the Dauphiné and faceted by low-index habit planes for the Brazil twin [4.136, Fig. 61]. In amethyst quartz the inserts are lamellae preferably parallel to the major rhombohedron faces.
- For crystals with a pronounced preference of a low-index planar twin boundary, the twin insert is a band-shaped lamella originating from the inclusion and proceeding with the growing crystal. An example is given by hexagonal potassium lithium sulfate (KLiSO_4 , merohedral reflection twin) grown from aqueous solution [4.148].

For the generation of twinning in melt-grown crystals, the reader is referred to Chap. 6 in this Handbook.

Propagation of Twin Boundaries

In contrast to a twin lamella, a (single) twin boundary cannot end *within* an otherwise perfect crystal. Therefore, a twin boundary emerging on a growth face must proceed with it during growth, whereby it should obey the theorem of minimum-energy orientation, postulated in Sect. 4.4 for growth dislocations. This means that the orientation of the twin boundary results from the competition to minimize the area of its surface within a growth layer (i.e., by orienting toward 90° with the grown face) and to minimize the boundary energy per unit area. Since, as a rule, the boundary energy has a pronounced and sharp minimum along a low-index lattice plane (similar to dislocations with pronounced Peierls energy, cf. *Deviations from Calculated Directions*), the boundary will follow this plane even for small angles between the twin contact plane and the growth face.

In mineralogy it is frequently observed that a twin boundary coincides with a large-area prominent growth face. A famous example is the polysynthetic lamellar twinning of the triclinic feldspar albite ([4.69, p. 410]). This indicates that a two-dimensional nucleus in twin position has formed on the growth face of the (previously untwinned) crystal [4.149, pp. 472–475]. Obviously, this process is triggered by defects in the growth face (e.g., by impurities, inclusions). If the twin nucleus spreads out over the growth face, the twin boundary coincides with the growth face. This mechanism seems to be possible only for twin boundaries of low energy, since the boundary energy of the large interface has to be supplied in one step, i.e., during spreading out of one single growth layer in twin position. The energy contribution of the first layer, however, may be quite small, because the structural alteration across the interface occurs only for second-nearest and more distant neighbors, so that the full boundary energy of the twin accumulates only after the deposition of a sufficiently thick package of growth layers. This is particularly the case if long-range (e.g., ionic) interactions are present. Thus, from an energetic point of view, the formation of twin boundaries coinciding with growth faces – after a two-dimensional nucleus in twin orientation has formed – appears probable. According to Hartmann [4.150], this kind of twin formation can only occur on *flat* or, with lower probability, on *stepped* faces (F- and S-faces, respectively). The critical step is the formation of the two-dimensional twin nucleus on these faces.

The formation of twin boundaries coinciding with the *actual* growth face, however, seems to be rather the exception, although in special cases, e.g., in polysynthetic lamellar twinning of the albite feldspar, it happens several times within the same crystal. It is pointed out that, for example, the planar low-index boundaries of Brazil twins in quartz *do not* develop parallel to prism or rhombohedron growth faces on which the twins are nucleated, although these faces are preferred (low-energetic) twin contact planes [4.136, 146]. This feature is obviously due to the special character of Brazil twins: they are merohedral inversion twins with full three-dimensional lattice coincidence.

Finally, boundaries of twins with more than two orientation states are considered. Such twins frequently occur in orthorhombic pseudo-hexagonal crystals (e.g., K_2SO_4 , $LiNH_4SO_4$, aragonite $CaCO_3$) and consist mostly of domains of three orientation states (triple twins) related by three equivalent twin mirror planes or twofold twin axes. An example is shown in Fig. 4.30a.

The crystals usually grow as *sector twins* starting from a common nucleus, with three or six twin components. In the latter case pairs of opposite sectors belong to the same orientation state. The twin boundaries mostly coincide with the twin mirror planes, but deviations leading to irregular boundaries may also occur (Fig. 4.30b). A twin boundary may coincide with a growth-sector boundary but usually does not (Fig. 4.30). An x-ray topographic study of pseudo-hexagonal growth twinning in $LiNH_4SO_4$ is presented by Docherty et al. [4.151].

For the sector-twin boundaries of pseudo-hexagonal crystals the angle $\gamma = 2 \arctan(b/a)$ (where a and b are the orthorhombic lattice parameters of the pseudo-hexagonal plane) plays an important role. For an exact fit of the sectors $\gamma = 120^\circ$ is required. Small misfits, e.g., $\gamma = 119.6^\circ$ for orthorhombic lithium ammonium sulfate [4.151] (Fig. 4.30), are tolerated for triple twins without further disturbances, but often induce cracks when the twins grow to a larger size. An example of extreme sectorial misfit occurs in orthorhombic aragonite $CaCO_3$ ($\gamma = 116.2^\circ$), which would generate a gap of 11.4° from the 360° closure. In this case the triple twin usually exhibits two boundaries coinciding quite perfectly with the two twin mirror planes $\{110\}$, whereas the third is irregular and strongly disturbed, thus closing the angular gap (Fig. 4.31b). A particularly interesting example is provided by nanocrystals of germanium nucleated in an amorphous Ge film deposited from the vapor on a NaCl cleavage plane (HRTEM study by Hofmeister [4.145]): pseudopentagonal sector twins by repeated (111) twin reflections and (111) twin contact planes are formed. The angle of one sector is theoretically 70.5° (the supplement to the tetrahedral angle 109.5°) and five of these angles leads to a gap of about 7.5° . This gap is compensated by slight widening of the sectors either by distortion or by the formation of stacking faults within a sector, whereby the five (111) twin boundaries of this fivefold sector twin remain perfect ([4.145] and [4.69, p. 439]).

4.5.4 Growth-Promoting Effect of Twin Boundaries

The growth-promoting influence of twin boundaries forming reentrant edges was already noticed by mineralogists in the 1890s and has later been described in detail by Buerger [4.149] and Hartmann [4.150]. This *twin-plane reentrant-edge effect* (TPRE effect after [4.137]) can occur only in faceted crystals and is pronounced for growth faces adjoining a reentrant edge,

which provides a self-perpetuating step source [4.137, 152–156]. It leads to crystals laterally extended in directions parallel to the twin interface (compared with untwinned crystal) and has also been observed for organic crystals of orthorhombic *n*-alkanes and paraffins [4.157, 158]. The TPRE effect has a particularly strong impact on the morphology of cubic crystals twinned by the spinel law: whereas untwinned cubic crystal exhibits an isometric shape, (111)- and (11 $\bar{2}$)-twinned crystals grow as plates parallel to the twin plane. The growth of (111) and (11 $\bar{2}$) platelets of cubic elemental and compound semiconductors from metal solutions using the TPRE effect has been studied in detail by Faust and John [4.137, and references therein]. Of particular significance for photographic products are tabular crystals of cubic silver halogenides, such as AgBr, AgCl, and AgI. The formation of tabular AgBr crystals by the TPRE mechanism is discussed by Jagannathan et al. [4.138, 139], Bögers et al. [4.140, 141], and more recently Lee et al. [4.156] using the hard-sphere model of Ming and Sunagawa [4.152, 153]. These authors also discuss the effect of two or more *parallel* twin planes (i. e., of twin lamellae).

A more drastic morphological change of cubic crystals is provided by two or more *intersecting* twin planes (*cross-twinning*). In this case the crystals grow as needles parallel to the intersection of the twin planes. Examples are presented and discussed by Wagner [4.159], Hamilton and Seidensticker [4.160] (critically reviewed by van de Waal [4.161]) for Ge (dendrites in $\langle 11\bar{2} \rangle$ direction), and Bögers et al. [4.142] for AgBr and AgCl (needles in $\langle 110 \rangle$ directions).

4.5.5 Formation of Twins after Growth

There are two causes for the formation of twins during cooling to room temperature after growth: phase transitions and ferroelastic switching [4.133].

Phase transition: Crystals often can only be grown at elevated temperatures, where they crystallize in another (*high-temperature*) phase of usually higher symmetry than they adopt at room temperature. On cooling below the transition temperature, twin domains

are formed, whereby the lost symmetry elements of the mother phase act as twin elements (twin laws) relating the twin domains. Examples: lithium niobate LiBO_3 is grown from the melt at $T_m = 1275^\circ\text{C}$ and undergoes a paraelectric–ferroelectric transition at T_c about 1140°C , whereby ferroelectric domains are formed. The high-temperature superconductor $\text{YBa}_2\text{Cu}_3\text{O}_{7-\delta}$, usually grown from flux, is subject to a transition at about 750°C from the tetragonal parent phase into an orthorhombic modification whereby it develops two nearly orthogonal systems of twin lamellae parallel to the two $\{110\}$ mirror planes of the tetragonal mother phase, lost in the transition [4.162]. These lamellae are ferroelastic and can be changed or even removed (detwinning) by mechanical stress. An example related to mineralogy is provided by quartz, which is stable in its trigonal phase below 575°C (α -quartz, point group 32) and hexagonal (β -quartz, point group 622) above this temperature. The transition from the hexagonal to the trigonal modification invariably leads to the formation of Dauphiné twinning (due to the loss of the twofold axis in the sixfold axis). The shape and arrangement of twin domains generated by crystal growth or by phase transformation (e.g., for Dauphiné twins) is quite different. In mineralogy these different features of twin textures are helpful for the determination of the conditions of mineral formation.

Ferroelastic switching: The twin domains of ferroelastic crystals switch by mechanical stress from one orientation state into the other. This occurs quite easily at elevated temperatures where the coercitive stress is strongly reduced. Thus, in a ferroelastic crystal grown without twinning, twin domains may be introduced by stress developed during cooling to room temperature. Here again inclusions forming stress centers are the main reason. The ferroelastic twin pattern is often correlated to the growth defects of the crystal, e.g., with growth striations [4.163, Fig. 100], [4.6, p. 379]. Postgrowth formation of twins by ferroelastic switching has been observed in ammonium sulfate $(\text{NH}_4)_2\text{SO}_4$ [4.151] and Rochelle salt [4.163, p. 184], both grown from aqueous solution.

4.6 Perfection of Crystals Grown Rapidly from Solution

Until the 1980s the opinion prevailed among crystal growers that highly perfect crystals could only be obtained from solution by very slow growth. This has been disproved by the pioneering work of Zaitseva, Smol-

sky, and Rashkovich [4.34, 57], who showed that, by well-devised construction of the growth apparatus and careful pretreatment and strong stirring of the solution, large KDP crystals of high perfection can be grown

from aqueous solution. Their work was the basis of the growth of huge, highly perfect KDP and DKDP crystals of up to 60 cm edge lengths under high supersaturation within a time period of only a few weeks (e.g., [4.17, 35, 36, 164]). The rapid growth of KDP and ADP is described in detail in Chap. 22 of this Handbook. In the present section the growth defects of a slowly grown KDP and a rapidly grown ADP crystal, revealed by x-ray topography, are compared. In addition, the rapid growth of potassium alum, mixed (K,NH₄)-alum, and sodium chlorate [4.165] is reported.

In recent years, various studies of the perfection of rapidly grown KDP crystals have been published, e.g., [4.17, 37, 48, 58]. The most striking difference between slowly and rapidly grown KDP crystals appears in their morphology: crystal grown slowly develops the shape of an *obelisk*, because under low supersaturation, the {100} prism faces are inhibited by impurities so that the crystals grow nearly exclusively on {101} pyramid faces. In order to obtain bulky crystals, large (001) seed plates are used, which lead to a large capping zone (Figs. 4.2, 4.21a, and 4.23). In highly supersaturated and strongly stirred solutions, however, the {110} prism and {101} pyramid faces have essentially the same growth velocity. This allows growth to be started with small *point seeds* with a correspondingly small capping zone. The proper shape and mounting of the point seed and its impact on the habit of the grown crystal has been stud-

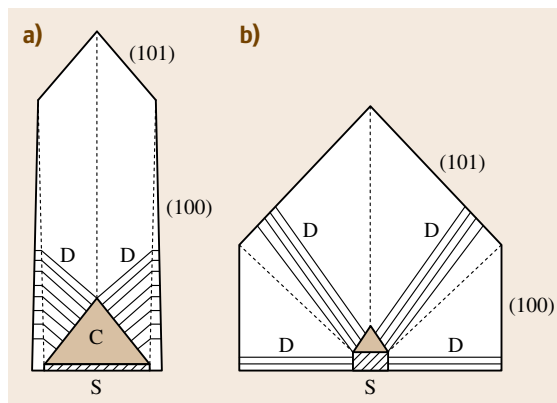


Fig. 4.32a,b Typical morphology and dislocation distribution of KDP and ADP crystal (a) slowly grown on a (001) seed plate S and (b) rapidly grown on a *point seed* S. D: dislocation lines, C: strongly disturbed regeneration (*capping*) zone (Figs. 4.21 and 4.23). In (b) this zone is small. *Dashed lines*: growth-sector boundaries. Note that here another (equivalent) labeling of faces is chosen than in Figs. 4.5, 4.21, and 4.23: prism {100}, dipyrmaid {101}

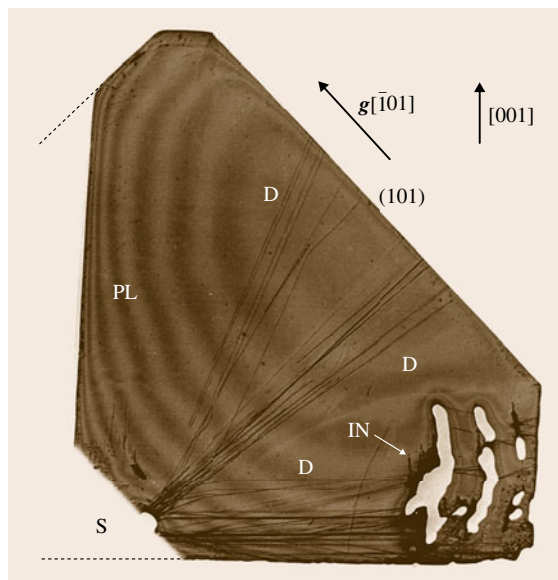


Fig. 4.33 X-ray topograph (MoK α radiation, reflection $\bar{1}01$) of a (010) plate (about 2.5 mm thick, horizontal extension about 60 mm, tetragonal axis vertical) cut from an ADP crystal rapidly grown within 10 days (including the seeding-in process and regeneration period) to a size with {100} edge lengths of about 110 mm. S: Location of the seed. The crystal has grown with about the same growth rates (about 15 mm/day in the end phase) on all {100} and {101} faces. Since the plate was too large for the x-ray topography crystal holder, a part was cut off at the left side. The crystal is highly perfect, as indicated by the x-ray *Pendellösung* fringes (rounded soft contrast bands PL) of constant plate thickness. Only a few dislocations D originate from a liquid inclusion at the point seed (which was out of the x-ray beam). IN: Large liquid inclusions which have formed on the right (100) face due to growth-face instabilities intentionally provoked by decreasing the temperature by 4 °C in one step at 50 °C after about 40 mm of perfect growth. Note that these inclusions have formed on only one of the four prism faces: the four {101} faces stayed also inclusion free. Reflection $g(\bar{1}01)$, MoK α . After [4.165]

ied by Zaitseva et al. [4.112]. The typical morphology of slowly and rapidly grown KDP and ADP crystals, the development of their growth sectors, and the arrangement of dislocations is shown in Fig. 4.32.

The typical growth defects and their distribution in slowly and rapidly grown crystals are apparent from the x-ray topographs shown in Figs. 4.5, 4.21a, 4.23, and 4.33. The crystals shown in the former three figures

were grown in the 1970s in the laboratory of *Bennema* (Delft and Nijmegen, The Netherlands) in a three-vessel growth system [4.26] at constant temperature of about 30 °C and supersaturation of about 5.4% with growth rate of about 1 mm/day on the {101} faces. The crystals were mounted on a tree which rotated in the solution. They contain inclusions, inhomogeneous impurity distributions (in the form of striations, growth, and vicinal sectors), and dislocations. As pointed out already by *Zerfoss* [4.12], *Janssen-van Rosmalen* et al. [4.26, 32], and *van Enckevort* et al. [4.33], liquid inclusions, in particular the quasiperiodic liquid inclusions shown in Fig. 4.5, can be avoided by strong stirring.

An x-ray topograph of an *ADP* crystal rapidly grown in the author's laboratory is shown in Fig. 4.33 [4.165]. The crystal was grown on a point seed in a sealed 10l tank by temperature decrease from 55 to about 45 °C with about the same growth rates on {100} prism and {101} pyramid faces in 10 days to a width of 110 mm along the <100> edges and a height of about 80 mm. It was rotated in the solution on a platform at about 50 cycles/min with reversal of the rotation every 30 s. The rate of temperature decrease was 0.1–1 °C in the generation period and was then increased stepwise to 4 °C/day, dependent on the size of the crystal. It is obvious from Fig. 4.33 that this crystal is much more homogeneous and perfect than the crystals shown in Figs. 4.5, 4.21a, and 4.23. Only a few dislocations originate from the point seed into the prism and pyramid growth sectors. Due to growth

face instabilities, large liquid inclusions have formed on the right prism face, but have healed out perfectly during further growth. Interestingly these inclusions block more growth dislocations than they generate. Convincing proof of the homogeneity of this crystal is the appearance of x-ray *Pendellösung fringes*, which result from the slight thickness decrease toward the edges of the plate. Neighboring (010) crystal plates, not cutting through the seed and through the inclusions, are dislocation free.

Rapid crystal growth of very large, highly perfect crystals from aqueous solution has been reported only for *KDP*, its deuterated variant *DKDP*, and for *ADP* [4.36]. In order to check the applicability of this method to other materials, growth experiments have been carried out with some other compounds usually used in student laboratory courses: pure and mixed potassium and ammonium alums, sodium chlorate, and nickel sulfate hexahydrate [4.165]. The growth procedure was essentially the same as reported above for *ADP*. Apart from some failures due to spontaneous nucleation, large crystals of these materials with edge lengths up to 12 cm could be successfully grown within 7–10 days with growth rates up to 25 mm/day. Optical inspection and x-ray topographic studies indicate that the optical and structural perfection is high and not at all inferior to the quality of corresponding traditionally grown crystals. These results indicate that the rapid growth method is applicable to the growth of many crystals from solution.

References

- 4.1 T. Scheffen-Lauenroth, H. Klapper, R.A. Becker: Growth and perfection of organic crystals from undercooled melt, *J. Cryst. Growth* **55**, 557–570 (1981)
- 4.2 A.R. Lang: Techniques and interpretation in x-ray topography. In: *Diffraction and Imaging Techniques in Materials Science*, 2nd edn., ed. by S. Amelinckx, R. Gevers, J. Van Landuyt (North-Holland, Amsterdam 1978) pp. 623–714
- 4.3 A. Authier: X-ray and neutron topography of solution-grown crystals. In: *Crystal Growth and Materials (ECCG-1 Zürich)*, ed. by E. Kaldis, H.J. Scheel (North-Holland, Amsterdam 1976) pp. 516–548
- 4.4 B.K. Tanner: *X-ray Diffraction Topography* (Pergamon, Oxford 1976)
- 4.5 A.R. Lang: Topography. In: *Internat. Tables for Crystallography, International Union of Crystallography, Vol. C*, ed. by A.J.C. Wilson (Kluwer Academic, Dordrecht 1995) pp. 113–123
- 4.6 H. Klapper: X-ray topography of twinned crystals. In: *Progress in Crystal Growth and Characterization*, Vol. 14, ed. by P. Krishna (Pergamon, Oxford 1987) pp. 367–401
- 4.7 H. Klapper: X-ray topography of organic crystals. In: *Crystals: Growth, Properties and Characterization*, Vol. 13, ed. by N. Karl (Springer, Berlin, Heidelberg 1991) pp. 109–162
- 4.8 H. Klapper: Defects in non-metal crystals. In: *Characterization of Crystal Growth Defects by X-ray Methods*, ed. by B.K. Tanner, D.K. Bowen (Plenum, New York 1980) pp. 133–160
- 4.9 H. Klapper: X-ray diffraction topography: Application to crystal growth and plastic deformation. In: *X-Ray and Neutron Dynamical Diffraction: Theory and Applications*, Proc. NATO ASI, Erice 1996, NATO Science Series B, Physics Vol. 357, ed. by A. Authier, S. Logomarsino, B.K. Tanner (Plenum Press, New York 1996) p. 167–177

- 4.10 H. Klapper: Structural defects and methods of their detection. In: *Materials Science Forum*, Vol. 276–277, ed. by R. Fornari, C. Paorici (Trans Tech, Switzerland 1998) pp. 291–306
- 4.11 H. Klapper: Generation and propagation of dislocations during crystal growth, *Mater. Chem. Phys.* **66**, 101–109 (2000)
- 4.12 S. Zerfoss, S.I. Slawson: Origin of authigenic inclusions in synthetic crystals, *Am. Mineral.* **41**, 598–607 (1956)
- 4.13 G. Laemmlein: Sekundäre Flüssigkeitseinschlüsse in Mineralien, *Z. Kristallogr.* **71**, 237–256 (1929), in German
- 4.14 A.R.J. de Kock: Effect of growth conditions on semiconductor crystal quality. In: *Crystal Growth and Materials (ECCG-1 Zürich)*, ed. by E. Kaldis, H.J. Scheel (North Holland, Amsterdam 1976) pp. 661–703
- 4.15 A.A. Chernov, D.E. Temkin: Capture of inclusions in crystal growth. In: *1976 Crystal Growth and Materials (ECCG-1 Zürich)*, ed. by E. Kaldis, H.J. Scheel (North Holland, Amsterdam 1977) pp. 4–77, esp. 53–54
- 4.16 V.Y. Khaimov-Mal'kov: (a) The thermodynamics of crystallisation pressure; (b) Experimental measurement of crystallization pressure; (c) The growth conditions of crystals in contact with large obstacles. In: *Growth of Crystals*, Vol. 2, ed. A.V. Shubnikov, N.N. Sheftal (Consultants Bureau Inc., New York 1959) pp. 3–13 (a), 14–19 (b), 20–28 (c)
- 4.17 N. Zaitseva, J. Atherton, R. Rozsa, L. Carman, I. Smol'sky, M. Runkel, R. Ryon, L. James: Design and benefits of continuous filtration in rapid growth of large KDP and DKDP crystals, *J. Cryst. Growth* **197**, 911–920 (1999)
- 4.18 M.O. Kliia, I.G. Sokolova: The absorption of droplets of emulsion by a growing crystal during crystallization from solutions, *Sov. Phys. Crystallogr.* **3**, 217–221 (1958)
- 4.19 G. Wulff: Zur Frage der Geschwindigkeit des Wachstums und der Auflösung der Kristallflächen, *Z. Kristallogr.* **34**, 449–530 (1901), esp. 512–530, in German
- 4.20 R.F. Strickland–Constable: *Kinetics and Mechanisms of Crystallisation* (Academic, London, New York 1968) pp. 76–84
- 4.21 P. Bennema: Generalized Herring treatment of the equilibrium form. In: *Crystal growth: An introduction*, North-Holland Series in Crystal Growth I, ed. by P. Hartman (North-Holland, Amsterdam 1973), pp. 342–357
- 4.22 C. Herring: Some theorems on the free energies of crystal surfaces, *Phys. Rev.* **82**, 87–93 (1951)
- 4.23 C. Herring: The use of classical macroscopic concepts in surface energy problems. In: *Structure and Properties of Solid Surfaces*, ed. by R.G. Gromer, C.S. Smith (University of Chicago Press, Chicago 1953) pp. 5–72
- 4.24 W. Schnoor: Über das Wachstum von Auflösungskörpern und Kugeln aus Steinsalz, *Z. Kristallogr.* **68**, 1–14 (1928), in German
- 4.25 H.E. Buckley: *Crystal Growth* (Wiley, London, New York 1961)
- 4.26 R. Janssen–van Rosmalen, W.H. van der Linden, E. Dobinga, D. Visser: The influence of the hydrodynamic environment on the growth and the formation of liquid inclusions in large potassium hydrogen phosphate crystals, *Krist. Tech.* **13**, 17–28 (1978)
- 4.27 A. Faber: *Röntgentopographische Untersuchungen von Wachstumsstörungen durch alternierende Temperaturgradienten im Kali-Alaun. Studienarbeit* (Inst. f. Kristallographie, RWTH Aachen 1980), in German
- 4.28 W.M. Vetter, H. Totsuka, M. Dudley, B. Kahr: The perfection and defect structures of organic hourglass inclusion K_2SO_4 crystals, *J. Cryst. Growth* **241**, 498–506 (2002)
- 4.29 B. Kahr, R.W. Guernsey: Dyeing crystals, *Chem. Rev.* **101**, 893–953 (2001)
- 4.30 B. Kahr, L. Vasquez: Painting crystals, *Cryst. Eng. Commun.* **4**, 514–516 (2002)
- 4.31 A.A. Chernov, G.Y. Kuznetsov, I.L. Smol'skii, V.N. Rozhanski: Hydrodynamic effects during ADP growth from aqueous solutions in the kinetic regime, *Sov. Phys. Crystallogr.* **31**, 705–709 (1986)
- 4.32 R. Janssen–van Rosmalen, P. Bennema: The role of hydrodynamics and supersaturation in the formation of fluid inclusions in KDP, *J. Cryst. Growth* **42**, 224–227 (1977)
- 4.33 W.J.P. van Enckevort, R. Janssen–van Rosmalen, H. Klapper, W.H. van der Linden: Growth phenomena of KDP crystals in relation to the internal structure, *J. Cryst. Growth* **60**, 67–78 (1982)
- 4.34 N.P. Zaitseva, I.L. Smol'sky, L.N. Rashkovich: Study of rapid growth of KDP crystals by temperature lowering, *Sov. Phys. Crystallogr.* **36**, 113–115 (1991)
- 4.35 N.P. Zaitseva, J.J. De Yoreo, M.R. Dehaven, R.L. Vital, K.E. Montgomery, M. Richardson, L.J. Atherton: Rapid growth of large-scale (40–55 cm) KH_2PO_4 crystals, *J. Cryst. Growth* **180**, 255–262 (1997)
- 4.36 N. Zaitseva, L. Carman: Rapid Growth of KDP-type Crystals, *Progr. Cryst. Growth Charact. Mater.* **43**, 1–118 (2001)
- 4.37 I. Smol'sky, J.J. de Yoreo, N.P. Zaitseva, J.D. Lee, T.A. Land, E.B. Rudneva: Oriented liquid inclusions in KDP crystals, *J. Cryst. Growth* **169**, 741–745 (1996)
- 4.38 E. Scandale, A. Zarka: Sur l'origine des canaux dans les cristaux, *J. Appl. Cryst.* **15**, 417–422 (1982), in French
- 4.39 X.R. Huang, M. Dudley, W.M. Vetter, W. Huang, S. Wang, C.H. Carter Jr.: Direct evidence of micropipe-related pure superscrew dislocations in SiC, *Appl. Phys. Lett.* **74**, 353–355 (1999)

- 4.40 J. Heindl, H.P. Strunk, V.D. Heydemann, G. Pensl: Micropipes: Hollow tubes in silicon carbide, *Phys. Status Solidi (a)* **162**, 251–262 (1997)
- 4.41 H.P. Strunk, W. Dorsch, J. Heindl: The nature of micropipes in 6H-SiC single crystals, *Adv. Eng. Mater.* **2**, 386–389 (2000)
- 4.42 Th. Scheffen-Lauenroth: *Czochralski-Züchtung und Perfektion organischer Kristalle*. Diplomarbeit (Inst. f. Kristallographie, RWTH Aachen 1983), in German
- 4.43 E. Roedder: Fluid inclusions. In: *Reviews in Mineralogy*, Vol. 12, ed. by P.H. Ribbe (Mineralogical Society of America, BookCrafters, Inc., Chelsea 1984)
- 4.44 W. Bardsley, D.T.J. Hurle, M. Hart, A.R. Lang: Structural and chemical inhomogeneities in germanium single crystals grown under conditions of constitutional supercooling, *J. Cryst. Growth* **49**, 612–690 (1980)
- 4.45 J.E. Gegusin, A.S. Dziyuba: Gas evolution and the capture of gas bubbles at the crystallization front when growing crystals from the melt, *Sov. Phys. Crystallogr.* **22**, 197–199 (1977)
- 4.46 M. Göbbels: *Züchtung organischer Molekülkristalle aus entgasten unterkühlten Schmelzen*. Studienarbeit (Inst. f. Kristallographie, RWTH Aachen), in German
- 4.47 G. Engel, H. Klapper, P. Krempf, H. Mang: Growth-twinning in quartz-homeotypic gallium orthophosphate crystals, *J. Cryst. Growth* **94**, 597–606 (1989)
- 4.48 I.L. Smolsky, A.E. Voloshin, N.P. Zaitseva, E.B. Rudneva, H. Klapper: X-ray topographic study of striation formation in layer growth of crystals from solution, *Philos. Trans. Math. Phys. Eng. Sci.* **357**, 2631–2649 (1999)
- 4.49 T. Nishinaga, P. Ge, C. Huo, J. He, T. Nakamura: Melt growth of striation and etch-pit free GaSb under microgravity, *J. Cryst. Growth* **174**, 96–100 (1997)
- 4.50 P. Dold: Czochralski growth of doped germanium with an applied rotating magnetic field, *Cryst. Res. Technol.* **38**, 659–668 (2003)
- 4.51 P. Rudolph: Travelling magnetic fields applied to bulk crystal growth from the melt: The step from basic research to industrial scale, *J. Cryst. Growth* **310**, 1298–1306 (2008)
- 4.52 H. Scheel: Theoretical and experimental solutions of the striation problem. In: *Crystal Growth Technology*, ed. by H.J. Scheel, T. Fukuda (Wiley, New York 2003), Chap. 4
- 4.53 N. Herres, A.R. Lang: X-ray topography of natural beryl using synchrotron and conventional sources, *J. Appl. Cryst.* **16**, 47–56 (1983)
- 4.54 H. Klapper: Röntgentopographische Untersuchungen von Gitterstörungen in Benzil-Einkristallen, *J. Cryst. Growth* **10**, 13–25 (1971), in German
- 4.55 K. Maeda, A. Sonoda, H. Miki, Y. Asakuma, K. Fukui: Synergy of organic dyes for KDP crystal growth, *Cryst. Res. Technol.* **39**, 1006–1013 (2004)
- 4.56 I.L. Smol'skii, A.A. Chernov, G.Y. Kutznetsov, V.F. Parvov, V.N. Rozhanskii: Vicinal sectoriality in growth sectors of {011} faces of ADP crystals, *Sov. Phys. Crystallogr.* **30**, 563–567 (1985)
- 4.57 I.L. Smol'skii, N.P. Zaitseva: Characteristic defects and imperfections in KDP crystals grown at high rates. In: *Growth of Crystals*, Vol. 19, ed. by E.I. Givargizov, S.A. Grinberg (Plenum, New York 1995) pp. 173–185
- 4.58 J.J. De Yoreo, T.A. Land, I.N. Rashkovich, T.A. Onischenko, J.D. Lee, O.V. Monovskii, N.P. Zaitseva: The effect of dislocation cores on growth hillock vicinality and normal growth rates of KDP {101} surfaces, *J. Cryst. Growth* **182**, 442–460 (1997)
- 4.59 A.G. Shtukenberg, Y.O. Punin, E. Haegele, H. Klapper: On the origin of inhomogeneity of anomalous birefringence in mixed crystals: An example of alums, *Phys. Chem. Miner.* **28**, 665–674 (2001)
- 4.60 H. Klapper, R.A. Becker, D. Schmiemann, A. Faber: Growth-sector boundaries and growth-rate dispersion in potassium alum crystals, *Cryst. Res. Technol.* **37**, 747–757 (2002)
- 4.61 W.J.P. Van Enckevort, H. Klapper: Observation of growth steps with full and half unit-cell heights on the {001} faces of $\text{NiSO}_4 \cdot 6\text{H}_2\text{O}$ in relation to the defect structure, *J. Cryst. Growth* **80**, 91–103 (1987)
- 4.62 H. Kanda, M. Akaishi, S. Yamaoka: Impurity distribution among vicinal slopes of growth spirals developing on the {111} faces of synthetic diamonds, *J. Cryst. Growth* **108**, 421–424 (1991)
- 4.63 J.J. De Yoreo, Z.U. Rek, N.P. Zaitseva, B.W. Woods: Sources of optical distortion in rapidly grown crystals of KH_2PO_4 , *J. Cryst. Growth* **166**, 291–297 (1996)
- 4.64 K. Fujioka, S. Matsuo, T. Kanabe, H. Fujita, M. Nakajatsuka: Optical properties of rapidly grown KDP crystals improved by thermal conditioning, *J. Cryst. Growth* **181**, 265–271 (1997)
- 4.65 N. Zaitseva, L. Carman, I. Smolsky, R. Torres, M. Yan: The effect of impurities and supersaturation on the rapid growth of KDP crystals, *J. Cryst. Growth* **204**, 512–524 (1999)
- 4.66 T. Bullard, M. Kurimoto, S. Avagyan, S.H. Jang, B. Kahr: Luminescence imaging of growth hillocks in potassium hydrogen phthalate, *ACA Transaction* **39**, 62–72 (2004)
- 4.67 A.R. Lang, V.F. Miuskov: Dislocations and fault surfaces in synthetic quartz, *J. Appl. Phys.* **38**, 2477–2483 (1967), esp. p. 2482
- 4.68 A.R. Lang, V.F. Miuskov: Defects in natural and synthetic quartz. In: *Growth of Crystals*, Vol. 7, ed. by N.N. Sheftal (Consultants Bureau, New York 1969) pp. 112–123, esp. p. 122
- 4.69 T. Hahn, H. Klapper: Twinning of crystals. In: *International Tables for Crystallography*, Vol. D (Kluwer Academic, Dordrecht 2003) pp. 393–448
- 4.70 W. Schmidt, R. Weiss: Dislocation propagation in Czochralski grown gadolinium gallium garnet, *J. Cryst. Growth* **43**, 515–525 (1978)

- 4.71 B. Cockayne, J.M. Roslington, A.W. Vere: Microscopic strain in faceted regions of garnet crystals, *J. Mater. Sci.* **8**, 382–384 (1973)
- 4.72 W.T. Stacy: Dislocations, facet regions and grown striations in garnet substrates and layers, *J. Cryst. Growth* **24/25**, 137–143 (1974)
- 4.73 A. Shtukenberg, Y. Punin, B. Kahr: Optically anomalous crystals. In: *Springer Series in Solid State Science* (Springer, Berlin, Heidelberg 2007)
- 4.74 R. von Brauns: *Die optischen Anomalien der Krystalle* (S. Hirzel, Leipzig 1891), in German
- 4.75 B. Kahr, J.M. McBride: Optically anomalous crystals, *Angew. Chem. Int. Ed.* **31**, 1–26 (1992)
- 4.76 H. Klapper: Reconstruction of the growth history of crystals by analysis of growth defects. In: *Crystal Growth of Technologically Important Electronic Materials*, ed. by K. Byrappa, T. Ohachi, H. Klapper, R. Fornari (Allied Publishers PVT, New Delhi 2003)
- 4.77 J.N. Sherwood, T. Shiripathi: Evidence for the role of pure edge dislocations in crystal growth, *J. Cryst. Growth* **88**, 358–364 (1988)
- 4.78 H.L. Bhat, R.I. Ristic, J.N. Sherwood, T. Shiripathi: Dislocation characterization in crystal of potash alum grown by seeded solution growth and conditions of low supersaturation, *J. Cryst. Growth* **121**, 709–716 (1992)
- 4.79 R.I. Ristic, B. Shekunov, J.N. Sherwood: Long and short period growth rate variations in potash alum, *J. Cryst. Growth* **160**, 330–336 (1996)
- 4.80 E. Billig: Some defects in crystals grown from the melt I: Defects caused by thermal stresses, *Proc. R. Soc. Lond. A* **235**, 37–55 (1956)
- 4.81 V.L. Indenbom: Ein Beitrag zur Entstehung von Spannungen und Versetzungen beim Kristallwachstum, *Kristall und Technik* **14**, 493–507 (1979), in German
- 4.82 P. Möck: Comparison of experiments and theories for plastic deformation in thermally processed GaAs wafers, *Cryst. Res. Technol.* **35**, 529–540 (2000)
- 4.83 P. Rudolph: Dislocation cell structures in melt-grown semiconductor compound crystals, *Cryst. Res. Technol.* **40**, 7–20 (2005)
- 4.84 Y.M. Fishman: X-ray topographic study of the dislocations produced in potassium dihydrogen phosphate crystals by growth from solution, *Sov. Phys. Crystallogr.* **17**, 524–527 (1972)
- 4.85 G. Dhanaraj, M. Dudley, D. Bliss, M. Callahan, M. Harris: Growth and process induced dislocations in zinc oxide crystals, *J. Cryst. Growth* **297**, 74–79 (2006)
- 4.86 G. Neuroth: Der Einfluß von Einschlufbildung und mechanischer Verletzung auf das Wachstum und die Perfektion von Kristallen. Ph.D. Thesis (University of Bonn, Bonn 1996), (Shaker, Aachen 1996), in German
- 4.87 A.J. Forty: Direct observation of dislocations in crystals, *Adv. Phys.* **3**, 1–25 (1954)
- 4.88 G.G. Lemmlein, E.D. Dukova: Formation of screw dislocations in the growth process of a crystal, *Sov. Phys. Crystallogr.* **1**, 269–273 (1956)
- 4.89 M.I. Kozlovskii: Formation of screw dislocations in the growth of a crystal around solid particles, *Sov. Phys. Crystallogr.* **3**, 205–211 (1958/60)
- 4.90 M.I. Kozlovskii: Formation of screw dislocations at the junction of two layers spreading over the surface of a crystal, *Sov. Phys. Crystallogr.* **3**, 236–238 (1958/60)
- 4.91 M. Dudley, X.R. Huang, W. Huang, A. Powell, S. Wang, P. Neudeck, M. Skowronski: The mechanism of micropipe nucleation at inclusions in silicon carbide, *Appl. Phys. Lett.* **75**, 784–786 (1999)
- 4.92 W.T. Read: *Dislocations in Crystals* (McGraw-Hill, New York 1953) p. 47
- 4.93 D. Hull: *Introduction to Dislocations*, Vol. 2 (Pergamon, Oxford 1975) pp. 229–235
- 4.94 J.P. Hirth, J. Lothe: *Theory of Dislocations* (McGraw-Hill, New York 1968)
- 4.95 J. Weertmann, J.R. Weertmann: *Elementary Dislocation Theory* (Macmillan, New York 1964) p. 137
- 4.96 H. Klapper: Vorzugsrichtungen eingewachsener Versetzungen in lösungsgezüchteten Kristallen. Habilitation Thesis, (Technical University (RWTH) Aachen 1975), in German
- 4.97 J. Lothe: Force on dislocations emerging at free surfaces, *Phys. Nor.* **2**, 154–157 (1967)
- 4.98 J.B. Eshelby, W.T. Read, W. Shockley: Anisotropic elasticity with applications to dislocation theory, *Acta Metall.* **1**, 251–259 (1953)
- 4.99 H. Klapper, Y.M. Fishman, V.G. Lutsau: Elastic energy and line directions of grown-in dislocations in KDP crystals, *Phys. Status Solidi (a)* **21**, 115–121 (1974)
- 4.100 H. Klapper: Elastische Energie und Vorzugsrichtungen geradliniger Versetzungen in aus der Lösung gewachsenen organischen Kristallen. I. Benzil, *Phys. Status Solidi (a)* **14**, 99–106 (1972), in German
- 4.101 H. Klapper: Elastische Energie und Vorzugsrichtungen geradliniger Versetzungen in aus der Lösung gewachsenen organischen Kristallen. II. Thioharnstoff, *Phys. Status Solidi (a)* **14**, 443–451 (1972), in German
- 4.102 H. Klapper: Röntgentopographische Untersuchungen am Lithiumformiat-Monohydrat, *Z. Naturforsch.* **28a**, 614–622 (1973), in German
- 4.103 H. Klapper, H. Küppers: Directions of dislocation lines in crystals of ammonium hydrogen oxalate hemihydrate grown from solution, *Acta Cryst.* **A 29**, 495–503 (1973), (correction: read $K/\cos\alpha$ instead of $K\cos\alpha$)
- 4.104 D.F. Croxall, R.C.C. Ward, C.A. Wallace, R.C. Kell: Hydrothermal growth and investigation of Li-doped zinc oxide crystals of high purity and perfection, *J. Cryst. Growth* **22**, 117–124 (1974)
- 4.105 U. Alter, G. Voigt: Direction change of dislocations on passing a growth-sector boundary in quartz crystals, *Cryst. Res. Technol.* **19**, 1619–1623 (1984)

- 4.106 A. Sakai, H. Sunakawa, A. Usui: Defect structure in selectively grown GaN films with low threading dislocation density, *Appl. Phys. Lett.* **71**, 2259–2261 (1997)
- 4.107 Z. Liliental-Weber, M. Benamara, W. Snider, J. Washburn, J. Park, P.A. Grudowski, C.J. Eiting, R.D. Dupuis: TEM study of defects in laterally overgrown GaN layers, *MRS Internet J. Nitride Semicond. Res.* **4s1**, 4.6 (1999)
- 4.108 H. Sunakawa, A. Kimura, A. Usui: Self-organized propagation of dislocations in GaN films during epitaxial lateral overgrowth, *Appl. Phys. Lett.* **76**, 442–444 (2000)
- 4.109 P. Venégués, B. Beaumont, V. Bousquet, M. Vaille, P. Gibart: Reduction mechanisms of defect densities in GaN using one- or two-step epitaxial lateral overgrowth methods, *J. Appl. Phys.* **87**, 4175–4181 (2000)
- 4.110 S. Gradezcek, P. Stadelman, V. Wagner, M. Illegems: Bending of dislocations in GaN during epitaxial lateral overgrowth, *Appl. Phys. Lett.* **85**, 4648–4650 (2004)
- 4.111 J. Bai, J.-S. Park, Z. Cheng, M. Curtin, B. Adekore, M. Carroll, A. Lochtefeld, M. Dudley: Study of the defect elimination mechanism in aspect ratio trapping Ge growth, *Appl. Phys. Lett.* **90**, 101902 (2007)
- 4.112 N. Zaitseva, L. Carman, I. Smolsky: Habit control during rapid growth of KDP and DKDP crystals, *J. Cryst. Growth* **241**, 363–373 (2002)
- 4.113 G.R. Ester, P.J. Halfpenny: An investigation of growth-induced defects in crystals of potassium hydrogen phthalate, *Philos. Mag. A* **79**, 593–608 (1999)
- 4.114 G.R. Ester, R. Price, P.J. Halfpenny: The relationship between crystal growth and defect structure: A study of potassium hydrogen phthalate using x-ray topography and atomic force microscopy, *J. Phys. D: Appl. Phys.* **32**, A128–A132 (1999)
- 4.115 G. Neuroth, H. Klapper: Dislocation reactions in Czochralski-grown salol crystals, *Z. Kristallogr.* **209**, 216–220 (1994)
- 4.116 I.L. Smolsky, E.B. Rudneva: Effect of the surface morphology on the grown-in dislocation orientations in KDP crystals, *Phys. Status Solidi (a)* **141**, 99–107 (1994)
- 4.117 T. Watanabe, K. Izumi: Growth and perfection of tetraoxane crystals, *J. Cryst. Growth* **46**, 747–756 (1979)
- 4.118 K. Izumi: Lattice defects in normal alcohol crystals, *Jpn. J. Appl. Phys.* **16**, 2103–2108 (1977)
- 4.119 H. Klapper: Röntgentopographische Untersuchungen der Defektstrukturen im Thioharnstoff, *J. Cryst. Growth* **15**, 281–287 (1972), in German
- 4.120 F.C. Frank: The influence of dislocations on crystal growth, *Disc. Faraday Soc.* **5**, 48–54 (1949), and 66–68
- 4.121 C.F. Frank: Crystal growth and dislocations, *Adv. Phys.* **1**, 91–109 (1952)
- 4.122 W.K. Burton, N. Cabrera, F.C. Frank: The growth of crystals and the equilibrium structure of their surfaces, *Philos. Trans. R. Soc. Lond. A* **243**, 299–358 (1951), especially Part II, pp. 310–323
- 4.123 H.P. Strunk: Edge dislocation may cause growth spirals, *J. Cryst. Growth* **160**, 184–185 (1996)
- 4.124 N.-B. Ming: Defect mechanism of crystal growth and their kinetics, *J. Cryst. Growth* **128**, 104–112 (1993)
- 4.125 E. Bauser, H. Strunk: Analysis of dislocations creating monomolecular growth steps, *J. Cryst. Growth* **51**, 362–366 (1981)
- 4.126 F.C. Frank: "Edge" dislocations as crystal growth sources, *J. Cryst. Growth* **51**, 367–368 (1981)
- 4.127 L.J. Gilling, B. Dam: A "rough heart" model for "edge" dislocations which act as persistent growth sources, *J. Cryst. Growth* **67**, 400–403 (1984)
- 4.128 H. Gottschalk, G. Patzer, H. Alexander: Stacking-fault energy and ionicity of cubic III–V compounds, *Phys. Status Solidi (a)* **45**, 207–217 (1978)
- 4.129 T.W. Donnelly: Kinetic considerations in the genesis of growth twinning, *Am. Mineral.* **52**, 1–12 (1967)
- 4.130 H. Carstens: Kinetic consideration in the genesis of growth twinning: A discussion, *Am. Mineral.* **53**, 342–344 (1968)
- 4.131 T.W. Donnelly: Kinetic consideration in the genesis of growth twins: A reply, *Am. Mineral.* **53**, 344–346 (1968)
- 4.132 V. Janovec, T. Hahn, H. Klapper: Twinning and domain structures. In: *International Tables for Crystallography*, Vol. D (Kluwer, Dordrecht 2003) pp. 377–378
- 4.133 V. Janovec, J. Přívratská: Domain structures. In: *International Tables for Crystallography*, Vol. D (Kluwer, Dordrecht 2003) pp. 449–505
- 4.134 F.D. Bloss: *Crystallography and Crystal Chemistry* (Rinehart & Winston, New York 1971) pp. 324–338
- 4.135 C. Giacobozzo (Ed.): *Fundamentals of Crystallography* (University Press, Oxford 1992) pp. 80–87, and 133–140
- 4.136 C. Frondel: Silica minerals. In: *The System of Mineralogy*, Vol. III, 7th edn. (Wiley, New York 1962) pp. 75–99
- 4.137 J.W. Faust Jr., H.F. John: The growth of semiconductor crystals from solution using the twin-plane reentrant-edge mechanism, *J. Phys. Chem. Solids* **25**, 1407–1415 (1964)
- 4.138 R. Jagannathan, R.V. Mehta, J.A. Timmons, D.L. Black: Anisotropic growth of twinned cubic crystals, *Phys. Rev. B* **48**, 13261–13265 (1993)
- 4.139 R. Jagannathan, R.V. Mehta, J.A. Timmons, D.L. Black: Reply to comment on anisotropic growth of twinned cubic crystals, *Phys. Rev. B* **51**, 8655 (1995), following the comment by B.W. van de Waal, *Phys. Rev. B* **51**, 8653–8654 (1995)
- 4.140 G. Bögels, T.M. Pot, H. Meekes, P. Bennema, D. Bollen: Side-face structure for lateral growth of tabular silver bromide crystals, *Acta Cryst. A* **53**, 84–94 (1997)
- 4.141 G. Bögels, H. Meekes, P. Bennema, D. Bollen: The role of {100} side faces for lateral growth of tabular

- silver bromide crystals, *J. Cryst. Growth* **191**, 446–456 (1998)
- 4.142 G. Bögers, J.G. Buijnsters, S.A.C. Verhaegen, H. Meekes, P. Bennema, D. Bollen: Morphology and growth mechanism of multiply twinned AgBr and AgCl needle crystals, *J. Cryst. Growth* **203**, 554–563 (1999)
- 4.143 C.A. Wallace, E.A.D. White: The morphology and twinning of solution-grown corundum crystals. In: *Crystal Growth*, ed. by H.S. Peiser (Pergamon, Oxford 1967) pp. 431–435, supplement to *Phys. Chem. Solids*
- 4.144 M. Senechal: The genesis of growth twins, *Sov. Phys. Crystallogr.* **25**, 520–524 (1980)
- 4.145 H. Hofmeister: Forty years study of fivefold twinned structures in small particles and thin films, *Cryst. Res. Technol.* **33**, 3–25 (1998), especially Sect. 4
- 4.146 I. Sunagawa, L. Taijing, V.S. Balitsky: Generation of Brazil and Dauphiné twins in synthetic amethyst, *Phys. Chem. Miner.* **17**, 320–325 (1990)
- 4.147 A.C. MacLaren, D.R. Pitkethly: The twinning microstructure and growth of amethyst quartz, *Phys. Chem. Miner.* **8**, 128–135 (1982)
- 4.148 H. Klapper, T. Hahn, S.J. Chung: Optical, pyroelectric and x-ray topographic studies of twin domains and twin boundaries in KLiSO_4 , *Acta Cryst. B* **43**, 147–159 (1987)
- 4.149 M.J. Buerger: The genesis of twin crystals, *Am. Mineral.* **30**, 469–482 (1945)
- 4.150 P. Hartmann: On the morphology of growth twins, *Z. Kristallogr.* **107**, 225–237 (1956)
- 4.151 R. Docherty, A. El-Korashi, H.-D. Jennissen, H. Klapper, K.J. Roberts, T. Scheffen-Lauenroth: Synchrotron Laue topographic studies of pseudo-hexagonal twinning, *J. Appl. Cryst.* **21**, 406–415 (1988)
- 4.152 N.-B. Ming, I. Sunagawa: Twin lamellae as possible self-perpetuating steps sources, *J. Cryst. Growth* **87**, 13–17 (1988)
- 4.153 N.-B. Ming, K. Tsukamoto, I. Sunagawa, A.A. Chernov: Stacking faults as self-perpetuating step sources, *J. Cryst. Growth* **91**, 11–19 (1988)
- 4.154 H. Li, X.-D. Peng, N.-B. Ming: Re-entrant corner mechanism of fcc crystal growth of A-type twin lamella: The Monte-Carlo simulation approach, *J. Cryst. Growth* **139**, 129–133 (1994)
- 4.155 H. Li, N.-B. Ming: Growth mechanism and kinetics on re-entrant corner and twin lamellae in a fcc crystal, *J. Cryst. Growth* **152**, 228–234 (1995)
- 4.156 R.-W. Lee, U.-J. Chung, N.M. Hsang, D.-Y. Kim: Growth process of the ridge-trough faces of a twinned crystal, *Acta Cryst. A* **61**, 405–410 (2005)
- 4.157 R. Boistelle, D. Aquilano: Interaction energies at twin boundaries and effects of the dihedral re-entrant and salient angles on the grown morphology of twinned crystals, *Acta Cryst. A* **34**, 406–413 (1978)
- 4.158 I.M. Dawson: The study of crystal growth with the electron microscope II. The observation of growth steps in the paraffin n-hexane, *Proc. R. Soc. Lond. A* **214**, 72–79 (1952)
- 4.159 R.S. Wagner: On the growth of Ge dendrites, *Acta Metal.* **8**, 57–60 (1960)
- 4.160 D.R. Hamilton, R.G. Seidensticker: Propagation mechanism of germanium dendrites, *J. Appl. Phys.* **31**, 1165–1168 (1960)
- 4.161 B. van de Waal: Cross-twinning model of fcc crystal growth, *J. Cryst. Growth* **158**, 153–165 (1996)
- 4.162 G. Roth, D. Ewert, G. Heger, M. Hervieu, C. Michel, B. Raveau, B. D'Yvoire, A. Revcolevschi: Phase transformation and microtwinning in crystals of the high-Tc superconductor $\text{YBa}_2\text{Cu}_3\text{O}_{8-x}$, *Z. Phys. B* **69**, 21–27 (1987)
- 4.163 I.S. Zheludev: Crystallography and spontaneous polarisation. In: *Physics of Crystalline Dielectrics*, Vol 1 (Plenum Press, New York 1971)
- 4.164 M. Nakatsuka, K. Fujioka, T. Kanabe, H. Fujita: Rapid growth of over 50 mm/day of water-soluble KDP crystal, *J. Cryst. Growth* **171**, 531–537 (1997)
- 4.165 H. Klapper, I.L. Smolsky, A.E. Haegeler: Rapid growth from solution. In: *Crystal Growth of Technologically Important Electronic Materials*, ed. by K. Byrappa, T. Ohachi, H. Klapper, R. Fornari (Allied Publishers PVT, New Delhi 2003)

5. Single Crystals Grown Under Unconstrained Conditions

Ichiro Sunagawa

Based on detailed investigations on morphology (evolution and variation in external forms), surface microtopography of crystal faces (spirals and etch figures), internal morphology (growth sectors, growth banding and associated impurity partitioning) and perfection (dislocations and other lattice defects) in single crystals, we can deduce how and by what mechanism the crystal grew and experienced fluctuation in growth parameters through its growth and post-growth history under unconstrained condition. The information is useful not only in finding appropriate way to growing highly perfect and homogeneous single crystals, but also in deciphering letters sent from the depth of the Earth and the Space. It is also useful in discriminating synthetic from natural gemstones. In this chapter, available methods to obtain molecular information are briefly

5.1	Background	134
5.2	Smooth and Rough Interfaces: Growth Mechanism and Morphology	136
5.3	Surface Microtopography	139
5.4	Growth Forms of Polyhedral Crystals	143
5.5	Internal Morphology	146
5.6	Perfection of Single Crystals	152
	References	156

summarized, and actual examples to demonstrate the importance of this type of investigations are selected from both natural minerals (diamond, quartz, hematite, corundum, beryl, phlogopite) and synthetic crystals (SiC, diamond, corundum, beryl).

The morphology, perfection, and homogeneity of single crystals and the textures of polycrystalline aggregates vary depending on their growth conditions and are determined by the atomic process and mechanism of crystal growth, which occurs exclusively at the solid-liquid interface. Understanding how crystals grow at the atomic level is the key to understanding how and why single crystals can have various morphologies and degrees of perfection and homogeneity depending on their growth parameters. This will provide essential information for both the fundamentals and the applications of crystal growth. Based on such understanding, we may obtain useful hints to develop appropriate methods for the growth of single crystals with desired perfection and homogeneity. We may also decipher how and under what conditions crystals of terrestrial and planetary minerals, as well as biominerals, grew and what sort of changes they experienced, based on this understanding. The purpose of this chapter is to summarize presently available understanding of why and how the morphol-

ogy, perfection, and homogeneity of single crystals are determined by their growth process. Since crystals growing in dilute multicomponent solution phases or by the chemical vapor transport (CVT) process show much wider variations in these properties than crystals grown in simpler monocomponent melt phase or by the physical vapor transport (PVT) process, actual examples to demonstrate how morphology, perfection, and homogeneity are controlled during growth processes will be selected from the former crystals, grown under unconstrained conditions, such as natural minerals or synthetic crystals whose growth process cannot be traced in situ.

Growth of crystals takes place uniquely at the solid-liquid interface, and the growth mechanism and growth rate versus driving force relations are determined by the structure of this interface, i. e., whether the interface is smooth or rough, and the roughening transition of smooth interfaces depending on the growth parameters. The process and mechanism of crystal growth at

the atomic level are recorded in the surface microtopography of crystal faces. A surface microtopograph of as-grown faces provides information on the atomic processes of crystal growth. By examining this surface, the external morphology of crystals, i.e., the evolution of the bulk morphology of three-dimensional (3-D) crystals from polyhedral, to hopper, to dendritic forms (habitus and tracht) is determined. Also the origin of malformed morphologies of two-dimensional (2-D, epitaxial) and one-dimensional (1-D, whisker) crystals may be understood. Similarly, through growth

process, various internal morphologies such as growth sectors, intrasectorial sectors, growth banding, imperfections (dislocation distribution), and inhomogeneities (element partitioning) can be determined and recorded as internal morphologies in nearly perfect single crystals. By applying sensitive methods to visualize or measure perfection and heterogeneity in single crystals, we may obtain useful information about how a single crystal grows and how its perfection and homogeneity are determined, and the whole growth history may be analyzed based on this information.

5.1 Background

Single crystals of various compounds have been synthesized in various sizes and forms, ranging from millimeter to meter scale in size, and from 3-D bulk, to 2-D thin film, to 1-D whisker in form, to meet corresponding requirements for scientific or industrial purposes. Bulk single crystals of large sizes are synthesized to obtain slices for semiconductor, optoelectronic, magnetic, telecommunication, and sensor devices, or to obtain synthetic gemstones, whereas millimeter size is sufficient for protein crystals for crystal structure analysis. Recent interest in nanotechnology has expanded the size ranges down to nanometer scale, and form to include hierarchical structures.

Since the size, form, perfection, and homogeneity of single crystals are essential factors for their use, various growth techniques have been designed and developed to obtain single crystals of appropriate size yet with desired form, perfection, and homogeneity, including:

1. Selection of appropriate ambient phase (melt, solution, vapor), i.e., selection of condensed or diluted phase, and of suitable solvent components
2. Homogenization of ambient phase by internal stirring or external rotation, or by applying magnetic or low gravity field
3. Using seed or substrate crystal to suppress unnecessary nucleation and control crystallographic orientation
4. Controlling temperature or concentration to realize a steady-state yet high rate of growth
5. Minimizing dislocation generation by selection and treatment of seed or by changing boule shapes during growth, or by other techniques.

In the synthesis of Si single-crystal boules larger than a few tens of centimeters across and longer

than 1 m, techniques to control dislocation densities have been successfully realized to obtain so-called dislocation-free Si crystals. In the syntheses of compound semiconductors, ammonium dihydrogen phosphate $\text{NH}_4\text{H}_2\text{PO}_4$ (ADP), potassium dihydrogen phosphate KH_2PO_4 (KDP) or quartz single crystals, further efforts are still required to reach the same level as in Si crystals for the realization of *dislocation-free* crystals, although large-scale mass-production techniques and techniques to grow meter-size crystals are already well established. Polymer and protein single crystals are still in the state of characterizing dislocations and understanding how they are generated, whereas in nanometer-sized ultrafine crystals, control of morphology and hierarchical structure is the present main interest.

Compared with previous efforts to understand the nature and origin of crystals and control dislocations, less effort has been invested in understanding and controlling the chemical homogeneity of single crystals, i.e., element partitioning in relation to growth kinetics. The Burton–Prim–Slichter (BPS) formula [5.1] describing the relation between element partitioning and growth kinetics, proposed half a century ago, still plays an important role in this respect. This problem is still fresh in terms of the synthesis of perfectly homogeneous single crystals in solution systems more complicated than for the simpler melt growth of Si crystal.

In contrast to synthetic crystals, single crystals of natural minerals grow under given geological environments and unconstrained conditions. Their growth and postgrowth histories vary depending on geological environments and processes. In the growth and postgrowth histories, conditions may fluctuate or abruptly

change, which modifies the morphology, perfection, and homogeneity of the crystal. Such variations and fluctuations are recorded within nearly perfect single crystals in the form of macromorphology (external forms), micromorphology (surface microtopography of crystal faces), and internal morphology (growth sectors, intrasectorial sectors, growth banding, the spatial distribution of lattice defects, and associated element partitioning). The morphological features, perfection, and homogeneity of single crystals of natural minerals, both terrestrial and extraterrestrial in origin, therefore provide the key to decipher how mineral crystals grew [5.2,3], as their perfection and homogeneity were determined during growth in ambient phases with complicated compositions under unconstrained conditions, provided that these can be visualized and characterized at the nm to μm scale. We have various sophisticated methods to characterize perfection and homogeneity within a nearly perfect single crystal. Nanometer-level information relating to growth mechanisms can be secured through surface microtopographic observations of crystal faces by means of various sensitive optical microscopy and interferometry techniques such as phase-contrast microscopy (PCM), phase-shifting microscopy (PSM), differential interference contrast microscopy (DICM), laser-beam scanning (LBS) microscopy, phase-shifting interferometry (PSI), and multiple-beam interferometry (MBI), as well as atomic force microscopy (AFM) and scanning tunneling microscopy (STM) [5.3, 4]. X-ray topography (XRT) is a powerful method to visualize the three-dimensional distribution of line and planar lattice defects, and micro-area x-ray fluorescence (MXRF), cathode-ray luminescence (CL), and laser-beam tomography (LBT) are useful characterization techniques to visualize the distribution of point defects and impurities in nearly perfect single crystals [5.3].

Information obtained through characterization of single crystals grown under unconstrained conditions provides useful background knowledge for the design of new techniques to control the perfection and homogeneity of synthetic single crystals, and also to distinguishing natural from synthetic crystals, since these crystals provide the full range of information relating to how imperfections and heterogeneities are generated and induced in single crystals during growth and their postgrowth history. To point out just one example demonstrating the importance of knowledge about the growth process of natural minerals in developing a new method for industrial purposes, we may men-

tion the concept of *epitaxy*. Growth of guest phase on host phase with a definite crystallographic relation is known from many examples of natural minerals, and later this relation was used to grow thin films of single crystals to prepare electronic devices, by either vapor- or liquid-phase growth.

Since the perfection and homogeneity of single crystals are both related to the mechanism, kinetics, and process of growth, which are reflected in the morphological features of the crystals, it is essential to understand how and why morphological variations occur on growing crystals. To this end, single crystals grown from solution phase and under unconstrained conditions provide more useful information than those formed in simpler melt or vapor phases (physical vapor transport, PVT, or physical vapor deposition, PVD) under constrained conditions. It is the purpose of this chapter to summarize the presently available knowledge on the morphology, perfection, and homogeneity of single crystals of mainly natural minerals, but also synthetic crystals whose growth process cannot be traced in situ, such as synthetic crystals grown in high-temperature solution, high-pressure high-temperature solution, hydrothermal solution, and by chemical vapor transport (CVT) method. We pay most attention to single crystals grown from the solution phase and by CVT method, since they represent crystals grown in multi-component and more complicated systems, and show all phenomena relating to crystal growth. Although large single crystals can be synthesized by methods using condensed melt phase, e.g., Czochralski, Verneuil, and Bridgman–Stockbarger methods, the solid–liquid interfaces in these synthesis are generally rougher than in the case of diluted solution or vapor growth, and thus morphological changes are less enhanced. In diluted solution and vapor growth, the solid–liquid interface is generally smoother than in condensed melt growth, leading to more variable morphological variations [5.3]. As compared with melt and PVT growth, solute–solvent interaction is involved in solution and CVT growth, thus providing additional information. We therefore purposely select crystals grown from solution and CVT, both natural and synthetic, to investigate the associated problems, although they are more complicated than those grown from pure melt or by PVT. Most crystal growth in nature, including crystallization in magma, pegmatite, and hydrothermal veins, as well as in regional and contact metamorphic rocks, can be regarded as solution or CVT growth [5.2, 3, 5]. There is no pure melt or PVT growth in natural crystallization.

5.2 Smooth and Rough Interfaces: Growth Mechanism and Morphology

Crystal growth takes place uniquely at solid–liquid interfaces. Depending on the atomic structure of the solid–liquid interface, the growth mechanisms and normal growth rate R versus driving force $\Delta\mu/(k_B T)$ relations are different, resulting in different morphology. The larger the R , the earlier the face disappears from the growing crystal. To nucleate and grow a crystal, a driving force must overcome the respective energy barrier. Throughout this chapter, the driving force is expressed in a general form by the chemical potential difference between solid and liquid phases $\Delta\mu/(k_B T)$. The phase with the larger chemical potential will have to diminish while the phase with the smaller chemical potential will grow, until equilibrium is reached and $\Delta\mu = 0$. If we consider the growth of a solid phase from a vapor or solution at temperature T_B and solute concentration C , the chemical potential difference is obtained by $\Delta\mu = k_B T_B \ln S$, where $S = C/C_\infty$ is the supersaturation ratio defined with respect to the equilibrium concentration C_∞ .

It has been well established [5.3] that:

1. An adhesive-type growth mechanism operates on an atomically rough interface, whereas either two-dimensional nucleation growth (2-DNG) or a spiral growth mechanism operates on an atomically smooth interface.
2. Relations between normal growth rates R and driving forces $\Delta\mu/(k_B T)$ are different depending on the growth mechanism.
3. A smooth interface may transform to a rough interface with increasing growth temperature or driving force.

Taking all these factors into consideration, we may expect that the morphology of a single crystal will change with increasing driving force $\Delta\mu/(k_B T)$ (which can be correlated to the supersaturation σ or supercooling ΔT) from polyhedral, via hopper (skeletal), to dendritic forms (all being morphologies of single crystals). On further increases of the driving force, semispherulite to spherulite or more complicated morphologies of polycrystalline aggregate are expected to appear, as the nucleation rate increases. Two critical driving force conditions, $\Delta\mu/(k_B T^*)$ and $\Delta\mu/(k_B T^{**})$ are present with increasing driving force, judging from the growth rate versus driving force relations expected for different growth mechanisms [5.2,3,5]. Under driving force conditions above $\Delta\mu/(k_B T^{**})$, the interface is expected to be rough, while below this the interface will be smooth. Above $\Delta\mu/(k_B T^{**})$, the interface is rough and the principal growth mechanism is of adhesive type. The morphological stability of such an interface is lower, and more easily violated on rough than smooth interfaces. Morphological instability of a rough interface leads to cellular growth and the appearance of dendritic morphology. Below $\Delta\mu/(k_B T^{**})$, the interface is smooth and the principal growth mechanism is either 2DNG or spiral growth. Due to the presence of the Berg effect [5.6], i.e., a higher driving force along the edges or corners of a face on a polyhedral crystal than at the center of the face, growth layers originate near the edges and corners and advance inwards to the center of the face. Therefore, a crystal takes a hopper or skeletal form under the driving force condition between $\Delta\mu/(k_B T^*)$ and $\Delta\mu/(k_B T^{**})$. Below $\Delta\mu/(k_B T^*)$, spiral growth layers originating from the center of a face advance toward its periphery, leading to the formation of a polyhedral crystal bounded by flat low-index faces. In Fig. 5.1, the morphological evolution of a crystal is indicated schematically in re-

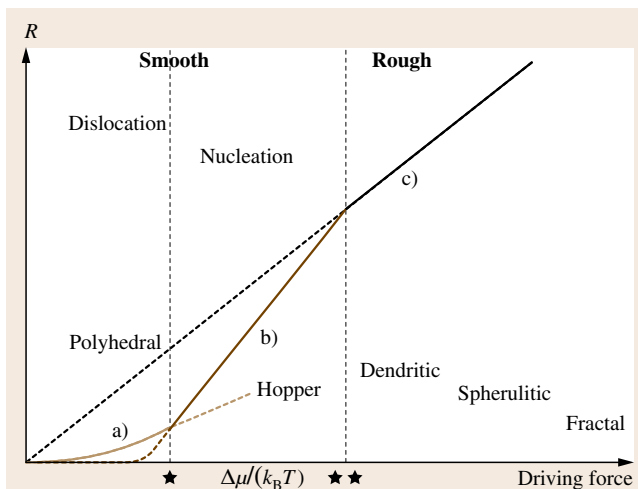


Fig. 5.1 Schematic illustration of the morphological evolution of a crystal on a normal growth rate R versus driving force $\Delta\mu/(k_B T)$ diagram. Curve (a) corresponds to spiral growth mechanism, curve (b) to 2DNG, and curve (c) to adhesive-type growth mechanism. Two critical driving forces $\Delta\mu/(k_B T^*)$ and $\Delta\mu/(k_B T^{**})$ are shown for one crystallographic face, and the regions where polyhedral, skeletal, dendritic, spherulitic, and fractal morphologies are expected are indicated (after [5.3,5])

lation to the driving force, interface roughness, growth mechanisms, and normal growth rate R versus driving force $\Delta\mu/(k_B T)$ relations [5.2, 3, 5]. The positions of $\Delta\mu/(k_B T^*)$ and $\Delta\mu/(k_B T^{**})$ on the driving force axis are different depending on the crystal face. The smoother the interface, the higher these values.

The morphological evolution from polyhedral, via hopper, to dendritic form with increasing driving force is expected theoretically and observed experimentally for many crystals grown in vapor and solution phases, such as snow crystals grown in vapor phase and silicate crystals formed in magmatic solution at elevated temperature. The reader may refer to [5.2, 3, 5] for details.

Under a driving force lower than the critical value $\Delta\mu/(k_B T^*)$ the morphology is polyhedral bounded by low-index crystal faces with slow normal growth rates. If growth continues for enough time and the crystal reaches equilibrium with the surrounding phase under a given thermodynamic condition and no further change is expected to occur, the crystal will be bounded only by the faces with the slowest, or second and third slowest, normal growth rates. The crystal morphology expected in the equilibrium state can be regarded as the *equilibrium form* under the given thermodynamic conditions. The sum of the surface free energy times the surface area will be minimum owing to the thermodynamic requirement of anisotropic material. In contrast, the equilibrium form of an amorphous material, such as a liquid, is a sphere. The equilibrium form was theoretically analyzed by Curie [5.7], Wulff [5.8], Gibbs [5.9], and more recently by Kern [5.10]. Through these analyses, a few important concepts relating to growth and morphology of crystals emerged, as summarized below:

1. The normal growth rates R of crystal faces are proportional to the surface energy γ . The smaller the surface energy, the slower the normal growth rate. This is strictly speaking valid only for molecular crystals [5.11, 12], but may be qualitatively applicable when the relative morphological importance of different faces is compared.
2. A polar diagram of *raspberry* shape, called a Wulff plot, can be drawn by connecting plots proportional to the surface energies.
3. The equilibrium form is obtained by connecting inscribed lines drawn on the cusps of the Wulff plot.
4. The equilibrium form corresponds to the form with minimum total surface free energy under a given thermodynamic condition, and not the growth forms, neither structure form.

In cubic crystals with equal axial lengths, polyhedral crystal will be bounded by only one crystallographically equivalent faces with the minimum surface energy. In anisotropic crystals, the equilibrium form of a polyhedral crystal is bounded by two or more crystallographic faces with the smallest, and second and third smallest, surface energies. Depending on the crystallographic system and axial relations, different characteristic growth forms appear, generally called the crystal habit, or more precisely habitus. Habitus is the characteristic form exhibited by a crystal species grown in an isotropic environment. Crystals belonging to the cubic system, or those with other systems but having nearly equal axial lengths, take equant habit. Crystals belonging to lower-symmetry systems, or with markedly different axial lengths, exhibit prismatic or platy habit. Crystals with much shorter axial length in the c -axis than the a - and b -axes take prismatic habit, whereas those with longer axial length in the c -axis take platy habit perpendicular to the c -axis. The expected polyhedral form of a given crystal is thus correlated to the symmetry elements involved in the unit cell, the crystal system, the crystal group, the space group or the chemical bonding in the crystal structure. Such morphology deduced from crystal structure alone can be called *structural form*, and be deduced theoretically based on types and symmetry elements, or by analyzing strong bonds in the structure, entirely neglecting the effect of thermodynamic or kinetic parameters. Examples of such analyses are the oldest Bravais–Friedel (B–F) law [5.13], an analysis based on leticular density or leticular spacing of unit-cell geometry, and Donnay–Harker’s (D–H) extension of the B–F law [5.14], in which symmetry elements involved in 230 space groups are taken into consideration. In these analyses, the order of morphological importance of the crystal faces can be deduced by calculating leticular densities or spacing. The higher the leticular density or the wider the leticular spacing, the higher the order of morphological importance. The order of morphological importance may be evaluated based on statistical observations of the frequency of occurrence and relative development of faces, or by comparing surface microtopographic characteristics of faces on a crystal. However, B–F or D–H analyses do not predict whether the face belongs to a smooth interface or rough interface, or the surface microtopography of crystal faces.

On the other hand, Hartman–Perdok’s periodic bond chain (PBC) theory [5.15–17] considers strong bond chains involved in crystal faces, and the connected net model of Bennema and van der Eerden [5.11] also

considers chemical bonding in the structure. These analyses can correlate the result to interface roughness, i. e., whether a face is rough or smooth, and quantitatively evaluate surface energy terms by calculating the attachment energies of slices E_{att} [5.12]. In the H–P theory, crystal faces containing more than two PBCs are called flat (F) faces, which correspond to smooth interfaces, whereas those containing no PBCs are called kinked (K) faces corresponding to rough interfaces. Stepped (S) faces containing only one PBC correspond to an intermediate between F and K faces, and appear by piling up of edges of growth layers developing on adjacent F faces. No growth layers will develop on S or K faces. When a crystal has more than one F face, their order of morphological importance is determined by the strength of the PBCs involved in the respective faces, and follows the order of attachment energies [5.11, 12]. These analyses can also predict the morphology of growth spirals on different faces.

All these models predict the morphologies of polyhedral crystals, based purely on the structural factor, entirely neglected the effect of external factors. These morphologies are thus considered the *structural form*. They can be different from actually observed morphology, i. e., *growth forms*, but can be used as a criterion for analyzing growth forms or the origin of their variation.

The morphology of polyhedral crystals is determined by the internal structural factor and external factors, and thus is not necessarily the same as the equilibrium or structural form. We have to take the following into consideration as possible factors affecting interface structures: ambient phases (condensed or diluted phases, involving solute–solvent interaction or not, and the strength of solute–solvent interaction), growth conditions (temperature, pressure, supercooling, supersaturation, diffusion, and convection), solvent and impurity components which modify surface or edge energy terms, and dislocations. Depending on how and under what conditions and by what processes polyhedral crystals are formed, different faces appear or disappear. Even crystallographically equivalent faces may develop with different sizes. Such morphology is called *growth forms* (plural), and offers information about how and under what conditions or conditional changes the crystal grew. Growth forms of polyhedral crystals may be bounded by more faces than the equilibrium or structural form, or by crystallographically equivalent faces of different sizes. In the same crystal habit (habitus) category, various forms may appear through different combinations and development

of crystal faces. *Tracht* is a term that denotes variation within the same category of habitus, due to the combination and development of different faces. Malformation of polyhedral forms from the ideal habitus occurs for various reasons, such as anisotropy in the crystal itself (spatial distribution and density of active dislocations for growth) or in the ambient phase (solution flow, convection, and the presence or absence of obstacles such as substrate surface or inclusions), and the presence or absence of seed. Information obtainable through variation in habitus and *tracht* tells us how the crystal grew and how the condition fluctuated throughout its growth history. Such information is very useful in analyzing conditional changes in the growth history of crystals whose growth process cannot be traced in situ (natural minerals, or crystals synthesized in enclosed systems), and to design appropriate methods to control the growth parameters to obtain single crystals of desired perfection and homogeneity.

It is to be noted that even ultrafine crystals of nanometer size show polyhedral morphology bounded by flat crystallographic faces. Ultrafine particles of not only metals but also various compounds show polyhedral morphology; for examples see [5.18] and many other papers. Only crystals smaller than 1 nm show forms without crystal faces.

Another morphology to be mentioned is whiskers. Depending on the anisotropy involved in growth sites, extremely anisotropic morphology appears. Such crystals are called whiskers, and have attracted both scientific and application interests, due to curiosity about the origin of their unusual morphology and their much higher perfection than 3-D bulk crystals. Most whiskers are straight, but topological whiskers, such as helical, coil, ribbon, and rope forms, are also known. A variety of mechanisms to account for whisker growth have been proposed, but only a few models have been established. The vapor–liquid–solid (VLS) mechanism [5.19] put forward as a possible mechanism for Si whisker formation is such a case. Detailed discussion on the mechanism of whisker formation will be given in Sect. 5.4. There are other well-established mechanism for whisker formations, and a discussion of possible mechanism is given in Sect. 5.4 and can also be found in [5.3].

We shall analyze in more detail in Sect. 5.4 possible reasons for the formation of various growth forms. However, before dealing with the macromorphology of crystals, it is necessary to understand at the atomic level how crystal growth proceeds. This is recorded in the form of the surface microtopography of crystal faces.

5.3 Surface Microtopography

Since growth (and dissolution) takes place exclusively at the solid–liquid interface, growth (and dissolution) process are recorded in the form of the surface microtopography of the crystal faces. Well-developed as-grown low-index faces corresponding to F faces show surface microtopography characterized by the development of step patterns resembling contour lines of a geographic map. They consist of flat terraces and sharp steps, with elemental height of nanometer order originating from screw dislocations, as well as bunched macrosteps with thicker step height. On terraced portion, which is usually atomically flat, islandlike layer formed by two-dimensional nucleation may occasionally be seen, where condition is changed to terminate the growth, leading to shoot up of the driving force. Islandlike layer formed by 2DNG mechanism is not commonly seen on inorganic crystal grown freely, but is more frequently encountered on protein crystals, probably due to the higher driving force conditions necessary to grow pro-

tein crystals and the larger size of the growth units involved in their growth. At least based on the author's experience of surface microtopographic observations of a wide variety of inorganic crystals, features conclusively demonstrating 2DNG have never been observed. The author is always careful to draw a conclusion about 2DNG based on islandlike patterns.

The surface microtopography of S faces is characterized by straight striations parallel to edges with adjacent F faces, whereas those of rough K faces show rugged, hummocky, rough surfaces. On both S and K faces, neither spiral step pattern nor two-dimensional island are observed. Surface microtopographs characteristic of smooth F, intermediate S, and rough K faces are illustrated schematically in Fig. 5.2a–c, respectively.

When F faces receive dissolution (etching), various etch figures appear, which include point-bottomed etch pits (P-type) formed at outcrops of dislocations, flat-bottomed etch pits (F-type) formed at outcrops of

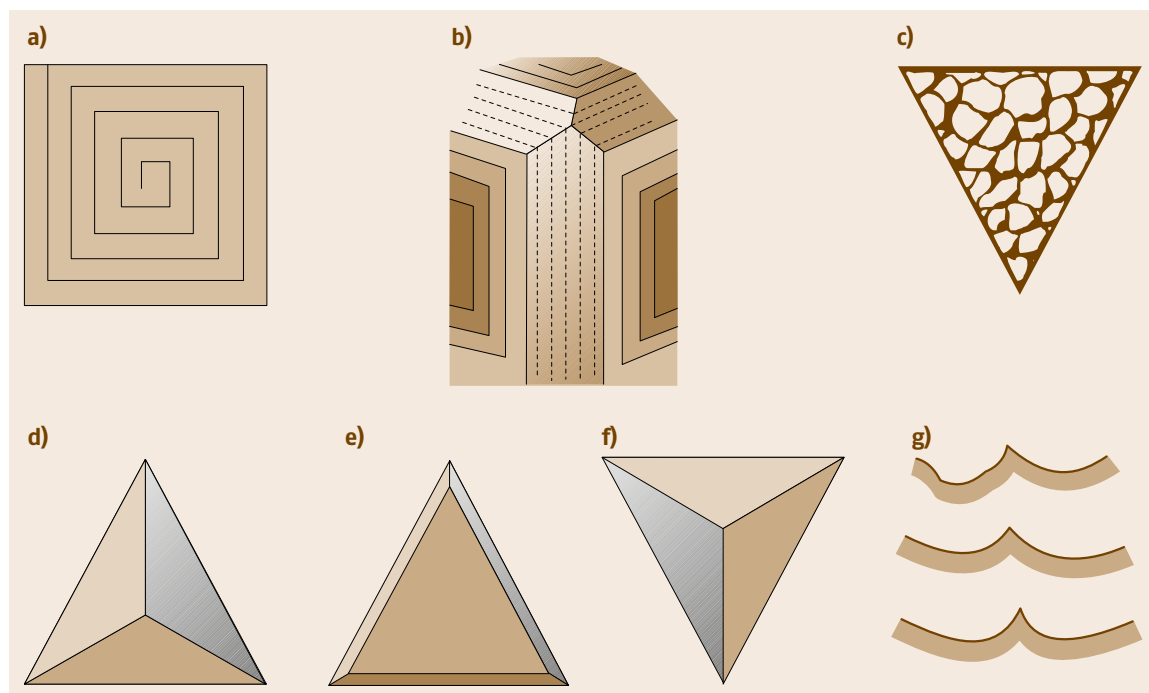


Fig. 5.2a–g Schematic illustrations of surface microtopographs expected to be observed on F (a), S (b), and K faces (c) formed by growth, and P-type (d), F-type (e) etch pits and etch hillock (f), and concave steps (g) due to two-dimensional recession of smooth growth steps on an F face. Microtopographs (a–c) are due to growth, whereas microtopographs (d–g) are due to dissolution (etching). Microtopographs (d–f) are illustrated by oblique illumination, whereas in (g), higher sides of steps are *shadowed*

point defects or impurity atoms, etch hillocks formed around obstacles such as dislocations decorated by impurities, and concave and rugged steps formed by two-dimensional recession of smooth growth steps. These are illustrated schematically in Fig. 5.2d–g.

If sophisticated methods to visualize and measure nanoscale steps are used, a spiral step pattern originating from isolated screw dislocations with elemental Burgers vector, and constant step separation can be seen on well-developed crystal faces. An elemental spiral originating from an independent screw dislocation has a profile consisting of atomically flat terraces and steep steps with height equal to the component of the Burgers vector perpendicular to the face, and with constant step separation. Depending on the growth conditions and ambient phases, the ratio of step separation λ to step height h varies. On crystals grown in very diluted vapor phase, the ratio is on the order of 1×10^3 – 1×10^5 , whereas on the same face of the same crystal grown

in less diluted solution phase it is on the order of 1×10^2 – 1×10^3 [5.20]. It is to be noted that the profile of an elemental growth spiral is such that, after walking on an extremely flat plateau for 1–10 km, one meets a sharp cliff 1 m in height. Phase-contrast (PCM), interference contrast (DICM), and phase shifting (PSM) microscopes can reveal such spiral steps with nanoscale height, and multiple-beam (MBI) and phase-shifting (PSI) interferometry can measure the height of such thin steps. The step height of an elemental spiral is equal to the unit cell height, or its fraction in the direction perpendicular to the face. The step separation of an elemental spiral corresponds to twice the radius of the critical two-dimensional nucleus under the given conditions. The step separation λ of an ideal elemental spiral is equal to $19r^*$, where r^* is the radius of the critical two-dimensional nucleus. r^* is determined by the edge free energy γ and the driving force $\Delta\mu = k_B T \ln S$ according to

$$r^* = 2\gamma \frac{\rho}{mk_B T \ln S}, \quad (5.1)$$

where m is the mass of one molecule and ρ is the density of the nucleus volume.

With increasing $\Delta\mu/(k_B T)$, λ becomes narrower when crystals grow in the same ambient phase. γ is modified by solute–solvent interaction and impurities adsorbed on the steps.

When the step separation is wider than the resolution limit of the microscopy adopted, the ideal spiral pattern is discernible. With increasing driving force, the step separation becomes narrower than this resolution and individual steps become impossible to resolve. Such growth spirals will appear in the form of growth hillocks with pointed summit, bounded by vicinal faces. If observation methods with higher horizontal resolution and equally high vertical resolution, such as atomic force microscopy (AFM), scanning tunneling microscopy (STM), or laser beam scanning microscope (LBSM) are applied, spiral steps may become discernible on the summit of such growth hillocks.

Growth spirals with elemental step heights take circular or polygonal form depending on the roughness of the spiral steps. A circular spiral appears when the step is rough, whereas a polygonal form appears when the step is smooth. So the same concept applied to the roughening transition of a smooth interface is applicable in this case too. The circular form appears under higher driving force conditions, whereas the polygonal form is seen when the driving force is below the critical value for the two-dimensional roughening tran-

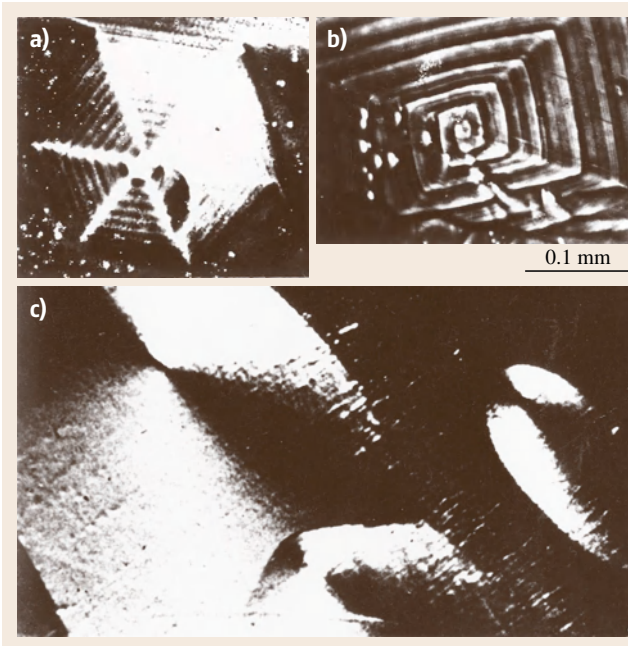


Fig. 5.3a–c Variation in the roundness of steps of growth spirals observed on different crystal faces of a hydrothermally grown synthetic beryl crystal. Regular hexagonal spirals are seen on the morphologically most important (0001) face (a), slightly rounded rectangular spirals are observed on the second important (1010) face (b), and rounded growth hillocks are observed on the far less important (2131) face (c). Growth features become more rounded with decreasing morphological importance

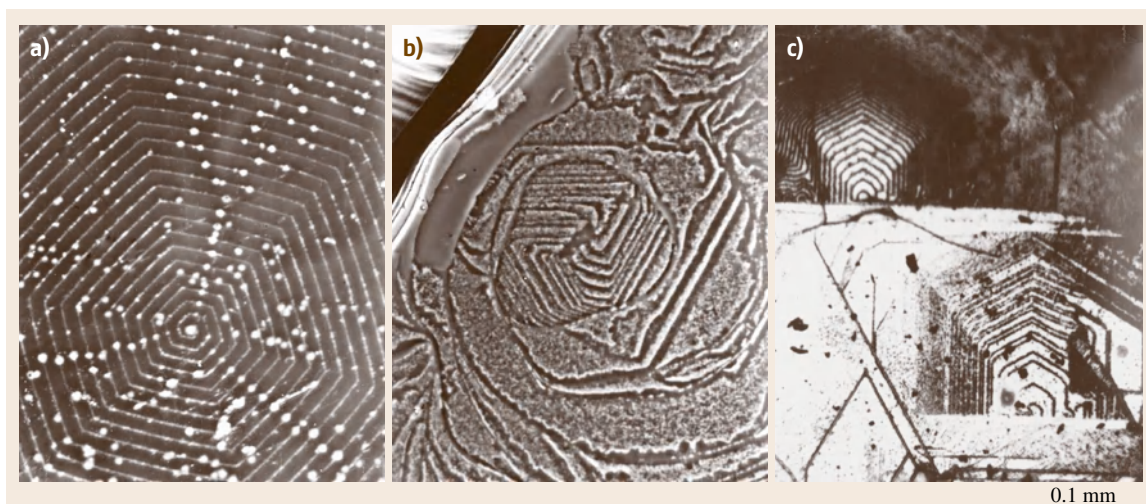


Fig. 5.4a–c Symmetry of polygonal growth spirals observed on crystals of different crystal systems: (a) hexagonal spiral observed on (0001) face of a hexagonal system, SiC, (b) triangular spiral observed on (0001) face of a trigonal system, hematite and (c) five-sided spiral containing only one mirror symmetry plane observed on (001) face of a monoclinic crystal, phlogopite. In (b), the crystal receives weak etching, forming rugged steps due to two-dimensional recession (dissolution) of smooth growth steps. In (c) spiral steps with height of 1 nm are decorated by selective nucleation of foreign crystals along the spiral steps

sition. The critical points for the roughening transition to take place may differ on the same crystal face depending on the growth parameters as well as on different faces on the crystal grown under the same conditions. On the same faces of crystals grown under different conditions, circular or polygonal spirals may be seen depending on the growth conditions. More polygonal spirals appear on crystals grown under lower driving force conditions than those grown under higher driving force conditions. Polygonal spirals may be observed on the morphologically most important face, whereas circular ones are seen on morphologically less important faces on the same crystal grown under the same conditions. Representative examples to demonstrate such variation is shown in Fig. 5.3. When spirals take the polygonal form, their symmetry follows that of the face,

since the steps are determined by PBCs involved in the face. Figure 5.4 shows representative examples of various morphologies of growth spirals observed on the faces of crystals belonging to different crystal systems.

Growth spirals with elemental step height bunch together to form thicker macrosteps while advancing

Fig. 5.5 An example of a step pattern observable on a whole face. More perturbed, bunched macrosteps appear closer to the edges of the face at the *bottom right*. All perturbed macrosteps seen at the lower right are bunched macrosteps originating from elemental spiral centers indicated by the *arrows*. Also note the wider step separation along the upper edges, which is considered as due to a higher driving force along the edge than at the center of the face, i. e., the Berg effect. Hematite (0001) ►



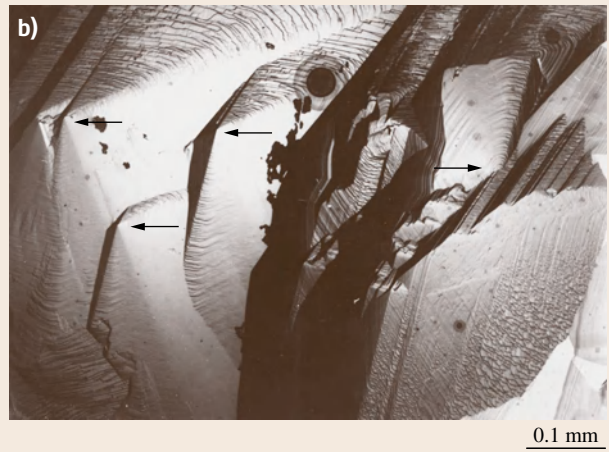


Fig. 5.6a–d Surface microtopographs of prism (a,b) and rhombohedral (c,d) faces of natural (a,c) and synthetic (b,d) quartz crystals. Arrows in (b) indicate spiral centers

laterally, due to either impurity adsorption along the step or fluctuations in the driving force over the surface. Since the advancing rate of a bunched macrostep is slower than that of elemental steps, the step pattern is perturbed more as it advances laterally. Since the driving force near the edges and corners of a crystal face is higher than at the center of a face due to the Berg effect [5.6], the step separation becomes narrower and the step pattern becomes more perturbed when advancing close to edges. Figure 5.5 shows such an example.

On real crystals, it is exceptional for a whole crystal face to be entirely covered by one spiral step pattern, with a constant step separation, originating from an outcrop of an independent screw dislocation. Several or a large number of growth spirals appear on one face, originating from several dislocations. So, step patterns observable on the same crystallographic face can differ from crystal to crystal, or among crystallo-

graphically equivalent faces, even if the crystal grew in similar ambient phases under similar growth conditions. However, overall surface microtopographs show characteristics corresponding to the crystal growth environment and conditions. The same hematite crystals occurring at different localities, but formed in similar ambient phases, i. e., natural CVT due to postvolcanic action, show surface microtopographic characteristics according to which different localities can be identified. Prism and rhombohedral faces of natural and synthetic quartz crystals show markedly different surface microtopographies according to which natural and synthetic crystals can be easily discriminated, even if both show the same hexagonal prismatic habit. In Fig. 5.6, surface microtopographs of prism (Fig. 5.6a,b) and rhombohedral (Fig. 5.6c,d) faces of natural (Fig. 5.6a,c) and synthetic (Fig. 5.6b,d) quartz are compared. The marked differences between natural and synthetic quartz crystals are due to the differences in growth rates (natural crystals grew slower under lower driving force conditions than synthetic crystals) and solution chemistry (natural quartz grows in neutral hydrothermal solution, whereas synthetic quartz in alkaline solution).

5.4 Growth Forms of Polyhedral Crystals

Polyhedral crystals bounded by flat crystallographic faces are formed by the spiral growth mechanism under conditions lower than $\Delta\mu/(k_B T^*)$. If a crystal grows in an isotropic environment, i. e., in an ambient phase with a concentric diffusion gradient toward the growing crystal, the growth form is determined simply by the relative normal growth rates of the faces present on the crystal surface. The morphology eventually reaches a form corresponding to a structural or equilibrium form. Crystallographically equivalent faces develop equally in size. If additional factors that may induce anisotropy in the mass transfer in the ambient phase or in the distribution of dislocation outcrops active as growth centers are involved, polyhedral growth forms deviate or are malformed from their ideal form. Even crystallographically equivalent faces will develop differently. As possible factors to induce such anisotropy, we may mention the following:

1. Convection or directional flow in the ambient phase, which induces anisotropy in mass transfer. This may result in not only modification of growth rates but also in the distribution of inclusions from which dislocations are newly generated.
2. The presence of seed or substrate surface. Seed modifies the growth form, and the surface of seed or substrate affects normal growth rates by newly generating dislocations on the interface.
3. The presence of reentrant corners or concentration of dislocations in twin junctions due to twinning. These provide sites for preferential growth.
4. Anisotropic distribution of active growth centers, i. e., outcrops of screw-type dislocations, for various reasons, such as new generation of dislocations from inclusions.
5. Impurity elements selectively adsorbed along growth steps or foreign compounds that selectively cover the growing surface due to epitaxial relation, or selective adsorption that suppresses the normal growth rate.

Since an ideally isotropic environment is not expected in real systems, actually observed polyhedral crystals show various forms which deviate or are malformed from ideally expected forms, i. e., the structural or equilibrium form. Even a simple octahedral crystal bounded by crystallographically equivalent {111} faces may only take polyhedral forms such as tetrahe-

dron, triangular or hexagonal plate, or even elongated rodlike form, due to anisotropic development of crystallographically equivalent faces. In Fig. 5.7, various polyhedral forms appearing due to anisotropic development of crystallographically equivalent {111} faces are shown. We shall in the following first analyze growth forms expected in an isotropic environment, and then proceed to the analysis of possible reasons for such deviations.

The normal growth rate R of a face growing by the spiral growth mechanism is determined by the height h , the separation between successive steps λ , and the advancing rate v of the spiral step $R = hv/\lambda$. Since h corresponds to the Burgers vector of dislocation, it is different on different faces. Since λ is equal to $19r_1^*$, and

$$\Delta G(r^*) = 16\pi\gamma^3 \frac{[v]^2}{3\Delta\mu^2}, \quad (5.2)$$

where r^* is the radius of the critical two-dimensional nucleus, γ is the edge free energy of the two-dimensional nucleus, v is the molar volume of the bulk nucleated phase, and $\Delta\mu$ is the chemical potential difference.

Important parameters that affect R , and hence modify the habitus and tracht of polyhedral crystals when

they grow in an isotropic environment, are those that modify the edge free energy and driving force. The following are considered to be the major factors:

1. Driving force, i. e., supercooling or supersaturation.
2. Ambient phase. Crystals of the same species growing from different ambient phases, i. e., those grown from melt, solution or vapor phase, will show different growth forms.
3. Solute–solvent interaction energy, i. e., crystals of the same species grown from solutions with different solvent compositions will show different growth forms.
4. Impurity elements, which modify the edge free energy by adsorbing on spiral growth steps. Foreign compounds which can selectively adsorb or epitaxially grow on particular faces. These may suppress the normal growth rate of rough or less smooth interfaces which grow with high growth rate in the pure system, resulting in marked morphological changes.

Examples demonstrating the effect of these factors are well known and can be found in older works by Wells [5.21] and Buckley [5.22]. Wells demonstrated various examples of variation of growth forms due to effects 1, 2, and 3, and Buckley summarized his observations on effect 4. Observations on the variation of habitus and tracht of mineral crystals in relation to their modes of occurrences and the analysis of their origins may be found in [5.2, 3, 5].

In real systems, polyhedral crystals grow in environmental phases that deviate from the ideal isotropic situation. Mass (or heat) transfer will be anisotropic due to convection or directional solution flow. It was noted as early as the 17th century by Hook [5.23] that alum crystals formed on the bottom of a beaker take hexagonal platy habit bounded by only {111} faces, as compared with the nearly simple octahedral habit of crystals formed on a string immersed in the solution, i. e., those growing in a nearly isotropic environment. Around a crystal growing on the bottom of a beaker, mass transfer to the face adhering to the bottom is strongly suppressed as compared with the faces directly facing to the solution, resulting in remarkable malformation from the ideal octahedral morphology.

Reentrant corners provided by twinning also play a similar role, resulting in triangular or hexagonal platy habit, since preferential growth occurs at a reentrant corner due either to the geometry or the concentration of dislocations in the twin junction plane.

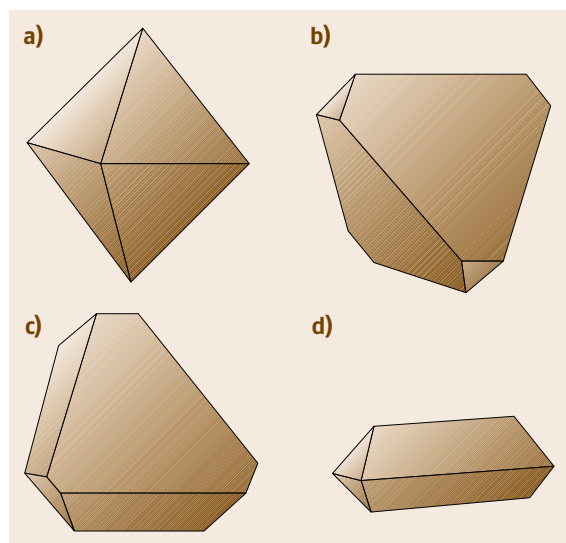


Fig. 5.7a–d A simple octahedral crystal bounded by {111} only (a) may take various malformed forms: tetrahedral (b), triangular platy (c) or elongated rodlike (d) due to anisotropy in either environmental factors or in the crystal itself

Convection or directional flow of solution is universally involved in mineral formation in hydrothermal veins in nature and in hydrothermal synthesis in the laboratory. When crystals grow in an impure system, precipitation and incorporation of solid grains of foreign minerals or mother liquid phase as inclusions in the growing crystal is also anisotropic, which will enhance growth rate anisotropy. Since such inclusions act as sites generating new dislocations, the density of outcropping dislocations on crystallographically equivalent faces become different, resulting in different growth rates. Depending on the conditions of solution flow, laminar or turbulent, the rate of mass transfer and the precipitation of foreign particles may be different. In turbulent flow, the growth rate is enhanced and more inclusions are included on the rear side of the solution flow than on the front side. Variation of normal growth rates or the precipitation and inclusion of foreign particles are recorded in the forms and sizes of growth sectors, the width of growth banding, and the distribution of centers of dislocation generation detectable in single crystals. Such internal morphology of single crystals offers important information for the analysis of growth history and conditional variations during growth. These will be described in more detail in Sect. 5.5.

When aiming to synthesize large single crystals of high perfection at high growth rate in the laboratory, seed crystals are generally used to suppress unnecessary spontaneous nucleation. Other techniques, such as the application of an alternating temperature to dissolve unnecessary nuclei, agitation and stirring of the solution, rotation of the crucible, application of a magnetic field, and growth under microgravity conditions, are applied to homogenize the ambient phase.

In preparing the seed, it is common to adopt a crystallographic orientation bounded by rough or less smooth interfaces to secure a higher growth rate and obtain forms appropriate for industrial use. The crystallographic orientations and surfaces of seed are generally chosen as different from those observed on freely grown forms. *Y*-bar seed for the hydrothermal synthesis of quartz and a seed plate parallel to $[21\bar{3}1]$, often used in the hydrothermal synthesis of emerald, are such examples. The seed surface is often treated by chemical etching before the onset of new growth. This results in markedly different as-grown morphology of syn-



Fig. 5.8a,b Natural quartz crystal grown without seed (a) and synthetic crystals grown on seed plate (Y-bar) (b). The *c*-axes are set vertically in both photographs ►

thetic crystals from those grown freely. Seed surfaces are usually those not seen on freely grown crystals, and belong to the category of rough interfaces. They often develop to a large size on synthetic crystal. On natural quartz crystals, $\{0001\}$ faces never appear unless a special effect is involved, whereas on synthetic quartz crystals these faces become large. In Fig. 5.8a,b natural and synthetic quartz crystals are compared with the same crystallographic orientation. Natural quartz crystals show hexagonal prismatic form elongated in the c -axis, and bounded by prism $\{10\bar{1}0\}$, two types of rhombohedral $\{10\bar{1}1\}$ and $\{01\bar{1}1\}$ faces, whereas synthetic crystals show prismatic form elongated along the Y -axis and perpendicular to the c -axis and bounded by basal $\{0001\}$, prism $\{10\bar{1}0\}$, $\{11\bar{2}0\}$, rhombohedral $\{10\bar{1}1\}$, $\{01\bar{1}1\}$ and trigonal pyramid $\{11\bar{2}2\}$ faces. $\{0001\}$, $\{11\bar{2}0\}$, and $\{11\bar{2}2\}$ faces are not commonly observed on freely grown quartz crystals. The difference is simply because the growth of synthetic quartz is forced to terminate before the crystal attains its final form. If growth proceeds further, synthetic quartz crystals will eventually show similar hexagonal prismatic form to natural quartz crystals. Spontaneously nucleated quartz crystals without seeds on the holder in the same autoclave take trigonal or hexagonal prismatic form, similar to natural crystals, except with more exaggerated trigonal symmetry than natural quartz.

Although not common, we may occasionally identify seed crystals in single crystals of natural minerals as well. The seed is formed elsewhere in a different geological environment and later incorporated into a new environment where further growth takes place later. Growth morphology may be different between the seed and the newly grown portion, and dislocations may be newly generated on the seed surface.

In epitaxial growth, the morphology of the guest crystal is different from that of freely grown crystal, since an additional interface energy and steps are introduced between the host crystal surface and the guest crystal due to their epitaxial relation. Epitaxially grown guest crystal usually takes more flattened or elongated forms. Many examples are known among mineral crystals.

5.5 Internal Morphology

Polyhedral crystals are bounded by several crystallographically equivalent or different faces that grow at different normal growth rates R . Crystal faces with smaller R become larger, whereas those with larger

Whiskers are single crystals with highly anisotropic forms. In most cases, they take straight forms, elongated in a certain crystallographic direction and bounded by low-index crystal faces [5.24]. Kinked whiskers are also sometimes observed. Recently, topological whiskers showing twisted, curved, helical, screw, Möbius ring, and other topological forms have been reported [5.25]. To account for the origin of such highly anisotropic morphology of single crystals, we have to assume the presence of a preferential unique growth site, where growth can occur while growth on other sites is suppressed. In the case of the vapor–liquid–solid (VLS) mechanism for Si whiskers [5.19], Si is continually supplied in vapor phase (V), which dissolves in Au particles to form a eutectic Au–Si liquid droplet (L), in which only Si nucleates and grows as whiskers (S). Since growth occurs only at the site of the nucleus, Si crystal grows as a whisker, with a cap of Au–Si eutectic liquid droplet at the tip, and Si is continually supplied from the vapor. In the eutectic solution (L) phase, for thermodynamic reasons (i. e., the lower melting point of the solution than of the pure solute and solvent phases and the phase to nucleate, and that growth in the solution is determined by the composition of the liquid phase), only Si is nucleated in the solution phase, providing a unique growth site, leading to whisker growth. Growth exclusively occurs at the root of whiskers in the eutectic liquid droplets. The VLS mechanism has been well established in many other example systems, including mineral crystals.

Another well-established mechanism for whisker formation was demonstrated in the case of KCl or NaCl crystals [5.26]. When KCl or NaCl aqueous solution in a wineskin is kept in the dark, whiskers of these crystals grow from the outer surface of the wineskin. These whiskers are hollow along their length, indicating that crystal growth occurs as soon as the solution is transported through capillaries in the skin and exposed on the skin surface or the tip of the hollow whisker, since supersaturation sharply increases. Growth uniquely occurs at the tip and, as long as the capillary is present, growth continues, leading to hollow whiskers.

R diminish in size or terminate as growth proceeds. So rough interfaces will disappear very soon from the external form, and only smooth faces will become large. Among smooth interfaces, the morphologically

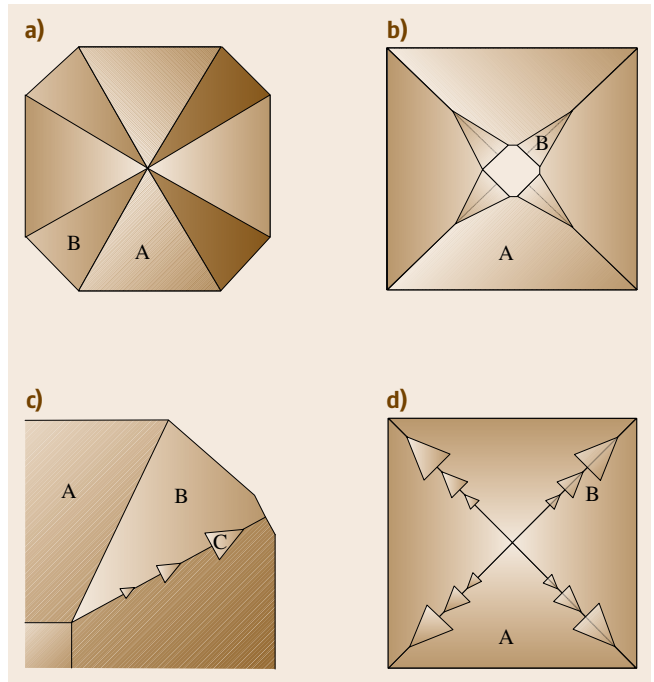
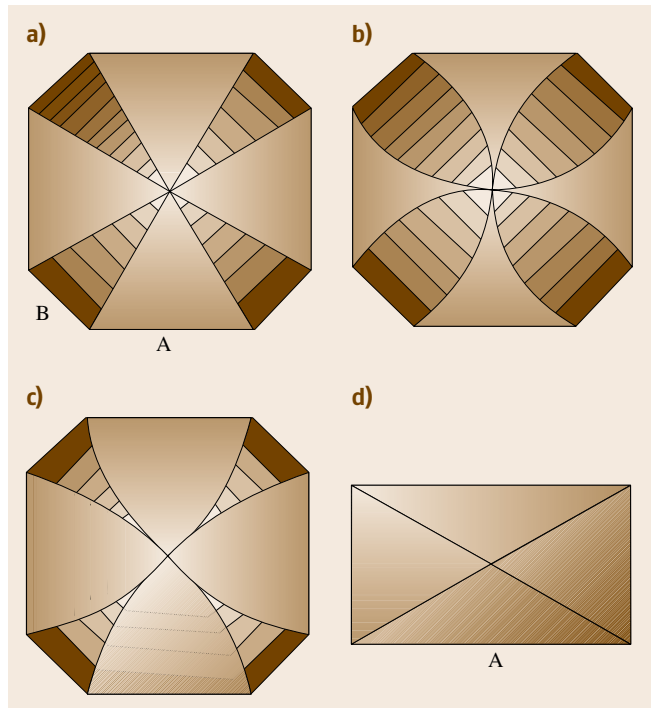
Fig. 5.9a–d Schematic illustration of growth sector boundaries. (a) Straight growth sector boundaries appear when R_A and R_B are constant; convex (b) or concave boundaries (c) appear when R_A or R_B is decreasing. Growth sector boundaries in a crystal bounded by crystallographically equivalent A faces, but with different growth rates are indicated in (d) ►

most important face develops as the largest face while morphologically less important faces develop smaller. Unless some factors suppress or enhance the normal growth rates, the final morphology is the same as that structurally expected. However growth forms are different from ideal forms. Even crystallographically equivalent faces grow at different R when a crystal grows in a real environmental phase in which flow or convection currents or substrate surface are present. The densities of active growth centers (outcrops of dislocations) will not be the same in a real system on growing surfaces of crystallographically equivalent faces, leading to different growth rates. Growth forms of polyhedral crystals may vary as they grow, due to variations and differences in the normal growth rates in different directions as well as changes in the growth conditions.

Through the growth process, pyramidal portions are formed in a single crystal, with their summits at the initiation of the face and the base at their terminations either within the crystal or on the final as-grown surface. These pyramidal portions observable in single crystals are called growth sectors, and can be visualized even in perfectly clean crystals by the naked eye when investigated by applying appropriate methods such as polarization microscopy, CL and laser-beam tomography, x-ray topography, and etching. In the Russian literature, they are called growth pyramids.

Depending on the growth history, various forms of growth sectors appear. If a face grows steadily throughout the whole growth history, the growth sector takes a regular pyramidal form with the summit at the center

Fig. 5.10a–d Schematic illustrating various types of growth sectors. (a) Two faces, A and B, grew at a constant growth rate. (b) The growth rate of sector B increases as growth proceeds and the sector terminates within the crystal. (c) Face C appears due to conditional change, and the corresponding growth sector soon terminates due to the original rapid growth rate. (d) Intermittent growth sectors, indicating repeated changes in growth conditions ►



of the crystal and the base at the final as-grown surface. The boundaries between the adjacent growth sectors detected when a crystal is bisected through the center may be straight, convex or concave, depending on the relative growth rates of the faces, as illustrated schematically in Fig. 5.9. Growth sector boundaries may be detected even between neighboring crystallographically equivalent faces. Since sector boundaries are places where advancing growth steps on the adjacent faces meet, where strain concentrates, they can be detected by appropriate methods. They are often seen by the concentration of mother liquid inclusions.

When one face grows at a much higher growth rate than the neighboring faces, the former growth sector becomes narrower and tapered as growth proceeds and the sector boundaries may terminate within the crystal. This forms a center cross pattern, with tapering growth sectors. If the face appears intermittently, zigzag sector boundaries appear. Figure 5.10a–d shows schematically various types of growth sectors. Clearly, morphologically important faces that behave as smooth interfaces under the growth condition form growth sectors that persist throughout the whole growth history, while morphologically less important faces that behave as less smooth or rough interfaces form tapering or intermittent

growth sectors. In these sectors, the summits and base are just opposite to ordinary observable growth sectors. The base of a pyramid appears first, and the boundaries are tapered as growth proceeds. This indicates that the face appeared when conditions changed to suppress the normal growth rate of the face, which otherwise grows with a higher growth rate. The presence of intermittent growth sectors indicates that an abrupt conditional change took place to suppress the normal growth rate of the face, leading to the appearance of the face, which soon disappears due to the rapid growth rate under the given conditions. Tapered growth sectors may represent either the coexistence of two smooth interfaces with different smoothness, or smooth and rough interfaces. In the case of the coexistence of smooth and rough interfaces, we have to assume an effect of external factors to suppress the normal growth rate of the rough interface. Otherwise, growth sectors corresponding to the rough interface will very quickly disappear from the crystal.

Even if the final morphology is a polyhedron bounded by flat faces, this does not automatically guarantee that the crystal took polyhedral form throughout its growth history, i. e., was formed exclusively under conditions lower than $\Delta\mu/(k_B T^*)$ throughout its whole growth history. They may start as spherulite or den-

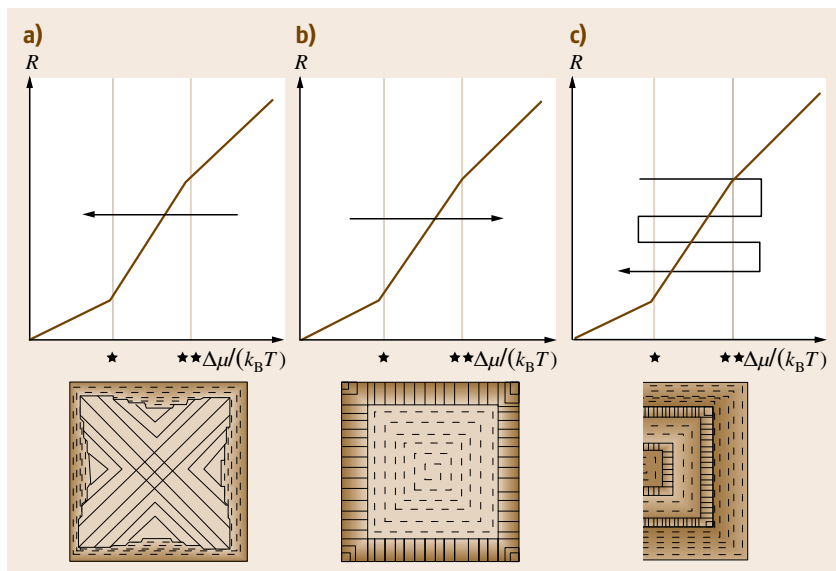


Fig. 5.11a–c Schematic illustrating the internal morphologies of single crystals formed first by dendritic growth followed by 2DNG and spiral growth (a). Fibrous (dendritic) overgrowth on earlier formed polyhedral crystal grown by 2DNG or spiral growth, due to a sharp increase of the driving force by conditional change at the latest stage, is indicated in (b). A case of repeated conditional change is indicated in (c). Corresponding conditional changes are indicated by *arrowed lines* on the respective growth rate versus driving force diagrams shown above

dritic forms under conditions higher than $\Delta\mu/(k_B T^{**})$, and 2DNG or spiral growth may take place later when the driving force drops below $\Delta\mu/(k_B T^*)$. The earlier formed dendritic or spherulitic forms may be found at the center of polyhedral crystals formed through such process, as illustrated schematically in Fig. 5.11. The skeleton and the present size of a polyhedral crystal may have been constructed during the earlier stage of dendrite formation.

So, through the analysis of internal morphology, we may assess how the as-grown morphology of a crystal has changed and which faces persisted and were morphologically important throughout its growth history, and how and why morphologically less important faces appeared or disappeared during the whole growth history of a crystal.

Although less distinct, growth sectors of smaller size can be detected within one growth sector when sensitive observation methods such as polarization microscopy or cathode luminescence tomography are used to detect chemical heterogeneity. Such growth sectors are called intrasectorial growth sectors, or vicinal sectoriality. They appear due to different advancing rates v of spiral growth layers or impurity incorporations between different vicinal faces of a spiral growth hillock developing on an F face. On the surface of an F face growing by spiral growth mechanism, a spiral growth hillock with polygonal form appears, being composed of a few vicinal faces and following the symmetry of the face. The vicinal faces appear by piling up of spiral steps, since the advancing rates of spiral growth layers are different in different directions. Due to the difference in the advancing rate, impurity concentrations can be different between different vicinal faces. This forms vicinal sectoriality or intrasectorial growth sectors. A good example of vicinal sectoriality was reported in [5.27], as revealed by CL on polygonal growth spirals developing on $\{10\bar{1}0\}$ face of synthetic quartz crystal. Brighter CL images corresponding to higher concentration of impurity Al are seen on only two among six vicinal faces forming a polygonal growth spiral. The higher concentration of Al in these vicinal faces results in the appearance and development of $s\{11\bar{2}1\}$, $x\{51\bar{6}1\}$ faces on natural quartz crystals and further to the appearance of $S\{11\bar{2}2\}$ faces on synthetic quartz crystals grown on seed [5.27]. Vicinal sectoriality is also reported on rhombohedral faces of calcite crystal [5.28]. The appearance of vicinal sectoriality due to impurity adsorption indicates that element partitioning is controlled by the growth kinetics.

Partitioning or the distribution of impurity elements is controlled by both thermodynamic factors and growth kinetics. Assuming growth under a constant thermodynamic condition, element partitioning is principally controlled by growth kinetics. The ratio of element partitioning between the ambient phase and crystal is defined by the effective distribution coefficient, K_{eff} . Elements with $K_{\text{eff}} < 1$ are incorporated less in the growing crystal and accumulate more in front of the growing crystal in the ambient phase, while those with $K_{\text{eff}} > 1$ are incorporated more into the crystal as growth proceeds. Burton et al. [5.1] indicated theoretically that K_{eff} depends on the normal growth rate R , the diffusion constant D , and the thickness of the diffusion boundary layer δ as

$$k_{\text{eff}} = \frac{k_0}{k_0 + (1 - k_0) \exp(-R\delta/D)}. \quad (5.3)$$

Since the normal growth rates differ depending on the crystallographic orientation and interface structures, element partitioning will be different between smooth and rough interfaces and among different crystallographic faces.

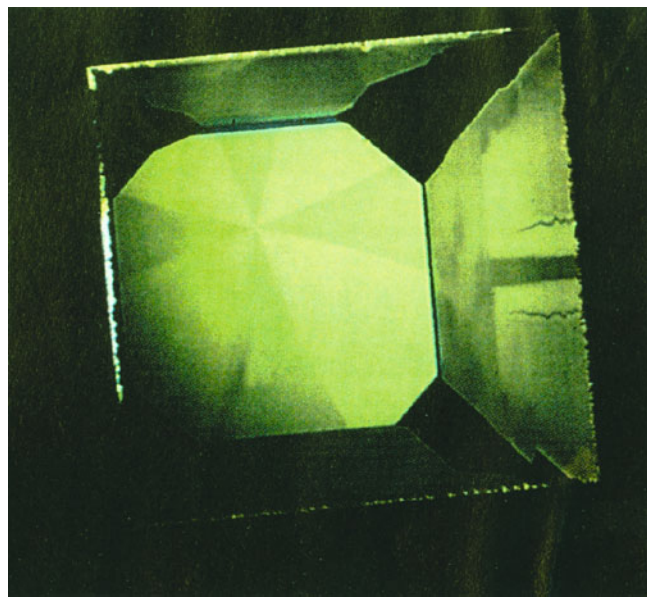


Fig. 5.12 Cathodoluminescence tomograph of cubo-octahedral crystal of HPHT synthetic diamond. CL intensity in $\{111\}$ growth sectors is high, whereas no or weaker CL intensity is seen in $\{100\}$ growth sectors, indicating selective and higher partitioning of nitrogen in morphologically more important $\{111\}$ growth sectors than in less important $\{100\}$ faces (courtesy of GAAJ)

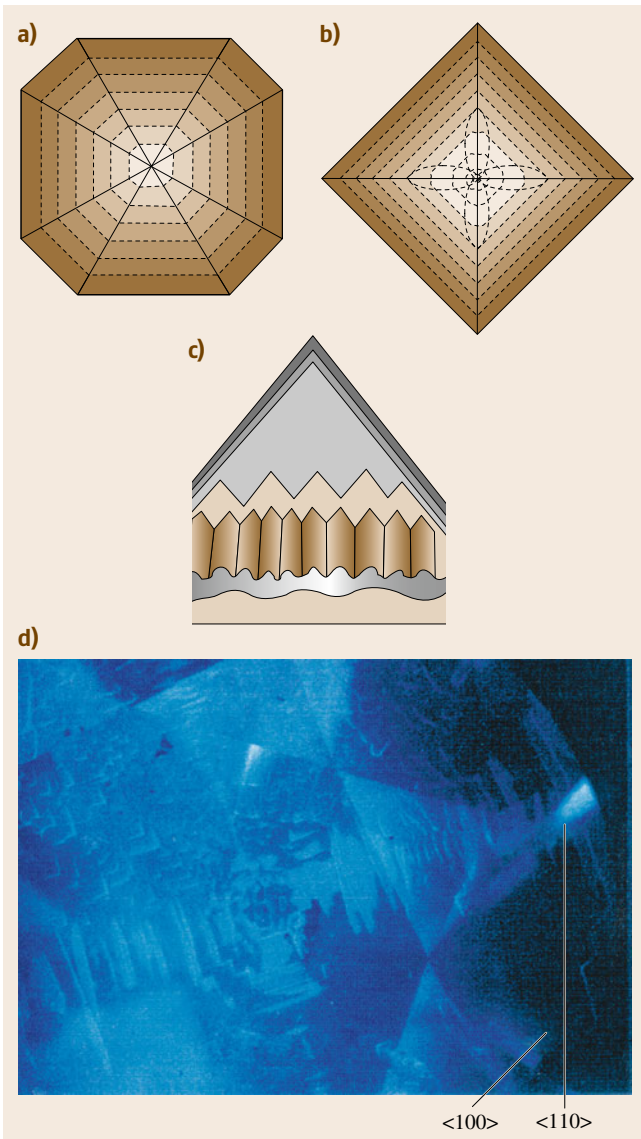


Fig. 5.13a–d Straight growth banding observable in the growth sectors corresponding to (a) two smooth interfaces and (b) one smooth interface and another rough interface, in which growth banding is not straight but hummocky. Transition of smooth to rough interface, followed by morphological instability of the interface to form cellular growth and the development of microfacets in the recovery process from rough to smooth interface, is indicated in (c). (d) CL tomography of a round, brilliant cut diamond, indicating the development of micro {111} facets during the recovery process from seed cuboid bounded by rough interfaces

The normal growth rate R of a rough interface is higher than that of a smooth interface. However, the lateral advancing rate v of growth layers on a smooth interface is much higher than the normal growth rate on a rough interface. The higher the growth rate or the step advancing rate, the higher the probability of incorporating impurity elements at the growth front. Therefore, it is anticipated that impurity elements with $K_{\text{eff}} < 1$ will be more concentrated in growth sectors of smooth interface than those of rough interface. This was initially observed in Si single crystals grown from the melt phase by Czochralski method. In melt growth of Si by CZ method, the solid–liquid interface follows an isothermal profile, the interface is mainly rough, and an adhesive-type growth mechanism operates principally. However, at the central portion of a growing single-crystalline boule, a facet of smooth {111} interface appears, forming a central, narrow growth sector formed by smooth interface surrounded by those formed by rough interface growth. It was found that Bi distributes more in the central growth sector of faceted growth on {111} smooth interface than in the major growth sectors of the rough interfaces. This anisotropic distribution of Bi was understood as due to the much higher advancing rate v of growth layers on a smooth interface than the normal growth rate R of a rough interface.

From the observation on Si crystal grown from the melt phase, it is anticipated that impurity elements with $K_{\text{eff}} < 1$ will be more concentrated in the growth sector of smooth face with the slowest normal growth rate than in growth sectors of both rough interface and smooth interface with lower morphological importance. Figure 5.12 shows an example demonstrating this: a CL tomograph of high-pressure high-temperature synthetic diamond crystal bounded by {111} and {100} faces showing brighter zones corresponding to higher concentration of nitrogen in {111} growth sectors than in {100} growth sectors, which show no CL intensity. In the growth of high-pressure high-temperature (HPHT synthetic) diamond, both {111} and {100} behave as smooth interfaces, but {111} is morphologically more important than {100} [5.29]. Natural diamonds also indicate higher concentration of nitrogen in smooth {111} growth sector than in rough {100} growth sector. In natural diamond growth, {111} behaves as a smooth interface, whereas {100} exclusively behaves as a rough interface. In synthetic quartz, Al impurity was found to be selectively adsorbed on growth

steps of certain vicinal faces of growth spirals developing on the morphologically most important $\{10\bar{1}0\}$ faces [5.27].

Impurity elements with $K_{\text{eff}} < 1$ accumulate more as growth proceeds, in the ambient phase, to form a concentration gradient in the diffusion boundary layer surrounding the growing crystal. This modifies the chemistry of the ambient phase in the diffusion boundary layer, affecting the normal growth rate, the critical driving force for 2DNG, diffusion rates, etc., and leads to the formation of a band with a gradient of impurity concentration parallel to the growing surface. Due to coupling of the accumulation of impurity on the growing interface, their diffusion, and the resulting change in the normal growth rate, an alternating succession of bands with varying concentration of impurity (and also point defects) appears parallel to the growing surface, even if the crystal grew under nearly constant growth conditions. Such bands may be less distinct and have nearly uniform and narrow spacing. When growth parameters change abruptly, a more distinct growth band is formed. So, within one growth sector, distinct but not uniformly spaced bands and less distinct but uniformly and narrowly spaced bands appear. Since these bands appear through growth and represent the morphology of the crystal at successive stages, this banding is called growth banding. Analysis of growth banding provides important information about how the crystal grew and the morphology changes throughout its growth process. Growth bands in the growth sectors of smooth interfaces exhibit straight banding, whereas in those of rough interface growth, hummocky growth banding appears (Fig. 5.13a,b). If a smooth interface transforms to a rough interface during growth due to a conditional change, and the rough interface changes to a smooth interface in further growth, the appearance of a wavy and hummocky band and its transformation to a cellular pattern, followed by transformation from a rough to smooth interface with the appearance of microfacets in the recovery process, may be traced by observation of growth banding (Fig. 5.13c,d). The evolution of the crystal morphology in the formation of single crystal may also be traced. Dissolution of earlier formed crystal followed by regrowth may be identified through the observation of the banding pattern in single crystal. All sorts of event may be discernible by the analysis of heterogeneities in single crystals. Figure 5.13a–c shows schematically a few cases to be expected, and Fig. 5.13d shows an actual example of the appearance of microfacets during the recovery process. Figure 5.14 shows schematically the internal morphology

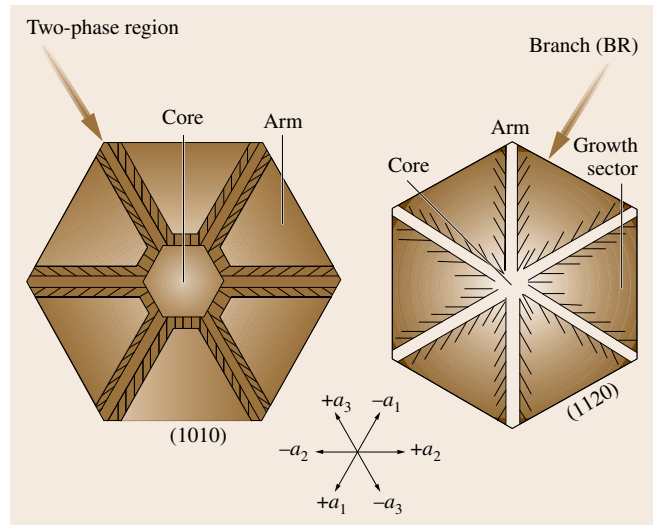


Fig. 5.14 Trapeiche emerald (left) and ruby (right), formed by dendritic growth forming the skeleton of the crystal, followed by growth on smooth interface filling the interstices of dendritic arms (after [5.30,31])

ogy of emerald and ruby crystals, indicating earlier formation of core portion by 2DNG or spiral growth, on which dendritic growth took place to form the arms and branches, followed by 2DNG or spiral growth filling the interstices of the dendritic arms. These are called trapeiche emerald or ruby. Various terms are used to express the corresponding portions, as indicated in the figure [5.30, 31], but the growth mechanism and history are the same in both minerals. The skeleton and the size of the present crystal are determined by this growth history.

If a polyhedral crystal receives weak dissolution (etching), corners, edges, and outcrops of point and line defects are preferential sites to be attacked. The polyhedral crystal will be rounded off with etch pits on the surfaces. Straight growth banding observable in growth sectors is cut by the rounded external surface. All natural diamond crystals show rounded morphology and etch pits, indicating that their characteristic rounded forms are due to dissolution experienced during the ascent period from depth to the Earth's surface, during which they experienced pressure–temperature conditions labile for diamond. When dissolution occurs to form rounded crystal, on which regrowth later took place, earlier straight growth banding is intersected by rounded discontinuity, followed later by the appearance of microfacets and straight growth banding. A wide variety of internal morphology is encoun-

tered in polyhedral single crystals of natural minerals, and their growth and postgrowth histories can be

analyzed if their internal morphology is properly analyzed.

5.6 Perfection of Single Crystals

Dislocations are generated where lattice planes advancing from different sources meet with mismatches or displacements during growth. There can be various origins of lattice mismatches during the growth process of a crystal. In the nucleation stage the nucleus may be bounded by rough interfaces, but soon smooth interface starts to appear. Lattice mismatch may occur through this transformation from rough to smooth interface at the earliest stage of growth. When dendritic arms conjugate, or when solid or liquid inclusions are enclosed into the growing crystal, lattice mismatch occurs at places where they are enclosed. When bunched macrosteps advancing on smooth interface meet, lattice mismatch may also occur. In these cases, dislocations with large

Burgers vector are often generated on the growing surface. Since such dislocations are energetically unfavorable, they dissociate into many dislocations with elemental Burgers vector. When seed crystal is used, its surface provides preferential sites to generate new dislocations, since inclusions are likely trapped on etched seed surface, from where dislocations are newly generated, together with dislocations inherited from the seed. A variety of spatial distributions of dislocations can therefore be encountered in single crystals grown freely under unconstrained conditions and with seed crystal. When crystals grow in the interstices of solid crystals of other minerals, such as in the formation of metamorphic rocks, numerous dislocation centers will be

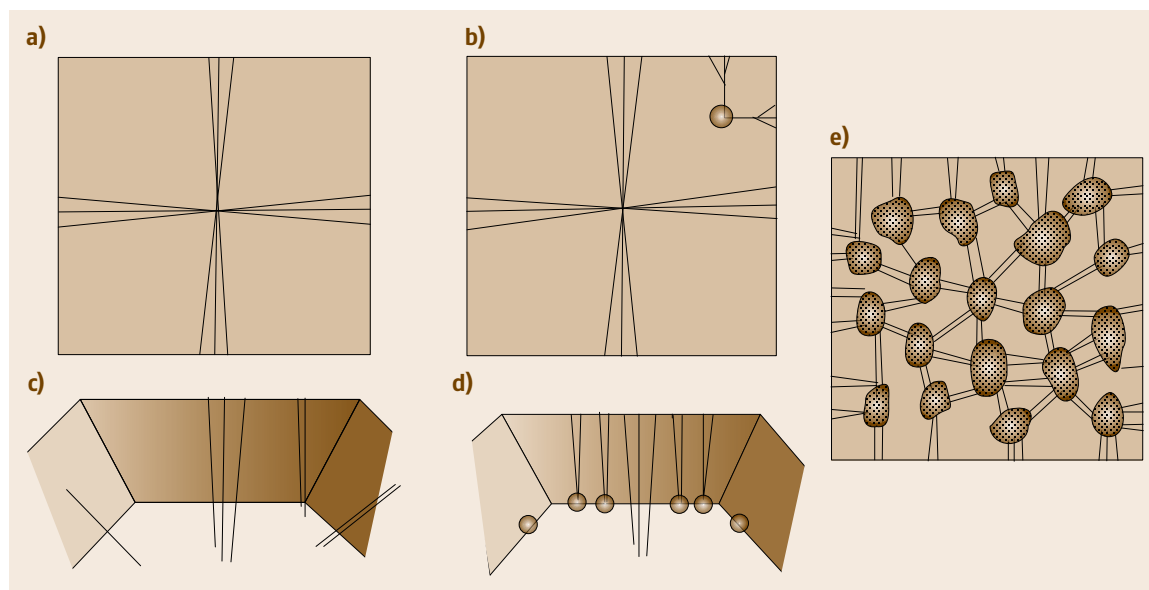


Fig. 5.15a–e Schematic illustrations of the spatial distribution of dislocations in single crystals. **(a)** Dislocations originating at the center of a crystal and radiating in a bundle nearly perpendicularly to the growing faces for energetic reasons. This is a representative distribution of dislocations observed in freely grown crystal in diluted vapor or solution phase under unconstrained conditions. **(b)** Dislocations are also generated from a point where an inclusion is enclosed. Dislocations with a large Burgers vector dissociate into many dislocations with elemental Burgers vector. **(c,d)** Comparison of the inheritance of dislocations in the seed to the newly grown portion **(c)** and the generation of new dislocations from inclusions formed on the seed surface **(d)**. **(c)** As-grown crystal is used as seed, whereas **(d)** etched crystal is used. **(e)** When growth occurs in the interstices of solid grains, such as expected in metamorphism, a single crystal may show a large number of points from where dislocations are generated

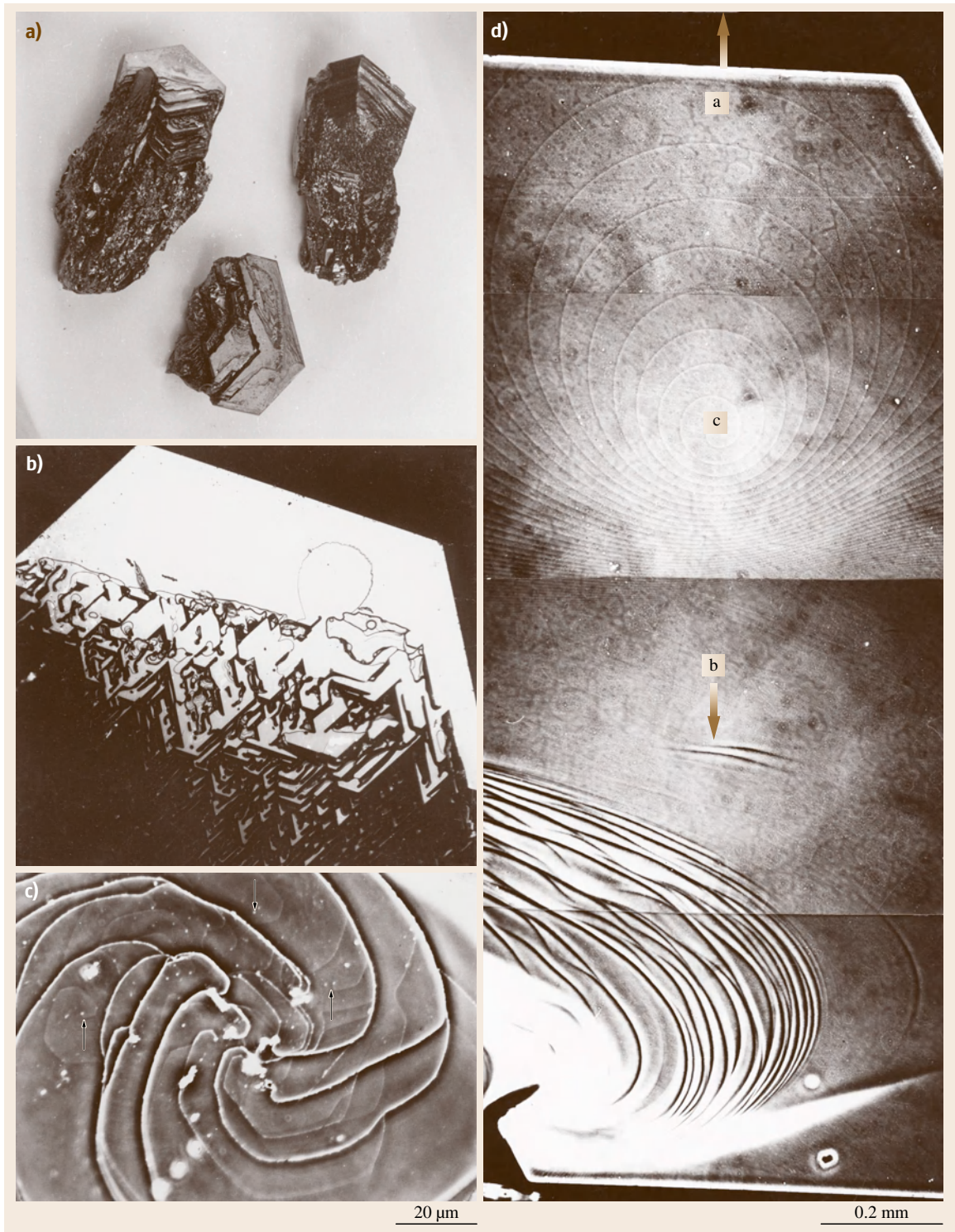


Fig. 5.16a–d How SiC crystals grow by the Acheson method (impure CVT) (a–c), and (d) by the Lely method (pure CVT or close to PVT). (a) Macro photograph of SiC crystals grown by the Acheson method, showing earlier dendritic growth followed by the appearance of {0001} face. (b) Ordinary reflection photomicrograph showing appearance of flat {0001} face through conjugation of microfacets of {0001} at the tips of dendrite arms, and (c) positive phase-contrast photomicrograph of growth spirals with larger and elemental (arrows) step heights, observable on flat {0001} surface such as shown in (b). Spiral steps originating from dislocations with larger Burgers vector show much brighter contrast than those originating from elemental (arrows) Burgers vector. Coexistence of growth spirals with larger and elemental Burgers vectors is due to the dissociation of dislocations with larger Burgers vector. (d) A positive phase-contrast photomicrograph showing an example of growth spirals commonly observed on SiC crystals synthesized by the Lely method. Arrows *a* and *b* indicate the direction to the center and the wall of the crucible, respectively, and *c* the spiral center. Step separation is eccentric from *c* to *a* and from *c* to *b*, due to the flow of source vapor (gradient) over the surface [5.32]. Bunching of spiral steps and perturbation of step morphology is seen in direction *b* ◀

observed in the crystals. These are illustrated schematically in Fig. 5.15, and a few representative examples will be described in the following.

A wide variety of spatial distributions of dislocations are observed in freely grown single crystals, such as natural minerals or crystals grown from solution phase. Since the spatial distribution of dislocations in single crystals provides important information relating how the crystal grew and what sort of conditional changes took place during its growth history, we may analyze these based on their investigations, coupled with observations of its surface microtopography and internal morphology. Three examples are now described.

SiC crystals synthesized by the Acheson method grow as dendrite at the initial stage on the wall of the reaction crucible. The dendritic arms conjugate together and the basal {0001} face starts to appear, inclined with respect to the length of the dendrites [5.33]. This can be seen clearly in Fig. 5.16a,b. Dislocations generated at the points where dendritic arms are close usually have large Burgers vector and dissociate into many dislocations with elemental Burgers vector. As a result, on the {0001} surface, coexistence of growth spirals with step heights corresponding to large and elemental Burgers vector is often observed. Figure 5.16c shows an example of growth spirals often observed on SiC crystals grown by the Acheson method. In the case of SiC crystals synthesized by the Lely method, more ideal growth spiral originating from independent dislocation are generally observed. However, these spirals often show eccentric step separation (Fig. 5.16d) due to the surface supersaturation gradient [5.32].

Figure 5.17 shows an x-ray topograph of a slice cut perpendicular to the *c*-axis of a prismatic quartz crystal occurring in a granitic pegmatite. Growth sectors corresponding to {10 $\bar{1}$ 1}, {0111}, and {10 $\bar{1}$ 0} faces and sector boundaries, growth banding, and dislocation bundles generated from inclusions are observed in contrast images. Distinct anisotropy in the development of growth sectors, in the spacing of growth banding, and in the distribution and density of inclusions and dislocation bundles can be noticed among crystallographically equivalent growth sectors. The observed anisotropies imply that the quartz crystal grew under the effect of solution flow. On the growing {10 $\bar{1}$ 1} and {10 $\bar{1}$ 0} faces, facing the solution flow, more inclusions are precipitated, from where more dislocations are newly generated than on the surface growing on the opposite side.

Figure 5.18a,b shows x-ray and CL tomographs of a pear-shaped brilliant cut diamond, respectively. The squarelike pattern at the center in Fig. 5.18a is an outline of a tiny cuboid crystal whose overall

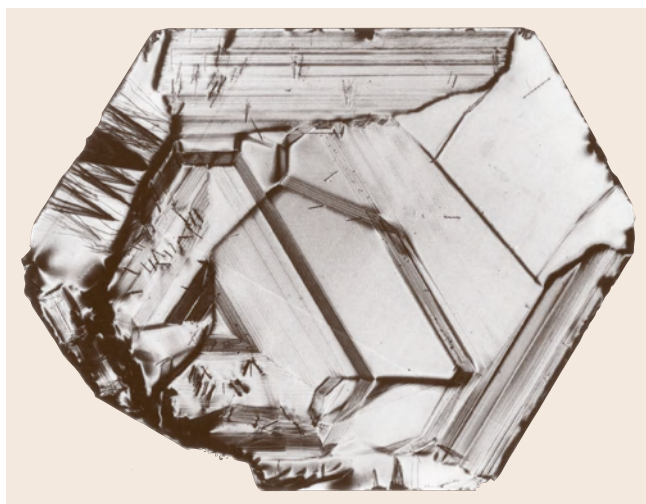


Fig. 5.17 X-ray topograph of a slice cut perpendicular to the *c*-axis of a prismatic quartz crystal from pegmatite (x-ray topography, courtesy of T. Yasuda)

form is close to cubic, although not bounded by flat {100} faces but by rough, near-{100} faces. The cuboid was formed elsewhere and transported into a different growth environment, where it acted as a seed for further growth under the new conditions. In Fig. 5.18a, it is noted that dislocations are newly generated on the surfaces of the seed cuboid and radiate in the form of bundles running parallel to $\langle 100 \rangle$, although there are also a few dislocations inherited from the seed. The Burgers vector of these dislocations is 100, which is different from those generally observed in most gem-quality diamonds, i.e., 110. In Fig. 5.18b, it is seen that growth of diamond on the seed transforms from rough {100} to smooth {111} morphology through the appearance of many {111} microfacets, indicating morphological evolution in the recovery process from rough to smooth interfaces [5.34]. The most likely place where the seed cuboid was formed is considered to be in ultrahigh-pressure high-temperature (UHPHT) metamorphic rocks formed by plate subduction. In these metamorphic rocks, minute diamond crystals are formed in porphyroblastic (crystals developed much larger than the coexisting ones) silicate minerals, such as garnet and zircon [5.35]. It is argued that these diamond crystals were formed in silicate-carbon liquid droplets formed by partial melting of porphyroblastic silicate mineral containing unmelted carbon [5.34]. The carbon source is assumed to be of organic origin, subducted from oceanic sediments. This explains the much higher concentration of diamond, attaining up to 2% in UHPHT metamorphic rock, as compared with the very low content of diamond (on the order of ppm) in mantle-originated ultramafic rocks. When these UHPHT metamorphic rocks are subducted deeper and digested in magma in the mantle, this diamond acts as a seed on which further diamond grows under much lower driving force conditions [5.34]. This example demonstrates that a large-scale geological movement or cycle is recorded in the form of the internal morphology, perfection, and homogeneity within a small crystal, provided that this information can be properly deciphered.

Natural diamond crystals experience a severe post-growth history. They grew in the depth of the Earth, under diamond-stable high-pressure high-temperature conditions, in silicate or carbonate solution phase, and were uplifted at great speed by volcanic action, to be quenched as a metastable phase through volcanic eruption. In the rapid ascent process, diamond crystals suffer partial dissolution, resulting in rounded forms and the formation of etch pits. They also experience plastic de-

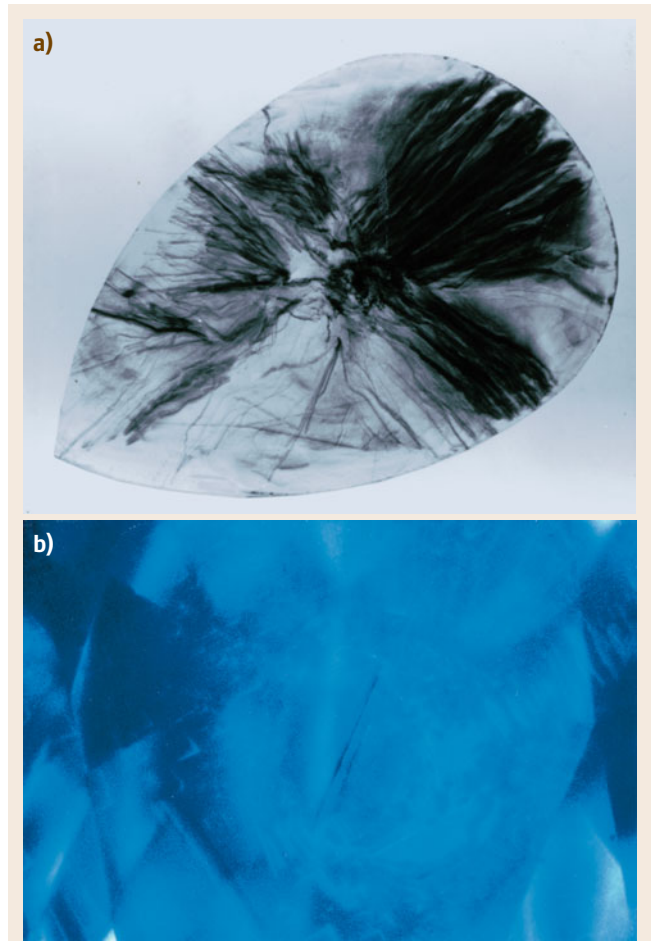


Fig. 5.18a,b X-ray topograph (a) and cathodoluminescence tomography (b) of a pear-shaped brilliant cut diamond. (a) demonstrates that most of this crystal was formed by growth under new conditions on a seed cuboid, seen at the center, which was formed elsewhere under different conditions and transported to the new conditions. Most dislocations with Burgers vector 100 are generated on the seed surface. (b) demonstrates that the morphology transformed from rough cuboid to octahedral bounded by smooth {111} faces via the appearance of a series of {111} microfacets, which is discernible from the distribution of brighter CL contrast corresponding to selective partitioning of impurity nitrogen to smooth {111} faces

formation, forming dislocation tangles and exsolution (precipitation) of impurity nitrogen. Natural diamonds are classified into type I and II, which differ in various physical properties related to their different nitrogen content. Type I contains higher nitrogen content and thus corresponds to C-N alloy, whereas type II contains

far less nitrogen and corresponds to pure C. Due to this difference, their plastic deformation behavior is different, type I being plastically stronger than type II. As a result, when both types experience the same stress history, type II suffers greater plastic deformation. Among natural diamond crystals, type II crystals exclusively show irregular forms without crystallographic faces, whereas type I crystals exhibit polyhedral form with rounded corners and edges. Type I crystals exhibit dislocation bundles radiating from the center of a crystal on x-ray topographs, whereas type II crystals show bending with portions of slightly different orientations, indicating that type II crystals are heavily deformed compared with type I crystals, and sometimes even broken into pieces [5.36].

Observations on the perfection, homogeneity, and internal morphology of natural diamond crystals

demonstrate that the whole growth and postgrowth histories are recorded in small crystals of diamond. We can see in a tiny diamond crystal the whole large-scale geological movements experienced by the crystal, provided that this record can be properly deciphered. Understanding the crystal growth mechanism, morphology, perfection, and homogeneity form the basis for properly reading this message sent from the depth of the Earth. It also indicates that natural and synthetic gemstones, including diamond, can be discriminated by these investigations, since both grow in solution phases but with different solvents (natural diamonds from silicate or carbonate, synthetic diamonds from metallic) and have different growth histories, although both are the same crystal species [5.29]. It is also possible to fingerprint two brilliant cut diamonds obtained and fashioned from one rough stone [5.34].

References

- 5.1 J.A. Burton, R.C. Prim, W.P. Slichter: The distribution of solute in crystals grown from the melt, Part 1, Theory, *J. Chem. Phys.* **21**, 1987–1991 (1953)
- 5.2 I. Kostov, R.I. Kostov: *Crystal Habits of Minerals* (Pensoft, Sofia 1999)
- 5.3 I. Sunagawa: *Crystals – Growth, Morphology and Perfection* (Cambridge Univ. Press, Cambridge 2005)
- 5.4 I. Sunagawa: Surface microtopography of crystal faces. In: *Morphology of Crystals, Part A*, ed. by I. Sunagawa (Reidel, Dordrecht 1987) pp. 321–365
- 5.5 I. Sunagawa: Growth of crystals in nature. In: *Materials Science of the Earth's Interior*, ed. by I. Sunagawa (Reidel, Dordrecht 1984) pp. 63–105
- 5.6 W.F. Berg: Crystal growth from solutions, *Proc. R. Soc. Lond. Ser. A* **164**, 79–95 (1938)
- 5.7 P. Curie: On the formation of crystals and on the capillary constants of their different faces, *J. Chem. Educ.* **47**, 636–637 (1970), translation of *Bull. Soc. Franc. Min. Cryst.* **8**, 145–150 (1885)
- 5.8 G. Wulff: Zur Frage der Geschwindigkeit des Wachstums und der Auflösung der Kristallflächen, *Z. Krist.* **34**, 449–530 (1901), in German
- 5.9 J.W. Gibbs: On the equilibrium of heterogeneous substances. In: *The Scientific Papers of J. W. Gibbs*, Vol. 1 (Longman Green, London 1906)
- 5.10 R. Kern: The equilibrium form of a crystal. In: *Morphology of Crystals, Part A*, ed. by I. Sunagawa (Reidel, Dordrecht 1987) pp. 77–206
- 5.11 P. Bennema, J.P. van der Eerden: Crystal graphs, connected nets, roughening transition and the morphology of crystals. In: *Morphology of Crystals, Part A*, ed. by I. Sunagawa (Reidel, Dordrecht 1987) pp. 1–75
- 5.12 P. Hartman: Modern PBC. In: *Morphology of Crystals, Part A*, ed. by I. Sunagawa (Reidel, Dordrecht 1987) pp. 269–319
- 5.13 A. Bravais: Les systemes formes par des pointes distribues regulierement sur un plan ou dans l'espace, *J. Ecol. Polytech.* **XIX**, 1–128 (1850), in French
- 5.14 J.D.H. Donnay, D. Harker: A new law of crystal morphology extending the law of Bravais, *Am. Mineral.* **22**, 446–467 (1937)
- 5.15 P. Hartman, W.G. Perdok: On the relations between structure and morphology of crystals. I, *Acta Cryst.* **8**, 49–52 (1955)
- 5.16 P. Hartman, W.G. Perdok: On the relations between structure and morphology of crystals. II, *Acta Cryst.* **8**, 521–524 (1955)
- 5.17 P. Hartman, W.G. Perdok: On the relations between structure and morphology of crystals. III, *Acta Cryst.* **8**, 525–529 (1955)
- 5.18 R. Uyeda: Crystallography of metal smoke particles. In: *Morphology of Crystals, Part B*, ed. by I. Sunagawa (Reidel, Dordrecht 1987) pp. 367–508
- 5.19 R.S. Wagner, W.C. Ellis: Vapor–liquid–solid mechanism of single crystal growth, *Appl. Phys. Lett.* **4**, 89–90 (1964)
- 5.20 I. Sunagawa: Vapor growth and epitaxy of minerals and synthetic crystals, *J. Cryst. Growth* **43**, 3–12 (1978)
- 5.21 A. Wells: Crystal habit and internal structure I + II, *Philos. Mag. Ser. 7* **37**, 184–236 (1946)
- 5.22 H.E. Buckley: *Crystal Growth* (Wiley, New York 1951)
- 5.23 R. Hook: *Micrographia* (Royal Society, London 1665)
- 5.24 E.I. Givargizov: *Highly Anisotropic Crystals* (Reidel, Dordrecht 1986)
- 5.25 I. Sunagawa, Y. Takahashi, H. Imai, S. Yamada: Topological whisker bundles of amphibole and frost

- column of quartz, *J. Cryst. Growth* **276**, 663–673 (2005)
- 5.26 Y. Aoki: Growth of KCl whiskers on KCl crystals including the mother liquids, *J. Cryst. Growth* **15**, 163–166 (1972)
- 5.27 M. Kawasaki: Growth-induced inhomogeneities in synthetic quartz crystals revealed by the cathodoluminescence method, *J. Cryst. Growth* **247**, 185–191 (2003)
- 5.28 R.J. Reeder, J.C. Grams: Sector zoning in calcite cement: Implication for trace element distributions in carbonates, *Geochim. Cosmochim. Acta* **51**, 187–194 (1987)
- 5.29 I. Sunagawa: The distinction of natural from synthetic diamonds, *J. Gemmol.* **24**, 489–499 (1995)
- 5.30 K. Nassau, K.A. Jackson: Trapiche emeralds from Chivor and Muzo, Colombia, *Am. Mineral.* **55**, 416–427 (1970)
- 5.31 I. Sunagawa, H.-J. Berhardt, K. Schmetzer: Texture formation and element partitioning in trapiche ruby, *J. Cryst. Growth* **206**, 322–330 (1999)
- 5.32 I. Sunagawa, I. Narita, P. Bennema, B. van der Hoek: Observation and interpretation of eccentric growth spirals, *J. Cryst. Growth* **42**, 121–126 (1977)
- 5.33 I. Sunagawa: Surface micro-topography of silicon carbide, *Sci. Rep. Tohoku Univ. Ser. III* **12**, 239–275 (1974)
- 5.34 I. Sunagawa, T. Yasuda, H. Fukushima: Fingerprinting of two diamonds cut from the same rough, *Gems Gemol. Winter*, 270–280 (1998)
- 5.35 N.V. Sobolev, V.S. Shetsky: Diamond inclusions in garnets from metamorphic rocks: A new environment for diamond formation, *Nature* **343**, 742–746 (1990)
- 5.36 I. Sunagawa: A discussion on the origin of irregular shapes of type II diamonds, *J. Gemmol.* **27**, 417–425 (2001)

6. Defect Formation During Crystal Growth from the Melt

Peter Rudolph

This chapter gives an overview of the important defect types and their origins during bulk crystal growth from the melt. The main thermodynamic and kinetic principles are considered as driving forces of defect generation and incorporation, respectively. Results of modeling and practical in situ control are presented. Strong emphasis is given to semiconductor crystal growth since it is from this class of materials that most has been first learned, the resulting knowledge then having been applied to other classes of material.

The treatment starts with zero-dimensional defect types, i.e., native and extrinsic point defects. Their generation and incorporation mechanisms are discussed. Micro- and macrosegregation phenomena – striations and the effect of constitutional supercooling – are added. The control of dopants by using the nonconservative growth principle is considered. One-dimensional structural disturbances – dislocations and their patterning – are discussed next. The role of high-temperature dislocation dynamics for collective interactions, such as cell structuring and bunching, is shown. In a further section second-phase precipitation and inclusion trapping are discussed. The importance of in situ stoichiometry control is underlined. Finally two special defect types are

6.1 Overview	159
6.1.1 Defect Classification	160
6.1.2 Consequences of Crystal Defects for Devices	161
6.2 Point Defects	163
6.2.1 Native Point Defect Generation	163
6.2.2 Extrinsic Point Defect Incorporation	170
6.2.3 Constitutional Supercooling – Morphological Instability	175
6.3 Dislocations	176
6.3.1 Dislocation Types and Analysis	177
6.3.2 Dislocation Dynamics	178
6.3.3 Dislocation Engineering	187
6.4 Second-Phase Particles	188
6.4.1 Precipitates	189
6.4.2 Inclusions	190
6.5 Faceting	191
6.6 Twinning	193
6.7 Summary	194
References	195

treated – faceting and twinning. First the interplay between facets and inhomogeneous dopant incorporation, then main factors of twinning including melt structure are outlined.

6.1 Overview

The quality of single crystals and devices made therefrom are very sensitively influenced by structural and atomistic deficiencies generated during the crystal growth process. It is the chief task of the crystal grower to determine the conditions for their control, minimization or even prevention. Crystalline imperfections include point defects, impurity and dopant inhomogeneities, dislocations, grain boundaries, second-phase and foreign particles, twins, and so on. Some defect types, such as point defects, are in thermodynamic equilibrium and are therefore always present. This is due to the thermal excitations and entropic disordering forces at temperatures $T > 0$. Further, each crystal is bounded by surfaces with interface characteristics deviating from

geneities, dislocations, grain boundaries, second-phase and foreign particles, twins, and so on. Some defect types, such as point defects, are in thermodynamic equilibrium and are therefore always present. This is due to the thermal excitations and entropic disordering forces at temperatures $T > 0$. Further, each crystal is bounded by surfaces with interface characteristics deviating from

volume perfection. These facts prevent the growth of ideal, perfect crystals. Hence, in practice only optimal crystals are achievable.

Over more than a half-century of development of melt growth, most of the important defect-forming mechanisms have become well understood. Historical aspects of this progress were recently summarized by Hurle and Rudolph [6.2, 3]. Today, there exists an enormous knowledge about defect genesis in as-grown crystals supported by demanding theoretical fundamentals and computational modeling. As a result, the present state of technology makes it possible to produce crystals of remarkably high quality with tailored parameters fitting the demands of the device industry quite well. However, that is not to say that all problems are already solved. Thus, the present chapter will also cover still open questions and help to find optimal measures of defect engineering.

In this section first the defect types will be categorized in the classical manner of zero-, one-, two- and three-dimensional defects. Then some effects of defects on device properties will be covered.

6.1.1 Defect Classification

The international standard crystal lattice defects (defects in short), sketched in Fig. 6.1, are usually classified according to their dimension as follows [6.1].

Zero-dimensional defects are *point defects*, often referred to by the unpopular name *atomic-size defects*, which include the intrinsic defect types va-

cancies, *interstitials*, and in compounds, *antisites*. If extrinsic atoms are invoked unintentionally (as residual *impurities*) or intentionally (as *dopants*) they occupy interstitial or substitutional (lattice) positions. At growth temperatures, point defects are isolated and usually electrically charged. The charge state of point defects can lead to their interaction with electrically active dopants, creating *point defect complexes*.

One-dimensional defects include all kinds of *dislocations*, i. e., perfect screw and edge dislocations, mixed dislocations, partial dislocations (always in connection with a stacking fault), and dislocation loops. The propagation and interaction of dislocations over mesoscopic distances is the subject of *dislocation dynamics*. The collective screening behavior of dislocations contributes to their rearrangement in dipoles, walls, and networks, as well as under simultaneous stress in cell patterns and bundles. Whether the cell patterning is driven energetically or by a self-organizing process in the framework of equilibrium or nonequilibrium thermodynamics, respectively, is still the subject of research.

Two-dimensional defects are grain boundaries, stacking faults, phase boundaries, facets, and twins. A *low-angle grain boundary* structure is formed by the mechanism of dynamic polygonization and still belongs conventionally to a single-crystalline state. In contrast, *large-angle grain boundary* structures are formed by polycrystalline growth due to spontaneous or foreign nucleation processes. *Facets* are formed along atomically smooth planes, indicating the tendency of high-quality crystals to form polyhedra. They cause extrinsic point-defect and temperature-field inhomogeneities due to their fast lateral growth kinetics and enhanced radiation reflectivity, respectively. Grown-in *twins* are originated by a false stacking sequence, especially when the two-dimensional nucleus on a growing facet is disoriented.

Three-dimensional defects include second-phase particles (*precipitates*), intrinsic vacancy conglomerates (*microvoids*), and foreign particles (*inclusions*). It is important to differentiate between precipitates and inclusions, which are mostly confused in the literature. Whereas precipitates and microvoids are formed by supersaturation-driven condensation of intrinsic point defects, i. e., interstitials and vacancies, respectively, inclusions are melt–solution droplets, gas bubbles, and foreign microparticles incorporated at the growing melt–solid interface, especially when the melt composition deviates from the congruent melting point or contaminations are present. The two types of defects

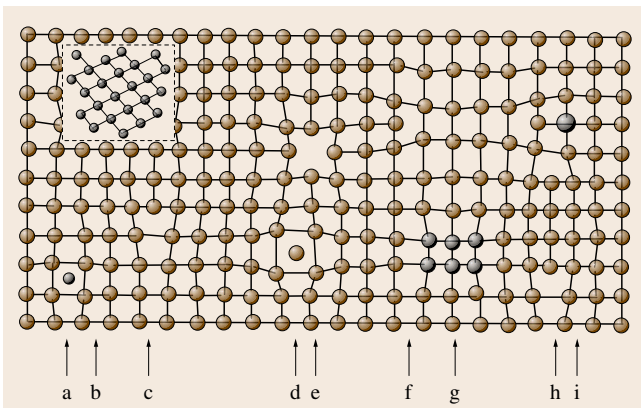


Fig. 6.1 Scheme of real crystal lattice with defects (after Föll [6.1]). a – interstitial impurity atom, b – incongruous inclusion, c – edge dislocation, d – self-interstitial atom, e – vacancy, f – vacancy-type dislocation loop, g – precipitate of impurity atoms, h – interstitial-type dislocation loop, i – substitutional impurity atom

usually differ in their size, being 10–100 nm for precipitates and 1–10 μm for inclusions.

6.1.2 Consequences of Crystal Defects for Devices

Defects have deleterious effects on the performance, reliability, and degradation behavior of devices. Following the early classification of *Pick* [6.4] defects influence the:

- Structural properties (vacancies and interstitials may change the lattice constant; grains affect the single crystallinity)
- Chemical properties (defects participate in chemical reactions; their redistribution causes composition inhomogeneities)
- Electronic properties (defects occupy a specific state in the band structure)
- Scattering properties, i.e., the defect interacts with particles (phonons, photons of any energy, electrons, positrons, etc.).

As can be seen, the interaction processes are many-sided and require wide interdisciplinary research with direct correlation to advanced technical progress. In fact, a large part of the worldwide technology progress depends on the control and manipulation of defects in crystals, above all in the semiconductor and optical industries, but also in biotechnology and many others. There are an enormous number of monographs and publications dealing with this topic. In the following, however, only selected examples of correlation between device characteristics and defects will be touched upon. An instructive review about defects in semiconductors and their electronic properties is given by *Mahajan* [6.5].

Point defects determine the basic properties of the materials used in devices. Parameters such as the specific resistance of semiconductors, conductance in ionic crystals, or diffusion properties in general, which may appear to be intrinsic properties of a material, are in fact defect dominated. In optical devices the transmittance, birefringence, and refractive index are influenced by the density and distribution of intrinsic and extrinsic point defects very sensitively. For instance, high-quality electrooptical and nonlinear optical devices of LiNbO_3 require an extremely accurate constant Li/Nb ratio (congruent composition) to ensure birefringence homogeneity of $(5\text{--}7) \times 10^{-5}$ [6.6]. Intrinsic point defects can influence the conduction type in semiconductors. For instance, vacancies and interstitials in silicon can

have distinct acceptor and donor energy levels within the bandgap, respectively [6.5]. As_{Ga} antisites in GaAs are deep-level donors (EL2). Their density, which depends on the deviation from stoichiometry, determines the compensation doping level by a shallow acceptor (carbon) in order to ensure semi-insulating property in high-frequency circuits [6.7]. Point defects and their diffusion have a strong impact on the noise characteristics through an interaction of charge carriers with the fluctuating local ionic surrounding. In (Hg,Cd)Te infrared photodiodes there is a linear dependence between the $1/f$ noise power and the fraction of ionized Hg vacancies providing p-type conductivity [6.8]. In some cases, however, a redistribution of extrinsic defects is even desirable. For instance, in micro laser waveguides for integrated optics (e.g., LiNbO_3 fibers) the accumulation of certain dopants (Mg) near the surface helps to concentrate the laser beam in the center by the effect of refractive-index cladding [6.9].

As is well known, *dislocations* are defects influencing the quality of nearly all types of devices insofar as they act as getters for point defects and dopants so that they can contribute to electrical and chemical inhomogeneity. They decrease transmission in lenses, affect light intensity in laser rods, and influence the mechanical stability in piezo- and acoustoelectric transducers. Dislocations in substrates are transformed as threading dislocations into the epitaxial layers grown on them. When an overcritical misfit between the lattice parameters of a substrate and epilayer exists, misfit dislocations are generated at their interface. Both threading and misfit dislocations play an important role in the rapid degradation of (Ga,Al)As/GaAs lasers. The degradation of light-emitting semiconductor diodes and lasers follows from the fact that dislocations cause nonradiative recombination and decrease luminescence efficiency. They reduce the minority-carrier lifetime and, when the spacing between them is comparable to the diffusion length, luminescence efficiency breaks down [6.10]. Dislocations can contribute to electronic behavior, especially, in diamond and zincblende structures where the cores of glide and shuffle set dislocations are associated with dangling bonds [6.5]. Recently it was shown that small screw dislocations and threading edge dislocations are the most common defects in 4H-SiC homoepitaxial devices produced by chemical vapor deposition on SiC substrates. As their densities increase, the breakdown voltage of Schottky devices is decreased [6.11]. The central parameter of field-effect transistors (FETs) is the turn-on threshold voltage (V_{th}), the fluctuations of which across a wafer

Table 6.1 Selected examples of defects in melt-grown crystals demonstrating their adverse effect on device quality (BPT – bipolar transistor, PD – photodiode, IR – infrared, KTN – $K(\text{Ta}_x\text{Nb}_{1-x})\text{O}_3$, ME – microelectronics, MC – multicrystalline, LED – light-emitting diode, LD – laser diode, PVE – photovoltaic efficiency, UV – ultraviolet, YAG – $\text{Y}_3\text{Al}_5\text{O}_{12}$, MOS – metal–oxide–semiconductor, HBT – heterostructure bipolar transistor, MMIC – monolithic microwave integrated circuit, NLO – nonlinear optic, AO – acoustooptic)

Material	Defect type	Device version	Adverse effect
<i>Zero-dimensional</i>			
Si	Interstitial Si_i	BPT, PD	Ionized donor level, carrier traps
CdTe	Vacancy V_{Cd}	Radiation detector	Shallow donor reducing electrical resistivity
(Hg,Cd)Te	Vacancy V_{Hg}	IR photodiodes	Increased $1/f$ noise power
GaAs	Antisite As_{Ga}	Radiation detector	Deep level trap reducing carrier lifetime
KTN	Ta-rich striations	Optical modulator	Optical inhomogeneity, refractive index change
<i>One-dimensional</i>			
Si	Dislocation loops	ME circuits	Swirl formation, shorts
Si	Dislocations	MC-Si solar cell	Affecting minority carrier lifetime
GaAs	Dislocations	LED, LD	Nonradiative recombination
(Cd,Zn)Te	Cell structure	Radiation detector	Impediment of electron transport
<i>Two-dimensional</i>			
Si	Grain boundaries	MC-Si solar cell	Decreasing PVE by impurity (Fe) gettering
InP	Twins	ME circuits	Decreasing usable crystal gain
CaF_2	Grain boundaries	UV lenses	Light scattering and radiation damage
YAG	Facets	Solid state laser	Refractive index variation, optical loss
<i>Three-dimensional</i>			
Si	V_{Si} clusters (voids)	MOS circuits	Gate oxide degradation by local thinning
GaAs	As precipitates	HBT, MMIC	Impairment of wafer polishing and epitaxy
LiNbO_3	Eutectic inclusions	NLO modulators	Light scattering, birefringence impairment
PbMoO_3	Pb-rich inclusions	AO transmitter	Light scattering, reduced transmission

must be minimal to ensure high device yield. In ion-implanted GaAs FETs a shift of V_{th} around dislocations was observed which has been explained not only by the dislocation presence but also by the enhanced GaAs antisites and As interstitials on dislocations [6.12]. Thus, in order to remove the decorating defects from dislocations today each as-grown GaAs crystal is postannealed before it is applied for device technology. Note that dislocations themselves are practically immune to post-growth thermal treatment.

Cellular structures of dislocations and *grain boundaries* are two-dimensional defects responsible for harmful optical and electrical inhomogeneities. For instance, across semi-insulating {100} GaAs wafers a mesoscopic resistivity variation is observed due to the accumulation of As_{Ga} antisite defects (EL2) within the cell

walls [6.13]. Subgrain boundaries also impede the electron transport, as in $\text{Cd}_{1-x}\text{Zn}_x\text{Te}$ radiation detectors [6.14]. In general, since grain boundaries are defects in the crystal structure, they tend to decrease the electrical and thermal conductivity of the material. Additionally, the high interfacial energy and relatively weak bonding in grain boundaries makes them preferred sites for the onset of corrosion and the precipitation of new phases from the solid. The presence of a small-angle grain boundary structure in melt-grown LiF crystals prevents their use in monochromators and x-ray analyzers due to the high light and x-ray diffraction scatterings, respectively [6.15]. Increasing quality is demanded for CaF_2 lenses, which are used in deep-ultraviolet (UV) semiconductor microlithography. The stepwise reduction of the exposing wavelength down to

157 nm, correlating with the smallest circuit structure size, requires a dramatic improvement of the growth and annealing conditions of CaF_2 crystals. The highest transmission and lowest radiation damage can be only achieved when the crystals are free of grain boundaries [6.16].

It is noteworthy that there is also a certain interest in crystals with mosaic structure. For instance, diffraction lenses for nuclear astrophysics show an improved reflection power when crystals with mosaicity of 20–50 arcs (e.g., $\text{Ge}_{1-x}\text{Si}_x$) are used [6.17]. Further, in nanocrystalline materials, controlled reduction of grain size to nanometer scale leads to many interesting new properties including a great increase in strength [6.18]. Therefore, the further development of knowledge about collective dislocation interactions in growing crystals is of general practical relevance for both targets, i.e., both suppressing and promoting cellularity.

6.2 Point Defects

At all temperatures above absolute zero, equilibrium concentrations of vacancies, self-interstitials, and in the case of compound semiconductors, antisite defects will exist. This is because point defects increase the configurational entropy, leading to a decrease in free energy. Thus, such native point defects are always presented in as-grown crystals. However, their concentration can be influenced by the growth conditions very sensitively. In silicon a nearly defect-free situation due to vacancy–interstitial annihilation can be achieved by selection of a certain relation between the temperature gradient and crystallization rate. In compound crystals *in situ* control of stoichiometric growth conditions can minimize the intrinsic defect density.

Extrinsic point defects are incorporated arbitrarily or deliberately as impurities or dopants, respectively. Today, the purification techniques of the starting charge materials are of such a high standard that total residual impurity concentrations fall below the frozen-in contents of native point defects. In elemental crystals (e.g., silicon) purity levels less than 10^{14} cm^{-3} and in compound crystals (e.g., GaAs) values below 10^{15} cm^{-3} can be achieved. Therefore, their influence on the crystal lattice parameter and electrical parameters is of secondary significance. Of course, due to a contaminated growth atmosphere or because of strong chemical affinities it can happen that certain arbitrary elements are introduced in enhanced concentrations, such as oxygen in

Precipitates and *inclusions* are second-phase particles of autonomous crystallographic structure and chemical composition forming an interfacial boundary with the matrix material. They induce local parameter and stress fluctuations and, therefore, mostly misfit dislocations [6.19,20]. In liquid encapsulation Czochralski (LEC) GaAs substrates arsenic precipitates affect the device properties of epitaxial-type metal-semiconductor field effect transistors (MESFETs). They also cause the formation of small surface oval defects on molecular beam epitaxy (MBE) layers [6.5]. Principally, inclusions impair the surface quality of wafers during the polishing process. In lenses and backside radiation detectors they reduce the transmission quality by light scattering.

Table 6.1 summarizes selected correlations between device quality impairments and the responsible defect types.

CaF_2 or carbon in silicon, for example. In contrast, for light-emitting devices the required dopant concentrations markedly exceed those of impurities and usually exceed 10^{18} cm^{-3} or amount even to 10^{21} cm^{-3} , as for Cr^{3+} in ruby laser crystals. In these cases homogeneous incorporation is of essential technological importance but is complicated by the natural segregation effect that may lead to macro- and microdistributions. A characteristic structural impairment during growth from doped or incongruent melts can arise from constitutional supercooling – the interplay between rejected dopants or excess atoms, diffusion, and heat transfer at the growing melt–solid interface. Growing-in dopants interact with native point defects, which are isolated and mostly ionized at growth temperatures. As a result, the physical efficiency of dopants can be reduced by compensation and complex formation.

It is the aim of the crystal grower to understand these interactions on the atomic scale and determine their correlations to the growth conditions in order to master chemical and electronic homogeneities as much as possible.

6.2.1 Native Point Defect Generation

Thermodynamics

All thermodynamic processes strive to minimize the free energy. Applied to the crystallization process this

means that the single-crystalline state is a normal one because the free thermodynamic potential G (free potential of Gibbs) is minimal if the *crystal growth units* (atoms, molecules) are perfectly packed in a three-dimensional ordered crystal structure, i. e., the atomic bonds are saturated regularly. Because the sum of the atomic bonds yields de facto the potential part H , i. e., the enthalpy part of the internal crystal energy $U = H - PV$ (where P is pressure, and V is volume), the process of ordering responsible for adjustment of the *crystal periodicity* is characterized by the minimization of enthalpy ($H \rightarrow \min$).

On the other hand, however, an ideally ordered crystalline state would imply an impossible minimal entropy S . Thus, the opposite process of increasing entropy, i. e., disordering ($S \rightarrow \max$) gains relevance with increasing temperature T . This is expressed by the basic equation of the thermodynamic potential of Gibbs

$$G = U + PV - TS = H(\downarrow) - TS(\uparrow) \rightarrow \min. \quad (6.1)$$

Hence, crystallization is composed of two opposite processes:

- i) Regular
- ii) Defective arrangement of the *growth units*.

Considering this dialectics of ordering and disordering forces at all temperatures above absolute zero it is not

possible to grow an absolutely perfect crystal. In reality *no ideal* but only an *optimal* crystalline state can be obtained. In other words, in thermodynamic equilibrium the crystal perfection is limited by incorporation of a given concentration of native point defects n .

Neglecting any effects of volume change, defect type, and defect interplay, at constant pressure the equilibrium defect concentration n can be determined from the change of thermodynamic potential by introducing the defect as

$$\Delta G = \Delta H_d - \Delta S_d T \rightarrow \min, \quad (6.2)$$

with $H_d = nE_d$, the change of internal energy due to the incorporation of n defects, depending on the total defect formation energy E_d , and $S_d = k_B \ln\{(N!)/[n!(N-n)!]\}$ the accompanying change of entropy (configurational entropy), where k_B is the Boltzmann constant and N the total number of possible sites. After substitution and application of Stirling's approximation for multiparticle systems such as a crystal ($\ln N! \approx N \ln N$, $\ln n! \approx n \ln n$, $\ln(N-n)! \approx (N-n) \ln(N-n)$) (6.2) becomes

$$\Delta G = nE_d - k_B T \times [N \ln N - n \ln n - (N-n) \ln(N-n)]. \quad (6.3)$$

Setting the first derivative of (6.3) as $\partial \Delta G / \partial n = 0$ to yield the energetically minimum defect concentration n_{\min} , and considering $N \gg n$, the *perfection limit* of a crystal is

$$n_{\min} = N \exp\left(\frac{-E_d}{k_B T}\right), \quad (6.4)$$

which is exponentially increasing with temperature. Setting $N = 5 \times 10^{22} \text{ atoms cm}^{-3}$ and $E_d = 1 \text{ eV}$ (the vacancy formation energy in metals) the minimum defect concentrations n_{\min} at 1000 and 300 K are about 5×10^{17} and 10^6 cm^{-3} , respectively. Note that, in the case of formation of vacancy–interstitial complexes (Frenkel defects), the value of $n_{\min}^{(F)}$ is somewhat modified and yields $\sqrt{N_{is} N} \exp(-E_d^{(F)}/k_B T)$, where N_{is} is the total number of interstitial positions depending on the given crystal structure, and $E_d^{(F)}$ is the energy of formation of a Frenkel defect. More fundamental details are given in Kröger's compendium [6.21], which remains even today one of the basic guides for the crystal grower.

Figure 6.2a,b shows the functions $\Delta G(n)$ and $n_{\min}(T)$ schematically. Due to the limitation of diffusion rate, a certain fraction of high-temperature defects

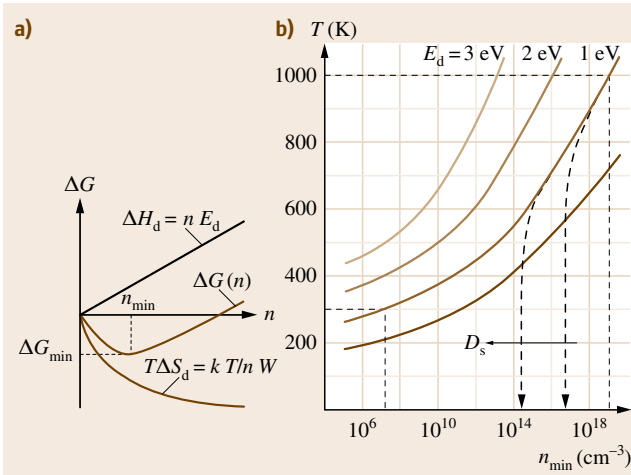


Fig. 6.2 (a) Schematic illustration of the equilibrium defect concentration (*perfection limit* n_{\min}) obtained by superposition of defect enthalpy H_d and entropy S_d using (6.2–6.4). (b) Minimum defect concentration versus temperature at various defect energies E_d according to (6.4). Dashed lines show the *freezing-in* courses of high-temperature defects for different migration coefficients D_s

freeze in during the cooling-down process of as-grown crystals (broken lines) and exceed the equilibrium concentration at room temperature markedly (Fig. 6.2b). In other words, in practical cases the intrinsic point-defect concentration is still far from thermodynamic equilibrium.

In principle, the total defect formation energy consists of various factors: $E_d = E_{\text{form}} + U_{\text{vib}} + S_{\text{vib}}T$ where E_{form} is the relevant defect formation energy, and U_{vib} and S_{vib} are the energy and entropy terms for the vibration contributions to the free energy. Of course, each contribution in its turn depends on temperature. Their exact experimental determination requires high-purity crystals and extremely precise analytical techniques, for instance, measurements of the thermal dependence of dilatation combined with precision x-ray analysis of the lattice constant. The native point defect concentration is proportional to the difference between the relative increase of length and the change of the lattice constant as $n \sim (\Delta L/L - \Delta a/a)$, whereas a positive or negative amount identifies the prevailing presence of vacancies or interstitials, respectively. No dilatation effect appears when the number of vacancies equals the number of interstitials. In principle, such measurements and most others begin to fail at defect concentrations below $\approx 10^{17} \text{ cm}^{-3}$. Therefore, theoretical treatments come to the fore, e.g., quasichemical, molecular dynamics (MD), ab initio, and first-principle calculations. Table 6.2 shows the formation energies and entropies of native point defects near the melting point in some important materials. The activation energies of defect migration are also given.

Note that these values for compound semiconductors differ in the literature markedly and Table 6.2 is only of approximate character. Additionally, one has to consider the multiple charge stages of native defects showing various energies depending on the position of the Fermi level [6.24].

It is clear that a given native point-defect content corresponds to each crystalline phase, like a *solute component* in a system with ideal mixing. Compound materials show a phase extent, termed the existence or homogeneity region, that deviates from the stoichiometric composition by a certain value. Assuming a conservative compound system AB with defect balance, the maximum deviation δ can be expressed in terms of the concentrations of the native point defects in each sublattice as [6.30]

$$\delta = \delta A - \delta B = \{[A_i] - [V_A] + 2[A_B] - 2[B_A]\} - \{[B_i] - [V_B] + 2[B_A] - 2[A_B]\}, \quad (6.5)$$

where $[A_i]$, $[B_i]$, $[V_A]$, $[V_B]$, $[A_B]$, and $[B_A]$ are the interstitial, vacancy, and antisite contents of A and B, respectively. In simple terms, by using (6.4) for each defect type in (6.5) the maximum equilibrium defect solubility in a given AB crystal at each temperature becomes identical to the solidus curve of the existence region in the phase diagram. Table 6.3 shows the maximum phase extents of some compound materials. As can be concluded from (6.4), in a cooling crystal the solidus curves take a retrograde course leading under realistic cooling rates to freeze in of high-temperature nonequilibrium defects (Fig. 6.2b). In standard-grown

Table 6.2 Selected formation energies, entropies, and activation energies of migration in selected materials (A, B_i – interstitial, $V_{A,B}$ – vacancy, A_B – antisite, k_B – Boltzmann constant, $^{\pm i}$ – charge stage and E_f in the mid-gap)

Material	Defect	Formation energy E_f (eV)	Formation entropy S_f (k)	Activation energy of migration E_m (eV)	Reference
Cu	Cu_i	1.1			[6.22]
	V_{Cu}	0.78–1.2	1.5	0.52–0.62	[6.22]
Si	Si_i	1.1, 3.46	1.4	0.937	[6.5, 23]
	V_{Si}	2.3, 2.48	–3.7	0.457	[6.5, 23]
GaAs	As_i	(5.5 ²⁺)			[(6.24)]
	V_{Ga}	2.59 (3.1 ²⁻)	32.9	1.7	[6.10] [(6.24)] [6.25]
	V_{As}	2.59 (3.7 ¹⁺)	1.1		[6.10] [(6.24)]
	As_{Ga}	3.21 (2.0 ²⁺)			[6.10] [(6.24)]
CdTe	Te_i	1.97 (3.67)			[6.26] [(6.27)]
	Cd_i	0.96	11.1	2.47–2.67	[6.28, 29]
	V_{Cd}	3.55, 3.84 (4.7)	–5.6		[6.29] [(6.27)]
	Te_{Cd}	0.81 (2.29)			[6.26] [(6.27)]

Table 6.3 Maximum widths of phase extent δ_{\max} of selected compounds [6.6, 19, 31]

Material	InP	GaAs	CdTe	CdSe	PbTe	SnTe	LiNbO ₃
δ_{\max} (mole fraction)	5×10^{-5}	2×10^{-4} (2×10^{-3})	1×10^{-4} (3×10^{-4})	5×10^{-4}	1×10^{-3}	1×10^{-2}	≈ 5
Side of maximum deviation and congruent melting point	In-rich	As-rich	Te-rich	Cd-rich	Te-rich	Te-rich	Nb ₂ O ₅ -rich

compound crystals the real intrinsic point-defect concentration at room temperature is between 10^{15} and 10^{17} cm^{-3} . This is about 7–9 orders of magnitude higher than the calculated values in thermodynamic equilibrium (if E_d is assumed to be 1–2 eV).

For silicon crystals near to the melting point it is accepted that vacancies and interstitials are simultaneously present in concentrations of about 10^{14} – 10^{15} cm^{-3} and that they can recombine very rapidly [6.32]. In the end, the ratio between them within the cooled crystal is determined by the relation of the atomistic transport processes (e.g., diffusion and thermodiffusion), the recombination rate, and the applied growth parameters (e.g., the temperature gradient and pulling velocity). The situation in compound materials, e.g., semiconductors such as $A^{\text{III}}B^{\text{V}}$ and $A^{\text{II}}B^{\text{VI}}$, is more complicated and less well studied. The equilibrium point defect concentrations at the melting point tend to be much higher than in Si. Hurle's calculations [6.30, 33] in GaAs of the concentrations of the principal native point defects at the melting temperature yield values about 10^{17} – 10^{19} cm^{-3} for $[V_{\text{Ga}}]$, $[Ga_i]$, and $[As_i]$, $[V_{\text{As}}]$, respectively. This is comparable to or even greater than the intrinsic carrier concentrations. Due to their isolated, and usually electrically charged, states they can influence the position of the Fermi level. This results in a complex interaction between electrically active dopants and the native point defects, which can exist in more than one charge state (Sect. 6.2.2).

Generation and Incorporation Kinetics

Principally, increasing the temperature raises the probability of thermal (vibrational) and entropy-driven (configurational) generation of Frenkel defects. Depending on the temperature gradients acting along the crystal and the cooling rate the initially coincident concentrations of vacancies and interstitials can differ markedly due to differing migration rates (Table 6.2). As a result, one defect type can move to the crystal surface, leaving defects of Schottky type. Further, during the crystallization process, point defects can be incorporated from the melt at the propagating melt–solid interface. Hence, one has to distinguish between:

- Intrinsic defect generation
- Incorporation from outside.

In any case, the principles of both energy minimization and electrical neutrality act as *regulators* of concentration and charge balancing as far as equilibrium conditions occur. Lowering the energy enhances the recombination probability of interstitials and vacancies during the cooling-down process of the growing crystal. Heat and mass flows, however, can lead to deviations from thermodynamic equilibrium.

During crystal pulling from the melt or unidirectional solidification, native point defects undergo various types of transport kinetics, i.e., capture at the interface due to the crystal translation or phase boundary propagation (often designated *convection*), Fickian diffusion by jumping via interstitial sites, kick-out or vacancy occupation mechanisms, and temperature-gradient-driven thermal diffusion (the Soret effect). Until now silicon is the material best studied. The prevailing transport mode at each temperature and in each crystal region has been estimated by dimensionless numbers of point defect dynamics [6.34]. The numbers of Péclet $Pe_{I,V} = \nu L / D_{I,V}(T)$, Damköhler $Da_{I,V} = k_r C_{V,I}^{\text{eq}}(T) L^2 / D_{I,V}(T)$, and Soret $ST_{(I,V)} = D_T / D_{I,V}(T) \approx \nu k_B T^2 / H_{I,V}^F G_T D_{I,V}$ compare the convection, recombination, and thermodiffusion, respectively, with Fickian diffusion, where ν is the crystal growth velocity, L is the characteristic length, k_r is the recombination reaction constant, $C_{V,I}^{\text{eq}}$ is the equilibrium concentration, D_T is the coefficient of thermodiffusion, $D_{I,V}(T)$ is the coefficient of Fickian diffusion of interstitials and vacancies, k_B is the Boltzmann constant, T is absolute temperature, $H_{I,V}^F$ is the formation enthalpy, and G_T is the temperature gradient at the melt–solid interface. Setting the parameters for silicon [6.23, 34] one can see that convective and Fickian diffusion flows are comparably strong and compete with each other in the hot crystal section, that recombination proceeds very fast at high temperatures, but that thermodiffusion contributes only marginally. Thus, variations of the pulling rate can shift point-defect transport between convection- and diffusion-dominated regimes.

As was proved experimentally [6.35], at high pulling rates the flux of vacancies dominates over that of self-interstitials. On the other hand, at low pulling rates or with high temperature gradients, interstitials are in excess. This fact is of high significance for in situ control of the native point defect type and content during growth (see later).

The situation in semiconductor and oxide compound crystals is not nearly as well understood as in silicon. There are still no detailed studies demonstrating the correlation between temperature gradient at the growing interface, crystallization rate, and content of the given intrinsic defect types. Of course, one reason is the presence of dislocations acting as effective getters (Sect. 6.3) that make it difficult to study the point defect dynamics in the pure form. In principle, as demonstrated in (6.5), the situation in multicomponent materials is additionally complicated due to the presence of equivalent defect types in each sublattice and the formation probability of antisites. It is established that the As_{Ga} antisite in $GaAs$ crystals, known as the neutral $EL2$ defect with charged states $EL2^+$ and $EL2^{2+}$, does not appear at the growth temperature but forms during the cooling-down process. In material grown from a near-congruent composition, i. e., slightly As -rich melt, the As_i content removes the $[V_{Ga}]$ by producing As_{Ga} as soon as the lowering temperature evokes supersaturation [6.33]. A nearly identical mechanism takes place in $CdTe$. In cooling Te -saturated samples the antisite Te_{Cd} does form and may become important as singly and doubly ionized mid-gap donors $Te_{Cd}^{1+,2+}$ responsible for compensation of the shallow native acceptor $V_{Cd}^{1-,2-}$ [6.36].

For understanding the defect trapping kinetics at a propagating melt–solid interface, first of all one has to clarify whether the front moves by atomically rough or smooth morphology. This can be estimated by the Jackson factor [6.37] $\alpha = (w/u)\Delta H/k_B T$, where ΔH is the enthalpy of crystallization, w is the number of nearest neighbors of an atom on the face, u is the number of nearest neighbors of an atom in the crystal, k_B is the Boltzmann constant, and T is absolute temperature (see also Sect. 6.5). Whereas metals show α values of about 1, i. e., a rough interface, dielectrics crystallize mostly with atomically smooth interfaces due to typical α values larger than 2. In between stand the semiconductor materials with their covalent bondings and, hence, α factors around 2. In this case the crystallographic binding structure along the crystallizing plane (w/u) determines whether the interface is microscopically smooth or rough. Semiconductors with diamond,

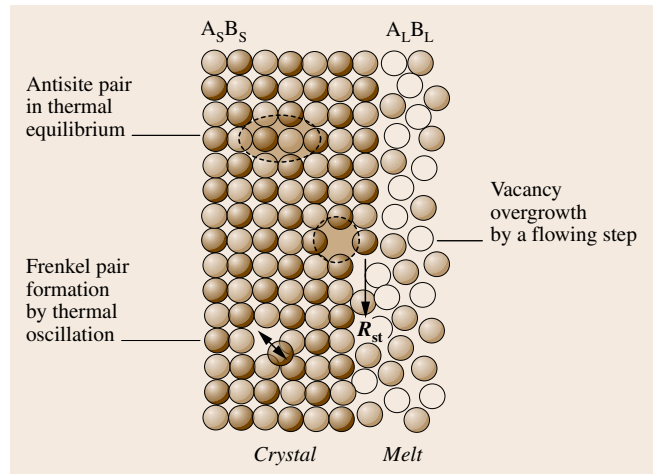


Fig. 6.3 Sketch of intrinsic point defect kinetics of an AB compound at an atomically flat melt–solid interface propagating by step-growth mechanism (R_{st} – lateral step-growth rate)

zincblende, and wurtzite structures grow from the melt along most directions by the atomically rough mode. They tend to form atomically smooth interfaces only on their most close-packed (i. e., $\{111\}$) planes (see also Sect. 6.5).

On atomically rough interfaces atoms can be added singly without the need for nucleation, i. e., at very low chemical potential difference between solid and liquid phases. As a result, possible defect sites are added to the crystal under quasi-equilibrium conditions. On the contrary, for atomically smooth planes much higher supercooling is required in order to initiate two-dimensional (2-D) nucleation followed by layer-by-layer growth. In such a case vacancies, interstitials and even foreign atoms, possibly delivered by the adjacent liquid boundary layer, can be overgrown very rapidly and, hence, incorporated in metastable states if their diffusion rate back to the melt is not high enough. The sketch in Fig. 6.3 demonstrates this situation. According to *Chernov* [6.38] equilibrium incorporation takes place only when the lateral step rate R_{st} fulfils the inequality

$$R_{st} < \frac{D_{IF}}{h}, \quad (6.6)$$

where D_{IF} is the interface diffusion coefficient (10^{-4} – 10^{-5} cm^2/s) and h is the step height. The actual step growth velocity can be estimated by the relation

$$R_{st} = \beta_i \Delta T, \quad (6.7)$$

where β_i is the kinetic step coefficient [6.38,39], which for silicon is 50 cm/(s K) [6.40], and ΔT is the supercooling, which has been determined at growing {111} facets of silicon crystals to be a maximum of 7 K [6.41]. Hence, at very high step flow rates, i. e., relatively high supercooling, nonequilibrium (metastable) point-defect incorporation can result.

It seems that the fluid phase should deliver sufficient imperfections due to its structural instability and disordered character. However, as recent MD simulations have demonstrated, between the liquid and crystal surface a characteristic transition region of several atomic layers exists, within which the thermal motion of the atoms decreases and the structure approaches the crystalline one [6.39]. In fact, as was ascertained by high-resolution in situ transmission electron microscopy, the {111} solid-liquid interface of Si has already a well-ordered transition layer on the atomic scale, which is compatible with defect-free 1 × 1 Si-{111} surface [6.42]. It can be assumed that the presence of such an ordered transition region should stabilize the growth kinetics against incorporation of an excess of deficiencies. According to Motooka's MD simulations [6.43], point defects are formed directly at the interface due to the density misfit between the liquid and solid phases.

Point Defect Engineering

In order to ensure specified electrical and optical qualities of single crystals and devices made therefrom the control of native point defects plays an important technological role, especially if harmful secondary reactions are evoked by point imperfections, such as precipitation (Sect. 6.4.1) and microvoid generation. From an experimental point of view, there are two possible ways of defect mastering:

- i) In situ control during the crystal growth process
- ii) Postannealing of the crystal bulk or pieces cut therefrom.

The first method is of increasing interest due to its cost benefits.

In the case of low-dislocation or even dislocation-free crystal growth, the complete native point defect dynamics come into play. The absence of dislocations leads to a quasihomogeneous defect interplay without catalytic effects. As a result the relatively high supersaturation promotes vacancy and/or interstitial condensations within the crystal volume, escalating to unfavorable micro and mesoconglomerations. For instance, in silicon at high pulling rates, vacancies

are incorporated in excess and condense during cooling down to form octahedral voids of ≈ 100 nm. On the other hand, at low pulling rates interstitials are in excess, forming a network of dislocation loops. In between, a defect-free region is obtained which is bounded by unwanted oxidation-induced stacking faults (OSF). The balance between the number of vacancies and interstitials is the controlling factor. Based on these experimental observations three ways to achieve microdefect-free silicon have been worked out [6.35]:

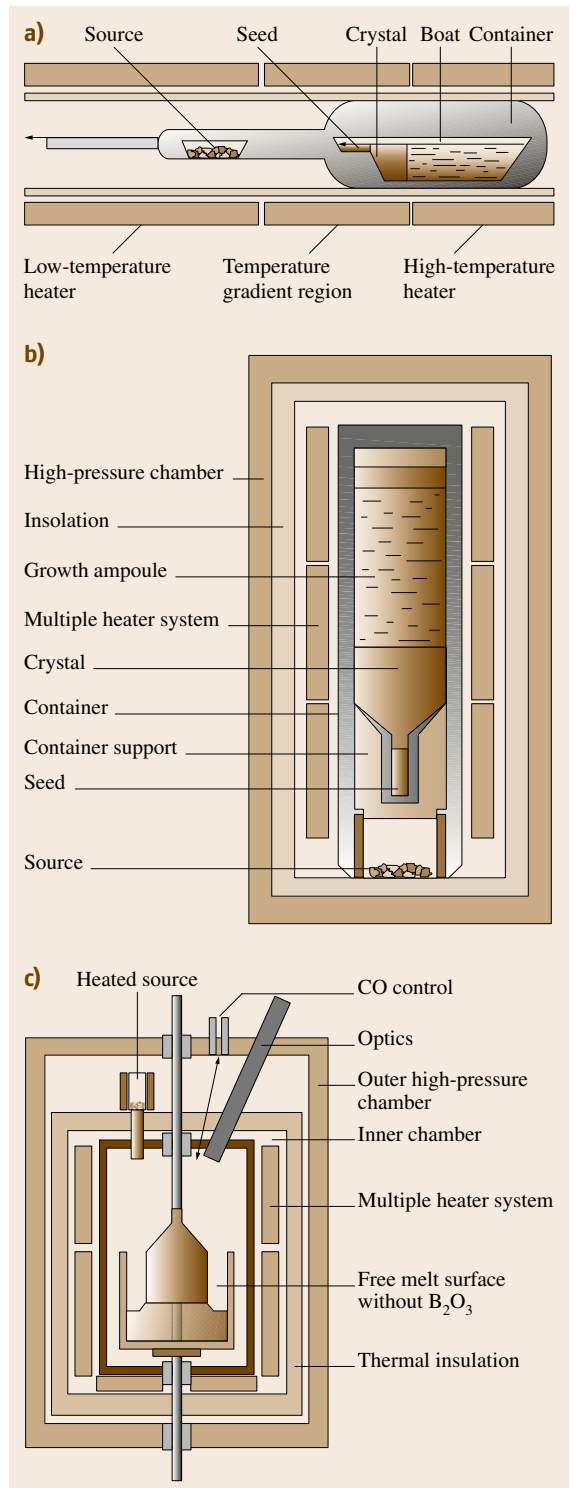
- i) Keeping the growth conditions within the defect-free regime, which is approximately $\pm 10\%$ around the critical ratio $v/G_T = 1.34 \times 10^{-3} \text{ cm}^2/(\text{K min})$, where v is the growth rate and G_T is the temperature gradient at the interface. However, such a small tolerance permits only very low pulling velocities of about 0.5 mm/min. Falster and Voronkov [6.44] described the in situ outdiffusion of interstitials. In this case, the crystals are pulled under interstitial-rich conditions and maintained at high temperatures for extended times, thus utilizing the very high migration speed of interstitials. However, extended cooling times with very low cooling rates are required.
- ii) Keeping a maximum pulling rate with fast cooling followed by a wafer annealing process to reduce the grown-in defect sizes.
- iii) Using a cost-optimized approach, a so-called *flash wafer* step [6.35], where only a thin Si layer of 0.5 μm is deposited onto the wafer surfaces. This combines maximum pull rate and fast cooling with low-cost treatment.

The in situ control of native point defects in compound crystals is coupled with the feasibility of accurate composition control during the growth process and, therefore, with exact knowledge of the phase diagrams. Taking the T - x -phase projections (where x is the mole fraction) one can find numerous AB compounds with a region of homogeneity containing the strict stoichiometric composition and extending to both sides of stoichiometry, such as CdTe and PbTe, for example [6.19]. However, there are also compounds with asymmetric phase extents shifted to anion or cation excess, even not including the stoichiometric composition, such as GeTe and SnTe, for example [6.45]. Also in LiNbO₃ the prevailing part of the existence region is located on the Nb₂O₃-rich side [6.46]. Unfortunately, for a lot of compounds the exact shape and width of the homogeneity region has not yet been clarified, especially when very small phase extents exist, as in InP, InAs,

Fig. 6.4a–c Crystal growth arrangements for in situ stoichiometry control by partial vapor pressure of the volatile element. **(a)** Horizontal Bridgman (HB) method. **(b)** Vertical gradient freeze (VGF) technique. **(c)** Vapor-pressure-controlled Czochralski (VCZ) method ▶

SiC, and PbMoO₄, or if phase relation analysis is difficult, as for ZnO and GaN. Even for GaAs only recently have thermochemical calculations [6.47, 48] confirmed the earlier and newer growth observations [6.49] that the phase extent is deviated exclusively towards the As-rich side. In principle, for materials with phase extents containing or touching the stoichiometric composition, it is obvious from theoretical calculations and annealing studies that stoichiometric growth conditions guarantee a minimum total native point defect concentration.

A method that has been well known for a long time is the in situ control of near-stoichiometric growth by applying a fixed-temperature vapor source of the volatile component in the horizontal Bridgman (HB) method without covering the melt [6.50]. In this technique there is direct contact of the vapor phase with the crystallizing melt–solid phase region, which guarantees near phase equilibrium conditions during the whole growth run (Fig. 6.4a). However, the technical limitation of the HB method for scaled-up production of crystals with diameters larger than 3 inches is commonly known. The vertical Bridgman (VB) and vertical gradient freeze (VGF) techniques have also been introduced, using an extra source for control of the vapor phase [6.51] (Fig. 6.4b). A certain transport transient of the vapor species has to be considered due to the complete covering of the crystallization front by the melt column. As a result the equilibrium temperatures for the vapor pressure source can somewhat differ between the techniques. Vapor-pressure-controlled HB, VB, and VGF have been successfully used to grow near-stoichiometric compound semiconductors, such as CdTe crystals [6.28]. If highly purified material is used even high-resistivity crystals can be obtained [6.52], due to intrinsic defect annihilation and compensation. However, ensuring a highly reproducible, stable intrinsic semi-insulating state over the whole crystal length during the whole growth run is very complicated due to native point defect segregation. A more promising method appears to be compensation doping (Sect. 6.2.2). In general, for VB and VGF, being obviously the most favorable melt growth techniques for semiconductor compounds, stoichiometric processing by in situ vapor pressure control is not yet possible on the industrial scale. The continuously decreasing



height of the melt column and segregation phenomena during the normal freezing process would require a well-controlled source temperature program that is well fitted to the growth rate. As a result, the stoichiometry is still tuned in cut wafers by postgrowth annealing if required for a given application [6.53].

Much less widely practiced is in situ control of stoichiometry in the Czochralski growth of semiconductor compounds. For this a modified technique without boric oxide encapsulant is required to influence the melt composition by the partial pressure of the volatile element. During the 1980s the hot-wall Czochralski (HWC) technique with As (P) source was advanced by Nishizawa et al. [6.54, 55] to analyze the variations of the physical parameters and dislocation density in GaAs and GaP crystals as functions of the melt composition. In recent years in situ control of the stoichiometry in GaAs by vapor-pressure-controlled Czochralski (VCz) technique [6.56] without boric oxide encapsulation has been under investigation [6.49, 57] (Fig. 6.4c). The mole fraction of the melt is controlled in the range of $0.45 \leq x_L \leq 0.50$ by partial arsenic pressures of 0.02–2.1 MPa, adjusted via the temperature of the As source from 540 to 650 °C. The authors [6.57] have demonstrated that near-stoichiometric growth conditions with a Ga-rich melt reduces the As_{Ga} antisite and V_{Ga} concentrations.

To date, for dielectric compounds, Czochralski growth experiments with precise in situ vapor pressure control are still rare. This is first of all due to the much higher growth temperatures and chemical aggressiveness of oxygen or fluorine, which make it difficult and expensive to insert a chemically resistant and gastight inner growth chamber with an extra source. However, some activities have been described. For instance, high-quality composition-controlled $Bi_{12}GeO_{20}$ (BGO) crystals were grown in an inner chamber made of platinum [6.58]. References [6.59, 60] describe a growth arrangement to control the stoichiometry of $PbMoO_4$ crystals with markedly improved optical transmission by using a MoO_3 evaporation source within a bell covering around the pulling crystal. Baumann et al. [6.6] demonstrated the importance of precise melt composition control for the growth of $LiNbO_3$ to obtain crystals with high axial homogeneity of birefringence.

6.2.2 Extrinsic Point Defect Incorporation

Thermodynamics

In growing crystals with dopant concentrations below the solubility limits, the matrix is regarded as con-

tributing one component in a phase diagram and the solute another. Thus, in growing such crystals from the melt, the system can be considered a binary one. The equilibrium between the chemical potentials of added species (i.e., solvent) i in the liquid and solid phases $\mu_{il}(x, T) = \mu_{is}(x, T)$ yields

$$\mu_{is}^0 + k_B T \ln x_{is} \gamma_{is} = \mu_{il}^0 + k_B T \ln x_{il} \gamma_{il}, \quad (6.8)$$

where μ^0 is the standard potential and γ is the interaction activity between i and atoms or molecules of the matrix. Setting $\mu_{il}^0 - \mu_{is}^0 = \Delta\mu_i^0 = \Delta h_i^0 - \Delta s_i^0 T$ and $s_i^0 = h_i^0/T_{mi}$, where h_i^0 and s_B^0 are the intensive standard enthalpy and entropy, respectively, T_{mi} is the melting point of the dopant, and $\Delta h_{Mis,l}^0 = k_B T \ln \gamma_{is,l}$ is the enthalpy of mixing, the transformed equation (6.8) becomes [6.31, 45]

$$\frac{x_{is}}{x_{il}} = k_0 = \exp \left[-\frac{\Delta h_i^0}{k} \left(\frac{1}{T} - \frac{1}{T_{mi}} \right) + \frac{\Delta h_{Mil} - \Delta h_{Mis}}{k_B T} \right], \quad (6.9)$$

where $k_{0i} = x_{is}/x_{il}$ is the (thermodynamic) *equilibrium distribution coefficient*, which can be assumed to be a constant for residual impurity or low dopant concentrations if the solidus and liquidus curves admit linearization. A more exact treatment, however, is provided by the description of the real solidus and liquidus courses by use of regression functions [6.61]. In most phase diagrams the solidus and liquidus courses can be approximated by polynomials. For instance, a polynomial of second order describes the temperature dependence of the solidus and liquidus as $T_{is,l} = p_{is,l} x_{is,l}^2 + q_{is,l} x_{is,l} + T_m$ where p and q are the regression coefficients and T_m is the melting point of the crystal matrix. The concentration dependence of the distribution coefficient then becomes $k_{0i}(x) = (p_{is} x_{is} + q_{is}) / (p_{il} x_{il} + q_{il})$. For the Al–Si system within the temperature region 660 °C (T_{mAl})–577 °C the coefficients are $p_{Sis} = 15.6065$, $q_{Sis} = -77.1694$, $p_{Sil} = -0.0371$, and $q_{Sil} = -6.2958$, for example [6.61].

Much more complicated is the situation of nonstoichiometric compound growth. Usually, the boundaries of the existence regions, being equivalent to the solidus curves of the excess component, show strong nonlinear T, x -behavior. Here a definition of the k_0 value for the given excess component becomes quite difficult, all the more so due to uncertainties in the shape of the phase extent. Such conditions take place during growth of semiconductor compounds. In [6.28, Fig. 4.5]

an attempt was made to estimate the segregation coefficients for Te and Cd in CdTe from the compound solidus courses on the Te- and Cd-rich sides. On the Te-rich side between the liquidus temperatures 1092 and 1080 °C, i. e., from the congruent melting point composition $x_{\text{cmp}} = 0.5 + 5 \times 10^{-6}$ up to a tellurium excess of $\delta x_{\text{Te}} = 5 \times 10^{-5}$, the k_0 value for Te changes between 0.8 and 0.1, respectively.

Interaction with Intrinsic Point Defects

Dopants can become incorporated on lattice sites or interstitial positions. In compounds, depending on their position in the periodic table, dopants may occupy either one or another or even both sublattice sites. In general, their incorporation efficiency is affected by the point defects that are present, which at growth temperatures are isolated and usually electrically charged [6.30]. The charge state of point defects depends on the position of the Fermi level, leading to their complex interaction with electrically active dopants. As a result the dopant solubility can be markedly influenced, and controversially, doping can affect the native point defect solubility.

The incorporation reaction of a dopant from the melt X_I with a neutral vacancy of the B sublattice V_B^0 in a AB semiconductor compound is assumed to be $X_I + V_B^0 = X_B^+ + e$, where X_B^+ is the substituting donor and e is a free electron. If the material is uncompensated the carrier concentration is $n = [X_B^+]$ and the segregation coefficient is

$$k_0 = \frac{[X_B^+]}{[X_I]}, \quad (6.10)$$

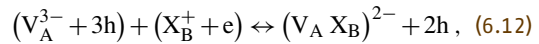
being constant as long as the dopant concentration is much lower than the intrinsic content of electron-hole pairs $n_i = [e_i] = [h_i]$ produced by the ionized native point defects. This follows from an effective value of the segregation coefficient k which was derived by *Chernov* [6.38] considering mass balance, electroneutrality, and k_0 from (6.10) as

$$k = \frac{k_0}{\sqrt{1 + \frac{[X_B^+]}{n_i}}} = \frac{k_0}{\sqrt{1 + \frac{[X_B^+]}{n_i}}}. \quad (6.11)$$

As can be seen, when $[X_B^+] \ll n_i$, the value of k equals the equilibrium distribution coefficient k_0 . However, once $[X_B^+]$ rises to $\approx n_i$ the effective segregation coefficient k begins to fall. In other words the dopant efficiency decreases. Physically, this is due to the growing charge state of the intrinsic point defect ($V_B^0 \rightarrow V_B^+ + e$)

in order to preserve the electroneutrality of the crystal $n = (n_i^2/n) + [X_B^+] + [V_B^+]$. This phenomenon has been well known for a long time from numerous melt-grown semiconductor compounds, such as GaAs doped with Te and Si [6.33] and CdTe doped with Ag and Cu [6.62].

The influence of the electron or hole concentration generated by the ionized dopants on the charge state of the native point defects is named the Fermi-level effect [6.63], whereby the degree of ionization depends on the position of the Fermi level [6.24]. For instance, the charge state of the Ga vacancy in GaAs changes from neutral V_{Ga}^0 in p-type material through double negatively charged V_{Ga}^{2-} in the midgap to a triple negatively charged V_{Ga}^{3-} in n-type material, which affects the compensation level and enhances the *complex formation* probability too. An example of a complex reaction in the common form is



as found in the form of $(\text{Te}_{\text{As}} V_{\text{Ga}})^{2-}$ or $(\text{Si}_{\text{Ga}} V_{\text{Ga}})^-$ in GaAs crystals.

Another factor influencing the incorporation efficiency of impurities and dopants is the nonstoichiometry of compounds. The greater the deviation from the stoichiometric composition during growth, the higher the possibility of vacancy generation within the compositionally impoverished sublattice. As a result the incorporation density of atoms at the growing interface occupying these vacant sites increases with nonstoichiometry. This was demonstrated in [6.62], where CdTe crystals were grown by vapor-pressure-controlled Bridgman method (Sect. 6.2.1) from different melt compositions containing Ag, Cu, and P dopants. Whereas Ag and Cu atoms occupy the Cd vacancies when growing proceeds from Te-rich melt, P takes up the Te vacancies on growth from Cd-rich melt. As has been demonstrated, the concentration of the neutral substitutions $[\text{Ag}_{\text{Cd}}^0]$, $[\text{Cu}_{\text{Cd}}^0]$, and $[\text{P}_{\text{Te}}^0]$, determined in as-grown crystal samples by absorption-calibrated photoluminescence [6.64], increased with Te or Cd enrichment of the melt, respectively. Figure 6.5 shows the variation of the substitutional concentration $[\text{Ag}_{\text{Cd}}^0]$ as a function of the starting silver concentration in the melt $[\text{Ag}_I]$ for various tellurium excess. At stoichiometric growth conditions the concentration of Ag_{Cd}^0 is drastically reduced down to $2 \times 10^{13} \text{ cm}^{-3}$. Compared with that, a Te excess of $5 \times 10^{17} \text{ cm}^{-3}$ leads to incorporation of Ag atoms on V_{Cd} sites at about one order of magnitude higher concentration (note the prevailing part of Ag atoms, is incorporated according k_0 in interstitial positions, probably acting as deep donors). The results underline the

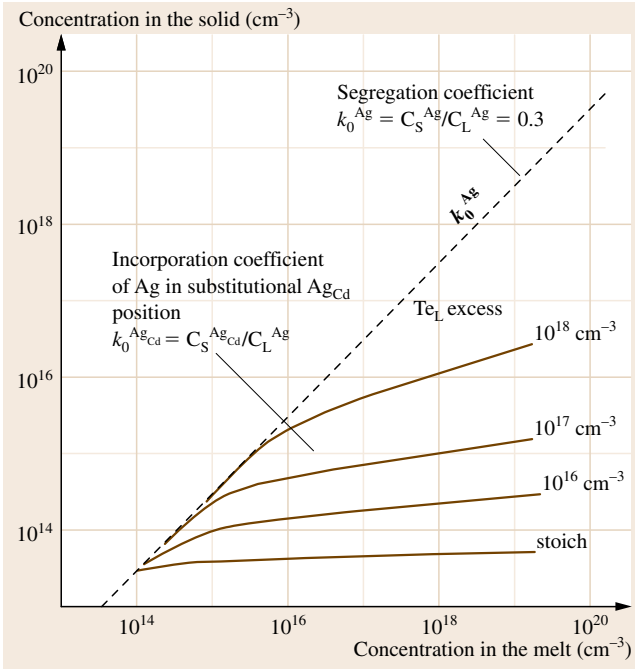


Fig. 6.5 Incorporation of silver atoms into substitutional Ag_{Cd} positions in CdTe crystals versus the degree of deviation from stoichiometry (Te excess) of the melt (after Rudolph et al. [6.62])

importance of in situ stoichiometry control in growth of both compound semiconductor crystals and dielectric crystals.

Segregation Phenomena

The redistribution of extrinsic atoms, arbitrarily or deliberately incorporated into a growing crystal, as well as the rearrangement of intrinsic point defects prove to be an essential challenge for the crystal grower. Such phenomena are due to the segregation effect and temperature gradients within the cooling crystal producing chemical and physical crystal inhomogeneities.

The deviation of the equilibrium segregation coefficient (6.9) from unity causes segregation phenomena during melt growth which can be treated in terms of an effective segregation coefficient $k_{\text{eff}} = x_{\text{is}}/x_{\text{il}}^{(\infty)}$, where $x_{\text{il}}^{(\infty)}$ is the mole fraction of the dopant in the melt far away from the interface. During an actual freezing process the solute is rejected ($k_0 < 1$) or preferentially absorbed ($k_0 > 1$) by the propagating solid–liquid interface, forming an enriched or depleted solute boundary layer in front of it.

The width δ_S of this boundary layer is determined by the growth rate R and by the diffusive and convec-

tive species transport in the melt, which is very often difficult to predict. A very popular model which is commonly used in melt growth was introduced by Burton, Prim, and Slichter (BPS) [6.65] for steady-state segregation

$$k_{\text{eff}} = \frac{k_0}{k_0 + (1 - k_0) \exp\left(\frac{-R\delta_S}{D}\right)}. \quad (6.13)$$

The advantage of this model is the ease of its use for plotting experimental data by fitting δ_S . By applying the Cochran flow solution at the surface of an infinite rotating disk, Levich [6.66] obtained the expression $\delta_S \approx 1.6D^{1/3}\nu^{1/6}\omega^{-1/2}$ (where D is the diffusion coefficient in the melt, ν is the kinematic viscosity of melt, and ω is the rotation frequency). Later, Ostrogoriski and Müller [6.67] quantified δ_S more physically for situations where natural convection rather than rotating disc flow dominated by considering its dependence on lateral convection velocity and the length of the interface. They defined $k_{\text{eff}} = (1 + \Lambda)/(1 + \Lambda/k_0)$ where $\Lambda = (v_D\delta_S)/(7.2\nu L)$, v_D is the convective velocity at the edge of the boundary layer, ν is the growth velocity, and L is the length of the interface. The value of k_{eff} is of central importance to explain macro- and microsegregation phenomena.

Macrodistribution

The macrodistribution describes the courses of a given solute concentration over its radius and along the as-grown crystal axis. Whereas the radial rearrangement is first of all affected by the shape of the melt–solid interface, the axial distribution depends on the growth velocity and level of convection in the melt. The degree of segregation depends on the extent to which the solute segregation coefficient (k_0) differs from unity. For instance, an enrichment of the dopants around the crystal center occurs at a concave- or convex-shaped interface and $k_0 < 1$ or > 1 , respectively. Against this, the solute is concentrated near the crystal periphery in the case of a convex interface and $k_0 > 1$. Therefore, only a nearly flat crystallization front can guarantee a homogeneous radial composition distribution.

The axial segregation function for unidirectional solidification in a completely mixed melt is described by the well-known Scheil equation (6.14), being valid for a stable planar crystal–melt interface and conservative mass balance, i. e., no solute evaporation from the melt or recharging into the melt takes place during the whole crystallization process. When the growth process is started with uniform melt concentration x_{i0} , the

concentration in the crystal x_{is} at a distance z from the initial growth face is

$$x_{is} = x_{i0} k_{\text{eff}} \left(\frac{1-z}{L_0} \right)^{k_{\text{eff}}-1}, \quad (6.14)$$

where L_0 is the length of the charge and the process considered is one in which the whole charge is initially molten and then frozen. From (6.13) and (6.14) it follows that k_{eff} equals unity at high growth rates or/and motionless melts, i. e., high values of δ_S in (6.13). In such cases high macroscopic distribution uniformity within the crystal can be reached. However, v is limited by the onset of morphological instability, as shown below. On the other hand, if the melt is stirred, the boundary layer is removed by the melt flow ($\delta_S \rightarrow 0$) and k_{eff} equals k_0 . In this case the axial distribution of the solute is typically inhomogeneous.

In order to obtain high axial chemical homogeneity in modern crystal growth processes often a nonconservative (open) system [6.68] with continuous dopant recharging (or extraction) is applied. This is practiced in the growth of semi-insulating GaAs crystals by applying carbon as a shallow acceptor for compensation of the deep intrinsic donor defects EL2 (As_{Ga}). As follows from (6.14), in the conservative case with complete melt mixing the C distribution, and hence the degree of compensation, which determines the electrical resistivity, becomes decreasing along the crystal axis due to $k_{\text{eff}}^C \approx k_0^C \approx 2$. By contrast, in a nonconservative system the axial distribution can be homogenized by proper in situ control of the CO fugacity within the growth chamber atmosphere delivering the C species for the melt via CO decomposition at the interface between boric oxide encapsulant and Ga-As melt. This is arranged by a controllable CO content within the working gas [6.69], a process well matured on the industrial scale [6.70]. Figure 6.6 compares the axial carbon distribution along GaAs crystals grown under nonconservative doping conditions [6.71]. For such case the Scheil equation (6.14) has to be modified as [6.72]

$$x_{is} = \frac{\eta k_{\text{eff}} x_{iv}}{k_{\text{eff}} + \eta - 1} \times \left(k_{\text{eff}} x_{i0} - \frac{\eta k_0 x_{iv}}{k_{\text{eff}} + \eta - 1} \right) \left(\frac{1-z}{L_0} \right)^{k_{\text{eff}} + \eta - 1}, \quad (6.15)$$

with

$$\eta = \frac{D_{i(\text{B}_2\text{O}_3)}}{h_{\text{B}_2\text{O}_3} v} \left(\frac{r_{\text{cruc}}^2}{r_{\text{cryst}}^2} - 1 \right). \quad (6.16)$$

x_{iv} is the concentration of dopant species in the gas phase at the upper interface of boric oxide, $D_{i(\text{B}_2\text{O}_3)}$ is the transport coefficient of the dopant species in boron oxide ($\approx 5 \times 10^{-8} \text{ cm}^2/\text{s}$ for carbon [6.72]), $h_{\text{B}_2\text{O}_3}$ is the height of the boric oxide encapsulant, and r_{cruc} and r_{cryst} are the radius of the crucible and crystal, respectively.

As is well known, a higher macroscopic homogeneity can be achieved by applying single-pass zone-melt techniques. A relative short first-to-freeze transient is followed by a compositionally uniform level region, the concentration of which equals that of the starting (polycrystalline) source rod, i. e., $x_{is} = x_{i0}$. The axial distribution function is

$$x_s = x_0 \left[1 - (1 - k_{\text{eff}}) \exp \left(\frac{-k_{\text{eff}} z}{L_z} \right) \right], \quad (6.17)$$

with zone length L_z and distance $z < L_0 - L_z$. The final part of solidification when $z > L_0 - L_z$ represents a normal freezing process and the concentration profile is given by (6.14). Single-pass zone growth is successfully used not only for production of extremely highly purified silicon by floating-zone melting [6.73] but also to obtain homogeneous mixed crystals of the

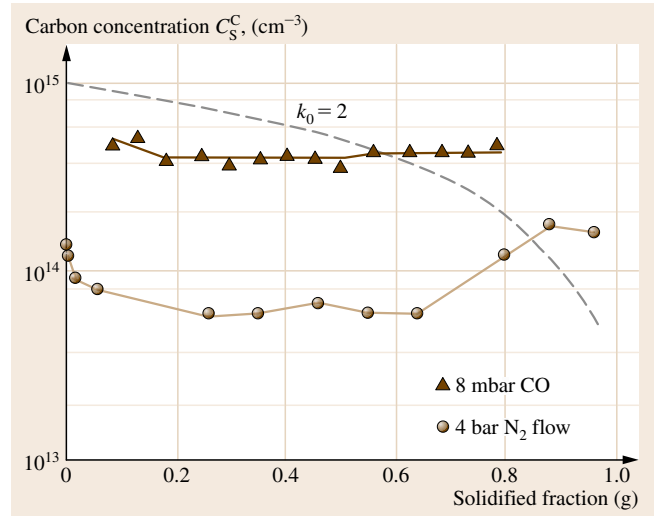


Fig. 6.6 Axial carbon distribution in LEC (\blacktriangle) and VCZ (\bullet) GaAs crystals grown under nonconservative conditions by controlled CO gas concentration (8 mbar) and rinsing nitrogen working gas (≈ 4 bar) [6.56], respectively. The dashed curve shows the theoretical Scheil distribution with $k_0 = 2$ (the equilibrium segregation coefficient of carbon) in case of conservative growth regime with complete melt mixing ($k_0 = k_{\text{eff}}$) and starting concentration $x_{\text{CO}} = 5 \times 10^{14} \text{ cm}^{-3}$

types $A_{1-x}B_x$ or $AB_{1-x}C_x$, even with widely spread liquidus and solidus curves. High-quality $Hg_{1-x}Cd_xTe$ and $Cd_{1-x}Zn_xTe$ crystals with axial uniformity of the constituents can be grown by the traveling-heater method (THM) from a Te-rich zone [6.74, 75]. Uniform oxide mixed crystals have been grown by a special heater-immersed zone melting technique [6.76]. Another use is microzone melting for the growth of various oxide fiber crystals by laser-heated pedestal growth (LHPG) [6.77]. Today this technique is applied for the production of nearly preparation-free microlasers for wavelength conservation by higher-harmonic generation [6.78].

Microinhomogeneities (Striations)

Microinhomogeneities are short-range composition fluctuations with characteristic spacing ranging from $1\text{ }\mu\text{m}$ to 1 mm , usually modulating the macrodistribution as *fine structure*. Such oscillations are found in nearly all crystals and are visible under light microscopy as *striations* on crystal cuts, especially after etching (Fig. 6.7a,b). They are one of the most investigated crystal defects [6.2, 3], and can seriously limit the device application of the given crystal (Sect. 6.1). Nonuniform segregation of solutes on the microscale is due to a variety of mechanisms, as recently summarized by Scheel [6.80]. Principally, one has to differentiate between kinetically and thermally induced striations.

Kinetic striations appear in the discontinuous (step-by-step) growth mode of atomically flat interfaces or facets (Sect. 6.5) when macrosteps are formed by bunching. Their repeated rapid lateral growth tends to trap the adjacent solute in alternating nonequilibrium concentration. At misoriented growth planes the propagation direction of the macrosteps, and hence striations, are inclined to the macroscopic course of the interface. This phenomenon is well known from liquid phase epitaxy (LPE) experiments [6.81].

Thermally induced striations are generated by non-steady growth velocities $\Delta v/v$, leading to variation of k_{eff} (6.13). Oscillating interface rates are caused by temperature fluctuations, which can be induced by:

- i) Rotation of Czochralski crystals in thermally asymmetric melts [6.82]
- ii) Convective instabilities [6.45, 67].

Vibrations and pressure fluctuations have also been identified as sources of growth rate variations. After Hurle's treatment [6.83], for certain frequencies of temperature oscillation, resonant coupling should occur between thermal and solute fields to give large compositional amplitudes.

For low-frequency oscillations with fluctuation periods $\tau > 2\delta_S/D$ (longer than about 10 s) the concentration changes are associated with growth rate R changes

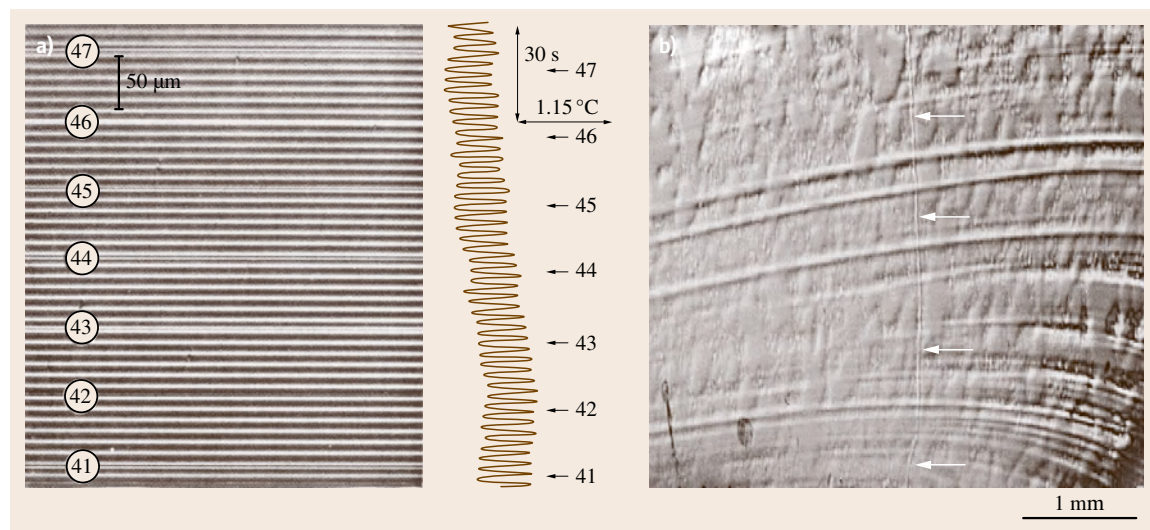


Fig. 6.7a,b Striations in semiconductor crystals. **(a)** Section of Te-doped InSb crystal grown in the presence of thermal oscillations in the melt [6.79] (after [6.45]; reproduced by permission of Springer). **(b)** Section of an undoped VCZ GaAs crystal grown from incongruent As-rich melt with compositional striations marking the interface shape. The arrows show the trace of a dislocation bundle propagating perpendicularly to the interface (courtesy of U. Juda from IKZ Berlin)

according to the steady-state BPS relation (6.13)

$$\begin{aligned} \frac{\Delta x_{is}}{x_{is}} &= \frac{\Delta R}{k_{\text{eff}}} \frac{\partial k_{\text{eff}}}{\partial R} \\ &= \frac{\Delta R}{R} \frac{(1-k_0) \left(\frac{R\delta_s}{D} \right) \exp\left(\frac{-R\delta_s}{D}\right)}{k_0 + (1-k_0) \exp\left(\frac{-R\delta_s}{D}\right)}. \end{aligned} \quad (6.18)$$

The maximum composition amplitude $[(\Delta x_{is}/x_{is})/(\Delta R/R)]_{\text{max}} = (1-k_0)(R\delta_s/D)$ occurs under conditions where $R\delta_s/D \ll 1$. By contrast, for high-frequency growth rate oscillations ($\tau < 2\delta_s/D$), the reaction time of the mass diffusivity is no longer able to follow the thermal agility. Thus, the amplitudes of the compositional fluctuations are increasingly reduced with increasing perturbation frequency f as

$$\frac{\Delta x_{is}}{x_{is}} = \frac{\Delta R}{R} (1-k_0) \frac{\frac{R\delta_s}{D}}{\left(\frac{2f\delta_s^2}{D}\right)^{1/2}}. \quad (6.19)$$

At frequencies higher than 10 Hz the relative concentration fluctuations fall to less than 10%. Therefore, low-frequency fluctuations affect the crystal homogeneity much more than do high-frequency ones. In other words, a melt–solid interface acts as a *low-pass filter*. Unfortunately, in crystal growth melts convective frequencies in the range of $0.1\text{--}0.5\text{ s}^{-1}$ are typical and the relation (6.18) must be used.

There are two general ways to damp temperature oscillations within the melt (when growth under microgravity is not considered):

- i) Brake the buoyancy convection streams
- ii) Minimize the temperature differences.

For the first method the application of various kinds of magnetic fields proves to be very effective for melts with electrical conductivity [6.84]. In the second case measures for temperature homogenization by using high-frequency melt mixing are required. From the above discussion, it follows that they are not dangerous for crystal homogeneity. Appropriate techniques are the accelerated crucible rotation technique (ACRT) [6.85] and ultrasonic vibration stirring [6.86].

Note that, for fundamental research and technology developments, the presence of striations proves to be of certain advantage because of their ability to mark the interface shape. Striation analysis along longitudinal crystal cuts reveals the time and course characteristics of the crystallization front during the whole growth process. Note that striations appear even in high-purity compound crystals grown from slightly

off-congruent melting point composition. For instance, in standard semi-insulating GaAs crystals grown from slightly As-rich melts, striations of very small and harmless amplitudes can be resolved by use of diluted Sirtl with light (DSL) etching [6.87] (Fig. 6.7b). They reflect the alternating incorporation of As-related native point defects [6.88]. For some materials it is important to consider the relatively high diffusion coefficients in the solid, leading to a leveling effect [6.89]. For instance, in melt-grown (Hg,Cd)Te mixed crystals, striations are not revealable due to the extremely high D_s^{Hg} .

6.2.3 Constitutional Supercooling – Morphological Instability

Under certain conditions, especially if the melt is not mixed by convection or stirring (i.e., if the solution boundary layer δ_s is well developed), the interface can become morphologically unstable. Both an enriched ($k_0 < 1$) or depleted ($k_0 > 1$) solute layer δ_s , showing a typically exponential concentration course (increasing or decreasing, respectively) at the growing interface, give rise to constitutional instability, especially if the corresponding liquidus temperatures of the concentration course exceed the actual temperature course

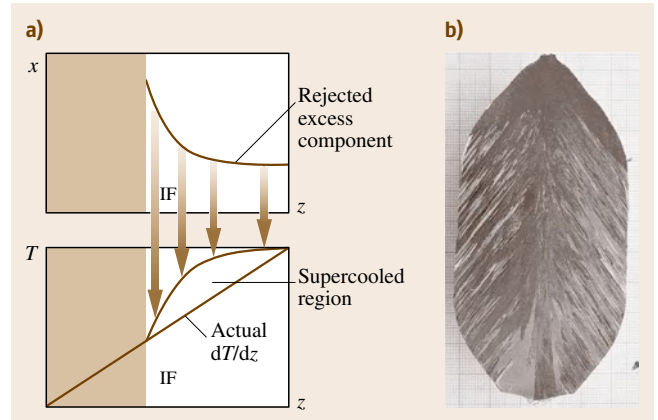


Fig. 6.8a,b Constitutional supercooling of the growing melt–solid interface. (a) Sketch demonstrating the supercooling effect at the interface due to the rejection of impurity, dopant or excess component (above x – z diagram) that leads to higher equilibrium melt temperature distribution compared with the actual temperature gradient (below T – z diagram; x – concentration, T – temperature, z – axial direction). (b) Undoped LEC InP crystal with features of morphological instability (cellular interface) grown from In-rich melt with too high a pulling rate (courtesy of M. Neubert and A. Kwasniewski from IKZ Berlin)

(Fig. 6.8a). Then random formation of a projection on the interface advances that portion of the interface into the region of increased supercooling, where it can grow more rapidly, causing lateral segregation of solute that suppresses growth in the neighboring region. As a result a close-packed array of such projections is formed on the length scale of the lateral diffusion distance D/ν . Such cellular interface morphology produces harmful columnar grain boundary structures with redistributed concentration and dislocation densities leading, finally, to polycrystallinity (Fig. 6.8b). This is exactly what happens in most metal alloy systems [6.90].

For semiconductors, however, faceted interfaces can be obtained. Once the amplitude of the projections grows to the point that their interface with the melt becomes tangential to a {111} faceting direction (Sect. 6.5), microfacets form on the interface [6.2, 3]. This occurs even if the dopant is not the cause of the constitutional supercooling. A noncongruent melt produces rejection of the component in excess and this lowers the liquidus temperature in exactly the same way as a solute. Because of the development of microfacets, the morphology of the resulting cellular structure is orientation dependent (not to be confused with the polygonized cell structure described in Sect. 6.3.2). In principle, dielectric (oxide) crystals that grow under conditions of constitutional supercooling always show faceted interfaces due to their atomically smooth interface kinetics on all important crystallographic planes.

First, Tiller et al. [6.91] deduced theoretically the condition for prevention of constitutional supercooling (i. e., preservation of morphological stability of the interface) as

$$\frac{G}{R} = \frac{m x_{il}(1 - k_0)}{k_0 D}, \quad (6.20)$$

where G is the temperature gradient in the melt at the interface and m the slope of the liquidus from the T - x -phase diagram projection (all other parameters are introduced above). Of course, relation (6.20) is an approximation that ignores some stabilizing factors. In particular, a face growing by an atomically flat mechanism is more stable against disturbances [6.38]. Further, the convection can stabilize the interface morphology by effective removal of the solute layer. Indeed, the

application of artificial melt mixing techniques, such as ACRT [6.85], ultrasonic vibration stirring [6.86] or time-dependent (i. e., rotating, alternating, traveling) magnetic fields [6.92–94], can help to ensure morphological stability very effectively.

A linear stability analysis predicting the exact conditions of onset of the morphological instability was later developed by Mullins and Sekerka [6.95], completing equation (6.20) by consideration of the heat diffusivity in the melt and solid. In subsequent years the theory was widely extended to include higher-order bifurcations and additional physical effects such as melt flow, atomic kinetics, Soret diffusion, applied electric fields, etc. All treatments showed that the Tiller criterion (6.20) can serve as a good approximation for the crystal grower. A detailed review is given in [6.96].

Constitutional supercooling can also appear during growth of undoped compound crystals growing from noncongruent melts. As shown above, in such cases the equilibrium segregation coefficient k_0 cannot be assumed to be constant. Wenzl et al. [6.97] modified the Tiller criterion (6.20), replacing the liquidus–solidus relation with the difference between the congruent melting composition x_{cmp} and the deviation from it in the melt x_1 . When x_{cmp} is close to the stoichiometric composition, as can be assumed for most compounds, one can set $x_{\text{cmp}} \approx 0.5$ and the undercritical growth velocity becomes [6.97]

$$R \leq \frac{GD}{(0.5 - x_1)} \left(\frac{dT}{dy} \right)^{-1}, \quad (6.21)$$

where D is here the diffusion coefficient of the excess component in the melt and dT/dy is the slope of the liquidus at the given x_1 . Obviously, R can be chosen relatively large close to the congruent melting point ($dT/dy \approx 0$). However, it falls drastically with increasing deviation and becomes for GaAs at $x_1 = 0.55$ (i. e., 5 at. % As excess, $D \approx 10^{-5} \text{ cm}^2/\text{s}$, $dT/dy \approx -200 \text{ K}$ [6.97]) about 4 mm/h, being markedly lower than the growth rate of standard crystals growing from near-stoichiometric melt composition. Figure 6.8b shows an image from the longitudinal cut of an InP crystal grown with overcritical growth velocity from an In-rich melt. The polycrystalline columnar structure induced by morphological instability is quite perceptible.

6.3 Dislocations

Contrary to native point defects (Sect. 6.2), dislocations are not in thermodynamic equilibrium, and hence in

principle are preventable. However, at present only silicon and germanium standard crystals can be grown

dislocation-free. This is because in compound crystals the situation is complicated by much higher intrinsic point defect content and lower critical resolved shear stress τ_{CRSS} (e.g., in GaAs and CdTe near the melting point, ≈ 0.5 MPa instead of ≈ 10 MPa in Si) markedly increasing the dislocation mobility and multiplication probability.

Dislocations in a growing crystal which come from the seed are termed grown-in dislocations. In the course of crystal cooling within a given temperature field the development of the dislocation density correlates closely with the thermomechanical stress induced by temperature nonlinearities within the crystal volume. It is the aim of dislocation engineering to achieve uniaxial low thermal gradients in order to minimize the elastic stress, and hence the dislocation density. To achieve this computational modeling of nonstationary plastic deformation proceeding within the crystal is today absolutely essential.

The phenomenon of dislocations interacting with each other at high temperatures is driven by mutual screening of the individual energetic fields and also by dissipative ordering processes in the framework of nonequilibrium thermodynamics. These processes, described by the principles of dislocation dynamics (DD), lead to characteristic collective rearrangements into cell patterns, bundles, and lineages. It can be shown experimentally that the cell size correlates with the mean dislocation density and acting elastic stress. Depending on material parameters, stress value, and the ripening level of dynamic polygonization, the cells transform into low-angle grain boundaries. Dislocation cells and bundles are not observed under low linear temperature gradients, stoichiometric growth conditions, and nearly flat interfaces. See also Chap. 4 in the present Handbook.

6.3.1 Dislocation Types and Analysis

Dislocations are linear crystallographic defects, or irregularities, within a crystal structure. Such linear defects cannot start or end within the crystal. They enter or leave the crystal through its surfaces, with the exception of dislocation loops closed within the crystal volume. The presence of dislocations strongly influences many of the properties of materials (Sect. 6.1) because of lattice distortion, local stress field, electrical activity, and getter ability for point defects. As defined by the angle between the dislocation line and the Burgers vector there are two primary dislocation types: *edge dislocations* and *screw dislocations* with an angle of 90° and 0° , respectively. *Mixed disloca-*

tions are intermediate combinations between these. In the diamond and zincblende structure 30° and 60° dislocations appear within the $\{111\}$ planes with Burgers vector $\mathbf{b} = a_0/\sqrt{2}$ along the $\langle 110 \rangle$ directions (a_0 = lattice constant). In semiconductor A^{III}–B^V compounds 60° dislocations are the prevailing ones, amounting in GaAs to 30% of all dislocation types present [6.98].

It is experimentally and theoretically well established that, independent of the growth method, the density and distribution of dislocations in melt-grown crystals are due to a thermoplastic relaxation of thermally, and to a much lower extent constitutionally, induced stress during growth. Principally, for growing crystals a differentiation between the terms *generation* and *multiplication* of dislocations is recommended. The formation of new dislocations within an ideal dislocation-free crystal under normal growth conditions is nearly impossible. Stresses of the order of the material strength limit $\tau \approx 10^{-2} - 10^{-1} G$ (where G is the shear modulus $\approx 10 - 70$ GPa) would be required, being much higher than that usually obtained in standard growth processes (around 10 MPa at most). Such values are not even high enough to penetrate Shockley partials in zincblende structures from microscopically stepped crystal surfaces, which requires stresses of at least ≈ 100 MPa [6.99]. Dislocations can be generated in the form of Frank loops due to collapsing vacancy agglomerations, interstitial disks, and interface misfits between foreign-phase inclusions and matrix (Fig. 6.1). The possibility of such origins is enhanced in nonstoichiometric material. The majority of dislocations in as-grown crystals, however, originate from glide- and climb-assisted elongation (bowing out) and multiplication (dissociation, cross-glide) of primary existing faults grown-in from the seed crystal.

There exist numerous reliable methods to analyze dislocations such as:

- i) High-resolution transmission electron microscopy (HRTEM)
- ii) X-ray Lang topography, enabling Burgers vector analysis
- iii) Laser scattering tomography (LST), ascertaining the spatial dislocation courses
- iv) Fully automatized etch pit density (EPD) mapping.

Even high-temperature synchrotron x-ray and transmission electron imaging techniques make it possible to study the dislocation kinetics at the crystallization front of some materials in situ [6.100]. As a result, knowledge about dislocation types and their mobility in correlation with the growth conditions as well as their

interaction with dopants is today well developed and a large number of related papers are available. For III–V compounds, a comprehensive summary was published by Sumino and Yonenaga [6.101], for example.

6.3.2 Dislocation Dynamics

Basic Considerations

Dislocations are the elementary carriers of plastic flow, relaxing the elastic stress, which affects the crystal structure. Plastic relaxation (i. e., deformation) of crystalline solids is related to the motion and multiplication of dislocations. This is a basic process within growing crystals by which dislocations are stored. The study of propagation and interaction of dislocations over mesoscopic distances is the subject of dislocation dynamics [6.102]. Because the collective behavior of dislocations is complicated, to date very little is known about the effects that individual dislocations have on each other when they come into close proximity, and more generally about the evolution of collections of strongly interacting dislocations near the melting point. In this chapter basic processes and some characteristic features of dislocation rearrangements into cells and bundles during crystal growth from the melt will be presented.

Dislocations can move within the glide plane by *glide* or *slip* in the direction of b (edge dislocations) or orthogonal to b (screw dislocation) or at a certain angle (30° and 60° dislocations). In addition, screw dislocation can *cross-slip* from one glide plane to another. *Climb* is the motion of dislocations perpendicular to the glide plane. Note that even climb and cross glide are responsible for spatial dislocation (see below).

The glide mobility v_g is given by

$$v_g = v_0 \tau_{\text{eff}}^m \exp\left(-\frac{E_a}{k_B T}\right), \quad (6.22)$$

where v_0 is the material constant, of the order of the magnitude of the Debye frequency, E_a is the activation energy (Peierls potential), $\tau_{\text{eff}} = \tau - A\sqrt{\rho_0}$ is the effective shear stress on dislocations, m is the stress exponent, τ is the acting shear stress, $A = Gb/2\pi(1-\nu)$ is the strain hardening factor, G is the shear modulus, ν is Poisson's ratio, and ρ_0 is the mobile dislocation density.

Usually, at higher temperatures, the process of climb constitutes the dominant mode of dislocation motion. It is thermally activated and therefore dependent upon the diffusivity of vacancies or interstitials to the dislocation core. A phenomenological expression for dislocation

climb velocity v_{cl} is given by [6.103]

$$v_{cl} = B \left(\frac{D_s}{b}\right) \left(\frac{G\Omega}{k_B T}\right) C_j \left(\frac{\gamma_{\text{SF}}}{Gb}\right)^2 \left(\frac{\tau}{G}\right), \quad (6.23)$$

where B is a constant on the order of 10^3 , Ω is the atomic volume, C_j is the concentration of jogs, and γ_{SF} is the stacking fault energy (all other parameters are introduced under relation (6.22)).

The cross-slip mechanism can proceed effectively only in case of relatively high stacking fault energy. Even in semiconductor compounds with zincblende structure containing characteristic partial dislocations (Shockley partials), cross-slip can be restrained due to a large equilibrium stacking fault distance between them, inversely related to the stacking fault energy γ_{SF} as $d_{\text{Sh}} = Ga_0^2/(24\pi\gamma_{\text{SF}})$. InP and CdTe crystals show the lowest stacking fault energies among the semiconductor compounds, and therefore reduced cross-slip probabilities (as a result, dislocation patterning is hindered).

As it is well known the stress force exerted by a dislocation on other dislocations is long range. Moving dislocations tend to minimize their individual stress field by mutual field screening that reduces the overall system energy. There are various mechanisms of dislocation interaction. When two dislocations of opposite Burgers vectors approach each other within a certain critical distance of separation they annihilate. The critical distance for *annihilation* of two screw dislocations is $y_s \approx Gb/2\pi\tau_g$, where τ_g is the shear stress required for dislocation glide. The value of y_s for metals is about 2 μm . However, their approach can also achieve a stable configuration, known as a *dipole*, if the dislocation pair remains both a distance greater than y_s apart and with a relative position angle of around 45°. Typical dipole lengths are on the order of tenths of a micron [6.103]. Dipoles are composed only of edge dislocations since screw dislocations annihilate easily by cross-slip. Furthermore, the attractive forces can lead to the formation of dislocation *junctions* and *walls*. The energy of a dislocation bounded in a stable wall configuration (e.g., a low-angle grain boundary) is about four times lower than the energy of a single dislocation.

Dislocations can multiply by cross-glide and the *Frank–Read mechanism*. In the latter case, multiplication occurs by pinning of the dislocation, bowing out and wrapping around the pinning points. Possible pinning points are precipitates and impurity clusters, but also junction segments produced by two dislocations [6.103]. Nabarro [6.104] discussed the bowing out

by multistep climb under conditions of vacancy supersaturation, known as the *Bardeen–Herring mechanism*.

The above-mentioned mechanisms of dislocation dynamics are considered to be the basic processes taking place during crystal growth from melt under the action of a thermoelastic stress field.

Dislocation Density Versus Thermomechanical Stress

Dislocations in a growing crystal come first of all from the seed (grown-in dislocations), or in special cases from lattice mismatches, e.g., at the interface between the crystal matrix and foreign inclusions, and are multiplied by viscous–plastic phenomena initiated by the thermoelastic stresses experienced by the crystal. Therefore, the content of dislocations is determined by the time- and space-dependent stress level during growth, which is related to the temperature field in the crystal growing and cooling-down procedure. Firstly, *Billig* [6.105] discovered that the dislocation density correlates with the imposed temperature gradient. *Indenbom* [6.106] specified that thermally induced stresses arise from temperature nonlinearity, i. e., divergence of the isotherm curvature from an idealized linear course, in other words not from the temperature profile but from its second derivative. Theoretically, this implies the simplified but quite useful formula

$$\sigma = \alpha_T E L^2 \left(\frac{\partial^2 T}{\partial z^2} \right) \approx \alpha_T E \delta T_{\max}, \quad (6.24)$$

where σ is the thermal stress, α_T is the coefficient of thermal expansion, E is the Young's modulus, L is the characteristic length (about the crystal diameter), T is temperature, z is the given coordinate (pulling axis), and δT_{\max} is the maximum deviation of the isotherm from a linear course. The extremely critical situation in most semiconductor compounds such as GaAs will be obvious by using the material constants near to the melting point ($\alpha_T = 8 \times 10^{-6} \text{ K}^{-1}$, $E = 7.5 \times 10^4 \text{ MPa}$). As can be seen, only very small isotherm deviations from linearity δT_{\max} of 1–2 K are enough to reach the critical-resolved shear stress (CRSS) for dislocation multiplication (0.5 MPa). This is one order of magnitude lower than in silicon, in which much greater isotherm curvatures are tolerated without disturbing dislocation-free growth. Even during pulling of a cylindrical crystal from the melt, steep temperature curvatures can occur due to different temperature gradients in the inner and outer regions of the crystal. From (6.24) follows a direct correlation between stress level and crystal diameter (characteristic length L) which has

been observed in reality. The larger the crystal diameter, the higher the mean dislocation density. For instance, in undoped 3, 4, and 6 inch **LEC** GaAs crystals typical mean dislocation densities are 2×10^4 , 5×10^4 , and $1 \times 10^5 \text{ cm}^{-2}$, respectively.

Modeling of Dislocation Density

From the discussion above it follows that both knowledge and control of the temperature field at all process stages are of essential significance. Due to the difficulties of measurement, numerical simulation is of increasing importance for heat flow, thermomechanical stress, and dislocation density analysis. Two approaches have been used so far [6.7]:

1. Calculation of the thermoelastic stress field (linear theory, isotropic and anisotropic analysis) of the crystal for a given temperature field using available computer packages and comparison of the resolved shear stress (RSS) in the glide systems or the von Mises invariant with the critical resolved shear stress (CRSS), taking into account its temperature dependence known from high-temperature creep experiments. The (local) dislocation density can then be concluded from the total excess shear stress $\sigma_{\text{ex}} = \sum_{i=1}^n \sigma_i^{\text{e}}$ (where n is the number of effective slip systems in the given crystal structure), where $\sigma_i^{\text{e}} = |\sigma_{\text{RSS},i}| - \sigma_{\text{CRSS}}$ for $|\sigma_{\text{RSS},i}| > \sigma_{\text{CRSS}}$ and $\sigma_i^{\text{e}} = 0$ for $|\sigma_{\text{RSS},i}| < \sigma_{\text{CRSS}}$, i. e., the maximum stress at any time of growth determines the local dislocation density. Examples of this approach can be found in *Jordan et al.* [6.107] and *Miyazaki et al.* [6.108].
2. Estimation of the local dislocation density from the constitutive law of Alexander and Haasen linking the relation between plastic shear rate and movement and density of dislocations $d\varepsilon/dt = \rho_0 v b$ (the Orowan equation) with the applied stress in the course of the cooling-down procedure of the crystal [6.109, 110]. The dislocation multiplication is proportional to the effective stress τ_{eff} , the mobile starting dislocation density ρ_0 , and velocity v , i. e., $d\rho/dt = K \tau_{\text{eff}} \rho_0 v$. By using (6.22) the differential equations of state become

$$\frac{d\varepsilon}{dt} = \rho_0 b v_0 \tau_{\text{eff}}^m \exp\left(\frac{E_a}{k_B T}\right), \quad (6.25)$$

$$\frac{d\rho}{dt} = K \rho_0 b v_0 \tau_{\text{eff}}^{m+1} \exp\left(\frac{E_a}{k_B T}\right), \quad (6.26)$$

where K is a multiplication constant (all other values are introduced below (6.22)). A detailed review

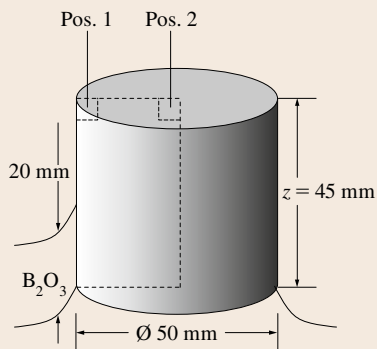
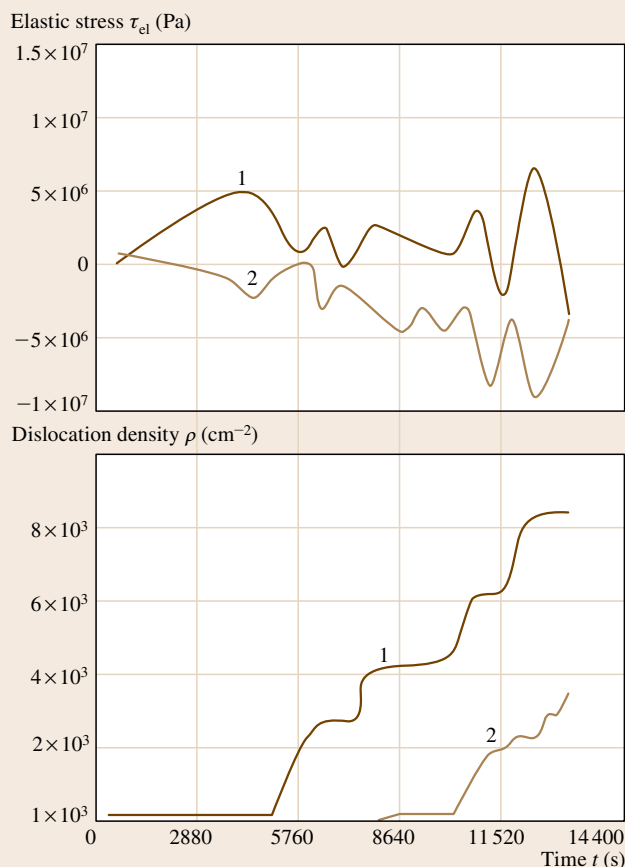
of this approach is given by Völkl [6.111]. Lo-honka et al. [6.112] extended this approach to the case of semiconductor compounds with zincblende structure. They considered the different dynamic characteristics of $\alpha(60^\circ)$, $\beta(60^\circ)$ and screw dislocations by modifying the Orowan equation to $d\varepsilon/dt = b(\rho_{0\alpha}v_\alpha + \rho_{0\beta}v_\beta + \rho_{0S}v_S)$. Note that, al-

though only screw dislocations contribute to the total plastic deformation, their dynamics depends also on the motion of $\alpha(60^\circ)$ and $\beta(60^\circ)$ dislocations formed together with screw dislocation loops [6.113], and which therefore have to be considered. Grondet et al. [6.114] included the annihilation of dislocations by pairs, leading to a certain decrease of dislocation density $d\rho^*/dt = d\rho/dt - d\rho^-/dt$ due to its proportionality to the square of the density of dislocation and their velocity: $d\rho^-/dt = A\rho_0^2v^2$ (A is a constant to be fitted by experimental results). This addition leads to a more realistic dislocation density, which becomes overestimated if this effect is neglected.

In general, approach 2 is the modern and more realistic way. As emphasized by Völkl [6.111], the plastic relaxation varies due to time-dependent experimental conditions and due to continuously acting dislocation dynamics. Therefore, the driving force for dislocation multiplication is given by the actual value of the elastic strain and not by the total deformation. Thus, one has to consider that the often-published *von Mises contours* (as part of approach 1), calculated along growing crystal cuts and cross-sections, reflect snapshots of the unrelaxed thermoelastic stress only. Certainly, they are usable for estimation of the dislocation density at the growing interface but not within the cooling crystal volume where the majority of the elastic strain is already relaxed by plastic deformation. Note that changing stress situations can appear during the growth run, as in the LEC case when the crystal emergences from the liquid encapsulant towards the streaming gas atmosphere, creating a thermoelastic shock, for example.

Recently Pendurti et al. [6.115] reported the global numeric modeling of the nonstationary elastic stress and related dislocation development in growing LEC InP crystals by considering the history of the thermal field in the furnace and crystal as well as the convection in the melt and vapor phase. Figure 6.9 shows their calculated elastic stress history and related dislocation density evolution at two selected crystal points.

Fig. 6.9 The history of elastic stress and dislocation density at the edge (1) and in the center (2) of a 2 inch InP crystal growing from the melt under a 20 mm-thick B_2O_3 layer (sketch at the bottom) calculated by a broadened Haasen–Alexander model with Grashof numbers of gas and melt of 10^8 and 10^6 , respectively, and rotational Reynolds number of 500 (after Pendurti et al. [6.115]) ◀



As the elastic stress alternates, the dislocation density increases stepwise accordingly. The authors found that gas convection has a significant effect on the total dislocation density – a quite important fact that had not yet been considered.

The modeling of thermoelastic stress fields and the related dislocation density during a crystal growth process based on constitutive principles of continuum mechanics has made marked progress during the last decade. For both semiconductor compounds [6.114, 115] and oxides [6.116] the comparison between the theoretical results and real structural quality (i. e., mean EPD distributions) along the growth axis and radius show good conformities. However, even today one is still unable to predict exactly the dislocation rearrangements in characteristic microstructures, such as cell patterns and dislocation lineages and bundles, observed in most as-grown crystals under evolving thermomechanical stresses (see below). There are numerous efforts to simulate correctly the three-dimensional dislocation dynamics representing the collective interaction processes [6.117]. However, because of the high computational cost of discrete simulations, present-day modeling is restricted to metals and small system sizes (typically about $10\mu\text{m}^3$) so that only the very first stages of dislocation cell patterning can be studied. Since the cell size of the incipient dislocation cell patterns is of the same order as the size of the simulation box, not much information about the spatial morphology of the emergent patterns can be obtained. Hence, further theoretical methods such as continuum and stochastic approaches are under current development [6.117].

Dislocation Patterning

During plastic relaxation the interacting dislocation populations tend to rearrange spontaneously into characteristic heterogeneous formations. They can be subdivided into two basic patterning phenomena observed in numerous as-grown crystals, i. e.:

- i) Dislocation *cell structuring*
- ii) Dislocation *bunching*.

In compounds and alloys, patterning leads to physical and chemical parameter inhomogeneities. Whereas (i) includes formations of three-dimensionally ordered honeycomb-like (often named mosaic) structures, group (ii) compiles local accumulations such as slightly wavy dislocation walls (lineages) and vein-like bundles and gnarls. Today, dislocation theory can explain the prop-

erties of individual dislocations reasonably well, but is still unable to solve their collective behavior in all its details [6.118]. Hence, the following sections will concentrate on some typical features and practical relationships only. For more theoretical understanding the recently published reviews [6.117, 119] are recommended.

Cellular Structuring

The self-rearrangement of dislocations present in cellular networks during single-crystal growth is typical of most substances used. Figure 6.10a shows such cells in a 4 inch GaAs wafer, revealed by a standard etching process. The cell structure can be analyzed in more detail by laser scattering tomography (LST), which takes advantage of dislocation decoration by precipitates of the excess component in the case of nonstoichiometric crystals [6.120] (Fig. 6.10b), or by high-resolution x-ray synchrotron topography (ST) [6.121] (Fig. 6.10c).

The cells are of globular-like shape, consisting of walls with high dislocation density separated by interiors of markedly dislocation-reduced or even dislocation-free material. Their size decreases with increasing average dislocation density, yielding diameters of 1–2 mm and $500\mu\text{m}$ at dislocation densities of $\rho \leq 10^4$ and $\approx 10^5\text{ cm}^{-2}$, respectively. Note that they are often termed mosaic structures due to their appearance in two-dimensional cuts. Such patterns are also well known from as-grown crystalline metals (e.g., Fe, Al, Ni, Mo), metallic alloys (e.g., Fe-Si, Ti_3Al , Cu-Mn), and dielectric crystals (e.g., LiF, CaF_2 , SrTiO_3 , quartz) [6.122]. However, some differing morphological details are noteworthy. For instance, in Mo, Cu-Mn, and GaAs the cell interiors are nearly free of dislocations and the walls are fuzzy and of certain thickness, consisting of many tangled dislocations (Fig. 6.10c). It is noteworthy that the tilt angle between the cells in high-quality GaAs standard crystals is around 10 arcs. Compared with that in CdTe, PbTe, and CaF_2 the mean disorientation angle is higher (> 20 arcs up to some arcmin) and the cell walls are very thin, of the order of one dislocation row, resembling classical low-angle grain boundaries. In these crystals the matrix shows mostly individual dislocations that can occasionally form a sub-cell structure. Finally, there are crystals in which cell structures are not well distinguishable in the as-grown state, as in InP, or even missing if special dopants are added, as for Si in GaAs or Se in CdTe [6.122]. After Rudolph [6.122] the most probable reasons for missing cell structures are:

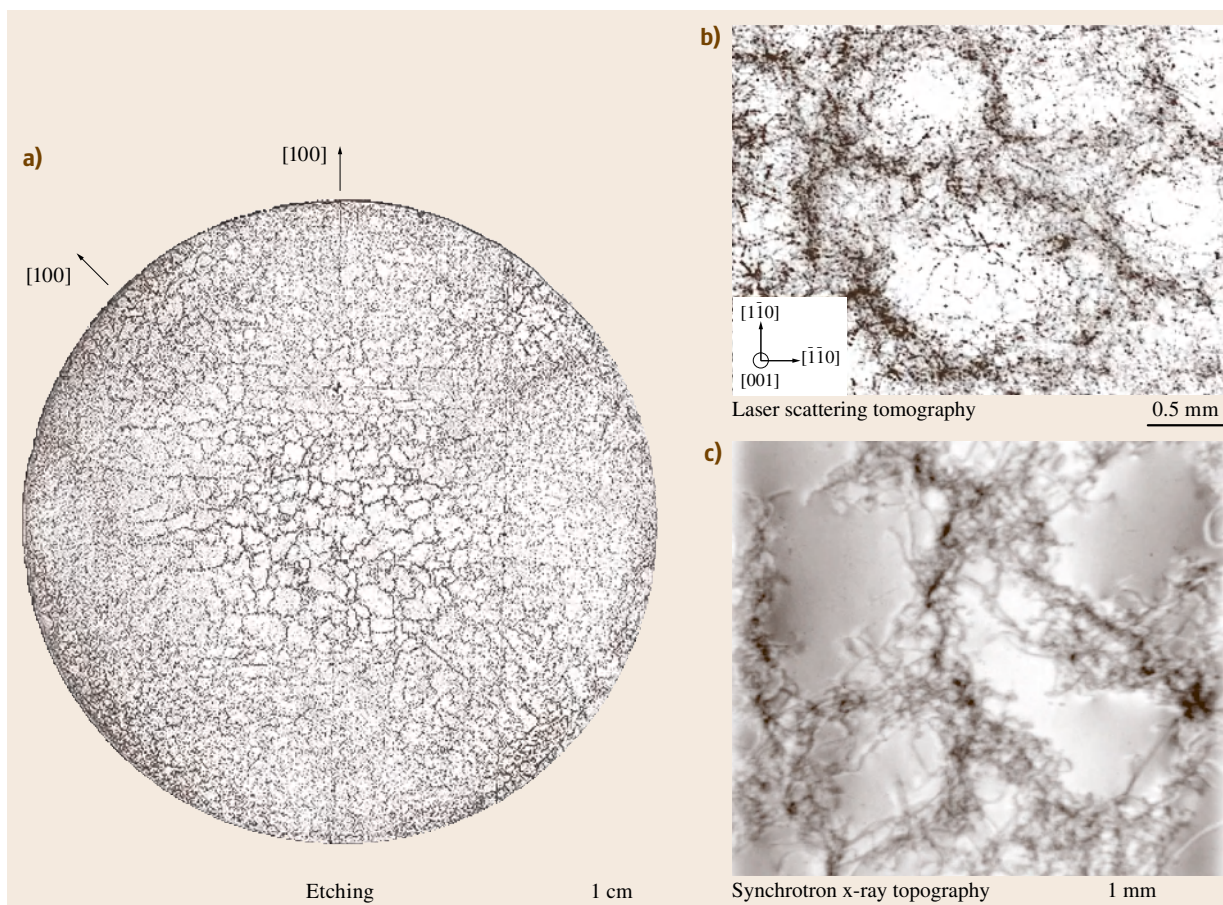


Fig. 6.10a–c Dislocation cell structures in GaAs crystals. **(a)** KOH-etched 4 inch wafer of a VGF crystal (after [6.56]). **(b)** LST analysis with integrated depth 2 mm (after [6.120]). **(c)** X-ray synchrotron topography (after [6.121, 122]) (reproduced by permission of Elsevier **(a,b)** and Wiley-VCH **(c)**)

- i) Low stacking fault energy preventing cross-slip
- ii) Small compound existence regions or stoichiometric growth conditions delivering only low native point-defect reservoir for climb
- iii) Retarded dislocation movement
- iv) Solution hardening by doping.

Undoped InP meets (i–iii). A possible explanation for the markedly differing wall morphologies in the cell structures in as-grown crystals is the different ripening levels within the framework of polygonization. Obviously, in Cu and GaAs the high tendency for dislocation screening by pronounced sessile junction formation leads to an entangled dislocation jungle within the walls being even stable against postannealing. Such mor-

phology resembles the so-called incidental dislocation boundaries (IDBs), which are assumed to be a result of statistical mutual trapping of dislocations. On the other hand CdTe, PbTe, and CaF₂ show typical characteristics of well-ripened low-angle grain boundaries, i.e., geometrically necessary boundaries (GNBs) [6.123].

Cell patterning is studied best in metals under an external load, but also in postdeformed elemental and semiconductor compound crystals. Today, there are a large number of papers dealing with cell patternings, especially in the field of metal physics and mechanics. For growing crystals, however, there is not yet detailed knowledge about the genesis of DD at high temperatures. In all probability, cellular substructures are due to the action of the internal thermomechanical stress field.

It can be assumed that cell formation is coupled with dynamic polygonization behind the growing interface where the plastic relaxation by dislocation multiplication takes place. There is a well-confirmed in situ observation on thin crystallizing and remelting Al plates by *Grange et al.* [6.124], who observed by real-time synchrotron x-ray topography that the cellular dislocation structure appears due to the thermally induced strain within the region already some millimeters behind the melt–solid phase boundary. Recently, *Jakobson et al.* [6.125] confirmed such fast dynamics by in situ x-ray reflection analysis on deforming Cu crystals. The observation strongly indicated that subgrain formation is initiated shortly after the onset of plastic deformation. This result is of great importance for understanding cell genesis in growing crystals, whereupon the cell pattern in the cooled crystal can be assumed to be identical to the structure formed under high temperatures, and is therefore generated by the initially acting thermoelastic stress.

Note that not all types of patterning can be attributed to DD that takes place within the crystal volume. As discussed in Sect. 6.2.3, in the case of morphological instability of a fluid–solid phase boundary induced by constitutional supercooling, the former planar shape changes into a characteristic cellular profile [6.90, 96]. As a result, a lamellar-like structure with longitudinally extended walls is formed. However, the distinction from dislocation patterning is sometimes not trivial, even when cross-sectional crystal wafers are investigated. The best way to distinguish between them is the application of analytical methods with three-dimensional (3-D) imaging such as LST to reveal the globular cell morphology typical of dislocation patterning [6.120]. Moreover, as is well known, dislocation cells may disappear completely if certain dopants are added, such as In in GaAs or Se in CdTe, although their presence could promote constitutional supercooling.

A systematic analysis of the origins and genesis of cell formation during growth of semiconductor compound crystals, especially GaAs, was started by *Rudolph et al.* [6.20, 126, 129]. First, the relation between the stored dislocation density ρ and the cell size (diameter) d has been determined. To deduce the 3-D cell diameters from the 2-D etch pit images obtained on cut wafers, a stereological analysis method was used, as described in [6.126]. Figure 6.11a shows this correlation taken from experimental data. The literature data of deformed metals are added [6.127]. For the GaAs samples with $\text{EPD} \geq 10^4 \text{ cm}^{-2}$ nearly the same correlation as in

deformed metals has been found, i. e.,

$$d \approx K \rho^{-1/2}, \quad (6.27)$$

with the factor of proportionality $K \approx 10\text{--}20$. This is surprising if one considers the marked differences between dislocation densities and cell dimensions in as-grown GaAs crystals and those in metals under load. The result shows that *Holt's* scaling relation [6.127] is

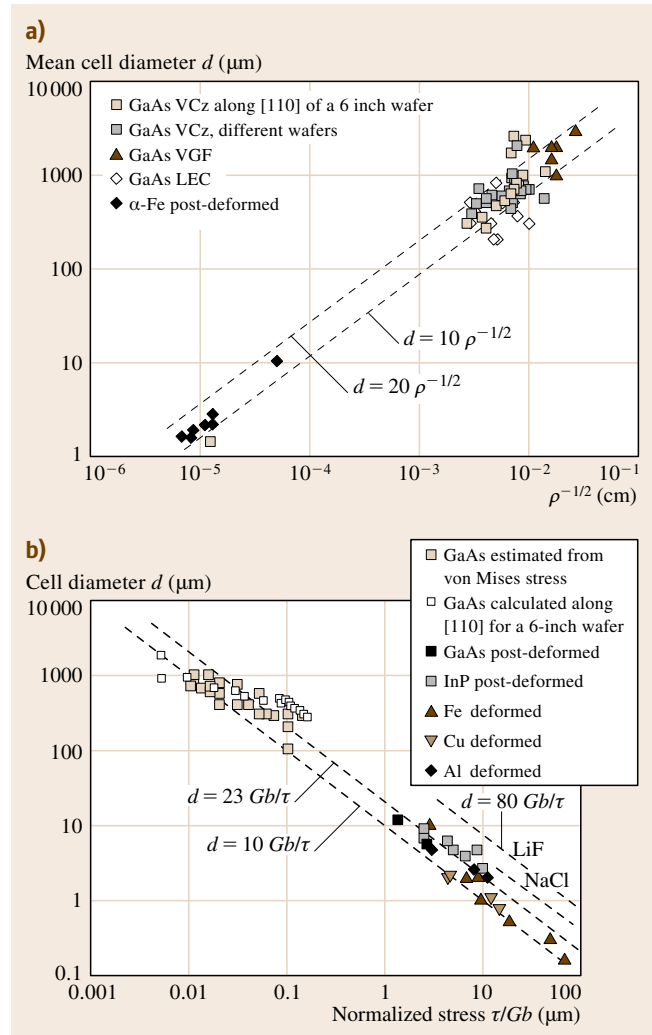


Fig. 6.11a,b Scaling of dislocation cell patterns in growing GaAs crystals in comparison with other crystalline materials post-deformed by mechanical stress (after [6.122, 126–128]). (a) Cell size d versus mean dislocation spacing $\rho^{-1/2}$, i. e., dislocation density ρ . (b) Cell size d versus flow stress τ (reproduced by permission of Wiley-VCH)

fulfilled over a wide range of materials and dislocation densities. At dislocation densities below $5 \times 10^3 \text{ cm}^{-2}$, however, the cells begin to dissociate.

Furthermore, the relation between acting stress and cell dimension was investigated. From postgrowth deformation experiments on numerous metals and dielectrics a universal relation between cell diameter and shear stress τ was found [6.130]:

$$d = \alpha K G b \tau^{-1}, \quad (6.28)$$

where α is another proportionality factor, G is the Young's shear modulus, and b is the Burgers vector. The analysis of this correlation in the case of growing crystals is more difficult due to the impracticality of in situ measurement of the acting thermomechanical stress values. As pointed out above, only the elastic term is responsible for dislocation movement, and thus for the collective dislocation rearrangement in cells. Considering that the subgrain generation is initiated shortly after the onset of plastic deformation [6.125] it can be assumed that the cell formation process takes place immediately behind the growing interface and is completed in the course of plastic relaxation. Thus, the frontal elastic strain acting immediately after the propagating phase boundary can be assumed to be the driving force. This stress value is today readily calculable by global modeling. Therefore, the authors [6.20, 126, 129] used the calculated frontal thermoelastic shear stresses of growth situations, being identical to the real growth positions of each crystal from which the EPD distributions and cell size measurements were taken. The correlation between d and τ^{-1} in the form of (6.28) with $\alpha K = K'$ is shown in Fig. 6.11b. For comparison, the results from deformed metals as well as the slopes for NaCl and LiF are included [6.128, 130]. As can be seen, for cell sizes smaller than $700 \mu\text{m}$ and calculated stresses larger than about 1 MPa, the functional slope is similar to those of deformed materials. Independent of the growth conditions, it was found that d is inversely proportional to τ^{-1} . Obviously, in this region dislocation glide is the prevailing driving force for cell formation, due to the fact that the stress is larger than the critical resolved shear stress. In the case of larger cell dimensions the trend changes, showing a slope smaller than -1 . In these regions a resolved shear stress of $\tau < 1 \text{ MPa}$ was calculated. One can suppose that, for such very low thermomechanical stress, even below the critical resolved shear stress ($\tau_{\text{CRSS}} \approx 0.5 \text{ MPa}$), glide-driven plastic relaxation can no longer be the prevailing driving force for cell formation. Other cell structuring mechanisms must become dominant, such

as point-defect-controlled diffusive creep. This could be in accordance with the observation that the residual dislocations in low-EPD GaAs VGF crystals probably no longer lie within the basal glide system [6.131, 132].

A number of theories have been proposed to account for the stress dependence of the cell size [6.117]. It is usually thought that the decreasing cell dimension with increasing stress is due to cell splitting in the course of growing stress, leading to progressive construction of new walls [6.118]. Newer papers favor a stochastic dynamics of the entire dislocation ensemble [6.117, 125] whereby the dislocation-free regions emerge and vanish in a fluctuating fashion in the course of the acting elastic stress. Until now, however, the question is whether the cell patterning is driven energetically or by a self-organizing process, in the former case by equilibrium, or in the latter by nonequilibrium thermodynamics where the entropy production is stopped, leading to dissipative structuring. There are well-known facts to be stated for energy-related processes. In the classical sense, the driving force for network formation is the reduction in strain energy resulting from the clustering (i. e., mutual field screening) of dislocations in cell boundaries. It is important to note that, for the formation of cells with globular morphology, in addition to dislocation glide, even spatial mechanisms such as climb and cross-glide are absolutely required [6.133]. However, the process of plasticity cannot be explained exclusively by equilibrium thermodynamics due to the presence of typical preconditions for irreversibility, such as temperature and stress gradients during the growth process. Hence, a growing crystal can be treated as a thermodynamically open system with continuous import and export of entropy. As a result, a rate of entropy is produced within the crystal, evoking self-ordered patterning of the stored dislocations. Much more fundamental co-working between crystal growers and theoretical physicists is required to clarify this still open problem.

Grain Boundaries

In numerous melt-grown compound crystals, such as in as-grown CdTe, PbTe, and CaF_2 , for example, the cell arrangement resembles the classical low-angle grain boundary structure. The grain matrix contains mostly isolated dislocations and the walls are formed very abruptly, consisting of only one row of dislocation pits. Sabinina et al. [6.134] investigated the cell wall structure in melt-grown CdTe samples by transmission electron microscopy and observed that the dislocations that constitute the boundaries are nearly all parallel

and most have the same Burgers vector. Such behavior is well known from the standard type of polygonized low-angle grain boundaries containing only the excess dislocations of similar Burgers vector after the annihilation process is completed. Obviously, in such crystals the DD contributes much more effectively to substructure ripening than in Cu and GaAs. Also, the larger disorientation angle between the neighboring cells refers to a typical polygonized grain-boundary structure. Tilt angles of 60–120 arcsec were reported for melt-grown CdTe crystals. Higher disorientation angles in the range of 2–30 arcmin, and in some cases even up to 3°, have been ascertained in PbTe crystals. Such a feature is also characteristic of dielectric materials such as CaF₂ and NaCl [6.135, 136]. It is obvious that in these crystals we have to deal with typical well-ripened grain boundaries, i. e., primary subboundaries, which are often superimposed by cellular structure and secondary subboundaries formed previously [6.136]. The scheme in Fig. 6.12 shows the possible stages of dislocation patterning during crystal growth beginning from cell formation towards a ripened small-angle (primary) grain-boundary structure. Depending on the dislocation mobility (highest in CdTe, PbTe), intrinsic point defect content (lowest in InP), and stacking fault energy (lowest in InP, CdTe), the ripening time and frozen-in contents are, however, different in various materials.

Conventionally, a low-angle grain boundary structure, formed by the above-discussed mechanism of dynamic polygonization, still belongs to a single-crystalline state. It is convenient to separate grain boundaries by the extent of the misorientation between two grains $\Theta[\text{rad}] = b/h$ (where h is the dislocation spacing within the grain boundary). Whereas a low-angle grain boundary is composed of an array of dislocations and its properties and structure (i. e., boundary energy) are a function of the misorientation, large-angle grain boundaries are those with a misorientation greater than 10–15° and are normally found to be independent of the tilt angle. A crystal with such grain structure is considered polycrystalline. It can be appear by:

- i) Spontaneous nucleation in unseeded melt growth processes
- ii) Disturbance of the heat balance between melt and solid phases
- iii) Prenucleation in a supercooled melt region before the growing interface.

Also a cellular interface shape, generated under conditions of morphological instability (Sect. 6.2.3), can

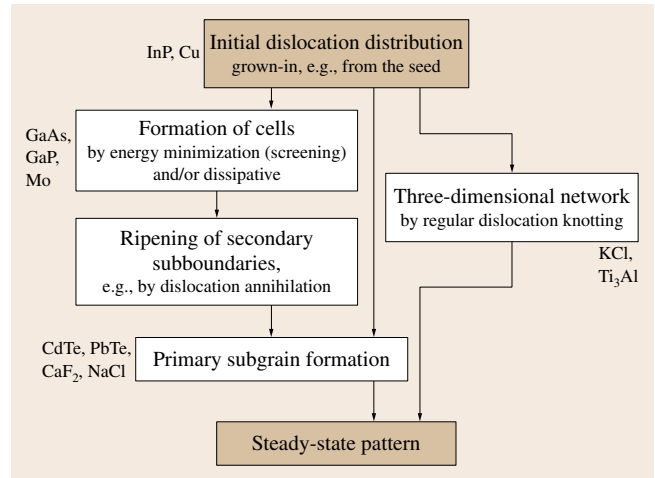


Fig. 6.12 Schematic demonstrating the different types and ripening stages of dislocation substructures that may develop from an initial uniform dislocation distribution. Some materials with typical related patterns, observed after crystallization, are added (after [6.136])

produce large-angle grain boundaries elongated parallel to the growth direction. Large-angle grain structure is a typical feature of cast solar silicon, affecting the photovoltaic efficiency (Table 6.1).

An interesting phenomenon can be observed during the Bridgman growth of semiconductor compounds with high ionicity, e.g., high degree of association in the melt (over 90%), such as CdTe and ZnSe [6.28, 137, 138]. There is a correlation between the number of large-angle grains and superheating of the melt before the crystallization process without an artificial seed is started (Fig. 6.13). Obviously, the high degree of association in slightly overheated melts causes stochastic preformation of structural elements (rings, chains, tetrahedrons), and their docking at the interface markedly affects the single crystallinity. Contrary to that, at a high level of superheating, the melt structure is altered to nearly monomolecular type, promoting nearly grain-free growth.

Dislocation Bunching

Dislocation bundles, often described as gnarls, tangles or clusters, mostly appear sporadically and in isolation. Once nucleated they may propagate through the whole growing crystal, typically parallel to the direction of solidification. Such defects have been detected in GaAs and InP crystals, independently of the growth method. Even in VGF crystals they have been observed. Typi-



Fig. 6.13 The number of grains with large-angle boundaries in VB-grown ZnSe crystals in dependence on the degree of superheating before crystallization. The growth process was started by spontaneous nucleation within the ampoule tip (after [6.138])

cally, they appear in cast silicon ingots too. They are also known from plastically deformed metals and are often called veins. Figure 6.14 shows such bundles as detected on etched wafers of some VCz GaAs crystals. As was revealed by EPD and LST analysis, such bundles consist of very high-density parallel-arranged sessile dislocations. Principally, one has to differ between two types of *bunching*. They can be originated from inclusions (type 1) and contain a characteristic core of the second phase, or they may consist of a high number of tangled dislocations only (type 2) [6.20]. At first glance the two types are often not distinguishable and a locally good resolving analysis is required to differentiate between them.

Today the genesis of type 1 defects is well understood [6.56, 97, 139]. For instance, in GaAs they appear if Ga-rich inclusions are presented. Possible preconditions are growth from Ga-rich melts and/or the use of nonstoichiometric seed crystals already containing

Ga inclusions. They have been also found in VB/VGF-grown CdTe crystals if growth from nonstoichiometric melts was employed [6.140]. In LEC crystals the main origin, however, is an unprotected dissociating crystal surface if it is in contact with too hot a gas ambience. In the case of GaAs the selective As evaporation releases Ga droplets penetrating into the crystal by a traveling solvent mechanism towards increasing temperature, i.e., following the growing interface [6.56, 97]. Usually, behind such defects, a tail of as-generated misfit dislocations are released [6.56, 139]. This mechanism makes LEC growth of semiconductor compounds in low temperature gradients impossible. Its prevention requires the protection of the crystal surface, whether by full encapsulation Czochralski measures (FEC), or VB/VGF or control of the thermodynamic equilibrium with the surrounding gas phase by partial pressure of the volatile component (VCZ mode). Considering these conditions, today type 1 defects are completely preventable.

There are various formation concepts for type 2 dislocation bundles. Mostly they appear at concave parts of the crystallization fronts where favorable conditions of dislocation focusing exist [6.141]. According to etching analysis, dislocation gnarls are mostly localized at the concave-to-convex transition regions on the (110) axis (Fig. 6.14a). Obviously, this has to do with collision of dislocation glides along the basis glide system $\langle 110 \rangle \{111\}$ according to the Schmidt contour. Once they are formed they follow the propagating crystallization front through the whole crystal, as was theoretically derived by Klapper et al. [6.141]. This fact was proved very carefully in GaAs crystals by Shibata et al. [6.142]. Wang et al. [6.143] attributed such bundles to localized composition variation, i.e., stoichiometry fluctuations, along the interface area, which create dislocation sources by vacancy agglomeration. Such instabilities are conceivable if convection-driven turbulence is present in the melt phase. Even newer concepts on stressed metals couple dislocation bunching with oscillating strain [6.144, 145]. The results of simulations demonstrated that, under cyclic loading regions of low and high dislocation density, a vein structure is formed. From that arises the question: do convective oscillations or even heating temperature fluctuations during a melt growth process play a similar stimulating role in dislocation bunching? Further investigations are required to solve this phenomenon. Generally, it is proved experimentally that the probability of bunching decreases with flattening of the growing interface. In fact, a slightly convex morphol-

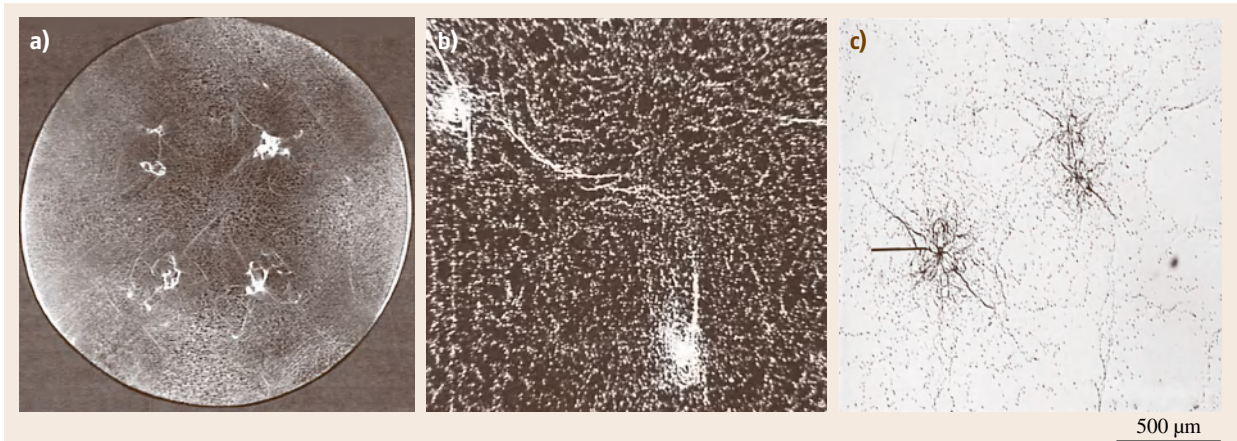


Fig. 6.14a–c Dislocation bunching in melt-grown crystals. **(a)** Dislocation bundles in a GaAs wafer positioned along $\langle 110 \rangle$ directions. The comparison with longitudinal striation analysis shows that the bundles are generated at the concave parts of a markedly w-shaped interface (after [6.20]) (reproduced by permission of Elsevier). **(b)** Magnified dislocation bundles in GaAs. **(c)** Dislocation bundles in cast silicon used for solar-cell production passing through the whole ingot as veins (see also Fig. 6.7b; **(c)** courtesy of U. Juda from IKZ Berlin)

ogy, if the ratio between the diameter of the interface curvature r_{IF} and the crystal radius r is > 0.5 , proves to be optimum for prevention of dislocation bunching [6.20].

A special case of slip line assembling has been found in *lineages* formed like wavy *dislocation walls*. According to [6.120] in GaAs such lineages are composed of an enormous number of slip lines piled up within thin stripes parallel to $\{110\}$. Due to their slope against the crystal edge when the interface was slightly convex they could be related to isotherm curvature. After Ono [6.146], lineages are the result of slip interactions leading to sessile dislocations by the Lomer–Cottrell mechanism. The degree of waving is influenced by high-temperature climb processes. Probably, they reflect a morphological feature of the growing interface and are, therefore, coupled with the melt–solid phase boundary. Today the exact origin of lineages is still unclear. From growth experiments it follows that they can be prevented by nearly flat interface shapes when only minimal thermoelastic stresses are present.

6.3.3 Dislocation Engineering

Dislocation engineering deals with practical measures of control of dislocation density and patterns or even their prevention in situ, i.e., during the crystal growth process. Generally, for dislocation-reduced growth of

compound and mixed crystals with large diameters, the proper combination of the following conditions are required:

- i) Use of a *dislocation-free seed* crystal, in order to prevent grown-in dislocations being the most serious sources of dislocation multiplication
- ii) Achievement of a strongly *uniaxial heat flow* with very small temperature gradients, i.e., nearly flat isotherms at all stages of the growth process
- iii) *Omission of fluid encapsulants* (boric oxide), the presence of which introduces marked thermomechanical stresses at the crystal periphery, and maybe its replacement by a *detached growth mode* [6.147]
- iv) In situ *stoichiometry control* by partial vapor pressure regulation over the melt in order to reduce the intrinsic point defect content which promotes high-temperature dislocation multiplication by climb and also cell structure formation
- v) Prevention of *constitutional supercooling* at the interface by proper selection of a noncritical G/R ratio
- vi) Minimization of atmospheric *pressure fluctuations* around the growing crystal to prevent heterogeneous dislocation rearrangements in bundles and veins.

The highest-temperature nonlinearities, and hence related thermal stress values, increasing very sensitively with diameter, appear in LEC crystals. Today, in such undoped 4 and 6 inch GaAs crystals, the

mean dislocation densities are $(5-7) \times 10^4$ and $(1-2) \times 10^5 \text{ cm}^{-2}$, respectively. The situation can be improved by using modified Czochralski growth with low thermal gradients, for which the vapor-pressure-controlled Czochralski (VCZ) method is available [6.56]. In 6 inch SI (semi-insulating) VCz crystals of more than 20 cm length (25 kg) the average etch pit density (EPD) along the $\langle 110 \rangle$ and $\langle 100 \rangle$ directions can be reduced to $(1.8-2.6) \times 10^4$ and $(2-3) \times 10^4 \text{ cm}^{-2}$, respectively. Minimum values of $(6-8) \times 10^3 \text{ cm}^{-2}$ were ascertained near the $r/2$ region (where r is the wafer radius). In 4 inch VCz crystals a somewhat lower average EPD of $(5-10) \times 10^3 \text{ cm}^{-2}$ was found [6.148].

The best EPD results, however, can be obtained by the VGF method, matured on the industrial scale since the mid-1990s as the most promising growth variant for important semiconductor (InP, GaAs, CdTe), fluoride (CaF_2), and oxide ($\text{Bi}_4\text{Ge}_3\text{O}_{12}$ (BGO), $\text{Pb}(\text{Mg}, \text{Nb})_{1-x}\text{Ti}_x\text{O}_3$ (PMNT), $\text{Pb}(\text{Zn}, \text{Nb})_{1-x}\text{Ti}_x\text{O}_3$ (PZNT)) compound crystals. The decisive technological measure proved to be the maintenance of a uniaxial heat flow through the growing crystal during the whole growth run by proper control of the cooling rate between a top and bottom heater flanked by a booster heater to avoid radial heat outflow [6.149]. In undoped GaAs VGF crystals with diameters between 3 and 6 inch, dislocation densities in the range from 500 to 5000 cm^{-2} have been reported [6.150, 151]. Müller and Birkmann [6.152] succeeded in the growth of Si-doped 4 inch GaAs crystals with the lowest EPD of 31 cm^{-2} by optimized VGF. The few residual dislocations in $\langle 100 \rangle$ -oriented crystals are accumulated cross-like along the $\langle 100 \rangle$ directions, obviously connected with the pronounced joint of the $\{111\}$ facets along the $\langle 100 \rangle$ directions in the crystal cone after the seed. This phenomenon favors growth with a flat bottom from a seed of the same diameter [6.153, 154] in order to maintain the rotational symmetry without pronounced faceting.

Another phenomenon to be controlled in situ is dislocation cell patterning. This problem has not yet been solved on an industrial scale. However, there are already some in-principal laboratory experiences usable for future melt growth improvements. First, independently of the materials used, the cell forma-

tion can be reduced very effectively by doping. No cell structuring was observed in GaAs doped with In or Si at concentrations $> 10^{18} \text{ cm}^{-3}$. Such an effect is due to the impurity gettering at the dislocation core increasing with temperature because of the increasing diffusion rate. As a consequence, the yield stress is enhanced by dislocation locking. No low-angle grain structure was found in CdTe and PbTe crystals when solution hardening by mixing components Se ($x > 0.4$) and Sn ($x > 0.15$) was provided, respectively. However, there is the drawback of segregation when dopants are added to the melt (Sect. 6.2.2) and the danger of morphological interface instability by constitutional supercooling (Sect. 6.2.3). Obviously, the best way to exclude dislocation patterning is reduction of the dislocation density by minimization of the thermomechanical stress. In undoped GaAs it was observed that at ρ values $< 5 \times 10^{-3} \text{ cm}^{-2}$ the cell structure began to disappear. However, for compound crystals with larger diameters over 100 mm the attainment of such low dislocation densities is not yet solved empirically when hardening dopants are not added. Hence, current efforts are directed to homogenization of the thermal field in the growing crystals in order to reduce the dislocation multiplication and mobility by minimizing the thermomechanical stress. Another important way to prevent cell patterning is the minimization of the native point defect content by in situ control of stoichiometry during growth. The stoichiometry can be regulated by the partial pressure of the volatile component over the melt, applying an extra heat source within the growth chamber [6.56]. Using such a VCz arrangement without boric oxide encapsulant, the cellular structure could be suppressed in undoped GaAs crystals when the stoichiometry was controlled by growth from Ga-rich melt composition [6.155, 156]. Recently, this result was confirmed theoretically [6.157]. The stored dislocation density can be reduced under stoichiometric growth conditions. This was achieved for GaAs by horizontal Bridgman growth [6.158], hot-wall Czochralski method [6.159], and VCz [6.155]. Tomizawa et al. explained it as a result of the lowest intrinsic point defect concentration taking part in dislocation motion and multiplication.

6.4 Second-Phase Particles

The presence of second-phase particles, often named COPs (crystal-originated particles), markedly affects the optical and electronic bulk quality as well as the

surface perfection of epitaxial substrates (Sect. 6.1.2). COPs are some of the most studied harmful objects in as-grown crystals. They are present even in un-

doped $A^{II}B^{VI}$ (e.g., CdTe [6.28, 140], ZnSe [6.137]), $A^{III}B^V$ (e.g., GaAs [6.160, 161]), and $A^{IV}B^{VI}$ (e.g., PbTe [6.162]) compounds, but also in numerous oxides (e.g., $Gd_3Ga_5O_{12}$ (GGG) [6.163]) and fluorides (e.g., CaF_2 [6.164]). One of the most serious consequences of compound crystal growth under conditions of native point defect formation is their condensation in precipitates and microvoids. This phenomenon is due to the retrograde behavior of the boundary of the compound existence region, and therefore related to nonstoichiometry (Sect. 6.2.1). In addition, foreign particles, melt–solution droplets of the excess component, and gas bubbles can be incorporated at the growing melt–solid interface.

As explained in detail by Rudolph et al. [6.28, 165], it is important to distinguish between these two different second-phase particle formation mechanisms:

- i) Precipitation
- ii) Inclusion incorporation.

A schematic sketch of the origins of both processes is shown in Fig. 6.15, where their relations to the phase diagram are also illustrated.

In the case of a particle with near-spherical geometry it is known that the total concentration of the second-phase component N_i (in cm^{-3}) can be estimated

according to the formula [6.28]

$$N_i = \frac{4\pi\rho_i N_A}{3A_i} \sum_{i=1}^n r_i^3 \rho_i, \quad (6.29)$$

where ρ_i and A_i are the density and the relative atomic mass of the second-phase component, respectively, N_A is Avogadro's constant, r_i is the particle radius, and i is an index for each class of particle diameter.

6.4.1 Precipitates

Fundamentals of Generation

Precipitates are formed due to the retrograde solubility of native point defects in nonstoichiometric solid compositions (Fig. 6.15). As the as-grown crystal is cooling down, the solidus is crossed and nucleation of the second phase takes place. Probably, Ostwald ripening has to be considered. Favored sites of precipitate ripening are dislocations, as has been concluded from IR laser scattering tomography (e.g., [6.120, 161]; Fig. 6.16). Average precipitate densities of about 10^8 and up to 10^{12} cm^{-3} have been found in GaAs [6.160] and CdTe [6.28], respectively. Typical sizes between 10–100 nm have been determined for As precipitates in GaAs [6.166] and Te precipitates in CdTe [6.167]. Half-empty precipitates have been found by transmission electron microscopy (TEM) in GaAs [6.168] and

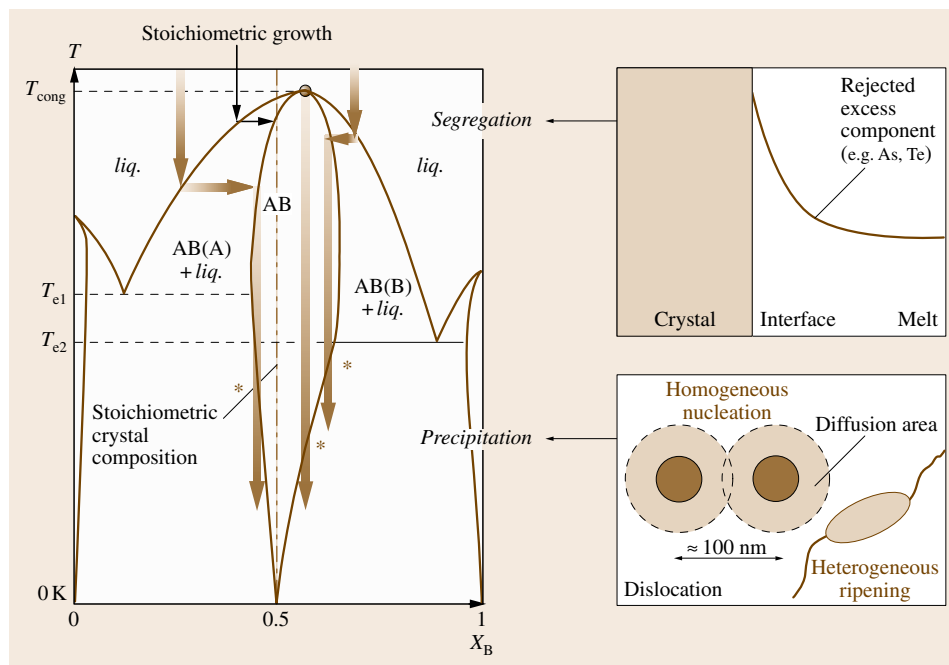


Fig. 6.15 Nonstoichiometry-related effects of second-phase particle formation in a growing compound crystal explained by a sketched phase diagram with elongated phase extent. The segregation evokes the rejection, and hence enrichment, of excess component at the interface that may lead to inclusion incorporation. Homogeneous (matrix) and heterogeneous (decoration) precipitations take place due to second-phase nucleation at the retrograde slope of the solidus curves, probably with subsequent Ostwald ripening

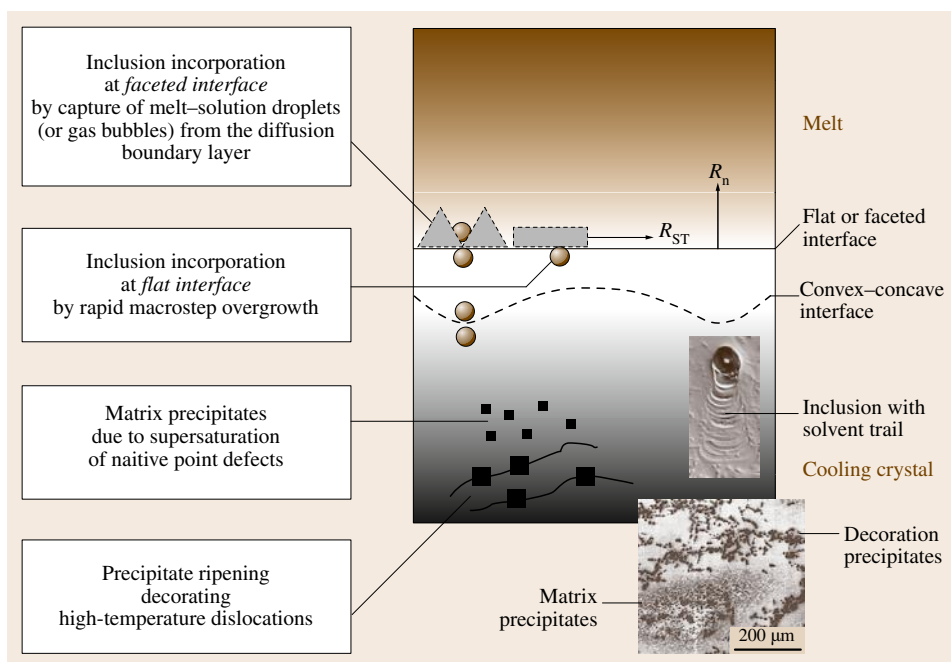


Fig. 6.16 Scheme of different inclusion incorporation and precipitation mechanisms during crystal growth from melt. Two images showing a Ga inclusion with traveling Ga-rich solvent trail and As precipitates in GaAs crystals (after [6.57, 161], reproduced by permission of Elsevier)

CdTe [6.169], probably caused by vacancy condensation in one of the sublattice components accompanied by conglomeration of excess atoms of the opposite sublattice.

In CdTe both tellurium and cadmium precipitates have been found [6.170]. This depends on the melt composition from which the crystal was grown (Te- or Cd-rich, respectively). According to the CdTe phase diagram their density can be effectively minimized by growth under near-stoichiometric conditions [6.28]. Contrary to this, in melt-grown GaAs crystals, only As precipitates were observed. Fornari et al. [6.166] found a correlation between As precipitate size and deviation from stoichiometry. Whereas at the stoichiometric melt composition ($x_L = 0.5$) the diameter is about 120 nm, from Ga-rich melts As precipitates of 40 nm diameter form, even when the mole fraction is markedly Ga-enriched ($x_L = 0.425$). This would be in accordance with a GaAs existence region located completely on the As-rich side, as obtained from current thermochemical calculations and stoichiometry-controlled VCz experiments [6.19, 47, 48].

Control of Precipitate Density

There are two effective ways to minimize the precipitation concentration:

- i) In situ control of stoichiometric crystal composition (see also Sect. 6.2.1)
- ii) Postgrowth annealing under controlled partial pressure.

As was demonstrated by Kießling et al. [6.57] in VCz growth of GaAs without boric oxide encapsulant, melt compositions less than or around a mole fraction of $x_L \approx 0.45$ yield near-stoichiometric crystals essentially without precipitation.

Oda et al. [6.53] developed a multiple postgrowth wafer annealing technology for semi-insulating GaAs. Highly uniform substrates with markedly decreased arsenic precipitate density were obtained. Postgrowth wafer annealing was also successfully used by other authors for InP, GaP, CdTe, and ZnSe wafers.

6.4.2 Inclusions

Incorporation Mechanisms

In contrast to precipitates, inclusions are formed by capture of melt-solution droplets, gas bubbles or foreign particles from the diffusion boundary layer adjacent to the growing interface and enriched by the rejected excess component (Fig. 6.15). Preferred sites are reentrant angles of grain boundaries and twins crossing the interface. Dinger and Fowler [6.171] found lineages

made of tellurium along the growth direction of CdTe crystals grown from Te-rich melt. They attributed this phenomenon to the enhanced cellular growth caused by constitutional supercooling. The inclusions are concentrated in the interlamella notches (Fig. 6.16). Typical inclusion diameters are 1–2 μm , but sizes up to 30 μm have been also observed in HB and VB CdTe crystals grown without Cd pressure control [6.28]. Their axial distribution increases slightly with increasing excess component by segregation. Melt–solution inclusions due to nonstoichiometric melt compositions show a specific crystallization genesis within the already solidified matrix [6.140]. Often they are embedded in a negative polyhedron formed by adjacent zincblende {111} planes. An inclusion could also be captured at a nearly flat interface by an overgrowth or embedding mechanism, as discussed by Chernov [6.38].

Prevention of Inclusion Trapping

There are two essential technological measures against inclusion incorporation:

- i) Growth from the congruent melting point (mostly located close to stoichiometry)
- ii) The choice of undercritical growth velocities.

Furthermore, accelerated crucible rotation techniques [6.85] and control by ultrasonic [6.86] or nonsteady magnetic fields [6.92–94] can be adopted as effective additional steps to disassemble phase boundary layers in melt-growth processes.

6.5 Faceting

When Hulme and Mullin [6.174] looked in the 1950s at the segregation of a number of solutes in InSb they found that the segregation coefficient was different for crystals grown in a $\langle 111 \rangle$ direction as compared with growth in any other direction. Using radiotracer

Fig. 6.17a,b Dopant redistribution in crystals grown with core facets. **(a)** Autoradiographs of a longitudinal section of $\langle 111 \rangle$ -oriented InSb crystals doped with Te. The *bright central column* in each section is a region of enhanced Te concentration where the crystals grew with a faceted interface (after [6.2,3]). **(b)** Optical diffraction along a longitudinal cut of an InP crystal doped with sulfur. The core region corresponding with {111} facet shows enhanced S concentration (after [6.173], reproduced by permission of Elsevier) ►

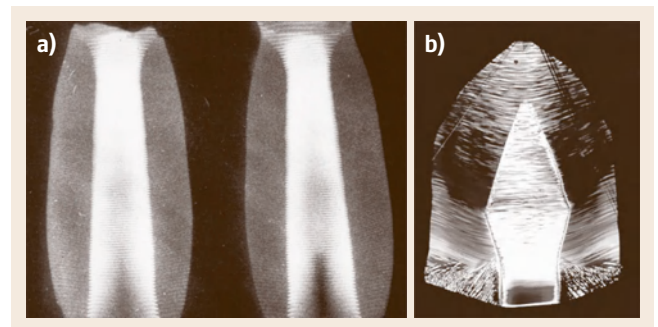
Note, even microgravity conditions are not favorable for the prevention of inclusion incorporation. Salk et al. [6.172] demonstrated during growth under microgravity that the danger of Te inclusion incorporation in CdTe is markedly increased. Due to the absence of convection in the melt the enrichment of the excess component at the interface, and hence the thickness of the diffusion boundary layer, is increased. This enhances the probability of inclusion capture. The growth of inclusion-reduced crystals in space proved to be successful only when well-controlled melt mixing by a rotating magnetic field was applied [6.172].

Chernov [6.38] estimated a critical interface rate R_{cr} to prevent inclusion or gas bubble incorporation that depends on the particle (bubble) radius r_{in} , the interface energy α , and the dynamical viscosity of the melt η as

$$R_{\text{cr}} \leq \left(\frac{0.11B}{\eta r_{\text{in}}} \right) \left(\frac{\alpha}{B r_{\text{in}}} \right)^{1/3}, \quad (6.30)$$

where B is a constant ($\approx 10^{-17} \text{ cm}^2 \text{ kg s}^{-2}$). For instance, in the growth of GaAs crystals from the melt with $\eta = 2.8 \times 10^{-5} \text{ kg cm}^{-1} \text{ s}^{-1}$ a solid spherical foreign particle with $r_{\text{in}} = 1.5 \times 10^{-3} \text{ cm}$ and $\alpha = 0.19 \text{ kg s}^{-2}$ would be rejected from the propagating interface if its normal rate R_{n} is $< 2 \text{ mm/h}$. Chernov showed that the hydrostatic pressing force of gaseous bubbles towards the interface plane is lower than that for solid particles. Hence, prevention of incorporation of microbubbles (e.g., of gaseous arsenic) of the same radius requires consideration of a somewhat enhanced critical velocity of about 8 mm/h.

techniques, they demonstrated that a nonequilibrium concentration was incorporated into those parts of the crystal that had been grown on a faceted interface [6.2, 3] (Fig. 6.17a).



Until today faceting plays a problematic role during crystal growth, especially of oxide materials [6.175, 176]. Facets are the macroscopic indication of a given crystallographic structure and express, therefore, the natural tendency of single crystals to form polyhedra. Hence, the higher the crystal quality, the more developed the facets. This means that they are not defects in reality, but rather a serious cause of dopant and solvent redistributions as well as thermal field inhomogeneities due to their enhanced radiation effects. Further, facets at the rim of a pulling crystal may affect meniscus stability. Careful observation of a growing LiNbO₃ crystal periphery has revealed sudden repelling of the melt from a facet followed by rewetting, i.e., the meniscus jumps several mm down and then up. Such meniscus instability can lead to spontaneous nucleation and subsequent growth of polycrystals [6.176].

Facets form on crystal planes, for which 2-D nucleation is required in order to initiate the growth of a new layer. On nonfaceted (atomically rough) surface atoms can be added singly without the need for nucleation. At a given growth temperature, all crystals will have some surfaces which are rough. However most crystals will have one or more surfaces that are atomically smooth requiring nucleation, especially dielectric materials. Jackson [6.37] proposed a simple relation (Jackson factor α) for the faceting probability

$$\alpha = \frac{\Delta H_{SL}}{k_B T_m} \frac{w}{u} \quad (6.31)$$

(T_m is the melting temperature; w is the number of nearest neighbors of an atom in the growing face; u is the

number of nearest neighbors of an atom in the crystal), which indicates that the magnitude of the entropy of fusion ΔH_{SL} of a material is the guide to its likelihood of forming facets during growth, i.e., materials having a low entropy of fusion (such as metals with $\alpha < 2$) have the lowest probability. In contrast, dielectric crystals with large ΔH_{SL} due to their strong ionic bond energy show a high α factor (> 2), and hence the greatest faceting probability. The common semiconductor materials, with their covalent bonding and $\alpha \approx 2$, tend to form facets during melt growth only on their most closely packed {111} planes, i.e., where the w/u ratio is nearest to unity, or in other words the surface energy is lowest. For instance, in silicon for the {100} and {111} planes the Jackson factors for $\alpha_{\{100\}}$ and $\alpha_{\{111\}}$ are 1.75 (atomically rough) and 2.63 (atomically smooth), respectively.

A further geometric requirement for facet formation during crystal growth from melts is that the radial temperature gradient be such that the freezing-point isotherm is convex when viewed from the crystal (Fig. 6.18a). This ensures that, if the crystal starts to lag behind the isotherm, it experiences increased supercooling at the facet, which ultimately promotes the nucleation of a new layer (note that, the higher the crystal perfection, i.e., the lower the dislocation density, the larger the supercooling). The lateral extension of the facet d is proportional to the supercooling ΔT [6.176] (Fig. 6.18a) as

$$d = 2\sqrt{\frac{2r_{IF}\Delta T}{G_r}}, \quad (6.32)$$

where G_r is the radial temperature gradient, ΔT is the undercooling, and r_{IF} is the radius of curvature of the interface. As can be seen, d increases with decreasing convexity of the interface, i.e., reducing radial temperature gradient. The rapid lateral growth tends to trap in the surface-adsorbed (equilibrium) solute concentration, thereby increasing the effective interface segregation coefficient of solutes that are preferentially adsorbed at the interface. The most dramatic effect occurs with Te-doping of InSb. Here the equilibrium segregation coefficient of Te is ≈ 0.5 , whereas the effective segregation coefficient on the {111} facets is ≈ 4.0 , giving the remarkable ratio 8 : 1 [6.177].

For several years the symptom of faceting at growing interfaces has been considered in numeric modeling of crystal growth processes [6.178]. To do this, the transport phenomena must be coupled with interfa-

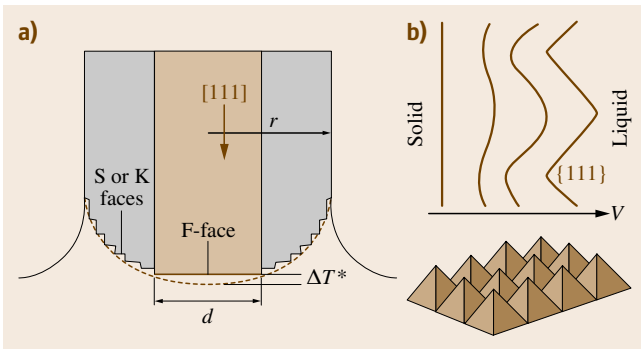


Fig. 6.18a,b Faceting phenomena at the growing melt–solid interface. **(a)** Sketch of Czochralski growth of a crystal with diamond or zincblende structure in $\langle 111 \rangle$ direction with convex interface where a $[111]$ facet is formed. **(b)** Morphological instability of a growing interface where microfacets are formed (after Hurle and Rudolph [6.2, 3])

cial attachment kinetics. Hence, the isotherm condition, typically employed at the melt–crystal interface, is replaced by an equation accounting for undercooling due to interface kinetics. As a result, the interplay between evolving thermal fields and anisotropic interface kinetics is investigated. In particular, the evolution of facets

6.6 Twinning

Grown-in twins are one of the most serious macroscopic defects, the presence of which makes a crystal of no commercial use because of the twin-induced growth disorientation over the whole crystal body (Fig. 6.19). To date, there is no absolutely reliable measure to prevent twinning due to the stochastic character of its appearance. However, one can rank the material and growth parameters most responsible for enhancing the twinning probability. *Gotschalk et al.* [6.181] correlated it with the stacking fault energy, whereupon the greatest danger of twinning exists in materials with high ionicity, showing the lowest stacking fault energies. In fact, InP and CdTe with degrees of ionicity of 42% and 72%, i. e., stacking fault energies of 18 and $11 \times 10^{-7} \text{ J/cm}^2$, respectively, show an extremely high twinning statistics among the semiconductor compounds. Growth conditions enhancing twin appearance are:

- i) Temperature instabilities, i. e., remelting of the interface
- ii) Presence of impurities
- iii) Foreign particles swimming on the melt surface
- iv) Interface contact with wetting inner container walls
- v) Morphological instability of the crystallization front

The recently successful twin-free growth of GaAs crystals from Ga-rich melts without boric oxide encapsulant by the VCz technique [6.156] refutes the former conclusion that twin-free growth was highly improbable for growth at marked deviation from stoichiometry, even of GaAs from Ga-rich melts [6.182].

In the diamond and zincblende structures, twinning is closely related to facet formation (Sect. 6.5) and specified by a rotation of the lattice by 60° about a $\langle 111 \rangle$ axis, the twin lying on the orthogonal $\{111\}$ plane. As a result, a former $[001]$ -oriented crystal after twinning becomes completely disoriented with the $[221]$ axis (Fig. 6.19a). It was recognized early on by *Billig* [6.183] that such twinning occurred principally on $\{111\}$ facets, which form adjacent to the three-phase boundary of melt, crystal, and ambient. *Billig* studied Ge crystals

and the dependence of their size on growth conditions, especially of oxide crystals such as $\text{Y}_3\text{Al}_5\text{O}_{12}$ (YAG), are explored. Of course, most realistic modeling of crystal growth systems involving partial faceting will usually require three-dimensional analysis techniques [6.179].

where the problem is not serious and totally avoidable with carefully controlled growth. The problem is more serious in the III–V compounds, notably In-containing ones such as InSb, InAs, and InP.

The mechanism by which such twins form during growth defied explanation for many years, but in 1995, *Hurle* [6.182] provided a possible thermodynamic description based on ideas due to *Voronkov* [6.184], which can explain the key features of the process. The model demonstrates that, because of the orientation dependence of interfacial energies in the presence of facets, there is a configuration of the three-phase boundary for which, for sufficiently large supercooling, the free

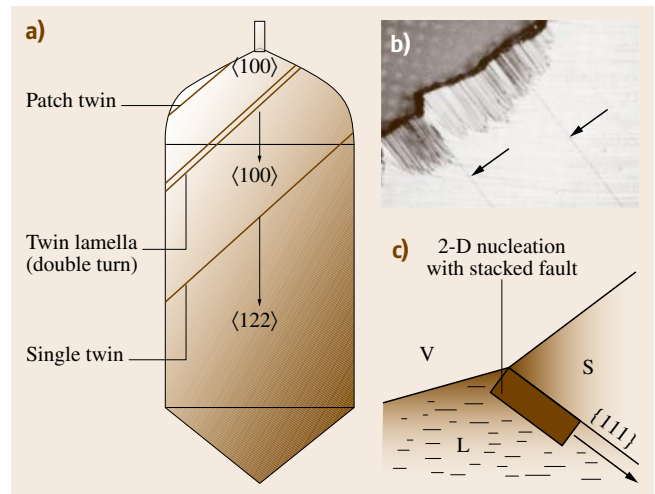


Fig. 6.19a–c Formation of grown-in twins in Czochozralski crystals with diamond and zincblende structures. **(a)** Sketch showing different kinds of twins and the misorientation of the whole crystal from the initial $[001]$ into $[122]$ direction after generation of a single twin. **(b)** Twinning on $\{111\}$ facets (white arrows) at the shoulder region of a InP crystal revealed by *Inada* [6.180] (reproduced by permission of Elsevier). **(c)** Scheme demonstrating the stacking fault (i. e., twinned) 2-D growth mode along the $\{111\}$ facets when a misoriented nucleus is generated at the vapor–liquid–solid (VLS) interface

energy of formation of a critical nucleus is actually lowered by forming that nucleus at the three-phase boundary in twinned orientation. This will occur only if a critical angle of conical growth presenting a portion of crystal surface normal to $\langle 111 \rangle$ is sampled during the growth.

Such a twinned nucleus is thermodynamically favored if the supercooling exceeds the critical value

$$\delta T^* = \left(\frac{\sigma T_m}{h \Delta H_{SL}} \right) A^*, \quad (6.33)$$

where σ is the twin plane energy, T_m is the melting temperature, h is the nucleus height, ΔH_{SL} is the latent heat of fusion, and A^* is the reduced work of formation of a nucleus intersecting the three-phase boundary. Experimental test of this model on InP had been provided by the groups of Müller [6.185] and Dudley [6.186, 187]. Especially Dudley et al. [6.187] found, by synchrotron x-ray anomalous scattering analysis of as-grown InP crystals, that not 60° twinning but 180° rotation between the matrix and the twins takes place. They observed that twinning immediately follows the formation of a $(1\bar{1}\bar{5})$ external shoulder facet which, upon twinning was converted to a $(\bar{1}11)$ one. This can only occur when the edge facets exist in a region where the shoulder angle is close to 74.21° . The result demonstrates the importance of shoulder geometry during growth. Additionally, it was ascertained that twin nucleation occurs preferentially on $\{111\}_P$ faces due to the 30% lower surface energy than those of $\{111\}_{In}$. In GaAs preferential twinning on $\{111\}_{As}$ planes has been reported, showing a 12% lower surface energy than that of the Ga-terminated one.

6.7 Summary

The most important defect types and possible origins during crystal growth from the melt have been discussed. Today, most of the defect-forming mechanisms are well understood. However, some important questions still remain to be solved. For instance, the influence of the degree of association of the melt on the growth kinetics, which probably plays an essential role in II–VI systems, requires further consideration. Further, the dislocation patterning and bunching mechanisms in correlation with the growth conditions are not yet completely decoded. Also, the main origin of twinning has not yet been revealed.

Many LEC and Bridgman experiments have demonstrated that the twin probability is markedly reduced if the temperature oscillations of the growth system, and therefore excursions of the angle of the contacting meniscus, are minimized. This is due to the reduced probability of encountering the critical angle described above when the meniscus angle fluctuations are reduced. In fact, Hosokawa et al. [6.188] succeeded in growing twin-free InP crystal with diameters up to 100 mm by careful maintenance of thermal stability during growth, which was achieved by VCz and applying damping magnetic fields around the melt.

An interesting correlation has been observed by Rudolph during the vertical Bridgman growth of CdTe [6.28] and ZnSe crystals [6.137] by self-seeding. The number of twins was reduced and even prevented when the melt was markedly overheated and held for a longer time before the nucleation process in the ampoule tip was started. Similar results were described by Khattak and Schmid [6.189], with reduced twin formation in CdTe by overheating of the melt to above 110 K. Such a phenomenon can be explained when the well-known high degree of melt association of these materials at low superheating is taken into account. Probably, at a few Kelvin above the melting point, there are still enough preserved melt associates, such as tetrahedra, which can be incorporated into the crystalline phase by a false stacking sequence (e.g., 60° rotated in relation to a correct stacked $\{111\}$ -plane). Witt [6.190] proposed a clustering model of the melt, whereupon the smallest cluster of relative stability capable of nucleating oblique twins comprises eight atoms. In general, more investigations of the melt structure and its influence on the growth kinetics are necessary.

Eminent success has been achieved in technological developments. During the last decade, computer-controlled vertical gradient freezing has matured to become the leading industrial production method for semiconductor compound crystals. However, that is not to say that all defects can be avoided. For example, the relatively poor thermal conductivity and low yield stresses of III–V and II–VI compounds as compared with Ge and Si mean that it is not possible to reduce the thermal stresses to a sufficiently low level to avoid dislocations.

Scaling up to achieve cost reduction is an ever-present pressure. Increasing crystal diameter increases

the thermal stresses experienced during cooling. Avoiding increased dislocation density requires continual refinement of furnace design, and here computer modeling plays a key role. An additional problem posed by scaling-up is the increased turbulence which occurs in the melt. The use of magnetic fields is being ex-

ploited to achieve damping of this turbulence. Recently, in the author's laboratory, the concept of simultaneous generation of heat and a traveling magnetic field by a heater placed within the growth chamber was successfully tested and its first industrial application started [6.191].

References

- 6.1 H. Föll: *Defects in Crystals*, Hyperscript, <http://www.tf.uni-kiel.de/matwis/amat/>
- 6.2 D.T.J. Hurler, P. Rudolph: A brief history of defect formation, segregation, faceting, and twinning in melt-grown semiconductors, *J. Cryst. Growth* **264**, 550–564 (2003)
- 6.3 R.S. Feigelson (Ed.): *50 Years Progress in Crystal Growth* (Elsevier, Amsterdam 2004) p. 109
- 6.4 H. Pick: Festkörperphysik, *Naturwissenschaft* **41**, 346–354 (1954), in German
- 6.5 S. Mahajan: Defects in semiconductors and their effects on devices, *Acta Mater.* **48**, 137–149 (2000)
- 6.6 I. Baumann, P. Rudolph, D. Krabe, R. Schälge: Orthoscopic investigations of the axial optical and compositional homogeneity of Czochralski grown LiNbO₃ crystals, *J. Cryst. Growth* **128**, 903–908 (1993)
- 6.7 P. Rudolph, M. Jurisch: Bulk growth of GaAs – An overview, *J. Cryst. Growth* **198/199**, 325–335 (1999)
- 6.8 N. Mainzer, E. Lakin, E. Zolotoyabko: Point-defect influence on 1/f noise in HgCdTe photodiodes, *Appl. Phys. Lett.* **81**, 763–765 (2002)
- 6.9 T. Fukuda, P. Rudolph, S. Uda: *Fiber Crystal Growth from the Melt* (Springer, Berlin 2004)
- 6.10 V. Swaminathan, A.T. Macrander: *Materials Aspects of GaAs and InP Based Structures* (Prentice Hall, Upper Saddle River 1991)
- 6.11 H. Chen, B. Raghotharmachar, W. Vetter, M. Dudley, Y. Wang, B.J. Skromme: Effects of different defect types on the performance of devices fabricated on a 4H-SiC homoepitaxial layer, *Mater. Res. Soc. Symp. Proc.* **911**, 1–6 (2006)
- 6.12 S. Miyazawa: Effect of dislocations on GaAs-MESFET Threshold voltage, and growth of dislocation-free, semi-insulating GaAs, *Prog. Cryst. Growth Charact. Mater.* **23**, 23–71 (1991)
- 6.13 J.R. Niklas, W. Siegel, M. Jurisch, U. Kretzer: GaAs wafer mapping by microwave-detected photoconductivity, *Mater. Sci. Eng. B* **80**, 206–209 (2001)
- 6.14 T.E. Schlesinger, J.E. Toney, H. Yoon, E.Y. Lee, B.A. Brunett, L. Franko, R.B. James: Cadmium zinc telluride and its use as a nuclear radiation detector material, *Mater. Sci. Eng. R* **32**, 103–189 (2001)
- 6.15 B.G. Ivanov, M.T. Kogan, V.M. Reiterov: Small-angle disorientation in Bridgman-Stockbarger-grown lithium fluoride crystals, *J. Opt. Technol.* **68**, 32–34 (2001)
- 6.16 P. Sadrabadi, P. Eisenlohr, G. Wehrhan, J. Stabilein, L. Parthier, W. Blum: Evolution of dislocation structure and deformation resistance in creep exemplified on single crystals of CaF₂, *Mater. Sci. Eng. A* **510**, 46–50 (2009)
- 6.17 H. Halloin, P. von Ballmoos, J. Evrard, G.K. Skinner, N. Abrosimov, P. Bastie, G. Di Cocco, M. George, B. Hamelin, P. Jean, J. Knödleseder, P. Laporte, C. Badenes, P. Laurent, R.K. Smither: Performance of CLAIRE, the first balloon-borne γ -ray lens telescope, *Nucl. Instrum. Methods Phys. Res. A* **504**, 120–125 (2003)
- 6.18 J.R. Weertman, D. Farkas, K. Hemker, H. Kung, M. Mayo, R. Mitra, H. Van Swygenhoven: Structure and mechanical behavior of bulk nanocrystalline materials, *MRS Bull.* **24**(2), 44–50 (1999)
- 6.19 P. Rudolph: Non-stoichiometry related defects at the melt growth of semiconductor compound crystals – A review, *Cryst. Res. Technol.* **38**, 542–554 (2003)
- 6.20 P. Rudolph, C. Frank-Rotsch, U. Juda, M. Naumann, M. Neubert: Studies on dislocation patterning and bunching in semiconductor compounds (GaAs), *J. Cryst. Growth* **265**, 331–340 (2004)
- 6.21 F.A. Kröger: *The Chemistry of Imperfect Crystals* (North-Holland Publ., Amsterdam 1973)
- 6.22 D.I. Takamura: Point defects. In: *Physical Metallurgy*, ed. by R.W. Cahn (North-Holland Publ., Amsterdam 1965), Chap. XIII–XX
- 6.23 E. Dornberger: Prediction of OFS ring dynamics and grown-in voids in Czochralski silicon crystals. Ph.D. Thesis (Universite Catholique de Louvain, Louvain-la-Neuve 1997)
- 6.24 K.M. Luken, R.A. Morrow: Formation energies and charge states of native defects in GaAs: A selected compilation from the literature, *Semicond. Sci. Technol.* **11**, 1156–1158 (1996)
- 6.25 J.L. Rouviere, Y. Kim, J. Cunningham, J.A. Rentschler, A. Bourret, A. Ourmazd: Measuring properties of point defects by electron microscopy: The Ga vacancy in GaAs, *Phys. Rev. Lett.* **68**, 2798–2801 (1992)
- 6.26 L. Yujie, M. Guoli, J. Wanqi: Point defects in CdTe, *J. Cryst. Growth* **256**, 266–275 (2003)
- 6.27 M.A. Berding, M. van Schilfgaarde, A.T. Paxton, A. Sher: Defects in ZnTe, CdTe, and HgTe: Total en-

- ergy calculations, J. Vac. Sci. Technol. A **8**, 1103–1107 (1990)
- 6.28 P. Rudolph: Fundamental studies on Bridgman growth of CdTe, Prog. Cryst. Growth Charact. Mater. **29**, 275–381 (1995)
- 6.29 R. Grill, J. Franc, P. Hoeschl, E. Belas, I. Turkevych, L. Turjanska, P. Moravec: Semiinsulating CdTe, Nucl. Instrum. Methods Phys. Res. A **487**, 40–46 (2002)
- 6.30 D.T.J. Hurle: Point defects in compound semiconductors. In: *Crystal Growth – From Fundamentals to Technology*, ed. by G. Müller, J.-J. Metois, P. Rudolph (Elsevier, Amsterdam 2004) pp.323–343
- 6.31 P. Rudolph: Elements of thermodynamics for the understanding and design of crystal growth processes. In: *Theoretical and Technological Aspects of Crystal Growth*, ed. by R. Fornari, C. Paorici (Trans Tech Publications, Switzerland 1998) pp.1–26
- 6.32 V.V. Voronkov, R. Falster, F. Quast: On the properties of the intrinsic point defects in silicon: A perspective from crystal growth and wafer processing, Phys. Status Solidi (b) **222**, 219–244 (2000)
- 6.33 D.T.J. Hurle: A comprehensive thermodynamic analysis of native point defect and dopant solubilities in gallium arsenide, J. Appl. Phys. **85**, 6957–7022 (1999)
- 6.34 R. Brown, D. Maroudas, T. Sinno: Modelling point defect dynamics in the crystal growth of silicon, J. Cryst. Growth **137**, 12–25 (1994)
- 6.35 E. Dornberger, J. Virbulis, B. Hanna, R. Hoelzl, E. Daub, W. von Ammon: Silicon crystals for future requirements of 300 mm wafers, J. Cryst. Growth **229**, 11–16 (2001)
- 6.36 M.A. Berding: Native defects in CdTe, Phys. Rev. **60**, 8943–8950 (1999)
- 6.37 K.A. Jackson: Liquid metals and solidification, Am. Soc. Met. (Cleveland, Ohio 1958) 174–180
- 6.38 A.A. Chernov: *Modern Crystallography III* (Springer, Berlin 1984)
- 6.39 I.V. Markov: *Crystal Growth for Beginners* (World Scientific, Singapore 1995)
- 6.40 A.A. Chernov: Notes on interface growth kinetics 50 years after Burton, Cabrera and Frank, J. Cryst. Growth **264**, 499–518 (2004)
- 6.41 K. Fujiwara, K. Nakajima, T. Ujihara, N. Usami, G. Sazaki, H. Hasegawa, S. Mizoguchi, K. Nakajima: In situ observations of crystal growth behavior of silicon melt, J. Cryst. Growth **243**, 275–282 (2002)
- 6.42 S. Arai, S. Tsukimoto, S. Muto, H. Saka: Direct observation of the atomic structure in a solid-liquid interface, Microsc. Microanal. **6**, 358–361 (2000)
- 6.43 T. Motooka, K. Nishihira, R. Oshima, H. Nishizawa, F. Hori: Atomic diffusion at solid/liquid interface of silicon: transition layer and defect formation, Phys. Rev. B **65**, 813041–813044 (2002)
- 6.44 R. Falster, V. Voronkov: Engineering of intrinsic point defects in silicon wafers and crystals, Mater. Sci. Eng. B **73**, 87–94 (2000)
- 6.45 F. Rosenberger: *Fundamentals of Crystal Growth I* (Springer, Berlin 1979)
- 6.46 S. Erdei, F.W. Ainger: Trends in the growth of stoichiometric single crystals, J. Cryst. Growth **174**, 293–300 (1997)
- 6.47 M. Jurisch, H. Wenzl: *Workshop on Simulations in Crystal Growth* (DGKK, Memmelsdorf 2002)
- 6.48 W. Dreyer, F. Duderstadt: *On the modelling of semi-insulating GaAs including surface tension and bulk stresses (EMS)* (Weierstraß-Institut, Berlin 2004), Treatise No. 995
- 6.49 P. Rudolph, F.-M. Kießling: Growth and characterization of GaAs crystals produced by the VCz method without boric oxide encapsulation, J. Cryst. Growth **292**, 532–537 (2006)
- 6.50 P. Rudolph, F.-M. Kießling: The horizontal Bridgman method, Cryst. Res. Technol. **23**, 1207–1224 (1988)
- 6.51 E. Monberg: Bridgman and related growth techniques. In: *Handbook of Crystal Growth*, Vol. 2a, ed. by D.T.J. Hurle (Elsevier, North-Holland 1994), Chap. 2
- 6.52 P. Rudolph, S. Kawasaki, S. Yamashita, S. Yamamoto, Y. Usuki, Y. Konagaya, S. Matada, T. Fukuda: Attempts to growth of undoped CdTe single crystals with high electrical resistivity, J. Cryst. Growth **161**, 28–33 (1996)
- 6.53 S. Oda, M. Yamamoto, M. Seiwa, G. Kano, T. Inoue, M. Mori, R. Shimakura, M. Oyake: Defects in and device properties of semi-insulating GaAs, Semicond. Sci. Technol. **7**, 215–223 (1992)
- 6.54 J. Nishizawa: Stoichiometry control for growth of III–V crystals, J. Cryst. Growth **99**, 1–8 (1990)
- 6.55 J. Nishizawa, Y. Oyama: Stoichiometry of III–V compounds, Mater. Sci. Eng. R **12**, 273–426 (1994)
- 6.56 M. Neubert, P. Rudolph: Growth of semi-insulating GaAs crystals in low-temperature gradients by using the vapour pressure controlled Czochralski method (VCz), Prog. Cryst. Growth Charact. Mater. **43**, 119–185 (2001)
- 6.57 F.-M. Kießling, P. Rudolph, M. Neubert, U. Juda, M. Naumann, W. Ulrici: Growth of GaAs crystals from Ga-rich melts by the VCz method without liquid encapsulation, J. Cryst. Growth **269**, 218–228 (2004)
- 6.58 U.A. Borovlev, N.V. Ivannikova, V.N. Shlegel, Y.V. Vasiliev, V.A. Gusev: Progress in growth of large sized BGO crystals by the low-thermal-gradient Cz technique, J. Cryst. Growth **229**, 305–311 (2001)
- 6.59 E. Pfeiffer: Untersuchungen zur Optimierung der Züchtungstechnologie von PbMoO₃-Einkristallen nach der Czochralski-Methode. Ph.D. Thesis (Humboldt-University, Berlin 1990), in German
- 6.60 E. Pfeiffer, P. Rudolph: German patent DD 290–226 (1989)
- 6.61 K. Hein, E. Buhrig (Eds.): *Kristallisation aus Schmelzen* (Verlag für Grundstoffindustrie, Leipzig 1983), in German
- 6.62 P. Rudolph, U. Rinas, K. Jacobs: Systematic steps towards exactly stoichiometric and uncompensated CdTe Bridgman crystals, J. Cryst. Growth **138**, 249–254 (1994)

- 6.63 E. Northrup, S.B. Zhang: Dopant and defect energetics: Si in GaAs, *Phys. Rev. B* **47**, 6791–6794 (1993)
- 6.64 H. Zimmermann, R. Boyn, C. Michel, P. Rudolph: Absorption-calibrated determination of impurity concentrations in CdTe from excitonic photoluminescence, *Phys. Status Solidi (a)* **118**, 225–234 (1990)
- 6.65 J.A. Burton, R.C. Prim, W.P. Slichter: The distribution of solute in crystals grown from the melt, *J. Chem. Phys.* **21**, 1987–1991 (1953)
- 6.66 V.G. Levich: *Physicochemical Hydrodynamics* (Prentice-Hall, Englewood Cliffs 1961)
- 6.67 A. Ostrogorsky, G. Müller: A model of effective segregation coefficient, accounting for convection in the solute layer at the growth interface, *J. Cryst. Growth* **121**, 587–598 (1992)
- 6.68 W.A. Tiller: Principles of solidification. In: *The Art and Science of Growing Crystals*, ed. by J.J. Gilman (Wiley, New York 1963), Chap. 15
- 6.69 N. Sato, M. Kakimoto, Y. Kadota: The carbon and boron concentration control in GaAs crystals grown by liquid encapsulated Czochralski method. In: *Semi-Insulating III–V Materials*, ed. by A. Milnes, C. Miner (Hilger, Bristol 1990)
- 6.70 M. Jurisch, F. Börner, T. Bünger, S. Eichler, T. Flade, U. Kretzer, A. Köhler, J. Stenzenberger, B. Weinert: LEC- and VGF-growth of Si GaAs single crystals – Recent developments and current issues, *J. Cryst. Growth* **275**, 283–291 (2005)
- 6.71 K. Jacob, C. Frank, M. Neubert, P. Rudolph, W. Ulrici, M. Jurisch, J. Korb: A study on carbon incorporation in semi-insulating GaAs crystals grown by the vapor pressure controlled Czochralski technique (VCZ), *Cryst. Res. Technol.* **35**, 1163–1171 (2000)
- 6.72 S. Eichler, A. Seidl, F. Börner, U. Kretzer, B. Weinert: A combined carbon and oxygen segregation model for the LEC growth of Si GaAs, *J. Cryst. Growth* **247**, 69–76 (2003)
- 6.73 J. Bohm, A. Lüdge, W. Schröder: Crystal growth by floating zone melting. In: *Handbook of Crystal Growth*, Vol. 2a, ed. by D.T.J. Hurle (Elsevier, North-Holland 1994), Chap. 4
- 6.74 R. Triboulet: The travelling heater method (THM) for $Hg_{1-x}Cd_xTe$ and related materials, *Prog. Cryst. Growth Charact. Mater.* **28**, 85–144 (1994)
- 6.75 C. Genzel, P. Gille, I. Hähner, F.-M. Kießling, P. Rudolph: Structural perfection of (Hg,Cd)Te grown by THM, *J. Cryst. Growth* **101**, 232–236 (1990)
- 6.76 H.J. Koh, Y. Furukawa, P. Rudolph, T. Fukuda: Oxide mixed crystals grown by heater-immersed zone melting method with multi-capillary holes, *J. Cryst. Growth* **149**, 236–240 (1995)
- 6.77 R.S. Feigelson: Pulling optical fibers, *J. Cryst. Growth* **79**, 669–680 (1986)
- 6.78 T. Fukuda, P. Rudolph, S. Uda (Eds.): *Fiber Crystal Growth from the Melt* (Springer, Berlin 2004)
- 6.79 K.M. Kim, A.F. Witt, H.C. Gatos: Crystal growth from the melt under destabilizing thermal gradients, *J. Electrochem. Soc.* **119**, 1218–1222 (1972)
- 6.80 H.J. Scheel: Theoretical and technological solutions of the striation problem, *J. Cryst. Growth* **287**, 214–223 (2006)
- 6.81 E. Bauser: Atomic mechanisms of LPE. In: *Handbook of Crystal Growth*, Vol. 3b, ed. by D.T.J. Hurle (Elsevier, North-Holland 1994), Chap. 20
- 6.82 J. Barthel, M. Jurisch: Oszillation der Erstarrungsgeschwindigkeit beim Kristallwachstum aus der Schmelze mit rotierendem Keimkristall, *Kristall und Technik* **8**, 199–206 (1973), in German
- 6.83 D.T.J. Hurle, E. Jakeman: Effects of fluctuations on measurement of distribution coefficient by directional solidification, *J. Cryst. Growth* **5**, 227–232 (1969)
- 6.84 D.T.J. Hurle, R.W. Series: Use of magnetic field in melt growth. In: *Handbook of Crystal Growth*, Vol. 2a, ed. by D.T.J. Hurle (Elsevier, North-Holland 1994), Chap. 5
- 6.85 H.J. Scheel: Accelerated crucible rotation: A novel stirring technique in high-temperature solution growth, *J. Cryst. Growth* **13/14**, 560–565 (1972)
- 6.86 G.N. Kozhemyakin: Imaging of convection in a Czochralski crucible under ultrasound waves, *J. Cryst. Growth* **257**, 237–244 (2003)
- 6.87 E. Gilioli, J.L. Weyher, L. Zanotti, C. Mucchino: Growth striations in GaAs as revealed by DSL photoetching, *Mater. Sci. Forum* **203**, 13–17 (1996)
- 6.88 J.L. Weyher, P.J. van der Wel, G. Frigerio, C. Mucchino: DSL photoetching and high spatial resolution PL study of growth striations in undoped semi-insulating LEC-grown GaAs, *Proceedings of the 6th Conference on Semi-Insulating III–V* (1990) pp. 161–166
- 6.89 R.T. Gray, M.F. Larrousse, W.R. Wilcox: Diffusional decay of striations, *J. Cryst. Growth* **92**, 530–542 (1988)
- 6.90 B. Billia, R. Trivedi: Pattern formation in crystal growth. In: *Handbook of Crystal Growth*, Vol. 1b, ed. by D.T.J. Hurle (Elsevier, North-Holland 1994), Chap. 14
- 6.91 W.A. Tiller, K.A. Jackson, J.W. Rutter, B. Chalmers: The redistribution of solute atoms during the solidification of metals, *Acta Metallurg.* **1**, 428–437 (1953)
- 6.92 P. Dold, K.W. Benz: Rotating magnetic fields: Fluid flow and crystal growth applications, *Prog. Cryst. Growth Charact. Mater.* **38**, 7–38 (1999)
- 6.93 C. Stelian, Y. Delannoy, Y. Fautrelle, T. Dufar: Solute segregation in directional solidification of GaInSb concentrated alloys under alternating magnetic fields, *J. Cryst. Growth* **266**, 207–215 (2004)
- 6.94 V. Socoliuc, D. Vizman, B. Fischer, J. Friedrich, G. Müller: 3D numerical simulation of Rayleigh-Bénard convection in an electrically conducting melt acted on by a travelling magnetic field, *Magnetohydrodynamics* **39**, 187–200 (2003)

- 6.95 W.W. Mullins, R.F. Sekerka: Stability of planar interface during solidification of a dilute alloy, *J. Appl. Phys.* **35**, 444–451 (1964)
- 6.96 S.R. Coriell, G.B. McFadden: Morphological stability. In: *Handbook of Crystal Growth*, Vol. 1b, ed. by D.T.J. Hurle (Elsevier, North-Holland 1994), Chap. 12
- 6.97 H. Wenzl, W.A. Oates, K. Mika: Defect thermodynamics and phase diagrams in compound crystals. In: *Handbook of Crystal Growth*, Vol. 1a, ed. by D.T.J. Hurle (Elsevier, North-Holland 1994), Chap. 3
- 6.98 P. Schlossmacher, K. Urban: Dislocations and precipitates in gallium arsenide, *J. Appl. Phys.* **71**, 620–629 (1992)
- 6.99 S. Brochard, J. Rabier, J. Grilhé: Nucleation of partial dislocations from a surface-step in semiconductors: a first approach of the mobility effect, *Eur. Phys. J. Appl. Phys.* **2**, 99–105 (1998)
- 6.100 G. Grange, C. Jourdan, A.L. Coulet, J. Gastaldi: Observation of the melting-solidification process of an Al crystal by synchrotron x-ray topography, *J. Cryst. Growth* **72**, 748–752 (1985)
- 6.101 K. Sumino, I. Yonenaga: Interactions of impurities with dislocations: Mechanical effects, *Solid State Phenom.* **85/86**, 145–176 (2002)
- 6.102 E. Nadgorny: Dislocation dynamics and mechanical properties of crystals. In: *Progress in Materials Science*, Vol. 31, ed. by J.W. Christian, P. Haasen, T.B. Massalski (Pergamon, Oxford 1988)
- 6.103 R.J. Amodeo, N.M. Ghoniem: Dislocation dynamics. I. A proposed methodology for deformation micromechanics; Dislocation dynamics. II. Applications to the formation of persistent slip bands, planar arrays, and dislocation cells, *Phys. Rev. B* **41**, 6958–6976 (1990)
- 6.104 R.N. Nabarro: Steady-state diffusional creep, *Philos. Mag.* **A 16**, 231–238 (1967)
- 6.105 E. Billig: Some defects in crystals grown from the melt, *Proc. R. Soc. Lond. Ser. A* **235**, 37–55 (1956)
- 6.106 V.L. Indenbom: Ein Beitrag zur Entstehung von Spannungen und Versetzungen beim Kristallwachstum, *Kristall und Technik* **14**, 493–507 (1979), in German
- 6.107 A.S. Jordan, A.R. von Neida, R. Caruso: The theory and practice of dislocation reduction in GaAs and InP, *J. Cryst. Growth* **70**, 555–573 (1984)
- 6.108 N. Miyazaki, H. Uchida, S. Hagihara, T. Munakata, T. Fukuda: Thermal stress analysis of bulk single crystal during Czochralski growth (comparison between anisotropic analysis and isotropic analysis), *J. Cryst. Growth* **113**, 227–241 (1991)
- 6.109 S. Motakef, A.F. Witt: Thermoelastic analysis of GaAs in LEC growth configuration: I. Effect of liquid encapsulation on thermal stresses, *J. Cryst. Growth* **80**, 37–50 (1987)
- 6.110 C.T. Tsai, A.N. Gulluoglu, C.S. Hartley: A crystallographic methodology for modeling dislocation dynamics in GaAs crystals grown from melt, *J. Appl. Phys.* **73**, 1650–1656 (1993)
- 6.111 J. Völkl: Stress in cooling crystals. In: *Handbook of Crystal Growth*, Vol. 2b, ed. by D.T.J. Hurle (Elsevier, North-Holland 1994), Chap. 14
- 6.112 R. Lohonka, G. Vanderschaeve, J. Kratochvil: Modelling of the plastic behaviour of III–V compound semiconductors during compressive tests, *Mater. Sci. Eng. A* **337**, 50–58 (2002)
- 6.113 K. Sumino, I. Yonenaga: Interactions of impurities with dislocations: mechanical effects, *Solid State Phenom.* **85/86**, 145–176 (2002)
- 6.114 S. Grondet, T. Duffar, F. Louchet, F. Theodore, N. Van Den Bogaert, J.L. Sentailler: A visco-plastic model of the deformation of InP during LEC growth taking into account dislocation annihilation, *J. Cryst. Growth* **252**, 92–101 (2003)
- 6.115 S. Pendurti, V. Prasad, H. Zhang: Modelling dislocation generation in high pressure Czochralski growth of InP single crystals: parts I and II, *Modelling Simul. Mater. Sci. Eng.* **13**, 249–297 (2005)
- 6.116 N. Miyazaki, Y. Matsuura, D. Imahase: Thermal stress analysis of lead molybdate single crystal during growth process: Discussion on relation between thermal stress and crystal quality, *J. Cryst. Growth* **289**, 659–662 (2006)
- 6.117 M. Zaiser: Dislocation patterns in crystalline solids – phenomenology. In: *Crystal Growth – From Theory to Technology*, ed. by G. Müller, J.-J. Metois, P. Rudolph (Elsevier, Amsterdam 2004) pp. 215–238
- 6.118 L. Kubin: Collective defect behavior under stress, *Science* **312**, 864–865 (2006)
- 6.119 F.R.N. Nabarro, M.S. Duesbery (Eds.): *Dislocations in Solids*, Vol. 11 (North-Holland, Amsterdam 2002)
- 6.120 M. Naumann, P. Rudolph, M. Neubert, J. Donecker: Dislocation studies in VCz GaAs by laser scattering tomography, *J. Cryst. Growth* **231**, 22–33 (2001)
- 6.121 T. Tuomi, L. Knuuttila, J. Riikonen, P.J. McNally, W.-M. Chen, J. Kanatharana, M. Neubert, P. Rudolph: Synchrotron x-ray topography of undoped VCz GaAs crystals, *J. Cryst. Growth* **237**, 350–355 (2002)
- 6.122 P. Rudolph: Dislocation patterning in semiconductor compounds, *Cryst. Res. Technol.* **40**, 7–20 (2005)
- 6.123 W. Pantleon: The evolution of disorientations for several types of boundaries, *Mater. Sci. Eng. A* **319–321**, 211–215 (2001)
- 6.124 G. Grange, C. Jourdan, A.L. Coulet, J. Gastaldi: Observation of the melting-solidification process of an Al crystal by synchrotron x-ray topography, *J. Cryst. Growth* **72**, 748–752 (1985)
- 6.125 B. Jakobson, H.F. Poulsen, U. Lienert, J. Almer, S.D. Shastri, H.O. Sørensen, C. Gundlach, W. Pantleon: Formation and subdivision of deformation structures during plastic deformation, *Science* **312**, 889–892 (2006)
- 6.126 C. Frank-Rotsch, U. Juda, F.-M. Kießling, P. Rudolph: Dislocation patterning during crystal growth of semiconductor compounds (GaAs), *Mater. Sci. Technol.* **21**, 1450–1454 (2005)

- 6.127 D.L. Holt: Dislocation cell formation in metals, *J. Appl. Phys.* **41**, 3197–3201 (1970)
- 6.128 J. P. Poirier: *Creep of Crystals – High-Temperature Deformation Processes in Metals, Ceramics*, Cambridge Earth Science Series (Cambridge Univ. Press, Cambridge 1985)
- 6.129 P. Rudolph, C. Frank-Rotsch, U. Juda, F.-M. Kießling: Scaling of dislocation cells in GaAs crystals by global numeric simulation and their restraints by in situ control of stoichiometry, *Mater. Sci. Eng. A* **400/401**, 170–174 (2005)
- 6.130 S.V. Raj, G.M. Pharr: A compilation and analysis of data for the stress dependence of the subgrain size, *Mater. Sci. Eng.* **81**, 217–237 (1986)
- 6.131 B. Birkmann, J. Stenzenberger, M. Jurisch, J. Härtwig, V. Alex, G. Müller: Investigations of residual dislocations in VGF-grown Si-doped GaAs, *J. Cryst. Growth* **276**, 335–346 (2005)
- 6.132 G. Müller, P. Schwesig, B. Birkmann, J. Härtwig, S. Eichler: Types and origin of dislocations in large GaAs and InP bulk crystals with very low dislocation densities, *Phys. Status Solidi (a)* **202**, 2870–2879 (2005)
- 6.133 B. Devincere, L.P. Kubin: Mesoscopic simulations of dislocations and plasticity, *Mater. Sci. Eng. A* **234–236**, 8–14 (1997)
- 6.134 I.V. Sabinina, A.K. Gutakovski, T.I. Milenov, N.N. Lykakh, Y.G. Sidorov, M.M. Gospodinov: Melt growth of CdTe crystals and transmission electron microscopic, *Cryst. Res. Technol.* **26**, 967–972 (1991)
- 6.135 L. Parthier, C. Poetsch, K. Pöhl, J. Stäblein, G. Wehrhan: About the influence of lattice-defects on the optical homogeneity of CaF₂ crystals for use in high performance microlithography, *Gemeinsame Jahrestagung der DGK und DGKK, Jena, Referate (Oldenburg, München 2004)* p. 5
- 6.136 S.V. Raj, I.S. Iskovitz, A.D. Freed: Modeling the role of dislocation substructure during class M and exponential creep, *NASA Technical Memorandum 106986*, 1–77 (1995)
- 6.137 P. Rudolph, N. Schäfer, T. Fukuda: Crystal growth of ZnSe from the melt, *Mater. Sci. Eng. R* **15**, 85–133 (1995)
- 6.138 P. Rudolph, K. Umetsu, H.J. Koh, T. Fukuda: Correlation between ZnSe crystal growth conditions from melt and generation of large-angle grain boundaries and twins, *Jpn. J. Appl. Phys.* **33**, 1991–1994 (1994)
- 6.139 J.P. Tower, R. Tobin, P.J. Perah, R.M. Ware: Interface shape and crystallinity in LEC GaAs, *J. Cryst. Growth* **114**, 665–675 (1991)
- 6.140 P. Rudolph, A. Engel, I. Schentke, A. Grochocki: Distribution and genesis of inclusions in CdTe and (Cd,Zn)Te single crystals grown by the Bridgman method and by the travelling heater method, *J. Cryst. Growth* **147**, 297–304 (1995)
- 6.141 H. Klapper: Generation and propagation of dislocations during crystal growth, *Mater. Chem. Phys.* **66**, 101–109 (2000)
- 6.142 M. Shibata, T. Suzuki, S. Kuma, T. Inada: LEC growth of large GaAs single crystals, *J. Cryst. Growth* **128**, 439–443 (1993)
- 6.143 F.-C. Wang, M.F. Rau, J. Kurz, M.F. Ehman, D.D. Liao, R. Carter: Correlation of growth phenomena to electrical properties of gnarl defects in GaAs. In: *Defect Recognition and Image Processing in III–V Compounds II*, ed. by E.R. Weber (Elsevier, Amsterdam 1987) p.117
- 6.144 J. Kratochvil: Self-organization model of localization of cyclic strain into PSBs and formation of dislocation wall structure, *Mater. Sci. Eng. A* **309/310**, 331–335 (2001)
- 6.145 O. Politano, J.M. Salazar: A 3D mesoscopic approach for discrete dislocation dynamics, *Mater. Sci. Eng. A* **309/310**, 261–264 (2001)
- 6.146 H. Ono: Dislocation reactions and lineage formation in liquid encapsulated Czochralski grown GaAs crystals, *J. Cryst. Growth* **89**, 209–219 (1988)
- 6.147 T. Duffar, P. Dusserre, F. Picca, S. Lacroix, N. Giacometti: Bridgman growth without crucible contact using the dewetting phenomenon, *J. Cryst. Growth* **211**, 434–439 (2000)
- 6.148 P. Rudolph, M. Czupalla, C. Frank-Rotsch, U. Juda, F.-M. Kießling, M. Neubert, M. Pietsch: Semi-insulating 4–6-inch GaAs crystals grown in low temperature gradients by the VCz method, *J. Ceram. Proc. Res.* **4**, 1–8 (2003)
- 6.149 M. Althaus, K. Sonnenberg, E. Küssel, R. Naeven: Some new design features for vertical Bridgman furnaces and the investigation of small angle grain boundaries developed during VB growth of GaAs, *J. Cryst. Growth* **166**, 566–571 (1996)
- 6.150 T. Kawase, Y. Hagi, M. Tasumi, K. Fujita, R. Nakai: Low-dislocation-density and low-residual-strain semi-insulating GaAs grown by vertical boat method. In: *1996 IEEE Semiconducting and Semi-insulating Materials Conference, IEEE SIMC-9, Toulouse 1996*, ed. by C. Fontaine (IEEE, Piscataway 1996) pp. 275–278
- 6.151 T. Bünger, D. Behr, S. Eichler, T. Flade, W. Fliegel, M. Jurisch, A. Kleinwechter, U. Kretzer, T. Steinegger, B. Weinert: Development of a vertical gradient freeze process for low EPD GaAs substrates, *Mater. Sci. Eng. B* **80**, 5–9 (2001)
- 6.152 G. Müller, B. Birkmann: Optimization of VGF-growth of GaAs crystals by the aid of numerical modelling, *J. Cryst. Growth* **237–239**, 1745–1751 (2002)
- 6.153 P. Rudolph, F. Matsumoto, T. Fukuda: Studies on interface curvature during vertical Bridgman growth of InP in a flat-bottom container, *J. Cryst. Growth* **158**, 43–48 (1996)
- 6.154 U. Sahr, I. Grant, G. Müller: Growth of S-doped 2" InP-crystals by the vertical gradient freeze technique. In: *Indium Phosphide and Related Materials*,

2007. IPRM. IEEE International Conference on 14–18 May 2001 in Nara, Japan, pp. 533–536
- 6.155 F.-M. Kießling, P. Rudolph, M. Neubert, U. Juda, M. Naumann, W. Ulrici: Growth of GaAs crystals from Ga-rich melts by the VCz method without liquid encapsulation, *J. Cryst. Growth* **269**, 218–228 (2004)
- 6.156 P. Rudolph, F.-M. Kießling: Growth and characterization of GaAs crystals produced by the VCz method without boric oxide encapsulation, *J. Cryst. Growth* **292**, 532–537 (2006)
- 6.157 B. Bakó, I. Groma, G. Györgyi, G. Zimányi: Dislocation patterning: The role of climb in meso-scale simulations, *Comput. Mater. Sci.* **38**, 22–28 (2006)
- 6.158 J.M. Parsey, F.A. Thiel: A new apparatus for the controlled growth of single crystals by horizontal Bridgman techniques, *J. Cryst. Growth* **73**, 211–220 (1985)
- 6.159 K. Tomizawa, K. Sassa, Y. Shimanuki, J. Nishizawa, Growth of low dislocation density GaAs by as pressure-controlled Czochralski method, *J. Electrochem. Soc.* **131**, 2394–2397 (1984)
- 6.160 P. Schlossmacher, K. Urban, H. Rüfer: Dislocations and precipitates in gallium arsenide, *J. Appl. Phys.* **71**, 620–629 (1992)
- 6.161 T. Steinegger, M. Naumann, M. Jurisch, J. Donecker: Precipitate engineering in GaAs studied by laser scattering tomography, *Mater. Sci. Eng. B* **80**, 215–219 (2001)
- 6.162 M. Mühlberg, D. Hesse: TEM precipitation studies in Te-rich as-grown PbTe single crystals, *Phys. Status Solidi (a)* **76**, 513–524 (1983)
- 6.163 K.-T. Wilke, J. Bohm: *Kristallzüchtung* (H. Deutsch, Thun, Frankfurt 1988) p. 356, in German
- 6.164 L. Su, Y. Dong, W. Yang, T. Sun, Q. Wang, J. Xu, G. Zhao: Growth, characterization and optical quality of CaF_2 single crystals grown by the temperature gradient technique, *Mater. Res. Bull.* **40**, 619–628 (2005)
- 6.165 P. Rudolph, M. Neubert, M. Mühlberg: Defects in CdTe Bridgman monocrystals caused by nonstoichiometric growth conditions, *J. Cryst. Growth* **128**, 582–587 (1993)
- 6.166 R. Fornari, C. Frigeri, R. Gleichmann: Structural and electrical properties of n-type bulk gallium arsenide grown from non-stoichiometric melts, *J. Electron. Mater.* **18**, 185–189 (1989)
- 6.167 R.S. Rai, S. Mahajan, S. McDevitt, D.J. Johnson: Characterisation of CdTe, (Cd,Zn)Te, and Cd(Te,Se) single crystals by transmission electron microscopy, *J. Vac. Sci. Technol. B* **9**, 1892–1896 (1991)
- 6.168 K. Sonnenberg: Defect studies in GaAs by NIR-microscopy with different contrast techniques, *IFF Bull.* **51**, 14–55 (1997)
- 6.169 J. Shen, D.K. Aidun, L. Regel, W.R. Wilcox: Characterization of precipitates in CdTe and $\text{Cd}_{1-x}\text{Zn}_x\text{Te}$ grown by vertical Bridgman–Stockbarger technique, *J. Cryst. Growth* **132**, 250–260 (1993)
- 6.170 H.G. Brion, C. Mewes, I. Hahn, U. Schäufele: Infrared contrast of inclusions in CdTe, *J. Cryst. Growth* **134**, 281–286 (1993)
- 6.171 R.J. Dinger, I.L. Fowler: Te inclusions in CdTe grown from a slowly cooled Te solution and by traveling solvent method, *Rev. Phys. Appl.* **12**, 135–139 (1977)
- 6.172 M. Salk, M. Fiederle, K.W. Benz, A.S. Senchenkov, A.V. Egorov, D.G. Matioukhin: CdTe and $\text{CdTe}_{0.9}\text{Se}_{0.1}$ crystals grown by the travelling heater method using a rotating magnetic field, *J. Cryst. Growth* **138**, 161–167 (1994)
- 6.173 J. Donecker, B. Lux, P. Reiche: Use of optical diffraction effects in crystals for growth characterization, *J. Cryst. Growth* **166**, 303–308 (1996)
- 6.174 K.F. Hulme, J.B. Mullin: Facets and anomalous solute distributions in InSb crystals, *Philos. Mag.* **41**, 1286–1288 (1959)
- 6.175 M.T. Santos, C. Marin, E. Dieguez: Morphology of $\text{Bi}_{12}\text{GeO}_{20}$ crystals grown along the (111) directions by the Czochralski method, *J. Cryst. Growth* **160**, 283–288 (1996)
- 6.176 P. Reiche, J. Bohm, H. Hermoneit, D. Schultze, P. Rudolph: Effect of an electrical field on the growth of lithium niobate single crystals, *J. Cryst. Growth* **108**, 759–764 (1991)
- 6.177 J.B. Mullin, K.F. Hulme: Orientation-dependent distribution coefficients in melt-grown InSb crystals, *J. Phys. Chem. Solids* **17**, 1–6 (1960)
- 6.178 Y. Liu, A. Virozub, S. Brandon: Facetting during directional growth of oxides from the melt: coupling between thermal fields, kinetics and melt/crystal interface shapes, *J. Cryst. Growth* **205**, 333–353 (1999)
- 6.179 O. Weinstein, S. Brandon: Dynamics of partially faceted melt–crystal interfaces III: Three-dimensional computational approach and calculations, *J. Cryst. Growth* **284**, 235–253 (2005)
- 6.180 M. Shibata, Y. Sasaki, T. Inada, S. Kuma: Observation of edge-facets in (100) InP crystals grown by LEC method, *J. Cryst. Growth* **102**, 557–561 (1990)
- 6.181 H. Gottschalk, G. Patzer, H. Alexander: Stacking fault energy and ionicity of cubic III–V compounds, *Phys. Status Solidi (a)* **45**, 207–217 (1978)
- 6.182 D.T.J. Hurle: A mechanism for twin formation during Czochralski and encapsulated vertical Bridgman growth of III–V compound semiconductors, *J. Cryst. Growth* **147**, 239–250 (1995)
- 6.183 E. Billig: Some defects in crystals grown from the melt, *Proc. R. Soc. Lond. Ser. A* **235**, 37–55 (1956)
- 6.184 V.V. Voronkov: Structure of crystal surfaces, *Sov. Phys. Cryst.* **19**, 573 (1975), (see also [6.179])
- 6.185 J. Amon, F. Dumke, G. Müller: Influence of the crucible shape on the formation of facets and twins in the growth of GaAs by the vertical gradient freeze technique, *J. Cryst. Growth* **187**, 1–8 (1998)
- 6.186 H. Chung, M. Dudley, D.J. Larson, D.T.J. Hurle, D.F. Bliss, V. Prasad: The mechanism of growth-twin formation in zincblende crystals: New insights from a study of magnetic liquid encapsulated

- Czochralski-grown InP single crystals, *J. Cryst. Growth* **187**, 9–17 (1998)
- 6.187 M. Dudley, B. Raghathamachar, Y. Guo, X.R. Huang, H. Chung, D.T.J. Hurle, D.F. Bliss: The influence of polarity on twinning in zincblende structure crystals: new insights from a study of magnetic liquid encapsulated, Czochralski grown InP single crystals, *J. Cryst. Growth* **192**, 1–10 (1998)
- 6.188 Y. Hosokawa, Y. Yabuhara, R. Nakai, K. Fujita: Development of 4-inch diameter InP single crystal with low dislocation density using VCZ method, *Indium Phosphide and Related Materials*, 1998, IPRM IEEE International Conference on 11–15 May 1998 in Tsukuba, Japan, pp. 34–37
- 6.189 C.P. Khattak, F. Schmid: Growth of CdTe crystals by the heat exchanger method (HEM), *SPIE* **1106**, 47–55 (1989)
- 6.190 A.F. Witt: Growth of CdTe under controlled heat transfer conditions, *Final Report*, DAAG No. 29–82–K–0119 (Mater. Proc. Center M.I.T., Cambridge 1986)
- 6.191 P. Rudolph: Travelling magnetic fields applied to bulk crystal growth from the melt: The step from basic research to industrial scale, *J. Cryst. Growth* **310**, 1298–1306 (2008)

Crystal Growth

Part B

Part B Crystal Growth from Melt Techniques

- 7 Indium Phosphide:
Crystal Growth and Defect Control
by Applying Steady Magnetic Fields**
David F. Bliss, Hanscom AFB, USA
- 8 Czochralski Silicon Single Crystals
for Semiconductor and Solar Cell Applications**
Koichi Kakimoto, Fukuoka, Japan
- 9 Czochralski Growth
of Oxide Photorefractive Crystals**
Ernesto Diéguez, Madrid, Spain
Jose Luis Plaza, Madrid, Spain
Mohan D. Aggarwal, Normal, USA
Ashok K. Batra, Normal, USA
- 10 Bulk Crystal Growth
of Ternary III–V Semiconductors**
Partha S. Dutta, Troy, USA
- 11 Growth and Characterization
of Antimony–Based Narrow–Bandgap III–V
Semiconductor Crystals
for Infrared Detector Applications**
Vijay K. Dixit, Indore, India
Handady L. Bhat, Bangalore, India
- 12 Crystal Growth of Oxides
by Optical Floating Zone Technique**
Hanna A. Dabkowska, Hamilton, Canada
Antoni B. Dabkowski, Hamilton, Canada
- 13 Laser–Heated Pedestal Growth
of Oxide Fibers**
Marcello R.B. Andreetta, São Carlos, Brazil
Antonio Carlos Hernandez, São Carlos, Brazil
- 14 Synthesis of Refractory Materials
by Skull Melting Technique**
Vyacheslav V. Osiko, Moscow, Russia
Mikhail A. Borik, Moscow, Russia
Elena E. Lomonova, Moscow, Russia
- 15 Crystal Growth of Laser Host Fluorides
and Oxides**
Hongjun Li, Shanghai, China
Jun Xu, Shanghai, China
- 16 Shaped Crystal Growth**
Vitali A. Tatartchenko, Puteaux, France

7. Indium Phosphide: Crystal Growth and Defect Control by Applying Steady Magnetic Fields

David F. Bliss

The application of steady magnetic fields during crystal growth of indium phosphide is described, and the effect of the magnetic fields on crystal properties is analyzed. The use of magnetic fields is one of many engineering controls that can improve homogeneity and crystal quality. This method is especially relevant to InP because of the high pressure requirement for crystal growth. Under high pressure, fluid flows in the melt and in the gas environment can become uncontrolled and turbulent, with negative effects on crystal quality and reproducibility. If properly configured, a steady magnetic field can reduce random oscillatory motion in the melt and reduce the likelihood of defect formation during growth. This chapter presents the history and development of magnetic-field-assisted growth of InP and an analysis of the effects of applied fields on crystal quality.

7.1	Historical Overview	205
7.2	Magnetic Liquid-Encapsulated Growth ...	206
7.2.1	Evolution of Crystal Growth Under Applied Magnetic Fields.....	206
7.2.2	Crystal Shaping Measures	207
7.2.3	Apparatus for Magnetically Stabilized Crystal Growth.....	209
7.3	Magnetic Field Interactions with the Melt	209
7.3.1	Hydrodynamic Principle	209
7.3.2	Effect of Magnetic Field on Crystal Twinning	210
7.4	Dislocation Density	216
7.4.1	Dislocation Reduction During Seeding	217
7.4.2	Analysis of Dislocations	219
7.5	Magnetic Field Effects on Impurity Segregation	220
7.5.1	Compensation Mechanism of InP:Fe	221
7.5.2	The Role of Hydrogen.....	222
7.5.3	Annealing Experiments	222
7.6	Optical Characterization of InP:Fe	224
7.7	Summary	226
	References	227

7.1 Historical Overview

The development of bulk InP crystal growth has been historically driven by the commercial telecommunications market for solid-state lasers. InP was chosen because it has a lattice match with the semiconductor compounds that serve as laser materials for fiber-optic communications. Small 2 in diameter wafers were sufficient from the outset to fabricate large volumes of discrete lasers with commercially viable yields. Because of the small size of the lasers, the demand for larger-diameter wafers was slow to gain momentum. Later, during the 1990s, new applications for optoelec-

tronic devices requiring larger-area InP substrates led to the development of 4 in diameter InP crystals. As recently as 2006, a new application for high-speed laser modulation was developed using 6 in InP wafers bonded to silicon [7.1].

Crystal growth of large-diameter InP boules places extreme control demands on the crystal growth environment, which becomes increasingly chaotic as the size of the melt increases. At the melting temperature of 1060 °C, the equilibrium vapor pressure of phosphorus over InP is 27 atm. Controlled crystal growth must

be performed in a pressure vessel exceeding 30 atm. Two principal issues arising from this pressure dependence are the synthesis of a stoichiometric InP compound and the containment of a highly volatile melt. Experiments on compound semiconductor crystal growth from volatile compounds in the 1960s focused on two possibilities: either the crystal must be grown in a completely sealed hot-wall ampoule (Bridgman or gradient freeze method), or the crystal can be pulled using an encapsulant under pressure. Using a pressure-balancing technique, a breakthrough came in 1962 when Metz and a group at Westinghouse [7.2] developed the liquid-encapsulated Czochralski (LEC) method for growth of PbSe and PbTe. The LEC method was later adapted for growth of InP using B_2O_3 as an encapsulant [7.3–5].

The state of the art today for bulk InP crystal growth is still divided between two competing technologies: top-seeded crystal pulling with liquid encapsulation and

vertical growth in a container with bottom seeding. Various names for these techniques have arisen from each unique laboratory research effort. In general, the pulling method has been the most cost-effective, but with high thermal gradients and a high level of strain during growth, the crystals may have high dislocation densities. On the other hand, vertical container growth offers a very low dislocation density because of its low-stress environment, but it is plagued by yield problems due to twinning and interface breakdown in heavily doped crystals. Two recent reviews [7.6, 7] have compared the growth, characteristics, and applications of InP crystals grown by both techniques. This chapter focuses on the development of techniques to control the turbulent melt environment using applied magnetic fields, and characterization to determine the electrical and optical properties of InP crystals after growth and thermal treatment.

7.2 Magnetic Liquid-Encapsulated Growth

Growth of InP in an axial magnetic field has two main advantages: melt stability contributes to reduced incidence of twinning and improved dopant uniformity. On the other hand, the radial temperature gradient is increased by an axial magnetic field because convective heat transfer in the melt is reduced. The resulting convex interface contributes to large hoop stresses during crystal growth, contributing to dislocation multiplication and propagation. On the other hand, if a cusped magnetic field is employed (with two opposing vertical magnetic fields), the radial thermal gradients are predicted to be flatter, since the nonuniform field will not affect radial fluid flow near the surface. Flattening the melt isotherm should reduce the dislocation density of InP crystals. In this chapter we will compare the cusped with the axial magnetic field for InP bulk crystal growth, and evaluate the practicality of imposing a strong axial magnetic field on the melt during growth. To determine if there are advantages in terms of process control, we compare crystallographic defects such as twins, dislocations, and striations under either controlled or uncontrolled environments during crystal growth. A major goal is to determine the effect on melt convection of magnetic field configuration, either axial or cusped.

7.2.1 Evolution of Crystal Growth Under Applied Magnetic Fields

In the 1960s several authors [7.8, 9] pointed out that the application of an external magnetic field would be useful to damp the time-dependent turbulent convective flows in melts during the growth of semiconductors. Experimental support for this concept did not appear in research laboratories until the 1980s [7.10, 11], and more recently it has attracted commercial interest for growth of InP crystals. There are two main advantages which result from magnetic field growth:

1. Thermal fluctuations are reduced, thereby stabilizing the microscopic growth rate, and consequently
2. The diffusion boundary layer is increased, enhancing the uniformity of dopant distribution.

Natural convection and forced convection are two coexisting forces during crystal pulling from the melt, and the magnitude and direction of fluid flow plays a crucial role in heat and mass transfer during growth. In Czochralski growth, both the thermal field and the solute distribution are dominated by convection. However, since most semiconductor melts are metallic in nature, changes to the flow dynamics can be made by applying

a magnetic field. With the application of a static magnetic field, convective forces in the liquid are restricted when the flow crosses the magnetic lines of flux by the Lorentz force \mathbf{L}

$$\mathbf{L} = \mathbf{j} \times \mathbf{B}, \quad (7.1)$$

where \mathbf{j} is the ionic current density vector and \mathbf{B} is the applied magnetic field. The characteristic ratio between the electromagnetic (EM) body force and the viscous force is Ha^2 , where the Hartmann number is

$$\text{Ha} = BR \left(\frac{\sigma}{\mu} \right)^{1/2}, \quad (7.2)$$

where B is the magnetic flux density of the magnetic field, R is the characteristic dimension of the melt, σ is the electrical conductivity of the melt, and μ is the dynamic viscosity of the melt. As the Hartmann number increases, the characteristic velocity of the melt is reduced. Although it is not practical to produce a magnetic flux density sufficiently large to eliminate all melt motion due to natural and forced convection, a strategy of controlling melt motion for dopant uniformity can be achieved with moderate magnetic fields. The model of Burton et al. [7.12] reveals the effect of melt convection on crystal growth. A diffusion boundary layer δ is assumed, beyond which the melt composition is maintained uniform by convection and inside of which transport is by diffusion only. The boundary layer is thus confined by the characteristic melt velocity. After steady state is reached, for an infinite liquid, one can define an effective distribution coefficient k_{eff}

$$\frac{C_S}{C_L} \equiv k_{\text{eff}} = \frac{k_0}{k_0 + (1 - k_0)e^{R\delta/D}}, \quad (7.3)$$

where R is the growth rate and D is the diffusion coefficient for the solute in the melt. This is a useful expression because it relates the composition of the growing crystal to convection conditions and the growth rate. It describes the dopant distribution provided that the thickness of the boundary layer is small compared with the extent of the crucible. For example, an increase in the growth rate or the boundary-layer thickness tends to enhance the effective distribution coefficient towards unity. In the case of an applied magnetic field, the diffusion boundary-layer thickness increases, and hence k_{eff} is closer to 1, resulting in a more uniform incorporation of the dopant. The dopant distribution in magnetic field growth has been modeled by several authors [7.13, 14]. Experimental confirmation of this model will be discussed in Sect. 7.3.2.

7.2.2 Crystal Shaping Measures

The prevailing crystal pulling method is liquid-encapsulated Czochralski growth, named after *Czochralski* [7.15], a Polish scientist who developed a pulling method for growth of metallic rods. Although his work was focused on thin metal rods, Czochralski's name has become associated with the characteristic shape of large single crystals pulled from the melt. Magnetic liquid-encapsulated Czochralski (MLEC) growth is a variant of Czochralski growth with improved control over melt turbulence by application of a static magnetic field. Crystal pulling is initiated immediately after seeding, and as the melt temperature is reduced, a sloped shoulder emerges from the melt with a grow-out angle between 60 and 80°. The phenomenon of growth twinning is a problem in the shoulder region because the shoulder angle may traverse a critical angle where twinning is likely to occur. As will be shown in Sect. 7.3.2, to avoid the problem of growth twinning, the shape of the crystal must be controlled reproducibly. In Fig. 7.1 we see an example of an InP MLEC crystal grown with a controlled shape to avoid the critical angle

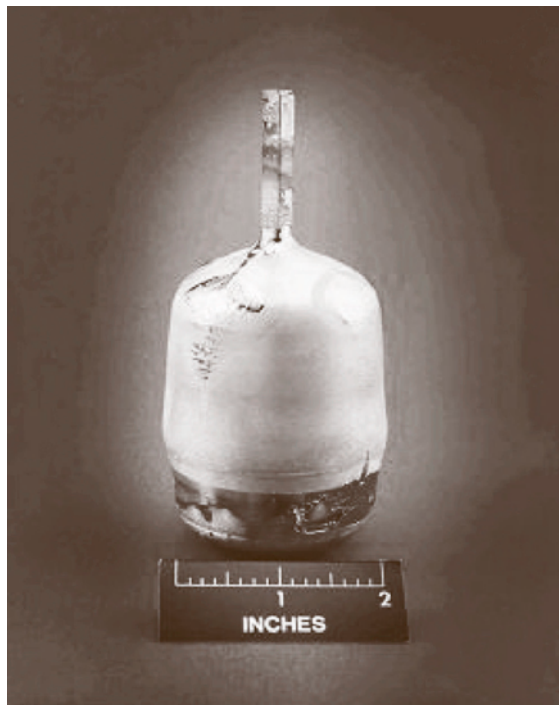


Fig. 7.1 MLEC InP Crystal with patch twins on the right shoulder (grown at the US Air Force Research Laboratory, Hanscom AFB)



Fig. 7.2 Twin-free MLEK InP crystal (grown at the US Air Force Research Laboratory, Hanscom AFB) ◀

for twinning. Despite the controlled angle, *patch* twins are visible on the shoulders. These twins are relatively benign, as most of the crystal remains usable.

Research at several laboratories has taken advantage of crystal shaping as a means to minimize the incidence of twinning [7.16]. Magnetically stabilized liquid-encapsulated Kyropoulos (MLEK) [7.17–19] growth is one such technique, where the crystal is grown with a flat top before initiation of pulling, in order to reduce the incidence of twins (Fig. 7.2). When pulling commences, the crystal has already reached full diameter, and the growth angle changes from perpendicular to parallel to the growth axis. At that moment the growth angle must pass through the critical range, but facet formation is reduced because thermal gradients near the periphery are steeper than at the center. This method relies on magnetic stabilization of the melt to suppress turbulent flows at the solid–liquid interface. Without the magnetic field, the flat top would become unstable because of perturbations due to the temperature fluctuations of natural convection.

It is worthwhile to note here a peculiar historical twist. The Kyropoulos method is named after Spyro Kyropoulos, a German scientist (1911–1967) who later emigrated to the USA. His technique for growth of large alkali halide crystals was conceived to avoid the cracking problems arising from container growth [7.20]. The Kyropoulos method was further developed during the 1930s and 1940s by several groups to grow large optical crystals of alkali halides for spectroscopy. Until World War II (WWII), it was considered to be one of the leading techniques for growing large single crystals. In a survey of crystal growth techniques from 1930 to 1946, Wells [7.21] referred to only three general methods for obtaining single crystals: Bridgman growth, Kyropoulos growth, and solid-state recrystallization. The Czochralski method was not considered as a method for large crystal growth. Nevertheless, after WWII when germanium and silicon crystal growth were demonstrated at Bell Labs and Texas Instruments, the name of the new process was assigned to Czochralski. Coincidentally, the language of science was shifting at that time from German to English, a fact that may explain the misunderstanding. Because of this historical twist, some clarification is in order to distinguish

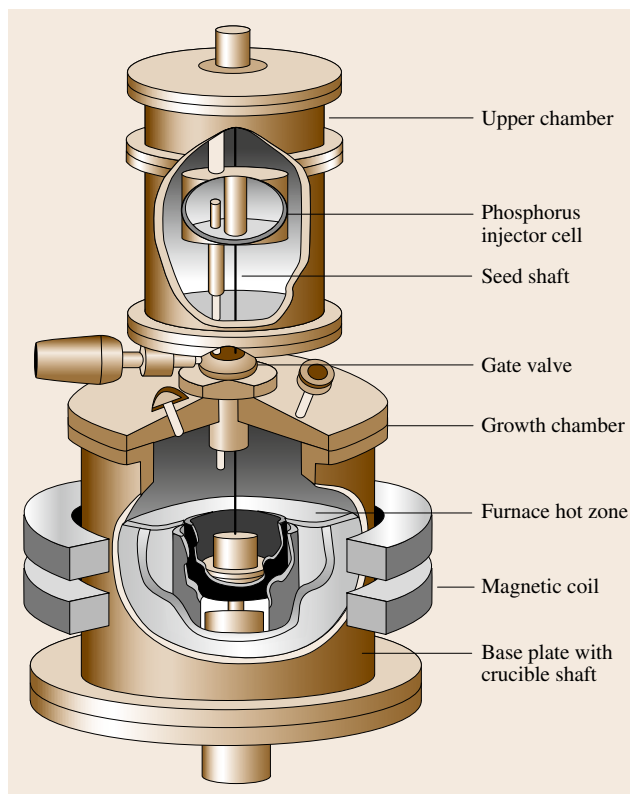


Fig. 7.3 Schematic diagram of a magnetic crystal growth furnace ◀

the two techniques. The main distinction is the pronounced difference between the crystal shapes, and the consequent differences between the curvatures of the solid–liquid interface. With the Kyropoulos method, the crystal forms an ellipsoid of rotation with its center deep in the melt. On the other hand, with the sloping shoulders of Czochralski growth, the solid–liquid interface is flatter.

7.2.3 Apparatus for Magnetically Stabilized Crystal Growth

The schematic diagram in Fig. 7.3 shows the basic components required for MLEC or MLEK growth. This custom furnace design was realized and is now in operation at the author's laboratory. Positioned around the outside of the growth chamber is a large Helmholtz

coil consisting of two toroidal magnets to provide an axisymmetric field up to 0.4 T. The two coils may be operated in tandem to provide an axial field, or in opposition to provide a cusped field. For a cusped field, the north pole of one coil points in the opposite direction to the other. The growth chamber is fabricated from nonmagnetic stainless steel to minimize screening losses and to allow the magnetic field to interact with the molten semiconductor. The water-cooled chamber is designed to operate at 20–40 atm ambient pressure. The upper chamber can be raised to allow access to the seed rod and a phosphorus ampoule. The upper chamber is separated by an isolation valve from the lower chamber, so that the phosphorus ampoule can be removed after in situ compounding of InP is completed. A seed is then attached to the seed rod, which can then be lowered into the growth chamber for crystal growth.

7.3 Magnetic Field Interactions with the Melt

The choice of magnetic field configuration and crystal shape are two types of engineering controls that can be exploited to improve the quality of InP crystals, with respect to twins, dislocations, and striations. In this chapter, the properties of InP crystals grown using these engineering controls are evaluated by synchrotron white-beam x-ray topography (SWBXT), chemical etching, and photoluminescence. Other controls, such as thermal gradient control and vapor pressure control, involving hardware modifications to the hot zone, are also considered for their practical application.

7.3.1 Hydrodynamic Principle

Although realizable magnetic flux densities are not large enough to eliminate melt motion altogether, a moderate magnetic field of 0.1–0.3 T can be used to tailor the melt motion for practical control of the crystal growth process. There are infinitely many ways to tailor the strength and configuration of the externally applied magnetic field, as well as the rotation rates, distribution of heat flux into and out of the melt, etc., so that models to accurately predict the system behavior are needed for process optimization. *Hurle and Series* [7.23] and *Walker* [7.24] reviewed the literature on the use of magnetic fields during bulk growth of semiconductors. Various components of fluid flow in InP melts have been modeled: melt-depletion flow [7.22], forced convection resulting from the rotational effects of the crystal and

crucible [7.25], and natural buoyant convection [7.26]. A global model combining the effects of pressure, thermal flux, magnetic field, and stress in the crystal was developed by *Zhang and Prasad* [7.27, 28]. The characteristic velocity U_c of melt motion in the magnetically

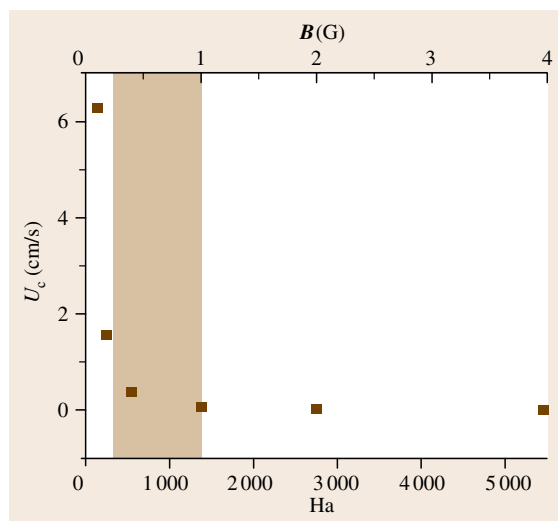


Fig. 7.4 Average melt velocity as a function of applied axial magnetic field and Hartmann number, calculated from the model of [7.22]. The shaded area shows the range where EM damping is sufficient for effective crystal growth control

damped melt is a critical indicator of EM suppression. This is shown graphically in Fig. 7.4, where calculated values of the average velocity are plotted against the Hartmann number [7.26]. The shaded area is the region where practical values of the magnetic flux can be used to control crystal shape and doping concentration for a given crucible design.

7.3.2 Effect of Magnetic Field on Crystal Twinning

The appearance of growth twins during the bulk crystal growth of InP is a recurrent yield-limiting problem. Because of their low stacking fault energy, indium-containing III–V compounds such as InP and InSb may have a higher tendency to form twins than other zincblende crystals. However, the general problem of twins in III–V crystal growth has been studied by experimentalists for many years [7.31, 32]. The first full theoretical treatment of twinning in III–V compound semiconductors was offered by Hurle in 1995 [7.29]. He observed that there were certain conditions under which internal (111) edge facets could be anchored to the three-phase boundary (TPB) at the solid–liquid–encapsulant interface. In addition, the appearance of an external shoulder facet coincides in many instances with the point of internal (111) facet anchoring. A diagram of the Hurle model in Fig. 7.5 shows the shouldering angle α and the angle ν between the edge facets and the extension of the crystal surface.

From a calculation of thermodynamic conditions for each orientation, Hurle derived a range of shouldering angles for which twinning was likely to occur. The model compared the undercooling at a high-index high-surface-energy external facet with that of a low-index low-surface-energy facet to determine if formation of a twin nucleus was energetically favorable. Hurle used this approach to predict the most dangerous shouldering angles for several zincblende crystals, including InP grown in the $\langle 001 \rangle$ and $\langle 111 \rangle$ directions. An experimental verification of this model was later published [7.33], where modifications to the Hurle theory were reported. These modifications were based on direct observations of the nucleation of twins on edge facets anchored to the TPB in S-doped MLEC-grown $\langle 001 \rangle$ InP single crystals using SWBXT and optical microscopy.

Undercooling at a facet during crystal pulling is determined by the nucleation process for a particular crystal face. Brice [7.30] pointed out that, to a simple approximation, the temperature gradient G in the solid at the interface depends on the radius of the crystal. If the curve of the interface passes through any low-index face, a facet will develop with undercooling ΔT . The crystal diameter is reduced by a chord formed by the facet, reducing the radius by a small amount (dimension c). As shown in Fig. 7.6, the undercooling at the center of the facet is given by

$$\Delta T = Gc. \quad (7.4)$$

The growth rate at the facet is controlled by this undercooling. The geometric relation between the facet half-width w and the temperature gradient can then be derived as

$$w^2 = c(2R - c), \quad (7.5)$$

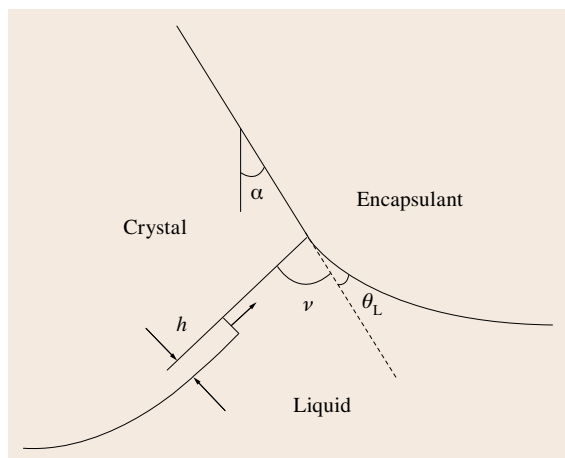


Fig. 7.5 Diagram showing the attachment of an internal edge facet to the three-phase boundary (TPB) (after [7.29])

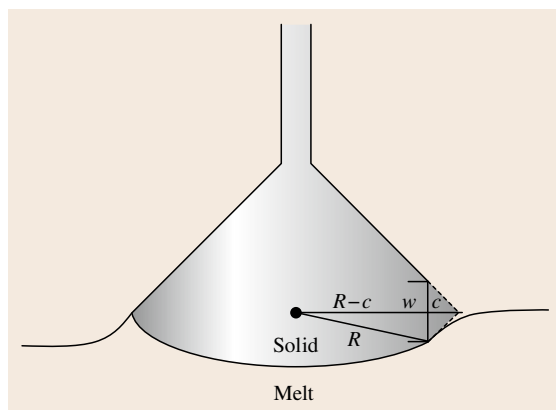


Fig. 7.6 Cross section (viewed from an angle slightly above the melt) schematic of a crystal with a shoulder facet (after [7.30])

and since the value of $R \gg c$ we can combine (7.3) and (7.4) to get

$$w^2 = \frac{2\Delta TR}{G}. \quad (7.6)$$

For a given crystal radius and a fixed growth rate, the undercooling is proportional to the square of the facet size. As the crystal diameter increases, so will the facet size, unless the undercooling is too small to sustain the facet. If undercooling is too large, the system becomes inherently unstable, and seeks a lower free energy.

In verifying the predicted relationship between twinning and growth angle, several [001] InP crystals were grown by the author with various shoulder angles from a 35° sloped shoulder to a 90° flat top. The incidence of twinning is generally higher in S-doped crystals than in crystals grown with other dopants, further motivating an investigation of the twinning defect. Study of the twins in these crystals by visual observation reveals a familiar pattern. Two kinds of twins exist: *patch twins*, which grow like epaulets on the shoulder, and *standard twins*, which grow on {111} planes passing through the boule center. Both types of twins nucleate on [110] ridge lines, but the patch twins are somewhat more benign in terms of wafer yield because they soon grow out of the crystal. A trend was observed after studying many crystals: twinning seems to occur more often on broad-shouldered crystals, but not so frequently on either low-angle shoulders or flat-top

crystals. However, these experiments show a marked difference in twinning probability depending on the field configuration.

Axial Field Growth

Magnetic stabilization using an axial magnetic field is a useful engineering control for controlling the InP growth process. As illustrated in Fig. 7.4, the melt velocity is reduced by an order of magnitude with an applied field of 0.2 T. Because of melt stabilization, dopant incorporation is more uniform, and shape control becomes reproducible. From the point of view of doping uniformity, it was possible to determine the effect on the solute boundary layer by comparing magnetically stabilized growth and standard LEC growth of InP [7.17]. To test the effect of magnetic fields on interface shape and dopant uniformity, two tin-doped crystals were grown, one without an applied magnetic field, and the other with an axial field of 0.2 T. Both were grown from melts weighing about 1 kg with tin concentrations of $5 \times 10^{19} \text{ cm}^{-3}$. After growth, these crystals were sliced into samples representing by weight each fraction of the grown crystal. The slices were then analyzed by glow-discharge mass spectrometry (GDMS). A plot of the tin concentration versus fraction grown was used to determine the effective distribution coefficient k_{eff} for each process. A comparison of the axial doping profiles revealed that k_{eff} is 2.5 times closer to unity for the magnetically stabilized growth. The

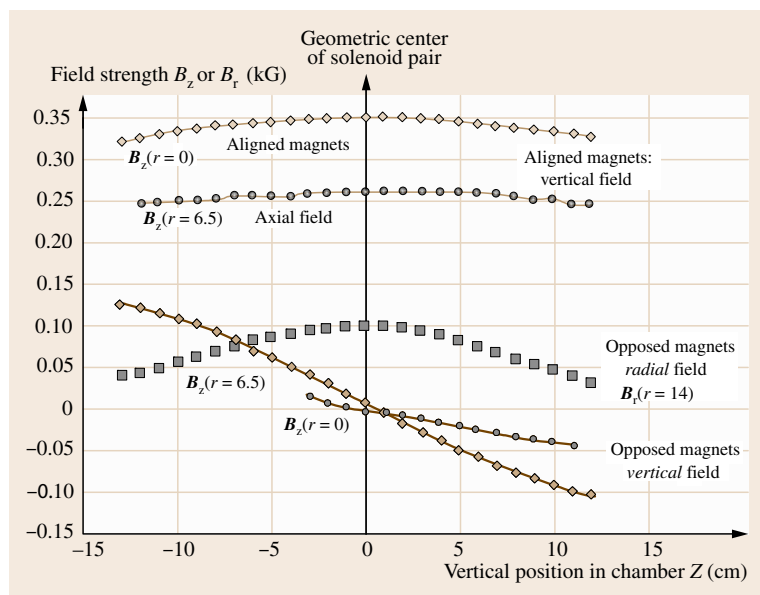


Fig. 7.7 A map of magnetic field strength for axial and cusped fields inside the crystal growth chamber at constant power

difference in k_{eff} indicates that static magnetic fields increase the boundary-layer thickness δ at the melt–solid interface. Considering the Burton, Prim and Schlichter (BPS) analysis in (7.3), one can see that k_{eff} is an exponential function of δ , since the growth rate R was the same in both cases, and the value of diffusivity D_L is assumed to be independent of the applied magnetic field. Using this analysis, the boundary-layer thickness is found to be 3.5 times larger for 0.2 T axial magnetic field growth compared with standard LEC growth.

Figure 7.7 shows the measured field strength within the chamber for cusped and axial fields. The axial field with aligned magnet pairs produced the highest magnetic field in the z -direction. Vertical scans were measured at the chamber center, and at 6.5 cm away from the center. The opposed magnet fields were measured in both the radial and axial directions. At the center, the vertical component B_z was zero, but small magnetic fields were measured at positions offset either vertically or radially.

Time-dependent temperature fluctuations in the melt were recorded with a sapphire optical thermometer and two thermocouples to reveal the effect of an axial magnetic field configuration on turbulent flow. For these measurements, the sensors were placed near the center of the melt at 2 and 12 mm from the crucible bottom (total InP depth approximately 31 mm and melt diameter 95 mm) with no crucible rotation. After the temperature reached steady state the magnet power was turned on and the field remained constant at 0.2 T. Figure 7.8 shows the off–on transient thermal behavior for the axially aligned field, where the temperature near center the

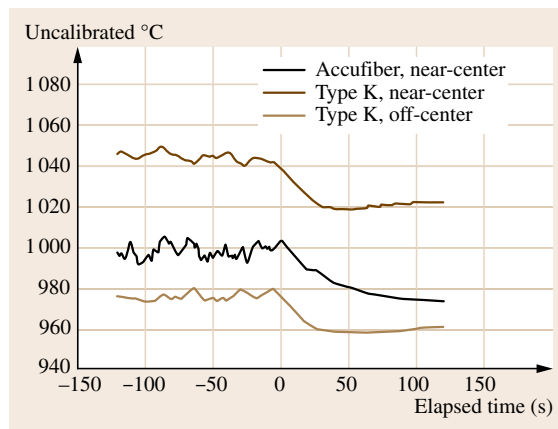


Fig. 7.8 Transient temperature fluctuations with no axial magnetic field ($t < 0$), and after axial magnetic field is turned on ($t > 0$)

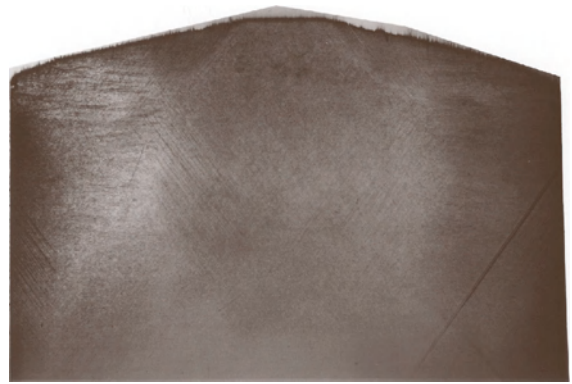


Fig. 7.9 SWBXT transmission topograph of (110)InP:Sn cross-sectional slice showing dislocations and darker slip bands but no edge facets or striations. $g = 004$, $\lambda = 0.5 \text{ \AA}$, scale: crystal diameter = 55 mm

drops rapidly to a 20 °C lower level and remains steady with minor fluctuations.

A topograph of an InP:Sn crystal grown under an axial magnetic field is shown in Fig. 7.9. Here the conical growth angle is $\alpha = 82^\circ$, and the presumed angle ν would be 115° if there were edge facets attached to the TPB. Technically, the angle ν is the angle between the (111) edge facets and the extension of the crystal surface, as defined in Fig. 7.5. In this case there are no edge facets to be seen either by x-ray or by infrared (IR) topography. Both iron- and tin-doped crystals were grown without twins in the axial magnetic field using the flat-topped configuration.

Cusped Field Growth

For InP growth in a cusped field [7.34], the magnetic stabilization effect is much weaker. Since the two magnets are opposed, much of the field strength is canceled, and in fact the axial field goes to zero at the center. Although the radial component of the magnetic field is about 0.1 T, this is not strong enough for convective damping. Without a strong applied magnetic field, random oscillatory flow still exists in the melt, and flat-top growth is not possible because of twin formation or dendritic growth. In order to obtain a single crystal under these conditions, the crystal must be pulled as in LEC growth, i. e., avoiding the critical 74° cone angle. A few crystals were successfully grown in this fashion, but with occasional twin formation. The appearance of (111) edge facets attaching to the TPB are observed in IR transmission micrographs, as shown in Fig. 7.10. A twin line extends from one of the smaller facets at the shoulder.

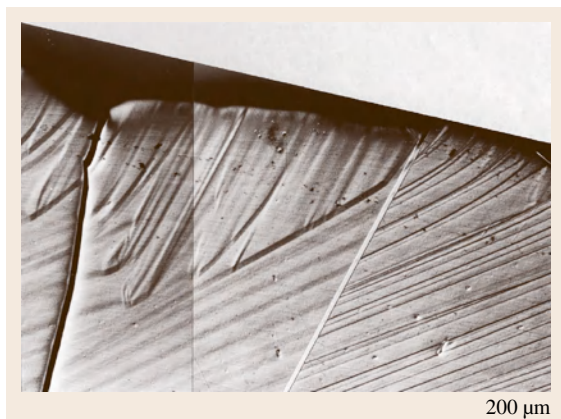


Fig. 7.10 Nomarski micrograph of the shoulder of an InP crystal grown in a cusped field, showing edge facets attached to the TPB and a twin line parallel to the (111) plane

A measurement of the transient temperature behavior in a cusped field shows only a small effect on turbulence at the moment when the magnet is turned on. Using the same temperature sensors as described above, time-dependent temperature fluctuations were recorded, again with no crucible rotation. After the temperature reached steady state the magnet power was turned on and the field remained constant at 0.2 T. Figure 7.11 shows the off-on transient thermal behavior for the cusped field, with opposed magnets. There is no discernible change in the temperature near the center, and a slight increase near the crucible edge. Thermal fluctuations are reduced by $\approx 25\%$ in amplitude, with more

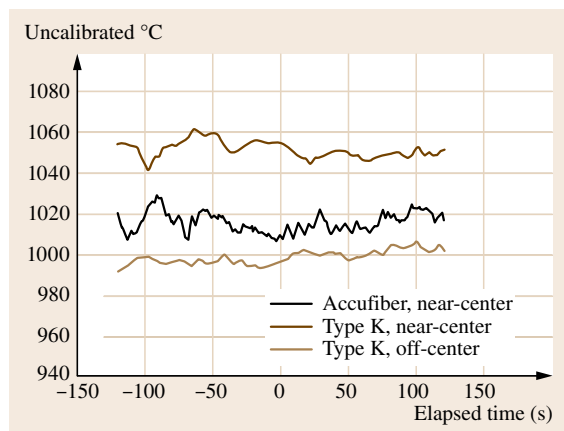


Fig. 7.11 Transient temperature fluctuations before ($t < 0$) and after ($t > 0$) cusped magnetic field is turned on

regular frequency, and there is a slight shift in average temperature.

Examination of the growth striations by IR transmission microscopy revealed some interesting differences between the axial and cusped magnetic fields [7.34]. For flat-topped crystals grown under axial field conditions, regular striations were observed which appeared to follow the rotational frequency. Calculating the rotational growth period by dividing the growth rate by the rotation rate gives $V/R = 50 \mu\text{m}$ as the length per rotational period. The observed striations showed a regular spacing corresponding to approximately $50 \mu\text{m}$. No facets were observed to be anchored to the TPB.

On the other hand, crystals grown in a cusped field exhibited a random striation pattern (Fig. 7.10), with striae periods as small as $30 \mu\text{m}$ and as large as $150 \mu\text{m}$. A large variation from center to edge was also observed, indicating that the interface shape is locally variant. Edge facets on (111) planes were observed near the top surface of the crystal, coinciding with the plane of twin formation.

The interface shape was examined with infrared transmission images taken with the IR camera for the two different magnetic configurations. For axial field growth the interface was convex at the seed end (radius of curvature $r = 5 \text{ cm}$). On the other hand, for crystals grown with a cusped field, the interface shape is sigmoidal, i. e., convex with a radius of 9 cm and deflected edges.

Figure 7.12 shows a detail from a scanned SWBXT image, recorded in transmission Laue geometry, from a (110) wafer cut from a S-doped, [001]-grown InP single crystal in which a twin was formed in a region where ($\bar{1}\bar{1}$) edge facets came into contact with the external shoulder of the crystal (i. e., were anchored at the TPB during crystal growth). On the right-hand side of this image a twin nucleates in a region containing anchored edge facets at the point where the shoulder angle reaches 74.21° . When viewed from above, a ($\bar{1}\bar{1}5$) external shoulder facet appears on the shoulder at the same point. After twinning, this ($\bar{1}\bar{1}5$) facet is replaced by a ($\bar{1}\bar{1}1$) facet. In this experiment, the external shoulder facets present before and after twinning were precisely identified using synchrotron white-beam back-reflection spot patterns [7.33].

Considering the left-hand side of this image, we observe anchored edge facets in several regions of differing shoulder angle, but none close enough to 74.21° to enable the creation of the ($\bar{1}\bar{1}5$) external shoulder facet required for the nucleation of a twin. Consequently no twinning is observed in this region, a confirmation

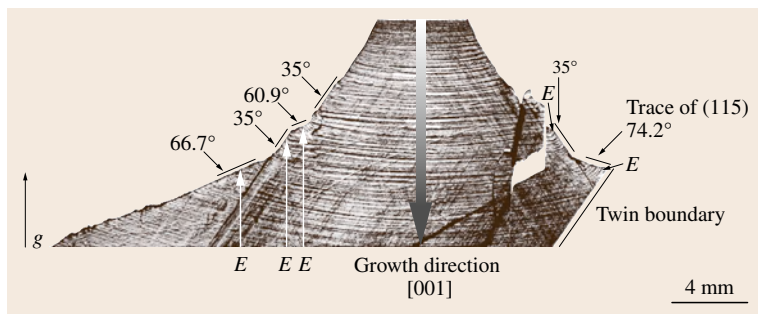


Fig. 7.12 SWBXT image recorded in transmission Laue geometry ($g = 004$, $\lambda = 0.45 \text{ \AA}$) showing the shoulder region of crystal. E indicates anchored edge facets. Local shoulder angles are indicated

of the importance of shoulder geometry. In the same boule, twinning was also observed to occur on the $(\bar{1}\bar{1}\bar{1})$ planes, leading to the conversion of a $(\bar{1}\bar{1}\bar{4})$ external shoulder facet to a $(\bar{1}\bar{1}0)$ one. In this case the twin, although nucleated in the shoulder region, grows out of the crystal. The local shoulder angle, in this case, must become equal to 70.53° , i.e., the shoulder must be parallel to $(\bar{1}\bar{1}\bar{4})$. Again, the presence of the various shoulder facets in the actual crystal was confirmed using synchrotron white-beam back-reflection spot patterns.

The concept of facet conversion resulting in a lower free energy is consistent with the Hurle model, but the model was modified by the authors [7.33] to agree with the observed geometry. For twinning in $\langle 001 \rangle$ growth of InP, the most dangerous shouldering angle was changed from 35.5 to 74.21° ; and the range of shoulder angles over which edge facets are thermodynamically favored to be anchored to the TPB was changed from $31^\circ < \nu < 86.5^\circ$ to $31^\circ < \nu < 112^\circ$, as illustrated in Fig. 7.13. A significant reduction in the estimated undercooling required to promote twinning was changed from ≈ 15 to $\approx 2^\circ\text{C}$.

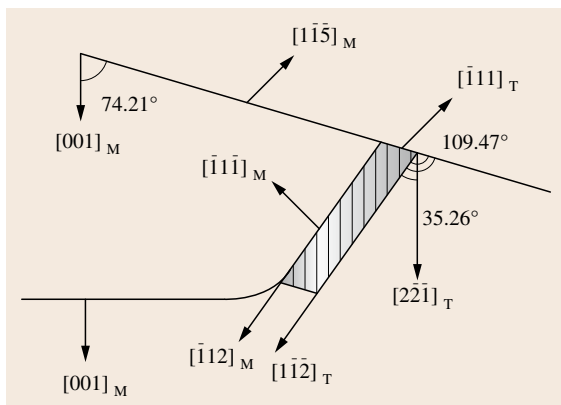


Fig. 7.13 Diagram of facets at TPB and a twin at the most likely growth angle for twin formation

Polarity of Twinning

Since the twin plane in InP is the polar $\{111\}$ family of planes, another important factor to be considered is the polarity of the observed twin planes. The question is: of the two types of edge facets, either $\{111\}_M$ or $\{\bar{1}\bar{1}\bar{1}\}_P$, anchored to the three-phase boundary, which has the higher propensity for generation of twins? Choosing the polarity of the seed face which is in contact with the melt in order to avoid twinning in $\langle 111 \rangle$ -grown InP has long been recognized [7.32]. However, an understanding of the influence of polarity on facet formation and twinning is not available for all zincblende structure crystals. In particular such understanding is lacking for InP.

In order to study the influence of polarity on faceting and twinning, it is important to be able to determine polarity unambiguously. Traditional practice has been to use chemical etching to distinguish between the two polar opposite faces of $\{111\}$ InP. The etching behavior of the In and P faces of InP are clearly different, but questions have been raised as to which surface is P- or In-terminated. Mullin et al. [7.35] report on the use of $6:3:1$ and $6:6:1 \text{ H}_2\text{O}:\text{HNO}_3:\text{HCl}$ in order to distinguish P faces from In faces in InP. Bachmann and Buehler [7.36], using the opposite indexing convention, confirm the usefulness of the $6:6:1$ etch in producing etch pits on the In face to discriminate between polar faces.

An experiment to confirm the etching method and to determine the crystallographic polarity of the $\{111\}$ edge facets by x-ray anomalous scattering was reported by Dudley [7.37]. To generate significant anomalous scattering for the case of InP, a characteristic radiation with a wavelength close to the In absorption edge ($\lambda_K = 0.444 \text{ \AA}$) was used. In this SWBXT study, plots of diffracted intensity as a function of Bragg angle corresponding to the $(\bar{1}\bar{1}\bar{1})$ and $(\bar{1}\bar{1}\bar{1})$ reflections, and also a plot of the ratio of the intensities of these reflections, were used to verify the etching results (Fig. 7.14a,b).

It can be seen that, for both reflections, the diffracted intensity changes abruptly at the absorption edge due to the drastic variation of the absorption coefficient. More important, the intensity values of the two reflections are significantly different in the vicinity of the absorption edge. The calculated ratios $|F_{111}^P/F_{111}^{\text{In}}|^2$ and $|F_{111}^P/F_{111}^{\text{In}}|$ are also shown in Fig. 7.14. These two curves represent the theoretical diffracted intensity ratios according to the kinematical and dynamical x-ray diffraction models, respectively. One would expect that, for a single crystal containing defects, the diffraction generally would contain both dynamical and kinematical contributions. It can clearly be seen that the profile of the ratios of the measured intensities is similar in shape to the theoretical predictions. Therefore, synchrotron x-ray anomalous scattering shows unambiguously that $(1\bar{1}1)$ is a P face while $(\bar{1}\bar{1}\bar{1})$ is an In face. These results are consistent with etching figures from either Br/methanol or 6:6:1 etchants that produce a smooth surface on the P face, while producing triangular pits on the In face.

With the polarity of $(1\bar{1}1)$ and $(\bar{1}\bar{1}\bar{1})$ being unambiguously defined, we can now define the polarity of the twins in InP, to say that twinning is observed to nucleate on only $\{1\bar{1}\bar{1}\}_P$ facets. Quite clearly, the preference for twinning on $\{1\bar{1}\bar{1}\}_P$ facets is related to the high incidence of twinning observed by Bonner [7.38] when growing InP in the $[111]_{\text{In}}$ direction. The preferred seed orientation is with the P face in contact with the melt. Similar results were reported by Steinemann and Zimmerli [7.39] for GaAs, which exhibited a preference for twinning on $\{\bar{1}\bar{1}\bar{1}\}_{\text{As}}$ planes. The effect of seed polarity on twinning incidence could be accounted for if the surface energy of the In-terminating facet was significantly higher than the P-terminating one. Hurle [7.29] cited the results of the model calculations of Oshcherin [7.40], who reports a value for the surface energy of the Ga-terminating facet that is $\approx 12\%$ higher than that of the As-terminating one. Surface energy values were reported by Oshcherin also for InP. Calculated values of the surface energy of $\{111\}_{\text{In}}$ faces were reported to be more than 30% larger than those for $\{1\bar{1}\bar{1}\}_P$ faces.

Twinning Summary

As a result of these studies, we have a better understanding of the fundamental causes of, and methods to control, twinning in InP crystal growth. Specifically, the magnetic field configuration, the dopant species, and the conical growth angle are three important parameters

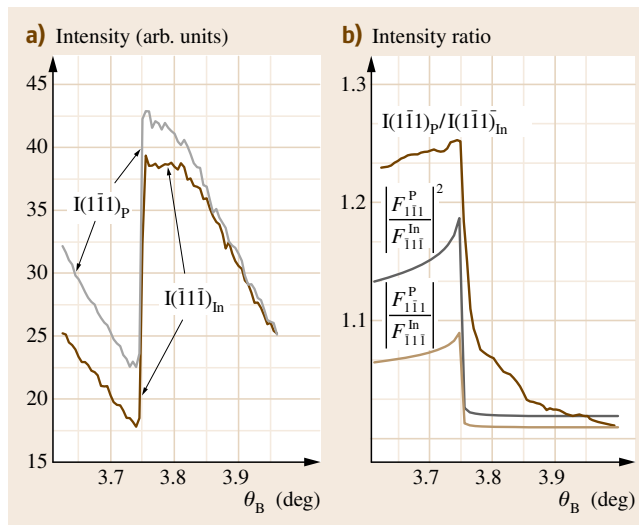


Fig. 7.14a,b Plots of (a) observed intensity versus Bragg angle plots for the two reflections, and (b) observed ratios of diffracted intensity as a function of Bragg angle from the $(1\bar{1}1)_P$ and $(\bar{1}\bar{1}\bar{1})_{\text{In}}$ planes, and calculated ratios of diffracted intensity according to kinematical theory, i.e., $|F_{111}^P/F_{111}^{\text{In}}|^2$ and dynamical theory, i.e., $|F_{111}^P/F_{111}^{\text{In}}|$

for control of twinning. Trade-offs can be made among these variables to minimize the occurrence of twins.

Although there are many possible causes of twinning in InP, two major causes which can be influenced by engineering controls are:

1. Uncontrolled crystal shape. In shaping the crystal from a narrow seed to a full-diameter body, the conical growth angle is a function of the imposed thermal gradient and the crystal pulling rate.
2. Sudden perturbations in the melt. Because InP crystals are grown with the encapsulant surface exposed to high pressure, temperature gradients in the liquid are steep (50–110°/cm). Uncontrolled oscillatory flows can cause severe thermal perturbations in the melt, resulting in rapid changes in the solid–melt interface shape.

The modified Hurle model, which predicts the incidence of twinning in the growth of III–V semiconductor compounds, focuses on uncontrolled shape as the primary cause of twinning. However, this is not the only factor in controlling twin nucleation in InP. The choice of dopant and magnetic field configuration are also

important. A comparison between the theoretical predictions of the incidence of twinning and experimental observation of the incidence of twinning in MLEC-grown [001] InP reveals the following:

1. X-ray topographic observations, etching studies, and IR transmission microscopy revealed the occurrence of twins nucleated at {111} edge facets anchored to the TPB. For (100) seeded InP crystals, this condition is most likely to occur when the angle ν between the edge facet and the extension of the crystal surface, falls in the range $31^\circ < \nu < 112^\circ$. For crystals grown with the angle $\nu > 112^\circ$ in which edge facets do not appear to be attached to the TPB, twin-free crystals can be grown by using the axial magnetic field configuration.
2. The conical growth angle α where twinning is most likely is 74.2° , where a {115} external shoulder facet is converted to a {111} shoulder facet. The most favorable angle for conical growth is 35.3° , where diagonal twins are minimized, for (100)-oriented InP crystals. However, this angle allows the possibility to produce patch twins. At a growth angle of 35.3° , the dominant {111} matrix facets typically appear on the crystal shoulders and these facets are favored because of their low surface energy. On the other hand, at a growth angle of 74° , the $\{115\}_M \rightarrow \{111\}_T$ transformation follows exactly the crystallographic orientation relationships of 180° rotation twins. In other words, a {111} external facet would be introduced by twinning if the external surface of the growing crystal becomes parallel to a {115} lattice plane just prior to twinning.
3. Of all the impurity elements used as dopants in this series of experiments, sulfur appears to be the most likely to cause twins. S-doped crystals also exhibit large shoulder facets during growth, an indication that sulfur doping increases undercooling. Other dopants, such as tin, even at the same high concentration, are not as likely to cause twinning.
4. The axial magnetic field configuration is preferred over the cusped field for controlling twins. With the axial field, there are more options to take advantage of crystal shaping as a means of reducing twins. However, because of the increased radial thermal gradient, the axial magnetic field increases thermal stress in the crystal.
5. Close examination of {110} cross-sectional views of S-doped InP crystals reveals that the edge facets may actually increase and then decrease in size before twinning nucleates, suggesting that a critical undercooling may not control the twinning process. Rather, the critical point at which the twin nucleates seems to be associated with production of the {115} shoulder facet, which upon twinning, converts to a {111} shoulder facet.

7.4 Dislocation Density

The primary cause of the high dislocation density in pulled crystals of InP is thermoelastic stress during crystal growth. A high density of dislocations can degrade the performance of photodetectors [7.41] and it affects the properties and performance of many other InP-based devices [7.42]. Dislocations may also change the mechanical properties of InP and contribute to point defect and impurity migration [7.43]. To reduce the dislocation density, sulfur doping is a preferred method, because of its lattice-hardening effect. The need for crystals with low dislocation density is increasing, because these structural defects can limit the performance of advanced monolithic microwave integrated circuits (MMICs) and optoelectronic integrated circuits (OEICs).

High dislocation density is less of a problem with vertical gradient freeze (VGF) or vertical Bridgman (VB) crystals, where the temperature gradient is signif-

icantly reduced compared with LEC growth. Densities of less than 500 cm^{-2} are generally reported for VGF crystals. Thermoelastic stresses are lower in the vertical configuration of container growth because the temperature gradients are so low. Thermal gradients at the solid-melt interface are on the order of 10–15 K/cm in the VGF process, very low compared with typical LEC growth at 60–80 K/cm or higher. For pulled crystals, the steep temperature gradient is the price one must pay to provide stability to the crystal growth environment. Without such steep gradients, diameter control is more difficult, twinning probability is increased, and surface decomposition occurs as the crystal grows out of the encapsulant.

Despite conditions of very steep thermal gradients, for Czochralski silicon growth it is possible to grow large crystals that are virtually dislocation free because the use of *Dash* [7.44] seeding eliminates dislocations

Table 7.1 Results of dislocation reduction experiments

Crystal/ dopant	Seeding condition	Growth rate (mm/h)	Clearance length (mm)	Interface shape	Mechanism	Origin of dislocation
InP:S crystal A	Hot seed	0–27	12	Convex	Glide	Stress induced
InP:S crystal B	Cold seed	0–54	18	Convex	Glide	Stress induced

that emanate from the seed. For InP growth, a similar technique [7.45] demonstrated that dislocation-free InP could be grown, but only up to 15 mm in diameter. When the diameter exceeds that, dislocations are generated at the periphery of the boule (not from the seed) due to the combination of tensile stresses and defects forming at the crystal surface. Reducing the density of dislocations in InP has been the subject of considerable effort during recent decades. The question has been raised of how best to reduce or minimize dislocation generation during InP bulk growth. One approach is the combination of magnetic field stabilization to reduce random thermal fluctuations together with Dash seeding to reduce dislocations from the seed.

7.4.1 Dislocation Reduction During Seeding

In principle, the formation of new dislocations within a crystal under normal growth conditions is nearly impossible. Stresses approaching the shear modulus (10–70 GPa) would be required to generate a new dislocation in the bulk. Thermoelastic stress during InP crystal growth rarely exceeds 10 MPa, and yet the dislocation density in pulled crystals is often greater than $5 \times 10^4 \text{ cm}^{-3}$. This has led many to assume that all dislocations are generated from the seed. If this is true, a seeding technique that removes the grown-in dislocations could result in defect-free single crystals. A controlled seeding test for InP crystal growth was employed [7.46] to suppress the propagation of dislocations from the seed–melt interface. This study showed how the strategy of necking can be exploited to effectively eliminate dislocations in MLEC InP. Dislocations formed at the seed–melt interface are seen to glide out of the neck region. Understanding this mechanism of dislocation reduction in InP crystal growth may lead to better control of dislocation formation and migration. This study showed the origin of the dislocations to be induction by thermal stress rather than by replication of dislocations growing directly from the seed. The results of the experiments are tabulated in Table 7.1.

One source of dislocations is generated at the seed–crystal interface, and these dislocations may propagate through the crystal. The Dash seeding approach, discovered in 1958 [7.44], increases the pulling rate of the narrow neck until a defect-free condition appears. Dash speculated that dislocations leave the crystal, in the necked region, due to climb caused by vacancy supersaturation. One difference between compound semiconductors and silicon may be the mechanism of dislocation formation. In the case of Dash’s silicon model, the dislocations are grown in at the solid–liquid interface and propagate along the growth direction until they move out of the narrow neck by the climb mechanism. On the other hand, for InP there is no evidence of straight-line axial dislocations; rather, it appears that segments of dislocations from the seed are threading into the newly grown crystal. The dislocations arise from stress in the solid, and they propagate

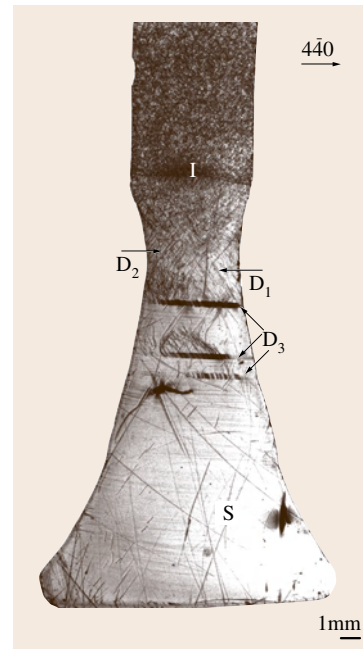


Fig. 7.15
SWBXT
transmission
topograph of
sample A, an
InP:S seed-neck
region, showing
dislocation
clusters D_1 , D_2 ,
and D_3 and
scratches S

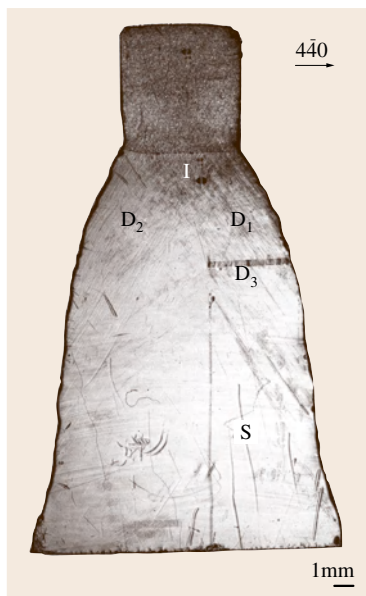


Fig. 7.16 SWBXT transmission topograph of sample B, an InP:S seed-neck region, showing dislocation clusters D_1 , D_2 , and D_3 and scratches S

Details of the mechanism leading to dislocation density reduction during necking were revealed, and the strategy of necking as an effective means to eliminate defects in InP was exploited. The effectiveness of the necking process as a strategy for reducing the dislocation density in MLEC-grown InP crystals was discussed.

Figures 7.15 and 7.16 show scanned transmission topographs recorded from two (110) InP slices. Figure 7.17 shows a geometric sketch of the dislocations in both crystals. Sample A (Fig. 7.15) has a narrow neck, whereas sample B (Fig. 7.16) expands in diameter from the seed. These crystals formed different shapes due to different growth conditions during initial seeding. For sample B, the initial temperature was slightly colder than normal – a condition called a *cold seed*. In contrast, the initial melt temperature for sample A was higher, and the meniscus diameter was smaller; this is called a *hot seed*. As the temperature was reduced, solidification proceeded to move down the narrow meniscus until the diameter started to increase. Comparing these two samples with different shapes, it

by slip-induced glide along the closest-packed {111} planes.

Bliss et al. [7.46] demonstrated crystal growth with a controlled seeding technique that suppressed the propagation of dislocations from the seed-melt interface.

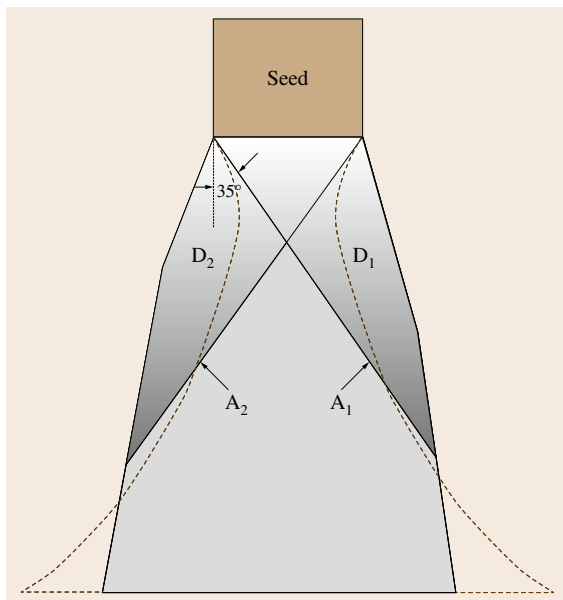


Fig. 7.17 Geometric sketch of the dislocations in both sample A and B

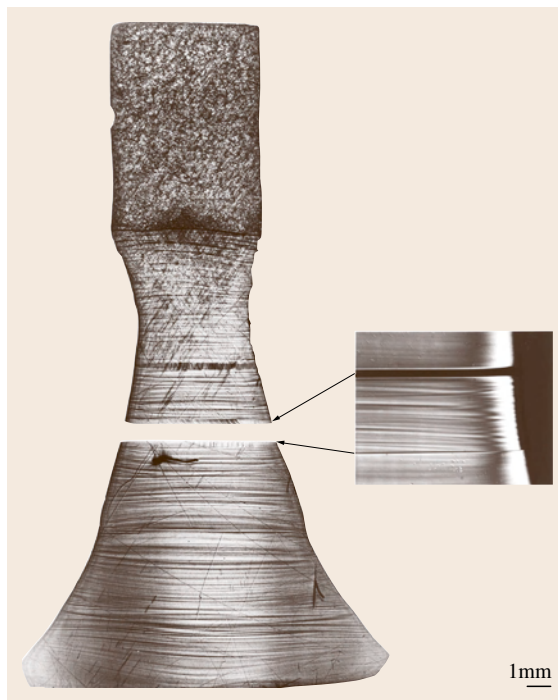


Fig. 7.18 SWBXT transmission topograph of sample A, a (110) slice of InP:S seed-neck region, with $g = 004$. *Inset*: Nomarski image of the etched surface around the twin lamella

is possible to evaluate the effectiveness of the necking process.

The diffraction vector for both topographs in Figs. 7.15 and 7.16 is $4\bar{4}0$, and the radiation wavelength is about 0.48 \AA , slightly larger than the indium K-absorption edge (0.44 \AA). In the figures the seed-crystal interface is represented; D_1 and D_2 are two groups of dislocations lying on $(1\bar{1}1)$ and $(\bar{1}11)$ planes, respectively. D_3 are dislocations lying on $(11\bar{1})$ planes, which are 35° from the (110) surface. A twin lamella intersects the surface in Fig. 7.15, bounded by two D_3 clusters, as can be seen more clearly in Fig. 7.18, the 004 topograph of sample A. By analyzing the projection lengths of the short, straight segments of D_3 dislocations, it was determined that they are parallel to the $(11\bar{1})_p$ twin plane. The dislocation density in the D_3 clusters is higher even than the dislocations in the seed (above $2 \times 10^4 \text{ cm}^{-2}$), so that individual dislocations cannot easily be resolved. The D_3 dislocation cluster indicates that there is plastic deformation along the twin plane. Thus, the dislocations are channeled by the twin lamella. The subsequent stress upon cooling is relaxed by the growth of D_3 clusters of dislocations adjacent to the twin lamella.

Most of the dislocations appear as intermittent short lines in both samples. The angles between the dislocation lines and the $[00\bar{1}]$ growth direction are about 35° . In Fig. 7.17 the dashed lines represent the cross-sectional shape of sample A while the solid lines correspond to sample B. A_1 and A_2 are two lines drawn from the bottom edges of the seed, at 35° to the growth axis. Most of the dislocations are distributed in the region of crystal above the lines A_1 and A_2 . Below this

region, very few dislocations can be found. Such dislocation configurations have been reproducibly observed in almost all MLEC-grown necked InP crystals. This demonstrates that these dislocations are closely related to the seed-crystal interface.

7.4.2 Analysis of Dislocations

In order to characterize the Burgers vector of the dislocations observed, transmission topographs with various diffraction g vectors were taken. Figures 7.19 and 7.20 show enlarged topographs near the seed-crystal interface of sample A, where the diffraction vectors are (a) $3\bar{3}3$ and (b) $3\bar{3}\bar{3}$. For the topographs in Figs. 7.19 and 7.20, some of the dislocations disappear because of the extinction conditions

$$\begin{aligned} \text{Screw: } & g \cdot b = 0, \\ \text{Edge: } & \begin{cases} g \cdot b = 0, \\ g \cdot (b \times l) = 0, \end{cases} \end{aligned} \quad (7.7)$$

where b is the dislocation Burgers vector and l is the dislocation line direction.

The extinction conditions for D_1 and D_2 dislocations are summarized in Table 7.2. From the extinction criteria of dislocation contrast on x-ray topographs [7.47], it can be determined that both D_1 and D_2 are segments of dislocations with mainly screw character. As shown in Table 7.2, D_1 can be explicitly determined as composing the dislocations with the line directions of $[011]$ and $[10\bar{1}]$ and Burgers vectors $\frac{1}{2}[011]$ and $\frac{1}{2}[10\bar{1}]$, respectively. In the case of D_2 , the

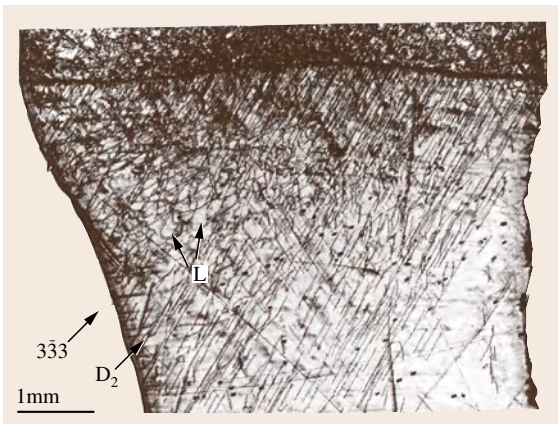


Fig. 7.19 Magnified x-ray topograph of neck region from sample A, showing D_2 defects

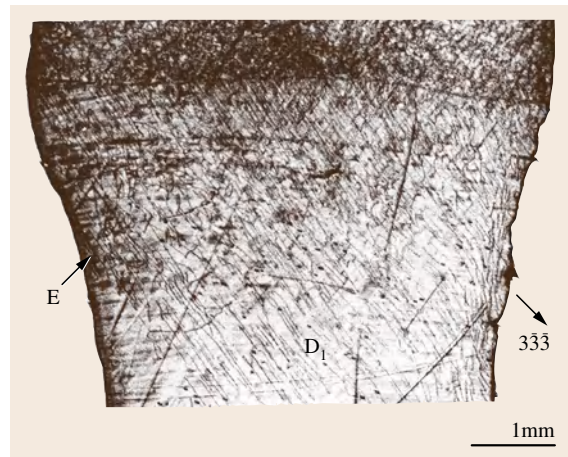


Fig. 7.20 Magnified x-ray topograph of neck region from sample A, showing D_1 defects

Table 7.2 Summary of x-ray data for allowed and extinct diffraction vectors for D₁ and D₂ dislocations

Dislocations	Visible	Invisible	Assigned slip system
D ₁	004, 440, 242 etc.	333, 422	(111) ₂ ¹ [011]
	004, 440, 422 etc.	333, 242	(111) ₂ ¹ [101]
D ₂	004, 440, 422 etc.	333, 242	(111) ₂ ¹ [101]
	004, 440, 242 etc.	333, 422	(111) ₂ ¹ [011]

dislocation lines are mainly along [101] and [011] with Burgers vectors of $\frac{1}{2}[101]$ and $\frac{1}{2}[011]$, respectively.

Unlike Dash’s straight axial growth dislocations, which originate in the seed, the topographs presented here show dislocations that consist of short segments lining up on three {111} planes. Careful observation of the spatial distribution and projected directions of these short dislocation segments, as determined above, confirms that they cannot be traced directly back to the seed, and therefore they cannot be growth dislocations. In addition, dislocation half-loops, indicating glide processes, can be observed in the topographs. These half-loops contain segments with line directions that are either parallel to the growth front or curve back against the growth front, which cannot occur if the dislocation is a growth dislocation [7.48]. It is thus apparent that most of the dislocations observed in these samples are not growth dislocations but are generated by postgrowth plastic deformation, i.e., by dislocation movement or interaction following crystal growth (behind the growth front). This is not surprising, considering the stresses generated due to the steep temperature gradients during MLEC growth. These straight segments of dislocations with mainly screw character

are the remnants of dislocation loops generated via the stress-induced multiplication of dislocation segments from the seed, which thread into the newly grown region of crystal. As is common in crystals with the zincblende structure, the velocities of edge dislocations are greater than their screw counterparts. Consequently, rapidly moving edge segments, which in this case escape through the outer periphery of the necked region, may leave behind a remnant of trailing screw segments. The dislocation loops will expand in such a fashion that the screw segments will enlarge laterally as well as extending their lengths. Therefore, the screw segments may not be directly traced back to the seed interface. No clear evidence is found supporting the conjecture of Dash [7.44] that the reduced dislocation density resulting from the necking process is associated with the climb-induced motion of dislocations.

These experiments demonstrate that most of the dislocations in MLEC-grown InP crystals originate from the seed–crystal interface, propagate via slip processes on {111} planes, and eventually exit the crystal through the periphery of the necked region. It is apparent that one can effectively limit the dislocation regions by choosing proper growth conditions, i.e., by adopting the necking technique. At least for small-diameter crystals, a pyramid-shaped sector which is nearly dislocation free is formed below the dislocation regions. However, the defect-free region cannot be successfully expanded as the crystal grows to full diameter. New dislocations are observed at the periphery as the crystal diameter increases. These dislocations are clearly not generated from the seed, but rather they seem to be propagating from the outer edge where faults exist at the shoulder surface.

7.5 Magnetic Field Effects on Impurity Segregation

Incorporation of dopant impurities from the melt into the crystal is dependent on the applied magnetic field, as described in Sect. 7.2.2. The use of impurity doping requires control of uniformity on both the macroscale and microscale. The magnetic field has been shown to contribute to axial as well as radial uniformity. This is important because all of the commercial uses of InP material require impurity doping in the crystal. Unlike GaAs bulk material, where a native defect EL2 contributes the deep level responsible for semi-insulating electronic properties, in the case of InP the dopant impurity iron must be added to provide the deep-level defect. Iron is the only impurity species

that can compensate the residual shallow donors of InP to produce semi-insulating material with resistivity at least $10^7 \Omega \text{ cm}$. However, the distribution of iron in the crystal can have two possible negative consequences. Macrosegregation of impurities can lead to yield problems; if maximum solubility is reached, precipitate formation, or interface breakdown due to constitutional supercooling will occur. On the other hand, the microsegregation of impurities can lead to striations, especially pronounced in the case of sulfur doping. And for the case of iron, with a solubility limit of $3 \times 10^{17} \text{ cm}^{-3}$, at high doping concentrations the nucleation of precipitates becomes a problem.

7.5.1 Compensation Mechanism of InP:Fe

It is known that Fe substitutes for In in InP and primarily adopts the neutral Fe^{3+} state (so called to denote its oxidation state). However, some of the iron is compensated by shallow donors to form Fe^{2+} , and the ratio between the ionized and neutral concentrations, $\text{Fe}^{2+}/\text{Fe}^{3+}$ was shown [7.49] to vary linearly with the free carrier concentration n . A linear dependence of n on $\text{Fe}^{2+}/\text{Fe}^{3+}$ is expected since both quantities are proportional to the term in the Fermi distribution function $\exp[-E_F/(k_B T)]$, where E_F is the Fermi energy and k_B is the Boltzmann constant. The free carrier concentration can be expressed as

$$n \cong N_C \exp\left(-\frac{E_C - E_A}{k_B T}\right) \frac{[\text{Fe}^{2+}]}{[\text{Fe}^{3+}]} \frac{g(\text{Fe}^{3+})}{g(\text{Fe}^{2+})}, \quad (7.8)$$

where N_C is the density of states in the conduction band and g represents the degeneracies of the two iron defect states. The energy difference $E_C - E_A$ is simply the change in Gibbs free energy associated with the transfer of an electron from the occupied iron acceptor level to the conduction band. The Gibbs free energy can be expressed in terms of the enthalpy H and entropy S as $G = H - TS$. The above equation can then be rewritten as

$$n \cong N_C \exp\left(-\frac{H}{k_B T}\right) \exp\left(\frac{S}{k_B}\right) \frac{[\text{Fe}^{2+}]}{[\text{Fe}^{3+}]} \frac{g(\text{Fe}^{3+})}{g(\text{Fe}^{2+})}. \quad (7.9)$$

The slope of an Arrhenius plot of $\log n$ versus $1/T$ gives the change in enthalpy H or the activation energy extrapolated to temperature $T = 0$; this value of 0.63 eV is the same as that measured by temperature-dependent Hall effect or by deep level transient spectroscopy (DLTS). However, the entropy S can also be extracted to give the temperature shift of the iron acceptor level. Zach determined this value and found that the temperature shift was different from the temperature shift of the bandgap [7.49]. This is illustrated in Fig. 7.21, which shows the relative shift of the bandgap versus the deep defect level. The results indicate that the thermodynamic position of the $\text{Fe}^{2+}/\text{Fe}^{3+}$ level at room temperature is 0.49 eV below the conduction band, and it is this energy that determines the carrier concentration. For example, referring to (7.9), the room-temperature carrier concentration for a half-occupied iron acceptor level, $\text{Fe}^{2+}/\text{Fe}^{3+} = \frac{1}{2}$, would be $n \cong 10^9 \text{ cm}^{-3}$. In this circumstance, with Fe-doping levels even twice as high as residual shallow donors, at room temperature InP material is still conducting.

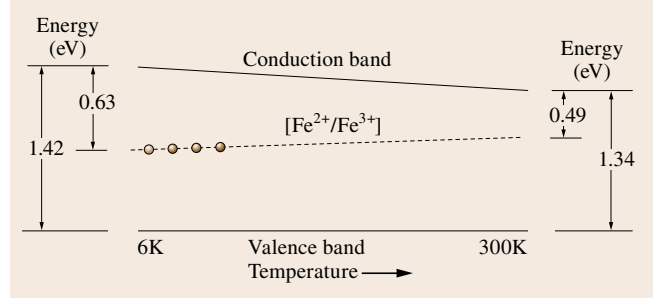


Fig. 7.21 Energy band diagram versus temperature for InP:Fe, showing the shift in bandgap energy (slope = $3.8 \times 10^{-4} \text{ eV/K}$) and the shift in the Fe acceptor ionization energy (slope = $4.7 \times 10^{-4} \text{ eV/K}$)

The Fermi energy can only be reduced to the mid-gap level as the occupancy of the iron acceptor level decreases, so that for $\text{Fe}^{2+}/\text{Fe}^{3+} = \frac{1}{10}$, the free carrier concentration will be $n \cong 10^7$. In other words, for typical semi-insulating InP with residual donor concentrations of $1\text{--}3 \times 10^{15} \text{ cm}^{-3}$, a minimum Fe doping level of $1\text{--}3 \times 10^{16} \text{ cm}^{-3}$ is required.

Zach [7.49] calculated the temperature shift of the iron level from the conduction band to be $-4.7 \times 10^{-4} \text{ eV/K}$. This value was later verified [7.50] by an optical experiment using two-wave mixing photorefractive and absorptive gain to evaluate the $\text{Fe}^{2+}/\text{Fe}^{3+}$ ratio in InP:Fe. As they varied the temperature of the crystal they observed that the wavelength of absorption gain was strongly dependent on temperature. For example, when the wavelength is fixed at 973 nm a null absorption gain is obtained at a crystal temperature of 285 K, while for a wavelength fixed to 991 nm a null gain is obtained at a crystal temperature of 330 K. The null point corresponds to the disappearance of the photorefractive space-charge grating because the creation of holes exactly compensates the creation of electrons ($\sigma_p p_{T0} = \sigma_n n_{T0}$). In this terminology, p_{T0} refers to Fe^{3+} and n_{T0} refers to Fe^{2+} . These results were explained by the temperature dependence of the iron level position as a function of temperature. That is, a shift of the iron level introduces a change in the optical cross sections. Using the temperature for which the absorption gain is null at $\lambda = 991$ and 973 nm, the temperature shift of the iron level with respect to the conduction band was found to be

$$\begin{aligned} \frac{dE_{\text{Fe-CB}}}{dT} &= \frac{E_{991 \text{ nm}} - E_{973 \text{ nm}}}{T_{991 \text{ nm}}^{I_a=0} - T_{973 \text{ nm}}^{I_a=0}} \\ &\approx -5.1 \times 10^{-4} \text{ eV/K}. \end{aligned} \quad (7.10)$$

This value is in close agreement with the value obtained by Zach. Significantly, the compensation model has been confirmed by both optical and electrical experiments.

7.5.2 The Role of Hydrogen

In semi-insulating InP material the concentration of ionized acceptors Fe^{2+} appears to be higher than the measured concentrations of Si and S. The donor impurities that compensate the iron acceptors in InP cannot all be accounted for through trace impurity analysis by glow-discharge mass spectroscopy (GDMS). Additional residual donors, not detected by impurity analysis, are present in these samples. It has been proposed that the other donor which contributes to the ionized Fe^{2+} concentration is hydrogen [7.52].

Several studies [7.53–55] of the absorption spectra of hydrogen in InP have established the structure of hydrogen-related complexes. The local vibrational mode (LVM) absorption at 2315.6 cm^{-1} in LEC InP shown in Fig. 7.22 is due to the P–H stretching modes in an environment that has tetrahedral symmetry [7.55]. Isotopic co-doping with deuterium and hydrogen was used [7.52] to investigate the LVM in InP. The splitting in the D–H spectrum was consistent with a defect having tetrahedral symmetry, and the authors proposed that the absorption is due to a fully passivated indium vacancy $[\text{V}_{\text{In}}(\text{PH}_4)]$. Investigation of the electrical prop-

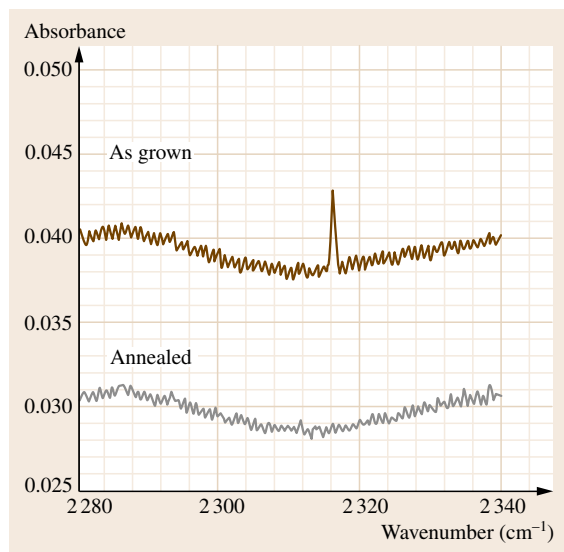


Fig. 7.22 Infrared absorption spectra in the range of the InP:H LVM line before and after annealing (after [7.50])

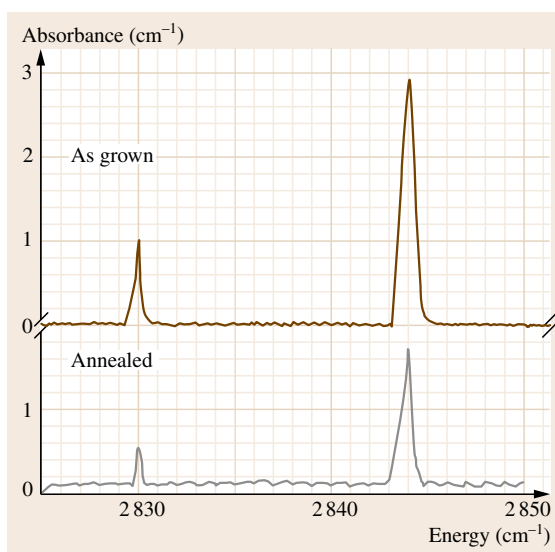


Fig. 7.23 Infrared absorption spectra in the range of the Fe^{2+} intracenter absorption before and after annealing (after [7.51])

erties of the hydrogen defect in InP [7.56] showed that this defect has a characteristic donor behavior.

The $\text{V}_{\text{In}}\text{H}_4$ defect disappears during annealing at $\approx 900^\circ\text{C}$ under a phosphorus overpressure, as shown in Fig. 7.22. For undoped bulk InP a reduction in free carrier concentration and an increase in mobility after annealing is also observed, consistent with a decrease in the donor-related $\text{V}_{\text{In}}\text{H}_4$ defect. For the case of Fe-doped material, annealing experiments [7.51, 57] showed the role of hydrogen-related donors in controlling resistivity. In these experiments the Fe^{2+} absorption peak was measured quantitatively to determine the residual shallow donor concentration. For semi-insulating Fe-doped material, annealing reduces the Fe^{2+} absorption peak as seen in Fig. 7.23. The change occurs without any measurable increase in Fe^{3+} by diffusion or other mechanisms. How to quantify the effect of hydrogen in Fe-doped InP is the key to understanding the $\text{V}_{\text{In}}\text{H}_4$ defect – and crucial for producing semi-insulating InP with a minimum concentration of iron.

7.5.3 Annealing Experiments

It has become apparent in the last few years that post-growth thermal treatment can bring about modification of the intrinsic defect concentrations in InP crystals [7.58–63]. It is now understood that the conversion

Table 7.3 Effect of annealing and cool-down on Fe-doped InP samples

Sample cool-down procedure	[Fe ²⁺] (cm ⁻³) as grown	[Fe ²⁺] (cm ⁻³) annealed	Δ[Fe ²⁺] (cm ⁻³)	VH ₄ integrated absorption (cm ⁻²)
Slow cool	3.3 × 10 ¹⁵	1.5 × 10 ¹⁵	1.8 × 10 ¹⁵	0.089
Fast cool	3.3 × 10 ¹⁵	1.7 × 10 ¹⁵	1.6 × 10 ¹⁵	0.097

from n-type to semi-insulating behavior by annealing at $\approx 950^\circ\text{C}$ is a consequence of the escape of shallow donors (the VH₄ defect) and the presence of a residual concentration of iron. Some commercial vendors now offer undoped InP that is wafer-annealed under FeP₂ atmosphere to provide semi-insulating properties with high mobility [7.64]. Some questions still persist, however, concerning the precise mechanism of thermal conversion. Does high-temperature treatment annihilate the VH₄ defect complex, or does it merely stimulate the diffusion to free surfaces? Likewise, if iron atoms are *electrically active* only on substitutional In sites, what happens to the InP crystal when iron diffusion occurs through an interstitial mechanism? After annealing, are some iron atoms quenched into inactive interstitial sites? The annealing experiments discussed in [7.65] were designed to answer some of these questions.

In order to determine the activation behavior of iron, Fe-doped InP crystals were grown by the MLEC method, such that the total iron concentration ranged from 1×10^{16} to $1 \times 10^{17} \text{ cm}^{-3}$ from seed to tail. The conductivity type of these crystals was semi-insulating (i. e., with free carrier concentration $n < 2 \times 10^8 \text{ cm}^{-3}$). The crystals were cut into rectangular $1 \times 1 \times 2 \text{ cm}^3$ polyhedra. Optical absorption spectra in the range $500\text{--}3500 \text{ cm}^{-1}$ (60–300 meV) were measured with a Digilab 80E-V vacuum Fourier-transform spectrometer. Samples were mounted in an exchange gas optical cryostat and cooled to temperatures between 6.5 and 12 K. The highest instrumental resolution used was 0.125 cm^{-1} , and standard measurements were performed at 0.25 cm^{-1} resolution.

These crystals were annealed in quartz ampoules with sufficient phosphorus to provide an overpressure of 5 atm at 900°C , well above the equilibrium partial pressure of P over InP. After being held at 900°C for 36 h the samples were cooled either slowly or rapidly to room temperature. Slow cooling was performed at a rate of less than 1 K/min, whereas rapid cooling was in excess of 5 K/min.

The results of the annealing experiments can be summarized as follows: In the case of slowly cooled samples, measurements of the hydrogenated vacancy VH₄ from the integrated absorption at 2316 cm^{-1}

showed virtually complete annihilation of the defect after annealing. In these same samples, the Fe²⁺ absorption lines were measured before and after annealing. The results are tabulated in Table 7.3.

The reduction in the Fe²⁺ concentration after annealing is directly proportional to the reduction of integrated absorption due to the hydrogen defect. The following quantitative calibration correlates the hydrogen–vacancy complex with the change in Fe²⁺ (equivalent to the net donor concentration)

$$[\text{V}_{\text{In}}\text{H}_4] = 4.2 \times 10^{16} (\text{cm}^{-1}) \times \text{Absorbance} (\text{cm}^{-2}). \quad (7.11)$$

For as-grown InP crystals with net donor concentration less than $4 \times 10^{15} \text{ cm}^{-3}$, the measured absorbance value for the 2316 cm^{-1} feature is slightly less than 0.1 cm^{-2} . This explains why undoped InP crystals are always n-type with *intrinsic* free carrier concentrations of $2\text{--}4 \times 10^{15} \text{ cm}^{-3}$. After annealing, the net donor concentration will be reduced so that it is possible to convert n-type InP with low iron doping to become semi-insulating.

For the case of the rapidly cooled sample, the results are somewhat different. It can be seen from the data in Table 7.3 that the annealing process is somewhat less efficient than for the slowly cooled sample. The change in Fe²⁺ concentration is not as large, indicating that VH₄ donor annihilation is either incomplete or that new compensating acceptors have been introduced during cool-down. Annihilation of VH₄ donors appears to be complete because of the total disappearance of the absorption peak at 2316 cm^{-1} . However, the mechanism of acceptors being quenched in during cool-down remains a possibility. Two observations concerning the quenched sample spectrum in Fig. 7.24 may supply clues to the answer. First, a sharp peak is found at 2204 cm^{-1} . This peak has been identified [7.66] as an LVM belonging to VH₂, an intermediary in the breakup of the VH₄ defect. As the number of H atoms in the vacancy decreases, the P–H bonds lengthen and the frequency of the vibrational mode decreases. As each hydrogen atom is removed from the vacancy, an electron is removed from the highest occupied state. The

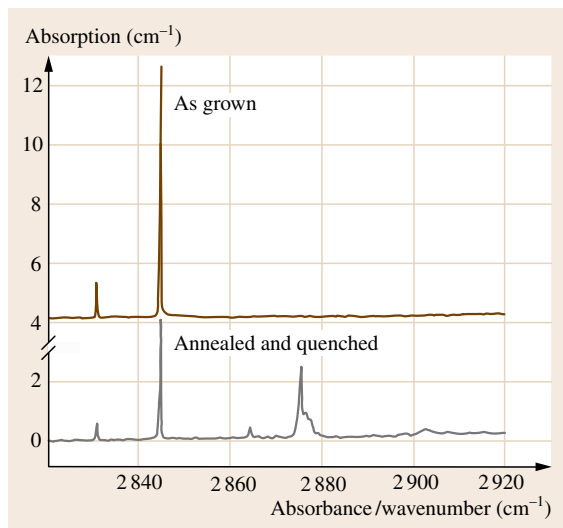


Fig. 7.24 A comparison of the absorption peaks in the vicinity of Fe^{2+} intracenter absorption, before and after annealing with rapid cooling

resulting defects, $\text{V}_{\text{In}}\text{H}_2$, $\text{V}_{\text{In}}\text{H}$, and V_{In} , have been identified as single, double, and triple acceptors, respectively, thereby compensating the residual donor concentration. The appearance of the VH_2 defect is likely contributing to the inefficient thermal conversion of quenched InP samples.

Another interesting feature in the IR absorption spectrum of rapidly cooled samples is seen in Fig. 7.24. Before annealing, in the upper plot, two peaks associated with the Fe^{2+} intracenter electronic transition are seen at 2830 and 2844 cm^{-1} . After annealing followed by rapid cooling, the integrated area of the two peaks is reduced, but not as much as for slowly cooled samples, and some new absorption lines emerge at 2864 cm^{-1} and a possible triplet centered around 2877 cm^{-1} . The new peaks are not identified in the literature, and it is not certain if they are caused by electronic transi-

tions or by local vibrational modes. However, because of their similar spacing and proximity to the well-known iron peaks, one could suspect an iron-related defect. Possibly a high-temperature defect becomes quenched in the rapidly cooled samples. For example, if iron diffuses at high temperature by an interstitial mechanism, it is likely that rapid cooling could leave some iron atoms on inactive sites. Substitutional iron (Fe^{3+}) and a low $\text{Fe}^{2+}/\text{Fe}^{3+}$ ratio are required for semi-insulating InP. If iron is trapped on interstitial sites, this will also contribute to the inefficiency of thermal conversion.

Fornari has observed [7.67] that the electrical activity of Fe in as-grown InP is dependent on the annealing cycle which occurs naturally during crystal growth. In other words, the concentration of active iron in a given cross section of the ingot depends on the thermal history and the concentration of In vacancies in that section. This observation led to the development of undoped semi-insulating InP wafers obtained by Fe diffusion [7.68]. In this new approach, unintentionally doped InP crystals were grown and sliced into wafers, which were then annealed at high temperature in an iron phosphide atmosphere. Subsequent electrical characterization showed that the wafers became semi-insulating with resistivities above $10^7 \Omega \text{ cm}$, and mobilities of 3000–4000 $\text{cm}^2/(\text{Vs})$. They also showed that Fe-diffused wafers are more uniform than Fe-doped crystals grown from the melt.

High-temperature annealing of InP has been shown to be an effective way to improve semi-insulating crystal properties. The anneal not only reduces the hydrogen-related donor complexes but also apparently causes Fe redistribution. The concentration of indium vacancies is critical to the annealing process. Substitutional iron requires an indium vacancy in order to be electrically active, just as hydrogen becomes a donor only in the configuration $\text{V}_{\text{In}}\text{H}_4$. With this understanding, it is possible to lower the critical threshold concentration of Fe in semi-insulating InP.

7.6 Optical Characterization of InP:Fe

In order to understand the spatial distribution of iron in InP, a mapping tool that can distinguish between the ionized state Fe^{2+} and the unoccupied Fe^{3+} is needed. Recent advances in optical characterization have developed scanning photocurrent (sPC) as a complement to scanning photoluminescence (PL) measurements [7.69]. Photocurrent mapping experi-

ments are carried out at liquid-nitrogen temperature to improve the contrast [7.70]. The photocurrent is excited by extrinsic light (either $\lambda = 1.32$ or 1.06 μm from a continuous wave (CW) Nd:YAG laser), which implies a probing depth equal to the wafer thickness; on the other hand, PL utilizes above-bandgap excitation wavelength, so the probed depth is on the order of

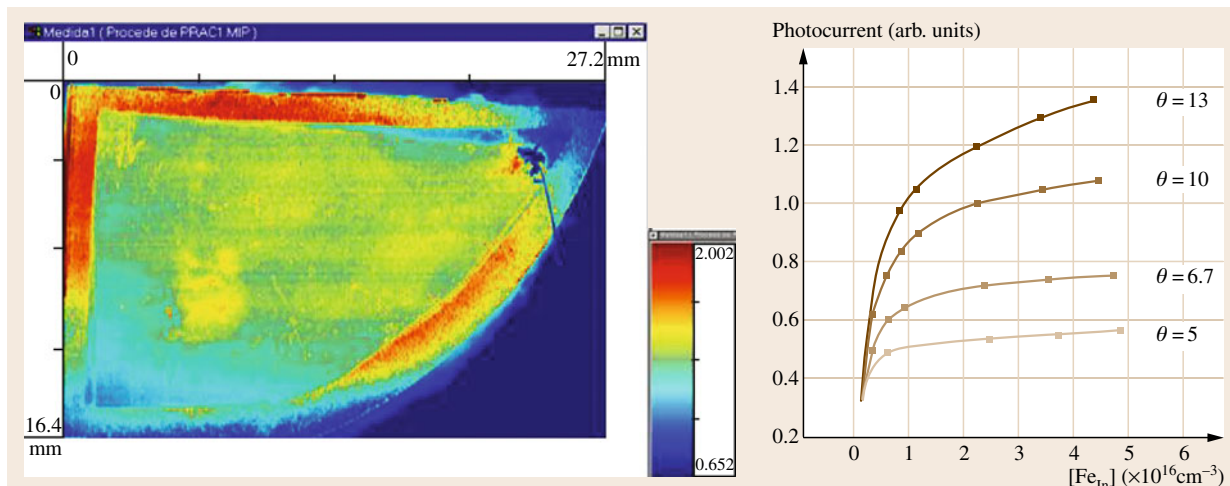


Fig. 7.25 Scanning PC measurement of InP:Fe with photocurrent intensity as a function of Fe_{In} and the compensation ratio $[\text{Fe}^{3+}]/[\text{Fe}^{2+}]$ (after [7.71])

the minority-carrier diffusion length, or about $1\ \mu\text{m}$. In order to explain the photoconductivity (PC) contrast, a model was developed [7.71] for Fe-doped InP and a direct correlation was found between the PC intensity and the compensation ratio $[\text{Fe}^{3+}]/[\text{Fe}^{2+}]$. This is just the opposite of the PL intensity. It would seem that the contrast in PC images will always be anticorrelated to that of PL images. In fact, the comparison is more subtle, as shown graphically in Figs. 7.25 and 7.26, where the calculated brightness varies with total Fe concen-

tration, considering the compensation ratio as a slope parameter.

Now one can compare the PL and PC images of the same Fe-doped InP wafer to determine if the iron is active or inactive, i.e., substitutional or interstitial. If the two images are anticorrelated as expected, then the compensation ratio will be rather uniform across the wafer. On the other hand, if the both PL and PC images show bright areas at the same location, interesting new possibilities arise. If some areas are correlated and

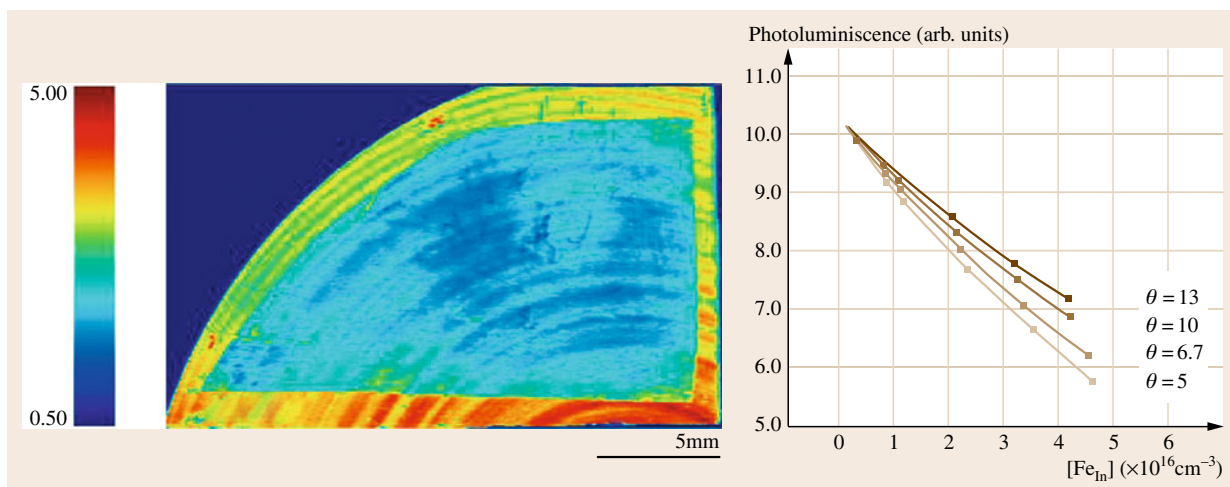


Fig. 7.26 Scanning PC measurement of InP:Fe with photoluminescence intensity as a function of Fe_{In} and the compensation ratio $[\text{Fe}^{3+}]/[\text{Fe}^{2+}]$ (after [7.71])

others anticorrelated, this indicates a nonuniform compensation ratio. Figures 7.25 and 7.26 contain PL and PC images of the same quarter wafer grown for this study of iron distribution. A visual comparison of the two images reveals a bright PC area, which coincides with a bright PL area. This correlated region is a region of low iron concentration but with high compensation. If this is true, it means that the Fe^{2+} concentration must be very low in this region. That means that both the iron atoms and the residual donors are reduced during the crystal growth and cooling process, possibly by a gettering mechanism.

High PL intensity is indicative of low Fe^{3+} concentration. The concentration may be reduced either because the total iron concentration here is low, or because some of the total iron atoms have migrated to inactive sites. On the other hand, high PC intensity indicates a high $[\text{Fe}^{3+}]/[\text{Fe}^{2+}]$ compensation ratio. Since the bright region must contain a low Fe^{3+} concentration, then the ionized Fe^{2+} must be even lower to account for the high PC intensity.

7.7 Summary

The use of applied magnetic fields during liquid-encapsulated crystal growth has been explored as a means to control defect formation in InP crystals. Since magnetic field growth was first suggested as a means to control crystal defects, experimental work has proceeded at several laboratories to understand its effects on melt growth. However, its use has never been adopted for commercial production. The risk may be too high when there is so small a body of knowledge on the subject. This chapter gives a practical review of the advantages and disadvantages of magnetic fields for liquid-encapsulated growth of InP. With the aid of computer modeling, it is possible to design a system with the proper configuration of magnetic field that will optimize the growth properties of InP. Avoidance of twinning, crystal shape control, and control of dopant distribution are goals that should be of interest for commercial production.

This chapter has also contributed to a practical understanding of how dislocations are generated

The PL and PC images present clear evidence that both iron and residual donors are diffusing in the solid during crystal growth. Furthermore, it appears from the annealing experiments that rapid cooling can increase wafer inhomogeneity. Two possible interpretations have been considered. First, the iron may diffuse interstitially, and remain at interstitial sites during rapid cool-down. Second, the iron and residual donors may be precipitating on dislocations by the mechanism of gettering. Either explanation could account for the inhomogeneity seen in the PL and PC images.

In summary, there is no concrete proof that interstitial iron atoms exist at room temperature in InP crystals. However, it can be inferred that the presence of interstitial iron contributes to the inhomogeneity of InP electrical and optical properties. This research has demonstrated that iron atoms as well as residual donors are diffusing rapidly through the crystal and forming precipitates during growth and cooling. Therefore, control over the annealing and cooling cycle is a prime factor in producing semi-insulating InP wafers.

and the mechanism by which they propagate in LEC InP. Dislocations are generated after growth, several millimeters away from the solid-liquid interface. Experiments to control dislocation density by Dash seeding were made possible by magnetic stabilization, but except for small-diameter crystals, the dislocation density is not reduced by magnetic fields, either axial or cusped.

Finally, the activity of iron as a dopant species to control the semi-insulating behavior of InP has been discussed. The simple process of Fe melt-doping is shown to have practical limitations. Control of compensating species and consideration of where the Fe sits in the crystal structure of InP can now be understood in the light of annealing studies. The most uniform crystals may be those that are grown without intentional Fe dopant, and then sliced and annealed to allow iron diffusion after growth. New tools for mapping the charge state of iron in InP have contributed greatly to clarify our understanding of iron activation.

References

- 7.1 J.E. Bowers, H. Park, A.W. Fang, R. Jones, O. Cohen, M. Paniccia: A technology for integrating active photonic devices on SOI wafers, *Proc. Int. Conf. InP Relat. Mater.* (Princeton 2006) pp. 218–221
- 7.2 E.P.A. Metz, R. Miller, R. Mazelsky: A technique for pulling single crystals of volatile materials, *J. Appl. Phys.* **33**, 2016–2017 (1962)
- 7.3 B. Mullin, R. Heritage, C. Holiday, B. Straughan: Liquid encapsulation crystal pulling at high pressures, *J. Cryst. Growth* **3–4**, 284 (1968)
- 7.4 K.J. Bachmann, E. Buehler: The growth of InP crystals from the melt, *J. Electron. Mater.* **3**, 279 (1974)
- 7.5 L. Henry, E.M. Swiggard: InP growth and properties, *J. Electron. Mater.* **7**, 647–657 (1978)
- 7.6 D.F. Bliss: InP bulk crystal growth and characterization. In: *InP-Based Materials and Devices: Physics and Technology*, ed. by O. Wada, H. Hasegawa (Wiley, New York 1999), Chap. 5
- 7.7 I.R. Grant: Indium phosphide crystal growth. In: *Bulk Crystal Growth of Electronic, Optical and Optoelectronic Materials*, ed. by P. Capper (Wiley, Chichester 2005), Chap. 4
- 7.8 H. Utech, M. Flemings: Elimination of solute banding in indium antimonide crystals by growth in a magnetic field, *J. Appl. Phys.* **37**, 2021–2024 (1966)
- 7.9 H. Chedzey, D. Hurle: Avoidance of growth-striae in semiconductor and metal crystals grown by zone-melting techniques, *Nature* **210**, 933–934 (1966)
- 7.10 H. Miyairi, T. Inada, M. Eguchi, T. Fukuda: Growth and properties of InP single crystals grown by the magnetic field applied LEC method, *J. Cryst. Growth* **79**, 291–295 (1986)
- 7.11 S. Bachowski, D.F. Bliss, B. Ahern, R.M. Hilton: Magnetically stabilized Kyropoulos and Czochralski growth of InP, 2nd Int. Conf. InP Relat. Mater. (Denver, 1990) pp. 30–34
- 7.12 J. Burton, R. Prim, W. Slichter: The distribution of solute in crystals grown from the melt. Part I Theoretical, *J. Chem. Phys.* **21**, 1987–1991 (1953)
- 7.13 T. Hicks, N. Riley: Boundary layers in magnetic Czochralski crystal growth, *J. Cryst. Growth* **96**, 957–968 (1989)
- 7.14 D. Hurle, R. Series: Effective distribution coefficient in magnetic Czochralski growth, *J. Cryst. Growth* **73**, 1–9 (1985)
- 7.15 J. Czochralski: Ein neues Verfahren zur Messung der Kristallisationsgeschwindigkeit der Metalle, *Z. Phys. Chem.* **92**, 219 (1918), in German
- 7.16 S. Yoshida, S. Ozawa, T. Kijima, J. Suzuki, T. Kikuta: InP single crystal growth with controlled supercooling during the early stage by a modified LEC method, *J. Cryst. Growth* **113**, 221–226 (1991)
- 7.17 D. Bliss, R. Hilton, J. Adamski: MLEK crystal growth of large diameter (100) indium phosphide, *J. Cryst. Growth* **128**, 451–456 (1993)
- 7.18 D. Bliss, R. Hilton, S. Bachowski, J. Adamski: MLEK crystal growth of (100) indium phosphide, *J. Electron. Mater.* **20**, 967–971 (1991)
- 7.19 S. Ozawa, T. Kimura, J. Kobayashi, T. Fukuda: Programmed magnetic field applied liquid encapsulated Czochralski crystal growth, *Appl. Phys. Lett.* **50**, 329–331 (1987)
- 7.20 S. Kyropoulos: Ein Verfahren zur Herstellung grosser Kristalle, *Z. Anorg. Allg. Chem.* **154**, 308–311 (1926), in German
- 7.21 A.F. Wells: *Crystal Growth*, Annual Reports on the Progress of Chemistry (Chemical Society, London 1946) pp. 62–87
- 7.22 J.L. Morton, N. Ma, D. Bliss, G. Bryan: Diffusion-controlled dopant transport during magnetically-stabilized liquid-encapsulated Czochralski growth of compound semiconductor crystals, *ASME J. Fluids Eng.* **123**(4), 893–898 (2001)
- 7.23 D.T.J. Hurle, R.W. Series: Use of a magnetic field in melt growth. In: *Handbook of Crystal Growth*, Vol. 2A, ed. by D.T.J. Hurle (Elsevier, Amsterdam 1994) pp. 261–285
- 7.24 J.S. Walker: Models of melt motion, heat transfer, and mass transport during crystal growth with strong magnetic fields. In: *Progress in Crystal Growth and Characterization of Materials*, Vol. 38, ed. by K.W. Benz (Elsevier, Amsterdam 1999) pp. 195–213
- 7.25 N. Ma, J. Walker, D. Bliss, G. Bryant: Forced convection during liquid encapsulated crystal growth with an axial magnetic field, *J. Fluids Eng.* **120**, 844–850 (1998)
- 7.26 J.L. Morton, N. Ma, D.F. Bliss, G.G. Bryant: Magnetic field effects during liquid-encapsulated Czochralski growth of doped photonic semiconductor crystals, *J. Cryst. Growth* **250**(1/2), 174–182 (2003)
- 7.27 Y.F. Zou, H. Zhang, V. Prasad: Dynamics of melt-crystal interface and coupled convection-stress predictions for Czochralski crystal growth processes, *J. Cryst. Growth* **166**, 476–482 (1996)
- 7.28 H. Zhang, V. Prasad, D.F. Bliss: Modeling of high pressure, liquid-encapsulated Czochralski growth of InP crystals, *J. Cryst. Growth* **169**, 250–260 (1996)
- 7.29 D. Hurle: A mechanism for twin formation during Czochralski and encapsulated vertical Bridgman growth of III–V compound semiconductors, *J. Cryst. Growth* **147**, 239–250 (1995)
- 7.30 J.C. Brice: Facet formation during crystal pulling, *J. Cryst. Growth* **6**, 205–206 (1970)
- 7.31 K.F. Hulme, J.B. Mullin: Indium antimonide: A review of its preparation, properties and device applications. In: *Solid State Electron*, Vol. 5 (Pergamon, London 1962) pp. 211–247
- 7.32 W. Bonner: Reproducible preparation of twin-free InP crystals using the LEC technique, *Mater. Res. Bull.* **15**, 63–72 (1980)

- 7.33 H. Chung, M. Dudley, D.J. Larson Jr., D.T.J. Hurle, D.F. Bliss, V. Prasad: The mechanism of growth-twin formation in zincblende crystals: new insights from a study of magnetic liquid encapsulated Czochralski-grown InP single crystals, *J. Cryst. Growth* **187**, 9–17 (1998)
- 7.34 G.G. Bryant, D.F. Bliss, D. Leahy, R. Lancto, N. Ma, J. Walker: Crystal growth of bulk InP from magnetically stabilized melts with a cusped field, *Proc. Int. Conf. InP Relat. Mater.* (Hyannis 1997) pp. 416–419
- 7.35 J.B. Mullin, A. Royle, B.W. Straughan: The preparation and electrical properties of InP crystals grown by liquid encapsulation, *Int. Symp. GaAs Relat. Compd.*, Aachen (IOP, London, Bristol 1970) pp. 41–49
- 7.36 K.J. Bachmann, E. Buehler: The growth of InP crystals from the melt, *J. Electron. Mater.* **3**, 279–302 (1974)
- 7.37 M. Dudley, B. Raghothamachar, Y. Guo, X.R. Huang, H. Chung, D.T.J. Hurle, D.F. Bliss: The influence of polarity on twinning in zincblende structure crystals: new insights from a study of magnetic liquid encapsulated Czochralski grown InP single crystals, *J. Cryst. Growth* **192**, 1–10 (1998)
- 7.38 W.A. Bonner: InP synthesis and LEC growth of twin-free crystals, *J. Cryst. Growth* **54**, 21–31 (1981)
- 7.39 A. Steinemann, U. Zimmerli: Growth peculiarities of GaAs single crystals, *Solid State Electron.* **6**, 597–604 (1963)
- 7.40 B.N. Oshcherin: On surface energies of $A^N B^{8-N}$ semi-conducting compounds, *Phys. Status Solidi (a)* **34**, K181–K186 (1976)
- 7.41 E. Beam, H. Temkin, S. Mahajan: Influence of dislocation density on I - V characteristics of InP photodiodes, *Semicond. Sci. Technol.* **7**, A229–A232 (1992)
- 7.42 R.K. Jain, D. Flood: Influence of the dislocation density on the performance of heteroepitaxial InP solar cells, *IEEE Trans. Electron. Dev.* **40**, 1928–1933 (1993)
- 7.43 T. Lee, C. Burrus: Dark current and breakdown characteristics of dislocation-free InP photodiodes, *Appl. Phys. Lett.* **36**, 587–589 (1980)
- 7.44 W.C. Dash: Single crystals free of dislocations, *J. Appl. Phys.* **29**, 736–737 (1958)
- 7.45 S. Shinoyama, C. Uemura, A. Yamamoto, S. Tohno: Growth of dislocation-free undoped InP crystals, *Jpn. J. Appl. Phys.* **19**, L331–L334 (1980)
- 7.46 D.F. Bliss, J.Y. Zhao, G. Bryant, R. Lancto, M. Dudley, V. Prasad: Dislocation generation and propagation near the seed-crystal interface during MLEC crystal growth of sulfur-doped InP, *Proc. 11th Int. Conf. InP Relat. Mater.* (IEEE, Davos 1998) p. 163
- 7.47 M. Dudley: X-ray topography. In: *Encyclopedia of Advanced Materials*, Vol. 4, ed. by D. Bloor, R.J. Brook, M.C. Flemings, S. Mahajan (Pergamon, Oxford 1994) pp. 2950–2956
- 7.48 H. Klapper: *Characterization of Crystal Growth Defects by X-ray Methods*, ed. by B.K. Tanner, D.K. Bowen (Plenum Press, New York London 1980) p. 133
- 7.49 F.X. Zach: New insights into the compensation mechanism of Fe-doped InP, *J. Appl. Phys.* **75**, 7894 (1994)
- 7.50 M. Chauvet, S.A. Hawkins, G.J. Salamo, D.F. Bliss, G. Bryant: Evaluation of InP:Fe parameters by measurement of two wave mixing photorefractive and absorptive gain, *J. Electron. Mater.* **27**, 883–890 (1998)
- 7.51 J. Wolk, G. Iseler, G. Bryant, E. Bourret-Courchesne, D. Bliss: Annealing behavior of the hydrogen-related defect in LEC indium phosphide, *Proc. 9th Int. Conf. InP Relat. Mater.* (Hyannis 1997) pp. 408–411
- 7.52 F.X. Zach, E.E. Haller, D. Gabbe, G. Iseler, G.G. Bryant, D.F. Bliss: Electrical properties of the hydrogen defect in InP and the microscopic structure of the 2316 cm^{-1} hydrogen related line, *J. Electron. Mater.* **25**, 331–335 (1996)
- 7.53 J. Pankove, N. Johnson: *Hydrogen in Semiconductors* (Academic, Orlando 1991)
- 7.54 B. Pajot, J. Chevallier, A. Jalil, B. Rose: Spectroscopic evidence for hydrogen-phosphorus pairing in zinc-doped InP containing hydrogen, *Semicond. Sci. Technol.* **4**, 91–93 (1989)
- 7.55 R. Darwich, B. Pajot, B. Rose, D. Robein, B. Theys, R. Rahbi, C. Porte, F. Gendron: Experimental study of the hydrogen complexes in indium phosphide, *Phys. Rev. B* **48**, 48 (1993)
- 7.56 C. Ewels, S. Oberg, R. Jones, B. Pajot, P. Briddon: Vacancy- and acceptor-H complexes in InP, *Semicond. Sci. Technol.* **11**, 502–507 (1996)
- 7.57 A. Zappettini, R. Fornari, R. Capelletti: Electrical and optical properties of semi-insulating InP obtained by wafer and ingot annealing, *Mater. Sci. Eng. B* **45**, 147–151 (1997)
- 7.58 R. Fornari, A. Brinciotti, E. Gombia, R. Mosca, A. Huber, C. Grattepain: Annealing-related compensation in bulk undoped InP, *Proc. 8th Conf. Semi-insulating III-V Mater.*, ed. by M. Godlewski (World Scientific, Warsaw 1994) pp. 283–286
- 7.59 G. Hirt, D. Wolf, G. Müller: Quantitative study of the contribution of deep and shallow levels to the compensation mechanisms in annealed InP, *J. Appl. Phys.* **74**, 5538–5545 (1993)
- 7.60 P.B. Klein, R.L. Henry, T.A. Kennedy, N.D. Wilsey: Semi-insulating behavior in undoped LEC InP after annealing in phosphorus. In: *Defects in Semiconductors*, Vol. 10–12, ed. by H.J. von Bardeleben *Materials Science Forum* (Trans. Tech. Pubs. 1986) pp. 1259–1264
- 7.61 K. Kainosho, H. Shimakura, H. Yamamoto, O. Oda: Undoped semi-insulating InP by high pressure annealing, *Appl. Phys. Lett.* **59**, 932–934 (1991)
- 7.62 D. Wolf, G. Hirt, G. Müller: Control of low Fe content in the preparation of semi-insulating InP by wafer annealing, *J. Electron. Mater.* **24**, 93–97 (1995)
- 7.63 K. Kainosho, M. Ohta, M. Uchida, M. Nakamura, O. Oda: Effect of annealing conditions on the uni-

- formity of undoped semi-insulating InP, *J. Electron. Mater.* **25**, 353–356 (1996)
- 7.64 K. Kuriyama, K. Ushiyama, T. Tsunoda, M. Uchida, K. Yokoyama: Uniformity of deep levels in semi-insulating InP obtained by multiple-step wafer annealing, *J. Electron. Mater.* **27**, 462–465 (1998)
- 7.65 Q. Ye, J.A. Wolk, E.D. Bourret-Courchesne, D.F. Bliss: Annealing behavior of the hydrogen-vacancy complex in bulk InP, *MRS Symp. Proc. H*, Vol. 513 (1998) pp. 241–246
- 7.66 C.P. Ewels, S. Öberg, R. Jones, B. Pajot, P.R. Bridgdon: Vacancy- and acceptor-H complexes in InP, *Semicond. Sci. Technol.* **11**, 502–507 (1996)
- 7.67 R. Fornari: On the electrical activity of Fe LEC indium phosphide, *Semicond. Sci. Technol.* **14**, 246–250 (1999)
- 7.68 R. Fornari, T. Görög, J. Jimenez, E. De la Puente, M. Avella, I. Grant, M. Brozel, M. Nicholis: Uniformity of semi-insulating InP wafers obtained by Fe diffusion, *J. Appl. Phys.* **88**, 5225–5229 (2000)
- 7.69 M. Avella, J. Jimenez, A. Alvarez, R. Fornari, E. Giglioli, A. Sentiri: Uniformity and physical properties of semi-insulating Fe-doped InP after wafer annealing, *J. Appl. Phys.* **82**, 3836–3845 (1997)
- 7.70 A. Alvarez, M. Avella, J. Jiménez, M.A. Gonzalez, R. Fornari: Photocurrent contrast in semi-insulating Fe-doped InP, *Semicond. Sci. Technol.* **11**, 941–946 (1996)
- 7.71 M. Avella, J. Jiménez, A. Alvarez, M.A. Gonzalez, L.F. Sanz: A photocurrent study of semiinsulating Fe-doped InP, *Mater. Sci. Eng. B* **28**, 111–114 (1994)

8. Czochralski Silicon Single Crystals for Semiconductor and Solar Cell Applications

Koichi Kakimoto

This chapter reviews growth and characterization of Czochralski silicon single crystals for semiconductor and solar cell applications. Magnetic-field-applied Czochralski growth systems and unidirectional solidification systems are the focus for large-scale integrated (LSI) circuits and solar applications, for which control of melt flow is a key issue to realize high-quality crystals.

8.1 Silicon Single Crystals for LSIs and Solar Applications	232
8.1.1 Conventional Czochralski Silicon.....	232
8.1.2 Magnetic Czochralski (MCZ) Silicon ..	235

8.2 Control of Crystal Defects in Czochralski Silicon	237
8.2.1 Criterion for Characteristic Defect Formation .	237
8.2.2 Effect of Pulling Rate and Temperature Gradient	238
8.3 Growth and Characterization of Silicon Multicrystal for Solar Cell Applications	239
8.3.1 Recent Development of Crystalline Silicon for Solar Cells..	240
8.4 Summary	240
References	241

Over the past 50 years, single crystals of semiconductors such as silicon (Si), gallium arsenide (GaAs), and indium phosphide (InP) have become increasingly key materials in the fields of computer and information technology. Attempts to produce pure silicon (i.e., a defect-free single crystal of silicon) were motivated by the desire to obtain ultralarge-scale integrated circuits (ULSIs) in which microvoids of about 10 nm diameter [8.1] are formed during crystal growth. Research over the past decade on crystal growth of silicon has focused on analysis of the formation of such microvoids during crystal growth using mass-transfer and reaction equations and on the temperature field in the crystals, obtained from global modeling. Control of solid-liquid interface shapes of GaAs and InP has been extensively studied to find a way to prevent the formation of dislocations and polygonization during crystal growth [8.2–5].

Microvoids are formed by the agglomeration of vacancies introduced at the solid-liquid interface of silicon. In most past studies, it has been difficult to reduce the total number of such microvoids in a whole crystal because the vacancy flux in silicon crystals must be controlled to reduce the probability of agglomeration.

One of the key points for controlling the vacancy flux in crystals, especially that near a solid-liquid interface, is control of the convection of the melt, through which the shape of the solid-liquid interface can be controlled. From this point of view, efforts have been made to control the periodic and/or turbulent flow of melt inside a crucible of large diameter. Crystal growth industries have mainly focused on quantitative prediction of a solid-liquid interface, point defect distribution, oxygen concentration, and dislocation-free growth. Steady (DC) and/or dynamic (AC) [8.6–44] magnetic fields, including electromagnetic fields, are opening up new fields to meet the increasing demand for large-diameter crystals.

A transverse magnetic field (i.e., TMCZ) is the type that has been utilized for commercial production, especially for large-diameter crystals. A lot of research [8.45–49] on the TMCZ method has been published. Numerical calculation [8.50–68] of these transverse magnetic fields is one of the key issues to predict temperature and impurity distributions in the system. Most numerical studies on CZ-Si growth in a transverse magnetic field have been limited to three-

dimensional analysis of melt flow in a crucible by imposing a flat melt–crystal interface and external thermal boundary conditions in the models. However, since the real shape of the melt–crystal interface and the thermal field near it are of great interest commercially, three-dimensional (3-D) global modeling that takes into account the high degree of nonlinearity of the growth system, the inherent three-dimensionality of the melt

flow, and the thermal field under the influence of a transverse magnetic field is necessary. However, there have been few studies using such modeling.

This chapter reviews crystal growth and characterization of CZ silicon. The effects of magnetic fields such as vertical and TMCZ methods on convection of the melt are also discussed. A means for solving the problem of convection computationally is also described.

8.1 Silicon Single Crystals for LSIs and Solar Applications

Figure 8.1 shows the structure of a typical furnace for CZ growth of silicon crystals. The heater, crucible heater, and thermal shields are made of carbon and/or carbon composite. Polycrystalline silicon as a raw material is placed in a quartz crucible. The growth furnace is evacuated, then Ar gas is introduced into the furnace to prevent oxidation of the silicon crystal and the melt. Subsequently, a seed crystal is attached to the top of the melt, then pulled upwards to grow silicon single crystals. The grown crystal is detached from the melt after the end of growth. Finally, the crystal is cooled to room temperature. The diameters of the crystal and crucible are currently 300 and 1200 mm, respectively. The diameter of the crystal is now increasing to 450 mm

in research and development, where the requirement on defect density becomes critical. Therefore, precise control of growth conditions is of great importance to grow defect-free crystals.

8.1.1 Conventional Czochralski Silicon

A seed crystal is usually suspended by a wire, then touches the surface of the silicon melt. The crucible usually rotates to stabilize the flow of the melt through centrifugal forces. The pulling rate of the crystal is also controlled to keep the crystal diameter constant. Monitoring of the diameter is usually carried out by a camera that monitors the meniscus shape. The pulling rate of the crystal is kept at about 1 mm/min, which is important for production efficiency. Oxygen concentration in a crystal is usually controlled by adjusting the pressure and the flow rate of the Ar gas. The crystal and crucible are usually rotated to control impurity and oxygen concentrations as well as the shape of the interface between the crystal and the melt. Moreover, a cone is located near the melt–gas interface to rectify the gas flow just above the melt surface. This cone can control the evaporation rate of oxygen from the top of the melt, which enables control of the concentration of oxygen incorporated from the melt into the crystal.

Bulk crystalline silicon of high quality has become an essential material for today’s information society. The distribution of temperature in a crystal during growth affects the distribution of vacancies and the formation of voids in the crystal. Therefore, it is important to control the temperature distribution in a crystal through control of the flow of the melt. To date, the temperature distribution in the furnace has been controlled by selecting a configuration of the thermal shields based on a global model including heat and mass transfer by radiation, convection, and conduction.

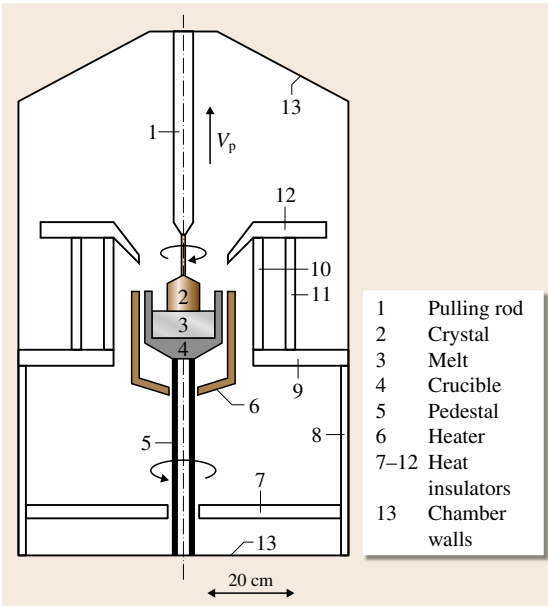


Fig. 8.1 Typical geometry of silicon Czochralski crystal growth furnace

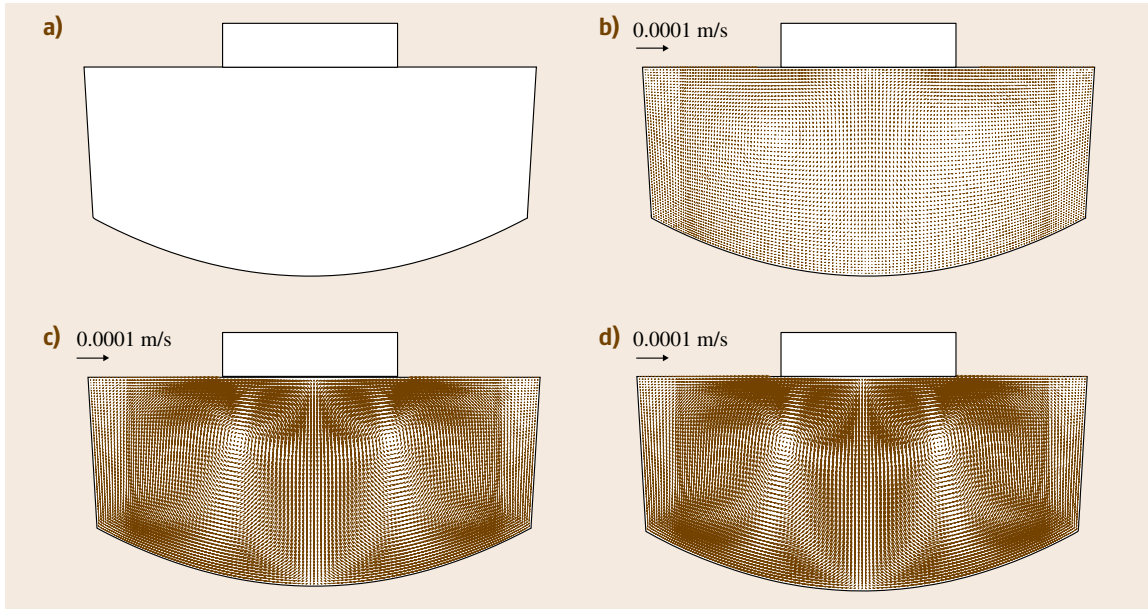


Fig. 8.2a–d Velocity profiles of Czochralski growth of silicon without temperature effect. (a) No forces, (b) with crystal rotation, (c) with crucible rotation, (d) with crystal and crucible rotations

Figure 8.2 shows velocity profiles of Czochralski growth of silicon without the effect of temperature, while Fig. 8.3 shows calculated temperature and velocity profiles of Czochralski growth of silicon including the effect of temperature. These figures clarify how crystal and/or crucible rotation and gravity affect the convection of the melt. This configuration contains melt and a crystal of silicon. Operating conditions in terms of the crystal (ω_s) and crucible (ω_c) rotation rates for Figs. 8.2 and 8.3 are listed in Table 8.1.

Figure 8.2a has no flow since there are no external or internal forces on the melt. Figure 8.2b shows the velocity profile with crystal rotation only, in which case the velocity is low. This is due to the low viscosity of the silicon melt, which cannot diffuse momentum effectively from the crystal to the melt. Figure 8.2c,d shows similar profiles with the crucible rotating, showing the large effect of crucible rotation on convection of the melt.

Figure 8.3 shows the temperature profiles under the conditions listed in Table 8.1. Figure 8.3a and b show almost the same profiles of temperature and velocity, similar to the relationship between Fig. 8.2a,b. This is because of the low viscosity of the melt.

Figure 8.3c,d shows a low velocity and a temperature profile similar to that for the conduction-dominated

case. This small velocity is attributed to the law of conservation of angular momentum in the rotating melt [8.26]. The momentum (Navier–Stokes) equation for the rotating melt contains terms for the Coriolis and centrifugal forces, as shown in (8.1), for the rotating coordinate system

$$\frac{\partial \mathbf{u}}{\partial t} = -\mathbf{u} \nabla \mathbf{u} - 2(\Omega \mathbf{k}) \times \mathbf{u} + (\Omega \mathbf{k}) \times (\Omega \mathbf{k}) \times \mathbf{r} + \frac{1}{\rho} \nabla p + \mu / \rho \Delta \mathbf{u} + \mathbf{g} \beta (T - T_0), \quad (8.1)$$

where \mathbf{u} and \mathbf{r} are the vectors of relative velocity on a rotational basis and position, respectively, Ω denotes the crucible rotation rate, p and μ represent the pressure and viscosity of the melt, and \mathbf{g} , β , and T_0 are the vectors of gravitational acceleration, the volume expansion coefficient, and the reference temperature

Table 8.1 Operating conditions of crystal (ω_s) and crucible (ω_c) rotation rates

Figure 8.2	a	b	c	d
ω_s	0	−3	0	−3
ω_c	0	0	10	10
Figure 8.3	a	b	c	d
ω_s	0	−3	0	−3
ω_c	0	0	10	10

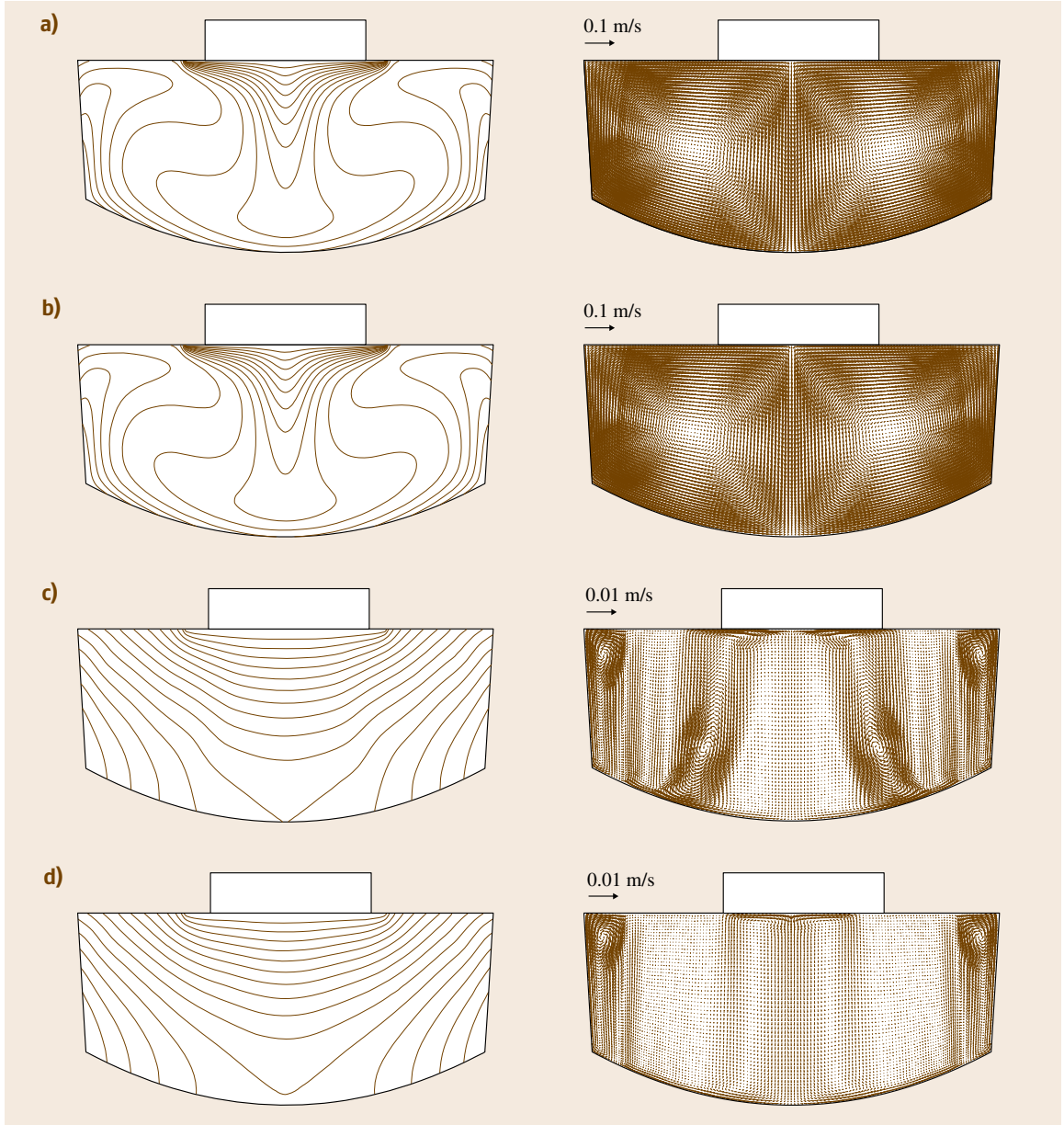


Fig. 8.3a–d Temperature and velocity profiles of Czochralski growth of silicon without temperature effect. **(a)** No forces, **(b)** with crystal rotation, **(c)** with crucible rotation, **(d)** with crystal and crucible rotations. Temperature difference between the contours is $\Delta T = 5$ K. Consequently, the centrifugal force always acts in the opposite direction. This means that the melt motion in the radial direction is suppressed by the crucible rotation

corresponding to specific mass, and the reference temperature of 1685 K, respectively. The second and third terms on the right-hand side of (8.1) express the Corio-

lis force and centrifugal acceleration, respectively. The vector \mathbf{k} in (8.1) is a unit vector in the z -direction. The centrifugal acceleration vector (\mathbf{a}_{cen}) can be expressed

as (8.2).

$$a_{\text{cen}} = \Omega^2 r = \frac{L^2}{r^3}, \quad (8.2)$$

where L is the angular momentum of the melt.

When a small volume element moves instantaneously from position r to $r' (= r + \Delta r)$, the excess force shown in (8.3) is caused by the conservation of angular momentum

$$\Delta a_{\text{cen}} = L^2 \left(\frac{1}{r^3} - \frac{1}{r'^3} \right). \quad (8.3)$$

8.1.2 Magnetic Czochralski (MCZ) Silicon

As the diameter of the crystal increases we need to stabilize the flow of the melt. There have been a lot of papers regarding the magnetic-field-applied Czochralski method, especially for large-diameter crystals [8.35–45]. Research on electromagnetic hydrodynamics has a long history in the field of steel and metal manufacturing processes. Since molten silicon, like molten steel or metal, has many free electrons, electromagnetic hydrodynamics can be used to control the convection in metalically conducting molten silicon through the application of magnetic and/or electric fields.

The electric current (\mathbf{J}) in the melt and the Lorentz force (\mathbf{F}) induced by the current in the case of a steady electromagnetic field are shown in (8.4) and (8.5), respectively, where σ_e , \mathbf{E} , \mathbf{B} , and \mathbf{v} are the electric conductivity of the melt, electric field, magnetic flux density, and velocity of the melt, respectively.

$$\mathbf{J} = \sigma_e (\mathbf{E} + \mathbf{v} \times \mathbf{B}), \quad (8.4)$$

$$\mathbf{F} = \mathbf{J} \times \mathbf{B}. \quad (8.5)$$

Due to the continuity condition on the electric current in the melt, (8.6) (a Poisson-type equation) should be satisfied, since there is no source of charge in this case:

$$\nabla \cdot \mathbf{J} = 0. \quad (8.6)$$

The typical magnetic fields used in the Czochralski method are shown in Fig. 8.4. Figure 8.4a and b show schematic diagrams of the vertical magnetic-field-applied Czochralski (VMCZ) and the transverse magnetic-field-applied Czochralski (TMCZ) method, respectively. One or two coils are set parallel to the pulling axis in VMCZ, while two coils are set perpendicular to the axis in TMCZ. For the cusp-shaped magnetic-field-applied Czochralski method there are two coils, which are set parallel to the axis with opposite current directions. Therefore, inhomogeneous magnetic fields are applied to the melt.

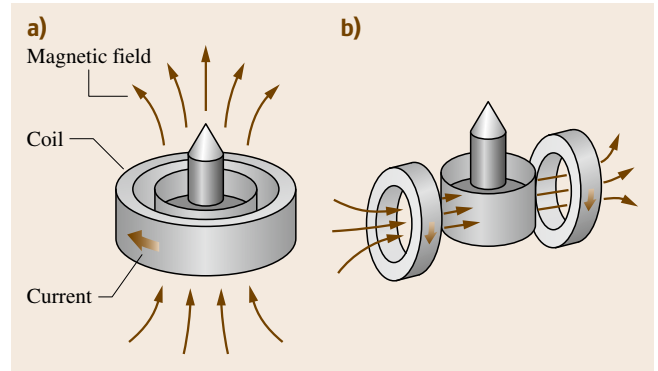


Fig. 8.4a,b Schematic diagram of a VMCZ (a) and TMCZ (b) system. Static current is applied to the cylindrical coil. Schematic diagram of electric currents and Lorentz forces under vertical magnetic fields

The vertical magnetic-field-applied Czochralski (VMCZ) method was one of the methods used in early works on magnetic-field-applied crystal growth. Magnetic fields are applied in the z -direction; therefore, motion of the melt in the radial and/or azimuthal directions reacts with the magnetic field, while melt motion in the vertical direction does not react with the field. Electric current is induced in the azimuthal direction by the radial motion of the melt under a vertical magnetic field. Therefore, the Lorentz force works in the opposite direction and suppresses the velocity of the melt in the radial direction.

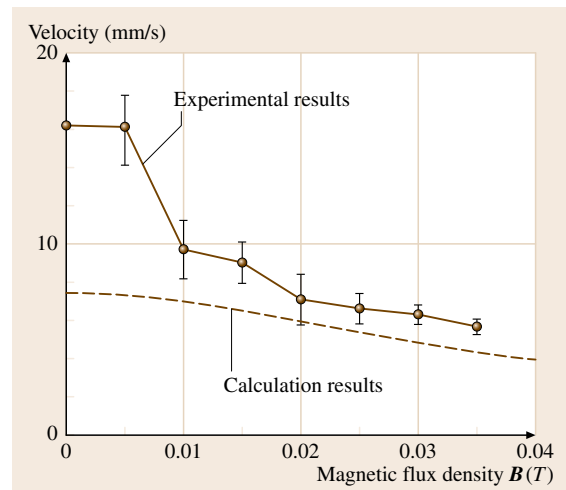


Fig. 8.5 Relationship between magnetic field and flow velocity in a meridional plane under vertical magnetic fields (after [8.35, 50])

Radial current, which is induced by a coupling with the azimuthal velocity and magnetic field, cannot flow through the crucible wall as it is electrically insulating. Thus, the Lorentz force cannot work, and the melt flows freely in the azimuthal direction.

Figure 8.5 shows experimental results for the melt velocity in a meridional plane obtained by a visualization technique using an x-ray radiography method [8.52]. The dots show experimental data while the lines show results of numerical calculation using a three-dimensional configuration of the melt. This figure clearly shows that there is a reduction in melt motion in the meridional plane. It was clarified from the visu-

alization that the motion in the azimuthal direction was not suppressed.

The TMCZ system has a nonaxisymmetric configuration, and temperature and velocity fields therefore have twofold symmetry. Although this system has such a symmetry, it has been used for actual production of silicon for charge-coupled devices (CCDs), since the system enables crystals with low oxygen concentration to be produced. CCDs should have homogeneous and low oxygen concentration for reduction of inhomogeneity of image cells in the devices.

An elliptic temperature distribution due to inhomogeneous heat transfer in the melt can be seen in

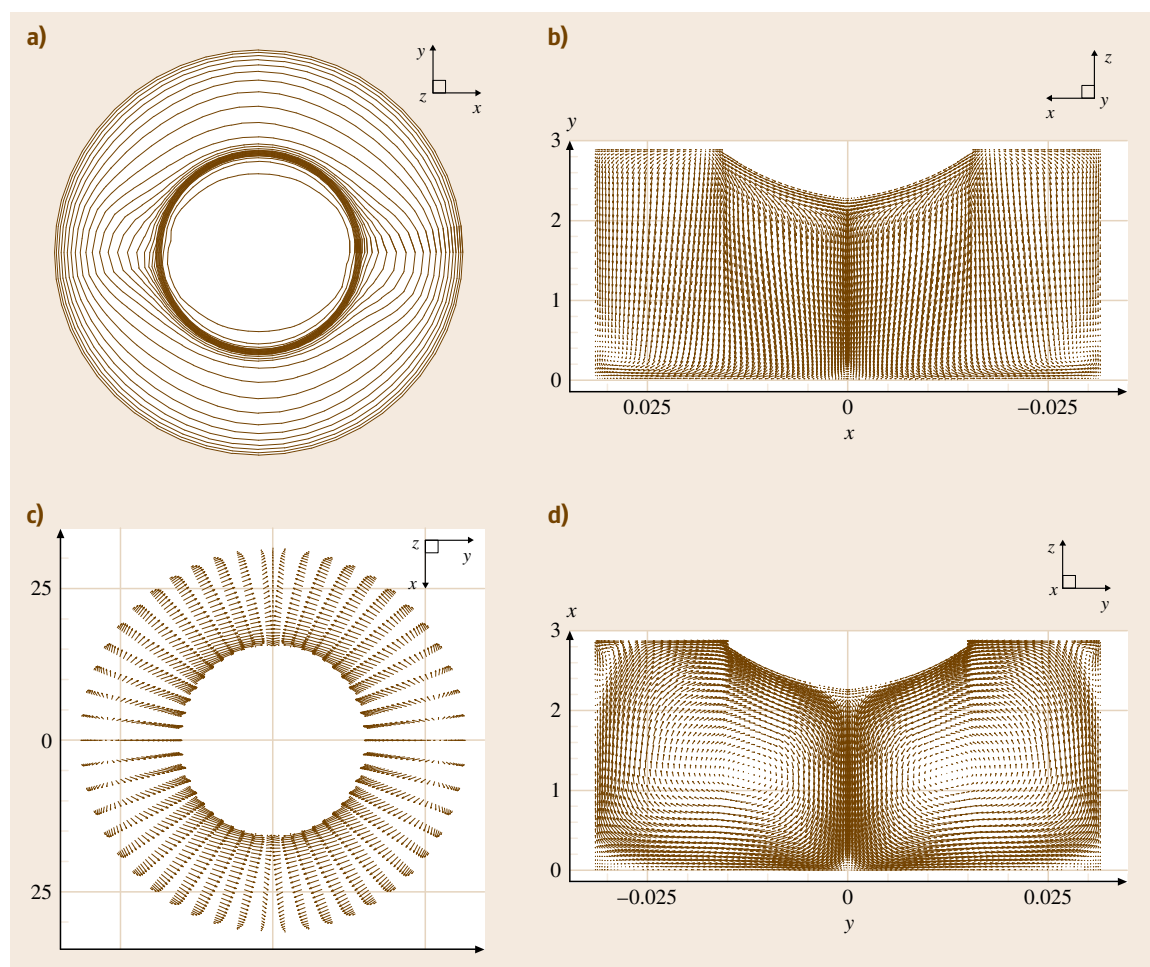


Fig. 8.6a–d Temperature and velocity distribution in silicon melt with a transverse magnetic field applied in the x -direction. Distributions of temperature (a) and velocity (c) at the top of the melt. Velocity distributions in planes perpendicular (b) and parallel (d) to the magnetic field. Temperature difference between the contours is 2 K. Average velocities of (b), (c) and (d) are 0.2, 0.18 and 0.19 mm/s, respectively

Fig. 8.6a. As shown schematically in Figure 8.6a,b, only down-flow is formed in a plane parallel to the magnetic field, while two roll cells are formed in a plane perpendicular to the field. Consequently, thin boundary layers of velocity, temperature, and oxygen near the crucible wall are formed.

This phenomenon is a characteristic of a transverse magnetic field, which is static and nonaxisymmetric. If an axisymmetric magnetic field such as a vertical or cusp-shaped field is used, the melt rotates with the same angular velocity as the crucible.

8.2 Control of Crystal Defects in Czochralski Silicon

Microvoids are formed by agglomeration of vacancies that are introduced at a solid–liquid interface of silicon [8.1, 51–55]. In most past studies, it has been difficult to reduce the total number of such microvoids in a whole crystal because the vacancy flux in silicon crystals must be controlled to reduce the probability of agglomeration.

One of the key points for controlling the vacancy flux in crystals, especially that near a solid–liquid interface, is control of the convection of melt, by which the shape of the solid–liquid interface can be controlled. From this point of view, efforts have been made to control the periodic and/or turbulent flow of melt inside a crucible of large diameter. Crystal growth industries have mainly focused on quantitative prediction of a solid–liquid interface, point defect distribution, oxygen concentration, and dislocation-free growth.

8.2.1 Criterion for Characteristic Defect Formation

Point defects such as a vacancy and an interstitial atom form clusters which become microvoids and dislocation clusters. Such defects degrade characteristics of LSIs by formation of leakage current paths. The microvoids and dislocation clusters are formed by supersaturation of vacancy and interstitial atoms during the crystal cooling, respectively. If the total number of vacancy and interstitial atoms is the same, they can compensate, and perfect crystal will then be formed. However, such condition cannot be realized due to differences in their equilibrium concentrations at melting point and their diffusion constants. The interstitial atoms migrate fast near the melting point while vacancies move with the pulling speed since their diffusion constant is small.

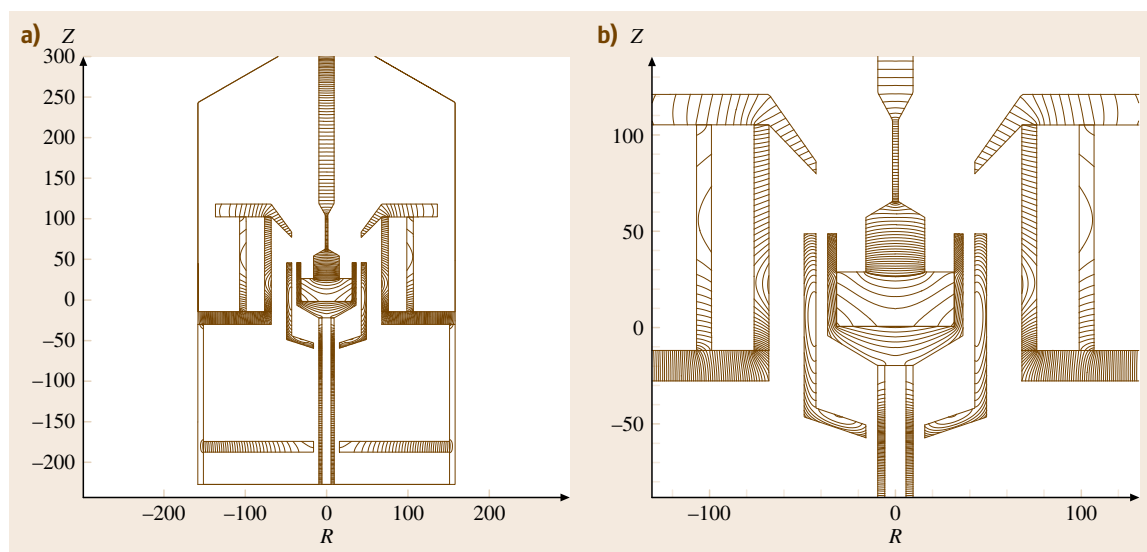


Fig. 8.7 (a) Temperature distribution in a global model with a two-dimensional configuration. (b) A zoomed temperature distribution in a global model with a two-dimensional configuration. Temperature difference between the contours is 5 K

Volonkov proposed (8.7) as the criterion to obtain perfect crystals [8.52]

$$\frac{V}{G} = 0.62, \quad (8.7)$$

where V and G are the crystal pulling rate and the temperature gradient of the crystal, respectively.

The flux of vacancy transfer in a crystal is determined by the crystal pulling speed since vacancies, with a slow diffusion constant, move with the pulled crystals. However, the flux of interstitial atoms in a crystal is determined by the temperature gradient of the crystal since interstitial atoms diffuse based on the gradient of the equilibrium concentration. Such concentration gradients are defined by the temperature gradient in a crystal. Therefore, the dominant defect can be determined by the relationship expressed by (8.7).

To obtain a perfect crystal one has to control the flux of defects in a crystal. We need to control these fluxes by controlling the temperature distribution in the furnace and the shape of the solid–liquid interface, which affects the temperature gradient in the crystal. We usually use a global model that can predict the temperature distribution in a furnace, including the shape of the solid–liquid interface. The global model contains conduction, convection, and radiation of heat and mass transfer in the furnace.

Figure 8.7a,b [8.55] shows two-dimensional temperature distributions in a furnace at Kyushu University. We can recognize temperature distributions in each part of the crystal, crucible, melt, heater, and thermal shields. If the system is completely axisymmetric, a two-dimensional configuration can be imposed due to the almost axisymmetric configuration of a Czochralski furnace. However, many studies have shown that flow in the melt has a three-dimensional structure. Therefore, we have to change the configuration from two to three dimensional.

8.2.2 Effect of Pulling Rate and Temperature Gradient

We usually use magnetic fields to control temperature gradient in a crystal through control of the flow of the melt. The results of a series of computations with various intensities of magnetic field and various crystal pulling rates are summarized in Figs. 8.8 and 8.9. Figure 8.8 shows the axial temperature gradients in both the crystal and the melt at a melt–crystal interface as a function of crystal pulling rate. Solid lines show the results with and without a magnetic field, while dashed lines

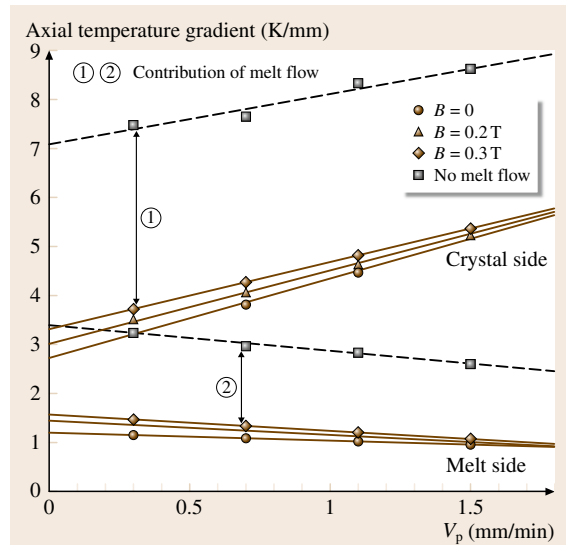


Fig. 8.8 Axial temperature gradients in the crystal (*upper part*) and melt (*lower part*) near the interface as a function of pulling rate of a crystal at different intensities of the applied magnetic field (after [8.55])

show the results without convection in the melt, approximately corresponding to the case with a magnetic field intensity of infinite value. The arrows in the figure show the contribution of the convection of the melt. The val-

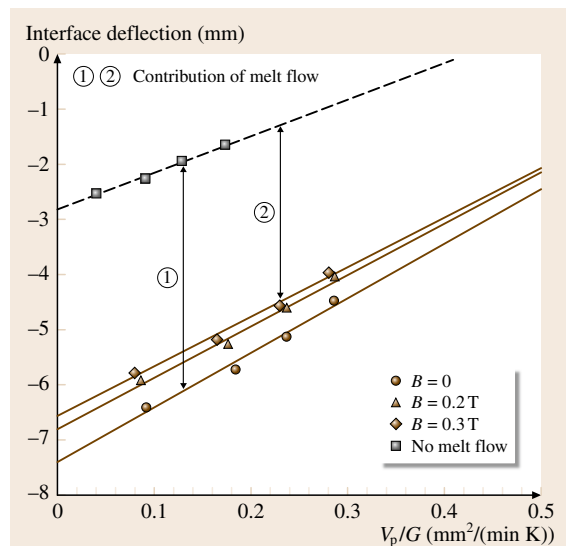


Fig. 8.9 Interface deflection as a function of pulling rate of a crystal at different intensities of the applied magnetic field (after [8.55])

ues of the axial temperature gradients in the melt and crystal were obtained by averaging in the central area of the interface. The values of the axial temperature gradients in the melt and crystal at the interface are not identical even when the crystal pulling rate is zero since the thermal conductivity of the crystal is not equal to that of the melt.

These results show that the axial temperature gradients in the melt and crystal near the interface increase with increasing magnetic field intensity. With increasing crystal pulling rate, the temperature gradient near the interface in the crystal increases, while that in the melt decreases. Meanwhile, the difference between the case with finite (including zero) magnetic field intensity and the case without melt convection becomes smaller. Since this difference is due to the melt convection, this result indicates that the contribution of melt flow becomes smaller with increasing crystal pulling rate.

These phenomena can be explained as follows. When we apply a magnetic field of large intensity natural convection of the melt is suppressed, resulting in a more inhomogeneous temperature distribution in the melt. Therefore, the temperature gradient in the melt increases with increasing magnetic field intensity. Meanwhile, because of heat balance between the liquid and solid at the interface, the temperature gradient in the crystal near the interface also increases accordingly. However, melt convection still remains, even if we apply a magnetic field with a relatively large intensity to the melt. As a result, even when a relatively large magnetic field of 0.3 T is applied to the system, the temperature gradients near the interface in both the crystal and the melt are far from those without melt convection, as shown in Fig. 8.8. On the other hand, since a larger crystal growth rate always results in lower heater power, the temperature on the sidewall of the melt becomes smaller due to the lower heater power. The temperature

difference becomes smaller and the temperature distribution becomes less inhomogeneous in the melt. This in turn leads to weaker melt convection due to decrease in the thermal buoyancy force induced by the temperature gradient in the melt. Therefore, with increase in the crystal pulling rate, both the axial temperature gradient in the melt near the interface and the contribution of melt convection decrease. However, since the heat released due to solidification at the interface is proportional to the crystal growth rate and it is transported away from the interface through the crystal, a larger axial temperature gradient field is generated in the crystal near the interface when the crystal pulling rate is increased.

Figure 8.9 shows the interface deflection toward the melt as a function of the ratio between the crystal pulling rate (V_p) and the temperature gradient in the crystal near the interface (G). The values of the interface deflection and the parameter V_p/G were obtained by averaging in the central area of the interface. The arrows in the figure show the contribution of convection in the melt. The interface moves upward to the crystal side with increase in either the magnetic field intensity or the value of the parameter V_p/G . This tendency is consistent with that of the axial temperature gradient in the crystal near an interface shown in Fig. 8.8. This is because the interface shape is mainly determined by the temperature distribution in the crystal close to the interface and the melt convection in the crucible. As explained in the previous section, when a magnetic field of large intensity is applied to the system or a larger pulling rate is applied to the crystal, the melt convection is suppressed and the axial temperature gradient in the crystal near the interface increases. The melt–crystal interface then moves upward to the crystal side in order to accommodate the increased axial temperature gradient in the crystal near the interface and the contribution of melt convection in the crucible becomes smaller.

8.3 Growth and Characterization of Silicon Multicrystal for Solar Cell Applications

Casting is a key method for large-scale production of multicrystalline silicon for use in highly efficient solar cells [8.56, 69–71]. Since the efficiency of solar cells depends on the quality of the multicrystalline silicon, which is in turn determined by the crystallization process, it is important to investigate and optimize the

casting process to control the distributions of temperature and iron in a silicon ingot during the solidification process. Moreover, dislocation plays an important role in the efficiency of solar cells. Such properties should be controlled carefully by using a large-scale calculation in order to obtain silicon crystals for solar cells.

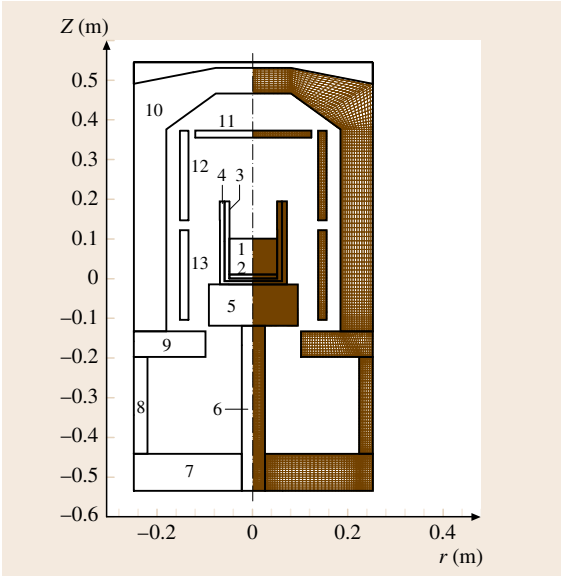


Fig. 8.10 Configuration and computation grid of a casting furnace. The melt, a crystal, a crucible, a crucible holder and pedestals are denoted as 1, 2, 3, 4, 5, and 6, respectively. Thermal shields are labeled 7–11. The numbers 12 and 13 indicate multiple heater

8.3.1 Recent Development of Crystalline Silicon for Solar Cells

Numerical simulation has become a powerful tool for investigation and optimization of the casting process and crystal growth process with the development of computer technology and computational techniques [8.56, 57]. Since a casting furnace has a highly nonlinear conjugated thermal system, transient simulation with global modeling is an essential tool for investigation and improvement of the casting process. We developed a transient code with a global model for the casting process and carried out calculations to investigate the distributions of temperature and iron in a silicon ingot during the casting process.

8.4 Summary

Crystal growth and characterization of Czochralski silicon single crystals for semiconductor and solar cell application is a key technology for information and renewable energy. Such activity enables us to open up

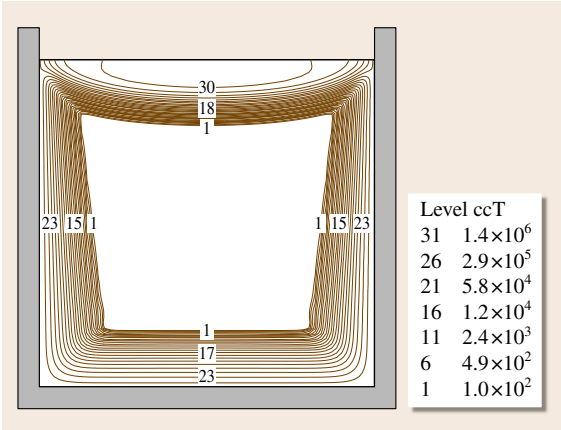


Fig. 8.11 Distribution of iron concentration in a solidified silicon ingot after the solidification process. The scale of iron concentration should be multiplied by $1 \times 10^{10} \text{ cm}^{-3}$. The periphery of the crystal contains on the order of $1 \times 10^{15} \text{ cm}^{-3}$

Time-dependent distributions of iron and temperature in a silicon ingot were investigated. Figure 8.10 shows a typical casting furnace for production of multicrystalline silicon for solar cells.

Figure 8.11 shows the distribution of iron concentration in a solidified silicon ingot that had been cooled for 1 h during the cooling process. The figure shows a vertical cross-section of the iron concentration in the crystal. The scale of the iron concentration should be multiplied by $1 \times 10^{10} \text{ cm}^{-3}$; therefore, the periphery of the crystal contains on the order of $1 \times 10^{15} \text{ cm}^{-3}$.

Areas with high iron concentration were formed at the top of the melt due to segregation of iron. Moreover, areas with high concentration of iron were formed close to the crucible walls. Such areas were formed by diffusion, which occurred during solidification and the cooling process. This is based on the small activation energy of iron diffusion in solid silicon. The central area of the ingot has a low concentration of iron after the solidification process, as shown in Fig. 8.11.

a new world through technological breakthroughs. Both experimental and numerical studies on crystal growth help us to understand and derive new concepts for new crystal growth technology.

References

- 8.1 M. Itsumi, H. Akiya, T. Ueki: The composition of octahedron structures that act as an origin of defects in thermal SiO₂ on Czochralski silicon, *J. Appl. Phys.* **78**, 5984–5988 (1995)
- 8.2 K. Koai, A. Seidel, H.-J. Leister, G. Müller, A. Koehler: Modeling of thermal fluid-flow in the liquid encapsulated Czochralski process and comparison with experiments, *J. Cryst. Growth* **137**, 41–47 (1994)
- 8.3 H.-J. Leister, M. Peric: Numerical-simulation of a 3-D Czochralski flow by a finite volume multi-grid-algorithm, *J. Cryst. Growth* **123**, 567–574 (1992)
- 8.4 H. Yamagishi, M. Kuramoto, Y. Shiraishi: CZ crystal growth development in super silicon crystal project, *Solid State Phenom.* **57–8**, 37–39 (1997)
- 8.5 Y.C. Won, K. Kakimoto, H. Ozoe: Transient three-dimensional flow characteristics of Si melt in a Czochralski configuration under a cusp-shaped magnetic field, *Numer. Heat Transf.* **A36**, 551–561 (1999)
- 8.6 K.-W. Yi, M. Watanabe, M. Eguchi, K. Kakimoto, T. Hibiya: Change in velocity in silicon melt of the Czochralski (CZ) process in a vertical magnetic field, *Jpn. J. Appl. Phys.* **33**, L487–L490 (1994)
- 8.7 M.G. Williams, J.S. Walker, W.E. Langlois: Melt motion in a Czochralski puller with a weak transverse magnetic-field, *J. Cryst. Growth* **100**, 233–253 (1990)
- 8.8 A.E. Organ, N. Riley: Oxygen-transport in magnetic Czochralski growth of silicon, *J. Cryst. Growth* **82**, 465–476 (1987)
- 8.9 J.S. Walker, M.G. Williams: Centrifugal pumping during Czochralski silicon growth with a strong transverse magnetic-field, *J. Cryst. Growth* **137**, 32–36 (1994)
- 8.10 J. Baumgartl, M. Gewald, R. Rupp, J. Stierlen, G. Müller: Studies of buoyancy driven convection in a vertical cylinder with parabolic temperature profile, *Proc. 7th Eur. Symp. Mater. Fluid Sci. Microgravity*, Oxford (1989) pp.10–15
- 8.11 L.N. Hjellming, J.S. Walker: Melt motion in a Czochralski crystal puller with an axial magnetic-field-uncertainty in the thermal constants, *J. Cryst. Growth* **87**, 18–32 (1988)
- 8.12 S. Kobayashi: Numerical-analysis of oxygen-transport in magnetic Czochralski growth of silicon, *J. Cryst. Growth* **85**, 69–74 (1987)
- 8.13 M. Akamatsu, K. Kakimoto, H. Ozoe: Effect of crucible rotation on the melt convection and the structure in a Czochralski method, *Transp. Phenom. Therm. Sci. Process Eng.* **3**, 637–642 (1997)
- 8.14 K.-W. Yi, K. Kakimoto, M. Eguchi, M. Watanabe, T. Shyo, T. Hibiya: Spoke patterns on molten silicon in Czochralski system, *J. Cryst. Growth* **144**, 20–28 (1994)
- 8.15 K. Kakimoto, H. Ozoe: Oxygen distribution at a solid-liquid interface of silicon under transverse magnetic fields, *J. Cryst. Growth* **212**, 429–437 (2000)
- 8.16 R.A. Brown, T.A. Kinney, P.A. Sackinger, D.E. Bornside: Toward an integrated analysis of Czochralski growth, *J. Cryst. Growth* **97**, 99–115 (1989)
- 8.17 H. Hirata, N. Inoue: Study of thermal symmetry in Czochralski silicon melt under a vertical magnetic field, *Jpn. J. Appl. Phys.* **23**, L527–L530 (1984)
- 8.18 H. Hirata, K. Hoshikawa: Silicon crystal growth in a cusp magnetic-field, *J. Cryst. Growth* **96**, 747–755 (1989)
- 8.19 H. Hirata, K. Hoshikawa: Homogeneous increase in oxygen concentration in Czochralski silicon-crystals by a cusp magnetic-field, *J. Cryst. Growth* **98**, 777–781 (1989)
- 8.20 H. Hirata, K. Hoshikawa: Silicon crystal growth in a cusp magnetic field, *J. Cryst. Growth* **96**, 747–755 (1989)
- 8.21 K. Hoshi, T. Suzuki, Y. Okubo, N. Isawa: Extended Abstracts, *Electrochem. Soc. Spring Meet.*, Vol. 80–1 (The Electrochem. Soc., Pennington 1980) p. 811
- 8.22 K. Hoshikawa: Czochralski silicon crystal growth in the vertical magnetic field, *Jpn. J. Appl. Phys.* **21**, L545–L547 (1982)
- 8.23 K. Hoshikawa, H. Kohda, H. Hirata: Homogeneity of vertical magnetic field applied LEC GaAs crystal, *Jpn. J. Appl. Phys.* **23**, L195–L197 (1984)
- 8.24 K. Kakimoto, L.J. Liu: Numerical study of the effects of cusp-shaped magnetic fields and thermal conductivity on the melt-crystal interface in CZ crystal growth, *Cryst. Res. Technol.* **38**, 716–725 (2003)
- 8.25 K. Kakimoto: Use of an inhomogeneous magnetic fields for silicon crystal growth, *Proc. 2nd Workshop High Magn. Fields*, ed. by H. Schneider-Muntau (World Scientific, New York 1997) pp. 21–24
- 8.26 K. Kakimoto: Flow instability during crystal growth from the melt, *Prog. Cryst. Growth Charact.* **30**, 191–215 (1995)
- 8.27 K. Kakimoto, Y.W. Yi, M. Eguchi: Oxygen transfer during single silicon crystal growth in Czochralski system with vertical magnetic fields, *J. Cryst. Growth* **163**, 238–242 (1996)
- 8.28 K. Kakimoto, Y.W. Yi: Use of magnetic fields in crystal growth from semiconductor melts, *Physica B* **216**, 406–408 (1996)
- 8.29 K.M. Kim, W.E. Langlois: Computer-simulation of boron transport in magnetic Czochralski growth of silicon, *J. Electrochem. Soc.* **133**, 2586–2590 (1986)
- 8.30 A.E. Organ, N. Riley: Oxygen-transport in magnetic Czochralski growth of silicon, *J. Cryst. Growth* **82**, 465–476 (1987)

- 8.31 Z.A. Salnick: Oxygen in Czochralski silicon crystals grown under an axial magnetic field, *J. Cryst. Growth* **121**, 775–780 (1992)
- 8.32 T. Suzuki, N. Isawa, Y. Okubo, K. Hoshi: Oxygen in Czochralski silicon crystals grown under a transverse magnetic field, *Semiconductor Silicon 1981*, ed. by H.R. Huff, R.J. Kriegler, Y. Takeishi (The Electrochem. Soc., Pennington 1981) pp. 90–94
- 8.33 R.N. Thomas, H.M. Hobgood, P.S. Ravishankar, T.T. Braggins: Oxygen distribution in silicon crystals grown by transverse magnetic fields, *Solid State Technol.* **April**, 163–170 (1990)
- 8.34 M. Watanabe, M. Eguchi, K. Kakimoto, T. Hibiya: The baroclinic flow instability in rotating silicon melt, *J. Cryst. Growth* **128**, 288–292 (1993)
- 8.35 M. Watanabe, M. Eguchi, K. Kakimoto, T. Hibiya: Flow mode transition and its effects on crystal-melt interface shape and oxygen distribution for Czochralski-grown Si single crystals, *J. Cryst. Growth* **151**, 285–290 (1995)
- 8.36 M.J. Wargo, A.F. Witt: Real-time thermal imaging for analysis and control of crystal-growth by the Czochralski technique, *J. Cryst. Growth* **116**, 213–224 (1995)
- 8.37 K.-W. Yi, M. Watanabe, M. Eguchi, K. Kakimoto, T. Hibiya: Change in velocity in silicon melt of the Czochralski (CZ) process in a vertical magnetic field, *Jpn. J. Appl. Phys.* **33**, L487–L490 (1994)
- 8.38 Y. Gelfgat, J. Krumins, B.Q. Li: Effects of system parameters on MHD flows in rotating magnetic fields, *J. Cryst. Growth* **210**, 788–796 (2000)
- 8.39 Y. Gelfgat, E. Jpriede: The influence of combined electromagnetic fields on the heat and mass transfer in a cylindrical vessel with the melt, *Magnetohydrodynamics* **31**, 102–110 (1995)
- 8.40 R.U. Barz, G. Gerbeth, Y. Gelfgat: Numerical simulation of MHD rotator action on hydrodynamics and heat transfer in single crystal growth processes, *J. Cryst. Growth* **180**, 388–400 (1997)
- 8.41 T. Kaiser, K.W. Benz: Taylor vortex instabilities induced by a rotating magnetic field: A numerical approach, *Phys. Fluids* **10**, 1104–1110 (1998)
- 8.42 F.-U. Brucker, K. Schwerdtfeger: Single-crystal growth with Czochralski method involving rotational electromagnetic stirring of the melt, *J. Cryst. Growth* **139**, 351–356 (1994)
- 8.43 J. Virbulis, T. Wetzal, A. Muiznieks, B. Hanna, E. Dornberger, E. Tomzig, A. Muhlbauer, W. von Ammon: Stress-induced dislocation generation in large FZ- and CZ-silicon single crystals – Numerical model and qualitative considerations, *Proc. 3rd Int. Workshop Model. Cryst. Growth* (2000) pp. 31–33
- 8.44 L.J. Liu, T. Kitashima, K. Kakimoto: Three-dimensional calculation of Si-CZ growth, *Proc. Int. Symp. Process. Technol. Market Dev. 300 mm Si Mater. (ISPM-300mm Si)*, Beijing (2003) pp. 2551–2555
- 8.45 O. Grabner, G. Mueller, E. Tomzig, W. von Ammon: Effects of various magnetic field configurations on temperature distributions in Czochralski silicon melts, *Microelectron. Eng.* **56**, 83–88 (2001)
- 8.46 K. Kakimoto, K.-W. Yi, M. Eguchi: Oxygen transfer during single silicon crystal growth in Czochralski system with vertical magnetic fields, *J. Cryst. Growth* **163**, 238–242 (1996)
- 8.47 A. Krauze, A. Muiznieks, A. Muhlbauer, T. Wetzal, L. Gorbunov, A. Pedchenko, J. Virbulis: Numerical 2-D modelling of turbulent melt flow in CZ system with dynamic magnetic fields, *J. Cryst. Growth* **266**, 40–47 (2004)
- 8.48 H. Ozoe, M. Iwamoto: Combined effects of crucible rotation and horizontal magnetic field on dopant concentration in a Czochralski melt, *J. Cryst. Growth* **142**, 236–244 (1994)
- 8.49 P. Sabhapathy, M.E. Salcudean: Numerical study of Czochralski growth of silicon in an axisymmetric magnetic field, *J. Cryst. Growth* **113**, 164–180 (1991)
- 8.50 K. Kakimoto, H. Watanabe, M. Eguchi, T. Hibiya: Direct observation by X-ray radiography of convection of molten silicon in the Czochralski growth method, *J. Cryst. Growth* **88**, 365–370 (1988)
- 8.51 K. Nakamura, S. Maeda, S. Togawa, T. Saisyoji, T. Tomioka: Effect of the shape of crystal-melt interface on point defect reaction in silicon crystals, *ECS Proc.* **17**, 31–33 (2000)
- 8.52 V. Voronkov: The mechanism of swirl defects formation in silicon, *J. Cryst. Growth* **59**, 625–643 (1982)
- 8.53 W. von Ammon, E. Dornberger, H. Oelkrug, H. Weider: The dependence of bulk defects on the axial temperature gradient of silicon crystals during Czochralski growth, *J. Cryst. Growth* **151**, 273–277 (1995)
- 8.54 K. Nakamura, T. Saisyoji, J. Tomioka: Grown-in defects in silicon crystals, *J. Cryst. Growth* **237**, 1678–1684 (2002)
- 8.55 L. Liu, S. Nakano, K. Kakimoto: An analysis of temperature distribution near the melt-crystal interface in silicon Czochralski growth with a transverse magnetic field, *J. Cryst. Growth* **282**, 49–59 (2005)
- 8.56 D. Franke, T. Rettelbach, C. Habler, W. Koch, A. Muller: Silicon ingot casting: process development by numerical simulations, *Sol. Energy Mater. Sol. Cells* **72**, 83–92 (2002)
- 8.57 M. Ghosh, J. Bahr, A. Muller: Silicon ingot casting: process development by numerical simulations, *Proc. 19th Euro. Photovolt. Sol. Energy Conf., Paris* (2004) pp. 560–563
- 8.58 D. Vizman, S. Eichler, J. Friedrich, G. Müller: Three-dimensional modeling of melt flow and interface shape in the industrial liquid-encapsulated Czochralski growth of GaAs, *J. Cryst. Growth* **266**, 396–403 (2004)
- 8.59 A. Krauze, A. Muiznieks, A. Muhlbauer, T. Wetzal, W. von Ammon: Numerical 3-D modelling of turbulent melt flow in a large CZ system with horizontal DC

- magnetic field. II. Comparison with measurements, *J. Cryst. Growth* **265**, 14–257 (2004)
- 8.60 L.J. Liu, K. Kakimoto: D global analysis CZ-Si growth in transverse magnetic field with rotating crucible and crystal, *Cryst. Res. Technol.* **40**, 347–351 (2005)
- 8.61 K. Kakimoto, L.J. Liu: Numerical study of the effects of cusp-shaped magnetic fields and thermal conductivity on the melt-crystal interface in CZ crystal growth, *Cryst. Res. Technol.* **38**, 716–725 (2003)
- 8.62 J.J. Derby, R.A. Brown: Thermal-capillary analysis of Czochralski and liquid encapsulated Czochralski crystal growth, *J. Cryst. Growth* **75**, 227–240 (1986)
- 8.63 F. Dupret, P. Nicodeme, Y. Ryckmans, P. Wouters, M.J. Crochet: Global modeling of heat-transfer in crystal growth furnaces, *Int. J. Heat Mass Transf.* **33**, 1849–1871 (1990)
- 8.64 M. Li, Y. Li, N. Imaishi, T. Tsukada: Global simulation of a silicon Czochralski furnace, *J. Cryst. Growth* **234**, 32–46 (2002)
- 8.65 V.V. Kalaev, I.Y. Evstratov, N.Y. Makarov: Gas flow effect on global heat transport and melt convection in Czochralski silicon growth, *J. Cryst. Growth* **249**, 87–99 (2003)
- 8.66 L. Liu, K. Kakimoto: Partly three-dimensional global modeling of a silicon Czochralski furnace II. Model application: Analysis of a silicon Czochralski furnace in a transverse magnetic field, *Int. J. Heat Mass Transf.* **48**, 4492–4497 (2005)
- 8.67 L. Liu, S. Nakano, K. Kakimoto: An analysis of temperature distribution near the melt-crystal interface in silicon Czochralski growth with a transverse magnetic field, *J. Cryst. Growth* **282**, 49–59 (2005)
- 8.68 L. Liu, K. Kakimoto: Partly three-dimensional global modeling of a silicon Czochralski furnace. I. Principles, formulation and implementation of the model, *Int. J. Heat Mass Transf.* **48**, 4481–4491 (2005)
- 8.69 E.W. Weber: Transition-metal profiles in a silicon crystal, *Appl. Phys.* **A30**, 1–15 (1983)
- 8.70 W. Zuhleiner, D. Huber: Czochralski crystal growth of silicon. In: *Crystal-Growth, Properties and Applications*, Vol. 8, ed. by J. Grabmaier (Springer, Berlin, Heidelberg 1988) pp. 1–12
- 8.71 D. Macdonald, A. Cuevas, A. Kinomura, Y. Nakano, J.J. Geerligs: Transition-metal profiles in a multicrystalline silicon ingot, *J. Appl. Phys.* **97**, 33523–33527 (2005)

Czochralski Growth of Oxide Photorefractive Crystals

Ernesto Diéguez, Jose Luis Plaza, Mohan D. Aggarwal, Ashok K. Batra

Czochralski crystal growth is one of the major methods of crystal growth from melt for bulk single crystals for commercial and technological applications. Most crystals, such as semiconductors and oxides, are grown from melt using this technique due to the much faster growth rates achievable. A detailed description of the process can only be given for specific materials; there is no universal crystal pulling system available commercially. The details of the basic principle and the design of automatic diameter control Czochralski crystal growth system elements are given in this chapter so as to enable any researcher to design and fabricate his/her own system. This chapter is devoted to the growth of bulk oxide photorefractive materials such as lithium niobate and sillenite crystals including the development in these materials during the last decade. A number of problems (and possible solutions) encountered by the authors during growth in their respective laboratories over the last two decades are discussed.

Section 9.2 provides the introduction to crystals and crystal growth mechanism and various methods of growing photorefractive crystals. Section 9.3 discusses in detail the Czochralski method of crystal growth, including selection of appropriate components for setting up a crystal growth system such as the heating system design, and raising, lowering, and rotation mechanisms. Section 9.4 discusses the growth and properties of lithium niobate crystals. A brief introduction to other photorefractive crystals is given in Sect. 9.5. The details of the growth and properties of sillenite crystals are given in Sect. 9.6. Section 9.7 summarizes the present state of these two important crystals in terms of growth and applications.

9.1	Background	246
9.2	Crystal Growth	246
9.2.1	Czochralski Method of Crystal Growth	246
9.3	Design and Development of Czochralski Growth System	247
9.3.1	Furnace Construction	247
9.3.2	Heating Methods.....	247
9.3.3	Temperature Control Techniques	248
9.3.4	Common Crucible Materials	249
9.3.5	Crystal Rotation and Pulling Arrangement	249
9.3.6	The Czochralski Crystal Growth System	249
9.3.7	Automatic Diameter Control for Czochralski Crystal Growth Technique	251
9.4	Growth of Lithium Niobate Crystals and Its Characteristics	252
9.4.1	Crystal Growth of Lithium Niobate ..	252
9.4.2	Mold-Pushing Melt-Supply Double-Crucible Czochralski Apparatus	255
9.4.3	Congruent Lithium Niobate Crystal Growth by Automatic Diameter Control Method	255
9.4.4	Poling of Lithium Niobate	257
9.4.5	Periodically Poled Lithium Niobate Structures.....	258
9.4.6	Doped Lithium Niobate Crystals.....	260
9.4.7	Relevant Properties and Characteristics	261
9.5	Other Oxide Photorefractive Crystals	262
9.6	Growth of Sillenite Crystals and Its Characteristics	264
9.6.1	Growth of Bulk Sillenite Crystals.....	264
9.6.2	Solid-Liquid Interface	266
9.6.3	Core Effect.....	267
9.6.4	Morphology and Faceting.....	268
9.6.5	Other Growth Defects.....	269
9.6.6	Doping of Sillenites	270
9.6.7	Relevant Properties	271
9.6.8	Growth of Photorefractive Bismuth Silicon Oxide Crystals	272
9.7	Conclusions	273
	References	273

9.1 Background

With the rapid growth of the electronic and optoelectronic industries, the demand for crystalline materials has increased dramatically over the past few decades. The requirement for better, cheaper, and larger single crystals has driven extensive research and development in crystal growth. A major factor behind such growth is the advent of high-power and efficient solid-state lasers, in combination with the use of materials that exhibit large second- or third-order nonlinearities [9.1–3]. In such conditions, nonlinear optics is becoming an important technology in the design of new laser sources emitting in the visible or near infrared. Nonlinear optics also enables the attainment of new functionalities in laser systems and in optoelectronic signal transmission and processing. The class of nonlinear phenomena based on the photorefractive effects in electrooptic crystals will undoubtedly play a major role in these various applications of laser photonics. Since its discovery, photorefraction has stimulated much basic research, covering both fundamental materials studies and their applications in dynamic holography, laser beam control, and optical processing. For many years the challenge was only to understand the basic mechanisms of photorefraction giving rise to this effect in different crystals, which drove research and development in this area. More and more materials were found to be photorefractive. New electrooptic interactions were discovered. The fields of nonlinear optics, optical spectroscopy, electrooptics, ferroelectrics, electronic transport, and Fourier optics were brought together to develop a complete

understanding of the complex microscopic mechanism involved. Another important aspect of photorefractive materials is their ability to perform efficient energy transfer between a signal and a reference beam interfering in the volume of the crystal. This property opens up a wide range of applications, including image amplification, optical phase conjugation with gain, and self-pumped optical cavities. To achieve these results and develop applications requires us to optimize nonlinear material properties, and therefore the choice of the best material is a critical issue. Nonlinear photorefractive optics is now well established and has reached scientific maturity. It contributes to stimulate basic research in solid-state physics and to investigate in detail the mechanisms of charge transport in different types of ferroelectric or semiconductor crystals such as LiNbO_3 , BaTiO_3 , KNbO_3 , $\text{Bi}_{12}\text{SiO}_{20}$ or GaAs.

The Czochralski method is most popular and useful for the growth of large oxides crystals. This chapter is devoted to the growth of bulk photorefractive materials from the Czochralski method, summarizing the development in these materials during the last decade. We focus our attention on the two most important photorefractive materials, LiNbO_3 and sillenites, which are considered the most relevant, especially because in these two materials all the problems and circumstances inherent to bulk crystal growth of photorefractive oxide materials are concentrated. For this reason the chapter includes various sections devoted to each of these materials.

9.2 Crystal Growth

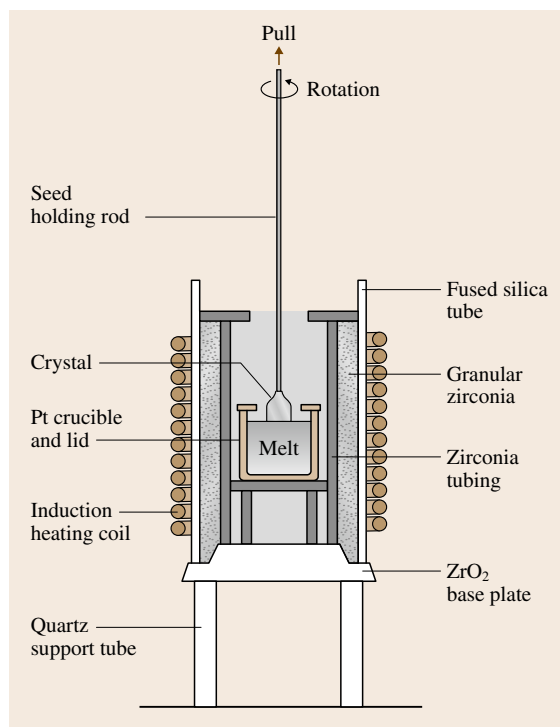
9.2.1 Czochralski Method of Crystal Growth

The CZ technique is named after J. Czochralski. Czochralski's invention was discovered essentially by accident. As the story goes, the young Czochralski, then chief of AEG's metal laboratory in Berlin, was studying the crystallization of metals. A crucible containing molten tin was left on his table for slow cooling and crystallization. Czochralski was preparing his notes on the experiments carried out during the day when at some point, lost in thought, he dipped his pen into this crucible instead of the inkwell placed near the crucible. He withdrew it quickly and saw a thin thread of so-

lidified metal hanging at the tip of the nib. Thus, the discovery was made. He had discovered a phenomenon never observed before: crystallization by pulling from the surface of a melt. However, careful observation of this accidental process provided a discovery of great importance. Later, the nib slot, in which crystallization was initiated, was replaced by a special narrow capillary and later by a seed crystal of the material to be grown [9.4]. *Teal* and *Little* also grew germanium single crystals by similar technique [9.5]. In the recent past, *Brandle* has given a detailed description of Czochralski growth of oxides along with current status [9.6].

Fig. 9.1 A basic diagram of the Czochralski method ►

A basic diagram of the CZ method is illustrated in Fig. 9.1 with various components to explain the process. To be considered as a possible candidate for crystal growth by the Czochralski technique, the material should have a relatively low vapor pressure. The crucible material should be nonreactive with the crystal growth material above its melting point. The Czochralski system is based on the following principle: the material is melted in a crucible and is kept for a certain time at a temperature above the melting point, then the temperature is reduced to a value slightly above the freezing point. The freezing point is judged by cooling the melt until crystals start to appear on the surface, then the temperature is slightly lowered and a seed (cut in the appropriate orientation) is inserted into the melt. It is kept at that position for a little while, then the pulling mechanism is started. The seed forms a crystallization center if the temperatures have been chosen correctly. If the crystal starts growing very fast and becomes visible to the naked eye, then the temperature of the melt needs to be increased by a degree or so; the melt must not be overheated as this would cause the crystal to dissolve and separate from the melt. The diameter of the pulled crystal is controlled by manipulating the temperature of the melt and the pulling rate. Suitable engineering of both axial and radial temperature gradients



is needed to grow single crystals of desired dimensions reliably.

9.3 Design and Development of Czochralski Growth System

In this section, various components and instruments used for developing the automatic diameter control CZ technique are discussed so that the reader can set up his/her own system. The major components are: furnace design, heating methods viz. resistive or inductive, temperature control techniques, crucible selection, and crystal rotation and pulling arrangement [9.7].

9.3.1 Furnace Construction

The furnace used for crystal pulling can vary from the very simple, e.g., a resistance wound heating element, to one which is extremely complex because of thermal and chemical constraints placed upon it by the crystal. Two types of furnaces can be used; the first type is for oxide crystal growth and is generally composed of ceramic and noble-metal parts, whereas the second type is for semiconductor growth and is usually composed

of graphite and fused-silica parts. For growing lithium niobate crystals, a resistance or inductive furnace can be utilized.

9.3.2 Heating Methods

Selection of the heating method depends on the operational temperature needed to grow single crystals of the desired material. This normally depends on the melting temperature, which can be determined from the phase diagram, which is essentially a first road map for the crystal grower. The basis for selection of the heating method is also determined by the following factors: the method of heat transfer (radiation, conduction or convection), the rate of heating or thermal transfer, the degree of uniformity of the temperatures, the shape of the temperature gradients, the precision needed in controlling the temperature, the furnace atmosphere, and

Table 9.1 Some useful properties of common resistance and heating elements

Material and trade name	Maximum operating temperature (°C)	Permissible atmosphere
Kanthal	1250	Oxidizing or reducing
Sintered SiC (Globar)	1600	Oxidizing
MoSi ₂ (Kanthal Super)	1650	Oxidizing
Graphite	2500	Inert or vacuum
Tungsten	3000	Inert or vacuum
Nichrome	1200	Oxidizing or reducing
Platinum	1450	Oxidizing or reducing

the cost of the heating equipment. The variety of heating methods for crystal growth may be categorized mainly in two categories, viz. resistance heating or induction heating. Some useful properties of common resistance heating element materials are listed in Table 9.1. As can be seen, resistance-heated furnaces are normally limited to lower temperature ranges (up to 1600 °C) and can have one of the several types of elements listed in the table. A general advantage of resistance-heated furnaces over other types is their greater electrical efficiency and reduced operational costs.

High-frequency heating is of major importance in crystal growth because a large range of temperatures can be achieved with a reasonably high efficiency of energy transfer and it can be used in a variety of processes. Radiofrequency (RF) induction heating provides the cleanest and most readily available method of heating precious-metal crucibles, although in the interest of economy, resistance heating is sometimes used, especially for lower-melting-point materials. Induction heating normally occurs in a conducting material due to eddy currents induced in the conductor by the electromagnetic field from a high-frequency current-carrying coil (the RF work coil) that surrounds the charge. The useful RF band is typically 100 kHz to 10 MHz, although for relatively large metallic ingots, frequencies in the medium frequency band (0.5–10 kHz) are useful and advantageous. In fact, most of the heat is generated in the skin layer over the coupled flux volume of the conductor. If a nonconducting crucible is required, a graphite susceptor should be utilized, which is heated first and then conducts heat to the charge in the crucible.

This source of heating is generally used for higher-melting oxides such as sapphire (Al₂O₃) and garnets;

however, it can be used for the growth of semiconductor materials. Usually RF generators operate in the above-mentioned frequency range and with a wide power range of 10–100 kW. For general laboratory use, a 10–30 kW RF generator is suitable and provides the capability to grow crystals up to about 30–50 mm in diameter.

9.3.3 Temperature Control Techniques

Thermocouples are routinely used for measuring the temperatures in these systems. There are a large number of thermocouple available including Chromel/Alumel, Pt-Pt10%Rh, and Pt-Pt13%Rh. Junctions between two thermocouples metals are produced by either fusing the two wires in a gas flame or by spot welding. Mechanical and brazed connections can also be used. Nowadays cold junction compensation is available for all types of thermocouples in any temperature measuring thermocouple thermometer. Basically these provide a zero suppression in accordance with the electromotive force (EMF) generated by the cold junction. Some of the most commonly used thermocouples are listed in Table 9.2.

Most conventional temperature controllers, whether analog or microprocessor based, are three-mode proportional–integral–differential (PID) controllers. This means that the control algorithm is based on a proportional gain, an integral action, and a derivative action. The proportional band simply amplifies the error between the set point and the measured value to establish a power level. The term *proportional band* (PB) expresses the gain of the controller as a percentage of the span of the instrument. A 25% PB equates to a gain of 4, whereas a 10% PB corresponds to a gain of 10. Given the case of a controller with a span of 1000 degrees, a PB of 10% defines a control range of 100 degrees around the set point. If the measured value is 25 degrees below the set point, the output level will be 25% heat. The proportional band determines the magnitude of the

Table 9.2 Most commonly used temperature sensors

Type and trade name	Thermocouple/sensor elements	Range (°C)
K	Chromel/Alumel	0–999
J	Iron/Constantan	0–500
R	Pt /13%Rh-Pt	0–1760
S	Pt /10%Rh-Pt	17–1760
B	Pt / 6% Rh-Pt /30%Rh	24–1820
C	W/5%Re-W/26%Re	17–2320
Spot pyrometer	Optical pyrometer	600–3000

response to an error. If the proportional band is too small, meaning high gain, the system oscillates and is overresponsive. A wide proportional band, i.e., low gain, could lead to control *wander* due to a lack of responsiveness. The ideal situation is achieved when the proportional band is as narrow as possible without causing oscillation.

Integral action, or automatic reset, is probably the most important factor governing control at a set point. The integral term slowly shifts the output level as a result of an error between the set point and the measured value. If the measured value is below the set point the integral action will gradually increase the output power level in an attempt to correct this error. Expressed as a time constant, the longer the integral time constant, the more slowly the power level will be shifted (the fewer repeats/min, the slower the response). If the integral term is set to a fast value the power level will be shifted too quickly, thus causing oscillation since the controller is trying to work faster than the load can change. Conversely, an integral time constant which is too long will result in very sluggish control. The derivative action or rate provides a sudden change in output power level as a result of a quick change in measured value. If the measured value drops quickly the derivative term will provide a large change in output level in an attempt to correct the perturbation before it goes too far. Derivative action is probably the most misunderstood of the three. It is also most beneficial in recovering from small perturbations.

An optical pyrometer is another well-accepted noncontact temperature measuring device. Optical pyrometers work for temperatures up to 3000 °C.

9.3.4 Common Crucible Materials

The chemical and physical stability of the crucible in the processing environment are important factors that dictate the selection of the material used to fabricate

it. The design and choice of the material for the crucible are critical. The crucible should not contaminate or stress the crystal. If possible it should have a thermal conductivity similar to that of the charge to ensure that planar isotherm profiles exist in the vicinity of the melting point of the charge, thus ensuring that the crystallizing interface is near planar. For crystal growth of metals, quartz and graphite are most often used. Some of the common materials used to make crucibles are listed in Table 9.3.

9.3.5 Crystal Rotation and Pulling Arrangement

A schematic of the crystal pulling arrangement used in author's laboratory is presented in Fig. 9.2. In this arrangement, circular motion of the motor is converted to linear motion by using a lead screw with a specific pitch. A rotation motor is attached to the cantilever arm. A load cell measures the weight of the growing crystal and also holds the seed rod. A gearbox arrangement is used to adjust the pulling rate, and the rotation rate is adjusted separately using a stepper motor and its controller.

9.3.6 The Czochralski Crystal Growth System

Using the above-described components, automatic diameter control for a CZ system has been designed and fabricated [9.8, 9]. The system consists of an electrical furnace with global heat elements that generates the required temperature gradient, seed rotation and lowering mechanisms, and an Hottinger Baldwin Messtechnik GmbH (HBM) electronic balance/load cell which can measure the weight of a growing crystal to the nearest 0.1 g. The temperature of the furnace goes up to 1500 °C, controlled using a Eurotherm 818 temperature controller. The data for the control thermocouple and from the balance are monitored by a personal computer, which through a central program, written in Visual Basic 6.0/BASIC (described below), sets the temperature controller to the required temperature set point. Two different stepper motors interfaced to a personal computer control the pulling and rotation of seed crystals. A photograph of the CZ crystal growth system used in the authors' laboratory using an induction heating system is shown in Fig. 9.3. Figure 9.4 shows a block diagram of the complete setup of the same Czochralski crystal growth system. An isometric view of a Czochralski crystal puller used in the laboratory at Alabama A&M University is shown in Fig. 9.5.

Table 9.3 Some commonly used crucible materials

Materials	Max. operating temperature (°C)	Melting point (°C)
Platinum	1500	1770
Silica	1550	1700
Alumina	1800	2040
Iridium	2100	2466
Molybdenum	2300	2620
Tungsten	2800	3410 ± 20
Graphite	3000	3652

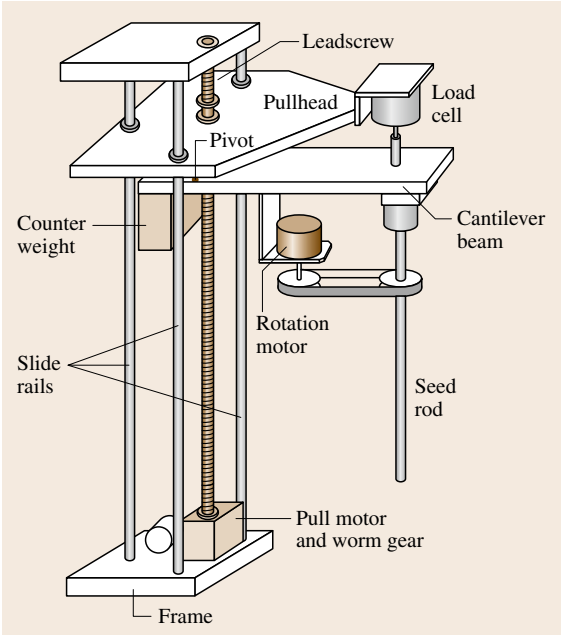


Fig. 9.2 Schematic diagram of the crystal rotation and pulling mechanisms with load cell for weighing the growing crystal

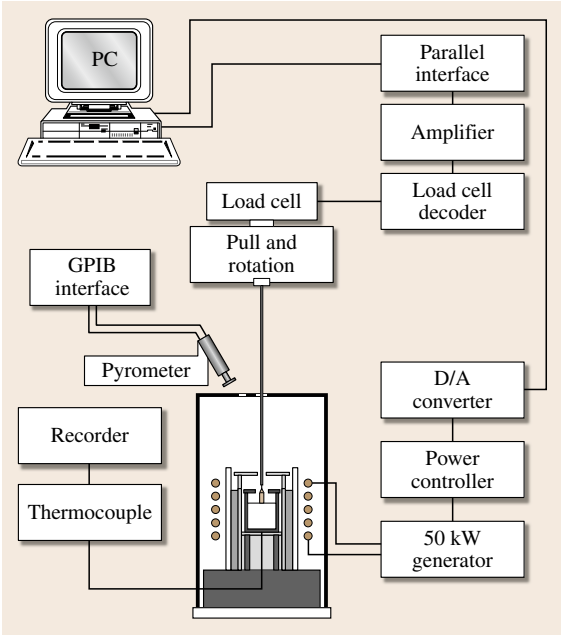


Fig. 9.4 Block diagram of the complete experimental set up for the Czochralski crystal growth technique (GPIB – general purpose interface bus, D/A – digital to analog)



Fig. 9.3 Growth chamber with crystal pulling and rotation system for Czochralski crystal growth

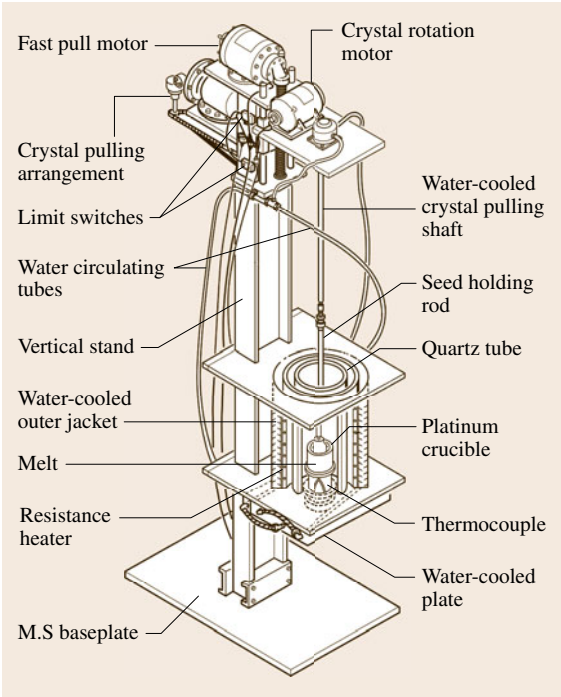


Fig. 9.5 An isometric view of Czochralski crystal puller at Alabama A&M University (M.S – mild steel) ►

9.3.7 Automatic Diameter Control for Czochralski Crystal Growth Technique

In order to reproducibly grow high-quality single crystals the best control techniques need to be considered. In this subsection we will discuss the use of automatic diameter control systems for Czochralski crystal growth from melt [9.9, 10]. Various techniques for automatic diameter control are available, including optical methods (i.e., analysis of a video or x-ray image of the growing crystal) as well as weight monitoring, which consists of weighing the crystal and seed holder, as used in the authors' laboratory in the present system, or by weighing the crucible and its contents. The relative merits of some of these systems are reviewed in the literature [9.7]. Briefly, optical methods depend on the availability of a clear optical path to view the growth interface, which may be difficult to maintain over the time required for growth. Weighing the crucible gives a poorer ratio of signal (weight change per unit time) to total weight than weighing only the crystal and seed holder. In addition, if induction heating is used, the radiofrequency (RF) field exerts a vertical force on the crucible (proportional to the instantaneous power) which must be taken into account to obtain accurate weight change data. To control the crystal growth process and achieve/maintain a specific crystal diameter, a program in Visual Basic 6.0 was designed and developed. The Visual Basic program has near-real-time access to all data, control characteristics, and user-friendly interfaces for user interaction with the software and access to archival data. The algorithm, written in Visual Basic, provides control of the complete crystal profile during seed extension and growth of the crystal to the desired diameter, termination of the growth process, and cooling of the grown crystal to room temperature. The slope of crystal weight over time is used to compute the diameter of crystal. All the parameters required for growth runs need to be optimized for each material, and the desired sizes of crystal are stored in a parameters file. The parameters stored in the file are crystal density, melt density, crucible diameter, seed length, seed diameter, cone angle crystal diameter and growth rate, control loop parameters including proportional–integral–derivative (PID) values for different stages of growth, fitting factors for minimizing noise during data acquisition, and feedback values. The controlled parameter is the power to the furnace through the Eurotherm 818 process controller. In the current application, the weight reading is taken at 6 s intervals but

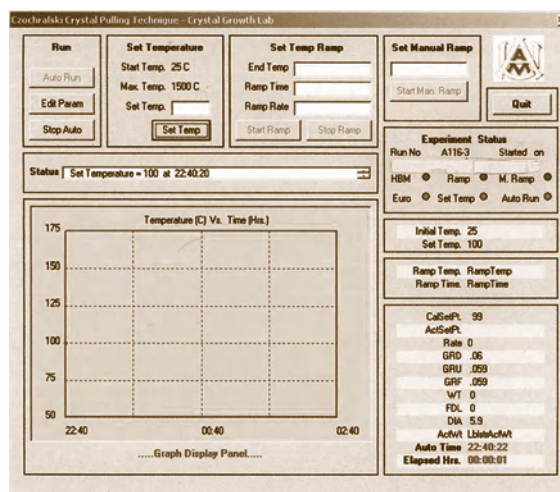


Fig. 9.6 Main parameter screen of the automatic diameter control software written in Visual Basic for the Czochralski crystal growth system

can be varied. At start up, the program asks for a history file name and parameter file to be used. After selecting the desired file corresponding to the crystal to be grown, the user enters the main parameter screen, as shown in Fig. 9.6. The main parameter screen exhibits various choices/command buttons to activate functions such as:

1. Set manual ramp
2. Ramp time
3. Ramp rate
4. End ramp
5. Edit parameter
6. Stop auto
7. Program end
8. Quit

When the *Auto* command button is pressed, it calls a subroutine to read crystal weight, calculates and displays relevant growth parameters, graphically displays temperature versus time, stores data in the history file, and sets the power level based on the calculated parameters.

In this program, one can set the desired growth profile of the crystal in terms of parameters such as seed length, cone profile, and desired crystal diameter. In the auto mode, this automatic diameter control program performs the desired functions and eventually a crystal with uniform diameter is obtained.

For a detailed description of crystal growth from melt, the text by *Hurle* is recommended [9.11].

9.4 Growth of Lithium Niobate Crystals and Its Characteristics

After more than 40 years of research into LiNbO_3 (LN), hundreds of publications have been devoted to this very important material, one of the most important photorefractive (PR) materials ever known, considering the huge number of applications it finds in our daily life.

LN is an excellent material, very attractive due to its nonlinear, electrooptic, piezoelectric, acoustical, and photorefractive properties, high electrooptic coefficient, transparency range, and the availability of large and good-quality single crystals. For these reasons, there are a huge number of applications of LN in a lot of fields such as linear and nonlinear optical devices, acoustooptic modulators, second-harmonic generation, integrated optics applications, and bulk and waveguide optoelectronic devices. In addition, LN occupies an important place in the field of laser materials, since *Johnson and Ballman* [9.12] reported for the first time pulsed stimulated emission by using Nd-doped congruent LN (Nd:CLN) crystals five decades ago.

The two principal topics that have been addressed in the last decade from the point of view of materials preparation can be summarized as the development of large stoichiometric bulk crystals and periodic structures. In the former case, CLN is commercially available, but stoichiometric LN (SLN) is still in its infancy, although there are high expectations for the Asiatic research area [9.13–15]. In the latter case, the interest emerges from LN's applications in electrooptical linear device fabrication.

CLN crystals are commercially grown on large scale by the Czochralski (CZ) method [9.16]. However it has been recognized lately that many properties of SLN crystals appear to be superior to those of CLN. The former shows larger electrooptic and nonlinear effects than those of CLN crystal [9.17, 18]. In addition, the SLN crystal coercive field has been reported to be much lower, approximately one-fifth that of CLN crystal at room temperature [9.19, 20].

Congruent lithium niobate is a very well-known material with congruent melting point and a Li/Nb ratio of about 48.6/51.4 mol %. This means that CLN is Li deficient and that Nb antisites are simultaneously present. Although these intrinsic defects represent a disadvantage of CLN which limits its technical applications, the possibility to fill these vacancies with a large number of dopants has been an extraordinary input for the applications of LN. One could say that the properties of CLN can be tailored with low concentration of a given dopant. A few examples support this statement:

active rare-earth ions allow laser action in the visible–infrared (IR) region; transition metals such as Fe and Mn increase the PR sensitivity; Ti diffusion leads to the fabrication of excellent optical waveguides; and Mg increases the resistance against optical damage. On the other hand, the applications of CLN often normally require monodomain samples, which involves an extra process for poling the initially unpoled material by applying high electric fields. These two key issues, congruency and poling processes, will be of special interest in the following paragraphs.

Stoichiometric or nearly stoichiometric lithium niobate (nSLN) is extremely important compared with CLN for several reasons: low concentration of intrinsic defects, large electrooptic coefficient, shorter absorption edge, lower coercive electric fields required for ferroelectric domain switching, lower optical damage in PR experiments, higher nonlinear optical coefficient, and lower extraordinary refractive index with constant ordinary index. Bearing in mind these properties and the future and attractive applications of SLN crystals, many efforts are being conducted towards research into this important material.

In the last decade, extensive research has been carried out in order to solve the problems related to the preparation of bulk single crystals. Now, at the beginning of the 21st century, the major scientific problems related to the preparation of bulk single crystals have been solved and now it is time for industrial developments. Below, some of the advances reported in the literature in the last decade in the field of the preparation and growth defects of LN crystals are briefly reviewed. However, we would like to remark that it would be impractical to summarize fully the large effort applied by hundreds of researchers worldwide on this topic (see, for example, two of the most recent books devoted to this material [9.1, 2]).

9.4.1 Crystal Growth of Lithium Niobate

Considering the phase diagram [9.10] and the physical and chemical properties of LN, the conventional Czochralski (CZ) growth method is practically the only way for growing bulk single crystals, and there are no significant publications related to its growth by other methods. The phase diagram is illustrated in Fig. 9.7.

The experimental conditions of the CZ method for growth of LN are well established and can be summarized as follows:

1. There are a large number of authors who use the oxide Nb_2O_5 and the lithium carbonate Li_2CO_3 as starting materials. In this case it is necessary to carry out a two-step sintering process: (1) heating at $700\text{--}850^\circ\text{C}$ for 2–12 h according to the temperature used for drying and calcination of carbonate, and (2) heating at around 1150°C for 2–4 h for sintering, followed by a grinding process at room temperature (RT) [9.21–27]. However, this process can be avoided using commercial LN of the highest chemical grade, which enables the growth of LN crystals with excellent physical properties. The same statements hold for growing other niobates or tantalates [9.27].
2. The standard growth parameters can be summarized as follows [9.23, 26, 28–34]: for CLN a pulling rate of 2–4 mm/h, with a rotation rate of 30–40 rpm, with axial temperature gradients in the solid–liquid interface (SLI) close to 10 K/cm. This value is easily attainable in resistance furnaces. However, active or passive afterheaters are recommended to be used with induction heaters. The growth process is generally terminated by a cooling process with cooling rates in the range 20–30 K/h followed by a fast cooling to RT. However some authors use an annealed step at 1000°C for 24 h to remove strains [9.30].

For SLN the pulling rate must be decreased to a value between 0.2 and 1 mm/h while the rotation

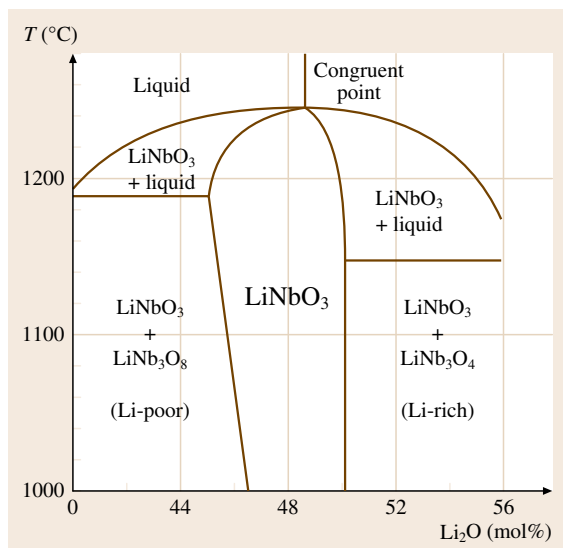


Fig. 9.7 Phase diagram of the $\text{Li}_2\text{O}-\text{Nb}_2\text{O}_5$ system for growing lithium niobate crystals

rate is in the range of 5–15 rpm. The axial temperature gradient is kept at relatively lower values compared with for CLN, while the cooling rates employed are generally the same as for CLN. As an example, Fig. 9.8 shows a schematic diagram and a picture of standard CZ equipment currently used for growing bulk LN crystals [9.35, 36]. It is also

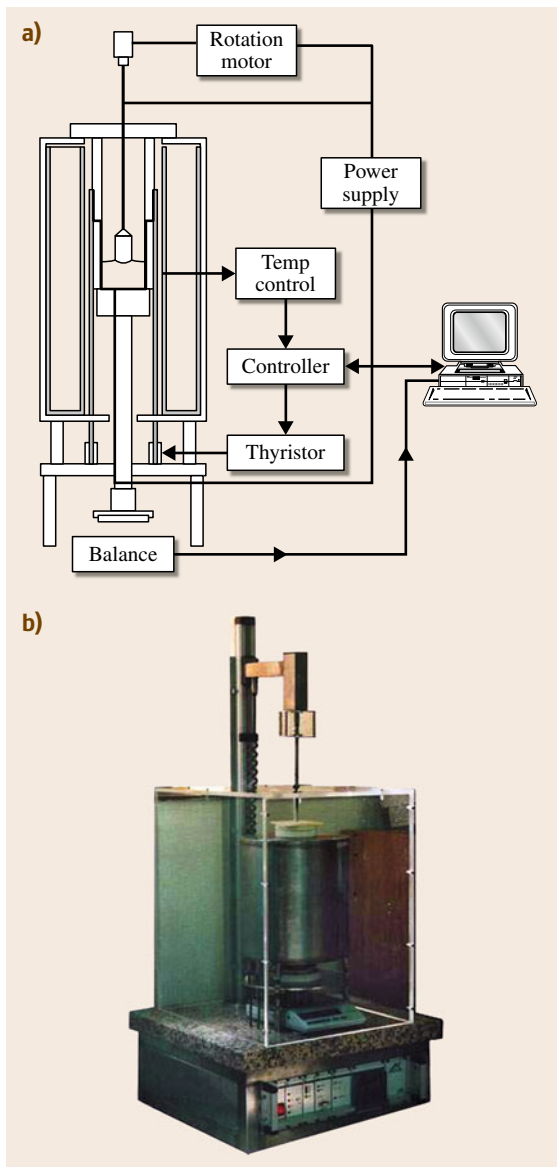


Fig. 9.8 (a) Schematic diagram and (b) conventional Czochralski crystal growth equipment with diameter control system

important to have excellent diameter control to obtain high-quality crystals. Figure 9.9 shows a CLN crystal grown by using a system like that shown in Fig. 9.8b.

3. However, the growth of bulk SLN crystals by the conventional CZ method is difficult and requires special conditions and/or technology, which are summarized in the following paragraphs.

Off-stoichiometric melts can be used with excess Li_2O in the growth process with a Li/Nb molar ratio of 1.38–1.41 [9.23–26, 30]. The yield of SLN obtained by using this process is about 10%. In this case a compositional inhomogeneity along the ingot is found, with a Li concentration difference from top to bottom in the range of 0.3–4 mol %. This inhomogeneity along the growth axis represents a great disadvantage of the off-stoichiometric melt growth process. This compositional variation increases as the Li_2O concentration in the melt increases with time.

SLN bulk crystals generally have a single-domain structure. However when an unpoled CLN seed is used in an stoichiometric melt growth, there is a diffusion of Li at high temperature from the stoichiometric melt to the CLN seed, giving rise to a compositional gradient along the length of the seed. This phenomenon induces a space-charge electric field, which in turn leads to the seed self-poling [9.37].

SLN crystals can also be successfully grown without any further experimental modification in the standard CZ technology by using K_2O -rich CLN melts. This can be considered as a mixture of oxides K_2O - Li_2O - NbO_5 where the ratio of Li/Nb is the same as that used for SLN melts [9.31, 32].

The derivative of the mass variation versus time obtained during the growth of this crystal is also shown in Fig. 9.9.

A concentration in the range 6–8 wt % of K_2O is necessary to obtain SLN crystals; other alkali oxides such as Na_2O , Rb_2O , and Cs_2O can also be used in lower concentrations, but in this case it is more difficult to obtain high-quality SLN [9.24]. The experimental conditions to be used in a K_2O -rich CLN melt growth of SLN crystals are the standard ones normally used in the CZ method. However, the rotation and pulling rates have to be low due to the higher viscosity of the melt, with values in the ranges 8–10 rpm and 0.1–0.3 m/h, respectively. The benefits of K_2O in growing SLN are related to the fact that K ions provide a similar chemical environment to that of Li ions.

It has also been proven that K is not incorporated into the crystal, while other alkali ions such as Cs and Na are entrapped in microinclusions [9.24]. Another advantage of K_2O is the lowering of the crystallization temperature close to 20°C . As a rule, all SLN crystals obtained from K_2O -rich melts have monodomain nature, with the advantage that, when using unpoled CLN seeds, they will be self-poled during the experiment [9.38].

The use of a double crucible in the CZ (DCCZ) method has proved to be an efficient approach for growing SLN, as described in [9.13, 27, 39] and references therein. The experimental setup of DCCZ is based on the use of a double crucible and/or a powder supply control in an extra upper crucible: although the experimental conditions are very strict and are generally difficult to attain in any standard crystal growth laboratory, crystals of up to 7.5–10 cm can be grown. Other benefits of this method include a constant surface melt level, which has two important consequences: constant convection throughout the growth process, and a fully stoichiometric crystal as a result of the composition adjustment of the melt supplied by the extra upper crucible. The DCCZ method is also very efficient for obtaining homogeneously doped CLN and SLN bulk crystals. Another recently developed, modified version of the double-crucible method is described in the following subsection.

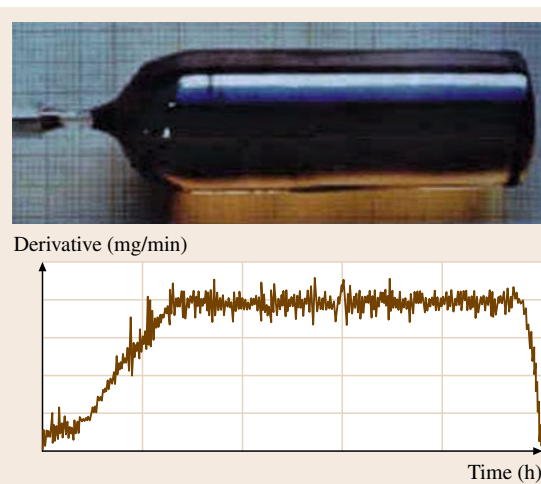


Fig. 9.9 Congruent lithium niobate crystal grown using the system shown in Fig. 9.8 and the derivative of mass variation with time

9.4.2 Mold-Pushing Melt-Supply Double-Crucible Czochralski Apparatus

The double-crucible Czochralski (DCCZ) growth apparatus consisted of three parts: the double crucible, the continuous supply system, and the Czochralski growth system. The double crucible consists of a growth crucible and a melt-supplying crucible. The two crucibles are connected by some holes. The continuous supply system consists of a mold made of Pt, which is placed in the melt-supply crucible, and a lowering mechanism. When pulling the crystal, the mold is lowered to push the melt from the melt-supply crucible into the growth crucible. The lowering rate of the mold is controlled independently by the lowering mechanism; the rate is controllable and can be adjusted in real time according to the rate of change of the crystal weight. A schematic drawing of the growth apparatus is shown in Fig. 9.10. The diameter of the as-grown crystal is controlled by an automatic weighing system, which controls the heating power. The composition of the as-grown crystal is influenced by the area ratio of the cross section of the crystal to that of the mold, the compositions of the melts in the two crucibles, and the velocity ratio of crystal pulling to mold lowering. Compared with the common DCCZ method, this technique avoids the problems related to the powder supply, inconsistency of melt composition, complexity, and the high price of the growth device. Researchers into this approach called it the mold-pushing melt-supplying (MPMS) technique [9.40].

Growth of near-stoichiometric LiNbO_3 crystals was illustrated by the authors [9.40].

In this work, the purity of the raw materials (Li_2CO_3 and Nb_2O_5) was 99.99%. The Li_2O content of the melt in the growth crucible was set to be 58 mol %, whereas in the melt supply crucible it was 50 mol %. The diameter of the as-grown crystal was kept unchanged throughout the whole run, while the rate of lowering was set to be equal to that of crystal pulling. The c -axis seed crystal was rotated at 5–15 rpm and both the pulling rate of the crystal and the lowering rate of the mold were 0.5–1.0 mm/h. The melt height in the growth crucible was kept unchanged during the whole process of crystal growth by controlling the melt supply from the melt-supply crucible. The diameter of the as-grown crystal was about 43 mm. The height of the crystal was 45 mm. The crystal was clear, without inclusions, free of cracks, and light yellow in color.

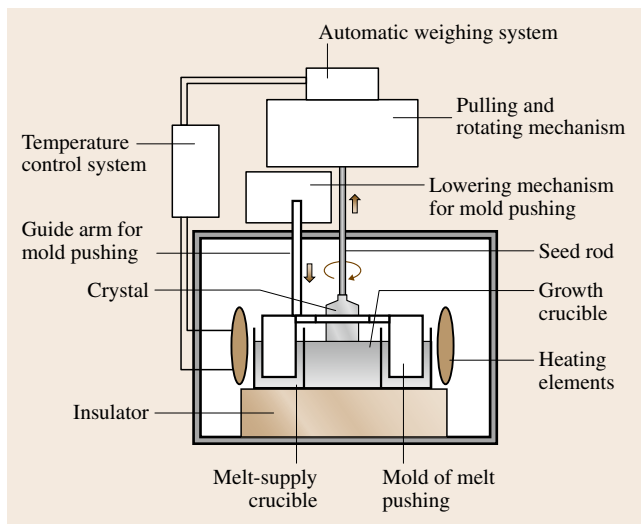


Fig. 9.10 Schematic diagram of mold pushing melt supply using DC Czochralski crystal growth system

9.4.3 Congruent Lithium Niobate Crystal Growth by Automatic Diameter Control Method

The apparatus described in Sect. 9.3.7 has been used for growing lithium niobate crystals [9.7–10]. A platinum crucible is filled with 300 g LN powder (purchased from Johnson Matthey, grade 99.9999% purity). The system is heated from room temperature to a temperature above

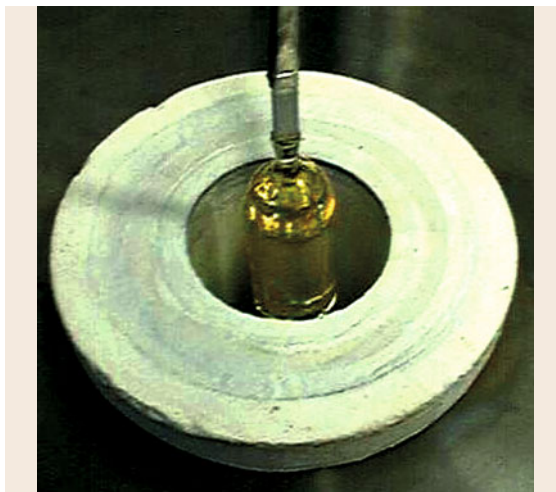


Fig. 9.11 A lithium niobate single crystal pulled from a Czochralski crystal growth system after cooling to room temperature



Fig. 9.12 A lithium niobate single crystal after necking of the seed crystal

1260 °C during a 24 h period using ramping mode. After this, the temperature is increased at a rate of 2 K every 30 min until all the charge is molten (complete molten state is in the vicinity of 1260 °C). A 5 mm-diameter seed oriented in the $\langle 001 \rangle$ direction is dipped into the melt. At this stage, the weight of the dipped seed is monitored so that the seed does not melt, and after 2–3 h of equilibration it is slowly pulled at a rate of 2 mm/h. The



Fig. 9.13 A number of pure and doped lithium niobate crystals grown at Alabama A&M University

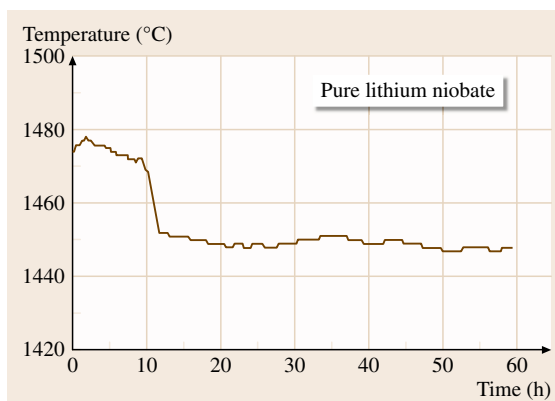


Fig. 9.14 Growth temperature versus time profile of the growth of lithium niobate crystal

rotation of the seed is kept at around 20 rpm. At this time the necking process begins. When the seed crystal starts to grow initially, the system is put into *Auto* mode by pressing the *Auto Run* button. After the crystal has grown to the desired size, and the crystal is withdrawn from the melt, the auto mode is stopped and the cool-down ramp is started to bring it to room temperature in 48 h. Figure 9.11 shows a grown crystal of LN being pulled out of the furnace after growth. Figure 9.12 shows a photograph of another LN single crystal along with the seed that, grown in the authors' laboratory. Figure 9.13 shows a photograph of pure and doped lithium niobate crystals.

From the history file, the growth data are analyzed, and the relevant parameters are plotted and presented

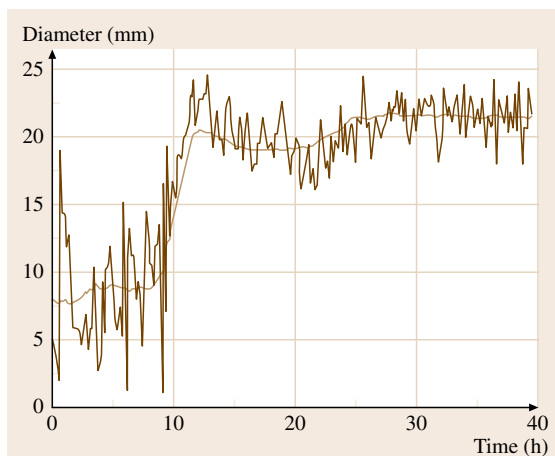


Fig. 9.15 Full diameter growth profile of lithium niobate crystal

in Figs. 9.14 and 9.15. After an initial adjustment, the power (temperature) rose during the 6 h period of growth at the diameter of the seed and then ramped down to allow the crystal to grow to its final desired diameter. The remainder of the growth shows an increase in power (temperature) due to increasing heat loss from the crystal surface. As the temperature fluctuates the automatic diameter program kicks in and controls the heat flow so that the curve of crystal diameter versus time (Fig. 9.15) is almost uniform. The irregularities in the curve represent the processing time during which the software calculates the diameter of the crystal.

9.4.4 Poling of Lithium Niobate

LN is a ferroelectric material at RT with a Curie temperature of around 1210 °C. In normal growth conditions, bulk CLN crystal has multidomain nature, while bulk SLN crystals have monodomain structure when any poling process is used. The top zone is a +Z surface while the bottom one corresponds to a -Z surface [9.30]. The origin of the internal field is related to nonstoichiometric point defects, such as lithium vacancies and niobium antisites, where hydrogen itself does not seem to play an active role [9.41]. When an external field reverses the polarization direction, the internal field tends to realign parallel to the new polarization direction with increasing temperature.

LN-based devices normally require monodomain crystals in order to eliminate undesirable multiplicity of ferroelectric domains. In order to produce poled LN crystals several techniques have been developed for use either during or after the growth process of bulk crystals. Let us summarize the most recent published results on this topic:

1. By far the most well-established poling technique is that based on the use of an external electric field applied to samples obtained from a bulk CLN ingot. For CLN, electric fields greater than the coercive field of 21 kV/mm are applied by using an appropriated mask with conductive electrodes. The process is carried out under controlled temperature of the order of 200 °C, followed by thermal annealing, and cooling of the sample while maintaining the electric field [9.25, 41–43]. The electrodes are based on a saturated aqueous solution of salts such as LiCl or KNO₃, with well-defined silicone rings. The poling process can be monitored in several ways, such as by measuring the charge delivered to the crystal,

controlling the poling current under different experimental conditions, and analyzing the switching times, domain stabilization, back-switching phenomenon, etc. [9.43]. These results are important for the design of effective recipes which can be very useful for the fabrication of more complicated domain structures. In all these applications the nature of the LN plays a key role because the switching electric field dramatically decreases with increasing Li content, in such a way that for SLN this electric field has a zero value, according to its monodomain nature [9.42].

2. The poling process in CLN crystals can be carried out in situ during the growth experiment by applying current densities in the range 1–3 mA/cm² across the growing crystal. In these experiments the seed holder acts as the negative electrode and the bottom of the Pt crucible as the positive one [9.25, 42]. The current density value is reduced when the Li concentration increases during the growth experiment, being one order of magnitude lower in quasi-SLN crystals. Moreover, small current densities help to reduce any possible problems related with the melt electrolysis and/or seed decomposition, which result in catastrophic consequences for the crystal growth. The constant current density induces a transient voltage due to the domain polarization which follows an experimental law, with a profile similar to the external shape of the crystal, which can be related to the microscopic domain polarization [9.44]. As a consequence this method can be used for growing bulk monodomain CLN single crystals along the full length of the crystal.
3. A similar approach is the poling of the whole crystal after the growth process in the same experimental CZ equipment, at temperatures close to the melting point when the remaining melt is solidified [9.22]. This process gives good results, although the use of an appropriate ratio between the applied electric field and the switching time is essential in order to prevent formation of new defects due to the high ionic conductivity at high temperature.
4. Patterned domains can also be prepared by using special techniques, for example, electron-beam writing and pulsed laser at given wavelengths below and close to the absorption edge [9.18, 45]. Both techniques have the advantage of creating ferroelectric surface domains with micro- and nanoscale dimensions, which can be analyzed in situ with appropriate microscopy facilities.

9.4.5 Periodically Poled Lithium Niobate Structures

In the last decade extensive research has been devoted to periodic LN structures. A variety of potential and promising applications have been found based on both periodic and aperiodic poled LN (PPLN and APPLN) and opposite domain LN (ODLN). Periodic structures considered as the organization of domains in a given way can be successfully applied to the fabrication of optoelectronic devices. Other structures such as ODLN, in which the polarization vector is aligned head to head and tail to tail, can be used in acoustic devices [9.46].

PPLN are structures where the polarization vector point is antiparallel, showing exceptional properties that are extremely useful for fabrication of electrooptic devices such as those conceived for the generation of light in the low-wavelength region through the quasi-phase-matched second-harmonic generation process (QPM SHG).

Although both structures, PPLN and ODLN, have extraordinary importance, we will focus our attention on PPLN structures considering the huge number of applications and possibilities for the future development of superior nonlinear optical media.

It is well known that birefringent phase-matching frequency requires single-domain crystals, while periodic-domain structures show the effect of QPM frequency conversion. These periodic modulations of the sign of the nonlinear coefficient can be obtained in ferroelectric crystals by periodically alternating the sign of the electric field of their ferroelectric domains. The benefits of PPLN structures over single-domain LN can be summarized as follows:

1. The highest value of the component of the second-order nonlinear tensor in the QPM wave-mixing process involved.
2. The reduction of photorefractive (PR) damage without the need for codoping of crystals with elements such as Mg as is the case for LN. Moreover, this SHG capability combined with LN's properties for hosting laser ions allows the development of optoelectronic devices such as self-frequency-doubling lasers, simultaneous multi-self-frequencies, and many other possibilities. Therefore, considering that the fabrication of new important devices requires microengineering of the domain structures, the first prerequisite is the manufacture of PPLN structures with controlled domain thickness.

The fabrication of PPLN structures can be performed sample by sample or just in the bulk crystal. In the former case, the most well-known and efficient technique for the preparation of these structures is the patterning of the surface by using standard optical lithography and suitable photoresist masks followed by the application of an external electric field [9.27, 47]. There are intrinsic drawbacks associated with this process: the high electric fields needed for inverting domains; domain widening due to intrinsic difficulties during the preparation of regular gratings with thickness of several μm ; preprocessing of the sample in order to prevent it from breaking; limitations in the preparation of low-period structures; problems associated with the inverted domain depth; flip-back effects in which reversed domains can revert to their original orientation when the poling field is dropped to zero; control of the poling pulse length, which must be large enough to prevent flip-back; the presence of a leakage current superimposed on the poling current; post-bake and cooling processes needed to suppress the pyroelectrically induced surface charge on the crystal surface; the thermal history of the sample prior the poling process; etc.. In spite of these problems associated with the preparation of PPLN structures by the application of an external electric field, this is the most widely used method due to the possibility of defining standard conditions to be applied in a fixed way.

A more sophisticated process for PPLN fabrication is the engineering of microdomains by applying a voltage between the tip and back electrodes in a high voltage atomic force microscope (AFM) [9.48]. The evolution of the domain generation process is similar to that of the conventional approach based on the application of an electric field. However in this AFM-based technique the nucleation begins near the charged tip working as an active nucleus center for domain formation. This process has been successfully applied to LN and TaLiO₃ structures using thick single-crystal samples.

Another interesting method for preparation of PPLN structures is off-centered CZ, which enables generation of periodic domains during the crystal growth process without applying any external electric field [9.49–52]. In this case, the formation of domain structures is related to the ratio between the rotation and pulling rates in a CZ system where the seed holder is displaced from the central symmetry axis of the furnace. Furthermore, when this ratio between the rotation and pulling rates changes during a growth process, aperiodic domains (APPLN) are formed. The off-centered CZ method is

based on the interplay between the forced convection existing in the melt and an appropriate ratio of rotation and pulling rates. Nevertheless one must also consider the effect of the **SLI**, which affects the formation of **PPLN** structure [9.53]. Furthermore, it is necessary to perform a quenching process after finishing the **PPLN** preparation, as slow cooling rates destroy the **PPLN** structures. Two advantages of this method can be mentioned. First the preparation of a large volume of **PPLN** structures, and second the ability to engineer **PPLN**-doped simultaneously with rare active laser ions and/or codoped with other interesting impurities such as Mg.

An issue which has been a matter of controversy is the domain composition in **PPLN** structures. It seems already well established that the positive domains contain higher Li concentration compared with the negative ones, which are Nb rich. In addition, the dopant concentration remains constant along the positive and negative domains, as has been proven for Nd, Er, and Y [9.54]. The influence of diffusion processes on ferroelectric domains has also been analyzed. For example the diffusion of fluorine ions along the positive domains has been ascertained by using secondary-ion mass spectrometry (**SIMS**) after a **HF** etching process [9.55]. Different etching rates between positive and negative domains have also been observed. This behavior can be understood by considering that Li outdiffusion occurs during the formation of periodic structures. This process, in turn, favors fluorine indiffusion preferentially in the positive domains, which are associated with positive charge regions as a consequence of Li outdiffusion.

Rare-earth (**RE**)-doped **PPLN** structures have additional physical properties which are advantageous for optical processes such as self-frequency doubling and self-frequency addition, as they combine nonlinear processes with host crystals containing **RE** elements [9.47, 51, 54, 56–58]. The possibility to fabricate **PPLN**-based optical devices has been proven in Er-, Nd-, and Yb-doped and Mg:Zn codoped **PPLNs**, the later two dopants being used in order to fully reduce the **PR** damage and obtain stable laser action at **RT**. However, it is also necessary to consider some drawbacks, such as the maximum limit in **RE** concentration which can be reached in the **PPLN** structures. This is the case of Er:**PPLN**, with a segregation coefficient of 1.2, where it is possible to create **PPLN** structures in the range of 0.5–1 mol %. However for lower Er concentration values irregular structures are obtained, while for concentrations higher than 1 mol %, disordered structures and clusters are formed. Similar behavior has been observed in Hf-doped **PPLN** structures, where the concentra-

tion induces polydomain structures for values higher than 0.5 mol %, or inhomogeneous structures for values lower than 0.25 mol %. This can be explained according to the Hf location in the **LN** lattice as has been previously described [9.53, and references therein]. It can be concluded that the behavior of Hf in **PPLN** structures can be considered as an exceptional case which induces a periodic modulation in Nb and Hf concentration as a function of the initial Hf concentration [9.53].

A critical issue in **PPLN** structures arises from the difficulty in visualizing them nondestructively using general techniques such as optical microscopy and low-voltage scanning electron microscopy. Nevertheless, there are other approaches which can also be used for this purpose [9.59]:

1. Considering the bulk of periodic structures as a volume diffraction grating, the use of a laser beam on a periodic structure supplies information about spatial frequency and orientation. In addition, the diffraction efficiency gives information about the magnitude of the periodic changes, where the number of diffracted spots and the spot size is the result of the properties of the domain. Light diffraction from periodic domains can be understood assuming that the refractive index changes at regions close to the domain walls, where the accumulated charge at the domain edges is probably due to the alternating Li/Nb ratio giving rise to a periodic change in the dielectric constant and hence in the refractive index of the sample.
2. Scanning force microscopy (**SFM**) has the advantage of simultaneous correlation of topographic and electrostatic images. Negative domains exhibit greater hardness, and positive ones show stronger attractive forces in the electrostatic image. Therefore, the etching rate in negative domains is faster than in positive ones. The contrast shown by the electrostatic images is explained according to the difference in the dielectric polarization, probably due to different Li/Nb ratio between the domains.

RE-doped **PPLN** and **APPLN** structures are promising materials for the development of optical devices based on nonlinear optical frequency conversion and the generation of visible laser radiation from efficient lasers operating in the near infrared. Some interesting examples of these kind of optical applications are: laser-diode pumped **PPLN**:Yb,Mg microchip laser sources; self-frequency mixing in **APPLN**:Nd [9.60]; multi-self-frequency conversion in **APPLN**:Nd [9.57], etc.

9.4.6 Doped Lithium Niobate Crystals

The main motivation for doping crystals of inorganic materials is for study of the nature of the different compounds. Fundamental questions appear in the chemistry of solids regarding the behavior of dopants during crystal growth, the charge state of these dopants, and the positions they occupy in the crystalline lattice. The modification of various physical and chemical crystal properties is also another powerful motivation for doping.

Er, Pr, Yb [9.61–66], Nd, Fe, Zn, Mg [9.67, 68], Zn [9.69, 70] In [9.71, 72], and Sc [9.73] can be considered as the most widely used dopants in LN. Most of them (Mg, Fe, Zn, In, Sc, etc.) have been studied as they are considered optical-damage-resistant elements and therefore would offer the best solution for the optical damage which severely limits the holographic storage, one of the most important applications of LN. In particular Nd is of primary importance due to its applications in laser technology. However, one of the main problems associated with LN-based continuous-wave (CW) laser oscillation technology is the difficulty in achieving this effect in these crystals (Nd:CLN). This is due to the high photorefractive damage (optical damage) which induces severe changes in the birefringence when the laser intensity is high [9.74–76]. However, it was soon recognized that this difficulty could be easily overcome by codoping Nd:CLN crystals with Mg (Nd:Mg:CLN), which successfully enables laser oscillation [9.77]. In addition an increased thermal conductivity has been reported in this material, which is advantageous even if other laser properties are almost the same.

Many studies have been devoted to the study of Nd segregation in LN crystals [9.78], through which the Nd effective distribution coefficient k_{eff} has been calculated to be 0.12. However, at relatively low Nd concentrations, Nd-doped LN normally exhibits a uniform Nd concentration along the pulling direction, enabling the growth of high-quality Nd-doped LN crystals. However the growth difficulties increase for highly Nd-doped Nd:Mg:SLN crystals.

Regarding Mg-doped LN, chemical analysis has been developed and the k_{eff} value reported for Mg in Nd:Mg:SLN crystal is 1. In addition, this value does not seem to be altered when codoping with Nd.

Some other studies have also been conducted in order to establish if CLN and SLN require the same amount of Mg in order to reduce, to the same level, the photorefractive damage. It has been demonstrated that, while 5 mol % Mg is needed [9.79] in CLN, only

1 mol % Mg is enough in SLN crystals grown from Li-rich solutions (Li-58 mol % self-flux) in order to obtain the same photorefractive damage suppression effect [9.80,81]. Lower required Mg dopant concentration has been reported for different growth methods. For example, in SLN crystal grown from $\text{K}_2\text{O-Li}_2\text{O-Nb}_2\text{O}_3$ flux [9.82], 0.2 mol % Mg is already enough to suppress the photorefractive damage. Therefore, it can be stated that Mg-doped SLN (Mg:SLN) crystals offer a great deal of advantages over congruent crystals as the difficulty to obtain high-quality crystals increases when increasing Mg doping concentration.

Doping of LN aimed at the drastic reduction of optical damage results in a secondary effect affecting the photoconductivity. This optical property drastically increases for dopant concentrations exceeding a certain threshold value [9.83]. Some recent works devoted to study of the increasing photoconductivity in LN established a relationship between this effect and a reduced Fe^{3+} electron trapping cross section which, in turn, is related to the substitutional site occupied by the Fe^{3+} ions [9.84]. In fact, laser-induced refractive index variations have been correlated to the Fe site in the LN lattice [9.85]. Extensive research has recently been conducted on these lines regarding Fe dopant in LN. For example, Zhen et al. [9.86] studied Zn:Fe:LiNbO₃ with different ZnO concentrations and several Li/Nb ratios, concluding that the optical damage increased for certain ZnO concentrations above a threshold value.

Further research devoted to the reduction of the optical damage in high-power laser applications has recently been reported [9.87]. As previously stated, due to the lower intrinsic defects in SLN, a smaller amount of MgO is enough to enhance the photorefractive damage threshold up to 2 MW/cm² [9.82]. However this is not the only type of optical damage which can be found in LN. There is another kind of damage, the so-called dark trace, which still appears in MgO-doped LN crystals. Dark trace occurs when illuminating LN with a high-power laser beam, thus limiting the potential use of this material in high-power applications. ZnO doping in LN has been reported as the solution to this problem, demonstrating the effective removal of the dark trace [9.70,87]. These authors reported that ZnO doping of SLN could increase the optical resistance to the same level reported for CLN with 4–6 mol % ZnO doping (120 MW/cm²).

Laser and holographic image recording applications have deeply motivated extensive research into Pr-doped LN [9.82–87]. However the crystal emission mechanisms of this important material are still not well

understood. In the past the quenching of the $3P_0$ population was associated with multiphonon processes. Only very recently [9.88] have other mechanisms, including exciton trapping to Pr^{3+} ions, been proposed.

Ti has also been used as a dopant in LN waveguides in order to reduce one of the well-known intrinsic drawbacks of LN when applied to the fabrication of optical modulators: the so-called direct-current (DC) drift [9.89–92]. This effect consists of the time variation of the bias voltage in an optical modulator. DC-drift characteristics are normally measured by the detection of the optical modulator output intensity. Polarization-induced space charge and ion migrations are the two driving forces inducing DC drift. The dielectric nature of LN induces electrical relaxation related to this effect. Two approaches have been used in order to reduce this effect: the first one consists of using a buffer layer over the LN waveguide; the second is mainly related to the proton impurities reduction in the LN wafer [9.93–98].

9.4.7 Relevant Properties and Characteristics

Thermal conductivity is one of the most important parameters for laser materials. High values of this physical property are desirable for laser applications. There are various methods available to determine the parameters involved in the mathematical expression for thermal conductivity, i.e., the thermal diffusivity and specific heat. Amongst these, the laser-flash method [9.97] is currently used for measuring thermal diffusivity while differential scanning calorimetry (DSC) is normally used for measuring specific heat. Thermal conductivity of LN crystals is sensitive to nonstoichiometric defects (Nb antisites). In particular, for Nd:Mg:SLN crystals it was found to be about 1.3 times as large as that of the Nd,Mg codoped congruent LN (Nd:Mg:CLN) [9.78]. These authors showed that, while density and specific heat were almost insensitive to nonstoichiometric defects (Nb antisites) and dopants, the thermal conductivity strongly depends on these two parameters.

Elastic properties have also been extensively studied in LN crystals. New methods have recently been introduced to improve the accuracy compared with early data about the elastic constants of this crystal. As an example, we can mention the work carried out by Hasse et al. [9.79], who used a novel method consisting of laser Doppler acoustic spectroscopy in order to obtain the 16 independent piezoelectric coefficients, the elastic constants, and the anelastic coefficients of LN single crystals.

Regarding the optical properties of LN, many studies have been carried out in order to ascertain the absorption and emission spectra of pure and doped lithium niobate crystals. Among these we can mention, as an example, the optical absorption and emission spectra obtained from Nd:Mg:SLN crystals which have been analyzed and compared with those of Nd:Mg:CLN crystals. The two spectra were found to be very similar to one another [9.99].

Another important measurement which is often developed in LN crystals is analysis of the OH^- absorption band, whose peak position is generally determined in order to estimate whether the resistance to photorefractive damage in a crystal is weak or not. Fourier-transform infrared (FTIR) spectroscopy is commonly used to obtain the OH^- absorption peak. In the case of Mg:CLN crystals with photorefractive damage the OH^- band peak is located at $2.87\ \mu m$. On the other hand, in the case of Mg-doped crystals without damage, it is located at $2.83\ \mu m$ [9.100, 101].

Photorefractivity is another advantageous physical property exhibited by LN crystals. This effect has been related to the hole polaron bound to Li vacancies and to three further, electronic polaronic structures, namely the free Nb_{Nb}^{5+} small (to intermediate) polaron, the Nb_{Li}^{4+} electron bound to the antisite defect, and the $Nb_{Li}^{4+}-Nb_{Nb}^{4+}$ bipolaron [9.98, 102].

Photorefractive properties in LN allow refractive index variations which can be electrooptically induced, in turn, by ionic distribution variations. These phenomena can all be used in order to permanently fix volume phase holograms recorded in LN for a long period of time, by using, for example, thermal fixing [9.103–107]. The use of the PR properties of LN for hologram thermal fixing involves three main stages. First the sample is submitted to a short heating process (a few minutes) at temperatures in the range of $120-160^\circ C$ in order to accommodate the holograms. During this process, ion migration effectively screens the initially recorded space-charge distribution. In a second stage, the ions are frozen in their new lattice positions by cooling the sample at room temperature. In the last stage, the charge distribution has to be developed by uniform illumination of the sample. Therefore fixed volume holograms can be contained by electrooptically induced variations of the refractive index generated by the above-mentioned charge distributions. Holograms lifetimes as long as 540 years have been reported recently in Fe-doped (0.1 mol %):Mg codoped (5.5 mol %) LN crystals.

The electrical conductivity of LN has also been studied for many years. It is well known that this phys-

ical property can be enhanced for concentrations of divalent ions above a certain threshold (4.5 mol %). Some researchers attributed this electrical conductivity enhancement to faster recovery or complete removal of optical damage [9.103]. Photoconductivity measurements have been developed in Cr-doped and Mg-codoped LN crystals [9.108]. In this case, the photocurrent has been explained by considering two main involved physical processes, namely, Cr^{3+}

ionization and generation of $\text{Nb}_{\text{Nb}}^{4+}$ small polarons acting as charge carriers. These experiments also showed that there exists a threshold temperature (140 K) below which photoconductivity is suppressed.

Other LN physical properties have also been shown to be strongly affected by the presence of divalent ions, such as changes in the lattice constants, and variations in the refractive indexes and in the location of the absorption edge [9.109–113].

9.5 Other Oxide Photorefractive Crystals

The list of other oxide photorefractive (PR) crystals [9.1] can be organized into two groups: pure niobates (KNbO_3 , KN), tantalates (LiTaO_3 , LTA; KTaO_3 , KTA), and titanates (BaTiO_3 , BTi), and their mixture compounds, e.g., niobates ($\text{Sr}_x\text{Ba}_{1-x}\text{Nb}_2\text{O}_6$, SBN), titanates ($\text{Ba}_{1-x}\text{Ca}_x\text{TiO}_3$, BCTi), and tantalates ($\text{KTa}_{1-x}\text{Nb}_x\text{O}_3$, KTA_N); and in the second group other PR oxides such as tellurites (Bi_2TeO_5) and germanates ($\text{Pb}_5\text{Ge}_3\text{O}_{11}$), although the importance of the former group is very well recognized due the huge number of established applications. Considering the impossibility of ordering these PR oxides according to importance, we include just a few words concerning the topics that have received the concentrated attention of researchers worldwide over the last decade.

The importance of LTA is well recognized due to their pyroelectric, piezoelectric, and optical properties. Just some brief comments about these applications:

1. Due to the unusually high electric field induced by external thermal gradients, large crystals up to 1 cm^3 have been used recently in order to induce nuclear fusion [9.114]. LTA offers the possibility to fabricate small, compact nuclear-fusion devices by using a small single crystal located in a chamber filled with deuterium gas, where a small furnace is used in order to supply heat to the crystal, creating a huge potential difference due to the pyroelectric effect. In turn, this potential is effectively used in order to accelerate the deuterium ions against a deuterated target, enabling the delivery of neutrons by nuclear fusion.
2. LTA crystals are also important for other applications such as multiplexing, demultiplexing, ultrafast optical amplifiers, and waveguide lasers [9.115–117]. However, LTA crystals are far less widespread despite the much higher optical damage threshold of LTA crystals compared with LN. Very recent

works have been devoted to exploiting the PR properties of LTA crystals for optical waveguides fabrication [9.118]. In another field, poled LTA crystals have also recently been investigated due to their potential applications in optically integrated devices [9.114].

3. Like LN, LTA crystals also show an extremely large piezoelectric effect [9.119, 120]. These physical property together with its optical nonlinearity offer great potential for fabricating sensors, transducers, actuators, etc. In particular, for acoustic applications, large piezoelectric constants and electromechanical coupling factors are required. Several recent works have been devoted to ascertaining how to improve and enhance these parameters [9.19, 121, 122].

On the other hand, SBN crystals show ferroelectricity with Curie temperatures of between 320 and 470 K for $0.25 < x < 0.73$. The ferroelectric properties of SBN critically affect their application in optical storage and light-wave amplification devices. Some studies have been conducted in order to measure the modification of their ferroelectric properties with RE doping. Following this idea an effective lowering of the phase-transition temperature T_c has been achieved [9.123, 124]. SBN also exhibits outstanding piezoelectric, electrooptic, pyroelectric, and nonlinear optical properties. In this way, amongst the many recent works on SBN on the last topic, we can mention those based on the analysis of emission and excitation spectra obtained from RE-doped SBN crystals. These studies have shown that the intrinsic disorder of the host strongly affects the spectral bands through inhomogeneous broadening [9.125]. Broad emission bands in the near infrared have also been reported for Cr-doped SBN crystals [9.126].

There are other specific features concerning the physical and chemical characteristics and properties

of the PR oxides: **LTa** is less sensitive to PR damage than **LN**, although it has the same structure with Li deficiency and a large number of Ta antisites, with a ferroelectric transition at 690 °C [9.15, 127–129]. **BTi** presents a transition at 120 °C from cubic to ferroelectric tetragonal phase, being stable at **RT** [9.1]. **SBN**, which has a lattice parameter that depends on the chemical composition of the solid solution [9.130] and a tetragonal tungsten bronze structure over a wide solid-solution range, presents a very small thermal conductivity with a value 1/60 of that of sapphire, which influences the form of the **SLI** during melt growth [9.131, 132]; **KTaN**, which shows similar valence state and ionic radius to Ta/Nb, presents difficulties for growing bulk single crystal with constant Ta/Nb ratio [9.133]; **BCTi** presents a great drawback due to the phase transition from tetragonal to orthorhombic at **RT** which deteriorates the optical quality [9.1].

Some of the preceding comments can affect the conditions of single-crystal growth, although there are a lot of similarities in the crystal growth method if one compares these PR oxides with the previous **LN** crystals. The **CZ** method, with the modifications discussed in the previous section on **LN**, is applicable to these PR oxides, although some features are specific:

- Top seed solution growth (**TSSG**) with optimized flux composition, generally in a solution rich in K_2O and in a process which requires extraordinary technical conditions, is used for **KN** [9.127].
- A variant of **DCCZ** with an automatic powder feeding system for obtaining crystals of 10 cm diameter [9.27, 129] or special parameters in the classical **CZ** method [9.128, 129] or **TSSG** with Li_2O excess [9.134] is used in the case of **LTa**.
- For **SBN** crystals a congruent composition is claimed for Sr composition of 0.61 mol % [9.135]; the double-crucible Stepanov technique with sophisticated dies is used, where the roll of the geometry of the die is fundamental to obtaining high-quality large (several cubic centimeters) crystals, although the vertical Bridgman method can exceptionally be used up to 25 mm crystal diameter [9.135], in both cases with free striations. As a consequence of the anomalous values of the thermal conductivity, a concave **SLI** is normally obtained due to the heat of solidification; a flat interface is very difficult to obtain [9.131].

- A curious method, named the step cooling technique by spontaneous nucleation, is used for **KTaN** with a gradient temperature accuracy of 0.1 K, and excess K_2CO_3 as a flux [9.133].

The growth defects that appear in **LN** crystals are still present in these PR oxides, although in a more quantitative way. In **LTa** crystals, multidomain ingots are obtained, which require a conventional poling process after growth, with a continuous core of inclusions along the crystal boule and growth defects such as twin planes, growth twins, and cracks which destroy the crystal quality [9.15, 27, 129, 136]; otherwise the importance of the seeding process and tail design seems to have a great importance in reducing the formation of mechanical twins and cracks [9.27, 129]. In **SBN**, although striations correlated with the temperature fluctuation appear, the authors claim that in general the crystals have very high optical homogeneity, are free of cracks, and have good transparency [9.20, 135, 137], although one must consider that growth by the **CZ** method is technically difficult, with highly faceted radial morphology [9.135].

The stoichiometry in PR oxide crystals is generally speaking a common characteristic considering that all of them are a mixture of more than two oxides. In **LTa** crystals there is a continuous change of Li_2O content, probably due to the Li outdiffusion from the crystal surface, an effect which is greater in near-stoichiometric crystals [9.15]. **SBN** has an open structure and the composition ratio of Sr/Ba can vary locally; considering the different ionic sizes of Sr and Ba, which gives rise to different preferred sites, its properties can be easily tailored [9.131, 132].

Doping of crystals with an appropriate impurity opens up the possible applications of PR oxides. Some singular results are the following: in **LTa**, doping with Nb helps to obtain crystals with highly homogeneous optical quality [9.136]; the PR response increases by two orders of magnitude by codoping of ZnO in **LTa:Fe** compared with **LTa:Fe** [9.128]. Some other dopants show interesting results: in **SBN** the effective coefficient of Nd is close to unity [9.137, 138]; different valence states have been analyzed by electron paramagnetic resonance (**EPR**) in **BTi** doped with Rh as well as Fe [9.1]; Bi_2TeO_5 , being a competitor for data storage applications with **LN:Fe**, is an interesting host for dopants such as Cr, V, Mo [9.1] etc.

9.6 Growth of Sillenite Crystals and Its Characteristics

The term *sillenite compounds* is applied to the series of materials which show structural similarities to γ - Bi_2O_3 . This family of compounds is very well known since the early 1970s when the first bulk crystals were grown by using CZ technique. With a structure containing Bi_2O_3 as the primary oxide compound, more than 60 single crystals have been obtained where the second oxide is a tetravalent oxide – general formula MO_2 with $\text{M} = \text{Ge}, \text{Si}, \text{Ti}$ – such as GeO_2 , SiO_2 , and TiO_2 as the most common ones. The general ratios between the two oxides is 6 : 1 and 2 : 3, giving the formulas $\text{Bi}_{12}\text{MO}_{20}$ and $\text{Bi}_4\text{M}_3\text{O}_{12}$. However this ratio can largely vary according to the phase diagram. Other $\text{Bi}_x\text{M}_y\text{O}_z$ double oxides are also known, where the cation M can be $\text{Ga}, \text{Zn}, \text{Ba}$, etc., with ratio between the two oxides different from that previously mentioned [9.139].

Bismuth sillenites $\text{Bi}_{12}\text{MO}_{20}$ (BMO, with $\text{M} = \text{Si}, \text{Ge}, \text{Ti}$ representing a tetravalent ion occupying a tetrahedral site in a body-centered cubic cell with space group I23 [9.135–137], play an important role as the main building blocks for the development of applications in the visible spectral range. These photorefractive crystals are of great importance in holographic applications, phase conjugation, and optical switching. In particular, sillenite crystals have recently found a prominent place in the field of metrology for the development of compact holographic interferometers [9.140–144]. As an example, we can mention holographic thermal fixing in $\text{Bi}_{20}\text{SiO}_{20}$ (BSO) single crystal [9.145, 146]. Extensive studies in terms of optimum dopants or thermal treatment have also been devoted to the enhancement of BMO photorefractive properties in the near infrared. This range is of great importance due to the recent development of laser diodes operating in this spectral region [9.147]. The early investigations around 1967 on the physical properties of sillenite crystals were mainly focused on congruently melting $\text{Bi}_{12}\text{SiO}_{20}$ and $\text{Bi}_{12}\text{GeO}_{20}$, and on the substitution of Si and Ge by other elements such as Ti, Ga , and Zn [9.148]. However in the last few years this research has also been directed towards the Bi_2O_3 - B_2O_3 system [9.149], where in addition to the well-known boron sillenite, there are two other compounds with relevant physical properties and applications: $\text{Bi}_4\text{B}_2\text{O}_9$ and BiB_3O_6 . The former crystallizes in the monoclinic structure (space group $P2_1/c$) and has been reported to show an extreme indicatrix dispersion [9.145]. The new material BiB_3O_6 , which crystallizes in the centrosymmetric monoclinic space group $C2$, presents extremely

good properties for effective frequency conversion devices [9.150].

Furthermore the most important sillenites used in photorefractive PR devices are those with formula $\text{Bi}_{12}\text{MO}_{20}$ ($\text{M} = \text{Ge}, \text{Si}, \text{Ti}$), so-called BGO, BSO, and BTO, respectively; those compounds, with chemical formula $\text{Bi}_4\text{M}_3\text{O}_{12}$, are relevant for manufacturing scintillator devices. Attending to the goal of this chapter, we will focus our attention on PR sillenite compounds.

BGO, BSO, and BTO are well known as good piezoelectric, excellent acoustooptic, and extraordinary electrooptic materials. In particular their high optical activity and high-speed PR response in the visible range make these materials of prominent interest. Regarding these important properties, PR sillenites are used extensively in a large number of applications: light spatial modulators, imaging treatment, hologram recording phase conjugation, optical-fiber electric field sensors, etc. Although good and excellent reviews have been published in the last decade, the last book, published by Gunter and Huignard [9.1], provides an excellent summary of the most recent and important applications of PR materials.

For these reasons, high-quality crystals with appropriate dopant concentrations are required. This is not an easy task in these compounds due to at least two main reasons that arise from the crystal growth process: the presence of a central core and the tendency for faceting. These questions will be discussed below.

9.6.1 Growth of Bulk Sillenite Crystals

The growth of PR sillenites compounds has been developed since the early 1970s. BGO and BSO have congruent melting points, while BTO melts incongruently at 875°C , where it decomposes into Bi_2O_3 and $\text{Bi}_4\text{Ti}_3\text{O}_{12}$ [9.151, 152]. In spite of this drawback in the BTO compounds growth process, very high-quality reproducible crystals have been obtained with TiO_2 concentration in the range of 8–10 mol %, with slightly different compositions amongst authors. A solid solution with a clear retrograde solidus curve has been demonstrated, and good reproducibility of the growth process can be achieved with low standard deviation of the lattice constant [9.87, 152, 153]. Several works have shown that other sillenites with cations such as $\text{Zn}, \text{Ga}, \text{Ba}$, etc. present some substantial differences compared with the common ones such as narrow temperature and compositional ranges [9.139].

The starting materials for growing sillenites are commonly oxides such as Bi_2O_3 , GeO_2 , SiO_2 , and TiO_2 . As a general rule high-chemical-quality starting materials must be used in order to avoid several problems during the growth process, and to avoid the fatal consequences that impurities in ppm amounts present in the starting materials would have in the final bulk crystal. When oxide compounds are used as starting materials, a sintering process must be developed at around 800°C for 24 h, followed by a grinding process at RT; this process is not mandatory as it could be done during the growth process, maintaining the starting products at the same temperature and for the same period of time as in the sintering process [9.154, 155]. Nevertheless, longer periods of time in the melted phase will increase the risk of evaporation of the constituent Bi_2O_3 .

A variety of techniques have been proposed for growing bulk PR sillenites crystals such as Czochralski, Stepanov, Hydrothermal, and Bridgman methods. Among these, the CZ technique is without doubt the most widely used one, with very well-established growth parameters.

Typical growth parameters for bulk BGO and BSO crystals are the followings: pulling rate 0.3–1.8 mm/h; rotation rate 10–45 rpm; temperature gradient over the melt of 10–35 K/cm; and cooling rate 15–25 K/h. Furthermore for BTO crystals the growth parameters are stricter with narrower ranges, i.e.: pulling rate 0.1–0.3 mm/h; rotation rate 10–20 rpm; axial temperature gradient over the melt 10–20 K/cm; and cooling rate 10–20 K/h [9.134, 151, 153–159]. Proper selection of the growth parameters is of primary importance due to its influence on the solid–liquid interface (SLI).

Some modifications in the CZ growth method have been published in the last decade which could be summarized as:

1. Zone melting CZ, consisting of a modified CZ technique where two crucibles are used: an outer crucible which continuously feeds the inner crucible, where the standard CZ process is followed. There are two critical steps: the adjustment of the outer crucible at the exact position for the crystal growth to reach the adequate temperature profile, and the removal of both crucibles after the process is finished [9.154].
2. A pulling down method which continuously feeds the bulk growing crystal in a similar way as is done

in the micro-pulling down method resembling the Verneuil process [9.160]; the melt is fed downwards by the action of gravity, and a molten zone is formed over the solidified material. The main difficulty in this technical approach is to obtain an adequate temperature gradient to reach a constant diameter and a controlled solid–liquid interface. Nevertheless, the great advantage is the removal of Bi_2O_3 evaporation by controlling the correct feeding.

3. The Bridgman technique is rarely used for the growth of PR sillenite compounds; nevertheless some approaches have been developed using Pt tubes encapsulated inside a ceramic tube. Al_2O_3 powder is also used between them in order to avoid thermal expansion problems which occur during the growth process [9.87]; the advantages of this modification are associated with benefits in the growth crystals claimed by the authors: lower dislocations density and striation free. Nevertheless one could say that the method is out of use compared with the standard CZ method.
4. Growth experiments in microgravity conditions [9.161] have been carried out with a similar technical Bridgman approach to the previous one and compared with the same experiments carried out on the ground; the results obtained support the ideas obtained in other recent microgravity growth experiments:
 - a) In microgravity conditions the crystallinity is better according to the results of rocking curves, which demonstrate at least two times better quality of crystals grown under microgravity conditions.
 - b) The phenomena of dewetting is observed, which is a great advantage of using the Bridgman method.
 - c) When doped crystals are studied, there is a compositional homogeneity along the ingot, with nearly constant dopant concentration, while results on the ground follow the Sheil law with variation in the dopant composition along the ingot.
 - d) Under the same experimental conditions, the solid–liquid interface is slightly convex under microgravity conditions compared with the concave one which appears on the ground.

In summary, the results of microgravity growth experiments show better perspectives than ground-based experiments.

9.6.2 Solid–Liquid Interface

The solid–liquid interface (SLI) in PR sillenites is a scientific topic which has been studied through the last decades due to its great influence on the quality of the bulk crystals. In fact, it is important to recognize that it is necessary to have complete control of the SLI in order to obtain good-quality PR sillenite crystals. Let us summarize the most important results obtained in the last decade:

1. The form of the SLI can be concave, flat or convex as seen from the melt. It is well recognized that an extremely large concave SLI will lead to dramatic consequence in the crystal such as increased stress, higher dislocations density, and microcracking; on the other hand, an extremely large convex interface will be the origin of core phenomena, which negatively affect the quality of PR sillenite bulk crystals [9.139].
2. The SLI is a consequence of the fluxes which exist in the melt, resulting from competition between free and forced convection, which are themselves governed principally by two growth parameters: the axial temperature gradient and the rotation rate; in fact, three zones must be considered: the shoulder zone, where the free convection is the dominant process and where a strong convex SLI is expected unless the rotation is drastically increased; the body zone, where the balance between forced convection and free convection must be obtained and a flat interface is normally obtained; and the last part of the growth process with a low value of the melt depth, where forced convection is dominant and a strong concave SLI is expected. All these situations have been analyzed and precisely identified by simulation tools using commercial codes [9.151].
3. The most important growth parameters that influence the SLI are: the axial temperature gradient, the pulling rate, and the rotation rate, which must be precisely controlled [9.139, 151, 153, 162, 163]:
 - a) The axial temperature gradient for crystal growth of PR sillenites is on the order of 10–20 K/cm, which is easily obtainable with resistance furnaces but very difficult to obtain with RF furnaces; in both cases the use of passive or active afterheaters is highly recommended, although the use of active afterheaters where the temperature is modified during the growth process can be more efficient.
 - b) The pulling rate must be kept within the limits discussed before, in which case its influence on the SLI is minimum.
 - c) The rotation rate is a decisive growth parameter to achieve an adequate SLI, together with the axial temperature gradient [9.130].
4. For standard growth conditions, as is normally the case in a general CZ process, the SLI changes throughout the growth process as a consequence of:
 - a) The change in crystal diameter from the shoulder to the body and from the last part to freezing
 - b) The reduction of melt height when the crystal is pulled up.

In an adequate, standard CZ process with constant rotation and pulling rates, in the initial stage of shoulder growth the SLI is convex and faceted; then this rounded shape changes from convex to flat, remaining so until a slightly concave shape is formed as the melt is reduced. These results are clearly visible when a crystal is withdrawn at different times during the growth process; furthermore simulations carried out considering specific growth parameters support these changes in the SLI [9.151, 162].
5. The consequence of a nonflat interface are thermal stresses, core phenomena, faceted interfaces, crystal cracking, impurity inhomogeneities, gas bubble entrapment, etc.
6. A flat or nearly convex interface is required to get high-quality PR sillenite bulk crystals.
7. A flat or nearly convex interface can be obtained with particular experimental conditions such as: variations in the rotation rate during the first step of the growth process during shoulder formation, a constant rotation rate during the growth of the body of the crystals, and with further variation in the rotation rate during the last part until freezing of the melt. When this situation occurs with a perfectly oriented seed crystal, we can say that we approach near-equilibrium conditions, and the result is the crystal shown in Fig. 9.16.

Furthermore, some other arrangements have been proposed such as metallic shields located on the seed holder to modify the radiation effect and as a consequence to influence the SLI [9.130, 139, 140]. Experimental results together with simulation data have shown the great influence that metallic or ceramic shields located on the seed holder have, flattening a deep interface [9.140].

From the above considerations on the SLI, two general conclusions can be drawn:



Fig. 9.16 Perfectly oriented BSO crystal obtained from nearly equilibrium conditions

1. The control of the SLI is extraordinary important to obtain high-quality crystals, and for this reason it is necessary to take special care of the growth parameters that modify the SLI, especially the axial temperature gradient and the rotation rate.
2. To obtain high-quality crystal a planar or slightly curved convex solid–liquid interface is necessary.

9.6.3 Core Effect

The core effect in PR sillenite materials has been one of the main scientific topics that have been studied for many years, due to its catastrophic consequences on the quality of crystals; see [9.139, 151, 153, 156–161] and references therein. One could say that the core effect is one of the main problems to solve in the preparation of bulk PR sillenite crystals. Let us comment on the most recent ideas which have been published in this field:

1. The core is a darker area that appears along the central part of the bulk crystal, normally full of defects and bubbles, which spreads from the shoulder part of the crystal and extends along the whole crystal, occupying a cross section of several millimeters, destroying its final crystal quality.
2. The core appears at the first stage of the growth process, just after the touching of the seed in the CZ method if no special conditions are used, a sit-

uation in the seeding process which also happens during growth by the Bridgman method in microgravity conditions, where similar defects in the core region were observed, as revealed by interferograms [9.161]. The core appears at this stage of the growth unless some conditions such as a high rotation rate are used in order to avoid the convex SLI. In fact, higher rotation rates at the shoulder position compared with the standard rotation value must be used to avoid the formation of the core region [9.156].

3. The shape of the core depends on the direction of the seed crystal. In fact when the growth direction is along the [100] and [110] directions, the core is favored and facets with several orientations are formed, while for the [111] growth direction it is easier to obtain core-free crystals for a nearly flat interface [9.157], although one must comment that there is not complete agreement between authors on this point [9.156]. Also, while for convex interfaces the core is central, for concave interfaces the core spreads out across the diameter of the crystal, forming a crown in the sample perpendicular to the growth direction; it is therefore clear that the shape of the core is related to SLI curvature [9.157, 162].
4. In general there is a consensus about the origin of the core and the relationship between the core and the facets: in some cases the core appears when there is a large convex interface at the liquid, where small facets are tangential to the interface, and in fact a faceted region is located in the core zone [9.147, 158]; in other cases, the core could be the result of small facets, and in these facets the concentration of impurities would be larger compared with the nonfacet region [9.139]. Nevertheless, it seems that in CZ growth the core effect can be avoided if one facet occupies the entire interface, which is not possible in the Bridgman method, where the core can occupy about half of the area of the grown crystal [9.139].
5. On the other hand, very recent results [9.164] show that specular reflection due to the shoulder side surface drastically changes the temperature fields and results in the appearance of a thin, cool area near the crystal axis which provokes large convexity of the SLI that may be responsible for the formation of the dark core in the center of the crystal. In this way, the angle and length of the shoulder will be of extraordinary importance for the formation of the core. In fact, experiments carried out in this regard have shown that, when a large shoulder of several

- centimeters is used and the diameter of the crystal is limited to 1 cm, the core area disappears along the whole crystal.
6. There have been several studies devoted to impurity analysis of the core. It seems that deep studies on this subject have concluded that the concentration of coloring impurities such as Fe, Mn, Ni, and Co is higher in the core, while the concentration of bleaching impurities such as Ca, Al, Mg, P, and Cl is lower [9.139]. One must indicate at this point that, when the starting materials used for crystals growth are of highest commercial quality, impurities of Fe are ever present at concentrations of a few ppm, as has been detected in the core of PR sillenites by EPR measurements. In fact EPR studies show that Fe^{3+} ions occupy the positions of Si and Ge. Also, in the growth of BSO and BGO bulk crystals, analysis of the core shows a lower concentration of the cations Si and Ge, respectively, compared with noncore regions [9.156]. For this reason one must conclude that the core in PR sillenites is an impurity-getter region.
 7. Moreover, the optical properties of the core region are different compared with those of noncore region, for example, the refractive index, which is at least five times lower in the core region [9.156]. On the other hand the cathodoluminescence emission band centered at 640 nm appears in both regions, being of higher intensity in the core region; one must therefore consider that, during electron radiation of the noncore region, the intensity of the 640 nm emission increases in intensity due to an ionized impurity such as Cr, Fe or Bi antisites as potential candidates, and as a consequence one could conclude that these emission centers are present in the core region [9.165]; for this reason one could say that in the original noncore region and under electron irradiation it is possible to create a *core* region with the same orange color and properties as the original core region.
 8. There is agreement about the influence of the shoulder angle on the formation and extinction of the core. In fact, by increasing the cone angle, the dark core is reduced, which is explained as a consequence of the flattening of the SLI, and at the same time by smoothing of T irregularities [9.157]. The consequence of this effect is very important, because if one could relate the appearance of the core to the shoulder cone, it would be necessary to strictly control the shape and angle of the shoulder in the first stages of the growth process.
 9. A general rule for the disappearance of the core is the presence of a nearly flat interface, which completely eliminates the core region [9.153, 163]. There are some other experimental conditions which reduce or eliminate the core formation:
 - a) With temperature axial gradients lower than 10°C in the vicinity of the SLI, which can be obtained either with passive afterheaters in resistance furnaces or with active afterheaters on induction heaters [9.156];
 - b) The rotation rate is probably the most critical condition, because using a critical rotation rate in the shoulder part will eliminate the core [9.156].
- In consequence, one must conclude that the core region can be avoided if some critical conditions are fulfilled.

9.6.4 Morphology and Faceting

PR sillenites can develop a polyhedral external morphology formed by the intersection of the narrow facets located at the outer part of the interface with the free surface of the melt. In fact, if special care is not taken during the growth process, such as the seed orientation, these facets are ever present and form a disordered external shape, due to this strong tendency for faceting and growth in typical habits [9.139]. Understanding facet formation during the growth process is rather complicated because there is interplay between the continuum transport phenomena and the interface growth kinetics.

The key question for the evolution of the external morphological is a balance between kinetic phenomena and thermal gradients. In fact the thermal conditions at the free surface around the crystals critically depend upon the radiant heat transfer from the melt surface and the structure of the flow field within the melt. These two conditions must be considered both in experimental conditions during the growth process and in simulation studies which can be carried out in order to understand the morphology of PR sillenite materials.

The shape of PR sillenite compounds is related to the radiative exchange that occurs during the growth process due to the growth regimes that occur throughout a complete growth experiment [9.166]. In fact, three regimes can be described:

1. During the shouldering step, radiative exchange occurs between the free melted surface and the upper surface of the growth chamber; in this case, taking

into account that the radiation losses are very high due to the low temperature of the upper surface, and at the same time considering the relatively uniformity of the radiation losses in the radial direction, both conditions will encourage a faceted exterior shape.

2. During the growth of the crystal body, the thermal losses decrease due to heat exchange between the melt surface and the growing crystal; in this case the radial gradient becomes larger, and as a consequence the crystal has a circular cross section.
3. Nevertheless, during the last part of the growth process and due to the reduced melt height, the dominant mechanism of convection is forced convection with a decrease in natural convection, which reduces the radial gradient, resulting in a crystal which exhibits a polar habit.

All three of these regimes influence the formation of a faceted crystal, and for this reason one must control the growth conditions in order to understand the appearance of facets in the crystal. Also, for a given radial temperature gradient and a nonflat interface, an induced stress appears in the growing crystal which will produce a polarization in the PR sillenite crystals in a given direction, resulting in preferential growth of facets [9.159]. In this way, considering the similar magnitude of the piezoelectric coefficients of the PR sillenites, one could conclude that these materials will exhibit similar behavior in terms of facet formation when grown under the same conditions.

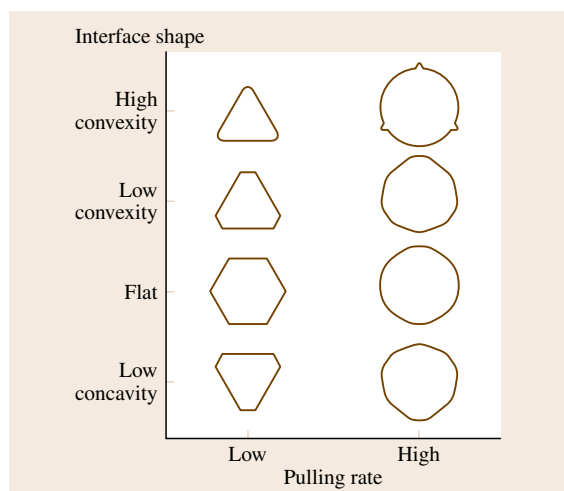


Fig. 9.17 Different morphologies in sillenite crystals for different experimental conditions

There are several factors which influence the morphology and facets in PR sillenite crystals, and all of them must be considered simultaneously. One must control the rotation rate, the pulling rate, and the axial and temperature gradients, as the most important factors. In fact all of these are growth parameters that control the SLI, and for this reason one must always consider the form of the SLI. Figure 9.17 shows an example of the morphology that appears in PR sillenite crystals for different combinations of experimental conditions for pulling rate and interface shape. For example, a constant pulling rate combined with a variable rotation rate with a low axial temperature gradient will be the most adequate set of growth parameters for obtaining near-equilibrium interface kinetics in order to eliminate inversion of the morphology in such a way that the seed direction will predict the faceted crystal and the orientation of the facets in the growing crystal [9.159]. Therefore, if one controls the seed orientation and applies adequate growth parameters, one can obtain experimental growth conditions that yield near-equilibrium conditions and thereby a crystal with controlled facetting.

9.6.5 Other Growth Defects

One could say that a perfect PR sillenite crystal without growth defects is in reality a dream, after considering the previous comments about the solid-liquid interface, the core effect, and the morphology of these materials. Furthermore, there are other growth defects that must be considered, about which a few comments are given below:

1. There are always native defects in PR sillenites crystals such as Bi antisites as a consequence of the phase diagram of these compounds. Nevertheless deeper studies have shown that a complex formed by a Bi antisite and an oxygen vacancy, or even more so the same Bi antisite with an oxygen divacancy, could be the most common native defect in these materials [9.1, 167]. In fact, one cannot avoid these defects because they are intrinsic and always present, although one can increase their concentration by going outside the congruent composition in the phase diagram.
2. The presence of growth striations is related to temperature fluctuations at the interface during the growth process [9.160]. In fact, these temperature fluctuations can result in deviations from stoichiometry and variation in impurity concentration when

a dopant is used, and in some cases the appearance of metastable phases [9.139]. Furthermore, larger temperature fluctuations will create problems associated with constitutional supercooling. For all of these reasons, growth striations are problems associated with a system with segregation coefficients different from unity, and they can be measured, for example, by resulting variations in the optical density [9.130]. Nevertheless there is not a clear relationship between temperature oscillations and growth striations, as happens in other materials.

3. The use of oxides such as Bi_2O_3 as starting materials could be a source of Pt inclusions due to the high reactivity of bismuth with the wall crucible [9.139]. In fact, in single crystals obtained with completely sintered BMO materials, these Pt inclusions can be totally avoided. Nevertheless deeper studies of BSO single crystals have shown the presence of Pt inclusions in dendrite form [9.139]. Some other inclusions and large precipitates have been found after uncontrolled remelting growth originating from a process of constitutional supercooling [9.132, 168].
4. The presence of other phases with different composition is another type of inclusion that must be considered [9.139]. The most common of these is $\gamma\text{-Bi}_2\text{O}_3$, followed by Bi_2SiO_5 and Bi_2GeO_5 , although careful control of the melt temperature can eliminate these phases. It is recognized that superheating above the melting temperature on the order of 25°C is required for the growth process, with the additional benefit of eliminating other structures different from the bulk BMO. Nevertheless lower or higher superheating temperatures must be clearly avoided.
5. Another growth defect in BMO crystals is the presence of bubbles, which often appear in various zones of the crystal such as the core. The bubbles are attributed to constitutional supercooling, which often occurs when the compositional difference between the melt and the growing crystal is large, probably as a consequence of Bi_2O_3 evaporation. This circumstance can be avoided in the zone-melting double-crucible Czochralski technique due to the thin melting zone used in the growth process [9.154, 160].
6. The first method to apply to reduce the dislocation density in a bulk crystal is the use of appropriate growth parameters. Nevertheless the second approach is the use of a seed of the highest quality; otherwise, at the seed-crystal junction the original

dislocations present in the seed will propagate into the bulk crystal as individual or bundles of dislocations [9.137, 139]. For this reason, a neck is strictly necessary in PR sillenite bulk crystal growth by CZ technique.

9.6.6 Doping of Sillenites

A vast range of elements have been tried as dopants in sillenite crystals. For example Tassev et al. [9.169] reported the optical activity of $\text{Bi}_{12}\text{Si}_{12}\text{O}_{20}$ (BSO), $\text{Bi}_{12}\text{GeO}_{20}$ (BGO), and $\text{Bi}_{12}\text{TiO}_{20}$ (BTO) crystals doped with Al, P, and V and codoped with Al and P. They demonstrated important changes near the absorption shoulder in the absorption spectra of these crystals in the range of 480–590 nm. These dopants have been shown to have an important effect on the rotatory power of the crystals.

Chromium in a wide range of concentrations has also been studied as a dopant in sillenite crystals [9.170]. Extensive research has been devoted to explaining the optical absorption background [9.171] and optical activity [9.172] of Cr-doped BGO crystals. The relevance of local structure properties such as the location and local lattice distortion on the optical properties and applications has been extensively demonstrated in the literature [9.173, 174]. Strong variations in the optical and physical photorefractive properties of BTO single crystals has been reported by Mokrushina et al. [9.175] and Mokrushina [9.53], showing at least two charge states occupying probably different positions in the sillenite unit cell. This dopant shifts the absorption edge towards lower frequencies and a new absorption band appears in the near infrared when the chromium concentration in the crystals is increased.

Other rare-earth ions such as Nd^{3+} in sillenite crystals are also of primary importance for new optical devices. As a result of this promising future, Nd:BGO crystals have been widely investigated. Second-harmonic generation, optical rotation, and the fabrication of laser-diode-pumped microchip lasers are some of the challenging topics for deep study in Nd^{3+} -doped sillenites [9.173, 176–179].

Very recently some interesting studies have been devoted to the behavior of several dopants in the sillenite crystal structure, in particular when impurity ions are located at trigonal Bi^{3+} sites. As an example, we can mention recent work on dopants such as Cr^{3+} and Nd^{3+} ions in BGO crystals [9.180]. The local structures of these ions at the Bi^{3+} sites have been analyzed. It has

been demonstrated that, contrary to the general assumption that these impurities are located exactly at Bi sites, they undergo center displacements related to these sites.

Other dopants have been used in order to induce photorefractive and photochromic properties in sillenite crystals. As an example we can mention some recent works on ruthenium-doped BSO and BTO crystals [9.140, 181, 182]. Ru ions can be readily incorporated into sillenite crystals such as BSO. This ion is normally located at Bi substitutional sites, enhancing the photorefractive properties of sillenite crystals at long wavelengths (red light) [9.183].

Electrical conductivity properties in sillenite crystals have also been recently investigated. In particular, electrical properties as a function of temperature have been analyzed in BTO crystals. The results show that the electrical resistance of this material can be modeled as a thermistor with negative temperature coefficient [9.184].

9.6.7 Relevant Properties

The mechanical properties of sillenites have been studied, and the elastic constants have been determined for some sillenite crystals [9.170], including the borate sillenites. The stronger Coulomb contribution of Si^{4+} , Ti^{4+} , and Ge^{4+} compared with B^{3+} seems to be the reason why the elastic constants corresponding to boron sillenites are slightly smaller than those corresponding to Si, Ti, and Ge.

Photorefractivity occurs in photoconductive crystals with a noncentrosymmetric structure when two coherent beams are used to create an interference pattern. In illuminated areas, electrons (holes) are ionized from a defect (intrinsic or extrinsic) to the conduction or valence band of the material. Once in this state, they can move (diffusion or drift regime) to dark areas and be efficiently trapped on the same or a different defect. A space-charge field is thus created, implying a modulation of the refractive index via the electrooptic (Pockels) effect. When trapping occurs at a level different from the original one, a modification of the absorption spectrum (photochromism) is frequently observed, especially at low temperature, due to the change in the concentration of intrinsic or extrinsic defects.

Recent studies have been devoted to analysis of the influence of holes bound to acceptor defects on the optical properties of sillenite crystals. Lattice distortion generally induces a strong localization of these systems at one of the oxygen legends related to the defect. Strong and wide absorption bands, usually in the visible

region, have been reported to occur in these materials, and were related to polaron stabilization energies close to 1 eV. The formation of polarons in sillenite crystals can be characterized as follows: ideal MO_4 tetrahedra are considered as the building blocks of sillenite crystals, where M is regarded as the cation and can be Ti^{4+} , Si^{4+} or Ge^{4+} . In real samples, such as the well-known sillenite $\text{Bi}_{12}\text{MO}_{20}$ crystal, Bi antisite acceptors can be formed as a large number of the M ions can be replaced by Bi^{3+} ions. These kinds of ions present the very stable $6s^2$ configuration, which is why an electron will be taken from one of the four O^{2-} ions [9.185] instead of from the Bi^{3+} , thus forming a bound O^- polaron [9.186–188]; this is an example of where O^- is formed by direct electron ionization to the conduction band. Previous analyses [9.189, 190] have demonstrated that this defect corresponds to the localization of a hole at an oxygen site with a trigonal C_{3v} noncentrosymmetric nature in the paramagnetic state. Therefore space charges generated by inhomogeneous illumination are transposed into refractive index changes via the Pockels effect. This photorefractive effect shows quite a fast response to illumination variations, mainly related to the high mobility of the electrons in the conduction band, forming large polarons [9.191].

All of the statements above show that the main intrinsic absorption of the sillenites, causing their typical honey-yellow coloration, is due to charge transfer excitations of an O^- bound polaron next to Bi^{3+}M antisite defects [9.60]. Very recently, the Bi-richest sillenite, $\text{Bi}_{24.5}\text{BO}_{38.25}$, has been successfully grown by the TSSG method [9.170]. The high values obtained for the refractive indexes of this boron sillenite compared with silicon sillenites were attributed to its high Bi content.

As previously mentioned, BSO [9.192] can be used for holographic applications. Hologram thermal fixing in BSO is induced by hydrogen impurities. This BSO material exhibits some differences compared with other crystals such as Fe-doped LN, including higher fixing temperatures (220 °C in BSO versus 140 °C in Fe:LN) and higher activation energy (1.44 eV) compared with Fe-doped LN (0.95 eV) [9.145, 146]. As a result, thermally fixed room-temperature lifetimes in BSO are much longer than those of holograms recorded in LN. Holographic fixing has also been achieved in other sillenites, such as BTO [9.193]. In this case, the fixing method consisted of the application of an alternating-current (AC) field under simultaneous heating at 90 °C. Two key material properties in holographic technology are: (1) high enough diffraction efficiencies and

(2) fast responses for processing of unfixed holograms. In this sense, sillenites are very promising materials for practical holographic applications, as long extrapolated hologram lifetimes of 10^4 years have been reported for particular materials such as BSO crystals [9.145].

9.6.8 Growth of Photorefractive Bismuth Silicon Oxide Crystals

For a typical $\text{Bi}_{12}\text{SiO}_{20}$ single-crystal growth run, 6 moles of Bi_2O_3 and 1 mole of SiO_2 (522.9 g of Bi_2O_3 and 11.237 g of SiO_2) are thoroughly mixed and loaded into a platinum crucible that is 5 cm in diameter and 5 cm high. The charge of 534.1 g is calculated to fill the crucible to 1.25 cm below the top with molten $\text{Bi}_{12}\text{SiO}_{20}$. From the phase diagram (Fig. 9.18), the melting point of $\text{Bi}_{12}\text{SiO}_{20}$ is about 910°C [9.10]. The charge is then melted at around 920°C in an induction furnace and the remaining material is loaded into the hot crucible. After all the material has been added, the charge is allowed to remain molten for 20 h. A seed crystal is slowly lowered to touch the melt surface in the center of the crucible. The seed is rotated at between 10–20 rpm and, for best results, pulled at between 2–2.5 mm/h.

If the interface is flat and the boule is a great deal smaller in diameter than the crucible, the interface will be elevated above the mean height of the melt and a column of liquid will be weighed along with the crystal. In

the more common case of oxide crystals, the interface is not flat but rather convex toward the melt and the boule diameter is > 0.5 times the crucible diameter.

Thus, part of the interface extends below the level of the melt and that part of the solid is buoyed up by the liquid so that the measured weight is less than that of the crystal.

In both cases, however, the shape of the melt surface is not flat near the crystal and near the crucible wall. If the melt wets the solid crystal, the melt surface will rise to come into contact with the solid at a small angle, leaving a concave curved ring of liquid above the mean surface of the melt. If the melt does not wet the solid, the curvature is convex and the melt surface is lowered to a level near the surface of the solid.

From above, the surface of the melt appears to have a particular temperature due to the actual temperature of the melt and the additional influences of the radiation from the bulk of the melt and the inner surface of the crucible containing the melt. Both are modified by the emissivity of the liquid surface, the reflection of ambient light (if any), the reflectivity of the liquid surface, and the angle of incidence of the ambient light.

For the flat portion of the melt surface, the contribution of ambient reflections is quite small since the light would have to come from the (relatively cold) top of the furnace setup. However, if the surface is curved concavely, light is reflected from the inside of the crucible

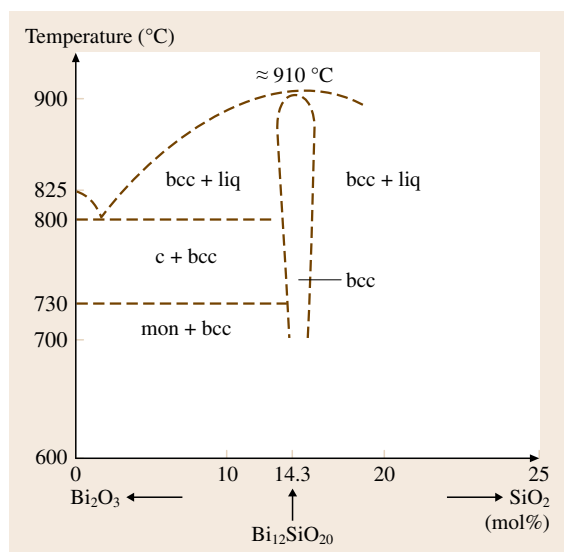


Fig. 9.18 Phase diagram the Bi_2O_3 - SiO_2 system for growth of $\text{Bi}_{12}\text{SiO}_{20}$ crystals



Fig. 9.19 BSO crystal grown using automatic control at Alabama A&M University

wall above the melt level, which is the hottest part of the growth environment. Thus, the meniscus wetting the growing crystal should appear hotter than the flat melt surface. If the melt does not wet the solid, the meniscus is convex and will reflect the crystal surface above it, which is colder than the melt and generally has a lower emissivity than the liquid. Thus the ring in this case should appear darker than the flat melt surface.

Radiative heat loss (proportional to the fourth power of the temperature) produces large temperature gradi-

ents in the crystals as they cool from their melting point, resulting in thermal stress that can result in shattering of the crystal some time after it has reached room temperature. These effects are minimized by the use of afterheaters.

Typical dimensions of successfully grown BSO crystals are 22 mm diameter and 75 mm long, and their typical weight is 250–300 g. A photograph of a BSO crystal grown using automatic diameter control is shown in Fig. 9.19.

9.7 Conclusions

The principal circumstances relating to the bulk growth of the photorefractive materials lithium niobate (LiNbO_3) and sillenites have been reviewed. Both of these kinds of crystals are grown by Czocharlski method, with similar problems originating from similar effects. This implies that they have similar solid–liquid interface and other crucial growth parameters. In LiNbO_3 the two most important problems to solve are their stoichiometry and the growth conditions to obtain periodic structures, which have been practically solved through interesting research solutions. Lithium niobate has an extensive array of properties that have made it one of the most widely used ferroelectric materials, with one of its major applications being the manufacture of surface acoustic wave devices, employed in high-speed signal filtering in televisions and mobile phones. In fact,

this material is often dubbed the silicon of nonlinear optics. It is widely sought after for applications for acoustic wave transducers, optical amplitude and phase modulators, second-harmonic generators, Q-switches, beam deflectors, phase conjugators, optical waveguides, holographic memory elements, and holographic data-processing devices. In sillenites, there is still a long way to go to reach the final goal of obtaining large high-quality bulk crystals, because problems inherent to their physicochemical properties such as the core effect and the solid–liquid interface are ever present. However, it can be seen that, in the last decade, there have been a large number of publications and an extraordinary high level of effort with the final result that most of these problems have been solved, as summarized in this chapter.

References

- 9.1 P. Günter, J.P. Huignard: *Photorefractive Materials and Their Applications 2* (Springer, Berlin 2007)
- 9.2 J. Frejlich: *Photorefractive Materials* (Wiley, New York 2007)
- 9.3 K.K. Wong: *Properties of Lithium Niobate* (Inspec, London 2002)
- 9.4 J. Czocharlski: Ein neues Verfahren zur Messung der Kristallisationsgeschwindigkeit der Metalle, *Z. Phys. Chem.* **92**, 219–221 (1918), in Germany
- 9.5 G. Teal, J.B. Little: Growth of germanium single crystals, *Phys. Rev.* **78**, 647 (1950)
- 9.6 C.D. Brandle: Czocharlski growth of oxides, *J. Cryst. Growth* **264**, 593–604 (2004)
- 9.7 M.D. Aggarwal, W.S. Wang, K. Bhat, P.G. Penn, D.O. Frazier: Photonic crystals: crystal growth processing and physical properties. In: *Handbook of Advanced Electronic and Photonic Materials and Devices*, Vol. 9, ed. by H.S. Nalwa (Academic Press, New York 2001) pp.193–228
- 9.8 M.D. Aggarwal, T. Gebre, A.K. Batra, M.E. Edwards, R.B. Lal, B.G. Penn, D.O. Frazier: Growth of nonlinear optical materials at Alabama A and M University, *Proc. SPIE*, Vol. 4813 (2002) pp. 51–65
- 9.9 T. Gebre, D.E. Edwards, M.D. Aggarwal, A.K. Batra, M.E. Edwards, D. Patel, L. Huey, R.B. Lal: Electrooptic characterization and Czocharlski growth technique of pure and doped lithium niobate crystals, *Proc. SPIE*, Vol. 5560, ed. by F.T. Yu, R. Guo, S. Yin (2004) pp.17–25, *Photorefractive Fiber and Crystal Devices: Materials, Optical Properties, and Applications IX*
- 9.10 A.K. Batra, T. Gebre, J. Stephens, M.D. Aggarwal, R.B. Lal: Growth and characteristics of single crystals of lithium niobate, *Proc. Mater. Res. Soc. Symp.*, Vol. 747 (2003) pp. 365–370
- 9.11 D.T.J. Hurle: *Crystal Pulling From the Melt* (Springer, Berlin 1993)
- 9.12 L.F. Johnson, A.A. Ballman: Coherent emission from rare earth ions in electro-optic crystals, *J. Appl. Phys.* **40**, 297–302 (1969)

- 9.13 Y. Furukawa, K. Kitamura, E. Suzike, K. Niwa: Stoichiometric LiTaO₃ single crystal growth by double crucible Czochralski method using automatic powder supply system, *J. Cryst. Growth* **197**, 889–895 (1999)
- 9.14 X. Li, K. Terabe, H. Hatano, K. Kitamura: Domain patterning in LiNbO₃ and LiTaO₃ by focused electron beam, *J. Cryst. Growth* **292**, 324–327 (2006)
- 9.15 D. Shumov, J. Rottenberg, S. Samuelson: Growth of 3-inch diameter near-stoichiometric LiTaO₃ by conventional Czochralski technique, *J. Cryst. Growth* **287**, 296–299 (2006)
- 9.16 P.F. Bordui, R.G. Norwood, C.D. Bird, G.D. Calvert: Compositional uniformity in growth and poling of large-diameter lithium niobate crystals, *J. Cryst. Growth* **113**, 61–68 (1991)
- 9.17 T. Fujiwara, M. Takahashi, M. Ohama, A.J. Ikushima, Y. Furukawa, K. Kitamura: Comparison of electro-optic effect between stoichiometric and congruent LiNbO₃, *Electron. Lett.* **35**, 499–501 (1999)
- 9.18 T. Fujiwara, A.J. Ikushima, Y. Furukawa, K. Kitamura: *New Aspects of Nonlinear Optical Materials and Devices* (Tech. Dig. Meet., Okazaki 1999)
- 9.19 M. Nakamura, M. Sekita, S. Takekawa, K. Kitamura: Crystal growth and characterization of Nd, Mg co-doped near-stoichiometric LiNbO₃, *J. Cryst. Growth* **290**, 144–148 (2006)
- 9.20 V. Gopalan, T.E. Mitchell, Y. Furukawa, K. Kitamura: The role of nonstoichiometry in 180° domain switching of LiNbO₃ crystals, *Appl. Phys. Lett.* **72**, 1981–1983 (1998)
- 9.21 L. Arizmendi, V. de Andrés, E.J. de Miguel-Sanz, M. Carrascosa: Determination of proton diffusion anisotropy by thermal decay of fixed holograms with *K*-vector perpendicular to the *c*-axis in LiNbO₃:Fe, *Appl. Phys.* **80**, 351–354 (2005)
- 9.22 V. Bermúdez, P.S. Dutta, M.D. Serrano, E. Diéguez: In situ poling of LiNbO₃ bulk crystals below the Curie temperature by application of electric field after growth, *J. Cryst. Growth* **169**, 409–412 (1996)
- 9.23 T. Zhang, B. Wang, S. Fand, D. Ma: Growth and photorefractive properties of an Fe-doped near-stoichiometric LiNbO₃ crystal, *J. Phys. D Appl. Phys.* **38**, 2013–2016 (2005)
- 9.24 G. Dravec, Á. Péter, K. Polgár, L. Kovács: Alkali metal oxide solvents in the growth of stoichiometric LiNbO₃ single crystal, *J. Cryst. Growth* **286**, 334–337 (2006)
- 9.25 G. Bhagavannarayana, G.C. Budakoti, K.K. Maurya, B. Kumar: Enhancement of crystalline, piezoelectric and optical quality of LiNbO₃ single crystals by post-growth annealing and poling, *J. Cryst. Growth* **282**, 394–401 (2005)
- 9.26 S.H. Yao, X.B. Hu, J.Y. Wang, H. Liu, L. Gao, X.F. Cheng, X. Yin, X.F. Chen: Growth and characterization of near stoichiometric LiNbO₃ single crystal, *Cryst. Res. Technol.* **42**, 114–118 (2007)
- 9.27 S. Kumaragurubran, S. Takekawa, M. Nakamura, K. Kitamura: Growth of 4-in diameter MgO-doped near-stoichiometric lithium tantalate single crystals and fabrication of periodically poled structures, *J. Cryst. Growth* **292**, 332–336 (2006)
- 9.28 V. Bermúdez, M.D. Serrano, J. Tornero, E. Diéguez: Er incorporation into congruent LiNbO₃ crystals, *Solid State Commun.* **112**, 699–703 (1999)
- 9.29 T.P.J. Han, F. Jaque, V. Bermúdez, E. Diéguez: Luminescence of the Cr⁺³ R-lines in pure and MgO co-doped near stoichiometric LiNbO₃:Cr crystals, *Chem. Phys. Lett.* **369**, 519–524 (2003)
- 9.30 M. Nakamura, M. Sekita, S. Takekawa, K. Kitamura: Crystal growth and characterization of Nd, Mg co-doped near-stoichiometric LiNbO₃, *J. Cryst. Growth* **290**, 144–148 (2006)
- 9.31 T.P. Han, F. Jaque, V. Bermúdez, E. Diéguez: The role of the Mg⁺² ions in Cr⁺³ spectroscopy for near-stoichiometric LiNbO₃ crystals, *J. Phys. Condens. Matter* **15**, 281–290 (2003)
- 9.32 S. Kar, R. Bhatt, V. Shukla, R.K. Choubey, P. Sen, K.S. Bartwal: Optical behaviour of VTE treated near stoichiometric LiNbO₃ crystals, *Solid State Commun.* **137**, 283–287 (2006)
- 9.33 R.K. Choubey, P. Sen, S. Kar, G. Bhagavannarayana, K.S. Bartwal: Effect of codoping on crystalline perfection of Mg:Cr:LiNbO₃ crystals, *Solid State Commun.* **140**, 120–124 (2006)
- 9.34 Y. Furukawa, K. Kitamura, S. Takekawa, K. Niwa, Y. Yajima, H. Iyi, I. Mnushkina, P. Guggenheim, J.M. Martin: The correlation of MgO-doped near-stoichiometric LiNbO₃ composition to the defect structure, *J. Cryst. Growth* **211**, 230–236 (2000)
- 9.35 M. Mühlberg, M. Burianek, H. Edongue, C. Poetsch: Bi₄B₂O₉ – Crystal growth and some new attractive properties, *J. Cryst. Growth* **240**, 740–744 (2002)
- 9.36 J.C. Rojo, E. Diéguez, J. Jeffrey, J. Derby: A heat shield to control thermal gradients, melt convection and interface shape during shouldering in Czochralski oxide growth, *J. Cryst. Growth* **200**, 329–334 (1999)
- 9.37 V. Bermúdez, P.S. Dutta, M.D. Serrano, E. Diéguez: Effect of crystal composition on the domain structure of LiNbO₃ grown from Li-rich melts by the Czochralski technique, *J. Cryst. Growth* **172**, 269–273 (1997)
- 9.38 V. Bermúdez, P.S. Dutta, M.D. Serrano, E. Diéguez: On the single domain nature of stoichiometric LiNbO₃ grown from melts containing K₂O, *Appl. Phys. Lett.* **70**, 729–731 (1997)
- 9.39 J. Sun, Y. Kong, L. Zhang, W. Yan, X. Wang, J. Xu, G. Zhang: Growth of large-diameter nearly stoichiometric lithium niobate crystals by continuous melt supplying system, *J. Cryst. Growth* **292**, 351–354 (2006)
- 9.40 Y. Zhen, E. Shi, Z. Lu, S. Chi, S. Wang, W. Zhang: A novel technique to grow stoichiometric lithium niobate single crystals, *J. Cryst. Growth* **211**, 895–898 (2005)
- 9.41 V. Gopalan, T.E. Mitchell: The role of nonstoichiometry in 180° domain switching of LiNbO₃ crystals, *Appl. Phys. Lett.* **72**, 1981–1983 (1998)

- 9.42 V. Bermúdez, L. Huang, D. Hui, S. Field, E. Diéguez: Role of stoichiometric point defect in electric-field-poling lithium niobate, *Appl. Phys. A* **70**, 591–594 (2000)
- 9.43 F. Yazdani, M.L. Sundheimer, A.S.L. Gomes: Ferroelectric domain inversion in congruent lithium Niobate, *Proc. SBMO/IEEE MTT-S IMOC* (2003) pp. 453–458
- 9.44 V. Bermúdez, P.S. Dutta, M.D. Serrano, E. Diéguez: Transient electrical field characteristics due to polarization of domains in bulk LiNbO₃ during Czocharlski growth, *J. Appl. Phys.* **81**, 862–864 (1997)
- 9.45 C.E. Valdivia, C.L. Sones, J.G. Scott, S. Mailis, R.W. Eason: Nanoscale surface domain formation on the +z face of lithium niobate by pulsed ultraviolet laser illumination, *Appl. Phys. Lett.* **86**, 022906–3 (2005)
- 9.46 V. Bermúdez, F. Caccavale, E. Diéguez: Domain walls characterization of the opposite domain lithium niobate structures, *J. Cryst. Growth* **219**, 413–418 (2000)
- 9.47 K. Nakamura, J. Kurz, K. Parameswaran, M.M. Fejer: Periodic poling of magnesium-oxide doped lithium niobate, *J. Appl. Phys.* **91**, 4528–4534 (2002)
- 9.48 M. Molotskii, A. Agronin, P. Urenski, M. Shvebelman, G. Rosenman, Y. Rosenwaks: Ferroelectric domain breakdown, *Phys. Rev. Lett.* **90**, 107601–107604 (2003)
- 9.49 E. Kokanyan, E. Diéguez: New perspectives of lithium niobate crystals, *J. Optoelectron. Adv. Mater.* **2**, 205–214 (2000)
- 9.50 V. Bermúdez, D. Callejo, R. Vilaplana, J. Capmany, E. Diéguez: Engineering of lithium niobate domain structure through the off-centered Czocharlski growth technique, *J. Cryst. Growth* **237**, 677–681 (2002)
- 9.51 V. Bermúdez, J. Capmany, J. García Solé, E. Diéguez: Growth and second harmonic generation characterization of Er³⁺ doped bulk periodically poled LiNbO₃, *Appl. Phys. Lett.* **73**, 593–595 (1998)
- 9.52 V. Bermúdez, M.D. Serrano, E. Diéguez: Bulk periodic poled lithium niobate crystals doped with Er and Yb, *J. Cryst. Growth* **200**, 185–190 (1999)
- 9.53 D. Callejo, V. Bermúdez, E. Diéguez: Influence of Hf ions in the formation of periodically poled lithium niobate structures, *J. Phys. Condens. Matter* **13**, 1337–1342 (2001)
- 9.54 V. Bermúdez, D. Callejo, F. Caccavale, F. Segato, F. Agulló-Rueda, E. Diéguez: On the compositional nature of bulk doped periodic poled lithium niobate crystals, *Solid State Commun.* **114**, 555–559 (2000)
- 9.55 V. Bermúdez, F. Caccavale, C. Sada, F. Segato, E. Diéguez: Etching effect on periodic domain structures of lithium niobate crystals, *J. Cryst. Growth* **191**, 589–593 (1998)
- 9.56 V. Bermúdez, M.D. Serrano, P.S. Dutta, E. Diéguez: Opposite domain formation in Er-doped LiNbO₃ bulk crystals grown by the off-centered Czocharlski technique, *J. Cryst. Growth* **203**, 179–185 (1999)
- 9.57 J. Capmany, V. Bermúdez, D. Callejo, J. García Solé, E. Diéguez: Continuous wave simultaneous multi-self-frequency conversion in Nd³⁺ doped aperiodically poled bulk lithium niobate, *Appl. Phys. Lett.* **10**, 1225–1227 (2000)
- 9.58 J. Capmany, D. Callejo, V. Bermúdez, E. Diéguez, D. Artigas, L. Torner: Continuous-wave self-pumped optical parametric oscillator based on Yb³⁺ doped bulk periodically poled LiNbO₃ (MgO), *Appl. Phys. Lett.* **79**, 292–295 (2001)
- 9.59 V. Bermúdez, A. Gil, L. Arizmendi, J. Colchero, A.M. Baró, E. Diéguez: Techniques of observation and characterization of the domain structure in periodically poled lithium niobate, *J. Mater. Res.* **15**, 2814–2820 (2000)
- 9.60 J. Capmany, J.A. Pereda, V. Bermúdez, D. Callejo, E. Diéguez: Laser frequency converter for continuous-wave tunable Ti:sapphire laser based on aperiodically poled LiNbO₃:Nd³⁺, *Appl. Phys. Lett.* **79**, 1751–1753 (2001)
- 9.61 A. Lorenzo, L.E. Bausá, J. García Solé: Optical spectroscopy of Pr³⁺ ions in LiNbO₃, *Phys. Rev. B* **51**, 16643–16650 (1995)
- 9.62 A. Lorenzo, H. Jarežic, B. Roux, G. Boulon, L.E. Bausá, J. García Solé: Lattice location of Pr³⁺ ions in LiNbO₃, *Phys. Rev. B* **52**, 6278–6284 (1995)
- 9.63 J.E. Muñoz-Santiuste, A. Lorenzo, L.E. Bausá, J. García Solé: Crystal field and energy levels of Pr³⁺ centres in LiNbO₃, *J. Phys. Condens. Matter* **10**, 7653–7664 (1998)
- 9.64 R. Piramidowicz, I. Pracka, W. Wolinski, M. Malinowski: Blue-green emission of Pr³⁺ ions in LiNbO₃, *J. Phys. Condens. Matter* **12**, 709 (2000)
- 9.65 W. Gryk, B. Kuklinski, M. Grinberg, M. Malinowski: High pressure spectroscopy of Pr³⁺ in LiNbO₃, *J. Alloy. Compd.* **380**, 230 (2004)
- 9.66 Y.S. Bai, R.R. Neugaonkar, R. Katchu: High-efficiency nonvolatile holographic storage with two-step recording in praseodymium-doped lithium niobate by use of continuous-wave lasers, *Opt. Lett.* **22**, 334–336 (1997)
- 9.67 G. Zhong, J. Jian, Z. Wu: Measurements of optically induced refractive index damage in lithium niobate, *Proc. 11th Int. Conf. Quantum Electron. (IEEE, New York 1990)* p. 631
- 9.68 M. Nakamura, M. Sekita, S. Takekawa, K. Kitamura: Crystal growth and characterization of Nd, Mg co-doped near-stoichiometric LiNbO₃, *J. Cryst. Growth* **290**, 144–148 (2006)
- 9.69 X.H. Zhen, Q. Li, Y.H. Xu: Influence of microscopic defects on optical damage resistance of Zn:Fe:LiNbO₃ crystals, *Cryst. Res. Technol.* **41**, 276–279 (2006)
- 9.70 T.R. Volk, V.I. Pryalkin, N.M. Rubinina: Optical-damage-resistant LiNbO₃:Zn crystal, *Opt. Lett.* **15**, 996 (1990)
- 9.71 T.R. Volk, N.M. Rubinina: A new optical damage resistant impurity in lithium niobate crystals: indium, *Ferroelectr. Lett.* **14**, 37–43 (1992)

- 9.72 Y. Kong, J. Wen, H. Wang: New doped lithium niobate crystal with high resistance to photorefractive – LiNbO₃:In, *Appl. Phys. Lett.* **66**, 280–281 (1995)
- 9.73 J.K. Yamamoto, K. Kitamura, N. Iyi, S. Kimura, Y. Furukawa, M. Sato: Increased optical damage resistance in Sc₂O₃-doped LiNbO₃, *Appl. Phys. Lett.* **61**, 2156–2158 (1992)
- 9.74 I.P. Kaminov, L.W. Stulz: Nd:LiNbO₃ laser, *IEEE J. Quantum Electron.* **QE-11**, 306–308 (1975)
- 9.75 Y. Furukawa, K. Kitamura, S. Takekawa, K. Niwa, Y. Yajima, N. Iyi, I. Mnushkina, P. Guggenheim, J.M. Martin: The correlation of MgO-doped near-stoichiometric LiNbO₃ composition to the defect structure, *J. Cryst. Growth* **211**, 230–236 (1990)
- 9.76 M.H. Li, Y.H. Xu, R. Wang, X.H. Zhen, C.Z. Zhao: Second harmonic generation in Zn-doped Li-rich LiNbO₃ crystals, *Cryst. Res. Technol.* **36**, 191–195 (2001)
- 9.77 A. Cordova-Plaza, T.Y. Fan, M.J.F. Digonnet, R.L. Byer, H.J. Shaw: Nd:MgO:LiNbO₃ continuous-wave laser pumped by a laser diode, *Opt. Lett.* **13**, 209 (1988)
- 9.78 M. Nakamura, M. Sekita, S. Takekawa, K. Kitamura: Crystal growth and characterization of Nd, Mg co-doped near-stoichiometric LiNbO₃, *J. Cryst. Growth* **290**, 144–148 (2006)
- 9.79 H. Ledbetter, H. Ogi, N. Nakamura: Elastic, anelastic, piezoelectric coefficients of monocrystal lithium niobate, *Mech. Mater.* **36**, 941–947 (2004)
- 9.80 D.A. Bryan, R. Gerson, H.E. Tomaschke: Increased optical damage resistance in lithium niobate, *Appl. Phys. Lett.* **44**, 847–849 (1984)
- 9.81 Y. Furukawa, K. Kitamura, S. Takakawa, A. Miyamoto, M. Terao, N. Suda: Photorefractive in LiNbO₃ as a function of [Li]/[Nb] and MgO concentrations, *Appl. Phys. Lett.* **77**, 2494–2496 (2000)
- 9.82 M. Nakamura, S. Higuchi, S. Takekawa, K. Terabe, Y. Furukawa, K. Kitamura: Optical damage resistance and refractive indices in near-stoichiometric MgO-doped LiNbO₃, *Jpn. J. Appl. Phys.* **41**, L49 (2002)
- 9.83 Á. Péter, K. Polgár, L. Kovács, K. Lengyel: Threshold concentration of MgO in near-stoichiometric LiNbO₃ crystals, *J. Cryst. Growth* **284**, 149–155 (2005)
- 9.84 T. Volk, N. Rubinina, M. Wöhlecke: Optical-damage-resistant impurities in lithium niobate, *J. Opt. Soc. Am. B* **11**, 1681 (1994)
- 9.85 R. Gerson, J.E. Firchhoff, H.E. Halliburton, D.A. Bryan: Microscopic mechanism of suppressing photorefractive in LiNbO₃:Mg,Fe crystals, *J. Appl. Phys.* **60**, 3553–3557 (1986)
- 9.86 J.J. Liu, W.L. Zhang, G.Y. Zhang: Microscopic mechanism of suppressing photorefractive in LiNbO₃:Mg,Fe crystals, *Solid State Commun.* **98**, 523–526 (1996)
- 9.87 C.B. Tsai, W.T. Hsu, M.D. Shih, Y.Y. Lin, Y.C. Huang, C.K. Hsieh, W.C. Hsu, R.T. Hsu, C.W. Lan: Growth and characterizations of ZnO-doped near-stoichiometric LiNbO₃ crystals by zone-leveling Czochralski method, *J. Cryst. Growth* **289**, 145–150 (2006)
- 9.88 C. Koepke, K. Wisniewski, D. Dyl, M. Grinberg, M. Malinowski: Evidence for existence of the trapped exciton states in Pr³⁺-doped LiNbO₃ crystal, *Opt. Mater.* **28**, 137–142 (2006)
- 9.89 H. Nagata, J. Ichikawa: Progress and problems in reliability of Ti:LiNbO₃ optical intensity modulators, *Opt. Eng.* **34**(11), 3284–3293 (1995)
- 9.90 X. Liang, X. Xuewu, T.C. Chong, Y. Shaoning, Y. Fengliang, T.Y. Soon: Lithium in-diffusion treatment of thick LiNbO₃ crystals by the vapor transport equilibration method, *J. Cryst. Growth* **260**, 143 (2004)
- 9.91 V.V. Atuchin, T.I. Grigorieva, I.E. Kalabin, V.G. Kesler, L.D. Pokrovsky, D.I. Shevtsov: Comparative analysis of electronic structure of Ti:LiNbO₃ and LiNbO₃ surfaces, *J. Cryst. Growth* **275**(1/2), e1603–e1607 (2005)
- 9.92 H. Nagata, Y. Li, W.R. Bosenberg, G.L. Reiff: DC drift of x-cut LiNbO₃ modulators, *IEEE Photon. Technol. Lett.* **16**, 2233–2235 (2004)
- 9.93 S. Yamada, M. Minakata: DC drift phenomena in LiNbO₃ optical waveguide devices, *Jpn. J. Appl. Phys.* **20**, 733–737 (1981)
- 9.94 R.A. Beaker: Circuit effect in LiNbO₃ channel-waveguide modulators, *Opt. Lett.* **10**, 417–420 (1985)
- 9.95 H. Nagata, K. Kiuchi: Temperature dependence of DC drift of Ti:LiNbO₃ optical modulators with sputter deposited SiO₂ buffer layer, *J. Appl. Phys.* **73**(9), 4162–4164 (1993)
- 9.96 H. Nagata, K. Kiuchi, S. Shimotsu, J. Ogiwara, J. Minowa: Estimation of direct current bias and drift of Ti:LiNbO₃ optical modulators, *J. Appl. Phys.* **76**(3), 1405–1408 (1994)
- 9.97 X.H. Zhen, Q. Li, Y.H. Xu: Influence of microscopic defects on optical damage resistance of Zn:Fe:LiNbO₃ crystals, *Cryst. Res. Technol.* **41**(3), 276–279 (2006)
- 9.98 W.J. Parker, R.J. Jenkins, C.P. Butler, G.L. Abbott: Flash method of determining thermal diffusivity, heat capacity, and thermal conductivity, *J. Appl. Phys.* **32**, 1679–1684 (1961)
- 9.99 P. Herth, T. Granzow, D. Schaniel, T. Woike, M. Imlau, E. Krätzig: Evidence for light-induced hole polarons in LiNbO₃, *Phys. Rev. Lett.* **95**, 067404–067408 (2005)
- 9.100 O.F. Schirmer: O²⁻ bound small polarons in oxide materials, *J. Phys. Condens. Matter* **18**, 667–704 (2006)
- 9.101 A.L. Shluger, A.M. Stoneham: Small polarons in real crystals, *J. Phys. Condens. Matter* **5**, 3049 (1993)
- 9.102 O.F. Schirmer, O. Thiemann, M. Wöhlecke: Defects in LiNbO₃ – I. Experimental aspects, *J. Phys. Chem. Solids* **52**, 185–200 (1991)
- 9.103 L. Arizmendi: Photonic applications of lithium niobate crystals, *Phys. Status Solidi (a)* **201**, 253–283 (2004)
- 9.104 B.K. Das, H. Suche, W. Sohler: Single-frequency Ti:Er:LiNbO₃ distributed Bragg reflector waveguide laser with thermally fixed photorefractive cavity, *Appl. Phys. B* **73**, 439–442 (2001)

- 9.105 J. Hukriede, D. Runde, D. Kip: Fabrication and application of holographic Bragg gratings in lithium niobate channel waveguides, *J. Phys. D Appl. Phys.* **36**, R1–R16 (2003)
- 9.106 I. Nee, O. Beyer, M. Müller, K. Buse: Circuit effect in LiNbO₃ channel-waveguide modulators, *J. Opt. Soc. Am. B* **20**, 1593–1602 (2003)
- 9.107 L. Arizmendi, F.J. López-Barberá: Lifetime of thermally fixed holograms in LiNbO₃ crystals doped with Mg and Fe, *Appl. Phys. B* **86**, 105–109 (2007)
- 9.108 L. Arizmendi, C. de las Heras, F. Jaque, A. Suchocki, S. Kobayakov, T.P.J. Han: Photoconductivity in LiNbO₃ crystals, codoped with MgO and Cr₂O₃, *Appl. Phys. B* **87**, 123–127 (2007)
- 9.109 L. Arizmendi, F. Agulló-López: LiNbO₃: A paradigm for photorefractive materials, *MRS Bulletin* **19**, 32–38 (1994)
- 9.110 J. Díaz-Caro, J. García-Solé, D. Bravo, J.A. Sanz-García, F.J. López, F. Jaque: MgO codoping-induced change in the site distribution of Cr³⁺ ions in LiNbO₃, *Phys. Rev. B* **54**, 13042–13046 (1996)
- 9.111 F. Jaque, T.P.J. Han, G. Lifante: Comparative study of the singularity in the optical properties of congruent doped LiNbO₃ crystals, *J. Lumin.* **248**, 102–103 (2003)
- 9.112 G.A. Torchia, J.A. Sanz-García, J. Díaz-Caro: Redistribution of Cr³⁺ ions from Li⁺ to Nb⁵⁺ sites in ZnO codoped LiNbO₃:Cr crystals, F. Jaque, T.P.J. Han, *Chem. Phys. Lett.* **288**, 65–70 (1998)
- 9.113 S.A. Basun, A.A. Kaplyanskii, A.B. Kutsenko, V. Dierolf, T. Troester, S.E. Kapphan, K. Polgár: Optical characterization of Cr³⁺ centers in LiNbO₃, *Appl. Phys. B* **73**, 453–461 (2001)
- 9.114 B. Naranjo, J.K. Gimzewski, S. Putterman: Observation of nuclear fusion driven by a pyroelectric crystal, *Nature* **434**, 1115–1117 (2005)
- 9.115 S. Tascu, P. Moretti, S. Kostitskii, B. Jacquier: Optical near-field measurements of guided modes in various processed LiNbO₃ and LiTaO₃ channel waveguides, *Opt. Mater.* **24**, 297–302 (2003)
- 9.116 Y.N. Korkishko, V.A. Fedorov, S.M. Kostitskii, A.N. Alkaev, E.I. Maslennikov, E.M. Paderin, D.V. Apraksin, F. Laurell: Proton exchanged LiNbO₃ and LiTaO₃ optical waveguides and integrated optic devices, *Microelectron. Eng.* **69**, 228–236 (2003)
- 9.117 P. Nekvindova, J. Špírková, J. Červená, M. Budnar, A. Razpet, B. Zorko, P. Pelicon: Annealed proton exchanged optical waveguides in lithium niobate: differences between the X- and Z-cuts, *Opt. Mater.* **19**, 245–253 (2002)
- 9.118 L. Salavcová, J. Špírková, F. Ondráček, A. Macková, J. Vacík, U. Kreissig, F. Eichhorn, R. Groetzschel: Study of anomalous behaviour of LiTaO₃ during the annealed proton exchange process of optical waveguide's formation – comparison with LiNbO₃, *Opt. Mater.* **29**, 913–918 (2007)
- 9.119 Z.D. Gao, Q.J. Wang, Y. Zhang, S.N. Zhu: Etching study of poled lithium tantalate crystal using wet etching technique with ultrasonic assistance, *Opt. Mater.* **30**(6), 847–850 (2008)
- 9.120 X.-H. Du, J. Zheng, U. Belegundu, K. Uchino: Crystal orientation dependence of piezoelectric properties of lead zirconate titanate near the morphotropic phase boundary, *Appl. Phys. Lett.* **72**, 2421–2423 (1998)
- 9.121 X.-H. Du, J. Zheng, K. Uchino: Crystal orientation dependence of piezoelectric properties in lead zirconate titanate: theoretical expectation for thin films, *Jpn. J. Appl. Phys.* **36**, 5580–5587 (1997)
- 9.122 W. Yue, J. Yi-jian: Crystal orientation dependence of piezoelectric properties in LiNbO₃ and LiTaO₃, *Opt. Mater.* **23**, 403–408 (2003)
- 9.123 T. Volk, V. Salobutin, L. Ivleva, N. Polzkov, R. Pankrath, M. Wöhlecke: Atomic structure of Sr_{0.75}Ba_{0.25}Nb₂O₆ single crystal and composition-structure-property relation in (Sr,Ba)Nb₂O₆ solid solutions, *Sov. Phys. Solid State* **42**, 2066–2071 (2000)
- 9.124 T. Volk, L. Ivleva, P. Lykov, N. Polozkov, V. Salobutin, R. Pankrath, M. Wöhlecke: Effects of rare-earth impurity doping on the ferroelectric and photorefractive properties of strontium-barium niobate crystals, *Opt. Mater.* **18**, 179–182 (2001)
- 9.125 M. Bettinelli, A. Speghini, A. Ródenas, P. Molina, M.O. Ramírez, B. Capote, D. Jaque, L.E. Bausá, J. García Solé: Luminescence of lanthanide ions in strontium barium niobate, *J. Lumin.* **122**, 307–310 (2007)
- 9.126 T.P.J. Han, F. Jaque, D. Jaque, J. García-Solé, L. Ivleva: Luminescence life time and time-resolved spectroscopy, of Cr³⁺ ions in strontium barium niobate, *J. Lumin.* **119**, 453–456 (2006)
- 9.127 T. Tagaki, T. Fujii, Y. Sakabe: Growth and characterization of KNbO₃ by vertical Bridgman method, *J. Cryst. Growth* **259**, 296–301 (2003)
- 9.128 R. Ilangoan, G. Ravi, C. Subramanian, P. Ramasamy, S. Sakai: Growth and characterization of potassium tantalate niobate single crystals by step-cooling technique, *J. Cryst. Growth* **237**, 694–699 (2002)
- 9.129 G. Ravi, R. Jayavel, S. Takekawa, M. Kanamura, K. Kitamura: Effect of niobium substitution in stoichiometric lithium tantalite (SLT) single crystals, *J. Cryst. Growth* **250**, 146–151 (2003)
- 9.130 M. Ulex, R. Pankrath, K. Betzler: Growth of strontium barium niobate: the liquidus-solidus phase diagram, *J. Cryst. Growth* **271**, 128–133 (2004)
- 9.131 S. Kuraragurubaran, S. Takekawa, M. Nakamura, K. Kitamura: Growth of 4-in diameter near-stoichiometric lithium tantalate single crystals, *J. Cryst. Growth* **285**, 88–95 (2005)
- 9.132 S. Fang, B. Wang, T. Zhans, F. Ling, R. Wang: Growth and photorefractive properties of Zn, Fe double-doped LiTaO₃ crystal, *Opt. Mater.* **28**, 207–211 (2006)
- 9.133 H.S. Lee, J.P. Wilde, R.S. Feigelson: Bridgman growth of strontium barium niobate single crystals, *J. Cryst. Growth* **187**, 89–101 (1998)

- 9.134 J.B. Gruber, T.H. Allik, D.K. Sardar, R.J. Yow, M. Scripsick, B. Wechsler: Crystal growth and spectroscopic characterization of $\text{Yb}^{+3}\text{:LiTaO}_3$, *J. Lumin.* **117**, 233–238 (2006)
- 9.135 S. Takekawa, Y. Furukawa, M. Lee, K. Kitamura: Double crucible Stepanov technique for the growth of striation – free SBN single crystal, *J. Cryst. Growth* **229**, 238–242 (2001)
- 9.136 L.I. Ivleva, T.R. Volk, D.V. Isakov, V.V. Gladkii, N.M. Polozkov, P.A. Lykov: Growth and ferroelectric properties of Nd-doped strontium–barium niobate crystals, *J. Cryst. Growth* **237**, 700–702 (2002)
- 9.137 C. Nitash, M. Göbbels: Phase relations and lattice parameters in the system $\text{SrO–BaO–Nb}_2\text{O}_5$ focusing on SBN ($\text{Sr}_x\text{Ba}_{1-x}\text{Nb}_2\text{O}_6$), *J. Cryst. Growth* **269**, 324–332 (2004)
- 9.138 S. Aravazhi, A. Tapponnier, D. Günther, P. Günther: Growth and characterization of barium-doped potassium tantalite crystals, *J. Cryst. Growth* **282**, 66–71 (2005)
- 9.139 H.A. Wang, C.H. Lee, F.A. Kröger, R.T. Cox: Point defects in $\alpha\text{-Al}_2\text{O}_3\text{:Mg}$ studied by electrical conductivity, optical absorption, and ESR, *Phys. Rev. B* **27**, 3821–3841 (1983)
- 9.140 F. Ramaz, L. Rakitina, M. Gospodinov, B. Briat: Photorefractive and photochromic properties of ruthenium-doped $\text{Bi}_{12}\text{SiO}_{20}$, *Opt. Mater.* **27**, 1547–1559 (2005)
- 9.141 M.P. Georges, V.S. Scauffaire, P.C. Lemaire: Compact and portable holographic camera using photorefractive crystals. Application in various metrological problems, *Appl. Phys. B* **72**, 761–765 (2001)
- 9.142 A.R. Lobato, S. Lanfredi, J.F. Carvalho, A.C. Hernandez: Synthesis, crystal growth and characterization of γ -phase bismuth titanium oxide with gallium, *Mater. Res.* **3**, 92–96 (2000)
- 9.143 M. Valant, D. Suvorov: Processing and dielectric properties of sillenite compounds $\text{Bi}[\text{12}]\text{M}[\text{20–}\delta]$ ($\text{M} = \text{Si, Ge, Ti, Pb, Mn, Bi}_{1/2}\text{P}_{1/2}$), *J. Am. Ceram. Soc.* **84**(12), 2900–2904 (2001)
- 9.144 M. Valent, D. Suvorov: Synthesis and characterization of a new sillenite compound – $\text{Bi}_{12}(\text{B}_{0.5}\text{P}_{0.5})\text{O}_{20}$, *J. Am. Ceram. Soc.* **85**, 355–358 (2002)
- 9.145 L. Arizmendi, J.F. López-Barberá, M. Carrascosa: Twelve-fold increase of diffraction efficiency of thermally fixed holograms in $\text{Bi}_{12}\text{SiO}_{20}$, *J. Appl. Phys.* **97**, 073505–073507 (2005)
- 9.146 E.M. de Miguel-Sanz, M. Carrascosa, L. Arizmendi: Effect of the oxidation state and hydrogen concentration on the lifetime of thermally fixed holograms in $\text{LiNbO}_3\text{:Fe}$, *Phys. Rev. B* **65**, 165101 (2002)
- 9.147 B. Briat, V.G. Grachev, G.I. Malovichko, O.F. Schirmer, M. Wöhlecke: Defects in inorganic photorefractive materials and their investigations. In: *Photorefractive Materials*, Vol. 2, ed. by P. Günter, J.P. Huignard (Springer, Berlin 2007), Chap. 2
- 9.148 B. Briat, C.L. Boudy, J.C. Launay: Magnetic and natural circular dichroism of $\text{Bi}_{12}\text{GeO}_{20}$: Evidence for several paramagnetic centres, *Ferroelectrics* **125**, 467–469 (1992)
- 9.149 M. Burianek, S. Haussühl, M. Kugler, V. Wirth, M. Mühlberg: Some physical properties of boron sillenite: $\text{Bi}_{24.5}\text{B}_{0.38.25}$, *Cryst. Res. Technol.* **41**, 375–378 (2006)
- 9.150 H. Hellwig, J. Liebertz, L. Bohatý: Exceptional large nonlinear optical coefficients in the monoclinic bismuth borate BiB_3O_6 (BIBO), *Solid State Commun.* **109**, 249–251 (1999)
- 9.151 J.F. Carvalho, A.C. Hernandez: Large $\text{Bi}_{12}\text{TiO}_{20}$ single crystals: A study of intrinsic defects and growth parameters, *J. Cryst. Growth* **205**, 185–190 (1999)
- 9.152 S. Miyazawa, T. Tabata: $\text{Bi}_2\text{O}_3\text{–TiO}_2$ binary phase diagram study for TSSG pulling of $\text{Bi}_{12}\text{TiO}_{20}$ single crystals, *J. Cryst. Growth* **191**, 512–516 (1998)
- 9.153 A. Majchrowski, M.T. Borowiec, J. Žmija, H. Szymczak, E. Michalski, M. Barański: Crystal growth of mixed titanium sillenites, *Cryst. Res. Technol.* **37**, 797–802 (2002)
- 9.154 C.W. Lan, H.J. Chen, C.B. Tsai: Zone-melting Czochralski pulling growth of $\text{Bi}_{12}\text{SiO}_{20}$ single crystals, *J. Cryst. Growth* **245**, 56–62 (2002)
- 9.155 M.T. Santos, L. Arizmendi, D. Bravo, E. Diéguez: Analysis of the core in $\text{Bi}_{12}\text{SiO}_{20}$ and $\text{Bi}_{12}\text{GeO}_{20}$ crystals grown by the Czochralski method, *Mater. Res. Bull.* **31**, 389–396 (1996)
- 9.156 J.C. Rojo, E. Diéguez: *Bismuth Germanate, Titanate and Silicate, Encyclopedia of Materials: Science and Technology* (Elsevier, Amsterdam 2001)
- 9.157 V. Bermúdez, O.N. Budenkova, V.S. Yuferev, M.G. Vasiliev, E.N. Bystrova, V.V. Kalaev, J.C. Rojo, E. Diéguez: Effect of the shouldering angle on the shape of the solid–liquid interface and temperature fields in sillenite-type crystals growth, *J. Cryst. Growth* **279**, 82–87 (2005)
- 9.158 S. Kumaragurubaran, S.M. Babu, K. Kitamura, S. Takegawa, C. Subramanian: Defect analysis in Czochralski grown $\text{Bi}_{12}\text{SiO}_{20}$ crystals, *J. Cryst. Growth* **239**, 233–237 (2001)
- 9.159 M.T. Santos, C. Marín, E. Diéguez: Morphology of $\text{Bi}_{12}\text{GeO}_{20}$ crystals grown along the $\langle 111 \rangle$ directions by the Czochralski method, *J. Cryst. Growth* **160**, 283–288 (1996)
- 9.160 S. Maida, M. Higuchi, K. Kodaira: Growth of $\text{Bi}_{12}\text{SiO}_{20}$ single crystals by the pulling–down method with continuous feeding, *J. Cryst. Growth* **205**, 317–322 (1999)
- 9.161 Y.F. Zhou, J.C. Wang, L.A. Tang, Z.L. Pan, N.F. Chen, W.C. Chen, Y.Y. Huang, W. He: Space growth studies of Ce-doped $\text{Bi}_{12}\text{SiO}_{20}$ single crystals, *Mater. Sci. Eng. B* **113**, 179–183 (2004)
- 9.162 M.T. Santos, J.C. Rojo, A. Cintas, L. Arizmendi, E. Diéguez: Changes in the solid–liquid interface during the growth of $\text{Bi}_{12}\text{SiO}_{20}$, $\text{Bi}_{12}\text{GeO}_{20}$ and LiNbO_3 crystals grown by the Czochralski method, *J. Cryst. Growth* **156**, 413–420 (1995)

- 9.163 J. Martínez-López, M. González-Mañas, J.C. Rojo, B. Capelle, M.A. Caballero, E. Diéguez: X-ray topographic characterization of growth defects in sillenite type crystals, *Ann. Chim. Mater.* **22**, 687–690 (1997)
- 9.164 O.N. Budenkova, M.G. Vasiliev, V.S. Yuferev, N. Bystrova, V.V. Kalaev, V. Bermúdez, E. Diéguez, Y.N. Makarov: Simulation of global heat transfer in the Czochralski process for BGO sillenite crystals, *J. Cryst. Growth* **266**, 103–108 (2004)
- 9.165 A. Cremades, M.T. Santos, A. Remón, J.A. García, E. Diéguez, J. Piqueras: Cathodoluminescence and photoluminescence in the core region of $\text{Bi}_{12}\text{GeO}_{20}$ and $\text{Bi}_{12}\text{SiO}_{20}$ crystals, *J. Appl. Phys.* **79**, 7186–7190 (1996)
- 9.166 J.C. Rojo, C. Marín, J.J. Derby, E. Diéguez: Heat transfer and the external morphology of Czochralski-grown sillenite compounds, *J. Cryst. Growth* **183**, 604–613 (1998)
- 9.167 N. de Diego, F. Plazaola, J. del Río, M.T. Santos, E. Diéguez: Positron annihilation in $\text{Bi}_{12}\text{XO}_{20}$ ($\text{X} = \text{Ge}, \text{Si}, \text{Ti}$) structures, *J. Phys. Condens. Matter* **8**, 1301–1306 (1996)
- 9.168 H.S. Horowitz, A.J. Jacobson, J.M. Newsam, J.T. Lewandowski, M.E. Leonowicz: Solution synthesis and characterization of sillenite phases: $\text{Bi}_{24}\text{M}_2\text{O}_{40}$ ($\text{M} = \text{Si}, \text{Ge}, \text{V}, \text{As}, \text{P}$), *Solid State Ion.* **32/33**, 678–690 (1989)
- 9.169 V. Tassev, G. Diankov, M. Gospodinov: Optical activity of doped sillenite crystals, *Mater. Res. Bull.* **30**, 1263–1267 (1995)
- 9.170 M. Burianek, S. Haussühl, M. Kugler, V. Wirth, M. Mühlberg: Some physical properties of boron sillenite: $\text{Bi}_{24.5}\text{BO}_{38.25}$, *Cryst. Res. Technol.* **41**(4), 375–378 (2006)
- 9.171 H. Marquet, M. Tapiero, J.C. Merle, J.P. Zielinger, J.C. Launa: Determination of the factors controlling the optical background absorption in nominally undoped and doped sillenites, *Opt. Mater.* **11**, 53–65 (1998)
- 9.172 V.L. Tassev, G.L. Diankov, M. Gospodinov: Measurement of optical activity and Faraday effect in pure and doped sillenite crystals, *Proc. SPIE* **2529**, 223–230 (1995)
- 9.173 D. Bravo, F.J. Lopez: The EPR technique as a tool for the understanding of laser systems, the case of Cr^{3+} and Cr^{4+} ions in $\text{Bi}_4\text{Ge}_3\text{O}_{12}$, *Opt. Mater.* **13**, 141–145 (1999)
- 9.174 D. Bravo, A. Martin, A.A. Kaminskii, F.J. Lopez: EPR spectra of Cr^{3+} ions in $\text{LiNbO}_3\text{:ZnO}$ and $\text{LiNbO}_3\text{:CaO}$, *Radiat. Eff. Defects Solids* **135**, 261–264 (1995)
- 9.175 E.V. Mokrushina, A.A. Nechitailov, V.V. Prokofiev: A method for determining the charge state of chromium in Cr-doped $\text{Bi}_{12}\text{SiO}_{20}$ and $\text{Bi}_{12}\text{TiO}_{20}$, *Opt. Commun.* **123**, 592–596 (1996)
- 9.176 A.K. Jazmati, G. Vazquez, P.D. Townsend: Second harmonic generation from RE doped BGO waveguides, *Nucl. Instrum. Methods B* **166–167**, 592–596 (2000)
- 9.177 A.K. Jazmati, P.D. Townsend: Optical rotation in a $\text{Bi}_4\text{Ge}_3\text{O}_{12}\text{:RE}$ surface modified by He-ion beam implantation, *Nucl. Instrum. Methods B* **148**, 698–703 (1999)
- 9.178 J.B. Shim, J.H. Lee, A. Yoshikawa, M. Nikl, D.H. Yoon, T. Fukuda: Growth of $\text{Bi}_4\text{Ge}_3\text{O}_{12}$ single crystal by the micro-pulling-down method from bismuth rich composition, *J. Cryst. Growth* **243**, 157–163 (2002)
- 9.179 X.Q. Feng, G.Q. Hu, Z.W. Yin, Y.P. Huang, S. Kapphan, C. Fisher, F.Z. Zhou, Y. Yang, D.Y. Fan: Growth, laser and magneto-optic properties of Nd-doped $\text{Bi}_4\text{Ge}_3\text{O}_{12}$ crystals, *Mater. Sci. Eng. B* **23**, 83–87 (1994)
- 9.180 S.Y. Wu, H.N. Dong: Investigations on the local structures of $\text{Cr}^{3+}(3d^3)$ and $\text{Nd}^{3+}(4f^3)$ ions at the trigonal Bi^{3+} sites in $\text{Bi}_4\text{Ge}_3\text{O}_{12}$, *Opt. Mater.* **28**, 1095–1100 (2006)
- 9.181 V. Marinova, M.L. Hsieh, S.H. Lin, K.Y. Hsu: Effect of ruthenium doping on the optical and photorefractive properties of $\text{Bi}_{12}\text{TiO}_{20}$ single crystals, *Opt. Commun.* **203**, 377–384 (2002)
- 9.182 V. Marinova, S.H. Lin, V. Sainov, M. Gospodinov, K.Y. Hsu: Light-induced properties of Ru-doped $\text{Bi}_{12}\text{TiO}_{20}$ crystals, *J. Opt. A. Pure Appl. Opt.* **5**, S500–S506 (2003)
- 9.183 K. Buse, H. Hesse, U. van Stevendaal, S. Loheide, D. Sabbert, E. Kratzig: Photorefractive properties of ruthenium-doped potassium niobate, *Appl. Phys. A* **59**, 563–567 (1994)
- 9.184 S. Lanfredi, M.A.L. Nobrea: Conductivity mechanism analysis at high temperature in bismuth titanate: A single crystal with sillenite-type structure, *Appl. Phys. Lett.* **86**, 081916 (2005)
- 9.185 B. Briat, V.G. Grachev, G.I. Malovichko, O.F. Schirmer, M. Wöhlecke: Defects in inorganic photorefractive materials and their investigations. In: *Photorefractive Materials and Their Applications*, Vol. 2, ed. by P. Gunter, J.P. Huignard (Springer, Berlin 2007)
- 9.186 B. Briat, A. Hamri, N.V. Romanov, F. Ramaz, J.C. Lounay, O. Thiemann, H.J. Reyher: Magnetic circular dichroism and the optical detection of magnetic resonance for the Bi antisite defect in $\text{Bi}_{12}\text{SiO}_{20}$, *J. Phys. Condens. Matter* **7**, 6951–6959 (1995)
- 9.187 H.J. Reyher, U. Hellwig, O. Thiemann: Optically detected magnetic resonance of the bismuth-on-metal-site intrinsic defect in photorefractive sillenite crystals, *Phys. Rev. B* **47**, 5638–5645 (1993)
- 9.188 I. Biaggio, R.W. Hellwarth, J.P. Partanen: Band mobility of photoexcited electrons in $\text{Bi}_{12}\text{SiO}_{20}$, *Phys. Rev. Lett.* **78**, 891–894 (1997)
- 9.189 W. Rehwald, K. Frick, G.K. Lang, E. Meier: Doping effects upon the ultrasonic attenuation of $\text{Bi}_{12}\text{SiO}_{20}$, *J. Appl. Phys.* **47**, 1292–1294 (1976)
- 9.190 P.K. Grewal, M.J. Lea: Ultrasonic attenuation in pure and doped $\text{Bi}_{12}\text{GeO}_{20}$, *J. Phys. C Solid State Phys.* **16**, 247–257 (1983)

- 9.191 B.K. Meyer, H. Alves, D.M. Hofmann, W. Kriegseis, D. Forster, F. Bertram, J. Christen, A. Hoffmann, M. Strassburg, M. Dworzak, U. Haboeck, A.V. Rodina: Bound exciton and donor–acceptor pair recombinations in ZnO, *Phys. Status Solidi (b)* **241**, 231–260 (2004)
- 9.192 S.L. Lee, C.K. Lee, D.C. Sinclair: Synthesis and characterisation of bismuth phosphate-based sillenites, *Solid State Ion.* **176**, 393–400 (2005)
- 9.193 D.C.N. Swindells, J.L. Gonzalez: Absolute configuration and optical activity of laevorotatory $\text{Bi}_{12}\text{TiO}_{20}$, *Acta Crystallogr. B* **44**, 12–15 (1988)

Bulk Crystal

10. Bulk Crystal Growth of Ternary III–V Semiconductors

Partha S. Dutta

Ternary semiconductor substrates with variable bandgaps and lattice constants are key enablers for next-generation advanced electronic, optoelectronic, and photovoltaic devices. This chapter presents a comprehensive review of the crystal growth challenges and methods to grow large-diameter, compositionally homogeneous, bulk ternary III–V semiconductors based on As, P, and Sb compounds such as GaInSb, GaInAs, InAsP, AlGaSb, etc. The Bridgman and gradient freezing techniques are the most successfully used methods for growing ternary crystals with a wide range of alloy compositions. Control of heat and mass transport during the growth of ternary compounds is crucial for achieving high-quality crystals. Melt mixing and melt replenishment methods are discussed. The scale-up issues for commercial viability of ternary substrates is also outlined.

10.1	III–V Ternary Semiconductors	282
10.2	Need for Ternary Substrates	283
10.3	Criteria for Device-Grade Ternary Substrates	284
10.4	Introduction to Bridgman Crystal Growth Techniques ..	286
10.4.1	Bridgman Techniques	286
10.4.2	Gradient Freezing Techniques	288
10.4.3	Seed Generation for New Materials	289
10.4.4	The Seeding Process	290
10.4.5	Growth Rate Determination Methods	290
10.5	Overview of III–V Binary Crystal Growth Technologies	292
10.5.1	Phase Equilibria for Binary Compounds	292
10.5.2	Binary Compound Synthesis	293
10.5.3	Single-Crystal Growth Processes	297
10.5.4	Cleaning Procedures for Growth Chamber, Crucible, and Charge	299
10.6	Phase Equilibria for Ternary Compounds ..	300
10.6.1	Pseudobinary Phase Diagram	300
10.6.2	Ternary Phase Diagram	300
10.6.3	Quaternary Phase Diagram	301
10.7	Alloy Segregation in Ternary Semiconductors	302
10.8	Crack Formation in Ternary Crystals	304
10.8.1	Phenomena of Crack Formation ...	304
10.8.2	Elimination of Cracks	306
10.8.3	Crystal Growth Rate for Crack-Free Ternary Crystals	308
10.9	Single-Crystalline Ternary Seed Generation Processes	308
10.9.1	Bootstrapping Method	308
10.9.2	Directional Solidification by Normal Freezing	309
10.9.3	Directional Solidification by Solute Diffusion and Precipitation	310
10.9.4	Growth of Lattice-Mismatched Ternary on Binary Using Quaternary Grading	311
10.10	Solute Feeding Processes for Homogeneous Alloy Growth	311
10.10.1	Growth from Large-Volume Melts ..	311
10.10.2	Solute Feeding Using Double-Crucible Configuration	312
10.10.3	Solute Feeding in the Vertical Bridgman Method ..	313
10.10.4	Solute Feeding by Crucible Oscillation	314
10.10.5	Growth Using Compositionally Graded Feed	315
10.10.6	Periodic Solute Feeding Process ...	315
10.11	Role of Melt–Solid Interface Shapes	318
10.12	Conclusion	321
	References	321

10.1 III–V Ternary Semiconductors

Ternary compounds are synthesized by mixing three elements. These are also referred to as pseudobinary or tertiary compounds or alloys. From the periodic table, one can mix two group III elements and one group V element to form ternaries such as $\text{Ga}_{1-x}\text{In}_x\text{As}$. Alternatively one could mix one group III element and two group V elements to form ternaries such as $\text{InP}_{1-y}\text{As}_y$. Here x and y are mole percentages. The values of x and y are between 0 (0 mol %) and 1 (100 mol %). *Pseudobinary* is an equivalent term since a ternary compound such as $\text{Ga}_{1-x}\text{In}_x\text{As}$ can be viewed as comprising of x mol % of InAs and $(1-x)$ mol % of GaAs. Ternary compounds are attractive as substrate materials for electronic and optoelectronic applications since one can tune the lattice parameter or the bandgap energy of the ternary materials by choosing appropriate chemical compositions [10.1–7].

Figure 10.1 shows the lattice parameters and bandgap energies of the III–V semiconductors [10.1]. The values of bandgap and lattice parameter of the binary compounds such as GaAs, InP, GaSb, InSb, etc. are based on experimental data. Curves joining two binary compounds would represent different ternary compounds. For example, a curve between GaAs and InAs would represent the ternary $\text{Ga}_x\text{In}_{1-x}\text{As}$ ($0 < x < 1$) compound. The curves shown in the literature are primarily extrapolated based on experimental data points of few alloy compositions.

The lattice constants of ternary compounds (a_t) varies linearly with composition (x) between the two

binary lattice constants (a_1 and a_2). This is known as *Vegard’s law*

$$a_t = xa_1 + (1-x)a_2 \tag{10.1}$$

For example

$$a(\text{Ga}_{1-x}\text{In}_x\text{As}) = x a(\text{InAs}) + (1-x)a(\text{GaAs}) \text{ .}$$

The lattice constants for binary compound semiconductors are listed in Table 10.1.

The bandgap of any ternary compound varies non-linearly with the alloy composition (x or y). The

Table 10.1 Lattice constant, direct (D) and indirect (I) bandgap energy, and corresponding wavelength for As-, P-, and Sb-based III–V binary semiconductors

Material	Lattice constant (Å)	Bandgap energy (eV)	Bandgap wavelength (μm)
AlP	5.467	2.45 (I)	0.50
AlAs	5.660	2.14 (I)	0.58
AlSb	6.136	1.63 (I)	0.76
GaP	5.4512	2.268 (I)	0.55
GaAs	5.6532	1.424 (D)	0.87
GaSb	6.0959	0.725 (D)	1.70
InP	5.8687	1.34 (D)	0.92
InAs	6.0583	0.356 (D)	3.5
InSb	6.4794	0.18 (D)	6.88

Table 10.2 Dependence of bandgap on alloy composition for As-, P-, and Sb-based ternary semiconductors

Alloy	Direct energy gap (eV)
$\text{Al}_x\text{In}_{1-x}\text{P}$	$1.34 + 2.23x$
$\text{Al}_x\text{Ga}_{1-x}\text{As}$	$1.424 + 1.247x, 0 < x < 0.45$ $1.424 + 1.087x + 0.438x^2, x > 0.45$
$\text{Al}_x\text{In}_{1-x}\text{As}$	$0.356 + 2.35x + 0.24x^2$
$\text{Al}_x\text{Ga}_{1-x}\text{Sb}$	$0.726 + 1.10x + 0.47x^2$
$\text{Al}_x\text{In}_{1-x}\text{Sb}$	$0.18 + 1.621x + 0.43x^2$
$\text{Ga}_x\text{In}_{1-x}\text{P}$	$1.34 + 0.511x + 0.6043x^2, 0 < x < 0.55$
$\text{Ga}_{1-x}\text{In}_x\text{As}$	$0.356x + 1.425(1-x) - 0.436x(1-x)$
$\text{Ga}_{1-x}\text{In}_x\text{Sb}$	$0.18x + 0.726(1-x) - 0.415x(1-x)$
$\text{GaP}_x\text{As}_{1-x}$	$1.424 + 1.172x + 0.186x^2$
$\text{InP}_x\text{As}_{1-x}$	$0.356 + 0.675x + 0.32x^2$
$\text{InAs}_y\text{Sb}_{1-y}$	$0.356y + 0.18(1-y) - 0.58y(1-y)$
$\text{GaAs}_y\text{Sb}_{1-y}$	$1.424y + 0.726(1-y) - 1.2y(1-y)$

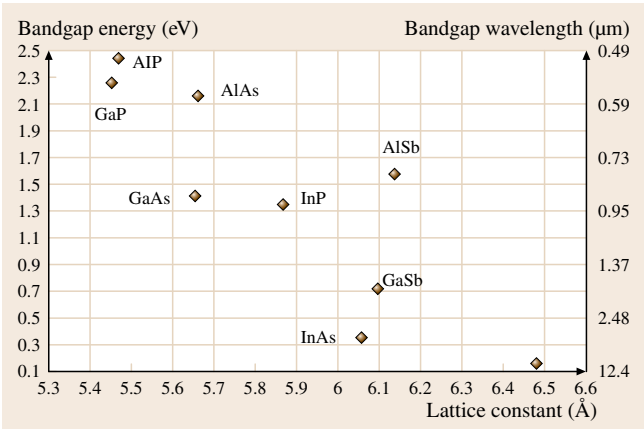


Fig. 10.1 Lattice constant, bandgap energy, and corresponding wavelength for As-, P-, and Sb-based III–V binary semiconductors

experimentally measured bandgap (E_g) for a ternary alloy can be fitted to a quadratic equation [10.1]

$$E_g(x)[\text{eV}] = xE_1 + (1-x)E_2 - cx(1-x), \quad (10.2)$$

where E_1 is the bandgap at $x = 1$, E_2 is the bandgap at $x = 0$, and the *composition independent* constant c is the bowing parameter accounting for the nonlinearity.

The above equation (10.2) can be rearranged as

$$E_g(x) = a + bx + cx^2,$$

where

$$a = E_2, \quad b = E_1 - E_2 - c, \quad c = c.$$

Table 10.2 summarizes the bandgap equations for various III–V ternary compounds. The bandgaps and lattice parameters shown in Fig. 10.1 as well as listed in Tables 10.1 and 10.2 are for compounds with the same crystal structure (zincblende or cubic). If the crystal structure changes, the lattice parameter and bandgap of the same material will be different. For example, the II–VI compound ZnS can exist in hexagonal or cubic phase.

10.2 Need for Ternary Substrates

For most semiconductor devices, multilayered thin-film structures comprising various ternary and quaternary compounds (also known as heterostructure) are necessary (Fig. 10.2). Ideally one would like to grow the entire thin-film structure on a substrate with same lattice constant (referred to as lattice-matched substrate). Unfortunately, device-grade single-crystal substrates of only binary compounds (such as GaAs, GaSb, InP, GaP, InAs, and InSb) with a few discrete lattice constants are commercially available (Fig. 10.1). Hence thin epitaxial layers are grown on binary substrates using liquid-phase epitaxy (LPE), metalorganic vapor-phase epitaxy (MOCVD or OMVPE) or molecular-beam epitaxy (MBE) techniques, as shown in Fig. 10.2. Due to the lattice mismatch between the epilayer and the

substrate, misfit dislocations originate at the growth interface and propagate into the device layers [10.1, 8]. Typical misfit dislocation density is in the range of 10^6 – 10^9 cm^{-2} [10.8]. Such a high density of dislocations leads to degradation of the electrical and optical characteristics of the devices. To reduce this misfit dislocation density, a variety of buffer layers are grown between the substrate and the device layers. However, the buffer layer technology necessary to relieve misfit-related stresses is not optimized for all systems, and often devices exhibit poor characteristics due to interfacial defects. Hence substrates with variable lattice constants are highly desirable to enhance the performance of electronic and optoelectronic devices.

The availability of substrates with tunable bandgap and lattice constant would also open up numerous possibilities of interesting bandgap engineering in homo- and heteroepitaxial devices with improved performances, new features, reduced fabrication complexity, and better cost effective. Some appropriate examples are: GaInAs laser diodes on lattice-matched substrates with high characteristics temperature [10.9–11], low-cost, high-quantum-efficiency photodetector [10.12, 13], and thermophotovoltaic cells [10.14] with diffused p-n homojunction on GaInSb bulk substrates, high-efficiency tandem solar cells [10.15], and antimonide-based quantum well and superlattice structures lattice matched to GaSb for high-efficiency mid-infrared sources and detectors [10.16]. Future devices with improved performances are being sought for a variety of military and civilian applications. These include: infrared (IR) imaging sensors for missile and surveillance systems; IR sources for deceptive jamming system; monitoring and detecting environmental pollution, fire, greenhouse-gas fluxes, industrial gas purity, trace moisture in corrosive

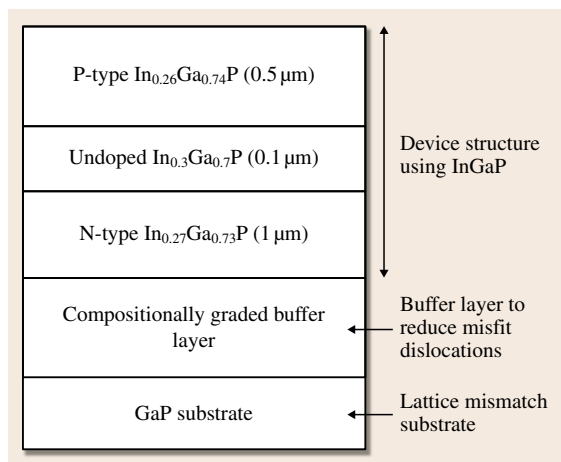


Fig. 10.2 A typical III–V ternary-based optoelectronic device structure grown on a lattice-mismatched binary substrate using a compositionally graded buffer layer

gases, and microleaks of toxic gases; high-performance and economical off-grid heat-electricity cogeneration systems; automobiles with ultralow emission (hybrid fuel–thermophotovoltaic); high sensitivity piezosensors and actuators; and quantum computing using electron spin coupling. Ternary substrates will provide a broad base of multicomponent alloy semiconductors with compatible heterostructure devices for these applications.

Bulk single-crystal substrates of ternary semiconductors are still not available from any commercial

vendor in spite of four decades of research on ternary substrates. The reason is not due to the lack of market for these substrates, but due to inherent problems in growing them from melt [10.17–31]. The development of electronic, optoelectronic, and photovoltaic devices based on ternary lattice-matched substrates has not been successful due to the poor substrate quality of mixed alloys and/or low yield of wafers with the same alloy composition. This chapter lays out the challenges and potential solutions that could be adopted for future commercial development of ternary substrates.

10.3 Criteria for Device-Grade Ternary Substrates

For successful incorporation of ternary substrates into future commercial device technologies, the wafers need to meet several important criteria as discussed below:

- (a) Single crystal wafers of 2 in (50 mm) or larger diameter must be available. Most commercial epitaxial growth and device fabrication equipment is geared towards handling wafers of 50 mm or larger. Hence the growth and fabrication conditions for any specific device structure need to be optimized using the geometries that will ultimately be used in large-scale production.
- (b) The spatial compositional inhomogeneity across the entire wafer should be minimal (less than 0.5 mol %). Variations in composition will lead to differences in final device characteristics fabricated across the wafer.
- (c) Wafers should be completely free from cracks, metallic inclusions, and multiphase regions. These are commonly observed defects in ternary crystals and hence a great deal of care is necessary to avoid them during growth.
- (d) The dislocation density should be similar to that in existing high-quality commercial binary substrates (less than 1000 cm^{-2}). Since the dislocations in the substrate propagate into the epilayers, lower dislocation density in the starting wafer is always desirable for better yield of reliable devices [10.1].
- (e) A wide range of doping should be possible in the substrate material in order to achieve desirable optical and electrical properties [10.32–38]. For electronic devices, semi-insulating substrates are necessary. For infrared photodetector applications with back illumination (radiation incident from the back of the substrate) or for light-emitting diodes, the substrate must be optically transparent for wavelengths that are being detected or emitted in the epilayers. The electrical resistivity or optical transparency can be altered by suitable impurity doping of the bulk crystal. Even if lattice matching is achieved using a certain substrate material, if they do not have the necessary electrical or optical characteristics, the substrates are of little use for end applications. For example: high-purity undoped substrates of GaSb are completely opaque for radiation with wavelengths less than its bandgap [10.35–37]. This is due to large concentration of native defects such as vacancies and antisites in the grown crystals. These defects act as p-type dopants, leading to optical absorption by free carrier mechanisms and low electrical resistivity. High-resistivity (semi-insulating) GaSb substrates are not commercially available. The optical transparency of GaSb (for below bandgap radiation) as well as its resistivity can be enhanced by impurity compensation [10.32, 37].
- (f) Ternary crystals tend to be brittle than binary crystals and can be damaged during wafer slicing and polishing. This is due to high built-in strain in the crystals. Ensuring that the crystals can be processed into wafers is crucial. This requires proper thermal conditions during crystal growth and postgrowth annealing treatments.
- (g) The wafer should have high-quality polished and chemically treated surface to enable epigrowth (also referred to as *epiready* surfaces) of high-quality layers. Certain materials such as AlSb, even if available as high-quality substrates, cannot be easily adopted for epigrowth or device fabrication due to the challenges with the surface oxidation. Similarly, antimonide-based wafer surfaces such as GaSb or

InSb need special chemical processing before growing device-quality epilayers. Hence developing the polishing recipe for each substrate material is necessary for their application.

- (h) Finally, the cost of the final wafers should not be significantly higher than that of commercially available binary substrates. Though bulk substrates contribute to a small fraction of the cost for the entire device, high cost of the substrates poses a barrier for adoption unless it is clearly established that, by using lattice-matched substrates, significant improvements in device characteristics can be achieved.

These attributes can be translated into numerous constraints during crystal growth. As will be discussed in this chapter, many of the requirements are counteractive, and appropriate trade-offs in the growth conditions are necessary.

The growth conditions that are necessary for high-quality ternary crystals have been summarized below:

1. Crack-free and inclusion-free crystals can be grown by avoiding constitutional supercooling. That means that the crystal growth rate must be lower than the rate at which excess constituents rejected at the melt–crystal interface (due to segregation) are mixed back into the growth melt. This requires forced convective mixing in the growth melt and near the melt–crystal interface.
2. Low dislocation density and strain can be achieved if the growth takes place under a low temperature gradient and the crystals are cooled slowly after solidification.
3. High yield refers to obtaining wafers of the same composition from a single ingot. This is possible only when the crystal grown has the same composition along the growth direction. This requires replenishment of the melt with the constituents to maintain the same melt composition during the entire growth.
4. Rapid or uncontrolled melt replenishment leads to high level of supersaturation in the melt with the replenished constituents. This triggers polycrystalline growth due to random nucleation in the melt. To maintain single-crystallinity during growth, the rate at which the solute is fed to the melt must be precisely controlled at all times to match the crystal growth rate. This requires special solute feeding processes and forced convective mixing in the melt.
5. Low cost of final wafers directly relates to the growth rate of the crystal and the volume of starting melt versus the volume of final crystal. This would require: (a) consuming the entire melt during the growth and (b) rapidly transporting the dissolved constituents (replenishing elements or compounds) to the growth interface by forced convection. In addition, rapid dissolution of the replenished constituents (solute) is necessary. This would require that the dissolution of the solute occurs in a melt zone that is always undersaturated.
6. Compositionally homogeneous wafer would translate to uniform composition in the crystal perpendicular to the growth direction. This would require a planar melt–crystal interface during growth. This can be achieved by balancing the heat transfer at the melt–crystal interface by a combination of temperature gradient imposed by the furnace and the forced convective mixing in the growth melt. At the same time, temperature fluctuations due to forced convection in the growth melt (leading to composition fluctuation and local constitutional supercooling) must be eliminated. This can be achieved by having a low temperature gradient near the liquid–solid interface.
7. Large-diameter wafers are necessary for commercial applications. Hence any technology that is being developed for growth of alloy semiconductors must scale up to dimensions required for practical usage. This would require optimization of the heat and mass transport processes between various melt zones during growth for the length scales of interest. This is purely dictated by the design of the experimental setup and the process parameters. Bridgman and gradient freezing types of method are becoming more popular for large-diameter binary crystal growth with very low defect content. Hence the advancement made for binary growth could be adopted for future ternary crystal growth technology.

To achieve these goals, a lot of effort in engineering of the heat and mass transport processes during the growth of ternary alloys from melts is necessary. In this chapter, we discuss the interdependencies between various experimental parameters and their effects on the compositional homogeneity of ternary crystals. The focus will be on the Bridgman techniques as it offers a variety of beneficial attributes that are necessary for ternary crystal growth processes. In the next section, we briefly review the Bridgman and gradient freezing directional solidification processes.

10.4 Introduction to Bridgman Crystal Growth Techniques

10.4.1 Bridgman Techniques

The Bridgman technique (also referred to as the Bridgman–Stockbarger method) is one of the oldest techniques used for growing crystals [10.39]. The crystal growth can be implemented in either a vertical (vertical Bridgman technique) or horizontal system configuration (horizontal Bridgman technique). Schematics of the two configurations are shown in Figs. 10.3 and 10.4. The growth systems typically consist of a single- or multizone furnace. A single-zone furnace has a parabolic temperature profile with the highest temperature being at the center along the length of the furnace, as shown in Figs. 10.3 and 10.4. On both sides of the hottest section, a temperature gradient exists that is used during the crystal growth. For a multizone furnace, specific temperature gradients between different zones can be established as described later.

The principle of crystal growth using Bridgman technique is based on directional solidification by translating a molten charge (melt) from the hot to the cold zone of the furnace, as depicted in Figs. 10.3 and 10.4. The presence of a seed at the end of the crucible (container) ensures single-crystal growth along specific crystallographic orientation. The process for generat-

ing the *first* single crystalline seed of any new material has been described in Sect. 10.4.3. Using the single-crystal seed, the entire growth process takes place in the following sequence. At the beginning of the experiment, the crucible with the polycrystalline charge and seed is placed inside the growth chamber. Then the chamber is evacuated by a vacuum pump and refilled with inert gas. The temperature of the furnace is then raised. A proportional–integral–differential (PID) control mechanism controls the power to the heater elements, maintaining the desired temperatures. The PID controller also controls the power during the heating and cooling stages of the furnace. After the furnace is heated to a temperature above the melting point of the polycrystalline charge, the crucible is slowly translated into the hot zone to melt the polycrystalline charge completely and bring it into contact with the seed. Section 10.4.4 presents the intricacies of the seeding process. After the melt touches the seed, a portion of the seed is remelted to expose a fresh growth interface. The melt is thoroughly mixed using forced convection generated by rotating the crucible (using stepper motor control, for example). The homogenization of the melt can also occur by natural convection and diffusion in the melt without any forced convection. Hence melts can be homogenized by simply leaving the melt at temper-

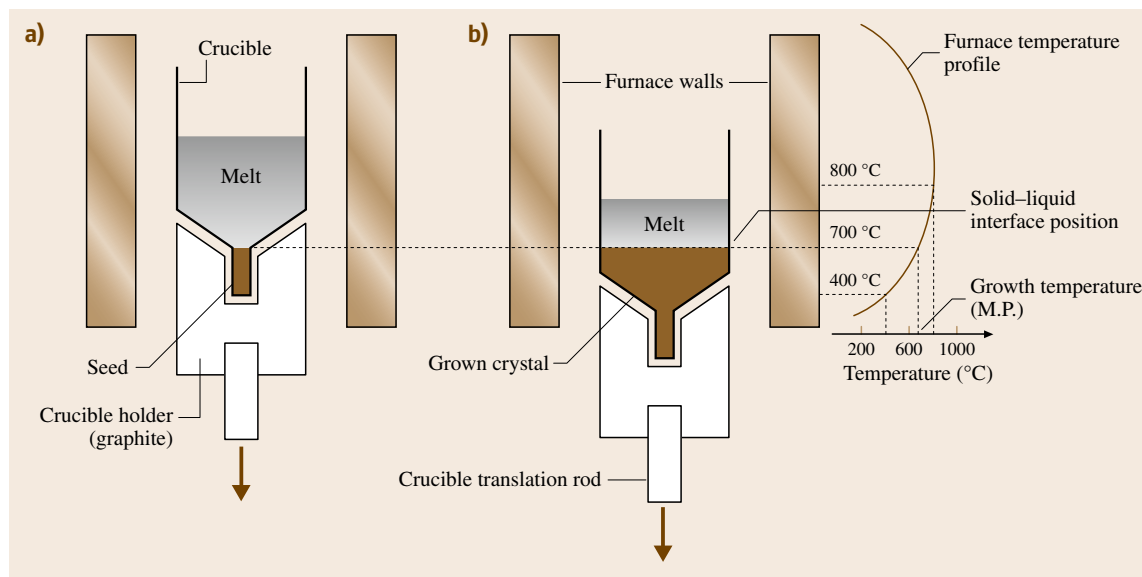


Fig. 10.3a,b Schematic diagram of a vertical Bridgman (VB) crystal growth process in a single-zone furnace: (a) at the beginning of the experiment and (b) with partially grown crystal

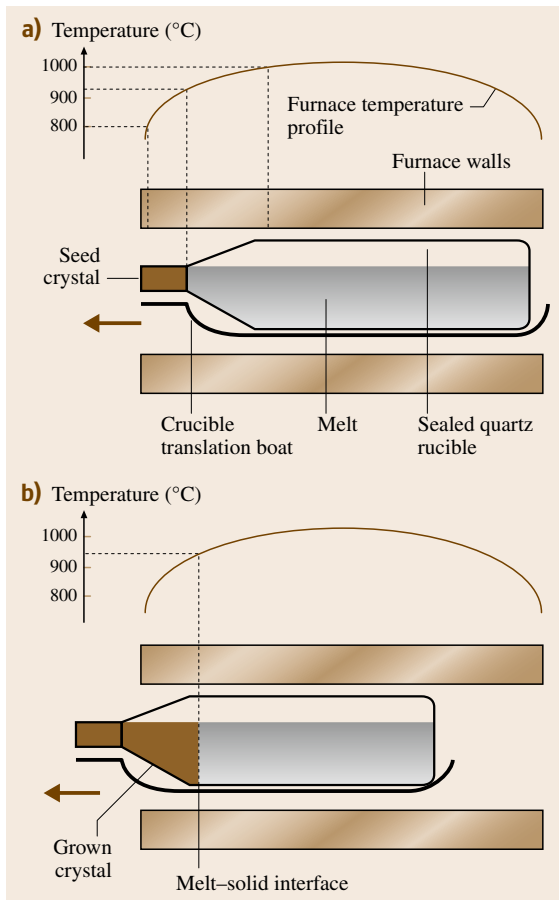


Fig. 10.4a,b Schematic diagram of a horizontal Bridgman (HB) crystal growth process in a single-zone furnace: **(a)** at the beginning of the experiment and **(b)** with partially grown crystal

atures higher than its melting point for a long duration. After the melt is completely mixed, crystal growth is initiated by cooling the melt from the seed end. This is done by translating the crucible slowly into the cooler section of the furnace. As the crucible is translated, the temperature at the bottom of crucible falls below the solidification temperature (the melting point of the material) and hence the melt starts to become a solid at the bottom of the crucible (at the seed–melt interface). After the melt has been completely translated below the melting point of the material, the entire molten charge converts to a solid ingot (also known as a boule). The crucible holder (typically made out of graphite) is connected to a stainless-steel shaft, which in turn is connected to a linear slide operated with the use

of a computer-controlled stepper motor assembly. The computer program controls the lowering rates of the crucible, and hence the rate of crystallization (growth rate) can be accurately controlled over long periods of time.

The growth rates for different crystals need to be optimized in order to grow single crystals with high crystalline quality. For example, the typical growth rate for III–V binary semiconductors is in the range of 0.5–3 mm/h, while for ternary crystals it is in the range of 0.1–1 mm/h. The shaft supporting the crucible can also be rotated with the help of a high-torque stepper motor. As will be discussed later, this is essential for efficient mixing of the melt during growth. After the entire molten charge is directionally solidified, the temperature of the furnace is decreased slowly to reach room temperature. The postgrowth cooling rate must be controlled in order to avoid thermal shock (due to rapid cooling) to the solid ingot that could lead to mechanical cracks in the crystal. Typical cooling rates are in the range of 10–50 °C/h, depending on the material. At the end of the experiment, the crystal is removed from the crucible and sliced to prepare the substrates. Figure 10.5 shows a typical vertical Bridgman grown ingot of GaInSb from the author's laboratory.

Though the concept of vertical and horizontal Bridgman techniques is similar, there are certain advantages and disadvantages of the two methods. The wafers extracted from vertical Bridgman grown crystals are perfectly circular in shape, unlike the D-shaped wafers from horizontal Bridgman grown crystals. For



Fig. 10.5 Vertical Bridgman grown $\text{Ga}_{1-x}\text{In}_x\text{Sb}$ single crystal (from the author's laboratory)

large-scale epitaxial growth on the substrates and device fabrication, circular wafers are certainly beneficial. The primary advantages of the horizontal Bridgman grown crystals are the high crystalline quality (such as low dislocation density) of the crystals and the stoichiometry control along the entire length of the crystal. In the horizontal Bridgman method (Fig. 10.4a,b), the crystal experiences lower stress due to the free surface on the top of the melt. During the growth, the solid does not touch the crucible on the top and hence is free to expand. Another advantage of the horizontal growth process is the enhanced mixing in the melt due to thermal convection (flows due to temperature gradient) at every location in the melt along the growth direction. As will be discussed later, this helps in ensuring stoichiometry (the composition of the crystal) along the length of the crystal by maintaining an overpressure of the volatile species such as the group V elements during III–V semiconductor growth.

Finally, it must be mentioned that, in the Bridgman techniques, the relative motion between the crucible and the furnace is all that matters. Instead of using crucible translation, the crucible can be kept stationary and the furnace translated to achieve directional solidification. In numerous cases, the crucible system design containing the melt, seed, and the overpressure elements is complex (as will be discussed below for GaAs and InP crystal growth) and hence translating the crucible poses

problems. It becomes much easier to translate the furnace along the crystal growth direction. The gradient freezing techniques discussed below is a sophisticated method to achieve the same effect without translating the crucible or furnace.

10.4.2 Gradient Freezing Techniques

The gradient freezing technique is analogous to the Bridgman technique discussed above except for the fact that the temperature gradient is translated along the melt to implement directional solidification [10.40–44]. The schematic of the gradient freeze method is shown in Fig. 10.6. The principle can be implemented in either vertical (VGF) or horizontal (HGF) configurations, as in the case of Bridgman methods. In the gradient freezing techniques, the crucible with the seed and the melt as well as the furnace system is kept stationary. The temperature gradient, as shown in Fig. 10.6, is moved along the crystal growth direction starting from the seed–melt interface to the end of the crystal. This is accomplished by a multiple-zone furnace system wherein the power to each zone is programmed and controlled by individual PID controllers. The use of multiple heater zones is necessary to maintain the same temperature gradient at the melt–solid interface during the entire crystal growth experiment. If a single-zone furnace is used, the temperature gradient at the

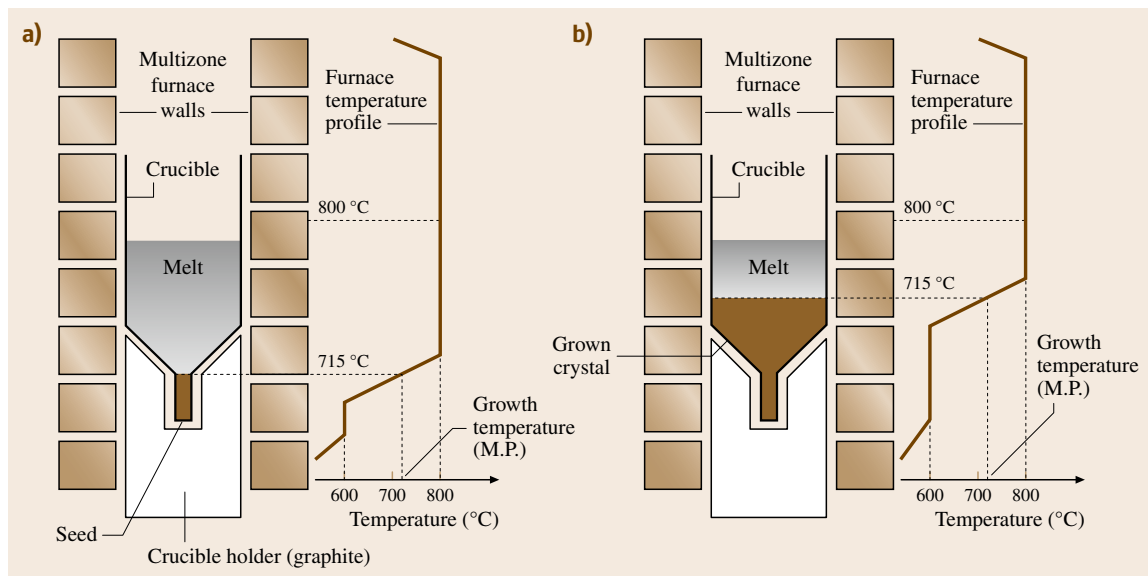


Fig. 10.6a,b Schematic diagram of a vertical gradient freeze (VGF) crystal growth process in a multizone (eight-zone) furnace: (a) at the beginning of the experiment and (b) with partially grown crystal

melt–solid interface changes at different locations in the furnace leading to variation in crystal growth rate with time. Since the heat flux through the growing crystal and melt changes with time, the multiple-zone system ensures continuously varying power to individual zones so as to maintain the same temperature gradient at the liquid–solid interface. The quality of the crystals grown by this method is far superior to that produced by traditional methods such as liquid encapsulated Czochralski (LEC). Since LEC growth takes place under a large temperature gradient (typically several tens of °C/cm), the dislocation density in grown crystals is of the order of $10\,000\text{ cm}^{-2}$ [10.1, 42, 45]. Wafer breakage in the device production process due to large thermal stress in the wafers is a significant problem. On the other hand, the temperature gradient used in the Bridgman or gradient freezing methods is very small ($1\text{--}10\text{ °C/cm}$). Hence a dislocation density less than 500 cm^{-2} has been achieved in VGF-grown crystals. As a result of this, the VGF and HGF techniques have received widespread commercial usage for both III–V and II–VI semiconductor crystal growth [10.40–44].

In a typical crystal growth experiment, the crucible with the charge is placed in the growth chamber. Then the chamber is evacuated by a vacuum pump and refilled with inert gas. The power to the individual element is increased with time to melt the polycrystalline charge completely and bring it into contact with the seed. A portion of the seed is also remelted to expose a fresh growth interface (Fig. 10.6a). Crystal growth is initiated by cooling the melt from the seed end. The temperature gradient at each and every point along the growth direction can be controlled very accurately due to the multiple zones (Fig. 10.6b). The sophisticated thermal controls also make gradient freezing systems more complex than typical Bridgman systems. Unlike simple resistance heater wires wound around tubes as in Bridgman-type systems, gradient freezing units have advanced heater designs. Some systems have water cooling tubes between the heater plates to ensure sharp and controllable temperature gradients along the length of the furnace.

For semiconductor crystal growth, oxygen in the melt must be eliminated completely. Hence crystal growth chambers are designed to be vacuum-tight as well as to withstand high internal gas pressures. After loading the crucible with charge, the growth chamber is evacuated to a high vacuum (1 mTorr or less pressure) and repeatedly flushed with an inert gas mixture such as argon/hydrogen or hydrogen/nitrogen to ensure the removal of moisture and oxygen from inside the chamber.

During the charge synthesis and growth, the chamber is filled with an inert gas and a pressure is maintained beyond the vapor pressure of the melt in the chamber.

10.4.3 Seed Generation for New Materials

For single-crystal growth of any material, a single-crystalline seed of specific orientation is necessary. For a new material under development, single-crystal seeds are not available. Single-crystal seeds can be generated by vertical Bridgman growth using specially tipped crucibles [10.39] as shown in Fig. 10.7. There are two ways this can be made possible. In the first scenario (Fig. 10.7a), a natural seed selection process can occur at the tip region of the crucible. A specific nucleus can grow faster than the others and outgrow the rest of the nuclei. However this process is completely random and cannot be expected to repeat in every experiment. Hence a more predictive way of selecting an individual seed orientation is via the necking process (similar to what is being done in the Czochralski crystal growth process). In this process (Fig. 10.7b), randomly nucleated grains are subjected to a filtering process at the necking point in the crucible so that only one orientation reaches the main body of the crucible and grows into a bulk ingot. However, the production of a single-crystal grain cannot always be guaranteed by either of these processes. Random secondary nuclei from the crucible walls, such as shown in Fig. 10.7b, are often seen. Hence liquid encapsulation with low-melting-point liquids or crucible coating, e.g., with carbon, is necessary to avoid the melt touching the crucible wall during growth. This process,

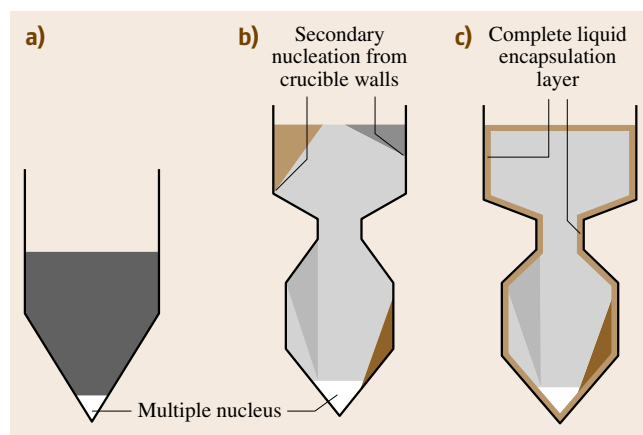


Fig. 10.7a–c Single-crystal seed generation processes: (a) by natural selection, (b) by necking, and (c) by necking and liquid encapsulation

depicted in Fig. 10.7c, is the most predictive way to ensure a single-crystal seed generation process. Due to the random nature of the initial seed orientation, the single-crystal seed is then oriented along a preferred crystallographic direction using the x-ray orientation method. The ingot is then mined to obtain a seed with a specific orientation for further crystal growth experiments. For a cylindrical seed, a diamond core drill could be used. For rectangular-shaped seeds, the ingot can be sliced using a blade or a wire saw.

10.4.4 The Seeding Process

The initial stage of the crystal growth experiments wherein a single-crystalline seed is contacted with the molten charge is crucial and requires adequate care and experience. High-quality single-crystal seeds are precious and used repeatedly for a large number of experiments. The seeds are smaller in diameter with respect to the final diameter of the grown crystals. For example, a typical seed diameter is 5 mm (with 5–6 cm in length), while the grown crystals could be 50–75 mm in diameter. The seed needs to be partially remelted (≈ 0.5 cm) to expose a fresh growth interface and then the crystal growth is started. Unlike in the Czochralski growth method, the seed–melt interface during Bridgman growth (in most cases) cannot be observed due to the opacity of the crucible, melt, and/or the growth chamber. Hence for precise remelting of the seed during crystal growth, one needs to conduct a priori thorough analysis of the thermal environment of the growth chamber. Translating the crucible into the hot zone even by 1 mm could sometimes remelt the entire length (and hence loss) of the seed. This is due to the heat transfer from the melt to the seed by conduction and convection in the hot melt. For Bridgman and gradient freezing types of crystal growth experiments, in order to ensure the exact seeding position in the furnace, prior experimentation needs to be done with dummy melts and seeds. Since the heat transfer between the furnace, crucible, melt, and growth chamber is quite complex, any optimization of the seeding position needs to be carried out using a specific set of crucible diameter, crucible holder design, crucible material (pyrolytic boron nitride (pBN), silica, graphite, alumina, etc.), melt depth, seed length, etc. If any of the above parameters is altered during the actual crystal growth experiment, the seeding position will change.

For the seeding position determination, two sets of experiments need to be carried out. In the first experiment, a polycrystalline charge (of the same material

to be grown) is melted into a crucible with the exact shape as is to be used in the final crystal growth experiment. The melt is then directionally solidified as in the real crystal growth experiment. The polycrystalline ingot, which is shaped like a crystal with a seed at the end (Fig. 10.3b), is removed from the crucible and then chemically etched to make the surface shiny (as described in Sect. 10.5.4). In the second experiment, this polycrystalline ingot is placed inside an identical crucible (as in the first experiment). The crucible is then slowly translated into the hot zone of the furnace to remelt the ingot to a desired point and then directionally solidified by translating the crucible back into the cold zone. After the experiment, one can easily observe the interface between the remelted and unmelted portions of the ingot. By repeating this process, one can identify the crucible location in the furnace that will provide the desired seed–melt interface. Since this process is rigorous, once the crucible location has been identified for proper seeding, it is advisable to maintain the same conditions during actual crystal growth experiments. Slight changes such as an increase or decrease in melt height or thickness of crucible wall could lead to a large variation in the seeding interface location. Hence in large-scale crystal production, the design of the entire crystal growth systems is properly analyzed and crystal growth conditions are kept unchanged.

10.4.5 Growth Rate Determination Methods

The crystal growth rate is an important factor that dictates the crystalline quality and microstructure of the grown crystals. For crystals grown from melt in crucibles using Bridgman or gradient freezing techniques, precise determination of growth rates requires considerable experimental effort. There are a few techniques that have been developed and used for determining the growth rate of crystals, as briefly discussed below [10.46–65]. The choice of technique is decided by the crystal growth temperature, and the optical, electrical, and thermal properties of the melt, crystal, and crucible material.

Depending on the crystal to be grown, a proper choice of crucible material is necessary based on its chemical reactivity with the melt. There may be more than one option for the crucible material for any specific melt. The final selection of the crucible material is made based on several other factors such as heat transfer and thermal configurations, use of melt encapsulations, the thermal expansion coefficient of the grown crystal, application of external fields during growth, etc. Hence,

based on the crucible material, a specific growth rate determination method is used. For example, crucible material such as silica (quartz) is optically transparent and hence the melt–crystal interface can be directly visualized during growth if a transparent furnace configuration is used. On the other hand crucibles made of pyrolytic boron nitride (pBN), alumina, graphite, etc. are opaque and hence indirect methods for melt–solid interface visualization are necessary. The thermal conductivity of the crucible material contributes to the heat transport from the hot zone to the cold zone of the furnace and thus has a significant effect on the melt–crystal interface shape and the growth rate of crystals. In the case of crystals grown under applied electric and magnetic fields, it is important to select a crucible material with appropriate electrical conductivity.

For crystals with low growth temperature (below 1000°C) that can be grown in a transparent crucible such as silica, the determination of growth rate is relatively straightforward. Since furnaces with optically transparent walls can be used for low growth temperatures, one can directly observe the melt and crystal inside the crucible. In these furnaces, a resistive heating coil is enclosed inside a transparent or semitransparent silica tube. Usually the furnace wall is coated with a thin film of reflective metal such as gold to reduce radiative heat losses. By in situ observation of the length of solidified melt with time (due to directional cooling), one can easily calculate the growth rate. This method has been used for determining the growth rate of optically transparent crystals as well as metal and semiconductor crystals [10.28, 46]. In the case of optically transparent material, the transparencies of the melt and the solid need to be different in order to observe a clear demarcation at the melt–crystal interface. For metallic or semiconductor crystals, typically the optical reflectivities of the melt and the solidified crystal are different, thus providing a clear delineation at the melt–crystal interface. This method cannot be used when the crystals need to be grown in an opaque crucible such as pBN or when a furnace with opaque insulation wall is used. Typically, for growth temperature exceeding 1000°C, the furnace wall is insulated with alumina or quartz wool and is opaque. In such scenarios, there are four methods for determining the growth rate, namely, melt quenching, Peltier interface demarcation (PD), periodic external field application, and real-time radiosopic x-ray/ γ -ray visualization.

In the traditional melt quenching method [10.47–49], the crystal growth experiment is terminated by rapid cooling of the melt after a certain period. When

the solidified ingot is sliced along the growth direction, one can easily observe two interfaces. The first interface is seen at the seeding point (at the first-to-freeze position on the seed crystal). The second interface is seen where the growth is terminated by rapid quenching. By measuring the distance between the two interface positions and the total growth duration, one can obtain the average growth rate. The sliced specimens generally requires metallographic preparation via coarse grinding and fine polishing (using abrasive powders or polishing slurries) followed by chemical etching (with a suitable etchant solution) to reveal the interface demarcation striations under Nomarski interference contrast microscopy. The quenching method is a universal technique that can be used for any material system irrespective of optical, electrical, and thermal properties. However it gives no information on the evolution of the solid–liquid interface position during growth. This is a major limitation since the crystal growth rate varies with time during the experiment as a result of varying heat flow through the melt and the crystal (due to changing axial temperature gradient in the melt and solid) as well as alloy segregation (as in the case of ternary and quaternary semiconductor alloys).

For crystals and melts with good electrical conductivity, the PD can be employed [10.50–56]. In a typical experiment, two electrical contacts are made: one at the top of the melt using an appropriate electrode material (that will not react with the melt) and one at the bottom of the seed crystal. In this method, thermoelectric effects induced by a current pulse passing through the melt and the directionally solidifying sample results in the creation of a rapid thermal perturbation at the solid–liquid interface. A series of perturbations result in concentration variations which, after being revealed by postgrowth metallography, delineate the instantaneous interface shape at successive times during growth and enable one to follow the time evolution of the solid–liquid interface. This method has been successfully used for metallic alloys and semiconductor materials. Since electric current needs to flow through the melt and the crystal, it is difficult to implement the PD process in materials with low electrical conductivity.

An elegant way of determining the crystal growth rate is by the application of periodic external fields during growth [10.57–60] such as by rotating magnetic fields or alternating electric fields. In the absence of an applied magnetic field, growth striations appear in the crystals due to natural convection. If the melt convection is suppressed by applied fields, the striations are not seen. By periodically switching on and off the ex-

ternal magnetic fields, one can create or suppress the growth striations. Postgrowth analysis of the specimens by selective chemical etching reveals the regions with striations and striation-free zones. By correlating the length of the individual zones with the field application durations, one can easily determine the growth rate. This technique cannot be used if the growth conditions have been optimized to obtain striation-free crystals without external fields. The application of alternating electric field has been found to alter the microstructure of the crystalline material. Hence, by switching on and off the field, one will obtain regions with different microstructures. The growth rate can be determined easily by postgrowth analysis of the cross-sectional view of the specimen after metallography.

A technique which is very attractive for real-time interface shape monitoring as well as growth rate determination is the use of x-rays and gamma-rays [10.61–

65]. This technique is based on the differential transmission of the x-rays or gamma-rays through the solid and the liquid phases. This difference in transmittance could be due to: (a) density difference between the liquid and solid phases, (b) crystalline structure (long- or short-range ordering), (c) dopant (impurity) distribution in the two phases (due to impurity segregation), etc. In the case of dopant distribution, the absorption coefficient of the radiation increases with increasing impurity concentration. This results in image contrast between the solid and liquid phases due to differences in the amount of radiation absorbed (or transmitted) through the individual regions (solid or liquid). One advantage of the radiosopic system is the ability to melt a single sample, solidify it, remelt it, and then change experimental parameters for a different case study. In this manner one can produce a large range of data in a single experiment.

10.5 Overview of III–V Binary Crystal Growth Technologies

Since the focus of this chapter is on ternary crystal growth, the topic of binary III–V bulk crystal growth (excluding the nitrides) using Bridgman or gradient freezing types of processes will be briefly reviewed. This is done to highlight the fundamental differences between the growth conditions of binary versus ternary compounds and the additional advances necessary for ternary crystal growth.

10.5.1 Phase Equilibria for Binary Compounds

Binary compounds such as GaAs, InP, GaSb, etc. are synthesized by mixing the individual elements such as gallium, indium, arsenic, phosphorus, antimony, etc. beyond the melting points of the compounds. Table 10.3 lists the melting points of As-, P-, and Sb-based III–V compounds [10.66, 67]. For compound synthesis, one needs to review the thermodynamic phase diagram. Figure 10.8 shows a schematic phase diagram typical of any III–V binary compound (except the nitrides). This schematic diagram depicting GaAs is not the actual phase diagram, but rather a sketch to explain the important features of the phase formation during compound synthesis and crystal growth. Due to their very high melting temperatures and extreme vapor pressures (exceeding 40 000 atm), GaN, AlN, and InN cannot be grown from stoichiometric melts by Czochralski or Bridgman-type techniques [10.68].

The phase diagrams of various III–V binary compounds can be found in the literature [10.66, 67]. According to the phase diagram shown in Fig. 10.8, the most stable phase is the one where the ratio of group III to group V mole fraction is close to 1 [10.1, 69]. Due to the narrow stability region, the solidus is shown by a vertical line at a composition of 50 at. % (the stoichiometric composition). As shown in Fig. 10.8, the

Table 10.3 Melting points of elements and III–V binary compounds

Material	Melting point (°C)
Ga	29.8
In	156.6
Al	660.4
Sb	630.7
P (red)	416 (sublimes)
As	614 (sublimes)
AlP	> 2000
GaP	1480
InP	1062
AlAs	1740
GaAs	1238
InAs	942
AlSb	1065
GaSb	712
InSb	527

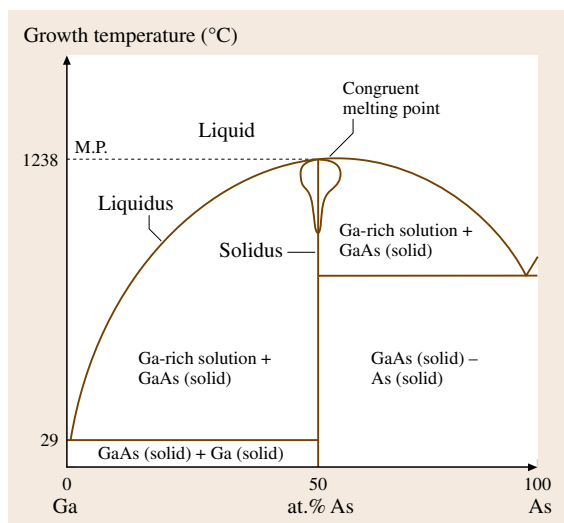


Fig. 10.8 Schematic binary phase diagram of III–V semiconductor (depicting GaAs)

stoichiometric melting point for GaAs is 1238 °C. The congruent melting point is typically slightly shifted from the stoichiometric composition. In the case of GaAs, the congruent melting point is on the arsenic-rich side of the phase diagram [10.69], and in the case of GaSb it is on the Ga-rich side [10.16]. The slight deviation from stoichiometry leads to point defects (native defects such as vacancies, interstitials, and antisites of group III and V elements) in the crystals, which affect the electrical and optical properties of the grown crystals [10.1, 16, 69].

Referring to Fig. 10.8, above the liquid curve (melting temperature), a uniform liquid region (melt) exists. Depending on the ratio of gallium to arsenic, the melting temperature varies. Irrespective of the growth temperature, the composition of the solid (solidus) that precipitate out of the liquid is always the stoichiometric compound GaAs. On the gallium-rich side, the melting point can be as low as 29 °C, which is the melting point of liquid gallium. However the solubility of arsenic in gallium decreases sharply as the temperature decreases. As the melt temperature is decreased, GaAs precipitates out first and then the excess gallium or arsenic solidifies. This phase formation property is used advantageously to grow binary compounds from group III- or group V-rich solutions at temperatures lower than the stoichiometric melting point. On both sides of the stoichiometric melting point, equilibrium regions with solid GaAs and Ga-rich or As-rich solution exist. Below a specific temperature, regions shown as solid GaAs

plus solid arsenic or solid gallium exist, depending on the excess element in the starting melt.

Due to the high vapor pressure of the group V elements, III–V compounds generally dissociate above the melting points. However, the dissociation rate depends on the partial vapor pressures. Antimony is the least volatile species amongst the group V elements. The partial vapor pressure of antimony at the melting point of GaSb (712 °C) is 3×10^{-6} Torr. Typically, during 10 h of GaSb growth, 10^{-3} moles of Sb would be lost from the melt [10.16]. The rate of antimony loss from AlSb melt at 1300 °C is ≈ 0.25 g/h [10.70]. The next most volatile species is arsenic. The vapor pressure of arsenic in equilibrium with GaAs melt at its melting point (1238 °C) is 1 atm. The phosphorus vapor pressure is the highest. At the melting point of InP (1062 °C), the vapor pressure in equilibrium with InP melt is ≈ 27 atmosphere. For comparison, the partial pressure of Ga, In, and Al is less than 10^{-6} Torr at the melting points of various compounds. To avoid evaporation of the group V element from the melt, pressure above the partial vapor pressure needs to be applied to the melt. This requires specially made high-pressure stainless-steel vessels, inside which the furnace is assembled.

10.5.2 Binary Compound Synthesis

In this section, we describe Bridgman or gradient freezing types of process that are being used for synthesizing the binary compounds [10.1, 16, 39–44, 66, 71–73, and references therein]. In this process, the starting ma-

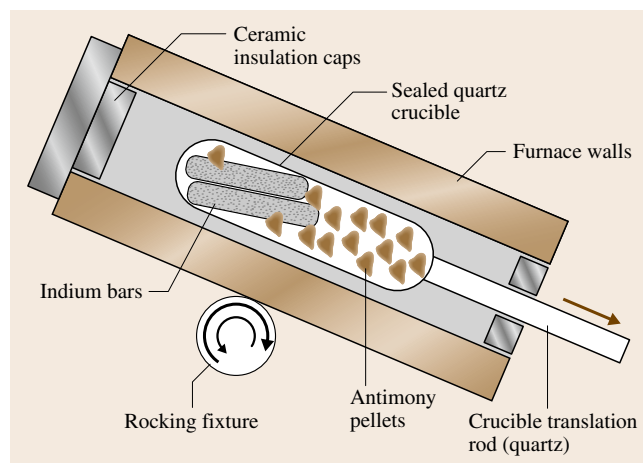


Fig. 10.9 InSb polycrystalline charge synthesis in a sealed crucible using a rocking furnace

terials (charge) consisting of equal mole fractions of the group III and group V elements are weighed and placed into a crucible. Depending on the compound to be synthesized, the placement of the elemental charges inside the crucible could be different, as described below. The crucible with the charge is then heated beyond the melting point of the binary compound and the compound synthesized in liquid form. Thereafter the melt is directionally solidified and slowly cooled to room temperature. Amongst the group V el-

ements, arsenic and phosphorus tend to be extremely volatile. Hence an overpressure of the group V element is necessary during the synthesis. Different configurations are used for compound synthesis and crystal growth of InP, GaAs, GaSb, AlSb, etc. Schematic diagrams of the experimental setups used for synthesizing arsenide-, phosphide-, and antimonide-based compounds are shown in Figs. 10.9–10.15. In this section, we summarize the general schemes for the compound synthesis.

Antimonide-Based Compounds

GaSb and InSb are the easiest compounds from the point of view of synthesis. The vapor pressure of antimony is very low at the melting points of the compounds. Hence both InSb and GaSb can be synthesized by simply melting and mixing the two constituents elements at a temperature beyond the melting point of the binary. The synthesis could be carried out either in a sealed (Fig. 10.9) or open crucible (Fig. 10.10). Inside the sealed crucibles, the vacuum level is typically 10^{-6} Torr or less. For open crucibles, inert-gas ambient is necessary. For synthesis of InSb, indium and antimony are mixed in equal mole fraction (1 : 1). Hence 114.82 g of indium and 121.75 g of antimony are necessary. The two elements are then heated to at least 20°C more than the melting point of InSb (527°C) and thoroughly mixed for several hours (10–12 h). Melt mixing could be implemented in sealed crucibles by rocked the crucible along with the furnace like a see-saw as shown in Fig. 10.9. At the end of the homogenization process, the furnace is held horizontal or vertical and the crucible is translated out of the furnace at a rate of 3–5 mm/h to directionally solidify the melt.

Figure 10.10a shows a schematic of GaSb synthesis in an open crucible configuration. The crucible is packed with antimony, gallium, and alkali halide salt (for melt encapsulation). The entire charge is heated to beyond the melting point of GaSb (712°C) and the compound is synthesized by mixing the melt. For melt homogenization, the crucible can be rotated with a stationary stirrer in the melt, as shown in Fig. 10.10a. Another efficient approach for melt mixing is by using a baffle or a plate with holes made out of the same material as the crucible (Fig. 10.10b). The baffle or mixing plate can be moved back and forth from the top to the bottom of the melt, creating turbulent flow through the narrow regions across the moving object. This leads to very rapid mixing. Hence large melts can be thoroughly mixed in minutes as opposed to hours (as is necessary with crucible rotation or rock-

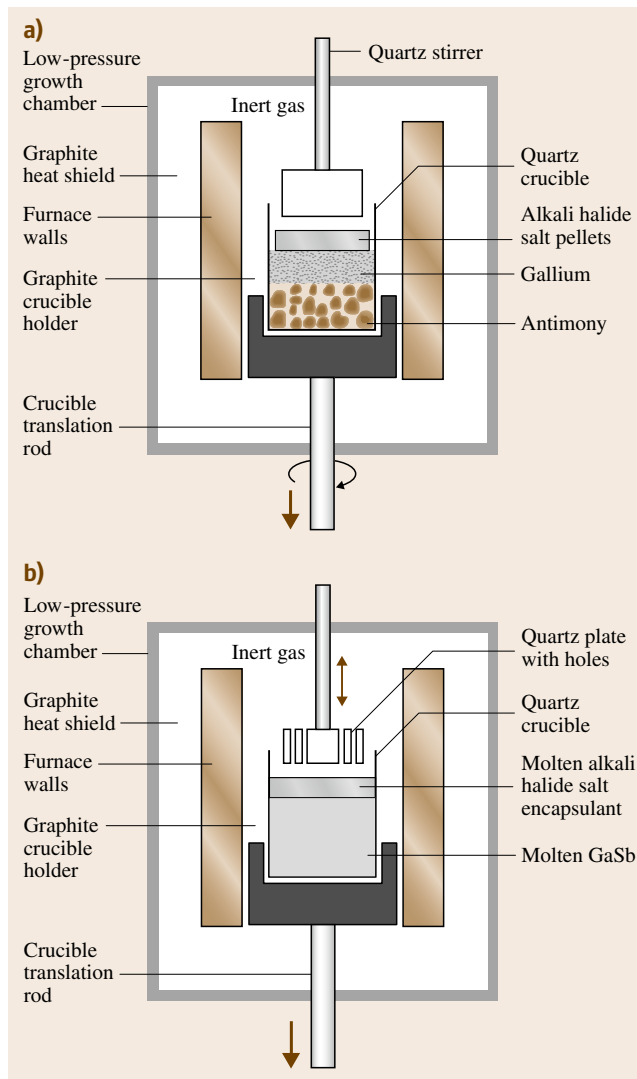


Fig. 10.10a,b GaSb polycrystalline charge synthesis in an open crucible by (a) using a stirrer and (b) using a quartz baffle for melt mixing

ing). After the melt has been completely homogenized, it is directionally solidified by translating the crucible at a rate of 3–5 mm/h in a furnace with a temperature gradient of 10–15 °C/cm until the entire liquid turns solid. After that the furnace is slowly cooled to room temperature at a rate of 15–20 °C/h. The presence of alkali halide salt encapsulation on the top of the melt helps avoid volatilization of antimony from the melt surface. As discussed earlier, the usage of liquid encapsulation during single-crystal growth is crucial to avoid melts touching the crucible walls and polycrystalline growth. The synthesis process for InSb and GaSb is exactly the same except for the synthesis temperature.

For AlSb, the problem is the sticking of the aluminum with crucible materials such as silica, pBN or graphite. Recently, a new process for synthesis and growth of AlSb in silica crucibles using alkali halide

salts as encapsulants has been demonstrated [10.71]. The adhesion of AlSb melt to silica crucible could be eliminated by employing a LiCl/KCl encapsulation [10.72] in conjunction with excess antimony in the melt. This process is shown schematically in Fig. 10.11a–c. The placement of the elements in the crucible (as shown in Fig. 10.11a) is crucial for successful synthesis of the compound without rupturing the crucible during the experiment. Care should be taken to avoid the elemental aluminum coming into contact with the silica crucible. The LiCl/KCl (58 : 42 mol %) eutectic salt mixture first melts and covers the crucible walls. Then the antimony melts and encapsulates the aluminum until it melts. The temperature of the melt is then increased to beyond the melting point of AlSb (1065 °C). The rest of the synthesis steps are similar to those for GaSb shown in Fig. 10.10.

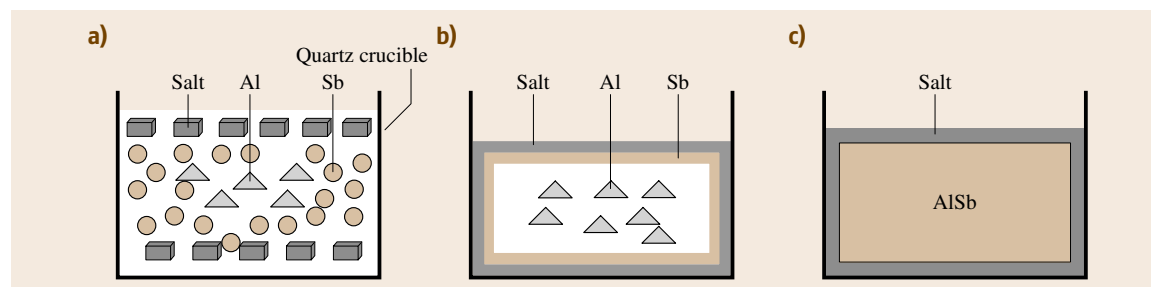


Fig. 10.11a–c Materials stacking scheme for AlSb synthesis in a quartz crucible

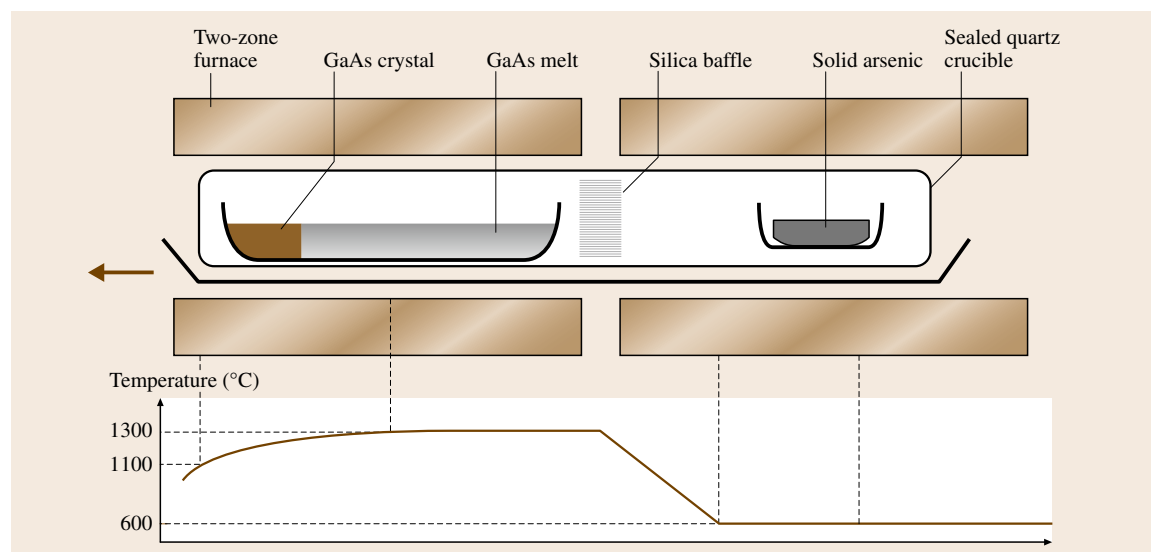


Fig. 10.12 GaAs synthesis inside sealed tube using a horizontal Bridgman configuration

Arsenide-Based Compounds

There are three general synthesis procedures for arsenic-based compounds. The configurations are shown in Figs. 10.12–10.14. Here we provide the specific examples of GaAs synthesis.

For GaAs, the synthesis is done under excess pressure of As. In the horizontal Bridgman method shown in Fig. 10.12, a sealed quartz tube containing 7 N pure gallium at one end separated and 6 N pure arsenic at the

other end is used. The quartz tube is placed in a two-zone furnace. The arsenic is kept between 600–620 °C (which results in ≈ 1 atm of arsenic vapor pressure) in the lower-temperature zone. The quartz boat containing the gallium is kept in the higher-temperature zone of the furnace above the melting point of GaAs (1238 °C). The arsenic vapor reacts with gallium to form the GaAs melt. A quartz baffle with narrow constrictions (silica baffle) between the two zones controls the transport of the arsenic. After the melt is homogenized for 12–24 h, the melt is directionally solidified by translating the crucible in a temperature gradient (10–20 °C/cm) at a rate of 1–3 mm/h. After the entire melt solidifies, the ingot is cooled slowly to room temperature over a period of 48 h.

Another method for synthesizing GaAs is the injection method (Fig. 10.13). In this method, the group V volatile element such as arsenic is contained in a quartz ampoule and heated to form vapors. The vapors are transported into the B₂O₃-covered molten gallium to form the compound (GaAs). The melt is maintained at a temperature higher than the melting point of GaAs. The pressure on the top of the melt must be maintained in the range 1–2 MPa (≈ 10 –20 atm). After the synthesis, the charge is directionally solidified and slowly cooled to room temperature. Since B₂O₃ reacts with quartz and crucible ruptures during cooling, pyrolytic boron nitride (pBN) crucibles are necessary for this process.

Direct synthesis of GaAs can be implemented by using the configuration shown in Fig. 10.14. The arsenic and gallium are packed together as shown in the figure with boric oxide as an encapsulant. The chamber in the pressure must be maintained to around 60 atm during the synthesis using nitrogen or argon. The synthesis of GaAs occurs around 700 °C by an exothermic reaction. After the compound is formed, the temperature is increased above the melting point of GaAs (1238 °C) and the pressure of the chamber can be reduced to 5–10 atm. The melt is then directionally solidified as in the previous cases.

Phosphide-Based Compounds

Phosphide-based materials such as InP and GaP have much higher vapor pressures than arsenide-based compounds. Hence specific modifications in configurations are necessary for the synthesis and growth of phosphide-based compounds. A stainless-steel-lined pressure vessel designed for 150–170 atm and continuous operation at 60–70 atm is necessary for InP growth. The direct synthesis method, which is the preferred syn-

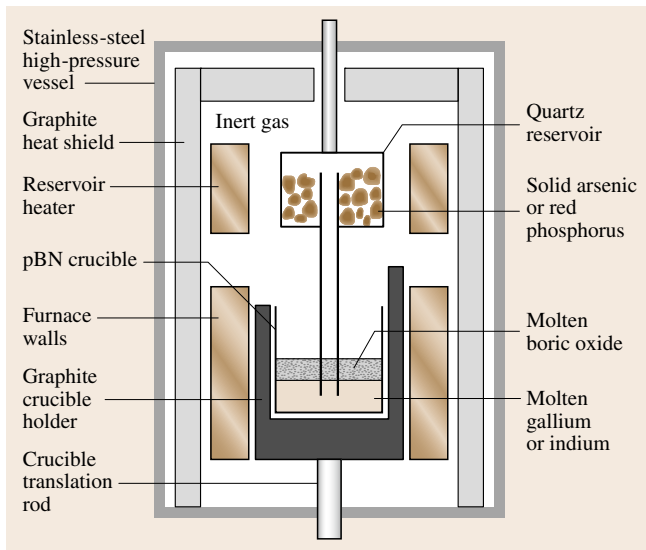


Fig. 10.13 GaAs and InP synthesis using a As and P injection method inside a high-pressure chamber

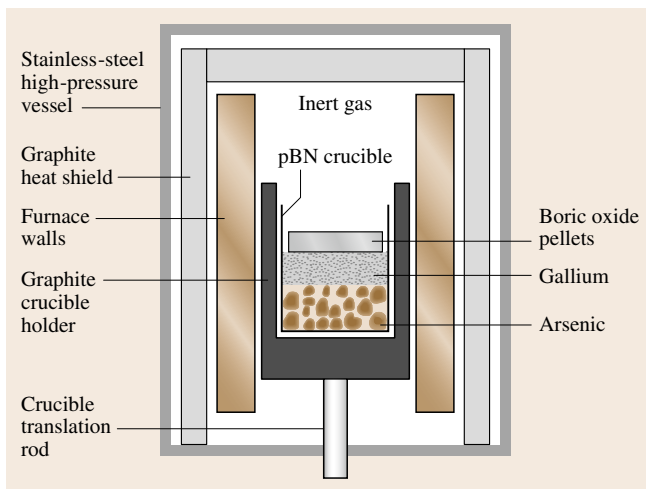


Fig. 10.14 Direct synthesis of GaAs in an open crucible inside a high-pressure chamber

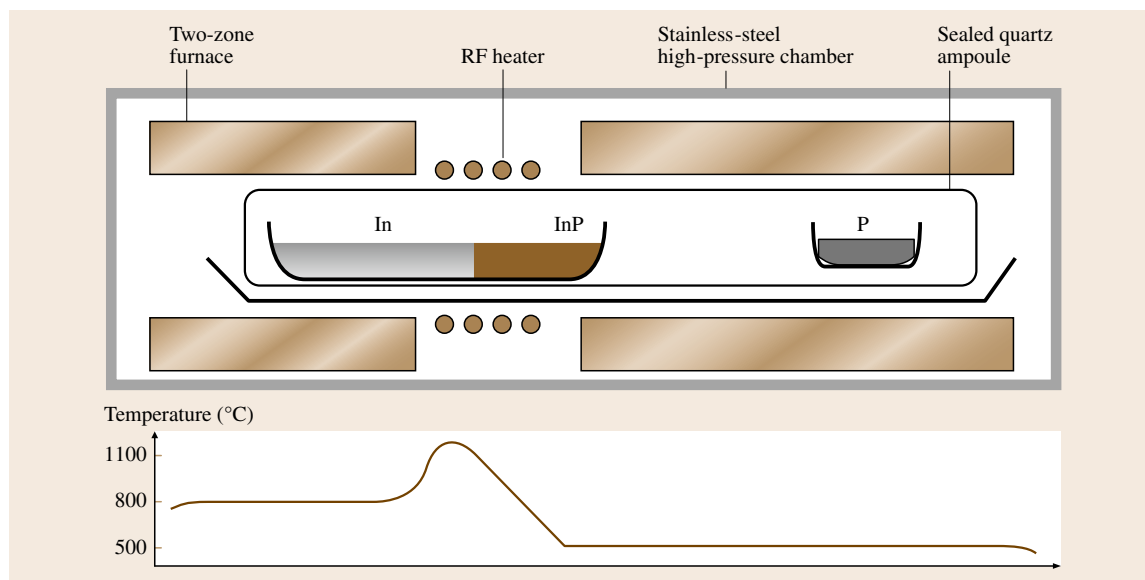


Fig. 10.15 InP synthesis inside a sealed tube using a horizontal Bridgman configuration with multizone heaters (RF heater refers to radio frequency heater coil)

thesis method for GaAs, is not possible for InP. Special handling procedures for phosphorus are necessary due to significant risk of ignition.

Two common InP synthesis techniques are the horizontal Bridgman (or gradient freezing) and the injection methods, as shown in Figs. 10.12 and 10.13. In the horizontal Bridgman process with a two-zone furnace (Fig. 10.12), indium is kept in a boat at one end and red phosphorus at the other end, and the silica tube sealed under 10^{-6} Torr. The sealed quartz crucible is kept inside a stainless-steel pressure vessel with preferably 45–50 atm of inert gas overpressure to avoid rupturing of the crucible. The red phosphorus is slowly heated to around 550°C to maintain a phosphorus pressure of 27 atm. The indium boat is maintained at 1075–1080°C. The phosphorus transports to the indium boat to form InP. After the homogenization of the melt, which could take 16–24 h, the melt is directionally solidified at a cooling rate of 0.5°C/h until the entire melt solidifies and the solid reaches around 1000°C. The crystal is then cooled to room temperature over a period of 30–40 h. Another common horizontal Bridgman-type configuration used for InP synthesis is shown in Fig. 10.15. The three-zone temperature profile resembles a zone-refining process and makes it easy to control the phosphorus vapor pressure on the melt and to avoid the supercooling effects seen in InP.

For the injection method shown in Fig. 10.13, the red phosphorus reservoir is maintained around 550°C and the indium is heated to 1080°C for the compound formation. The inert gas pressure in the chamber is maintained around 45–50 atm. The phosphorus vapors diffuse through the boric oxide to form InP. The melt is then homogenized and directionally solidified.

10.5.3 Single-Crystal Growth Processes

During the growth of binary compounds from melt, the macroscopic composition of the melt and the growing crystal remains constant (segregation coefficient equal to unity). Hence there is no need for solute replenishment processes (unlike in ternary crystal growth). Single-crystal growth is carried out by using a presynthesized polycrystalline charge and a seed. In addition, melt encapsulation is necessary for two reasons: (a) to avoid the escape of volatile species from the melt, and (b) to avoid contact between semiconductor melt and crucible walls during growth so that secondary nuclei, which lead to polycrystalline grains, do not originate. Details of crystal growth configurations and conditions can be found in the literature [10.1, 16, 40–44, 66, 71, 73, and references therein]. In this section, we present the schematics of the growth setups and summarize the growth conditions.

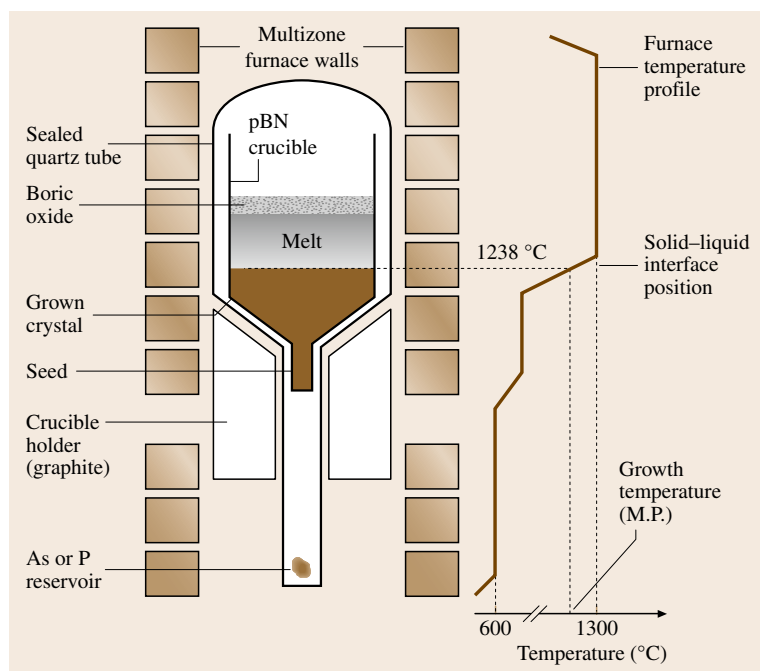


Fig. 10.16 Single-crystal growth of GaAs or InP inside a sealed tube using the vertical gradient freeze (VGF) method

Two typical VGF growth setups used for GaAs and InP are shown schematically in Figs. 10.16 and 10.17. In the sealed tube configuration (Fig. 10.16), a reservoir of a small amount of As or P is kept at a lower

temperature (the same as that used during synthesis) to maintain an adequate vapor pressure over the melt surface. In the open tube configuration (Fig. 10.17), the entire melt is pressured with an inert gas at a level of 10–20 atm for GaAs and 45–50 atm for InP growth. pBN crucibles along with ultralow-water-content boric oxide (B_2O_3) encapsulation is used. The boric oxide melts at 450 °C and has a low viscosity at the growth temperatures of GaAs and InP. The typical furnace temperature gradient is in the range of 5–10 °C/cm and the crystal growth rate is in the range of 0.5–2 mm/h. Growth of low-dislocation-density large-diameter (typically 100–150 mm) GaAs and InP has been demonstrated using the VGF technique. Semi-insulating GaAs crystals with a diameter of 200 mm are being produced today by VGF.

For the growth of GaSb and InSb, B_2O_3 encapsulation is not suitable since it is very viscous at low temperatures [10.73]. Instead of B_2O_3 , alkali halide eutectic salts such as LiCl/KCl (58 : 42 mol %) and NaCl/KCl (50 : 50 mol %) with low melting temperatures (between 350 and 600 °C) and significantly lower viscosity are used. These alkali halide salts do not react with the antimonide-based compounds and have no effect on the electrical and optical properties of the grown crystals [10.72]. Silica (quartz) crucibles are commonly

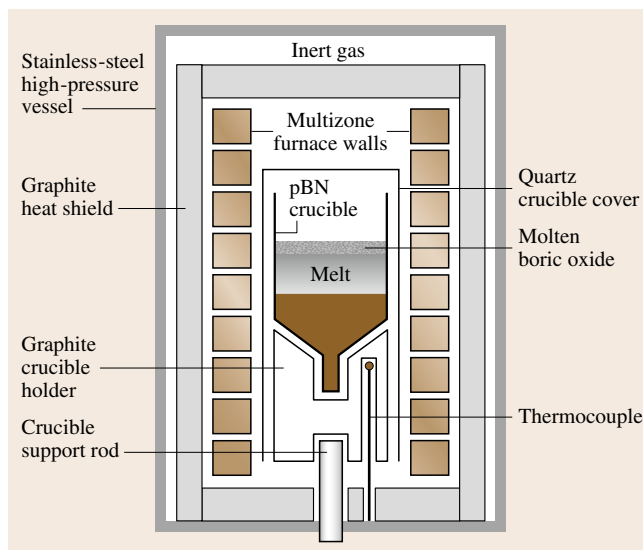


Fig. 10.17 Single-crystal growth of GaAs or InP in an open crucible using the vertical gradient freeze (VGF) method

used for GaSb and InSb growth. It should be noted that melt encapsulation for GaSb or InSb growth is not an absolute necessity. The vapor pressure of Sb is significantly lower compared with that of P or As. Nevertheless, alkali halide salt encapsulation does help in reducing the probability of polycrystalline growth from the crucible walls. Typically, thick oxide layers are present on GaSb and InSb polycrystalline surfaces (even after chemical etching). When the polycrystalline charge is melted, an oxide scum develops on the surface of the liquid. The scum in contact with the crucible walls enhances the sticking of the melt to the crucible and hence polycrystalline grains are formed. The salts help in dissolving the oxide scum and lead to a cleaner melt surface and avoid sticking of the melt with the crucible walls. The growth setup for GaSb and InSb is much simpler since there is no need for a high-pressure vessel. Typical vertical Bridgman or VGF can be used for single-crystal growth of low-dislocation-density GaSb and InSb. The typical furnace temperature gradient used for 50 mm diameter crystals is in the range of 5–15 °C/cm and the crystal growth rate is in the range of 1–3 mm/h.

10.5.4 Cleaning Procedures for Growth Chamber, Crucible, and Charge

Due to the high-purity nature of the semiconductor materials, the growth chambers, crucibles, and charge require special cleaning procedures. The growth chambers need to be cleaned prior to every experiment. Stainless-steel chamber surfaces must be scrubbed and cleaned to remove deposits of elemental and compounded species such as arsenic, antimony, GaAs, etc. from previous experiments. Proper safety masks, handling, and disposal procedures must be followed. After scrubbing, the chamber surfaces could be rinsed and wiped with an organic solvent such as methanol. If silica tubing is used in the growth chamber, they need to be chemically cleaned following the same procedures as for the crucibles as described below. All graphite parts such as the crucible holder must be cleaned with organic solvents (successively in xylene, acetone, and methanol) and then baked at high temperature (≈ 1200 °C) under high vacuum (less than 1 mTorr pressure) or under a flowing argon/hydrogen gas mixture.

Two most common crucible materials for III–V semiconductors are high-purity silica (quartz) and py-

rolytic boron nitride (pBN). High-purity, low-porosity graphite is also a suitable material. However due to difficulty in handling graphite, it is not used for bulk crystal growth. Prior to crystal growth, the silica and pBN crucibles need to be degreased in warm xylene followed by acetone and methanol. Depending on the residue material left behind from the previous experiment, such as GaAs or GaSb, the crucibles are chemically treated in a suitable chemical etchant solution to remove the residues. Typical etchants consist of acids such as nitric acid (HNO_3), hydrofluoric acid (HF) and glacial acetic acid (CH_3COOH) mixed in various volume ratios [10.74]. The crucibles are finally rinsed in high-purity deionized (DI) water and methanol, and dried with nitrogen gas.

For polycrystalline charge synthesis, the elemental constituents are accurately weighed according to the melt composition required. Elements with purity level of 6 N (99.9999%) or 7 N (99.99999%) are commercially available and used these days. The elements are available in various forms; for example, gallium comes in squeeze bottles or in the form of solidified rods; indium comes in tear drops or bar forms; while antimony, phosphorus, and arsenic come in small pellets. If the elements are opened from packed containers, they can be used the experiments without any cleaning. However, oftentimes the elemental charge possesses a thick oxide layer on the surface. Hence it is necessary to clean the charge before synthesizing compounds. Common cleaning procedures involve acid rinsing the oxide layer from the surface of the elements followed by cleaning in high-purity water, methanol rinsing, and nitrogen drying. Typical etchants for elemental cleaning includes hydrochloric (HCl), nitric (HNO_3), and hydrofluoric (HF) acids [10.66]. When polycrystalline compounded materials such as GaAs, GaSb, InSb, etc. are used for single-crystal growth experiments, they are etched in a variety of acids that act as etchants for the specific compound [10.74]. One such etchant that is widely used is a mixture of HNO_3 , CH_3COOH , and HF in the volume ratio 5 : 3 : 3, respectively. The polycrystalline charges are finally washed in high-purity water, rinsed with methanol, and dried by blowing nitrogen gas. Since there are numerous options for chemicals used in cleaning elemental and compound charges, no specific recommendations are made here. Every crystal grower adopts specific cleaning procedures based on the ease of handling certain chemicals, and experience.

10.6 Phase Equilibria for Ternary Compounds

There are three types of phase diagrams that can be used for the growth of ternary compounds, namely pseudobinary, ternary, and quaternary phase diagrams [10.17,29,30,66,75–77]. In this section, we will discuss the methods to use these phase diagram for determining melt or solution composition and the growth temperature for growing a crystal of specific composition.

10.6.1 Pseudobinary Phase Diagram

The most common phase diagrams used for melt growth of ternary crystals are the pseudobinary plots, as shown in Fig. 10.18 (depicting the GaInSb system [10.77]). These are known as pseudobinary diagrams because a ternary crystal such as $\text{Ga}_{0.6}\text{In}_{0.4}\text{Sb}$ can be thought of as a mixture of two binary compounds, namely, 60 mol % of GaSb and 40 mol % of InSb. In this diagram there are two curves: liquidus and solidus. The melting points of the two constituent binaries are shown on the y-axis at the two ends points. The melting points for pure InSb and pure GaSb are 527 and 712 °C, respectively. Any point on the liquidus curve represents the temperature above which the ternary of a specific composition is completely liquid. For example, $\text{Ga}_{0.6}\text{In}_{0.4}\text{Sb}$ or a mixture of 60 mol % GaSb and 40 mol % InSb will be completely liquid above 660 °C. When the individual binaries are mixed together, the InSb first melts at 525 °C and starts dissolving GaSb. As the temperature is increased, the amount of GaSb dissolved increases, resulting in a melt composition with increasing GaSb mole fraction or decreasing InSb mole

fraction. The ternary compounds can also be prepared by mixing individual elements such as Ga, In, Sb, etc. For example, $\text{Ga}_{0.6}\text{In}_{0.4}\text{Sb}$ can be prepared by mixing 60 mol % Ga, 40 mol % In, and 100 mol % Sb. The liquidus and solidus temperatures are independent of the preparation methodologies.

The solidus represents the temperature below which a ternary of specific composition is completely solid. For example, $\text{Ga}_{0.6}\text{In}_{0.4}\text{Sb}$ will be completely solid below 570 °C. Between the liquidus temperature and the solidus temperature for a specific ternary composition, there exist a two-phase region, as shown in Fig. 10.18, where a portion of the material is in liquid state and the rest is in solid state. In pseudobinary phase diagrams, there exist a single growth temperature and a single melt composition for any solid composition. For example, for growing $\text{Ga}_{0.8}\text{In}_{0.2}\text{Sb}$ crystals, the melt composition must be $\text{Ga}_{0.30}\text{In}_{0.70}\text{Sb}$ and the growth temperature is 605 °C. A horizontal line connecting a point in the liquidus and solidus is known as a tie-line. This is different than the ternary and quaternary phase diagrams (to be discussed next), where a specific solid composition can be obtained at numerous liquid compositions and growth temperatures.

10.6.2 Ternary Phase Diagram

Using the pseudobinary phase diagrams discussed above, the growth temperature of any ternary crystal is restricted to lie the melting points of the two constituent binaries. Growth of crystals from solution at lower temperatures has many advantages such as reduced native defects and lower dislocation densities that result in superior materials properties. Ternary phase diagrams can be used to grow crystals at low temperatures. Figure 10.19 shows a typical ternary phase diagram for the GaInSb system. This diagram is a schematic drawn to demonstrate the features of the ternary phase diagrams. The three vertices on the equilateral triangle represent the three constituent elements comprising the ternary compound. For GaInSb growth, the constituents are Ga, In, and Sb. The melting point of Ga, In, and Sb are 29, 156, and 630 °C, respectively. The low melting point of one or two constituent elements helps to decrease the growth temperature significantly. Each point within the triangular area represents a specific solution (liquid) composition (Ga : In : Sb in mol %). The lines drawn parallel to each face are used to determine the solution composition. For example, as one traverses the

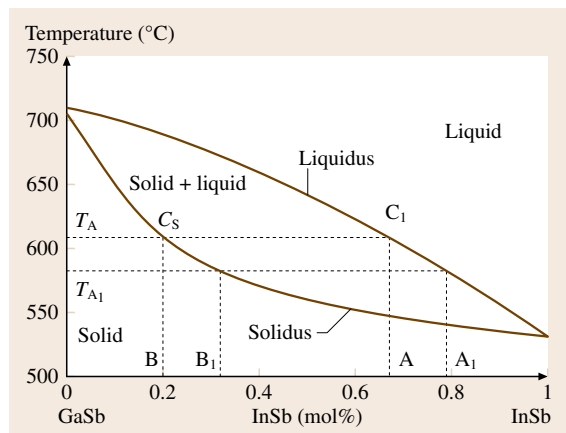


Fig. 10.18 Schematic pseudobinary phase diagram of a III–V ternary compound (depicting GaInSb)

space from the Sb vertex of the triangle downwards, the Sb content changes from 100 mol % to 0 mol % at the opposite face (which connects In and Ga). The same methodology can be applied for calculating the In and Ga compositions. The compositions of the liquid at the four circular dots in Fig. 10.19 have been calculated by drawing three straight lines parallel to each triangle axis, intersecting at the circular dot. The compositions for In, Ga, and Sb are then estimated by measuring the distance between the point of interest and each vertex of the triangle.

Referring to Fig. 10.19, the liquidus are shown by solid lines and the solidus are shown by dashed lines. Each liquidus curve corresponds to a specific solution (liquid) temperature. For example, the two liquidus shown correspond to 575 and 625 °C. Each solidus curve corresponds to a specific ternary solid composition. For example, the two solidus curves shown correspond to gallium mole fractions of 0.7 and 0.8 in the crystal. For the growth of crystal of any desired composition from a solution, one needs to find a specific solution composition and the growth temperature. This is done by finding a point in the ternary phase plane where the solidus and liquidus curves cross each other such as the points (In,Ga,Sb: 50,15,35 and 35,35,32) in Fig. 10.19. Hence, to grow a crystal of $\text{Ga}_{0.7}\text{In}_{0.3}\text{Sb}$ at 575 °C, the solution composition should be (In : Ga : Sb = 50 : 15 : 35 by mol %). It should be pointed out that there is more than one option for the growth temperature and liquid composition for the same crystal composition. It is also interesting to note that, even though the liquid compositions are completely nonstoichiometric ($\text{Ga}_x\text{In}_y\text{Sb}_z$; $0 < x, y, z < 1$), the grown solids are stoichiometric, of the form $\text{Ga}_{1-x}\text{In}_x\text{Sb}$ ($0 < x < 1$).

10.6.3 Quaternary Phase Diagram

Recently, it has been demonstrated that quaternary melts can be used to grow ternary crystals [10.29, 30, 78]. The growth of $\text{Ga}_{1-x}\text{In}_x\text{As}$ from stoichiometric $\text{Ga}_{1-x}\text{In}_x\text{As}_y\text{Sb}_{1-y}$ melt has been clearly demonstrated [10.29, 78]. Other III–V ternary systems such as GaInP, GaAsSb, and AlGaP, can also be grown from GaInPSb, GaInAsSb, and AlGaPSb melts, respectively [10.30]. The use of a quaternary melt enables the growth of ternary crystals at lower temperature compared with that possible using pseudobinary phase diagrams. Figure 10.20 shows a schematic phase diagram of the Ga-In-As-Sb system at 950 °C. The four constituent binaries for Ga-In-As-Sb are GaAs,

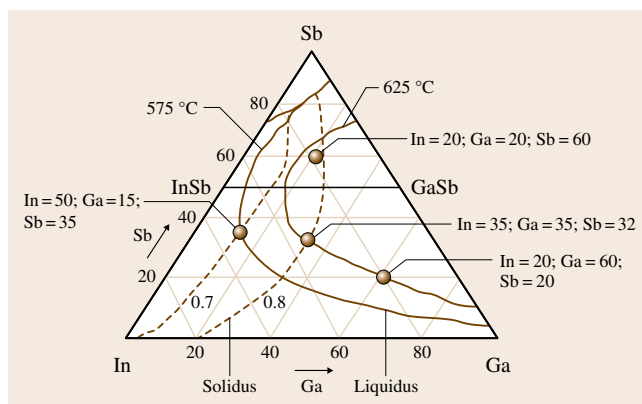


Fig. 10.19 Schematic ternary phase diagram of a III–V ternary compound (depicting GaInSb)

InAs, InSb, and GaSb. The quaternary phase diagram shows a liquidus curve and a solidus curve connected with tie-lines across the two-phase regions. The melt composition for growing a specific solid composition can be obtained by selecting a specific tie-line in the phase diagram. Like in the case of the ternary phase diagrams, depending on the growth temperature, the liquid composition for growing a particular solid composition varies. For example, the liquid composition of Ga-In-As-Sb to grow $\text{Ga}_{0.2}\text{In}_{0.8}\text{As}$ at 950 °C and 1000 °C are different. Using MTDATA, the National Physical Laboratory (NPL, UK) database for metallurgical thermochemistry, phase diagrams for the $\text{In}_x\text{Ga}_{1-x}\text{As}_y\text{Sb}_{1-y}$ system have been calculated for a wide temperature range [10.29, 30]. For temperatures below the melting point of InAs (942 °C),

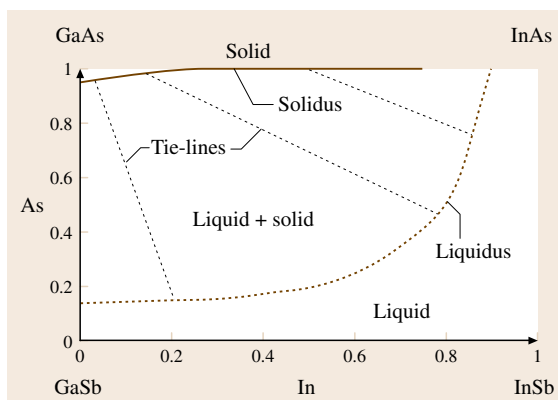


Fig. 10.20 Schematic quaternary phase diagram for III–V ternary compound growth (depicting GaInAs) from quaternary melt

$\text{Ga}_{1-x}\text{In}_x\text{As}$ (with residual Sb) and $\text{Ga}_{1-x}\text{In}_x\text{As}_y\text{Sb}_{1-y}$ solids can be grown from the Ga-In-As-Sb quaternary melts. Above the InAs melting point, only ternary $\text{Ga}_{1-x}\text{In}_x\text{As}$ is formed from the $\text{Ga}_{1-x}\text{In}_x\text{As}_y\text{Sb}_{1-y}$ melt. Figure 10.20 clearly shows that a wide range of GaInAs compositions could be grown using Ga-In-As-Sb melt at temperatures as low as 950 °C. Due to the fact that the first-to-freeze solid is ternary, the melt composition changes to a nonstoichiometric Ga-In-As-Sb from a stoichiometric starting melt (excess Sb in the solution). Hence replenishment of depleted species is necessary to keep the melt stoichiometric at all times.

The growth of a ternary from quaternary melt occurs at higher temperatures compared with growth from ternary solutions. Nevertheless, there are several tech-

nical advantages in using the quaternary melt. Since the quaternary melts can be prepared from presynthesized binary compounds, it enables the usage of liquid encapsulations during the growth. The metal-rich ternary solutions (such as Ga, In, Al) tend to stick to the crucible, making them difficult to mix and posing problems during Bridgman growth. Also the solubility of compounds in ternary solutions is significantly lower than in quaternary melts. This impacts the crystal growth rates. Another advantage of using the quaternary melts is seeding during a typical Bridgman growth. Due to the numerous technical benefits of the quaternary melts for ternary growth at low temperatures, this method will receive significant interest in the future, especially for crystals with high growth temperature (such as phosphides and arsenides).

10.7 Alloy Segregation in Ternary Semiconductors

All three types of phase diagrams discussed above for the growth of ternary crystals exhibit a common phenomenon. The solid composition precipitating out of the melt or solution is different from the liquid composition. This leads to alloy segregation, as discussed here. For the sake of simplicity, we will only discuss the pseudobinary phase diagrams since in this case one only needs to track the changes in concentration of one of the binary constituents. For example, during the growth of $\text{Ga}_{1-x}\text{In}_x\text{Sb}$, either the change in InSb concentration or GaSb concentration needs to be analyzed. The InSb and GaSb concentrations are complementary to each other. On the other hand, while using ternary or quaternary phase diagrams, the individual elemental concentrations such as Ga, In, As, Sb, etc. need to be analyzed since the concentration of each elemental species varies independently during the growth.

As shown in Fig. 10.18, pseudobinary phase diagrams exhibit a separation between the solidus and liquidus curves. Starting from a melt of alloy composition (A), when the liquid is cooled below the liquidus temperature T_A , the composition of the solid precipitating out of the liquid will have a composition corresponding to the point on the solidus (B) at the temperature T_A . Since the solid composition (B) is different than the liquid composition (A), the melt composition will change as soon as the solid starts precipitating out of the liquid. During crystal growth, the rejected species accumulate in front of the interface and spread into the liquid phase by diffusion and mixing induced by convection. From the phase diagram, it is clear that the

rejected species is the lower-melting binary constituent. For example, during the growth of $\text{Ga}_{1-x}\text{In}_x\text{Sb}$, the precipitating solid is rich in GaSb compared with the liquid. Hence the excess InSb is rejected into the melt at the solidification interface and the melt composition changes to a point indicated by A_1 in Fig. 10.18. The next precipitation event occurs at a lower temperature shown by T_{A_1} with the precipitating solid of composition B_1 . This continues and hence, during normal directional solidification process from melt as in Bridgman or Czochralski growth, the melt composition continuously changes with time, as in turn does the composition of the solidifying crystal.

The changing alloy composition in the solid can be theoretically analyzed using the fundamental equilibrium distribution (partition) coefficient or chemical segregation coefficient, k_0 . This can be derived from the equilibrium phase diagram by the ratio of the solidus (C_s) and liquidus concentration (C_l) of a species at a given temperature (Fig. 10.18) as follows

$$k_0 = \frac{C_s}{C_l} \quad (10.3)$$

In general, segregation depends on the growth rate and hence is described by an effective distribution coefficient, k_{eff} . If the melt is mixed continuously during a directional solidification crystal growth experiment, the alloy concentration in the solid is given by the well-known equation [10.79–82]

$$C_s = k_{\text{eff}} C_0 (1 - g)^{k_{\text{eff}} - 1} \quad (10.4)$$

where g is the fraction of melt solidified and C_0 the initial concentration of the melt (at the beginning of the growth). In this equation k_{eff} does not vary with alloy concentration, an assumption which is invalid for ternary crystal growth, as discussed below.

In a typical crystal growth experiment, the rejected species at the solid–liquid interface takes a finite time to diffuse back into the melt, giving rise to a completely homogeneous melt. The mixing rate of the rejected species with the rest of the melt can be enhanced by increasing the temperature gradient across the melt–solid interface, decreasing the cooling rate of the melt (decreasing the crystal growth rate), and by using forced convection. There are limitations with each of these processes. Large temperature gradients lead to temperature fluctuations, almost inevitably producing striations. Slow cooling increases the duration for crystal growth, which is undesirable for a variety of reasons (increase in cost, reduced equipment lifetime, unexpected long-term instability in furnace power, enhanced degradation of grown crystals due to volatilization of elements from the surface of the crystals and melt, etc.). Forced mixing has its own limitations such as complicated fluid patterns and associated temperature and solutal fluctuations. Thus, under normal conditions, the growth process is dominated by a stagnant (or diffusion) boundary layer of thickness δ , beyond which stirring in the bulk liquid ensures a uniform bulk concentration. Within the diffusion boundary layer, the composition of the rejected species changes continuously starting from the crystal surface to the end of the boundary layer [10.81]. Burton, Prim, and Slichter (BPS) derived the following equation to correlate the boundary-layer thickness with the effective segregation coefficient [10.81]

$$k_{\text{eff}} = \frac{k_0}{k_0 + (1 - k_0) \exp(-\Delta)}, \quad (10.5)$$

$$\Delta = R\delta/D,$$

where k_0 is the equilibrium segregation coefficient as estimated from the equilibrium phase diagram, D is the diffusion coefficient of the rejected species in the melt, R is the crystal growth rate, and δ is the thickness of the boundary layer. For crystal grown with forced convection, the boundary-layer thickness δ is given by

$$\delta = 1.6D^{\frac{1}{3}}\nu^{\frac{1}{6}}\Omega^{-\frac{1}{2}}, \quad (10.6)$$

where ν is the kinematic viscosity of the melt, Ω is the rotational rate of the crystal or seed (in the case of Czochralski growth), and D is the diffusion coefficient.

As can be seen from the above equation, when Δ approaches zero, k_{eff} equals k_0 . In the above equation, the

diffusion coefficient D is a fundamental material property and dependent on the alloy composition as well as the temperature. For example, the diffusion coefficient of InSb in GaInSb melt at 550 °C is different from that at 600 °C. Similarly, the diffusion coefficient of InSb in a Ga melt at 550 °C is different from that in GaInSb melt at the same temperature. The diffusion boundary-layer thickness can be altered by the hydrodynamic mixing in the melt as a result of natural and forced convection as well as diffusion. In the analysis shown above, k_0 is assumed to be constant with time. However during ternary crystal growth, the liquid concentration moves along the liquidus. For each corresponding liquidus and solidus points, the segregation coefficient is different. Hence the k_0 needs to be varied for analyzing the solid concentration along the crystal growth direction. Figure 10.21 shows the theoretically calculated gallium mole fraction along the length of $\text{Ga}_{1-x}\text{In}_x\text{Sb}$ crystals for different starting melt compositions, assuming completely homogeneous melt at all times. In these plots, the difference in segregation coefficient with change in melt composition was taken into account. The segregation coefficient as a function of alloy composition was extracted from the phase diagram of GaInSb, as depicted in Fig. 10.18. As clearly seen in Fig. 10.21, the solid composition changes continuously in the crystal due to changes in the melt composition. The rate at which the alloy composition changes along the crystal is dependent on the extent of separation between the liquidus and solidus curves, which is a material-dependent

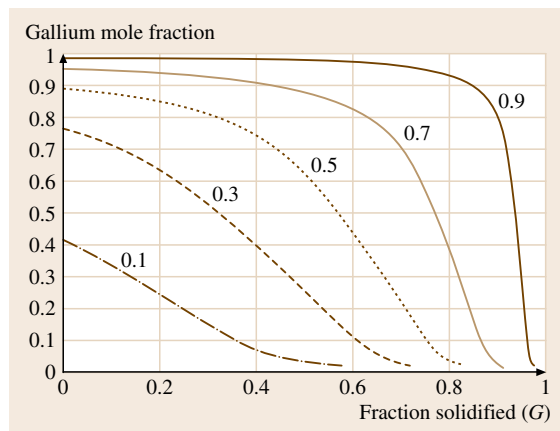


Fig. 10.21 Theoretical gallium concentration along the growth axis for $\text{Ga}_x\text{In}_{1-x}\text{Sb}$ crystals grown from different starting melt compositions (under normal freezing conditions). The fractions next to each curve represent the gallium mole fraction in the starting melt

property. A narrow gap between the two curves is desirable for growing homogeneous crystals and avoiding defects such as cracks in the crystals, as discussed in the next section.

The other extreme for alloy segregation behavior is observed under steady-state diffusion in a convection-free melt. This is represented by the well-known equation for diffusion-controlled segregation as [10.80, 82]

$$\frac{C_s(x)}{C_0} = k_0 + (1 - k_0) \left[1 - \exp \left(-\frac{k_0 R x}{D} \right) \right], \quad (10.7)$$

where $C_s(x)$ is the alloy concentration in the solid at a distance x measured from the beginning of the growth. In this scenario, the alloy composition in the diffusion boundary layer increases with time since there is no convective flow in the melt to extract the species from the diffusion boundary layer. This leads to a rapid increase in the alloy composition in the solid (initial transient) followed by a uniform region in the crystal. Figure 10.22 shows a typical diffusion-controlled alloy composition profile in a solid (10.7). For the sake of comparison, a normal freezing curve (10.4) with the same segregation coefficient has been included. While plotting (10.7), the parameter x has been normalized to the solidified fraction g . The uniform region in the diffusion-controlled profile appears very attractive for growing uniform ternary crystals. However, the technical problem lies in the fact that it is very difficult to achieve pure diffusion-controlled conditions. This would require complete elimination of convec-

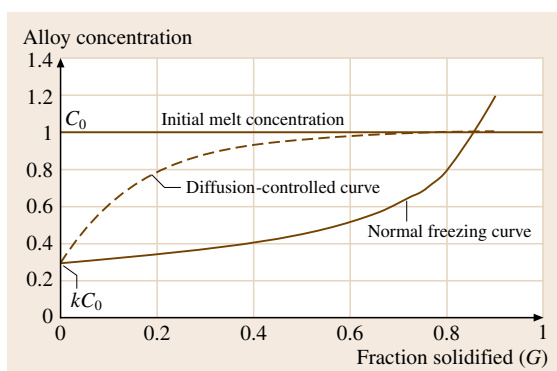


Fig. 10.22 Theoretical alloy composition profiles along the growth axis for crystals grown with complete melt mixing (normal freezing) and in the absence of melt convection (diffusion-controlled growth)

tion in the melt. Melt convections can be reduced by using magnetic fields [10.83–85], submerged baffles in the melt [10.86, 87], and under microgravity conditions [10.88–93]. However, these approaches have not been used in large-scale ternary crystal growth. There are other technical issues such as composition and length of the diffusion boundary layer necessary for growing ternary crystals with alloy compositions that are far from the binary compositions. Hence for the rest of this chapter, we will focus on the alloy composition changes that are typically seen in experiments with normal freezing conditions.

10.8 Crack Formation in Ternary Crystals

10.8.1 Phenomena of Crack Formation

One of the consequences of the alloy segregation is the cracking of the crystals during growth. If the growth rates are not low enough, constitutional supercooling occurs close to the liquid–solid interface, resulting in composition fluctuation and sudden transition from single to polycrystals. The local compositional inhomogeneity in the solid along with the wide difference in the lattice constants and the thermal expansion coefficients of constituent binary compounds introduces considerable strain, and invariably leads to cracking of the crystals. For the GaInSb system, the lattice parameter varies from 6.096 Å (for GaSb) to 6.479 Å (for InSb) and the thermal expansion coefficient from 7.75×10^{-6} to $5.37 \times 10^{-6} \text{ } ^\circ\text{C}^{-1}$ [10.1]. Figure 10.23

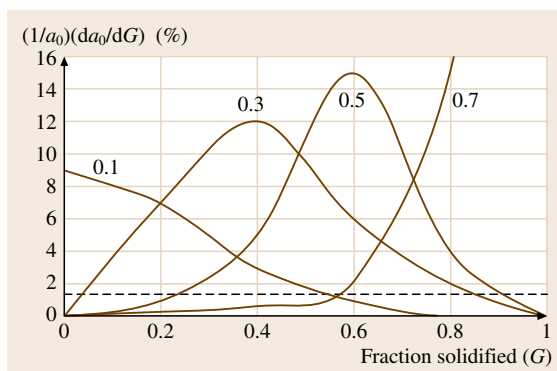


Fig. 10.23 Theoretical misfit strain gradient versus fraction of solidified melt calculated from the theoretical concentration curves shown in Fig. 10.21 for $\text{Ga}_x\text{In}_{1-x}\text{Sb}$ crystals

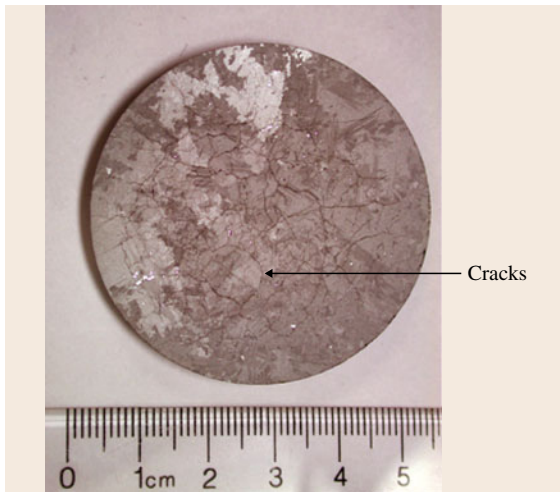


Fig. 10.24 Typical microcracks seen in ternary III–V crystals. The composition of the wafer shown here is $\text{Ga}_{0.7}\text{In}_{0.3}\text{Sb}$

shows the theoretical misfit strain gradient curves calculated using the theoretical alloy composition profiles shown in Fig. 10.21 and the lattice parameter a_0 for each composition using Vegard's law (10.1). It has been empirically observed that crystals inevitably crack if the misfit strain gradient exceeds 1–2% [10.17]. It is obvious that an alloy system with larger separation between the solidus and liquidus line has higher strain gradient than those with smaller separation. Moreover, cracking may occur even below 1% misfit strain gradient if there is a thermal strain caused by the large temperature gradient in the solid or during rapid cooling for the crystals. Figure 10.24 shows microcracks in a wafer sliced from a $\text{Ga}_{0.7}\text{In}_{0.3}\text{Sb}$ polycrystal grown using the vertical Bridgman method. The growth conditions used for this crystal were not optimized for avoiding cracks (as discussed below).

Cracks in crystals make the wafers completely unusable for any basic research or device applications. Hence eliminating cracks in the crystals by optimizing growth conditions is the first task for any ternary crystal growth. The cracks can be somewhat eliminated by zone leveling, slow cooling or prolonged annealing of the solidified ingot [10.17]. However, the concentration gradient does not smoothen completely by thermal treatment due to the low solid-state diffusion coefficients of III–V compounds. Hence microscopic cracks and stresses remain. Cracks can be avoided if and only if smooth change in alloy composition is ensured in the

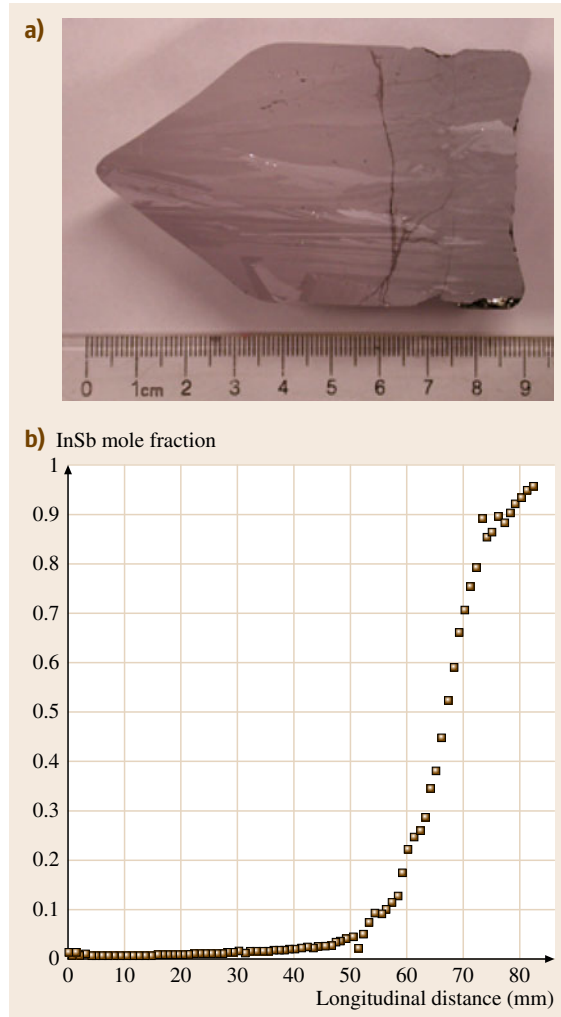


Fig. 10.25 (a) Cross section of a GaInSb crystal showing strain-gradient-related cracks and (b) the longitudinal composition profile measured along the center of the crystal

crystals during growth. Referring to Fig. 10.23, strain-related cracks originate in the crystal where the strain gradient exceeds 1–2%, as shown by the horizontal dashed line. For a crystal grown with starting gallium mole fraction of 0.7 in the melt, cracks should appear when the fraction solidified (G) is close to 60%. This has been experimentally confirmed during growth of GaInSb . Figure 10.25a shows a cross section of a crystal with a visible crack around 6 cm from the bottom of the crystal. This coincides with the longitudinal composition profile measured in the same crystal as shown in Fig. 10.25b. The region where the composition starts

changing rapidly (between 60 and 70 mm) is exactly where the crack in the crystal appears. It is interesting to observe that the cracks propagate across multiple grains (seen in both Figs. 10.24 and 10.25a) and the crack network cannot be correlated with the polycrystalline grain structure. Strain-related cracks seem to occur after the solidification front (melt–solid interface) had crossed the respective position. This clearly indicates that these cracks are not due to constitutional supercooling during growth, but are rather due to strain in the crystal. Rapid change in composition such as in Fig. 10.25b can also lead to constitutional supercooling and interface breakdown with sudden change in the grain structure and the appearance of cracks. However these cracks are easily distinguishable from strain-related cracks. Since there are two origins of cracks, different crystal growth conditions are necessary to eliminate them.

10.8.2 Elimination of Cracks

Misfit strain-related cracks are related to the rate at which the alloy composition and more importantly the lattice parameter and other physical properties such as thermal expansion coefficient change along the length of the crystal. Hence these cracks can be eliminated by ensuring gradual changes in alloy composition that will result in a strain gradient lower than that which initiates cracking. This is especially important during the seed formation process, as described in the next section. Since the materials properties for binary compounds vary significantly, the density of cracks varies for each ternary compound. Theoretical analysis of strain gradient as in Fig. 10.23 coupled with experimental trials is necessary to determine the compositional gradient in the crystal that will not lead to cracking.

Cracks originating from the constitutional supercooling process can be eliminated by avoiding supercooling during growth. This requires thinning the diffusion boundary layer at the melt–solid interface. Supersaturation in the boundary layer results in spurious nucleation and the formation of polycrystals [10.94,95]. A boundary layer with a diffusion-controlled (exponential) concentration distribution ahead of the growth interface causes constitutional instability. A region of constitutional supercooling emerges if the equilibrium liquidus temperature gradient exceeds the actual temperature gradient in the melt at the solid–liquid interface [10.82]. The composition of the diffusion boundary layer (enriched with the lower-melting-point binary compound such as InSb during the growth of

GaInSb) depends on the melt volume, the growth rate, and the degree of melt stirring. Theoretical analysis [10.80] has shown that, for preventing constitutional supercooling, the ratio of the temperature gradient in the melt near the growth interface (G) to the growth rate (R) should exceed a critical value given by

$$\frac{G}{R} \geq \frac{mC_0(1-k_0)}{k_0D}, \quad (10.8)$$

where m is the slope of the liquidus in the phase diagram.

Since avoiding constitutional supercooling is absolutely necessary during ternary growth, the role of melt stirring is crucial. Melt stirring can also enhance the growth rates by thinning the diffusion boundary layer at the growth interface. Melt stirring and homogenization can be achieved by natural convection, diffusion, and forced convection. Mass transport by natural convection takes place in most growth experiments due to the thermal convection caused by the temperature differences as well as the solutal convection caused by the density difference arising from the variation in solute concentration [10.96]. The natural convection and diffusion phenomena are weak. As a result of this, growth rates that are necessary for crack-free crystals are very low. Figure 10.26 shows the experimental crystal growth rates that were found to result in crack-free GaInSb crystals of different composition [10.18]. It is clear from the figure that, by using forced convection in the melt,

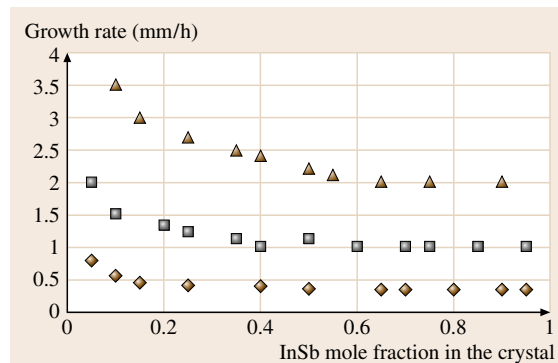


Fig. 10.26 Growth rate necessary for crack-free GaInSb crystals as a function of InSb mole fraction in the solid: crystals grown using temperature gradient of (◆) 10 °C/cm and (◻) 20 °C/cm without forced convection; (▲) crystals grown using 10 °C/cm temperature gradient with forced convection in the melt

the growth rates can be increased. For melts without any forced convection, a larger axial temperature gradient ($20\text{ }^{\circ}\text{C}/\text{cm}$) helps to increase growth rates for crack-free crystals. This is expected from *Tiller's* analysis [10.80], as discussed earlier. While increasing the axial temperature gradient helps to avoid constitutional supercooling, it increases the melt–solid interface curvature, due to which the radial composition profile in the wafers varies (as discussed later). Hence a lower temperature gradient is necessary for the growth of ternary compounds, which also helps in eliminating strain-related cracks in the crystal. To avoid constitutional supercooling under a lower temperature gradient, either the crystal growth rate needs to be decreased or melt stirring (by forced convection) needs to be enhanced. There are no thermal and solutal convection cells in the homogenized solution due to stirring and thus the supersaturation is not likely to go beyond the critical values for spontaneous nucleation. The second effect of homogenization is that the growing crystal always faces a homogeneous diffusion field, and thus inhomogeneities in crystals such as striations are avoided or decreased to a minimum level. Forced convection leads to a decrease in the metastable region and supersaturation. This decrease in supersaturation corresponds to a narrowing of the metastability range, so that no enhanced spontaneous nucleation is seen. Stirring decreases the diffusion boundary layer and reduces the inhomogeneous supersaturation across the growing crystal, which allows a faster stable growth rate than without stirring [10.97].

Fluid mixing patterns used for forced convection can be very complicated and significantly impact on crystalline quality. Melt mixing schemes reported in the literature [10.18, 25, 98, 99] during ternary crystal growth include: unidirectional rotation of the crucible, the accelerated crucible rotation technique (ACRT), and mixing the melt using baffles and stirrers. Unidirectional rotation, even at high rotation rates (100–200 rpm), does not result in effective mixing for large-diameter crystals (50 mm and higher). In ACRT, the crucible is periodically accelerated and decelerated (around the growth axis) to promote efficient mixing of the melt, as shown in Fig. 10.27. However, there can be dead (unmixed) zones even in a thoroughly mixed melt, especially at the center of the crystal [10.99]. These types of unmixed zones lead to compositional fluctuations in the grown crystals. Hence it is essential to optimize the rotation schemes for each crucible diameter, melt size, and fluid viscosity in the ACRT scheme. In the baffle mixing scheme [10.25], the melt is homogenized very efficiently either by rotating the baffle in

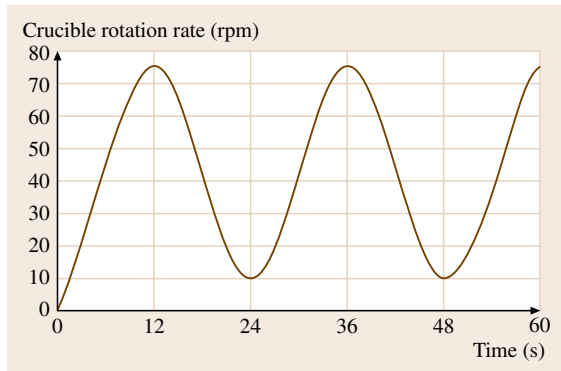


Fig. 10.27 Accelerated crucible rotation rates used for melt mixing and solute transport during vertical Bridgman growth of ternary crystals

the melt or by translating the baffle perpendicular to the growth interface, similar to shown in Fig. 10.10b (for polycrystalline charge synthesis). In the case where the baffle is translated perpendicular to the growth interface, obtaining single crystals is quite difficult due to thermal fluctuations at the melt–solid interface. Very small-sized grains are observed by using this process. In the case of stirrer mixing, a stationary stirrer is held inside the melt with a uniformly rotating crucible. The stirrer also helps in efficient solute transport during solute feeding processes (discussed later). The stirrer mixing scheme is simple and can be easily adopted for large melt mixing. In the future, it will be worthwhile investigating the effect of magnetic field stirring on the crack elimination process.

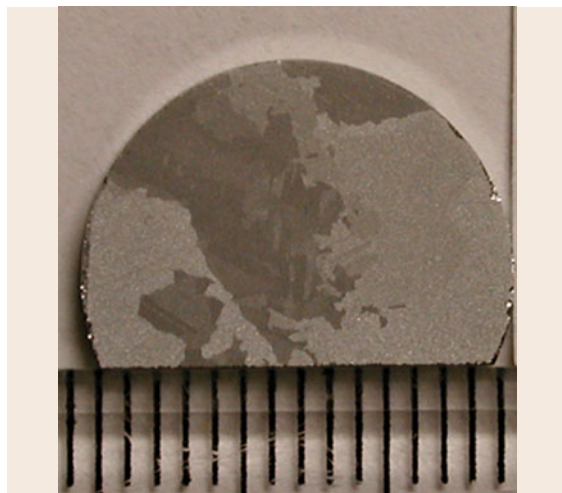


Fig. 10.28 Crack-free ternary wafer of $\text{Ga}_{0.76}\text{In}_{0.24}\text{Sb}$

10.8.3 Crystal Growth Rate for Crack-Free Ternary Crystals

As is evident from Fig. 10.26, crystal growth rates can be enhanced by a factor of four by efficient melt mixing. Typical growth rates for the GaInSb system are in the range of 0.3–0.5 mm/h (with 10 °C/cm thermal gradient). By using the optimized ACRT scheme, as shown in Fig. 10.27, the growth rate for crack-free crystals can be increased to 2 mm/h under the same thermal gradient (10 °C/cm). Figure 10.28 shows a crack-free polycrystalline wafer of Ga_{0.76}In_{0.24}Sb grown using the ACRT scheme. The growth rate was ≈ 1 mm/h, similar to that used for the cracked wafer

shown in Fig. 10.24. In general, for III–V ternary crystals, with an axial temperature gradient of ≈ 10 °C/cm, the maximum growth rate for crack-free single crystals is in the range of 0.02–0.5 mm/h, depending on the specific alloy system and its composition [10.18]. These rates are significantly lower than the binary growth rates (1–3 mm/h) under similar thermal gradient. A delicate balance between heat and mass transport strategies is necessary for ternary single-crystal growth without cracks. By using efficient melt stirring, the crystal growth rates for ternary materials can approach those for binary compounds grown under the same temperature gradient and group V overpressure.

10.9 Single-Crystalline Ternary Seed Generation Processes

For III–V ternary alloys, single-crystal growth poses a major challenge. Unlike for binary compounds, growth of spontaneously nucleated single-crystal ternary seeds such as from the tip of a crucible in the Bridgman method has not been possible. The preferred method for generating a seed of any ternary composition is by starting from a binary seed. However there is a major criterion that needs to be satisfied. It has been empirically observed that, for alloy systems with wide lattice mismatch between the end binaries (GaAs–InAs, GaSb–InSb, InAs–InSb, etc.), the first-to-freeze section of the crystal must have a composition less than or equal to 5 mol % with respect to the seed in order to maintain single-crystallinity [10.19–21, 100]. For example, during the growth of single-crystal Ga_{1–x}In_xAs on a GaAs seed, the first-to-freeze Ga_{1–x}In_xAs should have $x < 0.05$ [10.100]. With $x > 0.05$, polycrystalline growth occurs on a single-crystal seed [10.100]. Hence the compositional grading during ternary seed generation needs to be carefully controlled to obtain single-crystal seeds.

There are three common ways of generating a compositionally graded ternary seed starting from a seed of a binary compound, as discussed below.

10.9.1 Bootstrapping Method

The most common method is the *bootstrapping* process, wherein seeding is initiated from a binary seed and successive experiments are performed with increasing solute concentration to reach the target alloy composition in the seed. Figure 10.29 schematically depicts the axial composition in a single-crystal GaInAs seed

generated by the bootstrapping method. For example: to generate a Ga_{1–x}In_xAs seed, one would start from a GaAs or InAs seed and grow successive ingots of step-graded GaInAs. The maximum allowable step-like change in composition between the last-to-freeze of any ingot with the first-to-freeze of the next ingot must be equal or less than 5 mol %, as shown in Fig. 10.29. Due to change in the segregation coefficients with alloy composition (dictated by the pseudobinary phase diagrams), there is an increase in the InAs concentration during growth beyond each step. Bonner and coworkers [10.101, 102] employed this method to grow ternary seeds of Ga_{1–x}In_xAs up to $x = 0.12$ by using the Czochralski technique. Tanaka et al. [10.23] employed multistep pulling solute feeding Czochralski

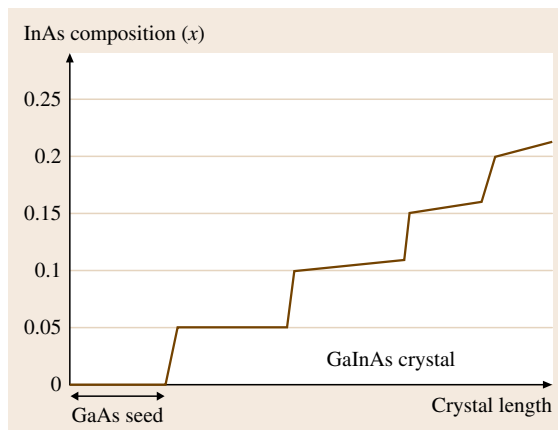


Fig. 10.29 Composition profile (schematic) of a GaInAs single-crystal seed generated by the bootstrapping process

method to grow $\text{Ga}_{1-x}\text{In}_x\text{Sb}$ single crystals using composition steps of $x = 0.04, 0.08, 0.12$, and 0.18 . Though the bootstrapping technique is the most straightforward way of generating single-crystal ternary seeds, it has several limitations. First of all, seed generation with concentrated alloy composition (e.g., $x = 0.5$) can be time consuming since the step in alloy composition in each growth run can only be 5 mol %. For vertical Bridgman growth, it is very difficult to use this method. The melt composition for successive growth in contact with the previous seed needs to be carefully monitored to avoid excessive dissolution of the seed crystal.

10.9.2 Directional Solidification by Normal Freezing

This method is based on the intrinsically changing axial composition profile in a crystal that has been directionally solidified by normal freezing, as depicted in Fig. 10.21 [10.100, 103, 104]. The process is shown schematically in Fig. 10.30a–d. In this process, a binary seed such as GaAs is used. A GaInAs melt is prepared by dissolving InAs and GaAs with the appropriate melt composition that would lead to a first-to-freeze ternary crystal region with 5 mol % compositional step as required for the ternary seed generation process. The melt is directionally solidified by Bridgman or gradient freezing method to obtain a ternary graded

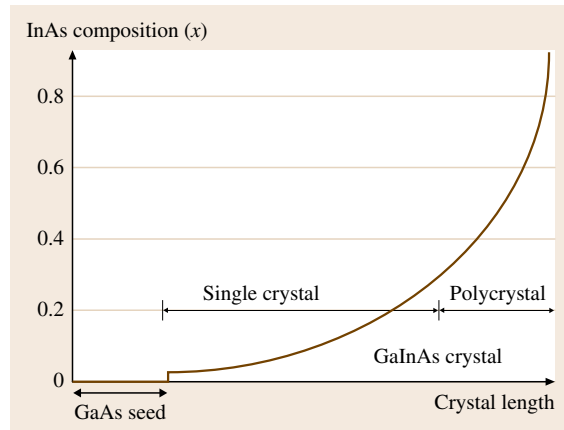


Fig. 10.31 Composition profile (schematic) in a directionally solidified ternary single-crystal seed

crystal. Figure 10.31 schematically depicts the axial InAs composition profile in a vertical Bridgman grown GaInAs crystal. Depending on the composition of the seed necessary for the actual crystal growth experiment, the crystal could be sliced at an appropriate axial position along the length of the crystal. The main problem with this approach is when the composition starts changing rapidly in the crystal; microscopic fluctuation of the composition and polycrystallinity occur due to constitutional supercooling unless the growth rate is significantly reduced. Hence only a part of crystal is sin-

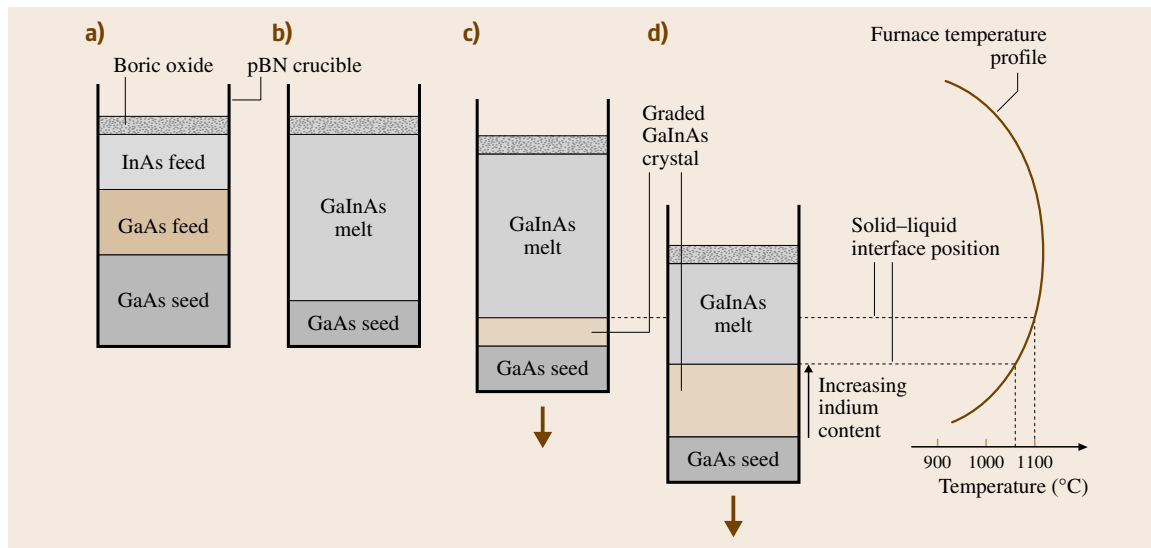


Fig. 10.30a–d GaInAs single-crystal seed generation by vertical Bridgman method (the arrows in (c) and (d) indicate the lowering of the crucible to the cold zone of the furnace during crystal growth)

gle and a bootstrapping process is necessary to change the composition of the seed beyond the point where the single- to polycrystal transition occurs. Even if one manages to grow a complete single crystal by reducing the growth rate, using a seed with a steep change in composition still remains a problem. During the subsequent crystal growth experiment, the seed needs to be dissolved slightly by contact with the ternary melt. However, any dissolution in the steep compositionally graded region will change the composition of the seed at the growth interface. Hence using the compositionally graded seed for a lattice-matched crystal growth experiment is not practical.

10.9.3 Directional Solidification by Solute Diffusion and Precipitation

This process is based on solute diffusion in the melt due to a concentration gradient [10.18, 98, 105, 106]. A schematic diagram of the approach is shown in Fig. 10.32a–d for growing GaInAs seeds. For GaInAs graded seed growth, the lower melting binary (InAs) is used as a seed. The charges in the crucible are stacked as shown in Fig. 10.32a. The crucible is placed in a temperature gradient in such a way that the InAs feed and a portion of the InAs seed remelts to dissolve a portion of the GaAs feed, forming a GaInAs melt. While selecting the temperature profile in the furnace, care should be taken to avoid melting of the GaAs feed. The dissolved GaAs from the feed diffuses towards the seed due to the concentration gradient. Once the solute content in the melt at any point reaches the solidus composition (corresponding to the solidus temperature), solidifica-

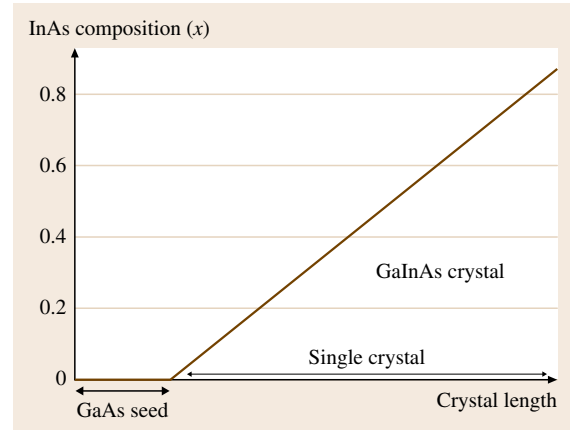


Fig. 10.33 Composition profile (schematic) of a GaInAs single-crystal seed generated by solute dissolution and diffusion

tion occurs. The growth rate is thus limited by the solute diffusion rate. During the growth, neither the crucible nor the furnace is translated. The composition profile in the graded crystal will depend on the temperature profile imposed by the furnace and the solidus curve in the pseudobinary phase diagram. As the GaAs in the melt precipitates and the crystal grows, the melt gets richer in InAs and hence more GaAs is dissolved from the feed. Ultimately, a crystal is obtained with compositional grading from InAs towards GaAs. Theoretically, if the furnace temperature profile matches the solidus temperature curve of the phase diagram, the compositional grading in the crystal will be linear, as depicted in Fig. 10.33.

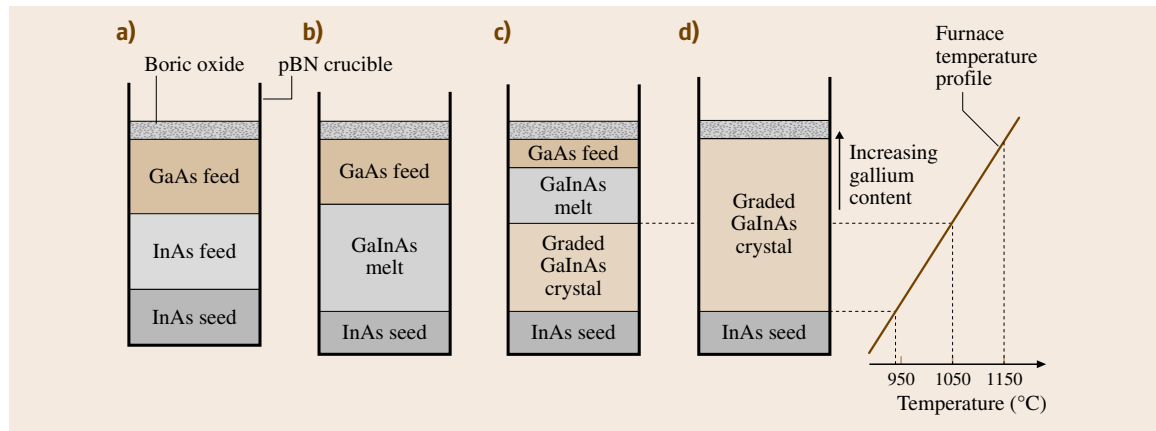


Fig. 10.32a–d GaInAs single-crystal seed generation using solute dissolution and diffusion method (with stationary crucible and furnace)

10.9.4 Growth of Lattice-Mismatched Ternary on Binary Using Quaternary Grading

One of the interesting aspects of the thermochemistry shown in Fig. 10.20 is the growth of ternary compounds from quaternary melts [10.29, 30, 78]. The concept is shown schematically in Fig. 10.34a. By using a GaAs seed and a GaInAsSb melt of a specific composition at a specific growth temperature, one can grow a GaInAs ternary crystal of uniform composition. The composition of the uniform ternary crystal is dependent on the quaternary melt composition and growth temperature. By carefully analyzing the region between the ternary crystal and the binary seed, a quaternary transition region has been observed where the composition changes from the binary to the ternary. The thickness of this graded quaternary region can be in the range of 10–100 μm , depending on the melt composition. In this process, no efforts are made to control the growth conditions to grow the graded quaternary intermediate layer. The compositional grading occurs spontaneously during the growth process. Figure 10.34b shows a compositionally homogeneous $\text{Ga}_{0.86}\text{In}_{0.14}\text{As}$ grown on GaAs substrate using a quaternary $\text{Ga}_{0.07}\text{In}_{0.93}\text{As}_{0.06}\text{Sb}_{0.94}$ melt at 700 $^{\circ}\text{C}$ [10.78]. The GaInAs ternary region does contain residual Sb (less than 1 mol %). However, for all practical purposes, it can be considered a ternary compound. The effect of residual antimony on the lattice parameter and bandgap is negligible. This process could be used in the future to grow ternary seeds of a desired

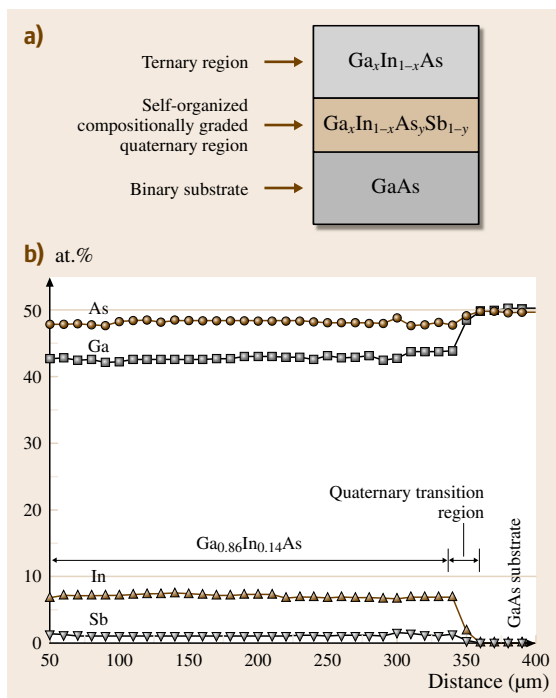


Fig. 10.34 (a) GaInAs seed generation using a self-organized quaternary grading method and (b) experimental composition profile for $\text{Ga}_{0.86}\text{In}_{0.14}\text{As}$ grown on GaAs

composition starting from a binary seed and quaternary melt by simple Bridgman or gradient freezing method without the need for any sophisticated grading procedures.

10.10 Solute Feeding Processes for Homogeneous Alloy Growth

Having grown a ternary single-crystal seed of the desired composition, the next step is to grow a ternary crystal of homogeneous composition from which a large number of wafers (of the same composition) can be sliced. We know that the melt composition as well as the ternary crystal composition changes continuously during the experiment (due to alloy segregation). Hence to grow homogeneous crystals, it is necessary to develop melt replenishment processes that can maintain the composition of the melt constant over the entire duration of the crystal growth experiment. In this section, we discuss the various melt replenishment methods and their limitations.

10.10.1 Growth from Large-Volume Melts

One simple idea would be to grow a small crystal from a huge volume of melt [10.107]. Referring to Fig. 10.21, few wafers of constant composition could be extracted from the first-to-freeze section of the crystal. The melt could then be reused for the next experiment by replenishing with fresh material to account for the extracted wafers. However, this is not a practical solution. Contamination of the melt by impurities from repeated use, the large crystal growth systems required, and the possibility of damaging the crucible during cooling of the melt make this process unattractive for ternary substrate

technology. For large-scale crystal growth production, it is desirable to consume the entire melt during a single experiment. Hence, growth from large-volume melts is not practiced for commercial applications.

10.10.2 Solute Feeding Using Double-Crucible Configuration

Melt replenishment during growth is also known as solute feeding. Many interesting solute feeding concepts have been tried by different researchers. The simplest of these processes is the solute feeding in the Czochralski (CZ) configuration [10.108–112]. Figure 10.35a shows

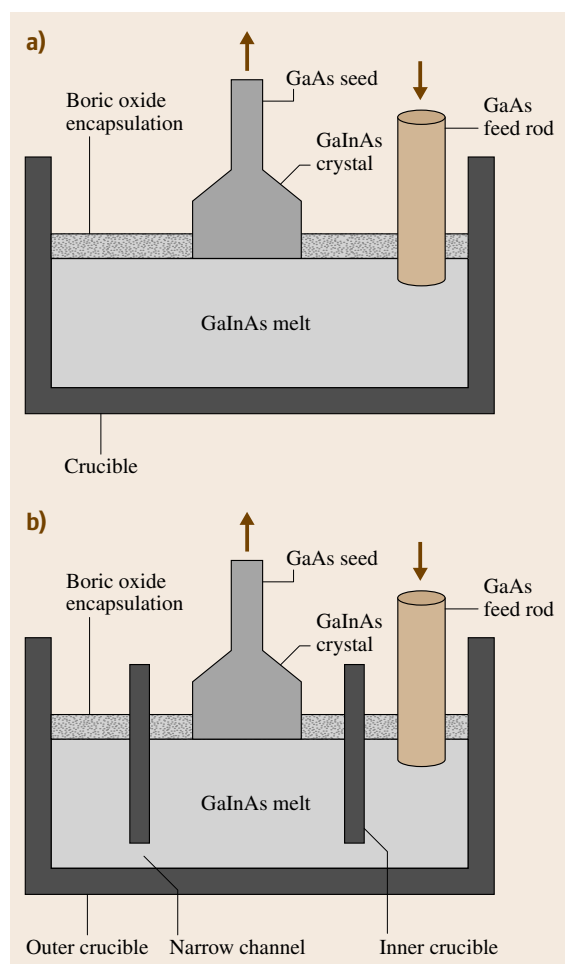


Fig. 10.35a,b Solute feeding in (a) single-crucible and (b) double-crucible Czochralski (CZ) growth configurations

a schematic diagram of this process for GaInAs growth. As the melt becomes depleted in GaAs, the feed rod is inserted to dissolve and maintain the composition of the melt at the liquidus composition. The problem with this process is the uncontrolled dissolution of the feed rod. If the radial temperature in the growth melt is uniform, the feed rod dissolves slower than the crystal pulling rate. This is due to the long duration it takes for the melt to uniformly develop the undersaturation level after the GaAs is depleted by the growing crystal. Hence the feed rod tends to dissolve at a slower rate than the rate at which the GaAs is depleted in the melt. This leads to fluctuation in the composition of the growing crystal. On the other hand, if the radial temperature at the edge of the crystal is increased to enhance the dissolution of the feed rod, rapid transport of GaAs to the growth interface often leads to rapid polycrystalline growth. Hence the feed dissolution rate and GaAs depletion rate need to be matched. This is quite challenging given the fact that the melt height changes during growth in the CZ technique, and thus so does the radial temperature gradient. To restrict the rapid transport of solute from the feed to the growth interface, a double-crucible CZ method as shown in Fig. 10.35b can be employed. In this configuration, the depleting component can be added to the outer crucible instead of the inner crucible. The temperature of the outer crucible is higher than that of the inner crucible, due to which the solubility of the GaAs feed in the GaInAs melt is higher. The narrow gap between the two crucibles controls the feeding rate of GaAs from the outer to inner crucible. This method also shares one of the limitations of the single-crucible CZ technique: once the outer melt is supersaturated with GaAs, the dissolution of the feed rod stops. The outer melt supersaturation level decreases only when the GaAs has been transported to the inner melt and the inner and outer melt have homogenized. Hence the feed rod does not dissolve continuously during the growth, which leads to fluctuations in the alloy composition in the crystal.

Variations on the double-crucible CZ configuration (refer to Fig. 10.36) have been attempted to control the solute transport rate between the inner and outer crucibles [10.23, 106, 113–116]. In both of these configurations, a piston attached below the outer crucible is used to keep the volume of the melt constant in the inner crucible. The diameter (Fig. 10.36a) or the length (Fig. 10.36b) of the channel is varied to control the solute feeding rate. The limitation with these processes is the blocking of the channels by the transporting solute. A change in liquidus temperature occurs along the

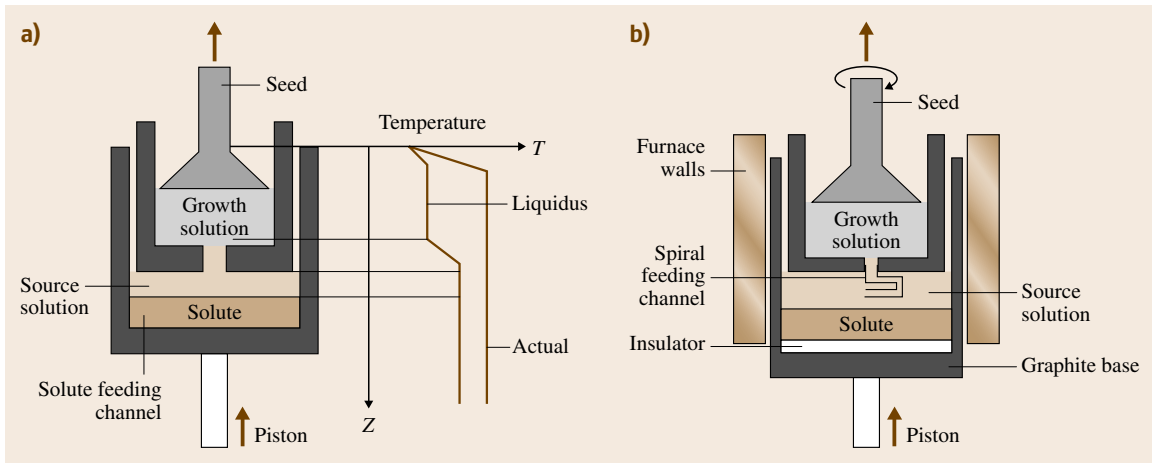


Fig. 10.36a,b Solute feed rate control in the double-crucible CZ method by optimizing (a) feeding channel diameter and (b) feeding channel length

length of the supply channel, as shown in Fig. 10.36a. This leads to precipitation of the solute in the channel towards the lower-temperature side. If the channel width is made larger to solve this problem, back-diffusion of species from the inner to the outer crucible takes place, which leads to variations in the composition of the grown crystal. Another problem is the optimization of the length of the spiral feeding channel (Fig. 10.36b). The diffusion rate of species in the channel dictates the growth rate of the crystal. A shorter channel leads to

back-diffusion of species from the inner to the outer melt, changing the composition of the growth solution. On the other hand, a longer channel leads to slow diffusion of species from the outer to the inner melt.

10.10.3 Solute Feeding in the Vertical Bridgman Method

The double-crucible CZ concept for solute feeding can be applied to the Bridgman or gradient freeze type

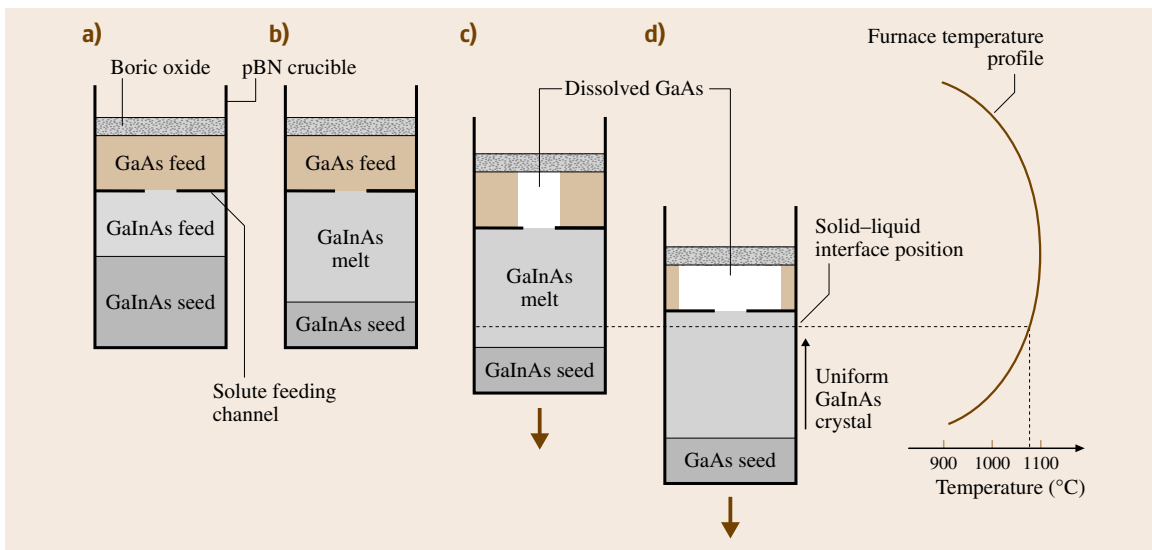


Fig. 10.37a–d Continuous solute feeding during vertical Bridgman growth

methods [10.21, 104]. Figure 10.37 shows a continuous solute feeding process during vertical Bridgman growth of GaInAs. In this configuration, a ternary single-crystal seed of GaInAs of the desired composition (solidus composition) is placed in a flat-bottomed crucible. A GaInAs polycrystalline homogeneous feed with the liquidus composition is placed on the seed. A GaAs polycrystalline solute feed is stacked on the GaInAs feed, separated by a quartz plate with a hole (Fig. 10.37a). The entire stack is then heated to the

growth temperature to melt the GaInAs feed and a small portion of the feed (Fig. 10.37b). The crucible is translated as in a vertical Bridgman growth process to initiate the crystal growth (Fig. 10.37c). The composition of the growing crystal is same as the ternary seed. The GaAs that is being depleted in the growth melt is continuously replenished by the feed at the top. The diameter of the hole restricts the dissolution rate of the GaAs feed. This helps to avoid rapid transport of GaAs from the feed to the growth interface, thus eliminating the possibility of polycrystalline growth [10.104]. The technical challenge with this configuration is the variation in the melt level during growth due to differences in the density of the melt versus the solid. When the GaInAs feed melts, the melt height lowers and the GaAs feed does not touch the melt unless a special mechanism is used to lower the feed. When the crystal grows, the solid expands, due to which the melt height increases. Hence there should be proper mechanism for moving the GaAs feed up into the crucible.

10.10.4 Solute Feeding by Crucible Oscillation

The method for synthesizing GaSb and InSb in sealed crucible as depicted in Fig. 10.9 can be adopted to perform solute feeding process during ternary growth [10.117]. Figure 10.38 shows the rocking furnace configuration for GaInAs growth. At one end of the crucible, the GaAs seed is placed, onto which a graded-composition GaInAs crystal is first grown towards the lower-temperature region of the furnace (as in the Bridgman method). Thereafter the furnace is tilted periodically such that the GaInAs melt touches the GaAs feed to replenish the depleted species. The crucible is continuously translated to continue the growth. Since the GaAs level in the ternary melt is kept constant by dissolving the feed, the composition of the grown crystal is homogeneous. For radial compositional homogeneity, the crucible can be rotated during growth. In this process, the temperature gradient across the crucible length plays a significant role in the crystalline quality. If thermal fluctuation occurs due to the oscillating melt, the grain size could be extremely small in the crystal. To avoid excessive feed dissolution or rapid precipitation at the growth interface, a low axial temperature gradient is desirable. However this increases the probability of constitutional supercooling. Hence efficient melt mixing by forced convection (continuous

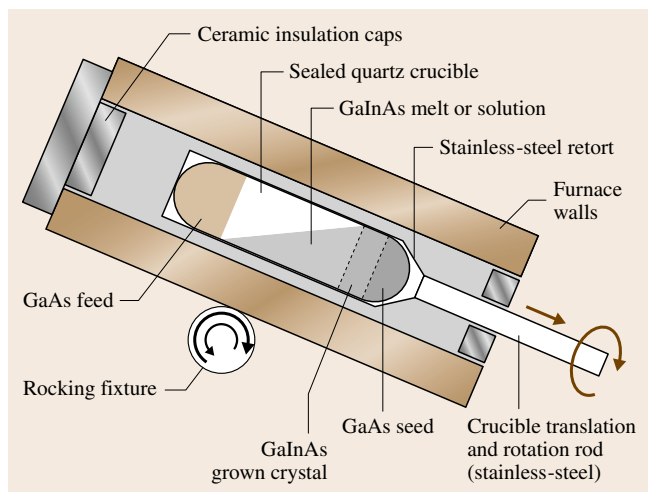


Fig. 10.38 Solute dissolution and feeding in a rocking furnace assembly

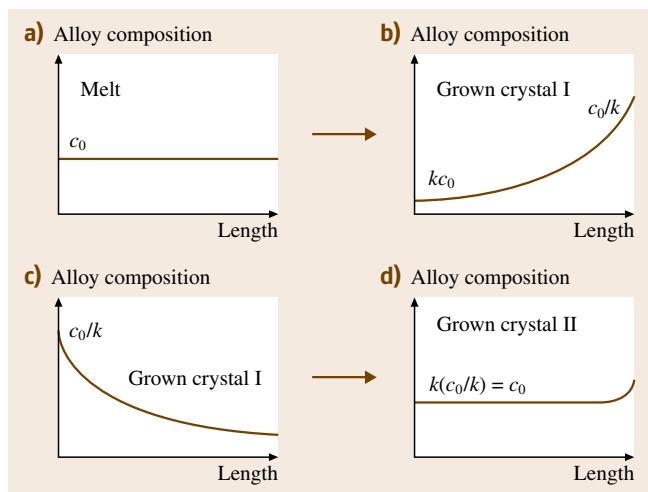


Fig. 10.39a–d Growth of homogeneous ternary by sequential normal freezing and zone growth methods

oscillation) in conjunction with a slow growth rate is necessary for this process.

10.10.5 Growth Using Compositionally Graded Feed

The graded concentration solute feeding process is depicted in Fig. 10.39 [10.118]. In this method, starting from a homogenous melt of composition C_0 , a crystal is first grown using the Bridgman or gradient freezing method. The axial alloy composition in the grown crystal is shown in Fig. 10.39b. According to segregation phenomenon, the composition in the crystal starts from kC_0 (k being the segregation coefficient) and continuously builds up beyond C_0/k . The crystal is then reversed and a traveling zone heater is traversed across the crystal starting from the C_0/k side. The final composition in the crystal is uniform and equal to C_0 . A traveling heater method (THM) can also be used to practice this concept [10.119]. This method needs a purely diffusive growth condition. Such conditions can only be found in microgravity situations. Convective flow in the liquid zone will change the solute concentration and result in nonuniform growth. Magnetic fields can be used to dampen convective flows. However for large-scale ternary substrate production, this method is not suited.

10.10.6 Periodic Solute Feeding Process

From the processes described above, it is clear that any large-scale ternary crystal growth process will require mechanisms for precise control of melt composition. Another technical problem is the preparation of the growth melt during the experiment. Ensuring that the melt composition is in equilibrium with the seed composition is crucial for avoiding excessive seed dissolution. The rate of solute dissolution and transport to the growth interface also needs to be controlled to achieve high crystalline quality and growth rates suitable for commercial applications. To address all of these technical issues collectively, the process shown in Fig. 10.40 has been developed and successfully employed for large-diameter ternary crystal growth. In this process, starting from a binary seed, the graded ternary seed and the homogeneous ternary crystal is grown in a single experiment. The schematic of the experimental growth configuration and crystal growth sequence for GaInSb is shown in Fig. 10.40a–d [10.28, 98, 120, 121].

To start with, a InSb single-crystalline seed is placed at the bottom of the crucible along with InSb polycrystalline charge. A GaSb polycrystal feed is suspended from the top of the growth chamber. After heating and stabilizing the furnace to obtain a specific temperature gradient, the crucible is raised into the furnace.

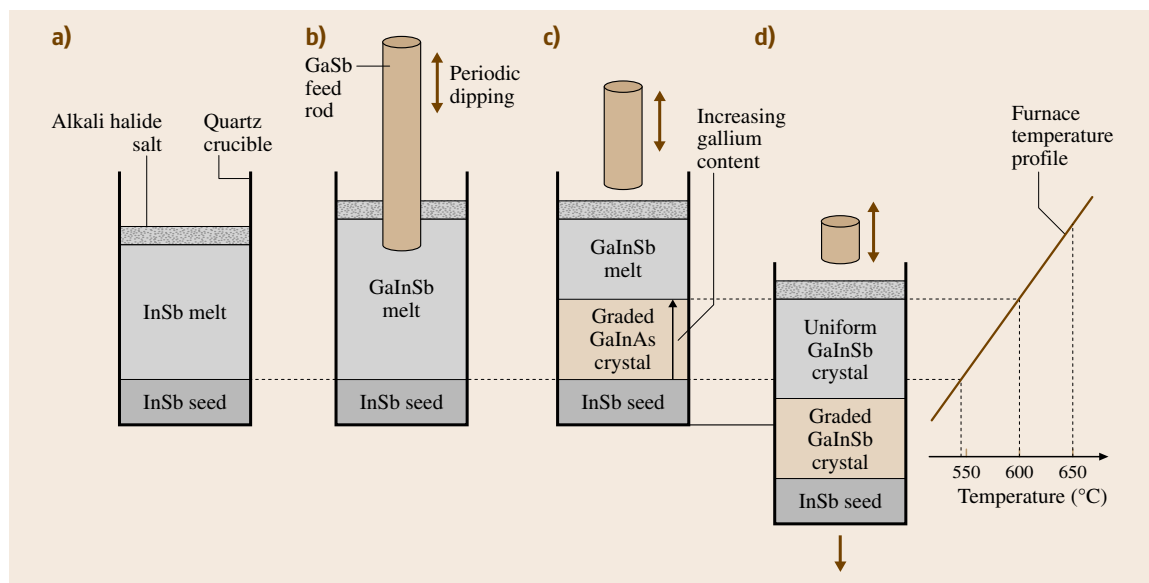


Fig. 10.40a–d Periodic solute feeding process for growth of graded-composition ternary seed and homogeneous ternary crystal in a single experiment by sequentially using solute diffusion and normal freezing processes

The InSb feed melts along with part of the InSb seed to obtain a melt–solid interface (Fig. 10.40a). At this point, the GaSb feed is lowered and allowed to touch the top of the InSb melt for a few seconds. The crucible is set to perform accelerated crucible rotation (ACRT), as shown in Fig. 10.27, and a homogeneous GaInSb melt is prepared (Fig. 10.40b). The GaSb feed is lowered periodically to touch the GaInSb melt. The dissolved species is transported rapidly to the InSb seed interface as a result of ACRT melt mixing. Crystal growth is initiated in the crucible as a result of the increasing level of the solute concentration at the solid–liquid interface with time. When the solute concentration in the melt near the seed interface reaches the liquidus composition, precipitation takes place and GaInSb starts growing on InSb (Fig. 10.40c). The crucible is kept at the same position in the furnace while the ACRT continues. As the GaSb feed is periodically lowered to touch the melt for few seconds, more solute is dissolved and transported to the growth interface and the crystal growth continues. Crystal grown by this method is compositionally graded along the growth axis with increasing gallium concentration in $\text{Ga}_{1-x}\text{In}_x\text{Sb}$ (decreasing indium concentration). The rate of compositional grading is decided by the solidus temperature in the pseudobinary phase diagram and the axial furnace temperature gradient. The axial composition in the crystal is graded until a desirable alloy composition is achieved and then a homogeneous composition crystal length is grown. During the compositionally graded crystal growth, the melt–solid interface automatically rises from the cooler to the hotter zone in the furnace. Thus the melt–solid interface shape changes continuously during the growth. The effect of temperature gradient on the melt–solid interface shape and the radial compositional variation will be discussed in the next section. To grow crystal with axially uniform composition, the crucible is translated into the lower-temperature zone of the furnace while the GaSb feed dissolution is continued by the periodic dipping method. While the GaSb at the melt–solid interface is depleted by preferential incorporation in the crystal, it is being replenished by the feed dissolution. Hence the melt–solid interface remains at the same position in the furnace until the entire melt has solidified (Fig. 10.40d).

The periodic solute feeding process described above in conjunction with efficient melt mixing provides complete control over the composition profile in the graded seed and the homogeneous crystal [10.120]. The entire experimental process could be automated using programmable stepper motors for the periodic solute

feeding, ACRT, and crucible translation processes. The main advantage of this process is the single experiment in which a ternary homogeneous crystal of any alloy composition can be obtained starting from a binary single-crystal seed and polycrystalline binary feed materials. For high-quality crystal growth, the periodic solute feeding process parameters need to be fine-tuned. This is necessary to precisely control the rate at which solute depletes and replenishes in the melt. The major process parameters that affect the crystalline quality include: the solute dipping time and frequency, the mixing strategy of the melt for solute transport, and the thermal gradient in the melt. Dipping time denotes the actual time that the melt is in contact with the feed. This determines the amount of feed introduced in the melt over one period of the dipping cycle. Due to the temperature gradient in the melt, the top of the melt (higher-temperature zone) is usually undersaturated. Hence there exists a danger of uncontrolled dissolution if the solute feeding rod is dipped for longer than the required time. Thus precise control of dipping time is required. Excess dissolution of the solute can promote random nucleation in the entire melt volume. Additionally, this can lead to an oversupply of the solute to the growth interface leading to small grains or causing a change in grain structure, as shown in Fig. 10.41. Dipping frequency defines the period of the dipping cycle and should depend on the growth rate. It takes finite time for the solute to reach the growth surface. Further, the growth kinetics determines the actual growth rate. The thermal gradient in the melt dictates the melt homogenization efficiency. For lower thermal gradients, the time for melt homogenization is longer than for high thermal gradient. Hence the dipping frequency needs to be lower for lower thermal gradients in order to prevent constitutional supercooling and so-

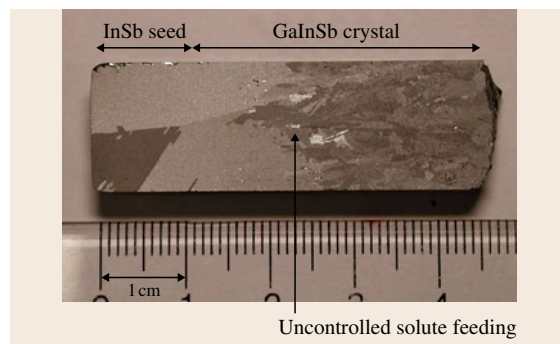


Fig. 10.41 Transition from large to small grains due to uncontrolled (rapid) solute feeding process during growth

lute precipitation in the melt. Mixing of the melt greatly affects the crystal growth. Efficient mixing can remove the excess solute rejected at the growth interface in less time than without mixing, thereby decreasing the possibility of constitutional supercooling. This suppresses the chances of interface breakdown, leading to conditions conducive for single-crystal growth. Based on experimental crystal growth results, a set of optimized periodic solute feeding parameters for GaInSb growth include: solute contact area of 20 mm, solute dipping time of 2–3 s, solute dipping frequency of 3–4 times per hour, temperature gradient near the melt–solid interface of 15 °C/cm, and ACRT melt mixing process. Figure 10.42 shows elemental composition profiles of Ga, In, and Sb for the graded GaInSb seed (shown in Fig. 10.41) grown using the periodic solute feeding process with the optimized parameters. The superior control of the composition profile shown in this diagram clearly demonstrates the effectiveness of the periodic solute feeding process. Beyond 47 mm, the solute feeding process was discontinued and the crystal was directionally solidified, giving rise to a composition profile as expected from the normal freezing process. This process has been demonstrated for the growth of homogeneous $\text{Ga}_{0.3}\text{In}_{0.7}\text{Sb}$ crystals [10.120].

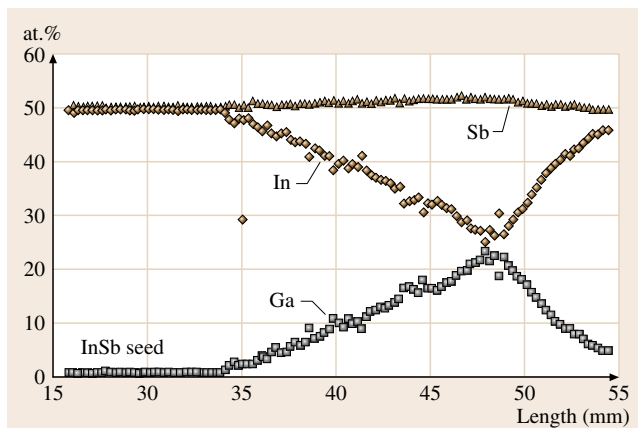


Fig. 10.42 Elemental composition profile along the growth direction of the GaInSb graded seed crystal grown using periodic solute feeding process shown in Fig. 10.40

Another method for periodic solute feeding process is shown in Fig. 10.43. In this process, the higher-melting binary is used as the starting seed material for the ternary crystal growth. In Fig. 10.43, the process for GaInSb growth starting from GaSb seed is illustrated. The experiment starts with a GaSb single-

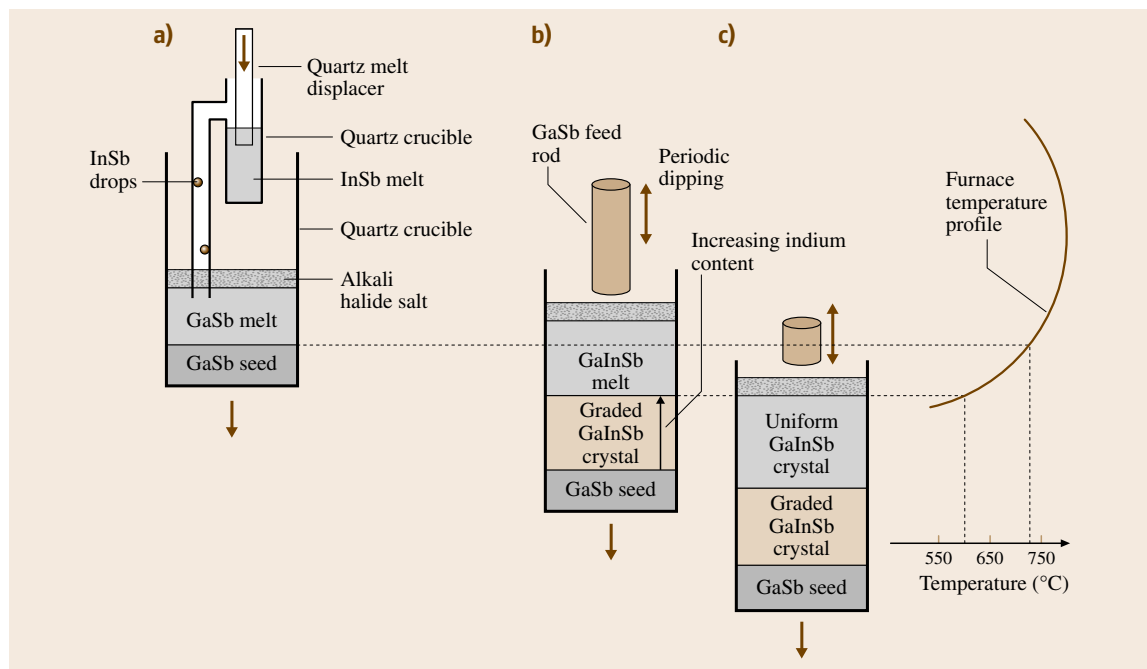


Fig. 10.43a–c Periodic solute feeding process for growth of graded-composition ternary seed and homogeneous ternary crystal in a single experiment by vertical Bridgman method

crystalline seed and a GaSb melt in the crucible. The lower-melting-point binary (InSb in this case) is present in a quartz melt displacer. After the furnace has been heated, the GaSb feed melts to form a melt–solid interface. The crucible is set for accelerated crucible rotation (ACRT) as in the previous case. By pressing the piston, the InSb can be periodically fed into the GaSb melt. After the initial InSb melt is dispensed into the growth melt to form GaInSb, the crucible is translated towards the lower-temperature zone of the furnace as in Bridgman growth. The graded-composition GaInSb ternary starts from the GaSb seed with increasing InSb content in the crystal. The InSb concentration in the melt increases with time as it is fed into the melt periodically. After the graded GaInSb seed growth, a GaSb feed is introduced into the melt periodically as in the previous case. The crucible translation is continued while the GaSb feed is periodically fed into the melt (Fig. 10.43c). This step results in a compositionally uniform GaInSb region as before (Fig. 10.40d). Care must be taken to ensure that the GaSb feed shown in Fig. 10.43b,c is introduced into the lower-temperature zone of the furnace without melting. The process illustrated in Fig. 10.43 can also be implemented by the gradient freezing process. In that case, the furnace temperature is decreased below the melting point of GaSb before it is introduced into the GaInSb melt for the homogeneous growth re-

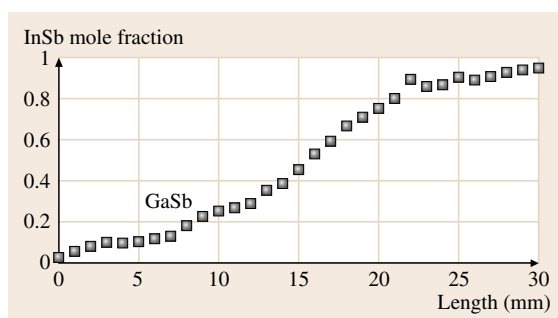


Fig. 10.44 InSb mole fraction along the growth direction of GaInSb crystal grown using the first step of the process (feeding InSb) shown in Fig. 10.43

gion. Figure 10.44 shows the axial InSb mole fraction in a GaInSb crystal grown by the periodic InSb feeding process. The composition of the crystal was continuously varied from GaSb to InSb, showing the flexibility of the process for controlling the alloy concentration in the crystal.

The periodic solute feeding process described in this section can be universally applied for the growth of any ternary alloy system. The same experimental configurations that are being used for the respective binary growth can be used with the addition of the periodic solute feeding mechanism.

10.11 Role of Melt–Solid Interface Shapes

The melt–solid interface shape during crystal growth plays a significant role in the quality of the grown crystals [10.100, 122, 123]. As shown in Fig. 10.45, with

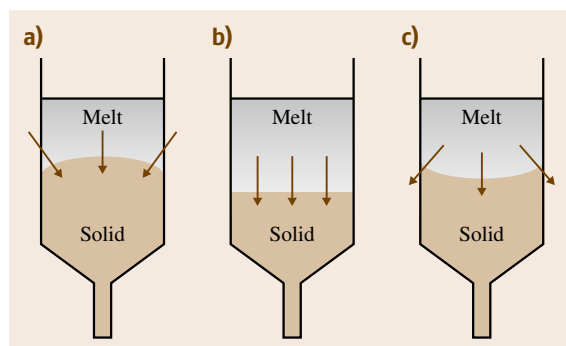


Fig. 10.45a–c Melt–solid interface shapes observed during vertical Bridgman growth: (a) convex, (b) planar, and (c) concave interface shapes

respect to the solid, the melt–solid interface shape could be (a) convex, (b) planar or (c) concave. The shape represents the isotherm corresponding to the melting point of the material [10.124]. A convex interface with respect to the solid is created when the temperature gradient at the growth interface is low since the heat extraction through the grown crystal becomes dominant, whereas the concave interface towards the melt is formed when the temperature gradient is large because heat is lost out through the crucible. The concave interface as shown means that the temperature at the center is higher than that around the edges. The arrows in the figure indicate the direction of heat flow, which is perpendicular to the melt–solid interface at every point. The curvature of the interface is dictated by the complex heat transfer between various components in the growth system (furnace, crucible, melt, crystal, encapsulant, gas, crucible holders, etc.). In general, a concave interface shape is the least desirable since it encourages polycrystalline

grains to originate from the walls of the crucible and grow into the crystal. The convex interface shape is desirable from the point of view of grain elimination (any polycrystalline grain will grow outwards to the edge of the crucible). However a convex interface tends to produce twinning in the crystal. Both concave and convex interfaces will produce nonuniform stress along the radial direction, thus producing a high dislocation density in localized regions across the wafer. The planar interface is the ideal for crystal growth. A significant amount of computational modeling and experimental research is being conducted to study the interface shape in real crystal growth configurations [10.125–127]. This is being done to identify thermal and growth conditions under which a planar melt–solid interface could be obtained.

The shape of the melt–solid interface determines the radial compositional profile in ternary crystals [10.100]. A planar interface is absolutely necessary for obtaining wafers with uniform alloy composition. Hence it is very important to understand the heat transfer processes during ternary crystal growth and identify suitable conditions that could lead to planar interface during growth. In general, for a Bridgman-type configuration, the primary heat flow mechanisms are: radiative heat transfer from the hot zone of furnace to the melt, convection and conduction in the melt, conduction in the solid (crystal) and radiative heat transfer from the crystal to the cold zone of the furnace [10.128]. Other effects such as latent heat release at the melt–solid interface, convective flow, etc. make secondary contributions. Convection in the liquid can be driven by several forces. In the presence of gravitational forces, the most importance source of convective flow is due to the density differences caused by temperature and composition differences in the liquid. Additional flow can be driven by the volume change accompanying the phase change. If free surfaces (i. e., liquid–vapor, liquid–liquid) are present, Marangoni convections due to the surface tension gradient originating from the difference of temperature and solute concentration occur. The density-driven convective flow due to the temperature difference can be prevented if the temperature increases with height (the stabilizing condition, as in the case of vertical Bridgman configuration) and no temperature gradient is present in the radial direction even in the presence of gravitational forces [10.96]. If a solute is present, the growth process will result in compositional differences ahead of the growth interface because the rejected solute from the crystal is lower or higher in density than the solvent; these composition differences may result in a thermoso-

lateral convective instability [10.96]. A global model incorporating the materials properties of all the components present in the growth chamber is necessary to predict the melt–solid interface shape to a high degree of accuracy. In this section, we will discuss the experimental parameters that alter the melt–solid interface curvature during ternary crystal growth using Bridgman or gradient freeze type methods.

During Bridgman growth of ternary crystals, the temperature gradient in the melt, at the melt–solid interface, and in the crystal plays a significant role in determining the curvature of the interface [10.121].

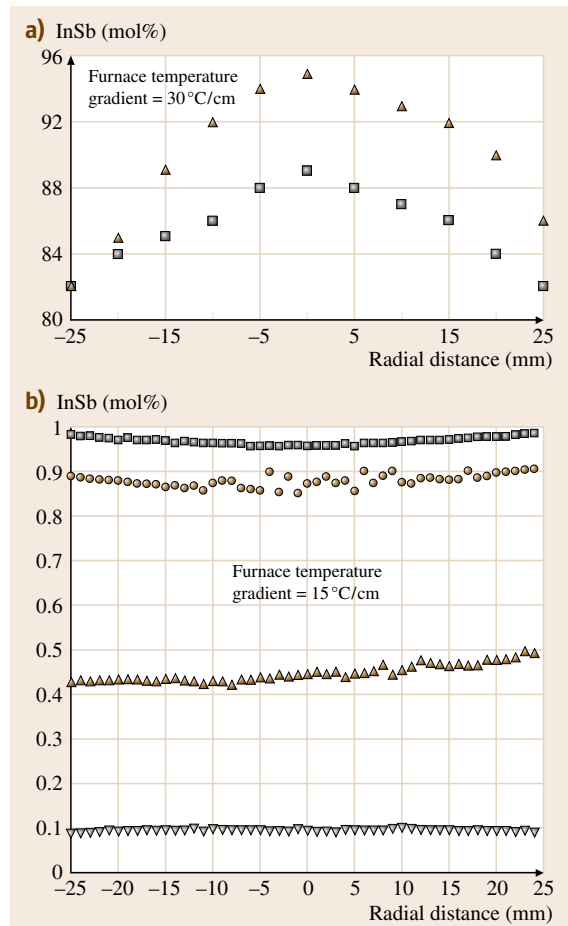


Fig. 10.46a,b Correlation of melt–solid (MS) interface shape with radial InSb composition profile in GaInSb crystals: **(a)** concave M–S interface resulting in convex InSb profile (Δ: without melt stirring, □: with melt stirring) and **(b)** planar M–S interfaces resulting in uniform InSb profiles (with melt stirring)

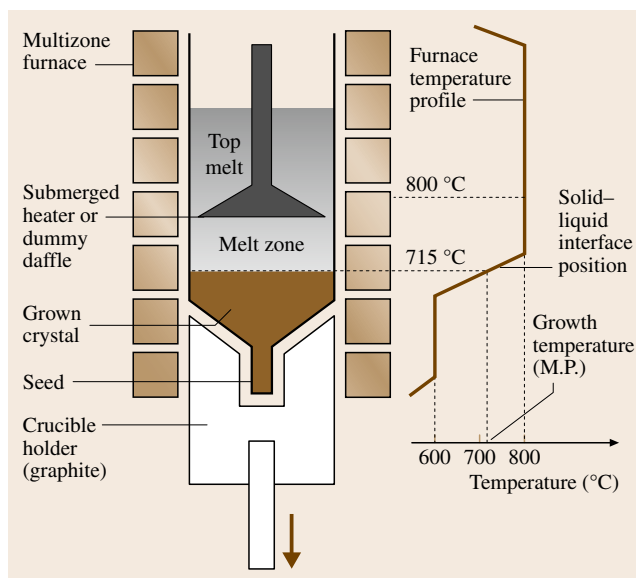


Fig. 10.47 Schematic diagram of vertical Bridgman growth configuration with submerged heater or baffle in the melt used for flattening the melt–solid interface shape

Interestingly, the effect of forced convection on the interface curvature seems to be weaker than the effect of temperature gradient. Figure 10.46 shows the radial InSb composition profiles for vertical Bridgman grown GaInSb crystals with furnace temperature gradients of 30 and 15 °C/cm. Under an axial temperature gradient of 30 °C/cm, the growth interface is highly concave with respect to the solid (leading to a convex InSb radial profile). Figure 10.46a also shows the radial InSb profile for a crystal grown using melt stirring (stationary stirrer in the melt with constant crucible rotation of 100rpm, as in Fig. 10.10a). The curved compositional profile clearly indicates that high axial gradients lead to curved interfaces which are very difficult to flatten even with strong fluid stirring. The convex radial profile is also seen in the crystal grown with ACRT (Fig. 10.27). This clearly demonstrates the strong influence of temperature gradient on the interface curvature. Higher temperature gradients are known to produce concave melt–solid interface shapes. Lowering the gradient would certainly flatten the interface. However very low gradients must be avoided since the probability of constitutional supercooling will be enhanced with low gradients. For ternary crystals with diameter of 50 mm, the optimum temperature gradient is in the

range of 10–15 °C/cm, wherein constitutional supercooling can be avoided by suitable melt stirring and a flat interface could be achieved. Figure 10.46b shows the radial InSb composition profiles in a GaInSb crystal grown with a temperature gradient of 15 °C/cm and with melt stirring using ACRT (Fig. 10.27). The interface curvature is extremely flat, except towards the end of growth where the interface curvature varies slightly. If melt stirring is not used under the same gradient of 15 °C/cm, constitutional supercooling was observed for growth rate of 0.7 mm/h or higher. Hence a combination of low temperature gradient and low growth rate or melt stirring is necessary to obtain a flat interface without constitutional supercooling [10.121].

A sophisticated method for achieving planar melt–solid interface shape during crystal growth is shown in Fig. 10.47 [10.86, 87]. In this configuration (the submerged heater method, SHM), a heater is enclosed inside a quartz disc-shaped hollow enclosure (baffle). A shallow growth melt is contained between the baffle and the growth interface. Heat is axially supplied to the melt by the disc-shaped heater submerged in the melt, which is held at a temperature higher than the melting point of the materials and is extracted downward through the crystal during the growth. This results in flattening of the melt–solid interface. It is also possible to use the submerged baffle without power. The thermal conductivity of the baffle on its own could flatten the interface without the addition of extra heat. This scheme enables the crystal to grow under steady-state conditions due to the low level of convection in the small melt zone and the continuous and stable replenishment of melt and impurities. While the crucible is lowered, the large melt above the baffle provides a liquid feed to the small melt enclosed between the crystal and the baffle. The downward flow in the gap between the crucible and the baffle inhibits back-diffusion, and buoyancy-driven convection is not expected since the top is hotter than the bottom in the small melt zone. The submerged baffle can also be rotated to create forced convection in the growth melt. This has been employed to eliminate cracks in GaInSb ternary crystals [10.25]. Advanced fluid flow patterns [10.129] will be necessary to achieve a high degree of compositional homogeneity in ternary crystals. In the future, a combination of ACRT [10.130–132], magnetic fields [10.133], and SHM [10.87] could enable the necessary heat and mass transport for growing compositionally tailored device-grade ternary crystals.

10.12 Conclusion

Ternary single-crystal substrates are important for advanced photonic, electronic, and photovoltaic-based power generation device structures. Large-scale crystal growth technology for growing reliable device-grade ternary substrates is still in its infancy and requires substantial engineering development. The Bridgman or gradient freezing process is the most suitable method for growing large-diameter III–V ternary bulk crystals. Ternary crystal growth requires low temperature gradient and low growth rate. Typical temperature gradient and growth rate are in the range of 5–15 °C/cm and 0.02–0.5 mm/h, respectively. A low temperature gradient helps to ensure a planar melt–solid interface shape, which is necessary for a uniform radial composition in the crystal as well as reducing the strain level in the crystal to avoid cracking. Low growth rates are necessary to avoid constitutional supercooling and interface breakdown, which lead to transition from single- to polycrystal growth and the generation of microcracks. Melt stirring using forced

convection is crucial to avoid constitutional supercooling during growth. Stirring also helps in enhancing crystal growth rate. Special conditions are necessary for ternary single-crystal seed generation. The rate of compositional grading along the crystal during the seed generation process should be maintained below a specific level in order to avoid strain-gradient-related cracks in the crystal. Precise melt composition control using solute replenishment is absolutely essential for the growth of compositionally homogeneous crystals. In this chapter, an advanced crystal growth process has been described that could lead to growth of high-quality device-grade and commercially viable ternary substrates. The proof of concept for the process has been successfully demonstrated by laboratory-scale large-diameter crystal growth experiments. It is anticipated that the single-step process for seed generation and homogeneous crystal growth could be universally employed for all III–V ternary compounds.

References

- 10.1 V. Swaminathan, A.T. Macrander: *Materials Aspects of GaAs and InP Based Structures* (Prentice Hall, New Jersey 1991)
- 10.2 M. Neuberger: III–V ternary semiconducting compounds–data tables. In: *Handbook of Electronic Materials*, Vol. 7 (IFI/Plenum, New York 1972)
- 10.3 O. Madelung, M. Schulz (eds): Landolt–Börnstein, numerical data and functional relationships. In: *Science and Technology, Semiconductors*, Vol. 22(A) (Springer, New York 1987)
- 10.4 W.B. Pearson: *A Handbook of Lattice Spacings and Structures of Metals and Alloys*, Vol. 1 (Pergamon, New York 1956), Vol. 2 (1967)
- 10.5 M.B. Panish, M. Illegems: Phase equilibria in ternary III–V systems, *Prog. Solid State Chem.* **7**, 39–83 (1972)
- 10.6 H.C. Casey Jr., M.B. Panish: *Heterojunction Lasers, Part B – Materials and Operating Characteristics*, Quantum Electronics Series (Academic, New York 1978)
- 10.7 I. Vurgaftman, J.R. Meyer, L.R. Ram-Mohan: Band parameters for III–V compound semiconductors and their alloys, *J. Appl. Phys.* **89**(11), 5815–5875 (2001)
- 10.8 Special issue on: Compliant and alternative substrate technology, *J. Electron. Mater.* **29** (2000)
- 10.9 K. Otsubo, H. Shoji, T. Kusunoki, T. Suzuki, T. Uchida, Y. Nishijima, K. Nakajima, H. Ishikawa: High T_0 (140 K) and low-threshold long-wavelength strained quantum well lasers on InGaAs ternary substances, *Electron. Lett.* **33**, 1795–1797 (1997)
- 10.10 H. Ishikawa: Theoretical gain of strained quantum well grown on an InGaAs ternary substrate, *Appl. Phys. Lett.* **63**, 712–714 (1993)
- 10.11 K. Otsubo, Y. Nishijima, T. Uchida, H. Shoji, K. Nakajima, H. Ishikawa: 1.3 μm InGaAs/InAlGaAs strained quantum well laser on InGaAs ternary substrates, *Jpn. J. Appl. Phys.* **38**, L312–L314 (1999)
- 10.12 H.X. Yuan, D. Grubisic, T.T.S. Wong: GaInSb photodetectors developed from single crystal bulk grown materials, *J. Electron. Mater.* **28**, 39–42 (1999)
- 10.13 T. Refaat, M.N. Abedin, V. Bhagwat, I.B. Bhat, P.S. Dutta, U.N. Singh: InGaSb photodetectors using InGaSb substrate for 2 μm applications, *Appl. Phys. Lett.* **85**(11), 1874–1876 (2004)
- 10.14 P.S. Dutta, J.M. Borrego, H. Ehsani, G. Rajagopalan, I.B. Bhat, R.J. Gutmann, G. Nichols, P.F. Baldasaro: GaSb and GaInSb thermophotovoltaic cells using diffused junction technology in bulk substrates,, *AIP Conf. Proc.* **653**, 392–401 (2002)
- 10.15 J. Merrill, D.C. Senft: Directions and materials challenges in high performance photovoltaics, *J. Miner. Met. Mater. Soc. (JOM)* **59**(12), 26–30 (2007)
- 10.16 P.S. Dutta, H.L. Bhat, V. Kumar: The physics and technology of gallium antimonide: An emerging

- optoelectronic material, J. Appl. Phys. **81**, 5821–5870 (1997)
- 10.17 K.J. Bachmann, F.A. Thiel, H. Schreiber Jr.: Melt and solution growth of bulk single crystals of quaternary III–V alloys, Prog. Cryst. Growth Charact. **2**, 171–206 (1979)
- 10.18 P.S. Dutta: III–V ternary bulk substrate growth technology: a review, J. Cryst. Growth **275**, 106–112 (2005)
- 10.19 W.A. Bonner, B.J. Skromme, E. Berry, H.L. Gilchrist, R.E. Nahory: Bulk single crystal GaInAs: LEC growth and characterization, Proc. 15th Int. Symp. GaAs Relat. Compd., Vol. 96, ed. by J.S. Harris (Institute of Physics, Bristol 1989) pp. 337–342
- 10.20 W.A. Bonner, B. Lent, D.J. Freschi, W. Hoke: Substrate quality of III–V single crystals for II–VI device applications: Growth and characterization, Proc. SPIE **2228**, 33–43 (1994)
- 10.21 S. Kodama, Y. Furumura, K. Kinoshita, H. Kato, S. Yoda: Single crystalline bulk growth of $\text{In}_{0.3}\text{Ga}_{0.7}\text{As}$ on GaAs seed using the multi-component zone melting method, J. Cryst. Growth **208**, 165–170 (2000)
- 10.22 A. Mitric, T. Duffar, C. Diaz-Guerra, V. Corregidor, L.C. Alves, C. Garnier, G. Vian: Growth of GaInSb alloys by vertical Bridgman technique under alternating magnetic field, J. Cryst. Growth **287**(2), 224–229 (2006)
- 10.23 A. Tanaka, J. Shintani, M. Kimura, T. Sukegawa: Multi-step pulling of GaInSb bulk crystal from ternary solution, J. Cryst. Growth **209**, 625–629 (2000)
- 10.24 J.P. Garandet, T. Duffar, J.J. Favier: Vertical gradient freeze growth of ternary GaSb–InSb crystals, J. Cryst. Growth **106**, 426–436 (1990)
- 10.25 P.S. Dutta, A.G. Ostrogorsky: Suppression of cracks in $\text{In}_x\text{Ga}_{1-x}\text{Sb}$ crystals through forced convection in the melt, J. Cryst. Growth **194**, 1–7 (1998)
- 10.26 P.S. Dutta, A.G. Ostrogorsky: Melt growth of quasi-binary $(\text{GaSb})_{1-x}(\text{InAs})_x$ crystals, J. Cryst. Growth **198/199**, 384–389 (1999)
- 10.27 P.S. Dutta, A.G. Ostrogorsky: Strong band gap narrowing in quasi-binary $(\text{GaSb})_{1-x}(\text{InAs})_x$ crystals grown from melt, J. Cryst. Growth **197**, 1–6 (1999)
- 10.28 P.S. Dutta, H.J. Kim, A. Chandola: Controlling heat and mass transport during the vertical Bridgman growth of homogeneous ternary III–V semiconductor alloys, Trans. Indian Inst. Met. **60**(2–3), 155–160 (2007)
- 10.29 P.S. Dutta, T.R. Miller: Engineering phase formation thermo-chemistry for crystal growth of homogeneous ternary and quaternary III–V compound semiconductors from melts, J. Electron. Mater. **29**, 956–963 (2000)
- 10.30 P.S. Dutta, T.R. Miller: Multicomponent homogeneous alloys and method for making same, US Patent 6613162 B1 (2003)
- 10.31 P.S. Dutta, A.G. Ostrogorsky: Alloys and methods for their preparation, US Patent 6273969 B1 (2001)
- 10.32 R. Pino, Y. Ko, P.S. Dutta: High-resistivity GaSb bulk crystals grown by the vertical Bridgman method, J. Electron. Mater. **33**(9), 1012–1015 (2004)
- 10.33 A. Chandola, H.J. Kim, S. Guha, L. Gonzalez, V. Kumar, P.S. Dutta: Below band-gap optical absorption in $\text{Ga}_x\text{In}_{1-x}\text{Sb}$ alloys, J. Appl. Phys. **98**, 093103–093109 (2005)
- 10.34 H.J. Kim, A. Chandola, S. Guha, L. Gonzalez, V. Kumar, P.S. Dutta: Influence of native defects on the infrared transmission of undoped $\text{Ga}_{1-x}\text{In}_x\text{Sb}$ bulk crystals, J. Electron. Mater. **34**(11), 1391–1398 (2005)
- 10.35 A. Chandola, R. Pino, P.S. Dutta: Below bandgap optical absorption in tellurium-doped GaSb, Semicond. Sci. Technol. **20**, 886–893 (2005)
- 10.36 R. Pino, Y. Ko, P.S. Dutta: Native defect compensation in III–V antimonide bulk substrates, Int. J. High-Speed Electron. Syst. **14**(3), 658–663 (2004)
- 10.37 R. Pino, Y. Ko, P.S. Dutta: Enhancement of infrared transmission in GaSb bulk crystals by carrier compensation, J. Appl. Phys. **96**(2), 1064–1067 (2004)
- 10.38 R. Pino, Y. Ko, P.S. Dutta, S. Guha, L. Gonzalez: Burstein–Moss shift in impurity-compensated bulk $\text{Ga}_{1-x}\text{In}_x\text{Sb}$ substrates, J. Appl. Phys. **96**(9), 5349–5352 (2004)
- 10.39 W.D. Lawson, S. Nielsen: *Preparation of Single Crystals* (Butterworths Scientific Publications, London 1958)
- 10.40 W.A. Gault, E.M. Monberg, J.E. Clemens: A novel application of the vertical gradient freeze method to the growth of high quality III–V crystals, J. Cryst. Growth **74**, 491–506 (1986)
- 10.41 I.R. Grant: InP crystal growth. In: *Bulk Crystal Growth of Electronic, Optical and Optoelectronic Materials*, ed. by P. Capper (Wiley, England 2005), Chap. 4
- 10.42 M.R. Brozel, I.R. Grant: Growth of GaAs. In: *Bulk Crystal Growth of Electronic, Optical and Optoelectronic Materials*, ed. by P. Capper (Wiley, England 2005), Chap. 2
- 10.43 T. Asahi, K. Kainosho, K. Kohiro, A. Noda, K. Sato, O. Oda: Growth of III–V and II–VI single crystals by the vertical gradient freeze method. In: *Crystal Growth Technology*, ed. by H.J. Scheel, T. Fukuda (Wiley, England 2003), Chap. 15
- 10.44 T. Kawase, M. Tatsumi, Y. Nishida: Growth technology of III–V single crystals for production. In: *Crystal Growth Technology*, ed. by H.J. Scheel, T. Fukuda (Wiley, England 2003), Chap. 16
- 10.45 P. Rudolph, M. Jurisch: Fundamental and technological aspects of Czochralski growth of high quality semi-insulating GaAs crystals. In: *Crystal Growth Technology*, ed. by H.J. Scheel, T. Fukuda (Wiley, England 2003), Chap. 14
- 10.46 N.B. Singh, S.S. Mani, J.D. Adam, S.R. Coriell, M.E. Glicksman, W.M.B. Duval, G.J. Santoro, R. De-

- Witt: Direct observations of interface instabilities, *J. Cryst. Growth* **166**, 364–369 (1996)
- 10.47 P. Capper, J.J.G. Gosney, C.L. Jones, M.J.T. Quelch: Quenching studies in Bridgman-grown $\text{Cd}_x\text{Hg}_{1-x}\text{Te}$, *J. Cryst. Growth* **63**, 154–164 (1983)
- 10.48 P.S. Dutta, K.S. Sangunni, H.L. Bhat, V. Kumar: Experimental determination of melt–solid interface shapes and actual growth rates of gallium antimonide grown by vertical Bridgman technique, *J. Cryst. Growth* **141**, 476–478 (1994)
- 10.49 R.K. Route, M. Wolf, R.S. Feigelson: Interface studies during vertical Bridgman CdTe crystal growth, *J. Cryst. Growth* **70**, 379–385 (1984)
- 10.50 R. Singh, A.F. Witt, H.C. Gatos: Application of the Peltier effect for the determination of crystal growth rates, *J. Electrochem. Soc.* **115**, 112–113 (1968)
- 10.51 Y. Dabo, H. Nguyen Thi, S.R. Coriell, G.B. McFadden, Q. Li, B. Billia: Microsegregation in Peltier interface demarcation, *J. Cryst. Growth* **216**, 483–494 (2000)
- 10.52 L.L. Zheng, D.J. Larson Jr.: Thermoelectric effects on interface demarcation and directional solidification of bismuth, *J. Cryst. Growth* **180**, 293–304 (1997)
- 10.53 N. Duhanian, T. Duffar, C. Marin, E. Dieguez, J.P. Garandet, P. Dantan, G. Guiffant: Experimental study of the solid–liquid interface dynamics and chemical segregation in concentrated semiconductor alloy Bridgman growth, *J. Cryst. Growth* **275**, 422–432 (2005)
- 10.54 J.M. Bly, M.L. Kaforey, D.H. Matthiesen, A. Chait: Interface shape and growth rate analysis of Se/GaAs bulk crystals grown in the NASA crystal growth furnace (CGF), *J. Cryst. Growth* **174**, 220–225 (1997)
- 10.55 C.A. Wang, J.R. Carruthers, A.F. Witt: Growth rate dependence of the interface distribution coefficient in the system Ge–Ga, *J. Cryst. Growth* **60**, 144–146 (1982)
- 10.56 D.H. Matthiesen, M.E.K. Wiegel: Determination of the Peltier coefficient of germanium in a vertical Bridgman–Stockbarger furnace, *J. Cryst. Growth* **174**, 194–201 (1997)
- 10.57 B. Fischer, J. Friedrich, H. Weimann, G. Muller: The use of time-dependent magnetic fields for control of convective flows in melt growth configurations, *J. Cryst. Growth* **198/199**, 170–175 (1999)
- 10.58 M.P. Volz, J.S. Walker, M. Schweizer, S.D. Cobb, F.R. Sofran: Bridgman growth of germanium crystals in a rotating magnetic field, *J. Cryst. Growth* **282**, 305–312 (2005)
- 10.59 Y. Ma, L.L. Zheng, D.J. Larson Jr.: Microstructure formation during BiMn/Bi eutectic growth with applied alternating electric fields, *J. Cryst. Growth* **262**, 620–630 (2004)
- 10.60 L.N. Brush, B.T. Murray: Crystal growth with applied current, *J. Cryst. Growth* **250**, 170–173 (2003)
- 10.61 T.A. Campbell, J.N. Koster: In situ visualization of constitutional supercooling within a Bridgman–Stockbarger system, *J. Cryst. Growth* **171**, 1–11 (1997)
- 10.62 T.A. Campbell, J.N. Koster: Visualization of liquid–solid interface morphologies in gallium subject to natural convection, *J. Cryst. Growth* **140**, 414–425 (1994)
- 10.63 T.A. Campbell, J.N. Koster: Radioscopic visualization of indium antimonide growth by the vertical Bridgman–Stockbarger technique, *J. Cryst. Growth* **147**, 408–410 (1995)
- 10.64 T. Schenk, H. Nguyen Thi, J. Gastaldi, G. Reinhart, V. Cristiglio, N. Mangelinck-Noel, H. Klein, J. Hartwig, B. Grushko, B. Billia, J. Baruchel: Application of synchrotron X-ray imaging to the study of directional solidification of aluminium-based alloys, *J. Cryst. Growth* **275**, 201–208 (2005)
- 10.65 P.G. Barber, R.K. Crouch, A.L. Fripp, W.J. Debnam, R.F. Berry, R. Simchick: A procedure to visualize the melt–solid interface in Bridgman grown germanium and lead tin telluride, *J. Cryst. Growth* **74**, 228–230 (1986)
- 10.66 R. K. Willardson, H.L. Goering: Preparation of III–V compounds, *Compound Semiconductors*, Vol. 1 (Reinhold Publishing Corporation, New York 1962)
- 10.67 M. Hansen (Ed.): *Constitution of Binary Alloys* (McGraw–Hill, New York 1958)
- 10.68 I. Grzegory, M. Bockowski, S. Porowski: GaN bulk substrates grown under pressure from solution in gallium. In: *Bulk Crystal Growth of Electronic, Optical and Optoelectronic Materials*, ed. by P. Capper (Wiley, England 2005), Chap. 6
- 10.69 P. Rudolph: Thermodynamic fundamentals of phase transitions applied to crystal growth processes. In: *Crystal Growth Technology*, ed. by H.J. Scheel, T. Fukuda (Wiley, England 2003), Chap. 2
- 10.70 C.T. Lin, E. Schonherr, H. Bender: Growth and characterization of doped and undoped AlSb single crystals, *J. Cryst. Growth* **104**, 653–660 (1990)
- 10.71 R. Pino, Y. Ko, P.S. Dutta: Adhesion-free growth of AlSb bulk crystals in silica crucibles, *J. Cryst. Growth* **290**, 29–34 (2006)
- 10.72 T. Duffar, J.M. Gourbil, P. Boiton, P. Dusserre, N. Eustathopoulos: Full encapsulation by molten salts during the Bridgman growth process, *J. Cryst. Growth* **179**, 356–362 (1997)
- 10.73 P.S. Dutta, A.G. Ostrogorsky, R.J. Gutmann: Bulk growth of GaSb and $\text{Ga}_x\text{In}_{1-x}\text{Sb}$, Proc. 3rd NREL Conf. Thermophotovolta. Gener. Electr., AIP Conf. Proc., Vol. 401 (1997) pp.157–166
- 10.74 A.R. Clawson: Guide to References on III–V semiconductor chemical etching, *Mater. Sci. Eng. R* **31**, 1–438 (2001)
- 10.75 K. Ishida, H. Tokunaga, H. Ohtani, T. Nishizawa: Data base for calculating phase diagrams of III–V alloy semiconductors, *J. Cryst. Growth* **98**, 140–147 (1989)

- 10.76 G.B. Stringfellow: Calculation of ternary and quaternary III–V phase diagrams, *J. Cryst. Growth* **27**, 21–34 (1974)
- 10.77 T.C. Yu, R.F. Brebrick: Thermodynamic analysis of the In–Ga–Sb System, *Metall. Mater. Trans. A* **25**, 2331–2340 (1994)
- 10.78 A. Kumar: Growth of Thick Lattice Mismatched Layers of GaInAsSb on GaAs Substrates from Quaternary Melts. Ph.D. Thesis (Rensselaer Polytechnic Institute, Troy, New York 2006)
- 10.79 W.G. Pfann: *Zone-melting* (Wiley, New York 1959)
- 10.80 W.A. Tiller: *The Science of Crystallization: Macroscopic Phenomena and Defect Generation* (Cambridge Univ. Press, New York 1991)
- 10.81 J.A. Burton, R.C. Prim, W.P. Slichter: The distribution of solute in crystals grown from the melt. Part I. Theoretical, *J. Chem. Phys.* **21**, 1987–1991 (1953)
- 10.82 W.A. Tiller, K.A. Jackson, J.W. Rutter, B. Chalmers: The redistribution of solute atoms during the solidification of metals, *Acta Metall.* **1**, 428–437 (1953)
- 10.83 S. Sen, R.A. Lefever: Influence of magnetic field on vertical Bridgman–Stockbarger growth of InGaSb, *J. Cryst. Growth* **43**, 526–530 (1978)
- 10.84 H.P. Utech, M.C. Flemings: Elimination of solute banding in indium antimonide crystals by growth in a magnetic field, *J. Appl. Phys.* **37**, 2021–2024 (1966)
- 10.85 J. Kang, T. Fukuda: Growth exploration of compositionally uniform bulk semiconductors under a high magnetic field of 80 000 Gauss, *Mater. Sci. Eng. B* **75**, 149–152 (2000)
- 10.86 A.G. Ostrogorsky: Numerical simulation of single crystal growth by submerged heater method, *J. Cryst. Growth* **104**, 233–238 (1990)
- 10.87 A.G. Ostrogorsky, G. Müller: Normal and zone solidification using the submerged heater method, *J. Cryst. Growth* **137**, 64–71 (1994)
- 10.88 A.F. Witt, H.C. Gatos, M. Lichtensteiger, M.C. Lavine, C.J. Herman: Crystal growth and steady-state segregation under zero gravity: InSb, *J. Electrochem. Soc.* **122**, 276 (1975)
- 10.89 J.F. Yee, M.–C. Lin, K. Sarma, W.R. Wilcox: The influence of gravity on crystal defect formation in InSb–GaSb alloys, *J. Cryst. Growth* **30**, 185–192 (1975)
- 10.90 K. Okitsu, Y. Hayakawa, T. Yamaguchi, A. Hirata, S. Fujiwara, Y. Okano, N. Imaishi, S. Yoda, T. Oida, M. Kumagawa: Melt mixing of the In/GaSb/Sb solid combination by diffusion under microgravity, *Jpn. J. Appl. Phys.* **36**, 3613–3619 (1997)
- 10.91 Y. Hayakawa, K. Balakrishnan, H. Komatsu, N. Murakami, T. Nakamura, T. Koyama, T. Ozawa, Y. Okano, M. Miyazawa, S. Dost, L.H. Dao, M. Kumagawa: Drop experiments on crystallization of InGaSb semiconductor, *J. Cryst. Growth* **237–239**, 1831–1834 (2002)
- 10.92 A. Eyer, H. Leister, R. Nitsche: Floating zone growth of silicon under microgravity in a sounding rocket, *J. Cryst. Growth* **71**, 173–182 (1985)
- 10.93 C.H. Su, Y.G. Sha, S.L. Lehoczky, F.R. Szofran, C.C. Gillies, R.N. Scripa, S.D. Cobb, J.C. Wang: Crystal growth of HgZnTe alloy by directional solidification in low gravity environment, *J. Cryst. Growth* **234**, 487–497 (2002)
- 10.94 K. Hashio, M. Tatsumi, H. Kato, K. Kinoshita: Directional solidification of $\text{In}_x\text{Ga}_{1-x}\text{As}$, *J. Cryst. Growth* **210**, 471–477 (2000)
- 10.95 W.W. Mullins, R.F. Sekerka: Stability of a planar interface during solidification of a dilute binary alloy, *J. Appl. Phys.* **35**, 444–451 (1964)
- 10.96 G.B. McFadden, S.R. Coriell: Thermosolutal convection during directional solidification. II. Flow Transitions, *Phys. Fluids* **30**(3), 659–671 (1987)
- 10.97 D. Elwell, H.J. Scheel: *Crystal Growth from High-Temperature Solutions* (Academic, London 1975)
- 10.98 H.J. Kim: Bulk Crystal Growth Process for Compositionally Homogeneous GaInSb Substrates. Ph.D. Thesis (Rensselaer Polytechnic Institute, Troy, New York 2005)
- 10.99 K.J. Vogel: Solute Redistribution and Constitutional Supercooling Effects in Vertical Bridgman Grown InGaSb by Accelerated Crucible Rotation Technique. Ph.D. Thesis (Rensselaer Polytechnic Institute, Troy, New York 2004)
- 10.100 Y. Nishijima, K. Nakajima, K. Otsubo, H. Ishikawa: InGaAs single crystal using a GaAs seed grown with the vertical gradient freeze technique, *J. Cryst. Growth* **197**, 769–776 (1999)
- 10.101 D. Reid, B. Lent, T. Bryskiewicz, P. Singer, E. Mortimer, W.A. Bonner: Cellular structure in LEC ternary $\text{Ga}_{1-x}\text{In}_x\text{As}$ crystals, *J. Cryst. Growth* **174**, 250–255 (1997)
- 10.102 W.A. Bonner, R.E. Nahory, H.L. Glichrist, E. Berry: Semi-insulating single crystal GaInAs: LEC growth and Characterization, *Semi-Insulating III–V Materials* (1990) pp. 199–204
- 10.103 K. Nakajima, T. Kusunoki, K. Otsubo: Bridgman growth of compositionally graded $\text{In}_x\text{Ga}_{1-x}\text{As}$ ($x = 0.05 - 0.30$) single crystals for use as seeds for $\text{In}_{0.25}\text{Ga}_{0.75}\text{As}$ crystal growth, *J. Cryst. Growth* **173**, 42–50 (1997)
- 10.104 Y. Nishijima, K. Nakajima, K. Otsubo, H. Ishikawa: InGaAs single crystal with a uniform composition in the growth direction grown on an InGaAs seed using the multicomponent zone growth method, *J. Cryst. Growth* **208**, 171–178 (2000)
- 10.105 T. Suzuki, K. Nakajima, T. Kusunoki, T. Katoh: Multicomponent zone melting growth of ternary InGaAs bulk crystal, *J. Electron. Mater.* **25**(3), 357–361 (1996)
- 10.106 A. Watanabe, A. Tanaka, T. Sukegawa: Pulling technique of a homogeneous GaInSb alloy under solute-feeding conditions, *Jpn. J. Appl. Phys.* **32**, L793–L795 (1993)

- 10.107 H.-J. Sell: Growth of GaInAs bulk mixed crystals as a substrate with a tailored lattice parameter, *J. Cryst. Growth* **107**, 396–402 (1991)
- 10.108 W.F. Leverton: Floating crucible technique for growing uniformly doped crystals, *J. Appl. Phys.* **29**, 1241–1244 (1958)
- 10.109 T. Kusunoki, K. Nakajima, K. Kuramata: Constant Temperature LEC growth of uniform composition InGaAs bulk crystals through continuous supply of GaAs, *Inst. Phys. Conf. Ser.* **129**, 37–42 (1992)
- 10.110 K. Nakajima, T. Kusunoki: Constant temperature growth of uniform composition InGaAs bulk crystals by supplying GaAs, *Inst. Phys. Conf. Ser.* **120**, 67–71 (1991)
- 10.111 T. Kusunoki, C. Takenaka, K. Nakajima: Growth of ternary $\text{In}_{0.14}\text{Ga}_{0.86}\text{As}$ bulk crystal with uniform composition at constant temperature through GaAs supply, *J. Cryst. Growth* **115**, 723–727 (1991)
- 10.112 T. Ashley, J.A. Beswick, B. Cockayne, C.T. Elliott: The growth of ternary substrates of indium gallium antimonide by the double crucible Czochralski technique, *Inst. Phys. Conf. Ser.* **144**, 209–213 (1995)
- 10.113 A. Tanaka, A. Watanabe, M. Kimura, T. Sukegawa: The solute-feeding Czochralski method for homogeneous GaInSb alloy pulling, *J. Cryst. Growth* **135**, 269–272 (1994)
- 10.114 A. Tanaka, T. Yoneyama, M. Kimura, T. Sukegawa: Control of GaInSb alloy composition grown from ternary solution, *J. Cryst. Growth* **186**, 305–308 (1998)
- 10.115 M.H. Lin, S. Kou: Czochralski pulling of InSb single crystals from a molten zone on a solid feed, *J. Cryst. Growth* **193**, 443–445 (1998)
- 10.116 M.H. Lin, S. Kou: Dopant segregation control in Czochralski crystal growth with a wetted float, *J. Cryst. Growth* **132**, 461–466 (1993)
- 10.117 T. Ozawa, Y. Hayakawa, M. Kumagawa: Growth of III–V ternary and quaternary mixed crystals by the rotationary Bridgman method, *J. Cryst. Growth* **109**, 212–217 (1991), see also [10.134]
- 10.118 K. Kinoshita, H. Kato, S. Matsumoto, S. Yoda: Growth of homogeneous $\text{In}_{1-x}\text{Ga}_x\text{Sb}$ crystals by the graded solute concentration method, *J. Cryst. Growth* **216**, 37–43 (2000)
- 10.119 K. Kinoshita, H. Kato, M. Iwai, T. Tsuru, M. Muramatsu, S. Yoda: Homogeneous $\text{In}_{0.3}\text{Ga}_{0.7}\text{As}$ crystal growth by the traveling liquidus-zone method, *J. Cryst. Growth* **225**, 59–66 (2001)
- 10.120 A. Chandola: Bulk Crystal Growth and Infrared Absorption Studies of GaInSb. Ph.D. Thesis (Rensselaer Polytechnic Institute, Troy, New York 2005)
- 10.121 H. Kim, A. Chandola, R. Bhat, P.S. Dutta: Forced convection induced thermal fluctuations at the solid-liquid interface and its effect on the radial alloy distribution in vertical Bridgman grown $\text{Ga}_{1-x}\text{In}_x\text{Sb}$ bulk crystals, *J. Cryst. Growth* **289**, 450–457 (2006)
- 10.122 J.C. Brice: *The Growth of Crystals from Liquids* (North-Holland, Amsterdam 1973)
- 10.123 P.S. Dutta, K.S. Sangunni, H.L. Bhat, V. Kumar: Growth of gallium antimonide by vertical Bridgman technique with planar crystal-melt interface, *J. Cryst. Growth* **141**, 44–50 (1994)
- 10.124 C.E. Chang, W.R. Wilcox: Control of interface shape in the vertical Bridgman-Stockbarger technique, *J. Cryst. Growth* **21**, 135–140 (1974)
- 10.125 A. Yeckel, J.J. Derby: Computer modeling of bulk crystal growth. In: *Bulk Crystal Growth of Electronic, Optical and Optoelectronic Materials*, ed. by P. Capper (Wiley, England 2005), Chap. 3
- 10.126 A. Yeckel, J.J. Derby: Computational simulations of the growth of crystals from liquids. In: *Crystal Growth Technology*, ed. by H.J. Scheel, T. Fukuda (Wiley, England 2003), Chap. 6
- 10.127 V.I. Polezhaev: Modeling of technologically important hydrodynamics and heat/mass transfer processes during crystal growth. In: *Crystal Growth Technology*, ed. by H.J. Scheel, T. Fukuda (Wiley, England 2003), Chap. 8
- 10.128 C.L. Jones, P. Capper, J.J.G. Gosney: Thermal modeling of Bridgman crystal growth, *J. Cryst. Growth* **56**, 581–590 (1982)
- 10.129 H.P. Greenspan: *The Theory of Rotating Fluids* (Cambridge Univ. Press, London 1968)
- 10.130 H.J. Scheel, R.H. Swendsen: Evaluation of experimental parameters for growth of homogeneous solid solutions, *J. Cryst. Growth* **233**, 609–617 (2001)
- 10.131 H.J. Scheel, E.O. Schulz-Dubois: Flux growth of large crystals by accelerated crucible-rotation technique, *J. Cryst. Growth* **8**, 304–306 (1971)
- 10.132 H.J. Scheel: Accelerated crucible rotation: A novel stirring technique in high-temperature solution growth, *J. Cryst. Growth* **13/14**, 560–565 (1972)
- 10.133 J.B. Mullin: The Role of Magnetic Fields in Crystal Growth, Special Issue of *Prog. Cryst. Growth Charact. Mater.* **38**, 1–6 (1999), see whole issue
- 10.134 T. Ozawa, Y. Hayakawa, K. Balakrishna, F. Ohnishi, T. Koyama, M. Kumagawa: Growth of $\text{In}_x\text{Ga}_{1-x}\text{As}$ bulk mixed crystals with a uniform composition by the rational Bridgman method, *J. Cryst. Growth* **229**, 124–129 (2001)

11. Growth and Characterization of Antimony-Based Narrow-Bandgap III–V Semiconductor Crystals for Infrared Detector Applications

Vijay K. Dixit, Handady L. Bhat

Materials for the generation and detection of 7–12 μm wavelength radiation continue to be of considerable interest for many applications such as night vision, medical imaging, sensitive pollution gas monitoring, etc. For such applications HgCdTe has been the main material of choice in the past. However, HgCdTe lacks stability and uniformity over a large area, and only works under cryogenic conditions. Because of these problems, antimony-based III–V materials have been considered as alternatives. Consequently, there has been a tremendous growth in research activity on InSb-based systems. In fact, InSb-based compounds have proved to be interesting materials for both basic and applied research. This chapter presents a comprehensive account of research carried out so far. It explores the materials aspects of indium antimonide (InSb), indium bismuth antimonide ($\text{InBi}_x\text{Sb}_{1-x}$), indium arsenic antimonide ($\text{InAs}_x\text{Sb}_{1-x}$), and indium bismuth arsenic antimonide ($\text{InBi}_x\text{As}_y\text{Sb}_{1-x-y}$) in terms of crystal growth in bulk and epitaxial forms and interesting device feasibility. The limiting single-phase composition of $\text{InAs}_x\text{Sb}_{1-x}$ and $\text{InBi}_x\text{Sb}_{1-x}$ using near-equilibrium technique has been also addressed. An overview of the structural, transport, optical, and device-related properties is presented. Some of the current areas of research and development have been critically reviewed and their significance for both understanding the basic physics as well as device applications are discussed. These include the role of defects and impurity on structural, optical, and electrical properties of the materials.

11.1	Importance of Antimony-Based Semiconductors	329
11.2	Phase Diagrams	330
11.2.1	InSb	330
11.2.2	$\text{InAs}_x\text{Sb}_{1-x}$	330
11.2.3	$\text{InBi}_x\text{Sb}_{1-x}$	331
11.3	Crystal Structure and Bonding	331
11.3.1	Crystal Structure and Bonding of InSb	331
11.3.2	Structural Properties of $\text{InAs}_x\text{Sb}_{1-x}$..	332
11.3.3	Crystal Chemical Aspect of Bi Substitution in InSb	333
11.4	Material Synthesis and Purification	333
11.4.1	Volatilization	333
11.4.2	Zone Refining	333
11.5	Bulk Growth of InSb	334
11.5.1	Zone Melting	334
11.5.2	Vertical and Horizontal Bridgman Methods	334
11.5.3	Bulk Growth of $\text{InAs}_x\text{Sb}_{1-x}$	335
11.5.4	Bulk Growth of $\text{InBi}_x\text{Sb}_{1-x}$	337
11.5.5	Growth of Thick Layers of InSb, $\text{InAs}_x\text{Sb}_{1-x}$, and $\text{InBi}_x\text{Sb}_{1-x}$, by Liquid-Phase Epitaxy	337
11.6	Structural Properties of InSb, $\text{InAs}_x\text{Sb}_{1-x}$, and $\text{InBi}_x\text{Sb}_{1-x}$	340
11.6.1	InSb	340
11.6.2	$\text{InAs}_x\text{Sb}_{1-x}$	342
11.6.3	$\text{InBi}_x\text{Sb}_{1-x}$	344
11.6.4	InSb, $\text{InAs}_x\text{Sb}_{1-x}$, and $\text{InBi}_x\text{Sb}_{1-x}$ Grown on GaAs	345
11.7	Physical Properties of InSb, $\text{InAs}_x\text{Sb}_{1-x}$, and $\text{InBi}_x\text{Sb}_{1-x}$	346
11.7.1	Band Structure of InSb, $\text{InAs}_x\text{Sb}_{1-x}$, and $\text{InBi}_x\text{Sb}_{1-x}$	346
11.7.2	Transport Properties of InSb, $\text{InAs}_x\text{Sb}_{1-x}$, and $\text{InBi}_x\text{Sb}_{1-x}$	347
11.7.3	Optical Properties of InSb, $\text{InAs}_x\text{Sb}_{1-x}$, and $\text{InBi}_x\text{Sb}_{1-x}$	352
11.7.4	Thermal Properties of InSb and Its Alloys	356
11.8	Applications	357
11.9	Concluding Remarks and Future Outlook	359
	References	360

Tremendous efforts have been applied in the development of infrared (IR) detectors and sensor materials. Much of the research on IR optoelectronic has been focused mostly on military needs, with particular emphasis on the development of high-performance detectors operating in the 3–5 and 7–12 μm wavelength bands. In recent years civilian needs have become more dominant due to the development of IR light-emitting diodes (LED) and lasers, which provide low-cost sensitive pollution monitoring systems that detect trace gases by their fundamental vibrational–rotational absorption bonds [11.1]. Other applications include fire-fighting, environmental monitoring, fiber-optic and free-space optical communication systems, landfill gas monitoring, fuel-gas analysis, personal safety, sports, medicine, and a variety of horticultural uses that include total organic carbon dioxide measurement. For all these applications HgCdTe (MCT) has been the main material of choice in the past, but it has proved to be a difficult compound to prepare due to the high vapor pressure of Hg and weak Hg bond. Also its material parameters change with time, resulting in poor mechanical and thermal properties [11.2]. Because of these problems associated with MCT, antimony (Sb)-based III–V materials have been considered as more attractive alternatives. Also they have stronger covalent bonds between indium (In) and Sb, which makes them stable compounds. In particular, InSb-based materials such as $\text{InAs}_x\text{Sb}_{1-x}$, $\text{InBi}_x\text{Sb}_{1-x}$, and $\text{InBi}_x\text{As}_y\text{Sb}_{1-x-y}$ have been extensively explored for many years [11.2–12]. In this chapter, we will review mostly the investigations carried out on these materials for the past two decades. The review highlights the current status of understanding of the crystal growth process and various physical properties of InSb, $\text{InBi}_x\text{Sb}_{1-x}$, $\text{InAs}_x\text{Sb}_{1-x}$, and $\text{InBi}_x\text{As}_y\text{Sb}_{1-x-y}$. While InSb continues to be grown commercially, very few reports are available on the growth of large-sized crystals and wafers with high quality. Some recent studies have surely led to better understanding of the problems associated with the enhancement of the size and quality of the grown crystals.

Substantial bowing in the energy gap to values below those of InSb (0.17 eV) and InAs (0.38 eV) occurs in indium arsenic antimonide. The energy gap of $\text{InAs}_x\text{Sb}_{1-x}$ continuously decreases with increasing x and attains a minimum value of 0.1 eV for $x = 0.4$, at room temperature [11.13–19]. Further-

more, the very low effective mass of $\text{InAs}_x\text{Sb}_{1-x}$ across the compositional range raises the prospect of using this material extensively for detector applications. Although the benefits of alloying As in InSb were discovered more than 34 years ago and have been studied since then, all studies have been carried out on bulk samples made from crudely prepared polycrystals [11.19, 20]. The main growth limitations in $\text{InAs}_x\text{Sb}_{1-x}$ arise from the wide separation between the liquidus and solidus curves in the temperature–composition phase diagram and the very low diffusion rates in the solid phase. Hence most bulk crystal growth (near equilibrium) has been carried out using gradient freeze and zone recrystallization and with long annealing duration, usually resulting in polycrystals.

$\text{InBi}_x\text{Sb}_{1-x}$ is a very interesting material because it is composed of the semimetal InBi and the semiconductor InSb and hence the bandgap energy and lattice constant can be varied over a wide range. Consequently, these crystals are also useful for the applications mentioned above. However, this alloy is even more difficult to grow in single-crystal form because of the wide separation between the liquidus and solidus lines in its phase diagram. This leads to constitutional supercooling in the solution below the growth interface. Hence, the composition ratio in the grown crystals will not be the same as that in the solution. Recently Dixit et al. [11.9, 12] reported successful growth of $\text{InAs}_x\text{Sb}_{1-x}$ and $\text{InBi}_x\text{Sb}_{1-x}$ single crystals using the rotatory Bridgman method (RBM). Efforts are also being made for possible integration of these materials onto suitable semi-insulating and IR-transparent substrates. CdTe is the only semi-insulating and lattice-matched substrate available for this purpose, but it is very difficult to prevent In_2Te_3 precipitate formation at the interface during growth [11.21, 22]. Hence, Si, GaAs, and InP have been used as substrates for epitaxial growth of these materials [11.23–25]. In spite of the large lattice mismatch between GaAs and these materials, there are many reports on the growth of these heterostructures using molecular-beam epitaxy (MBE) [11.26, 27], metalorganic vapor-phase epitaxy (MOVPE) [11.28–32], liquid-phase epitaxy (LPE) [11.5, 10, 33–35], and melt epitaxy (ME) [11.36–38]. The lattice-mismatched heteroepitaxy affects the structural, optical, and electrical properties of these materials and these issues have been addressed in this review.

11.1 Importance of Antimony-Based Semiconductors

After silicon, germanium, and gallium arsenide, indium antimonide is perhaps the most studied semiconductor. This is because it has the smallest energy gap (0.17 eV) among the III–V binary semiconductors. InSb has a strong band nonparabolicity, a very large g factor and is intrinsic at room temperature [11.40–50]. Due to these intrinsic properties, its physics is qualitatively different from that of other common semiconductors. The ease with which quantum phenomena can be seen and cleanly modeled has for a long time made it a favorite of semiconductor researchers. Two material-specific parameters that define the utility of a possible device are the energy gap and the effective mass. These can be tuned by strained epitaxy to some extent. However, alloying of two or more semiconductors drastically widens the available parameter space of various physical properties. Most physical properties (energy gap, effective mass, and lattice constant) of the alloy are continuous functions of the alloy composition and interpolate between the end members as a polynomial of low order. The energy gap of InSb, although the smallest among the III–V binaries, is not small enough to be used in practical long-wavelength infrared detectors. Hence the material has to be engineered so that its gap is within one of the wavelength windows where the atmospheric gases are transparent, i.e., 3–5 and 7–12 μm . The desired gap tailoring can be accomplished by alloying with low-bandgap semiconductors or semimetal.

InSb–InAs is one of the interesting alloy of this class because the substitution of a fraction of antimony sites in InSb with isovalent arsenic reduces the energy gap to a value lower than the energy gap of either of the parent compounds; it consequently has the lowest energy gap among the III–V semiconductors. This system also has one of the largest bowing parameters among the semiconductor alloys (Fig. 11.1a) [11.13]. Therefore the effects of alloy disorder in determining the physical properties may be expected to be more significant. By alloying with a suitable fraction of InAs, a room-temperature energy gap in both atmospheric wavelength windows can be achieved.

The desired energy gap tailoring can be accomplished by alloying with InBi also (Fig. 11.1b). Since Bi is much larger than Sb it produces rapid reduction of the bandgap of InSb at the rate of 36 meV/%Bi [11.51–54]. Incorporation of Bi in InAsSb produces an even larger reduction in bandgap (55 meV/%Bi) as determined by absorption and photoluminescence studies. *Ma*

et al. [11.54] reported Bi incorporation in $\text{InAs}_x\text{Sb}_{1-x}$ lattice and decrease in the bandgap energy of MOVPE-grown epilayer. The high quality of these layers was evidenced by the production of photoluminescence. Huang et al. [11.51] calculated the expected bandgap energies for the $\text{InBi}_x\text{As}_y\text{Sb}_{1-x-y}$ alloys having the optimum Bi concentration by linearly interpolating the values of dE_g/dx between InAs and InSb, yielding $dE_g/dx = -55 \pm 19x$ (meV/%Bi). The variation of the energy gap with alloy composition manifests in the optical and electrical properties of respective materials.

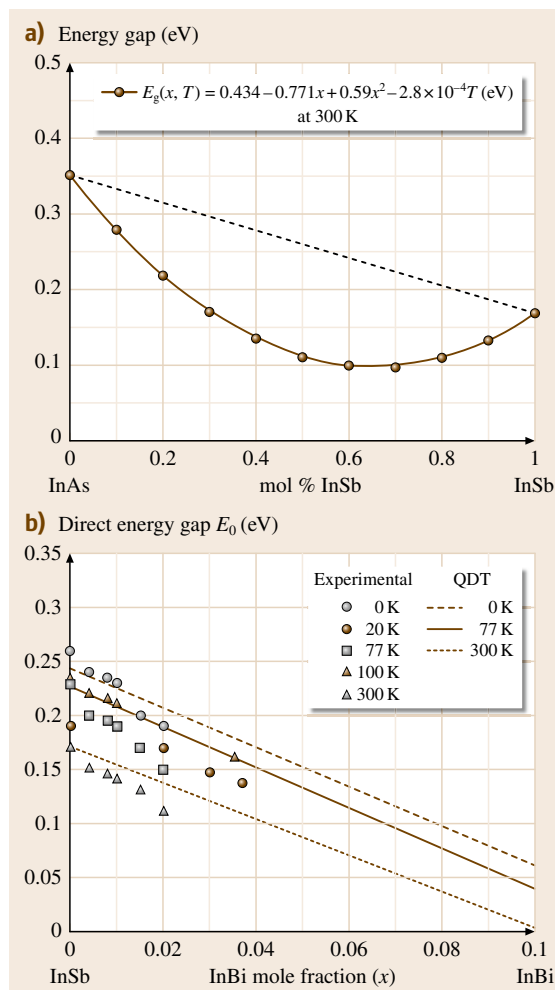


Fig. 11.1a,b Energy gap bowing for (a) $\text{InAs}_x\text{Sb}_{1-x}$, and (b) $\text{InBi}_x\text{Sb}_{1-x}$ (after [11.13, 39])

11.2 Phase Diagrams

In order to grow homogeneous and stoichiometric bulk and epitaxial single crystals of binaries and ternaries it is essential to understand the phase diagrams of these materials. The phase diagram of InSb, $\text{InAs}_x\text{Sb}_{1-x}$, and $\text{InBi}_x\text{Sb}_{1-x}$ are briefly described below.

11.2.1 InSb

The phase diagram of InSb was determined by *Liu and Peretti* [11.56] and is reproduced in Fig. 11.2a. It is characterized by the presence of two eutectics occurring at 0.8 and 68.2 at. % Sb. From the diagram it is clear that at the extreme left there exists a phase consisting of pure In (α -phase) with a melting point of 156°C. At the extreme right is elemental Sb (γ -phase) with a melting point of 630°C. InSb has a congruent melting temperature below the melting point of one of its constituents. This leads to certain differences between solution growth and congruent melt growth in terms of composition of In and Sb. Of interest in the phase diagram is the β -phase in the indium–antimony system, which has a congruent melting temperature of 525°C. The transition from solid to liquid phase occurs at composition of 50 at. %. This is the point where the crystal is grown stoichiometrically. Alloys with a deviation as small as 0.5% from the stoichiometric ratio show phase separation, making the phase very sensitive to composition. The β -phase divides the diagram into

two subsystems, namely the In–InSb (the $\alpha + \beta$ -phase) and the InSb–Sb (the $\beta + \gamma$ -phase) alloys. Also represented are the $L + \alpha$ - and the $L + \gamma$ -phases. Above the curve, InSb is in the liquid phase. For the growth of InSb epilayers using LPE, In–InSb region is preferred over other region, because In has a lower vapor pressure compared with Sb.

11.2.2 $\text{InAs}_x\text{Sb}_{1-x}$

Shih and Peretti [11.55] investigated the phase diagram of the InAs–InSb system and obtained a degenerate eutectic diagram with the terminal solid solution with 2% InSb. *Goryunova and Fedorova* [11.58] also reported

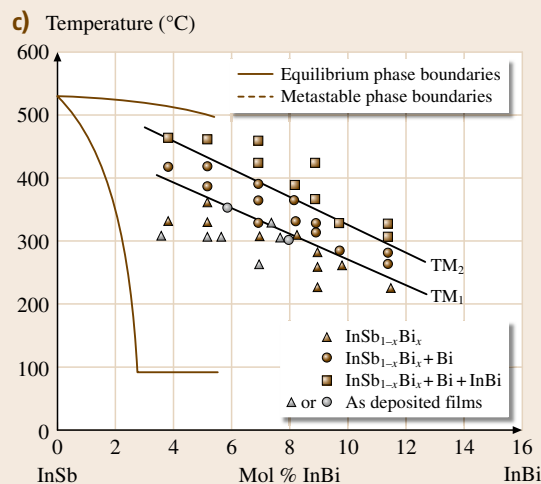
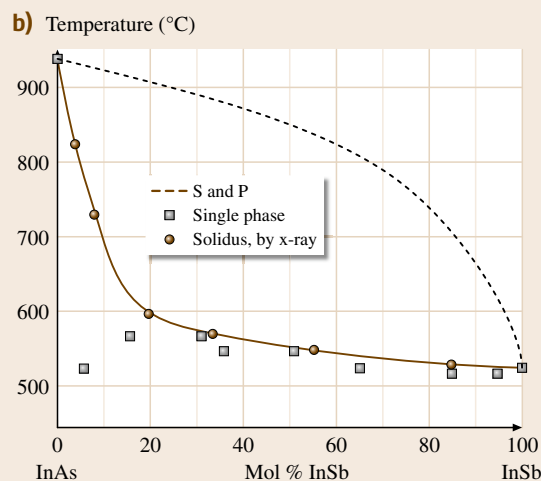
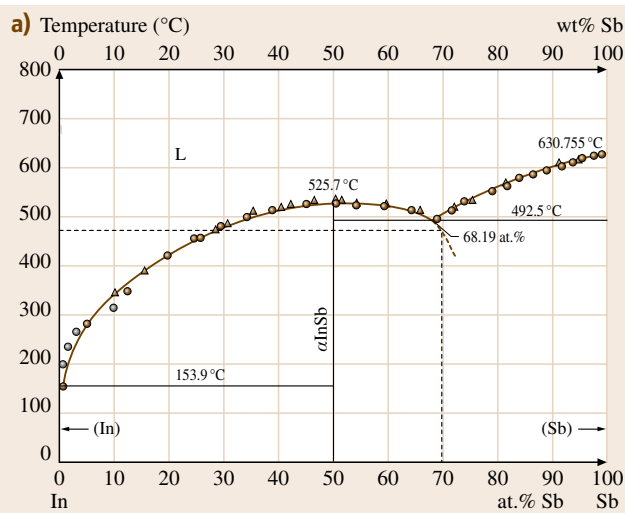


Fig. 11.2a–d Equilibrium phase diagrams of (a) InSb, (b) InSb–InAs, and (c) InSb–InBi (after [11.55–57])

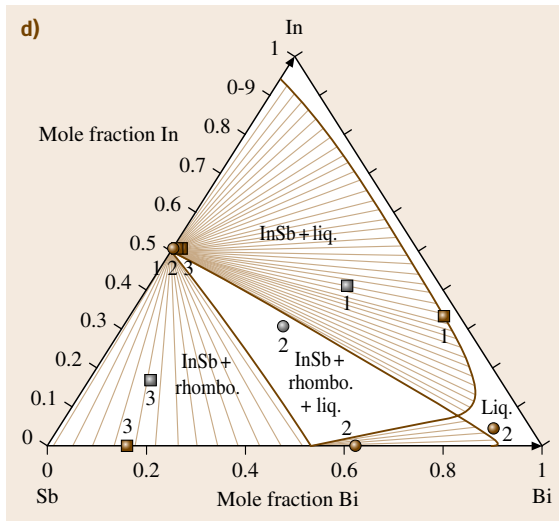


Fig. 11.2 (d) Equilibrium phase diagrams of $\text{InBi}_x\text{Sb}_{1-x}$ at 300 K (after [11.62])

investigation on the same system with a maximum terminal solid solution with $\approx 3\%$ InSb, which was in reasonable agreement with the result of *Shih* and *Peretti* [11.55]. Later, *Woolley* et al. [11.59] showed the complete solid solution for all compositions. *Stringfellow* and *Greene* [11.60] also reported the full phase diagram of $\text{InAs}_x\text{Sb}_{1-x}$. The analysis was carried out using x-ray and differential thermal analysis. They made $\text{InAs}_x\text{Sb}_{1-x}$ polycrystalline samples for the complete range of composition and annealed them at 525°C for 3 months. Alloys over a considerable range of composition were approaching a single-phase state, but alloys in the approximate range of 90–40 mol % InAs showed an apparent two-phase equilibrium condition when investigated by x-ray methods. When alloys of the same composition were first annealed to single phase at 550°C followed by annealing at 525°C for approximately 3 months, no indication of any splitting into a two-phase condition could be observed by x-ray investigation. The complete phase diagram for

all composition is shown in Fig. 11.2b. It would thus appear that at these compositions the diffusion rates in the solid are so low that, even at temperatures only $\approx 50^\circ\text{C}$ below the solidus, equilibrium cannot be attained under normal practical conditions, and the form of the equilibrium diagram at temperature below 550°C cannot be determined. *Dutta* and *Miller* [11.61] also reported studies on the phase diagram of this material.

11.2.3 $\text{InBi}_x\text{Sb}_{1-x}$

The phase diagram of $\text{InBi}_x\text{Sb}_{1-x}$ was determined by *Joukoff* and *Jean-Louis* [11.63] using differential thermal analysis (DTA) only up to 6 at. % Bi. They found that the maximum equilibrium solubility limit of Bi was 2.6 at. % in InSb, but *Zilko* and *Greene* [11.57] reported that in metastable conditions the solubility of Bi in InSb is 12 at. %. As can be seen from Fig. 11.2c wide separation exists between the liquidus and solidus lines in the phase diagram, which leads to constitutional supercooling in the solution below the growth interface. Hence, the composition ratio in the grown crystals will not be same as that in the solution. Two metastable phase boundaries T_{M1} and T_{M2} are also shown in Fig. 11.2c. Below the T_{M1} phase boundary InBi–InSb forms one single stable $\text{InBi}_x\text{Sb}_{1-x}$ phase, while in the region between the two-phase boundaries (T_{M1} and T_{M2}) the solution forms stable $\text{InBi}_x\text{Sb}_{1-x}$ and Bi phase. In the region above T_{M2} the solution forms stable $\text{InBi}_x\text{Sb}_{1-x}$, InBi, and Bi phases. Very recently *Minic* et al. [11.62] reported thermodynamic predictions for the equilibria of the InSbBi system. They estimated the phase diagram at 300°C and compared it with experimental results obtained by scanning electron microscopy (SEM) analysis (Fig. 11.2d). They experimentally determined that liquid and rhombohedral phases of $\text{In}_{0.31}\text{Sb}_{0.38}\text{Sn}_{0.31}$ sample contained higher contents of bismuth compared with the prediction, which suggests the need for the introduction of ternary interaction parameters for the calculation.

11.3 Crystal Structure and Bonding

For understanding the optical and electrical properties of InSb, $\text{InAs}_x\text{Sb}_{1-x}$, and $\text{InBi}_x\text{Sb}_{1-x}$ crystals it is essential to understand the crystal structures and bonding of these materials, which are briefly described below.

11.3.1 Crystal Structure and Bonding of InSb

The structure of InSb was first determined by *Goldschmidt* [11.43] and later in detail by *Iandelli* [11.64] using conventional x-ray structure determination tech-

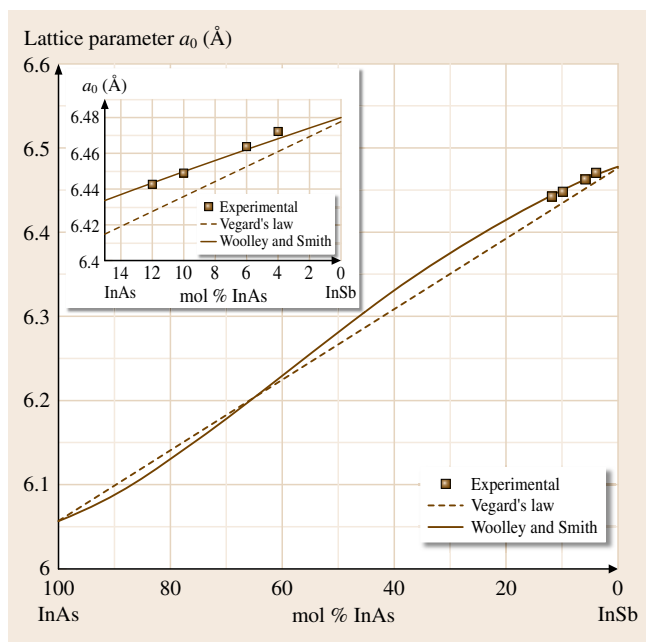


Fig. 11.3 Lattice parameter variation of InAsSb with composition (after [11.5, 20])

niques and found to be of zincblende type. The space group of InSb is $F\bar{4}3m$ [11.43] and hence it belongs to the point group $\bar{4}3m$. In the structure, each In atom is coordinated to four Sb atoms and vice versa. The presence of dissimilar atoms in the lattice imparts a directional character to the lattice. Hence, the direction from the In to the Sb is not equivalent to that from Sb to In. Thus, due to the lack of center of symmetry, the 111 direction forms the polar axis and there is a distinction between the [111] and the $\bar{1}\bar{1}\bar{1}$ directions. Conventionally, the direction from group III to V atom is $\bar{1}\bar{1}\bar{1}$ and from group V to III atom is [111]. In the zincblende structure, the crystal viewed perpendicular to [111] direction appears as sheets of alternate group III and V atoms stacked over one another. Dewald [11.65], while studying the growth of oxide layers on InSb, noticed a difference in the growth kinetics of (111) and $(\bar{1}\bar{1}\bar{1})$ surfaces. This difference in the behavior of the two surfaces was also noticed by other workers [11.66] during the observation of etch pits on InSb using CP4 ($\text{HF} : \text{HNO}_3 : \text{CH}_3\text{COOH} : \text{H}_2\text{O} = 3 : 5 : 3 : 20$) etchant. For example, it has been shown that dislocation etch pits appear on $(\bar{1}\bar{1}\bar{1})$ and not on (111) face. Also, growth of InSb crystals is easier on $(\bar{1}\bar{1}\bar{1})$ face than on (111) face. The bonding between In and Sb is a combination of two idealized states (purely ionic and

purely covalent states) as represented by the equation below

$$\Phi = a_{\text{ionic}}\Phi_{\text{ionic}} + a_{\text{covalent}}\Phi_{\text{covalent}} \quad (11.1)$$

This means that the bonding is of mixed nature and is characterized by the ionicity, which is the ratio of a_{ionic} to a_{covalent} [11.68]. This lends a mixed character to the lattice, giving rise to a net polarity along certain directions.

11.3.2 Structural Properties of $\text{InAs}_x\text{Sb}_{1-x}$

There are not many reports on the structural properties of $\text{InAs}_x\text{Sb}_{1-x}$ except for a study on the variation of lattice parameter with composition [11.20]. The variation of lattice parameter with composition is shown in Fig. 11.3. The experimental curve (solid line) obtained by Woolley and Warner [11.20] for the whole compositional range (in polycrystalline samples) crosses Vegard's line at approximately 67 mol % InAs, indicating that Vegard's law is not satisfied except at one point ($x = 0.67$). Recently Dixit et al. [11.5, 69] also reported similar observation up to 12% As. Their results are shown in the inset of Fig. 11.3. The maximum difference in the lattice parameters (6.330 Å) obtained from experimental curve (from Woolley and Warner's work) and the Vegard line is 0.030 Å at 33% InSb.

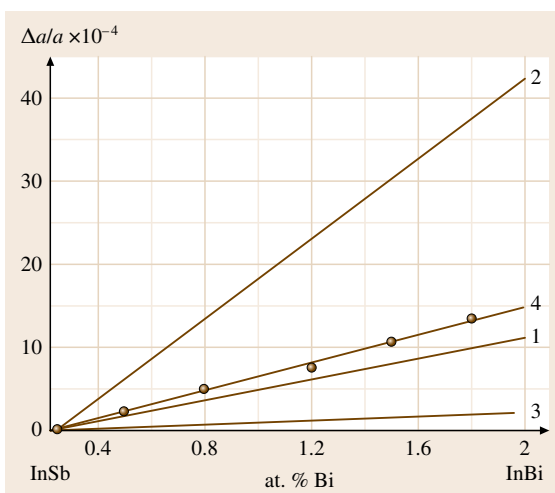


Fig. 11.4 Relative change of lattice parameter of InBiSb for Bi in (1) antimony position, (2) interstitial position, and (3) indium position, and (4) experimental curve (after [11.67])

11.3.3 Crystal Chemical Aspect of Bi Substitution in InSb

A large region of the phase diagram of $\text{InBi}_x\text{Sb}_{1-x}$ system corresponds to the region of primary crystallization of solid solutions based on InSb. Since In forms two stable compounds with Bi, depending on the composition and temperature of the molten solution, Bi can occur in three basic forms, Bi, InBi, and In_2Bi , in the melt [11.66]. By varying the crystallization conditions, one can follow how various forms of Bi in the melt influence its solubility in InSb as well as structural properties of $\text{InBi}_x\text{Sb}_{1-x}$. The character of Bi in the crystal lattice of InSb was determined by comparing the exper-

imental composition dependence of the lattice parameter a with that calculated theoretically for substitutional and interstitial solid solutions and also by studying the spectra of diffuse scattering of x-rays. The values of a were measured with a precision of $\pm 5 \times 10^{-5} \text{ \AA}$ [11.70]. By comparing the theoretical and experimental composition dependences of the relative change in the lattice parameters of $\text{InBi}_x\text{Sb}_{1-x}$, one can determine the position of Bi in InSb, as shown in Fig. 11.4. The results indicate that, when the relative change in the lattice parameter with Bi composition is large, Bi goes into interstitial position, whereas when it is small Bi goes into In position. For moderate change in the lattice parameter with Bi composition, Bi goes into Sb position.

11.4 Material Synthesis and Purification

Since the discovery of InSb material, considerable attention has been devoted to its growth in single-crystal form [11.71–75]. Growth of good-quality InSb single crystal depends on the purity of the source materials and homogeneous synthesis of the starting materials. InSb is synthesized by taking stoichiometric amounts of In and Sb in a quartz ampoule, kept in an atmosphere of pure argon or hydrogen. The charge is melted and mixed in the molten state inside the quartz ampoule and stirred either mechanically or electromagnetically. Synthesized InSb carries impurities either from the source materials or from growth environment. Use of high-purity source materials helps to avoid severe contamination of the synthesized compound. For purification of InSb two important techniques have been used, viz. volatilization and zone refining.

11.4.1 Volatilization

In volatilization, the melt is kept at an elevated temperature for very long periods, so that impurities that have higher volatility evaporate out of the melt. In InSb, cadmium (Cd), an elemental acceptor impurity, is effectively removed by volatilization. In the case of InSb, antimony has a higher vapor pressure compared with In. Hence, Sb escapes from the charge during volatilization. Therefore, whenever this process is adopted, Sb is taken in excess to compensate for its escape from the melt during volatilization.

11.4.2 Zone Refining

In zone refining (a technique developed by *Pfann* [11.76]), purification takes place because of the impurity atom's preference to stay either in the molten zone or in the solid zone (depending on the value of a segregation coefficient) as it moves along the ingot. This preference for the impurity is measured by defining an equilibrium distribution coefficient, k_{eq} , given by C_s/C_l , the ratio of the concentration of the impurity in the solid and liquid phases. The larger the deviation of k from 1, the easier it is to remove the impurity through zone refining. *Harman* [11.77] carried out extensive experiments on zone refining of InSb and found two main impurities, viz. Zn and Te, that segregated from the ingot. While Zn had an acceptor-like characteristic in InSb, Te showed donor-like properties. *Strauss* [11.78] determined the distribution coefficients of various elements such as Cd, Zn, Se, and Te in InSb. Zinc has a k_{eff} of 2.3–3.5 in InSb, which makes it fairly easy to be zone refined, whereas Te has a k_{eff} of 1 in InSb, which makes it almost impossible to remove from InSb. One can use the relation $c(x) = k_{\text{eff}}c_0(1 - g)^{k_{\text{eff}}} - 1$ to find the concentration at any location (x) of the growth front in different conditions, where g is the fraction of crystallized material and c_0 is the initial concentration. Here it is assumed that k_{eff} does not vary with concentration or temperature. Recent studies show that k_{eff} depends on growth rate also. Hence, k^* may in principle differ from k_{eff} and may depend on the growth rate, interface orientation, and solute concentration. Hence it is more

appropriate to use the following equation

$$k_{\text{eff}} = \frac{k^*}{k^* + (1 - k^*) \exp\left(\frac{-f\delta}{D}\right)}, \quad (11.2)$$

where f is the growth rate, δ is the diffusion thickness ($\delta = 1.6D^{1/3}\nu^{1/6}\omega^{-1/2}$), which is a function of rotation rate ω , the viscosity of the liquid ν , and the diffusion coefficient D of the impurity in the liquid. Under conditions of stirring at the interface, k^* is close to k_{eff} , but the two are quite different in real experimental situations. In fact, for certain impurities, very strong dependence of k^* on the crystallographic direction of ingot to be refined has been noticed, as is the case for Te in InSb. This anisotropic segregation created many difficulties for Te removal. It was thus difficult to remove Te ef-

fectively, as it always depended on ingot orientation and the ingots used were usually polycrystalline. However, the observation of the dependence of k^* on ingot orientation by Mullin and Hulme [11.79] showed that k^* is about 0.5 in the off-[111] direction and this can be effectively used to segregate Te from InSb ingots whose axis is crystallographically inclined away from [111] direction. In fact, k^* was not found to vary much on facets other than (111). Thus, researchers began to use off-[111] ingots for the refining process. Hence, the anisotropic segregation of Te in InSb, which posed problems earlier, was cleverly used to advantage in the refining process. However, this necessitated the use of oriented InSb ingots for the refining process rather than polycrystalline ingots as previously sought.

11.5 Bulk Growth of InSb

Since the discovery of InSb a large number of workers have performed growth experiments on InSb using a variety of techniques. Prominent examples are briefly described here.

11.5.1 Zone Melting

In the early stages, the growth technique used in the case of InSb was predominantly *zone melting* so that the refining and the growth could be carried out together. It was often found that multiple refining passes led to single-crystal growth. Mueller and Jacobson [11.80] used seeds of orientations [110], [111], and [211] to grow single crystals. Coherent twins were seen to occur, with the twin boundaries parallel to {111} planes. It was also observed that twinning occurred more readily when an [111] A surface was exposed to the melt. Superior growth characteristics of [111] B direction as compared with [111] A were demonstrated [11.81].

11.5.2 Vertical and Horizontal Bridgman Methods

Parker et al. [11.82] reported the growth of InSb single crystals by the horizontal Bridgman technique. Single crystals grown after refining had an etch pit density (EPD) of 10^5 cm^{-2} with carrier mobility of $919000 \text{ cm}^2/(\text{V s})$ (at 80 K). InSb was also grown by vertical Bridgman technique in quartz crucibles to yield single crystals with mobilities on the order of $10^4 \text{ cm}^2/(\text{V s})$ [11.71]. Bagai et al. [11.72] used semi-circular heaters to refine and grow single crystals with

high mobility by horizontal Bridgman technique. Although the growth of InSb has been tried by a variety of methods, and single crystals have been obtained, various problems continue to plague its production. The origin of most defects is traced to the growth environment, particularly the temperature. Impurity striation which was a common problem in Czochralski (CZ) grown InSb was also encountered in the Bridgman configuration. Zhou et al. [11.83] applied accelerated crucible rotation technique (ACRT) to the directional solidification of Te:InSb in a Bridgman system with a view to reduce rotational striation. Alternate methods such as the application of magnetic field during growth have also been attempted to tackle this problem [11.84, 85]. The magnetic field is known to reduce temperature fluctuations by damping convection in the melt. Better axial homogeneity in Te:InSb was observed by growth in a magnetic field. In the last decade great strides have been made in rheology and temperature modeling during growth to map the exact thermal environment in the growth chamber. Such studies have yielded a variety of information that provides greater insight into the growth phenomena. In situ observation of the growth of InSb by Bridgman method [11.86] has shown considerable supercooling during growth. This raises serious doubts as to whether the growth of the crystal under such a situation is from a homogeneous melt, a condition essential for growth. There has been a lot of work to understand the role that the crystal-melt interface plays during growth. Growth constrained by the crucible, such as in Bridgman technique, has been modeled [11.87–89], and the role that the ther-

mal properties of the melt and solid play in growth and interface shapes has been studied. A variety of quenching and etching techniques [11.90] have been developed to mark the growth history. Such experiments help researchers to study the origin of defects such as striation and coring, which lead to crystal inhomogeneity. Feedback from such studies helps to improve growth conditions. *Campbell and Koster et al.* [11.91] studied interface visualization through radiographic technique and calibrated interface temperature measurements to study growth of InSb from off-stoichiometric melts. Recently sequential-freeze technology has further been used for the study of segregation [11.92, 93]. This system has been used to test the effects of microgravity [11.94, 95] on growth. Large-sized InSb wafers are being produced (up to 100 mm diameter) in cutting-edge commercial product by Firebird Technology [11.96].

Czochralski Growth

Parker et al. also reported the growth of InSb by the CZ technique [11.82]. Polycrystalline zone-refined feed

material was used as the starting charge for growth. In fact, crystals grown by CZ from zone-refined ingots as the starting material gave the best results, yielding an EPD as low as 500 cm^{-2} . *Allred and Bate* [11.97] grew single-crystal InSb by CZ technique along $\langle 111 \rangle$ and $\langle 110 \rangle$ directions. They used radioactive Se and Te as dopants to trace dopant homogeneity in the pulled crystals. It was observed through contact radiography that the dopant formed a central core in the crystal where it was incorporated in large amounts, termed the coring effect. This was seen particularly for crystals grown along $\langle 111 \rangle$ directions. When grown along directions such as $\langle 110 \rangle$, it was seen that the dopant was preferentially incorporated in the $\{111\}$ facets that occurred at the edges of $\langle 110 \rangle$ boules. *Terashima* [11.98] introduced InN in InSb melt during the CZ growth to improve the crystals in terms of EPD. This was proposed to be the effect of nitrogen doping of the melt via InN. *Hurle et al.* [11.99] performed growth experiments of InSb from off-stoichiometric solutions which were either In or Sb rich. There exist many reports on the growth of InSb crystals using Czochralski method and the formation of various types of defects [11.97–102].

Traveling Heater Method (THM)

Benz and Müller [11.103] conducted various experiments on growth of InSb by the traveling heater method. The THM is a solvent method, and inclusion of the solvent from the feed is common in crystals grown by this method. Both vertical and horizontal configurations have been used and have obtained single crystals with no inclusion. The defect densities in the grown crystals were evaluated to be about 1000 cm^{-2} . The optimized growth rate for the growth of inclusion-free crystals was about 2.5 mm/day. It was found that higher growth rates led to solvent inclusions. The results were similar in the horizontal case. *Hamaker and White* [11.104] used the temperature gradient zone melting (TGZM) technique to study the growth kinetics in InSb. Thus InSb bulk crystals can be grown by many techniques, but at present the economical and large-sized crystals are produced by Bridgman methods. Also at present there is no incentive to use more sophisticated technique for growth of InSb. Some crystals grown in the authors' laboratory are shown in Fig. 11.5 [11.11, 69, 105, 106].

11.5.3 Bulk Growth of $\text{InAs}_x\text{Sb}_{1-x}$

Woolley and Warner [11.20] have reported two methods for the preparation of $\text{InAs}_x\text{Sb}_{1-x}$ alloys, viz. slow directional freezing and slow zone recrystallization of

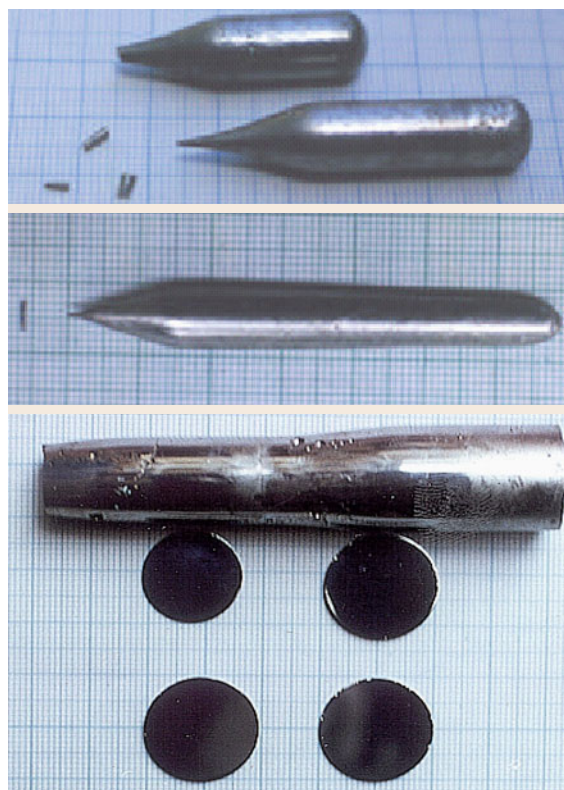


Fig. 11.5 InSb crystals and wafers of different sizes

suitable ingots. All the ingots were produced by melting together appropriate amounts of high-purity InAs and InSb. In slow directional freezing, ingots were prepared using equimolar proportions of InSb and InAs. Initially a furnace with a temperature gradient of 10 K/cm was used and temperature was controlled by an on-off controller, so that the time required to freeze the ingot completely was $\approx 2\text{--}3$ months. It was found that each end of the ingot was in good single-phase condition and the composition varied from 3 mol % to 12 mol % of InSb at one end and 88 mol % to 98 mol % at the other end. In between these regions however there was some 3 cm of the ingot where there was a very rapid change in composition with position and

where the material was not in equilibrium condition. An alternate method for preparing ingots of $\text{InAs}_x\text{Sb}_{1-x}$ alloys is the zone recrystallization technique. Here larger temperature gradients are used so that constitutional supercooling could be less of a problem, and the rate of movement of the freezing surface is directly controlled by the movement of the heater. *Glazov and Poyarkov* [11.107] reported homogeneous growth of this material in thin-foil form using rapid quenching. Recently *Dixit et al.* [11.9] reported growth of bulk single crystals of $\text{InAs}_x\text{Sb}_{1-x}$ for $0 \leq x \leq 0.05$ using RBM (Fig. 11.6). The phase diagram of In–As–Sb, which has been well studied both theoretically and experimentally [11.55, 61], was used to determine the

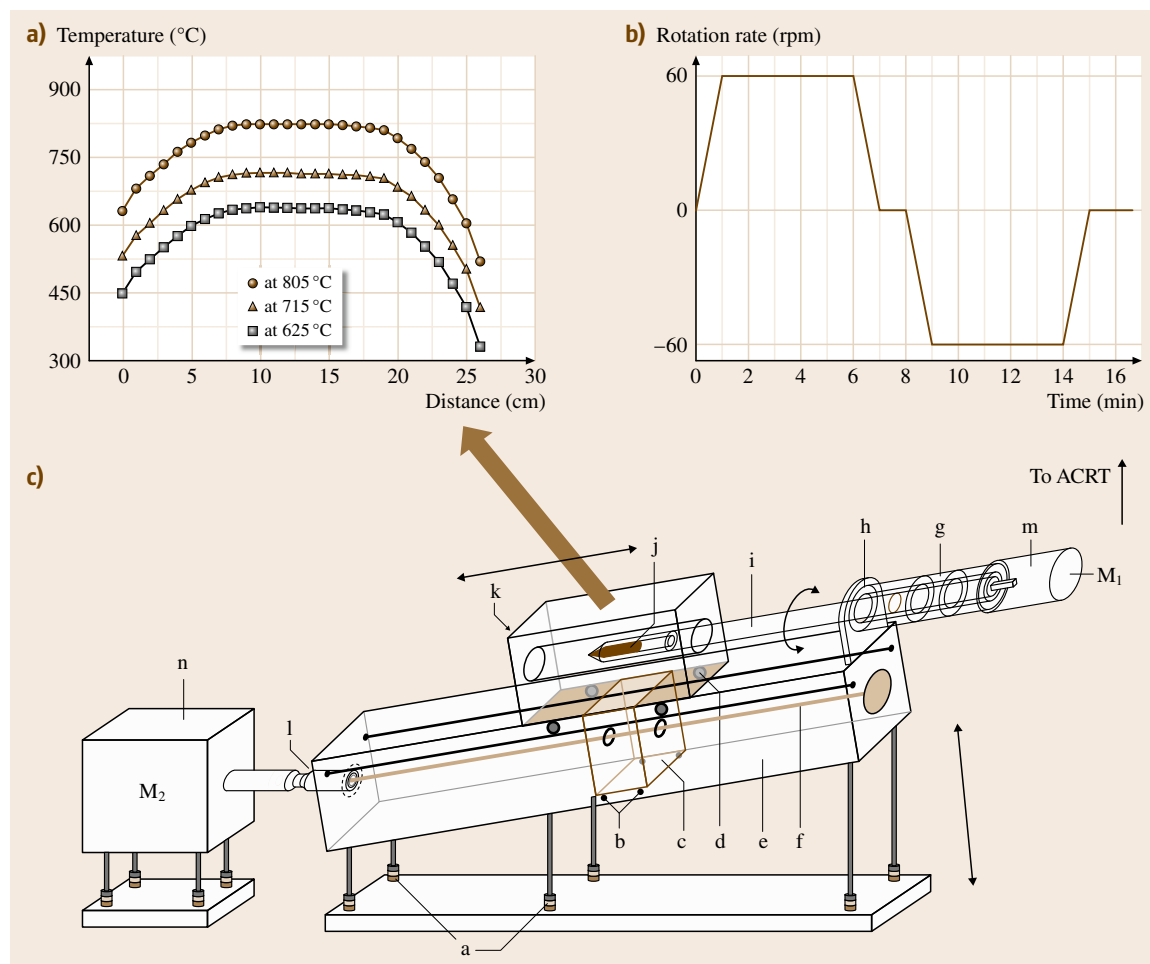


Fig. 11.6 (c) Schematic of RBM growth apparatus: (a – Antivibration mount, b – wheels, c – guided coupler, d – platform, e – aluminum frame, f – threaded lead screw, g – ball bearing, h – Wilson seal, i – quartz tube, j – ampoule, k – furnace, l – universal coupler, m – motor M_1 , and n – geared motor M_2). (a) Temperature profile of the furnace and (b) ACR sequence

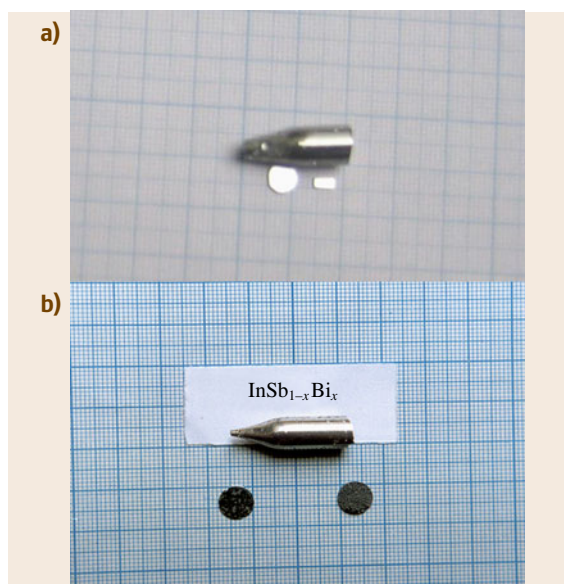


Fig. 11.7a,b Ingot and wafers of (a) $\text{InAs}_x\text{Sb}_{1-x}$ and (b) $\text{InBi}_x\text{Sb}_{1-x}$

initial reaction temperatures; these were in the range of 600–700 °C for various compositions in their experiments. $\text{InAs}_x\text{Sb}_{1-x}$ was synthesized by diffusing arsenic into high-purity InSb. Although various molar proportions, viz. $\text{InSb} : \text{As} = 95 : 5, 90 : 10, 85 : 15, 80 : 20$, and $75 : 25$, were tried, it was found that homogeneous single crystals of $\text{InAs}_x\text{Sb}_{1-x}$ could be grown only up to starting proportion of 90 : 10, beyond which the grown crystals were inhomogeneous and often phase separated. It was observed experimentally that the liquid–solid interface was slightly concave and symmetric with respect to ampoule axis. Typical size of the grown crystals was 8 mm diameter and about 45 mm length. The ingots were single crystalline up to ≈ 35 mm, after which they were multigrain. Wafers were made from the 10–20 mm region from the tip of the ingot. Figure 11.7a shows a typical crystal and wafers. If extensive work is carried out in these directions, bulk growth of $\text{InAs}_x\text{Sb}_{1-x}$ leading to large-size device-quality wafers can be achieved.

11.5.4 Bulk Growth of $\text{InBi}_x\text{Sb}_{1-x}$

Compared with $\text{InAs}_x\text{Sb}_{1-x}$ it is even more difficult to synthesize and grow single crystals of $\text{InBi}_x\text{Sb}_{1-x}$. The first work on synthesis and growth of $\text{InBi}_x\text{Sb}_{1-x}$ was reported by Jean-Louis et al. [11.108], followed by Joukoff and Jean-Louis [11.63]. The growth was

carried out using Czochralski technique, using $\langle 111 \rangle$ -oriented InSb seed rods of 3 mm diameter. Single crystal of $\text{InBi}_x\text{Sb}_{1-x}$ could be obtained from a melt up to 30% InBi, which yielded $x = 0.001$, insufficient for development of detectors in the 8–12 μm atmospheric window. Hence they attempted growth with 70% InBi melt, which did not give single crystal. In the intermediate range of 50–60 % they could obtain single crystal up to $x = 0.026$. Later, in 1991, Ozawa et al. [11.109] reported growth of $\text{InBi}_x\text{Sb}_{1-x}$ using RBM. They could grow $\text{InBi}_x\text{Sb}_{1-x}$ single crystals with x varying from 0.016 to 0.03 from the seed region to the end of the ingot. This indicated that the segregation coefficient of Bi in InSb was less than unity. They could enhance the Bi content up to ≈ 5 at. % by codoping with gallium [11.110]. Dixit et al. [11.12] also reported growth of bulk single crystals of $\text{InBi}_x\text{Sb}_{1-x}$ with $x = 0.067$ using RBM. $\text{InBi}_x\text{Sb}_{1-x}$ was synthesized using various molar proportions (1 : 1, 1 : 3, 1 : 4, and 1 : 5) of InSb and InBi. It was found that, compared with 1 : 1 and 1 : 3, 1 : 4 yielded higher Bi concentration in $\text{InBi}_x\text{Sb}_{1-x}$ crystal as well as better homogeneity. However further increase of InBi molar ratio to 1 : 5 led to formation of InBi and In_2Bi precipitates. Similar compositional ratio (1 : 4) was also employed by Kumagawa et al. [11.110]. Typical size of the grown crystals are 8 mm diameter and about 25 mm length. Figure 11.7b shows the grown crystal and wafers. Microgravity experiments on the growth yielded crystals with reduced segregation of InBi [11.94]. This is one avenue that could be explored for higher incorporation of Bi in the crystal, thereby improving suitability for device applications.

11.5.5 Growth of Thick Layers of InSb, $\text{InAs}_x\text{Sb}_{1-x}$, and $\text{InBi}_x\text{Sb}_{1-x}$, by Liquid-Phase Epitaxy

LPE, although a widely used general laboratory preparation technique, has not found much favor with these materials, mainly due to the low temperatures of growth, limited by the melting point of InSb. However, recently there has been renewed activity on LPE growth of these materials. Here we present a comprehensive report on the growth of InSb-based epitaxial layers grown using LPE. These layers mimic the bulk-like properties and can also be used as virtual epi-ready wafers for further growth of multilayered structures.

InSb Epilayers

Various efforts have been made to adapt LPE for growth of InSb. Kumagawa et al. [11.111] reported dopant

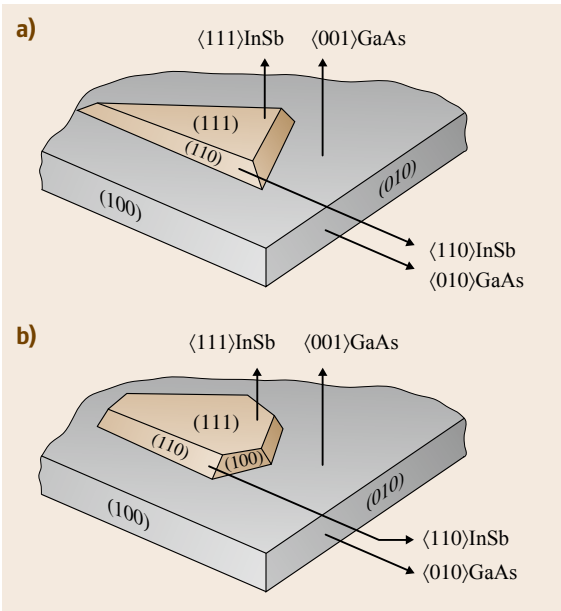


Fig. 11.8a,b The two typical shapes of growth islands: (a) triangular (60° angle) and (b) truncated triangular

modulation in InSb layers grown by liquid-phase electroepitaxy (LPEE). *Melngailis* and *Calawa* [11.112] reported growth of planar InSb laser structures by LPE. They used a stearic acid encapsulant for growth to avoid oxide layer formation during growth. *Holmes* and *Kamath* [11.113] have used infinite solution epitaxy to grow binary InSb and discussed the growth of continuous layers with constant ternary composition. However, other than a few early papers on homoepitaxy [11.111, 113], there are no reports on successful growth InSb/GaAs by LPE. Recently, *Dixit* et al. [11.10] reported successful epitaxial growth of

this material on SI-GaAs substrate by LPE with extremely low ramp cooling rates. Growth was carried out on (001) semi-insulating GaAs substrate in a boat-slider-type LPE unit [11.114, 115]. The optimized III/V mass ratio used for the growth was ≈ 3.45 . A ramp cooling routine was adopted with the intention of providing a driving force $\beta \propto \Delta T/T_g$ [11.116] (where ΔT denotes the supercooling of the solution and T_g the initial growth temperature) at every point of growth and induce orderly epitaxial growth. The sliding was achieved by an improvised electromechanical system. Films were grown under varied conditions of supersaturation by changing the ramp rate R and the cooling temperature step ΔT . During the course of this study, it was noticed that higher cooling rates led to formation of interesting island morphology. The two typical shapes were (a) triangular (60° angle) and (b) truncated triangular islands (Fig. 11.8). The results from various growth experiments are presented in Table 11.1. It is seen that the growth rate r ($\mu\text{m/h}$) and the ramp rate R have a direct correspondence as expected. Furthermore, as can be seen from Table 11.1, oriented films were grown only at $R = 0.2$ K/h, with ΔT of 2 K. Although oriented films were obtained by this way, coverage was low and morphology was poor. By increasing the growth temperature while keeping other conditions the same the growth rate could be decreased (#48A to #33B in Table 11.1), which is in agreement with *Elwenspoek's* work [11.116]. By initiating the growth at 423 °C and decreasing the ramp rate to 0.2 K/h, oriented films of 3 μm thickness could be grown.

InAs_xSb_{1-x} Epilayers

Until the 1990s growth of InAs_xSb_{1-x} by LPE was achieved only for very high arsenic concentrations (for 3–5 μm gap) and on nearly lattice-matched InAs and

Table 11.1 Summary of various InSb/GaAs thin-film growth experiments

#	R (K/h)	T_g (°C)	ΔT (K)	r ($\mu\text{m/h}$)	hkl_{max}	Other peaks	$I_{004}/\sum I_{hkl}$	Thickness (μm)
43A	3	410	5	240	(111)	(311) (220) (004)	0.1	400
40A	2.5	410	10	85	(331)	(220)	0	330
50A	1.8	410	5	45	(004)	(220) (311)	0.63	120
45A	0.5	410	5	30	(004)	(311) (220)	0.62	300
48A	0.2	410	2	27	(004)	–	1	270
13B	3	423	11	14.7	(004)	–	1	54
20B	1.5	423	5	3	(004)	–	1	10
30B	0.8	423	3	1.6	(004)	–	1	6
33B	0.2	423	3	0.4	(004)	–	1	4
5C	0.2	423	2	0.7	(004)	–	1	7
7C	0.2	423	2	0.3	(004)	–	1	3

Table 11.2 Summary of various InAs_xSb_{1-x}/GaAs thin-film growth experiments

#	<i>R</i> (K/h)	<i>T</i> _g (°C)	ΔT (K)	<i>r</i> (μm/h)	<i>hkl</i> _{max}	Other peaks	<i>I</i> ₀₀₄ / $\sum I_{hkl}$	<i>t</i> (μm)	Composition (<i>x</i>)	
									EDAX	X-ray
11D	2.5	453	3	16.67	(004)	(220)	0.85	20	0.12±0.01	0.12±0.004
21D	1.5	450	3	6.5	(004)	(220)	0.85	13	0.10±0.01	0.12±0.004
39D	0.8	448	3	2.67	(004)	–	1	10	0.06±0.01	0.45±0.004
43D	0.6	446	3	2.10	(004)	–	1	8	0.06±0.01	0.42±0.004

Table 11.3 Summary of various InBi_xSb_{1-x}/GaAs thin-film growth experiments

#	<i>R</i> (K/h)	<i>T</i> _g (°C)	ΔT (K)	<i>r</i> (μm/h)	<i>hkl</i> _{max}	Other peaks	<i>I</i> ₀₀₄ / $\sum I_{hkl}$	Thickness (μm)
13C	2.5	355	5	7.5	(004)	(220)	0.73	15
20C	1.5	353	3	5.0	(004)	(220)	0.89	10
30C	0.6	351	2	1.79	(004)	–	1	6
33C	0.2	351	2	0.2	(004)	–	1	2

GaSb substrates [11.117, 118]. However, there does not seem to be any work on LPE growth of this system for low values of *x*. This is primarily due to problems associated with the low growth temperature and large lattice mismatch. Recently a few more results have been published on this growth by authors such as Dixit et al. [11.5], Peng et al. [11.34], and Gao et al. [11.37], employing LPE or melt epitaxy (ME). Dixit et al. [11.5] grew InAs_xSb_{1-x} layers in the same boat-slider-type LPE unit used to grow InSb. Prior to growth, indium-rich InAsSb solution was prepared with indium and previously grown InAs_xSb_{1-x} crystals [11.9]. The optimized In/(Sb + As) mass ratio used for the growth was ≈ 2.93. The solution temperature was increased to 5 °C above the growth temperature of 446 °C, and baking for 6 h was used to allow proper homogenization. Here also a ramp cooling routine was used. The results obtained under various growth conditions are summarized in Table 11.2. Large growth rates force nucleation with off-(100) orientation, while oriented growth takes place on (100) GaAs at lower growth rates. It is to be noted that, when growth temperature increases above 446 °C, the arsenic incorporation into InSb increases due to the diffusion of arsenic from the GaAs substrate itself [11.119, 120]. Hence growth temperature was restricted to 446 °C. This led to the limitation of As incorporation to only 6 at. % in InAs_xSb_{1-x} epitaxial layers. Also it was observed that the quality of the interface deteriorated with increasing arsenic composition. This is due to a miscibility gap in the phase diagram. Recently, relatively thick films (100–200 μm) were grown by Gao et al. [11.37] using ME at 600 °C. Very recently Peng et al. [11.34] also reported predominantly oriented growth of InAs_xSb_{1-x} films with up

to 30% As incorporation using conventional LPE. In this work, layers were grown at constant growth temperatures rather than employing a ramp cooling routine. Constant growth temperature helps the compositional uniformity of the InAs_xSb_{1-x} films in the growth direction, similar to the observation of Dixit et al. [11.5] (by very slow growth rate condition).

InBi_xSb_{1-x} Epilayers

Literature on LPE growth of InBi_xSb_{1-x} is very limited. There are only a few reports on homoepitaxy of InBi_xSb_{1-x}. Ufimsev et al. [11.121] reported the growth for *x* = 0.01–0.02. Gao and Yamaguchi [11.122] also reported homoepitaxy of InBi_xSb_{1-x} using LPE, wherein they found that surface morphology was strongly dependent on cooling rate. Also Bi metal particles appeared on the surface of the epilayer. The cutoff wavelength reported for this film was 14 μm. Many reports can however be found in the literature on the heteroepitaxy of InBi_xSb_{1-x} using a variety of other techniques. Dixit et al. [11.123] also reported growth of InBi_xSb_{1-x} on GaAs using the boat-slider-type LPE unit. The optimized In/(Sb + Bi) mass ratio used for the growth was ≈ 1.86. The solution temperature was increased to ≈ 50 °C above the growth temperature (351 °C), and baking for a period of 6 h in ultra-pure hydrogen ambient was used for homogenization. Table 11.3 gives the correlation between imposed supersaturation ΔT (K) and the thickness of the grown films.

Work on the growth of InBi_xAs_ySb_{1-x-y} by a variety of techniques has also been reported, including LPE [11.4, 8, 53, 124–126]. However, extensive work is needed for the development of the Sb-based stable detectors for the long-wavelength region.

11.6 Structural Properties of InSb, InAs_xSb_{1-x}, and InBi_xSb_{1-x}

Structural information is crucial for developing any technology. Particularly it is very important to understand the role of alloying and mismatch epitaxy in these systems. Structural information about these materials is obtained using various characterization techniques. The most commonly used techniques include high-resolution x-ray diffraction (HRXRD), chemical etching, x-ray topography, atomic force microscopy (AFM), scanning electron microscopy (SEM), and transmission electron microscopy (TEM).

11.6.1 InSb

Composition

Although InSb growth is very well studied, care must be taken to obtain crystals in stoichiometric form. Hence the starting material for all growth runs should be synthesized in one batch to avoid any batch-to-batch variation in composition, and care must be taken in transferring the material and to maintain accuracy to the level of $\mu\text{g/g}$ of charge. Also, due to the vapor pressure difference, composition differences of the starting material have to be taken into account. The typical results of energy-dispersive x-ray analysis (EDAX) for samples made from grown InSb crystals showed that the crystals were radially and axially homogeneous. The typical radial composition profile for 20 mm InSb wafer is given in Table 11.4.

Orientation Determination

The crystallographic orientation of the grown crystals can be determined from x-ray diffraction experiments. The Laue pattern shows fourfold symmetry for $\langle 001 \rangle$ and threefold symmetry for $\langle 111 \rangle$ InSb wafer. From powder x-ray diffraction scans of the wafer one can

determine the growth direction of the crystals. For example, a single peak corresponding to (111) and $(1\bar{1}\bar{1})$ planes is obtained for wafers made from crystals grown by horizontal and vertical Bridgman techniques.

Chemical Etching

InSb is the most perfect material among the III–V semiconductors available to date. For chemical etching, usually CP4 etchant has been found to be very effective (Fig. 11.9). Chemical etching producing pits has been used to quantify dislocations. In InSb, a one-to-one correspondence has been established between dislocations and etch pits. The pit count, EPD, gives an order of magnitude estimate of the dislocation content in the crystals. Typically $10\text{--}100\text{ cm}^{-2}$ etch pit density is specified in commercially available InSb. However, the best results are only 1 etch pit in 50 cm^2 . T-shaped and *star*-type arrays of etch pits are more prominent in InSb due to an inherent difference between the (111) and $(\bar{1}\bar{1}\bar{1})$

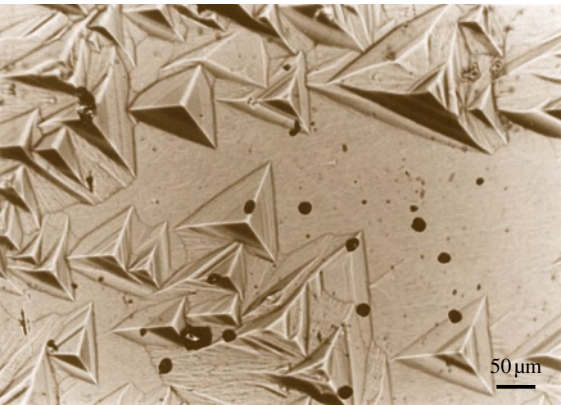



Fig. 11.9 Etch pit pattern on (111) InSb wafer

Table 11.4 Compositional profile of InSb wafer; *a*, *b*, *c*, *d* are marked in the schematic of the wafer shown at the top of the table

<div><div></div><div>Compositional profile</div></div>					
From <i>a</i> to <i>b</i>	Atomic percentage		From <i>c</i> to <i>d</i>	Atomic percentage	
	In	Sb		In	Sb
1. (1 mm)	50.10	49.85	1. (1 mm)	50.09	49.91
2. (6 mm)	50.07	49.93	2. (7 mm)	50.11	49.89
3. (12 mm)	50.19	49.81	3. (13 mm)	50.19	49.81
4. (19 mm)	50.10	49.9	4. (20 mm)	50.23	49.77

planes [11.96]. Also this polarity influences many other properties; for example, damage depth and chemical attack rates are different for 111B (Sb planes) and 111A (In planes).

Slip System

{111} are the slip planes for InSb. The slip direction is one of the $\langle 110 \rangle$ directions. If InSb crystals are compressed or bent by applying stress above a critical value, arrays of slip dislocations can be produced, which can be viewed as etch pit arrays defining the traces of the {111} planes.

Twinning

During growth, a 60° lattice rotation about any III–V bond in a $\langle 111 \rangle$ direction preserves the tetrahedron of opposite species but in a lattice mirrored across the (111) plane, since both the nearest and second nearest neighbors remain at their normal distance; the energy required for this twinned growth is exceptionally low. For this reason twinning across the set of {111} planes is the principal complication in growing single crystals of InSb. Various other types of twinning are also reported along {211} and {111} planes for III–V as well as IV semiconductors but not in InSb [11.96, 127]. *Terashima* [11.98] reported Y-shaped defects in (111) pulled InSb crystals and these defects are eliminated by growing the crystal using a seed inclined at $5\text{--}10^\circ$ from (111) towards $\langle 110 \rangle$.

High-Resolution X-Ray Diffraction Study

An ideal crystal on interaction with a x-ray beam diffracts a beam of extremely narrow width at the Bragg angle. However, in practice one sees a width of diffracted beam or rocking curve width of several hundreds of arc seconds in angular spread. This was first explained by *Darwin* [11.128], considering the crystal to be a macromosaic of crystals of slightly differing orientations. These macromosaics receive the x-ray at different incident angles and hence there is a finite spread in the resultant diffracted beam. Also, defects in the lattice such as vacancies, interstitial, dislocations, twins, and small-angle grain boundaries distort the lattice and contribute to broadening of the rocking curve. The relative widths of diffraction curves have been found useful for comparing the crystalline perfection of many semiconductors. Such studies have been made on InSb and are described by *Auleymer* [11.129]. High-resolution x-ray diffraction study is very effective for determining the crystalline quality [11.130] of InSb crystals. *Gartstein* and *Cowley* [11.131] and

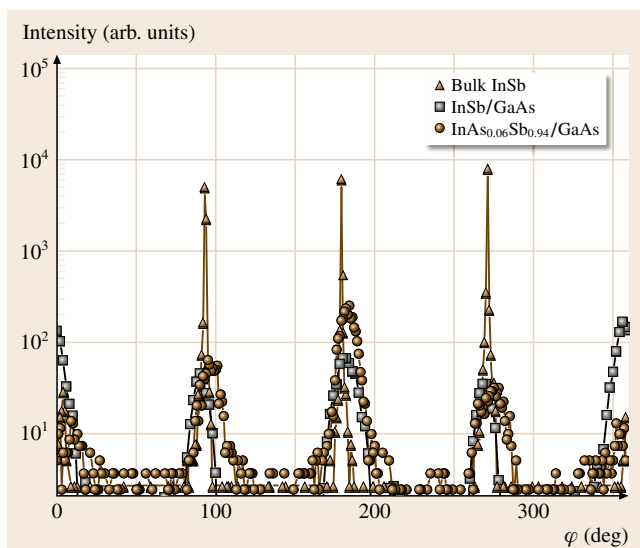


Fig. 11.10 X-ray diffraction patterns (ϕ scan) of single crystal and epilayers in asymmetric (115) reflection over 360° azimuths

Gartstein et al. [11.132] discuss the x-ray diffraction study of perfect and In^+ -ion-implanted InSb single crystals. The rocking curves of these crystals are relatively large; however substantial reduction in radiation damage by permanent magnetic fields is noticed. Recently, *Dixit* [11.11, 69] carried out HRXRD studies on bulk InSb and Li:InSb using a Philips X'PERT high-resolution x-ray diffractometer. A ϕ scan of an asymmetric reflection was performed to determine the single-crystal nature of the bulk InSb crystal. As seen in Fig. 11.10 the ϕ scan over 360° azimuths gave four distinct peaks separated by 90° intervals with no scattering between them, confirming the single-crystalline nature of InSb. Subsequently several symmetric and asymmetric rocking curves were recorded. The rocking curve width (full-width at half-maximum, FWHM) was found to be $18''$ (Fig. 11.11), which is approaching the theoretical limit of the rocking curve width for 004 reflection of InSb. Employing MOCVD *Gaskill* et al. [11.29] have grown layers of InSb on InSb substrates with rocking curve width of $34''$, approaching the theoretical limit of $11''$ for InSb. Interesting studies on the structural dynamics of InSb using time-resolved x-ray diffraction were reported by *Chin* et al. [11.133]

Synchrotron Radiation Topographic Study

Surowiec and *Tanner* [11.134] reported transmission x-ray topography studies on the dislocation configurations around microindentations on {111} surfaces

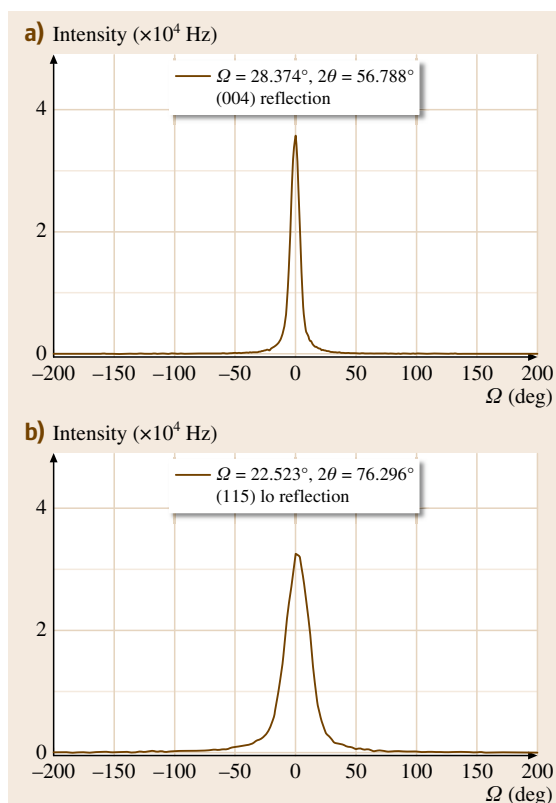


Fig. 11.11a,b Representative $\omega/2\theta$ scans of InSb for (a) (004) reflection and (b) (115) lo reflection

of InSb. Glide occurs on only B-type {111} planes, and the most extended dislocation loops occur around A-surface indents. Glide occurs on inclined {111} planes and the loops have extended screw segments parallel to the surface. The mobility of these dislocations is about two or three times less than the former type. Direct evidence for the formation of edge dislocation barriers from reactions between dislocations gliding in the (111) plane is reported. Dixit et al. [11.69] also carried out synchrotron x-ray topographic study on high-quality InSb crystals. Reflection topographs of polished surfaces were taken with the normal tilted 5° from 024 reflection. A diffraction wavelength of 1.30 \AA was used, and the sample-to-film distance was 20 cm. Results are shown in Fig. 11.12a,b. As can be seen from the figure, the topographic images are free from asterism. Surfaces show some polishing effects but they are free from any dislocation. Figure 11.12b shows some white circular features which are due to metal inclusions.

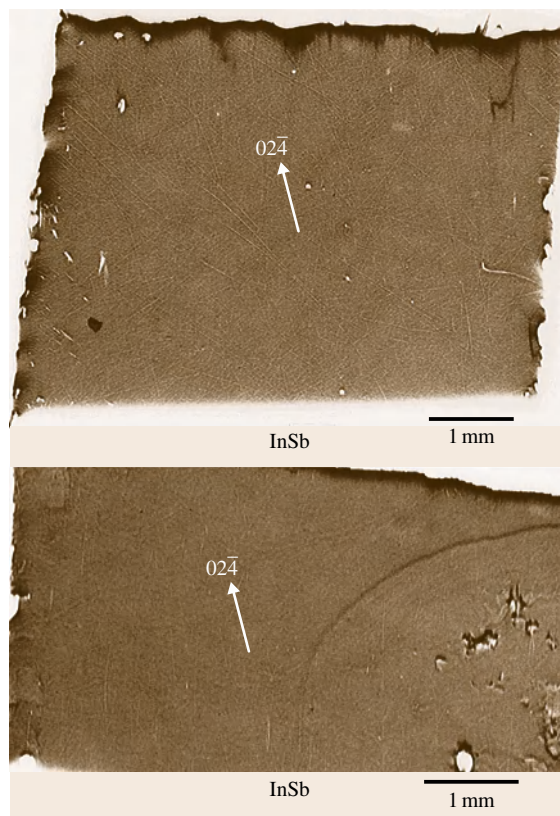


Fig. 11.12 Synchrotron reflection topographs of InSb wafers

11.6.2 $\text{InAs}_x\text{Sb}_{1-x}$

Dixit et al. [11.9, 69] estimated arsenic content in grown $\text{InAs}_x\text{Sb}_{1-x}$ crystal by measuring the melting point using differential scanning calorimetry and inferred that it must be more than 3 at.% (Fig. 11.13). The composition x in $\text{InAs}_x\text{Sb}_{1-x}$ crystals grown from starting proportions of 95 : 5 and 90 : 10 was 0.02 and 0.05, respectively, as determined from EDAX. Further confirmation of the composition was made using x-ray photoelectron spectroscopy (XPS). The binding energies were measured with respect to the 1s peak at 285 eV with a precision of $\pm 0.1 \text{ eV}$. XPS of core-level regions of In(3d), Sb(3d), and As(3d) are shown in Fig. 11.14. Spin-orbit doublet peaks of In($3d_{5/2,3/2}$), Sb($3d_{5/2,3/2}$), and As($3d_{5/2,3/2}$) show shifts compared with the respective metals [11.135]. The surface concentration ratio In(3d)/Sb(3d) has been estimated using the following

equation

$$\frac{C_{\text{In}}}{C_{\text{Sb}}} = \frac{I_{\text{In}} \sigma_{\text{Sb}} \lambda_{\text{Sb}} D_{\text{E}}(\text{Sb})}{I_{\text{Sb}} \sigma_{\text{In}} \lambda_{\text{In}} D_{\text{E}}(\text{In})}, \quad (11.3)$$

where C , I , σ , λ , and D_{E} are the concentration, intensity, photoionization cross section, mean escape depth [11.135–137], and geometric factor respectively. Integrated intensities of metal peaks have been

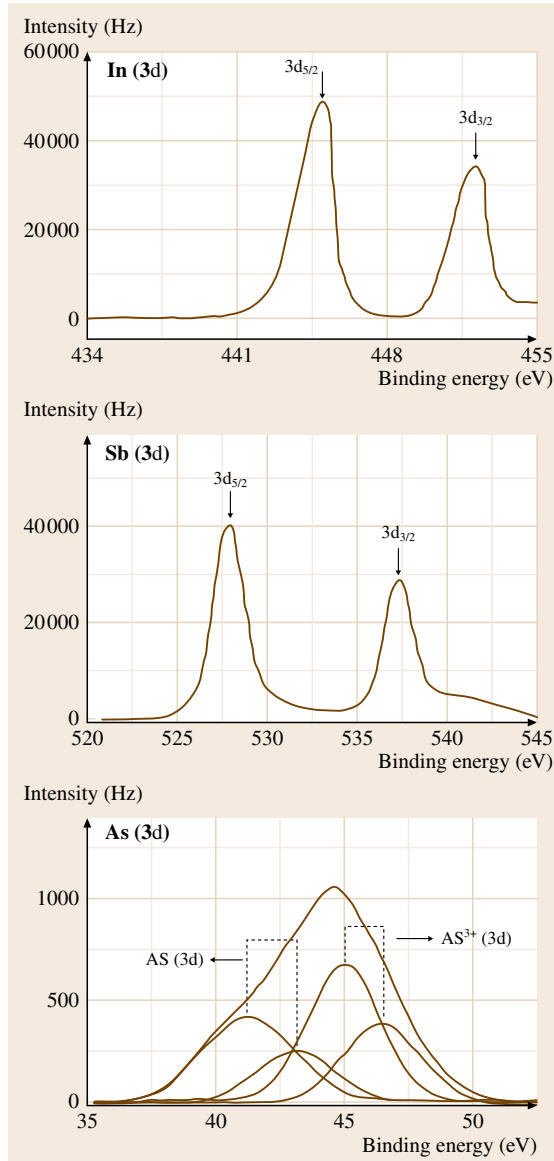


Fig. 11.14 X-ray photoelectron spectra of $\text{InAs}_{0.05}\text{Sb}_{0.95}$ for In, Sb, and As

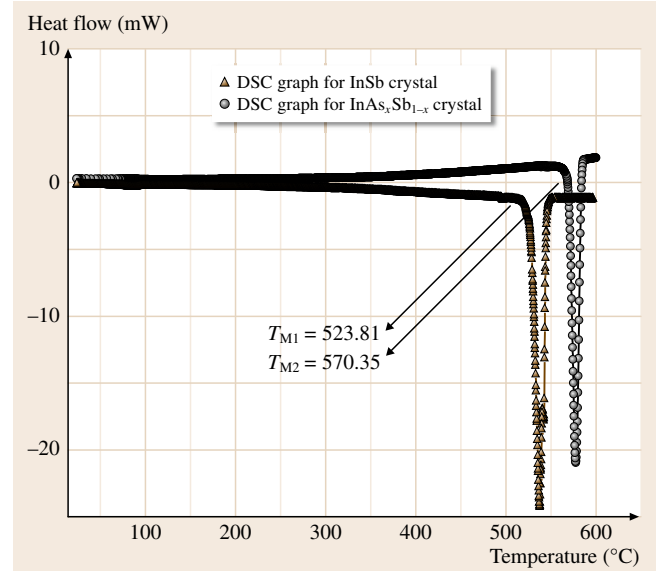


Fig. 11.13 Differential scanning calorimetry curves of $\text{InAs}_x\text{Sb}_{1-x}$ for $x = 0$ and 0.05

taken into account for calculating the concentrations. Surface concentration ratios of $\text{In}(3d)/\text{Sb}(3d)$ and $\text{As}(3d)/\text{Sb}(3d)$ can also be calculated using similar equations. The composition has been estimated to be $\text{InAs}_{0.055}\text{Sb}_{0.945}$, which is close to the bulk composition obtained from EDAX. From EDAX and XPS results

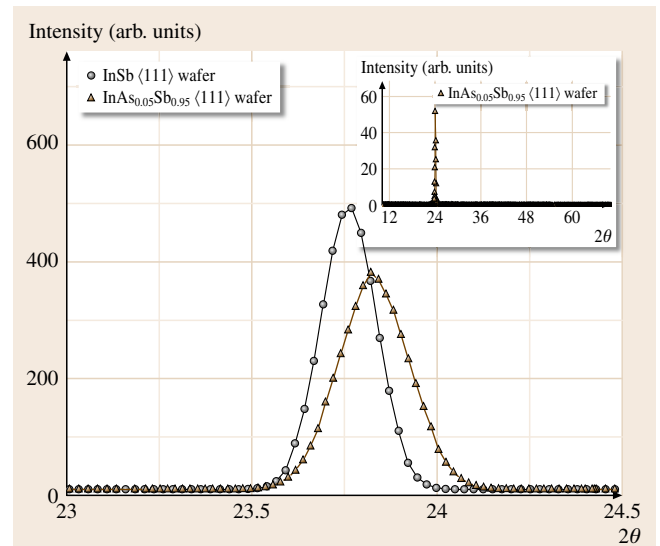


Fig. 11.15 X-ray diffraction peaks of single-crystal wafers of InSb and $\text{InAs}_{0.05}\text{Sb}_{0.95}$ for (111) reflection

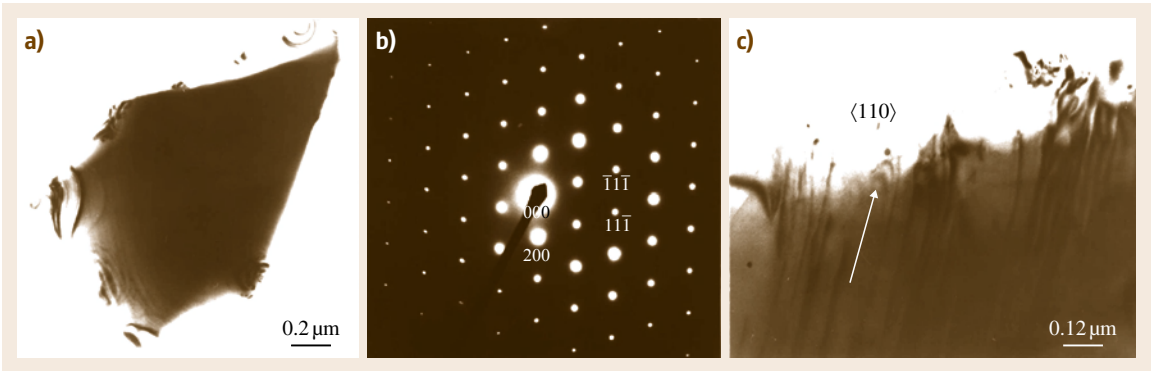


Fig. 11.16 (a) Bright-field image of $\text{InAs}_{0.05}\text{Sb}_{0.95}$, (b) selected-area diffraction pattern of (a), and (c) bright-field image showing dislocations along the $\langle 110 \rangle$ direction

it was concluded that the grown crystals were radially homogeneous but the As composition decreased from tip to the other end of the ingot. The lattice parameter

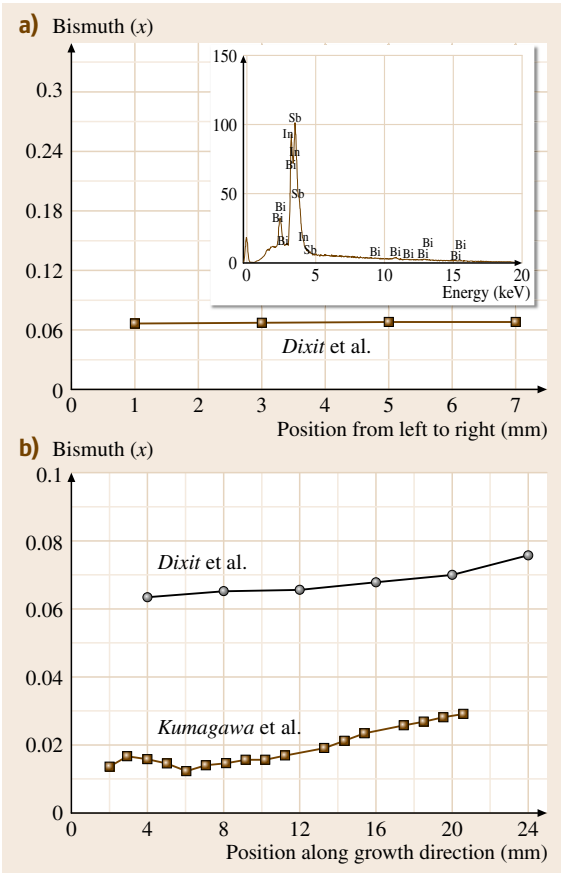
of $\text{InAs}_{0.05}\text{Sb}_{0.95}$ as calculated from XRD powder patterns is $6.460 \pm 0.006 \text{ \AA}$ and matches reasonably with that obtained from Vegard's law. $\text{InAs}_{0.05}\text{Sb}_{0.95}$ showed lattice contraction relative to that of InSb, as confirmed by XRD (Fig. 11.15). Dixit et al. [11.9] also obtained bright-field TEM images of $\text{InAs}_{0.05}\text{Sb}_{0.95}$ along with its selected-area electron diffraction pattern, confirming the absence of twinning (Fig. 11.16). However in the bright-field image, dislocations were observed primarily along $\langle 110 \rangle$ direction (Fig. 11.16). The estimated dislocation density was $\approx 10^8 \text{ cm}^{-2}$. This is comparable to those found for $\text{InAs}_x\text{Sb}_{1-x}$ alloy grown by other techniques [11.138].

11.6.3 $\text{InBi}_x\text{Sb}_{1-x}$

So far, the highest value of x in $\text{InBi}_x\text{Sb}_{1-x}$ bulk single crystals is 0.064 ± 0.01 , as determined from EDAX (inset in Fig. 11.17a). Dixit et al. [11.12] found that the Bi content in crystal grown by RBM increases from the tip to the upper end of the ingot, confirming that the equilibrium segregation coefficient of Bi in InSb is less than unity. Compared with Kumagawa et al. [11.110], they could achieve higher Bi incorporation into the crystals with better radial and axial homogeneity, as can be seen from Fig. 11.17. From powder x-ray diffraction patterns recorded for $\text{InBi}_x\text{Sb}_{1-x}$ the lattice parameter was calculated and found to be $6.489 \pm 0.006 \text{ \AA}$. The composition of Bi as evaluated by Vegard's law

$$a_{\text{InBi}_x\text{Sb}_{1-x}} = xa_{\text{InBi}} + (1-x)a_{\text{InSb}} \quad (11.4)$$

Fig. 11.17 (a) Radial and (b) axial compositional profiles of $\text{InBi}_x\text{Sb}_{1-x}$ crystal; inset in (a) shows a typical EDAX spectrum ◀



is 6.79 at. %, which is in reasonable agreement with the EDAX result, where

$$\begin{aligned} a_{\text{InBi}} &= 6.640 \text{ \AA} \quad [11.39] \quad \text{and} \\ a_{\text{InSb}} &= 6.478 \text{ \AA}, \\ a_{\text{InBi}_x\text{Sb}_{1-x}} &= 6.490 \pm 0.006 \text{ \AA}. \end{aligned}$$

11.6.4 InSb, InAs_xSb_{1-x}, and InBi_xSb_{1-x} Grown on GaAs

Dixit et al. [11.10, 115] carried out extensive HRXRD studies on these heterostructures grown using LPE. A ϕ scan of an asymmetric reflection recorded on InSb/GaAs gave four distinct layer peaks separated by 90° intervals with negligible scattering between them (Fig. 11.10). Layers show structural coherence with substrates as confirmed from various reflections (Fig. 11.18). The tilt angle T_{1s} of the epilayer to the substrate was estimated by using the relation

$$T_{1s} = \frac{1}{2} [(\Delta\omega_1 - \Delta\omega_3)^2 + (\Delta\omega_2 - \Delta\omega_4)^2]^{1/2}, \quad (11.5)$$

where the $\Delta\omega_i$ are the peak separations at 90° intervals. The tilt was found to be quite small and was about 0.01°. Strain parameters were evaluated by a least-squares routine for the following relationship [11.139]

$$\Delta\omega = k_1\epsilon_{\perp} + k_2\epsilon_{\parallel}, \quad (11.6)$$

where $k_1 = \cos^2\phi \tan\theta_B + 1/2 \sin 2\phi$ and $k_2 = \sin^2\phi \times \tan\theta_B - 1/2 \sin 2\phi$, in which θ_B is the substrate Bragg angle and ϕ is the angle between the reflecting plane (hkl) and the sample surface (001) with ϕ being positive (negative) for low (high) glancing incidence. The perpendicular and in-plane x-ray strain parameters, ϵ_{\perp} and ϵ_{\parallel} , in the above relationship are defined [11.140]

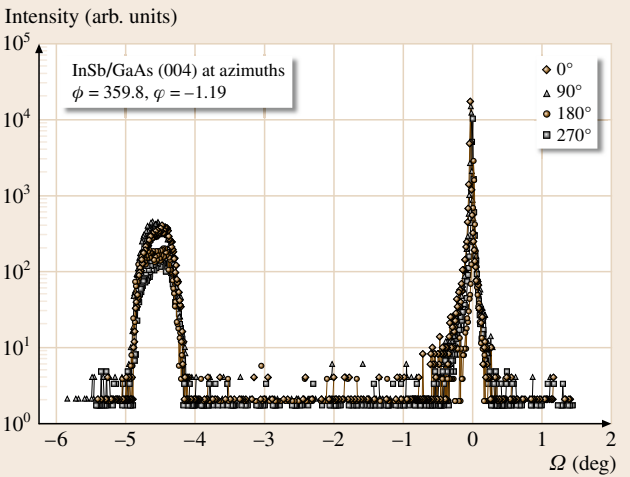


Fig. 11.18 Representative ω scans of InSb/GaAs for (004) reflection at four azimuths

with respect to the substrate lattice parameter as

$$\epsilon_{\parallel} = \frac{a_{\parallel} - a_s}{a_s}, \quad \epsilon_{\perp} = \frac{a_{\perp} - a_s}{a_s}, \quad (11.7)$$

where a_{\parallel} and a_{\perp} are the in-plane and out-of-plane lattice constants, respectively. The results of the least-square analysis are $\epsilon_{\parallel} = (99 \pm 10) \times 10^{-3}$ and $\epsilon_{\perp} = (108 \pm 3) \times 10^{-3}$, indicating considerable in-plane strain relaxation expected for the large mismatch. From these results they determined $a_{\parallel} = 6.213 \text{ \AA}$ and $a_{\perp} = 6.264 \text{ \AA}$, both approaching the standard lattice constant of InSb. The in-plane and out-of-plane residual strains as evaluated from a_{\parallel} and a_{\perp} are 0.0409 and 0.033, respectively, which are quite small. All the films shows almost complete relaxation, hence extensive dislocation network is to be expected, which was estimated using the FWHM of symmetric (004) reflec-

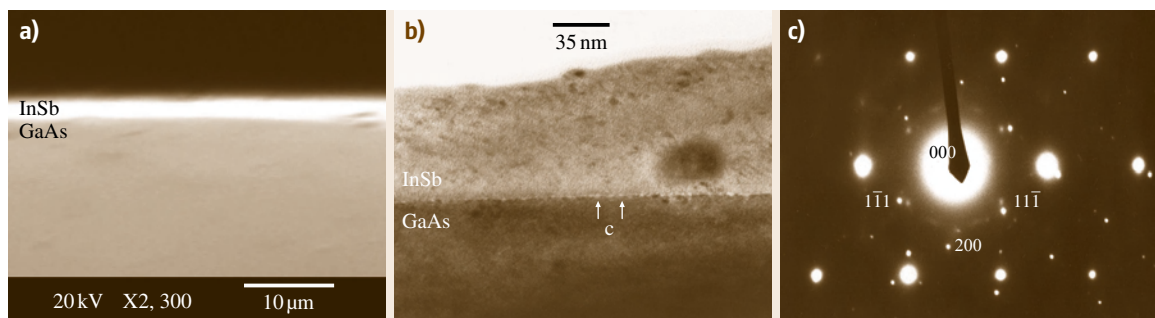


Fig. 11.19 (a) Scanning electron micrograph of InSb/GaAs interface, (b) bright-field image of the InSb/GaAs cross-section, and (c) selected-area diffraction pattern of ((b))

tion. With the magnitude of the Burger's vector taken as $1/(2\sqrt{2})a$ (which is the case for 60° misfit dislocation), where a is $(a_{\text{InSb}} + a_{\text{GaAs}})/2$ [11.141], the estimated average dislocation density is in the range $1.3 \times 10^9 - 4.7 \times 10^{10} \text{ cm}^{-2}$, which compares favorably with the values reported for epitaxial layers grown by MBE and MOCVD [11.28, 29].

The cross section of the film (cleaved sample) observed under a scanning electron microscope (SEM), shown in Fig. 11.19a, clearly reflects reasonable sharpness of the interface between the InSb layer and GaAs substrate. The bright-field cross-sectional TEM image,

taken with a JEM-200CX transmission electron microscope, indicates a sharp interface with very small coalescing islands (marked "C" in Fig. 11.19b). The selected-area electron diffraction pattern of an InSb–GaAs interface is shown in Fig. 11.19c. The diffraction spots occur in pairs, corresponding to InSb and GaAs, respectively, indicating that the layer and the substrate are epitaxially oriented. Very similar results were obtained for $\text{InAs}_x\text{Sb}_{1-x}/\text{GaAs}$ and $\text{InBi}_x\text{Sb}_{1-x}/\text{GaAs}$ heterostructures, confirming that heteroepitaxy is more dominant than alloying effects for these structures for small composition.

11.7 Physical Properties of InSb, $\text{InAs}_x\text{Sb}_{1-x}$, and $\text{InBi}_x\text{Sb}_{1-x}$

It is known that III–V compounds have band structures nearly similar to those of group IV semiconductors, although there are some differences which arise from the lack of inversion symmetry in their crystal structures. The effective mass of electrons in the conduction band varies from compound to compound and is the smallest for InSb-based materials amongst all III–V compounds. The effective masses of heavy holes, however, do not seem to vary much in these compounds. The strong interaction between the valence and conduction bands results in nonparabolicity at the bottom of the conduction band in these materials. Hence their electrical and optical properties are different from various other compound semiconductors.

11.7.1 Band Structure of InSb, $\text{InAs}_x\text{Sb}_{1-x}$, and $\text{InBi}_x\text{Sb}_{1-x}$

The band structure of InSb was calculated using the $\mathbf{k} \cdot \mathbf{p}$ perturbation approach [11.142]. Various authors have postulated the band structure of InSb and experiments have verified the same. Experiments show that the minimum of the conduction band in indium antimonide lies at the center of the zone and that the band is spherically symmetrical. The most direct evidence for the spherical symmetry of the band has come from microwave cyclotron resonance experiments [11.143]. For a band with spherical symmetry, the longitudinal magnetoresistance should be zero, and it has been found experimentally in n-type InSb that it is indeed an order of magnitude smaller than the transverse magnetoresistance [11.144]. The effective mass of electrons at the bottom of the conduction band in InSb is only $0.013(\pm 0.001)m_0$ [11.143]. This very small effective

mass means that the band has very high curvature and very low density of states at its minimum. As a result a small number of electrons fill the band to high energy levels [11.143]. Hence material becomes degenerate at relatively low electron densities and the height of the Fermi level above the bottom of the conduction band increases rapidly with electron concentration. At a temperature T the conduction band is filled up to a level which is about $4k_B T$ below the Fermi level, so that in an impure sample the transitions are to a level well above the bottom of the conduction band. In this case the optical energy gap increases with electron concentration as

$$\Delta E = \Delta E_0 + \left(1 + \frac{m_e}{m_h}\right)(\zeta - 4k_B T), \quad (11.8)$$

where ζ is the height of the Fermi level above the bottom of the band and ΔE_0 is the difference between the conduction-band minimum and the valence-band maximum. A striking property of electrons in the conduction band of indium antimonide is their very large magnetic moment, which is a consequence of interaction between the conduction and valence bands [11.145]. The g factor can be evaluated from

$$g = 2 \left[1 - \left(\frac{m_0}{m_e} - 1 \right) \left(\frac{\Delta}{3E_g + 2\Delta} \right) \right], \quad (11.9)$$

where Δ is the spin–orbit interaction and E_g is the energy gap. The measured g values decrease from -50.7 for $2 \times 10^{14} \text{ cm}^{-3}$ to -48.8 for $3 \times 10^{15} \text{ cm}^{-3}$ electron concentration. The theoretical work on InSb suggests the existence of three valence bands: a *heavy-hole* band V_1 , a *light-hole* band V_2 , degenerate with V_1 at $\mathbf{k} = 0$, and a band V_3 due to spin–orbit coupling (Fig. 11.20a).

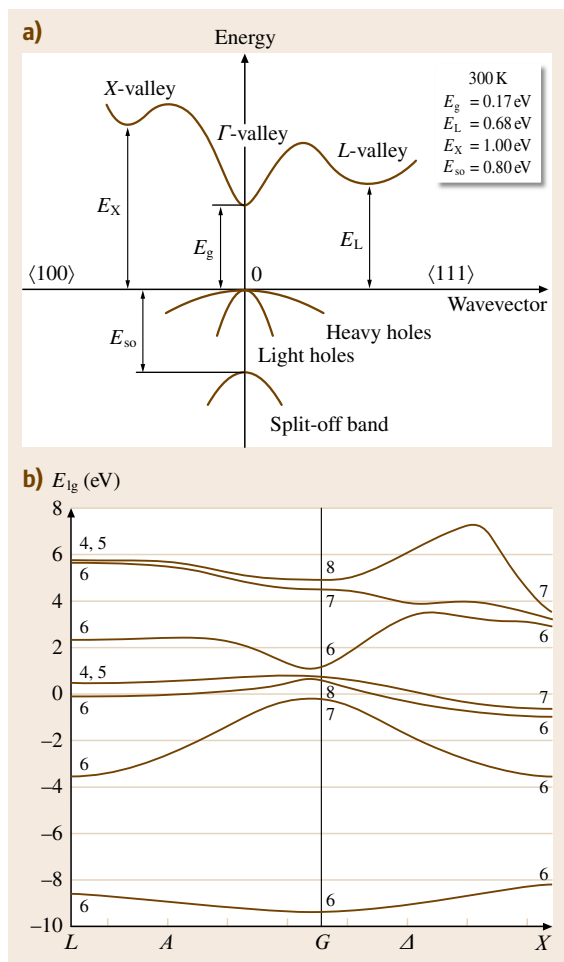


Fig. 11.20a,b Band structures of (a) InSb and (b) InBiSb (after [11.149])

The effective mass of the heavy hole lies in the range $0.55m_0 < m_h < 0.72m_0$ and that of the light hole is $0.015m_0$. The spin-orbit splitting of the valence band is estimated to be about 0.8 eV. The maximum of the valence band is not exactly at $k = 0$ but is displaced in the $\langle 111 \rangle$ direction, although it is difficult to resolve this displaced maxima experimentally because of the small energy (10^{-4} eV). Since the momentum offset is so small in InSb it behaves as a direct-gap semiconductor. Magnetoresistance measurements have been used to measure the shape of the valence band [11.146]. The band structure for $\text{InAs}_x\text{Sb}_{1-x}$ has also been studied within the framework of $k \cdot p$ theory and using this the variations of effective masses and g factor with composition were reported. By modifying the $k \cdot p$

theory and taking into account a multiband approximation as well as modified matrix elements the precise values of m and the g factor were obtained by *Hermann and Weisbuch* [11.147]. Furthermore, spin-orbit splitting of $\text{InAs}_x\text{Sb}_{1-x}$ has been studied by several authors [11.147, 148]. They reported values quite different from those calculated by a virtual-crystal approximation in which fluctuations in the crystal potential had been neglected. However, for very small values of x ($0 < x < 0.07$) both give similar values.

The band structure of $\text{InBi}_x\text{Sb}_{1-x}$ has been studied extensively by *Vyklyuk et al.* [11.149]. They calculated the electronic band structure of $\text{InBi}_x\text{Sb}_{1-x}$ for $x = 0.05$ using a local empirical pseudopotential with spin-orbit interaction in the virtual-crystal approximation (Fig. 11.20b). Utilizing this band structure they calculated the absorption coefficient, which closely matches experimental values.

11.7.2 Transport Properties of InSb, $\text{InAs}_x\text{Sb}_{1-x}$, and $\text{InBi}_x\text{Sb}_{1-x}$

InSb

Intrinsic carrier concentration is of fundamental importance for semiconductors and their application in devices. Knowledge of the intrinsic carrier concentration should help in understanding the performance of detectors. At moderate carrier densities, the degeneracy in InSb varies considerably in the temperature range of measurements [11.150]. This has a significant effect in determining the temperature dependence of transport properties. At room temperature, the intrinsic carrier density in InSb is $\approx 2.02 \times 10^{16} \text{ cm}^{-3}$, which is often larger than the background doping. Therefore, even in n-type doped samples, transport experiments must be considered in the light of ambipolar conduction [11.151]. Figure 11.21 shows a plot of the intrinsic carrier concentration n_i as a function of temperature. Since the heavy holes are ≈ 50 times heavier than the light holes (which have almost the same effective mass as the conduction electrons) they have a correspondingly larger relative population density at a given temperature. The purest InSb crystals reported contained less than 10^{13} donors/ cm^3 [11.152], but most of the information available on electrical properties refers to crystals with impurity concentration greater than 10^{14} cm^{-3} . The Hall coefficient in n-type samples varies little with temperature below 100 K. Above 150 K the purest sample is intrinsic. In n-type InSb the donor levels are merged with the conduction band, and at temperatures below the intrinsic range,

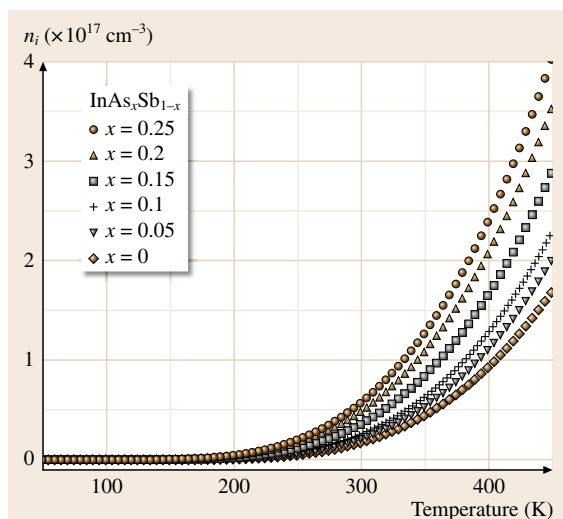


Fig. 11.21 Calculated intrinsic carrier concentration in InSb and $\text{InAs}_x\text{Sb}_{1-x}$ as a function temperature

the concentration of conduction electrons does not decrease with temperature. Thus at this point material behaves like a metal, with few charge carriers of high mobility.

The temperature dependence of conductivity and Hall data were reported by many groups [11.153–155]. Vinogradova and coworkers [11.156, 157] have reported room-temperature mobilities higher than $100\,000\text{ cm}^2/(\text{V s})$ in specimens with donor concentration of 10^{13} cm^{-3} . A more likely value for samples with donor concentration lower than $5 \times 10^{14}\text{ cm}^{-3}$ is 78 000 or 65 000, where the Hall factor (r_H) is taken as 1 or $\frac{3}{8}\pi$, respectively. The highest value reported for electron mobility at 77 K is $1.1 \times 10^6\text{ cm}^2/(\text{V s})$ for samples with donor concentration of $8 \times 10^{12}\text{ cm}^{-3}$ [11.152]. The highest reliable hole mobility value at room temperature is $750\text{ cm}^2/(\text{V s})$ and that at 77 K is $10\,000\text{ cm}^2/(\text{V s})$. The mobility ratio (b) is also temperature dependent and for pure specimens is $\approx 6.3 T^{1/2}$ above 250 K. At room temperature b is just 100. In impure specimens b is rather lower because the mobility of electrons is affected more than that of holes by impurity scattering. Madelung and Weiss [11.158] using resistivity data measured the thermal energy gap in InSb at 0 K to be 0.265 eV. Hrostowski et al. [11.153] also estimated it to be between 0.26 and 0.29 eV. Recently Bansal and Venkataraman [11.151] probed the effect of Landau level formation on the population of intrinsic electrons in InSb near room temperature in magnetic fields up to 16 T. Although the measured magnetic field

dependence of the Hall coefficient is qualitatively similar to the published results, it is shown that the data may also be explained by simply including ambipolar conduction. Thus, the inference on band depopulation drawn from previous measurements on InSb is inconclusive unless both the Hall and magnetoresistive components of the resistivity tensor are simultaneously measured and modeled. When the model includes both depopulation and ambipolar conduction, reasonable agreement with theory can be achieved. Drachenko et al. [11.159] experimentally reevaluated the effective mass of electron in InSb for two different g -factor values. It was found that the effective mass m_e was equal to $0.0127m_0$ at 80 K for $g = 54$. On the other hand, taking the experimental value of g -factor reported by Miura et al. [11.160] as 70, m_e was evaluated as

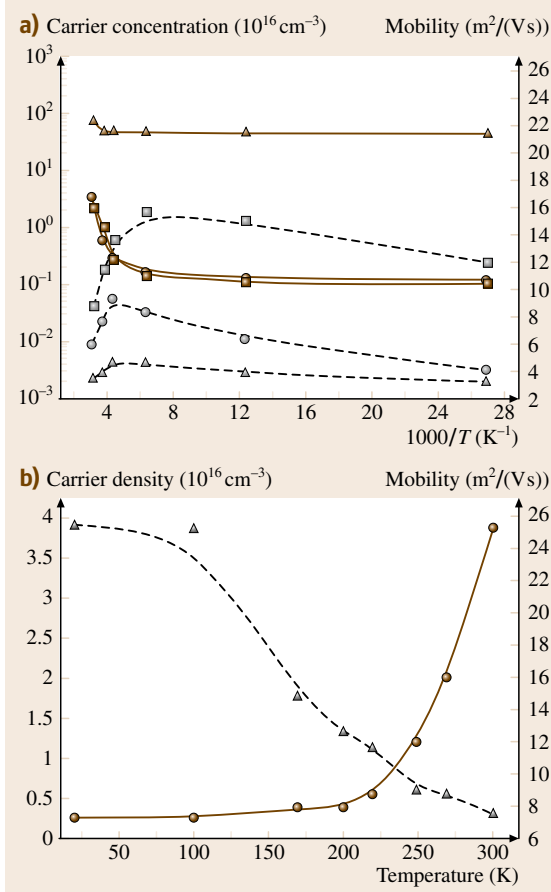


Fig. 11.22 (a) Hall data for InSb wafers grown from starting materials of different purity and (b) temperature-dependent Hall data of high-quality InSb wafer

0.0133 m_0 , which is very close to the recommended value (0.0135 m_0) for InSb at helium temperatures. A very comprehensive account of band structure effects and transport calculations in narrow-gap semiconductors can be found in the book by Nag [11.161] and review articles by Zawadzki [11.162]. Recently Bansal and Venkataraman [11.151] and Dixit et al. [11.10, 115] have reported transport properties of these materials in both the bulk and epitaxy forms. Strong effects of impurities in the starting materials on carrier density variation as a function of temperature have been noticed (Fig. 11.22a) [11.115]. The bulk InSb sample may be taken as a reference against which the effects of epitaxy and alloying can be compared. The temperature dependence of the measured carrier concentration and mobility for a bulk InSb sample is shown in Fig. 11.22b. The background doping of bulk InSb is a reasonable indicator of its properties. The low-temperature mobility and carrier concentration of bulk sample were at least an order of magnitude better than those of InSb epitaxial films grown from starting materials of the same purity (5 N).

InAs_xSb_{1-x}

Apart from disorder contributions, transport in InSb–InAs alloys may also be treated in a similar way to that of InSb. Only the band parameters, viz. the energy gap, the spin–orbit splitting, the effective masses, and phonon energies, need to be suitably determined at a given alloy concentration. For this the simplest method has been suggested by van Vechten [11.148] in a disordered virtual-crystal model for his quantum dielectric theory [11.163]. The first calculation of the intrinsic carrier concentration in InAs_xSb_{1-x} was carried out by Rogalski and Jozwikowski [11.18], who used a three-band approximation of $\mathbf{k} \cdot \mathbf{p}$ theory. The intrinsic carrier concentration and the reduced Fermi energy were calculated for InAs_xSb_{1-x} with $0 \leq x \leq 1$ and $50 \text{ K} \leq T \leq 300 \text{ K}$. By fitting the calculated non-parabolic n_i values to the expression for parabolic bands, the following equation for the intrinsic carrier concentration has been obtained

$$n_i = (1.35 + 8.50x + 4.22 \times 10^{-3}T - 1.53 \times 10^{-3}xT - 6.73x^2)T^{3/2}E_g^{3/4} \times \exp\left(\frac{-E_g}{2k_B T}\right) 10^{14}. \quad (11.10)$$

The calculated intrinsic carrier concentration in InAs_xSb_{1-x} (for lower values of As) as a function of temperatures has already been shown in Fig. 11.21.

As can be seen from Fig. 11.21, with increasing arsenic content the intrinsic carrier density increases. The conduction-band effective mass m_e was determined by Berolo et al. [11.164] for the whole range of compositions. The resultant conduction band effective mass m_e was given as

$$\frac{1}{m_e(x)} = \frac{1}{m_{ce}} + \frac{\delta E}{3} \left[\frac{1}{m_{hh}E_{gv}} + \frac{1}{m_{lh}E_{gv}} + \frac{1}{m_s(E_{gv} + \Delta_v)} - \frac{1}{m_{ce}} \left(\frac{2}{E_{gv}} + \frac{1}{E_{gv} + \Delta_v} \right) \right]. \quad (11.11)$$

In order to determine $m_e(x)$, all the parameters of above equation should be known. Here the difference $\delta E = E_{gv} - E_g$ is determined by the effects of the aperiodic potential due to disorder. E_{gv} and Δ_v are obtained

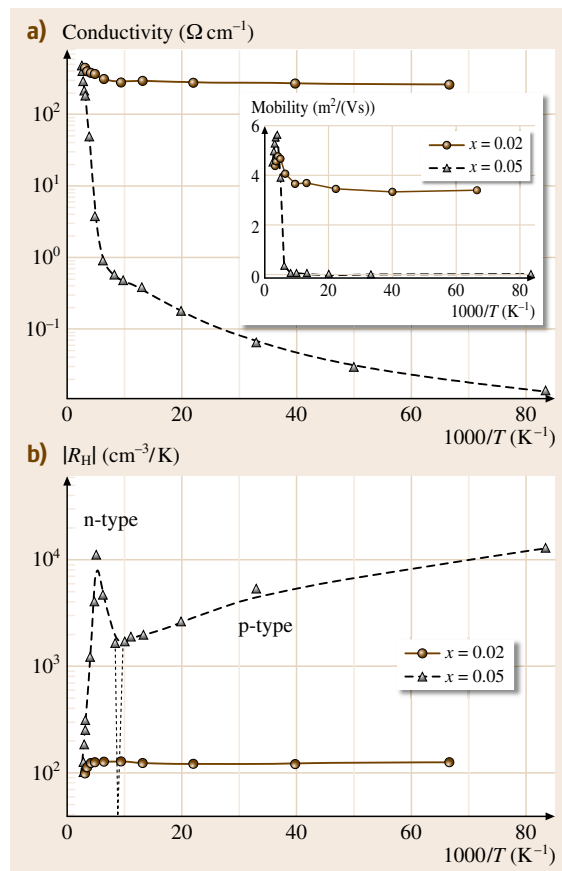


Fig. 11.23a,b Temperature dependence of (a) conductivity and mobility (inset) of InAs_xSb_{1-x} and (b) Hall coefficient

using the virtual-crystal approximation (VCA), which can be approximated by the expressions $E_{gv} = 0.351 - 0.0176x$ and $\Delta_v = 0.39 - 0.42x$ at 300 K. m_{lh} and m_{hh} are the light- and heavy-hole effective masses and m_{ce} is the effective mass for the conduction band in the absence of conduction–valence band mixing.

Resistivity and low-field (< 0.2 T) Hall coefficient for $\text{InAs}_x\text{Sb}_{1-x}$ samples with $x = 0.02$ and 0.05 were reported between 12 and 300 K [11.9]. The room-temperature (RT) mobility in the samples for $x = 0.02$ was $4.5 \times 10^4 \text{ cm}^2/(\text{V s})$ and that for $x = 0.05$ was $5.6 \times 10^4 \text{ cm}^2/(\text{V s})$. All samples with $x = 0.02$ were n-type and showed intrinsic behavior above ≈ 250 K. The representative results for $x = 0.02$ samples shown in Fig. 11.23a and b give a RT carrier concentration of $6.4 \times 10^{16} \text{ cm}^{-3}$ and a background doping of $5 \times 10^{16} \text{ cm}^{-3}$. On the other hand $\text{InAs}_{0.05}\text{Sb}_{0.95}$ shows a type conversion from n to p at 110 K. Below 77 K, the Hall coefficient and resistivity did not saturate and the conductivity below 30 K was strongly activated, indicating the presence of trap states. Further evidence of their presence is given by the pronounced tail in the absorption edge for this sample (as discussed in the next section). The hole mobility continuously dropped with decreasing temperature to $175 \text{ cm}^2/(\text{V s})$ at 15 K.

$\text{InBi}_x\text{Sb}_{1-x}$

Akchurin et al. [11.67] carried out experimental investigation on the behavior of Bi in $\text{InBi}_x\text{Sb}_{1-x}$ solid

solutions. It was found that bismuth doping in InSb strongly increases the electron density, which is due to the formation of Bi donor level [11.67]. An x-ray structure investigation indicated that this level is due to a complex state of Bi in the InSb lattice, representing a simultaneous combination of the substitutional and interstitial components. In the entire range of composition $\text{InBi}_x\text{Sb}_{1-x}$ shows n-type behavior. The electron mobility of $\text{InBi}_x\text{Sb}_{1-x}$ films decreases as the Bi concentration increases. This decrease of mobility is attributed to random alloy scattering [11.67]. The temperature dependence of resistivity also reveals the donor nature of Bi in $\text{InBi}_x\text{Sb}_{1-x}$ [11.67]. Dixit et al. [11.12] also showed the donor nature of Bi in $\text{InBi}_x\text{Sb}_{1-x}$ system.

InSb , $\text{InAs}_x\text{Sb}_{1-x}$, and $\text{InBi}_x\text{Sb}_{1-x}$ Grown on GaAs

For these materials, the unintentional background doping levels for the epitaxial layers were all similar, at around $\approx 10^{16} \text{ cm}^{-3}$, almost an order of magnitude higher than that in pure bulk InSb prepared under similar conditions. The mechanism for this unintentional n-type doping is not clear, although material contamination during growth (or use of the starting material of lower purity [11.115]) was seen to increase the background doping levels and reduce the mobility (Fig. 11.24). The room-temperature mobility is $30\,000$ – $50\,000 \text{ cm}^2/(\text{V s})$ for InSb, $\text{InAs}_x\text{Sb}_{1-x}$, and $\text{InBi}_x\text{Sb}_{1-x}$ epilayers when grown from starting materials of the same purity (5 N). At around 275 K, the number of thermally generated electron–hole pairs become comparable to this background doping level and therefore the carrier concentration shows an activated behavior above this temperature. The activated region, when fitted to a relation $n_i = AT^{3/2} \exp(-E_g/2k_B T)$, yielded zero-temperature energy gap values of 0.23, 0.20, and 0.19 eV for InSb, $\text{InAs}_{0.06}\text{Sb}_{0.94}$, and $\text{InBi}_{0.04}\text{Sb}_{0.96}$, respectively, in reasonable agreement with more precise estimation from optical measurements (described in the next section). A comparison with published results indicates that both the carrier density and the mobility match with the results published on InSb, $\text{InAs}_x\text{Sb}_{1-x}$, and $\text{InBi}_x\text{Sb}_{1-x}$ epitaxial layers on GaAs, grown by MBE or MOCVD. Since between 10 and 250 K, an anomaly was observed in the carrier concentration for all the epitaxial layers, the measured Hall coefficient (R_H) showed a maximum at some intermediate temperature. In the past this has been attributed to multicarrier conduction, with contributions from interfacial, bulk, and possibly a sur-

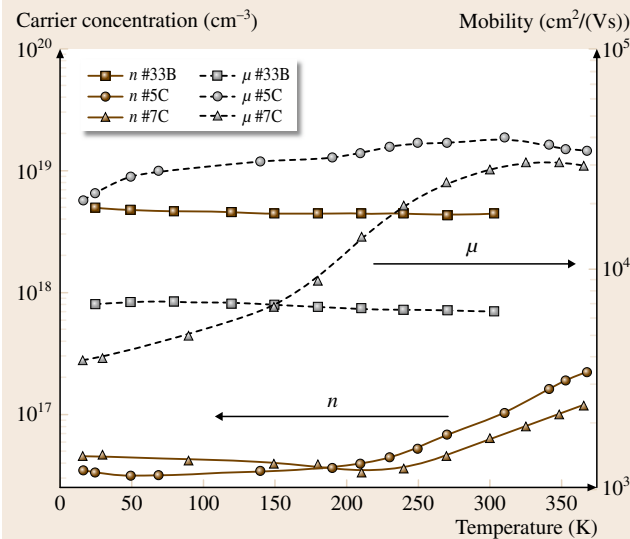


Fig. 11.24 Temperature dependence of carrier concentration and mobility of InSb/GaAs

face layer, each with a different mobility, separately contributing to the total conductivity. However, LPE-grown epilayers are relatively thick and the observed properties did not correlate with film thickness. An

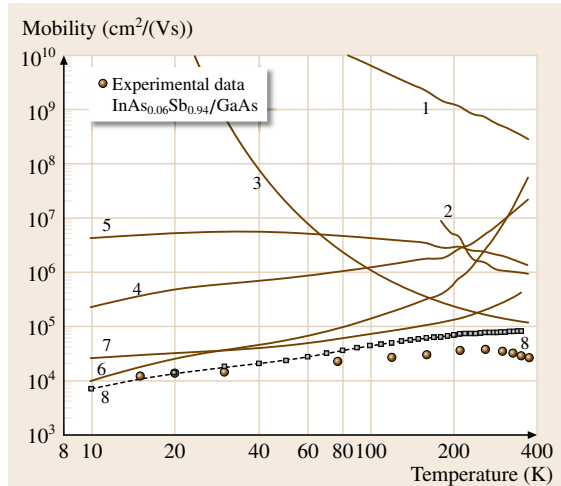


Fig. 11.25 Calculated temperature dependence of mobility due to various scattering mechanisms for $\text{InAs}_{0.06}\text{Sb}_{0.94}/\text{GaAs}$. (1) Acoustic phonon, (2) electron-hole, (3) polar optical, (4) ionized impurity, (5) alloy, (6) charged dislocation, (7) strain in dislocations, and (8) experimental data points

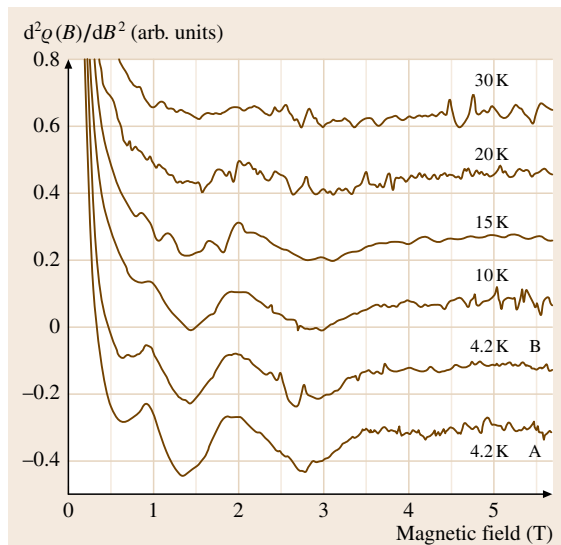


Fig. 11.26 Second derivative of the magnetoresistance signal of $\text{InAs}_{0.06}\text{Sb}_{0.94}$ measured at different temperatures. The electric field in B is twice that in A

alternative explanation in terms of variation of Hall factor (r_H) with the sample temperature and hence its degeneracy is more appropriate in this case. The Hall factor is exactly unity for a strongly degenerate sample but can take a larger value in nondegenerate samples, especially when long-range scattering potentials are active in limiting the sample mobility (e.g., $r_H = 1.93$ for ionized impurity scattering). The Hall factor for a partially degenerate gas, as in this case, can increase the measured Hall coefficient by $\approx 10\%$, which could explain the anomaly seen at most temperatures. The calculated temperature dependence of mobility due to various scattering mechanisms is shown in Fig. 11.25.

Magnetoresistance measurements were performed on $\text{InAs}_x\text{Sb}_{1-x}/\text{GaAs}$ by Bansal et al. [11.6]. The magnetoresistance signal starts as quadratic initially and becomes linear at higher magnetic fields (B), which is the expected behavior in the extreme quantum regime (Fig. 11.26). There was no magnetic-field-induced freeze-out observed at 4.2 K since, at background carrier densities of $\approx 10^{16} \text{ cm}^{-3}$, the impurity-band wavefunctions, even at 6 T magnetic field, have a spatial extent larger than the interimpurity separation because of the very small effective mass. There was no appreciable change in resistance or magnetoresistance between 4.2 and 30 K, again indicating that parallel conduction effects are not important since these are known to give an appreciable temperature dependence. Unlike in metals, the oscillations are not periodic in $1/B$ because of a considerable magnetic field dependence of the Fermi energy and unequal Landau level spacing due to nonparabolic energy dispersion. The amplitude of oscillations is extremely sensitive to sample homogeneity and therefore, although the $\mu B > 1$ condition was easily met, the oscillation amplitudes were small. This was the first time a Shubnikov signal in InAsSb has been observed. These results were further investigated in detail by Drachenko et al. [11.159], who reported the first experimental data for the calculation of the effective mass for $\text{InAs}_x\text{Sb}_{1-x}$. Using the expression for $E_g(T, x)$ in $\text{InAs}_x\text{Sb}_{1-x}$ alloys, they obtained m_e of $0.0122m_0$ and $0.0117m_0$ for $\text{InAs}_{0.04}\text{Sb}_{0.96}$, and $\text{InAs}_{0.06}\text{Sb}_{0.94}$ respectively.

$\text{InBi}_x\text{Sb}_{1-x}$ and $\text{InBi}_x\text{As}_y\text{Sb}_{1-x-y}$ also show n-type behavior over the entire temperature range. The maximum electron mobility was $3.54 \times 10^4 \text{ cm}^2/(\text{V s})$ and carrier concentration was $9.2 \times 10^{16} \text{ cm}^{-3}$ at 300 K for $\text{InBi}_x\text{Sb}_{1-x}$. Similarly $\text{InBi}_x\text{As}_y\text{Sb}_{1-x-y}$ has maximum electron mobility of $3.1 \times 10^4 \text{ cm}^2/(\text{V s})$ and carrier concentration of $8.07 \times 10^{16} \text{ cm}^{-3}$ at 300 K [11.8, 123].

11.7.3 Optical Properties of InSb, InAs_xSb_{1-x}, and InBi_xSb_{1-x}

The interest in antimonides is (to a large extent) because their energy gap is in the infrared. Optical properties of InSb have, of course, been long studied and are well understood [11.165, 166]. This section extends the studies to optical properties to determine the effect of alloying and heteroepitaxy on them.

InSb

In InSb, as the photon energy decreases past the value corresponding to the energy gap (0.17 eV), transmission shows a sudden increase until saturation, after which it remains constant or oscillatory (depending on the scattering process). From the position and shape of this *absorption edge* we obtain information on the nature of transition from valence band to conduction band. With further lowering of the photon energy (0.14 eV) the optical properties are affected by interaction between the photons and free carriers, and resulting transition takes place within the valence or the conduction bands. At still lower energy (0.09 eV) there can be interaction between photons and the lattice. The optical properties in this region are influenced both by the lattice and the free carriers and are being studied using Raman spectroscopy. The absorption edge of InSb is extremely steep and the absorption coefficients change by two orders of magnitude within a range of 0.01–0.04 eV. The position of the absorption edge will be dependent on pressure since compression of the lattice also changes the energy gap. The dimensions of the lattice also change when temperature is altered, but here there is an additional effect on the optical properties because the change in lattice vibration affects the width of the energy levels.

The wavelength dependence of free carrier absorption is therefore dependent on the scattering mechanism. At temperatures at which $k_B T \gg h\nu$, the square-law dependence is applicable for both acoustic and nonpolar optical scattering. When photon energy is greater than $k_B T$, the absorption is proportional to $\lambda^{3/2}$ for acoustic scattering but for optical scattering the dependence is more complicated. For impurity scattering, the absorption coefficient (α) is proportional to λ^3 . Kurnick and Powell [11.167] found that in InSb the free electron absorption had a λ^2 dependence, but the free-hole absorption was independent of wavelength. At 9 μm , the free-electron optical cross section ($= \alpha/n$) is $2.3 \times 10^{-17} \text{ cm}^2$ but the hole cross section is 40 times larger. The electron cross section is in good agreement with the theoretical value [11.167]. Measurements by Spitzer and Fan [11.168] on n-type InSb were extended to 35 μm and their results show that the square-law dependence is not obeyed at wavelengths longer than 12 μm . However, Moss [11.169] pointed out that the refractive index of InSb is not constant in this wavelength region. This theory gives the wavelength dependence of the product $\eta\alpha$ (where η is refractive index), and if the results of Spitzer and Fan are used in conjunction with

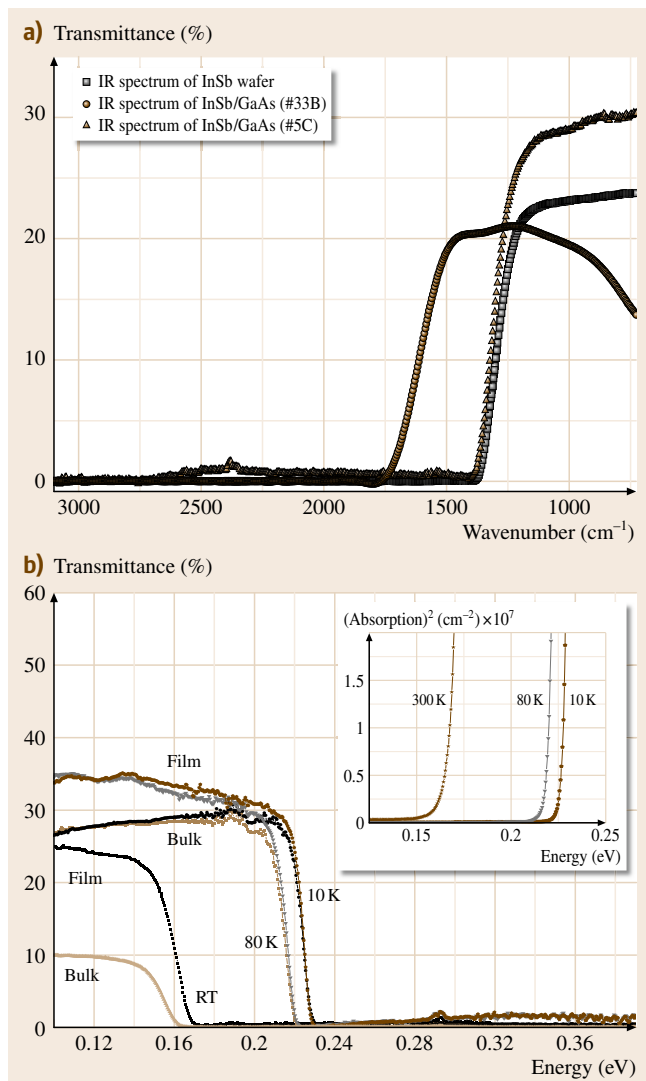


Fig. 11.27a,b Infrared spectra of InSb wafer and InSb/GaAs at (a) room temperature (b) different temperatures. The inset shows absorption squared versus energy plots at different temperatures

refractive index values, it is found that the product $\eta\alpha$ is proportional to λ^2 .

Recently Dixit et al. [11.115] observed that the absorption edge is shifted from the expected value towards higher energy to a different extent depending on the purity of the starting materials (Fig. 11.27a) similar to other report in literature [11.170]. Hence it is clear that the energy gap of InSb is very sensitive to impurities. The temperature dependence of the absorption edge is not significant for heavily doped materials because the Fermi level lies inside the conduction band. On the other hand the absorption edge for moderately doped or undoped InSb is very sensitive to temperature, as shown in Fig. 11.27b. The absorption coefficient was calculated from the transmission T , using the well-known expression that accounts for multiple reflections within the sample, viz. $T = ((1 - R)^2 e^{-\alpha d}) / ((1 - R)^2 e^{-2\alpha d})$. Here d is the thickness of the sample and $R = 0.4$ is the reflection coefficient, assumed to be constant in the spectral range of measurement. This equation is easily inverted by substituting $z = e^{-\alpha d}$ and then solving the quadratic equation in z . The energy gap, E_g , was obtained by fitting $\alpha = A(h\nu - E_g)^{1/2}$, to the experimental data around the absorption edge. Here α is the absorption coefficient in cm^{-1} , ν is the incident photon frequency, and A is a constant depending on the electron and hole effective masses and the optical transition matrix elements. The onset of absorption fits very well to the above relation, indicating a direct energy gap (inset of Fig. 11.27b). The energy gap was measured to be 0.172, 0.225, and 0.235 eV for RT, 80, and 10 K, respectively. The analysis of the temperature dependence of E_g is usually done by a three-parameter fit to Varshni's empirical relation [11.171], $E_g(T) = E_{gv}(0) - (\alpha T^2)/(\beta + T)$, where α and β are constants and $E_{gv}(0)$ is the energy gap at zero temperature. The energy gap of a semiconductor varies with temperature due to three distinct effects attributable to phonons [11.172]. These, all of similar importance, are the anharmonic (thermal expansion) and harmonic (Debye–Waller factor) phonon effects, and the temperature-dependent renormalization of the gap due to the electron–phonon self-energy correction (Fan's term). The value of the energy gap at different temperatures and the least-square fits to the above equation show good agreement. The fits yield $E_{gv}(0)$, α , and β as 0.235 ± 0.003 eV, $3.1 \pm 1.1 \times 10^{-4}$ eV/K, and 452 ± 190 K, respectively. These values and the temperature dependence of the energy gap are very similar to previous results [11.170], although these measurements were on wafers made from large-size crystals.

InAs_xSb_{1-x}

Woolley and Warner [11.13] carried out optical studies on InAs_xSb_{1-x} samples made by directional freeze and zone recrystallization methods. Although the energy values are determined on crudely prepared single crystal and polycrystals, the variation of energy gap with composition and temperature is reliable. The room-temperature values of E_g have been determined over the whole composition range. It is found that E_g falls as one compound is added to the other, the measured value of E_g reaching a minimum of 0.10 eV at approximately 60 mol % InSb. The variation of optical energy gap with alloy composition at room temperature has already been shown in Fig. 11.1a. For alloys near the center of the composition range the energy gap reduces. Due to the smaller energy gap and larger carrier concentration these alloys become degenerate at room temperature and hence the Fermi level goes into the conduction band. Thus the actual energy gap for the compounds in the intermediate range may in fact be smaller than the measured value because of the Moss–Burstein effect. The bandgap bowing in alloy systems has been explained by virtual-crystal analysis [11.173]. The energy gap variation in InAs_xSb_{1-x} as a function of x is given as

$$E_g(x, T) = 0.434 - 0.771x + 0.59x^2 - 2.8 \times 10^{-4}T \text{ [eV]}. \quad (11.12)$$

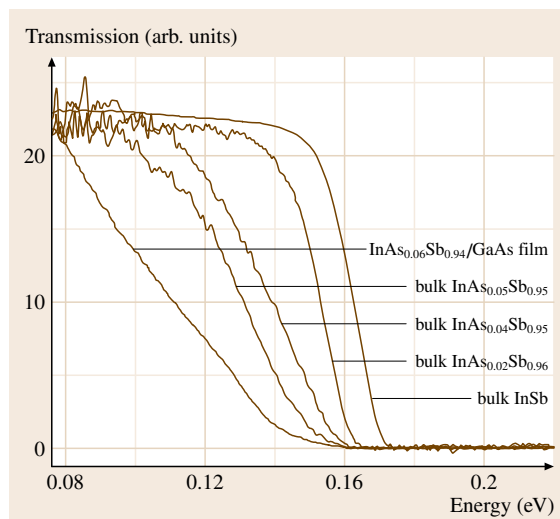


Fig. 11.28 Room-temperature transmission spectra of InAs_xSb_{1-x} for various x values up to 0.6

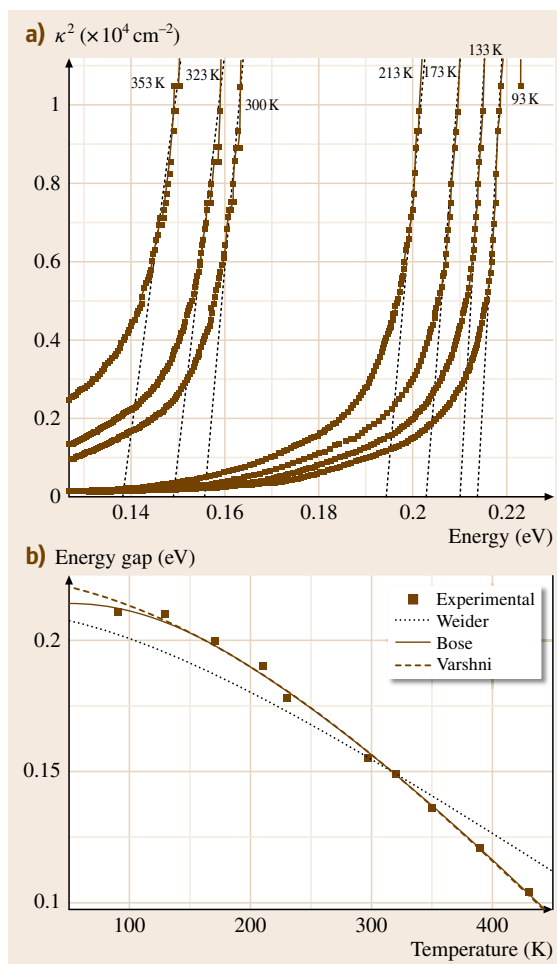


Fig. 11.29 (a) Plots of absorption squared versus energy for $\text{InAs}_x\text{Sb}_{1-x}$. Straight lines imply a direct bandgap. (b) Temperature dependence of energy gap. Data fitted to equations of Bose and Varshni. Wieder and Clawson's formula is also plotted (after [11.176])

The absorption edge shifts to lower energy for $\text{InAs}_x\text{Sb}_{1-x}$ as x increases. The room-temperature transmission spectra for $\text{InAs}_x\text{Sb}_{1-x}$ as a function of x are shown in Fig. 11.28. The value of the energy gap was evaluated to be 0.17, 0.16, and 0.15 eV for $x = 0, 0.02$, and 0.05, respectively. The temperature dependence of the energy gap and free carrier absorption in a high-quality $\text{InAs}_{0.05}\text{Sb}_{0.95}$ single crystal were also studied between 90 K and 430 K through the absorption spectra [11.7] (Fig. 11.29a). The value of the energy gap at different temperatures along with the least-square fits to the above equation

as well as Bose ($E_g(T) = E_{g\text{BE}}(0) - 2a_B/(\exp(\theta_{\text{BE}}/T) - 1)$ [11.174, 175]) and Varshni ($E_g(T) = E_{g\text{v}}(0) - (\alpha T^2)/(\beta + T)$) equations are shown in Fig. 11.29b. The fits yield $E_{g\text{v}}(0)$, α , and β as 0.223 ± 0.003 eV, $7.1 \pm 2.3 \times 10^{-4}$ eV/K, and 675 ± 370 K, respectively. For $E_{g\text{BE}}(0)$, $2a_B$, and θ_{BE} the values are 0.214 ± 0.002 eV, 0.107 ± 0.01 eV, and 466 ± 46 K, respectively. It can be seen that the Bose and Varshni equations give nearly identical fits for $T > 125$ K (Fig. 11.29b). Below 125 K the Bose fit is better, as is usually the case. The value of $E_{g\text{BE}}(0)$ agrees with the relation $E_{g(0)} = 0.4324 - 0.8831(1-x) + 0.6853(1-x)^2$, which gives $E_{g(0)} = 0.212$ eV for 5 at. % arsenic. Through measurements on flash-evaporated films and using data from other groups, Wieder and Clawson [11.176] fitted the energy gap to the above equation. Owing to its inherent appeal and widespread use, this equation is also plotted in Fig. 11.29b, although the agreement is not good except at room temperature. Bansal et al. [11.7] showed that on the low energy side (< 100 meV) free electrons become the dominant source of absorption for $\text{InAs}_{0.05}\text{Sb}_{0.95}$. Due to the vast difference in strength, the contributions of band-to-band transitions and free carrier absorption (FCA) can be separated by a minimum in absorption which occurs at an intermediate energy. The temperature dependence of the absorption coefficient as a function of wavelength (14–25 μm) is shown in Fig. 11.30a. The studied sample was p-type at low temperatures and hence the FCA increased around RT when the sample became intrinsic and the Hall coefficient changed sign. Absorption below room temperature due to holes was too weak to be resolved from the higher-order interband absorption background because of their much larger effective mass. Using the value of the carrier concentration of this sample at 300 K, the FCA cross section was measured to be $7.35 \times 10^{-16} \text{ cm}^2$ at 15 μm . The curves in the figure can be fitted to a power law of the form $\alpha = k\lambda^p$. The experimentally determined value of the exponent p is ≈ 1.5 near room temperature and is the one theoretically expected for acoustic-phonon-assisted FCA. The FCA exponent shows a steady drop with increasing temperature above 300 K; several reasons have been given for this. Firstly, above 350 K, there is an enhanced probability for second-order interband transitions accompanying the abrupt increase in the optical phonon occupancy (optical phonon energy 300 K). These broaden the absorption edge by ≈ 25 meV and overlap with FCA, making the total absorption curve flatter and extraction of the exponent unreliable. Secondly, beyond 400 K, where the pho-

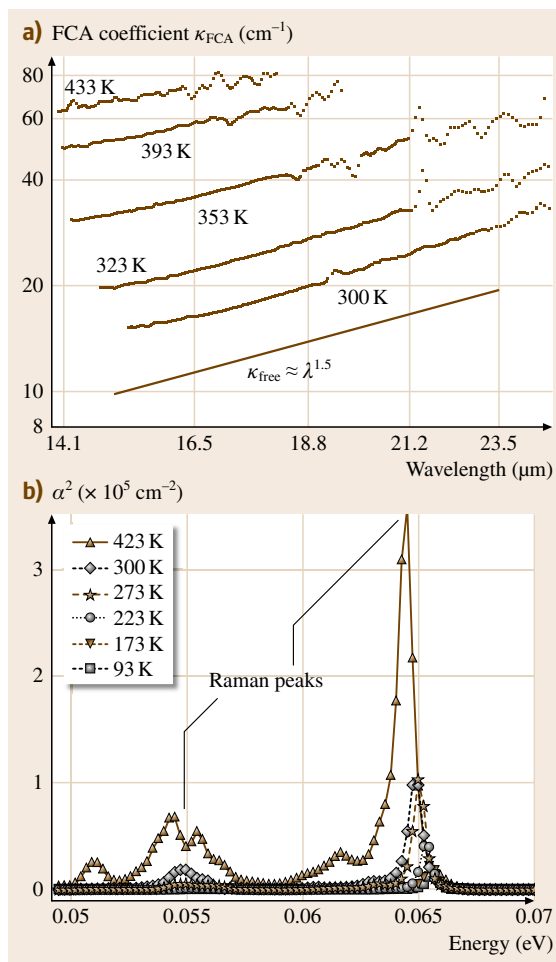


Fig. 11.30 (a) FCA spectra of $\text{InAs}_{0.06}\text{Sb}_{0.94}$ at different temperatures. Also $\kappa_{\text{FCA}} \approx (\lambda)^{1.5}$ is plotted for comparison (after [11.7]) (b) Raman peaks of $\text{InAs}_{0.06}\text{Sb}_{0.94}$ at different temperatures (after [11.5])

ton energy is $\approx 2k_{\text{B}}T$, classical analysis may become applicable. This, when accompanied by an increase in the optical phonon occupancy, could also lead to a sharp drop in the value of the relaxation time, τ , due to enhanced electron–optical phonon scattering. As τ reaches close to 10^{-14} s, deviation from the quadratic to a non-power-law behavior is expected, which could also lead to the observed reduction in the value of p . At high temperatures, multiphoton absorption by IR-active lattice modes is significantly enhanced. This is seen as noise in the high-temperature absorption spectra appearing around the second harmonic of the Raman peaks [11.177] (≈ 50 meV) (Fig. 11.30b).

$\text{InBi}_x\text{Sb}_{1-x}$

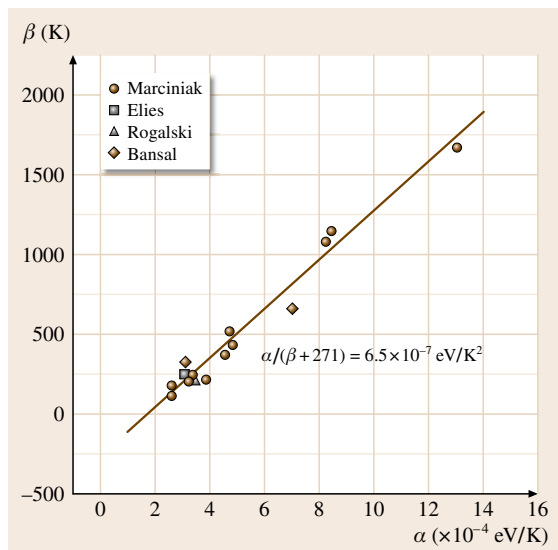
Quantum dielectric theory (QDT) has been used to predict the direct energy gap E_{g} of $\text{InBi}_x\text{Sb}_{1-x}$ semiconductor alloy up to 10 mol % InBi [11.39]. The calculated composition dependence of E_{g} for $\text{InBi}_x\text{Sb}_{1-x}$ is in good agreement with experimental results with a predicted semiconductor–semimetal transition (77 K) at $x = 0.124$. Figure 11.1b shows the E_{g} variation with InBi predicted using QDT for $\text{InBi}_x\text{Sb}_{1-x}$ at 0, 77, and 300 K, along with experimental results. E_{g} (77 K) values corresponding to 8–12 μm are obtained at $x = 0.043$ –0.070. The first-order calculation of E_{g} versus x follows the simple relation E_0 (eV) = $0.23 - 1.85x$ at 77 K. Vyklyuk and coworkers [11.149] have obtained the absorption coefficient of $\text{InBi}_x\text{Sb}_{1-x}$ in 0–10 eV range. The calculation of the absorption coefficient was based on the electron energy of $\text{InBi}_x\text{Sb}_{1-x}$ using a local empirical pseudopotential method with a virtual-crystal approximation including spin–orbital interaction. The energy dependence of the absorption coefficient of $\text{InBi}_x\text{Sb}_{1-x}$ showed an increase with Bi content and a shift in the absorption curve to lower energies [11.149]. The absorption edge of $\text{InBi}_x\text{Sb}_{1-x}$ at RT showed a shift towards lower energy [11.12]. Bandgap as estimated from the IR absorption edge is 0.113 ± 0.009 eV, which is very close to the value obtained from Fig. 11.1b [11.39]. They also noted that the free-carrier absorption was more in $\text{InBi}_x\text{Sb}_{1-x}$ crystal compared with InSb.

InSb, $\text{InAs}_x\text{Sb}_{1-x}$, and $\text{InBi}_x\text{Sb}_{1-x}$ Epilayers Grown on GaAs

Figure 11.27a,b also shows the absorption edge for InSb epitaxial layer at room temperature. The transmission spectra for the bulk and thin film are almost coincident, indicating that disorder effects are not strong enough to affect the optical absorption properties. Therefore, the effect of mismatched epitaxy is not evident in the optical absorption near the energy gap. This is in contrast to transport measurements, where heteroepitaxy was seen to be the most important factor affecting carrier mobility. Temperature-dependent optical absorption edge measurements on heteroepitaxial InSb are also shown in Fig. 11.27b. The difference in the cutoff energies between the spectra at 10, 80, and 300 K clearly shows the nonlinearity of the temperature dependence of the energy gap at low temperatures.

Figure 11.28 shows the transmission spectra measured for $\text{InAs}_x\text{Sb}_{1-x}$ with different alloy concentrations. As expected, the absorption edge clearly shifts to lower photon energies as the composition of arsenic

is increased. There is also an enhanced band tailing as the alloy fraction increases. Such band tails have been previously observed in similar anion-substituted mismatched alloy $\text{InP}_x\text{Sb}_{1-x}$ [11.178], and have been attributed to the formation of localized states as a result of composition fluctuations. It has been argued that composition and strain fluctuations effectively act as quantum wells which can trap electrons. A Gaussian distribution of their widths results in an exponentially decreasing density of localized states below the mobility edge. Recently, similar observations were reported by Gao et al. [11.179] on $\text{InAs}_x\text{Sb}_{1-x}/\text{GaAs}$ ($x < 0.06$) grown using ME. They also explain their results through composition fluctuations. Very recently Bansal et al. [11.180] further studied this and distinguished three absorption region: band to band, Urbach edge, and free-carrier absorption regions. They modeled the Urbach region and determined a structural disorder energy of 30 meV for $\text{InAs}_x\text{Sb}_{1-x}$. The RT energy gap for $\text{InAs}_x\text{Sb}_{1-x}$, calculated by assuming a cutoff at the mid-transmittance wavelength [11.181], is as low as 0.1 eV. However a more reliable estimation, i.e., fitting the absorption coefficient to the relation $\alpha = A(E_g - h\nu)^{1/2}$, gave a value of 0.133 eV for $\text{InAs}_{0.06}\text{Sb}_{0.94}/\text{GaAs}$. Wieder and Clawson's relation [11.176] gives the expected energy gap to be 0.146 eV for $x = 0.06$ at 300 K. Results for the bulk $\text{InAs}_{0.05}\text{Sb}_{0.95}$ sample showed perfect agreement with the above relation. Therefore, the 13 meV discrepancy is either due to error associated with calculating the energy gap (due to band tailing) or to a decrease in the gap due to residual strain. The residual strain, as evaluated from x-ray measurements, corresponds to a shift in the gap, $\Delta E = 2b(C_{11} + 2C_{12}/C_{11})e_{xx}$, where b is the deformation potential, C_{11} and C_{12} are the stress components, and e_{xx} is the in-plane residual strain, which is 0.0184 as evaluated from HRXRD. This yields a splitting energy (ΔE) of 15 meV, which may also explain the difference between the values for bulk and epitaxial $\text{InAs}_x\text{Sb}_{1-x}$. The change in E_g value with temperature for a $\text{InAs}_{0.06}\text{Sb}_{0.94}/\text{GaAs}$ sample along with fits to Varshni's and Bose–Einstein-type relations are also shown in Fig. 11.30. Varshni parameters for this curve are $E_g(0) = 0.193 \pm 0.007$ eV, $\alpha = 3.01 \pm 3.1 \times 10^{-4}$ eV/K, and $\beta = 341 \pm 60$ K. The Bose–Einstein fit yields $E_{g\text{BE}(0)} = 0.19$ eV, $2a_B = 0.051$, and $\theta_{\text{BE}} = 395$ K. The set of Varshni parameters are different from those obtained for bulk crystal. Marciniak et al. [11.182] have suggested a straight-line relationship between α and β , where $\alpha/(271 + \beta) = 6.5 \times 10^{-7}$ eV/K². Both the parameters



controlling the heat flow during growth, are 0.123 and $0.0474 \text{ W cm}^{-1} \text{ K}^{-1}$, respectively [11.185]. The specific heat of the melt and solid InSb are found to be 0.234 and 0.242 J/(g K) , respectively, and the latent heat of fusion of InSb is 108 J/g . Significant thermal param-

eters required for the growth are reported by Duffer et al. [11.94]. Dixon and Furdyna [11.186] reported the static dielectric constant of InSb lattice as 16.8 ± 0.2 . There do not seem to be detailed reports on the thermal properties of other considered alloys.

11.8 Applications

InSb and related crystals are used in many applications. Here we emphasize only infrared detector and galvanomagnetic sensor applications.

Infrared Photodetectors

The properties of InSb as a material for infrared detectors have been extensively discussed for more than 46 years now. At room temperature the intrinsic carrier density in narrow-gap materials is in the range $10^{15} - 10^{17} \text{ cm}^{-3}$ and the thermal generation rate is $10^{23} - 10^{24} \text{ cm}^{-3} \text{ s}^{-1}$. This results in a high noise level in photodetectors at room temperature. Ashley and Elliot [11.187] used *nonequilibrium* operation, which resulted in better detector performance at room temperature. The structure designed to achieve nonequilibrium (higher operating temperature) conditions is $p^+p^+\pi n^+$ or $p^+p^+\nu n^+$, where π and ν refer to intrinsic materials (either p- or n-type), which form an active region, and p^+ refers to wider-bandgap materials. The active region has a low doping level and therefore is intrinsic at RT. The n- and p-type contacts are made to the active region via regions with larger energy gap or higher doping level or both, so that under appropriate bias conditions minimal transport of minority carriers through the active region is ensured. At zero bias, the band structure of the devices ensures little transport of the minority carriers from the contact regions so that additional noise is minimized. The detectivity (D^*) of these devices is $2.5 \times 10^9 \text{ cm Hz}^{1/2} \text{ W}^{-1}$. For certain applications, particularly those requiring low temperature, it is often desirable to narrow the spectral responsivity, thereby increasing the detectivity by reducing the influence of background radiation. This can be achieved either by an external filter or by embodying the filter in the photodetector structure. Djuric et al. [11.188] made use of a remarkable technique which involves self-filtering based on the Moss–Burstein effect. The structure is an $n^+ - p$ -InSb photodiode (p-type InSb wafer and a heavily doped InSb layer using LPE). The quantum efficiency of the Moss–Burstein effect decreases almost linearly with wavelength. This allows approximately constant

sensitivity over a wide range of wavelengths when choosing appropriate material parameters. Later Bloom and Nemirovsky [11.189] concentrated on the fabrication of these detectors by reducing the surface recombination rates. Michel et al. [11.190] also developed InSb photovoltaic structures on GaAs using MBE and demonstrated a near-bulk value for the carrier lifetime in spite of large dislocation densities.

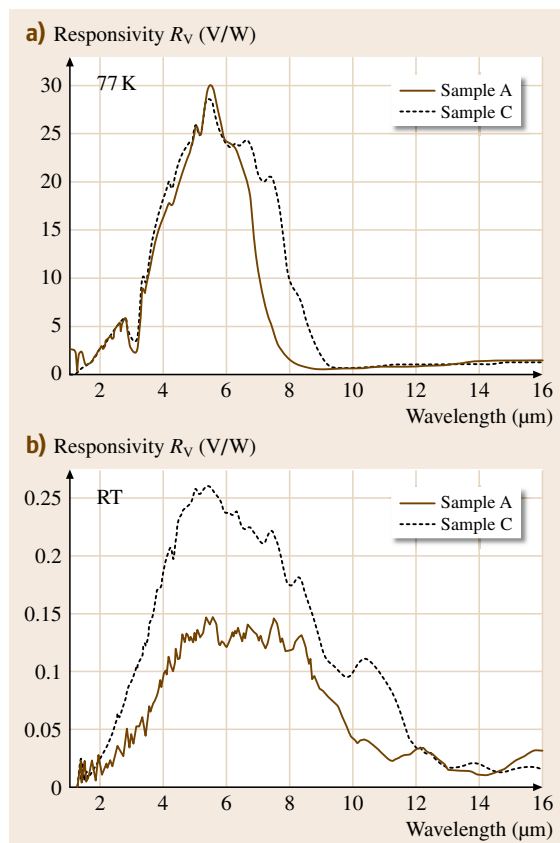


Fig. 11.32a,b Spectral responsivity of the photoconductors fabricated on InAsSb at (a) 77 K and (b) room temperature (after [11.34])

The highest carrier lifetime of 240 ns was reported for an InSb heteroepitaxial structure by these authors. InSb/InAs_xSb_{1-x}/InSb ($p^+ \pi n^+$) photovoltaic devices grown by LP-MOVPE and operated at room temperature in 8–13 μm was reported by Kim et al. [11.3]. Also, better performance was reported for photoconductors developed on p-InAs_xSb_{1-x}/p-InSb/GaAs [11.3]. Very recently Peng et al. [11.34] developed infrared photodetectors in the 8–13 μm range using LPE. They fabricated photoconductors from LPE-grown InAsSb/GaAs, and a notable photoresponse beyond 8 μm was observed at RT. In particular, for InAs_{0.3}Sb_{0.7}/GaAs, a photoresponse up to 13 μm with maximum responsivity of 0.26 V/W was obtained at RT (Fig. 11.32). Hence, InAsSb/GaAs heterostructures grown using LPE demonstrate attractive properties suitable for room-temperature, long-wavelength infrared radiation. Details of the detectors fabricated employing MBE and MOVPE can be found in [11.191, 192].

Galvanomagnetic Applications

The most common, semiconductor-based magnetic field sensors are silicon (Si)-based Hall sensors. In general, the higher the mobility of the semiconductor and the thinner the active region, the better the galvanomagnetic device. The room-temperature mobility of undoped InSb is ≈ 55 times higher than that of Si. Hence InSb should be preferred over Si for use in Hall sensors. In fact, bulk InSb wafers have been used for many years in the fabrication of magnetic field sensors, such as magnetoresistors and Hall sensors. Magnetic field sensors are, in turn, used in conjunction with permanent magnets to make contactless potentiometers and rotary encoders. This sensing technology offers the most reliable way to convert a mechanical movement into an electrical signal, and is widespread in automotive applications. Recent developments in the growth of thin epitaxial layers of InSb on semi-insulating GaAs substrates have resulted in the development of magnetoresistors with excellent sensitivity and operating temperatures up to 285 °C which are also cost effective. Hall sensors and magnetotransistors of thin n-InSb films outperform their Si-based counterparts even with integrated amplification. Oszwaldowski [11.194] also suggested very specific Hall sensors that can be made from heavily doped ($1\text{--}2 \times 10^{18} \text{ cm}^{-3}$) n-type InSb films. with these sensors they could achieve magnetic field sensitivity $\geq 0.05 \text{ V/T}$ and temperature coefficient of the output voltage $\leq 0.01\% \text{ K}^{-1}$, which are very difficult to achieve by any other Hall sensor. Heremans et al. [11.195] and Heremans [11.196] have described

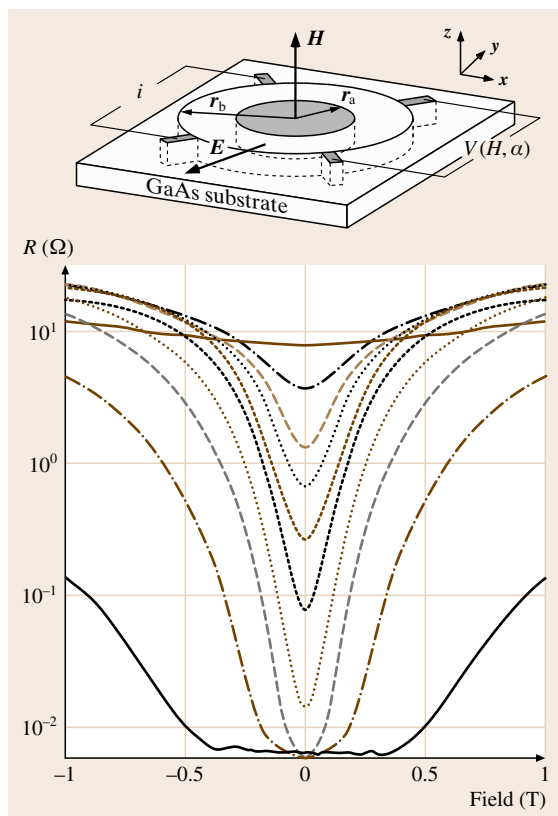


Fig. 11.33 RT resistance up to 1 T of a composite van der Pauw disk (vdP) of InSb and Au for a number of values of $a = 5r_a/r_b$. Inset schematic diagram of a cylindrical Au inhomogeneity (radius r_a) embedded in a homogeneous InSb vdP disk (radius r_b) (after [11.193])

device design criteria, materials requirements, and a direct comparison of the three types of galvanomagnetic devices, and have given the following guidelines for selecting sensors in different applications. According to them, NiFe-based magnetoresistors are preferred for sensing magnetic fields below 0.005 T, typical in magnetic read-out applications; Si Hall sensors with integrated amplification are useful in low-frequency applications in the field range of 0.005–0.03 T; and InSb-based magnetoresistors are most suitable in field ranges above 0.03 T but are not sensitive to the polarity of the field.

Recently Solin et al. [11.193] reported enhanced room-temperature geometric magnetoresistance in homogeneous nonmagnetic indium antimonide with an embedded concentric gold inhomogeneity (Fig. 11.33). The room-temperature geometric magnetoresistance is

as high as 100%, 9100%, and 750 000% at magnetic fields of 0.05, 0.25, and 4.0 T, respectively. They found that for inhomogeneities of sufficiently large diameter relative to that of the surrounding disk, the resistance

is field-independent up to an onset field ≈ 0.4 T, above which it increases rapidly. These results have been understood in terms of field-dependent deflection of current around the inhomogeneity.

11.9 Concluding Remarks and Future Outlook

In this chapter we have described and discussed certain specific characteristics of InSb, InSb-based ternary and quaternary crystals, and their thin films on highly mismatched semi-insulating GaAs substrates, with reference to infrared detection and galvanomagnetic applications. The use of these material systems as an alternative for such applications relies on the production of high-quality materials with low background doping level and defect density. While basic material quality is dictated by crystal growth conditions, the physical properties of the material are profoundly influenced by the process cycles and the conditions under which the devices are operated. Hence in making a good device, it is important to understand the material issues that are related to device performance and to achieve synergies between material preparation and device fabrication. Some of the issues which have been address in this review are:

1. How does mismatch heteroepitaxy affect the structural properties when the films are far beyond their critical thickness?
2. What do the interfaces look like?
3. Does strain modify the optical gap usefully?
4. How does the electron mobility depend on composition given that alloy scattering is negligible?
5. What role do dislocations play?

for which reasonable understanding has been provided.

It was found that scattering from dislocations, introduced as a result of GaAs heteroepitaxy, degrades mobility at low temperatures. However, room-temperature transport properties are comparatively unaffected. Bright-field cross-sectional TEM imaging shows a sharp interface with very small coalescing islands and the selected-area diffraction pattern indicates that the layer and the substrate are epitaxially oriented. Very similar results were obtained on $\text{InAs}_x\text{Sb}_{1-x}/\text{GaAs}$ and $\text{InBi}_x\text{Sb}_{1-x}/\text{GaAs}$ heterostructures. The energy gap of 0.133 eV for $\text{InAs}_{0.06}\text{Sb}_{0.94}/\text{GaAs}$ shows a 13 meV reduction due to residual strain. This reduction is very useful to shift

the energy gap to well within the 8–12 μm range. The interesting observation of band tailing as a result of alloying has been modeled through Urbach tail characteristics. Shubnikov–de Haas oscillations are observed in $\text{InAs}_{0.04}\text{Sb}_{0.96}$ and the effective mass of $\text{InAs}_x\text{Sb}_{1-x}$ for low values of x is reported. The temperature dependence of the energy gap and the behavior of free-carrier absorption have been reported for InAsSb alloy for a composition for which the energy gap is 15% lower than that of InSb. The values of fundamental material parameters, such as the zero-temperature gap and its temperature coefficients, the effective mass, etc., were evaluated and analyzed within the existing theoretical models. From the FCA spectra, it was concluded that, for 5% arsenic, alloy scattering is not the mobility-limiting mechanism near RT, which is useful for reliably modeling and evaluating the performance of optical and electrical devices made from these alloys.

Although successful reports on the growth of InSb, $\text{InAs}_x\text{Sb}_{1-x}$, and $\text{InBi}_x\text{Sb}_{1-x}$ crystals and their epitaxial films on semi insulating GaAs using liquid-phase epitaxy are presented in this chapter, a number of issues still remain to be addressed. In growth utilizing nonequilibrium techniques, whether one can increase the composition of As and Bi in single crystals of $\text{InAs}_x\text{Sb}_{1-x}$ and $\text{InBi}_x\text{Sb}_{1-x}$ remains to be explored. Reduction in the film thickness of these materials using LPE is another challenge which further opens the scope for improving heteroepitaxy of these materials. From structural, optical, and transport studies, it is clear that InSb–InAs and InSb–InBi alloying cannot be understood by simply using the conventional theories of alloy disorder.

A large electronegativity and size difference between the host and substituted anions also lead to considerable structural disorder in the form of local strains, defects, and at times compositional fluctuations. Thermodynamic analysis using empirical theories of bond energies can help to produce quantitative estimates of these effects. Such a calculation would be useful in determining the practical limits on the quality of samples grown under equilibrium conditions. $\text{InAs}_x\text{Sb}_{1-x}$,

$\text{InBi}_x\text{Sb}_{1-x}$, and $\text{InBi}_x\text{As}_y\text{Sb}_{1-x-y}$ are some of the many systems in the general class of highly mismatched alloys. A comparative analysis of other systems such as InPAs , InPSb , InNAs , and GaPSb over a wider compositional range would be useful in drawing generic conclusions regarding the properties of mismatched alloys. Experimental data on these systems are still limited. Shan et al. [11.197] have recently proposed a band

anticrossing model to explain the large bowing in dilute nitride systems. Since it is the only theory that can be rigorously compared against experiment, it would be interesting to look for the anticrossing gap in $\text{InAs}_x\text{Sb}_{1-x}$, $\text{InBi}_x\text{Sb}_{1-x}$, and $\text{InBi}_x\text{As}_y\text{Sb}_{1-x-y}$ if they exist. Such and other interesting issues, when properly addressed, will fix these materials firmly in the realm of modern technology.

References

- 11.1 C.H. Wang, J.G. Crowder, V. Mannheim, T. Ashley, D.T. Dutton, A.D. Johnson, G.J. Pryce, S.D. Smith: Detection of nitrogen dioxide using a room temperature operation mid-infrared InSb light emitting diode, *Electron. Lett.* **34**, 300–3001 (1998)
- 11.2 J.J. Lee, J.D. Kim, M. Razeghi: Room temperature operation of 8–12 μm InSbBi infrared photodetectors on GaAs substrates, *Appl. Phys. Lett.* **73**, 602–604 (1998)
- 11.3 J.D. Kim, S. Kim, D. Wu, J. Wojkowski, J. Xu, J. Piotrowski, E. Bigan, M. Razeghi: 8–13 μm InAsSb heterojunction photodiode operating at near room temperature, *Appl. Phys. Lett.* **67**, 2645–2647 (1995)
- 11.4 K.Y. Ma, Z.M. Fang, D.H. Jaw, R.M. Cohen, G.B. Stringfellow, W.P. Kosar, D.W. Brown: Organometallic vapor phase epitaxial growth and characterization of InAsBi and InAsSbBi , *Appl. Phys. Lett.* **55**, 2420–2422 (1989)
- 11.5 V.K. Dixit, B. Bansal, V. Venkataraman, H.L. Bhat, K.S. Chandrasekharan, B.M. Arora: Studies on high resolution x-ray diffraction, optical and transport properties of $\text{InAs}_x\text{Sb}_{1-x}/\text{GaAs}$ ($x \leq 0.06$) heterostructure grown using liquid phase epitaxy, *J. Appl. Phys.* **96**, 4989–4995 (2004)
- 11.6 B. Bansal, V.K. Dixit, V. Venkataraman, H.L. Bhat: Transport, optical and magnetotransport properties of hetero-epitaxial $\text{InAs}_x\text{Sb}_{1-x}/\text{GaAs}$ ($x \leq 0.06$) and bulk $\text{InAs}_x\text{Sb}_{1-x}$ ($x \leq 0.05$) crystals: experiment and theoretical analysis, *Physica E* **20**, 272–277 (2004)
- 11.7 B. Bansal, V.K. Dixit, V. Venkataraman, H.L. Bhat: Temperature dependence of the energy gap and free carrier absorption in bulk $\text{InAs}_{0.05}\text{Sb}_{0.95}$ single crystals, *Appl. Phys. Lett.* **82**, 4720–4722 (2003)
- 11.8 V.K. Dixit, K.S. Keerthi, P. Bera, M.S. Hegde, H.L. Bhat: Structural and compositional analysis of $\text{InBi}_x\text{As}_y\text{Sb}_{1-x-y}$ films grown on $\text{GaAs}(001)$ substrates by liquid phase epitaxy, *Appl. Surf. Sci.* **220**, 321–326 (2003)
- 11.9 V.K. Dixit, B. Bansal, V. Venkataraman, H.L. Bhat: Structural, optical, and electrical properties of bulk single crystals of $\text{InAs}_x\text{Sb}_{1-x}$ grown by rotatory Bridgman method, *Appl. Phys. Lett.* **81**, 1630–1632 (2002)
- 11.10 V.K. Dixit, B. Bansal, V. Venkataraman, G.N. Subbanna, K.S. Chandrasekharan, B.M. Arora, H.L. Bhat: High-mobility InSb epitaxial films grown on a $\text{GaAs}(001)$ substrate using liquid-phase epitaxy, *Appl. Phys. Lett.* **80**, 2102–2104 (2002)
- 11.11 V.K. Dixit, B.V. Rodrigues, R. Venkataraghavan, K.S. Chandrasekharan, B.M. Arora, H.L. Bhat: Effect of lithium ion irradiation on transport and optical properties of Bridgman grown n- InSb single crystals, *J. Appl. Phys.* **90**, 1750–1755 (2001)
- 11.12 V.K. Dixit, B.V. Rodrigues, H.L. Bhat: Growth of $\text{InBi}_x\text{Sb}_{1-x}$ crystals by rotatory Bridgman method and their characterization, *J. Cryst. Growth* **217**, 40–47 (2000)
- 11.13 J.C. Woolley, J. Warner: Optical energy-gap variation in InAs-InSb alloys, *Can. J. Phys.* **42**, 1879–1885 (1964)
- 11.14 W.M. Coderre, J.C. Woolley: Electrical properties of $\text{InAs}_x\text{Sb}_{1-x}$ alloys, *Can. J. Phys.* **46**, 1207–1214 (1968)
- 11.15 C.E.A. Grigorescu, R.A. Stradling: Semiconductor optical and electro-optical devices. In: *Handbook of Thin Film Devices*, Vol. 2, ed. by M.H. Francombe (Academic, New York 2000) pp. 27–62
- 11.16 M.Y. Yen, B.F. Levine, C.G. Bethea, K.K. Choi, A.Y. Cho: Molecular beam epitaxial growth and optical properties of $\text{InAs}_x\text{Sb}_{1-x}$ in 8–12 μm wavelength range, *Appl. Phys. Lett.* **50**, 927–929 (1987)
- 11.17 J.D. Kim, D. Wu, J. Wojkowski, J. Piotrowski, J. Xu, M. Razeghi: Long-wavelength InAsSb photoconductors operated at near room temperatures (200–300 K), *Appl. Phys. Lett.* **68**, 99 (1996)
- 11.18 A. Rogalski, K. Jozwikowski: Intrinsic carrier concentration and effective masses in $\text{InAs}_x\text{Sb}_{1-x}$, *Infrared Phys.* **29**, 35–42 (1989)
- 11.19 I. Kudman, L. Ekstrom: Semiconducting properties of InSb-InAs alloys, *J. Appl. Phys.* **39**, 3385–3388 (1968)
- 11.20 J.C. Woolley, J. Warner: Preparation of InAs-InSb alloys, *J. Electrochem. Soc.* **111**, 1142–1145 (1964)
- 11.21 K. Sugiyama: Molecular beam epitaxy of InSb films on CdTe , *J. Cryst. Growth* **60**, 450–452 (1982)
- 11.22 R. Venkataraghavan, K.S.R.K. Rao, M.S. Hegde, H.L. Bhat: Influence of growth parameters on the surface and interface quality of laser deposited

- InSb/CdTe heterostructures, *Phys. Status Solidi (a)* **163**, 93–100 (1997)
- 11.23 B.V. Rao, T. Okamoto, A. Shinmura, D. Gruznev, M. Mori, T. Tambo, C. Tatsuyama: Growth temperature effect on the heteroepitaxy of InSb on Si(111), *Appl. Surf. Sci.* **159/160**, 335–340 (2000)
- 11.24 S.D. Parker, R.L. Williams, R. Droopad, R.A. Stradling, K.W.J. Barnham, S.N. Holmes, J. Lavery, C.C. Phillips, E. Skuras, R. Thomas, X. Zhang, A. Staton-Beven, D.W. Pashley: Observation and control of the amphoteric behaviour of Si doped InSb grown on GaAs by MBE, *Semicond. Sci. Technol.* **4**, 663–676 (1989)
- 11.25 M. Mori, Y. Nizawa, Y. Nishi, K. Mae, T. Tambo, C. Tatsuyama: Effect of current flow direction on the heteroepitaxial growth of InSb films on Ge/Si(001) substrate heated by direct current, *Appl. Surf. Sci.* **159/160**, 328–334 (2000)
- 11.26 S.V. Ivanov, A.A. Boudza, R.N. Kutt, N.N. Ledentsov, B.Y. Meltser, S.S. Ruvimov, S.V. Shaposhnikov, P.S. Kopev: Molecular-Beam epitaxial growth of InSb/GaAs(100) and InSb/Si(100) heteroepitaxial layers (Thermodynamic analysis and characterization), *J. Cryst. Growth* **156**, 191–205 (1995)
- 11.27 P.E. Thompson, J.L. Davis, J. Waterman, R.J. Wagner, D. Gammon, D.K. Gaskill, R. Stahlbush: Use of atomic layer epitaxy buffer for the growth of InSb on GaAs by molecular beam epitaxy, *J. Appl. Phys.* **69**, 7166–7172 (1991)
- 11.28 B.S. Yoo, M.A. McKee, S.G. Kim, E.H. Lee: Structural and electrical properties of InSb epitaxial films grown on GaAs by low pressure MOCVD, *Solid Stat. Commun.* **88**, 447–450 (1993)
- 11.29 D.K. Gaskill, G.T. Stauf, N. Bottka: High mobility InSb grown by organometallic vapor-phase-epitaxy, *Appl. Phys. Lett.* **58**, 1905–1907 (1991)
- 11.30 M.C. Debnath, T. Zhang, C. Roberts, L.F. Cohen, R.A. Stradling: High-mobility InSb thin films on GaAs(001) substrate grown by the two-step growth process, *J. Cryst. Growth* **267**, 17–21 (2004)
- 11.31 T.R. Yang, Y. Cheng, J.B. Wang, Z.C. Feng: Optical and transport properties of InSb thin films grown on GaAs by metal organic chemical vapor deposition, *Thin Solid Films* **498**, 158–162 (2006)
- 11.32 T.R. Yang, Z.C. Feng, W. Lu, W.E. Collins: Far infrared reflectance spectroscopy of InSb thin films grown on GaAs by metal-organic vapor deposition, *Proc. XIXth Int. Conf. Raman Spectrosc.*, ed. by P.M. Fredericks, R.L. Frost, L. Rintoul (2004) pp. 629–630
- 11.33 A. Kumar, P.S. Dutta: Growth of long wavelength $\text{In}_x\text{Ga}_{1-x}\text{As}_y\text{Sb}_{1-y}$ layers on GaAs from liquid phase, *Appl. Phys. Lett.* **89**, 162101–162103 (2006)
- 11.34 C. Peng, N.F. Chen, F. Gao, X. Zhang, C. Chen, J. Wu, Y. Yu: Liquid-phase-epitaxy-grown $\text{InAs}_x\text{Sb}_{1-x}$ /GaAs for room-temperature 8–12 μm infrared detectors, *Appl. Phys. Lett.* **88**, 242108–242110 (2006)
- 11.35 C.M. Ruiz, J.L. Plaza, V. Bermúdez, E. Diéguez: Study of induced structural defects on GaSb films grown on different substrates by the liquid phase epitaxy technique, *J. Phys.: Condens. Matter* **14**, 12755–12759 (2002)
- 11.36 Y.Z. Gao, H. Kan, M. Aoyama, T. Yamaguchi: Germanium and zinc-doped p-type InAsSb single crystals with a cutoff wavelength of 12.5 μm , *Jpn. J. Appl. Phys.* **39**, 2520–2522 (2000)
- 11.37 Y.Z. Gao, H. Kan, F.S. Gao, X.Y. Gong, T. Yamaguchi: Improved purity of long-wavelength InAsSb epilayers grown by melt epitaxy in fused silica boats, *J. Cryst. Growth* **234**, 85–90 (2002)
- 11.38 Y.Z. Gao, X.Y. Gong, Y.S. Gui, T. Yamaguchi, N. Dai: Electrical properties of melt-epitaxy-grown $\text{InAs}_{0.04}\text{Sb}_{0.96}$ layers with cutoff wavelength of 12 μm , *Jpn. J. Appl. Phys.* **43**, 1051–1054 (2004)
- 11.39 S.A. Barnett: Direct E_0 energy gaps of bismuth-containing III–V alloys predicted using quantum dielectric theory, *J. Vac. Sci. Technol. A* **5**, 2845–2848 (1987)
- 11.40 Y. Amemiya, H. Tareo, Y. Sakai: Electrical properties of InSb-based mixed crystals, *J. Appl. Phys.* **44**, 1625–1630 (1973)
- 11.41 W. Zawadzki: Electron transport in small-gap semiconductors, *Adv. Phys.* **23**, 435 (1974), and In: *Handbook on Semiconductors* ed. by T.S. Moss (North-Holland, Amsterdam 1982) p. 713
- 11.42 A. Thiel, H. Koelsch: Studies on indium, *Z. Anorg. Chem.* **66**, 288–321 (1910), in German
- 11.43 V.M. Goldschmidt: Crystal structure and chemical constitution, *Trans. Faraday Soc.* **25**(253), 253–282 (1929)
- 11.44 H. Welker: Über neue halbleitende Verbindungen, *Z. Naturforsch.* **A 7**, 744–749 (1952)
- 11.45 L. Pincherle, J.M. Radcliffe: Semiconducting intermetallic compounds, *Adv. Phys. Philos. Mag. Suppl.* **5**, 271–322 (1956)
- 11.46 H. Welker, H. Wiess: *Solid State Physics*, Vol. 3 (Academic, New York 1956)
- 11.47 F.A. Cunnell, E.W. Saker: *Progress in Semiconductors*, Vol. 2 (Heywood, London 1959)
- 11.48 R.A. Smith: *Semiconductors* (Cambridge Univ. Press, Cambridge 1959)
- 11.49 M.J. Whelan: Properties of some covalent semiconductors. In: *Semiconductors*, ed. by J.B. Hannay (Rheinhold, New York 1959)
- 11.50 H.J. Hrostowski: Infrared absorption of semiconductors. In: *Semiconductors*, ed. by J.B. Hannay (Rheinhold, New York 1959)
- 11.51 K.T. Huang, C.T. Chiu, R.M. Cohen, G.B. Stringfellow: InAsSbBi alloys grown by organometallic vapor phase epitaxy, *J. Appl. Phys.* **75**, 2857–2863 (1994)
- 11.52 Q. Du, J. Alperin, W.T. Wang: Molecular beam epitaxial growth of GaInSbBi for infrared detector applications, *J. Cryst. Growth* **175**, 849–852 (1997)
- 11.53 T.P. Humphreys, P.K. Chiang, S.M. Bedair, N.R. Parikh: Metalorganic chemical vapor depo-

- sition and characterization of the In-As-Sb-Bi material system for infrared detection, *Appl. Phys. Lett.* **53**, 142–144 (1988)
- 11.54 K.Y. Ma, Z.M. Fang, D.H. Jaw, R.M. Cohen, G.B. Stringfellow, W.P. Kosar, D.W. Brown: Organometallic vapor phase epitaxial growth and characterization of InAsBi and InAsSbBi, *Appl. Phys. Lett.* **55**, 2420–2422 (1989)
- 11.55 C.H. Shih, E.A. Peretti: The phase diagram of the system InAs-Sb, *Trans. Am. Soc. Met.* **46**, 389–396 (1954)
- 11.56 T.S. Liu, E.A. Peretti: The indium-antimony system, *Trans. Am. Soc. Met.* **44**, 539–548 (1951)
- 11.57 J.L. Zilko, J.E. Greene: Growth and phase stability of epitaxial metastable $\text{InBi}_x\text{Sb}_{1-x}$ films on GaAs, *J. Appl. Phys.* **51**, 1549–1564 (1980)
- 11.58 N.A. Goryunova, N.N. Fedorova: On the question of the isomorphism of compounds of III–BV type, *J. Tech. Phys. Moscow* **24**, 1339–1341 (1955)
- 11.59 J.C. Woolley, B.A. Smith, D.G. Lee: Solid solution in the GaSb-InSb system, *Proc. Phys. Soc. B* **69**, 1339–1343 (1956)
- 11.60 G.B. Stringfellow, P.E. Greene: Calculation of III–V ternary phase diagram In–Ga–As and In–As–Sb, *J. Phys. Chem. Solids* **30**, 1779–1780 (1969)
- 11.61 P.S. Dutta, T.R. Miller: Engineering phase formation thermo-chemistry for crystal growth of homogeneous ternary and quaternary III–V compound semiconductors from melts, *J. Electron. Mater.* **29**, 956–963 (2000)
- 11.62 D. Minic, D. Manasijevic, D. Zivkovic, Z. Zivkovic: Phase equilibria in the In–Sb–Bi system at 300 °C, *J. Serb. Chem. Soc.* **71**, 843–847 (2006)
- 11.63 B. Joukoff, A.M. Jean-Louis: Growth of $\text{InBi}_x\text{Sb}_{1-x}$ single crystals by Czochralski method, *J. Cryst. Growth* **12**, 169–172 (1972)
- 11.64 A. Iandelli: MX₂-Verbindungen der Erdalkali- und Seltenen Erdmetalle mit Gallium, Indium und Thallium, *Z. Anorg. Allg. Chem.* **330**(3), 221–232 (1941), in German
- 11.65 J.F. Dewald: The kinetics and mechanism of formation of anode films on single crystal InSb, *J. Electrochem. Soc.* **104**, 244–251 (1957)
- 11.66 G.N. Kozhemyakin: Influence of ultrasonic vibration on the growth of InSb crystals, *J. Cryst. Growth* **149**, 266–268 (1995)
- 11.67 R.K. Akchurin, V.G. Zinov'ev, V.B. Ufimtsev, V.T. Bublik, A.N. Morozov: Donor nature of bismuth in indium antimonide, *Sov. Phys. Semicond.* **16**, 126–129 (1982)
- 11.68 L. Pauling: *The Nature of Chemical Bond* (Oxford Univ. Press, London 1940)
- 11.69 V.K. Dixit: Bulk and Thin Film Growth of Pure and Substituted Indium Antimonide for Infrared Detector Applications. Ph.D. Thesis (Indian Institute of Science, Bangalore 2004)
- 11.70 W.L. Bond: Precision lattice constant determination, *Acta Crystallogr.* **13**, 814–818 (1960)
- 11.71 R. Krishnaswamy: Compounding, zone refining and crystal growing of Indium Antimonide, *J. Indian Chem. Soc.* **LII**, 60–63 (1975)
- 11.72 R.K. Bagai, G.L. Seth, W.N. Borle: Growth of high purity indium antimony crystals for infrared detectors, *Indian J. Pure Appl. Phys.* **21**, 441–444 (1983)
- 11.73 T.A. Campbell, J.N. Koster: In situ visualization of constitutional supercooling within a Bridgman–Stockbarger system, *J. Cryst. Growth* **171**, 1–11 (1997)
- 11.74 D.B. Gadkari, K.B. Lal, A.P. Shah, B.M. Arora: Growth of high mobility InSb crystals, *J. Cryst. Growth* **173**, 585–588 (1997)
- 11.75 M.H. Lin, S. Kou: Czochralski pulling of InSb single crystals from a molten zone on a solid feed, *J. Cryst. Growth* **193**, 443–445 (1998)
- 11.76 W.G. Pfann: Principles of zone melting, *J. Met.* **4**, 747–753 (1952)
- 11.77 T.C. Harman: Effect of zone refining variables on the segregation of impurities in indium antimonide, *J. Electrochem. Soc.* **103**, 128–132 (1956)
- 11.78 A.J. Strauss: Distribution coefficients and carrier mobilities in InSb, *J. Appl. Phys.* **30**, 559–563 (1959)
- 11.79 J.B. Mullin, K.F. Hulme: Orientation dependent distribution coefficients in melt grown InSb crystals, *J. Phys. Chem. Solids* **17**, 1–6 (1960)
- 11.80 R.K. Mueller, R.L. Jacobson: Growth twins in indium antimonide, *J. Appl. Phys.* **32**, 550–551 (1961)
- 11.81 A.R. Murray, J.A. Baldrey, J.B. Mullin, O. Jones: A systematic study of zone refining of single crystal indium antimonide, *J. Mater. Sci.* **1**, 14–28 (1966)
- 11.82 S.G. Parker, O.W. Wilson, B.H. Barbee: Indium antimonide of high perfection, *J. Electrochem. Soc.* **112**, 80–81 (1965)
- 11.83 J. Zhou, M. Larrousse, W.R. Wilcox, L.L. Regel: Directional solidification with ACRT, *J. Cryst. Growth* **128**, 173–177 (1993)
- 11.84 K.M. Kim: Suppression of thermal convection by transverse magnetic field, *J. Electrochem. Soc.* **129**, 427–429 (1982)
- 11.85 J. Kang, Y. Okano, K. Hoshikawa, T. Fukuda: Influence of a high vertical magnetic field on Te dopant segregation in InSb grown by the vertical gradient freeze method, *J. Cryst. Growth* **140**, 435–438 (1994)
- 11.86 A.G. Ostrogorsky, H.J. Sell, S. Scharl, G. Müller: Convection and segregation during growth of Ge and InSb crystals by the submerged heater method, *J. Cryst. Growth* **128**, 201 (1993)
- 11.87 P.S. Dutta, H.L. Bhat, V. Kumar: Numerical analysis of melt–solid interface shapes and growth rates of gallium antimonide in a single-zone vertical Bridgman furnace, *J. Cryst. Growth* **154**, 213–222 (1995)
- 11.88 R. Venkataraghavan, K.S.R.K. Rao, H.L. Bhat: The effect of growth parameters on the position of the melt–solid interface in Bridgman growth of indium antimonide, *J. Phys. D Appl. Phys.* **30**, L61–L63 (1997)

- 11.89 N.K. Udayshankar, K. Gopalakrishna Naik, H.L. Bhat: The influence of temperature gradient and lowering speed on the melt-solid interface shape of $\text{Ga}_x\text{In}_{1-x}\text{Sb}$ alloy crystals grown by vertical Bridgman technique, *J. Cryst. Growth* **203**, 333–339 (1999)
- 11.90 P.G. Barber, R.K. Crouch, A.L. Fripp, W.J. Debnam, R.F. Berry, R. Simchick: Modelling melt-solid interfaces in Bridgman growth, *J. Cryst. Growth* **97**, 672–674 (1989)
- 11.91 T.A. Campbell, J.N. Koster: Growth rate effects during indium-antimony crystal growth, *Crystal. Res. Technol.* **34**, 275–283 (1999)
- 11.92 M.J. Hui, K. Beatty, K. Blackmore, K. Jackson: Impurity distribution in InSb single crystals, *J. Cryst. Growth* **174**, 245–249 (1997)
- 11.93 T.A. Campbell, J.N. Koster: Compositional effects on solidification of congruently melting InSb, *Crystal. Res. Technol.* **33**, 717–731 (1998)
- 11.94 T. Duffar, C. Potard, P. Dusserre: Growth analysis of the InSb compound by a calorimetric method in microgravity results of the Spacelab-D1 experiment, *J. Cryst. Growth* **92**, 467–478 (1988)
- 11.95 R. F. Redden, W. F. H. Micklethwait: Final Report to the Canadian Space Agency, MiM/QUELD Increment II (1998)
- 11.96 W.F.H. Micklethwaite: Bulk growth of InSb and related ternary alloys. In: *Bulk Growth of Electronic, Optical and Optoelectronic Materials*, ed. by P. Capper (Wiley, Chichester 2005)
- 11.97 W.P. Allred, R.T. Bate: Anisotropic segregation in InSb, *J. Electrochem. Soc.* **108**, 258–261 (1961)
- 11.98 K. Terashima: Growth of highly homogeneous InSb single crystals, *J. Cryst. Growth* **60**, 363–368 (1982)
- 11.99 D.T.J. Hurle, O. Jones, J.B. Mullin: Growth of semiconducting compounds from non-stoichiometric melts, *Solid Stat. Electron.* **3**, 317–320 (1961)
- 11.100 J.W. Faust Jr., H.F. John: The growth of semiconductor crystals from solution using the twin-plane reentrant-edge mechanism, *J. Phys. Chem. Solids* **23**, 1407–1415 (1962)
- 11.101 K. Morizane, A.F. Witt, H.C. Gatos: Impurity distributions in single crystals. I. Impurity striations in nonrotated InSb crystals, *J. Electrochem. Soc.* **114**, 51–52 (1966)
- 11.102 H.C. Gatos, A.J. Strauss, M.C. Lavine, T.C. Harmon: Impurity striations in unrotated crystals of InSb, *J. Appl. Phys.* **32**, 2057–2058 (1961)
- 11.103 K.W. Benz, G. Müller: GaSb and InSb crystals grown by vertical and horizontal travelling heater method, *J. Cryst. Growth* **46**, 35–42 (1979)
- 11.104 R.W. Hamaker, W.B. White: Mechanism of single-crystal growth in InSb using temperature-gradient zone melting, *J. Appl. Phys.* **39**, 1758–1765 (1968)
- 11.105 N.K. Udayshankar, H.L. Bhat: Growth and characterization of indium antimonide and gallium antimonide crystals, *Bull. Mater. Sci.* **24**, 445–453 (2001)
- 11.106 R. Venkataraghavan, K.S.R.K. Rao, H.L. Bhat: The effect of temperature gradient and ampoule velocity on the composition and other properties of Bridgman-grown indium antimonide, *J. Cryst. Growth* **186**, 322–328 (1998)
- 11.107 V.M. Glazov, K.B. Poyarkov: InSb-InAs alloys prepared by rapid quenching (10^6 – 10^8 K/s), *Inorg. Mater.* **36**, 991–996 (2000)
- 11.108 A.M. Jean-Louis, B. Ayrault, J. Vargas: Properties of $\text{InSb}_{1-x}\text{Bi}_x$ alloys. 2. Optical absorption, *Phys. Status Solidi (b)* **34**, 341–342 (1969)
- 11.109 T. Ozawa, Y. Hayakawa, M. Kumagawa: Growth of III-V ternary and quaternary mixed crystals by the rotationary Bridgman method, *J. Cryst. Growth* **109**, 212–217 (1991)
- 11.110 M. Kumagawa, T. Ozawa, Y. Hayakawa: A new technique for the growth of III-V mixed crystal layers, *Appl. Surf. Sci.* **33/34**, 611–618 (1988)
- 11.111 M. Kumagawa, A.F. Witt, M. Lichtensteiger, H.C. Gatos: Current-controlled growth and dopant modulation in liquid phase epitaxy, *J. Electrochem. Soc.* **120**, 583–584 (1973)
- 11.112 I. Melngailis, A.R. Calawa: Solution regrowth of planar InSb laser structures, *J. Electrochem. Soc.* **113**, 58–59 (1966)
- 11.113 D.E. Holmes, G.S. Kamath: Growth-characteristics of LPE InSb and InGaSb, *J. Electron. Mater.* **9**, 95–110 (1980)
- 11.114 R. Venkataraghavan, N.K. Udayshankar, B.V. Rodrigues, K.S.R.K. Rao, H.L. Bhat: Design and fabrication of liquid phase epitaxy system, *Bull. Mater. Sci.* **22**, 133–137 (1999)
- 11.115 V.K. Dixit, B.V. Rodrigues, R. Venkataraghavan, K.S. Chandrasekharan, B.M. Arora, H.L. Bhat: Growth of InSb epitaxial layers on GaAs(001) substrates by LPE and their characterizations, *J. Cryst. Growth* **235**, 154–160 (2002)
- 11.116 M. Elwenspoek: On the estimate of the supersaturation of nonelectrolyte solutions from solubility data, *J. Cryst. Growth* **76**, 514–516 (1986)
- 11.117 A.S. Popov, A.M. Koinova, S.L. Tzeneva: The In-As-Sb phase diagram and LPE growth of InAsSb layers on InAs at extremely low temperatures, *J. Cryst. Growth* **186**, 338–343 (1998)
- 11.118 L.O. Bubulac, A.M. Andrews, E.R. Gertner, D.T. Cheung: Backside illuminated InAsSb/GaSb broadband detectors, *Appl. Phys. Lett.* **36**, 734 (1980)
- 11.119 M.C. Wagener, J.R. Botha, A.W.R. Leitch: Substitutional incorporation of arsenic from GaAs substrates into MOVPE grown InSbBi thin films, *Physica B* **308–310**, 866–869 (2001)
- 11.120 M.C. Wagener, J.R. Botha, A.W.R. Leitch: Characterization of secondary phases formed during MOVPE growth of InSbBi mixed crystals, *J. Cryst. Growth* **213**, 51–56 (2000)

- 11.121 V.B. Ufimtsev, V.G. Zinovev, M.R. Raukhan: Heterogeneous equilibria in the system In-Sb-Bi and liquid phase epitaxy of InSb based solid solution, *Inorg. Mater.* **15**, 1371-1374 (1979)
- 11.122 Y.Z. Gao, T. Yamaguchi: Liquid phase epitaxial growth and properties of InSbBi films grown from In, Bi and Sn solutions, *Cryst. Res. Technol.* **34**, 285-292 (1999)
- 11.123 V.K. Dixit, K.S. Keerthi, P. Bera, H.L. Bhat: Growth of $\text{InBi}_x\text{Sb}_{1-x}$ films on GaAs(001) substrates using liquid phase epitaxy and their characterization, *J. Cryst. Growth* **241**, 171-176 (2002)
- 11.124 K.T. Huang, C.T. Chiu, R.M. Cohen, G.B. Stringfellow: $\text{InBi}_x\text{As}_y\text{Sb}_{1-x-y}$ alloys grown by organometallic vapor-phase epitaxy, *J. Appl. Phys.* **75**, 2857-2862 (1994)
- 11.125 Q. Du, J. Alperin, W.T. Wang: Molecular beam epitaxial growth of GaInSbBi for infrared detector applications, *J. Cryst. Growth* **175/176**, 849-852 (1997)
- 11.126 M. Oszwaldowski, T. Berus, J. Szade, K. Józwiak, I. Olejniczak, P. Konarski: Structural properties of InSbBi and InSbAsBi thin films prepared by the flash-evaporation method, *Cryst. Res. Technol.* **36**, 1155-1171 (2001)
- 11.127 P. Haasen: Twinning in indium antimonide, *J. Met.* **209**, 30-32 (1957)
- 11.128 C.G. Darwin: The reflexion of x-rays from imperfect crystals, *Philos. Mag.* **43**, 800-829 (1922)
- 11.129 J. Auleytner: *X-Ray Methods in the Study of Defects in Single Crystals* (Pergamon, Oxford 1967)
- 11.130 P.F. Fewster: *X-Ray Scattering from Semiconductors* (Imperial College Press, London 2000)
- 11.131 E. Gartstein, R.A. Cowley: The intensity patterns with a multocrystal diffractometer observed at a synchrotron source, *Z. Naturforsch. A* **48**, 519-522 (1992)
- 11.132 E. Gartstein, Y. Khait, V. Richter: An x-ray diffraction study of implantation damage in InSb reduced by a magnetic field, *J. Phys. D Appl. Phys.* **28**, A291-A294 (1995)
- 11.133 A.H. Chin, R.W. Schoenlein, T.E. Glover, P. Balling, W.P. Leemans, C.V. Shank: Ultrafast structural dynamics in InSb probed by time-resolved x-ray diffraction, *Phys. Rev. Lett.* **83**, 336-339 (1999)
- 11.134 M.R. Surowiec, B.K. Tanner: X-ray topography study of dislocations around indents on {111} surfaces of indium-antimonide, *J. Appl. Cryst.* **20**, 499-504 (1987)
- 11.135 D. Briggs, M.P. Seah: *Practical Surface Analysis by Auger and x-ray Photoelectron Spectroscopy* (Wiley, New York 1984), , Appendix 4
- 11.136 J.H. Scofield: Hartree-Slater subshell photoionization cross sections at 1254 and 1487 eV, *J. Electron Spectrosc. Relat. Phenom.* **8**, 129-137 (1976)
- 11.137 D.R. Penn: Quantitative chemical analysis by ESCA, *J. Electron. Spectrosc. Relat. Phenom.* **9**, 29-40 (1976)
- 11.138 R.J. Egan, V.W.L. Chin, T.L. Tansley: Dislocation scattering effects on electron mobility in InAsSb, *J. Appl. Phys.* **75**, 2473-2476 (1994)
- 11.139 C. Bocchi, C. Ferrari, P. Franzosi, A. Bosacchi, S. Franchi: Accurate determination of lattice mismatch in the epitaxial AlAs/GaAs system by high-resolution x-ray diffraction, *J. Cryst. Growth* **132**, 427-434 (1993)
- 11.140 C.R. Wie: High resolution x-ray diffraction characterization of semiconductor structures, *Mater. Sci. Eng. R* **13**, 1-56 (1994)
- 11.141 X. Weng, R.S. Goldman, D.L. Partin, J.P. Heremans: Evolution of structural and electronic properties of highly mismatched InSb films, *J. Appl. Phys.* **88**, 6276-6286 (2000)
- 11.142 E.O. Kane: Band structure of indium antimonide, *J. Phys. Chem. Solids* **1**, 249-261 (1957)
- 11.143 G. Dresselhaus, A.F. Kip, C. Kittel, G. Wagoner: Cyclotron and spin resonance in indium antimonide, *Phys. Rev.* **98**, 556-557 (1955)
- 11.144 H.P.R. Frederikse, W.R. Hosler: Galvanomagnetic effects in n-type indium antimonide, *Phys. Rev.* **108**, 1136 (1957)
- 11.145 L.M. Roth, B. Lax, S. Zwerdling: Theory of optical magneto-absorption effects in semiconductors, *Phys. Rev.* **114**, 90-103 (1959)
- 11.146 H.P.R. Frederikse, W.R. Hosler: Galvanomagnetic effects in p-type indium antimonide, *Phys. Rev.* **108**, 1146-1151 (1957)
- 11.147 C. Hermann, C. Weisbuch: $k \cdot p$ perturbation theory in III-V compounds and alloys reexamination, *Phys. Rev. B* **15**, 823-833 (1977)
- 11.148 J.A. van Vechten, O. Berolo, J.C. Woolley: Spin-orbit splitting in compositionally disordered semiconductors, *Phys. Rev. Lett.* **29**, 1400-1403 (1972)
- 11.149 J.I. Vykylyuk, V.G. Deibuk, I.M. Rarenko: Calculation of absorption coefficients of $\text{InBi}_x\text{Sb}_{1-x}$ solid solutions, *Semicond. Phys. Quantum Electron. Optoelectron.* **3**, 174-177 (2000)
- 11.150 S.D. Smith, T.S. Moss, K.W. Taylor: The energy-dependence of electron mass in indium antimonide determined from measurements of the infrared Faraday effect, *J. Phys. Chem. Solids* **11**, 131-139 (1959)
- 11.151 B. Bansal, V. Venkataraman: Magnetic field induced band depopulation in intrinsic InSb: a revisit, *J. Phys.: Condens. Matter* **17**, 7053-7060 (2005)
- 11.152 C. Hilsun, A.C. Rose-Innes: *Semiconducting III-V Compounds* (Pergamon, New York 1961) pp. 128-
- 11.153 H.J. Hrostowski, F.J. Morin, T.H. Geballe, G.H. Wheatley: Hall effect and conductivity of InSb, *Phys. Rev.* **100**, 1672-1672 (1955)
- 11.154 H. Fritzsche, K. Lark-Horovitz: Electrical properties of p-type indium antimonide at low temperatures, *Phys. Rev.* **99**, 400-405 (1955)
- 11.155 R. Barrie, J.T. Edmond: A study of the conduction band of InSb, *J. Electron.* **1**, 161-170 (1955)

- 11.156 K. Vinogradova, V. Galavanov, D. Nasledov: Production of high purity indium antimonide by zone fusion, *Sov. Phys. Tech. Phys.* **2**, 1832–1839 (1957)
- 11.157 K. Vinogradova, V. Galavanov, D. Nasledov, L. Soloveva: Production of high purity single crystals of InSb by zone melting, *Sov. Phys. Solid. Stat.* **1**, 364–367 (1959)
- 11.158 O. Madelung, H. Weiss: Die elektrischen Eigenschaften von Indiumantimoniden, *Z. Naturforsch.* **9a**, 527–534 (1954)
- 11.159 O. Drachenko, B. Bansal, V.V. Rylkov, J. Galibert, V.K. Dixit, J. Leotin: InAsSb/GaAs hetero-epitaxial crystals studied by cyclotron resonance measurements, 12th Int. Conf. Narrow Gap Semicond. (Toulouse, 2005)
- 11.160 N. Miura, G. Kido, S. Chikazumi: Infrared cyclotron resonance in InSb, GaAs and Ge in very high magnetic fields, *Solid State Commun.* **18**, 885–888 (1976)
- 11.161 B.R. Nag: *Electron Transport in Compound Semiconductors* (Springer, Berlin 1980)
- 11.162 W. Zawadzki: Electron transport in small gap semiconductors, *Adv. Phys.* **23**, 435–455 (1974)
- 11.163 J.A. van Vechten, T.K. Bergstresser: Electronic structures of semiconductor alloys, *Phys. Rev. B* **1**, 3351–3358 (1970)
- 11.164 O. Berolo, J.C. Woolley, J.A. van Vechten: Effect of disorder on conduction band effective mass, valence band spin orbit splitting and direct band gap in III–V alloys, *Phys. Rev. B* **8**, 3794–3798 (1973)
- 11.165 E.J. Johnson: Optical properties of III–V compounds. In: *Semiconductors and Semimetals*, Vol. 3, ed. by R.K. Willardson, A.C. Beer (Academic, New York 1967) pp. 154–
- 11.166 C.E.A. Grigorescu, R.A. Stradling: Antimony-based infrared materials and devices. In: *Handbook of Thin Film Devices*, Vol. 2, ed. by M.H. Francombe (Academic, New York 2000)
- 11.167 S.W. Kurnick, J.M. Powell: Optical absorption in pure single crystal InSb at 298 K and 78 K, *Phys. Rev.* **116**, 597–604 (1959)
- 11.168 W.G. Spitzer, H.Y. Fan: Infrared absorption in indium antimonide, *Phys. Rev.* **106**, 1893–1894 (1955)
- 11.169 T.S. Moss: *Optical Properties of Semiconductors* (Butterworths, London 1959)
- 11.170 O. Madelung (Ed.): *Semiconductors – Basic Data* (Springer, Berlin 1996)
- 11.171 Y.P. Varshni: Temperature dependence of energy gap in semiconductors, *Physica* **34**, 149–150 (1967)
- 11.172 M. Cardona: Renormalization of the optical response of semiconductors by electron-phonon interaction, *Phys. Status Solidi (a)* **188**, 1209–1232 (2001)
- 11.173 R.H. Parmenter: Energy levels of a disordered alloy, *Phys. Rev.* **97**, 587–598 (1955)
- 11.174 L. Malikova, W. Krystek, F.H. Pollak, N. Dai, A. Cavus, M.C. Tamargo: Temperature dependence of the direct gaps of ZnSe and $\text{Zn}_{0.56}\text{Cd}_{0.44}\text{Se}$, *Phys. Rev. B* **54**, 1819–1824 (1996)
- 11.175 L. Vina, S. Logothetidis, M. Cardona: Temperature dependence of the dielectric function of germanium, *Phys. Rev. B* **30**, 1979–1991 (1984)
- 11.176 H.H. Wieder, A.R. Clawson: Photo-electronic properties of $\text{InAs}_{0.07}\text{Sb}_{0.93}$ films, *Thin Solid Films* **15**, 217–221 (1973)
- 11.177 Y.B. Li, S.S. Dosanjh, I.T. Ferguson, A.G. Norman, A.G. de Oliveira, R.A. Stradling, R. Zallen: Raman scattering in $\text{InAs}_x\text{Sb}_{1-x}$ alloys grown on GaAs by molecular beam epitaxy, *Semicond. Sci. Technol.* **7**, 567–570 (1992)
- 11.178 E.H. Reihlen, M.J. Jou, Z.M. Fang, G.B. Stringfellow: Optical absorption and emission of $\text{InP}_{1-x}\text{Sb}_x$ alloys, *J. Appl. Phys.* **68**, 4604–4609 (1990)
- 11.179 Y.S. Gao, X.D. Gong, T. Yamaguchi: Optical properties of InAsSb single crystals with cutoff wavelengths of 8–12 μm grown by melt-epitaxy, *J. Appl. Phys.* **45**, 5732–5734 (2006)
- 11.180 B. Bansal, V. K. Dixit, V. Venkataraman, H. L. Bhat: Alloying induced degradation of the absorption edge of $\text{InAs}_x\text{Sb}_{1-x}$, *Appl. Phys. Lett.* **90**, 101905(1–3) (2007)
- 11.181 Y.Z. Gao, H. Kan, F.S. Gao, X.Y. Gong, T. Yamaguchi: Improved purity of long-wavelength InAsSb epilayers grown by melt epitaxy in fused silica boats, *J. Cryst. Growth* **234**, 85–90 (2002)
- 11.182 M.A. Marciniak, R.L. Hengehold, Y.K. Yeo, G.W. Turner: Optical characterization of molecular beam epitaxially grown InAsSb nearly lattice matched to GaSb, *J. Appl. Phys.* **84**, 480–488 (1998)
- 11.183 B. Bansal: Construction of a 17 Tesla Pulsed Magnet and Effect of Arsenic Alloying and Heteroepitaxy on Transport and Optical Properties of Indium Antimonide. Ph.D. Thesis (Indian Institute of Science, Bangalore 2004)
- 11.184 L. Bernstein, R.J. Beals: Thermal expansion and related bonding problems of some III–V compound semiconductors, *J. Appl. Phys.* **32**, 122–123 (1961)
- 11.185 A. Jordan: Estimated thermal diffusivity, Prandtl number and Grashof number of molten GaAs, InP GaSb *J. Cryst. Growth* **71**, 551–558 (1985)
- 11.186 J.R. Dixon, J.K. Furdyna: Measurement of the static dielectric constant of the InSb lattice via gyrotropic sphere resonances, *Solid State Commun.* **35**, 195–198 (1980)
- 11.187 T. Ashley, C.T. Elliott: Operation and properties of narrow gap semiconductor devices near room temperature using nonequilibrium techniques, *Semicond. Sci. Technol.* **6**, C99–C105 (1991)
- 11.188 Z. Djuric, V. Jovic, M. Matic, Z. Jaksic: IR photodetector with exclusion effect and self-filtering n^+ layer, *Electron. Lett.* **26**, 929–931 (1990)
- 11.189 I. Bloom, Y. Nemirovsky: Surface passivation of backside-illuminated indium antimonide focal plane array, *IEEE Trans. Electron. Dev.* **40**, 309–314 (1993)

- 11.190 E. Michel, J. Xu, J.D. Kim, I. Ferguson, M. Razeghi: InSb infrared photodetectors on Si substrates grown by molecular beam epitaxy, *IEEE Photon. Technol. Lett.* **8**, 673–675 (1996)
- 11.191 M. Razeghi: Overview of antimonide based III–V semiconductor epitaxial layers and their applications at the center for quantum devices, *Eur. Phys. J. PA* **23**, 149–205 (2003)
- 11.192 A. Rogalski: Heterostructure infrared photodiodes, *Semicond. Phys. Quantum Electron. Optoelectron.* **3**, 111–120 (2000)
- 11.193 S.A. Solin, T. Thio, D.R. Hines, J.J. Heremans: Enhanced room-temperature geometric magnetoresistance in inhomogeneous narrow-gap semiconductors, *Science* **289**, 1530–1532 (2000)
- 11.194 M. Oszwaldowski: Hall sensors based on heavily doped n-InSb thin films, *Sens. Actuators A* **68**, 234–237 (1998)
- 11.195 J. Heremans, D.L. Partin, C.M. Thrush, L. Green: Narrow gap semiconductor magnetic field sensors and applications, *Semicond. Sci. Technol.* **8**, S424–S430 (1993)
- 11.196 J. Heremans: Solid state magnetic field sensors and applications, *J. Phys. D Appl. Phys.* **26**, 1149 (1993)
- 11.197 W. Shan, W. Walukiewicz, J.W. Ager III, E.E. Haller, J.F. Geisz, D.J. Friedman, J.M. Olson, S.R. Kurtz: Band anticrossing in GaInNAs alloys, *Phys. Rev. Lett.* **82**, 1221–1224 (1999)

12. Crystal Growth of Oxides by Optical Floating Zone Technique

Hanna A. Dabkowska, Antoni B. Dabkowski

Single crystals of various congruently and incongruently melting oxides have been recently grown by the floating zone (FZ) and traveling solvent floating zone (TSFZ) techniques. For the incongruently melting materials, the use of solvent with an experimentally determined composition allows the establishment of the *practical* steady state much faster, leading to better, more stable growth. Growth conditions for different oxides are compared. Important problems in crystal characterization and assessment of micro- and macrodefects are briefly presented.

12.1	Historical Notes	367
12.2	Optical Floating Zone Technique – Application for Oxides	368
12.3	Optical Floating Zone and Traveling Solvent Crystal Growth Techniques	369
12.4	Advantages and Limitations of the Floating Zone Techniques	370

12.5	Optical Floating Zone Furnaces	371
12.6	Experimental Details of Ceramics and Rod Preparation for OFZT	372
12.7	Stable Growth of Congruently and Incongruently Melting Oxides	373
12.8	Constitutional Supercooling and Crystallization Front Stability	375
12.9	Crystal Growth Termination and Cooling	377
12.10	Characterization of Crystals Grown by the OFZ Technique	377
12.11	Determination of Defects in Crystals – The Experimental Approach	380
12.12	Details of Conditions for Growth of Selected Oxide Single Crystals by OFZ and TSFZ Methods	383
12.13	Conclusions	386
	References	386

12.1 Historical Notes

W. G. Pfann, a metallurgist at Bell Laboratories, developed zone refining, a precursor of floating zone crystal growth, in 1951. Pfann's process [12.1] involved placing the material to be crystallized in a crucible rather than suspending it in space as is the case in today's floating zone process. In 1952 Theurer, also at Bell Laboratories, created the floating zone process. Slightly later and independently, von Emeis at Siemens [12.2] as well as Keck and Golay [12.3] of the US Army Signal Corps developed a similar technique. Keck and Golay used *incandescent heating* with a short cylindrical tantalum heater rather than an optical system

and published their results in 1952. As Theurer's diary showed his priority in the invention, Bell Laboratories was eventually assigned a US patent [12.4]. According to Mühlbauer [12.5] the first firm to commercialize the float zone technique was Siemens in the early 1950s. They used the process in the course of manufacturing silicon, and patent for the technique known as the floating zone method was granted to them in 1953. They became the first company to produce ultrapure silicon single crystals for semiconductor devices by applying induction (radiofrequency, RF) heating to melt a narrow part of a cylindrical rod of polycryst-

talline material. Passing this molten zone along the rod transformed the ceramics into single crystals. In this case surface tension together with the electromagnetic force (*levitation*) supported the melt. The first company to manufacture a floating zone apparatus commercially was Ecco Corporation, North Bergen, NJ, in 1953.

The further development and production of float zone (FZ) silicon crystals took place in many countries. Detailed historical notes about the development of FZ technique can be found in [12.5]. Until the end of the 1950s, crystal diameter size did not exceed 25 mm, whereas during the 1960s and 1970s a dramatic increase from 33 to 50 and 75 mm was achieved. This diameter enlargement was a prerequisite for the development and fabrication of high-power discrete devices such as thyristors and others. The 100 mm crystal appears at the end of the 1970s, the 125 mm one in 1986, the world-wide first 200 mm (100) dislocation-free silicon crystal was grown at Wacker-Siltronic Company in September 2000.

Ferrites became important materials for microwave applications in the late 1950s and the floating zone tech-

nique was an obvious choice for crystal growth, but direct RF heating cannot be easily apply to oxides. Optical heating (*arc image furnaces*) utilizing carbon arc and elliptical mirrors was introduced for crystal growth of magnesium ferrite and sapphire by *De La Rue* and *Halden* [12.6] as a replacement for flame melting in the Verneuil method. His apparatus was based on earlier concepts and experiments with *image furnaces*, see *Null* and *Lozier* [12.7]. The concept of the image furnace was adopted to zone melting (in the geometry later call *pedestal growth*) for silicon by *Poplawsky* and *Thomas* [12.8] and soon *Poplawsky* applied this technique to ferrites [12.9]. The carbon arc heating is not an easy method to control, so at the same time the floating zone growth of yttrium iron garnet, $\text{Y}_3\text{Fe}_5\text{O}_{12}$ (YIG) was performed with RF heated MoSi_2 susceptor – which is also a kind of infrared (IR) optical heating – by *Abernethy* et al. [12.10]. As interest in ferrites was growing, soon more convenient halogen lamps and even more powerful xenon arc lamps were introduced and the apparatus for crystal growth of ferrites was developed by the groups of *Akashi* [12.11] and *Shindo* [12.12] in Japan.

12.2 Optical Floating Zone Technique – Application for Oxides

More recently the floating zone technique using halogen lamps and ellipsoidal mirrors (often called optical floating zone, OFZ) has been employed for crystal growth of a wide range of materials, including metals, oxides, and semiconductors [12.13–16]. With a growing number of optical systems around the world this technique is gaining popularity as the method of choice for the growth of various nonconventional oxides including high-temperature superconductors and new magnetic materials [12.17].

Crystals grown by the optical floating zone technique are of high quality but relatively small (usually not larger than a few millimeters in diameter and a few centimeters in length) so the majority of work is concentrated on new materials grown mainly for research purposes.

Recently high-quality crystals of $\beta\text{-Ga}_2\text{O}_3$ as large as 1 inch in diameter have been reported [12.18] but the only oxides grown by this technique for indus-

trial applications are still $\text{Y}_3\text{Fe}_5\text{O}_{12}$ [12.12, 14, 19] and TiO_2 [12.20].

In this chapter the advantages and disadvantages of the FZ technique for the growth of crystals of congruently and incongruently melting oxides and their solid solutions are discussed. For incongruently melting materials a variation of the FZ technique, called the traveling solvent floating zone (TSFZ), technique is used. Both methods are suitable for the growth of solid solutions.

The list of oxide materials grown by FZ and TSFZ methods includes simple oxides such as $\beta\text{-Ga}_2\text{O}_3$ or TiO_2 , as well as, complex oxides such as the spin Peierls material CuGeO_3 [12.17], high-temperature superconductors such as $\text{Bi}_2\text{Sr}_2\text{CaCu}_2\text{O}_n$ (BiSCCO) [12.17, 21], and frustrated antiferromagnets such as $\text{RE}_2\text{Ti}_2\text{O}_7$ (RE = rare earth) [12.22, 23].

The origin of most common macro- and microdefects – often seriously influencing crystal properties – is also briefly presented.

12.3 Optical Floating Zone and Traveling Solvent Crystal Growth Techniques

The idea of the optical floating zone is presented in Fig. 12.1. Two ceramic rods are mounted in such a way that their tips meet at the focal point of ellipsoidal mirrors. Halogen or xenon lamps of appropriate power sit at the other focal points of these mirrors. Any crystal growth process performed by the optical floating zone starts by melting the tips of polycrystalline rods, bringing them together and establishing a liquid called the *floating zone* between the bottom (seed) rod and a top (feed) rod (Fig. 12.2).

After the zone is created it starts moving upwards (either by moving the mirrors up or by moving the seed-and-feed setup down), the liquid cools and the material eventually crystallizes on the seed rod. During growth the rods rotate either in the same or in opposite directions with experimentally established rates. The rate of rotation is important as it is responsible for a pattern of forced convection flows within the zone and – as a result – for mixing of material, for the shape of the crystallization front (solid–liquid interface), and for the defects resulting from it. The rotation speed is optimized experimentally for each material and varies from 0 to 50 rpm. Successful growth requires a very stable zone. Stability of this zone depends on the quality of the starting rods as well as the alignment of both the feed and the seed rods. This is achieved by rigidly fixing the seed

rod to the lower shaft. The feed rod can either be attached equally rigidly to the top holder or can hang loosely from a hook. Rigid mounting requires a very high-quality (straight and dense) rod and a very precise alignment. Another important factor is the alignment of the lamp and mirrors. Mirrors are usually factory preadjusted, but alignment of lamps critically influences the temperature distribution within the zone.

It is advisable to start the growth on a crystalline, oriented seed, as this facilitates the beginning of crystallization and controls the appropriate orientation. It also prevents the soaking of the molten zone into the porous seed rod.

During the growth process only few parameters can be controlled. The pulling rate can be adjusted and this controls average growth rate. Due to the heat of crystallization this parameter also influence temperature near the crystallization front. The lamp power setting directly controls molten zone temperature, temperature gradients and also influences size and shape of the floating zone. The rate of rotation of both rods controls stirring of molten material which influence both, temperature distribution and composition within molten zone. Finally, adjusting the feeding rate controls the size of the zone.

There has been an intensive effort to model the silicon process [12.24, 25] but only a few modeling attempts have been made to understand what is happening inside the oxide molten zone [12.26–28]. The majority of modeling works deal with the floating zone method itself, investigating temperature oscillation in the zone [12.29], detailed lamp irradiation and thermal flows analysis [12.30, 31] or assessing the interface

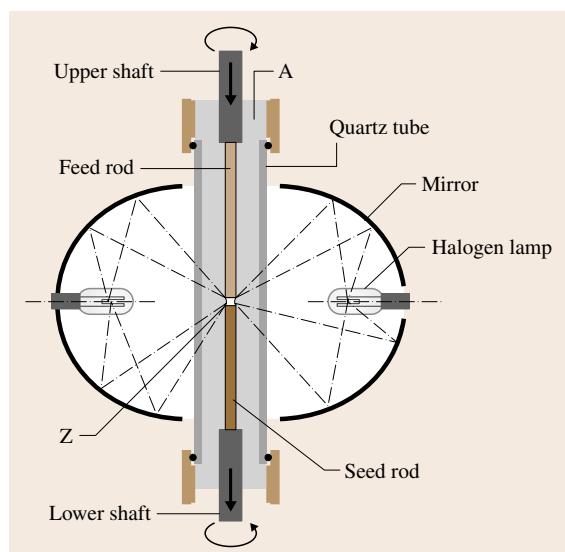


Fig. 12.1 Schematic diagram of optical floating zone apparatus (A – atmosphere, Z – floating zone)

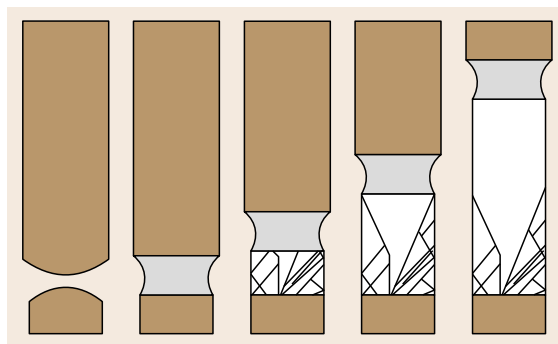


Fig. 12.2 Stages for nucleation on ceramic rods (see also Fig. 12.17)

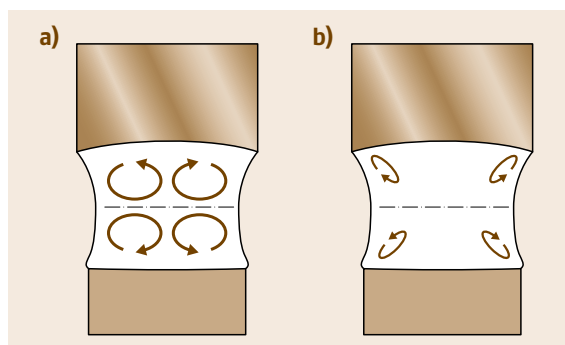


Fig. 12.3a,b Convection flows in the molten zone. (a) Combined buoyancy and forced convection for counter-rotation. (b) Marangoni convection (after Brice [12.32])

shape [12.27]. The recent and most likely the most advanced three-dimensional (3-D) modeling, performed by Lan [12.28] for optical heating with two elliptical mirrors in the horizontal configuration, suggests that the temperature distribution is less symmetrical and that the pattern of convection cells is more complex than the one presented by Brice [12.32] in an older, simpler description of Si growth with RF heating. External heating (either optical or RF) causes significant overheating of the liquid zone surface. High temperature gradients in the molten zone lead to strong buoyancy as well as Marangoni convection [12.29]. If the feed and seed rods counter-rotate the convection patterns become even more complicated. To explain these patterns the existence of upper and lower convection cells has been suggested. A schematic explanation of convection flows in the molten zone is shown on Fig. 12.3. Because

the flows on the cells' interface should be collinear, one can expect only limited liquid exchange and – for incongruently melting materials – upper and lower cells having distinctively different chemical compositions.

Using growth of $\text{Y}_3\text{Al}_5\text{O}_{12}$ as an example of a congruently melting material (melting point, $\text{mp} = 1970^\circ\text{C}$) grown in a double elliptical mirror system, Lan [12.28] concluded that the overheating (above mp of the material) is higher than 600°C , with azimuthal differences of more than 400°C (in the plane of lamps) and a temperature gradient near liquid–crystal interface in the range of $1500^\circ\text{C}/\text{cm}$. As this model assumes no rotation, the realistic values of the temperature gradients as well as overheating with rotation will most likely be lower.

Very high thermal gradients, even with a small size of the liquid zone (typically 0.4 cm^3 for 0.7 cm rod diameter), cause fast convection flows. Indeed, the results of Lan's modeling suggest that the liquid velocity in the zone is in the range of up to a few cm/s .

In order to do the modelling one needs experimental values of material properties such as the surface tension, wetting angle, melt viscosity, and density as well as the optical properties, emissivity factor and thermal conductivity of the melt and the crystal. The change of these properties with temperature should be known as well. Although this information is available for $\text{Y}_3\text{Al}_5\text{O}_{12}$ [12.33], it is not yet available for the majority of oxides.

Due to experimental challenges and the high temperatures involved unfortunately it is not yet feasible to directly compare this modeling with experimental results.

12.4 Advantages and Limitations of the Floating Zone Techniques

The greatest advantages of the OFZ technique come from the fact that no crucible is necessary and that both congruently and incongruently melting materials can be grown. This allows for growth of large-sized crystals that was not possible before. The relatively high thermal gradient on the crystallization front characteristic of this method decreases the chance of constitutional supercooling and allows for faster growth of incongruently crystallizing materials (see the discussion in Sect. 12.7). It is also important to note that oxides with the highest melting temperatures can be grown using xenon lamps. The growth can be conducted at high pressure (up to 70 atm , depending on the furnace model) and in a controlled gas atmosphere. Solid solutions with controlled

and uniform chemical composition can be prepared because – in contrast to crucible methods – the steady state, in principle, can be achieved. This is beneficial for crystallization of incongruently melting materials and for doped materials (with distribution coefficient different than 1), as well as materials in which, due to cation substitution, the congruently melting composition is not stoichiometric. The floating zone technique, when supported by characterization methods such as differential thermal analysis (DTA) or/and x-ray diffraction, is also an effective approach for the construction and investigation of phase diagrams [12.15].

There are some limitations to the growth of crystals by the OFZ method. As a rule this method is not

suitable for materials with high vapor pressure, low surface tension or high viscosity as well as for materials that undergo a phase transition during cooling (because such crystals usually crack after growth) [12.34, 35].

The small volume of liquid in the zone makes the stability of this crystal growth method susceptible to fluctuations of power and/or short-time oscillations of

gas pressure. Together with very high thermal gradients at the liquid–solid interface this leads to difficulties in achieving and maintaining a flat crystallization front and stable growth rate, which can result in many defects and growth instabilities [12.36]. Significant thermal and mechanical stresses limit the size and quality of crystals obtained. This problem is reduced if an afterheater is applied [12.14, 37, 38].

12.5 Optical Floating Zone Furnaces

Several types of optical floating zone furnaces are commercially available on the market, with two [12.14, 39, 41] or four [12.15, 40] ellipsoid mirrors. The idea of the furnace using only one mirror was also tested in 1969 [12.11, 13]. All these furnaces employ halogen or xenon arc lamps of different power as an energy source and – as already mentioned before – the growth can be carried in a controlled gas atmosphere and/or at high pressure. Using high pressure is advantageous in the case of crystallizing materials with high vapor pressure at crystallization temperature. As the diffusion coefficient is inversely proportional to pressure, higher pressure will slow the vapor transport from the source

(the molten zone or its hottest regions) to the coolest part of the system (quartz tube). Furthermore, using gas with higher molecular mass (for example Ar instead of N₂) reduces the rate of evaporation. Additionally, the capability of FZ systems to apply high pressure is useful when high partial pressure of oxygen (p_{O_2}) is required to stabilize higher oxidation state of cation(s) and – as a result – crystallization of the appropriate phase. Oxygen pressure as high as 70 atm was used to growth of single crystals of ferrites [12.14] whereas for growth of layered cuprates application of O₂ stabilizes Cu²⁺ [12.17, 42, 43].

The main difference between the commercially available furnaces is that in one system the lamps

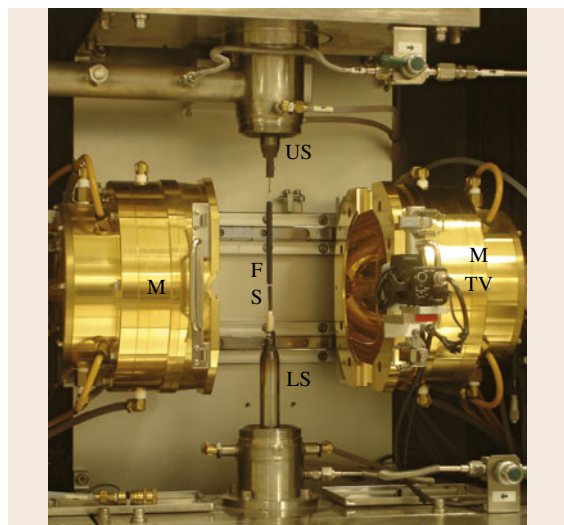


Fig. 12.4 Two (metallic) mirrors optical system of Nippon Electric Co. (now Canon). Mirrors are moved from their operational positions and the quartz tube is not installed for clarity of the view. M – mirrors, F – feed rod, S – seed rod, US – upper shaft, LS – lower shaft, TV – camera (after [12.39])

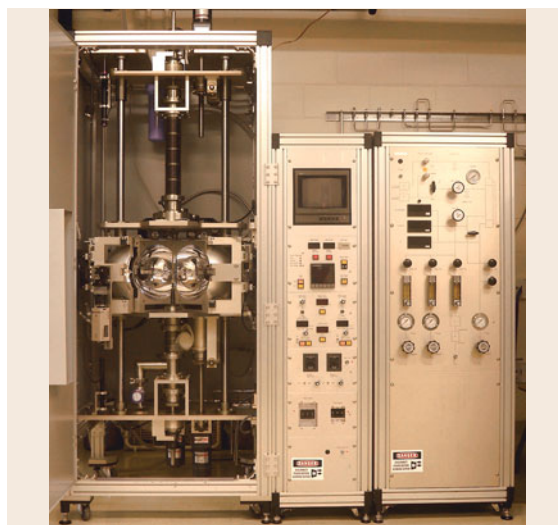


Fig. 12.5 General view of a crystal system machine (after [12.40]). The door to the four mirror optical system is open, and also the two front mirrors are open on their hinges to improve the view. The pressure control panel is on the *right side*

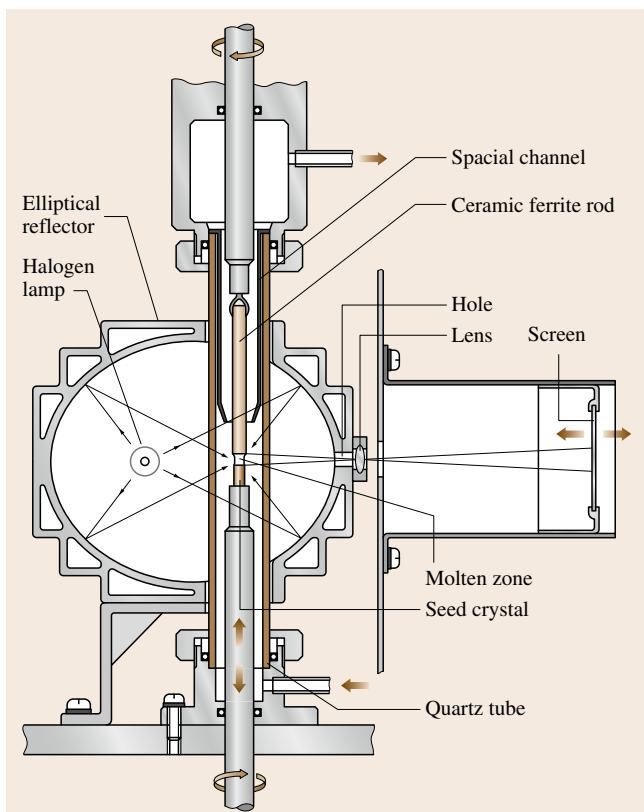


Fig. 12.6 Schematic drawing of a single elliptical mirror furnace (after Akashi et al. [12.11])

move (Crystal System [12.40]), whereas in the others (NEC [12.39] and URN2-ZN [12.41]) the rods move while the lamps stay in one position. In addition in the URN2-ZN apparatus the elliptical mirrors are configured in such a way that the optical axis of the system is vertical and the mechanical axis (of the rods) overlap. The single xenon lamp is at the focus of the lower mirror and the FZ at the focus of the upper one. This optical system is more complex and access to the growth chamber seems to be more complicated, but one gains a uniform azimuthal temperature distribution and less overheating of liquid.

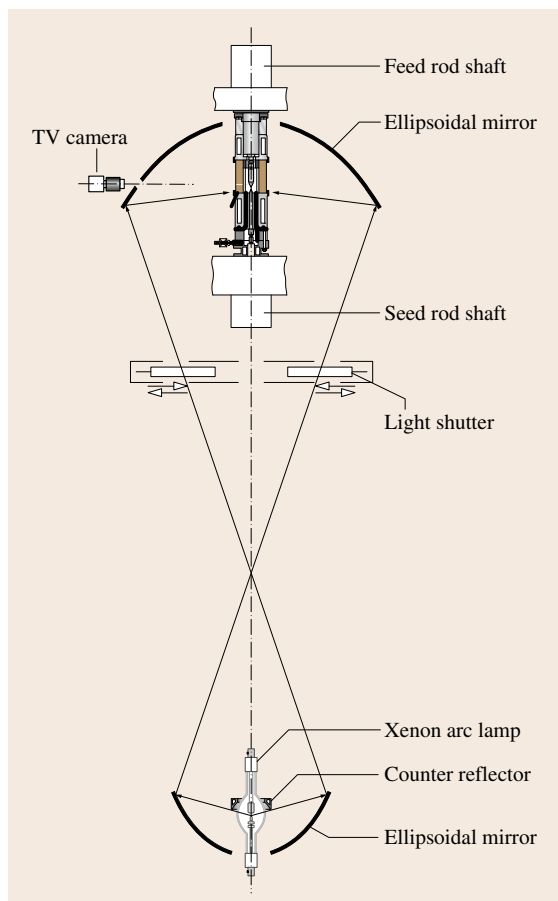


Fig. 12.7 Schematic drawing of URM2-ZN design with vertical optical axis (after [12.41])

The practical, commercial realizations of OFZ are presented in Figs. 12.4 and 12.5 and drawings of other designs are presented on Figs. 12.6 and 12.7.

All of the furnaces are usually equipped with video cameras, allowing in situ observation of the crystal growth process during experiments. There are also options that allow for remote control of the process via the Internet. This is helpful for adjusting growth conditions during lengthy experiments.

12.6 Experimental Details of Ceramics and Rod Preparation for OFZT

Stability of the growth process – and the quality of the obtained crystal – depends strongly on the stability of the zone. This depends on the stability of the power and of the feed and seed rod shaft translations.

Modern equipment is capable of stabilizing the power supplied to the halogen lamp with relative accuracy better than 10^{-4} , and the rate of shaft translation is realized with similar accuracy. Stability of the gas pres-

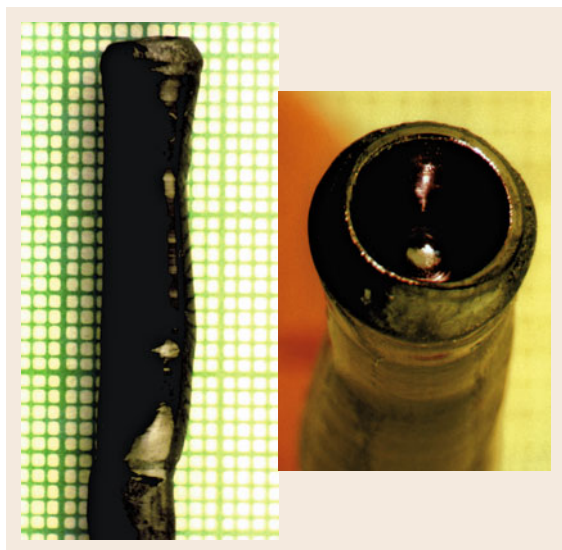


Fig. 12.8 CoTiO_3 crystal (growth rate 1 mm/h) showing internal cavity caused by a stable bubble seriously interrupting growth

sure (and flow) is important for a constant temperature distribution as well, as even small fluctuations have to be avoided. Furthermore, achieving a stable liquid zone requires a homogeneous, uniformly dense ceramic rod acting as the source of material for crystallization. Gas bubbles incorporated into the feed rod can seriously influence the zone, interrupting the crystal growth process (Fig. 12.8).

Successful preparation of starting rods for crystal growth requires: muffle furnaces for preliminary ceramics preparation, furnaces with controlled atmosphere appropriate for rod sintering, a hydrostatic press, as well grinders and/or mortars, as the particle size after grinding is crucial for obtaining good-quality rods.

The first step in rod preparation is a typical ceramics synthesis. The batch of powders is weighed accordingly to the chemical reaction and is prepared by ball-mixing and then by manual or automatic grinding in the mortar.



Fig. 12.9a–c Steps for preparation of ceramic feed rods of $\text{SrCu}_2(\text{BO}_3)_2$: (a) sintered in air, (b) sintered in O_2 , (c) pre-melted in O_2

The powders are pelletized and annealed at an appropriate temperature and specific time. The quality of the prepared ceramics is assessed by x-ray diffraction and – if found to be acceptable – the material is reground and formed as a rod (typically 8–10 mm in diameter and 120–150 mm long) by either cold or hot pressing. The pressure has to be experimentally selected to avoid *over-pressing*, with the typical range being 800–2500 atm. Polyvinyl alcohol, glycerol or other common additives are often used to reduce internal friction during pressing, allowing the production of denser, less porous ceramic rods. The pressed rod is later sintered at an optimized temperature and appropriate atmosphere.

The density of as-obtained ceramic rods (Fig. 12.9) should be measured and compared with the crystallographic density. This ratio depends as much on the material as on the quality of preparation and varies dramatically from under 60 to above 90%. In many cases, when evaporation is not an issue it is suggested to premelt (grow very fast) a less dense rod before performing the final crystal growth. This was found to be especially important for slower-grown, incongruently melting compounds (e.g., high temperature superconductors (HTSC) or $\text{SrCu}_2(\text{BO}_3)_2$). In the furnaces mentioned above, crystals up to 100–150 mm long and 10 mm in diameter can be grown, but the typical size of a good-quality grown crystal is usually smaller.

12.7 Stable Growth of Congruently and Incongruently Melting Oxides

Differential thermal analysis (DTA) should be routinely performed for all (attempted) new materials to establish their melting properties. For many new materials this is often not possible as DTA apparatus rated above 1500 °C are not common and analysis at elevated tem-

peratures is often limited by a lack of appropriate crucible materials. In this case the melting properties are determined during preliminary growth. Depending on those properties either the direct crystallization or the traveling solvent zone (TSZ) approach is applied.

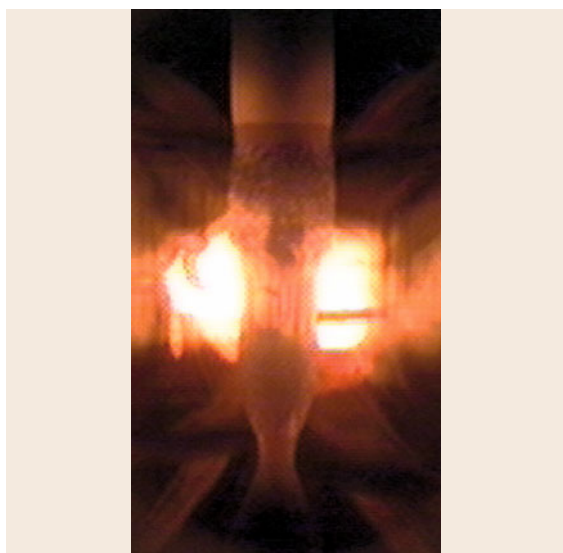


Fig. 12.10 Growth of congruently melting Al_2O_3 in an NEC furnace. Note *necking* on the lower part of the crystal

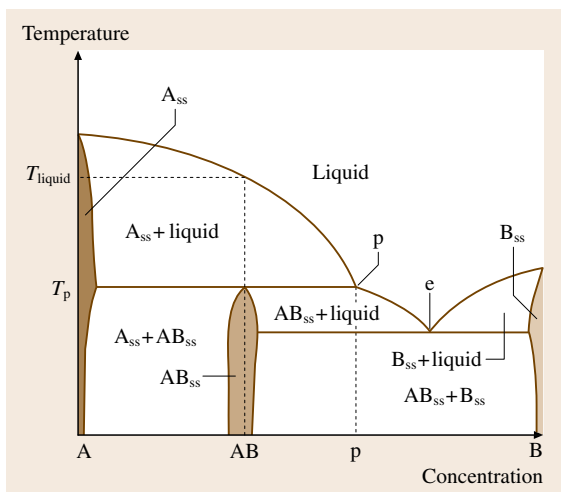


Fig. 12.11 Generic phase diagram of compound AB melting with peritectic decomposition

For congruently melting oxides the composition of ceramic rods, growing crystal, and the melt is the same. The crystal growth process in this case is relatively fast, and the growth rates vary from 1 to as high as 50 mm/h. Rods rotate in opposite directions so that temperature uniformity as well as mixing of material inside the molten zone is achieved (Fig. 12.10).

When an incongruently melting material (Fig. 12.11) is being grown one has to use a solvent (flux) to make

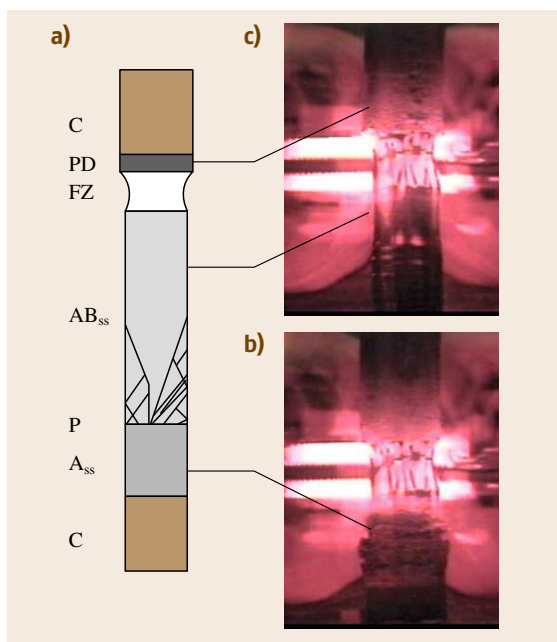


Fig. 12.12 (a) Simplified description of the creation of self-flux and growth of an incongruently melting oxide; C – ceramic rods with composition AB , A_{ss} – precipitation of phase A_{ss} . P – composition of liquid is passing peritectic point P, AB_{ss} – crystallization of AB_{ss} begins. FZ – floating zone, PD – peritectic decomposition of ceramic AB . On the beginning of growth primary phase A_{ss} crystallizes from FZ and liquid is continuously enriched in compound B until it reach peritectic composition P where AB_{ss} becomes primary phase solidifying with multiple nuclei. Grains with favoured orientation are growing faster and a single crystal of AB_{ss} can be grown. (b,c) growth of incongruently melting $\text{Ba}_x\text{La}_{1-x}\text{CuO}_4$ in a Crystal System furnace; image (c) recorded 23 h after image (b)

crystallization possible. The composition of the flux can be suggested on the basis of information from the appropriate phase diagram [12.44]. If this is not feasible it is suggested to use the self-flux approach. In such a case the zone is created by melting the ceramic rod (with composition similar to the composition of the required crystal) and carefully adjusting the temperature and growth speed until the evolution of the composition of liquid zone stabilizes growth with the required composition. In the case of peritectic transformation, the crystal growth starts with the precipitation of high-temperature primary phase on the seed rod (Fig. 12.12).

The zone composition then changes towards and beyond the peritectic liquid composition until a nearly

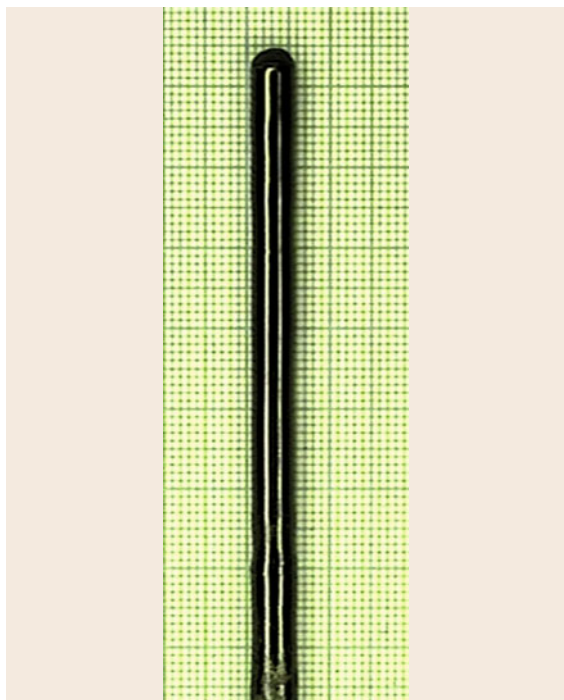


Fig. 12.13 Single crystal of incongruently melting $\text{La}_{2-x}\text{Ba}_x\text{CuO}_4$ grown by TSFZ technique (1 mm/h, 180 kPa O_2)

steady state is established and crystallization of the required phase begins. If the zone is quenched at this point it is possible to analyze the composition of the self-flux [12.45, 46].

In subsequent growths, to speed-up the process of achieving the nearly steady state, it is recommended to use a flux pellet with appropriate composition and size to create the molten zone. The flux pellet is synthesized and mounted between the feed and seed rods. As the temperature increases it melts and the rods become joined. At this point, the temperature has to be carefully adjusted again to allow for the establishment of a steady state, and then the growth starts. Dissolving the feed rod into the liquid in the zone continually restores the amount of material solidifying from the zone on the seed rod. The growth should be slow, due to the slow mass transport through the diffusion layer at the solid–liquid interface. For complex oxides such as $\text{Bi}_2\text{Sr}_2\text{Ca}_2\text{Cu}_3\text{O}_{10}$ [12.47] or $\text{SrCu}_2(\text{BO}_3)_2$ [12.48] it can be as slow as 0.1–0.2 mm/h, allowing crystallization of appropriate phase from a melt of significantly different composition.

Some materials decompose during growth and lose one of the components due to evaporation. In this case a small addition of the evaporating constituent to the feed rod proved to be successful (e.g., 1–1.5% CuO in $\text{Ba}_x\text{La}_{1-x}\text{CuO}_4$ [12.42, 49], see Fig. 12.13).

12.8 Constitutional Supercooling and Crystallization Front Stability

For complex oxides the congruently melting composition is quite often not exactly stoichiometric. This effect is well known for LiNbO_3 and was also observed for RE garnets (where the smaller RE ions usually occupying dodecahedral position also substitute smaller cations at octahedral positions). In such a case the evolution of the molten zone composition helps to produce crystals with composition close to stoichiometric. In the case of peritectic-type melting of binary (or more complex) compounds with solubility in the solid phase (i.e., with distribution coefficient $\neq 1$) the composition of liquid and solid in equilibrium are different (Figs. 12.11 and 12.12). Convection and/or mechanical mixing stir the majority of the volume of the liquid phase and this volume has a relatively uniform composition, but the layer in the vicinity of the crystallization front is nearly stagnant. This layer is depleted of the species that are incorporated into the crystal and enriched in those species rejected from the solid state. In contrast

to the volume of the well-stirred convection cell, mass transport in this layer is mostly driven by diffusion (*diffusion layer*) and a significant gradient of concentration is observed. For a distribution coefficient $k \ll 1$ this effect is more pronounced, and still more pronounced for the peritectic-type transition. As a result of this concentration gradient the solidus temperature decreases towards the solid–liquid interface. For lower thermal gradients in the diffusion layer a part of this layer can be supercooled more than liquid in close vicinity to the solid–liquid interface (Fig. 12.14), an effect referred to as *constitutional supercooling* [12.32, 50, 51].

As the growth rate is proportional to the degree of supercooling any positive fluctuation in the growth rate will lead to a further increase of growth rate (as it forces solid–liquid interface deeper into more supercooled liquid). The regions of the adjoining liquid will be even more depleted from crystal constituency and locally the solidus temperature will be even lower.

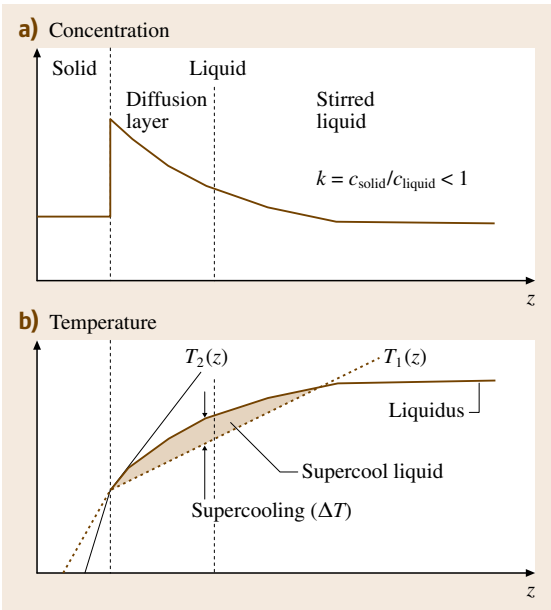
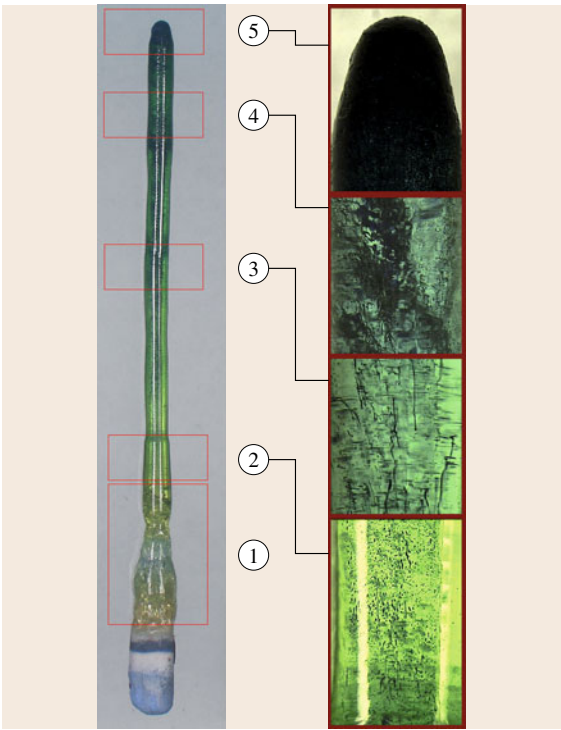


Fig. 12.14a,b Constitutional supercooling. **(a)** Concentration of dopant with distribution coefficient < 1 near the solid–liquid interface. **(b)** Conditions for constitutional supercooling near solid–liquid interface in the case of lower thermal gradient for temperature distribution $T_1(z)$

This causes crystallization front instability. Solute-rich channels form with the general direction parallel to the crystallization direction, which is not necessarily the pulling direction (note that both convex and concave crystallization fronts were observed in OFZ experiments) [12.52]. *Microfaceting* and *cellular growth* are often observed. For materials with high growth-rate anisotropy (especially for crystals with layered crystallographic structures such as CuGeO_3 [12.43] or $\text{Bi}_2\text{Sr}_2\text{CaCu}_2\text{O}_n$ [12.53]) this can result in platelike growth. Other defects such as flux tubes, precipitations,



and dendrite growth can also be expected as a result of crystallization front instability (Figs. 12.15 and 12.16).

To avoid constitutional supercooling the growth rate should be decreased. This measure reduces concentration gradients and the possibility of supercooling. Higher thermal gradients (on the solid–liquid interface) can also be suggested as a remedy. Unfortunately this action will cause even larger temperature gradients in the growing crystal, which can result in cracking during cooling (Fig. 12.15).

Control of the thermal gradient in the liquid near the crystallization front is a challenging problem. One

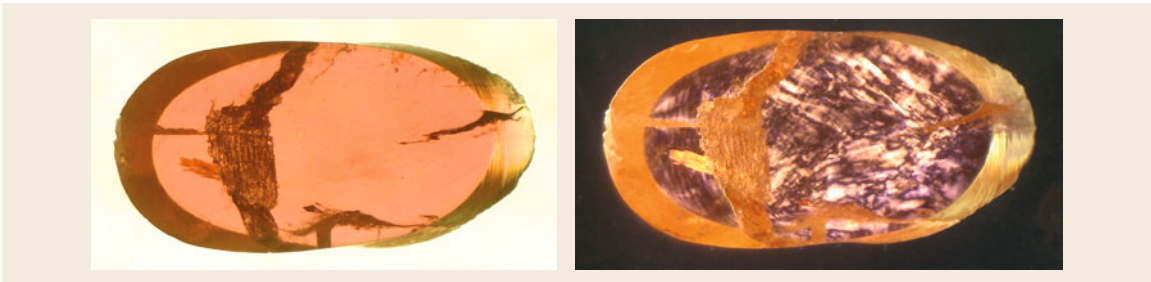


Fig. 12.15 Cut and polished slice of $\text{Dy}_2\text{Ti}_2\text{O}_7$ for defects observation. Transmission and dark field (crossed polarizers) macrophotographs

Fig. 12.16 Influence of evolution of composition of the molten zone on the crystallization process and defects in a *green sapphire* crystal grown by optical FZ. Al_2O_3 doped with $< 2\%$ of transition-metal oxides. Growth rate 8 mm/h in air, 25 rpm (counter-rotation). Transmission macrophotograph. (1) Initial part of growth. Nucleation begins on a ceramic seed rod with composition identical to the feed rod. The composition of molten zone is similar to that of the ceramic, resulting in low concentration of dopant in the crystal (*low coloration*). A multigrain crystal evolves into a single crystal after necking. Thermal stress during cooling causes cracks in the multigrain region. (2) Beginning of single-crystal growth. The concentration of dopant in the molten zone increases, as does the concentration of dopant in the crystal (*green coloration*). Isolated precipitations are seen as *dark spots* elongated in the growth direction (*white vertical strips* are caused by light reflection inside crystal). (3) Central part of the growth. The concentration of dopant in the solid (*greener coloration*) increases as a result of significantly higher accumulation of dopant in the molten zone. The density of precipitations increases due to more severe constitutional supercooling conditions. Note the striations, related to growth rate instability. These striations visualize a nearly flat crystallization front. (4) Advanced part of the growth. The concentration of dopant in the solid (*more green*) is higher due to the accumulation of dopant in the molten zone. This relative increase of dopants is lesser than observed in the lower part of crystal showing a tendency to stabilize. The density of precipitations is high. (5) The final part of the growth crystal growth termination. The crystal grows faster for a brief period of time and then the molten zone solidifies quickly (paraboloid tip). The fast growing part has a high density of precipitates and higher dopant concentration (*very green*). Very high concentration of dopant (and defects) is present in the solidified tip; this part of boule crystal is opaque ◀

of the possible approaches – anisotropic heating – was successfully applied by Watauchi et al. [12.54] for growth of congruently melting CuGeO_3 and incongruently melting $\text{Sr}_{14}\text{Cu}_{24}\text{O}_{41}$.

These effects are also depicted in Fig. 12.16. Single crystals of *green sapphire* (Al_2O_3 with $< 2 \text{ mol } \%$ of transition-metal oxides added, dopant segregation coefficient < 1) have been grown with constant pulling rate and dopant accumulate in the FZ as growth

progress. As the concentration of dopant increases, so does the degree of constitutional supercooling, creating increasing amount of defects. As the growth was not long enough the *steady state* could not be achieved (as it is an asymptotic process), but coloration of the upper part of the crystal indicates that as the crystal grows the dopant concentration apparently stabilizes – in contrast to the crucible methods.

12.9 Crystal Growth Termination and Cooling

As most of the heat is supplied to the crystal via the liquid zone, growth termination generates difficult-to-avoid *thermal shock* to the crystal. To lower the thermal shock the tip of as-grown crystal should be left in the hot zone during the lamp cooling process. The rate of lamp cooling should be related to the growth rate as switching off the lamps rapidly results in cracks in the crystal.

In some cases, it is advisable to relax the stresses created during the growth and cooling process by annealing the as-grown crystal at elevated temperature, then cooling it slowly to room temperature. After growth, annealing in a specific atmosphere often helps to reduce the number of defects present [12.51].

12.10 Characterization of Crystals Grown by the OFZ Technique

A good crystal – as defined by the *end user* – is in fact a crystal sample optimized for measurements or analysis by a particular method. Such a sample is usually oriented and cut to the required size. Special preparation of the surface of the crystal may also be necessary.

Large single crystals of silicon grown by the FZ method are of extremely good quality and can be dislocation free, but even they are not perfect as they have striations, oxygen incorporation, and other minute defects that influence or limit some demanding applica-

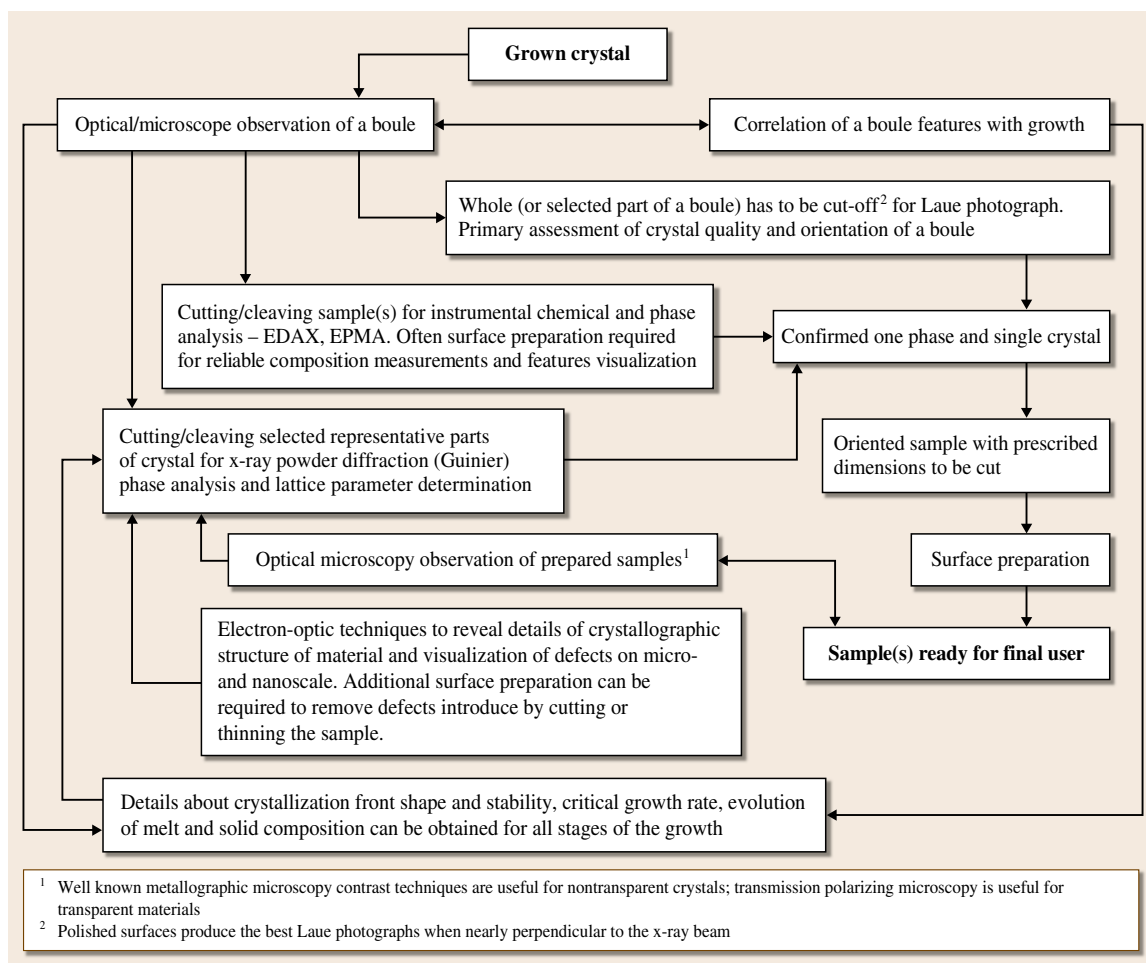


Fig. 12.16 Experimental approach to characterization of crystals grown by optical floating zone techniques

tions [12.55]. Improving the quality of a substantial size crystal in real life is a challenging and time-consuming task. It is mostly driven by specific applications or user demands – the silicon with its steady improvement is the best example.

Oxide crystals grown by OFZ method are not an exception to this rule and a lot of time and effort has been spent perfecting them. The more complicated the chemical formula of the attempted material, the more time is required to grow high-quality (although still not perfect) single crystals.

Careful characterization of both preprepared ceramics and the resulting crystals is essential for producing high-quality materials for further applications. This characterization depends as much on the material itself as on the purpose of its production.

Full characterization of a crystal involves a lot of time and manpower and is rarely performed. As growers using floating zone technique are interested mostly in investigating specific effects (e.g., superconducting properties) they often neglect detailed characterization of the crystals obtained. Even more unsettling is the fact that reviewers of renowned journals accept works done on crystals with virtually no characterization mentioned. This creates a vicious circle, as a generation of students believes that anything grown is a single crystal. Figure 12.16 suggests the basic experimental approach to characterization and quality improvement of crystals grown by the OFZ technique.

The existence of the required phase is usually confirmed by x-ray powder diffraction. Powder diffraction



Fig. 12.17 Cross section of the initial part of $\text{Sr}_{14}\text{Cu}_{24}\text{O}_{41}$ crystal grown at 1 mm/h in 8 atm O_2 . Note the visible grain boundaries on the axial cross section and a core on the cross section perpendicular to the boule axis

also allows the assessment of the uniformity of the material and addresses the problem of the existence of more than one phase. Accurate values of crystallographic lattice parameters can be measured by a Guinier camera with either Si or KCl as the internal standard, using a minute amount of material cut or cleaved from selected, characteristic parts of a boule. This information is important when crystals of solid solutions are obtained.

The observation of an as-grown transparent boule under an optical and/or polarizing microscope can reveal different defects in the crystal and their evolution during the growth process. It can also monitor the continuity of the growth and facilitate the observation of how changes of growth conditions (applied power, growth, and feed rate as well as speed of rotation) influence the quality of material grown (Fig. 12.17).

For nontransparent materials the surface features often mask the volume ones. This makes orientation of an as-grown FZ crystal very challenging. The majority of crystals grown by OFZ technique do not show distinctive facets (due to the high thermal gradients); usually they are round or oblong in cross section (Figs. 12.17 and 12.18). In this case sectioning of a grown boule and special surface preparation such as polishing and chemical etching are necessary before orientation by x-ray methods.

If as-grown crystals show distinctive facets then the facet quality may indicate overall crystal quality, and their shape and the angles between them as well as optical properties of materials can be used to orient the crystal. The existence of facets suggests a convex interface and can also be connected to growth striations. X-ray topography, discussed in detail in [12.56], con-



Fig. 12.18 Single crystal of $\text{SrCu}_2(^{11}\text{BO}_3)_2$ grown at 0.25 mm/h in 280 kPa (abs.) O_2

firmed a compositional difference between faceted and nonfaceted regions for YIG crystals [12.13, 57].

The Laue photography technique is a versatile method for crystal orientation (especially with available software [12.58]) and can also provide a preliminary assessment of the as-grown rod quality, answering the basic question of whether the material is a single crystal, multigrain sample (*blocks*) or polycrystalline boule with some degree of texture, etc. As the penetration of x-rays is in the micrometer range, the confirmation of crystallinity of a whole boule requires multiple Laue photographs (Fig. 12.19). If the Laue technique is used to assess local crystal quality, which relies on visual analysis of the shape of diffraction spots, its sensitivity is considerably limited and produces qualitative results only. For crystals of high quality collecting a *rocking curve* (ω -scan, which allows us to determine the full-width at half-maximum, **FWHM**) or pole figures using multiaxis diffractometers (preferably on polished and chemically treated

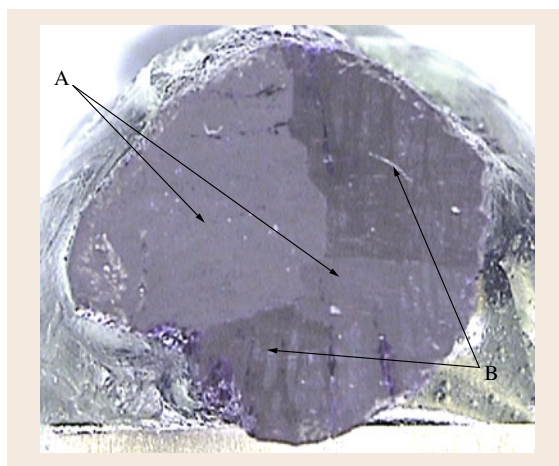


Fig. 12.19 Two grains in $\text{SrCu}_2(\text{BO}_3)_2:\text{Mg}$ crystal. Regions marked A have nearly identical crystallographic orientation, but different from that in regions marked B, which are also co-oriented (characterization by Laue photography, courtesy of S. Dunsiger)

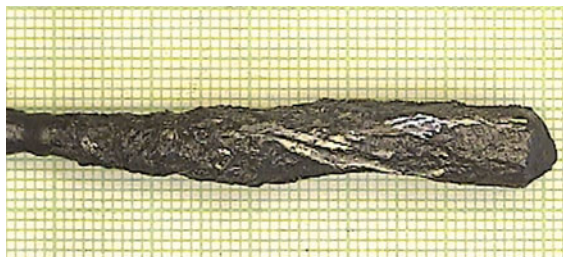


Fig. 12.20 Single crystal of $\text{Sr}_{1.95}\text{Na}_{0.05}\text{Cu}_2(^{11}\text{BO}_3)_2$ grown at 0.25 mm/h in 280 kPa (abs.) O_2

surfaces) addresses problems related to mosaic spread, grains, and twinning in a more quantitative manner. The rocking curve method can also be used for neutron diffraction [12.59].

Solving crystallographic structure provides the ultimate description of the crystal. Single-crystal x-ray diffraction is performed on a selected, small (and usually perfect) piece of as-grown material and consequently does not provide information about the entire grown crystal.

Both x-ray and electron diffraction provide very valuable surface information. Neutrons, on the other hand, provide information about the entire volume of the crystal due to their low absorption by the majority of materials. Neutron diffraction techniques – if available – provide an excellent confirmation of the total crystal quality because all the substantial grains present in the as-grown crystal can be detected. This

is especially important in the case of nontransparent crystals where the assessment of the quality of the whole boule can be performed without labor-intensive and destructive sectioning, surface preparation, etc. For example, high-resolution, elastic neutron scattering measurements on $\text{SrCu}_2(^{11}\text{BO}_3)_2$ confirmed that slowly (less than 0.3 mm/h) grown crystals (Fig. 12.18) are a single domain each, with a mosaic spread of the (110) Bragg peak of 0.3° . Note, that in this case, to avoid high thermal neutrons absorption in ^{10}B ($\approx 20\%$ of natural abundance) ^{11}B isotope enriched to 99.6% has been used [12.60].

Similar analysis performed on $\text{Sr}_{1.95}\text{Na}_{0.05}\text{Cu}_2(^{11}\text{BO}_3)_2$ (Fig. 12.20) revealed the presence of 11 grains in similarly sized crystal grown in the same conditions.

Energy-dispersive x-ray analysis (EDAX) and electron microprobe analysis (EPMA) can confirm the exact chemical formula of crystals and solid solutions grown in different conditions. They also allow advanced phase analysis of obtained materials. Good oxide standards are essential for quantitative analysis.

Single crystals of oxides are generally investigated by the crystal users, according to physical properties and predicted applications. Investigation of these properties and their changes with different dopants and growth conditions are now the main purpose of growing crystals by OFZ and TSFZ methods. The majority of crystals grown for research purpose have unique magnetic, electrical, and crystallographic properties, which are investigated and reported in specific journals.

12.11 Determination of Defects in Crystals – The Experimental Approach

All crystals contain defects and impurities that influence their physical properties. To observe and assess the growth features an oriented crystal has to be cut and polished. Which defects are expected determines the way in which the sample is prepared for observation (Figs. 12.15–12.19). It should be specified what defects are expected in crystals grown by a given method, as many defects interfere with measurements and applications.

An excellent discussion of the defects present in oxide crystals grown from low-temperature solutions is given by Rudolf [12.61], from high-temperature solutions by Elwell and Scheel [12.50], and for oxides grown by Czochralski method by Hurle [12.51].

The defects present in oxide crystals grown by the optical FZ technique are similar to those found in crys-

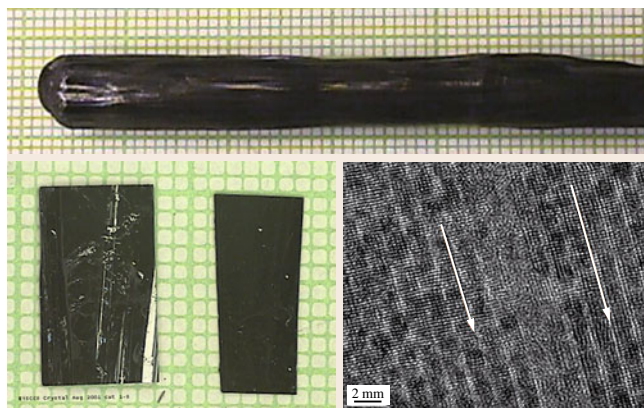
tals grown by other methods, but some result from the specific growth conditions in the OFZ, such as the very high temperature gradients (for both FZ and TSFZ methods) and growth from flux (for TSFZ method). In the next paragraph those defects and the reasons for their appearance are discussed.

Increasingly available and advanced electron-optics techniques with easily accessible instrumentation such as scanning electron microscopy (SEM), transmission electron microscopy (TEM), high-resolution transmission electron microscopy (HRTEM), electron energy-loss spectroscopy (EELS), and high-angle annular dark field in scanning transmission electron microscope (HAADF-STEM) answer many questions related to the real structure of crystal and the presence of defects on the scale from millimeters down to atomic

Fig. 12.21 *Top*: Single crystal of BiSCCO 2212 grown by TSFZ technique. *Left*: plates cleaved from this crystal. *Right*: HRTEM image of the (100) plane with grain boundary at the center. The arrows in the image indicate the direction of the *b*-axis in each grain (courtesy Y. Zhu) ►

resolution. Additional sample preparation is necessary to fully utilize the potential of these techniques. A leading experimental work on defect characterization, using STEM, EELS, and TEM techniques on cleaved $\text{Bi}_2\text{Sr}_2\text{CaCu}_2\text{O}_n$ crystals grown slowly (0.21 mm/h) by TSFZ method (Fig. 12.21) has recently been published by Zhu et al. [12.62].

Figure 12.22 presents a comparison between known crystallographic structure and a HAADF-STEM image. This very sophisticated method of characterization of crystal grown by TSFZ method visualizes the displacement of Bi atoms in crystallographic lattice by intensity modulation; the results are consistent with (but much clearer than) those obtained with conventional high-resolution TEM on the same crystal sample. Figure 12.23 shows a detailed analysis of grain boundary performed on a HAADF image. The line defect has a lattice parameter suggesting that it is an intergrowth of Bi-2201 phase in Bi-2213 crystal. Stacking defects are characteristic for BiSCCO superconductors and other



layered compounds, but it is common to find few hundred by few hundred nm area of the perfect atoms arrangements – see Fig. 12.24 in the crystal of $(\text{La}, \text{Ba})_2\text{CuO}_4$ grown by TSFZ.

Local macrodefects (already mentioned in the section about instabilities in crystal growth), i.e., *microfaceting* (Fig. 12.20) and *cellular (grain) growth*, as well as *grain boundaries* (Figs. 12.12, 12.17, and 12.25), *flux tubes*, *precipitations*, and *dendrite growth* [12.62, 63] are all present as a result of crystallization front instability. They are often observed under

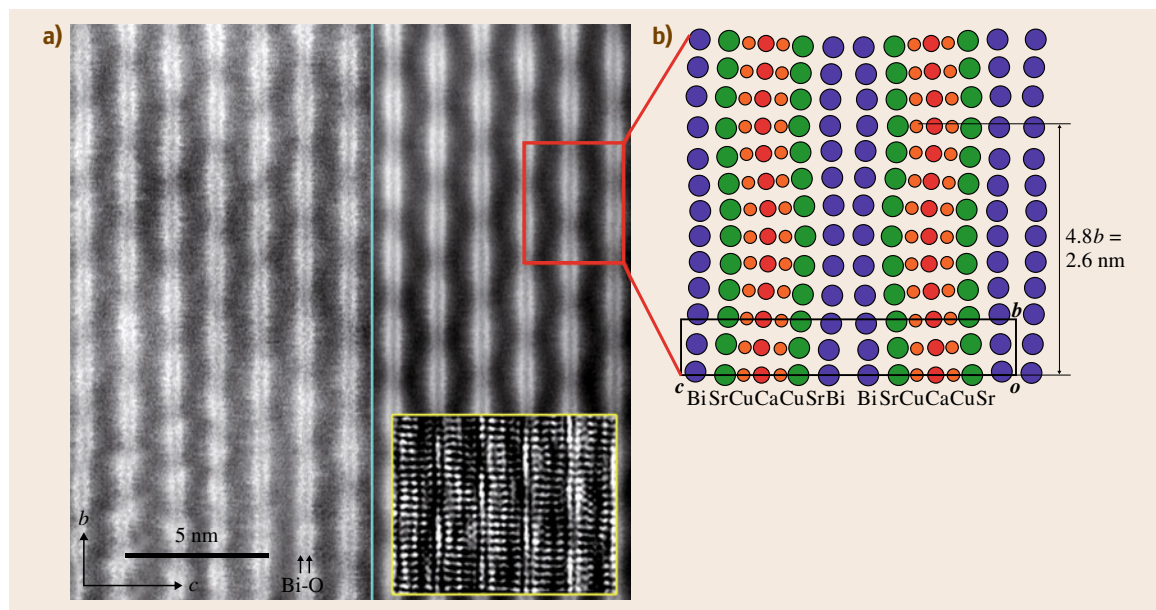


Fig. 12.22 (a) High-resolution HAADF image of Bi-2212. The double bright fringes correspond to Bi-O bilayer and dark ribbons to atomic layers of lighter elements. Compared with model of Bi-2212 incommensurate modulated structure (b) (after [12.62], courtesy Elsevier 2006)

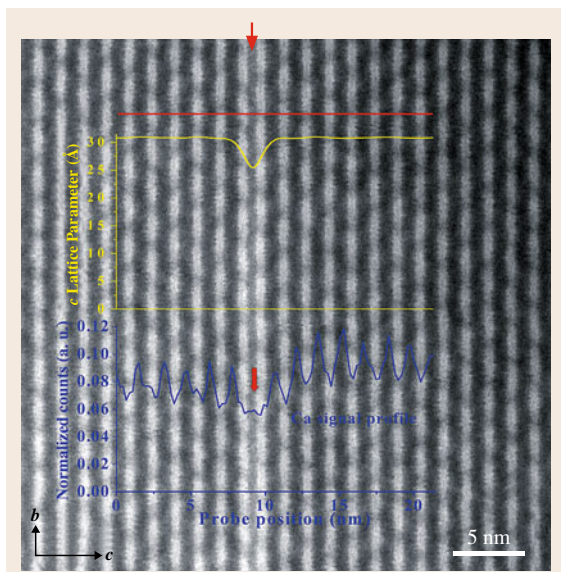


Fig. 12.23 HAADF images of BISCCO-2212 with intergrowth of 2201 phase. *Yellow profile*: calculated lattice parameter c ; over the intergrowth $c = 25.5 \text{ \AA}$, indicating that this defect is an intergrowth of 2201. *Blue profile*: normalized Ca signal related to the local concentration of Ca, indicating absence of Ca in this layer (after [12.62], courtesy Elsevier 2006)

polarizing microscope and/or by x-ray topography. These defects are more pronounced at the beginning of crystallization and can also be eliminated with the

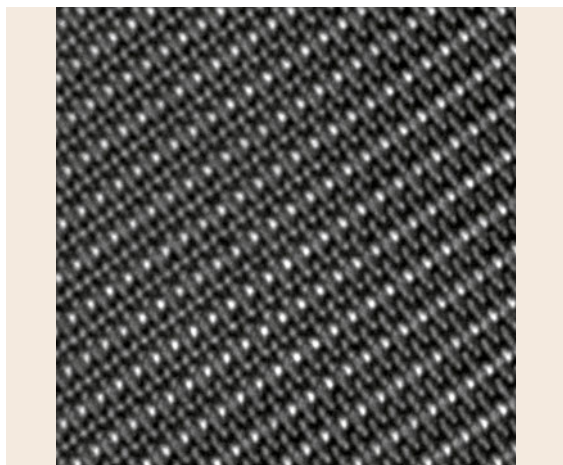


Fig. 12.24 HRTEM of perfect crystal of $\text{La}_{1.9}\text{Ba}_{0.1}\text{CuO}_4$ grown by TSFZ method (image courtesy of G. Botton and C. Maunders)

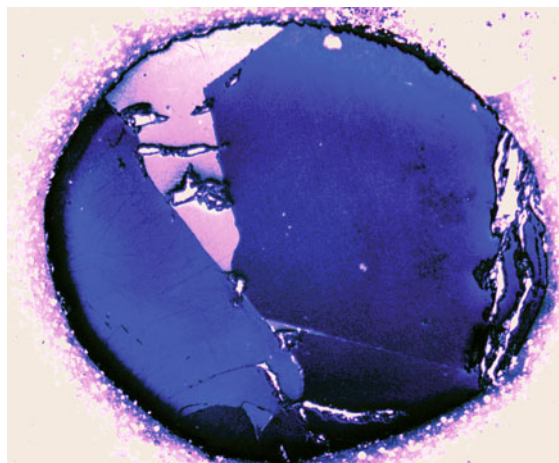


Fig. 12.25 Macrograph of polished cross section of La_2CuO_4 crystal grown 1 mm/h on seed, with visible large grains (polarized light, false colors)

use of a crystalline (preferably oriented) seed and/or necking procedure (Fig. 12.10). Crystal quality can be further improved by adjusting the rotation so as to maintain a flat crystallization front and slower growth rate.

Impurities, inclusions, and precipitates (e.g., in $(\text{La}, \text{Sr})_2\text{CuO}_4$ [12.63] or YVO_4 [12.64, 65]) are particles of the same or different phases embedded into otherwise good crystals. They can be generated by instabilities in the growth conditions leading to a noticeable amount of undissolved material in the molten zone. A slight change in stoichiometry of the starting rod can sometimes result in inclusion-free crystals as was proved for crystals of Mg_2TiO_4 grown from ceramic rod with $\text{Mg} : \text{Ti}$ ratio of $2 : 1.01$ [12.46]; a small excess of CuO is also used for various cuprates [12.21, 66, 67]. Dense feed rods and slower growths have been suggested for reducing the number of inclusions. Inclusions – on their own – are also the main cause of dislocations. The number of *precipitates* (such as the presence of Al_2O_3 in NiAl_2O_4 [12.52] or carbonates and BiO_x phase detected in $\text{Bi}_2\text{Sr}_2\text{CaCu}_2\text{O}_n$ [12.62, 68]) can sometimes be reduced with a slower growth rate or change of growth atmosphere.

Cracks, caused by mechanical stress due to cooling (e.g., in $\text{Ca}_2\text{Al}_2\text{SiO}_7$ [12.69] or SrZrO_3 [12.70]), can be diminished with the use of an afterheater [12.70, 71]. Sometimes, severe cracks are the result of phase transitions during cooling (e.g., CaTiSiO_5 , Fig. 12.26). Change of the growth atmosphere (from air to N_2) proved to be helpful in the above case [12.35].

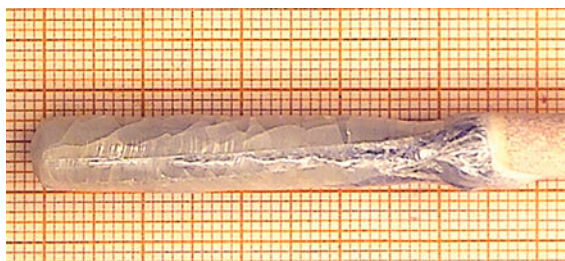


Fig. 12.26 CaTiSiO_5 undergoes phase transition during the final stage of cooling (about 235°C). Initially transparent crystal cracked only when cooled to near room temperature; H. Dabkowska, A. Dabkowski, unpublished results

Gas bubbles are trapped inside crystals grown by the FZ method because the shape of the solid–liquid interface causes the bubbles to concentrate in the core region of the crystals (Fig. 12.8). This effect is often caused by either solubility of O_2 in the liquid phase or partial decomposition of oxides. It can be controlled to some extent by atmosphere composition, as described for Al_2O_3 [12.72, 73] and Li_3VO_4 [12.74].

Striations are caused by fluctuations of the temperature of the liquid near the crystallization front, originating from convection flows. Temperature fluctuations cause fluctuations of the growth rate, and as a result there are changes in chemical composition (as the effective segregation coefficient depends on the growth rate). Striations may be used as indicators of the shape of the solid–liquid interface [12.13, 65]. Optical

observations on polished and etched YIG revealed the internal structure of a crystal, providing valuable information about the growth mechanism [12.12]. This proved that too fast a growth rate leads to *cellular growth*, which can often be corrected by lowering the growth speed.

Sheet defects [12.15, 17, 54] and *eutectic solidification* can be revealed by careful observation of the cross section of as-grown crystal when the coexistence of two or more phases is noticed. Mao et al. [12.75] combined microscope observation of polished Sr_2RuO_4 crystal with x-ray Laue photography and detected the presence of layered intergrowth of different phases (Sr and SrRuO_3) in the crystal. On the basis of this analysis it was possible to optimize the starting composition of the feed rod and the growth conditions, reducing the level of impurities and defects and increasing the T_c of ruthenate. Sometimes it is possible to understand and modify the physical properties of material by identifying defects resulting from the crystal growth. For example, eutectic solidification in crystals grown by OFZ was discussed by Troileux et al. in $\text{La}_{2-x}\text{Sr}_x\text{CuO}_4$ [12.76] and by Fittipaldi et al. [12.77] in the Sr–Ru–O system.

Twin boundaries analyzed by x-ray diffraction depend mostly on the crystallographic structure of the material (e.g., $\text{Mg}_3\text{V}_2\text{O}_8$ [12.78] and $\text{La}_{1-x}\text{Ca}_x\text{MnO}_3$ [12.79]).

The influence of convection on dopant segregation is discussed in [12.36, 80, 81].

12.12 Details of Conditions for Growth of Selected Oxide Single Crystals by OFZ and TSFZ Methods

In Table 12.1 examples of oxides grown by FZ and TSFZ techniques and the growth conditions employed are listed. Crystals grown with the application of a sol-

vent are marked with a dagger, and references referring to defects in each oxide crystal are marked with an asterisk.

Table 12.1 Examples of oxide crystals grown by optical floating zone technique and traveling solvent optical floating zone technique (marked by †). References discussing defects in obtained crystals are marked by *

Material	Growth rate (mm/h)	atmosphere	rotation (rpm)	References and comments
Al_2O_3	10–1500	Air	0–200	[12.72, 73]*
$\text{BaCo}_2\text{Si}_2\text{O}_7$	1	Air	20–30	H. Dabkowska, unpublished
$\text{Ba}_3\text{Cr}_2\text{O}_8$	10	2 atm Ar	–	[12.82]
$\text{BaFe}_{12}\text{O}_{19}$ †	6	70 atm O_2	–	[12.14]*
BaTiO_3 †	1	O_2/Ar 1 : 1	20	[12.83]
$\text{Ba}_{1-x}\text{Sr}_x\text{TiO}_3$	1–2	O_2	–	[12.38]
$\text{Bi}_2\text{Sr}_2\text{CaCu}_2\text{O}_n$ †	0.2–0.35	O_2	20–30	[12.21, 34, 53, 61, 62, 68, 84–88]

Table 12.1 (cont.)

Material	Growth rate (mm/h)	atmosphere	rotation (rpm)	References and comments
Bi ₂ Sr ₂ CaCu ₂ O _n :Y [†]	0.5	–	–	[12.89, 90]
Bi ₂ Sr ₂ CaCu ₂ O _n :Li [†]				
Bi ₂ Sr ₂ Ca ₂ Cu ₃ O ₁₀ [†]	0.05	O ₂ /Ar 1 : 4	10	[12.47]
Bi ₂ Sr ₂ CuO ₆ [†]	1.5	–	–	[12.91, 92]
Bi ₁₂ TiO ₂₀ [†]	0.25	O ₂ flow	35–45	[12.93]
Ca ₁₂ Al ₁₄ O ₃₃	0.2	–	–	[12.94]*
CaAl ₂ O ₄	4	Ar – O ₂ , Ar, Ar – H ₂	21	[12.95]
Ca ₂ Al ₂ SiO ₇	3	Low pressure	25	[12.69]*, [12.96]
Ca ₂ CuO ₃ [†]	1	1 atm O ₂	20–30	[12.97]
CaCu ₃ Ti ₄ O ₁₂ [†]	6	O ₂	30	[12.98, 99]
Ca ₂ FeMoO ₆	60	0.25–0.5 atm N ₂	–	[12.100]*
Ca _{0.5} La _{0.5} MnO ₃	2.5–10	Air, Ar/O ₂	–	[12.101]
Ca ₂ MgSi ₂ O ₇	2–3	Air, O ₂	30–45	[12.96]
CaTiSiO ₅	0.5–12	Air	15–30	[12.34, 35, 61, 84]* phase transition
Ca ₂ RuO ₄	45	Ar/O ₂ 9 : 1	–	[12.102]*
Ca _{2–x} La _x RuO ₄		10 atm		
Ca _{2–x} Sr _x RuO ₄	20–50	9Ar : 1O ₂ 10 atm	30–50	[12.103]*
CaYAlO ₄	3–5	Ar, O ₂ , N ₂ , air, O ₂ /N ₂	15–20	[12.104]* color centers
Ca _{2+x} Y _{2–x} Cu ₅ O ₁₀ [†]	0.5	O ₂	15	[12.105, 106]*
CdCu ₃ Ti ₄ O ₁₂ [†]	6	O ₂	30	[12.99]
CoTiO ₃	5	O ₂	20	HAD, not published
Co ₃ (VO ₄) ₂ [†]	0.5–3	Air	20–30	[12.107]
CuGeO ₃	1–10	1 atm O ₂	30	[12.17]*, [12.43, 54, 108]
Fe ₃ O ₄ [†]	6	CO ₂	–	[12.13]*
Ga ₂ O ₃	5–10	Air, Ar	15–30	[12.18]* volatile
GeCo ₂ O ₄	15–30	Air	–	[12.109] evaporation, low viscosity
GeNi ₂ O ₄	40	10 atm, O ₂	–	[12.109] evaporation, low viscosity
Gd ₃ Fe ₅ O ₁₂ [†]	1.5	70 atm O ₂	–	[12.14]
La ₂ CuO ₄ [†]	0.5–1	O ₂	25–30	[12.43, 110]
La _{2–x} Sr _x CuO ₄ [†]	1–15	O ₂ , air	40	[12.63]*, [12.76, 111–114]
La _{2–x} Ba _x CuO ₄ [†]	0.5–0.7	10 ^{–2} atm O ₂	30	[12.49]*, [12.63, 106, 110, 114–118]
(La _{1–x} Ca _x) ₂ CaCu ₂ O _{6+δ} [†]	0.35–1	10 atm O ₂	–	[12.45]*
(La _{1–x} Ca _x) ₂ CaSrCu ₂ O ₆ [†]	0.5	10 atm O ₂	–	[12.119]*
La _{14–x} Ca _x Cu ₂₄ O ₄₁ [†]	1–1.5	13 atm O ₂	40	[12.120]
LaCoO ₃	20	O ₂	–	[12.121, 122]
LaFeO ₃ , YFeO ₃	20	O ₂	–	[12.123]
LaMnO ₃	10	Air	–	[12.123]
La _{0.8} Sr _{0.2} MnO ₃	3–10	Air, Ar/O ₂	15–50	[12.101, 124–127]
La ₂ NiO ₄	20	O ₂	30–50	[12.71]*
La _{2–x} Sr _x NiO _{4+δ}	3–5	5–7 atm Ar : O ₂	40	[12.59]
LaTiO ₃	50	30% H ₂ in Ar	–	[12.123]
LiNbO ₃	9	–	–	[12.26, 27, 36]* laser heated
Li ₃ VO ₄ , β(II)-Li ₃ VO ₄ [†]	0.5–1	Ar, O ₂ , air	–	[12.37, 74]*
LuFe ₂ O ₄ [†]	1	Air	–	[12.128]*
LuFeCoO ₄ [†]	1	CO ₂ /CO	–	[12.128]*

Table 12.1 (cont.)

Material	Growth rate (mm/h)	atmosphere	rotation (rpm)	References and comments
MgFe ₂ O ₄ [†]	5	50 atm O ₂	–	[12.14]
Mg ₂ SiO ₄ :Cr	–	Ar/O ₂	–	[12.129]
MgTi ₂ O ₄ [†]	1–5	O ₂	30	[12.46]* inclusions, precipitates
Mg ₃ (VO ₄) ₂ [†]	0.5	O ₂ /N ₂ , O ₂	16–18	[12.78]*
Na _x CoO ₂	2	O ₂	–	[12.130–132]
Nd ₂ CuO ₄ [†] , Nd _{1.85} Ce _{0.15} Cu _{4–8} [†]	0.5–0.7	O ₂ flow, O ₂ /Ar, 8 atm O ₂	30	[12.113]*, [12.133]
Nd _{0.7} Sr _{0.3} MnO ₃	2.5–10	Air/O ₂	–	[12.101]
Nd _{1+x} Sr _{2–x} Mn ₂ O ₇	2–8	Air	25–30	[12.134]
NdTiO ₃ , Nd _{1–x} TiO ₃	25	Ar/H ₂ 95 : 5	15	[12.135]
NiAl ₂ O ₄	2.5–10	1–3 atm O ₂	5–40	[12.52]*
Ni ₃ (VO ₄) ₂ [†]	0.5–3	Air	20–30	[12.121]
Pr _{1+x} Sr _{2–x} Mn ₂ O ₇	2–8	Air	25–30	[12.134]
RE ₃ Ga ₅ O ₁₂ [†]	10	Air	–	[12.14]
REBa ₂ Cu ₃ O _{7–y} [†] (RE = Y, La, Pr, Nd, Sm)	–	10 ^{–2} atm O ₂	–	[12.136]*
REFeO ₃ [†]	3–10	70 atm O ₂	–	[12.14]
RE ₂ Ti ₂ O ₇ (RE = rare earth)	5–20	Ar, O ₂	10–20	[12.22, 34, 61, 84]*, [12.23]
SrAl ₂ O ₄	4	Ar–O ₂ , Ar, Ar–H ₂	21	[12.95]
Sr ₃ Cr ₂ O ₈	10/20/08	2 atm Ar	–	H. Dabkowska, unpublished
Sr ₂ CuO ₂ Cl ₂	5	Ar, Ar/O ₂	30	[12.137]*
SrCuO ₂ [†]	0.5–2	1 atm O ₂	–	[12.43, 138, 139]
Sr ₂ CuO ₃ [†]	1	1 atm O ₂	–	[12.43, 138]
SrCu ₂ (BO ₃) ₂ [†] SrCu ₂ (BO ₃) ₂ :Mg, La, Na [†]	0.2–0.5	O ₂	10–20	[12.42, 48, 60, 140] low surface tension
Sr ₁₄ Cu ₂₄ O ₄₁ [†]	1	5 atm	–	[12.34, 42, 43, 54, 61, 84, 138]
Sr _{14–x} Ca _x Cu ₂₄ O ₄₁ [†]	1	10 atm O ₂	–	[12.141]
SrFe ₁₂ O ₁₉ [†]	6	50 atm O ₂	–	[12.14]
Sr ₃ Fe ₂ O _{7–x} [†]	1–5	0.2–3 atm O ₂	10–15	[12.142]
Sr ₂ RuO ₄ , Sr ₂ RuO ₄ :Ti	25–45	Ar/O ₂ 2 : 1	–	[12.34, 61, 75, 84]*, [12.143] volatile
Sr ₃ Ru ₂ O ₇	15–20	Ar/O ₂ 1 : 9	–	[12.82, 144, 145]* volatile
SrTiO ₃ , SrTiO ₃ :La	15	15 atm	20–30	[12.14, 146]
SrZrO ₃	5–65	Air	3–25	[12.70]* evaporation
TiO ₂	5	Air, O ₂	30	[12.14], [12.20]* ZrO ₂ added
Y ₃ Al ₅ O ₁₂	5	Air	–	[12.14, 28], [12.147]*
YCrO ₃	20	Ar	–	[12.123]
Y ₃ Fe ₅ O ₁₂ [†]	1.5–3	15–30 atm O ₂	–	[12.10, 14], [12.17, 19, 57]*
Y ₃ Fe _{5–x} Al _x O ₁₂ [†]	6	O ₂	–	[12.12, 13]*, [12.19]
Y ₃ Fe _{5–x} Ga _x O ₁₂ [†]	1.5–3	20–30 atm O ₂	–	[12.14]
YFe ₂ O ₄ [†]	2–10	CO ₂ /H ₂	30	[12.148]*
YTiO ₃	50	30% H ₂ in Ar	–	[12.123]
YVO ₄ :Er, Ho, Tm	5–20	7% H ₂ in Ar, O ₂	20–30	[12.64]*, [12.65, 123]
YbCoGaO ₄	1.7	Air	15–30	[12.34, 61, 84, 149]
YbFeMgO ₄ [†]	1	Air	–	[12.128]*
ZnO [†]	0.5–1	Air	20	[12.150]*

12.13 Conclusions

The field of crystal growth by the optical floating zone and traveling solvent floating zone techniques is definitely expanding. With a growing number of highly computerized furnaces the quality and amount of works reported on new and already known materials is rising. The main advantage of both discussed floating zone techniques lies in the high purity of the obtained crystals resulting from the absence of a container. This feature also allows us to melt and grow high-quality, relatively large and uniform crystals of oxides for which there is no container (crucible) – either because of very high melting point or the melt being very aggressive – and which cannot be obtained by other methods. Both of these methods also make it possible to prepare solid solutions of oxides, modifying their properties according to the future applications.

Numerical modeling of the floating zone silicon process has turned out to be an excellent tool for modern crystal growth practice. Chains of models that cover the complete floating-zone process have been developed over the years [12.24, 25]. Now it is possible to simulate numerically the growth situations precisely enough to improve the final crystal quality even for very large diameters. Further modeling efforts, especially for other materials for which it is possible to compare modeling predictions with experimental observations, are necessary to improve the understanding of transport processes in the molten zone and of heat transport in

the whole system. Only then will it be possible to explain the changes observed in growth features as growth conditions change.

Apart from crystallizing new materials, future work in this area should also include:

- Investigation of phase diagrams
- Understanding/assessing high-temperature properties of molten oxides and salts
- Creating a user-friendly theoretical approach connecting crystal growth conditions with obtained results.

There is also the crucial but nearly untouched problem of automation of crystal growth. The automatic diameter control systems have proven to be useful in the Czochralski crystal growth of oxides [12.51] and one can expect that this approach can be successfully applied to grow them by the optical floating zone process as well.

It took about 50 years of research and financing to grow very high-quality, large single crystals of single element Si by FZ technique. Now the challenge is to follow this with growth of other technologically important materials. To achieve this continuous cooperation between a crystal grower and crystal user is necessary. Without good characterization of the crystals grown no progress in crystal growth can be achieved.

References

- 12.1 W.G. Pfann: Principles of zone-melting, *J. Met. Trans. AIME* **4**, 747 (1952)
- 12.2 R. Von Emeis: Tiegelfreies Ziehen von Silicium-Einkristallen, *Z. Naturforsch.* **9A**, 67 (1954), in German
- 12.3 H. Keck, M.J.E. Golay: Crystallization of silicon from a floating liquid zone, *Phys. Rev.* **89**, 1297 (1953)
- 12.4 H.C. Theuerer: Method of processing semiconductive materials, US Patent 3060123 (1962)
- 12.5 A. Mühlbauer: Innovative induction melting technologies: A historical review, *Int. Scientific Colloq. Modell. Mater. Process.* (Riga 2006)
- 12.6 R.E. De La Rue, F.A. Halden: Arc-image furnace for growth of single crystals, *Rev. Sci. Instrum.* **31**, 35–38 (1960)
- 12.7 M.R. Null, W.W. Lozier: Carbon arc image furnaces, *Rev. Sci. Instrum.* **29**, 163–170 (1958)
- 12.8 R.P. Poplawsky, J.E. Thomas Jr.: Floating zone crystals using arc image furnace, *Rev. Sci. Instrum.* **31**, 1303–1308 (1960)
- 12.9 R.P. Poplawsky: Ferrite crystals using arc image furnace, *J. Appl. Phys.* **33**, 1616–1617 (1961)
- 12.10 L.L. Abernethy, T.H. Ramsey Jr., J.W. Ross: Growth of yttrium iron garnet single crystals by the floating zone technique, *J. Appl. Phys.* **32**, 3765 (1961)
- 12.11 T. Akashi, K. Matumi, T. Okada, T. Mizutani: Preparation of ferrite single crystals by new floating zone technique, *IEEE Trans. Magn.* **5**, 285–289 (1969)
- 12.12 I. Shindo, N. Ii, K. Kitamura, S. Kimura: Single crystal growth of substituted yttrium iron garnets $Y_3Fe_{5-x}(Ga,Al)_xO_{12}$ by the floating zone method, *J. Cryst. Growth* **46**, 307–313 (1979)
- 12.13 S. Kimura, K. Kitamura: Floating zone crystal growth and phase equilibria: A review, *J. Am. Ceram. Soc.* **75**(6), 1140–1146 (1992)
- 12.14 A.M. Balbashov, S.K. Egorov: Apparatus for growth of single crystals of oxide compounds by floating zone melting with radiation heating, *J. Cryst. Growth* **52**, 498–504 (1981)

- 12.15 I. Shindo: Determination of the phase diagram by the slow cooling float zone method: The system MgO-TiO_2 , J. Cryst. Growth **50**, 839–851 (1980)
- 12.16 B. Moest, V.G. Glebovsky, H.H. Brongersma, R.H. Bergmans, A.W. Denier van der Gon, V.N. Semenov: Study of Pd single crystals grown by crucibleless zone melting, J. Cryst. Growth **192**, 410–416 (1998)
- 12.17 A. Revcolevschi, J. Jegoudez: Growth of large high-Tc single crystals by the floating zone method: A review, Progr. Mater. Sci. **42**, 321–339 (1997)
- 12.18 E.G. Villora, K. Shimamura, Y. Yoshikawa, K. Aoki, N. Ichinose: Large-size $\beta\text{-Ga}_2\text{O}_3$ single crystals and wafers, J. Cryst. Growth **270**, 420–426 (2004)
- 12.19 A.M. Balbashov, A.A. Tsvetkova, A.Y. Chervonenkis: Imperfections in crystals of yttrium-iron garnet grown from nonstoichiometric melts, Neorg. Mater. **11**, 108–111 (1975)
- 12.20 M. Higuchi, K. Kodaira: Effect of ZrO_2 addition on FZ growth of rutile single crystals, J. Cryst. Growth **123**, 495–499 (1992)
- 12.21 G.D. Gu, T. Egi, N. Koshizuka, P.A. Miles, G.J. Russell, S.J. Kennedy: Effect of growth conditions on crystal morphology and superconductivity of Bi-2212 oxide, Physica C **263**, 180–184 (1996)
- 12.22 J.S. Gardner, B.D. Gaulin, D.M. Paul: Single crystal growth by the floating zone method of a geometrically frustrated pyrochlore antiferromagnet $\text{Tb}_2\text{Ti}_2\text{O}_7$, J. Cryst. Growth **191**, 740–745 (1998)
- 12.23 J.C.P. Ruff, B.D. Gaulin, J.P. Castellán, K.C. Rule, J.P. Clancy, J. Rodriguez, H.A. Dabkowska: Structural fluctuations in the spin-liquid state of $\text{Tb}_2\text{Ti}_2\text{O}_7$, Phys. Rev. Lett. **99**, 237202 (2007)
- 12.24 A. Mühlbauer, A. Muiznieks, J. Virbulis, A. Lüdge, H. Riemann: Interface shape, heat-transfer and fluid-flow in the floating-zone growth of large silicon-crystals with the needle-eye technique, J. of Crystal Growth **151**, 66 (1995)
- 12.25 A. Rudevics, A. Muiznieks, G. Radnieks: Transient modeling of FZ crystal growth process and automatic adjusting of the HF inductor current and feed rod velocity, Proc. Joint 15th Riga and 6th Int. Conf. Fundam. Appl. MHD, Vol. 2 (2005) p. 229
- 12.26 J.C. Chen, H.-K. Wu: Numerical computation of heat flow, fluid flow and interface shapes in the float zone of lithium niobate during a melting process, J. Heat Mass Transf. **39**, 3707–3716 (1996)
- 12.27 C.J. Chen, H. Chieh: Measurement of the float-zone interface shape for lithium niobate, J. Cryst. Growth **149**, 87–95 (1995)
- 12.28 C.W. Lan: Three-dimensional simulation of floating-zone crystal growth of oxide crystals, J. Cryst. Growth **247**, 597–612 (2003)
- 12.29 Y.K. Yang, S. Kou: Temperature oscillation in a tin liquid bridge and critical Marangoni number dependency on Prandtl number, J. Cryst. Growth **222**, 135–143 (2001)
- 12.30 D. Rivas, C. Vazquez-Espi: An analysis of lamp irradiation in ellipsoidal mirror furnaces, J. Cryst. Growth **223**, 433–445 (2001)
- 12.31 S. Otani, T. Tanaka, Y. Ishizawa: Control of heat-flow to feed rod in floating zone system, J. Cryst. Growth **87**, 175–179 (1988)
- 12.32 J.C. Brice: *Crystal Growth Processes* (Blackie, Glasgow, London 1986)
- 12.33 V.J. Fratello, C.D. Brandle: Physical-properties of a $\text{Y}_3\text{Al}_5\text{O}_{12}$ melt, J. Cryst. Growth **128**, 1006–1010 (1993)
- 12.34 H.A. Dabkowska, B. D. Gaulin: *Crystal Growth of Technologically Important Electronic Materials*, ed. by K. Byrappa, T. Ochachi, M. Klapper, R. Fornari (Allied Publishers PVT, New Delhi 2003) pp. 341–354
- 12.35 I. Tanaka, T. Obuchi, H. Kojima: Growth and characterization of titanite (CaTiSiO_5) single crystals by the floating zone method, J. Cryst. Growth **87**, 169–174 (1988)
- 12.36 C.J. Chen, Y.-C. Lee, C. Hu: A simple method of examining the propagation of defects in the floating-zone solidification process of lithium niobate, J. Cryst. Growth **166**, 151–155 (1996)
- 12.37 W. Itoyama, K. Iishi, S. Sakata: Growth of $\beta(\text{II})\text{-Li}_3\text{VO}_4$ single crystals by the floating zone technique with the aid of a heat reservoir, J. Cryst. Growth **158**, 534–539 (1996)
- 12.38 H. Kojima, M. Watanabe, I. Tanaka: Crystal growth of strontium substituted barium-titanate ($\text{Ba}_{1-x}\text{Sr}_x\text{TiO}_3$) by the floating-zone method, J. Cryst. Growth **155**, 70–74 (1995)
- 12.39 NEC now: CANON MACHINERY Inc. 85 Minami Yamada-cho Kusatsu-city Shiga pref. 525–8511 Japan
- 12.40 I. Shindo: Crystal System Inc., 9633 Kobuchisawa, Yamanashi 408 Japan
- 12.41 A. Balbashov: Private communications, Moscow Power Engineering Institute Technical University, 14 Krasnokazarmennaya, Moscow, 111250, Russia
- 12.42 H.A. Dabkowska, B.D. Gaulin: Growth of single crystals of selected cuprates by the optical floating zone technique, J. Optoelectron. Adv. Mater. **9**, 1215–1220 (2007)
- 12.43 A. Revcolevschi, U. Ammerahl, G. Dhalenne: Crystal growth of pure and substituted low-dimensionality cuprates CuGeO_3 , La_2CuO_4 , SrCuO_2 , Sr_2CuO_3 and $\text{Sr}_{14}\text{Cu}_{24}\text{O}_{41}$ by the floating zone and travelling solvent zone methods, J. Cryst. Growth **198/199**, 593–599 (1999)
- 12.44 E.M. Levin, C.R. Robins, H.F. McMurdie: *Phase Diagrams for Ceramists* (Am. Ceram. Soc, Columbus 1964), and the next volumes; recently edited and published by NIST & ACS
- 12.45 G.D. Gu, M. Hucker, Y.J. Kim, J.M. Tranquada, H. Dabkowska, G.M. Luke, T. Timusk, B.D. Gaulin, Q. Li, A.R. Moodenbaugh: Crystal growth and superconductivity of $(\text{La}_{1-x}\text{Ca}_x)_2\text{CaCu}_2\text{O}_{6+\delta}$, J. Phys. Chem. Solids **67**, 431–434 (2006)

- 12.46 I. Shindo, S. Kimura, K. Kitamura: Growth of Mg_2TiO_4 by the floating zone method, *J. Mater. Sci.* **14**, 1901–1906 (1979)
- 12.47 T. Fujii, T. Watanabe, A. Matsuda: Single-crystal growth of $\text{Bi}_2\text{Sr}_2\text{Ca}_2\text{Cu}_3\text{O}_{10+\delta}$ (Bi-2223) by TSFZ method, *J. Cryst. Growth* **223**, 175–180 (2001)
- 12.48 H.A. Dabkowska, A.B. Dabkowski, G.M. Luke, S.R. Dunsiger, S. Haravifard, M. Cecchinell, B.D. Gaulin: Crystal growth and magnetic behaviour of pure and doped $\text{SrCu}_2(\text{BO}_3)_2$, *J. Cryst. Growth* **306**, 123–128 (2007)
- 12.49 T. Adachi, T. Noji, Y. Koike: Crystal growth, transport properties and crystal structure of the single-crystal $\text{La}_{(2-x)}\text{Ba}_x\text{CuO}_4$ ($x = 0.11$), *Phys. Rev. B* **64**, 144524–1–6 (2001)
- 12.50 D. Elwell, H.J. Scheel: *Crystal Growth from High-Temperature Solutions* (Academic, London 1975)
- 12.51 D.T.J. Hurle: *Crystal Pulling from the Melt* (Springer, Berlin, New York 1993)
- 12.52 R. Subramanian, M. Higuchi, R. Dieckman: Growth of nickel aluminate single crystals by the floating-zone method, *J. Cryst. Growth* **143**, 311–316 (1994)
- 12.53 G.D. Gu, K. Takamuku, N. Koshizuka, S. Tanaka: Growth and superconductivity of $\text{Bi}_{2.1}\text{CuSr}_{1.9}\text{Ca}_{1.0}(\text{Cu}_{1-y}\text{Fe}_y)_2\text{O}_x$ single-crystal, *J. Cryst. Growth* **137**, 472–478 (1994)
- 12.54 S. Watauchi, M. Wakiyama, I. Tanaka: Control of the anisotropic growth rates of oxide single crystals in floating zone growth, *J. Cryst. Growth* **229**, 423–427 (2001)
- 12.55 A. Mühlbauer, A. Muiznieks, J. Virbulis: Analysis of the dopant segregation effects at the floating zone growth of large silicon crystals, *J. Cryst. Growth* **180**, 372–380 (1997)
- 12.56 O.B. Raghothamachar, G. Dhanaraj, J. Bai, M. Dudley: Defect analysis in crystals using x-ray topography, *Microsc. Res. Tech.* **69**, 343–358 (2006)
- 12.57 K. Kitamura, S. Kimura, Y. Miyazawa, Y. Mori, O. Kamada: Stress-birefringence associated with facets of rare-earth garnets grown from the melt – a model and measurement of stress-birefringence observed in thin-sections, *J. Cryst. Growth* **62**, 351–359 (1983)
- 12.58 OrientExpress is a part of LMGP suite for Windows by Jean Laugier and Bernard Bochu (Laboratoire des Matériaux et du Génie Physique de l'Ecole Supérieure de Physique de Grenoble <http://www.inpg.fr/LMGP/>). Program can be downloaded from the LMGP Crystallography software suite website at: <http://www.ccp14.ac.uk/ccp/web-mirrors/lmgp-laugier-bochu/> (last accessed August 6, 2009)
- 12.59 D. Prabhakaran, P. Isla, A.T. Boothroyd: Growth of large $\text{La}_{2-x}\text{Sr}_x\text{NiO}_{4+\delta}$ single crystals by the floating-zone technique, *J. Cryst. Growth* **237**, 815–819 (2002), Part 1
- 12.60 S. Haravifard, S.R. Dunsiger, S. El Shawiish, B.D. Gaulin, H.A. Dabkowska, M.T.F. Telling, J. Bonca: In-gap excitation and finite triplet lifetimes in the dilute singlet ground state system $\text{SrCu}_{2-x}\text{Mg}_x(\text{BO}_3)_2$, *Phys. Rev. Lett.* **97**, 247206 (2006)
- 12.61 P. Rudolf: *Crystal Growth of Technologically Important Electronic Materials*, ed. by K. Byrappa, T. Ohashi, M. Klapper, R. Fornari (Allied Publishers PVT Ltd., New Delhi 2003) pp. 407–417
- 12.62 Y. Zhu, Y.M. Niewczas, M. Couillard, G.A. Botton: Single atomic layer detection of Ca and defect characterization of Bi-2212 with EELS in HA-ADF STEM, *Ultramicroscopy* **106**, 1076–1081 (2006)
- 12.63 K. Zhang, R. Mogilevsky, D.G. Hinks, J. Mitchell, A.J. Schultz, Y. Wang, V. Dravid: Crystal Growth of $(\text{La},\text{Sr})_2\text{CuO}_4$ by float zone melting, *J. Cryst. Growth* **169**, 73–78 (1996)
- 12.64 X.-L. Yan, X. Wu, J.-F. Zhou, Z.-G. Zhang, X.-M. Wang: Growth of laser single crystals Er:YVO_4 by floating zone method, *J. Cryst. Growth* **220**, 543–547 (2000)
- 12.65 X.-L. Yan, X. Wu, J.-F. Zhou, Z.-G. Zhang, X.-M. Wang, X.-M. Fu, P.-M. Jiang, Y.-D. Hu, J.-D. Hu, J.-L. Qiu: Growth of Tm:Ho:YVO₄ laser single crystals by the floating zone method, *J. Cryst. Growth* **212**, 204–210 (2000)
- 12.66 R.S. Dusinger, Y. Zao, Z. Yamani, W.J.L. Buyers, H.A. Dabkowska, B.D. Gaulin: Incommensurate spin ordering and fluctuations in underdoped $\text{La}_{2-x}\text{Ba}_x\text{CuO}_4$, *Phys. Rev. B* **77**, 224410 (2008)
- 12.67 Y. Zhao, B.D. Gaulin, J.P. Castellán, J.P.C. Ruff, S.R. Dunsiger, G.D. Gu, H.A. Dabkowska: High-resolution x-ray scattering studies of structural phase transitions in underdoped $\text{La}_{2-x}\text{Ba}_x\text{CuO}_4$, *Phys. Rev. B* **76**, 184121 (2007)
- 12.68 A. Maljuk, B. Liang, C.T. Lin, G.A. Emelchenko: On the growth of overdoped Bi-2212 single crystals under high oxygen pressure, *Physica C* **335**, 140–146 (2001)
- 12.69 N. Britos, A.-M. Lejus, B. Viana, D. Vivien: Crystal growth and spectroscopy of Tm^{3+} doped $\text{Ca}_2\text{Al}_2\text{SiO}_7$, *Eur. J. Solid State Inorg. Chem.* **32**, 415–428 (1995)
- 12.70 D. Souptel, G. Behr, A.M. Balbashov: SrZrO_3 Single crystal growth by floating zone technique with radiation heating, *J. Cryst. Growth* **236**, 583–588 (2002)
- 12.71 K. Dembinski, J.M. Bassat, J.P. Coutures, P. Odier: Crystal growth of La_2NiO_4 by the floating zone method with a CW CO_2 laser – Preliminary characterizations, *J. Mater. Sci. Lett.* **6**, 1365–1367 (1987)
- 12.72 M. Saito: Growth process of gas bubble in ruby single crystals by floating zone method, *J. Cryst. Growth* **74**, 385–390 (1986)
- 12.73 M. Saito: Gas-bubble formation of ruby single-crystals by floating zone method with an infrared radiation convergence type heater, *J. Cryst. Growth* **71**, 664–672 (1985)
- 12.74 S. Sakata, W. Itoyama, I. Fujii, K. Iishi: Preparation of low temperature Li_3VO_4 single crystal by float-

- ing zone technique, *J. Cryst. Growth* **135**, 555–560 (1994)
- 12.75 Z.Q. Mao, Y. Maeno, H. Fukazawa: Crystal growth of Sr_2RuO_4 , *Mater. Res. Bull.* **35**, 1813–1824 (2000)
- 12.76 L. Trouilleux, G. Dhalenne, A. Revcolevschi, P. Monod: Growth and anisotropic magnetic behavior of aligned eutectic-type structures in the system $\text{La}_{2-x}\text{Sr}_x\text{CuO}_4$ copper oxide, *J. Cryst. Growth* **91**, 268–273 (1988)
- 12.77 R. Fittipaldi, A. Vecchione, D.S. Sisti, S. Pace, S. Kittaka, Y. Maeno: Micro-crystallographic structure of $\text{Sr}_2\text{RuO}_4/\text{Sr}_3\text{Ru}_2\text{O}_7$ eutectic crystals grown by floating zone method, *IUCr XXI Congr. (Osaka 2008)*, MS13.5 C34
- 12.78 J.D. Pless, N. Erdman, D. Ko, L.D. Marks, P.C. Stair, K.R. Pöppelmeier: Single-crystal growth of magnesium orthovanadate, $\text{Mg}_3(\text{VO}_4)_2$ by the optical floating zone technique, *Cryst. Growth Des.* **3**, 615–619 (2003)
- 12.79 B.I. Belevtsev, D.G. Naugle, K.D.D. Rathnayaka, A. Parasiris, J. Fink-Finowicki: Extrinsic inhomogeneity effects in magnetic, transport and magnetoresistive properties of $\text{La}_{1-x}\text{Ca}_x\text{MnO}_3$ ($x \approx 0.33$) crystal prepared by the floating-zone method, *Physica B: Cond. Matter* **355**, 341–351 (2005)
- 12.80 C. Winkler, G. Amberg, T. Carlberg: Radial segregation due to weak convection in a floating Zone, *J. Cryst. Growth* **210**, 573–586 (2000)
- 12.81 J.-C. Chen, G.-H. Chin: Linear stability analysis of thermocapillary convection in the floating zone, *J. Cryst. Growth* **154**, 98–107 (1995)
- 12.82 A.A. Aczel, H.A. Dabkowska, P.R. Provencher, G.M. Luke: Crystal growths and characterization of the new spin dimmer system $\text{Ba}_3\text{Cr}_2\text{O}_8$, *J. Cryst. Growth* **310**, 870–873 (2008)
- 12.83 J. Furukawa, T. Tsukamoto: BaTiO_3 single crystal growth by traveling solvent floating zone technique, *Jpn. J. Appl. Phys.* **30**, 2391–2393 (1991)
- 12.84 H. Klapper: *Crystal Growth of Technologically Important Electronic Materials*, ed. by K. Byrappa, T. Ohashi, M. Klapper, R. Fornari (Allied Publishers PVT Ltd., New Delhi 2003) pp. 603–615
- 12.85 S. Takekawa, H. Nozaki: Single crystal growth of the superconductor $\text{Bi}_{2.0}(\text{Bi}_{0.2}\text{Sr}_{1.8}\text{Ca}_{1.0})\text{Cu}_{2.0}\text{O}_8$, *J. Cryst. Growth* **92**, 687–690 (1988)
- 12.86 G. Balakrishnan, D.McK. Paul, M.R. Lees: Superconducting properties of doped and off-stoichiometric $\text{Bi}_2\text{Sr}_2\text{CaCu}_2\text{O}_8$ single crystals, *Physica B* **194–196**, 2197–2198 (1994)
- 12.87 P. Murugakoothan, R. Jayavel, C.R.V. Rao, C. Subramanian, P. Ramasamy: Growth and characterization of $\text{Bi}_2\text{Sr}_2\text{Ca}_1\text{Cu}_2\text{O}_y$ by the floating zone method, *Mater. Chem. Phys.* **31**, 281–284 (1992)
- 12.88 Y. Huang, B.-L. Wang, M.-Y. Hong, M.-K. Wu: Single crystal preparation of $\text{Bi}_2\text{Sr}_2\text{CaCu}_2\text{O}_x$ superconductor by the travelling solvent floating zone method, *Physica C* **235–240**, 525–526 (1994)
- 12.89 K. Takamuku, K. Ikeda, T. Takata, T. Miyatake, I. Tomeno, S. Gotoh, N. Koshizuka: Single crystal growth and characterization of $\text{Bi}_2\text{Sr}_2\text{Ca}_{1-x}\text{Y}_x\text{Cu}_2\text{O}_y$ by TSFZ method, *Physica C* **185–189**, 451–452 (1991)
- 12.90 T. Horiuchi, K. Kitahama, T. Kawai, S. Kawai, S. Hontsu, K. Ogura, I. Shioyaki, Y. Kawate: Li substitution to Bi–Sr–Ca–Cu–O superconductor, *Physica C* **185–189**, 629–630 (1991)
- 12.91 B. Liang, A. Maljuk, C.T. Lin: Growth of large superconducting $\text{Bi}_{2+x}\text{Sr}_{2-y}\text{CuO}_{6+\delta}$ single crystals by traveling solvent floating zone method, *Physica C: Superconduct. Appl.* **361**, 156–164 (2001)
- 12.92 M. Matsumoto, J. Shirafuji, K. Kitahama, S. Kawai, I. Shigaki, Y. Kawate: Preparation of $\text{Bi}_2\text{Sr}_2\text{CuO}_6$ single crystals by the travelling solvent floating zone method, *Physica C* **185–189**, 455–456 (1991)
- 12.93 S. Miyazawa, T. Tabata: Bi_2O_3 – TiO_2 binary phase diagram study for TSSG pulling of $\text{Bi}_{12}\text{Ti}_{20}$ single crystals, *J. Cryst. Growth* **191**, 512–516 (1998)
- 12.94 S. Watauchi, I. Tanaka, K. Hayashi, M. Hirano, H. Hosono: Crystal growth of $\text{Ca}_{12}\text{Al}_4\text{O}_{33}$ by the floating zone method, *J. Cryst. Growth* **237**, 801–805 (2002)
- 12.95 T. Katsumata, T. Nabae, K. Sasajima, T. Matsuzawa: Growth and characteristic of long persistent SrAl_2O_4 - and CaAl_2O_4 -based phosphors crystals by floating zone technique, *J. Cryst. Growth* **83**, 361–365 (1998)
- 12.96 N.I. Shindo: Single crystal growth of akermanite ($\text{Ca}_2\text{MgSi}_2\text{O}_7$) and gehlenite ($\text{Ca}_2\text{Al}_2\text{SiO}_7$) by the floating zone method, *J. Cryst. Growth* **46**, 569–574 (1979)
- 12.97 J. Wada, S. Wakimoto, S. Hosoya, K. Yamada, Y. Endoh: Preparation of single crystal of Ca_2CuO_3 by TSFZ method, *Physica C* **244**, 193–195 (1997)
- 12.98 Y.J. Kim, S. Wakimoto, S.M. Shapiro, P.M. Gehring, A.P. Ramirez: Neutron scattering study of antiferromagnetic order in $\text{CaCu}_3\text{Ti}_4\text{O}_{12}$, *Solid State Commun.* **121**, 625 (2002)
- 12.99 C.C. Homes, T. Vogt, S.M. Shapiro, S. Wakimoto, M.A. Subramanian, A.P. Ramirez: Charge transfer in the high dielectric constant materials $\text{CaCu}_3\text{Ti}_4\text{O}_{12}$ and $\text{CdCu}_3\text{Ti}_4\text{O}_{12}$, *Phys. Rev. B* **67**, 092106 (2003)
- 12.100 L.B. Barbosa, D.R. Ardila, J.P. Andreeta: Growth of double perovskite $\text{Ca}_2\text{FeMoO}_6$ crystals by a floating zone technique, *J. Cryst. Growth* **254**, 378–383 (2003)
- 12.101 C. Kloc, S.-W. Cheong, P. Matl: Floating-zone crystal growth of perovskite manganites with colossal magnetoresistance, *J. Cryst. Growth* **191**, 294–297 (1998)
- 12.102 H. Fukazawa, S. Nakatsuji, Y. Maeno: Intrinsic properties of the mott insulator $\text{Ca}_2\text{RuO}_{4+\delta}$ ($\delta = 0$) studied with single crystals, *Physica B* **281**, 613–614 (2000)
- 12.103 S. Nakatsuji, Y. Maeno: Synthesis and single crystal growth of $\text{Ca}_{2-x}\text{Sr}_x\text{RuO}_4$, *J. Solid State Chem.* **156**, 26–31 (2001)

- 12.104 W. Wanyan, X. Yan, X. Wu, Z. Zhang, B. Hu, J. Zhou: Study of single-crystal growth of $\text{Tm}^{3+}:\text{CaYAlO}_4$ by the floating-zone method, *J. Cryst. Growth* **219**, 56–60 (2000)
- 12.105 K. Oka, H. Yamaguchi, T. Ito: Crystal growth of $\text{Ca}_{2+x}\text{Y}_{2-x}\text{Cu}_5\text{O}_{10}$ with edge sharing CuO_2 chains by the traveling-solvent floating-zone method, *J. Cryst. Growth* **229**, 419–422 (2001)
- 12.106 T. Ito, K. Oka: Growth and transport properties of single crystalline $\text{La}_{2-x}\text{Ba}_x\text{CuO}_4$, Part 1, *Physica C* **235**, 549–550 (1994)
- 12.107 G. Balakrishnan, O.A. Petrenko, M.R. Lees, D.M.K. Paul: Single crystals of the anisotropic Kagome staircase compounds $\text{Ni}_3\text{V}_2\text{O}_8$ and $\text{Co}_3\text{V}_2\text{O}_8$, *J. Phys. Cond. Matter* **16**, L347–L350 (2004)
- 12.108 G. Dhalenne, A. Revcolevschi, J.C. Rouchaud, M. Fedoroff: Floating zone crystal growth of pure and Si- or Zn-substituted copper germanate CuGeO_3 , *Mater. Res. Bull.* **32**, 939–946 (1997)
- 12.109 S. Hara, Y. Yoshida, S.I. Ikeda, N. Shirakawa, M.K. Crawford, K. Takase, K. Tanako, K. Sekizawa: Crystal growth of germanium-based oxide spinels by the float zone method, *J. Cryst. Growth* **283**, 185–192 (2005)
- 12.110 X.L. Yan, J.F. Zhou, X.J. Niu, X.L. Chen, Q.Y. Tu, X. Wu: Crystal growth of La_2CuO_4 and $\text{La}_{2-x}\text{Ba}_x\text{CuO}_4$ by the travelling solvent floating zone method, *J. Cryst. Growth* **242**, 161–166 (2002)
- 12.111 I. Tanaka, H. Kojima: Superconducting single crystals, *Nature* **337**, 21 (1985)
- 12.112 I. Tanaka, K. Yamane, H. Kojima: Single crystal growth of superconducting $\text{La}_{2-x}\text{Sr}_x\text{CuO}_4$ by the TSFZ method, *J. Cryst. Growth* **96**, 711–715 (1989)
- 12.113 A.M. Balbashev, D.A. Shulyatev, G.K. Panova, M.N. Khlopkin, N.A. Chernoplekov, A.A. Shikov, A.V. Suetin: The floating zone growth and superconductive properties of $\text{La}_{1.85}\text{Sr}_{0.15}\text{CuO}_4$ and $\text{Nd}_{1.85}\text{Ce}_{0.15}\text{CuO}_4$ single crystals, *Physica C* **256**, 371–377 (1996)
- 12.114 H. Kojima, Y. Yamamoto, Y. Mori, M.K.R. Khan, H. Tanabe, I. Tanaka: Single crystal growth of superconducting $\text{La}_{2-x}\text{M}_x\text{CuO}_4$ ($\text{M} = \text{Ca}, \text{Sr}, \text{Ba}$) by the TSFZ method, *Physica C* **293**, 14–19 (1997)
- 12.115 T. Ito, K. Oka: New technique for the crystal growth of $\text{La}_{2-x}\text{Ba}_x\text{CuO}_4$ ($x \leq 0.5$), *Physica C* **231**, 305–310 (1994)
- 12.116 J.D. Yu, J.D. Yanagida, H. Takashima, Y. Inaguma, M. Itoh, T. Nakamura: Single crystal growth of superconducting $\text{La}_{2-x}\text{Ba}_x\text{CuO}_4$ by TSFZ method, *Physica C* **209**, 442–448 (1993)
- 12.117 L.S. Jia, X.L. Yan, J.F. Zhou, X.L. Chen: Effect of pulling rates on quality of $\text{La}_{2-x}\text{Ba}_x\text{CuO}_4$ single crystal, *Physica C: Supercond. Appl.* **385**, 483–487 (2003)
- 12.118 I. Tanaka, H. Kojima: Single crystal growth of 2–1–4 system superconductors by the TSFZ method, *Int. Workshop Superconduct. (Honolulu 1992)* pp. 146–149
- 12.119 G.D. Gu, M. Hucker, Y.J. Kim, J.M. Tranquada, Q. Li, A.R. Moodenbaugh: Single crystal growth and superconductivity of $(\text{La}_{1-x}\text{Sr}_x)_2\text{CaCu}_2\text{O}_{6+\delta}$, *J. Cryst. Growth* **287**, 318–322 (2006)
- 12.120 U. Ammerahl, A. Revcolevschi: Crystal growth of the spin-ladder compound $(\text{Ca},\text{La})_{14}\text{Cu}_{24}\text{O}_{41}$ and observation of one-dimensional disorder, *J. Cryst. Growth* **197**, 825–832 (1999)
- 12.121 C. Zobel, M. Kriener, D. Bruns, J. Baier, M. Grüninger, T. Lorenz, P. Reutler, A. Revcolevschi: Evidence for a low-spin to intermediate-spin state transition in LaCoO_3 , *Phys. Rev. B* **66**, 020402 (2002)
- 12.122 P. Aleshkevych, P.M. Baran, S.N. Barilo, J. Fink-Finowicki, H. Szymczak: Resonance and non-resonance microwave absorption in cobaltites, *J. Phys. Cond. Matter* **16**, L179–L186 (2004)
- 12.123 T.-H. Arima, Y. Tokura: Optical study of electronic structure in Perovskite-type RMnO_3 ($\text{R} = \text{La}, \text{Y}; \text{M} = \text{Sc}, \text{Ti}, \text{V}, \text{Cr}, \text{Mn}, \text{Fe}, \text{Co}, \text{Ni}, \text{Cu}$), *J. Phys. Soc. Jpn.* **64**, 2488–2501 (1995)
- 12.124 Y. Tomioka, A. Asamitsu, Y. Tokura: Magneto-transport properties and magnetostructural phenomenon in single crystals of $\text{La}_{0.7}(\text{Ca}_{1-y}\text{Sr}_y)_{0.3}\text{MnO}_3$, *Phys. Rev. B* **63**, 024421 (2000)
- 12.125 A.M. De Leon-Guevara, P. Berthet, J. Berthon, F. Millot, A. Revcolevschi: Controlled reduction and oxidation of $\text{La}_{0.85}\text{Sr}_{0.15}\text{MnO}_3$ single crystals, *J. Alloys Compd.* **262/263**, 163–168 (1997)
- 12.126 A. Urushibara, Y. Moritomo, T. Arima, A. Asamitsu, G. Kido, Y. Tokura: Insulator-metal transition and giant magnetoresistance in $\text{La}_{1-x}\text{Sr}_x\text{MnO}_3$, *Phys. Rev. B* **51**, 14103–14109 (1995)
- 12.127 D. Prabhakaran, A.I. Coldea, A.T. Boothroyd, S. Blundell: Growth of large $\text{La}_{1-x}\text{Sr}_x\text{MnO}_3$ single crystals under argon pressure by the floating zone technique, *J. Cryst. Growth* **237**, 806–809 (2002)
- 12.128 J. Iida, S. Takekawa, N. Kimizuka: Single-crystal growth of LuFe_2O_4 , LuFeCoO_4 and YbFeMgO_4 by the floating zone method, *J. Cryst. Growth* **102**, 398–400 (1990)
- 12.129 J.L. Mass, J.M. Burlitch, S.A. Markgraf, M. Higuichi, R. Dieckmann, D.B. Barber, C.R. Pollock: Oxygen activity dependence of the chromium (IV) population in chromium-doped forsterite crystals grown by the floating zone technique, *J. Cryst. Growth* **165**, 250–257 (1996)
- 12.130 D.P. Chen, H.C. Chen, A. Maljuk, A. Kulakov, H. Zhang, P. Lemmens, P.C.T. Lin: Single-crystal growth and investigation of Na_xCoO_2 and $\text{Na}_x\text{CoO}_2 \cdot y\text{H}_2\text{O}$, *Phys. Rev. B* **70**, 024506 (2004)
- 12.131 C.T. Lin, D.P. Chen, P. Lemmens, X.N. Zhang, A. Maljuk, P.X. Zhang: Study of intercalation/deintercalation of Na_xCoO_2 single crystals, *J. Cryst. Growth* **275**, 606–616 (2005)
- 12.132 D. Prabhakaran, A.T. Boothroyd, R. Coldea, N.R. Charnley: Crystal growth of Na_xCoO_2 under different atmospheres, *J. Cryst. Growth* **271**, 74–80 (2004)

- 12.133 L.S. Jia, X.L. Yan, X.L. Chen: Growth of semiconducting Nd_2CuO_4 and as-grown superconductive $\text{Nd}_{1.85}\text{Ce}_{0.15}\text{Cu}_{4-z}$ single crystals, *J. Cryst. Growth* **254**, 437–442 (2003)
- 12.134 G. Balakrishnan, M.R. Lees, D.M. Paul: Single-crystal growth and properties of the double-layered manganese oxides, *J. Phys. Cond. Matter* **9**, L471–L474 (1997)
- 12.135 A.S. Sefat, J.E. Greedan, G.M. Luke, M. Niewczas, J.D. Garrett, H. Dabkowska, A. Dabkowski: Anderson–Mott transition induced by hole doping in $\text{Nd}_{1-x}\text{TiO}_3$, *Phys. Rev. B* **74**, 104419 (2006)
- 12.136 T. Ito, K. Oka: Crystal growth of $\text{REBa}_2\text{Cu}_3\text{O}_{7-y}$ and ambient atmosphere, *Physica C* **235**, 355–356 (1994), Part 1
- 12.137 N.T. Hien, J.J.M. Franse, J.J.M. Poethuizen, A.A. Menovsky: Growth and characterization of bulk $\text{Sr}_2\text{CuO}_2\text{Cl}_2$ single crystals, *J. Cryst. Growth* **171**, 102–108 (1997)
- 12.138 A. Revcolevschi, A. Vietkine, H. Moudden: Crystal growth and characterization of chain cuprates SrCuO_2 , Sr_2CuO_3 and spin-ladder $\text{Sr}_{14}\text{Cu}_{24}\text{O}_{41}$, *Physica C* **282–287**, 493–494 (1997)
- 12.139 N. Ohashi, K. Fujiwara, T. Tsurumi, O. Fukunaga: Growth of orthorhombic SrCuO_2 by a travelling solvent floating zone method and its phase transformation under high pressure, *J. Cryst. Growth* **186**, 128–132 (1998)
- 12.140 H. Kageyama, K. Onizuka, T. Yamauchi, Y. Ueda: Crystal growth of the two-dimensional spin gap system $\text{SrCu}_2(\text{BO}_3)_2$, *J. Cryst. Growth* **206**, 65–67 (1999)
- 12.141 U. Ammerahl, G. Dhalenne, A. Revcolevschi, J. Berthon, H. Moudden: Crystal growth and characterization of the spin-ladder compound $(\text{Sr,Ca})_{14}\text{Cu}_{24}\text{O}_{41}$, *J. Cryst. Growth* **193**, 55–60 (1998)
- 12.142 A. Maljuk, J. Strempfer, C. Ulrich, M. Sofin, L. Capogna, C.T. Lin, B. Keimer: Growth of $\text{Sr}_3\text{Fe}_2\text{O}_{7-x}$ single crystals by the floating zone method, *J. Cryst. Growth* **273**, 207–212 (2004)
- 12.143 Y. Maeno, H. Hashimoto, K. Yoshida, S. Nishizaki, T. Fujita, J.G. Bednorz, F. Lichtenberg: Superconductivity in a layered Perovskite without copper, *Nature* **372**, 532–534 (1994)
- 12.144 R.S. Perry, Y. Maeno: Systematic approach to the growth of high-quality single crystals of $\text{Sr}_3\text{Ru}_2\text{O}_7$, *J. Cryst. Growth* **271**, 134–141 (2006)
- 12.145 R. Fittipaldi, A. Vecchione, S. Fusanobori, K. Takizawa, H. Yaguchi, J. Hooper, R.S. Perry, Y. Maeno: Crystal growth of the new Sr_2RuO_4 – $\text{Sr}_3\text{Ru}_2\text{O}_7$ eutectic system by a floating-zone method, *J. Cryst. Growth* **282**, 152–159 (2006)
- 12.146 K. Uematsu, O. Sakurai, N. Mizutani, M. Kato: Electrical properties of La-doped SrTiO_3 (La: 0.1 to 2.0 at %) single crystals grown by xenon-arc image floating zone method, *J. Mater. Sci.* **19**, 3671–3679 (1984)
- 12.147 A. Sugimoto, Y. Nob, K. Yamagishi: Crystal-growth and optical characterization of $\text{Cr,Ca-Y}_3\text{Al}_5\text{O}_{12}$, *J. Cryst. Growth* **140**, 349–354 (1994)
- 12.148 I. Shindo, N. Kimizuka, S. Kimura: Growth of YFe_2O_4 single-crystals by floating zone method, *Mater. Res. Bull.* **11**, 637–643 (1976)
- 12.149 H.A. Dabkowska, A. Dabkowski, G.M. Luke, B.D. Gaulin: Crystal growth structure and magnetic behaviour of ytterbium cobalt gallium oxide YbCoGaO_4 , *J. Cryst. Growth* **234**, 411–414 (2002)
- 12.150 K. Oka, H. Shibata, S. Kashiwaya: Crystal growth of ZnO , *J. Cryst. Growth* **237**, 509–513 (2002)

13. Laser-Heated Pedestal Growth of Oxide Fibers

Marcello R.B. Andreetta, Antonio Carlos Hernandez

The laser-heated pedestal growth (LHPG) technique, when compared with conventional growth methods, presents many advantages, such as high pulling rates, a crucible-free process, and growth of high and low melting point materials. These special features make the LHPG technique a powerful material research tool. We describe the background history, theoretical fundamentals, and how the features of LHPG affect the growth of oxide fibers. We also present a list of materials processed by laser heating in recent decades, such as LiNbO_3 , Sr-Ba-Nb-O , $\text{Bi}_{12}\text{TiO}_{20}$, Sr_2RuO_4 , Bi-Sr-Ca-Cu-O , $\text{ZrO}_2\text{:Y}_2\text{O}_3$, LaAlO_3 , and also the eutectic fibers of $\text{Al}_2\text{O}_3\text{:GdAlO}_3$, $\text{Al}_2\text{O}_3\text{:Y}_2\text{O}_3$, and $\text{ZrO}_2\text{:Al}_2\text{O}_3$.

13.1	Fiber-Pulling Research	394
13.2	The Laser-Heated Pedestal Growth Technique	399
13.2.1	Source Preparation and Seeding	400

13.2.2	Automatic Diameter Control Applied to LHPG	401
13.3	Fundamentals	402
13.3.1	Conservation of Mass	402
13.3.2	Balance of Heat Transfer	403
13.3.3	Mechanical Stability	404
13.3.4	Growth Under Controlled Atmosphere	405
13.3.5	Dopant Distribution	406
13.3.6	Pulling Crystalline Fibers Under Electric Field	407
13.4	Fiber Growth Aspects	409
13.4.1	Congruent Melting Fibers: The Search for Stoichiometry	409
13.4.2	Incongruently Melting and Evaporating Fibers	416
13.4.3	Eutectic Fibers	416
13.5	Conclusions	418
	References	419

Laser technology has been applied for many years to process a wide range of materials and devices. The characteristics that make laser radiation very attractive for this purpose are its coherence and collimation, which allow the adjustment of the energy distribution with conventional optical elements as well as location of the heat source outside the preparation chamber. The main applications of laser materials processing technology are: perforation, cutting and welding, sintering, surface thermal treatment, unidirectional solidification applied to fiber pulling, material texturing, and production of aligned eutectic materials.

Among all the laser-heated crystalline fiber-pulling techniques that have appeared over the last 40 years, laser-heated pedestal growth (LHPG) has become one of the most powerful tools in new and conventional materials research. The main advantages of this technique are its high pulling rates (about 60 times faster than

conventional Czochralski technique) and the possibility to produce very high melting point materials. Besides that, it is a crucible-free technique, which allows the pulling of high-purity single crystals and composite fibers, avoiding mechanical stress and contamination due to the crucible material during the solidification process.

In addition to all of these advantages of the LHPG technique, the crystal geometric shape, its flexibility for small diameters, and its low cost make single-crystal fibers (SCF) produced by LHPG even more suitable to substitute for many of today's bulk devices, especially with respect to high melting point materials. However, for this purpose the SCF must have equal or superior optical and structural qualities compared with bulk devices.

In this chapter we describe the laser-heated pedestal growth technique as a powerful materials research tool

and its features, such as the high axial thermal gradients at the solid–liquid interface. In order to produce this chapter, the authors analyzed more than 300 original scientific papers dealing with laser-heated pedestal growth. The publication dynamics on laser-heated fiber growth using the laser-heated floating-zone-like technique are presented in Fig. 13.1. Those are the results of the last two decades of research. From these data we can verify the great increase in publication rate over the last two decades, showing the importance of this technique in materials science. We also present the historical evolution, theoretical fundamentals, and how the unique features of the LHPG technique affect the quality of the pulled fibers and make it possible to pull incongruently melting and evaporating materials, as well as its influence on the microstructures of eutectic oxide composites.

13.1 Fiber-Pulling Research

The first publications on fiber preparation from the melt date back to the beginning of the 20th century and were restricted to research on metal wires. The origin of this research started with the physicists *Baker* [13.1] and *da Costa Andrade* [13.2], who wrote in his personal reminiscences: “I continued my work on the creep of metals and accidentally made the first single crystal metal wires” [13.3]. However, in the same period, there was also the need to understand one of the topical areas of physical chemistry that had lasted for 50 years: the measurement of crystallization velocities [13.4,5]. It was with this idea in mind that *Czochralski* presented in 1918 a new *method for measurement of the crystallization velocity of metals* where he actually pulled fibers of low melting point metals from their melts [13.6]. Soon after this, *Gomperz* [13.7] used floating dies to control the fiber diameter [an early Stepanov or edge-defined film-fed growth (EFG) process] [13.5].

In the 1950s, single-crystal fiber attracted the attention of researchers due to its high crystalline perfection and outstanding mechanical properties. Those fibers were produced mainly by vapor-phase reactions [13.8]. Research into fiber pulling from the melt, especially for nonconducting materials, remained somewhat latent for approximately 20 years until the end of World War II (1945), the transistor revolution (1947), and the creation of the laser (1960). The works of *Labelle* and *Malvsky* [13.9,10] on the pulling of sapphire fibers from the melt opened a new perspective in fiber research.

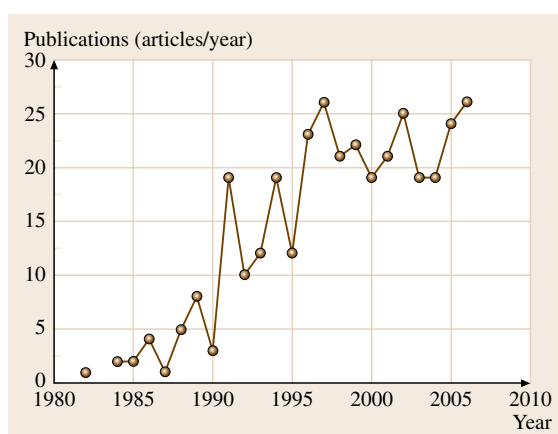


Fig. 13.1 Publication dynamics of laser-heated fiber pulling research

In their work of 1971 they grew sapphire fibers by the now famous die-shapes growth method known as edge-defined film-fed growth (EFG) [13.8]. Due to its outstanding mechanical strength, these sapphire fibers were considered good candidates to be used as structural composites.

It was only in 1972 that fiber pulling from the melt received a major contribution. Due to the interest of industry in creating a technique for producing fibers with small diameter, high mechanical strength, and high purity, the floating zone technique was considered. It was *Haggerty* [13.11] who developed the method of four focused laser beams to create a laser-heated floating zone for fiber production. However, this was not the first time that lasers had been used in the growth of bulk samples, as demonstrated by the work of *Cockayne* and *Gasson* [13.12]. Haggerty grew fibers of Al_2O_3 , Y_2O_3 , TiC , and TiB_2 and investigated their mechanical properties. He concluded that, even without optimization of the growth process, the room-temperature strength of $\text{Cr}:\text{Al}_2\text{O}_3$ fibers could reach $9.65 \times 10^9 \text{ N/m}^2$, which had previously been observed only with small, *whisker* single crystals.

In the late 1970s, the development in fiber-optic communication and the need for miniaturization of optical devices, such as miniature solid-state lasers, provided a major impulse for the laser-heated fiber growth technique. During this period, we can highlight the works of *Burrus*, *Stone*, and *Coldren* on the production

of high melting point oxide fibers (Nd:YAG, Nd:Y₂O₃, and Al₂O₃:Cr) and also the room-temperature operation of miniature lasers using Nd:YAG and Nd:Y₂O₃ fibers grown by the two focused laser beam heated pedestal growth method [13.13–15].

Until 1980, the laser-heated technique applied to crystal growth used only two or four laser beams focused over the source material. This condition usually leads to the creation of large radial thermal gradients in the molten zone that could be deleterious for growing crystal [13.8]. The main contribution on the subject of radial thermal flow in the laser-heated crystal growth technique was made by *Fejer* and *Feigelson* [13.16, 17]. They incorporated into the focusing system a special optical component known as a *refluxicon* [13.18], consisting of an inner cone surrounded by a larger coaxial cone section, both with a reflective surface, which converts the cylindrical laser beam into a larger-diameter hollow cylinder surface. This optical component allowed the energy to be distributed radially over the molten zone, reducing the radial thermal gradients [13.19]. This new version of the laser floating zone technique became known as laser-heated pedestal growth, or simply **LHPG**.

In the setup based on the Stanford version of the **LHPG** technique, a CO₂ laser (continuous wave (CW), $\lambda = 10.6 \mu\text{m}$) or Nd:YAG laser (CW, $\lambda = 1.06 \mu\text{m}$) can be used with the laser cavity cooled by water or air flow, depending on the nominal laser power. It is quite common to use a He–Ne laser, propagating parallel to CO₂ laser beam, to act as a guide for the eye in the opti-

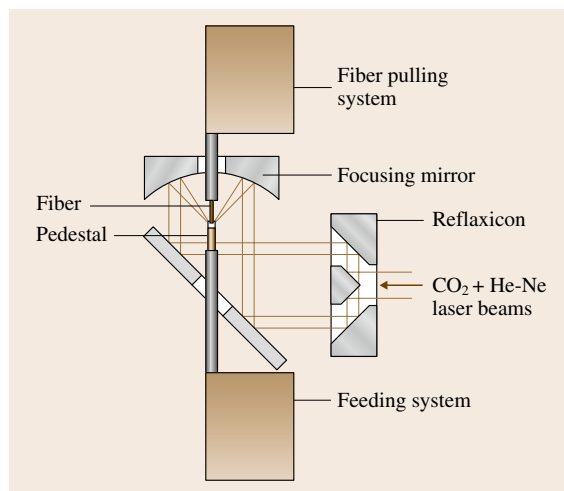


Fig. 13.2 Schematic drawing of the laser-heated pedestal growth (**LHPG**) technique (after [13.16–19])



Fig. 13.3 LiNbO₃ single-crystal fiber growth and its molten zone by the **LHPG** technique

cal alignment. The laser beams are guided into a closed chamber through a ZnSe window and hit the refluxicon [13.18], where they are converted as mentioned above into a cylindrical shell and guided to a spherical or parabolic mirror, and focused over the source material as shown in Fig. 13.2. The focusing mirror has a hole in its center to allow the seed holder to be placed in its optical axis and also to avoid vapor material deposition onto the optical mirrors during fiber pulling. The use of a growth chamber allows for a controlled growth atmosphere (special gases or vacuum). There are normally two windows in the growth chamber for visualization of the growth process: it is possible to see the molten zone by using magnifying lenses and with a video system mounted 90° off-axis from the first one. This video system has a microscope attached to it, allowing the viewing of the molten zone and the growing fiber (Fig. 13.3).

Since the implantation of the **LHPG** system at Stanford University laboratories, several modifications have been proposed to improve it. Table 13.1 lists some of these modifications in the **LHPG** technique over the last decades. The first modification to the **LHPG** system was made by *Fejer* himself (1985) when he implemented high-speed diameter control of the fiber during the pulling process [13.20]. Diameter control proved to be essential to obtain high-quality single-crystal fibers and also to improve the efficiency of resulting fiber-optical devices (such as waveguides and solid-state lasers) by decreasing the light scattering at the surface of the fiber.

Due to the fact that the **LHPG** technique has very localized heating, it generates a very large thermal gradient at the growth interface (on the order of

Table 13.1 Laser-heated fiber-pulling technique: evolution/modifications over the past decades

Year	Authors	Improvement	Reference
1971	Haggerty	Four laser beams focused at the molten zone	[13.11]
1982	Fejer et al.	Refluxicon – LHPG	[13.16]
1985	Fejer et al.	Fiber diameter control	[13.20]
1992	Uda and Tiller	Resistive afterheater	[13.21]
1993	Sugiyama et al.	Optical afterheater	[13.22]
1994	Phomsakha et al.	Gaussian reflector	[13.23]
1995	Yokoo et al.	Indirect laser heating (organic compounds) – ILHPG	[13.24]
1995	Imai et al.	Gas flux to increase axial thermal gradient	[13.25]
1996	Brueck et al.	Ultrahigh-vacuum LHPG	[13.26]
1997	Brenier et al.	Ferroelectric domain inversion by in situ electric field poling	[13.27]
1997	Nubling and Harrington	New refluxicon without shadows in the molten zone	[13.28]
1999	Ardila et al.	LHPG in a high isostatic pressure environment	[13.29]
2001	Ardila et al.	Bifocal spherical mirror	[13.30]
2001	Laversenne et al.	Gradient crystals (pedestal preparation)	[13.31]
2002	Andreeta et al.	Thermal gradient control by the modification of the focal spot	[13.32]
2003	Andreeta et al.	Automatic diameter control based on artificial vision	[13.33]
2004	Carrasco et al.	Electrical-assisted LHPG – EALHPG	[13.34]
2005	Lo et al.	Double-clad fiber crystal	[13.35]

10^3 – 10^4 °C/cm). Uda and Tiller [13.21] used a Pt–Rh(10%) resistive afterheater in order to control the axial thermal gradient at the solid–liquid growth interface [13.21] (Fig. 13.4a). They showed that Cr^{3+} doping concentration in LiNbO_3 single-crystal fiber is affected by an electric field generated at the growing interface, which is proportional to the axial temperature gradient. They could also calculate the diffusion coefficient for Cr in the liquid phase ($3.8 \times 10^{-6} \text{ cm}^2/\text{s}$). Sugiyama et al., in 1993 [13.22], proposed the use of an optical afterheater in order to create a more homogeneous temperature distribution around the growing fiber, to allow the pulling of larger-diameter (0.5–1.0 mm) high-quality *a*-axis strontium barium niobate (**SBN**) fibers for holographic applications (Fig. 13.4b). Larger-diameter fibers presented optical inhomogeneity resulting from internal stress induced during solidification and from anisotropic growth kinetics in the radial direction. Sugiyama et al. reported the improvement in the fiber morphology and also in the fiber composition homogeneity with the use of the afterheater. In the Fejer version of the **LHPG** technique, the arrangement results in very tight focusing on the shoulder of the molten

zone. Phomsakha et al. proposed the use of a Gaussian reflector [13.23] to substitute the refluxicon (Fig. 13.4c). In this way, they achieved a condition for sapphire fiber pulling where not only is the laser radiation spread more evenly over the molten zone but it also impinges on a short length of the newly grown fiber. In this configuration the fiber-pulling limit for high-quality sapphire fibers was extended from 2–3 mm/min to as high as 20 mm/min using He atmosphere. The authors believe that the appropriate distribution of the laser beam in the vicinity of the molten zone is important in minimizing the magnitude of convection currents, which could improve the sapphire fiber quality and allow greater pulling speed.

In 1995 Yokoo et al. modified the **LHPG** system in order to grow low melting point organic compounds [13.24]. The **LHPG** system in its original configuration cannot be applied directly to grow organic single fibers due to their very low melting point and poor thermal conductivity. Even though sublimation occurs more easily due to direct and localized heating by the laser in those compounds, this does not allow for stabilization of the molten zone. The new configura-

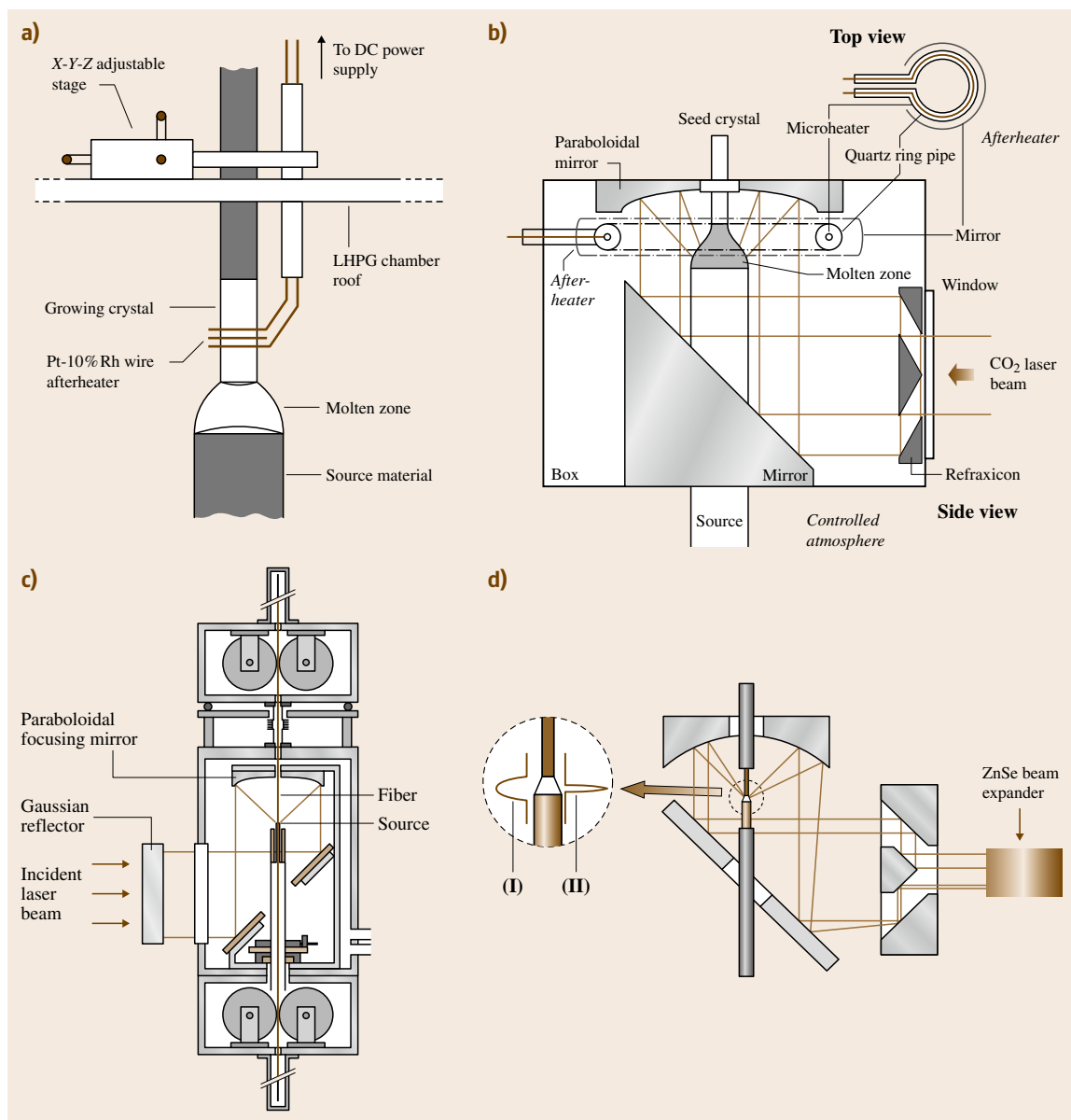


Fig. 13.4a–d Modifications to the LHPG system over the years to control/modify the temperature gradient at the solid–liquid interface. (a) Resistive afterheater (after [13.21]), (b) optical afterheater (after [13.22]), (c) Gaussian reflector replacing the refraxicon device (after [13.23]) and (d) Creation of a controlled optical aberration at the focusing point; (I) divergent laser beam and (II) parallel laser beam (after [13.32])

tion is based on the insertion of a glass tube to stop the laser beam before it reaches the material to be melted, and the introduction of a gas flow. The authors called this new method indirect laser-heated pedestal growth (ILHPG). The source rod and seed crystal are inserted

into the glass tube from opposite sides of the tube. The CO₂ laser beam is focused onto the glass tube circularly with an axially symmetric irradiance pattern. The laser beam is absorbed by the glass and retransmitted by black-body radiation emission from its inner surface.

As a result, direct and localized heating of the source rod is avoided. With this configuration they were able to produce single-crystal fibers of 2-adamantylamino-5-nitropyridine (AANP). The authors were able to produce AANP crystal fibers with lengths of more than 20 mm and diameters ranging from 300 μm to 2 mm. In addition, it has been experimentally confirmed that the efficiency of second-harmonic generation (SHG) for rod-like AANP crystal grown by the LHPG method is higher than that for conventional AANP crystal grown by Bridgman–Stockbarger method.

While many researchers were making efforts to decrease or homogenize the axial and radial temperature gradient at the solid–liquid interface, respectively, Imai and coworkers (1995), for the growth of potassium niobium tantalate (KTN) fibers, went in the opposite direction [13.25], observing that the thermal axial gradient was not high enough to prevent constitutional supercooling. The authors constructed a gas blower whose nozzle encircled the fiber symmetrically. The flow surrounds the fiber, the molten zone, and the pedestal-like tube. With this modification the authors were able to pull KTN fiber of 400 μm at pulling rates up to 0.4 mm/min, 50 times faster than the conventional top seed solution growth method, suppressing the constitutional supercooling phenomenon. However the fibers still had cracks and showed striations, located mainly at the center.

Brueck et al., in 1996, used an ultrahigh-vacuum (UHV) modified LHPG to grow metal fibers, returning, in a way, to the birth of fiber research [13.26]. They grew UPt_3 and UNi_2Al_3 in order to study their electric property, which is strongly affected by impurities and oxidation. The fibers were about 600 μm in diameter and showed superconductivity behavior down to 400 and 600 mK for UPt_3 and UNi_2Al_3 , respectively. UNi_2Al_3 fiber presented a higher temperature transition when compared with Czochralski single crystals (300 mK) due to the higher crystal quality.

In 1997 Nubling and Harrington introduced a new version of the reflexicon [13.28]. The inner cone was made from a ZnSe window with an Ag-coated diamond-turned cone in the center. By using a window and reflecting cone, they eliminated the need for supporting spokes for the cone and thus the laser beam was not obscured. The entire optical system could produce a calculated spot size as small as 22 μm . For larger-diameter fiber they were able to adjust the spacing between the reflexicon elements so that it was possible to create a larger focused spot that led to more stable growth. In the same year, Brenier et al. devel-

oped a method for producing periodic poling lithium niobate (PPLN) [13.27] single-crystal fiber. They added two identical tungsten electrodes, 250 or 750 μm in diameter, parallel to the growth direction (a -axis) and 6 mm apart, near the growth interface. They applied a 200 V periodic alternating voltage signal and created an electric field parallel and antiparallel to the c -axis. With this configuration they were able to produce periodic alternating ferroelectric domains separated by 1.68 μm with a typical period of 204 ms for the electric field and a pulling speed of 120 mm/h. In 1999 Ardila et al. developed a system to grow single-crystal fiber in a high isostatic pressure environment [13.29]. The authors have shown that fiber growth of $\text{LiNbO}_3\text{:Er}$ and $\text{Ca}_3\text{V}_2\text{O}_8\text{:Er}$ are favored by a high O_2 isostatic pressure during the pulling process. In the case of $\text{Ca}_3\text{V}_2\text{O}_8$ fiber the best results were obtained by a 10 bar O_2 pressure.

Two years later, Ardila et al. proposed another modification to the LHPG technique [13.30]. This time they introduced a bifocal spherical mirror to focus the CO_2 laser. With this modification to the optical system, they managed to create an optical afterheater with the same laser beam as used to melt the compound. They were able to grow c -axis LiNbO_3 with 2 mm diameter without cracks, doubling the diameter obtained with the previous focusing mirror. In the same year, Laversenne et al. [13.31] developed a process to produce concentration-gradient crystals. They describe a methodology to produce pedestals with two different composition (or concentration) regions. During the growth process the liquid phase continuously changes its composition, thus allowing crystallization at the beginning with one composition and finishing with another. This means that, in the same experiment, one may create a *spectroscopic library* (with different doping concentrations) for the determination of the optimum desired properties.

Andreeta et al. proposed in 2002 a modification to the alignment of the LHPG system that allowed the creation of an optical aberration at the focusing point of the CO_2 laser beam [13.32]. In this way it was possible to decrease the axial gradient while maintaining the annular radial distribution in the fiber growth. The authors have shown that the introduction of a 1° deviation from the original parallel laser beam entering the reflexicon could expand the width of the laser beam focused at the molten zone by a factor of 10 (Fig. 13.4d). This leads to a reduction of about 1000 $^\circ\text{C}/\text{cm}$ in the axial temperature gradient at the growing interface (from 3800 $^\circ\text{C}/\text{cm}$ to 2700 $^\circ\text{C}/\text{cm}$) for the Bi–Sr–Ca–Cu–O (BSCCO)

system used as a model material. The following year *Andreeta et al.* published an article describing another approach for automatic diameter control in the **LHPG** technique [13.33]. In this new approach an optical image of the molten zone is digitized and its height and the fiber diameter are monitored by a microcomputer, in an attempt to effectively control the shape of the molten zone and not only the fiber diameter itself.

In 2004, *Carrasco et al.*, using a Nd:YAG-LHPG technique, introduced an electric current flow through the crystallization interface in **BSCCO** fiber pulling [13.34]. They showed that the direction of current flux modifies the fiber quality and also that the choice of appropriate current direction and intensity can improve the texture of the **BSCCO** fibers produced.

Finally, in 2005, *Lo et al.* [13.35] developed a method to produce YAG fibers with a clad structure by introducing a previously grown fiber with a diameter of 68 μm into a fused-silica capillary tube with 76 and 320 μm inner and outer diameter, respectively. They then applied the **LHPG** technique again in the tube with

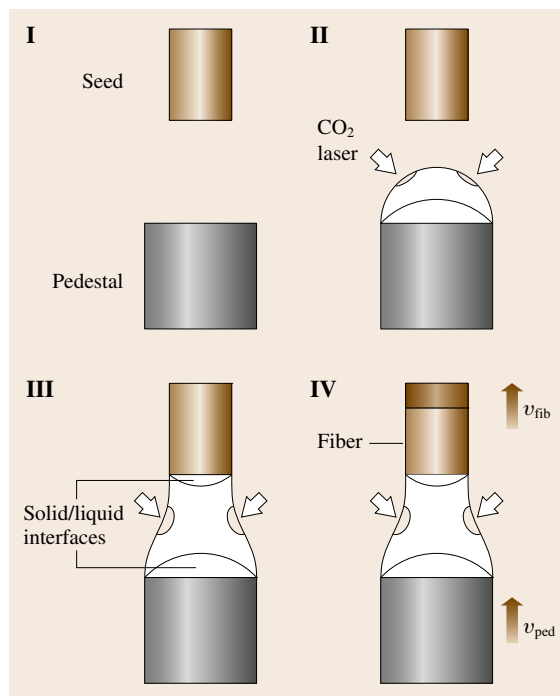
the fiber and pulled in the downward direction. The result was a core (YAG fiber with 25 μm in diameter) and two more layers. The outer layer proved to be of SiO_2 whereas the inner layer was a mixture of YAG and SiO_2 .

The history of fiber research is very rich and, as mentioned earlier, started before many of the traditional crystal growth techniques, such as Czochralski. The introduction of laser heating for the production of fiber-shaped materials expanded the previous physical limitations for new materials development. High melting point materials could be developed with minimal material lost. Due to its versatility and to achieve the fiber quality needed for some applications, almost once a year a new version/modification appears in the literature for the **LHPG** technique. Some of the changes and proposals for modification to the **LHPG** system described earlier are restricted to the developers' laboratory, mainly due to difficulties in their implementation. However, all of them slightly extended the potential of the **LHPG** technique to create new features for the development of new materials and also to improve the quality of known materials.

13.2 The Laser-Heated Pedestal Growth Technique

The **LHPG** technique, as described in Sect. 13.1, is basically a miniature floating-zone-like method where the heating element is substituted by a focused laser ring to generate the molten zone. The pulling process starts with basically four steps inside the growth chamber, as illustrated in Fig. 13.5. The first step is to align the seed and the pedestal mechanically, both centralized in the optical axis of the laser beam. The next step is to create a small molten zone on top of the pedestal, by turning on the laser and slowly increasing the laser power. In the following step the seed is introduced into the liquid and a molten zone is formed. Finally, the motors start the fiber pulling and rotation, as indicated in step IV of Fig. 13.5. In the following sections the experimental aspects of this technique are presented in terms of source and

Fig. 13.5 Schematic drawing of the four steps performed in the **LHPG** technique: (I) mechanical alignment of the seed and the pedestal and (II) creation of a small molten zone on the top of the pedestal. (III) The seed is then introduced in the liquid phase and there is creation of a molten zone. (IV) The motors are started and the fiber-pulling process begins ►



seed preparation and automatic diameter control (ADC) systems.

13.2.1 Source Preparation and Seeding

The source material (pedestals) used to grow single-crystal fibers can be prepared by cutting a previous bulk-grown crystal or dense ceramic or by the cold extrusion process. Pedestals obtained from bulk crystals or dense ceramics usually have a square section, which is not the best geometry to fit the cylindrical focusing laser beam. In this way one more step is needed before the fiber growth process, if one wants to avoid the corners of the square section pedestal going inside the liquid phase during the pulling process, destabilizing the contact angle. To avoid this effect it is necessary to round the pedestal.

In the cold extrusion process, an organic binder (such as polyvinyl alcohol) is added to the material of reacted or unreacted powder until it achieves a plastic-like consistency, and then it is forced, with a manual press, through a 5 mm long 1 mm diameter stainless-steel cylindrical tube [13.36]. This source material does not need to be cut, as it already has a convenient geometric shape. The pedestals are then allowed to dry at ambient temperature for at least 3 h, and can then be used as a source for crystal growth. This method for producing source materials has many advantages over conventional approaches, such as the small amount of materials needed and the possibility of producing source rods from reagents (green-rods), which also enables better stoichiometric control. When green rods are used in the LHPG system, the three steps in material

preparation are reduced to just one (synthesis, sintering, and crystal growth). In previous works, we have shown that the fiber quality of high melting point materials is related to the pedestal heat treatment previous to the growth process [13.37, 38]. The longer the pedestal heat treatment prior to the growth process, the darker the resulting fiber. The origin of the dark color of the fiber may be related to the creation of oxygen vacancies when the pedestal is processed at high temperatures, since changes in the stoichiometry were within experimental error. Crystals grown from an unreacted source (cold extrusion process) are colorless and show good transparency, as shown in Fig. 13.6.

Another feature of the LHPG technique is the possibility to prepare pedestals with compositional variation, such as in the method developed by *Laversenne et al.* [13.31] to create a different doping concentration along the fiber axis. This method was also used by *Barbosa et al.* [13.39] by conveniently joining two cold-extruded sections of CaMoO_4 and SrMoO_4 . The obtained fiber was pure CaMoO_4 at one end and pure SrMoO_4 at the other, both single crystals, with a continuous lattice parameter variation between the two pure sections (a gradient crystal fiber). This kind of crystal can be useful for x-ray optics applications.

The seeds used in the LHPG system must have the same characteristics as for any other crystal growth technique. However, since LHPG is a very powerful tool for new materials development, it is usual to use wires (Pt, Au, etc.) or small pieces of the pedestal (polycrystalline material) as a startup seed for the pulling process due to the impossibility of obtaining previous oriented crystals by any other growth technique. As would be expected, it has been shown that the seed plays a major role in the quality of the grown fiber. *Lu et al.* [13.40] studied seeding effects in the Bi–Sr–Ca–Cu–O system. They used Pt and Au wires to start the pulling process. The use of wires of Pt creates a very high thermal gradient at the wire–melt interface, thus nucleating grains that are aligned with the preferential growth direction perpendicular to the wire surface. While most of the grains grow out of the fiber, some of them grow parallel to the fiber axis and later dominate the grain structure. Grain selection usually takes place in the first 1–4 mm of the grown fiber, and depends on the diameter. For the same materials Au wires did not show the same results. The difference between Pt and Au wire seeding, according to the authors, is due to the reduced wettability or higher thermal conductivity of Au. Due to the considerably larger thermal conductivity of gold wires, the laser power (melt temperature)

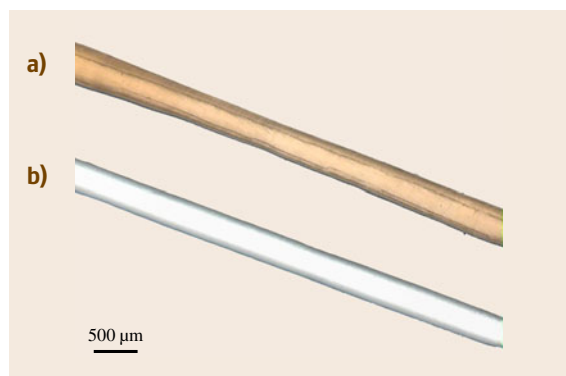


Fig. 13.6a,b Single-crystal LaAlO_3 fibers produced from different types of pedestals: (a) LaAlO_3 fiber grown from prereacted pedestal, and (b) LaAlO_3 fiber grown from unreacted pedestal (green-rod)

had to be increased significantly to cause the melt to adhere to the gold wire, and then decreased abruptly to create a normal-sized molten zone. In this way, higher-temperature phases dominate the beginning of the pulling process ($\text{CaO} + \text{liquid}$ and $\text{CaSrCu}_2\text{O}_4 + \text{liquid}$). *Chen* and coworkers [13.41] have shown that it is possible to pull stoichiometric LiNbO_3 single-crystal fibers from pedestals with 50 mol % Li_2O , if a seed with 58 mol % Li_2O is used. Using this strategy, in the beginning of the growth process an excess of Li_2O is inserted into the molten zone due to a small fraction of the seed that melts. In this way, since the early stages of the growth process, the crystal is allowed to solidify to 50 mol % Li_2O . In other words, when the solidified crystal composition reaches 50 mol % Li_2O , the fiber will have the same composition as the pedestal (source).

Another interesting work was performed by *Ishibashi* et al. [13.42], who studied facet suppression in the growth of $\text{YAG}:\text{Ca}:\text{Cr}$ fiber by the LHPG technique. This is a major issue for optimization of solid-state laser efficiency and holographic recording. In order to improve the laser operation efficiency, the authors studied the best crystallographic seed orientation in the growth of $\text{YAG}:\text{Ca}:\text{Cr}$ fibers. They found that facet suppression occurs for a crystallographic oriented seed at 15° from $\langle 100 \rangle$ to $\langle 110 \rangle$. For SBN single-crystal fibers, *Sugiyama* et al. [13.22] reported that the only way to obtain ridge fiber (facet suppression) is to use a ridge-fiber crystal as a seed.

13.2.2 Automatic Diameter Control Applied to LHPG

Despite the precautions intended to ensure stable growth conditions, as will be described in the following sections, it is found that excessive variations in the fiber diameter occur during open-loop growth. It is thus necessary to design closed-loop systems to regulate fiber diameter during the growth process. These systems contain basically two major components: a real-time dimension measurement apparatus and a proportional controller feeding back to the laser and/or motor speed ratio. Two main approaches have been developed to control the fiber diameter in the LHPG system. The first is based on quasisinusoidal interference fringes as the measurement technique observed in the far field of a fiber side-illuminated by a beam of coherent light [13.20]. The second method is based on artificial vision of the molten zone of the growing fiber [13.33].

The theoretical diameter variation resolution $(\Delta\phi/\phi)_{\min}$ of the system based on the interference

fringes can be obtained from a ray-tracing analysis, as shown in (13.1)

$$\left(\frac{\Delta\phi}{\phi}\right)_{\min} = \left(\frac{s}{f}\right)g(n, \theta), \quad (13.1)$$

where s is the distance between two adjacent elements in a photodiode array, f is the focal length of the lens that projects the interference pattern onto the photodiode array, and $g(n, \theta)$ is a geometrical factor dependent on the refraction index of the fiber n and the angle between the laser beam and the detector θ . This factor is obtained from ray-tracing analysis and is typically between 0.4 and 1.0. The quantity s/f can be described as the angular resolution of the optical system. The monotonic improvement in the resolution with increasing focal length predicted by (13.1) is eventually limited by signal-to-noise considerations. *Feyer* et al. [13.20] have shown that this ADC system allows the production of fibers with diameter fluctuations as small as 0.02%.

Another way to introduce an automatic diameter control system is to use the measurements of a charge-coupled device (CCD) camera image of the growing fiber as a feedback for the CO_2 laser and the fiber-pulling motor [13.33]. The video hardware captures the image, which is recorded and processed by a personal computer (PC) in gray scale mode. The black-body radiation from the molten zone and the high temperature gradient at the melting (pedestal) and crystallization (fiber) interfaces (10^3 – 10^4 °C/cm) make it easy to identify those interfaces positions, due to the good contrast in the image at those points in the LHPG technique. The software uses those positions to measure the fiber diameter and the height of the molten zone. In this way, two predefined areas in the image are measured. The first area is a vertical rectangle (3×354 pixels) and the

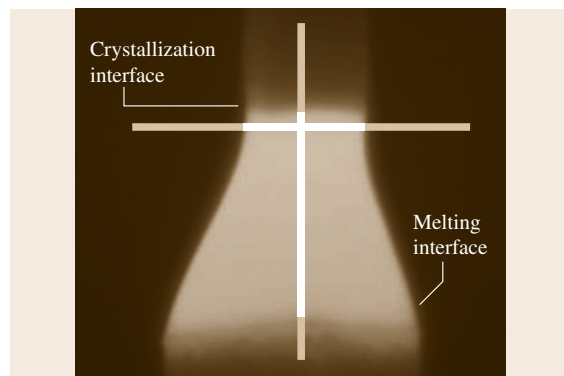


Fig. 13.7 Measurements on a captured image of a growing LaAlO_3 fiber (after [13.33])

other one is a horizontal rectangle (354×3 pixels), as shown in Fig. 13.7. The software recognizes the value of all the pixels (from 0 to 255) inside these areas. The next step is to count the number of white pixels inside the predefined area (molten material). The number of these pixels is proportional to the height of the molten zone (vertical) and to the fiber diameter (horizontal). Based on the vertical pixel count, the software recognizes the position of the crystallization interface, using this information to take the horizontal measurement just a few pixels below the crystallization interface (because of the better contrast on the molten zone). After selecting the desired diameter and molten zone height, the software modifies the laser power and pulling rate to match the number of pixels established by the crystal grower (the set point). One advantage of this system is that it is independent of the material used (opaque or transparent). Diameter control of better than 2% was obtained for growth of LaAlO_3 single-crystal fibers, using unreacted pedestals with an appropriate mixture of La_2O_3 – Al_2O_3 , with diameter fluctuation intentionally introduced in the pedestal up to 20% (Fig. 13.8). It has been shown that this ADC system can reduce the overall fiber diameter to less than 1% for dense pedestals, with regions on the order of 1 cm with near-zero variations.

13.3 Fundamentals

Many of the unique features of the LHPG technique are consequences of the very small liquid-phase volume necessary to grow crystals and in the following sections we shall discuss both experimental and theoretical aspects of the pulling process.

13.3.1 Conservation of Mass

It is possible to correlate the pedestal and fiber cross-section areas with their respective pulling rates if we consider that all molten materials from the pedestal are crystallized as a single-crystal fiber. If we are allowed to consider that the pedestal used has the same density of the growing crystal fiber, we can further simplify this relation as shown in (13.2)

$$\begin{aligned} \rho_{\text{fib}} r_{\text{fib}}^2 v_{\text{fib}} &= \rho_{\text{ped}} r_{\text{ped}}^2 v_{\text{ped}} \\ \text{if: } \rho_{\text{fib}} &= \rho_{\text{ped}} \quad r_{\text{fib}} = r_{\text{ped}} \sqrt{\frac{v_{\text{ped}}}{v_{\text{fib}}}}, \end{aligned} \quad (13.2)$$

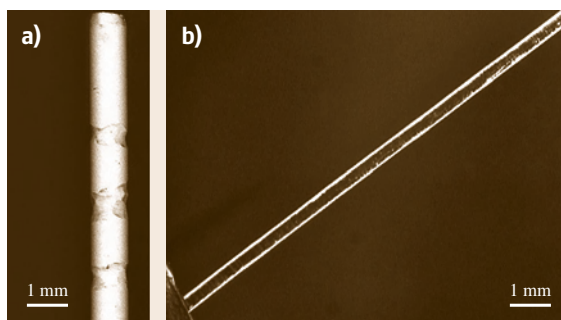


Fig. 13.8a,b A fiber pulled from a pedestal prepared with diameter fluctuations of up to 20%. (a) Unreacted pedestal (green rod) with the introduced diameter variation and (b) fiber pulled from the same pedestal showing that the diameter fluctuation was corrected by the automatic diameter control system (ADC)

Both systems have their advantages and limitations. The interference system showed better resolution results, however it is dependent on the fiber transparency, which affects the resolution of the apparatus: $g(n, \theta) = g(\theta) \approx 1/\theta$. On the other hand, the artificial vision system, although more versatile, is not adequate for low melting point materials ($< 800^\circ\text{C}$) due to their poor black-body emission.

where ρ_{fib} , r_{fib} , v_{fib} , and ρ_{ped} , r_{ped} , v_{ped} are the density, fiber radius, and pulling rates of the fiber and pedestal, respectively.

In laser-heated pedestal growth, the laser power and pulling rates are parameters that we can modify during the crystal growth process. It is evident that the crystal diameter will be constant if all the physical parameters remain unchanged. However, it is reasonable to assume that small imperfections in the pedestals may occur. In this way, if some variation of the source cross-sections remains, it is necessary to change one of the growth parameters in order to keep the fiber diameter constant. The simplest solution is to modify the pulling rate, assuming that the pedestal upward pulling rate remains unchanged.

That is why a fast and effective diameter control system is important, allowing for only very small changes in the pulling rate to correct for possible nonuniformity of the geometry of the pedestals used.

13.3.2 Balance of Heat Transfer

A schematic representation of the most important heat fluxes during fiber pulling is illustrated in Fig. 13.9. The energy delivered by the CO₂ laser that is used to keep the molten zone height is: conducted through the fiber and pedestal, lost to the growth chamber by irradiation, due to the black-body emission, and convection to the fluid inside, when present. There is also the latent heat of solidification and melting generated at the fiber-liquid and pedestal-melt interfaces.

In the LHPG system it is reasonable to assume heat transfer in one dimension, considering the heat fluxes in a semi-infinite cylinder, moving with velocity v in the z -direction [13.43]. The equation for the heat transfer can be written as

$$\frac{d^2 Y}{dZ^2} - 2(\text{Bi}_{\text{total}})Y - 2\text{Pe} \frac{dY}{dZ} = 2\text{Pe} \frac{dY}{d\tau}, \quad (13.3)$$

where $Y = (T - T_0)/(T_i - T_0)$, $Z = z/a$, and $\tau = v_{\text{fib}}t/a$; T_0 is the ambient temperature in the surroundings of the growing fiber, T_i is the growing temperature interface, a is the fiber radius, $\text{Bi} = ha$ is the total Biot number, h is the effective cooling constant (convective and radiative), and Pe is the Péclet number defined as $\rho c_p v_{\text{fib}} a / 2K$, where ρ is the solid density, c_p is the thermal capacity, and K is the solid thermal conductivity. From the solution of this equation it is possible to obtain an analytical solution for the thermal gradient at the crystal-liquid interface ($G_{s,i}$) as shown

in (13.4)

$$G_{s,i} = \left(\frac{dT}{dz} \right)_{z=0} = -(T_i - T_0) \left\{ \left[\text{Pe}^2 + 2(\text{Bi}) \right]^{\frac{1}{2}} - \text{Pe} \right\} \left(\frac{1}{a} \right). \quad (13.4)$$

The laser-heated pedestal growth method produces steeper thermal gradients at the growing interface than any other crystal growth method (ranging from 10^3 – 10^4 °C/cm). This high temperature gradient at the growing interface is responsible for the high pulling rate in this technique, allows the pulling rate to be mm/min instead of mm/h as is typical for conventional crystal growth methods. However, these same elevated thermal gradients also have some disadvantages, one of which is that it produces greater thermal stresses which restrict the maximum crystal diameter that can be grown before cracks develop. Brice [13.44] has shown that this maximum diameter can be determined based on the mechanical and thermal properties of the compound (13.5)

$$\left| \frac{dT}{dz} \right|_{\text{max}} \approx \frac{4\varepsilon_b}{\alpha a^{\frac{3}{2}}} \left(\frac{1}{h} \right)^{\frac{1}{2}}, \quad (13.5)$$

where $|dT/dz|_{\text{max}}$ is the absolute value of the maximum allowed thermal gradient at the growth interface, ε_b is the breaking strain, α is the coefficient of linear thermal expansion, a is the radius of the fiber, and h is the cooling constant.

The temperature gradient at the crystallization interface, in a conventional LHPG system, has a strong dependence on the fiber diameter. Andreetta [13.45] used lithium niobate as a material model due to its technological importance, for a study on the effects of the temperature gradients at the solid-liquid interface on the maximum attainable fiber diameter without cracks. For temperature measurements a very small Pt/Pt-Rh thermocouple (60 μm in diameter) attached to the pulling system was used. The thermocouple was inserted into the liquid phase and pulled through the solid-liquid interface. Single-crystal fibers of 40 mm in length and ranging from 300 to 1200 μm in diameter were pulled from single-crystal pedestals, along the c -axis. With this system it was possible to measure the high axial thermal gradient at the solid-liquid interface as a function of fiber radius (Fig. 13.10). From this data and the maximum diameter, above which the fiber cracks (13.5), we determined for lithium niobate a critical radius of 470 μm (Fig. 13.10).

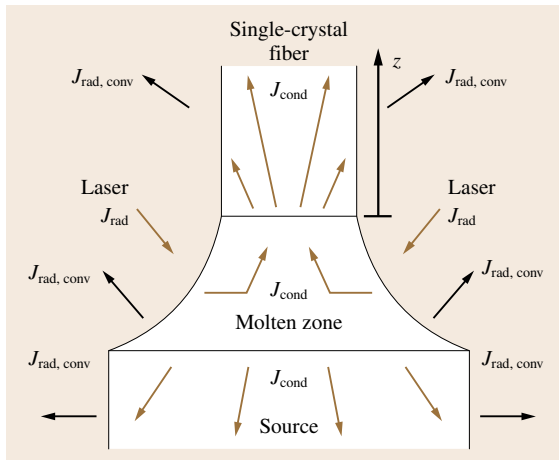


Fig. 13.9 Schematic drawing of the heat fluxes acting during the single-crystal fiber growth process

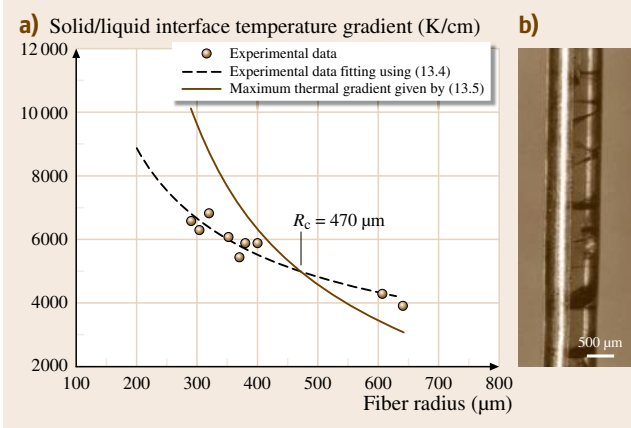


Fig. 13.10a,b Temperature gradient at the solid–liquid interface during LiNbO₃ single-crystal fiber growth. **(a)** The *continuous* line represents the maximum thermal gradient that the material can handle before it cracks (13.5) and the *dashed* line is the fitting of the temperature gradient measurements based on (13.4). $R_c = 470 \mu\text{m}$ is the critical radius above which fiber cracking results during the growth process. **(b)** LiNbO₃ single-crystal fiber with 1 mm diameter, showing cracks produced by generated thermal stress

The high axial temperature gradient at the solid–liquid interface results in a wide number of advantages, including higher growth rates, ferroelectric domain alignment during growth (LiNbO₃), and the possibility of obtaining high-temperature metastable phases of certain compounds. Another important effect of the high axial temperature gradient is to prevent constitutional supercooling. The condition for constitutional supercooling can be written as

$$\frac{G}{v} \leq \frac{mC_s}{D_l} \left(\frac{1-k_0}{k_0} \right), \quad (13.6)$$

where G is the absolute value of the temperature gradient at the solid–liquid interface, v is the pulling rate, m is the absolute value of the liquidus slope, C_s is the concentration in the solid phase, D_l is the diffusion coefficient of the solute in the liquid, and k_0 is the equilibrium distribution coefficient (the ratio between the solid and liquid concentration $-C_s/C_l$). The smaller the fiber radius, the greater the pulling rate allowed before constitutional supercooling occurs. Lu et al. [13.40] systematically studied the influence of constitutional supercooling on the growth of Bi₂Sr₂Ca₁Cu₂O₈ crystal fibers. They found a critical value for the constitutional supercooling ($1.0 \times 10^{12} \text{ K s/m}^2$) below which the pulled fiber became polycrystalline. They also esti-

mated that, for a fiber 30 μm in diameter, the maximum speed allowed should be around 26 mm/h.

Unfortunately, the same axial temperature gradient is also responsible for a high level of stress in the grown fiber. The thermal stresses induced by temperature gradients are the main cause of the formation of various crystallographic defects in the fiber. The expression for approximate calculation of the dislocation density (N_d) in terms of the axial temperature gradient was performed by Prokofiev et al. for the Bi₁₂SiO₂₀ (BSO) compound [13.46], yielding

$$N_d = \frac{\alpha}{b} \frac{dT}{dz} - \frac{2\varepsilon_b}{ba}, \quad (13.7)$$

where b is the Burger's vector and dT/dz is the axial temperature gradient at the crystallization interface. Using the calculated values of the axial temperature gradient, it is possible to evaluate the dislocation density in the fiber. The calculated value of N_d for BSO fibers was $5 \times 10^5 \text{ pits/cm}^2$ for fibers with 1 mm diameter, which is in good agreement with the value estimated by the chemical etching method ($1 \times 10^5 \text{ pits/cm}^2$). Prokofiev et al. also estimated that a BSO fiber with diameter below 100 μm should be free-dislocation.

13.3.3 Mechanical Stability

The shape of the molten zone is a very important growth parameter, especially in a floating-zone-like technique such as LHPG. The variation of the contact angle is responsible for the diameter fluctuation of grown fibers. The stability of a liquid trapped between two cylindrical plates has been studied for more than a century. Interest in this topic starts mainly from the 1950s due to the importance of the new (at that time) technology of semiconductors crystals.

For an analysis of the molten zone shape of the miniature floating zone let us consider an isotropic molten zone with length L , volume V , and surface area S , suspended between two axial solid cylinders of radius r_{fib} and r_{ped} . Kim et al. [13.47] studied the maximum stable zone length for sapphire and silicon crystals. The value found was $L_{\text{max}} = \pi\phi$, where ϕ is the fiber diameter.

If we consider also that the liquid–fiber and liquid–pedestal contact angles are ψ_{fib} and ψ_{ped} , respectively, and that the total energy involved in the liquid is composed of potential gravitational and surface energy, the molten zone will acquire the shape that allows for total

energy minimization as shown in (13.8)

$$E_T = E_g + E_s = \pi \rho g \int_0^L r^2(z) z dz + 2\pi \sigma \int_0^L \left(\sqrt{1 + \left(\frac{dr}{dz} \right)^2} \right) r(z) dz, \quad (13.8)$$

where g is the acceleration due to gravity, ρ is the density of the liquid, and σ is the surface tension. Since the effect of gravity on LHPG is very small, it can be neglected in comparison with the surface energy [13.19]. In this way, the problem is reduced to the minimization of the surface energy. Figure 13.11 illustrates several profiles of molten zones obtained for different fiber-pedestal diameter reductions, based on the numerical solution of the minimization of the surface energy of the liquid phase. *Saitou et al.* [13.48] developed an analytical solution for the liquid-phase profile in the floating zone technique for a pedestal-crystal diameter ratio of 1. They showed that minimization of the surface free energy (13.8) followed by application of the principle of variation led to the dimensionless expression

$$\frac{dx}{dy} = \frac{\frac{y^2}{2} + \lambda y + C_0}{\sqrt{1 - \left(\frac{y^2}{2} + \lambda y + C_0 \right)^2}}. \quad (13.9)$$

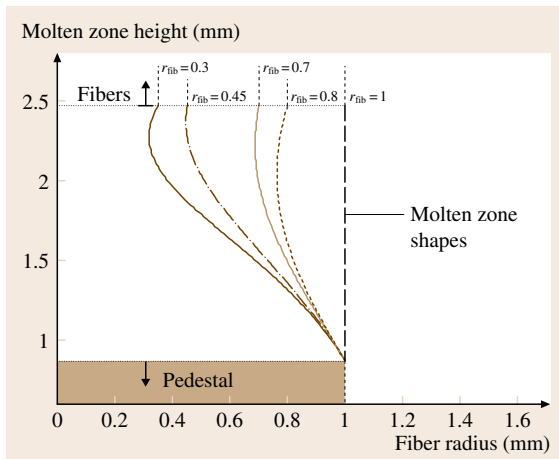


Fig. 13.11 Molten zone profile shapes obtained for different fiber-pedestal diameter reductions, obtained by numerical solution of the minimization of the surface energy of the liquid phase (the pedestal radius was normalized to 1) (after [13.19])

Solving (13.9) and returning to the dimensional form we obtain (13.10) [13.49]

$$x(y) = \frac{y^3}{6C^2} + \frac{\lambda y^2}{2C} + C_0 y + C_1 C, \quad (13.10)$$

where λ , C_0 , and C_1 are constants (given in terms of the floating zone height, pedestal diameter, and molten zone surface area), C is the capillary constant (defined as $C = (2\sigma/\rho g)^{1/2}$), σ is the surface tension, ρ is the liquid density, and g is the acceleration due to gravity [13.48].

When minimization of the energy takes place, considering an isotropic system, another way to look at the problem is to realize that equilibrium of the molten zone is reached when there is also balance of the surface tensions at the liquid-solid-gas junction. This junction defines what is called the wetting angle and it is possible to express the contact angle by

$$\cos \varphi_0 = \frac{\sigma_{l,g}^2 + \sigma_{s,g}^2 - \sigma_{s,l}^2}{2\sigma_{l,g}\sigma_{s,g}}, \quad (13.11)$$

where $\sigma_{l,g}$, $\sigma_{s,g}$, and $\sigma_{s,l}$ are the liquid-gas, solid-gas, and solid-liquid surface tensions, respectively.

When the wetting angle reaches this equilibrium value, the growth process is stable and there should be no diameter fluctuations. However in real crystal growth processes we are faced with nonideal situations which cause fluctuations of the floating zone shape, thus modifying the contact angle. Again for the LHPG technique, there is always the need for good diameter control to obtain high-quality fibers.

13.3.4 Growth Under Controlled Atmosphere

The growth atmosphere and the nature of the solid and liquid phases are also factors that influence the molten zone profile. The effects of external pressure on the melt properties and equilibrium of solid and liquid phases began to be studied in the first decades of the 20th century [13.50]. Fiber growth under different atmospheres using laser-heated systems was first explored in the pioneering work of *Haggerty* [13.11]. He grew fibers under air, Ar, Cl₂, H₂, and CH₃ alone or in combination. It was noticed that the mechanical strength of the fiber was dependent on the growth atmosphere used. *Ardila et al.* reported fiber pulling under controlled high external pressure [13.29]. In this work they modified the LHPG technique to grow crystal fibers in a system that could handle up to 15 atm of oxidizing, reducing or inert gas and studied the profile of the liquid phase. They used various materials, such as Ba_{0.77}Ca_{0.23}TiO₃ (BCT), CaMoO₄

(CMO), $\text{Ca}_2\text{FeMoO}_6$ (CFMO), and $\text{Ca}_{1-x}\text{Sr}_x\text{MoO}_3$ (CSMO) with $0 \leq x \leq 1$ [13.49, 51]. The values for the capillary constant and surface tension coefficient for all of these compounds were quite similar.

Phomsakha and coworkers studied the effect of the atmosphere on Al_2O_3 single-crystal fiber pulling [13.23]. They report that the best atmosphere is He gas, but if the pressure is increased to 15–20 Torr the fiber transmission decreases. They found that the optimum pressure was 5 Torr of He. Lower pressure values allow for vaporization that leaves oxygen in the melt, which is the main cause of the formation of microvoids. Other gases, such as N_2 , Ar, and air presented lower transmission measurements. Wu et al. [13.52] grew Ti-doped sapphire fibers under various atmosphere (N_2 , H_2 , Ar) in order to improve the Ti concentration in the fiber. They found that the use of an N_2 atmosphere increased the Ti fiber concentration when compared with experiments performed in air atmosphere, although the fibers presented dark regions on the surface and in the interior. In pure H_2 atmosphere, quite a large amount of white fog-like matter volatilized from the melting zone and was deposited onto the surfaces of the fiber and the furnace wall. The cross section of grown fiber was not circular and the grown fiber was useless [13.52]. However, a mixture of H_2 and Ar gas resulted in fibers without inclusions or bubbles inside. This last mixture allowed the researchers to obtain high-quality laser elements.

13.3.5 Dopant Distribution

As in any crystal growth process, the control of the dopant distribution along the crystalline matrix is desirable for many technological applications such as laser hosts and periodic poled ferroelectric crystals. Sharp et al. developed a model based on mass conservation for fiber pulling [13.53], shown in (13.12)

$$\frac{C_f(z)}{C_{S0}} = k_{\text{eff}} \left[C' e^{-\beta \frac{z}{v}} + \frac{\alpha'}{\beta} \left(1 - e^{-\beta \frac{z}{v}} \right) + \frac{\alpha'(C' - 1)}{(\beta - \gamma)} \left(e^{-\gamma \frac{z}{v}} - e^{-\beta \frac{z}{v}} \right) \right]. \quad (13.12)$$

Assuming that $\alpha' = \pi r_{\text{fib}}^2 v / V$; $\beta = (\alpha' k_{\text{eff}} + 1 / \tau_{\text{ev}})$; $\gamma = (v r_{\text{fib}}^2) / (\eta r_{\text{ped}})$, $C_f(z)$ is the fiber concentration at a point z , C_{S0} is the source concentration, k_{eff} is the effective distribution coefficient, C' is the fractional loss of dopant from the source rod at $z = 0$ due to evaporation, r_{fib} , r_{ped} , v , η , τ_{ev} , and V are the fiber radius, pedestal radius, pulling rate, characteristic length (not usually susceptible to measurement),

the evaporation constant, and the molten zone volume, respectively [13.53]. With this model, Sharp et al. could describe the observed concentration profile for Ti: Al_2O_3 fiber growth. Some CW laser applications at high power levels may require periodically doped crystals, as in the case of periodically poled $\text{LiNbO}_3\text{:Hf}$ and $\text{LiNbO}_3\text{:Nd}^{3+}$ (PPLN) [13.54]. The intrinsic characteristics of the growing process (high pulling rates, unidimensional growth-like process, and small molten volumes) usually led to the growth of homogenous dopant distribution in the crystal fiber.

However it is possible to intentionally change this distribution profile by modifying the growth conditions, such as introducing a sinusoidal temperature fluctuation at the molten zone [13.54]. In this case the dopant concentration can be expressed as a function of growth time, by applying also the mass conservation of the dopant. It is assumed that the dopant is supplied from the incoming pedestal. Dopant loss results from evaporation from the surface of the molten zone and from dopant being taken up by the growing fiber. Thus, the evaporation may be characterized by an evaporation time constant τ_{ev} defined as the time it takes for the concentration of dopant in the melt to decrease by a factor of e^{-1} when the fiber and pedestal are in a stationary state, i.e., at zero growth rate. Hence, the dopant concentration in the melt, considering the oscillation effects, can be expressed by (13.13)

$$\begin{aligned} \frac{dC_m}{dt} = & \frac{\pi r_{\text{ped}}^2 C_s(t) v_{\text{ped}}}{V} - \frac{\pi r_{\text{ped}}^2 k_{\text{eff}} C_m \frac{dF_p(t)}{dt}}{V} \\ & - \left[\frac{\pi r_{\text{fib}}^2 k_{\text{eff}} C_m v_{\text{fib}}}{V} + \left(\frac{\pi r_{\text{fib}}^2 k_{\text{eff}} C_m \frac{dF_f(t)}{dt}}{V} \right) \right] \\ & - \left(\frac{C_m}{V} \frac{dV}{dt} \right) - \frac{1}{\tau_{\text{ev}}} C_m, \end{aligned} \quad (13.13)$$

where C_m is the melt concentration, $C_s(t)$ is the initial pedestal concentration due to the instabilities at the startup of the melting process [13.54], r_{fib} and r_{ped} are the fiber and pedestal radii, respectively, $k_{\text{eff}} = C_f / C_m$ is the effective distribution coefficient, C_f is the fiber concentration, v_{ped} and v_{fib} are the pedestal and fiber pulling rates, respectively, V is the molten zone volume that was approximated to a conical section. $F_p(t)$ and $F_f(t)$ are functions for the periodical input oscillations, which were $A_p \sin(\omega t)$ and $A_f \sin(\omega t)$ for the pedestal melting and fiber growth, respectively [13.54]. The total molten zone oscillation amplitude is $A_p + A_f$.

Equation (13.13) can be numerically solved. The experimental input data required for the program were oscillation amplitude, r_{fib} , r_{ped} , k_{eff} , v_{ped} , v_{fib} , and fre-

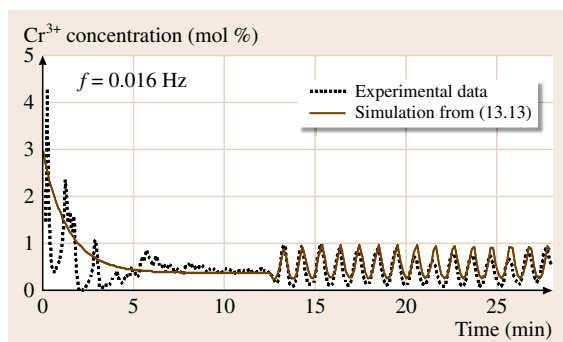


Fig. 13.12 Axial concentration profile measurement (dashed lines) for a frequency of 16 mHz molten zone oscillations, and corresponding simulation (continuous line) (after [13.33])

quency. The evaporation time constant τ_{ev} was used to minimize the difference between the calculated and measured Cr^{3+} concentration profile. The typical τ_{ev} values lay within a range of 3–4 min for several experiments, similarly to the $Al_2O_3:Ti$ fiber growth performed by Sharp et al. [13.53] without periodic oscillations. A good match between the measured and the calculated concentration profile with an oscillating molten zone can be verified when they are plotted together, as shown in Fig. 13.12. This means that the growth interface position corresponded directly with the periodic input program. With this new approach to single-crystal fiber growth, it is possible to predict and set the distance between two dopant concentration maxima. Also it is possible to pull fibers with alternating uniform and periodic concentration doping profiles regions.

Up to now it has been considered that the pulling of the fibers is unidimensional. Although for the thermal and composition axial profile this is a good approximation, the radial distribution must be considered to explain some of the observed growth aspects. Liu et al. recently observed that $Al_2O_3:Mg$ fibers present defects at their centers [13.55]. The radial Mg concentration showed that the center of the fiber is richer in Mg atoms. They proposed that this high concentration is due to Marangoni convection that creates a flow from the surface towards the center. This thermocapillary convection causes the flow to drift from the hot side (near the center, at the external part of the floating zone) to the cold side (at the solid–melt interface) along the melt–gas interface and then back from the cold side to the hot side near the axial center. This is highlighted as the main cause of excess dopant at the fiber center. Constitutional supercooling is then the responsible for the

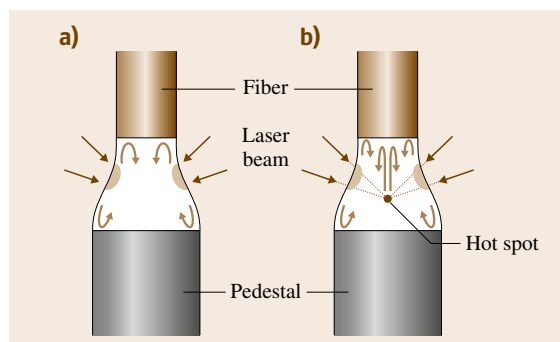


Fig. 13.13a,b Two possible configurations for the convection pattern inside the molten zone in a fiber-pulling process: (a) Laser radiation absorption in the opaque melt occurs at the liquid surface, leading to Marangoni convection, and (b) semitransparent melt, leading to the creation of a hot spot inside the molten zone at the focus point, generating flow competition with the Marangoni convection

creation of fiber defects at the center. Figure 13.13 illustrates two possible configurations for the fluid flow in the molten zone during fiber pulling. Figure 13.13a represents a molten zone opaque to the laser source, and thus all energy is absorbed in the liquid surface, creating a flow as Liu et al. described [13.55]. Figure 13.13b illustrates the condition for a material that is semitransparent to the applied laser source. In this condition a hot spot may be formed in the liquid center, creating competition between the two liquid flows. Erdei et al. [13.56] suggested that the configuration shown in Fig. 13.13b may be the cause of the radial segregation of Ba in the SBN fiber growth process. In the same work, the authors suggested that the radial dependence of the effective distribution coefficient can be expressed by

$$k_{\text{eff}}(r) = \frac{k_0}{k_0 + (1 - k_0)e^{-v\frac{\delta(r)}{D}}}, \quad (13.14)$$

where $k_{\text{eff}}(r)$ is the radial effective distribution coefficient, k_0 is the equilibrium distribution coefficient, v is the pulling speed, D is the diffusion coefficient of the element in the liquid phase, and $\delta(r)$ is the radial thickness distribution of the diffusion layer that forms ahead of the solidification interface during stationary growth.

13.3.6 Pulling Crystalline Fibers Under Electric Field

During crystallization of ionic melts, Uda et al. [13.21] have shown that an electric field will be present in both the liquid and solid, arising for at least two rea-

sons: differential partitioning of opposite-valence ions to place a net charge of one sign on the liquid boundary layer (crystallization electromotive force, EMF) and a Seebeck coefficient produced by the temperature dependence of the equilibrium ion concentration. The thermoelectric potential difference $\Delta\varphi$ between a location at temperature T_1 in the solid and a location at temperature T_2 in the liquid is given by [13.21]

$$\Delta\varphi = \alpha_s(T_1 - T_i) + \alpha_l(T_i - T_2) + \alpha_i v, \quad (13.15)$$

where v is the pulling rate, T_i is the interface temperature, α_i is the crystallization EMF coefficient, and α_s and α_l are the thermoelectric coefficients for the solid and liquid, respectively. The electric field generated at the interface during fiber pulling of some ferroelectric compounds is sufficient to orient the ferroelectric domains in situ, as in the case of LiNbO_3 [13.19].

Tiller et al. [13.58] investigated the effect of a strong interface field during the growth of TiO_2 -based crystals pulled by LHPG technique. According to the authors, when the field-driven flux is appreciably greater than the interface partitioning flux, a stationary-state solute

profile in the solid of an anomalous nature can be maintained. A steady-state solute profile requires the following to hold [13.58]

$$\left(\frac{D_s C_s}{kT}\right) q_s E_s \gg V k_0 C_l^i, \quad (13.16)$$

where D_s , C_s , q_s , and E_s are the diffusion coefficient, solute concentration, effective solute charge, and electric field, respectively, while k_0 is the solute distribution coefficient and C_l^i is the concentration in the liquid phase at the growth interface.

Using the electrical-assisted laser floating zone technique (EALFZ), Carrasco et al. studied the effect of a direct electrical current applied through the solidification interface for superconducting oxide materials [13.34]. In the EALFZ process the fiber can be grown with a direct current (DC) by connecting the positive and negative poles, respectively, to the seed and feed rod samples, or by a reverse current (RC) if the negative and positive poles are connected to the seed and feed rod samples, respectively. The application of a DC current during the EALFZ process can

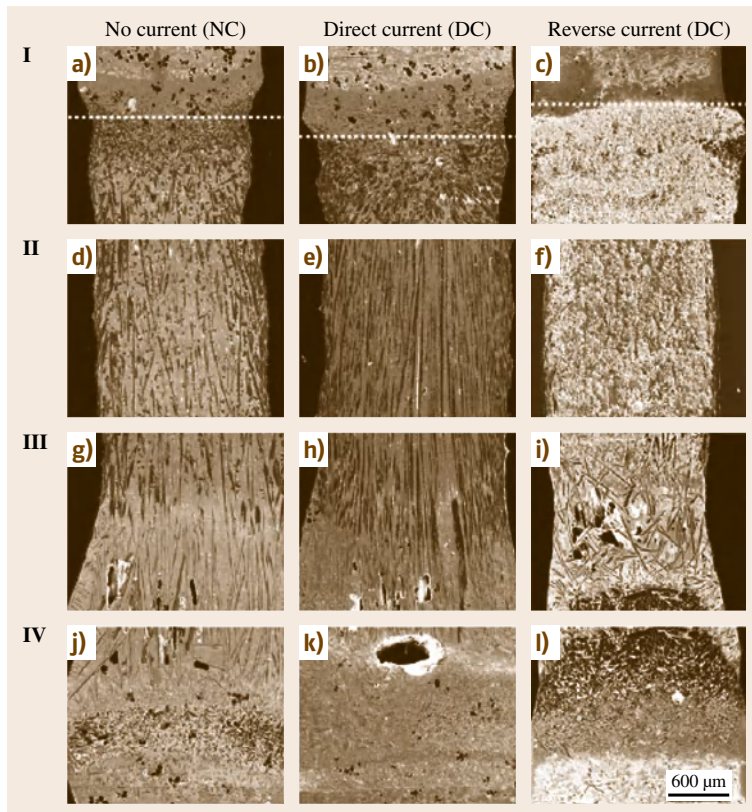


Fig. 13.14a–l Scanning micrograph of longitudinal sections of BSCCO fiber grown at $R = 15$ mm/h without current (NC fiber) (a,d,g,j) with direct current (DC fiber), (b,e,h,k) and with reverse current (RC fiber) (c,f,i,l). Region I – seeding initial transient. Region II – fiber steady-state region. Region III – frozen melt. Region IV – melting interface. The dotted line corresponds to the seed–fiber interface (after [13.57])

drive the system towards equilibrium, since it drastically changes the solidification features, namely the solute ion distribution, phase equilibrium, and crystal growth kinetics [13.57] (Fig. 13.14). Accordingly, important changes in phase structure, crystal morphology, and grain alignment are observed. The presence of the electric field through the solid–liquid interface accelerates the solute ions until a drift velocity R' ($R' = \mu E$) is reached. In this way, the original Burton–Prim–Slichter (BPS) theory equation for the effective distribution coefficient is modified to [13.34, 59]

$$k_{\text{eff}} = \frac{1 + \frac{R'}{R}}{1 + \left[\frac{1}{k_0} \left(1 + \frac{R'}{R} \right) - 1 \right] \exp \left[\left(-\frac{R\delta}{D} \right) \left(1 + \frac{R'}{R} \right) \right]}, \quad (13.17)$$

where R is the interface velocity, k_0 is the equilibrium distribution coefficient, D is the diffusion coefficient of the element in the liquid phase, and δ is the thickness of the diffusion layer that forms ahead of the solidification interface during stationary growth. Thus, the effective distribution coefficient k_{eff} is a set of two competition processes:

1. The rejection/acceptation of the solute for $k_0 < 1$ and $k_0 > 1$, respectively, by the solid–liquid interface
2. The mobility difference of the solute and solvent ions under the applied electric field in the diffusion layer.

When ions move towards the solid–liquid interface due to the application of a direct current (R' positive) the electrical field will increase k_{eff} . On the contrary, a decrease in k_{eff} is observed for the condition of R' negative, when the ions move away from the interface. It is important to point out that, in the presence of an electrical field and for a given value of interface velocity R ,

the effective distribution coefficient can exhibit values over a wide range, even outside of the normal range situated between k_0 and unity [13.34]. Useful examples of the effect of the electric current on k_{eff} were given by Pfann [13.60]:

1. The refinement of an ingot from an element for which k_0 is close to unity, by increasing the absolute value of $(1 - k_{\text{eff}})$
2. Segregation hindrance by making k_{eff} close to unity
3. Simultaneous zone refining even when solutes have k_0 values lying on opposite sides of the unity, forcing them to move to the same side of an ingot.

An external alternating electric field can also be applied to a LHPG fiber during the pulling process without physical contact with the growing fiber. This is performed in order to produce periodic inversion of ferroelectric domains, such as in the method developed by Brenier et al. described in Sect. 13.1. Lee et al. showed that assuming a uniform electric field E in the fiber cross-section, the accumulated E field, $E_{\text{acc}}(\bar{z})$ that the grown fiber experiences at position \bar{z} during the poling process can be expressed by the convolution integral [13.61]

$$E_{\text{acc}}(\bar{z}) = E_0 \int_{-\infty}^{+\infty} \text{rect} \left(\frac{(\bar{z} - z)}{W_e} - \frac{1}{2} \right) \sin \left(\frac{2\pi f z}{v} \right) dz, \quad (13.18)$$

where E_0 is the electric field at start point in the center of the poling region, W_e is the effective poling length, f is the applied electric field frequency, rect is the rectangular function (also known as the rectangle function, rect function, unit pulse, or the normalized boxcar function) [13.61], and v is the pulling rate. With this process, magnesium-doped lithium niobate can be periodically poled with controllable distance between the inverted domains.

13.4 Fiber Growth Aspects

As stated previously, the LHPG technique is a very powerful tool for producing single crystals of various compounds, as shown in Fig. 13.15. Table 13.2 lists the different compounds produced using the LHPG technique. The following sections present practical features and aspects of the pulling process using the laser-heated pedestal growth technique, such as pulling of stoichiometric fibers, incongruently melt/evaporating

materials, and directional solidification on eutectic compounds.

13.4.1 Congruent Melting Fibers: The Search for Stoichiometry

Congruently melting materials are the easiest type of compound to pull successfully in single-crystal form.

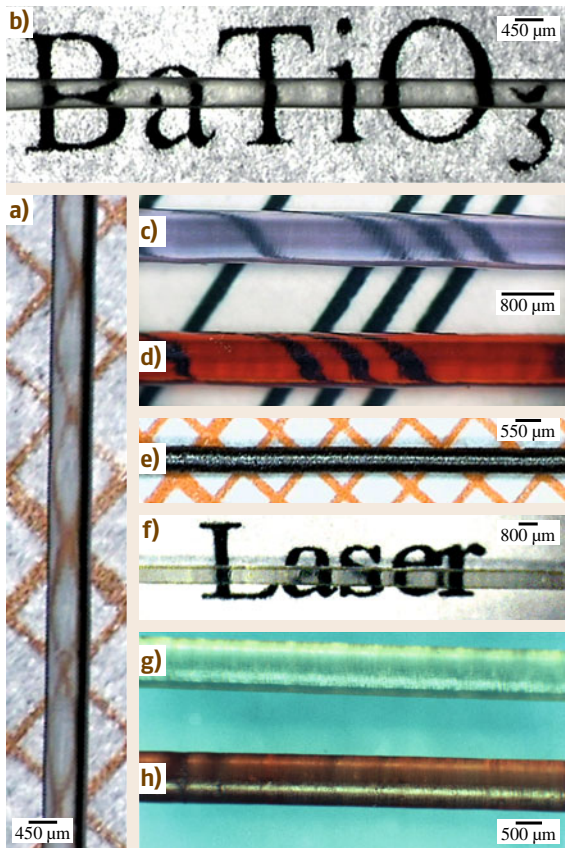


Fig. 13.15a–h Single-crystal fibers of various compounds pulled by the LHPG technique: (a) SrTiO₃, (b) BaTiO₃, (c) GdAlO₃:Nd³⁺, (d) GdAlO₃:Cr³⁺, (e) La_{0.67}Ca_{0.33}MnO₃, (f) LaVO₄, (g) Al₂O₃ (sapphire), and (h) Al₂O₃:Cr³⁺ (ruby)

However, the stoichiometric line in the phase diagram is in reality a region (termed the existence region), i. e., it may extend over a certain homogeneity range [13.62].

Stoichiometry variations can impair the electric, ferroelectric, magnetic, optical, and other characteristics of these single crystals. For many compounds of interest, congruently melting compositions have been detected which are nonstoichiometric, thereby giving rise to unwanted effects such as thermodynamic instabilities, precipitates, intrinsic impurities, and deviations of the distribution coefficient of cations from unity [13.62].

Due to their technological importance, Li(Nb, Ta)O₃, YVO₄, and SBN (Sr_{0.61}Ba_{0.39}NbO₃) have been studied in order to achieve stoichiometry composition along the fiber length. Besides the composition variation of metal elements along the crystal growth axis, those compounds also present oxygen deficiency. Since the congruency originates from the defect structure of niobates, tantalates or vanadates, the oxygen vacancy also plays an important role in the growth of highly homogeneous crystals. In other words, metal oxides having different oxygen stoichiometry will possess different congruent compositions [13.56]. Another effect of the oxygen-deficient phases is that they can form solid solutions with their pentavalent variant, as was observed for YVO₄ by Erdei et al. [13.80]. These solid-solution formations cannot be eliminated by simple melt growth techniques. The oxygen deficiency can also slightly modify the Li:Nb, Li:Ta or Y:V stoichiometries in LiNbO₃, LiTaO₃, and YVO₄ during the growth processes. In this way, it is possible to verify that there is not one general precise value for the exact congruent composition in the niobate, tantalate or vanadate families. Erdei et al. identified that slightly oxygen-deficient SBN connected with Nb₂O_{5–x} creates a solid solution with the pentavalent niobium–SBN system [13.56, 62].

In order to grow high-quality single-crystal fibers with near-stoichiometric composition and high homogeneity along the fiber length it is possible to distinguish three basic strategies to achieve the goal of stoichiom-

Table 13.2 Pure and doped fibers pulled by laser-heated pedestal growth technique

Compound	Doping	Applications/characteristics	References
Al ₂ O ₃	Cr ³⁺	Temperature sensor	[13.63–68]
	C	Radiation dosimetry	[13.69]
	Pure	Optical transmission	[13.28, 70–72]
	Pure	Mechanical	[13.73, 74]
	Ti ³⁺	Graded-index fiber – laser action	[13.52, 75]
	Yb ³⁺	Spectroscopy	[13.76]
	Er ³⁺ , Yb ³⁺	Temperature sensor	[13.77, 78]
	Mg	Mechanical	[13.55]
	Pure	Growth process/synthesis	[13.23]
	Ti	Growth process/synthesis	[13.53, 79]

Table 13.2 (cont.)

Compound	Doping	Applications/characteristics	References
Eutectic $\text{Al}_2\text{O}_3\text{-Y}_3\text{Al}_5\text{O}_{12}$	Pure	Mechanical	[13.81–84]
	Pure	Growth process/synthesis	[13.85]
Eutectic $\text{Al}_2\text{O}_3\text{-Y}_3\text{Al}_5\text{O}_{12}\text{-ZrO}_2$	Pure	Mechanical	[13.86]
Eutectic $\text{Al}_2\text{O}_3\text{-ZrO}_2$	Pure	Mechanical	[13.87–90]
	Pure	Mechanical	[13.84, 91–93]
	Y (eutectic)	Growth process/synthesis	[13.94]
$\text{Ba}(\text{Mg}_{0.33}\text{ME}_{0.67})\text{O}_3$, ME = Ta, Nb	Pure	Dielectric	[13.95]
		Spectroscopy	[13.96]
		Spectroscopy	[13.97]
		Growth process/synthesis	[13.98]
$\text{Ba}(\text{Ti}_{1-x}\text{Zr}_x)\text{O}_3$	Pure	Ferroelectric	[13.99]
	Pure	Dielectric	[13.100, 101]
$\text{Ba}_{1-x}\text{M}_x\text{TiO}_3$	M = Sr	Dielectric	[13.102–104]
	M = Ca	Growth process/synthesis	[13.105, 106]
$\text{Ba}_2\text{NaNb}_5\text{O}_{15}$	Nd^{3+}	Growth process/synthesis	[13.107, 108]
	Nd^{3+}	Spectroscopy	[13.109–114]
	Yb^{3+}	Spectroscopy	[13.115]
$\text{Ba}_2\text{NdNbO}_6$	Pure	Spectroscopy	[13.116]
BaTiO_3	Pure	Photorefractive effect	[13.117]
	Pure	Growth process/synthesis	[13.118–120]
$\text{Bi}_{12}\text{MEO}_{20}$; ME = Si, Ti	Pure	Photorefractive effect	[13.121]
		Optical activity	[13.122]
		Growth process/synthesis	[13.46, 123–127]
Bi-Sr-Ca-Cu-O	Pure	Superconductivity	[13.34, 128–130]
	Pure	Superconductivity	[13.57, 131–134]
	Pure	Superconductivity	[13.135–138]
	Pure	Superconductivity	[13.139–143]
	Pure	Magnetic	[13.144–148]
	Ag	Superconductivity	[13.149, 150]
	Pb	Superconductivity	[13.151, 152]
		Growth process/synthesis	
	Pure		[13.153–157]
	Pure		[13.32, 158–161]
	Pure		[13.162–166]
	Pure		[13.40, 167–170]
	Ti		[13.171]
	Ag		[13.172, 173]
	Pb		[13.174–177]
$\text{Ca}_{1-x}\text{Yb}_x\text{F}_{2+x}$	Yb^{3+}	Spectroscopy	[13.178]
$\text{Ca}_3(\text{VO}_4)_2$	Nd^{3+}	Spectroscopy	[13.179]
	Er^{3+}	Growth process/synthesis	[13.51]
$\text{Ca}_{9.5+0.5x}((\text{PO}_4)_{6-x})(\text{BO}_3)_x$ $((\text{BO}_2)_{1-x}\text{O}_x)$	Yb^{3+}	Spectroscopy	[13.180]

Table 13.2 (cont.)

Compound	Doping	Applications/characteristics	References
CaAl ₄ O ₇	Ce ³⁺	Spectroscopy	[13.181]
	Eu ²⁺ , Nd ³⁺	Spectroscopy	[13.182]
	Tb ³⁺ , Ce ³⁺	Spectroscopy	[13.183]
CaF ₂	Yb ³⁺	Spectroscopy/laser action	[13.184, 185]
CaM ₂ O ₆ ; M = Nb, Ta	Nd ³⁺	Spectroscopy	[13.186]
	Nd ³⁺	Spectroscopy	[13.187]
	Pure	Growth process/synthesis	[13.188]
	Pure		[13.189]
CaMoO ₄	Pure	Growth process/synthesis	[13.190]
CaMoO ₄ -SrMoO ₄	Pure	Growth process/synthesis	[13.39]
CaTiO ₃	Pure	Growth process/synthesis	[13.191]
Co, Fe, and Co-Fe alloy	Pure	Growth process/synthesis	[13.192]
Dy ₂ O ₃	Pure	Refraction index	[13.193]
EuAlO ₃	Ti ³⁺ -Ti ⁴⁺	Growth process/spectroscopy	[13.194]
Gd ₂ O ₃	Eu ³⁺	Luminescence	[13.195]
	Nd ³⁺	Spectroscopy	[13.196]
	Er ³⁺	Spectroscopy	[13.197]
	Yb ³⁺	Spectroscopy	[13.31]
Gd ₃ Sc ₂ Al ₃ O ₁₂	Cr ³⁺	Graded-index fiber	[13.75]
GdAlO ₃	Er ³⁺	Spectroscopy	[13.198]
	Ti ³⁺ -Ti ⁴⁺	Growth process/spectroscopy	[13.194]
Eutectic GdAlO ₃ -Al ₂ O ₃	Pure	Growth process/synthesis	[13.36]
GdTaO ₄	Pure	Growth process/synthesis	[13.199]
GdTaO ₄ -RETaO ₄ ; RE = Er, Yb	Pure	Growth process/synthesis	
		X-ray optics	[13.200]
		X-ray optics	[13.201]
K ₂ NdNb ₅ O ₁₅	Pure	Spectroscopy	[13.116]
K ₂ O-WO ₃ binary system	Pure	Growth process/synthesis	[13.202]
K ₃ Li _{2-x} ME _{5+x} O _{15+2x} ; ME = Nb, Ta	Pure	Dielectric	[13.203]
	Pure	Ferroelectric	[13.204]
	Nd ³⁺	Second-harmonic generation	[13.107, 108, 205]
		Growth process/synthesis	
	Pure		[13.206–210]
La _{1-x} ME _x MnO ₃ ; ME = Sr, Ca	Pure		[13.25]
		Magnetic	[13.211–213]
		Magnetic	[13.212–214]
		Growth process/synthesis	[13.215]
LaAlO ₃		Growth process/synthesis	
	Pure		[13.38]
	Cr ³⁺		[13.33, 54]
LaLuO ₃	Ce	Spectroscopy	[13.216]
La-Sr-Cu-O	Pure	Superconductivity	[13.217]
Li _{1-x} Nb _{1-x} W _x O ₃	Nd ³⁺	Growth process/synthesis	[13.218]
LiB ₃ O ₅	Pure	Growth process/synthesis	[13.219]

Table 13.2 (cont.)

Compound	Doping	Applications/characteristics	References
LiNbO ₃	Pure	Ferroelectric	[13.220, 221]
	Pure	Spectroscopy	[13.222–225]
	Nd:MgO	Second-harmonic generation	[13.226]
	Fe	Spectroscopy	[13.227, 228]
	Er ³⁺ :Sc ₂ O ₃	Visible and IR luminescence	[13.229]
	Nd ³⁺ :Sc ₂ O ₃	Spectroscopy	[13.230]
	Yb ³⁺ :Sc ₂ O ₃	Spectroscopy/laser action	[13.231]
		Growth process/synthesis	
	Pure		[13.30, 41, 232–235]
	Pure		[13.236–239]
	Fe		[13.240]
	MgO		[13.27, 61, 241–244]
	Mg, Zn		[13.245]
	Mg, Ti		[13.246]
	Cr		[13.21]
LiTaO ₃	Pure	Growth process/synthesis	[13.247]
LiYF ₄	Yb ³⁺	Spectroscopy/laser action	[13.248]
		Growth process/synthesis	
	Nd ³⁺ Tm ³⁺		[13.249] [13.249]
Lu ₂ O ₃	Pure	Refraction index	[13.193]
	Yb ³⁺	Spectroscopy/laser action	[13.31]–[13.231]
Lu ₄ Al ₂ O ₉	Ce	Spectroscopy	[13.216]
Mg ₂ SiO ₄	Cr	Growth process/synthesis	[13.250]
MgAl ₂ O ₄	Pure	Mechanical	[13.251]
		Growth process/synthesis	
	Ni		[13.252]
MgO-Nb ₂ O ₅ binary system: (Mg, Nb) ₂ O _{4.2} , Mg ₅ Nb ₄ O ₁₅ , Mg ₄ Nb ₂ O ₉ , MgNb ₂ O ₆	Pure	Growth process/synthesis	[13.253]
Eutectic MgTiO ₃ -CaTiO ₃	Pure	Growth process/synthesis	[13.254]
MTi ₂ O ₇ ; M = La, Nd	Pure	Piezoelectricity	[13.255]
		Piezoelectricity	[13.255]
NaF	U, Cu	Photoluminescence	[13.256]
Nb ₂ O ₅ :MO ₂	M = Ti	Dielectric	[13.257–260]
	M = Si	Dielectric	[13.260]
RE _{1-x} La _x VO ₄ ; RE = Y, Gd	Nd ³⁺	Spectroscopy	[13.261, 262]
	Tm ³⁺	Spectroscopy	[13.263]
		Growth process/synthesis	
	Pure		[13.80, 264–266]
	Nd ³⁺ Nd ³⁺		[13.267–271] [13.267, 268]
RETiNbO ₆	RE = Nd; Pr; Er	Spectroscopy	[13.272–274]
Sc ₂ O ₃	Pure	Refraction index	[13.193]
	Yb ³⁺	Spectroscopy/laser action	[13.231, 275]
ScTaO ₄	Pure	Growth process/synthesis	[13.276]

Table 13.2 (cont.)

Compound	Doping	Applications/characteristics	References
Sr(Al _{0.5} M _{0.5})O ₃	M = Ta; Nb	Dielectric	[13.95]
	M = Ta; Nb	Spectroscopy	[13.277]
	M = Ta; Nb	Growth process/synthesis	[13.278]
Sr ₂ RuO ₄	Pure	Growth process/synthesis	[13.279]
SrAl ₂ O ₄	Ce ³⁺	Photoconductivity	[13.181, 280]
	Eu ²⁺ , Dy ³⁺	Spectroscopy	[13.182]
	Tb ³⁺ , Ce ³⁺	Phosphorescence	[13.281]
Sr-Ca-Ti-O	Pure	Dielectric	[13.282]
SrHfO ₃	Pure	Growth process/synthesis	[13.283]
SrTiO ₃	Pure	Growth process/synthesis	[13.37, 118]
SrVO ₃	Pure	Growth process/synthesis	[13.29, 284]
Sr _x Ba _{1-x} Nb ₂ O ₆	Pure	Dielectric	[13.285–287]
	Ce	Photorefractive	[13.288–290]
	Nd	Spectroscopy	[13.291]
	Pure	Growth process/synthesis	[13.22, 56, 292–294]
Ta ₂ O ₅	Ti	Spectroscopy	[13.295]
TiO ₂	Pure	Growth process/synthesis	[13.296]
UNi ₂ Al ₃	Pure	Growth process/synthesis	[13.26]
UPt ₃	Pure	Growth process/synthesis	[13.26]
Y ₂ O ₃	Tb ³⁺ , Ce ³⁺	Spectroscopy	[13.297, 298]
	Eu ³⁺	Spectroscopy	[13.299–303]
	Yb ³⁺	Spectroscopy/laser action	[13.31, 298, 304–306]
	Ho ³⁺	Spectroscopy	[13.298, 304]
	Er ³⁺	Spectroscopy	[13.304]
	Tm ³⁺	Spectroscopy/laser action	[13.306]
	Tb ³⁺	Spectroscopy/laser action	[13.306]
	Tm ³⁺ , Pr ³⁺	Spectroscopy	[13.298]
	Er ³⁺ , Yb ³⁺	Spectroscopy/laser action	[13.307]
Y _{2-x} Sc _x O ₃	Eu ³⁺	Spectroscopy	[13.308]
Y ₃ Al ₅ O ₁₂	Tm ³⁺	Fluorescence/laser action	[13.309, 310]
	Nd ³⁺	Optical sensor/thermotherapy	[13.311–314]
	Nd ³⁺	Laser action	[13.315]
	Ca, Cr	Coloration/laser action	[13.42, 316]
	Cr ⁴⁺ , Cr ³⁺	Fluorescence	[13.311, 317]
	Cr ³⁺	Fluorescence/temperature sensor	[13.318]
	Er ³⁺	Fluorescence/temperature sensor	[13.319]
	Pr ³⁺	Spectroscopy	[13.320]
	Yb ³⁺	Spectroscopy	[13.321]
	Cr ⁴⁺	Growth process/synthesis	[13.35, 322, 323]
Y ₃ Fe ₅ O ₁₂	Ti ³⁺		[13.324]
	Pure	Growth process/synthesis	[13.325–328]
YAlO ₃	Nd ³⁺	Laser action	[13.329]
Yb ₂ O ₃	Pure	Refractive index	[13.193]

Table 13.2 (cont.)

Compound	Doping	Applications/characteristics	References
Y-Ba-Cu-O	Pure Pure Pure	Superconductivity Magnetic Crystal growth/synthesis	[13.134,330] [13.331] [13.332,333]
ZnLiNbO ₄	Pure	Growth process/synthesis	[13.334]
ZrO ₂ :Y ₂ O ₃	Pure Er ³⁺ , Pr ³⁺ Er ³⁺ Pure	IR waveguide Photoluminescence Mechanical Growth process/synthesis	[13.308] [13.335] [13.336,337] [13.338]
Eutectic ZrO ₂ -CaO-NiO	Pure	Mechanical Growth process/synthesis	[13.93] [13.339]
Eutectic ZrO ₂ -MgO	Pure	Mechanical	[13.93]
α -(Ba _{1-x} Sr _x)Nb ₂ O ₆ : β -(Na _{1-y} K _y)NbO ₃	Pure	Dielectric	[13.340]
β -BaB ₂ O ₄	Pure	Growth process/synthesis	[13.341,342]
(1-x)Pb(Mg _{0.33} Nb _{0.67})O ₃ -xPbTiO ₃	Pure	Growth process/synthesis	[13.343]
(Gd _{1-x} Nd _x) ₂ (SiO ₄)O	Pure	Growth process/synthesis	[13.344]
(La _{1-x} Nd _x) _{9.33} {(SiO ₄) ₆ O ₂ } _{0.67}	Pure	Growth process/synthesis	[13.344]
(Lu _{1-x} Nd _x) ₂ Si ₂ O ₇	Pure	Growth process/synthesis	[13.344]
2-adamantylamino-5-nitropyridine (AANP)	Organic	Growth process/synthesis	[13.24]
A ₂ B ₂ O ₇ (A = La, Nd, Ca, B = Ti, Nb)	Pure	Dielectric	[13.345]
Miscellaneous:			
Compiled information (reviews)			[13.346–351]
Several oxides and fluorides matrix			[13.352–356]
La _{0.7} Sr _{0.3} MnO ₃			[13.357]
LiNbO ₃	–	–	[13.358]
Mixed-oxide perovskites			[13.359]
Al ₂ O ₃			[13.360]
Simulation/modeling	–	–	[13.361–363]

etry control: seed compositions, self-adjusting melt composition, and pulling rate.

The seed composition strategy was already discussed in the seeding aspects of the LHPG technique (Sect. 13.2.1). Another strategy is to allow the system to self-adjust its melt composition. In the case of SBN fiber pulling, Erdei et al. observed that, after a transient composition at the beginning of fiber growth, the melt self-adjusted its composition and a high-quality fiber was obtained. Although a slightly off-congruent source rod composition was used the *composition-control system* of the LHPG technique modifies both the floating zone composition and the highly complex segregation effects, and can produce fibers that are homogeneous

in the growth direction [13.56]. However, the intensive convection flows generated in the molten zone are highlighted as responsible for the radial composition variations, as described earlier in Sect. 13.3.5. In another work, Erdei et al. also prepared YVO₄ single-crystal fibers, and the authors identified that the Y/V stoichiometry ratio was mainly caused by deficiency of oxygen due to vanadium oxide dissociation. However, it was Huang et al. [13.364] who was able to produce high-quality single-crystal fibers from stoichiometric-composition pedestals. The authors successfully applied pulling rates above 1 mm/min in order to avoid vanadium oxide dissociation and in this way obtained stoichiometric YVO₄ single-crystal fibers. The same

strategy was used by Burlot et al. [13.247] for growth of LiTaO_3 in order to avoid loss of Li_2O . The best results were obtained for pulling speeds of 0.7 mm/min. Nagashio et al. [13.232] also used high pulling rates in the LHPG technique to obtain near-stoichiometric LiNbO_3 fibers. They found that high pulling rates (4.1 mm/min) associated with a small molten zone length were the best conditions to avoid Li_2O evaporation, and thus to obtain stoichiometric fibers. Also, according to the Burton–Prim–Slichter (BPS) theory, the increased pulling rate leads the effective distribution coefficient (k_{eff}) to approach the value of 1 [13.59].

13.4.2 Incongruently Melting and Evaporating Fibers

An important characteristic of the LHPG technique is the possibility of growing incongruently melting and evaporating materials. Growth of incongruently melting bulk oxide single crystal is usually achieved by high-temperature solution growth, which is a slow and complicated technique. The source material in this technique must be rich in one or more elements to compensate for the incongruent melting. However in the LHPG system it has been shown that it is possible to grow such materials, $\text{Bi}_{12}\text{TiO}_{20}$ (BTO) for example, without the need for enrichment with excess Bi_2O_3 in the source composition. In other words, it is possible to grow incongruently melting materials from a source with the same composition as the grown fiber. According to Feigelson [13.8], the liquid composition in such growth experiments changes gradually until it naturally reaches the composition necessary for crystal growth, similar to the effect observed for SBN fiber growth (Sect. 13.4.1). This implies that, at the beginning of the process, the crystallizing solid must have a non-stoichiometric composition to allow the liquid phase to change gradually. With the LHPG technique it was possible to growth single-crystal fibers of BTO compound with 300–1200 μm diameter and up to 70 mm length (Fig. 13.16). The pulling rates typically used in



Fig. 13.16 The side of a $\text{Bi}_{12}\text{TiO}_{20}$ single crystal fiber grown from a stoichiometric pedestal, evidencing the natural face on the $[1\bar{1}0]$ crystallographic direction

this process were 6–18 mm/h, much higher than the few millimeters per day available with high-temperature solution methods.

By conveniently controlling the pulling and feeding ratio, it is also possible to grow materials with incongruent evaporation, such as Sr_2RuO_4 . The conventional method for growing Sr_2RuO_4 single crystals was floating zone melting, but due to the high evaporation rates of Ru_2O_3 , only single crystals of a few millimeters had been grown. Using the LHPG technique, and with a prereacted powder and then extruded source material with SrRuO_3 composition, it was possible to growth Sr_2RuO_4 single-crystal fibers up to 30 mm in length and 0.8–1.0 mm in diameter [13.279]. The best results were obtained with pulling rates of 0.3 mm/min with a feeding (source) rate of 0.4 mm/min. This again was only possible because of the high temperature gradients at the growth interface, allowing the growth velocities to be higher than in the conventional floating zone technique, and that a small amount of material stays at a high temperature for a short period of time, minimizing the ruthenium oxide evaporation.

13.4.3 Eutectic Fibers

The properties of materials are dependent not only on their composition, but also on their microstructure. In this way, phase distribution, size, and shape as well as interface characteristics play a crucial role in determining the behavior of composites [13.93]. The eutectic microstructure can be separated into three basic morphologies: lamellar, fibrous, and what is known as *Chinese script*.

The entropy of melting plays a very important role in determining the final microstructure of a eutectic. In 1966, Jackson and Hunt [13.365] demonstrated that irregular microstructures such as the *Chinese script* are formed during faceted–nonfaceted growth, in which one phase has high while the other has low entropy of melting. Eutectic compounds, despite the complexity of their microstructure, obey the following relationship [13.365]

$$\lambda_e^2 v = C, \quad (13.19)$$

where λ_e is the mean spacing between the phases, v is the pulling rate, and C is a constant.

The Al_2O_3 – $\text{ZrO}_2(\text{Y}_2\text{O}_3)$ system, called **ZA**, is one of the eutectic systems that have been systematically studied by the LHPG technique [13.87, 90, 92]. Farmer and Sayir [13.90] studied the fracture strength of 68 mol % Al_2O_3 in the ZA hypoeutectic composition

at varying Y_2O_3 content in fibers ranging from 1.0 to 1.8 mm in diameter. Their experiments showed that the Y_2O_3 composition has a major influence on the eutectic microstructure. Pure ZA eutectics have a lamellar microstructure at a pulling rate of 40 mm/h, although with the inclusion of Y_2O_3 the melt became constitutionally supercooled and a planar growth front in not maintained. Under conditions of large undercooling, the leading phase Al_2O_3 facets on the r -planes $\{1\bar{1}02\}$ and a transition from lamellar to ZrO_2 rod morphology occur. In this new condition, the fracture strength increases from 0.7 to 1 GPa. This increase is more strongly influenced by partial stabilization of the ZrO_2 than by the change in the phase morphology. With 1.1 mol % or less of Y_2O_3 the observed morphology shows excess Al_2O_3 accommodated in Al_2O_3 -rich colony boundary regions and formation of Al_2O_3 -rich facets on the fiber exterior in small-diameter (1.0 mm) fibers. With Y_2O_3 composition greater than 1.1 mol %, the system is highly supercooled and primary Al_2O_3 dendrites nucleate. The authors also observed, for compositions in the range 3.5–7.6 mol % Y_2O_3 , the formation of large amounts of $\text{Y}_3\text{Al}_5\text{O}_{12}$ within the colony boundary [13.90]. Peña et al. [13.94] pulled fibers with 1.5 mm diameter with a composition of 9 mol % Y_2O_3 . The authors reported that they were successful in producing fiber with highly homogeneous morphology. This was accom-

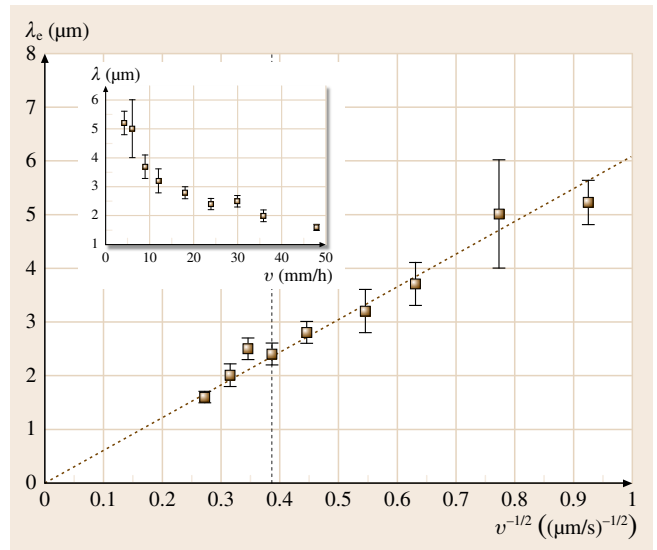
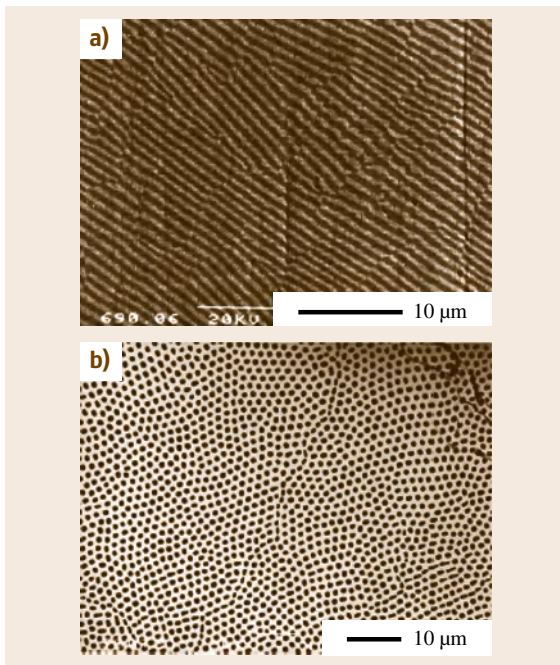


Fig. 13.17 Dependence of the mean spacing between the phases on the pulling rate of $\text{Al}_2\text{O}_3/\text{GdAlO}_3$. Only the *Chinese script* microstructure is present in all fibers on the right side of the vertical line (after [13.36])

plished by the use of very low pulling rate (10 mm/h), which in other words, increased the value of the ratio G/v , avoiding the constitutional supercooling condition. Francisco et al. [13.87] studied the influence of the processing conditions on the eutectic microstructure and reported a transition from coupled to dendrite growth at about 50 mm/h with axial gradient of 6×10^5 K/m, regardless of the rotation speed used.

Another eutectic explored by the LHPG system is Al_2O_3 -YAG. Pastor et al. [13.82] pulled 1 mm diameter fibers from pedestals containing 81.5 mol % Al_2O_3 and 18.5 mol % Y_2O_3 , the known eutectic composition. The fibers showed a *Chinese script*-type homogeneous microstructure. Due to the characteristics of its complex microstructure the hardness was fairly isotropic and the longitudinal strength of eutectics pulled at low and medium rates remained practically constant up to 1700 K.

The substitution of YAG by GdAlO_3 produced another interesting aluminate eutectic system ($\text{Al}_2\text{O}_3/\text{GdAlO}_3$) with the *Chinese script* microstructure. Andreea et al. [13.36] reported the pulling of $\text{Al}_2\text{O}_3/\text{GdAlO}_3$ eutectic fibers by LHPG technique using unreacted pedestals with a mixture of 77 mol %

Fig. 13.18a,b SEM photographs of (a) $\text{ZrO}_2(\text{CaO})\text{-NiO}$, and (b) transverse section of $\text{ZrO}_2\text{-MgO}$ (after [13.93]) ◀

Al_2O_3 and 23 mol % Gd_2O_3 . The average fiber diameter was $600\text{ }\mu\text{m}$ and the pulling rate ranged from 4.2 to 48.0 mm/h . In transversal analysis of the fibers, it could be observed that for pulling rates higher than 24 mm/h a transition from homogeneous to a complex regular microstructure appeared, with circular regions with larger GdAlO_3 phases, and even cellular arrangements with a fibrous pattern inside. Using pulling rates lower than 24 mm/h and with temperature gradients of $6 \times 10^5\text{ K/m}$, the high value of G/v prevented constitutional supercooling and fibers without the complex regular microstructure could be obtained. The Jackson and Hunt relationship [13.365] that holds for this compound was determined to be $\lambda^2 v = 40\text{ }\mu\text{m}^3/\text{s}$ (Fig. 13.17).

Orera et al. [13.93] explored the optical properties of the eutectics with regular microstructure to

be used as waveguide devices (Fig. 13.18). The eutectics have atomic-scale interfaces, producing sharp refractive index transitions between the phases, which lead to diffraction, interference, polarization effects, etc. Orera et al. also studied the waveguide effect of the fibrous microstructure of the eutectics. The authors showed that the $\text{CaF}_2\text{--MgO}$ eutectics can produce single-mode waveguides in the third optical window ($1500\text{--}1600\text{ nm}$). They also reported the cutoff wavelength, i.e., the most energetic light that can propagate in single-mode form, for the CaO--ZrO_2 ($\lambda_c = 1700\text{ nm}$), $\text{Al}_2\text{O}_3\text{--ZrO}_2$ ($\lambda_c = 500\text{ nm}$), and $\text{CaF}_2\text{--MgO}$ ($\lambda_c = 1300\text{ nm}$) eutectic systems. Since in the calcium fluoride eutectic light is guided by MgO fibers, it forms an optical-fiber bunch integrated in a crystal matrix which can be used for optical image transfer, giving a density higher than $40\,000\text{ pixels/mm}^2$.

13.5 Conclusions

The laser-heated pedestal growth technique (LHPG) has been presented as a powerful research tool for crystal growth of new and conventional compounds. In order to understand the state of the art of this technique, we report a historical background that led us to the beginning of the 20th century, when Baker and da Costa Andrade, one of Laue's and Bragg's coworkers, developed the first metallic single-crystal wires. One of the greatest breakthroughs in fiber research was, however, achieved by Fejer and coworkers with the introduction of an optical component (the reflexicon) to yield what is nowadays called the LHPG technique. This can be verified by the large increase in the number of papers published on the subject after the publication of Fejer and Feigelson's papers in the 1980s. The publication dynamics for laser-heated fiber growth over the last two decades shows that this technique is already well established, with more than 20 papers produced each year and more than 80 new and conventional different crystallographic matrices being produced. It must be noted that in this chapter only fiber pulling by LHPG technique was considered, which means that other fiber-pulling techniques such as the pulling down, melt extraction, and vapor reaction techniques were not included, which would certainly further increase the volume of scientific production.

The trends in the laser-heated pedestal technique can be separated into three basic lines. The first obvious trend is basic research into the fiber-pulling process, since the technique allows visualization of the molten zone and crystallization interfaces. In this way, it is possible to gain access to many solidifying parameters such as temperature gradients, interface shape, and contact angle. These are important, especially for very high melting point ($> 2500\text{ }^\circ\text{C}$) compounds, and are virtually impossible to measure in other conventional, crucible techniques. The second line is the miniaturization of some of today's devices by substituting bulk crystals with crystalline fiber. Along these lines it is possible to include the design of completely new devices based on the shape properties of fibers, such as high-temperature thermometers and infrared (IR) waveguides. Finally, with the approach of the data storage limit in semiconductor technology that could lead to holographic storage, and the need for new and efficient scintillators, ferroelectric compounds, and solid-state laser hosts, the most promising use of the laser-heated pedestal growth in the near future is its association with the combinatorial approach for new materials development. The LHPG technique can be used to test the possibility to grow large single crystals of the chosen compound and look more deeply into its physical properties.

References

- 13.1 B.B. Baker: On the stretching and breaking of sodium and potassium, *Proc. Phys. Soc. Lond.* **25**, 235 (1912)
- 13.2 E.N.C. da Andrade: Regular surface markings stretched wires of soft metals, *Philos. Mag.* **27**, 869 (1914)
- 13.3 P.P. Ewald (Ed.): *Fifty Years of X-ray Diffraction* (Oosthoek, Utrecht 1962)
- 13.4 P. Rudolph: What do we want with fiber crystals? An introductory overview, *Adv. Mater. Res.* **6**, 1–46 (2004)
- 13.5 H.J. Scheel: Historical aspects of crystal growth technology, *J. Cryst. Growth* **211**, 1–12 (2000)
- 13.6 J. Czochralski: Ein neues Verfahren zur Messung der Kristallisationsgeschwindigkeit der Metalle, *Z. Phys. Chem.* **92**, 219 (1918), in German
- 13.7 E.V. Gomerz: Untersuchungen an Einkristall-drähten, *Z. Phys. A* **8**, 184–190 (1922), in German
- 13.8 R.S. Feigelson: *Growth of Fiber Crystals. Crystal Growth of Electronic Materials* (North-Holland, Amsterdam 1985)
- 13.9 H.E. Labelle Jr., A.I. Mlavsky: Growth of sapphire filaments from the melt, *Nature* **216**, 574–575 (1967)
- 13.10 H.E. Labelle Jr., A.I. Mlavsky: Growth of controlled profile crystals from the melt: Part I – Sapphire filaments, *Mater. Res. Bull.* **6**, 571 (1971)
- 13.11 J.S. Haggerty: Production of fibers by a floating zone fiber drawing technique, Final Report NASA-CR-120948 (1972)
- 13.12 B. Cockayne, D.B. Gasson: The machining of oxides using gas lasers, *J. Mater. Sci.* **5**, 837 (1970)
- 13.13 C.A. Burrus, J. Stone: Single-crystal fiber optical devices: A Nd:YAG fiber laser, *Appl. Phys. Lett.* **26**, 318 (1975)
- 13.14 J. Stone, C.A. Burrus: Nd:Y₂O₃ single-crystal fiber laser: Room temperature CW operation at 1.07 and 1.35 μ m wavelength, *J. Appl. Phys.* **49**, 2281 (1978)
- 13.15 C.A. Burrus, L.A. Coldren: Growth of single crystal sapphire-clad ruby fibers, *Appl. Phys. Lett.* **31**, 383 (1977)
- 13.16 M.M. Fejer, R.L. Byer, R.S. Feigelson, W. Kway: Growth and characterization of single crystal refractory oxide fibers, advances in Infrared Fibers II, SPIE, Proc. 2nd Meet. Los Angeles (Bellingham 1982), A83–46621 22–74
- 13.17 M.M. Fejer, J.L. Nightingale, G.A. Magel, R.L. Byer: Laser-heated miniature pedestal growth apparatus for single-crystal optical fibers, *Rev. Sci. Instrum.* **55**, 1791–1796 (1984)
- 13.18 W.R. Edmonds: The reflexicon: A new reflective optical element and some applications, *Appl. Opt.* **12**, 1940 (1973)
- 13.19 M.M. Fejer: Single crystal fibers: Growth dynamics and nonlinear optical interactions. Ph.D. Thesis (Stanford Univ., Stanford 1986)
- 13.20 M.M. Fejer, G.A. Magel, R.L. Byer: High speed high-resolution fiber diameter variation measurement system, *Appl. Opt.* **24**, 2362 (1985)
- 13.21 S. Uda, W.A. Tiller: The influence of an interface electric field on the distribution coefficient of chromium in LiNbO₃, *J. Cryst. Growth* **121**, 93–110 (1992)
- 13.22 Y. Sugiyama, I. Hatakeyama, I. Yokohama: Growth of *a* axis strontium barium niobate single crystal fibers, *J. Cryst. Growth* **134**, 255–265 (1993)
- 13.23 V. Phomsakha, R.S.F. Chang, N. Djeu: Novel implementation of laser heated pedestal growth for the rapid drawing of sapphire fibers, *Rev. Sci. Instrum.* **65**, 3860–3861 (1994)
- 13.24 A. Yokoo, S. Tomaru, I. Yokohama, H. Itoh, T. Kaino: A new growth method for long rod-like organic nonlinear optical crystals with phase-matched direction, *J. Cryst. Growth* **156**, 279–284 (1995)
- 13.25 T. Imai, S. Yagi, Y. Sugiyama, I. Hatakeyama: Growth of potassium tantalate niobate single crystal fibers by the laser-heated pedestal growth method assisted by a crystal cooling technique, *J. Cryst. Growth* **147**, 350–354 (1995)
- 13.26 E. Brueck, H.J. Gelders, B.J. Harrison, A.A. Menovsky: Laser-heated fibre pedestal growth under UHV conditions, *J. Cryst. Growth* **166**, 394–397 (1996)
- 13.27 A. Brenier, G. Foulon, M. Ferriol, G. Boulon: The laser-heated-pedestal growth of LiNbO₃:MgO crystal fibres with ferroelectric domain inversion by in situ electric field poling, *J. Phys. D* **30**, L37–L39 (1997), rapid communication
- 13.28 R.K. Nubling, J.A. Harrington: Optical properties of single-crystal sapphire fibers, *Appl. Opt.* **36**, 5934–5940 (1997)
- 13.29 D.R. Ardila, J.P. Andreeta, C.T.M. Ribeiro, M.S. Li: Improved laser-heated pedestal growth system for crystal growth in medium and high isostatic pressure environment, *Rev. Sci. Instrum.* **70**, 4606–4608 (1999)
- 13.30 D.R. Ardila, L.B. Barbosa, J.P. Andreeta: Bifocal spherical mirror for laser processing, *Rev. Sci. Instrum.* **72**, 4415–4418 (2001)
- 13.31 L. Laversenne, Y. Guyot, C. Goutaudier, M.T. Cohen-Adad, G. Boulon: Optimization of spectroscopic properties of Yb³⁺-doped refractory sesquioxides: cubic Y₂O₃, Lu₂O₃ and monoclinic Gd₂O₃, *Opt. Mater.* **16**, 475–483 (2001)
- 13.32 M.R.B. Andreeta, E.R.M. Andreeta, A.C. Hernandez, R.S. Feigelson: Thermal gradient control at the solid-liquid interface in the laser-heated pedestal growth technique, *J. Cryst. Growth* **234**, 759–761 (2002)
- 13.33 M.R.B. Andreeta, L.C. Caraschi, A.C. Hernandez: Automatic diameter control system applied to the

- laser heated pedestal growth technique, *Mater. Res.* **6**, 1 (2003)
- 13.34 M.F. Carrasco, M.R. Soares, V.S. Amaral, J.M. Vieira, R.F. Silva, F.M. Costa: Bi-Sr-Ca-Cu-O superconducting fibers processed by the laser floating zone technique under different electrical current intensities, *Supercond. Sci. Technol.* **19**, 373–380 (2006)
- 13.35 C.Y. Lo, K.Y. Huang, J.C. Chen, C.Y. Chuang, C.C. Lai, S.L. Huang, Y.S. Lin, P.S. Yeh: Double-clad Cr⁴⁺:YAG crystal fiber amplifier, *Opt. Lett.* **30**, 129–131 (2005)
- 13.36 E.R.M. Andreeta, M.R.B. Andreeta, A.C. Hernandez: Laser heated pedestal growth of Al₂O₃/GdAlO₃ eutectic fibers, *J. Cryst. Growth* **234**, 782–785 (2002)
- 13.37 D.R. Ardila, M.R.B. Andreeta, S.L. Cuffini, A.C. Hernandez, J.P. Andreeta, Y.P. Mascarenhas: Single-crystal SrTiO₃ fiber grown by laser heated pedestal growth method: Influence of ceramic feed rod preparation in fiber quality, *Mater. Res.* **1**, 11 (1998)
- 13.38 M.R.B. Andreeta, E.R.M. Andreeta, A.C. Hernandez: Laser-heated pedestal growth of colorless LaAlO₃ single crystal fiber, *J. Cryst. Growth* **275**, e757–e761 (2005)
- 13.39 L.B. Barbosa, D.R. Ardila, E.M. Kakuno, R.H. Campanin, C. Cusatis, J.P. Andreeta: Processing of crystals with controlled lattice parameter gradient by the LHPG technique, *J. Cryst. Growth* **250**, 67–71 (2003)
- 13.40 Z. Lu, L.V. Moulton, R.S. Feigelson, R.J. Raymakers, P.N. Peszkin: Factors affecting the growth of single crystal fibers of the superconductor Bi₂Sr₂CaCu₂O₈, *J. Cryst. Growth* **106**, 732–741 (1990)
- 13.41 C.Y. Chen, J.C. Chen, Y.J. Lai: Investigations of the growth mechanism of stoichiometric LiNbO₃ fibers grown by the laser-heated pedestal growth method, *J. Cryst. Growth* **275**, e763–e768 (2005)
- 13.42 S. Ishibashi, K. Naganuma, I. Yokohama: Cr,Ca: Y₃Al₅O₁₂ laser crystal grown by the laser-heated pedestal growth method, *J. Cryst. Growth* **183**, 614–621 (1998)
- 13.43 H.S. Carslaw, J.C. Jaeger: *Conduction of Heat in Solids* (Oxford Univ. Press, London 1959)
- 13.44 J.C. Brice: The cracking of Czochralski grown crystals, *J. Cryst. Growth* **42**, 427 (1977)
- 13.45 M.R.B. Andreeta: Implantação da técnica de crescimento de Cristais por fusão a laser e a preparação de fibras monocristalinas óxidas. Master Thesis (Universidade de São Paulo, São Paulo 1996), in Portuguese
- 13.46 V.V. Prokofiev, J.P. Andreeta, C.J. de Lima, M.R.B. Andreeta, A.C. Hernandez, J.F. Carvalho, A.A. Kamshilin, T. Jääskeläinen: The relation between temperature gradients and structural perfection of single-crystal Bi₁₂SiO₂₀ and Bi₁₂TiO₂₀ fibers grown by the LHPG method, *Opt. Mater.* **4**, 433–436 (1995)
- 13.47 K.M. Kim, A.B. Dreeben, A. Schujko: Maximum stable zone length in float-zone growth of small diameter sapphire and silicon crystals, *J. Appl. Phys.* **50**, 4472 (1979)
- 13.48 M. Saitou: Shape and stability of a floating liquid zone between two solids, *J. Appl. Phys.* **82**, 6343–6345 (1997)
- 13.49 D.R. Ardila, L.V. Cofre, L.B. Barbosa, J.P. Andreeta: Study of floating zone profiles in materials grown by the laser-heated pedestal growth technique under isostatic atmosphere, *Cryst. Res. Technol.* **3**(9), 855–858 (2004)
- 13.50 A.L. Greer: Too hot to melt, *Nature* **404**, 134 (2000)
- 13.51 C.T.M. Ribeiro, D.R. Ardila, J.P. Andreeta, M.S. Li: Effects of isostatic oxygen pressure on the crystal growth and optical properties of undoped and Er³⁺-doped Ca₃(VO₄)₂ single-crystal fibres, *Adv. Mater. Opt. Electron.* **10**, 9–15 (2000)
- 13.52 L.S. Wu, A.H. Wang, J.M. Wu, L. Wei, G.X. Zhu, S.T. Ying: Growth and laser properties of Ti:sapphire single-crystal fibers, *Electron. Lett.* **31**, 1151–1152 (1995)
- 13.53 J.H. Sharp, T.P.J. Han, B. Henderson, R. Illingworth, I.S. Ruddock: Dopant incorporation in single-crystal fibre growth by the laser-heated miniature pedestal growth technique, *J. Cryst. Growth* **131**, 457–464 (1993)
- 13.54 M.R.B. Andreeta, L.C. Caraschi, F. Agulló-Rueda, A.C. Hernandez: Periodic doping in single crystal fibers grown by laser-heated pedestal growth technique, *J. Cryst. Growth* **242**, 395–399 (2002)
- 13.55 C.M. Liu, J.C. Chen, C.H. Chiang, L.J. Hu, S.P. Lin: Mg-doped sapphire crystal fibers grown by laser-heated pedestal growth method, *Jpn. J. Appl. Phys.* **45**, 194–199 (2006)
- 13.56 S. Erdei, L. Galambos, I. Tanaka, L. Hesselink, L.E. Cross, R.S. Feigelson, F.W. Ainger, H. Kojima: Inhomogeneities and segregation behavior in strontium-barium niobate fibers grown by laser-heated pedestal growth technique – Part II, *J. Cryst. Growth* **167**, 670–680 (1996)
- 13.57 M.F. Carrasco, R.F. Silva, J.M. Vieira, F.M. Costa: Electrical field freezing effect on laser floating zone (LFZ)-grown Bi₂Sr₂Ca₂Cu₄O₁₁ superconducting fibers, *Supercond. Sci. Technol.* **17**, 612–619 (2004)
- 13.58 W.A. Tiller, C.T. Yen: Some consequences of a strong interface field-effect operating during the growth of TiO₂-alloy crystals from the melt, *J. Cryst. Growth* **109**, 120 (1991)
- 13.59 J.A. Burton, R.C. Prim, W.P. Slichter: The distribution of solutes in crystals grown from the melt: Part I: Theoretical, *J. Chem. Phys.* **21**, 1987 (1953)
- 13.60 W.G. Pfann, R.S. Wagner: Simple method of measuring stress relaxation, *Trans. Metall. Soc. AIME* **224**, 1083 (1962)
- 13.61 L.M. Lee, C.C. Kuo, J.C. Chen, T.S. Chou, Y.C. Cho, S.L. Huang, H.W. Lee: Periodical poling of MgO doped lithium niobate crystal fiber by modulated pyroelectric field, *Opt. Commun.* **253**, 375–381 (2005)

- 13.62 S. Erdei, F.W. Ainger: Trends in the growth of stoichiometric single crystals, *J. Cryst. Growth* **174**, 293 (1997)
- 13.63 Y.T. Wang, D.S. Wang, W.Q. Ge, L.C. Cui: A sapphire fibre thermal probe based on fast Fourier transform and phase-lock loop, *Chin. Phys.* **15**, 975–979 (2006)
- 13.64 H.C. Seat, J.H. Sharp, Z.Y. Zhang, K.T.V. Grattan: Single-crystal ruby fiber temperature sensor, *Sens. Actuators A* **101**, 24–29 (2002)
- 13.65 K.T.V. Grattan, Z.Y. Zhang, T. Sun, Y. Shen, L. Tong, Z. Ding: Sapphire-ruby single-crystal fibre for application in high temperature optical fibre thermometers: Studies at temperatures up to 1500 °C, *Meas. Sci. Technol.* **12**, 981–986 (2001)
- 13.66 Y. Shen, Y. Wang, L. Tong, L. Ye: Novel sapphire fiber thermometer using fluorescent decay, *Sens. Actuators A* **71**, 70–73 (1998)
- 13.67 H.C. Seat, J.H. Sharp: Dedicated temperature sensing with c axis oriented single crystal ruby ($\text{Cr}^{3+}:\text{Al}_2\text{O}_3$) fibers: Temperature and strain dependences of R-line fluorescence, *IEEE Trans. Instrum. Meas.* **53**, 140–154 (2004)
- 13.68 Y.H. Shen, L.M. Tong, Y.Q. Wang, L.H. Ye: Sapphire-fiber thermometer ranging from 20 to 1800 °C, *Appl. Opt.* **38**, 1139–1143 (1999)
- 13.69 D. Bloom, D.R. Evans, S.A. Holmstrom, J.C. Polf, S.W.S. McKeever, V. Whitley: Characterization of Al_2O_3 single crystals grown by the laser-heated pedestal growth technique for potential use in radiation dosimetry, *Radiat. Meas.* **37**, 141–149 (2003)
- 13.70 R.K. Nubling, J.A. Harrington: Single-crystal laser-heated pedestal-growth sapphire fibers for Er:YAG laser power delivery, *Appl. Opt.* **37**, 4777–4781 (1998)
- 13.71 E.K. Renwick, E.E. Robertson, I.S. Ruddock, R. Illingworth: Optical transmission properties of single crystal fibres, *Opt. Commun.* **123**, 477–482 (1996)
- 13.72 A.G. Sinclair, G. McCormack, J.H. Sharp, I.S. Ruddock, R. Illingworth: Uniaxial crystalline fibers – optical methods for determining their physical characteristics, *Meas. Sci. Technol.* **4**, 1501–1507 (1993)
- 13.73 G.N. Merberg, J.A. Harrington: Optical and mechanical-properties of single-crystal sapphire optical fibers, *Appl. Opt.* **32**, 3201–3209 (1993)
- 13.74 H.F. Wu, A.J. Perrotta, R.S. Feigelson: Mechanical characterization of single-crystal $\alpha\text{-Al}_2\text{O}_3$ fibers grown by the laser-heated pedestal growth technique, *J. Mater. Sci. Lett.* **10**, 1428–1429 (1991)
- 13.75 J.H. Sharp, R. Illingworth, I.S. Ruddock: Graded-index characteristics in single-crystal fibers, *Opt. Lett.* **23**, 109–110 (1998)
- 13.76 J.K. Krebs, U. Happek: Yb^{3+} energy levels in $\alpha\text{-Al}_2\text{O}_3$, *J. Lumin.* **94**, 65–68 (2001)
- 13.77 H.C. Seat, J.H. Sharp: $\text{Er}^{3+}+\text{Yb}^{3+}$ -codoped Al_2O_3 crystal fibres for high-temperature sensing, *Meas. Sci. Technol.* **14**, 279–285 (2003)
- 13.78 J.H. Sharp, C.W.P. Shi, H.C. Seat: Er-doped sapphire fibre temperature sensors using upconversion emission, *Meas. Control* **34**, 170 (2001)
- 13.79 J.H. Sharp, T.J.P. Han, B. Henderson, R. Illingworth: Instability in the growth of $\text{Ti}:\text{Al}_2\text{O}_3$ single-crystal fibres, *J. Cryst. Growth* **140**, 79–83 (1994)
- 13.80 S. Erdei, G.G. Johnson, F.W. Ainger: Growth studies of YVO_4 crystals (II). Changes in Y–V–O–stoichiometry, *Cryst. Res. Technol.* **29**, 815–828 (1994)
- 13.81 J. Ramírez Rico, A.R. Pinto Gómez, J. Martínez Fernández, A.R. de Arellano López, P.B. Oliete, J.I. Peña, V.M. Orera: High-temperature plastic behavior of $\text{Al}_2\text{O}_3\text{--Y}_3\text{Al}_5\text{O}_{12}$ directionally solidified eutectics, *Acta Mater.* **54**, 107–3116 (2006)
- 13.82 J.Y. Pastor, J. Llorca, A. Salazar, P.B. Oliete, I. Francisco, J.I. Peña: Mechanical properties of melt-grown alumina-yttrium aluminum garnet eutectics up to 1900 K, *J. Am. Ceram. Soc.* **88**, 1488 (2005)
- 13.83 A. Laidoune, H. Lahrach, Y. Kagamitani, K. Leb-bou, F. Carrillo, C. Goutaudier, O. Tillement: Growth of polycrystalline fibers with eutectic composition $\text{Al}_2\text{O}_3/\text{Y}_3\text{Al}_5\text{O}_{12}$ for composite reinforcement, *J. Phys. IV* **113**, 129–134 (2004)
- 13.84 A. Salazar, J.Y. Pastor, J. Llorca, J.I. Peña, I. Francisco, P.B. Oliete: Mechanical properties of $\text{Al}_2\text{O}_3\text{--ZrO}_2(\text{Y}_2\text{O}_3)$ and $\text{Al}_2\text{O}_3\text{--YAG}$ eutectic composites processed by laser-heating floating zone, *Bol. Soc. Esp. Ceram. Vidr.* **44**, 193–198 (2006), in Spanish
- 13.85 C.S. Frazer, E.C. Dickey, A. Sayir: Crystallographic texture and orientation variants in $\text{Al}_2\text{O}_3\text{--Y}_3\text{Al}_5\text{O}_{12}$ directionally solidified eutectic crystals, *J. Cryst. Growth* **233**, 187–195 (2001)
- 13.86 J.I. Peña, M. Larsson, R.I. Merino, I. de Francisco, V.M. Orera, J. Lorca, J.Y. Pastor, A. Martín, J. Segurado: Processing, microstructure and mechanical properties of directionally-solidified $\text{Al}_2\text{O}_3\text{--Y}_3\text{Al}_5\text{O}_{12}\text{--ZrO}_2$ ternary eutectics, *J. Eur. Ceram. Soc.* **26**, 3113–3121 (2006)
- 13.87 I. Francisco, R.I. Merino, V.M. Orera, A. Larrea, J.I. Peña: Growth of $\text{Al}_2\text{O}_3/\text{ZrO}_2(\text{Y}_2\text{O}_3)$ eutectic rods by the laser floating zone technique: Effect of the rotation, *J. Eur. Ceram. Soc.* **25**, 1341–1350 (2005)
- 13.88 J.Y. Pastor, J. Lorca, P. Poza, I. de Francisco, R.I. Merino, J.I. Peña: Mechanical properties of melt-grown $\text{Al}_2\text{O}_3\text{--ZrO}_2(\text{Y}_2\text{O}_3)$ eutectics with different microstructure, *J. Eur. Ceram. Soc.* **25**, 1215–1223 (2005)
- 13.89 N.R. Harlan, R.I. Merino, J.I. Peña, A. Larrea, V.M. Orera, C. González, P. Poza, J. Llorca: Phase distribution and residual stresses in melt-grown $\text{Al}_2\text{O}_3\text{--ZrO}_2(\text{Y}_2\text{O}_3)$ eutectics, *J. Am. Ceram. Soc.* **85**, 2025 (2002)
- 13.90 S.C. Farmer, A. Sayir: Tensile strength and microstructure of $\text{Al}_2\text{O}_3\text{--ZrO}_2$ hypo-eutectic fibers, *Eng. Fract. Mech.* **69**, 1015–1024 (2002)

- 13.91 J.Y. Pastor, P. Poza, J. Llorca, J.I. Peña, R.I. Merino, V.M. Orera: Mechanical properties of directionally solidified $\text{Al}_2\text{O}_3\text{--ZrO}_2(\text{Y}_2\text{O}_3)$ eutectics, *Mater. Sci. Eng. A* **308**, 241–249 (2001)
- 13.92 J.A. Pardo, R.I. Merino, V.M. Orera, J.I. Peña, C. González, J.Y. Pastor, J. Llorca: Piezospectroscopic study of residual stresses in $\text{Al}_2\text{O}_3\text{--ZrO}_2$ directionally solidified eutectics, *J. Am. Ceram. Soc.* **83**, 2745–2752 (2001)
- 13.93 V.M. Orera, R.I. Merino, J.A. Pardo, A. Larrea, J.I. Peña, C. González, P. Poza, J.Y. Pastor, J. Llorca: Microstructure and physical properties of some oxide eutectic composites processed by directional solidification, *Acta Mater.* **48**, 4683–4689 (2000)
- 13.94 J.I. Peña, R.I. Merino, N.R. Harlan, A. Larrea, G.F. Fuente, V.M. Orera: Microstructure of Y_2O_3 doped $\text{Al}_2\text{O}_3\text{--ZrO}_2$ eutectics grown by the laser floating zone method, *J. Eur. Ceram. Soc.* **22**, 2595–2602 (2002)
- 13.95 A.S. Bhalla, R.A. Guo: Design of dielectric substrates for high T_c superconductor films, *Acta Phys. Pol. A* **92**, 7–21 (1997)
- 13.96 I.G. Siny, R.W. Tao, R.S. Katiyar, R.A. Guo, A.S. Bhalla: Raman spectroscopy of Mg–Ta order-disorder in $\text{BaMg}_{1/3}\text{Ta}_{2/3}\text{O}_3$, *J. Phys. Chem. Solids* **59**, 181–195 (1998)
- 13.97 R.L. Moreira, M.R.B. Andreeta, A.C. Hernandez, A. Dias: Polarized micro-Raman spectroscopy of $\text{Ba}(\text{Mg}_{1/3}\text{Nb}_{2/3})\text{O}_3$ single crystal fibers, *Cryst. Growth Des.* **5**, 1457–1462 (2005)
- 13.98 R.A. Guo, A.S. Bhalla, L.E. Cross: $\text{Ba}(\text{Mg}_{1/3}\text{Ta}_{2/3})\text{O}_3$ single-crystal fiber grown by the laser-heated pedestal growth technique, *J. Appl. Phys.* **75**, 4704–4708 (1994)
- 13.99 Z. Yu, R.Y. Guo, A.S. Bhalla: Growth of $\text{Ba}(\text{Ti}_{1-x}\text{Zr}_x)\text{O}_3$ single crystals by the laser heated pedestal growth technique, *J. Cryst. Growth* **233**, 460–465 (2001)
- 13.100 Z. Yu, R.Y. Guo, A.S. Bhalla: Growth of $\text{Ba}(\text{Ti}_{1-x}\text{Zr}_x)\text{O}_3$ single crystal fibers by laser heated pedestal growth technique, *Ferroelectr. Lett. Sect.* **27**, 113–123 (2000)
- 13.101 Z. Yu, R.Y. Guo, A.S. Bhalla: Dielectric behavior of $\text{Ba}(\text{Ti}_{1-x}\text{Zr}_x)\text{O}_3$ single crystals, *J. Appl. Phys.* **88**, 410–415 (2000)
- 13.102 D. Garcia, R. Guo, A.S. Bhalla: Dielectric properties of $\text{Ba}_{1-x}\text{Sr}_x\text{TiO}_3$ single crystal fibers grown by laser heated pedestal growth technique, *Integr. Ferroelectr.* **42**, 57–69 (2002)
- 13.103 D. Garcia, R. Guo, A.S. Bhalla: Growth and properties of $\text{Ba}_{0.9}\text{Sr}_{0.1}\text{TiO}_3$ single crystal fibers, *Mater. Lett.* **42**, 136–141 (2000)
- 13.104 D. Garcia, R.Y. Guo, A.S. Bhalla: Field dependence of dielectric properties of BST single crystals, *Ferroelectr. Lett. Sect.* **27**, 137–146 (2000)
- 13.105 J.C. Chen, C.Y. Chen: Growth of $\text{Ba}_{1-x}\text{Ca}_x\text{TiO}_3$ single-crystal fibers by a laser heated pedestal method, *J. Cryst. Growth* **236**, 640–646 (2002)
- 13.106 L.B. Barbosa, D.R. Ardila, J.P. Andreeta: Crystal growth of congruent barium calcium titanate by LHPG, *J. Cryst. Growth* **231**, 488–492 (2001)
- 13.107 G. Foulon, M. Ferriol, A. Brenier, M.T. Cohen-Adad, M. Boudeulle, G. Boulon: Nonlinear single-crystal fibers of undoped or Nd^{3+} -doped niobates: Growth by LHPG, spectroscopy and second harmonic generation, *Opt. Mater.* **8**, 65–74 (1997)
- 13.108 G. Foulon, A. Brenier, M. Ferriol, M.T. Cohen-Adad, G. Boulon: Nonlinear single-crystal fibers of Nd^{3+} -doped niobates ($\text{Ba}_2\text{NaNb}_5\text{O}_{15}$ and $\text{K}_3\text{Li}_{2-x}\text{Nb}_{5+x}\text{O}_{15+2x}$) Grown by LHPG, spectroscopy and self-frequency doubling, *J. Lumin.* **72–74**, 794–796 (1997)
- 13.109 I. Noiret, J. Schamps, J. Lamiot, G. Boulon, A. Brenier: Phase transitions in the 5 at % Nd^{3+} -doped $\text{Ba}_2\text{NaNb}_5\text{O}_{15}$ self-doubling laser crystal, *Phys. Rev. B* **69**, 104110 (2004)
- 13.110 G. Foulon, A. Brenier, M. Ferriol, T. Cohen-Adad, G. Boulon: Laser heated pedestal growth and spectroscopic properties of neodymium doped $\text{Ba}_2\text{NaNb}_5\text{O}_{15}$ single crystal fibers, *Chem. Phys. Lett.* **249**, 381 (1996)
- 13.111 M. Ferriol, G. Foulon, A. Brenier, G. Boulon: Phenomenological investigation of inhomogeneities in Nd^{3+} -doped $\text{Ba}_2\text{NaNb}_5\text{O}_{15}$ single-crystal fibres grown by the laser-heated pedestal growth technique, *J. Mater. Sci.* **33**, 1227–1232 (1998)
- 13.112 G. Foulon, M. Ferriol, A. Brenier, M.T. Cohen-Adad, G. Boulon: Growth by LHPG, structure and spectroscopy of Nd^{3+} -doped $\text{Ba}_2\text{NaNb}_5\text{O}_{15}$ nonlinear single-crystal fibres, *Acta Phys. Pol. A* **90**, 63–72 (1996)
- 13.113 G. Foulon, M. Ferriol, A. Brenier, G. Boulon, S. Lecocq: Obtention of good quality $\text{Ba}_2\text{NaNb}_5\text{O}_{15}$ crystals: Growth, characterization and structure of Nd^{3+} -doped single-crystal fibres, *Eur. J. Solid State Inorg. Chem.* **33**, 673–686 (1996)
- 13.114 M. Ferriol: Crystal growth and structure of pure and rare-earth doped barium sodium niobate (BNN), *Prog. Cryst. Growth Charact. Mater.* **43**, 221–244 (2001)
- 13.115 F.C. Romo, C. Goutaudier, Y. Guyot, M.T. Cohen-Adad, G. Boulon, K. Lebbou, A. Yoshikawa, T. Fukuda: Yb^{3+} -doped $\text{Ba}_2\text{NaNb}_5\text{O}_{15}$ (BNN) growth, characterization and spectroscopy, *Opt. Mater.* **16**, 199–206 (2001)
- 13.116 X. Qi, H.G. Gallagher, T.P.H. Han, B. Henderson, R. Illingworth, I.S. Ruddock: Laser heated pedestal growth and spectroscopic properties of $\text{K}_2\text{NdNb}_5\text{O}_{15}$ and $\text{Ba}_2\text{NdNb}_5\text{O}_{15}$ crystals, *Chem. Phys. Lett.* **264**, 623–630 (1997)
- 13.117 F. Ito, K.I. Kitayama: Observation of the photorefractive effect in single-domain BaTiO_3 crystal fiber, *Appl. Phys. Lett.* **61**, 2144–2146 (1992)
- 13.118 M. Saifi, B. Dubois, E.M. Vogel: Growth of tetragonal BaTiO_3 single crystal fibers, *J. Mater. Res.* **1**, 452 (1996)

- 13.119 Y.C. Lee, J.C. Chen: The effects of temperature distribution on the barium titanate crystal growth in an LHPG system, *Opt. Mater.* **12**, 83–91 (1999)
- 13.120 J.C. Chen, Y.C. Lee, S.P. Lin: A new technique to eliminate the 90° in BaTiO₃ crystal fibers, *Jpn. J. Appl. Phys.* **39**, 1812–1814 (2000)
- 13.121 E. Nippolainen, E. Raita, V.V. Prokofiev, A.A. Kamshilin, T. Jääskeläinen: Photorefractive fibers for adaptive correlation filtering of a speckle-pattern displacement, *Opt. Mater.* **14**, 1–4 (2000)
- 13.122 R.M. Ribeiro, A.B.A. Fiasca, P.A.M. dos Santos, M.R.B. Andreetta, A.C. Hernandez: Optical activity measurements in the photorefractive Bi₁₂TiO₂₀ single crystal fibers, *Opt. Mater.* **10**, 201–205 (1998)
- 13.123 J.C. Chen, L.T. Liu, C.C. Young: A study of the growth mechanism of bismuth silicon oxide during LHPG method, *J. Cryst. Growth* **199**, 476–481 (1999)
- 13.124 V.V. Prokofiev, J.P. Andreetta, C.J. Lima, M.R.B. Andreetta, A.C. Hernandez, J.F. Carvalho, A.A. Kamshilin, T. Jääskeläinen: Microstructure of single-crystal sillenite fibers, *Radiat. Eff. Defects Solids* **134**, 209–211 (1995)
- 13.125 V.V. Prokofiev, J.P. Andreetta, C.J. de Lima, M.R.B. Andreetta, A.C. Hernandez, J.F. Carvalho, A.A. Kamshilin, T. Jääskeläinen: Growth of single-crystal photorefractive fibers of Bi₁₂SiO₂₀ and Bi₁₂TiO₂₀ by the laser-heated pedestal growth method, *J. Cryst. Growth* **137**, 528–534 (1994)
- 13.126 V.V. Prokofiev, J.P. Andreetta, C.J. de Lima, M.R.B. Andreetta, A.C. Hernandez, J.F. Carvalho, A.A. Kamshilin, T. Jääskeläinen: The influence of temperature-gradients on structural perfection of single-crystal sillenite fibers grown by the LHPG method, *Opt. Mater.* **4**, 521–527 (1995)
- 13.127 V.V. Prokofiev, A.A. Kamshilin, T. Jääskeläinen: The formation and stability of the molten zone in single-crystal fiber growth by the LHPG method, *Adv. Cryst. Growth Mater. Sci. Forum* **203**, 71–75 (1996)
- 13.128 M.F. Carrasco, V.S. Amaral, R.F. Silva, J.M. Vieira, F.M. Costa: Annealing time effect on Bi-2223 phase development in LFZ and EALFZ grown superconducting fibres, *Appl. Surf. Sci.* **252**, 4957–4963 (2006)
- 13.129 M.F. Carrasco, J.H. Monteiro, V.S. Amaral, R.F. Silva, J.M. Vieira, F.M. Costa: The effect of annealing temperature on the transport properties of BSCCO fibres grown by LFZ and EALFZ, *Mater. Sci. Forum* **514–516**, 338–342 (2006)
- 13.130 M.F. Carrasco, A.B. Lopes, R.F. Silva, J.M. Vieira, F.M. Costa: Enhancement of Bi-2223 phase formation by electrical assisted laser floating zone technique, *J. Phys. Chem. Solids* **67**, 416–418 (2006)
- 13.131 M.F. Carrasco, V.S. Amaral, J.M. Vieira, R.F. Silva, F.M. Costa: The effect of current direction on superconducting properties of BSCCO fibres grown by an electrically assisted laser floating zone process, *Supercond. Sci. Technol.* **19**, 15–21 (2006)
- 13.132 A. Leyva, C.M. Cruz, M. Mora, K. Shtejer, J.C. Díez, L.A. Angurel, I. Piñera, Y. Abreu: The effects of ¹³⁷Cs and ⁶⁰Co γ radiation on the magnetic susceptibility of BSCCO textured thin rods, *Nucl. Instrum. Methods Phys. Res. Sect. B* **239**, 281–285 (2005)
- 13.133 M.F. Carrasco, F.M. Costa, R.F. Silva, F. Gimeno, A. Sotelo, M. Mora, J.C. Díez, L.A. Angurel: Textured Bi-Sr-Ca-Cu-O rods processed by laser floating zone from solid state or melted precursors, *Physica C* **415**, 163–171 (2004)
- 13.134 X. Wang, G.W. Qiao: Electron-microscopic studies on BSCCO and YBCO superconducting wires made by the laser heated pedestal growth technique, *Physica C* **185**, 2443–2444 (1991)
- 13.135 A. Salazar, J.Y. Pastor, J. Llorca, E. Natividad, F.J. Gimeno, L.A. Angurel: Effect of thermal cycling on the strength and superconducting properties of laser floating zone textured Bi-2212 rods, *Physica C* **384**, 443–450 (2003)
- 13.136 E. Natividad, J.A. Gomez, L.A. Angurel, A. Salazar, J.Y. Pastor, J. Llorca: Influence of the post-annealing cooling rate on the superconducting and mechanical properties of LFZ textured Bi-2212 rods, *Supercond. Sci. Technol.* **15**, 1512–1518 (2002)
- 13.137 E. Martinez, T.J. Hughes, C. Díez, L.A. Angurel, Y. Yang, C. Beduz: Self-field AC losses of textured Bi₂Sr₂CaCu₂O_{8+ δ} thin rods, *Physica C* **310**, 71–75 (1998)
- 13.138 F.M. Costa, R.F. Silva, J.M. Vieira: Influence of epitaxial growth on superconducting properties of LFZ Bi-Sr-Ca-Cu-O fibres. Part II. Magnetic susceptibility and transport properties, *Physica C* **289**, 171–176 (1997)
- 13.139 H. Yusheng, Z. Jincang, H. Aisheng, W. Jingsong, H. Yujing: Bi-based superconducting fibers prepared from amorphous materials, *Supercond. Sci. Technol.* **4**, S154–S156 (1991)
- 13.140 G.W. Qiao, J.S. Zhang, J.G. Huang, M. Jiang, Y.L. Ge, Y.Z. Wang, Z.Q. Hu: An investigation of melt-textured high T_c superconductor wires made by laser heated pedestal growth technique, *Physica C* **162–164**, 907–908 (1989)
- 13.141 G.F. de la Fuente, D. Beltrán, R. Ibáñez, E. Martinez, A. Beltrán, A. Segura: Crystal fibers of Bi-Sr-Ca-Cu-O materials grown by the laser floating zone method, *J. Less Common Met.* **150**, 253–260 (1989)
- 13.142 J.Z. Sun, R.S. Feigelson, D. Gazit, D. Fork, T.H. Geballe, A. Kapitulnik: Properties of high-T_c oxide fibers from laser heated pedestal growth, *IEEE Trans. Magn.* **25**, 2014–2016 (1989)
- 13.143 R.S. Feigelson, D. Gazit, D.K. Fork, T.H. Geballe: Superconducting Bi-Ca-Sr-Cu-O fibers grown by the laser-heated pedestal growth method, *Science* **240**, 1642–1645 (1988)
- 13.144 E. Martínez, L.A. Angurel, J.C. Díez, A. Larrea, M. Aguiló, R. Navarro: Grain texture and bulk magnetic anisotropy correlation in polycrystalline

- Bi₂Sr₂CaCu₂O_{8+δ} thin rods, *Physica C Appl.* **333**, 93–103 (2000)
- 13.145 E. Martínez, L.A. Angurel, J.C. Díez, F. Lera, R. Navarro: Magnetic relaxation of highly textured Bi₂Sr₂CaCu₂O_{8+δ} polycrystalline fibres, *Physica C* **271**, 133–146 (1996)
- 13.146 E.R. Yacoby, Y. Yeshurun, D. Gazit, R.S. Feigelson: Magnetic Irreversibility in Bi₂Sr₂CaCu₂O₈ fibers irradiated by neutrons, *Phys. Rev. B* **50**, 13027–13030 (1994)
- 13.147 Y.L. Ge, Y.N. Jiao, Y.S. Yang, C.S. Liu, Q.M. Liu, Z.Q. Hu: Bi system superconducting fibers by the laser-heated pedestal growth method in stable magnetic-field, *Chin. Sci. Bull.* **39**, 475–479 (1994)
- 13.148 A. Badía, Y.B. Huang, G.F. de la Fuente, M.T. Ruiz, L.A. Angurel, F. Lera, C. Rillo, R. Navarro: Magnetic and electric transport properties of Ag/(Bi,Pb)–Sr–Ca–Cu–O superconducting fibres, *Cryogenics* **32**, 969–974 (1992)
- 13.149 M. Mora, A. Sotelo, H. Amaveda, M.A. Madre, J.C. Díez, L.A. Angurel, G.F. de la Fuente: Ag addition effect on laser textured Bi-2212 samples, *Bol. Soc. Esp. Ceram. Vidr.* **44**, 199–203 (2005)
- 13.150 A. Sotelo, M. Mora, M.A. Madre, H. Amaveda, J.C. Díez, L.A. Angurel, G.F. de la Fuente: Ag distribution in thick Bi-2212 floating zone textured rods, *J. Eur. Ceram. Soc.* **25**, 2947–2950 (2005)
- 13.151 A. Sotelo, M. Mora, M.A. Madre, H. Amaveda, J.C. Díez, L.A. Angurel, M.C. Mayoral: Study of the variation of the *E*–*I* curves in the superconducting to normal transition of Bi-2212 textured ceramics by Pb addition, *Bol. Soc. Esp. Ceram. Vidr.* **45**, 228–232 (2006)
- 13.152 Y. Huang, G.F. de la Fuente, A. Sotelo, A. Badia, F. Lera, R. Navarro, C. Rillo, R. Ibañez, D. Beltran, F. Sapiña, A. Beltran: (Bi,Pb)₂Sr₂Ca₂Cu₃O_{10+δ} superconductor composites: Ceramics vs. fibers, *Physica C* **185–189**, 2401–2402 (1991)
- 13.153 D. Gazit, P.N. Peszkin, R.S. Feigelson: Growth of Bi-based superconducting ribbons, *J. Cryst. Growth* **98**, 541–544 (1989)
- 13.154 M.C. Mayoral, J.M. Andrés, M.T. Bona, L.A. Angurel, E. Natividad: Approximation to the laser floating zone preparation of high temperature BSCCO superconductors by DSC, *Thermochim. Acta* **409**, 157–164 (2004)
- 13.155 E. Natividad, J.C. Díez, L.A. Angurel, J.M. Andrés, A.C. Ferrando, M.C. Mayoral: Radial changes in the microstructure of LFZ-textured Bi-2212 thin rods induced by stoichiometry modifications, *Physica C* **383**, 379–387 (2003)
- 13.156 E. Natividad, J.C. Díez, J.I. Peña, L.A. Angurel, R. Navarro, J.M. Andrés, A.C. Ferrando: Correlation of radial inhomogeneties and critical current at 77 K in LFZ Bi-2212 textured thin rods, *Physica C* **372–376**, 1051–1054 (2002)
- 13.157 F.M. Costa, R.F. Silva, J.M. Vieira: Phase transformation kinetics during thermal annealing of LFZ Bi–Sr–Ca–Cu–O superconducting fibers in the range 800–870 °C, *Physica C* **323**, 23–41 (1999)
- 13.158 E. Martínez, L.A. Angurel, J.C. Díez, R. Navarro: Analysis of the length scales in the induced critical currents of Bi₂Sr₂CaCu₂O_{8+y} thick fibres, *Physica C* **289**, 1–21 (1997)
- 13.159 D. Gazit, P.N. Peszkin, L.V. Moulton, R.S. Feigelson: Influence of growth rate on the structure and composition of float zone grown Bi₂Sr₂CaCu₂O₈ superconducting fibers, *J. Cryst. Growth* **98**, 545–549 (1989)
- 13.160 F.M. Costa, R.F. Silva, J.M. Vieira: Influence of epitaxial growth on superconducting properties of LFZ Bi–Sr–Ca–Cu–O fibres. Part I. Crystal nucleation and growth, *Physica C* **289**, 161–170 (1997)
- 13.161 L. Yang, F.M. Costa, A.B. Lopes, R.F. Silva, J.M. Vieira: On the half unit cell intergrowth of Bi₂Sr₂Ca₃Cu₄O₁₂ with other superconducting phases in two-step annealed LFZ fibres, *Physica C* **398**, 31–36 (2003)
- 13.162 H. Miao, J.C. Díez, L.A. Angurel, J.I. Peña, G.F. de la Fuente: Phase formation and microstructure of laser floating zone grown BSCCO fibers: Reactivity aspects, *Solid State Ion.* **101–103**, 1025–1032 (1997)
- 13.163 F.M. Costa, A.P. Gonçalves, C. Abilio, M.M. Godinho, M. Almeida, J.M. Vieira: Crystallization process, phase chemistry and transport-properties of superconducting fibers prepared by the LFZ method followed by isothermal annealing, *Physica C* **235**, 513–514 (1994)
- 13.164 J. Zhang, A. He, Y. He, Y. Huo, F. Liu, S. Cao: Preparation, structure and properties of Bi-based superconducting fibers grown by laser-floating-zone-growth method, *Appl. Supercond.* **1**, 1987–1993 (1993)
- 13.165 C.J. Kim, M.R. De Guire, C.J. Allen, A. Sayir: Growth and characterization of Bi–Sr–Ca–Cu–O superconducting fibers, *Mater. Res. Bull.* **26**, 29–39 (1991)
- 13.166 D. Gazit, R.S. Feigelson: Laser-heated pedestal growth of high T_c Bi–Sr–Ca–Cu–O superconducting fibers, *J. Cryst. Growth* **91**, 318–330 (1998)
- 13.167 J.S. Zhang, J.G. Huang, M. Jiang, Y.L. Ge, Y.Z. Wang, G.W. Qiao, Z.Q. Hu: Preparation of Bi–Sr–Ca–Cu–O superconductors by laser floating zone melting technique, *Mater. Lett.* **8**, 46–48 (1989)
- 13.168 Y.L. Ge, Y.N. Jiao, Y.S. Yang, C.S. Liu, Q.M. Liu, Z.Q. Hu: Bi system superconducting fibers by the laser-heated pedestal growth method in stable magnetic-field, *Chin. Bull.* **39**, 475–479 (1994)
- 13.169 G.F. de la Fuente, R. Navarro, F. Lera, C. Rillo, J. Bartolome, A. Badia, D. Beltran, R. Ibanez, A. Beltran, E. Sinn: LFZ growth of (Bi,Pb)–Sr–Ca–Cu–O superconducting fibers, *J. Mater. Res.* **6**, 699–703 (1991)
- 13.170 J.M. Brenner, R.S. Feigelson, D. Gazit, P.N. Peszkin: Effects of heat-treatment on the superconducting properties of Bi₂Sr₂CaCu₂O_x fibers produced by the

- laser-heated pedestal growth method, *Mater. Sci. Eng. B* **5**, 351–357 (1990)
- 13.171 M. Mora, L.A. Angurel, J.C. Díez, R.J. Drost, P.H. Kes: Microstructural changes of LFZ Bi–2212 thin rods due to Ti addition, *Physica C* **372–376**, 1179–1182 (2002)
 - 13.172 A. Larrea, E. Snoeck, A. Badía, G.F. de la Fuente, R. Navarro: Microstructure, interfaces and magnetic behaviour of thick Ag/BSCCO composite fibres, *Physica C* **220**, 21–32 (1994)
 - 13.173 D. Gazit, P.N. Peszkin, R.S. Feigelson, J. Sun, T.H. Geballe: Preparation of high temperature superconductor–metal wire composites, *Mater. Res. Bull.* **24**, 467–474 (1989)
 - 13.174 G.F. de la Fuente, M.T. Ruiz, A. Sotelo, A. Larrea, R. Navarro: Microstructure of laser floating zone (LFZ) textured (Bi,Pb)–Sr–Ca–Cu–O superconductor composites, *Mater. Sci. Eng. A* **173**, 201–204 (1993)
 - 13.175 E. Snoeck, A. Larrea, C. Roucau: Microstructure of (Bi,Pb)–Sr–Ca–Cu–O fibres study by electron microscopy, *Physica C* **198**, 129–136 (1992)
 - 13.176 H. Yusheng, H. Yujing, L. Menglin, M. Sining, C. Liying, W. Ying, Z. Jincang, H. Aisheng, W. Jinsong, Y. Xiaohua: Fabrication, characterization and welding of Bi(Pb)–Sr–Ca–Cu–O superconducting fibres, *Supercond. Sci. Technol.* **4**, 158–164 (1991)
 - 13.177 J.C. Zhang, A.S. He, Y.J. Huo, J.S. Wang, Y.S. He: Bi(Pb)–Sr–Ca–Cu–O Superconducting fibers without postgrowth heat-treatment, *Chin. Phys.* **12**, 174–179 (1992)
 - 13.178 M. Ito, C. Goutaudier, Y. Guyot, K. Lebbou, T. Fukuda, G. Boulon: Synthesis and spectroscopic characterization of Yb^{3+} in $\text{Ca}_{1-x}\text{Yb}_x\text{F}_{2+x}$ crystals, *J. Phys. IV* **119**, 201–202 (2004)
 - 13.179 L.H.C. Andrade, D.R. Ardila, J.P. Andreeta, M.S. Li: Optical properties of Nd^{3+} -doped $\text{Ca}_3(\text{VO}_4)_2$ single crystal fiber, *Opt. Mater.* **22**, 369–375 (2003)
 - 13.180 R. Ternane, G. Boulon, Y. Guyot, M.T. Cohen-Adad, M. Trabelsi-Ayedi, N. Kbir-Ariguib: Crystal growth, structural and spectroscopic characterization of undoped and Yb^{3+} -doped oxyborapatite fibers, *Opt. Mater.* **22**, 117–128 (2003)
 - 13.181 D.D. Jia: Relocalization of Ce^{3+} 5d electrons from host conduction band, *J. Lumin.* **117**, 170–178 (2006)
 - 13.182 W. Jia, H. Yuan, L. Lu, H. Liu, W.M. Yen: Crystal growth and characterization of Eu^{2+} , Dy^{3+} : SrAl_2O_4 and Eu^{2+} , Nd^{3+} : CaAl_2O_4 by the LHPG method, *J. Cryst. Growth* **200**, 179–184 (1999)
 - 13.183 D. Jia, W. Jia, X.J. Wang, W.M. Yen: Quenching of thermo-stimulated photo-ionization by energy transfer in CaAl_4O_7 : Tb^{3+} , Ce^{3+} , *Solid State Commun.* **129**, 1–4 (2004)
 - 13.184 G. Boulon, M. Ito, C. Goutaudier, Y. Guyot: Advances in growth of fiber crystal by the LHPG technique. Application to the optimization of Yb^{3+} -doped CaF_2 laser crystals, *J. Cryst. Growth* **292**, 230–235 (2006)
 - 13.185 M. Ito, C. Goutaudier, Y. Guyot, K. Lebbou, T. Fukuda, G. Boulon: Crystal growth, Yb^{3+} spectroscopy, concentration quenching analysis and potentiality of laser emission in $\text{Ca}_{1-x}\text{Yb}_x\text{F}_{2+x}$, *J. Phys. Condens. Matter* **16**, 1501–1521 (2004)
 - 13.186 A.S.S. Camargo, R.A. Silva, J.P. Andreeta, L.A.O. Nunes: Stimulated emission and excited state absorption in neodymium-doped CaNb_2O_6 single crystal fibers grown by the LHPG technique, *Appl. Phys. B* **80**, 497–502 (2005)
 - 13.187 A.S.S. Camargo, C.R. Ferrari, A.C. Hernandez, L.A.O. Nunes: Structural and spectroscopic characteristics of neodymium doped CaTa_2O_6 single crystal fibres grown by the laser heated pedestal growth technique, *J. Phys. Condens. Matter* **16**, 5915–5923 (2004)
 - 13.188 C.R. Ferrari, A.S.S. Camargo, L.A.O. Nunes, A.C. Hernandez: Laser heated pedestal growth and optical characterization of CaTa_2O_6 single crystal fiber, *J. Cryst. Growth* **266**, 475–480 (2004)
 - 13.189 R.A. Silva, A.S.S. Camargo, C. Cusatis, L.A.O. Nunes, J.P. Andreeta: Growth and characterization of columbite CaNb_2O_6 high quality single crystal fiber, *J. Cryst. Growth* **262**, 246–250 (2004)
 - 13.190 L.B. Barbosa, D.R. Ardila, C. Cusatis, J.P. Andreeta: Growth and characterization of crack-free scheelite calcium molybdate single crystal fiber, *J. Cryst. Growth* **235**, 332–337 (2002)
 - 13.191 Y.J. Jiang, R.Y. Guo, A.S. Bhalla: Growth and properties of CaTiO_3 single crystal fibers, *J. Electroceram.* **2**, 199–203 (1998)
 - 13.192 S. Hayashi, W.L. Kway, R.S. Feigelson: Pulling microcrystals of Co, Fe and Co–Fe alloys from their melts, *J. Cryst. Growth* **75**, 459–465 (1986)
 - 13.193 O. Medenbach, D. Dettmar, R.D. Shannon, R.X. Fischer, W.M. Yen: Refractive index and optical dispersion of rare earth oxides using a small-prism technique, *J. Opt. A* **3**, 174–177 (2001)
 - 13.194 L. Merkle, H.R. Verdum, U. Braunch, G.F. de la Fluente, E. Behrens, L.M. Thomas, T.H. Allik: Growth and characterization of the spectra of EuAlO_3 :Ti and GdAlO_3 :Ti, *J. Opt. Soc. Am.* **6**, 2342–2347 (1990)
 - 13.195 C. Louis, K. Lebbou, M.A. Flores-Gonzalez, R. Bazzi, B. Hautefeuille, B. Mercier, S. Roux, P. Perriat, C. Olagnon, O. Tillement: Correlation of the structure and the luminescence properties of Eu^{3+} -doped Gd_2O_3 oxide between fiber single crystal and the nano-size powders, *J. Cryst. Growth* **265**, 459–465 (2004)
 - 13.196 A. Brenier, G. Boulon: Laser heated pedestal growth and spectroscopic investigations of Nd^{3+} -doped Gd_2O_3 single crystal fibres, *J. Lumin.* **82**, 285–289 (1999)
 - 13.197 D. Jia, L. Lu, W.M. Yen: Erbium energy levels relative to the band gap of gadolinium oxide, *Opt. Commun.* **212**, 97–100 (2002)
 - 13.198 A. Brenier, A.M. Jurdy, H. Verweij, M.T. Cohen-Adad, G. Boulon: Up-conversion dynamics in GdAlO_3 : Er^{3+} single crystal fibre, *Opt. Mater.* **5**, 233–238 (1996)

- 13.199 R.A. Silva, G. Tirao, C. Cusatis, J.P. Andreeta: Growth and structural characterization of M-type GdT₂O₇ single crystal fiber, *J. Cryst. Growth* **274**, 512–517 (2005)
- 13.200 R.A. Silva, G. Tirao, C. Cusatis, J.P. Andreeta: Growth and characterization of single crystal fiber with controlled concentration gradient in GdT₂O₇–ErT₂O₇ system, *J. Cryst. Growth* **294**, 447–451 (2006)
- 13.201 R.A. Silva, G. Tirao, C. Cusatis, J.P. Andreeta: Growth and X-ray characterization of Gd_xYb_{1–x}TaO₄ ($0 \leq x \leq 1$) single crystals with large lattice spacing gradient, *J. Cryst. Growth* **277**, 308–313 (2005)
- 13.202 E. Gallucci, C. Goutaudier, G. Boulon, M.T. Cohen-Adad: Growth of KY(WO₄)₂ single-crystal: Investigation of the rich WO₃ region in the K₂O–Y₂O₃–WO₃ ternary system. The K₂O–WO₃ binary system, *Eur. J. Solid State Inorg. Chem.* **34**, 1107–1117 (1997)
- 13.203 S.A. Amin, R. Guo, A.S. Bhalla: Dielectric and thermal expansion properties of LHPG grown potassium lithium niobate single crystals, *Ferroelectr. Lett. Sect.* **25**, 37–44 (1999)
- 13.204 M. Matsukura, T. Takeyama, T. Karaki, M. Adachi: Domain structures in K₃Li_{2–x}Nb_{5+x}O_{15+2x} single-crystal fibers produced by the laser-heated pedestal growth technique, *Jpn. J. Appl. Phys.* **40**, 5783–5785 (2001)
- 13.205 G. Foulon, A. Brenier, M. Ferriol, G. Boulon: Non-linear laser crystal as a blue converter: laser heated pedestal growth, spectroscopic properties and second harmonic generation of pure and Nd³⁺-doped K₃Li_{2–x}Nb_{5+x}O_{15+2x} single crystal fibres, *J. Phys. D Appl. Phys.* **29**, 3003–3008 (1996)
- 13.206 M. Matsukura, J. Murakami, T. Karaki, M. Adachi: Diameter control of K₃Li_{2–x}Nb_{5+x}O_{15+2x} single-crystal fibers, *Jpn. J. Appl. Phys.* **39**, 5658–5661 (2000)
- 13.207 M. Matsukura, T. Karaki, T. Takeyama, T. Fujii, M. Adachi: Growth of K₃Li_{2–x}Nb_{5+x}O_{15+2x} single-crystal fibers, *Jpn. J. Appl. Phys.* **38**, 5638–5640 (1999)
- 13.208 M. Ferriol, G. Boulon: Potassium lithium niobate: single-phase domain boundary in the 30 mol K₂O isopleth of the ternary system Li₂O–K₂O–Nb₂O₅ and characterization of single-crystal fibers, *Mater. Res. Bull.* **34**, 533–543 (1999)
- 13.209 M. Matsukura, Z.M. Chen, M. Adachi, A. Kawabata: Growth of potassium lithium niobate single-crystal fibers by the laser-heated pedestal growth method, *Jpn. J. Appl. Phys.* **36**, 5947–5949 (1997)
- 13.210 M. Ferriol, G. Foulon, A. Brenier, M.T. Cohen-Adad, G. Boulon: Laser heated pedestal growth of pure and Nd³⁺-doped potassium lithium niobate single-crystal fibers, *J. Cryst. Growth* **173**, 226–230 (1997)
- 13.211 D.L. Rocco, R.A. Silva, A. Magnus, G. Carvalho, A.A. Coelho, J.P. Andreeta, S. Gama: Magnetocaloric effect of La_{0.8}Sr_{0.2}MnO₃ compound under pressure, *J. Appl. Phys.* **97**, 10M317 (2005)
- 13.212 G.J. Snyder, R. Hiskes, S. Carolis, M.R. Beasley, T.H. Geballe: Intrinsic electrical transport and magnetic properties of La_{0.67}Ca_{0.33}MnO₃ and La_{0.67}Sr_{0.33}MnO₃ MOCVD thin films and bulk material, *Phys. Rev. B* **53**, 14434–14444 (1996)
- 13.213 E. Martínez, L.A. Angurel, J.C. Díez, F. Lera, R. Navarro: Magnetic relaxation of highly textured Bi₂Sr₂CaCu₂O_{8+δ} polycrystalline fibres, *Physica C* **271**, 133–146 (1996)
- 13.214 C.A. Cardoso, F.M. Araujo-Moreira, M.R.B. Andreeta, A.C. Hernandez, E.R. Leite, O.F. de Lima, A.W. Mombru, R. Faccio: Physical properties of single-crystalline fibers of the colossal-magnetoresistance manganite La_{0.7}Ca_{0.3}MnO₃, *Appl. Phys. Lett.* **83**, 3135–3137 (2003)
- 13.215 F. Büllersfeld, F. Ritter, W. Assmus: Crystal growth and twins in La_{1–x}Sr_xMnO₃, *J. Magn. Magn. Mater.* **226–230**, 815–817 (2001)
- 13.216 L. Zhang, C. Madej, C. Pedrini, B. Moine, C. Du-jardin, A. Petrosyan, A.N. Belsky: Elaboration and spectroscopic properties of new dense cerium-doped lutetium based scintillator materials, *Chem. Phys. Lett.* **268**, 408–412 (1997)
- 13.217 P.A. Morris, B.G. Bagley, J.M. Tarascon, L.H. Green, G.W. Hull: Melt growth of high-critical-temperature superconducting fibers, *J. Am. Ceram. Soc.* **71**, 334 (1988)
- 13.218 G. Foulon, A. Brenier, M. Ferriol, A. Rochal, M.T. Cohen-Adad, G. Boulon: Laser-heated pedestal growth and optical properties of Nd³⁺-doped Li_{1–x}Nb_{1–x}W_xO₃ single-crystal fibers, *J. Lumin.* **69**, 257–263 (1996)
- 13.219 Y.Y. Ji, S.Q. Zhao, Y.J. Huo, H.W. Zhang, M. Li, C.O. Huang: Growth of lithium triborate (LB0) single-crystal fiber by the laser-heated pedestal growth method, *J. Cryst. Growth* **112**, 283–286 (1991)
- 13.220 Y.J. Lai, J.C. Chen, K.C. Liao: Investigations of ferroelectric domain structures in the MgO:LiNbO₃ fibers by LHPG, *J. Cryst. Growth* **198–199**, 531–535 (1999)
- 13.221 Y.S. Luh, R.S. Feigelson, M.M. Fejer, R.L. Byer: Ferroelectric domain structures in LiNbO₃ single-crystal fibers, *J. Cryst. Growth* **78**, 135–143 (1986)
- 13.222 E.K. Renwick, I.S. Ruddock: Birefringent and non-linear optical assessment of single crystal lithium niobate fibres, *J. Phys. D Appl. Phys.* **38**, 3387–3390 (2005)
- 13.223 S.Z. Yin: Lithium niobate fibers and waveguides: Fabrications and applications, *Proc. IEEE* **87**, 1962–1974 (1999)
- 13.224 J.J. Carey, E.K. Renwick, I.S. Ruddock: Optical fibre polariser based on GRIN single crystal fibre, *Electron. Lett.* **35**, 1486–1488 (1999)
- 13.225 E.K. Renwick, M.P. MacDonald, I.S. Ruddock: GRIN single crystal fibres, *Opt. Commun.* **151**, 75–80 (1998)
- 13.226 W.X. Que, Y. Zhou, Y.L. Lam, Y.C. Chan, C.H. Kam, Y.J. Huo, X. Yao: Second-harmonic generation using an *a* axis Nd:MgO:LiNbO₃ single crystal fiber

- with Mg-ion in diffused cladding, *Opt. Eng.* **39**, 2804–2809 (2000)
- 13.227 P. Bourson, M. Aillierie, M. Cochez, M. Ferriol, Y. Zhang, L. Guilbert: Characterization of iron substitution process in Fe:LiNbO₃ single crystal fibers by polaron measurements, *Opt. Mater.* **24**, 111–116 (2003)
 - 13.228 M. Cochez, M. Ferriol, P. Bourson, M. Aillierie: Influence of the dopant concentration on the OH[−] absorption band in Fe-doped LiNbO₃ single-crystal fibers, *Opt. Mater.* **21**, 775–781 (2003)
 - 13.229 R. Burlot, R. Moncorgé, G. Boulon: Visible and infrared luminescence properties of Er³⁺-doped Sc₂O₃:LiNbO₃ crystal fibers, *J. Lumin.* **72–74**, 135–138 (1997)
 - 13.230 R. Burlot, R. Moncorgé, G. Boulon: Spectroscopic properties of Nd³⁺ doped Sc₂O₃:LiNbO₃ crystal fibers, *J. Lumin.* **72–74**, 812–815 (1997)
 - 13.231 G. Boulon: Yb³⁺-doped oxide crystals for diode-pumped solid state lasers: Crystal growth, optical spectroscopy, new criteria of evaluation and combinatorial approach, *Opt. Mater.* **22**, 85–87 (2003)
 - 13.232 K. Nagashio, A. Watcharapasorn, R.C. DeMattei, R.S. Feigelson: Fiber growth of near stoichiometric LiNbO₃ single crystals by the laser-heated pedestal growth method, *J. Cryst. Growth* **265**, 190–197 (2004)
 - 13.233 Y.J. Lai, J.C. Chen: Effects of the laser heating and air bubbles on the morphologies of c axis LiNbO₃ fibers, *J. Cryst. Growth* **231**, 222–229 (2001)
 - 13.234 J.C. Chen, Y.C. Lee: The influence of temperature distribution upon the structure of LiNbO₃ crystal rods grown using the LHPG method, *J. Cryst. Growth* **208**, 508–512 (2000)
 - 13.235 J.C. Chen, Y.C. Lee, C. Hu: Observation of the growth mechanisms of lithium niobate single crystal during a LHPG process, *J. Cryst. Growth* **174**, 313–319 (1997)
 - 13.236 J.C. Chen, C. Hu: Measurement of the float-zone interface shape for lithium niobate, *J. Cryst. Growth* **149**, 87–95 (1995)
 - 13.237 S. Uda, W.A. Tiller: Microbubble formation during crystallization of LiNbO₃ melts, *J. Cryst. Growth* **152**, 79–86 (1995)
 - 13.238 Y.S. Luh, M.M. Fejer, R.L. Byer, R.S. Feigelson: Stoichiometric LiNbO₃ single-crystal fibers for non-linear optical applications, *J. Cryst. Growth* **85**, 264–269 (1987)
 - 13.239 C. Hu, J.C. Chen: Experimental observation of interface shapes in the float zone of lithium niobate during a CO₂ laser melting, *Int. J. Heat Mass Trans.* **39**, 3347–3352 (1996)
 - 13.240 Y.J. Lai, J.C. Chen: The influence of heavy iron-doping on LiNbO₃ fibers and their growth, *J. Cryst. Growth* **212**, 211–216 (2000)
 - 13.241 M. Ferriol, A. Dakki, M.T. Cohen-Adad, G. Foulon, A. Brenier, G. Boulon: Growth and characterization of MgO-doped single-crystal fibers of lithium niobate in relation to high temperature phase equilibria in the ternary system Li₂O–Nb₂O₅–MgO, *J. Cryst. Growth* **178**, 529–538 (1997)
 - 13.242 W. Que, Y. Zhou, Y. Lam, Y. Chan, C. Kam, L. Zhang, X. Yao: Magnesium-ion diffusion to lithium niobate single-crystal fiber with MgF₂ as diffusion source, *Jpn. J. Appl. Phys.* **38**, 5137–5142 (1999)
 - 13.243 W. Que, S. Lim, L. Zhang, X. Yao: Characteristics of lithium niobate single-crystal fiber with magnesium-ion-indiffused cladding, *J. Am. Ceram. Soc.* **80**, 2945 (1997)
 - 13.244 A. Dakki, M. Ferriol, M.T. Cohen-Adad: Growth of MgO-doped LiNbO₃ single-crystal fibers: Phase equilibria in the ternary system Li₂O–Nb₂O₅–MgO, *Eur. J. Solid State Inorg. Chem.* **33**, 19–31 (1996)
 - 13.245 Z.L. Feng, Y. Liao, Z.F. Jiao, X. Wang: Preparation of LiNbO₃:Zn+Mg single crystal fibers, *Cryst. Res. Technol.* **31**, K27–K28 (1996)
 - 13.246 H. Li, Z. Feng, X. Wang, L. Wang, Z. Jiao, X. Xu: Growth and characterization of LiNbO₃:Mg+Ti monocrystalline fibers, *Cryst. Res. Technol.* **30**, 763–765 (1995)
 - 13.247 R. Burlot, M. Ferriol, R. Moncorgé, G. Boulon: Li₂O evaporation during the laser heated pedestal growth of LiTaO₃ single-crystal fibers, *Eur. J. Solid State Inorg. Chem.* **35**, 1–8 (1998)
 - 13.248 G. Boulon, Y. Guyot, M. Ito, A. Bensalah, C. Goutaudier, G. Panczer, J.C. Gacon: From optical spectroscopy to a concentration quenching model and a theoretical approach to laser optimization for Yb³⁺-doped YLiF₄ crystals, *Mol. Phys.* **102**, 1119–1132 (2004)
 - 13.249 L.B. Shaw, R.S.F. Chang: Rare-earth doped YLF grown by the laser-heated pedestal growth technique, *J. Cryst. Growth* **112**, 731–736 (1991)
 - 13.250 W. Jia, L. Lu, B.M. Tissue, W.M. Yen: Valence and site occupation of chromium ions in single-crystal forsterite fibers, *J. Cryst. Growth* **109**, 323–328 (1991)
 - 13.251 J. Sigalovsky, J.S. Haggerty, J.E. Sheehan: Growth of spinel single-crystal fibers by the laser-heated floating-zone technique and their characterization as high-temperature reinforcements, *J. Cryst. Growth* **134**, 313–324 (1993)
 - 13.252 L.H. Wang, M.H. Hon, L.F. Schneemeyer, G.A. Thomas, W.L. Wilson: Growth of single crystal fibers for 3 μm optical amplifiers by the laser-heated pedestal growth method, *Mater. Res. Bull.* **33**, 1793–1799 (1998)
 - 13.253 E. Bruck, R.K. Route, R.J. Raymakers, R.S. Feigelson: Crystal-growth of compounds in the MgO–Nb₂O₅ binary-system, *J. Cryst. Growth* **128**, 842–845 (1993)
 - 13.254 Y. Jiang, R. Guo, A.S. Bhalla: LHPG grown crystal fibers of MgTiO₃–CaTiO₃ eutectic system, *J. Phys. Chem. Solids* **59**, 611–615 (1998)
 - 13.255 J.K. Yamamoto, A.S. Bhalla: Piezoelectric properties of layered perovskite A₂Ti₂O₇ (A = La and Nd) single-crystal fibers, *J. Appl. Phys.* **70**, 4469–4471 (1991)

- 13.256 V.Y. Ivanov, A.N. Tcherepanov, B.V. Shul'gin, T.S. Koroleva, C. Pédrini, C. Dujardin: Photoluminescence properties of NaF:U,Cu bulk and fiber crystals, *Opt. Mater.* **28**, 1123–1127 (2006)
- 13.257 H. Manuspiya, R. Guo, A.S. Bhalla: Nb₂O₅-based oxide ceramics and single crystals—investigation of dielectric properties, *Ferroelectr. Lett. Sect.* **31**, 157–166 (2005)
- 13.258 H. Manuspiya, R. Guo, A.S. Bhalla: Nb₂O₅-based oxide ceramics and single crystals—investigation of dielectric properties, *Ceram. Int.* **30**, 2037–2041 (2004)
- 13.259 H. Choosuwana, R. Guo, A.S. Bhalla: Dielectric behaviors of Nb₂O₅(0.95):0.05TiO₂ ceramic and single crystal, *Mater. Lett.* **54**, 269–272 (2002)
- 13.260 H. Choosuwana, R. Guo, A.S. Bhalla, U. Balachandran: Growth studies of (Nb₂O₅)(1–x):xTiO₂ and (Nb₂O₅)(1–x):xSiO₂ single crystals and their dielectric behaviors, *Ferroelectrics* **262**, 1285–1293 (2001)
- 13.261 F.S. Ermeneux, C. Goutaudier, R. Moncorgé, M.T. Cohen-Adad, M. Bettinelli, E. Cavalli: Comparative optical characterization of various Nd³⁺:YVO₄ single crystals, *Opt. Mater.* **13**, 193–204 (1999)
- 13.262 A.S.S. de Camargo, L.A.O. Nunes, D.R. Ardila, J.P. Andreeta: Excited-state absorption and 1064-nm end-pumped laser emission of Nd:YVO₄ single-crystal fiber grown by laser-heated pedestal growth, *Opt. Lett.* **29**, 59–61 (2004)
- 13.263 A.S.S. de Camargo, M.R.B. Andreeta, A.C. Hernandez, L.A.O. Nunes: 4.8 μm emission and excited state absorption in LHPG grown Gd_{0.8}La_{0.2}VO₄:Tm³⁺ single crystal fibers for miniature lasers, *Opt. Mater.* **28**, 551–555 (2006)
- 13.264 C.H. Huang, J.C. Chen: Nd:YVO₄ single crystal fiber growth by the LHPG method, *J. Cryst. Growth* **229**, 184–187 (2001)
- 13.265 S. Erdei, G.G. Johnson, F.W. Ainger: Growth-studies of YVO₄ crystals (II) – changes in Y–V–O stoichiometry, *Cryst. Res. Technol.* **29**, 815–828 (1994)
- 13.266 S. Erdei, F.W. Ainger: Crystal growth of YVO₄ using the LHPG technique, *J. Cryst. Growth* **128**, 1025–1030 (1993)
- 13.267 M.R.B. Andreeta, A.S.S. de Camargo, L.A.O. Nunes, A.C. Hernandez: Transparent and inclusion-free RE_{1–x}La_xVO₄ (RE = Gd,Y) single crystal fibers grown by LHPG technique, *J. Cryst. Growth* **291**, 117–122 (2006)
- 13.268 A.S.S. Camargo, L.A.O. Nunes, M.R.B. Andreeta, A.C. Hernandez: Near-infrared and upconversion properties of neodymium-doped RE_{0.8}La_{0.2}VO₄ (RE = Y,Gd) single-crystal fibres grown by the laser-heated pedestal growth technique, *J. Phys. Condens. Matter* **14**, 13887–13889 (2002)
- 13.269 D.R. Ardila, A.S.S. Camargo, J.P. Andreeta, L.A.O. Nunes: Growth of yttrium orthovanadate by LHPG in isostatic oxygen atmosphere, *J. Cryst. Growth* **233**, 253–258 (2001)
- 13.270 L. Sangaletti, B. Allieri, L.E. Depero, M. Bettinelli, K. Lebbou, R. Moncorgé: Search for impurity phases of Nd³⁺:YVO₄ crystals for laser and luminescence applications, *J. Cryst. Growth* **198–199**, 454–459 (1999)
- 13.271 C. Goutaudier, F.S. Ermeneux, M.T. Cohen-Adad, R. Moncorgé, M. Bettinelli, E. Cavalli: LHPG and flux growth of various Nd:YVO₄ single crystals: A comparative characterization, *Mater. Res. Bull.* **33**, 1457–1465 (1998)
- 13.272 X. Qi, T.P.J. Han, H.G. Gallagher, B. Henderson, R. Illingworth, I.S. Ruddock: Optical spectroscopy of PrTiNbO₆, NdTiNbO₆ and ErTiNbO₆ single crystals, *J. Phys. Condens. Matter* **8**, 4837–4845 (1996)
- 13.273 X. Qi, R. Illingworth, H.G. Gallagher, T.P.J. Han, B. Henderson: Potential laser gain media with the stoichiometric formula RETiNbO₆, *J. Cryst. Growth* **160**, 111–118 (1996)
- 13.274 X. Qi, T.P.J. Han, H.G. Gallagher, B. Henderson, R. Illingworth, I.S. Ruddock: Optical spectroscopy of PrTiNbO₆, NdTiNbO₆ and ErTiNbO₆ single crystals, *J. Phys. Condens. Matter* **8**, 4837–4845 (1996)
- 13.275 G. Boulon, A. Brenier, L. Laversenne, Y. Guyot, C. Goutaudier, M.T. Cohen-Adad, G. Métrat, N. Muhlstein: Search of optimized trivalent ytterbium doped-inorganic crystals for laser applications, *J. Alloys Compd.* **341**, 2–7 (2002)
- 13.276 D. Elwell, W.L. Kway, R.S. Feigelson: Crystal growth of a new tetragonal phase of ScTaO₄, *J. Cryst. Growth* **71**, 237–239 (1985)
- 13.277 R.W. Tao, A.R. Guo, C.S. Tu, I. Siny, R.S. Katiyar: Temperature dependent Raman spectroscopic studies on microwave dielectrics Sr(Al_{1/2}Ta_{1/2})O₃ and Sr(Al_{1/2}Nb_{1/2})O₃, *Ferroelectr. Lett. Sect.* **21**, 79–85 (1996)
- 13.278 R.Y. Guo, A.S. Bhalla, J. Sheen, F.W. Ainger, S. Erdei, E.C. Subbarao, L.E. Cross: Strontium aluminum tantalum oxide and strontium aluminum niobium oxide as potential substrates for HTSC thin-films, *J. Mater. Res.* **10**, 18–25 (1995)
- 13.279 D.R. Ardila, M.R.B. Andreeta, S.L. Cuffini, A.C. Hernandez, J.P. Andreeta, Y.P. Mascarenhas: Laser heated pedestal growth of Sr₂RuO₄ single-crystal fibers from SrRuO₃, *J. Cryst. Growth* **177**, 52–56 (1997)
- 13.280 D.D. Jia, X.J. Wang, W. Jia, W.M. Yen: Temperature-dependent photoconductivity of Ce³⁺-doped SrAl₂O₄, *J. Lumin.* **119**, 55–58 (2006)
- 13.281 D. Jia, R.S. Meltzer, W.M. Yen, W. Jia, X. Wang: Green phosphorescence of CaAl₂O₄:Tb³⁺,Ce³⁺ through persistence energy transfer, *Appl. Phys. Lett.* **80**, 1535–1537 (2002)
- 13.282 M.H. Lente, J. de Los, S. Guerra, J.A. Eiras, T. Mazon, M.R.B. Andreeta, A.C. Hernandez: Microwave dielectric relaxation process in doped-incipient ferroelectrics, *J. Eur. Ceram. Soc.* **25**, 2563–2566 (2005)

- 13.283 M.R.B. Andreeta, A.C. Hernandez, S.L. Cuffini, J.A. Guevara, Y.P. Mascarenhas: Laser heated pedestal growth of orthorhombic SrHfO_3 single crystal fiber, *J. Cryst. Growth* **200**, 621–624 (1999)
- 13.284 D.R. Ardila, J.P. Andreeta, H.C. Basso: Preparation, microstructural and electrical characterization of SrVO_3 single crystal fiber, *J. Cryst. Growth* **211**, 131–137 (2000)
- 13.285 C. Huang, A.S. Bhalla, R. Guo, L.E. Cross: Dielectric behavior of strontium barium niobate relaxor ferroelectrics in ceramics and single crystal fibers, *Jpn. J. Appl. Phys.* **45**, 165–167 (2006)
- 13.286 J.K. Yamamoto, D.A. McHenry, A.S. Bhalla: Strontium barium niobate single-crystal fibers—optical and electrooptic properties, *J. Appl. Phys.* **70**, 3215–3222 (1991)
- 13.287 C. Huang, A.S. Bhalla, R. Guo, L.E. Cross: Dielectric behavior of strontium barium niobate relaxor ferroelectrics in ceramics and single crystal fibers, *Jpn. J. Appl. Phys.* **45**, 165–167 (2006)
- 13.288 M. Miyagi, Y. Sugiyama, S. Yagi, I. Hatakeyama: Photorefractive properties of Ce-doped strontium barium niobate single-crystal fibers at 830 nm, *Jpn. J. Appl. Phys.* **33**, L1417–L1419 (1994)
- 13.289 Y. Sugiyama, S. Yagi, I. Yokohama, I. Hatakeyama: Holographic recording in cerium doped strontium barium niobate a axis single crystal fibers, *Jpn. J. Appl. Phys.* **31**, 708–712 (1992)
- 13.290 Y. Sugiyama, I. Yokohama, K. Kubodera, S. Yagi: Growth and photorefractive properties of a axis and c axis cerium-doped strontium barium niobate single-crystal fibers, *IEEE Photonics Technol. Lett.* **3**, 744–746 (1991)
- 13.291 J.J. Romero, M.R.B. Andreeta, E.R.M. Andreeta, L.E. Bausá, A.C. Hernandez, J.G. Solé: Growth and characterization of Nd-doped SBN single crystal fibers, *Appl. Phys. A* **78**, 1037–1042 (2004)
- 13.292 L. Galambos, S. Erdei, I. Tanaka, L. Hesselink, L.E. Cross, R.S. Feigelson, F.W. Ainger, H. Kojima: Inhomogeneities and segregation behavior in strontium-barium niobate fibers grown by laser-heated pedestal growth technique – Part I, *J. Cryst. Growth* **166**, 660–669 (1996)
- 13.293 J.K. Yamamoto, S.A. Markgraf, A.S. Bhalla: $\text{Sr}_x\text{Ba}_{1-x}\text{Nb}_2\text{O}_6$ single crystal fibers: Dependence of crystal quality on growth parameters, *J. Cryst. Growth* **123**, 423–435 (1992)
- 13.294 J.P. Wilde, D.H. Jundt, L. Galambos, L. Hesselink: Growth of $\text{Sr}_{0.61}\text{Ba}_{0.39}\text{Nb}_2\text{O}_6$ fibers: New results regarding orientation, *J. Cryst. Growth* **114**, 500–506 (1991)
- 13.295 P.S. Dobal, R.S. Katiyar, Y. Jiang, R. Guo, A.S. Bhalla: Structural modifications in titania-doped tantalum pentoxide crystals: A Raman scattering study, *Int. J. Inorg. Mater.* **3**, 135–142 (2001)
- 13.296 T. Kotani, H.L. Tuller: Growth of TiO_2 single crystals and bicrystals by the laser-heated floating-zone method, *J. Am. Ceram. Soc.* **81**, 592 (1998)
- 13.297 D.D. Jia, X.J. Wang, W.M. Yen: Delocalization, thermal ionization, and energy transfer in singly doped and codoped CaAl_4O_7 and Y_2O_3 , *Phys. Rev. B* **69**, 235113 (2004)
- 13.298 Y. Guyot, R. Moncorgé, L.D. Merkle, A. Pinto, B. McIntosh, H. Verdun: Luminescence properties of Y_2O_3 single crystals doped with Pr^{3+} or Tm^{3+} and codoped with Yb^{3+} , Tb^{3+} or Ho^{3+} ions, *Opt. Mater.* **5**, 127–136 (1996)
- 13.299 M.A. Flores-Gonzalez, K. Lebbou, R. Bazzi, C. Louis, P. Perriat, O. Tillement: Eu^{3+} addition effect on the stability and crystallinity of fiber single crystal and nano-structured Y_2O_3 oxide, *J. Cryst. Growth* **277**, 502–508 (2005)
- 13.300 G.P. Flinn, K.W. Jang, J. Ganem, M.L. Jones, R.S. Meltzer, M. Macfarlane: Sample-dependent optical dephasing in bulk crystalline samples of $\text{Y}_2\text{O}_3\text{:Eu}^{3+}$, *Phys. Rev. B* **49**, 5821–5827 (1994)
- 13.301 K. Jang, I. Kim, S. Park: Optical dephasing of Eu^{3+} in yttrium oxide crystals, *J. Phys. Soc. Jpn.* **67**, 3969–3971 (1998)
- 13.302 M.J. Sellars, R.S. Meltzer, P.T.H. Fisk, N.B. Manson: Time-resolved ultranarrow optical hole burning of a crystalline solid: $\text{Y}_2\text{O}_3\text{:Eu}^{3+}$, *J. Opt. Soc. Am. B* **11**, 1468–1473 (1994)
- 13.303 G.P. Flinn, K.W. Jang, J. Ganem, M.L. Jones, R.S. Meltzer, R.M. Macfarlane: Anomalous optical dephasing in crystalline $\text{Y}_2\text{O}_3\text{-Eu}^{3+}$, *J. Lumin.* **58**, 374–379 (1994)
- 13.304 F. Auzel, G. Baldacchini, L. Laversenne, G. Boulon: Radiation trapping and self-quenching analysis in Yb^{3+} , Er^{3+} , and Ho^{3+} doped Y_2O_3 , *Opt. Mater.* **24**, 103–109 (2003)
- 13.305 G. Boulon, L. Laversenne, C. Goutaudier, Y. Guyot, M.T. Cohen-Adad: Radiative and non-radiative energy transfers in Yb^{3+} -doped sesquioxide and garnet laser crystals from a combinatorial approach based on gradient concentration fibers, *J. Lumin.* **102–103**, 417–425 (2003)
- 13.306 C. Goutaudier, F.S. Ermeneux, M.T. Cohen-Adad, R. Moncorgé: Growth of pure and RE^{3+} -doped Y_2O_3 single crystals by LHPG technique, *J. Cryst. Growth* **210**, 693–698 (2000)
- 13.307 L. Laversenne, S. Kairouani, Y. Guyot, C. Goutaudier, G. Boulon, M.T. Cohen-Adad: Correlation between dopant content and excited-state dynamics properties in Er^{3+} - Yb^{3+} -codoped Y_2O_3 by using a new combinatorial method, *Opt. Mater.* **19**, 59–66 (2002)
- 13.308 K.W. Jang, R.S. Meltzer: Homogeneous and inhomogeneous linewidths of Eu^{3+} in disordered crystalline systems, *Phys. Rev. B* **52**, 6431–6439 (1995)

- 13.309 Y.H. Shen, W.Z. Zhao, J.L. He, T. Sun, K.T.V. Grattan: Fluorescence decay characteristic of Tm-doped YAG crystal fiber for sensor applications, investigated from room temperature to 1400 °C, *IEEE Sens. J.* **3**, 507–512 (2003)
- 13.310 R.S.F. Chang, H. Hara, S. Chaddha, S. Sengupta, N. Djeu: Lasing performance of a Tm-YAG minirod grown by the laser-heated pedestal growth technique, *IEEE Photonics Technol. Lett.* **2**, 695–696 (1990)
- 13.311 Y.H. Shen, S.Y. Chen, W.Z. Zhao, J. Chen, L.H. Ye, J.G. Gu, K.T.V. Grattan: Growth characteristics and potential applications in optical sensors of composite Cr⁴⁺:yttrium-aluminum-garnet (YAG)-Nd³⁺:YAG crystal, *Rev. Sci. Instrum.* **74**, 1187–1191 (2003)
- 13.312 S.B. Zhang, Z.C. Ding, M.Y. Dong, B.H. Zhou, L.M. Tong: Study of optical-properties of Nd-YAG single-crystal optical fiber, *Chin. Phys.* **12**, 428–432 (1992)
- 13.313 L.M. Tong, D. Zhu, Q.M. Luo, D.F. Hong: A laser pumped Nd³⁺-doped YAG fiber-optic thermal tip for laser thermotherapy, *Lasers Surg. Med.* **30**, 67–69 (2002)
- 13.314 L.M. Tong, J.Y. Lou, Y.F. Xu, Q.M. Luo, N. Shen, E. Mazur: Highly Nd³⁺-doped Y₃Al₅O₁₂ crystal fiber tip for laser thermotherapy, *Appl. Opt.* **41**, 4008–4012 (2002)
- 13.315 C.Y. Lo, P.L. Huang, T.S. Chou, L.M. Lee, T.Y. Chang, S.L. Huang, L.C. Lin, H.Y. Lin, F.C. Ho: Efficient Nd:Y₃Al₅O₁₂ crystal fiber laser, *Jpn. J. Appl. Phys.* **41**, L1228–L1231 (2002)
- 13.316 B.M. Tissue, W.Y. Jia, L.Z. Lu, W.M. Yen: Coloration of chromium-doped yttrium-aluminum-garnet single-crystal fibers using a divalent codopant, *J. Appl. Phys.* **70**, 3775–3777 (1991)
- 13.317 J.C. Chen, C.Y. Lo, K.Y. Huang, F.J. Kao, S.Y. Tu, S.L. Huang: Fluorescence mapping of oxidation states of Cr ions in YAG crystal fibers, *J. Cryst. Growth* **274**, 522–529 (2005)
- 13.318 L. Ye, J. Zhang, Y. Shi: Growth and characteristics of Cr³⁺:YAG crystal fiber for fluorescence decay temperature sensor, *Rev. Sci. Instrum.* **77**, 054901 (2006)
- 13.319 Z. Zhang, J.H. Herringer, N. Djeu: Monolithic crystalline fiber optic temperature sensor, *Rev. Sci. Instrum.* **68**, 2068–2070 (1997)
- 13.320 X. Wu, W.M. Dennis, W.M. Yen: Temperature dependence of cross-relaxation processes in Pr³⁺-doped yttrium aluminum garnet, *Phys. Rev. B* **50**, 6589–6595 (1994)
- 13.321 A. Yoshikawa, G. Boulon, L. Laversenne, H. Canibano, K. Lebbou, A. Collombet, Y. Guyot, T. Fukuda: Growth and spectroscopic analysis of Yb³⁺-doped Y₃Al₅O₁₂ fiber single crystals, *J. Appl. Phys.* **94**, 5479–5488 (2003)
- 13.322 Y.S. Lin, C.C. Lai, K.Y. Huang, J.C. Chen, C.Y. Lo, S.L. Huang, T.Y. Chang, J.Y. Ji, P. Shen: Nano-structure formation of double-clad Cr⁴⁺:YAG crystal fiber grown by co-drawing laser-heated pedestal, *J. Cryst. Growth* **289**, 515–519 (2006)
- 13.323 J.Y. Ji, P. Shen, J.C. Chen, F.J. Kao, S.L. Huang, C.Y. Lo: On the deposition of Cr_{3–8}O₄ spinel particles upon laser-heated pedestal growth of Cr:YAG fiber, *J. Cryst. Growth* **282**, 343–352 (2005)
- 13.324 T. Kotani, J.K.W. Chen, H.L. Tuller: Striation formation in Ti-doped Y₃Al₅O₁₂ fibers grown by the laser heated floating zone method, *J. Electroceram.* **2**, 113–118 (1998)
- 13.325 T.C. Mao, J.C. Chen, C.C. Hu: Characterization of the growth mechanism of YIG crystal fibers using the laser heated pedestal growth method, *J. Cryst. Growth* **282**, 143–151 (2005)
- 13.326 J.C. Chen, C.C. Hu: Quantitative analysis of YIG, YFeO₃ and Fe₃O₄ in LHPG-grown YIG rods, *J. Cryst. Growth* **249**, 245–250 (2003)
- 13.327 C.C. Hu, J.C. Chen, C.H. Huang: Effect of pulling rates on the quality of YIG single crystal fibers, *J. Cryst. Growth* **225**, 257–263 (2001)
- 13.328 H.J. Lim, R.C. DeMattei, R.S. Feigelson, K. Rochford: Striations in YIG fibers grown by the laser-heated pedestal method, *J. Cryst. Growth* **212**, 191–203 (2000)
- 13.329 J.J. Romero, E. Montoya, L.E. Bausá, F. Agulló-Rueda, M.R.B. Andreeta, A.C. Hernandez: Multiwavelength laser action of Nd³⁺:YAlO₃ single crystals grown by the laser heated pedestal growth method, *Opt. Mater.* **24**, 643–650 (2004)
- 13.330 A.M. Figueredo, M.J. Cima, M.C. Flemings, J.S. Haggerty, T. Hara, H. Ishii, T. Ohkuma, S. Hirano: Properties of Ba₂YCu₃O_{7–δ} filaments directionally solidified by the laser-heated floating zone technique, *Physica C* **241**, 92–102 (1995)
- 13.331 H. Ishii, T. Hara, S. Hirano, A.M. Figueredo, M.J. Cima: Magnetization behavior and critical current density along the *c* axis in melt-grown YBCO fiber crystal, *Physica C* **225**, 91–100 (1994)
- 13.332 M. Jiang, J.G. Huang, Y.Z. Wang, C. Zhang, D.C. Zeng, X. Wang, G.W. Qiao: Solidification characteristics of textured 123 phase in YBCO by laser floating zone leveling (LFZL) method, *J. Cryst. Growth* **130**, 389–393 (1993)
- 13.333 X.P. Jiang, J.G. Huang, Y. Yu, M. Jiang, G.W. Qiao, Y.L. Ge, Z.Q. Hu, C.X. Shi, Y.H. Zhao, Y.J. Wang, G.Z. Xu, Y.E. Zhou: The crystal growth of Y-Ba-Cu-O by laser floating zone melting, *Supercond. Sci. Technol.* **1**, 102–106 (1988)
- 13.334 M. Ferriol, Y. Terada, T. Fukuda, G. Boulon: Laser heated pedestal growth and characterization of zinc lithium niobate crystals, *J. Cryst. Growth* **197**, 221–227 (1999)
- 13.335 F.S. Vicente, A.C. Hernandez, A.C. Castro, M.F. Souza, M.R.B. Andreeta, M.S. Li: Photoluminescence spectrum of rare earth doped zirconia fibre and power excitation dependence, *Radiat. Eff. Defects Solids* **149**, 153–157 (1999)

- 13.336 J. Martínez Fernández, A.R. Pínto Gómez, J.J. Quispe Cancapa, A.R. de Arellano López, J. Llorca, J.Y. Pastor, S. Farmer, A. Sayir: High-temperature plastic deformation of Er_2O_3 -doped ZrO_2 single crystals, *Acta Mater.* **54**, 2195–2204 (2006)
- 13.337 A. Ridruejo, J.Y. Pastor, J. Llorca, A. Sayir, V.M. Orera: Stress corrosion cracking of single-crystal tetragonal $\text{ZrO}_2(\text{Er}_2\text{O}_3)$, *J. Am. Ceram. Soc.* **88**, 3125 (2005)
- 13.338 L.M. Tong: Growth of high-quality Y_2O_3 - ZrO_2 single-crystal optical fibers for ultra-high-temperature fiber-optic sensors, *J. Cryst. Growth* **217**, 281–286 (2000)
- 13.339 J.I. Peña, H. Miao, R.I. Merino, G.F. de la Fuente, V.M. Orera: Polymer matrix synthesis of zirconia eutectics for directional solidification into single crystal fibres, *Solid State Ion.* **101–103**, 143–147 (1997)
- 13.340 Y.J. Jiang, R.Y. Guo, A.S. Bhalla: Single crystal growth and ferroelectric properties of $\alpha(\text{Ba}_{1-x}\text{Sr}_x)\text{Nb}_2\text{O}_6:\beta(\text{Na}_{1-y}\text{Ky})\text{NbO}_3$ solid solutions, *J. Appl. Phys.* **84**, 5140–5146 (1998)
- 13.341 J.G. Hou, D.Y. Tang, C.T. Chen, L.H. Ye, J.Q. Chen, Z.C. Ding: Growth of beta-barium metaborate single-crystal fibers along the phase matching direction, *Chin. Phys. Lett.* **7**, 568–571 (1990)
- 13.342 D.Y. Tang, R.K. Route, R.S. Feigelson: Growth of barium metaborate (BaB_2O_4) single crystal fibers by the laser-heated pedestal growth method, *J. Cryst. Growth* **91**, 81–89 (1988)
- 13.343 Y.H. Bing, A.S. Bhalla, R.Y. Guo: One-dimensional crystal growth near morphotropic phase boundary $(1-x)\text{Pb}(\text{Mg}_{1/3}\text{Nb}_{2/3})\text{O}_3$ - $x\text{PbTiO}_3$ crystal fibers, *Ferroelectr. Lett. Sect.* **33**, 7–14 (2006)
- 13.344 G.F. de La Fuente, L.R. Black, D.M. Andrauskas, H.R. Verdún: Growth of Nd-doped rare earth silicates by the laser floating zone method, *Solid State Ion.* **32–33**, 494–505 (1989)
- 13.345 J.K. Yamamoto, A.S. Bhalla: Microwave dielectric-properties of layered perovskite $\text{A}_2\text{B}_2\text{O}_7$ single-crystal fibers, *Mater. Lett.* **10**, 497–500 (1991)
- 13.346 P. Rudolph, T. Fukuda: Fiber crystal growth from the melt, *Cryst. Res. Technol.* **34**, 3–40 (1999)
- 13.347 R.S. Feigelson: Pulling optical fibers, *J. Cryst. Growth* **79**, 669–680 (1986)
- 13.348 R.S. Feigelson: Opportunities for research on single-crystal fibers, *Mater. Sci. Eng. B* **1**, 67–75 (1988)
- 13.349 C. Goutaudier, K. Lebbou, Y. Guyot, M. Ito, H. Canibano, A. El Hassouni, L. Laversenne, M.T. Cohen-Adad, G. Boulon: Advances in fibre crystals: Growth and optimization of spectroscopic properties for Yb^{3+} -doped laser crystals, *Ann. Chim.* **28**, 73–88 (2003)
- 13.350 R.S. Feigelson, W.L. Kway, R.K. Route: Single-crystal fibers by the laser-heated pedestal growth method, *Opt. Eng.* **24**, 1102–1107 (1985)
- 13.351 R.S. Feigelson, W.L. Kway, R.K. Route: Single-crystal fibers by the laser-heated pedestal growth method, *Proc. Soc. Photo-Opt. Instrum. Eng.* **484**, 133–141 (1984)
- 13.352 W.M. Yen: Synthesis, characterization, and applications of shaped single crystals, *Phys. Solid State* **41**, 693–696 (1999)
- 13.353 W.M. Yen: Rare earth ions as spectroscopic probes of dynamic properties of insulators, *J. Alloys Compd.* **193**, 175–179 (1993)
- 13.354 S.M. Jacobsen, B.M. Tissue, W.M. Yen: New methods for studying the optical-properties of metal-ions in solids, *J. Phys. Chem.* **96**, 1547–1553 (1992)
- 13.355 B.M. Tissue, L.Z. Lu, M. Li, W.Y. Jia, M.L. Norton, W.M. Yen: Laser-heated pedestal growth of laser and IR-upconverting materials, *J. Cryst. Growth* **109**, 323–328 (1991)
- 13.356 C.T. Yen, D.O. Nason, W.A. Tiller: On controlled solidification studies of some TiO_2 binary-alloys, *J. Mater. Res.* **7**, 980–991 (1992)
- 13.357 J. Baszynski, W. Kowalski, C.A. Cardoso, F.M. Araujo-Moreira, M.R.B. Andreeta, A.C. Hernandez: Current-induced conductance jumps in mechanically controllable junctions of $\text{La}_{0.7}\text{Sr}_{0.3}\text{MnO}_3$ manganites, *Czechoslov. J. Phys.* **54**, D39–D42 (2004)
- 13.358 R.C. Santana, M.C. Terrile, A.C. Hernandez, M.R.B. Andreeta, G.E. Barberis: Electron spin resonance study of Fe^{3+} in LiNbO_3 single crystals: Bulk and fibres, *Solid State Commun.* **103**, 61–64 (1997)
- 13.359 R.Y. Guo, P. Ravindranathan, U. Selvaraj, A.S. Bhalla, L.E. Cross, R. Roy: Modified mixed-oxide perovskites $0.7\text{Sr}(\text{Al}_{1/2}\text{B}_{1/2})\text{O}_3$ - 0.3LaAlO_3 and $0.7\text{Sr}(\text{Al}_{1/2}\text{B}_{1/2})\text{O}_3$ - 0.3NdGaO_3 ($\text{B} = \text{Ta}^{5+}$ or Nb^{5+}) for high T_c superconductor substrate applications, *J. Mater. Sci.* **29**, 5054–5058 (1994)
- 13.360 S.L. Fu, J.S. Jiang, J.Q. Chen, Z.C. Ding: The growth of single-crystal fibers directly from source rods made of ultrafine powders, *J. Mater. Sci.* **28**, 1659–1662 (1993)
- 13.361 G.W. Young, J.A. Heminger: Modeling the time-dependent growth of single-crystal fibers, *J. Cryst. Growth* **178**, 410–421 (1997)
- 13.362 M.J.P. Nijmeijer, D.P. Landau: Simulation of optical fiber growth in three dimensions, *Comput. Mater. Sci.* **7**, 325–335 (1997)
- 13.363 L.H. Wang, B.J. Tsay, M.H. Hon: A thermoelastic analysis in a semi-infinite cylindrical single crystal during laser-heated pedestal growth, *J. Chin. Inst. Eng.* **21**, 101–108 (1998)

13.364 C.H. Huang, J.C. Chen, C. Hu: YVO_4 single-crystal fiber growth by the LHPG method, *J. Cryst. Growth* **211**, 237–241 (2000)

13.365 K.A. Jackson, J.D. Hunt: Lamellar and rod eutectic growth, *Trans. Metall. Soc. AIME* **236**, 1129–1142 (1966)

Synthesis of

14. Synthesis of Refractory Materials by Skull Melting Technique

Vyacheslav V. Osiko, Mikhail A. Borik, Elena E. Lomonova

This chapter discusses methods of growing refractory oxide single crystals and synthesis of refractory glasses by skull melting technique in a cold crucible. It shows the advantages of radiofrequency (RF) heating of dielectric materials in a cold crucible and points out some specific problems regarding the process of growing crystals by directional crystallization from the melt and by pulling on a seed from the melt. The distinctive features of the method of directional crystallization from the melt are discussed in detail on the example of technology of materials based on zirconia, i. e., cubic single crystals and partly stabilized single crystals. It is shown that the size and quality of crystals are functions of the process conditions, such as thermal conditions under crystallization, growth rate, and chemical composition. We provide an overview of research on the structure, phase composition, and physicochemical properties of crystals based on zirconia. The optical, mechanical, and electric properties of these crystals make them suitable for a number of technical and industrial applications in optics, electronics, materials processing, and medicine. In this chapter, we also consider some problems regarding the synthesis of refractory glasses by skull melting technique. The physicochemical and optical properties of glasses are given and their practical applications in technology are discussed. We note that one of the better developed and most promising applications of skull melting technique is the immobilization of liquid and solid waste

14.1	Overview	433
14.2	Techniques for Growth of Single Crystals in a Cold Crucible	435
14.2.1	Directional Crystallization of the Melt	437
14.2.2	Crystal Growth by Pulling on a Seed from the Melt in a Cold Crucible	441
14.3	Growth of Single Crystals Based on Zirconium Dioxide	443
14.3.1	Crystal Structure of Zirconium Dioxide	445
14.3.2	Phase Diagrams of the ZrO_2 - Y_2O_3 System	445
14.3.3	Stabilization of Cubic and Tetragonal Structures in Zirconia-Based Materials.....	447
14.3.4	Cubic Zirconia Crystals (Fianits).....	448
14.3.5	Growth, Properties, and Application of PSZ Crystals.....	459
14.4	Glass Synthesis by Skull Melting in a Cold Crucible	465
14.4.1	Refractory Glasses of the R_2O_3 - Al_2O_3 - SiO_2 ($R = Y, La$, Rare-Earth Element) Systems.....	467
14.4.2	Immobilization of Radioactive Waste in Stable Solid Blocks	468
14.5	Conclusion	469
	References	469

(also radioactive waste) into solid-state materials by vitrification.

14.1 Overview

Refractory single crystals have a wide range of applications in modern technology. Successful development of fields and branches such as microelectronics, fiber

optics, laser techniques, metallurgy, and mechanical engineering would be impossible without elements based on refractory crystals and glasses as significant compo-

nents. In order to promote the development of refractory materials technology it is necessary to find solutions to a number of problems relating to obtaining materials of a required chemical composition with predetermined properties, including

- Development of crystal growth methods and material synthesis techniques at temperatures higher than 2000 °C
- Growing single crystals and casting glasses with perfect internal structure
- Obtaining ultrapure materials where the uncontrolled impurity content does not exceed 10^{-4} wt % and in some cases even 10^{-6} wt %
- Controlled synthesis of materials in oxidation–reduction gas environments
- High production efficiency with minimal harm to the environment

The main challenge is to provide a complex solution to these problems, i. e., in the ideal case the developed technology will meet all these requirements. It is our opinion that the technology surveyed in this chapter can provide a complex approach to the problems related to the production of refractory crystalline materials and glasses, even though it also has certain shortcomings. This technology is based on the skull melting (SM) method in a cold crucible (CC), which follows two main principles:

- Keeping the melt in a solid shell (skull) with a chemical composition identical to that of the melt
- An inductive (i. e., contact-free) method of heating the material

These principles were proposed by various scientists a rather long time ago; for instance, the method of melting metal in an arc furnace with a water-cooled metal plate has been known since 1905 [14.1]. Later on there appeared some work on the method of inductive melting of metals and semiconductors in a CC [14.2, 3]. In the 1960s French scientists published their research on the method of inductive melting in CC of specific refractory oxides (Al_2O_3 , ZrO_2 , Y_2O_3 , TiO_2 , and UO_2) and complex chemical compounds based on them [14.4–8]. After that a number of publications appeared on the inductive heating of glass in cooled quartz and ceramic crucibles for vitrification of radioactive waste [14.9], as well as on the synthesis of ultrapure glasses in cooled quartz crucibles for fiber-optic communication lines [14.10, 11]. At the same time, independent re-

search started at the Physical Institute of the USSR Academy of Sciences, aiming at developing technology for refractory materials production by the SM method. In the course of this research, appropriate equipment was designed and developed, conditions of melting and crystallization of various chemical compounds were systematically and thoroughly studied, and large-sized single crystals were grown from solid solutions based on zirconia and hafnia, as well as single crystals of rare-earth oxides, alumina, scandia, and yttria [14.12–15].

To date there have been quite a few publications discussing the modeling of inductive melting of dielectric materials in a CC. The basic properties of a thermal balance for so-called internal melting, which is very similar to SM, were discussed in [14.16, 17]. Some theoretical assumptions made in [14.16, 17] were applied to SM [14.18, 19], and this analytical model was used to account for quantitative description of losses in an RF coil and a crucible. The dependency between the form of a melted zone and the parameters of the system was calculated, a comparison with experimental data was made, and the stability of a melted zone was investigated [14.18, 19]; similar research is reported in [14.20–22]. The experience has shown that the new technology has a number of definite advantages and can successfully be used to synthesize refractory materials, including single-crystal growth. Some of these advantages are:

- There is no upper limit on the temperature (up to 3000 °C and higher).
- There is no contact with alien chemical substances and, therefore, the obtained materials are exceptionally pure. The purity of the resulting material can even exceed the purity of the original material in terms of some impurities (either volatile matters or those which are easily segregated during crystallization).
- The process can be carried out in any atmosphere, including an oxidizing one (air or oxygen).
- Any type of chemical reaction with the melt is possible, in both single-phase and multicomponent systems.
- Melting process can be interrupted or carried out continuously, without any restrictions on the melt volume.
- There are no specific requirements on grain-size composition of the initial materials.
- It is a waste-free technology, since the crystalline scrap from previous melting processes and other waste can be remelted.

- It becomes possible to obtain a large volume of melt, which facilitates convective mass and impurities transport and leads to better-quality single crystals.
- The melt composition can be changed during synthesis by adding different components to the melt via its open surface.

The most striking result of the developed **SM** technology is the industrial technology of growth and production of crystals based on zirconia. This is the only existing method for zirconia crystal production for

industrial purposes. Each month several hundred tons of crystals are manufactured, with production concentrated mostly in the USA, China, South Korea, Russia, and Taiwan. More than 90% of grown crystals are used in jewelry and the rest is used in some technical applications. In this chapter we give an overview of experimental and theoretical research on **SM** in a **CC** and the results of this research, with special attention paid to the technology of zirconia-based single-crystal growth and the application of this method to glass synthesis.

14.2 Techniques for Growth of Single Crystals in a Cold Crucible

The development of the **SM** technique of nonmetal materials in a **CC** promoted progress in the field of technology of refractory materials, in particular single crystals. As has already been mentioned, the technique allows the melt to be held at very high temperature (up to 3000 °C or higher) to keep it in a stable state for crystallization under controlled conditions. During the last 40 years of the development of this technique a large variety of single crystals of refractory oxides and compounds have been grown, their properties have been

investigated, and some industrial technologies and special equipment have been developed. The procedure of **SM** and crystallization from the melt under direct radiofrequency (**RF**) heating has been described in many studies [14.15, 23–25] and consists of several steps: (1) start melting, (2) formation of the main volume of the melt, (3) setting the melt–solid shell system in equilibrium (homogenization), and (4) crystallization of the melt (Fig. 14.1).

The necessity for start heating of dielectric materials and its practical implementation are discussed in detail in [14.25, 26]. Normally the metal used to initiate the start heating is the same as in the initial oxide charge. The metal and the surrounding charge are heated by the absorption of **RF** energy and the exothermic oxidation of the metal. In each particular case, the exact contribution of each process depends on the physicochemical properties of the metal used. Moreover, the process is affected by the conditions under which the start melting is carried out, i. e., the composition of the gas atmosphere, the position of the seed metal in the charge, the amount of seed metal, the particle size of the initial charge powder, etc. The time of start melting is largely determined by these factors. Graphite is rather frequently used in start melting because it completely oxidizes in air without any contamination of the melt. Being economical, this technique is very often employed in industrial production of many refractory materials and crystals. As a rule, bar-shaped graphite pieces are linked to obtain a ring with diameter smaller than that of the **CC**. Graphite is also used for melting complex oxide compounds and glasses, when it is sometimes positioned in the refractory ampoule, made of, for example, quartz, in the form of a heating rod. The rod is inserted into the center of the crucible filled with the

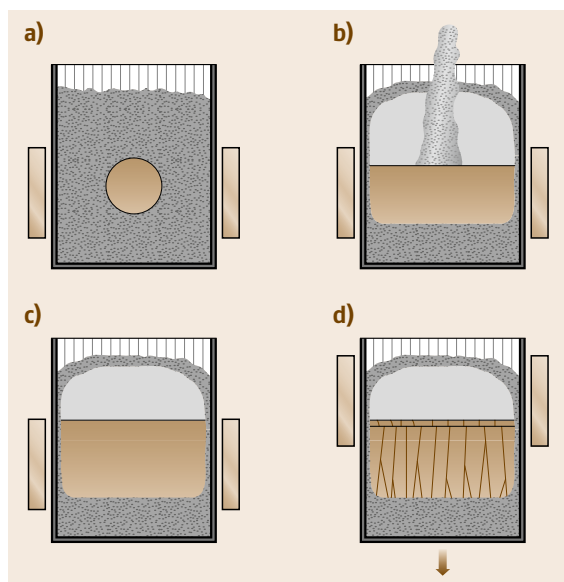


Fig. 14.1a–d Main stages of crystal growth technology in a cold crucible: (a) start melting, (b) formation of the main volume of the melt, (c) homogenization, and (d) crystallization

initial powder charge. As the initial volume of the melt increases in the crucible, the rod is drawn out by means of various tools.

After start melting is complete, the melt volume should be increased gradually by the melting of ambient solid phase of the charge. The charge is usually composed of either oxide powders or their mixture with previously melted material. The melt volume increases until the charge in a CC is melted completely except for a thin layer of powder adjusting to the walls of the CC. This layer with a thin layer of crystallized melt together forms a polycrystalline solid (shell) or skull. Additional portions of the charge can be gradually poured into the melt until the desired volume of melt is reached. The use of either previously melted or preliminary compacted materials allows the desired volume of the melt to be achieved without additional pouring. In this case all the material is charged into the CC at once and the start melting occurs in the upper part of the charge, while the charged crucible is set at its lowest position. As the melt forms, the crucible is moved upwards to melt the whole charge, until the highest position is reached. This technique is less laborious but more time consuming and, thus, is less economical with respect to energy consumption.

When the volume of the melt reaches the desired value, the melt is exposed for a certain time under a constant energy input in order to achieve thermal and spatial equilibrium between the melt and the skull. The principal feature of the resulting stationary state of the system is a constant volume of the melt, i. e., the immobility of the melt–solid phase (skull) interface. The conditions of the phase equilibrium are discussed in [14.12]. Despite some rough approximations made in the analysis, it provides a simple and clear evaluation of the peculiarities of the phase equilibrium in the melt–solid system in a CC (Fig. 14.2). The following approximations are made in the analysis:

1. The temperature of the melt is equal over the volume, except for a thin layer adjacent to the skull (assuming complete stirring of the melt).
2. The temperature (T_L) at any point of the melt–solid interface is equal to the melting point and does not change.
3. The RF field energy is absorbed by the melt only and the field is uniform inside the inductor.

The amount of heat given off by the melt to the surface of the solid phase (Q_1) can be expressed as $Q_1 = \alpha(T_M - T_L)F\tau$, where α is the heat emission co-

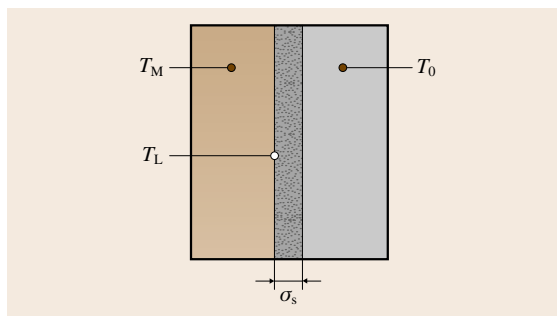


Fig. 14.2 Illustration of melt–solid equilibrium in a cold crucible

efficient, T_M is the temperature of the melt, T_L is the temperature at the solid–liquid interface (which equals the melting point), F is the heat-emitting surface, and τ is time. The amount of heat transported through a solid layer of thickness σ_s and thermal conductivity λ can be expressed by $Q_2 = \lambda/\sigma_s(T_L - T_0)F\tau$, where T_0 is the heat carrier temperature. For stationary conditions $Q_1 = Q_2$, i. e., $(\lambda/\sigma_s)\alpha = (T_M - T_L)/(T_L - T_0)$, where $(T_M - T_L) = \Delta T$ is the parameter characterizing the overheating of the melt. If we assume λ , α , and T_0 to be independent of σ_s , then $\sigma_s \Delta T = \text{const}$.

The above analysis leads to the following conclusions:

- An essential feature of the skull melting technique is the necessary overheating of the melt ΔT , the value of which greatly affects the process of crystal growth in a CC (if $\Delta T \rightarrow 0$, then $\sigma_s \rightarrow \infty$).
- There is always a solid skull in a CC because complete melting of the solid phase requires infinite overheating (if $\sigma_s \rightarrow 0$, then $\Delta T \rightarrow \infty$).
- Increasing or decreasing the melt temperature (T_M) changing the skull thickness σ_s .
- Convection of the melt determines the value of the heat emission coefficient α , thus affecting the phase equilibrium.
- Any process in the skull resulting in a change of its thermal conductivity (e.g., sintering or fusion penetration) will disturb the phase equilibrium and therefore cause variation in either the melt temperature (T_M) or the skull thickness (σ_s).

After the thermal equilibrium in a CC has been established, crystallization of the melt takes place. The crystallization can be carried out by various techniques. For producing molten polycrystalline materials a fast mass crystallization is quite suitable. Single-crystal

growth is performed either by means of a directional crystallization, which is similar to the Bridgman–Stockbarger technique, or by pulling a seed similarly to in the Czochralski or Kyropoulos growth techniques. Applications of the other methods of single-crystal growth (e.g., crystallization from the flux solution or Stepanov technique) are also possible. The majority of single crystals are produced by either directional crystallization or by pulling a seed from the melt in a CC.

14.2.1 Directional Crystallization of the Melt

Most single crystals grown from a CC are produced by means of directional crystallization of the melt. The choice of this technique is motivated by its relative technical simplicity, which does not require any additional heat sources or complicated design of the thermal unit. Directional crystallization is usually carried out by lowering the crucible containing the melt out of the induction coil at a certain rate. Electromagnetic interaction between the lower part of the charge and the induction coil decreases as this part moves away from the inductor, so the released power also decreases. Gradual cooling then results in the crystallization of the melt at the bottom of the crucible. When using large-volume CCs, it is more convenient to conduct directional crystallization by moving the induction coil upwards, the container being fixed; this prevents technical problems associated with the design of the drive assembly for the heavy (> 1000 kg) charged crucible, and should ensure reliable operation and uniform crystallization rate in order to grow good-quality crystals.

Less frequently, crystallization is conducted by gradual reduction of the power. This procedure is less reliable, as it may lead to spatial instability and uncontrollable solidification of the melt [14.15–18]. Therefore, it is suitable only for crystallization of high-stability melts. The melt stability depends on the electrical and thermophysical properties of the material. Thus, to ensure a reliable and economical process, it is desirable to use melts which have sufficiently high electrical conductivity over a wide range of temperatures and with low thermal conductivity of the solid phase. The feasibility of SM for crystal growth also depends on a number of physicochemical properties of the material used. High evaporation rates of melt components may reduce the volume of the melt, causing the system to become unstable or resulting in uncontrolled crystallization of the melt. However, more frequently, volatility of a certain component causes a deviation

from stoichiometry of the grown crystals. If this is the case, it is necessary either to correct the melt composition during growth or to use ambient atmospheres that prevent this deviation.

A CC usually consists of isolated sections and has gaps, so in the case of melt penetration, the melt can leak out, which can disturb the crystallization process. Leakage is prevented by the surface tension of the melt, which is determined by the surface tension coefficient, the size of gaps between the sections of the crucible, and the wettability of the wall. Therefore, it is easier to work with melts, possessing high surface tension. For single-crystal growth, direct crystallization in a CC has a number of advantages compared with other well-known crucible-less techniques (e.g., Verneuil or floating-zone technique); for instance, this method allows a considerable volume of the melt to be created, which promotes convective transfer of the main constituents and impurities and provides better quality of crystals. In addition, this method can be used to grow crystals in any atmosphere. The open surface of the melt makes it possible to vary the melt composition by adding various components and facilitates purification of the melt of volatile impurities and gases. However, single-crystal growth by directional crystallization in a CC faces some general difficulties, mainly associated with peculiarities of the direct RF heating of dielectric materials. With this method of heating the melt itself, being a transient power load in the oscillatory circuit of the RF generator, is a heat-absorbing body. The interaction between the load (melt) and the generator is rather complicated. Melting and crystallization occurring in the skull result in changes of the volume and electrical conductivity of the melt, which affect operation. This is problematic for rigorous control of the input power required to sustain the stability of crystallization. On the one hand, if the input power drops below a certain critical point, this may lead to loss of coupling between the melt and the RF field and, consequently, spontaneous crystallization. On the other hand, if the melt is overheated (i. e., excess input power), this results in melt penetration through the skull, leakage of the melt through the gaps between the CC sections, and disruption of the stability of crystallization (up to complete interruption of the process). Another control problem relates to the absence of visual monitoring of the process and direct measurements of the temperature of the melt and crystals during the growth. The high melting temperatures of the materials usually processed by this technique (such as zirconia, with a melting point of $\approx 3000^\circ\text{C}$) and the presence of the RF field hinder

any temperature measurements, except irradiative ones. Only the melt surface lends itself to direct observations and measurements, when the upper thermal screen (or core) is removed.

Just after the crystallization has been completed, annealing of the crystals is carried out directly in the growth furnace. Annealing is an important stage of the process, necessary to relieve any residual stress in order to prevent fracturing of the crystals. In a conventional growth furnace, there is usually a zone with a certain temperature gradient, where the crystals can slowly cool to the ambient temperature. This, however, becomes impossible when using direct RF heating for crystal growth because the electric conductivity of materials sharply decreases in the process of crystallization. The absorption of the RF field power decreases too, which results in uncontrollable cooling of grown crystals. The cooling rate depends on the volume of the crystallized material (i. e., its thermal inertia). Given that crystals are placed in a water-cooled crucible, the cooling rate of the crystal in zones adjacent to the wall is significantly higher.

The method of directional solidification in a CC essentially differs from the conventional *hot* techniques of crystal growth, e.g., the Bridgman–Stockbarger method, in which nucleation occurs only at the interface between the crystal and a considerable volume of the melt, followed by directional crystallization over a temperature gradient field. In these furnaces a certain gradient of temperature is created and maintained during the growth. The growth usually starts with complete melting of the charge in a crucible, and then, at the stage of initial nucleation, several crystals are formed. Further growth of one of the nuclei at the *crystal–melt* interface

is performed by various techniques: a conical bottom, a capillary or constrictions on the bottom, and seeding. The task of growing large and good-quality crystals by this method is solved empirically by appropriate selection of crucible shape, temperature gradients, and the rates of lowering the crucible or cooling of the furnace. In directional crystallization in a CC the melt is in permanent contact with the skull of the same composition formed on the bottom and walls of the crucible. Therefore, polynuclear crystallization takes place. Crystallization begins in the lower part of the crucible from the crystal grains of the skull. As crystallization proceeds, the number of crystals is reduced considerably due to selection according to growth rate. As a result, a bulk of column-shaped single crystals is obtained. It is impossible to use any device to limit the quantity of crystals growing from the bottom and the walls of the crucible because of the very high temperatures and RF field. In general, seed crystals allow to increase the size and decrease the amount of growing crystals, but in practice this is rather problematic. Therefore, the quantity and size of the crystals are determined by the composition of the melt and the growth process conditions.

The peculiar distribution of temperature fields inside a CC is another important feature of the method. On the one hand, the distribution is determined by the RF field energy release in the melt, which depends on the melt properties at a current temperature, and on the other, by heat removal through the walls and bottom of the crucible maintained by the heat carrier (water). Growing good-quality crystals is determined by proper control of the temperature and temperature gradients in the melt and solid phase. Therefore, the distribution of temperature fields in a CC is extremely important. The patterns of temperature distribution both at the surface and inside the oxide melt under direct RF heating, as well as a number of technological conditions influencing these patterns, have been studied [14.27] using glass-forming melts in the temperature range 1000–1500 °C as a model system. The temperature distribution was shown to be determined by both the process parameters (absorbed RF power, position of a CC with respect to the induction coil, and the size and shape of a crucible) and the properties of the melt (temperature dependencies of the viscosity and electric conductivity). Typical temperature distribution patterns in the glass-forming melt under direct RF heating in a CC are presented in Fig. 14.3 for various viscosities. As this figure shows, a decrease in melt viscosity (most of non-glass-forming oxides) results in a signifi-

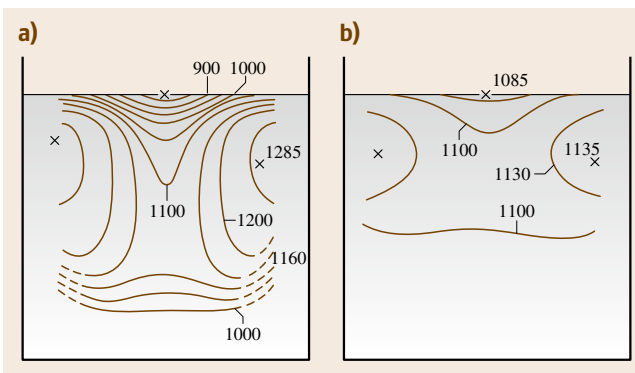


Fig. 14.3a,b Temperature distributions (°C) in oxide melts with different viscosities: (a) 45.6Na₂O + 54.4SiO₂; (b) 55.4Na₂O + 44.6SiO₂

cant decrease of the temperature gradients in the melt, the general pattern of temperature distribution being the same.

A simplified model can help explain the temperature distribution patterns under direct RF heating. Most of the RF energy is released in a certain active layer of the melt, the thickness of which depends on the RF generator frequency and the electric conductivity of the melt, whereas the rest of the melt is heated by conduction of heat from this part. This type of heating can be roughly compared to the one produced by a virtual heat source in the form of a hollow cylinder placed into the melt. The height and diameter of the source are determined by the induction coil height and RF field penetration depth (the thickness of the active layer), respectively. It is clear that, in this model, the radial temperature gradients will be determined by the diameter of the CC and by the input power, and the axial ones by the position of the melt with respect to the induction coil and the heat losses.

For the directional crystallization method of crystal growth, the temperature distribution in the lower part of the melt controlling the crystallization front is of primary importance, but there are no data available for refractory materials. Nevertheless, even on the basis of a model, some conclusions could be made, which were later confirmed in practice. Thus, the maximum temperature is achieved at the level corresponding to the center of the RF coil, while in the upper and lower parts of the melt the temperature is lower due to the heat sink through the lower part of a crucible and heat losses from the surface of the melt. The ratio of heat flows removed from the top and bottom of the crucible determines the position of the maximum temperature zone, related to the melt depth and the values of the axial gradients. At the same time, the axial gradients are higher in the area that corresponds to the RF field energy release (i. e., at the periphery) than in the central zone. Such a temperature distribution results in an increase of temperature in the melt layer above the crystal bulk growing from the bottom with increasing height. Consequently, thermal convection in the melt is hindered. The effect of electrodynamic stirring depends on the applied RF field frequency and is negligible for frequencies of 0.5–10 MHz [14.26]. The most intensive convective stirring occurs in the upper part of the melt. Radial temperature gradients in the heating zone suppress growth of crystals from the walls of a CC into the melt. However, if the melt is overheated, the crystallization front becomes concave and shifts below the heating zone (i. e., lower than the RF coil). This is associated with in-

tense growth of crystals adjacent the skull and leads to an increase in the total number of the crystals, although the crystals become smaller. In order to suppress this growth, it is desirable to reduce overheating to a minimum and to maintain the heat sink from the bottom so that the crystallization front is either in the active heating zone or as close to it as possible. This is favorable for decreasing the total number of nucleating crystals and improving the quality of single crystals [14.28–31], because it brings the crystallization front near to the zone of intense convective stirring.

The following question thus arises: how to control the temperature distribution in the melt. First, this can be done by changing the pattern of energy absorption in the melt, which is largely determined by the value of the resistivity of the melt, its temperature dependency, and the RF field frequency. The former two parameters are properties of the material itself and so are predefined. The optimal electromagnetic field frequency is also predetermined by the electric properties of the material; it can be varied within a narrow range, but these variations do not significantly affect the temperature fields in the melt. For example, if the resistivity of the melt is $0.1 \Omega \text{ cm}$ then frequency variation from 5 to 1 MHz results in changing of the penetration depth from ≈ 0.7 to $\approx 1.6 \text{ cm}$. Even for small crucibles (e.g., 10 cm in diameter) this change could not significantly influence the values of temperature gradients. It is also possible to change the electromagnetic field configuration by changing the RF coil design, insertion of additional short-circuited turns, magnetic enhancers, etc. [14.25, 26, 31].

In our opinion, the simplest and most efficient way to control temperature gradients in the melt is to use those means that involve heat removal from the melt through the walls and the bottom of the crucible, as well as from the melt surface. To control heat removal through the walls of a cold crucible and from the melt surface heat shields are used. In order to keep the crucible bottom warmer, a part of the charge at the bottom is not subjected to melting at the stage of formation of the main volume of melt. This part is located below the heating zone and has the same composition as the main charge. This thermal shield decreases heat loss through the crucible bottom, balances the radial temperature gradients in the melt, reduces axial gradients in a growing crystal, decreases electromagnetic losses related to the absorption of energy by a massive metal bottom at start melting, and affects nucleation and degeneration of crystals in polynuclear crystallization. Low axial gradients and uniform thermal properties at

the melt–solid interface help to decrease the number of nucleated crystals and to increase the size of individual single crystals.

The upper thermal shields are formed when the melt volume formation is nearly completed. Thermal radiation from the melt surface at high temperatures has high intensity, which leads to fast sintering of the powder charge above the melt. This sintered layer (crust) functions as an upper thermal shield. Such insulating layers of sintered material with composition identical to the melt readily occur in small-diameter cold crucibles. It is much more difficult to form the upper thermal shield in crucibles with larger diameters, although the role of such a shield becomes more important for crystal growth in large-diameter crucibles because the upper thermal shield decreases heat losses associated with radiation, increases the surface temperature, and consequently reduces the probability of spontaneous crystallization in the upper part of the melt, which is frequently the case in refractory melts. Reducing the heat losses results in better performance by decreasing the electricity cost, which is of primary importance for high-capacity installations. Surface heating (skin effect) and high temperature gradients in **SM** require special technological procedures for balancing thermal fields in the melt in order to achieve uniform melting and stable crystal growth over the whole diameter of the crucible. If the input power is insufficient and efficient upper thermal shielding is absent, the central part of the melt becomes overcooled, which results in the formation of small and imperfect crystals in this area. In the worst case, the material in the central part of a crucible remains unmelted or crystallizes rapidly.

In the absence of shielding, low radial and high axial temperature gradients in the melt and in growing crystals lead to the formation of many small crystals, whereas large-sized single crystals are desirable. It is possible to control the ratio between axial and radial gradients by applying thermal shielding in the top and bottom parts of the melt, thus optimizing the gradients for growing large-sized single crystals. Appropriate selection of the thermal conditions is usually carried out experimentally because of the difficulties in regulating melting and crystallization in this method. Moreover, thermal shields help to increase the mass of the charge in a cold crucible, and, consequently, to slow down the cooling of the crystals after growth to prevent fracturing in large crystal bulks. The shape of a **CC** influences the temperature distribution inside a crucible, and hence the thermal conditions of crystal growth. If the crucible diameter is increased while the penetration depth and

input power are kept constant, then the radial gradients are reduced, leading to the formation of a convex or flat crystallization front. With constant heating parameters (frequency and power) and physical properties of the melt (electric conductivity and viscosity), changing the crucible diameter-to-height ratio affects heat removal from the growing crystals. The ratio of the melt volume to the square of the cooling surface decreases with increasing **CC** diameter. This reduces energy loss through the walls of a crucible and makes the process more economical. Heat removal from the growing crystals at the bottom mainly occurs through the bottom and side (lateral) walls in the lower part of the charge below the active heating zone. Therefore, the amount of heat removed from the growing crystals is reduced with the increase of crucible diameter for the same reasons: given that the height of this part remains the same, the larger the crucible diameter, the less cooling surface (through which the heat transfers from growing crystals) there is for a unit volume of solid phase.

Thus, there are two important factors for growing crystals from the melt in a **CC**: first, the power released in the melt should be accurately determined and correlated with the volume of the melt, and second, there is a need for proper control of the heat removal through the bottom of the **CC** and via the surface of the melt. Optimizing these parameters allows the shape of the crystallization front and its position with respect to the active heating zone to be varied. Unfortunately, as mentioned above, some of the processing parameters in a **CC**, such as the temperatures in the melt and in the solid phase, the melt volume, and the crystallization rate, are extremely difficult to control. These parameters can only be assessed by the final results of the crystallization after the process has been completed. Some attempts have been made to develop techniques that can provide indirect but reliable data on the melting directly in the course of the process. Continuous monitoring of the **RF** generator parameters combined with analysis of the generator loading status enables an elucidation of the mechanisms occurring in a **CC** [14.32–36].

To date a considerable variety of single crystals of simple and complex oxides and oxide solid solutions have been grown by directional crystallization. The conditions of crystallization and the dimensions of the crystals grown by this method are reviewed in [14.23]. It has been shown that the oxides of transition metals have the necessary electrical and thermophysical properties at high temperatures, which makes them suitable for **RF** heating, melting, maintaining in the molten state, and

further crystallization in a CC. CoO, Fe₃O₄, and TiO₂ single crystals up to 1–3 cm³ have been grown [14.37]. The scope of the technique has been demonstrated by magnetite single-crystal growth [14.38], before which good-quality magnetite (Fe₃O₄) single crystals were grown in platinum crucibles by the Bridgman technique. However, this approach was expensive since, following growth, the crucibles were cut to release the crystal, and, moreover, the crucibles were destroyed because of the diffusion of iron into the platinum. Thus, SM has obvious advantages in this case. In order to maintain the oxygen stoichiometry of magnetite it is crucial to create an atmosphere with a certain oxygen activity and to keep it under control. To solve this problem, the process was carried out in a CO/CO₂ buffered atmosphere with a fixed fugacity of O₂. The growth process consisted of two stages. In the first stage the charge is melted in air up to a desirable volume, and in the second stage the chamber is evacuated to allow the gas mixture to flow through it. The melt was kept in this atmosphere for 1.5 h to achieve equilibrium conditions, and then the crucible was lowered. A drop in the growth rate to 7.5 mm/h was mentioned to be necessary to attain the equilibrium between the melt and the gas phase and to grow larger crystals. Similar conditions were required to grow monoxides of some transition metals (Mn_{1-x}O, Co_{1-x}O, Fe_{1-x}O, and Ni_{1-x}O) with interesting electrical, optical, and magnetic properties, which can vary with the oxygen stoichiometry. The equipment used for growth in a CC was the same as in the previous case. After studying the effects of atmosphere on the phase composition of single crystals of transition-metal monoxides it was established that the excess of oxygen in the Fe_{1-x}O melt led to the formation of Fe₃O₄ inclusions, whereas metallic inclusions M⁰ occurred under a relatively reducing atmosphere. The importance of crystal annealing at subsolidus temperatures, which improves homogeneity of the crystals and completely eliminates the magnetite phase, was also demonstrated in these studies. With an adequate buffer oxygen atmosphere 1 cm-long (Fe₃O₄)_{1-x}(FeTiO₄)_x single crystals were grown. The atmosphere was controlled throughout the process, including the melting stage. Studies on the phase composition of grown crystals proved this method to be applicable to the growth of ferrite crystals of any composition. The same facilities and technology were also used to grow Ln₂NiO₄ (Ln = La, Pr) single crystals. Later on, single crystals of high-temperature superconductors [14.20, 39], several complex oxides (e.g., CeO₂-Y₂O₃) [14.40], oxide eutectics [14.41], and

other oxide compounds and compositions were synthesized and studied [14.42].

14.2.2 Crystal Growth by Pulling on a Seed from the Melt in a Cold Crucible

The method of crystal growth by pulling on a seed from the melt (Czochralski technique) in a hot crucible has been widely and successfully used for a variety of oxide crystals. Its application is conditioned by a strictly defined temperature distribution in the melt and at the crystallization front, as well as by a constant temperature at the crystallization front. The process of crystal growth by SM is of a great interest but it is associated with the some principal difficulties discussed above. The temperature distribution in the surface area of the melt is of primary importance for crystal growth by pulling on a seed. The isotherm patterns (Fig. 14.3) show the temperature distribution in the melt. Temperature gradients in the melt can be changed by varying the position of the RF coil with respect to the melt surface or by adjusting the input power. There are various additional factors affecting the formation of temperature gradients in the melt, such as optimizing the shape and the dimensions of a crucible, setting the optimal frequency, using thermal shields or additional heat sources, RF coil design, and some other parameters.

Let us now consider some practical applications of single-crystal growth by pulling on a seed from a CC. The synthesis of corundum and ruby single crystals was the first important scientific and practical result using this technique [14.12, 31, 43]. One of the conditions required for single-crystal growth by pulling on a seed was established to be the following: the specific heat flow from the melt though a crystal has to exceed the specific heat losses from the open surface of the melt. Thermal shields above the melt were used to decrease the heat losses associated with radiation. Besides, a cup-shaped crucible and RF coil were used to improve phase stability and to prevent crystal growth from the skull at the crucible surface caused by changing the input power (Fig. 14.4) [14.31]. The technique was used to grow ruby and corundum single crystals of various orientations, up to 160 mm in length and up to 35 mm in diameter. The pulling rate was in the range of 10–30 mm/h with seed rotation speed of 20–140 rpm.

The method of forming temperature gradients at the melt surface by means of thermal shielding was also applied for growing SrTiO₃ [14.44, 45] and Bi₁₂GeO₂₀ [14.46] single crystals. The Bi₁₂GeO₂₀ crystals were grown in a tubular crucible of 90 mm

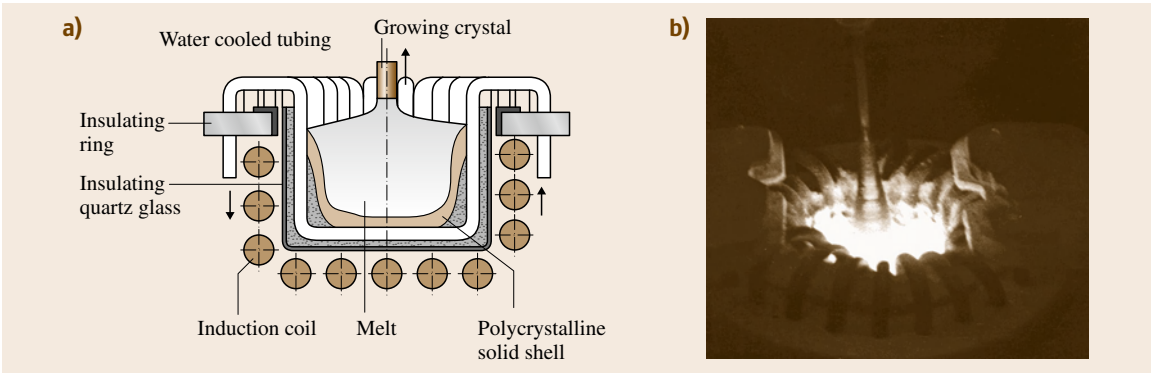


Fig. 14.4a,b Schematic of the unit for growing Al_2O_3 crystals from cup-shaped cold crucible (a) and photograph of growing crystal (b)

diameter and 60 mm height. The scheme of the heating unit for crystal growth is shown in Fig. 14.5.

The thermal and electrophysical properties of the melt allowed for adjusting the temperature by varying the input power over a wide range of values, while keeping the phase stability undisturbed. The consistency of input power supply was ensured by anode current stabilization. Convectional flows were observed on the melt surface. The intensity of the flows decreased when the input power was decreased, the convection pattern on the surface became regular, and the flows were oriented from the periphery to the center. Thermal shields provided more stable convection patterns, which made the intensity of the flows decrease. Figure 14.6 illustrates the temperature distribution on the melt surface measured by a pyrometer according to the observed convective flow pattern.

The grown crystals were up to 15 mm in cross-section and up to 100 mm in length (Fig. 14.7).

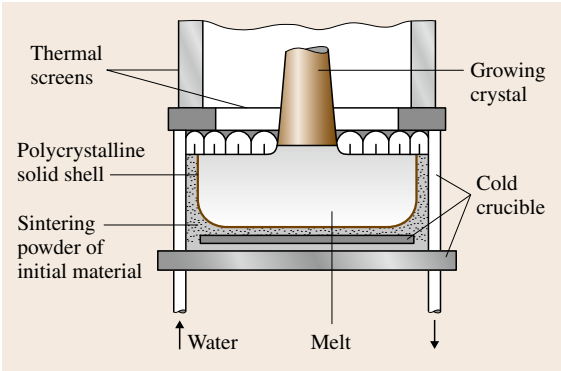


Fig. 14.5 Schematic of the unit for growing $\text{Bi}_{12}\text{GeO}_{20}$ crystals

In some cases the crystals were faceted while being grown, although crystal edge outlets of the fourth-order symmetry at the crystal surface were more frequently

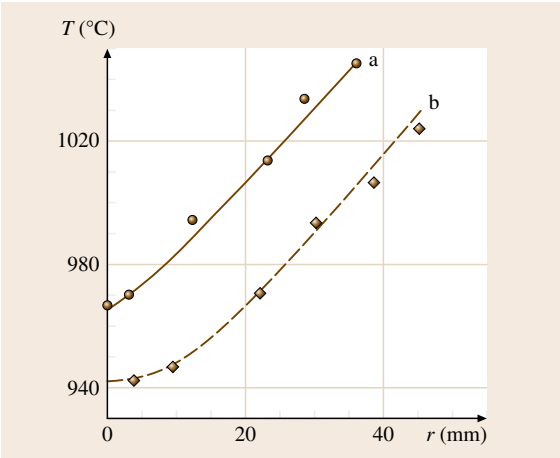


Fig. 14.6 Temperature distribution on the surface of the melt for input power of (a) 2.90 kW and (b) 2.50 kW

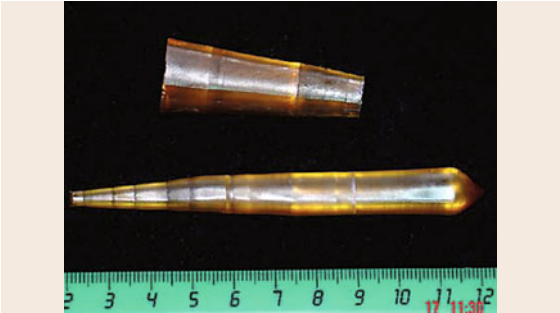


Fig. 14.7 $\text{Bi}_{12}\text{GeO}_{20}$ crystals

Table 14.1 Concentration of copper in Bi₁₂GeO₂₀ crystals grown in a copper water-cooled crucible

Material	Concentration of Cu, wt%
Initial charge	$1 \times 10^{-2} \pm 5 \times 10^{-4}$
Skull	$9.3 \times 10^{-2} \pm 1.6 \times 10^{-2}$
Crystal top	$1 \times 10^{-1} \pm 2 \times 10^{-2}$
Crystal center	$7.5 \times 10^{-2} \pm 1.3 \times 10^{-2}$
Crystal bottom	$1.4 \times 10^{-2} \pm 2.5 \times 10^{-3}$

observed. Bi₁₂GeO₂₀ crystal grown in platinum crucibles is associated with the occurrence of platinum macroinclusions up to 0.5 mm. These inclusions are due to the chemical activity of the melt, which destroys the crucible surface, and to the metal particles becoming entrapped by a growing crystal. If a CC is used, this problem does not arise. However, X-ray spectral analysis revealed the presence of Cu (the material of a cold crucible) in crystals (Table 14.1). The measured concentration of Cu in the skull and in crystals was somewhat higher than in the initial charge and this was shown to be dependent on a number of technological parameters, such as overheating of the melt during start melting and during crystal detachment, the number of remeltings of the crystallized melt (the recycling factor), and the duration of growth. The presence of Cu did not result in inclusion formation and did not distort the optical homogeneity of crystals. A study of the optical properties of crystals revealed no influence of small copper impurities on the main properties of the material.

Another method for temperature fields formation in the melt was proposed in [14.47] for Nd₃Ga₅O₁₂ crystal growth. The growth was associated with significant turbulent convection on the melt surface. To suppress the convection and maintain the necessary radial temperature gradient, a *double-crucible* technique was applied, which consists of the insertion of a split iridium cru-

cible into the melt. On the bottom of the CC there was an iridium ring, which was heated by an additional RF coil. The ring was used to produce a start melt and as an additional heating source to ensure a constant volume of melt during growth. The technique allowed Nd₃Ga₅O₁₂ crystals of 35 mm cross-section and 90 mm length to be grown, the quality of which was comparable to that of crystals grown from heated crucibles by Czochralski technique.

An interesting development of the SM technique is presented in [14.48], which proposes to combine direct RF melting with radiative heating of the melt surface. Start melting is carried out by means of three powerful optic concentrators with xenon arc lamps used as light sources. The CC can be moved vertically or rotated. The radiation from these three light sources makes it possible to control the thermal field pattern in the melt by changing the position of the focal spot with respect to the axis of the crucible rotation and by adjusting the radiative power. There are alumina thermal shields and a platinum electric resistance furnace above the melt, which help to decrease the temperature gradients in the pulled crystal and the performance of subsequent annealing. Radiative heating sources in this model allow to form certain thermal patterns in the melt at a certain radiative-to-RF heating power ratio, which facilitates crystal growth by pulling on a seed. The technique was applied to grow MnZnFe₂O₄ crystals. The SM method for crystal growth is very promising, primarily for the synthesis of new refractory compounds (in the form of crystals) from the melt. However, the analysis of thermal fluxes in the melt and the development of methods to monitor and control the process to achieve a certain thermal field configuration remain the most complicated problems in this growth technique. This might be the reason why there are so few publications devoted to crystal growth by pulling on a seed from a CC.

14.3 Growth of Single Crystals Based on Zirconium Dioxide

Crystals of pure ZrO₂ are used very rarely because of destructive phase transformations. However, it was shown [14.49] that stabilizing the cubic phase by adding MgO, CaO, Sc₂O₃, Y₂O₃ or CeO₂ could prevent these phase transformations. In this case a metastable cubic solid solution with fluorite structure is formed at room temperature.

The high melting point (2700–2800 °C), the high chemical activity of the melt, and the occurrence

of polymorphic transformations made the growth of ZrO₂-based single crystals very difficult. That is why single crystals of pure ZrO₂ were obtained by low-temperature techniques such as flux growth, vapor deposition or hydrothermal method [14.50–54]. These processes are of a very long duration, while the size of the crystals obtained is rather small. Single crystals of solid solutions based on ZrO₂ were grown from the melt by crucible-free techniques (arc and floating-zone

melting) [14.55–59]. However, large-scale industrial production of ZrO_2 -based single crystals became possible only when the above-described SM method was applied. During the development of the method and its application for single-crystal growth, the first publications on the synthesis of ZrO_2 -based single crystals appeared [14.7, 12, 31, 60–62].

Research on some properties of single crystals of cubic solid solutions based on ZrO_2 (CZ) showed that these crystals possess unique optical, mechanical, and electrical characteristics, namely, they are optically isotropic, have high refraction index $n_d = 2.15 - 2.2$, and are transparent in the range 260–7500 nm; these crystals are very hard (8.5 by Moos), have a high melting point (2700–2800 °C), and demonstrate ionic conductivity at temperatures above 300 °C [14.13, 15, 31]. This combination of properties makes CZ crystals promising materials for many technical and industrial applications, including optical, electronic, instrument-making, and high-temperature techniques.

The first practical application of CZ crystals was in jewelry. The similarity of CZ's refractivity index to that of diamond and its high dispersion cause a special play of light under various lighting conditions. These properties make CZ crystals one of the best materials for the imitation of diamond. The possibility of crystal growth of various colors enables the imitation of other natural gemstones, as well as the creation of new gemstones of original colors. Development of the industrial technology, the creation of the first apparatus for crystal production, and the production of the first crystals were accomplished in the Physical Institute of the Academy of Sciences of the USSR (FIAN) as early as the beginning of the 1970s. Exactly this application gave great impetus to the setting up of the industrial production of these crystals and the creation of new equipment for RF heating. Industrial technology for the production of CZ crystals was first elaborated in Russia in FIAN. Mass production of these crystals, which were given the name *fianites*, was already organized at the beginning of the 1970s. In most countries these crystals are known as *cubic zirconia*. World production of CZ crystals for jewelry is inferior only to that of silicon and synthetic quartz crystals, thus occupying the third place.

The following problems remain topical in the modern technology of CZ crystals:

- Enlarging of the color range
- Increasing the size of crystals
- Increasing the optical perfection and uniformity of crystals for technical applications

A little later, in the middle of the 1970s, interest towards high-strength and high-viscosity materials based on ZrO_2 arose. One such material is partly stabilized zirconium dioxide (PSZ) – a solid solution of yttrium oxide or other rare-earth or alkaline-earth oxides in ZrO_2 . In 1975 the attention of researchers was concentrated on the creation of two-phase materials characterized by high destruction viscosity due to inherent phase transitions similar to martensitic transformations in steel. Thus, Harvey [14.63] obtained and extensively studied a material based on ZrO_2 partially stabilized by CaO. The new material was named *ceramic steel*. Ceramics of even higher characteristics were obtained when Y_2O_3 was used as a stabilizer and the tetragonal phase (TZP) was synthesized [14.64, 65]. The transformational mechanism of hardening was proposed in [14.66]. These results gave great impetus to the development of fundamental research on ZrO_2 -based material and studies on its synthesis and applications. An up-to-date review on the transformational mechanism of hardening of constructional ceramics is given in [14.67], where the theoretical aspects of transformational hardening are analyzed and experimental results on the microstructure and mechanical properties of ZrO_2 -based materials are presented.

Essential conditions for the preparation of high-strength high-viscosity construction ceramics are small grain size (10–100 nm) and that the residual porosity of the material be close to zero. Methods of non-porous ceramics preparation include high-temperature sintering, sintering under pressure, and hot pressing under isostatic conditions [14.68–70]. In order to obtain high-strength ceramics with high destruction viscosity by these methods one should use ultrafine (grain size ≈ 10 –200 nm) and highly homogeneous, uniform fused mixture. Nowadays much attention is paid to the preparation of ultrafine oxide particles as starting materials for the production of nonporous ceramics [14.71, 72]. The peculiarities of ceramic materials include randomness of the distribution of initial components, defects in the material structure (which may cause a significant scatter in material properties), and the presence of pronounced grain boundaries, which influence the properties of such materials significantly.

The SM method allows high-strength crack-resistant material with zero porosity without sharp grain boundaries to be obtained by directional crystallization of the melt. The possibility of synthesis under air, the lack of special requirements concerning grain composition and homogeneity of the initial materials, as well

as the practically waste-free character of the technology (i. e., the possibility of recycling crystalline waste) make this method very promising for the synthesis of these hard construction materials resistant to aggressive (in particular, oxidizing) gas atmosphere over a broad temperature range.

14.3.1 Crystal Structure of Zirconium Dioxide

Zirconium dioxide has several polymorphic modifications [14.73–75]. Monoclinic (m), tetragonal (t), and cubic (c) modifications of ZrO_2 exist at ambient pressure. The thermal stability range of the m-phase extends to 1160°C; that of the t-phase extends from 1160 to $\approx 2370^\circ\text{C}$; and that of the c-phase extends from $\approx 2370^\circ\text{C}$ to the melting point of ZrO_2 , $\approx 2680^\circ\text{C}$. Cubic phase of ZrO_2 is a nondistorted structure of the fluorite type, belonging to the $Fm\bar{3}m$ space group with lattice parameter $a = 5.07 \text{ \AA}$. The oxygen coordination number is 4, and the zirconium coordination number regarding oxygen positions is 8 [14.76, 77]. Tetragonal phase of ZrO_2 exhibits a slightly distorted fluorite structure, belonging to the $P4_2/nmc$ space group with lattice parameters $a = b = 5.085 \text{ \AA}$, $c = 5.166 \text{ \AA}$, and $a/c = 1.016$ [14.74–76]. The c-phase becomes unstable upon a decrease in temperature and is transformed to the t-modification by means of a small distortion of the fluorite structure. The symmetry of the initial structure is distorted as a result of small translocations of atoms, mainly of oxygen ions. Oxygen ions become shifted from their ideal positions (1/4, 1/4, 1/4) in the fluorite lattice but this does not lead to a change in the coordination number of zirconium. Four oxygen ions located at a distance of 2.065 \AA from each other occupy the apices of a tetrahedron; the other four ions occupy distorted tetrahedral positions and are located at a distance of 4.455 \AA from each other. On the whole, the lattice of the t-phase displays a minute elongation along the c -axis as compared with the lattice of the c-phase. Monoclinic phase of ZrO_2 belongs to the space group $P2_1/c$, with the following lattice parameters $a = 5.169 \text{ \AA}$, $b = 5.232 \text{ \AA}$, $c = 5.341 \text{ \AA}$, $\beta = 99^\circ 15'$, and $Z = 4$ [14.77–79]. The next phase transition, occurring at 1200°C , causes the transition from the t-form to the m-form. The latter form is stable under normal conditions, widely spread in the Earth's crust, and known as the mineral baddeleyite. Its structure is a result of further distortion of the c-phase of ZrO_2 , but the distortion is so pronounced that a completely new structural type emerges. The zirconium coordination number decreases from 8 to 7. Half of the oxygen atoms in the

baddeleyite structure are four-coordinated and the others are three-coordinated. It is important to emphasize that the structure of m- ZrO_2 is extremely stable, this being confirmed by the existence of m- ZrO_2 over a broad temperature range and the extreme stability of the mineral baddeleyite under natural conditions. Twinning is characteristic of the monoclinic structure. The twinning plane is constituted by oxygen ions – $\{100\}_m$ or $\{110\}_m$.

Pure $\alpha\text{-Y}_2\text{O}_3$ (cubic) has a volume-centered lattice and is isostructural to Mn_2O_3 . This structural type can be derived from the CaF_2 structure by deletion of a quarter of all nonmetallic atoms [14.80].

14.3.2 Phase Diagrams of the $\text{ZrO}_2\text{--Y}_2\text{O}_3$ System

Yttrium oxide is the most widely used stabilizing oxide for the growth of ZrO_2 -based crystals. That is why the $\text{ZrO}_2\text{--Y}_2\text{O}_3$ system will be extensively discussed in this chapter. The first phase diagram for the $\text{ZrO}_2\text{--YO}_{1.5}$ system was published in 1951 [14.81]. Many publications have appeared since then, but the experimental data obtained are often contradictory and the data for some parts of the phase diagram are not yet sufficiently reliable. The characteristic presence of wide solid-solution regions based on either ZrO_2 or Y_2O_3 was disclosed already during the first studies of the $\text{ZrO}_2\text{--Y}_2\text{O}_3$ system. The most reliable phase diagrams were plotted at the end of the 1970s [14.82–87] (Fig. 14.8).

These diagrams show that the ordered compound $\text{Zr}_3\text{Y}_4\text{O}_{12}$ formed at Y_2O_3 content of 40 mol % exists along with solid solutions. This compound was first synthesized and described in [14.82]. $\text{Zr}_3\text{Y}_4\text{O}_{12}$ displays a rhombohedral-type symmetry (space group $R\bar{3}$), is isostructural to UY_6O_{12} , and undergoes incongruent decomposition at $1523 \pm 50 \text{ K}$ [14.84], i. e., the structure is disordered to yield a fluorite phase.

Special attention was paid to the part of the phase diagram corresponding to zirconia-rich compositions because these materials are of great practical interest. A series of complicated phase transformations depending on the thermal history, grain size or particle size is observed in this part of the system. The presence of metastable states is common. A detailed analysis of these phase transformations is given in [14.88, 89]. A decrease in the temperature of the t–m phase transition accompanied by the increase in yttrium content is a characteristic property of this region of the phase diagram. A narrow two-phase (m–t) region exists in a range of temperatures above the temperatures to which the m-

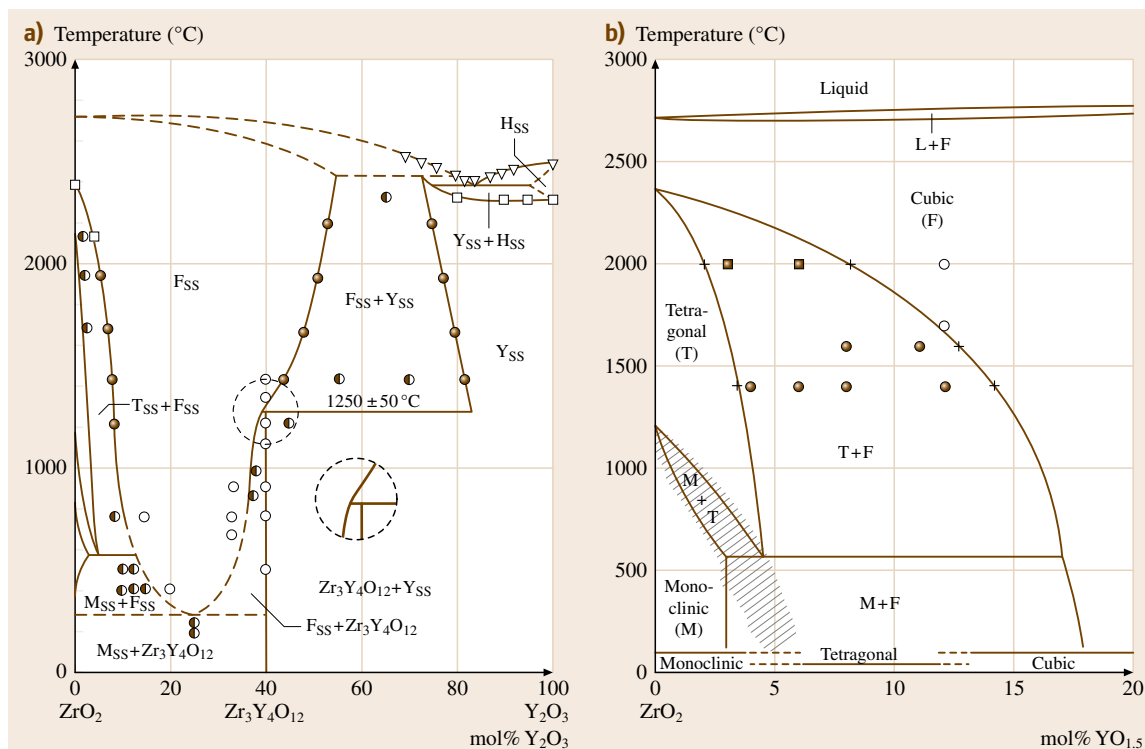


Fig. 14.8a,b ZrO₂-Y₂O₃ phase diagrams: (a) after [14.82]; (b) after [14.83]

phase corresponds. This two-phase region is followed by the so-called transformable t-phase region. The t-phase, which is transformed into the m-phase upon cooling, exists in the composition range of 0–5 mol % YO_{1.5}. However, if the grain size of the ceramic sample is low enough (0.2–1 μm), the transformation of the material with YO_{1.5} content of 3–4 mol % into m-phase may not occur spontaneously at room temperature but takes place upon significant mechanical loading. The complexity and low rate of the m-t diffusion phase transition make the determination of equilibrium phase boundaries in the two-phase m+t region very difficult. Practically, the t ↔ m transition boundary was determined using various methods: differential thermal analysis, dilatometry, acoustic studies, and Raman spectroscopy. The data obtained in these studies were very incoherent, depending on the method of sample preparation, thermal history, presence and size of grains, purity of starting materials, etc. The samples were obtained by oxide mixtures sintering [14.87, 89] or by crystallization of the melt in a CC [14.90–92].

A two-phase region of untransformable tetragonal (t') and c solid solutions corresponds to higher YO_{1.5}

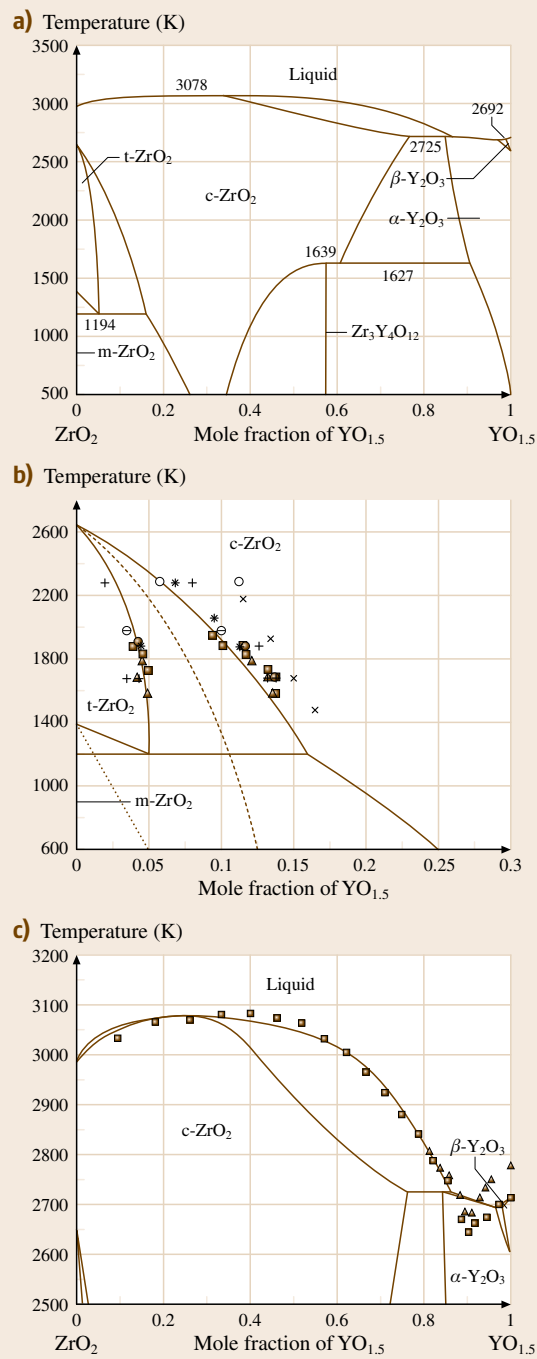
concentrations. Samples containing 4–13 mol % YO_{1.5} undergo a phase transformation into t'-ZrO₂ upon rapid cooling, starting from temperatures corresponding to the temperatures of existence of the c-ZrO₂ solid solution. This phase is named untransformable because it does not turn into the m-ZrO₂ phase. Upon an increase in yttrium oxide content the tetragonal distortion of the structure (*c/a*) decreases and its lattice parameters become very similar to the cubic parameters of the fluorite lattice. Such phase transitions in metallic systems are well known [14.93]. Their main features are the lack of changes of the chemical composition (the lack of diffusion) and a collective shifting of atoms during the transition (cooperative transformation). This transition is defined mainly by the rate of phase boundary migration. Various models of the phase transition process of this type were proposed, the choice of the model being determined by the temperature [14.94]. In the case of ZrO₂-YO_{1.5} the c ↔ t' transition occurs in the two-phase region c+t. The nature and properties of the t'-phase as well as its formation from the c-phase upon a phase transition are reviewed in detail in [14.95]. The boundaries of the two-phase region of c+t existence

Fig. 14.9a–c Phase diagrams for the $\text{ZrO}_2\text{--Y}_2\text{O}_3$ system calculated by CALPHAD [14.99]. Experimental data from: (○) [14.81], (+) [14.83], (×) [14.84], (●) [14.100], (Δ, □) [14.88], (*) [14.83], (◐) [14.101] dotted line: t–m transition temperature; dashed line: t–c transition temperature ►

were studied by many researchers [14.81, 84, 87, 95]. The use of various methods of sample synthesis and phase boundary determination causes a scattering of the values. For example, in the temperature range of 1823–2273 K the two-phase region t + c extends from 3–4 mol % to 10–13 mol % $\text{YO}_{1.5}$. Further increase of $\text{YO}_{1.5}$ concentration to 15 mol % $\text{YO}_{1.5}$ and above results in the formation of completely stabilized c solid solutions of fluorite type. The liquidus curves for the whole composition range were first plotted in [14.96]. Eutectic formation was detected at Y_2O_3 concentration of 87.1 mol % and temperature of 2643 K. Melting points of 2983 and 2712 K were determined for pure ZrO_2 and pure Y_2O_3 by the authors of this work. The calculation of phase diagrams (CALPHAD) method was used to give a complete description of the thermodynamic properties and equilibrium phase boundaries of the system $\text{ZrO}_2\text{--YO}_{1.5}$ [14.97–99]. The calculated phase diagram of the $\text{ZrO}_2\text{--Y}_2\text{O}_3$ system as well as separate fragments supplemented with points marking the experimental values is presented in Fig. 14.9.

14.3.3 Stabilization of Cubic and Tetragonal Structures in Zirconia-Based Materials

Stability in the whole temperature range including room temperature should be imparted to one of the high-temperature modifications of ZrO_2 in order to grow single crystals from the melt. The ratio of the cation (R_c) and anion (R_a) ionic radii was shown to be the critical parameter for fluorite lattice stability [14.102]. The face-centered anion package in the $Fm\bar{3}m$ lattice is possible if $R_c/R_a \geq 0.736$. If the parameter value is less than this value, the cubic structure cannot exist because forces of electrostatic repulsion inevitably distort the dense ion package when distances between the anions are small. For ZrO_2 this ratio is 0.66. The cubic lattice can be stabilized if the cation size is increased and the effective anion size is decreased. This may be achieved in two ways: by replacing the zirconium cation by a cation of a larger radius or by creating vacancies in the anionic sublattice (i. e., by introducing cations of lower charge). In order to achieve the required increase in the



ratio of the ion radii in the ZrO_2 lattice the lattice parameters should be increased by approximately 4%. In some cases stabilization is also achieved by introduction

of oxides with cations having a lower radius than that of the zirconium ion. Therefore, the cation radius is not a decisive factor for the formation of the ZrO_2 c-phase. The stable lattice is the one corresponding to the state of minimum free energy. Apart from the radii of the cation and anion, the character of the interaction between the electron shells of the lattice components is of a great significance for this state. References [14.103, 104] state that the bond between oxygen and the introduced cation must be more heteropolar than the bond between oxygen and the zirconium ion. In this case the fluorite structure is formed. The mechanism of stabilization of high-temperature modifications and the role of the oxygen vacancies formed upon heterovalent replacement of zirconium cations by lower-valency cations of the stabilizing oxide are discussed in several publications [14.105–107]. The degree of stabilization depends on the nature of the stabilizing oxide and its concentration. Oxides structurally similar to ZrO_2 are commonly used. According to crystallochemical conceptions, stable solid solutions can be formed in this case. Such oxides include Y_2O_3 , and oxides of rare-earth elements and alkaline-earth elements.

Tetragonal solid solution based on ZrO_2 can be obtained by decreasing the stabilizing oxide concentration. Single-phase samples with t-structure can be prepared only under strictly determined conditions [14.64, 65, 85, 108]. The stability of the t- ZrO_2 structure depends on factors such as density, composition, grain size, length of intergrain boundaries, and annealing conditions. As mentioned above, two forms of t- ZrO_2 exist [14.94, 100, 101, 109]: the t'- ZrO_2 , rich in Y_2O_3 , and the t- ZrO_2 , which is depleted of Y_2O_3 and can undergo a martensitic transition into the m-phase. The t'-phase is predominant in materials obtained by sharp quenching of c-solid solutions. Single crystals grown by directional crystallization of the ZrO_2 -3 mol % Y_2O_3 melt composition in a CC have a strongly twinned t-structure [14.110]. Cooling at a low rate facilitates the t \rightarrow m phase transition, i. e., the t-phase was not the t'-phase in spite of being richer in Y_2O_3 than the equilibrium t-phase. ZrO_2 -based ceramics with 2–9 mol % Y_2O_3 stabilizer, obtained by sintering, consists of two or three phases mainly. Monoclinic or t- ZrO_2 can be present in such materials in the form of coherent precipitates in a t- or c-matrix, according to the ratio of the crystallographic parameters of these phases.

The best conditions for preparation of samples consisting only of the t'-phase by directional crystallization of melt in a CC are Y_2O_3 concentration of

3 mol % and high cooling rate (> 400 K/h). These results are consistent with the experimental conditions determined in [14.111]. For the study of the t'-phase, crystals grown by SM were reheated up to 2150°C (stability region of the c-phase) for 10 min and then quickly cooled to room temperature (cooling time of 60 min) [14.112]. The c \rightarrow t transformation is accompanied by the formation of a domain structure in the crystals [14.109, 112, 113]. Orientation dispersion and the crystallographic correlations between domains are determined by both the prototype (c-phase) symmetry and the symmetry of the t'-phase formed from the c-phase. Domains form ordered colonies of two alternative variants separated by habitus planes $\{110\}$, which are the twinning planes. If the material contains only the t'-phase, then colonies occupy all of its volume, directly adjoining each other. They border on each other along the $\{110\}$ planes and are elongated along the $\langle 111 \rangle$ direction, forming a spiral-like structure. Detailed investigation of the domain structure of the t'-phase was performed in [14.112, 114–116]. It was found that tetragonal domains occupy all of the volume of t'- ZrO_2 . Their spatial arrangement must be highly symmetric in order to minimize the energy of coherent deformations [14.112]. Three-dimensional spatial arrangement of the colonies in pure t- ZrO_2 obviously differs from that in PSZ, where colonies of t-uniform domains are inserted into the uniform matrix [14.115, 117]. Colonies and their substructures are a result of the optimal accommodation of spontaneous stress caused by the c \rightarrow t transition. Upon a c \rightarrow t phase transition, the c-axis of the elementary cell is slightly elongated. In t'- ZrO_2 containing 3 mol % Y_2O_3 the elongation did not exceed 1%. This is approximately half that of the t-distortion for pure ZrO_2 with $c/a = 1.02$ [14.112]. Correspondingly, the domain c-axes are not orthogonal: the angle between them equals 89.4° in the case of a 1% distortion. It has been found that the domains inside the colony are separated by coherent low-energy twinning planes $\{110\}$.

14.3.4 Cubic Zirconia Crystals (Fianits)

As mentioned, the above-described SM method was most successfully applied for the development of an industrial technology for ZrO_2 -based single-crystal growth. Crystals up to 60 mm in length and up to 20 mm in cross section had been grown already at the beginning of the 1970s using the technology elaborated in Russia. Such crystals were obtained in the first industrial equipment including a CC of 180–200 mm in diameter.

The power of the RF generator was 60 kW, and the frequency was 5.28 MHz. The weight of the melt was up to 15–20 kg. Further development of the technology was aimed at achieving a larger size and higher quality of the crystals as well as at lowering their price. Using large melt volumes for crystal growth is the simplest and most efficient way of achieving these objectives because it allows:

- Growth of a much larger quantity of crystals during one crystallization cycle at the same crystallization rate. This allows lowering of the production costs.
- Lowering the heat losses through the walls of a CC and the corresponding lowering of the RF generator input power; the ratio of cooled surface area to the melt volume is much less in larger CC.
- Improving the crystallization conditions in order to obtain high-quality crystals. When the melt volume is large, the system has a high thermal inertia which levels out random oscillations of RF output power on the crystallization front.
- Preventing the formation of cracks in large crystals during the cooling of the crystalline ingot. At large melt volumes the cooling rate of the crystals after complete of the crystallization is much lower.

This was confirmed with experience on industrial equipment with a CC of 400 mm in diameter, output power of 160 kW, and RF frequency of 1.76 MHz. The weight of the melt was 80–100 kg. Nowadays large-scale production of single crystals is mainly performed in facilities with CC diameter up to 1000 mm, power of 800 kW, and frequency of 400–800 kHz. The weight of the melt is 600–1500 kg. The weight of individual crystals reaches 15 kg.

Growth of CZ Crystals

The scheme of manufacturing of CZ crystals is shown in Fig. 14.10. The main technological stages are the following: preparation of the initial mixture, loading of the initial mixture into the CC, SM of the material, directional crystallization of the melt, extraction and separation of the crystal ingot, crystal cutting and sorting, and processing of the material and offcuts. The most important stages of the technological process will be discussed below.

The oxides used as starting material are weighed and thoroughly mixed in a ratio corresponding to the predetermined concentration. In the case of mass production, various quantities of crystalline melted material of the same composition from previous melts are

added to the initial mixture [14.25, 30, 118]. ZrO_2 and Y_2O_3 are the main raw materials, their purity being of great significance for the crystallization conditions and the degree of structural perfection of the crystals. The presence of some trace contaminants in the oxides used for crystal growth by directional crystallization in the CC is highly undesirable. These contaminants influence both the growth process and the quality of the single crystals obtained. Atomic emission spectroscopy studies have shown that the concentration of contaminants in the crystals obtained is 5–100 times less than that in the starting oxides due to the evaporation of the volatile oxides (namely, oxides of As, Pb, Cu, etc.) and the segregation of impurities (Si, Ti, Al, W, etc.) during directional crystallization [14.25, 30] (Table 14.2).

Requirements concerning the purity of the starting materials depend on the field of application of the crystals. For example, the content of Si, Ti, Al, and W in oxides used to synthesize crystals of high optical uniformity and structural perfection for optical applications must not exceed 10^{-4} – 10^{-5} wt %.

Putting the initial materials into the CC is an important technological stage that greatly influences the reproducibility and crystal yield in the cycle, as well as the size and quality of crystals. The method of loading influences the processes of start melting, the formation of the melt volume, and the thermal conditions under which further melting and subsequent crystallization of the melt proceed. As already mentioned, thermal shielding of the melt plays an important role during SM in a CC. The lower thermal shield is formed during crucible loading. As a rule, crystalline melted pieces of the previous processes and the initial powders of the same composition are used to form the shield. The position of the shield is determined experimentally to create appropriate thermal conditions for crystallization. If large quantities of crystalline material are used, circular loading of the CC is often performed [14.118]. Circular loading ensures the formation of a dense, reliable sintered skull. Thus heat losses are decreased and leakage of the melt from the CC through intersection gaps is prevented. As a result, the stability of the melting process becomes higher. In the case of a large-diameter CC this loading method ensures reproducibility of the start melting process and creates the optimal conditions for the formation of large melt volumes required for obtaining large crystals at the lowest power values possible.

During the melting of the initial charge the molten zone approaches the CC walls; emission of radiation through the intersection gaps situated in the upper part of the charge begins and gradually becomes more in-

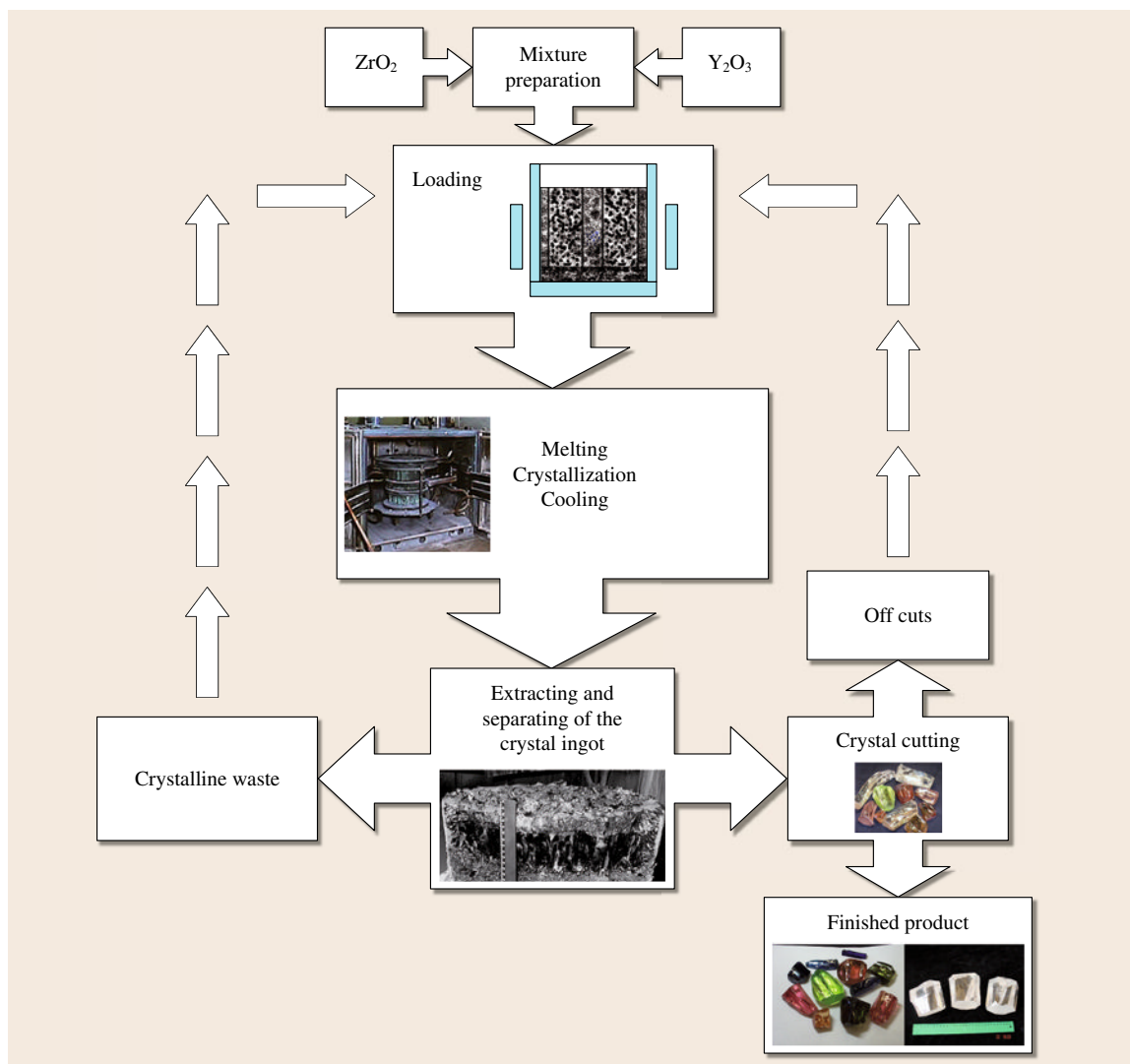


Fig. 14.10 Process flowsheet of the production of crystals based on zirconia

tense. The importance of providing an upper shield for the melt upon crystal growing by directional crystallization from the melt in large CCs was mentioned above. Choice of the size of the upper thermal shield and the method of its formation vary depending on the method of melt volume formation during start melting. If portions of the initial powders are not added during melt volume formation, then the remaining sintered arch of powdered material acts as a heat shield. If initial powders are added during the process of melt formation, then crystalline material (of the same composition) of previous processes can be used for shield formation.

This material is loaded after the completion of melt formation. This material does not melt because it remains above the RF coil level during loading; only partial melting of the lower part of the shield may occur. Studies on the initial melt volume formation in the CC have shown [14.33–36] that the same volume can be formed in different ways (Fig. 14.11).

The character of melting depends on the characteristics of the starting material. Studies were carried out for ZrO_2 powders of different dispersity. The experimental data showed that more power is needed for the melting of a less porous (porosity ε_1) powder than for a more

Table 14.2 Results of the analytical determination of impurities concentrations in the initial ZrO_2 and ZrO_2 –15 mol. % Y_2O_3 crystals grown at 10 mm/h

Element	Concentration, wt% $\times 10^{-5}$			
	Initial ZrO_2	Crystal		
		Bottom of the crystal	Middle of the crystal	Top of the crystal
Fe	2.0	< 0.1	< 0.5	1.0
Ca	3.0	1.1	1.6	1.8
Si	5.1	0.1	0.5	1.0
Mn	0.2	< 0.1	< 0.1	< 0.1
Cu	1.0	< 0.1	< 0.1	< 0.1
Mg	1.2	0.5	1.1	1.4
Al	0.5	< 0.1	< 0.1	< 0.1
Nb	0.4	0.1	0.1	0.3
W	< 0.1	< 0.01	–	–
Ti	0.5	< 0.1	0.1	0.4
Be	< 0.1	< 0.01	< 0.01	0.01
Sr	4.3	1.5	2.1	3.3

porous one (porosity ε_2). Properties of the initial material (in particular the powder porosity) determine the direction of the melt spreading during the stage of start melting, as well as the structure of the skull. It was confirmed that two modes of melting of a porous dielectric exist: the stationary mode and the quasiperiodic mode. The mode observed is determined by the ratio of the threshold power density (depending on the porosity of the initial powder) and the density of power released in the charge. This experimental data confirmed the theoretical model of induction melting of dielectrics proposed in [14.119]. It was shown that the direction of melt spreading during the initial stage of melting influences the volume and the shape of the molten bath

formed, the value of power released in the melt, the value of melt overheating, and the power of heat losses in the charge. The preferable variant of spreading during melting is spreading towards the bottom of the CC. In this case less power is needed for the molten bath formation, the melt overheating is less pronounced, and the melting process is more stable without leakage of melt through the gap between the sections. The mode of initial melt formation is especially important when large CC or charges of large mass are used, or when power is limited. The use of the above-mentioned circular loading method considers the advantages of melt volume formation by spreading of the melt towards the bottom of the CC and thus promotes the formation of large melt

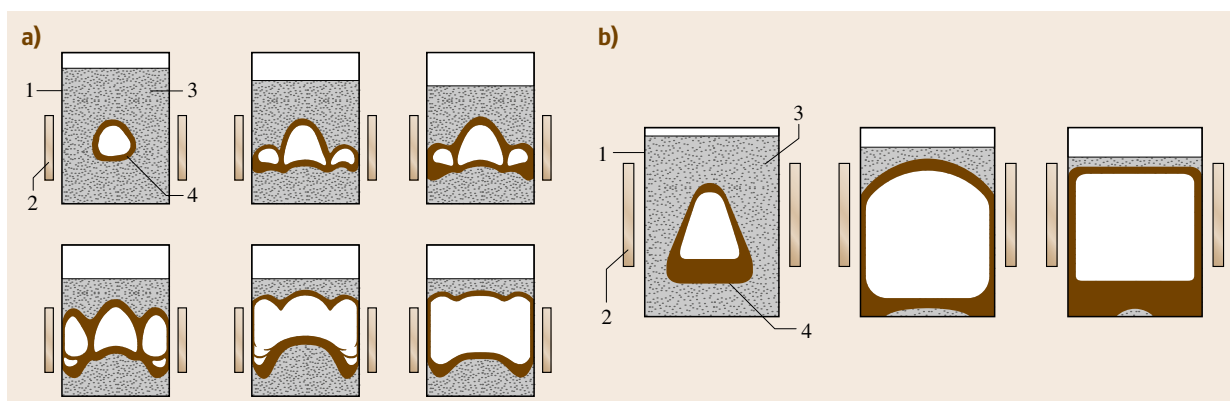


Fig. 14.11a,b Schematic of the melt propagation at melting initial powder with different particle size ε_1 (a) and ε_2 (b). 1 – Cold crucible; 2 – induction coil; 3 – powder of initial materials; 4 – melt

volumes at minimal power values. After the end of melting, the melt is homogenized to achieve thermal and phase equilibrium.

Crystallization of the melt begins on the bottom of the CC on crystal grains of the solid skull. Only a restricted number of crystals of those initially formed remain during growth. As a result of crystallization, a columnar block of single crystals grows. The size of CZ crystals grown by SM technique is influenced by:

- The conditions of formation of the initial melt volume determining the temperature gradients on the interface, which influence the geometry of the crystallization front and the position of this front relative to the heating zone
- The conditions of nucleation on the skull
- The conditions of degeneration during mass crystallization
- The chemical composition of the initial melt (the nature and concentration of the stabilizing oxide and the presence of impurities)

The melt–solid interface geometry may be concave, flat or convex depending on the conditions of the melt volume formation. The last two types are preferable for crystal growth in the CC as well as for traditional directional crystallization in hot crucibles because they promote a decrease in the number of growing crystals and a consequent increase of crystal size; they also ensure low thermal strains and high purity of the growing crystal. The experience of growing CZ crystals by SM technique shows that larger crystals are formed when the crystallization front is flat or convex, other conditions being equal. In the case of a concave crystal-

lization front the number of crystals formed increases, while their size, especially the size of the crystals in the central part of the ingot, decreases (Fig. 14.12). The actual crystallization front may have a more complex shape and change its geometry during crystallization corresponding to changes in thermal conditions.

Nucleation. The nucleation process determines the size and quantity of growing crystals. Authors [14.120] have described the peculiarities of SM of porous dielectrics during the stage of melting wave propagation, when capillary spreading of the melt takes place inside the pores of the dielectric powder. During this process the melt impregnates the solid phase and crystallizes in it, then slow melting of the crystallized layer takes place, and then the situation cycles. These processes of capillary spreading determine the local structure of the interface on which the single-crystal growth begins. The melt from the heated zone causes partial melting of the upper layer of the lower thermal shield. This layer being nonuniform and porous, the melt penetrates into the surface layer nonuniformly. The photograph of the fragment of the lower part of a crystal (Fig. 14.13) clearly shows that inclusions of unmolten initial powder and bubbles are present in the crystal.

The Laue pattern of this part of the crystal indicated that the atomic planes are heavily distorted near the inclusions but the crystal structure remains single-crystalline. Nonuniformity of the nucleation interface leads to the formation of a great number of crystals and thus decreases the cross-sectional size of isolated crystal. So, the lower thermal shield influences the nucleation process greatly. When this shield is lacking, the thin skull is substantially nonuniform due to the random

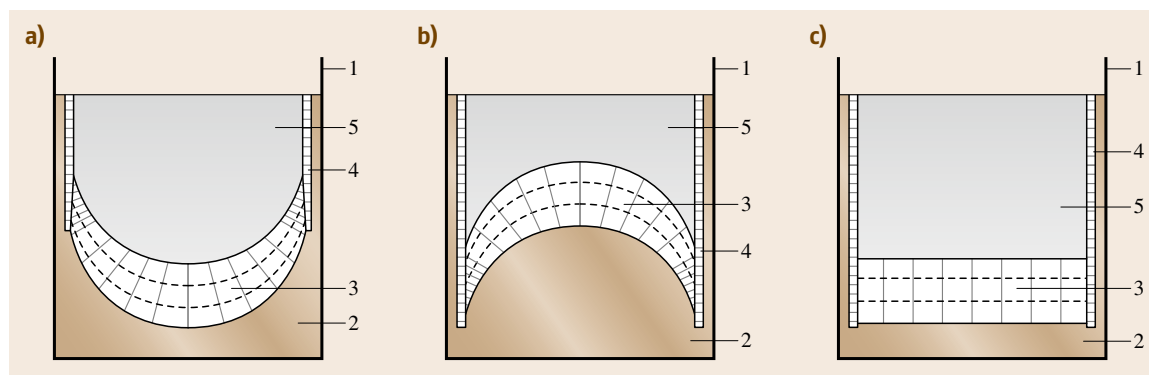


Fig. 14.12a–c Crystal growth in a cold crucible with different shapes of crystallization front: (a) concave crystallization front, (b) convex crystallization front, and (c) flat crystallization front. 1 – cold crucible; 2 – polycrystalline solid shell; 3 – crystals grown from bottom of the crucible; 4 – crystals grown from sides of the crucible; 5 – melt



Fig. 14.13 Section of the bottom part of the crystal

character of heat removal in different regions (even direct contact of the melt with the bottom of the CC is possible). This nonuniformity is significantly decreased if a dense heat-insulating layer is formed. This causes a significant decrease in the number of seeded crystals and the increase of the size of crystals already at the nucleation stage. Besides, such a shield allows the use of seeds placed on it. Unfortunately, this seeding process is uncontrolled, has a random character, and requires experimental selection of conditions to increase its repeatability. Nevertheless, crystals were grown on seeds of different orientations [(100), (111), and (101)] and X-ray studies showed that the crystals inherited the crystallographic orientation of the seeds.

Degeneration. The degeneration process consists of a decrease in the number of seeding crystals and is accompanied by an increase in the cross-sectional size of some crystals at the expense of a decrease in the size of other crystals. The problems of competitive growth were analyzed in studies of mass crystallization [14.121–125]; the selection of crystals according to their size was shown to be a result of these processes and so-called *geometric selection*. The mechanism of this process is the following: crystals survive the competition only if their direction of fastest growth is close to the normal of the nucleation surface. As a result, all crystals separated from the nucleation surface by a distance greatly exceeding the mean distance between the nuclei are elongated and their geometric axes are almost parallel to each other: the so-called columnar structure occurs. The formation of such a structure is influenced by only geometric factors, the influence of external conditions (for example, the direction of heat transfer from the growing crystal) being small. It was supposed that the influence of external factors could be only indirect and result in a change of facet growth rate and

crystal habitus. Quantitative experiments on geometric selection [14.126, 127] showed that the linear density of the number of surviving crystals $n(h)$ decreases proportionally to the height $n \sim 1/h$. The probabilistic assessment [14.128] yielded the same result for the two-dimensional case and a dependence expressed by the formula $n \sim 1/\sqrt{h}$ for the three-dimensional case. The aspect ratio depends on the crystal habitus in both cases.

A theory of crystal degeneration based on studies of the mass crystallization of metals with a face-centered lattice was proposed by Tiller [14.123–125]. It was supposed that grooves formed by boundary surfaces of crystals exist on the interfaces of growing crystals. The depth of the grooves was supposed to depend on the temperature gradients in the solid phase and the melt, as well as on the orientation of the neighboring crystals. The inclination of groove slopes is determined by crystal orientation. Thus a crystal with $\langle 111 \rangle$ orientation relative to the growth axis has a greater slope inclination than a crystal with $\langle hkl \rangle$ orientation, so it will hang over the latter crystal and finally displace it. Such grooves were observed upon growing CZ crystals [14.129]. It was noted that, upon consideration of the degradation process in the framework of Tiller's theory, a decrease of the heat power released in the melt causes a decrease of the mean temperature of the melt and a corresponding decrease of axial gradients at the crystallization front. The decrease in the gradient causes an increase in the depth of the groove between the growing crystals and makes the degeneration process more efficient.

The melt volume influences the size of CZ crystals: larger crystals can be grown in large-volume CCs, exceeding 200 mm in diameter [14.25, 30, 118]. In the case of small crucibles (90–100 mm) the high ratio of the cooling surface area to the melt volume and high heat losses through the CC walls require a higher melt overheating. Significant melt overheating deleteriously influences the degeneration conditions and the shape of the crystallization front [14.129]. The growth rate influences the degeneration process of CZ crystals in the following way: a decrease in the growing rate leads to an increase in the crystal size [14.30, 118]. This corresponds to Tiller's theory of degeneration, which states that the ratio of the rate of displacement of the competing nuclei to the axial growth rate is higher when the growth rates are lower and thus the displacement process becomes more efficient. The influence of melt composition (in particular, the nature and concentration of the stabilizing oxide) on the crystal size was stud-

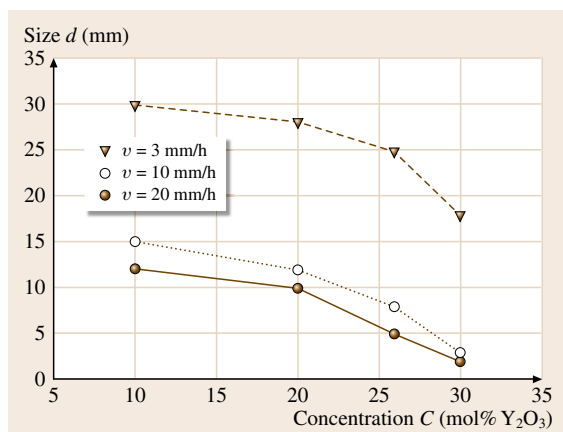


Fig. 14.14 Mean size of $\text{ZrO}_2\text{-Y}_2\text{O}_3$ crystals versus Y_2O_3 concentration and growth rate

ied in [14.25, 30]. The dependence of the *mean size* of the crystals obtained at different crystallization rates (3, 10, and 20 mm/h) in a CC of 130 mm diameter on the Y_2O_3 concentration is shown in Fig. 14.14. The *mean size* $d = D/n$, where D is the diameter of the ingot and n is the number of crystals in ingot cross-section, was used to compare crystals from different ingots.

The growth conditions were selected for the crystallization front to remain flat throughout the process and for the melt height to be approximately the same for different compositions (the melt height was about ≈ 50 mm, thus being less than the crucible diameter, and this diminished the influence of the degeneration processes). Figure 14.14 demonstrates that an increase in Y_2O_3 concentration (especially above 20 mol %) causes a decrease in the *mean size* of crystals. Consequently, the growth rate must be significantly decreased to maintain an acceptable size of crystals at high Y_2O_3 concentrations.

As mentioned before, impurities that influence the growth of crystals are present in the starting materials. Besides, large quantities of additives may be introduced into the crystals to vary the physicochemical properties of crystals (optical, spectral, electrical, mechanical, and others). These additives significantly influence the crystallization process and, consequently, the size of crystals. It is well known that directional crystallization of multicomponent melts with component distribution coefficients (K) not equal to 1 is accompanied by segregation of the component decreasing the crystallization temperature, into the melt, and its accumulation at the crystallization front (if $K < 1$). In Tiller's theory, grooves on crystal interfaces act as sinks for such ad-

mixtures. Thus, the segregation of admixtures inhibits the lateral growth of crystals, and causes an increase in the groove depth and retardation (or complete stop) of the degeneration process. Therefore the introduction of additives, as well as the use of initial mixture with high levels of impurities requires correction of the growing conditions.

Many studies of mass crystallization of metals have been devoted to the problem of preferential orientation of grains in the ingots [14.121–123]. The growth rates anisotropy attempted to give an explanation of the preferential orientation of grains in the ingots: the anisotropy was believed to be due to the anisotropy of the heat conductivity in the crystal. Higher heat conductivity in the temperature gradient direction was suggested to be the cause of the difference in the grain growth rates. However, this is possible only for crystals characterized by anisotropy of heat conductivity, whereas heat conductivity anisotropy is known to be low for most crystals and to be zero for cubic crystals. Experiments on bicrystal growth showed that the equilibrium temperature of the crystal contacting the melt depends on the crystallographic orientation relative to the interface. Dependence of the preferential crystallographic orientation on the growth rate, value of overcooling, and presence of admixtures in the starting material was also noted in these experiments. The problem of preferential crystallographic orientation of CZ crystals grown by SM technique has not been studied in detail. The preferential crystallographic orientation of CZ crystals was shown to be $\langle 110 \rangle$ [14.13, 25, 31, 130, 131]. However, experience shows that the deviation of the crystal growth axis from this direction may often amount to tens of degrees. The correlation structure and morphology of CZ crystals was studied in [14.132]. Single crystals of $\text{M}_x\text{Zr}_{1-x}\text{O}_{2-x/2}$ ($\text{M} = \text{Y}, \text{Er}, \text{Yb}$) with $0.3 < x < 0.57$, i.e., crystals with high stabilizer content, were studied. In accordance with the phase diagram, formation of the ordered compound $\text{Zr}_3\text{Y}_4\text{O}_{12}$ was observed at $x = 0.4$. The phenomenon of short-range order was shown to influence the crystal morphology significantly. The interpretation of results was based on the analysis of structural characteristics of ordered rhombohedral phases of the type Y_6UO_{12} by the method of Hartman and Perdok [14.133]. This method supposes the crystal habitus to be determined by chains of strong bonds. This work clearly demonstrates how the lattice symmetry, the nature of the solid solution, and the crystal growth conditions influence the shape of CZ crystals.

Properties of CZ Crystals

CZ crystals grown by **SM** technique have been studied rather extensively with regard to chemical and phase compositions, determination of the range of stabilizer concentrations allowing preparation of cubic solid solution crystals from the melt, determination of the phase stability of the crystals, and characterization of growth defects [14.25, 28–31, 61, 134–140]. The structure of crystals was studied in detail by X-ray analysis, Raman spectroscopy, electron paramagnetic resonance, neutron diffraction, etc. [14.91, 113, 141–146]. Lattice parameters and the mechanism of cubic solid solution stabilization were also studied [14.144–149]. A number of investigations have been devoted to the physico-chemical properties of crystals: electrical and optical properties [14.150–154], spectral generation characteristics of the activated crystals [14.155–163], and thermophysical and mechanical properties [14.164–177]. Studies of these properties of crystals are of a great significance for practical applications. It should be mentioned that the possibility of using crystals for different applications is to a great extent determined by the perfection of crystals. Therefore types of imperfections appearing in **CZ** crystals as well as causes of the appearance of imperfections and possible ways of their elimination will be discussed in the following section.

Defects in CZ Crystals

Growth striations, cellular structure, and inclusions of extrinsic phases are imperfections characteristic of **CZ** crystals [14.28, 29, 138, 139] (Fig. 14.15a–h).

Growth striations. Growth striations are observed in crystals of various compositions as layers with different refraction indices. They appeared as alternating layers perpendicular to the direction of growth of the crystals (Fig. 14.15a). Appearance of striations in $\text{ZrO}_2\text{--R}_2\text{O}_3$ crystals is indicative of nonuniformity of the components distribution during the crystallization process, in particular of nonuniform distribution of the stabilizing oxide. Local concentration measurements showed that Y_2O_3 concentration fluctuations do not exceed 1 mol %. Such factors as the stabilizing oxide concentration, crystal growth rate, and nature of melt stirring were found to influence the striae density [14.25, 28, 29]. A considerable increase in the density of the striations was observed at concentrations close to 30 mol % R_2O_3 , as well as upon an increase in lowering rate above 16 mm/h. When the lowering rate was decreased from 16 to 1 mm/h (for $\text{ZrO}_2\text{--}8\text{--}20$ mol % R_2O_3 compositions and **CC** of 90–200 mm in diameter), the striae

density decreased from ≈ 20 to $\approx 8\text{ cm}^{-1}$. When forced stirring by reverse rotation of the crucible was used at low lowering rates, striae density decreased and reached 1 cm^{-1} . As is known, nonuniform impurity distributions in crystals is caused by irregular growth rate, resulting in corresponding changes of the effective distribution coefficient and impurity concentration. Growth rate changes may be caused either by peculiarities of the instrumentation or by the processes taking place at the crystallization front. Striations caused by factors of the first type are usually called instrumental while those caused by factors of the second type are called fundamental. Under real conditions, factors of both type usually act simultaneously.

Instrumental striations may be caused by shortcomings of the crystal growth equipment (unstable functioning of the mechanical drives and **RF** generator output power, oscillations of the coolant flow, etc.) and also by changes of the growth rate caused by temperature oscillations in the melt due to convection. A study of the causes of growth striation formation [14.28, 29] showed that striations are caused by oscillations of the stabilizing oxide concentration (these oscillations are due to constitutional supercooling during growth) and can be eliminated by decreasing the lowering rate to 1–2 mm/h and introducing forced stirring by reverse rotation of the crucible with the melt. It was shown that instrumental instability can cause striations in this case, but this is not the main cause of striations. More uniform crystals are formed upon an increase of the melt volume. Increase of the melt volume causes an increase in the thermal inertia of the crystallization system. High thermal inertia significantly reduces the influence of oscillations of the power supplied by the **RF** generator and removed by water from a **CC**, i. e., suppresses the temperature fluctuations, maintaining the stationary state in the system. This results in stabilization of the crystallization front and increases the homogeneity of crystals. This situation was observed upon growing **CZ** crystals from a **CC** of more than 400 mm in diameter when the density of the growth striations decreased to $1\text{--}2\text{ cm}^{-1}$ upon decreasing the rate to 2–3 mm/h without forced stirring. The determination of the K of components of solid solution in ZrO_2 is very important for growing homogeneous **CZ** crystals.

Distribution Coefficients of the Solid Solution Components

The K of a component denotes the ratio of concentrations of this component in a liquid and solid phase having a common interface. Actually one usually deals

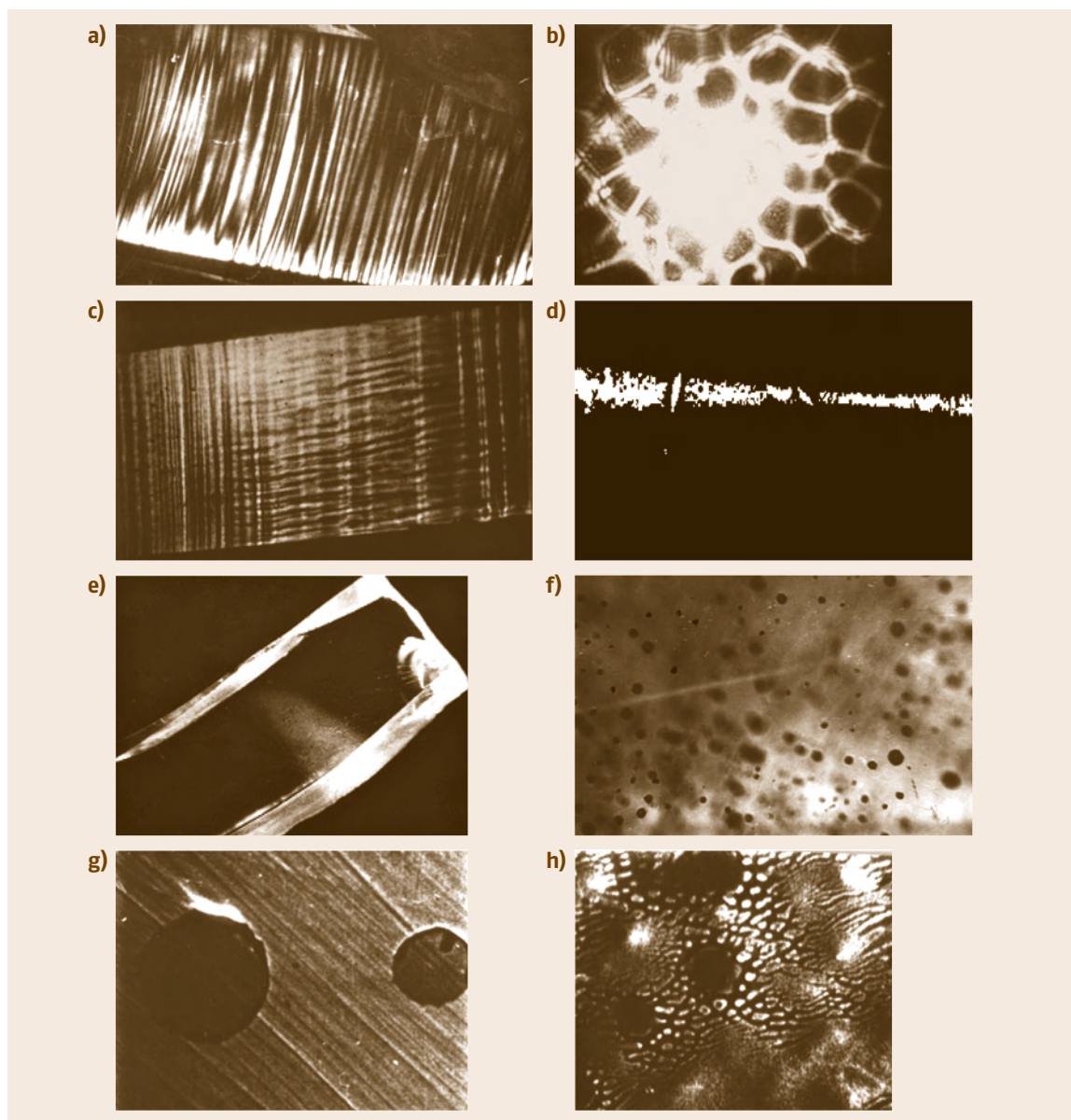


Fig. 14.15a–h Defects in cubic zirconia single crystals: (a) growth striae; (b) cellular structure; (c) growth striae and cellular structure; (d) light scattering of laser beam in the crystal; (e) light scattering in the defect area; (f) inclusions in the boundaries of cells; (g) inclusions containing SiO_2 ; (h) SiO_2 inclusions on the surface of ZrO_2 –10 mol % Y_2O_3 crystals

with effective distribution coefficients (K_{eff}) which differ from the equilibrium coefficients (K_0). K_0 characterizes the ratio of concentrations corresponding to the solidus and liquidus curves of the phase diagram having a common node. The directional crystalliza-

tion processes take place with finite rate, so greater or lesser deviations from equilibrium occur. To determine the value of K_{eff} , the distribution of the components along with the axis of the crystal is measured. Quantitative element analysis was performed by electron probe

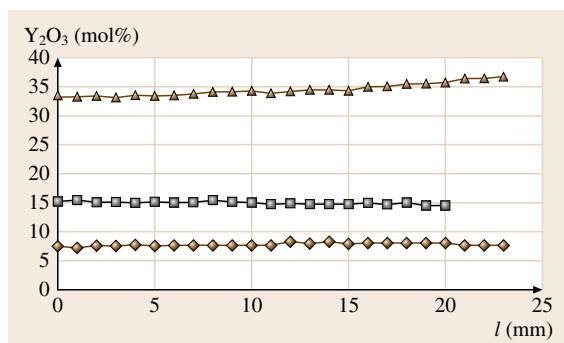


Fig. 14.16 Distribution of Y_2O_3 concentration in ZrO_2 - Y_2O_3 crystals of different compositions. Initial composition (mol.% Y_2O_3): (▲) – 35; (□) – 15; (◆) – 7.5

microanalysis [14.25, 28, 30, 31] or by optical spectroscopy [14.134, 135]. The experimental results were approximated by the equation $C(g) = kC_0(1 - g)^{k-1}$, which is commonly used to describe the processes of normal directional crystallization [14.25, 28, 30, 31]. An example of measurements of the stabilizing oxide concentrations in ZrO_2 - Y_2O_3 crystals of different composition is given in Fig. 14.16.

A more detailed study of the Y_2O_3 distribution curves in crystals taken from different parts of the ingot showed that periodic nonuniformity of crystal composition along the growth direction occurs, resulting from oscillations of the crystal growth rate [14.28]. Waves in concentration curves of crystals taken from different parts of the ingot did not coincide, this being indicative of differences in crystallization conditions along the ingot cross-section (the crystallization front not being flat). Sometimes sudden changes of concentration were observed in the distribution curves. Such changes can occur due to an abrupt change of power supplied by a RF generator, causing a dramatic change of the crystallization rate, or to quick uncontrolled growth caused by constitutional supercooling. As a rule, such sharp concentration changes took place at the end of crystal growth. This is due to accumulation of the displaced admixtures in the melt and enhancement of the constitutional supercooling, which disturb the stable growth of crystals, causing the formation of inclusions and cellular structure. Besides, the coupling between the RF field and the melt is deteriorated when the amount of melt decreases, and this results in quick uncontrolled crystallization of the remaining melt. Changing the lowering rate of a CC in the range of 1–16 mm/h and changing the concentration of the stabilizing oxide weakly influenced the character of the distribution curves. The

Table 14.3 Effective distribution coefficients of Y_2O_3 in the ZrO_2 - Y_2O_3 system

C (mol% Y_2O_3)	Growth rate (mm/h)	K_{eff}
5	16	1.08 ± 0.05
8	16	1.06 ± 0.05
10	1	1.12 ± 0.03
10	5	1.05 ± 0.02
10	8	1.02 ± 0.02
10	30	1.07 ± 0.02
15	16	1.02 ± 0.02
20	16	1.00 ± 0.01
30	16	1.01 ± 0.02

values of K_{eff} for different growth rates and compositions are presented in Table 14.3. The values of K_{eff} of Y_2O_3 calculated from these data are close to 1 and only slightly depend on the growth rate and initial concentration of Y_2O_3 .

The values of K_{eff} for Gd – Yb oxides are close to those of Y_2O_3 in cubic solid solutions based on ZrO_2 and also slightly depend on the growth rate and initial concentration of stabilizing oxide [14.25, 30]. The values of K_{eff} for rare-earth oxides from the left part of the lanthanide series (Ce–Nd) in cubic solid solutions based on ZrO_2 were found to be less than 1 [14.25] (Table 14.4).

Data on the dependence of K_{eff} in CZ crystals with 12 mol % Y_2O_3 doped with 1.2265 wt % Nd_2O_3 on growth rate are shown in Table 14.5 [14.134]. Using the data obtained, the authors determined that, for Nd_2O_3 , $K_0 = 0.426$ and the diffusion layer is approximately 1 mm thick.

Cellular structure [14.25, 28–31] was observed in crystals extracted from the central part of the ingot and, as a rule, in the top part of the crystals (Fig. 14.15b). The top of the crystals exhibiting cellular structure had a characteristic *rudded* appearance; if the cellular structure was highly developed, boundaries between smooth shiny surface and uneven wavy surface could be clearly seen on the sides of the crystals. Regions exhibiting lamellar and cellular structure can alternate in the same crystal (Fig. 14.15c). The appearance of cellular structure is accompanied by a decrease in the striae density. The formation of cellular structure is caused by the destabilization of the smooth crystallization front upon growing [14.178–180]. Most authors consider constitutional supercooling of the melt near the phase interface to be the cause of destabilization of the smooth front and its transformation into the cellu-

Table 14.4 Effective distribution coefficients of Nd₂O₃ and CeO₂ in the ZrO₂-0Y₂O₃-Nd₂O₃-CeO₂ system

Composition	V (mm/h)	<i>K</i> _{eff} Nd ₂ O ₃	CeO ₂	Y ₂ O ₃
ZrO ₂ -(12-25 mol %) Y ₂ O ₃ -(0.74-4.40 mol %) Nd ₂ O ₃	5	0.62 ± 0.04	–	1.045 ± 0.03
ZrO ₂ -(9-11 mol %) Y ₂ O ₃ -(2-2.5 mol %) Nd ₂ O ₃ -1 mol % CeO ₂	5	0.58 ± 0.08	0.42 ± 0.04	1.09 ± 0.02
ZrO ₂ -3 mol % Y ₂ O ₃ -0.3 mol % Nd ₂ O ₃ -0.4 mol % CeO ₂	10	0.87 ± 0.08	0.78 ± 0.02	1.13 ± 0.01

lar type [14.180]. Constitutional supercooling alone was shown to be insufficient for the formation of cellular structure; a threshold value of constitutional supercooling depending on the chemical composition of the melt and the direction of growth had to be achieved. Studies of CZ crystals [14.25, 28–31] showed that the cellular structure appears at the end of the growth stage, most often in crystals situated in the central part of the crystalline ingot. This is connected both with the accumulation of admixtures in the melt before the crystallization front during crystal growth and with the character of the temperature distribution in the CC. Cellular structure, appearing as a *constriction* in the middle of the crystal, was formed at high growth rates (> 10 mm/h) in the absence of stirring.

Oxides of Si, Al, Ti, and W cause the appearance of imperfections deleterious to the optical uniformity of the crystals. Of all the contaminants mentioned, SiO₂ exerts the most negative influence on the growth and perfection of crystals. Even small quantities of SiO₂ promote disruptions of crystal growth and the appearance of cellular structure regions. Decreasing the growth rate and using forced stirring improves the efficiency of impurity segregation and the crystal quality [14.25, 28–30].

Inclusions [14.25, 29–31]. Large isolated inclusions and bubbles are seldom observed in CZ crystals; inclusions formed by light-diffusing particles of 10–0.08 μm in size are observed much more often. Light scattering can be observed either visually or by the scattering of a laser beam passing through the crystal (Fig. 14.15d). The occurrence of light-scattering regions depends on the composition of the melt and the growth conditions. Single crystals may be completely opalescent or exhibit broad opalescent bands in the top central part of the ingot (Fig. 14.15e). Research [14.25, 29–31] showed that band-shaped light-scattering regions coincide with regions of cellular growth. It was established that light-scattering inclusions may be formed during melt crystallization in CZ crystals either on all the phase interface or on the boundaries of the cellular structure (Fig. 14.15f,g). Growth of CZ crystals in a wide range of concentration of the stabilizing oxide at growth

rates of 1–2 mm/h showed that light scattering by the whole crystals is characteristic of compositions with 8–12 mol % R₂O₃ (R = Y, Gd) [14.25]. X-ray diffraction patterns of these crystals were not indicative of the appearance of new phases. Scattering in these crystals was caused by particles of the second phase with size of 1–0.1 μm. Under the same growth conditions, increasing the concentration of the stabilizing oxide to above 14 mol % R₂O₃ (R = Y, Yb) or above 16 mol % Gd₂O₃ completely eliminated light scattering in the crystals. The appearance of light-scattering particles may be connected either with the presence of impurities becoming less soluble upon a decrease in temperature (in this case it depends on the melt composition) or with the decomposition of the fluorite-type solid solution. Low concentration of the second phase and the very small size of its particles complicates direct determination of the phase structure and composition. It is worth mentioning that heat treatment of ZrO₂-12 mol % Y₂O₃ crystals at 2100 °C for 3 h under vacuum and subsequent quenching (at cooling rate of 1000 °C/h) led to elimination of light scattering. Large inclusions of the second phase (> 0.5 μm) are an extreme case of inhomogeneity of the crystal and are usually located in regions of highly developed cellular structure. As a rule, such inclusions are caused by the presence of unde-

Table 14.5 Effective distribution coefficients of Nd₂O₃ in the ZrO₂-12 mol % Y₂O₃-1.2265 wt % Nd₂O₃ system

V (mm/h)	<i>K</i> _{eff}
4	0.51 ± 0.016
4	0.52 ± 0.025
6	0.54 ± 0.013
6	0.54 ± 0.013
8	0.61 ± 0.025
8	0.60 ± 0.03
10	0.63 ± 0.006
10	0.68 ± 0.038
12	0.68 ± 0.019
12	0.65 ± 0.013
14	0.73 ± 0.06
14	0.70 ± 0.06

sirable impurities in the initial mixture. The type of inhomogeneity caused by the presence of admixtures is determined by the nature and concentration of the admixture (SiO_2 , TiO_2 , Al_2O_3 , WO_3). Large (4–10 μm in size) silicon-containing inclusions of the second phase were detected in the boundaries of cells (Fig. 14.15f,g). The density of such inclusions in the top part of the crystal varies from 4.5×10^2 to $26 \times 10^2 \text{ mm}^{-3}$.

Electron probe microanalysis of the inclusion composition showed that the concentration of SiO_2 in the inclusions is very high ($\approx 60 \text{ mol } \%$). The spherical shape of such inclusions and their compositional nonuniformity suggest that trapping of the liquid phase occurs. The melting point of the SiO_2 -enriched drops being lower than that of $\text{ZrO}_2\text{--R}_2\text{O}_3$, these liquid drops become trapped in the solid crystal matrix. The concentration of Y_2O_3 in the inclusions is also higher than in the matrix because R_2O_3 , being oxides of basic character, accumulate in the drops due to chemical affinity towards SiO_2 , which is more acidic than ZrO_2 . The process of chemical differentiation takes place either upon drop formation or upon drop cooling (in the latter case it is due to diffusion from the solid matrix). High content of stabilizing oxide in the inclusions (up to 28 mol % in the case of $\text{ZrO}_2\text{--}12 \text{ mol } \% \text{ Y}_2\text{O}_3$) may cause decomposition of the cubic solid solutions and formation of m-ZrO_2 if the concentration of SiO_2 is sufficiently high and the concentration of the stabilizing oxide is low. However, the probability of this process is low if the Y_2O_3 concentration in the cubic crystals is high. Apart from forming inclusions inside the crystal, the second phase can form precipitates on the surface of blocks (Fig. 14.15h). In this case a matted deposit appears on some parts of the crystal facets, which is usually smooth and very shiny [14.25, 29–31].

14.3.5 Growth, Properties, and Application of PSZ Crystals

The SM technology of PSZ crystals is similar to the above-described growth process of CZ crystals. The growing PSZ crystal exhibits a c-structure during the first stage of synthesis from melt; phase transitions in the crystal occur upon cooling of the solid phase. The $\text{c} \rightarrow \text{t}$ phase transformation is accompanied by the formation of domain structure in the crystals [14.130–132]. PSZ crystals are used mainly for scientific research on the mechanism of hardening, structural, micro- and nanostructural research, studies on phase transformations, and physicochemical properties [14.109, 112, 116, 149, 181–183]. Although the advantages in mechan-

ical properties (high hardness, strength, and fracture toughness) of PSZ crystals, especially at elevated temperatures, have apparently been demonstrated, practical applications of PSZ as construction material have not yet been reflected in the literature.

Large uniform blocks of material without cracks are required for practical applications. This is why the influence of composition and growth conditions on the size and mechanical properties of crystals was investigated [14.184–187]. The stabilizing oxide concentration range (2.5–4 mol % Y_2O_3) allowing the preparation of large (up to 40 mm in cross-section, up to 120 mm in length) uniform PSZ crystals not containing fractures has been established [14.188]. PSZ crystals of the composition $\text{ZrO}_2\text{--}2.5\text{--}4 \text{ mol } \% \text{ Y}_2\text{O}_3$ are white and nontransparent, with a smooth shiny surface. The crystal surface becomes rough and matted upon a decrease in Y_2O_3 content. The crystal size is significantly decreased at Y_2O_3 concentration $< 1 \text{ mol } \%$. Crystals containing 5–8 mol % Y_2O_3 are semitransparent and contain a large number of fractures in the volume. Experiments on the growth of crystals in a CC of 130 mm diameter showed that rate decrease from 40 to 3 mm/h led to a significant increase in the crystal cross-section size (from 3–7 mm to 20–40 mm) [14.185, 186] (Fig. 14.17).

However, growing the crystals at 3 mm/h rate results in a considerable increase in the number of fractures in the crystals. The cooling rate in the crucible of 130 mm diameter being too high for crystals of a large size, residual thermal stresses are probably relieved by means of fracture formation in the crystals. Research into the influence of thermal conditions on crystal growth showed that the quantity of large cross-section crystals is significantly increased upon an increase of the height of the bottom thermal shield. Most crystals have a smooth shiny surface.

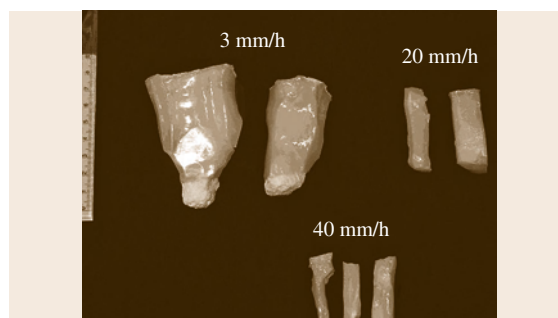


Fig. 14.17 PSZ crystals grown at 3, 20, and 40 mm/h in a cold crucible with 130 mm diameter

Table 14.6 Effective distribution coefficient of Y₂O₃ in the ZrO₂-Y₂O₃ system in PSZ

C (mol% Y ₂ O ₃)	K _{eff} 10 mm/h	20 mm/h	40 mm/h
2.5	1.04 ± 0.01	1.07 ± 0.01	–
3	1.006 ± 0.007	1.025 ± 0.006	1.02 ± 0.02
3.5	1.150 ± 0.009	1.023 ± 0.005	1.027 ± 0.007
4	0.98 ± 0.09	1.001 ± 0.008	1.002 ± 0.009
5	1.03 ± 0.01	–	–
8	1.041 ± 0.007	–	–

Therefore, the most appropriate conditions for the preparation of large, smooth-faceted PSZ crystals are growth rate about 10 mm/h with enlarged bottom thermal shield. Studies of the chemical composition of the crystals showed that microcontaminants from the starting materials are segregated during growth of PSZ crystals in the same way as for CZ crystals. Decreasing the crystallization rate results in a decrease in contaminant concentrations compared with in the initial mixture [14.185]. The distribution of the main components of the solid solution (at crystallization rates of 3–40 mm/h) is fairly uniform, the value of K_{eff} Y₂O₃ in ZrO₂ being close to 1 [14.186] (Table 14.6).

Investigation of the crystal phase composition of as-grown crystals (growth rate 3–10 mm/h) by Raman spectroscopy revealed that molten ZrO₂ was m-phase; crystals containing 2 mol % Y₂O₃ were a mixture of m- and t-phases; crystals containing 2.5 mol % Y₂O₃ contained small m-phase regions, the larger part of the crystal being t-phase; at concentration range 3–5 mol % the crystals were t-phase; at Y₂O₃ concentration of 8–35 mol % the crystals were constituted by a cubic solid solution of fluorite structure [14.185, 186]. X-ray diffraction patterns of powdered samples prepared from PSZ crystals (growth rate 3–10 mm/h) showed that the m-phase is present in crystals containing 2.0–3.5 mol % Y₂O₃ while only the peaks of a highly symmetric phase are present in the pattern of crystals containing 4.0–5.0 mol % Y₂O₃. Apparently, t→m transformation occurred under powdering. Analysis of the same powders by Raman spectroscopy has confirmed that such a transformation in fact took place, indicated by the occurrence of the m-phase in powdered samples containing up to 3.5 mol % Y₂O₃. Differences in the phase composition of bulk and powdered samples show that X-ray diffraction analysis of powders more appropriately reflects the phase composition of materials subjected to intensive mechanical impact, while Raman spectroscopy allows a more detailed determination of the phase composition of bulk crystal samples. It

was shown that PSZ crystals grown in a CC of 130 mm in diameter are not sharply quenched, therefore they contain the t-phase as well as the t'-phase, and so the m-phase appears upon mechanical impact [14.186]. The incorporation of admixtures (oxides of Ce, Nd, Tb, Co, etc.) was also shown to influence the number of fractures [14.189–191].

The shape of the crystal growth surface precisely reflects the microstructure of the material, which is influenced by the composition as well as crystallization and annealing conditions. Scanning electron microscopic studies of the as-grown crystals showed that the crystal surface morphology is influenced by the stabilizing oxide concentration in the solid solution [14.185, 186, 189, 191]. Microphotographs of the as-growth crystal surfaces with different content of the stabilizing oxide (Y₂O₃) are shown in Fig. 14.18.

Relief of the growth facets of pure ZrO₂ crystals which had undergone a t→m transformation is typical for martensitic transitions (Fig. 14.18a,b). This transition is accompanied by a significant volume change (up to 5 vol. %) and causes fracturing. A regular microcrack network in the form of rhombs can be clearly seen in Fig. 14.18a. The cracks of each subset are apparently parallel to each other and the angle of intersection is close to 30°. Microcracks can be also seen on the growth surface of ZrO₂–2.0 mol % Y₂O₃ samples (Fig. 14.18c,d), but these microcracks are sufficiently shorter and many of them are warped. Both the elements of the above-described structure and the so-called *tweed* structure characteristic of samples with higher Y₂O₃ content can be seen on the surface. *Tweed* structure is characterized by element intersection angle close to 80–90°. The surface of crystals containing 2.5 mol % Y₂O₃ (Fig. 14.18e,f) is practically devoid of cracks, while the elements of the *tweed* structure occupying the larger part of the crystal surface can be clearly seen. However, only isolated elements of the *tweed* structure are present in some regions of the crystal surface (Fig. 14.18f). The existence of two characteristic

types (type 1 and type 2) of growth surface was detected for ZrO_2 crystals containing 3.0 mol % Y_2O_3 (Fig. 14.18g–j). Type 1 is characterized by *smooth* facets (Fig. 14.18g), while type 2 is characterized by *matted* facets (Fig. 14.18h,i). The boundary of the smooth and matted facets is shown in Fig. 14.18j.

Surface morphology of any of these types may be characteristic either for all facets of the crystal block or only for some of them, being present as an individual facet. The surface of type 1 comprises a rather regular structure, which is similar to the *tweed* one. It consists of tiny elongated rectangles (1–10 μm in length and 0.5–3 μm in width) grouped parallel to each other. The angle of orientation of groups relative to each other is close to 80–90°. The surface of type 2 has a more pronounced relief than the one described above and consists of parallel convex rectangles, which are larger than the elements of type 1 structure (up to 50 μm in length and > 5 μm in width). More pronounced relief of the structure forms the matted appearance of the facet. Figure 14.18 clearly shows that smaller structural elements with sizes characteristic of the smooth (type 1) surface coexist with larger surface elements on type 2 surfaces.

Matted surfaces occur in the central and lower part of the crystal bulk, their appearance being dependent on the melt volume and crystal length. At the same time, single-crystalline blocks are often accreted by these facets, so separation of such blocks sometimes leads to destruction of the crystals. It seems that this process is influenced by cooling conditions during crystal growth, which determine the phase composition and microstructure of the crystals. The absence of matted facets on the crystal surface at growth rate of 3 mm/h is worth mentioning. Practically, large crystals are no growing together. There are few such crystals in the ingot, and stress is relieved mainly on the block boundaries and partly in the block volume. The latter process results in crystal fracturing. The matted crystal surface is formed if the initial melt contains significant quantities of contaminants with K value much lower than 1. However, such surfaces differ from that described above by the presence of a characteristic tarnish of the segregated admixtures (Fig. 14.19).

Further increase of the stabilizing oxide concentration results in the appearance of various types of island structures; namely, islands consisting of parallel structural elements without perpendicular crossing appear on a *tweed* structure background in the case of ZrO_2 containing 3.5 mol % Y_2O_3 (Fig. 14.20a,b).

Crystals containing 4.0 mol % Y_2O_3 are characterized by a smooth unstructured surface on which small

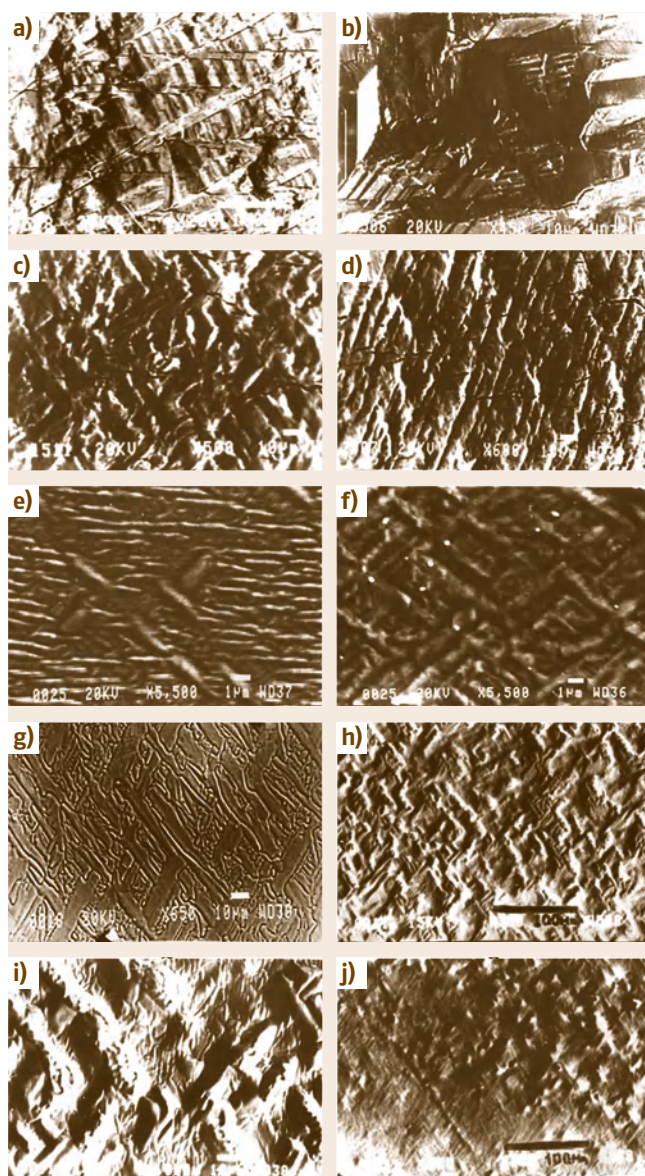


Fig. 14.18a–h Morphology of as-grown facets of PSZ crystals of $(1-x)\text{ZrO}_2$ - $x\text{Y}_2\text{O}_3$ mol % compositions (**a,b**) $x = 0$; (**c,d**) $x = 2.0$; (**e,f**) $x = 2.5$; (**g,h**) $x = 3.0$

islands with a pronounced microstructure occur very rarely (Fig. 14.21). The appearance of an island structure can be indicative of incompleteness of the phase transitions occurring during the cooling of the crystal. As a result, Y_2O_3 is unevenly redistributed between two t-phases at temperatures corresponding to the two-phase region of the phase diagram. It is obvious that phases

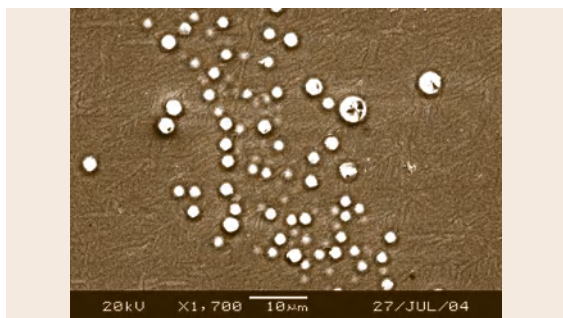


Fig. 14.19 Surface of facets of ZrO_2 -3 mol % Y_2O_3 grown at 3 mm/h with SiO_2 inclusions (magnification 1700 \times)

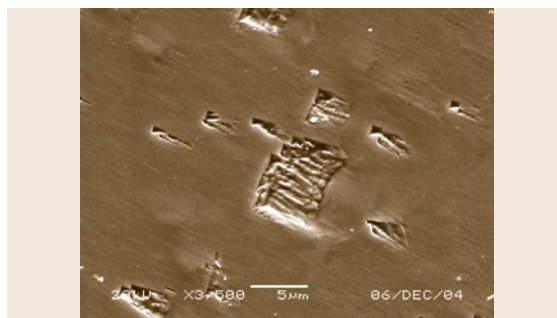


Fig. 14.21 Surface of facets of ZrO_2 -4 mol % Y_2O_3 grown at 10 mm/h

with different Y_2O_3 content can differ in microstructure.

Nanostructure of ZrO_2 -3 mol % Y_2O_3 crystals was studied by high-resolution transmission electron microscopy (TEM) as well as by x-ray analysis. The latter method was used to estimate the size of coherent scattering regions according to the broadening of the diffraction reflexes [14.112, 114, 115, 186]. A model of ordered domain colonies occupying all the volume of the crystal at the minimum of deformation energy was proposed [14.112]. TEM studies of the ZrO_2 -3 mol %

Y_2O_3 crystal revealed the presence of colonies formed by *parquet* structure domains (30–100 nm in width, 400–800 nm in length) (Fig. 14.22).

Laminated structure with a period of about 10 nm is observed in the colonies, indicating the presence of a lamellar domain structure in each colony. Their size is estimated to be (0.1–0.5) \times (10–20) nm. An estimate of the coherent scattering region size (D) in the ZrO_2 -3 mol % Y_2O_3 crystal by X-ray structure analysis yields a value of 87–310 nm, which corresponds rather well to the above estimates of the colony size. A scanning electron microscopic study of the crystal surface microstructure at 25 000 \times amplification allowed estimation of the size of the smallest structural elements. The width was estimated to be 70–300 nm and the length was estimated to be 300–900 nm. These estimated values are close to the sizes of colonies observed during the TEM study. Therefore, the microstructure of as-grown facet of the crystals reflects the inner crystal structure (the structure of colonies). Research on

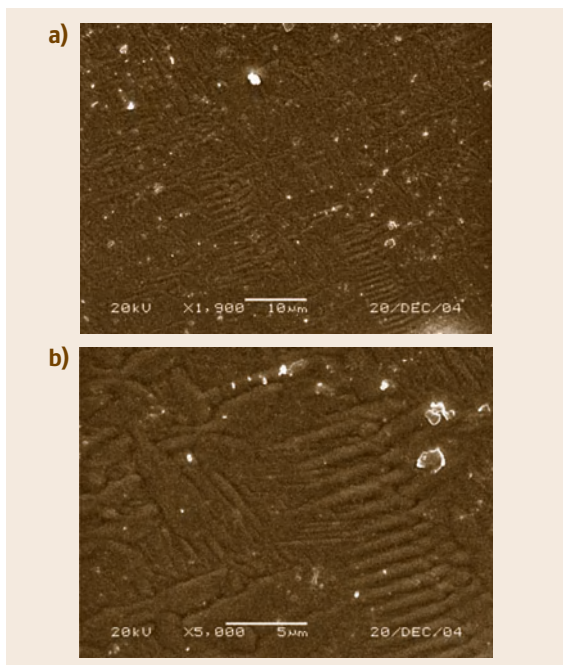


Fig. 14.20a,b Surface of facets of ZrO_2 -3.5 mol % Y_2O_3 grown at 10 mm/h. (a) 1900 \times ; (b) 5000 \times

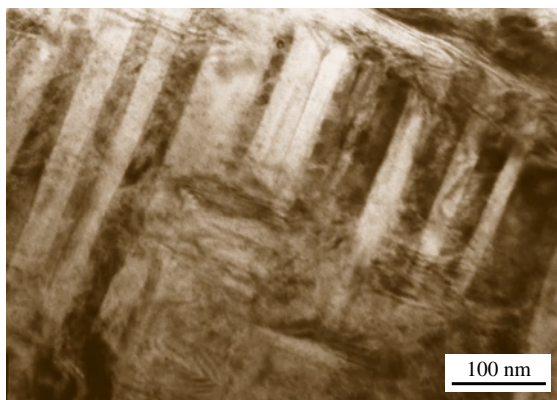


Fig. 14.22 Nanostructure of ZrO_2 -3 mol % Y_2O_3 crystal grown at 10 mm/h

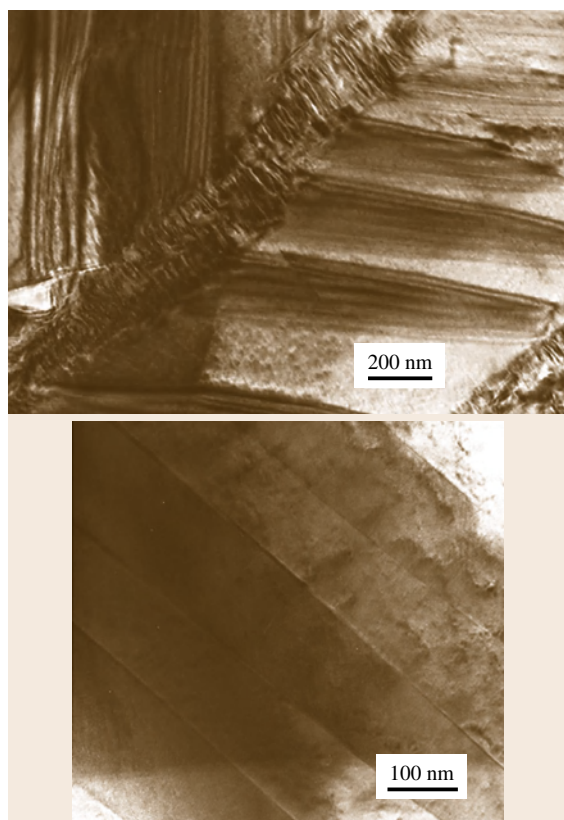


Fig. 14.23 Nanostructure of ZrO_2 –2.5 mol % Y_2O_3 crystal grown at 10 mm/h

the nanostructure of ZrO_2 –2.5 mol % Y_2O_3 crystals showed that the formation of the domain structure just begins at this Y_2O_3 concentration (a system of parallel domains with some elements of the tweed structure is formed) (Fig. 14.23).

Only isolated regions with nonpronounced domain structure were detected in ZrO_2 –4 mol % Y_2O_3 crystals (Fig. 14.24).

This corresponds to the results of research on the microstructure of growth surface of PSZ crystals as determined by their composition. The doping of PSZ crystals with additional admixtures in small quantities (≈ 0.1 mol %) affects the microstructure and mechanical properties of the crystals [14.189, 191]. These studies revealed that sample breaking strength is connected with the structure of the crystal surface, which reflects the microstructure of layers adjacent to the surface.

The oxygen-isotope method was used to study the peculiarities of oxygen redistribution during formation

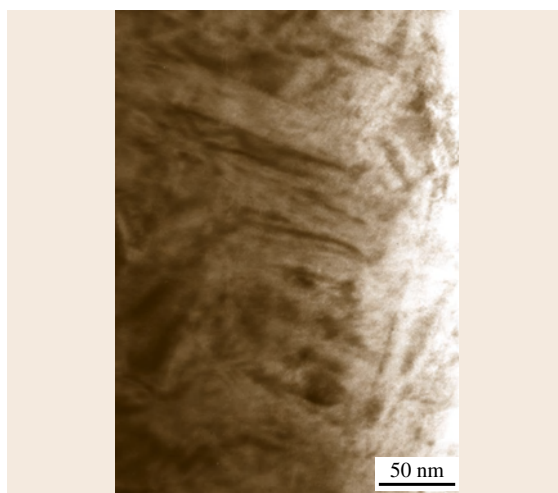


Fig. 14.24 Nanostructure of ZrO_2 –4 mol % Y_2O_3 crystal grown at 10 mm/h

and stabilization of the structure of substitutional solid solutions $\text{Zr}_{1-x}^{+4}\text{Y}_x^{+3}\text{O}_{2-0.5x}^{-2}\text{V}_{0.5x}^0$ and further annealing of the crystals under various gas atmosphere. The mobility of oxygen was shown to depend on the chemical composition of the crystal and the conditions of heat treatment. The existence of correlation between oxygen mobility in PSZ crystals and their electrical and mechanical properties was confirmed [14.192]. It was also shown that maximum oxygen mobility is found in PSZ crystals containing 2.5–4.0 mol % Y_2O_3 . The optimal composition range of PSZ crystals ensuring the nanocrystalline structure, high mechanical characteristics, and high oxygen mobility was found by physicochemical methods to be ZrO_2 –2.5–4.0 mol % Y_2O_3 .

Significant anisotropy of strength properties (elastic characteristics, threshold values of strength, deformation properties, specific fracture energy, fracture strength, and hardness) was detected in studies of the dependence of these properties on Y_2O_3 concentration, presence of additives, growth rate, crystallographic orientation, and heat treatment conditions. It should be mentioned that stabilizing oxide concentration exerts a determining influence on strength properties [14.116, 181, 193–197]. The following high values of strength properties were determined for PSZ crystals: dynamic modulus of elasticity of 400–500 GPa, ultimate compression strength of 4000 MPa, ultimate bending strength of 1600 MPa, fracture toughness of $15 \text{ MPa m}^{0.5}$, and hardness of 15 GPa.

Results of the studies of the tribological properties of PSZ crystals are presented in [14.195–197].

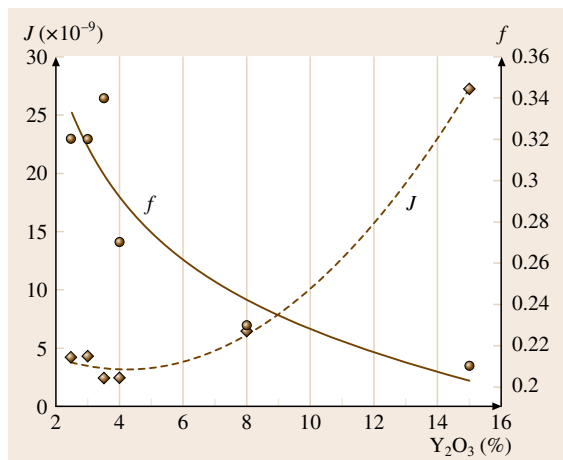


Fig. 14.25 Effect of Y_2O_3 concentration on wearing intensity (J) and friction coefficient (f)

The main tribotechnical properties and the mechanism of wearing of the PSZ crystals were determined in experiments including x-ray and electron microscopic analyses of friction surfaces. PSZ crystals containing

2.5–4.0 mol % Y_2O_3 were the most wear resistance. The intensity of wear was $(2.5\text{--}4.3) \times 10^{-9}$, the friction coefficient was 0.32–0.34, and microhardness was 11.8–15.08 GPa (assessed with instrumental steel U10A as counterbody) (Fig. 14.25).

The predominant wear mechanism of the PSZ crystals was shown to be a two-stage mechanical (fatigue) mechanism involving the destruction of the surface layer of secondary structures formed upon friction with subsequent destruction of deeper layers of the bulk material. The results obtained show that synthesis of high-strength fracture-proof materials by directional crystallization of melt requires consideration of many factors: the K_{eff} values of the additives used, growth rate, temperature gradients in the melt, the nature and concentrations of the stabilizing oxide and the third additive, and cooling and annealing conditions.

PSZ crystals possess a number of properties giving them advantage over metals and high-strength dielectric materials (including ceramics). Due to their lack of grain boundaries PSZ crystals are characterized by high strength (comparable to the strength of metals), fracture toughness, and hardness. They are also char-

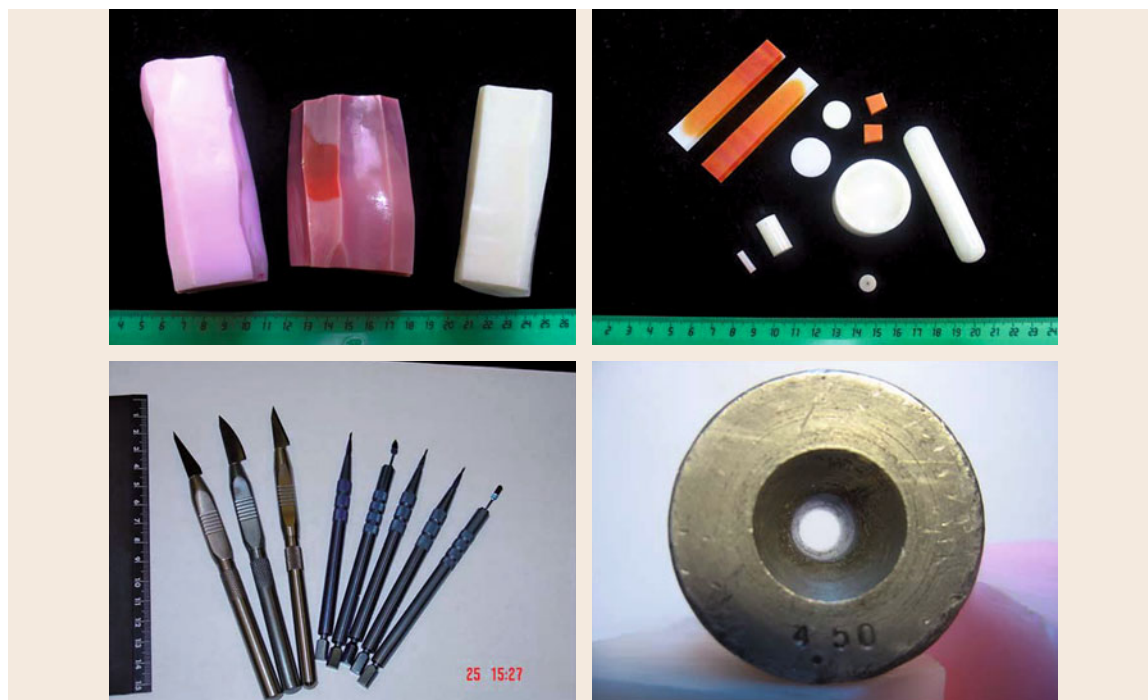


Fig. 14.26 Technical articles and components fabricated from PSZ crystals. PSZ crystals (top left); cutting elements, rolls and grinding tool fabricated from PSZ (top right); medicine scalpels with cutting edge from PSZ (bottom left); wire drawing die with insert from PSZ (bottom right)

acterized by low friction coefficient and high abrasive wear resistance, and high resistance to acids, alkali, and water vapor. Deterioration of mechanical characteristics of PSZ crystals placed in oxidizing atmosphere at high temperatures (up to 1400 °C) is much less pronounced than that of metals (which are intensely oxidized) or construction ceramics, which are prone to recrystallization. Besides, the mechanical properties of the crystals are improved upon temperature decrease (at −140 °C the improvement amounts to 70%). Such materials can be used to produce details of appliances functioning under extreme conditions: at high mechanical loadings, in aggressive media, at elevated temperatures, without lubrication, etc. Such appliances include bearings, support prisms, guide plates, and motor valves. Due to the existence of domain nanostructure in PSZ crystals and high mechanical strength of these crystals they may be used in the manufacturing of instruments with very sharp cutting edges, for example, high-quality medi-

cal scalpels and instruments for precision machining of various materials (metal, wood, glass, crystals, etc.).

The biological inertness of this material [14.183, 198, 199] enables its use in the manufacturing of implants for medicine. Comparative mechanical and biomedical tests were performed for PSZ crystals, CZ crystals, PSZ ceramics, and Al₂O₃ single crystals [14.182]. PSZ crystals were shown to be somewhat stronger than other materials and displayed the highest fracture toughness. Studies on implants made of ZrO₂-based materials showed that these implants neither provoke an inflammatory reaction in tissues nor cause pathological changes in the internal organs of animals. The results of investigations show that PSZ crystals can be used as a material for various implants. Some articles manufactured from PSZ crystals are shown in Fig. 14.26 to give examples of practical applications of this material.

14.4 Glass Synthesis by Skull Melting in a Cold Crucible

In this section some questions about using SM technique for glass synthesis will be analyzed. Use of this method is justified if the synthesis of a specific type of glass by traditional methods is impossible or very difficult. These glass types include:

- Optical and laser glasses for which high chemical purity is required; for example, in glasses for fiber-optical communication lines the content of transition-metal contaminants must not exceed 10^{−5}–10^{−6} wt %
- Glasses prepared from highly reactive melts and/or materials capable of interacting with the crucible material
- High-temperature glasses of various compositions which must be synthesized at temperatures exceeding 1600 °C.

Let us analyze the peculiarities of the use of this method for glass synthesis.

Glass is an amorphous material, undergoing a smooth transition from solid state to glass-like state upon heating. Glass-forming melts differ from other oxide melts by their high viscosity (depending on the melt composition, the viscosity may be several orders of magnitude higher than that of typical oxide melts) and a smooth temperature dependence of viscosity and electric conductivity. Besides, the absence of a solid–liquid phase transition and the corresponding dramatic change

in electric conductivity enhance the phase stability of the melt and make keeping of the melt in a stationary state easier. That is why in the case of induction melting in the cold crucible the skull consists of a thin layer of initial powdered mixture adjacent to crucible walls and a layer of solid glass, the thickness of the latter layer being influenced by the temperature distribution in the melt.

Various types of crucibles are used according to the composition of a specific glass type. Synthesis of silicate glasses was performed in water-cooled quartz crucibles [14.10, 11]. As quartz is a typical dielectric, effective supply of the alternating electromagnetic field energy to the melt without losses in the crucible material is enabled. The use of such crucibles imposes considerable limitations on the temperature of glass synthesis. Other drawbacks of quartz crucibles are the impossibility of repeated use and a requirement for stringent control of the melt temperature to avoid the risks of crucible destruction and water getting into the melt. Metallic crucibles for glass synthesis also have some peculiarities. Aluminum is the preferred crucible material. Beside individual oxides, salts (carbonates, nitrates, oxalates, etc.) are often used as starting materials for glass synthesis. Upon thermal decomposition of salts, interaction of the decomposition products with the crucible material and transfer of small quantities of crucible material into the melt may occur. In the case of aluminum

crucibles, a thin layer of Al_2O_3 present on the surface of aluminum prevents the heterogeneous chemical reactions. Besides, Al_2O_3 is often present in glasses and therefore embedding of small amounts of Al_2O_3 into the melt does not cause a significant change in the properties of glass. Aluminum oxide is an optically inactive admixture, so its presence does not influence the optical properties of glass. Metallic crucibles must be dismountable in order to ensure quick extraction of the glass block for further annealing. The use of combined crucibles, i. e., metallic crucibles with thin-walled quartz crucibles inserted into them, has also been reported [14.26].

In the case of glass synthesis, the initial melt volume cannot be created by introducing small pieces of a metal directly into the initial mixture, because this would lead to contamination of the melt by metal and the reduction products dispersed in the melt volume. The high viscosity of glass-forming melts leads to a dramatic decrease in the metal burning-out rate [14.31]. Start melting is usually performed by placing a quartz ampoule filled with pieces of graphite or low-resistance Si into the fusion mixture. Afterwards the ampoule is removed from the melt. To make start melting easier and to prevent the evaporation of low-melting-point components, one should first melt the low-melting-point components and then introduce the refractory ones into the melt; for example, glass synthesis in the system $\text{Li}_2\text{O}-\text{Al}_2\text{O}_3-\text{SiO}_2-\text{ZrO}_2$ was begun with the melting of the $\text{Li}_2\text{O}-\text{SiO}_2$ composition, which melts at $1100-1200^\circ\text{C}$ [14.200].

Homogenization of the melt is an important technological stage of high-quality optical glass synthesis. Complicated physicochemical processes connected with the melting of individual components of the fusion mixture and the occurrence of solid-phase chemical reactions and reactions in the melt are finished at this stage. Nonuniform temperature distribution in the melt exerts a significant influence on the dissolution of the fusion mixture components not yet involved in chemical reactions and the removal of the previously formed gas bubbles. At first, bubbles are removed from the maximum temperature zone, which is situated at a distance of 10–20 mm from the crucible walls (Fig. 14.3). Intensive convection in the melt, which promotes the removal of gas bubbles and leveling of the chemical composition of the melt, is an important consequence of the existence of high temperature gradients in the melt. Mechanical stirring by a water-cooled stirrer or by gas bubbling through the melt is used to intensify these processes [14.11, 31]. These methods are used in

combination with the melt temperature increase, which causes a decrease in viscosity and an increase in the rate of convective mass transfer.

After glass synthesis in the CC, annealing cannot be performed in the same crucible because, when the temperature of the melt being cooled reaches a value determined by the temperature dependence of the conductivity, the melt ceases to absorb the energy of the RF electromagnetic field. After this, intensive cooling of the glass by the water-cooling crucible walls and glass fracturing occurs. Therefore a method of glass extraction from the crucible with subsequent annealing in the furnace is essential. One of the methods consists of pouring the melt into a mold and further annealing of the glass. However, the risk of contamination of the central part of the glass block by bubbles and nonmolten particles of the fusion mixture from the periphery of the block is very high during this operation. Another method consists of extracting the glass block at a specific temperature, which is determined experimentally for every glass composition. The periphery of the glass block being cooled much quicker than the central part, the extraction temperature must be high enough to prevent fracturing of the peripheral part, but not too high, otherwise softening of the peripheral part and leakage of the viscous glass mass may occur due to heating by the inner hot part. In the case of glass synthesis in cooled quartz crucibles, a crucible with glass is simply transferred into the annealing furnace. Thin-walled crucibles are used to prevent glass fracturing caused by the difference of glass and quartz thermal expansion coefficients. The quartz crucible fractures and exfoliates during annealing, while the glass block remains a monolith.

A significant factor limiting the use of this method for the synthesis of glass with enhanced crystallization ability should be mentioned. The presence of the skull increases the possibility of glass crystallization because the initial mixture crystalline particles are ready nuclei contacting the melt directly. Under certain conditions initial mixture particles may provoke the crystallization of the whole glass volume. The possibility of preparation of glasses with enhanced crystallization ability in the cold crucible depends on a multitude of factors: melt volume, thickness of the viscous glass layer (which is determined by the power released in the melt as well as by the temperature dependence of the viscosity and electrical conductivity of the melt), the cooling rate of melt, and the rates of nucleation and crystal growth. Therefore quantitative assessment of this possibility is very difficult. As for qualitative analysis, it is clear that the crystal nuclei must not be able to grow through the

Table 14.7 Thermal expansion coefficients (K_{te}) and transformation (T_l) and softening (T_g) temperatures in glass of the $\text{La}_2\text{O}_3\text{--Al}_2\text{O}_3\text{--SiO}_2$ system [14.201]

Composition (mol%)			K_{te} (20–800 °C) ($\times 10^{-7}$, °C $^{-1}$)	T_g (°C)	T_l (°C)
SiO_2	Al_2O_3	La_2O_3			
50.1	32.8	17.0	64.0	855	820
55.0	28.4	16.6	62.5	860	825
59.1	34.7	6.3	43.2	895	850
71.6	26.4	2.0	33.7	920	900
72.0	21.5	6.3	38.9	910	865
68.3	25.6	6.1	39.1	905	860

whole melt volume while the temperature of the melt being cooled is in the range of possible crystallization. Otherwise, a block of crystallized glass is formed.

14.4.1 Refractory Glasses of the $\text{R}_2\text{O}_3\text{--Al}_2\text{O}_3\text{--SiO}_2$ ($\text{R} = \text{Y}, \text{La}$, Rare-Earth Element) Systems

Investigation of the properties of glasses formed in this system was performed by several research groups and showed that these glasses possess a combination of valuable properties [14.201–207]. High refractive indices and high mechanical strength combined with high deformation temperature, relatively small values of thermal expansion coefficient (K_{te}), very low electric conductivity, and extremely high resistance to the action of alkalis make these glasses promising materials for use at high temperatures in chemically aggressive media. Besides, glasses formed in this system are devoid of oxides of alkaline or alkaline-earth metals and can be structurally different from traditional alkaline glasses. This undoubtedly makes them objects of scientific interest; for example, a nuclear magnetic resonance study of glasses of the $\text{SiO}_2\text{--Al}_2\text{O}_3\text{--Y}_2\text{O}_3$ system revealed the presence of tetra-, penta-, and hexacoordinated Al^{3+} ions in the glass structure, as well as a rather complicated structure of the silicon–oxygen framework [14.208].

Synthesis of glasses of the $\text{R}_2\text{O}_3\text{--Al}_2\text{O}_3\text{--SiO}_2$ ($\text{R} = \text{Y}, \text{La}$, rare-earth element) systems was performed by SM in a CC [14.201, 203]. Synthesis was performed under air at temperature of $\approx 2000^\circ\text{C}$ in water-cooled metal crucibles of 90–120 mm in diameter. Pieces of graphite were used for initial melting. The glass blocks obtained had a mass of 2–6 kg (depending on the crucible size) and did not contain any inclusions or bubbles. The practically important values of the K_{te} and characteristic temperatures for glasses of various compositions are presented in Table 14.7.

High values of the softening temperatures (855–920 °C) combined with relatively low K_{te} values ($33.7\text{--}64$) $\times 10^{-7}$ make these glasses promising materials for use in electrovacuum technologies for welding and sealing of W and Mo. Apart from being convenient for the preparation of relatively large quantities of glass, the SM technique proved to be very convenient for studies on glass formation in various systems. This method allows obtaining a range of samples of various compositions in one experiment. The glass-formation range in the system $\text{La}_2\text{O}_3\text{--Al}_2\text{O}_3\text{--SiO}_2$ was studied in [14.201]. Samples for these investigations were prepared as follows: first, a two-component mixture $\text{Al}_2\text{O}_3 + \text{SiO}_2$ of predetermined composition was melted in the cold crucible. After keeping of the melt at the temperature 1800–2000 °C for 1 h, a mixture

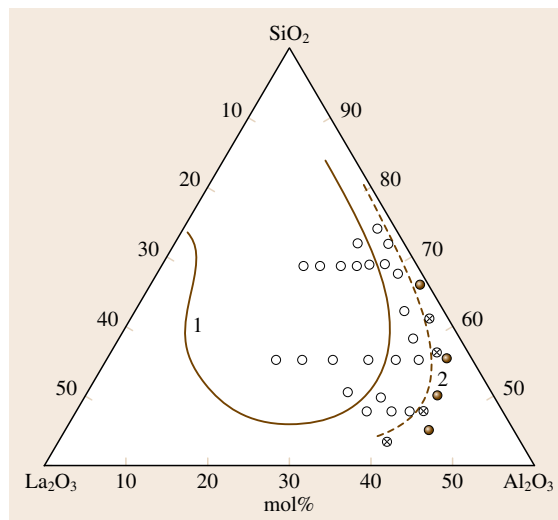


Fig. 14.27 Glass-forming region in the $\text{La}_2\text{O}_3\text{--Al}_2\text{O}_3\text{--SiO}_2$ system at different synthesis temperatures: 1 – 1600 °C, 2 – 2000 °C; (○ – glass, ● – sintered, ⊗ – surface crystallized) (after [14.201])

Table 14.8 Compositions and properties of the glasses with high concentrations of rare-earth element ions

Composition (mol%)	Young's modulus ($\times 10^{-8}$ Pa)	Hardness ($\times 10^{-7}$ Pa)	K_{te} ($\times 10^7$ °C $^{-1}$)	Thermal conductivity (W/(m K))	Poisson's ratio
43.2SiO ₂ –28.5Al ₂ O ₃ –26.4Y ₂ O ₃ –1.9Nd ₂ O ₃	1230	830	56.7	1.1	0.259
29.6SiO ₂ –34.3Al ₂ O ₃ –36.1Nd ₂ O ₃	1080	770	62.4	1.0	–
51.7SiO ₂ –26.0Al ₂ O ₃ –22.3Nd ₂ O ₃	1160	800	54.6	0.9	–
37.6SiO ₂ –32.9Al ₂ O ₃ –26.6Yb ₂ O ₃ –2.9Ho ₂ O ₃	1250	810	–	0.6	–
47.7SiO ₂ –32.6Al ₂ O ₃ –19.3Yb ₂ O ₃ –0.4Er ₂ O ₃	1270	–	44.0	0.55	–
48.2SiO ₂ –27.5Al ₂ O ₃ –24.3Tb ₂ O ₃	1125	730	55.8	0.7	–
53.2SiO ₂ –24.4Al ₂ O ₃ –20.6La ₂ O ₃ –1.8Nd ₂ O ₃	990	–	–	0.7	0.15

of SiO₂ + La₂O₃ with a predetermined composition was added in small (30–50 g) portions. After the addition of each portion the melt was homogenized for 10 min and then drops of the glass mass weighing 1–3 g were extracted with a quartz rod and quenched on a water-cooled metal surface. After this evaluation of the chemical compositions of the samples by electron probe microanalysis, microscopic analysis and X-ray diffraction analyses were performed. The results of the study compared with the literature data available are presented in Fig. 14.27.

The increase of the glass synthesis temperature to 2000 °C evidently leads to a considerable broadening of the glass-forming range in this system. Thus, at a SiO₂ content of 65–75 mol % the addition of only \approx 2 mol % of La₂O₃ results in the formation of transparent glass. It is also worth noting that this system allows obtaining glasses with a SiO₂ content less than 50 mol %. These glasses are of interest for structural research because a continuous silicon–oxygen framework cannot exist in them.

Another interesting feature of the glasses of the R₂O₃–Al₂O₃–SiO₂ system is the possibility of obtaining glasses with extremely high concentrations of rare-earth element ions, in particular the Nd³⁺, Yb³⁺, and Tb³⁺ ions. It is impossible to obtain such glasses using conventional alkaline glass matrices. The weight of glass blocks obtained amounted to 5 kg, and the rare-earth metal-ion content amounted to 10²² cm^{–3}. The properties of some of the glasses synthesized are presented in Table 14.8.

The study of the luminescence spectra of the Sm³⁺ and Eu³⁺ ions present in lanthanaluminate glass was performed using the method of selective laser excitation of luminescence and revealed the absence of microphases with drastically different symmetries in the surroundings of the active ions, i. e., the activator

ions in the glass were not segregated [14.209, 210]. Glasses synthesized in cold crucibles at high temperatures are characterized by low content of hydroxyl groups OH[–], even without using special dehydration methods (the peak value of absorption coefficient at the wavelength 3 μ m is about \approx 3–4 cm^{–1}) [14.211]. Glasses with Nd³⁺ concentration up to 1.1 \times 10²² cm^{–3} are characterized with peak absorption coefficients of 290, 130, 150, and 40 cm^{–1} at wavelengths of 590, 745, 810, and 890 nm, respectively. High thermophysical and mechanical characteristics of such glasses (Table 14.8) combined with their stability at high temperatures make them promising materials for thin, optically dense, selective filters. Glasses with a high content of Tb³⁺ ions are also of considerable practical interest. This ion possesses magneto-optical activity, that is, it can alter the phase of linearly polarized light when magnetic field is applied. Measurements of the magneto-optical properties of the Tb₂O₃–Al₂O₃–SiO₂ glass containing 9.5 \times 10²¹ Tb³⁺ ions/cm³ showed that the Verdet constant equals –0.33 min/Oe cm at the wavelength of 630 nm. Such a high value of the Verdet constant combined with the high value of the laser damage threshold (1.7 \times 10⁹ W/cm²) and high heat conductivity opens wide perspectives for the use of this glass in various Faraday rotator devices in high-power laser systems.

14.4.2 Immobilization of Radioactive Waste in Stable Solid Blocks

During the last few years the SM method was widely applied for the immobilization of liquid and solid wastes (including radioactive waste) in stable solid blocks (phosphate and borosilicate glasses, mineral-like compositions) [14.212]. Improvement of the efficiency of radioactive waste neutralization is one of the main

tasks of the atomic power generation industry. Waste recycling is a complex problem. It includes various technological stages (preparation and delivery of waste for recycling, melting, pouring into containers, collection and processing of the gases released, etc.). The melting unit is the most important element of such systems. Until recently all existing programs of waste vitrification relied on the use of traditional melting furnaces with hot crucibles, working in the 1100–1150 °C temperature range. Phosphate and borosilicate glasses are commonly used as matrices for waste immobilization. However, the low operate temperatures of such furnaces impose considerable limitations on the vitrification process. The use of a CC enables working at higher temperatures

and removes the restrictions inherent to conventional melting units. Thus, higher temperatures provide broad possibilities for the design and application of new glass-forming and crystalline matrices for waste immobilization, including the possibility of introducing a higher concentration of waste matter into the matrices already being used, and processing of a wider range of waste matters (for example, heat-insulating materials) without the introduction of fluxing additives [14.213]. Other advantages of this technology include the small dimensions of the melting unit and high productivity of waste processing. Research and industrial *cold-crucible* systems are widely used nowadays in Russia, the USA, France, Germany, Italy, and South Korea [14.214].

14.5 Conclusion

This chapter on the application of skull melting of dielectric oxide materials in a cold crucible has illustrated the dynamic development of the method, which provides a basis for industrial-scale technologies as the development and manufacturing of the corresponding equipment has increased. The range of materials synthesized by means of this technique has

become increasingly wide. Development of the technique for growth of PSZ crystals and nuclear waste vitrification can be pointed out as two of the most promising directions. Nevertheless, it is apparent that the potential of the method has not been exhausted, particularly in the field of single-crystal growth of refractory compounds.

References

- 14.1 W.V. Bolton: Das Tantal, seine Darstellung und seine Eigenschaften, *Z. Electrochem.* **11**, 45–51 (1905), in German
- 14.2 H.F. Sterling, R.W. Warren: High temperature melting without contamination in cold crucibles, *Metallurgia* **67**, 301–307 (1963)
- 14.3 A.A. Neustruev, G.L. Khodorovskii: *Vacuum skull furnaces* (Metallurgija, Moscow 1967), in Russian
- 14.4 R. Collongues, M. Perez y Jorba: Sur le chauffage et la fusion sans creuset par induction haute fréquence de la zircone stabilisée, *C. R. Acad. Sci.* **257**, 1091–1093 (1963), in French
- 14.5 B. Gayet, J. Holder, G. Kurka: Fusion du bioxyde d'uranium par induction de la haute fréquence, *Rev. Haut. Temp. Reftact.* **1**, 153–157 (1964), in French
- 14.6 M. Perez y Jorba, R. Collongues: Sur le chauffage et la fusion sans creuset par induction haute fréquence de quelques oxydes réfractaires, *Rev. Haut. Temp. Reftact.* **1**, 21–25 (1964), in French
- 14.7 C. Deportes, B. Lorang, G. Vitter: Sur une amélioration du procédé de fusion en auto-creuset des oxydes réfractaires, *Rev. Haut. Temp. Reftact.* **2**, 159–161 (1965), in French
- 14.8 Y. Roulin, G. Vitter, C. Deportes: Nouveau dispositif de fusion en autocreuset. Fusion d'oxydes réfractaires dans une enceinte multitubulaire, *Rev. Int. Haut. Temp. Reftact.* **6**, 153–158 (1969), in French
- 14.9 J. Moulin, I. Reboux: Nouveaux développements dans la fusion électrique des verres réfractaires, *Verres Reftact.* **26**, 123–127 (1972), in French
- 14.10 B. Scott, H. Rawson: Techniques for producing low loss glasses for optical fibre communication system, *Glass Technol.* **14**, 115–124 (1973)
- 14.11 B. Scott, H. Rawson: Preparation of low loss glasses for optical fibre communication system, *Optoelectronics* **5**, 285–288 (1973)
- 14.12 V.I. Aleksandrov, V.V. Osiko, V.M. Tatarintsev: *Report FIAN* (FIAN, Moscow 1968), in Russian
- 14.13 V.I. Aleksandrov, E.E. Lomonova, A.A. Majer, V.V. Osiko, V.M. Tatarintsev, V.T. Ydovenchik: Physical properties of zirconia and hafnia single crystals, *Bull. Lebedev Phys. Inst. (FIAN)* **11**, 3–7 (1972), in Russian

- 14.14 V.I. Aleksandrov, V.V. Osiko, A.M. Prokhorov, V.M. Tatarintsev: Novel method of preparation of refractory single crystals and melted ceramic materials, *Herald Rus. Acad. Sci.* **12**, 29–36 (1973), in Russian
- 14.15 V.I. Aleksandrov, V.V. Osiko, A.M. Prokhorov, V.M. Tatarintsev: Synthesis and crystal growth of refractory materials by RF melting in a cold container, *Top. Mater. Sci.* **1**, 421–480 (1978)
- 14.16 R.F. Sekerka, R.A. Hartzell, B.J. Farr: Instability phenomena during the RF-heating and melting of ceramics, *J. Cryst. Growth* **50**, 783–806 (1980)
- 14.17 R.A. Hartzell, R.F. Sekerka: Mathematical modeling of internal centrifugal zone growth of ceramics and ceramic metal composites, *J. Cryst. Growth* **57**, 27–42 (1982)
- 14.18 C. Gross, W. Assmus, A. Muiznieks, G. Raming, A. Muehlbauer, C. Stenzel: Power consumption of skull melting, Part I: analytical aspects and experiments, *Cryst. Res. Technol.* **34**, 319–328 (1999)
- 14.19 A. Muiznieks, G. Raming, A. Muehlbauer, C. Gross, W. Assmus, C. Stenzel: Power consumption of skull melting, Part II: numerical calculation of the shape of the molten zone and comparison with experiment, *Cryst. Res. Technol.* **34**, 329–338 (1999)
- 14.20 T. Behrens, M. Kudryash, B. Nacke, D. Lopuch, A. Martynow, I. Loginov: Induction skull melting of Y_2O_3 –BaO–CuO in a cold crucible, *Int. Sci. Coll. Modelling for Electromagnetic Processing* (Hannover 2003) pp. 249–254
- 14.21 B. Nacke, T. Behrens, M. Kudryash, A. Jakovics: Skull melting technology for oxides and glasses, *Conf. Fundamental and Applied MHD*, Vol. 2 (Riga 2005) pp. 241–244
- 14.22 A.V. Shkulkov: Attractor formation in induction skull-melting systems and its effect on crystal structure, *Bull. Rus. Acad. Sci. Phys.* **68**, 1000–1006 (2004)
- 14.23 V.V. Osiko, M.A. Borik, E.E. Lomonova: Crucible-free methods of growing oxide crystals from the melt, *Annu. Rev. Mater. Sci.* **17**, 101–122 (1987)
- 14.24 E.E. Lomonova, V.V. Osiko: Growth of zirconia crystals by skull-melting technique. In: *Crystal Growth Technology*, ed. by H.J. Scheel, T. Fukuda (Wiley, Chichester 2003) pp. 461–484
- 14.25 Y.S. Kuzminov, E.E. Lomonova, V.V. Osiko: *Refractory Materials from a Cold Crucible* (Nauka, Moscow 2004)
- 14.26 Y.B. Petrov: *Inductive Melting of Oxides* (Energoatomizdat, Leningrad 1983), in Russian
- 14.27 V.I. Aleksandrov, A.L. Blinov, M.A. Borik, V.V. Osiko: Investigation of temperature distribution in viscous oxide melts under process of skull melting in a cold crucible, *Izv. AS USSR, Inorg. Mater.* **19**, 443–447 (1983), in Russian
- 14.28 V.I. Aleksandrov, S.H. Batygov, V.F. Kalabuhova, S.V. Lavrishev, E.E. Lomonova, V.A. Mizina, V.V. Osiko, V.M. Tatarintsev: Itria distribution and inhomogenities into cubic ZrO_2 – Y_2O_3 crystals, *Izv. AS USSR, Inorg. Mater.* **16**, 99–104 (1980), in Russian
- 14.29 V.I. Aleksandrov, S.H. Batygov, V.F. Kalabuhova, S.V. Lavrishev, E.E. Lomonova, V.A. Mizina, V.V. Osiko, V.M. Tatarintsev: Effect SiO_2 on growth and perfection of stabilized ZrO_2 , *Izv. AS USSR, Inorg. Mater.* **16**, 1800–1804 (1980), in Russian
- 14.30 V.I. Aleksandrov, M.A. Vishnyakova, V.F. Kalabuhova, E.E. Lomonova, V.A. Panov: Growth of zirconia single crystals by direct crystallization in a cold container, *Proc. Indian Natl. Sci. Acad.* **2**, 133–144 (1991)
- 14.31 V.I. Aleksandrov, V.V. Osiko, A.M. Prokhorov, V.M. Tatarintsev: Refractory materials preparation by skull melting in a cold container, *Rus. Chem. Rev.* **47**, 385–427 (1978), in Russian
- 14.32 V.I. Aleksandrov, V.P. Voitsitskii, E.E. Lomonova, V.V. Osiko, N.P. Khaneev: Study of melting and crystallization processes in a cold container with direct radio-frequency heating, *Instrum. Exp. Tech.* **3**, 231–234 (1991), in Russian
- 14.33 V.I. Aleksandrov, V.P. Voitsitskii, E.E. Lomonova, V.V. Osiko, N.P. Khaneev: Study of dielectric materials melting in a cold container with direct radio-frequency heating, *Izv. AS USSR, Inorg. Mater.* **27**, 983–987 (1991), in Russian
- 14.34 V.I. Aleksandrov, V.P. Voitsitskii, E.E. Lomonova, V.V. Osiko, N.P. Khaneev: Investigation of melting and crystallization processes in a cold container with direct radio-frequency heating, *Izv. AS USSR, Inorg. Mater.* **27**, 2167–2171 (1991), in Russian
- 14.35 V.I. Aleksandrov, V.P. Voitsitskii, E.E. Lomonova, V.V. Osiko, N.P. Khaneev: Control method of melt propagation on a initial stage of direct radio-frequency melting in a cold container, *Instrum. Exp. Tech.* **4**, 212–217 (1992), in Russian
- 14.36 V.I. Aleksandrov, V.P. Voitsitskii, E.E. Lomonova, V.V. Osiko, N.P. Khaneev: Monitoring of melt propagation direction on a initial stage of direct radio-frequency melting in a cold container, *J. Tech. Phys.* **62**, 180–186 (1992), in Russian
- 14.37 B.T. Melekh, F.F. Andreeva, N.F. Kartenko, I.V. Korokin, V.B. Smirnov: Features of direct induction melting and crystal growth of refractory oxide transition elements, *Izv. AS USSR, Inorg. Mater.* **18**, 98–101 (1982), in Russian
- 14.38 R. Aragon, H.R. Harrison, R.H. McCallister, C.J. Sandberg: Skull melting single crystal growth of magnetite (Fe_3O_4)–ulvospinel (Fe_2TiO_4) solid solution members, *J. Cryst. Growth* **61**, 221–228 (1983)
- 14.39 V.I. Aleksandrov, A.L. Blinov, M.A. Borik, V.G. Veselago, V.V. Voronov, V.M. Ivanovskaja, V.A. Misina, V.V. Osiko, V.T. Udovenchik, V.A. Fradkov, M.A. Chernikov: Synthesis and crystal growth of $YBa_2Cu_3O_{6.5+x}$ from the melt by direct radio-frequency heating in a cold container, *7 All-Union Conf. on Crystal Growth*, Vol. 2 (Moscow 1988), pp. 378–379, in Russian

- 14.40 M. Hartmanova, E.E. Lomonova, V. Navratil, P. Sutta, F. Kudracik: Characterization of yttria-doped ceria prepared by directional crystallization, *J. Mater. Sci.* **40**, 5679–5683 (2005)
- 14.41 L. Mazerolles, D. Michel, M.J. Hytch: Microstructures and interfaces in directionally solidified oxide-oxide eutectics, *J. Eur. Ceram. Soc.* **25**, 1389–1395 (2005)
- 14.42 W.-J. Jang, K. Imai, M. Hasegawa, H. Takei: Growth and structure of $\text{La}_2\text{NiO}_{4+\delta}$ ($0.19 \geq \delta \geq 0.12$) single crystals, *J. Cryst. Growth* **152**, 158–168 (1995)
- 14.43 V.I. Aleksandrov, V.V. Osiko, V.M. Tatarintsev: Melting of refractory dielectric materials by radio-frequency heating, *Instrum. Exp. Tech.* **5**, 222–225 (1970), in Russian
- 14.44 V.I. Aleksandrov, M.A. Vishnyakova, Y.K. Voron'ko, V.F. Kalabuchova, E.E. Lomonova, V.A. Misina, V.V. Osiko: Crystal growth of SrTiO_3 by Czochralski method from a cold crucible, *Izv. AS USSR, Inorg. Mater.* **19**, 104–108 (1983), in Russian
- 14.45 V.I. Aleksandrov, S.H. Batygov, M.A. Vishnyakova, Y.K. Voron'ko, V.F. Kalabuchova, E.E. Lomonova, V.V. Osiko: Optical properties of SrTiO_3 single crystal grown by Czochralski method, *Izv. AS USSR, Inorg. Mater.* **19**, 265–268 (1983), in Russian
- 14.46 V.I. Aleksandrov, I.A. Gerasimova, A.V. Kolesnikov, E.E. Lomonova, V.V. Osiko, V.A. Panov, P.A. Makarov, A.V. Archakov, N.G. Gorashchenko, A.A. Mayer: Growth of sillenite (BGO) single crystals from cold container, *Russ. J. Inorg. Chem.* **35**, 878–883 (1990)
- 14.47 D. Mateika, R. Lauien, M. Liehr: Czochralski growth by double container technique, *J. Cryst. Growth* **65**, 237–242 (1983)
- 14.48 A.M. Balbashov, A.J. Chervonenkis: *Magnetic Materials for Electronics* (Energija, Moscow 1979), in Russian
- 14.49 O. Ruff, F. Ebert: Contributions on ceramics of high refractory materials. I. The forms of zirconium dioxide, *Z. Anorg. Allg. Chem.* **180**, 19–41 (1929)
- 14.50 B.J. Curtis, J.A. Wilkinson: Preparation of mixed oxide crystals by chemical transport, *J. Am. Ceram. Soc.* **48**, 49–50 (1965)
- 14.51 V.A. Kysnetsov, O.V. Sidorenko: Crystallization of ZrO_2 and HfO_2 in hydrothermal conditions, *Cristallogr. Rep.* **13**, 748–749 (1968), in Russian
- 14.52 A.M. Anthony, V. Loc: Preparation de monocristaux de zircone pure monoclinique, *C. R. Acad. Sci.* **260**, 1383–1385 (1965), in French
- 14.53 A.B. Chase, J.A. Osmer: Growth of single crystals of ZrO_2 and HfO_2 from PbF_2 , *Am. Mineral.* **51**, 1811–1888 (1966)
- 14.54 W. Kleber, L. Ickert, J. Doerschel: Ein Beitrag zum Wachstum von Zirkoniumdioxid-Einkristallen aus Schmelzenlosungen, *Krist. Tech.* **1**, 237–248 (1966)
- 14.55 M. Yokoyama, T. Ota, I. Yamai: Flux growth of yttria-stabilized zirconia crystals, *J. Cryst. Growth* **75**, 630–632 (1986)
- 14.56 T. Yamakawa, N. Ishizawa, K. Uematsu, N. Mizutani, M. Kato: Growth of yttria partially and fully stabilized zirconia crystals by xenon arc image floating zone method, *J. Cryst. Growth* **75**, 623–629 (1986)
- 14.57 M. Yoshimura, T. Hiuga, S. Somiya: Crystal growth of yttria stabilized zirconia (YSZ) under hydrothermal conditions, *J. Cryst. Growth* **71**, 277–279 (1985)
- 14.58 T.B. Reed: Growth of refractory crystals using the induction plasma torch, *J. Appl. Phys.* **32**, 2534–2535 (1961)
- 14.59 A. Saiki, N. Ishizawa, N. Mizutani, M. Kato: Directional crystal growth of yttria-stabilized zirconia by the arc image floating-zone method, *J. Mater. Sci. Lett.* **6**, 568–570 (1987)
- 14.60 D. Michel, M. Perez y Jorba, R. Collongues: Sur l'elaboration de monocristaux de zircone stabiliseret sur certaines proprieles de la solution solide cubique $\text{ZrO}_2\text{-CaO}$, *C. R. Acad. Sci. C.* **266**, 1602–1604 (1968), in French
- 14.61 D. Michel, M. Perez y Jorba, R. Collongues: Growth from skull-melting of zirconia rare earth oxide crystals, *J. Cryst. Growth* **43**, 546–548 (1978)
- 14.62 A.M. Anthony, R. Collongues: Modern methods of growing single crystals of high-melting point oxides. In: *Preparative Methods in Solid State Chemistry*, ed. by P. Hagenmuller (Academic, New York 1972) pp.147–249
- 14.63 R.C. Garvi, R.H. Hannink, R.T. Pascoe: Ceramic steel, *Nature* **258**, 703–704 (1975)
- 14.64 T.K. Gupta, J.H. Bechtold, R.C. Kuznicki, L.H. Cadoff, B.R. Rossing: Stabilization of tetragonal phase in polycrystalline zirconia, *J. Mater. Sci.* **12**, 2421–2426 (1977)
- 14.65 T.K. Gupta: Sintering of tetragonal zirconia and its characteristics, *Sci. Sinter.* **10**, 205–216 (1978)
- 14.66 D.L. Porter, A.H. Heuer: Mechanisms of toughening partially stabilized zirconia (PSZ), *J. Am. Ceram. Soc.* **60**, 183–184 (1977)
- 14.67 R.H.J. Hannink, P.V. Kelly, B.C. Muddle: Transformation toughening in zirconia-containing ceramics, *J. Am. Ceram. Soc.* **83**, 461–487 (2000)
- 14.68 M.E. Mashburg, W.E. Coblenz: Reactio-formed ceramics, *J. Am. Ceram. Soc.* **67**, 356–363 (1988)
- 14.69 R. Chaim, M. Hefetz: Effect of grain size on elastic modulus and hardness of nanocrystalline $\text{ZrO}_2\text{-3 wt \% -Y}_2\text{O}_3$ ceramic, *J. Mater. Sci.* **39**, 3057–3061 (2004)
- 14.70 K. Tzushima, K. Heda, M. Shimada: Strength and fracture toughness in isostatically hot pressed composites of Al_2O_3 and Y_2O_3 partially stabilized ZrO_2 , *J. Am. Ceram. Soc.* **68**, C4–C5 (1985)
- 14.71 M. Hoch, K.M. Nair: Densification characteristics of ultrafine powders, *Ceramurg. Int.* **2**, 88–97 (1976)
- 14.72 K.S. Mazdiyasi: Powder synthesis from metal-organic precursors, *Ceramurg. Int.* **8**, 42–56 (1982)
- 14.73 C.J. Howard, R.J. Hill, B.E. Reichert: Structures of the ZrO_2 polymorphs at room temperature by

- high-resolution neutron powder diffraction, *Acta Crystallogr. B* **44**, 116–120 (1980)
- 14.74 G. Teufer: Crystal structure of tetragonal ZrO_2 , *Acta Crystallogr.* **15**, 1187 (1962)
- 14.75 R.J. Ackermann, S.P. Garg, E.G. Rauh: High-temperature phase diagram for the system Zr-O , *J. Am. Ceram. Soc.* **60**, 341–345 (1977)
- 14.76 D.K. Smith, C.F. Cline: Verification of existence of cubic zirconia at high temperature, *J. Am. Ceram. Soc.* **45**, 249–250 (1962)
- 14.77 J. McCullough, K. Trueblood: The crystal structure of baddeleyite (monoclinic ZrO_2), *Acta Crystallogr.* **12**, 507–511 (1959)
- 14.78 N.V. Belov: Crystallographic structure of baddeleyite, *Crystallogr. Rep.* **5**, 460–461 (1960), in Russian
- 14.79 D.K. Smith, H.W. Newkirk: The crystal structure of baddelyite (monoclinic ZrO_2) and its relation to the polymorphism of ZrO_2 , *Acta Crystallogr.* **18**, 983–991 (1965)
- 14.80 R. Cupres, R. Wollast: Polymorphism conversion of pure zirconia, *Ber. Dtsch. Keram. Ges.* **40**, 527–532 (1963)
- 14.81 P. Duwez, F.H. Brown, F. Odell: The zirconia-yttria system, *J. Electrochem. Soc.* **38**, 356–362 (1951)
- 14.82 S.P. Ray, V.S. Stubican: Fluorite related ordered compounds in the $\text{ZrO}_2\text{-CaO}$ and $\text{ZrO}_2\text{-Y}_2\text{O}_3$ system, *Mater. Res. Bull.* **12**, 549–556 (1977)
- 14.83 H.G. Scott: Phase relationships in the yttria-zirconia system, *J. Mater. Sci.* **10**, 1527–1535 (1975)
- 14.84 V.S. Stubican, R.C. Hink, S.P. Ray: Phase equilibria and ordering in the system $\text{ZrO}_2\text{-Y}_2\text{O}_3$, *J. Am. Ceram. Soc.* **61**, 17–21 (1978)
- 14.85 V.S. Stubican, G.S. Gorman, J.R. Hellmann, G. Senft: Phase relationships in some ZrO_2 systems. In: *Advances in Ceramics Vol. 12: Science and Technology of Zirconia II*, ed. by N. Claussen, M. Rühle, A.H. Heuer (Am. Ceram. Soc., Columbus 1984) pp. 96–106
- 14.86 V.S. Stubican: Phase equilibria and metastabilities in the systems $\text{ZrO}_2\text{-MgO}$, $\text{ZrO}_2\text{-CaO}$, and $\text{ZrO}_2\text{-Y}_2\text{O}_3$,. In: *Advances in Ceramics Vol. 12: Science and Technology of Zirconia II*, ed. by N. Claussen, M. Rühle, A.H. Heuer (Am. Ceram. Soc., Columbus 1984) pp. 71–95
- 14.87 C. Pascual, P. Duran: Subsolidus phase equilibria and ordering in the system $\text{ZrO}_2\text{-Y}_2\text{O}_3$, *J. Am. Ceram. Soc.* **66**, 23–27 (1983)
- 14.88 M. Rühle, N. Claussen, A.H. Heuer: Microstructural studies of Y_2O_3 -containing tetragonal ZrO_2 polycrystals (Y-TZP). In: *Advances in Ceramics Vol. 12: Science and Technology of Zirconia II*, ed. by N. Claussen, M. Rühle, A.H. Heuer (Am. Ceram. Soc., Columbus 1984) pp. 352–370
- 14.89 A.H. Heuer, M. Rühle: Phase transformations in ZrO_2 -containing ceramics. II. The martensitic reaction in t- ZrO_2 . In: *Advances in Ceramics Vol. 12: Science and Technology of Zirconia II*, ed. by N. Claussen, M. Rühle, A.H. Heuer (Am. Ceram. Soc., Columbus 1984) pp. 14–32
- 14.90 C.H. Perry, D.W. Liu, R.P. Ingel: Phase characterization of partially stabilized zirconia by Raman spectroscopy, *J. Am. Ceram. Soc.* **68**, 184–187 (1985)
- 14.91 Y.K. Voron'ko, A.A. Sobol, S.N. Ushakov, L.I. Tsimbal: Tetragonal structure formation in partly stabilized zirconia, *Izv. AS USSR, Inorg. Mater.* **30**, 803–808 (1994), in Russian
- 14.92 M.A. Aboimov, M.A. Borik, G.A. Gogotsi, V.F. Kalabuchova, E.E. Lomonova, V.A. Mizina: Phase transitions in crystals of partially stabilized zirconia, *Inorg. Mater.* **33**, 285–291 (1997)
- 14.93 M. Hillert: Critical limit for massive transformation, *Metall. Mater. Trans. A* **33**, 2299–2308 (2002)
- 14.94 H.G. Scott: Phase relationships in the yttria-rich part of the yttria-zirconia system, *J. Mater. Sci.* **12**, 311–316 (1977)
- 14.95 C.A. Anderson, J. Gregg, T.K. Gupta: Diffusionless transformations in zirconia alloys,. In: *Advances in Ceramics Vol. 12: Science and Technology of Zirconia II*, ed. by N. Claussen, M. Rühle, A.H. Heuer (Am. Cer. Soc., Columbus, OH 1984), pp.78–85
- 14.96 A. Rouanet: Diagrams of solidification and diagrams of high temperature phases in the zirconia-erbium oxide, zirconia-yttrium oxide and zirconia-ytterbium oxide systems, *C. R. Acad. Sci. Ser. C* **267**, 1581–1584 (1968)
- 14.97 Y. Du, Z. Jin, P. Huang: Thermodynamic assessment in the $\text{ZrO}_2\text{-Y}_{0.15}$ system, *J. Am. Ceram. Soc.* **74**, 1569–1577 (1991)
- 14.98 N.S. Jacobson, Z.-K. Liu, L. Kaufman, F. Zhang: Thermodynamic modeling of $\text{Y}_{0.15}\text{-ZrO}_2$ system, *J. Am. Ceram. Soc.* **87**, 1559–1566 (2004)
- 14.99 M. Chen, B. Hallstedt, L.J. Gauckler: Thermodynamic Modeling of the $\text{ZrO}_2\text{-Y}_{0.15}$ system, *Solid State Ion.* **170**, 255–274 (2004)
- 14.100 V. Lantery, A.H. Heuer, T.E. Mitchell: Tetragonal phase in the system $\text{ZrO}_2\text{-Y}_2\text{O}_3$. In: *Advances in Ceramics Vol. 12: Science and Technology of Zirconia II*, ed. by N. Claussen, M. Rühle, A.H. Heuer (Am. Ceram. Soc., Columbus 1984), pp.118–130
- 14.101 T. Yagi, A. Saiki, N. Ishizawa, N. Mizutani, M. Kato: Analytical electron microscopy of yttria partitioning in the yttria-partially-stabilized zirconia-crystal, *J. Am. Ceram. Soc.* **69**, C3–C4 (1986)
- 14.102 G.B. Bokij: *Crystal Chemistry* (Nauka, Moscow 1971), in Russian
- 14.103 V.P. Gorelov, S.F. Pal'guev: Examination of oxygen vacancy model in solid solution $\text{ZrO}_2\text{-Y}_2\text{O}_3$, *Izv. AS USSR, Inorg. Mater.* **13**, 181–182 (1977), in Russian
- 14.104 H.H. Möbius: Sauerstoffionenleitende Festelektrolyte und ihre Anwendungsmöglichkeiten, *Z. Chem.* **2**, 101–106 (1962), in German
- 14.105 S. Fabris, A.T. Paxton, M.W. Finnis: A stabilization mechanism of zirconia based on oxygen vacancies only, *Acta Mater.* **50**, 5171–5178 (2002)

- 14.106 E.V. Stefanovich, A.L. Shluger, C.R.A. Catlow: Theoretical study of the stabilization of the cubic-phase ZrO_2 by impurities, *Phys. Rev. B* **49**, 11560–11571 (1994)
- 14.107 S. Fabris, A.T. Paxton, M.W. Finnis: Relative energetics and structural properties of zirconia using a self-consistent tight-binding model, *Phys. Rev. B* **63**, 094101–13 (2001)
- 14.108 F.F. Lange: Transformation toughness, Part I: Size effects associated with the thermodynamics of constrained transformation, *J. Mater. Sci.* **17**, 225–234 (1982)
- 14.109 D. Michel, L. Mazerolles, M. Perez y Jorba: Fracture of metastable tetragonal zirconia crystals, *J. Mater. Sci.* **18**, 2618–2628 (1983)
- 14.110 F.R. Chien, F.J. Uvic, V. Prakash, A.H. Heuer: Stress-induced transformation and ferroelastic deformation adjacent microhardness indents in tetragonal zirconia single crystals, *Acta Mater.* **46**, 2151–2171 (1998)
- 14.111 J. Lefevre: Fluorite-type structural modifications in system having a zirconium and hafnium oxide based, *Ann. Chem.* **8**, 117–149 (1963)
- 14.112 D. Baither, B. Baufeld, U. Messerschmidt, F.H. Foitzik, M. Rühle: Ferroelasticity of t' -zirconia: I, high electron microscopy studies of the microstructure in polydomain tetragonal zirconia, *J. Am. Ceram. Soc.* **80**, 1691–1698 (1997)
- 14.113 Y.K. Voron'ko, M.A. Zufarov, B.V. Ignat'ev, V.V. Osiko, E.E. Lomonova, A.A. Sobol': Raman scattering in tetragonal single crystals ZrO_2 - Gd_2O_3 and ZrO_2 - Eu_2O_3 , *Opt. Spectrosc.* **51**, 569–571 (1981), in Russian
- 14.114 K.M. Prettyman, J.-F. Jue, A.V. Virkar, C.R. Hubbard, O.B. Cavin, M.K. Ferber: Hysteresis effects in 3 mol % yttria-doped zirconia (t' -phase), *J. Mater. Sci.* **27**, 4167–4174 (1992)
- 14.115 D. Baither, B. Baufeld, U. Messerschmidt: Morphology of tetragonal precipitates in Y_2O_3 -stabilized ZrO_2 crystals, *Phys. Status Solidi (a)* **137**, 569–576 (1993)
- 14.116 A.H. Heuer, V. Lanteri, A. Dominguez-Rodriguez: High-temperature precipitation hardening of two phase Y_2O_3 -partially-stabilized ZrO_2 single crystals: A first report, *J. Amer. Cer. Soc.* **69**, 285–287 (1986)
- 14.117 V. Lanteri, T.E. Mitchell, A.H. Heuer: Morphology of tetragonal precipitates in partially stabilized ZrO_2 , *J. Am. Ceram. Soc.* **69**, 564–569 (1986)
- 14.118 V.I. Aleksandrov, M.A. Borik, M.A. Vishnyakova, V.P. Voitsitskii, V.F. Kalabuchova, E.E. Lomonova, V.V. Osiko: Method of single crystal preparation (modification), RF Patent 2133787 (1999), in Russian
- 14.119 A.G. Merjanov, V.A. Raduchev, E.N. Rumanov: Heat waves of melting in dielectric crystals, *Dokl. AS USSR* **253**, 330–334 (1980), in Russian
- 14.120 E.N. Rumanov: *Heat Wave of Elementary Substance Melting* (Preprint OIHF AS USSR, Chernogolovka, 1982) p. 20, in Russian
- 14.121 B. Chalmers: *Theory of Solidification* (Metallurgija, Moscow 1968), in Russian
- 14.122 A. Hellawell, P.M. Herbert: The development of preferred orientations during the freezing of metals and alloys, *Proc. R. Soc. London Ser. A* **269**, 560–573 (1962)
- 14.123 W.A. Tiller: Preferred growth direction of metals, *J. Met.* **9**, 845–855 (1957)
- 14.124 A. Rosenberg, W.A. Tiller: The relationship between growth forms and the preferred direction of growth, *Acta Metall.* **5**, 565–573 (1957)
- 14.125 W.A. Tiller: Solute segregation during ingot solidification, *J. Iron Steel Inst.* **215**, 447–457 (1959)
- 14.126 G.G. Lemlein: Geometric selection in growing crystal aggregate, *Dokl. AS USSR* **48**, 177–180 (1945), in Russian
- 14.127 A.V. Chubnikov: About geometric selection rule during formation crystal aggregate, *Dokl. AS USSR* **51**, 679–681 (1946), in Russian
- 14.128 A.N. Kolmogorov: On the issue of "geometric selection" crystals, *Dokl. AS USSR* **65**, 681–684 (1949), in Russian
- 14.129 V.V. Osiko, D.L. Penyaz, N.P. Khaneev: Study of directional crystallization process in a cold container with direct radiofrequency heating, *J. Cryst. Growth* **128**, 1193–1196 (1993)
- 14.130 R.P. Ingel, D. Lewis, B.A. Bender, P.W. Rice: Temperature dependence of strength and fracture toughness of ZrO_2 single crystals, *J. Am. Ceram. Soc.* **65**, C150–C152 (1982)
- 14.131 R.P. Ingel, D. Lewis, B.A. Bender, P.W. Rice: Room temperature strength and fracture of ZrO_2 - Y_2O_3 single crystals, *J. Am. Ceram. Soc.* **65**, C108–C109 (1982)
- 14.132 D. Michel: Relation between morphology and structure for stabilized zirconia crystals. In: *Advances in Ceramics, Vol. 24 Science and Technology of Zirconia III*, ed. by S. Somiya, N. Yamamoto, H. Yanahida (Am. Ceram. Soc., Columbus 1988) pp. 455–461
- 14.133 P. Hartman, W.G. Perdok: On the relations between structure and morphology of crystals, *Acta Crystallogr.* **8**, 525–531 (1955)
- 14.134 H. Römer, K.-D. Luther, W. Assmus: Measurement of the distribution coefficient of neodymium in cubic zirconium dioxide, *J. Cryst. Growth* **130**, 233–237 (1993)
- 14.135 H. Römer, K.-D. Luther, W. Assmus: The distribution coefficients of rare earth ions in cubic zirconium dioxide, *J. Cryst. Growth* **141**, 159–164 (1994)
- 14.136 H. Römer, K.-D. Luther, W. Assmus: Determination of the distribution coefficients of the rare earth ions Er^{3+} and Nd^{3+} in yttria-stabilized c- ZrO_2 single crystals, *Z. Kristallogr.* **209**, 311–314 (1994)
- 14.137 V.B. Glushkova, V.V. Osiko, L.G. Shcherbakova, V.I. Aleksandrov, Y.N. Paputskii, V.M. Tatarintsev: Study of features monocrystalline solid solution in

- ZrO₂-Y₂O₃ system, *Izv. AS USSR, Inorg. Mater.* **13**, 2197-2201 (1977), in Russian
- 14.138 D.B. Zhang, X.M. He, J.P. Chen, J.C. Wang, Y.F. Tang, B.L. Hu: Research on crystal growth and defects in cubic zirconia, *J. Cryst. Growth* **79**, 336-340 (1986)
 - 14.139 A. Baermann, W. Guse, H. Saalfeld: Characterization of different (Me,Zr)O₂ single crystals grown by the "skull-melting" technique, *J. Cryst. Growth* **79**, 331-335 (1986)
 - 14.140 W.-S. Kim, I.-H. Suh, Y.-M. You, J.-H. Lee, C.-H. Lee: Synthesis of yttria-stabilized zirconia crystals by skull-melting method, *Neues Jb. Miner. Monatsh.* **3**, 136-144 (2001)
 - 14.141 E.V. Alekseev, O.N. Gorshkov, E.V. Chuprunov, V.A. Novikov, A.P. Kasatkin, G.K. Fukin: Investigation into the specific features of the changes in the crystal structure of stabilized zirconia upon thermochemical reduction, *Crystallogr. Rep.* **51**, 632-635 (2006)
 - 14.142 H. Kahlert, F. Frey, H. Boysen, K. Lassak: Defect structure and diffuse scattering of zirconia single crystals at elevated temperatures and simultaneously applied electric field, *Appl. Cryst.* **28**, 812-819 (1995)
 - 14.143 J.S. Thorp, A. Aypar, J.S. Ross: Electron spin resonance in single crystal yttria stabilized zirconia, *J. Mater. Sci.* **7**, 729-734 (1972)
 - 14.144 R.I. Merino, V.M. Orera, O. Povill, W. Assmus, E.E. Lomonova: Optical and electron paramagnetic resonance characterization of Dy³⁺ in YSZ single crystals, *J. Phys. Chem. Solids* **58**, 1579-1585 (1997)
 - 14.145 R.I. Merino, V.M. Orera, E.E. Lomonova, S.K. Batygov: Paramagnetic electron traps in reduced stabilized zirconia, *Phys. Rev. B* **52**, 6150-6152 (1995)
 - 14.146 D. Gomez-Garcia, J. Martinez-Fernandez, A. Dominguez-Rodriguez: Recent advances in electron-beam-induced damage models in yttria fully stabilized zirconia single crystals, *Philos. Mag. Lett.* **81**, 173-178 (2001)
 - 14.147 R.P. Ingel, D. Lewis III: Lattice parameters and density for Y₂O₃-stabilized zirconia, *J. Am. Ceram. Soc.* **69**, 325-332 (1986)
 - 14.148 V.I. Aleksandrov, G.E. Val'jano, B.V. Lukin, V.V. Osiko, A.E. Rautbort, V.M. Tatarintsev, V.N. Filatova: Crystal structure of stabilized zirconia, *Izv. AS USSR, Inorg. Mater.* **12**, 273-277 (1978), in Russian
 - 14.149 R.H. Ingel, D. Lewis, B.A. Bender, R.W. Rice: Physical, microstructural and thermomechanical properties of ZrO₂ single crystals. In: *Advances in Ceramics Vol. 12: Science and Technology of Zirconia II*, ed. by N. Claussen, M. Rühle, A.H. Heuer (Am. Ceram. Soc., Columbus 1984) pp. 408-414
 - 14.150 A. Cheikh, A. Madani, A. Touati, H. Boussett, C. Monty: Ionic conductivity of zirconia based ceramics from single crystals to nanostructured polycrystals, *J. Eur. Ceram. Soc.* **21**, 1837-1841 (2001)
 - 14.151 M. Hartmanova, J. Schneider, V. Navratil, F. Kundracik, H. Schulz, E.E. Lomonova: Correlation between microscopic and macroscopic properties of yttria stabilized zirconia. 1. Single crystals, *Solid State Ion.* **107**, 136-137 (2000)
 - 14.152 D.S. Thorp, H.P. Buckley: The dielectric constants of current-blackened single crystal yttria-stabilized zirconia, *J. Mater. Sci.* **8**, 1401-1408 (1973)
 - 14.153 S.P.S. Badwal: Electrical conductivity of single crystal and polycrystalline yttria-stabilized zirconia, *J. Mater. Sci.* **19**, 1767-1776 (1984)
 - 14.154 N. Bonanos, E.P. Butler: Ionic conductivity of monoclinic and tetragonal yttria-zirconia single crystals, *J. Mater. Sci. Lett.* **4**, 561-564 (1985)
 - 14.155 V.I. Aleksandrov, S.H. Batygov, Y.K. Voron'ko, B.I. Denker, E.E. Lomonova, V.V. Osiko, V.M. Tatarintsev: Coloured centres in cubic ZrO₂ single crystals, *Izv. AS USSR, Inorg. Mater.* **11**, 664-667 (1975), in Russian
 - 14.156 V.I. Aleksandrov, M.A. Vishnyakova, V.P. Voitsitskii, E.E. Lomonova, M.A. Noginov, V.V. Osiko, V.A. Smirnov, A.F. Umiskov, I.A. Shcherbakov: Fianite (ZrO₂-Y₂O₃:Er³⁺) laser emitting the 3 μm range, *Sov. J. Quant. Electron.* **19**, 1555-1556 (1989)
 - 14.157 V.I. Aleksandrov, M.A. Vishnyakova, V.P. Voitsitskii, Y.K. Voron'ko, E.E. Lomonova, V.A. Mizina, A.A. Sobol, S.N. Ushakov, L.I. Tsimbal: Spectroscopic properties solid solution ZrO₂-Y₂O₃ single crystals doped with Cr and Nd, *Izv. AS USSR, Inorg. Mater.* **26**, 1251-1255 (1990), in Russian
 - 14.158 A.V. Prokof'ev, W. Assmus, A.I. Shelykh, I.A. Smirnov, B.T. Melekh: Absorption edge of zirconium dioxide crystals doped with rare earth ions, *Phys. Solid State* **38**, 2739-2743 (1996)
 - 14.159 H. Römer, K.-D. Luther, W. Assmus: Coloured zirconia, *Cryst. Res. Technol.* **29**, 787-794 (1994)
 - 14.160 S.E. Paje, J. Llopis: Photoluminescence decay and time-resolved spectroscopy of cubic yttria-stabilized zirconia, *Appl. Phys. A* **59**, 569-574 (1994)
 - 14.161 V.I. Aleksandrov, N.A. Abramov, M.A. Vishnyakova, V.F. Kalabukhova, E.E. Lomonova, N.R. Miftiahedina, V.V. Osiko: High temperature disproportionation of fianit, *Izv. AS USSR, Inorg. Mater.* **19**, 100-103 (1983), in Russian
 - 14.162 L. Thome, J. Fradin, J. Jagielski, A. Gentils, S.E. Enescu, F. Garrido: Radiation damage in ion-irradiated yttria-stabilized cubic zirconia single crystals, *Eur. Phys. J. Appl. Phys.* **24**, 37-48 (2003)
 - 14.163 T. Hojo, H. Yamamoto, J. Aihara, S. Furuno, K. Sawa, T. Sakuma, K. Hojou: Radiation effects on yttria-stabilized zirconia irradiated with He or Xe ions at high temperature, *Nucl. Instrum. Methods Phys. Res. B* **241**, 536-542 (2005)
 - 14.164 R. Mevrel, J.-C. Laizet, A. Azzopardi, B. Leclercq, M. Poulain, O. Lavigne, D. Demange: Thermal diffusivity and conductivity of Zr_{1-x}Y_xO_{2-x/2} (x = 0,

- 0.084 and 0.179) single crystals, *J. Eur. Ceram. Soc.* **24**, 3081–3089 (2004)
- 14.165 J. Martinez-Fernandez, A.R. Pínto Gómez, J.J. Quispe Cancapa, A.R. de Arellano López, J. Llorca, J.Y. Pastor, S. Farmer, A. Sayir: High-temperature plastic deformation of Er_2O_3 -doped ZrO_2 single crystals, *Acta Mater.* **54**, 2195–2204 (2006)
- 14.166 A.H. Heuer: Indentation induced cracks and the toughness anisotropy of 9.4 mol yttria-stabilized cubic zirconia single crystals, *J. Am. Ceram. Soc.* **74**, 855–862 (1991)
- 14.167 A. Dominguez-Rodriguez, K.P.D. Lagerlof, A.H. Heuer: Plastic deformation and solid solution hardening of Y_2O_3 -stabilized ZrO_2 , *J. Am. Ceram. Soc.* **69**, 281–284 (1986)
- 14.168 D. Holmes, A.H. Heuer, P. Pirouz: Dislocation structure around Vickers indents in 9.4 mol Y_2O_3 -stabilized cubic ZrO_2 single crystals, *Philos. Mag. A* **67**, 325–342 (1993)
- 14.169 A. Pajares, F. Guiberteau, A. Dominguez-Rodriguez, A.H. Heuer: Microhardness and fracture toughness anisotropy in cubic zirconium oxide single crystals, *J. Am. Ceram. Soc.* **71**, C332–C331 (1988)
- 14.170 A. Pajares, F. Guiberteau, A. Dominguez-Rodriguez, A.H. Heuer: Indentation-induced cracks and toughness anisotropy of 9.4 mol%-yttria-stabilized zirconia cubic single crystals, *J. Am. Ceram. Soc.* **74**, 859–862 (1991)
- 14.171 K.J. McClellan, A.H. Heuer, L.P. Kubin: Localized yielding during high temperature deformation of Y_2O_3 -fully-stabilized cubic ZrO_2 single crystals, *Acta Mater.* **44**, 2651–2662 (1996)
- 14.172 F. Guiberteau, F.L. Cumbrera, A. Dominguez-Rodrigues, E. Fries, J. Castaing: X-ray Berg-Barrett topography of the deformation substructure of stabilized zirconium oxide single crystals deformed at 1673 K, *J. Appl. Cryst.* **27**, 406–410 (1994)
- 14.173 D. Gomez-Garcia, J. Martinez-Fernandez, A. Dominguez-Rodriguez: Recent advances in electron-beam-induced damage models in yttria fully stabilized zirconia single crystals, *Phil. Mag. Lett.* **81**, 173–178 (2001)
- 14.174 M. Barch, A. Tikhonovsky, U. Messerschmidt: Plastic deformation of yttria stabilized cubic zirconia single crystals II: Plastic instabilities, *Phys. Status Solidi (a)* **201**, 46–58 (2004)
- 14.175 G.A. Gogotsi, D.Y. Ostrovoi, E.E. Lomonova: Deformation behavior of cubic ZrO_2 single crystals, *Refractories* **3**, 15–19 (1992), in Russian
- 14.176 R.P. Ingel, D. Lewis III: Elastic anisotropy in zirconia single crystals, *J. Am. Ceram. Soc.* **71**, 265–271 (1988)
- 14.177 I.L. Chisty, I.L. Fabelinskij, V.F. Kitaeva, V.V. Osiko, Y.V. Pisalevskij, I.M. Sil'vestrova, N.N. Sobolev: Experimental study of the properties of ZrO_2 - Y_2O_3 and HfO_2 - Y_2O_3 solid solution, *J. Raman Spectrosc.* **6**, 183–192 (1977)
- 14.178 C.F. Bolling, W.A. Tiller: Growth from the melt. II. Cellular interface morphology, *J. Appl. Phys.* **31**, 2040–2045 (1960)
- 14.179 V.G. Fomin, M.G. Mil'vidskii, R.S. Beletskaja: Study of heavy doped silicon single crystals with cellular structure, *Crystallogr. Rep.* **13**, 172–173 (1968), in Russian
- 14.180 A.N. Kirgintsev, L.I. Isaenko, V.A. Isaenko: *Impurity Distribution Under Direct Crystallization* (Nauka, Novosibirsk 1977), in Russian
- 14.181 A.H. Heuer, V. Lantery, A. Dominguez-Rodriguez: High-temperature precipitation hardening of Y_2O_3 partially-stabilized ZrO_2 (Y-PSZ) single crystals, *Acta Metall.* **37**, 559–567 (1989)
- 14.182 G.A. Gogotsi, E.E. Lomonova, V.G. Pejchev: Strength and fracture toughness of zirconia crystals, *J. Eur. Ceram. Soc.* **11**, 123–132 (1993)
- 14.183 G.A. Gogotsi, E.E. Lomonova, Y. Furmanova, I.M. Savitskaya: Zirconia crystals suitable for medicine: 1. Implants, *Ceramurg. Int.* **20**, 343–348 (1994)
- 14.184 V.I. Aleksandrov, S.H. Batygov, Y.K. Voron'ko, M.A. Vishnyakova, V.F. Kalabuchova, E.E. Lomonova, V.V. Osiko: Effect Pr_2O_3 on ZrO_2 crystal growth from melt, *Izv. AS USSR, Inorg. Mater.* **23**, 349–352 (1987), in Russian
- 14.185 M.A. Borik, E.E. Lomonova, V.V. Osiko, V.A. Panov, O.E. Porodinkov, M.A. Vishnyakova, Y.K. Voronko, V.V. Voronov: Partially stabilized zirconia single crystals: growth from the melt and investigation of the properties, *J. Cryst. Growth* **275**, e2173–e2179 (2005)
- 14.186 V.V. Alisin, M.A. Borik, E.E. Lomonova, A.F. Melsharov, G.V. Moskvitin, V.V. Osiko, V.A. Panov, V.G. Pavlov, M.A. Vishnjakova: Zirconia-based nanocrystalline synthesized by directional crystallization from the melt, *Mater. Sci. Eng. C* **25**, 577–583 (2005)
- 14.187 M.A. Borik, Y.K. Voron'ko, E.E. Lomonova, V.V. Osiko, V.A. Sarin, G.A. Gogotsi: Mechanical properties of the PSZ crystal grown by skull melting technique: influence of technology conditions. In: *Fracture Mechanics of Ceramics, Vol.13, Crack-Microstructure Interaction, R-curve Behavior, Environmental, Effects in Fracture, and Standardization*, ed. by R.S. Bradt, D. Munz, M. Sakai, V.Y. Shevchenko, K. White (Kluwer/Plenum, New York, Boston, London, Moscow 1999), pp.485–496
- 14.188 G.A. Gogotsi, E.E. Lomonova, V.V. Osiko: Mechanical characteristics zirconia single crystals for constructional applications, *Refractories* **8**, 14–17 (1991), in Russian
- 14.189 G.A. Gogotsi, V.I. Galenko, B.A. Ozerskii, E.E. Lomonova, V.A. Mizina, V.F. Kalabukhova: Prochno strength and fracture toughness of zirconia single crystals with yttrium and terbium oxides, *Refractories* **6**, 2–8 (1993), in Russian

- 14.190 S.N. Dub, G.A. Gogotsi, E.E. Lomonova: Hardness and fracture toughness of tetragonal zirconia single crystals, *J. Mater. Sci. Lett.* **1**, 446–449 (1995)
- 14.191 G.A. Gogotsi, S.N. Dub, B.A. Ozerskii, D.Y. Ostrovoi, G.E. Khomenko, S.H. Batygov, M.A. Vishnjakova, V.F. Kalabukhova, S.V. Lavrishchev, E.E. Lomonova, V.A. Mizina: Zirconia single crystals with yttrium and terbium oxides, *Refractories* **7**, 2–10 (1995), in Russian
- 14.192 V.V. Alisin, K. Amosova, V.P. Voitsitskii, V.V. Voronov, V.A. Grinenko, E.E. Lomonova, N.I. Medvedovskaya, V.I. Ustinov: Influence of temperature on oxygen redistribution in nanocrystal-zirconia-based materials with high mechanical characteristics. In: *Perspektivnie Materiali I Tehnologii: Nanokompozity*, Vol.2, ed. by A.A. Berlin, I.G. Assovsky (Toruss, Moscow 2006) pp.183–193
- 14.193 J. Martinez-Fernandez, M. Jimenez-Melendo, A. Dominguez-Rodriguez: Microstructural evaluation and stability of tetragonal precipitates in Y_2O_3 -partially stabilized ZrO_2 single crystals, *Acta Metall. Mater.* **43**, 593–601 (1995)
- 14.194 J. Martinez-Fernandez, M. Jimenez-Melendo, A. Dominguez-Rodriguez, A.H. Heuer: Microindentation-induced transformation in 3.5 mol yttria-partially-stabilized zirconia single crystals, *J. Am. Ceram. Soc.* **74**, 1071–1081 (1991)
- 14.195 V.V. Osiko, V.V. Alisin, M.A. Vishnjakova, Z.V. Ignat'eva, E.E. Lomonova, V.G. Pavlov: Tribological properties of nanocrystalline material based on zirconia, *Frict. Wear* **26**, 285–289 (2005), in Russian
- 14.196 V.V. Osiko, V.V. Alisin, M.A. Vishnjakova, Z.V. Ignat'eva, E.E. Lomonova, V.G. Pavlov: Effect Y_2O_3 stabilisator content on tribological properties of nanocrystalline material based on zirconia, *Zavod. Lab. Diagn. Mashin* **4**, 47–52 (2006), in Russian
- 14.197 K.V. Frolov, V.V. Osiko, V.V. Alisin, M.A. Vishnjakova, Z.V. Ignat'eva, E.E. Lomonova, A.F. Melshanov, G.V. Moskvitin, V.G. Pavlov, M.S. Pugachev: Mechanical and tribological properties of nanocrystalline material based on zirconia, *Probl. Mashinost. Nadezn. Mashin* **4**, 3–8 (2006), in Russian
- 14.198 P. Christel, A. Meunier, M. Heller, Y.P. Torre, C.N. Peille: Mechanical properties and short-term in vivo evaluation of yttrium oxide-partially-stabilized zirconia, *J. Biomed. Mater. Res.* **23**, 45–61 (1989)
- 14.199 C. Piconi, G. Maccauro: Zirconia as a ceramic biomaterial, *Biomaterials* **20**, 1–25 (1999)
- 14.200 V. Nezhentsev, Y. Petrov, A. Zhilin, O. Dymshits: Use of induction furnaces with a cold crucible for melting hard glasses (review), *Steklo Keram.* **9**, 9–11 (1986)
- 14.201 V.I. Aleksandrov, M.A. Borik, G.H. Dechev, N.I. Markov, V.A. Myzina, V.V. Osiko, V.M. Tatarintsev, R.Y. Khodakovskaja: Synthesis and investigations of $La_2O_3-Al_2O_3-SiO_2$ glasses, *Glass Phys. Chem.* **6**, 170–173 (1980), in Russian
- 14.202 B.À. Sakharov, Ò.S. Sedyh, Å.P. Rashevskaja: Study of system $Y_2O_3-SiO_2-Al_2O_3$, *Trudy Giredmet* **52**, 83–87 (1974), in Russian
- 14.203 V.I. Aleksandrov, M.A. Borik, V.B. Glushkova, R.E. Krivosheev, N.I. Markov, V.V. Osiko, V.M. Tatarintsev: Synthesis and some properties of refractory glasses in $R_2O_3-Al_2O_3-SiO_2$ system, *Glass Phys. Chem.* **3**, 177–180 (1977), in Russian
- 14.204 A. Makishima, Y. Tamura, T. Sakaino: Elastic moduli and refractive indices of aluminosilicate glasses containing Y_2O_3 , La_2O_3 and TiO_2 , *J. Am. Ceram. Soc.* **61**, 247–249 (1978)
- 14.205 A. Makishima, T. Shimohira: Alkaline durability of high elastic modulus aluminosilicate glasses containing Y_2O_3 , La_2O_3 and TiO_2 , *J. Non-Cryst. Solids* **39/40**, 661–666 (1980)
- 14.206 G.E. Malashkevich, V.N. Tadeush, V.V. Kuznetsova, A.K. Cherches, N.I. Bliznyuk, V.G. Mikhalevich, M.B. Rzhetskii: Physicochemical and spectral luminescence properties of a glass based on the $SiO_2-Al_2O_3-La_2O_3-Nd_2O_3$ system, *J. Appl. Spectrosc.* **37**, 926–929 (1982)
- 14.207 J. Shelby, S. Minton, C. Lord, M. Tuzzolo: Formation and properties of yttrium aluminosilicate glasses, *Phys. Chem. Glasses* **33**, 93–98 (1992)
- 14.208 J. Kohli, J. Shelby, J. Frye: A structural investigations of yttrium aluminosilicate glasses using ^{29}Si and ^{27}Al magic angle spinning nuclear magnetic resonance, *Phys. Chem. Glasses* **33**, 73–78 (1992)
- 14.209 T.T. Basiev, Y.K. Voron'ko, V.V. Osiko, A.M. Prokhorov: Laser spectroscopy doped crystals and glasses. In: *Spectroscopy of Crystals*, ed. by A.A. Kaplyanskii (Leningrad, Nauka 1983) pp.57–82, in Russian
- 14.210 M. Weber: Laser excited fluorescence spectroscopy in glass. In: *Laser Spectroscopy of Solids*, ed. by W.M. Yen, P.M. Selzer (Springer, Berlin-Heidelberg, New-York 1981) pp.189–239
- 14.211 G.E. Malashkevich, N.N. Ermolenko, V.I. Aleksandrov, M.A. Borik, G.M. Volokhov, A.S. Gigevich, G.A. Denisenko, A.V. Mazovko, V.N. Tadeush: Spectral-luminescent and thermomechanical characteristics of silicate-borate glasses activated with Yb^{3+} and Er^{3+} ions, *Izv. AS USSR, Inorg. Mater.* **6**, 1053–1055 (1987), in Russian
- 14.212 Y.I. Matunin, A.V. Demin, T.V. Smelova: Behavior of uranium and rare-earth elements in glasses synthesized in an induction melter with a cold crucible, *At. Energy* **83**, 795–800 (1997)
- 14.213 N.D. Musatov, V.G. Pastushkov, P.P. Poluektov, T.V. Smelova, L.P. Sukhanov: Compaction of

radioactive thermal-insulation materials and construction debris by melting in a cold crucible, *At. Energy* **99**, 602–606 (2005)

14.214 K. Guilbeau, A. Giordana, W. Ramsey, N. Shulyak, A. Aloy, R. Soshnikov: Induction-melting technology, *Am. Ceram. Soc. Bull.* **83**, 38–40 (2004)

15. Crystal Growth of Laser Host Fluorides and Oxides

Hongjun Li, Jun Xu

Following the discovery of the first laser action based on ruby, hundreds of additional doped crystals have been shown to lase. Among those, many crystals, such as $\text{Ti}:\text{Al}_2\text{O}_3$, $\text{Nd}:\text{Y}_3\text{Al}_5\text{O}_{12}$, $\text{Nd}:\text{YVO}_4$, $\text{Yb}:\text{Y}_3\text{Al}_5\text{O}_{12}$, $\text{Yb}:\text{Ca}_5(\text{PO}_4)_3\text{F}$, and $\text{Cr}:\text{LiCAF}$ have come to practical application, and are being widely used in scientific research, manufacturing and communication industries, military applications, and other fields of modern engineering. These crystals are mainly oxides and fluorides, which are grown from melt. This chapter reviews the major results obtained during recent years in the growth of various crystalline oxides and fluorides for laser operation, with emphasis on crystals doped with the additional ions Ti^{3+} , Nd^{3+} , and Yb^{3+} . On the other hand, special attention is paid to discuss the elimination of growth defects in these crystals. Limited by the length of this chapter, for each crystal, only outstanding defects are considered herein.

15.1 Crystal Growth of Laser Fluorides and Oxides from Melt	479
15.1.1 Laser Crystal Growth from the Melt	480
15.1.2 Czochralski Technique (CZ)	480

15.1.3 Temperature Gradient Technique (TGT)	482
15.1.4 Heat-Exchanger Method (HEM)	483
15.1.5 Vertical Bridgman Technique (VBT) ..	484
15.1.6 Horizontal Bridgman Technique (HBT)	485
15.1.7 Laser-Heated Pedestal Growth Method (LHPG)	486
15.1.8 Flux Technique (FT)	487
15.2 Laser Crystal Defects	487
15.2.1 Ti:sapphire	487
15.2.2 Nd-Doped Laser Crystals	489
15.2.3 Yb-Doped Laser Crystals	492
15.2.4 Other Activator-Doped Laser Crystals	498
15.3 Crystal Growth Techniques	
Characterization	501
15.3.1 Czochralski (CZ) Process	501
15.3.2 Temperature Gradient (TGT)	501
15.3.3 Heat-Exchanger Method (HEM)	502
15.3.4 Vertical Bridgman Technique (VBT) ..	502
15.3.5 Horizontal Bridgman Technique (HBT)	502
15.3.6 Laser-Heated Pedestal Growth (LHPG)	503
15.3.7 Flux Technique (FT)	503
References	503

15.1 Crystal Growth of Laser Fluorides and Oxides from Melt

The development of many advanced fields in modern engineering is, to a large extent, governed by the success achieved in the techniques of crystal growth. On the other hand, the demand for new crystals for advanced technologies has stimulated the improvements in growth techniques of these crystals. Certainly, this concerns only a few very important crystals.

In 1960, laser action was first demonstrated on the basis of a ruby laser rod (or Cr^{3+} -doped Al_2O_3) [15.1], indicating the birth of a new subdiscipline of science:

the laser technique. In the 1970s, the discovery of Nd^{3+} -doped yttrium aluminum garnet ($\text{Nd}:\text{YAG}$) [15.2] crystal prompted the rapid development of the solid-state laser. In the 1980s, the invention of Ti^{3+} -doped sapphire ($\text{Ti}:\text{Al}_2\text{O}_3$) [15.3] made it possible to produce ultra-intense and ultrafast lasers, based on which the intralase technique has been employed widely in both basic and applied science fields. In the 1990s, the successful fabrication of $\text{Nd}:\text{YVO}_4$ [15.4] led to a new period of development for the laser technique:

the all-solid-state laser. Simultaneously, the advent of cheap diode-laser pump sources brought about the practical application of Yb-doped materials such as Yb:YAG [15.5] and Yb:Sr₅(PO₄)₃F (Yb:S-FAP) [15.6], which have shown great capability in high-power laser systems. Entering the 21st century, research into laser materials is expanding extensively in the forms of single crystal, glass, ceramics, and fiber. Owing to their advantages of simple fabrication processes, lower costs, and greater perfection, laser fiber [15.7] and polycrystalline ceramics [15.8] are challenging the dominant status of traditional materials.

In spite of the hundreds of additional doped crystals that have been shown to lase, few crystals have proven to be useful in practical circumstances. In fact, the gap between demonstration exercises of laser action and the engineering of practical systems is often wide and difficult to bridge.

In order to develop and test new laser crystals, it is first crucial to identify the appropriate means by which to grow and fabricate the crystal. To further optimize the crystal growth conditions, it is necessary to understand the physical properties of the melt and solid. In order to improve the crystal quality, it is important to clarify the formation mechanism of growth defects in the crystal so as to find proper ways to eliminate them. While the methods and issues associated with crystal growth occupy the bulk of this chapter, we begin with a discussion of the important growth techniques and their modifications for laser crystal growth. Our attention is focused on the insights and issues involved in the development, melt-growth, and defect elimination of the main laser oxides and fluorides. Since our approach will entail discussion from the perspective of laser materials, only crystals doped with the most attractive additional ions, such as Ti³⁺, Nd³⁺, and Yb³⁺, will be addressed.

15.1.1 Laser Crystal Growth from the Melt

After the development of the first laser, which was based on a Verneuil-grown ruby, almost all of the classical crystallization techniques have been applied to analyze growth characteristics and provide high-quality laser crystals and the development of new laser crystals. In the 1960s, flux methods were widely used to grow the rare-earth aluminum and gallium garnets, both pure and doped, as well as some of the rare-earth orthoaluminate hosts. The emphasis later was on melt techniques, as they provided both larger crystal size and faster growth rates. Among these, the Czochralski technique (CZ)

employing iridium crucibles and radiofrequency (RF) heating was the most adaptable and widely used for the majority of high-temperature laser oxides, while the vertical Bridgman technique (VBT) was commonly used for laser fluorides. On the other hand, static growth techniques, such as the heat-exchange method (HEM) and temperature gradient technique (TGT), have been becoming efficient methods for the growth of large-sized laser crystals, while two other promising techniques, the micro-pulling-down method (μ -PD) and the laser-heated pedestal growth method (LHPG), are especially used for fiber crystal growth.

15.1.2 Czochralski Technique (CZ)

The CZ method is named after *Jan Czochralski* who introduced an early version of the present-day process in 1916, and published it as a method for studying the crystallization rate of metals [15.9]. Further modifications by *Teal* and *Little* [15.10] brought the technique closer to the process known today as the Czochralski, or CZ, method. The application of this technique and its consequent development was stimulated by the invention of the laser in 1960, since when it has been used for oxide crystal production [15.11, 12].

The CZ furnace geometry is relatively simple, as shown in Fig. 15.1, and is usually constructed of either Al₂O₃ or stabilized ZrO₂ ceramics. The crucible can be either Pt or Ir, depending upon the melting point of the material and/or the atmosphere required for the growth process.

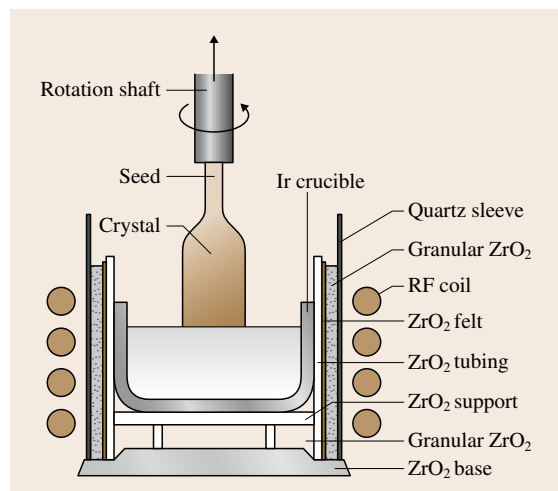


Fig. 15.1 Schematic drawing of a typical Czochralski furnace used for the growth of oxide-based laser crystals

The crucible is heated by means of an RF generator operating in the range of 10–400 kHz. With the development of solid-state RF generators, the trend is toward lower frequencies, preferably in the range 10–30 kHz. These lower frequencies have the distinct advantage of producing more uniform heating of crucible, which is necessary for the growth of large-diameter crystals, and in the case of the higher-melting oxide systems that must use ZrO_2 insulation, avoiding coupling of the RF energy directly into the ceramic parts of the furnace.

The growth and control of the crystal is dependent upon the radial temperature gradient in the liquid and the vertical gradient through the length of the furnace. For smaller growth systems (typically using crucibles less than 75 mm in diameter), the adjustment of the radial and vertical thermal gradients can be easily accomplished by varying the ceramic insulation and its dimension. However, once beyond this size, a suitable liquid radial gradient becomes more difficult to establish, thereby making seeding and the initial cone section of the crystal more difficult to control, hence the need for an automatic diameter control system. Although several methods of diameter control have been developed [15.14–17], the one mostly widely used is that of weighing the crystal while it is growing. In this case, a load cell with a sensitivity of ± 0.1 g is placed in line with the rotation shaft to which the seed crystal is attached. As the crystal is pulled from the melt, the change in weight is used to generate a control signal that modifies the generator output power to the crucible, thereby controlling the diameter through small changes in the liquid temperature. Typical systems are easily capable of maintaining a 75 mm-diameter crystal to within ± 1 mm.

The CZ growth process is, by far, the most commonly used process for the growth of laser materials and is employed over a wider span of materials and melting points than any other melt-growth method, ranging from mixed compounds such as nitrates, through germinates, fluorides, molybdates, tantalates, and garnets, to single oxides such as sapphire and yttria. To circumvent various kinds of problems encountered during crystal growth, numerous modifications have been made to improve the standard CZ growth process.

During the growth of Nd:YAG crystals, the Nd segregation problem always exists. Nd concentration increases as crystal growth proceeds so that, if we want to keep uniformity of concentration within 0.1 at. %, solidification is restricted to 20–30% of melt in crucible. To achieve higher solidification, Katsurayama and coworkers [15.13] developed a double-crucible method with

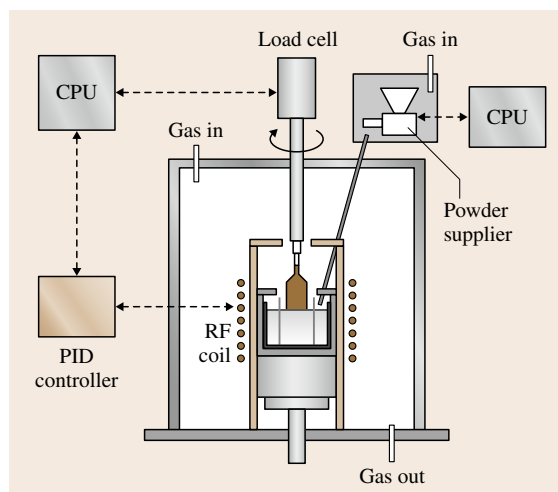


Fig. 15.2 Schematic diagram of crystal growth apparatus with automatic powder supply system [15.13] (CPU – central processing unit, PID – proportional–integral–derivative)

automatic powder supply (Fig. 15.2). In this system, material powder is continuously supplied into the crucible to maintain the concentration of Nd in the melt. As a result, the Nd concentration fluctuation in the grown crystal has been reduced to as low as 0.02 at. % when 30% of melt is solidified. On the other hand, Kanchanavaleerat et al. [15.18] modified the growth parameters to grow highly doped Nd:YAG crystals with excellent optical quality, as shown in Fig. 15.3, and the laser testing shows that the highly doped Nd:YAG rods have very good efficiency due to low passive losses.

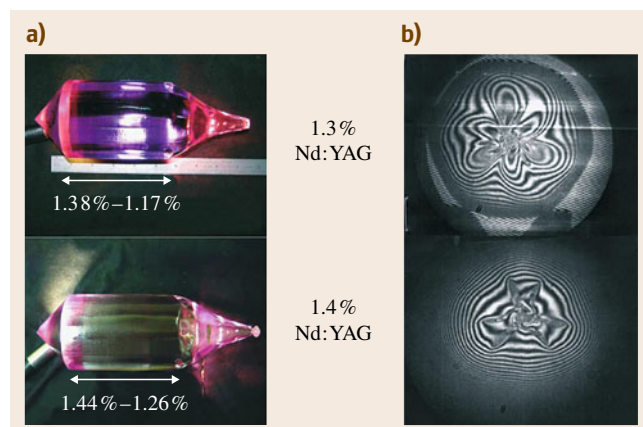


Fig. 15.3 (a) Highly doped Nd:YAG crystals, (b) Zygo interferogram

Boulon et al. [15.19] indicated that Y_2O_3 , Sc_2O_3 , and Lu_2O_3 sesquioxides have the highest laser potentialities in the continuous wave (CW) regime. However, due to their high melting points, about 2420°C , the growth of the sesquioxides is rather difficult. The major problem is that the high temperature restricts the choice of crucible materials, which has to be mechanically stable at the melting point and resistant to chemical reactions with the melt as well as with the surrounding thermal insulation. The results of Fornasiero et al. [15.20] reveal that rhenium fulfills these requirements to the greatest extent. Rhenium is sensitive to oxidizing atmospheres but resistant to melts of Al_2O_3 and rare-earth oxides. The melting point of rhenium is 3180°C . To avoid the react of the hot crucible and the ceramic zirconia insulation at high temperatures, Fornasiero designed a holding construction which consisted of rhenium rods directly welded to the crucible. The crucible was suspended in a thermally insulating tube of zirconia felts so that it was completely surrounded by gas. To reduce the radiation losses from the free melt surface, rings and funnels were inserted into the crucible a few millimeters above the melt. Through the above modifications of the conventional CZ configuration, several crystals with typical length of 5 mm and diameter of 10 mm have been grown [15.20].

Shimamura et al. reported the growth of Ce:LiCAF crystals without either the use of HF gas or the hydrofluorination of raw materials [15.21]. Instead, a growth chamber was evacuated to about 10^{-2} Torr prior to growth, and high-purity Ar (99.9999%) gas was used as a growth atmosphere. Under these conditions, a deposit of a white foreign substance, composed of volatile fluorides and oxyfluoride, was found on the surface of the grown crystals. In order to avoid its formation and to grow high-quality crystals with higher reproducibility, several modifications such as high-vacuum atmosphere prior to growth, use of CF_4 gas instead of Ar, and growth with a low temperature gradient, were required [15.21]. Such modifications are also needed for the growth of other fluorides, e.g., LiYF₄ (YLF), BaLiF₃, and CaF₂ [15.22, 23].

15.1.3 Temperature Gradient Technique (TGT)

The temperature gradient technique (TGT) is a typical static directional solidification technique, which was invented by Zhou et al. [15.24] in 1979; Shanghai Institute of Optics and Fine Mechanics (SIOM) obtained a patent on TGT in 1985 [15.25].

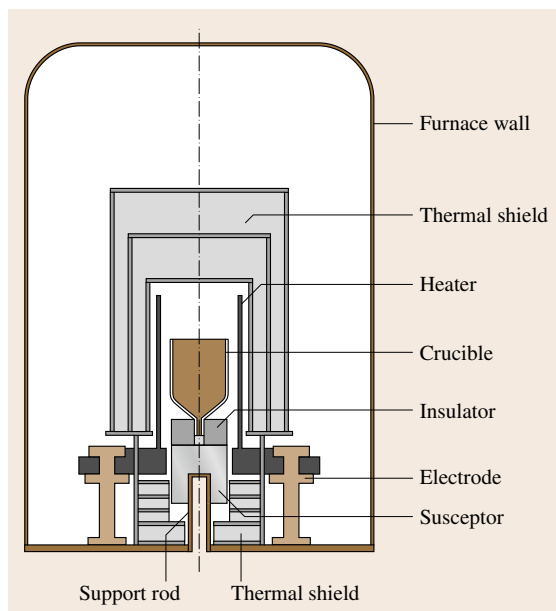


Fig. 15.4 Schematic diagram of a TGT furnace

A schematic diagram of the TGT furnace is shown in Fig. 15.4. It consists of a molybdenum crucible, graphite heating element, and molybdenum heat shields. The cylindrical graphite heating element is designed as an electric circuit with appropriate linear resistance from the top to the middle by making holes with a certain distribution. The cylinder is placed in the graphite electrodes, which are cooled by water. The temperature gradient of the upper part is produced by the linear resistance of the heating element, whereas that in the lower part depends on the extraction of heat by water flowing in the tubes through the electrodes. Besides these, the temperature field near the seed is influenced by the heat conductivity of the water-cooled center rod. In TGT, there are no moving parts. The growth process is accomplished by dropping the temperature at designed rates with a high-precision temperature program controller.

Large-sized laser oxide and fluorides, such as Ti:sapphire [15.26], Nd:YAG [15.27], Yb:YAlO₃ (Yb:YAP) [15.28], and Na,Yb:CaF₂ [15.29] shown in Fig. 15.5, have been grown successfully by the TGT method. Taking the growth of Ti:sapphire as an example, the basic growth process of TGT can be described as follows. A cylindrical seed with the selected orientation is placed into the seed hole of the molybdenum crucible, and the high-purity starting materials are placed in the crucible. The furnace is loaded for the

growth process, outgassed to $(2-4) \times 10^{-3}$ Pa; when the temperature at the bottom of crucible is about 1400°C , high-purity Ar is fed into furnace; then the material is melted and kept molten for several hours. After the temperature field has stabilized, crystallization is started by slow cooling ($1.3-3$ K/h). The solid-liquid interface advances upwards as the temperature drops. The whole crystallization process is completed automatically. During the growth process, it is essential that the temperature and thermal field are very stable, and an important factor is the flow stability of the circulating cooling water so that the solid-liquid interface advances with constant velocity.

The typical size of TGT-grown Ti:sapphire boules is $\varnothing 110 \times 80$ mm², the titanium doping levels are between 0.05 and 0.52 wt %, the absorption coefficient at 490 nm is from 1 to 7.5 cm^{-1} , the absorption coefficient can be as high as 10 cm^{-1} in some case (the theoretical limit is 11 cm^{-1} for absorption coefficient at 490 nm), and the figure of merit (FOM) of Ti:sapphire crystals is in the range 150–400. Besides the mentioned advantages, there are other advantages of TGT-grown Ti:sapphire, such as low dislocation density, low scattering, and high perfection, which are very important factors determining laser performance [15.31].

For TGT-grown Nd:YAG crystals, high doping concentration of neodymium is a distinct character. Highly doped (2.5 at. %) Nd:YAG shows high absorption coefficients at the 808 nm laser diode (LD)-pumping wavelength up to 7.55 cm^{-1} , nearly three times higher than 1 at. % Nd:YAG [15.32]. Therefore, a short crystal length (e.g., 1 mm) is preferred, and compact microchip lasers can be constructed by using 2.5 at. %-doped Nd:YAG. Almost the same output has been achieved preliminarily in both (111)-cut 1 mm-long Nd:YAG and *a*-cut 1 mm-long YVO₄ microchip lasers with a very short (9 mm) laser cavity. In particular, the broader and smoothly varying absorption bandwidth allows less stringent requirements on temperature control.

In the growth of Yb:CaF₂ crystals, it is notable that a lid was employed to seal the crucible to reduce volatilization of the materials. Sometimes, small amounts of PbF₂ or ZnF₂ acting as scavengers were added to the CaF₂ raw materials to eliminate residual moisture prior to growth.

15.1.4 Heat-Exchanger Method (HEM)

The heat-exchanger method (HEM) for growing large sapphire boules was invented by Schmid and Viechnicki at the Army Materials Research Lab in Watertown, MA,

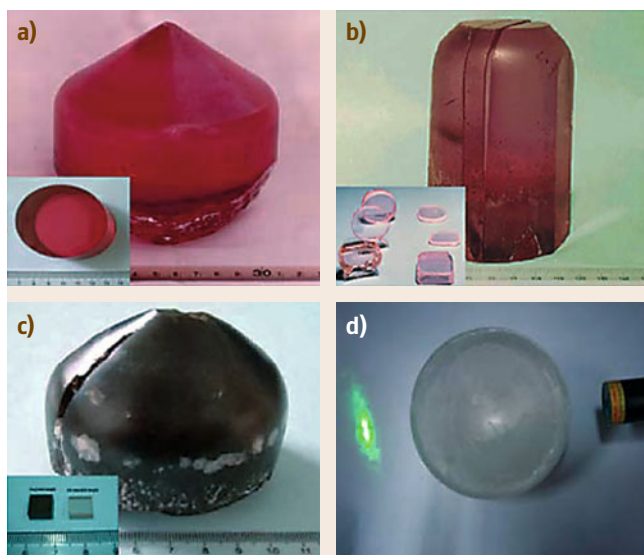


Fig. 15.5a–d Crystal boules and fabricated samples of Ti:sapphire (a), Nd:YAG (b), Yb:YAP (c) and Na, Yb:CaF₂ (d) grown by TGT

in 1967 [15.33]. The modern implementation of Schmid and Viechnicki's heat-exchanger method at Crystal Systems in Salem, MA, is shown in Fig. 15.6 [15.30].

It consists of a water-cooled chamber containing a well-insulated heat zone. A high-temperature heat exchanger is introduced from the bottom of the furnace

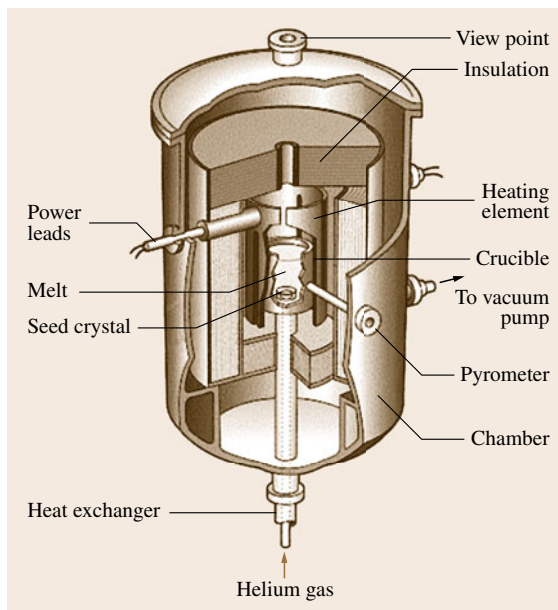


Fig. 15.6 Schematic of a HEM furnace [15.30]



Fig. 15.7 A 10 cm-diameter $\text{Ti:Al}_2\text{O}_3$ crystal grown by HEM [15.34]

into the heat zone. The heat exchanger is a closed-end tube with an injection tube through which a controlled flow of coolant gas is introduced. A crucible with a seed crystal positioned at the bottom and loaded with charge is placed on top of the heat exchanger. The furnace chamber can be evacuated with a vacuum pump or back-filled with a gas for controlled atmosphere processing. Heat is supplied by the graphite resistance to melt the charge; the seed is prevented from melting by flowing minimal coolant gas through the heat exchanger. After partial melting of the seed, gas flow is increased to cool the seed and initiate crystallization of melt onto the seed. The furnace is held at constant temperature during growth of the crystal, which proceeds out from the seed in three dimensions. After crystallization is complete, the furnace temperature and the helium flow are decreased and the boule is slowly annealed in situ. The long, slow cool-down produces crystals of the highest quality.

HEM has been successfully utilized for the growth of the world's largest sapphire boules with diameter of 340 mm and mass of 82 kg [15.36]. By this method, more than 95% of the melt can be converted into high-quality crystalline material. HEM was capable of growing laser crystals such as Ti:sapphire (as shown in Fig. 15.7) [15.34], Co:MgF_2 [15.34, 37], Nd:YAG [15.38], and Ti:YAP [15.39].

Recently, a modified HEM technique has been employed in the production of high-melting (about 2400°C) sesquioxides, such as $\text{Yb:Sc}_2\text{O}_3$ and $\text{Yb:Y}_2\text{O}_3$ [15.35]. Due to the high melting point (m.p.) of yttria and scandia, rhenium (m.p. 3180°C) was selected

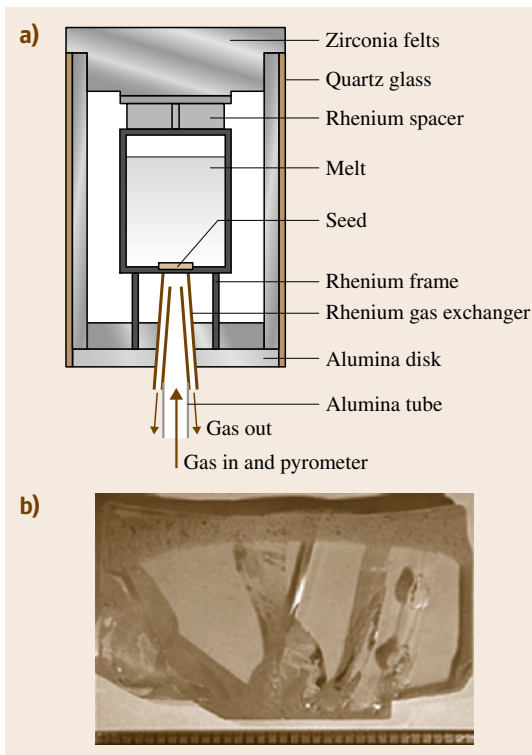


Fig. 15.8a,b Insulation HEM setup for the growth of high-melting sesquioxide crystals (a) and the grown Sc_2O_3 crystal (b) [15.35]

as the crucible material, and the crucible was completely surrounded by gas since no insulation materials could be found that would be stable when in direct contact with the crucible at the required temperature. The growth setup is shown in Fig. 15.8a. During the growth process, the crucible was heated by an RF generator under an atmosphere of 0.01% O_2 , 10–15% H_2 , and 85–90% N_2 at pressure of 1 bar. Eventually, crystals with vertical volumes of small, single crystals were obtained (Fig. 15.8b), owing to the use of a polycrystalline seed.

15.1.5 Vertical Bridgman Technique (VBT)

The vertical Bridgman technique (VBT) was first used by *Bridgman* in 1925 [15.40] and especially exploited by *Stockbarger* in 1936 and 1949 [15.41, 42]. This technique is commonly known as the Bridgman–Stockbarger method, although sometimes the names of *Tammann* (1925) and *Obreimov* (1924) are associated with the technique. *Buckly* [15.43] discussed the histor-

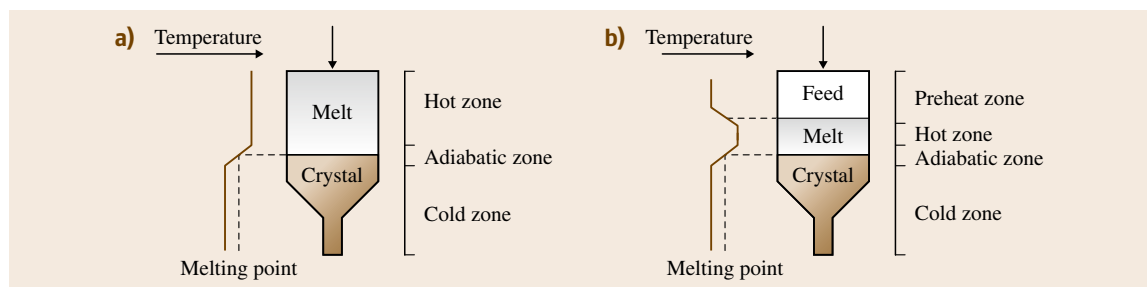


Fig. 15.9a,b A classical (a) and a modified (b) vertical Bridgman process

ical aspects of the technique and assigned the name to the original researcher.

In the Bridgman process, an ampoule containing the materials to be crystallized is translated from a zone hotter than the melting point, through a temperature gradient, to a zone cooler than the melting point in order to solidify the material (Fig. 15.9a). Equivalently, the temperature can be translated through a stationary ampoule by moving the furnace relative to the ampoule.

The vertical Bridgman technique has been applied to the growth of oxide crystals since the late 1960s [15.44]. In apparatus for this purpose a resistively heated tungsten furnace and crucibles (tubes) fabricated from molybdenum are used. Several complex oxide crystals have been grown by this technique, including Nd:YAG, and the first lasing material Nd:YAlO₃. This technique has proved to have great potential in both materials research and in the production of oxide laser crystals. Various Bridgman-grown crystals possessing application quality are now available, including Nd:YAG, Er:YAG, Tm³⁺,Cr³⁺:YAG, Tm³⁺,Cr³⁺,Ho³⁺:YAG, Er:LuAG, Pr:YAlO₃, Pr:LuAlO₃, and Nd:LuAlO₃ [15.44]. Improvements of crystalline and chemical perfection of crystals, obtained as a result of better understanding of the basic physical processes occurring during crystallization in this configuration, have resulted in larger-scale use of this technique for oxide crystal growth. In addition, VBT has been widely used for the growth of large-sized commercial CaF₂ crystals for optical applications [15.45]. Certainly, this technique can be modified for the growth of ion-doped CaF₂ crystals or other fluorides for laser applications.

Figure 15.9b illustrates a modification of the Bridgman technique in which a third zone, cold relative to the melting point, is added to the top of the furnace. This is referred to as the moving melt zone or the traveling heater method. In this case the melt volume is small compared with the ampoule. The advantages of this

configuration are twofold. First, steady-state conditions may be established in the small melt volume for growth of crystals with nonunity segregation coefficient to level out changes in dopant concentration along the length of the crystal. Second, the upper interface produces a temperature gradient that drives buoyant convection, thereby increasing mixing in the melt. This can be important for growth of multicomponent systems.

15.1.6 Horizontal Bridgman Technique (HBT)

The horizontal Bridgman technique (HBT), also known as the Bagdasarov method, is a method for refractory single-crystal growth proposed by Bagdasarov in 1964 [15.46]. In HBT, presented schematically in Fig. 15.10, the crystallizing material (in the form of powder, crystal crackles or ceramics) is placed in a boat-like crucible, melted by moving the crucible through the heating zone, and then crystallized. To obtain a strictly oriented crystal the single crystal seed is mounted on the top of the crucible (boat) and both the moment of seeding and the formation of the growth front are observed visually.

HBT allows repeated crystallizations to be carried out when additional chemical purification of the raw

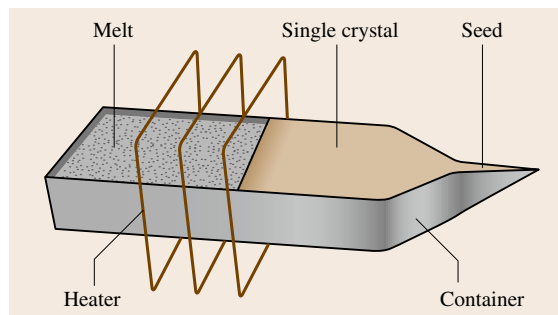


Fig. 15.10 Horizontal Bridgman technique scheme

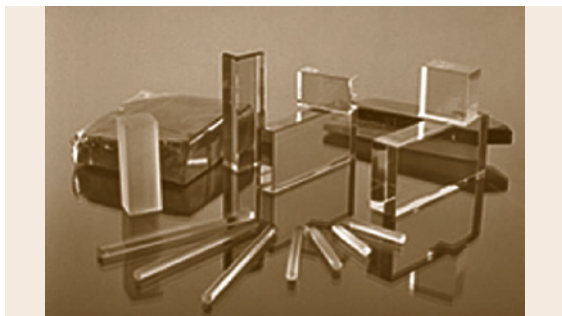


Fig. 15.11 Nd:YAG and Er:YAG crystals grown by HBT [15.46]

material is required. It is also possible to carry out a continuous crystallization process by directed shifting of the crucible echelon through the crystallization zone. With the HBT method it is technically easy to create a controlled temperature field, which is crucial for the growth of high-perfection large-size single crystals. This method makes it possible to obtain large slabs with almost perfect edges and of any given crystallographic orientation.

Initially, this method was designed in order to grow large-size, Nd-doped, high-perfection yttrium–aluminum garnet laser crystals. Later, it turned out to have potential for the growth of yttrium–erbium–aluminum garnet. The crystals have a typical size of $130 \times 130 \times 25 \text{ mm}^3$ as well as high optical homogene-

ity, as shown in Fig. 15.11. Recently, it is reported that HBT could be used to produce a new type of Nd:YAG crystal with emission property two times higher than from conventional Nd:YAG crystals [15.46].

15.1.7 Laser-Heated Pedestal Growth Method (LHPG)

Poplawsky [15.48] was the first to initiate crystal growth using a pedestal growth process based on melting materials by the energy created by an image furnace. Then, in 1972, Haggerty et al. developed the laser-heated pedestal growth method (LHPG), which was improved later by Feigelson [15.49] at Stanford University.

Figure 15.12 illustrates LHPG crystal growth. In this technique a float zone is created at the top of a vertical feed rod by using a focused laser beam. Motion of the float zone is generated by vertical displacement of the feed. During this translation, the feed progressively melts and, behind the float zone, a crystallized rod is formed. The float zone remains in equilibrium with the feed and the crystallized rod due to surface tension. The source rod materials containing the desired host and dopant materials can be used as oriented fiber single crystals or polycrystalline reacted materials prepared by solid-state reaction. A seed crystal, once dipped into the molten zone, is withdrawn at some rate faster than the source material is fed in. By conservation of melt volume, this leads to the crystalline fiber

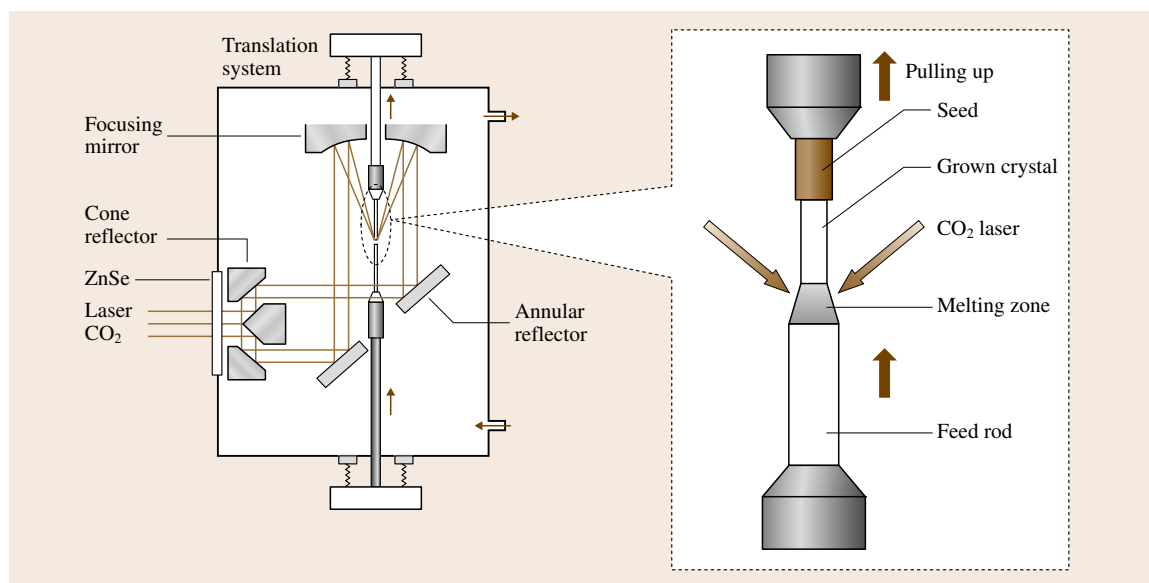


Fig. 15.12 Schematic diagram of the laser optics used in the LHPG technique [15.47]

growing at some constant fraction of the source rod diameter.

A great variety of oxide and fluoride crystal fibers doped with rare-earth and transition metal ion activators in a great range of concentrations have been pulled by the **LHPG** technique [15.47, 50]. Specially, because of the lack of crucible and the use of a CO₂ laser, the **LHPG** technique is well adapted to high-refractory crystals such as yttria, scandia, and lutecia sesquioxides, as well as garnets [15.19, 51].

In the combinatorial approach proposed by *Boulon* [15.19], the **LHPG** technique is applied to a feed rod constituted by two ceramics parts, A and B, with different compositions. When the molten zone moves along the feed rod, there is mutual solubilization of A and B. As the solubilized amounts of A and B vary, the composition of the molten zone changes continuously, inducing a progressive and continuous composition gradient along the crystallized rod. This new approach is an efficient tool for measuring optical, spectroscopic or thermal properties in any type of inorganic optical materials in which either activator ion or nominal composition concentrations can be changed.

15.1.8 Flux Technique (FT)

The flux technique (**FT**) is based on growth of crystals from a nonaqueous solution. As a rule, a mixture of salts is used as a solvent. In the 1960s, flux methods were widely used to grow the rare-earth aluminum [15.52–54] and gallium [15.55] garnets, both pure and doped, as well as some of the rare-earth orthoaluminate hosts [15.56]. The emphasis later was on melt techniques, as they provided both larger crystal

size and higher growth rates. At present, a modified **FT** method, the top-seeded solution growth method (**TSSG**), is widely applied to produce those crystals that cannot be grown from melt easily, Nd:YVO₄ [15.57], Yb:KY(WO₄)₂ (Yb:KYW) [15.58], Nd:KGd(WO₄)₂ (Nd:KGW) [15.59], and Yb:YAl₃(BO₃)₄ (Yb:YAB) [15.60]. Sometimes, **TSSG** is also described as a high-temperature solution growth method or a modified Czochralski technique.

Among the Yb³⁺-doped oxide crystals for diode-pumped solid-state lasers, **KYW** and **KGW** were evaluated to be the hosts with the greatest lasing potential in the **CW** regime [15.19]. **FT** is obvious the choice for the growth of single crystals such as **KGW**, since **KGW** crystal has a phase transition at 1005 °C (**KYW** at 1014 °C) below its melting point (1075 °C). A typical growth procedure of such crystals is described as follows [15.58].

The starting materials with flux, such as K₂WO₄ or K₂W₂O₇, are mixed and placed into the platinum crucible. The fully charged crucible is then placed into the furnace. It is important that the charged crucible be kept at a constant temperature of 1050 °C for 3–4 days to let the solution melt completely and homogeneously. The saturation temperature of the solution is determined exactly by repeated seeding. The seed contacts the melt at a temperature 5 K above the saturation temperature and is kept at constant temperature for half an hour to dissolve the outer surface of the seed. During the growth period, the crystal is slowly cooled at a rate of 1 K/day and rotated at a rate of 4.5 rpm. When the growth process ended, the crystal is pulled up from the melt surface and cooled to room temperature at a rate of 15 K/h.

15.2 Laser Crystal Defects

The main defects which can degrade the performance of melt-grown crystals are now generally recognized to be any which can absorb, reflect, refract or scatter magnetic, optical, acoustic or electrical energy either generated within or incident upon the material. Thus, dislocations, color centers, facet, striations, twins, voids, cellular structures, precipitates, inclusions, and more destructive defects such as cracks are all important defects that have to be eliminated or controlled. Due to the great variety of defects, only those frequently encountered and those specific to the concerned host materials are discussed herein.

15.2.1 Ti:sapphire

Ti:sapphire single crystal is one of the most attractive broadly tunable solid-state laser materials. Both **CW** and pulsed lasers have been demonstrated with very high efficiency over a tuning range in excess of 300 nm centered at 800 nm. In order to develop this material to meet the needs of current commercial laser systems a variety of growth techniques, such as **HEM** [15.34], **VGF** (vertical gradient freeze) [15.61], **CZ** [15.62], and **TGT** [15.26], have been used to grow Ti:sapphire crystals. Residual infrared absorption and

mosaic structure are the main defects in as-grown Ti:sapphire crystals.

Residual Infrared Absorption

The efficiency at which a laser can operate is fundamentally impacted by its gain-to-loss ratio. As a consequence, the presence of absorptive loss at laser wavelengths can potentially reduce the efficiency, or even render the system inoperable. These parasitic losses generally arise from the presence of unwanted impurities or from unanticipated oxidation states of the laser ion. Parasitic absorption losses can be more harmful to laser performance than an equivalent amount of loss resulting from scattering, since the absorption often leads to additional heating of the medium. Since many solid-state amplifiers operate in the grain regime of 3–30%/cm, losses on the order of 1%/cm can seriously impair laser performance [15.63].

In Ti:sapphire, parasitic losses are mainly induced by the presence of a relatively weak, broad infrared absorption band that peaks between 800 and 850 nm [15.64–67]. Aggarwal and coworkers [15.68] proposed that the residual absorption in these crystals is largely due to $\text{Ti}^{3+}/\text{Ti}^{4+}$ ion pairs, and also indicated that annealing such crystals at high temperatures ($\approx 1600^\circ\text{C}$) in a reducing atmosphere (an Ar/ H_2 mixture) decreased the residual absorption without significantly changing the main absorption, whereas annealing in an oxidizing atmosphere (Ar/ O_2 mixture) increased the residual absorption and simultaneously decreased the main absorption. The decrease in the main absorption, which was also observed in earlier experiments on Ti:sapphire crystals grown by the Czochralski method [15.69–71], results from the oxidation of Ti^{3+} ions to Ti^{4+} ions. Mohapatra and Kroger [15.71] concluded that charge compensation is probably accomplished by the formation of an Al vacancy for every three Ti^{3+} ions converted to Ti^{4+} . The main absorption could be restored by annealing oxidized samples in a reducing atmosphere [15.69–71].

As noted above, the residual infrared absorption could be eliminated with careful attention to the redox conditions in the melt and also by postannealing techniques [15.72, 73].

Basal Slip

Because of its rhombohedral structure and its resulting anisotropic properties, sapphire exhibits different crystalline habits and structure perfections when growing along different directions [15.74]. Generally it is difficult to grow high-quality sapphire single crystal along

the [0001] direction because this orientation is not preserved in the grown crystal [15.74], due to the weakening action of the main slip systems. The slip systems of sapphire reported so far are $(0001)1/3\langle 11\bar{2}0 \rangle$ basal slip, $\{11\bar{2}0\}\langle 1100 \rangle$ prism slip, and $\{10\bar{1}1\}1/3\langle \bar{1}101 \rangle$ pyramidal slip [15.75, 76]. Among those, basal slip is known to be the easiest slip system at elevated temperatures.

In HEM or CZ systems an interface is developed which is convex towards the liquid. With such an interface a boule grown along the [0001] orientation always exhibits solidification stress. So, typically, sapphire is often grown in $[11\bar{2}0]$, $[10\bar{1}0]$, and $[1\bar{1}02]$ orientations to avoid basal slip. For zero-birefringence optics, the [0001] orientation is required, and components can be obtained from $[11\bar{2}0]$ - and $[10\bar{1}0]$ -oriented boules by fabricating pieces orthogonal to the growth direction [15.77]. However, this limits the size and homogeneity of fabricated components. As will be discussed in Sect. 15.3.2, the TGT system has a rather more stable thermal field than any other system, and the solid–liquid interface in the TGT system is much flatter (slightly convex). This made it easier to grow [0001]-oriented boules [15.78, 79], thereby enhancing the perfection of fabricated components, which results in a good laser performance, as described below [15.31].

The concentration of titanium along the radius in Ti:sapphire crystal grown by TGT is nearly unity. Figure 15.13 shows the distribution of the absorption coefficient at 514 nm ($\alpha_{514\text{ nm}}$) along the growth axis of Ti:sapphire crystal grown by HEM and TGT. It can be seen that the concentration of Ti^{3+} in HEM-grown Ti:sapphire is not high, and the concentration gradi-

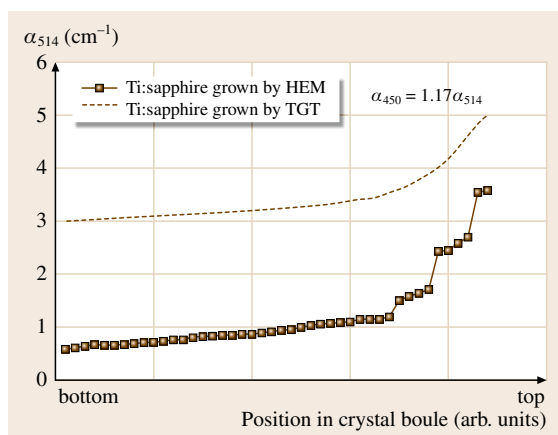


Fig. 15.13 Distribution of the absorption coefficient at 514 nm ($\alpha_{514\text{ nm}}$) along the growth axis of Ti:sapphire crystal grown by HEM and TGT

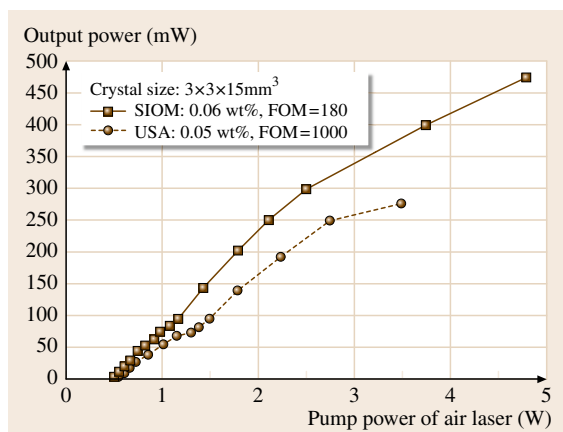


Fig. 15.14 CW laser performance of Ti:sapphire crystals grown by TGT and HEM in the same laser systems without water cooling

ent is large in the highly doped section ($1\text{--}3.6\text{ cm}^{-1}$). The concentration of Ti^{3+} in TGT-grown Ti:sapphire is higher, and the absorption coefficient can reach as high as 5 cm^{-1} . Figure 15.14 shows the CW laser performance of Ti:sapphire crystals grown by TGT and HEM without water cooling in the same laser system. Although the FOM, mainly determined by the $\text{Ti}^{3+}/\text{Ti}^{4+}$ ratio in the crystal, of HEM-grown Ti:sapphire is as high as 1000, 5.5 times higher than that of the TGT-grown one, the laser performance (efficiency and output power) of TGT-grown Ti:sapphire crystal is obviously better. These results show that the laser performance of Ti:sapphire depends not only on the FOM, but more on the crystal perfection. Furthermore, ultrashort pulse performance in China (12 fs) and in other counties (8 fs) was also achieved using TGT-grown Ti:sapphire crystals. High gain was obtained in TGT-grown highly doped Ti:sapphire crystals in RIKEN, Japan in 1994, and was 100 times higher than the data reported for Ti:sapphire crystals grown by HEM at that time [15.31].

15.2.2 Nd-Doped Laser Crystals

Nd-ion-based lasers are among the mostly used solid-state laser systems. They find applications in many areas, including the generation of the highest energy per pulse for laser-induced fusion purpose. Nd:YAG is by far the most useful material, owing to its unique combination of excellent thermomechanical properties and high gain cross section at $1.064\text{ }\mu\text{m}$. Nd:YLF offers lower thermal lensing and longer storage time compared with Nd:YAG, although it is also a much less robust

crystal. The Nd:YAP crystal does not exhibit the thermal birefringence problems experienced by Nd:YAG, but crystal growth of this medium has been hampered by several problems, including a tendency to twin. Nd:FAP and Nd:YVO₄ crystals possess the important properties of very large emission cross sections.

In spite of possessing many advantages, high-quality Nd-doped laser crystals are not easy to obtain due to the presence of many growth defects such as striations, facets, inclusions, the low distribution coefficient of Nd in host materials, etc.

Striations

Temperature fluctuations can give rise to striations in the growing crystal, which are often detrimental to laser performance [15.80]. These fluctuations can arise both from imperfect temperature/power control in the heating elements as well as from periodic or turbulent flows in the melt.

Striations can be eliminated or reduced in a number of ways. In pure compounds, growth at the congruently melting composition is an obvious solution. However, with deliberately doped or slightly impure materials the lowest temperature gradients and smallest melt depths compatible with crystal diameter control and the avoidance of other defects must be employed in order to limit convection.

Striations represent a useful built-in record of the interface shape at any point in the crystal and are thus widely employed in studying defects and morphology changes related to the solid-liquid interface. Figure 15.15 illustrates the striations observed in CZ and TGT-grown Nd:YAG crystals. It shows that the CZ configuration tends to produce a conical interface shape, while TGT has a flatter shape. Such a discrepancy results mainly from differences in the melt geometries, thermal and boundary conditions, and heating methods.

In CZ growth of laser crystals, the time constant of the system is generally set by the melt and the crys-

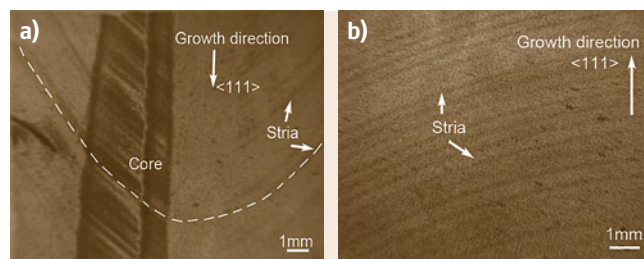


Fig. 15.15a,b Striations in CZ-grown (a) and TGT-grown (b) Nd:YAG crystals, observed by synchrotron radiation topography

tal, since induction heating of the crucible is usually the method of choice. The thin-walled crucible has a negligible impact on the time constant of the furnace. On the other hand, in TGT, VBT or HEM growth, the furnace time constant is often much longer because of the use of massive heating elements (either inductive or resistive). This large mass dampens the inevitable temperature fluctuations from the power supply. Rather than inductively heating the crucible, a relatively massive resistive heater is used that radiates to crucible. The crucible mass can be as large as required. For inductive heating, a massive susceptor can also be used, even for higher-melting materials such as Nd:YAG. A susceptor is a material used for its ability to absorb electromagnetic energy and convert it to heat.

In TGT, VB or HEM growth, with the melt above the crystal, the vertical temperature gradient is stabilizing with respect to natural convection (hot above cold), as opposed to the CZ configurations, which is destabilizing. In this context, stabilizing and destabilizing refer to the tendency to establish buoyancy-driven flows. For systems in which hotter fluid rests on top of colder fluid, such as in TGT, VB, and HEM growth, the lower density associated with the hotter fluid on top means that it will tend to remain in that position; hence this is stable. For systems in which hotter fluid is below colder fluid, such as for CZ growth, the colder upper fluid will tend to fall due to its higher density; this is unstable with respect to convection. In addition to TGT and HEM growth, keeping the crucible and growing crystal stationary will reduce temperature fluctuations result-

ing from mechanical vibration, and thus further enhance thermal stability in the melt.

In TGT, VB or HEM systems, the temperature gradient can be as small as practically required, depending on thermodynamic considerations. This can be important for controlling thermal stresses or selective evaporation from multicomponent systems. In Czochralski growth, appreciable temperature gradients are required to control the diameter. In fact, Surek [15.81] showed by analysis that, when heat transfer effects are neglected isothermally, the CZ process is unstable; small perturbations will produce large fluctuations in crystal diameter.

Facets

During the growth of Nd:YAG crystal along [111] crystallographic axis under conditions which produce a deep interface, i.e., the growing end of the crystal has an essentially conical shape, convex into the melt, the interface geometry, combined with {211} facets near the tip, generates a nonhomogeneous central core [15.82] surrounded by a six-lobed strain pattern (Fig. 15.16c). The presence of facets limits the size of the slab that can be harvested from the boule and degrades the uniformity of the crystal.

Ming et al. [15.83] indicated that the core will appear at the region where the facet planes are parallel to the solid-liquid interface. Since the interface shapes in TGT and CZ configurations are commonly different, it is certain that the distribution of cores in crystals grown by these methods will be different: one is at the center, while the other is at the periphery (Fig. 15.16).

In the CZ configuration, Nd:YAG naturally grows with a deep interface because of radiative heat loss through the cooler, upper part of the furnace. In effect, the cold part of the furnace pushes the melt/crystal interface down into the melt via this long-range radiative exchange. In the CZ configuration, the interface shape can be controlled to give an approximately planar surface by increasing the crystal rotation rate to a critical value that depends on the crystal diameter [15.84–87], but this approach increases the risk of temperature fluctuations.

For some garnets, e.g. $\text{Dy}_3\text{Al}_5\text{O}_{12}$, the planar interface shape is produced at lower crystal rotation rates as compared with $\text{Y}_3\text{Al}_5\text{O}_{12}$ [15.88], while at higher rates it transforms to a concave one [15.89]. This behavior has been attributed to intensive absorption in the infrared associated with Dy^{3+} ions that overlaps with the maximum wavelength of spectral density of the thermal radiation used for melting [15.88]. In order to adapt this approach to laser crystal growth, impurity ions that are

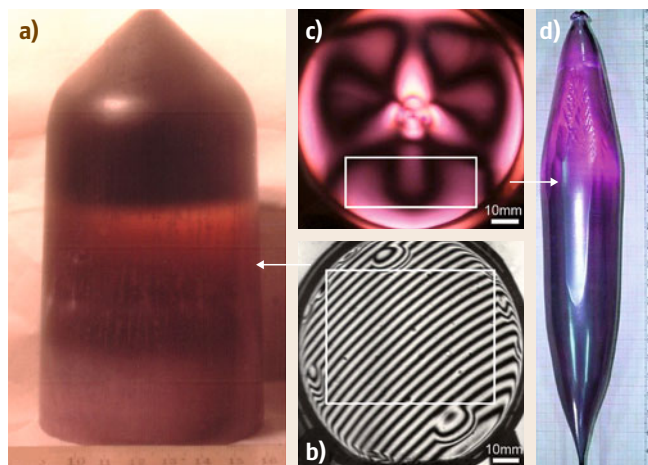


Fig. 15.16a–d Distributions of facet-induced cores in $\varnothing 75$ mm TGT-grown YAG (a,b) and in $\varnothing 80$ mm CZ-grown Nd:YAG (c,d); the white frames indicate the available aperture for laser elements

spectroscopically indifferent with respect to the lasing ions must be selected. It has been seen, for example, that additions to **YAG** melts of small amounts of Pr^{3+} , Sm^{3+} or Zr^{3+} [15.90], producing intensive absorption lines in the infrared region, also affect the shape of the interface.

In the **TGT** or **VBT** configurations, the low temperature gradients give an approximately planar solid–liquid interface except near the crucible wall, where the interface becomes slightly convex towards the melt and it is here that the facets occur [15.27, 91]. In the case of the $\langle 100 \rangle$ axis, which is normally accepted as the most preferable for Bridgman growth of garnets [15.90], the facets are eliminated further to the crystal peripheral region due the larger angle between the growth axis and the facets plane.

Scattering and Inclusions

The sources of scattering and inclusions can be either extrinsic (impurities) or intrinsic, such as solid-state exsolution of a compound from a congruently melting, nonstoichiometric crystal.

For small intrinsic defects, often nothing can be done to eliminate them. In general, there are two ways in which small intrinsic defects can be eliminated or reduced in number. Point defects can sometimes be quenched before agglomeration take place. However, quenching implies the presence of large temperature gradients that are often problematic, producing either large thermal stresses or intense melt convection. The second means of elimination is solid-state diffusion of species over macroscopic distances. This mechanism is only applicable for small ions such as lithium or sodium, since the diffusion coefficients must be very large for this to be practical. Large defects, on the order of tens or hundreds of microns, of some intrinsic composition are indicative of other problems in the growth process. These can result from temperature fluctuations leading to large undercooling in portions of the melt, or from insufficient mixing in a multicomponent system, leading to localized composition nonuniformities. In these cases significant changes in growth conditions, or a different growth process, may be in order.

Extrinsic defects are generally controlled by a combination of suitable purification of starting materials and atmosphere control. In the growth of fluorides, this generally involves the use of reactive atmosphere processing using either **HF**, CF_4 , SF_6 or other species to react with oxide impurities to form volatile byproducts [15.92, 93]. In addition, fluorides crystals are often grown in either **HF**, such as **YLF**, or in vacuum to further minimize contamination. Sometimes gettering

compounds such as PbF_2 are employed to react with oxide impurities prior to growth.

The presence of inclusions in oxide crystals is usually a result of the formation and precipitation of a second phase in the primary liquid phase during the crystal growth process. One example is the formation of an oxygen-deficient phase in many of the gallium-containing garnets. In this case, simply increasing the oxygen partial pressure of the growth atmosphere is sufficient to eliminate this source of inclusions. Similar types of oxygen-deficient phases, usually appearing as submicron particles, i. e. smoke, have been observed in **YAG**, sapphire, and Y_2SiO_5 (**YSO**) and can be eliminated by appropriate adjustment of the oxygen partial pressure of the growth atmosphere [15.94].

A second source of inclusions can be associated with the dopant ion, as is the case in the growth of **Nd:YAG**. In the $\text{Y}_3\text{Al}_5\text{O}_{12}$ system, the distribution coefficient for **Nd** in **YAG** is relatively low (less than 0.2). Therefore to achieve approximately a 1 at. % **Nd** doping level in the crystal, the liquid must contain approximately 5 at. % **Nd**. Furthermore, since the distribution coefficient is much less than unity, as the growth of the crystal proceeds, the concentration of **Nd** in the liquid increases. Usually, when only about 20% of the liquid is crystallized, approximately a 20% change in the dopant ion concentration through the length of the crystal is produced. Variations in the dopant concentration beyond this amount often have detrimental effects on the laser performance of the material. Thus a low dopant ion distribution coefficient also imposes another limit on the useful amount of material that can be crystallized from the melt. The desire for large fabricated components therefore enforces the use of large quantities of starting material and large crucibles in **CZ** growth of **Nd:YAG** using the batch process. However, the batch process introduces complexity into the growth of a crystal through the progressive decrease in melt height. As the melt height decreases, transfer of heating power to the melt is affected and the strength of convective melt flow and mixing is reduced. The thermal environment of the crystal is also altered as the melt level falls, exposing the crystal to a greater area of the hot crucible wall. This tends to lower the temperature gradient in the melt, which enhances the risk of constitutional supercooling [15.87]. In order to circumvent some of the shortcomings of the standard process, development of an automated **CZ** growth process was initiated to achieve steady-state conditions through addition to the melt to maintain constant melt height and constant concentration of dopant in the melt [15.19, 87].

On the other hand, the compound $\text{Nd}_3\text{Al}_5\text{O}_{12}$ does not exist among the rare-earth aluminum garnets. Consequently, this system is not a solution between two different rare-earth aluminum garnets, but is a solution between NdAlO_3 (a perovskite phase) and $\text{Y}_3\text{Al}_5\text{O}_{12}$ [15.63]. Unfortunately at the required Nd liquid concentration, one is very close to the solubility limit of NdAlO_3 in YAG. Small temperature fluctuations from external or internal source, e.g., the heating power or a change in the cooling-water temperature, will easily result in constitutional supercooling, thereby exceeding the solubility limit of NdAlO_3 in YAG, which causes localized precipitation of the perovskite phase. Once in the crystal, they cannot be removed by subsequent processing such as annealing.

A similar example occurs in the growth of substituted $\text{Gd}_3\text{Ga}_5\text{O}_{12}$ (GGG) [15.95, 96]. In this case, Mg^{2+} , Ca^{2+} , and Zr^{4+} are added to the liquid in a ratio such that the resulting distribution coefficients are nearly equal to unity. However, this results in a Zr^{4+} liquid concentration (0.65 atoms per formula unit) that is very close to the solubility limit of $\text{Gd}_2\text{Zr}_2\text{O}_7$ in GGG (approximately 0.7 atoms per formula unit). Again, local temperature fluctuations near the growth interface can produce an excess of Zr^{4+} that results in the precipitation of submicron $\text{Gd}_2\text{Zr}_2\text{O}_7$ particles in the liquid, which are trapped by the growing crystal.

In both of these examples, not only are scattering sites produced in the crystal, but generally associated with these inclusions are region of strain [15.97]. In some cases, the induced strain is of sufficient magnitude that it can result in the formation of clusters of dislocations that propagate down the crystal axis and are roughly normal to the growth interface. For a crystal of 25–50 mm in diameter, these dislocations will continue down the crystal axis for approximately another 3–7 cm before reaching the crystal surface, thus further degrading its optical quality. Although the formation and subsequent entrapment of a second phase can be localized, its influence on the optical quality of the crystal can extend far beyond the local environment. As in the case of inclusions, subsequent processing such as annealing will have little, if any, effect on this type of defect. Thus the formation of optical-quality oxide materials must be accomplished during the crystal growth of the material and cannot necessarily be achieved after the growth process is complete.

Both of these cases illustrate the fact that a stable thermal environment is necessary for the growth of optical-quality single crystals suitable for laser applications. Thus much of the effort in the growth of many of

these materials is devoted to the design of the growth equipment, its power source, and the furnace geometry.

A third source of scattering sites in oxide materials can result from contamination of the liquid by the crucible material, either Pt or Ir. These scattering centers can vary from submicron to tens of microns in size. Unlike inclusions generated by the precipitation of a second phase, these inclusions always appear as either triangular or pseudo-hexagonal particles with an aspect ratio of at least 10 : 1. Furthermore, these are flat, thin particles, and tend to align themselves parallel to the growth interface when trapped by the growing crystal. Thus the larger cross section of the particle presents itself to the optical path of the resulting laser rods, which greatly increases the possibility of damage. Both Ir and Pt particles can be formed in the liquid by numerous chemical paths [15.98]; for example, the presence of H_2O in either the starting powder or the growth atmosphere usually results in a high density of particles in many oxide systems. Of the two metals usually used for oxide growth, Ir is more prone to oxidation than is Pt. Consequently, for those oxide systems that require iridium as a crucible, the elimination of Ir particles is always a concern. Special attention must be paid to powder preparation, crucible cleaning and charging, and growth atmosphere to avoid any possible set of conditions that could result in the transport via oxidation of the crucible material into the bulk charge.

15.2.3 Yb-Doped Laser Crystals

The most promising ion that can be used in a non-Nd laser in the same range of emission wavelength is Yb^{3+} . The Yb^{3+} ion has some advantages over the Nd^{3+} ion as a laser-emitting center due to its very simple energy-level scheme, consisting of only two levels: the $^2F_{7/2}$ ground state and the $^2F_{5/2}$ excited state. There is no excited-state absorption to reduce the effective laser cross section, no up-conversion, no concentration quenching. The intense Yb^{3+} absorption lines are well suited for laser-diode pumping near 980 nm and the small Stokes shift between absorption and emission reduces the thermal loading of the material during laser operation. The disadvantage of Yb^{3+} is that the final laser level of the quasi-three-level system is thermally populated, increasing the threshold.

Among new directed searches for novel laser crystals, one important approach is the use of Yb^{3+} active ion in an inertial-fusion energy diode-pumped solid-state laser. $\text{Ca}_5(\text{PO}_4)_3\text{F}$ (FAP) and YAG were soon recognized to be favorable hosts for lasing in the

nanosecond pulse regime. This fact was supported by an evaluation of the spectroscopic properties of several Yb^{3+} -doped crystals useful for laser action [15.99,100].

Although, compared with Nd-doped crystals, ytterbium can easily be incorporated into the host materials due to its relatively small ionic radii, many defects induced by doping effects are still present in Yb-doped crystals, and significantly impact on their thermal and spectral properties.

Lattice Distortion

The lattice parameters of YAG and YbAG were measured to be 1.2011597 ± 0.000034 and 1.1937997 ± 0.000054 nm, respectively, and there is only a 1.8% difference in unit-cell size [15.101, 102]. Figure 15.17 shows the Yb^{3+} concentration dependence of lattice parameter. It can be seen that lattice parameter is a linear function of Yb^{3+} concentration, and a linear equation can be obtained as follows:

$$\alpha(x) = 1.20076 - 0.007072x \text{ nm}.$$

From this equation, the densities of crystals with different Yb^{3+} concentration can be estimated from the cell volume and molecular weight of Yb:YAG.

As discussed above, compared with the CZ method, the temperature and thermal field of TGT are very stable and convection that disturbs the solid-liquid interface does not appear. Therefore, Yb^{3+} ions can more easily

substitute at the position of Y^{3+} sites. From the results of cell parameters shown in Table 15.1, it can be seen that the effect of Yb^{3+} on the crystal lattice deformation in TGT-grown Yb:YAG crystals is smaller than that in CZ-grown Yb:YAG crystals. The cell structure of TGT-grown Yb:YAG crystals is steadier.

Different from the typical four-level Nd:YAG laser, the quasi-three-level nature of Yb:YAG requires high pump density in order to overcome the deleterious effect of the lower laser level reabsorption at room temperature; moreover, the laser performance decreases significantly with increasing temperature [15.103]. So it is favorable to keep the temperature of Yb:YAG crystal as low as possible. Obviously, knowledge of the effect of doping on thermal properties of crystal is helpful for both designing laser systems or improving crystal performance.

Figure 15.18a shows that the thermal diffusivity decreases with increasing Yb^{3+} concentration, and values of thermal diffusivity at 50°C are 1.72×10^{-6} , 1.62×10^{-6} , and $1.54 \times 10^{-6} \text{ m}^2/\text{s}$ for single crystals with doping level 5 at. %, 10 at. %, and 25 at. %, respectively. Figure 15.18b shows that the specific heat increases as the temperature increases in the measured range, and the variation of temperature has a strong influence on highly doped Yb:YAG crystals [15.104]. The thermal conductivity was calculated from the thermal diffusivity and specific heat capacity, as displayed in Fig. 15.12c, and we can see the apparent influence of Yb^{3+} doping concentration on the thermal conductivity. In Yb:YAG crystals, the main mechanism of heat transfer is by phonons. Yb doping into YAG crystals inevitably induces structural distortion in crystals. The defects in crystals remarkably reduce the phonon mean free path, and the thermal conductivity decreases as Yb doping concentration increases. The deterioration of thermal properties of highly doped Yb:YAG will more easily lead to thermo-optic aberrations, lensing, and birefringence. Therefore, in order to acquire high beam quality and stable laser output from highly doped Yb:YAG media, an efficient cooling system must be adopted [15.105, 106].

The result of Chenais et al. [15.107] shows that the thermal conductivity of Yb:GGG, although lower than that of Yb:YAG at weak Yb^{3+} concentrations, becomes

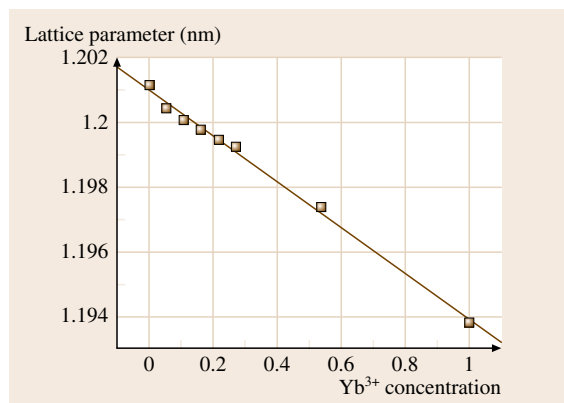


Fig. 15.17 Lattice parameter as a function of Yb^{3+} concentration

Table 15.1 Cell parameters of Yb:YAG crystals

Growth method	Yb^{3+} concentration (at.%)	α (nm)	β	V (nm^3)
CZ	5.4	1.200424 ± 0.000063	90.0	1.72983
TGT	5.4	1.200704 ± 0.000052	90.0	1.73104

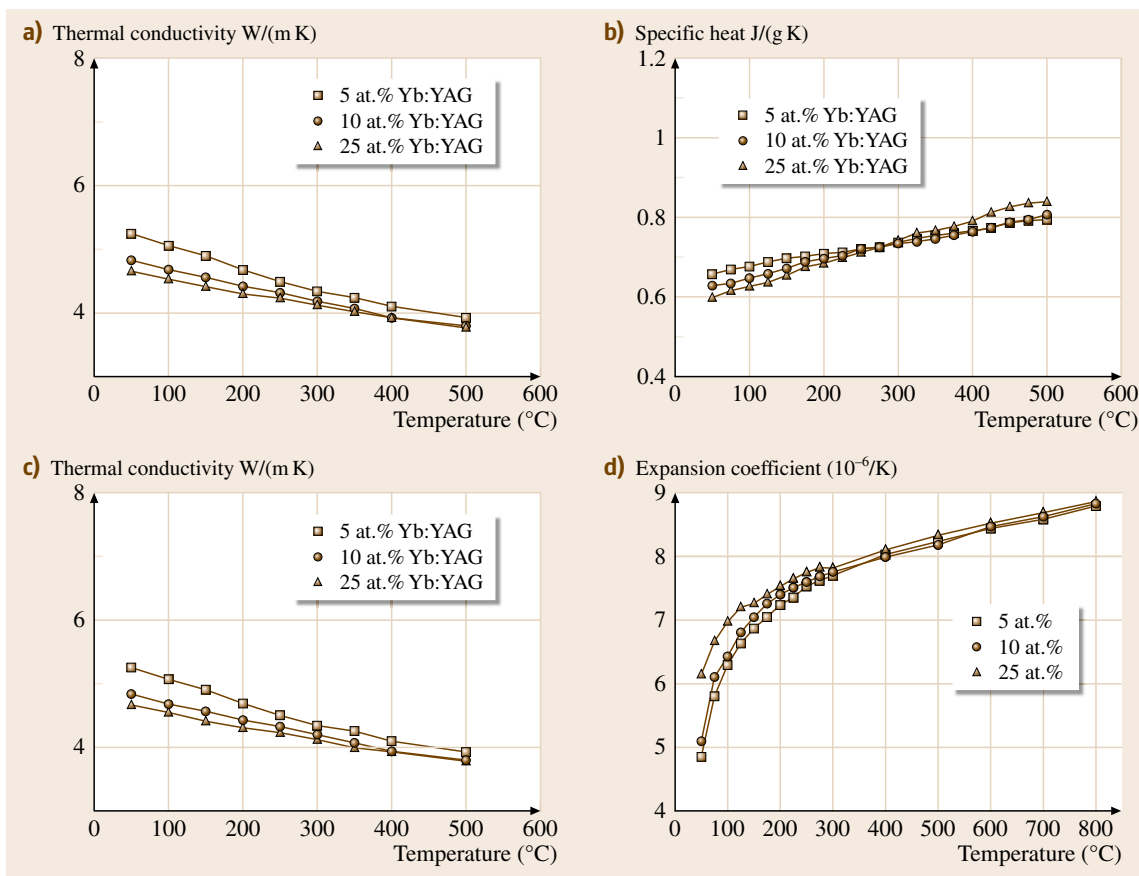


Fig. 15.18a–d Thermal diffusivity (a), specific heat (b), conductivity (c), and expansion coefficient (d) of Yb:YAG crystals as a function of temperature for several Yb³⁺ doping concentrations

higher for doping levels above 5×10^{20} ion/cm³. This means that Yb:GGG exhibits a lower quantum defect and better thermal conductivity, and thermal loading is lower than in Yb:YAG for high doping levels.

Color Centers

Color centers in oxide-based crystals constitute a complex problem, as some centers can be removed by annealing in oxidizing atmosphere [15.108] and others by annealing under reducing or vacuum conditions [15.109, 110]. Color center formation, in general, is attributed to change of lattice defects associated, primarily, with unintentionally introduced impurities.

In CZ-grown Yb:YAG, a particular color center was found [15.111–113], whose absorption spectra are shown in Fig. 15.19. The inert growth atmosphere brought about a lot of oxygen vacancies and formed

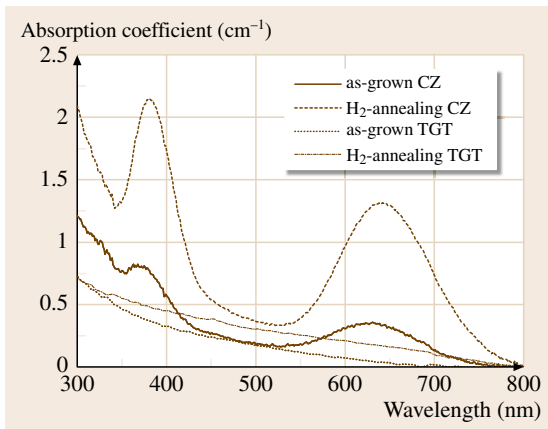


Fig. 15.19 Absorption spectra of color centers in Yb:YAG crystals

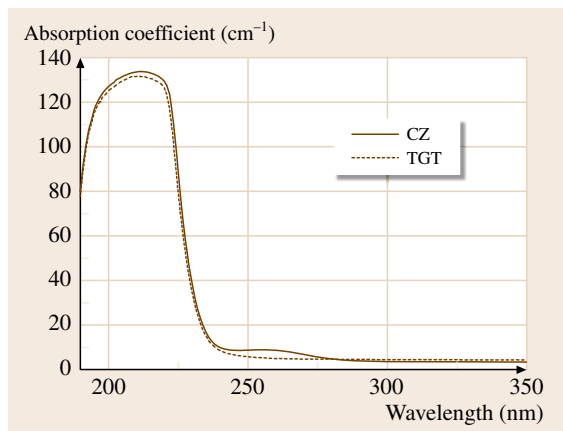


Fig. 15.20 UV absorption spectra of Yb:YAG crystals

Re-F type color centers and Yb^{2+} , which are detrimental to the intrinsic spectroscopic performances of Yb:YAG. They degraded the Yb^{3+} intrinsic absorption at 900–1050 nm and the emission intensity at 1028–1060 nm, and shortened the fluorescence lifetime of Yb^{3+} in YAG host. The color center's two absorption bands are located at wavelengths of 368 and 623 nm, respectively. Each absorption peak increases in intensity after annealing the sample in hydrogen at 1400 °C for 12 h, and the main band positions move from 368 to 381 nm and from 623 to 642 nm, respectively. The absorption spectra of TGT-grown Yb:YAG crystals are also shown in Fig. 15.19. Although also grown in an inert atmosphere, and even when annealing the sample in hydrogen atmosphere, TGT-grown Yb:YAG crystals do not exhibit the same absorption bands. The results indicate that there is no Yb^{2+} and color center absorption in TGT-grown Yb:YAG crystal, which is of great use for the laser performance of Yb:YAG.

The ultraviolet (UV) absorption spectra after annealing in oxygen shows a weak peak around 255 nm in CZ-grown Yb:YAG crystals, as shown in Fig. 15.20. Chen et al. [15.114] used optical absorption and electron paramagnetic resonance (EPR) techniques to study iron impurities in YAG crystals and considered that the absorption band at 255 nm was attributable to a Fe^{3+} charge-transfer band that was made up of contributions from substitutional Fe^{3+} ions in octahedral and tetrahedral sites. The role of Fe impurity ions in color center formation has also been demonstrated by other technologists in YAG [15.115], YAlO_3 [15.116, 117], and Al_2O_3 [15.118, 119].

For Yb:YAP crystals [15.120], three irradiation-induced color center absorption bands, located at

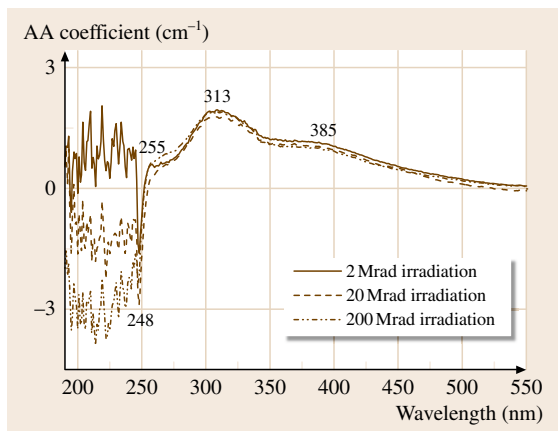


Fig. 15.21 Absorption spectra of color centers in Yb:YAP crystals

wavelengths 248, 309, and 385 nm, respectively, were observed (Fig. 15.21). The significant additional absorption (AA) peak at 248 nm is believed to be caused by the slight shift of the charge-transfer absorption edge of Yb^{3+} ions induced by the charge density redistribution. Based on the result discussed above, combined with the data reported by Matkovski [15.121] for the absorption band at 263 nm corresponding to Fe^{3+} ions in Nd:YAP, Fe^{3+} ions are considered to be responsible for the absorption band at 256 nm in Fig. 15.21. The 313 nm band has been observed by Matkovski [15.121] in absorption spectra of Nd:YAP and pure YAP crystals and was attributed to Fe^{2+} in YAP host. Kaczmarek suggested that a 313 nm band in γ -ray-irradiated Cr;Tm;Ho:YAG is most probably correlated to Fe^{2+} ions. Therefore, it is reasonable to

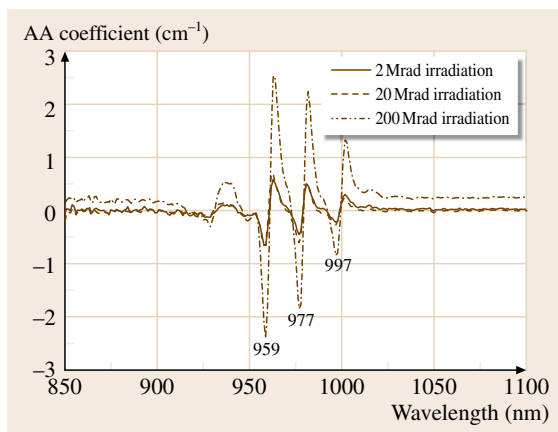


Fig. 15.22 UV absorption spectra of Yb:YAP crystals

believe that the 313 nm bands in Yb:YAP are also associated with the same kind of impurity. The increased AA value of the 313 nm band clearly indicates that the concentration of Fe^{2+} ions increased after γ -ray irradiation. The preexisting Fe^{3+} ions in Yb:YAP captured the electrons produced by γ -ray irradiation and the following interaction takes place: $\gamma + \text{Fe}^{3+} \rightarrow \text{Fe}^{2+}$. Yb^{3+} ions in Yb:YAP crystal could also capture the free electrons induced by γ -ray irradiation and as a result the transition $\text{Yb}^{3+} \rightarrow \text{Yb}^{2+}$ takes place, as shown in Fig. 15.22. The broad absorption band centered at about 385 nm shown in Fig. 15.21 has attracted more attention due to its complicated origin. According to the results of Sugak et al. [15.122], one broad absorption band located at 385–666 nm occurred in γ -irradiated Nd:YAP and the absorption induced in this region is caused by color centers intrinsic to the YAP lattice. Furthermore, a similar band was also observed in Pr:YAP under γ -ray irradiation [15.123]. Matkovski et al. [15.121] found that color centers in this region created in YAP crystals are associated with the crystal host and that their nature does not depend strongly on the type of dopant, even for high dopant concentrations. Because the Yb:YAP crystal was grown in inert atmosphere, a lot of oxygen vacancies are produced in the crystal. In analogy with the charge-recharge process of Fe and Yb ions, these O^{2-} vacancies in Yb:YAP crystal would capture one or two electron(s) to form F^+ or F centers. It has been shown that cation vacancy would be the most common defect intrinsic to the YAP lattice [15.124]. Consequently, it is most probable that the broad AA band centered at 385 nm is correlated with the cation vacancies and F-type center.

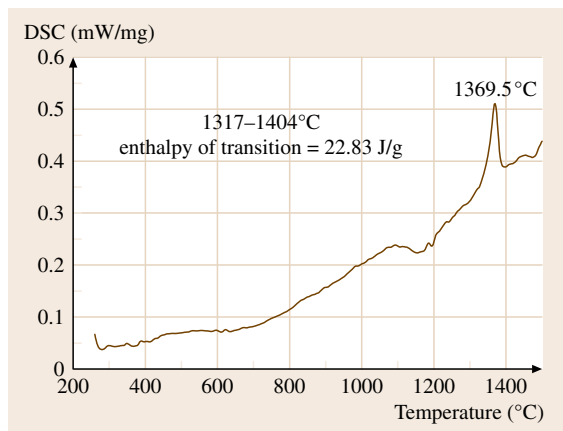


Fig. 15.23 Differential scanning calorimetry (DSC) curve of Yb:YAG

Commonly, color centers may be annealed out or reduced in number at high temperature under oxidizing, reducing or vacuum atmosphere depending on the center's origination. In the case of Yb:YAG, it is notable that annealing at high temperature increases the possibility of scattering formation due to a phase transition occurring at 1369.5 °C, as shown in Fig. 15.23, so a relatively lower temperature should be adopted when annealing.

Fluorescence Quenching

The effective stimulated-emission cross section (σ) and radiative lifetime (τ) are two important parameters for the assessment of a laser crystal [15.125]. Knowledge of both σ and τ is essential when evaluating laser system performance parameters such as saturation intensity and threshold pump power; for example, the threshold pump power is inversely proportional to the product of the effective emission cross section and the radiative lifetime of the lasing crystal [15.126].

Figure 15.24 shows the relationship of measured fluorescence lifetime of Yb:YAG crystals with temperature. At higher temperatures (above 200 K), the fluorescence lifetime increases as the Yb^{3+} concentration increases in the YAG host because of radiative trapping and reabsorption effects. The measured lifetime is longer than the radiative lifetime in these cases. At lower temperatures (below 80 K), the measured fluorescence lifetime of Yb in YAG is nearly the same for each concentration, similar to the results reported by Patel et al., [15.127] except for the 30 at. % Yb:YAG crystal. The decreased lifetime ob-

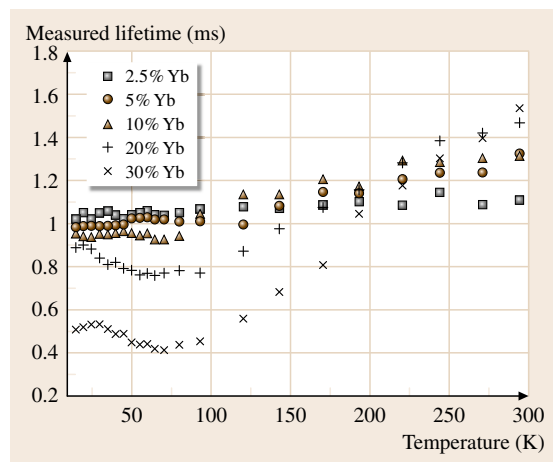


Fig. 15.24 Measured lifetime of Yb:YAG crystals as a function of temperature

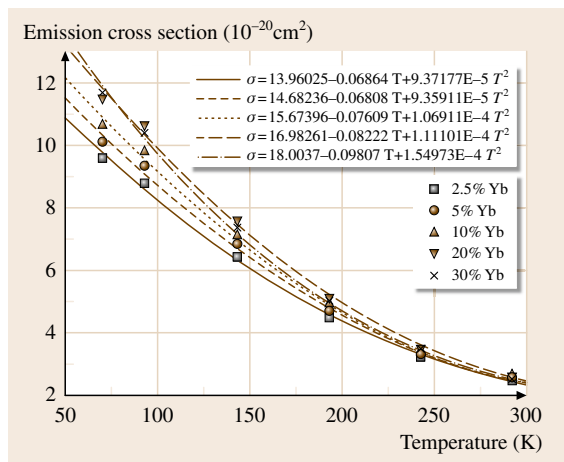


Fig. 15.25 Emission cross sections of Yb:YAG as a function of temperature for five concentrations of Yb; the indicated polynomial fits were obtained by the least-squares method

served for the 30 at. % crystal at the lowest temperatures may be due to the presence of more impurities in the highly doped crystal, which cause significant fluorescence quenching. These impurities may be other rare-earth ions that are hard to eliminate from the Yb starting material.

Using the measured lifetime at the lowest temperature as the radiative lifetime of different concentrations of Yb:YAG crystals, the effective emission cross section of Yb:YAG crystals can be calculated from the Füchtbauer–Ladenburg (F–L) formula [15.125]. Figure 15.25 shows the dependence of the effective emission cross section of these Yb:YAG crystals on temperature. The emission cross section increases as the temperature decreases.

Dislocations

Dislocation structures in oxides etc. have been widely studied using chemical etching procedures to reveal dislocations as individual pits. Such procedures can be misleading as great care is needed to distinguish dislocation etch pits from etch pits caused by inclusion or surface damage. X-ray topography has provided significant information but a useful innovation has been the application of electron microscopy to such studies because of the inherent resolution improvement at shorter wavelengths.

Generally, the symmetry of an etch pit is in accordance with the symmetry of the crystal face, and the shapes of etch pits on different faces are different for the

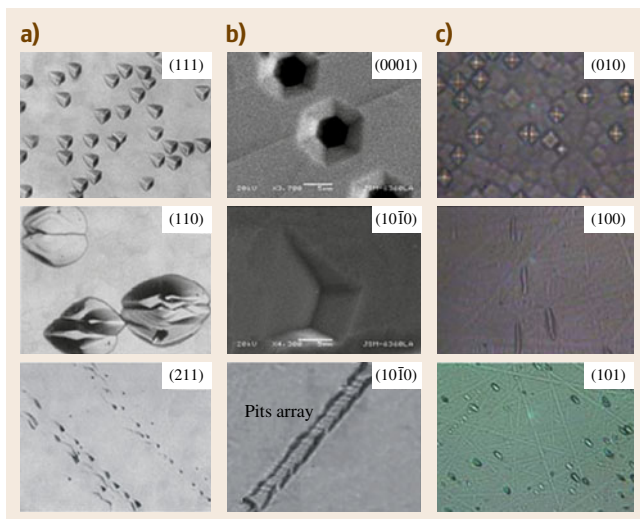


Fig. 15.26a–c Etch patterns formed on different faces of Yb:YAG (a), Yb:FAP (b), and Yb:YAP (c)

same crystal [15.128]. The change of etching conditions may also affect etch-pit morphology.

For Yb:YAG crystals [15.129], under the same etching conditions, the pits on the (111) face have two

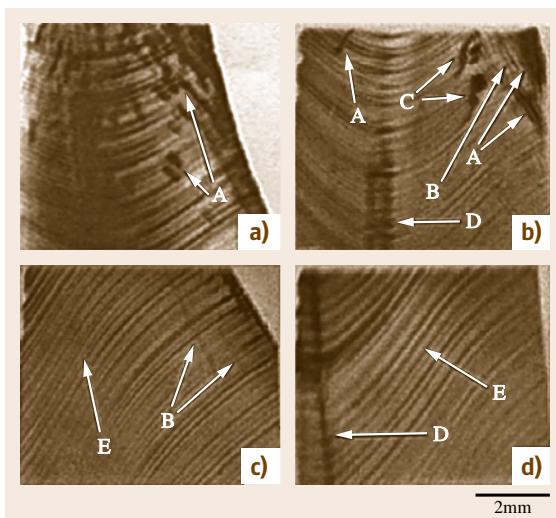


Fig. 15.27a–d Transmission synchrotron topography of (110) slices of Yb:YAG parallel to the [111] growth axis with (121) reflection. (a–d) From the upper parts to the middle of the crystal. A: dislocation bundles originated from seed/crystal interfaces; B: dislocation lines; C: dislocation bundles originating from impurity or inclusions; D: core and side core; E: growth striations

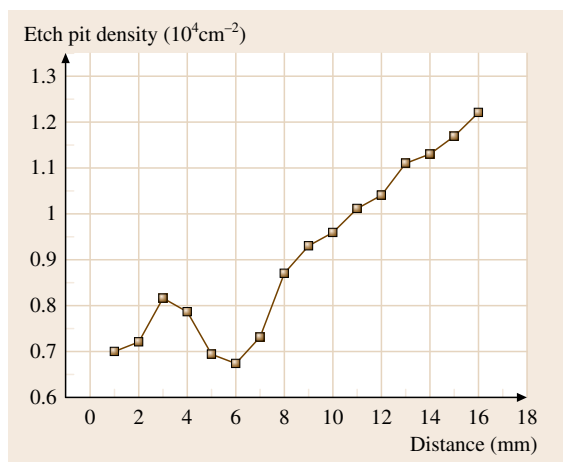


Fig. 15.28 Radial distribution of etch-pit density on (0001) face of Yb:FAP crystal

shapes: one is triangular, and the other is six-sided. The pit pattern on (211) is triangular with a tail and the pit pattern on (110) is a distorted rhombus. In Yb:FAP crystals, etch pits associated with dislocations emerging on the (0001) plane are hexagonal, while those on the (10 $\bar{1}$ 0) plane have an irregular shape. For Yb:YAP, the etch pits have rhombus shape on the (010) face, haricot-beam shape on the (100) face, and elliptic form on the (101) face. The typical etching patterns are shown in Fig. 15.26.

For Yb:YAG (111) slices, more etch pits can be observed in the initial growth period, which implies that the crystal is imperfect, and with an increase of distance from the seed the number of pits decreases gradually and they are mainly centered at the periphery of the sections. In the middle parts of Yb:YAG crystal, there are few etch pits, which implies that the crystal is perfect. Figure 15.27 shows the transmission synchrotron topography of a (110) slice of Yb:YAG crystal with (121) reflection, displaying typical growth defects in Yb:YAG. This shows that dislocation bundles and dislocation lines distribute towards the crystal periphery in the upper parts of the Yb:YAG crystal. However, in the middle parts of Yb:YAG crystal, they vanish, as shown in Fig. 15.27d. These experimental results are in good agreement with those obtained by chemical etching. Such a rule can also be demonstrated by the radial distribution of etch-pit density along the diameter of Yb:FAP crystal [15.130], as shown in Fig. 15.28.

According to the observations in Fig. 15.27a–c, the growth dislocations may originate from the following sources: (1) dislocations already existing in the

seed; (2) dislocations produced by nucleation at the seed–crystal interface, where some defects such as mechanical damage of the seed end, aggregation of impurity particles and inclusions, and thermal shock stress exist, as shown in Fig. 15.27a,b. These dislocations are the main types of source in the as-grown Yb:YAG crystals; (iii) dislocations emerging from impurity particles and inclusions trapped within the crystal during crystal growth. Comparing Fig. 15.27a–c, it can be seen that the propagation direction of the dislocations is perpendicular to the solid–liquid interface and as a result the dislocations are mainly found at the periphery of the upper parts. This rule can be explained by the minimum-energy principle, since the dislocations take the shortest path and locate in the lowest-energy state only when they take this route. Schmidt [15.131] found a similar rule in GGG crystal and calculated the propagating path of dislocations with Klapper theory [15.132]. Therefore, in order to obtain high-quality Yb:YAG crystal, it is necessary to choose high-quality seeds free from dislocations and grow the initial part of the crystal with a highly convex solid–liquid interface to eliminate dislocations. Usually, the neck technique is applied to eliminate dislocations originating from the seed or introduced by thermal shock during dipping of a seed crystal into the melt.

15.2.4 Other Activator-Doped Laser Crystals

While flashlamp-pumped ruby lasers are now primarily an artifact of the past, many of the common transition-metal lasers still appear to be a useful system for some specialized applications. Alexandrite, Cr:LiCaAlF₆ (Cr:LiCAF), and Cr:LiSrAlF₆ (Cr:LiSAF) lasers operate on the vibronic sideband of Cr, and consequently have a much lower threshold than ruby, which renders them much more useful. Cr:LiCAF was found to lase very efficiently. Forsterite (Mg₂SiO₄:Cr⁴⁺) was found to be an exciting new tunable laser material, and MgF₂:Co²⁺ proved not to require cryogenic cooling if it is pumped on a timescale short compared with the excited-state storage time of 40 μ s. Otherwise, several researchers have carefully assessed whether the Mn³⁺ ion might prove to be a useful laser ion [15.63].

While all of the rare-earth ions have been lased, systems based on Er, Tm, and Ho, besides Yb and Nd, have thus far proved to be the most useful. The Cr,Tm:YAG laser material is characterized by a particularly low gain cross section and, as a result, is most efficiently operated in a quasi- or true-CW type of mode. The Cr,Tm,Ho:YAG crystal has been found to be a very

efficient flashlamp-pumped system that operates near $2.09\text{ }\mu\text{m}$, since Cr^{3+} and Tm^{3+} can act as sensitizers of Ho^{3+} to enhance the absorption of flashlamp light. Later, it was noted that the Tm,Ho:YLF crystal is similar to the YAG system. Finally, the Er:YAG crystal has turned out to be useful as a long-wavelength system. The $2.3\text{ }\mu\text{m}$ lasers are particularly useful for novel medical procedures and for applications requiring eye-safe laser output.

During the growth of these crystals, the defects that should be specially mentioned are absorptions at the laser wavelength induced by impurities and the thermal stresses formed in the crystals.

Absorption at Laser Wavelength

As discussed above in Sect. 15.2.1, the presence of absorptive loss at the laser wavelength can strongly degrade the performance of melt-grown crystals. An example similar to the presence of Ti^{4+} in Ti^{3+} :sapphire is the unintended incorporation of Cr^{4+} into tetrahedral Ga-sites of the $\text{Gd}_3\text{Sc}_2\text{Ga}_3\text{O}_{12}$ (GSGG) garnet when the crystal is co-doped with Nd^{3+} and Cr^{3+} [15.133]. This problem is complicated by the interplay of numerous growth conditions, such as volatilization of Ga_2O_3 from the melt, oxidation of the crucible, requirement for calcium additives to stabilize growth, and scattering centers under certain conditions. This problem has been particularly vexing because the absorption strength of the tetrahedral Cr^{4+} is orders of magnitude greater than that of the normal Cr^{3+} (on the octahedral Sc^{3+} site), thereby requiring that much less than 1% of the Cr ions be incorporated in the tetravalent state. It is worthwhile to note that, ironically, the Cr^{4+} ion was later recognized to be useful as a saturable absorber in Q-switching applications and then as a laser ion in the forsterite crystal (Mg_2SiO_4). Other examples of the presence of interfering oxidation states of chromium include Cr^{2+} in Cr^{3+} -doped LiCAF and LiSAF [15.134], while Cr^{3+} is found to absorb pump radiation in Cr^{4+} -doped forsterite [15.135].

The growth atmosphere can have a profound effect on the oxidation state of dopants and impurities and hence on the quality of the crystal via the phase diagram. For example, Nd:YLF is generally grown in an HF atmosphere to maintain low concentration of YOF forming from oxide impurities [15.136]. Cr^{4+} :forsterite is grown under oxidizing conditions [15.135], while Ti^{3+} :sapphire is grown under moderately reducing conditions [15.137]. For the gallium-containing garnets, i.e., GGG and GSGG, the formation of a reduced Gd–Ga compound that is insoluble in the molten gar-

net can be prevented by the addition of 2–3 vol. % oxygen to the growth atmosphere (N_2) [15.98]. In addition to preventing the formation of a second phase, the addition of oxygen to the growth atmosphere reduces the evaporation of Ga_2O_3 from the liquid surface. In general, for most oxide material systems, the addition of small (≈ 500 ppm) to moderate (approximately 2.5% by volume) amounts of oxygen to the growth atmosphere will prevent the partial reduction of the oxide constituents.

Furthermore, during the growth of oxide-based laser materials, the lasing action is dependent upon the dopant ion being in a particular oxidation state, e.g., Cr^{4+} in forsterite [15.138, 139]. Maintaining the correct oxidation state of Cr^{4+} can require a growth atmosphere that is more oxidizing than that required to prevent partial decomposition of the constituent oxides. Postgrowth annealing of the crystal has also been used to convert the dopant ion to the desired valence state. However, the impact of this process is highly dependent upon either cation or anion valencies in the lattice. Therefore, the preferred approach is to produce these crystals by adjusting the initial growth conditions and starting materials to directly yield the desired dopant oxidation state.

The converse can also be true. For Cr,Nd:GSGG and Cr,Nd:GGG , the presence of Cr^{4+} introduces a broad absorption band in the $1\text{ }\mu\text{m}$ region. In this case, it was found that low-level divalent impurities such as Ca^{2+} in the starting materials were charge-compensated in the lattice by the conversion of Cr^{3+} to Cr^{4+} . The elimination of Cr^{4+} in the crystal was achieved by the addition of another tetravalent ion such as Ti^{4+} into the starting composition, thereby providing the growing crystal with a readily available source of another tetravalent ion [15.140, 141].

Thermal Stresses

Thermal stresses result from nonlinear temperature fields in growing crystals, scale linearly with the second derivative of temperature (assuming no external traction forces), and often scale quadratically with the length scale over which they occur [15.142]. The details are actually much more complicated, particularly in noncubic crystals. However, increasing the size of a crystal increases the imposed thermal stress, subject to the degree to which it can be controlled. In CZ growth, radial temperature gradients are required to maintain control over the growth process. Curvature along the growth direction is generally nonlinear, but in principle could be linearized through suitable furnace design to minimize thermal stresses. In TGT, VBT or HEM growth, radial

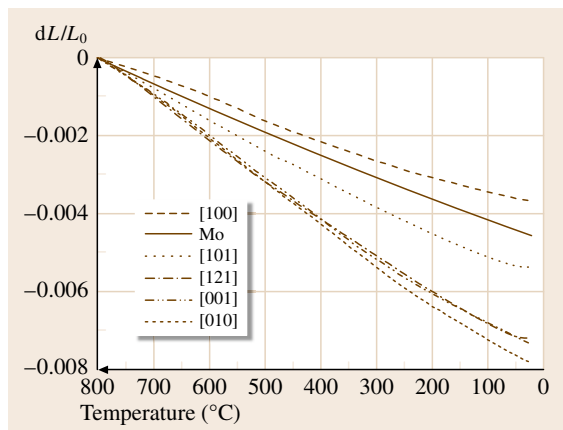


Fig. 15.29 Thermal contraction curves along several typical directions of **YAP** crystal

(lateral) temperature gradients can be minimized since the crystal takes the shape of the ampoule. However, the ampoule itself can also act as a source of stress in the crystal usually during cool-down.

For robust oxide crystals such as Nd:**YAG** and Ti:sapphire, scaling up the growth process may ultimately be successful for obtaining larger crystals suitable for large slabs. For fluorides, which have much lower fracture toughness, the thermal stresses present in the **CZ** process may ultimately limit the sizes that can be grown. The **TGT** and Bridgman process does not require lateral thermal gradients for stability, and the furnace can be designed to minimize these gradients. As was noted above, however, use of the **TGT** and Bridgman process can lead to other stress problems due to the different thermal contraction coefficients of the crystal and crucible. A typical example is the cracking and twinning defects occurred in **TGT**-grown **YAP** crystals using a Mo crucible. **YAP** possesses a deformed perovskite-like structure, and is highly anisotropic in its coefficient of thermal expansion (CTE), with approximate values of $4.2 \times 10^{-6} \text{ K}^{-1}$, $11.7 \times 10^{-6} \text{ K}^{-1}$, and $5.1 \times 10^{-6} \text{ K}^{-1}$ along the *a*-, *b*-, and *c*-axes, respectively. As shown in Fig. 15.29, since the CTE of the Mo crucible is higher than that along the *a*-axis in **YAP**, the crystal is compressed along its *a*-axis by the crucible as it cools, hence leading to cracking and twinning. Such defects can be reduced or even eliminated by growing **YAP** crystal using an *a*-oriented seed or tungsten crucible since the tungsten has a lower CTE, as shown in Fig. 15.30.

Cr:**LiCAF** is also anisotropic in its CTE. Along the *a*-axis the CTE is approximately $2.2 \times 10^{-6} \text{ K}^{-1}$, while

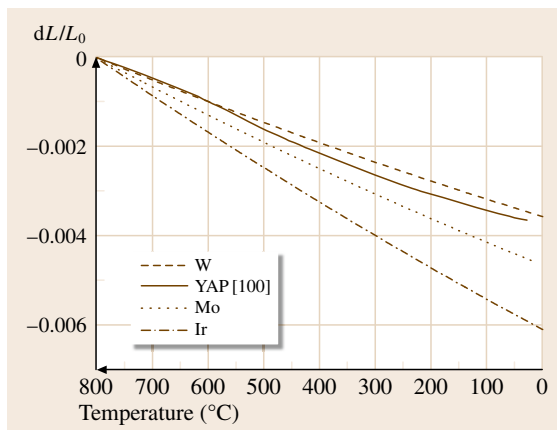


Fig. 15.30 Thermal contraction curves of several common crucible materials in comparison with that along the [100] direction of **YAP**

along the *c*-axis the CTE is only $3.6 \times 10^{-6} \text{ K}^{-1}$. Since the graphite ampoule has a CTE of $8 \times 10^{-6} \text{ K}^{-1}$, the crystal is compressed along its *c*-axis by the ampoule as it cools. For slab growth, this places the two broad faces of the slab under compression. Materials generally do not fail under compression, and this is probably not a problem for Cr:**LiCAF**. However, by pinning the crystal (either partially or completely) along the *c*-axis, the slab is put under tension in the orthogonal directions since the CTE is larger than that of graphite. Evidence of failure in tension in the form of long, linear fractures that run the length of slab has been seen by *Atherton et al.* [15.63]. They tried to compensate for this fracture mode by using compressible graphite foam inserts in the ampoule to take up the imposed stress along the *c*-axis. While this clearly helped, it did not eliminate the fracture problem entirely. In addition, there also exist small, nonlinear temperature gradients in the crystal as it cools down, thus creating another type of stress field. Calculations have indicated that these stresses are at least an order of magnitude smaller than the traction-induced stresses, but they may still be important, especially given the experience with the foam inserts.

Should the need for large slabs of Cr:**LiCAF** (or Cr:**LiSAF** and other analogues) arise in the future, further modification of the ampoule in the form of lower-CTE graphite, a softer foam insert or an ampoule design that opens as it cools could be utilized to address the traction-induced stress problem. The furnace itself can be modified to further linearize the temperature field imposed on the crystal as it cools to minimize thermal stresses.

15.3 Crystal Growth Techniques Characterization

15.3.1 Czochralski (CZ) Process

The **CZ** process is by far the most commonly used process for the growth of laser materials. The main **CZ** characteristics are as follows.

Advantages of CZ

An appropriate thermal field is easy to establish for various crystals with a wider span of materials and melting points than any other melt-growth method. Not only by varying the ceramic insulation and its dimensions but by changing the rotation rate of the crystal, the adjustment of radial and vertical thermal gradients in the melt can be easily accomplished. Moreover, the convenience of the observation of the growing crystal makes it possible to adjust the growth parameter promptly, which is essential for realizing real-time control of the growth process.

Where **CZ** is used, crystals grow from the free surface of the melt without contacting with crucible. Therefore, defects induced by contact stress and parasitic nucleation can be eliminated, and the selection of crucible material is no longer limited by the mismatch of **CTE** between crystal and crucible.

In **CZ**, a neck process can be easily employed to eliminate dislocations originating from the seed and thermal shock. Compared with other methods, **CZ** can provide a higher growth rate to obtain a relatively large crystal with good perfection.

Disadvantages of CZ

The **CZ** furnace is usually constructed of either Al_2O_3 or stabilized ZrO_2 ceramics, which contact directly with the crucible. This configuration leads to a weakly oxidizing atmosphere in the furnace. Such conditions may result in the oxidation of crucible and introduce pollutants into the melt.

In **CZ** growth, appreciable temperature gradients are usually needed to control the diameter of the growing crystal. Otherwise, the space above the crucible is commonly opening due to the presence of the lift mechanism. Such a configuration increases the loss of heat. In addition, the growing crystal can act as a light-conduction tunnel for radiative heat loss. So **CZ** often has higher temperature gradients, which will introduce thermal stress into the crystal.

15.3.2 Temperature Gradient (TGT)

The **TGT** method has the following advantages and disadvantages with respect to the **CZ** technique.

Advantages of TGT

Since the crystal shape is dictated by the crucible, there is no need for sophisticated diameter control based on weight gain or various optical techniques. This aspect is especially significant when growing relatively large sample.

For application where large crystal plates are required, the **TGT** process can be effectively utilized. This is especially valuable for crystals in which significant scale-up is required.

In **TGT** growth with the melt above the crystal, the vertical temperature gradient is stabilizing with respect to natural convection (hot above cold), as opposed to the **CZ** configurations, which is destabilizing, as discussed in Sect. 15.2.2. In addition, the furnace, crucible, and crystal are fixed in space, so this configuration is mechanically simple, which enhances the temperature stability.

In **TGT** growth, the temperature gradient can be as small as practically required, depending on thermodynamic considerations. This can be important for controlling thermal stresses or selective evaporation from multicomponent systems. In **CZ**, appreciable temperature gradients are required to control the crystal diameter.

Disadvantages of TGT

Because the crystal is growing in contact with the crucible, two problems can arise. One is spurious nucleation on the crucible wall that gives rise to large-angle grain boundaries. This problem is magnified when insufficient temperature gradients are utilized. The second problem stems from stress imposed on the crystal during cool-down for the cases where the crucible has a large coefficient of thermal expansion for contraction, or where adhesion due to wetting of the crucible wall occurs. The magnitude of this problem is determined by the strength of the crystal and of the adhesion.

Poor mixing in **TGT** growth stems from the lack of convection in the melt due to the stabilizing temperature gradient discussed above. This aspect is only a disadvantage for growth of multicomponent systems

that either grow noncongruently or show selective evaporation of one or more of the components. In this case, convection is absolutely required to homogenize the melt continually.

Blind seeding is a commonly cited disadvantage of the **TGT**, **VB**T, and **HEM** techniques. A combination of diagnostics (usually strategically placed thermocouples) and experience can overcome this disadvantage, even for growth in very low temperature gradients.

15.3.3 Heat-Exchanger Method (HEM)

The **HEM** process shares most of the advantages and disadvantages of **TGT** method. The most important differences are noted below.

Advantages of HEM

One of the unique features of **HEM** is that there are no significant temperature gradients built into the heat zone. The temperature gradients required for crystal growth are controlled by the furnace and heat-exchanger temperatures. For a given material, the furnace temperature determines the temperature gradients in the liquid, and the heat-exchanger temperature determines the temperature gradients in the solid. These temperatures are sensed and controlled externally and, therefore, the temperature gradients can be varied during the growth cycle. This unique feature allows independent control of temperature gradients in the liquid and solid during most of the growth cycle. Once the growth cycle is established, the furnace and heat exchanger temperatures can be readily automated using microprocessors.

Disadvantages of HEM

The **HEM** process usually uses helium gas as the heat-exchanger medium, which is very expensive. Furthermore, the common growth cycle is very long, so the consumption of helium gas is high.

15.3.4 Vertical Bridgman Technique (VB

One of the most distinguishing characters of **VB**T is the translation of the crucible vertically through a hot zone with a temperature gradient designed to crystallize the materials. This feature leads to both advantages and disadvantages of the growth process relative to **TGT**.

Advantages of VB

In **VB**T growth, only sufficient temperature gradients are needed near the solid–liquid interface, whilst else-

where a small one is enough. However in **TGT** growth, a linear temperature gradient is required all along the crucible from the bottom to the top. Apparently, this will increase the difficulty of establishing the thermal field, especially for high-melting-temperature crystals.

For complicated thermodynamic systems, the Bridgman process can be utilized by adding a third zone to the furnace (Fig. 15.9b). If large crystals, especially slabs, are required, this may be the only practical route to growing these crystals.

Disadvantages of VB

The employment of the lift mechanism will give rise to flow vibration on the solid–liquid interface, and enhance the risk of striation formation, which can degrade crystal performance.

15.3.5 Horizontal Bridgman Technique (HBT)

In the **HBT**, the crucible is translated horizontally through the hot zone, in contrast with **VB**T, which leads to some advantages and disadvantages, as noted below.

Advantages of HBT

By using either a boat or a sealed crucible that is not completely filled with starting material, the problem of a crucible imposing stresses on the crystal during cool-down can be overcome. This assumes that either the crystal has a larger coefficient of thermal expansion than the crucible in one or more directions, or that it does not adhere to the crucible during cool-down.

As in this method the melt height is much smaller than the dimension of its surface, this condition is good for effective withdrawal of the impurities at the expense of evaporation. For multicomponent systems, as discussed above, the lack of a stabilizing temperature field can be an advantage. This produces more intense convection that may be crucial for multicomponent systems. Besides, the open surface of the melt provides the opportunity to insert the activating impurity at any stage of crystallization.

HBT possesses the advantage that crystallization is carried out under conditions facilitating the evaporation of extraneous impurities. As a result the chemical purity of the crystal is enhanced on average by one order of magnitude compared with the raw material.

Disadvantages of HBT

The more intense flows generated by the horizontal Bridgman configuration can produce a highly concave

interface shape. This can be counteracted by suitable modification of the externally imposed furnace temperature profile, but the process is interactive and definitely not straightforward.

Melt flows in the horizontal configuration can be vigorous, and in addition to complicating control of interface shape, they can also produce striations. This problem can only be overcome by modifying the temperature gradients or the ampoule geometry.

15.3.6 Laser-Heated Pedestal Growth (LHPG)

LHPG and the related float zone growth technique are microvariants of the **CZ** growth method. Several advantages of **LHPG** have become apparent, not only in the growth of fibers for applications but, more importantly, as a general way to explore material synthesis and the properties of crystal growth. Other practical advantages of the **LHPG** method have also become apparent, as follows.

The **LHPG** relies on surface tension to maintain the integrity of the melt and hence it does not require crucibles, nor does the enclosure containing the fiber growth region possess walls heated to high temperatures as is the case in crystal growth furnaces. Both crucible and furnace surfaces are generally understood to be the primary sources of contamination in normal crystal growth, hence it follows that the absence of these surfaces allows the growth of very pure crystal materials. The impurity levels found in **LHPG** fibers are solely determined by the purity of the starting materials of the source rod. Furthermore, it is also generally accepted

that thermal gradients within the melt container are responsible for introducing stresses and other defects in bulk crystals. Because of this, **LHPG** pulled fibers can be made practically stress free.

The source rod length as well as the melt volume in **LHPG** is typically small, of the order of 10 mm and 1 mm³, respectively. The cost of the chemical compounds required for the growth of single-crystal fibers is, as a consequence, relatively small. Because of this, it is possible to grow fiber crystals of materials which would be prohibitively expensive to grow by traditional methods, especially on a basis. The small volume of the growth area also facilitates the introduction of external perturbations during synthesis of the crystal. The application of an external field to the melt may influence the growing process by encouraging the inclusion of domains or the formation of other stoichiometric combinations.

One of the most attractive features of the **LHPG** methods is the rapidity with which fibers can be grown by this method. The information feedback made possible by this allows for rapid readjustment of stock compositions and growth conditions for optimized materials.

15.3.7 Flux Technique (FT)

The **FT** is interesting from the point of view of the peculiarities of crystallization, especially at relatively low temperature. For those crystals that cannot be easily grown from melt, **FT** may be the most useful method to obtain them. The relatively low growth rate is an obvious disadvantage of this technique.

References

- 15.1 T.H. Maiman: Stimulated optical radiation in ruby masers, *Nature* **187**, 493–494 (1960)
- 15.2 H.G. Danielmeyer, F.W. Ostermayer: Diode-pump-modulated Nd:YAG laser, *J. Appl. Phys.* **43**, 2911–2913 (1972)
- 15.3 P.F. Moulton: Spectroscopic and laser characteristics of Ti:Al₂O₃, *J. Opt. Soc. Am. B* **3**, 125–133 (1986)
- 15.4 L. De Shazer: Vanadate crystals exploit diode-pump technology, *Laser Focus World* **30**, 88 (1994)
- 15.5 P. Lacovara, H.K. Choi, C.A. Wang, R.L. Aggarwal, T.Y. Fan: Room-temperature diode-pumped Yb:YAG laser, *Opt. Lett.* **16**, 1089–1091 (1991)
- 15.6 R. Scheps, J.F. Myers, S.A. Payne: End-pumped Yb-doped fluorapatite laser, *IEEE Photon. Technol. Lett.* **5**, 1285–1288 (1993)
- 15.7 Y. Jeong, J.K. Sahu, D.N. Payne, J. Nilsson: Ytterbium-doped large-core fiber laser with 1.36 kW continuous-wave output power, *Opt. Exp.* **12**, 6088–6092 (2004)
- 15.8 A. Ikesue, T. Kinoshita, K. Kamata, K. Yoshida: Fabrication and optical properties of high-performance polycrystalline Nd:YAG ceramics for solid-state lasers, *J. Am. Ceram. Soc.* **78**, 1033–1040 (1995)
- 15.9 J. Czochralski: A new method for the measurement of crystallization rate of metals, *Z. Ver. Deutsch. Ing.* **61**, 245–351 (1917)
- 15.10 G.K. Teal, J.B. Little: Growth of germanium crystals, *Phys. Rev.* **78**, 647 (1950)
- 15.11 A.E. Paladino, B.D. Roiter: Czochralski growth of sapphire, *J. Am. Ceram. Soc.* **47**, 465–468 (1964)

- 15.12 B. Cockayne, M. Chesswas, D.B. Gasson: Single-crystal growth of sapphire, *J. Mater. Sci.* **2**, 7–11 (1967)
- 15.13 M. Katsurayama, Y. Anzai, A. Sugiyama, M. Koike, Y. Kato: Growth of neodymium doped $\text{Y}_3\text{Al}_5\text{O}_{12}$ single crystals by double crucible method, *J. Cryst. Growth* **229**, 193–198 (2001)
- 15.14 K.J. Gärtner, K.F. Rittinghaus, A. Seeger, W. Uelhoff: An electronic device including a TV-system for controlling the crystal diameter during Czochralski growth, *J. Cryst. Growth* **13/14**, 619 (1972)
- 15.15 T.R. Kyle, G. Zydzik: Automated crystal puller, *Mater. Res. Bull.* **8**, 442–450 (1973)
- 15.16 R.C. Reinert, M.A. Yatsko: Crystal weighing mechanism for growth monitoring of Czochralski grown crystals, *J. Cryst. Growth* **21**, 283–286 (1974)
- 15.17 D.T.J. Hurlle: Control of diameter in Czochralski and related crystal growth techniques, *J. Cryst. Growth* **42**, 473–482 (1977)
- 15.18 E. Kanchanavaleerat, D. Cochet-Muchy, M. Kokta, J. Stone-Sundberg, P. Sarkies, J. Sarkies, J. Sarkies: Crystal growth of high doped Nd:YAG, *Opt. Mater.* **26**, 337–341 (2004)
- 15.19 G. Boulon: Yb^{3+} -doped oxide crystals for diode-pumped solid state lasers: crystal growth, optical spectroscopy, new criteria of evaluation and combinatorial approach, *Opt. Mater.* **22**, 85–87 (2003)
- 15.20 L. Fornasiero, E. Mix, V. Peters, K. Petermann, G. Huber: Czochralski growth and laser parameters of RE^{3+} -doped Y_2O_3 and Sc_2O_3 , *Ceram. Int.* **26**, 589–592 (2000)
- 15.21 K. Shimamura, H. Sato, A. Bensalah, V. Sudesh, H. Machida, N. Sarukura, T. Fukuda: Crystal growth of fluorides for optical applications, *Cryst. Res. Technol.* **36**, 801–813 (2001)
- 15.22 S.L. Baldochi, K. Shimamura, K. Nakano, N. Mujilatu, T. Fukuda: Growth and optical characteristics of Ce-doped and Ce:Na-codoped BaLiF_3 single crystals, *J. Cryst. Growth* **200**, 521–526 (1999)
- 15.23 S. Licia Baldochi, K. Shimamura, K. Nakano, N. Mujilatu, T. Fukuda: Ce-doped LiYF_4 growth under CF_4 atmosphere, *J. Cryst. Growth* **205**, 537–542 (1999)
- 15.24 F. Cui, Y. Zhou, J. Qiao: Growth of high quality monocrystal sapphire by seed-induced temperature gradient technique (STGT), *J. Chin. Ceram. Soc.* **8**, 109–113 (1980)
- 15.25 Y. Zhou: A temperature gradient furnace for growing high-melting crystals, *Chin. Patent* 85100534.9 (1985)
- 15.26 Y. Zhou, H. Xia, Z. Huang, M. Lu, P. Deng, J. Qiao, Q. Zhang, B. Hu: Growth of large-size Ti: Al_2O_3 tunable laser crystal, *SPIE* **1627**, 230–233 (1992)
- 15.27 Y. Zhou: Growth of high quality large Nd:YAG crystals by temperature gradient technique (TGT), *J. Cryst. Growth* **78**, 31–35 (1986)
- 15.28 G. Zhao, H. Li, J. Zhu, M. Jie, X. He, J. Xu: The temperature gradient technique (TGT) growth and optical properties of Yb-doped YAlO_3 single crystal, *J. Cryst. Growth* **280**, 483–489 (2005)
- 15.29 L. Su, J. Xu, H. Li, L. Wen, W. Yang, Z. Zhao, J. Si, Y. Dong, G. Zhou: Crystal growth and spectroscopic characterization of Yb-doped and Yb,Na-codoped CaF_2 laser crystals by TGT, *J. Cryst. Growth* **277**, 264–268 (2005)
- 15.30 D.C. Harris: A peek into the history of sapphire crystal growth, *Proc. SPIE* **5078**, 1–11 (2003)
- 15.31 J. Dong, P. Deng: Ti:sapphire crystal used in ultrafast lasers and amplifiers, *J. Cryst. Growth* **261**, 514–519 (2004)
- 15.32 J. Xu, Y. Zhou, H. Li, P. Deng: Growth of high-doped Nd:YAG laser crystals, *Proc. SPIE* **3889**, 420–421 (2000)
- 15.33 F. Schmid, D. Viechnicki: Growth of sapphire disks from the melt by a gradient furnace technique, *J. Am. Ceram. Soc.* **53**, 528 (1970)
- 15.34 C.P. Khattak, A.N. Scoville: Growth of laser crystals by heat exchanger method (HEM), *SPIE* **681**, 58–61 (1986)
- 15.35 V. Peters, A. Bolz, K. Petermann, G. Huber: Growth of high-melting sesquioxides by the heat exchanger method, *J. Cryst. Growth* **237–239**, 839–883 (2002)
- 15.36 C.P. Khattak, P.J. Guggenheim, F. Schmid: Growth of 15-inch diameter sapphire boules, *Proc. SPIE* **5078**, 47–53 (2003)
- 15.37 C.P. Khattak, F. Schmid: Growth of large-diameter crystals by HEM for optical and laser application, *SPIE* **505**, 4–8 (1984)
- 15.38 J.L. Caslavsky, D. Viechnicki: Melt growth of Nd: $\text{Y}_3\text{Al}_5\text{O}_{12}$ (Nd:YAG) using the heat exchange method (HEM), *J. Cryst. Growth* **46**, 601–606 (1979)
- 15.39 C.P. Khattak, F. Schmid, K.F. Wall, R.L. Aggarwal: Growth and characterization of Ti: YAlO_3 for turnable solid state laser applications, *Proc. SPIE* **1104**, 95–99 (1989)
- 15.40 P.W. Bridgman: Certain physical properties of single crystals of tungsten, antimony, bismuth, tellurium, cadmium, zinc, and tin, *Proc. Am. Acad. Arts Sci.* **60**, 305–383 (1925)
- 15.41 D.C. Stockbarger: The Production of large single crystals of lithium fluoride, *Rev. Sci. Instrum.* **7**, 133–136 (1936)
- 15.42 D.C. Stockbarger: The production of large artificial fluorite crystals, *Disc. Faraday Soc.* **5**, 294–299 (1949)
- 15.43 H.E. Buckley: *Crystal Growth* (Wiley, New York 1951) pp. 71–99
- 15.44 A.G. Petrosyan: Crystal growth of laser oxides in the vertical Bridgman configuration, *J. Cryst. Growth* **139**, 372–392 (1994)
- 15.45 J. Xu, M. Shi, B. Lu, X. Li, A. Wu: Bridgman growth and characterization of calcium fluoride crystals, *J. Cryst. Growth* **292**, 391–394 (2006)
- 15.46 K.S. Bagdasarov: <http://www.bagdasarovcrystals.com/v1/> (2007)

- 15.47 G. Boulon, M. Ito, C. Goutaudier, Y. Guyot: Advances in growth of fiber crystal by the LHPG technique. Application to the optimization of Yb^{3+} -doped CaF_2 laser crystals, *J. Cryst. Growth* **292**, 230–235 (2006)
- 15.48 R.P. Poplawsky: Ferrite crystals using an arc image furnace, *J. Appl. Phys.* **33**, 1616 (1962)
- 15.49 R.S. Feigelson: Pulling optical fibers, *J. Cryst. Growth* **79**, 669–680 (1986)
- 15.50 W.M. Yen: Synthesis, characterization, and applications of shaped single crystals, *Phys. Solid State* **41**, 693–696 (1999)
- 15.51 L. Laversenne, C. Goutaudier, Y. Guyot, M.T. Cohen-Adad, G. Boulon: Growth of rare earth (RE) doped concentration gradient crystal fibers and analysis of dynamical processes of laser resonant transitions in RE-doped Y_2O_3 (RE = Yb^{3+} , Er^{3+} , Ho^{3+}), *J. Alloys Compd.* **341**, 214–219 (2002)
- 15.52 R.A. Lefever, J.W. Torpy, A.B. Chase: Growth of single crystals of yttrium aluminum garnet from lead oxide–lead fluoride melts, *J. Appl. Phys.* **32**, 962–963 (1961)
- 15.53 R.C. Linares: Substitution of aluminum and gallium in single-crystal yttrium iron garnets, *J. Am. Ceram. Soc.* **48**, 68–70 (1965)
- 15.54 L.G. van Uitert, W.H. Grodkiewicz, E.F. Dearborn: Growth of large optical-quality yttrium and rare-earth aluminum garnets, *J. Am. Ceram. Soc.* **48**, 105–108 (1965)
- 15.55 J.W. Nielsen: Garnet gemstones, US Patent 3091540 (1963)
- 15.56 G. Garton, B.M. Wanklyn: The rare earth aluminates, *J. Cryst. Growth* **1**, 164–166 (1967)
- 15.57 S. Erdei, B.M. Jin, F.W. Ainger, B. Keszei, J. Vandlik, A. Suveges: Possible trends for the growth of low scattering $\text{Nd}:\text{YVO}_4$ laser crystals; phase relations–growth techniques, *J. Cryst. Growth* **172**, 466–472 (1997)
- 15.58 X. Han, G. Wang, T. Tsuboi: Growth and spectral properties of $\text{Er}^{3+}/\text{Yb}^{3+}$ -codoped $\text{KY}(\text{WO}_4)_2$ crystal, *J. Cryst. Growth* **242**, 412–420 (2002)
- 15.59 C. Pujol, M. Aguil, F. Diaz, C. Zaldo: Growth and characterisation of monoclinic $\text{KGd}_{1-x}\text{RE}_x(\text{WO}_4)_2$ single crystals, *Opt. Mater.* **13**, 33–40 (1999)
- 15.60 N.I. Leonyuk, E.V. Koporulina, V.V. Maltsev, O.V. Pilipenko, M.D. Melekhova, A.V. Mokhov: Crystal growth and characterization of $\text{YAl}_3(\text{BO}_3)_4$ doped with Sc, Ga, Pr, Ho, Tm, Yb, *Opt. Mater.* **26**, 443–447 (2004)
- 15.61 E. Fahey, A.J. Strauss, A. Sanchez, R.L. Aggarwal: Growth of $\text{Ti}:\text{Al}_2\text{O}_3$ crystals by a gradient-freeze technique. In: *Tunable Solid State Lasers II*, Springer Series in Optical Sciences, Vol. 52, ed. by A.B. Budgor, L. Esterowitz, L.G. DeShazer (Springer, New York 1987) pp. 82–88
- 15.62 R. Uecker, D. Klimm, S. Ganschow, P. Reiche, R. Bertram, M. Robberg, R. Fornari: Czochralski growth of $\text{Ti}:\text{sapphire}$ laser crystals, *Proc. SPIE* **5990**, 599006–1–5990006–9 (2005)
- 15.63 L.J. Atherton, S.A. Payne, C.D. Brandle: Oxide and fluoride laser crystals, *Annu. Rev. Mater. Sci.* **23**, 453–502 (1993)
- 15.64 P.F. Moulton: Spectroscopic and laser characteristics of $\text{Ti}:\text{Al}_2\text{O}_3$, *J. Opt. Soc. Am. E* **3**, 125–133 (1986)
- 15.65 P. Albers, E. Stark, G. Hube: Continuous-wave laser operation and quantum efficiency of titanium-doped sapphire, *J. Opt. Soc. Am. B* **3**, 134–139 (1986)
- 15.66 G.F. Albrecht, J.M. Eggleston, J.J. Ewing: Measurements of $\text{Ti}^{3+}:\text{Al}_2\text{O}_3$ as a lasing material, *Opt. Commun.* **52**, 401–404 (1985)
- 15.67 R.C. Powell, J.K. Caslavsky, Z. AlShaieb, J.M. Bowen: Growth, characterization, and optical spectroscopy of $\text{Al}_2\text{O}_3:\text{Ti}^{3+}$, *J. Appl. Phys.* **58**, 2331–2336 (1985)
- 15.68 R.L. Aggarwal, A. Sanchez, M.M. Stuppi, R.E. Fahey, A.J. Strauss, W.R. Rapoport, C.P. Khattak: Residual infrared absorption in As grown and annealed crystals of $\text{Ti}:\text{Al}_2\text{O}_3$, *IEEE J. Quantum Electron.* **24**, 1003–1008 (1988)
- 15.69 G.A. Keig: Influence of the valence state of added impurity ions on the observed color in doped aluminum oxide single crystals, *J. Cryst. Growth* **2**, 356–360 (1968)
- 15.70 T.P. Jones, R.L. Coble, C.J. Mogab: Defect diffusion in single crystal aluminum oxide, *J. Am. Ceram. Soc.* **52**, 331–334 (1969)
- 15.71 K.S. Mohapatra, F.A. Kroger: Defect structure of $\alpha\text{-Al}_2\text{O}_3$ doped with titanium, *J. Am. Ceram. Soc.* **60**, 381–387 (1977)
- 15.72 M.R. Kokta: Processes for enhancing $\text{Ti}:\text{Al}_2\text{O}_3$ tunable laser crystal fluorescence by annealing, US Patent 4587035 (1986)
- 15.73 M.R. Kokta: Processes for enhancing fluorescence of tunable titanium-doped oxide laser crystals, US Patent 4988402 (1991)
- 15.74 K.S. Bagdasarov, E.R. Dobrovinskaya, V.V. Pishchik, M.M. Chernick, Y.Y. Kovalev, A.S. Gershun, I.F. Zvyagintseva: Low dislocation density single crystals of corundum, *Sov. Phys. Crystallogr.* **18**, 242–245 (1973)
- 15.75 C.T. Bodur, J. Chang, A.S. Argon: Molecular dynamics simulations of basal and pyramidal system edge dislocations in sapphire, *J. Europ. Ceram. Soc.* **25**, 1431–1439 (2005)
- 15.76 A. Nakamura, T. Yamamoto, Y. Ikuhara: Direct observation of basal dislocation in sapphire by HRTEM, *Acta Mater.* **50**, 101–108 (2002)
- 15.77 C.P. Khattak, A.N. Scoville, F. Schmid: Recent developments in sapphire growth by heat exchanger method (HEM), *SPIE* **683**, 32–35 (1986)
- 15.78 J. Xu, Y. Zhou, G. Zhou, J. Xu, P. Deng: Producing large (0001)-oriented sapphire for optical applications, *SPIE* **3557**, 11–14 (1998)
- 15.79 J. Xu, Y. Zhou, G. Zhou, K. Xu, P. Deng, J. Xu: Growth of large-sized sapphire boules by temperature gra-

- dient technique (TGT), *J. Cryst. Growth* **193**, 123–126 (1998)
- 15.80 J.R. Carruthers: Origins of convective temperature oscillations in crystal growth melts, *J. Cryst. Growth* **32**, 13–26 (1976)
- 15.81 T. Surek: Theory of shape stability in crystal growth from the melt, *J. Appl. Phys.* **47**, 4384–4393 (1976)
- 15.82 J. Basterfield, M.J. Prescott, B. Cockayne: An X-ray topographic study of single crystals of melt-grown yttrium aluminium garnet, *J. Mater. Sci.* **3**, 33–40 (1968)
- 15.83 N. Ming, Y. Yang: Facet and vicinical growth of YAG by Czochralski, *Acta Phys. Sin.* **28**, 285–295 (1979)
- 15.84 B. Cockayne, M. Chesswas, D.B. Gasson: The growth of strain-free $\text{Y}_3\text{Al}_5\text{O}_{12}$ single crystals, *J. Mater. Sci.* **3**, 224–225 (1968)
- 15.85 G. Zydzik: Interface transitions in Czochralski growth of garnets, *Mater. Res. Bull.* **10**, 701–707 (1975)
- 15.86 B. Cockayne, B. Lent: A complexity in the solidification behaviour of molten $\text{Y}_3\text{Al}_5\text{O}_{12}$, *J. Cryst. Growth* **46**, 371–378 (1979)
- 15.87 E.W. O'Dell, D.J. Nelson, D. Narasimhan, R.C. Morris, J.E. Marion: Development of a large scale Nd:YAG growth process, *SPIE* **1223**, 94–102 (1990)
- 15.88 B. Cockayne, M. Chesswas, D.B. Gasson: Facetting and optical perfection in Czochralski grown garnets and rubies, *J. Mater. Sci.* **4**, 450–456 (1969)
- 15.89 Y. Miyazawa, M. Mori, S. Honma: Interface shape transitions in the Czochralski growth of $\text{Dy}_3\text{Al}_5\text{O}_{12}$, *J. Cryst. Growth* **43**, 541–542 (1978)
- 15.90 A.G. Petrosyan: Crystal growth of laser oxides in the vertical Bridgman configuration, *J. Cryst. Growth* **139**, 372–392 (1994)
- 15.91 P. Deng, J. Qiao, B. Hu, Y. Zhou, M. Zhang: Perfection and laser performances of Nd:YAG crystals grown by temperature gradient technique (TGT), *J. Cryst. Growth* **92**, 276–286 (1988)
- 15.92 R.C. Pastor: Effect of RAP purification on materials characterization, *J. Cryst. Growth* **75**, 54–60 (1986)
- 15.93 M. Robinson: Processing and purification techniques of heavy metal fluoride glass (HMFG), *J. Cryst. Growth* **75**, 184–194 (1986)
- 15.94 C.D. Brandle, A.J. Valentino, G.W. Berkstresser: Czochralski growth of rare-earth orthosilicates (Ln_2SiO_5), *J. Cryst. Growth* **79**, 308–315 (1986)
- 15.95 D. Mateika, J. Herrnring, R. Rath, C. Rusche: Growth and investigation of $\{\text{Gd}_{3-x}\text{Ca}_x\}[\text{Ga}_{2-y-z}\text{Zr}_y\text{Gd}_z](\text{Ga}_3)_2\text{O}_{12}$ garnets, *J. Cryst. Growth* **30**, 311–316 (1975)
- 15.96 D. Mateika, C. Rusche: Coupled substitution of gallium by magnesium and zirconium in single crystals of gadolinium gallium garnet, *J. Cryst. Growth* **42**, 440–444 (1977)
- 15.97 D.C. Miller: Defects in garnet substrates and epitaxial magnetic garnet films revealed by phosphoric acid etching, *J. Electrochem. Soc.* **120**, 678–685 (1973)
- 15.98 C.D. Brandle, D.C. Miller, J.W. Nielsen: The elimination of defects in Czochralski grown rare-earth gallium garnets, *J. Cryst. Growth* **12**, 195–200 (1972)
- 15.99 G. Boulon, A. Brenier, L. Laversenne, Y. Guyot, C. Goutaudier, M.T. Cohen-Adad, G. Metrat, N. Muhlstein: Search of optimized trivalent ytterbium doped-inorganic crystals for laser applications, *J. Alloys Compd.* **341**, 2–7 (2002)
- 15.100 D. De Loach, S.A. Payne, L.L. Chase, L.K. Smith, W.L. Kway, W.F. Krupke: Evaluation of absorption and emission properties of Yb^{3+} doped crystals for laser applications, *IEEE J. Quantum Electron.* **29**, 1179–1191 (1993)
- 15.101 X. Xu, Z. Zhao, J. Xu, P. Deng: Distribution of ytterbium in Yb:YAG crystals and lattice parameters of the crystals, *J. Cryst. Growth* **255**, 338–341 (2003)
- 15.102 P. Lacovara, H.K. Choi, C.A. Wang, R.L. Aggarwal, T.Y. Fan: Room-temperature diode-pumped Yb:YAG laser, *Opt. Lett.* **16**, 1089–1090 (1991)
- 15.103 F. Lu, M. Gong, H. Xue, Q. Liu, W. Gong: Analysis on the temperature distribution and thermal effects in corner-pumped slab lasers, *Opt. Lasers Eng.* **45**, 43–48 (2007)
- 15.104 X. Xu, Z. Zhao, J. Xu, P. Deng: Thermal diffusivity, conductivity and expansion of $\text{Yb}_{3x}\text{Y}_{3(1-x)}\text{Al}_5\text{O}_{12}$ ($x=0.05, 0.1$ and 0.25) single crystals, *Solid State Commun.* **130**, 529–532 (2004)
- 15.105 S.A. Payne, R.J. Beach, C. Bibeau, C.A. Ebbers, M.A. Emanuel, E.C. Honea, C.D. Marshall, R.H. Page, K.I. Schaffers, J.A. Skidmore, S.B. Sutton, W.F. Krupke: Diode arrays, crystals, and thermal management for solid-state lasers, *IEEE J. Quantum Electron.* **3**, 71–81 (1997)
- 15.106 D.J. Ripin, J.R. Ochoa, R.L. Aggarwal, T.Y. Fan: 300-W cryogenically cooled Yb:YAG laser, *IEEE J. Quantum Electron.* **41**, 1274–1277 (2005)
- 15.107 S. Chenais, F. Druon, F. Balembois, P. Georges, A. Brenier, G. Boulon: Diode-pumped Yb:GGG laser: comparison with Yb:YAG, *Opt. Mater.* **22**, 99–106 (2003)
- 15.108 J.B. Willis, M. Dixon: Assessment and control of imperfections in crystals for laser devices, *J. Cryst. Growth* **3–4**, 236–240 (1968)
- 15.109 V.A. Antonov, P.A. Arsenev, I.G. Linda, V.L. Farshendiker: Studies of some point defects in YAlO_3 and GdAlO_3 single crystals, *Phys. Status Solidi (a)* **5**, K63–K68 (1973)
- 15.110 B. Cockayne, B. Lent, J.S. Abell, I.R. Harris: Cracking in yttrium orthoaluminate single crystals, *J. Mater. Sci.* **8**, 871–875 (1973)
- 15.111 P. Yang, P. Deng, J. Xu, Z. Yin: Growth of high-quality single crystal of 30 at. % Yb:YAG and its laser performance, *J. Cryst. Growth* **216**, 348–351 (2000)
- 15.112 H. Qiu, P. Yang, J. Dong, P. Deng, J. Xu, W. Chen: The influence of Yb concentration on laser crystal Yb:YAG, *Mater. Lett.* **55**, 1–4 (1998)

- 15.113 X. Xu, Z. Zhao, G. Zhao, P. Song, J. Xu, P. Deng: Comparison of Yb:YAG crystals grown by CZ and TGT method, *J. Cryst. Growth* **257**, 297–300 (2003)
- 15.114 C.Y. Chen, G.J. Pogatshnik, Y. Chen, M.R. Kokta: Optical and electron paramagnetic resonance studies of Fe impurities in yttrium aluminum garnet crystals, *Phys. Rev. B* **38**, 8555–8561 (1988)
- 15.115 K. Mori: Transient colour centres caused by UV light irradiation in yttrium aluminium garnet crystals, *Phys. Status Solidi (a)* **42**, 375–384 (1977)
- 15.116 T.I. Butaeva, K.L. Ovanesyan, A.G. Petrosyan: Growth and spectral investigations of oxide laser crystals with Pr^{3+} ions, *Cryst. Res. Technol.* **23**, 849–854 (1988)
- 15.117 R.F. Belt, J.R. Latore, R. Uhrin, J. Paxton: EPR and optical study of Fe in Nd:YAlO₃ laser crystals, *Appl. Phys. Lett.* **25**, 218–220 (1974)
- 15.118 J. Kvapil, J. Kvapil, J. Kubelka, R. Autrata: The role of iron ions in YAG and YAP, *Cryst. Res. Technol.* **18**, 127–131 (1983)
- 15.119 J. Kvapil, B. Perner, M. Košelja, J. Kvapil: Absorption background and laser properties of YAP:Nd, *Czech. J. Phys.* **40**, 99–108 (1990)
- 15.120 Y. Dong, G. Zhou, J. Xu, G. Zhao, F. Su, L. Su, H. Li, J. Si, X. Qian, X. Li, J. Shen: Color centers and charge state recharge in γ -irradiated Yb:YAP, *Opt. Mater.* **28**, 1377–1380 (2006)
- 15.121 A. Matkovski, A. Durygin, A. Suchocki, D. Sugak, G. Neuroth, F. Wallrafen, V. Grabovski, I. Solski: Photo and gamma induced color centers in the YAlO₃ and YAlO₃:Nd single crystals, *Opt. Mater.* **12**, 75–81 (1999)
- 15.122 D. Sugak, A. Matkovski, D. Savitski, A. Durygin, A. Suchocki, Y. Zhydashchik, I. Solskii, I. Stefaniuk, F. Wallrafen: Growth and induced color centers in YAlO₃–Nd single crystals, *Phys. Status Solidi (a)* **184**, 239–250 (2001)
- 15.123 S.M. Kaczmarek: Role of the type of impurity in radiation influence on oxide compounds, *Cryst. Res. Technol.* **34**, 737–743 (1999)
- 15.124 V.G. Baryshevsky, M.V. Korzhik, B.I. Minkov, S.A. Smirnova, A.A. Fyodorov, P. Dorenbos, C.W.E. van Eijk: Spectroscopy and scintillation properties of cerium doped YAlO₃ single crystals, *J. Phys. Condens. Matter* **5**, 7893–7902 (1993)
- 15.125 J. Dong, M. Bass, Y. Mao, P. Deng, F. Gan: Dependence of the Yb³⁺ emission cross section and lifetime on temperature and concentration in yttrium aluminum garnet, *J. Opt. Soc. Am. B* **20**, 1975–1979 (2003)
- 15.126 T.Y. Fan, R.L. Byer: Diode laser pumped solid-state laser, *IEEE J. Quantum Electron.* **24**, 895–912 (1988)
- 15.127 F.D. Patel, E.C. Honea, J. Speth, S.A. Payne, R. Hutcheson, R. Equall: Laser demonstration of Yb₃Al₅O₁₂ (YbAG) and materials properties of highly doped Yb:YAG, *IEEE J. Quantum Electron.* **37**, 135–144 (2001)
- 15.128 R. Sang: *Etching of Crystal Theory, Experiment and Application* (North-Holland, Amsterdam 1987) p. 303
- 15.129 P. Yang, P. Deng, Z. Yin, Y. Tian: The growth defects in Czochralski-grown Yb:YAG crystal, *J. Cryst. Growth* **218**, 87–92 (2000)
- 15.130 P. Song, Z. Zhao, X. Xu, P. Deng, J. Xu: Defect analysis in Czochralski-grown Yb:FAP crystal, *J. Cryst. Growth* **286**, 498–501 (2006)
- 15.131 W. Schmidt, R. Weiss: Dislocation propagation in Czochralski grown gadolinium gallium garnet (GGG), *J. Cryst. Growth* **43**, 515–525 (1978)
- 15.132 H. Klapper, H. Koppers: Directions of dislocation lines in crystals of ammonium hydrogen oxalate hemihydrate grown from solution, *Acta Cryst. A* **29**, 495–503 (1973)
- 15.133 W.F. Krupke, M.D. Shinn, J.E. Marion, J.A. Caird, S.E. Stokowski: Spectroscopic, optical, and thermomechanical properties of neodymium- and chromium-doped gadolinium scandium gallium garnet, *J. Opt. Soc. Am. B* **3**, 102–114 (1986)
- 15.134 S.A. Payne, L.L. Chase, L.J. Atherton, J.A. Caird, W.L. Kway, M.D. Shinn, R.S. Hughes, L.K. Smith: Properties and performance of the LiCaAlF₆:Cr³⁺ laser material, *Proc. SPIE* **1223**, 84 (1990)
- 15.135 P. Pan, H. Zhu, S. Yan, Y. Chai, S. Wang, Y. Hou: Distribution and valence of chromium in forsterite crystals grown by the Czochralski technique, *J. Cryst. Growth* **121**, 141–147 (1992)
- 15.136 R. Uhrin, R.F. Belt, V. Rosati: Preparation and crystal growth of lithium yttrium fluoride for laser applications, *J. Cryst. Growth* **38**, 38–44 (1977)
- 15.137 M.R. Kokta: Process for enhancing Ti:Al₂O₃ tunable laser crystal fluorescence by controlling crystal growth atmosphere, US Pat 4711696 (1987)
- 15.138 C.B. Finch, G.W. Clark: Czochralski growth of single-crystal Mg₂SiO₄ (forsterite), *J. Cryst. Growth* **8**, 307–308 (1971)
- 15.139 H. Takei, T. Kobayashi: Growth and properties of Mg₂SiO₄ single crystals, *J. Cryst. Growth* **23**, 121–124 (1974)
- 15.140 C.D. Brandle, V.J. Fratello, A.J. Valentino, S.E. Stokowski: Effects of impurities and atmosphere on the growth of Cr-doped gadolinium scandium gallium garnet. I, *J. Cryst. Growth* **85**, 223–228 (1987)
- 15.141 V.J. Fratello, C.D. Brandle, A.J. Valentino, S.E. Stokowski: Effects of impurities and atmosphere on the growth of Cr-doped gadolinium scandium gallium garnet. II, *J. Cryst. Growth* **85**, 229–233 (1987)
- 15.142 B.A. Bolev, J.H. Weiner: *Theory of Thermal Stresses* (Wiley, New York 1960) p. 586

Shaped Cryst

16. Shaped Crystal Growth

Vitali A. Tatartchenko

Part B | 16

Crystals of specified shape and size (shaped crystals) with controlled defect and impurity structure have to be grown for the successful development of modern engineering. Since the 1950s many hundreds of papers and patents concerned with shaped growth have been published. In this chapter, we do not try to enumerate the successful applications of shaped growth to different materials but rather to carry out a fundamental physical and mathematical analysis of shaping as well as the peculiarities of shaped crystal structures. Four main techniques, based on which the lateral surface can be shaped without contact with the container walls, are analyzed: the Czochralski technique (CZT), the Verneuil technique (VT), the floating zone technique (FZT), and technique of pulling from shaper (TPS). Modifications of these techniques are analyzed as well. In all these techniques the shape of the melt meniscus is controlled by surface tension forces, i.e., capillary forces, and here they are classified as capillary shaping techniques (CST). We look for conditions under which the crystal growth process in each CST is dynamically stable. Only in this case are all perturbations attenuated and a crystal of constant cross section grown *without any special regulation*. The dynamic stability theory of the crystal growth process for all CST is developed on the basis of Lyapunov's dynamic stability theory. Lyapunov's equations for the crystal growth processes follow from fundamental laws. The results of the theory allow the choice of stable regimes for crystal growth by all CST as well as special designs of shapers in TPS. SCG experiments by CZT, VT, and FZT are discussed but the main consideration is given to TPS. Shapers not only allow crystal of very complicated cross section to be grown but provide a special distribution of impurities. A history of TPS is provided later in the chapter, because it can only be

described after explanation of the fundamental principles of shaping. Some shaped crystals, especially sapphire and silicon, have specified structures. The crystal growth of these materials, and some metals, including crystal growth in space, is discussed.

16.1 Definitions and Scope of Discussion:	
SCG by CST	510
16.2 DSC – Basis of SCG by CST	512
16.2.1 Lyapunov Set of Equations	513
16.2.2 Capillary Problem – Common Approach	514
16.2.3 The Equation of Crystal Dimension Change Rate	515
16.2.4 The Equation of the Crystallization Front Displacement Rate	516
16.2.5 SA in a System with Two Degrees of Freedom	516
16.3 SA and SCG by CZT	517
16.3.1 Capillary Problem	517
16.3.2 Temperature Distribution in the Crystal–Melt System	517
16.3.3 SA and Crystal Growth	519
16.4 SA and SCG by VT	519
16.4.1 Practical Results of the Theoretic Analysis	519
16.4.2 SA-Based Automation of VT	521
16.5 SA and SCG by FZT	522
16.6 TPS Capillary Shaping	522
16.6.1 Capillary Boundary Problem	522
16.6.2 Stability Analysis	529
16.6.3 Experimental Tests of the Capillary Shaping Statements	530
16.6.4 Impurity Distribution	534
16.6.5 TPS Definition	537
16.6.6 TPS Brief History	537

16.7	TPS Sapphire Growth	539	16.8.2	Local Electronic Properties of Shaped Silicon	549
16.7.1	Modifications of TPS	540	16.8.3	TPS Silicon Growth	551
16.7.2	Crystal Defects.....	541	16.9	TPS Metals Growth	551
16.7.3	Applications	545	16.10	TPS Peculiarities	552
16.8	TPS Silicon Growth	546	References		552
16.8.1	Shaped Silicon Structure	546			

16.1 Definitions and Scope of Discussion: SCG by CST

Modern engineering usually uses device details fabricated from crystals in the shape of plates, rods or tubes. Sometimes the shapes can be more complicated. Traditional ways of the detail fabrication (a growth of a bulk crystal and its machining) bring a loss of expensive material (often up to 90%) as well as an appearance of structure defects. Therefore, crystals of specified shape and size with controlled defect and impurity structure have to be grown. It allows using the crystals as final products with minimal additional machining as well as without one.

The problem of shaped crystal growth seems to be simply solved by profiled container crystallization just as in the case of casting. Indeed, it is possible to find a realization of this idea by the vertical or horizontal Bridgman techniques for growth of silicon, fluoride, sapphire or YAG crystals with different cross

Fig. 16.2 Cylindrical crystal growth by VT: H_2 – hydrogen flow; O_2 – mixed oxygen and powder flow; R – crystal radius; l_1 – melt surface position relative to the burner; l – crystallization front position relative to the burner; $h = l - l_1$ is the melt meniscus height; V – crystal displacement rate; ω – crystal rotation rate ►

section of the crucible used [16.1–3]. But in these cases the crucible material should satisfy a whole set of requirements: it should neither react with the melt nor be wetted by it. Even if all these requirements are satisfied, perfect-crystal growth is not secured: the crucible serves as a source of noncontrolled nucleation as well as internal residual stresses. In addition, if a crucible material is wetted by the melt, the crucible usually has been made from a thin foil and used only once [16.2, 3].

Therefore, the techniques of crystal lateral surface shaping without contact with container walls have to be considered as the candidates for a shaped crystal growth. Since early sixties, both theoretical and practical aspects of the shaped crystal growth by these techniques have been developed. The main information

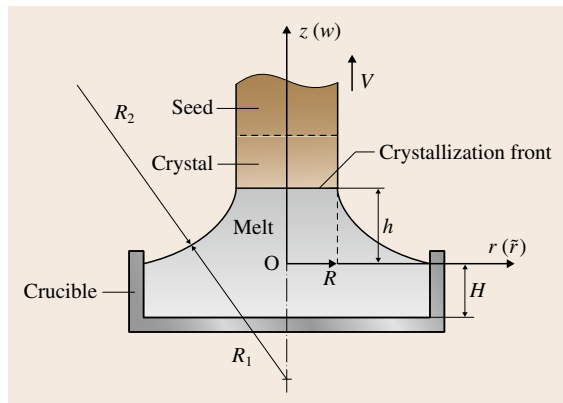


Fig. 16.1 Cylindrical crystal growth by CZT: R – crystal radius; h – crystallization front height; V – crystal pulling rate; H – melt level in crucible; $wO\tilde{r}$ or zOr – coordinate systems; R_1 and R_2 – main radii of liquid surface curvature

Fig. 16.4a–j Melt growth of crystalline rod by TPS (a–j): pulling up (a–e, h, i) or lowering down (f, g, j) with rate V ; shaping on the shaper surfaces (a, c, g–i); shaping on the shaper edges (b, d–f, j); positive melt pressure d (b, f, g, j); negative melt pressure d (d, e); C, G are counters of contact meniscus with shaper; n – normal vector to the shaper walls; d_0 – shaper depth; R – crystal radius; r_0 – edge counter radius; h – crystallization front height; Θ – wetting angle; ψ_0 – growth angle; α_d – meniscus inclination angle with respect to positive r -direction at the point of the contact with the shaper; $\alpha_1 = \pi - \alpha_d$; β – angle of cone shaper wall inclination; r_1 – cone radius on the melt free surface level ►

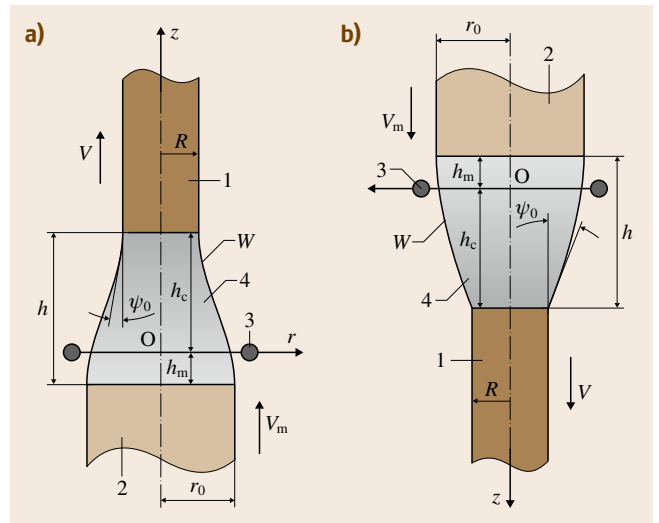
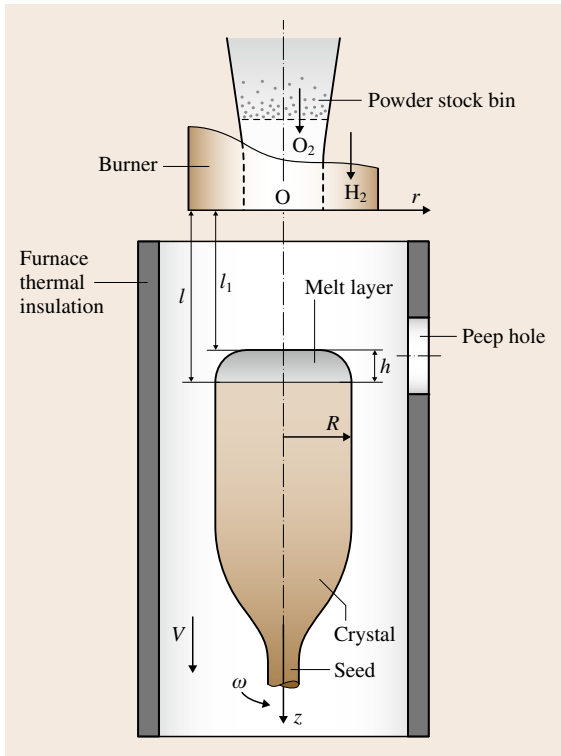
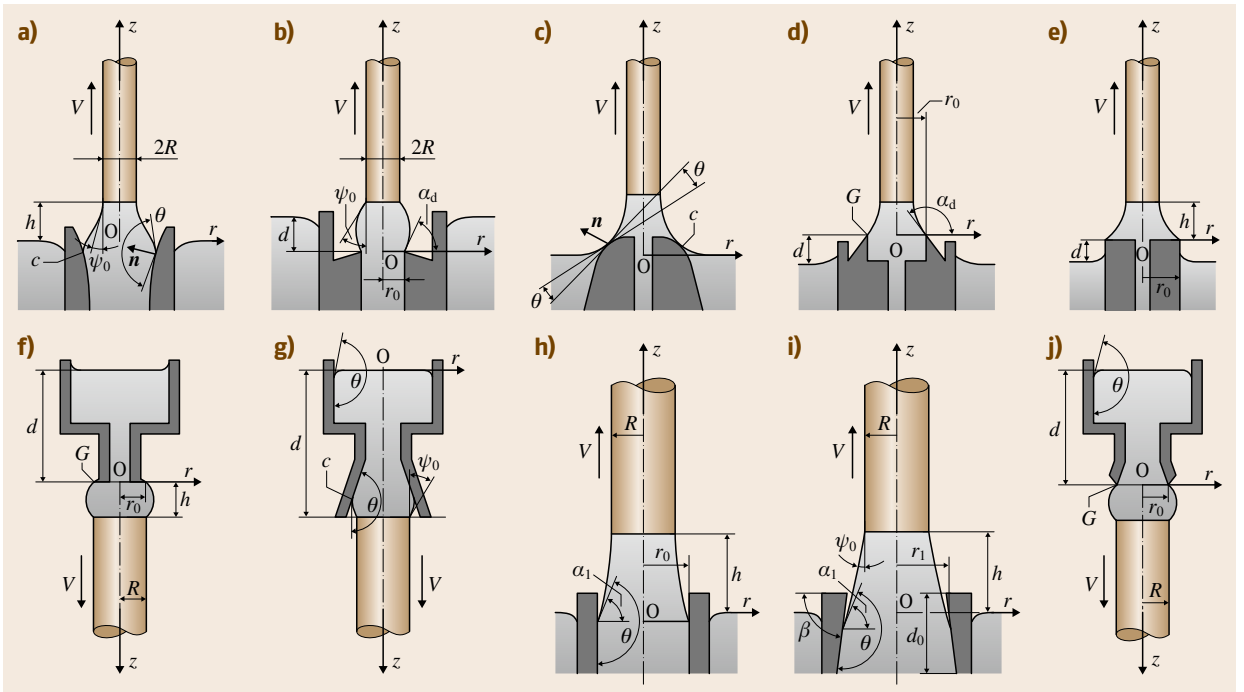


Fig. 16.3a,b Cylindrical crystal growth by FZT. (a) Pulling up, (b) lowering down: (1) growing crystal with radius R ; (2) feeding rod with radius r_0 ; (3) heater; (4) melted zone; h_c , h_m – positions of crystallization front and melting front relative to the heater, respectively; $h = h_c + h_m$ is the length of the melted zone; W – volume of the melted zone; ψ_0 – growth angle; V – rate of growing crystal displacement relative to the induction heater; V_m – the same for the melting rod



concerned with all of them was published in some books and reviews [16.4–10], in the proceedings of three international conferences [16.11–13] and in hundreds of papers.

The few *classical* techniques of this type are well known: the Czochralski technique (CZT, Fig. 16.1), the Verneuil technique (VT, Fig. 16.2), the floating zone technique (FZT, Fig. 16.3). For all these techniques the shapes and the dimensions of the crystals grown are controlled by the shapes and the dimensions of meniscus of melt existing at the vicinity of interface crystal–melt. A shape of meniscus is controlled by the surface tension forces of the melt – capillary forces. Let the above-mentioned techniques (some *no classical* ones will be added below) be classified as capillary shaping techniques (CST). As a rule, all these techniques are used to grow crystals of nonregular cylindrical shape. On the other hand, all of them have

been used for shaped crystal growth as well. For shaped crystal growth it is necessary to guarantee a special shape for the melt meniscus and a dynamical stability of the crystal growth process. But in any case, all above mentioned techniques allow obtaining only simple shaped crystals (cylinders, plates or tubes) and they have to be modified for the growth of more complicated ones. It has to be mentioned that *classical* Kyropoulos technique also belongs to CST but, in fact, it has never been used for the shaped growth because of specific thermal growth conditions [16.8].

Some possible schemes of the modification of *classical* CST are shown on the Fig. 16.4a–j. The schemes Fig. 16.4a–e,h,i differ from CZT by the presence of a shaper at the melt. The schemes Fig. 16.4f,g,j may be classified as FZT modified with lowering down where the melting rod is replaced by a shaper with a melt inside.

16.2 DSC – Basis of SCG by CST

As the crystal is not restricted by crucible walls its cross section depends upon the growth regimes. Any deviations of pulling or lowering (for a down growth) rate, as well as temperature conditions result in changes of the crystal cross section (pinches formation). A lot of defects (an increased amount of inclusions, nonuniform impurity distributions, subgrain formation) are observed at the pinch locations. It is not the pinches themselves, that seem to cause defect formation, but some deviation of the growth conditions (mainly, the crystallization rate) from the optimal ones indicated by a change in the crystal dimensions. Therefore, the stabilization of the crystal cross section as well as the crystallization front position has to be achieved. Why is it very important the stabilization of the crystallization front position? We can see from the schemes of CST (Figs. 16.1–16.4) that, if the crystallization front position is unmoved, a crystal growth speed is exactly equal to the one of pulling or lowering of a seed. A displacement of the crystallization front position changes the real crystal growth, see (16.10). As a result, in spite of the pulling or lowering rate stabilization, there is defect formation.

The modern systems of regulation using weight or crystal diameter detectors allow obtaining the cylindrical crystals by CST. These systems effect with a change of a power or pulling rate. Sometimes, the regulation is not stable and there is a permanent perturbation of the crystallization front position. The solution is to analyze

theoretically the dynamic stability of concrete schemes of crystal growth and to select on the basis of this analysis the stable ones. In the dynamically stable system, the perturbations of parameters attenuate because of internal processes and, without any additional active regulation, it is possible to provide crystals of specified shape and of controlled cross section. If the active regulator is included in the system under investigation, this dynamically stable system can improve the shape and the quality of crystals.

For the first time, a comparative theoretical analysis of a dynamic stability of crystallization process for CZT and TPS had been carried out by the author of this chapter in 1971. The very impressive result was published in 1973 [16.14]. It was explained why it is difficult to pull crystals of constant cross section by CZT and easy by TPS: the use of a shaper allows obtaining a dynamic capillary stability of the crystal growth process. In the same year, the first paper concerning the investigation of VT dynamic stability was published [16.15]. In 1974 the investigation of CZT, TPS, VT and FZT stability was presented at the 4th International Conference of Crystal Growth in Japan [16.16]. The analysis of capillary and heat stability in detail using Lyapunovs approach was published in 1976 [16.17]. In 1976 Surek published only capillary stability analysis [16.18] repeating our main results for CZT and TPS from [16.14].

16.2.1 Lyapunov Set of Equations

The main results of stability analysis for all CST [16.4–10] were obtained by applying of the Lyapunovs approach [16.19]. With respect to Lyapunov, the crystallization techniques under consideration have to be characterized by a finite number n of the variables (degrees of freedom) X_i which can arbitrarily vary in the process of crystallization. Each CST has to include, as a minimum, crystal dimension R and crystallization front position h as degrees of freedom, i.e. a minimal degree of freedom quantity $\min n$ have to be two. Sometimes, it is sufficient for the dynamic stability analysis (CZT, Fig. 16.1; TPS, Fig. 16.4). But for VT, $\min n = 3$ (Fig. 16.2): R, l, h ; for the FZT, $\min n = 4$ (Fig. 16.3): R, W, h_c, h_m . It has to be mentioned that the $\min n$ depends also on the cross section of the crystal to be grown. For instance, for a tube crystal, the internal diameter, as well as the external one, are the degrees of freedom. Therefore, $\min n = 3$ for CZT and for TPS.

If n exceeds $\min n$, the analysis is more fruitful. Sometimes we can use several iterations. The first iteration can include the stability investigating for $\min n$. After that, one or more variables can be added. For instance, in [16.6, pp. 71–145], the stability of TPS as a system with $\min n$ was investigated. As a second step [16.6, pp. 155–159], the melt pressure was added as a third degree of freedom and a complimentary information concerning the influence of pressure perturbation on the stability of growth was obtained. So, we can confirm that $\min n \geq 2$ but we can not propose any simple choosing of $\min n$ as well as optimal n . For us, in every case, it has been a result of very special investigation.

To realize a mathematical analysis of stability, a set of equations (16.1) for derivation of each degree of freedom X_i with respect to time t as a function of all n degrees of freedom X_1, \dots, X_n , their other (except i) $n - 1$ derivatives, time t , and parameters of process C (a temperature of melt, a velocity of pulling, a regime of cooling, etc.) has to be obtained

$$\begin{aligned} \frac{dX_i}{dt} &= f_i \left(X_1, X_2, \dots, X_n, \right. \\ &\quad \left. \frac{dX_1}{dt}, \frac{dX_2}{dt}, \dots, \frac{dX_{n-1}}{dt}, t, C \right), \\ i &= 1, 2, \dots, n. \end{aligned} \quad (16.1)$$

To find the explicit function f_i , a set of fundamental laws have to be used. The set should include:

1. The Navier–Stokes equation for a melt with the boundary conditions on the meniscus free surface (the Laplace capillary equation)
2. The continuity equation (the law of crystallizing substance mass conservation)
3. The heat transfer equations for the liquid and the solid phases with the equations of heat balance at the crystallization front and at the melting front as the boundary conditions (the law of energy conservation)
4. The diffusion equation (impurity mass conservation)
5. The growth angle certainty condition
6. Some others.

The set of these equations is general for all the crystallization techniques under consideration (but it does not mean that each time we use all of them) while the specific features of each of crystallization schemes are characterized by the set of boundary conditions and concrete values of the parameters included in the equations.

Equation 16.1 with zero left side corresponds to the system under conditions of equilibrium ($X_i = X_i^0$): the growth of crystals of constant cross section X_1^0 with stationary crystallization front position X_2^0 etc.

$$f_i (X_1^0, X_2^0, \dots, X_n^0, t, C) = 0. \quad (16.2)$$

We are looking for the stable solutions of (16.1). According to Lyapunov [16.19], the solutions of (16.1) are stable if they are stable for the linearized set of equations

$$\frac{dX_i}{dt} = \sum_{k=1}^n \frac{\partial f_i}{\partial X_k} \delta X_k = \sum_{k=1}^n A_{ik} \delta X_k. \quad (16.3)$$

Here, $\delta X_k = X_k - X_k^0$, $\partial f_i / \partial X_k = A_{ik}$, all partial derivatives are taken with $X_k = X_k^0$. The stability of (16.3), in turn, is observed when all the roots S in the characteristic equation (16.4)

$$\det \left(\frac{\partial f_i}{\partial X_k} - S \delta_{ik} \right) = 0 \quad (16.4)$$

have negative real components (δ_{ik} is the Kronecker delta [16.19]). This equilibrium will be unstable if (16.4) has at least one root with a positive real component. If an imaginary number can be found among the roots, additional study including an allowance for the nonlinear terms in (16.3) is required.

Calculation of the time-dependent non stationary functions f_i is usually rather difficult. These difficulties can be avoided using a quasi-stationary approach.

We successfully have been used it in the most of our dynamic stability investigations and can show other examples of the same approach. For instance, *Mullins and Sekerka* [16.20] applied it to the temperature and impurity distribution problem while studying the morphological stability of the crystallization-front shape. However, in each particular case, the quasi-stationary approach has to be justified.

A number of constraints imposed on the systems and perturbations occurring in the course of Lyapunov stability study should be noted. Stability is examined over an infinitely long period of time. In this case, the perturbations are considered to be small and are imposed on the initial conditions only, i.e. after the perturbations, the same forces and energy sources affect the system as before the perturbations.

16.2.2 Capillary Problem – Common Approach

Melt Meniscus Shaping Conditions

For the capillary shaping techniques, the crystal cross section is determined by the melt meniscus section formed by the crystallization surface. The melt meniscus shape can be calculated on the basis of the Navier–Stokes equation, the Laplace capillary equation being the free-surface boundary condition.

The full-scale solution of this problem offers considerable mathematical difficulties. Therefore, to simplify the problem formulation, the contributions of various factors of meniscus shaping should be estimated: the inertial forces associated with the melt flow, the capillary forces, the gravity forces, viscous and the thermocapillary forces [16.6, 21]. The relative effect of the first three factors can be estimated by means of dimensionless numbers: the Weber number $We = \rho V^2 L / \gamma$, characterizing comparative action of the inertial and capillary forces, the Froude number $Fr = V / (gL)^{1/2}$ characterizing comparative action of the inertial and gravity forces; the Bond number $Bo = \rho g L^2 / \gamma$, characterizing comparative action of the gravity and capillary forces. Here ρ denotes the liquid density, L the liquid meniscus characteristic dimensions, γ the liquid surface tension coefficient, V is the liquid flow rate, and g relates to the gravity acceleration. When the Weber and Froude numbers are small, the melt flow can be neglected. The Bond number defines the region of capillary or gravity force predominance (Fig. 16.5). The effect of the inertial force as compared with the gravity and capillary ones proves to be negligible, if liquid flow rate is considered to

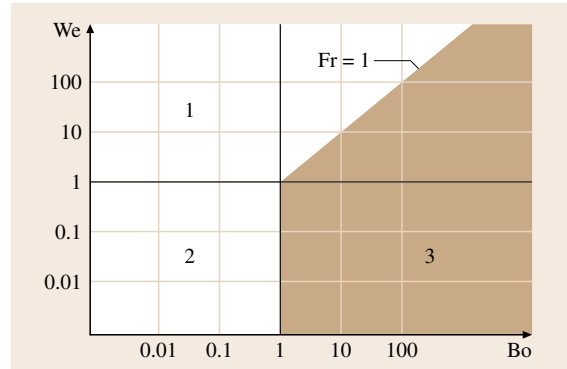


Fig. 16.5 Inertial (1), capillary (2), and gravitational force effects (3) on the melt column shaping (We , Bo , and Fr are characteristic Weber, Bond and Froude numbers, respectively)

be equal to the crystallization rate. Indeed, if we assume that the linear dimensions of the meniscus lie within the range of 10^{-3} – 10^{-2} m, $\rho \approx 10^{-3} \text{ kg m}^{-3}$, $\gamma \approx 1 \text{ N m}^{-1}$ the liquid meniscus shaping can be examined in the hydrostatic approximation up to the fluid speed of 0.1 – 1.0 m s^{-1} .

Convective flows, whose rates can substantially exceed the crystallization rate, can occur in a liquid column in addition to the flow associated with crystallization. These flow effects on meniscus shaping and on liquid-phase heat-transfer as well as the influence of the two latter factors can be found in [16.6].

The Meniscus Surface Equation

In the hydrostatic approximation, the equilibrium shape of the liquid surface is described by the Laplace capillary equation [16.22]

$$\frac{\gamma}{R_1} + \frac{\gamma}{R_2} + \rho g w = \text{const} . \quad (16.5)$$

Here, R_1 and R_2 denote the main radii of liquid surface curvature. They have to be located in two perpendicular planes. As a rule one of the planes coincides with the diagram plane (R_2 , Fig. 16.1) and second one is perpendicular to it (R_1 , Fig. 16.1). The w -axis is directed vertically upwards. The value of const. depends upon w -coordinate origin selection and is equal to the pressure p on the liquid in the plane $w = 0$. In particular, if the w -coordinate origin coincides with the plane of the liquid surface, const. = 0 (Fig. 16.1).

In this chapter our study will be restricted to considering meniscus possessing axial symmetry (Figs. 16.1–16.4). Such meniscus is obtained during melt

pulling of straight circular cylinder, tube-shaped crystals as well as a flat part of ribbon. We will find the equation of such meniscus surface, by introducing the cylindrical coordinates w, \tilde{r} . The problem of liquid meniscus shape calculation for an axially symmetric meniscus is reduced to finding the shape of a profile curve $w = f(\tilde{r})$, the liquid surface meniscus being obtained by rotating this curve around the w -axis. Let us introduce the capillary constant a , and pass to the dimensionless coordinates and parameters

$$\left(\frac{2\gamma}{\rho g}\right)^{1/2} = a, \quad \frac{w}{a} = z, \\ \frac{\tilde{r}}{a} = r, \quad \frac{pa}{2\gamma} = d.$$

This transition means that the capillary constant serves as a linear dimension unit, and the weight of a liquid column of one capillary constant high corresponds to the pressure equal to one unit. The approach allows application of the calculated results to any substance and magnitude of gravity, with the scale changing alone. Then (16.5) takes the form

$$z''r + z'(1 + z'^2) \pm 2(d - z)(1 + z'^2)^{3/2}r = 0. \quad (16.6)$$

For large Bond numbers ($Bo \gg 1$, Fig. 16.5) gravity prevails (this condition corresponds to growing big diameter crystals with $R \geq 5a$) and (16.6) can be simplified

$$z''r \pm 2(d - z)(1 + z'^2)^{3/2}r = 0. \quad (16.7)$$

For small Bond numbers ($Bo \ll 1$, Fig. 16.5) capillarity prevails (this condition corresponds to growing small diameter crystals $R < a$ as well as it was easily satisfied in our TPS experiments on the board of space stations [16.6] when the capillary constant is high) and (16.6) can also be simplified to give

$$z''r + z'(1 + z'^2) \pm 2d(1 + z'^2)^{3/2}r = 0. \quad (16.8)$$

Static Stability of the Melt Meniscus as well as the dynamic stability of crystal growth process has to be provided. A presence of static stability means that the melt meniscus exists for all values of crystallization parameters. An analysis of the stability can be realized on the basis of Jacobis equation investigation. For the TPS, this analysis was realized in [16.23, 24].

Growth Angle Certainty – Common Boundary Condition for CST

As the Laplace capillary equation is a second order differential one, formulation of a boundary problem for melt meniscus shape calculation requires assignment of two boundary conditions. The first of them is determined by the structural features of each specific CST and will be analyzed in details below. But second of the boundary conditions (the crystal–melt interface condition) is mutual for all CST. This condition follows from the growth angle certainty.

Let the angle ψ_0 (Figs. 16.3, 16.4a,b), made by the line tangent to the meniscus and the lateral surface of the growing crystal, be called the growth angle. The growth angle should not be confused with the wetting angle. The wetting angle characterizes particular equilibrium relative to the liquid movement along a solid body and is not directly associated with crystallization [16.6]. In the first studies of the CZT and TPS, a crystal of constant cross section was considered to grow in case $\psi_0 = 0$. Judging by a purely geometric diagram of liquid–solid phase conjugation, such assumption is quite natural. However, experimental and theoretical investigations of the crystal growth process showed that the geometrical condition $\psi_0 = 0$ is not satisfied while growing crystals of constant cross sections and ψ_0 is a physical characteristic of the crystals. Particular case $\psi_0 = 0$ is available only for some metals. Experimental determinations of the ψ_0 have included direct measurements as well as indirect calculations. Indirect techniques, as a rule, are more precise [16.6]. In our experiments [16.6, 25], we studied shapes of crystallized drops obtained on the bottom of silicon, germanium and indium antimonide crystals detached from the melts in the process of pulling by the CZT. The values of $\psi_0 = 25 \pm 1^\circ$ for indium antimonide, $\psi_0 = 11 \pm 1^\circ$ for silicon, and $\psi_0 = 12 \pm 1^\circ$ for germanium were obtained. Theoretical investigations have shown that ψ_0 is an anisotropic value as well as it depends on the crystallization speed. In [16.6], a reader can find a discussion of the problem in detail. In this chapter, for the dynamic stability analysis, we will use ψ_0 as a constant value for the crystal to be grown.

16.2.3 The Equation of Crystal Dimension Change Rate

Proceeding from the condition of growth angle certainty, we can obtain an equation for the crystal characteristic dimension change rate dR/dt that is common for all CST. On the diagram (Fig. 16.6) a vector

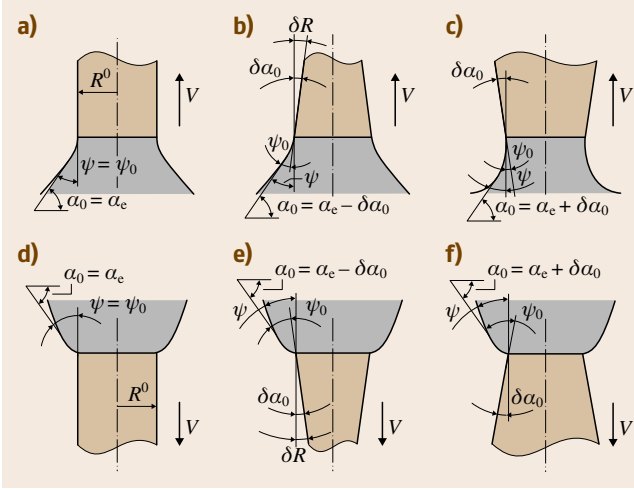


Fig. 16.6a–f Crystal growth by CST: pulling up (a–c); lowering down (d–f); $\alpha_0 = \alpha_e$: growth of constant cross section crystal (a,d); $\alpha_0 < \alpha_e$: growth of widening cross section crystal (b,e); $\alpha_0 > \alpha_e$: growth of narrowing cross section crystals (c,f); V is the crystal displacement rate; other symbols given in the text

R is located within the diagram plane and represents the radius for a straight circular cylinder-shaped crystal. For a plate it is its half-thickness. Now we introduce the angles made by the line tangent to the meniscus on the three-phase line with the horizontal α_0 and with the vertical ψ (the crystal grows in the vertical direction). When the angles α_0 and ψ add up to the $\frac{\pi}{2}$, a crystal of constant cross section R^0 grows. In this case, the angle ψ is equal to the growth angle ψ_0 and the value of the angle α_0 is denoted α_e . If $\psi \neq \psi_0$ the crystal lateral surface declines from the vertical on the angle $\psi - \psi_0 = \alpha_0 - \alpha_e = \delta\alpha_0$ the crystal changes its dimension $\delta R = R - R^0$ in accordance with (Fig. 16.6)

$$\frac{dR}{dt} = V_c \tan(\delta\alpha_0) = V_c \tan(\alpha_0 - \alpha_e). \quad (16.9)$$

The angle $\delta\alpha_0$ is the angle of crystal tapering at any moment, the crystallization rate V_c is equal to the difference in rates between pulling and front displacement

$$V_c = V - \frac{dh}{dt}. \quad (16.10)$$

Near the stationary state that we need for (16.3), deviations dh/dt as well as $\delta\alpha_0$ have to be negligible. Hence, the crystallization rate V_c can be replaced by the rate of the pulling V and $\tan(\delta\alpha_0) \approx \delta\alpha_0$. The angle α_0 together with the meniscus shape as a function of R , h and other parameters can be determined by solving the capillary boundary problem whose equation was discussed

above. Assuming that the capillary problem is solved, i. e., the function $\alpha_0(X_1^0, X_2^0, \dots, X_n^0, t, C) = 0$ is found, (16.9) can be represented by

$$\frac{dR}{dt} = \sum_{k=1}^n \frac{\partial \alpha_0}{\partial X_k} \delta X_k = \sum_{k=1}^n A_{ik} \delta X_k. \quad (16.11)$$

16.2.4 The Equation of the Crystallization Front Displacement Rate

The equation of the crystallization front displacement rate belongs to the set (16.3) and as well as (16.11) is common for all CST. It follows from the heat-balance condition on the crystallization front

$$-\lambda_S G_S(h) + \lambda_L G_L(h) = \zeta V_c. \quad (16.12)$$

Here λ_S and λ_L denote thermal conductivities of the solid and liquid phases respectively, $G_S(h)$ and $G_L(h)$ are the temperature gradients in the solid and liquid phases at the crystallization front, h is a crystallization front position, ζ denotes the latent melting heat of a material unit volume, V_c is the crystallization rate. In accordance with (16.10), we obtain a (16.1)-type equation for dh/dt

$$\frac{dh}{dt} = V - \zeta^{-1} [\lambda_L G_L(h) - \lambda_S G_S(h)]. \quad (16.13)$$

The equation of (16.3)-type is

$$\frac{dh}{dt} = \zeta^{-1} \sum_{k=1}^n \left[\lambda_S \left(\frac{\partial G_S}{\partial X_k} \right) - \lambda_L \left(\frac{\partial G_L}{\partial X_k} \right) \right] \delta X_k. \quad (16.14)$$

Now the functions $G_L(h)$ and $G_S(h)$ have to be found, which can be done by solving the Stefans problem – a nonstationary thermal conductivity problem with interface boundary as a heat source.

16.2.5 SA in a System with Two Degrees of Freedom

If only the crystal radius R and the crystallization front position h are regarded as variable parameters, (16.11) and (16.14) look like

$$\frac{dR}{dt} = A_{RR} \delta R + A_{Rh} \delta h, \quad (16.15)$$

$$\frac{dh}{dt} = A_{hR} \delta R + A_{hh} \delta h, \quad (16.16)$$

where the notations $A_{RR} = -V(\partial\alpha_0/\partial R)$; $A_{Rh} = -V(\partial\alpha_0/\partial h)$; $A_{hR} = \zeta^{-1}[\lambda_S(\partial G_S/\partial R) - \lambda_L(\partial G_L/\partial R)]$;

$A_{hh} = \zeta^{-1}[\lambda_S(\partial G_S/\partial h) - \lambda_L(\partial G_L/\partial h)]$ have been used. The solutions of the set (16.15), (16.16) are

$$\delta R = C_1 \exp(S_1 t) + C_2 \exp(S_2 t), \quad (16.17)$$

$$\delta h = C_3 \exp(S_1 t) + C_4 \exp(S_2 t). \quad (16.18)$$

Here S_1 and S_2 are the roots of the characteristic equation (16.4) that, for our case, reads

$$S^2 - (A_{RR} + A_{hh})S + (A_{RR}A_{hh} - A_{Rh}A_{hR}) = 0. \quad (16.19)$$

To estimate the stability of the set of equations (16.15) and (16.16) there is no need to solve the equations themselves but the Routh–Gurwitz conditions [16.6] can be used. For the set (16.15) and (16.16) to be stable, it is necessary and sufficient that the coefficients satisfy the inequalities

$$A_{RR} + A_{hh} < 0, \quad (16.20)$$

$$A_{RR}A_{hh} - A_{Rh}A_{hR} > 0. \quad (16.21)$$

The stability types mentioned are *rough* in the sense that the system stability remains unchanged within a wide range of values of the coefficients $A_{ik}(i, k = R, h)$. If at least one of the inequalities (16.20), (16.21) is replaced by the equality, the roots of the characteristic equation

(16.19) are either imaginary or zero. In this case we can not judge the system's stability by its linear approximation, and the nonlinear model should be analyzed.

The coefficients A_{RR} and A_{hh} indicate direct correlation between dR/dt and δR , as well as dh/dt and δh , i. e., self-stability of the parameters. The coefficients A_{Rh} and A_{hR} represent the effect of the change in one value on the rate of change of the other value, i. e., inter-stability of the parameters. It can be concluded from the analysis of (16.20) and (16.21) that the crystal growth system is stable if

$$A_{RR} < 0, \quad A_{hh} < 0, \quad A_{Rh}A_{hR} < 0, \quad (16.22)$$

$$A_{RR} < 0, \quad A_{hh} < 0, \quad A_{Rh}A_{hR} > 0, \quad (16.23)$$

$$|A_{RR}A_{hh}| > |A_{Rh}A_{hR}|, \quad (16.24)$$

$$A_{RR} < 0, \quad A_{hh} > 0, \quad |A_{RR}| > |A_{hh}|, \quad (16.25)$$

$$A_{Rh}A_{hR} < 0, \quad |A_{RR}A_{hh}| < |A_{Rh}A_{hR}|, \quad (16.26)$$

$$A_{RR} > 0, \quad A_{hh} < 0, \quad |A_{RR}| < |A_{hh}|, \quad (16.27)$$

$$A_{Rh}A_{hR} < 0, \quad |A_{RR}A_{hh}| < |A_{Rh}A_{hR}|. \quad (16.28)$$

We can see, that negative values of A_{RR} and A_{hh} coefficients to be, is a very important condition for the crystal growth system stability. Below, we will use the following terminology. There is a capillary stability in the system if $A_{RR} < 0$ and there is a heat stability if $A_{hh} < 0$.

16.3 SA and SCG by CZT

16.3.1 Capillary Problem

A solution of the boundary capillary problem allows finding coefficients A_{RR} and A_{Rh} . In [16.6], the reader can find the investigation of the problem in detail. Here are the brief results. The problem includes (16.6) with $d = 0$ and the two boundary conditions

$$\left. \frac{dz}{dr} \right|_{r=R} = -\tan \alpha_0, \quad (16.29)$$

$$z|_{r \rightarrow \infty} = 0. \quad (16.30)$$

The boundary problems numerical solution is presented on the Fig. 16.7 and

$$A_{RR} > 0; \quad A_{RR}|_{r \rightarrow \infty} \rightarrow 0, \quad (16.31)$$

$$A_{hR} < 0; \quad A_{hR}|_{r \rightarrow \infty} \rightarrow \approx 4V. \quad (16.32)$$

For the numerical calculation the dimensionality of A_{ik} is s^{-1} ; all angles have to be measured in radians, the units of length is the capillary constant a and speed of pulling is a/s .

16.3.2 Temperature Distribution in the Crystal–Melt System

A solution of the boundary heat problem allows finding A_{hh} and A_{hR} coefficients. There exists a great number of works dealing with calculation of the temperature fields in the crystal–melt system. They form a group of the Stefan problems in which a crystal–melt boundary is a heat source. However, owing to the variety of growth schemes and presence of a great number of factors that are to be taken into account for the thermal conductivity problems, for instance, complex temperature dependence of the thermophysical characteristics of various matters as well as convective flows in melts, a complete mathematical description of heat patterns during crystal growth is very difficult. Obtaining the solution in its analytical form is usually achieved by significant simplifications. With this end in view, the following equation from [16.26] allowing simple analytical solutions will be used to analyze the heat conditions in the

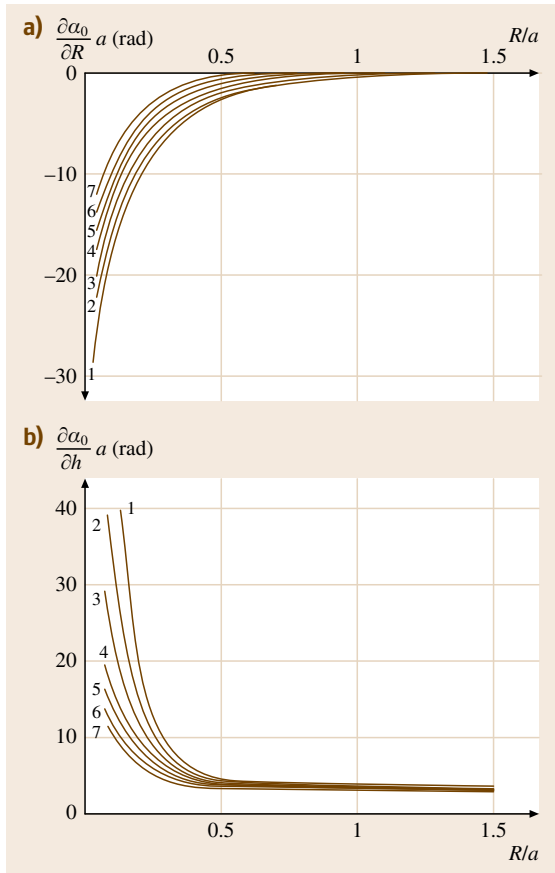


Fig. 16.7a,b For CZT (a) $\partial\alpha_0/\partial R$ and (b) $\partial\alpha_0/\partial h$ versus crystal radius for various values of the growth angle ψ_0 : (1) 15°; (2) 5°; (3) 0°; (4) 10°; (5) 20°; (6) 30°; (7) 40°. Capillary constant a is used as a unit of all dimensions

crystallization process

$$k_i^{-1} \frac{\partial T_i}{\partial t} = \frac{d^2 T_i}{dz^2} - V k_i^{-1} \frac{dT_i}{dz} - \mu_i \lambda_i^{-1} F (T_i - T_e) . \quad (16.30)$$

Here $i = L, S$ ($i = L$ for a liquid, $i = S$ for a solid body), T_i denotes the temperature, k_i is the thermal diffusivity coefficient, z is the vertical coordinate, μ_i denotes the coefficient of heat-exchange with the environment, F denotes the crystal (meniscus) cross section perimeter-to-its area ratio, T_e is the environment temperature, λ_i is the thermal conductivity coefficient.

There are few peculiarities for the use of (16.30):

1. It describes the temperature distribution of the crystal–melt system in a one-dimensional approxi-

mation that means that the temperature in the crystal (meniscus) cross section is averaged and isotherms are flat.

2. The heat exchange with the environment is allowed for not in the form of the boundary condition but by introducing heat run-offs on the lateral surface in the form of an additional term in the equation.
3. It gives a good description of real temperature distribution for small Biot numbers ($Bi = \mu_i R \lambda_i^{-1} \ll 1$) – this can be observed during growth of small diameter or thickness wall crystals, for low coefficients of convective heat transfer from the crystal (melt) surface, and high thermal conductivities.
4. Heat exchange is allowed for by the Newton law that means the convective heat exchange is much higher than the heat losses caused by radiation (the heat losses caused by free convection are comparable with the heat losses caused by radiation at the surface temperatures of $\approx 1000^\circ\text{C}$ and even higher in case specimen surface blowing is provided).
5. The equation is not available for vacuum pulled refractory materials and this for the radiation heat-exchange, the Stefan–Boltzmann law should be necessarily allowed for which leads to considerable nonlinearity of the problem; in this case a linearization of the crystal–surface radiation law described in [16.6] can be applied that allows (16.30) to be used up to temperatures of 2000°C .

In Sect. 16.2.1 we discussed a possibility to use a quasi stationary approximation, according to which temperature distribution in the crystal–melt system at any moment of time satisfies the stationary thermal conductivity equation with instantaneous values of all the process parameters. For this approximation to be applied, the time of crystallization front relaxation to the stationary state should be significantly longer than the characteristic time of temperature relaxation. As a rule, this condition is satisfied [16.6]. So, we can use (16.30) with left part set to zero for the calculation of G_S and G_L .

As an example of A_{hh} and A_{hR} calculation, we consider a growth of a long crystal (the limiting case is a continuous pulling), with good thermal screening of the melt column provided. So, we use (16.30) with zero left part for crystal as well as for the melt meniscus with $\mu_L = 0$. Boundary conditions of the problem are the following:

1. The melt temperature at the bottom of the liquid column at the level of the melt free surface is fixed: $T_L|_{z=0} = T_m$.

2. The crystallization-front temperature is equal to the melting temperature T_0 : $T_L|_{z=h} = T_S|_{z=h} = T_0$.
3. The temperature of the crystal end is equal to the environment temperature: $T_S|_{z \rightarrow \infty} = T_e$.

The solution of (16.30) with these boundary conditions [16.6] allows obtaining A_{hh} and A_{hR}

$$A_{hh} = -\zeta^{-1} \lambda_L h^{-2} (T_m - T_0) , \quad (16.31)$$

$$A_{hR} = \zeta^{-1} \mu_s R^{-2} \zeta_S^{-1} (T_0 - T_e) ; \quad (16.32)$$

where

$$\zeta_S = \left(\frac{1}{4} V^2 k_S^{-2} + 2 \mu_s \lambda_S^{-1} R^{-1} \right)^{1/2} .$$

So, on the basis of the capillary and heat boundary problems solution, the signs and the values of CZT growth stability coefficients are found. The signs are $A_{RR} > 0$; $A_{Rh} < 0$; $A_{hR} > 0$; $A_{hh} < 0$, if the melt is superheated ($T_m > T_0$).

16.3.3 SA and Crystal Growth

It can be concluded that:

1. The capillary stability is absent for all diameters of crystal.
2. Heat stability can be realized.

3. It is a chance to satisfy conditions (16.25) and to have the crystal growth stable if the following two inequalities can be fulfilled.

$$\left| \frac{\partial \alpha_0}{\partial R} \right| < \lambda_L V^{-1} \zeta^{-1} h^{-2} (T_m - T_0) , \quad (16.33)$$

$$\left| \frac{\partial \alpha_0}{\partial R} \right| < \left| \frac{\partial \alpha_0}{\partial h} \right| h^2 \mu_s R^{-2} \lambda_L^{-1} \zeta_S^{-1} \times (T_0 - T_e) (T_m - T_0)^{-1} . \quad (16.34)$$

Practically it means that a constant cross section crystal can be grown if the diameter of crystal is bigger than a melt capillary constant and the melt is superheated. If a crystal has a smaller diameter, superheating has to be high as well as a special combination of a process crystal growth parameters given the inequalities (16.33) and (16.34) has to be realized. Our experience of CZT crystal growth without a special diameter regulation as well as the growth of cylindrical crystals of silver [16.27] and of big diameter silicon tubes [16.28] confirms the conclusions of this paragraph. It has to be mentioned a necessity of very good stabilization of the pulling speed: it was shown [16.29] even a stable system can not compensate a sudden speed change and as a result there is a pinch formation.

16.4 SA and SCG by VT

At the beginning of seventies, our attention in some experiments was turned to the fact that growth of corundum crystals of small diameters ≈ 5 mm (they are grown especially as seed crystals) was easy. Practically the growth regime required no correction by an operator. The crystals had smooth surfaces and cylindrical shapes. This stimulated our works on the VT dynamic stability investigation. As was mentioned above, the analysis had been carried out with 3 degrees of freedom for cylindrical crystals (Fig. 16.2) and with 4 ones for tubular ones. The limited volume of the chapter does not allow us to give further details about the theoretical model. The reader can find them in [16.6, 15, 30–32]. Let us notice some peculiarities of the problem formulation for VT and the main conclusions. *First of all*, the mass balance condition in a system including a charge feeder, a melt layer, and a crystal has been used as a third equation for the set (16.2). *Second peculiarity* concerned with a heat problem formulation. As a rule, when formulating the heat problem for crystal growth

from melts, the melt temperature has been specified as the boundary condition (Sect. 16.3.2). This boundary condition for the VT does not correspond to the real situation. Crystal displacement in the furnace muffle results in melt-temperature change on its surface. This is a reason why the heat conditions of the technique under consideration will be allowed for by specifying the density Q of the heat flow fed from the burner onto the surface of the melted layer. With the gas flow specified, the density of the heat flow Q depends on the distance between the burner and the level of the melt surface $Q(l)$. The function $Q(l)$ is determined by the burner design and the gas debit.

16.4.1 Practical Results of the Theoretic Analysis

Round Cylindrical Crystals

For the process to be stable the following three conditions have to be fulfilled:

1. The diameter of crystal $2R$ has to be small ($R < a$). We can see that the situation is the opposite one to the CZT.
2. Change in the heat flow density $Q(l)$ along the furnace muffle in the vicinity of the growth zone at the distance of an order of R should not exceed the crystallization heat.
3. The heat flow density value $Q(l)$ in the vicinity of growth zone has to be decreased if the distance between the melt surface and the burner l_1 is increased.

The result of the theoretical investigation explains why growth of corundum crystals of small diameters (≈ 5 mm) is easy. They grow in the dynamically stable regime; it means that there are internal mechanisms for dissipation of perturbations. With respect to our terminology, the capillary stability exists for $R < a$ (for the sapphire melt $a = 6$ mm).

In spite of the capillary stable growth is impossible for the cylindrical round sapphire crystals with the diameters more than 12 mm, the theoretical model allows a minimizing of the crystallization process perturbations while growing big diameter crystals. For this, the previous two conditions have to be fulfilled (evidently, without the crystal dimension limitation) and also:

- The temperature of a muffle wall has to be increased.
- The irregularity of the density distribution of the charge flow falling on the melted layer has to be decreased.

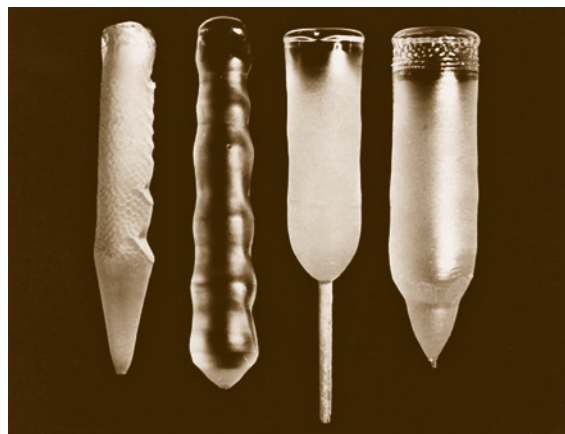


Fig. 16.8 Corundum cylindrical crystals grown by VT in optimized (two right ones) and nonoptimized (two left ones) regimes

These requirements of the crystallization conditions (we classify them as optimized) are in good agreement with our experimental results [16.15, 30–32]. In the experiments such hydrogen- and oxygen-flow debits in a three-channel burner had set that a crystal grown closer to the burner had a larger diameter. This condition corresponds to the heat-flow density increase when approaching the burner. Preheating the gas before feeding it into the burner and increasing the furnace muffle temperature were also used. As a rule, no parameter control to maintain constant cross section of the crystal was required. Crystals, grown under these conditions, exhibited a smoother surface and improved optical and structural characteristics. In the Fig. 16.8, corundum crystals of 40 mm diameter, grown in 1972 without any automatic control by the author of this chapter with collaborators from the Leningrad State Optical Institute, are presented.

Tube Shaped Crystals

The theoretical analysis states: Crystallization of tubes of arbitrary outer diameters is stable if the tube wall thickness is smaller than some critical thickness. This thickness is smaller than the capillary constant a and depends both on the heat conditions of the process and on the outer diameter of the tube. It increases with the outer diameter increase. In our experiments [16.6, 32] tubes with an outer diameter of 16–25 mm with walls 3–4 mm thick were grown (Fig. 16.9). A crystallization apparatus fitted with a four-channel burner providing charge supply via the central and periphery channels was used. It was experimentally stated the optimal gas distribution in the burner channels: oxygen-hydrogen-oxygen-hydrogen. Crystal growth was initiated from



Fig. 16.9 Six corundum single crystals (five tubes and one cylindrical crystal) grown by VT in the same regime

a seed 3–4 mm in diameter. Firstly, a seed cone was grown. The cone was widened by feeding the charge through the central channel, the periphery oxygen flow rate being increased. As soon as the crystal diameter reached the specified value 20–22 mm the charge was fed through the periphery channel. A little later (10–15 min) charge supply from the central tank was cut off and within 30–60 min the rate of the central oxygen flow was reduced. This growth regime has provided smooth transition from a solid crystal to a tube. The sink rate was smoothly increased. After that the process of stationary growth went on. Tubes up to 120 mm in length were grown. Usually no parameter control to maintain constant cross section of the tube was required, i. e., stable growth conditions the existence of which had been theoretically predicted could be attained. Figure 16.9 shows some of the tubes grown in 1981 by the authors of this chapter with collaborators from the Solid State Institute of the Russian Academy of Science. Three of the tubes are cut (one of them along the axe, and two ones obliquely) to show the tube walls. For the comparison, a cylindrical crystal of the same diameter, grown in the same furnace, is shown on the figure. The irregular crystal shape indicates that for it this regime is not optimal from the point of view of stability that is not at variance with our theoretical prediction.

Plate Shaped Crystals

The theoretical results are applicable for the growth of plate shaped crystals: The crystal plates of less than two capillary constants thick (12 mm for sapphire) have to grow stably. Information of corundum crystal plate growth by VT can be found in our review [16.8].

16.4.2 SA-Based Automation of VT

As was shown above, when passing to crystals with diameters exceeding the two capillary constants crystallization stability is lost. Practically it means that the crystallization front position and crystal dimensions are changed during the crystal growth process. In this case, an operator controls the parameters by changing the gas debit, charge feed and crystal sinking rate using his experience and intuition. Automatic system of control provides better result. When developing systems of growing crystal automatic diameters control, a problem of the laws of automatic control of the process parameters under some changes in crystal dimensions arises. Up to publication of our paper [16.33] the required laws of parameters control were defined from the re-

sults of empirical search. In [16.33] it was shown that the laws can be performed on the basis of the crystal growth stability analysis. In this instance the controllable parameters side by side with the crystal diameter, the liquid–gas interface position and the melt meniscus height can be required as the degrees-of-freedom of the crystal growth process. For VT the density of the heat flow from the burner Q , (it is regulated by the changing of the gases debit P), the rate of crystal sinking V and the powder charge flow rate Ω can be used as controllable parameters. Usually, P as well as Ω is used as controllable parameters on the stage of crystal widening. But after the crystal has already widened from the seed dimension up to the desired diameter, the control is provided by Ω regulation. In our approach Ω has to be regarded as an additional 4th degree-of-freedom for the cylindrical crystal. But coefficients of the linear equation for W are unknown. They have to be found from the necessary and sufficient conditions of the set of 4 equations stability of (16.3)-type. The problem can have several solutions. Each of them can be used as the regulation law in the control system. In this case our system of crystal growth including the regulator has to be stable. In [16.33] three different Ω change laws, allowed stable growth, were found. Fig. 16.10 illustrates corundum crystals grown with one of the stable laws of Ω regulation and the proportional one. The crystals were grown in 1979 by the author of this chapter with collaborators from the Institutes of Crystallogra-

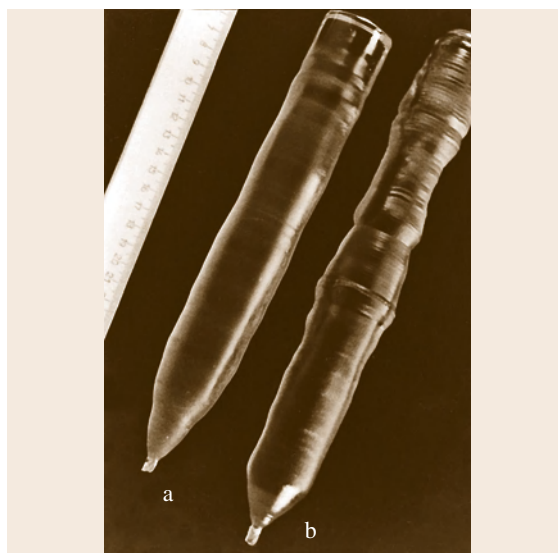


Fig. 16.10 Corundum crystals grown by VT using stable (a) and unstable (b) laws of powder charge control

phy and Solid State Physics of the Russian Academy of Science. A standard industrial Verneuil furnace was used for the experiments. A comparison of crystals from Figs. 16.8 and 16.10 shows that a design of the fur-

nace corresponding optimized, from the point of view of stability, growth conditions can provide the same (or even better) crystal quality as using of automatic system control.

16.5 SA and SCG by FZT

The FZT has been widely used for different materials crystal growth, especially: semiconductors (RF heating), high-melting metals and dielectrics (electron beam, plasma or laser heating). There are a lot of publications concerning a FZT theoretical study but only two aspects have been the investigation topics: a static meniscus stability, melt flows included, and impurity segregation. Only few papers have been devoted the dynamic stability analysis. Reference [16.18] has been the first of them. However, this analysis has not been completed as a heat conditions of crystallization have not been taken into account and a capillary part of the problem has been violently simplified. As a result, in [16.18] a capillary stability proved to exist in all versions of FZT. Our analysis based on the Lyapunovs theory [16.34, 35] is more common and includes the following main points:

1. Min $n = 4$ were chosen (Fig. 16.3).
2. The crystal up pulling as well as down lowering with different diameters ratio of the growing crystal and the rod to be melted were analyzed.
3. Equation (16.11) for $\partial R/\partial t$ was obtained as a result of the capillary boundary problem with the boundary condition of the angle growth certainty on the crystallization front.
4. It has been shown the boundary condition of the angle certainty is not available for the melting front [16.6, 36].

5. The equation for dW/dt was obtained from the mass balance of melted and crystallized substances.
6. Equation (16.14) for dh_c/dt was obtained as a result of the solution of (16.30) near the crystallization front as well as for dh_m/dt near the melting front.

The analysis of the result is rather complicated because four Routh–Gurvitz inequalities have to be simultaneously satisfied. Here are the main conclusions:

1. The capillary stability exists ($A_{RR} < 0$) for big growing crystal and melted rod diameters ($R > a$, $r_0 > a$) with all ratios of them (R/r_0).
2. For small ($R < a$, $r_0 < a$) crystal and rod diameters, $A_{RR} < 0$ if $R > R_{\min} \approx \frac{1}{2}r_0$.
3. The biggest negative value of A_{RR} coefficient corresponds to $R = r_0$.
4. The capillary stability exists for both direction of growth (up or down) but down lowering is the preferable one.

As for practical using of FZT for shaped crystal growth, besides widely spreaded round shape rode, the ribbon-to-ribbon (RTR) technique [16.37] has to be mentioned. A ribbon was used for a feeding as well as a ribbon crystal was grown. RTR achieved silicon ribbons for a solar cells application of a width 75 mm, a thickness 0.1 mm, and a 3–9 cm/min growth rate with laser heating being used.

16.6 TPS Capillary Shaping

While analyzing stability of TPS as a system with two degrees of freedom, the equations (16.15)–(16.25) have to be used. Therefore, we can proceed to the analysis of the melt-column shaping conditions in TPS.

16.6.1 Capillary Boundary Problem

For axisymmetrical case, the Laplace capillary equations (16.6)–(16.8) will be used in our analysis. As was mentioned above, each equation is a second order differ-

ential one and a boundary problem for a melt meniscus shape calculation strictly requires assignment of two boundary conditions. The first of them is (16.26), common for all CST but the second one is determined by the structural features of each specific TPS. A shaper is used for melt-column shaping in TPS (Fig. 16.4). The functions of the shaper in TPS are wide and we will discuss all of them later. At the moment, we characterize the shaper as a device to control the melt-column shape only. This problem is a fundamental one for

a shaped crystal growth by TPS and we will discuss it in detail. In a mathematical description of the problem, a shaper function is to determine the meniscus shape by means of fixation of a capillary problem second boundary condition. For the first time, the characterization of shapers from this point of view was accomplished by us in 1967 [16.38, 39]. In the most cases, the shaper (Fig. 16.4) is characterized by its wall or free edge curvature radius r_0 in the horizontal plane, the angle β made by its wall with the horizontal. The wetting angle Θ formed by the melt and the shaper surface, is a very important shaper characteristic. If this angle exceeds 90° , the shaper material is not wetted by the melt (Fig. 16.4a,b,g–j); if it is smaller, the melt wets the shaper material (Fig. 16.4c–f). Shaping is accomplished either on the surfaces (Fig. 16.4a,c,g–i) or on the sharp edges (Fig. 16.4b,d–f,j) of the shaper. It corresponds to the following boundary conditions of the capillary boundary problem:

Catching Boundary Condition

In case the shaper material is wetted by the melt, the melt is easily caught by its sharp edge. This boundary condition will be termed the *catching condition*. There is a possibility of providing the catching conditions at nonwetttable shaper free-edges which will be discussed below. The catching condition means that a counter line on the meniscus surface is fixed by the edge of the shaper, i. e., it coincides with the edge counter of the shaper. It does not matter if the edge counter is internal (Fig. 16.4d,j) or external (Fig. 16.4e,f), if the pulling up (Fig. 16.4d,e) or down lowering (Fig. 16.4f,j) is used for the shape crystal growth. The catching condition has the following mathematical form in the cylindrical coordinate system

$$z|_G = d(r, \phi). \quad (16.35)$$

Here G is the counter of the shaper edge, d is the distance from the shaper edge to the coordinate plane. In case the shaper is flat and is positioned parallel to the melt plane, $d = \text{const.}$ For axisymmetric flat shaper edges the condition (16.35) has the following form

$$z|_{r=r_0} = \text{const.} = d, \quad (16.36)$$

where r_0 is a shaper edge counter radius. If the coordinate plane coincides with the free level of the melt, d represents the pressure of feeding the melt to the shaper. In this case, the pressure is included in the boundary condition and in the Laplace capillary equation, $\text{const.} = 0$. If the coordinate plane coincides with the shaper edge plane (Fig. 16.4b,d–f,j) the right part of

(16.36) is equal zero and the pressure d is included in the Laplace capillary equation (16.5–16.8) as a parameter ($\text{const.} = d$). The pressure being positive, the shaper edges are positioned below the melt free-surface level and vice versa.

Angle Fixation Boundary Condition (the Wetting Condition)

If the melt has a contact with the shaper surface, it makes the wetting angle, Θ with the shaper surfaces (Fig. 16.4a,c,g–i). This boundary condition will be termed the *angle fixation condition or wetting condition*. It can be realized for nonwetttable shaper material (Fig. 16.4a,g–i) as well as for wetttable one (Fig. 16.4c), for pulling up (Fig. 16.4a,c,h,i) as well as for lowering down (Fig. 16.4g) shaped crystal growth. The condition means that shaper walls fix the meniscus angle on a counter C belonging to the shaper surface by forming the angle of wetting. The condition has the following forms:

In common case, where \mathbf{n} denotes the direction of the normal towards the shaper wall, C is a counter of the contact of the meniscus with the shaper walls

$$\left[1 + \left(\frac{\partial z}{\partial x} \right)^2 + \left(\frac{\partial z}{\partial y} \right)^2 \right]^{-1/2} \frac{\partial z}{\partial \mathbf{n}} \Big|_C = -\cos \Theta. \quad (16.37)$$

The shapers of complicated surfaces (Fig. 16.4a,c) can illustrate this condition although in the figure they represent a particular case of the cylindrical symmetry system (z, r coordinates) whereas, for the common case, the use of x, y, z coordinate system is necessary.

For an axisymmetrical problem (a rod, a tube) on the vertical shaper walls (Fig. 16.4h)

$$\frac{dz}{dr} \Big|_{r=r_0} = \tan \left(\Theta - \frac{\pi}{2} \right) = -\tan \alpha_1. \quad (16.38)$$

For circular cone shaper walls formed the angle β with the horizontal (Fig. 16.4i)

$$\frac{dz}{dr} \Big|_{r=r_1-z \cot \beta} = \tan \left(\Theta + \beta - \frac{\pi}{2} \right) = -\tan \alpha_1. \quad (16.39)$$

Wetting-to-Catching Condition Transition

With the melt pressure increasing, the catching boundary condition at the nonwetttable shaper free-edges can be obtained. Figure 16.11a illustrates this transition with the pressure to be increased by gradual shaper immersing into the melt. The diagram is based on [16.40]

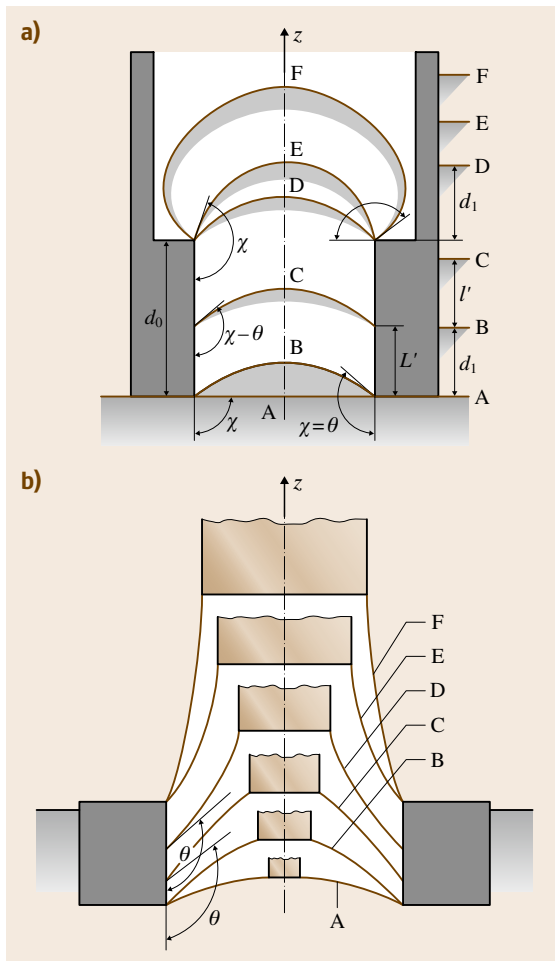


Fig. 16.11a,b Transition of the shaper lower free-edge catching boundary condition (meniscus A) to the wetting condition (menisci B, C, D) and further to the shaper upper free-edge catching condition (menisci E, F); (a) pressure changes (the horizontal lines denote successive positions of the liquid free surface); (b) the seed-shaper dimension ratio changes; χ is the angle between the line tangent to the melt surface and the shaper wall, θ is the wetting angle

describing the particle buoyancy conditions for the flotation processes. A nonwettable shaper, with a hole of d_0 depth, possessing vertical walls is considered. The angle χ between the line tangent to the liquid surface and the shaper wall is introduced. Let us analyze a number of shaper successive positions. *Position A*: The shaper touches the melt with its lower plane. The lower-plane immersion depth is equal to zero. The line

tangent to the liquid surface coincides with the liquid surface. Angle χ is $\frac{\pi}{2}$. The catching condition holds at the lower free edge of the shaper. With the shaper being immersed into the liquid, the angle χ increases, and when the shaper lower plane reaches some depth d_1 , (*position B*) the angle χ will be equal to the wetting angle θ , (within the immersion depth range from 0 to d_1 the catching condition holds at the lower free edge). With further shaper immersing into the liquid, χ remains equal to the wetting angle θ . The liquid-shaper wall contact line goes up by the value of L^1 , the shaper immersion depth, the distance between this line and the free surface level remaining equal to d_1 (*position C*). As soon as the immersion depth is equal to $d_0 + d_1$, the liquid-shaper contact line coincides with the shaper sharp edge (*position D*), and with further pressure increase, the catching condition at the shaper upper free edge holds (*position E*). In this case the angle χ will increase until the wetting angle θ is formed by the liquid and the shaper surface [16.40]. For the horizontal shaper surface $\chi = \frac{\pi}{2} + \theta$ (*position F*). Further increase in pressure is impossible as it will lead to liquid spreading over the shaper surface and the shaper will not operate properly. But if shaper's free edges are sharp, pressure increase is possible (Fig. 16.4b) up to the loss of the meniscus' static stability.

The presence of a seed or a profile being pulled considerable changes into the conditions of the transition described. It means that the condition at the upper boundary (along the crystal-melt contact line) can affect the character of the condition at the lower boundary (along the melt-shaper contact line). The diagram, that will be proved when solving the boundary problem, is given in Fig. 16.11b. By changing the seed-to-shaper hole dimension ratio alone, the catching boundary condition at the lower free edge (menisci A, B), the wetting condition on the shaper walls (menisci C, D), the catching boundary condition at the upper free edge (menisci E, F) can be achieved. The very important conclusion is the following: the wetting boundary condition means the angle χ is fixed but the counter of the meniscus with the shaper contact is movable. Its position on the shaper walls depends on the melt pressure and the crystal-shaper dimensions ratio.

Certainly, we could change a melt pressure by any other way as well as a growth direction does not matter. For instance, by changing a melt pressure or the crystal-shaper edge dimensions ratio, it is possible to realize the scheme of either Fig. 16.4g or j.

A comparison of Fig. 16.11a and b diagrams shows that there are two very different situations: before seed-

ing and after seeding (during pulling). In the second case, even for non wettable shaper walls, the meniscus, changing its curvature with forming a negative pressure inside, raises the melt above the shaper edge, up to the crystallization front (the same situation exists in CZT).

Hereafter it will be shown that the catching boundary condition usually leads to more capillary stability of the process, therefore, the ways of achieving the catching condition at the shaper free edges in TPS should be specified: *Firstly*, a melt-wettable material should be used for the shaper, and the latter should be designed in such a way that the melt could raise up to the shaper free-edges due to capillary forces (Fig. 16.4d–f). *Secondly*, for melt-nonwettable materials, the melt column should be embraced from outside, providing additional pressure on the liquid to make the melt–shaper contact point touch the shaper sharp edge (Fig. 16.4b,j). *Thirdly*, for poorly wettable shaper materials, the crystal–shaper dimensions ratio should be used in order that it could ensure melt column contact with the shaper sharp edges, compare Fig. 16.4g and j.

Influence of the Wetting-Angle Hysteresis on Capillary Boundary Conditions

While analyzing all the capillary effects, the existence of wetting-angle hysteresis should be taken into consideration. The wetting angle hysteresis reveals itself in the fact [16.40] that the wetting angle of liquid run on a solid body is larger than that of liquid run off a solid body. This means that the stationary wetting angle depends upon the process of meniscus formation (on-run or off-run). This results, for example, in the fact that a higher pressure is to be applied to create the catching condition at the shaper free edge than that required to keep it unchanged. In case the catching condition is created by the seed, this condition can remain unchanged in the process of growth, with the clearance between the shaper free edge and the growing crystal changing.

A Comparison of the Catching Boundary Condition and the Angle Fixation One

The comparison can be done on the basis of the previous description of transition one to another. It exhibits a big difference of these two boundary conditions: The catching one fixes a coordinate of the meniscus end counter but an angle of the inclination of the meniscus is not fixed. The wetting one fixes an angle of inclination of the meniscus end counter but not a coordinate. In this case the meniscus is movable (Fig. 16.11b). Its position on the shaper wall depends on the second

boundary condition (a seed or growing crystal presence as well as a growing crystal dimension and a growth angle) and can be found as a result of the capillary boundary problem solution. So, for capillary shaping by walls, a shaper has to be designed taking account for this phenomena as well as the angle-wetting hysteresis. We carefully explain this difference because there is a big misunderstanding of this key problem for capillary shaping. Let us analyze some of wrong approaches. For the boundary capillary problem solution, Stepanov et al. [16.41] use the idea of Tsivinskii from [16.42], where, for the axisymmetrical meniscus described the Laplace equation (16.5), it was suggested to replace $1/R_2$ (Fig. 16.1) by a linear function of the vertical co-

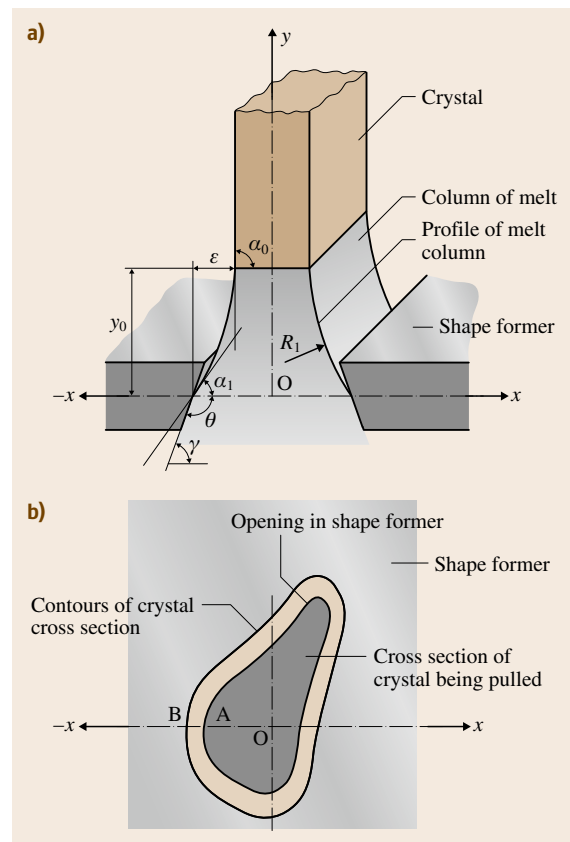


Fig. 16.12a,b Arrangement for producing a crystal with cross section of arbitrary form. Melt column parameters: y_0 represents the melt column height, α is the inclination of the profile curve tangent to the x axis (α_0 at $y = 0$ and α_{01} at $y = y_0$), and R_1 is the radius of curvature of the melt column surface, lying in a plane perpendicular to the tangent (R^0 at $y = 0$ and R^{01} at $y = y_0$) (after [16.41])

ordinate. There are, as minimum, four mistakes in this approach (Fig. 16.12):

1. The axisymmetrical meniscus is applied for the growth of arbitrary cross section crystals
2. A priori, we need to know if the meniscus is concave, convex or concave-convex
3. A priori, for concave-convex meniscus, we need to know the coordinates of the inflection point
4. We need to know y_0 , α_0 , and α_{01} .

The fourth mistake is the worst. Indeed, the fixation of these parameters means that we need to use three boundary conditions for the second order differential equation: a fixation of the angle growth on the crystal-melt boundary and the catching as well as the wetting boundary conditions on the shaper. But it is nonsense. Authors of this approach had published a lot of papers including cumbersome formulas that never have been used or verified. The main argument of the authors: this approach is applied for CZT – there are a lot of experimental evidences of it. But it is clear, why the approach works for CZT. The second boundary condition for CZT (16.27) confirms the vertical coordinate strives for the zero on the infinity. Automatically it means that the first derivative also strives for the zero on the infinity. So, this is the well known in mathematics peculiarity of the boundary condition on the infinity and, as a result, we have three boundary conditions. For

the first time we had explained nonapplicability of this approach to the TPS in [16.43] (1969) and later in our reviews [16.5, 6, 9]. But many journals have continued publishing including *Pet'kov* and *Red'kin* paper [16.44] concerned with the investigation of the shaped growth dynamic stability. In our paper [16.45] we once more explained nonapplicability of this approach.

More Precise Definition of the Catching Boundary Condition

Nevertheless, we understood that there is a weak point in our approach: From the formal point of view we are right – mathematical formulation of the problem requires two boundary conditions. But from the physical point of view a melt has to form a wetting angle with a shaper surface. This discrepancy was explained in [16.23]. The paper contains well-grounded mathematical proof but here we only illustrate the main idea. Figure 16.13 presents one specific case: the growth of round cylindrical crystal with respect to scheme Fig. 16.4d. The shaper edges are replaced by circular coaxial tours of four different curvature radii r_S (the last $r_S \rightarrow 0$). The example corresponds to middle-range bond numbers $Bo \approx 1$. The shaper radius $r_0 = 1$. The unit of lengths measurement is the capillary constant a which is equal for silicon 7.6 mm, for sapphire 6 mm, for germanium 4.8 mm, for indium antimonide 3.7 mm [16.6]. It means that for silicon the diameter of the shaper edges circle is 15.2 mm, for sapphire 12 mm. The origin of the z -coordinate is located on the melt free surface. The negative melt pressure $d = -1$, e.g. the melt free surface is located on the distance a lower than the shaper edge (Fig. 16.4). Three set of profile curves (a profile curve is a section of the meniscus by the figure plane) are presented on the Fig. 16.13. Each set consists of four profile curves and is characterized by the same value of the angle α_d -meniscus inclination angle with respect to positive r -direction at the point of the contact with the shaper. The lower end of each profile curve is located on the surface of a torus and forms the wetting angle $\Theta = 10^\circ$ with the surface of the torus. The each torus corresponds to the shaper edge of a different radius of curvature r_S : $r_S = 0.09$ (0.68 mm for Si) for the all three profile curves of set d , $r_S = 0.06$ (0.46 mm for Si) for the curves c , $r_S = 0.03$ (0.23 mm for Si) for curves b , $r_S \rightarrow 0$ for curves a . The upper end of each profile curve forms the angle 10° with the vertical. It corresponds to crystal growth of the respective dimension with the growth angle $\psi_0 = 10^\circ$: $R \approx 0.45$ (the crystal of 7 mm diameter for Si) for set 1, $R \approx 0.7$ (the crystal of 10.6 mm diameter for Si) for set 2, $R \approx 0.9$

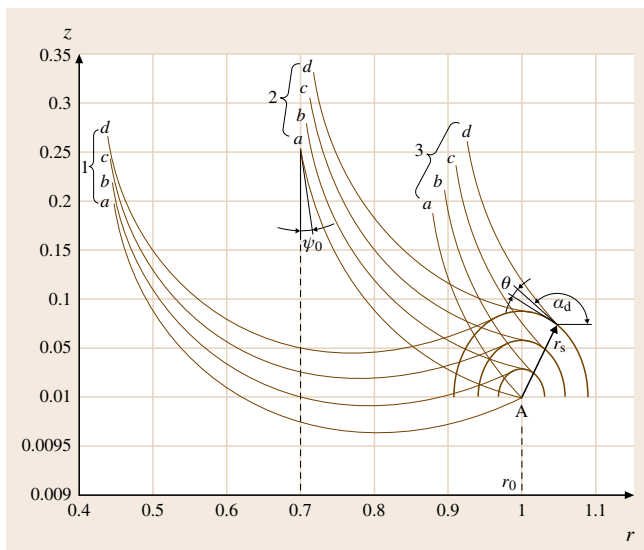


Fig. 16.13 Mid-range Bo . Profile curves $z(r)$, starting from surfaces of toruses ($b-d$) of different radius r_S and from a sharp edge of the shaper (a) (after [16.23])

(the crystal of 16 mm diameter for Si) for set 3. The crystallization front is located on the height (from the plane of the shaper edges) 0.20 (1.5 mm for Si) for sets 1 and 3, 0.30 (2.2 mm for Si) for set 2.

So, on the microlevel, the melt forms the wetting angle with the torus surfaces and we have a normal physical wetting condition. If the crystal changes its dimension the contact point also changes its position on the torus surface but, in any case, its position will be in the vicinity (torus radius r_S) of the point A. With the r_S decreasing, a location of the lower end of the profile curve is more definite near the point A with the coordinates ($r_0 = 1$, $z = 1$). If the torus radius is infinitely small we have, in macroscopic sense, the catching of the meniscus on the sharp shaper edge (in point A). So, the catching condition is just a useful mathematical approach to satisfy a capillary boundary problem. From the physical point of view it defines a wetting boundary condition on the sharp edges of the shaper. It seems, everything is clear. But in spite of the publication of our papers [16.23, 45], the history of application of the approach from [16.42] to TPS has not been finished [16.46].

Capillary Boundary Problem Solution

The solution of the problem we are dividing on three parts with respect to the Bond numbers Bo : large, middle-range and small ones. For large and small Bo , the Laplace equation has the forms (16.7) and (16.8), respectively. A solution of the boundary problems for both of them can be obtained in analytical form (sometimes with the using of special functions). For a middle-range Bo a numerical solution is needed. A comparison of the analytical and numerical solutions shows that, with a sufficient accuracy for practice, we can use:

1. The large Bo approximation for the growth of cylindrical round rods or tubes of $10a$ minimal diameter (remind that for the silicon it corresponds 76 mm, for the sapphire 60 mm)
2. The small Bo approximation for the growth of cylindrical round rods or tubes of a maximal diameter (remind that for the silicon it corresponds 7.6 mm, for the sapphire 6 mm) on the Earth surface as well as for the very big diameters crystals growth under microgravity conditions

A solution of a boundary capillary problem allows to obtaining very interesting information concerning a capillary shaping as a function of a shaper design, melt pressure, wetting angle. The information can include:

1. A shape of meniscus-conditions of existence of concave, convex and convexo-concave ones
2. A range of parameters for existence of catching and wetting boundary conditions
3. Design of a shaper and a range of parameters for existence of a meniscus with the definite growth angle ψ_0
4. The same with the fixed crystallization front position
5. Signs and values A_{RR} and A_{Rh} coefficients [16.6, 23, 24, 47].

Here are few examples of this kind.

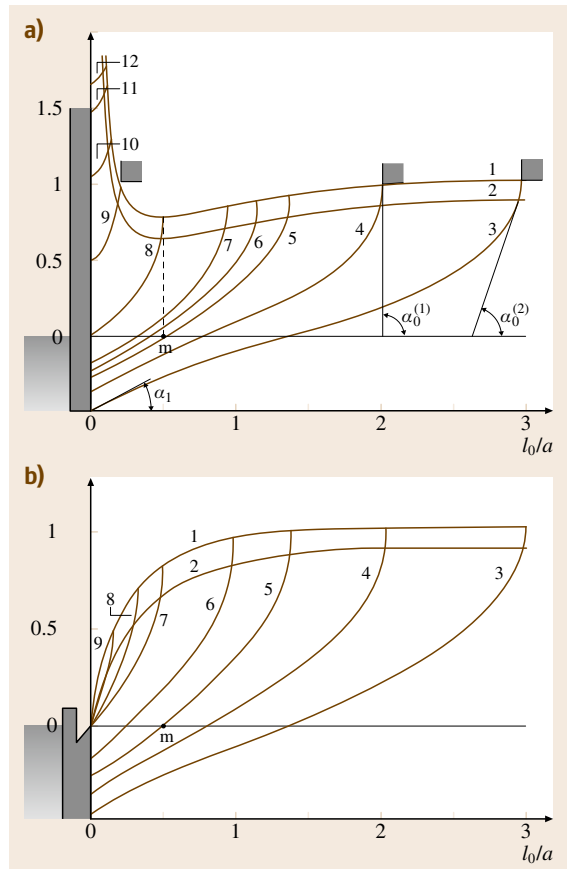


Fig. 16.14a,b Large Bo : (a) Wetting boundary condition ($\theta = 135^\circ$); convex-concave (3–7) and concave (8–12) profile curves $z(r)$; boundary 1 ($\psi_0 = 0$) and 2 ($\psi_0 = 15^\circ$) curves $h(R)$; (b) transition from the wetting boundary condition (3–6) to the catching condition (7–9) by changing the shaper design

Large Bo: Let us formulate the following crystal growth conditions (Fig. 16.14) which corresponds to the scheme Fig. 16.4h [16.6,47]: To the right, where $r = r_0$, the non wetted shaper wall is located. The line tangent to the melt surface in the melt–shaper contact point makes the wetting angle Θ with the shaper wall. Let us introduce the angle $\alpha_1 = \Theta - \frac{\pi}{2}$. To the left, where $r = R$, the edge of a melt-growing flat crystalline tape or that of a circular cylindrical crystal of a large diameter is situated. Let the angle α_0 (Fig. 16.6a), made by the line tangent to the melt surface at the melt–crystal growing contact point and the negative direction of the r -axis, be specified (while growing crystals of constant cross sections, the angle $\alpha_0 = 1/2\pi - \psi_0$ is the complement of the growth angle ψ_0). Let l_0 denotes the clearance between the crystal edge and the shaper: $l_0 = r_0 - R$. Let us consider what process parameter data can be obtained with such problem formulation. According to our terminology, we have the angle-fixation boundary conditions (or wetting conditions) on both the ends of the r -variation interval: the equation (16.7), boundary conditions (16.26) and (16.38). The analytical solution of the problem was obtained in the Legendre elliptical functions (e.g. [16.6]) and is presented on the Fig. 16.14a for the following parameter values: $\Theta = 135^\circ$ ($\alpha_1 = 45^\circ$), $\psi_0 = 15^\circ$ ($\alpha_0 = 75^\circ$) and $\psi_0 = 0$ ($\alpha_0 = 90^\circ$). The origin of the z -coordinate coincides with the free melt surface. The profile curves 3–12 are the sections of the melt meniscus by the diagram plane. Each profile curve corresponds to the definite distance l_0 between the growing crystal and the shaper wall. The edges of the crystals are located on the one of two boundary curves $h(R)$ corresponding two different growth angles: (1) for $\psi_0 = 0$ and (2) for $\psi_0 = 15^\circ$. Based on this boundary problem solution, the following conformities can be established:

1. With the angle fixation boundary condition satisfied at both the ends of the l_0 -variation interval, the vertical coordinates of the liquid–solid phase contact points with respect to the melt free surface are not fixed but depend on the relation between the angles at both the ends of the interval and on the value of the clearance between the shaper and the crystal being pulled. It is a confirmation the scheme Fig. 16.11b.
2. There exists some minimum value m of the clearance between the shaper and the crystal being pulled (for our parameter values it is equal approximately to one capillary constant a) when the meniscus lies both above and below the melt free surface. When

this gap is smaller than m , the point of the meniscus contact with the shaper wall is located higher of the melt free surface.

3. The meniscus part, located below the melt surface is convex, the meniscus part, located above the melt surface is concave.
4. A higher crystallization front position corresponds to a smaller growth angle.
5. For the crystal–shaper gap being more than capillary constant a the crystallization front height doesnot exceed capillary constant. For smaller gaps, the crystallization front height can be infinitely tall.
6. Any change in the melt level during pulling will produce the following effect on the crystal dimensions: with the level decreasing, the tape thickness (or the rod diameter) can be kept unchanged only in case the crystallization front is lowered by the same value. With the crystallization front position kept unchanged, the tape thickness or the crystal diameter will decrease with the melt lowering and vice versa. It means that the melt level can be qualified as one of degrees of freedom. We investigated these phenomena (e.g. [16.6]).
7. $|\partial\alpha_0/\partial h| > 0$; $|\partial\alpha_0/\partial R| > 0$ for $l_0 < m$; $|\partial\alpha_0/\partial R| < 0$ for $l_0 > m$. It means that there is a capillary stability ($A_{RR} < 0$) only if the gap between the shaper wall and the pulling crystal is more than capillary constant ($l_0 > m \approx a$).

Now, let us modify the shaper design: let us locate a sharp shaper edge on the melt free surface level. The solution of the new boundary problem is presented on Fig. 16.4b. Let us discuss new results:

1. For $l_0 > m \approx a$, the situation is the same as in previous case.
2. But for $l_0 < m \approx a$, the situation is dramatically changed: the catching boundary condition is realized (this is a second confirmation of the scheme of Fig. 16.11b) and, as a result, either for $l_0 < m \approx a$, $|\partial\alpha_0/\partial R| > 0$, i.e., the capillary stability exists for all range of l_0 variations.
3. On the other hand, a crystallization front $h(R)$ has to be located much lower than in the previous case. In particular, $h(R)|_{R \rightarrow r_0} \rightarrow 0$.

Middle-ranged Bo: For a middle-ranged Bo ($Bo \approx 1$), three profile curves a of the sets 1–3 on the Fig. 16.13 present an example of the numerical solution of the capillary boundary problem with the catching boundary condition that corresponds to Fig. 16.4d Therefore, we use (16.6) and the boundary conditions

(16.26) and (16.36). The results were discussed above but the two peculiarities have to be mentioned here:

1. A middle part of the meniscus, corresponding to the crystal radius $R \approx 0.5$, is located lower than the shaper edge.
2. The highest crystallization front position corresponds to the crystal radius $R \approx 0.7$.

Small Bo: As an example of the capillary boundary problem solution for a small Bo ($Bo \ll 1$), studied in detail in the analytical form with using of the Legendre elliptical functions in [16.6, 47], we show (Fig. 16.15) a melt pressure influence on the shape of profile curves $z(r)$, with the boundary condition of catching in the point r_0 (the shaper radius $r_0 = 0.05$), as well as on the boundary curves $h(R)$ (1–4), corresponding to the growth angle $\psi_0 = 0$. Hence, we use the equation (16.8) and the boundary conditions (16.26) and (16.36). It is very important to mention that in the capillary problem with small Bo it is neglected by the influence of gravity. This is a reason, why these results are applicable for the growth of different size crystals in microgravity conditions. As for the growth in the condition of normal gravity, the results are applicable for filaments growth (for sapphire, for instance, the case under consideration corresponds to growth of a filament of 0.6 mm diameter)

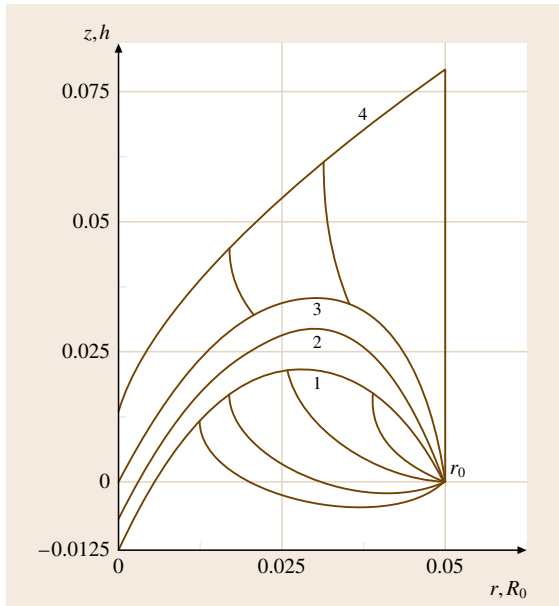


Fig. 16.15 Small Bo: Boundary curves $h(R)$ 1–4 and some profile curves $z(r)$ for shaper with $r_0 = 0.05$, under various pressures d : -10 (1), -5 (2), 0 (3), 10 (4)

with pulling up as well as lowering down. Consequently, the schemes Fig. 16.4b,d–f,j are described in the frame of this model. Here are some peculiarities of the results presented on the Fig. 16.15:

1. The order of magnitude of the crystallization front position is the same as the shaper radius for all values pressures under investigation. In our example, $r_0 = 0.05$. It means that for sapphire, for instance, the crystallization front is located on the distance 0.5–0.6 mm from the plane of sharp shaper edges.
2. For all boundary curves, except 4, $h(R)|_{R \rightarrow r_0} \rightarrow 0$.
3. The boundary curve 4 is the particular one. From the theoretical study [16.6], it follows that if d corresponds to the value from the formula $2dr_0 = 1$, the boundary curves for all r_0 values (but only from the range of small Bo values) has to have the shape similar to the curve 4. The main particularity of this curve is the following one: $h(R)|_{R=r_0} = 0.5\pi r_0$. Hence, for this particular pressure, if the diameter of pulling crystal is equal to the shaper edge diameter, the very special meniscus in the shape of the right circular cylinder exists.
4. All boundary curves, except 4, have a maximum. The maximum position corresponds to $R = R_m \approx 0.7r_0$ and it divides all range of the crystal dimensions on two parts for which: $\partial\alpha_0/\partial R > 0$ if $R > R_m$ and $\partial\alpha_0/\partial R < 0$ if $R < R_m$. It means that for d values characterized the formula $2dr_0 < 1$, there is a capillary stability ($A_{RR} < 0$) only if the gap between the shaper edge and the pulling crystal is less than $0.3r_0$.

16.6.2 Stability Analysis

Signs of capillary coefficients A_{RR} and A_{Rh} are presented on Fig. 16.16. For the stability estimation, heat coefficients (16.31) and (16.32) can be used: $A_{hh} < 0$, $A_{hr} > 0$. With respect to Fig. 16.16, we can choose a shaper design to have a capillary stability: $A_{RR} < 0$, $A_{Rh} < 0$. Therefore, with respect to (16.22) inequalities fulfilled, a dynamic stability of a shaped crystal growth will be provided.

Here we formulated a common problem of stability for growth of arbitrary cross section crystals by TPS. But only the simplest case (a growth of a round cylindrical crystal in the thermal condition described by the one dimensional thermoconductivity equation) was analyzed. Complimentary information on the topic can be found in our reviews [16.6, 9] and papers [16.23, 24]. It includes:

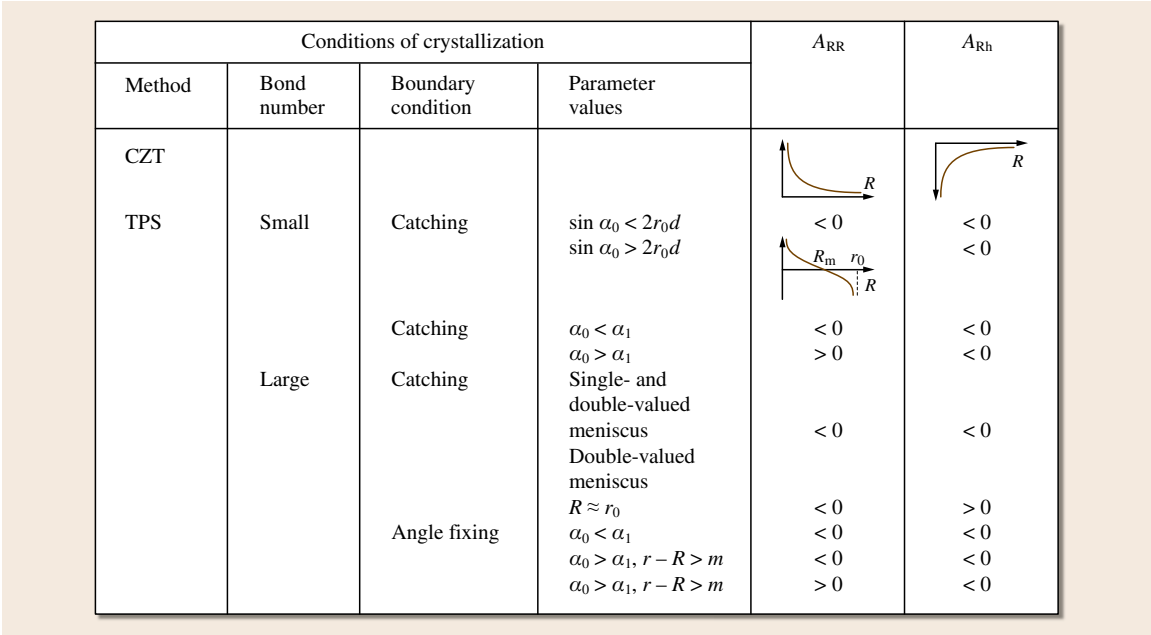


Fig. 16.16 CZT and TPS capillary coefficients for different Bo values and different capillary boundary conditions

1. Investigation of the meniscus static stability.
2. Investigation of tubes growth dynamic stability – three degrees of freedom stability problem where internal tube diameter is a third degree of freedom.
3. Investigation of a melt pressure influence on the dynamic stability – three degrees of freedom stability problem where melt pressure is a third degree of freedom.
4. Crystal cross section shape stability. So, some problems are solved but for theory up to now, there have been a lot of problems to be solved. The main of them is the stability of complicated shape crystal growth and an influence of crystallographic anisotropy.

Now, for preliminary analysis of the capillary shaping conditions before the experiments, we use rough estimations. For instance, for ribbon growth, an approximation including three steps, we proposed [16.6]:

1. A solution of the capillary problem with large Bo for the ribbon flat part
2. A solution of the capillary problem with small Bo for the ribbon edge
3. A joining of two solutions on the boundary near ribbon edge with the condition of the same growth angle for two parts.

16.6.3 Experimental Tests of the Capillary Shaping Statements

Growth Angle Certainty

A growth angle certainty is one of the main capillary shaping theory statements. This is a reason, why we carried out special experiments to examine it [16.6, 48]. A growth of thin sapphire crystal from a shaper with 0.8 mm diameter was carried out (Fig. 16.16). By changing the slope between the crystallization front and the surface of the skew shaper by means of a different heating, various boundary conditions were created for left and right sections of the same crystal. In Fig. 16.16a the rod of a constant cross section grows: the angles ψ_1 between the crystallization front and the growth direction are different on the left and on the right crystal sides; constancy of the diameter is provided by maintaining the angle $\alpha_0 = \alpha_e (\alpha_e = \pi/2 - \psi_0)$ all over the perimeter. In Fig. 16.17b on the left $\alpha_0 = \alpha_e$, on the right $\alpha_0 < \alpha_e$, the right side of the crystal widens. In Fig. 16.17c deviation α_0 from the equilibrium value α_e on the right side has led to crystal contraction. In the transient region, the crystal surface is convex on the Fig. 16.17b and concave on the Fig. 16.17c, which corresponds to the capillary stability presence.

Integration of the equation (16.9) in the range of the crystal radius R change from R_0 to the final value R_{01}

gives the following formula

$$\ln D = - \left(\frac{d\alpha_0}{dR} \right) z, \quad (16.40)$$

where

$$D = \frac{R - R_{01}}{R_0 - R_{01}}.$$

Linear dependence $\ln D$ versus z has to be a proof of the (16.9) correctness. Figure 16.18 presents the data processing from Fig. 16.17b,c.

The Space Experiments. We carried out some model experiments in the microgravity conditions (small Bo) to test some capillary shaping theory statements [16.6, 49–54].

Simulation Experiments. Crystal growth experiments under microgravity conditions in the Space were preceded by simulating the liquid column shape with using immiscible liquids of equal densities [16.6, 49–51]. A meniscus of the alcohol/water solution was formed between two glass tubes, surrounded by the equal-in-density mineral oil (Fig. 16.19). Pressure d in meniscus was equal to the weight of column of the alcohol solution in the upper tube. The lower tube (3) of $2r_0 = 13.12$ mm diameter imitated the shaper, and the upper one (1) of $2R$ in diameter – the crystal. For a right circular cylindrical meniscus (2) existence, a pressure 16.8 dyn/cm^2 was determined experimentally (Fig. 16.19a). A convex meniscus (2) (Fig. 16.19b) was formed under pressure 27.14 dyn/cm^2 . The sphere menisci (4) on the ends of the lower tubes (3) were used for the pressure estimation as well as, with a certain pressure, for a surface tension value on the two liquids boundary. The same types of the experiments were carried out by us on the board of a flight laboratory with the 20 s microgravity time.

Crystallization of Copper Under Short-Time Microgravity Conditions. The simulation experiments with liquids were only the first step to estimate the crystal growth real conditions. Moreover, a doubt appeared that a shaped crystal growth under microgravity could be realized because, sometimes, in simulation experiments, the liquid flew on the crystal surface [16.6, 49]. Therefore, we crystallized the copper under the capillary shaping, on a high-altitude rocket, with 20 min time of microgravity [16.6, 50, 51]. The metal has a relatively low melting point (1083°C), resistance to overloading (it is important for rocket launching as well as for a cap-

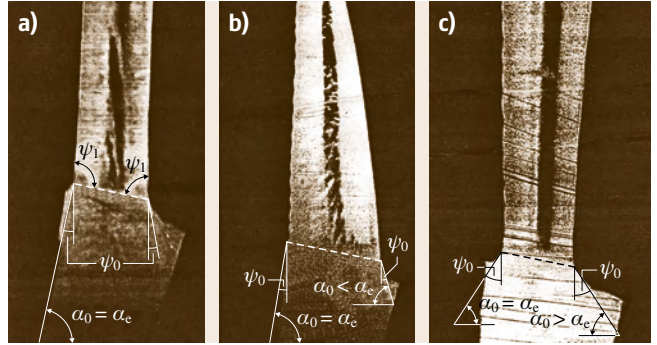


Fig. 16.17a–c TPS growth of a thin sapphire filament, the shaper being skew: (a) constant cross section, (b) widening from the right, (c) constriction from the right

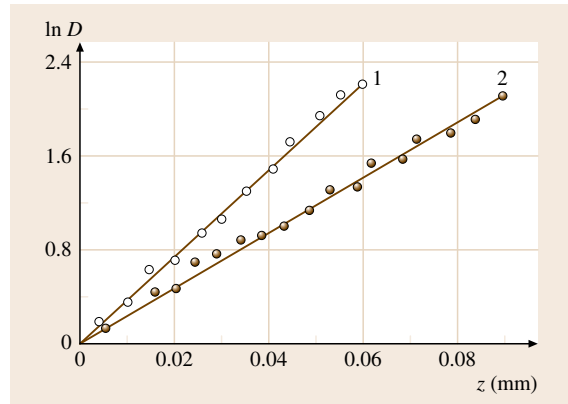


Fig. 16.18 Sapphire filament constriction (1) and widening (2) in the transient range

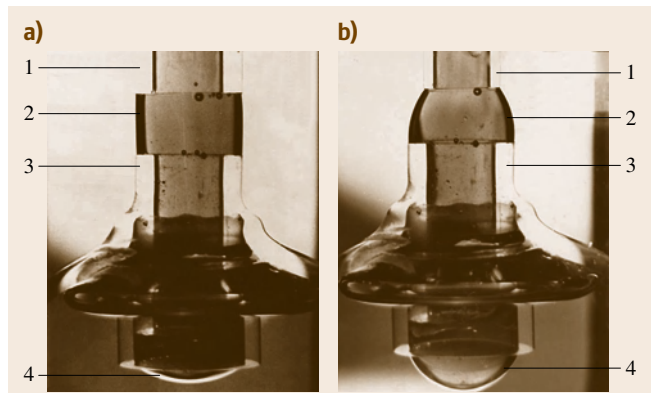


Fig. 16.19a,b Meniscus model of pulling a circular rod under zero-g conditions: (a) right circular cylinder, (b) convex

sule landing), and its physical-chemical properties are well known.

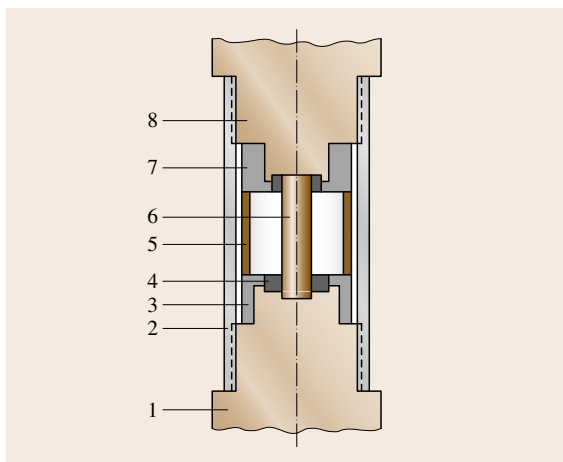


Fig. 16.20 Design of the capsule used to investigate the crystallization process from a melt under microgravity conditions (notations given in the text)

The technique of capillary shaping was preliminary used to produce a rod specimen in an evacuated enclosure. This enables us to reduce the amount of gas in the metal. Specimen (6) in the form of a cylinder, 5–8 mm in diameter, and about 5–6 mm long (Fig. 16.20) was placed between two molybdenum shapers (1) and (8) into which copper (4) was fused preliminary. This guaranteed complete wetting of the shaper during the space experiment. Two graphite guard rings (3) and (7) were introduced to prevent the escape of the melt beyond the sharp lip of the shaper. These rings were supported by the graphite spacer (5), which also acted as a thermal shield. Both shapers were pushed into the coupling tube (2). The above design ensured rigidity, simplicity of assembly, and constant separation between the shapers. Tungsten-rhenium thermocouples were mounted near the ends of the specimens to estimate the temperature distribution along its length. The capsule was inserted into a heating device using the energy of the exothermic chemical reaction. The device did not contain any movable parts. The experiment was carried out by the following way. When a microgravity conditions had achieved, the specimen was completely melted. After that during the microgravity existence, a directional crystallization of the melt column was realized by the heat removing from the upper shaper. On the high-altitude rockets, we had no photographic facilities for recording the crystallization process. Therefore, the shapes of the crystallized specimens had examined experimentally and was compared with the calculated for $\psi_0 = 0$ ones. Figure 16.21 confirms:

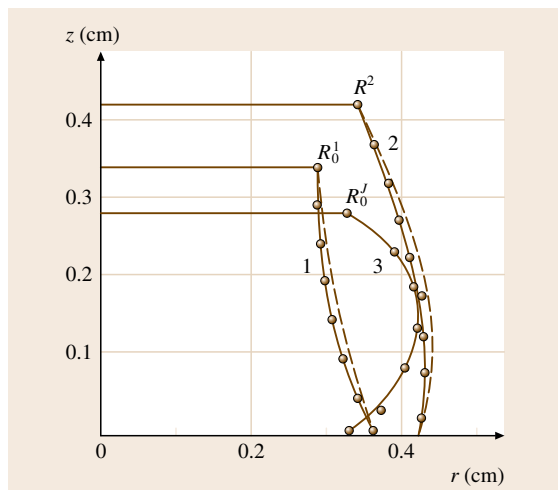


Fig. 16.21 Calculated profile curves of the melted copper columns (dotted line) and crystallized specimens (continuous line) for different (1, 2, 3) internal meniscus pressures; experimental data for the crystallized specimen shape are indicated by bullets

1. Our model of capillary shaping is applicable for a crystal growth in the conditions of microgravity.
2. Under recorded by the thermocouples crystallization speed 5–7 mm/min, $\psi_0 = 0$ for Cu crystallization.
3. The melt did not flow on the crystal surface during the crystallization; therefore, the crucible-free zone melting and capillary shaping crystal growth could be realized in the space.

A little later, these crystallization processes were realized in the *shape* and *ribbon* experiments.

Shape Experiment. The main idea of the experiment was to realize a crystal growth by using the right cylindrical melt column which can not exist in the terrestrial condition (except a filament growth). Under microgravity (Figs. 16.15 and 16.19a), such a column of melt is formed if $R = r_0$; $\alpha_0 = \frac{\pi}{2}$ under pressure d , satisfying equality $2dr_0 = 1$, but, reaching the altitude $h \approx \pi r_0$, it loses static stability and transforms first to a meniscus, its profile curve having an ambiguous projection onto the abscissa axis, and then with increasing h , it falls into two independent meniscus. At $h < \pi r_0$ and $d = 0$, a meniscus is a catenoid; with increasing pressure its curvature in the axial cross section decreases, reaching infinity at $2dr_0 = 1$. When pressure increases above this value the meniscus becomes convex (Fig. 16.19b).

A cylindrical meniscus can be used for a crystal growth only at $\psi_0 = 0$, which means that a metal should be chosen for the material grown experimentally (for metals the angle of growth is usually close to zero). In 1984, under microgravity, at *Salyut* orbital space probe, crystallization of indium was carried out by big group of Russian scientists governed by the author of this chapter [16.6, 50, 52]. The advantage of indium is its low melting temperature (156 °C). It is very important for the simplicity of the space furnace and the limited energy power on the space craft board. Here are some other In physical characteristics: a comparatively high density in a solid state (7.28 g/cm³) which only slightly differs from that of the melt (7.03 g/cm³), the surface tension of the melt $\gamma = 592$ erg/cm², and capillary constant under terrestrial conditions $a = 0.41$ cm.

Figure 16.22 depicts a scheme of the growth device. A plastic case (1) with a lid (2) has a graphite container (3) filled with indium preliminary. A resistive heater (4), separated by a foam-polyurethane layer (5), is used. The heat is delivered to the container through a copper capsule (6), which also serves for holding a copper cap (7) (shaper itself) and supplied with a hole for leveling the inert gas pressure inside and outside the container (3). The meniscus of melt (8) is formed first between the initial copper rod (9), fastened to a rod (10), and the edge of the shaper (7). The meniscus shape is fixed by a photo camera with an illumination system of windows (11). The most important part of this setup was the system of maintaining a pressure inside of meniscus by means of a melt meniscus formed near the crucible bottom. The pressure depends on the radius R of the graphite container and a wetting angle. The idea had been suggested by the author of this chapter and was used either for the *ribbon* experiments. Figure 16.23 depicts the shape of a drop (a), formed at the edge of the shaper, and of the meniscus of melt (b). Pressure, which had been found from the shape of the drop (Fig. 16.23a), exceeded approximately by 40% that required for formation of a cylindrical column. A reason of non accuracy is evident – there are a lot of factors (a hysteresis included) governed by the wetting angle. Some of them could be found only under real space conditions and could not be taking into account before. Unfortunately, we did not have any possibility to repeat the same experiment with the correction. But the main aim of the experiment was achieved: the typical shape of a meniscus has the ratio $h/r_0 \approx 3.6$ (10 mm) that one order exceeds terrestrial TPS growth conditions. After the seed rod was wetted with the melt, it was pulled at the speed $V \approx 3$ mm/min. The pulling

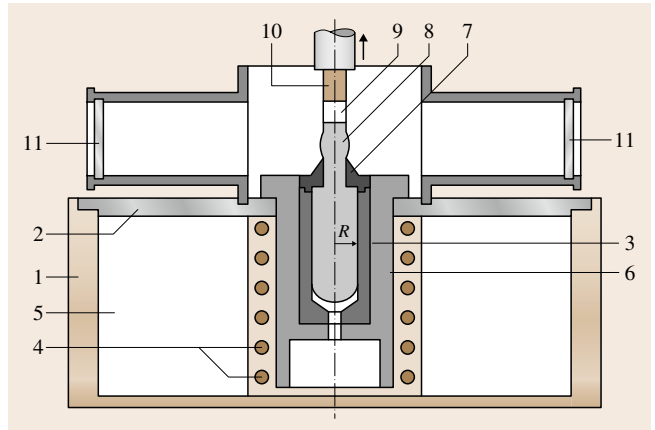


Fig. 16.22 Experimental setup for space crystal growth (notations given in the text) in the *shape* experiment

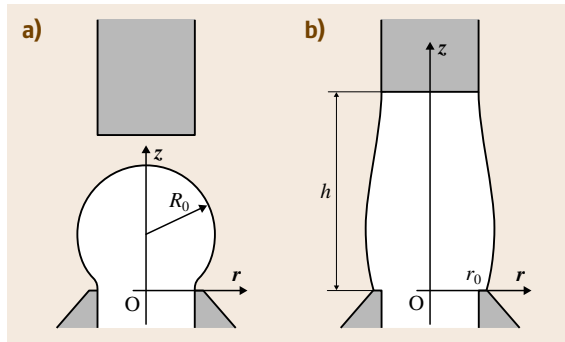


Fig. 16.23a,b Melt drop at the edge of the shaper (a) and the meniscus formed thereupon (b) in the *shape* space experiment

speed of the test indium specimen, grown with the analogous device in terrestrial conditions, could not be elevated above 0.2 mm/min. The flight specimen diameter was ≈ 5.6 mm, whereas it was 2.9–3.2 mm of the test one. No special regulation systems were used, but it is evident that both pulling processes were stable. The both samples were mainly single crystals in structure.

Ribbon Experiment. The crystallization of ribbons from the melt of Ge and GaAs in the orbital station *Mir* is the next example of TPS realization at microgravity conditions [16.6]. The melt is placed in a fixed gap between two non wettable flat plates (Fig. 16.24). The right part of the melt is a free surface of the $1/r$ curvature which depends on the wetting angle and the distance $2r_0$ between the plates. It was the same idea,

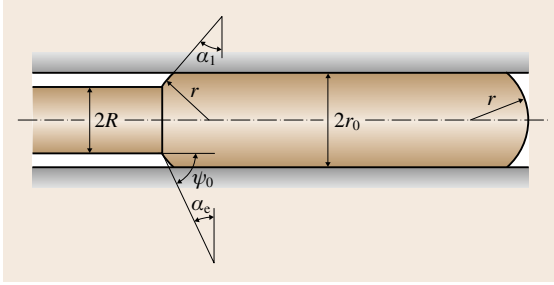


Fig. 16.24 Schematic drawing of tape growth in the *ribbon* space experiment

which before had been realized in the *shape* experiment, to maintain a definite pressure inside the growth meniscus by the curvature of the melt free surface. The growth meniscus projection in the gaps between the walls and the growing crystal are the circular arcs of the same radius r . It is the realization of *TPS* with the wetting boundary conditions on the walls of the shaper. The employment of unwetted walls has to be successful, if the following inequality is fulfilled

$$\alpha_1 = \Theta - \frac{\pi}{2} > \alpha_0 = \frac{\pi}{2} - \psi_0, \quad (16.41)$$

that is

$$\Theta > \pi - \psi_0.$$

Here Θ is the wetting angle and ψ_0 is the growth angle.

The ribbon thickness $2R$, the capillary coefficients A_{RR} and A_{Rh} are the following ones

$$2R = \frac{2r_0 \sin \alpha_0}{\sin \alpha_1}, \quad (16.42)$$

$$A_{RR} = \frac{-V \sin \alpha_1}{r_0 \cos \alpha_0}, \quad (16.43)$$

$$A_{Rh} = \frac{-V \sin \alpha_1}{r_0 \sin \alpha_0}. \quad (16.44)$$

The both capillary coefficients are negative and there is a capillary stability. For the common dynamic stability estimation, the heat coefficients (16.31) and (16.32) can be used: $A_{hh} < 0$, $A_{hR} > 0$. Therefore, with respect to (16.22) inequalities fulfilled, the dynamic stability of the scheme under investigation is provided.

At the flight experiments, Ge and GaAs ribbons were grown between pyrocarbon plates. Unfortunately, a heating regime was not optimal, the seeds were melted and the ribbon structures were polycrystalline [16.6]. But smooth surfaces and constant thicknesses of the ribbons, grown without any special regulation, is an evidence of the process stability.

16.6.4 Impurity Distribution

Impurity distribution in crystals grown by the Bridgman, *CZT* and *FZT* is studied rather thoroughly, however extension of the mechanisms known to thin-profile growth using *TPS* can lead to wrong conclusions. Application of the Burton–Prim–Slichter equation [16.55] to calculation of the impurity distribution effective coefficient K requires specification of the boundary diffusion layer thickness. In case this thickness is assumed to be equal to the total height of the meniscus and the shaper capillary channel, $K = 1$ for any impurity [16.56] that does not correspond to reality. The present section gives a model of impurity transfer for the *TPS* under consideration that allows relating K -values to the parameters of capillary shaping and feeding [16.6, 57]. Figure 16.25a illustrates the case of a thin tape growth.

Stationary process is considered; it is assumed that the melt in the zone of the meniscus and the capillary channel is not stirred and the conditions of complete stirring are maintained in the crucible. Under the assumptions made, an impurity transfer in the meniscus is described by

$$D \left(\frac{d^2 C}{dr^2} + r^{-1} \frac{dC}{dr} \right) = -V \frac{dC}{dr}, \quad (16.45)$$

with the following boundary condition at the crystallization front

$$-D \frac{dC}{dr} \Big|_{r=r_0} = V_0 (1 - K_0) C(r_0). \quad (16.46)$$

Here C denotes impurity concentration in the melt, D is the diffusion coefficient, K_0 is the impurity distribution equilibrium coefficient, others notations are given in Fig. 16.25a.

The polar coordinate system chosen allows easy specification of the melt-flow rate distribution in the meniscus $V(r) = V_0 r_0 / r$. Then (16.45) is rearranged into the following form

$$\frac{d^2 C}{dr^2} + r^{-1} \left(1 + \frac{V_0 r_0}{D} \right) \frac{dC}{dr} = 0. \quad (16.47)$$

Impurity transfer in the capillary channel is described by the equation

$$D \frac{d^2 C}{dz^2} = -V_c \frac{dC}{dz}, \quad (16.48)$$

with the following boundary condition

$$C|_{z \rightarrow \infty} \rightarrow C_\infty. \quad (16.49)$$

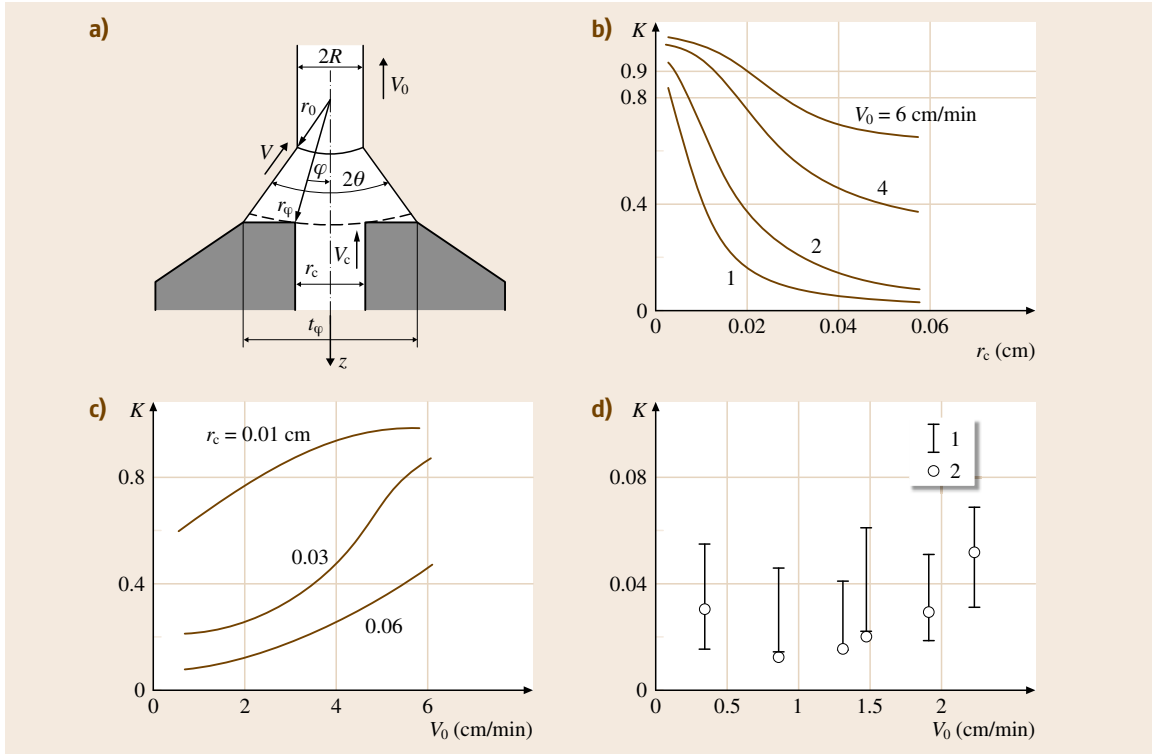


Fig. 16.25a–d Calculating the impurity distribution effective coefficient K (a) diagram; (b) $K = f(r_c)$ – calculated; (c) $K = f(V_0)$ – calculated; (d) comparison of experimental (1) and calculated (2) K -values from (16.50) for the In distribution in thin-walled shaped Si crystal

It is assumed that the impurity concentration in the bulk of the melt C_∞ is constant in the process of tape growth. The solution of the problem relates the value of the impurity distribution effective coefficient K to the parameters of the crystallization conditions (V_0 and $2R$), with the conditions of capillary shaping (t_ϕ , r_c , Θ) and the impurity characteristics (D and K_0)

$$K = K_0 / \left\{ K_0 \left[1 + \left(\frac{\Theta r_c}{\phi t_\phi} - 1 \right) \cos \phi \right] + (1 - K_0) (1 - \cos \phi) \left(\frac{2R}{t_\phi} \right)^{V_0 R / D \sin \Theta} \right\} \quad (16.50)$$

If the width of the capillary channel r_c reaches its maximum value t_ϕ , equation (16.50) is reduced to

$$K = K_0 / \left[K_0 (1 + (1 - K_0) \times (1 - \cos \phi) \left(\frac{2R}{t_\phi} \right)^{V_0 R / D \sin \Theta} \right] \quad (16.51)$$

Figure 16.25b shows $K = f(r_c)$ calculated for aluminum impurities in silicon. The following values are used: $K_0 = 0.002$, $D = 0.53 \times 10^{-3} \text{ cm}^2 \text{ s}^{-1}$, $2R = 0.03 \text{ cm}$, $t_\phi = 0.06 \text{ cm}$. Figure 16.25c presents $K = f(V_0)$ calculated from (16.51) for various r_c values. It is obvious that K increases with V_0 (and as a result V_c) increasing. Under actual conditions of growing thin-walled profiled silicon crystals $K_{Al} < 1$. Processing of the data of [16.58] gives the value of $K_{Al} = 0.039$ in silicon, which agrees very well with the value of $K_{Al} = 0.3\text{--}0.4$ calculated from (16.50) in accordance with the initial data of [16.58].

Figure 16.26 gives data on sulfur distribution along the axis of a TPS silicon tape obtained by laser emission microanalysis (LEM). The ratio of the sulfur spectral line strength J_S to that of silicon J_{Si} (the ratio is proportional to the concentration of the element analyzed in the silicon matrix) is plotted on the ordinate. The rate of tape pulling was equal to 12 mm/min. Increase of sulfur concentration in the silicon tape in the process of its pulling shows that $K_S < 1$ (it is assumed that

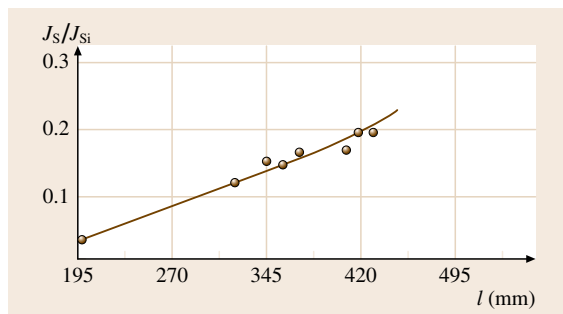


Fig. 16.26 Sulfur distribution along the length of a silicon tape (LEM data)

for sulfur impurity in silicon $K_0 = 0.001 \times 10^{-3}$). While analyzing other impurities, no explicit regularities were observed.

To verify the main equation (16.50) a series of 0.01 mass indium-doped silicon tapes was grown. The mass of each tape-shaped crystal did not exceed 7% of that of silicon charged into the crucible. The tape thickness $2R$, the shaper transverse dimension t_φ , the capillary slot dimension r_c , the growth rate V_0 were measured. Then photometrical spectral lines of indium in the crystals grown and in the crucible residue were drawn. The measurement accuracy of the indium distribution effective coefficient was equal to (40–50%). The results obtained are depicted in Fig. 16.25d. Vertical arrows indicate experimental results, circles show the values calculated from (16.50) in accordance with the above mentioned

parameters. The values of $D = 0.52 \times 10^{-3} \text{ cm}^2 \text{ s}^{-1}$, $K_0 = 0.4 \times 10^{-3}$ are assumed for indium impurity in silicon. The results shown in Fig. 16.25d do not allow plotting K versus the growth rate V_0 since the thickness of a silicon tape, $2R$, decreases with V_0 increasing (the value of $2RV_0$ practically was constant in the experiments), and they can only demonstrate satisfactory agreement between calculated and experimental values. The values of K calculated from the Burton–Prim–Slichter equation are equal to 0.8–0.9, i.e., they are some orders of magnitude greater than the experimental values.

Impurity distribution along the widths profiled crystals is to a great extent determined by the technique used to feed the melt to the growth meniscus. In Fig. 16.27a,b resistivity ρ distributions across of silicon tapes, grown under the conditions of the two versions of meniscus melt replenishment, are compared. The shaper shown in Fig. 16.27d possesses one long capillary slot, while the shaper given in Fig. 16.27e has two short slots at its end faces. The same feeding system was used for the sapphire ribbon growth. A diffusion reflection of light (Fig. 16.27c) indicates a bubbles concentration at the center of ribbon. The following explanation of nonuniformity of impurity distribution across the crystal (Fig. 16.27a–c) observed can be offered. In the case of horizontal melt flow in the meniscus from the shaper edges towards its center, impurities with $K < 1$ driven off by the growing crystal accumulate in the central part of the meniscus. Hence, corresponding distribution of

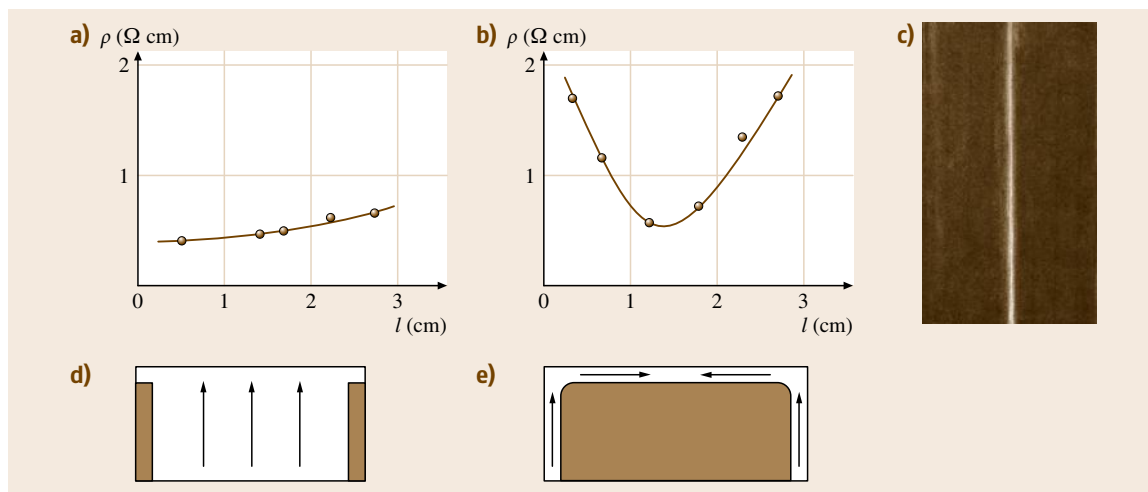


Fig. 16.27a–e Impurity distribution across ribbons using two different versions of melt replenishment of the meniscus: (a) silicon ribbon and (d) corresponding feeding scheme; (b) silicon and (c) sapphire ribbon and (e) corresponding feeding scheme

capillary channels in the shaper allows controlling impurity distribution at the cross section of crystals being grown.

16.6.5 TPS Definition

On the basis of the theoretical analysis, accomplished above, we can define TPS:

TPS is the shape crystal growth technique which uses a solid body (shaper) to define a melt meniscus shape by means of either catching (on edges of the shaper) or wetting (on surfaces of the shaper) capillary boundary condition to obtain the crystal of predominant cross section and impurity distribution as a result of pulling it in a dynamically stable regime.

This definition follows from our analysis of capillary catching and wetting boundary conditions, completed in 1967 and published for the first time in 1968 [16.38], as well as from our dynamical stability analysis with a capillary shaping, completed in 1970 and published for the first time in 1973 [16.14]. Now, on the basis of this definition, we can analyze a TPS development history.

16.6.6 TPS Brief History

A development of shaped crystal growth for industrial application was begun from the set of papers [16.59–63] published in 1958–1959. The papers [16.59, 60] informed that during 1938–1941, Russian scientist A.V. Stepanov had carried out experiments concerning pulling of shaped polycrystalline and single-crystalline specimens (sheets, tubes and so on) from melts of some metals, especially aluminum and its alloys. The Second World War interrupted these experiments and they have been continued since 1950s in the Physical and Technical Institute of the USSR Academy of Sciences. During 1950–1958 few Stepanovs collaborators, especially postgraduated students *Shakch-Budagov* and *Goltsman*, continued these experiments with low-melting metals and alkaline halides. The papers [16.61–63] described the main results of these experiments. The author of this chapter has been a participant of the below described events because in 1959 he began a scientific activity as the undergraduated student in the Stepanov's laboratory.

In 1963 Stepanov formulated his global idea [16.64]:

it is necessary to find a way to pull all types of industrial profiles from melts of aluminum, steel and

other alloys. It could save energy, and eliminate extruding, rolling, cutting and many other types of mechanical treatments.

It was a basis of large investigations in the field carried out in the Stepanov's laboratory. Two main directions were being developed:

1. Polycrystalline metals and alloys
2. Semiconductors single crystals.

The author of this chapter was nominated as the head of the first direction. First of all, *Stepanov* and *Tatartchenko* decided to demonstrate the possibilities of the technique as widely as possible. For this, *Tatartchenko* designed an installation for the continuous production of aluminum tubes. During development of the installation, a lot of technical problems were solved [16.65]. The installation was completed in 1963. It contained two connected crucibles: the first for feeding and a second for the pulling of 6 mm diameter tube, automatically wound on a coil. During testing of the installation, specimens of tubes with a length up to 4000 m and a speed of pulling up to 15 m/h were obtained. The installation was made very compact to demonstrate its operation at different exhibitions. In 1964, the installation was shown in Italy. There was a full success: many articles described a new metallurgical technique. After that, a second variant of the installation was developed for the production of the aluminum profiles of different complicated cross sections with lengths up to 3 m [16.10]. The operation of it was demonstrated at exhibitions in Hungary (twice in 1967), in Italy (1968), in Czechoslovakia (1971). Examples of aluminum profiles obtained with this installation are presented in Fig. 16.28. A possibility to use the technique for steel profiles and combined aluminum-steel profiles pulling was either demonstrated by the author of this chapter [16.66] (Fig. 16.29).

In the application of the technique for single crystals pulling, the laboratory intensively was working with the huge industrial germanium project. Some industrial laboratories and plants were included in the project and, at the end of the 60s, in the former Soviet Union, about 85% of the germanium was produced as shaped crystals. For instance, for electronic applications, instead of one crystal by the CZT, 26 round cylindrical crystals with the diameter of 10.0 ± 0.1 mm we pulled, from the same crucible, without any special control [16.10]. The author of this chapter participated in the project by developing the theory described above as well as the application of the theory for the technology (e.g. [16.67]).



Fig. 16.28 Aluminum heat exchangers and other profiles grown by TPS in Stepanov's laboratory by the author of this chapter with collaborators

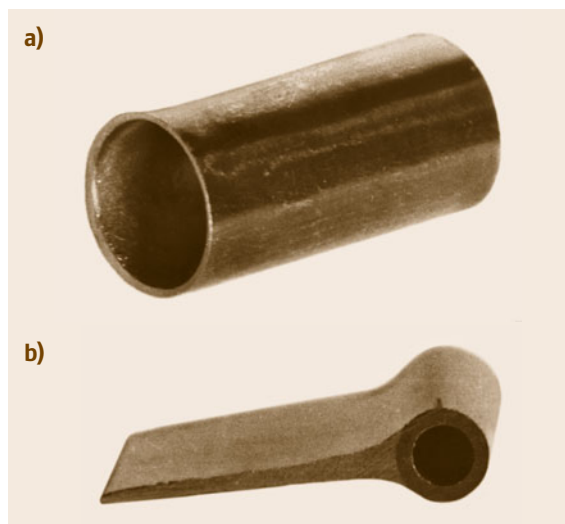


Fig. 16.29a,b Steel tube (a) and steel tube with Al rib (b) grown by TPS in Stepanov's laboratory by the author of this chapter

Up to 1967 shaped crystal growth was developing only in the former Soviet Union. The publication of the information concerning shaped filaments growth [16.68, 69] and especially edge defined film fed growth (EFG) [16.70] changed the situation drastically: Shaped crystal growth appeared in the USA. It was a beginning of shaped crystal growth spreading in many

scientific groups, especially for the sapphire and silicon growth. As for former Soviet Union, the shaped crystal growth direction has continued the development. Since 1968 every year, Russian National Conferences has been organised with publication of the special Proceedings (e.g. [16.38]) as well as special issues of Bulletin of the Academy of Sciences of the USSR, Physical Series (e.g. [16.39]). All variants of pulling techniques from the shaper were named Stepanov's technique. In 1972, A.V. Stepanov died. His laboratory has continued to work. The author of this chapter was invited as the head of the Crystal Growth department in the Solid State Physics Institute of the Academy of Sciences of the USSR. In the frame of the department, the shaped crystal growth laboratory was organized with the stuff of 40 persons. Many theoretical and experimental aspects of shaped growth, Space growth included, were developed there. The main competitor during long time was being the Tyco laboratory where EFG growth was developing for sapphire and silicon. In 1978, the author of this chapter visited the Tyco laboratory and had very interesting discussion with La Belle, the author of EFG patent. That time, it was impossible to imagine that he would work in this laboratory (later Saphikon, and Saint-Gobain Crystals) as the chief scientist twenty four years later.

Now, shaped crystal growth is widely spreaded but there are a lot of titles used, especially EFG and Stepanov's technique. We are sure the situation must be clarified. As for us, since 1980s, we have preferred not to use the title Stepanov's technique neither EFG. We insist to combine all these techniques by the title *technique of pulling from shaper (TPS)*. Here are the reasons of that.

A priority in applying of a shaper (holes in plates placed onto the melt surface for shaping melt-pulled crystals) belongs to Gomperz [16.71]. In 1922, he used mica plates floating on melt surfaces to pull Pb, Zn, Sn, Al, Cd, Bi thin filaments through holes in the plates. Sometimes the filaments had a single crystalline structure. In 1923, the same technique was used either for filaments pulling [16.72]. In 1929, for Zn single crystalline filaments growth, for the first time, a single crystalline seed was used [16.73]. In 1929, the technique was titled Czochralski-Gomperz technique [16.74, 75]. In 1928, P. Kapitza, later the Nobel Prize rewarded, used this technique for Bi rods growth [16.76]. So, during 1922–1931, six papers concerned with a shaper using were published. Moreover, the technique was titled as a CZT modification Czochralski-Gomperz technique. Hence, Stepanov

does not have a priority. Never in his publications, have we found any of these six references. What about the explanation of the shaper functions? He is one of our coauthors of [16.38, 39] papers, explaining catching and wetting boundary conditions. On the other hand, at the same time his name as a coauthor we can see in the [16.41] publication, the no applicability of which to shaped growth we explained in some our papers, among them with Stepanov's participation [16.43]. This absurd situation does not need any comments [16.7]. In [16.64] Stepanov pretended to have invented:

the principle of shape formation from a melt, using capillary forces or some other actions (except of crucible walls) on the melt, of the cross section or an element of a cross section of solid profile its following crystallisation.

This is a typical *umbrella* formulation which covers CZT, VT, FZT techniques as well as electromagnetic, ultrasonic, inertial and other possibilities of shaping. It can not be discussed seriously. At the same manuscript we read:

A shaper should be distinguished from a die. A die is the embodiment of a brute force. A shaper is a more spiritual system. Its aim, first of all, is to provide a delicate effect on the curvature and shape

of the mobile column of the liquid melt stretching itself behind the crystal by creating new boundary conditions along its contour.

We agree that there is a big difference between a die and shaper, but in spite of Stepanov's big role in the TPS spreading [16.7], *new boundary conditions* never have been specified in Stepanov's papers. We think there is sufficient quantity of arguments not to use the title Stepanov's technique. On the contrary, our capillary shaping analysis of TPS, that has been done in 1968 [16.38] is completed: It is impossible to suggest something new, beside catching or wetting if using a shaper. From this point of view EFG technique is simply TPS with catching boundary condition. Probably, this is because of a low level of patent experts that the independent EFG patent exists. Edge defined condition for meniscus was published in our paper [16.39] as catching boundary conditions before the EFG patent appearance. We only agree that capillary feeding was described in the EFG patent for the first time. Certainly, many shaped growth schemes of TPS have peculiarities and we will discuss some of them below.

Now we will describe shaped crystal growth of few materials. The most impressive results of TPS industrial application were obtained for sapphire and silicon. Furthermore structures of shaped sapphire and silicon have a lot of peculiarities.

16.7 TPS Sapphire Growth

Sapphire belongs to the family of corundum crystals. The term corundum designates α -aluminum oxide. Pure corundum crystals are colourless and are named *leucosapphire* ones. But now the name *sapphire* crystals is very often used, although historically the title *sapphire* crystals has been applied to the blue corundum ones. Different colours of corundum can be obtained by the addition of different metallic oxides to aluminum one. Natural and synthetic red ruby contains 1–7% chromium oxides. Synthetic alexandrite is produced by the addition of vanadium oxide. 1% titanium and 2% iron oxides give a blue colour. Nickel oxide gives a yellow colour. An addition of vanadium and cobalt oxides imparts a green colour. Green crystals are also produced if the chromium content exceeds 8%.

The application of TPS for sapphire is an example of the most successful one because of coexistence of few factors [16.8]: First of all, it is a demand for

advance techniques of a material with unique physical and chemical properties: high melting point, exceptional hardness, transmission over a wide band of wavelengths, radiation and chemical resistance. Secondly, exceptional hardness of sapphire hinders its machining if it could be grown by other techniques. Thirdly, it has been impossible to growth very big crystals (for instance, optical windows 320 x 500 mm² for aircrafts and spacecrafts) by using other crystal growth techniques. Fourthly, chemically resistant and wettable materials (W, Mo, Ir) have been found for shapers.

La Belle and *Mlavsky* were the first who grew shaped sapphire crystals. In [16.68] there was information concerning shaped filament growth without any detail. In [16.69, 70, 77] edge defined film fed growth, EFG, technique was described. EFG corresponds to the scheme Fig. 16.4e, i.e., TPS with a catching boundary

condition. A peculiarity of EFG is a capillary feeding. The capillary together with wettable shaper facilitates a seeding. It is important to repeat once more that the capillary from Fig. 16.4e serves only for feeding and does not participate in the capillary shaping: the meniscus, caught on the edge of a shaper, changes its curvature with forming a negative pressure inside, and raises the melt above the shaper edge, up to the crystallization front.

16.7.1 Modifications of TPS

The presence of the shaper in TPS allows many manipulations during growth. The variable shaping technique VST described for the first time in [16.79], gives a possibility to change a cross section of crystal (periodically if it is necessary) during of pulling. Monocrystalline sapphire profiles, grown by TPS and VST by the authors with collaborators in the Solid State Physics Institute of Academy of Sciences of Russia, are presented on the Fig. 16.30. VST is based on controlling the melt mass flow towards the crystallization interface when passing to a new specific cross section shape. One of VST variants described in [16.78] is shown on the Fig. 16.31. The scheme allows not only changing the shape of the crystal but also its composition. It works by the following way: At the beginning both channels 5 and 6 plunged in the melts but, only through capillary channel 5, melt reaches the shaper edge. As a result, during a first stage, a tube (cross section A) grows. Because of a vacuum, formed inside of the growing tube, the other melt through non capillary channel 6 reaches the shaper edges and, during a second stage, the rod of two different compositions grows (section B). During the thirds stage shown on the diagram, the feeding

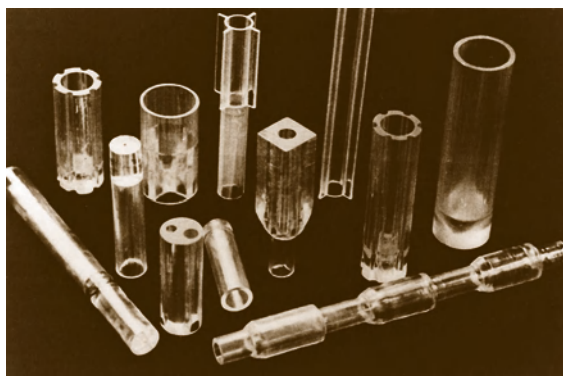


Fig. 16.30 Monocrystalline sapphire profiles grown by TPS and VST

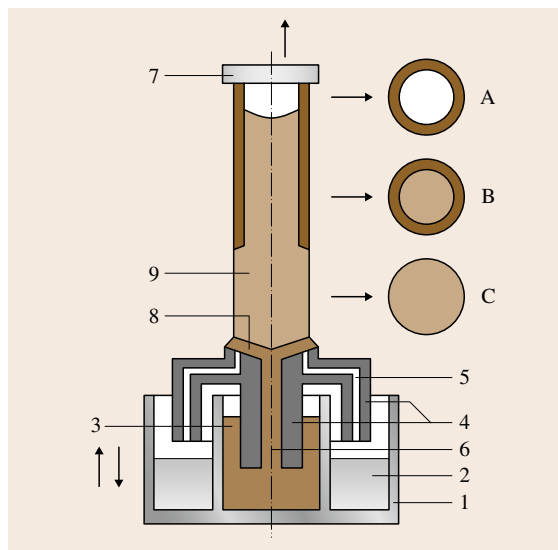


Fig. 16.31 The scheme from [16.78] for growth at various cross sections and various compositions crystals: 1 – crucible; 2 – undoped melt; 3 – doped melt; 4 – shaper; 5 – capillary feeding channel; 6 – noncapillary feeding channel; 7 – seed; 8 – meniscus; 9 – growing crystal; A, B, C – cross sections of the different parts of the growing crystal

through the channel 5 is eliminated by the crucible lowering (section C). By the similar way, changing of shaper plunging in the melt, different edges or walls of the shaper can operate by turns. As a result, we obtain a variety of shaped crystals, examples of which are presented on the Fig. 16.30. There is very interesting modification of TPS used especially for a dome growth [16.80]. There the seed is rotated around horizontal axes.

The local shaping technique, LST [16.81], shapes only an element of the crystal that we need to grow. During growth, the horizontal displacement of the seed and shaper with respect to each other in combination with rotation and pulling of the seed allows obtaining a variety of shape crystals. Figure 16.32 presents a tube growth: A shaper of a diameter q shapes an element of the tube of thickness $p = r_2 - r_1$. The seed is rotated with the angle speed ω and is moved up with the speed V . A middle tube radius R is equal to a distance between the shaper center and the axe of the seed rotation. Practically any complicated body of revolution, for instance, a dome with the thin wall, can be obtained by this technique. A dynamic stability investigation of LST was carried out in [16.81]. It has to be mentioned that

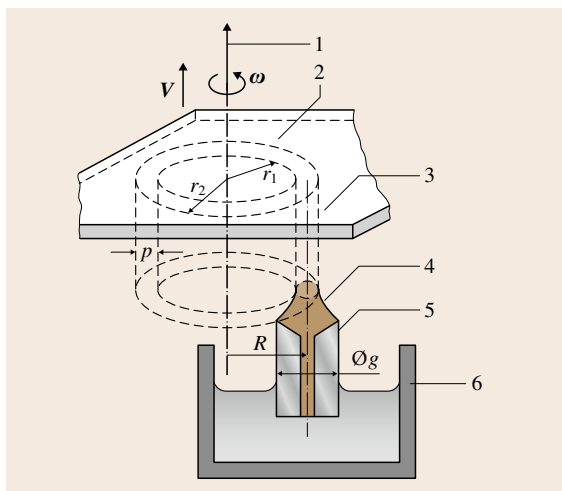


Fig. 16.32 Local shaping technique scheme: 1 – rotation axis, 2 – seed crystal, 3 – growing tube, 4 – melt meniscus, 5 – shaper, 6 – crucible

40 years ago **LST** was being used in our experiments with aluminum growth as well as a vacuum inside of a tube grown for a seeding. Some specimens are shown on the Fig. 16.28.

16.7.2 Crystal Defects

In compared with other crystal growth techniques, the peculiarities of **TPS** crystal defect structures are mainly determined by two factors:

1. High growth speed which, as a rule, one or two orders more
2. Small thickness.

Bubbles are the major defects in shaped corundum crystals (e.g. Fig. 16.27c). There are two aspects of the problem concerned with its appearance in the crystal. The first of them is an enrichment of the melt by gas and the bubble formation in the melt. The second one is a capture of the bubbles by grown crystal.

A vacuum treatment of the melt before the crystal growth reduces the bubble contents in the crystals. This is a proof that a dilution of gases in the melt is one of the sources of its gas enrichment. But there is a more important gas source for the corundum melt. In spite of the aluminum oxide is stable under normal conditions; its heating is accompanied with thermal dissociation, evaporation of some reaction products and coagulation of others. Mass spectroscopic analysis shows [16.82] that the products of dissociation of aluminum oxide are

O^+ , O_2^+ , Al^+ , AlO^+ , Al_2O^+ , AlO_2^+ , $Al_2O_2^+$. The intensity of thermal dissociation depends greatly on the temperature and environment. It is the most intensive if the hydrogen is presented, less intensive in the vacuum and the least intensive in the inert atmosphere (argon, nitrogen). The **VT** improves this thesis. One of the first bubble formation versions in **VT** corundum crystals was concerned with the gas adsorption on the surface of feeding powder particles. But the hypothesis is at variance with the following experimental fact. The γ - Al_2O_3 powder is more friable than α - Al_2O_3 and, therefore, adsorbs more gas on the surface. But corundum crystals grown from γ - Al_2O_3 charge have less bubble inclusions. So, the charge dissociation has to be the main reason of bubble formation because of the hydrogen presence, and α - Al_2O_3 powder is worse because of sticking of α - Al_2O_3 powder particles.

The crucible and shaper presence complicates the situation. Although the problem is not completely understood at this time, the thermal dissociation of the melt because the chemical interaction of the melt with the crucible material seems to be very important cause of the gas appearance in the melt. Here is the list of chemical activity of the main container materials for sapphire crystal growth (from the best to the worst): Ir, W, Mo, Nb, Ta, Zr. As rule, only three first materials are used for the containers. The reaction of Al_2O_3 with refractory metals is generally believed to involve two stages. For example with Mo: $Al_2O_3 \rightarrow Al_2O + O_2$; $Mo + O_2 \rightarrow MoO_2$. In reality, the presence above mentioned aluminum oxide dissociation products does the situation much more complicated. Mass spectroscopic measurements point to the presence of MoO, MoO_2 , MoO_3 ions.

The diluted gases and the gas products of the above mentioned reactions are impurities in the melt and assist a gas inclusions formation in the crystals. Here are two possibilities:

1. As rule, dilution of gases is decreased with the temperature. The liberated gases form the bubbles. The crystal catches the bubble existed in the melt.
2. A nuclear bubble forms on the interface, grows and catches by the crystal.

The surface energies estimation [16.83] deduced that the interface is not an effective heterogeneous site for bubble formation. We agree that this deduction is correct for a flat interface but cavities on the interface can be effective bubble nucleation spots. In any case, the melt layer near the interface has to be preferable for the bubble formation because of enrichment of the diluted

gas rejected by the growing crystal. Direct experiments of the melted zone quenching [16.84] improved this mechanism of the bubble formation.

As other impurities, bubbles can form striations, parallel to the interface. The striations are concerned with the variations of growth rate and captures of the bubbles situated in the melt layer near the crystallization front. Sometimes it is a result of constitutional supercooling. Sometimes long tube similar bubble can be found in the corundum crystals. A mechanism of this type bubble formation suggested in [16.85,86].

In each case, the caverns on the interface, formed as a result of morphological stability loss, provokes the bubbles capture, especially for the big growth rate. In our experiments [16.5,6,87] with ribbons and tubes grown by TPS in the *C*-direction the following results were obtained. At the crystallization rate of order of 0.2 mm/min the bubble practically were absent. In [16.88] the critical growth rate (0.5 mm/min for sapphire) has been calculated below which a foreign particle is not trapped by the grown crystal. The interface is plane below this rate. At crystallization rates 0.75–1.5 mm/min the bubble distribution is in the shape of a treelike pile-up with a branch diameter of up to 1 mm (Fig. 16.33). The ends of ribbon are bubbles free, probably, because of gas diffusion to the melt surface and leaving of the melt. The same result was obtained in [16.83] where small diameter crystals were bubbles free.

The distribution of bubbles over a specimen section normal to the growth direction is shown in Fig. 16.34a,b. The following explanation is proposed for the bubble distribution observed. The plane interface becomes morphologically unstable. Macroscopic concavities, with a diameter to 1 mm, arise on the crystallization front; these concavities are characterized by an enhanced trapping of bubbles. We suppose that the change of position of the concavities on the crystallization front with time depends on the pattern of the convective flows in the melt that leads to the bubble distribution shown in Figs. 16.33 and 16.34a. This process is in accordance with the Mullins and Sekerka [16.20] theory for the lowest frequencies. When growing shaped sapphire crystals at rates of 1–3 mm/min the interface has, as a rule, a convex central part and concave peripheral sections that traps the bubbles (Fig. 16.34b).

As the growth rate is increased further, the entire solid–liquid interface becomes unstable. The crystallization front becomes faceted, with the new interface shape becoming stabilized by the faceting. Figure 16.35

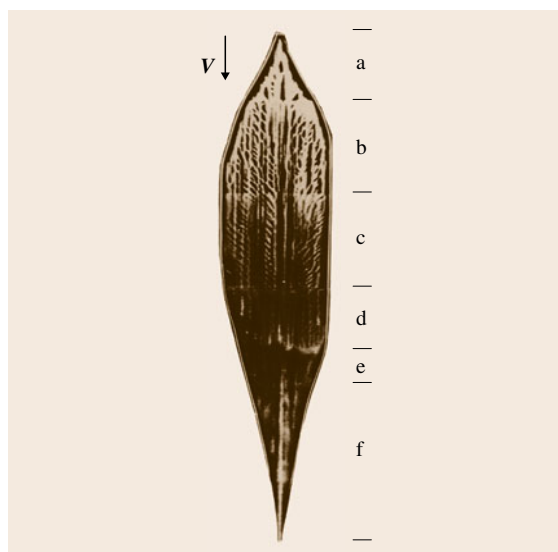


Fig. 16.33 Bubbles in a sapphire ribbon pulled with step changes in the rate V : the arrow indicates the growth direction, V mm/min = 0.75 (a); 1.0 (b); 1.25 (c); 1.5 (d); 1.75 (e); 2.0 (f)

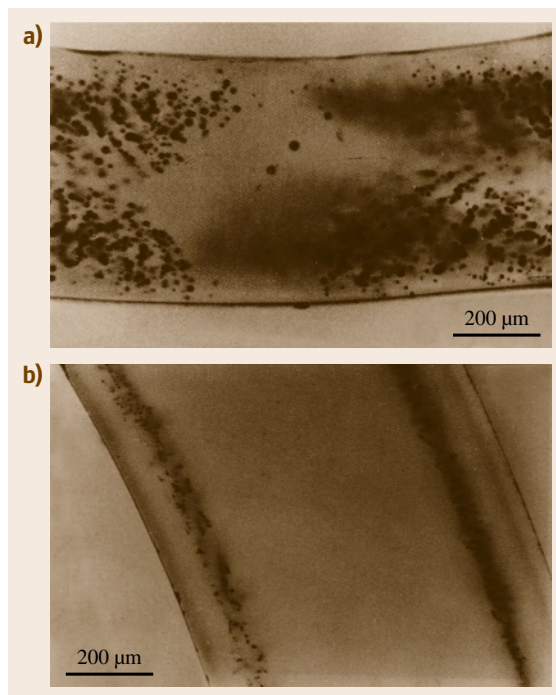


Fig. 16.34a,b Cross section of sapphire ribbon pulled with rate of V (mm/min) = 0.75 (a); 2.0 (b)

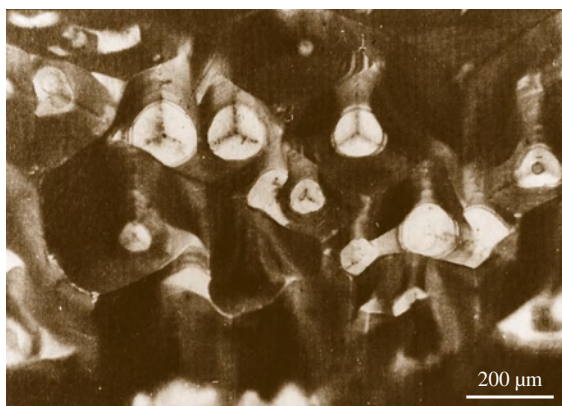


Fig. 16.35 Interface of decanted sapphire ribbon grown with $V = 3 \text{ mm/min}$

shows the decanted crystallization front of a tube faceted by rhombohedral planes. The bubbles distribution in the crystal is a hexagonal pattern and corresponds to the positions of grooves on the interface. Always the bubble agglomerations correspond to cavity positions. The decanted crystallization front of a tube faceted by the $\{11\bar{2}0\}$ and $\{10\bar{1}1\}$ planes is shown in Fig. 16.36a. From geometrical considerations

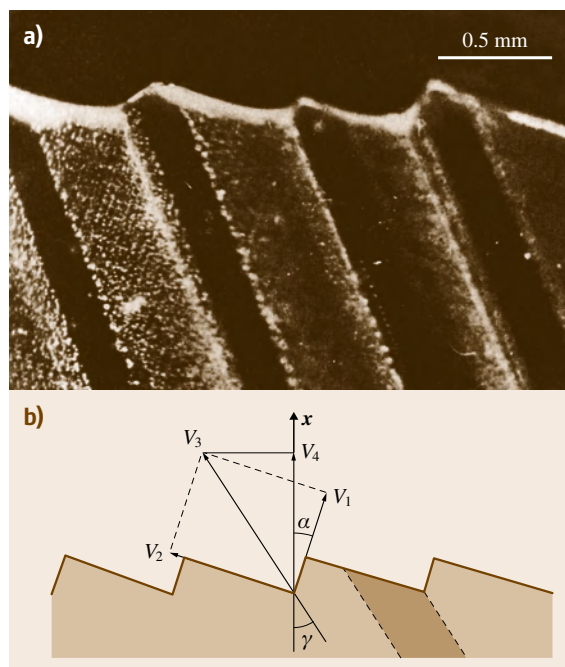


Fig. 16.36 (a) View and (b) schematic of the decanted crystallization front of a tube pulled at $V > 5 \text{ mm/min}$

(Fig. 16.36b), it is apparent that the angle γ between the crystal pulling direction and the direction of the band of void pile-up depends on the ratio of two mentioned faces growth rates.

Solid inclusions are the second type of inclusions. Container material gives metal particle inclusions, sometimes as a result of complicated chain of chemical reactions mentioned above – volatile oxides formation, gas transport in the melt and decomposition of oxides with metal inclusion formation. Experiments show that the small particle of container metal (Ir, Mo), as rule, presents at the crystal. Innumerable experimental data demonstrate that the density of small dimensions (about $10 \mu\text{m}$) inclusions (bubbles and metal particles) is a few orders of magnitude greater than of large dimensions (about $1000 \mu\text{m}$) ones. The low growth speed and low gradients favor to crystal growth with minimum inclusions. Here is an example (American 80/50 standard) of bubbles and solid inclusions requirement for window-grade corundum: maximal allowable size is $500 \mu\text{m}$, and maximal allowable sum of diameters within any 20 mm – diameter circle is $1000 \mu\text{m}$. As rule, modern technology of TPS sapphire meets this requirement.

Dislocations, Low Angle Grain Boundaries, Internal Stresses

Four possible mechanisms of dislocation appearance in the corundum crystals can be postulated:

1. Intergrowth from seed
2. Formation on rough defects (inclusions, grain boundaries, twins) during growth
3. Condensation of vacancies during growth and cooling
4. Plastic deformation during growth and annealing.

Theoretically all dislocations can be identified. The dislocation identification of the first and the second types is evident. The third type dislocations, as rule, have a circle shape because they are a result of collapse of flat round discs obtained by a condensation of nonequilibrium vacancies. The geometry of the last type dislocations depends on two plastic deformation glissile systems $\{0001\} \langle 11\bar{2}0 \rangle$ and $\{11\bar{2}0\} \langle 10\bar{1}0 \rangle$ in the corundum crystals. The first source can be eliminated by necks formation. The second one – by crystal growth without rough defects. The third mechanism concerned with a fundamental physical phenomena, but their density are not significant for the corundum crystals. As to the plastic deformation, it is a main source of dislocations in the corundum crystals.

The defect structure of **TPS** crystals is formed as a result of complex interactions of growth, in situ annealing and cooling. A systematic investigation of the defect structure of **TPS** grown sapphire crystals was carried out both by the optical polarization method and by the technique of widely diverging x-ray beams [16.5, 6, 87]. The tube samples with diameters of 4–40 mm and wall thickness in the range 0.5–3 mm were investigated.

It has been established that, in the absence of low-angle grain boundaries propagating from the seed, the initial part of the crystal does not contain subgrain (or low-angle grain) boundaries. Then, as the crystal grows the dislocation density increases and subgrain boundaries are formed. The disorientation of adjacent subgrains increases with distance from the seed, reaches a certain limit, and then decreases slightly with further growth. The decrease is probably associated with a rearrangement of the subgrain structure; i. e. subgrains with large disorientations branch into a series of subgrain boundaries with smaller disorientations. In addition, there is a decrease in the density of subgrain boundaries which are at large angles to the growth direction. The subgrain boundaries which remain are approximately parallel to the growth direction; the density of these boundaries (with disorientation as high as 5–10° stays constant.

It should be noted that, at high crystallization rates, crystals which are free of low-angle grain boundaries can sometimes be grown. This is probably explained by the fact that the time spent by the growing crystal in the plastic zone is not long enough for polygonization processes to occur. The presence of bubbles is a source of additional stresses which gives rise to dislocation generation and boundary formation. Sub grain boundaries are frequently observed to form along planes of bubbles pile-up. So, we can conclude that the quality of crystals at the beginning, at lower temperature gradient, was better.

Our experience of sapphire crystals growth by different techniques, **TPS** included, allows a statement that only temperature gradient less than 2 K/mm gives the possibility to grow the crystals without low angle boundaries and the dislocation density on the level $\leq 10^3 \text{ cm}^{-2}$. Certainly, the dislocation density is a relative characteristic of crystal because the crystal quality can be characterized only taking into account, as minimum, six dependent parameters:

1. The dislocation density
2. The density of low angle boundaries
3. The degree of subgrain disorientation

4. Residual stresses value
5. Twins
6. Impurity inhomogeneities.

Twins

In the temperature lower than 800 °C single crystal sapphire is essentially brittle and is not deformed by usual dislocation mechanism. A twinning is only mode of deformation. The following two main rhombohedral twin systems in sapphire were identified: $\{01\bar{1}2\} \langle 0\bar{1}11 \rangle$, $\{0\bar{1}14\} \langle 02\bar{2}1 \rangle$.

Twinning process consists of two distinct stages: the twin nucleation and the twin growth. The nucleation stress is higher than growth stress. In [16.89] the nucleation stress for 600 °C was determined experimentally. It is high and strictly depends on surface treatment. It was found as 13–18 kg/mm² for polished specimens and 36–41 kg/mm² for polished and heat treated ones. During growth the stress of twin formation has to be average. It corresponds to the residual stress $\approx 20 \text{ kg/mm}^2$, where the twins can be more often found.

Faceting, Inhomogeneities of Impurity

Faceted growth is a normal mode of some growth techniques. The singular faces appearance on the interface in **CZT** is not very important for sapphire growth but assists nonhomogeneity in ruby growth because the coefficient of chrome distribution is different for faceted and nonfaceted interface. But for **TPS** faceting may be serious defects.

The geometrical form of **TPS** tubes can differ slightly from ideal for reasons of a crystallographic nature. According to the Curie theorem, in the process of growth, there is an interaction between the crystal symmetry and that of the medium (i. e. the thermal environment in which the crystal grows). In the grown crystal, only those elements of symmetry are exhibited which are common both for the crystal and for the medium. That is the reason why grown crystals are faceted depending on the orientation. If a sapphire tube is pulled in the directions $\langle 10\bar{1}0 \rangle$, $\langle 11\bar{2}0 \rangle$ or intermediate ones with $\rho = 90^\circ$ (ρ is the angle between the *C*-axis and the pulling direction), the close-packed basal plane (0001) becomes parallel to the growth direction and facets the tube [16.5, 6, 87]. If ρ differs slightly from 90°, a steplike faceting by the basal plane appears on the lateral surface of the tube. Tubes grown in the [0001] direction are faceted on the outside by $\{11\bar{2}0\}$ planes and on the inside by $\{10\bar{1}0\}$ prismatic planes. Faceting is reduced if the temperature gradient at the

interface increases. The faceting can be explained because of supercooling that singular face needs to grow with the same speed as an isothermal part of interface.

Impurity inhomogeneities are important for ruby crystals. There are macroscopic and microscopic periodic inhomogeneities (striations) along axes of growth. Macroscopic ones concerned with the impurity concentration changing during the growth because of the coefficient of distribution that is not equal of one. **TPS** allows growing of crystals with macroscopically homogeneous distribution of impurity. Microscopic inhomogeneity concerned with the periodic changing of growth parameters or constitutional supercooling.

Growth Direction

The corundum crystal growth in the direction of *C*-axis is very difficult for all techniques of the melt growth, except **TPS**. **TPS** allows growing of all profile crystals in *C*-direction without any problems. And what is more, if we grow corundum filaments without seeds, the spontaneous orientation of the filament coincides with *C*-axis. What is the reason? For many melt growth techniques the growth in the *C*-direction requires an appearance of the singular *C*-plane on the interface. *C*-plane has the lowest growth speed. **TPS** crystals, the filaments especially, grow with high speed. The interface loses morphologic stability and is faceted by the rhombohedral faces, as it is shown on Fig. 16.35. So, *C*-plane does not participate in the growth. As for filament orientation, the orientation of *C*-axes is the most preferable orientation for its growth with respect to Curie principle. On the other hand, the filament interface also is faceted by the rhombohedral faces.

16.7.3 Applications

Special Windows

Application for modern airborne optical reconnaissance systems is one of the most impressive fields of **TPS** sapphire using [16.8]. Practically **TPS** does not have any competitors here. Below are the evidences that **TPS** sapphire meets all requirements for this application:

1. The maximal dimensions achieved are $315 \times 480 \text{ mm}^2$ [16.90]. It is necessary up to 750 mm diameter.
2. It has *high optical transmission* in the 3–5 μm wavelength atmospheric transmission window.
3. Sapphire has a *hardness 9 on the Moose scale* (the hardness of diamond is 10). It is the most durable commercially available infrared window material. It

has the best resistance to erosion by rain and sand of any available window materials.

4. It also has *excellent thermal shock resistance*. But its thermal shock resistance is limited by loss of mechanical strength at high temperature from 70 kg/mm² at room temperature to 20 kg/mm² at 600 °C. Doping or ion implantation with Mg, Ti can double the compressive strength at 600 °C. Heat treatment at 1450 °C in an air atmosphere enriched with oxygen increases compressive strength by 1.5 times. Neutron irradiation with 1×10^{22} neutrons increases the *C*-axes compressive strength by a factor of 3 at 600 °C.
5. It is available routinely with *minimal optical scatter*.
6. *High refractive index uniformity* is achieved because of simple oxide composition. For stringent optical applications, *C*-axes optics is preferred as this is zero birefringence orientation.

Domes

The requirements for rocket nose cones correspond mentioned above ones. The traditional technique of dome production is a mechanical treatment of big sapphire crystals. The effort of production concerned with minimization of treatment by a growth of crystals having a shape close to dome. **TPS** has suggested some successful examples of this kind [16.80, 81, 91].

Substrates

An application of sapphire in electronics as substrate for silicon on sapphire devices was rather large at 1970s. In that case the face {1102} was used. The requirements were not very rigid. But since 1990s, sapphire has been becoming the main substrate material for blue and white laser diodes. The face {0001} is used for the epitaxy. The requirements to the wafers concerning a crystal structure and orientation as well as polishing quality are very high. Sometimes special misorientation of wafer is used to get better deposited layer. It is evident, that this **TPS** application is very promising. But practically there are no publications concerning this topic, except rare ones [16.92], probably because of technological secrets.

Construction Material

Sapphire is increasingly becoming the material of choice for engineers faced with the design challenges of extreme conditions, such as those found in high-temperature, high-pressure or aggressive chemical environment. There are a lot of examples of this **TPS** sapphire product using in the former Saphikon (now

Saint-Gobain Crystals) catalog. The industrial technique of welding of sapphire pieces is developed there. Sapphire tubes, plates and more complicated assemblies are used a superior alternative to quartz, alumina, and silicon carbide: in semiconductor processing applica-

tion (plasma containment tubes, process gas injectors, thermocouple protectors); in spectroscopy and chemical and biological analysis; lamps and lamp envelopes (high intensity lamps, flash-lamps, ultraviolet sterilizations); GaAs backer/carriers; mail sorting optical windows.

16.8 TPS Silicon Growth

Silicon is the second example of the TPS successful industrial application. But this case is not similar to the sapphires one. All numerous attempts to grow shaped Si crystals of electronic grade quality have not been successful because shaped silicon is characterized by the presence of a defect structure influencing its electronic properties. At the same time, a quality of big surface thin sheets obtained is acceptable for no expensive solar cells industrial production. We carried out a complex investigation of shaped ribbons and tubes defect structures [16.93, 94]. The aims of these investigations were to understand why it is difficult to obtain a single crystal structure as well as what is an electric activity of different defects. Its influence on the lifetime of secondary charge carriers is of particular importance, since the efficiency of solar elements is determined primarily by the lifetime of the secondary carriers. It is well known that inhomogeneity of the properties results from the inhomogeneous distribution of electrically active defects. The processes occurring at the solid-liquid (S-L) interface essentially affect formation of defects and their electronic properties as well. The simultaneous study of electric and photoelectric properties of sheet and tube crystals, its defect structure and the S-L interface was carried out. The graphite and the quartz were used as materials for crucibles and the graphite – for shapers.

16.8.1 Shaped Silicon Structure

Shaped silicon crystals possess characteristic defects of their crystalline structures including flat boundaries (most often those of the twinning type), dislocations and pileups thereof as well as SiC particles and particle-aggregations. As a result of twinning along intersecting planes, which can be observed at the initial stage of growth, a stable and quasi-equilibrium structure characterized by existence of defect areas (flat boundaries) perpendicular to the tape plane and parallel to the pulling direction. In this case the silicon tape surface orientation is {110} and the crystallographic axis $\langle 211 \rangle$ coincides with the direction of pulling. Such orientation is formed and maintained irrespective of the seed

orientation and can be attained directly at the seed-crystal contact boundary in case the seed orientation is {110} $\langle 211 \rangle$ or a stable-structure section of the previously grown silicon tape is used as a seed. Figure 16.37 gives a photograph of the surface of a silicon tape of a stable defect structure: SiC inclusion surrounded with dislocation pileups can be observed on the tape surface.

As a result of x-ray structure analysis it was established that the orientation of silicon-tape surfaces can deflect within the range of 15° from {110}. Considerable dimensional fragments of defect structures identical to those of tapes are observed in silicon tubes (Fig. 16.38a). The tube-surface orientation in the vicinity of such a fragment deflects from {110} due to surface curvature. This change in orientation does not cause additional structure defects up to the values equal to 15° and as soon as that value reaches 15° surface orientation abruptly changes because there appears a *severely defect spot* that provides an indispensable turn of the crystal orientation in such a way so that the system of twin-boundary planes should be again approximately perpendicular to the tube surface. Either grain boundaries of a general type or dislocation pileups can act as such defect areas (Fig. 16.38b)



Fig. 16.37 Defect structure of a silicon tape: selective chemical etching pattern, 120 \times ; an SiC inclusion is located in the *center*; the label “H.p.” indicates the direction of crystal growth

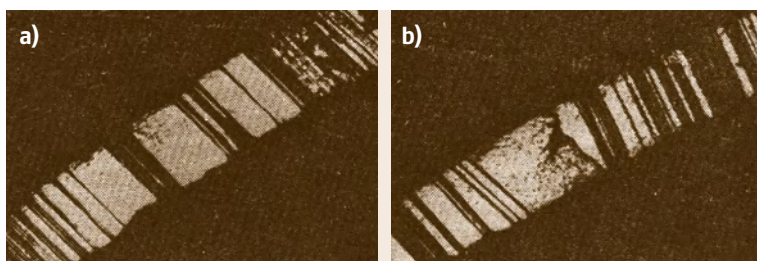


Fig. 16.38a,b Defect structures of silicon tubes (cross-sectional fragments): selective chemical etching pattern, 200 \times : (a) typical structure; (b) defect area providing rotation of the system of twin-boundary planes

Apparently, the number of *severely defect spots* and correspondingly the number of fragments of steady structures is determined by the necessity of closing the system of fragments into a cylinder. Since the angular magnitude of an arc of 30° corresponds to the variation of the tube surface orientation of 15° from {110}, the overall number of defect spots is equal to at least twelve, which is experimentally proved. It should also be noted that this linear length of *severely defect spots* along the perimeter of a tube depends little on its diameter, therefore the relation of the volume of *severely defect spots* to crystal volume should quickly decrease with the tube diameter increasing.

Defect structures of silicon tapes were studied by the TEM. With a ≈ 200 magnification, the defect structure pattern proved to be similar to that of selective etching (Fig. 16.37). It was observed that the width of defective areas is equal to $\approx 5\mu\text{m}$ and the width of monocrystalline regions between them varies from 10–500 μm . Interpretation of fine structures of defect areas, that look like dark lines parallel to the direction of pulling in the pattern of selective chemical etching (Fig. 16.37) revealed that each area represents a set of microtwins 40–200 Å wide (Fig. 16.39). Small-angle

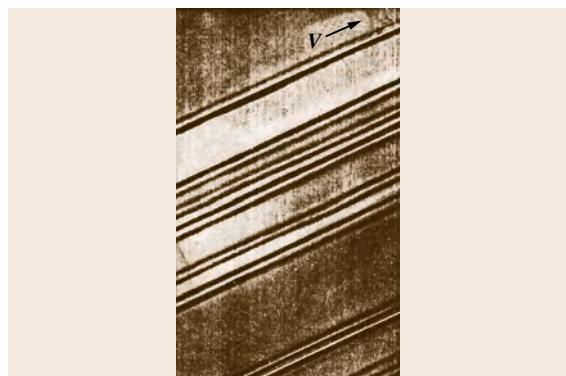


Fig. 16.39 TEM image of a silicon tape: flat defect area structure in the form of a system of microtwins; magnification 160 000; V denotes the direction of crystal growth

disorientation of monocrystalline sections adjacent to the defect area is caused by such set of microtwins. Disorientation measured by the Kikuchi-line technique varied from 40 to 4°. Besides defect areas of twinning nature, other types of defects were observed in 2% of cases. Those included multilayer lattice defects, small-angle dislocation boundaries as well as separate dislocations and inclusions.

To interpret the defect structure and macroscopic pattern of profiled silicon crystal growth, a model, according to which the crystallization front tends to be shaped by the most slowly growing crystal faces {111} while high rates are provided by availability of inlet angles with their vertexes coinciding with twin boundaries, was postulated (Fig. 16.40a). To check the model offered, experiments on investigation of the crystallization front shape visualized by impulse changes in the crystal-pulling rate were carried out. In this case local changes in crystal thickness follow the changes in crystallization front shape, so does the horizontal hatching observed on the surface of profiled silicon crystals (Fig. 16.40d).

Crystallization front shaping by faces {111} proved to be observed only in the vicinity of high-energy boundaries of a general type and at twin boundaries of higher orders, e.g., {111}–{115}. Crystallization front deflection from the flat one does not exceed 2 μm in the coherent-twin region. The overall crystallization front area made by faces {111} is not large; the major part of the crystallization front follows the crystallization isotherm and corresponds to the face close to {112} and in separate cases to {110} (Fig. 16.40b,c) each of which can grow according to the normal mechanism, i. e., both layer-by-layer and normal mechanisms of growth take place when shaped crystals grow.

The specific features of the crystallization front revealed might be associated with the impurity influence on the face free energy or on the growth kinetics. Therefore it can be assumed that front shaping and perhaps inlet angle formation at twin boundaries are not necessary for high rates of profiled silicon crystal growth to be put

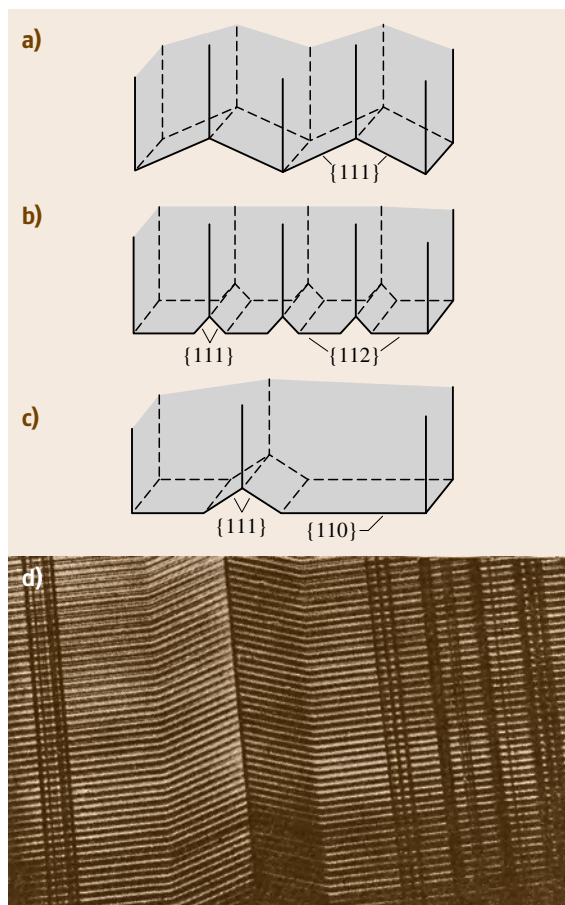


Fig. 16.40 (a) Crystallization front cut by $\{111\}$ planes in accordance with the postulated model; (b,c) experimentally observed crystallization front shape; (d) correspondence between the crystallization front shape and the horizontal hatching on the surface of profiled crystals

into practice. It can be confirmed by the fact that in separate cases silicon tapes with wide (up to 10–15 mm) monocrystalline areas can be grown.

It was noticed that in the process of silicon tube growth the melt meniscus height strongly influences the character of defect formation in crystals. With the crystallization front in a tube sinking, the number of boundaries of a general type increases, i.e., profile defect structure depends on the interaction efficiency in the crystallization front–shaper system. The shaper influence is mainly determined by the distortions (thermal and capillary) introduced by the silicon carbide layer formed on the operating free edges of a graphite shaper when it interacts with the silicon melt.

Besides such indirect influence on the structure of profiles, silicon carbide entering the crystal subsurface layer in the form of SiC particles greatly affects the quality of the material produced. SiC microcrystals measuring 25–30 μm , produced in the melt meniscus, form a carbide layer growing on the shaper free edges. When bulges appear on the layer the meniscus becomes distorted and on the crystal surface there appear distinctive furrows and in separate cases bulges along the direction of pulling that break when SiC particles and aggregations thereof results from random fluctuations of the crystallization front when particles reaching the size of the meniscus escape the carbide layer. The number and the size of simultaneously entrapped particles depend on the amplitude of front fluctuations and on the mean height of the meniscus. The mechanism of carbide inclusion entrapment offered is confirmed by the results of silicon tube growth when the number of SiC particles entrapped sharply decreases for a high meniscus since the number of particles whose dimensions reach the meniscus height decreases.

The number of carbide inclusions in shaped silicon crystals can be decreases in several ways: by using crucibles made of graphite of high density; by replacing the

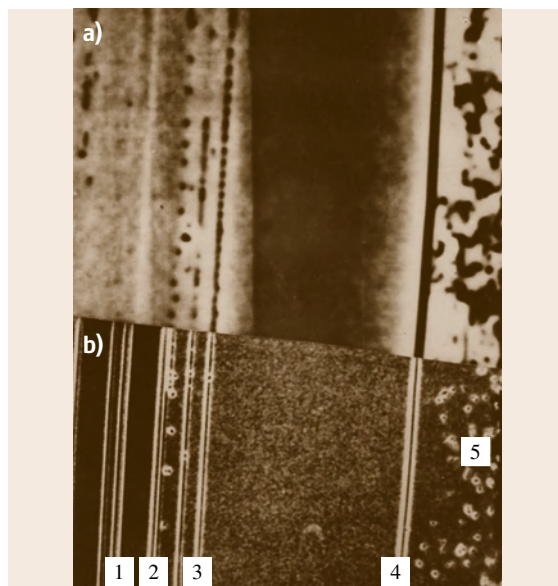


Fig. 16.41a,b The patterns (a) of spatial distribution of the secondary carrier current (EBIC, dark regions correspond to increased recombination) and (b) selective chemical etching; recombination boundaries: (1) inactive, (2) intermittent active, (3) low active, (4) high active, and (5) active dislocations

graphite container for crucibles with a protective layer-coated container; by maintaining a high melt meniscus (easy to secure when growing closed profiles). Besides, experiments on alloying shaped silicon with rare-earth elements showed that no SiC inclusions can be found on profile surfaces for any meniscus height in case at least 0.05 mass % of gadolinium dopant is introduced into silicon melt.

16.8.2 Local Electronic Properties of Shaped Silicon

The electric and photoelectric properties of crystals have been studied by local methods at $T = 300\text{ K}$: electron-beam induced current (EBIC), spreading re-

sistance (SR), light-beam induced voltage (LBIV) and light-beam induced current (LBIC). EBIC-method is the widely used one. In the case of the SR method, the local conductivity of the sample was detected by an acicular probe displaced on the crystal surface with $8\text{ }\mu\text{m}$ step. In this case the spatial resolution of the method was $30\text{ }\mu\text{m}$. The LBIV method was used for measuring the potential difference at the edges of a sample locally illuminated by a scanning light beam of $5\text{ }\mu\text{m}$ in diameter. This method made it possible to reveal the built-in electric fields caused by the defects of the crystal structure. In order to apply the LBIC method, a p-n junction was prepared or tin and indium oxide film was grown on the silicon surface, and then the current of minority carriers generated by a method analogous to the LBIV

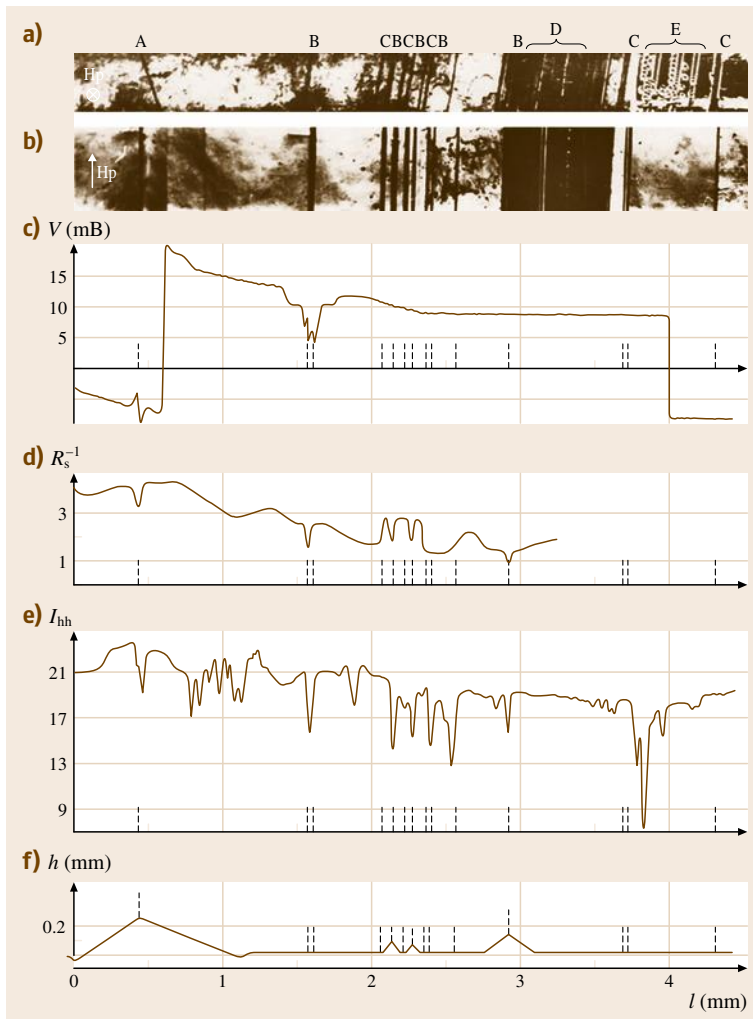


Fig. 16.42 Local study of the defect structure (a,b), electric properties (c-e), and S-L interface shape (f) of a silicon ribbon: (a) defect structure of the transverse cross section of an etched silicon ribbon, A-E indicate different types of defects, the label “Hp” indicates the growth direction; (b) structural defects on the surface of an etched ribbon, the label “Hp” indicates the growth direction; (c) distribution of photo-EMF obtained by the LBIV method across the ribbon; (d) spatial distribution of crystal conductivity, obtained by the spreading resistance method (arbitrary unit); (e) spatial distribution of minority carriers across the ribbon obtained by the LBIC method (arbitrary unit); (f) shape of the S-L interface crystal is shown above the curve, and the melt is below; at $l \geq 2\text{ mm}$ the height h of the S-L interface distortion is expanded by a factor of 10. The dashed lines in (c-f) show the locations of some twin boundaries in (b)

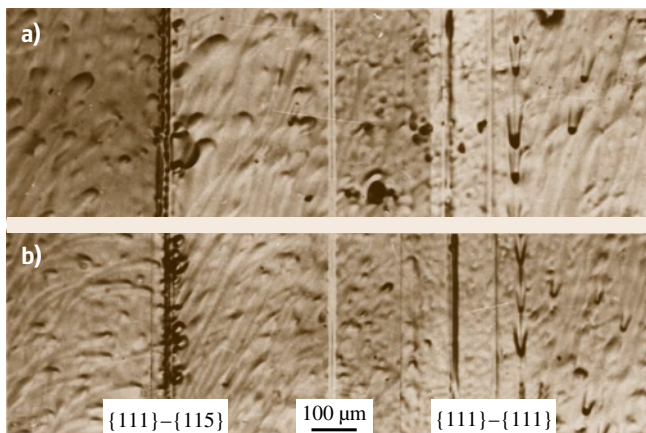


Fig. 16.43a,b Morphology of the melting crystal surface in the region of twin boundaries $\{111\}$ – $\{115\}$ at $l = 0.43$ mm, and $\{111\}$ – $\{111\}$ at $l = 2.2$ mm. The distances from the melting front are (a) 5 mm and (b) 3 mm

method was recorded. Effective centers of recombination were revealed by the LBIC method.

The spatial distribution of crystal defects was analyzed by the method of selective chemical etching. In addition, the structure of boundaries was examined with a scanning electron microscope. The morphology of the S–L interface was investigated as it is written above (Fig. 16.40d). Preliminary EBIC investigations of shaped crystals show that the electrical activity of twin boundaries as centers of increased recombination of nonequilibrium charge carriers differs (Fig. 16.41): there are electrically inactive boundaries, which are evidently coherent, boundaries with discontinuous activity, and boundaries of moderate and high activity. In the latter case, the boundaries are evidently incoherent. The combined results are presented on the Fig. 16.42 analyzed in detail in [16.94]. Here are brief results. The most important are defects whose electrical activity, as recombination centers of nonequilibrium carriers, is constant all along the silicon ribbon. It can be seen from comparing the LBIC spectra (Fig. 16.42e) with the pattern of selective chemical etching (Fig. 16.42b), that there are three types of such defects, at least. They are narrow bands of submicrons defects, accumulations or agglomerations of point defects with the coordinate $l = 0.8$ – 1.2 mm extended along the crystal growth direction. Dislocation etch pits are not visible here. The rows of dislocations denoted by index E in Fig. 16.42a and some twin boundaries are highly electrically active. Twin boundaries are the main defects. Its electric activity, as shown by the analysis in detail, de-

pends on structural properties as well as enriching by impurities.

We have assumed that the decreased melting temperature of boundaries enriched with impurities may affect the S–L interface structure. Therefore, experiments were performed on melting shaped silicon crystals. It has turned out that melting starts on the surface and melt drops are formed in the vicinity of impurity inclusions. Fig. 16.43 shows that their concentration at the boundary with the coordinate $l = 0.43$ mm (Fig. 16.42) is of order of 400 cm^{-1} , which is in accordance with a density of inclusions equal to 10^5 cm^{-2} found along this boundary after crystal cleavage. At the distance 5 mm from the melting front of reference single crystalline regions, separate drops coalesce and make up a uniform melt band of $10 \mu\text{m}$ in width. The process of melting thus proceeds mainly along the boundary, and a crystal can be divided into two parts by melting.

So, the main defects of the shaped silicon are the following ones: SiC inclusions, block boundaries, acute-angle boundaries, monocrystalline sections with

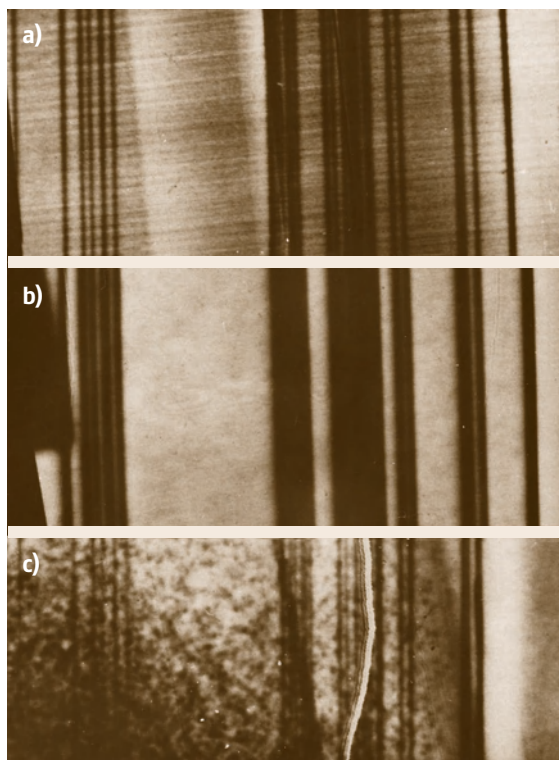


Fig. 16.44a–c Influence of annealing on the EBIC contrast of a silicon strip: (a) initial sample; (b) annealed at 450°C for 50 h; (c) annealed at 1000°C for 50 h (130 \times)

reduced lifetime, incoherent twin boundaries, dislocations, and coherent twin boundaries. The electrical activity of the structural defects falls in the order listed: in the region of the SiC inclusion, the lifetime of secondary carriers $\tau \leq 10^{-8}$ s, increasing to a magnitude of the order of 10^{-6} s in monocrystalline regions of Si crystals with a resistivity of the order of $1 \Omega \text{ cm}$.

The concentration of electrically active defects may possibly be reduced at the stage of crystal growth by improving the procedure. Decreasing of electrical activity of crystal defects in postgrowth treatment is a promising method of increasing the efficiency of solar elements. It has been established that annealing crystals at temperature of the order of 500°C is a largely ineffective. In the EBIC spectra shown in Fig. 16.44, the regions of increased recombination of nonequilibrium carriers in the vicinity of the boundaries are seen to be only slightly broaden. However, annealing at 1000°C leads to an increase in lifetime of the secondary carriers as a result of the decrease in electrical activity of the boundaries.

16.8.3 TPS Silicon Growth

The first experiments in the field of shaped silicon growth, especially for solar cells, were carried out more than thirty years ago. More than twenty different techniques have been tested. Information concerning this activity with numerous bibliographies can be found in [16.11–13]. The recent situation was analyzed in [16.95] review where four shaped silicon growth techniques are estimated as promising. There are TPS-EFG production of octagon profiles of 5 m length with 8 faces of 12.5 cm width and 0.3 mm thickness: RWE Schott Solar produces more than 200 000 kg/year with solar cell efficiency 14%. There is no any sawing loss because a laser cutting is used. In the frame of R&D project, a growth of tubes with the diameter of 0.5 m was realized [16.96].

Three other techniques are the following ones:

1. Evergreen Solar uses the string ribbon technique – a vertical growth from free melt surface between two metal strings

16.9 TPS Metals Growth

What are the results of TPS application for metals and alloys? On the basis of our big experience in the field, we can conclude: when we find a material for the shaper (both wetted or nonwetted, but chemically inert) we

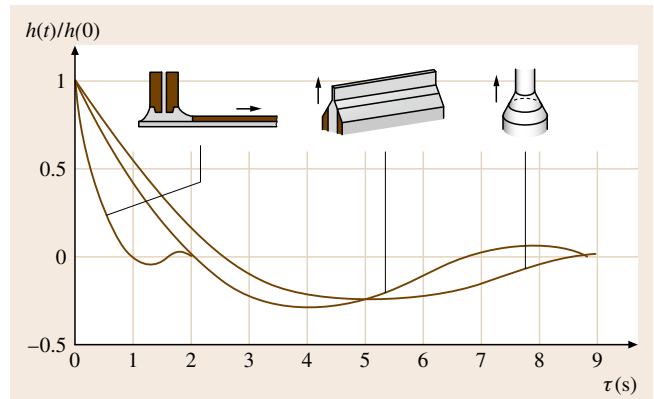


Fig. 16.45 Calculated curves of attenuation of crystallization front perturbation for a silicon tape

2. AstroPower uses the Silicon Film technique – a horizontal growth on a substrate with separation of the ribbon from the substrate
3. ECN uses RGS – the horizontal growth on a substrate when the substrate is used as a part of the solar cell.

We suggested this variant of shaped silicon growth 22 years ago with the name two shaping elements technique, TSET [16.97]. The scheme of the technique can be seen on the Fig. 16.45. When a graphite cloth is used as the substrate we title the technique the silicon on cloth, SOC.

At the conclusion of the silicon shaped growth discussion, let us show how the stability theory can be used for a crystal growth process characterization. On the Fig. 16.45 the curves of attenuations of crystallization front perturbation are presented. The special experiments were carried out for TSET. The relocation time was calculated as a function of the growth speed. It was found that it is decreased with the speed increasing up to the growth speed 6 cm/min and is not changed with the farther speed increasing. Two speeds (1.5 and 6 cm/min) were used in the experiments. The surface quality of the ribbons grown with the speed 6 cm/min was much better. The amplitude of the roughness was five times less.

can pull profiles from pure metals and eutectic alloys. The profiles have good quality surfaces (sometimes like a mirror). It is easy to grow low-melting metal single crystals by this technique. But there is no any technical

application. As for refractory metal single crystals, for instance Mo that is used for foil production, it is very difficult to find a material for shaper.

Polycrystalline profiles could be used for many applications, for instance heat exchangers from alloys of aluminum (Fig. 16.28). But when we need alloys of high mechanical properties, the composition of alloys is complicated. There is a big gap between the temperatures of liquidus and solidus. Dendrite crystals appear in the meniscus and the problem of profile pulling is rather difficult both from point of view of surface quality and

internal structure. So, TPS is difficult to compete with extrusion. On the other hand, the structure and mechanical properties of profiles are better than ones of cast profiles. We think the history is not finished yet. The problem of industrial application is not easy and a lot of efforts will need from numerous researchers. First of all alloys of special compositions have to be developed. Our success in the TPS application for the special steel [16.66] (Fig. 16.29a) and never published before stainless steel with aluminum rib (Fig. 16.29b) were promising but unfortunately have not been continued.

16.10 TPS Peculiarities

1. The crystals have the shape that we need for the most rational practical using.
2. The technique can be applied for any matters if a material for the shaper (both wetted or nonwetted, but chemically inert) is found.
3. The range of crystal dimensions is large: filaments of 0.02 mm diameter; tubes of 0.5 m diameter; plates $480 \times 320 \times 10 \text{ mm}^3$.
4. A growth speed, as rule, is much higher than in other crystal growth techniques.
5. Crystal, as rule, has a special structure concerned with the interface faceting.
6. Shaper influences on the interface shape.
7. The separation of growth zone from the melt in the crucible allows realization of continuous feeding by the raw material during growth process. As a result, we can have a short time of the melt presence before the growth, if it is necessary. Periodical change of the doping also is possible.
8. A distribution of impurities along the axis of crystal is more uniform. Indeed, if a coefficient of distribution of impurities is not equal to one during crystal growth a quantity of impurities changes along an axis of crystals in the most of crystal growth techniques. A solution of this problem can be found by localization of the melt at the zone of growth without stirring it with other melt volume. This situation we have, for instance, in using of additional crucible of small volume for CZT. The more effective result gives the capillary feeding at the TPS.
9. The using of special systems of capillaries for feeding allows controlling a distribution of impurities at the cross section of crystal.
10. A combination of doped and undoped parts is achieved in the same crystal.
11. The dynamic stability theory, developed for TPS, was successfully used for other CST as well as for analysis of cylindrical pores (negative crystals) growth and the radial instability of vapor whisker growth [16.5, 6].

References

- 16.1 A. Horowitz, S. Biderman, D. Gazit, Y. Einav, G. Ben-Amaz, M. Weiss: The growth of dome-shaped sapphire crystals by the gradient solidification method (GSM), *J. Cryst. Growth* **128**, 824–828 (1993)
- 16.2 D. Petrova, O. Pavloff, P. Marinov: Optical quality and laser characteristics of YAG:Nd crystals grown by the Bridgman–Stockbarger method, *J. Cryst. Growth* **99**, 841–844 (1990)
- 16.3 C.S. Bagdasarov: Problems of synthesis of refractory optic crystals. In: *Rost Kristallov*, Vol. 11, ed. by E.I. Givargizov (Transl. Growth of Crystals, Consultants Bureau, New York 1978) pp. 169–195, in Russian
- 16.4 V.A. Tatartchenko: Growth of shaped crystals from the melt. In: *Encyclopedia of Materials: Science and Technology*, ed. by K.H.J. Buschow, R.W. Cahn, M.C. Flemings, B. Ilshner, E.J. Kramer, S. Mahajan, P. Veyssière (Elsevier Science, Amsterdam 2001) pp. 3697–3703
- 16.5 V.A. Tatartchenko: Shaped crystal growth. In: *Handbook of Crystal Growth*, Vol. 2b, ed. by

- D.T.J. Hurle (North-Holland, Amsterdam 1994) pp.1011–1110
- 16.6 V.A. Tatartchenko: *Shaped Crystal Growth* (Kluwer Academic, London 1993)
- 16.7 V.A. Tatartchenko: The life of Alexander Stepanov and a brief history of shaped crystal growth, *J. Jpn. Assoc. Cryst. Growth*, **28**, 55–59 (2001)
- 16.8 V.A. Tatartchenko: Sapphire crystal growth and applications. In: *Bulk Crystal Growth of Electronic, Optical and Optoelectronic Materials*, ed. by P. Capper (Wiley, London 2005) pp.299–338
- 16.9 V.A. Tatartchenko: *Stable Crystal Growth* (Nauka–Science, Moscow 1988), in Russian
- 16.10 P.I. Antonov, L.M. Zatulovskiy, A.S. Kostigov, D.I. Levinzon, S.P. Nikanorov, V.V. Peller, V.A. Tatartchenko, V.S. Juferev: *Preparation of Shaped Single Crystals and Products by Stepanov's Technique* (Nauka–Science, Moscow 1981), in Russian
- 16.11 G.W. Cullen, T. Surek, P.I. Antonov (Eds.): Shaped crystal growth, *J. Cryst. Growth* **50**(1), 1–396 (1980)
- 16.12 J.P. Kalejs, T. Surek, V.A. Tatartchenko (Eds.): Shaped crystal growth, *J. Cryst. Growth* **82**(1/2), 1–268 (1987)
- 16.13 J.P. Kalejs, T. Surek (Eds.): Shaped crystal growth, *J. Cryst. Growth* **104**(1), 1–199 (1990)
- 16.14 V.A. Tatartchenko: Influence of capillary phenomena on the stability of the crystallization process during the pulling of shaped specimens from the melt, *Phys. Chem. Mater. Treat.* **6**, 47–53 (1973), in Russian
- 16.15 V.A. Tatartchenko, G.I. Romanova: Stability of crystallization by Verneulle technique, *Sov. Single Cryst. Tech.* **2**, 48–53 (1973), in Russian
- 16.16 V.A. Tatartchenko: Stability of profiled pattern crystallization from the melt, 4th Int. Conf. Cryst. Growth Abstr. (Tokyo 1974) pp. 521–522
- 16.17 V.A. Tatartchenko, E.A. Brener: Stability of crystallization from a melt with a capillary shaper, *Izv. Akad. Nauk SSSR, Ser. Fiz.* **40**, 1456–1467 (1976), in Russian – Translation in *Bull. Acad. Sci. USSR Phys. Ser.* **40**, **7**, 106–115 (1976)
- 16.18 T. Surek: Theory of shape stability in crystal growth from the melt, *J. Appl. Phys.* **47**, 4384–4393 (1976)
- 16.19 G.A. Korn, T.M. Korn: *Mathematical Handbook for Scientists and Engineers* (McGraw–Hill, New York 1961) pp.282–284
- 16.20 V.W. Mullins, F.R. Sekerka: Stability of the flat interface during crystallization of dilute binary alloys, *J. Appl. Phys.* **35**, 444–455 (1964)
- 16.21 V.A. Tatartchenko: Survey of quantitative analyses of the effects of capillary shaping on crystal growth, *J. Cryst. Growth* **82**, 74–80 (1987)
- 16.22 L.D. Landau, E.M. Lifchits: *Mecanique des Fluids* (Mir, Moscow 1971) p. 289
- 16.23 V.A. Tatartchenko, V.S. Uspenski, E.V. Tatartchenko, J.P. Nabot, T. Duffar, B. Roux: Theoretical Model of Crystal Growth Shaping Process, *J. Cryst. Growth* **180**, 615–626 (1997)
- 16.24 V.A. Tatartchenko, V.S. Uspenski, E.V. Tatartchenko, B. Roux: Theoretical investigation of crystal growth shaping process with the wetting boundary condition, *J. Cryst. Growth* **220**, 301–307 (2000)
- 16.25 G.A. Satunkin, V.A. Tatartchenko, V.I. Shaitanov: Determination of the growth angle from the shape of a crystal lateral face and solidified separation drops, *J. Cryst. Growth* **50**, 133–139 (1980)
- 16.26 H.S. Carslaw, J.C. Jaeger: *Conduction of Heat in Solids* (Clarendon, Oxford 1959) p.148
- 16.27 K.J. Bachmann, H.J. Kirsch, K.J. Vetter: Programmed Czochralski growth of metals, *J. Cryst. Growth* **7**, 290–295 (1970)
- 16.28 A.A. Alioshin, N.I. Bletsan, S.I. Bogatyriov, V.N. Fedorenko: Silicon furnace components for micro-electronic applications fabricated from shaped silicon tubes, *J. Cryst. Growth* **104**, 130–135 (1990)
- 16.29 V.A. Tatartchenko, A.I. Saet: Thermal regime of profile pulling from melt, *J. Eng. Phys.* **13**(2), 255–258 (1967), in Russian – Translation in *J. Eng. Phys. USA*
- 16.30 G.I. Romanova, V.A. Tatartchenko, N.P. Tichonova: Stability of crystallization at the crystal growth by the gas flame technique, *Trudi Goi* **54**(188), 10–13 (1976), in Russian – *Sov. Proc. State Opt. Inst., Leningrad*
- 16.31 V.A. Borodin, E.A. Brener, V.A. Tatartchenko: Investigation of the crystallization process in the Verneulle technique, *Cryst. Res. Technol.* **16**, 1187–1197 (1982)
- 16.32 V.A. Borodin, E.A. Brener, T.A. Steriopolo, V.A. Tatartchenko, L.I. Chernishova: Growing single crystal corundum tubes by Verneulle technique in stable conditions, *Cryst. Res. Technol.* **16**, 1199–1207 (1982)
- 16.33 V.A. Borodin, E.A. Brener, V.A. Tatartchenko, V.I. Gusev, I.N. Tsigler: Automation of the Verneulle technique on the basis of stability analysis, *J. Cryst. Growth* **52**, 505–508 (1981)
- 16.34 E.A. Brener, G.A. Satunkin, V.A. Tatartchenko: Some aspects of the macroscopic theory of oriented crystallization from the melt. IV. The floating zone techniques, *Acta Phys. Acad. Sci. Hung.* **47**, 159–165 (1979)
- 16.35 E.A. Brener, G.A. Satunkin, V.A. Tatartchenko: Macroscopic theory of crystallization from a melt with capillary shaping. The floating-zone method. In: *Growth of Crystals*, Vol.14, ed. by E.I. Givargizov (Nauka Science, Moscow 1983) pp.153–158, in Russian – Translation in *Growth of Crystals*, Vol. 14 (Consultants Bureau, New York 1987), 181–186

- 16.36 E.A. Brener, V.A. Tatartchenko, V.E. Fradkov: Differences between the mass transfer processes at a crystal surface near a three-phase line during crystallization and melting, *Kristallografiya* **27**, 205–206 (1982), in Russian – Translation in *Sov. Phys. Crystallogr.* **27** 127–128 (1982)
- 16.37 I.A. Lesk, A. Baghdadi, R.W. Gurtler, R.J. Ellis, J.A. Wiese, M.G. Coleman: Ribbon-to-ribbon crystal growth, *Proc. 12th IEEE Photovolta. Spec. Conf.* (IEEE, New York 1976) pp. 163–167
- 16.38 V.A. Tatartchenko, A.I. Saet, A.V. Stepanov: The shape of liquid column on producing of specified shape product by crystallization of melt, *Proc. 1st Conf. Stepanov's Growth Semiconduct. Single Cryst.* (Ioffe Phys.-Techn. Inst., Leningrad 1968) pp. 83–97, in Russian
- 16.39 V.A. Tatartchenko, A.I. Saet, A.V. Stepanov: Boundary conditions of capillary shaping at crystallization from melts, *Izv. Akad. Nauk SSSR, Ser. Fiz.* **33**, 1954–1959 (1969), in Russian – Translation in *Bull. Acad. Sci. USSR, Phys. Ser. USA*
- 16.40 N.K. Adam: *The physics and Chemistry of surfaces* (Clarendon, Cambridge 1930)
- 16.41 S.V. Tsivinskii, P.I. Antonov, A.V. Stepanov: Melt column form in crystal pulling process, *Sov. Phys. Tech. Phys.* **15**, 274–277 (1970), American translation of *Sov. Zh. Tek. Fiz.*
- 16.42 S.V. Tsivinskii: Application of capillary phenomena theory to manufacturing articles of predominant shape directly from the melt by Stepanov's method, *J. Eng. Phys.* **5**(9), 59–63 (1962), in Russian – Translation in *J. Eng. Phys. USA*
- 16.43 V.A. Tatartchenko, A.V. Stepanov: Calculation of the height of liquid column in crystal growth from melts, *Izv. Akad. Nauk SSSR Ser. Fiz.* **33**, 1960–1962 (1969), in Russian – Translation in *Bull. Acad. Sci. USSR, Phys. Ser. USA*
- 16.44 I.S. Pet'kov, B.S. Red'kin: Stability analysis of movable menisci, *J. Cryst. Growth* **104**, 20–22 (1990)
- 16.45 V.A. Tatartchenko, J.P. Nabot, T. Duffar, E.V. Tatartchenko, B. Roux: Some problems of stability of movable meniscus, *J. Cryst. Growth* **148**, 415–420 (1995)
- 16.46 L.L. Kuandykov, P.I. Antonov: Shaped melt column optimal choice on the basis of an equilibrium growth angle value, *J. Cryst. Growth* **222**, 852–861 (2001)
- 16.47 V.A. Tatartchenko: Capillary shaping in crystal growth from melts, I. Theory, *J. Cryst. Growth* **37**, 272–284 (1977)
- 16.48 V.A. Tatartchenko, G.A. Satunkin: Capillary shaping in crystal growth from melts, II. Experimental results for sapphire, *J. Cryst. Growth* **37**, 285–288 (1977)
- 16.49 V.A. Tatartchenko, S.K. Brantov: A model for a capillary shaper under conditions of weightlessness, *Izv. Akad. Nauk SSSR, Ser. Fiz.* **40**, 1468–1484 (1976), in Russian – Translation in *Bull. Acad. Sci. USSR Phys. Ser. USA* **40**, 116–129 (1976)
- 16.50 Y.A. Osipian, V.A. Tatartchenko: Crystal growth from melt by capillary shaping technique, *Adv. Space Res.* **8**(12), 16–34 (1988)
- 16.51 M.S. Agafonov, G.A. Gavrillov, L.I. Gubina, V.A. Kislov, L.V. Leskov, Y.B. Levin, V.V. Savichev, V.A. Tatartchenko, N.I. Timofeeva: Crystallization from the melt by the Stepanov method under zero-gravity conditions, *Izv. Akad. Nauk SSSR, Ser. Fiz.* **43**, 1935–1939 (1979), in Russian – Translation in *Bull. Acad. Sci. USSR, Phys. Ser.* **43**(9), 124–128 (1979)
- 16.52 V.A. Tatartchenko, S.K. Brantov, L.V. Leskov, V.L. Levto, M.S. Agafonov: Experimental results of the crystallization of indium by the Stepanov method in conditions of micro-gravitation, *Izv. Akad. Nauk SSSR, Ser. Fiz.* **49**, 708–710 (1985), in Russian – Translation in *Bull. Acad. Sci. USSR, Phys. Ser.* **49**(4), 77–79 (1985)
- 16.53 V.A. Tatartchenko: Stability of melt crystal growth under microgravity condition, *Adv. Space Res.* **11**(7), 307–321 (1991)
- 16.54 L.A. Slobozhanin, M.A. Svechkareva, V.A. Tatartchenko: Stability of melt meniscus during growth of crystals by the technique of pulling from shaper under zero-gravity conditions, *J. Cryst. Growth* **133**, 273–280 (1993)
- 16.55 J.A. Burton, P.C. Prim, W.P. Slichter: The distribution of solute in crystals grown from the melt. Part I. Theoretical, *J. Chem. Phys.* **21**, 1987–1991 (1953)
- 16.56 J.C. Swartz, T. Surek, B. Chalmers: EFG (edge-defined, film-fed growth) process applied to the growth of silicon ribbons, *J. Electron. Mater.* **4**, 255–264 (1975)
- 16.57 S.K. Brantov, V.A. Tatartchenko: On effective coefficient of impurity distribution at the Stepanov thin-walled crystal growth (EFG), *Cryst. Res. Technol.* **18**, K59–K64 (1983)
- 16.58 J.P. Kalejes: Impurity redistribution in EFG, *J. Cryst. Growth* **44**, 329–334 (1978)
- 16.59 A.V. Stepanov: A new technique of production of sheets, of tubes, of rods with different cross sections from a melt, *J. Tech. Phys.* **29**, 382–393 (1959), in Russian – Translation in *Sov. Phys. Tech. Phys. USA*
- 16.60 A.V. Stepanov: A new technique of products fabrication from a melt, *Mech. Eng. Bull.* **11**, 47–50 (1959), in Russian
- 16.61 A.L. Shakch-Budagov, A.V. Stepanov: A new technique of production of sheets, of tubes, of rods with different cross sections from a melt, *J. Tech. Phys.* **29**, 394–405 (1959), in Russian – Translation in *Sov. Phys. Tech. Phys. USA*
- 16.62 B.M. Goltsman, A.V. Stepanov: A technique of production of sheets and tubes directly from a melt of aluminum and its alloys, *Bull. Acad. Sci.*

- USSR, Metall. Fuel Ser. **5**, 49–53 (1959), in Russian
- 16.63 B.M. Goltsman: A pulling of crystalline sheets and tubes from a melt, *Opt. Mech. Ind.* **11**, 45–46 (1958), in Russian
- 16.64 A.V. Stepanov: *The Future of Metals Machining* (Lenizdat, Leningrad 1963), in Russian
- 16.65 V.A. Tatartchenko, A.V. Stepanov: The installation for investigation of crystallization parameters influence on the structure properties of crystallized specimens. In: *Machines and Devices for Testing of Materials*, ed. by G.V. Kurdiumov (Metallurgy, Moscow 1971), in Russian
- 16.66 V.A. Tatartchenko, V.V. Vakhrushev, A.S. Kostygov, A.V. Stepanov: Profile shaping in iron alloys of high carbon content, *Izv. Akad. Nauk SSSR, Ser. Fiz.* **35**, 511–513 (1971), in Russian – Translation in *Bull. Acad. Sci. USSR, Phys. Ser. USA*
- 16.67 G.V. Sachkov, V.A. Tatartchenko, D.I. Levinzon: Control of the capillary shaping process for single crystals grown from a melt, *Izv. Akad. Nauk SSSR, Ser. Fiz.* **37**, 2288–2291 (1997), in Russian – Translation in *Bull. Acad. Sci. USSR, Phys. Ser.*
- 16.68 H.E. La Belle, A.I. Mlavsky: Growth of sapphire filaments from the melt, *Nature* **216**, 574–575 (1967)
- 16.69 H.E. La Belle, A.I. Mlavsky: Growth of controlled profile crystals from the melt. Part 1. Sapphire filaments, *Mater. Res. Bull.* **6**, 571–580 (1971)
- 16.70 H.E. La Belle, A.I. Mlavsky: Growth of controlled profile crystals from the melt. Part 2. Edge-defined film fed growth (EFG), *Mater. Res. Bull.* **6**, 581–590 (1971)
- 16.71 E.V. Gomperz: Untersuchungen an Einkristall-drähten, *Z. Phys.* **8**, 184–190 (1922), in German
- 16.72 H. Mark, M. Polanyi, E. Schmid: Vorgänge bei der Dehnung von Zinkkristallen, *Z. Phys.* **12**, 58–77 (1923), in German
- 16.73 E. Grüneisen, E. Goens: Untersuchungen an Metallkristallen, *Z. Phys.* **26**(4/5), 235–273 (1924), in German
- 16.74 A.G. Hoyem, E.P.T. Tyndall: An experimental study of the growth of zinc crystals by the Czochralski-Gomperz method, *Phys. Rev.* **33**, 81–89 (1929)
- 16.75 A.G. Hoyem: Some electrical properties of spectroscopically pure zinc crystals, *Phys. Rev.* **38**, 1357–1371 (1931)
- 16.76 P. Kapitza: The study of the specific resistance of bismuth crystals and its change in strong magnetic field and some allied problems, *Proc. R. Soc. Lond. Ser. A*, **119**(782), 358–443 (1928)
- 16.77 H.E. LaBelle: EFG, the invention and application to sapphire growth, *J. Cryst. Growth* **50**, 8–16 (1980)
- 16.78 V.N. Kurlov, S.V. Belenko: The growth of sapphire shaped crystals with continuously modulated dopants, *J. Cryst. Growth* **191**, 779–782 (1998)
- 16.79 V.A. Borodin, V.V. Sidorov, T.A. Steriopolov, V.A. Tatartchenko: Variable shaping growth of refractory oxide shaped crystals, *J. Cryst. Growth* **82**, 89–94 (1986)
- 16.80 J.W. Locher, H.E. Bennet, P.C. Archibald, C.T. Newmyer: Large diameter sapphire dome: Fabrication and characterization, *Proc. SPIE* **1326**, 2–10 (1990)
- 16.81 V.A. Borodin, V.V. Sidorov, S.N. Rassolenco, T.A. Steriopolov, V.A. Tatartchenko, T.N. Yalovets: Local shaping technique and new growth apparatus for complex sapphire products, *J. Cryst. Growth* **104**, 69–76 (1990)
- 16.82 K.S. Bagdasarov: Synthesis of large single crystals of corundum. In: *Ruby and Sapphire*, ed. by L.M. Belyaev (National Bureau of Standards, Washington, DC 1980) pp.15–38, Translation from Russian
- 16.83 M. Saito: Gas-bubble formation of ruby single crystals by floating zone melt growth with an infrared radiation convergence type heater, *J. Cryst. Growth* **71**, 664–672 (1985)
- 16.84 M. Saito: Growth process of gas-bubble in ruby single crystals by floating zone method, *J. Cryst. Growth* **74**, 385–390 (1986)
- 16.85 A.V. Zhdanov, G.A. Satunkin, V.A. Tatartchenko, N.N. Talyanskaya: Cylindrical pores in a growing crystal, *J. Cryst. Growth* **49**, 659–660 (1980)
- 16.86 V.A. Tatartchenko: Cylindrical pores in a growing crystal, *J. Cryst. Growth* **143**, 294–300 (1994)
- 16.87 V.A. Tatartchenko, T.N. Yalovets, G.A. Satunkin, L.M. Zatulovsky, L.P. Egorov, D.Y. Kravetsky: Defects in shaped sapphire crystals, *J. Cryst. Growth* **50**, 335–340 (1980)
- 16.88 A.A. Chernov, D.T. Temkin, A.M. Melnikova: Theory of inclusion capture at the melt crystal growth, *Kristallographia (Sov. Crystallography)* **21**(4), 652–660 (1976)
- 16.89 E. Savrun, C. Toy, W.D. Scott, D.C. Harris: Is sapphire inherently weak in compression at high temperature?, *Proc. SPIE* **3705**, 12–16 (1999)
- 16.90 J.W. Locher, S. Zanella, H. Bates, V.A. Tatartchenko: Production of large sapphire crystals by EFG, *Abstracts 14th Int. Conf. Cryst. Growth (Grenoble 2004)* p. 560
- 16.91 V.N. Kurlov, B.M. Epelbaum: Fabrication of near-net-shaped sapphire domes by noncapillary shaping method, *J. Cryst. Growth* **167**, 165–180 (1997)
- 16.92 V.S. Yuferev, V.M. Krymov, L.L. Kuandykov, S.I. Bakholdin, Y.G. Nosov, I.L. Shulpina, P.I. Antonov: The growth of sapphire ribbons with basal facet surface, *J. Cryst. Growth* **275**, 785–790 (2005)
- 16.93 J. Shi, G. Geitos, N.V. Abrosimov, S.K. Brantov, S.A. Erofeeva, V.A. Tatartchenko: Some structural and electrophysical properties of silicon ribbons produced by Stepanov's method, *Izv. Akad. Nauk SSSR, Ser. Fiz.* **43**, 1992–1994 (1979), in Russian – Translation in *Bull. Acad. Sci. USSR, Phys. Ser. USA* **43**, 164–165 (1979)

- 16.94 N.V. Abrosimov, A.V. Bazhenov, V.A. Tatartchenko: Growth features and local electronic properties of shaped silicon, *J. Cryst. Growth* **82**, 203–208 (1987)
- 16.95 J.P. Kalejs: An overview of new developments in crystalline silicon ribbon material technology for solar cells, *Proc. 3rd World Conf. Photovolta. Energy Convers.* (Osaka 2003)
- 16.96 D. Garcia, M. Ouellette, B. Mackintosh, J.P. Kalejs: Shaped crystal growth of 50 cm diameter silicon thin-walled cylinders by EFG, *J. Cryst. Growth* **225**, 566–571 (2001)
- 16.97 S.K. Brantov, B.M. Epelbaum, V.A. Tatartchenko: Unidirectional growth of silicon layers on a graphitized fabric substrate, *Mater. Lett.* **2**, 274–277 (1984)

Solution **Part C**

Part C Solution Growth of Crystals

17 Bulk Single Crystals Grown from Solution on Earth and in Microgravity

Mohan D. Aggarwal, Normal, USA
Ashok K. Batra, Normal, USA
Ravindra B. Lal, Normal, USA
Benjamin G. Penn, Huntsville, USA
Donald O. Frazier, Huntsville, USA

18 Hydrothermal Growth of Polyscale Crystals

Kullaiah Byrappa, Mysore, India

19 Hydrothermal and Ammonothermal Growth of ZnO and GaN

Michael J. Callahan, Hanson, USA
Qi-Sheng Chen, Beijing, China

20 Stoichiometry and Domain Structure of KTP-Type Nonlinear Optical Crystals

Michael Roth, Jerusalem, Israel

21 High-Temperature Solution Growth: Application to Laser and Nonlinear Optical Crystals

Joan J. Carvajal, Tarragona, Spain
Maria Cinta Pujol, Tarragona, Spain
Francesc Díaz, Tarragona, Spain

22 Growth and Characterization of KDP and Its Analogs

Sheng-Lai Wang, Jinan, Shandong, China
Xun Sun, Jinan, China
Xu-Tang Tao, Jinan, China

17. Bulk Single Crystals Grown from Solution on Earth and in Microgravity

Mohan D. Aggarwal, Ashok K. Batra, Ravindra B. Lal, Benjamin G. Penn, Donald O. Frazier

The growth of crystals has been of interest to physicists and engineers for a long time because of their unique properties. Single crystals are utilized in such diverse applications as pharmaceuticals, computers, infrared detectors, frequency measurements, piezoelectric devices, a variety of high-technology devices, and sensors. Solution crystal growth is one of the important techniques for the growth of a variety of crystals when the material decomposes at the melting point and a suitable solvent is available to make a saturated solution at a desired temperature. In this chapter an attempt is made to provide some fundamentals of growing crystals from solution, including improved designs of various crystallizers.

Since the same solution crystal growth techniques could not be used in microgravity, authors had proposed a new cooled sting technique to grow crystals in space. Authors' experiences of conducting two Space Shuttle experiments relating to solution crystal growth are also detailed in this work. The complexity of these solution growth experiments to grow crystals in space are discussed. These were some of the earliest experiments performed in space, and various lessons learnt are described.

A brief discussion of protein crystal growth, which also shares the basic principles of the solution growth technique, is given along with some flight hardware information for such growth in microgravity.

17.1	Crystallization:	
	Nucleation and Growth Kinetics	561
17.1.1	Expression for Supersaturation	561
17.1.2	Effects of Convection in Solution Growth	563
17.1.3	Effect of Impurities	564
17.2	Low-Temperature Solution Growth	566
17.2.1	Solution Growth Methods	566
17.3	Solution Growth by Temperature Lowering	567
17.3.1	Solvent Selection and Solubility	567
17.3.2	Design of a Crystallizer	569
17.3.3	Solution Preparation and Starting a Growth Run	573
17.4	Triglycine Sulfate Crystal Growth: A Case Study	574
17.4.1	Growth of Single Crystals of Triglycine Sulfate	574
17.4.2	Growth Kinetics and Habit Modification	576
17.5	Solution Growth of Triglycine Sulfate Crystals in Microgravity	582
17.5.1	Rationale for Solution Crystal Growth in Space	583
17.5.2	Solution Crystal Growth Method in Space	583
17.5.3	Results and Discussion	588
17.6	Protein Crystal Growth	592
17.6.1	Protein Crystal Growth Methods	592
17.6.2	Protein Crystal Growth Mechanisms	593
17.6.3	Protein Crystal Growth in Microgravity	593
17.7	Concluding Remarks	594
	References	594

The growth of crystals with tailored physical and chemical properties, the characterization of crystals with advanced instrumentation, and their eventual conversion into devices play vital roles in science and technology. Crystal growth is an important field of materials science, involving controlled phase transformation. Growth of crystals from solution at low temperature is one of the important techniques in the fields of pharmaceutical, agriculture, and materials science. Crystal growth acts as a bridge between science and technology for practical applications. In the past few decades, there has been growing interest in the crystal growth process, particularly in view of the increasing demand for materials for technological applications. The strong influence of single crystals in present-day technology is evident from recent advances in the fields of semiconductors, transducers, infrared detectors, ultrasonic amplifiers, ferrites, magnetic garnets, solid-state lasers, nonlinear optics, piezoelectrics, acousto-optics, photosensitive materials, and crystalline thin films for microelectronics and computer applications. All these developments could only be achieved due to the availability of single crystals such as silicon, germanium, and gallium arsenide, and also through the discovery of nonlinear optical properties in some inorganic, semiorganic, and organic crystals. Researchers have always sought new materials for growth of single crystals for new applications and the modification of present crystals for various applications. Any crystal growth process is complex; it depends on many parameters, which can interact. A complete description of a process may well be impossible, since this would require the specification of too many variables. This is why crystal growth is sometimes called an art as well as a science, but like other crafts, it can provide great satisfaction after successful crystal growth of a desired material.

Solid-state materials can be classified into single crystals, polycrystalline, and amorphous materials depending upon the arrangement of their constituent molecules, atoms or ions. An ideal crystal is one in which the surroundings of any atom would be exactly the same as the surroundings of every similar atom in three dimensions. However, real crystals are finite and contain defects. The consistency of the characteristics of devices fabricated from a crystal depends on the homogeneity and defect contents of the crystal. Hence, the process of producing single crystals, which offer homogeneous media at the atomic level with directional properties, attracts more attention than any other

process. The methods of growing crystals are mainly dictated by the characteristics of the material and the desired size of the crystal. The method of growing crystals at low and high temperature can be broadly divided into the following six categories:

1. Growth from aqueous solution (low-temperature growth)
2. Growth by gel method (low-temperature growth)
3. Growth from flux or top-seeded solution growth method (high-temperature growth)
4. Hydrothermal growth (high-temperature growth)
5. High-pressure growth (high-temperature growth)
6. Growth by electrodeposition.

Growth of bulk crystals from aqueous solution is technically very important. Besides bulk crystal growth, this method is also used for purification of materials and separation of impurities. Growth of large single crystals from aqueous solution is of interest for essentially two reasons. First, there is a growing need for solution-grown crystals in the area of high-power laser technology, such as potassium dihydrogen phosphate (KDP)-type crystals. Second, research in this area of crystal growth and the corresponding in-depth examination of several key parameters provides fundamental case studies generating theory and technology that are applicable to all solution crystal growth processes, including new aqueous growth systems and high-temperature solution growth.

In this chapter, the fundamental aspects of solution growth and the various methods of bulk crystal growth from solution are described, along with solution crystal growth in the microgravity environment of space. Based on extensive experience of the authors in growing inorganic and organic crystals on Earth and in space, the authors have tried to provide a lucid explanation of the fundamentals of solution crystal growth and crystal growth systems. However, enough details are given on fabrication of crystallizers, associated instruments, and techniques that new researchers may be able to design and set up his/her own solution crystal growth system after review of this chapter. Furthermore, growth and perfection of a technologically important crystal from aqueous solution based on the case study of triglycine sulfate is presented. The effects of various parameters such as the design of the seed holder, seed morphology, the characteristics of the solution such as pH, the growth temperature, dopants, impurities, and microgravity on the physical properties are presented in detail.

17.1 Crystallization: Nucleation and Growth Kinetics

The study and investigation of crystal growth implies the determination of growth laws and growth mechanisms, and the explanation of the final result, i. e., the crystal habit. These aspects are interconnected. Since the growth rate of a face depends on its growth mechanisms and contributes to define the crystal habit, detailed knowledge of these aspects is essential for production of crystals of specific physical or morphological properties. Crystal growth is due to deposition of solute particles on crystal faces, which can grow layer by layer at different rates. The growth rate of a face, i. e., the advancement of its surface in the normal direction per unit time, depends upon both internal and external factors. Internal factors include the surface structure of faces, which in turn are related to the bulk crystal structure, and their degree of perfection. Defects usually occur in the crystals and can emerge at the surface, affecting the growth kinetics. The external factors include the supersaturation, the solute concentration, which is related to solubility, the temperature of the solution, the composition of the solution, mechanical conditions such as the use of stirring, and the presence of impurities or a magnetic or gravitational field. The crystal growth of a face is a succession of complex processes that take place at the interface between the liquid and solid phase. This therefore implies transport of matter and energy across the interface, which is the site of major importance in crystal growth.

In the following section, the fundamentals of nucleation and crystal growth in low-temperature solution are described.

17.1.1 Expression for Supersaturation

The supersaturation of a system can be expressed in a number of ways. A basic unit of concentration as well as temperature must be specified. The concentration driving force (ΔC), the supersaturation ratio (S), and the relative supersaturation (σ) are related to each other as follows.

The concentration driving force is

$$\Delta C = C - C^*, \quad (17.1)$$

where C is the actual concentration of the solution and C^* is the equilibrium concentration at a given temperature.

The supersaturation ratio is

$$S = \frac{C}{C^*}. \quad (17.2)$$

The relative supersaturation is

$$\sigma = \frac{C - C^*}{C^*} \quad \text{or} \quad \sigma = S - 1. \quad (17.3)$$

If the concentration of a solution can be measured at a given temperature and the corresponding equilibrium saturation concentration is known, then the supersaturation can be estimated.

The required supersaturation can be achieved either by cooling/evaporation or by the addition of a precipitant. *Meirs* and *Isaac* reported a detailed investigation on the relationship between supersaturation and spontaneous crystallization [17.1]. The results of their analysis are shown in Fig. 17.1, which shows three zones, termed regions I, II, and III. The lower continuous line indicates the normal solubility of the salt concerned. The temperature and concentration at which spontaneous crystallization occurs are represented by the upper broken curve, generally referred to as the supersolubility curve. This curve is not well defined, as the solubility curve and its position in the diagram depend on the degree of agitation of the solution. The three zones are defined as:

- I. The stable (undersaturated) zone, where crystallization is not possible.
- II. The metastable zone, where spontaneous crystallization is improbable. However, if a seed crystal is placed in such a metastable solution, growth will occur.

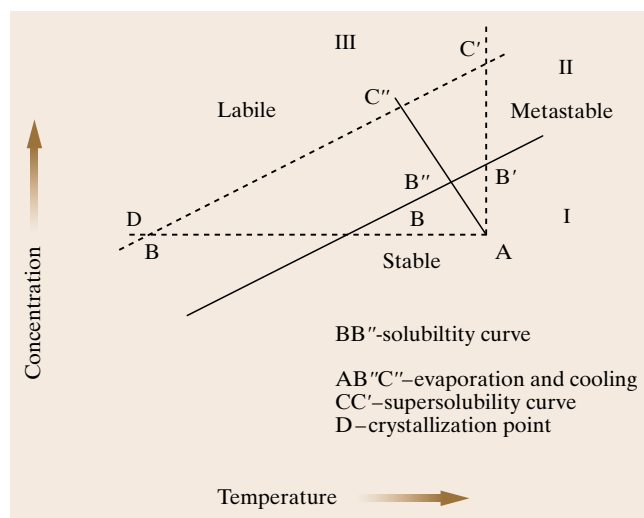
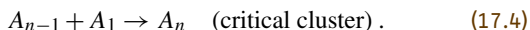


Fig. 17.1 Meirs and Issac solubility curve

III. The unstable or labile (supersaturation) zone, where spontaneous crystallization is more probable.

The achievement of supersaturation is not sufficient to initiate crystallization. The formation of embryos or nuclei with a number of minute solid particles present in the solution, often termed centers of crystallization, is a prerequisite. Nucleation may occur spontaneously or can be induced artificially. Broadly speaking, nucleation can be classified into primary and secondary. All types of nucleation, whether homogeneous or heterogeneous, in systems that do not contain crystalline matter are described as primary. On the other hand, nucleation generated in the vicinity of crystals present in a supersaturated system is termed secondary nucleation.

The formation of stable nuclei occurs only by the addition of a molecule (A_1) until a critical cluster is formed



Subsequent additions to the critical cluster result in nucleation followed by growth. The growth units (ions or molecules) in a solution can interact with one another, resulting in a short-lived cluster. Short chains or flat monolayers may be formed initially, and eventually the lattice structure is built up. This process occurs very rapidly and continues in regions of very high supersaturation. Many nuclei fail to achieve maturity and simply dissolve due to their unstable nature. If the nuclei grow beyond a certain critical size, they become stable under the average conditions of supersaturation in the bulk of the solution.

The formation of a solid particle within a homogeneous solution results from the expenditure of a certain quantity of energy. The total quantity of work W required for the formation of a stable nucleus is equal to the sum of the work required to form the surface W_S (a positive quantity) and the work required to form the bulk of the particle W_V (a negative quantity).

$$W = W_S + W_V. \quad (17.5)$$

The change in Gibbs free energy (ΔG) between the crystalline phase and the surrounding mother liquor results in a driving force, which stimulates crystallization. This ΔG is the sum of the surface free energy and the volume free energy

$$\Delta G = \Delta G_S + \Delta G_V. \quad (17.6)$$

For a spherical nucleus

$$\Delta G = 4\pi r^2 \gamma + \frac{4}{3}\pi r^3 \Delta G_V, \quad (17.7)$$

where r is the radius of the nucleus, γ is the interfacial tension, and ΔG_V is the free energy change per unit volume.

For rapid crystallization, $\Delta G < 0$; the first term in the above equation expresses the formation of new surface, and the second term expresses the difference in chemical potential between the crystalline phase (μ) and the surrounding mother liquor (μ_0). At the critical condition, the free energy formation obeys the condition $d\Delta G/dr = 0$. Hence the radius of the critical nucleus is expressed as

$$r^* = \frac{2\gamma}{\Delta G_V}. \quad (17.8)$$

The critical free energy barrier is

$$\Delta G^* = \frac{16\pi\gamma^3 v^2}{3(\Delta\mu)^2}. \quad (17.9)$$

The number of molecules in the critical nucleus is

$$I^* = \frac{4}{3}\pi\gamma(r^*)^3. \quad (17.10)$$

The crucial parameter between a growing crystal and the surrounding mother liquor is the interfacial tension γ . This complex parameter can be determined by conducting nucleation experiments.

Growth of crystals from the vapor, melt or solution occurs only when the medium is supersaturated. The process involves at least two stages [17.2]:

1. Formation of stable three-dimensional (3-D) nuclei
2. Development of the stable 3-D nuclei into crystals with well-developed faces.

The formation of 3-D nuclei is usually discussed in terms of reduction in the Gibbs free energy of the system. At a given supersaturation and temperature, there is a critical value of the free energy at which 3-D nuclei of a critical radius are formed. Only those nuclei which are greater than the critically sized nucleus are capable of growing into crystals of visible size by the attachment of growth species (i.e., molecules, atoms or ions) at energetically favorable growth sites such as kinks (K) in the ledges (L) of a surface. The surfaces of growing crystals may be flat (F), stepped (S) or kinked (K). However, crystals of visible size are usually bounded by slowly growing F-faces which grow by the attachment of growth units at energetically favorable sites. Figure 17.2 shows different positions for the attachment of growth units at a flat crystal-medium interface of a simple cubic lattice. A growth unit attached at a surface terrace (T), smooth ledge (L) or kink (K)

site has one, two or three out of the six potential nearest neighbors, respectively. Therefore, a growth unit arriving at a surface terrace, ledge or kink simply loses one, two or three degrees of freedom. If ϕ is the binding energy per pair, the corresponding binding energy of a growth unit attached at these sites is ϕ , 2ϕ , and 3ϕ , respectively. Since the probability of capture of a growth unit at a given site depends on the term $\exp(n\phi/k_B T)$ (where n is the number of bonds formed, k_B is the Boltzmann constant, and T is the temperature in Kelvin), the growth unit has a much higher probability of becoming a part of the crystal at a kink site than at a ledge or surface terrace. Consequently, in contrast to ledges, the contribution of kinks is overwhelmingly high in the rate v of displacement of a step along the surface and in the rate R of displacement of the surface normal to it. Similarly, the contribution to the face growth rate R by the direct attachment of growth units at the terrace is negligible.

From the above discussion, it may be concluded that the kinetics of crystal growth may, in general, be considered to occur in the following stages:

1. Transport of growth units to the growing surface by bulk diffusion and their capture onto the surface terrace
2. Migration of growth units adsorbed onto the terrace to the step by surface diffusion and their capture at the step
3. Migration of growth units adsorbed onto the step to the kink site and their integration into the kink
4. Transport of the released heat of the reaction and solvent molecules from the solvated atoms/molecules.

One or more of the above stages may control the growth rate but the slowest one is always rate limiting. However, it should be noted that growth kinetics, characterized by the rates v' and R , depends on the crystal structure, the structure of the crystal–medium interface (i.e., rough or smooth), the presence of dislocations emerging on the growing face, the supersaturation of the growth medium, the growth temperature, stirring, and impurities present in the growth medium. It is also these factors that ultimately determine the surface morphology of the crystal.

To explain the crystal growth processes, various theories, models, and role of impurities have been proposed in the past. Some of these are listed below. For details, one can refer to various excellent references, and references therein [17.2–36]. The important growth models are: (i) the two-dimensional nucleation model, (ii) the

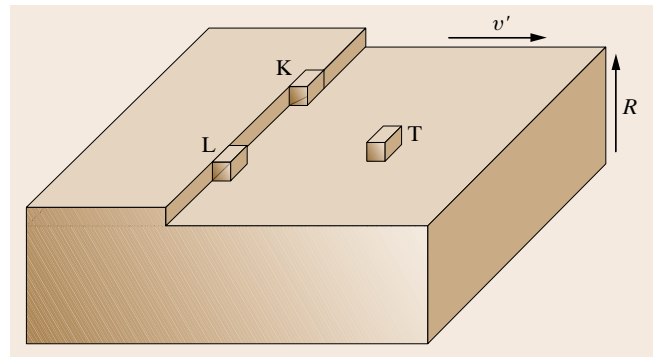


Fig. 17.2 Different positions for the attachment of growth units at a flat crystal–medium interface of a simple cubic lattice

spiral growth model, (iii) the bulk diffusion model, and (iv) growth by a group of cooperating screw dislocations.

17.1.2 Effects of Convection in Solution Growth

Convection is comprised of two mechanisms: energy transfer due to random molecular motion (diffusion) and energy transferred by bulk or macroscopic motion of the fluid. This fluid motion is associated with the fact that, at any instant, large numbers of molecules are moving collectively or as aggregates. Such motion, in the presence of a temperature gradient, contributes to heat transfer. Because the molecules in the aggregate retain their random motion, the total heat transfer is then due to a superposition of energy transport by the random motion of the molecules and by the bulk motion of the fluid. It is customary to use the term *convection* when referring to this cumulative transport and the term *advection* when referring to transport due to bulk fluid motion.

Natural Convection

Convective heat flow can be classified as natural (or free) convection or forced convection according to the nature of the fluid flow. Natural convection is due to the density difference of a solution near a crystal and far from it. This density difference is due primarily to the change in concentration of a solution during growth or the dissolution of a crystal; and, secondly, due to the absorption or evolution of heat in the fluid. In natural convection, fluid motion is due to buoyancy forces within the fluid. Buoyancy is due to the combined presence of a fluid density gradient and a body force that

is proportional to density. In practice, the body force is usually the gravitational force. Free convection flows may occur in the form of a plume. The well-known convective flow pattern for solution growth is associated with fluid rising from the bottom of the crystal. During the growth of a crystal, solution rises because the solution near a crystal is less dense as a result of a reduction in its concentration, and the temperature is higher because of the evolution of the heat of crystallization. With this depletion of the heavier solute, the solution around the crystal becomes lighter and, thus, rises. When a crystal is dissolved, the direction of motion is opposite (downward). Under these conditions, the diffusion of molecules is supplemented by the more energetic convective transport of matter.

Diffusion is the distribution of a substance by random motion of individual particles. It is due to the presence of a gradient of the chemical potential in the system. A gradient is defined as the increment of a function in an infinitely short distance, along the direction of the most rapid variation of the function. Diffusion always reduces this gradient. Molecular diffusion is observed in viscous media and at low supersaturations, as well as in the growth of crystals, in thin films of liquids, and in capillaries. In molecular diffusion the transport of matter to a crystal is slower than under other diffusion conditions. The thickness of the boundary layer increases with time and the concentration gradient gradually decreases. Therefore, the rate of growth decreases with time. The time interval during the formation of a boundary diffusion layer represents the non-steady-state condition. During this initial period, the rate of growth varies considerably. The thickness of the boundary layer depends on the difference between the densities of different parts of the solution (i.e., on the rate of growth of a crystal), the viscosity of the solution, and the dimensions of the crystal. The presence of the boundary near the crystal and the orientation of the crystal itself affect the nature of the convection currents and the thickness of the boundary layer at different crystal faces.

Forced Convection

Forced convection is produced by the action of external forces such as the forced motion of a crystal in the solution. There is no basic difference between forced and natural convection. When the velocity of motion of a solution with respect to a crystal is increased, the thickness of the boundary layer increases and the supply of matter to a face of the crystal increases. Therefore, by increasing the rate of motion of a solution, we can in-

crease the growth rate of the crystal faces. However, we cannot continue this process indefinitely. A temperature gradient constitutes the driving potential for heat transfer. Similarly, a concentration gradient of a species in a mixture (or solution) provides the driving potential for mass transfer. Both conduction heat transfer and mass diffusion are transport processes that originate from molecular activities. Crystal growers are actually concerned with two aspects of nutrient-to-crystal transport:

1. The mass flux across an interface, which we will call the interfacial flux and which determines the crystal growth rate
2. The concentration profile of growth species in the nutrient adjacent to the crystal, which is an essential parameter in morphological stability discussions.

Let us now introduce the dimensionless numbers that govern forced and free convection. The Grashof number Gr is

$$Gr = \frac{g\beta\Delta TL^3}{\nu^2}, \quad (17.11)$$

where g is gravitational acceleration (m/s^2), $\beta = 1/\rho(\delta\rho/\delta T)$ is the thermal expansion coefficient (where ρ is density), ΔT is the temperature difference between the horizontal surfaces that are separated by L , and ν is kinematic viscosity (m^2/s). The Grashof number Gr plays the same role in free convection that the Reynolds number plays in forced convection. The Reynolds number Re is

$$Re = \frac{VL}{\nu} = \frac{\rho VL}{\mu}, \quad (17.12)$$

where V is velocity (m/s), L is the characteristic length (m), ν is kinematic viscosity (m^2/s), ρ is density, and μ is viscosity ($\text{kg}/(\text{s m})$). The Reynolds number Re provides a measure of the ratio of the inertial to viscous forces acting on a fluid element. In contrast, the Grashof number Gr , indicates the ratio of the buoyancy force to the viscous force acting on the fluid.

17.1.3 Effect of Impurities

We will now define impurities, which are inherently present, and additives or dopants, which are deliberately added. The former are naturally present in the growth environment and are unwanted; the latter are deliberately added in order to control nucleation, improve crystal quality, increase the size, and change the crystal habit or other physical properties. This topic

has received great attention since it is of relevant theoretical and practical interest in the growth of crystals of industrial importance. The ability of impurities to change the growth behavior has been studied by many authors [17.23–36]. It is well known that the influence of impurities on the crystal form and the growth rate is based on the adsorption of ions, atoms or molecules of foreign species at kinks, ledges, and terraces of a growing crystal. The change of the crystal form is based on a difference in adsorption energies on different faces. Impurity molecules will be preferentially adsorbed on surfaces where the free adsorption energy is maximum. It has been possible to predict this preferred surface using computational approaches [17.37]. Recently the mechanisms and models of adsorption of impurities during the growth of bulk crystals have been surveyed by Sangwal, including kinetic effects of impurities on the growth of single crystals from solution [17.36].

The solvent itself is an impurity. High temperatures and high supersaturations increase growth rate, but in the presence of a solvent the effect of temperature is stronger, since it promotes water desorption and growth kinetics much more than supersaturation, as found for sucrose [17.38, 39]. Anomalies found by Chernov and Sipyagin [17.40] at 10 and 40 °C in growth rates disappeared when ethanol, which is known to disrupt the bulk structure of water, was added to the solution. Indeed, water adsorbed on crystal surfaces has properties differing from those of free water. This is attributed to the different structures of the adsorbed layer which undergo phase-like transformations at these temperatures.

Impurity adsorption can be studied indirectly through the adsorption isotherm, i. e., the fraction θ of adsorbed sites which are occupied as the impurity concentrations C_i increase. The simplest model of localized adsorption, i. e., situated at lattice sites, is the Langmuir isotherm

$$K_a C_i = \frac{\theta}{1 - \theta}, \quad (17.13)$$

where K_a is the temperature-dependent adsorption constant, which is different for each crystal face. Other models, which take into account the interactions between adsorbed impurities or the occupation probability, have been proposed.

Impurities can act in different ways. When they interact with the solute or solvent, they can have strong influences on the solubility and consequently on the supersaturation and kinetic processes. When impurities are adsorbed on crystals, they can have thermodynamic

and kinetic effects. The dominant effect is on the rates of exchange in which the adsorbed molecule or ions and growth units are involved. If the former are exchanged more rapidly than the latter, adsorption mainly affects surface and edge free energy. For a face, a decrease of γ_i (interfacial energy of face i) results in, according to the Gibbs equation,

$$\Delta\gamma_i = k_B T \ln(1 - \theta)/S, \quad (17.14)$$

where S is the area of the adsorption site. Similarly, the edge free energy is decreased. These effects should cause an increase in the nucleation and growth rate. If the exchange rate of the adsorbed molecules is slower, impurities can strongly decrease the kinetic coefficients ($R_F = K\sigma^2$ at low supersaturation and $R_F = K'\sigma$ at high supersaturation, where K and K' are kinetic coefficients that depend on the temperature and growth mechanisms, R_F is the growth rate of face F , and σ is the relative supersaturation). So that as a final result the kinetic effects dominate the thermodynamic ones and a decrease in growth rate and impingement flux occur. The interpretation of impurity effects can be done on a structural and kinetic basis:

1. Low concentrations of impurity can form an adsorbed monolayer on the surface even in undersaturated solutions, due to the structural relationship between the two-dimensional (2-D) crystal face and the adsorbed layer (as in the case of NaCl grown in the presence of CdCl_2 , where a monolayer of $\text{Na}_2\text{CdCl}_2 \cdot 3\text{H}_2\text{O}$ is formed). The main influence is on the crystal habit.
2. The kinetic interpretation considers the possibility of adsorption on the different surface sites. If impurities are adsorbed at the kinks, the advancement rate of the edge is hindered even at very low impurity concentrations and the growth rate is strongly decreased and even blocked. Adsorption can also occur on the surface with so strong bonds that impurity molecules cannot move and form a barrier through which the steps have to filter. The spreading of steps beyond this barrier demands supersaturation higher than a critical value for each impurity concentration. In this case impurities are incorporated. Such additives are tailor-made to modify the crystal habit for industrial needs. The molecules of these impurities are similar to those of crystals, but contain some structural differences, so that when they are incorporated into the crystal they disrupt some bonds and change the growth rate of the faces.

17.2 Low-Temperature Solution Growth

Among the various methods of growing single crystals [17.41–43], solution growth at low temperature occupies a prominent place owing to its versatility and simplicity. Growth from solution occurs close to equilibrium conditions and hence crystals of high perfection can be grown.

Solution growth is the most widely used method for the growth of crystals when the starting materials are unstable or decompose at high temperatures. This method demands that the materials must crystallize from solution with prismatic morphology. In general, this method involves seeded growth from a saturated solution. The driving force, i.e., the supersaturation, is achieved either by lowering the temperature or solvent evaporation. This method is widely used to grow bulk crystals that have high solubility and solubility variation with temperature. After many modifications and refinements, the process of solution growth now yields good-quality crystals for a variety of applications. Growth of crystals from solution at room temperature has many advantages over other growth methods, though the rate of crystallization is slow. Since growth is carried out close to room temperature, the density of structural imperfections in solution-grown crystals is relatively low.

17.2.1 Solution Growth Methods

Low-temperature solution growth can be subdivided into the following categories: (i) the slow cooling method, (ii) the slow evaporation method, (iii) the temperature gradient method, and (iv) the chemical/gel method.

Slow Cooling Method

Slow cooling is the best way to grow crystals by solution technique. The main disadvantage of the slow cooling method is the need to use a narrow temperature range. The possible range of temperature is usually narrow and hence much of the solute remains in the solution at the end of the growth run. To compensate for this effect, a large volume of solution is required. A wide range of temperature may not be desirable because the properties of the grown crystal may vary with temperature. Even though this method has the technical difficulty of requiring a programmable temperature control, it is widely used with great success. In this method, growth occurs without any secondary nucleation in the solution, if the supersaturation is fixed

within the metastable zone limit. A large cooling rate changes the solubility beyond the metastable zone width and multinucleation occurs at the expense of the seed crystal. A balance between temperature lowering and the growth rate has to be maintained. Growth at low supersaturation prevents strain and dislocation formation at the interface. Supersaturation can be increased after initial growth to achieve a reasonable growth rate.

Slow Evaporation Method

This method is similar to the slow cooling method in terms of the apparatus requirements. The tem-

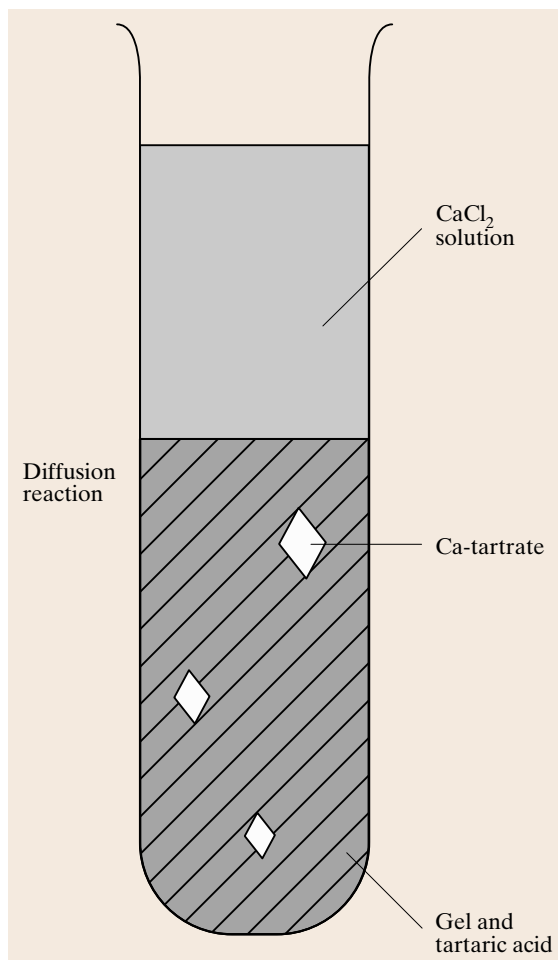


Fig. 17.3 Schematic diagram of the gel crystal growth process

perature is fixed and provision is made for evaporation. With nontoxic solvents such as water, it is permissible to allow evaporation into the atmosphere. Typical growth conditions involve a temperature stabilization of about $\pm 0.05^\circ\text{C}$ and rates of evaporation of a few mm^3/h . The evaporation technique has the advantage that the crystals grow at fixed temperature, but inadequacies of the temperature control system still have a major effect on the growth rate. This method can be used effectively for materials with very low temperature coefficient of solubility.

Temperature Gradient Method

This method involves the transport of materials from a hot region containing the solute material to be grown in a cooler region, where the solution is supersaturated and the crystal grows. The main advantages of this method are

1. Crystal growth at fixed temperature

2. Insensitivity to changes in temperature, provided that both the source and growing crystal undergo the same change
3. Economy of solvent and solute.

On the other hand, a small temperature difference between the source and the crystal zones has a large effect on the growth rate.

Chemical/Gel Method

The gel method is exceedingly simple. One procedure is to prepare a gel using commercial waterglass, adjusted to a specific gravity of 1.06 g/cm^3 . Gel is then mixed with 1 M tartaric acid and allowed to gel in a test tube. Once the gel is formed, some other solution can be placed on top (1 M CaCl_2 solution), as shown in Fig. 17.3. In the course of time, crystals of calcium tartrate tetrahydrate are formed in the gel. In a nutshell, one solution diffuses through the gel and reacts with the other solution to form crystals of appropriate chemicals [17.44].

17.3 Solution Growth by Temperature Lowering

The growth of crystals from low-temperature solutions occupies a prominent place, especially when materials are not stable at elevated temperatures. A number of concepts for solution crystal growth systems can be found in the literature. One of the best concepts for growth of both inorganic and organic crystals from solution is by temperature lowering of a solution, provided that the material has a positive temperature coefficient of solubility. In this method, a saturated solution of the material to be grown is prepared at a chosen temperature and kept at this temperature for 24 h. Then a seed holding rod is inserted into the growth chamber and its rotation is initiated. The growth process is initiated by lowering the temperature slowly. The temperature of the solution is lowered at a preprogrammed rate, typically $0.05\text{--}2.0^\circ\text{C}/\text{day}$, depending on the solubility of the chosen material. The complete crystallization process may take from one to several weeks. To terminate the growth process the grown crystals are taken out of the solution without thermal shock.

Solution crystal growth is a highly complex process and depends on various growth parameters such as the quality of the seed, the growth temperature, the temperature lowering rate, the character of the solution, the seed rotation speed, and stirring of the solution, besides

other conditions. To grow good-quality crystals, these parameters have to be optimized for each crystal.

17.3.1 Solvent Selection and Solubility

A solution is a homogeneous mixture of a solute in a solvent. Generally, the solute is the component present in a smaller quantity. For a given solute, there may be different solvents. Apart from high-purity starting materials, solution growth requires a good solvent. The solvent must be chosen by taking into account the factors:

1. High solubility for the given solute
2. Good solubility gradient
3. Low viscosity
4. Low volatility
5. Low corrosion.

If the solubility is too high, it is difficult to grow bulk single crystals and, if it is too small, solubility restricts the size and growth rate of the crystals. Solubility data at various temperatures is essential to determine the level of supersaturation. Hence, the solubility of the solute in the chosen solvent must be determined before starting the growth process. If the solubility gradient is very

Table 17.1 Solubility parameters δ of water and some organic solvents at 25 °C

Solvent	δ (MPa ^{1/2})	Solvent	δ (MPa ^{1/2})
Water	47.9	Acetic acid	20.7
Methanol	29.6	1,4-Dioxane	20.5
Ethanol	26.0	Carbondisulfide	20.4
Formamide	39.3	Cyclohexanone	20.3
<i>N</i> -Methyl-formamide	32.9	Acetone	20.2
1,2-Ethanediol	29.9	1,2-Dichloroethane	20.0
Tetrahydrothiophene-1,1-dioxide	27.4	Chlorobenzene	19.4
<i>N,N</i> -Dimethylformamide	24.8	Chloroform	19.0
Dimethylsulfoxide	24.5	Benzene	18.8
Acetonitrile	24.3	Ethylacetate	18.6
1-Butanol	23.3	Tetrahydrofuran	18.6
Cyclohexanol	23.3	Tetrachloromethane	17.6
Pyridine	21.9	Cyclohexane	16.8
<i>tert</i> -Butanol	21.7	<i>n</i> -Hexane	14.9
Aniline	21.1	Perfluoro- <i>n</i> -heptane	11.9

small, slow evaporation of the solvent is the other option for crystal growth to maintain supersaturation in the solution. Growth of crystal from solution is mainly a diffusion-controlled process; the medium must be less viscous to enable faster transference of the growth units from the bulk solution to the growth site by diffusion. Hence a solvent with lower viscosity is preferable. Most important single crystals, such as potassium dihydrogen phosphate (KH₂PO₄) and L-arginine phosphate monohydrate (LAP), are grown in aqueous solutions or in solvents that are mixtures of water and miscible organic solvents. Of all known substances, water was the first to be considered for use as a solvent because it is non-toxic, most abundant, and low cost. A proper choice of solvent based on a knowledge of its chemical reactivity helps one to avoid undesired reactions between solute and solvent. Except that, in general, the solubility of the growth materials in solvents is required to be sufficiently large, the solubility parameter δ can often be used in estimating the solubility of nonelectrolytes in organic solvents

$$\delta = \left(\frac{\Delta U}{V_m} \right)^{1/2} = \left(\frac{\Delta H - RT}{V_m} \right)^{1/2}, \quad (17.15)$$

where V_m is the molar volume of the solvent, ΔU is the molar energy, and ΔH is the molar enthalpy; δ is a solvent property that measures the work necessary to separate the solvent molecules. Often a mixture of two solvents, one having a δ value higher than that of a solute and the other lower, is a better solvent than either

of the two solvents separately [17.45]. A selection of δ -values is given in Table 17.1.

Another property, that is, the dipole moments between the solute and solvent, may also be considered for selecting solvent for crystal growth. Most typical organic solvents have a dipole moment less than about 3 debye. Therefore, in the case of a solute having a similar value of dipole moment, a much wider choice of solvents is possible.

Solubility Determination

Solubility is an important parameter for crystal growth from solution at low temperature. Before any solution growth technique can be applied, determination of congruent or incongruent solubility and the establishment of absence of compound formation with pure or mixed solvents must be achieved. In the latter cases, a special compositional and thermal regime will be necessary to crystallize the desired phase. A simple apparatus for solubility studies is shown in Fig. 17.4. Visual inspection allows the determination of the solubility. Upon cooling, crystallized material is obtained for solid-phase analysis. This apparatus is easily fabricated and is very convenient for measuring solubility. The following is a description of how this has been achieved. The solute and solvent are weighed into a glass ampoule. The ampoule is sealed and rotated in a bath controlled by a thermostat, the temperature of which is increased in steps of 0.5 °C every 1–2 h. The final disappearance of the solute yields the saturation temperature. The accuracy of this measurement is within ± 0.5 °C.

However, the time needed to reach equilibrium for most covalent organic materials is usually shorter than that of sparingly soluble salts, although the settling times before analyses may be longer. In many soluble salts, such as potassium dihydrogen phosphate, KH_2PO_4 (**KDP**), triglycine sulfate $(\text{NH}_2\text{CH}_2\text{COOH})_3\text{H}_2\text{SO}_4$ (**TGS**), and ethylene dithiotetrathiafulvalene $(\text{CH}_2\text{NH}_2)_2\text{C}_2\text{H}_4\text{O}_6$ (**EDT**), the solubility is strongly temperature dependent. On the other hand, for some soluble salts, such as LiIO_3 and $\text{Li}_2\text{SO}_4 \cdot \text{H}_2\text{O}$, the solubility is not dependent on temperature and even has a negative slope.

Various techniques for measuring solubility, such as methods based on the vortex flow caused by concentration and optical effects, can be found in the literature. However, accurate measurement of supersaturation is usually difficult. Some new methods such as holographic phase-contrast interferometric microphotography and trace fluorescent probe have been developed. Using these techniques, the concentration distributions and thickness of the boundary layers under different convection conditions can be measured with greater accuracy. Although these methods still need more development and refinement to become more generally applicable, they are promising alternatives for the determination of supersaturation of easily soluble compounds. Of course, if the solubility is known, supersaturation can be calculated by measuring the temperature of the solution and its equilibrium temperature. The problem is that equilibrium temperature measurements are not always easy.

17.3.2 Design of a Crystallizer

When designing a crystallizer for growing crystals from solution by the temperature lowering method, the following conditions should be met [17.43, 46, 47]:

1. A range of operating temperature from room temperature to 80°C , depending on the solvent
2. The choice of hydrodynamic conditions in the solution
3. Measurements of growth parameters such a growth rate
4. Arrangement for taking grown crystals out of the crystallizer without any thermal shock
5. Arrangement for changing the saturation/temperature decrease rate
6. The possibility of interchanging different kinds of seed holders
7. Long-term operating reliability.

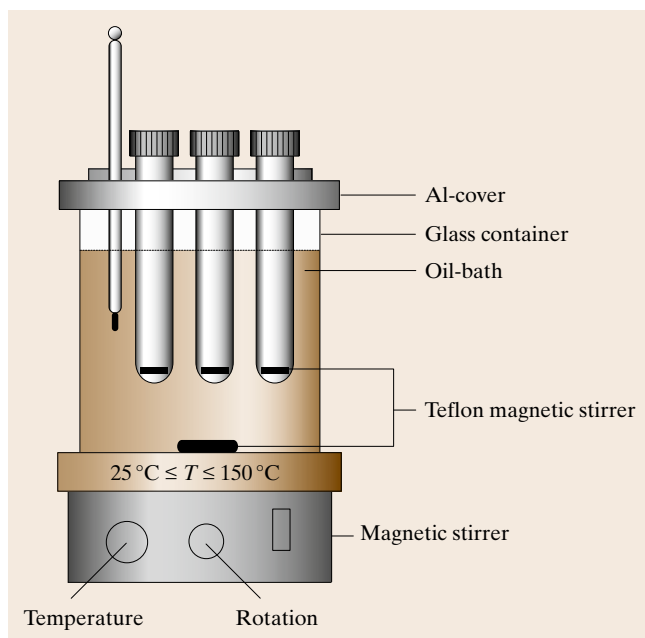


Fig. 17.4 Apparatus for solubility studies as well as equilibration of feed material and growth solution

Since these types of solution crystallizers are not available on the market, one has to design and fabricate one's own system based on one's requirements. A description of a modified crystallizer for growing large crystals from solutions along with the design of a versatile electronic reciprocating control system to change and reciprocate the motor speed containing the seed holding rod for solution growth crystallizer is given below.

In this system, the rotation rate and number of revolutions in the clockwise and counterclockwise direction can be adjusted as desired. This electronic system alleviates the problem of jerky motion of the seed holder [17.48] during reciprocation as in earlier electromechanical systems designed by the authors. Good-quality crystals of important nonlinear optical materials such as 2-methyl-4-nitroaniline:methyl-(2,4-dinitrophenyl)-aminopropanoate (**MNA:MAP**), L-arginine phosphate (**LAP**), L-histidine tetrafluoroborate (**LHFB**), L-arginine tetrafluoroborate (**LAFB**), and others such as triglycine sulfate and potassium dihydrogen sulfate have been successfully grown in authors' laboratory using this system [17.47, 49–54]. The complete crystallization apparatus along with the electronic circuit can be easily fabricated in the laboratory with readily available components.

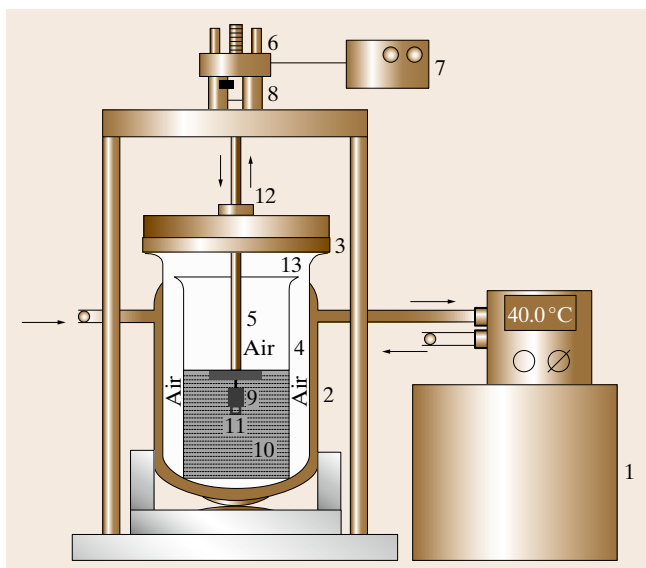


Fig. 17.5 Schematic diagram of a new type of crystallizer for growing organic crystals. (1) Circulating bath, (2) jacketed reaction kettle, (3) RTV/Teflon seal, (4) crystallizer jar, (5) Teflon seed holder, (6) reversible motor, (7) circuit for reciprocating and controlling the stirring rate of seed holder, (8) arrangement for pulling the crystal during growth, (9) Teflon tape cover, (10) solution, (11) seed crystal, (12) Teflon seal, and (13) glass lid

A Typical Solution Crystal Growth Crystallizer

A schematic diagram of a modified solution crystal growth system that the authors designed and fabricated after designing a number of crystallizers [17.48, 55–57] in our laboratory is shown in Fig. 17.5. It consists of a 250 ml crystallizer jar (4), which holds the growth solution that is placed inside a 2.5 l glass-jacketed kettle (2). The linear and reciprocating motion of the Teflon seed holder (5) is controlled by a rack–pinion arrangement (8) and electronic circuit (7), respectively. A reversible motor (6) is used for rotating the seed holder. The temperature of the growth solution is controlled and programmed by circulating water using a NesLab bath (1). To prevent evaporation of the solvent, a specially designed oil–Teflon seal (3) and/or room temperature vulcanizing silicone RTV/Teflon seal (3) are used. The main advantages of our crystal growth system are: (i) better temperature stability even with sudden fluctuations in room temperature, (ii) better control over evaporation of organic solvents, (iii) a mechanical screw-type arrangement for pulling the seed crystal at a controlled rate, (iv) the possibility of varying the seed orientation and type, and (v) a versatile

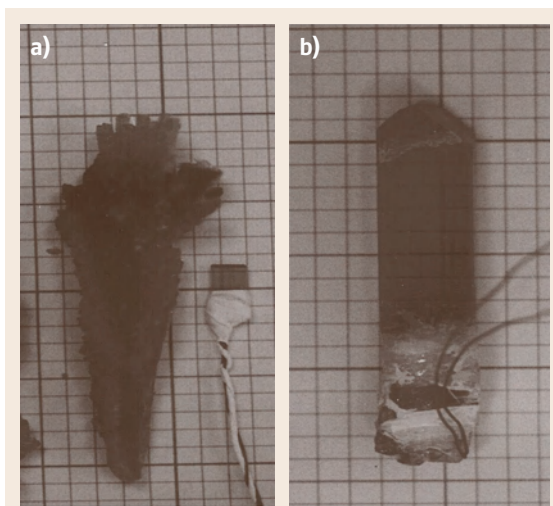


Fig. 17.6a,b MNA:MAP seed: (a) with aloe-vera-tree-type growth and (b) without aloe-vera-tree-type growth

electronic reciprocating control system to change and reciprocate the motor speed containing the seed holding rod. Better temperature stability was accomplished by loading the growth solution into a beaker kept inside the jacketed vessel.

An air gap provides extra insulation. Moreover, spontaneous nucleation at the bottom of the growth vessel, which hampers growth and impacts on the crystal yield, is completely eliminated. By providing an extra lid on the inside beaker and a Teflon seal over the jacketed vessel, the evaporation of the solvent was dramatically reduced. The inner beaker is filled halfway with solution rather than three-quarters as is usually done, and the growing crystal is pulled in a controlled fashion. Since filling of the inner beaker to three-quarters is not required, not only is the crystal annealed in situ but also spurious aloe-vera-tree-like growth near the seed in some crystals such as MNA:MAP is greatly reduced or completely eliminated.

Figure 17.6a shows the seed crystal along with a MNA:MAP crystal grown using the usual technique, i.e., without pulling the growing crystal. Figure 17.6b shows the same crystal grown with pulling where aloe-vera-tree-type growth is avoided. Furthermore, large crystals can be grown from a smaller amount of expensive mother liquor when the crystal is pulled while growing.

Another modified solution growth crystallizer was also designed in our laboratory, whose three-dimensional cutout view with reciprocating seed ar-

rangement and other components is illustrated in Fig. 17.7. It uses a magnetic stirrer to keep the temperature of the water bath uniform at a particular temperature. A layer of silicon oil on the surface of water was found to reduce the evaporation of water to a minimum, which is a big improvement over earlier designs.

Besides temperature control, the uniform rotation of seeds is required so that stagnant regions or recirculating flows are not produced, otherwise inclusions in the crystals will be formed. To study and achieve uniform and optimum transport of solute to the growing crystals, various seed rotation mechanisms have been used in the past. Unidirectional rotation of the seed leads to the formation of cavities in central regions of a crystal face because of lesser solute transport to this region than to edges and corner of the growing crystal. Furthermore, nonuniform solute supply favors the formation of thick layers which subsequently lead to the trapping of inclusions and the generation of dislocations. Periodic rotation of the growing crystal in opposite directions suppresses edge formation but does not eliminate the formation of the central cavity. To avoid these defects and stagnant regions in the solution, eccentric or clockwise and counterclockwise motion of the seed holder is used when growing crystals from solutions. Several mechanisms [17.48, 55, 58] have been used in the past to generate reciprocating motion of the seed holder, such as electromechanical [17.55] and rack–pinion methods [17.48]. In the electromechanical system, a connection of the motor polarity is reversed mechanically by using a microswitch. In this mechanical system, there is a jerky motion on reversal, which sometimes causes seeds to fall down. The jerky motion also creates a turbulent flow in the fluid and hence nonuniform transfer of solute to the growing faces, which may lead to the formation of defective crystals. Also, the microswitch has to be changed frequently due to mechanical failure. Furthermore, the effect of seed rotation rates on the growth rate and the quality of the crystals cannot be systematically studied because the rotation rate cannot be varied. In the rack–pinion arrangement, there is no jerking motion but one has to change gears to change rotation and reversal rate, which is quite an involved process.

To address these drawbacks, in our Crystal Growth Laboratory at Alabama A&M University, a versatile solid-state electronic circuit for reciprocating the direction of the seed holder was designed along with added features in such a way as to vary the rotation rate and stopping time on reversal, and control the timing for

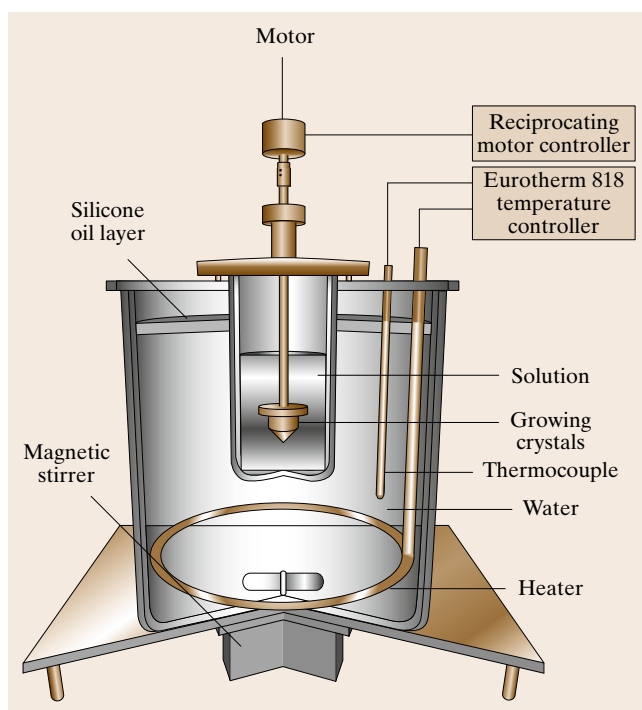


Fig. 17.7 A modified crystallizer with arrangement to stop water evaporation

clockwise and counterclockwise motion of the crystal/seed holder [17.56]. These design features will allow crystal growers to study more clearly the effect of seed rotation rate on the growth and quality of the grown crystals, thereby optimizing this important parameter for growing better-quality crystals.

A schematic diagram of the basic electronic circuit for reciprocating motion control is shown in Fig. 17.8. In Fig. 17.8, the timer (chip LM 555, U3) produces a square-wave timing pulse. It may be set to a particular frequency (POT1) and duty cycle (POT2) in combination with a timing capacitor (C3) and reset if necessary by a switch (S2). The timing waveform is divided by the J–K flip-flop chip 74LS112 (U1) to one-half of the timer frequency. Parasitic oscillations are suppressed by three capacitors (C1, C2, and C4). The two waveforms are combined by a NAND gates chip SN7400 (U2) to turn on two transistors (Q1 and Q2) alternately to control the solid-state relays (1 and 2) which connect alternate sides of the motor capacitor to the 110 V_{AC} return line. Similarly, the transistors (Q3 or Q4) alternately turn on the indicator lamps (LED1 and LED2). Current limiting and bias is provided by resistors (R1 through R8). Motor rotation speed is controlled by a potentiometer.

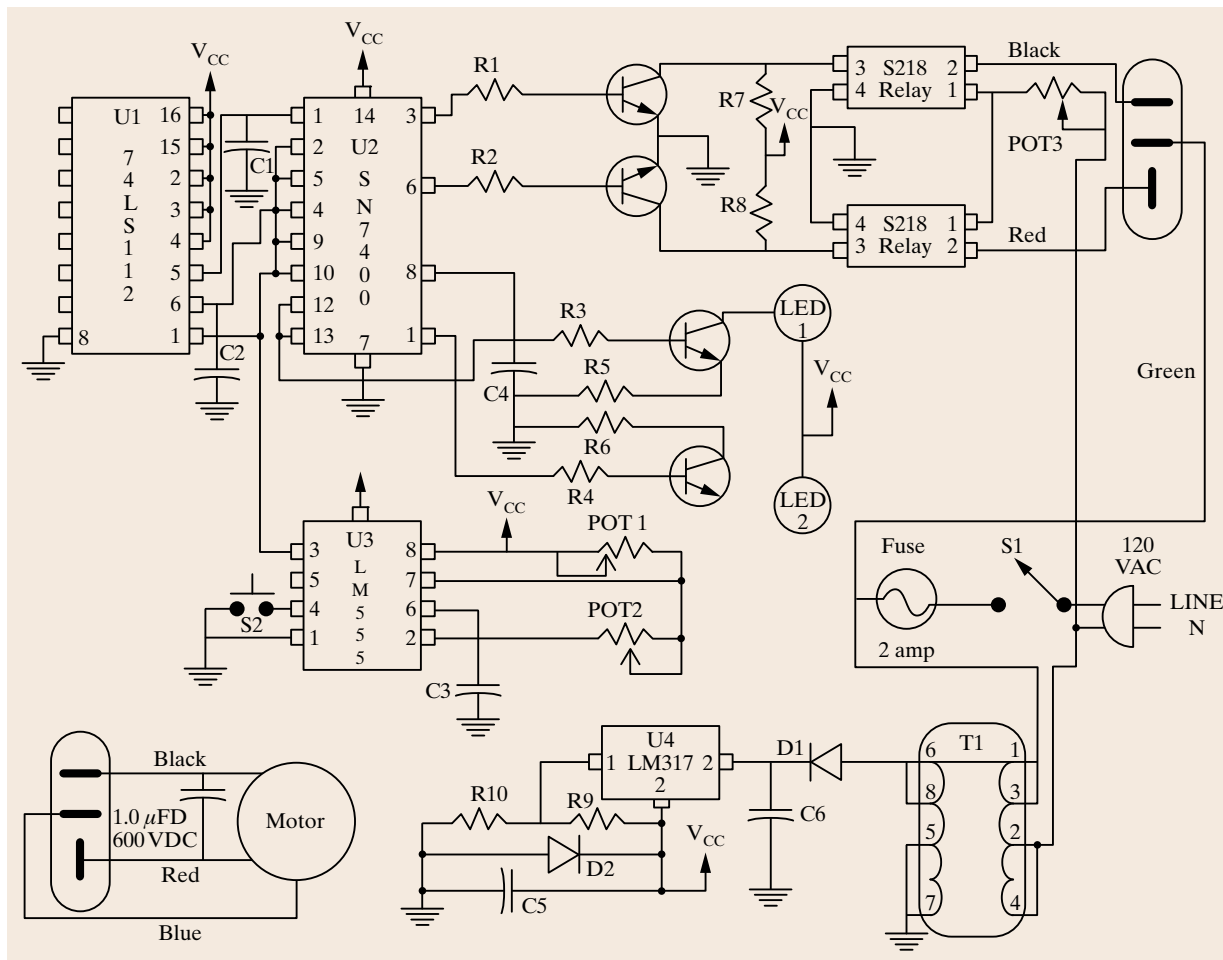


Fig. 17.8 Diagram of electronic circuit for control of the reciprocating motion of the seed holder for solution crystallizer

ter (POT3). A power supply consisting of a step-down transformer (T1), a voltage regulator (U4), and an associated filtering circuit (D1, D2, C5, and C5), and voltage

setting divider (R9 and R10) provides 5 V_{DC} to the circuit. The operation of the circuit causes the following sequence of states in the system: during first interval, the seed holder motor runs counterclockwise; during the second interval, the motor comes to a stop; during the third interval, the motor runs clockwise; and during the fourth interval, the motor again comes to stop. Then the entire cycle of operation is repeated, and the intervals can be varied as needed for a particular crystal growth experiment.

Crystal Seed Holder

In order to ensure the best growth conditions, it is necessary to use a special crystal holder because the success of an experiment may depend upon its suitability. The selection of the crystal holder and the method for attach-

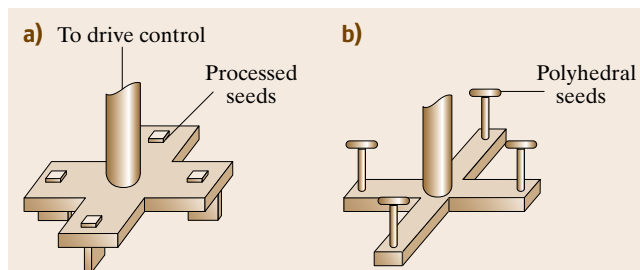


Fig. 17.9a,b Plexiglas seed holders for solution-growth crystallizers: (a) with processed seeds and (b) with polyhedral seeds

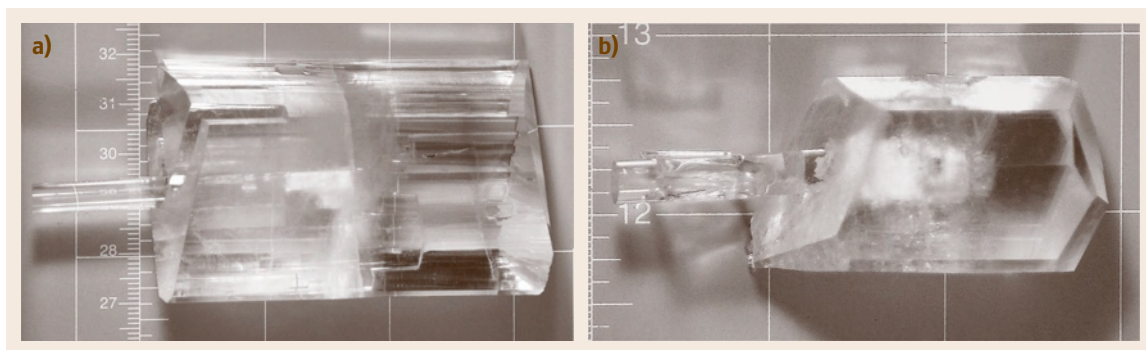


Fig. 17.10a,b Photographs of crystals grown at Alabama A&M University: (a) L-histidine tetrafluoroborate and (b) L-pyroglutamic acid crystals

ing a seed to it are no less important than the selection of the growth method. A crystal holder should ensure that a seed is held securely in a desired orientation and that the seed and therefore the growing crystal can be moved in any required manner. Also, the crystal holder should not become deformed at the selected speed and direction of the motion or by the weight of the final crystal grown on it. The crystal holder material should be chemically inert in the solution of the substance being crystallized.

A schematic diagram of two plexiglas seed holders that were specially designed, fabricated, and successfully used by the authors for aqueous solution crystal growth are shown in Fig. 17.9.

Preparation of the Seed Crystal and Mounting

A seed is a small fragment of a crystal or a whole crystal which is used to start the growth of a larger crystal in a solution. This seed must meet the following requirements:

1. It should be a single crystal free of cracks or boundaries.
2. It should be free of inclusions.
3. Its surface should be free of any sharp cleaved edges.
4. It must be grown under the same conditions as those to be used in growing the desired single crystals.

Following the above requirements in preparing the seed crystals will result in the growth of high-quality crystals, if other criteria such as solution preparation are performed carefully as well. Prior to crystal growth, seed crystals are mounted on plexiglas rods using 100% silicon rubber Dow Corning Silastic 732 RTV adhesive.

17.3.3 Solution Preparation and Starting a Growth Run

For solution preparation it is essential to have the solubility data of the growth material at different temperatures. Sintered glass filters of different pore sizes are used for solution filtration. The clear solution, saturated at the desired temperature, is poured into the growth vessel. For growth by slow cooling, the vessel is sealed to prevent solvent evaporation. Before starting the crystal growth process, a small crystal suspended in the solution is used to test the saturation. By varying the temperature, a situation is obtained where neither growth nor dissolution occurs. The test seed is then replaced with a good-quality seed. All unwanted nuclei and the surface damage on the seed are removed by dissolving at a temperature slightly above the saturation point. Growth is initiated after lowering the temperature to the equilibrium saturation. Controlled solvent evaporation can also be used in initiating the growth. The quality of the grown crystal depends on (a) the nature of the seed, (b) the cooling rate employed, and (c) the agitation of the solution.

Various new nonlinear optical crystals which hold promise for use in optical processing devices such as L-arginine phosphate, L-histidine tetrafluoroborate, L-arginine tetrafluoroborate, 2-methyl-4-nitroaniline:methyl-(2,4-dinitrophenyl)-aminopropanoate (MNA:MAP) and L-pyroglutamic acid have been successfully grown using the above-mentioned reciprocating system in combination with the temperature lowering technique, as described by the authors [17.47, 49–51]. Some of these crystals are shown in Fig. 17.10. In the investigators' observation and experience, there is significant improvement in the quality of grown crystals and success rates of the growth runs, as evident from the

transparency and lower scattering observed using laser illumination. This electronic system for reciprocal motion control of solution growth crystallizers has been in use in our laboratory for several years, and continues to work satisfactorily.

It is worth mentioning that this simple and versatile crystallization apparatus can be fabricated in any college, university or scientific laboratory from read-

ily available components. Besides its use in physics or chemistry laboratory experiments, it can also be used for doing extensive research on the effect of important parameters such as seed rotation rate, stopping time of reversal, and number of rotations in the clockwise or counterclockwise direction on the quality and growth rate of technologically important crystals.

17.4 Triglycine Sulfate Crystal Growth: A Case Study

Triglycine sulfate (TGS) is one of the most important ferroelectric materials. The ferroelectric nature of triglycine sulfate, $(\text{NH}_2\text{CH}_2\text{COOH})_3 \cdot \text{H}_2\text{SO}_4$, usually abbreviated as TGS, was discovered by Matthias et al. and discussed by Jona and Shirane [17.59]. The crystal structure of TGS was reported by Hoshino, Okaya, and Pepinsky and discussed in the above reference. In the ferroelectric phase below the Curie temperature ($T_C \approx 49^\circ\text{C}$), the symmetry is monoclinic with space group $P2_1$. Above the Curie temperature, the structure gains an additional set of mirror planes in the space group $P2_1/m$. It has been reported that the lattice parameters are $a = 9.42 \text{ \AA}$,

$b = 12.64 \text{ \AA}$, $c = 5.73 \text{ \AA}$, and $\beta = 110^\circ 23'$ and that the structure contains three independent glycine molecules. One of the structures, designated as glycine II, has a zwitterion configuration $(\text{NH}_3)^+\text{CH}_2\text{OO}^-$, and the other two, $(\text{NH}_3)^+\text{CH}_2\text{COOH}$. TGS may be called glycine-diglycinium sulfate with chemical formula $((\text{NH}_3)^+\text{CH}_2\text{COO}^-) \cdot ((\text{NH}_3^+)\text{CH}_2\text{COOH})_2 \cdot \text{SO}_4^{2-}$. The projection of the structure along the c -direction is illustrated in Fig. 17.11. Glycine I deviates only slightly from the plane m' at $y = \frac{1}{4}$ on which the $[\text{SO}_4]^{2-}$ tetrahedra also lie, whereas glycine II and III are approximately related by inversion through $(\frac{1}{2}, \frac{1}{2}, \frac{1}{2})$ [17.60].

17.4.1 Growth of Single Crystals of Triglycine Sulfate

Single crystals of TGS have usually been grown from aqueous solution by the temperature lowering or solvent evaporation method. The authors have successfully grown TGS crystals using the crystallizer whose schematic diagram is shown in Fig. 17.12 [17.57]. The outside water bath, with a capacity of about 12 l, and the inside smaller cubical growth cell with 1 l capacity were made out of Plexiglas. Temperature control of the crystallizer was achieved using 250 W immersion heaters controlled by YSI 72 proportional temperature controllers to an accuracy of $\pm 0.1^\circ\text{C}$. Uniformity of the temperature throughout the bath was achieved with the help of a fluid circulation pump. The bath temperature is monitored at two points during the crystal growth using NIST (National Institute of Standards and Technology) calibrated thermometers. The crystals were grown by slow cooling of the solution at any desired rate.

TGS crystals are doped with L-alanine to enhance its performance and check depoling for their use in infrared sensor element. A rotating disc technique [17.61] has been applied to grow uniformly L-alanine-doped TGS crystals using a large-area seed crystal having large

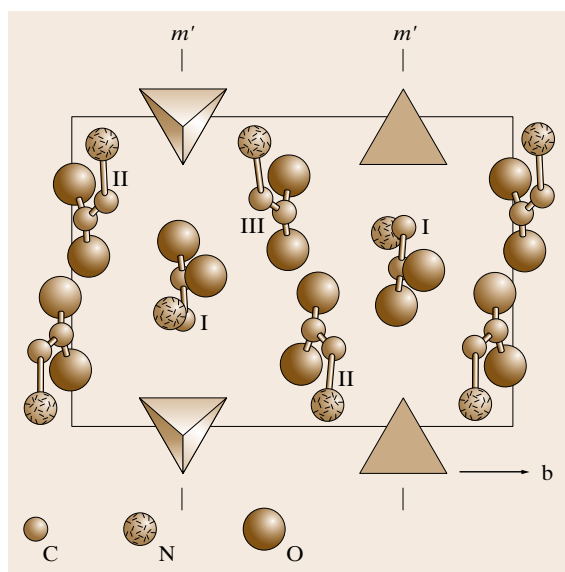


Fig. 17.11 Projection of the structure of TGS crystal along the c -direction: m' represents the set of pseudomirror planes in which glycine I molecules are inverted on ferroelectric switching

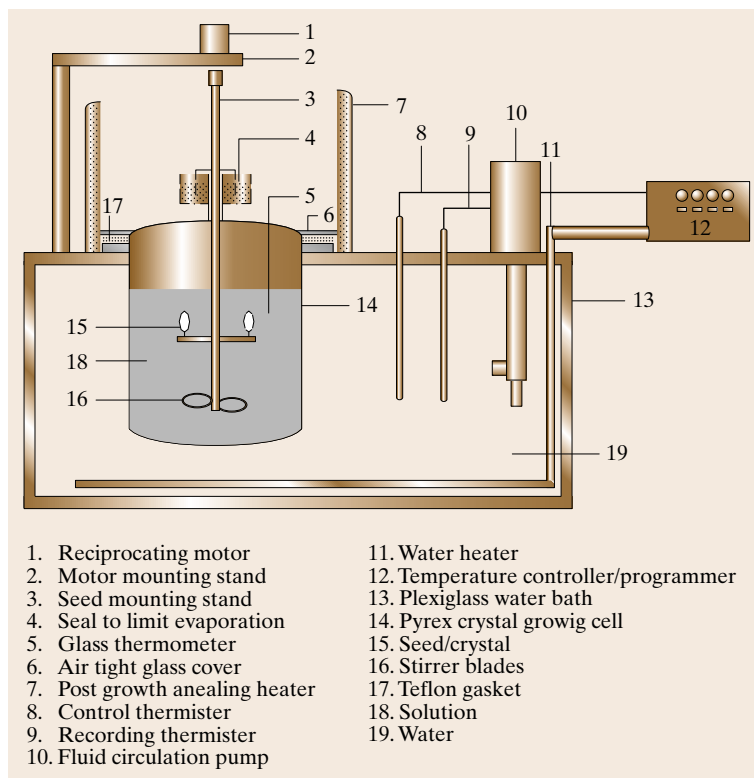


Fig. 17.12 Schematic diagram of reciprocating motion crystallizer

(010) face. A conventional crystallizer was modified to allow growth under suitable hydrodynamic conditions in order to stabilize growth on the (010) face. Such a crystallizer is shown in Fig. 17.13. In this crystallizer, a seed crystal in the form of a disc was held in a circular holder with the (010) face exposed to the solution. The disc was attached to the end of a spindle that was rotated at 340 rpm. This creates a uniform boundary layer of solution over the crystal's exposed face. The container with 30 l capacity was heated by a hot plate spaced from its bottom surface and regulated to hold the temperature within $\pm 0.01^\circ\text{C}$. The solution rises from the bottom of the vessel but hotter liquid is prevented from reaching the crystal directly by a plexiglas baffle. A growth rate of 1 mm/day was maintained by lowering the temperature uniformity at $0.05^\circ\text{C}/\text{day}$. The resulting crystals were found to be visibly of good quality, without defects propagating from the seed. In addition to uniform doping and growth of high-quality crystal, the method has several other useful features such as short growth time, with decreased cost and reuse of seeds, and that growth occurs within a narrow temperature range. *Brezina et al.* [17.62] designed a crystallizer

for growing L-alanine-doped deuterated triglycine sulfate (DTGS) crystals by isothermal evaporation of D_2O . *Satapathy et al.* [17.63] have described a novel technique for mounting the TGS seeds and a crystallizer. *Banan* [17.64] has also described a crystallizer and a seed holder for growing pure and doped TGS crystals.

TGS crystals weighing more than 100 g have been grown from solution with ethyl alcohol additions [17.65]. When alcohol is mixed in an aqueous solution of TGS, part of the water in the solution associates with alcohol, which concentrates the solution. Thus, the supersaturation can be controlled to a certain degree, making it easier to grow TGS crystals.

To achieve success in growing crystals from aqueous solutions, it is important to prepare a solution with a well-determined saturation temperature, solubility profile, and absence of any foreign particles. For our investigation, TGS solution was prepared using high-purity crystalline triglycine sulfate from BDH, UK. The solubility of TGS at various temperature were determined and compared with information available from various sources. TGS solution was prepared at 40°C saturation temperature. To prepare saturated solution,

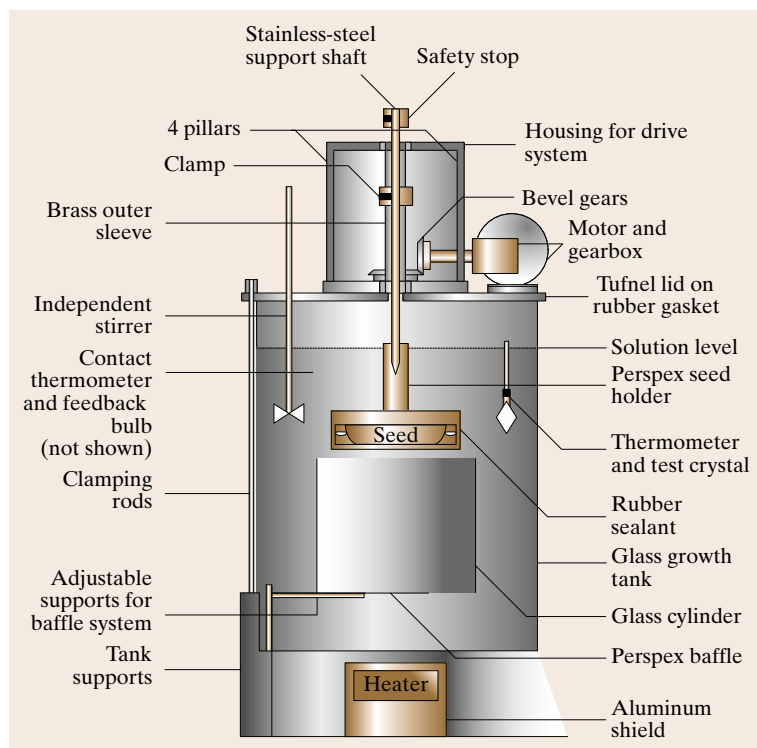


Fig. 17.13 Apparatus for spinning disc growth

464 g TGS was weighed and dissolved in 1000 cm³ distilled water. The mixture was heated to 50 °C and mixed thoroughly using a Teflon-coated magnetic stirrer. The solution was then filtered through a 5 μm filter funnel using a vacuum unit. After filtration, this solution was transferred to the growth chamber. To start the growth run, the bath temperature was kept at 45 °C. The solution was poured into the growth cell. Then the temperature was reduced to 41.5 °C, 1.5 °C above the saturation temperature and allowed to stabilize over night. The saturation temperature was again checked by the technique of crystal insertion into the solution as well as refractive index measurements. For each saturation point the refractive index was measured at different temperatures beforehand using an Abbe refractometer. The starting growth temperature was adjusted based on the result of this procedure. After this the seed crystal holder was placed in an oven and heated to 45 °C. Prior to transfer to the growth cell, all precautions were taken to keep the seeds as well as the holder surface free of dust and foreign particles. The preheated seed crystals holder were then inserted into the growth cell and holder attached to the reciprocating apparatus. The seed crystals were slightly dissolved and the growth run started.

The bath temperature was reduced by 0.1 °C/day initially and at the final stage of growth by 0.2 °C/day. The removal of the grown crystals from the mother liquor requires some care. Mishandling may induce defects, thus destroying the scientific value of the crystal or even fracturing it altogether. To avoid cracking the crystals due to thermal shock, the crystals were wrapped in a lint-free paper towel maintained at final growth temperature. The crystals were then transferred to an oven kept at an appropriate temperature. The temperature of the oven was slowly lowered to room temperature. Grown crystals can be easily removed from the seed holder by slight finger force, as RTV 732 adhesive was used for mounting the seed crystal.

17.4.2 Growth Kinetics and Habit Modification

Triglycine sulfate crystal normally grows with the habit shown schematically in Fig. 17.14a. A photograph of the TGS crystal grown at authors' laboratory is shown in Fig. 17.14b. It is observed that the $V_{(010)}$ growth rate is much faster than $V_{(001)}$. So the (010) face, as seen in Fig. 17.14, is very small or not present. Both

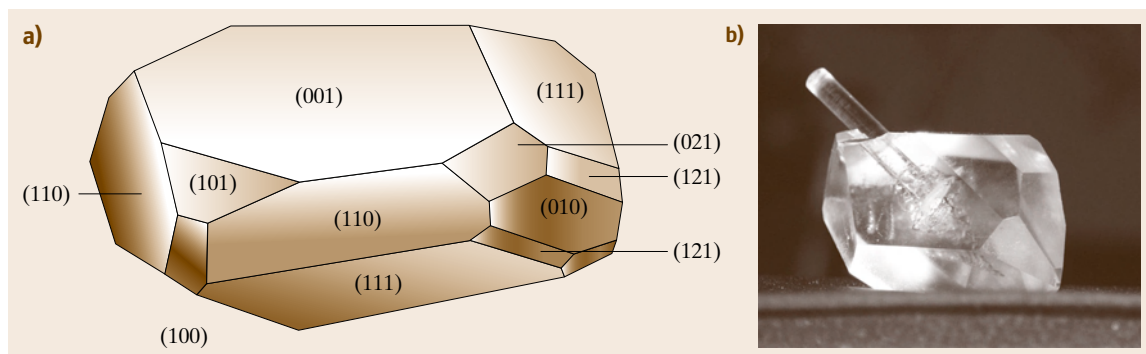


Fig. 17.14a,b Normal growth habit of TGS crystal. (a) Normal growth habit of TGS crystal, (b) photograph of as grown crystal of TGS at Alabama A&M University

growth kinetics and habit modifications of TGS have been extensively studied over the past few decades. The work published so far has resulted in a description sufficient for reliable growth of this crystal as described above. A number of studies of the growth kinetics of TGS grown from aqueous solution have been reported in the literature [17.66–71]. Novotny et al. [17.69] studied the growth of the (110) face of TGS crystals grown isothermally above the phase transition, at higher supersaturation ($\sigma > 10^{-3}$), and under constant hydrodynamically controlled conditions. The researchers observed that the ratio of growth rates along the individual axes is $V_a : V_b : V_c = 0.67 : 1 : 0.25$. On the basis of the measured dependence of the linear growth rate on the supersaturation (σ), it was found that the growth of the (110) face is probably controlled by volume diffusion of TGS molecules towards the surface of the growing crystal. Increasing the supersaturation caused a reduction of the number of faces in the prismatic zone of the crystal and an increase of the dislocation density in the (110) faces. Measurements of the growth rates [17.69] of (110) and (001) faces as a function of supersaturation of the solution were also analyzed on the basis of the surface diffusion model of Burton, Cabrera, and Frank (BCF) [17.67]. It was shown that surface diffusion is responsible for the low growth rates of (001) faces; in the case of (110) faces, the mechanism is less important at higher values of supersaturation than volume diffusion. Rashkovich [17.68] investigated the growth of (001) faces below the transition temperature. The results were qualitatively consistent with the dislocation model of crystal growth, but the growth at low supersaturation did not agree with the BCF model [17.67]. Reiss et al. [17.71] studied the growth of crystals at 33.55 °C at relative supersaturations of 0.004

and 0.045. In their study, the BCF law is fitted to the growth rate data. They also found that qualitative aspects of the growth are consistent with the BCF model.

The role of pH, impurities, degree of supersaturation, growth temperature and technical parameters, including seed preparation and attachment etc. on growth kinetics has also been quantitatively investigated by various investigators [17.72–90]. The results are described below.

Effect of Seed Crystal

It has been observed that morphology does not change much for seed crystals obtained at different temperatures [17.80]. However, at higher temperatures (35–45 °C) seeds tend to be elongated in the (001) direction, while seeds grown at lower temperatures are nearly isometric. Morphological study of the crystals grown using the above-cited seeds showed dependency of the crystal habit on the characteristics of the seed. The grown crystals tended to be elongated when elongated seeds were used. Crystals with large (010) faces grew when cleaved platelets were used for seeding. Crystals with high transparency and lower dislocation densities were obtained when the crystal growth tem-

Table 17.2 Crystal growth data for TGS crystals grown on poled and unpoled seeds [17.72]

TGS crystals	Crystal yield weight (g/(day °C))	Growth velocity $V_{(010)}$ (mm/(day °C))
(010) poled seed	0.618	1.05
(010) unpoled seed	0.621	1.16
(0 $\bar{1}$ 0) poled seed	0.624	1.20
(0 $\bar{1}$ 0) unpoled seed	0.637	1.25

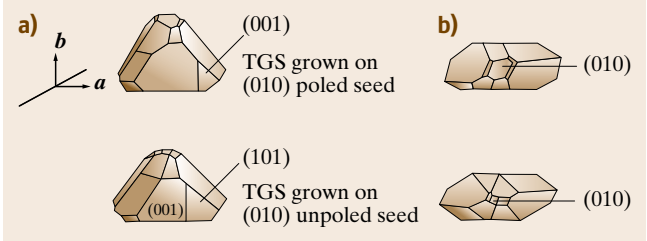


Fig. 17.15a,b Growth habits of **TGS** crystals grown on (a) poled and (b) unpoled seeds

perature was kept the same as that used to grow the seed. Crystal growth was seriously impaired when cleaved platelets were used as seeds, because of unwanted nucleation that started growing during the growth process. *Banan et al.* [17.82] studied the effect of using poled seed on the morphology and growth rate of **TGS** crystals. Table 17.2 summarizes the normalized growth data for two crystal growth runs using poled and unpoled seeds, and Fig. 17.15 gives the morphology of resulting **TGS** crystals. A number of interesting effects on the growth rate and morphology of these crystals were observed. Generally, the growth rate along the ($-b$ -axis) (010) was faster than along the ($0\bar{1}0$) ($+b$ -axis). The well-developed (010)/(0 $\bar{1}0$) faces, which are generally not present or less developed in pure **TGS** crystals, were prominent and large in crystals grown on poled seed. In this way, the identification of the ferroelectric axis in the **TGS** crystal becomes easier, and cleaving normal to the ferroelectric axis for preparation of pyroelectric infrared (IR) element can be economically accomplished. It can be inferred from Table 17.2 that growth velocity along the [010] axis of **TGS** crystal is affected by using a poled seed crystal. The decrease in growth rate along the [010] direction in the case of poled seed helps in the emergence of larger (010) face.

Effect of Growth Temperature and Supersaturation

The effect of crystal morphology and quality on growth temperature using the seed also grown at the same

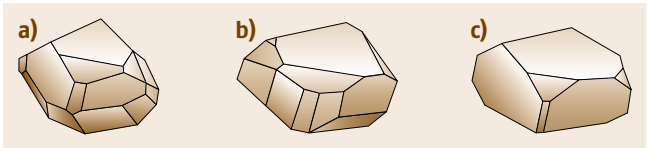


Fig. 17.16a–c Change of growth habits of **TGS** with growth temperature and supersaturation: (a) 32 °C, 0.7×10^{-3} (b) 32 °C, 3.0×10^{-3} , and (c) 52 °C, 3.0×10^{-3}

Table 17.3 Growth rates of various faces of **TGS** versus solution pH [17.76]

pH	$V_{(001)}$ (10^{-3} mm/h)	$V_{(010)}$ (10^{-3} mm/h)	$V_{(100)}$ (10^{-3} mm/h)
2.70	71.6	291.5	260.9
2.14	49.6	118.2	117.6
1.25	207.0	262.0	109.0
1.00	144.6	156.2	43.9
0.30	109.9	120.9	40.5

growth temperature, and from the same solution, has also been studied [17.80]. The change in morphology was not substantial, but the rate of growth in different directions changed with temperature, and relative change in the size of the faces was observed. Extra nuclei hindered growth at higher temperature (40 °C), and the crystals were of poor quality with low transparency. The change in habit of **TGS** crystals [17.76] as a function of temperature and supersaturation is shown in Fig. 17.16.

Effect of Solution pH

The influence of solution pH on the growth, morphology, and quality of **TGS** crystals has been studied by a number of workers. It was observed that crystal quality is not greatly affected by pH variation [17.80]. The influence of growth solution pH on growth rates of various faces: {(001), (010), (100)} and habit of **TGS** was studied by *Tsedrik et al.* [17.76].

At pH < 1, diglycine sulfate (**DGS**) was formed. Table 17.3 gives average values of the growth rate V of (001), (010), and (100) faces of **TGS** crystals versus pH of the solution as well as **DGS** grown at pH 0.3. Values of $V_{(100)}$ decreased monotonously with lowering pH, and $V_{(001)}$ and $V_{(100)}$ had a local minima near the pH value corresponding to the stoichiometric (pH = 2.14) value and a local maxima around pH = 1.25. The crystal habit is defined by the growth rates of the faces. Figure 17.17 shows the dependence of crystal habit on pH [17.76]. The most isometric crystals were obtained at pH = 1.55, when $V_{(100/001)} \approx 1$ (Fig. 17.17c). Almost all crystals at low pH had gaps on the (111) and ($11\bar{1}$) faces (Fig. 17.17d,e). The above observed changes in morphology of **TGS** single crystals with the pH of the solution were apparently affected by different capture of incidental impurities, which are always present in the solutions. Chemical (structural) impurities captured by the crystal faces reduced the growth rates of the corresponding faces, and mechanical impurities (defects) increased these rates. At low pH values,

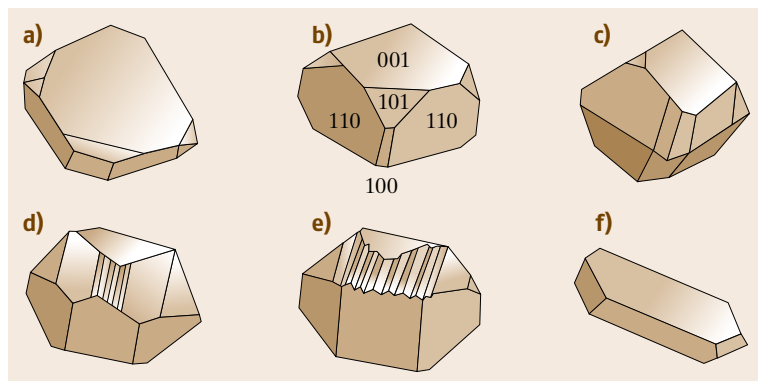


Fig. 17.17a–f Change of habit of **TGS** crystals with solution pH: (a) 2.75, (b) 2.1, (c) 1.55, (d) 1.23, (e) 1.0, and (f) 0.3 (**DTGS**)

chemical impurities played the predominant role. Their entry into the growing crystal was increased with reducing pH. Table 17.3 clearly shows that the growth rate of all faces decreased with reducing pH, starting with $\text{pH} = 1.25$. The gaps on the (111) and $(11\bar{1})$ faces were connected with strong hindering of the growth layers by the adsorbed impurities (Fig. 17.17d,e). At high pH (> 2) another kind of impurity (mechanical defects) has a predominant influence on crystal morphology. Their entry increased with rising pH, so the growth rates of all faces increased (Table 17.3). At $\text{pH} = 1.55$ the action of impurities of both kinds was comparable, and mostly isometric crystals were formed (Fig. 17.17c). Recently, it has been shown [17.91] that the growth rate of (010) face of **TGS** and L-alanine doped triglycine sulfo-phosphate (**ATGSP**) crystals varies with the pH of the solution.

With the same supersaturation, the growth rate of **TGS** crystals was slowest in the neutral solution ($\text{pH} = 2.25$). It grew faster in both acidic ($\text{pH} = 1.73\text{--}2.25$) and alkaline solution ($\text{pH} = 2.25\text{--}2.52$). In alkaline solution, the growth rate of **TGS** varied faster with changing pH value. However, if the pH was too high, then the (010) face capped quickly. The variation of growth rate of L-alanine-doped triglycine sulfo-phosphate (**ATGSP**) with pH was not similar to that of **TGS**. The growth rate of **ATGSP** crystals in a neutral solution ($\text{pH} = 2.5$) was the fastest, and it was slower in both acidic ($\text{pH} = 2.20\text{--}2.50$) and alkaline ($\text{pH} = 2.5\text{--}2.85$) solutions. The above results demonstrate that, on the basis of the pH of a solution, one can grow crystals at higher growth rates.

Effect of Impurities on TGS Crystal Growth

The presence of impurities in the process of crystal growth results in modification of the crystal shape and growth rates. Various workers have studied the effects

of inorganic and organic impurities on the kinetics of growth of doping **TGS** crystals. It was observed that Ni-doped crystals were very similar in habit to pure **TGS** crystals, while in the case of Cu- and Fe-doped crystals, the numbers of developed faces were strongly reduced [17.70]. In the presence of Ni, Co, and Cu ions, the rate of crystallization decreased [17.81]. An odd behavior was found while growing Cr-doped crystals. The addition of Cr with a concentration of 1% changed the regime of crystallization owing to the high chemical activity of these ions. At a concentration of about 3%, the rate of crystallization became very fast even without lowering the temperature [17.81]. In Pd-doped crystals, the ratios of the growth rate along the c -axis to the growth rate along the a - and b -axes slightly decreased as the crystal grew larger [17.85]. For medium-sized crystals (≈ 30 g), the average relative growth rate along the c -axis was larger by more than an order of magnitude in Pd-doped crystals than in pure **TGS**. Pd-doped crystals also developed other faces which have not been observed before. *Banan et al.* [17.82] studied the effect of Ce-, Cs-, L-alanine, and L-alanine + Cs on the growth and morphology of **TGS** crystals. Table 17.4 shows the crystal growth data, and Fig. 17.17 shows their habit. The well-developed $(010)/(0\bar{1}0)$ faces, which were generally not present or less developed in pure **TGS** crystals are obtained with L-alanine- or Cs-doped crystals. Moreover, (101) faces obtained in crystals doped with L-alanine and in crystals doped with Cs and L-alanine were more dominant than pure **TGS** crystals. Also, the axial velocities, $V_{(001)}$ and $V_{(100)}$, were affected by doping (Table 17.4). Lower growth rates were especially obvious in Cs-doped crystals. The crystals became plate-like for $V_{(010)}/V_{(001)} \approx 28.0$; and the habits was strongly disturbed (Fig. 17.18). L-Alanine-doped crystals developed a habit which was asymmetric about the (010) plane. The growth rate in

Table 17.4 Growth data of doped TGS crystals [17.82]

	Crystal yield (g/(day °C))	$V_{(010)}$ (mm/(day °C))	$V_{(001)}$ (mm/(day °C))	$V_{(010)}$ (mm/(day °C))
TGS	0.171	0.88	0.34	2.58
TGS + Ce	0.021	0.079	0.047	1.68
TGS + Cs	0.009	0.198	0.007	28.20
TGS + L-alanine	0.192	0.89	0.44	2.02
TGS + L-alanine + Cs	0.132	0.65	0.063	10.30

the positive *b*-direction was higher than in the negative *b*-direction [17.29]. In D-alanine and L-alanine-doped TGS crystals, (101) faces developed more prominently than (001) faces, so the deuterated L-alanine-doped triglycine sulfate (DLATGS) crystals seemed to be thinner than pure TGS crystals. The (010) faces were more developed in aniline-doped crystals [17.84]. Recently, Seif et al. [17.92] studied the dependence of growth rate of the faces of TGS and KDP crystals on concentration of Cr(III) [17.92]. They proposed the following hypothesis to explain the effect of impurities on TGS and KDP crystals. It has long been known that, when a solute crystallizes from its supersaturated solution, the presence of impurities can often have a spectacular effect on the crystal growth kinetics and the habit of the crystalline phase. The impurities exhibit a marked

specificity in their action as they are absorbed onto growing crystal surfaces. Adsorption of impurities onto crystal faces changes the relative surface free energies of the face and may block sites essential to the incorporation of new solute molecules into the crystal lattice and hence slow down the growth. The habit is thus determined by slow-growing faces. Furthermore, in the TGS:Cr(III) system dope with metal ions, metal-glycine complexes are formed in solution and enter the crystal lattice in the process of growth. The structure and type of metal ion complexes formed in the TGS lattice will determine the growth rate and hence the crystal habit.

It is also worthwhile to describe the effect of the same impurity on different types of crystals. The growth kinetic data of TGS and KDP crystals grown in the

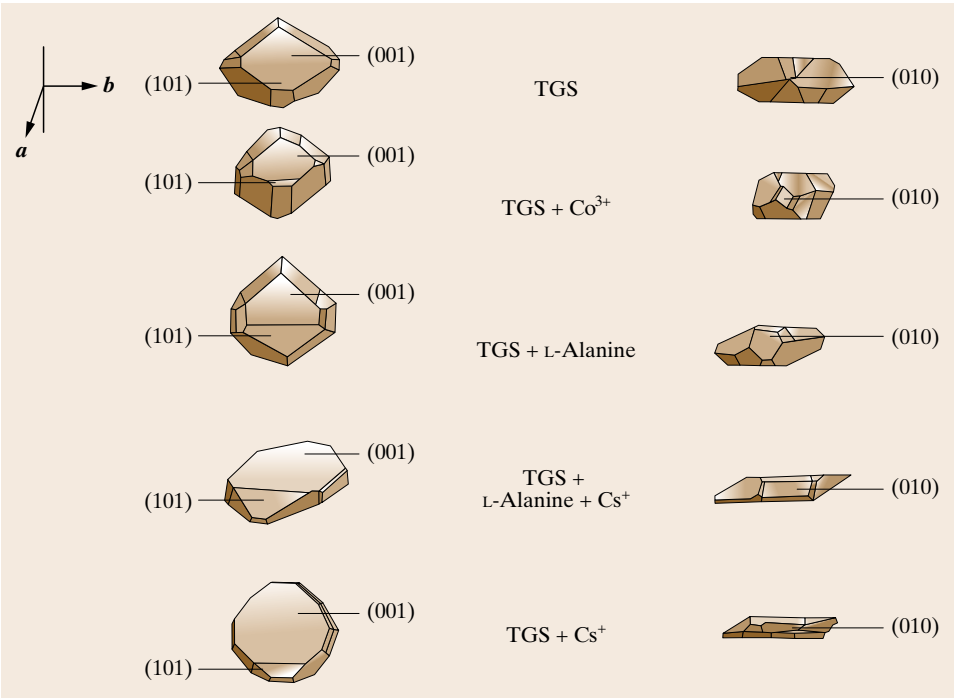


Fig. 17.18 Growth habits of doped TGS crystals

presence of Cr(III) ions are presented in Figs. 17.19 and 17.20. This data show the effect of impurity concentration on the growth rate of different faces of TGS and KDP crystals grown under constant, low supersaturation. In the case of KDP crystal, the mean growth rate along the [001] direction increases while along the [100] direction it remains almost constant with an increase in the concentration of Cr(III) in the solution/crystal with a slight fall below 7000 ppm. A similar type of effect of Fe(III) on growth rate of KDP crystal has been reported by Owczarek and Sangwal [17.25]. $\text{Cr}_2(\text{SO}_4)_3$ molecules are considered to dissolve as an active complex such as $[\text{Cr}(\text{H}_2\text{O})_2(\text{OH})]^{2+}$, $[\text{Cr}(\text{H}_2\text{O})_4(\text{OH})_2]^+$ or $[\text{Cr}_2(\text{SO}_4)_2(\text{H}_2\text{O})_7(\text{OH})]^+$ and are assumed to become adsorbed on the crystal faces, thereby suppressing the growth rate. The impurities adsorbed on the surface of growing crystal at low supersaturation impede movements of steps by different mechanisms depending on the site of adsorption. Models of different types which describe the adsorption process and growth reduction have been reported in the literature [17.26, 27, 36, 93]. The models assume that the impurity species (ions, molecules or atoms)

are adsorbed on the crystal surface into kinks, ledges, and terraces of growing surfaces. As soon as kinks and steps are occupied by impurity particles, there is a reduction in growth rates due to coverage of the crystal faces. This decrease in the growth rate can be explained on the basis of a model proposed by Sangwal and Mielniczek-Brzoska [17.32] based on their recent studies involving the Cu(II)–ammonium oxalate monohydrate crystal system. As shown in Fig. 17.19, the decrease in growth rate of (100) face of KDP crystals should be a kinetic effect involving a reduction in the value of the kinetic coefficient ($\beta = a\nu \exp(-W/k_B T)$), where a is the dimension of growth units perpendicular to the step, ν is the frequency of vibration of molecules/atoms on the surface (s^{-1}), W is the activation energy for growth, k_B is the Boltzmann constant, and T is temperature (in Kelvin) for motion of steps on the surface. Above a certain critical concentration of impurity, there is no kinetic effect of impurity on growth kinetics. This may be due to the fact that all the active centers for crystallization are blocked, thus reducing the growth rate to zero. In our study, no growth of the {100} face was observed with more than 8000 ppm Cr(III) im-

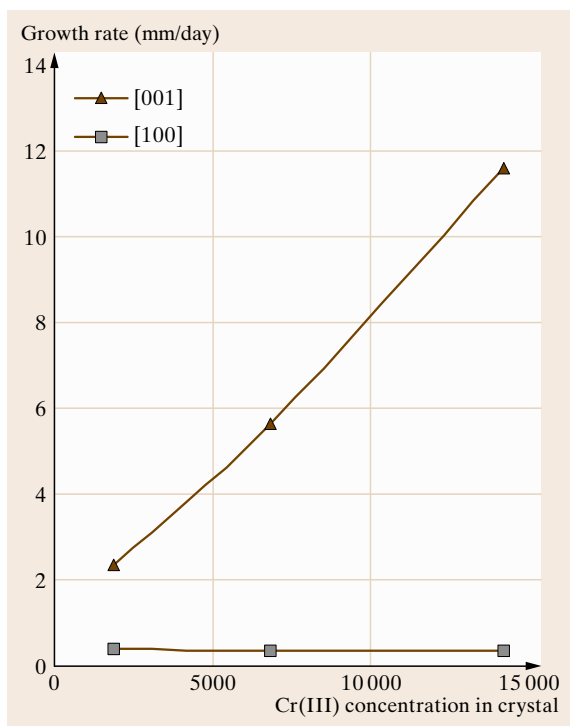


Fig. 17.19 Dependence of growth rate of the faces of KDP crystals on concentration of Cr(III)

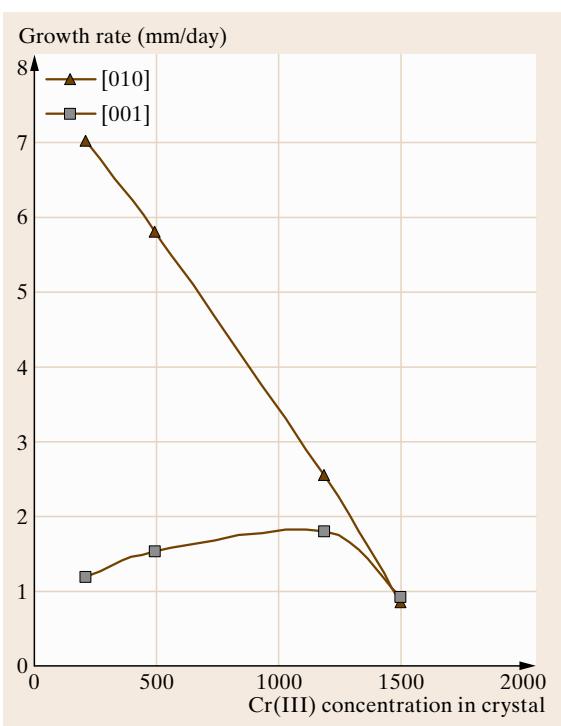


Fig. 17.20 Dependence of growth rate of the faces of TGS crystals on concentration of Cr(III)

purity in the **KDP** solution. An increase in growth rate along the [001] direction of **KDP** crystals may be caused by a decrease in the free energy of the face (thermodynamic effect); the surface energy decreases with an increase in impurity concentration, and hence increase in the growth rate. The above discussion suggests that the kinetic or thermodynamic effect depends on the structure of the crystal face, i.e., atomic arrangement, besides other factors.

Figure 17.20 shows that in the case of **TGS** crystals, the growth rate along the [010] direction decreases with an increase in the concentration of Cr(III) in the growth solution. This decrease in growth rate is due to the kinetic effect as explained above for the **KDP** crystal system. However, there is a slight increase in the growth rate along the [001] direction, with maxima around 1300 ppm Cr(III), and then there is a decrease. According to layer growth models, the consequence of a decrease in the edge free energy is an increase in the growth rate. Additionally, a decrease in the edge free en-

ergy may cause the growth mechanism to change. This effect of an initial increase followed by a subsequent decrease in growth rate with increasing concentration of impurity has been suggested by *Davey* [17.94], to opposite effects of thermodynamic and kinetic parameters. Furthermore, that ability of additives to form complexes with adventitious impurities present in a growth medium cannot be ruled out, as it can alter the atomic arrangement in crystal faces. To explain the effect of impurities on growth in more detail, one needs to collect more experimental data, including studies of the micromorphology of crystal surfaces as well as growth kinetics.

Effects of various organic dopants such as L-asparagine, L-tyrosine, L-cystine, guanidine, L-valine, and other dopants on morphology, growth, mechanical, and some physical properties of **TGS** have also been reported in the recent past [17.91, 95–99]. However, no explanation is given for change in the morphology of crystals by the authors of these publications.

17.5 Solution Growth of Triglycine Sulfate Crystals in Microgravity

The US National Aeronautics and Space Administration (**NASA**) has carried out about 115 Space Transportation Systems (**STS**) space flight missions (**STS-1** to **STS-127**) from 1980 to the present day [17.100].

The authors were associated with two **NASA** missions called Spacelab-3 and the International Microgravity Laboratory (**IML-1**) on which single crystals of triglycine sulfate were grown from solution in microgravity for a period of 7 days aboard a Space Shuttle.

The general goal of the programs within **NASA**'s Microgravity Research Division was to conduct basic and applied research under microgravity conditions (10^{-6} g) that would increase our understanding of fundamental physical, chemical, and biological processes specifically biotechnology, combustion science, fluid physics, fundamental physics, and materials science.

The microgravity environment of space provides a unique opportunity to further our understanding of various materials phenomena involving the molten, fluidic, and gaseous states by reducing or eliminating buoyancy-driven effects. Microgravity experiments in space are affected by residual microaccelerations on the spacecraft deriving from atmospheric drag, reaction control systems, momentum wheels, gravity gradients, crew involvement, and other disturbances. Mostly there

is no actual suggestion by the scientific community as to the microgravity level required for their experiments. The general opinion is that microgravity will reduce the influence of convection, buoyancy, and sedimentation. Hardly any quantitative estimates have been made.

The anticipated results of microgravity materials science research range from establishing baselines for fundamental materials processes to generating results with more direct commercial significance. **NASA**'s objectives for the microgravity materials science program include:

- Advancing our knowledge base for all classes of materials
- Designing and facilitating the execution of microgravity experiments that will help achieve this goal
- Determining road maps for future microgravity studies
- Contributing to **NASA**'s Human Exploration and Development of Space enterprise
- Contributing to the national economy by developing enabling technologies valuable to the US private sector.

To accomplish these goals, the materials science program has tried to expand both its scientific scope and

research community's involvement in microgravity research. Based on their requirements for experimental facilities most of the current materials science microgravity experiments can be divided into four general categories. The first category involves melt growth experiments, such as those used for processing multicomponent alloys from the liquid. The experiments in this category frequently require high temperatures and closed containers or crucibles to prevent elemental losses. The second group includes aqueous or solution growth experiments for materials such as triglycine sulfate and zeolite. These experiments usually require moderate to low temperatures. Hydrothermal processing of inorganic compounds and sol-gel processing also fit in this category. The third category of experiments involves vapor or gaseous environments, such as those used for growing mercury iodide or plasma processing. Unlike the first three categories that use containers for the parent materials and products, the fourth category involves processes and experiments that require containerless processing environments. Examples of these experiments include the formation of metallic and nonmetallic glasses during levitation melting and solidification, float-zone growth of crystals, and measurement of thermophysical properties such as diffusion coefficients and surface tension.

17.5.1 Rationale for Solution Crystal Growth in Space

In the microgravity environment of space, several physical phenomena taken for granted on Earth change dramatically. Convection in solution due to density differences is greatly reduced. Crystallization and solidification are two processes that can benefit from microgravity environment. As a part of the US National Aeronautics and Space Administration (NASA) microgravity and applications program, a study of TGS crystals growth from solution was carried out on Spacelab-3 (SL-3) and first International Microgravity Laboratory (IML-1) missions in 1985 and 1992, respectively. Crystals from solution are usually grown in a closed container of limited volume. Thus, any convection that is generated tends to lead to a circular to steady laminar convection, due to buoyancy. The density differences in the fluid can arise from both temperature and concentration variations. On Earth buoyancy-driven convection may cause microscopic gas/solution inclusions and fluctuating dopants incorporation and other defects in the crystals. Besides degrading pyroelectric device performance, the growth yield of useful crystals

is also severely impacted due to incorporation of these types of defects. In a low-gravity environment, convection is greatly suppressed and diffusion becomes the predominant mechanism for thermal and mass transport. Thus, growth in microgravity can eliminate these problems and enhance our knowledge about the science of crystal growth.

17.5.2 Solution Crystal Growth Method in Space

Since the ground solution technique could not be used in the microgravity environment of space, the authors developed a new method known as the cooled sting technique to grow crystals in space from solution, as described below.

Cooled Sting Technique

As the conventional techniques of solution crystal growth cannot be used for growing crystals in space, a new technique was proposed and developed [17.100–102]. On Earth, in the absence of stirring, conventional techniques of solution crystal growth cause a lowering of concentration of the solution in the vicinity of the growing crystal, resulting in an upward flow of solution. At constant temperature this reduction in concentration would cause the growth rate to decrease rapidly. In a 1g environment, most solution growth techniques are directed towards increased convection mass transport by applying forced convection with very slow programmed cooling of a saturated solution. However, in the absence of convection, a change of temperature must move inward toward the crystal by conduction. The characteristic time for this to occur is $T = L^2 \rho C_p / k$, where L is the distance over which the heat must be conducted, ρ is the density, C_p is the heat capacity, and k is the thermal conductivity of solution. For water, it takes 48 min for a temperature change of 1 °C to be felt at a distance of 2 cm. This is too slow to keep a constant growth rate. So a unique technique was developed by the authors, which uses programmed cooling of the seed crystal itself. This is accomplished by using a cold finger (*sting*) in direct contact with the seed crystal, which allows temperature lowering in accordance with a predetermined polynomial [17.103, 104] for maintaining a supersaturated TGS solution near the surface of the crystal. Because of the L^2 dependence of T , it takes less time for a change of sting temperature to be transmitted through the growing crystal and to be felt at the surface. The construction of the ground-based cooled sting and solution growth apparatus [17.103, 104] are

illustrated in Figs. 17.21 and 17.22, respectively. In this case, crystals are grown by lowering the sting/seed and solution temperature, thereby creating a desired supersaturation.

Flight Hardware

The experiment in space utilizes the fluid experiments system (FES) and crystals are grown by a new technique developed by the authors called the *cooled sting technique* as described earlier [17.101–103]. This technique utilizes heat extraction from the seed crystal through a copper rod (sting), thereby creating the desired supersaturation near the growing crystal. The sting temperature profile follows a predetermined polynomial so as to obtain uniform growth. Figure 17.23 shows a detailed diagram of the flight cell with sting incorporated in the experimental module. The FES is an

apparatus with the crystal growth cell as an integral part. It was developed by NASA and fabricated by TRW, CA.

The cell is designed to allow a variety of holographic diagnostics and real-time schlieren viewing of the crystal and the surrounding fluid. Schlieren images are transmitted down a link as black-and-white video to reveal flow patterns and variation in fluid density. Holograms that are recorded in space give 3-D information that leads to quantitative determination of concentration fields surrounding the crystal and motion of particles, if present, to determine g-jitters. The modified FES incorporates holographic tomography which enables the taking of optical data through the cell at multiple angles. During the SL-3 mission, two TGS crystals (named FES-2 and FES-3) were grown using (001)-oriented seed-type disc (as shown in Fig. 17.24). The objectives

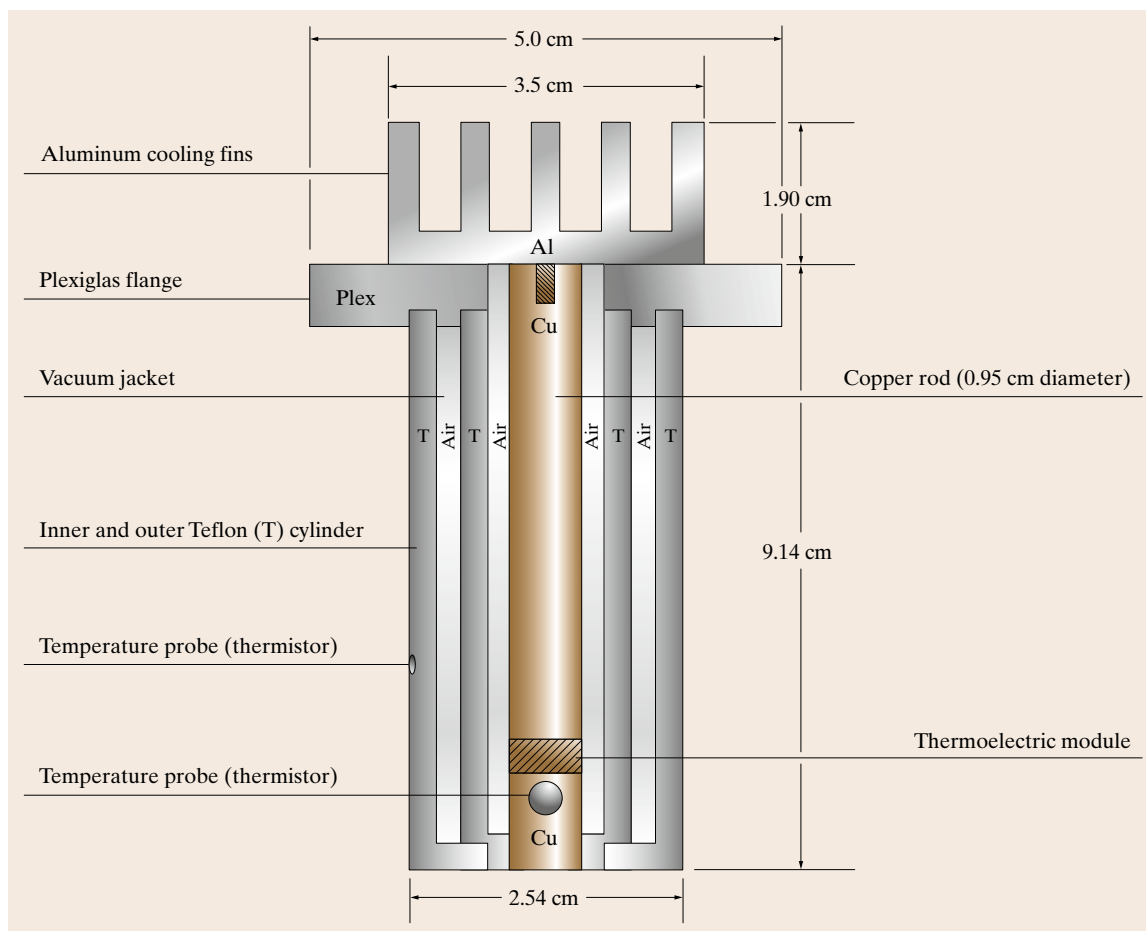


Fig. 17.21 Laboratory version of cooled sting assembly for the proposed crystal growth technique for microgravity

of the **IML-1** flight experiments were: (a) to grow **TGS** crystals, (b) to perform holographic tomography of fluid field in the test cell in three dimensions, (c) to study fluid motion due to g-jitter by multiple-exposure holography of tracer particles (200, 400, and 600 μm), and (d) to study the influence of g-jitter on crystal quality and growth rate. One of the authors (R. B. Lal) was the principal investigator of the Spacelab-3 and **IML-1** experiments. The coinvestigators were A. K. Batra, J. Trolinger, and W. R. Wilcox. During the **IML-1** flight, due to serious hardware problems, only one

TGS crystal was grown on a (010)-oriented seed crystal. The growth surface of seed crystal was a natural (010) face (unlike experiments performed in **SL-3**, in which processed seeds were used) cut from a polyhedral **TGS** crystal, with a thickness of about 3.5 mm. In **TGS**, the crystal growth rate is fast (maximum) in the [010] direction. On the ground, good-quality crystals are grown on (001)-oriented seed because growth on (010) face is nonuniform and multifaceted. Thus, it was important to investigate the growth on an (010)-oriented seed in the absence of buoyancy-driven convection,

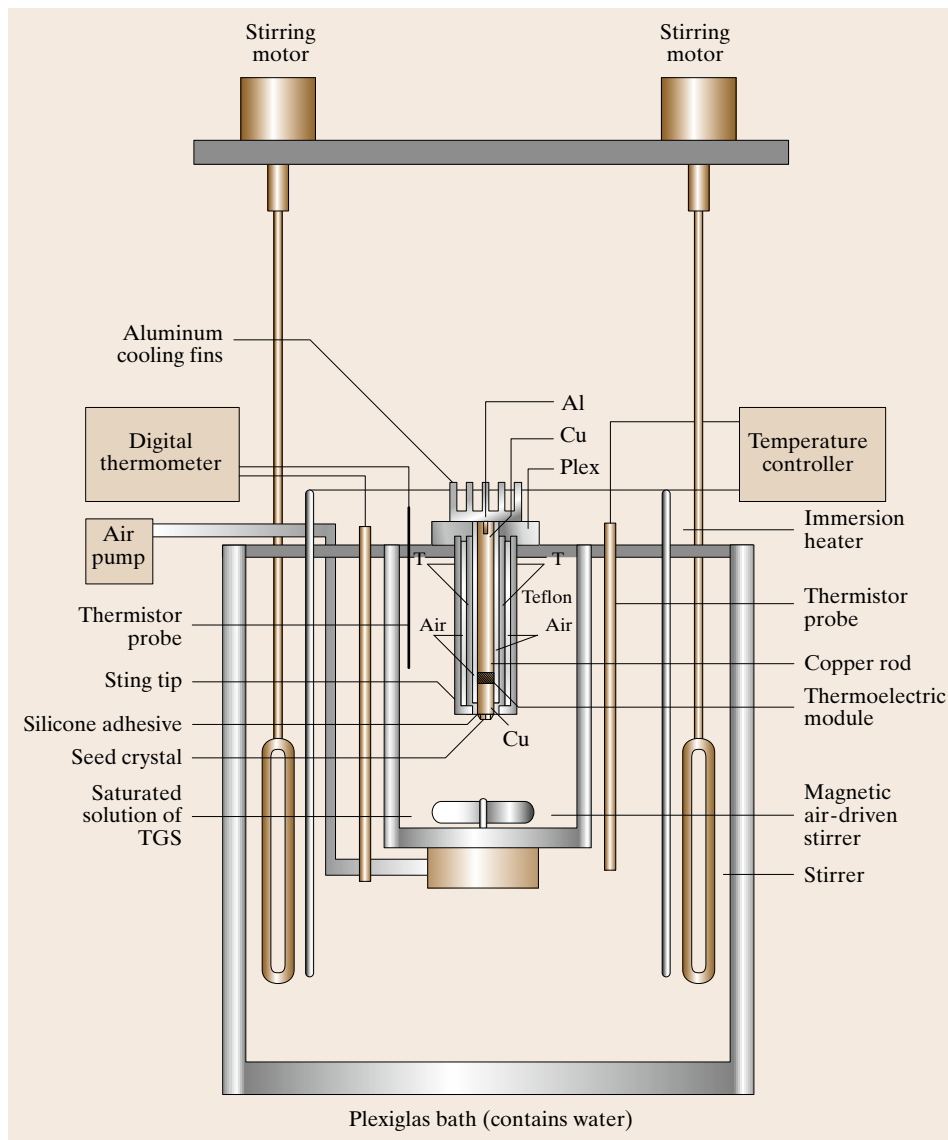


Fig. 17.22 Schematic diagram of the ground-based cooled sting solution growth apparatus

where growth is expected to be mainly diffusion controlled. This crystal was grown with undercooling of 4 °C for about 4 h. The growth rate was estimated to be about 1.6 mm/day and the quality of the grown crystal was substantially good. This can be attributed to a smooth transition from dissolution to growth in space experiment.

Flight Optical System

The fluids experiment system (FES) is a fully instrumented space flight chamber that can characterize the growth process through diagnostics of the crystal environment. Figure 17.25 shows the layout of optical system. Optical diagnostic instruments include two holographic cameras and a schlieren system, the output of which can be viewed in real time by television (TV) downlink. The optical and electronic instruments provide measures of solution concentration, temperature, convection, growth rate, and crystal properties during growth.

By recording light passing through the cell as well as light scattered from the crystal, holography provided diagnostics of the fluid through holographic interferometry, and particle diagnostics through three-dimensional particle imaging velocimetry. Figure 17.26 shows the

layout of the optical system in which a 4 inch diameter, collimated He-Ne (Spectra Physics 107) laser beam passes through a double window into the crystal growth chamber, through the TGS solution, and across the surface of the crystal, finally emerging from a second set of windows. The beam then continues to the hologram plane, which is approximately 20 cm away, where it is mixed with a collimated reference wave on 70 mm-format roll film. The film is drawn flat on the platen by a vacuum in a unique film implementation of hologram recording for interferometry. In addition to the use of vacuum platens for recording and reconstruction, a special reconstruction process, necessary for holographic interferometry with film, described below, was developed to account for the imperfect optical quality of the film. A second holocamera views the crystal face directly from a lateral window [17.105]. Four types of holograms were produced, including singly exposed and multiply exposed holograms. The back-lighting of the crystal was accomplished in two different ways, each with advantages and limitations; one method employs the direct laser beam and a second employs a diffuse beam, produced by inserting a diffuser into the object beam path before the beam enters the first cell window. The diffuse beam illuminates the field with

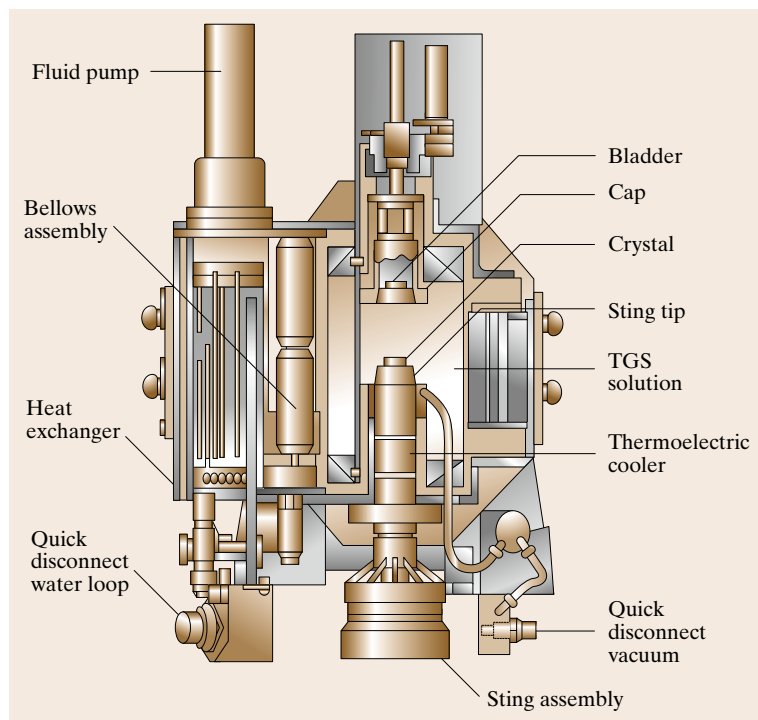


Fig. 17.23 Flight crystal growth cell designed and developed by NASA

many directions and is convenient for some types of viewing. However, such illumination is not useful for interferometry or schlieren in this system. Direct illumination is also used for interferometry and schlieren. With conventional optics, the direct illumination beam would provide a single illumination and viewing angle through the field.

Our previous experience in Spacelab-3 had taught us that more than one viewing angle is desirable. We achieved multiple viewing angles in **IML-1** through the use of windows equipped with holographic optical elements (**HOEs**). The input window contains **HOEs** that convert the single input beam into three beams that pass over the crystal at angles of 0 and $\pm 23.5^\circ$. The opposite window contains **HOEs** that redirect these beams to the recording film plane so that they can all be recorded and separated again during reconstruction.

Consequently, each recording comprises three superimposed, but independently viewable, holograms. The schlieren system is viewed by **TV**, allowing real-time viewing both by the crew and by the **TV** downlink. A primary use of the schlieren system is to view and judge the transition of the crystal from a dissolution phase to a growth phase since control of this transition is considered to be critical in producing a high-quality crystal. The knife-edge in the schlieren system was set so that, when the crystal was dissolving, light rays entering the resulting higher-refractive-index region above the crystal would be refracted in the direction of the crystal and be removed by the knife-edge, appearing dark in the image. When the transition from dissolution to growth occurred, the region immediately above the crystal would be depleted of solute, thus reducing the refractive index and causing the refracted rays to pass

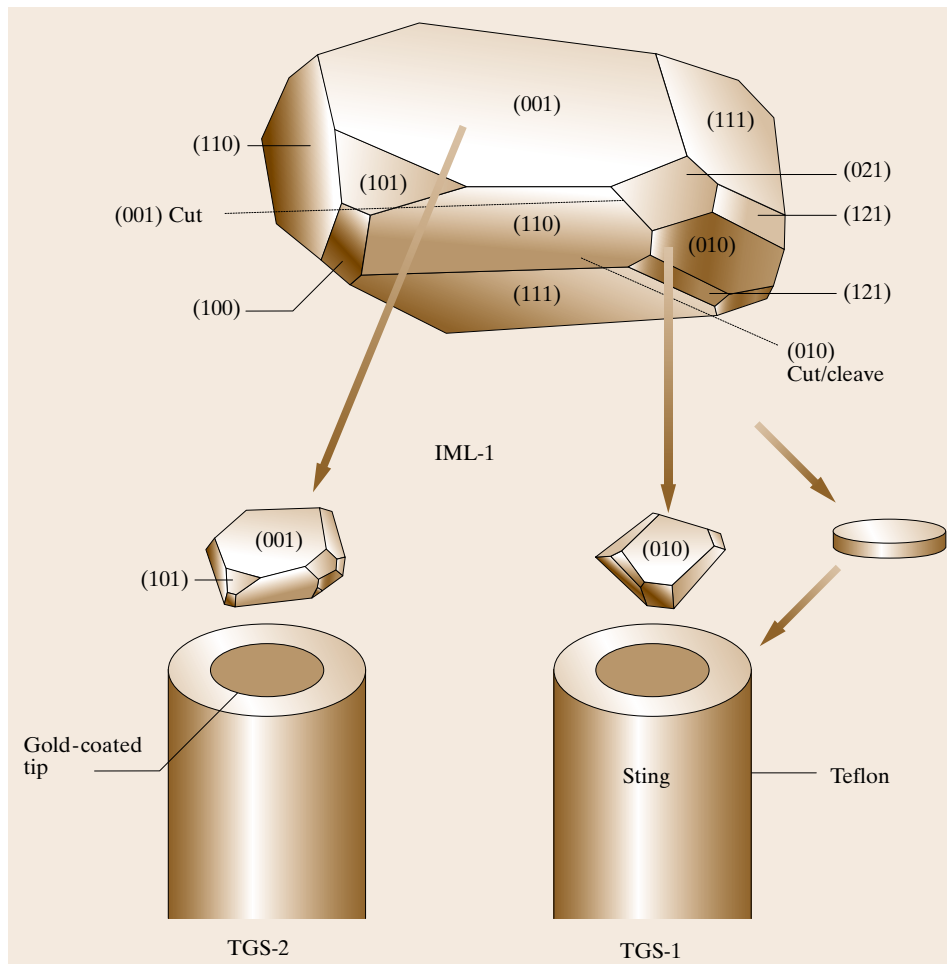


Fig. 17.24 TGS seed crystals used for growth runs on NASA's first International Microgravity Laboratory-1 (IML-1) mission

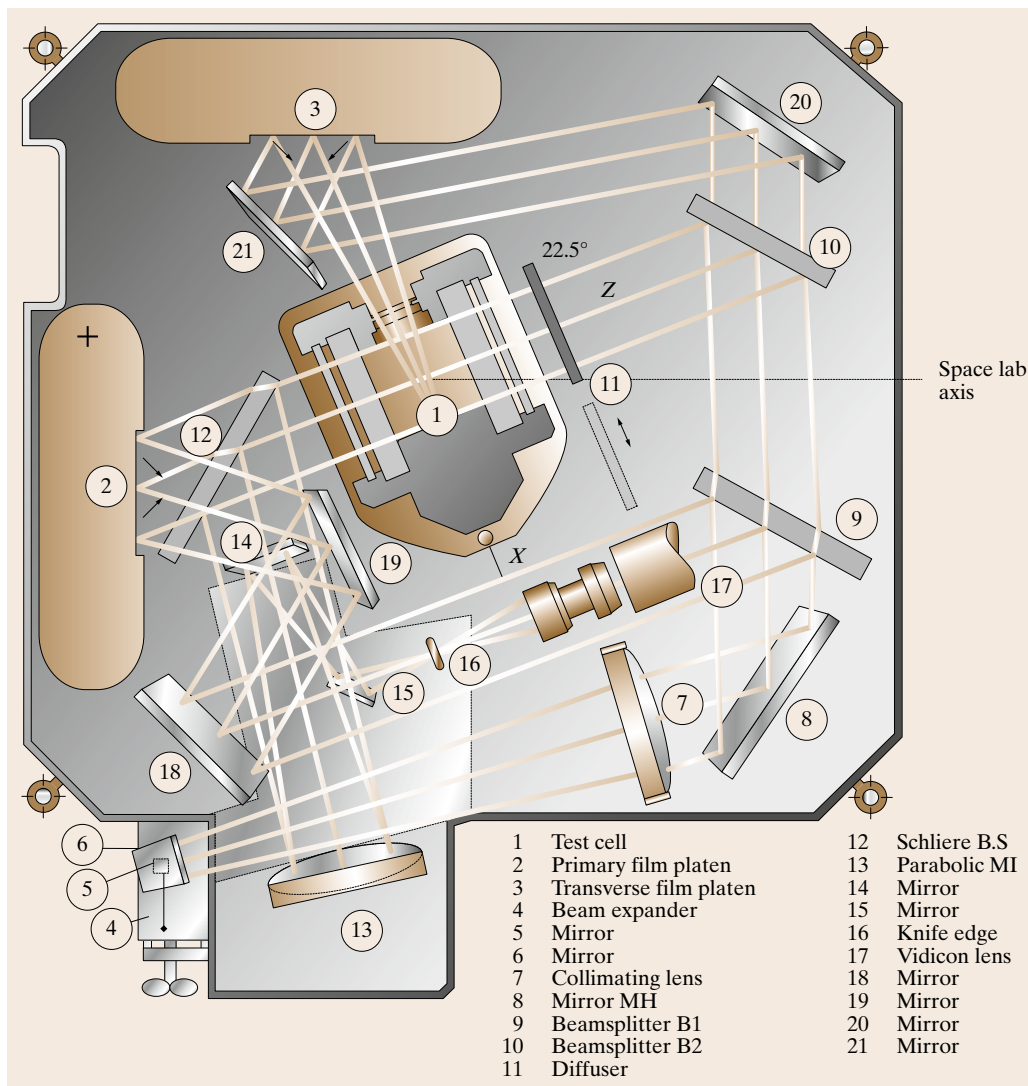


Fig. 17.25
Modified fluid
experiment
system (FES)
optical system
with various
components

above the knife edge, causing a bright region to appear above the crystal within the larger, dark region of higher concentration. The method proved to be an extremely sensitive way to identify the transition from dissolution to growth.

17.5.3 Results and Discussion

The flight TGS crystals were examined with a high-resolution monochromatic synchrotron x-radiation diffraction technique, both before and after slicing for the fabrication of infrared detectors to check the lattice

regularity, identify inclusions and dislocations, draw inferences about growth mode and stability, and locate the interface between the seed and the new growth. The experiments were performed at the National Synchrotron Light Source at Brookhaven National Laboratory in collaboration with B. Steiner of the US National Institute of Standards and Technology (NIST). The performance of materials is determined by their structure; in this performance, irregularity typically plays a leading role. The growth of crystals in low-*g* has long been of interest because of the anticipation that reduction in gravitational forces would strongly affect crystal growth and

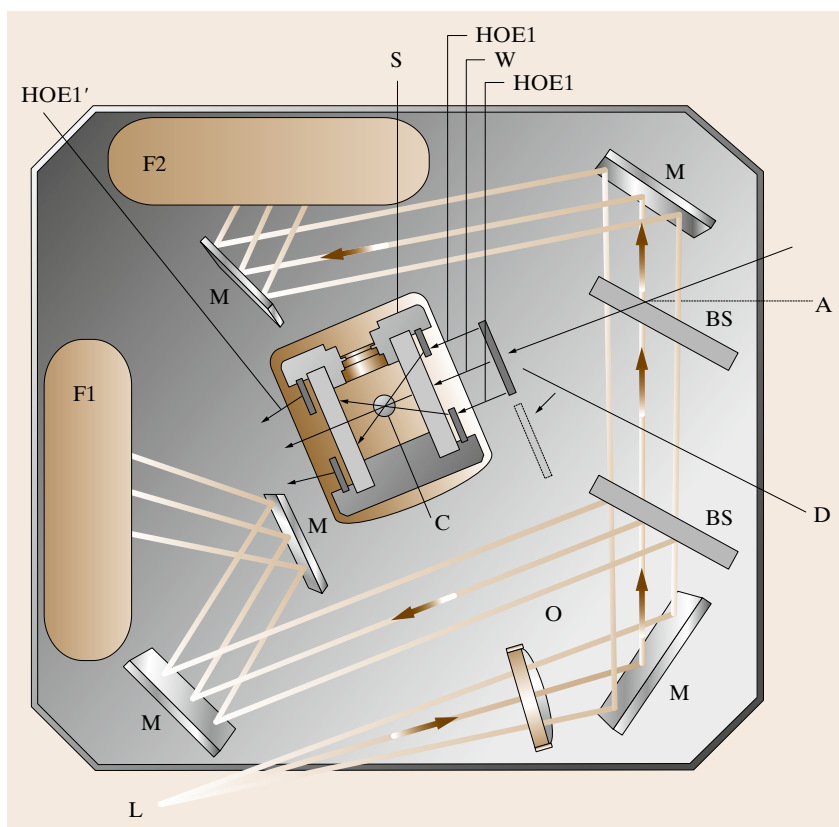


Fig. 17.26 Detailed optical layout for the fluid experiment system (FES) designed and developed by TRW. HOE 1': note that ray emerges at an angle to simplify separation. A – Angle between optical axis and space shuttle axis, M – mirror, BS – beamsplitter, C – crystal, O – lens, D – removable diffusor, F1 – hologram 1, F2 – hologram 2, L – He-Ne laser underneath, S – side window, W – window

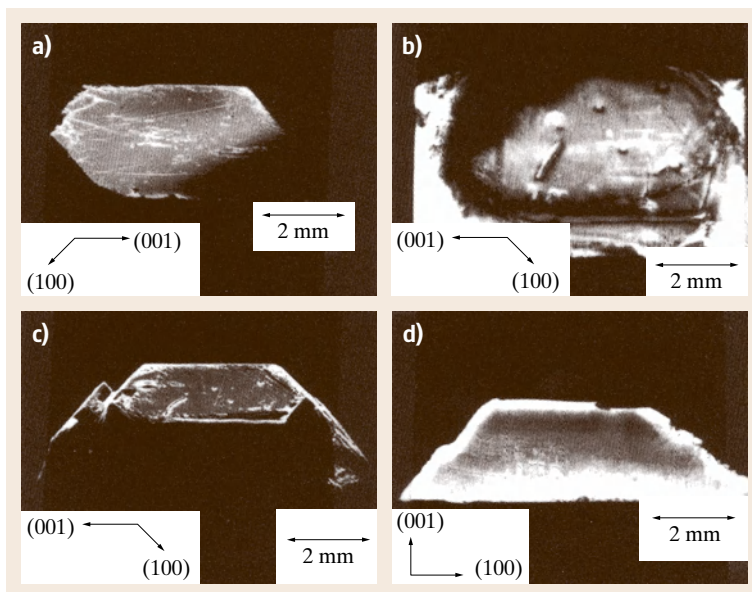


Fig. 17.27a–d High-resolution synchrotron x-ray radiation diffraction imaging of 1g- and microgravity-grown TGS crystals. (a) Uncut flight seed crystal, (b) high-resolution $(\bar{1}10)$ diffraction image of the interior of the IML-1 crystal, (c) space-grown crystal with polystyrene particles, (d) cut edge of the IML-1 crystal

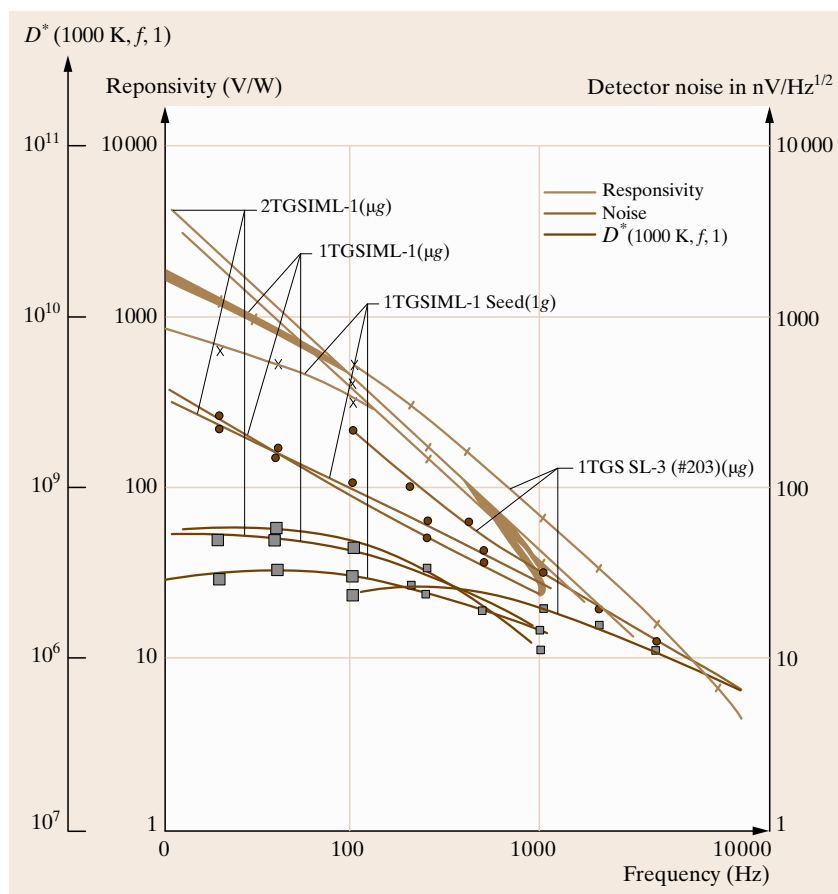


Fig. 17.28 Relevant parameters of infrared detectors fabricated from 1g- and microgravity-grown TGS crystals

thereby the nature of resulting irregularities. Many factors affect crystal growth, and because these can interact strongly with one another, the understanding of the structural variation necessary for its effective exploitation has not been fully achieved. Gaining knowledge of irregularities in space- and Earth-grown crystals, developed in conjunction with an understanding of their genesis and detailed effects on properties, is an important challenge. Such knowledge is also expected to contribute to dramatically improving single-crystal production, both in space and on the Earth. The local acceptance angle for diffraction from the uncut flight TGS-1 crystal of 1–2 arcsec (Fig. 17.27) indicates extraordinary crystal quality [17.106]. Polystyrene particles that had been included in the space-grown material in IML-1 experiment are observed as small imperfections in Fig. 17.27b. Also, clearly distinguishable in Fig. 17.27b is the faceted growth mode. Two sets of edge dislocations in the seed, one [101] ori-

ented and the other [001] oriented, were noted as well in images taken in Laue geometry, but they appear not to have affected the space growth. Observation of the cut edge of the crystal (Fig. 17.27d) shows continuity between the seed at the top and space grown part. The demarcation between the seed and the space-grown material is indistinct. High-resolution imaging of terrestrial crystals has shown that the surface treatment of the seed crystal is critical to growth perfection. The ground control TGS crystals were of extremely high perfection. Slice next to many possible flight seeds were examined by high-resolution diffraction imaging. The selection of the flight seed was based on the perfection of the slice next to the seed crystal.

Infrared detectors from the flight and ground control crystals were fabricated at EDO/Barnes Engineering Division, Shelton, CT. The detectivity (D^*) and other parameters for these infrared detectors are shown in

Table 17.5 Detector characteristics of space-grown TGS crystals

Crystal (TGS)	Noise (nV/Hz ^{1/2})	Responsivity (V/W)	Detectivity (1000 K, f , 1) $\times 10^{-8}$	f (Hz)	Remarks
SL-3/FES2-TGS (μ g grown)	320	510	0.99	100	Area = 0.3×3 mm ² , blackened
IML-1TGS seed (1g grown)	418	320	2	100	Area = 1×1 mm ² , no window
IML-1TGS (μ g grown)	90	400	4.2	100	Area = 1×1 mm ²
IML-1TGS (1g grown)	98	420	4.5	100	Area = 1×1 mm ²
IML-1TGS (μ g grown)	100	340	3	100	Area = 1×1 mm ²

Fig. 17.28. The detector characteristics are given in Table 17.5. The detectivity (D^*) for IR detectors fabricated from the IML-1 crystal shows an improvement over the ground-grown crystals and crystals grown on Spacelab-3.

The motion of three different-sized particles were mapped using techniques described elsewhere [17.105, 107]. The combined effects of fluid convection, particle interaction, residual gravity, Space Shuttle maneuvers, and g-jitters have been observed. However, the interferograms show several noteworthy features. When the crystal enters a growth phase, the solution in the region near the crystal is depleted of solute, thus reducing its refractive index below that of the surrounding fluid, creating a hemispherical cap of fringes over the crystal, as shown in Fig. 17.29. The stability of this cloud in the interferograms confirmed that the crystal was growing in a diffusion-controlled process. The cloud did show, however, that the process was not completely axisymmetric, due to equipment-related problems that were encountered during the mission.

To sum up, in spite of problems with the operation of the FES, two important objectives were attained in the IML-1 experiment: (a) a high-quality TGS crystal was grown, (b) the particle dynamics experiment was successful.

In spite of limited time and fast growth, the growth on the (010) face was substantially uniform over a period of 18 h. The growth on the (010) face on ground is mostly nonuniform. Polystyrene particles of three sizes that had been occluded by the growing TGS were observed as small imperfections in the grown crystal. The observations of the cut edge of the flight crystal (TGS-1) show continuity between the seed at the bottom and the space growth at the top, indicating a high degree of epitaxy of the space-grown material. The demarcation between the seed and the space-grown material is indistinct, indicating a smooth transition from dissolu-

tion to growth so that solvent inclusions are not formed between the seed and the grown layer. Experiments on Earth have shown that such inclusions tend to result in dislocations that propagate through subsequently grown material and degrade properties. The infrared detectors fabricated from the TGS-1 flight crystal show improved detectivity (D^*) compared with ground samples and even with detectors fabricated from crystals grown on Spacelab-3. The dielectric loss in the IML-1 crystal is lower than in ground crystals and in crystals grown in Spacelab-3.

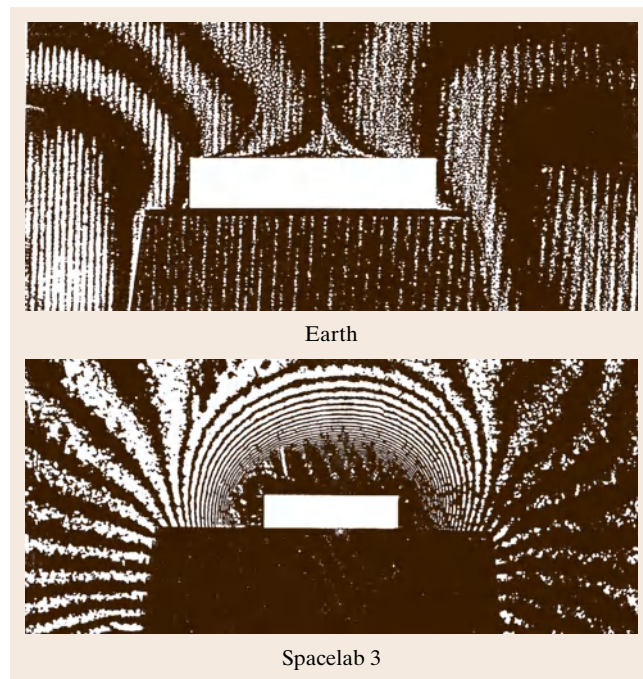


Fig. 17.29 Interferograms of concentration field in TGS solution on Earth and in microgravity onboard Spacelab-3

17.6 Protein Crystal Growth

The human body contains thousands of different proteins, which play essential roles in maintaining life. A protein's structure determines the specific role that it plays in the human body; however, researchers lack detailed knowledge about the structures of many proteins. The crystallization of proteins has three major applications: (1) structural biology and drug design, (2) bioseparations, and (3) controlled drug delivery. In the first application, protein crystals are used with the techniques of crystallography to ascertain the three-dimensional structure of the molecule. This structure is indispensable for correctly determining the often complex biological functions of these macromolecules. The design of drugs is related to this, and involves designing a molecule that can exactly fit into a binding site of a macromolecule and block its function in a disease pathway. Producing better-quality crystals will result in more accurate 3-D protein structure, which in turn means that the protein's biological function can be known more precisely, also resulting in improved drug design. The second application, bioseparations, refer to the downstream processing of the products of fermentation. Typically, the desired product of the fermentation process is a protein (e.g., insulin), which then needs to be separated from biomass. Crystallization is one of the commonly employed techniques for separation of protein. It has the advantage of being a benign separation process, that is, it does not cause the protein to unfold and lose its activity. The other application of protein, controlled drug delivery, is also very important. Most drugs are cleared by the body rapidly following administration, making it difficult to achieve a constant desired level over a period of time. When the drug is a protein such as insulin or α -interferon, administering the drug in the crystalline form shows promise of achieving such controlled delivery. The challenge is to produce crystals of relatively uniform size so that dosage can be correctly prescribed.

17.6.1 Protein Crystal Growth Methods

Protein crystallization is inherently difficult because of the fragile nature of protein crystals. Proteins have irregularly shaped surfaces, which result in the formation of large channels within any protein crystal. Therefore, the noncovalent bonds that hold the lattice together must often be formed through several layers of solvent molecules. In addition, to overcoming the

inherent fragility of protein crystals, successful production of x-ray-worthy crystals is dependent upon a number of environmental factors because so much variation exists among proteins, with each one requiring unique conditions for successful crystallization. Therefore, attempting to crystallize a protein without a proven protocol can be very tedious. Some factors that require consideration are protein purity, pH, concentration of protein, temperature, and the precipitants. In order to initiate crystallization the protein solution has to be brought to a thermodynamically unstable state of supersaturation. The solution can be brought back to the stable equilibrium state through precipitation of the protein, which is the most frequent process, or through crystallization. The supersaturation state can be achieved by several techniques: evaporation of solvent molecules, change of ionic strength, change of pH, change of temperature or change of some other parameter.

Two of the most commonly used methods for protein crystallization fall under the category of vapor diffusion [17.108–110]:

1. Hanging drop method
2. Sitting drop method.

Both of these methods entail the use of a droplet containing purified protein, buffer, and precipitants in higher concentration. Initially, the droplet of protein solution contains an insufficient concentration of precipitant for crystallization, but as water vaporizes from the drop and transfers to the reservoir, the precipitant concentration increases to a level optimal for crystallization. Since the system is in equilibrium, these optimum conditions are maintained until the crystallization is complete. Figures 17.30 and 17.31 depict

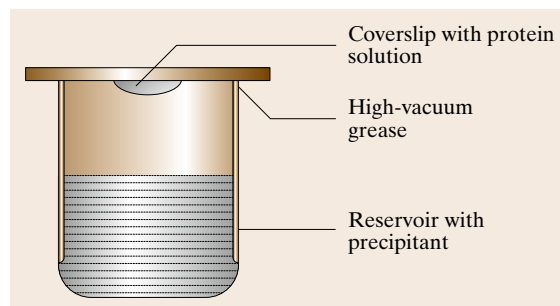


Fig. 17.30 Schematic diagram of the hanging drop method

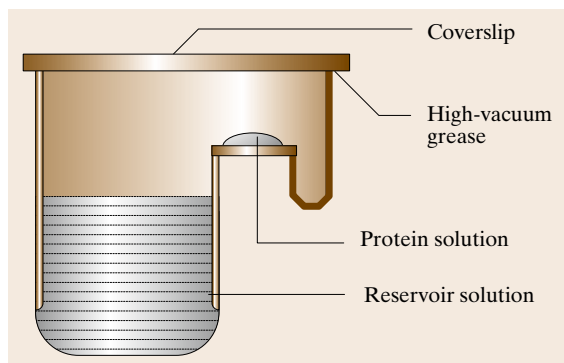


Fig. 17.31 Schematic diagram of the sitting drop method

the hanging drop and sitting drop systems, respectively. The hanging drop method differs from the sitting drop method in the vertical orientation of the protein solution drop within the system. It is important to mention that both methods require a closed system, that is, the system must be sealed off from outside using an airtight container. It is worth mentioning that the reservoir solution usually contains buffer and precipitant. The protein solution contains the same compounds, but in lower concentrations. The protein solution may also contain trace metals or ions necessary for precipitation; for instance, insulin is known to require trace amounts of zinc for crystallization.

17.6.2 Protein Crystal Growth Mechanisms

From the presence of well-defined facets on most protein crystals one can unambiguously conclude that growth occurs via the spreading of layers from growth step sources such as dislocations and 2-D nuclei. This has been confirmed on a molecular level. Ex situ electron microscopy observations have resolved individual growth steps on (010) and (110) faces of tetragonal lysozyme [17.111] that, contrary to recent claims [17.112, 113], are of monomolecular height. In situ atomic force microscopy of lysozyme has produced particularly instructive images of growth step generation at screw dislocations outcrops and of 2-D nucleation-induced islands.

Most recent atomic force microscopy observations on a larger number of other proteins and viruses [17.114] have reproduced the whole body of growth morphology and kinetics scenarios known for inorganic solution growth. These include layer spreading from dislocations and 2-D nuclei, interaction between growth steps from sources of different activ-

ities, and impediment of step propagation by foreign particles. Particle engulfment was observed to often result in dislocation formation. Crystallites that impinged on the interface became either epitaxially aligned with main crystal, or remained misaligned and caused various defects during further growth. There even appears to be some indication of kinetic roughening on certain facets of some proteins [17.115].

17.6.3 Protein Crystal Growth in Microgravity

The microgravity environment aboard spacecraft in low Earth orbit provides a convection- and sedimentation-free environment for the study and applications of fluid-based systems. With the advent of the US Space Shuttle, scientists had regular access to such environments and many experiments were initiated, including those in protein crystallization. After many trials it became clear that, for several proteins, crystallization in microgravity environment resulted in bigger and better crystals. In some instances, crystals that could not be crystallized at all on the ground were found to crystallize in space. Conversely, for numerous proteins the space environment was found to be no better or was worse than ground-based conditions. As a result of these observations, NASA has become one of the leading federal agencies in prompting and funding protein crystallization research. Efforts are directed at both utilizing the space environment to improve the crystallization of novel proteins and at fundamental studies of the causes (if any) of the improvement in protein crystals produced in microgravity. The results from flying more, and studying in more detail, have significantly altered attitudes towards space-based protein crystal growth. Persuasive explanations have emerged, and a strong theoretical model has emerged to explain why space-based growth is better.

Since the inception of protein crystal growth in microgravity research by *Littke* and *John* [17.116], several research groups have developed microgravity hardware and experiments [17.116–121]. Some of those are listed below:

1. Handheld protein crystallization apparatus for microgravity (HH-PCAM) [17.122]
2. Diffusion-controlled crystallization apparatus for microgravity (DCAM) [17.123]
3. High-density protein crystal growth system (HDPCG) [17.124]
4. Protein crystal growth facility (PCF) [17.125]

5. A multiuser facility-based protein crystallization apparatus for microgravity (PCAM) [17.122]
6. Advanced protein crystallization facility (APCF) [17.123].

Several thousand individual protein crystal growth experiments have been flown using the PCAM facility hardware aboard the US Space Shuttle. According to the developer of this facility, this hardware represents a pioneering development in design and deployment of space flight hardware based on disposable interface elements [17.122]. Furthermore, it has resulted in an ultrahigh-resolution structure and first example of neutron diffraction achieved as a result of protein crystal growth in microgravity [17.125–127]. Additionally, using this facility, fundamental differences in protein partitioning in microgravity have been documented, which represent the first direct ex-

perimental observation of the factors contributing to quality improvements in the growth of protein crystals in microgravity [17.128]. The other important hardware, referred to as the diffusion-controlled crystallization apparatus for microgravity (DCAM), utilizes the dialysis method and allows the equilibration rate of each individual experiment to be passively controlled from several days to several months. It is worth mentioning that precision control rate of supersaturation has routinely produced macrocrystals of size 5 mm to 1.25 cm for a variety of protein in this hardware. Analysis of serum albumin, ferritin, lysozyme, bacteriorhodopsin, and nucleosome core particles exhibit superior diffraction properties as compared with ground-based controls [17.123]. Further improvements of the hardware is ongoing for the International Space Station, where x-ray analysis can be done aboard the Space Station [17.124].

17.7 Concluding Remarks

Bulk high-quality single crystals are required for use in fabricating devices for various technological applications. Since crystal growth is a complicated process that depends on many parameters that can interact, the complete process is not well understood. This is one of the reasons to grow crystals in microgravity of space, to separate omnipresent convection on Earth and have only diffusion-controlled growth. The authors have attempted to give a comprehensive overview of the various problems encountered in the solution growth of single crystals on Earth and in space experiment based on their experience over almost three decades. The solutions of the various problems encountered during growth on ground and in spaceflight experiments are described. This chapter will serve as a foundation for those who desire to initiate a research program in the growth of bulk single crystals of technological importance that can be grown from low-temperature solution technique. A brief review of crystal growth fundamentals is presented, including key

techniques for solution crystal growth such as solubility determination and the design of various crystal growth systems including mechanical and electronic crystal motor reciprocating arrangements. Three generations of modifications to solution crystallizers designed and fabricated in the laboratory and a crystallizer for space growth based on the cooled sting technique advanced by the authors are described. A number of solution-grown crystals grown at Alabama A&M University are shown. A detailed description of the crystal growth experiments on an important infrared material, triglycine sulfate, and the difficulties encountered in the space crystal growth experiment aboard the Space Shuttle in the NASA Spacelab-3 and first International Microgravity Laboratory (IML-1) missions are given. Since basic principles of solution growth technique are shared by protein crystal growth, basic techniques of protein crystal growth are briefly mentioned and efforts towards protein crystal growth in microgravity are also discussed.

References

- 17.1 H.A. Meirs, F. Isaac: The spontaneous crystallization, *Proc. R. Soc. Lond. A* **79**, 322–325 (1987)
- 17.2 K. Sangwal: Growth kinetics and surface morphology of crystals grown from solutions: recent observations and their interpretations, *Prog. Cryst. Growth Charact. Mater.* **36**(3), 163–248 (1998)
- 17.3 I.F. Nicolau: Growth kinetics of potassium-dihydrogen phosphate crystals in solution, *Krist. Tech.* **9**(11), 1255–1263 (1974)

- 17.4 R. Janssen-Van Rosmalen, P. Bennema, J. Gar-side: The influence of volume diffusion on crystal growth, *J. Cryst. Growth* **29**, 342–352 (1975)
- 17.5 A. Chianese: Growth and dissolution of sodium perborate in aqueous solutions by using RDC technique, *J. Cryst. Growth* **91**, 39–49 (1988)
- 17.6 K. Sangwal: On the mechanism of crystal growth from solutions, *J. Cryst. Growth* **192**, 200–214 (1998)
- 17.7 Y. Wang, X.L. Yu, D.I. Sun, S.T. Yin: Mass transport and growth kinetics related to the interface supersaturation of lithium formate monohydrate, *Cryst. Res. Technol.* **36**(4/5), 441–448 (2001)
- 17.8 N. Zaitseva, L. Carman: Rapid growth of KDP-type crystals, *Prog. Cryst. Growth Charact. Mater.* **43**, 1–118 (2001)
- 17.9 I.V. Melikhov, L.B. Berliner: Crystallization of salts from supersaturated solutions; diffusion kinetics, *J. Cryst. Growth* **46**, 79–84 (1979)
- 17.10 P. Bennema: Spiral growth and surface roughening: development since Burton, Cabrera and Frank, *J. Cryst. Growth* **69**, 182–197 (1984)
- 17.11 X.Y. Liu, K. Malwa, K. Tsukamoto: Heterogeneous two dimension nucleation and growth kinetics, *J. Chem. Phys.* **106**(5), 1870–1879 (1997)
- 17.12 A.F. Izmailov, A.S. Myerson: Momentum and mass transfer in supersaturation solutions crystal growth from solution, *J. Cryst. Growth* **174**, 263–368 (1997)
- 17.13 M. Rak, K. Izdebski, A. Brozi: Kinetic Monte Carlo study of crystal growth from solution, *Comput. Phys. Commun.* **138**, 250–263 (2001)
- 17.14 F. Rosenberger, B. Mutaftschiev (Eds.): *Interfacial Aspects of Phase Transformation* (Reidel, Dordrecht 1982)
- 17.15 A.A. Chernov: Present day understanding of crystal growth from aqueous solutions, *Prog. Cryst. Growth Charact.* **26**, 121–151 (1993)
- 17.16 R. Mohan, A.S. Myerson: Growth kinetics: A thermodynamic approach, *Chem. Eng. Sci.* **57**, 4277–4285 (2002)
- 17.17 C.M. Pina, A. Putnis, J.M. Astilleros: The growth mechanisms of solid solutions crystallization from aqueous solutions, *Chem. Geol.* **204**, 145–161 (2004)
- 17.18 I. Sunagawa, K. Tsukamoto, K. Maiwa, K. Onuma: Growth and perfection of crystals from aqueous solution: Case studies on Barium nitrate and K-Alum, *Prog. Cryst. Charact.* **30**, 153–190 (1995)
- 17.19 W.R. Wilcox: Influence of convection on the growth of crystals from solution, *J. Cryst. Growth* **65**, 133–142 (1983)
- 17.20 I.V. Markov: *Crystal Growth for Beginners* (World Scientific, Hoboken 2004)
- 17.21 I. Sunagawa: *Crystals Growth, Morphology and Perfection* (Cambridge Univ. Press, Cambridge 2005)
- 17.22 T. Ogawa: A phenomenological analysis of crystal growth from solutions as an irreversible process, *Jpn. J. Appl. Phys.* **16**(5), 689–695 (1977)
- 17.23 S. Veintemillas-Verdaguer: Chemical aspects of the effect of impurities in crystal growth, *Prog. Cryst. Growth Charact.* **32**, 76–109 (1996)
- 17.24 K. Sangwal: Kinetics effects of impurities on the growth of single crystals from solutions, *J. Cryst. Growth* **203**, 197–212 (1999)
- 17.25 I. Owczarek, K. Sangwal: Effect of impurities on the growth of KDP crystals: Mechanism of adsorption on (101) faces, *J. Cryst. Growth* **102**, 574–580 (1990)
- 17.26 K. Sangwal: Effects of impurities on the crystal growth processes, *Prog. Cryst. Charact.* **32**, 3–43 (1996)
- 17.27 E. Kirkova, M. Djarova, B. Donkova: Inclusions of isomorphism impurities during crystallization from solutions, *Prog. Cryst. Growth Charact.* **32**, 111–134 (1996)
- 17.28 M. Rauls, K. Bartosch, M. Kind, S. Kuch, R. Lacmann, A. Mersmann: The influence of impurities on crystallization kinetics – A case study on ammonium sulfate, *J. Cryst. Growth* **312**, 116–128 (2000)
- 17.29 E. Mielniczek-Brzoska, K. Gielzak-Kocwin, K. Sangwal: Effects of Cu(II) ions on the growth of ammonium oxalate monohydrate crystals from aqueous solutions: Growth kinetics, segregation coefficient and characterization of incorporation sites, *J. Cryst. Growth* **212**, 532–542 (2000)
- 17.30 K. Sangwal, E. Mielniczek-Brzoska, J. Bore: Effect of Mn(II) ions on the growth of ammonium oxalate monohydrate crystals from aqueous solutions: Growth habit and surface morphology, *Cryst. Res. Technol.* **38**(2), 103–112 (2003)
- 17.31 N. Kubota, M. Yokota, J.W. Mullin: Supersaturation dependence of crystal growth in solutions in the presence of impurity, *J. Cryst. Growth* **182**, 86–94 (1997)
- 17.32 K. Sangwal, E. Mielniczek-Brzoska: On the effect of Cu(II) impurities on the growth kinetics of ammonium oxalate monohydrate crystals from aqueous solutions, *Cryst. Res. Technol.* **36**(8–10), 837–849 (2001)
- 17.33 K. Sangwal, E. Mielniczek-Brzoska, J. Bore: Study of segregation coefficient of cationic impurities in ammonium oxalate monohydrate crystals during growth from aqueous solutions, *J. Cryst. Growth* **244**, 183–193 (2002)
- 17.34 K. Sangwal, T. Palcznska: On the supersaturation and impurity concentration dependence of segregation coefficient in crystals grown from solutions, *J. Cryst. Growth* **212**, 522–531 (2002)
- 17.35 P.S. Delineshev: Growth of crystals in the presence of impurities, a hypotheses based on a kinetic approach, *Cryst. Res. Technol.* **33**(6), 891–897 (1998)
- 17.36 K. Sangwal: Kinetic effects of impurities on the growth of single crystals from solutions, *J. Cryst. Growth* **203**, 197–212 (1999)
- 17.37 A.S. Myerson, S.M. Jang: A comparison of binding energy an metastable zone width for adipic acid

- with various additives, *J. Cryst. Growth* **156**, 459–466 (1995)
- 17.38 D. Aquilano, M. Rubbo, G. Mantovani, G. Sgualdino, G. Vaccari: Equilibrium and growth forms of sucrose crystals in the $\{h0l\}$ zone, *J. Cryst. Growth* **74**, 10–20 (1986)
- 17.39 D. Aquilano, M. Rubbo, G. Mantovani, G. Sgualdino, G. Vaccari: Equilibrium and growth forms of sucrose crystals in the $\{h0l\}$ zone, *J. Cryst. Growth* **83**, 77–83 (1987)
- 17.40 A.A. Chernov, V.V. Sipyagin: Peculiarities in crystal growth aqueous solutions connected with their structure. In: *Current Topics in Materials Science*, Vol. 5, ed. by E. Kaldis (North-Holland, Amsterdam 1980) pp. 279–333
- 17.41 K. Byrappa, H. Klapper, T. Ohachi, R. Fornari (Eds.): *Crystal Growth of Technologically Important Electronic Materials* (Allied, New Delhi 2003)
- 17.42 M.D. Aggarwal, T. Gebre, A.K. Batra, M.E. Edwards, R.B. Lal, B.G. Penn, D.O. Frazier: Growth of nonlinear optical materials at Alabama University, *Proc. SPIE* **4813**, 52–65 (2002)
- 17.43 M.D. Aggarwal, W.S. Wang, K. Bhat, B.G. Penn, D.O. Frazier: Photonic crystals: crystal growth processing and physical properties. In: *Handbook of Advanced Electronic and Photonic Materials and Devices*, Vol. 9, ed. by H.S. Nalwa (Academic, New York 2001) pp. 193–228
- 17.44 H.K. Henisch: *Crystal Growth in Gels* (Dover, New York 1970)
- 17.45 A.F. Barton: *Handbook of Solubility Parameters and Other Cohesion Parameters* (CRC, Boca Raton 1983)
- 17.46 J. Novotny: A crystallizer for the investigation of conditions of growth of single crystals from solutions, *Krist. Tech.* **6**(3), 343–352 (1971)
- 17.47 M.D. Aggarwal, J. Choi, W.S. Wang, K. Bhat, R.B. Lal, A.D. Shields, B.G. Penn, D.O. Frazier: Solution growth of a novel nonlinear optical material: L-histidine tetrafluoroborate, *J. Cryst. Growth* **204**, 179–182 (1999)
- 17.48 A.K. Batra, S.C. Mathur: Reciprocating arrangement for solution crystal growth, *Res. Ind.* **29**, 20–22 (1984)
- 17.49 W.S. Wang, M.D. Aggarwal, J. Choi, K. Bhat, T. Gebre, A.D. Shields, B.G. Penn, D.O. Frazier: Solvent effects and polymorphic transformation of organic nonlinear optical crystal L-pyrogutamic acid in solution growth processes. I. Solvent effects and growth morphology, *J. Cryst. Growth* **198/199**, 578–582 (1999)
- 17.50 C. Owens, K. Bhat, W.S. Wang, A. Tan, M.D. Aggarwal, B.G. Penn, D.O. Frazier: Bulk growth of high quality nonlinear optical crystals of L-arginine tetrafluoroborate (L-AFB), *J. Cryst. Growth* **225**, 465–469 (2001)
- 17.51 R.B. Lal, H.W. Zhang, W.S. Wang, M.D. Aggarwal, H.W.H. Lee, B.G. Penn: Crystal growth and optical properties of 4-aminobenzophenone crystals for NLO applications, *J. Cryst. Growth* **174**, 393–397 (1997)
- 17.52 H.W. Zhang, A.K. Batra, R.B. Lal: Growth of large methyl-(2,4-dinitrophenyl)-aminopropanoate: 2-methyl-4-nitroaniline crystals for nonlinear applications, *J. Cryst. Growth* **137**, 141–144 (1994)
- 17.53 M.R. Simmons: An investigation of crystals matrices of single crystals doped with rare earth ions. M.Sc. Thesis (Alabama Univ., Alabama 2002)
- 17.54 J.-M. Chang, A.K. Batra, R.B. Lal: Growth and characterization of doped TGS crystals for infrared devices, *Cryst. Growth Des.* **2**(5), 431–435 (2002)
- 17.55 M.D. Aggarwal, R.B. Lal: Simple low-cost reciprocating crystallizer for solution crystal growth, *Rev. Sci. Instrum.* **54**, 772–773 (1983)
- 17.56 A.K. Batra, C.R. Carmichael-Owens, M. Simmons, M.D. Aggarwal, R.B. Lal: Design of a solution crystal growth crystallizer with versatile electronic reciprocal motion control for a crystal holder, *Cryst. Res. Technol.* **40**(8), 757–760 (2005)
- 17.57 A.K. Batra, M.D. Aggarwal, R.B. Lal: Growth and characterization of doped DTGS crystals for infrared sensing devices, *Mat. Lett.* **57**, 39–43 (2003)
- 17.58 R.B. Lal, M.D. Aggarwal: Reciprocating crystallizer: Automatic crystallizer grows crystals from aqueous solutions, *NASA Tech. Briefs* **8**, 419 (1984)
- 17.59 F. Jona, S. Shirane: *Ferroelectric Crystals* (Dover, New York 1993)
- 17.60 R.B. Lal, A.K. Batra: Growth and properties of triglycine (TGS) sulfate crystals: Review, *Ferroelectrics* **142**, 51–82 (1993)
- 17.61 E.A.D. White, J.D.C. Wood, V.M. Wood: The growth of large area, uniformly doped TGS crystals, *J. Cryst. Growth* **32**, 149–156 (1976)
- 17.62 B. Brezina, M. Havrankova, M. Vasa: Enhanced growth of non-polar $\{001\}$ growth sectors of deuterated triglycine sulfate doped with L-alanine (LADTGS), *Cryst. Res. Technol.* **27**(1), 13–20 (1992)
- 17.63 S. Satapathy, S.K. Sharma, A.K. Karnal, V.K. Wadhawan: Effects of seed orientation on the growth of TGS crystals with large (010) facets needed for detector applications, *J. Cryst. Growth* **240**, 196–202 (2002)
- 17.64 M. Banan: Growth of pure and doped triglycine sulfate crystals for pyroelectric infrared detector applications. M.Sc. Thesis (Alabama A&M Univ., Alabama 1986)
- 17.65 D. Zhao-De: A new method of growth of ferroelectric crystal, *Ferroelectrics* **39**, 1237–1240 (1981)
- 17.66 F. Moravec, J. Novotny: Study on the growth of triglycine sulphate single crystals, *Krist. Techn.* **7**, 891–902 (1972)
- 17.67 W.K. Burton, N. Cabrera, F.C. Frank: The growth of crystals and the equilibrium structure of their surfaces, *Philos. Trans. R. Soc. Lond.* **243**, 299–358 (1951)

- 17.68 L.N. Rashkovich: Interferometric investigation of growth rate of {001} faces of triglycine sulfate at various supersaturation and temperature, *Sov. Phys. Crystallogr.* **28**, 454–458 (1983)
- 17.69 J. Novotny, F. Moravec, Z. Solc: The role of surface and volume diffusion in the growth of TGS single crystals, *Czech. J. Phys. B* **23**, 261–266 (1973)
- 17.70 J. Novotny, F. Moravec: Growth of TGS from slightly supersaturated solutions, *J. Cryst. Growth* **11**, 329–335 (1971)
- 17.71 D.A. Reiss, R.L. Kroes, E.E. Anderson: Growth kinetics of the (001) face of TGS below the ferroelectric transition temperature, *J. Cryst. Growth* **84**, 7–10 (1987)
- 17.72 M. Banan, R.B. Lal, A.K. Batra, M.D. Aggarwal: Effect of poling on the morphology and growth rate of TGS crystals, *Cryst. Res. Technol.* **24**(3), K53–K55 (1989)
- 17.73 F. Moravec, J. Novotny: A contribution to the study of the influence of impurities on the growth and some physical properties of TGS single crystals, *Krist. Techn.* **6**(3), 335–342 (1971)
- 17.74 R.V. Whipples, R.S. Cosier, L.K. Bye: Orthorhombic diglycine sulphate, *J. Mater. Sci.* **7**(12), 1476–1477 (1972)
- 17.75 E. Dominquez, R. Jimenez, J. Mendiola, E.J. Vivas: Diglycine sulphate – An interesting new dielectric crystal species, *J. Mater. Sci.* **70**(3), 363–364 (1972)
- 17.76 M.S. Tsedrik, V.N. Ulasen, G.A. Zaborovski: Growing TGS and TGSe single crystals at various pH of solution, *Krist. Techn.* **10**(1), 49–54 (1975)
- 17.77 E.J. Weidmann, E.A.D. White, V.M. Wood: Induced growth anisotropy in TGS crystals, *J. Mater. Sci. Lett.* **7**, 719–720 (1972)
- 17.78 L. Szczepanska: Growth investigations of single crystal sulphates containing molecular glycine groups, *Krist. Techn.* **11**, 265–271 (1976)
- 17.79 L. Prokopova, J. Novotny, Z. Micka, V. Malina: Growth of triglycine sulphate crystals doped by cadmium phosphate, *Cryst. Res. Technol.* **36**, 1189–1195 (2001)
- 17.80 G.R. Pandya, D.D. Vyas: On growth and morphological studies of TGS single crystals, *Cryst. Res. Technol.* **16**, 1353–1358 (1981)
- 17.81 R.B. Lal, S. Etminan, A.K. Batra: Effect of simultaneous organic and inorganic dopants on the characteristics of triglycine sulfate crystals, *Proc. 9th IEEE Int. Symp. Appl. Ferroelectr.* (1994) pp. 695–697
- 17.82 M. Banan, A.K. Batra, R.B. Lal: Growth and morphology of triglycine sulphate (TGS) crystals, *J. Mater. Sci. Lett.* **8**, 1348–1349 (1989)
- 17.83 N. Nakatani: Ferroelectric domain structure and internal bias field in DL- α -alanine-doped triglycine sulfate, *Jpn. J. Appl. Phys.* **30**(12A), 3445–3449 (1991)
- 17.84 J. Eisner: The physical properties of TGS single crystals, grown from aqueous TGS solutions containing aniline, *Phys. Status Solidi* **43**, K1–K4 (1977)
- 17.85 F. Moravec, J. Novotny, J. Strajblova: Single crystals of triglycine sulphate containing palladium, *Czech J. Phys.* **23**, 855–862 (1977)
- 17.86 A.S. Sidorkin, A.M. Kostsov: Exoelectron emission from a ferroelectric crystal of triglycine sulfate with defects, *Sov. Phys. Solid State* **33**(8), 1383–1384 (1991)
- 17.87 L. Yang, A.K. Batra, R.B. Lal: Growth and characterization of TGS crystals grown by cooled sting technique, *Ferroelectrics* **118**(1–4), 85–89 (1991)
- 17.88 N. Nakatani: Ferroelectric domain structure and internal bias field in DL- α -alanine doped triglycine sulfate, *Jpn. J. Appl. Phys.* **30**, 3445–3449 (1991)
- 17.89 B. Brezina, M. Havrankova: Orientation of structure and crystals of TGS and TGS doped with D, al or L, al, *Cryst. Res. Technol.* **20**, 781–786 (1985)
- 17.90 G.M. Loiacono, J.P. Dougherty: *Final Technical Report* (Night Vision and Electro-optics Laboratories, Fort Belvoir 1978), Contract No. DAAK70–77–C–0098
- 17.91 G. Arunmozhi, E. De Matos Gomes, J. Ribeiro: Dielectric properties of L-asparagine doped TGS (Asp-TGS) crystals, *Ferroelectrics* **295**, 87–95 (2003)
- 17.92 S. Seif, K. Bhat, A.K. Batra, M.D. Aggarwal, R. B. Lal: Effect of Cr(III) impurity on the growth kinetics of potassium dihydrogen phosphate and triglycine sulfate grown from aqueous solutions, *Mater. Lett.* **58**, 991–994 (2004)
- 17.93 V.A. Kuznetov, T.M. Okhrimenko, M. Rak: Growth promoting effect of organic impurities on growth kinetics of KAP and KDP crystals, *J. Cryst. Growth* **193**, 164–173 (1998)
- 17.94 R.J. Davey: *Industrial Crystallization*, Vol. 78, ed. by E.J. de Jong, S.J. Jancic (North-Holland, Amsterdam 1979) pp. 169–198
- 17.95 O.W. Wang, C.S. Fang: Investigation of the solution status of TGS and ATGSP crystals, *Cryst. Res. Technol.* **27**, 245–251 (1992)
- 17.96 K. Meera, R. Muralindharan, A.K. Tripathi, P. Ramasamy: Growth and characterization of l-threonine, dl-threonine, l-methionine admixed TGS crystals, *J. Cryst. Growth* **263**, 524–531 (2004)
- 17.97 G. Su, Y. He, H. Yao, Z. Shi, Q. Wu: A new pyroelectric crystal L-lysine-doped THS (LLTGS), *J. Cryst. Growth* **209**, 220–222 (2000)
- 17.98 J. Novotny, J. Zelinkay, F. Moravec: Broadband infrared detectors on the basis of PATGS/Pt(IV) single crystals, *Sens. Actuators A* **119**, 300–304 (2005)
- 17.99 S. Kalainathan, M.B. Margaret, T. Trusan: Morphological changes of L-asparagine doped TGS crystal, *Cryst. Eng.* **5**, 71–78 (2002)
- 17.100 <http://www.nasa.gov/missions/index.html> (last accessed August 9, 2009)
- 17.101 R.B. Lal, R.L. Kroes: Solution growth of crystal on Spacelab-3, *Proc. 24th AIAA Sci. Meet.* (Reno 1985)
- 17.102 R.B. Lal, M.D. Aggarwal, R.L. Kroes, W.R. Wilcox: A new technique of solution crystal growth, *Phys. Status Solidi (a)* **80**, 547–551 (1983)

- 17.103 A.K. Batra, R.B. Lal, M.D. Aggarwal: Electrical properties of TGS crystals grown by new technique, *J. Mater. Sci. Lett.* **4**, 1425–1427 (1985)
- 17.104 R.B. Lal, M.D. Aggarwal, A.K. Batra, R.L. Kroes: Solution growth of crystals in zero-gravity, final technical report (NASA, Washington 1987), NASA contract number NAS8–32945
- 17.105 R.B. Lal: Solution growth of crystals in low-gravity, final technical report (1995), NASA contract number NAS8–36634
- 17.106 B. Steiner, R. Dobbryn, D. Black, H. Burdette, M. Kuriyama, R. Spal, L. van den Berg, A. Fripp, R. Simchick, R.B. Lal, A.K. Batra, D. Mathiesen, B. Ditchek: High resolution diffracting imaging of crystals grown, Microgravity and closely related terrestrial crystals (NIST, Gaithersburg 1991), Technical Note 1287
- 17.107 R.B. Lal, A.K. Batra, J.D. Trolinger, W.R. Wilcox: TGS crystal growth experiment on the first international microgravity laboratory (IML-1), *Microgravity Q.* **4**(3), 186–198 (1994)
- 17.108 D.E. McRee: *Practical Protein Crystallography* (Academic Press, San Diego 1993) pp. 1–23
- 17.109 G. Rhodes: *Crystallography Made Crystal Clear* (Academic, San Diego 1993) pp. 8–10
- 17.110 G. Rhodes: *Crystallography Made Crystal Clear* (Academic, San Diego 1993) pp. 29–38
- 17.111 S.D. Durbin, G. Feher: Studies of crystal growth mechanisms of proteins by electron microscopy, *J. Mol. Biol.* **212**, 763–774 (1990)
- 17.112 E. Forsythe, M.L. Pusey: The effects of temperature and NaCl concentration on tetragonal lysozyme face growth rates, *J. Cryst. Growth* **139**, 89–94 (1994)
- 17.113 A. Nadaraja, E.L. Forsythe, M.L. Pusey: The averaged face growth rates of lysozyme crystals: The effect of temperature, *J. Cryst. Growth* **151**, 163–172 (1995)
- 17.114 W. Littke, C. John: Protein single crystal growth under microgravity, *Science* **225**, 203–204 (1984)
- 17.115 F. Rosenberger: Protein crystallization, *J. Cryst. Growth* **166**, 40–54 (1996)
- 17.116 W. Littke, C. John: Protein single crystal growth under microgravity, *J. Cryst. Growth* **76**, 663–672 (1986)
- 17.117 L.J. DeLucas, F.L. Suddath, R.S. Snyder, R. Naumann, M.B. Broom, M.L. Pusey, V. Yost, B. Herren, D.C. Carter, B. Nelson, E.J. Meehan, A. McPherson, C.E. Bugg: Preliminary investigations of protein crystal growth using the space shuttle, *J. Cryst. Growth* **76**, 681–693 (1986)
- 17.118 L.J. DeLucas, C.D. Smith, H.W. Smith, V.K. Senadhi, S.E. Senadhi, S.E. Ealick, D.C. Carter, R.S. Snyder, P.C. Weber, F.R. Salemme, D.H. Ohlen-dorf, H.M. Einspahr, L.L. Clancy, M.A. Navia, B.M. Mc-Keever, T.L. Nagabhushan, G. Nelson, A. McPherson, S. Koszelak, G. Taylor, D. Stammers, K. Powell, G. Darby, C.E. Bugg: Protein crystal growth in microgravity, *Science* **246**, 651–653 (1989)
- 17.119 S. Simic-Stefani, M. Kawaji, H.U. Hu: G-jitter induced motion of a protein crystal under microgravity, *J. Cryst. Growth* **294**, 373–384 (2006)
- 17.120 A. McPherson: Virus and protein crystal growth on earth and in microgravity, *J. Phys. D* **26**, B104–B112 (1993)
- 17.121 D.C. Carter, T.E. Dowling: Protein crystal growth apparatus for microgravity, US Patent 5643540 (1997)
- 17.122 D.C. Carter, B. Wright, T. Miller, J. Chapman, P. Twigg, K. Keeling, K. Moody, M. White, J. Click, J.R. Ruble, J.X. Ho, L. Adcock-Downey, T. Dowling, C.-H. Chang, P. Ala, J. Rose, B.C. Wang, J.-P. Declercq, C. Evrard, J. Rosenberg, J.-P. Wery, D. Clawson, M. Wardell, W. Stallings, A. Stevens: PCAM: A multi-user facility-based protein crystallization apparatus for microgravity, *J. Cryst. Growth* **196**, 610–622 (1999)
- 17.123 D.C. Carter, B. Wright, T. Miller, J. Chapman, P. Twigg, K. Keeling, K. Moody, M. White, J. Click, J.R. Ruble, J.X. Ho, L. Adcock-Downey, G. Bunick, J. Harp: Diffusion-controlled crystallization apparatus for microgravity (DCAM): Flight and ground-based applications, *J. Cryst. Growth* **196**, 602–609 (1999)
- 17.124 L.J. DeLucas, K.M. Moore, M.M. Long, R. Rouleau, T. Bray, W. Crysel, L. Weise: Protein crystal growth in space, past and future, *J. Cryst. Growth* **237–239**, 1646–1650 (2002)
- 17.125 J.P. Declercq, C. Evrard, D.C. Carter, B.S. Wright, G. Etienne, J. Parelo: A crystal of a typical EF-hand protein grown under microgravity diffracts x-rays beyond 0.9 resolution, *J. Cryst. Growth* **196**, 595–601 (1999)
- 17.126 S. Gorti, E.L. Forsythe, M.L. Pusey: Measurable characteristics of lysozyme crystal growth, *Acta Cryst. D* **61**, 837–843 (2005)
- 17.127 <http://science.nasa.gov/ssl/msad/pcg/> (last accessed August 9, 2009)
- 17.128 D.C. Carter, K. Lim, J.X. Ho, B.S. Wright, P.D. Twigg, T.Y. Miller, J. Chapman, K. Keeling, J. Ruble, P.G. Vekilov, B.R. Thomas, F. Rosenberger, A.A. Chernov: Lower dimmer impurity incorporation may result in higher perfection of HEWL crystals grown in microgravity: a case study, *J. Cryst. Growth* **196**, 623–637 (1999)

18. Hydrothermal Growth of Polyscale Crystals

Kullaiah Byrappa

Part C | 18

In this chapter, the importance of the hydrothermal technique for growth of polyscale crystals is discussed with reference to its efficiency in synthesizing high-quality crystals of various sizes for modern technological applications. The historical development of the hydrothermal technique is briefly discussed, to show its evolution over time. Also some of the important types of apparatus used in routine hydrothermal research, including the continuous production of nano-size crystals, are discussed. The latest trends in the hydrothermal growth of crystals, such as thermodynamic modeling and understanding of the solution chemistry, are elucidated with appropriate examples. The growth of some selected bulk, fine, and nanosized crystals of current technological significance, such as quartz, aluminum and gallium berlinites, calcite, gemstones, rare-earth vanadates, electroceramic titanates, and carbon polymorphs, is discussed in detail. Future trends in the hydrothermal technique, required to meet the challenges of fast-growing demand for materials in various technological fields, are described. At the end of this chapter, an Appendix 18.A containing a more or less complete list of the characteristic families of crystals synthesized by the hydrothermal technique is given with the solvent and pressure-temperature (PT) conditions used in their synthesis.

Crystals are the unacknowledged pillars of modern technology owing to their ever-increasing applications in various technologies such as electronics, microelectronics, magnetics, optics, nonlinear optics, photonics, optoelectronics, magnetoelectronics, biomedicine, biophotonics, biotechnology, nanotechnology, etc. Accordingly the size and quality of crystals control their application potential, as the properties also vary greatly with size, i. e., from bulk crystals to nanocrystals, due to the quantization effect. Hence, a new ter-

minology (*polyscale crystals*) has become more appropriate in recent years for contributions like this devoted to the hydrothermal growth of crystals of different compositions and sizes. When the hydrothermal technique was initiated in the mid 19th century, the focus was essentially on mineral synthesis, also in the form of bulk single crystals. During World War II the importance of the hydrothermal technique was realized with the tremendous success in the growth of larger-size quartz crystals, and the focus shifted to the design of different types of autoclaves which could hold fluids under high-pressure and high-temperature conditions over a longer period. A greater variety of crystals hitherto unknown or without natural counterparts was synthesized during the 1960s and 1970s. Although there was a slight decline in the popularity of the hydrothermal technique during the 1980s, it has now picked up as one of the best methods to grow not only bulk crystals, but also fine and nanocrystals with desired shape, size, and properties. Hence, there has been a sudden surge in activities related to hydrothermal research in the last decade, because of the high-quality crystals of different sizes that can be grown well under hydrothermal conditions. This is further supported by the overwhelming success in the field of thermodynamic modeling and solution chemistry under hydrothermal conditions, which have drastically reduced the PT conditions required for crystal growth.

18.1	History of Hydrothermal Growth of Crystals	603
18.2	Thermodynamic Basis of the Hydrothermal Growth of Crystals ..	606
18.2.1	Hydrodynamic Principles of the Hydrothermal Growth of Crystals	606

18.2.2 Thermodynamic Modeling of the Hydrothermal Growth of Crystals	608	18.4 Hydrothermal Growth of Some Selected Crystals	620
18.2.3 Solutions, Solubility, and Kinetics of Crystallization under Hydrothermal Conditions	610	18.4.1 Quartz.....	620
18.3 Apparatus Used in the Hydrothermal Growth of Crystals ..	615	18.4.2 Aluminum and Gallium Berlinites .	625
18.3.1 Morey Autoclave.....	617	18.4.3 Calcite	628
18.3.2 Tuttle–Roy Cold–Cone Seal Autoclaves.....	617	18.4.4 Gemstones	629
18.3.3 General–Purpose Autoclaves and Others	618	18.4.5 Rare–Earth Vanadates.....	633
		18.5 Hydrothermal Growth of Fine Crystals	634
		18.6 Hydrothermal Growth of Nanocrystals	637
		18.7 Concluding Remarks	640
		18.A Appendix.....	641
		References	646

The term *hydrothermal* is purely of geological origin. It was first used by the British geologist *Sir Roderick Murchison* (1792–1871) to describe the action of water at elevated temperature and pressure, in bringing about changes in the Earth’s crust leading to the formation of various rocks and minerals. It is well known that the largest single crystal formed in nature (a beryl crystal of > 1000kg) and some of the largest quantities of single crystals created by man in one experimental run (quartz crystals of several 1000 kg) are both of hydrothermal origin [18.4]. The technique is very important for its technological efficiency in developing high-quality crystals of different sizes. The term *polyscale* is relatively new and refers to different sizes of crystals, covering

bulk single crystals, small crystals, and micrometer to nanosize crystals [18.5]. This concept becomes more relevant with the progress achieved in nanotechnology, wherein the quantization size effect explains the changes in the physical properties of the crystalline materials with size. The hydrothermal technique is becoming one of the most important tools for advanced materials processing, particularly owing to its advantages in the processing of nanostructural materials for a wide variety of technological applications such as electronics, optoelectronics, catalysis, ceramics, magnetic data storage, biomedicine, biophotonics, etc. The hydrothermal technique greatly helps in processing monodispersed and highly homogeneous nanocrystals [18.6]. The hydrothermal technique refers to any

Table 18.1 Different terminologies used in the hydrothermal technique

Conventional hydrothermal	Solvothermal	Supercritical hydrothermal	Related terminologies	Multi-energy hydrothermal
Aqueous solvent; Refers to conditions above atmospheric temperature and pressure; Suitable for high quality; Bulk, fine nanocrystals [18.1]	Nonaqueous solvents; Low to high temperature conditions; Suitable for good quality; Bulk, fine nanocrystals [18.1,2]	Critical to supercritical conditions; Both aqueous and nonaqueous solvents; Suitable for fine and nanocrystals; Rapid [18.3]	Ammonothermal, glycothermal, lyothermal, alcohothermal, carbonothermal, etc. depending upon the specific solvent used; Spray pyrolysis; Suitable for fine to nanocrystals and thin films [18.1,2]	Hydrothermal in combination with extra energy likesuch as microwave, electrochemical, sonar, mechanochemical, biomolecular, sol–gel, etc. Extremely efficient for thin films, fine to nanocrystals; Epitaxy, etc. Very fast processing [18.2]

homogeneous (nanocrystals) or heterogeneous (bulk single crystals) reaction in the presence of aqueous solvents or mineralizers under high-pressure and high-temperature conditions to dissolve and recrystallize (recover) materials that are relatively insoluble under ordinary conditions. *Byrappa* and *Yoshimura* define *hydrothermal* as any homogeneous or heterogeneous chemical reaction in the presence of a solvent “(whether

aqueous or nonaqueous) above the room temperature and at pressure greater than 1 atm in a closed system” [18.1, 2]. However, chemists prefer to use the term *solvothermal*, meaning “any chemical reaction in the presence of a nonaqueous solvent or solvent in supercritical or near-supercritical conditions”. Table 18.1 gives different terminologies used by different specialists for hydrothermal technology.

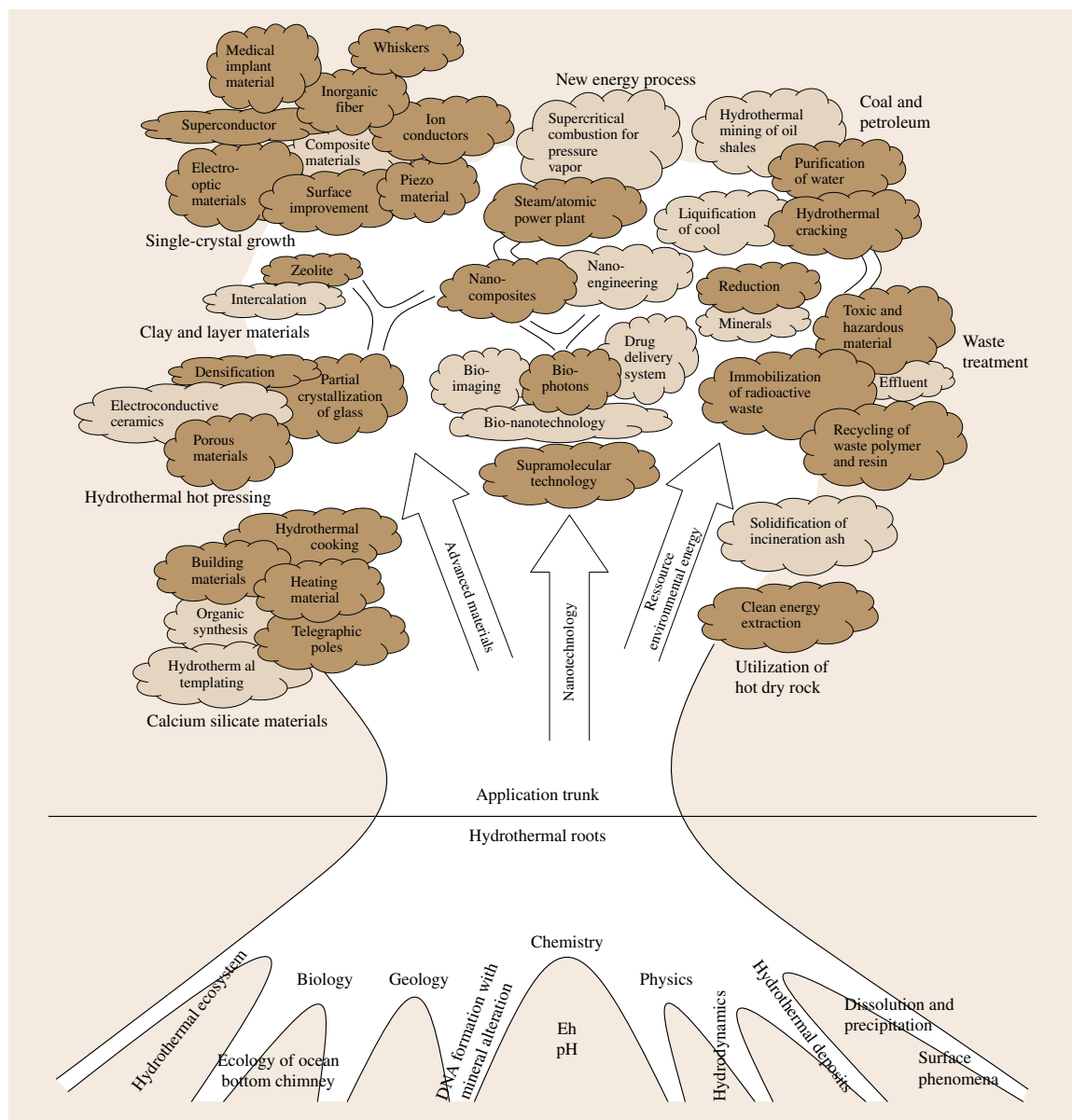


Fig. 18.1 Hydrothermal tree showing different branches of science and technology (after [18.6])

In recent years, the addition of energy into the hydrothermal process, such as in hydrothermal-electrochemical, hydrothermal-mechanochemical, hydrothermal-microwave, hydrothermal-sonar, hydrothermal-sol-gel, hydrothermal-biomolecular, etc., methods has made the process extremely effective and fast. It also leads us to a new concept of chemistry at the speed of light [18.2, 6]. However, this new process is only suitable for the preparation of fine to nanosize crystals, and thin films with high crystallinity and desired properties. In recent years, capping agents, organic molecules, surfactants, etc., have become popular for use in crystal growth in order to achieve growth in the desired crystallographic direction and stunt growth in the undesired crystallographic directions under hydrothermal conditions. Such developments have made the hydrothermal technique unique in terms of its ability to fabricate functional products with in situ control over their growth. All these recent developments in the last 10 years have completely changed the concept of hydrothermal growth of crystals. Earlier, researchers had always considered hydrothermal growth of crystals to be a high-temperature and high-pressure technique that was very expensive and slow in terms of growth rate. However, a new generation of hydrothermal researchers now consider it to be a simple technique that requires mild to low temperature/pressure, which is not expensive, and which is fast with a maximum product yield. Thus hydrothermal technique is being popularly employed by physicists, chemists, ceramists, hydrometallurgists, material scientists, biologists, engineers, geologists, technologists, and so on. Figure 18.1 shows the various branches of science either emerging from the hydrothermal technique or closely linked with it. One could firmly say that this family tree will keep expanding its branches and roots in the years to come.

Here, the author uses the term *hydrothermal* only in a broad sense covering a set of all the above-mentioned variations given in Table 18.1 to describe chemical reactions taking place in the presence of a solvent – aqueous or nonaqueous – under subcritical or supercritical conditions in a closed system. Similarly, the hydrothermal method has been widely accepted since the 1960s and practically all inorganic species, from native elements to the most complex silicates, germinates, phosphates, and others, have been obtained by this method. The technique is being employed on an industrial scale to prepare bulk to nanosize crystals for piezoelectric, optoelectronic, magnetic, ceramic, photonic, etc., applications. It offers several

advantages over the conventional techniques of crystal growth in terms of purity, homogeneity, crystal symmetry, metastable-phase formation, reproducibility, lower crystallization temperature, single-step processing, simple equipment, lower energy requirements, fast reaction times, desired polymorphic modifications, growth of ultralow-solubility materials, etc.. For example, it is the only method that has been successfully employed to produce large-size single crystals of α -quartz on an industrial scale. Similarly compounds with elements in oxidation states that are difficult to obtain (especially transitional-metal compounds) by other ordinary methods can be synthesized well under hydrothermal conditions, for example, ferromagnetic chromium(IV) oxide. The synthesis of metastable phases such as subiodides of tellurium (Te_2I) can be carried out more easily under hydrothermal conditions [18.7]. The scope of the present chapter has been limited to the hydrothermal growth of crystals – bulk single crystals to selected nanocrystals – instead of describing the application of the entire hydrothermal technology that deals with the hydrothermal reactions, hydrothermal treatment of various organic and inorganic materials including recycling, frequently employed on a large scale. Also it is impossible to discuss the growth of each and every crystalline compound available in the literature, as they exceeds several hundred; the focus is limited to selected crystals of current interest and also some exceptionally major works of the past. The following aspects have been covered in the present chapter:

1. The history of hydrothermal growth of crystals
2. The thermodynamic basis of the hydrothermal growth of crystals
3. Hydrothermal apparatus and safety measures to be adopted
4. Hydrothermal growth of selected crystals:
 - a) Bulk crystals
 - b) Small crystals
 - c) Nanocrystals
5. Future trends in the hydrothermal growth of crystals.

The theory of hydrothermal growth of crystals dealing with the growth mechanism is a recent subject; hence more emphasis is placed on the experimental aspects of crystal growth under hydrothermal conditions. However, the growth mechanism is briefly discussed for those compounds where this is available in the literature.

18.1 History of Hydrothermal Growth of Crystals

The history of hydrothermal growth of crystals has been elaborated in several works by *Byrappa* and co-workers [18.1, 2, 6, 7]. Here, the history of the hydrothermal growth of crystals is discussed briefly. The hydrothermal technique was initiated by Earth scientists during the middle of the 19th century to understand the genesis of rocks and minerals by simulating the natural conditions existing under the Earth's crust and crystallizing them in the laboratory. The first hydrothermal experiment was carried out by *Schafthaul* in 1845 to synthesize quartz crystals upon transformation of freshly precipitated silicic acid in Papin's digester [18.8]. Followed by this there were quite a few works by French and German mineralogists on the hydrothermal synthesis of minerals [18.9–12]. However, the size of the crystals obtained in general did not exceed thousands or hundreds of a millimeter. Thus, it was well known that the majority of the early hydrothermal experiments carried out during the 1840s to the early 1900s mainly dealt with fine to nanocrystalline products, which were discarded as failures due to the lack of sophisticated electron microscopic techniques available during that time to observe such small-sized products. Many times, when the bulk crystals or single crystals of several millimeter sizes were not obtained in the products, the experiments were considered as failures and the materials were washed away. Perhaps the greatest contribution during the 19th century in the field of hydrothermal synthesis of crystals was by *De Senarmont*, the founder of hydrothermal synthesis in geoscience. He synthesized mineral carbonates, sulfates, sulfides, and fluorides using glass liners in autoclaves [18.11]. *Bunsen* first used thick-walled glass tubes to contain high-temperature high-pressure liquids and prepare strontium and barium carbonates [18.9]. Although *Saint-Claire Deville* attempted to transform bauxite into corundum under hydrothermal conditions using NaOH as a mineralizer, the experimental results were not definite; perhaps he was the first to use a mineralizer other than water [18.13]. *Von Chrustschoff* first proposed the noble-metal lining of autoclaves to prevent corrosion [18.14]. Before this the glass tubes that were used were frequently attacked under hydrothermal conditions, and earlier researchers do not mention anything about the precautions taken in this regard. With the introduction of steel autoclaves and noble-metal linings, the tendency to reach higher-pressure/temperature conditions began. However, the majority of works up to 1880 continue to pertain to quartz, feldspar, and related

silicates. *Hannay* claimed to have synthesized artificial diamond by the hydrothermal technique [18.15]. Similarly, *Moissan* also claimed to have synthesized diamond as large as 0.5 mm artificially from charcoal [18.16]. Though, the success of these experiments was treated as dubious, they certainly provided a further stimulus for hydrothermal research, particularly the development of high-pressure techniques. Perhaps the first large crystals obtained using this technique in the 19th century were by *Friedel* and *Sarasin* (1881), who synthesized hydrated potassium silicate, 2–3 mm long [18.17]. Then, in 1891 *Friedel* obtained corundum crystals by heating a solution of NaOH with excess Al_2O_3 at a high temperature for that time: 530–535 °C [18.18].

Towards the end of the 19th century, *Spezia* from the Torino Academy of Science began his classical work on the seeded growth of quartz. His contribution to the field of hydrothermal growth of crystals is remembered even today. *Spezia* (1896) found that plates of quartz kept at 27 °C for several months with water under a pressure of 1750–1850 atm did not lose their weight and also showed no etch figures; thus, he concluded that pressure alone has no influence on the solubility of quartz [18.19]. *Spezia* studied the solubility of quartz in such great detail that the growth of bulk single crystals of quartz became possible [18.20]. So before the end of the 19th century, a large number of minerals had been synthesized, and experiments had been carried out on a wide variety of geological phenomenon ranging from the origin of ore deposits to the origin of meteorites. According to *Morey* and *Niggli*, around 150 mineral species including diamond had been synthesized by 1900 [18.21]. *Morey* quotes a horrible experience of one of the earliest hydrothermal experiments in which, after reacting a mixture of colloidal silicon, colloidal ferric hydroxide, colloidal ferrous oxide, lime water, magnesium hydroxide, and potassium hydroxide in glass for 3 months at 550 °C, some fine crystals of hornblende were obtained, which had no bearing on the petrogenesis or the phase equilibria of the mineral system [18.22]. This was definitely due to lack of knowledge in areas of solvent chemistry, thermodynamics, kinetics, and compound solubility.

The entire activity on the hydrothermal research was concentrated in Europe, and there was no activity in North America or Asia, including Japan, China, India, and Taiwan, which are included today in the top ten countries actively engaged in hydrothermal research.

Perhaps the first published work from North American on hydrothermal research was by *Barus*, who essentially worked on the impregnation of glass with water to such an extent that it melted below 200 °C by using steel autoclaves [18.23]. Following this, Allen published his classic work on the growth of quartz crystals 2 mm long using steel autoclaves with copper sealing. The first commercialization of the hydrothermal technique took place in the early 20th century to leach bauxite, an aluminum ore, by Bayer's process. However, this is not related to crystal growth. The establishment of the Geophysical Laboratory at the Carnegie Institute of Washington in 1907 probably marked the most important milestone in the history of hydrothermal research. The credit goes to pioneers such as Bridgman, Cohen, Morey, Niggli, Fenner, and Bowen in the early 20th century, who changed the scenario of hydrothermal research. They carried out an impressive amount of basic research, along with their European counterparts. However, the total research effort was small and the study passed into a period of dormancy except for phase equilibria studies in some systems relevant to natural systems. This was connected with the need for materials with a combination of high strength and corrosion resistance at high temperatures. Although, a great deal of research was carried out during the 20th century, the facilities for large-scale hydrothermal research before the end of World War II were virtually nonexistent, with the exception of at the University of Chicago and Harvard University. This situation changed dramatically with the development of test-tube-type pressure vessels by Tuttle, later modified by Roy. These test-tube-type pressure vessels are some of the most versatile autoclaves used worldwide today; also popularly known as batch reac-

tors, that could hold temperatures up to 1150 °C at lower pressures and pressure up to 10 kbar at lower temperatures (the modified titanium zirconium molybdenum (TZM) autoclaves).

The actual impetus for hydrothermal growth of crystals began during World War II with the growth of quartz. Here, in contrast to the very slow growth rate achieved by earlier workers such as *De Senarmont* and *Spezia*, captured German reports show that *Nacken*, using natural α -quartz as seed crystals and vitreous silica as the nutrient, had grown quartz crystals in an isothermal system and succeeded in obtaining a large quartz crystal from a small seed [18.25, 26]. *Nacken* (1884–1971) worked on the synthesis of various crystals from 1916 onwards, but left this field. In 1927 or 1928, he started working only on the hydrothermal growth of quartz crystals. On *Nacken's* work, Sawyer writes (cited by Bertaut and Pauthenet, 1957) that, "... *Nacken* made quartz crystals of 1" diameter by using hydrothermal method and the conditions are given as ..." followed by some biographical data. Similarly, *Nacken's* emphasis on quartz growth has also been documented by Sawyer. Almost at the same time, *Nacken* made emerald single crystals by the hydrothermal method and also beryl or corundum crystals for watch bearings. He prepared a large number of synthetic emeralds by using a trace of chromium to produce color and could obtain hexagonal prisms of emerald weighing about 0.2 mg in a few days [18.27]. Figure 18.2 shows the first large-size manmade quartz crystals obtained by *Nacken* [18.24]. At almost this time, Russian researchers were producing bulk quartz crystals using old discarded cannon barrels as autoclaves. Unfortunately, these works were not published. However, the author of this chapter had an opportunity to interact on several occasions with the late *Prof. Shternberg*, from the Institute of Crystallography, Academy of Sciences (erstwhile USSR), who was mainly responsible for such great and unpublished Russian work [18.28].

With the publication of *Nacken's* work in 1950, several laboratories around the world began working on large-scale production of quartz crystals. During the 1960s, interest in the hydrothermal method was boosted in connection with the industrial growth of good-quality quartz single crystals and the successful growth of most complex inorganic compounds. Perhaps this is the beginning of the growth of crystals which did not have natural analogues. During the 1970s, there was a question about the search for and growth of hitherto unknown compounds of photoconductors, ferromagnets, lasers, and piezo- and ferroelectrics,

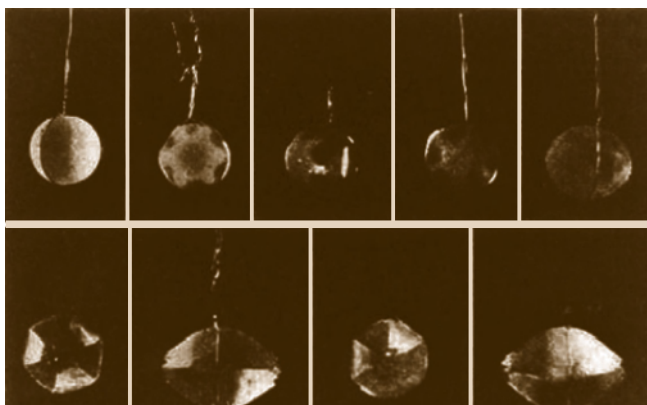


Fig. 18.2 The first manmade large-size crystals of quartz, obtained by *Nacken* [18.24]

and the hydrothermal method attracted great attention. Several established laboratories in the world began to study systematically various aspects of the hydrothermal growth of crystals such as the physicochemical principles, kinetics, designing new apparatus, growing new compounds, and so on. Specific aspects of the hydrothermal method as a modeling tool to understand the natural processes of mineral formation changed dramatically into an important method characteristic for inorganic chemistry. During the 1980s, a new sealing method for large-size autoclaves was designed, viz. Grey-Loc sealing, which facilitates the construction of very large-size autoclaves with a volume of 5000 l [18.29]. Toyo Electric Co., Japan, houses the world's largest autoclave for the growth of quartz crystals.

Towards the end of the 1970s, on the whole, the hydrothermal field experienced a declining trend for two reasons: there was no major scope for further work on the growth of large-size single crystals of quartz on the one hand, and on the other hand, large-scale attempts to grow larger crystals of other compounds investigated during the 1960s and 1970s failed miserably. It was unanimously decided that the hydrothermal technique was not suitable for the growth of large crystals other than quartz. The focus at this time was on Czochralski, molecular chemical vapor deposition (MOCVD), and molecular-beam epitaxy (MBE). This is mainly connected to the general approach of the hydrothermal researchers to grow large single crystals without looking into the hydrothermal solvent chemistry and the kinetics of the crystallization process. However, the Nobel Symposium organized by the Swedish Academy of Sciences, during September 17–21, 1979, on *The Chemistry and Geochemistry of Solutions at High Temperatures and Pressures* is remembered as an eye-opener. The presence of pioneers in the field of hydrothermal physical chemistry such as *Franck, Seeward, Helgeson, Pitzer*, and so on, drew the attention of hydrothermal crystal growers and a new trend was set to look into the hydrothermal solvent chemistry and the physical chemistry of the hydrothermal systems [18.30–33]. Following this, *Prof. Somiya*, Japan, organized the first ever International Symposium on Hydrothermal Reactions, in 1982, which was attended largely by specialists from different branches of science such as physical chemistry, inorganic chemistry, solid-state physics, material scientists, organic chemists, hydrometallurgists, hydrothermal engineers, etc. [18.34]. This was the dawn of modern hydrothermal research, and since

then new avenues in the field of hydrothermal research are being explored. As evident from the recent literature data, the hydrothermal technique is one of the most efficient techniques for the growth of high-quality crystals of GaN, ZnO, GaPO₄, etc. as well as traditional quartz crystals. Obviously there is a surge in the activities related to hydrothermal growth of crystals. This is greatly supported by developments in thermodynamic modeling and also understanding of the fluid dynamics in autoclaves through simulation.

There is a great difference between the hydrothermal research carried out during the previous century and the early 21st century. During the mid-20th century the hydrothermal technique was at its peak and the focus was mainly on the high-temperature and high-pressure regime of crystal growth, because of lack of knowledge on the solubility of several compounds and also on the selection of an appropriate solvent. The First International Hydrothermal Symposium (1982) held at the Tokyo Institute of Technology, Japan, brought together specialists from the interdisciplinary branches of science [18.34]. Since then knowledge on the physical chemistry and the PVT relationship in hydrothermal systems has greatly improved, which helped in drastically reducing the temperature and pressure conditions required for crystal growth. Similarly solvothermal and supercritical processing have been developed, which use a variety of other solvents such as organic and organometallic complexes in the synthesis, thereby moving this technique towards “green” chemistry. Table 18.2 presents trends in the hydrothermal growth of crystals, taking the hydrothermal

Table 18.2 Current trends in hydrothermal technology [18.5]

Crystal	Earlier works	Present Author
Li ₂ B ₄ O ₇	$T = 500\text{--}700\text{ }^{\circ}\text{C}$ $p = 500\text{--}1500\text{ bar}$	$T = 240\text{ }^{\circ}\text{C}$ $p \leq 100\text{ bar}$
Li ₃ B ₅ O ₈ (OH) ₂	$T = 450\text{ }^{\circ}\text{C}$ $p = 1000\text{ bar}$	$T = 240\text{ }^{\circ}\text{C}$ $p = 80\text{ bar}$
NaR(WO ₄) ₂ R = La, Ce, Nd	$T = 700\text{--}900\text{ }^{\circ}\text{C}$ $p = 2000\text{--}3000\text{ bar}$	$T = 200\text{ }^{\circ}\text{C}$ $p \leq 100\text{ bar}$
R:MVO ₄ R = Nd, Eu, Tm; M = Y, Gd	Melting point > 1800 °C	$T = 100\text{ }^{\circ}\text{C}$ $p \leq 30\text{ bar}$
LaPO ₄	Synthesized at > 1200 °C	$T < 120\text{ }^{\circ}\text{C}$ $p < 40\text{ bar}$
Zoisite	$T = 500\text{ }^{\circ}\text{C}$ $p = 5\text{ kbar}$	$T = 250\text{ }^{\circ}\text{C}$ $p \leq 100\text{ bar}$

technique towards green technology for sustained human development, since it consumes less energy, no or little solid/liquid waste, no recovery treatment, no hazardous processing materials, high selectivity, a closed

processing system, etc. [18.5]. Hydrothermal chemistry has to be understood precisely in order to grow crystals under soft and environmentally benign conditions.

18.2 Thermodynamic Basis of the Hydrothermal Growth of Crystals

The thermodynamic basis of the hydrothermal growth of crystals is perhaps the least explored aspect in the literature. As such, there is no major review or book dealing with this aspect, although some significant developments have occurred in this area since the Nobel Symposium organized by the Royal Swedish Academy of Sciences in 1978, followed by the First International Symposium on Hydrothermal Reactions, organized by the Tokyo Institute of Technology in 1982, helped in setting a new trend in hydrothermal technology by attracting physical chemists in large numbers. Hydrothermal physical chemistry today has enriched our knowledge greatly through a proper understanding of hydrothermal solution chemistry. The behavior of the solvent under hydrothermal conditions dealing with aspects such as structure at critical, supercritical, and subcritical conditions, dielectric constant, pH variation, viscosity, coefficient of expansion, density, etc., are to be understood with respect to pressure and temperature. Similarly, thermodynamic studies have yielded rich information on the behavior of solutions at various pressure–temperature conditions. Since most hydrothermal crystal growth experiments are carried out under conditions with temperature gradients in standard autoclaves, growth occurs due to the recrystallization of the solid substance, including dissolution in the liquid phase and convective mass transfer of the dissolved part of the substance to the growth zone or seed, and also through the dissolution of the mixture of the nutrient components with the help of their convective mass transport into the growth zone and interaction of the dissolved components on the seed surface. However, there are several macro- and microprocesses occurring at the interface boundary of the solution and the crystal/seed. Therefore, the composition and concentration of the solution, and the temperature, pressure, and hydrodynamic conditions and surface contact of the phases are some of the basic physical and chemical parameters that determine the regime and rate of dissolution of the nutrient, the mass transport, and the possibility of the formation of new phases.

18.2.1 Hydrodynamic Principles of the Hydrothermal Growth of Crystals

The hydrodynamic principles of growth of crystals under hydrothermal conditions have been studied by several groups since the 1990s using numerical modeling to understand the fluid flow in an autoclave. There are quite a few publications on this aspect. In order to grow good-quality crystals with minimum possible defects, one has to understand the flow dynamics. *Laudise* and *Nielsen* were perhaps the first to draw the attention of hydrothermal crystal growers to the thermal conditions during growth, which lead to strong buoyancy-driven flow carrying nutrient from the lower dissolution chamber to the upper growth chamber [18.35]. Then *Klipov* and *Shmakov* studied the shape and morphology of the surfaces, the growth rate, the macroscopic defects, and the inclusion density of hydrothermally grown quartz crystals, and found a strong correlation with the fluid flow around the crystals [18.36]. *Ezersky* et al. have studied the hydrodynamics under hydrothermal conditions using a shadowgraph technique [18.37, 38]. This helped the authors to understand the spatiotemporal structure of hydrothermal waves in Marangoni convection. *Roux* et al. have developed both two-dimensional (2-D) axisymmetric and three-dimensional (3-D) models for hydrothermal crystal growth, by focusing on the bulk flow pattern in an autoclave [18.39]. Their 2-D axisymmetric model gave an unrealistic nonaxisymmetric flow pattern, while their 3-D model considers a square cross-section for the container instead of a circular or cylindrical one actually used in hydrothermal experiments. However, the results obtained were based on very low Rayleigh numbers (up to 6×10^4), corresponding to very small autoclaves, which cannot be applied to the larger autoclaves used for bulk or commercial crystal growth. *Chen* et al. [18.40, 41] have studied the flow dynamics by using a numerical model with a higher Rayleigh numbers and developed a comprehensive 3-D model for the hydrothermal growth of crystals. The

significant aspect of their work is the introduction of a fluid-superposed porous raw material bed in the lower dissolution chamber of the autoclave. This model predicts a strong 3-D flow in the autoclave and a strong temperature fluctuation. However, the best works to date on the numerical modeling of flow pattern dynamics comes from *Evans* and group [18.42–45]. Their 3-D modeling is based on industrial-scale hydrothermal autoclaves with various aspect ratios with nonuniform heating conditions. The nonuniform heating is introduced on the surface of the lower dissolving chamber and the upper growing chamber of an autoclave with or without a baffle at the middle height. It was found that the circumferentially nonuniform surface temperature has dramatic effects on the fluid flow and therefore the temperature distribution in the bulk fluid. With a temperature deviation, the flow is three dimensional. When only the dissolving chamber is subjected to circumferentially nonuniform heating, a baffle is essential to create a uniform growth environment in the growth chamber. It is evident from their work that, in order to obtain high-quality single crystals, wall-temperature control on the growth chamber wall is more important than on the dissolving chamber wall. Figure 18.3 shows the velocity distributions and temperature contours for an autoclave without a baffle and with a 15% baffle, respectively. The velocity field is much stronger in the case without a baffle than that with a baffle. The numerical study of the effects of various baffles (with 2–25% opening) on the fluid flow and temperature fields have been investigated by these authors. Accordingly a smaller opening leads to a weaker flow field and a more uniform temperature profile. A multihole baffle establishes a more uniform temperature in the upper chamber than does a single-hole baffle of the same area opening. The number of holes in the multihole baffle has significant effects, while the hole arrangements affect the thermal condition only near the baffle.

The flow pattern, with a high flow velocity in the upper growing chamber, could have a significant negative effect on solute transport from the solution to the seed crystals and therefore on the crystal growth rate and quality. The strong flow also leads to strong distortion of the temperature field. A nonuniform temperature field in the growth region is not desirable for growing uniform high-quality crystals. A significant development in the field of numerical modeling of heat transfer processes and flow fields under hydrothermal conditions is the work related to the crystal growth of beryl, AlPO_4 , and GaPO_4 [18.46, 47]. These studies have yielded some insight into the flow pattern under hydrothermal con-

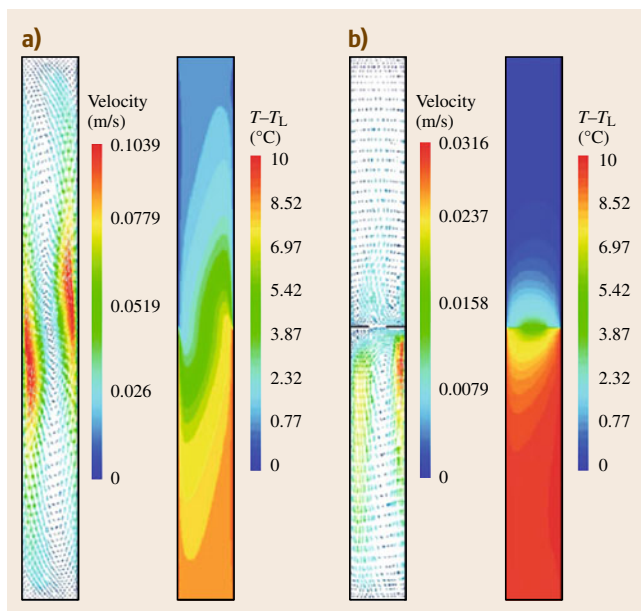


Fig. 18.3a,b Velocity pattern and isotherms in the symmetry plane. $\Delta T = 10^\circ\text{C}$. On the lower chamber $\Delta T = 0.1^\circ\text{C}$ only. (a) Without baffle; and (b) with a 15% area baffle opening at the median plane

ditions. For example, the influence of a rotating solid crystal or a seed crystal inside the autoclave has also been considered in such numerical modeling.

However, most of these models on numerical flow patterns are based on several assumptions and are applied mainly to simple or single-phase systems. Also, the nature of the fluid is important and the flow dynamics will vary with the type of fluid; and 3-D simulation models of the flow in the autoclave show that the turbulent flow is not in fact 3-D. The effect of the simultaneous existence of the crystals and the raw materials has not been considered in most of these models. Thus there is an incomplete picture on the whole with respect to the flow dynamics. A lot more experimental and theoretical investigations are needed to clarify and complete the description of the hydrothermal flow dynamics.

During the late 1980s to early 1990s a good number of publications appeared on the physicochemical foundation of crystal growth under hydrothermal conditions. Balitsky and Bublikova carried out detailed physicochemical investigations on malachite bulk crystal growth. Similarly Kuznetsov has reviewed the physical chemistry of hydrothermal crystal growth of II–VI compounds. Further, Popolitov has reviewed the physical chemistry of the hydrothermal growth of tellurium dioxide crystals. The reader can get more valuable

information in the book *Hydrothermal Growth of Crystals* [18.4]. However, all these studies are again based on several assumptions and indirect approaches with less bearing on the thermodynamic modeling principles.

18.2.2 Thermodynamic Modeling of the Hydrothermal Growth of Crystals

A key limitation to the conventional hydrothermal method has been the need for time-consuming empirical trial-and-error methods as a means of process development. Currently, research is being focused on the development of an overall rational-engineering-based approach that will speed up process development. The rational approach involves four steps:

1. Computation of thermodynamic equilibria as a function of chemical processing variables
2. Generation of equilibrium diagrams to map the process variable space for the phases of interest
3. Design of hydrothermal experiments to test and validate the computed diagrams
4. Utilization of the processing variables to explore opportunities for controlling reactions and crystallization kinetics.

Hydrothermal crystallization is only one of the areas where our fundamental understanding of hydrothermal kinetics is lacking due to the absence of data related to the intermediate phases forming in solution. Thus our fundamental understanding of hydrothermal crystallization kinetics is in the early stage, although the importance of studies of the kinetics of crystallization was realized with the commercialization of the synthesis of zeolites during the 1950s and 1960s. In the absence of predictive models, we must empirically define the fundamental role of temperature, pressure, precursor, and time on the crystallization kinetics of various compounds. Insight into this would enable us to understand how to control the formation of solution species, solid phases, and the rate of their formation. In recent years, thermochemical modeling of chemical reactions under hydrothermal conditions has become very popular. The resulting thermochemical computation data helps in the intelligent engineering of the hydrothermal processing of advanced materials. The modeling can be successfully applied to very complex aqueous electrolyte and nonaqueous systems over wide ranges of temperature and concentration and is widely used in both industry and academy. For example, OLI Systems Inc., USA, provides software for such

thermochemical modeling, and using such a package, aqueous systems can be studied within the temperature range -50 – 300 °C, pressure ranging from 0 to 1500 bar, and concentration 0–30 M in molal ionic strength; for nonaqueous systems the temperature range covered is 0–1200 °C and pressure from 0 to 1500 bar, with species concentration from 0 to 1.0 mol fraction.

Such a rational approach has been used quite successfully to predict the optimal synthesis conditions for controlling phase purity, particle size, size distribution, and particle morphology of lead zirconium titanates (PZT), hydroxyapatite (HA), and other related systems [18.48–50]. The software algorithm considers the standard state properties of all system species as well as a comprehensive activity coefficient model for the solute species. Table 18.3 gives an example of thermodynamic calculations and the yield of solid and liquid species outflows at $T = 298$ K, $p = 1$ atm, $I = 0.049$ M, and $\text{pH} = 12.4$.

Using such a modeling approach, theoretical stability field diagrams (also popularly known as yield diagrams) are constructed to obtain 100% yield. Assuming that the product is phase-pure, the yield Y can be expressed as

$$Y_i = 100 \frac{m_i^{\text{ip}} - m_i^{\text{eq}}}{m_i^{\text{ip}}} \% , \quad (18.1)$$

where m^{ip} and m^{eq} are the input and equilibrium molal concentrations, respectively, and the subscript i indicates the designated atom. Figures 18.4 and 18.5 show stability field diagrams for the PZT and HA systems.

From Fig. 18.4 it is observed that the region shaded represents 99% yield of PZT, although the PZT forms within a wide range of KOH and Ti concentrations. The figure clearly illustrates the region where all the solute species transform towards 100% product yield. Simi-

Table 18.3 Thermodynamic calculations for the HAp system

Species name	Inflows (mol)	Outflows	
		Liquid/mol	Solid/mol
H ₂ O	55.51	55.51	8.1×10^{-2}
Ca(OH) ₂	0.1	7.2×10^{-6}	
CaO			
Ca ²⁺		1.5×10^{-2}	
Ca(OH) ⁺		4×10^{-3}	
H ⁺		4.45×10^{-13}	
OH [−]		3.41×10^{-2}	
Total	55.61	55.56	8.1×10^{-2}

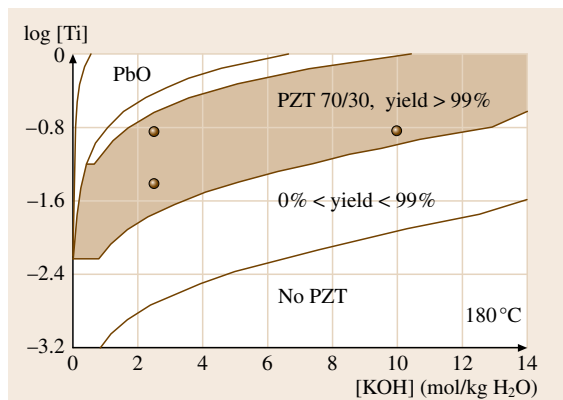


Fig. 18.4 Calculated stability field diagram for the PZT system at 180°C with KOH as the mineralizer (after [18.48])

larly, from Fig. 18.5, it is observed that all the Ca species participate in the reaction to form HA, thus leading to 100% yield of HA in the region denoted by a black square. Thick dotted lines indicate the boundary above which 99% Ca precipitates as HA. The other regions mark mixed-phase precipitation such as hydroxyapatite, monetite, and other calcium phosphate phases.

Such thermodynamic studies help to intelligently engineer the hydrothermal process and also to obtain a maximum yield for a given system. This area of research has great potential for application in crystal growth, including of nanocrystals. However, in the majority of cases, the conventional and nonconventional (composition diagrams) phase diagrams are still constructed based on phase equilibria studies carried out under hydrothermal conditions for systems of interest. Nonconventional phase diagrams (composition diagrams) plotted for equilibrium conditions are popular, especially among Russian workers, and are known as NC diagrams or TC diagrams, where N stands for the nutrient composition, T stands for experimental temperature, and C stands for solvent concentration. There are hundreds of such diagrams in the literature. Figure 18.6 represents an NC diagram for the system $\text{Na}_2\text{O}-\text{RE}_2\text{O}_3-\text{SiO}_2-\text{H}_2\text{O}$, showing the distribution of silicon-oxygen radical groups in the rare-earth silicates under hydrothermal conditions with fixed pressure and temperature conditions [18.51]. The solid lines indicate the regions of monophasic crystallization, and dashed lines indicate the beginning of crystallization of the excess component. Similarly there is one more type of composition diagrams used routinely in crystal growth to select the conditions of crystallization of

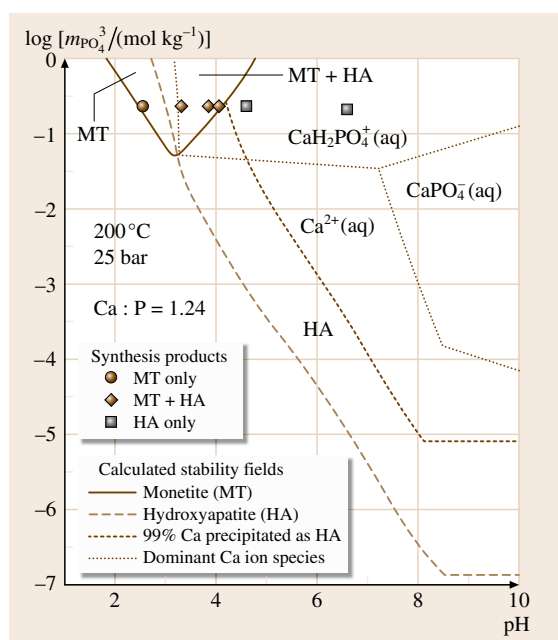


Fig. 18.5 Calculated stability field diagram for the HAP system at 200°C and 25 bar with Ca : P ratio of 1.24 (after [18.50])

various phases in a given system. Figure 18.7 represents the concentration versus temperature diagram for the system $\text{K}_2\text{O}-\text{La}_2\text{O}_3-\text{P}_2\text{O}_5-\text{H}_2\text{O}$ [18.52]. This dia-

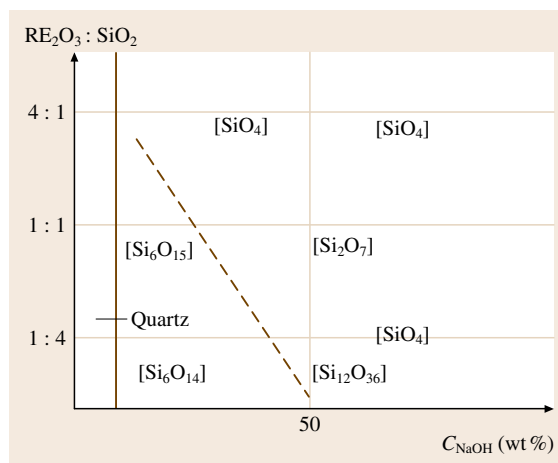


Fig. 18.6 NC diagram for the system $\text{Na}_2\text{O}-\text{RE}_2\text{O}_3-\text{SiO}_2-\text{H}_2\text{O}$ giving the distribution of silicon-oxygen radical groups in the rare-earth silicates under hydrothermal conditions with fixed pressure and temperature conditions (after [18.51])

gram helps in selecting the experimental temperature for the growth of rare-earth orthophosphate crystals. These nonconventional phase diagrams are relatively easy to obtain and are highly useful for the growth of single crystals as they clearly depict the growth conditions.

In addition to such unconventional phase diagrams, researchers frequently use standard phase diagrams such that shown in Fig. 18.8 for the potassium titanyl phosphate (KTP) system [18.53]. This type of phase diagram occurs in the thousands for various compounds, and is commonly used in crystal growth. Such phase diagrams give in general the phase boundaries and the phase formation within a given system under fixed PT conditions, and help to select the conditions for crystal growth.

18.2.3 Solutions, Solubility, and Kinetics of Crystallization under Hydrothermal Conditions

This is one of the most important aspects of the hydrothermal growth of crystals. Initial failures in the hydrothermal growth of a specific compound are usually the result of lack of proper data on the type of solvents, the solubility, and the solvent–solute interaction. A hydrothermal solution is generally considered as a thermodynamically ideal one, yet in the case of strong and specific interaction between the solute and the solvent, or among the components of the soluble substance in them, significant deviations from Raoult's law occur. Consequently, real hydrothermal solutions differ from ideal solutions and their understanding requires knowledge of the influence of the solvent in

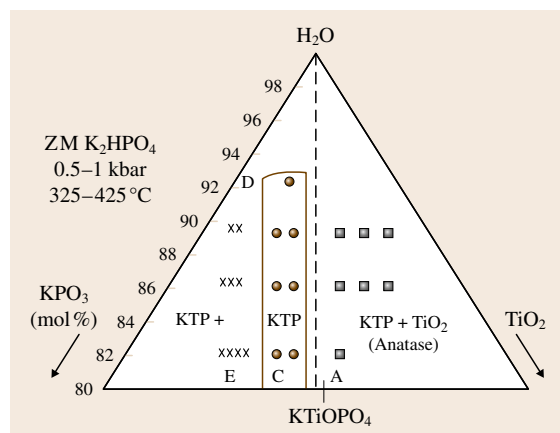


Fig. 18.8 Phase diagram for the KTP system (after [18.53])

the process of dissolution and crystallization of various compounds. Obviously, as shown in most of the experiments, the type of solvent and its concentration determine a specific hydrothermal process and its important characteristics such as the solubility of the starting materials, the quantity of the phases, their composition, and the output of the phases, kinetics, and growth mechanism of single crystals.

At the moment there is no theory which can explain and estimate solubility in real solutions. However many of the problems connected with solubility can be explained on the basis of overall physicochemical principles or laws.

In some cases, it is always better to use the empirical rule that solubility becomes high in solvents with higher dielectric constant (ϵ) and for types of chemical bond which are close to those of the solute substance. Deviation from this takes place when specific interactions between the solid substance and solvent occur.

The synthesis and recrystallization of a specific compound and the growth of single crystals on the seed are all carried out using different solvents on the basis of physicochemical considerations.

The following conditions are adopted in selecting the most suitable mineralizers:

1. Congruence of the dissolution of the test compounds
2. A fairly sharp change in the solubility of the compounds with changing temperature or pressure
3. A specific quantitative value of the absolute solubility of the compound being crystallized
4. The formation of readily soluble mobile complexes in the solution

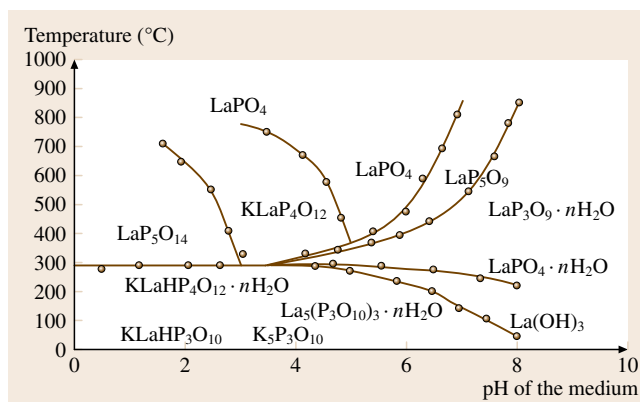


Fig. 18.7 Concentration versus temperature diagram for the system K_2O – La_2O_3 – P_2O_5 – H_2O (after [18.52])

5. A specific redox potential of the medium, ensuring the existence of ions of the required valence.

Additionally the solvent should have the desired viscosity, insignificant toxicity, and very weak corrosion activity with respect to the apparatus. These factors fulfill the requirements of the hydrothermal mineralizer (solvent) in addition to determining the values of solubility of the compound under investigation. Some of the basic properties of the hydrothermal medium, such as viscosity, dielectric constant, compressibility, and coefficient of expansion, are discussed here briefly in the context of crystal growth. Since diffusion is inversely proportional to solvent viscosity, one can expect very rapid diffusion in hydrothermal growth. This leads to the growth of perfect single crystals with well-developed morphology. We can expect higher growth rates, a narrower diffusion zone close to the growing interface, and less likelihood of constitutional supercooling and dendritic growth. It is thus no wonder that quartz growth rates as high as 2.5 mm/day without faults or dendritic growth have been observed [18.54].

Let us consider briefly the role of water as a solvent in the hydrothermal growth of crystals. Water is always the major component of hydrothermal solutions, with various chemical compositions in the laboratory and nature. All solutions used in hydrothermal experiments vary from one another in their properties, their ability to dissolve and crystallize, and the nature of the linking between water and electrolyte. Moreover, the properties of each solution depend upon physicochemical aspects and the structure of the pure water. The formation of associates and complexes in the aqueous solutions of electrolytes is possible because of the presence of structural water, i.e., water molecules with directional hydrogen bonding. Several chemical changes arise from changes in ionic dissociation of the solution. Therefore, it is better to understand the characteristics of the pure water under hydrothermal conditions. The hydrogen ions show an influence on the solubility of various compounds under hydrothermal conditions. Figure 18.9 shows the viscosity of water as a function of density and temperature [18.55]. It has been demonstrated that the mineralizer solutions (typically 1 M NaOH, Na_2CO_3 , NH_4F , K_2HPO_4 , etc.) have properties quite close to those of water. For 1 M NaOH at room temperature, $\eta_{\text{solution}}/\eta_{\text{water}} = 1.25$ [18.56] and one can expect that the viscosity of hydrothermal solutions can be as much as two orders of magnitude lower than ordinary solutions. The mobility of molecules and ions in the supercritical range is much higher than under normal

conditions. Also electrolytes which are completely dissociated under normal conditions tend to associate with rising temperature [18.57].

Hasted et al. (1948) observed that the dielectric constant of electrolyte solutions (ϵ) can be regarded as a linear function of molarity up to 1–2 M, depending on the electrolyte [18.58]. Franck [18.55] discussed ionization under hydrothermal conditions and made careful and complete conductivity studies, showing that the conductance of hydrothermal solutions remains high despite the decrease in ϵ , because this effect is more than compensated for by an increase in the ion mobility brought about by the decreased viscosity under hydrothermal conditions. Figure 18.10 shows the dielectric constant of water [18.59]. Thermodynamic and transport properties of supercritical water are remarkably different from those of ambient water. Supercritical water is unique as a medium for chemical processes. The solubility of nonpolar species increases, whereas that of ionic and polar compounds decreases as a result of the drop of the solvent polarity, and the molecular mobility increases due to a decrease in the solvent viscosity (η). Drastic changes of ionic hydration are brought about by the decrease in the dielectric constant (ϵ) and density (ρ). Largely as a consequence of the dramatic decrease in the dielectric constant of water with increasing temperature at constant pressure and/or de-

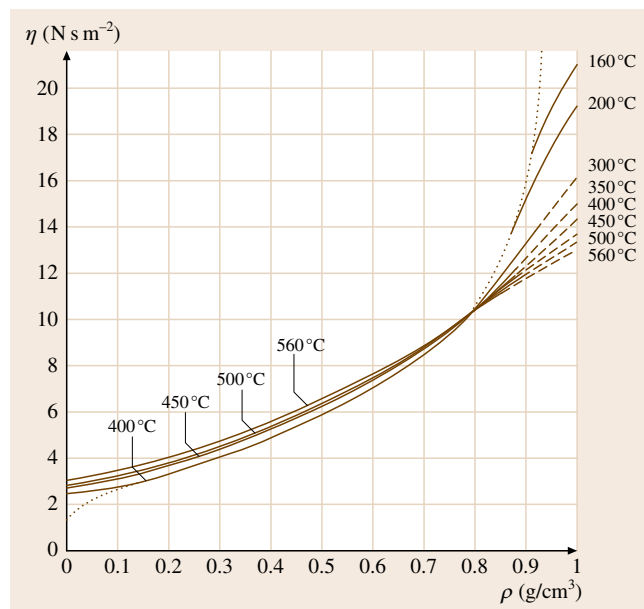


Fig. 18.9 Viscosity of water as a function of density and temperature (after [18.55])

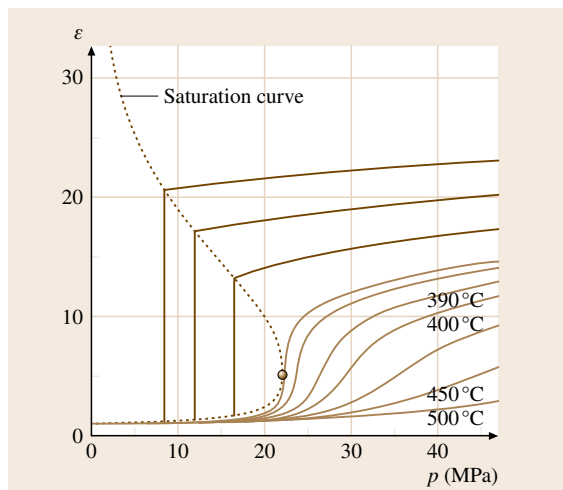


Fig. 18.10 Dielectric constant of water around the critical point (after [18.59])

creasing pressure at constant temperature, *completely* dissociated electrolytes at low temperatures and pressures may become highly associated in the supercritical region.

Water is an environmentally safe material and cheaper than other solvents, and it can act as a catalyst for the transformation of desired materials by tuning temperature and pressure. Studies of the structure dynamics and reactivity of supercritical water have led to a better understanding of how complicated compounds are adaptively evolved from simple ones in hydrothermal reactions. It is important to elucidate how the structure and dynamics of supercritical water are controlled by intermolecular interactions (ρ) as well as kinetic energies (T). This is a new frontier of solution chemistry. The **PVT** data for water up to 1000 °C and 10 kbar is known accurately enough (to within 1% error) [18.60, 62, 63]. At very high-**PT** conditions (1000 °C and 100 kbar), water is completely dissociated into H_3O^+ and OH^- , behaving like a molten salt, and has a higher density of the order of 1.7–1.9 g/cm³. Figure 18.11 shows the temperature–density diagram of water, with pressure as a parameter [18.60].

In hydrothermal crystal growth, the **PVT** diagram of water proposed by *Kennedy* is very important even today for reasons of simplicity (Fig. 18.12), although there are several recent diagrams available with greater accuracy [18.61]. Usually, in most routine hydrothermal experiments, the pressure prevailing under the working conditions is determined by the degree of filling

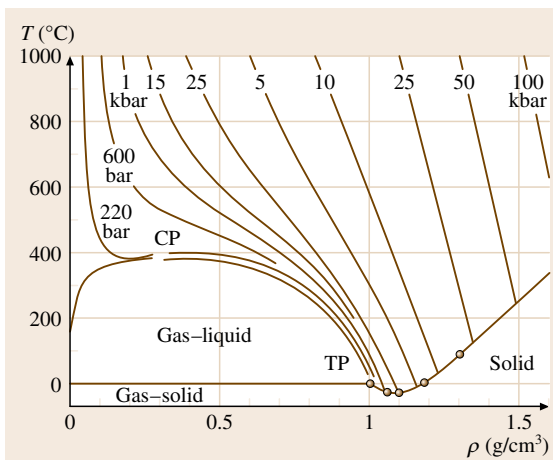


Fig. 18.11 Temperature–density diagram of water with pressure as a parameter (after [18.60])

and the temperature. When concentrated solutions are used, the critical temperature can be several hundred degrees above that of pure water. The critical temperatures are not known for the, usually complex, solutions at hand; hence one cannot distinguish between sub- and supercritical systems for reactions below 800 °C. Although the temperature in the growth zone and the actual vapor pressure are not known to 100% accuracy, the **PVT** diagram of *Kennedy* is routinely used by most hydrothermal crystal growers. The **PVT** relations for several other systems, such as AlPO_4 and SiO_2 , have been reviewed in [18.52, 64, 65].

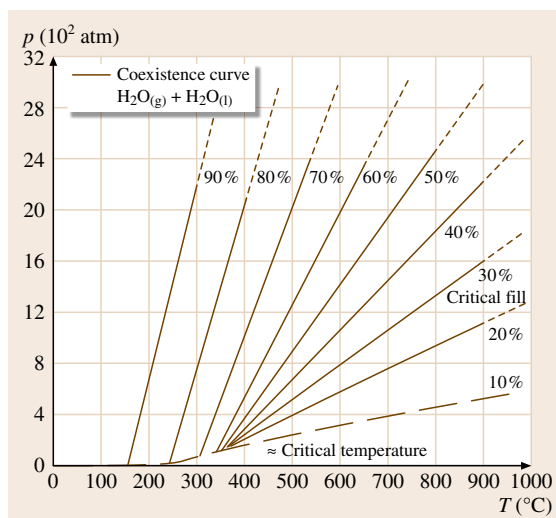


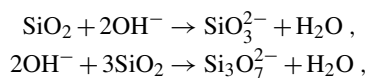
Fig. 18.12 **PVT** diagram of water (after [18.61])

Solubility

Solubility is one of the most important aspects of hydrothermal crystal growth. The early failures in the growth of bulk crystals using the hydrothermal technique were mainly due to the lack of solubility data on those compounds. This topic was almost neglected until the works of Spezia, who studied the solubility of quartz in detail and gave a new direction to hydrothermal growth of crystals. During the 1960s, new methods of investigating the solubility and the new experimental setup for the determination of solubility under hydrothermal conditions were proposed [18.66, 67]. There are two basic methods of determining the solubility under hydrothermal conditions: (a) the sampling technique, and (b) the weight loss method [18.68, 69]. Both methods have their merits and demerits. In many cases the solubility obeys the van't Hoff equation and is linearly dependent on solution density [18.70]. The ratio of solubility to mineralizer concentration often gives clues to the species present [18.71]. Some dedicated equipment have been designed and fabricated for solubility studies under hydrothermal conditions [18.72]. Herein we describe the different types of solubility under hydrothermal conditions by selecting appropriate examples such as quartz, berlinite, gallium orthophosphate, and potassium titanyl phosphate, because of their contrasting solubilities. As mentioned earlier (Sect. 18.1) the earliest hydrothermal researchers used only water as the solvent. Today we use a great variety of mineralizers, both aqueous and nonaqueous solvents, and also mixed solvents in many cases. However, Hannay and Hogarth used alcohol as the solvent [18.73], although that work did not draw the attention of scientists until recently. Although water can be a good solvent under very high-pressure and high-temperature conditions, the use of acids, salts, bases, and mixtures of them considerably reduces the PT conditions required for crystallization. The commonly used nonaqueous solvents are NH_3 , HF, HCl, HBr, Br_2 , S_2Cl_2 , S_2Br_2 , SeBr_2 , $\text{H}_2\text{S} + \text{N}(\text{C}_2\text{H}_5)_3$, NH_4Cl , $\text{C}_2\text{H}_5\text{OH}$, CS_2 , CCl_4 , C_6H_6 , CH_3NH_2 , etc. In the last 15 years, the growth conditions for a variety of crystals have been further reduced with the use of some high-molar acid solvents such as HCl, H_2SO_4 , H_3PO_4 , HNO_3 , HCOOH , etc. which has reduced the growth temperature to below 300°C . This reduction in the growth temperature considerably reduces the working pressure, which in turn helps in the use of simple apparatus. Even silica autoclaves can be used, which facilitates direct visibility of the growth medium just as in any other low-temperature solution growth. This has greatly attracted the atten-

tion of crystal growers in the last decade, and a great variety of compounds which hitherto were produced only at high temperature and pressure have been today obtained at lower-PT conditions. Hence the mineralizer plays an important role in the hydrothermal growth of crystals and has given a new perspective to the method.

Solubility of Quartz. The first systematic study of the solubility of quartz was carried out by Spezia, which opened up the trend for the growth of bulk crystals on the whole using the hydrothermal method [18.20]. The solubility of quartz in pure water was found to be too low for crystal growth (0.1–0.3 wt %), but the solubility could be markedly increased by the addition of OH^- , Cl^- , F^- , Br^- , I^- , and acid media, which act as mineralizers. For example, the reactions



show the formation of various complexes or species during the hydrothermal crystallization of quartz. Hosaka and Taki have used Raman spectra to identify and quantify such species [18.74].

In pure aqueous solutions (even at 400°C and 25 000 psi), the solubility of quartz is too low to allow growth to take place in any reasonable time. Alkaline additions, such as NaOH, Na_2CO_3 , KOH, and K_2CO_3 , are all effective as mineralizers in this pressure and temperature range. However, higher molarity of the alkaline solutions introduce other alkali silicates along with quartz. Therefore, a moderate molarity and especially mixed mineralizers are more effective to achieve higher growth rate. Laudise and Ballman have measured the solubility of quartz in 0.5 M NaOH as a function of temperature [18.75] and even today the classical work carried out by Laudise and group remains the standard one as far as quartz growth under hydrothermal conditions is considered. Figure 18.13 shows the solubility curve for quartz in 0.5 M NaOH as a function of temperature and percentage fill [18.75]. An important result of solubility determinations is the delineation of the pressure, temperature, and composition regions where the temperature coefficient of solubility is negative. These regions are to be avoided in the growth of quartz, since it requires a different setup to avoid the loss of seed crystals. In recent years, for quartz crystal growth, mixed solvents are used in most cases.

Solubility of Berlinite. The solubility of berlinite was first determined by John and Kordes in orthophosphoric

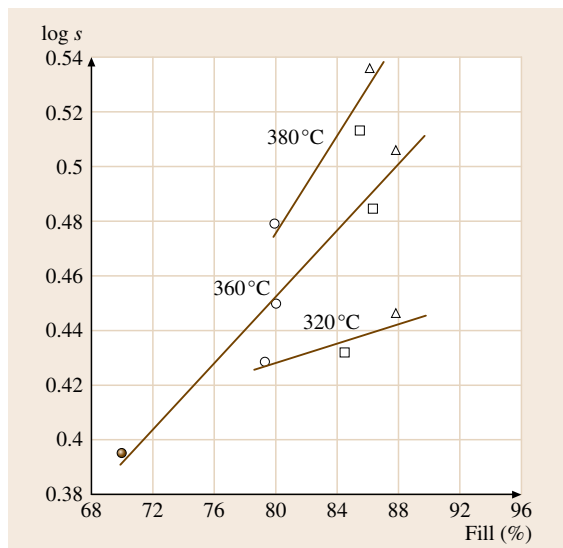


Fig. 18.13 Quartz solubility dependence on percentage fill (after [18.75])

acid above 300 °C and was found to be positive [18.76]. Subsequently *Stanley* reported a negative solubility for berlinite in 6.1 M H_3PO_4 [18.77]. The solubility of AlPO_4 varies widely with the type of solvent used. Some authors claim that solubility of AlPO_4 in HCl is similar to that in H_3PO_4 . The most important difference is the higher solubility at comparable mineralizer concentration. The authors of [18.78] have studied the solubility of AlPO_4 in some new solvents such as HCOOH , NH_4Cl , Na_2CO_3 , $\text{NH}_4\text{H}_2\text{PO}_4$, NaF , KF , and LiF . The solubility of AlPO_4 (in wt %) as a function of temperature and at a pressure of 2 kpsi, in 2 M HCOOH solution is shown in Fig. 18.14.

Solubility of Gallium Orthophosphate. Gallium orthophosphate has been studied extensively for the past 12 years owing to its excellent piezoelectric properties, which are much better than those of conventional α -quartz. The solubility of gallium orthophosphate is quite interesting, although it is isostructural and iso-electronic with α -quartz and berlinite. Several studies exist on the solubility of GaPO_4 [18.79–82]. GaPO_4 shows a negative coefficient of solubility, like berlinite, with some significant differences between the two. Figure 18.15 shows a more precise solubility curve for GaPO_4 crystals [18.82]. The solubility of another very important crystal, ZnO , has been discussed in detail by M.J. Callahan et al. in this Handbook.

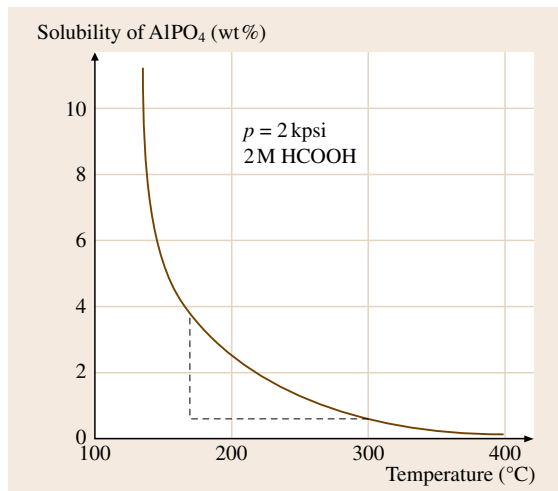


Fig. 18.14 Solubility of AlPO_4 (in wt %) as a function of temperature at a pressure of 2 kpsi, in 2 M HCOOH solution (after [18.78])

Kinetics of Crystallization under Hydrothermal Conditions

Studies related to the kinetics of crystallization under hydrothermal conditions began during the 1950s and 1960s with the commercialization of the synthesis of zeolites, and the large-scale growth of bulk crystals of quartz. Subsequently, several other crystals, such as GaPO_4 , AlPO_4 , malachite, ZnO , calcite, and ruby, were studied in detail. The anisotropy in the rate of growth of different faces during growth on the seed, if understood

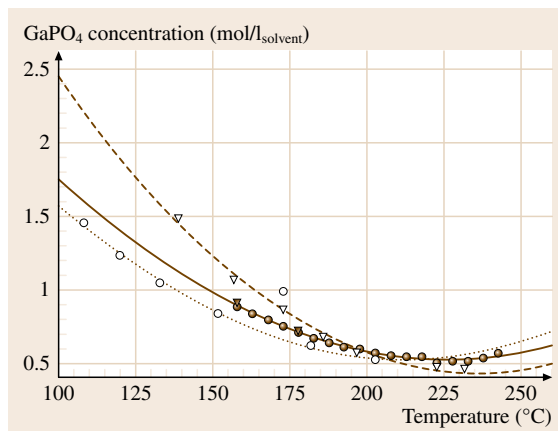


Fig. 18.15 Solubility curve of GaPO_4 under hydrothermal conditions in 15 M phosphoric acid: Δ and ∇ correspond to the crystallization data; \circ and \bullet correspond to the dissolution data (Δ , \circ after [18.79]; ∇ , \bullet after [18.80])

clearly, can allow the orientation of the seeds in such a way that the fastest growth can be achieved within a short time without compromising crystal quality. The crystallization kinetics of ZnO crystals under hydrothermal conditions have been discussed in this Handbook by the other authors (Callahan et al., Chap. 19). However, the crystallization kinetics are discussed in general for one or two selected compounds in this section. Various general laws characterizing the relationship between the anisotropy of the rates of growth of the faces and the chemical nature of the solvent have been studied by several workers.

The high activation energies of the growth of the faces, combined with other factors – the anisotropy of the rates of growth of the faces, the marked dependence of the rate of crystallization on the composition of the solution, etc. – provide strong evidence in support of the suggestion that, in hydrothermal crystallization under conditions of excess mass transfer, a primary role is played by surface processes taking place directly at the crystal–solution interface. It should be remembered that the activation energy of diffusion in solutions usually does not exceed 4–5 kcal/mol [18.83], while the activation energies of dissolution rarely exceed ≈ 10 kcal/mol. These values are much lower than the activation energies of growth, indicating that diffusion in the solution and dissolution of the charge do not limit the rate of crystallization with increase in the concentration of the solution. The rate of crystallization can increase in two ways. For crystals which do not contain components of the solvent, the rate increases sharply at low concentrations and remains practically unchanged at high concentrations. Similarly, in some cases, an increase in the rate of growth of the faces

with increase in pressure has been observed. Pressure apparently does not have any significant direct effect on the rate of growth crystals, but it may have an influence through other parameters: mass transfer and solubility.

Kuznetsov reported the effects of temperature, seed orientation, filling, and temperature gradient (ΔT) on the growth kinetics of corundum crystals [18.84]. The activation energies calculated were 32 kcal/mol for the (1011) face and 17.5 kcal/mol for the (1120) face. Kaneko and Imoto have investigated the effects of pressure, temperature, time, and Ba:Ti ratio on the kinetics of a hydrothermal reaction between barium hydroxide and titania gels to produce barium titanate powders [18.85]. Ovramenko et al. conducted kinetics studies to compute the activation energy (E_a) of 21 kJ/mol [18.86]. In contrast, Hertl calculated an activation energy of 105.5 kJ/mol [18.87]. Riman and group have investigated the crystallization kinetics of various perovskite-type oxides using the computation modeling under hydrothermal conditions, and were able to construct speciation and yield diagrams [18.88, 89].

Thermodynamic modeling, solubility studies, and kinetics of crystallization under hydrothermal conditions is still an attractive field of research in the hydrothermal growth of crystals. During the 1980s and 1990s, external energy such as microwave, sonar, mechanochemical, and electrochemical, was employed to enhance the crystallization kinetics under hydrothermal conditions, especially in the preparation of fine crystals; and now in the last half-decade, the processes have been better understood to prepare crystalline particles with desired shape and size [18.90, 91].

18.3 Apparatus Used in the Hydrothermal Growth of Crystals

Designing an ideal hydrothermal apparatus, popularly known as an autoclave, is the most difficult task and perhaps impossible to define, because each project has different objectives and tolerances. Obviously several autoclave designs exist to meet requirements for a specific objective such as the study of phase equilibria, solubility, growth of bulk or small crystals, continuous production of nanocrystals, etc. However, an ideal hydrothermal autoclave should have the following characteristics irrespective of the goal:

1. Inertness to acids, bases, and oxidizing agents
2. Ease of assembly and disassembly
3. Sufficient length to obtain a desired temperature gradient
4. Leakproof, with unlimited resistance to the required temperature and pressure
5. Rugged enough to bear high-pressure and high-temperature experiments for long duration, so that no machining or treatment is needed after each experimental run.

The most commonly used autoclaves in hydrothermal research are listed in Table 18.4. The last four types listed are useful for the preparation of nanocrystals and powders under extreme conditions. When selecting

a suitable autoclave, the first and foremost parameter is the experimental temperature and pressure conditions and its corrosion resistance in that pressure temperature range for a given solvent or hydrothermal fluid. If the reaction is taking place directly in the vessel, the corrosion resistance is of course a prime factor in the choice of autoclave material. The most successful materials are corrosion-resistant high-strength alloys, such as 300-series (austenitic) stainless steel, iron, nickel, cobalt-based superalloys, and titanium and its alloys. However, the hydrothermal experimenter should pay special attention to systems containing hydrogen, nickel, etc., which can be dangerous under high-PT conditions in the presence of some solvents. Therefore, selection of autoclaves, PT conditions, and the chemical media under hydrothermal conditions are extremely important to know before running actual experiments. Glass autoclaves were used in the 19th century for lower-PT conditions. In recent days in some laboratories thick quartz tubes are used for lower-temperature experiments [18.92]. Autoclaves are usually provided with liners made of various materials depending upon the type and purpose of the crystals to be grown. For example, quartz growth can be carried out in regular stainless-steel autoclaves without any lining or liners. If high-quality and high-purity quartz crystals are de-

Table 18.4 Autoclaves

Type	Characteristic data
Pyrex tube 5 mm i.d., 2 mm wall thickness	6 bar at 250 °C
Quartz tube 5 mm i.d., 2 mm wall thickness	6 bar at 300 °C
Flat plate seal, Morey type	400 bar at 400 °C
Welded Walker-Buehler closure 2600 bar at 350 °C	2000 bar at 480 °C
Delta ring, unsupported area	2300 bar at 400 °C
Modified Bridgman, unsupported area	3700 bar at 500 °C
Full Bridgman, unsupported area	3700 bar at 750 °C
Cold-cone seal, Tuttle–Roy type	5000 bar at 750 °C
Piston cylinder	40 kbar, 1000 °C
Belt apparatus	100 kbar, > 1500 °C
Opposed anvil	200 kbar, > 1500 °C
Opposed diamond anvil	Up to 500 kbar > 2000 °C

sired then platinum or gold liners should be used. Even glass, copper, silver, Teflon, etc., tubes can be used, depending upon the PT conditions and the hydrothermal media. Autoclave lining is not new and in fact began

Table 18.5 Materials used as reactor linings

Material	T (°C)	Solutions	Remarks
Titanium	550	Chlorides Hydroxides Sulfates Sulfides	Corrosion in >25% NaOH solution in >10% NH ₄ Cl solution (at 400 °C)
Armco iron	450	Hydroxides	Gradual oxidation producing magnetite
Silver	600	Hydroxides	Gradual recrystallization and partial dissolution
Platinum	700	Hydroxides Chlorides Sulfates	Blackening in chlorides in the presence of sulfur ions Partial dissolution in hydroxides
Teflon	300	Chlorides Hydroxides	Poor thermal conduction
Tantalum	500	Chlorides	Begins to corrode in 78% NH ₄ Cl solution
Pyrex	300	Chlorides	
Copper	450	Hydroxides	Corrosion reduced in the presence of fluoride ions and organic compounds
Graphite	450	Sulfates	Pyrolytic graphite most suitable for linings
Nickel	300	Hydroxides	
Quartz	300	Chlorides	
Gold	700	Hydroxides Sulfates	Partial dissolution in hydroxides

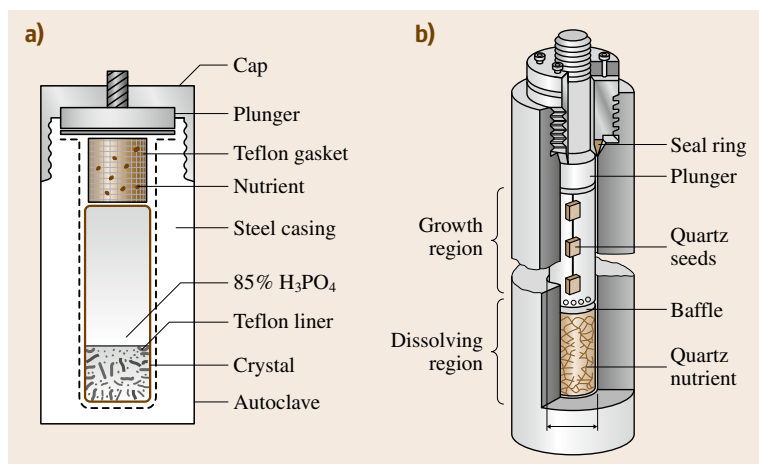


Fig. 18.16a,b The internal liner assembly. (a) Berlinite with negative temperature coefficient of solubility has the seed crystals (growth zone) at the bottom and nutrient (dissolution zone) at the top [18.78]. (b) Quartz with positive temperature coefficient of solubility has the nutrient (dissolution zone) at the bottom and the seed crystals (growth zone) in the top (courtesy of *Laudise* [18.94])

during the 19th century. Table 18.5 gives a list of the materials used as linings [18.93].

The internal assembly of the liners in hydrothermal experiments varies with the type of compounds to be grown and their solubility. For example, quartz and berlinite have contrasting solubility, and accordingly their crystal growth insists upon a completely different experimental setup, as shown in Fig. 18.16.

Here, only the standard designs used in hydrothermal research related to phase equilibria studies, solubility, kinetics, and crystal growth will be discussed, since the number of autoclave designs available in the literature exceeds more than 100.

18.3.1 Morey Autoclave

This autoclave was designed in 1913 by *Morey* with a simple sealing gasket; its volume is generally 25–100 ml [18.21]. It is widely used in hydrothermal research and a cross-section of a typical Morey autoclave is shown in Fig. 18.17. The usual dimensions of are 10–20 cm length and 2.5 cm inner diameter. The closure is made by a Bridgman unsupported area seal gasket made of copper, silver or teflon. Therefore it is also called a flat plate closure autoclave. The autoclave generates an autogeneous pressure depending on the degree of filling, the fluid, and the temperature. The autoclave is limited to $\approx 450^\circ\text{C}$ and 2 kbar in routine use. In later versions, the pressure can be directly measured and adjusted during an experiment by providing an axial hole through the closure nut, but this sometimes causes compositional changes as the material is transported to the cooler region. A thermocouple is inserted in the well close to the sample and the vessel is placed

inside a suitable furnace so that the entire Morey autoclave and closure lie within the element of the furnace. At the end of the run the vessel is quenched in a jet of air followed by dipping in water and the closure seal is broken.

18.3.2 Tuttle–Roy Cold-Cone Seal Autoclaves

This consists of a longer vessel in which the open end and seal are outside the furnace, hence the term *cold-cone seal* (although in fact the seal is far from being cold). Pressure is transmitted to the sample, which is contained in a sealed capsule, through a hole in the clo-

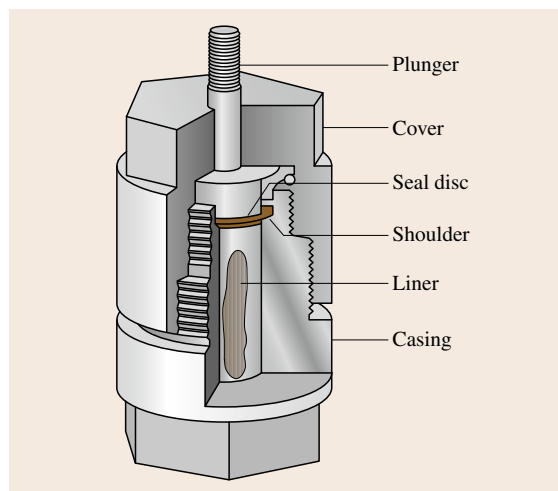


Fig. 18.17 Cross-section of a typical Morey autoclave [18.21]

sure. The capsules are normally made of noble metals (platinum, gold or silver). These vessels may be operated closure up, closure down, or horizontally. The ratio of the vessel diameter to the wall diameter determines the strength of the vessel. In most standard Tuttle vessels this ratio is 4%. Using steallite 25, experiments can be carried out at 900 °C and 1 kbar or 750 °C and 3 kbar for long-term use (from hours to weeks). Roy and Tuttle made many hydrothermal experimental runs for several months in the late 1950s. Moreover, the reaction could be *quenched* by lowering the furnace quickly and surrounding the bomb with a container of water [18.95]. Figure 18.18 shows the cross section of a Tuttle–Roy autoclave [18.95].

Around 1950, Roy and Osborn [18.96] also designed a simple universal pressure intensifier for compressing (virtually) all gases (H_2 , N_2 , CO_2 , and NH_3) or liquids such as H_2O from the compressed gas tank pressures of about 100–200 bar to 5 kbar. From 1950 onwards *test-tube racks* of hydrothermal vessels including such compressors were used worldwide for hydrothermal research, mainly in the geochemical community. Figure 18.19 shows the advertisement of Leco Company, TemPress Research (Bellefonte, USA), which was set up by Tuttle, Roy, and Licastro to make these key

tools for hydrothermal research available worldwide. This continues to the present day, mainly due to the overriding convenience and simplicity of the design.

These autoclaves are highly useful for hydrothermal researchers to carry out phase equilibria studies, solubility, high-temperature/pressure synthesis, nanocrystals synthesis, etc. Today they are also called batch reactors by several researchers and are popularly used for nanomaterials synthesis. The advent of new materials, particularly molybdenum-based alloys, has extended the temperature capabilities of cold-seal vessels to about 1150 °C at pressure above 4 kbar (so-called **TZM** vessels). The prospects of new refractory alloys extending up to this range are encouraging. These cold-seal vessels are safe, inexpensive, simple, and operationally routine. Unlike the Morey type of autoclaves, in the Tuttle cold-seal vessel the pressure is built up by an external pump and the pressure medium is usually distilled water with a little glycol added to inhibit corrosion. For higher fluid pressure, a hydraulic intensifier or air-driven pump is used with argon or nitrogen as the pressure medium. Normally, several vessels run from a single pump, where each vessel is connected to a high-pressure line by a valve and T-junction. The (two-way) valve isolates the vessels from the line. Each vessel is connected to a separate Bourdon gauge with a safety glass dial and blowout block. An autocontroller is normally used. The types of pressure tubing, valves, and fittings used depend on the operating pressures. Normally stainless-steel alloy is used up to 13 kbar, and size is recommended to be 1.4 inch outer diameter and 1/16 inch inner diameter. Although there has been rather little evolution in the basic design of cold-seal pressure vessels, marked changes have occurred in the controllers and pumps.

18.3.3 General-Purpose Autoclaves and Others

Other autoclaves, such as welded closures and modified Bridgman autoclaves, were used as the workhorses during the 1950s to 1980s; now their usage has reduced significantly because handling of them is quite cumbersome. However, these autoclaves contributed enormously to the development of both the hydrothermal technique itself and the growth of bulk crystals.

For the synthesis of crystals under hydrothermal conditions, these days very simple general-purpose autoclaves are used. Such autoclaves are commercially

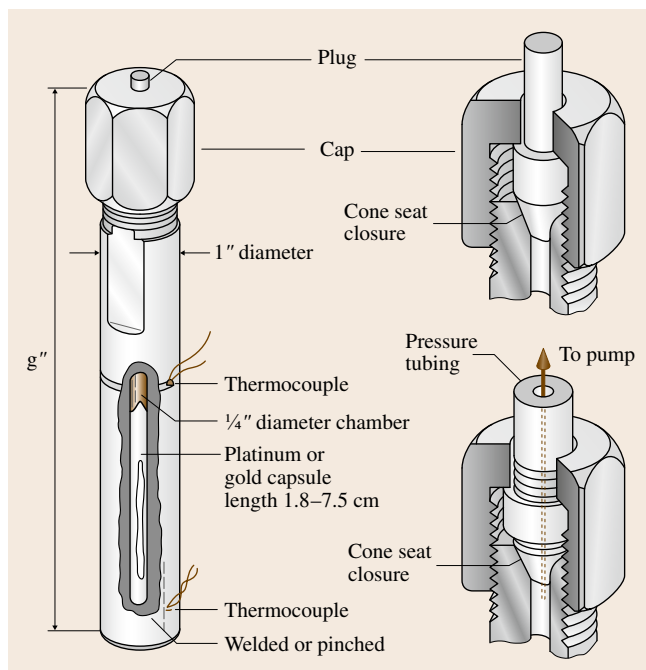


Fig. 18.18 Cross-section of the Tuttle–Roy autoclaves [18.95]

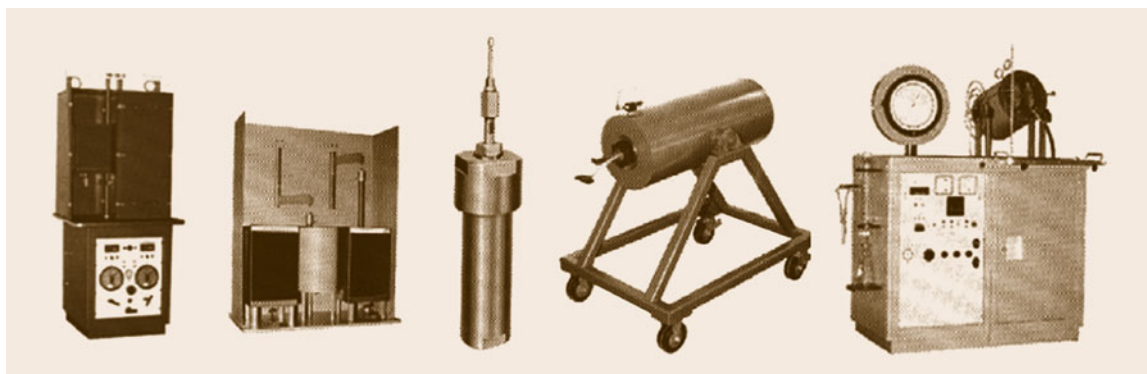


Fig. 18.19 Various test-tube-type cold-cone closure autoclaves (after [18.95])

available from many sources. Also several laboratories fabricate such autoclaves in their laboratories. Figure 18.20 shows the general-purpose autoclave used at the author's laboratory.

Many other designs are available today to meet the specific requirements, such as stirred autoclaves (Fig. 18.21), which are very useful to stir the mixture during the hydrothermal synthesis, to extract the contents from inside the reactor during the experiments, and also to pump in the desired gas into the reactor at any given time. The internal pressure can be read directly. The products can be quenched readily by the circulation of chilled water through the cooling coils running inside the autoclave. These additional advantages have helped greatly to understand the hydrothermal crystallization mechanism, kinetics, and the metastable phases more precisely.

In the last two decades the use of continuous-flow reactors has become very popular to synthesize small, micrometer-sized crystals to nanocrystals with a high degree of control over the shape and size of the crystals.



Fig. 18.20 General-purpose autoclaves popularly used for hydrothermal synthesis

These reactors operate at or above the supercritical conditions of the solvents – both aqueous and nonaqueous in nature. The method is also popularly known as the supercritical fluid (SCF) technology. With the invention of *green chemistry* in the early 1990s, there was a surge in the popularity of SCF technology. Today SCF technology has replaced organic solvents for the fabrication of a number of nanocrystals. Also it is emerging as an alternate to most existing techniques for designing and crystallizing new drug molecules.

Several designs and variations are available today for continuous-flow reactors to generate small to nanocrystals within the shortest possible time. The solubility of the materials has no major role to play in these flow systems. The use of capping agents and surfactants helps to control the size and shape of the nanocrystals and also to modify the surface characteristics of the crystals produced. By this method a great variety of crystals starting from metal oxides to silicates, vanadates, phosphates, germanates, titanates, etc., are produced for a wide range of modern technological applications within a few seconds. Hence, this technique is highly suitable for the commercial production of nanocrystals. The technique has been reviewed extensively and the reader can find additional information in several works [18.97–99]. Figure 18.22 shows a continuous-flow semi-pilot-scale reactor used in the crystallization of nanocrystals.

There are many more reactor designs for special purposes, such as rocking autoclaves, PVT apparatus, multichamber autoclaves, fluid sampling autoclaves, micro-autoclaves, autoclaves for visual examination, hydrothermal hot-pressing, vertical autoclaves, continuous-flow reactors, hydrothermal-electrochemical autoclaves, autoclaves for solubility measurements, autoclaves for kinetic study, pendulum autoclave, hor-



Fig. 18.21 Commercially available stirred autoclaves [18.100]

izontal autoclaves for controlled diffusion study, and so on. The reader can find details of the construction and working mechanism of these autoclaves from the source [18.1].

Safety and maintenance of autoclaves is the prime factor one has to bear in mind while carrying out experiments under hydrothermal conditions. It is estimated that for a 100 cm^3 vessel at 20 000 psi, the stored energy is about $15\,000\text{ lbf/in}^2$. Figure 18.23 shows the autoclaves ruptured because of pressure surges.

Hydrothermal solutions – either acidic or alkaline – at high temperatures are hazardous to human beings if the autoclave explodes. Therefore, the vessels should

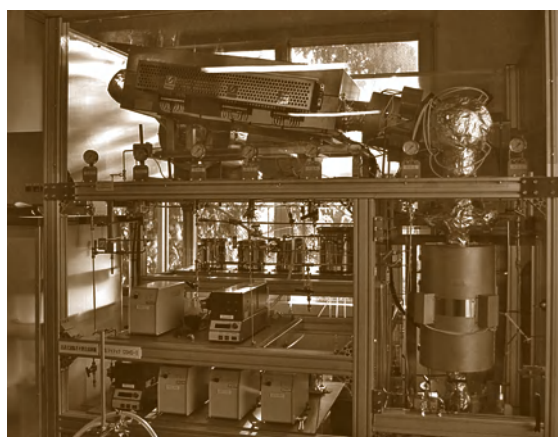


Fig. 18.22 The semi-pilot plant scale continuous-flow reactor used in the crystallization of nanocrystals [18.6]

have rupture discs calibrated to burst above a given pressure. Such rupture discs are commercially available for various ranges of bursting pressure. The most important arrangement is that provision should be made for venting the live volatiles in the event of rupture. Proper shielding of the autoclave should be given to divert the corrosive volatiles away from personnel. In the case of a large autoclave, the vessels are to be placed with proper shielding in a pit.

18.4 Hydrothermal Growth of Some Selected Crystals

As mentioned earlier, in this chapter only the growth of some selected crystals of current technological significance will be discussed. However, a more or less complete list of the compounds obtained under hydrothermal conditions is given in the form of a table at the end of this chapter, as Appendix 18.A.

18.4.1 Quartz

Advances in the hydrothermal method of growing crystals have been linked very closely with the progress achieved in the field of quartz growth ever since the technique was discovered. Quartz (SiO_2) exists in both crystalline and amorphous forms in nature. The crystalline form has over 22 polymorphic modifications. Among them, α -quartz is the most important one, which transforms into β -quartz above 573°C . In order to grow this low-temperature modification of quartz, only the hydrothermal technique is suitable. α -quartz, as

a piezoelectric crystal, has the ability to convert electric waves into mechanical waves and vice versa. Because of this property α -quartz is widely used in the electronics industries. In recent years, quartz for *tuning forks* has become essential for timing functions in electronic watches and in timing circuits for computers and telecommunications.

The principal source of electronics-grade natural quartz is Brazil. Today, the electronics industries are largely inclined to use synthetic quartz, because natural quartz crystals are generally irregular in shape, automatic cutting is cumbersome, and the yield is low. Many countries in the world, such as the USA, Japan, the UK, Germany, Russia, Poland, China, Belgium, and Taiwan, have entered the world market. Over 3000 t of quartz is produced annually for a variety of applications. The production of high-quality defect-free quartz has a large potential market among all electronic materials. Japan alone produces more than 50% of the

world's production, followed by the USA and China. More recently several other Japanese companies such as Kyocera, Shin-Etsu, Asahi Glass Co., etc. have started producing quartz for highly specialized applications. Perhaps Toyo is the largest single company in the world producing quartz. About 50% of the quartz produced goes into devices in the automotive industries, 30% of production goes into frequency control-devices, and the remaining 20% goes into optical devices. The total cost involved in the production of quartz is:

End users: \approx US\$ 1 000 000 000 000

Equipment: \approx US\$ 5 000 000 000

Components: \approx US\$ 100 000 000.

Thus, quartz takes the first place in value and quantity of single-crystal piezoelectric materials produced. Much of the research related to quartz today is confined to industry, while only scant publications emerge from research laboratories on new applications of quartz and the preparation of nanoscale silica particles. Otherwise, it is mainly research and development (R&D)-based industries that carry out research on the production of high-quality quartz and its applications, and these results are not published.

After the successful growth of quartz (Fig. 18.2) by Nacken in the 1940s, Walker synthesized large-size crystals of quartz (Fig. 18.24), much bigger than the size of the crystals produced by Nacken [18.101]. Subsequently major research activity was initiated at AT&T Bell Labs, and the most important contributions to the quartz growth came from the workers such as Ballman, Laudise, Kolb, and Shtenberg during the 1970s. Figure 18.25 shows the quartz crystals obtained at AT&T Bell Labs during the 1970s, the biggest crystals of that period. Each autoclave could produce around 70 kg of quartz crystals during the 1970s. In contrast, today in Japan, in one experimental run, about 4000–4500 kg of quartz is produced using the world's largest autoclave with a volume of 5000 l. Figure 18.26 shows the growth of quartz crystals in the world's largest autoclave at Toyo Communications Ltd., Japan. The early success in producing commercial quartz crystals in Japan during the post-war period paved the way for the entry of several others into the field. Some of the prominent contributors were Professor Noda, Doimon, Kiyooru, Dr. Itoh, and Dr. Taki. Today Japan is the world's largest producer of synthetic quartz for a variety of applications, followed by China.

In recent years mixed solvents are being used in the growth of quartz. High-quality quartz crystals have been obtained in NaCl and KCl solutions, NaOH, and

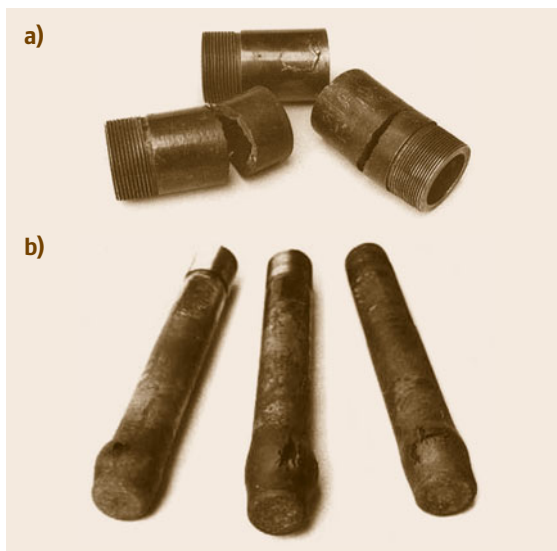


Fig. 18.23a,b Ruptured autoclaves. (a) General-purpose autoclaves, (b) Tuttle–Roy autoclaves

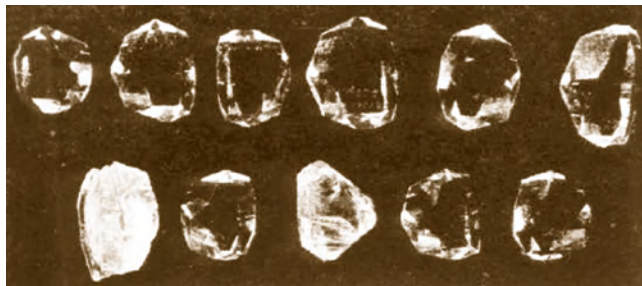


Fig. 18.24 Quartz crystals obtained by Walker [18.101]

Na_2CO_3 solutions (10%) [18.102, 103]. It has been observed that the high-frequency applications of α -quartz require sheets with small thickness, of the same order of size as the defects (such as inclusions, etch pits, and dislocations). Thus the pressure can promote new solvents viable for hydrothermal growth, especially by reducing their concentrations. The recent experimental results have shown the following enthalpy values calculated for α -quartz

$$\Delta H_T = 2395 \pm 5 \text{ cal/mol}, \quad \text{for NaOH (1 M)}, \\ 200 \text{ MPa} \leq p \leq 350 \text{ MPa};$$

$$\Delta H_T = 4001 \pm 2 \text{ cal/mol}, \quad \text{for Na}_2\text{CO}_3 \text{ (1 M)}, \\ 150 \text{ MPa} \leq p \leq 350 \text{ MPa}.$$

In the growth of α -quartz, available nutrient material, such as small-particle-size α -quartz, silica glass, high-



Fig. 18.25 Quartz crystals obtained at AT&T Bell Labs during the 1970s [18.102]

quality silica sand or silica gel, is placed in a liner made of iron or silver with a suitable baffle and a frame holding the seed plates. A mineralizer solution with a definite molarity is poured into the liner to achieve the required percentage fill. The increased solubility in the presence of mineralizer increases the supersaturation without spontaneous nucleation and consequently allows more rapid growth rates on the seeds. Figure 18.16b shows a cross-section of a modified Bridgman autoclave used in the growth of quartz crystals.

The commercial autoclaves used have 10 inch inner diameter, and are 10 ft long unlined. These autoclaves can work at conditions up to 30 000 psi and 400 °C. Most of these experiments are carried out for 25–90 days to obtain full-size crystals of 4 cm in the z -direction and 12.5–15 cm in the y -direction. The temperature gradient is varied according to the nutrient used. About 1 N NaOH or Na_2CO_3 is the most commonly used mineralizer. The solubility change with temperature is smaller in NaOH and slightly larger in Na_2CO_3 . The temperature of the autoclave at the nutrient zone is usually kept at 355–369 °C and, in the growth zone, kept at 350 °C. The addition of lithium improves the growth rate, and small amounts of Li salts are routinely added to the solution [18.104].

The solubility is also, to some extent, a function of increasing pressure. The pressure is controlled by the percentage fill of the autoclave and is usually about 80% for hydroxyl mineralizer (20 000 psi internal pressure).

In most experiments the percentage opening of the baffle is 20%, although lower values are used by several workers. However, the actual percentage opening of the baffle area and its geometry are not disclosed, especially by commercial growers.

The optimum growth conditions for synthesis of quartz based on the work in Bell Laboratories are [18.105, 106]:

Dissolution temperature:	425 °C
Growth temperature:	375 °C
Pressure:	15 000–25 000 psi.
Mineralizer concentration:	0.5–1.0 M NaOH
Temperature gradient (ΔT):	50 °C
% fill:	78–85%
Growth rate in (0001):	1.0–1.25 mm/day.

The quality of the grown crystals is also a function of the seed orientation and its quality. Strained seeds generally produce strained growth regions [18.107]. The seeds are polished to a very fine finish before use. Most high-quality crystals are grown using seeds with the surface perpendicular to the z -direction, since this region has the lowest aluminum concentration. Though most quartz production consists of y bar crystals, that is, small crystals ($z = 20$ –25 mm, 64 mm seed) capable of several y bar per crystal, *pure* z bars are also produced, representing 10–20% of production. However, for medium- and high-quality grades we notice a rise in demand for crystals of very large dimensions and upper-medium quality, especially in the USA, for manufacturing wafers used in surface wave applications [18.108]. Earlier, most seeds used were natural quartz cut in a definite orientation, but in recent years this practice is only used when a high-quality crystal is desired.

The growth of quartz crystals has been understood precisely with reference to the growth temperature, temperature gradient, percentage fill, solubility, percentage of baffle opening, orientation and nature of seed, and type of nutrient. Also many kinetic studies have been carried out [18.35, 109]. Figure 18.27 shows the growth rate of quartz as a function of seed orientation [18.109]. The solubility of quartz has been studied as a function of temperature, and the growth rate as a function of seed orientation and percentage fill. Figure 18.28 shows hydrothermally grown quartz crystals.

The type of crystal to be grown depends on the application, as different properties are required in each case. For optical use, high uniformity, low strain, and low inclusion counts are needed, since all of these can affect transparency. For surface acoustic wave de-



Fig. 18.26 Growth of quartz crystals in the world's largest autoclave at Toyo Communications Ltd., Japan (courtesy of S. Taki). Dissolution temperature: 425 °C; growth temperature: 375 °C; pressure: 15 000–25 000 psi; mineralizer concentration: 0.5–1.0 M NaOH; temperature gradient (ΔT): 50 °C; percentage fill: 78–85%; growth rate of (0001): 1.0–1.25 mm/day

vices, large pieces that can take a very high-quality surface finish are needed. The quality of the material required for resonators used in time and frequency devices varies with the application. The more precise the need, the more stringent the requirements. For most applications, a truly high-quality material is not needed. For high-precision uses, such as in navigational devices and satellites, a very high-quality material must be used. Most recent research on quartz growth is for improved resonator performance, which requires the growth of high-quality low-dislocation quartz. Figure 18.29 shows the fabrication of resonators from a single crystal.

Several criteria are used to evaluate the quality of quartz crystals. The most commonly used criterion is the Q value or quality factor, which is a measure of the acoustic loss of the material. It is important for a resonator to have high electrical Q value and superior frequency–temperature characteristics. In a piezoelectric resonator, electrical energy and mechanical energy are interconvertible. In such a case, Q is expressed as

$$Q = \frac{[X]}{R}, \quad (18.2)$$

where X is the inductive or capacitive reactance at resonance and R is the resistance.

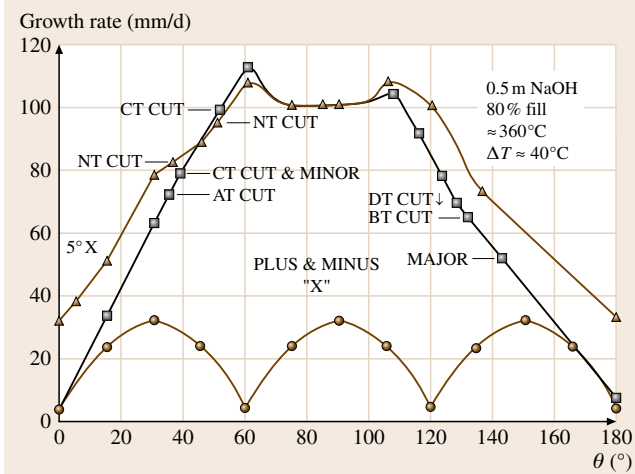


Fig. 18.27 Growth rate of quartz as a function of seed orientation [18.109]

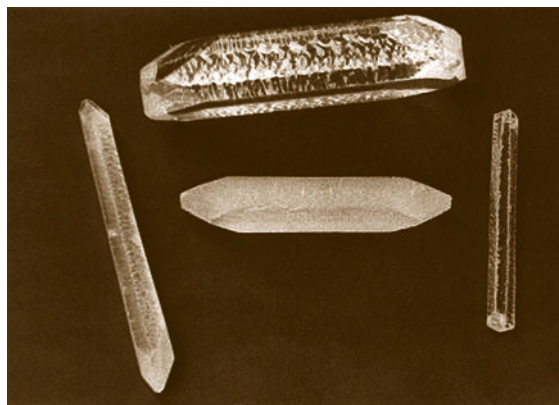


Fig. 18.28 Hydrothermally grown quartz crystals



Fig. 18.29 Fabrication of resonators from a single crystal

The acoustic Q for natural α -quartz crystal varies in the range 1 to 3×10^6 , while for synthetic quartz crystals the value drops to 2×10^5 to 1×10^6 . Thus in the last two decades, the main objective among quartz crystal growers has been to improve Q , which in turn leads to a low concentration of physicochemical and structural defects.

The growth rate is determined by the ratio of increase in thickness of the seed and the duration of the run. The growth rate along the main crystallographic axes R_c is determined by dividing the thickness of the layer grown on the seed, $(h_1 - h_0)/2$, by the run duration t , and is expressed in millimeters per day. It has also been known for quite some time that, qualitatively, acoustic Q is inversely proportional to growth rate and directly related to chemical impurities. The internal friction (the inverse of the mechanical Q) is dependent on the growth rate of synthetic quartz crystals. *Martin* and *Armington* have studied the effect of growth rate on the aluminum content at low growth rates [18.110]. Al^{3+} and H^+ are the most deleterious impurities in quartz used for frequency and timing applications, and they also influence the growth rates. Similarly the percentage fill and pressure strongly influence the growth rate of quartz.

For any crystal growth, seed crystals play a vital role in controlling the quality, growth rate, and morphology of the grown crystals. Usually, in the case of quartz for higher-frequency applications, a smaller x -axis dimension is needed. z -Growth material is desired for resonators, as it has been shown that this material has about an order of magnitude lower aluminum concentration. In the majority of crystal growth experiments, in general the thickness of the seed crystal is usually 1–2 mm. Until recently, it was necessary to use natural seeds for the preparation of low-dislocation crystals. However, most crystals grown from synthetic seeds contain large numbers of dislocations, of the order of several hundred per square centimeters. These results in the formation of etch channels in the resonator, which weaken it mechanically and can be a problem when electronic devices are deposited on the surface. When a seed perpendicular to the z -axis (but from the x -growth region) is used, the dislocation density can be reduced to below ten and sometimes to zero dislocations per square centimeter [18.111]. The purity of the crystals produced using seeds cut from the x -region is as good as that from crystals produced from the usual z -seed.

In the growth of quartz crystals, the nutrient has a profound effect on the quality of the grown crystal.

It is well known that most of the impurities and in turn the defects in the grown crystals come from the nutrient and only to some extent from the autoclave walls. Nutrient selection is one of the attractive research topics in crystal growth on the whole. Even in the 19th century, researchers tried the use of several varieties of nutrient to obtain quartz under hydrothermal conditions. There are several reasons for using varieties of nutrients, including: to obtain high-purity crystal, to obtain higher solubility in the desired **PT** conditions for a given solvent, to achieve higher growth rate, to obtain higher yield, and to lower the **PT** conditions for growth. In the case of quartz, to obtain high-quality crystals, even α -cristobalite has been used as a nutrient [18.112].

Tables 18.6 and 18.7 show the distribution of impurities in different sectors of synthetic quartz. Hence, attention has to be paid to the solvent, nutrient, seed orientation, and seed quality in order to obtain high-quality crystals, as well as the experimental **PT** conditions.

In the growth of α -quartz for high-frequency device applications (24–100 MHz or more), the existence of defects, either physicochemical or structural, in synthetic quartz crystals leads to critical modifications of devices. Low-defect, high-purity synthetic quartz should have the characteristics given in Table 18.8 [18.113]. Sweeping is one of the most popularly used techniques in recent years to enhance the performance of quartz resonators. Sweeping, or solid-state electrolysis or electrodiffusion, is generally performed under vacuum, air, hydrogen or a desired atmosphere. During sweeping, the crystal is placed in an electric field and heated. Then, migration of the impurities and some modifications are induced within the

Table 18.6 Impurities in different sectors in synthetic quartz

Sector	Al	Na	Li
Z	5	1	0.5
+X	31	9	5
−X	122	40	5
S	85	26	16

Table 18.7 Dislocation density in different seeds

Seed	Mineralizer	Etch channel density
Z	Hydroxide	253
Z	Carbonate	247
X+	Hydroxide	1
X+ (reused)	Hydroxide	14

Table 18.8 Desirable and achieved parameters in synthetic quartz [18.113]

Parameter	Desirable	So far achieved
Etch channel density	$< 10/\text{cm}^2$	< 86
Inclusion density	$< 10/\text{bar}$	
Impurity concentration (ppb)		
Al	< 200	700
Li	< 300	300
Na	< 500	1640
K	< 40	300
Fe	< 100	1800
Q ($3500/3800\text{ cm}^{-1}$)	$< 2.5 \times 10^6$	$< 2.5 \times 10^6$
Strain	None	Variable
Fringe distortion	$< 0.05\text{ RMS}$	Variable

crystal. Sweeping reduces the formation of etch tunnels. The effect of sweeping is to remove lithium and sodium deposited interstitially in the lattice during the growth. These ions are usually trapped along an angstrom-wide tunnel, which is parallel to the z -axis in the quartz crystal lattice. These ions, in an interstitial position, interact with substitutional aluminum impurities in the lattice to form Al-Li centers, which have been shown to be weakly bonded and are the cause of low radiation tolerance in a resonator. In the sweeping process, these are replaced by Al-OH or Al-hole centers, which have a much higher radiation tolerance. The sweeping is carried out at $500\text{--}550^\circ\text{C}$ usually for a period of 7 days or even more to remove alkalis. However, it should be remembered that sweeping cannot become a routine process even if the same experimental conditions are always applied.

There are several other techniques employed for the fabrication of piezoelectric high- to ultrahigh-frequency devices based on quartz resonators. The important ones are: chemical polishing, ion beam etching (IBE). The reverse thermodynamic relations are employed for the refinement of chemical polishing. Several solvents such as HF and NH_4HF_2 , NaOH, $\text{KOH} \cdot x\text{H}_2\text{O}$, and $\text{NaOH} \cdot x\text{H}_2\text{O}$ are employed [18.114].

Similarly, the industrial chemical etching process is specially dedicated for large thickness removals without damaging the blank surface texture. This is most useful for frequency applications of quartz, because the mechanical grinding and lapping introduce surface stresses. Fluoride media is the most popular for this type of chemical polishing [18.115]. Recently, Cambon et al. tried industrial chemical etching successfully in

the temperature range $150\text{--}180^\circ\text{C}$ using concentrated NaOH solvents [18.116]. During the chemical etching process, several factors influence the process: kinetics, etching temperature, etching time, plate orientation, SiO_2 concentration, solvent concentration, wafer carrier geometry, and so on. By using this process about 3200 quartz plates can be processed in a single run. The resonators manufactured by this process have demonstrated a high level of performance, even higher than that of plates obtained by mechanical means.

In recent years there has been growing interest in morphological variations, growth-rate monitoring using various seed orientations, and computer simulation for the precise calculation of growth rates of various faces [18.117–119]. These studies greatly help in understanding the growth technology for commercial production of defect-free and economic quartz crystals.

The growth of bulk single crystals of quartz is still an attractive field of research, especially the growth of defect-free quartz crystals for space-grade applications. Understanding of solubility and the growth mechanism is still incomplete, although laser Raman spectroscopy and other advanced techniques such as computer simulation are yielding rich information about how to intelligently engineer the growth processes, thereby minimizing growth defects.

The preparation of quartz for other applications, such as photomask substrates for lithography, poly-Si thin-film transistor liquid-crystal displays (TFT-LCDs), and high-purity and high-precision polishing devices, is a new trend in science. For example, Shin-Etsu Chemical (Japan), Asahi Glass Co. (Japan), NDK America (USA), and APC International Ltd. (USA) are engaged in such research and development, whereas companies such as Sawyer Research Inc., General Electric (GE), Philips, and Toyo Communication are engaged in production of bulk crystals of quartz for oscillators, frequency devices, etc.

18.4.2 Aluminum and Gallium Berlinites

Berlinite (AlPO_4) and gallium berlinite (GaPO_4) are the two most important crystals that are isoelectronic and isostructural with α -quartz. These compounds are used to replace quartz in electronic devices because of their larger mechanical coupling factors than α -quartz, and because their resonant frequency is nearly independent of temperature for certain orientations [18.120–122]. Table 18.9 gives a comparison of some piezoelectric characteristics of these materials [18.123]. The growth of berlinite and gallium berlinite does not differ much

between the two materials because they both have a negative temperature coefficient of solubility, and hence a similar experimental arrangement is used for both. During the 1980s the growth of berlinite was studied extensively, and it was considered at one time as a replacement for α -quartz [18.124]. However, results were not encouraging for bulk crystal growth of berlinite on a par with that of α -quartz. Although the growth of gallium berlinite began sometime during the late 1980s, momentum picked up during 1995. It is important to discuss the growth of these crystals from a scientific point of view in order to learn about the hydrothermal technique in general, as these crystals – although isoelectronic and isostructural with α -quartz – have a completely contrasting experimental setup for their crystal growth.

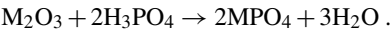
John and Kordes were the first to grow berlinite crystals successfully, followed by Stanley using completely different conditions [18.76, 77]. The greatest disadvantage in the growth of these berlinites is their negative temperature coefficient of solubility, which demands a special experimental setup. Although much progress has been achieved in the growth of these berlinite crystals, our knowledge on the growth of AlPO_4 and GaPO_4 is still comparable to that of quartz some 50 years ago, particularly with reference to size, crystal perfection, reproducibility, etc. The highly corrosive nature of the solvent is the major hindrance in the growth of bulk crystals of these berlinites.

The solubility of these berlinites has been discussed earlier. Although several reports have appeared on solubility measurements as a function of various parameters, there is still no unanimity in these results.

Berlinites could be best grown using the hydrothermal technique. α -Berlinite is stable up to 584°C , and below 150°C the hydrates and $\text{AlPO}_4 \cdot \text{H}_2\text{O}$ are stable. Therefore, the growth temperatures should be greater than 150°C but less than 584°C . However, solubility and PVT studies have clearly shown that crystal growth

must be carried out at less than 300°C because of the reverse solubility. Several versions of the hydrothermal growth of berlinite single crystals have been tried to suit the solubility. In contrast to aluminum berlinite, gallium berlinite has no phase transitions, and therefore some researchers have even synthesized this crystal using the flux growth method [18.125]. However, the quality of these flux-grown gallium berlinite crystals is far inferior to that of hydrothermally grown crystals. In the hydrothermal growth of these berlinites, usually acid mineralizers are used at various concentrations. Mixed acid mineralizers such as HCl , H_3PO_4 , H_2SO_4 , HCOOH , etc. are much more widely used in practice. However, other mineralizers such as NaOH , Na_3PO_4 , Na_2HPO_4 , NaHCO_3 , NaF , KF , LiF , NH_4HF_2 , NaCl , Na_2CO_3 , etc. have also been tried. More details can be found in [18.126].

Small crystals of both aluminum berlinite and gallium berlinite can be obtained through hydrothermal reactions of H_3PO_4 with various chemicals containing Al and Ga [18.94, 126, 127]



These fine crystals of berlinite can in turn be used as the nutrient to grow bigger bulk single crystals. Since the solubility of these compounds is negative, the seed is placed in the hotter zone in the bottom, while nutrient is placed in the upper cooler region. The most important modifications suggested from time to time in the growth of berlinite crystals are:

- 1. Crystal growth by slow heating method
- 2. Crystal growth by composite gradient method
- 3. Crystal growth by temperature gradient
- 4. Growth on seeds.

The crystal growth by slow heating method was mainly used for improving the quality of seeds and to enhance the size of the crystal, with conditions similar to those used for nucleation. A major drawback of this method is the impossibility of obtaining crystals of sufficient size in one operation due to the limited quantity of metal phosphate available in the solution. Usually Morey autoclaves are used to carry out crystal growth by the slow heating method ($T \leq 250^\circ\text{C}$; $p = 100\text{--}1000\text{ atm}$). The size of the crystals obtained through spontaneous nucleation is usually $0.1\text{--}4\text{ mm}$, depending upon the experimental conditions.

The crystal growth by composite gradient method gives more flexibility in adjusting the growth rates and avoids the preliminary work of crystal growth or nutrient preparation.

Table 18.9 Comparison of some piezoelectric characteristics (* AT cut)

Parameter	Quartz	Berlinite	Gallium berlinite
Coupling coefficient K (%)*	8.5	11.0	> 16.0
Surtension coefficient Q *	3×10^6	10^6	> 5×10^4
α - β phase transition ($^\circ\text{C}$)	573	584	No

The crystal growth with reverse temperature gradient method is much more versatile for these compounds in general. In this approach, the nutrient (either crystalline powder or fine grains of AlPO_4 usually obtained from the slow heating method) is kept in a gasket at the upper portion of the autoclave, which is cooler than the bottom of the liner that is kept at slightly higher temperature, forming the crystallization zone (Fig. 18.16a).

The crystal growth on seeds method uses spontaneously nucleated seeds and oriented seeds cut from grown crystals, usually mounted on a platinum frame placed in the bottom (hotter) region of an autoclave, and the nutrient (≈ 60 mesh particle size prepared by other methods) is placed above in a platinum gasket in the upper region (or in a Teflon gasket). Thus, the seeds are in the warmer, supersaturated region at the bottom of the autoclave and the temperature gradient achieved by cooling the top allows proper convection.

Figure 18.30 shows aluminum berlinite crystals grown by the hydrothermal method. The orientation of the seed is important, as in the case of quartz, because the growth rate and crystal quality depend upon the seed orientation. The following growth rates are shown for seeds whose faces are indicated below:

(0001) (basal plane):	0.25–0.50 mm/day
(102 $\bar{1}$) (x -cut):	0.23–0.30 mm/day
(1010) (y -cut):	0.12–0.15 mm/day
(011 $\bar{1}$) (minor rhombohedral face):	0.12 mm/day
(101 $\bar{1}$) (major rhombohedral face):	0.15 mm/day

The relative growth rates are in general agreement with the morphology of the equilibrium form, as judged from observing spontaneously nucleated crystals which are bounded by small prism faces and terminated by minor and major rhombohedral faces. The dissolution rate of aluminophosphate glass charge is three times greater than that of the crystalline charge [18.128].

The morphology of spontaneously crystallized aluminum berlinite crystals varies greatly, depending upon the type of solvent, its concentration, and the experimental temperature. The most commonly observed morphologies are hexagonal, rhombohedral, rods, needles, and equidimensional crystals. Impurities also play a prominent role in controlling the crystal morphology. In the growth of aluminum berlinite the typical experimental conditions used are:

Growth temperature:	240 °C
Pressure:	15–35 MPa
Solvents:	Mixed acid mineralizers

Nutrient:	Powdered nutrient, preferably aluminum phosphate glass
Filling:	80%
ΔT :	5 °C < T < 30 °C
Growth rate:	0.35 to 0.50 mm/day in H_3PO_4 0.35 to 0.45 mm/day in HCl 0.25 to 0.35 mm/day in HNO_3 0.2 to 0.3 mm/day in H_2SO_4 .

It is interesting to note that the berlinite crystals show internal structural defects on x-ray Lang topography. No fundamental differences were found by x-ray topography between the horizontal gradient, vertical gradient, and slow heating methods. The two principal imperfections readily observable in berlinite are crevice flawing and cracks. Although crystals appear quite transparent from the outside, they contain many internal defects. A combination of optimum growth conditions, reducing the water content, and using heat treatment to control the water distribution could be of great interest for improving the piezoelectric device potential of aluminum berlinite.

During the 1980s and early 1990s work on aluminum berlinite was at its peak, and then activity suddenly dropped, because of several difficulties associated with its growth as bulk crystal. However, crystal growth of gallium berlinite, which began during the late 1980s, is still an attractive field, and several research groups are actively engaged in bulk crystal growth of gallium berlinite. The solubility and crystal growth kinetics of gallium phosphate have been extensively studied by various groups [18.129–131] and basically resemble those of aluminum berlinite. The necessary conditions for crystal growth are:

1. Solubility of GaPO_4 nutrient is sufficient for crystal growth.
2. Convection of saturated fluids is intensive and not varying during the crystal growth cycle.
3. No formation of spontaneous crystallites.
4. Saturation of an initial solvent slowly appears, simultaneously with the end of seed etching (very soft restart conditions).

The typical growth conditions are:

Experimental temperature:	280 °C
Experimental pressure:	8 MPa
Mineralizer:	$\text{H}_3\text{PO}_4 + \text{H}_2\text{SO}_4$ (pH = 3–4 under ambient conditions).

The biggest disadvantage is that, in the case of seeded growth under retrograde solubility, it is often accompanied by precipitation of spontaneous crystals or degradation of growth surfaces because of the irreversible character of the mass transportation (high or low relation of ΔS to growth kinetic parameters).

Figure 18.31 shows gallium berlinite crystals obtained under hydrothermal conditions. The commonly appearing faces are $(10\bar{1}1)$, $(01\bar{1}1)$, $(10\bar{1}0)$, and $(10\bar{1}2)$. The growth rates along various crystallographic directions decrease in the sequence

$$\gamma(0001) \gg \gamma(01\bar{1}2) > \gamma(10\bar{1}0) > \gamma(01\bar{1}1) \\ > \gamma(10\bar{1}2) > \gamma(10\bar{1}1).$$

The common twins observed in GaPO_4 obey the Dauphiné, Brazil, and Laydolt's twinning laws.

The crystallization process, dissolution process, rate of crystallization (i.e., the amount of GaPO_4 crystal formed per unit time), action of solvent, its concentration and temperature regime, etc. have been studied in detail for GaPO_4 crystal growth by several workers [18.127, 132, 133]. Also characterization of defects has been carried out in detail [18.134–136].

Although the first stage of GaPO_4 crystal growth began with epitaxy of GaPO_4 on AlPO_4 seeds, the sub-

ject still remains popular. Several substrates including quartz have been used to grow GaPO_4 crystal.

If the size of the GaPO_4 crystals grown by the hydrothermal technique is increased sufficiently, it would become the best piezoelectric material replacing quartz.

18.4.3 Calcite

Calcite (Ca_2CO_3) is an important carbonate mineral. Pure and optically clear calcite is called Iceland spar. Calcite single crystals form an important optical material owing to its large birefringence and transparency over a wide range of wavelengths. These properties make it a significant material for polarized devices such as optical isolators and Q-switches. It also exhibits antiferromagnetic properties. Although there are many deposits of calcite in the world, the optically clear quality calcite, Iceland spar, has been depleted in recent years, leading to its shortage in nature. However, the demand for optically clear calcite single crystals is increasing greatly with the development of laser devices such as the optical isolator [18.137, 138]. Many researchers have tried to grow calcite single crystals at relatively low temperatures, since calcite crystals dissociate to form CaO and CO_2 above 900°C under atmospheric pressure. Various solvents have been used for hydrothermal growth of calcite, but none of them has been found to be the best to grow large single crystals.

The solubility of calcite is very interesting. The solubility is positive for increasing CO_2 pressure and negative for increasing temperature. This behavior of calcite has posed a real problem in the search for a suitable solvent to optimize the growth rate. Despite a large number of reports concerning calcite growth, hydrothermal reactions of calcite in chloride and other chloride solutions have appeared, because natural calcite crystals are formed in both chloride and carbonate hydrothermal solutions and these chloride solutions are almost analogous to natural carbonate thermal springs. Ikornikova has done extensive work on aspects of solubility, designing an apparatus to grow calcite crystals with changing CO_2 concentration as the pressure is reduced at constant temperature, crystal growth kinetics, and mechanism [18.139]. The following groups have carried out extensive studies on the solubility of calcite:

1. Ikornikova, Russia, during the 1960s and 1970s, using chloride solutions
2. Belt, USA, during the 1970s using carbonate solutions

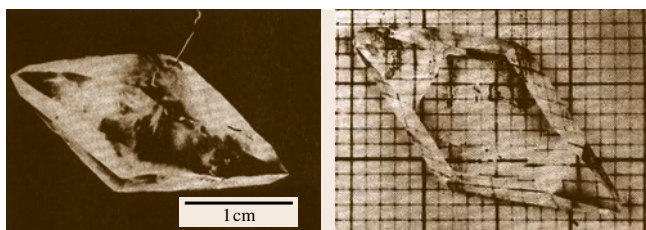


Fig. 18.30 Hydrothermally grown aluminum berlinite crystals (courtesy of Dr. Y. Toudic)

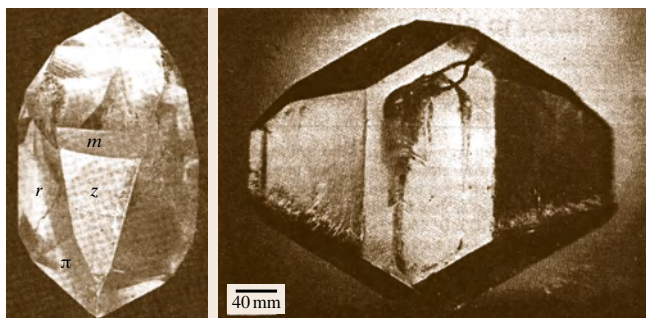


Fig. 18.31 Characteristic photographs of GaPO_4 crystals obtained by the hydrothermal method (courtesy of Prof. L. N. Demianets)

3. Hirano, Japan, during the 1980s and early 1990s using nitrate solutions
4. Kodaira, Japan, during the 1990s using $\text{H}_2\text{O}/\text{CO}_2$
5. Yamasaki, Japan, during the 1990s using ammonium acetate and other organic solvents.

Each of the last three groups claims superiority of their solvents over the others. Figure 18.32 shows solubility curves for calcite in different solvents. Yanagisawa et al. have studied the effect of pH of $\text{CH}_3\text{COONH}_4$ on the growth of calcite [18.142]. When as-cleaved seeds are used, the calcite crystals obtained are usually opaque or not transparent and the surfaces show a greater degree of defects such as growth hillocks, a lot of small secondary grown crystals, and strains. In contrast, crystals grown on etched seed crystals are usually transparent and their surfaces are very smooth. Figure 18.33 shows a characteristic photograph of calcite single crystal grown in NH_4NO_3 solution using as-cleaved and etched seeds. Earlier experiments on calcite single-crystal growth were carried out under higher-PT conditions. For example, Kinloch et al. carried out calcite crystal growth at temperature greater than 435°C with 1.72 kbar pressure using platinum liners and achieved about $50\ \mu\text{m}/\text{day}$ growth rate for the $\{1011\}$ face [18.137]. However, in recent years crystal growth has been carried out using lower-PT conditions using Teflon liners (below 250°C), and a growth rate of $> 120\ \mu\text{m}/\text{day}$ has been achieved. Also several types of nutrients such as natural limestone, natural Iceland spar, reagent-grade carbonates, etc., have been attempted in recent years to obtain high-quality calcite single crystals [18.143].

There are several works in the literature on the growth of other carbonates such as MnCO_3 (rhodochrosite), FeCO_3 (siderite), CdCO_3 (otavit), NiCO_3 , etc., using alkali chloride and carbonate solutions in the temperature range $300\text{--}500^\circ\text{C}$ and pressure up to 1 kbar with a temperature gradient [18.139].



Fig. 18.33 Characteristic photographs of calcite single crystal grown in NH_4NO_3 solution

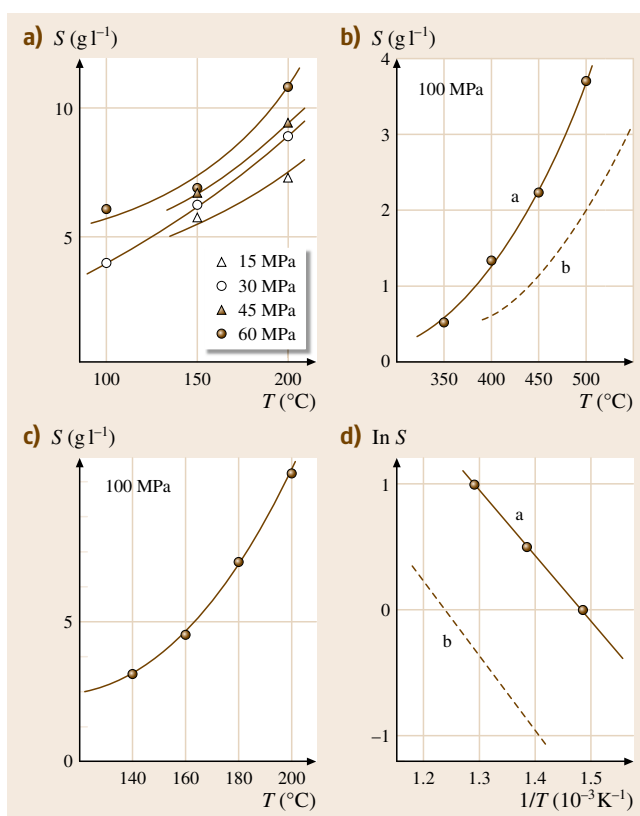


Fig. 18.32a–d Solubility curves for calcite in different solvents: (a) in 1 M NH_4NO_3 ; (b) in 1.5 M $\text{Ca}(\text{NO}_3)_2$ (a), 3 M NaCl (b); (c) in 3 M NH_4NO_3 ; (d) in 1.5 M $\text{Ca}(\text{NO}_3)_2$ (a), 3 M NaCl (b) (after [18.140, 141])

18.4.4 Gemstones

The hydrothermal method has been popularly used from the third quarter of the 19th century for the growth of gemstones such as corundum, ruby, emerald, and garnet [18.15, 16, 18]. During the 1960s and 1970s work on hydrothermal growth of gemstones reached its peak, when successful and high-quality crystals of emerald, colored quartz, amethyst, ruby, corundum, malachite, silicon nitride, garnet, etc. were obtained. However, today, like quartz, much of the research on the hydrothermal growth of gemstones is commercial and hence few publications appear from research laboratories. However, some publications appear periodically on the growth of new gemstones, for example, zeosite. As the sources of natural colored gemstones continue to shrink and the population of the world continues to grow, one could expect increased demand for mater-

ials such as synthetic emerald (tempered, however, by occasional reverses in the world economy). Here, in order to understand the hydrothermal growth of crystals in general, knowledge on the growth of gemstones is also essential. Therefore, a few selected gemstones grown using this hydrothermal technique will be discussed below.

Corundum

Corundum (Al_2O_3) is stable under hydrothermal conditions at $T > 400^\circ\text{C}$ [18.146, 147] and is soluble in alkali and carbonate solutions. The hydrothermal growth of corundum is achieved using a metastable-phase technique because of its very low solubility. Gibbsite ($\text{Al}(\text{OH})_3$) is used as a nutrient, $\alpha\text{-Al}_2\text{O}_3$ as a seed, and an alkaline solution as a solvent. A higher growth rate is obtained in KOH or K_2CO_3 solution than in NaOH or Na_2CO_3 solution. The solubility is lower in KOH or K_2CO_3 , but the interaction between the impurity absorbed beforehand onto the crystal surface and K^+ ions existing in the solution acts as a factor to augment the growth rate. As the pH of solution is lowered, thickness of the growth layer increases along the c -axis. The growth of corundum is extremely low in 6N HCl . Kashkurov et al. have studied the growth of large corundum crystals at pressures of up to 2000 atm and temperatures of up to 550°C in alkali solutions of various concentrations. Crystals weighing up to 1 kg were prepared by the hydrothermal technique, and the imperfect state of these crystals was apparently associated with internal stresses and the mosaic structure of seed crystals, which were prepared by Varneuil technique [18.148]. Figure 18.34 shows the solubility of corundum in potassium carbonate aqueous solutions.

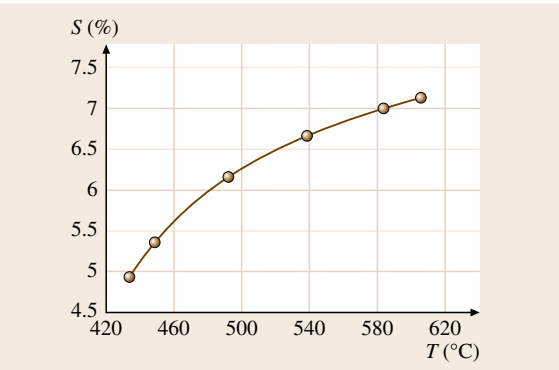


Fig. 18.34 Dependence of solubility of corundum in K_2CO_3 aqueous solutions (after [18.144])

The ideal experimental conditions for the growth of good-quality corundum crystals are:

- Temperature: 480°C
- Pressure: 1.33 kbar
- Mineralizer: 4 M K_2CO_3
- Fill: 85%
- ΔT : 30°C .

Using these experimental conditions colorless and transparent crystals with (211), (311), and (111) faces were obtained. Increasing the temperature yields a higher growth rate in the temperature interval $400\text{--}500^\circ\text{C}$.

Ruby and Sapphire

Ruby and sapphire crystals are grown using the hydrothermal method, with appropriate dopants added to experimental conditions similar to those described for corundum crystal growth. Sapphire was probably the second material after quartz to be grown in any size by the hydrothermal method. Similarly large ruby crystals could be grown using carbonate solutions. The solubilities of sapphire and ruby are the same as that of corundum and increase with temperature. Oxides of chromium and iron taken in the nutrient along with Na_2CO_3 solution strongly influence the crystallization of these two varieties of crystals than K_2CO_3 solution. However, when the concentration of these components in the nutrient is $> 1.6\%$ in 10% Na_2CO_3 solution, crystals barely grow. Figure 18.35 shows the growth rate of the (1011) face versus Cr_2O_3 concentration in the initial charge (10% Na_2CO_3 solution, 550°C , autoclave 60% filled). In carbonate and bicarbonate solutions, chromic oxide and aluminum oxide have substantially different solubilities and rates of dissolution.

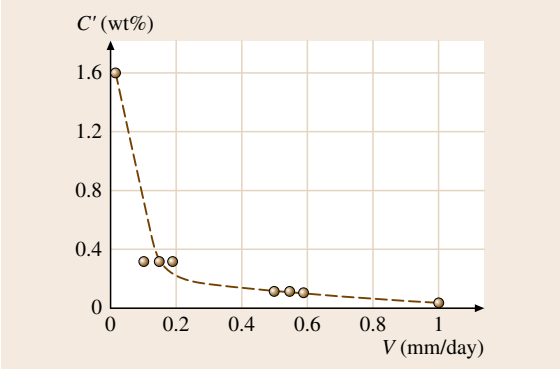


Fig. 18.35 Growth rate of (1011) face versus Cr_2O_3 concentration in the initial charge (after [18.145])

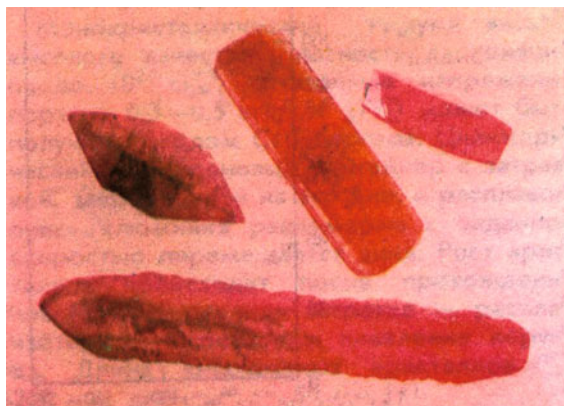


Fig. 18.36 Hydrothermally grown ruby crystals (courtesy of Prof. V. S. Balitskii)

Monchamp et al. have carried out very large-scale growth of sapphire and ruby with considerable success [18.149, 150]. Figure 18.36 shows hydrothermally grown ruby crystal [18.151]. Green crystals containing iron have been grown by carrying out the crystallization in welded liners directly, and essentially pure colorless crystals have been prepared by the use of silver tubes [18.150]. The overall features are similar to those for the growth of corundum crystals.

Emerald

Among the other gemstones grown popularly under hydrothermal conditions, emerald is one of the most important ones. It is also used as an effective tunable laser medium. The presence of Cr^{+3} in beryl ($\text{Be}_3\text{Al}_2(\text{SiO}_3)_6$) gives a green-colored emerald. The bluish-green variety is known as aquamarine. Gems that are greenish/yellow to iron-yellow and honey-yellow are called golden beryl. The rose-colored variety is called morganite or vorobyevite. Alkali elements such as Na^+ , Li^+ , and Cs^+ are sometimes present, replacing the beryllium at 0.25–5%. Artificial growth of beryl crystals began in the previous century itself. *Hautefeuille* and *Perrey* were the first to synthesize beryl crystals artificially [18.152]. Probably the earliest best work on hydrothermal growth of emerald was by *Nacken*. He made larger numbers of synthetic emeralds, using a trace of chromium to produce the color. Hexagonal prisms weighing about 0.2 g were grown in a few days. Several workers have reviewed the hydrothermal growth of emerald [18.153, 154]. *Lechleitner* of Innsbruck, Austria, released the first and not completely satisfactory product into the market during the 1960s and 1970s [18.155–157]. He used faceted

beryl gemstones as the seed and grew a thin layer of hydrothermal emerald on the surface, which was subsequently given a light polish (not necessarily on all faces). Such stones were marketed for a short time under the names *Emerita* and *Symerald*. The first completely synthetic hydrothermal emerald was put on the market by the Linde Division of the Union Carbide Corporation in 1965. The first patent on beryl revealed that it could be grown in a neutral to alkali medium (pH of 7–12.5) using mineralizers such as alkali or ammonium halides (e.g., $\text{NH}_4\text{F} + \text{NH}_4\text{OH}$ or KF), and that Fe, Ni, or Nd could be used as dopants [18.158]. The second patent dealt with the analogous growth of beryl in an acid medium (pH 0.2–4.5), using similar halide mineralizers but with an acid reaction (e.g., 8 N NH_4Cl) or with extra acid added [18.159]. Typical emerald growth conditions included a pressure of 10 000–20 000 psi at temperatures of 500–600 °C resulting from a 62% fill. A small temperature gradient of 10–25 °C was employed. The Al was supplied from gibbsite $\text{Al}(\text{OH})_3$, Be from $\text{Be}(\text{OH})_2$, Si from crushed crystals of quartz, and Cr from $\text{CrCl}_3 \cdot 6\text{H}_2\text{O}$. Growth rates as high as 0.33 mm/day could be attained. The pressure vessel was lined with gold.

Biron Mineral (Pvt.) Ltd., Australia, produces commercially popular Biron synthetic emerald, but the growth conditions remain unknown. However, chlorine, chromium, vanadium, some water, and also tiny gold crystals have been detected in these crystals [18.160, 161]. Today Russia produces the largest quantities of synthetic emerald in the world. Also there are several recent publications from Russian laboratories on synthetic emerald. This activity began in 1965 and the growth conditions used are:

Growth temperature:	590–620 °C
Temperature gradient:	45 °C 20–100 °C 70–130 °C
Pressure:	790–1481 atm
Solvent:	Acidic solution or fluorine bearing solutions of complex components
Nutrient:	Natural beryl or oxides of Be, Al, and Si
Vessel:	Stainless steel (200–800 ml)
Seed:	Plate cut parallel to (5510).

Cr^{3+} , Fe^{2+} , Fe^{3+} , Ni^{3+} , and Cu^{2+} have been detected through chemical analysis as color-associated transition elements. Fe^{2+} and Cu^{2+} ions were assigned to the tetrahedral sites, and Ni^{3+} , Cr^{3+} , and Fe^{3+} ions to the octahedral sites [18.162]. Evolution of ions

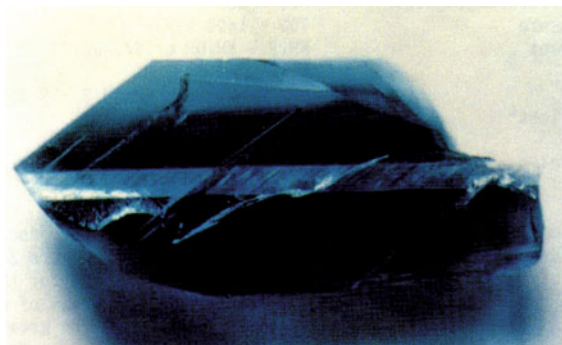


Fig. 18.37 As-grown crystals of regency emerald

from the inner wall of the autoclave is possible. It is, therefore, unknown which ions were added during the process of growth. The length of the crystal is 6.1 cm, width 1 cm, and thickness 0.7 cm. The solubility of emerald has been restudied recently using H_2SO_4 aqueous solution [18.163]. Also there are several works related to defect formation and zoning in emerald crystals obtained under hydrothermal conditions [18.164]. Figure 18.37 shows hydrothermally prepared regency emerald.

Colored Quartz

Throughout history, quartz has been the common chameleon of gemstones, standing in for more expensive gemstones ranging from diamond to jade. However, the incredible variety of quartz is now beginning to be appreciated for its own sake. Purple to violet amethyst and yellow to orange citrine are jewelry staples that continue to increase in popularity.

Ametrine combines the appeal of both amethyst and citrine as well as both the purple and yellow in one bicolored gemstone. Other major colors include the brownish smoky quartz, pink rose quartz, and colorless rock crystal quartz. Different colors and types of chalcedony, including agate, bloodstone, chrysoprase, and black onyx, have grown in popularity with growing appreciation for carved gemstones and art cutting and carving. Unusual quartz specialties such as drossy quartz, with its surface covered by tiny sparkling crystals, and rutilated quartz, which has a landscape of shining gold needles inside, are adding variety and nature's artistry to unusual one-of-a-kind jewelry. The hydrothermal growth of colored quartz is a major activity today owing to its commercial value. No colored synthetic quartz producing company has ever published the exact recipe of the growth of colored quartz.

The synthesis of amethyst was first described by *Tsinobar* and *Chentsova* [18.165]. After the growth of quartz on positive (r) and negative (z) seeds in an iron-containing alkaline solution, an amethystine color is produced by irradiation. The color intensity is high from the (z) to the (r) directions. This is due to the difference of growth rates between the positive and negative rhombohedra. This phenomenon has been exploited by a large group of researchers in growing a wide range of bicolored, color-zoned quartz crystals, which are very attractive as gemstones, for example, ametrine (amethyst-citrine) [18.166]. In alkaline solutions the growth rate of the positive rhombohedron is lower than that of the negative rhombohedron. So, the content of entrapped iron is higher in the positive than in the negative rhombohedron. This color inhomogeneity with the amount of entrapped iron is distinctly discerned at areas where Dauphiné twin quartz exists. A brown or green color is emitted from the basal surface of crystals, which is caused by nontrapping of structural iron in the basal surface and also a cut surface close to the basal surface [18.167]. The credit for hydrothermal growth of gem-quality colored quartz goes to pioneers such as *Tsinobar*, *Nassau*, and *Balitsky*. At present *Balitsky* is still very active in this area of research.

Purple-colored quartz has been synthesized under the following conditions [18.168]:

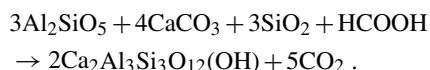
Growth temperature:	400–450 °C
ΔT :	25–50 °C
Pressure:	774–1260 atm
Solvent:	10 wt % NaCl; 10 wt % KCl,
Dopant:	Fe in the form of a metal; $\alpha\text{-Fe}_2\text{O}_3$ in the form of a powder
Vessel:	Platinum-lined (16.5 ml)
Irradiation:	$2 - 15 \times 10^6 \text{ R (Röntgen) } (^{60}\text{Co})$

When the amount of impurities exceeds a certain level the growth is inhibited and pits or crevice flaws are induced in the crystal. Also, the type of dopant and its concentration controls the degree of growth inhibition. Faint-pink-colored quartz can be obtained in the presence of iron and titanium ions. The type and concentration of impurity ions used by the industries producing these colored quartz crystals commercially are not exactly known. However, these synthetic colored quartz crystals are even called poor man's diamond, emerald, ruby, etc., because of their beauty and closeness to those expensive natural gemstones. Readers can find more extensive information on this subject in [18.151, 169].

Zoisite

The commercial name for zoisite is tanzanite, a calcium aluminum silicate hydroxide ($\text{Ca}_2\text{Al}_3\text{Si}_3\text{O}_{12}(\text{OH})$) having a very high commercial value that poses a real challenge to crystal growers to grow it as bulk single crystals. There are several groups throughout the world working on this, but the PT conditions involved are extreme. The special chatoyancy phenomena with vitreous luster observed in this crystal has made it a highly valuable gemstone. There are several imitations on the market as well.

Byrappa et al. have reported the synthesis of zoisite using mild hydrothermal conditions with sillimanite (Al_2SiO_5), calcium carbonate (CaCO_3), and quartz (SiO_2) in the ratio 3 : 4 : 3 [18.170]. Sillimanite gel was prepared using commercially available corundum (Al_2O_3) and quartz (SiO_2) gels. The advantages of gels as starting material is that numerous and complex phases can be intimately mixed. The experiments were carried out in general-purpose autoclaves using Teflon liners in the temperature range 10–250 °C with pressure of 60–80 bar in a desired solvent. The experimental temperature was raised slowly at the rate of 20 °C/h. Several mineralizers such as HCl, CH_3COOH , $\text{C}_2\text{H}_5\text{OH}$, glycol, methanol, NaOH, etc. have been tried, but only HCOOH and *n*-butanol were found to be the most suitable mineralizers to synthesize zoisite crystal. The probable reaction for zoisite synthesis when HCOOH is used as a mineralizer is as follows:



The usual pH conditions to obtain zoisite is between 1.6 and 1.8. The crystals were obtained through spontaneous nucleation in the size range 0.5–2 mm.

18.4.5 Rare-Earth Vanadates

R:MVO_4 (where R = Nd, Er, Eu; M = Y, Gd) form an important group of highly efficient laser-diode pumped microlasers, efficient phosphors, polarizer materials, and low-threshold laser hosts [18.171–174]. These crystals offer many advantages over the conventional Nd:YAG crystal, with larger absorption coefficient and gain cross section. Rare-earth vanadates are known as high-melting materials (> 1800 °C) with low solubility, and obviously their synthesis by any technique usually requires higher-temperature conditions. In spite of its excellent physical properties, high-tech applications have not been realized due to crystal growth difficulties. One of the major problems encountered in the

growth of RVO_4 crystals is the presence of oxygen imperfections (color centers and inclusions), which are introduced during the crystal growth processes. Although YVO_4 melts congruently [18.175], vanadium oxides vaporize incongruently, causing changes in Y/V ratio and oxygen stoichiometry in the melt. These undesired effects could generate additional phases and oxygen defects in the YVO_4 crystals grown, especially from the melt [18.176]. Efforts to eliminate these defects did not yield significant success with the flux and melt techniques. The instability of pentavalent vanadium at higher temperatures and the loss of oxygen through surface encrustation by the reaction of the melt with the crucible material further complicate the growth processes. In order to overcome most of the difficulties encountered in the melt and high-temperature solution techniques, the hydrothermal technique has been proposed as a solution [18.177–181]. Since the experiments are carried out in a closed system, the loss of oxygen can be readily prevented. The experiments are usually carried out in the temperature range of 240–400 °C at pressure of 40 bar to 1 kbar. The starting materials (oxides of rare earths and V_2O_5 with a desired solvent in a particular concentration) are held in Teflon or platinum liners depending upon the PT conditions of the experiments, and the Morey or Tuttle type of autoclaves are used. The solubility of rare-earth vanadates is shown in Fig. 18.38 and is found to be negative. It increases with the concentration of the solvent. Both acid and basic mineralizers are used in the growth of these vanadates. However, acid mineralizers are more effective, especially the mixed acid mineralizers ($\text{HCl} + \text{HNO}_3$ in a particular molar ratio).

The morphology of these crystals can be tuned to a desired shape using appropriate starting materials and

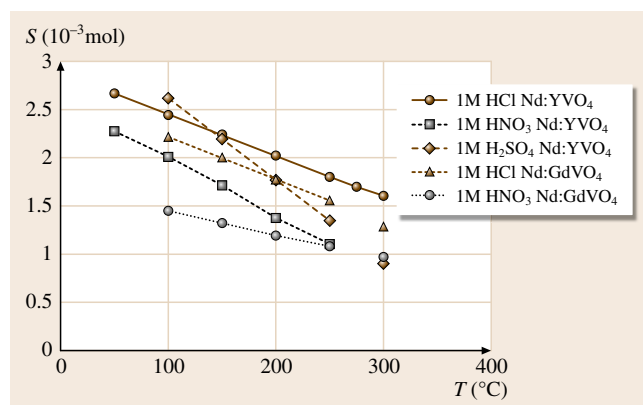


Fig. 18.38 Solubility of Nd:MVO₄ in different solvents

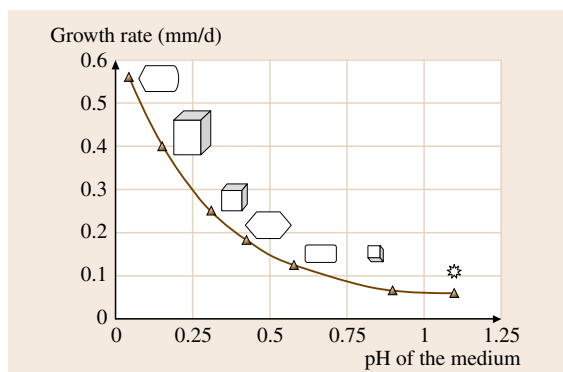


Fig. 18.39 Morphology variation with pH for Nd:YVO₄ crystals obtained from presintered nutrient in 1.5 M HCl + 3 M HNO₃ mineralizer (courtesy of K. Byrappa)

experimental conditions. Figure 18.39 shows the morphology of rare-earth vanadates and growth rate with pH of the medium. Both the chemical-reagent-grade nutrient and the presintered Nd:YVO₄ nutrient are used in the growth of rare-earth vanadates. In fact, the presintered nutrient gives better results. The most interesting part of this work is the need of an oxidizing agent such as hydrogen peroxide in the system, otherwise the crystals appear dark and opaque (Fig. 18.40). Often the crystals show twinning, depending upon the growth

conditions. Some attempts at in situ morphology control of these vanadates have been made. The readers can refer to the works of the present author [18.174, 177, 178].

On the whole there is a slow decline in activity on bulk growth of other materials such as potassium titanyl phosphate, potassium titanyl arsenate, mixed-framework rare-earth silicates, germinates, rare-earth tungstates, borates, phosphates, oxides of various metal like tellurium, zirconium, hafnium, and a variety of sulfides of lead, copper, mercury, silver, cadmium, etc. The growth of these crystals was extremely popular from the 1960s to the 1980s. Readers can obtain more information on the growth of these crystals in earlier publications [18.1, 2, 4, 7]. The trend in hydrothermal research shifted towards the growth of fine crystals of various compounds, especially a large family of piezoelectric ceramic crystals such as lead zirconium titanates (PZT), ferrites, hydroxyapatites, etc., during the 1990s and towards the turn of the 20th century focus shifted to the growth of nanocrystals. Hence, the growth of selected fine and nanocrystals is now discussed. Accordingly the chapter refers to polyscale crystals, because it covers bulk crystals to nanocrystals. It should be noted that bulk growth of other important current technological materials such as ZnO, GaN, etc. has been discussed separately by Callaghan et al. in Chap. 19 of this handbook.

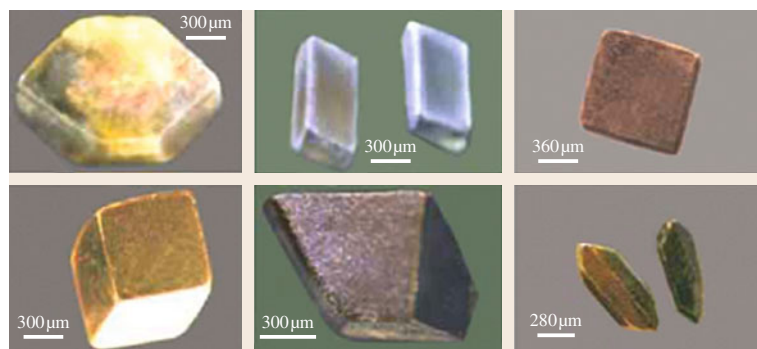


Fig. 18.40 Characteristic photographs of Nd:YVO₄ crystals (courtesy of K. Byrappa)

18.5 Hydrothermal Growth of Fine Crystals

The growth of fine crystals under hydrothermal conditions has been known since hydrothermal technology was born. The majority of early hydrothermal experiments carried out during the 1840s to early 1900s mainly dealt with fine to nanocrystalline products, which were discarded as failures due to the lack of so-

phisticated tools to examine the fine products except some chemical techniques [18.6]. During this period many experiments were carried out on the synthesis of fine crystals of zeolites, clays, some silicates, hydroxides, etc. [18.22]. When Barrer reported the hydrothermal synthesis of fine particles of zeolites during

the 1940s, it opened a new branch of science, viz. molecular sieve technology. During the late 1960s and 1970s, attempts were made to synthesize fine crystals of metal oxides using the hydrothermal method. This was a very popular field of research at that time [18.4, 182, 183]. Hydrothermal research during the 1990s marked the beginning of work on processing of fine to ultrafine crystals with controlled size and morphology. Today, it has evolved to be one of the most efficient methods of soft chemistry for the preparation of advanced materials such as fine to nanocrystals with controlled size and shape. Currently, the annual market value of electronic ceramics is over US\$ 1 billion, and the market for nanocrystals processing (US\$ 120 billion in 2002) is increasing at 15% annually, to reach US\$ 370 billion by 2010, and will jump to become a trillion-dollar industry by 2015, according to National Science Foundation (NSF) predictions.

Of all the ceramics, the PZT family has been studied most extensively using the hydrothermal technique. Since the early 1980s several thousands of reports have appeared on the preparation of these ceramics. Thermodynamic calculation and kinetics of these systems have been studied extensively (Figs. 18.4 and 18.5) [18.48, 50]. Several new variants/approaches to the processing of these electronic ceramic crystals have been reported to enhance the kinetics, shorten the processing time,

control the size and shape, maintain the homogeneity of the phases, and achieve reproducibility. A great variety of precursors and solvents have been attempted in the processing of these fine crystals. Similarly fine film formation of these on an appropriate substrate has been accomplished by several workers [18.184, 185]. Here only some selected crystals such as PZT and HAP will be discussed.

The important step in the synthesis of fine crystals of advanced materials is the use of surfactants and chelates to control the nucleation of a desired phase, such that the desired phase homogeneity, size, shape, and dispersibility can be achieved during the crystallization of these fine crystals. This marked the beginning of the study of precursor preparation for different systems, surface interactions with capping agents or surfactants, and polymerized complexes. The surfaces of the crystals can be altered to become hydrophobic or hydrophilic, depending upon the applications [18.186, 187]. Today this approach is playing a key role in preparing highly dispersed, oriented, and self-assembled fine to nanocrystals. Figure 18.41 shows the new chemical approach for preparation of precursors. Using such an approach a wide range of advanced materials such as the PZT family of ceramics, ferrites, phosphates, sulfides, oxides, hydroxyapatites, etc., as well as composites have been prepared as fine crystals for technological ap-

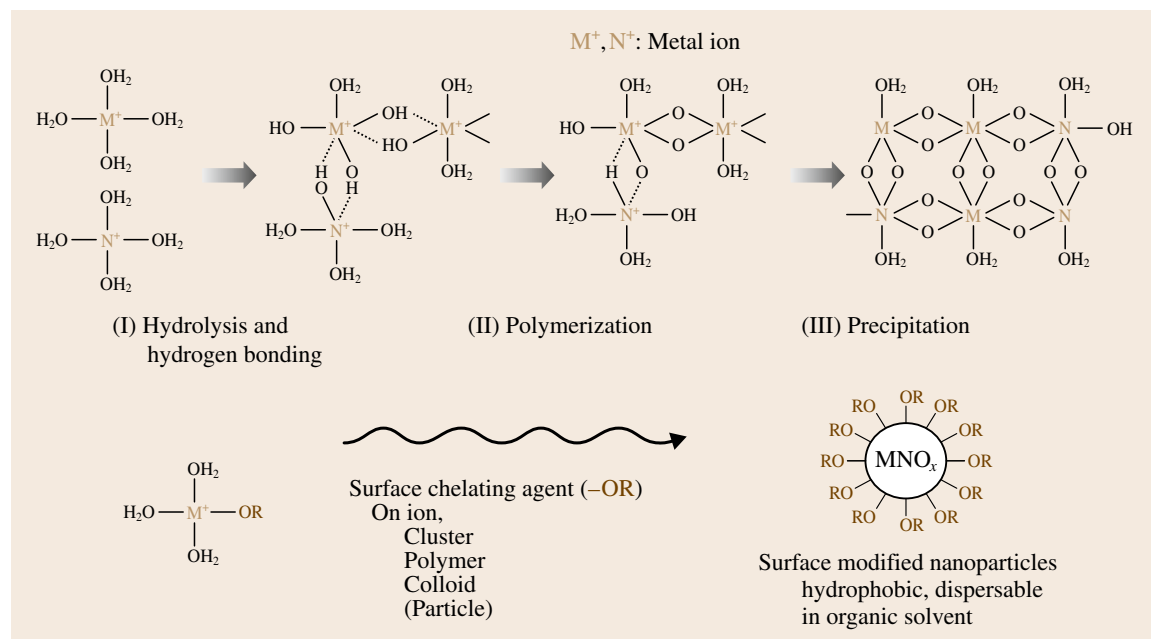


Fig. 18.41 A new preparative chemical approach for precursor preparation (courtesy of Prof. M. Yoshimura)

plications with preferred morphology such as whiskers, rods, needles, plates, spheres, etc., depending upon their application. This precursor-based chemical approach to hydrothermal synthesis has made tremendous progress in recent years and has also drastically reduced the temperature and pressure conditions required for crystal growth.

Riman and group have done extensive work on intelligent engineering of fine crystals of the **PZT** family and **HA** based on the thermodynamic modeling approach, and also calculated their crystallization kinetics in detail. Such studies not only helped in the hydrothermal synthesis of these fine crystals, but also in controlling their precise shape and size as per application requirements. Figures 18.42 and 18.43 show designer fine crystals of **PZT**, LiMn_2O_4 , **HA**, etc., prepared under hydrothermal conditions.

The majority of the **PZT** systems incorporate intolerable amounts of alkaline metals, which are introduced in the form of mineralizers. In recent years organic mineralizers have become popular with a large number of workers. For example, *Riman* and group have found that tetramethylammonium hydroxide $[\text{N}(\text{CH}_3)_4\text{OH}]$ is a favorable substitute for alkaline metal hydroxide mineralizer in producing phase-pure **PZT** [18.89]. Phase-pure MeTiO_3 ($\text{Me} = \text{Ca}, \text{Sr}, \text{Ba}$) can be obtained at input molalities of Ba , Sr , and Ca greater than 7×10^{-5} , 10^{-6} , and 5×10^{-5} M respectively. Otherwise, the relative location of the 99.995% yield regions for the three titanates will be similar to the pattern noted in the stability diagrams. In concentrated solutions, the consumption of OH^- ions is caused by the predominant

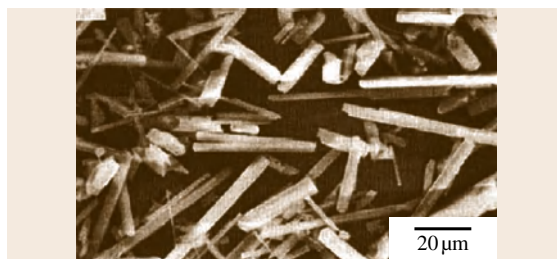


Fig. 18.43 SEM photograph of HAp crystals (courtesy of Dr. W. Suchanek)

reaction



Such an approach to understand the crystallization mechanism of the **PZT** family of crystals has been made by several workers and there are many commercial producers of these ceramic crystals, especially in the USA, Japan, and Europe.

Gersten has extensively reviewed the processing parameters for the synthesis of fine ferroelectric perovskite crystals by the hydrothermal method [18.49]. Accordingly, the first step in the growth of these fine particles is thermodynamic verification of the correct processing conditions for the reaction of the desired product. The chemical purity of the precursors should be high, and the pH adjusters or other additives should be decomposable at the calcination temperature. The supersaturation is influenced by the initial reagent concentration, pH, experimental temperature, stirring rate, type of mineralizer, and time. An increase in the supersaturation will result in a decrease in crystal size.

In recent years interest in fine **HA** crystals with desired size and shape has resulted in a rapid increase in the number of publications on HAp. Starting chemicals such as H_3PO_4 , $\text{Ca}(\text{OH})_2$, and lactic acid or other solvents are taken in a Teflon beaker, inserted into an autoclave, and hydrothermally treated in the temperature range $150\text{--}200^\circ\text{C}$ for a few hours under autogenous pressure. The molar ratios of solvent/ Ca and Ca/P are adjusted appropriately to get the desired phase of calcium phosphate. The morphology of the resultant **HA** can be controlled through the initial precursors and their ratios, besides the experimental temperature and duration. Even stirring influences the morphology of the crystals. For example, the diameter of the grains increases with increasing Ca/P molar ratio in the starting solution and is generally larger for high lactic acid/ Ca molar ratios. The aspect ratio of HAp crystals is in the

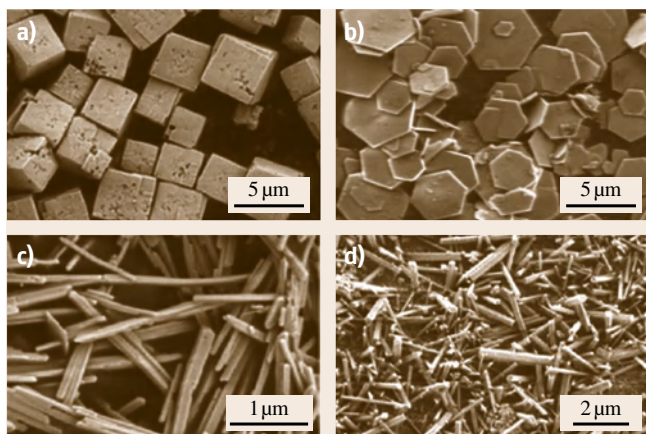


Fig. 18.42a–d Hydrothermally synthesized fine crystals: (a) **PZT**; (b) LiMn_2O_4 ; (c) PbTiO_3 ; (d) BaTiO_3 (courtesy of Prof. Richard E. Riman)

range of 5–20. It decreases with increasing Ca/P ratio and is lower in the case of high lactic acid/Ca ratios. When the lactic acid/Ca and Ca/P starting ratios are low, crystals have the shape of whiskers, whereas in other cases large, elongated grains form [18.188].

There is a steady flow of publications relating to the growth of fine crystals of oxides, silicates, vanadates, phosphates, tungstates, titanates, etc., for various applications. The interesting aspect of their growth is the

adaptability of the hydrothermal technique for all these compounds, which can be synthesized through spontaneous nucleation without many complications as in the case of bulk crystal growth. The reaction mixtures can be stirred at different rates and the crystals can also be produced continuously with the use of a flow reactor. There are many publications related to the use of flow reactors for continuous production of such fine crystals [18.97, 98].

18.6 Hydrothermal Growth of Nanocrystals

The hydrothermal technique is becoming one of the most important tools to synthesize nanocrystals for a wide variety of technological applications such as electronics, optoelectronics, catalysis, ceramics, magnetic data storage, biomedicine, biophotonics, etc. On the whole 21st century hydrothermal technology is more inclined towards nanotechnology owing to its advantages in obtaining high-quality, monodispersed, homogeneous nanocrystals with controlled size and shape, as well as the lower-*PT* conditions of the synthesis, simple apparatus, shorter duration, and lower cost of production. The most important advantage is that nanocrystals with desired physicochemical characteristics can be prepared, and desired surface charge can be introduced onto the nanocrystals in situ with the help of surface modifiers, capping agents, etc.

Hundreds of types of nanocrystals have been synthesized using hydrothermal technique, with over 10 000 publications in the last 8 years. The number of publications is increasing year by year and covers all groups of advanced materials such as metals, metal oxides, semiconductors including II–VI and III–V compounds, silicates, sulfides, hydroxides, tungstates, titanates, carbon, zeolites, etc. It is not possible to discuss the synthesis of all these nanocrystals using hydrothermal technology. Instead, the synthesis of some representative and technologically important nanocrystals will be discussed.

In recent years noble-metal particles (such as Au, Ag, Pt, etc.), magnetic metals (such as Co, Ni, and Fe), metal alloys (such as FePt, CoPt), multilayers (such as Cu/Co, Co/Pt), etc. have attracted the attention of researchers owing to their new interesting fundamental properties and potential applications as advanced materials with electronic, magnetic, optical, thermal, and catalytic properties [18.189–192]. The intrinsic properties of noble-metal nanoparticles strongly depend

upon their morphology and structure. The synthesis and study of these metals have implications for the fundamental study of the crystal growth process and shape control. The majority of the nanostructures of these metal alloys and multilayers form under conditions far from equilibrium [18.193]. Among these metals, alloys, and multilayers, shape anisotropy exhibits interesting properties. Both the hydrothermal and hydrothermal supercritical water techniques have been extensively used in the preparation of these nanoparticles.

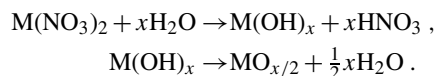
The synthesis of metal oxide nanocrystals under hydrothermal conditions is important because of its advantages in the preparation of highly monodispersed nanocrystals with control over size and morphology. There are thousands of reports in the literature, which also include a vast number of publications on supercritical water (SCW) technology for the preparation of metal oxides. The most popular among these metal oxides are TiO₂, ZnO, CeO₂, ZrO₂, CuO, Al₂O₃, Dy₂O₃, In₂O₃, Co₃O₄, NiO, etc. Metal oxide nanocrystals are of practical interest in a variety of applications, including high-density information storage, magnetic resonance imaging, targeted drug delivery, bio-imaging, cancer therapy, hyperthermia, neutron capture therapy, photocatalytic, luminescent, electronic, catalytic, optical, etc. The majority of these applications require nanocrystals of predetermined size and narrow size distribution with high dispersibility. Hence, a great variety of modifications are used in the hydrothermal technique.

Al'myasheva et al. and *Jiao et al.* have reviewed the hydrothermal synthesis of corundum nanocrystals under hydrothermal conditions [18.194, 195]. A high specific surface area corundum has been synthesized through the conversion of diasporite to corundum under hydrothermal conditions. This nanosized alumina has great application potential. The authors were able

to develop a new transitional alumina reaction sequence that gave rise to an intermediate alpha structure, α' - Al_2O_3 , with a very high surface area. Also they have investigated the thermodynamic basis and equilibrium relationships for the nanocrystalline phases. Qian and his group has studied extensively low temperature hydrothermal synthesis of a large variety of metal oxides under hydrothermal and solvothermal conditions [18.196]. Among the nanocrystals of the metal oxides, TiO_2 and ZnO occupy a unique place. Since the preparation of ZnO has been discussed in Chap. 19, only the synthesis of TiO_2 nanocrystals is discussed here. The synthesis of TiO_2 is usually carried out in small autoclaves of Morey type, provided with Teflon liners. The conditions selected for the synthesis of TiO_2 particles are: $T \leq 200^\circ\text{C}$, $p < 100$ bar. Such pressure/temperature conditions facilitate the use of autoclaves of simple design provided with Teflon liners. The use of Teflon liners helps to obtain pure and homogeneous TiO_2 particles. Though the experimental temperature is low ($\approx 150^\circ\text{C}$), TiO_2 particles with a high degree of crystallinity and desired size and shape could be achieved through a systematic understanding of the hydrothermal chemistry of the media [18.197]. A variety of surfactants are used to produce nanocrystals of the desired shape and size. Figure 18.44 shows TiO_2 nanocrystals obtained under supercritical hydrothermal conditions (400°C and pressure 30 MPa) in the presence of hexaldehyde.

Adschiri and co-workers [18.198, 199] have worked out in detail a continuous synthesis of fine metal ox-

ide particles using supercritical water as the reaction medium. They have shown that fine metal oxide particles are formed when a variety of metal nitrates are contacted with supercritical water in a flow system. They postulated that the fine particles were produced because supercritical water causes the metal hydroxides to rapidly dehydrate before significant growth takes place. The two overall reactions that lead from metal salts to metal oxides are hydrolysis and dehydration



Processing in SCW increases the rate of dehydration such that this step occurs while the particle size is small and the reaction rate is less affected by diffusion through the particle. Furthermore, the gas-like viscosity and diffusivity of water in the critical region lead to a negligible mass-transfer limitation. The net effect is that the overall synthesis rate is very large. The high temperature also contributes to the high reaction rate. Several metal oxides, including α - Fe_2O_3 , Fe_3O_4 , Co_3O_4 , NiO , ZrO_2 , CeO_2 , LiCoO_2 , α - NiFe_2O_4 , $\text{Ce}_{1-x}\text{Zr}_x\text{O}_2$, etc., have been prepared by this technique.

Hydrothermal synthesis of sulfides of various divalent, trivalent, and pentavalent metals constitutes an important group of materials for a variety of technological applications. They popularly form II–VI, III–VI, and V–VI group semiconductors, which are being studied extensively with respect to their different morphologies and particle size, which in turn greatly influence their properties. There are several hundred reports on these sulfides, such as CdS , PbS , ZnS , CuS , NiS , NiS_2 , NiS_7 , Bi_2S_3 , AgIn_5S_8 , MoS , FeS_2 , InS , and Ag_2S , prepared through hydrothermal or solvothermal routes with or without capping agents/surfactants/additives to alter their morphologies and sizes as desired.

Among II–VI group semiconductor nanocrystals, AX ($A = \text{Cd}, \text{Pb}, \text{Zn}$, $X = \text{S}, \text{Se}, \text{Te}$), CdS is an important one. These AX nanocrystals have important applications in solar cells, light-emitting diodes, nonlinear optical materials, optoelectronic and electronic devices, biological labeling, thermoelectric coolers, thermoelectronic and optical recording materials, etc. Furthermore, these compounds can exhibit varying structures such as zincblende, wurtzite, halite, etc. Several papers have been published recently reporting the synthesis of chalcogenides by the hydrothermal method [18.200–203]. On the whole, for crystallization of sulfides, nonaqueous solvents are found to be more favorable, also in terms of decreasing the PT conditions

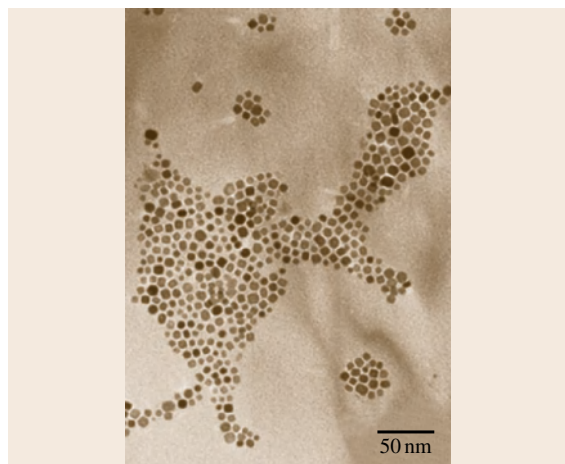


Fig. 18.44 TiO_2 nanocrystals prepared at 400°C and 30 MPa pressure using hexaldehyde as the surface modifier (courtesy of Prof. T. Adschiri)

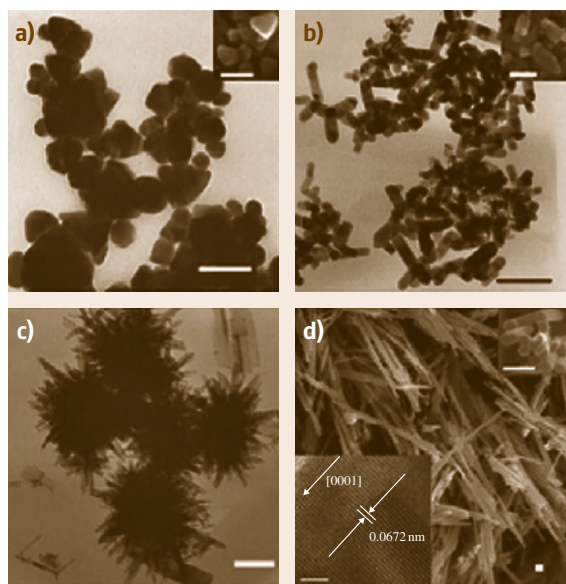


Fig. 18.45a–d TEM and SEM images of CdS products obtained at 180 °C for 5 h in mixed solvents with different volume ratios: (a) 5% ethylene, TEM image with SEM image as inset; (b) 15%, TEM image with SEM image as inset; (c) 65%, TEM image; (d) 100%, SEM image with the upper right inset showing a magnified picture of the hexagonal ends of the long rods, and the lower left inset showing the high-resolution TEM (HRTEM) image of a nanorod. The scale bars in the TEM and SEM images all represent 100 nm. The scale bar in the HRTEM image is 5 nm (courtesy of Prof. Yan Li)

required for crystallization. Qian's group has reported the hydrothermal synthesis (using nonaqueous solvents) of nanocrystalline CdS in some coordinating solvents such as ethylenediamine and pyridine [18.204–206]. Li et al. have used thioacetamide as the sulfide source, as it easily releases sulfide ions, a process which is beneficial for lowering the reaction temperature and shortening the reaction period [18.207]. The hydrothermal route is more popular than all the other methods reported in the literature because of the lower temperature, shorter duration, and control over the size and morphology. The experiments are usually carried out in the temperature range 150–200 °C. Figure 18.45 shows transmission electron microscopy (TEM) and scanning electron microscopy (SEM) images of CdS nanocrystals.

The synthesis of various carbon polymorphs such as graphite, diamond or diamond-like carbon, fullerenes, etc., has attracted considerable interest for a long time because of their importance in science and technology.

There are uncertainties about the phase stabilities of these polymorphs, as some of them do not find a place in the carbon pressure–temperature (PT) diagram and are also known for their contrasting physical properties. The exact physicochemical phenomena responsible for their formation are yet to be understood. Attempts to synthesize these forms under various conditions and with various techniques, sometimes even violating thermodynamic principles, have met with a fair amount of success. The stabilities of graphite and diamond in nature were mainly controlled by p – T – f_{O_2} in the C–O–H system [18.208–211]. The role of C–O–H fluids [18.212, 213], as well as the hydrothermal and organic origin of these polymorphs, especially with reference to diamond genesis, prompted material scientists to explore the possibility of synthesizing them at fairly low-pressure/temperature conditions. The hydrothermal technique is highly promising for reactions involving volatiles, as they attain the supercritical fluid state, and supercritical fluids are known for their greater ability to dissolve nonvolatile solids [18.214]. Silicon carbide powder has been used for the synthesis of carbon polymorphs [18.215, 216], and Gogotsi et al. [18.217] have reported decomposition of silicon carbide in supercritical water and discussed the formation of various carbon polymorphs. Basavalingu et al. have explored the possibilities of producing carbon polymorphs under hydrothermal conditions through decomposition of silicon carbide in the presence of organic compounds instead of pure water [18.218]. The organic compounds decompose into various C–O–H fluids; the main components are CO, OH, CO₂, and C₁H_x radicals. It is very well known that these fluids play a significant role in creating a highly reducing environment in the system and also assist in the dissociation of silicon carbide and precipitation of the carbon phase. The study of solid and gaseous inclusions in diamond also indicated the C–O–H fluids as the source for nucleation and growth of diamonds in nature [18.211].

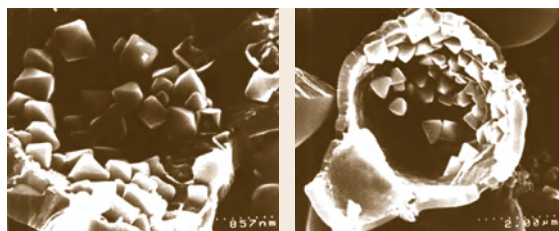


Fig. 18.46 SEM images of diamond nanocrystals with well-developed octahedral facets adhered to the inner walls of the broken spherical particles (courtesy of K. Byrappa)

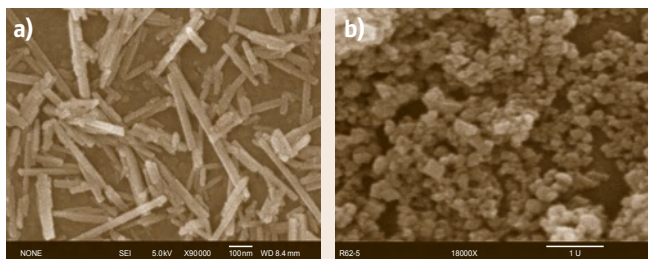


Fig. 18.47a,b SEM images of LaPO_4 and Nd:LaPO_4 . (a) LaPO_4 synthesized at 120°C for about 16 h; (b) LaPO_4 synthesized at 120°C for 30 h

The experiments were carried out in the pressure temperature range of 200–300 MPa and $600\text{--}800^\circ\text{C}$ using externally heated Roy–Tuttle test-tube-type autoclaves. Figure 18.46 shows SEM images of diamond nanocrystals with well-developed octahedral facets adhered to the inner walls of the broken spherical particles.

Very recently, great efforts have been made to develop new phosphor systems for white-LED, FED, and programmed data processor (PDP) applications based on rare-earth phosphate systems. Several authors have reported the synthesis of rare-earth phosphate compounds via different methods. However, the hydrothermal method has distinct advantages over the other methods for the preparation of these rare-earth orthophosphates as good-quality nanocrystals. The present author's laboratory has prepared LaPO_4 and Nd^{3+} -doped LaPO_4 under hydrothermal conditions. The effect of experimental temperature, solvents, the ratio of the starting materials, stirring, and experimental duration has been studied in great detail with respect to crystal size, morphology, and the crystallinity of the resultant products in order to find the

optimum experimental conditions for preparation of biophotonic materials. The experiments were carried out using Teflon-lined Morey autoclaves, Tuttle–Roy autoclaves, and stirred autoclaves. In a typical preparation, La_2O_3 and H_3PO_4 were taken in 1 : 1.2 molar ratio in a beaker containing water (14 ml) to prepare LaPO_4 , and Nd_2O_3 (1–6 mol %) was added for the preparation of $\text{Nd}^{3+}:\text{LaPO}_4$. The pH of the solution was adjusted to 1.4–2 using ethanol. Usually the experimental duration was from 12 to 16 h. Figure 18.47 shows nanocrystals of rare-earth orthophosphates prepared under hydrothermal conditions.

There are hundreds of reports on the hydrothermal preparation of nanocrystals for various applications: to mention a few, the preparation of AlPO_4 , ferrites, phosphors such as $\text{Eu}:\text{Y}_2\text{Sn}_2\text{O}_7$, $\text{Nd}:\text{YAlO}_3$, GaP , Ga_3P , vanadates, fluorides, carbonates, garnets, C_3N_4 , hydroxides, etc. using both hydrothermal and solvothermal routes [18.219–225]. On the whole, solvothermal routes or the use of nonaqueous solutions is becoming more popular even for ultra-high-melting compounds such as GaN and diamond. Furthermore, the solvothermal route can minimize the entry of undesired carbonate or hydroxyl molecules into the final compounds. Similarly, the stoichiometry of the starting materials, and in some cases the change in valency of the metals, can be well controlled when using both the hydrothermal and solvothermal routes. However, the experimenter has to bear in mind that, though nonaqueous solvents show very high reactivity, one has to understand the exothermic and endothermic reactions taking place inside the autoclave, the pressure surge, and the release or formation of highly dangerous components with high volatility. If these things are checked in advance then the method can be well suited to advanced nanomaterial synthesis.

18.7 Concluding Remarks

The hydrothermal technique has evolved into one of the most efficient methods to grow crystals of different size with desired properties. The importance of the hydrothermal technique for the preparation of highly strategic materials such as GaN and ZnO has been realized in recent years. Numerical modeling has contributed greatly to understand the hydrodynamic conditions, which in turn assists in improving the quality of the crystals without any macro- or microdefects even for an industrial-scale autoclave. The

recent progress in the thermodynamic modeling and also the solution chemistry of the hydrothermal media has greatly contributed to the drastic reduction in the PT conditions of the growth of crystals, even with ultralow solubility and high melting temperature. The generation of yield diagrams or stability field diagrams helps in the intelligent engineering of the crystal growth process, so that the yield is almost 100%, i.e., all the solute is converted into the product without any loss of the nutrient. The study of solubility in the success-

ful growth of crystals under hydrothermal conditions is essential, as is the kinetics of crystallization, which helps greatly in enhancing the growth rate. The application of additional energy such as microwave, sonar, mechanochemical, electrochemistry, biomolecules, etc. takes us into a different field of chemistry at the speed of light, because of the increased growth kinetics. The stirring of the precursor during the crystal growth under hydrothermal conditions also contributes to the size and shape of the crystals, especially in the case of fine crystal growth. In recent years, organic molecules, capping agents, and surfactants have been extensively used to introduce a desired surface charge to the crystal surface, and also the properties of the crystal surface can be altered to either hydrophobic or hydrophilic. Similarly the crystal size and shape can be altered with the help of such organic agents. This area of in situ crystal growth process is fast growing and making the

hydrothermal technique into one of the most efficient methods in crystal growth. However, our knowledge today on the growth of crystals such as diamond, gallium nitride, gallium berlinite, etc., is comparable to that of quartz some 60 years ago. Therefore, a collective multidisciplinary approach is essential to understand the hydrothermal technique in order to grow crystals of desired shape, size, and properties. Knowledge on the hydrothermal phase equilibrium is also essential and has to be supported by thermodynamic modeling and computation techniques. Although much of the recent work on the hydrothermal growth of bulk crystals such as quartz, gemstones, gallium nitride, etc., is treated as classified, there is still enormous scope for the application of this technique to grow crystals of technological significance. The number of publications on this important tool of materials processing is also increasing year by year.

18.A Appendix

Table 18.10 List of the polycrystals prepared under hydrothermal conditions. Aut. = autogenous pressure

Compound	Mineralizer(s)	Temperature (°C)	Pressure (kbar)	References
<i>Native elements</i>				
Au, Ag, Pt, Co, Ni, Te, As, Bi, C	NaOH, KOH, HCl, HI, HBR	400–600	> 0.60	[18.189–192] [18.218, 226]
Se	NaOH, KOH	–	–	[18.227]
Cd	NaOH, KOH	–	–	[18.228]
Pb, Cu	NaOH, KOH	450–550	> 0.05	[18.229]
<i>Oxides</i>				
CuO, Cu ₂ O	NaOH, KOH	350–450	0.65–0.8	[18.230]
BeO	NaOH, KOH	450–550	0.8	[18.231]
ZnO	NaOH, KOH, NH ₄ Cl	350–600	0.78–1.0	[18.232]
CdO	NaOH, Na ₂ CO ₃ , (NH ₄) ₂ SO ₄	250–500	0.3–2.0	[18.233]
NiO	NH ₄ Cl	300	0.3	[18.234]
HgO	NaOH	200–300	0.1	[18.235]
PbO	LiOH	450	0.6	[18.236]
Al ₂ O ₃ , emerald	NaOH, KOH, Na ₂ CO ₃ , K ₂ CO ₃	300–620	0.5–0.7	[18.27, 194, 195]
RE ₂ O ₃	H ₂ O	> 500	0.2–0.9	[18.237]
In ₂ O ₃	NaOH, NH ₄ Cl	350–600	0.4–3.0	[18.238]
V ₂ O ₃	NaOH	550–700	1.3	[18.239]
Sb ₂ O ₃	KF, Na ₂ CO ₃	460–600	1.0–1.5	[18.240]
Bi ₂ O ₃	NaOH, KOH	360–600	0.4–1.2	[18.241]
Au ₂ O ₃	Na ₂ CO ₃	300	3.0	[18.242]

Table 18.10 (continued)

Compound	Mineralizer(s)	Temperature (°C)	Pressure (kbar)	References
Fe ₃ O ₄	NaOH	350–405	0.75–0.8	[18.243]
MnO ₂	NaOH	450	0.75–0.8	[18.244]
TiO ₂	KF, NaF, NH ₄ F, NaOH, KOH	100–700	0.5–3.0	[18.197]
ZrO ₂ , HfO ₂	NaF, KF, NH ₄ F	520–690	1.0	[18.2, 34]
SnO ₂	NaOH, KOH	450–600	0.7	[18.245]
TeO ₂	HCl, HF, HI, HBr, HNO ₃	250–385	0.05–0.8	[18.246]
PbO ₂	NH ₄ OH	230–290	0.5	[18.247]
CrO ₂	HClO ₄ , HIO ₄ , NH ₄ ClO ₄	350–400	2.0	[18.248]
SiO ₂ , quartz	NaOH + Na ₂ CO ₃ , NaCl + KCl	350–370	1.5	[18.35]
Amethyst	NH ₄ F	210–450	–	[18.167]
GeO ₂	NaOH, KOH	350	1.0	[18.249]
K ₂ Te ₄ O ₉ · 3H ₂ O	K ₃ PO ₄ + H ₂ O	380	–	[18.250]
Y ₃ Fe ₅ O ₁₂	KOH	420	2.0	[18.251]
Y ₃ Al ₅ O ₁₂	K ₂ CO ₃ , Na ₂ CO ₃ , NaOH	350	2.0	[18.252]
ABi ₁₂ O ₂₀ (A = Ti, Si, Ge)	NaOH	500–570	1.5–2.0	[18.253]
NiFe ₂ O ₃	NH ₄ Cl	475	–	[18.109]
<i>Hydroxide</i>				
M(OH) ₂ (M = Be, Mg, Ca, Cd, Mn, Ni, Co)	NaOH, H ₂ O	100–550	0.6–4.0	[18.254]
RE(OH) ₃ (RE = La – Gd, Dy, Er, Yb)	NaOH	350–450	0.6	[18.254]
M(OH) ₃ (M = Cr, In)	NaOH	300–450	0.4–1.5	[18.254]
Al(OH) ₃	H ₂ O	< 150	0.04	[18.255]
MOOH, MOOD, In(OD) ₃ M = In, Cr, Gd, Sn	H ₂ O, D ₂ O	180–600	0.02–1.4	[18.256]
α-ScOOH, β-ScOOH	H ₂ O	162–350	0.006–0.17	[18.257]
Sr ₃ Cr ₂ (OH) ₁₂	H ₂ O	150–200	–	[18.258]
Malachite, azurite	–	–	–	[18.259]
<i>Garnets</i>				
A ₃ B ₂ Si ₃ O ₁₂ (A = Mn, Ca, Fe, Cd; B = Al, Fe, In, V, Cr)	CaCl ₂ , CdCl ₂ , NH ₄ Cl	400–900	0.4–30.0	[18.260, 261]
<i>Silicates</i>				
Li ₂ SiO ₃	LiOH	450	0.15	[18.262]
KHSiO ₂ O ₅	KOH	300	–	[18.263]
Al ₂ SiO ₅	H ₂ O	900	20.0	[18.264]
CaBSiO ₄ (OOH)	CaCl ₂ + HCl	300–400	0.3–0.35	[18.264]
Zn ₂ SiO ₄	HCl	400–500	0.4	[18.265]
Zn ₂ SiO ₄ · Mn ²⁺	Ethanol	220	Auts.	[18.266]
R ₂ Si ₂ O ₇ (R = La – Lu, Sc, Y, Cd)	H ₂ O	700	2.5	[18.267]
Na ₂ Fe ₅ TiSiO ₂₀	H ₂ O	500–700	0.5	[18.268]
Na ₂ R ₆ Si ₆ O ₂₄ (OH) ₂ (R = La, Y)	H ₂ O	500–700	2.0	[18.269]

Table 18.10 (continued)

Compound	Mineralizer(s)	Temperature (°C)	Pressure (kbar)	References
$M_4R_6Si_6O_{24}(OH)_2$ (M = Ba, Ca, Sr, Pb, Mn; R = La, Nd, Sm, Gd, Dy, Y)	H ₂ O	500–700	2.0	[18.269]
MPbSiO ₄ (M = Mn, Fe, Co, Ni, Zn, Mg, Cd, Be)	H ₂ O	300–500	2.0	[18.270]
MBe ₂ Si ₂ O ₇ (M = Ba, Sr, Pb)	H ₂ O	450–750	1.5–3.0	[18.271]
Na ₂ Be ₂ Si ₆ O ₁₄	NaOH	400–600	1.5–3.0	[18.272]
Na ₂ BeSi ₂ O ₆	NaOH, H ₂ O	400–600	–	[18.272]
Ca ₂ MgSi ₂ O ₇	H ₂ O	798	4.06	[18.273]
Na ₂ TiZnSiO ₇	NaOH	350–550	> 3.0	[18.274]
Ba ₂ TiSi ₂ O ₈	Ba(OH) ₂	200–500	> 2.0	[18.275]
Li ₄ Sn ₂ Si ₁₂ O ₃₀	LaOH	500–600	> 2.0	[18.276]
K ₂ SnSi ₃ O ₉	KOH	400–650	> 1.5	[18.277]
RbFeSi ₃ O ₈	RbOH	480	1.6	[18.278]
K ₂ CeSi ₆ O ₁₅	KOH	450	2.0	[18.279]
K ₃ NdSi ₆ O ₁₅	KOH + K ₂ CO ₃	400–600	2.0	[18.280]
K(Mn,Fe) ₂ (Zn,Mn) ₃ Si ₁₂ O ₃₀	KOH + KCl	580–600	0.8	[18.281]
K ₂ Mn ₂ Zn ₂ Si ₄ O ₁₅	KOH + KCl + MnCl ₂	580–600	0.8	[18.282]
FeMgAl ₄ Si ₂ O ₁₀ (OH) ₄	H ₂ O	650	9.2	[18.283]
Na ₂ MnZn(SiO ₃ OH) ₂ (OH) ₂	NaOH	450	> 0.5	[18.284]
Na ₄ Fe ₁₀ Ti ₂ Si ₁₂ O ₄₀	H ₂ O	700	1.0	[18.285]
Na ₃ CaMg ₂ Si ₈ O ₂₂ (OH) ₂	Na ₂ CO ₃	400–970	0.1–0.8	[18.286]
LiAlSi ₂ O ₆ · H ₂ O	H ₂ O	300–350	2.0	[18.287]
Na ₈ SnSi ₆ O ₁₈	NaOH	600	1.0	[18.288]
K ₂ ZrSi ₂ O ₇	KOH	310	0.5–1.0	[18.289]
RERE/SiO ₅ (RE = La, Ce, Pr, Sm)	NaOH + HCl	135–700	1.0	[18.290]
K ₂ ZrSi ₃ O ₈	KOH	350–450	0.5	[18.291]
(Na ₂ Ca)ZrSi ₃ O ₉ · H ₂ O	Na ₂ CO ₃	350–530	–	[18.292]
PbCa ₂ Si ₃ O ₉	H ₂ O	350	2.0	[18.293]
KLi ₂ AlSi ₄ O ₁₀ F ₂	H ₂ O	400–670	2.0–5.0	[18.294]
K ₃ Li ₃ Al ₃ Si ₆ O ₂₀ (F,OH) ₄	H ₂ O	400–670	2.0–5.0	[18.295]
<i>Sodalite</i>				
Mica	KOH, K ₂ CO ₃ , KHCO ₃	–	–	
Na ₈ Al ₆ Si ₆ O ₂₄ (OH) ₂ · nH ₂ O	NaOH	200–450	0.5	[18.296]
Na ₂ MgSiO ₄	NaOH	700	3.0	[18.297]
Na ₄ Zr ₂ Si ₃ O ₁₂	NaOH	600	3.0	[18.298]
NaAlSiO ₄ , Na ₂ Zn ₂ Si ₂ O ₇ , Na ₂ ZnSi ₃ O ₈ , Na ₂ ZnSiO ₄ , Na ₂ Mn ₂ Si ₂ O ₇	NaOH, NaOH + Na ₂ CO ₃	375–450	1.0–2.0	[18.299]
<i>Germanates</i>				
MGeO ₄ (M = Zr, Hf, U)	H ₂ O	150–300	1.0	[18.300]
Al ₂ GeO ₅	H ₂ O	400–700	0.5	[18.301]
Pb ₃ GeO ₅	KOH	450–500	0.6–1.2	[18.302]
Sb ₂ Ge ₂ O ₇	KF	400–550	0.6–1.2	[18.303]
Sb ₄ Ge ₃ O ₁₂	K ₂ CO ₃	450–550	0.6–1.2	[18.304]

Table 18.10 (continued)

Compound	Mineralizer(s)	Temperature (°C)	Pressure (kbar)	References
Bi ₄ Ge ₃ O ₁₂	NaOH	350–450	0.6–0.8	[18.305]
CaGeO ₃	H ₂ O	150–450	0.8–1.8	[18.306]
SrGeO ₃	NaOH	300–600	> 1.0	[18.307]
Mg ₅ GeO ₆ (OH) ₂	H ₂ O	470–570	> 0.3	[18.308]
Y ₂ GeO ₆ (OH,F) ₄	KF	450	1.5	[18.309]
Yb ₄ Ge ₃ O ₉ (OH,F) ₄	KF	450	1.0	[18.310]
Er ₄ Ge ₃ O ₉ (OH,F) ₄	CsF	450	0.6	[18.311]
M ₆ Ge ₄ O ₁₀ (OH) ₄ (M = Na, Li, Rb, K, Cs)	H ₂ O	180–500	0.1	[18.312]
Na ₂ LaGe ₄ (OH)	NaOH	450	1.0	[18.313]
Na ₂ TiGeO ₅ , Na ₂ Zn ₂ TiGeO ₇	NaOH	400–550		[18.314]
Na ₃ ZrHGe ₂ O ₈	NaOH	500	1.2–2.0	[18.315]
Na ₂ ZrGeO ₅ , Na ₂ ZrGe ₂ O ₇ , Na ₄ Zr ₂ Ge ₃ O ₁₂ , Na ₂ BeSiO ₂	NaOH	450–500	1.0	[18.316]
KAlGe ₂ O ₆ , NaFeGe ₂ O ₆	KOH, NaOH	450	1.0	[18.317]
NaAlGe ₃ O ₉	H ₂ O	800	10.0	[18.318]
AgAlGe ₃ O ₈	H ₂ O + O ₂	600	1.5	[18.319]
TiAlGe ₃ O ₈	H ₂ O	1000	2.5	[18.319]
MAlGe ₃ O ₈ (M = Li, Na, K, Rb, Cs)	H ₂ O	800–900	13.0–25.0	[18.319]
Na ₆ Sn ₄ Ge ₅ O ₂₀ (OH) ₂		450	1.0	[18.320]
Na ₂ SnGe ₂ O ₆ (OH) ₂		450	0.5	[18.321]
Na ₃ REGe ₂ O ₇ (RE = La, Nd, Eu)		800	1.5	[18.322]
Y ₇ Ge ₂ O ₁₂ (F,OH) ₅ , Sm ₄ Ge ₃ O ₉ (OH) ₆ , Y ₄ GeO ₆ (OH,F) ₄ , Nd ₄ GeO ₈ , Yb ₂ Ge ₂ O ₇ , RE ₃ GeO ₅ (OH) ₃ (RE = Gd, Sm, Dy, Er)	KF, CsOH, RbOH, NaOH	450–500	1.5–2.0	[18.323]
<i>Phosphates</i>				
AlPO ₄	H ₃ PO ₄ , H ₂ SO ₄ , HCl, HCOOH	150–300	0.03–0.2	[18.324]
ABO ₄ (A = Fe, Bi, Mn, Cr, Al, B; B = P, V, As)	NaOH, H ₃ PO ₄	200–900	0.03–50.0	[18.325, 326]
Ce(HPO ₄) ₂ · 33H ₂ O	H ₃ PO ₄	160	–	[18.327]
CuTi ₂ (PO ₄) ₃	H ₃ PO ₄	500	3.0	[18.328]
RbNbOPO ₄	H ₃ PO ₄	600	1.8	[18.329]
Cu ₃ (PO ₄) ₂ · H ₂ O	H ₃ PO ₄ + H ₂ O	220	–	[18.330]
NH ₄ Zr ₂ (PO ₄) ₃	NH ₄ Cl	250–300	0.1	[18.331]
(H ₃ O)Zr ₂ (PO ₄) ₃	H ₂ O	200	< 0.1	[18.332]
KMnO ₂ · O(PO ₄)(H ₃ PO ₄)	H ₂ O	400	3.0	[18.333]
NdP ₅ O ₁₄ , TmP ₅ O ₁₄	H ₃ PO ₄ , HCl + H ₃ PO ₄	240–300	0.05–0.1	[18.334]
MREP ₄ O ₁₂ (M = Le, Na, K, Rb, Cs; RE = La–Nd)	H ₃ PO ₄	300–500	0.1–0.5	[18.335]
(Na _{2/3} Zr _{1/3}) ₂ P ₂ O ₇	H ₃ PO ₄ + HCl	250	< 0.01	[18.336]
Na ₂ H ₃ Al(P ₂ O ₇) ₂	H ₃ PO ₄	200–250	0.01	[18.337]

Table 18.10 (continued)

Compound	Mineralizer(s)	Temperature (°C)	Pressure (kbar)	References
NaHMP ₂ O ₇ (M = Ni, Co)	H ₃ PO ₄	200–250	0.01	[18.338]
KH ₂ MoPO ₇	H ₃ PO ₄	180	< 0.01	[18.339]
NaH ₂ (MoO) ₂ (PO ₄) ₃ · $\frac{1}{2}$ H ₂ O	H ₃ PO ₄	600	1.8	[18.340]
KTP	K ₂ HPO ₄ + KPO ₃	425–600	10 kpsi	[18.53]
<i>Vanadates</i>				
TMAV ₃ O ₇ , TMAV ₄ O ₁₀	TMAOH, LiOH	200	Auts.	[18.174, 341–343]
TMAV ₈ O ₁₀		–	–	
Li _x V _{2–δ} O _{4–δ}		–	–	
R:MVO ₄ (R = Nd, Er, Eu; M = Y, Gd)		–	–	
γ-LiV ₂ O ₅		–	–	
<i>Borates</i>				
Zn ₄ B ₆ O ₁₂	NaOH	500	2.4	[18.344]
Li ₂ B ₄ O ₇	HCl	250	0.12	[18.345]
Li ₃ B ₅ O ₈ (OH) ₂	–	–	–	[18.346]
REBO ₃ (RE = Sm, Er, Gd, Eu, Tm, Yb)	1.4 Butanediol	315	Auts.	[18.347]
LiBO ₂ , LiZnBO ₃	NaOH, KOH	> 300	1.0	[18.344]
LiH ₂ B ₅ O ₉	HCOOH	> 240	0.01	[18.348]
<i>Carbonates</i>				
MCO ₃ (M = Ca, Mg, Sr, Ba)	NH ₄ Cl, LiCl, H ₂ CO ₃ , HNO ₃	200–450	0.6–0.8	[18.139]
<i>Chalcogenides</i>				
Cu ₉ S ₅ , Ag ₂ S		180–343	0.01–0.15	[18.349]
Cu ₂ S		312	0.01	[18.350]
α-MnS	Thiourea, benzene	100–200	–	[18.351]
PbS	Toluene	220	Auts.	[18.352]
MoS ₂	C ₂ H ₄ NS + NH ₃	160–195	Auts.	[18.353]
Ag ₂ Se		180–343	0.01–0.5	[18.354]
MSe (M = Zn, Cd, Hg, Co, Pb)		180–500	0.01–1.5	[18.355]
MTe (M = Zn, Cd, Pb, Hg, Co)		180–400	0.05–2.0	[18.356]
MS (M = Cu, Zn, Hg, Pb, Fe, Cd, Mn, Co, Ni)		190–640	0.05–2.0	[18.357]
Bi ₂ Se, Sb ₂ Se		180–343	0.01–1.4	[18.355]
Sb ₂ Si ₃ , In ₂ Si ₃ , Bi ₂ S ₃		180–343	0.01–0.15	[18.358]
Bi ₂ Fe ₃ Sb ₂ Te ₃		180–343	0.01–0.15	[18.359]
AgMS ₂ (M = Bi, Ga, In, Sb, Be)		180–343	0.01–0.15	[18.358]
CuMS ₂ (M = Ga, In, Fe)		–	–	
Cu ₈ MS ₆ , M = Ge, Sb		312	0.1	[18.350]
CuInTe ₂		265–343	0.05–0.15	[18.360]
Cu ₆ ZnAs ₂ S ₇ , Cu ₆ FeAs ₂ S ₇		180–343	0.01–0.05	[18.361]
AX (A = Cd, Pb, Zn, In; X = S, Se, Te)	Ethylenediamine	150–200	Auts.	[18.204–206]
<i>Titanates</i>				
PbTiO ₃ , PbTi ₃ O ₇ , PbZrO ₃	KF	450–700	0.8–3.0	[18.362]
MTiO ₃ (M = Ca, Co, Mn, Ba, Sr)	NaOH, KOH, KF	200–700	0.3–2.0	

Table 18.10 (continued)

Compound	Mineralizer(s)	Temperature (°C)	Pressure (kbar)	References
Na ₂ Ti ₂ O ₅ , Na ₂ Ti ₆ O ₁₃ , Na ₂ Ti ₃ O ₇ , Na ₂ Ti ₃ O ₇ · H ₂ O	NaOH, HCl, HCOOH	200–500	0.08–3.0	[18.363,364]
<i>Molybdates</i>				
MMoO ₄ (M = Cd, Sr, Pb, Ba)	NH ₄ Cl, NaOH, KOH	350–500	–	[18.365]
KLn(MoO ₄) ₂ (Ln = La – Yb)	K ₂ MoO ₄	525–600	–	[18.366]
K ₅ Ln(MoO ₄) (Ln = La – Yb)		–	–	
Ln ₂ MoO ₆ (Ln = Pr – Er)		–	–	
<i>Tungstates</i>				
MWO ₄ (M = Ba, Sr, Cd)	NH ₄ Cl	450	–	[18.365]
Li ₂ Fe(WO ₄) ₂	LiCl + Na ₂ WO ₄	575–600	1.0–1.5	[18.367]
MLn(WO ₄) ₂	LiCl, KCl, NH ₄ Cl	400–720	1.2–1.7	[18.368,369]
LnWO ₄ · OH (M = Li, Na, K, NH ₄ ; Ln = Ce, Pr, Nd)	LiCl + NH ₄ Cl	–	–	[18.366]
<i>Niobates, tantalates, arsenates, gallates, etc.</i>				
ABO ₄ (A = Al, Fe, Ga, B, Bi; B = P, V, As)	NaOH, NaF, KF, HBr, HI	> 500	2.0	[18.370]
LiNbO ₃	LiOH	650	2.0	[18.371]
LiGaO ₂	NaOH	360–420	–	[18.372]
Gd ₃ Ga ₅ O ₁₂	NaOH, Na ₂ CO ₃ , K ₂ CO ₃	350–605	1.5	[18.252]
Potassium titanyl arsenate (KTA)	KOH	590	1.8	[18.373]
<i>Chlorides, bromides, fluorides</i>				
Fe ₆ O ₁₁ Cl ₂ , TeOCl ₂ , CuBr, PbBr,	HCl, HBr, HI	100–200	0.1	[18.370]
AREF ₄ , AREF ₆ , A ₂ REF ₅ (A = Li, Na, K, Rb, Cs; RE = Nd, Sm, Eu, Gd, Tb, Yb, Ho, Y)	KF, H ₂ O	450–500	Auts.	[18.374]
<i>Nitrides</i>				
AlN, GaN, InN	Toluene, THF, trioctylamine NH ₃ + NH ₄ Cl, NH ₃ + NH ₄ Br, NH ₃ + NH ₄ I, (or admixture of all)	265–290 360–550	Auts. 1.4	 [18.375,376]
<i>Miscellaneous</i>				
α-ZrP	H ₃ PO ₄ , H ₂ O	120–280	Auts.	[18.377]
β-TiP	H ₃ PO ₄	300	Auts.	[18.378]

References

- 18.1 K. Byrappa, M. Yoshimura: *Handbook of Hydrothermal Technology* (Noyes, New York 2001)
- 18.2 M. Yoshimura, K. Byrappa: *J. Mater. Sci.* **43**, 2085–2103 (2007)
- 18.3 K. Byrappa, S. Ohara, T. Adschiri: *Adv. Drug Del. Rev.* **60**, 299–327 (2007)
- 18.4 K. Byrappa (Ed.): *Hydrothermal growth of crystals*, *Prog. Cryst. Growth Charact. Mater.* **21**, 1–365 (1990)

- 18.5 K. Byrappa: Hydrothermal processing of advanced materials. In: *Kirk-Othmer Encyclopedia of Chemical Technology* (Wiley, London 2005)
- 18.6 K. Byrappa, T. Adschiri: Prog. Cryst. Growth. Character. Mater. **53**, 117–166 (2007)
- 18.7 K. Byrappa: Hydrothermal growth of crystals. In: *Handbook of Crystal Growth*, Vol. 2, ed. by D.T.J. Hurle (Elsevier, Amsterdam 1994) p. 465
- 18.8 K.F.E. Schafthaul: Gelehrte Anz. Bayer. Akad. **20**, 557 (1845)
- 18.9 R. Bunsen: Bemerkungen zu einigen Einwüfen gegen mehrere Ansichten über die chemisch-geologischen Erscheinungen in Island, *Annalen* **65**, 70 (1848)
- 18.10 F. Wöhler: *Annalen* **65**, 80 (1848), cited by R. Bunsen
- 18.11 H. De Senarmont: *Ann. Chim. Phys.* **32**, 142 (1851)
- 18.12 M. Daurree: *Ann. Mines* **12**, 289 (1857)
- 18.13 H.E. Saint-Claire Deville: *Ann. Chim. Phys.* **61**, 309–314 (1857)
- 18.14 K. von Chrustschoff: *Am. Chem.* **3**, 281 (1873)
- 18.15 J.B. Hannay: *Proc. R. Soc. Lond.* **30**, 178–189 (1880)
- 18.16 R. Moissan: *Experimental Petrology, Basic Principles and Techniques* (Clarendon, Oxford 1973) p. 5, cited by A.D. Edgar
- 18.17 C. Friedel, E. Sarasin: *C. R.* **92**, 1374–1378 (1881)
- 18.18 C. Friedel: *Bull. Soc. Min.* **14**, 7–10 (1891)
- 18.19 G. Spezia: *Atti. Accad. Sci. Torino* **35**, 95–107 (1900)
- 18.20 G. Spezia: *Atti. Accad. Sci. Torino* **40**, 254–262 (1905)
- 18.21 G.W. Morey, P. Niggli: *J. Am. Chem. Soc.* **35**, 1086–1130 (1913)
- 18.22 G.W. Morey: *J. Am. Ceram. Soc.* **36**, 279–285 (1953)
- 18.23 C. Barus: *Am. J. Sci.* **6**, 270 (1898)
- 18.24 R. Nacken: *Chem. Z.* **74**, 745–749 (1950)
- 18.25 R. Nacken: Captured German Reports RDRC/13/18 (1946)
- 18.26 R. Nacken: US Office of Technical Services Reports PB-6948 (1946)
- 18.27 K. Nassau: *J. Cryst. Growth* **35**, 211–222 (1976)
- 18.28 A.A. Shternberg: private communication (Moscow 1981, 1982)
- 18.29 J. Asahara, K. Nagai, S. Harada: Synthetic crystals by large autoclaves – The reality and characterization, Proc. 1st Int. Symp. Hydrotherm. React., ed. by S. Somiya (Gakujutsu Bunkens Fukyu-Kai 1982) pp. 430–441
- 18.30 E.U. Franck: Survey of selected non-thermodynamic properties and chemical phenomena of fluids and fluids mixtures. In: *Chemistry and Geochemistry of Solutions at High Temperatures and Pressure*, Proc. Nobel Symp., Vol. 13/14, ed. by D.T. Rickard, F.E. Wickman (Pergamon, New York 1979) pp. 65–88
- 18.31 T.M. Seward: Metal complex formation in aqueous solutions at elevated temperatures and pressures. In: *Chemistry and Geochemistry of Solutions at High Temperatures and Pressure*, Proc. Nobel Symp., Vol. 13/14, ed. by D.T. Rickard, F.E. Wickman (Pergamon, New York 1979) pp. 113–132
- 18.32 H.C. Helgeson: Prediction of the thermodynamic properties of electrolytes at high pressures and temperatures. In: *Chemistry and Geochemistry of Solutions at High Temperatures and Pressure*, Proc. Nobel Symp., Vol. 13/14, ed. by D.T. Rickard, F.E. Wickman (Pergamon, New York 1979), pp. 133–178
- 18.33 K.S. Pitzer: Characteristics of very concentrated aqueous solutions. In: *Chemistry and Geochemistry of Solutions at High Temperatures and Pressure*, Proc. Nobel Symp., Vol. 13/14, ed. by D.T. Rickard, F.E. Wickman (Pergamon, New York 1979) pp. 249–272
- 18.34 S. Somiya (Ed.): Hydrothermal reactions, Proc. 1st Int. Symp. Hydrotherm. React. (Gakujutsu Bunkens Fukyu-Kai, 1982) pp. 430–441
- 18.35 R.A. Laudise, J.W. Nielsen: *Solid State Phys.* **12**, 149 (1961)
- 18.36 V.A. Klipov, N.N. Shmakov: Influence of convective flow on the growth of quartz crystals, Proc. 45th Annu. Symp. Freq. Control, IEEE (New York 1991) p. 29
- 18.37 A.B. Ezersky, A. Garcimartin, J. Burguete, H.L. Mancini, C. Pérez-García: *Phys. Rev. E* **47**, 1126–1131 (1993)
- 18.38 A.B. Ezersky, A. Garcimartin, H.L. Mancini, C. Pérez-García: *Phys. Rev. E* **48**, 4414–4422 (1993)
- 18.39 B. Roux, O. Louchart, O. Terhmina: *J. Phys. (France)* **4(C)**, 2–3 (1994)
- 18.40 Q.S. Chen, V. Prasad, A. Chatterjee: Modelling of fluid flow and heat transfer in a hydrothermal crystal growth system, Proc. Am. Soc. Mech. Eng. Heat Transf. Div. (1998) p. 119, HTD 361–4
- 18.41 Q.S. Chen, V. Prasad, A. Chatterjee, J. Larkin: *J. Cryst. Growth* **198/199**, 710 (1999)
- 18.42 E.A. Evans, H. Li, G.-X. Wang: Bulk flow of solution in an autoclave for crystal growth, Proc. CD IMECE 2001 (New York 2001), Paper No. HTD 24342
- 18.43 H. Li, E.A. Evans, G.-X. Wang: *J. Cryst. Growth* **256**, 146–155 (2003)
- 18.44 H. Li, G.-X. Wang, E.A. Evans: *J. Cryst. Growth* **271**, 257–267 (2004)
- 18.45 H. Li, E.A. Evans, G.-X. Wang: *J. Cryst. Growth* **275**, 561–571 (2005)
- 18.46 R.-U. Barz, M. Grassl: *J. Cryst. Growth* **249**, 345–353 (2003)
- 18.47 V.N. Popov, Y.S. Tsivinskaya, T.B. Bekker, K.A. Kokh, A.E. Kokh: *J. Cryst. Growth* **289**, 652–658 (2006)
- 18.48 M.M. Lencka, R.E. Riman: Thermodynamics of multicomponent perovskite synthesis in hydrothermal solution. In: *Handbook of Crystal Growth Technology*, ed. by K. Byrappa, T. Ohashi (Springer, Berlin Heidelberg 2003) p. 271
- 18.49 B. Gersten: Growth of multicomponent perovskite oxide crystals: Synthesis conditions of the hydrothermal growth of ferroelectric powders. In:

- Handbook of Crystal Growth Technology*, ed. by K. Byrappa, T. Ohashi (Springer, Berlin Heidelberg 2003) p. 299
- 18.50 R.E. Riman, W.L. Suchanek, K. Byrappa, C.W. Chen, P. Shuk, C.S. Oakes: *Solid State Ion.* **151**, 393 (2002)
- 18.51 O.V. Dimitrova: Investigations of the phase formations in the system $\text{Na}_2\text{O}-\text{RE}_2\text{O}_3-\text{SiO}_2-\text{H}_2\text{O}$ under hydrothermal conditions. Ph.D. Thesis (Moscow State University, Moscow 1975)
- 18.52 K. Byrappa, J.R. Paramesha: *Mater. Sci. Forum* **315–317**, 514–518 (1999)
- 18.53 R.A. Laudise, W.A. Sunder, R.F. Belt, G. Gashurov: *J. Cryst. Growth* **102**, 427–433 (1990)
- 18.54 R.A. Laudise, A.A. Ballman, J.C. King: *J. Phys. Chem. Solids* **26**, 1305 (1965)
- 18.55 E.U. Franck: *Pure Appl. Chem.* **24**, 13–30 (1970)
- 18.56 R.C. Weast (Ed.): *Handbook of Physics and Chemistry*, 64th edn. (CRC, Boca Raton 1983)
- 18.57 H.C. Helgeson: *Phys. Chem. Earth* **13/14**, 133 (1981)
- 18.58 J.B. Hasted, D.M. Ritson, C.H. Collie: *J. Chem. Phys.* **16**, 1 (1948)
- 18.59 M. Uematsu: Phase equilibria and static properties. In: *Supercritical Fluids – Molecular Interaction, Physical Properties, and New Applications*, Springer Series in Materials Processing, ed. by Y. Arai, T. Sako, Y. Takebayashi (Springer, Berlin Heidelberg 2002) p. 71
- 18.60 E.U. Franck: *Int. Corros. Conf. Ser.*, 109 (1973)
- 18.61 G.C. Kennedy: *Am. J. Sci.* **248**, 540–543 (1950)
- 18.62 S.D. Haman: *Phys. Chem. Earth* **13/14**, 89 (1981)
- 18.63 K. Todheide: *Ber. Bunsenges. Phys. Chem.* **86**, 1005 (1982)
- 18.64 E.D. Kolb, P.L. Key, R.A. Laudise, E.E. Simpson: *Bell Syst. Tech. J.* **61**, 639 (1983)
- 18.65 W.L. Marshall, E.V. Jones, J. Jones: *Inorg. Nucl. Chem.* **36**, 2313 (1974)
- 18.66 A.A. Shternberg: Controlling the growth of crystals in autoclaves. In: *Crystallization Processes Under Hydrothermal Conditions*, ed. by A.N. Lobachev (Consultants Bureau, New York 1973) pp. 225–240
- 18.67 L.N. Demianets, E.N. Emelyanova, O.K. Melnikov: Solubility of sodalite in aqueous solutions of NaOH under hydrothermal conditions. In: *Crystallization Processes Under Hydrothermal Conditions*, ed. by A.N. Lobachev (Consultants Bureau, New York 1973) pp. 125–150
- 18.68 G.W. Morey, J.M. Hesselgesser: *Am. J. Sci.*, 367 (1952)
- 18.69 R.A. Laudise: *J. Am. Chem. Soc.* **81**, 562 (1959)
- 18.70 R.A. Laudise: Hydrothermal growth of crystals. In: *Progress in Inorganic Chemistry*, Vol. 3, ed. by F.A. Cotton (Wiley, New York 1962)
- 18.71 D.J. Marshall, R.A. Laudise: Crystal growth by hydrothermal technique. In: *Crystal Growth*, ed. by H.S. Peiser (Pergamon, New York 1966) p. 557
- 18.72 N.Y. Ikornikova, A.N. Lobachev, A.R. Vasenin, V.M. Egrov, A.V. Autoshin: Apparatus for precision research in hydrothermal experiments. In: *Crystallization Processes Under Hydrothermal Conditions*, ed. by A.N. Lobachev (Consultants Bureau, New York 1973) p. 241
- 18.73 J.B. Hannay, J. Hogarth: *Proc. R. Soc. Lond.* **30**, 178 (1880)
- 18.74 M. Hosaka, S. Taki: *J. Cryst. Growth* **100**, 343 (1990)
- 18.75 R.A. Laudise, A.A. Ballman: *J. Phys. Chem.* **65**, 1396–1400 (1961)
- 18.76 V.M. John, S. Kordes: *Chem. Earth* **70**, 75–89 (1953)
- 18.77 J.M. Stanley: *Ind. Eng. Chem.* **468**, 1684–1689 (1954)
- 18.78 K. Byrappa, V. Venkatachalapathy, B. Puttaraju: *J. Mater. Sci.* **19**, 2855–2862 (1984)
- 18.79 M. Cochez, A. Ibanez, A. Goiffon, E. Philippot: *Eur. J. Solid State Ionorg. Chem.* **30(55)**, 509–519 (1993)
- 18.80 O.V. Zvereva, M.Y. Mininon, L.N. Demianets: *J. Phys. (France)* **4(C2)**, 19–24 (1994)
- 18.81 P. Yot, O. Cambon, D. Balitsky, A. Goiffon, E. Philippot, B. Capelle, J. Detaint: *J. Cryst. Growth* **224**, 294–302 (2001)
- 18.82 R.-U. Barz, M. Grassl, P. Gille: *J. Cryst. Growth* **245**, 273–277 (2002)
- 18.83 O.Y. Samoilov: *The Structure of Aqueous Solutions and the Hydration of Ions* (Akademy Nauk, Moscow 1957)
- 18.84 V.A. Kuznetsov: *Sov. Phys. Crystallogr.* **12**, 608–611 (1968)
- 18.85 S. Kaneko, F. Imoto: *Nippon Kagaku Kaishi* **6**, 985–990 (1975)
- 18.86 N.A. Ovramenko, L.I. Shvets, F.D. Ovcharenko, B.Y. Kornilovich: *Izv. Akad. Nauk USSR, Inorg. Mater.* **15**, 1982–1985 (1979)
- 18.87 W. Hertl: *J. Am. Ceram. Soc.* **71**, 879–883 (1988)
- 18.88 M.M. Lencka, R.E. Riman: *Chem. Mater.* **53**, 31–41 (1981), .
- 18.89 J.O. Eckert Jr., C.C. Hung-Houston, B.L. Gersten, M.M. Lencka, R.E. Riman: *J. Am. Ceram. Soc.* **79**, 2929–2939 (1996)
- 18.90 S. Komarneni: Enhanced reaction kinetics under microwave-hydrothermal conditions, *Proc. 2nd Int. Conf. Solvotherm. React.* (Takamatsu 1996) pp. 97–100
- 18.91 S.H. Zhung, J.H. Lee, P.M. Forster, G. Ferey, A.K. Cheetham, J.S. Chang: *Chem. Eur. J.* **12**, 7899–7905 (2006)
- 18.92 V.I. Popolitov: *Hydrotherm. Growth Crystals Prog. Cryst. Growth Charact. Mater.* **21**, 255–297 (1990)
- 18.93 B.N. Litvin, D.A. Tules: Apparatus for hydrothermal synthesis and growth of monocrystals. In: *Crystallization Process under Hydrothermal Conditions*, Studies in Soviet Science, ed. by A.N. Lobachev (Consultant Bureau, New York 1973), p.139
- 18.94 R.A. Laudise, E. Kaldis (Ed.): *Crystal Growth of Electronic Materials* (Elsevier, Amsterdam 1985) p.159
- 18.95 Leco Catalogue, Tem-Press Research Division, (Bellefonte, Pennsylvania 2005)
- 18.96 R. Roy, E.F. Osborn: *Econ. Geol.* **47**, 717–721 (1952)
- 18.97 T. Adschiri, K. Arai: Hydrothermal synthesis of metal oxide nanoparticles under supercritical con-

- ditions. In: *Supercritical Fluid Technology in Materials Science and Engineering*, ed. by Y.-P. Sun (Marcel Dekker, New York 2002) pp. 311–325
- 18.98 E. Reverchon, R. Adam: *J. Supercrit. Fluids* **37**, 1–22 (2006)
- 18.99 M. Goto (Ed.): *Proc. 8th Int. Symp. Supercrit. Fluids* (Kyoto 2006)
- 18.100 Catalogue of M/s Berghof, Germany; M/s Nit-tokoatsu, Japan
- 18.101 A.C. Walker: *Ind. Eng. Chem.* **36**, 250–256 (1953)
- 18.102 M. Hosaka, S. Taki: *J. Cryst. Growth* **52**, 837 (1981)
- 18.103 F. Lafon, G. Demazeau: *J. Phys. (France)* **4**(C2), 177–182 (1994)
- 18.104 R.A. Laudise, A.A. Ballman, J.C. King: *J. Phys. Chem. Solids.* **26**, 1305–1308 (1965)
- 18.105 R.A. Laudise: Hydrothermal crystal growth – some recent results. In: *Advanced Crystal Growth*, ed. by P.M. Dryburgh, B. Cockayne, K.G. Barraclough (Prentice Hall, New York 1987) pp. 267–288
- 18.106 R.A. Laudise, R.A. Sullivan: *Chem. Eng. Prog.* **55**, 55–59 (1959)
- 18.107 R.L. Barns, E.D. Kolb, R.A. Laudise, E.E. Simpson, K.M. Kroupa: *J. Cryst. Growth* **34**, 189–197 (1976)
- 18.108 X. Buisson, R. Arnaud: *J. Phys. (France)* **4**(C2), 25–32 (1994)
- 18.109 A.A. Ballman, R.A. Laudise: Solution growth. In: *Art and Science of Growing Crystals*, ed. by J.J. Gilman (Wiley, New York 1963) p. 231
- 18.110 J.J. Martin, A.F. Armington: *J. Cryst. Growth* **62**, 203–206 (1983)
- 18.111 A.F. Armington, J.J. Larkin: *J. Cryst. Growth* **71**, 799 (1985)
- 18.112 M. Hosaka, T. Miyata: *Mater. Res. Bull.* **28**, 1201–1208 (1993)
- 18.113 G.R. Johnson, R.A. Irvine, J.W. Foise: A parametric study of the variables involved in quartz growth, *IEEE Proc. 44th Annu. Symp. Freq. Control* (1990) pp. 216–221
- 18.114 M. Deleuze, O. Cambon, A. Goiffon, A. Ibanez, E. Philippot: *J. Phys. (France)* **4**(C2), 79–84 (1994)
- 18.115 K. Bräuer, E. Müller: *Cryst. Res. Technol.* **19**, 101–109 (1984)
- 18.116 O. Cambon, M. Deleuze, J.P. Michel, J.P. Aubry, A. Goiffon, E. Philippot: *J. Phys. (France)* **4**(C2), 85–91 (1994)
- 18.117 H. Iwasaki, F. Iwasaki, E.A. Marina, L.V. Balitskaya: Process for producing unsintered cristobalite silica, US Patent 4853198 (1989)
- 18.118 H. Iwasaki, F. Iwasaki, V.S. Balitsky, L.V. Balitskaya: *J. Cryst. Growth* **187**, 481 (1998)
- 18.119 H. Iwasaki, F. Iwasaki, M. Kurashige, K. Oba: *J. Cryst. Growth* **234**, 711 (2002)
- 18.120 Z.P. Chang, G.R. Barsch: *IEEE Trans. Sonics Ultrasonics* **23**, 127 (1976)
- 18.121 R.M. O'Connell, P.H. Corr: Temperature compensated cuts of berlinite and β -eucryptite: for saw devices, *Proc. 31st Annu. Freq. Control Symp.* (1977) pp. 182–186
- 18.122 E.D. Kolb, A.M. Glass, R.L. Rosenberg, J.C. Grenier, R.A. Laudise: Frequency dependence in quartz seed orientation, *Proc. 35th Ultrasonic Symp.* (New York 1981)
- 18.123 E. Philippot, D. Palmier, M. Pintard, A.A. Goiffon: *J. Solid State Chem.* **123**, 1–13 (1996)
- 18.124 K. Byrappa, S. Srikantaswamy: *Prog. Cryst. Growth. Charact. Mater.* **21**, 199 (1990)
- 18.125 M. Beaurain, P. Armand, P. Papet: *J. Cryst. Growth* **294**, 396–400 (2006)
- 18.126 B.H.T. Chai, M.L. Shand, I. Bucher, M.A. Gillee: Berlinite synthesis and SAW characteristics, *Proc. IEEE Ultrasonic Symp.* (1979) p. 557
- 18.127 V.I. Popolitov, I.M. Yaroslavskii: *Izv. Akad. Nauk USSR, Neorg. Mater.* **26**, 892 (1990)
- 18.128 I.M. Yaroshavskii, V.I. Popolitov: *Neorg. Mater. Izv. Akad. Nank SSSR* **26**, 1055–1059 (1990)
- 18.129 N. Prud'homme, D. Cachau-Herreillat, P. Papet, O. Cambon: *J. Cryst. Growth* **286**, 102–107 (2006)
- 18.130 D.V. Balitsky, E. Philippot, P. Papet, V.S. Balitsky, F. Pey: *J. Cryst. Growth* **275**, 887–894 (2005)
- 18.131 M. Haouas, F. Taulelle, N. Prud'homme, O. Cambon: *J. Cryst. Growth* **296**, 197–206 (2006)
- 18.132 W. Wallnofer, P.W. Krempel, F. Krispel, V. Willfurth: *J. Cryst. Growth* **198/199**, 487 (1999)
- 18.133 R.-U. Barz, M. Grassl, P. Gille: *J. Cryst. Growth* **237–239**, 843–847 (2002)
- 18.134 P. Hofmann, U. Juda, K. Jacobs: *J. Cryst. Growth* **275**, 1883–1888 (2005)
- 18.135 M. Grassl, R.-U. Barz, P. Gille: *Cryst. Res. Technol.* **37**, 531–539 (2002)
- 18.136 K. Jacobs, P. Hofmann, D. Klimm: *J. Cryst. Growth* **237–239**, 837–842 (2002)
- 18.137 D.R. Kinloch, R.F. Belt, R.C. Puttback: *J. Cryst. Growth* **24/25**, 610–613 (1974)
- 18.138 S. Hirano, K. Kikuta: *J. Cryst. Growth* **79**, 223–226 (1986)
- 18.139 N.Y. Ikornikova: *Hydrothermal Synthesis of Crystals in Chloride Systems* (Nauka, Moscow 1975) pp. 1–222, in Russian
- 18.140 S. Hirano, K. Kikuta: *J. Cryst. Growth* **94**, 351–356 (1989)
- 18.141 S. Hirano, T. Yogo, K. Kikuta, Y. Yoneta: *J. Ceram. Soc. Jpn.* **101**, 113–117 (1993)
- 18.142 K. Yanagisawa, Q. Feng, K. Ioku, N. Yamasaki: *J. Cryst. Growth* **163**, 285–294 (1996)
- 18.143 K. Yanagisawa, K. Kageyama, Q. Feng, I. Matsushita: *J. Cryst. Growth* **229**, 440–444 (2001)
- 18.144 V.N. Rummyantsev, I.G. Ganeev, I.S. Rez: Solubility of SiO_2 in alkali and carbonate solutions. In: *Crystal Growth*, Vol. 9 (Nauka, Moscow 1972) pp. 51–54
- 18.145 V.A. Kuznetsov, A.A. Shternberg: *Sov. Phys. Crystallogr.* **12**, 280–285 (1967)
- 18.146 R.L. Barus, R.A. Laudise, R.M. Shields: *J. Phys. Chem.* **67**, 835–840 (1963)
- 18.147 G. Yamaguchi, H. Yanagida, S. Sojma: *Bull. Soc. Chem. Jpn.* **35**, 1789–1791 (1962)

- 18.148 K.F. Kashkurov, P.I. Nikitichev, V.V. Osipov, L.D. Sizova, A.V. Simonov: *Sov. Phys. Crystallogr.* **12**, 837–839 (1968)
- 18.149 R.R. Monchamp, R.C. Puttbach, J.W. Nielson: *J. Cryst. Growth* **2**, 178 (1968)
- 18.150 R.A. Laudise, A.A. Ballman: *J. Am. Chem. Soc.* **80**, 2655–2657 (1958)
- 18.151 V.S. Balitsky, E.E. Lisinstina: *Synthetic Analogues and Imitation of Natural Gemstones* (Nedra, Moscow 1981)
- 18.152 P. Hautefeuille, A. Perrey: *C. R. Acad. Sci.* **106**, 1800–1810 (1888)
- 18.153 R. Webster: *Gems*, 3rd edn. (Newnes–Butterworths, London 1975)
- 18.154 M. Hosak: Hydrothermal Growth of Crystals, *Prog. Crystal Growth Charact.* **21**, 71–96 (1990)
- 18.155 B.W. Anderson: *Gem Testing*, 8th edn. (Butterworths, London 1971)
- 18.156 R.T. Liddicoat Jr.: *Handbook of Gem Identification*, 10th edn. (Gemmological Institute of America, Los Angeles 1975)
- 18.157 P.J. Yancey: Hydrothermal process for growing crystals having the structure of beryl in highly acid chloride medium, US Patent 3723337 (1973)
- 18.158 E.M. Flanigen: Hydrothermal process for growing crystals having the structure of beryl in an alkaline halide medium, US Patent 3567642 (1971)
- 18.159 E.M. Flanigen, N.R. Mumbach: Hydrothermal process for growing crystals having the structure of beryl in an acid halide medium, US Patent 3567643 (1971)
- 18.160 R.E. Kane, R.T. Liddicoat Jr.: *Gems Gemol.* **21**(3), 156 (1985)
- 18.161 K. Scarratt: *J. Gemmol.* **21**(5), 294 (1989)
- 18.162 K. Schmetzer: *J. Gemmol.* **21**(3), 145 (1988)
- 18.163 Z. Chen, G. Zhang, H. Shen, C. Huang: *J. Cryst. Growth* **244**, 339–341 (2002)
- 18.164 V.G. Thomas, S.P. Demin, D.A. Foursenko, T.B. Bekker: *J. Cryst. Growth* **206**, 203–214 (1999)
- 18.165 L.I. Tsinobar, I.G. Chentsova: *Kristallografiya* **4**, 633 (1959)
- 18.166 V.S. Balitsky, I.B. Machina, A.A. Marin, J.E. Shigley, G.R. Rossman, T. Lu: *J. Cryst. Growth* **212**, 255–260 (2000)
- 18.167 V.S. Balitsky: *J. Cryst. Growth* **41**, 100 (1977)
- 18.168 M. Hosaka, S. Taki: *J. Cryst. Growth* **64**, 572 (1983)
- 18.169 K. Nassau: *Gemstone Enhancement*, 2nd edn. (Butterworths, Boston 1994)
- 18.170 K. Byrappa, M.K. Devaraju, P. Madhusudan, A.S. Dayananda, B.V. Suresh Kumar, H.N. Girish, S. Ananda, K.M.L. Rai, P. Javeri: *J. Mater. Sci.* **41**, 1395 (2006)
- 18.171 B.C. Chakoumakos, M.M. Abraham, L.A. Batner: *J. Solid State Chem.* **109**, 197 (1994)
- 18.172 M. Prasad, A.K. Pandit, T.H. Ansari, R.A. Singh, B.M. Wanklyn: *Phys. Lett. A* **138**, 61 (1989)
- 18.173 B.H.T. Chai, G. Loutts, X.X. Chang, P. Hong, M. Bass, I.A. Shcherbakov, A.I. Zagumennyi: *Advanced Solid State Lasers, Technical Digest*, Vol. 20 (Optical Society of America, Washington 1994) p. 41
- 18.174 K. Byrappa, K.M.L. Rai, B. Nirmala, M. Yoshimura: *Mater. Sci. Forum* **506**, 315 (1999)
- 18.175 F.M. Levin: *J. Am. Ceram. Soc.* **50**, 381 (1967)
- 18.176 L.G. Vanuitret, R.C. Linares, R.R. Soden, A.A. Ballman: *J. Chem. Phys.* **36**, 702 (1962)
- 18.177 K. Byrappa, C. Ramaningaiiah, K. Chandrashekar, K.M.L. Rai, B. Basavalingu: *J. Mater. Sci.* **506**, 315 (1999)
- 18.178 K. Byrappa, B. Nirmala, K.M. Lokanatha Rai, M. Yoshimura: Crystal growth, size, and morphology control of Nd:RVO₄ under hydrothermal conditions. In: *Crystal Growth Technology*, ed. by K. Byrappa, T. Ohachi (Springer, Berlin, Heidelberg 2003) p. 335
- 18.179 H. Wu, H. Xu, Q. Su, T. Chen, M. Wu: *J. Mater. Chem.* **13**, 1223 (2003)
- 18.180 S. Erdei, B.M. Jin, F.W. Ainger: *J. Cryst. Growth* **174**, 328 (1997)
- 18.181 S. Erdei, M. Kilmkiewicz, F.W. Ainger, B. Keszei, J. Vandlik, A. Suveges: *Mater. Lett.* **24**, 301 (1995)
- 18.182 T. Mitsuda: *Ceram. Jpn.* **15**, 184 (1980)
- 18.183 S. Somiya: *J. Mater. Sci.* **41**, 1307 (2006)
- 18.184 K. Kajiyoshi, K. Tomono, Y. Hamaji, T. Kasanami, M. Yoshimura: *J. Am. Ceram. Soc.* **78**, 1521 (1995)
- 18.185 W.S. Cho, M. Yashima, M. Kakihana, A. Kudo, T. Sakata, M. Yoshimura: *J. Am. Ceram. Soc.* **80**, 765 (1997)
- 18.186 S. Ohara, T. Mousavand, T. Sasaki, M. Umetsu, T. Naka, T. Adschiri: *J. Mater. Sci.* **41**, 1445 (2006)
- 18.187 T. Mousavand: Synthesis of organic–inorganic hybrid nanoparticles by in-situ surface modification under supercritical hydrothermal conditions. Ph.D. Thesis (Tohoku University, Sendai 2007)
- 18.188 M. Yoshimura, H. Suda, K. Okamoto, K. Ioku: *J. Mater. Sci.* **29**, 3399–3402 (1994)
- 18.189 S. Forster, M. Antonietti: *Adv. Mater.* **10**, 195 (1998)
- 18.190 Y. Zhu, H. Zheng, Y. Li, L. Gao, Z. Yang, Y.T. Qian: *Mater. Res. Bull.* **38**, 1829 (2003)
- 18.191 V.F. Puentes, K.M. Drishnan, A.P. Alivisatos: *Science* **291**, 2115 (2001)
- 18.192 Q. Xie, Z. Dai, W. Huang, J. Liang, C. Jiang, Y.T. Qian: *Nanotechnology* **16**, 2958 (2005)
- 18.193 Z. Tian, J. Liu, J.A. Voigt, H. Xu, M.J. Mcdermott: *Nano Lett.* **3**, 89 (2003)
- 18.194 O.V. Al'myasheva, E.N. Korytkova, A.V. Maslov, V.V. Gusarov: *Inorg. Mater.* **41**, 460 (2005)
- 18.195 X. Jiao, D. Chen, L. Xiao: *J. Cryst. Growth* **258**, 158 (2003)
- 18.196 M. Wu, Y. Xiong, Y. Jia, J. Ye, K. Zhang, Q. Chen: *Appl. Phys. A* **81**, 1355 (2005)
- 18.197 K. Byrappa, K.M.L. Rai, M. Yoshimura: *Environ. Technol.* **21**, 1085 (2000)
- 18.198 T. Adschiri, K. Kanazawa, K. Arai: *J. Am. Ceram. Soc.* **75**, 1019 (1992)
- 18.199 T. Adschiri, Y. Hakuta, K. Arai: *Ind. Eng. Chem. Res.* **39**, 4901 (2000)

- 18.200 M. Schur, H. Rijnberk, C. Nather: *Polyhedron* **18**, 101 (1998)
- 18.201 C.L. Cahill, B. Gugliotta, J.B. Parise: *Chem Commun.* **16**, 1715 (1998)
- 18.202 G.C. Guo, R.M.W. Kwok, T.C.W. Mak: *Inorg. Chem.* **36**, 2475 (1997)
- 18.203 W. Wang, Y. Geng, P. Yan, F. Liu, Y. Xie, Y. Qian: *J. Am. Chem. Soc.* **121**, 4062 (1999)
- 18.204 Y. Li, H. Liao, Y. Fan, Y. Zhang, Y. Qian: *Inorg. Chem.* **38**, 1382 (1999)
- 18.205 S. Yu, J. Yang, Z. Han, Y. Zhou, R. Yang, Y. Qian, Y. Zhang: *J. Mater. Chem.* **9**, 1283 (1999)
- 18.206 Y. Li, H. Liao, Y. Fan, L. Li, Y. Qian: *Mater. Chem. Phys.* **58**, 87 (1999)
- 18.207 Y. Li, F. Huang, Q. Zhang, Z. Gu: *J. Mater. Sci.* **35**, 5933 (2000)
- 18.208 C.E. Melto, A.A. Giardini: *Am. Mineral.* **59**, 775 (1974)
- 18.209 M. Schrauder, O. Navon: *Nature* **365**, 42 (1999)
- 18.210 O. Navon: *Nature* **353**, 746 (1991)
- 18.211 G.D.J. Guthrie, D.R. Veblen, O. Navon, G.R. Rossman: *Earth Planet Sci. Lett.* **105**, 1 (1991)
- 18.212 R.C. De Vries: Synthesis of diamond under metastable conditions, *Ann. Rev. Mater. Sci.* **17**, 161–187 (1987)
- 18.213 R.C. DeVries, R. Roy, S. Somiya, S. Yamada: *Trans. Mater. Res. Soc. Jpn. B* **14**, 641 (1994)
- 18.214 C.A. Eckert, B.L. Knutsan, P.G. Debenedetti: *Nature* **383**, 313 (1996)
- 18.215 Y.G. Gogotsi, K.G. Nickel, P.J. Kofstad: *Mater. Chem.* **5**, 2313 (1995)
- 18.216 R. Roy, D. Ravichandran, P. Ravindranathan, A. Badzian: *J. Mater. Res.* **11**, 1164 (1996)
- 18.217 Y.G. Gogotsi, P. Kofstad, M. Yoshimura, K.G. Nickel: *Diam. Rel. Mater.* **5**, 151 (1996)
- 18.218 B. Basavalingu, J.M. Calderon Moreno, K. Byrappa, Y.G. Gogotsi: *Carbon* **39**, 1763 (2001)
- 18.219 X. Zhang, H. Liu, W. He, J. Wang, X. Zi, R.I. Boughton: *J. Cryst. Growth* **275**, 1913 (2005)
- 18.220 S. Krupanidhi, C.N.R. Rao: *Adv. Mater.* **16**, 425 (2004)
- 18.221 B. Huang, J.M. Hong, X.T. Chen, Z. Yu, X.Z. You: *Mater. Lett.* **59**, 430 (2005)
- 18.222 Y. Zhang, H. Guan: *Mater. Res. Bull.* **40**, 1536 (2005)
- 18.223 U.K. Gautam, K. Sardar, F.L. Deepak, C.N.R. Rao: *Pramana* **65**, 549 (2005)
- 18.224 H. Xu, W. He, H. Wang, H. Yan: *J. Cryst. Growth* **260**, 447 (2004)
- 18.225 M. Cao, X. He, X. Wu, C. Hu: *Nanotechnology* **16**, 2129 (2005)
- 18.226 A. Rabenau, H. Rau: *Naturwissenschaften* **55**, 336 (1968)
- 18.227 J.F. Balasico, R.B. White, R. Roy: *Mater. Res. Bull.* **2**, 913 (1967)
- 18.228 L.N. Demianets: *Hydrothermal Synthesis of Crystals* (Nauka, Moscow 1968), in Russian
- 18.229 L.N. Demianets, L.S. Garashina, B.N. Litvin: *Kristallografiya* **8**, 800 (1963)
- 18.230 I.P. Kuzmina: *Geol. Ore Depos.* **6**, 101 (1963)
- 18.231 P. Hartman: *Phys. Status Solidi* **2**, 585 (1962)
- 18.232 D. Ehrentraut, H. Sato, Y. Kagamitani, H. Sato, A. Yoshikawa, T. Fukuda: *Prog. Cryst. Growth Character. Mater.* **52**, 280 (2006)
- 18.233 J. Bauer, P. Kaczerosky: *Vysok. Skola Chem.–Tech. Praxe G.* **12**, 153 (1970)
- 18.234 E. Prochazkova, D. Rykl, V. Seidl: *Czechoslovakian Patent* 170391 (1973), No. 5939–73
- 18.235 I.P. Kuzmina, B.N. Litvin: *Crystal Growth* **4**, 160 (1964)
- 18.236 C.J.M. Rooymans, W.F. Langenhoff: *J. Cryst. Growth* **3–4**, 411 (1968)
- 18.237 V.B. Glushkova: *Polymorphism of Rare Earth Oxides* (Nauka, Leningrad 1967), in Russian
- 18.238 I.P. Kuzmina, N.M. Khaidukov: *Crystal Growth from High Temperature Aqueous Solutions* (Nauka, Moscow 1977), in Russian
- 18.239 H. Guggenheim: *Solid State Phys.* **12**, 780 (1961)
- 18.240 V.I. Popolitov, A.N. Lobachev, V.F. Perkin: *Kristallografiya* **17**, 436 (1972)
- 18.241 B.N. Litvin, V.I. Popolitov: *Hydrothermal Synthesis of Inorganic Compounds* (Nauka, Moscow 1984), in Russian
- 18.242 E.D. Kolb, A.J. Caporaso, R.A. Laudise: *J. Cryst. Growth* **19**, 242 (1973)
- 18.243 K. Byrappa, S. Srikanthaswamy, G.S. Gopalakrishna, V. Venkatachalapathy: *J. Mater. Sci.* **21**, 2202 (1986)
- 18.244 S.P. Fedoseeva: *J. Cryst. Growth* **8**, 59 (1972)
- 18.245 I.P. Kuzmina, B.N. Litvin: *Kristallografiya* **7**, 478 (1963)
- 18.246 V.I. Popolitov, A.N. Lobachev: *Izv. Akad. Nauk USSR: Inorg. Mater.* **8**, 960 (1972)
- 18.247 T. Eitzi, K. Iodji, K. Kendzi, S. Tatsuro: *Patent* 5248959 (1975), Japan No. 50–102484
- 18.248 G. Demazeau, P. Maestro: Hydrothermal growth of Cr_2O_3 , *Proc. 7th Int. AIRAPT Conf. (Le Creusot)*, Vol. 1 (1979) p. 572
- 18.249 I.P. Kuzmina: *Author's Abstract IKAN* (SSSR, Moscow 1968), in Russian
- 18.250 B.N. Litvin, V.I. Popolitov: *Hydrothermal Synthesis of Inorganic Compounds* (Nauka, Moscow 1984) p. 165, in Russian
- 18.251 R.A. Laudise, E.E. Kolb: *J. Am. Ceram. Soc.* **45**, 51 (1962)
- 18.252 G.I. Distler, S.A. Kobzareva, A.N. Lobachev, O.K. Melnikov, N.S. Triodina: *Krist. Tech.* **13**, 1025 (1978)
- 18.253 S.C. Abraham, P.B. Jameson, J.L. Bernstein: *J. Chem. Phys.* **47**, 4034 (1967)
- 18.254 B.N. Litvin, V.I. Popolitov: *Hydrothermal Synthesis of Inorganic Compounds* (Nauka, Moscow 1984) p. 216, in Russian
- 18.255 G. Ervin, E.F. Osborn: *J. Geol.* **59**, 381 (1951)
- 18.256 A.N. Christensen: *Acta Chem. Scand.* **20**, 896 (1966)
- 18.257 A.N. Christensen: *Acta Chem. Scand.* **30**, 133 (1976)
- 18.258 H. Schwarz: *Z. Naturforsch.* **22b**, 554 (1967)
- 18.259 V.S. Balitsky, T. Bublikova: *Prog. Cryst. Growth. Character. Mater.* **21**, 139 (1990)

- 18.260 B.V. Mill: Dokl. Akad. Nauk SSSR **156**, 814 (1964)
- 18.261 J. Ito, C. Frondel: Am. Mineral. **53**, 1276 (1968)
- 18.262 B.A. Maksimov, Y.A. Kharitonov, V.V. Ilyukhin, N.V. Belov: Dokl. Akad. Nauk SSSR **178**, 980 (1968)
- 18.263 M. Bihan, T.A. Katt, R. Wey: Bull. Soc. France Mineral. Crystallogr. **94**, 15 (1971)
- 18.264 D.E. Appleman, J.R. Clark: Am. Mineral. **50**, 679 (1965)
- 18.265 K. Kodaira, S. Ito, T. Matsushita: J. Cryst. Growth **29**, 123 (1975)
- 18.266 J. Wan, Z. Wang, X. Chen, L. Mu, W. Yu, Y. Qian: J. Lumin. **121**, 32 (2006)
- 18.267 Z. Ito, I. Harold: Am. Mineral. **53**, 778 (1968)
- 18.268 D.H. Lindsley: *Carnegie Inst. Annu. Rep.* (Direct. Geophys. Lab., Washington 1971) p. 188
- 18.269 J. Ito: Am. Mineral. **53**, 782 (1968)
- 18.270 J. Ito, C. Frondel: Am. Mineral. **52**, 1077 (1967)
- 18.271 J. Ito, C. Frondel: Arkiv. Min. Geol. **58**, 391 (1968)
- 18.272 G.V. Bukin: Mineralogical Museum, Akad. Nauk SSSR **19**, 131 (1969)
- 18.273 R.J. Harker, O.G. Tuttle: Am. J. Sci. **254**, 468 (1956)
- 18.274 P.A. Sandomirskii, M.A. Smirnov, A.V. Arakcheeva, N.V. Belov: Dokl. Akad. Nauk SSSR **227**, 856 (1976)
- 18.275 B.Y. Kornilovich, N.A. Ovramenko, F.D. Ovcharenko: Dokl. Akad. Nauk SSSR **261**, 245 (1981)
- 18.276 I.Y. Nekrasov, T.P. Dadze: J. Mineral. **3**, 287 (1980)
- 18.277 I.Y. Nekrasov, T.P. Dadze, N.V. Zayakina: Dokl. Akad. Nauk SSSR **261**, 479 (1981)
- 18.278 G.D. Brunton, L.A. Harris, O.C. Kopp: Am. Mineral. **57**, 1720 (1972)
- 18.279 E.E. Strelkova, O.G. Karpov, B.N. Litvin: Kristallografiya **22**, 174 (1977)
- 18.280 D.Y. Pushcharovskii, O.G. Karpov, E.A. Pobedinskaya, N.V. Belov: Dokl. Akad. Nauk SSSR **234**, 1323 (1977)
- 18.281 D.Y. Pushcharovskii, T. Baatarin, E.A. Pobedinskaya, N.V. Belov: Kristallografiya **16**, 899 (1971)
- 18.282 D.Y. Pushcharovskii, E.A. Pobedinskaya, N.V. Belov: Dokl. Akad. Nauk SSSR **185**, 395 (1969)
- 18.283 L.B. Halferdahl: J. Petrol. **2**, 49 (1961)
- 18.284 D.Y. Pushcharovskii, E.A. Pobedinskaya, B.N. Litvin, N.V. Belov: Dokl. Akad. Nauk SSSR **214**, 91 (1974)
- 18.285 R.N. Thomson, J.E. Chisholm: Mineral. Mag. **37**, 253 (1969)
- 18.286 C.F. Warren: Am. Mineral. **56**, 997 (1971)
- 18.287 D.J. Drysdale: Am. Mineral. **56**, 187 (1971)
- 18.288 A.N. Safronov, N.N. Nevskii, V.I. Ilyukhin, N.V. Belov: Dokl. Akad. Nauk SSSR **255**, 278 (1980)
- 18.289 R. Caruba, A. Baumer, G. Turco: C. R. Acad. Sci. Paris **270**, 1 (1970)
- 18.290 V.G. Chykhlanstev, K.V. Alyamovskaya: Izv. Akad. Nauk SSSR: Inorg. Mater. **6**, 1639 (1970)
- 18.291 N.G. Shymyaskaya, V.A. Blinov, A.A. Voronkov: Dokl. Akad. Nauk SSSR **208**, 1876 (1973)
- 18.292 M.C. Michel-Levy: Bull. Soc. France Mineral. Crystallogr. **84**, 2989 (1967)
- 18.293 J. Ito: Am. Mineral. **53**, 998 (1968)
- 18.294 J.L. Munoz: Am. Mineral. **53**, 1490 (1968)
- 18.295 A. Baronnet, M. Amouric, B. Chabot, F. Corny: J. Cryst. Growth **43**, 255 (1978)
- 18.296 L.N. Demianets, E.N. Emelyanova, O.K. Melnikov: Solubility of sodalite under hydrothermal conditions. In: *Crystallization Process Under Hydrothermal Conditions*, ed. by A.N. Lobachev (Consultant Bureau, New York 1973) p. 151
- 18.297 R.D. Shannon: Phys. Chem. Mineral. **4**, 139 (1979)
- 18.298 D. Tranqui, J.J. Capponi, J.C. Joubert, R.D. Shannon: J. Solid State Chem. **73**, 325 (1988)
- 18.299 J.W. Cobble: Rapp. Tech. Cent. Belge Etude Corros. **142**, 119 (1982)
- 18.300 R. Caruba, A. Baumer, G. Turco: Geochim. Cosmochim. Acta **39**, 11 (1975)
- 18.301 A. Baumer, G. Turco: C.R. Acad. Sci. D **270**, 1197 (1970)
- 18.302 A.A. Bush, S.A. Ivanov, S.Y. Stefanovich: Izv. Akad. Nauk SSSR: Inorg. Mater. **13**, 1656 (1977)
- 18.303 M.N. Tseitlin, G.F. Plakhov, A.N. Lobachev: Kristallografiya **18**, 836 (1973)
- 18.304 V.I. Popolitov, G.F. Plakhov, S.Y. Stefanovich: Izv. Akad. Nauk SSSR: Inorg. Mater. **17**, 1841 (1981)
- 18.305 B.N. Litvin: Hydrothermal chemistry of silicates and germinates. Ph.D. Thesis (Academy of Sciences Russia, Moscow 1978)
- 18.306 A.N. Lazarev, A.K. Shirivinskaya: Izv. Akad. Nauk SSSR: Inorg. Mater. **12**, 771 (1976)
- 18.307 T.N. Nadezhdina, E.A. Pobedinskaya, V.V. Ilyukhin, N.V. Belov: Dokl. Akad. Nauk SSSR **223**, 1086 (1977)
- 18.308 S.R. Lyon, E.S. Ehlers: Am. Mineral. **56**, 118 (1970)
- 18.309 B.A. Maksimov, Y.V. Nikolskii, Y.A. Kharitonov: Dokl. Akad. Nauk SSSR **239**, 87 (1978)
- 18.310 A.M. Dago, D.Y. Pushcharovskii, E.A. Pobedinskaya, N.V. Belov: Dokl. Akad. Nauk SSSR **250**, 857 (1980)
- 18.311 D.Y. Pushcharovskii, A.M. Dago, E.A. Pobedinskaya, N.V. Belov: Dokl. Akad. Nauk SSSR **251**, 354 (1980)
- 18.312 D.M. Roy, R. Roy: Am. Mineral. **39**, 957 (1954)
- 18.313 D.Y. Pushcharovskii, E.A. Pobedinskaya, O.V. Kudryasteva, B. Hettash: Kristallografiya **1**, 1126 (1976)
- 18.314 I.P. Kuzmina, O.K. Melnikov, B.N. Litvin: *Hydrothermal Synthesis of Crystals* (Nauka, Moscow 1968) p. 41
- 18.315 N.A. Nosirev: Investigations of germanate system in hydrothermal condition. Ph.D. Thesis (Institute of Crystallography, Moscow 1975)
- 18.316 Y.K. Egorov-Tismenko, M.A. Simonov, N.V. Belov: Dokl. Akad. Nauk SSSR **227**, 2 (1976)
- 18.317 I.I. Soloveva, V.V. Bakanin: Kristallografiya **12**, 591 (1967)
- 18.318 S. Kume, S. Ueda, M. Koizumi: J. Geophys. Res. **74**, 2145 (1969)
- 18.319 N. Kinomura: J. Am. Ceram. Soc. **56**, 344 (1973)
- 18.320 N.V. Belov: Dokl. Akad. Nauk SSSR **268**, 360 (1983)
- 18.321 A.N. Christensen: Acta Chem. Scand. **24**, 1287 (1970)
- 18.322 O. Jarchow, K.H. Kalska, H. Schenk: Naturwissenschaften **68**, 475 (1981)

- 18.323 L.N. Demianets, A.N. Lobachev, G.A. Emelchenko: *Rare Earth Germanates* (Nauka, Moscow 1980)
- 18.324 E.D. Kolb, R.A. Laudise: *J. Cryst. Growth* **43**, 313 (1978)
- 18.325 F. Dacheville, R. Roy: *Z. Kristallogr.* **111**, 451 (1959)
- 18.326 S. Srikantaswamy: Phases and crystallization in the system aluminum orthophosphate. Ph.D. Thesis (University of Mysore, India 1988)
- 18.327 R.G. Hermann: Ph.D. Thesis (Ohio University, Ohio 1972)
- 18.328 E.M. McCarron, J.L. Calabrese, M.A. Subramanian: *Mater. Res. Bull.* **22**, 1421 (1987)
- 18.329 J.M. Congo, P. Kierkegaard: *Acta Chem. Scand.* **20**, 72 (1966)
- 18.330 H. Effenberger: *J. Solid State Chem.* **57**, 1240 (1985)
- 18.331 A. Clearfield, B.D. Roberts, A. Clearfield: *Mater. Res. Bull.* **19**, 219 (1984)
- 18.332 M.A. Subramanian, B.D. Roberts, A. Clearfield: *Mater. Res. Bull.* **19**, 1417 (1984)
- 18.333 P. Lightfoot, A.K. Cheema, A.W. Sleight: *J. Solid State Chem.* **73**, 325 (1988)
- 18.334 K. Byrappa, S. Srikantaswamy, S. Gali: *J. Mater. Sci. Lett.* **9**, 235 (1990)
- 18.335 K. Byrappa, B.N. Litvin: *J. Mater. Sci.* **18**, 703 (1983)
- 18.336 S. Gali, K. Byrappa: *Acta Crystallogr. C* **46**, 2011 (1990)
- 18.337 S. Gali, A. Cardenas, K. Byrappa, G.S. Gopalakrishna: *Acta Cryst. C* **48**, 1650 (1992)
- 18.338 K. Byrappa, B.V. Umesh Dutt, D. Poojary, A. Clearfield: *J. Mater. Res.* **9**, 1519 (1994)
- 18.339 A. Clearfield: *Prog. Cryst. Growth. Charact. Mater.* **21**, 1 (1990)
- 18.340 R. Peascoe: Ph.D. Thesis (Texas University, Austin 1989)
- 18.341 T. Chirayil, P.Y. Zavalij, M.S. Whittingham: *Chem. Mater.* **10**, 2629 (1998)
- 18.342 K. Byrappa, C.K. Chandrashekar, B. Basavalingu, K.M.L. Rai, S. Ananda, M. Yoshimura: *J. Cryst. Growth* **306**, 94 (2007)
- 18.343 Y.W. Wang, H.Y. Xu, H. Wang, Y.C. Zhang, Z.Q. Song, H. Yan, C.R. Wan: *Solid State Ion.* **167**, 419 (2004)
- 18.344 L.N. Demianets: *Prog. Cryst. Growth. Charact. Mater.* **21**, 299 (1990)
- 18.345 K. Byrappa, K.V.K. Shekar: *J. Mater. Chem.* **2**, 13 (1992)
- 18.346 K. Byrappa, K.V.K. Shekar, S. Gali: *Cryst. Res. Technol.* **6**, 768 (1992)
- 18.347 S. Hosokawa, Y. Tanaka, S. Iwamoto, M. Inoue: *J. Mater. Sci.* **43**, 3079 (2008)
- 18.348 A. Cardenas, J. Solans, K. Byrappa, K.V.K. Shekar: *Acta Cryst. C* **49**, 645 (1992)
- 18.349 M. Elli, L. Cambi: *Atti. Accad. Naz. Lincei, Rend. Cl. Sci. Fis. Mat. Nat.* **39**, 87 (1965)
- 18.350 L. Cambi, M. Elli: *Chim. Ind. Ital.* **47**, 136 (1968)
- 18.351 S. Biswas, S. Kar, S. Chaudhuri: *J. Cryst. Growth* **284**, 129 (2005)
- 18.352 U.K. Gautam, R. Seshadri: *Mater. Res. Bull.* **39**, 669 (2004)
- 18.353 J.R. Ota, S.K. Srivastava: *J. Nanosci. Nanotechnol.* **6**, 168 (2006)
- 18.354 L. Cambi, M. Elli: *Chim. Ind. Ital.* **51**, 3 (1969)
- 18.355 L. Cambi, M. Elli: *Atti. Accad. Naz. Lincei. Rend. Cl. Sci. Fis. Mat. Nat.* **40**, 553 (1966)
- 18.356 E.D. Kolb, A.J. Caporaso, R.A. Laudise: *J. Cryst. Growth* **31/4**, 422 (1968)
- 18.357 N.K. Abrikosov, V.F. Bankina, L.V. Porestkaya: *J. Cryst. Growth* **7**, 176 (1967)
- 18.358 L. Cambi, M. Elli: *Chim. Ind. Ital.* **48**, 944 (1966)
- 18.359 L. Cambi, M. Elli: *Atti. Accad. Naz. Lincei. Rend. Cl. Sci. Fis. Mat. Nat.* **41**, 241 (1966)
- 18.360 L. Cambi, M. Elli: *Chim. Ind. Ital.* **50**, 94 (1968)
- 18.361 V.S. Balitsky, V.V. Komova, N.A. Ozerova: *Izv. Akad. Nauk SSSR Ser. Geol.* **12**, 93 (1971)
- 18.362 V.A. Kuznetsov, A.N. Lobachev (Ed.): *Crystal Processes Under Hydrothermal Conditions* (Consultant Bureau, New York 1973)
- 18.363 I. Keeman: *Z. Anorg. Allg. Chem.* **346**, 30 (1966)
- 18.364 K. Byrappa, B.V. Umesh Dutt, R.R. Clemente, S. Gali, A.B. Kulkarni: In: *Current Trends in Crystal Growth and Characterization*, ed. by K. Byrappa (MIT, Bangalore 1991) p. 272
- 18.365 L.N. Demianets: *Hydrothermal Synthesis of Crystals* (Nauka, Moscow 1968) p. 93, in Russian
- 18.366 L.Y. Kharchenko, V.I. Protasova, P.V. Klevstov: *J. Inorg. Chem.* **22**, 986 (1977)
- 18.367 P.V. Klevstov, N.A. Novgorodsteva, L.Y. Kharchenko: *Dokl. Akad. Nauk SSSR* **183**, 1313 (1968)
- 18.368 K. Byrappa, A. Jain: *J. Mater. Res.* **11**, 2869 (1996)
- 18.369 R.F. Klevstova, L.Y. Kharchenko, S.V. Borisov, V.A. Efremov, P.V. Klevstov: *Kristallografiya* **24**, 446 (1979)
- 18.370 V.I. Popolitov, B.N. Litvin: *Growth of Crystals Under Hydrothermal Conditions* (Nauka, Moscow 1986) p. 38
- 18.371 V.G. Hill, K. Zimmerman: *J. Electrochem. Soc. Solid State* **115**, 978 (1968)
- 18.372 E.D. Kolb, A.J. Caporaso, R.A. Laudise: *J. Cryst. Growth* **8**, 354 (1971)
- 18.373 R.F. Belt, J.B. Ings: *J. Cryst. Growth* **128**, 956 (1993)
- 18.374 A.V. Novoselova: *Izv. Akad. Nauk SSSR, Inorg. Mater.* **20**, 967 (1984)
- 18.375 J. Choi, E.G. Gillan: *J. Mater. Chem.* **16**, 3774 (2006)
- 18.376 D. Ehrentauf, N. Hoshino, Y. Kagamitani, A. Yoshikawa, T. Fukuda, H. Itoh, S. Kawabata: *J. Mater. Chem.* **17**, 886 (2007)
- 18.377 A. Clearfield, G.D. Smith: *Inorg. Chem.* **7**, 431 (1969)
- 18.378 S. Alluli, C. Ferraggiva, A. Laginestra, M.A. Massucci, N. Tomassini: *J. Inorg. Nucl. Chem.* **399**, 1043 (1977)

19. Hydrothermal and Ammonothermal Growth of ZnO and GaN

Michael J. Callahan, Qi-Sheng Chen

Zinc oxide (ZnO) and gallium nitride (GaN) are wide-bandgap semiconductors with a wide array of applications in optoelectronic and electronics. The lack of low-cost, low-defect ZnO and GaN substrates has slowed development and hampered performance of devices based on these two materials. Their anisotropic crystal structure allows the polar solvents, water and ammonia, to dissolve and crystallize ZnO and GaN at high pressure. Applying the techniques used for hydrothermal production of industrial single-crystal quartz to ZnO and GaN opens a pathway for the inexpensive growth of relatively larger crystals that can be processed into semiconductor wafers. This chapter will focus on the specifics of the hydrothermal growth of ZnO and the ammonothermal growth of GaN, emphasizing requirements for industrial scale growth of large crystals. Phase stability and solubility of hydrothermal ZnO and ammonothermal GaN is covered. Modeling of thermal and fluid flow gradients is discussed and simulations of thermal and temperature profiles in research-grade pressure systems are shown. Growth kinetics for ZnO and GaN respectively are reviewed with special interest in the effects of crystalline anisotropy on thermodynamics and kinetics. Finally, the incorporation of dopants and impurities in ZnO and GaN and how their incorporation modifies electrical and optical properties are discussed.

19.1 Overview of Hydrothermal and Ammonothermal Growth of Large Crystals	657
19.1.1 Comparison of Ammonia and Water as Solvents	657
19.1.2 Growth of Large Crystals by the Transport Growth Model....	659
19.2 Requirements for Growth of Large, Low-Defect Crystals	661
19.2.1 Thermodynamics: Solubility and Phase Stability.....	661
19.2.2 Environmental Effects on Growth Kinetics and Structure Perfection (Extended and Point Defects).....	664
19.2.3 Doping and Alloying	665
19.3 Physical and Mathematical Models	666
19.3.1 Flow and Heat Transfer	666
19.3.2 Porous-Media-Based Transport Model	666
19.3.3 Numerical Scheme.....	667
19.4 Process Simulations	669
19.4.1 Typical Flow Pattern and Growth Mechanism	669
19.4.2 Effect of Permeability on the Porous Bed.....	670
19.4.3 Baffle Design Effect on Flow and Temperature Patterns.....	670
19.4.4 Effect of Porous Bed Height on the Flow Pattern.....	672
19.4.5 Simulation of Reverse-Grade Soluble Systems	672
19.5 Hydrothermal Growth of ZnO Crystals	674
19.5.1 Growth Kinetics and Morphology .	674
19.5.2 Structural Perfection – Extended Imperfections (Dislocations, Voids, etc.)	676
19.5.3 Impurities, Doping, and Electrical Properties	678
19.5.4 Optical Properties.....	679
19.6 Ammonothermal GaN	681
19.6.1 Alkaline Seeded Growth	681
19.6.2 Acidic Seeded Growth	683
19.6.3 Doping, Alloying, and Challenges .	684
19.7 Conclusion	685
References	685

Gallium nitride (GaN) and zinc oxide (ZnO) are emerging semiconductor materials that will have an enormous impact in electronics and optoelectronics. GaN and ZnO both have the anisotropic wurtzite crystal structure (space group $P6_3mc$) as their thermodynamically stable phase. This anisotropy, along with a large ionic component in their chemical bonds, accounts for the high spontaneous and piezoelectric polarization found in both GaN and ZnO [19.1]. GaN and ZnO also have large saturation velocities, high mobilities, large radiation resistance, nonlinear optical properties, and are chemically and thermally robust. They both have direct bandgaps in the ultraviolet (UV) region (GaN, $E_g = 3.42$ eV at 300 K; ZnO, $E_g = 3.37$ eV at 300 K) and have the ability to form direct-bandgap alloys for the fabrication of quantum wells (AlN and InN with GaN and MgO and CdO with ZnO) [19.2–5].

Devices based on the GaN [19.2, 3] and ZnO [19.4, 5] material systems are currently or will be produced in the future for a myriad of applications including solid-state lighting, power electronics, high-power radio-frequency (RF) monolithic microwave integrated circuit (MMIC) arrays, terahertz detection, high-density optical storage, and UV–infrared (IR) detection. GaN-devices have seen rapid development in the last 10 years due to the overcoming of major technological hurdles in the early 1990s [19.6]. A multibillion-dollar market now exists for GaN green–violet light-emitting diodes (LEDs) and the overall GaN-device market is forecasted to increase by the tens of billions of dollars in the next several decades. GaN-based blue and violet laser diodes are in high demand for high-definition digital versatile disk (DVD) drives. ZnO-based devices have not seen penetration into the semiconductor marketplace because of its own set of technical hurdles yet to be overcome (P-doping, contacts, low-defect active layers, etc.) [19.7], but an intense research and development effort for commercial ZnO-based devices is currently progressing.

Semiconductor devices have typically been manufactured on *native* substrates that have nearly identical crystalline structure to the active device layers manufactured on them. Semiconductor substrates are normally cut from large single boules that have been grown by melt techniques, with variations of the Czochralski and Bridgman growth methods being the most common [19.8]. The melt techniques are generally preferred over vapor or solution methods for the growth of large single crystals, owing to the higher growth rates, which allow for lower costs and rapid scaling of boule diameters.

There is an important class of semiconductor materials where growth of large single crystals is problematic. These materials have different and in many cases superior electrical, optical, and structural properties compared with traditional semiconductors such as Si. ZnO and the group III nitrides: AlN, GaN, and InN are in this class of semiconductors, which also include SiC and diamond. The reactivity of molten ZnO and the relatively high oxygen overpressure (≈ 50 atm) required to melt ZnO makes the melt growth of large single-crystal ZnO boules difficult [19.9]. GaN also cannot be grown by traditional melt techniques due to the extreme pressures and temperatures required to prevent the dissociation of GaN to form molten GaN [19.10]. In fact, all of the group III nitrides decompose into their corresponding group III metal and N_2 well before their melting points when heated at atmospheric pressure.

Techniques for growing nitride thin films on Si, sapphire (Al_2O_3), and silicon carbide (SiC) substrates were developed in the 1980s and 1990s due to the lack of GaN substrates [19.6]. GaN thin-film growth on nonnative substrates such as sapphire produces a large number of threading dislocations and other defects caused by the large lattice and thermal expansion mismatch between GaN and the nonnative substrate. These defects are deleterious to device reliability and performance. Low-cost commercial GaN substrates would enable enhanced performance, increased yields, and allow rapid market penetration of nitride-based devices. Therefore, there has been a considerable amount of research in producing GaN wafers grown by non-molten techniques. The most widely developed is the hydride vapor-phase epitaxy (HVPE) technique. Several research institutes have demonstrated GaN-based devices, processed on HVPE GaN wafers with improved device metrics compared with nitride devices fabricated on SiC and sapphire wafers. Although an improvement over heteroepitaxy, GaN HVPE wafers are inferior in structural quality compared with Si or GaAs wafers. GaN-based laser diodes manufactured on HVPE GaN substrates have extremely low yields and reduced performance compared with the red diodes grown on low-defect GaAs substrates. HVPE GaN substrates are available only in limited quantities and are extremely expensive. Several other techniques such as high-pressure Ga flux and alkali fluxes have been investigated for the growth of large GaN crystals but have not produced the scale and quality that is required for high-volume low-cost GaN semiconductor wafers.

Large zinc oxide single crystals were first produced in the 1960s due to the interest in using single-crystal

ZnO for piezoelectric transducers and surface acoustic wave (SAW) devices. Renewed interest arose because of ZnO's potential as an isostructural, nearly lattice-matched substrate for group III nitride semiconductor device structures. Advances in fabricating ZnO and ZnMgO quantum wells on sapphire that exhibit strong optically stimulated UV emissions have further driven demand for development of ZnO substrates [19.11]. Zinc oxide boules up to 2 inch in diameter and 1 cm thick have been grown by vapor-phase transport [19.12], and melt-grown wafers of 2 in diameter are now also available [19.9]. Both processes typically yield wafers with dislocation densities of 10^4 – 10^5 cm $^{-2}$. Recently, the most promising method for the growth of inexpensive, large, low-defect ZnO boules is the hydrothermal method [19.13].

The similarity of water and ammonia as polar solvents allows GaN crystals to be grown in ammonia solvents (ammonothermal growth) similar to the hydrothermal growth of oxides crystals in high-pressure

water solutions. Large quantities of low-cost ZnO and GaN wafers could theoretically be manufactured by applying the same scaling techniques used for quartz growth to the hydrothermal growth of ZnO and ammonothermal growth of GaN.

This chapter will focus on the specifics of hydrothermal growth of large single crystals of zinc oxide (ZnO) and ammonothermal growth of gallium nitride (GaN). Ammonia and water will be compared as solvents and a brief overview of the temperature gradient method, which is the predominant technique employed for large-scale hydrothermal growth of single crystals, will be presented. Phase stability, adequate solubility, and optimization of thermal and fluid flow gradients in hydrothermal systems through modeling and simulation will be reviewed. Finally, growth kinetics for hydrothermal ZnO and ammonothermal GaN and how the incorporation of dopants and impurities influence the electrical and optical properties on these two important semiconductor materials will be discussed.

19.1 Overview of Hydrothermal and Ammonothermal Growth of Large Crystals

19.1.1 Comparison of Ammonia and Water as Solvents

Water's abundance, low toxicity, high purity, liquid phase at room temperature and atmospheric pressure, high dielectric constant, and its amphoteric properties make it the most widely used solvent. Several large crystals have been grown in water at ambient conditions such as aluminum potassium sulfate (ALUM) and potassium dihydrogen phosphate (KDP), but many compounds need higher temperatures to obtain the high solubility and kinetics for the growth of large crystals. Hundreds of different crystalline compounds have been grown by the hydrothermal technique, but only quartz crystals have been produced in the size and quantities that are required for semiconductor substrates. Ammonia is the most common anhydrous solvent because of the many similarities with water, as shown in Table 19.1. Ammonia is readily available, with 109 000 metric tons produced worldwide in 2004 [19.14]. Costs for ultrahigh-purity anhydrous ammonia have been driven down due to its use in the synthesis of Si $_2$ N $_3$ during complementary metal–oxide–semiconductor (CMOS) processing, and in the production of GaN LEDs.

Like water, ammonia is a polar molecule. Polar molecules have a nonuniform or anisotropic structure that causes positive and negative charges to form in opposite parts of the molecule. The old alchemist's

Table 19.1 Physical properties of ammonia and water

Property	Ammonia	Water
Boiling point (°C)	− 33.4	100
Freezing point (°C)	− 77.7	0
Critical temperature (°C)	132.5	374.2
Critical pressure (bar)	113	221
Density (g cm $^{-3}$)	0.68 (−33 °C)	0.96 (100 °C)
Ionic product	$\approx 10^{-29}$	10^{-14}
Heat of vaporization (kcal/mol)	5.58	9.72
Heat of fusion (kcal/mol)	1.35	2.0
Viscosity of liquid at 25 °C (cP)	0.135	0.891
Dielectric constant	22 (−33 °C)	80 (0 °C)
Dipole moment (D)	1.46	1.84
Polarizability (cm 3) ($\times 10^{24}$)	2.25	1.49
Specific conductance (Ω^{-1} cm $^{-1}$)	4×10^{-10} (−15 °C)	4×10^{-8}

adage: *similia similibus solvuntur* (i.e., like dissolves like), a basic rule of solution growth, holds for polar solvents, which tend to dissolve ionic and polar solids. Ammonia has a lower, but still relatively high, dielectric constant and lower dipole moment than water (the dielectric constant and dipole moment are measures of the degree of polarization of a molecule), and therefore has less ability to dissolve highly ionic compounds than water, but a greater ability to dissolve organic molecules. Thus, ammonia-based solutions have been used predominately for chemical synthesis of fertilizers, pharmaceutical products, and plastics. Water and ammonia are also both protic solvents, which means they can donate a hydrogen bond to a solvated compound. Ammonia has a slightly higher proton affinity than that of water, and thus is a more basic solvent than water and enhances the acidity of many compounds. Table 19.1 lists some of the physical properties of ammonia and water.

Byrappa and Yoshimura define hydrothermal growth as [19.15]

any heterogeneous chemical reaction in the presence of a solvent (whether aqueous or nonaqueous) above room temperature at a pressure greater than 1 atm in a closed system.

The term *solvothermal growth* has also been used generically when discussing both aqueous and nonaqueous solvents at above ambient conditions, but recently has been used more specifically when discussing the use of organic solvents at above ambient temperatures and pressures. The term *hydrothermal* is more commonly used when discussing aqueous (water-based) solvents, and the term *ammonothermal* has been recently adopted for discussing ammoniated (ammonia-based) solvents. Here we will define hydrothermal and ammonothermal as subclasses of the generic term of solvothermal growth as shown in Fig. 19.1 to avoid confusion while discussing differences and similarities of aqueous and ammoniated solvents.

Solvothermal crystal growth offers several advantages over better known methods such as melt growth. Solvothermal growth is a low-temperature process, which often makes possible the growth of materials that are difficult or impossible to melt, or materials which, on solidifying from a melt and cooling down, would undergo phase changes (because of such changes, α -quartz cannot be grown from the melt). Low-temperature solvothermal growth can also minimize or eliminate the incidence of temperature-induced point defects, as illustrated by the hydrothermal growth of $\text{Bi}_{12}\text{SiO}_{20}$ [19.16], and can produce large amounts of material by simultaneous growth on multiple seeds (over 4000 kg of single-crystal quartz has been produced in a single run [19.15]). Only a small amount of user intervention and monitoring is required during growth because of the extremely uniform temperature gradients that can be maintained and the absence of moving parts. Some disadvantages of solvothermal growth are the low growth rates and initial capital equipment costs, but these are offset by the ability to grow multiple crystals in a single run and the extended lifetimes of the autoclaves.

The autoclaves are made out of high-strength steels or special alloys. The vessel must be corrosion resistant and able to withstand the temperature and pressure requirements for long periods of time. Corrosive solutions employing concentrated acids and bases are sometimes required to increase the solubility to obtain acceptable growth rates. Therefore, to protect the autoclave, a noble-metal liner (e.g., silver, gold, platinum or Teflon depending upon the pressure and temperature (PT) conditions and the solvent medium) is used in this case. Superstrong high-content-nickel alloy autoclaves are used for ammonothermal growth of GaN due to the higher temperatures and pressures required for the growth of large crystals of GaN. These autoclaves currently have small volumes, but should be easily scalable to larger sizes, albeit at greater expense than current industrial-scale autoclaves. Four centimeter-diameter autoclaves have recently been used to grow GaN crystals [19.17].

Additional tasks must be preformed when ammonia is being used as a high-pressure solvent. Ammonia, which is a vapor at ambient temperatures and pressures, can be condensed at room temperature and atmospheric pressure into an autoclave immersed in a chilled alcohol bath, pumped into an autoclave using high-pressure pumps, or chilled and poured into an autoclave. Precautions have to be taken, such as the use of glove boxes and vacuum apparatus, for any reactants or products that are air or moisture sensitive, e.g., alkali metals and their amides and azides used as mineralizers. Ammonia is

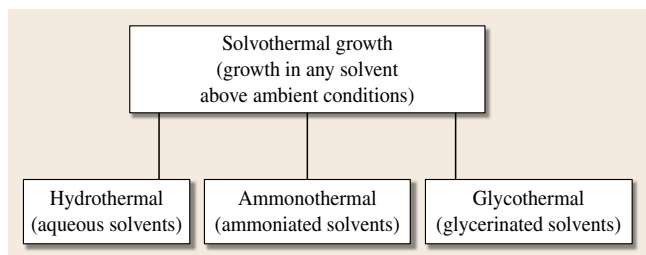


Fig. 19.1 Several subclasses of solvothermal growth

also toxic, so autoclaves with internal volumes greater than 50 cm³ should be run inside chemical exhaust cabinets in case of a seal leak or rupture. There are several publications that cover specific details of the apparatus and autoclaves used in both hydrothermal [19.15, 18] and ammonothermal reactions [19.19, 20].

19.1.2 Growth of Large Crystals by the Transport Growth Model

Solvothermal growth is typically performed for two reasons:

1. The desired material is not thermodynamically favorable at ambient conditions;
2. The kinetics is such that the growth rate of the desired material is extremely slow at ambient conditions.

The *transport growth model* (also called the *temperature-differential* or *dissolution–crystallization* model) is predominately used for solvothermal growth of large single crystals, due to the low growth rate of quartz and many other technologically important materials grown in high-pressure solvents. Table 19.2 shows the dissolution–crystallization mechanism which is kinetically enhanced by the addition of *mineralizers*. Ammonia, like water, is amphoteric and can be made either acidic or alkaline depending on which compounds or *complexing agents* are combined with it. These complexing agents, or *mineralizers*, ionize in the solvent; it is these cations (acidic ions) or anions (alkaline ions) that promote the high solubility of many solid-phase compounds at low temperature. Source material is dissolved to form an intermediate species (left to right flow in the reversible chemical reactions in Table 19.2). Subsequently, the intermediate species becomes supersaturated by an external force and crystallizes out as single-crystal deposits (right to left flow in reactions in Table 19.2).

The *transport growth model* and all solvothermal growth mechanisms are based on supersaturation. Fig-

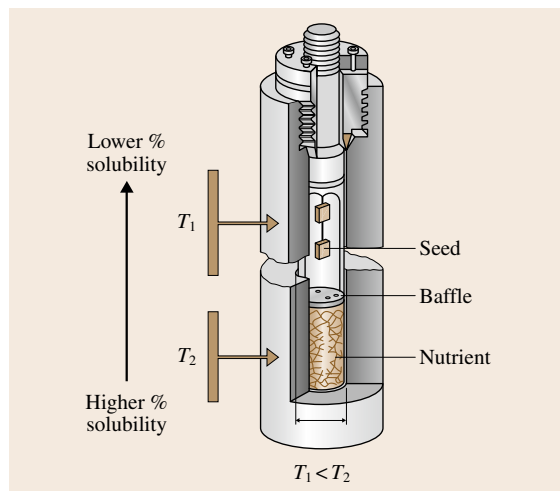


Fig. 19.2 Schematic of solvothermal crystal growth by the transport growth model (after [19.18])

ure 19.2 shows a schematic of the model. A temperature zone is established where the lower half of the autoclave, called the dissolution zone (T_2 in Fig. 19.2), is at a higher temperature than the upper half of the autoclave, called the crystallization zone (T_1 in Fig. 19.2). A baffle is placed between the two zones to help establish near-isothermal conditions in each zone. The solvent at the bottom of the vessel dissolves the nutrient until it reaches saturation. The solvated species is transported by the lower density fluid in the warmer dissolution zone, through natural fluid convection, to the cooler crystallization zone. Because of the lower temperature at the seed the solvated species becomes supersaturated, comes out of solution, and deposits on the seed (normal saturation conditions). Fluid convection returns the higher-density depleted solution to the lower-density fluid in the dissolution zone, where additional nutrient is dissolved. The cycle repeats as long as there is nutrient in the lower zone. Quartz [19.15], zinc oxide [19.21–27], GaN [19.20], and many other inorganic crystals have

Table 19.2 Comparison of dissolution–crystallization cycle of the hydrothermal and ammonothermal techniques

Hydrothermal: oxides	Ammonothermal: nitrides
Water: $2\text{H}_2\text{O} \rightarrow \text{H}_3\text{O}^+ + \text{OH}^-$	Ammonia: $2\text{NH}_3 \rightarrow \text{NH}_4^+ + \text{NH}_2^-$
ZnO in alkali water solution	GaN in ammonobasic solution
$\text{ZnO} + 2\text{H}_2\text{O} + 4\text{OH}^- \leftrightarrow \text{Zn}(\text{H}_2\text{O})_2(\text{OH})_4^-$	$\text{GaN} + (x-3)\text{NH}_2^- + 2\text{NH}_3 \leftrightarrow \text{Ga}(\text{NH}_2)_x^{3-x}$
Mineralizers	Mineralizers
Acids: HNO_3 , HCl , HI	Acids: NH_4Cl , NH_4I , HI
Bases: KOH , NaOH , LiOH	Bases: KNH_2 , NaNH_2 , LiNH_2

Table 19.3 Status of technology, ca. 2006, for solvothermal growth of SiO₂, ZnO, and GaN crystals (after [19.28])

Parameter	SiO ₂	ZnO	GaN
Autoclave inner diameter	0.65 m	≤ 0.2 m	≤ 0.03 m
Autoclave inner length	14 m	≤ 3 m	0.2–0.7 m
Volume	4.6 m ³	≤ 0.2 m ³	≤ 5 × 10 ^{−4} m ³
Seed size	70 × 45 × 230 mm ³	≈ 50 mm diameter	≤ 25 mm diameter
Seeds per batch	1400	112	1–4
Weight of crystal	1700 g	320 g; 20 mm thick	Few gram
Total yield per batch	2300 kg	36 kg	Few gram
Growth rate (<i>c</i> -axis)	25 μm/h	10 μm/h	≤ 2 μm/h
3-Run-per-year yield	6900 kg	108 kg	0.12 kg

been grown solvothermally by the transport growth model.

A recent publication by *Fukuda and Ehrentraut* [19.28] gives an outlook of industrial growth of hydrothermal ZnO crystals and ammonothermal GaN by projecting their current and future development path with that of quartz growth. Table 19.3 shows the current status of hydrothermal quartz, hydrothermal zinc oxide, and ammonothermal gallium nitride. Even with the slow growth rates of zinc oxide and gallium nitride (20–40% and 5–20% of the growth rate of quartz, respectively) under current solvothermal conditions it is theoretically possible to grow hundreds of kilograms of zinc oxide or gallium nitride in a single autoclave.

Hydrothermal zinc oxide crystals of several hundred grams have been grown with batch sizes in the tens of kilograms in small production autoclaves as shown in Table 19.3. An industrial-scale 500l autoclave was recently used to grow 200 ZnO crystals at a growth temperature of 330 °C. The run lasted

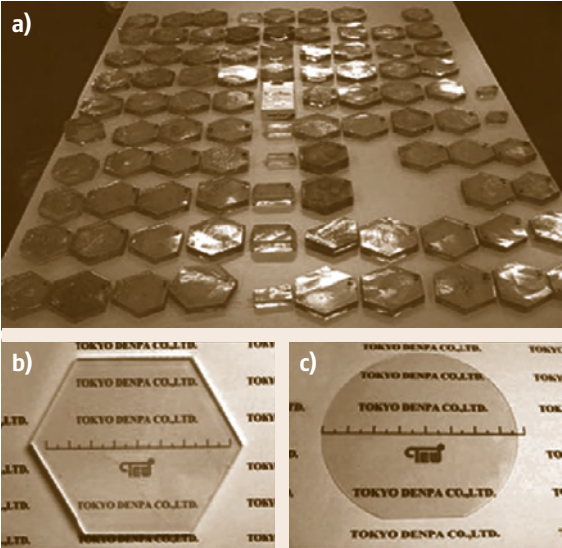


Fig. 19.3 (a) Two inch-size ZnO crystals produced during single growth run; (b) 3 inch ZnO crystal viewed down *c*-axis; (c) 3 inch (0001) ZnO wafer (after [19.13])

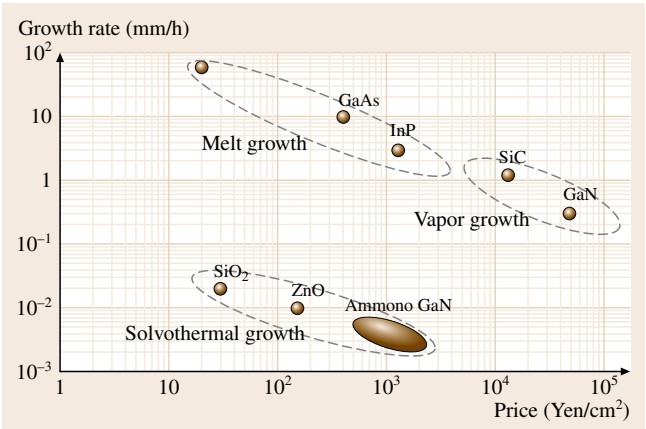


Fig. 19.4 Growth rates and cost of large-area single crystals (projected cost for ZnO and GaN) (after [19.28])

for 100 days and the weight of the crystals varied in the range 100–250 g [19.29]. If there is a large demand for ZnO wafers, economies of scale will allow for price reductions (200–400 US\$/cm² in 2006), as there is no reason ZnO crystals could not be grown in large industrial-scale autoclaves currently used to grown single-crystal quartz. Figure 19.3a shows 2 inch-diameter ZnO crystals grown in an autoclave with the equivalent dimensions as the *ZnO autoclave* listed in Table 19.3 [19.13]. Figures 19.3b and 19.3c show the largest current ZnO crystal and corresponding 3 inch-diameter wafer cut from the crystal.

Fukuda and Ehrentraut go on to apply SiO₂ quartz development to future ZnO and GaN development in order to project the cost of ZnO and GaN wafers when

their development cycle fully matures. The authors claim that hydrothermal ZnO and ammonothermal GaN wafers will be cost-competitive with traditional compound semiconductor wafers such as GaAs and InP in

the future. This comparison is shown in Fig. 19.4, which shows the potential of applying solvothermal growth techniques for industrial production of semiconductor wafers.

19.2 Requirements for Growth of Large, Low-Defect Crystals

19.2.1 Thermodynamics: Solubility and Phase Stability

In solvothermal growth of large crystals a *nutrient*, often the compound one intends to crystallize out as a single crystal, is dissolved in the solvent. The dissolved compound may form intermediate complexes or species in solution. In solvothermal growth, convective circulation and/or diffusion of these species throughout the solvent provides the primary mechanism for synthesizing crystalline compounds. A solvothermal growth system is designed to bring the soluble species into a region of the solvent medium where a change in conditions – e.g., in temperature, solvent composition, pH, or pressure – promotes crystal growth. Ideally, this change of conditions puts the soluble species in supersaturation, so the species must come out of solution – hopefully as the desired compound (e.g., ZnO, GaN) – until an equilibrium state (saturation) is achieved.

Thus, there are four fundamental thermodynamic requirements for the growth of high numbers of low-defect crystals by the hydrothermal/solvothermal method:

1. The desired material must have an adequate solubility at a given set of conditions (solvent, dissolution temperature, and pressure);
2. The solubility of the desired material must have adequate temperature dependence between the dissolution zone and crystallization zone;
3. The desired material must be the thermodynamically preferred material in the crystallization zone for a given set of conditions (solvent, crystallization temperature, and pressure);
4. The solvent must be thermodynamically stable at the temperatures and pressure needed to fulfill requirements 1–3 over long periods of time.

Low solubility will result in low growth rates; excessively high solubility will result in polycrystalline growth or spontaneous nucleation, which may be desirable for solvothermal powder synthesis, but prohibits

growth of low-defect-density single crystals. Typically, the nutrient should be 1–10 wt.% soluble in the solvent. Solubility can be increased by adding a proper complexing agent (mineralizer). Most mineralizers used in solvothermal growth change the pH of the solvent, making the solvent either acidic or alkaline, i.e., increasing the number of cations (H_3O^+ in water, NH_4^+ in ammonia) or anions (OH^- in water, NH_2^- or NH_2^{2-} in ammonia) that attack the nutrient material in ionic solutions. For zinc oxide and gallium nitride, a solubility of approximately 5% by weight in alkaline solution yields high-quality single crystals at reasonable growth rates.

Because temperature is used to create supersaturation for large crystals, solubility of the compound must have temperature dependence. Natural convection allows solute to transport to the seed interface, where varying the temperature gradient between the nutrient and seed controls crystal growth kinetics.

The third requirement above can be difficult to achieve because of the multicomponent nature of solvothermal growth. If an oxide such as zinc oxide is desired, the hydride, hydroxide or hydrate should not be thermodynamically favored for the specific mineralizer, temperature, and pressure conditions employed. Also, chemical elements that are components in the mineralizer must not contribute to the formation of undesirable solid compounds at the growth interface.

The final requirement is not readily apparent in hydrothermal growth. Water is stable as a liquid or supercritical fluid to temperatures above the maximum operating conditions of even small super-high-pressure research autoclaves. Ammonia however starts decomposing well below 500 °C at atmospheric pressure, and even under 3–4 kbar of pressure a significant percentage of ammonia will decompose above 500 °C [19.19]. This has two deleterious effects, first the change in solvent composition by ammonia decomposition over long periods of time will change the kinetic and possibly the thermodynamics of the growing GaN crystals, and secondly, hydrogen could have adverse effects on the autoclave vessels through hydrogen embrit-

tlement. The decomposition of ammonia is therefore one of the main issues that must be addressed for the growth of large crystals by the ammonothermal method.

The solubility and phase stability of ZnO in hydrothermal solvents and GaN in ammonothermal solvents are presented here.

Solubility of Hydrothermal ZnO

The solubility of hydrothermal zinc oxide in an OH[−] alkaline medium is shown in Fig. 19.5 [19.23]. Note that solubility increases with temperature. This is called *normal* or *forward-grade solubility*.

Zinc oxide is an amphoteric oxide, meaning it acts as an acid in alkaline solutions and as a base in acidic solutions. It is possible to grow hydrothermal zinc oxide in acidic solutions as well as the alkaline solutions shown in Fig. 19.6. McCandlish and Uhrin recently studied the solubility of ZnO in an acidic medium and grew ZnO at 100–250 °C, with growth rates up to 0.25 mm/day [19.30]. Figure 19.6 illustrates the solubility in acidic regimes. The squares signify 2 molal aqueous nitric acid and the circles signify a proprietary acidic solution. Note that the nitric acid solution exhibits normal solubility, whereas the proprietary solution exhibits decreasing solubility with increasing temperature (*retrograde* or *reverse-grade solubility*). To grow ZnO crystals under conditions of normal solubility the seed is placed in a colder region than the source material (Fig. 19.2); to grow under conditions of retrograde solubility, the seed is placed in the hotter region.

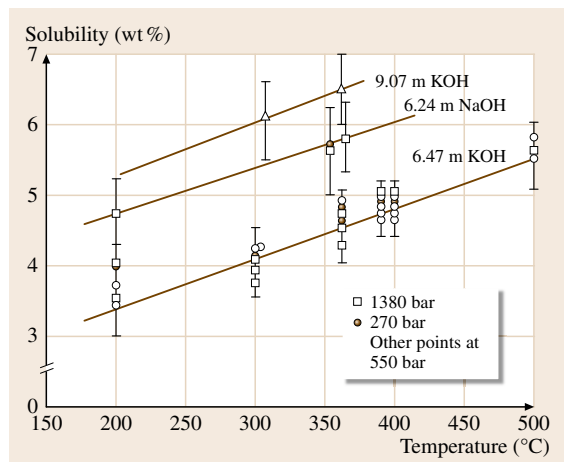


Fig. 19.5 Solubility of ZnO versus T in aqueous NaOH and KOH solutions (after [19.23])

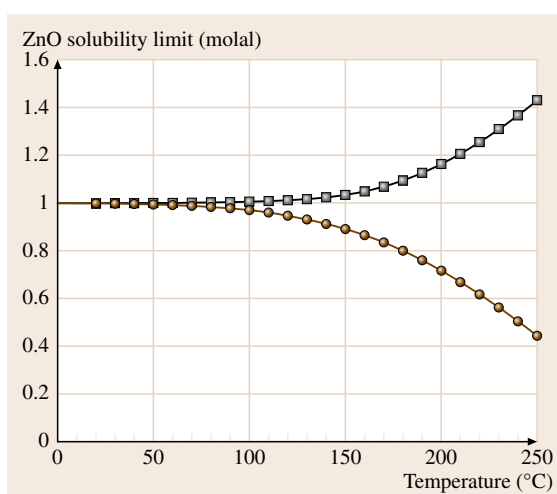


Fig. 19.6 Normal solubility of ZnO in 2 molal nitric acid (squares), and retrograde solubility of ZnO in a proprietary acid solution (circles) (after [19.30])

Phase Equilibrium of ZnO in Hydrothermal Solvents

Hüttig and Möldner studied the phase equilibrium of the ZnO–H₂O system to 40 °C and found zinc oxide to be the stable solid phase at pressures above 50 torr and temperatures above 35 °C [19.31]. Lu and Yeh experimentally showed that zinc oxide is the stable product up to pH = 12.5 in an aqueous ammonia solution at 100 °C [19.32]. Laudise and Ballman grew large zinc oxide crystals in alkaline media and found zinc oxide to be the stable product at 200–400 °C in 1.0 M NaOH [19.33]; subsequently it was found that zinc oxide can be grown in hydroxide solutions up to 10 M at temperatures exceeding 300 °C [19.27].

Recent advances in thermodynamic modeling of aqueous solution chemistry can aid in choosing conditions that achieve crystal growth of zinc oxide and other materials. A thermodynamic model of aqueous-based chemistry has been developed that computes the stability of zinc oxide in different aqueous regimes. The model uses commercial software (OLI Systems Inc., Morris Plains) and is detailed in several publications [19.34–36]. McCandlish and Uhrin initially modeled zinc oxide in the hydroxide system to validate the model against experimental data. Subsequently, a thermodynamic model was created for the growth of zinc oxide in acidic environments. Figure 19.7 shows the computed stability of ZnO at 150 °C as a function of pH with HNO₃ as the mineralizer [19.30].

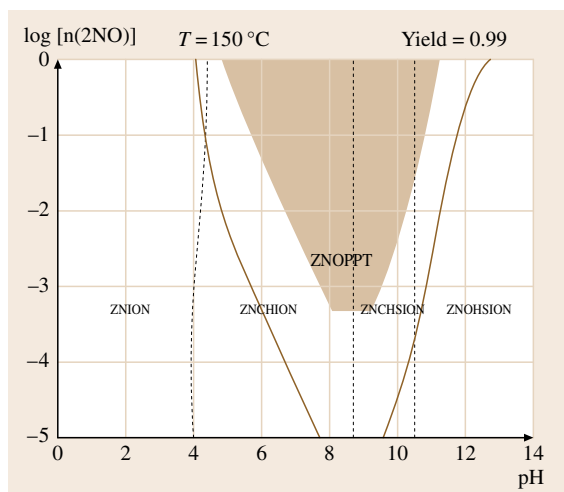


Fig. 19.7 Yield diagram for the precipitation of ZnO in 2 molal nitric acid at 150 °C as a function of pH; $\log [n(2NO)]$ signifies the log of the molar concentration of nitric acid in solution; ZNION, ZNCHION, ZNCHSION and ZNOHSION signifies the basic atomic chemical composition of the ionic compounds in solution for a given pH: Zn ion, ZnCH ion, ZnCHS ion, ZnOHS ion; ZnOPPT signifies ZnO crystallites that participated out of solution for a given pH (after [19.30])

Solubility of Ammonothermal GaN

Ammonothermal growth of GaN has retrograde solubility in alkaline solutions and normal solubility in acidic solutions. Figure 19.8 shows the solubility of polycrystalline GaN after a series of runs in the $\text{KNH}_2\text{-NH}_3$ system ($\pm 10\%$ variability in filling and molarity) [19.42]. The KNH_2 concentration is about 3.5 ± 0.5 M, the temperature gradient is around $10^\circ\text{C}/\text{cm}$, and the pressure is 1.3–2.4 kbar. The solubility of GaN in solutions of greater than 1 molal $\text{NaN}_3\text{-NH}_3$, $\text{KN}_3\text{-NH}_3$, $\text{KNH}_2\text{-NH}_3$, and $\text{NaNH}_2\text{-NH}_3$

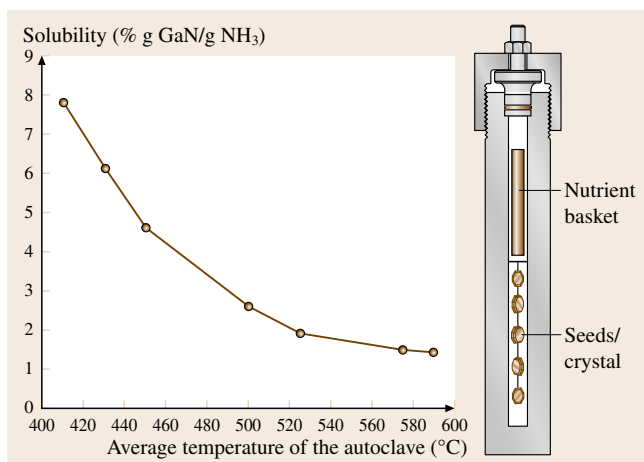


Fig. 19.8 Solubility of GaN polycrystalline in $\text{KNH}_2\text{-NH}_3$ system, 3.5 ± 0.5 M KNH_2 concentration (after [19.42])

has similar tendencies: a negative solubility coefficient and rather high solubility, in the range of 1–10% between 400 °C and 600 °C.

Using acidic mineralizers such as 0.4 M NH_4Cl , GaN has a normal solubility in ammonia [19.43]. The acidic conditions required the use of a Pt inner liner to protect the autoclave from corrosion. A growth rate of 0.02–0.03 mm/day can be achieved at a temperature of 550 °C and a pressure of less than 1.5 kbar. Normal solubility has also been claimed using other ammonium halide mineralizers [19.41,43].

Phase Equilibrium of GaN in Ammonothermal Solvents

The early work on ammonothermal synthesis of nitride powders was performed by *Jacobs* and *Schmidt* [19.19]. They synthesized several novel nitrogen-based compounds and designed apparatus specifically for ammonothermal powder synthesis. Later *Peters* [19.44]

Table 19.4 Growth conditions of ammonothermal synthesis of GaN microcrystals

Investigators	Mineralizers	Temperature ($^\circ\text{C}$)	Pressure (kbar)	Growth rate and habit
<i>Dwilinski</i> et al. [19.37]	KNH_2	550	1–5	Hexagonal microcrystals
<i>Purdy</i> [19.38]	NH_4Cl , NH_4Br or NH_4I	250–500	0.7	Mixed cubic and hexagonal microcrystals
<i>Ketchum</i> and <i>Kolis</i> [19.39]	KNH_2/KI	400	2.4	Hexagonal submillimeter-size plates
<i>Yoshikawa</i> et al. [19.40]	NH_4Cl	500	1.2	Hexagonal needle shape 0.02–0.03 mm/day
<i>Lan</i> et al. [19.41]	NH_4F , NH_4Cl , NH_4Br or NH_4I	450–600	1–2	Hexagonal microcrystals

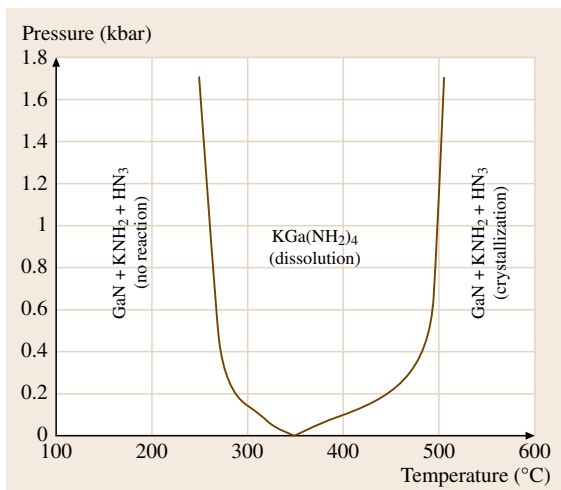


Fig. 19.9 Phase diagram of GaN in the GaN–KNH₂–NH₃ system (after [19.45]) (curves based on experiments between 0.3–2.4 kbar (5–35 kpsi); below 0.3 kbar the tendency is estimated).

and Dwilinski et al. [19.37] were the first to synthesize AlN and GaN microcrystals ammonothermally. The work on ammonothermal microcrystalline synthesis is summarized in Table 19.4.

Dwilinski et al. [19.37] obtained microcrystals of BN, AlN, and GaN by the ammonothermal method using lithium or potassium amide as mineralizer at pressures in the range 1–5 kbar and temperatures up to 550 °C. Ketchum and Kolis [19.39] grew ammonothermal single crystals of gallium nitride in supercritical ammonia at 400 °C and 2.4 kbar by using potassium amide (KNH₂) and potassium iodide (KI) as mineral-

izers. Hexagonal GaN crystals of $0.5 \times 0.2 \times 0.1 \text{ mm}^3$ were obtained. They also used potassium azide (KN₃) or sodium azide (NaN₃) to increase the solubility of GaN in ammonia [19.48].

The phase diagram of GaN in the GaN–KNH₂–NH₃ system is shown in Fig. 19.9 [19.45]. Unlike hydrothermal ZnO, high temperatures are needed to precipitate GaN out of an ammonothermal solution. The reaction $\text{KGa}(\text{NH}_2)_4 \leftrightarrow \text{KNH}_2 + \text{GaN} + 2\text{NH}_3$ did not produce GaN at temperatures below 400 °C. Pressure variations had little effect on the thermodynamics of GaN formation.

GaN has a metastable cubic phase that has been formed ammonothermally. Purdy et al. synthesized both cubic and hexagonal GaN by ammonothermal reactions of gallium metal or GaI₃ under acidic (NH₄Cl, NH₄Br or NH₄I) conditions [19.38, 49]. The reaction temperatures were 250–500 °C and pressures were up to 10 000 psi (0.6895 kbar).

Figure 19.10a shows well-defined cubic crystals grown in ammonia with the addition of lithium chloride to an acidic solution [19.46]. Hashimoto et al. [19.50] have shown that the ammonium halides (acidic mineralizer) and the alkali halide (neutral mineralizer) can form mixed cubic and hexagonal phases of GaN. Ehrentauf et al. [19.47] showed that pure hexagonal phases can be obtained in acidic ammonia solutions. Figure 19.10b shows that hexagonal formation is favored at lower temperatures in solutions for successively smaller halide cations. Pure phase hexagonal GaN was obtained at ≥ 470 °C for NH₄Cl mineralizer, ≥ 500 °C for NH₄Br mineralizer, and ≥ 550 °C for NH₄I mineralizer. If one takes into account the metastable nature of cubic GaN (Purdy [19.51] showed a correlation between cubic GaN formation and short-duration experiments), a phase conversion of the metastable cubic GaN to the stable hexagonal GaN could be possible in long-duration experiments as performed by Ehrentauf et al. [19.47].

19.2.2 Environmental Effects on Growth Kinetics and Structure Perfection (Extended and Point Defects)

The stable phase of ZnO and GaN has the wurtzite crystal structure, which is hexagonal with a space group of $P6_3mc$. The noncentrosymmetric structure of the wurtzite structure produces an anisotropy in which the opposite sides of a basal plane wafer have different atomic arrangements at their surfaces. This anisotropy in hexagonal GaN and ZnO also causes a nonsymmet-

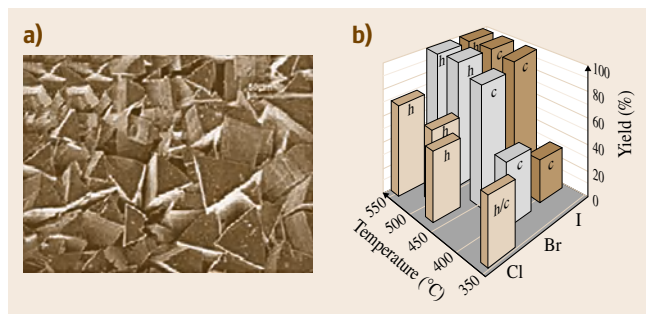


Fig. 19.10 (a) Ammonothermal cubic GaN formed under acidic conditions with the addition of lithium (after [19.46]); (b) temperature and mineralizer effect on phase stability of gallium nitride synthesized under acidic ammonothermal conditions (after [19.47]) (h – hexagonal, c – cubic)

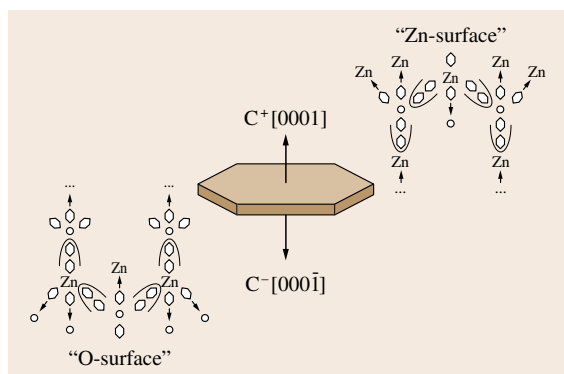


Fig. 19.11 Electronic charge distribution of zinc oxide basal faces (GaN has the same crystal structure as ZnO) (after [19.21,52])

rical charge state due to its anisotropic crystal structure. The C^+ side of the basal plane is comprised of a Zn-rich layer for ZnO or a Ga-rich layer for GaN, and the C^- is comprised of an O-rich layer for ZnO or a N-rich layer for GaN, as illustrated in Fig. 19.11 (a zinc oxide crystal is shown; gallium nitride has the exact same configuration).

The C^+ plane has a net positive surface charge because of the greater number of positive dangling bonds (Zn or Ga) on its surface, in contrast to the C^- plane, which has a net negative surface charge due to the greater number of negative dangling bonds (O or N). The resulting distribution of electric charge causes disparities, among the various growth planes, in growth rates, as well as in impurity incorporation, chemical etching, and optical and electrical properties.

Many anisotropic or polar crystals including inorganic and organic materials have been grown from solutions. When growing polar crystals from solutions, especially a highly polarized solution such as water or ammonia, investigations into the surface chemistry of the crystals and the composition of the growth medium need to be taken into consideration. Typically the solvent, the intermediate species in solution, and the crystal itself all have surface charge states. The intermediate species can be broken down into fundamental growth units that react with the crystal's growth facets. The structure of these growth units determines growth kinetics on the various polar faces of the crystal due in large part to the charge state of these faces in relation to the charge states of the fundamental growth units.

Impurities in solutions cause changes in molecular diffusion and atomic absorption on advancing crystal surfaces, which in turn, influences the growth kinetics of the crystal. Because ZnO and GaN have anisotropic crystal structures, impurities, even at small levels, can effect a change in growth rates along specific crystallographic axes which induce point and line defects. In addition, the concentrations of impurities incorporated in the various growth sectors of a polar crystal can vary. ZnO and GaN grown on their positive polar surfaces have different impurity concentrations, growth rates, and morphologies than material grown on the negative polar surfaces. In short, the growth characteristics (growth morphology, impurities distribution, and crystal quality) are influenced by the anisotropic nature of polar crystals. The influence of impurities on hydrothermal ZnO and ammonothermal GaN will be discussed in Sects. 19.4 and 19.5, respectively.

19.2.3 Doping and Alloying

Semiconductor wafers ideally should be conducting or insulating. The previous section discusses how impurities can dramatically influence the growth kinetics. Therefore, great care must be taken while applying doping in a solvothermal medium. The majority of dopants slow down growth rates because they block the diffusion and/or absorption of the matrix atoms to the lattice sites of the various surfaces of the crystal. Dopants can have different segregation coefficients in solution growth, similar to impurities in molten solidification. It is difficult to control growth morphology in anisotropic crystals grown from solution with high levels of impurities or dopants. As in any semiconductor crystal growth process, impurities must be reduced to the lowest possible levels. This will allow for the smallest levels of dopants introduced for the synthesis of semiconductor boules with the desired conductivity levels. Finally solvothermal has several advantages over molten techniques for the growth of alloy wafers, such as solid sources and low temperature gradients. Preliminary experiments of hydrothermal ZnMgO [19.53] and solvothermal AlGaIn [19.54] have been conducted.

Fluid flow and optimization of temperature zones are extremely important for the formation of low-defect crystals. The next two sections will discuss how to model fluid velocity and temperature gradient in a solvothermal system.

19.3 Physical and Mathematical Models

19.3.1 Flow and Heat Transfer

The hydrothermal and ammonothermal growth processes employ aqueous and ammoniated solvents under high temperatures and high pressures to dissolve and recrystallize materials that are relatively insoluble under ordinary conditions. After the system is pressurized, the solvent occupies most of the volume. The convection system for hydrothermal/ammonothermal growth consists of a porous bed whose height changes with the growth, a fluid layer overlying this porous bed, a metal baffle with holes (which lies above the porous bed), and solid seed plates whose size increase with the growth. Figure 19.12 shows the schematic of growth system that has been used experimentally to synthesize GaN [19.39]. The autoclave has an internal diameter of 0.932 cm, external diameter of 3.5 cm, internal height of 18.4 cm, and external height of 20.3 cm (Tem-Press MRA 138R with a volume of 12.5 ml). The thicknesses of the sidewall and bottom of the autoclave are 1.28 cm. The charge height is 1 cm, and the gap between the baffle and charge bed is 2 cm. A baffle made from 0.28 mm Ag foil is used to divide the autoclave into two parts: the upper and lower portions.

Hence the upper portion can be considered as a fluid layer with the assumption of incompressible flow

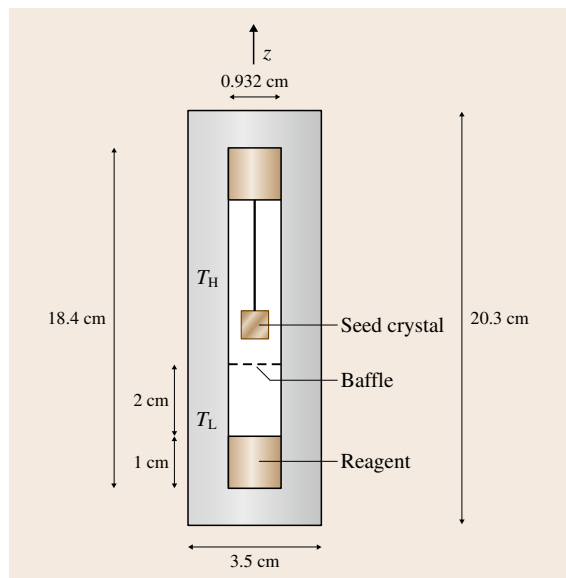


Fig. 19.12 Schematic of an ammonothermal growth system (after [19.55])

and the Boussinesq approximation [19.56, 57], and the Navier–Stokes equations can be used in the fluid layer. Suppose that the density has a linear temperature dependence of the form

$$\rho = \rho_0[1 - \beta(T - T_0)], \quad (19.1)$$

where ρ , β , and T are density, isobaric coefficient of expansion, and temperature, and ρ_0 and T_0 are constant reference values for the density and temperature, respectively.

In the solid region which comprises the autoclave walls, the baffle, and the seeds, only conductive heat transfer is considered. In the fluid region, convective heat transfer is considered.

19.3.2 Porous-Media-Based Transport Model

The nutrient particles (e.g., ZnO or GaN) in the bottom of the autoclave can be considered as a porous medium. In this case, the Darcy–Brinkman–Forchheimer model can be employed in the porous layer [19.58, 59]. The dimensionless parameters of the system are listed as follows

$$A = H/R, \quad \text{Gr} = g\beta R^3 \Delta T / \nu^2, \quad \text{Pr} = \nu / \alpha, \\ \text{Da} = K/R^2, \quad \text{Fs} = b/R,$$

where A , Gr , Pr , Da , and Fs denote the aspect ratio, Grashof number, Prandtl number, Darcy number, and Forchheimer number, respectively. H is the internal height of the autoclave, R is the internal radius of the autoclave, g is acceleration due to gravity, ΔT is the maximum temperature difference on the sidewall of the autoclave, ν is kinematic viscosity, α is thermal diffusivity, the permeability of porous matrix $K = d_p^2 \varepsilon^3 / [150(1 - \varepsilon)^2]$ with d_p as the average diameter of the nutrient particles, and the Forchheimer coefficient $b = 1.75 K^{0.5} / (\sqrt{150} \varepsilon^{1.5})$.

The governing equations in the porous and fluid layers can be combined by defining a binary parameter B as: $B = 0$ in the fluid layer and $B = 1$ in the porous layer, respectively. The porosity is $\varepsilon = 0$ in solid, $0 < \varepsilon < 1$ in porous layer, and $\varepsilon = 1$ in fluid layer, respectively. The combined governing equations in a cylindrical coordinate system are

$$\frac{\partial(\varepsilon \rho_f)}{\partial t} + \nabla \cdot (\rho_f \mathbf{u}) = 0, \quad (19.2a)$$

$$\begin{aligned} \frac{\rho_f}{\varepsilon} \frac{\partial \mathbf{u}}{\partial t} + \frac{\rho_f}{\varepsilon} (\mathbf{u} \cdot \nabla) \frac{\mathbf{u}}{\varepsilon} \\ = -\nabla p - \rho_f \beta (T - T_0) \mathbf{g} \\ + \nabla \cdot (\mu_e \nabla \mathbf{u}) - B \left[\left(\frac{\mu_f}{K} + \frac{\rho_f b}{K} |\mathbf{u}| \right) \mathbf{u} \right], \quad (19.2b) \end{aligned}$$

$$(\rho c_p)_e \frac{\partial T}{\partial t} + (\rho c_p)_f [(\mathbf{u} \cdot \nabla) T] = \nabla \cdot (k_e \nabla T), \quad (19.2c)$$

where μ , k , and c_p denote dynamic viscosity, thermal conductivity, and specific heat, respectively, and \mathbf{g} is the gravity vector. Subscripts f and e denote fluid and effective, respectively.

The following scales are used to nondimensionalize the governing equations: length, R ; velocity, $u_0 = v/R$; time, $t_0 = R^2/\nu$; pressure, $\rho \nu^2/R^2$; temperature, $T_H - T_L$. T_H and T_L are the high and low temperature applied on the sidewall of the autoclave, respectively. The resulting nondimensionalized equations are

$$\frac{\partial \varepsilon \bar{\rho}}{\partial t} + \frac{1}{r} \frac{\partial}{\partial r} (r \bar{\rho} u) + \frac{\partial}{\partial z} (\bar{\rho} w) = 0, \quad (19.3a)$$

$$\begin{aligned} \frac{\partial}{\partial t} \left(\frac{1}{\varepsilon} \bar{\rho} u \right) + \frac{1}{r} \frac{\partial}{\partial r} \left(\frac{1}{\varepsilon^2} r \bar{\rho} u u \right) + \frac{\partial}{\partial z} \left(\frac{1}{\varepsilon^2} \bar{\rho} w u \right) \\ = \bar{\mu} \left[\frac{1}{r} \frac{\partial}{\partial r} \left(r \frac{\partial u}{\partial r} \right) + \frac{\partial^2 u}{\partial z^2} - \frac{u}{r^2} \right] - \frac{\partial p}{\partial r} \\ - B \left(\frac{1}{\text{ReDa}} + \frac{\text{Fs}}{\text{Da}} |\mathbf{u}| \right) u, \quad (19.3b) \end{aligned}$$

$$\begin{aligned} \frac{\partial}{\partial t} \left(\frac{1}{\varepsilon} \bar{\rho} w \right) + \frac{1}{r} \frac{\partial}{\partial r} \left(\frac{1}{\varepsilon^2} r \bar{\rho} u w \right) + \frac{\partial}{\partial z} \left(\frac{1}{\varepsilon^2} \bar{\rho} w w \right) \\ = \bar{\mu} \left[\frac{1}{r} \frac{\partial}{\partial r} \left(r \frac{\partial w}{\partial r} \right) + \frac{\partial^2 w}{\partial z^2} \right] - \frac{\partial p}{\partial z} + \text{Gr} \Theta \\ - B \left(\frac{1}{\text{ReDa}} + \frac{\text{Fs}}{\text{Da}} |\mathbf{u}| \right) w, \quad (19.3c) \end{aligned}$$

$$\begin{aligned} \bar{\rho} \bar{c}_p \frac{\partial \Theta}{\partial t} + \frac{1}{r} \frac{\partial}{\partial r} (r \bar{\rho} u \Theta) + \frac{\partial}{\partial z} (\bar{\rho} w \Theta) \\ = \frac{1}{\text{Pr}} \bar{k} \left[\frac{1}{r} \frac{\partial}{\partial r} \left(r \frac{\partial \Theta}{\partial r} \right) + \frac{\partial}{\partial z} \left(\frac{\partial \Theta}{\partial z} \right) \right], \quad (19.3d) \end{aligned}$$

where $\bar{\rho} = \frac{\rho_e}{\rho_f}$, $\bar{\mu} = \frac{\mu_e}{\mu_f}$, $\bar{c}_p = \frac{c_{pe}}{c_{pf}}$, $\bar{k} = \frac{k_e}{k_f}$.

19.3.3 Numerical Scheme

The momentum equations (19.3b,c) and energy equation (19.3d) are solved using an in-house-developed finite-volume algorithm [19.60, 61]. The above conservation equations (19.3b–d) can be written in the

following general form

$$\begin{aligned} \frac{\partial}{\partial t} (rc \bar{\rho} \phi) + \frac{1}{r} \frac{\partial}{\partial r} (dr \bar{\rho} u \phi) + \frac{\partial}{\partial z} (d \bar{\rho} w \phi) \\ = \frac{\partial}{\partial r} \left(r \Gamma \frac{\partial \phi}{\partial r} \right) + \frac{\partial}{\partial z} \left(r \Gamma \frac{\partial \phi}{\partial z} \right) + r (S_C + S_p \phi), \quad (19.4) \end{aligned}$$

where ϕ is the generalized variable, Γ is the diffusion coefficient, and S_C is the volumetric source. The coefficients are defined as

$$c = \frac{1}{\varepsilon}, \quad d = \frac{1}{\varepsilon^2}, \quad \Gamma = \bar{\mu}, \quad S_C = -\frac{\partial p}{\partial r},$$

and

$$\begin{aligned} S_p = -B \left(\frac{1}{\text{ReDa}} + \frac{\text{Fs}}{\text{Da}} |\mathbf{u}| \right) - \frac{1}{r^2} \text{ for } (19.3b) \\ (\phi = u); \end{aligned}$$

$$c = \frac{1}{\varepsilon}, \quad d = \frac{1}{\varepsilon^2}, \quad \Gamma = \bar{\mu}, \quad S_C = -\frac{\partial p}{\partial z} + \text{Gr} \Theta,$$

and

$$S_p = -B \left(\frac{1}{\text{ReDa}} + \frac{\text{Fs}}{\text{Da}} |\mathbf{u}| \right) \text{ for } (19.3c) (\phi = w);$$

$$c = \bar{\rho} \bar{c}_p, \quad d = 1, \quad \Gamma = \frac{\bar{k}}{\text{Pr}}, \quad S_C = 0,$$

and

$$S_p = 0 \text{ for } (19.3d) (\phi = \Theta).$$

The grid used for this task is a structured trapezoidal mesh. For a typical primary point, the discretized form of the continuity (19.3a) in a generalized coordinate system (ξ, η) is then written as

$$\begin{aligned} \frac{\varepsilon \bar{\rho} - \varepsilon^0 \bar{\rho}^0}{\Delta t} r Ja \Delta \xi \Delta \eta \\ + [(r \bar{\rho} \alpha_\xi u_\xi)_e - (r \bar{\rho} \alpha_\xi u_\xi)_w] \Delta \eta \\ + [(r \bar{\rho} \alpha_\eta u_\eta)_n - (r \bar{\rho} \alpha_\eta u_\eta)_s] \Delta \xi \\ = S_{\text{NO}} \Delta \xi \Delta \eta, \quad (19.5) \end{aligned}$$

where Δt is the time step, the curvature source term arising from the nonorthogonal grid $S_{\text{NO}} = [(r \bar{\rho} \beta_\xi u_\eta)_e - (r \bar{\rho} \beta_\xi u_\eta)_w] \times \Delta \eta + [(r \bar{\rho} \beta_\eta u_\xi)_n - (r \bar{\rho} \beta_\eta u_\xi)_s] \Delta \xi$, α_ξ and β_ξ are the primary area and the secondary area over the control-volume face, which is represented by $\xi = \text{const}$, e.g., $\mathbf{u} \cdot \mathbf{e}^\xi h_\eta = \alpha_\xi u_\xi - \beta_\xi u_\eta$, where \mathbf{e}^ξ is the contravariant base vector, and h_η is the scale factor. So, $\alpha_\xi = h_\xi h_\eta^2 / (Ja)$ and $\beta_\xi = h_\xi h_\eta^2 (\mathbf{e}_\xi \cdot \mathbf{e}_\eta) / (Ja)$ [19.60, 61].

The momentum equations (19.3b,c) can be written as

$$\begin{aligned} & \frac{(rc\bar{\rho}\phi Ja - rc\bar{\rho}^0\phi^0 Ja^0)_P \Delta\xi \Delta\eta}{\Delta t} \\ & + [(r\alpha_\xi J_\xi)_e - (r\alpha_\xi J_\xi)_w] \Delta\eta \\ & + [(r\alpha_\eta J_\eta)_n - (r\alpha_\eta J_\eta)_s] \Delta\xi \\ & = [r(S_C + S_\phi)\phi Ja + S_\phi] \Delta\xi \Delta\eta, \end{aligned} \quad (19.6)$$

where the curvature source term S_ϕ arises from the nonorthogonal grid, and is given by $S_\phi = [(r\beta_\xi J_\eta)_e - (r\beta_\xi J_\eta)_w] \Delta\eta + [(r\beta_\eta J_\xi)_n - (r\beta_\eta J_\xi)_s] \Delta\xi$. The flux components in the ξ and η directions are $J_\xi = d\bar{\rho}u_\xi\phi - \frac{1}{h_\xi} \Gamma \frac{\partial\phi}{\partial\xi}$ and $J_\eta = d\bar{\rho}u_\eta\phi - \frac{1}{h_\eta} \Gamma \frac{\partial\phi}{\partial\eta}$, respectively.

Multiplying (19.5) by $d\phi$, subtracting it from (19.6), and multiplying the resulting equation by $(1+i)$ yields the discretized equation for u and v in the control volume [19.55, 61]

$$\begin{aligned} a_P\phi_P &= a_E\phi_E + a_W\phi_W + a_N\phi_N + a_S\phi_S \\ &\quad - (a_E + a_W + a_N + a_S)_{\text{conv}}\phi_P + S_\phi \\ &\quad - dS_{\text{NO}}\phi + b, \end{aligned} \quad (19.7)$$

where

$$\begin{aligned} a_P &= (1+i)rc\bar{\rho}Ja \frac{1}{\Delta t} - (1+i)rJaS_P \\ &\quad + (a_E + a_W + a_N + a_S)_{\text{cond}}, \\ b &= (1+i)rc\bar{\rho}^0Ja^0 \frac{1}{\Delta t} \phi_P^0 + (1+i)rJaSc + iS_{\text{conv}}, \end{aligned}$$

and

$$\begin{aligned} S_{\text{conv}} &= a_E\phi_E^0 + a_W\phi_W^0 + a_N\phi_N^0 + a_S\phi_S^0 \\ &\quad - (a_E + a_W + a_N + a_S)\phi_P^0 - dS_{\text{NO}}\phi^0. \end{aligned}$$

The subscripts *conv* and *cond* indicate convective and conductive terms, respectively. The discretization in time is first order when $i = 0$ and second order when $i = 1$.

The momentum equations can be written as

$$A_P u_P = (H_u)_P - (1+i) \frac{\partial p}{\partial r}, \quad (19.8a)$$

$$A_P w_P = (H_w)_P - (1+i) \frac{\partial p}{\partial z}, \quad (19.8b)$$

where the subscript P represents the central point of a finite volume

$$\begin{aligned} A &= (1+i)c\bar{\rho} \frac{1}{\Delta t} - (1+i)S_P \\ &\quad + [(a_E + a_W + a_N + a_S)_{\text{cond}}] / (rJa), \\ (H_u)_P &= [a_E u_E + a_W u_W + a_N u_N + a_S u_S \\ &\quad - (a_E + a_W + a_N + a_S)_{\text{conv}}\phi_P + S_\phi \\ &\quad - dS_{\text{NO}}\phi + b'] / (rJa), \end{aligned}$$

and b' represents b without the pressure term. The velocity component and pressure gradient in ξ direction are, respectively,

$$u_\xi = \frac{r'_\xi u + z'_\xi w}{h_\xi}, \quad (19.9a)$$

$$\frac{\partial p}{\partial \xi} = \frac{\partial p}{\partial r} r'_\xi + \frac{\partial p}{\partial z} z'_\xi, \quad (19.9b)$$

where the prime denotes the differential. By setting $(1+i)p$ as p , combining (19.8a,b), and using the procedures for pressure treatment as in [19.55, 62], we obtain

$$\begin{aligned} (u_\xi)_P &= \frac{(H_u - A_P u_P) r'_\xi + (H_w - A_P w_P) z'_\xi - \left(\frac{\partial p}{\partial \xi}\right)_P}{h_\xi A_P} \\ &\quad + (u_\xi)_P^0, \end{aligned} \quad (19.10)$$

and

$$\begin{aligned} (\bar{\rho} u_\xi \alpha_\xi)_P &= \left[(H_u - A_P u_P) r'_\xi + (H_w - A_P w_P) z'_\xi \right. \\ &\quad \left. - \left(\frac{\partial p}{\partial \xi}\right)_P \right] \bar{\rho} \alpha_\xi / (h_\xi A_P) + (\bar{\rho} u_\xi \alpha_\xi)_P^0. \end{aligned} \quad (19.11)$$

Substituting the above into the continuity equation, we obtain the pressure equation as

$$a_P p_P = a_E p_E + a_W p_W + a_N p_N + a_S p_S + b, \quad (19.12)$$

where

$$\begin{aligned} a_E &= D_e \Delta\eta, \\ a_P &= a_E + a_W + a_N + a_S, \\ D_e &= [\bar{\rho} \alpha_\xi / (h_\xi A)]_e, \\ b &= -\{[(H_\xi - Au_\xi)h_\xi]_e D_e + (\rho u_\xi \alpha_\xi)_e^0\} \Delta\eta \\ &\quad + \{[(H_\xi - Au_\xi)h_\xi]_w D_w + (\rho u_\xi \alpha_\xi)_w^0\} \Delta\eta \\ &\quad - \{[(H_\eta - Au_\eta)h_\eta]_n D_n + (\rho u_\eta \alpha_\eta)_n^0\} \Delta\xi \\ &\quad + \{[(H_\eta - Au_\eta)h_\eta]_s D_s + (\rho u_\eta \alpha_\eta)_s^0\} \Delta\xi \\ &\quad + S_{\text{NO}}, \end{aligned}$$

and

$$H_\xi = \frac{H_u r'_\xi + H_w z'_\xi}{h_\xi}.$$

For the temperature equation, profiled temperature boundary conditions are applied on the outer surfaces of the autoclave. The temperature profile set on the sidewall of the autoclave is $T = T_H$, $z < H_B - 0.5\delta_T$; $T = T_H - (T_H - T_L)(z - H_B + 0.5\delta_T)/\delta_T$; $H_B - 0.5\delta_T \leq$

$z < H_B + 0.5\delta_T$; $T = T_L$, $z > H_B + 0.5\delta_T$, where H_B is the height of the baffle and δ_T is the length of the portion of the wall where the temperature changes from T_H to T_L . The top and bottom of the autoclave are considered adiabatic. The temperature distribution is considered axisymmetric, $\partial T/\partial r = 0$, at $r = 0$.

For solving the momentum equations and the pressure equation inside the autoclave, the fluid boundaries were searched inside the autoclave in the r and z direc-

tions, respectively [19.55]. For example, when solving the equations using the tridiagonal matrix algorithm (TDMA) method, the fluid boundaries were searched in the r or z direction separately, and the equations were solved in different intervals of fluid space in this direction. In this way, the fluid field was obtained inside the autoclave that contains different shapes of baffles and seeds. A mesh size of 302×77 was used in the simulation, and the nondimensional time step was $\Delta t = 10^{-6}$.

19.4 Process Simulations

19.4.1 Typical Flow Pattern and Growth Mechanism

For the solubility curve with a positive coefficient of temperature, the growth zone is maintained at a lower temperature than that in the dissolving zone, thus the nutrient becomes supersaturated in the growth zone. The critical properties of ammonia are $T_c = 405.5$ K and $P_c = 112.8$ bar. The reduced pressure and reduced temperature at 2 kbar and 250°C for the growth condition in [19.39] are $P_r = 2000/112.8 = 17.7$ and $T_r = 523/405.5 = 1.3$. For $P_r = 10$ and $T_r = 1.3$, the viscosity and conductivity of ammonia are $\mu/\mu_1 = 4.3$ and $k/k_1 = 5.0$, where μ_1 and k_1 are the dynamic viscosity and the thermal conductivity at 250°C and atmospheric pressure [19.63].

Solubility data of GaN for mineralizers of KN_3 , KNH_2/KI were obtained in [19.39,55]. The solubility of GaN for mineralizer of 1.6 M KN_3 is high in the temperature range of $300\text{--}450^\circ\text{C}$. It seems that, by using azide as mineralizer, a high solubility of GaN can be obtained at low growth temperatures. For 0.8 M KNH_2/KI , the solubility is low in the range of $350\text{--}550^\circ\text{C}$. Mineralizer of 2–6 M KNH_2 or NaNH_2 was used to increase the solubility of GaN [19.55].

For charge particle size of 0.6 mm, $T_H - T_L$ applied on the sidewall of 50 K, and $\delta_T = 1$ cm, the aspect ratio, Grashof number, Prandtl number, Darcy number, and Forchheimer number for the system in [19.39] are $A = 40$, $\text{Gr} = 4.46 \times 10^6$, $\text{Pr} = 0.73$, $\text{Da} = 2.2 \times 10^{-5}$, and $\text{Fs} = 2.6 \times 10^{-3}$, respectively. The baffle has an opening of 30% in the cross-sectional area, including the central opening of 20% and a gap between the baffle and autoclave of 10% in the cross-sectional area. The reference velocity and time scale are $u_0 = 3.5 \times 10^{-5}$ m/s and $t_0 = 131$ s, respectively.

The flow pattern is shown in Fig. 19.13a. There are two flow cells rotating in different directions un-

der the baffle. The flow goes up along the sidewall driven by the buoyancy, which is caused by the high temperature applied on the lower part of the sidewall. Some flow penetrates through the gap between the baffle and the sidewall of the autoclave, and some flow goes inward along the baffle and then downward near the central opening of the baffle. The flow in the porous layer is much weaker than that in the fluid layer. The modified Grashof number can be used to measure the flow strength in the porous charge, $\text{Gr}^* = \text{Gr} \cdot \text{Da}$. In this case, the modified Grashof number is $\text{Gr}^* = 98.2$. The fluid flow cannot penetrate the porous layer, and heat and mass transfer in the porous layer are mainly by conduction and diffusion, respectively.

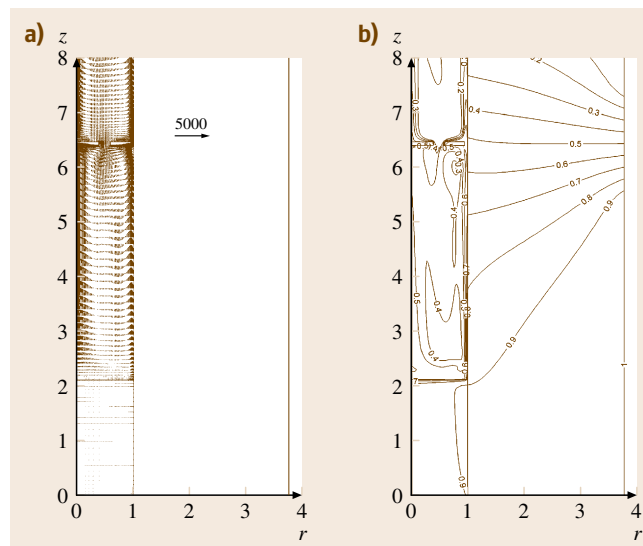


Fig. 19.13 (a) Fluid flow and (b) temperature distribution in an autoclave with internal diameter of 0.932 cm, internal height of 18.4 cm, particle size of 0.6 mm, and $\Delta T = 50$ K (after [19.55])

The temperature distribution is shown in Fig. 19.13b. The temperatures in the porous charge are almost the same as the high temperature T_H applied on the lower part of the sidewall of the autoclave. A large temperature gradient occurs near the fluid–charge interface. The aspect ratio in this case is 40 and the temperatures at $z > 20$ within the autoclave are almost the same as the low temperature T_L applied on the upper part of the sidewall of the autoclave.

19.4.2 Effect of Permeability on the Porous Bed

The optimum precursor sizes found in the ZnO growth experiments have been confirmed by numerical simulations [19.55]. When the charge particle size is increased from 0.6 mm to 3 mm, the Darcy number in the charge increases by 25 times and the modified Grashof number is $Gr^* = 2455$. Figures 19.14a and 19.14b show the flow pattern and temperature distribution in the autoclave, respectively. Significant convective effects are seen occurring in the charge (Fig. 19.14a), and the velocity is large in the porous layer. There are again two flow cells below the baffle. The flow moves upward through the gap between the baffle and the sidewall, and fluid flow is oscillating in the central hole. The flow structure above the baffle is complex and oscillating.

As can be seen from Fig. 19.14b, the temperature distribution in the charge is in the convection mode, and large temperature gradients appear near the interface between the charge and the sidewall of the autoclave. It is obvious that the particle size is an important factor to consider for successful growth of GaN by the ammonothermal method.

The constraints for ammonothermal growth include dissolving of the charge, nucleation on the sidewall, transfer of nutrient from charge to seed, and growth kinetics. Mass transfer between the charge and the fluid layer is important for successful growth. The flow strength in the fluid layer depends on the Grashof number, which is proportional to the temperature difference on the sidewall and the cube of the internal radius of the autoclave. Flow in the charge layer depends on the product of the Grashof and Darcy numbers, which is proportional to the square of the average diameter of particles. The flow strength in the porous layer is increased by increasing the size of the particles, or by putting particles in bundles as in the hydrothermal growth.

19.4.3 Baffle Design Effect on Flow and Temperature Patterns

The optimization of the baffle design has been performed numerically in [19.62] for the growth system used in [19.64] which has an internal diameter of 0.875 inch (2.22 cm), external diameter of 3 inch (7.62 cm), internal height of 14 inch (35.56 cm), and external height of 15 inch (38.10 cm) (Tem-Press MRA 378R with a volume of 134 ml) [19.64]. The thickness of the sidewall of the autoclave is 1 inch (2.54 cm). The baffle is located at a distance of 6 inch (15.24 cm) from the bottom of the autoclave. The charge particle size is 0.6 mm. $\Delta T = 50$ K is applied on the sidewall and the baffle thickness is 0.28 mm. The aspect ratio, Grashof number, Prandtl number, Darcy number, and Forchheimer number are, $A = 16$, $Gr = 6.0 \times 10^7$, $Pr = 0.73$, $Da = 3.8 \times 10^{-6}$, and $Fs = 1.1 \times 10^{-3}$, respectively. The reference velocity and time scale are $u_0 = 1.4 \times 10^{-5}$ m/s and $t_0 = 748$ s, respectively.

Figure 19.15a shows the flow pattern for a system with a baffle opening of 15% in the cross-sectional area, e.g., 10% in the central hole and 5% in the ring opening between the baffle and the sidewall of the autoclave. The flow is very weak in the porous layer, and the flow in the fluid layer is much stronger. The modified Grashof number, which is used to measure the flow strength in the porous charge, is $Gr^* = 228$. Thus, heat

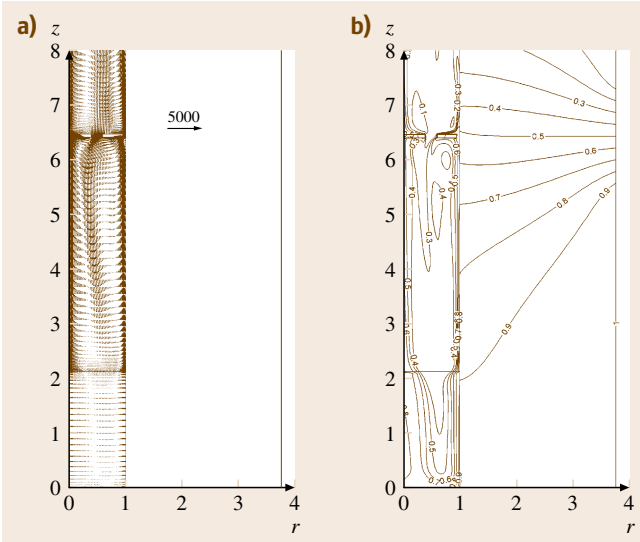


Fig. 19.14 (a) Fluid flow and (b) temperature distribution in a growth system with particle size of 3 mm and $\Delta T = 50$ K. The autoclave has an internal diameter of 0.932 cm and internal height of 18.4 cm (after [19.55])

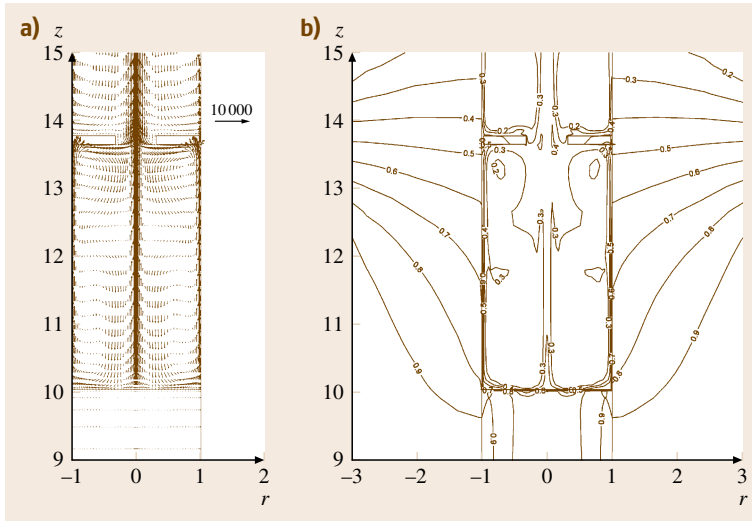


Fig. 19.15 (a) Fluid flow and (b) temperature field in a system with a baffle opening of 15% in the cross-sectional area (central opening of 10% and ring opening of 5%) (after [19.62])

and mass transfer in the porous layer is mainly by conduction and diffusion. This will constrain the nutrient transport between the charge and fluid layer, and cause nutrient deposition on the sidewall of the autoclave near the fluid–charge interface, as observed in experiments.

The temperature distribution is shown in Fig. 19.15b. The charge has a temperature of T_H as applied on the lower part of the autoclave. A large temperature gradient exists at the fluid–charge interface and the fluid–autoclave interface. Supersaturation in the fluid is

related to the temperature difference between the charge and the fluid layer. A large temperature gradient at the fluid–charge interface may cause a large supersaturation, and subsequently nucleation near the fluid–charge interface.

The mixing of flow across the baffle has been investigated. Figure 19.16 shows the changes of the vertical velocity at the center of the central hole opening in certain time period. The patterns of oscillations of velocity are repeatable for a longer time period than that

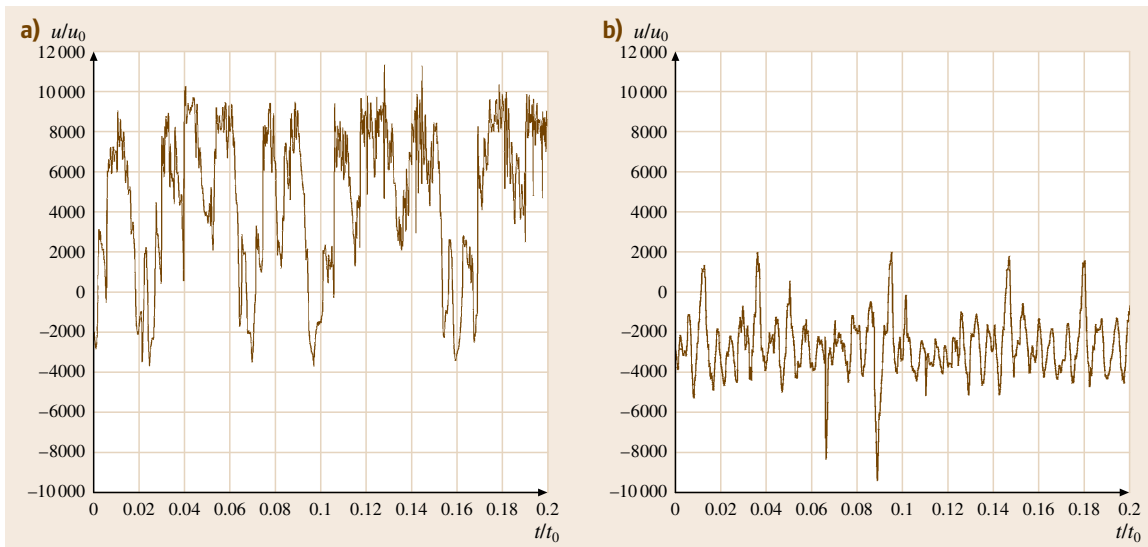


Fig. 19.16a,b Changes of the vertical velocity with time at the center of the central hole opening for baffle with (a) opening of 15% in the cross-sectional area, and (b) opening of 20% (after [19.62])

shown in Fig. 19.16. The heating on the bottom and cooling on the top promote Bénard-type convection in the fluid layer, which interacts with the vertical temperature boundary layer near the sidewall of the autoclave, causing the unsteady and oscillatory flow. For a long time period, it is observed that the amplitude of velocity oscillation in the center of the central hole is larger in the case of the 15% opening (Fig. 19.16a) than in the case of the 20% opening (Fig. 19.16b). The vertical velocity in the center of the central hole changes direction over time in the case of the 15% opening, while it is negative most of the time in the case of the 20% opening. In the case of the 20% opening, the fluid can go up through the ring opening of 10% in the cross-sectional area and return back through the central opening of the same size as the ring opening, so the flow is mixed more thoroughly across the baffle. Oscillation of the vertical velocity in the central hole can be decreased by reducing the difference between the sizes of the central opening and ring opening.

19.4.4 Effect of Porous Bed Height on the Flow Pattern

The influence of the height of the porous bed on transport phenomena in a hydrothermal system was investigated in [19.59]. Since the hydrothermal growth is a very slow process, it can be considered as qua-

sisteady, and the flow and temperature fields for given porous bed height under steady-state condition were obtained in [19.59]. Note that the height of the porous bed decreases as the polycrystalline charge dissolves and the solute moves up for deposition on the seed. Evidently the flow and temperature patterns will change with the porous bed height. *Chen et al.* [19.59] examined the effect of decreasing height in a case with $A = 3$, $\eta = 0.4$, $Pr = 1$, $Da = 10^{-4}$, and $Gr = 10^5$, where η denotes the ratio of the porous bed height and the overall height.

As shown in Fig. 19.17a, a small portion of the hot surface lies in the fluid region, which promotes a local recirculation on top of the porous layer because of the increased buoyancy effect in this region. The small cell now acts as a buffer restricting the fluid moving from the porous region to the fluid region. It gains fluid from both of the stronger cells and feeds back to them. When the Grashof number is low, the flow may show an axisymmetric pattern with two strong convective rolls and one weak cell. However, the axisymmetric nature of the flow field is completely destroyed at higher Grashof number. A convective roll may then appear in the central region directly above the porous bed and, depending on its location, the large convective rolls in the fluid region may shift. As can be expected, this does not influence the flow and temperature fields in the porous region in any appreciable manner as long as the Darcy number or permeability is low. From growth considerations, a change in flow pattern in the porous bed has no special meaning. However, a major shift in flow characteristics in the fluid region can significantly change the growth dynamics and quality of the crystal. The isotherm pattern is shown in Fig. 19.17b, which is distorted accordingly even though in the central region of the system.

19.4.5 Simulation of Reverse-Grade Soluble Systems

For the ammonothermal growth of GaN with a retrograde solubility, the predetermined amount of GaN particles is loaded above the baffle inside an autoclave (Fig. 19.18). GaN seeds are hung on a wire below the baffle. In this case, the solubility of GaN has a negative coefficient with respect to temperature, so that the growth zone in the lower part is maintained at a higher temperature than that in the upper part. The baffle opening is used to control the mixing of nutrients in two

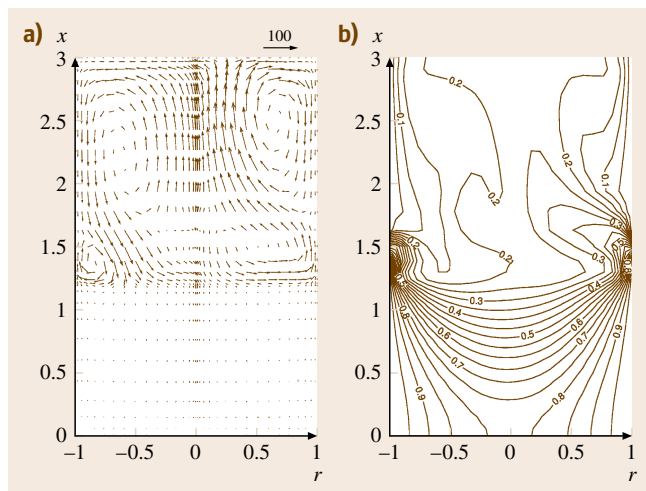


Fig. 19.17 (a) Fluid flow and (b) temperature distribution in a vertical cross-section of the autoclave; $A = 3$, $\eta = 0.4$, $Pr = 1$, $Da = 10^{-4}$, and $Gr = 10^5$ ($Gr^* = 10$) (after [19.59])

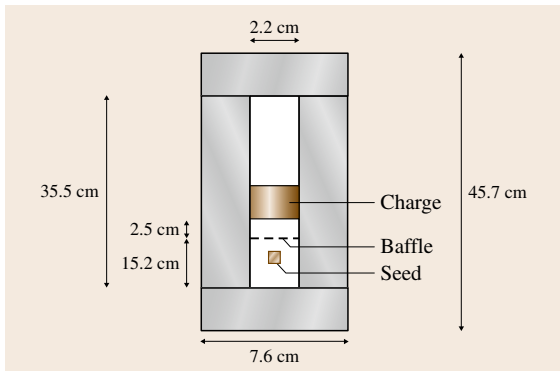


Fig. 19.18 Schematic of an ammonothermal growth system with retrograde solubility (after [19.65])

zones, and cause the transfer of nutrient from the upper part to the lower part.

By using a mineralizer of 2–3 M KNH_2 , GaN has a retrograde solubility in ammonia as in [19.64]. The solubility of GaN in ammonia changes from 10% by weight to 2% if temperature increases from 350 °C to 600 °C. With a fill of 60–85% and temperature of 600 °C, pressure is in the range of 25–45 kpsi. A typical run takes 14–21 days and deposition can be observed both on the seeds and on walls of the autoclave.

Numerical studies were performed for an autoclave used in [19.64]. The baffle is located at a distance of 6 inch (15.24 cm) from the bottom of the autoclave. The

charge of 4 inch in height is put 1 inch above the baffle, and the charge particle size is 0.6 mm. $\Delta T = 50$ K is applied on the sidewall and the baffle thickness is 0.28 mm.

Figure 19.19a shows the flow pattern for the growth system with retrograde solubility. The baffle openings are 15% of the cross-sectional area, including 10% in the central hole and 5% in the ring opening between the baffle and the sidewall of the autoclave. Since the GaN charge is put above the baffle, the flow is much stronger below the baffle, as shown in Fig. 19.19a. Highly oscillatory flow is observed across the central hole in the baffle. The flow in the central hole first moves downwards, sending nutrient to the growth zone at the bottom of the autoclave, then the flow moves upwards, sending exhausted fluid back to the dissolving zone in the porous layer. This process repeats with time. The opening of 15% causes very large flow oscillation across the baffle in this case.

The temperature distribution in the case of the retrograde solubility is shown in Fig. 19.19b. The temperature difference between the dissolving zone and growth zone is smaller than the temperature difference applied on the sidewall of the autoclave. A larger baffle opening means more fluid mixing across the baffle and less temperature difference between the two zones. In this case, the temperature across the baffle oscillates with time, and the magnitude of the oscillation of temperature is very large for baffle opening of 15%.

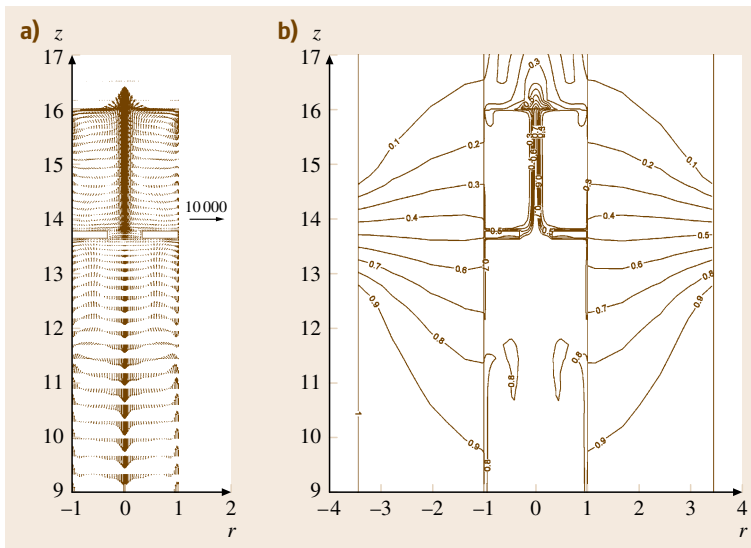


Fig. 19.19 (a) Fluid flow and (b) temperature distribution in an ammonothermal system with a retrograde solubility. Baffle opening is chosen as 15% in cross-sectional area (central opening of 10% and ring opening of 5%) (after [19.65])

19.5 Hydrothermal Growth of ZnO Crystals

19.5.1 Growth Kinetics and Morphology

Figure 19.20 shows the growth planes for hydrothermal zinc oxide crystals. Hydrothermal crystals are highly faceted due to the slow growth rates and lack of confinement during growth. Because each facet has an associated free energy, crystal growth rates can differ for different facets. Hydrothermal ZnO in an alkaline medium grows with the following facets: (0001) and (000 $\bar{1}$) monohedra (C^+ and C^- planes, respectively) and the six (10 $\bar{1}0$) prismatic faces (M planes). The six (10 $\bar{1}1$) pyramid faces (P planes) also can form under certain conditions, which will be describe in Sect. 19.5.2. *Laudise* and *Ballman* first observed the anisotropic growth rate on both spontaneous crystallites and crystals grown on seeds in 1 M NaOH [19.33]. ZnO crystals grown on a C^+ -plane seed and a M -plane seed are shown in Fig. 19.20.

Growth on the C^+ face is always faster than on the C^- face in hydroxide solutions above 1 M. Typical growth rates for 6 M KOH and 1 M LiOH are

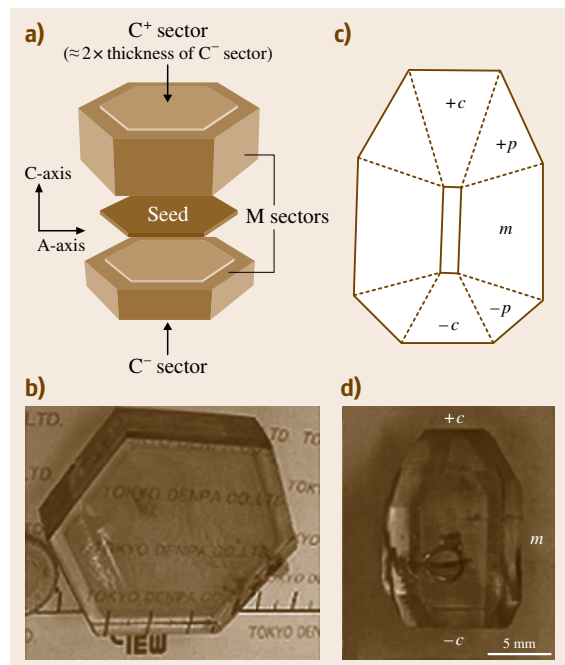


Fig. 19.20a–d Hydrothermal ZnO: (a) schematic and (b) crystal formed by growth on C^+ -plane seed (after [19.13]), (c) schematic and (d) crystal formed by growth on M -plane seed (after [19.66])

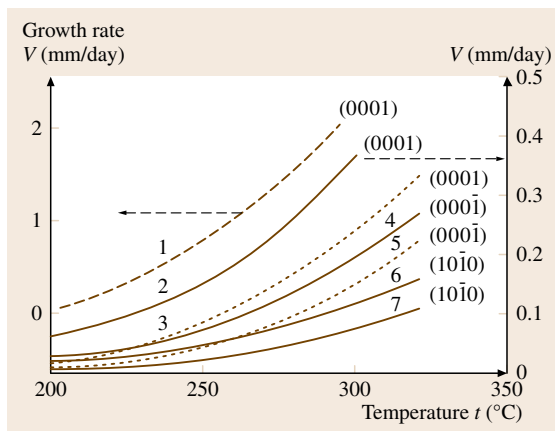


Fig. 19.21 Growth rates of the faces of the monohedra and the {10 $\bar{1}0$ } prism of ZnO single crystals in alkaline solutions as a function of temperature: (1) 5 M KOH and (2–7) 5.15 M KOH + 1.2 M LiOH as functions of temperature. Solid lines correspond to $\Delta t = 75^\circ\text{C}$; dashed lines to $\Delta t = 50^\circ\text{C}$ (after [19.67])

0.45 mm/day in the C^+ direction, and 0.22 mm/day in the C^- direction for growth on C^+ -plane seeds [19.24]. Growth rates on M -plane seeds average 0.2 mm/day in the direction normal to the M -plane [19.33]. *Demianets* et al. measured the growth kinetics on the different crystallographic faces by varying the type and concentration mineralizer, growth temperature, and temperature difference between the dissolution and crystallization zones [19.67]. Figure 19.21 shows more detailed kinetics of ZnO growth as a function of temperature. Note the effect that the addition of lithium, which improves the perfection of the ZnO crystal, has in decreasing the growth rate.

The authors went on to determine the elementary surface layers for the possible growth facets of ZnO. The elementary surface layers were then used to determine the relative theoretical growth velocities under ideal conditions (*the absence of any additional components in the crystallization medium*) for the different crystallographic faces of ZnO. The relationships of the velocities are

$$V(10\bar{1}0) < V(000\bar{1}) \sim V(0001) \\ < V(10\bar{1}1) < V(10\bar{1}2) < V(1\bar{1}20).$$

The sequence would be reversed to characterize the prevalence of the faces in the formed crystal. The ideal

velocities above would form simple shapes such as monohedra and prisms but water, a polar solvent, adds a great deal of complexity to the kinetics of crystal growth.

The anisotropy of the growth rates for the various crystal facets is related to the charge distribution on the facets and the charge of the ions in solution. Several researchers have studied the solubility and thermodynamic parameters of aqueous Zn species for natural hydrothermal systems. *Khodakovsky and Yelkin* concluded that $\text{Zn}(\text{OH})_4^{2-}$ is the dominant species in alkaline solution at the high temperatures and high pH values at which bulk crystals are grown [19.70]. *Bénézech et al.* investigated solubility of zinc oxide in 0.03–1.0 M sodium trifluoromethanesulfonate solutions to determine thermodynamic properties of the transport species in dilute acidic and alkaline solutions [19.60, 71]. The Gibbs free energy of formation, entropy, and enthalpy at 25 °C and 1 atm were determined for Zn^{2+} , $\text{Zn}(\text{OH})^+$, $\text{Zn}(\text{OH})_2^0$, and $\text{Zn}(\text{OH})_3^-$ by employing a hydrogen electrode concentration cell and periodic sampling of cell potentials. Solubility data at temperatures up to 200 °C for $\text{Zn}(\text{OH})^+$, $\text{Zn}(\text{OH})_2^0$, and $\text{Zn}(\text{OH})_3^-$, and at temperatures up to 290 °C for Zn^{2+} , were also obtained. The authors concluded that $\text{Zn}(\text{OH})_4^{2-}$ was the predominant species in OH^- solutions above 0.1 M NaOH. *Wang and Li et al.* performed systematic studies of the morphology and growth rates of zinc oxide powder in alkaline solutions [19.68, 69, 72]. Starting with $\text{Zn}(\text{OH})_2$ colloids as nutrient, they investigated morphological changes as a function of pH (Fig. 19.22).

The studies assumed that $\text{Zn}(\text{OH})_4^{2-}$ growth units were the predominant species in solution when hydrox-

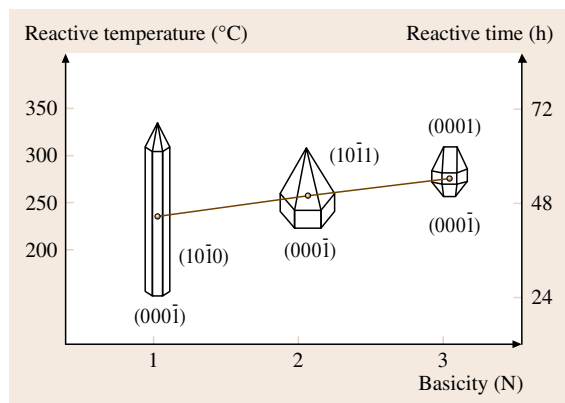


Fig. 19.22 Morphological changes of ZnO crystallites with increasing pH of the growth solution (after [19.68])

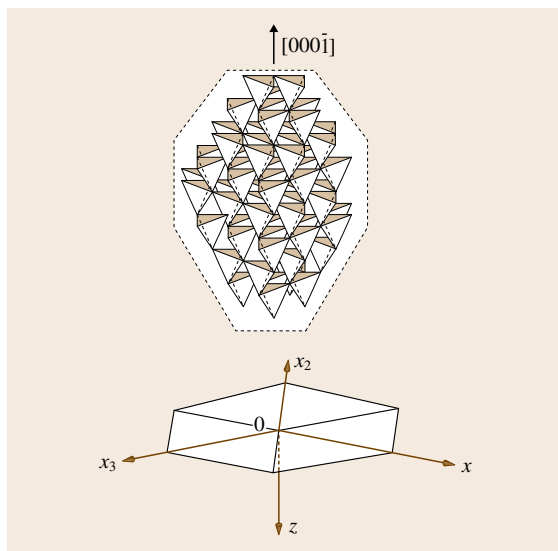


Fig. 19.23 ZnO crystal structure image represented in the form of the coordination tetrahedron along the x -direction (C^- surface made up of flat faces at top) (after [19.69])

ide colloids were dissolved. These growth units have a tetrahedral form and charge distribution similar to those of ZnO, which itself is a series of tetrahedra (Fig. 19.23). The corner (point) of a zinc oxide tetrahedron can bind with three hydroxide growth units, the edge with two growth units, and the face of the tetrahedron with only one growth unit. The viscosity of the hydrothermal growth solution is low, so the crystal interface structure plays a large role in kinetics. Thus analysis of Fig. 19.23 would predict the following relative growth rates under ideal conditions

$$V(0001) > V(01\bar{1}1) > V(0\bar{1}10) \\ > V(01\bar{1}1) > V(000\bar{1})$$

The hydroxide growth units cluster together by dehydration. In strong alkali solution these clusters are shielded by ions such as Na^+O^- , shielding the growth units and slowing down growth. *Wang et al.* contend that these mechanisms account for the growth rates and shape of bulk zinc oxide crystals in strong alkali solutions. *Demianets and Kostomarov* proposed a similar mechanism, but argued that $\text{Zn}(\text{OH})_4^{2-}$ dissociates into $\text{ZnO}_2^{2-} + 2\text{H}^+$, and that the ZnO_2^{2-} concentration increases with increasing pH [19.26]. Reaction of one ZnO_2^{2-} with the zinc surface of the crystal allows two ZnO units to form, whereas reaction on the oxygen

surface allows only one ZnO unit because of charge compensation.

Addition of lithium to the solution, as hydroxide or carbonate, improves the quality of the bulk zinc oxide crystals but also reduces the growth rate in the (0001) facet while increasing the rate on the (10 $\bar{1}$ 0) facets [19.67, 73]. This may be due to the shielding mechanism mentioned above. *Kuz'mina* et al. grew ZnO crystals grown in KOH solutions that had higher structural quality but more highly faceted than those grown in NaOH solutions [19.27]. *Suscavage* et al. used a 3 M NaOH:1 N KOH:0.1–0.5 N Li₂CO₃ solution which produced ZnO crystals with low defect densities and less P-plane faceting than KOH-grown crystals [19.21]. The mixed NaOH–KOH solvent had the added benefit of being less corrosive than KOH solutions. The crystal shown on the left-hand side in Fig. 19.20 [19.13] has negligible P-plane faceting and fits the kinetic models of Wang and Demainets discussed before. The low impurity levels in these crystals, high levels of lithium, and growth on fully faceted C-plane seeds may have suppressed formation of the P-plane in these crystals.

Sakagami found that hydrothermal zinc oxide crystals have tens of ppm excess zinc [19.25]. He therefore added H₂O₂ as an oxidizer; excess zinc was reduced to 1–2 ppm. The addition of an oxidizer such as hydrogen peroxide slows the growth rate on all faces, especially the C[−] facet [19.27]. Manganese and nickel had no effect on the kinetics but did color the crystals red and green, respectively. No effect of these dopants on the electrical resistance could be discerned [19.27]. Addi-

tion of NH₄⁺ increased the growth rate on the (10 $\bar{1}$ 0) facets, but crystal quality was degraded [19.27]. *Demianets* et al. published a more detailed paper on the effect of Li⁺ and several of the divalent and trivalent metals (Co²⁺, Fe²⁺, Mn²⁺, Fe³⁺, Mn³⁺, Sc³⁺, In³⁺) on growth kinetics and morphology of hydrothermal ZnO [19.67]. Figure 19.20 shows that, as metallic impurities are increased in the ZnO growth medium, P-plane facets are formed and C-axis growth rates decreases. The decrease in growth rates can be explained by the shielding effects impurities can have on the matrix compound (i. e. ZnO) as discussed in Sect. 19.2.

19.5.2 Structural Perfection – Extended Imperfections (Dislocations, Voids, etc.)

Because hydrothermal zinc oxide and quartz are both amphoteric single-component oxides, many insights into zinc oxide hydrothermal can be obtained from studies on hydrothermal quartz growth, which has been intensely investigated during the last 50 years. *Laudise* and *Barnes* [19.74] and *Armington* [19.75] have published excellent reviews on the growth of high-perfection quartz and on dislocation mechanisms. Extended imperfections that can be formed in both zinc oxide and quartz include the following:

- Seed veils and etch channels – small holes or channels filled with voids, water vapor or liquid, caused by etch tracks that form on seeds during initial growth

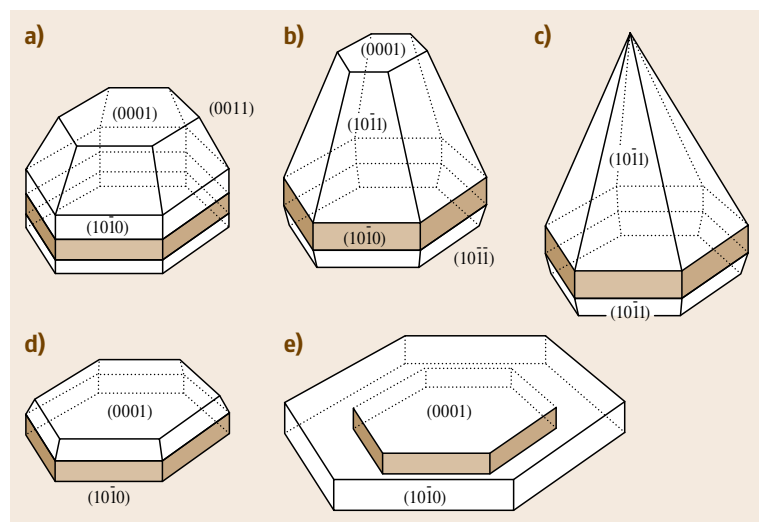


Fig. 19.24a–e Impurity effects on morphology of hydrothermal ZnO crystals (a) Li⁺, (b,c) Fe⁺, (d) Mn²⁺, (e) In³⁺ (after [19.67])

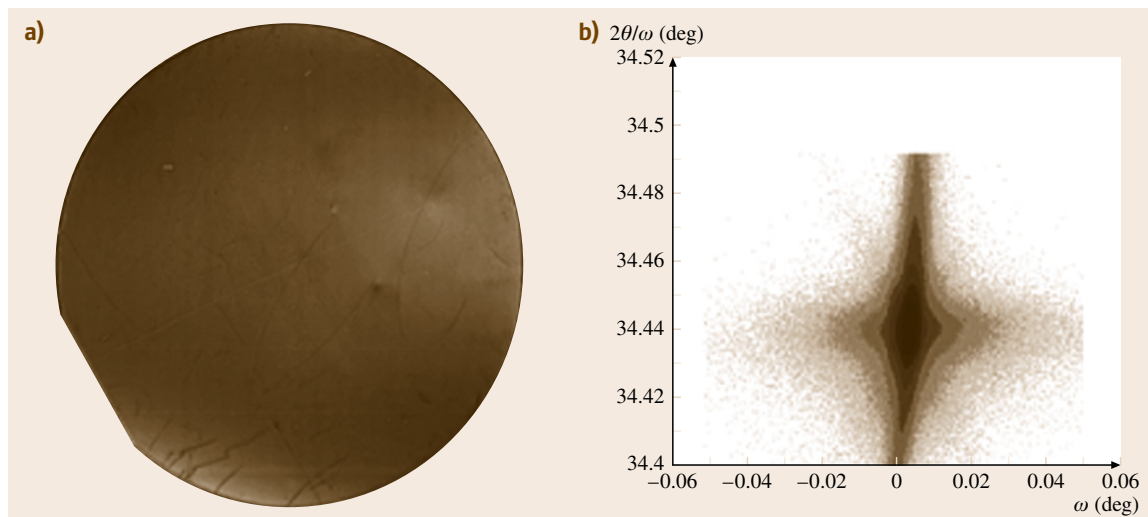


Fig. 19.25 (a) Reflection x-ray topograph of 2 inch ZnO wafer in C-axis projection. (b) (002) reciprocal-space map of corresponding wafer (after [19.13])

- Voids – small holes filled with air, water vapor or liquid; can occur whenever growth conditions change abruptly at the growth surface (impurity clusters, cracks, or crystalline particles from nutrient brought to growth interface by fluid flow)
- Crevice flaws – equivalent to dendritic growth in metals. Uneven or rough growth caused by a change of surface kinetics on growth faces. In extreme cases can cause gaps, cracks, and large numbers of dislocations
- Dislocations – equivalent to those in melt-grown bulk crystals. Strain-induced, because of impurity incorporation or intersection of growth planes, dislocations often propagate from seed into crystal
- Vertical etch channels – equivalent to micropipes that form in vapor-grown crystals. Dislocations decorated with impurities causing cylindrical voids that can reach from the seed to the surface of the crystal

All these imperfections have been observed in hydrothermal zinc oxide bulk crystals. *Laudise and Barnes* [19.74] stated that very small nutrient particle size resulted in low growth rates and flawed growth, and an optimal particle of several millimeters was determined, which was confirmed by *Chen et al.* [19.55] by numerical simulation. Addition of lithium, use of low dislocation-density seeds, and use of high purity nutrient also reduces the concentrations of most imperfections. Lithium may reduce imperfections by decreasing the surface free energy when lithium ions

incorporate at the growth interface. Lithium may also limit the incorporation of H_2O and OH^- into the crystal lattice at the growth interface [19.76–78].

Figure 19.25 shows a reflection x-ray topograph and the (002) reflection reciprocal-space map for a low-defect commercial 2 inch-diameter (0001) ZnO wafer. Both measurements demonstrate very low defect concentrations in the wafer analyzed [19.13]. Commercial hydrothermal ZnO wafers have measured etch pit densities in the range of 100 cm^{-2} and the full-width half-maximum (FWHM) of the rocking curve below 20 arcsec, another indication of the high crystallinity of hydrothermal ZnO wafers.

Synchrotron white-beam x-ray topography (SWBXT) in Laue configuration was performed on a series of crystals grown at AFRL-Hanscom [19.79]. To trace the growth history of the crystal, (10 $\bar{1}$ 0) crystal plates containing both the seed crystal and the bulk region were imaged. One set of topographs showed the usual propagation of edge dislocations from the seeds (Fig. 19.26). The growth sector (GS) boundary can also clearly be seen, marking a change of growth morphology.

On several other crystals the topographs revealed a capping phenomenon similar to that observed in KDP [19.80]. Figure 19.26b shows that the dislocation density is very high near the seed–crystal interface, revealing strain associated with growth initiation rather than dislocations propagating from the seed into the bulk. A growth band, possibly because of a fluctuation

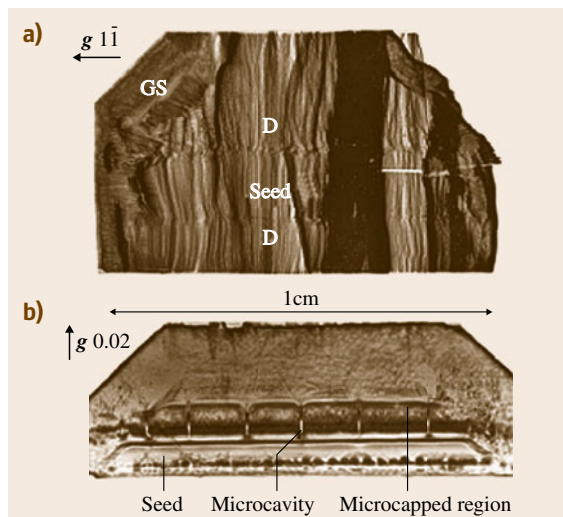


Fig. 19.26a,b Synchrotron white-beam x-ray topographs of ZnO seed–crystal interfaces (after [19.79]): (a) normal seed interface (D – dislocations, GS – growth sector boundary); (b) ZnO microcapped region, exhibiting microcavities and low dislocation generation above microcapped region in the C^+ direction

in the growth conditions, stops many of these dislocations. In some cases microcavities originating at the seed–crystal interface were observed; the cavities heal during subsequent growth, nucleating dislocations.

The cause of microcapping has not been established. One possible mechanism is seed etch-back during initial growth, due to fluctuations in the temperature gradient coupled with seed misalignment from C -plane orientation.

Surface studies on hydrothermal crystals showed the C^+ surface to be smooth and specular, with spiral hexagonal growth pyramids [19.27]. The C^- surface is more three-dimensional, with layer-like growth. The M -planes also have layered growth; the P -planes have a series of terraces. No in-depth study has addressed the mechanisms responsible for these various morphologies on the growth surfaces.

19.5.3 Impurities, Doping, and Electrical Properties

Generally the impurity concentrations in hydrothermal ZnO depend not only upon the purity of starting materials, but also upon the growth conditions (solution chemistry, growth temperature, etc.). Fe, Ag, Si, Na, Li, K, and Al are the primary impurities found in

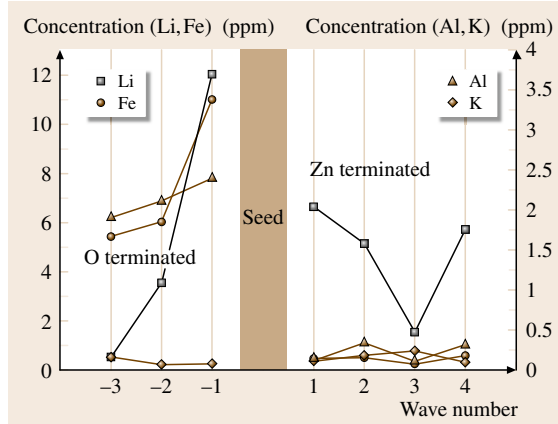


Fig. 19.27 Discharge mass spectroscopy (DMS) data for ZnO wafers sliced along the C^- and C^+ growth directions of a commercial 2 inch-diameter boule (after [19.13])

hydrothermal ZnO crystals. *Sekiguchi et al.* reported impurity concentration variations among crystals that were grown under various conditions of temperature and pressure but that otherwise were nominally identical [19.66]. Nonetheless, low-ppm impurity and sub- 10^{16} cm^{-3} donor/acceptor concentrations have been achieved [19.13, 21], demonstrating that hydrothermal ZnO crystals can have purities that rival or exceed the purities of bulk ZnO grown by other methods – purities, in fact, that rival or exceed those of III–V semiconductors such as InP and GaN. Figure 19.27 shows glow discharge mass spectroscopy (GDMS) data for ZnO wafers sliced along the C^- and C^+ growth directions of a commercial 2 inch-diameter boule [19.13]. High levels of lithium were incorporated in the crystal for growth in both the C^- and C^+ directions. The divalent and trivalent metals levels are two orders of magnitude lower in the wafers grown in the C^+ (Zn-terminated) growth direction.

The resistivity over a 2 inch hydrothermal wafer cut from the C^+ sector (Zn-terminated growth) was measured to be $380 \Omega \text{ cm} \pm 15\%$ [19.13].

Lithium is often added to hydrothermal solutions as hydroxide or carbonate because it improves crystallinity and morphology, as stated in the previous section. Li can therefore occur in concentrations of $>10 \text{ ppm}$ in hydrothermal ZnO [19.13, 21, 25, 66]; it has been employed to achieve resistivities as high as $10^{10} \Omega \text{ cm}$ by compensating native donors [19.18]. Lithium is anathema to most electronic and optical device fabricators, who fear that Li – typically a fast diffuser – will incorporate into devices and thereby *poison* them. This may

not be an insurmountable obstacle for device applications, as Li apparently can be removed from ZnO by annealing in a zinc atmosphere [19.77]. Also, using appropriate mineralizer solutions, it is possible to obtain high-quality as-grown hydrothermal ZnO crystals that have sub-ppm Li concentrations [19.21].

In, Ga, and Al are shallow donors in ZnO [19.82, 83]. As mentioned above, Li occupying the Zn site is believed to be an acceptor (interstitial Li is believed to be a donor [19.77]); addition of Li or Cu increases the resistivity of ZnO after annealing in air or Zn [19.22,24,76,77], probably by compensating donors. The donor/acceptor properties of Fe^{2+} and Fe^{3+} in ZnO are not known. The role of hydrogen in ZnO is controversial: recent theoretical calculations predict it should be a shallow donor [19.84], in overall agreement with experimental measurements performed in the 1950s that associated increases in electrical conductivity with hydrogen incorporation (reviewed in [19.85]); however, in recent work on MOCVD-grown ZnO films, the conductivity increase was attributed to passivation of acceptors [19.86]. Hydrothermal growth of ZnO in an effective overpressure of H_2 was achieved by adding Zn powder to the growth solution; unfortunately only the carrier concentrations after annealing in vacuum or air ($2\text{--}5 \times 10^{15} \text{ cm}^{-3}$), not carrier concentrations in as-grown ZnO, were reported [19.77].

Native defects such as oxygen vacancies or zinc interstitials have long been regarded as donor centers in ZnO (see, e.g., [19.84, 87] and references therein). In many cases, they may constitute the most numerous donor sites. Sakagami's observation that the ZnO electrical resistance increased when an oxidizing agent was added to the hydrothermal growth solution (equivalent to growth in an oxygen overpressure) [19.25] is indirect evidence that many donor defects result from imperfect zinc–oxygen stoichiometry.

Semi-insulating behavior in hydrothermal ZnO has, as already noted, been achieved through lithium doping [19.83] and growth in an effective oxygen overpressure [19.25]. Semi-insulating behavior, with a net room-temperature free electron concentration of $\approx 2 \times 10^{12} \text{ cm}^{-3}$, and electron mobility of $\approx 175 \text{ cm}^2/\text{Vs}$, was observed [19.21]. The cause of this behavior was found to be a donor center located 340 meV below the conduction band; the microscopic nature of this donor is not understood.

The presence of large growth facets on hydrothermal ZnO crystals facilitates study of electronic properties as a function of crystallographic orientation and surface polarity. Urbietta et al. employed scanning

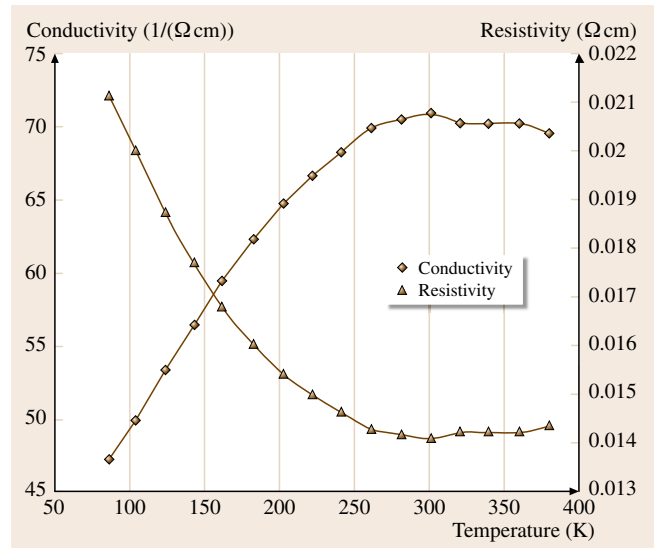


Fig. 19.28 Hall-effect data for indium-doped ZnO wafer (after [19.81])

tunneling microscopy and found clear differences in surface electronic structure that distinguished the C^+ (zinc-surface), C^- (oxygen-surface), and m (nonpolar surfaces) [19.88]. Sakagami et al. measured I – V and C – V characteristics on the crystallographic C^+ , C^- , and m faces [19.89]. Along all crystallographic axes studied, they observed nearly ohmic behavior when surfaces were zinc-rich and rectifying behavior when surfaces were oxygen rich. The authors' judgment that m -sectors are more suitable than c^+ and c^- sectors for making electrical contacts, if confirmed, has potential significance for device fabrication that could stimulate interest in ZnO crystal growth on nonbasal plane.

Hydrothermal conducting indium-doped ZnO was grown using sintered zinc oxide powder that was mixed with a small percentage indium oxide [19.81]. As previously stated, growth rates were dramatically reduced in the C -axis (Fig. 19.23c). Conductivity measurements for a $5 \times 5 \text{ mm}^2$ In:ZnO sample is shown in Fig. 19.28. The conductivity achieved is adequate for most semiconductor device applications that would benefit from conducting substrates.

19.5.4 Optical Properties

The most sensitive indications of crystal quality often come from optical measurements at near-liquid-helium temperatures, where excitonic and other bands indicate the underlying quality (or lack thereof) of the material.

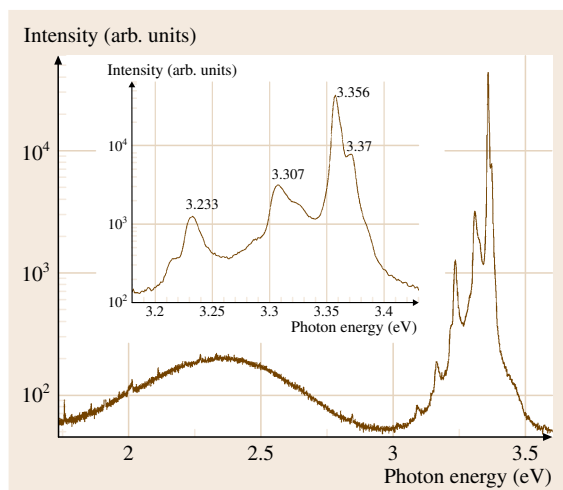


Fig. 19.29 Low-temperature broadband photoluminescence spectrum (after [19.13])

Broadband spectra at both high and low temperatures can provide useful information about impurities and native defects.

The broadband low-temperature photoluminescence (PL) spectrum of a 2 inch ZnO wafer is shown in Fig. 19.29. In addition to the UV band (excitonic and donor–acceptor bands at energies above 3 eV), there is a broad band centered at ≈ 2.3 eV. Similar broad extrinsic *orange* and *green* bands have been reported in several PL [19.90] and cathodoluminescence (CL) [19.91, 92] measurements of hydrothermal grown ZnO. Several authors have shown that the intensity of the UV band compared with the intensity of the broad-band can provide qualitative information on the crystal quality of hydrothermal ZnO [19.92, 93].

Conflicting mechanisms have been advanced for the origin of the green band. Reynolds et al. compared the ZnO green band to the *yellow band* in GaN (a wurtzitic crystal having a bandgap similar to that of ZnO), whose origin remains a matter of debate, and concluded that both bands arise from a transition between a shallow donor and a deep level [19.94]. However, Garces et al. concluded, from electron paramagnetic resonance (EPR) and PL spectra of unannealed and annealed vapor-phase-grown ZnO, that ZnO green bands are caused by emission from Cu^+ and Cu^{2+} ions, respectively [19.82].

Orange and green CL has been observed in the *m*, *c*, and *p* sectors of hydrothermal ZnO crystals. Strong green emission (in addition to near-band-edge emission, which is ignore for the purposes of this discussion)

was observed from C^+ (Zn-terminated) surfaces, and weak orange emission from C^- (oxygen-terminated) surfaces; green emission was observed from P^- surfaces (Zn-terminated) and orange emission from P^+ (oxygen terminated) surfaces; and there was weak orange emission from the (nonpolar) *M* face [19.66]. Combining these and related observations with the growth kinetic models, Sekiguchi et al. [19.66] and Urbietta et al. [19.95, 96] associated the occurrence of ZnO green and orange CL bands with impurity incorporation efficiencies (during crystal growth) that the growth model attributes to the polarization state of ZnO sectors (c^+ , c^- , *m*, etc.); similarly, UV and broadband luminescence efficiencies were associated with presumed incorporation rates of nonradiative recombination centers. In this vein, Sekiguchi et al. noted that orange emission was strongest in their sample that had the highest Li concentration and lower in a flux-grown crystal that contained virtually no Li; they also noted that use of H_2O_2 in the hydrothermal growth solution, which presumably lowered the concentration of oxygen vacancies, significantly reduced the orange emission [19.66]. An overview of visible luminescence in ZnO has more comprehensive information of the possible mechanisms

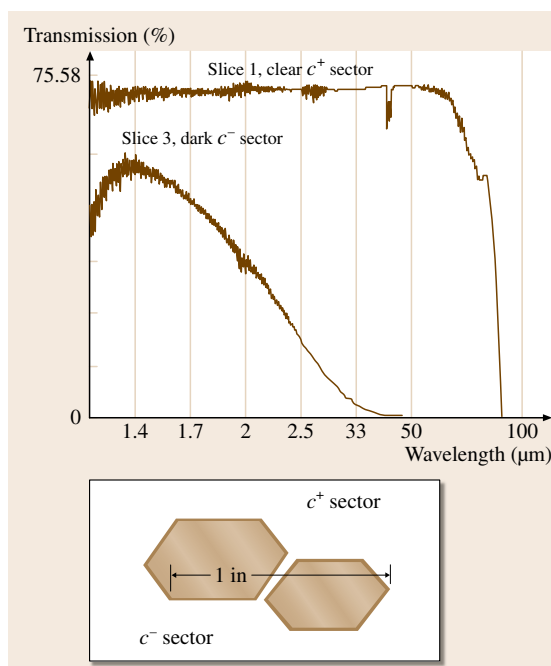


Fig. 19.30 IR transmission spectra of ZnO slices cut from c^+ and c^- growth sectors of a ZnO crystal (after [19.21])

of broadband emission in ZnO bulk crystals and thin films [19.97].

We complete our summary of the optical properties of hydrothermal ZnO by considering transmission spectra (Fig. 19.30) [19.98]. Insulating ZnO is transparent from the near-ultraviolet almost to 10 μm (the spectrum in Fig. 19.30 labeled *clear c^+ sector*). Elec-

trically conducting samples (e.g., the spectrum labeled *dark c^- sector*) exhibit a long-wavelength free-carrier absorption tail. The optical transparency shown in Fig. 19.30, together with the high laser breakdown strength of ZnO [19.98], have made ZnO the leading candidate for transparent conducting electrodes for high-power near-IR laser beam steering devices [19.99].

19.6 Ammonothermal GaN

19.6.1 Alkaline Seeded Growth

Callahan et al. [19.64] synthesized and grew GaN crystals in a retrograde configuration (Fig. 19.8) with 2–3 M KNH_2 concentration. Seeded growth experiments employed autoclaves with 2.2 cm internal diameter and 140 ml volume. Both sets of autoclaves are capable of sustained operation at 600 $^\circ\text{C}$ and pressures up to 4 kbar.

Polycrystalline GaN, synthesized by an in-house vapor process [19.100], was suspended in a scaffold near the bottom of the autoclave to obtain solubility data. Single-crystal *free-standing* gallium nitride up to 200 μm thick with a surface area of 1 cm^2 grown by hydride vapor-phase epitaxy (HVPE) was used as seeds and suspended by a wire scaffold near the bottom (warmer portion) of the autoclave. Seeded growth experiments were carried out for 5–30 days. Transported material nucleates on the walls of the autoclave, the wire scaffold, and on the GaN HVPE seeds. The mass of heterogeneously nucleated materials recovered from the

lower walls (crystallization zone) is often eight to ten times the weight gain of the seeds.

Single-crystal growth on the seeds occurred at a rate of up to 40 μm per day. Growth approaching 1 mm in thickness was achieved on multiple seeds. Etching studies were conducted to determine the polarity of the crystalline surfaces. Previous work [19.101] indicates that the C^+ face (gallium face) when exposed to phosphoric acid etchants shows little erosion of the bulk material. The nitrogen polar face (Fig. 19.31a) has flatter surface than the gallium polar face (Fig. 19.31b). A cleaved cross-section of as-grown gallium nitride is shown in Fig. 19.31c. Growth in the C^+ and C^- directions (gallium face and nitrogen face, respectively) exhibits a columnar-type growth, with much more pronounced grain boundaries seen in the growth on the gallium face. Under different experimental conditions growth rates of the C^+ and C^- planes differ, but are approximately equal. Substantial growth in the *a*-direction has also been observed.

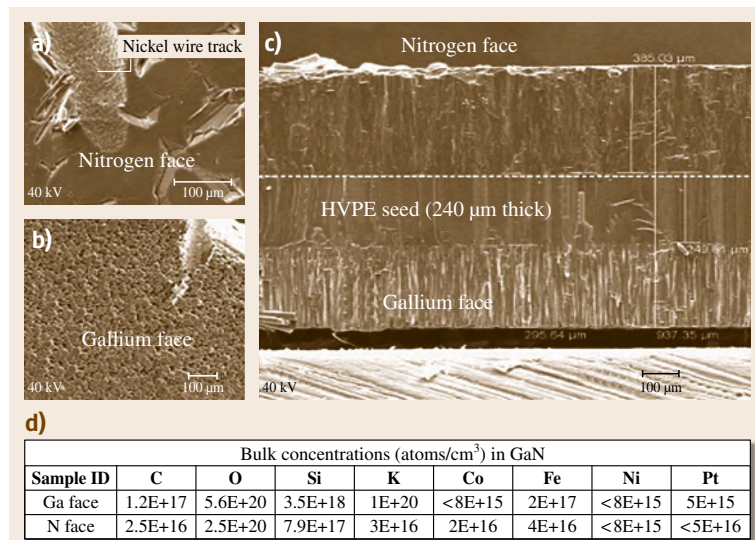


Fig. 19.31a–d Thick ammonothermal GaN growth (after [19.64]) (a) SEM image of nitrogen polar face. (b) SEM image of gallium polar face. (c) SEM image of a cleaved cross-section of gallium nitride grown on HVPE seed. (d) Impurity concentrations of Ga and nitrogen faces measured by secondary ion mass spectrometry (SIMS)

Secondary ion mass spectrometry (SIMS) were performed on as-grown ammonothermal gallium nitride crystal samples. The results from a characteristic sample are shown in Fig. 19.31d. Impurities do not incorporate into the bulk crystal homogeneously. Concentrations of impurities were different between the gallium and nitrogen surfaces of the bulk crystal. In general metallic impurities incorporated less on the nitrogen face than the gallium face. Figure 19.31d shows that the impurity levels for oxygen and hydrogen are above 10^{19} atoms per cm^3 for both faces. Potassium impurities for the mineralizer were 10^{19} cm^3 atoms per cm^3 on the gallium face and mid 10^{18} cm^3 atoms per cm^3 on the nitrogen face.

The reciprocal-space maps and reflection topographs are shown in Fig. 19.32 for an ammonothermal crystal grown under similar conditions as those in Fig. 19.31 [19.102].

It is evident that the ammonothermal growth has higher defects levels than the HVPE seed. When a thinner film of $\approx 50 \mu$ was grown [19.103] there was less columnar growth. The levels of impurities in the crystals and the nonuniform crystallinity of the HVPE seeds make quantitative analysis difficult.

The ammonothermal growth of 1 inch-size (0001) GaN crystal in a cylindrical high-pressure autoclave having an internal diameter of 40 mm was reported by Hashimoto et al. [19.17, 104]. About $15 \mu\text{m}$ -thick GaN films were uniformly grown on each side of the GaN seed, which has an oval shape of $3 \times 4 \text{ cm}^2$. The applied temperature and pressure were $625\text{--}675^\circ\text{C}$ and about 2.14 kbar. Basic mineralizers were used, resulting in retrograde solubility of GaN in supercritical ammonobasic solutions. The nutrient was placed in the colder region (upper region) and free-standing C-plane HVPE GaN seed crystals were placed in the hotter region (lower

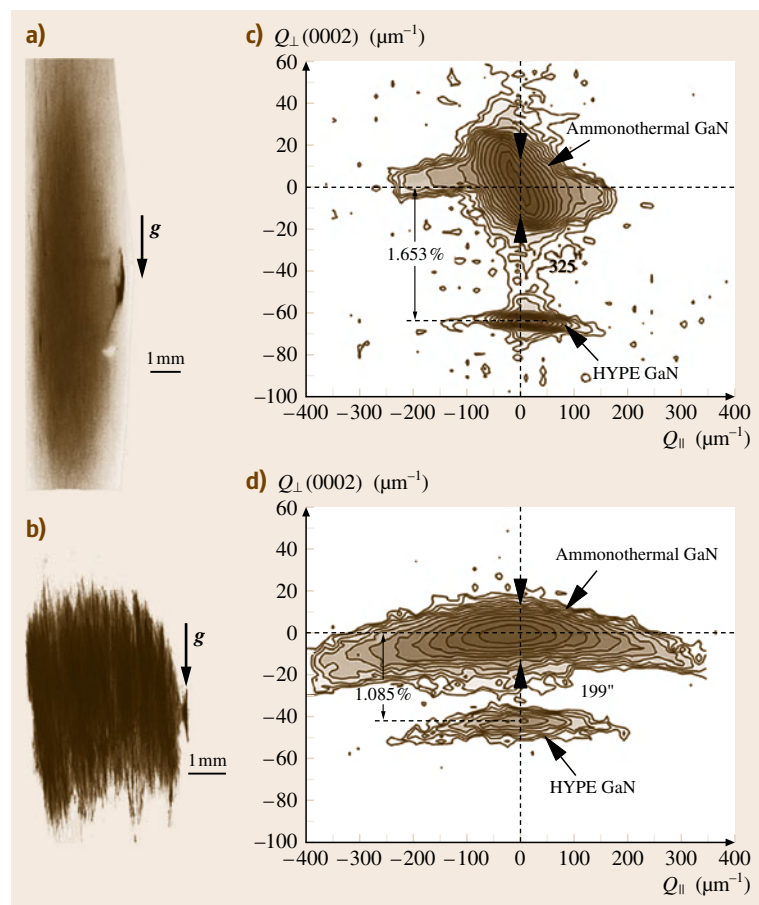


Fig. 19.32a–d Reciprocal-space maps and reflection topographs for ammonothermal GaN and HVPE seed grown with KNH_2 mineralizer (after [19.102])

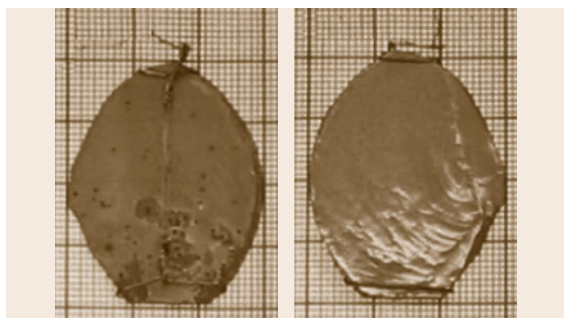


Fig. 19.33 Ammonothermal growth on $40 \times 30 \text{ mm}^2$ HVPE seed (after [19.17, 104])

region). A baffle divides the reactor into an upper region and a lower region to set a temperature difference between the dissolving region and the crystallization region. Uniform growth of GaN films on an over-1 inch oval-shaped seed crystal was achieved through fluid transport of Ga nutrient. Ga nutrient was transformed to GaN on the crucible wall, resulting in abrupt drop of the growth rate in about a day. The crystal is shown in Fig. 19.33.

Polycrystalline GaN nutrient and higher mineralizer concentration was used for longer growth runs. Due to thick wall of the autoclave, the temperature difference between the upper and lower regions of the fluid is estimated to be less than 50°C . The resulting ammonia pressure was about 1.8–1.9 kbar. The growth rates along C^+ (Ga face), C^- (N face) and M direction were 0.8, 3.6, and $6 \mu\text{m}/\text{day}$. The authors showed a defective growth interface with numerous voids and defects; as growth progressed the structure improved [19.106].

Dwilinski et al. recently reported on GaN crystals grown in alkaline ammonia with a dislocation density on the order of $5 \times 10^3 \text{ cm}^{-2}$ [19.107], which is several orders of magnitude lower than what has previously been reported. An x-ray rocking curve FWHM of 17 arcsec was measured on a 1 inch substrate cut from one of the GaN crystals and subsequently polished. There was no evidence of mosaicity or low-angle grain boundaries. X-ray rocking curves under 20 arcsec and radius of curvature on the order of 10^2 – 10^3 meters were measured on various crystals from separate growth runs. The authors did not disclose how the superior crystallinity of the GaN crystals was obtained.

Figure 19.34 is unpublished data [19.105] that shows photoluminescence (PL) of an alkaline ammonia sample, rack, and wall nucleation. The PL is improved over previous experiments. The broadband emission is reduced over previous runs [19.103] and there is no ev-

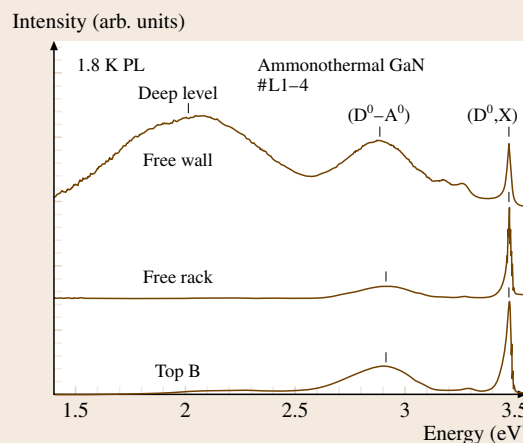


Fig. 19.34 Photoluminescence spectra of ammonothermal GaN (note the difference in broadband emission) (after [19.105])

idence of a PL signature at 3.4 eV that was identified as stacking-fault-related emission [19.108]. The wall nucleation has a greater number of broadband emissions. This might be evidence of impurities leaching from the autoclave.

19.6.2 Acidic Seeded Growth

Due to the corrosive nature of acidic solvents a platinum or silver liner must be used to contain the experiment. Figure 19.35 shows a scanning electron microscopy (SEM) image of acidic ammonothermal growth at a relatively low pressure of $\leq 170 \text{ MPa}$ and temperature in the range 500 – 550°C . The film was grown in standard configuration (forward-grade solubility). The authors increase the temperature and obtained columnar growth.

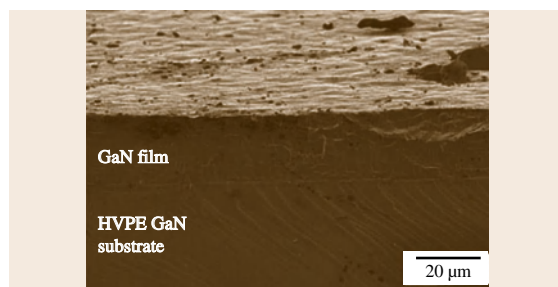


Fig. 19.35 Cross-sectional SEM image of $21 \mu\text{m}$ of ammonothermal growth on a HVPE seed using NH_4Cl as a mineralizer (after [19.43])

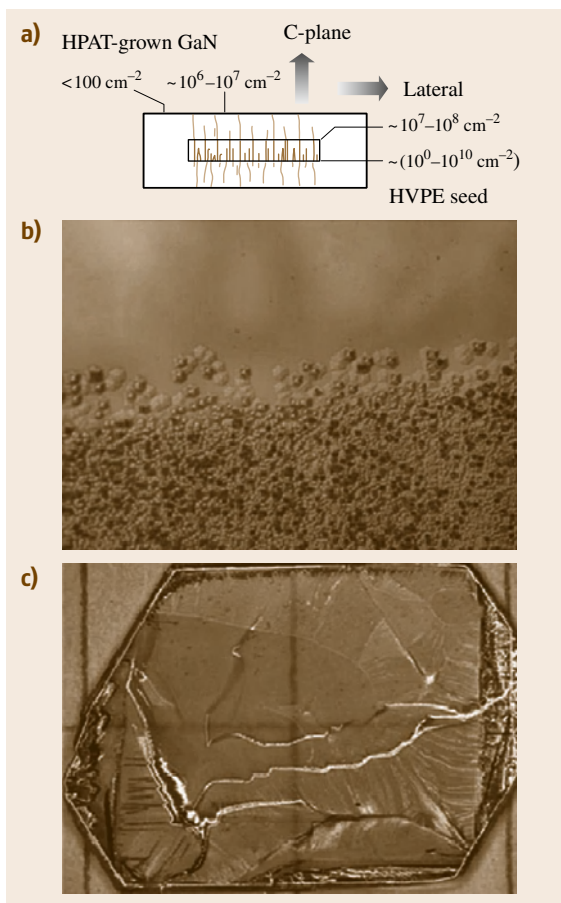


Fig. 19.36a–c GaN grown in high-pressure anvil cell at 700 °C; (a) schematic of growth; (b) SEM of low-defect/high-defect seed interface in the m-plane direction; (c) picture of large HVPE seed with ammonothermal growth showing smooth morphology (after [19.109])

Figure 19.36 shows a GaN crystal grown in a sealed capsule that is placed in a high-pressure cell with a solid pressure medium [19.109]. The cell is similar to the type used for piston-press and belt-press synthesis of diamond. The cell was heated between 600–1000 °C with a pressure in the range 5–20 kbar. The authors show a standard forward-grade solubility configuration for growth. The higher pressure and temperatures that this system can withstand allow for much higher growth rates than those that can be obtained in autoclaves. Figure 19.36a shows a schematic of the dislocation density of a crystal grown by the high-pressure ammonothermal technique (HPAT). Growth in the direction perpendicular to the HVPE seed was almost free of dislocations

and other defects. This shows the advantage of using the ammonothermal technique to obtain very low-defect material. The impurities in the crystals grown were reduced by two orders of magnitude (10^{20} – 10^{18}) from a previous publication. The authors fabricated a functional laser diode on one of the HPAT substrates.

19.6.3 Doping, Alloying, and Challenges

There has been synthesis of InGaN nanocrystals [19.110], polycrystalline AlN [19.111], and GaN microcrystals doped with transition-metal ions (Mn, Fe, and Cr) for dilute magnetic semiconductor applications [19.112]. Transition metals could also be used to increase resistance in GaN wafers. Finally, AlGaN microcrystalline balls were synthesized ammonothermally [19.54]. The Al metal nutrient was depleted before the end of the run. The result was two different compositions of AlGaN in the inner and outer portions of the ball, as seen in Fig. 19.37. It is surmised that an AlGaN alloy liquid droplets formed during the heating process and the AlGaN crystallized around the droplets.

Several challenges need to be overcome with ammonothermal technology in order to bring GaN-based crystal growth from research into full production. High-quality seeds, nutrient, equipment, and a complete understanding of the chemistry are required. Ammonothermal growth will leverage other growth technologies such as flux growth and HVPE growth for sources of seeds and nutrient. Electrical and optical characterization will proceed as large-area ammonothermal GaN crystals become available. Denis et al. published an excellent review of GaN bulk growth [19.113]. This technology is still in its infancy and there are many unique avenues to be explored.

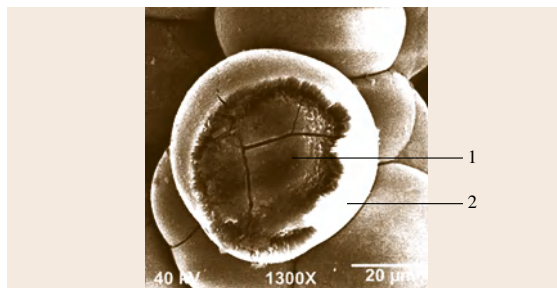


Fig. 19.37 Ammonothermal AlGaN balls (after [19.54]): 1 – $\text{Al}_{0.5}\text{Ga}_{0.5}\text{N}$; 2 – $\text{Al}_{0.25}\text{Ga}_{0.75}\text{N}$; nutrient – molar ratio of Al : Ga = 3 : 7 (Al nutrient was depleted during course of experiment)

19.7 Conclusion

Hydrothermal growth has produced very high-quality zinc oxide crystals. Nearly dislocation-free growth can be produced in zinc-terminated growth sectors and on nonpolar prism faces. Semi-insulating and conducting crystals have been grown, as well as crystals exhibiting superior low-temperature PL characteristics.

The various crystallographic faces of hydrothermal ZnO exhibit pronounced differences not only in the growth rates, but also in structural, electrical, and optical properties. The growth mechanisms, the incorporation of impurities, and the generation of native defects are (at least in part) connected to the polarity of the growth surfaces; however, the precise mechanisms – and especially the properties of impurities and native defects – have not been fully elucidated. Exploiting the faceted morphology of hydrothermal crystals may facilitate studies of these phenomena, many of which surely have counterparts in ZnO thin-film growth and ZnO bulk growth by other methods. Hydrothermal ZnO technology has progressed rapidly in the last 5 years with the capability to produce hundreds of wafers in a single run. Therefore economical growth of large, low-defect-density ZnO crystals is waiting for innovative strategies in ZnO device design and fabrication to spur demand for large-scale commercialization of ZnO-based devices and therefore ZnO substrates.

Significant progress has been made in acidic and alkaline ammonothermal growth of GaN. Forward solubility in ammonia has been determined when using acidic mineralizers such as NH_4Cl , in contrast with alkaline mineralizers such as KNH_2 , where a retrograde solubility was discovered. Several groups have

demonstrated that low-defect-density GaN can be produced using the ammonothermal technique, and growth on 1–2 inch-diameter GaN HVPE templates has been shown.

Process modeling and simulation based on physics are necessary in the scale-up of solvothermal systems. Forward solubility has been simulated for an autoclave with an internal diameter of 0.932 cm and internal height of 18.4 cm. The optimum precursor sizes found in the GaN growth experiments have been confirmed by numerical simulations. The fluid field can be significantly increased by an increase of the particle size from 0.6 mm to 3 mm. The optimization of the baffle design has been performed numerically and needs to be carefully selected to achieve a predefined temperature difference across the baffle, to achieve the necessary supersaturations required for the crystallization of single crystals at elevated growth rates.

Ammonothermal technology is a fertile ground for the production of many nitrogenated compounds that are difficult to synthesize by other techniques. The production of gallium nitride by the ammonothermal method requires a large amount of further investigation just as the production of quartz did in the early 20th century. In-depth phase, solubility, growth kinetics, and fluid dynamics studies need to be completed for a multiplicity of mineralizers, and high-strength vessels must be designed for the increased pressure requirements of supercritical ammonia. The cost advantages afforded by growing on multiple seeds simultaneously make this technique an attractive means for meeting the demand for high-quality gallium nitride substrates.

References

- 19.1 F. Bernardini, V. Fiorentini, D. Vanderbilt: Spontaneous polarization and piezoelectric constants of III–V nitrides, *Phys. Rev. B* **56**(R10), 24–27 (1997)
- 19.2 S.J. Pearton, C.R. Abernathy, F. Ren: *Gallium Nitride Processing for Electronics, Sensors and Spintronics* (Springer, Berlin Heidelberg 2006)
- 19.3 B. Gil: *Low-Dimensional Nitride Semiconductors* (Oxford Univ. Press, Oxford 2002)
- 19.4 C. Jagadish, S.J. Pearton: *Zinc Oxide, Thin Films and Nanostructures: Processing, Properties, and Applications* (Elsevier Science, Amsterdam 2006)
- 19.5 Ü. Özgür, Y.I. Alivov, C. Liu, A. Teke, M.A. Reshchikov, S. Doğan, V. Avrutin, S.-J. Cho, H. Morkoç: A comprehensive review of ZnO material and devices, *Appl. Phys. Rev.* **98**(041301), 1–103 (2005)
- 19.6 I. Akasaki: Key inventions in the history of nitride-base blue LED and LD, *J. Cryst. Growth* **300**, 2–10 (2007)
- 19.7 C. Klingshirn, R. Hauschild, H. Priller, M. Decker, J. Zeller, H. Kalt: ZnO rediscovered – once again!?, *Superlattice Microstruct.* **38**, 209–222 (2005)
- 19.8 H.J. Scheel: Historical aspects of crystal growth technology, *J. Cryst. Growth Technol.* **211**, 1–12 (2000)
- 19.9 J. Nause, B. Nemeth: Pressurized melt growth of ZnO boules, *Semicond. Sci. Technol.* **20**, S45–S48 (2005)
- 19.10 J. Karpiński, J. Jun, S. Porowski: High pressure thermodynamics of GaN, *J. Cryst. Growth* **66**, 1–10 (1984)

- 19.11 H.D. Sun, Y. Segawa, M. Kawasaki, A. Ohtomo, K. Tamura, H. Koinuma: Phonon replicas in ZnO/ZnMgO multiquantum wells, *J. Appl. Phys. Lett.* **91**(10), 6450–6457 (2002)
- 19.12 D.C. Look, D.C. Reynolds, J.R. Sizelove, R.L. Jones, C.W. Litton, G. Cantwell, W.C. Harsch: Electrical properties of bulk ZnO, *Solid-State Commun.* **105**, 399–401 (1998)
- 19.13 D. Ehrentraut, H. Sato, Y. Kagamitani, H. Sato, A. Yoshikawa, T. Fukuda: Solvothermal growth of ZnO, *Prog. Cryst. Growth Charact. Mater.* **52**, 280–335 (2006)
- 19.14 D.A. Kramer: Nitrogen (fixed) Ammonia. In: *US Geological Survey*, ed. by US Department of the Interior (United States Government Printing Office, Washington 2005) pp. 116–117
- 19.15 K. Byrappa, M. Yoshimura: *Handbook of Hydrothermal Technology* (William Andrew, New York 2001)
- 19.16 M.T. Harris, J.J. Larkin, J.J. Martin: Low-defect colorless Bi₁₂SiO₂₀ grown by hydrothermal techniques, *Appl. Phys. Lett.* **60**, 2162–2163 (1992)
- 19.17 T. Hashimoto, K. Fujito, M. Saito, J.S. Speck, S. Nakamura: Ammonothermal growth of GaN on an over-1-inch seed crystal, *Jpn. J. Appl. Phys.* **44**, L1570–L1572 (2005)
- 19.18 R.A. Laudise: *Hydrothermal Growth in The Growth of Single Crystals* (Prentice-Hall, New Jersey 1970) pp. 275–293
- 19.19 H. Jacobs, D. Schmidt: High-pressure ammonolysis in solid-state chemistry. In: *Current Topics in Materials Science*, Vol. 8, ed. by E. Kaldis (North Holland, Amsterdam 1982) pp. 381–427
- 19.20 B. Wang, M.J. Callahan: Ammonothermal synthesis of III-nitride crystals, *Cryst. Growth Des.* **6**(6), 1227–1246 (2006)
- 19.21 M. Suscavage, M. Harris, D. Bliss, P. Yip, S.Q. Wang, D. Schwall, L. Bouthillette, J. Bailey, M. Callahan, D.C. Look, D.C. Reynolds, R.L. Jones, C.W. Litton: High quality ZnO crystal, *Mater. Res. Soc. Symp. Proc.* **537**, 294–299 (1999)
- 19.22 R. R. Monchamp, R. C. Puttbach, J. W. Nielson: Hydrothermal growth of ZnO crystals (Airtron Division of Litton Industries, Morris Plains, technical report AFML-TR-67-144 1967)
- 19.23 R.A. Laudise, E.D. Kolb: The solubility of zincite in basic hydrothermal solvents, *Am. Mineral.* **48**(3), 642–648 (1963)
- 19.24 D.F. Croxall, R.C.C. Ward, C.A. Wallace, R.C. Kell: Hydrothermal growth and investigation of Li-doped zinc oxide crystals of high purity and perfection, *J. Cryst. Growth* **22**, 117 (1974)
- 19.25 N. Sakagami: Hydrothermal growth and characterization of ZnO single crystals of high purity, *J. Cryst. Growth* **99**, 905–909 (1990)
- 19.26 L. Demianets, D. Kostomarov: Mechanism of zinc oxide single crystal growth under hydrothermal conditions, *Ann. Chim. Sci. Mater.* **26**(1), 193–198 (2001)
- 19.27 I.P. Kuz'mina, A.N. Lobachev, N.S. Triodina: *Synthesis of Zincite by the Hydrothermal Method in Crystallization Process Under Hydrothermal Conditions* (Nauka, Moscow 1973) pp. 27–41
- 19.28 T. Fukuda, D. Ehrentraut: Prospects for the ammonothermal growth of large GaN crystals, *J. Cryst. Growth* **305**, 304–310 (2007)
- 19.29 E.V. Kortunova, P.P. Chvanski, N.G. Nikolaeva: The first attempts of industrial manufacture of ZnO single crystals, *J. Phys. IV France* **126**, 39–42 (2005)
- 19.30 L.E. McCandlish, R. Urhin: Mild conditions for hydrothermal growth of ZnO with potential for p-type semiconductor behavior, Poster Presentation at 5th Int. Conf. Solvotherm. React. Conf (East Brunswick, 2002), image supplied directly by L.E. McCandlish
- 19.31 G.F. Hüttig, H. Möldner: The specific heat of crystallized zinc hydroxide and calculation of the affinities between zinc oxide and water, *Z. Anorg. Chem.* **211**, 368–378 (1933)
- 19.32 C.H. Lu, C.H. Yeh: Influence of hydrothermal conditions on the morphology and particle size of zinc oxide powder, *Ceram. Int.* **26**, 351–357 (2000)
- 19.33 R.A. Laudise, A.A. Ballman: Hydrothermal synthesis of zinc oxide and zinc sulfide, *J. Phys. Chem.* **64**(5), 688–691 (1960)
- 19.34 M.M. Lencka, R.E. Riman: Synthesis of lead titanate: thermodynamic modeling and experimental verification, *J. Am. Ceram. Soc.* **76**, 2649–2659 (1993)
- 19.35 M.M. Lencka, A. Anderko, R.E. Riman: Hydrothermal precipitation of lead zirconate titanate solid solutions: thermodynamic modeling and experimental synthesis, *J. Am. Ceram. Soc.* **78**, 2609–2618 (1995)
- 19.36 M.M. Lencka, R.E. Riman: Thermodynamic modeling of hydrothermal synthesis of ceramic powders, *Chem. Mater.* **5**, 61–70 (1993)
- 19.37 R. Dwilinski, R. Doradzinski, J. Garczynski, L. Sierzputowski, J.M. Baranowski, M. Kaminska: AMMONO method of GaN and AlN production, *Diam. Relat. Mater.* **7**, 1348–1350 (1998)
- 19.38 A.P. Purdy: Ammonothermal synthesis of cubic gallium nitride, *Chem. Mater.* **11**, 1648–1651 (1999)
- 19.39 D.R. Ketchum, J.W. Kolis: Crystal growth of gallium nitride in supercritical ammonia, *J. Cryst. Growth* **222**, 431–434 (2001)
- 19.40 A. Yoshikawa, E. Ohshima, T. Fukuda, H. Tsuji, K. Oshima: Crystal growth of GaN by ammonothermal method, *J. Cryst. Growth* **260**, 67–72 (2004)
- 19.41 Y.C. Lan, X.L. Chen, M.A. Crimp, Y.G. Cao, Y.P. Xu, T. Xu, K.Q. Lu: Single crystal growth of gallium nitride in supercritical ammonia, *Phys. Status Solidi (c)* **2**(7), 2066–2069 (2005)
- 19.42 B. Wang, M.J. Callahan, K. Rakes, D.F. Bliss, L.O. Bouthillette, S.-Q. Wang, J.W. Kolis: Am-

- monothermal growth of GaN crystals in alkaline solutions, *J. Cryst. Growth* **287**, 376–380 (2006)
- 19.43 Y. Kagamitani, D. Ehrentaut, A. Yoshikawa, N. Hoshino, T. Fukuda, S. Kawabata, K. Inaba: Ammonothermal epitaxy of thick GaN film using NH_4Cl mineralizer, *Jpn. J. Appl. Phys.* **45**(5A), 4018–4020 (2006)
- 19.44 D. Peters: Ammonothermal synthesis of aluminium nitride, *J. Cryst. Growth* **104**, 411–418 (1990)
- 19.45 B. Wang, M.J. Callahan: Transport growth of GaN crystals by the ammonothermal technique using various nutrients, *J. Cryst. Growth* **291**, 455–460 (2006)
- 19.46 A.P. Purdy, R.J. Jouet, F.G. Clifford: Ammonothermal recrystallization of gallium nitride with acidic mineralizers, *Cryst. Growth Des.* **2**(2), 141–145 (2002)
- 19.47 D. Ehrentaut, N. Hoshino, Y. Kagamitani, A. Yoshikawa, T. Fukuda, H. Itoh, S. Kawabata: Temperature effect of ammonium halogenides as mineralizers on the phase stability of gallium nitride synthesized under acidic ammonothermal conditions, *J. Mater. Chem.* **17**, 886–893 (2007)
- 19.48 B. Raghoeamachar, W.M. Vetter, M. Dudley, R. Dalmau, R. Schlessler, Z. Sitar, E. Michael, J.W. Kolis: Synchrontron white beam topography characterization of physical vapor transport grown AlN and ammonothermal GaN, *J. Cryst. Growth* **246**, 271–280 (2002)
- 19.49 A.P. Purdy, S. Case, N. Murastore: Synthesis of GaN by high-pressure ammonolysis of gallium triiodide, *J. Cryst. Growth* **252**, 136–143 (2003)
- 19.50 T. Hashimoto, K. Fujito, R. Sharma, E.R. Letts, P.T. Fini, J.S. Speck, S. Nakamura: Phase selection of microcrystalline GaN synthesized in supercritical ammonia, *J. Cryst. Growth* **291**, 100–106 (2006)
- 19.51 A. Purdy: Growth of cubic GaN crystals from hexagonal GaN feedstock, *J. Cryst. Growth* **281**, 355–363 (2005)
- 19.52 A.N. Mariano, R.E. Hanneman: Crystallographic polarity of ZnO crystals, *J. Appl. Phys.* **34**, 384–389 (1963)
- 19.53 B. Wang, M.J. Callahan, L.O. Bouthillette: Hydrothermal growth and photoluminescence of $\text{Zn}_{1-x}\text{Mg}_x\text{O}$ alloy crystals, *Cryst. Growth Des.* **6**, 1256–1260 (2006)
- 19.54 M. J. Callahan, B. Wang, unpublished results
- 19.55 Q.-S. Chen, V. Prasad, W.R. Hu: Modeling of ammonothermal growth of nitrides, *J. Cryst. Growth* **258**, 181–187 (2003)
- 19.56 M. Carr: Penetrative convection in a superposed porous-medium-fluid layer via internal heating, *J. Fluid Mech.* **509**, 305–329 (2004)
- 19.57 V. Prasad: Convective flow interaction and heat transfer between fluid and porous layers. In: *Convective Heat and Mass Transfer in Porous Media*, ed. by S. Kakaç, B. Kilic, F.A. Kulacki, F. Arinc (Kluwer, Netherlands 1991) pp. 563–615
- 19.58 Q.-S. Chen, V. Prasad, A. Chatterjee, J. Larkin: A porous media-based transport model for hydrothermal growth, *J. Cryst. Growth* **198/199**, 710–715 (1999)
- 19.59 Q.-S. Chen, V. Prasad, A. Chatterjee: Modeling of fluid flow and heat transfer in a hydrothermal crystal growth system: use of fluid-superposed porous layer theory, *J. Heat Transf.* **121**, 1049–1058 (1999)
- 19.60 H. Zhang, V. Prasad, M.K. Moallemi: Numerical algorithm using multizone adaptive grid generation for multiphase transport processes with moving and free boundaries, *Num. Heat Transf.* **29**(B), 399–421 (1996)
- 19.61 H. Zhang, V. Prasad: An advanced numerical scheme for materials process modeling, *Comput. Model. Simul. Eng.* **2**, 322–343 (1997)
- 19.62 Q.-S. Chen, S. Pendurti, V. Prasad: Effects of baffle design on fluid flow and heat transfer in ammonothermal growth of nitrides, *J. Cryst. Growth* **266**, 271–277 (2004)
- 19.63 A.J. Chapman: *Heat Transfer* (Macmillan, New York 1984)
- 19.64 M. Callahan, B.-G. Wang, K. Rakes, D. Bliss, L. Bouthillette, M. Suscavage, S.-Q. Wang: GaN single crystals grown on HVPE seeds in alkaline supercritical ammonia, *J. Mater. Sci.* **41**, 1399–1407 (2006)
- 19.65 Q.-S. Chen, S. Pendurti, V. Prasad: Modeling of ammonothermal growth of gallium nitride single crystals, *J. Mater. Sci.* **41**, 1409–1414 (2006)
- 19.66 T. Sekiguchi, S. Miyashita, K. Obara, T. Shishido, N. Sakagami: Hydrothermal growth of ZnO single crystals and their optical characterization, *J. Cryst. Growth* **214/215**, 72–76 (2000)
- 19.67 L.N. Demianets, D.V. Kostomarov, I.P. Kuz'mina, S.V. Pushko: Mechanism of growth of ZnO single crystals from hydrothermal alkali solutions, *Cryst. Rep.* **47**, S86–S98 (2002), Supp 1
- 19.68 B.G. Wang: Understanding and controlling the morphology of ZnO crystallites under hydrothermal conditions, *Cryst. Res. Technol.* **32**, 659–667 (1997)
- 19.69 W.J. Li, E.W. Shi, W.Z. Zhong, Z.W. Yin: Growth mechanism and growth habit of oxide crystals, *J. Cryst. Growth* **203**, 186–196 (1999)
- 19.70 I.L. Khodakovskiy, A.Y. Yelkin: Measurement of the solubility of zincite in aqueous NaOH at 100, 150, and 200 °C, *Geokhimiya* **10**, 1490–1498 (1975)
- 19.71 P. Bénézeth, D. Palmer, D. Wesolowski: The solubility of zinc oxide in 0.03 m NaTr as a function of temperature with in-situ pH measurement, *Geochim. Cosmoch. Acta* **63**, 1571–1586 (1999)
- 19.72 B.G. Wang, E.W. Shi, W.Z. Zhong: Twinning morphologies and mechanisms of ZnO crystallites under hydrothermal conditions, *Cryst. Res. Technol.* **33**, 937–941 (1998)

- 19.73 M.M. Lukina, M.V. Lelekova, V.E. Khadzhi: Effect of lithium on the growth rate of zincite and quartz under hydrothermal conditions, *Sov. Phys. Crystallogr.* **15**, 530–531 (1970)
- 19.74 R.A. Laudise, R.L. Barnes: Perfection of quartz and its connection to crystal growth, *IEEE Trans. Ultrasonics Ferroelectr. Freq. Control.* **35**, 277–287 (1998)
- 19.75 A.F. Armington: Recent advances in the growth of high quality quartz, *Prog. Cryst. Growth Charact.* **21**, 97–111 (1990)
- 19.76 E.D. Kolb, R.A. Laudise: Hydrothermally grown ZnO crystals of low and intermediate resistivity, *J. Am. Ceram. Soc.* **49**, 302–305 (1966)
- 19.77 E.D. Kolb, S. Coriell, R.A. Laudise, A.R. Hutson: The hydrothermal growth of low carrier concentration ZnO at high water and hydrogen pressures, *Mater. Res. Bull.* **2**, 1099–1106 (1967)
- 19.78 I.P. Kuz'mina: Crystallization kinetics of zincite under hydrothermal conditions, *Sov. Phys. Crystallogr.* **13**(5), 803–805 (1969), translated from *Kristallogr.*, Vol. 13, No. 5
- 19.79 G. Dhanaraj, M. Dudley, D. Bliss, M. Callahan, M. Harris: Growth and process induced dislocation in zinc oxide crystals, *J. Cryst. Growth* **297**, 74–79 (2006)
- 19.80 H. Youping, Z. Jinbo, W. Dexang, S. Genbo, Y. Ming-shan: New technology of KDP crystal growth, *J. Cryst. Growth* **169**, 196–198 (1996)
- 19.81 B. Wang, M.J. Callahan, C. Xu, L.O. Bouthillette, N.C. Giles, D.F. Bliss: Hydrothermal growth and characterization of indium-doped-conducting ZnO crystals, *J. Cryst. Growth* **304**, 73–79 (2007)
- 19.82 N.Y. Garces, L. Wang, L. Bai, N.C. Giles, L.E. Halliburton, G. Cantwell: Role of copper in the green luminescence from ZnO crystals, *Appl. Phys. Lett.* **81**, 622–624 (2002)
- 19.83 E.D. Kolb, R.A. Laudise: Hydrothermally grown ZnO crystals of low and intermediate resistivity, *J. Am. Ceram. Soc.* **49**, 302–305 (1966)
- 19.84 C.G. Van de Walle: Hydrogen as a cause of doping in zinc oxide, *Phys. Rev. Lett.* **85**(5), 1012–1015 (2000)
- 19.85 R. Littbarski: Carrier concentration and mobility. In: *Current Topics in Materials Science*, Vol. 7, ed. by E. Kaldis (North-Holland, Amsterdam 1981) pp. 212–225
- 19.86 B. Theys, V. Sallet, F. Jomard, A. Lusson, J. Rommeluère, Z. Teukam: Effects of intentionally introduced hydrogen on the electric properties of ZnO layers grown by metalorganic chemical vapor deposition, *J. Appl. Phys.* **91**, 3922–3924 (2002)
- 19.87 D.C. Look, J.W. Hemsky, J.R. Sizelove: Residual native shallow donor in ZnO, *Phys. Rev. Lett.* **82**, 2552–2555 (1999)
- 19.88 A. Urbieto, P. Fernández, J. Piqueras, T. Sekiguchi: Scanning tunneling spectroscopy characterization of ZnO single crystals, *Semicond. Sci. Technol.* **16**, 589–593 (2001)
- 19.89 N. Sakagami, M. Yamashita, T. Sekiguchi, S. Miyashita, K. Obara, T. Shishido: Variation of electrical properties on growth sectors of ZnO single crystals, *J. Cryst. Growth* **229**, 98–103 (2001)
- 19.90 M. Yoneta, K. Yoshino, M. Ohishi, H. Saito: Photoluminescence studies of high-quality ZnO single crystals by hydrothermal method, *Phys. B* **376–377**, 745–748 (2006)
- 19.91 J. Mass, M. Avella, J. Jiménez, M. Callahan, E. Grant, K. Rakes, D. Bliss, B. Wang: Cathodoluminescence characterization of hydrothermal ZnO crystals, *Superlattice Microstruct.* **38**, 223–230 (2005)
- 19.92 L.N. Dem'yanets, V.I. Lyutin: Status of hydrothermal growth of bulk ZnO: latest issues and advantages, *J. Cryst. Growth* **310**, 993–999 (2008)
- 19.93 J. Mass, M. Avella, J. Jiménez, A. Rodríguez, T. Rodríguez, M. Callahan, D. Bliss, B. Wang: Cathodoluminescence study of ZnO wafer cut from hydrothermal crystals, *J. Cryst. Growth* **310**, 1000–1005 (2008)
- 19.94 D.C. Reynolds, D.C. Look, B. Jogai, H. Morkoç: Similarities in the bandedge and deep-centre photoluminescence mechanisms of ZnO and GaN, *Solid State Commun.* **101**, 643–646 (1997)
- 19.95 A. Urbieto, P. Fernández, J. Piqueras, C. Hardalov, T. Sekiguchi: Cathodoluminescence microscopy of hydrothermal and flux grown ZnO single crystals, *J. Phys. D Appl. Phys.* **34**, 2945–2949 (2001)
- 19.96 A. Urbieto, P. Fernández, C. Hardalov, J. Piqueras, T. Sekiguchi: Cathodoluminescence and scanning tunneling spectroscopy, *Mater. Sci. Eng.* **B91–92**, 345–348 (2002)
- 19.97 J. Mass, M. Avella, J. Jiménez, M. Callahan, E. Grant, K. Rakes, D. Bliss, B. Wang: Visible luminescence in ZnO. In: *New Materials and Processes for Incoming Semiconductor Technologies*, ed. by S. Dueñas, H. Castán (Transworld Research Network, Kerala 2006)
- 19.98 D. Bliss: Zinc oxide. In: *Encyclopedia of Advanced Materials*, ed. by D. Bloor, M.C. Flemings, R.J. Brook, S. Mahajan, R.W. Cahn (Pergamon, Oxford 1994) pp. 9888–9891
- 19.99 C. Woods, A.J. Drehman: Presentation, *Natl. Space Missile Mater. Symp.* (Monterey, 2001)
- 19.100 B. Wang, M. Callahan, J. Bailey: Synthesis of dense polycrystalline GaN of high purity by the chemical vapor reaction process, *J. Cryst. Growth* **286**, 50–54 (2005)
- 19.101 K. Lee, K. Auh: Dislocation density of GaN grown by hydride vapor phase epitaxy, *MRS Int. J. Nitride Semicond. Res.* **6**, 9 (2001)
- 19.102 B. Raghothamacher, J. Bai, M. Dudley, R. Dalmau, D. Zhuang, Z. Herro, R. Schlessler, Z. Sitar, B. Wang, M. Callahan, K. Rakes, P. Konkapaka, M. Spencer: Characterization of bulk-grown GaN and AlN single-crystals materials, *J. Cryst. Growth* **287**, 349–353 (2006)

- 19.103 M.J. Callahan, B. Wang, L. Bouthillette, S.-Q. Wang, J.W. Kolis, D. Bliss: Growth of GaN crystals under ammonothermal conditions, MRS Fall Meet. Symp. Proc. **798**, Y2.10 (2004)
- 19.104 T. Hashimoto, M. Saito, K. Fujito, F. Wu, J.S. Speck, S. Nakamura: Seeded growth of GaN by the basic ammonothermal method, J. Cryst. Growth **305**, 311–316 (2007)
- 19.105 Images provided by Prof. Brian Skromme's group, Arizona St. Univ.
- 19.106 T. Hashimoto, K. Fujito, F. Wu, B.A. Haskell, P.T. Fini, J.S. Speck, S. Nakamura: Structural characterization of thick GaN films grown on free-standing GaN seeds by the ammonothermal method using basic ammonia, Jpn. J. Appl. Phys. **44**(25), L797–L799 (2005)
- 19.107 R. Dwilinski, R. Doradzinski, J. Garzynski, L.P. Sierzputowski, A. Puchalski, Y. Kanaba, K. Yagi, H. Minakuchi, H. Hayashi: Excellent crystallinity of truly bulk ammonothermal GaN, J. Cryst. Growth **310**, 3911–3916 (2008)
- 19.108 J. Bai, M. Dudley, B. Raghothamachar, P. Gouma, B.J. Skromme, L. Chen, P.J. Hartlieb, E. Michaels, J. Kolis: Correlated structural and optical characterization of ammonothermally grown bulk GaN, Appl. Phys. Lett. **84**(17), 3289–3291 (2004)
- 19.109 M.P. D'Evelyn, H.C. Hong, D.-S. Park, H. Lu, E. Kaminsky, R.R. Melkote, P. Perlin, M. Lesczynski, S. Porowski, R.J. Molnar: Bulk GaN crystal growth by the high-pressure ammonothermal method, J. Cryst. Growth **300**, 11–16 (2007)
- 19.110 S.V. Bhat, K. Biswas, C.N.R. Rao: Synthesis and optical properties of In-doped GaN nanocrystals, Solid State Commun. **141**, 325–328 (2007)
- 19.111 B.T. Adekore, K. Rakes, B. Wang, M.J. Callahan, S. Pendurti, Z. Sitar: Ammonothermal synthesis of aluminum nitride crystals on group III-nitride templates, J. Electron. Mater. **35**, 1104–1111 (2006)
- 19.112 M. Zajac, J. Gosk, E. Grzanka, S. Stelmakh, M. Palczewska, A. Wyszomolek, K. Korona, M. Kamińska, A. Twardowski: Ammonothermal synthesis of GaN doped with transition metal ions (Mn, Fe, Cr), J. Alloys Compd. **456**, 324–338 (2008)
- 19.113 A. Denis, G. Goglio, G. Demazeau: Gallium nitride bulk crystal growth processes: a review, Mater. Sci. Eng. R **50**, 167–194 (2006)

20. Stoichiometry and Domain Structure of KTP-Type Nonlinear Optical Crystals

Michael Roth

In recent years the growth technologies of only a few inorganic oxide crystals, such as **BBO** (BaB_2O_4), **LBO** (LiB_3O_5), and the **KTP** (KTiPO_4) group of isomorphous compounds, have matured to a degree allowing their extensive integration into commercial laser systems in the form of nonlinear optical (**NLO**) and electrooptic (**EO**) devices. The **KTP**-type crystals are ferroelectrics at room temperature. They are also well known for their large birefringence, high **NLO** and **EO** coefficients, wide acceptance angles, thermally stable phase-matching properties, and relatively high damage threshold. These properties make them especially useful for high-power wavelength-conversion applications, such as the second-harmonic generation (**SHG**) and optical parametric oscillations (**OPO**), as well as for electrooptic phase modulation and Q-switching. Lately, a great deal of effort has been put into the development of periodically poled **KTP** (**PPKTP**) devices based on quasi-phase-matched (**QPM**) wavelength conversion. However, both birefringent and **QPM** properties of **KTP** crystals depend on their structural characteristics, such as morphology, chemical composition, point defect distribution (stoichiometric and impurities), and particularly the ferroelectric domain structure, which are closely related to the specific crystal growth parameters. Current research includes studies of nonstoichiometry and distribution of point defects, e.g., vacancies and impurities, as well as the basic mechanisms underlying ferroelectric domain formation during

20.1	Background	691
20.1.1	KTP Crystal Structure	692
20.1.2	Crystal Growth	694
20.2	Stoichiometry and Ferroelectric Phase Transitions	697
20.2.1	KTiPO_4 Crystals.....	697
20.2.2	RbTiPO_4 Crystals.....	700
20.2.3	Other KTP Isomorphs.....	702
20.3	Growth-Induced Ferroelectric Domains	703
20.3.1	Domains in Top-Seeded Solution-Grown KTP	704
20.3.2	Domain Boundaries.....	705
20.3.3	Summary of Ferroelectric Domain Structures	707
20.3.4	Single-Domain Growth	707
20.4	Artificial Domain Structures	708
20.4.1	Electric Field Poling	708
20.4.2	As-Grown Periodic Domain Structure	711
20.5	Nonlinear Optical Crystals	713
20.5.1	Optical Nonuniformity	713
20.5.2	Gray Tracks	715
	References	716

KTP crystal growth and cool-down. By controlling the stoichiometry and achieving single-domain growth of bulk crystals it is also possible to create as-grown periodic domain structures useful for nonlinear **QPM** applications.

20.1 Background

Potassium titanyl phosphate (**KTP**) belongs to the family of isomorphous compounds with generic composition of MTiOXO_4 , where $X = \{\text{P or As}\}$ and $M = \{\text{K, Rb, Tl,}$

NH_4 or Cs (for $X = \text{As}$ only)} [20.1]. All crystals of this family, including their solid solutions, are orthorhombic and belong to the noncentrosymmetric point group $mm2$

Table 20.1 Selected physical properties of KTP-family crystals

Crystal	KTP	RTP	KTA	RTA	CTA	References
Optical transparency (μm)	0.35–4.3	0.35–4.3	0.35–5.3	0.35–5.3	0.35–5.3	[20.2–4]
Birefringence, $n_z - n_x$ at 1.064 μm	0.0921	0.0884	0.0863	0.0782	0.0700	[20.4–8]
NLO susceptibilities (pm/V) at 1.064 μm						
d_{33}	16.9	17.1	16.2	15.8	18.1	[20.9, 10]
d_{32}	4.4	4.1	4.2	3.8	3.4	
d_{31}	2.5	3.3	2.8	2.3	2.1	
d_{24}	3.6	–	3.2	–	–	
d_{15}	1.9	–	2.3	–	–	
d_{eff} for type-II SHG	3.35	2.51	–	–	–	[20.4, 11]
SHG cutoff (μm) along						
x-direction	1.082	1.147	1.134	1.243	1.548	[20.11]
y-direction	0.994	1.038	1.074	1.138	1.280	
EO coefficients (pm/V) at 0.633 μm						
r_{33}	36.3	39.6	37.5	40.5	38.0	[20.10, 12]
r_{23}	15.7	17.1	15.4	17.5	18.5	
r_{13}	9.5	12.5	11.5	13.5	14.2	

at room temperature. The unique ferroelectric, EO, and NLO properties of the KTP-family crystals are stipulated by this specific structure. Table 20.1 gives a partial list of the important physical properties exhibited by the five more extensively studied KTP group members: KTiOPO₄ (KTP), RbTiOPO₄ (RTP), KTiOAsO₄ (KTA), RbTiOAsO₄ (RTA), and CsTiOAsO₄ (CTA).

All these crystals exhibit a broad optical transparency range allowing for NLO [20.13] and EO [20.14] interactions from the visible to the near- and mid-infrared. The larger birefringence and suitable dispersion of the orthophosphates, KTP and RTP, brings their phase-matching directions into the *x*–*y* plane for efficient second-harmonic generation (SHG) of the principal Nd:YAG laser radiation at 1.064 μm. Although not suitable for frequency doubling into the green, CTA includes the 1.32 μm line of the Nd:YAG laser in its phase-matchable wavelength interval within the *x*–*y* plane [20.9] allowing doubling into the red. In general, the transparency range of the orthoarsenates extends by 1 μm further into the mid-infrared (Table 20.1) and contains no orthophosphate overtone absorption at wavelengths shorter than 3.5 μm, which makes them particularly attractive for noncritically phase-matched (NCPM) eye-safe OPO (signal at ≈ 1.5 μm) with negligible absorption of the idler radiation at ≈ 3.3 μm [20.15]. It is noteworthy that a more detailed insight into the idler absorption problem in KTP, namely its reduced value for *z*-polarization, demonstrates that orthophosphates may also gener-

ate high-average-power eye-safe OPO [20.16]. All KTP-family crystals also feature large EO coefficients necessary for electrooptic modulation and switching [20.14], but mainly RTP, and especially RTP, are widely used for these applications [20.17, 18]. This may be associated with the fact that the orthoarsenates are apt to ferroelectric multidomain formation [20.19, 20], and their crystal growth is a costly process [20.21]. Therefore, the more technologically important KTP and RTP materials will be primarily discussed in terms of their defect structure and the structure–properties relationships versus the main processing parameters.

20.1.1 KTP Crystal Structure

The five KTP-family members identified above have identical crystal structures at room temperature. The orthorhombic structure ($a \neq b \neq c$, $\alpha = \beta = \gamma = 90^\circ$) of KTP belongs to the space group *Pna*2₁, as initially determined by Tordjman et al. in 1974 [20.22]. There are 64 atoms in a unit cell in the KTP-type lattice. This 64-atom group separates into four subgroups of 16 atoms each, and within each subgroup there are two inequivalent K (Rb) sites, two inequivalent titanium sites, two inequivalent P (As) sites, and ten inequivalent oxygen sites. Two of the latter oxygen sites represent bridging ions located between titanium ions, while the other eight are contained in PO₄ (AsO₄) groups where they link one Ti and one P (As) ion.

Table 20.2 Crystal lattice parameters of KTP-family crystals

Lattice constants (Å)	KTP [20.23]	RTP [20.24]	KTA [20.25]	RTA [20.26]	CTA [20.27]
<i>a</i>	12.819	12.952	13.125	13.264	13.486
<i>b</i>	6.399	6.4925	6.5716	6.682	6.682
<i>c</i>	10.584	10.555	10.786	10.7697	10.688

Lattice Parameters and Site Occupation

The room-temperature lattice constants of KTP-family crystals are given in Table 20.2. They change relatively little in going from KTP even to CTA. The values for KTP and RTP are very close, thus verifying that the PO₄ tetrahedra have much more influence on the lattice constants than the monovalent cations K and Rb. In KTA, the *a* and *b* lattice constants are approximately 1.2% larger than in KTP and the *c* lattice constant is about 2.1% larger than in KTP, thus reflecting the slightly larger size of the AsO₄ tetrahedron compared with PO₄. One 16-atom subgroup can be transformed into one of the other three subgroups by simple transformations within the unit cell. The [001] projection of the KTP structure is shown in Fig. 20.1.

The physical structure of the KTP-type crystal contains helical chains of distorted TiO₆ octahedra running parallel to the <011> crystallographic directions and forming a two-dimensional network in the *b*–*c* plane. The TiO₆ octahedra are linked at two corners by alternately changing long and short Ti(1)–O bonds which are commonly assumed as primarily responsible for the optical nonlinearity [20.28]. Other sources of optical nonlinearities have been invoked as well. Bond-polarizability calculations of KTP [20.29] show that the nonlinearity derives from the various K–O bonds and P(2)O₄ groups rather than from the TiO₆ groups. Nuclear magnetic resonance (NMR) studies of KTP [20.30] suggest that the large electric field gradients at the Ti sites and associated charge-transfer mechanisms are important factors establishing the necessary conditions for high nonlinear response. However, very recent stimulated Raman measurements show that, in KTP, the strongest vibrations occur in the direction collinear with the distortion of TiO₆ octahedra [20.31]. The other four oxygen ions around a titanium ion are parts of the PO₄ (or AsO₄) tetrahedra. These tetrahedra bond the –Ti–O–Ti–O– networks into a three-dimensional covalent (TiOPO₄) framework. The crystal structure is completed by potassium (or rubidium) ions occupying cavities, or cages, within this framework. These monovalent ions are either 8- or 9-coordinated with respect to oxygen, and they are denoted as K(1) and K(2), respec-

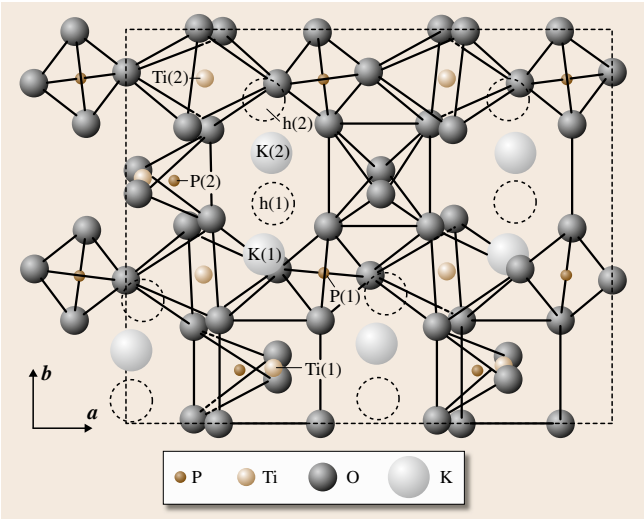


Fig. 20.1 A view of the KTP crystal structure along the *c*-axis direction

tively, in Fig. 20.1 representing the KTP structure. Each K atom is asymmetrically coordinated by O atoms in the two inequivalent sites, and at a short distance along the *b*-direction from each K atom there is a void similar in size and coordination to the K site. The voids are termed *hole sites*, h(1) and h(2) [20.32], and they are pseudosymmetrically related to the K(2) and K(1) sites respectively, as is apparent from Fig. 20.1. At high temperatures, above the transition to the ferroelectric (*Pna*2₁) to paraelectric (centrosymmetric) *Pnan* phase, the K(1) and h(1) as well as K(2) and h(2) sites merge along the *b*-direction into positions halfway between the room-temperature K sites and their associated holes sites. More refined studies of the crystallographically unique K(1) and K(2) sites reveal additional splittings of their positions [20.33, 34]. Also, the K(1) cage has a volume 25% smaller than the K(2) cage [20.35]. This may explain why the larger Rb atoms substituting for K atoms in mixed K_{*x*}Rb_{1–*x*}TiOPO₄ crystals occupy preferentially the larger K(2) sites, independently of the Rb incorporation mechanism, by crystal growth or ion exchange [20.36].

Ionic Conductivity

Finally, we refer again to Fig. 20.1 and conclude that there are additional consequences to the quite different environments for the K(1) and K(2) atoms. The K(2)O₉ cage forms a channel, parallel to the *c*-axis, which runs through the entire crystal structure and along which the K(2) atoms are expected to move relatively freely. On the other hand, the K(1) atom is constrained from a similar motion by the confinement of the P(1)O₄–Ti(2)O₆ chain which restricts its movement along the *c*-axis. Although the K(1)O₈ cage forms a channel along the *a*-axis, the K(1) atom does not show any significant movement along this axis even at high pressures [20.35]. Therefore, when KTP is described as a quasi-one-dimensional superionic conductor [20.37], with the conductivity σ_{33} being about three orders of magnitude higher than σ_{11} and σ_{22} [20.38], mainly K(2) ions can diffuse through cavities combined into channels along the *c*-axis direction via a vacancy mechanism [20.39]. Similar ionic conductivity anisotropy is valid also for KTA [20.2]. In RTP and RTA, σ_{33} is relatively smaller, since the activation energy for hopping of larger ions is higher [20.40,41]. The concentration of potassium/rubidium vacancies, or the degree of deviation from stoichiometry, depends on the crystal growth method and on specific growth parameters that will be discussed throughout the chapter.

20.1.2 Crystal Growth

KTP-family crystals decompose before melting (e.g., KTP decomposes at 1172 and 1158 °C in air and argon atmospheres, respectively [20.42]) and may be thus grown only from solutions. Relatively small but high-quality crystals can be grown from aqueous so-

lutions by the hydrothermal process. Larger crystals, yet requiring meticulous quality control, can be grown from high-temperature tungstate and molybdate fluxes or self-fluxes. All these methods are being used for commercial production of KTP-family crystal in their seeded versions, although unseeded small crystals are occasionally processed for research purposes. The typical morphology of a KTP crystal [20.43,44] grown on a seed fully immersed into the solution (by either of the methods mentioned above) is shown in Fig. 20.2.

The crystal exhibits 14 facets belonging to four families of crystallographic planes, namely: {100}, {110}, {011} and {201}. Accordingly, 14 growth sectors develop simultaneously on the submerged seed. The morphology can be altered depending also on the seed shape and the solution composition [20.45,46].

Hydrothermal Growth

A detailed description of the first attempts to grow a few millimeter-sized optical-quality KTP-family crystals hydrothermally was given by *Bierlein* and *Gier* in the patent literature [20.47,48]. Typically, the hydrothermal process involved growing the crystal in an autoclave having a growth region and a nutrient region, and an aqueous mineralizer solution was employed. For example, *Laudise* et al. [20.49] used a Pt-lined low-carbon steel autoclave (75% filled) at a constant pressure of about 1360 atm with baffle-separated flux-grown KTP crystals as a nutrient (at 435 °C) and a (2 M K₂HPO₄ + 0.5 M KPO₃) mineralizer and TiO₂ to grow KTP crystals at around 400 °C. Better quality crystals were obtained by growing on (201)- and (010)-oriented seeds at ≈ 0.07 – 0.14 mm/day rates. A typical commercial production of KTP crystals uses a potassium phosphate mineralizer at temperatures in the range of about 520–560 °C and pressures in the range of about 1700–2000 atm [20.50]. The relatively high temperatures and pressures employed in this process makes scale-up difficult and expensive, yet the use of more moderate conditions can lead to a problem of anatase (TiO₂) coprecipitation [20.51], making the process less useful. In principle, it has been shown that growth temperatures (< 500 °C) and pressure (< 1000 atm) can be reduced while using potassium-rich mineralizer solutions, but the growth rate becomes limited (< 0.13 mm/day) due to the relatively low solubility of KTiOPO₄ in the mineralizer [20.52].

Other types of mineralizers adopted for the hydrothermal growth of KTP involve the use of KF solutions, as suggested by *Jia* et al. [20.53,54]. By utilizing KF as a mineralizer, relatively lower temperature

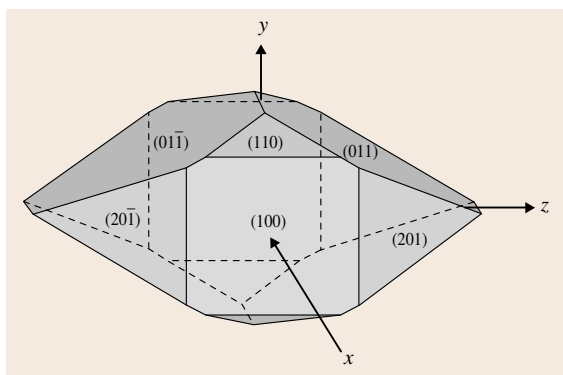
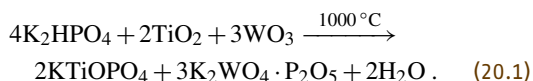


Fig. 20.2 Typical habit of an immersion-seeded KTP crystal

and pressure (≈ 1000 atm) can be employed for a hydrothermal KTP crystal growth process. In addition, the use of pure KF mineralizer provides a solubility of about 2% under the stated growth conditions, but like the process described by *Laudise et al.* [20.49], the higher solubility occurs near the phase-stability boundary (with respect to temperature, pressure, and mineralizer concentration), so the possibility of coprecipitation of an undesirable non-KTP phase exists. To avoid this disadvantage, *Cheng* [20.55] suggested complex aqueous solutions as mineralizers comprising both KF and potassium (rubidium) phosphates (arsenates) for hydrothermal production of KTP-family crystals, in amounts effective to assure solubility of the KTP-type crystals of at least about 1% by weight. Although grown under higher temperatures and pressures, optical-quality KTP and KTA crystals of at least 1 mm^3 volume could be recovered after a few hours rather than days and weeks. In the most recent report on hydrothermal KTP growth a process utilizing a ($2\text{ M K}_2\text{HPO}_4 + 0.1\text{ M KH}_2\text{PO}_4 + 1\text{ wt \% H}_2\text{O}_2$) solution as a mineralizer and crushed flux-grown KTP crystals as a nutrient was described [20.56]. Crystals with dimensions up to $14.5 \times 28 \times 17\text{ mm}^3$ have been grown on (011) and spherical seeds at a rate of 0.15 mm/day in the $400\text{--}540^\circ\text{C}$ temperature range and $1200\text{--}1500\text{ atm}$ pressure range. They exhibited an exceptionally high (for KTP) optical damage threshold of 9.5 GW/cm^2 .

Growth from Low-Viscosity Melts

In the early days of optical-grade KTP development, the only commercial process reported was the hydrothermal crystal growth technique requiring cumbersome high-pressure vessels with noble-metal liners and yielding relatively small crystals. Initial attempts to grow KTP crystals from phosphate fluxes at atmospheric pressure conditions [20.42] seemed to encounter the problem of high melt viscosity. *Ballman et al.* [20.57] were the first to report on the growth of up to 1 cm^3 KTP single crystals from a low-melting low-viscosity water-soluble tungstate flux. Tungstic anhydride was added to the potassium phosphate-titanium oxide melt, and KTP as a single stable phase formed according to the following reaction



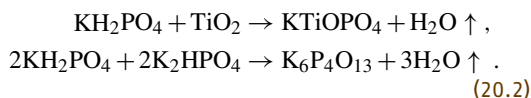
Iliev et al. [20.58] found that with a $\text{K}_2\text{O} : \text{P}_2\text{O}_5$ ratio of $0.9 : 0.1$ and 40 mol \% WO_3 in the melt, the flux

viscosity was as low as $10\text{--}15\text{ cP}$ in the $1050\text{--}850^\circ\text{C}$ temperature range. High-optical-quality KTP crystals up to $30 \times 20 \times 20\text{ mm}^3$ in size could be grown from the $\text{K}_2\text{O-P}_2\text{O}_5\text{-TiO}_2\text{-WO}_3$ system in the $930\text{--}700^\circ\text{C}$ temperature range at a rate of 0.9 mm/day [20.59]. Not only KTP, but also RTP, KTA, and RTA crystals were subsequently grown from both tungstate and molybdate fluxes [20.44]. However, optical inhomogeneities associated with tungsten-containing ($0.5\text{--}1.0\text{ wt \%}$) striations parallel to the $\{011\}$ faces were identified [20.60, 61]. Indeed, electron paramagnetic resonance (EPR) measurements show that tungsten enters KTP as an impurity occupying both the Ti(1) and Ti(2) sites as W^{5+} and, partly, the Ti(2) site as W^{4+} [20.62]. The tungsten impurity is found to cause detrimental multiplication of growth sectors in the case of $\langle 011 \rangle$ -seeded (and less $\langle 010 \rangle$ -seeded) KTP crystal growth from $3\text{K}_2\text{WO}_4 \cdot \text{P}_2\text{O}_5$ fluxes [20.63].

When small amounts of MoO_3 are added to the phosphate flux ($\text{K}_6\text{P}_4\text{O}_{13}$) in the case of spontaneous nucleation growth, only trace amounts of Mo are detected in the KTP crystal, but they prevent spurious nucleation and increase the crystal hardness necessary for improved polishing [20.64]. In a different attempt to reduce the melt viscosity, potassium halides were added to the phosphate flux to grow KTP [20.65] or RbI to grow RTP [20.66] crystals.

Growth from Self-Fluxes

The main crystal growth problems pointed out above were that the hydrothermal process yielded high-quality but small single crystals, and the use of tungstate fluxes resulted in incorporation of W impurities into the crystals, increasing the optical loss [20.60] and lowering their laser damage resistance [20.67]. Therefore, the development of most of the practical NLO devices unfolded in parallel with constant advancement of the seeded growth of large and ever-improving quality KTP-family crystals from self-fluxes, namely high-temperature solutions in alkali phosphates. In the early work [20.42, 68, 69], KTP crystals up to 1 cm^3 in size were grown from flux compositions within the $\text{KPO}_3\text{-K}_4\text{P}_2\text{O}_7$ system. The end components obtained by thermal decomposition of K_2HPO_4 and KH_2PO_4 together with TiO_2 were used for flux preparation, e.g., according to the following high-temperature reactions



More chemical routes for preparing self-fluxes of **KTP** and its isomorphs are given by *Iliev et al.* [20.70] and *Cheng et al.* [20.10]. $K_6P_4O_{13}$ (denoted as **K6** in the literature), with the K-to-P ratio $R = 1.5$, is the most popular solvent for **KTP** growth due to the moderate viscosity [20.71] and volatility [20.70] of the **KTP/K6** flux and relatively high solubility of **KTP**. Other solvents, such as $K_4P_2O_7$ (**K4**), $K_5P_3O_{10}$ (**K5**), $K_8P_6O_{19}$ (**K8**), $K_{10}P_8O_{25}$ (**K10**), $K_{15}P_{13}O_{40}$ (**K15**), and $K_{18}P_{16}O_{49}$, have been also studied, mainly in terms of **KTP** solubility [20.46, 72] in the 900–1100°C temperature range. The solubility decreases down this sequence due to the relative decrease of the concentration of $(P_2O_7)^{-4}$ anions in the flux, since all the above solvents can be viewed as composed of $(xKPO_3 + yK_4P_2O_7)$ [20.72]. In the case of **KTP** isomorphs, their solubility in similar self-fluxes (**RTP/R6** [20.73, 74], **KTA/K6**, **RTA/R5**, and **CTA/C5** [20.10], **KTA/K5** [20.75], and **RTP/R4** [20.76]) has been also reported.

Reproducible and controllable seeded growth of large-size **KTP** crystals from the **KTP/K6** flux has been repeatedly reviewed [20.77–79]. In view of the small

undercooling required for **KTP** nucleation, close to nongradient conditions in the growth furnace are appropriate. However, it is necessary to provide for a high degree of spatial temperature uniformity in order to avoid spurious nucleation. *Bordui et al.* [20.80] used a heat-pipe-based furnace for this purpose with submerged seeding. Others used three-zone [20.81] or five-zone [20.82] furnaces to produce large (200–300 g) and almost inclusion-free **KTP** crystals by the top-seeded solution growth (**TSSG**) method. *Angert et al.* [20.83] suggested a way to improve the yield of **KTP** crystal growth by combining the **TSSG** technique with seed pulling. Figure 20.3 shows the growth schemes typical for the submerged seed, top-seeded, and top-seeded with pulling configurations.

The convection-dominated mass transfer in submerged seed growth of **KTP** (left image in Fig. 20.3) was studied theoretically by *Vartak and Derby* [20.84], and some modeling problems were pointed out. An interesting approach to the submerged growth was put forward earlier by *Bordui and Motakef* [20.85] (modeling and experiment), who suggested an asymmetric 90° seed orientation and rotation at 50 rpm with periodic reversal in order to reduce the amount of inclusions. Their model was initially supported by numerical analyses performed by *Vartak et al.* [20.86], but a more recent boundary-layer analysis for flow and mass transfer [20.87] showed that the straightforward computational approach, such as the use of a spinning disk approximation, could provide satisfactory results only under experimental conditions not matching the realistic setups employed in the field. It is noteworthy that surface kinetics must be also considered in the growth of **KTP** crystals [20.46, 88].

Although the submerged seed method is still being used for commercial production by a few vendors, clearly the development of up to 14 growth sectors (Fig. 20.2) limits the use of such **KTP** crystals to fab-

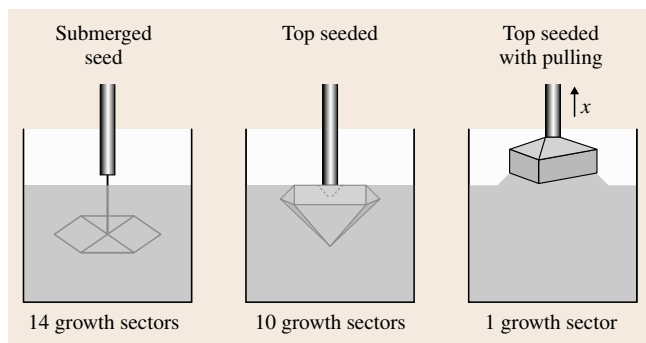


Fig. 20.3 Three configurations for seeded high-temperature solution growth of **KTP**-family crystals

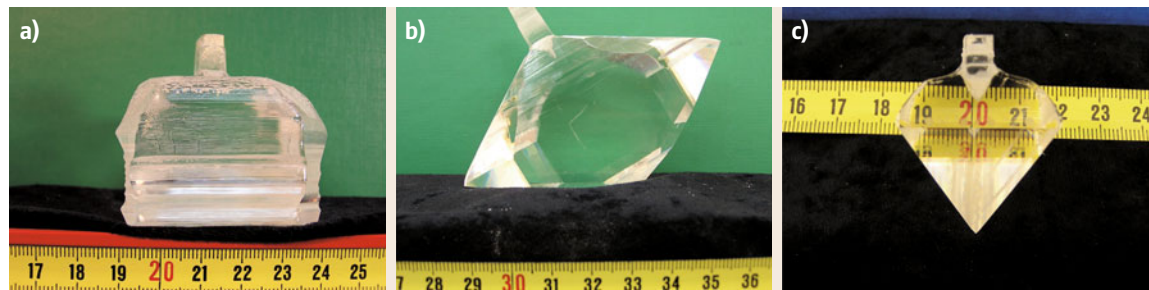


Fig. 20.4a–c **KTP** crystals grown by the top-seeded solution growth method with pulling in the (a) [100]-, (b) [010]-, and (c) [001]-directions

ricating only small optical elements, since elements cut from a single sector are required for high-quality performance [20.89]. Multiplication of growth sectors results in nonuniform growth rates [20.46, 63] and incorporation of trace impurities at the sector boundaries and may affect the ferroelectric domain structure to be discussed below. The same is true for the conventional top-seeding method, shown in the middle sketch of Fig. 20.3. In contrast, *TSSG* with pulling reduces the number of growth sectors formed. *Bolt* et al. [20.81] suggest the use of a [001]-oriented seed, since maximal linear growth rate can be achieved in this direction. (Note that the low growth rate in the [100] direction can be overcome by using seeds elongated in this direction [20.45] to grow

larger crystals.) However, in the case of [001] seeding, four growth sectors form, and the crystal is bound by the {201} and {011} facets. The use of [100]-oriented seeds is, therefore, favorable [20.83], since growth of a single growth sector crystal can be achieved. The corresponding configuration is shown on the right side of Fig. 20.3. With the largest (100) facet (Fig. 20.2) parallel to the growth front, as is typical for growth from the *KTP*/K6 flux, a planar solid-liquid interface bounds the crystal, assuring the best possible transverse uniformity of its physical properties. Photographs of three *KTP* crystals grown by the *TSSG* method with pulling on [100]-, [010]-, and [001]-directed seeds are shown in Fig. 20.4 to illustrate their distinct morphologies.

20.2 Stoichiometry and Ferroelectric Phase Transitions

Regardless of the growth method of *KTP*-family crystals from self-fluxes, say of MTiOXO_4 ($M = \{\text{K}, \text{Rb}\}$ and $X = \{\text{P}, \text{As}\}$) from $\text{MTiOXO}_4/\text{M}_6\text{X}_4\text{O}_{13}$, the M-to-X ionic ratio increases as the crystal grows out, leaving behind a solution that becomes gradually enriched in M cations. Obviously, the M-metal content in the growing crystal increases accordingly, presumably improving the associated stoichiometry; for example, in the initially solidifying portion of the *KTP* crystal grown from the *KTP*/K6 flux, large concentrations of potassium vacancies (500–800 ppm) have been detected [20.90]. These vacancies can be charge-compensated by holes trapped at bridging oxygen ions between two titanium ions [20.91] and by positively charged oxygen vacancies [20.92]. This is reflected in the high-temperature defect formation reaction [20.93]



where x is the concentration of potassium vacancies.

Most of the *KTP*-family crystals are high-temperature ferroelectrics [20.9] which undergo a second-order phase transition changing its point group symmetry from *mmm* in the high-temperature paraelectric phase to the *mm2* polar symmetry class in the low-temperature ferroelectric phase [20.94]. The ferroelectric phase transition (Curie) temperature, T_C , is very sensitive to the crystal stoichiometry and ionic substitution, which is manifested in the large spread of published Curie temperatures for all *KTP*-family crystals [20.95]. In this section we will discuss the correlation between the Curie temperatures and the defect structure, mainly stoichiometry, in *KTP* and *RTP* and

present the limited results available also on other related crystals.

20.2.1 *KTiOPO₄* Crystals

In *KTP*, addition of dopants, such as Ga, Al, and Ba, in the 400–2000 ppm concentration range is known to reduce the Curie temperature by several tens of degrees and modifies the Curie constant in the Curie–Weiss law [20.96, 97]. Isomorphic substitution of K and P ions by Rb, Cs or Tl and As reduces the Curie temperature by hundreds of degrees [20.97, 98]. Partial substitution of Na for K has been shown to initially increase the T_C from 944 °C for pure *KTP* to 956 °C and then decrease it to 914 °C for [Na] = 4 and 47 mol %, respectively [20.99]. A large diversity of Curie temperatures was reported for pure *KTP* crystals. The highest T_C values, 955–959 °C [20.97, 99, 100], were measured on hydrothermally grown crystals. A variety of lower T_C values was given for flux-grown *KTP* crystals: 952 °C [20.95] (second-harmonic generation (SHG) measurements), 947–951 °C [20.100], 946 °C [20.97], 944 °C [20.99], 934 °C [20.101], 910 °C [20.102] (dielectric measurements), and 892 °C [20.103] (birefringence measurements). Such scatter of data is beyond any imaginable experimental error and can be explained only in terms of variable stoichiometry of the *KTP* crystals grown from different solutions under variable growth conditions. *Angert* et al. [20.72] have studied the dependency of T_C on the composition of self-fluxes in great detail, and the main results will be presented below. The influence of high-temperature annealing on T_C has been addressed as well.

Curie Temperature Versus Composition

Curie temperatures of numerous crystals grown from different self-fluxes with varying initial concentrations were measured by a standard dielectric technique [20.72]. The results are reproduced in Fig. 20.5, where the measured T_C values are given as a function of weight concentration of KTP in each of the seven fluxes used, namely corresponding to KTP dissolved in the K4, K5, K6, K8, K10, K15, and K18 solvents with $[K]/[P]$ ratios (R) varying from 2 to 1.125. The lowest T_C value found was 898 °C and the highest was 960 °C, but these limits could be stretched even further upon broadening the KTP concentration and solvent composition ranges. Within the part of the crystallization field studied (of the K_2O - TiO_2 - P_2O_5 ternary system) the T_C dependencies can be approximated by straight lines for all fluxes employed. This provides the possibility of a quantitative representation of the T_C dependences on two parameters: R and the KTP concentration in the flux (C), which can be fitted by the equation

$$T_C(C, R) = 980 + (C + 0.24) \times (98R^3 - 555.6R^2 + 1074R - 733), \quad (20.4)$$

for $1 < R \leq 2$. Equation (20.4) allows to forecast or to choose any desirable initial T_C for the crystal, since it

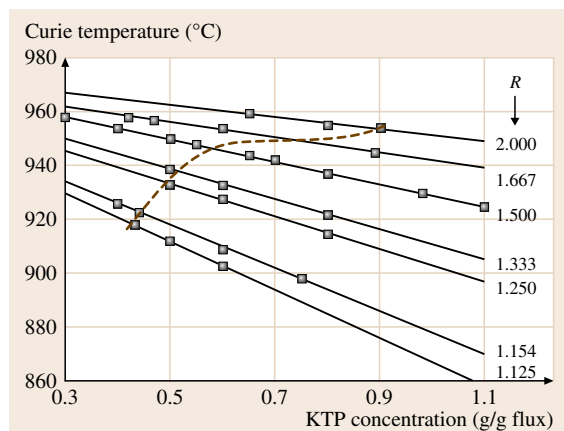


Fig. 20.5 Curie temperatures as a function of KTP concentration in the flux for seven different solvents ($K_4P_2O_7$, $K_5P_3O_{10}$, $K_6P_4O_{13}$, $K_8P_6O_{19}$, $K_{10}P_8O_{25}$, $K_{15}P_{13}O_{40}$, and $K_{18}P_{16}O_{49}$) corresponding to different potassium-to-phosphorus ratios (R). The dotted line crosses the slopes at compositions of equal Curie and crystallization temperatures (deduced from the measured solubilities of each flux)

holds for any arbitrary self-flux composition. In principle, the higher the T_C value, the more perfect the crystal in terms of stoichiometry or content of impurities, which may be important for many physical applications of this type of crystals.

It is apparent from Fig. 20.5 that, the lower the KTP concentration in any particular self-flux, the higher the Curie temperature of the solid. Also, for any given concentration, the Curie temperatures are higher for self-fluxes exhibiting higher values of R . These two observations can be combined into one conclusion, namely that higher overall concentrations of K in the solution result in higher Curie temperatures of KTP crystals. Moreover, this implies a gradual increase in T_C during growth of a large KTP crystal, since for any given self-flux the solution becomes richer in K while the crystal grows out. T_C increase of up to 20 °C along the growth direction in some large KTP crystals grown from the $K_6P_4O_{13}$ solvent are reported [20.72]. Such spatial variation of T_C in the crystal is obviously associated with compositional (mainly stoichiometry) gradients resulting in nonuniformity of the crystal physical properties. Indeed, Miyamoto et al. [20.104] have observed appreciable gradients in the refractive indices, $\Delta n_x/\Delta x = 1.2 \times 10^{-5} \text{ mm}^{-1}$ and $\Delta n_z/\Delta z = -2.0 \times 10^{-5} \text{ mm}^{-1}$, in a large TSSG KTP crystal.

Another a priori observation from Fig. 20.5 is that growth above the dotted line is supposed to yield single-ferroelectric-domain crystals, while growth below this line is apt to result in multidomain crystals, which is occasionally claimed [20.105]. However, in reality, multidomain KTP crystals are frequently obtained for growth below T_C , and single-domain crystals may form when growth is initiated above T_C [20.106]. This may be understood after a more detailed insight into the nature of compositional gradients arising from the variable potassium stoichiometry. Even a relatively large concentration of potassium vacancies of up to 800 ppm [20.90] is small in comparison with the overall amount of potassium ions. Therefore, the gradients of the latter are small in absolute terms. The diffusion coefficient of the K^+ ions at typical growth temperatures is small as well, e.g., $8 \times 10^{-10} \text{ cm}^2/\text{s}$ at 965 °C [20.107]. This explains why the growth-induced potassium concentration gradients essentially freeze in along the crystal. The associated gradients of ionized oxygen vacancies are, in contrast, relatively high, and they are responsible for the production of a built-in electric field according to the model proposed earlier by Kugel et al. [20.92]. This built-in field may be signifi-

cantly larger than the coercive field [20.92] depending on the magnitude of the existing concentration gradients of charged species. The resulting *memory* effects may have an impact on the ferroelectric domain formation.

Effect of Thermal Treatment

Direct proof for the existence of a close relationship between potassium nonstoichiometry and the Curie temperatures of **KTP** crystals has been found while monitoring the T_C variation in samples exposed to high-temperature annealing in air. A typical example of the results is shown in Fig. 20.6. A set of 1.35–1.5 mm thick *z*-cut samples exhibiting an initial T_C value of 950 °C has been maintained at 1000 °C in air for variable long periods of time. Exposure to high temperatures causes partial decomposition of the crystal surface, which manifests itself in the appearance of a translucent outer layer, a few tens of micrometer thick. This layer has been removed upon cooling to room temperature, leaving behind a transparent, colorless crystal. Figure 20.6 shows that the Curie temperature can be reduced by prolonged high-temperature annealing in air down to 883 °C, i.e., even beyond the lowest T_C values obtained in as-grown **KTP** crystals. This effect can be explained in terms of gradual potassium escape, or increasing potassium deficiency in the crystal, upon heat treatment [20.92, 107, 108]. A moderate increase in the Curie temperature following 400 h of heat treatment is not an artifact and has been repeatedly observed with a number of samples. This may result from as-yet

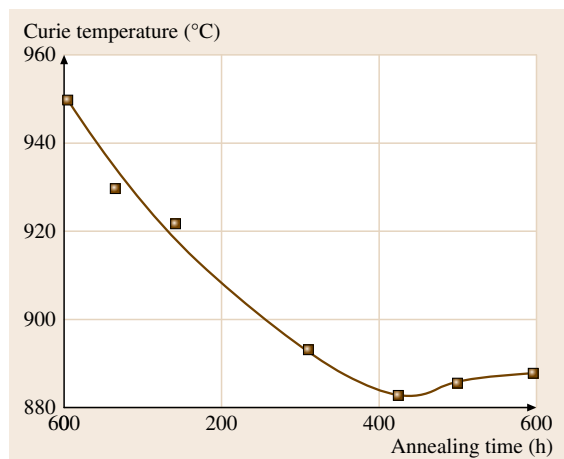


Fig. 20.6 Dependence of Curie temperature on time for long-term high-temperature annealing (at 1000 °C) of 1.35–1.5 mm thick **KTP** crystals grown from a 0.5 (g/g) **KTP**/ $\text{K}_6\text{P}_4\text{O}_{13}$ flux (after [20.72])

unknown kinetics of stoichiometry variation in high-temperature-annealed **KTP** crystals associated with the surface layer decomposition [20.108].

The existence of potassium nonstoichiometry in **KTP** crystals was realized a long time ago [20.109], but there was disagreement about the limits of its range. According to some reports, this range is narrow, less than 0.1 mol % [20.90], while others claim that it may exceed 10 mol % [20.108]. Our preliminary electron microprobe measurements indicate that the potassium deficiency may be of the order of a few mol. % and that phosphorus nonstoichiometry may exist as well [20.110]. An attempt to evaluate the **KTP** composition based on T_C measurements has been made only using ceramic **KTP** compounds synthesized at 800 and 900 °C [20.89], since the single crystal decomposes before melting. It is common to think that stoichiometry of as-grown **KTP** depends on the crystallization temperature alone [20.90]. However, this is true only for a single kind of self-flux (Fig. 20.5), when the saturable **KTP** concentration (solubility) is a direct function of temperature. A generally more correct statement is that **KTP** stoichiometry, and thus the Curie temperature, depend on the self-flux composition; for example, two crystals grown from 1.1 g/g $\text{K}_6\text{P}_4\text{O}_{13}$ and 0.4 g/g $\text{K}_{15}\text{P}_{13}\text{O}_{40}$ fluxes have an identical T_C value of 925 °C, yet their crystallization temperatures (1080 and 926 °C, respectively) are completely different.

Effect of Impurities

We have referred above to the gradients of potassium and oxygen vacancies V_K and V_O , respectively. However, the latter can be superimposed by the gradients of residual impurities on the various **KTP** cation and anion sites. Some impurities may create a charge-compensating effect and alter the magnitude of the built-in electric field. Depending on the valence and the nature of a substitutional site captured, impurity ions may enhance or diminish the concentration of oxygen vacancies that are normally charge-compensating the potassium vacancies. Table 20.3 gives a chart of the influence of various impurities located at different sites, assuming that the effective distribution coefficients (k_{eff}) of all impurities are less than one. The parallel arrows indicate enhancement of the V_O concentration gradients, while antiparallel arrows indicate their compensation with a consequent reduction in the value of the built-in electric field in the *z*-direction.

It should be noted that miscellaneous dopants are frequently introduced into the **KTP** crystals for a variety of reasons, such as alteration of their resistivity [20.90]

Table 20.3 Concentration gradients of oxygen vacancies in **KTP** crystals grown from self-fluxes and solutions with charge-compensating dopants ($k_{\text{eff}} < 1$)

Case	Type of doping	Direction of V_O concentration gradient induced by		
		V_K in self-flux	Doping	Result
1	Self-flux	↓	None	↓
2	A^{3+}/Ti^{4+}	↓	↓	↓ ↓
3	A^{5+}/Ti^{4+}	↓	↑	↓ or ↑
4	A^{6+}/Ti^{4+}	↓	↑	↓ or ↑
5	B^{2+}/K^+	↓	↑	↓ or ↑
6	Si^{4+}/P^{5+}	↓	↓	↓ ↓
7	F^-/O^{2-}	↓	↑	↓ or ↑

↓ Direction from the seed to a growing facet, ↑ direction from a growing facet to the seed,
 $A^{3+} = Sc^{3+}, Ga^{3+}, Al^{3+}, In^{3+}, Cr^{3+}$; $A^{5+} = Nb^{5+}, Ta^{5+}$; $A^{6+} = W^{6+}, Mo^{6+}$; $B^{2+} = Pb^{2+}, Ca^{2+}, Mg^{2+}$

or nonlinear optical properties [20.111, 112]. Lead oxide is deliberately added to the K6 self-flux [20.106] in order to enhance the crystal growth rate and to reduce the probability of spurious nucleation at the crucible wall. As a result, several hundred ppm of Pb^{2+} ions have been introduced into the crystal [20.113]. They cause a beneficial effect of significantly reducing the concentration of color centers responsible for the detrimental *gray-tracking* phenomenon [20.67] in frequency-doubling the 1.06 μm Nd:YAG laser. Most stable *gray-track* defects are attributed to the presence of oxygen-vacancy-associated Ti^{3+} centers in the **KTP** crystal. Addition of small amounts of Pb^{2+} ions substituting for K^+ ions provides charge compensation for potassium vacancies, and oxygen vacancies are no longer needed. (Gray-tracking will be discussed in more detail at the end of this chapter.) Reduction in the concentration of oxygen vacancies and their gradients has the effect of diminishing the built-in electric field and is, therefore, influencing the ferroelectric domain formation in **KTP** crystals during growth and cooling through the Curie temperature.

20.2.2 RbTiOPo₄ Crystals

Presently, **RTP** is viewed as a particularly useful member of the **KTP** family of crystals for electrooptic applications, such as high-frequency Q-switching and light modulation, due to its large electrooptic coefficients, high damage threshold, and the absence of piezoelectric ringing [20.14, 114]. The low-ionic-conductivity **RTP** crystals are required for low-leakage-current operation of the devices. Although the Rb^+ ion is larger than the K^+ ion, **RTP** is also a classical ionic conductor [20.39], and vacancy-assisted one-dimensional ionic

conductivity is expected. It is thus important to monitor the concentration of Rb vacancies, or the degree of Rb stoichiometry, which may and usually does depend on the crystal growth conditions. The fundamental ideas about such dependence for growing **RTP** crystals from self-fluxes can be based on the knowledge accumulated with **KTP** crystals as described above. In the present section, we will review the recent results on the variable stoichiometry of **RTP** crystals as assessed using the Curie temperature measurements by Roth et al. [20.76]. Some peculiar results distinct from those observed with **KTP** were revealed.

Differentiation of Growth Sectors
In similarity with **KTP**, an **RTP** crystal growing out from a particular flux, e.g., $Rb_6P_4O_{13}$ (R6), and becoming enriched in rubidium in course of the process is expected to be gradually more stoichiometric in terms of Rb^+ ions. To verify this, a 300 g **RTP** crystal (of Fig. 20.4a type) was grown from an R6 solvent by pulling on a [100]-oriented seed, and the Curie temperatures of the top and bottom parts of the boule were measured using the dielectric (capacitance) anomaly technique. The top part exhibited $T_C = 782^\circ C$, and the bottom part showed a higher T_C value by $5^\circ C$. This result was in accord with the expected improvement of rubidium stoichiometry. The absolute T_C values depend, of course, on the specific solute content and solvent composition in the flux, to be discussed below.

Before engaging in the analysis of Curie temperature dependencies on the flux chemical composition, we will address the peculiar effect revealed in the course of taking the capacitance versus temperature characteristics in some **RTP** samples. These characteristics frequently feature two peaks, pointing to the fact that

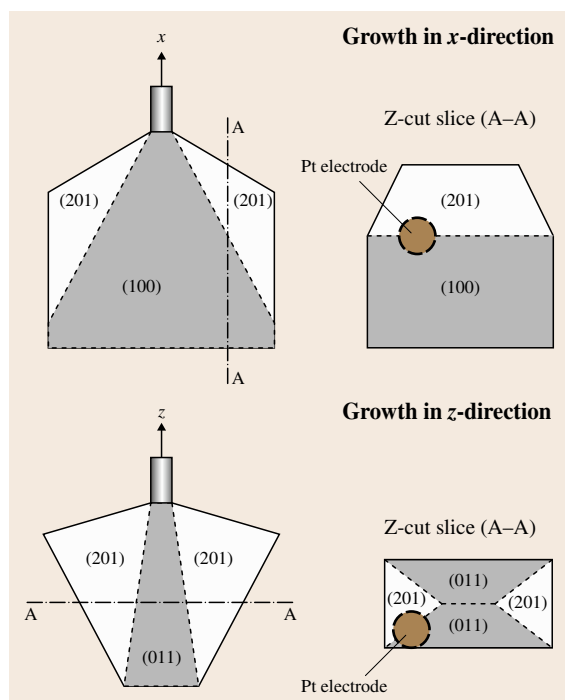


Fig. 20.7 Schematic representation of growth sectors developed in RTP crystals grown on *x*- and *z*-oriented seeds; *z*-cut slices may contain two growth sectors, which can be partially included in the area below the Pt electrode

two different Curie temperatures exist in the same sample. A close examination of such samples revealed that they were cut from crystal areas comprising two different growth sectors, and that the Pt electrodes covered areas containing both sectors. We recall that RTP crystals (like other *KTP*-family crystals) contain 14 growth sectors, displayed through four types of well-developed facets: $2 \times \{100\}$, $4 \times \{110\}$, $4 \times \{011\}$, and $4 \times \{201\}$, in its typical morphological habit (Fig. 20.2). The number of growth sectors and the volume and geometry of each particular sector depend on the growth direction and type (submerged, TSSG, with or without pulling). Figure 20.7 shows schematically the structure of main growth sectors in two RTP crystals grown by the TSSG method from R6 fluxes, one with pulling on an *x*-oriented [100] seed and the other without pulling and grown on a *z*-oriented [001] seed. Samples for T_C measurements were machined from *z*-cut slices along the A–A lines shown in the figure for both cases. Apparently, Pt electrodes could cover either a single growth sector or two sectors, and a double-peaked $C = C(T)$ characteristic was obtained in the latter case.

Curie Temperature Versus Composition

The intriguing result described above implies that the variation of the Curie temperature, or of the stoichiometry of RTP crystals, as a function of the flux chemical composition must be studied for each growth sector separately. In Fig. 20.8, the results for three differen-

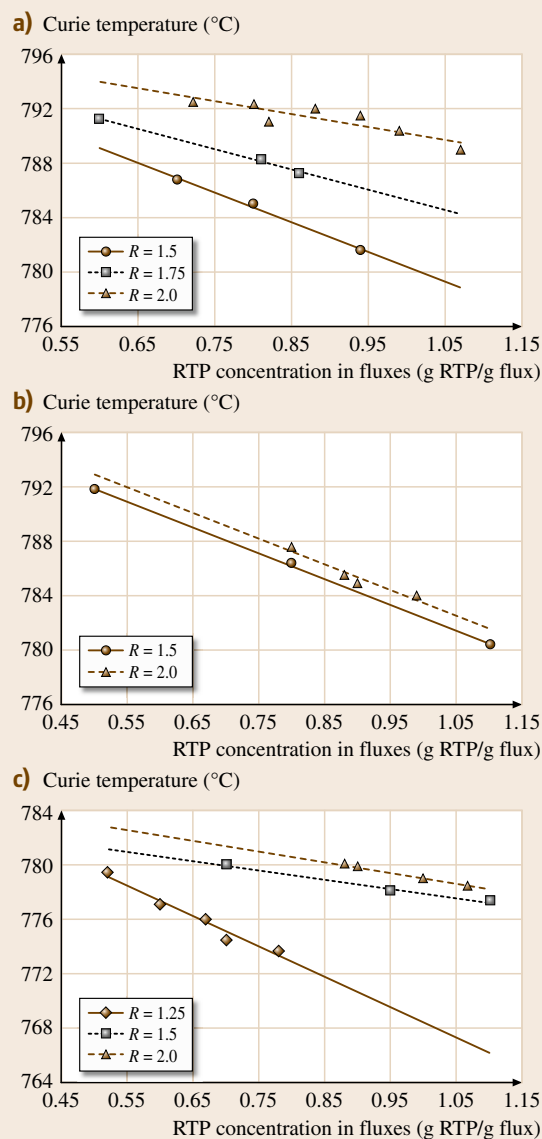


Fig. 20.8a–c Curie temperatures as a function of RTP concentration in the solution for various self-fluxes, measured separately for three growth sectors: (a) {100}, (b) {011}, and (c) {201}

tial growth sectors, of the {100}, {011}, and {201} types, are presented. For each sector, T_C as a function of RTP concentration (in weight units) is given for self-fluxes with different R ([Rb]/[P]) values. The nearly linear dependencies obtained are in complete similarity with the KTP case: (1) the lower the RTP concentration, in any self-flux, the higher the T_C value of the crystal, and (2) for any given RTP concentration, T_C is higher for self-fluxes with higher values of R . The combined result is that a higher Curie temperature corresponds to a higher overall concentration of the Rb ions in the solution, and therefore to higher rubidium content in the crystal. Naturally, the solution becomes gradually enriched in rubidium in the course of RTP crystal growth. The important practical consequence of this behavior is that a rubidium concentration gradient builds up in the as-grown crystal. This gradient is not averaged out during the cool-down stage, since the diffusion coefficient of the larger Rb^+ ions is presumably even smaller than that of K^+ ions.

The observed span of T_C values in RTP, from 770 to 800 °C, is much narrower than the corresponding range of Curie temperatures in KTP (880–960 °C). In addition, the slopes of the linear dependencies are shallower. We presume, therefore, that the overall extent of change of the Rb stoichiometry in RTP crystals is essentially smaller than the corresponding variation of K stoichiometry in KTP crystals. Another distinctive feature of RTP crystals is that they exhibit abrupt jumps in the Curie temperature over boundaries between any pair of simultaneously solidifying growth sectors of different types, as can be deduced from Fig. 20.8. It is noteworthy that a sign of a double peak in the $C(T)$ curve has been reported for the isomorphous CTA crystal [20.20], but has never been observed in nominally pure (undoped) KTP crystals. Only deliberately doped KTP may show double peaks due to the different distribution coefficients of dopants at various growth faces along the crystal–melt interfaces [20.76].

Extensive studies of nominally pure and deliberately doped RTP crystals exhibiting double peaks in their $C(T)$ curves, with a separation of over 10 °C between the T_C values on a single sample, cannot be explained by the presence of trace impurities. A different explanation must be invoked. It starts with the recognition that the RTP growth temperatures are typically 100–200 °C higher than the T_C values, and the crystals solidify in the pseudosymmetric *mmm* phase [20.116], in which the R(1) and R(2) sites are symmetrically identical [20.24]. However, the likely diverse formation mechanisms of native defects within the various growth

facets at high temperatures may cause a variation in the statistical distribution of the Rb ions between the Rb(1) and Rb(2) sites during cooling through the ferroelectric phase transition. The defects may be associated not only with the rubidium and charge-compensating oxygen vacancies, but also with other stoichiometric components, namely titanium and phosphorus ions. However, initial attempts to identify any deviation from the stoichiometric composition of these components using the electron-microprobe technique did not contribute positive results.

20.2.3 Other KTP Isomorphs

Only a limited attempt has been made to study the crystal stoichiometry versus flux composition dependencies in KTP isomorphs other than RTP. This is regrettable, since the arsenates, especially KTA, are very useful for OPO applications in the near-infrared [20.15], and optically uniform long *x*-cut elements are required. The same applies to RTA crystals used for periodically poled waveguide frequency-doubling devices [20.117]. In this section, some preliminary results on the arsenate isomorphs are given.

Curie Temperature Variation

In a recent work [20.118], a series of relatively small ($< 1 \text{ cm}^3$) KTP, RTP, KTA, and RTA crystals were grown by the TSSG method from high-temperature K6 and R6 self-fluxes containing different starting concentrations of the (KTP, KTA) and (RTP, RTA) solutes, respectively. Figure 20.9 shows the Curie tempera-

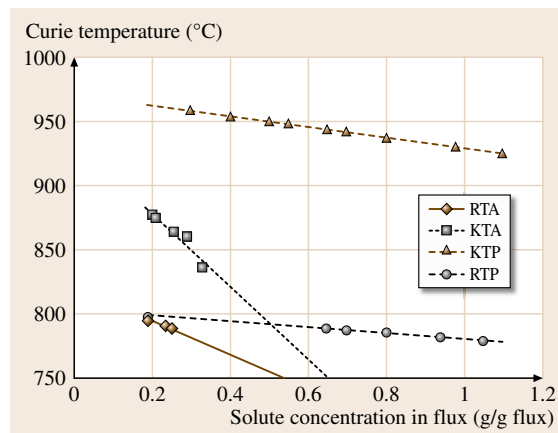


Fig. 20.9 Curie temperature dependence on solute (KTP, RTP, KTA, and RTA) concentration in the respective K6 or R6 flux for four KTP isomorphs (after [20.115])

ture dependencies of all the corresponding crystals on the solute concentration in the flux for comparison. The trend lines expanded for the two arsenate crystals do not represent accurate slopes, since only a few growth experiments have been carried out, at small solute concentrations. There is a difficulty in obtaining such crystals with reliably changing compositions from highly concentrated solutions, namely at higher growth temperatures, due to arsenic evaporation. However, the common rule for all isomorphs is quite apparent, namely, the more dilute the solution, the higher the Curie temperature, and the more stoichiometric the crystal. This reflects the fact that, at smaller solute concentrations, the crystal solidifies from solutions richer in (primarily) potassium or rubidium ions with respect to titanium.

In the preceding discussion, we have referred only to the potassium or rubidium stoichiometry. The reasons for such approach are that (1) titanium (oxide) alone is left behind during prolonged high-temperature annealing of *KTP*, while the potassium and phosphorus compounds evaporate [20.93], and (2) there is a general belief that PO_4 tetrahedra are the basic building blocks of the *KTP* structure [20.115], making phosphorus non-

stoichiometry less likely. On the contrary, the existence of potassium [20.90] and rubidium [20.119] vacancies in *KTP* and *RTP*, respectively, has been demonstrated.

Concluding Remarks

To summarize this section, large crystals of *KTP* and its isomorphs, such as *RTP*, *KTA*, and *RTA*, are found to exhibit gradual compositional changes in their stoichiometric components (primarily potassium or rubidium ions) during *TSSG* from self-fluxes. This has been verified by measuring the ferroelectric transition (Curie) temperatures of the various crystals grown from fluxes of different initial solute concentrations. Higher Curie temperatures of crystals solidified from dilute solutions indicate their improved stoichiometry, which translates into better performance in optical devices; for example, more stoichiometric *KTP* becomes highly resistant to the detrimental gray-tracking in *SHG* [20.89]. Better stoichiometry implies also lower coercive fields necessary for efficient processing of *KTP*-based periodically poled nonlinear optical devices (see Sect. 20.4.1 for more detail) and orders of magnitude higher electrical resistivity, which is particularly important for the use of *RTP* crystals in electrooptic devices [20.14].

20.3 Growth-Induced Ferroelectric Domains

Single-domain *KTP*-family crystals can be readily grown from high-temperature solutions well below the Curie temperature. However, high-temperature growth is of more practical interest due to the lower viscosity or significantly larger growth rates involved [20.83]. When the high-temperature growth results in multidomain crystals, the latter can be converted into single-domain structures by complex thermal annealing [20.105, 107]. The presence of multiple domains degrades the optical uniformity and, thus, the device performance of the crystals. Numerous questions associated with the domain structure and their formation during crystal growth, cooling through the Curie temperature, and thermal annealing are still not understood to a full extent. Historically, *Zumsteg* et al. [20.116] were the first to predict the existence of a ferroelectric domain structure in *KTP*-family crystals. *Bierlein* and *Ahmed* [20.120] used piezoelectric, electrooptic, and pyroelectric techniques to reveal the domain structure in hydrothermally grown *KTP* crystals. They found domains oriented parallel to the (100) crystal-

lographic plane and zigzag domain walls characteristic of a head-to-head domain configuration. A more complex domain structure was observed by *Loiacono* and *Stolzenberger* [20.121] in flux-grown *KTP* crystals. This structure, termed *dark line defects*, could not be ascribed any definite crystallographic orientation. Moreover, the domain pattern could not be altered by thermal cycling to above the Curie temperature and, thus, the domains were identified as possible nonferroelectric Dauphiné twins. *Shi* et al. [20.122] reported on the existence of a ferroelectric domain twin boundary in *KTP* parallel to the crystallographic (001) plane. They concluded, based on X-ray double-crystal diffraction measurements, that the (100) facet of *KTP* was formed by two symmetric vicinal planes with the interface between the vicinal planes being the 180° twin boundary. However, other authors [20.10, 83] pointed out that the (100) vicinal plane boundary and the corresponding 180° twinned domain wall might not coincide with the (001) plane but rather exhibit a considerably more complicated structure.

20.3.1 Domains in Top-Seeded Solution-Grown KTP

KTP crystals grown from highly concentrated solutions usually crystallize in the paraelectric phase above the Curie temperature (Fig. 20.5). The ferroelectric domain structure is formed upon postgrowth cooling, at a rate of $\approx 25\text{--}40^\circ\text{C}$ in a $2\text{--}5\text{ K/cm}$ temperature gradient. In order to visualize the domain structure, diverse techniques are employed, such as etching and piezoelectric measurements [20.107] or pyroelectric toning [20.123]. Below, visualization of the various **KTP** ferroelectric domain structures will be presented as obtained by simple etching in a 2 : 1 (molar ratio) $\text{KOH} : \text{KNO}_3$ solution at 220°C . The main parameters governing the kinetics of the diverse domain shape formation are elucidated in this section as well.

Bidomain Structure

TSSG of **KTP** crystals from the K6 self-flux by pulling on x -oriented seeds and initiated above the T_C (Fig. 20.4a) frequently results in a bidomain structure, namely the boule contains two large ferroelectric domains of opposite sign in a head-to-head configuration. Figure 20.10a shows the details of this structure through a crystal cross-section cut perpendicularly to the growth direction. Two central domains with vectors of spontaneous polarization P_s pointing towards the domain boundary, or inwards, usually exist. The domain boundary coincides with the z -plane or has an orientation very close to it (since this is not always a coherent boundary [20.107]) and crosses vertically the entire crystal. Additionally, the boule is enveloped by a thin domain layer, 0.5–2 mm thick, and a fragment of such envelope is shown in Fig. 20.10b. Its polarization is always opposite in sign to the neighboring main domain and positive towards the outer surface. The surface appears to be the Ti (or K) positive face of the crystal. The en-

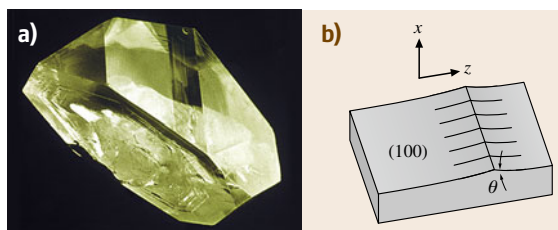


Fig. 20.11a,b Photograph of a hillock (a) on the flat (100) facet of a **TSSG KTP** and sketch of the associated edge-like perturbation (b)

velope domain is clearly formed during the slow crystal cooling above the melt. As a result, the outer crystal surface is charged positively, however can be reversed by an appropriate thermal treatment [20.83].

The origin of the bulk bidomain structure is of particular importance and interest. We recall that in the course of pulling **KTP** crystals on x -oriented seeds the growth interface is formed entirely by the large flat (100) facet. However, Bolt and Enckevort [20.124] have reported on the existence of one or several hillocks on the (100) facet, or the formation of growth surfaces vicinal to the (100) crystallographic plane at an angle of about 30° . In fact, they have observed such hillocks on top of all facets parallel to the z -direction. Our experimental observations are consistent with their reports as well. A sample photograph of a hillock on the (100) facet of a top-seeded **KTP** crystal is shown in Fig. 20.11a. These linear hillocks are essentially edge-like perturbations on flat facets, described by Chernov [20.125] over three decades ago, and they are due to temperature fluctuations at the growth interface. A sketch of the edge-like perturbation is given in Fig. 20.11b.

Kinetics of Domain Formation

As discussed above, potassium concentration gradients are developed in the growing **KTP** crystal perpendicularly to the growth interface. With the existence of vicinal surfaces inclined at small angles to the z -direction, small components of the concentration gradients in this direction inevitably emerge. If the associated built-in electric field is larger than the coercive field, the direction of the concentration gradient's z -component defines the domain direction when the crystal undergoes the ferroelectric transition upon cooling. A bidomain structure is thus formed, as shown in Fig. 20.12a. Subsequent temperature fluctuations may cause additional edge-like perturbations resulting in formation of new domains by a similar mechanism. Local

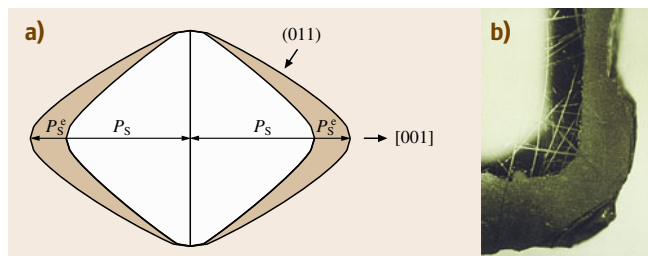


Fig. 20.10a,b Typical bidomain structure scheme in a (100) cross-section of an as-grown (above Curie temperature) **KTP** crystal (a) and a photograph ($\times 30$) of an envelope domain fragment (b)

variations in the magnitude of the built-in field may cause an opposite effect, namely healing of the main domain (also shown in Fig. 20.12a) leaving behind domain islands of opposite sign. Examples of such islands are shown in Fig. 20.12b, and their existence has been reported elsewhere [20.126] as well. Incorporation of residual impurities may play a role in this process, as follows from Table 20.3. Each half of the bidomain crystal can be monodomained using high-temperature thermal treatment [20.83].

If seeded growth above the Curie temperature is enforced in such a way that the crystal is always submerged in the solution, no envelope domain is formed, but the bidomain structure can be also readily obtained. Figure 20.13a shows a y-cut cross-section of such a crystal, which generally acquires the typical morphology sketched in Fig. 20.2. The (100)- and (201)-type growth sectors are defined by dotted lines in the drawing. Clearly, the (201)-type facet forms a large angle (about 31°) with the z-direction, which results in a large z-component of the concentration gradient and a large built-in electric field. Relatively small temperature fluctuations cannot reverse the domain sign in this case, and single-domain (201)-type sectors always grow. The same applies to the (011)-type growth sectors not shown in the picture. The bidomain formation within the (100)-type growth sector is also reflected in Fig. 20.13a; similar structure occurs in the (110)-type growth sectors, since the (110) crystallographic plane is also parallel to the z-axis. Figure 20.13b demonstrates that, when the growth is initiated below the Curie temperature, the compositional gradient may be so strong across the {201} and {011} facets that a double-domain structure rather than a single-domain occasionally occurs, with a configuration as shown.

20.3.2 Domain Boundaries

We have already demonstrated elsewhere [20.107] that the domain boundary within the (100) growth sector is diffuse rather than a sharp 180° twin boundary [20.10]. Similar diffuse boundaries exist within the (110) growth sector. Of special interest are the domain boundaries at the borders of growth sectors, which are formed at the edges of two meeting facets during growth. In the following, the various types and subtypes of ferroelectric domain boundaries will be described in more detail.

Classification of Boundaries

It should be pointed out that not only the intrasector boundaries, but also the edge boundaries between

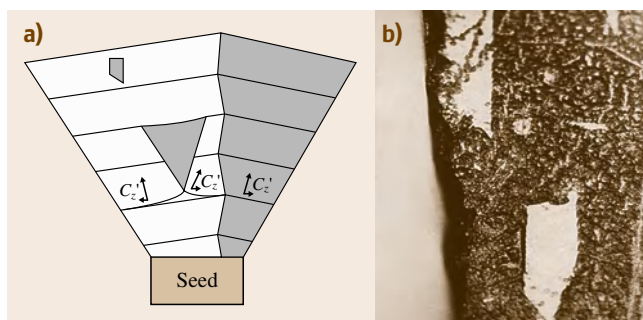


Fig. 20.12a,b Formation of ferroelectric domains in the (100) growth sector of K₂P₂O₇ due to edge-like perturbations: (a) schematic drawing, (b) image of etched surface parallel to the [100]-direction

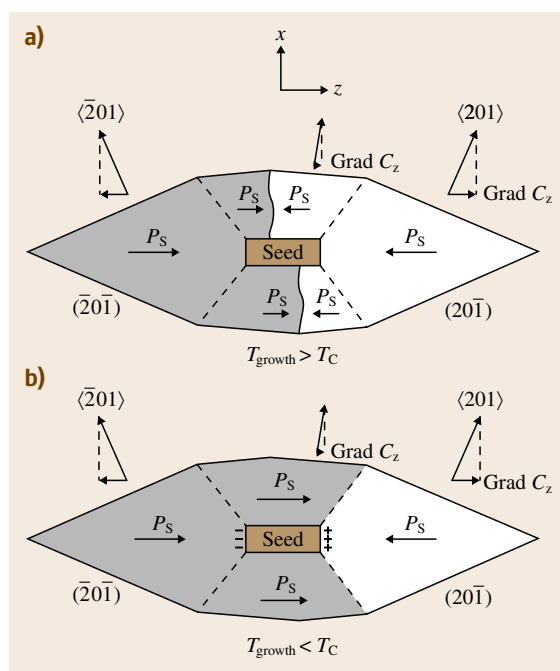


Fig. 20.13a,b Ferroelectric domain structure in immersion-seeded K₂P₂O₇ crystals (central cuts in the y-plane) grown above (a) and below (b) the Curie temperature

(100)- and (110)-type sectors are diffuse, while those between (011)- and (011-bar)-type sectors (Fig. 20.2) are always sharp. A boundary between (110)- and (011)-type growth sectors may not exist at all or appear in its special form shown in Fig. 20.14a. Such apex-like perturbations of the edge between the corresponding growth facets may arise [20.125] due to temperature fluctuations, and a z-component of the potassium con-

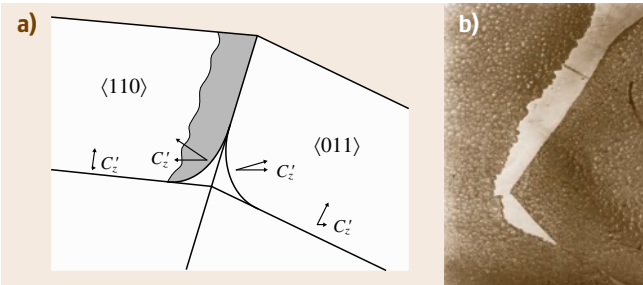


Fig. 20.14a,b Complex ferroelectric domain boundary between (110) and (011) growth sectors: **(a)** schematic drawing, **(b)** metallographic image (× 40)

centration gradient is created on the (110) facet. The associated built-in electric field may be large enough to reverse the domain sign near the boundary, but only within the (110) growth sector. This results in a special type of edge domain boundary, which is sharp on the (011) sector side and diffuse on the (110) sector side. Such complex boundaries are frequently observed experimentally, as shown in Fig. 20.14b.

The variety of domain boundaries and their extent depend directly on the number of growth sectors formed and on the kinetics of growth of each sector, which in turn depend on the growth method employed and on the chemical composition of the flux. According to *Loiacono et al.* [20.46], in the case of K6 flux, complex ions of $(\text{PO}_4)^{3-}$, $(\text{P}_2\text{O}_5)^{4-}$, and $(\text{P}_3\text{O}_{10})^{5-}$ are present in the solution in a ratio 3 : 8 : 1, leading to the ratio of 1 : 2 : 3 for growth rates in the *x*, *y*, and *z* crystallographic directions, respectively. They report on a relatively close to the former growth rate ratio of 1 : 1 : 3 for K8 and K15 fluxes, but a quite distinct ra-

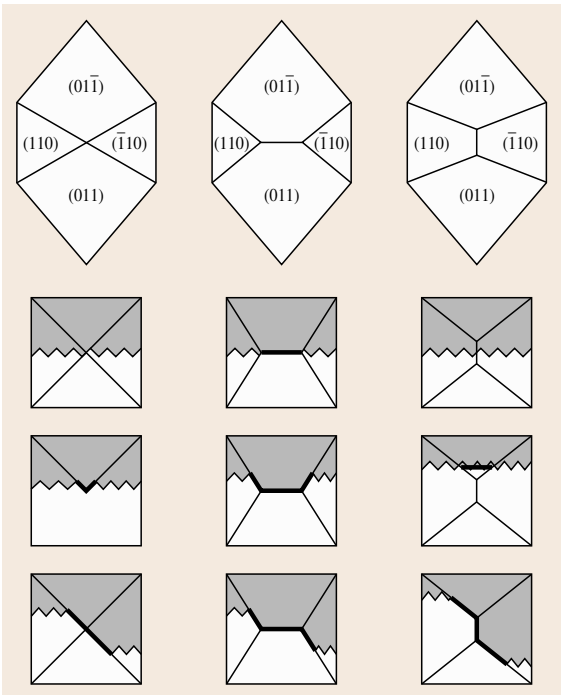


Fig. 20.15 Ferroelectric domain structure and types of domain boundaries in TSSG KTP crystals terminating with edges or sharp spikes in the *z*-direction

tio of 1 : 18 : 17 (extremely slow growth of the *x* facet) for the K4 flux. The differences in growth rates are reflected in the variation of morphological shapes of KTP crystals [20.43]. Certain facets may be overdeveloped or underdeveloped or not exit at all. A good example is the (001) facet that is expected to exist

Table 20.4 Classification of ferroelectric domain boundaries in KTP-type crystals*

Type of domain boundary		Details and comments
Edge boundary	– Full-size edge	Traces of intersection of growing planes; they are always sharp boundaries
	– Partial edge	{011}/{011}; {201} types never intersect
Intrasector boundary		{110}/{110}, {110}/{201}, {110}/{100}
	– Central	Inside {100} and {110} growth sectors (diffuse boundaries)
	– Streak	Adjacent to {011}/{110} edge (sharp on the {011} side, diffuse inside the {110} sector)
	– Dispersed	Contours of small domains inside the {100} and {110} growth sectors (irregular shape)
	– Envelope	External crystal surface (for TSSG – on top of the crystal, for SSSG – the entire surface)

* {201}/{100} and {201}/{011} boundaries *do not* exist

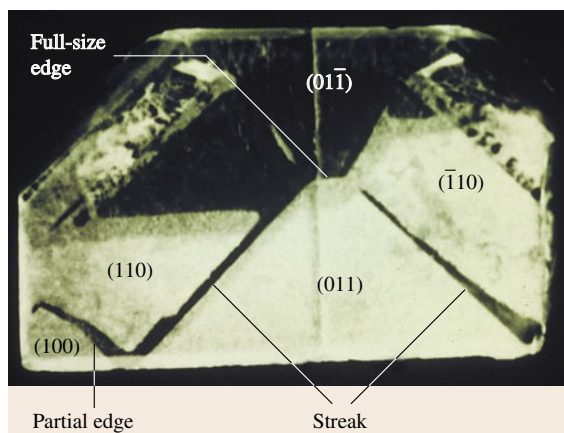


Fig. 20.16 Metallographic image of a full (011)-cut slice of a TSSG KTP crystal showing a real structure of ferroelectric domains and domain boundaries

theoretically [20.43], but which is rarely observed experimentally. Usually, only edges parallel to the x - (as in Fig. 20.2) or y -directions or just sharp spikes develop instead of this facet. These three cases are presented schematically in Fig. 20.15, where the central cut (perpendicularly to the y -axis) reveals the specific domain structure and the various domain boundaries of TSSG KTP crystals.

Similar types of diffuse and sharp domain boundaries can be found in crystals cut also along other crystallographic planes, but the y -cut slice reveals this variety sufficiently, allowing to suggest their presumably complete classification, which is summarized in Table 20.4. In this classification, the main distinction is made between domain boundaries forming at the borders of different growth sectors and within the growth sectors. Boundaries associated with the envelope domains discussed above and the irregular shape domains within the {100} growth sectors are added as a special case of intrasector boundaries. Figure 20.16 shows a real domain structure as revealed on the etched surface of a (011)-cut slice of a TSSG KTP crystal as well as part of the domain boundaries shown in Fig. 20.15 (for a y -cut surface) and listed in Table 20.4.

20.3.3 Summary of Ferroelectric Domain Structures

The foregoing analysis of the domain structure and boundaries applies to all KTP-type crystals grown by the TSSG method, both above and below the

corresponding Curie temperatures. The main features observed are as follows:

- The ferroelectric domain structure of high-temperature solution grown KTP crystals is defined by the nature of growth sector development.
- Domain formation within the (100)- and (110)-type growth sectors (containing central and streak boundaries) is governed by the elementary crystal growth mechanisms.
- (100)- and (110)-type growth sectors exhibit predominantly bidomain and rarely multidomain structures; (011)- and (201)-type growth sectors are single domain.
- The bidomain, or 180° twin domain, is not a twin in the crystallographic sense.
- The diverse domain boundaries can be classified into edge type (partial and full size) forming at intersections of growth sectors and intrasector type (central, streak, dispersed, envelope).
- Domain orientation is defined by the direction of the built-in electric field originating from the concentration gradients of stoichiometric components (mainly potassium in KTP) and cation impurities.

20.3.4 Single-Domain Growth

The kinetics of ferroelectric domain formation during growth of KTP crystals described above allows to suggest a number of avenues for growing single-domain crystals. A few examples are given below:

- Meniscus growth with pulling on (201)- or (011)-oriented seeds yields single-domain growth immediately, which becomes clear from the observation of Fig. 20.13. Large compositional gradients formed upon crystallization on {201} and {011} facets imply high built-in electrical fields, preventing domain inversion and keeping the body of the crystal enclosed within these facets' single domain. The drawback of this method is that *boot-like* growth occurs due to the lack of symmetry in these directions, and the crystals may hit the crucible wall before a large chunk of crystal is grown.
- TSSG with pulling on a z -oriented seed generally starts with a multidomain structure, but eventually converts into a single domain when the main body of the crystal is formed solely by the (201)- and (011)-type growth sectors as well.
- Bidomain growth is frequently also acceptable for practical applications, when the crystals are large

enough. Such growth has already been discussed above for the case of **TSSG** with pulling on x -oriented seeds. Naturally, the same applies to growth on $\langle 110 \rangle$ -oriented seeds. Hereby, there is always a danger of multidomain formation, which can be prevented by minimizing temperature fluctuations at the growth interface.

- **TSSG** with pulling in the y -direction behaves as follows: the $\langle 110 \rangle$ -type facets grow out fast, and the growth is governed by two $\langle 011 \rangle$ -type sec-

tors, resulting in a bidomain growth with a sharp $\langle 011 \rangle / \langle 0\bar{1}1 \rangle$ domain boundary.

We reiterate that growth of **KTP** or **KTA** below the Curie temperature, even by several tens of degrees, may result in similar domain formation features due to the large potassium concentration gradients, or large built-in electric fields involved. The rubidium isomorphs follow these rules very closely as well.

20.4 Artificial Domain Structures

Single-domain **KTP**-family crystals are indispensable for most nonlinear optical and electrooptic applications; for example, their excellent birefringent phase-matching properties, such as appreciable effective nonlinear coefficients, broad temperature tolerance, and large angular bandwidth, make them highly suitable for frequency doubling of near-infrared lasers. Unfortunately, in the useful type II phase-matching scheme, the optical birefringence is too small to allow for frequency doubling into the green by **KTA** or into the blue by **KTP** [20.127]. In the latter case, it is possible to obtain the important blue coherent radiation with **KTP** using sum-frequency generation [20.128] or broadening its birefringence range by doping [20.129] or with the thermally unstable KNbO_3 crystal [20.130]. However, all these methods are not attractive due to their technological complexity. An appropriate alternative is the use of quasi-phase-matching (**QPM**) based on periodic domain structures (**PDS**). The **QPM** technique, first suggested by *Armstrong et al.* [20.131], corrects the relative phase of the fundamental and secondary waves at regular intervals by means of structural periodicity built into the nonlinear medium. Phase-matching is thus achieved by periodic spatial modulation of the nonlinear coefficient along the direction of propagation. The most efficient implementation of **QPM** occurs when the sign of the nonlinear coefficient is periodically reversed, which can be achieved by periodic domain inversion in a ferroelectric material. This has been initially performed by means of fabricating several-micrometer-deep **KTP** waveguides by the ion-exchange method [20.132–134], in which Rb^+ and Ba^{2+} ions replace K^+ ions. Attempts to obtain deeper periodic domain structures involve scanned electron beams [20.135] in **KTP** and, more recently, atomic force microscopy (**AFM**) cantilever tips [20.136] in **RTP**. Well-controlled domain inver-

sion in more than 1 mm thick **KTP**-type crystals with down to a few μm small period structures has been obtained reproducibly using electrical field poling, and we will review this technique and structures in more detail below. As-grown periodic domain structures allowing for larger apertures and, thus, for higher-average-power laser applications will be discussed as well.

20.4.1 Electric Field Poling

Fabrication of **QPM PDS** by external electrical field poling has been initially implemented in LiNbO_3 [20.137, 138], where the coercive field is $\approx 21 \text{ kV/mm}$ (congruent crystals) and the wafer thickness is limited to 0.5 mm due to the high field (24 kV/mm) needed to produce domain inversion. The coercive field of **KTP** and its isomorphs is about an order of magnitude lower and, unlike LiNbO_3 , they do not suffer from photorefractive damage. The main problem of **KTP**-type crystals is the relatively high ionic conductivity, which may complicate the periodic poling. Among the techniques employed to overcome this problem are ion exchange in the surface layer and low-temperature poling. Alternatively, more stoichiometric (in potassium or rubidium) crystals exhibiting lower ionic conductivities can be used. These approaches will be discussed in more detail below.

Periodically Poled KTP

KTP is the most readily available material within the family, and the main bulk of published work in the field of **QPM** structures describes periodically poled **KTP** (**PPKTP**). The conventional process of periodic domain structure fabrication [20.137–139] is based on the application of an electric field to a photolithographically patterned electrode on the z -cut crystal surface, com-

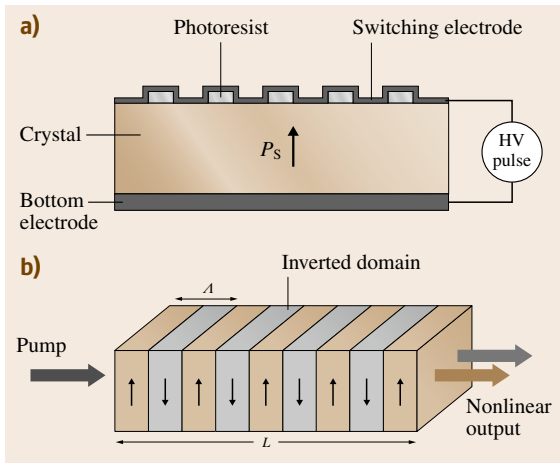


Fig. 20.17 (a) Conventional experimental setup for fabrication of domain gratings; (b) basic structure of electrically poled crystal for frequency conversion. The SHG efficiency, $\eta \propto d_{\text{eff}}^2 L$ [20.140], with L the crystal length, and the effective nonlinear coefficient for SHG of an order of m is given by [20.141] $d_{\text{eff}} = (2/\pi m) \sin(\pi m D) d_{33}$, where D is the duty cycle (ratio between inverted and uninverted domain widths). With $m = 1$ for the first-order interaction and $D = 0.5$, the optimal $d_{\text{eff}} = 2d_{33}/\pi$. Most importantly, the z -direction of light propagation with the highest nonlinear coefficient d_{33} can be chosen

prising a periodic array of metal and insulating stripes, as shown in Fig. 20.17a, or forming a grating. For SHG, the grating period (Λ) shown in Fig. 20.17b is related to the refractive indices of the fundamental (pump) and second-harmonic waves, $n_{2\omega}$ and n_ω , respectively, by

$$\Lambda = \frac{\lambda_\omega}{2(n_{2\omega} - n_\omega)}, \quad (20.5)$$

where λ_ω is the pump wavelength. For $\lambda_\omega = 0.84 \mu\text{m}$, frequency doubling into the blue requires PPKTP with $\Lambda = 4 \mu\text{m}$ [20.139], while for $\lambda_\omega = 1.06 \mu\text{m}$ (Nd:YAG laser) doubling into the green $\Lambda \approx 9 \mu\text{m}$ [20.142]. Much larger periods are sufficient for OPO, where they are deduced from the first-order ($m = 1$) phase-matching condition [20.138]

$$\frac{1}{\Lambda} = \frac{n_p}{\lambda_p} - \frac{n_s}{\lambda_s} - \frac{n_i}{\lambda_i}, \quad (20.6)$$

where n_p , n_s , and n_i are the pump, signal, and idler refractive indices, respectively. The signal and idler outputs are shown by arrows in Fig. 20.17b. For example, for an OPO interaction with $\lambda_p = 1.06 \mu\text{m}$, the period required is $\Lambda = 37.8 \mu\text{m}$ in PPKTP [20.143].

As shown in Fig. 20.17, the pulsed switching voltage is applied to the polar z -faces of the crystal through metal electrodes. The required periodic domain inversion is obtained if spontaneous polarization switching occurs only under the micrometer-wide metal stripes (top electrode) that are in intimate contact with the crystal and does not occur below the dielectric photoresist layers of the same width. If polarization switching below the insulating stripes is not prevented, domain broadening takes place below them [20.144], which degrades the duty cycle of the device (Fig. 20.17b). The resulting inverted domain narrowing is due to high tangential fields arising immediately below the dielectric barrier layer and causing depolarization by internal charge carriers [20.144]. The kinetics of depolarization thus depends strongly on the crystal electrical conductivity. In insulating ferroelectric crystals, e.g., LiNbO₃, the polarization relaxes very slowly ($\tau \approx 10^5$ s), while in KTP and its isomorphs exhibiting high ionic conductivity the relaxation process is very fast ($\tau \approx 0.2 \mu\text{s}$) [20.144]. One way of decreasing the relaxation time, or screening of depolarization, is the reduction of electrical conductivity by ion exchange.

A detailed experimental account of ion-exchange-assisted poling of KTP crystals was given by Karlsson and Laurell [20.145]. They made use of the fact that the larger Rb⁺ ions had a lower mobility than K⁺ ions in the KTP lattice and indiffused Rb⁺ ions, by immersing flux-grown KTP crystals in a RbNO₃ melt, to obtain low conductivity (\sim three orders of magnitude lower than the bulk) thin (2–5 μm) layers of Rb_{*x*}K_{1–*x*}TiOPO₄ at the two z -faces, where x varies gradually from 100% at the surface to 0% in the bulk. When voltage is applied to such crystal, the field in the exchanged layer is significantly higher than in the bulk, due to the difference in conductivity. At a certain voltage the coercive field is exceeded in the exchanged layer and an inverted domain nucleates. It continues growing towards the opposite side of the crystal under the influence of the remaining field in the bulk. The periodicity of the field near the surface is well defined, and the domains formed there can grow in a low field (lower than the coercive field) without significant broadening. Up to 1 mm thick PPKTP wafers could be fabricated using this method, and efficient first and higher-order green SH signals were obtained with 9.01 and 31 μm domain gratings [20.145] and blue SH with 6.09 μm gratings [20.146].

Another method of poling under reduced KTP ionic conductivity and requiring no chemical treatment of the crystal is the low-temperature polarization

switching suggested by *Rosenman et al.* [20.147]. They used 0.5 mm thick **KTP** wafers with a room-temperature conductivity of $10^{-7} \Omega^{-1}\text{cm}^{-1}$. The latter reduced to about $10^{-12} \Omega^{-1}\text{cm}^{-1}$ at $T = 170 \text{ K}$ due to the freeze-in of K^+ -ion migration. This increased the relaxation time τ by five orders of magnitude as well, and polarization switching under the dielectric layer stripes (Fig. 20.17) was prevented. One negative feature of the low-temperature poling method is that it causes a strong increase in the coercive field, but even at $T = 170 \text{ K}$ it is still twice as low as in LiNbO_3 [20.147]. High-quality **PPKTP** elements with $9 \mu\text{m}$ domain grating period were fabricated using this method for efficient frequency doubling into the green [20.142] and **OPO** [20.148], while no optical damage due to gray tracking (green-induced infrared absorption) was observed up to continuous pump power of 4.5 kW/cm^2 .

In spite of the tangible technological progress in **PPKTP** processing, many aspects of the field-induced ferroelectric domain formation still remain unclear, and additional research efforts have to be made for their understanding. Clearly, the domain propagation speed along the polar z -axis is orders of magnitude larger than that in the x - y plane [20.149] in consonance with the anisotropy of ionic conductivity. In addition, anisotropy in the domain wall propagation velocity between the x - and y -directions exists as well, being 6–30 times larger in favor of the latter [20.149, 150]. Room-temperature polarization reversal in conventional **KTP** superionic conductor results in spontaneous nucleation of domains in the crystal bulk, since the mobile potassium ions can screen the depolarization field of the nucleating domain [20.151]. Additional observations related to room-temperature poling include the widely known features, such as domain nucleation at the electrode edges, domain broadening due to charge deposition underneath the dielectric layer and overpoling by multiple pulses, lateral domain growth and merging before reaching the opposite electrode, and also nonuniformity of the domain growth kinetics across the wafer. The latter is attributed to the variable stoichiometry of the **KTP** crystal [20.152]. Some attempts to return to the doping schemes for increasing the **KTP** resistivity for poling have been made lately as well [20.153].

High-Potassium KTP

Improvement of the morphology of **PPKTP** domain structures by ion exchange or low-temperature poling discussed above incorporates also certain disadvantages. Ion exchange is a two-step method involving

chemical treatment of the crystal and resulting in variable success. Low-temperature poling requires application of external electric fields above the coercive field, which is as high as 12 kV/mm [20.147]. Therefore, a better alternative is to use more stoichiometric (in potassium) **KTP** crystals, exhibiting lower ionic conductivities and allowing poling at higher temperatures and lower voltages. Such an attempt has been made by *Rosenman et al.* [20.154], who have studied polarization reversal in three different **KTP** crystals denoted as **HK**, **IK**, and **LK** for high, intermediate, and low potassium content, since it is quite difficult to determine the exact potassium stoichiometry. The conductivities of the samples varied from 10^{-12} to $10^{-8} \Omega^{-1}\text{cm}^{-1}$ at room temperature. Both **HK** and **IK** samples exhibited a relatively long polarization switching relaxation time, $\tau \approx 0.18 \text{ s}$, which is sufficient for preventing domain broadening. Their measured room-temperature coercive field was less than 3 kV/mm , namely four times lower than that of **LK** at 170 K . The crystallographically more perfect 0.5 mm thick **IK** sample was used for actual poling at 248 K under a 4.6 kV/mm electric field. The duty cycle obtained was 50%, which indicated a complete lack of domain broadening. The element with a grating period of $24.7 \mu\text{m}$ was subsequently used for successful doubling of $1.55 \mu\text{m}$ radiation from a 18 mW diode laser into the deep red.

In a follow-up paper, *Jiang et al.* [20.155] grew **HK**-grade **KTP** crystals from a highly potassium-containing **K4** flux for electric poling application. Their results confirmed that crystals with better potassium stoichiometry exhibited significantly lower ionic conductivities and lower coercive fields, allowing successful room-temperature poling. Application of a less than 3 kV/mm electric field to a 1 mm thick **HK**-grade **KTP** crystal resulted in polarization reversal throughout the sample thickness, and **PPKTP** elements with grating periods of $60 \mu\text{m}$ could be obtained. A surprising detail pointed out by the authors was that periodic poling for the grating vectors along $[100]$ - and $[010]$ -directions gave similar results, which was presumably sample dependent, since it was never observed with the usual smaller $9 \mu\text{m}$ gratings.

KTP Isomorphs

Very few attempts have been made to produce **PPKTA** crystals, since in addition to the difficulties of arsenate growth the dielectric and ferroelectric properties of **KTA** are hardly better than those of **KTP** crystals. In fact, the arsenate crystallographic framework is even more open [20.25, 26], facilitating the enhanced chi-

ral mobility of the K⁺ ions in KTA. Consequently, the superionic-to-insulating transition occurs at even lower temperature than in KTP, and the crystal temperature must be reduced to 150 K for low-temperature poling [20.156]. The reported coercive field is as high as 90 kV/cm at $T = 150$ K, and 0.5 mm thick KTA wafers have been poled at this temperature under 5 kV switching bias to obtain PPKTA elements with grating periods of 37.4 and 39 μm . It was suggested that domain inversion hereby occurred by twinning across the (100) domain walls with As(1) acting as linking atoms [20.157]. KTA has better transparency in the infrared than KTP [20.15] and is preferred for OPO applications, hence the large grating periods prepared [20.156].

Periodically poled rubidium isomorphs, namely 1 mm thick PPRTP [20.158, 159] and 3 mm thick PPRTA [20.143, 160, 161], have been prepared as well. Unlike KTP and KTA, commercially available RTP and RTA crystals have low electrical conductivities in the 10^{-12} – $10^{-8} \Omega^{-1}\text{cm}^{-1}$ range [20.14, 143]. This is due to the larger size of Rb⁺ ions in comparison with K⁺ ions and thus their lower mobility along the polar axis. The much narrower span of the Curie temperatures in RTP crystals (Fig. 20.8) than in KTP (Fig. 20.5) also indicates a smaller deviation from stoichiometry, which is likely in the case of RTA as well. As a result, PDS in RTP and RTA can be obtained by electrical poling at room temperature. The reported room-temperature coercive fields of RTP vary from 2.65 to 6 kV/mm, obviously depending on the specific resistivity of the crystals used [20.40, 149]. Typically, ≈ 4 kV voltages are used for creating PPRTP homogeneous structures over more than 80% of the 1 mm depth [20.158]. Both HK KTP and RTP crystals can be successfully poled at room temperature for a variety of applications. Unfortunately, the commercial production of PPKTP devices existing to date is based mostly on the low-temperature poling technology. Voltage pulses as low as 5.3 kV are sufficient for obtaining 3 mm thick PPRTA elements, also at room temperature [20.143]. PPRTA, like PPKTA, is used mainly in OPO applications [20.143, 162–164] due to the lower absorption in the mid-infrared. The detailed study of the thermal dependences of refractive indices performed for RTP and RTA shows that PPRTP is more appropriate for applications that require immunity to thermal lensing, whereas PPRTA is suitable for realizing temperature-tuned nonlinear devices [20.165]. Of great current interest are PPRTP-based submicrometer-size ($\Lambda = 1.18 \mu\text{m}$) domain structures produced in a 200 μm thick RTP crystal

by applying a voltage of 650 V from a high-voltage atomic force microscope [20.136]. Such PPRTP nanodomain gratings are used, for example, in backward-propagating quasi-phase-matched converters [20.136] and noncollinear SHG [20.166]. It is noteworthy that, concurrently, 0.5 mm thick flux-grown KTP crystals have been poled by the ion-exchange-aided method with application four 1 ms long 1 kV pulses to produce submicrometer PPKTP gratings with a period as small as 800 nm [20.167]. The latter have been used for demonstrating electrically adjustable Bragg reflectivity.

20.4.2 As-Grown Periodic Domain Structure

Domain miniaturization in electrically poled PDS, discussed at the end of the previous paragraph, is of great interest for the development of novel photonic devices. However, the ability to produce large-aperture PDS for high-power QPM nonlinear optical devices is of equal technological importance. The straightforward way of generating periodic domains in the bulk of large ferroelectric crystals is to introduce appropriate temperature oscillations during their growth to induce striations associated with impurities. This has been attempted with other ferroelectric crystals, such as rare-earth-doped LiNbO₃ [20.168, 169] and Li-doped KTa_xNb_{1-x}O₃ [20.170]. In the case of KTP, the influence of the various impurities on the direction of impurity-related concentration gradients and, therefore, domain formation has been discussed in Sect. 20.2.1. An additional advantage of KTP over LiNbO₃ is that the latter grows (by Czochralski pulling from the melt) with a curved interface, whereas KTP exhibits a flat facet morphology. Until now, only a single attempt to grow a large KTP crystal with a periodic domain structure has been made [20.106], and it will be described comprehensively below.

Kinetics of Impurity Incorporation

It has been pointed out in Sect. 20.3.4 that TSSG growth of KTP crystals by pulling on z -oriented seeds eventually results in stable single-domain growth due to large potassium concentration gradients, or their vacancies, in the (201) and (011) growth directions. However, the presence of charge-compensating impurities, such as divalent ions (Mg²⁺ or Pb²⁺) on K⁺-sites, may minimize or eliminate these gradients and the associated built-in electric fields. In this case, periodic variation in the domain sign during crystal cooling through the Curie temperature can be achieved by imprinting a periodic variation in the impurity effective distribution coefficient

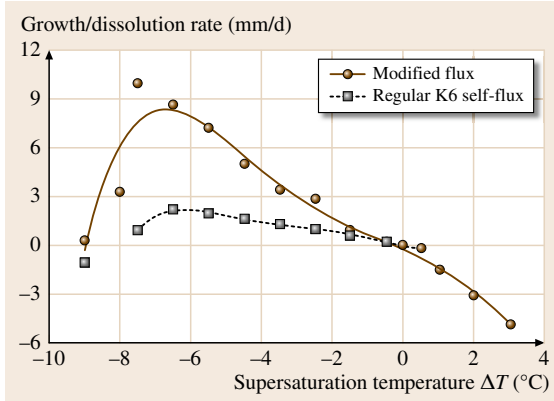


Fig. 20.18 Growth and dissolution rate of **KTP** in z -direction

cient [20.171]

$$k_{\text{eff}} = \frac{k^*}{k^* + (1 - k^*) \exp(-f^* \delta_D / D_L)}, \quad (20.7)$$

where k^* is the interface distribution coefficient, f^* is the interfacial linear growth rate, δ_D is the diffusion boundary layer, and D_L is the diffusion coefficient. Since $\delta_D \sim \sqrt{\nu/\omega}$, where ν and ω are the kinematic viscosity and crystal rotation rate, respectively, one way of altering k_{eff} is to introduce a variable rotation rate. This is complex, since the hydrodynamic flow may be altered and is then difficult to control. The second approach is to vary the growth rate by controlling the interface temperature.

The average linear growth rate can be expressed by [20.172]

$$\langle f \rangle = \frac{V}{A\rho} \left(\frac{dC_e}{dT} \right) \frac{\Delta T}{\Delta t}, \quad (20.8)$$

where V is the volume of the solution, A is the growing crystal area, ρ its density, C_e is the equilibrium concentration of the solute, dC_e/dT is the change of solubility per degree (known from the solubility curve), ΔT is the undercooling, and $\Delta T/\Delta t$ is the cooling rate. The magnitude of undercooling is defined by the width of the metastable zone, which has been studied experimentally for the regular K6 and modified K6 (addition of PbO) fluxes [20.106]. The results are reproduced in Fig. 20.18, showing the growth or dissolution rate as a function of undercooling.

Temperature Oscillations and Crystal Growth

It is apparent from Fig. 20.18 that the width of the metastable zone almost does not depend on the type

of flux, and its average value is 6.6 K. This is remarkably close to the theoretically estimated value of 6.67 K [20.173] for the K6 self-flux. The average undercooling, $\langle \Delta T \rangle$, must be of the order of half of the width of the metastable zone, or about 3.3 K, for normal **KTP** growth. If an additional periodic, e.g., sinusoidal, temperature oscillation is superimposed on the average undercooling, the actual undercooling can be expressed by

$$\Delta T = \langle \Delta T \rangle + B \sin(2\pi t/\tau), \quad (20.9)$$

where τ is the time period of temperature oscillation and the constant B must be chosen so that the undercooling does not exceed the limits of the metastable zone. As a result, growth rate oscillations will occur followed by variable (positive and negative) concentration gradients of the solute and production of a periodic domain structure. The domain metric period, Λ , depends on the

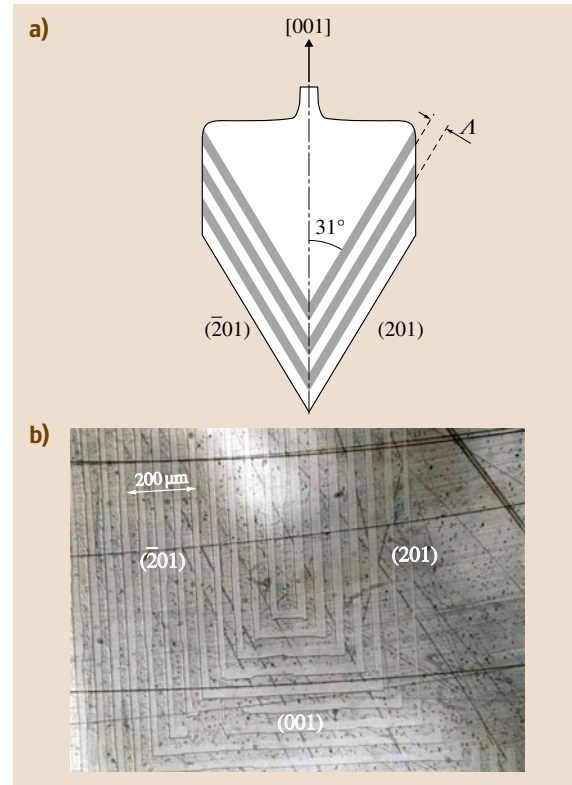


Fig. 20.19a,b Periodic ferroelectric domain structure in as-grown **KTP** crystal pulled in the z -direction: (a) schematic drawing of domain formation; (b) etched z -cut slice showing the rectangular periodic domain pattern within $\{201\}$ and $\{011\}$ growth sectors

average growth rate and the time period of temperature oscillations through the straightforward relation

$$\langle f \rangle \tau = \Lambda. \quad (20.10)$$

Growth experiments involving an undercooling oscillatory regime by multistep programming of the growth system's temperature controller yield large KTP crystals with a well-defined periodic domain structure. The geometry of such structure for TSSG with pulling in z -direction is presented schematically in Fig. 20.19a. When the {201} and {011} facets are fully developed, temperature oscillation is turned on, and the periodic domain structure is formed with period Λ . This is not the true period for nonlinear interactions; the latter is $\Lambda/\cos(31^\circ)$, since wafers are cut perpendicularly to the [001] axis in order to utilize the largest d_{33} nonlinear coefficient.

Figure 20.19b shows an etched surface of a fraction of a real z -cut slice, where clearly defined domain structures are visible within the {201} and {011} growth

sectors. The domain contours are straight since both the {201} and {011} are perfectly flat. The grating period in this picture is $50\text{ }\mu\text{m}$, but structures with Λ of $25\text{--}40\text{ }\mu\text{m}$ have been easily obtained. They can be effectively used for a variety of OPO applications. Frequency doubling requires smaller periods, such as $9\text{ }\mu\text{m}$, for SHG of the $1.06\text{ }\mu\text{m}$ radiation of the Nd:YAG laser, and there is no principal limitation in creating the narrower domain as-grown structures. The quality of the PDS is determined by the value of the duty cycle, $D = a/\Lambda$, where a is the actual inverted domain width. The optimal effective NLO coefficient and, thus, frequency conversion efficiency is obtained at $D = 0.5$ [20.142]. The D values in Fig. 20.19b are in the $0.2\text{--}0.5$ range along 10 mm of the wafer in the [100] direction (within a single growth sector), which are still useful for practical implementation of the as-grown PDS. It is noteworthy that in LiNbO₃ reasonable quality PDS can be obtained only along 1 mm due to the curved Czochralski growth interface where the inverted domains are obtained.

20.5 Nonlinear Optical Crystals

The combined knowledge of KTP-type crystal morphology development, compositional variations, and ferroelectric domain formation kinetics during growth allows one to adapt the crystal growth method to the requirements of particular applications. It has been pointed out in the previous section that TSSG of KTP crystals with pulling in the [001]-direction is most suitable for creating as-grown PDS. Crystals grown by top-seeding with pulling from K6-forming fluxes in the [100]-direction are the best choice for extracting x -oriented (for highest electrooptic coefficients) Q-switching elements, since the large flat (100) facet (Fig. 20.2) assures excellent transverse optical homogeneity needed for maximum extinction ratio [20.118]. This approach is specifically implemented in producing RTP Q-switching devices [20.14, 114]. Fortunately, TSSG with pulling in both [001]- and [100]-directions allows to obtain large volumes of single-domain crystals, as summarized in Sect. 20.3.4. In addition, establishment of compositional gradients during growth and poor potassium stoichiometry in general can not only influence the domain formation mechanisms (Sect. 20.3.1) but also affect the optical properties of KTP crystals. In the following, we will analyze the nonuniformity in the distribution of

refractive indices associated with compositional gradients [20.118] and generation of detrimental point defects related to potassium vacancies [20.89].

20.5.1 Optical Nonuniformity

Every application of nonlinear optical and electrooptic crystals requires variable degrees of optical uniformity. However, one has to make a distinction between the relative importance of transverse and longitudinal uniformity with respect to the direction of propagation of the laser beam. While x -oriented crystal pairs of electrooptic Q-switches are not too sensitive to longitudinal distribution of refractive indices [20.14], their inhomogeneity along the OPO interaction path may lead to phase mismatch and, consequently, to degradation of the OPO interaction efficiency. In this section, we will mainly focus on this latter example.

Distribution of Refractive Indices

The variation of refractive indices in large solution-grown KTP crystals, from the seed to the crystal periphery, has been studied experimentally by transmission interferometry and reported in a series of works by Sasaki et al. [20.60, 82, 104]. They have discovered the

existence of constant gradients of the refractive indices in different crystallographic directions of TSSG-grown KTP crystals, which are ascribed to compositional variation in the solute, in agreement with the Curie temperature variation described in Sect. 20.2.1. Particularly useful are the results of [20.82], where growth and characterization details of a large TSSG-grown crystal are given including the initial flux composition and saturation temperature, final crystal weight, and the end values of the refractive indices measured at 633 nm. With the knowledge of KTP solubility in K6 [20.10], their data allow to calculate the average variation of the refractive indices per degree for growing out crystal volumes upon the solution temperature reduction. The values obtained are [20.118]

$$\begin{aligned}\frac{\Delta n_{x,y}}{\Delta T} &\approx 10^{-7} \text{ K}^{-1} \quad \text{at 633 nm,} \\ \frac{\Delta n_z}{\Delta T} &\approx 2 \times 10^{-6} \text{ K}^{-1} \quad \text{at 633 nm.}\end{aligned}\quad (20.11)$$

Assuming, as a simplifying approximation, that Δn varies linearly with the increase of the solidified mass and depends weakly on wavelength, (20.11) are a universal result, independent of the specific method of solution growth (Fig. 20.3). In particular, this result can be applied to crystals obtained by TSSG with pulling, and their optical uniformity in specific crystallographic directions can be assessed if certain growth parameters are known.

Figure 20.20 shows a photograph of an almost ideal TSSG (meniscus-pulled in the [100]-direction) KTP crystal of ≈ 850 g weight. A nearly constant growth interface area has been maintained after developing the shoulders of the crystal by careful monitoring the tem-

perature reduction program and the pulling rate. The height of the nearly rectangular part of the crystal l is about 50 mm, and the temperature drop during its growth was 75 K. Using these parameters and the data of (20.11), the following average gradients of the refractive indices along the crystal length can be calculated

$$\begin{aligned}\frac{\Delta n_z}{\Delta l} &= 3 \times 10^{-5} \text{ cm}^{-1}, \\ \frac{\Delta n_{x,y}}{\Delta l} &= 1.5 \times 10^{-6} \text{ cm}^{-1}.\end{aligned}\quad (20.12)$$

OPO Interaction in KTP

[100]-Cut KTA and KTP crystals are widely used in frequency conversion of Nd-doped solid-state lasers to longer wavelengths by OPO, primarily for eye-safe lidar systems operating in the 1550 nm spectral region [20.15, 16]. One of the major advantages of KTP-family crystals is the ability to operate with noncritical phase matching (NCPM), allowing large acceptance angles of the incident beam. The basic configuration of the type II process in a KTP-type crystal pumped in the x -direction is shown in Fig. 20.21. In this interaction, a y -polarized pump (p) generates a y -polarized signal (s) and z -polarized idler (i) beams, and the corresponding frequencies are bound by the following equations:

$$\begin{aligned}n_y^p \omega^p &= n_y^s \omega^s + n_z^i \omega^i, \\ \omega^p &= \omega^s + \omega^i,\end{aligned}\quad (20.13)$$

which are the perfect NCPM phase-matching conditions, namely the momentum and energy conservation laws, respectively. (The frequencies can be recalculated from the known wavelengths, which for the Nd:YAG-

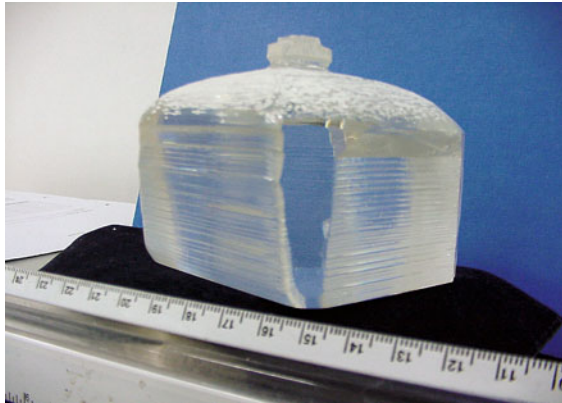


Fig. 20.20 TSSG KTP crystal meniscus pulled on a [100]-oriented seed

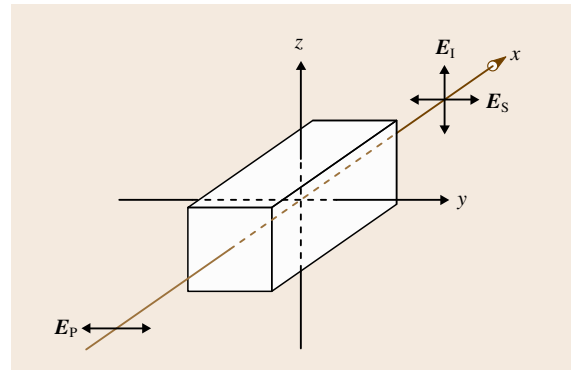


Fig. 20.21 Noncritical phase-matching scheme for type II OPO in the x - z plane of a KTP crystal (E_p , E_s , and E_i are the appropriate electric field polarization vectors)

induced **NCPM OPO** in **KTP** are $\lambda^p = 1064.2$ nm, $\lambda^s = 1576$ nm, and $\lambda^i = 3277$ nm [20.16].)

It is well known that the inherently present variation of the refractive indices due to gradual compositional changes inevitably causes a phase mismatch during the interaction. This mismatch can be evaluated by deriving the associated bandwidth of the generated signal wave $\Delta\omega^s$. If we disregard the negligible change in n_y [20.104] and assume that only $\Delta n_z \neq 0$, the signal bandwidth is given by

$$\Delta\omega^s = \frac{\Delta n_z^i}{n_z^i - n_y^s} \omega^i. \quad (20.14)$$

Keeping in mind that Δn_z does not vary dramatically with wavelength, the value of $\Delta n_z^i = 3 \times 10^{-5}$ for a 1 cm long crystal, from the first of (20.12), can be used as a rough approximation. The relevant refractive indices can be calculated from the Sellmeier equations for **KTP** [20.10] as $n_z^i = 1.7717$ and $n_y^s = 1.7362$. Final calculation using these parameters gives $\Delta\omega^s = 2.6 \text{ cm}^{-1}$, which is well within the **KTP/OPO** acceptance bandwidth of 9.02 cm^{-1} for a 1 cm interaction length [20.174]. This explains the high **NCPM OPO** conversion efficiency achieved even by pumping 20 mm long **KTP** crystals with a multimode laser [20.16].

It is also important to remember that, with a proper choice of the growth method, **KTP**-type crystals of sufficient optical uniformity can be obtained for both nonlinear optical and electrooptic applications. We recall that the main cause of inhomogeneity in the distribution of refractive indices along the growing crystal is the composition gradient, mainly of potassium ions, building up in the course of growth from self-fluxes. Such gradients are considerably smaller in the case of one-dimensional meniscus growth with pulling in the x -direction than in the case of three-dimensional submerged-seeded growth (Fig. 20.3).

20.5.2 Gray Tracks

In some applications where **KTP** is used to generate the second harmonic of the 1064 nm Nd:YAG laser radiation [20.175–179] or **OPO** pumped at 532 nm [20.180], detrimental optical absorption often builds up in the crystal bulk following intense high-repetition pulse or continuous-wave (**CW**) pumping. This phenomenon is termed gray-tracking, since darkening is observed along the laser beam path, which is attributed to formation of color centers absorbing in most of the visible 400–700 nm range [20.67] and emitting in the 700–1200 nm range under green laser excita-

tion [20.181]. The induced absorption diminishes the nonlinear output power and causes significant local heating, leading to severe beam distortion. It is imperative, therefore, to understand the nature of color centers involved and to find the means of their suppression.

Origin of Gray Track Centers

Gray tracks have been unambiguously related to the presence of Ti^{3+} ions [20.67, 178, 182], which are electron color centers induced photochemically via electron trapping by the constitutional Ti^{4+} ions. The latter can be reduced to Ti^{3+} also by high-temperature annealing in vacuum or by charge transfer (e.g., $\text{Fe}^{2+} \rightarrow \text{Ti}^{4+}$) from adjacent transition-metal impurities [20.108]. Yet, in thermally untreated and nominally pure **KTP** crystals, **EPR** and electron-nuclear double resonance (**ENDOR**) measurements have revealed four distinct types of Ti^{3+} centers as well [20.183, 184]. Two of them, appearing only in hydrothermal **KTP**, have a Ti^{3+} ion occupying the inequivalent Ti(1) and Ti(2) sites with a proton (in the form of an OH^- ion) bonded to an adjacent oxygen ion as a stabilizing entity for the electron trapping. The remaining two types of centers are present only in flux-grown crystals. One of them represents a self-trapped electron at the Ti(1) site stabilized by a neighboring divalent cation impurity, according to a tentative suggestion [20.184], but it is unstable above 140 K. The other is a Ti^{3+} ion located at the Ti(2) site adjacent to an oxygen vacancy and is stable at room temperature for days or weeks.

It is now well established that the reason for the existence of electron-trap-stabilizing OH^- ions (in hydrothermal crystals) and oxygen vacancies (in flux-grown crystals) is charge compensation of K^+ vacancies present to variable degrees in all **KTP** crystals [20.185], as also discussed in Sect. 20.2. In an attempt to reduce the concentration of oxygen vacancies, **PbO** was added to the **KTP** growth flux to form the modified flux referred to in Sect. 20.4.2. A Pb^{2+} ion, with its $6s^2$ closed shell configuration, has an ionic radius approximately 0.2 \AA smaller than a K^+ ion, and thus easily substitutes for the K^+ ion to provide charge compensation for one potassium vacancy. Oxygen vacancies are no longer needed to stabilize the Ti^{3+} color center if a sufficient amount of the Pb^{2+} dopant is present. Instead, $[\text{Ti}^{3+}\text{-Pb}^{2+}]$ centers may form under intense laser irradiation. Four types of these centers have been revealed by **EPR** and **ENDOR** measurements [20.113], but they are all unstable above 250 K and thus short-lived at room temperature. Of course, operation under the extreme conditions of high-

power, high-repetition-rate or CW pumping will cause the transient formation of large concentrations of Ti^{3+} centers with the detrimental optical absorption in the visible. Therefore, doping with lead is only a partial remedy. A better way to eliminate gray-tracking is the reduction of potassium vacancies, or improvement of potassium stoichiometry, in as-grown KTP crystals by using K-rich solvents and/or more dilute solutions as discussed in Sect. 20.2.

Kinetics of Gray Track Formation

Figure 20.5 shows explicitly that KTP crystals grown at lower temperatures, especially from self-fluxes with higher $[\text{K}]/[\text{P}]$ ratios, are more stoichiometric, exhibiting higher Curie temperatures. In order to test the influence of potassium stoichiometry, a comparative study of the kinetics of gray track formation in high- and low- T_C KTP crystals has been conducted [20.89]. This has been done using the green-radiation-induced infrared absorption (GRIIRA) method which has been initially developed for periodically poled LiNbO_3 [20.186]. In the quoted experiment [20.89], a 10 kW/cm^2 CW green (532 or 514 nm) excitation beam was used to induce the gray track damage, while the resulting infrared (1064 nm) absorption was monitored. At the initial stage of gray track formation, usually lasting from several seconds to several minutes, an increase in the infrared absorption can be observed. This increase (after the onset of green irradiation) is clearly seen in Fig. 20.22.

During the studied initial stage (80 s) the gray track is located within the green beam region and disappears fast when the green light is turned off. However, the first minute of the test is sufficient to determine the quality of the sample. The results of Fig. 20.22 clearly show that the infrared absorption of the HK KTP crystals with a higher potassium content (high- T_C) saturates deep below the level of 10^{-4} cm^{-1} while the similar absorption of a low- T_C crystal (LK) continues to rise linearly. Obviously, crystals with an improved potassium stoichiometry reveal a higher resistance to gray track formation. Such crystals may compete successfully with hydrothermal KTP (where the concentration of gray track centers is higher, but

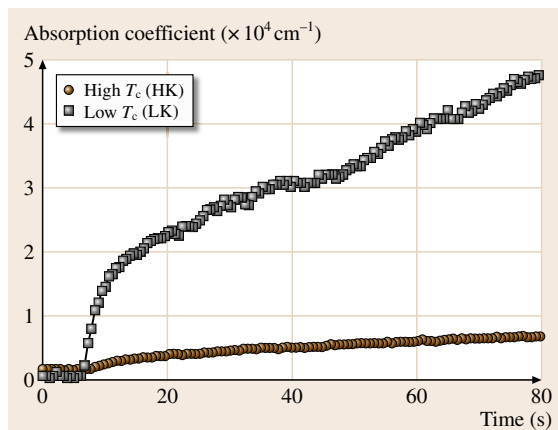


Fig. 20.22 Initial stages of gray-track formation in potassium-deficient (LK, low- T_C) and potassium-rich (HK, high- T_C) grown from self-fluxes

they are less stable [20.183, 184]) in high-power frequency doubling. Crystals grown from pure self-fluxes have an advantage also with respect to low-power applications, since their initial absorption never exceeds 10^{-5} cm^{-1} (Fig. 20.22). The known initial absorption of most hydrothermal KTP crystals is typically higher than 10^{-4} cm^{-1} , presumably due to the presence of impurities associated with the hydrothermal growth.

RTP crystals are seldom used for frequency doubling into the green [20.4] and, therefore, their susceptibility to gray track formation has not been investigated directly. However, very recent EPR and ENDOR studies have shown that room-temperature-stable Ti^{3+} centers stabilized by oxygen vacancies can be created also in this crystal [20.187]. The narrow range of Curie temperature variation in RTP (Fig. 20.8) and the usually observed high electrical resistivity of these crystals [20.14] imply that their concentration of stable Ti^{3+} electron trap centers is generally low. Nevertheless, current attempts to develop Yb and Nb co-doped RTP crystals as new self-doubling laser media [20.188] necessitates an examination of RTP crystals using the GRIIRA test, similarly to the one described above for KTP.

References

- 20.1 J.D. Bierlein, H. Vaherzele: Potassium titanyl phosphate: Properties and new applications, *J. Opt. Soc. Am. B* **6**, 622–633 (1989)
- 20.2 G.M. Loiacono, D.N. Loiacono, J.J. Zola, R.A. Stolzenberger, T. McGee, R.G. Norwood: Optical properties and ionic conductivity of KTiOAsO_4

- crystals, Appl. Phys. Lett. **61**, 895–897 (1992)
- 20.3 D.E. Spence, C.L. Tang: Characterization and applications of high repetition rate, broadly tunable, femtosecond optical parametric oscillators, IEEE J. Sel. Top. Quantum Electron. **1**, 31–43 (1995)
- 20.4 Y.S. Oseledchik, A.I. Pisarevsky, A.L. Prosvirin, V.V. Starshenko, N.V. Svitanko: Nonlinear optical properties of the flux grown RbTiOPO₄ crystal, Opt. Mater. **3**, 237–242 (1994)
- 20.5 T.Y. Fan, C.E. Huang, B.Q. Hu, R.C. Eckardt, R.L. Byer, R.S. Feigelson: Second harmonic generation and accurate index of refraction measurements in flux-grown KTiOPO₄, Appl. Opt. **26**, 2390–2394 (1987), .
- 20.6 C.-S. Tu, R.S. Katiyar, V.H. Schmidt, R.-M. Chien, R. Guo, A.S. Bhalla: Hypersonic anomalies and optical properties of RbTiOAsO₄ and KTiOPO₄ single crystals, Phys. Rev. B **59**, 251–256 (1999)
- 20.7 L.T. Cheng, L.K. Cheng, J.D. Bierlein, F.C. Zumsteg: Properties of doped and undoped single domain KTiOAsO₄, Appl. Phys. Lett. **62**, 346–348 (1993)
- 20.8 L.T. Cheng, L.K. Cheng, J.D. Bierlein, F.C. Zumsteg: Nonlinear optical and electro-optical properties of single crystal CsTiOAsO₄, Appl. Phys. Lett. **63**, 2618–2620 (1993)
- 20.9 L.K. Cheng, J.D. Bierlein: KTP and isomorphs – Recent progress in device and material development, Ferroelectrics **142**, 209–228 (1993)
- 20.10 L.K. Cheng, L.T. Cheng, J. Galperin, P.A. Morris Hotsenpiller, J.D. Bierlein: Crystal growth and characterization of KTiOPO₄ isomorphs from the self-fluxes, J. Cryst. Growth **137**, 107–115 (1994)
- 20.11 L.K. Cheng, L.T. Cheng, J.D. Bierlein: Phase-matching property optimization using birefringence tuning in solid solutions of KTiOPO₄ isomorphs, Appl. Phys. Lett. **64**, 1321–1323 (1994)
- 20.12 M. Roth, N. Angert, M. Tseitlin, G. Wang, T.P.J. Han, H.G. Gallagher, N.I. Leonyuk, E.V. Koporulina, S.N. Barilo, L.A. Kurnevich: Recent developments in crystal growth and characterization of nonlinear optical borate and phosphate materials, Proc. 3rd Int. Conf. Single Crystal Growth, Strength Probl. Heat Mass Transf., Vol. 2, ed. by V.P. Ginkin (Uch.-Izd., Obninsk 2000) pp. 416–426
- 20.13 D.N. Nikogosyan: *Nonlinear Optical Crystals: A Complete Survey* (Springer, New York 2005)
- 20.14 M. Roth, M. Tseitlin, N. Angert: Oxide crystals for electro-optic Q-switching of lasers, Glass Phys. Chem. **31**, 86–95 (2005)
- 20.15 M.S. Webb, P.F. Moulton, J.J. Kasinski, R.I. Burnham, G. Loiacono, R. Stolzenberger: High-average-power KTiOAsO₄ optical parametric oscillator, Opt. Lett. **23**, 1161–1163 (1998)
- 20.16 L.S. Lingvay, N. Angert, M. Roth: High-average-power KTP ring OPO, Proc. SPIE **3928**, 52–56 (2000)
- 20.17 X.D. Wang, P. Basseras, R.J.D. Miller, H. Vanherzeele: Investigation of KTiOPO₄ as an electro-optic amplitude modulator, Appl. Phys. Lett. **59**, 519–521 (1991)
- 20.18 S. Pearce, C.L.M. Ireland: Performance of a CW pump Nd:YVO₄ amplifier with kHz pulses, Opt. Laser Technol. **35**, 375–379 (2003)
- 20.19 M.G. Jani, J.T. Murray, R.R. Petrin, R.C. Powell: Pump wavelength tuning of optical parametric oscillations and frequency mixing in KTiOAsO₄, Appl. Phys. Lett. **60**, 2327–2329 (1992)
- 20.20 G.M. Loiacono, D.N. Loiacono, R.A. Stolzenberger: Crystal growth and characterization of ferroelectric CsTiOAsO₄, J. Cryst. Growth **131**, 323–330 (1993)
- 20.21 J. Nordborg, G. Svensson, R.J. Bolt, J. Albertsson: Top seeded solution growth of [Rb,Cs]TiOAsO₄, J. Cryst. Growth **224**, 256–268 (2001)
- 20.22 I. Tordjman, R. Masse, J.C. Guitel: Crystalline-structure of monophosphate KTiPO₅, Z. Krist. **139**, 103–115 (1974)
- 20.23 P.A. Thomas, A.M. Glazer, B.E. Watts: Crystal structure and nonlinear optical properties of KSnOPO₄ and their comparison with KTiOPO₄, Acta Crystallogr. B **46**, 333–343 (1990)
- 20.24 P. Delarue, C. Lecomte, M. Jannin, G. Marnier, B. Menaert: Evolution towards centrosymmetry of the nonlinear-optical material RbTiOPO₄ in the temperature range 293–973 K: Alkaline displacements and titanil deformations, Phys. Rev. B **58**, 5287–5295 (1998)
- 20.25 S.C. Mayo, P.A. Thomas, S.J. Teat, G.M. Loiacono, D.N. Loiacono: Structure and nonlinear-optical properties of KTiOAsO₄, Acta Crystallogr. B **50**, 655–662 (1994)
- 20.26 P.A. Thomas, S.C. Mayo, B.E. Watts: Crystal structures of RbTiOAsO₄, KTiO(P_{0.58}As_{0.42})O₄, RbTiOPO₄ and (Rb_{0.465}K_{0.535})TiOPO₄ and analysis of pseudosymmetry in crystals of the KTiOPO₄ family, Acta Crystallogr. B **48**, 401–407 (1992)
- 20.27 J. Protas, G. Marnier, B. Boulanger, B. Menaert: Crystal structure of CsTiOAsO₄, Acta Crystallogr. C **45**, 1123–1125 (1989)
- 20.28 M. Munowitz, R.H. Jarman, J.F. Harrison: Theoretical study of the nonlinear optical properties of KTiOPO₄: Effects of Ti–O–Ti bond angles and oxygen electronegativity, Chem. Mater. **5**, 1257–1267 (1993)
- 20.29 D. Xue, S. Zhang: The origin of nonlinearity in KTiOPO₄, Appl. Phys. Lett. **70**, 943–945 (1997)
- 20.30 P.A. Thomas, A. Baldwin, R. Dupree, P. Blaha, K. Schwartz, A. Samoson, Z.H. Gan: Structure-property relationships in the nonlinear optical crystal KTiOPO₄ investigated using NMR and ab initio DFT calculations, J. Phys. Chem. B **108**, 4324–4331 (2004)
- 20.31 V. Pasiskevicius, C. Canalias, F. Laurell: Highly efficient stimulated Raman scattering of picosecond pulses in KTiOPO₄, Appl. Phys. Lett. **88**, 041110 (2006)
- 20.32 P.A. Thomas, A.M. Glazer: Potassium titanyl phosphate, KTiOPO₄. II. Structural interpretation of

- twinning, ion exchange and domain inversion, *J. Appl. Cryst.* **24**, 968–971 (1991)
- 20.33 P. Delarue, C. Lecomte, M. Jannin, G. Marnier, B. Menaert: Behavior of the non-linear optical material KTiOPO_4 in the temperature range 293–973 K studied by x-ray diffractometry at high resolution: Alkaline displacements, *J. Phys. Condens. Matter* **11**, 4123–4134 (1999)
- 20.34 S.T. Norberg, N. Ishizawa: K-site splitting in KTiOPO_4 at room temperature, *Acta Crystallogr. C* **61**, i99–i102 (2006)
- 20.35 D.R. Allan, J.S. Loveday, R.J. Nelmes, P.A. Thomas: A high-pressure structural study of potassium titanyl phosphate (KTP) up to 5 GPa, *J. Phys. Condens. Matter* **4**, 2747–2760 (1992)
- 20.36 P.A. Thomas, R. Duhlev, S.J. Teat: A comparative structural study of a flux-grown crystal of $\text{K}_{0.86}\text{Rb}_{0.14}\text{TiOPO}_4$ and an ion-exchanged crystal of $\text{K}_{0.84}\text{Rb}_{0.16}\text{TiOPO}_4$, *Acta Cryst. B* **50**, 538–543 (1994)
- 20.37 S. Furusawa, H. Hayasi, Y. Ishibashi, A. Miyamoto, T. Sasaki: Ionic conductivity of quasi-one-dimensional superionic conductor KTiOPO_4 (KTP) single crystal, *J. Phys. Soc. Jpn.* **62**, 183–195 (1993)
- 20.38 J.D. Bierlein, C.B. Arweiler: Electro-optic and dielectric properties of KTiOPO_4 , *Appl. Phys. Lett.* **49**, 917–919 (1986)
- 20.39 B. Mohamadou, G.E. Kugel, F. Brehat, B. Wyncke, G. Marnier, P. Simon: High-temperature vibrational spectra, relaxation and ionic conductivity effects in KTiOPO_4 , *J. Phys. Condens. Matter* **3**, 9489–9501 (1991)
- 20.40 Q. Jiang, A. Lovejoy, P.A. Thomas, K.B. Hutton, R.C.C. Ward: Ferroelectricity, conductivity, domain structure and poling conditions of rubidium titanyl phosphate, *J. Phys. D Appl. Phys.* **33**, 2831–2836 (2000)
- 20.41 P. Urenski, N. Gorbatov, G. Rosenman: Dielectric relaxation in flux grown KTiOPO_4 and isomorphous crystals, *J. Appl. Phys.* **89**, 1850–1855 (2001)
- 20.42 J.C. Jacco, G.M. Loiacono, M. Jaso, G. Mizell, B. Greenberg: Flux growth and properties of KTiOPO_4 , *J. Cryst. Growth* **70**, 484–488 (1984)
- 20.43 R.J. Bolt, P. Bennema: Potassium titanyl phosphate KTiOPO_4 (KTP): Relation between crystal structure and morphology, *J. Cryst. Growth* **102**, 329–340 (1990)
- 20.44 L.K. Cheng, J.D. Bierlein, A.A. Ballman: Crystal growth of KTiOPO_4 isomorphs from tungstate and molybdate fluxes, *J. Cryst. Growth* **110**, 697–703 (1991)
- 20.45 X. Wang, X. Yuan, W. Li, J. Qi, S. Wang, D. Shen: Flux growth of large potassium titanyl phosphate crystals and their electro-optical applications, *J. Cryst. Growth* **237–239**, 672–676 (2002)
- 20.46 G.M. Loiacono, T.F. McGee, G. Kostecky: Solubility and crystal growth of KTiOPO_4 in polyphosphate solvents, *J. Cryst. Growth* **104**, 389–391 (1990)
- 20.47 J.D. Bierlein, T.E. Gier: Crystals of $(\text{K,Rb,Tl,NH}_4)\text{TiO(P,As)O}_4$ and their use in electrooptic devices, US Patent 3949323 (1976)
- 20.48 T.E. Gier: Hydrithermal process for growing a single crystal with an aqueous mineralizer, US Patent 4305778 (1981)
- 20.49 R.A. Laudise, R.J. Cava, A.J. Caporaso: Phase relations, solubility and growth of potassium titanyl phosphate, *KTP, J. Cryst. Growth* **74**, 275–280 (1986)
- 20.50 R.F. Belt, G. Gashurov, R.A. Laudise: Low temperature hydrothermal growth of KTiOPO_4 (KTP), *Proc. SPIE* **968**, 100–106 (1988)
- 20.51 R.A. Laudise, W.A. Sunder, R.F. Belt, G. Gashurov: Solubility and P–V–T relations and the growth of potassium titanyl phosphate, *J. Cryst. Growth* **102**, 427–433 (1990)
- 20.52 A. Ferretti, T.E. Gier: Hydrothermal process for growing optical-quality crystals, US Patent 5066356 (1991)
- 20.53 S.Q. Jia, P.Z. Jiang, H.D. Niu, D.Z. Li, X.H. Fan: The solubility of KTiOPO_4 (KTP) in KF aqueous solution under high temperature and high pressure, *J. Cryst. Growth* **79**, 970–973 (1986)
- 20.54 S.Q. Jia, H.D. Niu, J.G. Tan, Y.P. Xu, Y. Tao: Hydrothermal growth of KTP crystals in the medium range of temperature and pressure, *J. Cryst. Growth* **99**, 900–904 (1990)
- 20.55 L.K. Cheng: Hydrothermal aqueous mineralizer for growing optical-quality single crystals, US Patent 5500145 (1996)
- 20.56 C. Zhang, L. Huang, W. Zhou, G. Zhang, H. Hou, Q. Ruan, W. Lei, S. Qin, F. Lu, Y. Zuo, H. Shen, G. Wang: Growth of KTP crystals with high damage threshold by hydrothermal method, *J. Cryst. Growth* **292**, 364–367 (2006)
- 20.57 A.A. Ballman, H. Brown, D.H. Olson, C.E. Rice: Growth of potassium titanyl phosphate (KTP) from molten tungsten melts, *J. Cryst. Growth* **75**, 390–394 (1986)
- 20.58 K. Iliev, P. Peshev, V. Nikolov, I. Koseva: Physico-chemical properties of high-temperature solutions of the $\text{K}_2\text{O}-\text{P}_2\text{O}_5-\text{TiO}_2-\text{WO}_3$ system, suitable for the growth of KTiOPO_4 (KTP) single crystals, *J. Cryst. Growth* **100**, 225–232 (1990)
- 20.59 C.G. Chao, Z.Q. Qiang, T.G. Kui, S.W. Bao, T.H. Gao: Top seeded growth of KTiOPO_4 from molten tungsten solution, *J. Cryst. Growth* **112**, 294–297 (1991)
- 20.60 A. Yokotani, A. Miyamoto, T. Sasaki, S. Nakai: Observation of optical inhomogeneities in flux grown KTP crystals, *J. Cryst. Growth* **110**, 963–967 (1991)
- 20.61 D.P. Shumov, M.P. Tarassov, V.S. Nikolov: Investigation of optical inhomogeneities in KTiOPO_4 (KTP) single crystals grown from high-temperature tungsten-containing solutions, *J. Cryst. Growth* **129**, 635–639 (1993)
- 20.62 D. Bravo, X. Ruiz, F. Díaz, F.J. López: EPR of tungsten impurities in KTiOPO_4 single crystals grown from

- molten tungstate solutions, *Phys. Rev. B* **52**, 3159–3169 (1995)
- 20.63 J.H. Kim, J.K. Kang, S.J. Chung: Effects of seed orientation on the top-seeded solution growth of KTiOPO_4 single crystals, *J. Cryst. Growth* **147**, 343–349 (1995)
- 20.64 F.J. Kumar, S.G. Moorthy, C. Subramanian, G. Bocelli: Growth and characterization of KTiOPO_4 single crystals, *Mater. Sci. Eng. B* **49**, 31–35 (1997)
- 20.65 G. Marnier: Process for the flux synthesis of crystals of the KTiOPO_4 potassium titanyl monophosphate type, US Patent 4746396 (1988)
- 20.66 Y. Guillien, B. Ménart, J.P. Fève, P. Segonds, J. Douady, B. Boulanger, O. Picaud: Crystal growth and refined Sellmeier equations over the complete transparency range of RbTiOPO_4 , *Opt. Mater.* **22**, 155–162 (2003)
- 20.67 G.M. Loiacono, D.N. Loiacono, T. McGee, M. Babb: Laser damage formation in KTiOPO_4 and KTiOAsO_4 crystals: Grey tracks, *J. Appl. Phys.* **72**, 2705–2712 (1992)
- 20.68 T.E. Gier: Method for flux growth of KTiOPO_4 and its analogues, US Patent 4231838 (1980)
- 20.69 D. Shen, C. Huang: A new nonlinear optical crystal KTP, *Prog. Cryst. Growth Charact.* **11**, 269–274 (1985)
- 20.70 K. Iliev, P. Peshev, V. Nikolov, I. Koseva: Physico-chemical properties of high-temperature solutions of the $\text{K}_2\text{O}-\text{P}_2\text{O}_5-\text{TiO}_2$ system suitable for the growth of KTiOPO_4 (KTP) single crystals, *J. Cryst. Growth* **100**, 219–224 (1990)
- 20.71 P.F. Bordui, J.C. Jacco: Viscosity and density of solutions used in high-temperature growth of KTiOPO_4 (KTP), *J. Cryst. Growth* **82**, 351–355 (1987)
- 20.72 N. Angert, M. Tseitlin, E. Yashchin, M. Roth: Ferroelectric phase transition temperatures of KTiOPO_4 crystals grown from self-fluxes, *Appl. Phys. Lett.* **67**, 1941–1943 (1995)
- 20.73 Y.S. Oseledchik, S.P. Belokrys, V.V. Osadchuk, A.L. Prosvirin, A.F. Selevich, V.V. Starshenko, K.V. Kuzemchenko: Growth of RbTiOPO_4 single crystals from phosphate systems, *J. Cryst. Growth* **125**, 639–643 (1992)
- 20.74 C.V. Kannan, S. Ganesa Murthy, V. Kannan, C. Subramanian, P. Ramasamy: TSSG of RbTiOPO_4 single crystals from phosphate flux and their characterization, *J. Cryst. Growth* **245**, 289–296 (2002)
- 20.75 L.I. Isaenko, A.A. Merkulov, V.I. Tyurikov, V.V. Atuchin, L.V. Sokolov, E.M. Trukhanov: Growth and real structure of KTiOAsO_4 crystals from self-fluxes, *J. Cryst. Growth* **171**, 146–153 (1997)
- 20.76 M. Roth, N. Angert, M. Tseitlin, G. Schwarzman, A. Zharov: Ferroelectric phase transition temperatures of self-flux-grown RbTiOPO_4 crystals, *Opt. Mater.* **26**, 465–470 (2004)
- 20.77 M.E. Hagerman, K.R. Poeppelmeier: Review of the structure and processing-defect-property relationships of potassium titanyl phosphate: A strategy for novel thin-film photonic devices, *Chem. Mater.* **7**, 602–621 (1995)
- 20.78 M.N. Satyanarayan, A. Deepthy, H.L. Bhat: Potassium titanyl phosphate and its isomorphs: growth, properties and applications, *Crit. Rev. Solid State* **24**, 103–189 (1999)
- 20.79 J. Wang, J. Wei, Y. Liu, X. Yin, X. Hu, Z. Shao, M. Jiang: A survey of research on KTP and its analogue crystals, *Prog. Cryst. Growth Charact.* **40**, 3–15 (2000)
- 20.80 P.F. Bordui, J.C. Jacco, G.M. Loiacono, R.A. Stolzenberger, J.J. Zola: Growth of large single crystals of KTiOPO_4 (KTP) from high-temperature solution using heat pipe based furnace system, *J. Cryst. Growth* **84**, 403–408 (1987)
- 20.81 R.J. Bolt, M.H. van der Mooren, H. de Haas: Growth of KTiOPO_4 (KTP) single crystals by means of phosphate and phosphate/sulfate fluxes out of a three-zone furnace, *J. Cryst. Growth* **114**, 141–152 (1991)
- 20.82 T. Sasaki, A. Miyamoto, A. Yokotani, S. Nakai: Growth and optical characterization of large potassium titanyl phosphate crystals, *J. Cryst. Growth* **128**, 950–955 (1993)
- 20.83 N. Angert, L. Kaplun, M. Tseitlin, E. Yashchin, M. Roth: Growth and domain structure of potassium titanyl phosphate crystals pulled from high-temperature solutions, *J. Cryst. Growth* **137**, 116–122 (1994)
- 20.84 B. Vartak, J.J. Derby: On stable algorithms and accurate solutions for convection-dominated mass transfer in crystal growth modeling, *J. Cryst. Growth* **230**, 202–209 (2001)
- 20.85 P.F. Bordui, S. Motakef: Hydrodynamic control of solution inclusion during crystal growth of KTiOPO_4 (KTP) from high-temperature solution, *J. Cryst. Growth* **96**, 405–412 (1989)
- 20.86 B. Vartak, Y. Kwon, A. Yeckel, J.J. Derby: An analysis of flow and mass transfer during the solution growth of potassium titanyl phosphate, *J. Cryst. Growth* **210**, 704–718 (2000)
- 20.87 B. Vartak, A. Yeckel, J.J. Derby: On the validity of boundary layer analysis for flow and mass transfer caused by rotation during the solution growth of large single crystals, *J. Cryst. Growth* **283**, 479–489 (2005)
- 20.88 E.G. Tsvetkov, V.N. Semenenko, G.G. Khranenko, V.I. Tyurikov: Growth peculiarities and polar structures formation in potassium titanyl phosphate crystals, *J. Surf. Invest. X-Ray Synchrotron Neutron Tech.* **5**, 65–70 (2002), in Russian
- 20.89 M. Roth, N. Angert, M. Tseitlin, A. Alexandrovski: On the optical quality of KTP crystals for nonlinear optical and electro-optic applications, *Opt. Mater.* **16**, 131–136 (2001)
- 20.90 P.A. Morris, A. Ferretti, J.D. Bierlein, G.M. Loiacono: Reduction of the ionic conductivity of flux grown KTiOPO_4 crystals, *J. Cryst. Growth* **109**, 367–375 (1991)

- 20.91 M.G. Roelofs: Identification of Ti^{3+} in potassium titanyl phosphate and its possible role in laser damage, *J. Appl. Phys.* **65**, 4976–4982 (1989)
- 20.92 V.D. Kugel, G. Rosenman, N. Angert, E. Yashchin, M. Roth: Domain inversion in KTiOPO_4 crystal near the Curie point, *J. Appl. Phys.* **76**, 4823–4826 (1994)
- 20.93 M.E. Hagerman, V.L. Kozhevnikov, K.R. Poeppelmeier: High-temperature decomposition of KTiOPO_4 , *Chem. Mater.* **5**, 1211–1215 (1993)
- 20.94 D.K.T. Chu, H. Hsiung: Ferroelectric phase transition study in KTiOPO_4 – An optical 2nd harmonic generation study, *Appl. Phys. Lett.* **61**, 1766–1768 (1992)
- 20.95 K. Zhang, X. Wang: Structure sensitive properties of KTP-type crystals, *Chin. Sci. Bull.* **46**, 2028–2036 (2001)
- 20.96 T.F. McGee, G.M. Blom, G. Kostecky: Growth and characterization of doped KTP crystals, *J. Cryst. Growth* **109**, 361–366 (1991)
- 20.97 D.K.T. Chu, H. Hsiung, L.K. Cheng, J.D. Bierlein: Curie temperatures and dielectric-properties of doped and undoped KTiOPO_4 and isomorphs, *IEEE Trans. Ultrason. Ferroelectr. Fraq. Control* **40**, 819–824 (1993)
- 20.98 R.V. Pisarev, R. Farhi, P. Moch, V.I. Voronkova: Temperature-dependence of Raman-scattering and soft modes in TiTiOPO_4 , *J. Phys. Condens. Matter* **2**, 1555–1568 (1990)
- 20.99 G.M. Loiacono, R.A. Stolzenberger, D.N. Loiacono: Modified KTiOPO_4 crystals for noncritical phase matching applications, *Appl. Phys. Lett.* **64**, 16–18 (1994)
- 20.100 P.F. Bordui, R.G. Norwood, M.M. Fejer: Curie-temperature measurements on KTiOPO_4 single-crystals grown by flux and hydrothermal techniques, *Ferroelectrics* **115**, 7–12 (1991)
- 20.101 V.K. Yanovskii, V.I. Voronkova, A.P. Leonov, S.Y. Stefanovich: Ferroelectric properties of KTiOPO_4 type crystals, *Sov. Phys. Solid State* **27**, 1506–1516 (1985)
- 20.102 B.C. Choi, J.B. Kim, B.M. Jin, S.I. Yun, J.N. Kim: Dielectric properties of flux-grown KTiOPO_4 single crystals, *J. Korean Phys. Soc.* **25**, 327–331 (1992)
- 20.103 Y.V. Shaldin, R. Poprawski: Spontaneous birefringence and pyroelectricity in KTiOPO_4 crystals, *Ferroelectrics* **106**, 399–404 (1990)
- 20.104 A. Miyamoto, Y. Mori, Y. Okada, T. Sasaki, S. Nakai: Refractive index and lattice constant variation in flux grown KTP crystals, *J. Cryst. Growth* **156**, 303–306 (1995)
- 20.105 M.N. Satyanarayan, H.L. Bhat: Influence of growth below and above T_c on the morphology and domain structure in flux-grown KTP crystals, *J. Cryst. Growth* **181**, 281–289 (1997)
- 20.106 M. Roth, N. Angert, M. Tseitlin: Growth-dependent properties of KTP crystals and PPKTP structures, *J. Mater. Sci. Mater. Electron.* **12**, 429–436 (2001)
- 20.107 N. Angert, M. Tseitlin, L. Kaplun, E. Yashchin, M. Roth: Ferroelectric domain reversal in KTP crystals by high-temperature treatment, *Ferroelectrics* **157**, 117–122 (1994)
- 20.108 M.J. Martín, D. Bravo, R. Solé, F. Díaz, F.J. López, C. Zaldo: Thermal reduction of KTiOPO_4 crystals, *J. Appl. Phys.* **76**, 7510–7518 (1994)
- 20.109 P.A. Morris: Impurities in nonlinear optical oxide crystals, *J. Cryst. Growth* **106**, 76–88 (1990)
- 20.110 M. Roth, N. Angert, L. Weizman, A. Gachechiladze, M. Shachman, D. Remennikov, M. Tseitlin, A. Zharov: Development of KTP crystals for laser applications, *Ann. Isr. Phys. Soc.* **14**, 89–92 (2000)
- 20.111 L.T. Cheng, L.K. Cheng, R.L. Harlow, J.D. Bierlein: Blue light generation using bulk single crystals of niobium-doped KTiOPO_4 , *Appl. Phys. Lett.* **64**, 155–157 (1994)
- 20.112 V.I. Chani, K. Shimamura, S. Endo, T. Fukuda: Growth of mixed crystals of the KTiOPO_4 (KTP) family, *J. Cryst. Growth* **171**, 472–476 (1997)
- 20.113 K.T. Stevens, L.E. Halliburton, M. Roth, N. Angert, M. Tseitlin: Identification of Pb-related Ti^{3+} center in flux-grown KTiOPO_4 , *J. Appl. Phys.* **88**, 6239–6244 (2000)
- 20.114 E. Lebiush, R. Lavi, Y. Tsuk, N. Angert, A. Gachechiladze, M. Tseitlin, A. Zharov, M. Roth: RTP as a Q-switch for high repetition rate applications, *Proc. Adv. Solid State Lasers, TOPS* **34**, 63–65 (2000)
- 20.115 Y. Stefanovich, L.A. Ivanova, A.V. Astafyev: *Ionic and Superionic Conductivity in Ferroelectrics* (Nitekhim, Moscow 1989) p. 37, in Russian
- 20.116 F.C. Zumsteg, J.D. Bierlein, T.E. Gier: $\text{K}_x\text{Rb}_{1-x}\text{TiOPO}_4$: A new nonlinear optical material, *J. Appl. Phys.* **47**, 4980–4985 (1976)
- 20.117 W.P. Risk, G.M. Loiacono: Periodic poling and waveguide frequency doubling in RbTiOAsO_4 , *Appl. Phys. Lett.* **69**, 311–313 (1996)
- 20.118 M. Roth, M. Tseitlin, N. Angert: Composition-dependent electro-optic and nonlinear optical properties of KTP-family crystals, *Opt. Mater.* **28**, 71–76 (2006)
- 20.119 Y. Jiang, L.E. Halliburton, M. Roth, M. Tseitlin, N. Angert: Hyperfine structure associated with the dominant radiation-induced trapped hole center in RbTiOPO_4 crystals, *Phys. Status Solidi (b)* **242**, 2489–2496 (2005)
- 20.120 J.D. Bierlein, F. Ahmed: Observation and poling of ferroelectric domains in KTiOPO_4 , *Appl. Phys. Lett.* **51**, 1328–1330 (1987)
- 20.121 G.M. Loiacono, R.A. Stolzenberger: Observation of complex domain walls in KTiOPO_4 , *Appl. Phys. Lett.* **53**, 1498–1500 (1988)
- 20.122 L.P. Shi, J. Chrosch, J.Y. Wang, Y.G. Liu: Twinning in KTiOPO_4 crystals, *Cryst. Res. Technol.* **27**, K76–K78 (1992)
- 20.123 F. Laurell, M.G. Roelofs, W. Bindloss, H. Hsiung, A. Suna, J.D. Bierlein: Detection of ferroelectric

- domain reversal in KTiOPO_4 wave-guides, *J. Appl. Phys.* **71**, 4664–4670 (1992)
- 20.124 R.J. Bolt, W.J.P. Enckevort: Observation of growth steps and growth hillocks on the {100}, {210}, {011} and {101} faces of flux-grown KTiOPO_4 (KTP), *J. Cryst. Growth* **119**, 329–338 (1992)
- 20.125 A.A. Chernov: Stability of faceted shapes, *J. Cryst. Growth* **24/25**, 11–31 (1974)
- 20.126 N.R. Ivanov, N.A. Tikhomirova, A.V. Ginzberg, S.P. Chumakova, E.I. Eknadisyants, V.Z. Borodin, A.N. Pinskaya, V.A. Babanskikh, V.A. D'yakov: Domain structure of KTiOPO_4 crystals, *Crystallogr. Rep.* **39**, 593–599 (1994)
- 20.127 W.P. Risk, R.N. Payne, W. Lenth, C. Harder, H. Meier: Noncritically phase-matched frequency doubling using 994-nm dye and diode laser radiation in KTiOPO_4 , *J. Appl. Phys.* **55**, 1179–1181 (1989)
- 20.128 W.P. Risk, W.J. Kozlovsky: Efficient generation of blue-light by doubly resonant sum-frequency mixing in a monolithic KTP resonator, *Opt. Lett.* **17**, 707–709 (1992)
- 20.129 L.T. Cheng, L.K. Cheng, R.L. Harlow, J.D. Bierlein: Blue light generation using bulk single crystals of niobium-doped KTiOPO_4 , *Appl. Phys. Lett.* **64**, 155–157 (1994)
- 20.130 H. Mabuchi, E.S. Polzik, H.J. Kimble: Blue-light-induced infrared-absorption in KNbO_3 , *J. Opt. Soc. Am. B* **11**, 2023–2029 (1994)
- 20.131 J.A. Armstrong, N. Bloembergen, J. Ducuing, P.S. Pershan: Interaction between light waves in a nonlinear dielectric, *Phys. Rev.* **127**, 1918–1939 (1962)
- 20.132 J.D. Bierlein, D.B. Laubacher, J.B. Brown: Balanced phase matching in segmented KTiOPO_4 wave-guides, *Appl. Phys. Lett.* **56**, 1725–1727 (1990)
- 20.133 C.J. van der Poel, J.D. Bierlein, J.B. Brown: Efficient type I blue second harmonic generation in periodically segmented KTiOPO_4 waveguides, *Appl. Phys. Lett.* **57**, 2074–2076 (1990)
- 20.134 M.G. Roelofs, P.A. Morris, J.D. Bierlein: Ion exchange of Rb, Ba, and Sr in KTiOPO_4 , *J. Appl. Phys.* **70**, 720–728 (1991)
- 20.135 M.C. Gupta, W.P. Risk, A.C.G. Nutt, S.D. Lau: Domain inversion in KTiOPO_4 using electron beam scanning, *Appl. Phys. Lett.* **63**, 1167–1169 (1993)
- 20.136 G. Rosenman, P. Urenski, A. Agronin, A. Arie, Y. Rosenwaks: Nanodomain engineering in RbTiOPO_4 ferroelectric crystals, *Appl. Phys. Lett.* **82**, 3934–3936 (2003)
- 20.137 M. Yamada, N. Nada, M. Saitoh, K. Watanabe: First-order quasi-phase matched LiNbO_3 waveguide periodically poled by applying an external field for efficient blue second harmonic generation, *Appl. Phys. Lett.* **62**, 435–437 (1993)
- 20.138 L.E. Myers, R.C. Eckardt, M.M. Fejer, R.L. Byer, W.R. Bosenberg, J.W. Pierce: Quasi-phase-matched optical parametric oscillators in bulk periodically poled LiNbO_3 , *J. Opt. Soc. Am. B* **12**, 2102–2116 (1995)
- 20.139 Q. Chen, W.P. Risk: Periodic poling of KTiOPO_4 using an applied electric field, *Electron. Lett.* **30**, 1516–1517 (1994)
- 20.140 G.D. Boyd, D.A. Kleinman: Parametric interaction of focused Gaussian light beams, *J. Appl. Phys.* **39**, 3597–3639 (1968)
- 20.141 M.M. Fejer, G.A. Magel, D.H. Jundt, R.L. Byer: Quasi-phase-matched second harmonic generation: tuning and tolerances, *J. Quantum Electron. QE* **28**, 2631–2654 (1992)
- 20.142 A. Arie, G. Rosenman, V. Mahal, A. Skliar, M. Oron, M. Katz, D. Eger: Green and ultraviolet quasi-phase-matched second harmonic generation in bulk periodically-poled KTiOPO_4 , *Opt. Commun.* **142**, 265–268 (1997)
- 20.143 M. Peltz, U. Bäder, A. Borsutzky, R. Wallerstein, J. Hellström, H. Karlsson, V. Pasiskevicius, F. Laurell: Optical parametric oscillators for high pulse energy and high average power operation based on large aperture periodically poled KTP and RTA, *Appl. Phys. B* **73**, 663–670 (2001)
- 20.144 G. Rosenman, K. Garb, A. Skliar, D. Eger, M. Oron, M. Katz: Domain broadening in quasi-phase-matched nonlinear optical devices, *Appl. Phys. Lett.* **73**, 865–867 (1998)
- 20.145 H. Karlsson, F. Laurell: Electric field poling of flux grown KTiOPO_4 , *Appl. Phys. Lett.* **71**, 3474–3476 (1997)
- 20.146 M. Pierrou, F. Laurell, H. Karlsson, T. Kellner, C. Czeranowsky, G. Huber: Generation of 740 mW of blue light by intracavity frequency doubling with a first-order quasi-phase-matched KTiOPO_4 crystal, *Opt. Lett.* **24**, 205–207 (1999)
- 20.147 G. Rosenman, A. Skliar, D. Eger, M. Oron, M. Katz: Low temperature periodic poling of flux-grown KTiOPO_4 and isomorphic crystals, *Appl. Phys. Lett.* **73**, 3650–3652 (1998)
- 20.148 A. Garashi, A. Arie, A. Skliar, G. Rosenman: Continuous-wave optical parametric oscillator based on periodically poled KTiOPO_4 , *Opt. Lett.* **23**, 1739–1741 (1998)
- 20.149 C. Canalias, J. Hirohashi, V. Pasiskevicius, F. Laurell: Polarization-switching characteristics of flux-grown KTiOPO_4 and RbTiOPO_4 at room temperature, *J. Appl. Phys.* **97**, 124105 (2005)
- 20.150 P. Urenski, M. Lesnykh, Y. Rosenwaks, G. Rosenman: Anisotropic domain structure of KTiOPO_4 crystals, *J. Appl. Phys.* **90**, 1950–1954 (2001)
- 20.151 P. Urenski, M. Molotski, G. Rosenman: Bulk ferroelectric domain nucleation in KTiOPO_4 crystals, *Appl. Phys. Lett.* **79**, 2964–2966 (2001)
- 20.152 C. Canalias, S. Wang, V. Pasiskevicius, F. Laurell: Nucleation and growth of periodic domains during electric field poling in flux-grown KTiOPO_4 observed by atomic force microscopy, *Appl. Phys. Lett.* **88**, 032905 (2006)

- 20.153 J. Zhang, J. Wang, B. Ge, Y. Liu, X. Hu, G. Zhao, S. Zhu, R.I. Boughton: Growth, conductivity and periodic poled structure of doped KTiOPO_4 and its analogue crystals, *Opt. Mater.* **28**, 355–359 (2006)
- 20.154 G. Rosenman, P. Urenski, A. Arie, M. Roth, N. Angert, A. Skliar, M. Tseitlin: Polarization reversal and domain grating in flux-grown KTiOPO_4 crystals with variable potassium stoichiometry, *Appl. Phys. Lett.* **76**, 3798–3800 (2000)
- 20.155 Q. Jiang, P.A. Thomas, D. Walker, K.B. Hutton, R.C.C. Ward, P. Pernot, J. Baruchel: High potassium KTiOPO_4 crystals for the fabrication of quasi-phase matched devices, *J. Phys. D: Appl. Phys.* **36**, 1236–1241 (2003)
- 20.156 G. Rosenman, A. Skliar, Y. Findling, P. Urenski, A. Englander, P.A. Thomas, Z.W. Hu: Periodically poled KTiOAsO_4 crystals for optical parametric oscillation, *J. Phys. D: Appl. Phys.* **32**, L49–L52 (1999)
- 20.157 P. Pernot-Rejmánková, P.A. Thomas, P. Cloenets, F. Lorut, J. Baruchel, Z.W. Hu, P. Urenski, G. Rosenman: Periodically poled KTA crystal investigated using coherent X-ray beams, *J. Appl. Cryst.* **33**, 1149–1153 (2000)
- 20.158 H. Karlsson, F. Laurell, L.K. Cheng: Periodic poling of RbTiOPO_4 for quasi-phase matched blue light generation, *Appl. Phys. Lett.* **74**, 1519–1521 (1999)
- 20.159 A. Fragemann, V. Pasiskevicius, J. Nordborg, J. Hellström, H. Karlsson, F. Laurell: Frequency converters from visible to mid-infrared with periodically poled RbTiOPO_4 , *Appl. Phys. Lett.* **83**, 3090–3092 (2003)
- 20.160 H. Karlsson, F. Laurell, P. Hendriksson, G. Arvidsson: Frequency doubling in periodically poled RbTiOAsO_4 , *Electron. Lett.* **32**, 556–557 (1996)
- 20.161 H. Karlsson, M. Olson, G. Arvidsson, F. Laurell, U. Bäder, A. Borsutzky, R. Wallenstein, S. Wikström, M. Gustafsson: Nanosecond optical parametric oscillator based on large-aperture periodically poled RbTiOAsO_4 , *Opt. Lett.* **24**, 330–332 (1999)
- 20.162 G.T. Kennedy, D.T. Reid, A. Miller, A. Ebrahimzadeh, H. Karlsson, G. Arvidsson, F. Laurell: Near- to mid-infrared picosecond optical parametric oscillator based on periodically poled RbTiOAsO_4 , *Opt. Lett.* **23**, 503–505 (1998)
- 20.163 P. Loza-Alvarez, D.T. Reid, M. Ebrahimzadeh, W. Sibbett, H. Karlsson, P. Hendriksson, G. Arvidsson, F. Laurell: Periodically poled RbTiOAsO_4 femtosecond optical parametric oscillator tunable from 1.38 to 1.58 μm , *Appl. Phys. B* **68**, 177–180 (1999)
- 20.164 W. Chen, G. Mouret, D. Boucher, F.K. Tittel: Mid-infrared trace gas detection using continuous-wave difference frequency generation in periodically poled RbTiOAsO_4 , *Appl. Phys. B* **72**, 873–876 (2001)
- 20.165 I. Yutis, B. Kirshner, A. Arie: Temperature-dependent dispersion relations for RbTiOPO_4 and RbTiOAsO_4 , *Appl. Phys. B* **79**, 77–81 (2004)
- 20.166 S. Moscovich, A. Arie, R. Urenski, A. Agronin, G. Rosenman, Y. Rosenwaks: Noncollinear second-harmonic generation in sub-micrometer-poled RbTiOPO_4 , *Opt. Exp.* **12**, 2242 (2004)
- 20.167 C. Canalias, V. Pasiskevicius, R. Clemens, F. Laurell: Submicron periodically poled flux-grown KTiOPO_4 , *Appl. Phys. Lett.* **82**, 4233–4235 (2003)
- 20.168 D. Feng, N. Ming, J. Hong, Y. Yang, J. Zhu, Z. Yang, Y. Wang: Enhancement of second-harmonic generation in LiNbO_3 crystals with periodic laminar ferroelectric domains, *Appl. Phys. Lett.* **37**, 607–609 (1980)
- 20.169 V. Bermudez, E. Callejo, E. Dieguez: Effect of temperature annealing on periodically poled rare-earth doped lithium niobate crystal, *J. Optoelectron. Adv. Mater.* **5**, 55–59 (2003)
- 20.170 C.E.M. de Oliveira, G. Orr, N. Axelrod, A.J. Agranat: Controlled composition modulation in potassium lithium tantalate niobate crystals grown by off-centered TSSG method, *J. Cryst. Growth* **273**, 203–206 (2004)
- 20.171 J.A. Burton, R.C. Prim, W.P. Slichter: The distribution of solute in crystals grown from the melt. Part I. Theoretical, *J. Chem. Phys.* **21**, 1987–1991 (1953)
- 20.172 D. Elwell, H.J. Scheel: *Crystal Growth from High-temperature Solutions* (Academic, New York 1975) p.294
- 20.173 F.J. Kumar, D. Jayaraman, C. Subramanian, P. Ramasamy: Nucleation kinetic study of KTiOPO_4 crystallizing from high temperature solution, *J. Cryst. Growth* **137**, 535–537 (1994)
- 20.174 A.V. Smith: *SNLO nonlinear optics code*, available from: www.sandia.gov/imrl/x1118/xttab.htm
- 20.175 J.C. Jacco, D.R. Rockafello, E.A. Teppo: Bulk-darkening threshold of flux-grown KTiOPO_4 , *Opt. Lett.* **16**, 1307–1309 (1991)
- 20.176 R. Blachman, P.F. Bordui, M.M. Fejer: Laser-induced photochromic damage in potassium titanyl phosphate, *Appl. Phys. Lett.* **64**, 1318–1320 (1994)
- 20.177 B. Boulanger, M.M. Fejer, R. Blachman, P.F. Bordui: Study of KTiOPO_4 gray-tracking at 1064, 532 and 355 nm, *Appl. Phys. Lett.* **65**, 2401–2403 (1994)
- 20.178 M.P. Sripsick, D.N. Loiacono, J. Rottenberg, S.H. Goellner, L.E. Halliburton, F.K. Hopkins: Defects responsible for gray tracks in flux-grown KTiOPO_4 , *Appl. Phys. Lett.* **66**, 3428–3430 (1995)
- 20.179 J.P. Feve, B. Boulanger, G. Marnier, H. Albrecht: Repetition rate dependence of gray-tracking in KTiOPO_4 during second-harmonic generation at 532 nm, *Appl. Phys. Lett.* **70**, 1–3 (1997)
- 20.180 W.R. Bosenberg, D.R. Guyer: Single-frequency optical parametric oscillator, *Appl. Phys. Lett.* **61**, 387–389 (1992)
- 20.181 A. Deepthy, M.N. Saryanarayan, K.S.R.K. Rao, H.L. Bhat: Photoluminescence studies on gray tracked KTiOPO_4 single crystals, *J. Appl. Phys.* **85**, 8332–8336 (1999)

- 20.182 B.V. Andreev, V.A. Maslov, A.A. Mikhailov, S.K. Pak, O.P. Shaunin, I.A. Sherbakov: Exptimental study of the laser-induced absorption effect and the nature of color centers in potassium titanyl phosphate crystals, *Proc. SPIE* **1839**, 280–289 (1991)
- 20.183 M.P. Scripsick, G.J. Edwards, L.E. Halliburton, R.F. Belt, G.M. Loiacono: Effect of crystal growth on Ti^{3+} centers in KTiOPo_4 , *J. Appl. Phys.* **76**, 773–776 (1994)
- 20.184 S.D. Setzler, K.T. Stevens, N.C. Fernelius, M.P. Scripsick, G.J. Edwards, L.E. Halliburton: Electron paramagnetic resonance and electron–nuclear double–resonance study of Ti^{3+} centres in KTiOPo_4 , *J. Phys. Condens. Matter* **15**, 3969–3984 (2003)
- 20.185 P.A. Morris, M.K. Crawford, M.G. Roelofs, J.D. Bierlein, P.K. Gallagher, G. Gashurov, G. Loiacono: Proton effects in KTiPO_5 , *MRS Proc. Opt. Fiber Mater. Process.* **172**, 283–289 (1990)
- 20.186 R.G. Batchko, G.D. Miller, A. Alexandrovski, M.M. Fejer, R.L. Byer: *Limitations of High-Power Visible Wavelength Periodically Poled Lithium Niobate Devices due to Green-Induced Infrared Absorption and Thermal Lensing*, OSA Technical Digest, Vol. 6 (OSA, Washington 1998) pp. 75–76
- 20.187 Y. Jiang, L.E. Halliburton, M. Roth, M. Tseitlin, N. Angert: EPR and ENDOR study of an oxygen–vacancy–associated Ti^{3+} center in RbTiOPo_4 crystals, *Physica B* **400**, 190–197 (2007)
- 20.188 J.J. Carvajal, R. Solé, J. Gavalda, J. Massons, P. Segonds, B. Boulanger, A. Brenier, G. Boulon, J. Zaccaro, M. Aguiló, F. Díaz: Spectroscopic and second harmonic generation properties of a new crystal: Yb-doped RbTiOPo_4 , *Opt. Mater.* **26**, 313–317 (2004)

21. High-Temperature Solution Growth: Application to Laser and Nonlinear Optical Crystals

Joan J. Carvajal, Maria Cinta Pujol, Francesc Díaz

Growth methods based on high-temperature solutions, traditionally also known as flux growth methods, and especially the top-seeded solution growth (TSSG) and liquid-phase epitaxy (LPE) methods, are some of the most popular methods by which to grow single crystals. These methods have to be used when the grown materials melt incongruently, melt at very high temperatures, or suffer from polymorphic transitions below the crystallization temperature. In this chapter we review the main advances produced in these crystal growth techniques during recent years, both in bulk and epitaxial films, and for two families of oxide materials, specifically those commonly used for solid-state lasers and nonlinear optical crystals. We intend to focus on the application to the real problems related to crystal growth in solutions with different viscosities, while revisiting some of the main strategies developed to overcome these problems to enable growth of bulk single crystals and single-crystalline films with good optical quality.

21.1 Basics	726
21.1.1 Historical Background and Overview	726
21.1.2 Most Important Families of Laser and Nonlinear Optical Materials	727
21.2 High-Temperature Solution Growth	731
21.2.1 Top-Seeded Solution Growth (TSSG)	732
21.2.2 Liquid-Phase Epitaxy (LPE)	734
21.3 Growth of Bulk Laser and NLO Single Crystals by the TSSG Method	736
21.3.1 Crystal Growth from Low-Viscosity Solutions: Fluorides, Tungstates, and Vanadates	736
21.3.2 Crystal Growth from High-Viscosity Solutions: Phosphates and Borates	739
21.4 Liquid-Phase Epitaxy: Growth of Epitaxial Films of Laser and NLO Materials	746
21.4.1 Epitaxial Films of Laser Materials: Lanthanide-Doped KLuW on KLuW Substrates	746
21.4.2 Epitaxies Within the Structural Field of KTP ...	748
References	752

Interest in crystal growth technology started at the beginning of the 20th century, initially in the jewelry and watch industry, and later on in microelectronics (semiconductors), solid-state devices, and laser technology.

During the period 1900–1939, before World War II, the basis of high-temperature solution growth technology was developed, but industrial applications were limited almost only to the ruby single crystal, so the new crystal growth method, and the crystals grown from it, were limited to the academic level. The widespread technological application of single crystals began with the military application of piezoelectric single crystals for transducers in sonar and radar devices. In 1948, after World War II, the discovery of the transistor effect

substantially increased the demand for single crystals. The deficient performance of the first generation of transistors based on germanium, principally related to the existence of micro- and macrodefects in germanium single crystals, induced and impelled the study and improvement of high-temperature solution crystal growth methods.

After 1990, the expansion to large-scale industrial production of transistors and the progress in the field of electronics definitively motivated crystal growth as a new scientific field in the material science area. Semiconductors such as Si, GaAs, InAs, etc., and crystalline materials such as BaTiO₃, ferrites, yttrium iron garnet **YIG**, and yttrium aluminum garnet (**YAG**), among oth-

ers, have been obtained with a high enough level of perfection, and have been incorporated as core materials for different solid-state devices.

Now, technology uses thousands of single-crystal materials, especially in microelectronics, optoelectronics, optics, and laser technologies. Research is oriented to develop methods and technologies to control the crystallinity, purity, and homogeneity of the grown crystals. The most extended crystal growth methods, based on producing controlled solidification of a melt of the

stoichiometric composition of the material, are related to the production of semiconductor materials such as silicon and GaAs. However, several crystalline materials cannot be obtained from melt methods and have to be grown from a solution with a convenient solvent. In this chapter we discuss the high-temperature solution growth methodologies as some of the most suitable ways to obtain several optical materials, specifically in the fields of the laser and nonlinear optical technologies.

21.1 Basics

21.1.1 Historical Background and Overview

Crystal growth is a central step in the processing of solid-state laser and nonlinear optical (NLO) materials.

Crystal size, optical losses, and optical uniformity, as well as ultimate crystal cost, tend to be dominated by the crystal growth process. A variety of techniques are practiced, but for most materials, there emerges a preferred crystal growth technique. The process-dependent properties and limitations of a crystal tend to reflect the inherent nature of that growth technique.

In general, crystal growth from the melt is preferable whenever possible. However, other crystal growth methods have to be used when materials melt incongruently, when they suffer from polymorphic transitions below crystallization temperature, or when they melt at very high temperatures. In these cases high-temperature solution methods must be used, in processes analogous to crystal growth from aqueous solutions, but in which the solvent solidifies before reaching room temperature. The main advantage of these methodologies is that crystals are grown below their melting temperature, or in a fluid with lower viscosity than the melt. In high-temperature solution growth, thermal strain is minimized due to the relatively low growth temperature, the much smaller thermal gradients used in these methods compared with classical methods based on growth from melts, and the free growth into a liquid. These factors make crystal growth proceed in physical conditions near thermodynamic equilibrium, allowing crystals to grow in a way that minimizes the superficial energy, developing facets. However, these low growth rates, in general hundreds of times smaller than the growth rates that can be achieved in melt-based growth methods, constitute the main disadvantage of the high-temperature solution growth methods. This, together with the differences in linear growth rates among the different faces of

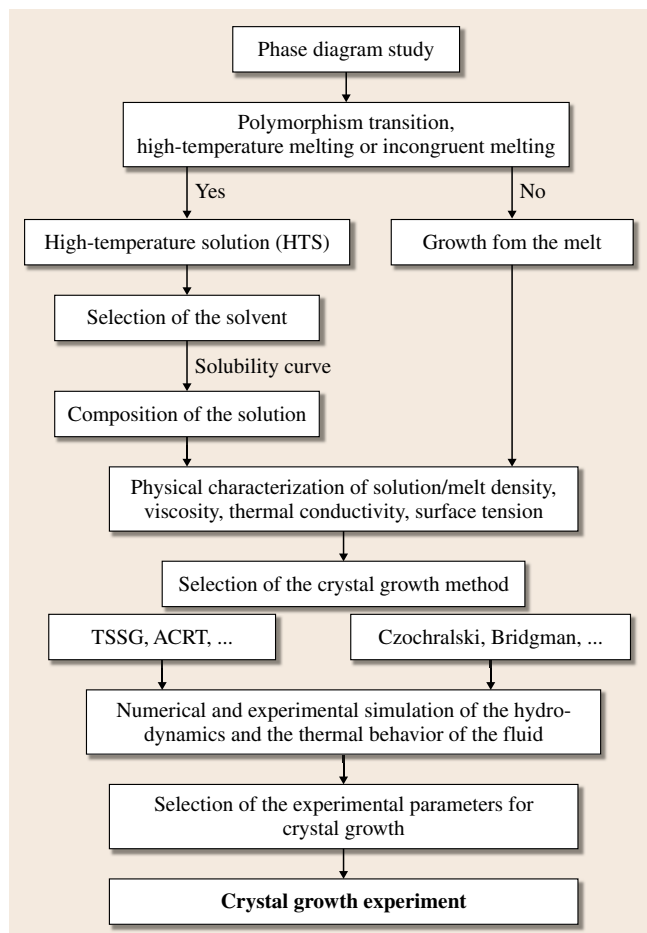


Fig. 21.1 Flow chart with the criteria used to determine the crystal growth method of a material from the melt or from high-temperature solutions ◀

Table 21.1 Structural, thermal, and optical properties of the most important families of inorganic SSL single crystal

	Space group of symmetry	Optical class	Moh's hardness	Thermal conductivity (W/m K)	Transparency range (nm)	Growth method	References
YAG	<i>Ia3d</i>	Isotropic	8.2–8.5	14	200–6000	Czochralski Floating zone μ -Pulling	[21.1, 2]
REVO ₄ ^a	<i>I4₁/amd</i>	Uniaxial	5	$c_{\parallel} = 5.23$ $c_{\perp} = 5.10$	400–5000	Czochralski HTS EDFF TSSG	[21.3–5]
YAP	<i>Pbnm</i>	Biaxial	\approx YAG	11	300–10 000	Czochralski	[21.6]
KREW ^b	<i>C2/c</i>	Biaxial	4.5–5	2.2–3.5	300–5000	TSSG INFC TNFC	[21.7–10]
RELF ^c	<i>I4₁/a</i>	Uniaxial	4–5	6	120–7500	Bridgman Czochralski VGF	[21.11, 12]
BaREF ^d	<i>C2/m</i>	Biaxial	3–3.5	6	125–12 000	Czochralski	[21.13, 14]
LiSAF	<i>P31c</i>	Uniaxial		3.3–3.6		Czochralski Bridgman TSSG	[21.15, 16]

^a Data for YVO₄; ^b Data for KGd(WO₄)₂; ^c Data for YLF; ^d Data for BaYF₈

the crystal, which lead to chemical and structural inhomogeneities in the crystal, has hampered the industrial production of crystals grown from high-temperature solution methods.

Figure 21.1 summarizes the criteria used to determine the possibility of use of growth methods based on melt, or when not possible, the use of growth methods based on high-temperature solutions.

21.1.2 Most Important Families of Laser and Nonlinear Optical Materials

Laser Materials

Kaminskii [21.17] mentioned that currently there are over 575 single crystals for solid-state laser (SSL) applications, among them, different structure fluorides, oxides, chlorides, bromides, and compounds with mixed anion pairs such as chlorine–oxygen, fluorine–oxygen, and sulfur–oxygen, which can produce continuous wave (CW) or pulsed stimulated emission (SE) generation over a very wide spectral range from ≈ 0.172 to $\approx 7.24 \mu\text{m}$.

The desirable properties of a good laser material are: feasibility of growth; high capacity to incorporate the active ions without affecting the structure; transparency in the suitable range; favorable spectroscopic properties for the active ions; high thermal conductivity; low and similar thermal expansion coefficients; inertness; low cost; and hardness, which favors polishing. They especially have to favor large absorption and emission cross sections, and have: a high gain coefficient; an optimum distance between the active ions (i.e., if laser transition is based on a scheme where cross-relaxation phenomena favors the population of the emitting level, the distance must be short to increase this populating level; on the other hand, if the laser emitting level could be depopulated by a cross-relaxation or energy transfer among active ions, then the distance must be longer); long lifetime to allow population inversion; and low phonon energy modes of the structure to avoid nonradiative transitions.

Table 21.1 lists the most important families of inorganic SSL single crystals, summarizing some of their main structural, thermal, and optical properties.

Oxides

Y₃Al₅O₁₂, Yttrium Aluminum Garnet (YAG). YAG crystallizes in the cubic system. The active ions substitute Y³⁺ in the structure in a *D*₂ position. It is a very stable compound with high robustness and high thermal conductivity. Optically YAG is isotropic. YAG is one of the most widely produced gain laser hosts. The Nd:YAG laser is by far the most commonly used solid-state laser since its first reported lasing at Bell Telephone Laboratories and RCA Laboratories in 1964. Tm-, Ho-, and Er-doped YAG lasers are also widely studied and used in the 2 μm region.

REVO₄, Rare-Earth Vanadate. Rare-earth vanadates crystallize in the tetragonal system. The trivalent active ions substitute the optically inert trivalent cations RE³⁺ at lattice sites with $\bar{4}2m$ symmetry. Optically they are positive uniaxial crystals, with $n_o = n_a = n_b$ and $n_e = n_c$. YVO₄ is a strongly birefringent material ($\Delta n = 0.2225$ at 633 nm at room temperature). Their advantages when compared with YAG are the high absorption and emission cross sections, broad bandwidths, and natural polarization of these materials.

YAlO₃, Yttrium Aluminum Perovskite (YAP). Several possible crystalline structures can be found in the literature for YAlO₃ [21.6]. The active lanthanide ions substitute the Y³⁺ in the lattice sites in *C*_{1h}. The physical properties of YAP, such as hardness, thermal conductivity, etc., are quite similar to those of YAG [21.18]. From the optical point of view, YAP is a biaxial, birefringent material (Δn , at 1.06 μm, $n_a = 1.929$, $n_b = 1.943$, and $n_c = 1.952$). The transparency region is from around 300 nm to 10 μm. The advantage of this material is related to its anisotropy, which allows the possibility of short tuning of the wavelength with the variation of the wavevector direction in the crystal, and the generation of linearly polarized output beams.

KRE(WO₄)₂, Potassium Double Tungstates (KREW). The monoclinic KREW is another well-known family of laser host compounds. The active lanthanide ions substitute the RE³⁺ cation in the structure at the local symmetry lattice site *C*₂. The physical properties of KREW materials are governed by their huge anisotropy. Their thermal conductivity is anisotropic, and depends also on the RE³⁺ cation. Optically, monoclinic KREW are biaxial crystals. The *N*_p orthogonal principal crystallooptic axis is parallel to the twofold symmetry axes. The other two principal axes are in the *a*-*c* plane. The

principal axis *N*_g is located at $\kappa = 18.5\text{--}21.5^\circ$ (angle value depending on the RE³⁺ of the host) clockwise to the *c*-crystallographic axis when the positive *b*-axis is pointing towards the observer. *N*_m is rotated at $\beta + \kappa - 90^\circ$ with respect to the *a* crystallographic axis in the clockwise direction. Their anisotropy is responsible for the large absorption and emission cross sections of the active ions. Furthermore, these crystals are also very interesting for their stimulated Raman scattering (SRS) properties, and recently for their high efficiency as laser optical cooling materials [21.19].

Fluorides

RELiF₄, Rare-Earth Lithium Fluoride (RELF). This material crystallizes in the tetragonal system. The active ions substitute the RE³⁺ in the *S*₄ positions of the structure. It is an anisotropic uniaxial crystal, with the optical axis along the *c* crystallographic direction. Its birefringence at 633 nm is $n_o = 1.443$ and $n_e = 1.464$, and at 1064 nm is $n_o = 1.448$ and $n_e = 1.470$. Fluoride crystals are useful for coherent optical sources in the ultraviolet (UV) wavelength region. It can host a high percentage of doping elements, and possesses a low thermal lensing effect, when compared with YAG.

BaREF₈, Barium Rare-Earth Fluoride (BaREF). These materials crystallize in the monoclinic system. The rare-earth dopant substitutionally enters the RE³⁺ sites, whose symmetry is *S*₄. The BaYF refractive index *n* is 1.5. Optically, BaREF₈ is a biaxial crystal. Their monoclinic structure compensates the thermal lens effect under strong pumping better than cubic crystals such as YAG. Additionally, these materials have low-energy phonons: the maximum phonon energy is 400 cm⁻¹.

LiSrAlF₆, Lithium Strontium Aluminum Fluoride (LiSAF). LiSAF crystals belong to the colquiriite fluoride family of crystals LiMAF (where M = Sr, Ga, Ca). These materials crystallize in the trigonal system. Optically, these materials are uniaxial. Among them, LiCaAlF₆:Cr (LiCAF:Cr) is more robust and has more advantageous thermo-optical properties. It exhibits higher scattering and smaller absorption and emission cross sections when compared with LiSAF. Cr³⁺-doped single crystals of this family have been described as efficient broadly tunable laser materials [21.20,21].

Nonlinear Optical Materials

Since its first demonstration in 1961 [21.22], nonlinear frequency conversion has been a field limited by

the available materials, with practical advances largely controlled by progress in making improved **NLO** materials. To date, the most important class of materials used in nonlinear optics has been inorganic single crystals. Organic materials, although promising, have yet to be produced with good enough chemical and mechanical properties to find broad practical application. Relatively few materials find application in nonlinear optics. The physics of the frequency conversion process places severe demands on potential **NLO** crystals. Beyond the **NLO** physics are the additional practical requirements of mechanical and chemical stability and the possibility for production in the form of adequately sized and uniform single crystals.

Table 21.2 lists the main inorganic **NLO** crystals together with their main structural, thermal, and optical properties.

Niobates. LiNbO_3 (**LN**) crystallizes in the trigonal system. Its **NLO** coefficients are relatively high, and the birefringence is of a magnitude, enabling phase matching for noncritical type I second-harmonic generation (**SHG**) of a 1064 nm fundamental at room temperature. Its thermal conductivity is very high. **LN** can suffer from photorefractive damage when illuminated with visible radiation. Certain Mg-doped **LN** crystals have been measured to have a photorefractive damage threshold more than 10^5 times greater than that of typical

Table 21.2 Structural, thermal, and optical properties of the main inorganic **NLO** single crystals [21.23]

	Space group of symmetry	Optical class	Thermal conductivity (W/m K)	Transparency range (nm)	NLO coefficients (pm/V)	Growth method
LN	$R3c$	Uniaxial	0.0015	350–5000	$d_{21} = d_{16} = -2.1$ $d_{22} = 2.1$ $d_{14} = d_{25} = d_{36} = 0$ $d_{31} = d_{15} = -4.3$ $d_{32} = d_{24} = -4.3$ $d_{33} = -27$	Czochralski VTE TSSG DC-Czochralski
KN	$Amm2$	Biaxial		400–5500	$d_{21} = d_{16} = 0$ $d_{22} = 0$ $d_{14} = d_{25} = d_{36} = 0$ $d_{31} = d_{15} = -11.3$ $d_{32} = d_{24} = -12.8$ $d_{33} = -19.5$	HTS
KTP	$Pna2_1$	Biaxial	2–3.3	350–4500	$d_{21} = d_{16} = 0$ $d_{22} = 0$ $d_{14} = d_{25} = d_{36} = 0$ $d_{31} = d_{15} = 2.0$ $d_{32} = d_{24} = 3.6$ $d_{33} = 8.3$	HTS Hydrothermal
KDP	$I\bar{4}2d$	Uniaxial	1.86–2.09	180–1800	$d_{21} = d_{16} = 0$ $d_{22} = 0$ $d_{14} = d_{25} = d_{36} = 0.37$ $d_{31} = d_{15} = 2.0$ $d_{32} = d_{24} = 3.6$ $d_{33} = 8.3$	Aqueous solution
β -BBO	$R3c$	Uniaxial	0.001–0.002	198–2600	$d_{21} = d_{16} = -2.3$ $d_{22} = 2.3$ $d_{14} = d_{25} = d_{36} = 0$ $d_{31} = d_{15} = 0.1$ $d_{32} = d_{24} = 0.1$ $d_{33} = 0$	HTS Metastable growth Czochralski

Table 21.2 (cont.)

	Space group of symmetry	Optical class	Thermal conductivity (W/m K)	Transparency range (nm)	NLO coefficients (pm/V)	Growth method
LBO	$Pna2_1$	Biaxial		160–2300	$d_{21} = d_{16} = 0$ $d_{22} = 0$ $d_{14} = d_{25} = d_{36} = 0$ $d_{31} = d_{15} = -0.67$ $d_{32} = d_{24} = 0.85$ $d_{33} = 0.04$	HTS
BIBO	$C2$	Biaxial		286–2500	$d_{222} = 2.53(4)$ $d_{211} = 2.3(2)$ $d_{233} = 1.3(1)$ $d_{231} = 2.3(2)$ $d_{112} = 2.8(2)$ $d_{332} = 0.9(1)$ $d_{312} = 2.4(3)$ $d_{132} = 2.4(3)$	Czochralski
AgGaS ₂	$I\bar{4}2d$	Uniaxial	0.01	500–13 000	$d_{21} = d_{16} = 0$ $d_{22} = 0$ $d_{14} = d_{25} = d_{36} = 17.5$ $d_{31} = d_{15} = 0$ $d_{32} = d_{24} = 0$ $d_{33} = 0$	Bridgman
LiIO ₃	$P6_3$	Uniaxial	8×10^{-4}	310–5000	$d_{21} = d_{16} = 0$ $d_{22} = 0$ $d_{14} = d_{25} = d_{36} = 0$ $d_{31} = d_{15} = 4.4$ $d_{32} = d_{24} = 4.4$ $d_{33} = 4.5$	Aqueous solution

undoped LN. Mg doping appears to have little effect on the NLO coefficients.

KNbO₃ (KN) is notable for its very large NLO coefficients and birefringence. The transmission range is similar to that of LN, although residual losses are generally higher and much less consistent from crystal to crystal. It suffers from significant processing limitations, due to the material’s low Curie temperature and its pyroelectric and ferroelastic character.

Phosphates. KTiOPO₄ (KTP) belongs to family of compounds with the general formula ABOXO₄ where A = K, Rb, Na, Cs, Tl, NH₄; B = Ti, Sn, Sb, Zr, Ge, Al, Cr, Fe, V, Nb, Ta, and X = P, As, Si, crystallizing in the orthorhombic system [21.24]. KTP single crystals are chemically inert. Optically they are biaxial crystals. The KTP transmission range, NLO coefficients, and birefringence are similar to

those of LN, although KTP’s residual absorption is notably higher. Perhaps most important for KTP are its very large thermal and angular phase-matching bandwidths for SHG of fundamental wavelengths near 1064 nm.

KH₂PO₄ (KDP) and its homologs are among the most widely used commercial NLO materials. Although members of the family have relatively low NLO coefficients, they feature good UV transmission, high birefringence, and relatively high resistance to laser damage. KDP is widely used to generate second, third, fourth, and fifth harmonics of 1.06 μm radiation.

Borates. Single crystals of the low-temperature phase of barium metaborate, β-BaB₂O₄ (β-BBO) and LiBO₃ (LBO) have found important applications for NLO devices. β-BBO has a wide transparent spectral range, and good mechanical properties. In general, borates

combine UV transparency, high-laser damage thresholds, and adequate birefringence for phase-matching a broad range of visible and UV interactions. β -BBO has larger nonlinear susceptibilities than LBO, and can be phase-matched more readily in the UV, but suffers from smaller angular acceptance and lower damage threshold, and is more hygroscopic.

BiB_3O_6 (BIBO) is another outstanding NLO crystal. It belongs to the monoclinic system. BIBO is an appropriate material for phase-matching condition for near-infrared (NIR) wavelengths. It possesses a large effective nonlinear coefficient and high damage threshold, and is nonhygroscopic. Its nonlinear coefficient is 3.5–4 times higher than that of LBO, and 1.5–2 times higher than that of β -BBO [21.25].

Chalcopyrites. The most important of these compounds are AgGaS_2 , AgGaSe_2 , and ZnGeP_2 . These materials exhibit broad transparency far into the infrared, sufficient birefringence to enable phase-matching over a major portion of the transparency range, and relatively high nonlinear coefficients. Laser damage resistance tends to be very low. The greatest limitation to application of the chalcopyrites has been optical loss.

LiIO_3 . Because of its large birefringence, lithium iodate, LiIO_3 is broadly phase-matchable, but suffers from large walk-off effects that limit conversion efficiencies despite its larger nonlinear susceptibility. Applications taking advantage of the broad tuning range are the most common.

21.2 High-Temperature Solution Growth

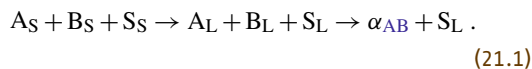
When compared with growth from the melt, crystal growth from solution produces remarkable improvements in the quality of the grown crystals, principally due to a much lower crystallization temperature. Using lower temperatures during the growth process means a lower density of structural defects and less contamination in the liquid phase from the crucible or the ambient. Furthermore, the low growth rate developed at lower temperatures enables better control of all the parameters involved in a stable growth process. Finally, careful choice of a suitable solvent can help reduce the viscosity of the solution, minimizing problems related to deficient mass transport that can generate solvent inclusions in the crystals. However, crystal growth by high-temperature solution (HTS) presents some disadvantages when compared with crystal growth techniques from the melt. Substitution, or generation of interstitial defects when the solvent contains ions alien to the grown material, and the relatively low crystal growth rates inherent to HTS techniques constitute the main disadvantages of these techniques, especially when scaling up these processes to industrial production.

Nevertheless, there is no doubt that HTS growth methods have a huge field of application and they constitute the basis of several of the current solid-state technologies, mainly in microelectronics and optoelectronic devices. Theoretically, this method presents no limits – it is always possible to find a suitable solvent and the most convenient crystallization conditions to obtain any material. In practice, however, it is not this

easy. Despite this, the list of materials that have been obtained by HTS methods is very long, covering materials from diamond or oxide compounds to metals. Hundreds of single-crystalline materials are grown by HTS-based methods, among them the magnetic ferrites developed in the 1970s, the superconductor materials such as $\text{YBa}_2\text{Cu}_3\text{O}_{7-x}$ (YBCO) developed during the 1980s and 1990s, many ferroelectric materials such as KTP, etc. Crystal growth from HTS is also one of the most popular growth methods as it does not require sophisticated equipment. At present, several research laboratories around the world are not only growing new and different crystalline materials, but are also studying and modeling the fundamentals of the transport processes involved in crystal growth using these HTS techniques.

The principle of crystal growth by HTS lies in choosing a suitable solvent S for the components A and B of a given α_{AB} phase, all solids at room temperature, with a lower solubility for the α_{AB} phase at a given temperature than for the initial components.

By heating the reagents it will be possible to induce HTS growth



The driving force for HTS growth is supersaturation of the $\alpha_{AB} + \text{S}_L$ solution. This supersaturation can be created by slow cooling of the solution, by evaporation of the solvent or by increasing the solute concentration at constant temperature.

To control spurious nucleation and improve the quality of the grown crystals, modifications to HTS methods have been applied through the years. Methods based on homogeneous nucleation used in the 1960s have been displaced by methods based on induced growth (secondary nucleation), which involve techniques such as rotation and pulling of the growing crystals that enhance mass transport conditions in the solution, avoid supersaturation gradients, and allow growth of larger crystals. Top-seeded solution growth and liquid-phase epitaxy are the most popular methods based on HTS growth technologies. In the next sections the main features of these two methods will be described.

21.2.1 Top-Seeded Solution Growth (TSSG)

To grow a crystal the first step, after having selected a suitable candidate solvent, is the study of the phase diagram of the different compounds that will be mixed to create the growth solution to determine the composition and temperature range in which the desired crystalline phase (solute into the solution) can be grown. As an example the phase diagram of $\text{K}(\text{Gd}_{0.5}\text{Nd}_{0.5})(\text{PO}_3)_4$ in the ternary system $(\text{Nd}_2\text{O}_3 + \text{Gd}_2\text{O}_3) - \text{K}_2\text{O} - \text{P}_2\text{O}_5$ is shown in Fig. 21.2a. Parameters such as the existence of other neighboring crystalline phases, the crystallization temperature, the solute-to-solvent ratio, etc. will influence the selection of the most suitable point of the phase diagram at which to perform the crystal growth

experiments. The solubility curve of the crystallizing phase in the chosen solvent must then be determined. Figure 21.2b shows the solubility curve of the KREW- $\text{K}_2\text{W}_2\text{O}_7$ system. When the solubility curve has been determined, the crystallization experiment can be performed by choosing the most suitable solute-solvent composition while accounting for the slope of the solubility curve. If the growth experiment is performed in a solution with a solute-solvent composition in region I of Fig. 21.2b, where the solubility curve shows a pronounced slope, a temperature fluctuation ΔT produces a small change in the concentration of solute Δc_1 . However, if the experiment is performed in a solution with a composition in region II, where the solubility curve has a flat slope, the same temperature fluctuation ΔT will produce a larger change in the concentration of solute Δc_2 that can lead to fluctuations in the supersaturation levels created in the solution. In order to obtain crystals with a lower density of defects it is important to avoid fluctuations in the supersaturation levels in the growth solution. Thus, region I is the most suitable region to grow crystals in these solutions, as it provides better control of the solutal fluctuations by small changes in the temperature.

The TSSG method represents an improvement of crystal growth from HTS methodologies as it restricts and forces crystal growth only at a point of the free surface of the solution, i.e., on a crystal seed in contact with the surface of the solution that can be rotated and pulled. Figure 21.3a shows the experimental con-

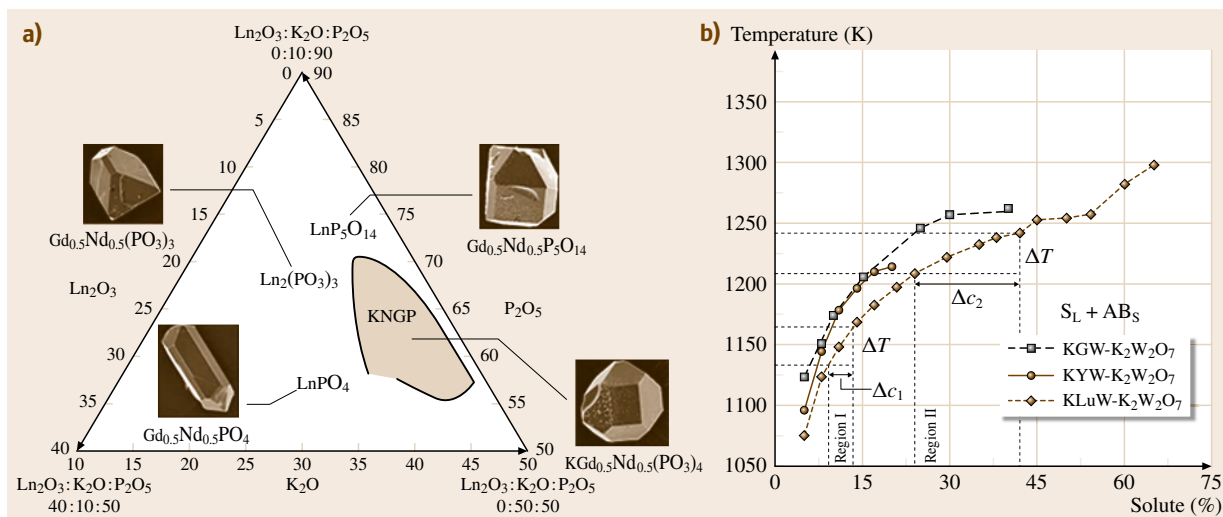


Fig. 21.2 (a) Crystallization region of $\text{KGd}_{0.5}\text{Nd}_{0.5}(\text{PO}_3)_4$ with solution isotherms in the $\text{Ln}_2\text{O}_3 - \text{K}_2\text{O} - \text{P}_2\text{O}_5$ system. SEM images of $\text{K}(\text{Gd}, \text{Nd})(\text{PO}_3)_4$ crystals and neighboring phases. (b) Solubility curve of KREW (RE = Gd, Y, and Lu) in $\text{K}_2\text{W}_2\text{O}_7$ solvent

figuration of the TSSG method. Before configuring the values of the TSSG parameters it is necessary to know the physicochemical properties of the solution such as density, viscosity, thermal conductivity, and surface tension [21.26]. This knowledge enables numerical and experimental simulation to determine the best solute-solvent composition and to know the hydrodynamics of the solution needed for a successful crystal growth experiment [21.27]. These experimental simulation studies will provide the most suitable values for parameters such as the aspect ratio (diameter/height) of the crucible that will contain the solution, axial and radial thermal gradients in the solution, rotation rate of the crystal seed, extent of the crucible's rotation, ratio between the size of the growing crystal and the crucible radius, etc. Figure 21.3b shows a nonaxisymmetric horizontal flow pattern of the solution obtained by visualization techniques in an experimental simulation of a growth experiment. The best conditions for real growth should avoid nonaxisymmetric flow patterns. Figure 21.3c shows an axial cross section of a growth solution by visualizing the flow established by a crystal/crucible counter-rotation configuration

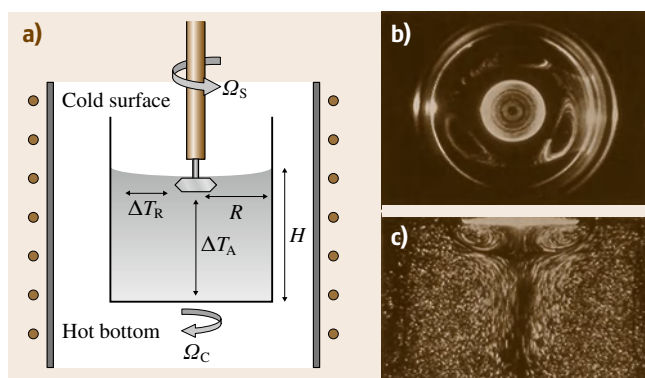


Fig. 21.3a–c TSSG method. (a) Scheme of the experimental configuration. (b) Nonaxisymmetric horizontal flow pattern obtained by visualization techniques of the solution. (c) Axial cross section of a solution of growth, visualizing the flow established by a crystal/crucible counter-rotation configuration

counter-rotation configuration. These experimental simulations have been obtained from liquid simulation under similar thermal and hydrodynamics conditions to

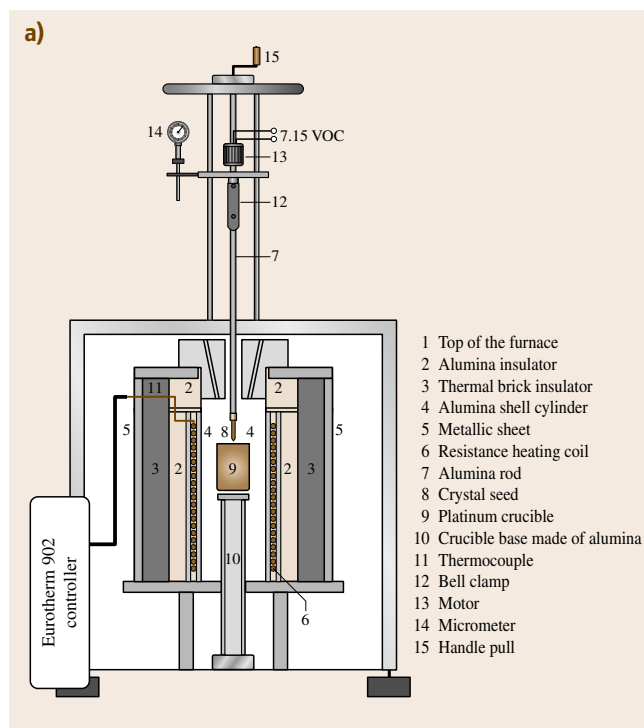


Fig. 21.4a,b TSSG method. (a) Schematic representation and (b) picture of a system used for the TSSG method including a single-thermal-zone vertical tubular furnace, the crystal seed attach, rotation, and pulling system, the crucible and its support, and temperature controller/programmer

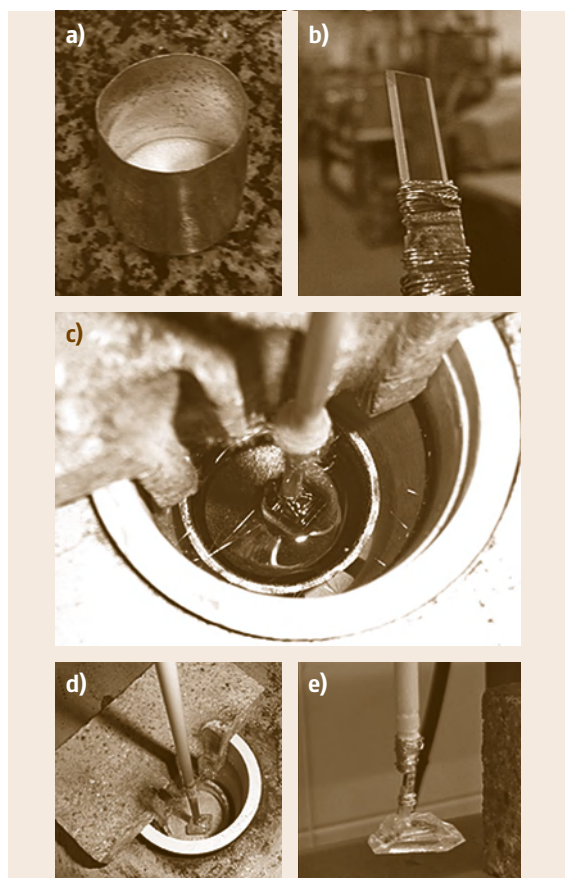


Fig. 21.5a–e Process of growth of a double tungstate single crystal by the TSSG method. (a) Platinum crucible containing the flux or solution at room temperature. (b) Crystal seed ready to be used for the crystal growth experiment. (c) Single crystal growing inside the solution. (d) Single crystal after being removed from the solution while cooling the furnace to room temperature. (e) Single crystal attached to the crystal seed at the end of the experiment

those of a real growth solution (equal Reynolds and Prandtl numbers). In high-viscosity solutions the use of angular acceleration of the crystal or the crucible, or both, with periodic changes in their direction of rotation, has also been used to improve the homogeneity of the solution. For very-high-viscosity systems a HTS alternative technology such as the accelerated crucible rotation technique (ACRT) must be used [21.28].

Figure 21.4 shows a schematic representation and a picture of the system used for the TSSG method. It includes a single-thermal-zone vertical tubular fur-

nace, the crystal seed attach, rotation, and pulling system, the crucible and its support, and the temperature controller/programmer. The furnace is heated by an electrical resistance, and the thermal insulation and the alumina shell cylinder can also be seen in the cross section of the furnace provided in the schematic representation. The seed attach, rotation, and pulling system consist of a series of high-precision mechanisms attached to two different stepper motors that allow simultaneous rotation and pulling of the crystal seed. Both the speed of rotation and the speed of pulling can be modified according to the voltage provided by the power source. The attach system can be moved up and down to locate the crystal seed precisely in contact with the surface of the solution. This movement can be monitored with a micrometric comparer for better precision. The support of the crucible allows it to be located at the correct height along the axis of the furnace to obtain the desired thermal gradient inside the solution. Finally, the heating or cooling rate and the temperature of the furnace are precisely controlled by the controller/programmer systems, connected to a thyristor.

Figure 21.5 shows a sequence of pictures representing the process of growth of a double tungstate single crystal using the TSSG method. Figure 21.5a shows a platinum crucible containing the flux or solution, which is a solid at room temperature. Figure 21.5b shows a crystal seed attached to an alumina rod and a platinum support ready for the crystal growth experiment. In Fig. 21.5c, the single crystal growing inside the solution while attached to the crystal seed can be seen. Figure 21.5d shows the single crystal after being removed from the solution and standing near the surface of the solution while the furnace is being cooled slowly to room temperature to avoid thermal cracking of the crystal. Finally, Fig. 21.5e shows the single crystal at the end of the crystal growth experiment still attached to the crystal seed.

21.2.2 Liquid-Phase Epitaxy (LPE)

The term epitaxy can be defined as the deposition of a single-crystal layer on a single-crystal substrate such that the crystalline structure of the substrate is continued into the layer. For a given substrate, the lattice parameter mismatch between the layer and the substrate is limited by a critical value, above which continuity of the crystalline construction across the substrate–layer interface is impossible. LPE is the growth of epitaxial layers, hereafter epilayers, from solutions at high temperatures.

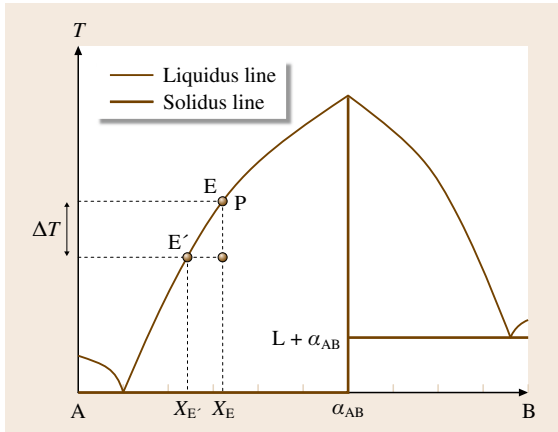


Fig. 21.6 Cooling effect in a binary diagram

The process of LPE growth involves three main steps:

1. Creation of supersaturation
2. Mass transport from solution to solid-liquid interface
3. Nucleation and surface attachment [21.29, 30]

1. *Creation of supersaturation.* Figure 21.6 introduces the fundamentals of LPE as a crystal growth method. A substrate is introduced into a solution, which is cooled by a discrete amount ΔT and the equilibrium liquid-phase composition is shifted from X_E to $X_{E'}$, which has a lower α_{AB} (solute) concentration. The decrease in solubility creates a supersaturated solution and yields deposition of α_{AB} solid phase onto the substrate.

The supersaturation created in the solution

$$\sigma = \frac{X_E(T) - X_{E'}(T)}{X_{E'}(T)} \quad (21.2)$$

is related to the change of free energy when crystallization occurs $\Delta G \approx RT\sigma$ and to the gradient of chemical potential $\Delta G \approx \Delta\mu$. The chemical potential at point P in Fig. 21.6 of the supersaturated solution is higher than its equilibrium value at the same temperature, point E' in Fig. 21.6. This constitutes the driving force of LPE growth, and induces heterogeneous nucleation, which exhibits a lower activation energy than homogeneous nucleation because the surface of the substrate catalyzes the crystal growth process.

2. *Mass transport from the solution to the solid-liquid interface.* When the epilayer starts to grow, and because of the limitations of mass transport near the

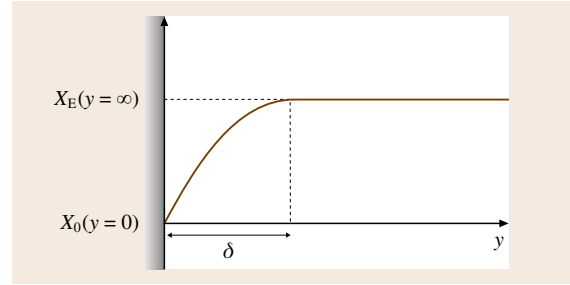


Fig. 21.7 Solutal boundary layer adjacent to substrate surface

substrate surface, a solutal boundary layer is established, as can be seen in Fig. 21.7.

The velocity of mass transport from the solution to the solid-liquid interface in stationary conditions is given by Fick's equation

$$\begin{aligned} R &= \frac{D_v}{\rho} \frac{X_{E'} - X_0}{\delta} = \frac{1}{\rho} \frac{D_v}{\delta} (X_{E'} - X_0) \\ &= \frac{1}{\rho} \frac{1}{\delta/D_v} (X_{E'} - X_0), \end{aligned} \quad (21.3)$$

where D_v is the volumetric diffusivity of the solute in the solution, ρ is the density, and δ is the thickness of the solutal boundary layer. The quotient δ/D_v is called the diffusional resistivity of mass transport.

In a situation of natural thermal convection under low Rayleigh number (low thermal gradients) and also in growth experiments with forced convection but with low Reynolds number (low rotational velocity of the substrate), the boundary thickness is given by

$$\delta \propto D_v^{1/3} \nu^{1/6} \omega^{-1/2}, \quad (21.4)$$

where ν is the kinematic viscosity and ω is the revolution rate of the substrate.

3. *Heterogeneous nucleation and surface attachment.* The capture of the atoms onto the surface of the

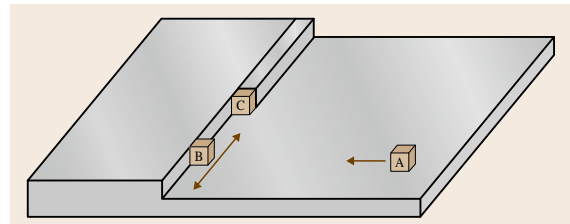


Fig. 21.8 Heterogeneous nucleation and surface attachment process on the substrate surface

- substrate takes place in a number of successive steps:
- a) The nucleation, or the formation of stable clusters of atoms on the surface of the substrate at sites such as A (Fig. 21.8)
 - b) The migration of atoms on the surface to the growth step by surface diffusion and their adsorption at sites such as B
 - c) Migration of the adsorbed atoms in B positions to energetically favorable sites such as C

- d) Removing the released heat from the global reaction and transport of the solvent from the lost solute–solvent solvation

The contributions of all surface processes on the kinetics of the crystal growth process can be evaluated by adding a new resistivity $1/\kappa$ to the crystal growth rate formula

$$R = \frac{1}{\rho} \left(\frac{1}{\kappa} + \frac{\delta}{D_v} \right)^{-1} (X_{E'} - X_0). \tag{21.5}$$

21.3 Growth of Bulk Laser and NLO Single Crystals by the TSSG Method

A favourable viscosity of the growth solution can be defined in the range 1–100 cP, while the maximum practical viscosity that allows development of a crystal growth process would be about 10 P. An ideal solvent was defined by *Elwell* and *Scheel* [21.29] as a solvent with a viscosity in the range 1–10 cP. However, it is not trivial to find compounds that can be used as solvents in high-temperature solutions with such viscosities. In this chapter we define low-viscosity solutions as those with viscosity below 40–50 cP, typical of fluorides, vanadates, and tungstates. Solutions containing phosphates and borates present a much higher viscosity, with values that can reach up to 10 P. Crystal growth using high-temperature solutions with low or high viscosities present different difficulties that we will try to summarize here, together with the strategies proposed to overcome these problems.

21.3.1 Crystal Growth from Low-Viscosity Solutions: Fluorides, Tungstates, and Vanadates

Double Tungstates MREW
(M = Na, K, Rb; RE = Y and Lanthanides)

The crystallization temperature of the required phase, the presence of other phases crystallizing at higher temperature, the nature of possible polymorphic phase transformations, and the melting character of the compound are the factors that determine the most suitable growth method to obtain single crystals of a particular MRE(WO₄)₂ compound. The Czochralski method is the most used method to obtain double tungstate compounds that melt congruently and do not show polymorphic transformations, such as Na-based double tungstates compounds with RE ions with large

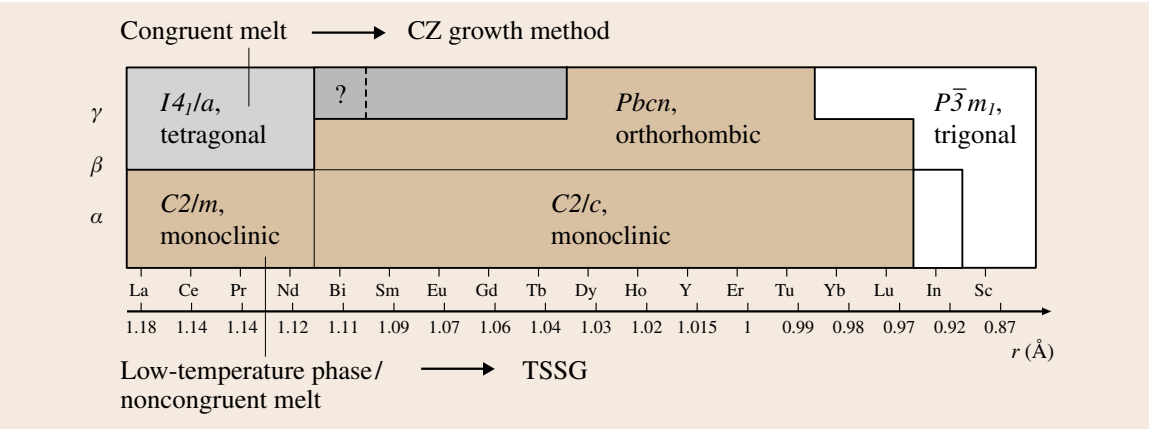


Fig. 21.9 Polymorphism of KREW compounds at room temperature, and recommended methods to grow the different crystal of this family of materials

Table 21.3 Concentration of precursor oxides to form a growth solution of KGdW using $K_2W_2O_7$ as a solvent, with a composition 85 mol % solvent–15 mol % solute

Molar ratio of oxides in the composition of growth: 30.85% K_2O – 2.5% Gd_2O_3 – 66.67% WO_3
Molar ratio of oxides in the solvent: 33.3% K_2O – 66.67% WO_3
Molar ratio of oxides in the solute: 16.6% K_2O – 16.6% Gd_2O_3 – 66.67% WO_3
Solvent: $(K_2O + 2WO_3) \times 0.85$
Solute: $(0.5K_2O + 0.5Gd_2O_3 + 2WO_3) \times 0.15$
Total: $0.925K_2O + 0.075Gd_2O_3 + 2WO_3 = 30.85\% K_2O - 2.5\% Gd_2O_3 - 66.67\% WO_3$

ionic radii, such as $NaGd(WO_4)_2$. However, melting is not congruent when the ionic radius of the lanthanide decreases [21.31]. On the other hand, KREW monoclinic single crystals are usually grown by the TSSG slow-cooling (SC) method, as they present a phase transformation at a lower temperature than the congruent melting temperature. Figure 21.9 summarizes the polymorphism of KREW compounds together with the recommended methods that can be used to grow these crystals.

The appropriate solvent for growing KREW crystals has been chosen among the stable compounds of the K_2O – WO_3 binary system [21.32,33] to avoid introduction of foreign ions in the solution that can contaminate the crystals. The most used solvents are K_2WO_4 and $K_2W_2O_7$. $K_2W_2O_7$ has a lower melting point when compared with the other stable compounds in the K_2O – WO_3 system, and due to a higher tungsten content, it exhibits a low viscosity during the growth process. K_2WO_4 was used as well [21.34], as a solvent for the growth of KREW, but it did not yield good homogenization of the solution and was more prone to evaporation. The solubility curves of the monoclinic KREW (RE = Gd, Y, and Lu) in $K_2W_2O_7$ are shown in Fig. 21.2b.

The limits of the solubility curve are given by the properties of this binary system. At around 45 mol % solute, the phase that crystallizes first when decreasing the temperature does not belong to the monoclinic system [21.35]. The lower limit at around 5 mol % solute is related to the economical profitability of the growth procedure. Although the monoclinic phase of KREW can be grown in the range 5–42 mol % solute, it is better to use a solution with < 15 mol % solute, where small variations of the temperature lead to small changes in supersaturation. The growth temperatures when using these solutions are around 1090–1230 K and guarantee a low economical cost for the growth procedure.

The thermal gradients in the solutions are usually low, in the range of 1.5 and 11.5 K/cm for axial and radial gradients, respectively, with the bottom and the

crucible wall as the hottest spots. Growth of double tungstates is very sensitive to thermal gradients [21.36, 37]. Large thermal gradients may crack the growing crystal due to the high anisotropy of the linear thermal expansion coefficients of monoclinic double tungstates. The solution was prepared by melting the mixed oxide precursors, weighed in stoichiometric ratio. Table 21.3 shows the molar ratio of the precursor oxides for the growth of $K_2W_2O_7$ /KGdW with composition 85 mol % solvent–15 mol % solute.

The solution was homogenized by keeping it at ≈ 50 K above the saturation temperature for several hours (up to 24 h in some cases). Then, the saturation temperature was determined by observing the growth/dissolution of an oriented prism crystal of KREW acting as a seed in contact with the surface of the solution.

For KGdW the saturation temperature was in the range 1173–1203 K, for KYbW it was in the range 1170–1195 K, and for KLuW it was in the range 1146–1162 K. The fact that to reach the same solubility value we have to increase the temperature in the sequence $T(\text{sol})_{KGdW} < T(\text{sol})_{KYbW} < T(\text{sol})_{KLuW}$, as observed in Fig. 21.2b, is translated to a lower temperature of crystal growth when decreasing the ionic radius of the lanthanide ion $T_{S,KGdW} > T_{S,KYbW} > T_{S,KLuW}$ for a fixed solute-to-solvent ratio.

Growth experiments could be made using the same growth conditions but not the same crystal seed orientation. Crystal seeds were cut with a parallelepipedal shape and oriented along the *b*-, *c*-, and *a**-directions. The use of *b*-oriented seeds allows us to apply a slightly faster cooling rate and consequently to obtain a higher growth rate than when using crystal seeds oriented along other orientations [21.7,38], still obtaining defect-free single crystals. Seeding along $\bar{1}11$ direction has also been reported [21.39]. The seed was rotated at a broad range of rotation velocities from 4.5 to 90 rpm. Once the saturation temperature was determined, the crystal seed was placed in contact with the surface of the solution and slow cooling was applied to cre-

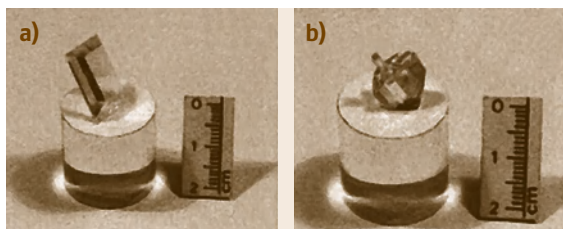


Fig. 21.10a,b Monoclinic undoped $\text{KGd}(\text{WO}_4)_2$. (a) Crystal grown on a b -oriented seed. (b) Crystal grown on a c -oriented seed

ate supersaturation. The temperature of the solution was usually decreased for $\approx 10\text{ K}$ at a cooling rate of $0.03\text{--}0.05\text{ K/h}$. After that, the crystals were removed slowly from the solution and cooled to room temperature at 15 K/h to avoid thermal shocks. The results obtained clearly showed that the crystal quality depended strongly on the cooling rate. The slower the applied cooling rate, the better the quality of the crystals.

In the growth of KHoW single crystals, *Borowiec et al.* [21.40] used programmed changes of the cooling rate to grow crystals with larger dimensions.

Pulling at rates of $2\text{--}5\text{ mm/day}$ has also been used to grow these crystals [21.40, 41]. In this way, crystals grow as cylinders bounded by $\{110\}$ and $\{011\}$ prisms and by $\{100\}$, $\{010\}$, and $\{001\}$ pinacoids [21.40].

Figure 21.10 shows some examples of KREW crystals grown by the TSSG method.

As the main application of these crystals is to be used as hosts for other active laser lanthanides ions,

it is worth mentioning the effects of lanthanide doping on the growth procedure. First, it is important to highlight the feasibility of growing highly doped lanthanide monoclinic tungstates, up to 100% stoichiometric KREW, with RE as the active ion, such as KerW and KYbW [21.42]. The difference of ionic radii between the RE constituting element of the KREW host and the doping Ln^{3+} cation governs the difficulty of the crystal growth process and the attainable limit of substitution. For example, when growing praseodymium-doped KGdW crystals, it was necessary to reduce the cooling rate to 0.02 K/h to obtain high-quality single crystals. The degree of substitution can be evaluated by the distribution coefficient $K_{\text{Ln}^{3+}}$, which provides the ratio between the lanthanide concentration in solution and the lanthanide concentration in the crystal. This measures how easy it is to dope the crystal with a particular ion. The distribution coefficient can be calculated by the following expression

$$K_{\text{Ln}^{3+}} = \frac{\{[\text{Ln}^{3+}]/([\text{Ln}^{3+}] + [\text{RE}^{3+}])\}_{\text{crystal}}}{\{[\text{Ln}^{3+}]/([\text{Ln}^{3+}] + [\text{RE}^{3+}])\}_{\text{solution}}} \quad (21.6)$$

Distribution coefficients close to 1 favor homogeneity of doping element inside the crystal. Figure 21.11 shows the distribution coefficient for lanthanide doping in KGdW . Figure 21.11a shows the dependence of the distribution coefficient on the ionic radii of the lanthanide doping ion: the larger the ion, the more difficult it is for it to enter the structure. Figure 21.11b shows that, the smaller the ionic radii difference between the rare-earth host and the lanthanide ion, the larger the distribution coefficient.

Fluorides

LiYF_4 (YLF) has been grown by the TSSG method [21.43] based on the phase diagram of the binary system $\text{LiF}\text{--}\text{YF}_3$, which presents a peritectic point at 49 mol % YF_3 and 1090 K, and a eutectic point at 19 mol % YF_3 and 970 K. Crystals were grown by pulling in a melt containing YF_3 and a slight excess of LiF over the stoichiometric amount in a purified helium atmosphere.

KYF_4 (KYF) and KLiYF_5 (KLYF) have also been grown by the TSSG method [21.44]. Crystals were grown by slow cooling of b -oriented crystal seeds, controlling their dimensions by pulling of the crystal from the solution and using weight control feedback. However, the existence of cleavage planes perpendicular to the b -axis limits growth to some extent.

Other fluorides such as LiCaAlF_6 and LiSrAlF_6 can also be grown by TSSG using inert or reactive gas atmospheres to avoid traces of H_2O and O_2 that can degrade

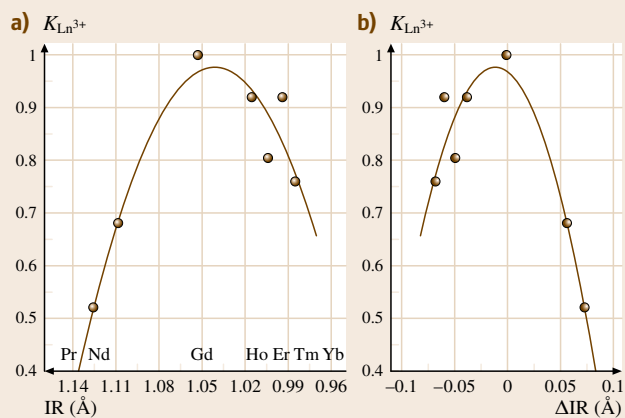


Fig. 21.11a,b Lanthanide doping distribution coefficient in KGdW crystal with RE = Gd, Y, Yb, and Lu. (a) Ionic radii (IR). (b) Difference between RE host and lanthanide ion

their optical quality. Wet chemical methods, ammonium salt methods, or hot hydrofluorination processes have to be used to obtain the high-purity halides to be used in these growth processes, as they are not commercially available [21.45]. The control of the diameter by a weight-sensing feedback system, and pulling of the growing crystal from the solution, have been used to grow these crystals.

Vanadates

REVO₄ single crystals are usually grown by the Czochralski method, but these compounds melt congruently at very high temperatures [21.46]. So, the TSSG method has also been reported as a suitable technique to grow these crystals. This technique allows one to avoid the formation of nonpentavalent vanadium oxides. Various fluxes have been used to grow these crystals: NaVO₃ [21.47], V₂O₅ [21.48], Pb₂V₂O₇ [21.4, 47], PbO + PbF₂ [21.49], and LiVO₃ [21.5]. However, PbO + PbF₂ is not very appropriate because of its toxicity, and Pb₂V₂O₇ has a high viscosity and a low solubility for these solutes. Large axial thermal gradients in the growth solution were used to grow crystals with this solvent on *c*-oriented crystal seeds rotated at 100 rpm [21.50]. LiVO₃ has a suitable solubility for YVO₄, low viscosity, low evaporation in the working temperature range, and no toxicity [21.51]. LiVO₃ is a very hygroscopic soluble in water, which facilitates crystal and crucible cleaning after the growth procedure. Crystals were grown by slow cooling of the solution. Rotation and pulling of nonoriented YVO₄ seeds have been used.

21.3.2 Crystal Growth from High-Viscosity Solutions: Phosphates and Borates

Crystal growth in highly viscous solutions is very difficult because the high viscosity limits the hydrodynamics and mass transport in the melted solution. It also creates a thick growth boundary layer and makes both heat extraction and impurity expulsion difficult. All these factors interfere with the growth process, resulting in many crystal macrodefects, such as inclusions. This, coupled with the tendency of the melt to supercool, makes this type of growth especially challenging.

Phosphates

KTP was first synthesized in 1890 by Ouyard, and was crystallized in a polycrystalline form from a flux by Masse and Grenier [21.52]. KTP melts incongruently at 1172 °C when heated in air [21.24, 53], and

therefore it cannot be grown directly from its melt. Various solvents have been used to grow KTP crystals from high-temperature solutions. Table 21.4 summarizes the chemical reactions used to synthesize KTP and its solvents. The crystallization region of KTP in the K₂O–P₂O₅–TiO₂ system was first studied by Voronkova and Yanovskii [21.54], and later in detail by Iliev et al. [21.55]. The solubility of KTP in this system has been shown to increase as the concentration of the anion (P₂O₇)^{4–} increases [21.56–58]. The viscosity of these solutions range from 50 to 80 cP, increasing as the TiO₂ content increases, due to the formation of [Ti(PO₄)₃]^{5–} complexes that polymerize upon addition of TiO₂ [21.55, 59].

KTP single crystals on crystal seeds were first grown from the phosphate system and patented by Gier [21.60]. Alexandrovskii et al. [21.61] used fused KPO₃ with excess K₂O for the same purpose. Loiacono et al. [21.58] reported that crystals of KTP grown in K₄P₂O₇ solvent resulted in a platy morphology. The growth process has been developed with slow cooling of the saturated solutions [21.54], and with gradient transport at constant ΔT [21.56]. However, the viscosity of phosphate solutions increases to unacceptable levels when decreasing the temperature. This leads to supersaturation gradients in the solution and results in spurious nucleation and solvent inclusion in the crystals. These inclusions can be a source of strain that cracks the crystals on cooling to room temperature. By imposing motion of the growing crystal, inclusion-free single crystals can be obtained, as this rotation improves the mass transport in the solution [21.62, 63]. Crystals can be rotated about the center of the surface of the solution or eccentrically, although the latter method does not use the crucible space as efficiently as the former one [21.57, 64]. The accelerated crucible rotation technique, by which the accelerating motion of the solution relative to the growing crystal surface prevents the adverse effects of constitutional supercooling, has also been used to improve the mass transport in the solution [21.56]. Strictly controlled cooling rates and a specially designed monitoring of crystal weight changes were employed to crystallize the largest KTP inclusion-free crystal reported [21.64]. Figure 21.12 shows some single crystals of the KTP family obtained by the TSSG method.

Dhanaraj et al. [21.65, 66] realized that using cooling rates that are too fast (1 K/h) in these viscous solutions resulted in coarse dendritic structures on the crystal surfaces and flux inclusion in the bulk of the crystal, due to a rapid increase in supersaturation, es-

Table 21.4 Chemical reaction of formation of **KTP** and several fluxes used for its growth from **TSSG** method

Formation of KTP
$\text{KH}_2\text{PO}_4 + \text{TiO}_2 \rightarrow \text{KTiOPO}_4 + \text{H}_2\text{O}$
$\text{K}_2\text{CO}_3 + 2\text{TiO}_2 + \text{P}_2\text{O}_5 \rightarrow 2\text{KTiOPO}_4 + \text{CO}_2$
$\text{K}_2\text{CO}_3 + 2\text{TiO}_2 + 2\text{NH}_4\text{H}_2\text{PO}_4 \rightarrow 2\text{KTiOPO}_4 + \text{CO}_2 + 2\text{NH}_3 + 3\text{H}_2\text{O}$
$\text{K}_2\text{TiO}(\text{C}_2\text{O}_4)_2 \cdot 2\text{H}_2\text{O} + \text{KH}_2\text{PO}_4 \rightarrow \text{KTiOPO}_4 + \text{H}_2\text{C}_2\text{O}_4 + \text{K}_2\text{C}_2\text{O}_4 + 2\text{H}_2\text{O}$
Formation of phosphate solvents
$3\text{K}_2\text{CO}_3 + 3\text{P}_2\text{O}_5 \rightarrow 2\text{K}_3\text{P}_3\text{O}_9 + 3\text{CO}_2$
$2\text{K}_2\text{HPO}_4 \rightarrow \text{K}_4\text{P}_2\text{O}_7 + \text{H}_2\text{O}$
$2\text{K}_2\text{CO}_3 + \text{P}_2\text{O}_5 \rightarrow \text{K}_4\text{P}_2\text{O}_7 + 2\text{CO}_2$
$\text{KH}_2\text{PO}_4 + 2\text{K}_2\text{HPO}_4 \rightarrow \text{K}_5\text{P}_3\text{O}_{10} + 2\text{H}_2\text{O}$
$3\text{K}_4\text{P}_2\text{O}_7 + \text{K}_3\text{P}_3\text{O}_9 \rightarrow 3\text{K}_5\text{P}_3\text{O}_{10}$
$2\text{K}_2\text{HPO}_4 + 2\text{KH}_2\text{PO}_4 \rightarrow \text{K}_6\text{P}_4\text{O}_{13} + 3\text{H}_2\text{O}$
$2\text{KH}_2\text{PO}_4 + 2\text{K}_2\text{HPO}_4 \rightarrow \text{K}_6\text{P}_4\text{O}_{13}$ (or $2\text{KPO}_3 \cdot \text{K}_4\text{P}_2\text{O}_7$) $+ 3\text{H}_2\text{O}$
$4\text{KH}_2\text{PO}_4 + \text{K}_2\text{CO}_3 \rightarrow \text{K}_6\text{P}_4\text{O}_{13} + 4\text{H}_2\text{O} + \text{CO}_2$
$3\text{K}_4\text{P}_2\text{O}_7 + 2\text{K}_3\text{P}_3\text{O}_9 \rightarrow 3\text{K}_6\text{P}_4\text{O}_{13}$
$4\text{KH}_2\text{PO}_4 + 2\text{K}_2\text{HPO}_4 \rightarrow \text{K}_8\text{P}_6\text{O}_{19} + 5\text{H}_2\text{O}$
$11\text{KH}_2\text{PO}_4 + 2\text{K}_2\text{HPO}_4 \rightarrow \text{K}_{15}\text{P}_{13}\text{O}_{40} + 12\text{H}_2\text{O}$
Formation of tungstate solvents
$6\text{K}_2\text{HPO}_4 + 6\text{WO}_3 \rightarrow 6\text{K}_2\text{WO}_4 + 3\text{P}_2\text{O}_5 + 3\text{H}_2\text{O}$
Formation of other solvent
$\text{NaF} + \text{KH}_2\text{PO}_4 \rightarrow \text{KNaPO}_3\text{F} + \text{H}_2\text{O}$
$5\text{KH}_2\text{PO}_4 + 2\text{BaCO}_3 \rightarrow \text{KBa}_2(\text{PO}_3)_5 \cdot 2\text{K}_2\text{O} + 2\text{CO}_2 + 5\text{H}_2\text{O}$

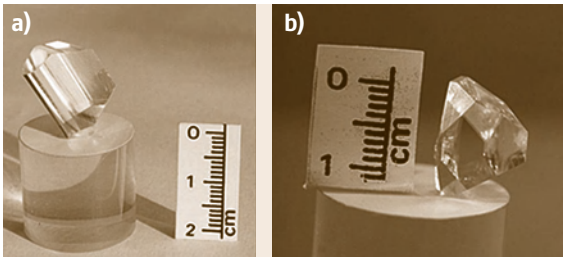


Fig. 21.12a,b Single crystal of **(a)** KTiOPO_4 and **(b)** RbTiOPO_4 obtained by the **TSSG** method in phosphate and tungstate fluxes

pecially during the final stages of growth. When growth is performed on *c*- and *b*-oriented seeds, since the {001} and {010} faces are fast-growing faces which do not occur on **KTP** naturally, a capping process takes place at the initial stages of growth, until the {201} and {011} faces, or the {110} and {011} faces, have appeared, respectively [21.67]. Crystals grown on [100]-oriented seeds showed inclusions parallel to {011} faces, although this seeding may yield large single-sector **KTP** crystals [21.68]. [201]-Oriented seeding produced a tilt

of the growing crystal to respect the rotation axis that improves the hydrodynamics of the solution, helping in melt mixing and allowing optimal utilization of the available melt volume by placing the long *c*-direction of the crystal along the body diagonal of the crucible [21.69]. **KTP** crystals have also been grown from phosphate fluxes by the **TSSG** method with pulling [21.67, 70] to avoid their multifaceted shape that leads to inefficient cutting of optical elements from **KTP** crystals [21.67]. As crystal growth proceeds on natural faces, they show relatively low dislocation densities, allowing one to obtain single crystals without inclusions or growth striations [21.70].

Carvajal et al. [21.71] developed a crystal growth system comprising a Pt stirrer immersed in the growth solution and two crystal seeds in contact with the solution surface, symmetrically distributed at about 1.5 cm from the rotation axis and 2 cm up the platinum turbine, as can be seen in Fig. 21.13. This system improved the mass transport conditions in the solution, thus minimizing problems associated with nonhomogeneous supersaturation in these viscous solutions. Stirring the solution decreases the frequency of spontaneous nucle-

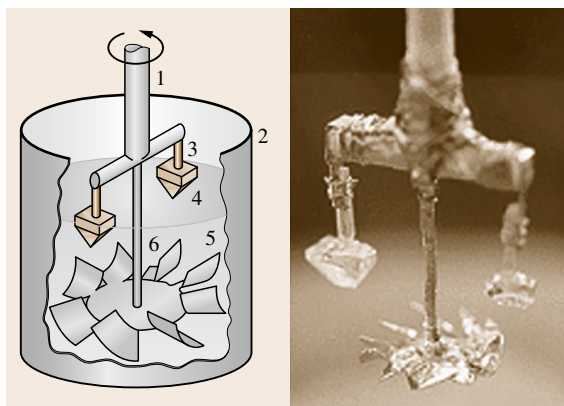


Fig. 21.13 Schematic and picture of the crystal growth system used in TSSG experiments to grow RbTiOPO_4 crystal and isostructurals that included a Pt turbine rotating together with the crystal seeds: (1) alumina rod, (2) platinum crucible, (3) crystal seeds, (4) growing crystals, (5) solution, and (6) platinum turbine

ation during the growth process and yields a higher quantity of high-quality inclusion-free single crystals of the KTP family.

Other KTP isostructurals, such as RbTiOPO_4 (RTP), which shows almost the same NLO properties of KTP , have been grown from these phosphate solutions. Oseledchik et al. [21.72] determined the crystallization region of RTP in the phosphate system and obtained crystals containing some inclusions, indicating the presence of unstable temperature control, high cooling rates, unsatisfactory temperature profile, and unsatisfactory dynamics of the melt flowing around the crystal.

An alternative to the improvement of the mass transport is the reduction of the viscosity of the solution by adding a modifier. Ballman et al. [21.73] proposed the low-viscosity, very fluid, non-glass-forming, water-soluble tungstate melts as a solvent, which greatly improves circulation and mixing during the crystallization process and results in a higher yield of inclusion-free material. Iliev et al. determined the phase diagram of KTP in the $\text{K}_2\text{O}-\text{P}_2\text{O}_5-\text{TiO}_2-\text{WO}_3$ system, as well as the viscosity of these solutions [21.74]. An increase in concentration of WO_3 results in a decrease of the solubility of KTP ; however, the shallower slope of the solubility curves indicates a low degree of supersaturation for a given temperature drop and allows for a more controllable growth process. The addition of lithium to these solutions further enhances the fluidity of the melt and helps in the crystal growth process [21.69]. However, the use of tungstate fluxes leads

to incorporation of tungsten ions in KTP crystals and reduces their optical transparency [21.75]. Striations and growth sectors were observed for all the existing faces on the crystals, which was attributed to changes in tungsten concentration in the crystal caused by variations in growth rates, temperature fluctuations in the furnace, or convective motion of the solution in the crucible [21.75, 76]. Carvajal et al. [21.71] determined the variation of the crystallization region of RTP when introducing WO_3 in the solution. The crystallization regions became narrower, and were displaced towards Rb_2O -rich regions when the concentration of WO_3 increased, as can be seen in Fig. 21.14. In these solutions the time of homogenization was shorter, the interval cooling of temperatures could be wider, and the cooling process to obtain high-quality crystals could be made faster than in phosphate fluxes.

Marnier proposed the use of alkaline halide (KF, KCl, and KBr) fluxes as an alternative to tungstate fluxes [21.77]. Alkaline halides also reduce the viscosity of the solution and enable a satisfactory growth rate at low temperature while enhancing the solubility of KTP and isostructurals. Sulfate-containing fluxes also reduce the viscosity of the solution due to the presence of SO_4^{2-} ions in the flux that breaks the titanate chains of the flux. However, a certain amount of incorporation of sulfur into the crystals takes place [21.67]. More recently, Suma et al. [21.78, 79] carried out rapid growth of KTP single crystals by using $\text{KBa}_2(\text{PO}_3) \cdot 2\text{K}_2\text{O}$ and KNaPO_3F as fluxes. The steepness of the solubility

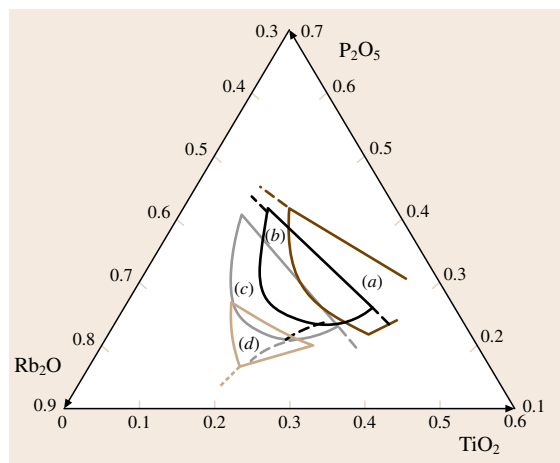


Fig. 21.14 Crystallization region of RbTiOPO_4 in the system $\text{Rb}_2\text{O}-\text{P}_2\text{O}_5-\text{TiO}_2-\text{WO}_3$ for (a) 0 mol % WO_3 (b) 10 mol % WO_3 (c) 20 mol % WO_3 , and (d) 30 mol % WO_3 in solution

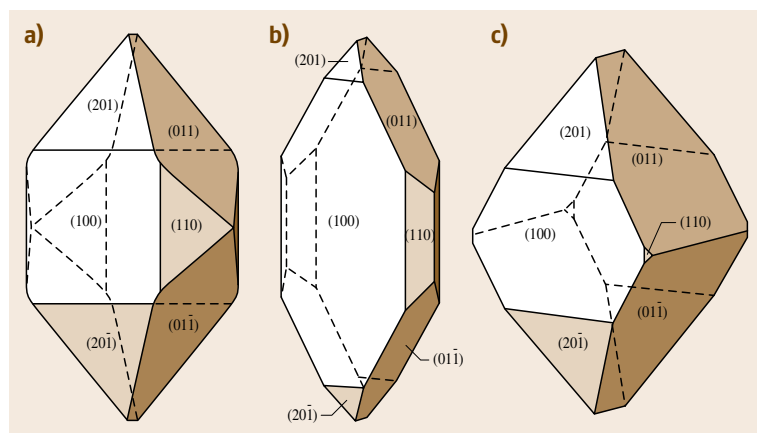


Fig. 21.15a–c Morphology of (a) RTP crystal, (b) RTP crystal doped with Nb grown on a thin crystal seed in the *a*-direction, and (c) RTP crystal doped with Nb grown on a thin crystal seed in the *a*-direction. The morphology of these crystals improved, where the {110} form tends to disappear, and the {011} and the {01 $\bar{1}$ } forms become larger, which provide a larger useful area of crystal in the *a*–*b* plane with benefits for applications in SHG

curve of KTP in these systems enables rapid cooling of the solution and fast growth of KTP.

In the last decade, much effort has been devoted to doping of KTP and isostructurals with various ions to change some of their physical properties, such as the crystal's optical transmission [21.80, 81], Curie temperature [21.82], ionic conductivity [21.83, 84], refractive indexes [21.85], and NLO properties [21.86, 87]. For this purpose, Nb is one of the most used ions with which KTP and isostructural crystals have been doped. However, this ion increases the difficulty of crystal growth: the growth solution is more viscous, the homogenization time increases, the saturation temperature increases, the solution is more prone to spurious nucleation, the efficiency of the crystal growth process decreases, crystals tend to crack, and they show more solution inclusions. Furthermore, these tendencies increase with increasing Nb concentration in the crystal. The crystal morphology is flat, long, and narrow, and especially small in size in the *a*-axis direction, suggesting that crystals may grow by a two-dimensional nucleation mechanism. When crystals were grown on *a*-oriented seeds, they showed poor transparency with many inclusions and twin-crystal flaws along the (100)-plane. In spite of this, this seeding orientation has a good effect on controlling spurious nucleation. When crystals were grown on *c*-oriented crystal seeds, they had a larger transparent area and fewer inclusions with no twin-crystal flaws. If the crystal seed was rotated, reversing the rotation direction periodically during the growth process, crystals showed even larger transparent areas. Using crystal seeds with the same composition as the crystal to be grown further reduced the number of cracks observed in the crystals [21.88]. By forcing crystal growth in the *a*-direction using crystal seeds with

a larger dimension in this direction than in any other crystallographic direction, crystals with typical dimensions of $5 \times 5 \times 5 \text{ mm}^3$ in the three crystallographic directions could be obtained [21.87]. Figure 21.15 summarizes these changes in morphology caused by Nb in RTP crystals.

$\text{KNd}(\text{PO}_3)_4$ (KNP) and $\text{KGd}(\text{PO}_3)_4$ (KGdP) single crystals have been grown by the TSSG technique [21.89, 90]. The crystallization regions of KNP, KGdP, and the intermediate $\text{KGd}_{0.5}\text{Nd}_{0.5}(\text{PO}_3)_4$ compound in the system $\text{Ln}_2\text{O}_3\text{--K}_2\text{O--P}_2\text{O}_5$ (where $\text{Ln} = \text{Nd}$ or Gd) have been studied [21.89–91]. Figure 21.2a shows a comparison of these crystallization regions. Although the viscosity of the solution is very high throughout the crystallization region, when the $\text{Ln}_2\text{O}_3/\text{K}_2\text{O}$ molar ratio ($\text{Ln} = \text{Nd}$ or Gd) is above $\frac{3}{97}$, it is so high that it hinders crystallization.

TSSG experiments were carried out with axial temperature gradients in the solution of 0.75–0.92 K/mm for KNP, and 1.2 K/mm for KGdP. Crystals were grown with constant rotation at 75 rpm using KNP or KGdP parallelepipedal oriented seeds located at the center of the solution surface, by slow cooling at 0.1 K/h for an interval of 15–20 K. To improve the mass transport in the solution, a platinum turbine similar to that described for KTP and isostructural crystals was used, resulting in better quality crystals. Seeding along the *a**-direction in the crystallographic reciprocal space and the *c**-crystallographic direction in the reciprocal space was suitable for growing KNP and KGdP single crystals. Seeding along the *b*-direction in the direct space was unsuitable because crystals tended to crack perpendicularly to this direction when they were too heavy. When solutions contained 65 mol % P_2O_5 or higher, small crystals with poor quality were obtained,

due to the high viscosity of the solution. KGdP:Nd crystals showed some inclusions, especially when the Nd content increased, which could be avoided when the cooling rate was decreased to 0.05 K/h.

Borates

LBO has been known since 1926; in 1958 the Li_2O – B_2O_3 phase diagram was studied [21.93], and in 1978 small **LBO** single crystals were grown. **LBO** is a peritectic compound that cannot be grown by congruent melting and solidification. It can be synthesized by the peritectic reaction, a process that is too slow and difficult to carry to completion. Thus, the sole method of obtaining **LBO** single crystals is the flux growth method [21.94]. However, fluxed melt systems for growing **LBO** make controlling the temperature gradients difficult, as the main heat transport occurs by means of radiation energy. This leads to the appearance of growth defects, such as inclusions, inhomogeneous distribution of uncontrolled impurities, and nonstoichiometry of composition [21.95].

LBO crystals have been grown in different solution compositions of the Li_2O – B_2O_3 system. Solutions containing B_2O_3 are, in general, too viscous. In this system, the most suitable region of **LBO** concentrations to grow **LBO** crystals is 72–82 wt % **LBO** as the viscosity has a relatively low value and changes slightly with concentration. If the concentration is lower than 72 wt %, the mass transport is rather difficult because of the high viscosity. At concentrations higher than 82 wt %, the initial values of the supersaturation are high and drive the crystallization process too fast and hard for operating [21.96]. Additionally, the steep temperature versus composition slope places tight constraints on the seeding temperature: too high a temperature resulted in melting the seed, whereas too low a temperature resulted in polycrystal forming. The melt also showed a strong tendency to supercool. Furthermore, as **LBO** is sensitive to thermal shocking it has to be cooled after growth at very low cooling rates (≈ 3 K/h) [21.97]. Use of small thermal gradients in the furnace favors the growth of good-quality crystals [21.94]. Properly thermally insulating the upper part of the growth chamber, reducing temperature gradients above the melt during growth, and lowering the melt from the crystal when growth was terminated instead of lifting the crystal away from the melt helped to reduce cracking in the crystals. This leaves the crystal in the heated position of the chamber, allowing better control of cooling and resulting in smaller thermal gradients in the crystal. However, growth in solution with insufficiently high

thermal gradients resulted in the appearance of large inclusions of fluxed melt and oxygen nonstoichiometry in the crystals. This is due to the presence of concentrations of inhomogeneities in the fluxed melt, which cannot be readily removed via the usual diffusion process during the period of their movement across the surface of the growing crystal because of the high viscosity of the fluxed melt. As the axial and radial thermal gradients increase near the crystallization front, the fluxed melts become more homogeneous and the quality of **LBO** crystals improves.

The surfaces of **LBO** crystals gradually decompose due to moisture present in the ambient atmosphere, forming a millimeter-thick, optically opaque, white, polycrystalline skin, replicating the original surface of the growing crystal. Upon cooling, severe cracking occurs on the crystal surfaces adjacent to this layer. The formation of this layer, and the subsequent cracking, can be avoided by growing crystals under dry nitrogen atmospheres [21.98].

Increasing rotation rates and the use of accelerated crucible rotation yields larger crystals due to the enhancement of forced convection. Seeding in the direction normal to widely developed faces is thought to enlarge the diameter of the crystal, as happens in **LBO** when using a seed normal to the (011) face compared with seeding in the [001] direction, while the thickness and the quality of crystal were almost the same, keeping the remaining growth conditions constant. In general, the forced convection in the solution caused by rotation is affected by the ratio of the crystal to crucible diameters. As the diameter of the growing crystal increases, the forced convection in the solution increases, which increases the crystal yield by increasing the mixing and the mass transfer in the solution. Figure 21.16 shows this effect in two **LBO** single crystals.

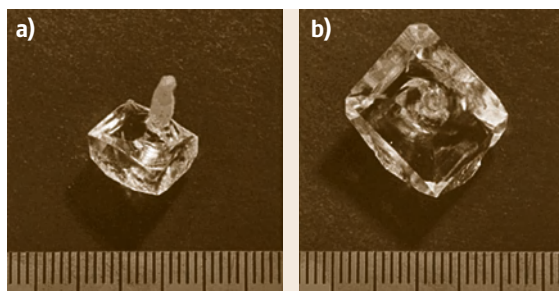


Fig. 21.16a,b **LBO** crystals grown by seeding in different directions while maintaining the rest of the conditions of growth [21.92]: (a) seeding along [001] and (b) seeding along [011]. Each scale is 1 mm

tals grown under the same conditions except for the seeding direction.

As the viscosity of the $\text{LBO-B}_2\text{O}_3$ system cannot be decreased by increasing the growth temperature because of the low decomposition temperature of LBO , it is very important to find new solvents which can reduce the viscosity while having sufficient solubility for LBO . B_2O_3 solutions form three-dimensional networks, mainly consisting of randomly oriented boroxol rings interconnected by B-O-B bridges, the structure of which may be altered by the addition of alkali oxides, reducing the viscosity of the solutions as a function of the O-to-B ratio. However, the phase region for the growth of LBO crystals is located near the maximum of the temperature-dependent viscosity curve, so the addition of small amounts of alkali oxides has little effect on the overall viscosity of the solution [21.99]. The addition of halide ions such as Cl^- and F^- can weaken the network in alkali borate melts. Cl^- anions do not take part in the boron-oxygen network, but lie in the space between the network as free ions. Therefore, the large size of the Cl^- anions and the electrical repulsion between the Cl^- ions and the $[\text{BO}_4]^{5-}$ ions is effective in reducing the viscosity of the melt. F^- ions terminate the network by forming B-F nonbridging bonds, thereby reducing the viscosity of the solution. In the $\text{Li}_2\text{B}_4\text{O}_7\text{-B}_2\text{O}_3\text{-NaCl}$ system, the viscosity of the solution and the seeding temperature were found to decrease as the amount of NaCl in the solution increased, while the metastable zone for crystallization of LBO became wider. This made it possible to increase the growth rate by up to 2–3 times for solutions containing 4 mol % NaCl with no obvious effect on crystal quality. The addition of MoO_3 also reduced the viscosity of the system. However, phases of enriched MoO_3 , which can be incorporated into the growing crystal, appear [21.100].

Although BBO melts congruently at 1369 K, the structural reordering that occurs during the phase transition at 1198 K causes cracking of grown crystals during cooling. Of all the growth techniques used to grow $\beta\text{-BBO}$, only in the TSSG method can large-sized crystals of $\beta\text{-BBO}$ be grown [21.101–105]. However, even when using this technique, the real success in growing $\beta\text{-BBO}$ came with the discovery of a suitable solvent for this material [21.106]. Up to now, B_2O_3 , BaF_2 , BaCl_2 , Li_2O , Na_2O and $\text{Na}_2\text{B}_4\text{O}_7$ [21.107], NaF [21.101], NaCl [21.108], $\text{Na}_2\text{O-NaF}$ [21.109], $\text{Na}_2\text{O-BO}_3$ [21.110], $\text{Na}_2\text{B}_2\text{O}_4$ [21.101], Na_2SO_4 , and CaF_2 [21.111] have been used as fluxes to grow $\beta\text{-BBO}$ crystals. Using B_2O_3 , Li_2O , $\text{Na}_2\text{B}_2\text{O}_4$, and $\text{Na}_2\text{B}_4\text{O}_7$ as fluxes limits the growth of $\beta\text{-BBO}$ crystals due to the

high viscosity of the solutions or narrow crystallizing range. Growth of $\beta\text{-BBO}$ using NaCl , Na_2SO_4 , BaCl_2 , BaF_2 , and CaF_2 as fluxes is difficult because of the high volatility of the solutions, and in some cases, because of the high-temperature hydrolysis that releases HCl vapor during growth. Na_2O is the flux which produced the best results, in terms of crystal size and defect density, when using the TSSG method with pulling to grow $\beta\text{-BBO}$ crystals [21.104].

In the $\text{BBO-Na}_2\text{O}$ pseudobinary diagram [21.101], there is a large temperature range from 1198 to 1028 K to grow $\beta\text{-BBO}$ crystals. Normally, after cooling the melts for 70–85 K, an onset of growth interface instability was observed, which could be readily detected since, before its occurrence, melt flow patterns could be clearly seen through the growing crystals, whereas after it happened, the melt convection was obscured. Above a certain diameter of the growing crystal, the free convection flow in the solution around the crystal in the direction from the crystal edge to its center is opposed by a counterflow of forced convection due to the rotation of the crystal. The interaction between these two flows below the crystal leads to a temperature instability, and hence to disturbance of the growth stability [21.110]. Moderate and steeper radial and axial temperature gradients have been used to grow $\beta\text{-BBO}$ crystals with this solvent. A suitable value for the vertical thermal gradient has been estimated to be $\approx 20\text{ K/cm}$. Nevertheless, large single crystal with optical quality could be grown 3–4 times faster in high thermal gradient furnaces, as it was possible to cool farther before encountering interface instabilities.

Pulling at a rate commensurate with the growth rate has also been applied to the growth of these crystals, which allows the growth of thicker crystals at higher growth rates in smaller crucibles, which prevents seed failure that occurs when crystals touch the crucible wall. However, during pulling, if a steep thermal gradient is used, the quality of the crystals grown will be poor, but if a moderate thermal gradient is used, it is difficult to control the diameter of the crystal. However, if the pulling method is not used, the crystals assumed a shallow lens shape typical of BBO crystals.

Normally, during the growth period, the seed was rotated. However, large rotation rates make the forced convection gradually overcome natural convection, eventually reversing the direction of radial fluid flow along the growth interface, resulting in lower supersaturation at the center of the growth interface and a change in the interface shape from convex to concave. As the highest-quality crystals are usually grown with a flat

or slightly convex interface, rotation rates have to be limited to avoid concave interfaces.

A major limitation of using *c*-axis oriented crystal seeds was the tendency toward interface breakdown after 15 mm of growth, and that crystals tended to show a higher defect density in the core region, corresponding to the center of the star-shaped convective flow pattern, where there is stagnation and little mixing due to crystal rotation. Boule cross sections were more elliptical, and faceting on the top surface of the boule was less pronounced, when using *a*- and *b*-oriented crystal seeds, growing in a nearly cylindrical shape when

pulled. However, crystals tended to fracture along the (0001) cleavage planes during cooling due to anisotropy in the thermal expansion.

Inclusions are generally linked to unstable growth conditions, and a standard method of improving the growth stability is by mechanical stirring of the solution. However, none of the conventional stirring techniques, including convective stirring, uniform crucible rotation, accelerated crucible rotation, and uniform boule rotations have produced any substantial change in the quality of β -BBO crystals. The change of the symmetry and the rotation of the thermal field that create inhomogeneous stationary and cyclically varying external thermal fields to control the convective heat and mass transfer, and the application of a vibrational temperature mode in the growth zone, has been proved to be very successful in the growth of β -BBO crystals. An appropriate commutation of the heating elements around the crucible creates a rotating thermal field that considerably intensifies the stirring both in the flux bulk and in the vicinity of the crystallization front, as can be seen in Fig. 21.17. Thus, the thickness of the diffuse layer at the crystallization front decreases and the concentration supercooling is delayed, making it possible to grow large β -BBO single crystals with circular cross section and high structural quality [21.112].

Another method used to improve the quality of the β -BBO crystals grown in BBO–Na₂O solution is continuous feeding during growth by adding pure BBO. This provides the possibility of isothermal growth at a suitable temperature. Gradual depletion of the solution during growth was constantly compensated by manual addition of pure BBO through an alumina tube that transferred the feed material to a small platinum crucible partially immersed in the melt whose bottom was punched, allowing for slow dissolution of the feed [21.103]. The main drawback of using this solvent is that β -BBO crystals contained up to 200 ppm of Na, which affects the optical transmission of the crystals, especially in the UV region [21.113].

Adding Nd₂O₃ to the BBO–Na₂O system with the aim of obtaining a new self-frequency-doubling material resulted in a strong stabilization effect of the β -BBO phase (Fig. 21.18). However, as the Nd₂O₃ concentration and the saturation temperature in the system become higher, the creeping of the solution along the crucible wall was stronger, which meant that relatively good β -BBO single crystals, doped with up to 2 mol % of Nd³⁺, were only obtained from solutions with low Nd₂O₃ concentration (12 mol %) [21.114].

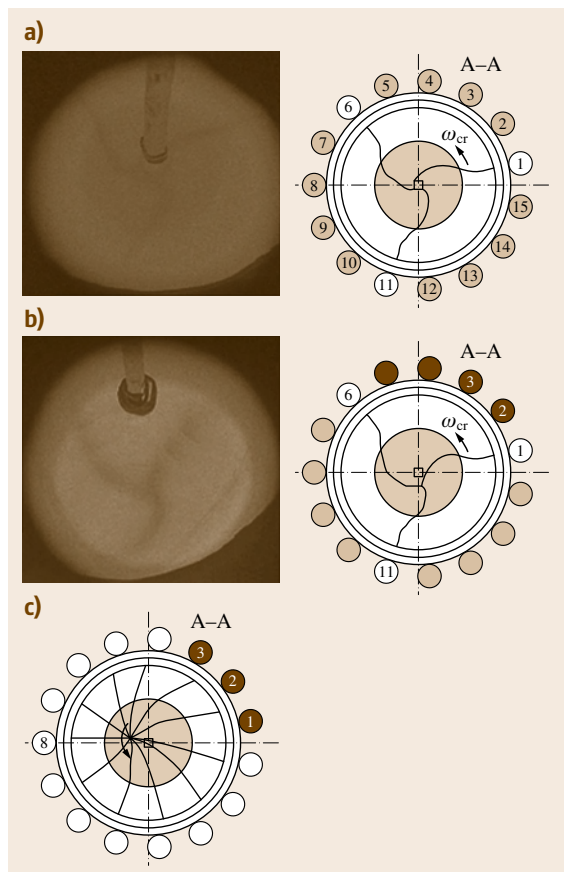


Fig. 21.17a–c Schematic of the setup for growing BBO crystal with the change of the symmetry and rotation of the thermal field and convective patterns observed on the free surface and through a growing BBO crystal [21.112]: (1–15) heating elements (dark color indicates switched-on elements, and white color indicates switches-off elements), (a) and (b) creation of thermal fields with a threefold and a quasi-threefold symmetry; (c) rotating thermal fields

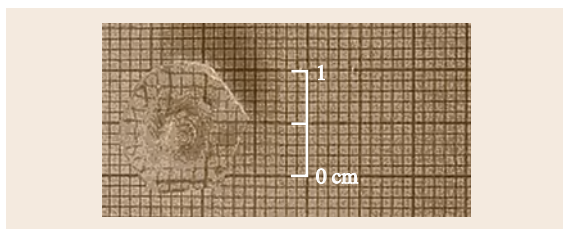


Fig. 21.18 Crystal of β -BaB₂O₄ growth in a solution of BBO–Na₂O

Roth and Perlov [21.104] determined the BBO–NaF pseudobinary diagram. Compared with the BBO–Na₂O system, in the BBO–NaF system the slope of the liquid curve is smoother and the maximal range of the BBO composition change wider, which allows higher yields of β -BBO crystals. The BBO–NaF pseudobinary phase diagram has a single eutectic point at a composition of 61 mol % NaF and a temperature of 1027 K. The solution viscosities are lower by about 15% on average over

the entire temperature range of interest when compared with BBO–Na₂O solutions. Although the volatility of BBO–NaF solutions is almost an order of magnitude higher than that of BBO–Na₂O, the average escape of 6 mg of solution per hour (mainly NaF) does not affect the crystal growth process considerably and can be corrected by adjusting the cooling rate during the growth process. A breakdown of the solid–liquid interface into a cellular structure also occurs at a certain stage of growth. However, the crystal yield before breakdown is larger than in the case of Na₂O-containing solutions. Crystals grown from NaF solutions had smaller diameters and larger thickness than those grown from Na₂O solution, which could be attributed to the low viscosity of the solution, which would make natural convection dominant over forced convection, and which resulted in vertical growth dominating radial growth [21.115]. Adding Na₂O to the BBO–NaF system reduces the volatility of the solutions to less than 1% during the entire growth process [21.107].

21.4 Liquid-Phase Epitaxy: Growth of Epitaxial Films of Laser and NLO Materials

The thin-disk laser approach was introduced by Giesen et al. in 1994 [21.116] to ameliorate the quality of the beam and the thermal loading using efficient longitudinal cooling; moreover the thermal lensing effect is also minimized, especially in the high-power regime [21.117]. The thickness of the active layer minimizes reabsorption phenomena in quasi-three-level systems such as ytterbium or 2 μ m thulium emissions. Some examples of thin-disk lasers have been realized [21.118, 119], including those which employ monoclinic KREW active layers [21.120, 121]. KREW materials are good hosts for thin-disk lasers due to the high absorption and emission cross sections of lanthanide-doped KREW. This has propelled, in recent years, the growth of single-crystalline thin films of these materials by LPE techniques.

Growth of thin films of NLO materials, specifically phosphate materials of the structural field of KTiOPO₄ (KTP), attracts attention as a means to fabricate optical waveguides. The confinement of light in a micrometer-sized waveguide and its propagation without appreciable diffraction greatly increases the optical fields, and the efficiencies of NLO processes [21.122]. Waveguides of KTP and related materials could be used to control or convert high-intensity optical beams

with input wavelengths extending from the visible to the infrared (IR) with thermal and mechanical stability [21.123].

21.4.1 Epitaxial Films of Laser Materials: Lanthanide-Doped KLuW on KLuW Substrates

For the thin-disk approach, as well as for waveguide lasers, homoepitaxial growth of lanthanide-doped KREW (RE = Y, Gd, Lu) by LPE has been recently reported for Yb:KYW films grown on KYW substrates [21.124, 125] and for Yb:KLuW films grown on KLuW substrates [21.126].

Successful growth of these epitaxial layers was demonstrated in a special vertical furnace with a wide zone of uniform temperature to achieve a zero temperature gradient in the solution. The most common solvent for this epitaxial growth is K₂W₂O₇ in a solution with a 5 mol % solute and 85 mol % solvent composition. Taking into account the solubility curves of KREW in K₂W₂O₇ (Fig. 21.2b), the average degree of supersaturation at 5 mol % solute is 0.16×10^{-2} g/K (g of solution). This low level of supersaturation allows the growth to occur near equilibrium. Also Yb:KYW

Table 21.5 Mismatch for $\text{Ln}^{3+}:\text{KLuW}/\text{KLuW}$ ($\text{Ln} = \text{Yb}$ and Tm) on different faces

Epitaxial layer	$f(010)$	$f(110)$	$f(310)$	$f(\bar{1}11)$
$\text{KLu}_{0.88}\text{Yb}_{0.12}\text{W}/\text{KLuW}$	−0.074	−0.081	−0.085	−0.089
$\text{KLu}_{0.78}\text{Yb}_{0.22}\text{W}/\text{KLuW}$	−0.107	−0.130	−0.142	−0.135
$\text{KLu}_{0.48}\text{Yb}_{0.52}\text{W}/\text{KLuW}$	−0.143	−0.220	−0.259	−0.211
KYbW/KLuW	−0.215	−0.354	−0.425	−0.324
$\text{KLu}_{0.97}\text{Tm}_{0.03}\text{W}/\text{KLuW}^*$	−0.069	−0.064	−0.062	−0.073
$\text{KLu}_{0.95}\text{Tm}_{0.05}\text{W}/\text{KLuW}^*$	−0.086	−0.087	−0.087	−0.090
$\text{KLu}_{0.925}\text{Tm}_{0.075}\text{W}/\text{KLuW}^*$	−0.085	−0.099	−0.106	−0.103
$\text{KLu}_{0.90}\text{Tm}_{0.10}\text{W}/\text{KLuW}^*$	−0.116	−0.136	−0.147	−0.140
$\text{KLu}_{0.80}\text{Tm}_{0.20}\text{W}/\text{KLuW}^*$	−0.198	−0.261	−0.293	−0.248

* The epitaxial layer stoichiometry is expressed by the initial solution composition (not corrected by distribution coefficient)

thin films on **KYW** substrates have been grown using a NaCl-KCl-CsCl solvent. Although this leads to precipitation of yttrium and tungsten oxides on the bottom of the crucible, this problem can be solved by following the methodology of *Kawaguchi et al.* [21.126] using **LPE** from a solid–liquid coexisting solution.

The step of homogenization of the flux is to increase the temperature 50 K above the expected saturation temperature for 24 h.

Before being placed in the furnace, the substrates must be carefully cleaned in $\text{HNO}_3 : \text{H}_2\text{O}$ (1 : 1 in volume), distilled water, acetone, and ethanol in 5 min steps each. They are then slowly introduced into the furnace to prevent thermal stress and kept at a constant temperature for about 1 h above the surface of the solution. The temperature of the solution is then reduced to 1 K above the saturation temperature and the substrate is introduced into the solution and kept at this temperature for 5 min, so that the outer layer of the substrate dissolves, without introducing defects into the subsequent epitaxial growth.

The growth of the epilayers is achieved by creating a ≈ 5 mol % supersaturation with a decrease of the saturation temperature by 2–6 K. The substrate is rotated at 15–60 rpm. In some experiments, a cooling rate of 0.67 K/h is used.

Wiping off the solution is not difficult due to its low viscosity. When the substrate is removed from the solution, it is still rotating while the whole system cools to room temperature.

Aznar et al. mentioned that on the (010) faces the epitaxial growth mainly exhibits a flat surface, which indicates a layer-by-layer growth mechanism. However *Romanuyk et al.* reported a three-dimensional (3-D) nucleation, also known as the Volmer–Weber growth mode [21.127].

The substrates were oriented perpendicular to the **b**-crystallographic direction, as preliminary studies of thin-film growth had demonstrated that epitaxial growth on the (010) face resulted in high-quality films at the fastest growth rate. Generally, higher density of growth steps is observed on epilayers grown on (310) and ($\bar{1}11$). A possible reason is the higher growth rate of these faces when compared with their neighboring faces. The layer–substrate mismatches on the ($\bar{1}11$) and (010) faces are rather similar. The lattice mismatch for Yb-doped **KLuW** thin films grown on **KLuW** substrates and Yb-doped **KYW** thin films grown on **KYW** substrates are listed in Table 21.5. No thermal mismatch data are available for these epitaxial layers.

Growth hillocks have been observed on Yb:**KLuW** films grown on **KLuW** substrates, which is a typically observed micromorphology that develops during the growth process.

Figure 21.19 shows the comparison of the thickness on different faces.

The chemical composition of the layer is usually measured by x-ray spectrometry or electron probe microanalysis to quantify the concentration and to calculate the distribution coefficient of the doping element in the epilayer, and also to determine if diffusion of the doping element into the substrate occurs. The distribution coefficient of the different lanthanide doping ions in the epilayers is near unity. No diffusion into the substrate has been observed. Higher doping levels of the epitaxial film will lead to an increase of the lattice mismatch and, consequently, difficulties in the growth of the epitaxial layers. When doping **KYW** with Yb the doping level obtained in the epitaxial films with high crystalline quality was 10 at. % in the growth solution. In the case of **KLuW**, it is possible to increase the dop-

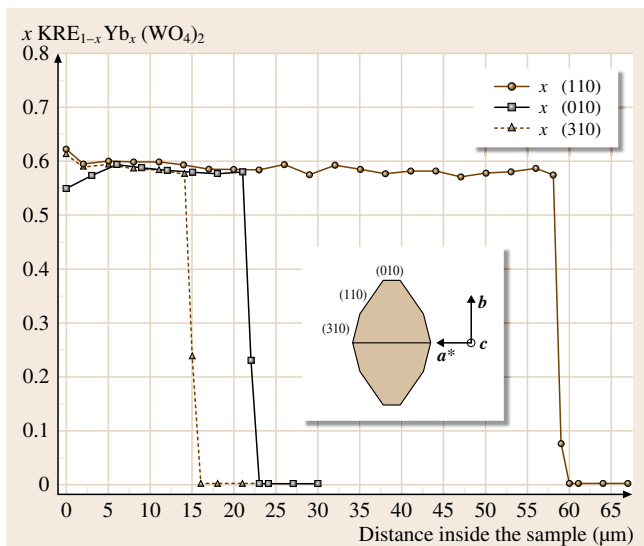


Fig. 21.19 Ytterbium concentration profile for the $\text{KLu}_{0.48}\text{Yb}_{0.052}\text{W}$ layer on KLuW substrates on three different faces: (310), (110), and (010) (after [21.128])

ing concentration to 50 at. % while maintaining high quality of the epitaxial layer.

Recently, the growth of thulium-doped epitaxial layers on KYW and KLuW substrates has been reported. For the KLuW host the doping level can reach 7.5 at. % substitution of lutetium by thulium while maintaining high film quality.

21.4.2 Epitaxies Within the Structural Field of KTP

Optical waveguides in KTP have been produced by ion exchange of K^+ by Rb^+ , Cs^+ or Tl^+ on the surface of a KTP substrate immersed in molten salts of Rb, Cs, and Tl [21.129]. A metal mask (e.g., Al, Au, Ti) has been used to fabricate channel waveguides by this procedure. These waveguides appear to be optically uniform over the width of the channel and show no evidence of lateral ion diffusion [21.130], which enables fabrication of high-density waveguide arrays and modulated index waveguides, while at the same time optimizing the electric-field overlap for modulators, switches, and nonlinear waveguide devices [21.123]. When $\text{Ba}(\text{NO}_3)_2$ is added to the molten RbNO_3 , the ion-exchange process changes not only the optical indices of the crystal but also its polarity, enabling the fabrication of not only Rb-exchanged quasi-phase-matched waveguides of KTP [21.131].

However, ion-exchange processes have their drawbacks. Due to the inherently diffusive and strongly anisotropic nature of the process, it is difficult to control the waveguide depth, producing guides with a broad, poorly defined index profile along the c -axis [21.24, 131]. This index profile, although satisfactory for many applications, is less effective for confinement of optical fields, especially in waveguiding second-harmonic generation [21.132] where variations of ionic conductivity due to crystal growth methods and with impurities make the device fabrication process difficult and results in poor yields.

Optical waveguides in KTP have been produced by proton or ammonium exchange [21.122], yielding a more step-like index profile by sol-gel chemistry [21.133] producing continuous KTP polycrystalline films with a grain size of $0.3 \mu\text{m}$, and by pulsed excimer laser ablation [21.134], allowing growth of KTP films on foreign substrates such as sapphire, silicon [21.135], and quartz.

Unlike other techniques used to fabricate waveguides, the LPE technique enables growth of a homogeneous single-crystal film and allows control of the thickness by adjusting the supersaturation of the solution and the growth time. Films with well-defined step-like refractive-index profile can be grown directly by LPE [21.131]. Good-quality single-crystal epitaxial layers of KTP suitable for producing optical waveguides can be obtained by LPE on substrates of the same family. This can be done by controlling the mismatch between the cell parameters of the substrate and those of the film using the solid solutions offered by this family of crystals. Thin films of $\text{KTiOP}_x\text{As}_{1-x}\text{O}_4$ were grown by Cheng et al. on KTP substrates using both tungstate and the pure phosphate–arsenate self-fluxes [21.132]. The KTA–KTP system was chosen, since the substitution of arsenic for phosphorus provides the desired refractive-index difference without compromising the nonlinearity of the material. $\text{KTiOP}_x\text{As}_{1-x}\text{O}_4$ films with a thickness of $5\text{--}50 \mu\text{m}$ were grown on polished KTP substrates. These substrates were polished with diamond-based polishing powder and finished with a 30 s chemical–mechanical polish in colloidal silica prior to epitaxial growth. A small ($\approx 0.75 \text{ mm}$) hole, drilled at one corner of the substrate, allows it to be tied vertically onto a crystal rotation–pulling head with a thin platinum wire to assist flux drainage after dipping. Slight etching of the substrate in warm dilute hydrochloric acid prior to the dipping improved the quality of the epitaxial layer. {100}, {011}, {110}, and {201} oriented plates cut from a single crystal grown

by the flux method were chosen as substrates. Although {001} films would be preferred in device applications, since the largest nonlinear optical coefficients of **KTP** lie in this plane, growth of high-quality {001} films has not been successful due to the fast growth and *c*-capping habit of **KTP**. The same problem was observed when growing thin epitaxial layers of **KTP** on {010} substrates. It should be noted that the use of substrates cut from hydrothermally grown crystals leads to optical degradation with the formation of fine white filaments in the substrate due to the precipitation of fine water-based inclusions [21.131].

The dipping setup [21.131] consisted of a 250 ml crucible placed at the bottom of a short-zone top-loading crucible furnace. The melt (≈ 200 ml) was homogenized overnight at ≈ 50 K above its liquidus temperature, which was determined accurately by repeated seeding. The substrate was introduced into the growth furnace slowly (≈ 5 – 25 mm/min) to avoid cracks due to thermal stress, and the flux was cooled to ≈ 1.5 – 3 K below the saturation point and allowed to equilibrate for 30 min prior to dipping the substrate into the melt. The substrate was spun unidirectionally at 10 rpm. The dipping time varied depending on the desired film thickness, the degree of supersaturation used, the choice of flux, and the growth temperature. Experimentally it was found that back-etching of the substrate in the same **LPE** solution prior to growth resulted in significantly better quality films. This was accomplished by taking advantage of the thermal inertia of the system and submerging the substrate before the melt reached the growth temperature. Upon completion of the dipping, the substrate–epitaxy was removed from the flux and washed with warm diluted hydrochloric acid.

Optical-quality films could be readily obtained using a 3–4 K supersaturation and a growth temperature of ≈ 1173 K. The observed growth rate was found to be weakly dependent on the orientation of the substrates. An abrupt increase in the arsenic concentration at the film–substrate interface was revealed, and resulted in an abrupt, step-like refractive index profile. It was concluded that the maximum lattice mismatch between the film and the substrate that still yields high-quality films was $\approx 1\%$, which corresponds to a $\approx 35\%$ increase in arsenic content in the $\text{KTiOAs}_x\text{P}_{1-x}\text{O}_4$ film. Film cracking was observed for films grown on substrates with larger lattice mismatch.

Significantly different growth properties were observed for tungstate and $\text{K}_6\text{P}_4\text{O}_{13}$ fluxes. First, a longer soak time was needed when using the $\text{K}_6\text{P}_4\text{O}_{13}$ flux. Second, under the same growth conditions (temperature

and supercooling), the growth rate normal to the natural face used as the substrate was substantially lower in the $\text{K}_6\text{P}_4\text{O}_{13}$ flux, necessitating supercooling roughly twice that used in tungstate flux to achieve a comparable growth rate. Third, films grown from $\text{K}_6\text{P}_4\text{O}_{13}$ flux tend to show film–substrate interfaces of poorer quality due to the slow dissolution kinetics of this flux, which makes the implementation of pregrowth etching difficult.

Appropriate replacement of the titanyl group via solid solution formation (e.g., Sn or Ge) or impurity doping could also generate epitaxial films with well-defined refractive index boundaries [21.24]. However, the growth of $\text{KTi}_{1-x}\text{Sn}_x\text{OPO}_4$ films proved to be difficult due to the anomalously slow dissolution properties of KSnOPO_4 . As an alternative, growth of $\text{KTi}_{1-x}\text{Ge}_x\text{OPO}_4$ thin films on **KTP** substrates using a 20% Ge solution has been tested [21.131]. Films ($10\text{ }\mu\text{m}$ thick) of $\text{KTi}_{0.96}\text{Ge}_{0.04}\text{OPO}_4$ on {011} **KTP** substrates were grown. Discouragingly, even with a low 4.3% Ge incorporation, numerous cracks perpendicular to the *c*-crystallographic direction were observed in thicker ($30\text{ }\mu\text{m}$) films because the $\text{KTi}_{0.96}\text{Ge}_{0.04}\text{OPO}_4$ films grew under tensile stress.

Cheng et al. [21.131] suggested that this situation can be improved by reversing the film–substrate configuration, such as growing **KTP** films on $\text{KTi}_{1-x}\text{Ge}_x\text{OPO}_4$ substrates. In this way, Solé et al. [21.85, 136] produced **KTP** thin films grown on $\text{KTi}_{1-x}\text{Ge}_x\text{OPO}_4$ substrates also using both tungstate and pure phosphate self-fluxes. These **LPE** experiments were performed in a special vertical furnace built to provide a wide enough region in which there was practically no axial gradient so that the epitaxial film thickness did not depend on the solution depth. Platinum cylindrical crucibles, 30 mm in diameter and 40 mm high, filled with about 50 g of solution with composition of $\text{K}_2\text{O} : \text{P}_2\text{O}_5 : \text{TiO}_2 = 49.8 : 33.2 : 17$ (mol %) in self-flux and $\text{K}_2\text{O} : \text{P}_2\text{O}_5 : \text{TiO}_2 : \text{WO}_3 = 42 : 14 : 14 : 30$ in tungstate flux were used. After homogenization of the solution, special attention was paid to determining the saturation temperature of the solution using a *c*-oriented seed rotating at 16 rpm. A new approach was used to study the quality of the films simultaneously on different substrates with different orientation. The epitaxial growth was made directly on the natural faces of as-grown single crystals of $\text{KTi}_{1-x}\text{Ge}_x\text{OPO}_4$. Thus, the growth conditions were forced to be the same for all the different orientations of the crystal faces used as substrates. The substrates were fixed using their own growth crystal seeds at the end of an alumina rod and cleaned for 5 min in $\text{HNO}_3 : \text{H}_2\text{O} = 1 : 1$ by volume,

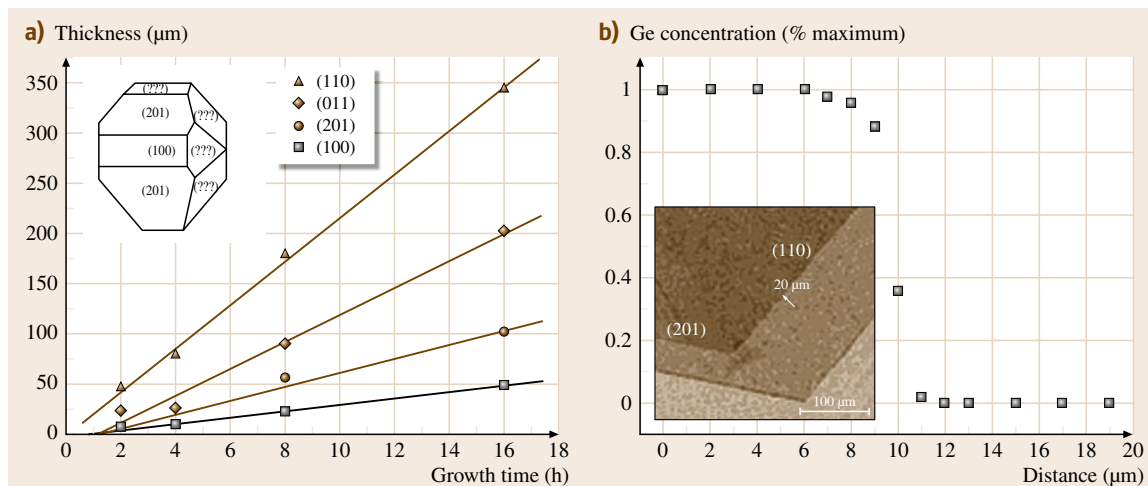


Fig. 21.20 (a) Epitaxial film thickness on different faces of a $\text{KTi}_{0.988}\text{Ge}_{0.012}\text{OPO}_4$ crystal as a function of the time of growth. The thin films were grown at 2 K below the saturation temperature of the solution. A morphology sketch with the difference faces of the $\text{KTi}_{0.988}\text{Ge}_{0.012}\text{OPO}_4$ crystal is included. (b) Normalized germanium concentration around the substrate–film interface determined by electron probe microanalysis. A scanning electron microscopy image of a cross section of the substrate–film interface taken with a secondary-electron detector is included. The difference in contrast indicates where the substrate–film interface is located, suggesting also a sharp interface (after [21.85])

for 5 min in distilled water, and for 5 min in ethanol. The whole cleaning process was carried out with crystal rotation. The crystal was then introduced into the furnace slowly to avoid cracks caused by thermal stress and heated for 30 min above the solution surface. The substrate was then dipped into the solution at a temperature 3–5 K above the saturation temperature for 1 h to dissolve the substrate surface before the beginning of growth. In tungsten solutions, the dissolution of the substrate was performed at 1 K above the saturation temperature for 10 min since this solution is significantly less viscous than the solution without WO_3 , and all these processes are much quicker. The temperature of the solution was maintained at 2 K below the saturation temperature for several hours to induce epitaxial growth when self-flux was used, or for several minutes when tungstate flux was used. The growth was performed at 1 K below the saturation temperature only when the growth time was long (16 h) and the degree of substitution was high. In all cases, the crystal rotation was maintained at 16 rpm. After the epitaxial growth, the crystal was removed from the flux and extracted from the furnace slowly to avoid thermal stresses in the crystal.

In general, the surface morphology and quality of the epitaxial films obtained depends on the crystal face on which they grew. Other parameters such as Ge content in the substrate and time of growth have signifi-

cantly less influence. The films on (201) and (100) faces were found to be of high quality and smooth. Films grown on (100) faces tended to show small macrosteps that could be a reproduction of the steps already existing on the substrates. The films on (011) and (110) faces tended to show small hillocks when the time of growth and the Ge in the substrate increased and a tendency for films grown on (011) face to be of best quality compared with those grown on (110) face. This difference in quality could be related to the faster velocity of film growth on these faces. The worst quality films grew on (101) face. This face, although it exists in $\text{KTi}_{1-x}\text{Ge}_x\text{OPO}_4$ crystals, is not a usual face in pure KTP. The defects in films grown on the (101) face are due to the faster growth velocity in pure KTP relative to the growth velocity on the other faces. In general, films grown on $\text{KTi}_{0.918}\text{Ge}_{0.082}\text{OPO}_4$ substrates showed some cracks. The quality of epitaxial growth in tungstate flux on (100), (201), and (011) faces was found to be good up to the highest concentration of Ge studied and the longest time studied. The epitaxy on (011) face, however, seemed to show a greater tendency to have macrosteps and growth hillocks than the other two faces. Similarly, when the Ge substitution for Ti in the substrate, and/or the growth time increased, the epitaxial film on (110) face showed a slight tendency to exhibit more defects.

A linear correlation between the epitaxial thickness and the time of growth was observed for all films grown on the faces of $\text{KTi}_{0.988}\text{Ge}_{0.012}\text{OPO}_4$. Figure 21.20a shows the epitaxial film thickness on the different faces as a function of the growth time for films grown at 2 K below the saturation temperature of the solution. The epitaxy on the (100) face showed the lowest rate of growth, followed by the film grown on the (201) face. The quality of these epitaxial films remained good even for long growth times and high concentrations of Ge in the substrate. The epitaxial films on (011) and (110) faces showed a faster rate of growth. Thus, when the time of growth increased, the density of defects also increased. Because of the poor quality of the epitaxial film on (101) face it was difficult to measure the epitaxial thickness accurately. For the case of growth in tungstate solutions, the epitaxy on (100) face showed the lowest rate of growth, followed by the films grown on (201), (011), and (110) faces, which showed similar rates of film growth. A sharp change in the germanium concentration at the substrate–film interface was observed. Figure 21.20b shows the normalized germanium concentration around the substrate–film interface.

The mismatch between the substrate and the film, defined as $f_{s(hkl)} = (S_{s(hkl)} - S_{0(hkl)})/S_{0(hkl)}$, where $S_{s(hkl)}$ and $S_{0(hkl)}$ are the areas obtained from the periodicity vectors of the substrate and the film, respectively, is listed for each face in Table 21.6. For {100} and {201} faces, these mismatches were positive, meaning the substrate was larger than the film. For {110} and {011} faces the mismatches were always negative, which is believed to produce films of lower quality. The different quality of the epitaxial films grown on the different crystal faces could also be explained by considering the position of titanium in the *KTP* structure with respect to the different planes that constitute the external morphology of the crystals used as the substrate on which the epitaxial films are grown. The Ti planes parallel to (100), (201), and (011) faces are regularly located in the structure and equidistant, while planes parallel to the (110) and (101) faces are not equidistant. Thus, the structural distortion produced by the Ge substitution in these planes was not distributed as homogeneously as in the case of the (100), (201), and (011) faces. This

could lead to a larger tendency to generate defects in the film.

Epitaxial $\text{Rb}_x\text{K}_{1-x}\text{TiOPO}_4$ films were grown from a 20% Rb solution on a *KTP* substrate [21.133]. Although the grown layer was measured to be 50 μm , the diffusion of Rb into the substrate at the growth temperature (≈ 1125 K) significantly broadened the waveguiding layer up to ≈ 125 μm . It is therefore more appropriate to view the liquid-phase epitaxy of $\text{Rb}_x\text{K}_{1-x}\text{TiOPO}_4$ on *KTP* as an ion-exchange waveguide fabrication process using molten tungstate instead of nitrate.

Liquid-phase epitaxy was also used as a tool to test the morphological stability of the (00 $\bar{1}$) face, which is a natural face in KTiOAsO_4 crystals and on *KTP* crystals. For this purpose, a *c*-cut *KTP* plate was submerged into a slightly supercooled (≈ 4 K) $\text{K}_6\text{P}_4\text{O}_{13}$ solution of *KTP* at 920 °C for ≈ 35 min. Smooth planar growth steps at the center of the *KTP* plate suggest that the (00 $\bar{1}$) face is indeed singular in *KTA*. Stable {01 $\bar{1}$ } and {20 $\bar{1}$ } lamellae extend rapidly along the (00 $\bar{1}$) and (20 $\bar{1}$) directions to form overhangs which eventually enclose the (001) and (00 $\bar{1}$) faces and thus eliminate them from the final growth form [21.137].

A completely new combination of both top-down and bottom-up approaches has been reported recently to grow two-dimensional (2-D) photonic crystals of *KTP* involving liquid-phase epitaxial techniques [21.138]. *KTP* rods grew inside the air holes of an ordered silicon matrix closely bound to a *c*-oriented *KTP* substrate and following the orientation of the substrate. The 2-D *KTP* patterning implemented can be summarized in a four-step procedure, shown in Fig. 21.21a, that involves preparation of a high-quality ordered macroporous silicon template, epitaxial growth of the *KTP* rods into the silicon template, polishing of the top or bottom surface of the *KTP* columns, and finally partial selective etching of the silicon matrix. A platinum wire was used to bind the silicon template to a *KTP* substrate. The template–substrate was dipped for 5 min into a high-temperature solution with a mol % composition $\text{K}_2\text{O} : \text{P}_2\text{O}_5 : \text{TiO}_2 : \text{WO}_3 = 42 : 14 : 14 : 30$ without any additional thermal gradient. We initiated the epitaxial growth of the *KTP* 2-D photonic structure

Table 21.6 Mismatches between $\text{KTi}_{1-x}\text{Ge}_x\text{OPO}_4$ substrates and *KTP* films

Epitaxial layer	$f(100)$	$f(201)$	$f(101)$	$f(110)$	$f(011)$
$\text{KTi}_{0.988}\text{Ge}_{0.012}\text{OPO}_4/\text{KTP}$	−0.003	0.006	0.018	−0.017	−0.007
$\text{KTi}_{0.955}\text{Ge}_{0.045}\text{OPO}_4/\text{KTP}$	0.009	0.032	0.060	−0.035	−0.009
$\text{KTi}_{0.918}\text{Ge}_{0.082}\text{OPO}_4/\text{KTP}$	−0.071	−0.029	0.023	−0.156	−0.107

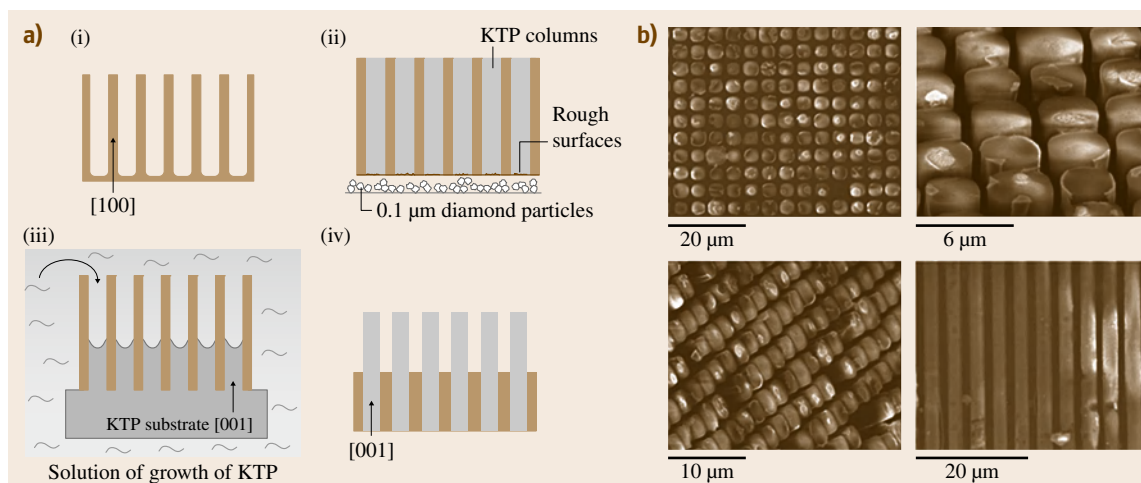


Fig. 21.21 (a) Schematic view of the four stages of growth of **KTP 2-D** photonic crystals: (i) preparation of the oriented **2-D** macroporous silicon membrane, (ii) the silicon template is attached to an oriented **KTP** substrate and then immersed in the growth solution of **KTP**. The direction of growth of the **KTP** rods is the same as oriented of the **KTP** substrate, **[001]**. (iii) After growth, the top of the rods is polished with diamond particles in order to obtain an optical-quality surface. (iv) Silicon is partially removed by selective chemical etching. (b) Scanning electron microscopy images of (i) the top of a **2-D** KTO phonic crystal after polishing and partially etching of the macroporous silicon template, (ii) side view of the **KTP** rods after removing the silicon template, (iii) a detailed view of a **2-D** **KTP** phonic crystal with a period of $4.5\ \mu\text{m}$, and (iv) side view of a plane of rods of a **2-D** **KTP** photonic crystal lattice

2 K below the saturation temperature, which provided a supersaturation in the solution of about 2%. The template–substrate–epitaxy composite was then removed from the solution, but kept inside the furnace above the surface of the solution while the furnace was cooled to room temperature at a rate of 15 K/h to avoid thermal stress that could result in cracks

either in the **2-D** photonic structures or in the substrate. The final **2-D** photonic structures are formed from independent rods of **KTP** with square cross section, perfectly aligned with the orientation of the **KTP** substrate. Figure 21.21b shows several scanning electron microscopy (SEM) images of these photonic structures.

References

- 21.1 M.M. Kujla: Defects in yttrium aluminium perovskite and garnet crystals: atomistic study, *J. Phys. Condens. Matter* **12**, 2953–2967 (2000)
- 21.2 V. Lupei: RE^{3+} emission in garnets: multisites, energy transfer and quantum efficiency, *Opt. Mater.* **19**, 95–107 (2002)
- 21.3 J. Petit, B. Viana, P. Goldner, D. Vivien, P. Louiseau, B. Ferrand: Laser oscillation with low quantum defect in Yb:GdVO_4 , a crystal with high thermal conductivity, *Opt. Lett.* **29**, 833–835 (2004)
- 21.4 S.H. Smith, G. Garton, B.K. Tanner: Top-seeded flux growth of rare-earth vanadates, *J. Cryst. Growth* **23**, 335–340 (1974)
- 21.5 S. Erdei: Growth of oxygen deficiency-free YVO_4 single crystal by top-seeded solution growth technique, *J. Cryst. Growth* **134**, 1–13 (1993)
- 21.6 D.I. Savytskii, L.O. Vasylechko, A.O. Matkovskii, I.M. Solskii, A. Suchocki, D.Y. Sugak, F. Wallrafen: Growth and properties of $\text{YAlO}_3\text{:Nd}$ single crystals, *J. Cryst. Growth* **209**, 874–882 (2000)
- 21.7 R. Solé, V. Nikolov, X. Ruíz, J. Gavalda, X. Solans, M. Aguiló, F. Díaz: Growth of $\beta\text{-KGd}_{1-x}\text{Nd}_x(\text{WO}_4)_2$ single crystals in $\text{K}_2\text{W}_2\text{O}_7$ solvents, *J. Cryst. Growth* **169**, 600–603 (1996)
- 21.8 M.C. Pujol, M. Aguiló, F. Díaz, C. Zaldo: Growth and characterisation of monoclinic $\text{KGd}_{1-x}\text{RE}_x(\text{WO}_4)_2$ single crystals, *Opt. Mater.* **13**, 33–40 (1999)
- 21.9 G. Métrat, N. Muhlstein, A. Brenier, G. Boulon: Growth by the induced nucleated floating crystal (INFC) method and spectroscopic properties of $\text{KY}_{1-x}\text{Nd}_x(\text{WO}_4)_2$ laser materials, *Opt. Mater.* **8**, 75–82 (1997)

- 21.10 A. Brenier, F. Bourgeois, G. Métrat, N. Muhlstein, M. Boudelle, G. Boulon: Spectroscopic characterization of Nd^{3+} -doped $\text{KY}(\text{WO}_4)_2$ single crystal, *J. Lumin.* **81**, 135–141 (1999)
- 21.11 D. Gabbe, A.L. Harmer: Scheelite structure fluorides: The growth of pure and rare earth doped LiYF_4 , *J. Cryst. Growth* **3**, 544 (1968)
- 21.12 K. Shimamura, H. Sato, A. Bensalah, V. Sudesh, H. Machida, N. Sarukura, T. Fukuda: Crystal growth of fluorides for optical applications, *Cryst. Res. Technol.* **36**, 801–813 (2001)
- 21.13 A. Agnesi, G. Carraro, A. Guandalini, G. Reali, E. Sani, A. Toncelli, M. Tonelli: 1-mJ Q-switched diode-pumped $\text{Nd}:\text{BaY}_2\text{F}_8$ laser, *Opt. Exp.* **12**, 3766–3769 (2004)
- 21.14 S. Bigotta, D. Parisi, L. Bonelli, A. Toncelli, M. Tonelli, A. Di Lieto: Spectroscopic and laser cooling results on Yb^{3+} -doped BaY_2F_8 single crystal, *J. Appl. Phys.* **100**, 013109 (2006)
- 21.15 R.F. Belt, R. Uhrin: Top seeded solution growth of $\text{Cr}^{3+}:\text{LiCaAlF}_6$ in HF atmosphere, *J. Cryst. Growth* **109**, 340–344 (1991)
- 21.16 D. Klimm, P. Reiche: Ternary colquiriite type fluorides as laser hosts, *Cryst. Res. Technol.* **34**, 145–152 (1999)
- 21.17 A.A. Kaminskii: Modern developments in the physics of crystalline laser materials, *Phys. Status Solidi (a)* **200**, 215–296 (2003)
- 21.18 A.A. Kaminskii: *Laser Crystals. Their Physics and Properties* (Springer, Berlin 1981)
- 21.19 C.E. Mungan, S.R. Bowman, T.R. Gosnell: Solid-state laser cooling of ytterbium-doped tungstate crystals, *Proc. Lasers 2000* (2001) pp. 819–826
- 21.20 A.N. Medina, A.C. Bento, M.L. Baesso, F.G. Gandra, T. Catunda, A. Cassanho: Temperature dependence of the Cr^{3+} site axial distortion in LiSrAlF_6 and LiSrGaF_6 single crystals, *J. Phys. Condens. Matter* **13**, 8435–8443 (2001)
- 21.21 S.A. Payne, L.L. Chase, H.W. Newkirk, L.K. Smith, W.F. Krupke: $\text{LiCaAlF}_6:\text{Cr}^{3+}$: A promising new solid-state laser material, *IEEE J. Quantum Electron.* **QE-24**, 2243–2252 (1988)
- 21.22 J.A. Armstrong, N. Bloembergen, J. Ducuing, P.S. Pershan: Interactions between light waves in a nonlinear dielectric, *Phys. Rev.* **127**, 1918–1939 (1962)
- 21.23 P.F. Bordui, M.M. Fejer: Inorganic crystals for nonlinear optical frequency conversion, *Annu. Rev. Mater. Sci.* **23**, 321–379 (1993)
- 21.24 M.E. Hagerman, K.R. Pöppelmeier: Review of the structure and processing defect property relationships of potassium titanyl phosphate: A strategy for novel thin film photonic devices, *Chem. Mater.* **7**, 602–621 (1995)
- 21.25 H. Hellwig, J. Liebertz, L. Bohaty: Exceptional large nonlinear optical coefficients in the monoclinic bismuth borate BiB_3O_6 (BIBO), *Solid State Commun.* **190**, 249–251 (1998)
- 21.26 R. Solé, X. Ruíz, R. Cabré, M. Aguiló, F. Díaz, V. Nikolov, P. Peshev: High temperature solutions of the $(0.4\text{Na}_2\text{O}-0.6\text{B}_2\text{O}_3)-\text{BaO}-((6-x)+x\text{CoSnO}_3)$ system. Physical properties, *Mater. Res. Bull.* **30**, 779–788 (1995)
- 21.27 X. Ruíz, M. Aguiló, J. Massons, F. Díaz: Numerical and experimental study of the forced convection inside a rotating disk-cylinder configuration, *Exp. Fluids* **14**, 333–340 (1993)
- 21.28 H.J. Scheel, E.O. Schulz-Dubois: Flux growth of large crystals by accelerated crucible-rotation technique, *J. Cryst. Growth* **8**, 304–306 (1971)
- 21.29 D. Elwell, H.J. Scheel: *Crystal Growth from High-Temperature Solutions* (Academic, London 1975)
- 21.30 M.G. Astles: *Liquid-Phase Epitaxial Growth of III-V Compound Semiconductor Materials and Their Device Applications* (Adam Hilger, New York 1990)
- 21.31 A.A. Maier, M.V. Provotorov, V.A. Balashov: Double molybdates and tungstates of the rare earth and alkali metals, *Russ. Chem. Rev.* **42**, 822–833 (1973)
- 21.32 E. Gallucci, C. Goutadier, G. Boulon, M.T. Cohen-Adad: Growth of $\text{KY}(\text{WO}_4)_2$ single crystal: Investigation of the rich WO_3 region in the $\text{K}_2\text{O}-\text{Y}_2\text{O}_3-\text{WO}_3$ ternary system. 1. The $\text{K}_2\text{O}-\text{WO}_3$ binary system, *Eur. J. Solid State Inorg. Chem.* **34**, 1107–1117 (1997)
- 21.33 R. Guérin, P. Cailliet: Sur les phases du système $\text{K}_2\text{WO}_4-\text{WO}_3$ et leur réduction par la vapeur de potassium, *C. R. Acad. Sci. Ser. C* **271**, 815–817 (1970), in French
- 21.34 G. Wang, Z.D. Luo: Crystal growth of $\text{KY}(\text{WO}_4)_2:\text{Er}^{3+},\text{Yb}^{3+}$, *J. Cryst. Growth* **116**, 505–506 (1992)
- 21.35 P.V. Kletsov, L.P. Kozeeva, L.Y. Kharchenko: Study on the crystallization and polymorphism of double potassium and trivalent metal tungstates, $\text{KR}(\text{WO}_4)_2$, *Sov. Phys. Crystallogr.* **20**, 732–735 (1976)
- 21.36 A. Majchrowski: *Supermaterials* (Kluwer, Dordrecht 2000)
- 21.37 A. Majchrowski, M.T. Borowiec, E. Michalski: Top seeded solution growth of $\text{KHo}(\text{WO}_4)_2$ single crystals, *J. Cryst. Growth* **264**, 201–207 (2003)
- 21.38 M.C. Pujol, R. Solé, J. Gavalda, J. Massons, M. Aguiló, F. Díaz: Growth and ultraviolet optical properties of $\text{KGd}_{1-x}\text{RE}_x(\text{WO}_4)_2$ single crystals, *J. Mater. Res.* **14**, 3739–3745 (1999)
- 21.39 K. Wang, J. Zhang, J. Wang, W. Yu, H. Zhang, Z. Wang, X. Wang, M. Ba: Predicted and real habits of flux grown potassium lutetium tungstate single crystals, *Cryst. Growth Des.* **5**, 1555–1558 (2006)
- 21.40 M.T. Borowiec, A. Majchrowski, V. Domuchowski, V.P. Dyakonov, E. Michalski, T. Zayarniuk, J. Żmija, H. Szymczak: Crystal growth and x-ray structure investigation of the $\text{KHo}(\text{WO}_4)_2$, *Proc. SPIE* **5136**, 20–25 (2003)

- 21.41 A.A. Kaminskii, J.B. Gruber, S.N. Bagaev, K. Ueda, U. Hömmerich, J.T. Seo, D. Temple, B. Zandi, A.A. Kornienko, E.B. Dunina, A.A. Pavlyuk, R.F. Klevtsova, F.A. Kuznetsov: Optical spectroscopy and visible stimulated emission of Dy^{3+} ions in monoclinic $\alpha\text{-KY}(\text{WO}_4)_2$ and $\alpha\text{-KGd}(\text{WO}_4)_2$ crystals, *Phys. Rev. B* **65**, 125108 (2002)
- 21.42 M.C. Pujol, M. Bursukova, F. Güell, X. Mateos, R. Solé, J. Gavalda, M. Aguiló, J. Massons, F. Díaz, P. Klopp, U. Griebner, V. Petrov: Growth, optical characterization, and laser operation of the stoichiometric crystal $\text{KYb}(\text{WO}_4)_2$, *Phys. Rev. B* **65**, 165121 (2002)
- 21.43 H.P. Jensen, A. Linz: Analysis of the optical spectrum of Tm^{3+} in LiYF_4 , *Phys. Rev. B* **11**, 92–101 (1975)
- 21.44 B. Chai, J. Lefaucheur, A. Pham, G. Lutts, J. Nicholls: Growth of high-quality single crystals of KYF_4 by TSSG method, *Proc. SPIE* **1863**, 131–135 (1993)
- 21.45 P. Hagenmüller: *Inorganic Solid Fluorides* (Academic, New York 1985)
- 21.46 E.M. Levin: The system $\text{Y}_2\text{O}_3\text{-V}_2\text{O}_5$, *J. Am. Ceram. Soc.* **50**, 381–382 (1967)
- 21.47 L.G. Van Uitert, R.C. Linares, R.R. Soden, A.A. Ballman: Role of f-orbital electron wave function mixing in the concentration quenching of Eu^{3+} , *J. Chem. Phys.* **36**, 702–705 (1962)
- 21.48 W. Hintzmann, G. Müller-Vogt: Crystal growth and lattice parameters of rare-earth doped yttrium phosphate, arsenate and vanadate prepared by the oscillating temperature flux technique, *J. Cryst. Growth* **5**, 274–278 (1969)
- 21.49 S.H. Smith, B.M. Wanklyn: Flux growth of rare earth vanadates and phosphates, *J. Cryst. Growth* **21**, 23–28 (1974)
- 21.50 B.M. Wanklyn: Use of a crystalline seal in flux growth – Rare-earth borates, vanadates and garnets, KNiF_3 and CsNiMF_6 ($M = \text{Fe, Cr}$), *J. Cryst. Growth* **54**, 610–614 (1981)
- 21.51 V.A. Timofeeva: Physicochemical aspects of flux crystallization of the oxide materials. In: *Growth of Crystals* (Consultants Bureau, New York 1988)
- 21.52 R. Masse, J.C. Grenier: Étude des monophosphates du type $M'\text{TiOPO}_4$ avec $M' = \text{K, Rb et Tl}$, *Bull. Soc. Fr. Mineral. Cristallogr.* **94**, 437–439 (1971), in French
- 21.53 M.N. Satyanarayan, A. Deepthy, H.L. Bhat: Potassium titanyl phosphate and its isomorphs. Growth, properties, and applications, *Crit. Rev. Solid State Mater. Sci.* **24**, 103–191 (1999)
- 21.54 V.I. Voronkova, V.K. Yanovskii: Growth of KTiOPO_4 -group crystals from a solution in a melt and their properties, *Inorg. Mater.* **24**, 273–277 (1988)
- 21.55 K. Iliev, P. Peshev, V. Nikolov, I. Koseva: Physicochemical properties of high-temperature solutions of the $\text{K}_2\text{O-P}_2\text{O}_5\text{-TiO}_2$ system suitable for the growth of KTiOPO_4 (KTP) single crystals, *J. Cryst. Growth* **100**, 219–224 (1990)
- 21.56 J.C. Jacco, G.M. Loiacono, M. Jaso, G. Mizell, B. Greenberg: Flux growth and properties of KTiOPO_4 , *J. Cryst. Growth* **70**, 484–488 (1984)
- 21.57 P.F. Bordui, J.C. Jacco, G.M. Loiacono, R.A. Stolzenberger, J.J. Zola: Growth of large single crystals of KTiOPO_4 (KTP) from high-temperature solution using heat pipe based furnace system, *J. Cryst. Growth* **84**, 403–408 (1987)
- 21.58 G.M. Loiacono, T.F. McGee, G. Kostecy: Solubility and crystal growth of KTiOPO_4 in polyphosphate solvents, *J. Cryst. Growth* **104**, 389–391 (1990)
- 21.59 P.F. Bordui, J.C. Jacco: Viscosity and density of solutions used in high-temperature solution growth of KTiOPO_4 , *J. Cryst. Growth* **82**, 351–355 (1987)
- 21.60 T.E. Gier: Method for flux growth of KTiOPO_4 and its analogues, US Patent 4231838 (1980)
- 21.61 A.L. Aleksandrovskii, S.A. Akhmanov, V.A. D'yakov, N.I. Zheludev, V.I. Pryalkin: Efficient nonlinear optical converters made of potassium titanyl phosphate crystals, *Sov. J. Quantum Electron.* **15**, 885–886 (1985)
- 21.62 P.F. Bordui, S. Motakef: Hydrodynamic control of solution inclusion during crystal growth of KTiOPO_4 (KTP) from high-temperature solution, *J. Cryst. Growth* **96**, 405–412 (1989)
- 21.63 B. Vartak, Y.I. Kwon, A. Yeckel, J.J. Derby: An analysis of flow and mass transfer during the solution growth of potassium titanyl phosphate, *J. Cryst. Growth* **210**, 704–718 (2000)
- 21.64 T. Sasaki, A. Miyamoto, A. Yokotani, S. Nakai: Growth and optical characterization of large potassium titanyl phosphate crystals, *J. Cryst. Growth* **128**, 950–955 (1993)
- 21.65 G. Dhanaraj, T. Shripathi, H.L. Bhat: Defect characterization of KTP single-crystals, *Bull. Mater. Sci.* **15**, 219–227 (1992)
- 21.66 G. Dhanaraj, H.L. Bhat: Dendritic structures on habit faces of potassium titanyl phosphate crystals grown from flux, *Mater. Lett.* **10**, 283–287 (1990)
- 21.67 R.J. Bolt, M.H. van der Mooren, H. de Haas: Growth of KTiOPO_4 (KTP) single crystals by means of phosphate and phosphate/sulphate fluxes out of a three-zone furnace, *J. Cryst. Growth* **114**, 141–152 (1991)
- 21.68 M. Roth, N. Angert, M. Tseitlin, A. Alexandrovski: On the quality of KTP crystals for nonlinear optical and electro-optic applications, *Opt. Mater.* **16**, 131–136 (2001)
- 21.69 L.K. Cheng, J.D. Bierlein, A.A. Ballman: Crystal growth of KTiOPO_4 isomorphs from tungstate and molybdate fluxes, *J. Cryst. Growth* **110**, 697–703 (1991)
- 21.70 N. Angert, L. Kaplun, M. Tseitlin, E. Yashchin, M. Roth: Growth and domain structure of potassium titanyl phosphate crystals pulled from high-temperature solutions, *J. Cryst. Growth* **137**, 116–122 (1994)

- 21.71 J.J. Carvajal, V. Nikolov, R. Solé, J. Gavalda, J. Massons, M. Rico, C. Zaldo, M. Aguiló, F. Díaz: Enhancement of the erbium concentration in RbTiOPO₄ by co-doping with niobium, *Chem. Mater.* **12**, 3171–3180 (2000)
- 21.72 Y.S. Oseledchik, S.P. Belokry, V.V. Osadchuk, A.L. Prosvirnin, A.F. Selevich, V.V. Starshenko, K.V. Kuzemchenko: Growth of RbTiOPO₄ single crystals from phosphate systems, *J. Cryst. Growth* **125**, 639–643 (1992)
- 21.73 A.A. Ballman, H. Brown, D.H. Olson, C.E. Rice: Growth of potassium titanyl phosphate (KTP) from molten tungstate melts, *J. Cryst. Growth* **75**, 390–394 (1986)
- 21.74 K. Iliev, P. Peshev, V. Nikolov, I. Koseva: Physico-chemical properties of high-temperature solution of the K₂O–P₂O₅–TiO₂–WO₃ system, suitable for the growth of KTiOPO₄ (KTP) single crystals, *J. Cryst. Growth* **100**, 225–232 (1990)
- 21.75 D.P. Shumov, M.P. Tarassov, V.S. Nikolov: Investigation of optical inhomogeneities in KTiOPO₄ (KTP) single crystals grown from high-temperature tungsten-containing solutions, *J. Cryst. Growth* **129**, 635–639 (1993)
- 21.76 A. Yokotani, A. Miyamoto, T. Sasaki, S. Nakai: Observation of optical inhomogeneities in flux grown KTP crystals, *J. Cryst. Growth* **110**, 963–967 (1991)
- 21.77 G. Marnier: Process for the flux synthesis of crystals of the KTiOPO₄ potassium titanyl monophosphate type, US Patent 4746396 (1988)
- 21.78 S. Suma, N. Santha, M.T. Sebastián: Growth of KTP crystals from potassium sodium fluoride phosphate solution, *Mater. Lett.* **34**, 322–325 (1998)
- 21.79 S. Suma, N. Santha, M.T. Sebastián: A new flux for the fast growth of potassium titanyl phosphate (KTP) single crystals, *J. Mater. Sci. Mater. Electron.* **9**, 39–42 (1998)
- 21.80 A. Miyamoto, Y. Mori, T. Sasaki, S. Nakai: Improvement of optical transmission of KTiOPO₄ crystals by growth in nitrogen ambient, *Appl. Phys. Lett.* **69**, 1032–1034 (1996)
- 21.81 J. Zhang, J. Wang, B. Ge, Y. Liu, X. Hu, R.I. Boughton: Growth, conductivity and generation of blue coherent laser of cesium doped KTiOPO₄ crystals, *J. Cryst. Growth* **267**, 517–521 (2004)
- 21.82 N. Angert, M. Tseitlin, E. Yashchin, M. Roth: Ferroelectric phase transition temperatures of KTiOPO₄ crystals grown from self-fluxes, *Appl. Phys. Lett.* **67**, 1941–1943 (1995)
- 21.83 P.A. Morris, A. Ferretti, J.D. Bierlein, G.M. Loiacono: Reduction of the ionic conductivity of flux grown KTiOPO₄ crystals, *J. Cryst. Growth* **109**, 361–366 (1991)
- 21.84 J. Zhang, J. Wang, B. Ge, Y. Liu, X. Hu, G. Zhao, S. Zhu, R.I. Boughton: Growth, conductivity and periodic poled structure of doped KTiOPO₄ and its analogue crystals, *Opt. Mater.* **28**, 355–359 (2006)
- 21.85 R. Solé, V. Nikolov, A. Vilalta, J.J. Carvajal, J. Massons, J. Gavalda, M. Aguiló, F. Díaz: Growth of KTiOPO₄ films on KTi_{1-x}Ge_xOPO₄ substrates by liquid-phase epitaxy, *J. Mater. Res.* **17**, 563–569 (2002)
- 21.86 J.Y. Wang, Y.G. Liu, J.Q. Wei, L.P. Shi, M. Wang: Crystal growth and properties of rubidium titanium oxide phosphate, RbTiOPO₄, *Z. Kristallogr.* **191**, 231–238 (1990)
- 21.87 S. Ganesa Moorthy, F.J. Kumar, C. Subramanian, G. Bocelli, P. Ramasamy: Structure refinement of nonlinear optical material K_{0.97}Ti_{0.97}Nb_{0.03}OPO₄, *Mater. Lett.* **36**, 266–270 (1998)
- 21.88 D.Y. Zhang, H.Y. Shen, W. Liu, W.Z. Chen, G.F. Zhang, G. Zhang, R.R. Zeng, C.H. Huang, W.X. Lin, J.K. Liang: Crystal growth, x-ray diffraction and nonlinear optical properties of Nb:KTiOPO₄ crystal, *J. Cryst. Growth* **218**, 98–102 (2000)
- 21.89 I. Parreu, R. Solé, J. Gavalda, J. Massons, F. Díaz, M. Aguiló: Crystallization region, crystal growth, and phase transitions of KNd(PO₃)₄, *Chem. Mater.* **15**, 5059–5064 (2003)
- 21.90 I. Parreu, R. Solé, J. Gavalda, J. Massons, F. Díaz, M. Aguiló: Crystal growth, structural characterization, and linear thermal evolution of KGd(PO₃)₄, *Chem. Mater.* **17**, 822–828 (2005)
- 21.91 I. Parreu, J.J. Carvajal, X. Solans, F. Díaz, M. Aguiló: Crystal structure and optical characterization of pure and Nd-substituted type III KGd(PO₃)₃: A new material for laser and nonlinear optical applications, *Chem. Mater.* **18**, 221–228 (2006)
- 21.92 H.G. Kim, J.K. Kang, S.H. Lee, S.J. Chung: Growth of lithium triborate crystals by the TSSG technique, *J. Cryst. Growth* **187**, 455–462 (1998)
- 21.93 B.S.R. Sastry, F.A. Hummel: Studies in lithium oxide systems: I, Li₂O–B₂O₃–B₂O₃, *J. Am. Ceram. Soc.* **41**, 7–17 (1958)
- 21.94 Z. Shuqing, H. Chooen, Z. Hongwu: Growth of lithium triborate (LBO) single crystal fiber by the laser-heated pedestal growth method, *J. Cryst. Growth* **112**, 283–286 (1990)
- 21.95 S.A. Guretskii, A.P. Ges, D.I. Zhigunov, A.A. Ignatenko, N.A. Kalanda, L.A. Kurnevich, A.M. Lugnets, A.S. Milanov, P.V. Molchan: Growth of lithium triborate single crystals from molten salt solution under various temperature gradients, *J. Cryst. Growth* **156**, 410–412 (1995)
- 21.96 D.P. Shumov, V.S. Nikolov, A.T. Nenov: Growth of LiB₃O₅ single crystals in the Li₂O–B₂O₃ system, *J. Cryst. Growth* **144**, 218–222 (1994)
- 21.97 T. Ukachi, R.J. Lane, W.R. Bosenberg, C.L. Tang: Phase-matched second-harmonic generation and growth of a LiB₃O₅ crystal, *J. Opt. Soc. Am. B* **9**, 1128–1133 (1992)
- 21.98 E. Bruck, R.J. Raymakers, R.K. Route, R.S. Feigelson: Surface stability of lithium triborate crystals grown

- from excess B_2O_3 solutions, *J. Cryst. Growth* **128**, 933–937 (1993)
- 21.99 J.W. Kim, C.S. Yoon, H.G. Gallagher: The effect of NaCl melt-additive on the growth and morphology of LiB_3O_5 (LBO) crystals, *J. Cryst. Growth* **222**, 760–766 (2001)
- 21.100 C. Parfeniuk, I.V. Samarasekera, F. Weinberg: Growth of lithium triborate crystals. I. Mathematical model, *J. Cryst. Growth* **158**, 514–522 (1996)
- 21.101 W. Chen, A. Jiang, G. Wang: Growth of high-quality and large-sized β - BaB_2O_4 crystal, *J. Cryst. Growth* **256**, 383–386 (2003)
- 21.102 W.R. Bosenberg, R.J. Lane, C.L. Tang: Growth of large, high-quality beta-barium metaborate crystals, *J. Cryst. Growth* **108**, 394–398 (1991)
- 21.103 D. Perlov, M. Roth: Isothermal growth of β -barium metaborate single crystals by continuous feeding in the top-seeded solution growth configuration, *J. Cryst. Growth* **137**, 123–127 (1994)
- 21.104 M. Roth, D. Perlov: Growth of barium borate crystals from sodium fluoride solutions, *J. Cryst. Growth* **169**, 734–740 (1996)
- 21.105 A. Liang, F. Cheng, Q. Lin, Z. Cheng, Y. Zheng: Flux growth of large single crystals of low temperature phase barium metaborate, *J. Cryst. Growth* **79**, 963–969 (1986)
- 21.106 R.S. Feigelson, R.J. Raymakers, R.K. Route: Solution growth of barium metaborate crystals by top seeding, *J. Cryst. Growth* **97**, 352–366 (1989)
- 21.107 L.H. Brixner, K. Babcock: Inorganic single crystals from reactions in fused salts, *Mater. Res. Bull.* **3**, 817–824 (1968)
- 21.108 P.F. Bordui, G.D. Calvert, R. Blachman: Immersion-seeded growth of large barium borate crystals from sodium chloride, *J. Cryst. Growth* **129**, 371–374 (1993)
- 21.109 Y.S. Oseledchik, V.V. Osadchuk, A.L. Prosvirnin, A.F. Selevich: Growth of high-quality barium metaborate crystals from Na_2O -NaF solution, *J. Cryst. Growth* **131**, 199–203 (1993)
- 21.110 V. Nikolov, P. Peshev, K. Khubanov: On the growth of β - BaB_2O_4 (BBO) single crystals from high-temperature solutions: II. Physicochemical properties of barium borate solutions and estimation of the conditions of stable growth of BBO crystals from them, *J. Solid State Chem.* **97**, 36–40 (1992)
- 21.111 Q. Huang, Z. Liang: Studies on flux systems for the single crystal growth of β - BaB_2O_4 , *J. Cryst. Growth* **97**, 720–724 (1989)
- 21.112 A.E. Kokh, N.G. Kononova, T.B. Bekker, V.A. Vlezko, P.V. Mokrushnikov, V.N. Popov: Change of symmetry and rotation of thermal field as a new method of control of heat and mass transfer in crystal growth (by example of β - BaB_2O_4), *Crystallogr. Rep.* **50**, 160–166 (2005)
- 21.113 S.C. Sabharwal, S.M. Goswami, S.K. Kulkarni, B.D. Padalia: Growth, optical transmission and x-ray photoemission studies of BaB_2O_4 single crystals, *J. Mater. Sci. Mater. Electron.* **11**, 325–329 (2000)
- 21.114 R. Solé, V. Nikolov, M.C. Pujol, J. Gavalda, X. Ruíz, J. Massons, M. Aguiló, F. Díaz: Stabilization of β - BaB_2O_4 in the system BaB_2O_4 - Na_2O - Nd_2O_3 , *J. Cryst. Growth* **207**, 104–111 (1999)
- 21.115 H.G. Kim, J.K. Kang, S.J. Park, S.J. Chung: Growth of the nonlinear crystals of lithium triborate and beta barium borate, *Opt. Mater.* **9**, 356–360 (1998)
- 21.116 A. Giesen, H. Hügel, A. Voss, K. Wittig, U. Brauch, H. Opower: Scalable concept for diode-pumped high-power solid-state lasers, *Appl. Phys. B* **58**, 363–372 (1994)
- 21.117 S. Chénais, F. Balembois, F. Druon, G. Lucas-Leclin, P. Georges: Thermal lensing in diode-pumped ytterbium lasers – Part I: theoretical analysis and wavefront measurements, *IEEE J. Quantum Electron.* **QE-40**, 1217–1233 (2004)
- 21.118 C. Stewen, K. Contag, M. Larionov, A. Giesen, H. Hügel: A 1-kW CW thin disc laser, *IEEE J. Sel. Top. Quantum Electron.* **6**, 650–657 (2000)
- 21.119 R. Paschotta, J. Aus der Au, G.J. Spühler, S. Erhard, A. Giesen, U. Keller: Passive mode locking of thin-disk lasers: effects of spatial hole burning, *Appl. Phys. B* **72**, 267–278 (2001)
- 21.120 U. Griebner, J. Liu, S. Rivier, A. Aznar, R. Grunwald, R.M. Solé, M. Aguiló, F. Díaz, V. Petrov: Laser operation of epitaxially grown $Yb:KLu(WO_4)_2$ - $KLu(WO_4)_2$ composites with monoclinic crystalline structure, *IEEE J. Quantum Electron.* **QE-41**, 408–414 (2005)
- 21.121 Y.E. Romanyuk, C.N. Borca, M. Pollnau, S. Rivier, V. Petrov, U. Griebner: Yb-doped $KY(WO_4)_2$ planar waveguide laser, *Opt. Lett.* **31**, 53–55 (2006)
- 21.122 M.G. Roelofs, A. Ferretti, J.D. Bierlein: Proton-exchanged and ammonium-exchanged waveguides in $KTiOPO_4$, *J. Appl. Phys.* **73**, 3608–3613 (1993)
- 21.123 J.D. Bierlein, H. Vanherzeele: Potassium titanyl phosphate-properties and new applications, *J. Opt. Soc. Am. B* **6**, 622–633 (1989)
- 21.124 A. Aznar, R. Solé, M. Aguiló, F. Díaz, U. Griebner, R. Grunwald, V. Petrov: Growth, optical characterization, and laser operation of epitaxial $Yb:KY(WO_4)_2/KY(WO_4)_2$ composites with monoclinic structure, *Appl. Phys. Lett.* **85**, 4313–4315 (2004)
- 21.125 Y.E. Romanyuk, I. Utke, D. Ehrentaut, V. Apostolopoulos, M. Pollnau, S. Garcia-Revilla, R. Valiente: Low-temperature liquid-phase epitaxy and optical waveguiding of rare-earth-ion-doped $KY(WO_4)_2$ thin layers, *J. Cryst. Growth* **269**, 377–384 (2004)
- 21.126 T. Kawaguchi, D.H. Yoon, M. Minakata, Y. Okada, M. Imaeda, T. Fukuda: Growth of high crystalline quality $LiNbO_3$ thin films by a new liquid phase epitaxial technique from a solid-liquid coexisting melt, *J. Cryst. Growth* **152**, 87–93 (1995)

- 21.127 E. Bauer: Phänomenologische Theorie der Kristallabscheidung an Oberflächen II, *Z. Kristallogr.* **110**, 395–431 (1958), in German
- 21.128 A. Aznar, O. Silvestre, M.C. Pujol, R. Solé, M. Aguiló, F. Díaz: Liquid-phase epitaxy crystal growth of monoclinic $\text{KLu}_{1-x}\text{Yb}_x(\text{WO}_4)_2/\text{KLu}(\text{WO}_4)_2$ layers, *Cryst. Growth Des.* **6**, 1781–1787 (2006)
- 21.129 J.D. Bierlein, A. Ferretti, L.H. Brixner, W.Y. Hsu: Fabrication and characterization of optical waveguides in KTiOPo_4 , *Appl. Phys. Lett.* **50**, 1216–1218 (1987)
- 21.130 A. Raizman, D. Eger, M. Oron: X-ray characterization of Rb exchanged KTP, *J. Cryst. Growth* **187**, 259–267 (1998)
- 21.131 L.K. Cheng, J.D. Bierlein, C.M. Foris, A.A. Ballman: Growth of epitaxial thin-films in the KTiOPo_4 family of crystals, *J. Cryst. Growth* **112**, 309–315 (1991)
- 21.132 L.K. Cheng, J.D. Bierlein, A.A. Ballman: $\text{KTiOP}_x\text{As}_{1-x}\text{O}_4$ optical wave-guides grown by liquid-phase epitaxy, *Appl. Phys. Lett.* **58**, 1937–1939 (1991)
- 21.133 M.A. Harmer, M.G. Roelofs: Sol-gel synthesis of thin-films of potassium titanyl phosphate for non-linear optical applications, *J. Mater. Sci. Lett.* **12**, 489–491 (1993)
- 21.134 F. Xiong, R.P.H. Chang, M.E. Hagerman, V.L. Kozhevnikov, K.R. Pöppelmeier, H. Zhou, G.K. Wong, J.R. Ketterson, C.W. White: Pulsed excimer-laser deposition of potassium titanyl phosphate films, *Appl. Phys. Lett.* **64**, 161–163 (1994)
- 21.135 P.M. Lundquist, H. Zhou, D.N. Hahn, J.B. Ketterson, G.K. Wong, M.E. Hagerman, K.R. Pöppelmeier, H.C. Ong, F. Xiong, R.P.H. Chang: Potassium titanyl phosphate thin-films on fused quartz for optical waveguide applications, *Appl. Phys. Lett.* **66**, 2469–2471 (1995)
- 21.136 R. Solé, V. Nikolov, A. Vilalta, J.J. Carvajal, J. Massons, J. Gavalda, M. Aguiló, F. Díaz: Liquid phase epitaxy of KTiOPo_4 on $\text{KTi}_{1-x}\text{Ge}_x\text{OPO}_4$ substrates, *J. Cryst. Growth* **237–239**, 602–607 (2002)
- 21.137 L.K. Cheng, L.T. Cheng, J. Galperin, P. Morris-Hotseppiller, J.D. Bierlein: Crystal-growth and characterization of KTiOPo_4 isomorphs from the self-fluxes, *J. Cryst. Growth* **137**, 107–115 (1994)
- 21.138 A. Peña, S. Di Finizio, T. Trifonov, J.J. Carvajal, M. Aguiló, J. Pallares, A. Rodriguez, R. Alcubilla, L.F. Marsal, F. Díaz, J. Martorell: Two dimensional KTP photonic crystal grown using a macroporous silicon template, *Adv. Mater.* **18**, 2220–2225 (2006)

Growth and

22. Growth and Characterization of KDP and Its Analogs

Sheng-Lai Wang, Xun Sun, Xu-Tang Tao

Crystals of potassium dihydrogen phosphate (KDP, KH_2PO_4) and its deuterated analogs (DKDP, $\text{K}(\text{D}_x\text{H}_{1-x})_2\text{PO}_4$) have been studied for their interesting electrical and optical properties, structural phase transitions, and ease of crystallization. They are the only nonlinear crystals currently applied in inertial confinement fusion (ICF), which has made them a hot topic of research for decades. To yield enough large crystals exceeding 50 cm in all three dimensions, the point-seed technique was recently developed. This method can grow crystals one order of magnitude faster than conventional methods. Recent developments in both the techniques and science of growth phenomena and defect formation under various conditions are described in this chapter, which also reviews significant advances in understanding of the fundamentals of KDP crystal growth, other growth methods to yield large high-quality crystals, growth defects and optical performance, and evaluations of crystal quality.

22.1	Background	759
22.2	Mechanism and Kinetics of Crystallization	761
22.2.1	Studies of KDP Crystal Surfaces	761
22.2.2	Nucleation Studies in Supersaturated Solution	763
22.2.3	Dislocation Mechanism	765
22.2.4	Growth on Two-Dimensional Nuclei	767
22.2.5	Growth from Crystal Edges	767
22.3	Growth Techniques for Single Crystals	769
22.3.1	Parameters Affecting Growth Rate ..	769
22.3.2	Stability of Solution	770
22.3.3	Conventional Methods	771
22.3.4	Rapid Growth from a Point Seed	773
22.4	Effect of Growth Conditions on Defects of Crystals	776
22.4.1	Impurity Effect	776
22.4.2	Supersaturation	779
22.4.3	Filtration	780
22.4.4	Hydrodynamic Effects	781
22.5	Investigations on Crystal Quality	783
22.5.1	Spectroscopic Studies	783
22.5.2	Homogeneity	784
22.5.3	Laser Damage Threshold	787
	References	789

22.1 Background

Crystals of potassium dihydrogen phosphate (KDP) and its isomorphs have been the subject of a wide variety of investigations for over half a century owing to their interesting electrical and optical properties, structural phase transitions, and ease of crystallization [22.1–4]. Today, these crystals are widely used in both laboratory and industrial settings to control the parameters of laser light, such as pulse width, polarization, and frequency, through first- and second-order electrooptic effects [22.4, 5]. Their application in inertial confinement fusion (ICF) research [22.6] has made them a hot topic of research for decades.

The very high-energy Nd-glass lasers used for ICF research need large plates of nonlinear crystals for electrooptic switches and frequency converters (Fig. 22.1). The lasers under construction in the USA and France with about $40 \times 40 \text{ cm}^2$ aperture require single-crystal boules with linear dimensions in the 50–100 cm range. KDP (KH_2PO_4) and its deuterated analogs DKDP ($\text{K}(\text{D}_x\text{H}_{1-x})_2\text{PO}_4$) are the only nonlinear crystals currently used for these applications due to their unique physical properties, which include transparency over a wide region of the optical spectrum, resistance to damage by laser radiation, and relatively high nonlin-

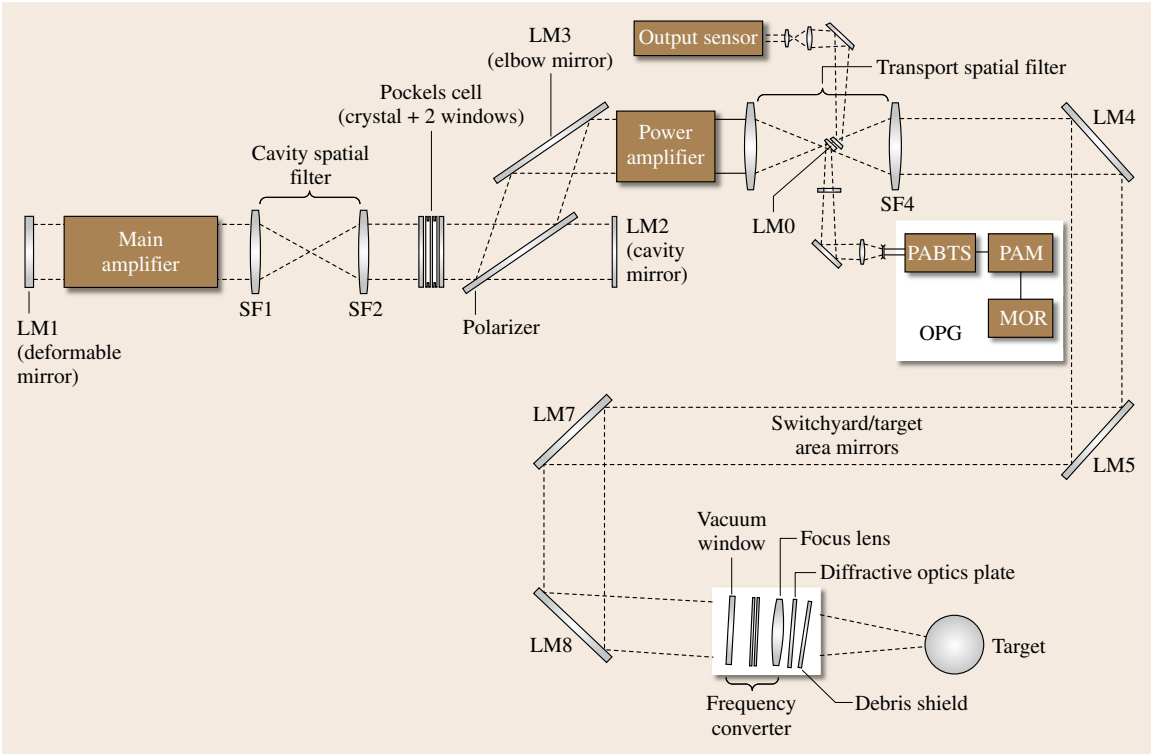


Fig. 22.1 Schematics of single NIF beamline showing positions of major optical components (after [22.7], with permission of ASM) (LM – laser mirror, SF – spatial filter, OPG – optical pulse generation)

ear efficiency, in combination with reproducible growth to large size and perfection.

The main limitation in growth of such large crystals by traditional techniques is the growth rates of only 0.5–1 mm/day typical for low-temperature solution growth, which leads to growth cycles exceeding 1–2 years. Work on rapid growth of KDP crystals started in the early 1980s when the world’s biggest laser of that time, Nova, was being built at the Lawrence Livermore National Laboratory (LLNL). New rapid growth techniques [22.9–11] explored at that time involved radical modification of standard crystallization equipment. However, the complicated designs proposed could not solve the problems such as hydrodynamic conditions [22.9] and control of high supersaturation needed to avoid defect formation and spontaneous nucleation [22.10]. As a result, the 27×27 cm² plates of KDP crystals for the frequency-conversion arrays on Nova were grown by traditional techniques.

Also, a rapid crystal growth method called the point-seed technique, based on the traditional solution growth process, was initiated at Moscow State Univer-

sity [22.12]. This technique demonstrated that KDP and DKDP crystals could be grown in standard Holden-

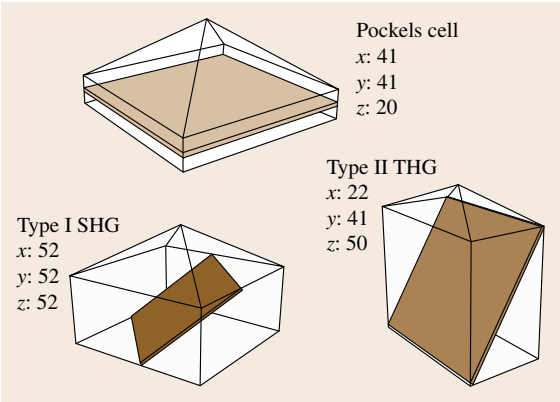


Fig. 22.2 The minimum size of KDP single-crystal boules (in cm) needed for obtaining Pockels cell and harmonic-generation plates of different types for the NIF project (after [22.8], with permission of Elsevier) (SHG – second harmonic-generation, THG – third harmonic-generation)

type rotary crystallizers without spontaneous nucleation and visible defects, one to two orders of magnitude faster than by conventional methods. Later this method was further developed and scaled for production of crystals for Nova's successor – the National Ignition Facility (NIF), under construction at LLNL [22.8]. To achieve economically useful yield, crystals grown for NIF should exceed 50 cm in all three dimensions (Fig. 22.2).

The development of new techniques required both technical solutions and scientific knowledge about growth phenomena, defect formation at varying degrees

of supersaturation, and growth rate. The purpose of this chapter is to describe recent developments in growth and characterization of KDP and its analogs. The chapter also includes significant advances in understanding the fundamentals of KDP crystal growth, developing growth methods to yield large-dimension high-quality crystals, and the relation between growth defects and optical performance. To this end, the chapter is divided into four sections encompassing the mechanism and kinetics of crystallization, growth techniques for single crystals, the effect of growth conditions on crystal defects, and problems with crystal quality.

22.2 Mechanism and Kinetics of Crystallization

As we know, since the growth of crystals takes place at the crystal–solution interface, structural information on the immersed solid is essential for understanding crystal growth from solution or melt. This is also a very important topic for KDP-type crystals, which can help us to understand the relaxations and possible reconstructions of the top layers, the influence of impurities on morphology, and even the possible reason for change in optical properties of crystals.

22.2.1 Studies of KDP Crystal Surfaces

The crystallographic theory of Hartman and Perdok aims to predict the morphology of growing crystals dominated by the so-called F (flat) faces, referred to by the Miller indices (hkl) [22.14, 15]. However, the theory has its limitations. Often more than one surface termination is possible for a given orientation (hkl) and it is impossible to predict which of the alternatives will control the crystal growth.

The theory predicts that the pyramidal faces {101} and the prismatic faces {100} of KDP are flat in solution [22.16, 17], in agreement with the observed habit of these crystals (Fig. 22.3a). For the prismatic {100} faces exactly one surface termination is predicted (Fig. 22.4). For the pyramidal {101} faces, however, two alternative terminations are theoretically possible. One has the negative H_2PO_4^- groups on the outside, and the other the positive K^+ ions (Fig. 22.3b). The difference in polarity of the layers and, especially, the differences in size and polarizability of the ions will result in a different surface free energy. From the surface morphology observed with interference-contrast reflection microscopy

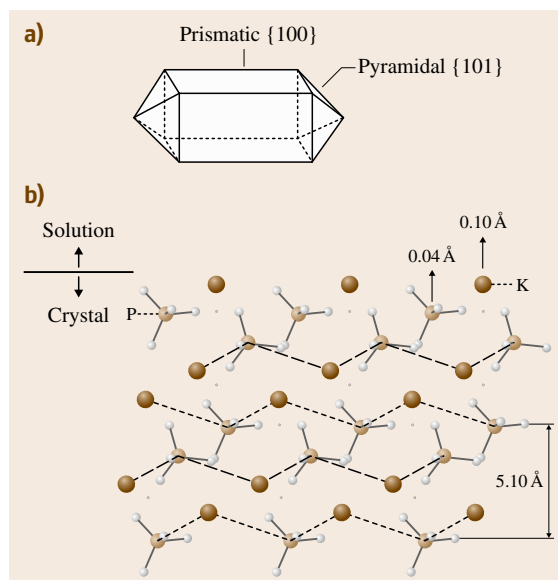


Fig. 22.3 (a) Growth habit of a KDP crystal with the prismatic and pyramidal faces indicated. (b) Schematic side view of the pyramidal face, KDP {101}, projected on the {111} plane. The big circles are the potassium atoms while the PO_4 groups are depicted as a circle for the phosphorus atom connected by sticks to the four neighboring oxygen atoms, shown as small white circles. The dots give the positions of the hydrogen atoms between two oxygen atoms. The layers with the K^+ ions on top are schematically indicated by the dashed lines and the layers with the H_2PO_4^- groups on top by the discontinuous lines. Arrows indicate the relaxations in the topmost layer as determined from fitting the experimental data (after [22.13])

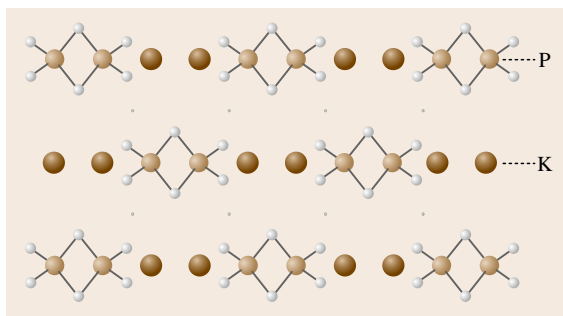


Fig. 22.4 The prismatic KD P{100} face projected on the {010} plane. Here only one termination is possible (after [22.13])

and considering the symmetry of the crystal [22.17, 18] it can be concluded that the surface is bounded by only one of the polar layers. This is confirmed by atomic force microscopy measurements where the height of the steps on the {101} face is always found to correspond to 0.5 nm, the thickness of double layers [22.19].

De Vries and coworkers used the technique of surface x-ray diffraction at a third-generation synchrotron radiation source to determine the structure of KDP crystal surfaces in air, vacuum, and solution [22.13, 20]. They measured the distribution of diffracted intensities along so-called crystal truncation rods (CTRs) [22.21], which is hardly influenced by the solution and mainly depends on the crystal surface atomic structure. All data show that the pyramidal {101} faces are terminated with K^+ atoms rather than with $H_2PO_4^-$ groups, while the prismatic {100} faces terminate in alternating rows of K^+ and $H_2PO_4^-$ ions (Fig. 22.5).

From the atomic structure of both faces, it is easy to be understood why small traces of trivalent metal ion impurities such as Fe^{3+} or Cr^{3+} block the growth of the prismatic faces, but affect the growth of the pyramidal faces to a much lesser extent [22.17, 22, 23]. With only K^+ ions on the surface of the crystal, metal impurities such as Fe^{3+} and Cr^{3+} ions will experience a large barrier to adsorption onto the positively charged face. The impurity content is limited by adsorption kinetics on the terraces rather than incorporation kinetics at the steps. On the prismatic faces, however, these ions can adsorb easily, and small amounts of Fe^{3+} or Cr^{3+} will already block the growth.

Furthermore, De Vries et al. present the results of experiments about the solid–liquid interface during growth, with and without the addition of Fe^{3+} impurities. The surface was roughened, as seen from the decrease in intensity in between the Bragg peaks. The

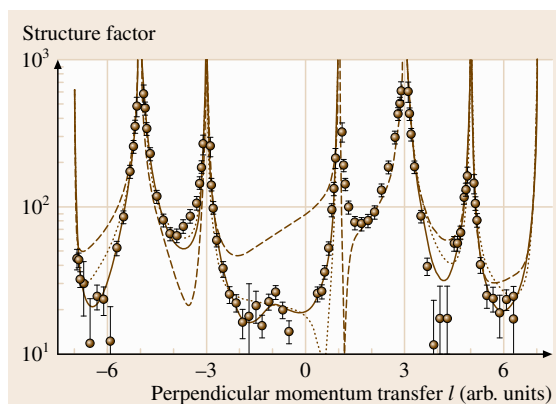


Fig. 22.5 Structure-factor amplitudes along the $(hk) = (10)$ crystal truncation rod for KDP {101} as a function of the diffraction index, which is expressed in reciprocal lattice units. The dotted line is a calculation for a bulk K^+ -terminated surface, the dashed curve for a $H_2PO_4^-$ -terminated one. The solid line is the best fit starting from a K^+ -terminated surface and allowing the K^+ ions and the $H_2PO_4^-$ groups in the top layer to relax (after [22.13])

overall shape of the CTR is unchanged, so no ordered layer of Fe^{3+} is formed on the surface. Apparently, the amounts of adsorbed Fe^{3+} are very small. These impurities locally pin the moving steps [22.24–26], which causes an increased meandering of the steps and thus leads to a rougher surface.

The molecular structure of interface boundary layers in the crystal growth of KDP and DKDP has been an interesting topic for a long period. The Raman spectra of saturated KDP solution show that only 40% of the phosphates exist as monomers and that anion–anion association via hydrogen bonds does cease at the dimer [22.27]. Lu et al. [22.28] studied the growth units of KDP crystal from the growth solution by using space group theoretical analyses and Raman spectra; the result proved that the growth unit is dimers of $[H_2PO_4^-]$ anions. Yu et al. [22.29] used holography to measure the thickness of boundary layers to be a few hundred micrometers during KDP crystal growth in free convection. Their real-time Raman microprobe experiments show that the smectic ordering structure of the anions–cations called the crystallization unit is formed within the boundary layer of KDP and DKDP growth solutions [22.30].

An in situ x-ray diffraction study of growth surface by Reedijk et al. [22.31] revealed interface-induced ordering in the first four layers of water molecules. The first two layers behave ice-like and are strongly bound

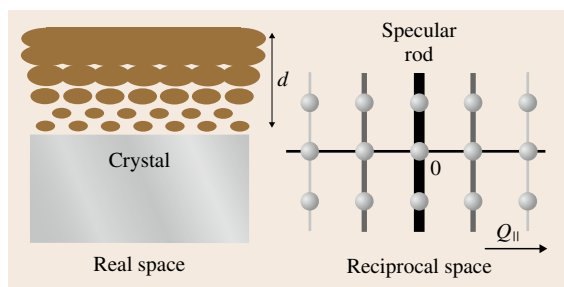


Fig. 22.6 Schematic drawing of a crystal covered with a partly ordered liquid layer of thickness d . The contribution of the (partially) ordered liquid to the substrate diffraction rods is strongest in the specular rod and diminishes at higher parallel momentum transfer (Q_{\parallel}) in reciprocal space (after [22.31])

to the surface. The next two layers are more diffuse and show only minor lateral and perpendicular ordering (Fig. 22.6). The highly ordered liquid at the interface is expected to slow down the incorporation and diffusion of the growth units.

Further research [22.33] on the solid–liquid interface structure of the {101} and {100} faces of KDP crystals in contact with growth solutions of different pH values showed in all cases several liquid layers with varying degrees of lateral and perpendicular order. The structural changes are large for the {101} face and small for the {100} face. The changes at the {101} face are likely due to the pH-dependent competition between K^+ and H_3O^+ bonding.

22.2.2 Nucleation Studies in Supersaturated Solution

Nucleation theory has developed since the early 18th century. Mullin [22.34] classified nucleation into two major group: primary nucleation and secondary nucleation, where nuclei are generated in the vicinity of crystals already present in a supersaturated system. Primary nucleation consists of homogeneous nucleation and heterogeneous nucleation. The study on the stability of solution by Zaitseva et al. [22.32] provided the basis to develop fast growth techniques for KDP and DKDP crystals.

Primary Nucleation

Cooling a solution with concentration C to a temperature T under its equilibrium temperature leads to a supersaturated solution. The supersaturation ΔC is $C - C_0$. In classic nucleation theory, the homogeneous

nucleation rate of the supersaturated solutions, i.e., the frequency of formation of a particle with critical nucleus in a unit volume, is expressed as

$$J = B_1 \exp \left(- \frac{16\pi\alpha^3\omega^3}{3k_B^3 T^3 \left(\ln \frac{C}{C_0} \right)^2} \right). \quad (22.1)$$

The induction period is inversely proportional to the nucleation rate, which leads to the expression

$$\text{int}_i = B + \frac{16\pi\alpha^3\omega^3}{3k_B^3 T^3 \left(\ln \frac{C}{C_0} \right)^2}. \quad (22.2)$$

Equations (22.1) and (22.2) express the width of the metastable zone in terms of the supersaturation and induction time for homogeneous nucleation. However, the quantitative estimation of these parameters for real crystallization systems using these equations is practically impossible because of the many unknown parameters, such as α , the specific free energy of the interface, that form the constants. It is not of much help in practical work because a real growth system obviously does not deal with homogenous nucleation. The presence of crystallizer walls, parts of equipment, and extraneous particles in the supersaturated solution makes heterogeneous nucleation more probable. Some theoretical calculations and experiments in pure containerless systems show that homogeneous nucleation occurs at extremely high concentrations, exceeding the solubility limit by several factors [22.35–37].

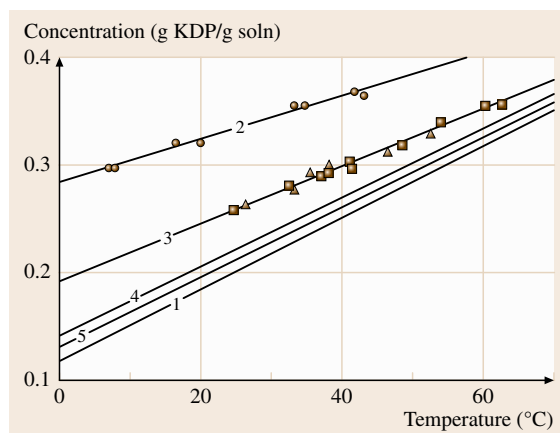


Fig. 22.7 Stability of supersaturated KDP solutions: (1) solubility curve; (2) and (3) metastable boundaries of solutions without (●) and with (■) a growing crystal, respectively; (▲) experiments with the empty platform; (4) and (5) traditional level of stability (after [22.32])

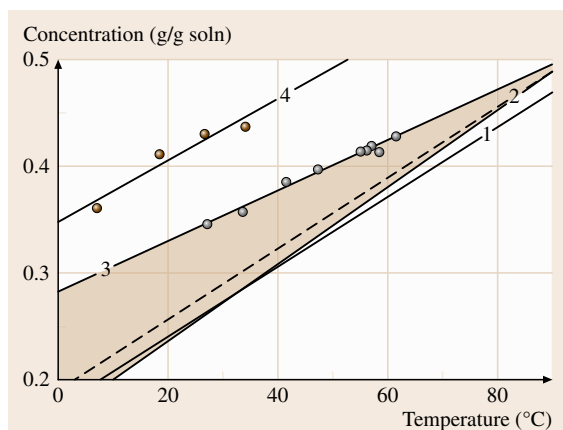


Fig. 22.8 Metastable zone of DKDP solutions ($X = 98\%$). (1) Monoclinic phase solubility. (2) Tetragonal phase solubility. (3) Metastable boundary in the presence of a growing crystal. The region of tetragonal crystals growth is shaded. For comparison the data of [22.38] are shown (dashed line). (4) Metastable boundary without crystals (after [22.32])

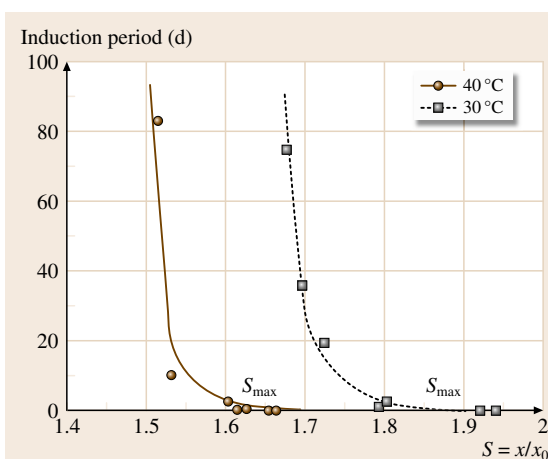


Fig. 22.10 Effect of supersaturation on induction period in KDP solutions (after [22.32])

In order to understand the nature of nucleation in a real crystallization system there was no other way but to perform experiments in the system. Zaitseva et al. measured the metastable zone of KDP solution by the polythermal method in standard Holden-type crystallizers with volumes of 5–20 l and 1000 l [22.32]. Figures 22.7–22.9 present the results, which show the maximum concentration and supersaturation reached without spontaneous nucleation in stirred KDP and DKDP solutions without growing crystals. The level of supersaturation that can be reached is much higher than that expected from previous studies [22.10, 38]. The experiments show a much narrower metastable zone when the solution is not filtered. The drop of stability is due to the effect of typical heterogeneous particles present in the salts generated during their commercial production. Insufficient overheating can cause a similar drop in stability as in the absence of filtration. Solution overheating of 80 °C can result in reproducible stability, independent of the saturation temperature. They found no correlation between spontaneous nucleation and the chemical purity of the solutions, which is different from other investigations [22.34, 39–41].

The induction period was also measured for various supersaturated solutions by the isothermal method in the same crystallizers [22.32]. The results (presented in Fig. 22.10) show a sharp increase of induction period at supersaturation of less than some certain values (35% for 40 °C, 50% for 30 °C). Experimentally this means that no precipitation was observed for 3 months with supercooling more than 30 °C below the saturation point.

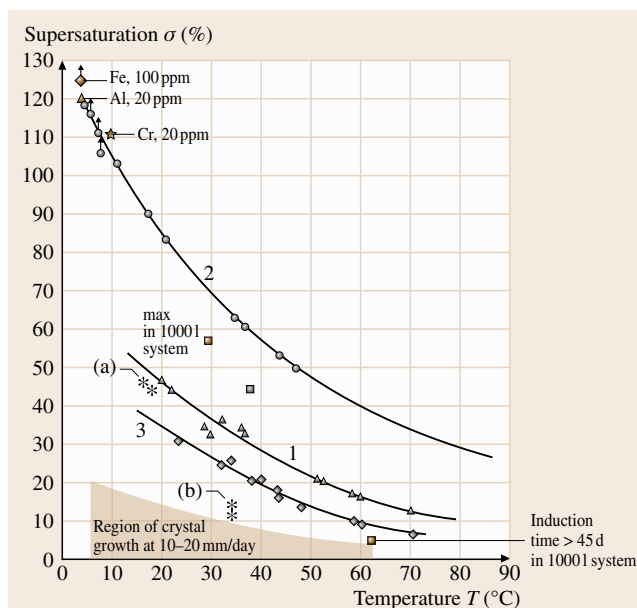


Fig. 22.9 Temperature dependence of supersaturation σ_{\max} reached in KDP solutions without spontaneous nucleation: (○) filtered and (△) unfiltered solutions without crystals overheated at 80 °C; (◇) filtered solution in the presence of a crystal overheated at 80 °C; (*) filtered (a) and unfiltered (b) solutions without crystals overheated at 54 °C (after [22.42])

Secondary Nucleation

Secondary nucleation is more difficult to explain in detail as there are at least three categories of secondary nucleation: apparent (small fragments washed from the surface of crystalline seeds), true (when the current level of supersaturation is higher than the supersaturation level or the solute particles present in solution), and contact nucleation (when a growing particle contacts the walls of the baffles, stirrer or other objects, thus leaving behind residual solute particles that have been broken off from primary crystals) [22.43].

Randolph and *Larsen* stated that, in either continuously stirred crystallizers or seeded batch crystallizers, the main source of secondary nuclei is the crystal suspension itself [22.44]. *Boiste* also agrees that a major source is the crystal surface; secondary nuclei form whenever the tiny embryos, or crystallites, that are removed from the surface and dispersed into a supersaturated solution exceed the critical size [22.45].

Secondary nucleation initiated by a well-faceted crystal is often treated as aggregates appearing and being held in a stagnant supersaturated (transitional boundary) layer under the influence of the force field of the crystal [22.46]. These aggregates are thought to be stripped off the crystal surface by fluid motion, providing secondary nuclei [22.46, 47]. However, there is still a certain contradiction, as supersaturation in the immediate vicinity of the growing crystal is lower than elsewhere in the solution.

Most empirical expressions based on the results obtained in real crystallization systems predict very narrow metastable regions with a width of a few degrees [22.38, 48–50]. However, the metastable zone reported by *Zaitseva* et al. is much larger than those listed above [22.32]. The experiments show that a defectless crystal does not produce any secondary nucleation and does not influence spontaneous nucleation from solution. The initial results shown in Figs. 22.7–22.9 show that the presence of a growing crystal reduces the solution stability, which was supposed to not be caused by secondary nucleation but rather by introduction of the platform into the otherwise closed system.

22.2.3 Dislocation Mechanism

The bulk of a faceted crystal is built up by deposition of surface layers parallel to the crystallographic faces. Recent experimental studies by means of optical interferometry [22.1] and atomic force microscopy (AFM) [22.25, 51] present clear evidence that the dislocation growth mechanism remains dominant during

the growth of KDP-type crystals. Dislocation bunches which give rise to growth hillocks on crystal faces form during seed regeneration. During further growth, dislocations arise from mutual displacement of the layers overlapping a solution inclusion or an extraneous particle. Two or more growth sources of the same activity can exist on a face simultaneously. The growth sources initiated during regeneration can be replaced by new leading hillocks that become more active under the changing conditions. The change of the leading hillock is inevitably accompanied by the formation of growth bands due to the appearance of new growth steps of various orientations [22.52]. When very strong and dense dislocation bunches form, cracking may occur due to great internal stress in the crystal during the growth process [22.53].

Dislocation hillocks on the pyramidal {101} and prismatic {100} faces of KDP and DKDP crystals have the different shapes shown in Fig. 22.11. The shapes of the hillocks reflect the crystallography of the face such that each hillock is comprised of a set of sectors with unique slopes and step. Growth occurs on monomolecular steps, and the hillocks on the {101} faces are shaped as trihedral pyramids with three neighboring slopes (vicinal sectors) of different steepness. The hillocks on the {100} faces have an elliptical shape that changes from almost round to nearly a parallelogram with four vicinal sectors at increasing supersaturation [22.1]. The intersection of the vicinal sectors of the hillocks form the edges of a hillock, called vicinal-sectoral boundaries, which are typically straight lines on both sets of faces. Intervicinal boundaries are the geometrical

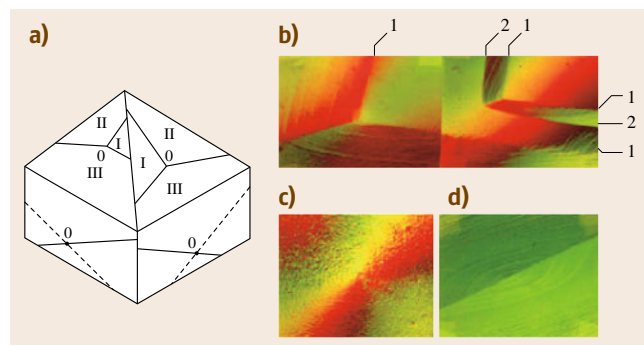


Fig. 22.11a–d Geometry and shape of the dislocation hillocks of KDP: (a) position on the adjacent faces; I, II, and III are vicinal sectors on {101} faces. (b) Micrograph of the hillocks on {101} face; 1 – vicinal boundaries; 2 – intervicinal boundary; as grown surface at $t = 30^\circ\text{C}$ and $\sigma = 0.06$; (c, d) growth hillocks on {100} face of KDP at low and high supersaturation, respectively (after [22.42])

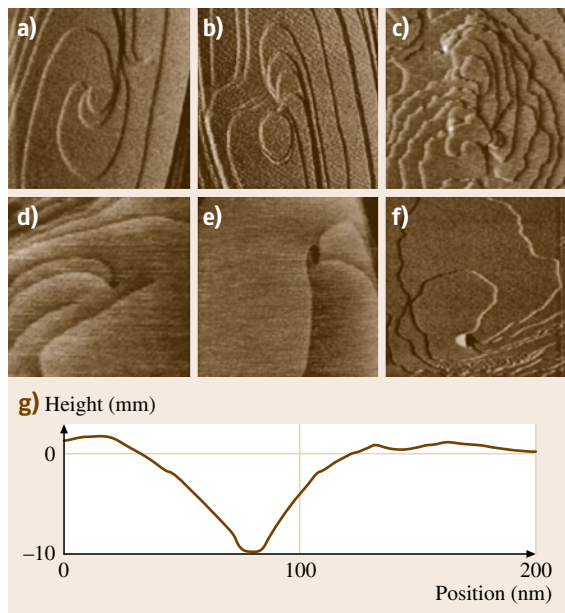


Fig. 22.12a–g AFM images of typical growth hillocks on {100} face of **KDP** showing complex structure of dislocation sources (a–c) and {101} face showing hollow cores at dislocation sources (d–f): cross-section of typical hollow core is shown in (g) (after [22.7]). (a) $1 \times 1 \mu\text{m}^2$; (b) $1.5 \times 1.5 \mu\text{m}^2$; (c) $2 \times 2 \mu\text{m}^2$; (d) $3 \times 3 \mu\text{m}^2$; (e) $2.6 \times 2.6 \mu\text{m}^2$; (f) $8.4 \times 8.4 \mu\text{m}^2$

points where the steps from the neighboring vicinal hillocks meet [22.42]. The position of the vicinal-sectorial boundaries is determined by the location of the dislocation outcrop on a crystal face. Their orientation, strictly connected with the crystal symmetry, can vary only within several degrees, depending on growth conditions [22.1, 54].

The AFM studies revealed that, for Burgers vectors in excess of one unit step, even simple sources exhibit hollow cores at the dislocation source on {101} faces (Fig. 22.12) [22.7, 19]. The shape of the cores demonstrates that the step edge energy is isotropic. X-ray projection topograph of a {101} **KDP** plate shows that the adjacent vicinal sectors are each slightly disoriented relative to the others, and the average difference of the lattice parameters is of the order of 10^{-6} of the average lattice parameter value (Fig. 22.13) [22.18, 55]. As a rule, the lattice deformations are maximal at these boundaries that form the vicinal sector I on {101} faces, whereas the steps of the vicinal sectors II and III smoothly convert into each other without clearly discernible deformations. Different impurities selectively

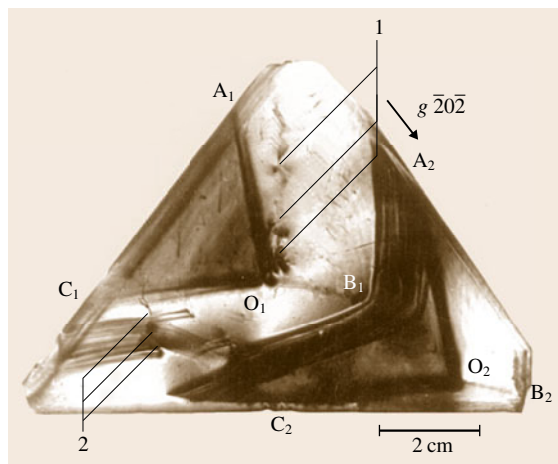


Fig. 22.13 Projection x-ray topograph of a plate cut parallel to the {101} dipyramid face of **KDP** crystal. O₁ and O₂, are tips of vicinal hillocks formed by dislocations, O₁A₁, O₁B₁, O₁C₁ and O₂A₂, O₂B₂, O₂C₂, are vicinal-sectorial boundaries, A₂B₁C₂ is an intervicinal boundary; 1, 2 are dislocations which do not form vicinal hillocks (after [22.42])

incorporate into the different vicinal sectors depending on their nature [22.55]. For example, Fe³⁺ and other metal impurities preferentially incorporate into sector I [22.56]. In **DKDP** crystals this defect can be

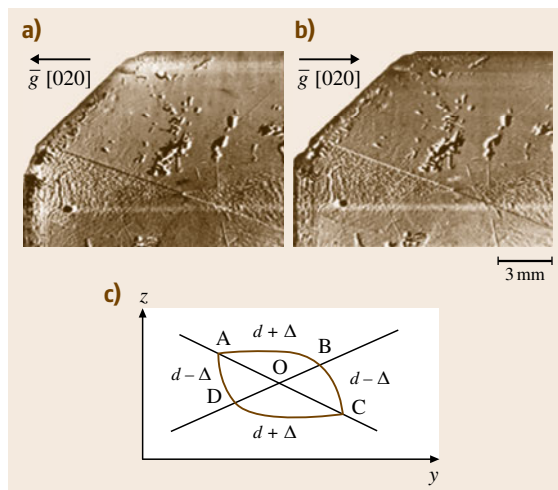


Fig. 22.14a–c X-ray topographic images of a vicinal hillock on the prismatic face of a **KDP** crystal (a,b) and diagram with notations for analyzing the contrast (c). d – lattice parameter, Δ – the difference of the parameter in adjacent vicinal sectors (after [22.42])

more pronounced because of the different composition of deuterium and hydrogen in the three vicinal sectors [22.42].

On the {100} face, the dislocation sources are often complex (Fig. 22.14). Vicinal hillocks on the face are shown in Fig. 22.11. Growth steps change their orientation on the edge AC abruptly, while on the edge BD the orientation changes more smoothly. The x-ray topograph reveals that the lattice parameters are greater in vicinal sectors AOB and COD than in sectors BOC and AOD [22.42]. Formation of these vicinal sectors can be also explained by the different incorporation of impurities into the differently oriented steps.

22.2.4 Growth on Two-Dimensional Nuclei

The main mechanism of growth was clear because the dislocation growth sources could be easily seen on the growing faces. At the same time, the growth of KDP {101} surfaces occurs also on islands formed by two-dimensional (2-D) nucleation (Fig. 22.16) at moderate supersaturations (10%) [22.19]. Furthermore, on the terraces of the vicinal hillocks formed by 2-D nucleation, island growth competes with step flow when the interisland spacing is comparable to the terrace width. For example, 2-D nucleation [22.57, 58] was found to contribute to the rapid growth of crystal on the *negative* pyramidal faces $\{10\bar{1}\}$ just above the platform (Fig. 22.15). All the dislocations formed during regeneration very quickly vanish from these negative pyramidal faces because of their orientation at some angle to the platform surface. The dislocation-free growth rate measured in the range of 63–60 °C at $a = 0.06$ is about one order of magnitude (1–1.5 mm/day) slower than for the case of dislocation growth (about 15–17 mm/day under the same conditions).

De Yoreo et al. [22.19] estimated that, at supersaturation below 5%, layer growth on {101} faces is dominated by the dislocation mechanism, and that growth on 2-D nuclei begins to compete at 5–10% supersaturation. Results from Alexandru [22.59] showed that growth by the dislocation mechanism on {100} surface is severely retarded by the stopper action of impurities, particularly towards smaller supersaturation. At supersaturation less than 8–10% the dislocation mechanism of growth appears to compete with 2-D nucleation mechanism at lower impurity concentration. The two-dimensional nucleation mechanism of growth becomes dominant at higher supersaturation.

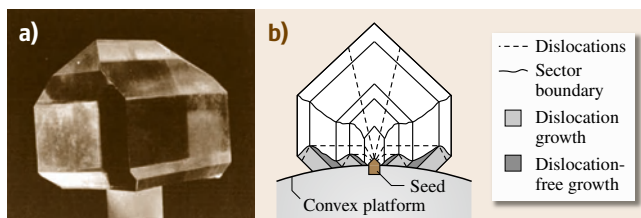


Fig. 22.15 (a) KDP crystal with clearly pronounced {101} low pyramids growing periodically by dislocation and dislocation-free mechanism; (b) schematic of dislocation geometry on convex-shaped platform (after [22.42])

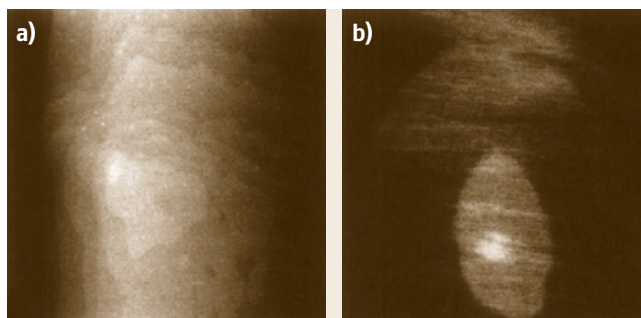


Fig. 22.16 (a) AFM image ($5.4 \times 5.4 \mu\text{m}^2$) of typical hillock on KDP {101} at which no dislocations are observed. (b) Higher-resolution ($715 \times 715 \text{ nm}^2$) image of one such hillock showing the topmost island, for which the radius is 42 nm (after [22.19])

22.2.5 Growth from Crystal Edges

Existing models of dislocation growth typically do not take into account mutual effects of growing crystal faces and participation of the edges in the growth process. The edges of faceted crystals are often considered as passive places where the steps produced on adjacent faces meet, although evidence of growth-step generation from the edges has been reported in many experimental works [22.60, 61].

Zaitseva et al. proposed a possible mechanism of growth-step generation from the edges of faceted crystals obtained from experimental observations with KDP crystals [22.62]. It suggests that growth from the crystal edges is initiated by the deviation of the edges from their crystallographic orientation and formation of incomplete shapes of singular facets. An incomplete crystallographic shape of a singular face is determined by the existence of concave angles formed by the edges in the plane of this face. These concave angles are sources of growth steps in the surface layer. The surface layer generated from a concave angle on a singular

crystal face completes the crystallographic shape of the face. Growth of this surface layer does not require the existence of a preceding layer of the same orientation.

Formation of the layers on the crystal edges, such as the *z*-cut seed regeneration process, can be observed during growth of KDP crystals. The thin surface layers can grow from the edges in crystallographic planes without pre-existing layers under them. A typical explanation for this phenomenon is attributed to a supersaturation gradient and better hydrodynamic conditions on the edges [22.63].

Experiments [22.62] including regeneration of singular faces with incomplete crystallographic shape (Fig. 22.17) and formation of the thin surface layers during joining of two equally oriented crystals were performed to clarify what effect such deviations produce during growth and formation of the surface structure. These experiments suggested that the process of step generation from the edges was connected with the de-

viation of faces from crystallographic orientations and shape, resulting from vicinal hillocks on the crystal surface.

The growth velocity of these layers has the same order of magnitude as the tangential growth rate V of a dislocation step. Estimations give values for the velocity of the thin-film advancement of 1×10^{-4} – 4×10^{-4} cm/s at temperature of 30 °C and supersaturation of about 0.09, while the value of V from [22.64] is 7×10^{-4} cm/s for about the same growth conditions. The measurements done at 60 °C gave higher values of about 1×10^{-3} cm/s at approximately the same supersaturation [22.62].

According to this mechanism, the crystal surface should be considered as an entire system. The structure of one separate face is connected with the phenomena that take place on the other faces through the crystal edges, which play an important role during crystal growth. During the growth of faceted crystals, this mechanism may work in combination with the dislo-

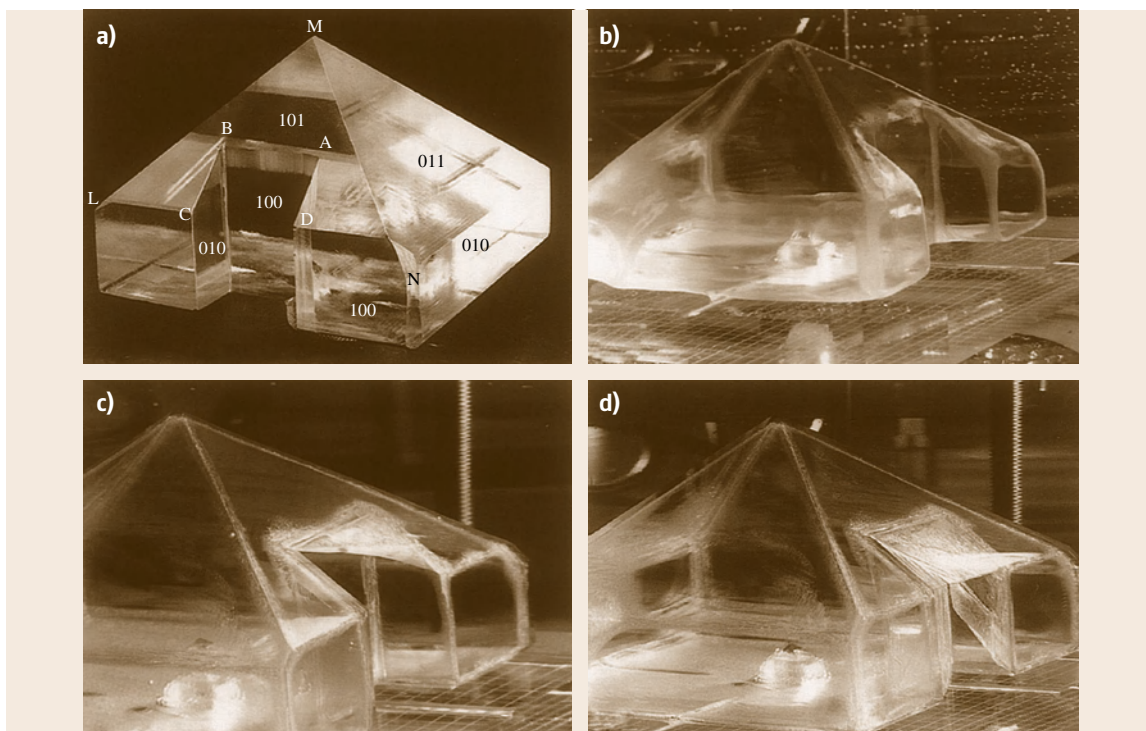


Fig. 22.17a–d Regeneration of KDP crystal surfaces of incomplete crystallographic shape: (a) initial crystal with a removed part; (b) first stage of the regeneration process; (c) formation of a thin surface layer from concave angles A and B on the edge of the {101} face; (d) formation of the {100} surface by thin layers; $t_0 = 65$ °C; $\sigma = 0.08$; crystal cross section about 10×10 cm² (after [22.62])

cation mechanism of growth. Dislocation sources of steps form vicinal slopes which lead to a deviation of the crystal faces and edges from their crystallographic orientation. The reconstruction of the complete crystallographic shape of adjacent faces occurs by the incorporation of building units into the crystal edges. This process results in the generation of growth steps to the deviated faces. The deviation from singularity caused by the presence of vicinal slopes of a crystal

face is compensated for and corrected by growth steps generated from the edges.

However, the question that still exists is why these crystals grow not by close packing of the volume but by creating thin surface layers and hollow spaces under them. Formation of the thin layers creates at least double the surface area. In this regard, close packing should be more beneficial because of minimization of the surface energy.

22.3 Growth Techniques for Single Crystals

There have been more than 80 years of research on the growth of KDP/DKDP crystals. The need for large single-crystal plates for use as Q-switches and laser radiation converters [22.6] has stimulated the development of growth techniques for KDP crystals, but the key problems to be solved are centered on the rapidly growing large-aperture crystals and improving the optical quality of the crystal.

22.3.1 Parameters Affecting Growth Rate

The growth rate of KDP crystals depends on many parameters, such as growth temperature, supersaturation of growth solution, impurities, and hydrodynamic conditions, as described in detail by Zaitseva et al. [22.55] and other authors [22.7, 66–68]. KDP/DKDP crystals typically grow by the screw dislocation mechanism. The growth rate R of a crystal face in the direction normal to it is given by the geometrical relation

$$R = pV. \quad (22.3)$$

Here p is the slope of the dislocation hillock and V is the tangential speed of the elementary steps. As follows from (22.3), the hillock structure and the step velocity affect the growth rate. In the kinetic limit, the step speed V is linearly connected with the supersaturation σ through

$$V = b\beta\sigma, \quad (22.4)$$

$$\beta = \beta_0 \exp(-E_A/k_B T), \quad (22.5)$$

where b and β_0 are constants, β is the kinetic coefficient, E_A is the activation barrier of the slowest stage of growth, T is the temperature, and k_B is the Boltzmann constant. According to (22.4) and (22.5), the step speed V can be increased by increasing either σ or T .

Increasing supersaturation has always been known as an obvious way to accelerate crystal growth. The shift of the growth process to higher temperature can also increase the growth rate by increasing the value of the kinetic coefficient [22.65, 69]. In agreement with the above analysis, the growth rates empirically measured by Zaitseva et al. [22.42] show very close relationship with temperature T and supersaturation σ , as shown in Fig. 22.18.

The slope p in the expression (22.3) is determined by the structure of a dislocation hillock. It depends on the amount of dislocations in the growth source m ; the distance between them, defined by the length $2L$; the el-

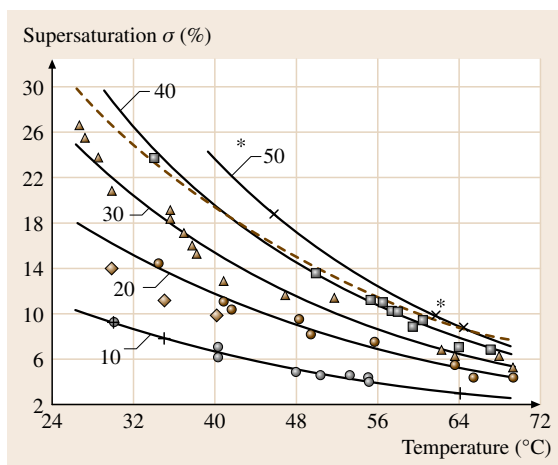


Fig. 22.18 Temperature dependence $\sigma(T)$ corresponding to approximately constant growth rates of KDP crystals R : 10 mm/day (\circ), 20 (\bullet), 30 (\blacktriangle), 40 (\square), 50 (\times), and 60 ($*$); + and \diamond are data from [22.65] for 10 and 20 mm/day, respectively. The dashed line is the boundary of the metastable zone (after [22.42], with permission of Elsevier)

elementary step height h ; and the critical radius r_c , given by

$$p = mh/(19r_c + 2L), \quad (22.6)$$

$$r_c = \omega\alpha/k_B T \sigma, \quad (22.7)$$

where ω is the volume of a molecule of the crystallizing matter and α is the specific free energy of a step edge. Expression (22.7) is obtained from the Gibbs–Thomson formula. According to (22.6) and (22.7), p (and hence R) can be increased by increasing σ or changing the number of dislocations in the growth source. Direct control of the growth rate by changing the dislocation structure is difficult because of the complicated relationship between the structure of a dislocation source, σ , and T [22.71]. However, as recently shown [22.68], for $\sigma > 5\%$ the activity of a growth hillock is dominated by the presence of strain-induced dislocation cores and is nearly independent of σ .

There are two more important parameters affecting growth rate: impurities and mass transfer, or hydrodynamic conditions. The metallic cations, especially those with high valency, were considered to greatly affect the growth rate. It is well known that metallic cations (such as Sn^{4+} , Fe^{3+} , Cr^{3+} , and Al^{3+}) affect the growth rate of prismatic faces of KDP crystals much more than the pyramidal ones [22.72]. Fe^{3+} and Al^{3+} ions can decelerate the growth rate of {100} faces [22.66]. With increasing impurity concentration of Fe^{3+} or Cr^{3+} ions, the crystal growth rate of {101} faces first increases and then decreases [22.67]. Sn^{4+} ions can decrease the growth rate of both {100} and {101} faces [22.73].

Anions with strong H-bond affinity such as oligophosphate, are easily adsorbed on the pyramidal faces and inhibit their growth, resulting in extended prismatic faces [22.74–76]. Organic materials such as glycol and ethylene diamine tetraacetic acid (EDTA) show growth-promoting effects on both pyramidal and prismatic faces at very low concentration [22.77], but the growth rate decreases with continuous increase of additive concentration.

Thus, the growth rate can be increased by purification of the raw material, as well as by shifting the growth process into the kinetic regime by increasing the velocity of the solution flow relative to the surface of the growing crystal [22.1, 34]. Unfortunately, wide variations in impurity levels and hydrodynamic conditions are limited because of their undesirable influence on the optical quality of growing crystals. Greater acceleration of the growth rate can obviously be obtained by increasing the supersaturation.

22.3.2 Stability of Solution

Conventional methods could tolerate the presence of some spontaneous crystals during the growth process, but spontaneous nucleation means termination of the growth run for rapid crystal growth. Zaitseva et al. [22.32] performed experiments to show that KDP solution has a wide metastable zone, which provided the basis to develop fast growth techniques for KDP crystals.

A number of methods are reportedly used to improve the stability of the growth solution. These include superheating of the solution to dissolve microcrystals, filtration to remove insoluble particles, reduction of rough surfaces in the crystallizer, and prevention of cavitations by solution stirring. Nakatsuka et al. [22.70] found that the maximum supersaturation reached 120% with overheating above the saturation temperature (by 25 K) at pH 3.2. They also found that lower pH was effective to yield higher supersaturation. Strong acoustic energy can be used to achieve greater solution supersaturation, replacing overheating (Fig. 22.19). The applied acoustic energy may greatly accelerate cluster disconnection. Zaitseva found that a continuous filtration system (CFS) (Fig. 22.20) could improve the stability and minimize the potential for spontaneous nucleation. They designed a continuous filtration system for 1000 l crystallizers to grow large KDP crystals [22.78]. Degassing the solution is also a useful means to prevent nucleation [22.79].

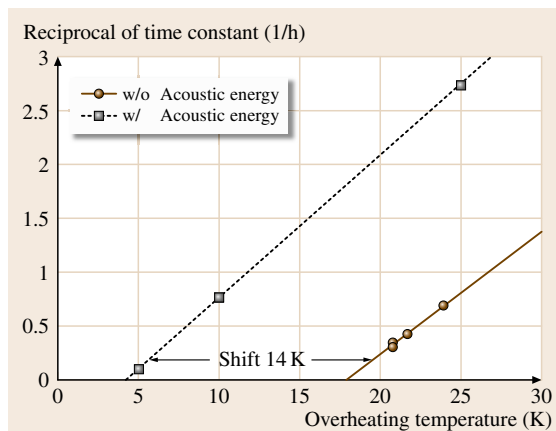


Fig. 22.19a,b The reciprocal of the time constant to reach a steady state of the supersaturation (a) without acoustic energy, and (b) with acoustic energy, as a function of overheating temperature (after [22.70], with permission of Elsevier)

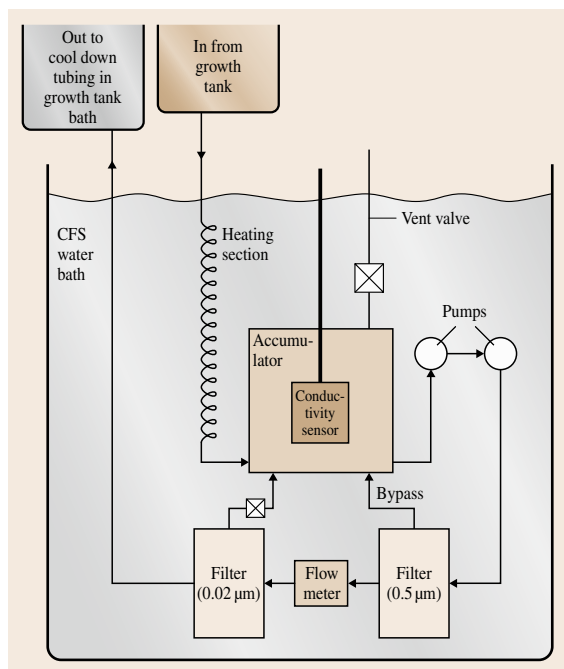


Fig. 22.20 Schematic of the continuous filtration system (CFS) (after [22.55], with permission of Elsevier)

There are some factors associated with crystallization systems that may cause spontaneous nucleation, which lowers the stability of solution during growth [22.42]. Insufficient sealing of the system leads to the possibility of nucleation on the liquid–vapor interface. Nucleation can occur from embryos retained in small cracks and cavities in the surface or joined parts of the equipment immersed in the solution. Nucleation can happen easily at spots of intensive evaporation or dry spots on the parts of the system with an interfacial boundary between solution and vapor that appear as a result of the absence of condensation of the solute on these parts. A classic example of such nucleation is crystallization on the walls of the crystallizer. Secondary nucleation occurs from the main crystal as a result of defect formation or friction between the crystal and supporting parts during the process of stirring.

The impurity composition of the raw material is typically considered an important factor affecting the stability of supersaturated solutions during growth. Some researchers have described the effect, both positive and negative, of different impurities on the stability of solutions [22.40, 73]. However, experiments performed by Zaitseva et al. [22.32] show no correlation between spontaneous nucleation and the chemical purity of the

solutions. Solutions intentionally doped with Fe, Cr, and Al were measured to have the same stability as regular ones up to very high supersaturation (Fig. 22.9).

22.3.3 Conventional Methods

The temperature-reduction method (TRM) and solution circulating method were two major conventional techniques used to grow large KDP/DKDP crystals before the development of rapid growth from point seed; there are many other methods for KDP/DKDP crystals growth, such as the gel growth and electrodialysis growth methods [22.81].

KDP/DKDP crystals are grown from aqueous solutions by using TRM [22.82, 83] in standard Holden-type crystallizers due to their positive temperature coefficient of solubility [22.32]. The growth equipment is simple, and supersaturation during growth is only controlled by the rate of temperature reduction (Fig. 22.21). Using this method it is difficult to maintain stabilization of supersaturation and the growth rate is generally slow, 1–2 mm/day. Sasaki [22.83] grew large KDP crystal of size, $400 \times 400 \times 600 \text{ mm}^3$ in 10 months by this method (Fig. 22.22).

Polymorphism of DKDP crystal gives rise to difficulties in the growth of useful tetragonal crystal by TRM. Due to the isotope effect, DKDP crystal may exist in two polymorphs: the tetragonal form (point group $42m$) and monoclinic form (point group 2). The tetragonal–monoclinic phase transition temperature decreases with increasing deuterium concentration in the crystal, which depends on that of the solu-

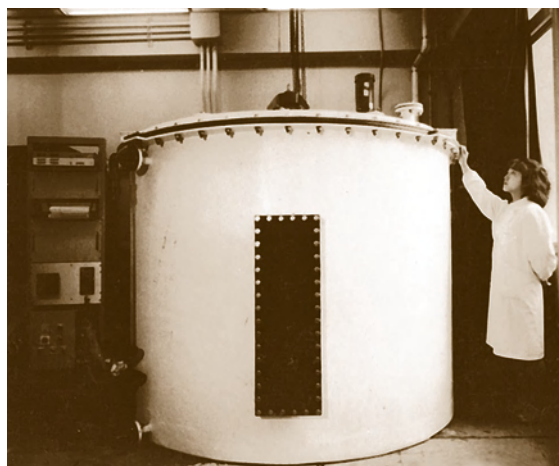


Fig. 22.21 A 1.5 m^3 growth vessel for large KDP crystals (TRM) (after [22.80])



Fig. 22.22 KDP crystals grown at 2 mm/day on average by TRM (size $40 \times 40 \times 60 \text{ cm}^3$, growth period 10 months) (after [22.83], with permission of Elsevier)

tion in which the crystal grows. The phase equilibrium transition point of 99.6 mol % deuterated solution is $21 \pm 0.5^\circ\text{C}$, whereas that of 90 mol % deuterated solution is $49 \pm 1^\circ\text{C}$. The growth of tetragonal DKDP crystal is very difficult once the tetragonal–monoclinic phase transition takes place or monoclinic phase spurious crystals appear. Thus the degree of deuteration of DKDP imposes strict temperature limits on the growth process; for example, tetragonal DKDP is difficult to grow in a solution of 99.3% deuterium concentra-

tion from a starting temperature higher than 43°C by TRM [22.38].

In the solution circulating method the supersaturation for crystal growth is maintained by circulating the supersaturated solution at constant temperature. Raw material can be added during growth. The system is usually composed of three tanks, namely, the saturation tank, buffer tank, and growth tank (Fig. 22.23) [22.83]. The supersaturation is provided by the difference in temperature between the saturation tank and growth tank. The three tanks are connected by tubes and the growth solution is circulated by using a pump, so crystal can be grown at constant temperature and supersaturation. This system is more complex and the tube is susceptible to blockage due to crystallization [22.82].

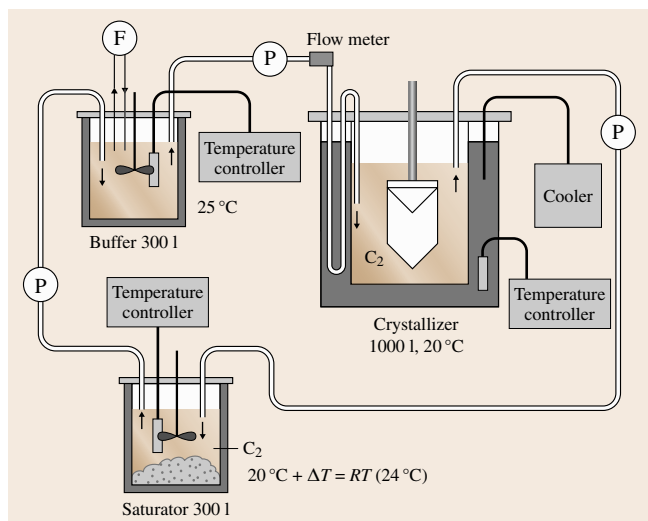


Fig. 22.23 Schematic diagram of the crystallizer with three-vessel solution circulating method (TVM) (after [22.83], with permission of Elsevier) (F – filter, P – pump)

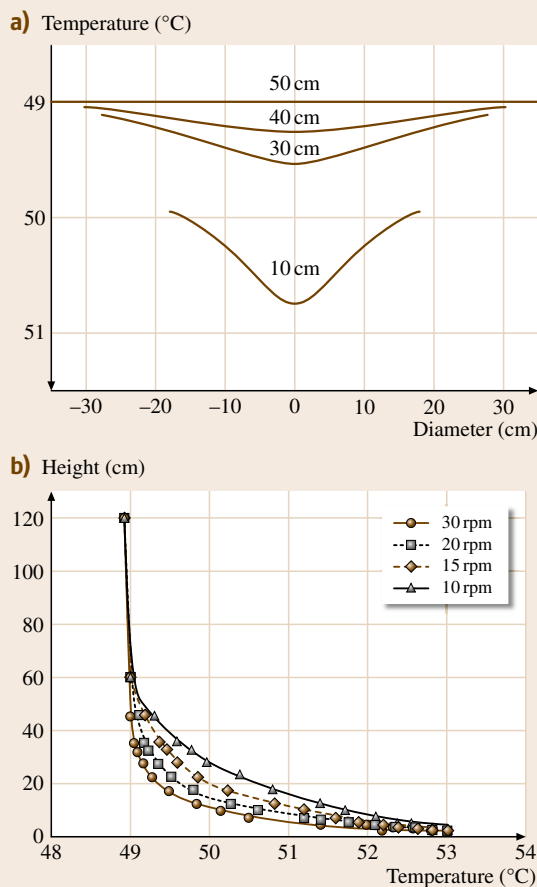


Fig. 22.24 (a) Radial temperature distribution at different height from the bottom of the crystallizer; (b) relation between crystal rotation rate and temperature distribution in axial direction (after [22.84])

In order to resolve the problem of blocking, *Sasaki* made the temperature of the growth tank lower than room temperature and the others higher [22.83]. *Lu* et al. [22.84] further modified the solution circulating system to resolve all of those problems. The stability of the growth solution and the growth temperature were improved by overheating the growth solution and adjusting the flux of solution and the temperature difference between the growth tank and saturation tank. Also, a suitable temperature gradient inside the growth tank was obtained along the radial and axial directions with respect to the crystal rotation rate (Fig. 22.24). The crystal growth rate was thereby increased 3–5 times over that of conventional TRM. Figure 22.25 shows the bulk KDP crystal grown by them.

Besides, *Vladimin* et al. [22.85] designed a method to grow KDP crystal at constant temperature and constant supersaturation. In this method, supersaturation was provided by adding solution. This method, which is very simple, has the advantage of solution circulating at constant temperature. It has only a tank without tubes, and can decrease the volume of the growth tank. Especially for growth of DKDP crystal, this method can effectively decrease the dosage of heavy water to reduce the cost of crystal growth.

22.3.4 Rapid Growth from a Point Seed

With the development of ICF, more and larger KDP/DKDP crystals with higher quality were needed.



Fig. 22.25 Bulk KDP crystal grown by solution circulating method (weight: 110 kg; size: 260 × 250 × 770 mm³)

However, the problem of low growth rate was particularly daunting. The main limitation on growth of large crystals by conventional techniques is the growth rates of only 1–2 mm/day for KDP and not faster than 1 mm/day in the case of DKDP crystal. In addition, the growth of each crystal required the production of seed material of equal cross-section, adding significantly to the production time. Difficulties in providing reliable equipment, high risk of failure, and defect formation during such long periods resulted in low yield and high cost of final crystals. These reasons stimulated the development of new techniques to accelerate the growth rate without the sacrificing optical quality of large crystals.

Work on rapid growth of KDP/DKDP crystals started in the early 1980s, aimed at conducting the growth process in the kinetic regime [22.9]. It improved the growth rate efficiently by increasing the velocity of the solution flow relative to the crystal surface. A high *z*-direction rate of 5–25 mm/day was achieved using a novel turbine to enhance mass transport [22.11]. Up to 150 × 150 × 80 mm³ KDP and DKDP crystals were grown at a rate of 0.5–1 mm/h by the technique of properly feeding the growing surfaces [22.86]. The quality of crystals was reported to remain the same as those grown by conventional technique, but the results proved that this was not the ultimate solution.

Zaitseva et al. [22.8, 32] realized that the primary factor controlling the growth rate was supersaturation, while a number of other researchers focused on increasing mass transport to the crystal surface. Results of nucleation and kinetic experiments made it possible to achieve stable growth rates that were one order of magnitude faster than conventional techniques. Rapid growth on both {100} and {101} faces of a point seed was carried out in Holden-type crystallizers (Fig. 22.26) at high supersaturation by using extensively purified raw material. The process is depicted in references [22.7, 42].

Growth solution was prepared by dissolving salt in water with saturation temperature depending on the required mass of the crystal. The solubility data in the temperature range $T = 10\text{--}80\text{ }^{\circ}\text{C}$ for KDP, and DKDP with 90% deuteration, are expressed as [22.42]

$$C_0 = 0.1165 + 3.0017 \times 10^{-3}T + 8.5768 \times 10^{-6}T^2, \quad (22.8)$$

$$C_0 = 0.1701 + 3.4817 \times 10^{-3}T + 2.8062 \times 10^{-6}T^2, \quad (22.9)$$

respectively.

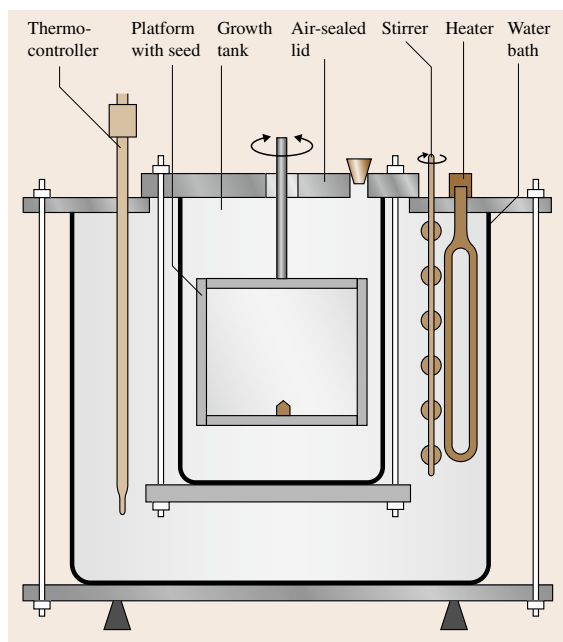


Fig. 22.26 Scheme of the crystallizer used for fast growth (after [22.32], with permission of Elsevier)

Solutions were filtered through submicrometer filters in two ways: prior to growth, or continuously during the whole growth process. After the filtration was stopped, all solutions were overheated for not less than 24 h. Both filtration and overheating were carried out in air-sealed crystallizers with continuous stirring at 80 °C.

Square seeds with T-shaped cross-section were cut from previously grown crystals without visible defects. A water-polished seed was glued into a square hole in the middle of the platform. After the glue had dried, the platform with the seed was assembled in an empty crystallizer and slowly heated to 80 °C. Growth solution that was overheated at the same temperature in a separate vessel was carefully introduced into the crystallizer without splashing. Alternatively, for small-scale growth, the platform with the seed was heated to 80 °C in hot water vapor in a separate crystallizer and then quickly introduced into the overheated solution.

After the seed had been introduced, the crystallizer was tightly sealed and the solution was maintained at 80 °C for 10–15 min. During this time, the seed was slightly dissolved to eliminate any surface crystallites. Additionally, all dry surfaces that could produce spontaneous nucleation were wetted by condensation of

the hot solvent vapor. This overheating time was limited by seed dissolution. Typically, the solution was cooled to the saturation temperature before the upper part of the seed had dissolved to the edge of the hole.

Continuous cooling was stopped when the temperature corresponded to the supersaturation for regeneration. Under these conditions, the regeneration process was completed in 1–2 h. During regeneration, the solution was stirred by reversible rotation of the platform at 40–60 rpm with a period of about 30 s in one direction and a 2–3 s pause. This platform rotation was also used during the crystal growth procedure that followed.

After the regeneration process was completed, the temperature reduction continued according to a program that provided stable growth at the desired growth rate. The process could be done completely automatically by using concentration sensors [22.87, 88]. Crystals could be grown at nearly constant growth rate using this procedure. The growth rate could be monotonically decreased toward the end of growth to avoid increasing supersaturation at lower temperature. When the growth was completed, the solution was removed from the crystallizer. If the process finished below or above room temperature T_r , the system was slowly heated or cooled to T_r before the crystal was taken out.

To meet the demands of the National Ignition Facility (NIF) for a large number of 0.5 m high-quality KDP/DKDP crystals, many scientific developments and engineering design changes were incorporated into the rapid growth crystallizer system (Figs. 22.26 and 22.27). The crystal is rotated alternately in one direction and then in the other using a symmetrically programmed schedule with controlled acceleration, de-

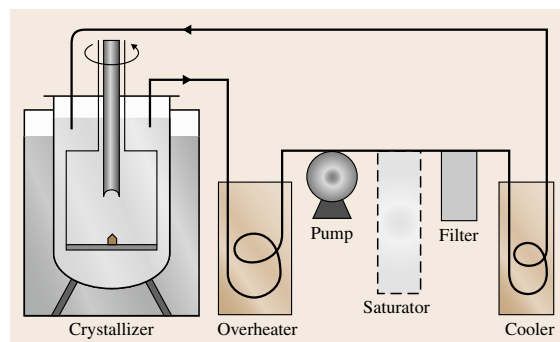


Fig. 22.27 Schematic diagram of the 1000 l crystallizer (after [22.7], with permission of ASM Int.)



Fig. 22.28 Photograph of the large 1000l crystallizer (after [22.7], with permission of ASM Int.)

celeration, and rotation rates. A special device, called a seed protector, is inserted within the platform shaft in order to cover the point seed during the filtration or overheating procedures [22.89]. The continuous filtration system shown in Fig. 22.20 contains three temperature-controlled sections: a superheater and filter (operating at 80°C), and the third section where the filtered solution is cooled to the growth temperature [22.78]. The details of this classical loop are designed such that the solution can be continuously filtered during the entire growth process at supersaturations up to 20% without generating spontaneous nucleation. Other important changes include a rigid and streamlined platform compatible with hot KDP solution that could rotate at sufficiently high rates without flexing, oscillating or creating a large wave at the solution–air interface [22.7], and a semi-automated system for temperature reduction [22.87]. Successful incorporation of these design elements led to a reliable method. By using this method, a KDP crystal of 317.97 kg was grown in 52 days in LLNL (ICF Monthly Highlights, January 2000 UCRL-TB-128550-00-04) (Fig. 22.29).

The combination of the regeneration conditions with a convex-shaped platform and continuous filtration makes it possible to control the KDP crystal habit for production. The ratio of dimensions along the

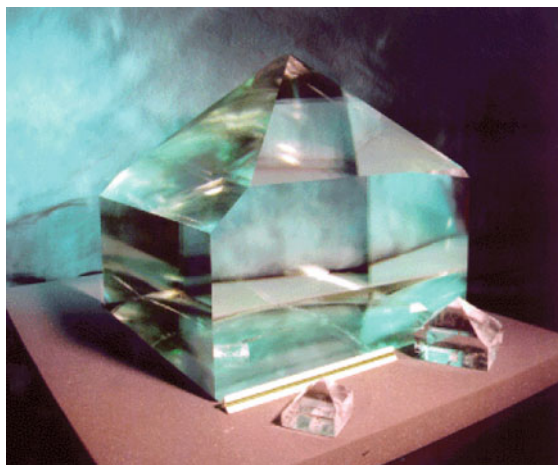


Fig. 22.29 First KDP crystal of the NIF SHG size ($53 \times 54 \times 55 \text{ cm}^3$) grown on the convex platform with continuous filtration (after [22.42], with permission of Elsevier)

crystallographic axes was controlled by two methods: (1) creation of special dislocation structures during the seed regeneration process and (2) change in the orientation of the seed [22.58]. These methods enable the growth of large crystals with specified habit without the deleterious effects of intentionally introduced chemical impurities. KDP and DKDP crystals of various habits were grown at rates of 10–20 mm/day to linear sizes near 90 cm (Fig. 22.30).

In addition, for DKDP crystal, growth by the point-seed rapid growth method not only decreases the growth period but also avoids the emergence of monoclinic DKDP crystal. This is very important for the growth of highly deuterated DKDP crystals [22.32, 53, 90].

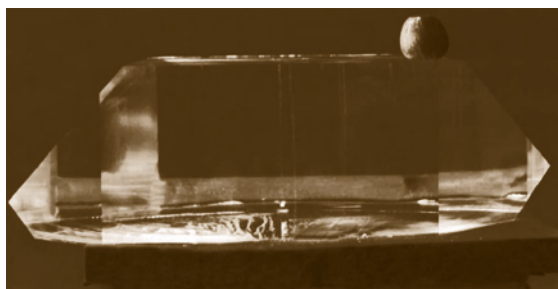


Fig. 22.30 DKDP crystal grown for THG on a horizontally oriented seed; $X : Y : Z = 1 : 2.2 : 3$; length $Z = 86 \text{ cm}$; convex platform (after [22.58], with permission of Elsevier)

22.4 Effect of Growth Conditions on Defects of Crystals

Growth conditions as well as the after-growth treatment [22.91, 92] affect the optical quality of crystals. Discussion of the mechanisms of growth and their influence on the defect formation process showed that the major factors that determine the defect structure of **KDP** crystals are the impurities content and the dislocation structure of the crystals. Vicinal sectorality, striations, and strain are the main parameters affecting the optical quality of crystals. Solution inclusions and cracks, which make crystals completely inappropriate for optical applications, are also largely influenced by the same factors.

22.4.1 Impurity Effect

Impurities, which originate from the precursors and from dissolution of the crystal growth tank, can be di-

vided into three main kinds: metal cations such as Al^{3+} , Fe^{3+} , Cr^{3+} , Ca^{2+} , Mg^{2+} , Na^+ , etc., anions such as SO_4^{2-} , NO_3^- , Cl^- , etc., and organic impurities such as **EDTA**, organic dyes, etc. The impurities, as well as the crystal growth rate, affect the defect structure of **KDP** crystal, which in turn affects the optical quality of **KDP** crystals.

The metallic cations, particularly those with high valency were considered to strongly affect the growth habit and optical properties of crystals. Trivalent metal cations such as Fe^{3+} , Cr^{3+} , and Al^{3+} have a deleterious effect on the growth of {100} faces of **KDP** [22.1]. Their introduction into the growth solution poisons the {100} faces, producing a region of no growth at low supersaturation commonly referred to as the *dead zone*. They also promote macrostep formation as the supersaturation is increased and growth begins. At impurity concentrations in the range 1–10 ppm, this phenomenon often results in the formation of solution inclusions [22.1, 93]. In addition, these impurities are strongly incorporated into the {100} face with effective segregation coefficient of the order of 10. In contrast, these impurities have little or no effect on the growth of the {101} faces and are strongly rejected with segregation coefficient of 1.0 [22.92]. This nearly hundredfold difference in impurity incorporation results in strong optical inhomogeneities which are manifested in the refractive indices, the linear and two-photon absorption coefficients, and the anomalous birefringence near the {100}/{101} boundaries of the crystal [22.94, 95]. It was found that a correlation exists between *foggy* inclusions (Fig. 22.31) at the corners of the prismatic sectors and aluminum concentrations in the growth solution when a certain concentration is exceeded [22.96].

Table 22.1 presents the relationship between the concentration of the most common impurities in initial solutions and their distribution in pyramidal and prismatic sectors of **KDP** crystals. From these results one can see that most impurities, especially trivalent metal cations, go preferably into the prismatic growth sectors. However, some impurities, such as Rb, have approximately the same low concentration in both prismatic and pyramidal parts of the crystals. Some impurities (B, Na, Mg, and Ca) seem to be completely rejected by the crystals.

Anions were traditionally considered to have slight effect on the quality and growth of **KDP** crystals. However, recent research gives us new insights into this hypothesis [22.74–76, 97, 98]. Some anionic impuri-

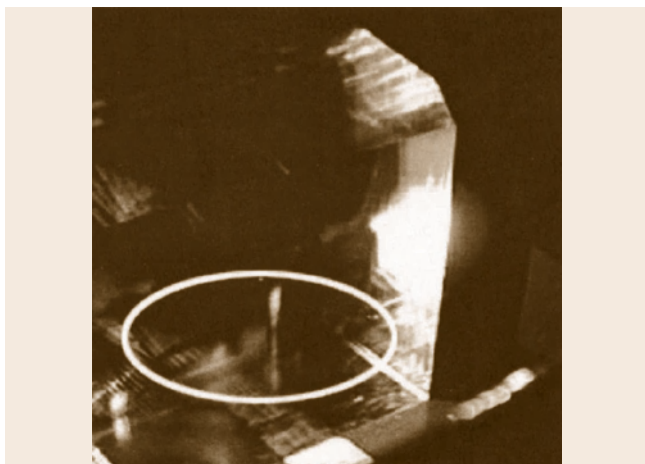


Fig. 22.31 Photograph of foggy inclusions along prism–prism boundary of NIF-size **KDP** boule grown in solution having high Al content during middle of growth run (after [22.7], with permission of ASM Int.)

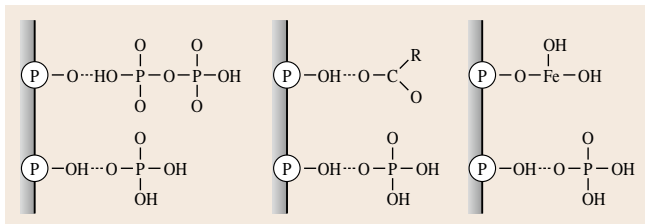


Fig. 22.32 Scheme of adsorption of anionic and cationic species (after [22.75], with permission of Elsevier)

Table 22.1 Distribution of impurity concentration C_i in raw material and pyramidal and prismatic sectors of KDP crystals

Impurity	MDL (ng/g KDP)	C_i raw material (ng/g KDP)	C_i pyramid (ng/g KDP)	C_i prism (ng/g KDP)
B	1000	14000	ND	ND
Na	300	86000	ND	ND
Mg	5	100	ND	D
Al	100	900	200	4400
Si	100	12000	D	390
Ca	100	3600	ND	ND
V	0.5	< 80	0.1	6.0
Cr	100	2000	490	11000
Fe	50	5300	110	12000
As	200	< 200	ND	D
Rb	10	10000	2600	2100
Sr	5	320	870	1800
Mo	10	790	66	1100
Sb	4	70	30	280
Ba	5	52	120	600

MDL – method detection limit, D – detected, ND – not detected

ties (sodium metaphosphate, potassium pyrophosphate, formic acid, acetic acid, oxalic acid, and tyrosine) were found to have an inhibiting effect on the growth of KDP crystals. Complete stoppage of pyramidal face growth was observed in the presence of high concentration of both $[H_{x-n}(PO_3)_x]^{n-}$ and $[H_2P_2O_7]^{2-}$. In these cases, the crystal habit was changed into a closed octahedron and the whole crystal stopped growing. The inhibition is assumed to be caused by the adsorption of these anions at the growing crystal surface, especially on pyramidal surface, through the formation of H-bonds between anions and H_2PO_4 groups (Fig. 22.32). When the doped metaphosphate concentration is high enough, mother-liquor macroinclusions occur along the sector boundaries and in pyramidal sectors (Fig. 22.33). In observations using laser tomography, the density of scatter increases with increasing concentration of doped metaphosphate. The scatters are suggested to be microsolution inclusions caused by the inhibition effect of metaphosphate on the growing faces. These anions have a harmful effect on the laser damage threshold due to possible incorporation (Table 22.2). Sulfate

Fig. 22.33a–e Photographs of KDP crystals grown on Z-cut plate seed from metaphosphate-doped solutions with addition of (a) 50 ppm, (b) 30 ppm, (c) 15 ppm, (d) 10 ppm, and (e) 1 ppm (after [22.76], with permission of Elsevier)

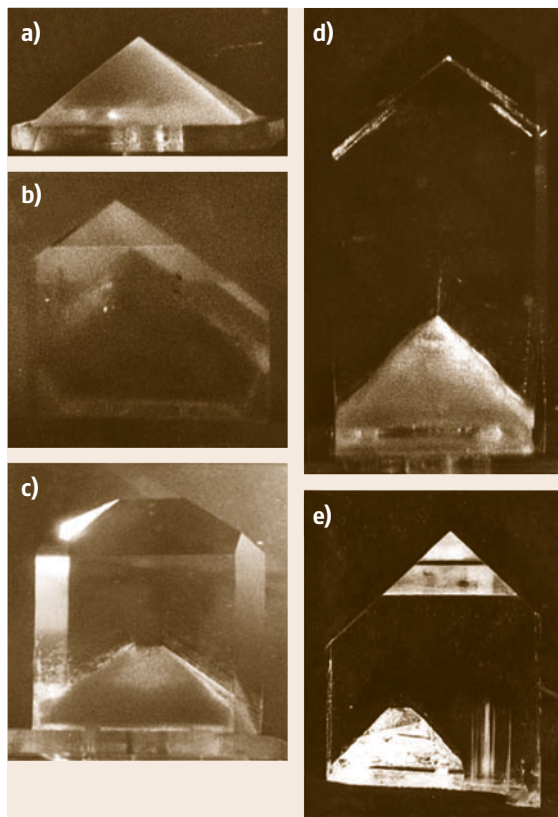


Table 22.2 The effect of anionic species on the optical properties of **KDP** crystal

Dopants	Mass ratio (ppm)	A (%/cm)	F_{th} (J/cm ²)
Potassium pyrophosphate	100	5.1	34.3
EDTA	300	5.5	52.0
Tyrosine	20	4.7	40.4
Tyrosine	50	4.8	40.4
Tyrosine	300	4.9	35.1
Formic acid	300	6.1	42.7
Oxalic acid	300	4.5	45.8
Pure KDP material		5.2	52.0

A – absorption coefficient; F_{th} – laser damage threshold, 1-on-1, 1.06 μ m, 10 ns

(SO_4^{2-}) anions, which can join into the **KDP** crystal lattices through H-bonding and electron attraction, have a great effect on the growth habit of **KDP** crystals at high dopant concentration. **KDP** crystals showed many defects such as mother liquor inclusions, parasite crystals, and cracks. Besides, SO_4^{2-} content also adversely affects crystal transparency. At high dopant concentration, **KDP** crystal transmittance decreases significantly in the ultraviolet region [22.98].

Organic additives such as glycerol, ethylene glycol, polyethylene glycol, and **EDTA** show growth-promoting effects on both pyramidal and prismatic faces at very low concentration [22.75–77, 99]. In **KDP** crystals grown in the presence of optimal amounts of organic additives, there is a decrease in the concentration of inorganic background impurities of the cations, an increase in the transparency in the (100) growth sector in a certain range, and an increase in optical uniformity and laser damage threshold.

The distribution of impurities in the **KDP** crystal is nonuniform, as is evident in crystals grown from solutions doped with impurities that can produce visible color. KH_2PO_4 shows a strong tendency to incorporate anionic dyes only on the {101} faces, presumably because these faces are terminated with K^+ ions [22.93]. However, impurities may inhomogeneously deposit not only between growth sectors, but also within a single growth sector depending on the crystal surface topography. Surfaces of crystals grown in the regime of lower supersaturation often propagate through dislocations that produce growth spirals or hillocks, and shallow-stepped pyramids with single or multiple dislocations at

the apex [22.100, 101]. Polygonization of hillocks partitions faces into vicinal regions, each having slightly different inclinations. Impurity partitioning among vicinal slopes and intrasectoral zoning result from selective interactions of impurities with particular stepped hillock slopes.

Zaitseva and coworkers [22.1] perfected KH_2PO_4 crystal growth conditions as a prerequisite to the development of the National Ignition Facility. Amaranth, which displayed exclusive affinity for the {101} surfaces of KH_2PO_4 [22.93, 102], was both inter- and intrasectorally zoned [22.92]. This observation required introduction of the dye during late growth, thereby coloring only a thin surface layer so that patterns of color were not confounded by moving dislocation cores. Figure 22.34 highlights the {101} faces of KH_2PO_4 /amaranth crystals. The heterogeneities resulted from amaranth having distinguished among the A, B, and C slopes of the polygonized hillocks prevalent on the pyramid faces. Incorporation followed the trend $B > A > C$. On the other hand, Chicago sky blue preferred C [22.103]. At low Chicago sky blue concentration, B remained colorless. The incorporation was associated with a critical temperature above which the dye was not captured. In situ interferometry [22.104] was used to show the influence of the dye on the surface morphology at different concentrations and KH_2PO_4 supersaturations.

The effect of impurities on the recovery of surfaces out of the dead zone was traditionally explained by the classic theory of Cabrera and Vermilyea in terms of pinning of elementary step motion by impurities [22.105]. In this model, impurities adsorbed on the terraces create a field of *impurity stoppers* that act to block the motion of elementary steps. When the average impurity spacing is less than a critical distance, whose magnitude is approximately given by the Gibbs–

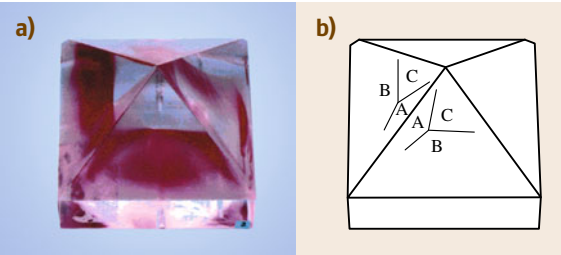


Fig. 22.34a,b Intrasectoral zoning in KH_2PO_4 /amaranth. (a) Photograph of KH_2PO_4 /amaranth crystal grown by Zaitseva et al. [22.55]. (b) Idealized representation of crystal in (a), illustrating the hillocks observed on the surface

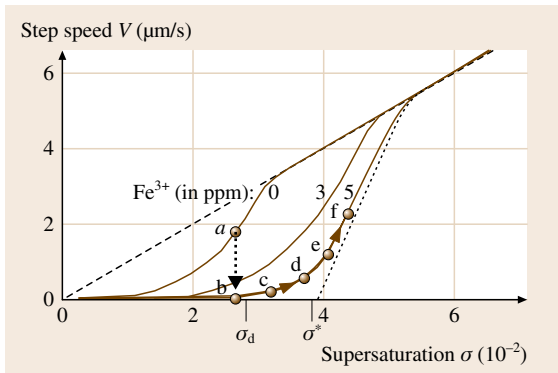


Fig. 22.35 Dependence of step velocity on supersaturation in the presence of Fe^{3+} (after [22.26], with permission of Macmillan)

Thomson critical diameter, the steps cannot advance. As the supersaturation is increased and the critical diameter becomes smaller, the steps begin to squeeze through the fence of impurities and the step speed rises rapidly. The dotted curve in Fig. 22.35 illustrates the prediction of such a model. No growth occurs below a percolation threshold given by σ^* , while for $\sigma > \sigma^*$, the step speed rises rapidly to its unimpeded value. While the model correctly predicts the rapid rise in step speed for $\sigma > \sigma^*$, no growth is predicted below σ^* , in contrast to what has been observed experimentally. Land et al. [22.106] considered that recovery of the KDP surface occurred through the movement of macrosteps (Fig. 22.36), which were mobile even when elementary steps remained pinned. This led to a slow increase in growth rate below σ^* , even for supersaturations in the region $\sigma_d < \sigma < \sigma^*$. At supersaturation near σ^* , elementary steps begin to straighten out and become mobile, but their speed is still considerably less than that of the macrosteps. Finally, at supersaturations in excess of σ^* , the surface once again consists of a combination of rapidly moving elementary steps and step bunches that resemble the step trains for the undoped solution. The elementary steps are now moving with a velocity that is close to that of the macrosteps.

De Yoreo et al. [22.54] point out that, although all the defects observed in KDP are also present in DKDP, there are some aspects of crystal quality which are peculiar to the deuterated crystals. DKDP crystals grown at rates of 1–15 mm/d have always been found to exhibit vicinal sectorality in their x-ray topograph. This inhomogeneity has a moderate effect on the optical uniformity.

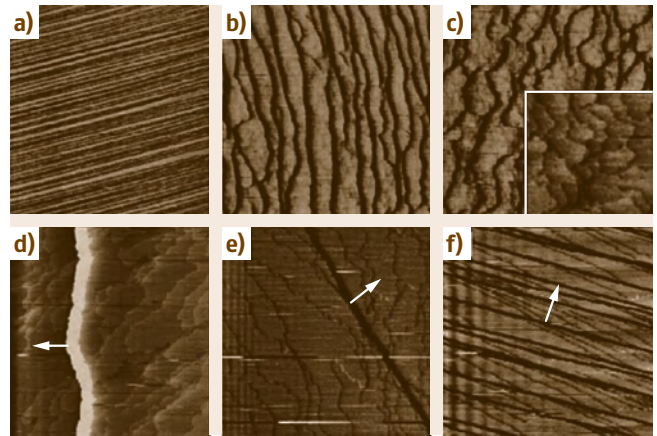


Fig. 22.36a–f Series of AFM images illustrating the process of impurity poisoning and recovery (after [22.7], with permission of ASM Int.): (a–c) $15 \times 15 \mu\text{m}^2$ scans collected at $\sigma = 0.04$ along heavy dashed line trajectory from point a to point b in Fig. 22.35 showing poisoning of surface by introduction of 12 ppm Fe^{3+} (per mole of KDP); time at the start of each scan is (a) 0 s, (b) 64 s, and (c) 106.7 s, and Fe-doped solution was introduced at $t = 42.7$ s (steps in image (c) are immobile and inset shows $6 \times 6 \mu\text{m}^2$ image of morphology of elementary steps on macrostep terraces); (d) $9 \times 9 \mu\text{m}^2$ image collected at point c in Fig. 22.35 (elementary steps are immobile and macrosteps are distorted but moving slowly); (e) $13 \times 13 \mu\text{m}^2$ image collected at point d in Fig. 22.35 (elementary steps are still immobile and macrosteps are straight and moving rapidly); (f) $12.5 \times 12.5 \mu\text{m}^2$ image collected at point e in Fig. 22.35 (elementary steps are now moving but more slowly than macrosteps)

22.4.2 Supersaturation

According to the dependence of growth-step velocity of KDP prism faces on the supersaturation, three regions can be defined, corresponding to the dead zone, the transition region of high $dV/d\sigma$, and the linear part of $V(\sigma)$ with high supersaturation and growth rate.

When crystals grow in the dead zone, large variation occurs in steepness, resulting from different incorporation of impurities into separate vicinal slopes. This variation produces large misorientation between small crystals formed during regeneration on melted faces and the z-cut of the seed. This misorientation makes the process of joining difficult, which leads to the formation of cracks and subindividual crystals [22.107–110]. As a result, the crystallographic shape fails to regenerate. Even when regeneration occurred successfully, subindividual crystals and cracks often appeared if growth was performed within the dead zone.

The transition region of high $dV/d\sigma$ is a region of surface instability that develops when elementary steps pass through the fence of impurity blockers with the accompanying macrostep bunching [22.1]. Solution inclusions form most likely in this region because of higher variations of supersaturation on the growing surface. Another reason for increasing instability is the formation of new hillocks, which are frequently observed during the transition. Besides, the change of leading hillock on the growing face in the region of low supersaturation and in the vicinity of the dead zone is inevitably accompanied by the formation of growth bands. This is due to the appearance of new growth steps of various orientations which lead to the formation of inhomogeneity.

When crystal grows at high supersaturation, corresponding to the linear part of $V(\sigma)$, no visible inclusions are formed on the vicinal slopes, despite the fact that microscopic investigation of the surface clearly shows the structure of bent macrosteps on both prismatic and pyramidal faces [22.111]. The formation of large, bent macrosteps is not a sufficient condition for inclusion formation. There is also no evidence that such bent macrosteps cause microsolution inclusions or dislocation since etching did not reveal any dislocation pits.

It can be concluded that, in order to minimize defect and inhomogeneity formation, crystals should be grown in the region of the dead zone (traditional growth) or in the region of the linear part of the dependencies $V(\sigma)$ (rapid growth).

22.4.3 Filtration

KDP crystals often contain hairlike inclusions that run roughly perpendicular to the growth direction (Fig. 22.37) [22.112]. They have the appearance of fine fibres a few centimeters in length, extending through the



Fig. 22.37 Hairlike inclusions in rapidly grown **KDP** crystals (after [22.7], with permission of ASM Int.)

crystal in the direction of growth and deflecting away from the z -axis; they occur in both dipyramidal and prismatic growth sectors. Most of these inclusions, which lie at angles to the z -axis that vary between 20 and 90°, are not continuous but rather consist of long chains containing from dozens to hundreds of liquid inclusions.

Many models of liquid inclusion formation have been proposed [22.113, 114]. A most likely source of hairlike inclusions is particle incorporation. During crystal growth, steps often close around particles, but do not cover them. Researchers at LLNL have observed this process in **KDP** during the passage of hundreds of layers. Figure 22.38 shows holes caused by this process in a number of crystals, including **KDP**. Apparently, once these holes are formed, they are difficult to fill in and result in the generation of hollow channels running at a high angle to the growth front. Given that the **KDP** crystals were grown by a temperature drop method, any channels which formed during growth would have contained solutions that became increasingly supersaturated as the temperature was decreased and thus might be expected to condense into chains of inclusions.

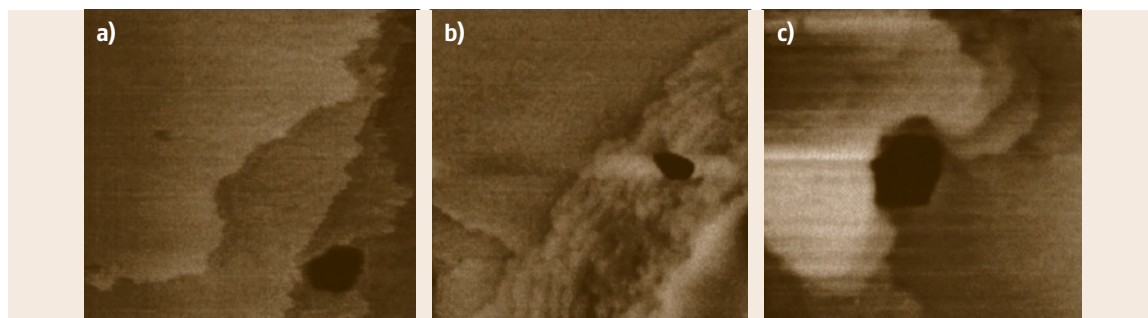


Fig. 22.38a–c Appearance of holes in crystals following inclusion of particle: (a) Canavalin, $6 \times 6 \mu\text{m}^2$; (b) Satellite Tobacco Mosaic virus, $12 \times 12 \mu\text{m}^2$; (c) **KDP**, $3 \times 3 \mu\text{m}^2$ (after [22.7], with permission of ASM Int.)

Filtration of solution before crystallization to remove extraneous solid particles and thereby improve the crystal quality and laser damage threshold is a standard procedure for experimental or commercial crystal growth. However, no matter how well the solution is filtered before crystal growth, a large number of particles appear very soon after the filtration is stopped. This phenomenon is especially pronounced during the growth of large bulk crystals in equipment containing moving and rotating parts that generate particulate contamination and spoil previously purified growth solutions.

The requirement of high damage threshold in NIF crystals stimulated the design of a continuous filtration system. The system removes growth solution from the tank, heats it to prevent spontaneous nucleation, and filters the solution through 0.02 μm -pore filters. The solution is then cooled before its injection back into the growth tank. This system filters the solution not only before the growth (prefiltration) but also during the entire growth process in a continuous mode.

Comparison of crystals grown with and without continuous filtration showed substantial difference in structure and number of defects. When crystals grow from only prefiltered solutions, the pyramidal face of the crystal generally has a large number of dislocation pits uniformly distributed over the whole crystal (Fig. 22.39). This high density of dislocations, which shows that the distribution of growth sources on the face is not stable, is more or less typical for all KDP and DKDP crystals grown without continuous filtration.

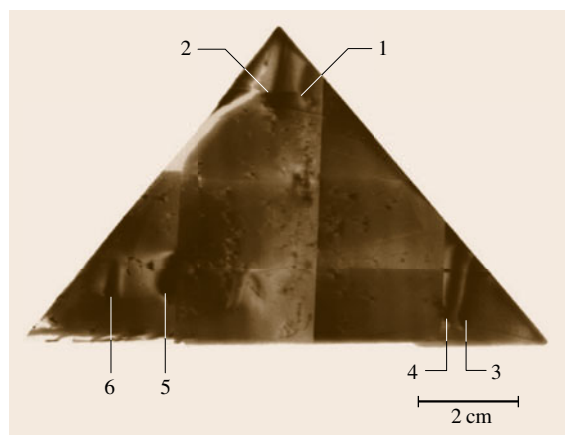


Fig. 22.39 X-ray synchrotron topographic image of dipyramidal face of a KDP crystal grown without continuous filtration. Black dots are dislocation outcrops on the face. (1–6) Vicinal hillocks tips (after [22.78], with permission of Elsevier)

Initial dislocation hillocks formed after seed regeneration are located approximately in the center of each face, but the location of vicinal hillocks far from the central part of the face does not correspond to the distribution bunches created on the seed during regeneration. These dislocations were formed during the process of growth. When crystals grow with continuous filtration, positions of the leading hillocks do not change, and the crystal surface preserves its simple structure during the entire growth, with one growth hillock approximately in the middle of each face, corresponding to the locations formed during regeneration.

These results indicate that, under continuous filtration, the formation of new dislocations is significantly reduced. Large amounts of dislocations lead to the possibility of formation of vicinal hillocks that can compete in step generation under changing growth parameters, such as temperature, supersaturation or hydrodynamic conditions. The change of leading dislocation hillocks on the growing crystal face always results in the formation of structural defects. The shift of dislocation hillocks to the asymmetrical position close to the edges leads to a higher probability of formation of liquid inclusions and new dislocations on them. This is why crystals grown with continuous filtration have much higher optical homogeneity compared with crystals grown under usual conditions.

22.4.4 Hydrodynamic Effects

Obtaining the optimal hydrodynamic conditions in a crystallizer is a principal factor ensuring high quality of crystals.

The surface structure of each face of KDP crystal consists of growth hillocks, intervicinal valleys, and additional valleys produced by the *bending* of macrosteps originating from a single growth hillock (Fig. 22.40). By ex situ measurement on the surface topography of rapidly grown KDP crystals using a precision coordinate measuring machine (CMM) [22.106], these valleys are observed to be precursors of morphological instability and the formation of solution inclusions on the crystal surface. Results from numerical simulations of the hydrodynamics [22.115] and mass transfer [22.116] for the conditions used in the rapid growth process show that the surface supersaturation field generated on these crystals is inhomogeneous due to the spatially and temporally varying boundary layer thickness on the rotating crystal surface. These simulations clearly indicate that the process of step bending can produce the features which are observed in experiment. The simulations have

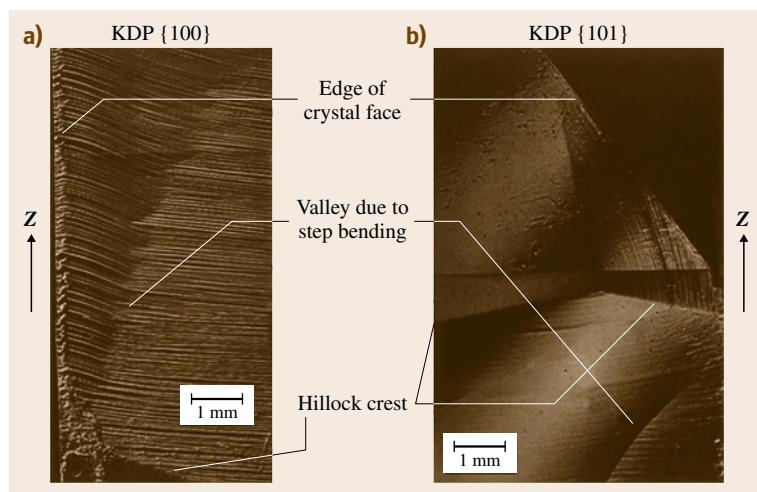


Fig. 22.40a,b Photographs of the typical surface structure resulting from step bending on the (a) {100} and (b) {101} face (after [22.106], with permission of Elsevier)

been used to explore the dependence of step bending on parameters such as crystal growth rate, rotation conditions, growth hillock location, and (for prismatic faces) impurity level [22.111]. It has been shown that the step bending and resulting valley formation is intensified by increasing crystal growth rate, by decreasing rotational speed, and (for the {100} face) by increasing the impurity level. It has also been shown that the resulting surface structure depends on the location and number of hillocks on the surface.

The crystallization process can be regarded as two stages: supply of crystallizing matter from solution to the crystallization surface through the diffusion boundary layer by molecular and convective diffusion, and the formation of a crystal. The former is rate-limiting if the supersaturation at the crystallization surface is lower compared with the bulk supersaturation, in which case the growth is said to proceed in the diffusion regime. The second stage is rate-limiting if the bulk supersaturation and crystal surface supersaturation are similar, in which case the growth regime is said to be kinetic. Crystals are generally considered to be in a mixed diffusion–kinetic regime. However, surface and bulk supersaturation should be made as close as possible to the kinetic regime so that the diffusion processes of supply of crystallizing matter do not limit the crystallization rate.

The traditional recommendation to approach the kinetic regime is to decrease the thickness of the diffusion layer by increasing the flow velocity or changing the flow geometry [22.36]. However, it can also be achieved by decreasing σ . Thus, to stay close to the kinetic regime, the growth rate should be lowered by increas-

ing the rotation rate of platform. The dependence of the growth rate R_z on the rotation rate of the platform can be determined in a rapid growth crystallizer [22.37]. At very slow rotation of 0–25 rpm, inclusions always form on some crystal faces. Between 25 and 40 rpm, crystals grow with and without inclusions. With faster rotation, formation of solution inclusions is extremely rare and one can be considered to be close to the kinetic regime.

The hydrodynamic conditions most likely affect the solution inclusion process indirectly through changes of the dislocation structure. Low flow velocity at slow rotation results in a greater gradient of the thickness of the diffusion layer along the faces and of the supersaturation at the crystallization surface. The growth hillocks move to the positions of favorable hydrodynamic conditions, i.e., close to the crystal edges and apexes. Morphological instability develops on the large vicinal slope, which covers the whole face. Formation of macrosteps and increasing slope of the vicinals leads to large deviation of the face from its singular orientation and initiates step generation from edges. This phenomenon produces thin surface layers that cover the deviated vicinals with the formation of liquid inclusions. Shift of the hydrodynamic conditions towards the kinetic regime decreases the gradient of the supersaturation along the faces, which makes location of the growth sources close to the edges less probable. In practice, the approach to the kinetic regime is achieved in large crystallizers by increasing the rotation rate of the platforms, as well as by continuous filtration. The combination of these conditions almost completely eliminates solution inclusions without decreasing the growth rate.

22.5 Investigations on Crystal Quality

The optical parameters used to evaluate KDP-type crystals for the ICF project mainly include transparency, optical homogeneity, and resistance to damage by laser radiation.

22.5.1 Spectroscopic Studies

Transparent Spectrum

Transmission in the KDP crystal spectra is from 250 to 1700 nm. For DKDP crystals, the deuterated crystals have higher transmission efficiency ($> 89\%$) at 1064 nm and lower optical absorption efficiency ($< 3\% \text{ cm}^{-1}$) than those of the undeuterated crystals (Fig. 22.41). The infrared (IR) absorption edges of the deuterated crystals are obviously red-shifted by 0.4–0.5 μm to about 2.0 μm in comparison with those of the undeuterated crystals (about 1.5 μm) so that DKDP crystals can be applied over a wider wavelength region. The infrared cutoff ratio of the hydrogen mode against the deuterium mode is 1/1.33, which nearly coincides with the ratio of the square root of the reduced mass of O–H against O–D, which is known to be 1/1.3743 [22.117].

Raman Spectra

The Raman spectra of KDP crystals exhibit a red-shift, similar to that observed in the transmission spectra [22.117]. The Raman peak 916 cm^{-1} of the H_2PO_4^- group in KDP crystal is red-shifted by 35 cm^{-1} to the 881 cm^{-1} Raman peak of the D_2PO_4^- group in DKDP

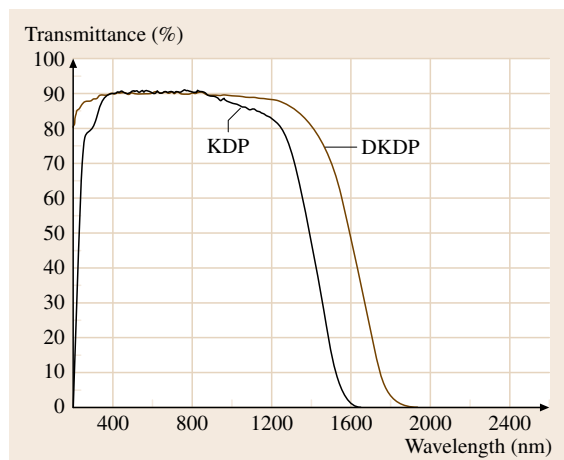


Fig. 22.41 Transmission spectra of Z-cut KDP/DKDP crystals (after [22.117], with permission of Elsevier)

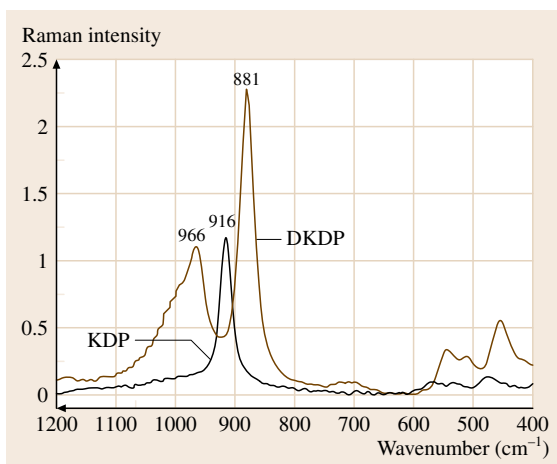


Fig. 22.42 Raman spectra of KDP/DKDP crystals (after [22.117], with permission of Elsevier)

crystal (Fig. 22.42). This red-shift is due to the isotope substitution effect. In the structure of the tetragonal phase, the PO_4 tetrahedra are coupled by potassium atoms, and four of these oxygen atoms are transformed to produce strong lines at 966 cm^{-1} in the DKDP crystal. These lines are not detected for the KDP crystal. This result confirms that the spectrum of Raman scattering in the deuterated crystal can be split into two parts related to internal and external vibrations.

Effect of Impurities on the Transmission Spectrum

Certain impurities have a discernible effect on the transmission of KDP crystals. For example, strong absorption in the wavelength region of 200–300 nm is a signature of metal impurities.

Many experiments have been done to investigate the dependence of near-ultraviolet (UV) absorption on the presence of impurities. Garces et al. [22.118] indicated that near-ultraviolet absorption is strongly related to the Fe^{3+} impurity in the growth solution. Near-ultraviolet optical absorption spectra taken from two KDP crystals are shown in Fig. 22.43. These data clearly indicate the presence of an intense 270 nm optical absorption band, along with additional absorption in the 200–230 nm region. They found a direct correlation between the Fe^{3+} content and the 270 nm band intensity. Wang et al. [22.73] also found that doping of Sn^{4+} lowers transmission near the ultraviolet region, as shown in Fig. 22.44.

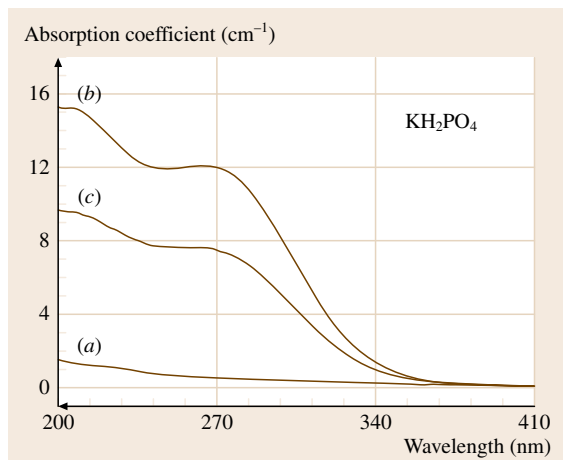


Fig. 22.43 Optical absorption of **KDP** crystals at room temperature (after [22.118], with permission of Elsevier)

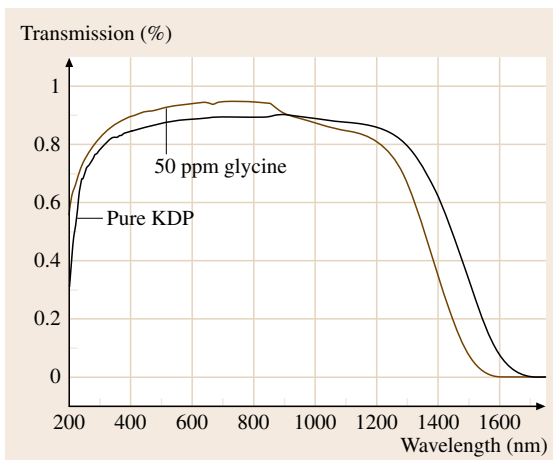


Fig. 22.45 Transmission curves of 50 ppm glycine doped **KDP** (after [22.119])

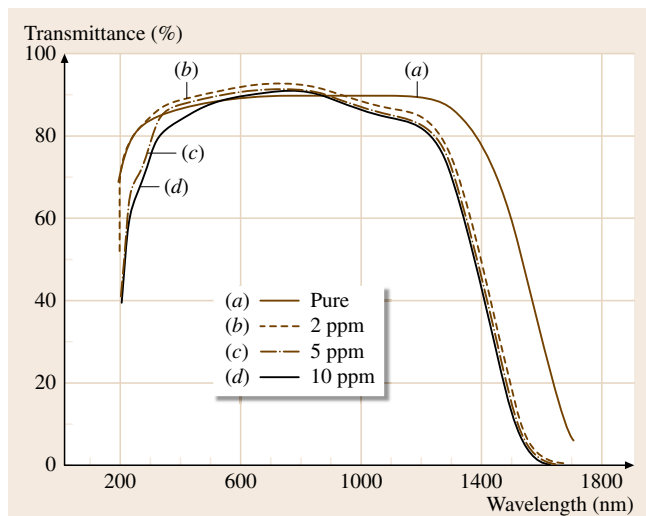


Fig. 22.44 Transmission spectra of **KDP** crystals grown from solution doped with different concentrations of Sn^{4+} ion by traditional temperature reduction method (after [22.73], with permission of Elsevier)

The effects of some anion and amino-acid impurities have been studied and reported by *Sum* and others [22.98, 119], showing that pyrophosphoric acid shortens the transparency range while the addition of a certain concentration of **EDTA** can extend the range of transparency. As shown in Figs. 22.45 and 22.46, other impurities such as boric acid, glycine, and sulfate can affect the transmittance of **KDP** crystal.

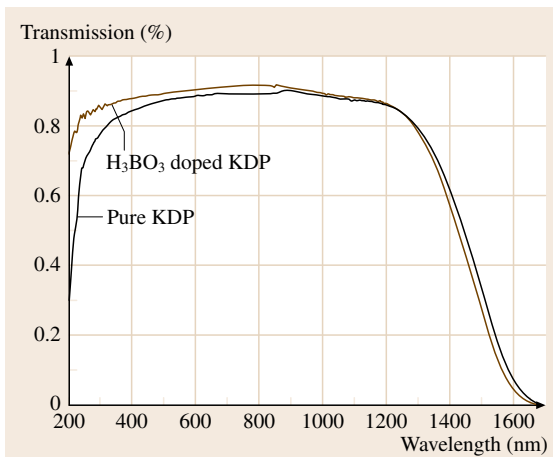


Fig. 22.46 Transmission curves of 10 ppm boric acid doped **KDP** (after [22.119])

Generally, metal impurities such as Fe^{3+} and Cr^{3+} are mainly responsible for the extra absorption in the near-ultraviolet band through an electron transition mechanism, while infrared and near-IR band shifts can be attributed to anion group and amino-acid impurities, as they can affect vibration in the **IR** band.

22.5.2 Homogeneity

Efficient operation of electrooptic devices such as Pockels cells and frequency converters requires crystals with a high degree of optical perfection. For a crystal to perform adequately when used in a laser system it must

maintain beam polarization, introduce minimal distortion of the spatial phase profile, and provide uniform phase matching for frequency conversion. All growth defects have the potential to degrade the performance of KDP and DKDP crystals either by altering the index of refraction or by generating inhomogeneities in the unit normal to the c -plane of the crystal. This latter phenomenon has been referred to as z -axis wander [22.94,95].

Variations in the refractive index are caused by two primary effects: impurities and strain. Impurities, even when uniformly distributed, generate compositional variations which can alter the diagonal components in the projection onto the plane of polarization of the refractive index tensor. These control the velocity and therefore the phase front of a transmitted beam. However, unless the impurities are of sufficient concentration to alter the crystal symmetry, the induced anomalous birefringence would be insignificant.

In contrast, strain due to externally applied stresses, inhomogeneities in impurity concentrations, foreign inclusions or structural defects such as dislocations, twin boundaries or low-angle grain boundaries can both alter the diagonal components and introduce off-diagonal components, the latter being the source of anomalous birefringence. From the theoretical relationships between optic index and applied strain, measured spatial variations in transmitted phase and depolarization of an incident beam can be related to the internal strain field of a crystal.

The primary effect of z -axis wander is to generate spatial nonuniformities in the critical phase-matching angle for frequency conversion. The same sources which are responsible for anomalous birefringence can be expected to lead to z -axis wander.

Regarding the techniques employed, x-ray topography [22.94,95], scatterometry [22.120], optical absorption [22.121], and secondary-ion mass spectrometry (SIMS) have been used to correlate optical distortions with defects in KDP crystals:

- X-ray topography and scatterometry reveal the presence of structural defects and inclusions.
- X-ray topography and optical absorption probe the large-scale impurity variations from growth bands, crystal sectorality, and vicinal sectorality.
- Secondary-ion mass spectrometry, and to some extent scatterometry, probes the small-scale distribution of impurity ions.

Effect of Dislocations

In conventionally grown crystals, high dislocation density near the seed cap results in a large degree of optical distortion. Because the majority of these dislocations emerge at high angles to the $\{101\}$ faces, as the crystal grows along the z -direction they pass to the $\{100\}$ faces. The resulting crystal has low dislocation density only far from the seed, as illustrated in Fig. 22.47a. Consequently, useful material can only be taken from areas that are remote from the seed cap.

In contrast, dislocations in rapidly grown crystals of both KDP and DKDP are a minor source of optical distortion. This is because regeneration of the point seed leads to discrete bunches of dislocations, as shown schematically in Fig. 22.47b.

The research of Smolsky et al. [22.122] indicates that a temperature change of 0.1 K is sufficiently high to form large secondary dislocation sources. The distribution of growth steps over the faces of a crystal during growth is not constant. They change not only because of the variations of the external growth conditions but also because of some internal factors. The steps generated

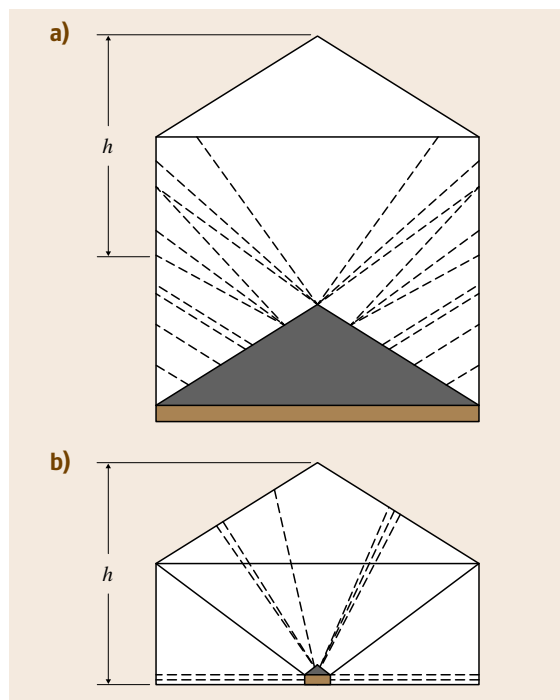


Fig. 22.47a,b Schematic of dislocation structure of (a) conventional and (b) rapidly grown KDP crystals (after [22.7], with permission of ASM Int.)

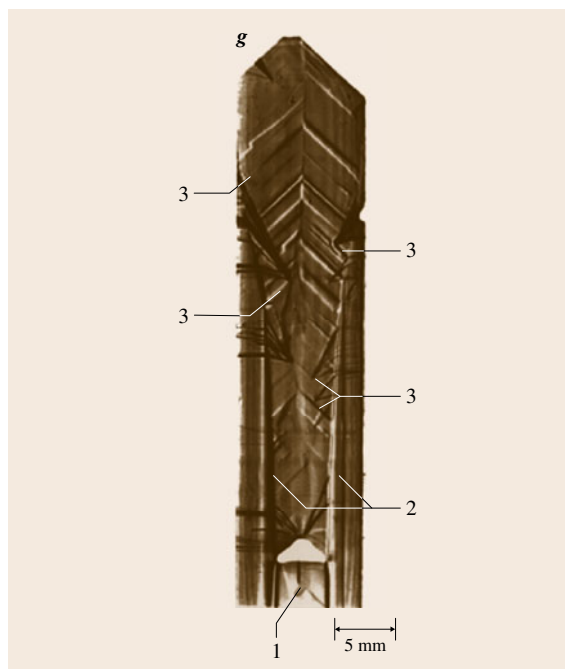


Fig. 22.48 Projection x-ray topograph of the X-cut of a KDP crystal. $\text{MoK}\alpha_1$ radiation, reflection vector $g[020]$: (1) seed; (2) sectorial boundaries between the prismatic and bipyramidal faces; (3) striation due to a lower activity of the leading growth hillocks at the face edge and the formation of new dislocation sources of steps (after [22.7], with permission of ASM Int.)

by new dislocations have new spreading directions on the face and density in accordance with the dislocation source position and activity. Therefore some stresses are formed between the old and new layers which, in turn, give rise to striation (Fig. 22.48).

De Yoreo's results [22.94] show a distinct dependence on position in the boule. Crystals from near the seed (grown first) show considerably more strain than those from near the end of the boule (grown last). This dependence may result from the distribution of dislocation as shown in Fig. 22.48.

Differences Across Sector Boundaries

There is evidence to show that the level of impurities changes sharply at $\{101\}/\{100\}$ boundaries, but remains fairly uniform within each sector, when the crystal is grown at 5 mm/day. In contrast, depolarization data shows that the strain is concentrated near the boundary, where the impurity level changes sharply, supporting the expectation that impurities per se are not the source

of strain but rather local variations in impurity levels [22.7].

Crystals grown at higher rates exhibit strong ultraviolet absorption in the $\{100\}$ sectors, but the contrast between the two sectors is greatly reduced, as is the strain at the boundary. In fact, the level of optical distortion due to the presence of sector boundaries is now at the level of background distortion due to other factors. Even in crystals with rather uniform transmitted wavefront (TWF), significant inhomogeneities in phase-matching angle have been observed [22.123].

Perhaps the most troublesome aspect of crystal sectorality is the strong tendency of iron to incorporate into the $\{100\}$ sectors, combined with its extremely high absorption coefficient in KDP at the third harmonic. In fact, of all the impurities that have been investigated in NIF development, iron appears to be the only impurity that generates significant optical absorption at 351 nm, which lies in the tail of an absorption band that peaks near 270 nm (Fig. 22.43).

Vicinal Sectorality

Within the $\{101\}$ sectors of KDP crystals, the boundaries between the three sectors of each vicinal hillock as well as the boundaries between neighboring hillocks subdivide the crystal into regions of contrasting lattice parameters. This vicinal sectorality has a distinct dependence on growth rate. High growth rate cause high depolarization losses [22.7]. Impurities are the source of vicinal sectorality in KDP. The UV absorption and impurity content increase sharply at the boundary.

Deuterated KDP Crystals

De Yoreo et al. [22.7] point out that all the defects observed in KDP are also present in DKDP. Besides, there are some aspects of crystal quality which are peculiar to the deuterated crystals. These peculiarities arise from the fact that, in practice, all DKDP crystals contain significant levels of hydrogen, unless deuterated salt is utilized. Consequently, all deuterated crystals contain hydrogen as a substitutional impurity species at levels from $\approx 1\%$ to more than 10%. Indeed, in NIF development work, DKDP crystals grown at rates from less than 1 to 15 mm/day have always been found to exhibit vicinal sectorality in their x-ray topograph. This inhomogeneity has a moderate effect on optical uniformity. Figure 22.49a shows the TWF profile from a 92% DKDP crystal grown at 9 mm/day that exhibits strong vicinal sectorality.

The fact that such sectorality is due to variations in hydrogen content is demonstrated in Fig. 22.49b which

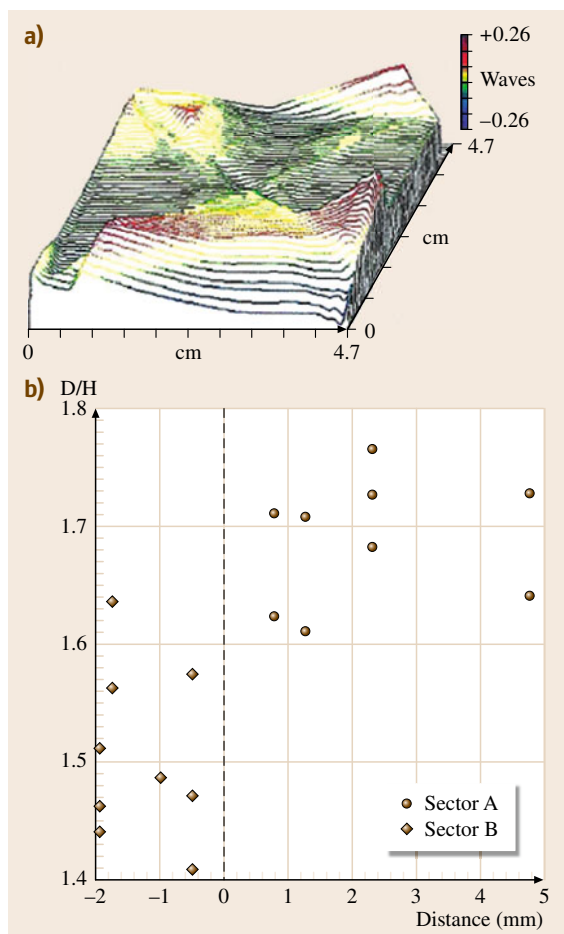


Fig. 22.49a,b Strong vicinal sectorality of 92% DKDP crystal grown at 9 mm/day (a) TWF profile; (b) profile of D/H ratio across vicinal sector boundary as determined from secondary-ion mass spectrometry (SIMS) (after [22.7], with permission of ASM Int.)

shows a SIMS profile of the D/H ratio collected across a vicinal sector boundary. Results demonstrate that the hydrogen content changes by 15% across the boundary. Other results have shown that the magnitude of this change depends inversely on growth temperature. The difference is optically undetectable for growth temperatures greater than about 60 °C.

A kind of inclusions also is found in the area of pyramidal–pyramidal sector boundary, the formation of which is related to the absorption of impurities. During the growth of pyramidal sector, the impurities are rejected from the sector and aggregate in the pyramidal–pyramidal sector boundary, causing lattice mismatch.

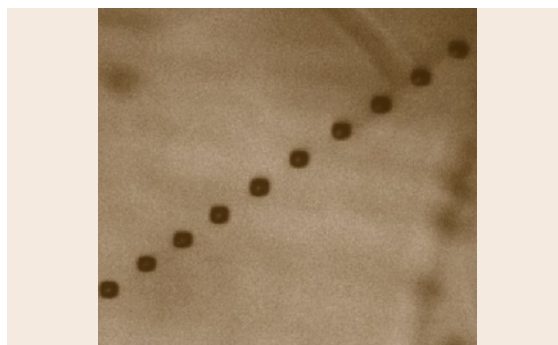


Fig. 22.50 Inclusions along Py–Pr sector (after [22.124])

This mismatch breaks the D-bond and creates a bunch of inclusions (Fig. 22.50) [22.124]. Similar results can be seen in the reports of Joshi and others [22.76, 105, 125].

In total, there are four possible sources of strain in crystals of $K(D_xH_{1-x})_2PO_4$. Each of them can act independently to produce strain in KDP–DKDP crystals [22.94]. First among these is dislocations, which produce strain fields that vary as $1/r$, where r is the distance from the dislocation. The second source is impurities, which gives rise to strain due to lattice mismatch. These first two factors are commonly found in the case of KDP crystals. The third one is the mixing of hydrogen and deuterium on the hydrogen sublattice, which generates strain due to the difference in structural parameters of KH_2PO_4 and KD_2PO_4 . Both the cell parameters and orientation of the PO_4 tetrahedron are different for the two end members of this solid-solution series [22.126, 127], consequently the mixed crystals will be strained. The fourth source of strain is that the tetragonal–monoclinic phase transition in this solid-solution series occurs at increasingly lower temperature as the deuterium level increases.

22.5.3 Laser Damage Threshold

The mechanisms of laser-induced damage are still not well understood. Many papers are devoted to it and several models have been proposed, such as lattice defects, interstitial inclusions and vacancies, multiphoton ionization, and two-photon absorption, etc. [22.128, 129]. Impurities in the raw material and growth conditions have been proved to have a direct relation with the bulk laser-induced damage threshold (LDT) of the crystal, including inorganic impurities, such as Fe^{3+} , anion impurities, and some organic materials [22.7, 119].

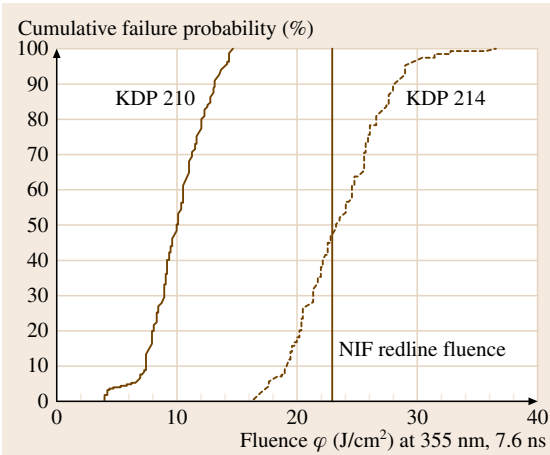


Fig. 22.51 Effect of continuous filtration of the 3ω damage performance of rapidly grown KDP. Samples were grown under nominally identical conditions with ultrahigh-purity salts. Sample 210 was prefiltered only, which resulted in high numbers of inclusions in the crystal, while sample 214 was continuously filtered during growth. Sample 214 represents the best damage performance of a rapid growth crystal to date (after [22.130])

Also, filtration before growth and continuous filtration during the growth process help to increase the LDT; investigations show that continuous filtration results in an increase in damage performance of $\approx 2\times$ over the entire cumulative failure distribution (CFD) range [22.130] (Fig. 22.51).

One should be aware that LDT is related to the laser conditions, such as wavelength, frequency, laser irradiation direction, and polarization, which makes it more complex [22.128, 133].

Effect of Postgrowth Treatment

Previous investigations of the effects of thermal annealing on KDP and KD*P damage performance [22.132–137] have indicated that it is possible to increase the 1ω

damage threshold ($R/1$) by approximately $1.5\times$ compared with the level without conditioning (Table 22.3). The 3ω thresholds, however, were not substantially affected by the annealing process.

LLNL testing showed that postgrowth thermal annealing of KDP crystals at 160°C appears to increase the damage performance of rapidly grown samples by $2.7\times$ at 1ω . The benefits of thermal annealing at 3ω are not as well defined as the dramatic increases seen at 1ω . On the other hand, thermal annealing appeared to suppress the low-fluence tail of the CFD at 3ω , thus leading to less expected damage at 1ω . When large-area beams were used to study the feasibility of online conditioning for NIF triplers, it was found that substantial conditioning was achievable in 8–12 shots of equal fluence interval. Analysis of scatter density versus fluence showed that the number of damage sites evolved exponentially. Furthermore, damage sites were stable against increases in fluence. Fujioka et al. [22.91] reported similar result. The full-width at half-maximum (FWHM) of x-ray diffraction of KDP crystals was detected to decrease obviously after conditioning at 165°C , as shown

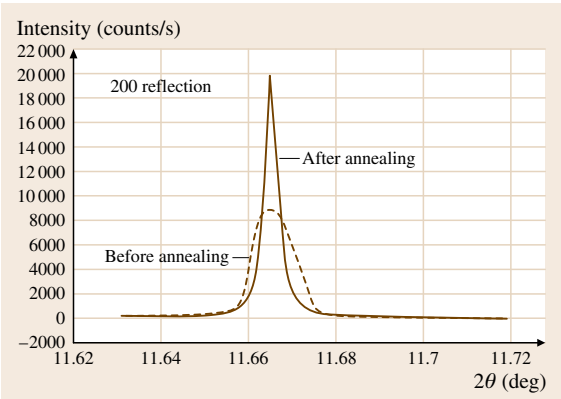


Fig. 22.52 Rocking curve of KDP crystal sample (200) double-crystal x-ray diffraction at same position before and after annealing at 165°C (after [22.131])

Table 22.3 Compilation of thermal annealing on KDP damage performance [22.132]

Sample	Sector	Growth temperature ($^\circ\text{C}$)	Growth (d)	Unannealed (J/cm^2)	Annealed (J/cm^2)	Annealed with SHG (J/cm^2)
F6-1	Pyramid	48	40	32	33	26
F6-2	Pyramid	63	30	17	23	18
F6-3	Pyramid	72	14	17	23	23
F6-4	Prism	71	20	23	40	30
F6-5	Prism	60	33	21	37	36
F6-6	Prism	25	48	17	40	28

in Fig. 22.52, which suggested that internal stress was released partly and the structural perfection of crystal was improved [22.131]. The result that the perfection of rapidly grown crystal improved more than those grown using conventional methods is consistent with the improvement of optical property by annealing [22.91].

DKDP is not amenable to thermal conditioning, because the crystals tend to fog or fall apart as a result of either decomposition or phase transformation at the temperatures used to anneal KDP. Consequently, laser conditioning is the only option [22.139].

Simulation of the Mechanism of LID

Understanding the susceptibility of KDP crystals to laser-induced damage (LID) at high laser fluence an order of magnitude below the expected intrinsic breakdown limits is a long-standing issue [22.7]. Recently, Carr et al. [22.128] employed a novel experimental approach in order to understand the mechanisms of laser-induced damage of KDP crystal. Two notable sharp steps in the damage threshold centered at 2.55 eV (487 nm) and 3.90 eV (318 nm) are clearly demonstrated in their experimental results (Fig. 22.53). Recent simulation study of KDP crystal seems to be targeted at the wavelength dependence of laser-induced damage to support the defect-assisted multistep photon mechanism proposed by Carr et al. [22.128].

The effect of neutral and charged H-interstitial and H-vacancy on laser damage was investigated by Liu et al. [22.140]. They reported that the bandgap of the neutral H-interstitial and positively charged H-vacancy are greatly reduced to 2.6 and 2.5 eV, respectively. This result is well consistent with the first sharp step at 2.55 eV and suggests that these two types of defects may be responsible for lowering the damage threshold in KDP crystal [22.128]. Wang et al. [22.141] explained that -2 charged O-interstitials are responsible for laser-induced local collapse.

In Liang's work [22.138], an ab initio study of $[\text{SO}_4]^{2-}$ in KDP is presented [22.142]. $[\text{SO}_4]^{2-}$ is such a common impurity ion in KDP raw materials that point defects of $[\text{PO}_4]^{3-}$ replaced by $[\text{SO}_4]^{2-}$ are easily created during crystal growth [22.143]. The same simulation model as that adopted by Liu et al. [22.140] and Wang et al. [22.141] was used, which made it

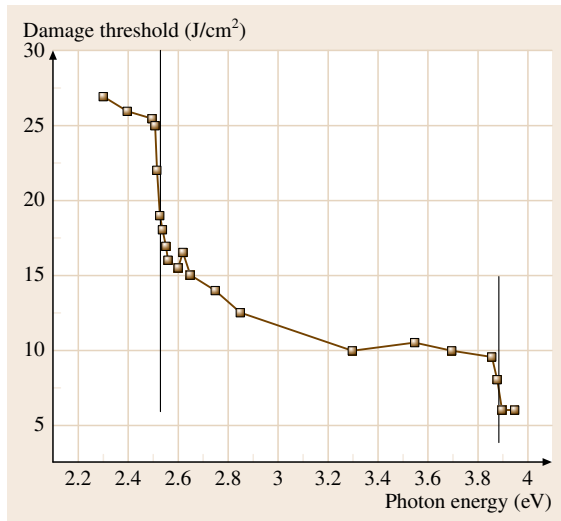


Fig. 22.53 Wavelength-dependent damage threshold (after 22.128)

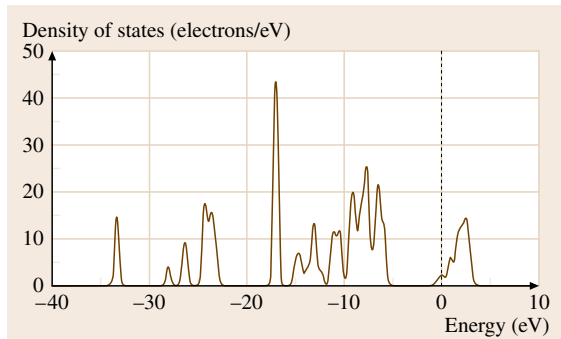


Fig. 22.54 Total density states of KDP ($[\text{SO}_4]^{2-}$) (after 22.138)

possible to compare between different works. In the density of states (DOS) of KDP containing $[\text{SO}_4]^{2-}$ (Fig. 22.54), it is shown that the bandgap has reduced to 3.90 eV (318 nm), which can induce laser absorption at 318 nm [22.138]. The results of this study are consistent with the experimental work of Carr et al. [22.128]. So, it can be speculated that sulfate substitution accounts to some extent for the second sharp step.

References

- | | |
|---|--|
| <p>22.1 L.N. Rashkovich: <i>KDP Family Single Crystals</i> (Adam-Hilger, New York 1991)</p> <p>22.2 Ferroelectrics 71 (1987)</p> | <p>22.3 Ferroelectrics 72 (1987)</p> <p>22.4 J.F. Nye: <i>Physical Properties of Crystals</i> (Oxford Univ. Press, New York 1985), Chap. 13</p> |
|---|--|

- 22.5 D. Eimerl: Electro-optic, linear, and non-linear optical properties of KDP and its isomorphs, *Ferroelectrics* **72**, 95 (1987)
- 22.6 J.D. Lindl: Review of development of the indirect-drive approach to inertial confinement fusion and the target physics basis for ignition and gain, *Phys. Plasmas* **2**, 3933 (1995)
- 22.7 J.J. De Yoreo, A. Burnham, P.K. Whitman: Developing KDP and DKDP crystals for the world's most powerful laser, *Int. Mater. Rev.* **13**, 113–152 (2002)
- 22.8 N.P. Zaitseva, J.J. De Yoreo, M.R. Dehaven, R.L. Vital, K.E. Montgomery, M. Richardson, L.J. Ather-ton: Rapid growth of large-scale (40–55 cm) KH_2PO_4 crystals, *J. Cryst. Growth* **180**, 255–262 (1997)
- 22.9 V.I. Bespalov, V.I. Bredikhin, V.P. Ershov, V.I. Katsman, N.V. Kiseleva, S.P. Kuznetsov: Optical properties of KDP and DKDP crystals grown at high rates, *Sov. J. Quantum Electron.* **12**, 1527–1528 (1982)
- 22.10 G.M. Loiacono, J.J. Zola, G. Kostecky: Growth of KH_2PO_4 crystals at constant temperature and supersaturation, *J. Cryst. Growth* **62**, 545–556 (1983)
- 22.11 J.F. Cooper, M.F. Singlenton, J. Zandelevich: Rapid growth of potassium dihydrogen phosphate crystals, *Proc. Int. Conf. Laser* 1984 (1984) pp. 567–572
- 22.12 L.N. Rashkovich: High-speed growth of large crystals for nonlinear optics from solution, *Vestn. Akad. Nauk SSSR* **9**, 15–19 (1984)
- 22.13 S.A. de Vries, P. Goettkindt, S.L. Bennett, W.J. Huisman, M.J. Zwanenburg, D.-M. Smilgies, J.J. De Yoreo, W.J.P. van Enckevort, P. Bennema, E. Vlieg: Surface atomic structure of KDP crystals in aqueous solution: An explanation of the growth shape, *Phys. Rev. Lett.* **80**, 2229 (1998)
- 22.14 P. Hartman: In: *Crystal Growth, An Introduction* (North-Holland, Amsterdam 1973) p. 367
- 22.15 P. Bennema: In: *Handbook of Crystal Growth*, Vol. 1a, ed. by T.J. Hurler (Elsevier Science Publishers, Amsterdam 1993) p. 477
- 22.16 P. Hartman: The morphology of zircon and potassium dihydrogen phosphate in relation to the crystal structure, *Acta Crystallogr.* **9**, 721–727 (1956)
- 22.17 B. Dam, P. Bennema, W.J.P. Van Enckevort: The mechanism of tapering on KDP-type crystals, *J. Cryst. Growth* **74**, 118–128 (1986)
- 22.18 W.J.P. Van Enckevort, R. Janssen-van Rosmalen, W.H. van der Linden: Evidence for spiral growth on the pyramidal faces of KDP and ADP single crystals, *J. Cryst. Growth* **49**, 502–514 (1980)
- 22.19 J.J. De Yoreo, T.A. Land, B. Dair: Growth morphology of vicinal hillocks on the {101} face of KDP: From step-flow to layer-by-layer growth, *Phys. Rev. Lett.* **73**, 838–841 (1994)
- 22.20 S.A. de Vries, P. Goettkindt, W.J. Huisman, M.J. Zwanenburg, R. Feidenhans'l, S.L. Bennett, D.-M. Smilgies, A. Stierle, J.J. De Yoreo, W.J.P. van Enckevort: X-ray diffraction studies of potassium dihydrogen phosphate (KDP) crystal surfaces, *J. Cryst. Growth* **205**, 202–214 (1999)
- 22.21 I.K. Robinson: Crystal truncation rods and surface roughness, *Phys. Rev. B* **33**, 3830–3836 (1986)
- 22.22 B. Dam, W.J.P. van Enckevort: In situ observation of surface phenomena on {100} and {101} potassium dihydrogen phosphate crystals, *J. Cryst. Growth* **69**, 306–316 (1984)
- 22.23 B. Dam, E. Polman, W.J.P. van Enckevort: *Industrial Crystallization*, Vol. 84, ed. by S.J. Jancic, E.J. de Jong (Elsevier Science Publishers, Amsterdam 1984) p. 97
- 22.24 N. Cabrera, D.A. Vermilyea: The growth of crystals from solution. In: *Growth and Perfection of Crystals*, ed. by R.H. Doremus, B.W. Roberts, D. Turnbull (Wiley, New York 1958) pp. 393–410
- 22.25 T.A. Land, T.L. Martin, S. Potapenko, G.T. Palmore, J.J. De Yoreo: Recovery of surfaces from impurity poisoning during crystal growth, *Nature* **399**, 442–445 (1999)
- 22.26 W.J.P. van Enckevort, A.C.J.F. van den Berg: Impurity blocking of crystal growth: A Monte Carlo study, *J. Cryst. Growth* **183**, 441–455 (1998)
- 22.27 M.K. Cerreta, K.A. Berglund: The structure of aqueous solutions of some dihydrogen orthophosphates by laser Raman spectroscopy, *J. Cryst. Growth* **84**, 577–588 (1987)
- 22.28 L.G. Wu, X.H. Rui, G.J. Teng, Z.S. Qi, C. Yong, Z.Y. Qi: Lattice vibration modes and growth mechanism of KDP single crystals studied by Raman spectroscopy, *Chin. J. Light Scatt.* **01**, 28–34 (2002)
- 22.29 X. Yu, X. Yue, H. Gao, H. Chen: Quantitative studies of solute boundary layers around crystals by holographic phase-contrast interferometric microphotography, *J. Cryst. Growth* **106**, 690–694 (1990)
- 22.30 X. Yu, J. Yu, Y. Wang, Z. Cheng, B. Yu, S. Zhang, D. Sun, G. Jiang: Microprobe of structure of crystal/liquid interface boundary layers, *Sci. China Ser. E* **3**, 43–51 (2001)
- 22.31 M.F. Reedijk, J. Arsic, F.F.A. Hollander, S.A. de Vries, E. Vlieg: Liquid order at the interface of KDP crystals with water: Evidence for icelike layers, *Phys. Rev. Lett.* **90**, 66103 (2003)
- 22.32 N.P. Zaitseva, L.N. Rashkovich, S.V. Bogatyreva: Stability of KH_2PO_4 and $\text{K}(\text{H},\text{D})_2\text{PO}_4$ solutions at fast crystal growth rates, *J. Cryst. Growth* **148**, 276–282 (1995)
- 22.33 D. Kaminski, N. Radenovic, M.A. Deij, W.J.P. van Enckevort, E. Vlieg: pH-dependent liquid order at the solid-solution interface of KH_2PO_4 crystals, *Phys. Rev. B* **72**, 245404 (2005)
- 22.34 J.W. Mullin: *Crystallization* (Butterworths, London 1993)
- 22.35 D. Kashchiev, D. Verdoes, G.M. van Rosmalen: Induction time and metastability limit in new phase formation, *J. Cryst. Growth* **110**, 373–380 (1991)

- 22.36 A.S. Myerson, A.F. Izmailov, H.-S. Na: Thermodynamic studies of levitated microdroplets of highly supersaturated electrolyte solutions, *J. Cryst. Growth* **166**, 981–988 (1996)
- 22.37 M. Bohenek, A.S. Myerson, W.M. Sun: Thermodynamics, cluster formation and crystal growth in highly supersaturated solutions of KDP, ADP and TGS, *J. Cryst. Growth* **179**, 213–225 (1997)
- 22.38 M.H. Jiang, C.S. Fang, X.L. Yu, M. Wang, T.H. Zheng, Z.S. Gao: Polymorphism and metastable growth of DKDP, *J. Cryst. Growth* **53**, 283–291 (1981)
- 22.39 M. Shanmugham, F.D. Gnanam, P. Ramasamy: Non-steady state nucleation process in KDP solutions in the presence of XO_4 impurities, *J. Mater. Sci.* **19**, 2837–2844 (1984)
- 22.40 O. Shimomura, M. Suzuki: The increase of temperature range in the region of supersaturation of KDP solution by addition of impurity, *J. Cryst. Growth* **98**, 850–852 (1989)
- 22.41 S. Nagalingam, S. Vasudevan, R. Dhanasekaran, P. Ramasamy: Effect of impurities on the nucleation of ADP from aqueous solution, *Cryst. Res. Technol.* **16**, 647–650 (1981)
- 22.42 N.P. Zaitseva, L. Carman: Rapid growth of KDP-type crystals, *Prog. Cryst. Growth Charact. Mater.* **43**, 1–118 (2001)
- 22.43 A.B. Ahza: Kinetics of milk fat crystallization in a continuous crystallizer, Ph.D. Thesis (University of Wisconsin–Madison 1995)
- 22.44 A.D. Randolph, M.A. Larson: *Theory of Particulate Processes. Analysis and Techniques of continuous crystallization*, 2nd edn. (Academic, San Diego 1988)
- 22.45 R. Boisteale: Fundamentals of nucleation and crystal growth. In: *Crystallization and Polymorphism of Fats and Fatty Acids*, Surfactant, Vol. 31, ed. by N. Garti, K. Sato (Marcel Dekker, New York 1988) pp. 189–226
- 22.46 J. Nývlt, O. Söhnel, M. Matichová, M. Bruol: *The Kinetics of Industrial Crystallization* (Academia, Prague 1985)
- 22.47 E.G. Denk Jr., G.D. Botsaris: Fundamental studies in secondary nucleation from solution, *J. Cryst. Growth* **13/14**, 493–499 (1972)
- 22.48 J. Synowiec: A method calculation of the limiting supersaturation of inorganic salt solutions, *Krist. Tech.* **8**, 701–708 (1973)
- 22.49 O. Söhnel: Metastable regions of aqueous solutions of inorganic soluble salts, *Krist. Tech.* **11**, 141–148 (1976)
- 22.50 A. Mersmann, K. Bartosch: How to predict the metastable zone width, *J. Cryst. Growth* **183**, 240–250 (1998)
- 22.51 T.A. Land, J.J. De Yoreo, T.L. Martin, G.T. Palmore: A comparison of growth hillock structure and step dynamics on KDP {100} and {101} surfaces using force microscopy, *Crystallogr. Rep.* **44**, 704–716 (1999)
- 22.52 I.L. Smolsky, N.P. Zaitseva: *Growth of Crystals*, Vol. 19, ed. by E.I. Givargizov, S.A. Grinberg (Plenum Publ. Corp., New York 1995) p. 173
- 22.53 A.A. Chernov, N.P. Zaitseva, L.N. Rashkovich: Secondary nucleation induced by the cracking of a growing crystal: KH_2PO_4 (KDP) and $K(H,D)_2PO_4$ (DKDP), *J. Cryst. Growth* **102**, 793–800 (1990)
- 22.54 H. Hilscher: Microscopic investigations of morphological structures on the pyramidal faces of KDP and DKDP single crystals, *Cryst. Res. Technol.* **20**, 1351–1361 (1985)
- 22.55 N.P. Zaitseva, L. Carman, I.L. Smolsky, R. Torres, M. Yan: The effect of impurities and supersaturation on the rapid growth of KDP crystals, *J. Cryst. Growth* **204**, 512–524 (1999)
- 22.56 C. Belouet, M. Monnier, J.C. Verplanke: Autoradiography as a tool for studying iron segregation and related defects in KH_2PO_4 single crystals, *J. Cryst. Growth* **29**, 109–120 (1975)
- 22.57 A.I. Malkin, A.A. Chernov, I.V. Alexeev: Growth of dipyramidal face of dislocation-free ADP crystals; free energy of steps, *J. Cryst. Growth* **97**, 765–769 (1989)
- 22.58 N.P. Zaitseva, L. Carman, I.L. Smolsky: Habit control during rapid growth of KDP and DKDP crystals, *J. Cryst. Growth* **24**, 363–373 (2002)
- 22.59 H.V. Alexandru, S. Antohe: Prismatic faces of KDP crystal, kinetic and mechanism of growth from solutions, *J. Cryst. Growth* **258**, 149–157 (2003)
- 22.60 A.A. Chernov: Stability of faceted shapes, *J. Cryst. Growth* **24/25**, 11–31 (1974)
- 22.61 H.J. Scheel, P. Niedermann: Growth mechanisms of $YBa_2Cu_3O_{7-x}$ platelet crystals from STM/SEM investigations, *J. Cryst. Growth* **94**, 281–284 (1989)
- 22.62 N.P. Zaitseva, I.L. Smolsky, L. Carman: Growth phenomena in the surface layer and step generation from the crystal edges, *J. Cryst. Growth* **222**, 249–262 (2001)
- 22.63 E.P. Lokshin: Growth and properties of KDP-group crystals, *Crystallogr. Rep.* **41**, 1061–1069 (1996)
- 22.64 L.N. Rashkovich, G.T. Moldazhanova: Growth kinetics and morphology of potassium dihydrogen phosphate crystal faces in solutions of varying acidity, *J. Cryst. Growth* **151**, 145–152 (1995)
- 22.65 J.W. Mullin, A. Amatavivadhana: Growth kinetics of ammonium and potassium dihydrogen phosphate crystals, *J. Appl. Chem.* **17**, 151–156 (1967)
- 22.66 L.N. Rashkovich, N.V. Kronskey: Influence of Fe^{3+} and Al^{3+} ions on the kinetics of steps on the {100} faces of KDP, *J. Cryst. Growth* **182**, 434–441 (1997)
- 22.67 T.A. Eremina, V.A. Kuznetsov, N.N. Eremin, T.M. Okhrimenko, N.G. Furmanova, E.P. Efremova, M. Rak: On the mechanism of impurity influence on growth kinetics and surface morphology of KDP crystals-II: Experimental study of influence of bivalent and trivalent impurity ions on growth kinetics and surface morphology of KDP crystals, *J. Cryst. Growth* **273**, 586–593 (2005)

- 22.68 J.J. De Yoreo, T.A. Land, L.N. Rashkovich, T.A. Onischenko, J.D. Lee, O.V. Monovskii, N.P. Zaitseva: The effect of dislocation cores on growth hillock vicinity and normal growth rates of KDP {101} surfaces, *J. Cryst. Growth* **182**, 442–460 (1997)
- 22.69 P.G. Vekilov, Y.G. Kuznetsov, A.A. Chernov: The effect of temperature on step motion; {101} ADP face, *J. Cryst. Growth* **121**, 44–52 (1992)
- 22.70 M. Nakatsuka, K. Fujioka, T. Kanabe, H. Fujita: Rapid growth over 50 mm/d of water-soluble KDP crystal, *J. Cryst. Growth* **171**, 531–537 (1997)
- 22.71 P.G. Vekilov, Y.G. Kuznetsov: Growth kinetics irregularities due to changed dislocation source activity; {101} ADP face, *J. Cryst. Growth* **119**, 248–260 (1992)
- 22.72 G.M. Loiacono, J.J. Zola, G. Kostecky: The taper effect in KH_2PO_4 type crystals, *J. Cryst. Growth* **58**, 495–499 (1982)
- 22.73 B. Wang, C.-S. Fang, S.-L. Wang, X. Sun, Q.-T. Gu, Y.-P. Li, X.-G. Xu, J.-Q. Zhang, B. Liu, X.-M. Mou: The effects of Sn^{4+} ion on the growth habit and optical properties of KDP crystal, *J. Cryst. Growth* **297**, 352–355 (2006)
- 22.74 Z.S. Gao, Y.P. Li, C. Wang, Z.K. Lu: Effect of metaphosphate on the growth in KDP crystal, *J. Synth. Cryst.* **23**(3/4), 52–55 (1994)
- 22.75 Y.-J. Fu, Z.-S. Gao, J.-M. Liu, Y.-P. Li, H. Zeng, M.-H. Jiang: The effects of anionic impurities on the growth habit and optical properties of KDP, *J. Cryst. Growth* **198/199**, 682–686 (1999)
- 22.76 S. Wang, Z.S. Gao, Y. Fu, X. Sun, J. Zhang, H. Zeng, Y. Li: Scattering centers caused by adding metaphosphate into KDP crystals, *J. Cryst. Growth* **223**, 415–419 (2001)
- 22.77 V.A. Kuznetsov, T.M. Okhrimenko, M. Rak: Growth promoting effect of organic impurities on growth kinetics of ADP and KDP crystals, *J. Cryst. Growth* **193**, 164–173 (1998)
- 22.78 N.P. Zaitseva, J. Atherton, R. Rozsa, L. Carman, I.L. Smolsky, M. Runkel, R. Ryon, L. James: Design and benefits of continuous filtration in rapid growth of large KDP and DKDP crystals, *J. Cryst. Growth* **197**, 911–920 (1999)
- 22.79 I. Owsczarek, B. Wojciechowski: Nucleation and growth behaviour of KDP from degassed and undegassed aqueous solutions, *J. Cryst. Growth* **84**, 329–331 (1987)
- 22.80 H.J. Scheel, T. Fukuda (Eds.): *Crystal Growth Technology* (Wiley, New York 2003) p. 446
- 22.81 I. Kolodyazhngl: *Abstracts of ICCG XI, P201A.21* (The Hague, 1995) pp. 18–23
- 22.82 M.S. Yan, D. Wu, J.B. Zeng, X. Zhang, Y. Guan, L. Wang: Growth of large cross section KDP-type crystals, *J. Synth. Cryst.* **115**, 1–4 (1986)
- 22.83 T. Sasaki, A. Yokotani: Growth of large KDP crystals for laser fusion experiments, *J. Cryst. Growth* **99**, 820–826 (1990)
- 22.84 Z.K. Lu, Z.S. Gao, Y.P. Li, C. Wang: Growth of large KDP crystals by solution circulating method, *J. Synth. Cryst.* **25**, 19–22 (1996)
- 22.85 V.M. Loginer: *Abstracts of ICCG XI, P203B.22* (The Hague, June 1995) pp. 18–25
- 22.86 V.I. Bespalov, V.I. Bredikhin, V.P. Ershov, V.I. Katsman, L.A. Lavrov: KDP and DKDP crystals for nonlinear optics grown at high rate, *J. Cryst. Growth* **82**, 776–778 (1987)
- 22.87 P.F. Bordui, G.M. Loiacono: In-line bulk supersaturation measurement by electrical conductometry in KDP crystal growth from aqueous solution, *J. Cryst. Growth* **67**, 168–172 (1984)
- 22.88 S.L. Wang, Y.J. Fu, W.C. Zhang, X. Sun, Z.S. Gao: In-line bulk concentration measurement by method of conductivity in industrial KDP crystal growth from aqueous solution, *Cryst. Res. Technol.* **35**, 1027–1034 (2000)
- 22.89 K. Montgomery, N.P. Zaitseva, J.J. De Yoreo, R. Vital: Device for isolation of seed crystals during processing of solutions, LLNL Docket No. IL-9643, DOE case No. S-82,943, US Patent 5904772
- 22.90 S.L. Wang, Z.S. Gao, Y.J. Fu, A.D. Duan, X. Sun, C.S. Fang, X.Q. Wang: Study on rapid growth of highly-deuterated DKDP crystals, *Cryst. Res. Technol.* **38**, 941–945 (2003)
- 22.91 K. Fujioka, S. Matsuo, T. Kanabe, H. Fujita, M. Nakatsuka: Optical properties of rapidly grown KDP crystal improved by thermal conditioning, *J. Cryst. Growth* **181**, 265–271 (1997)
- 22.92 M.J. Runkel, W.H. Williams, J.J. De Yoreo: Predicting bulk damage in NIF triple harmonic generators, *Proc. SPIE* **3578**, 322–335 (1998)
- 22.93 B. Kahr, S.-H. Jang, J.A. Subramony, M.P. Kelley, L. Bastin: Dyeing salt crystals for optical applications, *Adv. Mater.* **8**, 941–944 (1996)
- 22.94 J.J. De Yoreo, B.W. Woods: A study of residual stress and the stress-optic effect in mixed crystals of $\text{K}(\text{D}_{x}\text{H}_{1-x})_2\text{PO}_4$, *J. Appl. Phys.* **73**, 7780–7789 (1993)
- 22.95 J.J. De Yoreo, Z.U. Rek, N.P. Zaitseva, B.W. Woods: Sources of optical distortion in rapidly grown crystals of KH_2PO_4 , *J. Cryst. Growth* **166**, 291–297 (1996)
- 22.96 R.A. Hawley-Fedder, H.F. Robey III, T.A. Biesiada, M.R. DeHaven, R. Floyd, A.K. Burnham: Rapid growth of very large KDP and KD*P crystals in support of the National Ignition Facility, *Proc. SPIE* **4102**, 152–161 (2001)
- 22.97 S. Wang, Z.S. Gao, Y. Fu, J. Zhang, X. Sun, Y. Li, H. Zeng, G. Huang, J. Yang, Y. Zhuang, Z. Xue: Effects of metaphosphate doping on growth and properties of KDP crystals, *Acta Opt. Sin.* **22**, 753–757 (2002)
- 22.98 J. Zhang, S. Wang, C. Fang, X. Sun, Q. Gu, Y. Li, B. Wang, B. Liu, X. Mu: Growth habit and transparency of sulphate doped KDP crystal, *Mater. Lett.* **61**, 2703–2706 (2007)
- 22.99 S. Hirota, H. Miki, K. Fukui, K. Maeda: Coloring and habit modification of dyed KDP crystals as functions

- of supersaturation and dye concentration, *J. Cryst. Growth* **235**, 541–546 (2002)
- 22.100 W.J.P. van Enckevort: Surface microtopography of aqueous solution grown crystals, *Prog. Cryst. Growth Charact. Mater.* **9**, 1–50 (1984)
- 22.101 I. Sunagawa: In: *Materials Science of the Earth's Interior*, ed. by I. Sunagawa (Terra Scientific, Tokyo 1984) pp. 63–105
- 22.102 J.A. Subramony, S.-H. Jang, B. Kahr: Dyeing KDP, *Ferroelectrics* **191**, 293–300 (1997)
- 22.103 O.A. Gliko, N.P. Zaitseva, L.N. Rashkovich: Morphology and dynamics of crystal surfaces in complex molecular systems. In: *Materials Research Society Symposium Proceedings*, Vol. 620, ed. by J.J. De Yoreo, W. Casey, A. Malkin, E. Vlieg, M. Ward (Materials Research Society, Warrendale 2001)
- 22.104 L.N. Rashkovich, A.A. Mkrtchan, A.A. Chernov: *Kristallografiya* **30**, 380–387 (1985)
- 22.105 I.L. Smolsky, N.P. Zaitseva, E.B. Rudneva, S.V. Bogatyreva: Formation of “hair” inclusions in rapidly grown potassium dihydrogen phosphate crystals, *J. Cryst. Growth* **166**, 228–233 (1996)
- 22.106 H.F. Robey, S.Y. Potapenko, K.D. Summerhays: “Bending” of steps on rapidly grown KH_2PO_4 crystals due to an inhomogeneous surface supersaturation field, *J. Cryst. Growth* **213**, 340–354 (2000)
- 22.107 T.A. Land, J.J. De Yoreo: The evolution of growth modes and activity of growth sources on canavalin investigated by in situ atomic force microscopy, *J. Cryst. Growth* **208**, 623–637 (2000)
- 22.108 H.G. Van Bueren: *Imperfections in Crystals* (Interscience, New York 1960)
- 22.109 P. Feng, J.-K. Liang, G.-B. Su, Q.-L. Zhao, Y.-P. He, Y.-S. Hunag: Growth of KDP crystals by splicing parallel-seed in aqueous solution and its mechanism, *Cryst. Res. Technol.* **25**, 1385–1391 (1990)
- 22.110 P. Feng, J.-K. Liang, G.-B. Su, Y.-P. He, B.-R. Huang, Y.-S. Huang, Q.-L. Zhao: The growth of KDP crystals and its mechanism by splicing misoriented in aqueous solution, *Cryst. Res. Technol.* **26**, 289–295 (1991)
- 22.111 H.F. Robey, S.Y. Potapenko: Ex situ microscopic observation of the lateral instability of macrosteps on the surfaces of rapidly grown KH_2PO_4 crystals, *J. Cryst. Growth* **213**, 355–367 (2000)
- 22.112 I.L. Smolski, J.J. De Yoreo, N.P. Zaitseva, J.D. Lee, T.A. Land, E.B. Rudneva: Oriented liquid inclusions in KDP crystals, *J. Cryst. Growth* **169**, 741–746 (1996)
- 22.113 R. Brooks, A.T. Horton, J.L. Torgesen: Occlusion of mother liquor in solution-grown crystals, *J. Cryst. Growth* **2**, 279–283 (1968)
- 22.114 M.S. Joshi, B.K. Paul: Effect of supersaturation and fluid shear on the habit and homogeneity of potassium dihydrogen phosphate crystals, *J. Cryst. Growth* **22**, 321–327 (1974)
- 22.115 H.F. Robey, D. Maynes: Numerical simulation of the hydrodynamics and mass transfer in the large scale, rapid growth of KDP crystals. Part 1: Computation of the transient, three-dimensional flow field, *J. Cryst. Growth* **222**, 263–278 (2001)
- 22.116 H.F. Robey: Numerical simulation of the hydrodynamics and mass transfer in the large scale, rapid growth of KDP crystals. Part 2: Computation of the mass transfer, *J. Cryst. Growth* **259**, 388–403 (2003)
- 22.117 G. Li, L. Xue, G. Su, X. Zhuang, Z. Li, Y. He: Study on the growth and characterization of KDP-type crystals, *J. Cryst. Growth* **274**, 555–562 (2005)
- 22.118 N.Y. Garces, K.T. Stevens, L.E. Halliburton, M. Yan, N.P. Zaitseva, J.J. De Yoreo: Optical absorption and electron paramagnetic resonance of Fe ions in KDP crystals, *J. Cryst. Growth* **225**, 435–439 (2001)
- 22.119 X. Sun, X.-F. Cheng, Z.-P. Wang, Q. Gu, S. Wang, Y. Li, B. Wang, X. Xu, C. Fang: Effect of impurities on optical qualities of KDP crystal, *Laser Part. Beams* **16**, 830–834 (2004)
- 22.120 B. Woods, M. Runkel, M. Yan, M. Staggs, N.P. Zaitseva, M. Kozlowski, J.J. De Yoreo: Investigation of laser damage in KDP using light scattering techniques, *Proc. SPIE* **2966**, 20–31 (1997)
- 22.121 M. Yan: Chemistry and materials science, Progress Report UCID-20622-95 12–16 LLNL CA 1996
- 22.122 I.L. Smolsky, A.E. Voloshin, N.P. Zaitseva, E.B. Rudneva, H. Klapper: X-ray topography study of striation formation in layer growth of crystals from solutions, *Philos. Trans. R. Soc. Lond. A* **357**, 2631–2649 (1999)
- 22.123 J. Auerbach, P.J. Wegner: Modeling of frequency doubling and tripling with measured crystal spatial refractive-index nonuniformities, *Appl. Opt.* **40**, 1404–1411 (2001)
- 22.124 X. Sun, X. Xu, Z. Wang, Y. Fu, S. Wang, H. Zeng, Y. Li, X. Yu, Z. Gao: Inclusion in DKDP crystals, *Chin. Sci. Bull.* **46**(20), 1757–1760 (2001)
- 22.125 M.S. Joshi, A.V. Antony: Oriented inclusions in single crystals of potassium dihydrogen phosphate, *Krist. Tech.* **14**, 527–530 (1979)
- 22.126 R.J. Nemes, Z. Tun, W.F. Kuhs: A compilation of accurate structural parameters for KDP and DKDP, *Ferroelectrics* **71**, 125–141 (1987)
- 22.127 Z. Tun, R.J. Nemes, W.F. Kuhs, R.F.D. Stansfield: A high resolution neutron diffraction study of the effects of deuteration on the crystal structure of KH_2PO_4 , *J. Phys. C* **21**, 245–258 (1988)
- 22.128 C.W. Carr, H.B. Radousky, S.G. Demos: Wavelength dependence of laser-induced damage: Determining the damage initiation mechanisms, *Phys. Rev. Lett.* **91**, 127402 (2003)
- 22.129 K. Wang, C. Fang, J. Zhang, X. Sun, S. Wang, Q. Gu, X. Zhao, B. Wang: Laser-induced damage mechanisms and improvement of optical qualities of bulk potassium dihydrogen phosphate crystals, *J. Cryst. Growth* **287**, 478–482 (2006)

- 22.130 M. Runkel, R. Jennings, J.J. De Yoreo, W. Sell, D. Milam, N. Zaitseva, L. Carmen, W. Williams: An overview of recent KDP damage experiments and implications for NIF tripler performance, *Proc. SPIE* **3492**, 374–385 (1999)
- 22.131 S. Wang, L. Li, X. Hu, Z. Gao, Y. Fu, X. Sun, Y. Li, H. Zeng: The effect of thermal conditioning on microstructure of KDP crystals, *J. Funct. Mater.* **34**, 331–333 (2003)
- 22.132 M. Runkel, M.S. Maricle, R.A. Torres, J. Auerbach, R. Floyd, R. Hawley-Fedder, A. Burnham: Effect of thermal annealing and second harmonic generation on bulk damage performance of rapid-growth KDP type-I doublers at 1064 nm, *Proc. SPIE* **4347**, 389–399 (2001)
- 22.133 H. Yoshida, T. Jitsuno, H. Fujita, M. Nakatsuka, M. Yoshimura, T. Sasaki, K. Yoshida: Investigation of bulk laser damage in KDP crystal as a function of laser irradiation direction, polarization, and wavelength, *Appl. Phys. B* **70**, 195–201 (2000)
- 22.134 F. Rainer, L.J. Atherton, J.J. De Yoreo: Laser damage to production- and research grade KDP crystals, *Proc. SPIE* **1848**, 46–58 (1992)
- 22.135 F. Rainer, F. De Marco, M. Staggs, M. Kozlowski, L. Atherton, L. Sheehan: A historical perspective on fifteen years of laser damage thresholds at LLNL, *Proc. SPIE* **2114**, 9–23 (1994)
- 22.136 J. Swain, S. Stokowski, D. Milam, F. Rainer: Improving the bulk laser damage resistance of potassium dihydrogen phosphate by pulsed laser irradiation, *Appl. Phys. Lett.* **40**(4), 350–352 (1982)
- 22.137 J. Swain, S. Stokowski, D. Milam, G. Kennedy: The effect of baking and pulsed laser irradiation on the bulk laser threshold of potassium dihydrogen phosphate crystals, *Appl. Phys. Lett.* **41**(1), 12–16 (1982)
- 22.138 L. Liang, Z. Xian, S. Xun, S. Xueqin: Sulfate may play an important role in the wavelength dependence of laser induced damage, *Opt. Exp.* **14**, 12196–12198 (2006)
- 22.139 L.J. Atherton, F. Rainer, J.J. De Yoreo, I. Thomas, N. Zaitseva, F. De Marco: Thermal and laser conditioning of production and rapid-growth KDP and DKDP crystals, *Proc. SPIE* **2114**, 36–45 (1994)
- 22.140 C.S. Liu, N. Kioussis, S.G. Demos, H.R. Radousky: Electron- and hole-assisted reactions of H defects in hydrogen-bonded KDP, *Phys. Rev. Lett.* **91**, 15505 (2003)
- 22.141 K. Wang, C. Fang, J. Zhang, C. Liu, R. Boughton, S. Wang, X. Zhao: First-principles study of interstitial oxygen in potassium dihydrogen phosphate crystals, *Phys. Rev. B* **72**, 184105 (2005)
- 22.142 M.C. Payne, M.P. Teter, D.C. Allen, T. Arias, J. Joannopoulos: Iterative minimization techniques for ab initio total-energy calculations: Molecular dynamics and conjugate gradients, *Rev. Mod. Phys.* **64**, 1045–1097 (1992)
- 22.143 J.-Q. Zhang, S.-L. Wang, C.-S. Fang, X. Sun, Q. Gu, Y. Li, K. Wang, B. Wang, Y. Li, B. Liu: Effects of sulphate doping on the growth habit of KDP crystal, *J. Funct. Mater.* **36**, 1505–1508 (2005)

Crystal Growth

Part D

Part D Crystal Growth from Vapor

23 Growth and Characterization of Silicon Carbide Crystals

Govindhan Dhanaraj, Nashua, USA
Balaji Raghothamachar, Stony Brook, USA
Michael Dudley, Stony Brook, USA

24 AlN Bulk Crystal Growth by Physical Vapor Transport

Rafael Dalmau, Morrisville, USA
Zlatko Sitar, Raleigh, USA

25 Growth of Single-Crystal Organic Semiconductors

Christian Kloc, Singapore
Theo Siegrist, Tallahassee, USA
Jens Pflaum, Würzburg, Germany

26 Growth of III-Nitrides with Halide Vapor Phase Epitaxy (HVPE)

Carl Hemmingsson, Linköping, Sweden
Bo Monemar, Linköping, Sweden
Yoshinao Kumagai, Tokyo, Japan
Akinori Koukitu, Tokyo, Japan

27 Growth of Semiconductor Single Crystals from Vapor Phase

Ramasamy Dhanasekaran, Chennai, India

Growth and Characterization of Silicon Carbide Crystals

Govindhan Dhanaraj, Balaji Raghothamachar, Michael Dudley

Silicon carbide is a semiconductor that is highly suitable for various high-temperature and high-power electronic technologies due to its large energy bandgap, thermal conductivity, and breakdown voltage, among other outstanding properties. Large-area high-quality single-crystal wafers are the chief requirement to realize the potential of silicon carbide for these applications. Over the past 20 years, considerable advances have been made in silicon carbide single-crystal growth technology through understanding of growth mechanisms and defect nucleation. Wafer sizes have been greatly improved from wafer diameters of a few millimeters to 100 mm, with overall dislocation densities steadily reducing over the years. Device-killing micropipe defects have almost been eliminated, and the reduction in defect densities has facilitated enhanced understanding of various defect configurations in bulk and homoepitaxial layers. Silicon carbide electronics is expected to continue to grow and steadily replace silicon, particularly for applications under extreme conditions, as higher-quality, lower-priced large wafers become readily available.

23.1 Silicon Carbide – Background and History	797
23.1.1 Applications of SiC	798
23.1.2 Historical Development of SiC Crystal Growth	798
23.2 Vapor Growth	799
23.2.1 Acheson Method	799
23.2.2 Lely Method	799
23.2.3 Modified Lely Method	800
23.2.4 Sublimation Sandwich Method	800
23.2.5 Chemical Vapor Deposition	800
23.3 High-Temperature Solution Growth	801
23.3.1 Bulk Growth	801
23.3.2 Liquid-Phase Epitaxy	802
23.4 Industrial Bulk Growth by Seed Sublimation	802
23.4.1 Growth System	803
23.4.2 Seeding and Growth Process	804
23.5 Structural Defects and Their Configurations	805
23.5.1 Micropipes and Closed-Core Screw Dislocations	806
23.5.2 Basal Plane Dislocations in 4H-SiC	809
23.5.3 Threading Edge Dislocations (TEDs) in 4H-SiC	814
23.6 Concluding Remarks	816
References	817

23.1 Silicon Carbide – Background and History

Silicon carbide (SiC), one of the oldest known semiconductor materials, has received special attention in recent years because of its suitability for electronic and optoelectronic devices operating under high-temperature, high-power, high-frequency, and/or strong radiation conditions, where conventional semiconductor materials such as silicon, GaAs, and InP are considered to have reached their limits. SiC exists as a family of crystals with more than 200 polytypes and a bandgap

range of 2.4–3.3 eV. As a wide-bandgap material, SiC possesses many superior properties, e.g., a larger operating temperature range, a high critical breakdown field (E_{cr}), high resistance to radiation, and the ability to construct visible-range light-emitting devices [23.1]. It also distinguishes itself by a combination of high thermal conductivity (higher than that of copper), hardness second only to diamond, high thermal stability, and chemical inertness.

23.1.1 Applications of SiC

High-Temperature Applications

Current and future applications of electronic components have placed much more critical environmental requirements on semiconductors [23.2]; for example, high-temperature electronic components and systems can play an important role in many areas, e.g., aircraft, spacecraft, automotive, defense equipment, power systems, etc. For reliable functioning of electronic devices under extreme conditions they need to withstand high temperatures. SiC appears to be a desirable candidate because of its high working temperature as well as Debye temperature. As reported by *Chelnokov* and *Syrkin* [23.2], 6H-SiC is superior to Si, GaAs, GaN, and AlN for high-temperature application. SiC can also find applications in sensors for high-temperature, high-pressure, and highly corrosive environments (e.g., combustion systems, gas turbines, and in the oil industry) [23.3]; for example, pressure sensors based on SiC thin layers deposited on an insulator structure have been successfully used to measure the pressure in a combustion engine up to 200 bar at temperatures up to 300°C [23.4].

High-Power Devices

Power semiconductor devices are important for regulation and distribution of electricity. Since the efficient use of electricity depends on the performance of power rectifiers and switches, further improvements in efficiency, size, and weight of these devices are desirable. SiC has a high breakdown strength, and therefore it is possible to dope it at higher concentration while still having thinner layers for a given blocking voltage compared with corresponding Si devices [23.4]. Indeed, power losses can decrease dramatically with the use of SiC-based devices. Another desirable property of SiC for power application is its high thermal conductivity, which can facilitate quick dissipation of heat generated in the component. SiC power metal–oxide–semiconductor field-effect transistors (MOSFETs), diode rectifiers, and thyristors are expected to function over wider voltage and temperature ranges with superior switching characteristics.

High-Frequency Devices

Cellular phones, digital television (TV), telecommunication systems, and radars have made microwave technology an essential part of everyday life. Although some high-power microwave semiconductor components have existed for a long time, e.g., Gunn,

impact ionization avalanche transit time (IMPATT), and trapped plasma avalanche transit time (TRAPATT) diodes, these devices can only operate in parametric amplifiers, which are much more difficult to manufacture and tune. SiC-based microwave transistors are predicted to produce more efficient microwave systems and further expand their existing applications [23.4]. Silicon carbide static induction transistors (SITs) and metal semiconductor field effect transistors (MESFETs) have already been developed for these applications.

Optoelectronic Applications

The special physical and optical properties of SiC have been further exploited to fabricate bright blue and green light-emitting diodes (LEDs) [23.5]. In terms of manufacturing, there are several advantages to using SiC as a substrate material, such as easier handling and cheaper processing. SiC is also being used as a substrate for the growth of GaN, an important material for LEDs. Compared with GaN growth on sapphire substrates, it is possible to obtain structurally more perfect epitaxial GaN layers on SiC due to the smaller lattice mismatch and closer match of thermal expansion coefficients.

The primary requirement for SiC-based devices is the production of high-quality thin films, which in turn requires high-quality substrates.

23.1.2 Historical Development of SiC Crystal Growth

SiC has been known in the materials world since 1824. It was recognized as a silicide of carbon in 1895 and could be synthesized successfully by the Acheson process [23.6] using sand and coke. SiC-based LEDs were made as early as 1907 using small SiC crystals obtained from the cavities formed in the Acheson system. In 1955, *Lely* demonstrated the growth of SiC on a porous SiC cylinder by vapor condensation [23.7]. This method was further refined by *Hamilton* [23.8] and *Novikov* and *Ionov* [23.9], and is commonly referred to as the Lely method. Based on this method SiC platelets were prepared in the laboratory for several different applications. *Halden* [23.10] grew single crystals of SiC using Si melt solutions, but this method was not continued because of the difficulty in obtaining larger crystals. *Kendal* [23.11] later proposed a method of cracking of gaseous compounds containing C and Si at high temperature to form SiC crystallites, which is probably the basis for today's SiC chemical vapor deposition (CVD) technology.

A real breakthrough occurred in 1978 when *Tairov* and *Tsvetkov* [23.12] demonstrated seeded growth of

SiC using the sublimation method. Since Tairov and Tsvetkov used Lely's concept of vapor condensation, their method is commonly known as the modified Lely method. Further research on bulk growth is only a refinement and improvement of this technology. Commercially SiC wafers were first made available by Cree Research, Inc., in 1991 [23.13]. The availability of

SiC wafers in recent years has spurred extensive research on epitaxial growth. *Matsunami* group's [23.14] research in establishing step-controlled epitaxy is a notable development in optimizing SiC epitaxial growth morphology. Today, 100 mm SiC wafers are routinely available commercially, and overall defect densities show gradual improvement.

23.2 Vapor Growth

Unlike most semiconductor crystals, melt growth methods cannot be adopted for growth of silicon carbide since it is not possible to melt SiC under easily achievable process conditions. The calculated values show that stoichiometric SiC would melt only at above 10 000 atm and 3200 °C [23.15]. Because of these reasons, single crystals of silicon carbide are grown using techniques based on vapor growth, high-temperature solution growth, and their variants. Since SiC readily sublimates, physical vapor growth can be easily adapted and has become the primary method for growing large-size SiC boules. On the other hand, SiC can also dissolve in certain melts, e.g., silicon, which makes melt solution growth a possible technique. This method is predominantly used for growing single-crystal films.

23.2.1 Acheson Method

Commercial production of SiC was established as early as in 1892 [23.6] using the Acheson method. This process is primarily used for synthesis of low-purity polycrystalline material. The Acheson method also yields spontaneously nucleated SiC platelets of incomplete habit. In this process, a predetermined mixture of silica, carbon, sawdust, and common salt [23.16] (e.g., 50% silica, 40% coke, 7% sawdust, 3% salt) is heated by resistive heating of the core of graphite and coke placed at the center of the furnace. The furnace is heated to 2700 °C and maintained at that temperature for a certain amount of time, and then the temperature is gradually decreased. During the thermal cycle, different regions of the reactants are subjected to different temperatures. In between the outermost and innermost regions, the temperature reaches above 1800 °C and the mixture transforms to amorphous SiC. In the core region, SiC is formed first but as the temperature increases it decomposes into graphite and silicon. The decomposed graphite remains at the core and the silicon vapor reacts with the carbon in the adjacent cooler regions

to form SiC. Crystalline SiC is therefore formed outside the graphite layers. The common salt reacts with metallic impurities and escapes in the form of chloride vapors, improving the overall purity of the charge. The reaction yields predominantly 6H-SiC polycrystalline materials. Platelet crystals up to 2–3 cm are formed in some hollow cavities. This method does not yield reproducible quality and dimensions of single crystals and hence is not suitable for commercial production, although one can obtain SiC platelets suitable for use as seeds in physical vapor growth.

23.2.2 Lely Method

In the Lely method, developed in 1955 [23.7], SiC lumps are filled between two concentric graphite tubes [23.8]. After proper packing, the inner tube is carefully withdrawn, leaving a porous SiC layer inside the outer graphite tube called the crucible. The crucible with the charge is closed with a graphite or SiC lid and is loaded vertically into a furnace. The furnace is then heated to ≈ 2500 °C in an argon environment at atmospheric pressure. The SiC powder near the crucible wall sublimates and decomposes because of a higher temperature in this region. Since the temperature at the inner surface of the charge is slightly lower, SiC crystals start nucleating at the inner surface of the porous SiC cylinder. These thin platelets subsequently grow larger in areas if the heating is prolonged at this temperature. Since crystals are nucleated on the lumps of SiC (at the inner surface) and it is difficult to impose higher supersaturation, there is no control over the nucleation process, leading to platelets of incomplete hexagonal habit. The original Lely method was later improved by *Hamilton* [23.8] and others [23.9], where SiC charge is packed in between the two annular graphite cylinders. The outer cylinder (crucible) is thick whereas the inner cylinder is thin and porous and acts as a diaphragm. The sublimed SiC vapor passes through the small holes in the diaphragm, and crystals are nucleated at the inner

surface. Thick layers of SiC are also deposited on the lids at both ends. This modification offers slightly better control over the number of nucleation sites and yield, and crystals up to $20 \times 20 \text{ mm}^2$ have been grown using this method. Good-quality, larger crystals are obtained when the temperature variation in the cavity is small and the Ar pressure is maintained at about 1 atm [23.9]. Similar to the Acheson process, crystals of 6H polytype are predominantly produced by this method. The amount of crystals of other polytypes, such as 15R and 4H, depends on the growth temperature and dopant. Even though Lely platelets show good structural perfection, they have nonuniform physical and electrical characteristics. Also, since the yield is low ($\approx 3\%$), this method is not suitable for industrial production. The Lely method is, however, ideal for producing platelets of high structural perfection that can be used as seed crystals in bulk growth using other methods.

23.2.3 Modified Lely Method

In 1978, *Tairov* and *Tsvetkov* [23.12] developed the seeded sublimation growth technique, commonly known as the modified Lely method. They succeeded in suppressing the widespread spontaneous nucleation occurring on the (inner) graphite cylinder wall and achieved controlled growth on the seed (Fig. 23.1). This method also led to the control of polytypes to some extent. In the modified Lely method, growth occurs in argon environment at 10^{-4} –760 Torr in the temperature range of 1800–2600 °C and the vapor transport is facilitated by a temperature differential, $\Delta T = T_2 \approx T_1$, between the seed and the source material. The seed temperature T_1 is maintained slightly lower than the source temperature. The kinetics of the transport of Si- and C-containing species are primarily controlled by the diffusion process.

There are two different designs of the seeded sublimation growth system based on the locations of the charge and seed. In earlier work [23.17–19], the source SiC was placed in the upper half of the graphite crucible in a circular hollow cylindrical configuration between the crucible and a thin-walled porous cylinder (Fig. 23.1a). The seed platelet was held on a pedestal in the lower half of the crucible. Using this configuration, *Ziegler* et al. [23.17] grew 20 mm-diameter 24 mm-long crystals while *Barrett* et al. [23.18] succeeded in growing 6H-SiC of 33 mm diameter and 18 mm length. In the second configuration [23.15, 20–24] (Fig. 23.1b), which is commonly used today, the source material is held at the bottom of the crucible and the seed plate on the top. No graphite diaphragm is used in this configuration. This arrangement has a high yield (90%) [23.25] and has therefore become the industry standard for production of SiC boules.

23.2.4 Sublimation Sandwich Method

The sublimation sandwich method (SSM) is another variant of physical vapor transport (PVT) growth where the growth cell is partially open and the environment containing Si vapor may be used to control the gas-phase stoichiometry [23.26–30]. The source material consists of a SiC single-crystal or polycrystalline plate with small source-to-crystal distance (0.02–3 mm). There are several parameters, such as the source-to-substrate distance, small temperature gradient, and presence of Ta for gettering of excess carbon, that can be used to control the growth process. A high growth rate is achieved mainly due to the small source-to-seed distance and a large heat flux onto a small amount of source material with a low to slightly moderate temperature differential between the substrate and the source (0.5–10 °C). While growth of large boules is quite difficult, this method is quite promising for better-quality epitaxial films with uniform polytype structures.

23.2.5 Chemical Vapor Deposition

Chemical vapor deposition (CVD) is a popular method for growing thin crystalline layers directly from the gas phase [23.14, 31–33]. In this process a mixture of gases (source gases for Si and C, and carrier gas) is injected into the growth chamber with substrate temperatures above 1300 °C. Silane is the common Si source, and a hydrocarbon is used for C. Propane is quite popular, but methane is of interest because of its availability with very high purity, although it has lower carbon

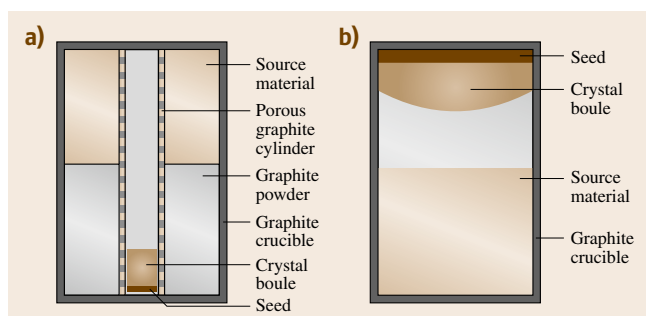


Fig. 23.1a,b Modified Lely method: (a) seed at the bottom, and (b) seed at the top

cracking efficiency. The carrier gas is high-purity H_2 , which also acts as a co-reactant. Conventional Si and C source molecules, called multiple-source precursors, have been used successfully, and reproducible CVD epitaxial films have been produced. However, the single-source CVD SiC precursor shows several advantages over the multiple-source precursors, including a lower growth temperature (less than 1100 °C).

The first successful large-area, heteroepitaxially grown 3C-SiC was obtained by *Nishinov et al.* [23.34] on a high-quality commercial Si wafer. With the availability of 6H-SiC wafers grown by the modified Lely method, homoepitaxial growth of 6H-SiC and heteroepitaxial growth of 3C-SiC have been achieved with good success [23.14]. SiC epitaxial growth is mainly performed on 4H and 6H substrates. Growth on the Si face is preferred because of the superior quality and well-understood doping behavior. In general, the quality of films obtained on the (0001) face is poor, but this problem can be overcome by using a wafer mis-oriented by 3–8° from the basal plane to control the morphology of the deposited epilayer [23.14], a process referred to as step-controlled epitaxy. Doping of the film is obtained in situ during the growth of each epilayer by flowing either a p-type or n-type source gas. The growth rates of CVD processes are low, a few tens of microns per hour, generally making it unsuitable for boule production. The rate can be increased by increasing the deposition temperature, but this makes control of the process much more difficult and also results in many other problems such as homogeneous nucleation in the gas phase. The high-temperature CVD (HTCVD) pro-

cess [23.35, 36] is an improved version that can yield thicker films and higher growth rates. In HTCVD the substrate is placed at the top of a vertically held graphite susceptor, similar to the crucible used in the modified Lely method, with holes at the bottom and top. The gaseous reactants are passed from the bottom of the susceptor upwards through the hole at the bottom. To maintain the growth for a long time and obtain the maximum deposition on the substrate, the temperature of the susceptor wall is kept high and the substrate temperature is kept slightly lower. In principle, SiC growth by this method can be continued for longer periods, and bulk crystals can be obtained. The hot-wall CVD reported by *Kordina et al.* [23.37] is probably a good method to produce uniform epitaxial films on large-diameter wafers. In this approach, the CVD reactor is made of a single graphite block with a protective SiC layer. It has an elliptical outer cross-section with a rectangular tapered hole which runs through the entire length. The substrate wafers are placed appropriately on both sides of the rectangular slit. The mixture of gaseous precursors with carrier gas is passed through the reactor from the end containing the larger hole. The tapered hole compensates for severe depletion of Si and C content in the reactant. The flow rate of the gas can be sufficiently large. This design provides good temperature homogeneity, and epitaxial films of excellent thickness uniformity can be obtained. The surface morphology of the film can be controlled by choosing off-*c*-oriented substrate. Recent technological developments have allowed the growth of uniform epitaxial films on wafers as large as 100 mm in diameter [23.38–41].

23.3 High-Temperature Solution Growth

23.3.1 Bulk Growth

Carbon is soluble in a Si melt, which enables growth of SiC from high-temperature solution. The solubility ranges from 0.01% to 19% in the temperature interval 1412–2830 °C [23.20], although at high temperatures the evaporation of silicon makes the growth unstable. The solubility of carbon can be increased by adding certain transition metals to the Si melt [23.42]. In principle, this can enable growth of SiC from saturated solution by seeded solution growth. Unfortunately there is no crucible material that can remain stable at the required temperatures and with these melts, and also the evaporation of the Si melt poses a serious prob-

lem at higher temperatures. It is also speculated that the incorporation of the added metals into the growing crystal is too high to be acceptable for semiconductor applications [23.20]. These difficulties restrict the application of this method to bulk growth of SiC. *Halden* [23.10], however, has grown SiC platelets from Si melt at 1665 °C on a graphite tip in Czochralski configuration. *Epelbaum et al.* [23.43] have obtained SiC boules of 20–25 mm diameter and 20 mm length at pull rate of 5–15 mm/h in the temperature range of 1900–2400 °C at Ar pressure of 100–120 bar. Even though solution-grown crystals free of micropipes have been produced, they contain a number of flat silicon inclusions and show rather high rocking-curve width.

Because of the high temperature and high pressure involved in this process, the method is not considered economic for large-scale production.

23.3.2 Liquid-Phase Epitaxy

Even though the high-temperature solution method for SiC poses enormous difficulties and is not popular for bulk growth, it has been successfully adopted for growth of thin films by liquid-phase epitaxy (LPE). Indeed, LPE has been used for production of several SiC-based optoelectronic devices [23.17]. In LPE, semiconductor-grade silicon is used as a solvent in a graphite crucible. Carbon from the graphite crucible dissolves in the Si melt and is transported to the surface of the SiC substrate, which is placed at the bottom of the crucible at a relatively lower temperature. Bright LEDs have been fabricated using this process. However this method suffers from several setbacks such as cracking of the film due to differential thermal contraction while solidifying and the cumbersome process of extraction of the substrate containing the epitaxial film by etching off the solidified Si. These problems can be overcome using a dipping technique [23.44]. In this improved process a SiC substrate attached to a graphite holder is dipped into the molten Si heated by an induction furnace and is kept in the lower-temperature region of the crucible. The substrate is withdrawn from the melt after obtaining growth of the epitaxial film of a desired thickness. The growth is performed in an Ar environment at 1650–1800 °C, and the typical growth rate is 2–7 μm/h. Doping is obtained by adding Al to the Si melt for p-type layer, and Si₃N₄

powder to Si for n-type. It is also possible to obtain n-type film by passing N₂ gas along with Ar. Epitaxial films obtained on (0001) 6H-SiC substrate have shown degradation in LED performance. This problem can be resolved by using substrates misoriented with respect to the *c*-axis by a few degrees (3–10°), which leads to better polytype control and improved surface morphologies [23.14]. The method is known as step-controlled epitaxy and has led to improved quality of the film and thereby reliable device performance. A better epitaxial surface morphology is obtained by this process, which has been explained based on the nucleation concept [23.14].

It is possible to lower the growth temperature range by selecting an alternative melt which has a higher solubility than Si. *Tairov et al.* [23.45] have used Sn and Ga melts in the temperature range of 1100–1400 °C and have produced LPE layers by using a sliding boat technique. *Dmitriev et al.* [23.46] have grown p–n junctions in the temperature range of 1100–1200 °C. In addition they have demonstrated container-free epitaxial growth of 6H- and 3C-SiC films in which the melt is held by an electromagnetic field. This method has the advantage of mixing induced by the electromagnetic forces [23.47]. Recently, *Syvajarvi et al.* [23.48] used a special sandwich configuration in LPE and succeeded in obtaining growth rates as high as 300 μm/h. One of the main attractions of LPE of SiC is the potential for filling of micropipes. The substrate, after filling of micropipes, does not reveal the presence of micropipes by either optical microscopy or etching [23.35]. However, detailed analysis is needed to understand the defect configuration around the filled core of the micropipes.

23.4 Industrial Bulk Growth by Seed Sublimation

Seeded sublimation growth, commonly known as the modified Lely method, is the only method that has been implemented by industry. The method has spurred intense worldwide research activity in recent years and has become a standard method for growing SiC crystals [23.12, 17–24, 49–51]. The instrumentation and technology involved in bulk growth of SiC are complex, and hence the availability of large-size crystals is still limited. This is primarily due to the fact that the operating temperatures are extreme, and monitoring and control are difficult [23.20]. Even today, only a few companies are successful in producing SiC boules of reasonable quality and size. The main

constraint is the difficulty in determining the optimum growth conditions for the modified Lely method, such as the right combination of pressure, temperature, temperature gradient, charge size, geometric configuration, etc. It is not feasible to determine the exact thermal conditions in the growth zone experimentally due to high operating temperatures and opacity of the graphite crucible. In spite of these limitations, great success has been achieved in the industrial production of SiC crystals in terms of crystal perfection and size [23.52–55]. Numerical modeling and simulation have been of great help in this endeavor [23.56].

23.4.1 Growth System

As described earlier, there are two main configurations for seeded sublimation growth (Fig. 23.1). The second configuration [23.20, 50, 54, 55], where the source material is held at the bottom of the crucible and the seed plate is fixed onto the crucible lid, is the system commonly used today (Fig. 23.1b). This arrangement yields a higher growth rate compared with the other approach, because of the smaller source-to-seed distance. Also, since the growing surface is facing downwards, there is no danger of incorporation of charge particles into the growing crystal as in the first case (Fig. 23.1a) where particulates can fall from the top. The main disadvantage of this configuration is that, in a system for growing larger-diameter boules, maintaining temperature uniformity in the source material becomes difficult. The first configuration is slightly less susceptible to temperature and pressure fluctuations. The operating temperature range of seeded sublimation growth is 1800–2600 °C [23.12], with the actual temperature for growth depending on many different process conditions. Induction furnaces operating at lower frequencies (4–300 kHz) [23.17, 58] are commonly used for the modified Lely method. The optimum operating frequency of the induction furnace is 10 kHz, which corresponds to a reasonably high skin depth for the graphite crucible. Recently, efficient solid-state induction furnaces have become readily available, and these low-frequency generators preferentially couple with the susceptor and crucible, with minimum induction on the graphite insulator. Additionally, in an induction furnace, it is possible to vary the temperature gradient at the initial stage as well as during the run. Another advantage of the induction furnace over the resistive furnace is the minimal thermal insulation required as the heat is generated directly on the susceptor and crucible. The dimensions and number of turns of the induction coil are selected based on geometric considerations, the temperature and temperature gradients desired, and heat losses.

The main chamber of the SiC growth system (Fig. 23.2) is a vertically mounted double-walled water-cooled assembly that consists of two concentric quartz tubes sealed with vacuum-tight end flanges using double O-ring seals on ground surfaces of the quartz tubes. Cooling water is circulated between the concentric quartz tubes from bottom to top, although Yakimova et al. [23.49] have shown that it is also possible to use an air-cooled quartz enclosure. The hot zone consists of a high-density graphite crucible

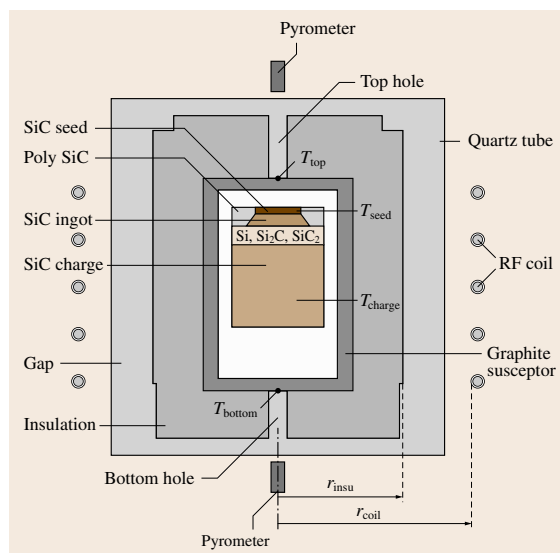


Fig. 23.2 Schematic of the SiC growth system (after [23.57])

and susceptor surrounded by rigid graphite insulation. Because of the higher resistivity of the rigid insulation compared with that of the graphite susceptor and crucible, heat is generated primarily on the susceptor by eddy currents induced by the low-frequency magnetic field. The graphite components of the growth chamber, particularly the crucible and susceptor, are treated at high temperatures in fluorine atmosphere to remove metallic impurities. The design of the hot zone is modified based on the requirements of the axial and radial gradient. This is accomplished with the help of computer modeling [23.56] and prediction of the temperature profile as a function of the growth front.

The normally practiced measurement procedure is to monitor temperatures of the top (T_1) and bottom (T_2) surfaces of the graphite crucible using two color pyrometers (Fig. 23.2). The temperatures are controlled by varying the output power of the induction furnace. Often, the induction coil is mounted on a motorized linear vertical translation stage, and the position of the coil is changed during the growth to vary the temperature gradient and the seed temperature. The vertical growth chamber is connected to a high-vacuum system to obtain initial degassing (at 10^{-7} Torr) as well as to maintain the required vacuum (e.g., 10–100 Torr) conditions during growth. Maintaining vacuum at a predetermined value, as closely as possible, is essential to control the growth rate.

23.4.2 Seeding and Growth Process

After repeated degassing and baking of the growth zone, the chamber is filled with Ar gas. The Ar partial pressure is maintained at about 600 Torr–1 atm while heating to the maximum required growth temperature (2200–2400 °C). The coil position is adjusted such that a desirable temperature gradient of 10–20 °C/cm is obtained. The seed temperature T_1 and the temperature differential ΔT can be varied by changing the coil position; however, T_1 and T_2 cannot be controlled independently. The Ar pressure is brought down to a lower value between 1 and 40 Torr at a predetermined pumping speed to initiate the growth smoothly. The axial temperature gradient influences the growth rate, whereas the radial temperature gradient changes the diameter of the crystal [23.56].

The main stages of the growth are:

1. Dissociative sublimation of SiC source
2. Mass transfer of gaseous species
3. Crystallization onto the seed

At a high temperature, the SiC source material decomposes into several Si- and C-containing species such as Si, C, SiC₂, and Si₂C. Since the crucible is made of graphite, vapor species will react with the graphite wall to form Si₂C and SiC₂, with the graphite crucible acting like a catalyst. Details of the reaction kinetics are described by *Chen et al.* [23.56]. The temperature difference between the seed and source ΔT works as a driving force and facilitates transport of vapor species, mainly Si, Si₂C, and SiC₂. The presence of the temperature gradient leads to supersaturation of vapor, and controlled growth occurs at the seed. Initially, a high-quality Lely plate is used as the seed crystal, and the diameter of the growing crystal is increased by properly adjusting the thermal conditions. To grow larger boules of approximately uniform diameter, wafers from previously grown boules are used as seed discs.

The seed crystal is attached to the graphite top using sugar melt [23.59], which decomposes into carbon and gets bonded to the graphite lid. Optimizing this bonding process is quite important, since the differential thermal expansion between the seed and the graphite lid can cause bending of the seed plate, leading to formation of domain-like structure, low-angle boundaries, and polygonization [23.60]. Micropipes can form at such low-angle boundaries. Any nonuniformity in seed attachment, such as a void between the seed and the lid, can cause variation in the temperature distribution, and the heat dissipation through the seed may be altered.

This can result in uneven surfaces and depressions in the growth front corresponding to the void. Evaporation of the back surface of the seed crystal can create thermally decomposed voids which can propagate further into the bulk [23.59]. These voids can then become sources for the generation of micropipes. Protecting the back surface of the seed with a suitable coating eliminates these voids. Seed platelet attachment to the graphite lid is one of the important technical aspects of industrial growth.

If the growth process is not optimized, polycrystalline deposition due to uncontrolled nucleation may occur. In addition to optimizing the Ar pressure and temperature gradient to achieve controlled nucleation, removal of a thin layer of the seed surface by thermal etching, obtained by imposing a reverse temperature gradient [23.61], has been found to be helpful. Etching is also possible by oscillatory motion of the induction coil. The in situ thermal etching helps in cleaning the surface of the seed crystal before starting growth. In some cases, a small amount of excess silicon is added to the charge in order to maintain the Si vapor concentration and stabilize the growth of certain polytypes. The growth of boule is initiated at a very slow rate and is increased progressively by decreasing the pressure.

Depending on the design of the crucible and supersaturation ratio, simultaneous growth of polycrystalline SiC, predominantly 3C, occurs particularly on the graphite lid surrounding the seed crystal. If the growth conditions are not optimal, the polycrystalline SiC can get incorporated into the boule near the periphery, leading to cracking due to high stresses. If the growth rate of the boule is higher than the growth rate of polycrystalline SiC, smooth growth of the boule dominating over the polycrystalline mass is favored. Design of the crucible for increasing the diameter of the boule is normally accomplished through modeling [23.56].

Bahng et al. [23.62] have proposed a method of rapid enlargement of the boule using a cone-shaped platform, where enlargement depends on the taper angle of the cone. It has been reported that, in this technique, the broadening of the boule is not affected by the growth of polycrystalline SiC. After obtaining the required diameter of boule, seed discs of larger diameter are prepared from these boules for further growth in a specifically designed hot zone suitable for promoting predominantly axial growth. As growth of the boule progresses, the temperature of the growing surface changes, which can be compensated by moving the induction coil. It is evident that the process parameters must be optimized for a particular crucible design, system geometry, and boule dimension.

Among the numerous SiC polytypes, only 6H, 4H, 15R, and 3C have been studied for different applications. Polytypes 6H and 4H have been studied extensively in bulk crystal as well as epitaxial form, whereas 3C has been investigated predominantly in epitaxial form. Recently, work on bulk growth of 15R has been initiated for MOSFET applications [23.63]. Crystals of 4H polytype are grown in a narrow temperature range of 2350–2375 °C at 5 mbar using (0001)C face of 4H seed plates [23.35]. A lower growth rate (0.1 mm/h) is used in the beginning and then increased to 0.5 mm/h after growing a 1 mm-long boule. Above 2375 °C the 4H polytype transforms into 6H; below 2350 °C, crystal quality becomes a limiting factor. Among the SiC polytypes, 6H is the most extensively studied, and the reported growth temperature ranges vary widely, although this may be due to differences in growth cell configuration and temperature measurement convention. Snyder et al. [23.53] have reported the growth of 100 mm 6H boules at 2100–2200 °C and 5–30 Torr Ar pressure with 10–30 °C/cm temperature gradient. The clearly established result is that (0001)Si face should be used for growth of 6H, whereas (0001)C face is needed for growth of 4H. It seems that, for bulk growth of 15R, seed platelets of the same polytype are required. Schulze et al. [23.64] have demonstrated growth of 15R crystals on (0001)Si seed face at 2150–2180 °C with 5 °C/cm gradient. However, Nishiguchi et al. [23.58] have shown that 15R polytypes can grow stably on both C and Si of (0001) face at seed temperature not exceeding 2000 °C with growth rate controlled between 0.1 mm/h to 0.5 mm/h. In addition to temperature there are several other parameters that can be used to control polytype formation.

Growth of SiC boule depends on many parameters, such as growth temperature, temperature gradient, Ar pressure, crystal temperature, source-to-crystal distance, and the porosity of the source material [23.56]. Preparative conditions of the source material alter the

vapor species concentrations and vary the growth conditions. Deviation from stoichiometry can lead to a lower growth rate. The growth rate increases as the seed crystal temperature increases. It also increases with the temperature differential ($T_2 \propto T_1$) and temperature gradient but decreases with the source-to-seed distance. The growth rate varies almost inversely with the Ar pressure, and the trend is consistent with 1/P dependence on the molecular diffusion coefficient [23.50]. There exists a saturation of growth rate at very low pressures, and one would tend to select this growth regime, but then control of the vapor composition becomes more difficult.

The growth rates have been measured by inducing growth bands by simultaneously introducing N₂ gas along with the Ar flow at different intervals and subsequent post mortem studies. In general, (0001) plate is used as a seed, and growth proceeds along the *c*-direction. Even though the crystal grows smoothly on (0001) plate, this is also the favorable orientation for nucleation of micropipes. There have been several attempts [23.65, 66] to grow crystals on non-(0001) orientation. Even though the micropipe density was reduced in the bulk, the generation of other types of defects such as stacking faults on the basal plane, which hinder electron transport in device applications, increased. Presently, seeding is restricted to (0001) orientation for industrial production of SiC boules.

Monitoring and controlling growth of SiC is very difficult because of the use of opaque graphite materials in the hot zone. Recently, radiography has been employed to study the growth interface during the growth process [23.67]. This imaging technique has also revealed the graphitization of the SiC source material, which could reduce the growth rate as well as affect the structural perfection of the growing boule. Attempts have also been made to study defect generation during the growth process using in situ x-ray topography [23.68].

23.5 Structural Defects and Their Configurations

Assessment of crystalline imperfections and growth inhomogeneities in grown crystals is necessary to understand how they are formed and for the development of engineering methods to eliminate them or minimize their effect in order to obtain high-quality crystals required for electronic applications. SiC crystals grown using different techniques can contain crystalline imper-

fections such as growth dislocations of screw character with closed or hollow cores (micropipes), deformation-induced basal plane dislocations, parasitic polytype inclusions, planar defects (stacking faults, microscopic twins, and small-angle boundaries), hexagonal voids, etc. that affect device performance. A review of SiC defect characterization efforts reveals that x-ray topog-

raphy, and in particularly synchrotron white-beam x-ray topography (SWBXT) [23.69–71], is superior to other techniques such as chemical etching, atomic force microscopy (AFM), scanning electron microscopy (SEM), transmission electron microscopy (TEM), and optical microscopy-based methods, although these other techniques can be used in a complementary manner. Defects imaged by x-ray topography are primarily discussed in this section.

23.5.1 Micropipes and Closed-Core Screw Dislocations

Origin of the Hollow Core and Frank's Theory

Among the various defects that exist in SiC crystals, screw dislocations lying along the [0001] axis are the most significant and are generally considered to be one of the major factors limiting the extent of the application of SiC. These screw dislocations (SDs) have been shown to have Burgers vectors equal to nc (where c is the lattice parameter along the [0001] direction in the hexagonal coordinate space and n is an integer), with hollow cores becoming evident with $n \geq 2$ for 6H-SiC and $n \geq 3$ for 4H-SiC [23.69]. These latter screw dislocations are generally referred to as micropipes (MPs), and their hollow cores can be understood from Frank's theory [23.73], which predicts that a screw dislocation whose Burgers vector exceeds a critical value in crystals with large shear modulus should have a hollow core with equilibrium diameter D related to the magnitude of the Burgers vector b by

$$D = \frac{\mu b^2}{4\pi^2\gamma}, \quad (23.1)$$

where μ is the shear modulus and γ is the specific surface energy. Experimentally, the diameter D can be measured directly using SEM or AFM, while the Burgers vector magnitude b can be obtained by determining the step height of the growth spiral on the as-grown surface using optical interferometry or AFM, or directly using x-ray topography. Detailed experimental results indicate a directly proportional relationship between D and b^2 for micropipes in both 6H- and 4H-SiC [23.69–71].

Growth Spirals and Screw Dislocations

Growth spirals observed on habit faces of as-grown SiC crystals [23.74, 75] are a clear manifestation of screw dislocations emerging on the growth surface. The emergence of screw dislocations on a habit face produces a ledge of height equal to the Burgers vector. The crys-

tal grows by attachment of molecules to the edge of this ledge. The ledge is self-perpetuating and continues to be present on the surface as long as the dislocation line intersects the surface. The ledge winds itself into a circular or polygonal spiral with a dislocation line at the center and, as the growth proceeds, the spiral apparently revolves. The step height of these spirals is equal to an integer times c . Depending on the sign of the Burgers vector the spiral can revolve in a clockwise or anticlockwise direction [23.69]. These spirals have been studied using phase-contrast microscopy [23.76], scanning electron microscopy (SEM) [23.76], and recently by atomic force microscopy (AFM) [23.77]. When two screw dislocations of the same sign are present very close to each other, their spirals spin without intersecting each other, which are called cooperative spirals. Two dislocations of opposite sign can form a closed loop.

Back-Reflection Observation of Screw Dislocations

Screw dislocations in (0001)SiC wafers, of both closed and hollow core (micropipes), can be effectively characterized using back-reflection geometry in SWBXT [23.78]. Figure 23.3, a typical back-reflection topograph taken from a (0001)SiC wafer (grown by Cree Research, Inc.), clearly reveals the screw dislocations, both hollow and closed core, as white circular spots surrounded by black rings. The distribution of micropipes and screw dislocations as well as their detailed structures can be obtained from such images.

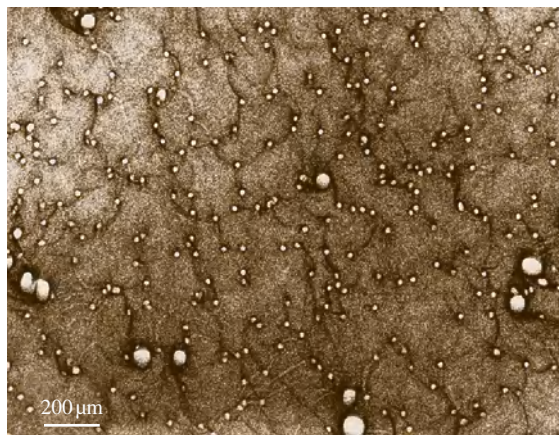


Fig. 23.3 SWBXT back-reflection images of closed-core (smaller white spots) and hollow-core (large white spots) screw dislocation in a (0001) 6H-SiC wafer. The faint lines connecting these screw dislocation images are basal plane dislocation images [23.72]

The circular white spots in Fig. 23.3 are not images of micropipes and closed-core screw dislocations but are actually related to diffraction effects associated with the long-range strain fields of the screw dislocations. Using a ray-tracing simulation based on the orientation contrast mechanism, a model for qualitative and quantitative interpretation of topographic observations in SiC has been developed [23.79–82]. It has been successfully used in back-reflection XRT to clarify the screw character of MPs and also to reveal the dislocation sense of threading screw dislocations (TSDs)/MPs, the Burgers vectors of threading edge dislocations (TEDs), the core structure of Shockley partial dislocations, and the sign of Frank partial dislocations [23.83–85]. Based on this ray-tracing principle, images of micropipes and screw dislocations can be rigorously simulated. Figure 23.4a shows a magnified image of an $8c$ micropipe in 6H-SiC, while Fig. 23.4b shows the simulated image of a screw dislocation with Burgers vector of $8c$ ($b \approx 12.1$ nm). It is apparent that the simulation is in excellent agreement with the recorded micropipe image. This proves that micropipes in SiC are indeed pure screw dislocations. The magnitude of the Burgers vector can be estimated from the diameter of the screw dislocation image, while the twist direction unambiguously indicates the dislocation sense, i.e., the direction of the Burgers vector [23.81]. Back-reflection section topographs of micropipes recorded with a $20\text{ }\mu\text{m}$ -wide slit-limited synchrotron beam can also reveal the sense of the screw dislocation (Fig. 23.5a–d).

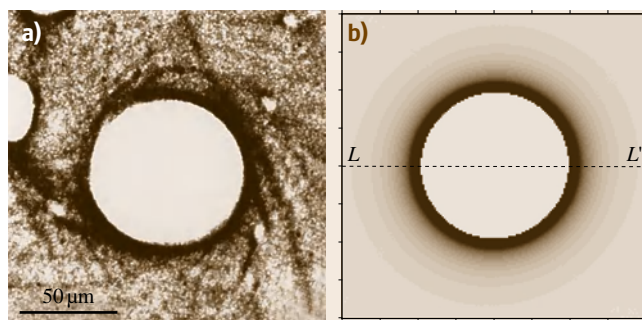


Fig. 23.4 (a) Back-reflection SWBXT image of an $8c$ micropipe taken from a (0001) surface of a 6H-SiC crystal, with sample-to-film distance of 20 cm. (b) Simulation of a screw dislocation with Burgers vector $|b| = 8c$ [23.80]

Grazing-Incidence Imaging of Screw Dislocations

In the grazing-reflection geometry, the incident beam makes an extremely small angle (less than 1°) with respect to the (0001) plane, but there is no limitation for the exit angle of the diffracted beam. This is an especially useful geometry for characterizing micropipes and screw dislocations as well as threading edge dislocations in SiC epitaxial films, since one can control the penetration depth of x-rays at will by adjusting the incidence angle. Figure 23.6a shows a $11\bar{2}8$ topograph taken with the recording x-ray film parallel to the (0001) surface, in which the oval-shaped white spots are images of micropipes. The simulated images based on the ray-tracing principle are shown in Fig. 23.6b, c [23.84].

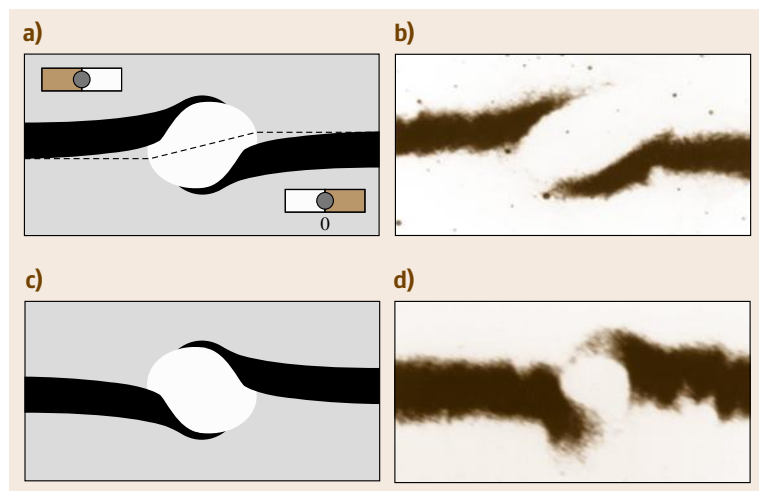


Fig. 23.5a–d Section topographs showing the senses of screw dislocations associated to micropipes. (a) and (b) are simulated and recorded images of a right-handed screw dislocation, respectively; (c) and (d) are simulated and recorded images of a left-handed screw dislocation [23.80]

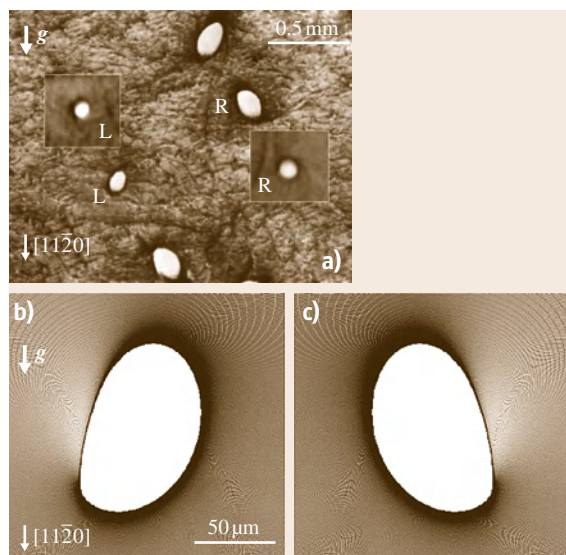


Fig. 23.6 (a) A $(11\bar{2}8)$ grazing-incidence SWBXT image of 4H-SiC. MPs appear as roughly oval shaped with various orientations and dimensions. The MPs can be divided into two groups according to the orientation of the white elliptical contrast. Examples of each kind are shown (marked by “L” and “R”). Their images in back-reflection geometry appear as complete circular shapes (*insets*, on a different scale), indicating that they are isolated MPs (not MP pairs or groups). Simulated $(11\bar{2}8)$ grazing-incidence x-ray topographic images of left-handed (b) and right-handed (c) 8c MPs at a specimen-to-film distance of 35 cm. Both images appear as roughly white ellipses canted clockwise (a) or counterclockwise (b) from vertical configuration [23.84]

The observed (Fig. 23.6a) and simulated (Fig. 23.6b,c) images correlate very well. Simulation shows that left-handed MPs appear as nearly elliptical features canted clockwise, while right-handed MPs are canted counterclockwise.

Model for the Origin of Screw Dislocations and Micropipes

Systematic observations of screw dislocation or micropipe formation processes using a variety of techniques [23.77, 86–89] suggest that a possible mechanism for nucleation of micropipes in SiC involves the incorporation of inclusions, which could be, for example, graphite particles, silicon droplets, or even voids, into the crystal lattice. Nucleation of screw dislocations at inclusions has been observed in several systems [23.90–92]. The formation of screw dislocation pairs from inclusions has been briefly proposed by

Chernov [23.93] for crystals grown from solution. This approach has been extended to explain the observed nucleation of screw dislocations in SiC [23.94]. This model assumes that two macrosteps of different heights, approaching each other on the growth surface, trap a layer of foreign material (solvent, void or impurity) on the growth surface. As a result of the higher rate of feeding of the protruding edge than the re-entrant edge, an overhanging ledge can subsequently be produced as the crystal attempts to overgrow the inclusion and incorporate it into its lattice. This overhanging ledge is vulnerable to deformation and vibrations and, when the macrostep meets the approaching macrostep, horizontal atomic planes which were at the same original height may no longer meet along the line where the two steps meet. If the layer of foreign material constituted a void (or transport gases), downward depression of the overhanging ledge may be expected, whereas if it constituted an impurity, deformation of the opposite-sense dislocations might be expected. In order to accommodate this misalignment, screw dislocations of opposite sign are created with Burgers vector magnitudes equal to the magnitude of the misalignment. Since the degree of misalignment depends on the relative size of the two approaching steps and the lateral and vertical extent of the inclusion, the production of dislocations with a range of Burgers vectors becomes possible. In fact, micropipe-related screw dislocations in SiC can have Burgers vectors as large as several tens of times the basic lattice constant along the c -axis [23.95]. In addition, in cases of large inclusions or groups of inclusions, the deformation of the protruding ledge may be spread over the length of the line along which they meet, resulting in the creation of distributed groups of opposite-sign screw dislocations. These groups may not necessarily be distributed symmetrically, but in all cases, the sum of all the Burgers vectors of the dislocations created must equal zero.

In SiC the sources of the growth steps involved in the above-described model can be the vicinal nature of the growth surface (which tends to be slightly dome shaped), two-dimensional (2-D) nucleation, as well as spiral steps associated with intersections of screw dislocations with the surface. Differences in step height are certainly conceivable when a vicinal step meets a spiral step and can even occur when two spiral steps associated with screw dislocations of different Burgers vector magnitude meet or if step bunching occurs for a group of dislocations. Moreover, the merging of 2-D grown islands also plays an important role in the formation of growth steps as well as voids. These various sources in

conjunction with the formation of inclusions thus provide opportunities for micropipes as well as closed-core screw dislocations to be created during growth.

23.5.2 Basal Plane Dislocations in 4H-SiC

The primary slip plane for hexagonal 4H- and 6H-SiC is the basal plane. It is therefore not surprising that deformation-induced dislocations on the basal plane are observed in both structures [23.97,98]. An example is shown in Fig. 23.7, which shows a transmission topograph recorded from a 4H-SiC basal plane wafer. Also shown in this figure is a grazing-incidence topograph recorded from the same region of the 4H-SiC crystal. Detailed Burgers vector analysis of these dislocations can be easily performed. Observation of the morphologies of the basal plane dislocation (BPD) loops clearly indicates that they are deformation induced and appear to have been nucleated both at the crystal edges and at the sites of micropipes/screw dislocations.

The Burgers vectors of the BPDs in SiC are $1/3\langle 11\bar{2}0 \rangle$, and two extra $(11\bar{2}0)$ half-planes are associated with an edge-oriented BPD, as the magnitude of its Burgers vector is twice the d -spacing of $(11\bar{2}0)$ plane. The BPD is energetically favorable to be dissociated

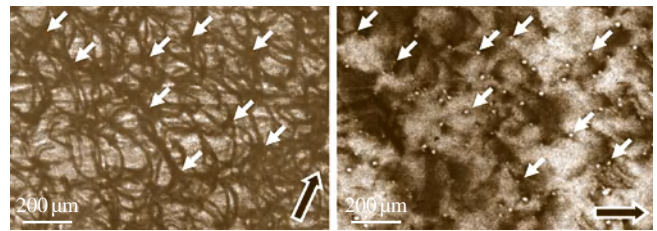


Fig. 23.7a,b Transmission x-ray topograph ((a), $g = [\bar{1}\bar{1}20]$) and grazing incidence ((b), $g = [11\bar{2}8]$) of 20 μm epilayer on 8° offcut 4H-SiC substrate. Circular basal plane dislocations (BPDs) anchored by SDs are seen. Some anchor points are marked by arrows

into two Shockley partial dislocations with a stacking fault (SF) area in between, and the equilibrium separation d of the two Shockley partial dislocations is given by $d = Gb^2/4\pi\gamma$, where G is the shear modulus, b is the magnitude of the Burgers vector of the Shockley partial dislocation, and γ is the energy of the SF. This equilibrium separation is $\approx 330 \text{ \AA}$ for 4H-SiC, assuming the SF energy to be 14.7 mJ/m^2 [23.99].

The dislocation character of a BPD is determined by the angle between its line direction and the Burgers vector. Figure 23.8 illustrates the various cases when

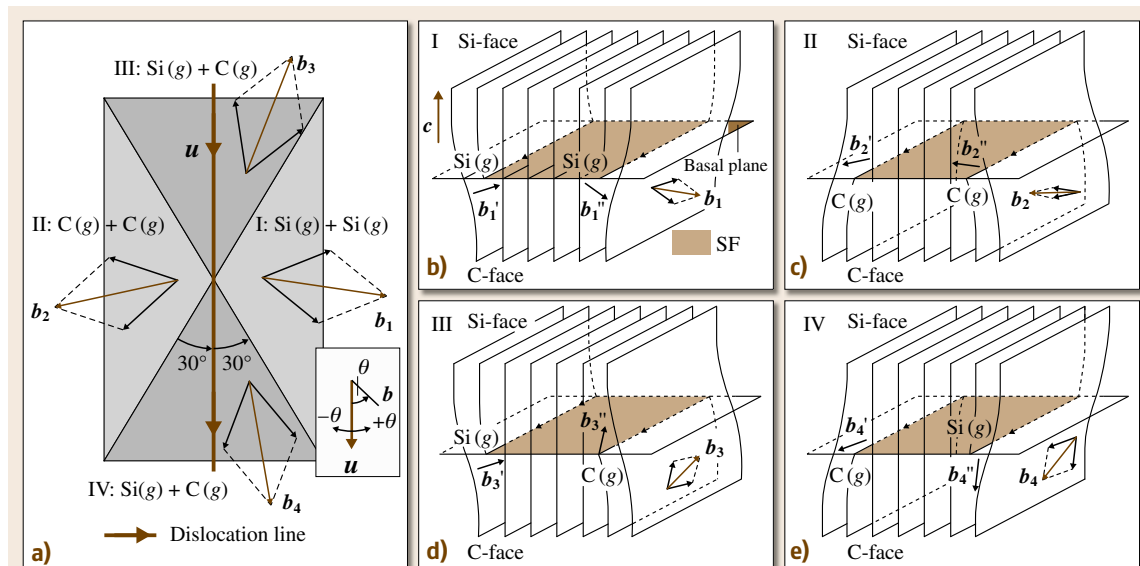


Fig. 23.8a-e Schematics showing Shockley partial dislocations of different core structures dissociated from a perfect BPD. (a) Four regions defined according to the direction of Burgers vector with respect to the line direction of the dislocation, assuming Si-face is facing up: (b) $30^\circ < \theta < 150^\circ$, the BPD is dissociated into two Si-core partials; (c) $210^\circ < \theta < 330^\circ$, the BPD is dissociated into two C-core partials; (d) $-30^\circ < \theta < +30^\circ$, one Si-core and one C-core; (e) $150^\circ < \theta < 210^\circ$, one Si-core and one C-core. θ is defined in the inset of (a) (after [23.96])

a perfect BPD is dissociated into Shockley partial dislocations [23.96]. The angle θ is the counterclockwise angle from the line direction to the Burgers vector direction (clockwise angles are negative); see the inset of Fig. 23.8a. In region I, in which $30^\circ < \theta < 150^\circ$, the extra half-plane(s) associated with the BPD extend toward the Si-face determined by the right-hand rule, $\mathbf{u} \times \mathbf{b}$. If $30^\circ < \theta < 150^\circ$, when the BPD with Burgers vector \mathbf{b}_1 is dissociated into two partial dislocations of Burgers vectors \mathbf{b}'_1 and \mathbf{b}''_1 (Fig. 23.8b), the angles between $\mathbf{b}'_1/\mathbf{b}''_1$ and their line directions (assuming the same line direction as the BPD) will be in the range (0° , 180°). The extra half-planes associated with the two partials can be subsequently determined again by right-hand rule: $\mathbf{u} \times \mathbf{b}'_1$ and $\mathbf{u} \times \mathbf{b}''_1$; both are extending toward the Si-face. Since the Shockley partials in SiC are glide set dislocations, both partials are Si-core. Under this circumstance, the SF will expand toward both directions, as both partials are mobile. Similar mechanism can be applied for regions II, III, and IV. In region II (Fig. 23.8c), both dissociated partials are C-core and neither of them advances, while for regions III (Fig. 23.8d) and IV (Fig. 23.8e), a Si-core and a C-core partial are formed and the SF expands as the Si-core partial advances. Notice that, if the Burgers vector of the BPD is at $30^\circ/150^\circ/210^\circ/330^\circ$ to its line direction, it is dissociated into a screw-oriented and a C-core or Si-core partial.

Susceptibility of Basal Plane Dislocations in 4H Silicon Carbide

Dissociation of basal plane dislocations (BPDs) into mobile silicon-core (Si-core) partial dislocations and subsequent advancement of these partial dislocations under forward bias pose a large challenge for the lifetime of SiC-based bipolar devices [23.100] since the expansion of Shockley stacking faults (SFs) associated with the advancement of Si-core partials causes the forward voltage to drop. Such expansion of basal SFs is activated by the electron-hole recombination-enhanced dislocation glide (REDG) process [23.101–103]. Through detailed x-ray topography analysis of a dislocation configuration formed after stacking fault expansion under forward bias, the susceptibility of basal plane dislocations to REDG has been determined. Figure 23.9 shows x-ray topographs (Fig. 23.9a–e) and the schematic configuration after advancement of the mobile partial. During the advancement of the partial, it interacted with a few threading screw dislocations (TSDs), and the final configuration obtained is shown in Fig. 23.9f. The Burgers vector \mathbf{b} of the original

BPD is determined to be $1/3(\bar{1}\bar{1}20)$, as indicated in Fig. 23.9f. Thus, the original BPD is screw oriented ($\theta = 0^\circ$) and it is dissociated into a C-core and a Si-core partial. This corresponds to the case in region IV

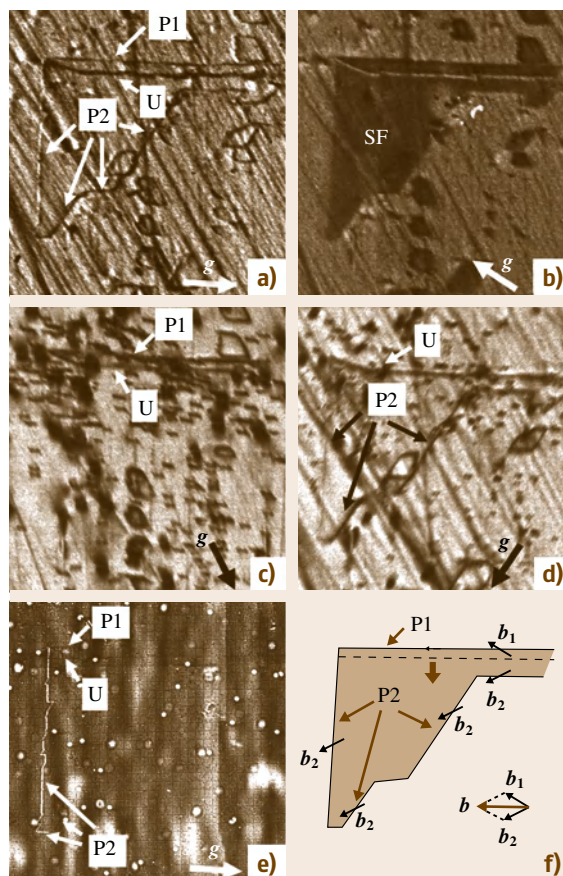


Fig. 23.9a–f REDG-activated SF after forward bias from a screw-oriented BPD. (a) $(11\bar{2}0)$ transmission topograph showing the partials (P1 and P2) bounding the SF. The SF area is out of contrast since $\mathbf{g} \cdot \mathbf{R}$ is equal to an integer; (b) $(\bar{1}010)$ transmission topograph showing the SF; (c) P2 is out of contrast in the $(2\bar{1}\bar{1}0)$ transmission topograph, indicating its Burgers vector of $1/3(0\bar{1}10)$; (d) P1 is out of contrast in the $(1\bar{2}10)$ transmission topograph, indicating its Burgers vector of $1/3(\bar{1}010)$; (e) (0008) back-reflection topograph. The sign of P1 and P2 can be determined; (f) schematics showing the SF configuration. The SF is obtained via expansion of Si-core partial toward the bottom edge of the view (dashed line) and interaction with TSDs. The Burgers vector of each partial segment is labeled; the Burgers vector \mathbf{b} of the original BPD can be obtained and it is screw-oriented (after [23.96])

of Fig. 23.8, in which θ is between -30° and $+30^\circ$. Thus, the susceptibility of the basal plane dislocations to REDG process is determined by the counterclockwise angle θ from the line direction to its Burgers vector. Basal plane dislocations with $30^\circ < \theta < 150^\circ$ are most detrimental, as both partials will advance under forward bias. If $-30^\circ < \theta < 30^\circ$ or $150^\circ < \theta < 210^\circ$, only one partial advances. Both partials are immobile if $210^\circ < \theta < 330^\circ$ [23.96].

The Nucleation Mechanism in 4H-SiC Homoepitaxial Layers

BPDs in 4H-SiC homoepitaxial layers result largely from replication, during growth, of BPDs which intersect the surface of the offcut SiC substrates, a process which can be mitigated by the conversion of the

BPDs into threading edge dislocations (TEDs) [23.105], which are not susceptible to REDG. While various schemes have been developed to increase the conversion rate to nearly 100% [23.106–109], BPDs which intersect the surface in screw orientation are observed to persist [23.110], and furthermore, they are observed to nucleate half-loop arrays. By recording the behavior of a half-loop array (HLA) from a Si-face epilayer using ultraviolet photoluminescence (UVPL) imaging, a model has been developed to explain the formation of HLAs. Figure 23.10a shows a screw-type BPD with Burgers vector $1/3[11\bar{2}0]$ intersecting the surface of the substrate, which is expected to be replicated during epitaxy, in contrast to those with significant edge components, which are likely to be converted into TEDs. As soon as the epilayer exceeds a critical thickness, as per

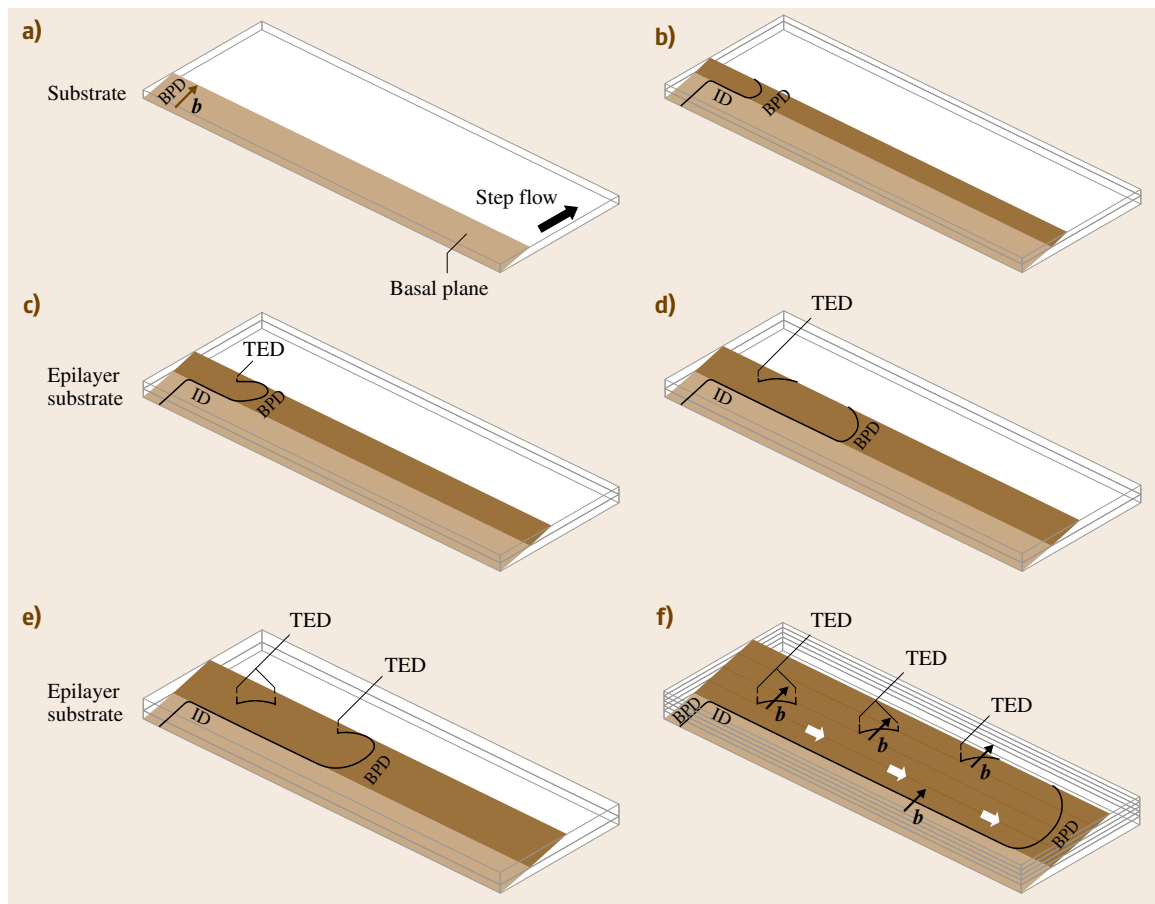


Fig. 23.10a–f Schematic showing the formation mechanism of a HLA. (a–e) Sequential stages in the process; (f) summary of process. The lighter-shaded planes in (a–f) indicate the basal plane on which the BPD lies in the substrate, while the darker one lies in the epilayer. See text for details of the mechanism (after [23.104])

the predictions of *Matthews and Blakeslee* [23.111], the threading segment of the screw-oriented **BPD** will be forced to glide sideways, leaving a trailing interfacial segment in its wake at or near the substrate–epilayer interface. During this glide process, the mobile threading segment adopts more edge character near the growth surface (Fig. 23.10b), rendering it susceptible to conversion to a **TED** during continued growth. Slip in SiC is confined to the basal plane, so that the sessile **TED** segment pins the surface intersection of the mobile **BPD** segment. During further growth, the **TED** segment is replicated while the mobile basal segment of dislocation pivots about the pinning point, as shown in Fig. 23.10c. At this juncture, part of the mobile **BPD** segment can escape through the epilayer surface (creating a surface step of magnitude equal to the Burgers vector), as shown in Fig. 23.10d, leaving two further **BPD** surface intersections which, since they are not in screw orientation, are susceptible to conversion to **TEDs**. Upon conversion, one of these **TEDs** is connected via a short **BPD** segment to the **TED** segment created in Fig. 23.10b, thus creating a half-loop comprising two **TEDs** and a connecting **BPD**. The other **TED** again acts as a pinning point for the still mobile segment of threading **BPD**, as shown in Fig. 23.10e, as the process repeats during continued growth as the **TED** segments further replicate and the threading **BPD** segment continues to glide. The net result of this process is an array of half-loops with short, large-edge-component **BPD** segments, all deposited on the exact same basal plane. The direction of the array is nearly perpendicular to the offcut direction, as summarized in Fig. 23.10f.

The value of this angle depends on the competition between the growth rate and the rate of sideways glide of the threading **BPD** segment.

Dislocation Behavior in SiC Single Crystals

Recently, the availability of 76 and 100 mm-diameter 4H-SiC wafers with extremely low **BPD** densities ($3\text{--}4 \times 10^2 \text{ cm}^{-2}$) has provided a unique opportunity to discern details of **BPD** behavior which were previously mostly unresolvable [23.113]. Figure 23.11a–d shows typical x-ray topographs from a section of such a 4H-SiC wafer (4° offcut towards $[11\bar{3}0]$). **BPDs** ($g = \bar{1}\bar{1}20$) belonging to the three $1/3\langle 11\bar{2}0 \rangle (0001)$ slip systems can be observed. For the dislocation inside the dashed frame pinned at points a–d, at point a, there is a **TSD** close to the surface intersection of the **BPD** which appears to be responsible for the pinning at that point, while no **TSD** is present at point d. Conversion of the **BPD** into a sessile **TED** at point d during growth creates an effective single-ended pinning point for the **BPD**. As the crystal grows, the **BPD** continues to glide, forming a spiral configuration around the **TED** pinning point, as shown schematically in Fig. 23.11e, thus operating as a single-ended Frank–Read source [23.112].

Figure 23.12a–d shows images of a $1/3[11\bar{2}0]$ basal plane dislocation exhibiting several loophole configurations that is pinned at five points a–e (Fig. 23.12a). The pinning at point a appears to have occurred close to the wafer surface at a **TSD**, while no **TSDs** are observed at any of the other pinning points. In this case, conversion of **BPD** segments into **TEDs** occurs during growth but also includes reconversion of the same **TED** into a **BPD**

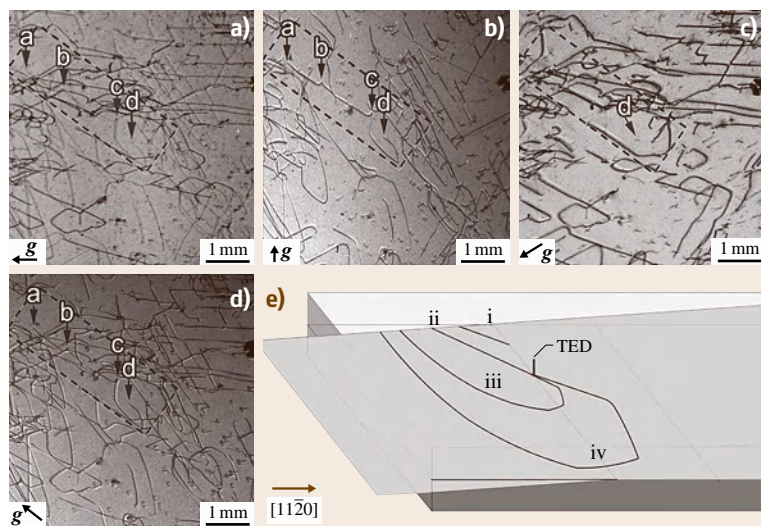


Fig. 23.11a–e SWBXT images showing **BPD** of interest inside dashed frame. Offcut direction is horizontal towards the right: (a) $g = \bar{1}\bar{1}20$; (b) $g = \bar{1}100$; (c) $g = 0\bar{1}10$; (d) $g = \bar{1}010$. (e) Schematic showing the originally screw-oriented **BPD** at position i being converted into a **TED** at its surface intersection at position ii and beginning to act as a single-ended Frank–Read source at positions iii and iv (after [23.112])

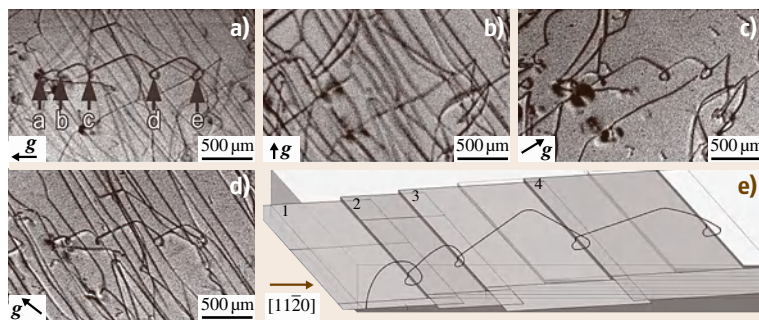


Fig. 23.12a–e SWBXT images showing dislocation loop configurations. Offcut direction is horizontal towards the right: (a) $g = \bar{1}\bar{1}20$; (b) $g = \bar{1}100$; (c) $g = 01\bar{1}0$; (d) $g = \bar{1}010$. (e) Schematic showing the deflection of the BPD gliding on basal plane 1 into a TED, which then acts as a pinning point as the BPD continues to glide, followed by deflection of the TED onto basal plane 2 through overgrowth by a macrostep. The process repeats through basal planes 3 and 4 (after [23.112])

in a process that repeats throughout the growth process. This is shown schematically in Fig. 23.12e. The initial BPD segment may have had screw orientation, but continued glide may cause it to move away from screw orientation at its growth surface intersection, rendering it susceptible to conversion into a TED. During further growth, this short TED segment acts as a single-ended pinning point for the BPD which continues to glide under thermal stress. This TED can be redirected back into the basal plane as a screw-oriented BPD through overgrowth by a macrostep traveling from left to right. Once back in the basal plane, the screw-oriented BPD, being glissile, begins to glide in spiral configuration about its single-ended TED pinning point. Again, once the BPD moves away from screw orientation, it becomes more susceptible to conversion into a TED and the whole process repeats, as shown schematically in Fig. 23.12e, leading to the type of configuration observed in Fig. 23.12a,c,d [23.112].

In Fig. 23.13a, the transmission topograph from near the edge of a 75 mm wafer reveals several long, mostly straight dislocation images running approximately in the radial direction, e.g., at AB and CD. These dislocations are growth induced and may have been redirected from an originally threading orientation onto the basal plane, for example, due to overgrowth by a macrostep. These dislocations are associated with several overlapping stacking faults (Fig. 23.13b), the contrast from which arises from the phase shift experienced by the x-ray wave fields as they cross the fault plane [23.115]. Detailed analysis of the fault contrast on different reflections [23.114] indicates that there are three different types of faults present here. The first type is a pure Shockley fault, the second is a fault comprising the sum of a Frank fault ($c/4$) and a Shockley fault, and the third is a pure Frank fault ($c/4$). Figure 23.14a shows the surface intersection of the TED core, where the two extra ($1\bar{2}10$) half-planes correspond to the $1/3[1\bar{2}10]$ Burgers vector. Note that, since the SiC structure com-

prises corner-sharing tetrahedra, overgrowth can only occur if the stacking position of the underside of the overgrowing step is able to maintain tetrahedral bonding with the top side of the terrace being overgrown, i.e., the stacking sequence rules, as, for example, described in [23.116], must be obeyed. As the macrostep advances over the surface outcrop, it is not able to admit the dislocation into itself so that the dislocation is necessarily deflected into the direction of step flow,

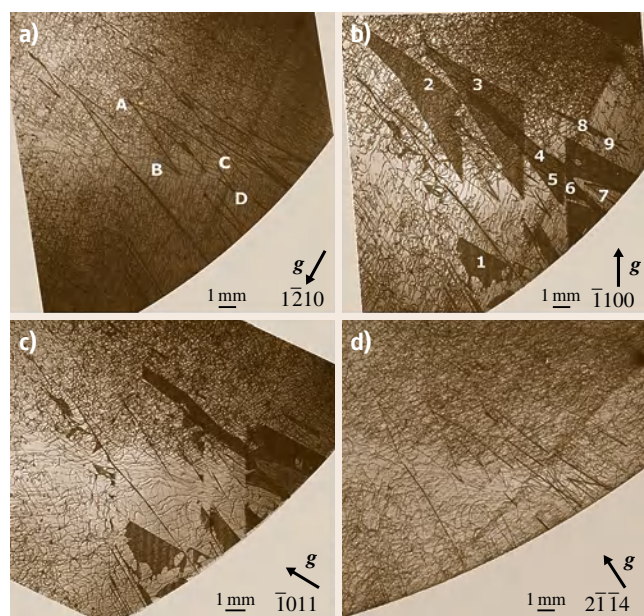


Fig. 23.13a–d SWBXT images recorded from a region near the edge of a 75 mm wafer cut with 4° offcut towards $[11\bar{2}0]$: (a) $1\bar{2}10$ reflection showing long straight dislocations, for example, at AB and CD; (b) $\bar{1}100$ reflection from the same area, showing stacking fault contrast. Faults of interest are numbered 1–9; (c) $\bar{1}011$ reflection from same area. Some of the fault images have disappeared on this image; (d) $2\bar{1}\bar{1}4$ reflection showing absence of all fault contrast [23.114]

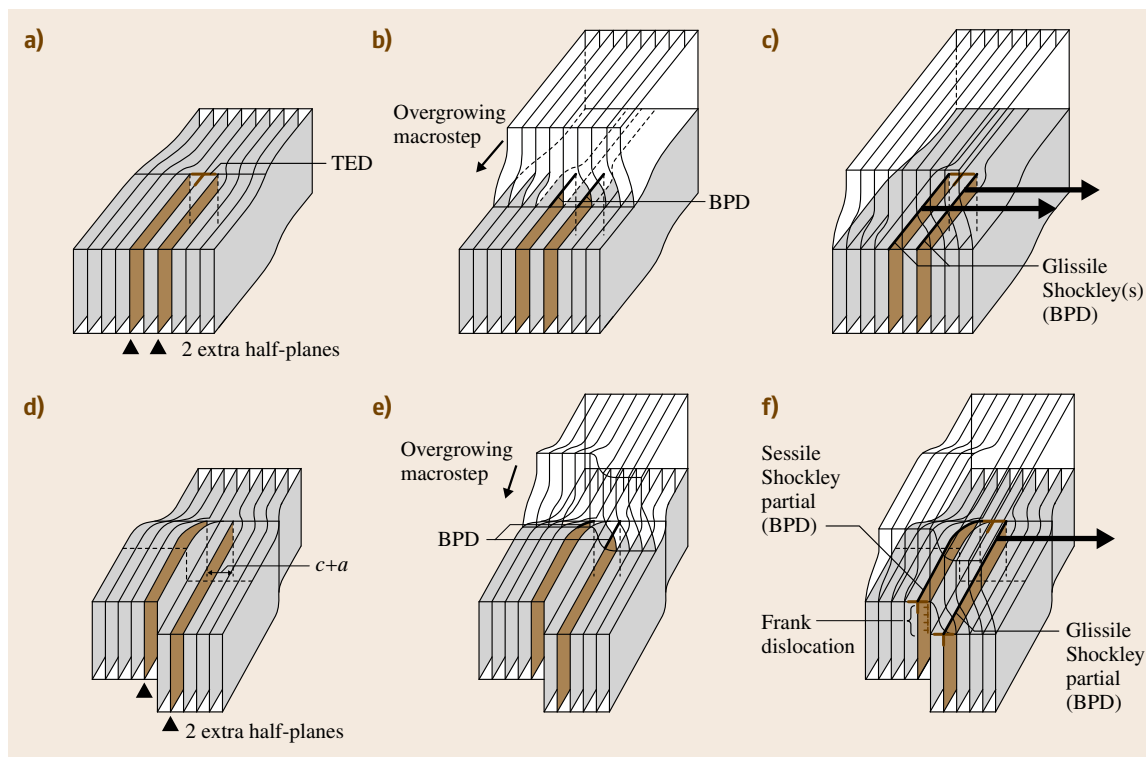


Fig. 23.14 (a–f) Overgrowth of the surface outcrop of a TED by a macrostep converting it to a BPD. Once on the basal plane, both Shockley partials are glissile and move in tandem; (b) overgrowth of a $c+a$ dislocation with a c -height step. After deflection, one Shockley is sessile and the other is glissile (after [23.114])

onto the basal plane. As this happens, the surface intersections of the two extra half-planes are frozen into the crystal and, in fact, define the line direction of the resulting BPD, as shown in Fig. 23.13b,c. If these surface intersections occur on an atomically flat terrace, the resulting BPD will comprise two extra half-planes on the exact same basal plane. Once on the basal plane, the BPD can become glissile (i.e., mobile) if sufficient basal plane shear stresses are available, and the glissile partials (comprising one extra half-plane each) will most likely separate to their equilibrium value of 20 nm and track each other as they move; i.e., the leading partial will fault the slip plane and the trailing partial will *unfault* the plane. If the surface intersections of the two extra half-planes occur on a region of surface such that they straddle the riser of a surface step which is parallel to them, it becomes possible for the overgrowth to result in two partials lying on slip planes separated by the height of the step, provided again that the overgrowth process does not breach the stacking rules [23.116].

Stacking faults are observed in the vicinity of what appear to be deflected threading dislocations. Detailed contrast analysis carried out on the faults is consistent with the Burgers vectors for the original threading dislocations of type $c+a$. The surface step (associated with the screw component) created at the surface intersection of the deflected dislocations creates a separation between the slip planes of the partials associated with the a component of the dislocations, causing one to be sessile and the other glissile. Glide of the glissile partial creates the stacking faults, which can be pure Shockley (if the original dislocation step is one unit cell high), Shockley plus $c/4$ (if the step is split into $c/4$ and $3c/4$ components), or $c/4$ if a second $c+a$ dislocation becomes involved [23.114].

23.5.3 Threading Edge Dislocations (TEDs) in 4H-SiC

In 4H-SiC, threading edge dislocations (TEDs) are dislocations with line directions roughly parallel to the

c -axis and Burgers vectors in the c -plane. TEDs have been observed to be one of the major components of the LAGBs, and they play critical roles in the defect structures in SiC, e.g., they act as a barrier for gliding BPDs if the spacing between adjacent TEDs is less than a critical value [23.117]. On {0001} wafer, TEDs have a $1/3\langle 11\bar{2}0 \rangle$ Burgers vector. Thus six different directions of the TED Burgers vector, $[\bar{1}\bar{1}20]$, $[12\bar{1}0]$, $[2\bar{1}\bar{1}0]$, $[1\bar{1}20]$, $[1\bar{2}\bar{1}0]$, and $[2\bar{1}10]$, exist on the 4H-SiC epilayers, although all with the same Burgers vector magnitude. Figure 23.15a shows a $(11\bar{2}8)$ topograph recorded from a 4H-SiC wafer [23.118]. The

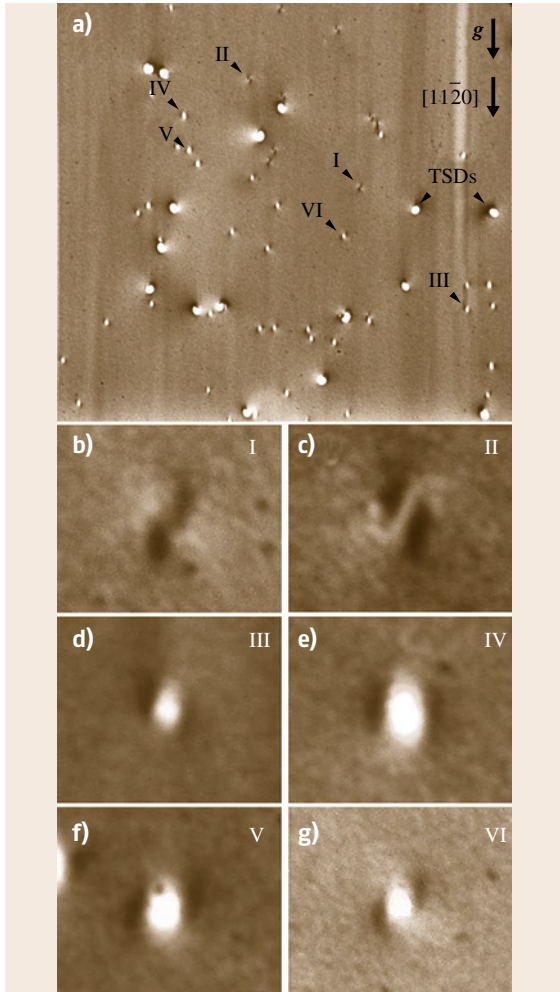


Fig. 23.15 (a) $(11\bar{2}8)$ topograph showing various images of TEDs. (b–g) Six different types of images of TEDs observed in the topographs, probably corresponding to the six types of TEDs

large roughly white circles are images of TSDs, as marked in the figure. Other than the TSDs, smaller features are also seen, corresponding to the TEDs with various Burgers vectors. They appear as two dark arcs, either separated by a white spot or canted to one side or the other of the g vector. By carefully examining the images of the TEDs in more than 50 topographs recorded, six different configurations of TEDs were observed and their highly magnified images are shown in Fig. 23.15b–g. The topographic images of the expected six types of TEDs have been simulated by ray-tracing method and are shown in Fig. 23.16. The schematics of the six types of TEDs are illustrated at the top of the figure, according to the extra atomic half-

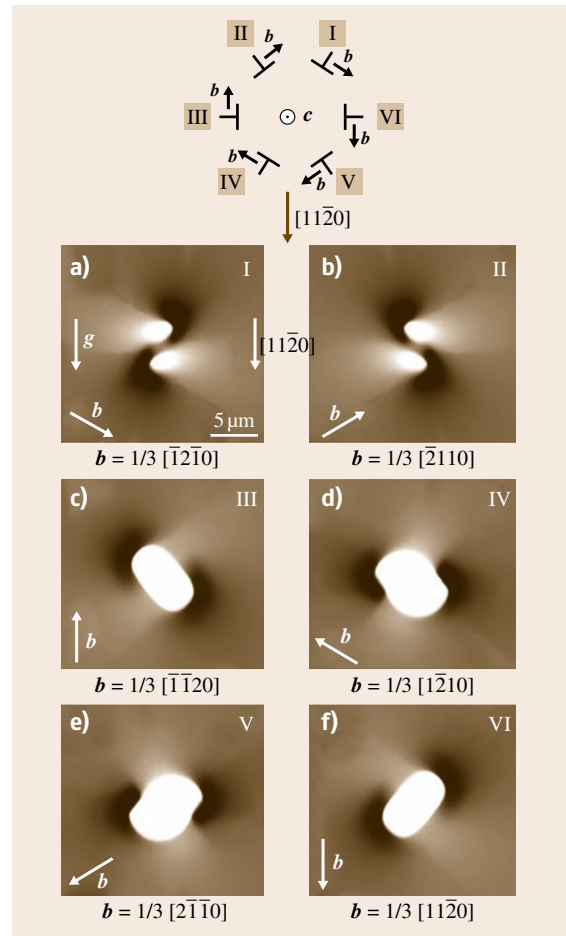


Fig. 23.16a–f Simulated $(11\bar{2}8)$ grazing-incidence XRT images of TEDs with six different Burgers vectors (a–f) Top: six types of TEDs are illustrated according to the position of the extra atomic half-planes associated with them

planes associated with them. They appear as two dark arcs canted to one side or the other of the g -vector, and these two dark arcs are either shifted vertically (Fig. 23.15a, b) or separated by an area of white contrast (Fig. 23.15c–f). Their Burgers vectors are at 60° , 120° , 180° , 240° , 300° , and 0° counterclockwise from the g -vector on the x-ray films for Fig. 23.15a–f, respectively. By comparing the simulated images in Fig. 23.15 and the observation in Fig. 23.16, one-to-one correspon-

dence can be seen. Thus, the Burgers vectors of the TEDs can be revealed from a single-reflection (1128) grazing-incidence x-ray topograph, based on their topographic contrast [23.118]. TED arrays in 4H-SiC prefer to be oriented along $(1\bar{1}00)$, and their Burgers vectors are perpendicular to the arrays. This is consistent with the fundamental dislocation theory that edge-oriented dislocations tend to align perpendicular to their Burgers vector to minimize the total strain energy.

23.6 Concluding Remarks

An extraordinary combination of physical and electronic properties makes silicon carbide a unique material for devices in high-power, high-frequency, high-temperature, and intense-radiation applications. Recent developments in SiC bulk growth and epitaxial film technology have greatly advanced SiC-based device technology. The modified Lely method has now become a standard process for industrial production of SiC boules. Wafers of 75 and 100 mm diameter are commercially available from numerous vendors. Dislocation densities have been reduced by optimizing the crystal growth technology in conjunction with modeling and computer simulation.

Defects, particularly micropipes, have nearly been eliminated by improving the growth technique, optimizing the process parameters, and developing better understanding of defect generation and propagation. Undesirable polytype inclusions have been understood reasonably well, and it is now possible to grow a single polytype using the modified Lely method. With the availability of 6H-SiC wafers, research on epitaxial growth has increased tremendously. High-quality films are being produced for different device applications using CVD techniques; in particular, HTCVD and hot-wall CVD have yielded films of good uniformity. Even though LPE of SiC is not as successful as CVD, recent developments such as container-free LPE growth show promise for better-quality films. In addition, the quality of the epitaxial film and thereby the functioning of the device have been greatly improved by using step-controlled epitaxy. High dopant incorporation can be achieved using the site-competition technique.

Defects present in SiC crystals have been characterized using x-ray topography and microscopy-based techniques such as chemical etching, AFM, SEM, TEM, and reflection and transmission optical microscopy. Even though many of these techniques are used in a complementary manner to obtain detailed informa-

tion on defects present in the crystal, x-ray topography, particularly SWBXT, is quite superior to other methods in revealing defects present in SiC crystals. Indeed, SWBXT has provided complete quantitative characterization of both closed-core and hollow-core (micropipes) screw dislocations as well as basal plane dislocations and threading edge dislocations. It has also given insights into the formation mechanisms of these defects and various interesting configurations that can be formed. Since SWBXT is capable of imaging defects in a full-size wafer with devices fabricated on it, this technique can be successfully used to study the influence of various defects on device performance.

The challenges in SiC growth still remain quality, size, and cost. To enable widespread use of SiC as a semiconductor, it is important that further progress be made in all of these areas. While micropipe defects have been nearly eliminated, other defects such as basal plane dislocations and screw dislocations need to be substantially reduced. Another important area is polytype control and infringement of polycrystalline growth directly under the seed. Since different polytypes of SiC have different properties and also polytype inclusions can become potential sources for defect generation, it is critical that a single polytype is maintained throughout the growth of the boule.

Control of the growth process requires sensing, measurement, and control strategies. However, the process does not allow much measurement, in fact, nothing inside the growth zone. Measurement of temperatures at only two locations, far away from the growth surface and the bulk of the SiC charge, gives very little information on the actual growth temperature and temperature gradient, two critical growth parameters. Also, it is difficult to determine experimentally the rate of sublimation, the chemical composition of the vapor, the growth interface shape, etc., which makes control of the process very difficult.

References

- 23.1 A.A. Lebedev, V.E. Chelnokov: Wide-gap semiconductors for high-power electronics, *Semiconductors* **33**, 999–1001 (1999)
- 23.2 V.E. Chelnokov, A.L. Syrkin: High temperature electronics using SiC: Actual situation and unsolved problems, *Mater. Sci. Eng. B* **46**, 248–253 (1997)
- 23.3 A. Lloyd, P. Tobias, A. Baranzahi, P. Martenson, I. Lundström: Current status of silicon carbide based high-temperature gas sensors, *IEEE Trans. Electron. Dev.* **46**, 561–566 (1999)
- 23.4 C.I. Harris, A.O. Konstantinov: Recent developments in SiC device research, *Phys. Scr.* **79**, 27–31 (1999)
- 23.5 V. Harle, N. Hiller, S. Kugler, B. Hahn, N. Stath: Industrial aspects of GaN/SiC blue light emitting diodes in Europe, *Mater. Sci. Eng. B* **61–62**, 310–313 (1999)
- 23.6 A.G. Acheson: *Br. Pat.* **17**, 911 (1892)
- 23.7 A.J. Lely: Darstellung von Einkristallen von Siliziumcarbid und Beherrschung von Art und Menge der eingebauten Verunreinigungen, *Ber. Dtsch. Keram. Ges.* **32**, 229–231 (1955)
- 23.8 D.R. Hamilton: The growth of silicon carbide by sublimation. In: *Silicon Carbide. A High Temperature Semiconductor*, ed. by J.R. Connor, J. Smilestons (Pergamon, Oxford 1960) pp. 45–51
- 23.9 V.P. Novikov, V.I. Ionov: Production of monocrystals of alpha silicon carbide, *Growth Cryst.* **6**, 9–21 (1968)
- 23.10 F.A. Halden: The growth of silicon carbide from solution. In: *Silicon Carbide. A High Temperature Semiconductor*, ed. by J.R. Connor, J. Smilestons (Pergamon, Oxford 1960) pp. 115–123
- 23.11 J.T. Kendal: The growth of silicon carbide from gaseous cracking. In: *Silicon Carbide. A High Temperature Semiconductor*, ed. by J.R. Connor, J. Smilestons (Pergamon, Oxford 1960) pp. 67–72
- 23.12 Y.M. Tairov, V.F. Tsvetkov: Investigation of growth processes of ingots of silicon carbide single crystals, *J. Cryst. Growth* **43**, 209–212 (1978)
- 23.13 Cree Research, Inc., 2810 Meridian Parkway, Durham, NC 27713, USA
- 23.14 H. Matsunami, T. Kimoto: Step controlled epitaxial growth of SiC: High quality homoepitaxy, *Mater. Sci. Eng. R* **20**, 125–166 (1997)
- 23.15 R.C. Glass, D. Henshall, V.F. Tsvetkov, C.H. Carter Jr.: SiC-seeded crystal growth, *MRS Bulletin* **22**, 30–35 (1997)
- 23.16 W.F. Knippenberg: Growth phenomena in silicon carbide: Preparative procedures, *Philips Res. Rep.* **18**, 170–179 (1966)
- 23.17 G. Ziegler, P. Lanig, D. Theis, C. Weyrich: Single crystal growth of SiC substrate material for blue light emitting diodes, *IEEE Trans. Electron. Dev.* **30**, 277–281 (1983)
- 23.18 D.L. Barrett, R.G. Seidensticker, W. Gaida, R.H. Hopkins: SiC boule growth by sublimation vapor transport, *J. Cryst. Growth* **109**, 17–23 (1991)
- 23.19 R.A. Stein, P. Lanig, S. Leibenzeder: Influence of surface energy on the growth of 6H and 4H-SiC polytypes sublimation, *Mater. Sci. Eng. B* **11**, 69–71 (1992)
- 23.20 R.C. Glass, D. Henshall, V.F. Tsvetkov, C.H. Carter Jr.: SiC seeded crystal growth, *Phys. Status Solidi (b)* **202**, 149–162 (1997)
- 23.21 D.L. Barrett, J.P. Mchugh, H.M. Hobgood, R.H. Hopkins, P.G. McMullin, R.C. Clarke: Growth of large SiC single crystals, *J. Cryst. Growth* **128**, 358–362 (1993)
- 23.22 A.R. Powell, S. Wang, G. Fechko, G.R. Brandes: Sublimation growth of 50 mm diameter SiC wafers, *Mater. Sci. Forum* **264–268**, 13–16 (1998)
- 23.23 I. Garcon, A. Rouault, M. Anikin, C. Jaussaud, R. Madar: Study of SiC single-crystal sublimation growth conditions, *Mater. Sci. Eng. B* **29**, 90–93 (1995)
- 23.24 Y.M. Tairov, Y.V.F. Tsvetkov: General principles of growing large-size single crystals of various silicon carbide polytypes, *J. Cryst. Growth* **52**, 146–150 (1981)
- 23.25 Y.M. Tairov: Growth of bulk SiC, *Mater. Sci. Eng. B* **29**, 83–89 (1995)
- 23.26 S.Y. Karpov, Y.N. Makarov, E.N. Mokhov, M.G. Ramm, M.S. Ramm, A.D. Roenkov, R.A. Talalaev, Y.A. Vodakov: Analysis of silicon carbide growth by sublimation sandwich method, *J. Cryst. Growth* **173**, 408–416 (1997)
- 23.27 S.Y. Karpov, Y.N. Makarov, M.S. Ramm: Simulation of sublimation growth of SiC single crystals, *Phys. Status Solidi (b)* **202**, 201–220 (1997)
- 23.28 Y.A. Vodakov, A.D. Roenkov, M.G. Ramm, E.N. Mokhov, Y.N. Makarov: Use of Ta-container for sublimation growth and doping of SiC bulk crystals and epitaxial layers, *Phys. Status Solidi (b)* **202**, 177–200 (1997)
- 23.29 E.N. Mokhov, M.G. Ramm, A.D. Roenkov, Y.A. Vodakov: Growth of silicon carbide bulk crystals by the sublimation sandwich method, *Mater. Sci. Eng. B* **46**, 317–323 (1997)
- 23.30 S.Y. Karpov, Y.N. Makarov, M.S. Ramm, R.A. Talalaev: Control of SiC growth and graphitization in sublimation sandwich system, *Mater. Sci. Eng. B* **46**, 340–344 (1997)
- 23.31 A. Henry, I.G. Ivanov, T. Egilsson, C. Hallin, A. Ellison, O. Kordina, U. Lindefelt, E. Janzen: High quality 4H-SiC grown on various substrate orientations, *Diam. Relat. Mater.* **6**, 1289–1292 (1997)
- 23.32 D.J. Larkin: An overview of SiC epitaxial growth, *MRS Bulletin* **22**, 36–41 (1997)
- 23.33 H. Matsunami: Progress in epitaxial growth of SiC, *Physica B* **185**, 65–74 (1993)

- 23.34 S. Nishinov, J.A. Powell, H.A. Will: Production of large-area single-crystal wafers of cubic SiC for semiconductors, *Appl. Phys. Lett.* **42**, 460–462 (1983)
- 23.35 R. Yakimova, R.E. Janzen: Current status and advances in the growth of SiC, *Diam. Relat. Mater.* **9**, 432–438 (2000)
- 23.36 O. Kordina, C. Hallin, A. Ellison, A.S. Bakin, I.G. Ivanov, A. Henry, R. Yakimova, M. Touminen, A. Vehanen, E. Janzen: High temperature chemical vapor deposition of SiC, *Appl. Phys. Lett.* **69**, 14561458 (1996)
- 23.37 O. Kordina, C. Hallin, A. Henry, J.P. Bergman, I. Ivanov, A. Ellison, N.T. Son, E. Janzen: Growth of SiC by “hot-wall” CVD and HTCVD, *Phys. Status Solidi (b)* **202**, 321–334 (1997)
- 23.38 C.H. Carter, V.F. Tsvetkov, R.C. Glass, D. Henshall, M. Brady, S.G. Muller, O. Kordina, K. Irvine, J.A. Edmond, H.S. Kong, R. Singh, S.T. Allen, J.A. Palmour: Progress in SiC: From material growth to commercial device development, *Mater. Sci. Eng. B* **61–62**, 1–8 (1999)
- 23.39 E. Janzen, O. Kordina: SiC Material for high-power applications, *Mater. Sci. Eng. B* **46**, 203–209 (1997)
- 23.40 M. Nakabayashi, T. Fujimoto, M. Katsuno, N. Ohtani, H. Tsuge, H. Yashiro, T. Aigo, T. Hoshino, H. Hirano, K. Tatsumi: Growth of crack-free 100 mm diameter 4H-SiC crystals with low micropipe densities, *Mater. Sci. Forum* **600–603**, 3–6 (2009)
- 23.41 R.T. Leonard, Y. Khlebnikov, A.R. Powell, C. Basceri, M.F. Brady, I. Khlebnikov, J.R. Jenny, D.P. Malta, M.J. Paisley, V.F. Tsvetkov, R. Zilli, E. Deyneka, H. Hobgood, V. Balakrishna, C.H. Carter Jr.: 100 mm 4HN-SiC wafers with zero micropipe density, *Mater. Sci. Forum* **600–603**, 7–10 (2009)
- 23.42 M. Syväjärvi, R. Yakimova, I.G. Ivanov, E. Janzen: Growth of 4H SiC from liquid phase, *Mater. Sci. Eng. B* **46**, 329–332 (1997)
- 23.43 B.M. Epelbaum, D. Hofmann, M. Muller, A. Winnacker: Top-seeded solution growth of bulk SiC: Search for the fast growth regimes, *Mater. Sci. Forum* **338–342**, 107–110 (2000)
- 23.44 A. Suzuki, M. Ikeda, N.T. Nagoa, H. Matsunami, T.J. Tanaka: Liquid phase epitaxial growth of 6H-SiC by the dipping technique for preparation of blue-light-emitting diodes, *J. Appl. Phys.* **47**, 4546–4550 (1976)
- 23.45 Y.M. Tairov, F.I. Raihel, V.F. Tsvetkov: Silicon solubility in tin and gallium, *Neorg. Mater.* **3**, 1390–1391 (1982)
- 23.46 V.A. Dmitriev, L.B. Elfimov, N.D. Il’inskaya, S.V. Rendakova: Liquid phase epitaxy of silicon carbide at temperatures of 1100–1200 °C, *Springer Proc. Phys.* **56**, 307–311 (1996)
- 23.47 V.A. Dmitriev, A. Cherenov: Growth of SiC and SiC–AlN solid solution by container free container free liquid phase epitaxy, *J. Cryst. Growth* **128**, 343–348 (1993)
- 23.48 M. Syväjärvi, R. Yakimova, H.H. Radamsom, N.T. Son, Q. Wahab, I.G. Ivanov, E. Janzen: Liquid phase epitaxial growth of SiC, *J. Cryst. Growth* **197**, 147–154 (1999)
- 23.49 R. Yakimova, M. Syväjärvi, M. Tuominen, T. Iakimov, R. Råback, A. Vehanen, E. Janz: Seeded sublimation growth of 6H and 4H-SiC crystals, *Mater. Sci. Eng. B* **61–62**, 54–57 (1999)
- 23.50 G. Augustine, H.M. Hobgood, V. Balakrishna, G. Dunne, R.H. Hopkins: Physical vapor transport growth and properties of SiC monocrystals of 4H polytype, *Phys. Status Solidi (b)* **202**, 137–148 (1997)
- 23.51 S.I. Nishizawa, Y. Kitou, W. Bahng, N. Oyanagi, M.N. Khan, K. Arai: Shape of SiC bulk single crystal grown by sublimation, *Mater. Sci. Forum* **338–342**, 99–102 (2000)
- 23.52 D. Hobgood, M. Brady, W. Brixius, G. Fechko, R. Glass, D. Henshall, J.R. Jenny, R. Leonard, D. Malta, S.G. Muller, V. Tsvetkov, C.H. Carter Jr.: Status of large diameter SiC crystal growth for electronic and optical applications, *Mater. Sci. Forum* **338–342**, 3–8 (2000)
- 23.53 D.W. Snyder, V.D. Heydemann, W.J. Everson, D.L. Barret: Large diameter PVT growth of bulk 6H SiC crystals, *Mater. Sci. Forum* **338–342**, 9–12 (2000)
- 23.54 R.R. Siergiej, R.C. Clarke, S. Sriram, A.K. Aggarwal, R.J. Bojko, A.W. Morse, V. Balakrishna, M.F. MacMillan, A.A. Burk, C.D. Brandt: Advances in SiC materials and devices: An industrial point of view, *Mater. Sci. Eng. B* **61–62**, 9–17 (1999)
- 23.55 S.G. Muller, R.C. Glass, H.M. Hobgood, V.F. Tsvetkov, M. Brady, D. Henshall, J.R. Jenny, D. Malta, C.H. Carter Jr.: The status of SiC bulk growth from an industrial point of view, *J. Cryst. Growth* **211**, 325–332 (2000)
- 23.56 Q.-S. Chen, V. Prasad, H. Zhang, M. Dudley: Silicon carbide crystals – Part II: Process physics and modeling. In: *Crystal Growth Technology*, ed. by K. Byrappa, T. Ohachi (Springer, Berlin, Heidelberg 2001) pp. 233–269
- 23.57 G. Dhanaraj, X.R. Huang, M. Dudley, V. Prasad, R.-H. Ma: Silicon carbide crystals – Part II: Process physics and modeling. In: *Crystal Growth Technology*, ed. by K. Byrappa, T. Ohachi (Springer, Berlin, Heidelberg 2001) pp. 181–232
- 23.58 T. Nishiguchi, S. Okada, M. Sasaki, H. Harima, S. Nishino: Crystal growth of 15R-SiC boules by sublimation method, *Mater. Sci. Forum* **338–342**, 115–118 (2000)
- 23.59 E.K. Sanchez, T. Kuhr, D. Heydemann, W. Snyder, S. Rohrer, M. Skowronski: Formation of thermal decomposition cavities in physical vapor transport of silicon carbide, *J. Electron. Mater.* **29**, 347–351 (2000)
- 23.60 M. Tuominen, R. Yakimova, R.C. Glass, T. Tuomi, E. Janzen: Crystalline imperfections in 4H SiC grown with a seeded Lely method, *J. Cryst. Growth* **144**, 267–276 (1994)

- 23.61 M. Anikin, R. Madar: Temperature gradient controlled SiC crystal growth, *Mater. Sci. Eng. B* **46**, 278–286 (1997)
- 23.62 W. Bahng, Y. Kitou, S. Nishizawa, H. Yamaguchi, M. Nasir Khan, N. Oyanagi, S. Nishino, K. Arai: Rapid enlargement of SiC single crystal using a cone-shaped platform, *J. Cryst. Growth* **209**, 767–772 (2000)
- 23.63 R. Schorner, P. Friedrichs, D. Peters, D. Stephani: Significantly improved performance of MOSFETs on silicon carbide using the 15R-SiC, *IEEE Electron. Device Lett.* **20**, 241–244 (1999)
- 23.64 N. Schulze, D. Barrett, M. Weidner, G. Pensl: Controlled growth of bulk 15R SiC single crystals by the modified Lely method, *Mater. Sci. Forum* **338–342**, 111–114 (2000)
- 23.65 J. Takahashi, M. Kanaya, Y. Fujiwara: Sublimation growth of SiC single crystalline ingots on faces perpendicular to the (0001) basal-plane, *J. Cryst. Growth* **135**, 61–70 (1994)
- 23.66 M. Touminen, R. Yakimova, E. Prieur, A. Ellison, T. Touni, A. Vehanen, E. Janzen: Growth-related structural defects in seeded sublimation-grown SiC, *Diam. Relat. Mater.* **6**, 1272–1275 (1997)
- 23.67 N. Oyanagi, S.I. Nishizawa, T. Kato, H. Yamaguchi, K. Arai: SiC Single crystal growth rate by in-situ observation using the transmission x-ray technique, *Mater. Sci. Forum* **338–342**, 75–78 (2000)
- 23.68 T. Kato, N. Oyangi, H. Yamaguchi, Y. Takano, S. Nishizawa, K. Arai: In-situ observation of SiC bulk single crystal growth by x-ray topography, *Mater. Sci. Forum* **338–342**, 457–460 (2000)
- 23.69 W. Si, M. Dudley, R. Glass, V. Tsvetkov, C.H. Carter Jr.: Experimental studies of hollow-core screw dislocations in 6H-SiC and 4H-SiC single crystals, *Mater. Sci. Forum* **264–268**, 429–432 (1998)
- 23.70 W. Si, M. Dudley, R. Glass, V. Tsvetkov, C.H. Carter Jr.: Hollow-core screw dislocations in 6H-SiC single crystals. A test of Frank's theory, *J. Electron. Mater.* **26**, 128–133 (1997)
- 23.71 M. Dudley, W. Si, S. Wang, C.H. Carter Jr., R. Glass, V.F. Tsvetkov: Quantitative analysis of screw dislocations in 6H-SiC single crystals, *Nuovo Cim. D* **19**, 153–164 (1997)
- 23.72 M. Dudley, S. Wang, W. Huang, C.H. Carter Jr., V.F. Tsvetkov, C. Fazi: White beam synchrotron topographic studies of defects in 6H-SiC single crystals, *J. Phys. D* **28**, A63–A68 (1995)
- 23.73 F.C. Frank: Capillary equilibria of dislocated crystals, *Acta Cryst.* **4**, 497–501 (1951)
- 23.74 A.R. Verma: Spiral growth on carborundum crystal faces, *Nature* **167**, 939 (1951)
- 23.75 S. Amelinck: Spiral growth on carborundum crystal faces, *Nature* **167**, 939–940 (1951)
- 23.76 A.R. Verma: *Crystal Growth and Dislocations* (Butterworths Scientific, London 1953)
- 23.77 J. Giocondi, G.S. Rohrer, M. Skowronski, V. Balakrishna, G. Augustine, H.M. Hobgood, R.H. Hopkins: An AFM study of super-dislocation/micropipe complexes on the 6H-SiC(0001) growth surfaces, *J. Cryst. Growth* **181**, 351–362 (1997)
- 23.78 M. Dudley, W. Huang, S. Wang, J.A. Powell, P. Neudeck, C. Fazi: White beam synchrotron topographic analysis of multipolytype SiC device configurations, *J. Phys. D* **28**, A56–A62 (1995)
- 23.79 X.R. Huang, M. Dudley, W.M. Vetter, W. Huang, C.H. Carter Jr.: Contrast mechanism in superscrew dislocation images on synchrotron back-reflection topographs, *Mater. Res. Soc. Symp. Proc.* **524**, 71–76 (1998)
- 23.80 X.R. Huang, M. Dudley, W.M. Vetter, W. Huang, S. Wang, C.H. Carter Jr.: Direct evidence of micropipe-related pure superscrew dislocations in SiC, *Appl. Phys. Lett.* **74**, 353–356 (1999)
- 23.81 X.R. Huang, M. Dudley, W.M. Vetter, W. Huang, W. Si, C.H. Carter Jr.: Superscrew dislocation contrast on synchrotron white-beam topographs: An accurate description of the direct dislocation image, *J. Appl. Crystallogr.* **32**, 516–524 (1999)
- 23.82 M. Dudley, X.R. Huang, W. Huang: Assessment of orientation and extinction contrast contributions to the direct dislocation image, *J. Phys. D* **32**, A139–A144 (1999)
- 23.83 Y. Chen, M. Dudley: Direct determination of dislocation sense of closed-core threading screw dislocations using synchrotron white beam x-ray topography in 4H silicon carbide, *Appl. Phys. Lett.* **91**, 141918 (2007)
- 23.84 Y. Chen, G. Dhanaraj, M. Dudley, E.K. Sanchez, M.F. MacMillan: Sense determination of micropipes via grazing-incidence synchrotron white beam x-ray topography in 4H silicon carbide, *Appl. Phys. Lett.* **91**, 071917 (2007)
- 23.85 I. Kamata, M. Nagano, H. Tsuchida, Y. Chen, M. Dudley: Investigation of character and spatial distribution of threading edge dislocations in 4H-SiC epilayers by high-resolution topography, *J. Cryst. Growth* **311**, 1416–1422 (2009)
- 23.86 N. Schulze, D.L. Barret, G. Pensl: Near-equilibrium growth of micropipe free 6H-SiC single crystals by physical vapor transport, *Appl. Phys. Lett.* **72**, 1632–1634 (1998)
- 23.87 V. Tsvetkov, R. Glass, D. Henshall, D. Asbury, C.H. Carter Jr.: SiC seeded boule growth, *Mater. Sci. Forum* **264–268**, 3–8 (1998)
- 23.88 V.D. Heydemann, E.K. Sanchez, G.S. Rohrer, M. Skowronski: Structural evolution of Lely seeds during the initial stages of SiC sublimation growth, *Mater. Res. Soc. Symp. Proc.* **483**, 295–300 (1998)
- 23.89 V. Balakrishna, R.H. Hopkins, G. Augustine, G.T. Donne, R.N. Thomas: Characterization of 4H-SiC monocrystals grown by physical vapor transport, *Inst. Phys. Conf. Ser.* **160**, 321–331 (1998)
- 23.90 S. Gits-Leon, F. Lefaucheux, M.C. Robert: Effect of stirring on crystalline quality of solution grown

- crystals – case of potash aluminum, *J. Cryst. Growth* **44**, 345–355 (1978)
- 23.91 H. Klapper, H. Koppers: Directions of dislocation lines in crystals of ammonium hydrogen oxalate hemihydrate grown from solution, *Acta Cryst. A* **29**, 495–503 (1973)
 - 23.92 G. Neuroth: Der Einfluß von Einschlußbildung und mechanischer Verletzung auf das Wachstum und die Perfektion von Kristallen. Ph.D. Thesis (University of Bonn, Bonn 1996)
 - 23.93 A.A. Chernov: Formation of crystals in solutions, *Contemp. Phys.* **30**, 251–276 (1989)
 - 23.94 M. Dudley, X.R. Huang, W. Huang, A. Powell, S. Wang, P. Neudeck, M. Skowronski: The mechanism of micropipe nucleation at inclusions in silicon carbide, *Appl. Phys. Lett.* **75**, 784–786 (1999)
 - 23.95 P. Krishna, S.-S. Jiang, A.R. Lang: An optical and x-ray topographic study of giant screw dislocations in silicon-carbide, *J. Cryst. Growth* **71**, 41–56 (1985)
 - 23.96 Y. Chen, M. Dudley, K.X. Liu, R.E. Stahlbush: Observations of the influence of threading dislocations on the recombination enhanced partial dislocation glide in 4H-silicon carbide epitaxial layers, *Appl. Phys. Lett.* **90**, 171930 (2007)
 - 23.97 S. Wang: Characterization of growth defects in silicon carbide single crystals by synchrotron x-ray topography. Ph.D. Thesis (State University of New York at Stony Brook, Stony Brook 1995)
 - 23.98 W.M. Vetter: Characterization of dislocation structures in silicon carbide crystals. Ph.D. Thesis (State University of New York at Stony Brook, Stony Brook 1999)
 - 23.99 M.H. Hong, A.V. Samant, P. Pirouz: Stacking fault energy of 6H-SiC and 4H-SiC single crystals, *Philos. Mag. A* **80**, 919–935 (2000)
 - 23.100 H. Lendenmann, F. Dahlquist, N. Johansson, R. Soderholm, P.A. Nilsson, J.P. Bergman, P. Skytt: Long term operation of 4.5 kV PiN and 2.5 kV JBS diodes, *Mater. Sci. Forum* **353–356**, 727 (2001)
 - 23.101 A. Galeckas, J. Linnros, P. Pirouz: Recombination-enhanced extension of stacking faults in 4H-SiC p-i-n diodes under forward bias, *Appl. Phys. Lett.* **81**, 883 (2002)
 - 23.102 J.D. Weeks, J.C. Tully, L.C. Kimerling: Theory of recombination-enhanced defect reactions in semiconductors, *Phys. Rev. B* **12**, 3286–3292 (1975)
 - 23.103 H. Sumi: Dynamic defect reactions induced by multiphonon nonradiative recombination of injected carriers at deep levels in semiconductors, *Phys. Rev. B* **29**, 4616–4630 (1984)
 - 23.104 N. Zhang, Y. Chen, Y. Zhang, M. Dudley, R.E. Stahlbush: Nucleation mechanism of dislocation half-loop arrays in 4H-silicon carbide homoepitaxial layers, *Appl. Phys. Lett.* **94**, 122108 (2009)
 - 23.105 S. Ha, P. Mieszkowski, M. Skowronski, L.B. Rowland: Dislocation conversion in 4H silicon carbide epitaxy, *J. Cryst. Growth* **244**, 257–266 (2002)
 - 23.106 Z. Zhang, T.S. Sudarshan: Basal plane dislocation-free epitaxy of silicon carbide, *Appl. Phys. Lett.* **87**, 151913 (2005)
 - 23.107 J.J. Sumakeris, J.P. Bergman, M.K. Das, C. Hallin, B.A. Hull, E. Janzen, H. Lendenmann, M.J. O'Loughlin, M.J. Paisley, S. Ha, M. Skowronski, J.W. Palmour, C.H. Carter Jr.: Techniques for minimizing the basal plane dislocation density in SiC epilayers to reduce V_f drift in SiC bipolar power devices, *Mater. Sci. Forum* **527–529**, 141 (2006)
 - 23.108 E.R. Stahlbush, B.L. VanMil, R.L. Myers-Ward, K.-K. Lew, D.K. Gaskill, C.R. Eddy Jr.: Basal plane dislocation reduction in 4H-SiC epitaxy by growth interruptions, *Appl. Phys. Lett.* **94**, 041916 (2009)
 - 23.109 R.E. Stahlbush, B.L. VanMil, K.X. Liu, K.K. Lew, R.L. Myers-Ward, D.K. Gaskill, C.R. Eddy Jr., X. Zhang, M. Skowronski: Evolution of basal plane dislocations during 4H-SiC epitaxial growth, *Mater. Sci. Forum* **600–603**, 317–320 (2009)
 - 23.110 H. Tsuchida, I. Kamata, M. Nagano: Investigation of defect formation in 4H-SiC(0001) and (0001) epitaxy, *Mater. Sci. Forum* **600–603**, 267–272 (2009)
 - 23.111 J.W. Matthews, A.E. Blakeslee: Defects in epitaxial multilayers: I. Misfit dislocations, *J. Cryst. Growth* **27**, 118–125 (1974)
 - 23.112 M. Dudley, N. Zhang, Y. Zhang, B. Raghothamachar, S. Byrappa, G. Choi, E.K. Sanchez, D. Hansen, R. Drachev, M.J. Loboda: Characterization of 100 mm diameter 4H-Silicon carbide crystals with extremely low basal plane dislocation density, *Mater. Sci. Forum* **645–648**, 291 (2010)
 - 23.113 M. Selder, L. Kadinski, F. Durst, T.L. Straubinger, P.L. Wellmann, D. Hofmann: Numerical simulation of thermal stress formation during PVT-growth of SiC bulk crystals, *Mater. Sci. Forum* **353–356**, 65 (2001)
 - 23.114 M. Dudley, S. Byrappa, H. Wang, F. Wu, Y. Zhang, B. Raghothamachar, G. Choi, E.K. Sanchez, D. Hansen, R. Drachev, M.J. Loboda: Analysis of dislocation behavior in low dislocation density, PVT-grown, four-inch silicon carbide single crystals, *Mater. Res. Soc. Symp. Proc.* **1246**, (2010) in press
 - 23.115 A. Authier, Y. Epelboin: Variation of stacking fault contrast with the value of the phase shift in x-ray topography, *Phys. Status Solidi (a)* **41**, K9–K12 (1977)
 - 23.116 P. Pirouz, J.W. Yang: Polytypic transformations in SiC: The role of TEM, *Ultramicroscopy* **51**, 189–214 (1993)
 - 23.117 Y. Chen, H. Chen, N. Zhang, M. Dudley, R. Ma: Investigation and properties of grain boundaries in silicon carbide, *Mater. Res. Soc. Symp. Proc.* **E 955**, 095510750 (2007)
 - 23.118 I. Kamata, M. Nagano, H. Tsuchida, Y. Chen, M. Dudley: Investigation of character and spatial distribution of threading edge dislocations in 4H-SiC epilayers by high-resolution topography, *J. Cryst. Growth* **311**, 1416–1422 (2009)

AlN Bulk Crystals

Rafael Dalmau, Zlatko Sitar

Part D | 24

Despite considerable research in thin-film growth of wide-bandgap group III nitride semiconductors, substrate technology remains a critical issue for the improvement of nitride devices. With applications ranging from high-power electronics to optoelectronics, an increasing number of nitride semiconductor devices are becoming commercially available. Currently, many of these devices are being grown heteroepitaxially on nonnative substrates, leading to a high defect density in the active layers, which limits device performance and lifetime. Aluminum nitride (AlN) is considered a highly desirable candidate as a native substrate material for III-nitride epitaxy, especially for AlGaN devices with high Al concentrations. AlN crystals have been grown by a variety of methods. High-temperature growth of AlN bulk crystals by physical vapor transport (PVT) has emerged as the most promising growth technique to date for production of large, high-quality single crystals. This chapter reviews recent growth and characterization results of AlN bulk crystals grown

24. AlN Bulk Crystal Growth by Physical Vapor Transport

- 24.1 PVT Crystal Growth 822
- 24.2 High-Temperature Materials Compatibility 825
- 24.3 Self-Seeded Growth of AlN Bulk Crystals . 827
- 24.4 Seeded Growth of AlN Bulk Crystals 829
 - 24.4.1 Growth on SiC Seeds 829
 - 24.4.2 Growth on AlN Seeds 831
- 24.5 Characterization of High-Quality Bulk Crystals 832
 - 24.5.1 Structural Properties 832
 - 24.5.2 Fundamental Optical Properties of AlN 835
 - 24.5.3 Impurities 838
- 24.6 Conclusions and Outlook 839
- References 839

by PVT and discusses several issues that remain to be addressed for continued development of this technology.

Wide-bandgap nitride semiconductors, AlN, GaN, and InN, have been identified as promising materials for a broad range of applications in electronics and optoelectronics [24.1]. Currently, epitaxial heterostructures involving these semiconductors are being grown by various techniques on a number of substrates [24.2–6]. The two most commonly used substrates, sapphire and SiC, are not closely lattice-matched to the III-nitride overlayers, leading to a high defect density in overgrown active layers, which limits device performance and lifetime. Additional limitations of the currently available substrates include cracking of the device layers due to the large thermal mismatch, and poor thermal conductivity. Thus, the performance of III-nitride semiconductor devices would be greatly improved by the

availability of native substrates. High-quality, single-crystalline AlN substrates with low dislocation densities are expected to decrease defect density in the overgrown device structures by several orders of magnitude and, thereby, greatly improve the performance and lifetime of III-nitride devices. AlN has a number of excellent properties that make it a highly desirable candidate as a substrate for III-nitride epitaxy. Its crystalline structure is the same as that of GaN, with a lattice mismatch in the *c*-plane of approximately 2.5%. Since AlN makes a continuous range of solid solutions with GaN, it plays an important role in GaN-based devices and is highly suited as a substrate for AlGaN devices with high Al concentrations or structures with graded layers. Its high thermal conductivity

makes it desirable for high-temperature electronic and high-power microwave devices where heat dissipation is critical. The direct, large optical bandgap of 6.1 eV [24.7] makes it suitable for ultraviolet applica-

tions down to wavelengths as short as 200 nm. This chapter reviews recent growth and characterization results of AlN bulk crystals grown by physical vapor transport (PVT).

24.1 PVT Crystal Growth

The vast majority of commercially grown semiconductor bulk crystals are grown from the melt using one of several methods, such as the Czochralski, Bridgman, and vertical gradient freeze methods. However, bulk crystal growth by physical vapor transport is an alternative when melt growth is not possible, such as when the melting point is too high, the material decomposes before it melts or the melt reacts with the crucible. Because of the high melting temperature and large dissociation pressure at the melting point of the III-nitrides [24.8], bulk crystal growth from the melt is precluded unless very high pressure is applied. Although the first AlN was synthesized in 1862 by *Briegleb* and *Geuther* [24.9] by the reaction between molten aluminum and nitrogen, it took more than a century before any sizeable single crystals of AlN were grown [24.10]. Past efforts to grow AlN bulk crystals have explored sublimation of AlN, vaporization of Al, and solution routes, with sublimation yielding the most voluminous AlN crystals to date. Crystal growth by other methods, such as hydride vapor-phase epitaxy [24.11], ammonothermal growth [24.12], or solution growth [24.13, 14], has been reported, but only crystals of either inferior quality or size have been produced thus far. In recent years, several research groups [24.15–18] independently developed processes and models for growth of AlN crystals which all converge to the same basic growth principle and process parameter space. All these efforts clearly demonstrate that AlN bulk crystals of very high quality and of sizes appropriate for use as III-nitride substrates can be produced by PVT.

In a typical PVT process an AlN powder source is sublimed within a closed or semi-open crucible, and the vapors are subsequently transported in nitrogen (N₂) atmosphere through a temperature gradient to a region held at a lower temperature than the source, where they recrystallize. The region where recrystallization takes place can consist of the crucible walls, in which case we speak of self-seeded growth, or it may consist of an intentionally selected seed crystal, in which case we have seeded growth. AlN growth can be achieved at tem-

peratures as low as 1800 °C; however, temperatures in excess of 2200 °C are required to achieve commercially viable growth rates. This high growth temperature, in combination with the highly reactive Al vapor, creates a challenge for the identification of appropriate crucible materials and has been a major obstacle in growth of high-purity, large-size AlN crystals.

Early kinetic theory formulation for the sublimation growth of AlN indicated that the useful growth temperature range was 2000–2400 °C, yielding growth rates ranging from 0.3 to 15 mm/h [24.19]. A two-dimensional model of mass transport in the gas phase was analyzed by *Liu* and *Edgar* [24.20], who determined that the activation energy for AlN growth was 681 kJ/mol, which is close to the heat of sublimation of AlN, 630 kJ/mol. To better describe growth at pressures below 100 Torr, a refined model [24.21] included the influence of surface kinetics (N₂ sticking coefficient), which is not a limiting factor at higher pressures. *Karpov* et al. [24.22] and *Segal* et al. [24.23] identified two mechanisms of vapor transport in AlN sublimation: at high pressure (760 Torr), vapor transport was controlled by diffusion in the gas phase, while at low pressure (10^{−4} Torr), it was dominated by drift of the reactive species, Al and N₂. Growth at low pressure required 350–400 °C lower temperature to achieve the same growth rate.

A one-dimensional model was developed for the high-temperature growth by *Noveski* et al. [24.24]. Gas-phase mass transfer of Al species was assumed to limit the overall growth rate. Thus an equation describing the temperature (*T*) and pressure (*p*) dependence of the growth rate (*v_G*) was derived by considering the transport of Al species through the N₂ gas,

$$v_G = k \frac{\exp\left(\frac{\Delta S - \frac{\Delta H}{T}}{R}\right) \Delta T}{RT^{1.2} p^{1.5} \delta}, \quad (24.1)$$

where the pre-exponential term *k* contains the diffusion coefficient of Al; ΔS and ΔH are the entropy and enthalpy of sublimation, respectively; *R* is the universal gas constant; and $\Delta T/\delta$ is the temperature gradient in the crucible. An apparent activation energy of

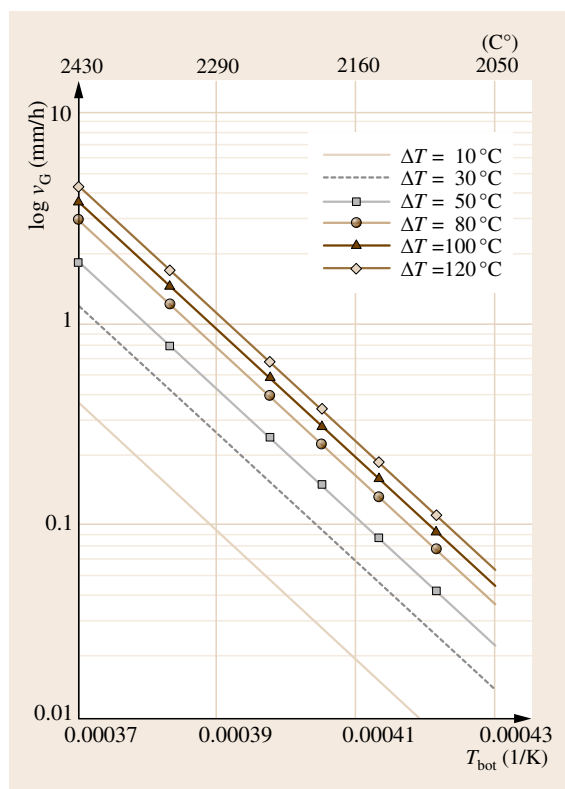


Fig. 24.1 Predicted growth rate as a function of temperature at the bottom of the crucible (T_{bot}) for different temperature differences (ΔT) along the crucible, 600 Torr pressure, and 10 mm source-to-seed distance (after [24.24], with permission)

638.1 kJ/mol was predicted. The theoretical model was experimentally validated by selecting growth parameters for which the model predicted a growth rate of 1 mm/h (Fig. 24.1). Sustained growth rates on the order of 1 mm/h were demonstrated, clearly showing that the growth rate is Al transport limited at total N_2 pressures in the range of 400–800 Torr.

The dependence of growth rate on temperature and pressure was also studied by Epelbaum et al. [24.25], who found that PVT transport of AlN was possible starting at 1850 °C, but temperatures exceeding 2100 °C were necessary to obtain stable growth of well-faceted crystals. The vapor pressure of Al as a function of temperature was calculated for different total system pressures (Fig. 24.2) and used to determine the corresponding AlN growth rates, under the assumption that reaction of adsorbed Al and N_2 species to form AlN is the rate-limiting growth step. According

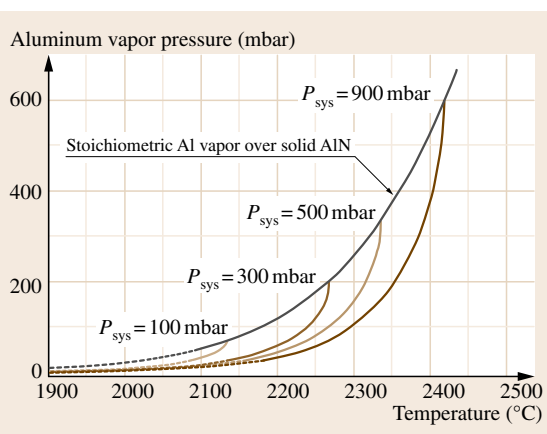


Fig. 24.2 Dependence of aluminum vapor pressure on temperature and system pressure (after [24.25], with permission of Trans Tech)

to the calculations, growth temperatures in excess of 2100 °C are required to obtain growth rates in excess of 1 mm/h for typical PVT process conditions (e.g., total pressure, thermal gradient). Experimentally observed growth rates in the range of 0.3–3 mm/h were achieved during growth of polycrystalline AlN boules up to 51 mm in diameter and 15 mm in length [24.25].

Two-dimensional simulations [24.26] demonstrated that at a given temperature both the powder source and the seed sublime below a critical pressure when the sum of the Al and N_2 partial pressures at the seed and source are greater than the ambient pressure. Under growth conditions below this critical pressure, the simulations showed that the gas phase is transported out of the growth cell and the sublimation growth fails. The simulations were used to explain the experimentally observed effect of growth temperature (T_g), source-to-seed temperature difference (ΔT), and ambient N_2 pressure on the growth rate [24.27]: For high ΔT , the source sublimation and crystal growth rates increased exponentially with temperature; as ΔT decreased, the sublimation rate continued to exhibit an exponential dependence with temperature, but the growth rate became a decreasing function of temperature, dropping sharply at temperatures greater than 2130 °C; finally, as the ambient nitrogen pressure was decreased, the growth rate initially increased, but then sharply dropped at a critical pressure. This critical pressure was found to increase from ≈ 50 Torr at 2100 °C to ≈ 120 Torr at 2200 °C. The simulation results are presented in Fig. 24.3, where the N_2 molar fraction distributions and the velocity vector fields in the crucible are shown for two differ-

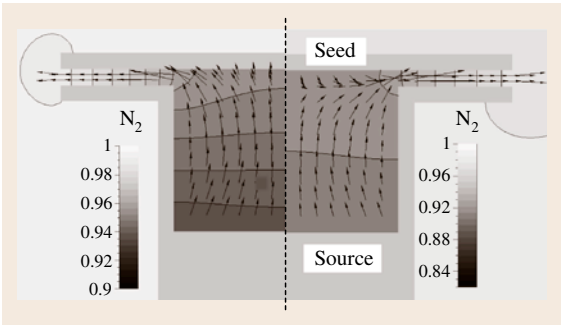


Fig. 24.3 Nitrogen molar fraction distributions and velocity vector fields in the crucible under different thermal conditions: (left) $\Delta T \approx 35$ K, $T_g \approx 2150$ °C; (right) $\Delta T \approx 10$ K, $T_g \approx 2215$ °C (after [24.27], with permission of Trans Tech)

ent growth regimes. In the first regime, T_g is 2150 °C and ΔT is about 35 °C. The Al/N₂ gas mixture evaporated from the source is divided into two flows, one of which deposits on the growing crystal, while the other is transported out of the crucible. In the second regime, T_g is higher, 2215 °C, and ΔT is lower, about 10 °C. Now, the gas flows evaporated from the source and seed are both transported out of the crucible, and the growth fails. When AlN crystal growth experiments were performed using the optimized conditions determined from the simulations, a distinct dependence

of the growth morphology on system pressure was observed. Crystals grown at close to atmospheric N₂ pressure had a hexagonal facet shape, with a nominally c-plane growth surface. At much lower pressures, the presence of many competing growth centers resulted in a rough, porous surface with a rounded shape. Under optimal growth conditions, growth proceeded from a single growth center and the surface exhibited distinct macroscopic steps, suggesting a layer growth mechanism.

The role of oxygen in the sublimation growth was also analyzed [24.28]. Closed-box thermodynamics calculations indicated that at elevated temperature Al₂O and AlO are the only major Al–O gaseous compounds, and that at temperatures less than ≈ 2350 °C the only condensed phase, solid AlN, is thermodynamically stable. Model calculations were performed for growth conditions where the growth rate is determined by the transport of Al-containing species from the source to the seed. After solving for the fluxes and partial pressures of all reactive species as a function of the source temperature (T_s), ΔT , total pressure (p_{tot}), and oxygen atomic fraction in the vapor averaged over the gas volume (X_O), the AlN growth rate was determined by the total aluminum flux from five Al-containing gaseous species: Al, Al₂, AlN, Al₂O, and AlO. The AlN growth rate as a function of temperature computed for pure and oxygen-contaminated N₂ atmospheres is shown in Fig. 24.4 for various oxygen atomic fractions and total

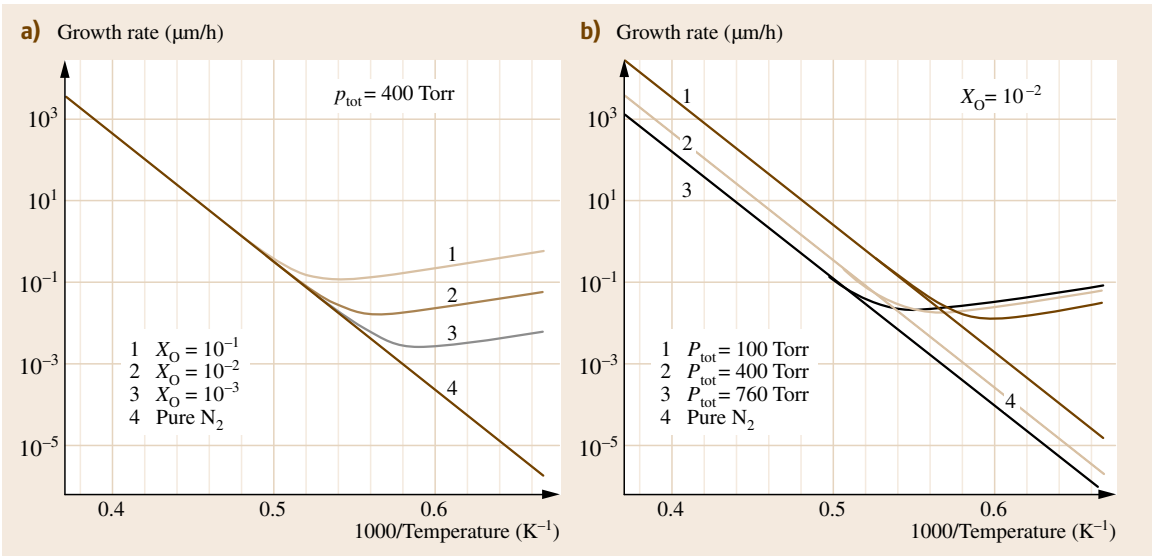


Fig. 24.4a,b The temperature variation of AlN growth rate computed for pure and oxygen-contaminated N₂ atmospheres, $\Delta T = 30$ K, and various X_O (a) or P_{tot} (b) (after [24.28], with permission of Wiley-VCH)

pressures. It is seen that the effect of oxygen on the growth rate is appreciable only for low growth temperatures and becomes negligible in the temperature range $1850^{\circ}\text{C} < T < 2350^{\circ}\text{C}$ typical for sublimation growth. In addition, the critical oxygen fraction in the vapor corresponding to Al_2O_3 inclusion generation on the AlN surface was determined [24.28]. It was found that, for typical growth temperatures, sufficient purification of AlN source powder is required to produce less than a 10^{-3} oxygen fraction in the vapor in order to avoid inclusion formation. High growth temperatures are also favorable for obtaining crystals free of inclusions.

The above analyses tend to assume, especially at high temperature, that the only gas-phase species of any significance are Al and N_2 . First-principles gas-phase composition calculations have indicated that Al_nN ($n = 2, 3, 4$) species, though present in much smaller mole fractions than Al and N_2 , are supersaturated with respect to the AlN crystal (Fig. 24.5) and may contribute to the growth [24.29]. Additional analysis of the model was used to show how these trace precursors contribute to mass transport and the growth rate [24.30]. The model predicts the existence of a small mass transport barrier whose height is dependent primarily on the amount of Al_3N in the vapor, and is sensitive to changes in the source temperature and total pressure. Results were used to predict the effective range of ΔT as a function of T_s and p_{tot} , yielding good agreement with published experimental data. However, little is known about the kinetics of these trace species. Their existence and the effect they have on AlN bulk crystal growth have yet to be determined experimentally.

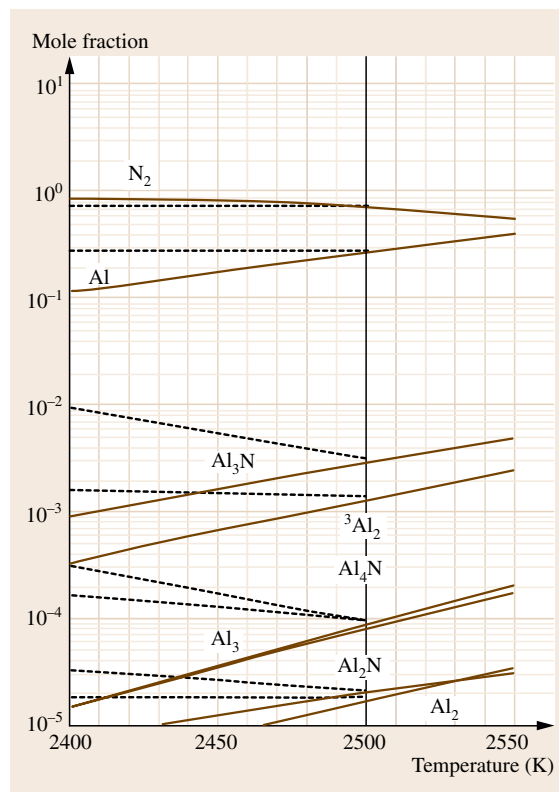


Fig. 24.5 Calculated equilibrium mole fractions of precursors for AlN sublimation growth at a nitrogen pressure of 400 Torr: boundary layer of an Al surface (solid lines); and boundary layer of the bulk gas (dashed lines) sublimed at $T = 2500\text{ K}$ (vertical line) (after [24.29], with permission of APS)

24.2 High-Temperature Materials Compatibility

By necessity, commercially viable growth rates are achieved at very high process temperatures (typically $> 2200^{\circ}\text{C}$), making furnace design and materials selection critical to the success of the overall process, both for achieving durability of growth hardware and keeping crystal impurity levels low. In particular, crucible materials must be refractory and compatible with elevated growth temperatures, inert to chemically aggressive Al vapor, a negligible source of contamination to the growth process, reusable for multiple growth runs, relatively inexpensive, and manufacturable in various shapes and dimensions [24.31].

In his early work, Slack [24.10] demonstrated successful growth using W crucibles; however, crucible

lifetime was limited and $\approx 50\text{ ppm}$ of W incorporation was reported. Some efforts have employed graphite or coated (SiC, NbC, TaC) graphite crucibles. Several independent studies show that pure graphite crucibles should be avoided due to incompatibility with Al, high levels of carbon in crystals, and the detrimental influence of carbon on growth morphology. Coated graphite crucibles reduce these shortcomings for low-temperature growth; however, these coatings deteriorate quickly above 2000°C , regardless of their thickness or deposition process, and thus do not offer a long-term stable growth environment.

There are several reports of crystal growth in boron nitride (BN) crucibles [24.16, 32, 33]. Sizeable transpar-

ent crystals with very low dislocation densities were grown; however, it seems that a BN growth environment produces highly anisotropic growth rates at high temperatures, where the growth rate in the a -direction is almost completely inhibited. As a result, coalescence and crystal-size expansion are difficult to achieve.

Compatibility of reactor materials at the high temperatures needed for crystal growth was addressed by *Epelbaum et al.* [24.35]. Crystals were grown from AlN powder with approximately 1% aluminum oxide impurity in a resistively heated reactor at temperatures of 1800–2200 °C using W or graphite heating elements. Different combinations of crucible materials and heating elements yielded results similar to those reported previously [24.36]. Crucibles made of graphite were readily attacked by the Al vapor, while graphite crucibles coated with SiC were unstable at temperatures above 1950 °C, leading to the formation of mixed AlN–SiC crystals varying in color from dark blue to light green. Problems were also associated with the combination of W crucible and heating element, namely degradation of W by aluminum vapor or by oxygen from impurities in the source. The most flexible reactor design was deemed to be a combination of W crucible and graphite heating element.

More recently, efforts with sintered tantalum nitride and tantalum carbide crucibles confirmed that these materials are more stable than any of the aforementioned crucible materials, with crucible lifetimes exceeding 500 h at growth temperatures exceeding 2200 °C [24.31,

37]. Well-faceted crystals with isotropic growth and very low dislocation densities were obtained. These materials have melting points around 3100 °C and 3900 °C, respectively, and thermodynamic calculations [24.34, 38] of the partial pressure of Ta over the solid carbide or nitride have indicated that these materials possess excellent high-temperature stability. Figure 24.6 shows the calculated partial pressures present over several solid crucible materials at 2300 °C in one atmosphere of N₂.

Several groups are developing proprietary processes for fabrication of suitable growth crucibles. Optimization of the sintering process parameters yielded better than 96% dense TaC shapes, which were successfully employed in PVT growth of 38 mm diameter AlN boules [24.31]. Elemental analysis demonstrated that Ta incorporation was below the detection limit (sub-ppm level). However, since TaC appears to possess a larger thermal expansion than AlN, TaC crucibles may exert a compressive stress upon AlN boules during cool-down, leading to the formation of stress-related defects. Thus, use of these crucibles requires that wall contact between the AlN boule and the crucible be avoided. In other work, chemically passivated TaC crucible surfaces were formed by carburization of Ta metal shapes [24.39, 40]. *Mokhov et al.* [24.39] carburized Ta crucibles with 1–2 mm thick walls at 2200–2500 °C in a carbon-containing atmosphere. Carburized crucibles were stable in an atmosphere of Al vapor and N₂ gas at 2300 °C for up to 500 h, after which surface cracks appeared, making them permeable to the vapor. *Hartmann*

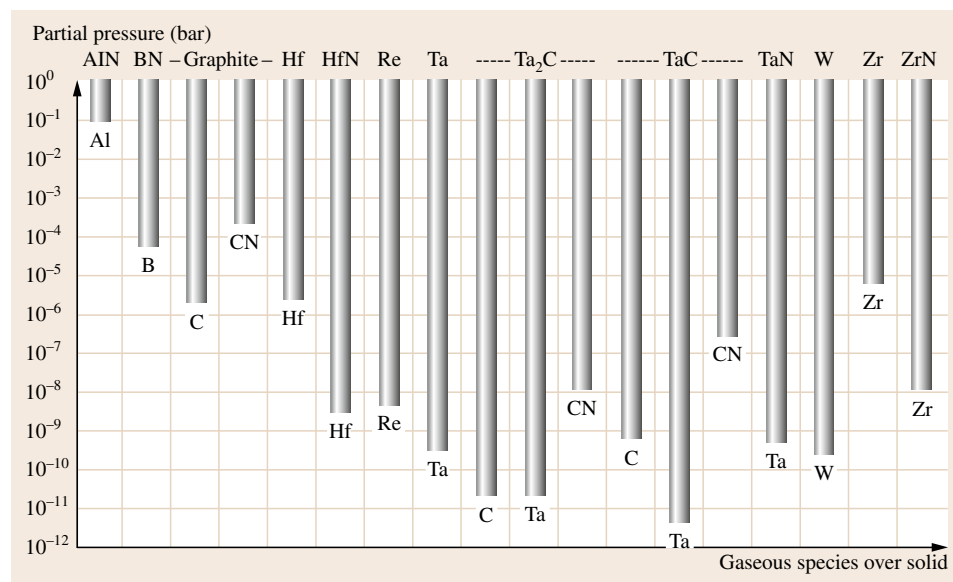


Fig. 24.6 Possible crucible contaminants: partial pressures present over solid crucible materials at 2300 °C in 1 atm nitrogen (after [24.34], with permission)

et al. [24.40] studied the reaction kinetics of Ta carburization, showing that the diffusion-controlled phase transformation follows the sequence $\text{Ta} \rightarrow \text{Ta}_2\text{C} \rightarrow \text{TaC}_{1-x}$. Incomplete carburization led to a mechanically stable layered structure of different phases, with Ta_2C at the center and TaC at the surface. When the car-

burization was allowed to proceed completely to TaC, grain coarsening and anisotropic lattice expansion of the polycrystalline material led to cracking along grain boundaries, rendering fully carburized crucibles unsuitable for PVT growth. Further evaluation of other inert, high-temperature materials may prove fruitful.

24.3 Self-Seeded Growth of AlN Bulk Crystals

Edgar et al. [24.17] reported on AlN crystal growth by sublimation in resistively heated furnaces with W or graphite heating elements. AlN needles and platelets freely nucleated from AlN source material in the cold zone of BN crucibles. Source temperatures were varied from 2000 to 2200 °C and reactor nitrogen pressures ranged from 300 to 800 Torr. Crystals grown in a furnace with W heating elements were either colorless or amber in color, while those grown in a furnace with a graphite heater were colorless. Observed morphologies included needles up to 4 mm in length and 0.5 mm in diameter, and thin plates. The plates were as large as 60 mm² and contained growth striations running the length of the crystals along the *c*-direction. These striations appear to be characteristic of crystals grown in BN environments. They are not seen in AlN grown in other types of crucibles [24.17,33].

AlN boules up to 10 mm in diameter were produced at Crystal IS [24.41] in conical crucibles. No seed crystals were used in the growth process and, typically, several nuclei formed on the crucible walls during the early stages of growth. As the crystal grew, growth competition between different nuclei resulted in single-crystal regions of varying sizes and orientations. A driving rate for growth was set by translation of the crucible relative to the thermal gradient in the reactor. Under adequate growth conditions (e.g., thermal gradient, reactor pressure) the crystal growth rate was equal to the driving rate, which was varied between 0.65 and 0.9 mm/h. Atomic force microscopy (AFM) imaging of the as-grown crystals revealed 0.25 nm high monolayer steps with straight segments. Step flow resulted from screw dislocations intersecting the growing surface. Screw dislocation density was estimated at $5 \times 10^4 \text{ cm}^{-2}$.

Wafering of these boules revealed several large grains and polycrystalline regions, or single-crystalline regions exhibiting severe cracking around the periphery [24.15,42,43]. Chemomechanical polishing (CMP) was used to obtain surfaces suitable for epitaxial growth. Final etching of vicinal surfaces in a mixture of

phosphoric and sulfuric acids or potassium hydroxide solution revealed that the N-terminated face was etched much faster and was rougher than the Al-terminated face.

More recently, growth of single-crystal boules up to 15 mm in diameter and several centimeters in length was reported [24.44]. These were used to prepare 0.5 mm thick wafers which were polished by CMP. Wafers exhibited some color variation, which was attributed to absorption by nitrogen vacancies, but were free of cracks. Synchrotron white-beam x-ray topography (SWBXT) was used to characterize the wafers' defect content. Contrast arising from surface damage was observed near the edges, probably due to imperfect polishing, while a high density of small inclusions was observed near the center. Typical dislocation densities were in the 800–5000 cm⁻² range; dislocations were distributed inhomogeneously, with higher concentrations near the wafer edge. Narrow x-ray rocking curve widths attested to the high quality of the material obtained.

Schlessner et al. [24.32] and Schlessner and Sitar [24.16] reported on growth of AlN by vaporization of metallic Al in a nitrogen atmosphere and by sublimation of an AlN source [24.32,45]. Growth temperatures ranged from 1800 °C to 2300 °C at reactor pressures of 250–750 Torr. Temperature gradients of 10–100 K/cm between the source material and crystal growth region were employed. In Al vaporization experiments, the crystal shape and fastest growth direction was found to depend strongly on the growth temperature: at relatively low temperatures (1800–1900 °C) long needles were grown, temperatures around 1900–2000 °C yielded twinned platelets, while *c*-platelets were formed at temperatures above 2100 °C. These *c*-plates grew at a rate of 5 mm/h in the *c*-plane and 0.2 mm/h along the *c*-axis. Vaporization experiments were performed for 2 h each at a constant growth temperature. Longer growth times did not yield substantially larger crystals. The observed slowdown in growth rate with time was attributed to a decreasing Al flux from the Al source over

time, which was due to the progressive formation of an Al-rich, polycrystalline AlN coating over the molten Al.

In order to overcome problems with the Al source instability in vaporization experiments, crystals were grown for longer periods of time by subliming AlN source material [24.32]. Sublimation yielded a stable Al flux over several days of growth. Experiments were carried out at higher temperatures of 2200–2300 °C in order to obtain vapor pressures of Al above AlN comparable with those above metallic Al in the vaporization experiments. Transparent AlN single crystals with dimensions as large as 13 mm were grown with growth rates exceeding 500 $\mu\text{m}/\text{h}$. These sublimation experiments were performed in BN crucibles and typically yielded fastest growth along the c -axis and crystals with surface striations along the c -direction, similar to those observed by Edgar et al. [24.33].

The natural growth habit of AlN bulk crystals was investigated by Epelbaum et al. [24.46]. Crystals were grown in the 2050–2250 °C temperature range using a low temperature gradient of 3–5 K/cm, intended to facilitate free nucleation of separate single crystals under conditions enhancing formation of natural crystal habit planes. A distinct dependence of morphology on growth temperature was observed: crystals grown at 2050 °C were nearly transparent six-sided prismatic

needles, 0.1–0.3 mm in diameter and 5–15 mm in length; columnar crystals 3 mm in length and 1.5 mm in diameter characterized primarily by $\{10\bar{1}1\}$ and $\{10\bar{1}2\}$ rhombohedral facets were grown at 2150 °C; finally, thick platelets of dark amber or brownish color grew at 2250 °C. The largest of these latter crystals was approximately $14 \times 7 \times 2 \text{ mm}^3$ (Fig. 24.7). Their morphology, orientation, and polarity was studied in greater detail. X-ray diffraction was used to index individual facets and their polarity was confirmed by etching in a molten KOH/NaOH eutectic at 250 °C for 3 min. The Al-polar (0001) and positive rhombohedral faces were characterized by mirror-like facets and transparent material of high crystalline quality, while the N-polar c -plane face contained micrometer-sized inclusions and was opaque. Since these freestanding crystals were grown under approximately isothermal conditions, they possessed a zonal structure corresponding to the simultaneous growth on multiple facets. Examination of polished cuts prepared from them revealed that the zones all belonged to the same single crystal, but exhibited different coloration, etching response, and optical properties (see the discussion in Sect. 24.5.2). Structural, optical, thermal, elemental, and electrical characterization results on single crystals and polycrystalline AlN boules were also reported [24.47–49].

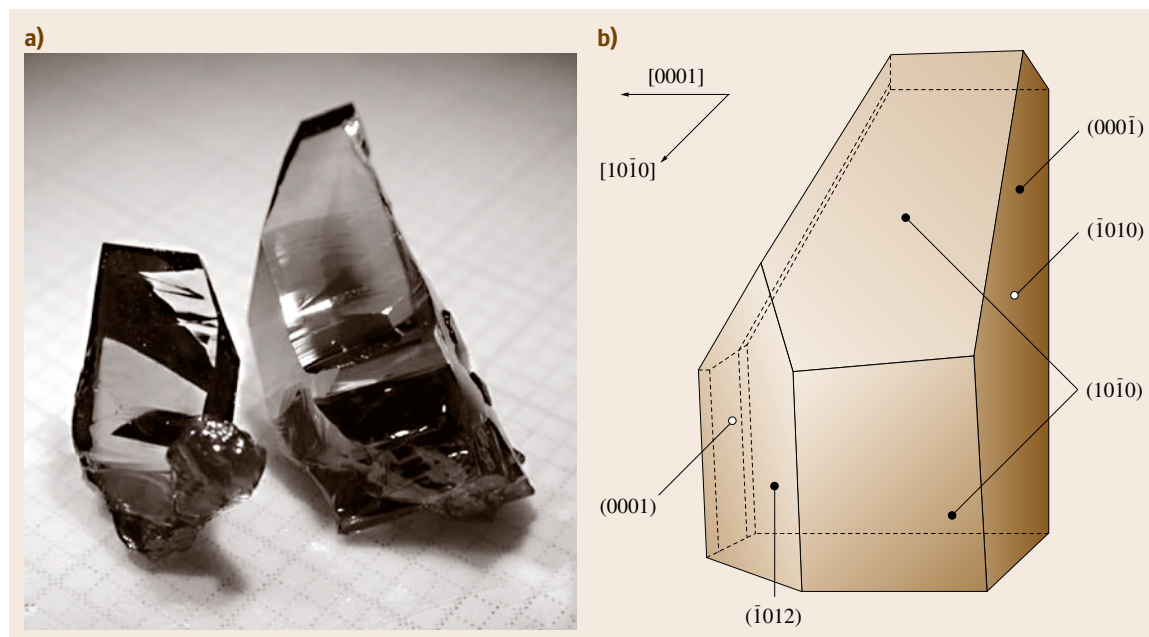


Fig. 24.7 (a) Selected crystals grown by spontaneous nucleation at 2250 °C showing typical growth habit (millimeter grid) and (b) characteristic growth faces of best formed AlN platelets (after [24.46], with permission of Elsevier)

24.4 Seeded Growth of AlN Bulk Crystals

Seeded growth of AlN on SiC has been studied as a way to exploit the availability of large, high-quality SiC substrates and to control the polarity and orientation of AlN crystals [24.50]. Due to the high process temperatures involved and the difference in thermal expansion between AlN and SiC, the stability of the SiC seeds and the cracking of the AlN layers are important issues that need to be addressed in establishing a reproducible seeded growth process on SiC. In contrast, seeded growth on recently available AlN native seeds eliminates many of the problems associated with heteroepitaxial growth, but is only beginning to be investigated. Techniques to avoid renucleation and maintain stable growth have been developed and led to considerable single-crystal size expansion [24.51, 52]. However, several questions, such as which orientation is most favorable for growth, still need to be addressed.

24.4.1 Growth on SiC Seeds

The growth of AlN crystals seeded on SiC substrates was first reported by Balkas et al. [24.36]. Single-crystal platelets were grown in a resistively heated graphite furnace by PVT. Growth temperature was varied from 1900°C to 2250°C. SiC-coated graphite crucibles were used in 10–15 h experiments. The source material was 99% dense sintered AlN, chosen to allow controllable source-to-seed separation, which was crucial for good crystal growth. Optimal separation was found to be between 1 and 5 mm. Single-crystal 6H-SiC(0001) substrates 10×10 mm² were used as seeds. Growth in a high temperature range (2100–2250°C) and a low temperature range (1950–2050°C) was investigated. Single crystals of ≈1 mm thickness that covered the entire SiC seed were grown at 2150°C and 4 mm separation distance. The growth rate was estimated at 0.5 mm/h. Due to the degradation of the SiC substrates at higher temperatures, isolated nucleation sites were formed on the seeds at temperatures above 2150°C, and 2×2 mm² hexagonal AlN crystals were grown. The crystals were colored from green to blue, indicating the incorporation of impurities. Secondary-ion mass spectrometry (SIMS) analysis confirmed the presence of Si and C in these crystals. Crystals grown in the low-temperature range were colorless and transparent, but growth rates were significantly lower, 30–50 μm/h. Cracking was always observed in as-grown crystals, due to the thermal ex-

pansion coefficient mismatch between SiC and AlN. X-ray diffraction (XRD) patterns confirmed the single-crystal nature of all crystals. Bright-field plan-view transmission-electron microscopy (TEM) and associated selected-area diffraction (SAD) indicated the high quality of the single crystals.

The growth of AlN crystals by sublimation on 6H-SiC seeds was more extensively investigated by Edgar et al. [24.17], Shi et al. [24.53–55], and Liu et al. [24.56–58]. Experiments were carried out in tungsten crucibles placed within the axial temperature gradient of a resistively heated furnace. The growth temperature was typically 1800°C. SiC wafers (on-axis and 3.5° off-axis) with silicon and carbon terminations were used as substrates. Direct growth [24.53] on as-received Si-terminated SiC resulted in the formation of discontinuous hexagonal subgrains of 1 mm² average size. No growth was observed on C-terminated as-received SiC. In order to promote two-dimensional growth on Si-terminated substrates, a 2 μm thick AlN buffer layer was deposited by metalorganic chemical vapor deposition (MOCVD). Continuous growth was achieved by the use of the buffer layer, although cracks formed during cool-down due to stress resulting from the thermal expansion coefficient mismatch. AFM images indicated that AlN grew by the step-flow growth mode.

The initial stages of AlN growth on SiC were studied by Liu et al. [24.58]. Fifteen minute growth runs were performed on as-received, on-axis, Si-terminated 6H-SiC(0001) substrates under various temperature and pressure conditions. During the initial stages of growth, AlN nucleated as individual hexagonal hillocks and platelets in an island-like growth mode. Nuclei size and density increased at constant pressure with increased growth temperature in the range of 1800–1900°C. At constant temperature, growth under reduced pressures yielded coalesced, irregularly shaped platelet crystals. Scanning Auger microprobe (SAM) measurements indicated varying relative compositions of Al, N, Si, and C on different crystal facets of the AlN nuclei. The surface morphology and stress in AlN crystals grown on SiC substrates were also characterized [24.56, 57]. AFM images revealed scratches and steps on as-received 6H-SiC substrates, which served as nucleation sites for individual AlN grains grown in a three-dimensional mode. On SiC substrates with an AlN MOCVD epilayer, however, AlN deposited in a two-dimensional growth mode without island formation. Surface mor-

phology varied across the sample, from flat surfaces to regions with large steps (120 nm) separated by large terraces (up to 5 μm). Root-mean-square (RMS) roughness for samples grown with an AlN epilayer was less than 5 nm, compared with 40 nm for crystals grown on as-received substrates. Stress-induced cracks were always observed in the AlN crystals. It was predicted [24.59] that AlN grown on 6H-SiC should be at least 2 mm thick in order to avoid cracking during cool-down from a growth temperature of 2000 °C. Raman spectroscopy revealed that crystals were under compressive stress at the surface and tensile stress (1 GPa) at the interface. Raman spectra indicated improved crystal quality with increasing AlN thickness.

The above method was modified in order to reduce cracking of AlN [24.54, 55]. After deposition of the MOCVD AlN epilayer, an $\text{AlN}_{0.8}\text{SiC}_{0.2}$ alloy layer was deposited by sublimation from a source mixture of AlN–SiC powders. Pure AlN was then sublimed on the alloy seed as above. The intermediate properties of the alloy layer helped reduce cracking in the overgrown AlN. In addition, the SiC powder source decreased the degradation of the SiC substrates during sublimation growth, allowing for longer growth times. Single-crystal AlN, $4 \times 6 \times 0.5 \text{ mm}^3$, was obtained after 100 h of growth. Characterization by XRD and Raman spectroscopy confirmed the high quality of the grown material. Thus, three problems identified with growth of AlN on SiC seeds were addressed by this method: (1) the presence of Si and C in the vapor

helped suppress the decomposition at high temperature of the SiC seed, (2) an AlN epilayer promoted two-dimensional growth, and (3) cracking of the AlN bulk layer was greatly reduced by an AlN–SiC alloy interlayer.

Dalmau et al. [24.50, 61] developed a two-step process for deposition of thick AlN layers on SiC, and for reduction of cracks in the grown layers. AlN layers up to 3 mm thick were grown on on-axis and off-axis, (0001)-oriented, Si-face SiC seeds by PVT from an AlN powder source. During the growth, the SiC seeds were gradually decomposed at high temperature, yielding freestanding AlN crystals up to 25 mm in diameter. In other samples, the AlN was delaminated from the SiC seeds. As-grown surfaces of layers grown on on-axis SiC seeds were characterized by sharp hexagonal hillocks, suggesting a dislocation-mediated island growth mode, while layers grown on off-axis seeds exhibited steps aligned perpendicular to the off-axis direction, characteristic of the step-flow growth. Crack-free AlN crystals were obtained from these layers and used to fabricate AlN wafers, as shown in Fig. 24.8. High-resolution rocking curves and reciprocal space maps of the (0002) reflection showed that the full-width at half-maximum intensity (FWHM) ranged from 282 to 1440 arcsec, indicating a tilt distribution in the grown layers caused by strain and/or the formation of low-angle grain boundaries as the AlN coalesced [24.60, 62]; nevertheless, these values were comparable to or better than those of the SiC seeds used in these experiments. SWBXT indicated that some strain-free crystals

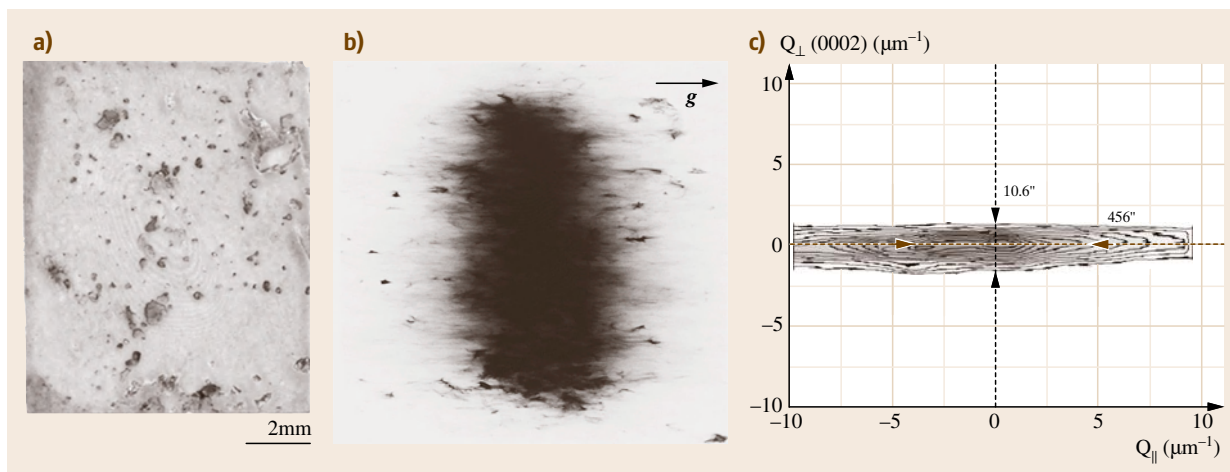


Fig. 24.8 (a) Bulk AlN crystal grown by gradually decomposing the SiC substrate; (b) transmission topograph ($g = [20\bar{2}1]$) showing inhomogeneous strain and high dislocation density; (c) reciprocal space map showing very low triple-axis ω – 2θ scan width (10.6 arcsec) (after [24.60], with permission of Trans Tech)

were obtained, but in all samples the density of dislocations was significantly higher ($> 10^6 \text{ cm}^{-2}$) than in self-seeded AlN crystals. Elemental characterization showed impurity concentrations comparable to those found in the AlN source powder (300 ppmw C and 200 ppmw Si), indicating negligible incorporation of C and Si during growth; the low triple axis ω - 2θ scan widths typically observed (≈ 11 arcsec) were characteristic of high-purity crystals and consistent with these results.

In other efforts, Sarney et al. [24.63] grew bulk AlN on on-axis and 3.5° off-axis, c -oriented 6H-SiC seeds. Sublimation from an AlN powder source in N_2 atmosphere was performed in the temperature range 2150 – 2200°C with 4 mm separation between the source and seed. The AlN grew well aligned with the substrate. As in previous work [24.36], cracks were observed in the AlN. Epelbaum et al. [24.64] studied AlN crystal growth on SiC substrates of different orientations. Layers of 200 – $500 \mu\text{m}$ thickness were deposited at seed temperatures around 2000°C in 350 mbar N_2 pressure. Growth on Si-face, c -oriented substrates was characterized by many hexagonal hillocks on the surface. In contrast, 10° off-axis and on-axis, a -plane substrates resulted in more stable growth. The smoothest morphology, typical of step-flow growth, was obtained with on-axis, a -plane substrates, however, cracks were also observed in the AlN layers. Epelbaum et al. [24.65] and Heimann et al. [24.66] suggested a possible vapor-liquid-solid mechanism, mediated by the presence of a molten AlOC_x layer on the surface of SiC, during seeded growth on SiC. Finally, successful seeded growth on C -face SiC was reported recently [24.67,68].

24.4.2 Growth on AlN Seeds

Reports on AlN growth on native seeds are limited, as these seeds have only recently become available. Seeded growth of AlN on native seeds by PVT was reported for the first time by Schlessner et al. [24.45]. Transparent, single-crystal c -platelets prepared by vaporization of Al in N_2 were used as seeds. They were mounted into the top of a BN growth crucible filled with AlN source material. Growth was carried out at 2200°C with a temperature gradient between the source and seed of approximately 3 K/mm . A small seed, 4 mm tall and 0.5 mm thick, grew over a total of 34 h into a 5 mm tall and 7 mm wide single crystal. Growth rates were highly anisotropic, with the fastest growth direction along the c -axis. Also, growth rates on the two c -faces of opposite polarity differed by a factor of 2–3, with the Al polarity showing slower and smoother growth. Crystal quality of the grown crystals was characterized by XRD. X-ray rocking curves around the (0002) reflection varied from 25 to 45 arcsec, indicating very high single-crystal quality of the material grown by seeded growth.

Noveski et al. [24.51,69] demonstrated a process for continuous growth of AlN on previously deposited material, resulting in significant expansion of single-crystal grains. Growth was performed in a radiofrequency (RF)-heated reactor at temperatures between 2050 and 2150°C and pressures of 450 – 500 Torr, yielding growth rates in the range of 0.1 to 0.3 mm/h . In this process, a starting layer of coalesced polycrystalline AlN was grown into boules up to 38 mm in length and 32 mm in diameter over the course of

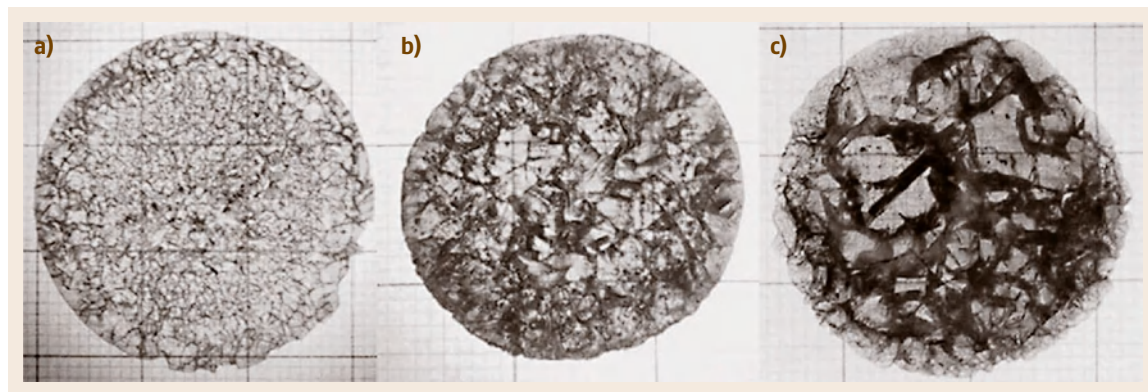


Fig. 24.9a–c Grain evolution observed in different cross-sections of a boule with a diameter of 32 mm: 0.5 mm thick slice, cut after the first 1 mm of growth (a); 1 mm thick slice cut at 22 mm boule length (b); 2 mm thick slice cut at 35 mm boule length, showing centimeter-size grains (c) (after [24.51])

several growth runs. Sublimation growth from a presintered AlN source was interrupted several times in order to replenish the source and keep the source-to-seed distance constant. Renucleation of AlN on the previous growth front after exposure of the boules to air was suppressed by using the inverted temperature gradient method. During the early stages of each run, the crystal growth region was maintained in an inverted temperature gradient, effectively desorbing surface contamination and part of the previously grown layer. In this manner, continuous expansion of previously formed single-crystalline grains was achieved (Fig. 24.9). Centimeter-sized, single-crystal grains were observed in polished cross-sections of boules, and epitaxial regrowth was demonstrated regardless of the orientation of individual grains.

In order to overcome problems associated with the formation of cracks in these polycrystalline boules, large single-crystal grains were harvested and used to prepare seeds for subsequent seeded growth [24.52, 70]. To ensure epitaxial regrowth, seeds were etched in a phosphoric and sulfuric acid mixture, followed by dilute hydrofluoric acid, prior to loading into the system, and were maintained in an inverted temperature gradient during the ramp to the growth temperature. Crystal growth was performed in an axial temperature gradient of 5–10 °C/cm, maintaining the source temperature at 2200–2250 °C and reactor pressure at 400–900 Torr. A (41 $\bar{5}$ 0)-oriented seed was expanded from 10 to 18 mm after several consecutive growth runs, representing a 45° crystal expansion angle (Fig. 24.10).

In related work, Herro et al. [24.71, 72] investigated seeded growth along the {0001} polar directions. {0001}-Oriented AlN single crystals were successfully

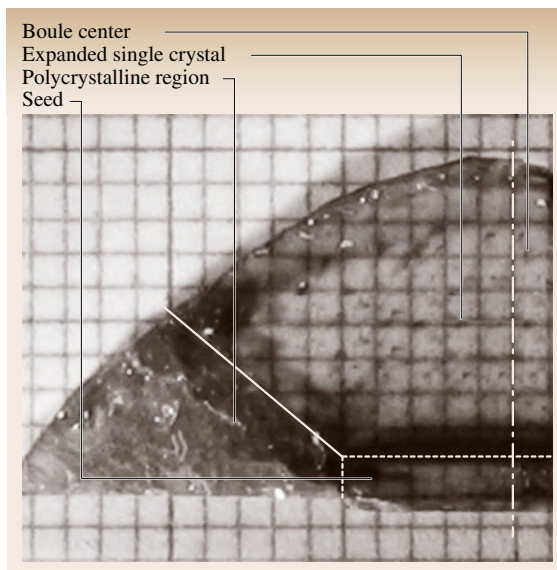


Fig. 24.10 Longitudinal cut of a crystal boule after several growth runs showing the crystal expansion angle (millimeter grid) (after [24.70])

grown along both polar directions, but more stable growth results were obtained on N-polar seeds. The growth surface of N-polar crystals was controlled by a single growth center, leading to a mirror-like growth facet. In contrast, the surfaces of crystals grown on Al-polar seeds showed numerous growth centers, leading to a deterioration of crystal quality, even though the same growth parameters were used for both types of seeds. These observations suggest that lower supersaturation is required to obtain stable growth in the Al-polar direction.

24.5 Characterization of High-Quality Bulk Crystals

As the size of AlN single crystals continues to increase, several characterization techniques are being used to assess the structural and optical properties of large bulk crystals, as well as to determine impurity incorporation, so that the concentration of extended defects and adverse growth contaminants may be minimized by adjusting the growth conditions. Availability of large, strain-free, high-quality bulk crystals has allowed investigators to study the fundamental properties of this material in more detail than has previously been possible with AlN ceramics or thin films. Recent exper-

imental findings have been used to confirm theoretical predictions about the band structure of AlN, leading to revised values for the fundamental bandgap.

24.5.1 Structural Properties

The equilibrium crystal structure (α -phase) of the III-nitrides, AlN, GaN, and InN, is the wurtzite (2H) structure. The stacking sequence of the (0001) close-packed wurtzite planes is ABAB... , comprising bilayer sheets of nitrogen and III-metal atoms; this structure

consists of two interpenetrating sublattices that contain the nitrogen and III-metal atoms in tetrahedral coordination. The space group of the wurtzite nitrides is $P6_3mc$, the same as that of the hexagonal (4H and 6H) polytypes of SiC.

X-ray diffraction topography is used to study a crystal's internal diffracting planes in order to discern local changes in the spacing and relative rotation of the planes [24.74]. X-ray topographs, two-dimensional projections of the distribution of diffracted intensity as a function of position in the sample, can be used to map defect structures in large, nearly perfect single crystals and to identify the crystallographic orientations of the diffracting planes. Images are produced by scattering a low-divergence area-filling beam from a set of Bragg planes onto a two-dimensional detector, typically high-resolution x-ray film. In addition, high-resolution x-ray diffraction (HRXRD) is also commonly employed to provide information about the orientation and perfection of single crystals. This technique can be used to generate a reciprocal space map (RSM) representing the two-dimensional intensity contour of the diffracted intensity about a given lattice reflection. These maps provide much more information than typical x-ray rocking curves, since the distribution of lattice tilts (i. e., orientations) and lattice dilations (i. e., d -spacings) can be read independently from the RSM. The lattice dilation distribution is correlated with the concentration

of point defects (e.g., vacancies or impurities) in the sampled crystal volume.

SWBXT studies of self-seeded crystals grown by sublimation of AlN powder revealed crystals to be virtually dislocation free [24.37, 60, 73, 75]. Overall dislocation densities were estimated to be around 10^3 cm^{-2} . Defects such as inclusions, growth sector boundaries, and growth dislocations were detected. The presence of Pendellösung fringes in the topographs (Fig. 24.11) was indicative of the high crystalline perfection attained in several samples. Triple-axis x-ray rocking curve **FWHM** of ω - 2θ scans of several large crystals ($\approx 10 \text{ mm}$) were as low as 7.2 arcsec, marginally larger than the theoretical limit of 6 arcsec, indicating a low density of point defects in these samples.

Characterization results reported for bulk single crystals grown at Crystal **IS** demonstrated that crystals were of high quality. X-ray topographs of an unevenly shaped polished wafer [24.76], approximately $7 \times 9 \text{ mm}^2$ in size, indicated no significant strain in the wafer and showed an overall dislocation density of $800\text{--}1000 \text{ cm}^{-2}$. The density of detected inclusions (presumably oxygen related) was on the order of 10^5 cm^{-3} . **FWHM** of high-resolution rocking curves ranged from 9 to 12 arcsec, indicating very good crystalline quality. The edge of the wafer in contact with the crucible wall contained cracks and slip bands, probably due to the thermal expansion mismatch between

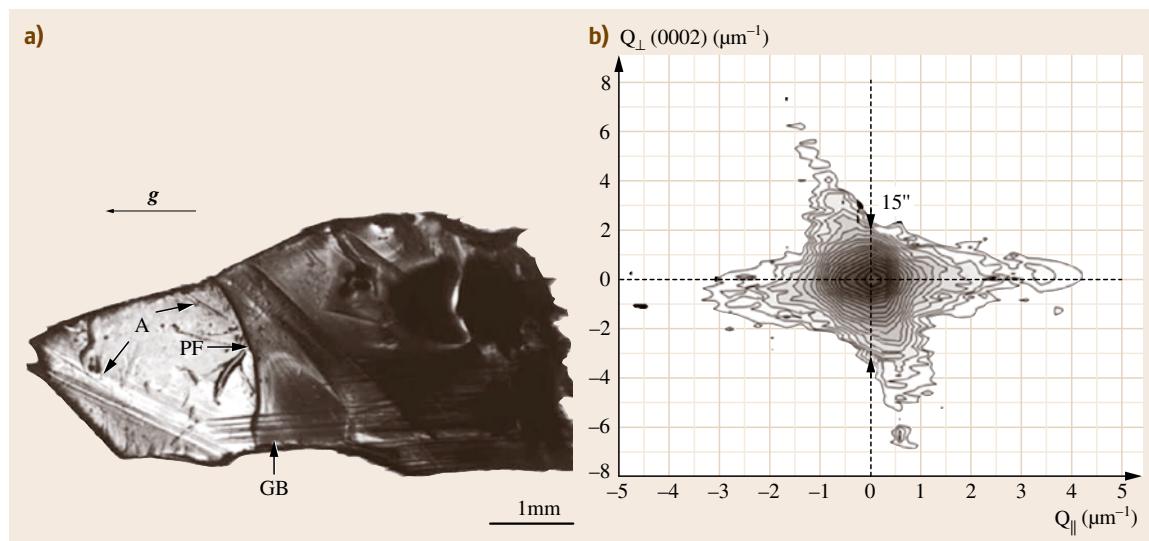


Fig. 24.11 (a) Transmission x-ray topograph ($g = [\bar{1}\bar{1}20]$, $\lambda = 0.54 \text{ \AA}$) from a dislocation-free, spontaneously nucleated AlN single crystal (A – surface artifacts, GB – growth bands, PF – pendellösung fringes); (b) (0002) reciprocal space map (triple-axis ω - 2θ scan width: 15 arcsec) (after [24.73], with permission)

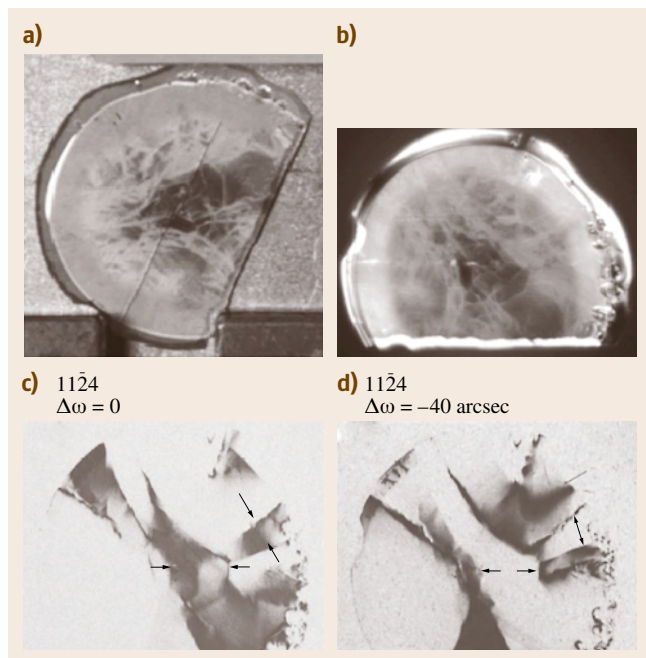


Fig. 24.12 (a) Optical image of an AlN substrate. The length of the flat is 22 mm. (b) The same substrate taken through crossed polarizers. (c,d) Two x-ray topography images of the same substrate taken at an angular distance of 40 arcsec. Small-angle grain boundaries are shown (black arrows). $\Delta\omega = 0$ refers to the maximum of the rocking curve. The picture at the right shows the intensity observed at 40 arcsec from the maximum of the rocking curve. Now the areas adjacent to the original black arrows show stronger diffraction intensity. The misalignment between these areas is small, on the order of 40 arcsec (after [24.77], with permission of Wiley-VCH)

the boule and crucible. Figure 24.12 shows a picture of a polished AlN substrate with a flat width of 22 mm, an image of the same substrate taken through crossed polarizers, and x-ray topography images taken at two different rocking angles [24.77]. X-ray topographs revealed the presence of small-angle grain boundaries throughout the wafer and individual dislocations at the wafer edge. No diffraction was observed from inclusions that were optically visible. The nature of these inclusions was not discussed.

Defects in polished AlN wafers were studied by XRD, optical microscopy, etch pit pattern delineation, and AFM [24.78]. A triple-axis rocking curve with a FWHM of 10 arcsec was reported. Figure 24.13 shows an optical image of an AlN surface where chemical etching was used to reveal dislocations (viewed as single dots) and slip bands (viewed as straight lines). These



Fig. 24.13 Nomarski image of prismatic slip bands as seen on on-axis oriented AlN after chemical etching (after [24.78], with permission)

slip bands were oriented parallel to the $\{1\bar{1}00\}$ directions, demonstrating the activation of prismatic glide in AlN single crystals. The density and shape of etch pits in chemically etched AlN were also studied. Etch pit densities for c -plane wafers varied from 1×10^3 to $3 \times 10^4 \text{ cm}^{-2}$, while etch pit patterns were used to distinguish between screw and edge dislocations. In addition, it was shown how subgrain boundaries may propagate as cracks into another grain. Also, etch pits on $\{1\bar{1}00\}$ prismatic planes were reported for the first time; the etch pit density was higher than on basal planes, averaging from 6×10^4 to $4 \times 10^5 \text{ cm}^{-2}$. AFM images of Al-polar, c -plane, epitaxially substrate surfaces prepared by CMP revealed atomic-level steps for near-on-axis substrates and for off-axis orientations up to 6° off-axis [24.79]. RMS roughness of $5 \times 5 \mu\text{m}^2$ scans was as low as 2.15 \AA . The presence of shallow pits, whose density decreased with increasing off-axis orientation, was observed on these Al-polar c -plane samples. However, the origin of the pits is still not well understood, but may be related to the polishing process. These pits were not observed in AFM scans of substrates with nonpolar orientations.

AFM studies [24.72] of Al- and N-polar c -plane AlN surfaces, obtained by seeded growth on AlN seeds, showed a significant difference in the step-and-terrace structures observed on the two different polar surfaces (Fig. 24.14). Single-unit-cell-high steps were observed on both surfaces, but the terrace width on N-polar AlN, 200–250 nm, was much larger than that observed on Al-polar AlN, 50–70 nm. Since seeded growth was

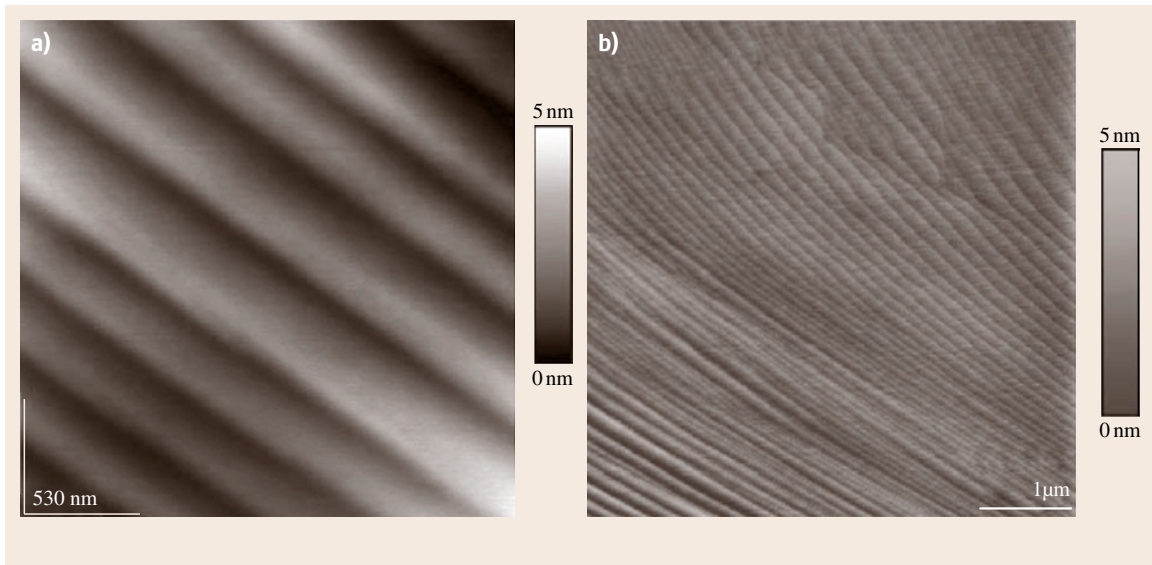


Fig. 24.14a,b AFM micrographs taken on as-grown AlN surfaces: (a) N-polar orientation; (b) Al-polar orientation. In both cases, single-unit-cell-high steps were observed (after [24.72], with permission)

performed on seeds of both polarities using the same growth conditions, thus ensuring equal supersaturations of Al vapor, these differences were attributed to the surface energy difference of the N- and Al-polar facets.

24.5.2 Fundamental Optical Properties of AlN

AlN has a direct bandgap at the center (Γ -point) of the Brillouin zone exceeding 6 eV. In general, there are still many details concerning the band structure and optical properties of AlN that require further investigation. For example, the band structure parameters near the Γ -point and the fundamental optical transitions were until very recently not well known. In the past, measurements of the bandgap have been performed by optical absorption [24.80–82] and ellipsometry [24.83]. Variations in the measured values were likely due to differences in crystal quality (e.g., impurity and defect concentrations). The room-temperature value commonly quoted in the literature was 6.2 eV. Band-edge luminescence has been investigated using cathodoluminescence (CL) [24.84] and photoluminescence (PL) [24.85].

Recently, though, measurements on high-quality bulk crystals have provided a more complete picture of the band structure. The conduction band has a sin-

gle minimum (Γ_{7c}) at the Γ -point. The valence band, on the other hand, is split at the Γ -point by the crystal field and the spin-orbit interaction. According to calculations [24.86], the spin-orbit splitting ranges from 11 to 20 meV. The crystal field splitting at the top of the valence band in AlN was predicted [24.87, 88] to be negative, in contrast to the other III-nitrides, but calculated values have ranged widely. However, this information gives a qualitative picture of the valence-band ordering at the Γ -point, and of the associated intrinsic free-exciton transitions. In order of increasing transition energies, these are Γ_{7v} (upper, A-exciton), Γ_{9v} (B-exciton), and Γ_{7v} (lower, C-exciton). The square of the dipole transition matrix elements between the conduction band and the three Γ -point valence states calculated by Li et al. [24.89] indicated that the A-exciton transition is nearly forbidden for light polarized perpendicular (\perp) to the wurtzite c -axis, while the B- and C-exciton transitions are nearly forbidden for light polarized parallel (\parallel) to the c -axis. This picture has recently been confirmed by Li et al. [24.89] and optical reflectivity measurements [24.7, 90] (Figs. 24.15 and 24.16) which have provided experimental values for the exciton resonances, the crystal field splitting parameter, and the fundamental bandgap of AlN. The fundamental bandgap energy of unstrained AlN was determined by Chen et al. [24.7] to be 6.096 eV at 1.7 K, while the crystal field splitting parameter was -230 meV and

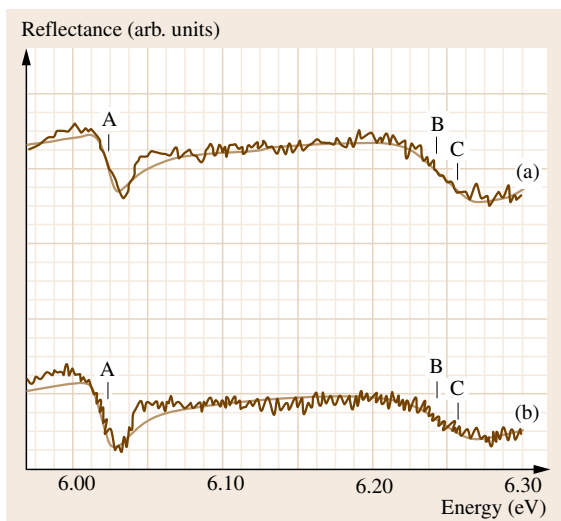


Fig. 24.15 Low-temperature partially polarized optical reflectance spectra from the *m*-face of a bulk AlN crystal with the *c*-axis parallel to the spectrometer slits (*graph a*) and the *c*-axis perpendicular to the slits (*graph b*). *Solid lines* are theoretical fits to the spectra. The bottom of the graph is a (different) finite signal level in each case, to show the features more clearly (after [24.7], with permission of AIP)

the exciton energies were 6.025, 6.243, and 6.257 eV for the A-, B-, and C-excitons, respectively. Note that the A transition is allowed for light polarized parallel to the *c*-axis. This may explain why earlier absorption measurements consistently resulted in larger values for the bandgap; these measurements were typically performed with light polarized perpendicular to the *c*-axis, and likely probed the B- or C-transitions. These results imply that (0001)-oriented devices grown with AlN or high-Al-content AlGaN alloys will be better edge emitters than surface emitters, and other orientations should be investigated for surface-emitting devices [24.7].

In other studies, the crystalline quality and orientation of a sample oriented with the *c*-axis in the plane of the crystal were evaluated by testing the selection rules for the $A_1(\text{TO})$, $E_1(\text{TO})$, and $E_2(\text{high})$ Raman modes [24.91, 92]. In the $x(\text{zz})x$ geometry, the allowed $A_1(\text{TO})$ and $E_1(\text{TO})$ modes were observed and the forbidden $E_2(\text{high})$ mode was not, while in the $x(\text{zy})x$ geometry, the $A_1(\text{TO})$ mode was suppressed and the $E_1(\text{TO})$ mode was enhanced, confirming the crystal's orientation and high crystalline quality. The superposition of different Raman modes and the presence of

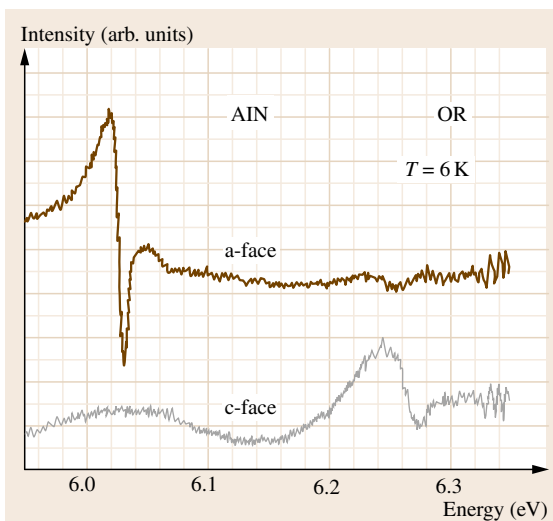


Fig. 24.16 Low-temperature optical reflectivity data at near-normal incidence for AlN samples oriented in two different crystallographic orientations (after [24.90], with permission of APS)

quasi-LO modes was observed in the spectra of a randomly oriented sample.

The dependence of phonon spectra on crystal orientation was also observed by Bickermann et al. [24.93]. Raman spectra of optical phonons in AlN were taken in backscattering geometry on different well-developed facets of a self-seeded bulk crystal (such as that shown in Fig. 24.7). The results indicated that facets belonging to the same crystal class showed very similar Raman spectra, while the appearance or absence of the $A_1(\text{LO})$, $A_1(\text{TO})$, $E_1(\text{LO})$, and $E_1(\text{TO})$ phonon bands in the spectra could be used to identify the basal *c*-plane facets unambiguously from the prismatic $\{10\bar{1}0\}$ facets (Fig. 24.17). *c*-Plane facets showed, in addition to the E_2 modes, only the $A_1(\text{LO})$ and $E_1(\text{TO})$ bands, while prismatic facets showed the $A_1(\text{TO})$ and both $E_1(\text{LO})$ and $E_1(\text{TO})$ bands. When facets with crystallographic orientations between the basal and prismatic planes were studied, i.e., rhombohedral facets, features corresponding to quasi-LO and quasi-TO phonons with mixed A_1 – E_1 symmetry appeared in the spectra.

The zonal dependence of the optical absorption and CL spectra of self-seeded crystals was also investigated [24.94]. Crystals exhibiting natural crystal habits of AlN with well-developed facets [24.46] were selected, cut in different orientations, and polished on both sides. The resulting samples included a number of different zones, which corresponded to volumes of the

crystal grown on a different facet. Thus, differences in impurity incorporation and/or defect formation, as reflected in the optical spectra, were correlated to growth on different facets or polar orientations of AlN. In the near-ultraviolet (near-UV) and visible range, Al-polar zones had the lowest absorption, followed by zones grown in the r - and a -directions, and finally by N-polar zones. These differences corresponded to differences in crystal coloration, with N-polar zones exhibiting the deepest amber coloration, which is primarily caused by a broad absorption band at 2.8 eV whose origin is still unclear but has in the past been assigned to nitrogen vacancies. In the mid-UV range, the peak position and intensity of the broad absorption bands observed varied depending on the zone. Zones grown on the Al-polar c -face exhibited a strong band at 4.6 eV, which was nearly absent in all other samples. Finally, in the 5.0–5.8 eV range, an increase in absorption was observed for zones grown in the c -direction regardless of polarity, while zones grown in r - or a -directions exhibited a local minimum; absorption in this range was attributed to nitrogen vacancies. The CL spectra of bulk crystals and polished cuts also showed intensity variations that were dependent on the investigated area. As shown in Fig. 24.18, r - and a -plane facets exhibited intense luminescence peaking at 3.8 eV, while this feature was absent on the Al-polar c -plane facet, where broad, weak bands at 2.5–2.8, 3.3, and 4.3 eV were present.

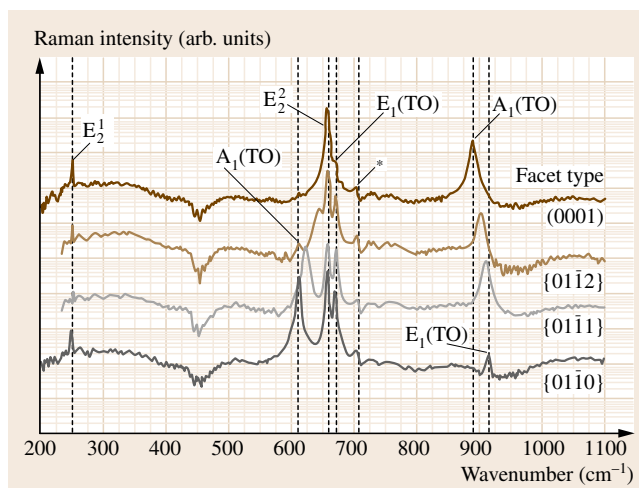


Fig. 24.17 Raman spectra taken in normal incidence on different facets of an AlN single crystal. A logarithmic intensity scale is used to show weak features. The symbols denote AlN phonon bands (after [24.93], with permission of AIP)

Optical transitions with energies in the 3–5 eV range are likely due to Al vacancies and their complexes with oxygen.

In other work, *Silveira et al.* [24.84, 95, 96] used CL to study self-seeded AlN crystals and homoepitaxial thin films of AlN grown on these crystals. Both

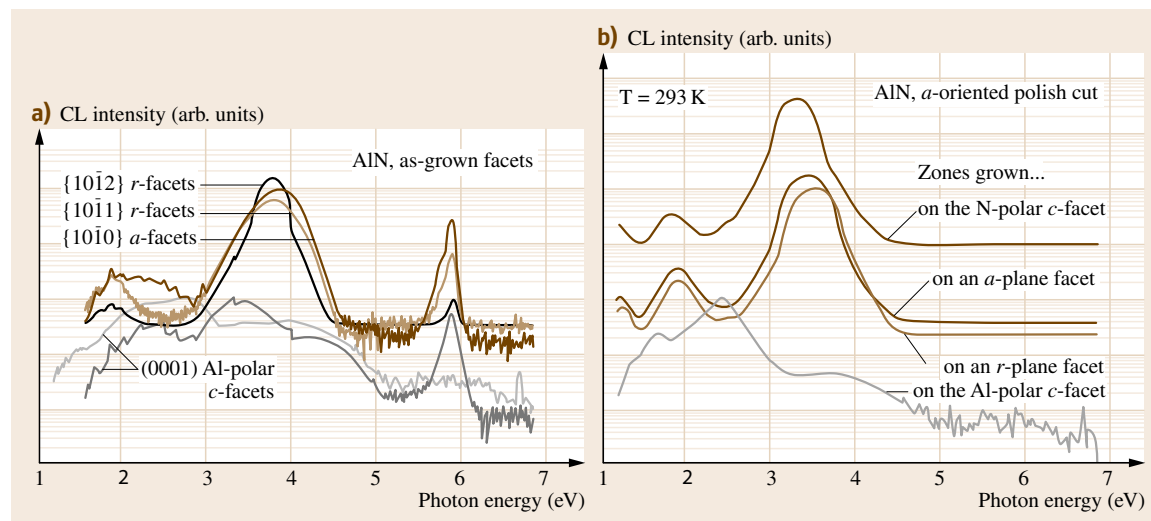


Fig. 24.18a,b Cathodoluminescence spectra of bulk AlN single crystals taken at room temperature. Logarithmic scale is used to show weak features; small jumps in the spectra (left) are measurement artifacts. (a) Spectra taken on different facet surfaces of an as-grown boule. (b) Spectra taken on different zones of an a -oriented polished cut (after [24.94], with permission of Wiley-VCH)

c-plane and *a*-plane wafers were cut from bulk crystals and polished by CMP. Strong emission was observed at the near-band-edge (NBE) region around 6 eV, and two additional bands were observed in the energy range between 2 and 5.5 eV. One of these bands (VB), at about 3.5 eV, was attributed to oxygen-related defects, while the second band (UVB), at about 4.4 eV, was tentatively assigned to oxygen-related complexes. The integrated intensity of the NBE emission showed a linear dependence with beam current up to 5 μ A, and this band was therefore related to exciton recombination processes. Analysis of the NBE CL spectrum of an *a*-plane sample revealed five transitions in this energy range. Based on the temperature dependence of the NBE spectra, features at 6.026 and 6.041 eV (6 K) were attributed to the free-exciton A- and B-transitions [24.96]. Similar assignments, based on thermal quenching studies, were made for features observed at 6.023 and 6.036 eV in the NBE spectra of a nominally *c*-plane AlN homoepitaxial film [24.84]. However, recent reflectivity measurements [24.90,91] demonstrate that these assignments are likely incorrect.

24.5.3 Impurities

Growth of high-purity AlN is a challenging task. As a result of the high affinity of Al for oxygen (the

standard Gibbs free energy of formation of Al₂O₃ at 298.15 K is highly negative, -1.582×10^6 J/mol [24.97]), oxygen is a common contaminant in AlN, and influences, among other things, the lattice parameters, thermal conductivity, luminescence, and defect structure of AlN. Early material property measurements on oxygen-contaminated AlN have been revised as higher-purity single-crystal material has become available. In addition, since commercially available AlN powder contains approximately 1% oxygen impurities, obtaining a high-purity AlN source powder is of interest to the crystal growth community. Calculations by Karpov et al. [24.28] have shown that AlN source purification is favorable for obtaining bulk crystals free of Al₂O₃ inclusions. Carbon is also a common contaminant in AlN, while metallic and other impurities are typically found at trace levels. Knowledge of the influence these different contaminants have on the growth process and fundamental properties of AlN is still limited, but recent investigations have provided some valuable data.

Dalmau et al. [24.36] reported that sintering of a commercially purchased AlN source powder at a temperature of 2200 °C resulted in a significant reduction of nearly all impurities, with the largest reductions observed for oxygen and carbon impurities (Table 24.1). Several investigators have incorporated source presin-

Table 24.1 Published GDMS analysis results for AlN (all values in ppmw; *T*: sintering/growth temperature, pressure: system pressure, NA: not available)

Sample	<i>T</i> (°C)	Pressure (Torr)	Crucible material	O	C	Si	W	Reference
1. As-received powder	NA	NA	NA	≈ 1000	≈ 3000	200	< 50	[24.37]
2. Sintered powder	2200	400	TaN	≤ 300	≤ 200	200	< 20	[24.37]
3. Self-seeded single crystal	1950/2070*	500/400*	BN	≤ 500	≤ 300	5.5	< 1	[24.91]
4. Self-seeded single crystal	1885/2030*	600/600*	TaN	≤ 1200	≤ 160	130	< 0.05	[24.91]
5. Self-seeded polycrystal	2100	500	TaC	≤ 50	≤ 50	40	< 1	[24.91]
6. Self-seeded polycrystal	2100	500	TaC	≤ 400	≤ 30	40	< 1	[24.91]
7. Self-seeded polycrystal	2250	< 750	W	≈ 86	≈ 100	2.5	7.9	[24.18]
8. Seeded single crystal	2200	400–900	NA	< 100	< 100	80	< 10	[24.52]

* Samples 3 and 4 were grown using a two-stage growth process; temperatures were gradually ramped between the two stages

tering as part of the PVT growth process [24.46, 70, 72]. Epelbaum et al. [24.60] identified how low-temperature transport of Al as suboxides during the ramp to growth temperature can lead to poisoning of the AlN seed surface during seeded growth on native seeds. Even when the AlN source is relatively pure (< 300 ppmw O), evaporation of a thin oxide layer on the source may occur at temperatures as low as 1750°C , leading to an accumulation of aluminum oxynitrides on the seed surface, which make the surface unsuitable for growth. However, the inverted temperature gradient method developed by Noveski et al. [24.51, 69] and used by others [24.52, 70–72] during seeded growth on native seeds represents a practical solution to the problem. This surface poisoning does not appear to be a problem during seeded growth on SiC seeds, possibly due to the different growth mechanism involved [24.64, 65].

Bulk AlN with low oxygen content was reported by Bickermann et al. [24.18, 98]. Polycrystals were grown in a vertical, cold-wall reactor equipped with W heating elements. Growth was performed in N_2 atmosphere, at pressures below 1000 mbar, using almost sealed crucibles. Source and crystal growth temperatures ranged from 2200 to 2350°C , and from 2100 to 2250°C , respectively. Dense, polycrystalline AlN boules up to 15 mm high and 51 mm in diameter were produced with growth rates between 0.2 and 2 mm/h. Boules were composed of *c*-textured crystalline grains, some as large as $5 \times 5 \text{ mm}^2$. Although the AlN source material contained significant amounts of various im-

purities (6000 ppmw oxygen, 300 ppmw carbon, and 500 ppmw metals), as determined by glow discharge mass spectrometry (GDMS), impurity incorporation into grown material was significantly lower (86 ppmw oxygen, 100 ppmw carbon, ≈ 22 ppmw metals). GDMS is a mass-spectrometric technique for the analysis of trace elements in bulk solid samples. It offers several advantages over other trace analysis techniques, including detection limits down to the sub-ppb range, wide dynamic range ($\approx 10^{11}$ range between minor and major components), relative matrix insensitivity, and applicability to a wide variety of materials systems. Table 24.1 shows the results of GDMS analysis on different AlN samples reported in the literature.

A number of researchers have used compositional analysis of AlN crystals together with measurements of optical properties (Sect. 24.5.2) in order to identify impurities that correlate with specific optical transitions. Slack et al. [24.99] reported an oxygen-related absorption region between 3.5 and 5.2 eV, with peak positions varying from 4.3 to 4.8 eV depending on the amount of oxygen impurity. These features are likely due to transitions involving Al vacancy–oxygen complexes. The influence of different impurities on the absorption and luminescence spectra of AlN has also been studied by other investigators [24.31, 91, 92, 98]. However, more work is needed before features observed in the absorption and luminescence spectra of high-quality bulk crystals can be unambiguously assigned to specific defect transitions.

24.6 Conclusions and Outlook

AlN crystal growth is a challenging task that has been attempted in the past via a variety of growth methods. Although several issues remain, PVT growth of AlN at high temperatures shows the most promising results and is the only growth technique that can produce high-quality low-dislocation-density crystals. This method has yielded AlN crystals of very high quality and of sufficient size for fabrication of the first devices. The recent demonstration of seeded growth with subsequent crystal-size expansion is certainly a crucial

milestone for future development of this technology that will lead to further expansion of single-crystal size. Lifetime and stability of growth crucibles and reactor parts remain a challenge that will need to be addressed in the quest for high-purity crystals and lower production cost. Further research is also needed to improve the understanding of the detrimental effects of various impurities in AlN, so that technologically relevant properties of AlN may be fully exploited by reducing the concentration of adverse growth contaminants.

References

- | | |
|--|---|
| <p>24.1 R. Dalmau, Z. Sitar: Sublimation growth of AlN crystals. In: <i>Encyclopedia of Materials: Science and Technology</i>, ed. by K.H.J. Buschow, R.W. Cahn, M.C. Flemings, B. Ilshner, E.J. Kramer,</p> | <p>S. Mahajan, P. Veyssi re (Elsevier, Oxford 2005) pp.1–9</p> |
| <p>24.2</p> | <p>O. Ambacher: Growth and applications of group III–nitrides, <i>J. Phys. D</i> 31, 2653–26710 (1998)</p> |

- 24.3 R. Gaska, C. Chen, J. Yang, E. Kuokstis, A. Khan, G. Tamulaitis, I. Yilmaz, M.S. Shur, J.C. Rojo, L.J. Schowalter: Deep-ultraviolet emission of AlGaIn/AlN quantum wells on bulk AlN, *Appl. Phys. Lett.* **81**, 4658–4660 (2002)
- 24.4 L. Liu, J.H. Edgar: Substrates for gallium nitride epitaxy, *Mater. Sci. Eng. R* **37**, 61–127 (2002)
- 24.5 B. Monemar: III–V nitrides – important future electronic materials, *J. Mater. Sci.* **10**, 227–254 (1999)
- 24.6 L.J. Schowalter, Y. Shusterman, R. Wang, I. Bhat, G. Arunmodhi, G.A. Slack: Epitaxial growth of AlN and Al_{0.5}Ga_{0.5}N layers on aluminum nitride substrates, *Appl. Phys. Lett.* **76**, 985–987 (2000)
- 24.7 L. Chen, B.J. Skromme, R.F. Dalmau, R. Schlesser, Z. Sitar, C. Chen, W. Sun, J. Yang, M.A. Khan, M.L. Nakarmi, J.Y. Lin, H.-X. Jiang: Band-edge exciton states in AlN single crystals and epitaxial layers, *Appl. Phys. Lett.* **85**, 4334–4336 (2004)
- 24.8 I. Grzegory, J. Jun, M. Boćkowski, S. Krukowski, M. Wróblewski, B. Lucznik, S. Porowski: III–V nitrides – Thermodynamics and crystal growth at high N₂ pressure, *J. Phys. Chem. Solids* **56**, 639–647 (1995)
- 24.9 F. Briegleb, A. Geuther: Ueber das Stickstoffmagnesium und die Affinitäten des Stickgases zu Metallen, *Ann. Chem.* **123**, 228–241 (1862)
- 24.10 G. A. Slack: Aluminum nitride crystal growth, Final Report, Contract No. F49620-78-C-0021 (1980) 1–31
- 24.11 A. Nikolaev, I. Nikitina, A. Zubrilov, M. Mynbaeva, Y. Melnik, V. Dmitriev: AlN wafers fabricated by hydride vapor phase epitaxy, *MRS Internet J. Nitride Semicond. Res.* **551**, W6.5.1–W6.5.5 (2000)
- 24.12 R. Dwiliński, R. Doradziński, J. Garczyński, L. Sierżputowski, M. Palczewska, A. Wyszomolek, M. Kamińska: AMMONO method of BN, AlN and GaN synthesis and crystal growth, *MRS Internet J. Nitride Semicond. Res.* **3**, 25.1–25.4 (1998)
- 24.13 C.O. Dugger: Synthesis of AlN single crystals, *Mater. Res. Bull.* **9**, 331–336 (1974)
- 24.14 M. Bockowski: Growth and doping of GaN and AlN single crystals under high nitrogen pressure, *Cryst. Res. Technol.* **36**, 771–787 (2001)
- 24.15 J.C. Rojo, G.A. Slack, K. Morgan, B. Raghothamachar, M. Dudley, L.J. Schowalter: Report on the growth of bulk aluminum nitride and subsequent substrate preparation, *J. Cryst. Growth* **231**, 317–321 (2001)
- 24.16 R. Schlesser, Z. Sitar: Growth of bulk AlN crystals by vaporization of aluminum in a nitrogen atmosphere, *J. Cryst. Growth* **234**, 349–353 (2002)
- 24.17 J.H. Edgar, L. Liu, B. Liu, D. Zhuang, J. Chaudhuri, M. Kuball, S. Rajasingam: Bulk AlN crystal growth: self-seeding and seeding on 6H–SiC substrates, *J. Cryst. Growth* **246**, 187–193 (2002)
- 24.18 M. Bickermann, B.M. Epelbaum, A. Winnacker: PVT growth of bulk AlN crystals with low oxygen contamination, *Phys. Status Solidi (c)* **0**, 1993–1996 (2003)
- 24.19 P.M. Dryburgh: The estimation of maximum growth rate for aluminum nitride crystals grown by direct sublimation, *J. Cryst. Growth* **125**, 65–68 (1992)
- 24.20 L. Liu, J.H. Edgar: Transport effects in the sublimation growth of aluminum nitride, *J. Cryst. Growth* **220**, 243–253 (2000)
- 24.21 L. Liu, J.H. Edgar: A global growth rate model for aluminum nitride sublimation, *J. Electrochem. Soc.* **149**, G12–G15 (2002)
- 24.22 S.Y. Karpov, D.V. Zimina, Y.N. Makarov, E.N. Mokhov, A.D. Roenkov, M.G. Ramm, Y.A. Vodakov: Sublimation growth of AlN in vacuum and in a gas atmosphere, *Phys. Status Solidi (a)* **176**, 435–438 (1999)
- 24.23 A.S. Segal, S.Y. Karpov, Y.N. Makarov, E.N. Mokhov, A.D. Roenkov, M.G. Ramm, Y.A. Vodakov: On mechanisms of sublimation growth of AlN bulk crystals, *J. Cryst. Growth* **211**, 68–72 (2000)
- 24.24 V. Noveski, R. Schlesser, S. Mahajan, S. Beaudoin, Z. Sitar: Mass transfer in AlN crystal growth at high temperatures, *J. Cryst. Growth* **264**, 369–378 (2004)
- 24.25 B.M. Epelbaum, M. Bickermann, A. Winnacker: Sublimation growth of bulk AlN crystals: Process temperature and growth rate, *Mater. Sci. Forum* **457–460**, 1537–1540 (2004)
- 24.26 S.Y. Karpov, A.V. Kulik, M.S. Ramm, E.N. Mokhov, A.D. Roenkov, Y.A. Vodakov, Y.N. Makarov: AlN crystal growth by sublimation technique, *Mater. Sci. Forum* **353–356**, 779–782 (2001)
- 24.27 E. Mokhov, S. Smirnov, A. Segal, D. Bazarevskiy, Y. Makarov, M. Ramm, H. Helava: Experimental and theoretical analysis of sublimation growth of bulk AlN crystals, *Mater. Sci. Forum* **457–460**, 1545–1548 (2004)
- 24.28 S.Y. Karpov, A.V. Kulik, I.N. Przhivalskii, M.S. Ramm, Y.N. Makarov: Role of oxygen in AlN sublimation growth, *Phys. Status Solidi (c)* **0**, 1989–1992 (2003)
- 24.29 Y. Li, D.W. Brenner: First principles prediction of the gas-phase precursors for AlN sublimation growth, *Phys. Rev. Lett.* **92**, 75503.1–75503.4 (2004)
- 24.30 Y. Li, D.W. Brenner: Influence of trace precursors on mass transport and growth rate during sublimation deposition of AlN crystal, *J. Appl. Phys.* **100**, 84901.1–84901.6 (2006)
- 24.31 R. Schlesser, R. Dalmau, D. Zhuang, R. Collazo, Z. Sitar: Crucible materials for growth of aluminum nitride crystals, *J. Cryst. Growth* **281**, 75–80 (2005)
- 24.32 R. Schlesser, R. Dalmau, R. Yakimova, Z. Sitar: Growth of AlN bulk crystals from the vapor phase, *Mater. Res. Soc. Symp. Proc.* **693**, I.9.4.1–I.9.4.6 (2002)
- 24.33 B. Liu, J.H. Edgar, B. Raghothamachar, M. Dudley, J.Y. Lin, H.X. Jiang, A. Sarua, M. Kuball: Free nucleation of aluminum nitride single crystals in HPBN crucible by sublimation, *Mater. Sci. Eng. B* **117**, 99–104 (2005)

- 24.34 G.A. Slack, J. Whitlock, K. Morgan, L.J. Schowalter: Properties of crucible materials for bulk growth of AlN, *Mater. Res. Soc. Symp. Proc.* **798**, Y10.74.1–Y10.74.4 (2004)
- 24.35 B.M. Epelbaum, D. Hoffman, M. Bickermann, A. Winnacker: Sublimation growth of bulk AlN crystals: materials compatibility and crystal quality, *Mater. Sci. Forum* **389–393**, 1445–1448 (2002)
- 24.36 C.M. Balkas, Z. Sitar, T. Zheleva, L. Bergman, R. Nemanich, R.F. Davis: Sublimation growth and characterization of bulk aluminum nitride single crystals, *J. Cryst. Growth* **179**, 363–370 (1997)
- 24.37 R. Dalmau, B. Raghothamachar, M. Dudley, R. Schlessner, Z. Sitar: Crucible selection in AlN bulk crystal growth, *Mater. Res. Soc. Symp. Proc.* **798**, Y2.9.1–Y2.9.5 (2004)
- 24.38 B. Liu, J.H. Edgar, Z. Gu, D. Zhuang, B. Raghothamachar, M. Dudley, A. Sarua, M. Kuball, H.M. Meyer III: The durability of various crucible materials for aluminum nitride crystal growth by sublimation, *MRS Internet J. Nitride Semicond. Res.* **9**, 6.1–6.11 (2004)
- 24.39 E.N. Mokhov, O.V. Avdeev, I.S. Barash, T.Y. Cheme-kova, A.D. Roenkov, A.S. Segal, A.A. Wolfson, Y.N. Makharov, M.G. Ramm, H. Helava: Sublimation growth of AlN bulk crystals in Ta crucibles, *J. Cryst. Growth* **281**, 93–100 (2005)
- 24.40 C. Hartmann, J. Wollweber, M. Albrecht, I. Rasin: Preparation and characterization of tantalum carbide as an optional crucible material for bulk aluminum nitride crystal growth via physical vapour transport, *Phys. Status Solidi (c)* **3**, 1608–1612 (2006)
- 24.41 L.J. Schowalter, J.C. Rojo, N. Yakolev, Y. Shusterman, K. Dovidenko, R. Wang, I. Bhat, G.A. Slack: Preparation and characterization of single-crystal aluminum nitride substrates, *MRS Internet J. Nitride Semicond. Res.* **551**, W6.7.1–W6.7.6 (2000)
- 24.42 J.C. Rojo, G.A. Slack, K. Morgan, L.J. Schowalter, M. Dudley: Growth of self-seeded aluminum nitride by sublimation-recondensation and substrate preparation, *Mater. Res. Soc. Symp. Proc.* **639**, G1.10.1–G1.10.6 (2001)
- 24.43 J.C. Rojo, L.J. Schowalter, K. Morgan, D.I. Florescu, F.H. Pollack, B. Raghothamachar, M. Dudley: Single-crystal aluminum nitride substrate preparation from bulk crystals, *Mater. Res. Soc. Symp. Proc.* **680E**, E.2.1.1–E.2.1.7 (2001)
- 24.44 L.J. Schowalter, G.A. Slack, J.B. Whitlock, K. Morgan, S.B. Schujman, B. Raghothamachar, M. Dudley, K.R. Evans: Fabrication of native, single-crystal AlN substrates, *Phys. Status Solidi (c)* **0**, 1997–2000 (2003)
- 24.45 R. Schlessner, R. Dalmau, Z. Sitar: Seeded growth of AlN bulk single crystals by sublimation, *J. Cryst. Growth* **241**, 416–420 (2002)
- 24.46 B.M. Epelbaum, C. Seitz, A. Magerl, M. Bickermann, A. Winnacker: Natural growth habit of bulk AlN crystals, *J. Cryst. Growth* **265**, 577–581 (2004)
- 24.47 M. Bickermann, B.M. Epelbaum, A. Winnacker: Structural properties of AlN crystals grown by physical vapor transport, *Phys. Status Solidi (c)* **2**, 2044–2048 (2005)
- 24.48 M. Bickermann, B.M. Epelbaum, M. Kazan, Z. Herro, P. Masri, A. Winnacker: Growth and characterization of bulk AlN substrates grown by PVT, *Phys. Status Solidi (a)* **202**, 531–535 (2005)
- 24.49 M. Bickermann, B.M. Epelbaum, A. Winnacker: Structural, optical, and electrical properties of bulk AlN crystals grown by PVT, *Mater. Sci. Forum* **457–460**, 1541–1544 (2004)
- 24.50 R. Dalmau, R. Schlessner, B.J. Rodriguez, R.J. Nemanich, Z. Sitar: AlN bulk crystals grown on SiC seeds, *J. Cryst. Growth* **281**, 68–74 (2005)
- 24.51 V. Noveski, R. Schlessner, B. Raghothamachar, M. Dudley, S. Mahajan, S. Beaudoin, Z. Sitar: Seeded growth of bulk AlN crystals and grain evolution in polycrystalline boules, *J. Cryst. Growth* **279**, 13–19 (2005)
- 24.52 D. Zhuang, Z.G. Herro, R. Schlessner, B. Raghothamachar, M. Dudley, Z. Sitar: Seeded growth of AlN crystals on nonpolar seeds via physical vapor transport, *J. Electron. Mater.* **35**, 1513–1517 (2006)
- 24.53 Y. Shi, Z.Y. Xie, L.H. Liu, B. Liu, J.H. Edgar, M. Kuball: Influence of buffer layer and 6H-SiC substrate polarity on the nucleation of AlN grown by the sublimation sandwich technique, *J. Cryst. Growth* **233**, 177–186 (2001)
- 24.54 Y. Shi, B. Liu, L. Liu, J.H. Edgar, E.A. Payzant, J.M. Hayes, M. Kuball: New technique for sublimation growth of AlN single crystals, *MRS Internet J. Nitride Semicond. Res.* **6**, 5.1–5.6 (2001)
- 24.55 Y. Shi, B. Liu, L. Liu, J.H. Edgar, H.M. Meyer III, E.A. Payzant, L.R. Walker, N.D. Evans, J.G. Swadener, J. Chaudhuri, J. Chaudhuri: Initial nucleation study and new technique for sublimation growth of AlN on SiC substrate, *Phys. Status Solidi (a)* **188**, 757–762 (2001)
- 24.56 L. Liu, B. Liu, Y. Shi, J.H. Edgar: Growth mode and defects in aluminum nitride sublimed on (0001) 6H-SiC substrates, *MRS Internet J. Nitride Semicond. Res.* **6**, 7.1–7.5 (2001)
- 24.57 L. Liu, D. Zhuang, B. Liu, Y. Shi, J.H. Edgar, S. Rajasingam, M. Kuball: Characterization of aluminum nitride crystals grown by sublimation, *Phys. Status Solidi (a)* **188**, 769–773 (2001)
- 24.58 B. Liu, Y. Shi, L. Liu, J.H. Edgar, D.N. Braski: Surface morphology and composition characterization at the initial stages of AlN crystal growth, *Mater. Res. Soc. Symp. Proc.* **639**, G3.13.1–G3.13.6 (2001)
- 24.59 L. Liu, B. Liu, J.H. Edgar, S. Rajasingam, M. Kuball: Raman characterization and stress analysis of AlN grown on SiC by sublimation, *J. Appl. Phys.* **92**, 5183–5188 (2002)

- 24.60 B. Raghathamachar, R. Dalmau, M. Dudley, R. Schlessler, D. Zhuang, Z. Herro, Z. Sitar: Structural characterization of bulk AlN single crystals grown from self-seeding and seeding by SiC substrates, *Mater. Sci. Forum* **527–529**, 1521–1524 (2006)
- 24.61 R. Dalmau, R. Schlessler, Z. Sitar: Polarity and morphology in seeded growth of bulk AlN on SiC, *Phys. Status Solidi (c)* **2**, 2036–2039 (2005)
- 24.62 B. Raghathamachar, M. Dudley, R. Dalmau, R. Schlessler, Z. Sitar: Synchrotron white beam x-ray topography (SWBXT) and high resolution triple axis diffraction studies on AlN layers grown on 4H- and 6H-SiC seeds, *Mater. Res. Soc. Symp. Proc.* **831**, E8.24.1–E8.24.6 (2005)
- 24.63 W.L. Sarney, L. Salamanca-Riba, T. Hossain, P. Zhou, H.N. Jayathirtha, H.H. Kang, R.D. Vispute, M. Spencer, K.A. Jones: TEM study of bulk AlN grown by physical vapor transport, *MRS Internet J. Nitride Semicond. Res.* **551**, W5.5.1–W5.5.6 (1999)
- 24.64 B.M. Epelbaum, M. Bickermann, A. Winnacker: Seeded PVT growth of aluminum nitride on silicon carbide, *Mater. Sci. Forum* **433–436**, 983–986 (2003)
- 24.65 B.M. Epelbaum, P. Heimann, M. Bickermann, A. Winnacker: Comparative study of initial growth stage in PVT growth of AlN on SiC and on native AlN susbtrates, *Phys. Status Solidi (c)* **2**, 2070–2073 (2005)
- 24.66 P. Heimann, B.M. Epelbaum, M. Bickermann, S. Nagata, A. Winnacker: The initial stage in PVT growth of aluminum nitride, *Phys. Status Solidi (c)* **3**, 1575–1578 (2006)
- 24.67 K. Balakrishnan, M. Banno, K. Nakano, G. Narita, N. Tsuchiya, M. Imura, M. Iwaya, S. Kamiyama, K. Shimono, T. Noro, T. Takagi, H. Amano, I. Akasaki: Sublimation growth of AlN bulk crystals by seeded and spontaneous nucleation methods, *Mater. Res. Soc. Symp. Proc.* **831**, E11.3.1–E11.3.7 (2005)
- 24.68 S. Wang, B. Raghathamachar, M. Dudley, A.G. Timmerman: Crystal growth and defect characterization of AlN single crystals, *Mater. Res. Soc. Symp. Proc.* **892**, FF30.06.1–FF30.06.6 (2006)
- 24.69 V. Noveski, R. Schlessler, J. Freitas Jr., S. Mahajan, S. Beaudoin, Z. Sitar: Vapor phase transport of AlN in an RF heated reactor: Low and high temperature studies, *Mater. Res. Soc. Symp. Proc.* **798**, Y2.8.1–Y2.8.6 (2004)
- 24.70 D. Zhuang, Z.G. Herro, R. Schlessler, Z. Sitar: Seeded growth of AlN single crystals by physical vapor transport, *J. Cryst. Growth* **287**, 372–375 (2006)
- 24.71 Z.G. Herro, D. Zhuang, R. Schlessler, R. Collazo, Z. Sitar: Growth of large AlN single crystals along the [0001] directions, *Mater. Res. Soc. Symp. Proc.* **892**, FF21.01.1–FF21.01.6 (2006)
- 24.72 Z.G. Herro, D. Zhuang, R. Schlessler, R. Collazo, Z. Sitar: Seeded growth of AlN on N- and Al- polar (0001) AlN seeds by physical vapor transport, *J. Cryst. Growth* **286**, 205–208 (2006)
- 24.73 B. Raghathamachar, J. Bai, M. Dudley, R. Dalmau, D. Zhuang, Z. Herro, R. Schlessler, Z. Sitar, B. Wang, M. Callahan, K. Rakes, P. Konkapaka, M. Spencer: Characterization of bulk grown GaN and AlN single crystal materials, *J. Cryst. Growth* **287**, 349–353 (2006)
- 24.74 M. Dudley, X. Huang: X-ray topography. In: *Encyclopedia of Materials: Science and Technology*, ed. by K.H.J. Buschow, R.W. Cahn, M.C. Flemings, B. Ilshner, E.J. Kramer, S. Mahajan, E. Veyssi re (Elsevier, Oxford 2001) pp. 9813–9825
- 24.75 B. Raghathamachar, W.M. Vetter, M. Dudley, R. Dalmau, R. Schlessler, Z. Sitar, E. Michaels, J.W. Kolis: Synchrotron white beam topography characterization of physical vapor transport grown AlN and ammonothermal GaN, *J. Cryst. Growth* **246**, 271–280 (2002)
- 24.76 B. Raghathamachar, M. Dudley, J.C. Rojo, K. Morgan, L.J. Schowalter: X-ray characterization of bulk AlN single crystals grown by the sublimation technique, *J. Cryst. Growth* **250**, 244–250 (2003)
- 24.77 L.J. Schowalter, S.B. Schujman, W. Liu, M. Goorsky, M.C. Wood, J. Grandusky, F. Shahedipour-Sandvik: Development of native, single crystal AlN substrates for device applications, *Phys. Status Solidi (a)* **203**, 1667–1671 (2006)
- 24.78 R.T. Bondokov, K.E. Morgan, R. Shetty, W. Liu, G.A. Slack, M. Goorsky, L.J. Schowalter: Defect content evaluation in single-crystal AlN wafers, *Mater. Res. Soc. Symp. Proc.* **892**, FF30.03.1–FF30.03.6 (2006)
- 24.79 S.B. Schujman, W. Liu, N. Meyer, J.A. Smart, L.J. Schowalter: Atomic force microscope studies on native AlN substrates, *Mater. Res. Soc. Symp. Proc.* **892**, FF30.05.1–FF30.05.6 (2006)
- 24.80 J. Pastr  k, L. Roskocov  : Optical absorption edge of AlN single crystals, *Phys. Status Solidi (b)* **26**, 591–597 (1968)
- 24.81 W.M. Yim, E.J. Stofko, P.J. Zanzucchi, J.I. Pankove, M. Ettenberg, S.L. Gilbert: Epitaxially grown AlN and its optical band gap, *J. Appl. Phys.* **44**, 292–296 (1973)
- 24.82 G.A. Slack, T.F. McNelly: AlN single crystals, *J. Cryst. Growth* **42**, 560–563 (1977)
- 24.83 T. Wethkamp, K. Wilmers, C. Cobet, N. Esser, W. Richter, O. Ambacher, M. Stutzmann, M. Cardona: Dielectric function of hexagonal AlN films determined by spectroscopic ellipsometry in the vacuum-UV range, *Phys. Rev. B* **59**, 1845–1849 (1999)
- 24.84 E. Silveira, J.A. Freitas Jr., M. Kneissel, D.W. Treat, N.M. Johnson, G.A. Slack, L.J. Schowalter: Near-bandedge cathodoluminescence of an AlN homoepitaxial film, *Appl. Phys. Lett.* **84**, 3501–3503 (2004)

- 24.85 E. Kuokstis, J. Zhang, Q. Fareed, J.W. Yang, G. Simin, M.A. Khan, R. Gaska, M. Shur, C. Rojo, L. Schowalter: Near-band-edge photoluminescence of wurtzite-type AlN, *Appl. Phys. Lett.* **81**, 2755–2757 (2002)
- 24.86 I. Vurgaftman, J.R. Meyer: Band parameters for nitrogen-containing semiconductors, *J. Appl. Phys.* **94**, 3675–3696 (2003)
- 24.87 M. Suzuki, T. Uenoyama, A. Yanase: First-principles calculations of effective-mass parameters of AlN and GaN, *Phys. Rev. B* **52**, 8132–8139 (1995)
- 24.88 J.M. Wagner, F. Bechstedt: Properties of strained wurtzite GaN and AlN: Ab initio studies, *Phys. Rev. B* **66**, 115202.1–115202.20 (2002)
- 24.89 J. Li, K.B. Nam, L. Nakarmi, J.Y. Lin, H.X. Jiang, P. Carrier, S.H. Wei: Band structure and fundamental optical transitions in wurtzite AlN, *Appl. Phys. Lett.* **83**, 5163–5165 (2003)
- 24.90 E. Silveira, J.A. Freitas Jr., O.J. Glembocki, G.A. Slack, L.J. Schowalter: Excitonic structure of bulk AlN from optical reflectivity and cathodoluminescence measurements, *Phys. Rev. B* **71**, 41201 (2005)
- 24.91 M. Strassburg, J. Senawiratne, N. Dietz, U. Haboeck, A. Hoffmann, V. Noveski, R. Dalmau, R. Schlessner, Z. Sitar: The growth and optical properties of large, high-quality AlN single crystals, *J. Appl. Phys.* **96**, 5870–5876 (2004)
- 24.92 J. Senawiratne, M. Strassburg, N. Dietz, U. Haboeck, A. Hoffmann, V. Noveski, R. Dalmau, R. Schlessner, Z. Sitar: Raman, photoluminescence and absorption studies on high quality AlN single crystals, *Phys. Status Solidi (c)* **2**, 2774–2778 (2005)
- 24.93 M. Bickermann, B.M. Epelbaum, P. Heimann, Z.G. Herro, A. Winnacker: Orientation-dependent phonon observation in single-crystalline aluminum nitride, *Appl. Phys. Lett.* **86**, 131904 (2005)
- 24.94 M. Bickermann, P. Heimann, B.M. Epelbaum: Orientation-dependent properties of aluminum nitride single crystals, *Phys. Status Solidi (c)* **3**, 1902–1906 (2006)
- 24.95 E. Silveira, J.A. Freitas Jr., G.A. Slack, L.J. Schowalter: Cathodoluminescence studies of large bulk AlN crystals, *Phys. Status Solidi (c)* **0**, 2618–2622 (2003)
- 24.96 E. Silveira, J.A. Freitas, G.A. Slack, L.J. Schowalter, M. Kneissl, D.W. Treat, N.M. Johnson: Depth-resolved cathodoluminescence of a homoepitaxial AlN thin film, *J. Cryst. Growth* **281**, 188–193 (2005)
- 24.97 D.R. Lide (Ed): *CRC Handbook of Chemistry and Physics*, 74th edn (CRC Press, Boca Raton 1993) Chap. 5, p. 5
- 24.98 M. Bickermann, B.M. Epelbaum, A. Winnacker: Characterization of bulk AlN with low oxygen content, *J. Cryst. Growth* **269**, 432–442 (2004)
- 24.99 G.A. Slack, L.J. Schowalter, D. Morelli, J.A. Freitas Jr: Some effects of oxygen impurities on AlN and GaN, *J. Cryst. Growth* **246**, 287–298 (2002)

25. Growth of Single-Crystal Organic Semiconductors

Christian Kloc, Theo Siegrist, Jens Pflaum

Organic semiconductor crystal growth presents a very different set of challenges than their inorganic counterparts. Although single crystals of organic semiconductors can be grown by the same techniques used for inorganic semiconductors, the weak intermolecular bonds, low melting temperatures, and high vapor pressures and solvent solubilities require specific modifications to crystal growth techniques of these materials. Bulk crystals of only a handful of different materials have been grown from the melt. The Czochralski, Bridgman, and general melt growth techniques are hampered by the high vapor pressure, which causes fast evaporation of the material during the growth process. However, the significant vapor pressure of organic semiconductors makes gas-phase growth methods suitable for most of them. In general, multistep synthesis of organic molecules produces impure materials which need extensive purification. Small crystals, mostly for structure determinations, have been grown from organic solvents. Zone melting has been used for a few materials, but many organic molecules decompose before reaching the melting temperature. The crystal growth of volatile molecules in a stream of flowing gas is therefore a widely used method that combines purification and crystal growth. Although gas-phase grown crystals tend to be small in size, they have high structural quality and superior

25.1	Basics	845
25.2	Theory of Nucleation and Crystal Growth	847
25.2.1	Stability Criteria for Nuclei	847
25.2.2	Thermodynamic Considerations of Crystal Growth	847
25.2.3	Growth Morphology in Relation to Symmetry	848
25.2.4	Structural Defects	848
25.3	Organic Materials of Interest for Semiconducting Single Crystals	848
25.4	Pregrowth Purification	850
25.4.1	Zone Refinement	851
25.4.2	Sublimation and Its Modifications ..	852
25.5	Crystal Growth	854
25.5.1	Melt Growth	855
25.5.2	Growth from the Gas Phase	857
25.5.3	Solvent-Based Growth Methods	862
25.6	Quality of Organic Semiconducting Single Crystals	862
25.7	Organic Single-Crystalline Field-Effect Transistors	863
25.8	Conclusions	864
	References	865

rior purity and are therefore preferred for physical property measurements.

25.1 Basics

Most organic molecular crystals are transparent materials that behave like insulators, with electrical resistivities in the range of 10^{13} – 10^{18} Ω cm at room temperature. However, some organic molecules with delocalized π -electrons such as conjugated hydrocarbons, phthalocyanines, oligothiophenes, etc. may form colored crystals indicating a small energy gap between

the highest occupied (**HOMO**) and the lowest unoccupied (**LUMO**) molecular orbitals. Crystals made from such substances often show significant absorption and emission of visible light, and photoconductivity and electrical conductivity, and in general behave more like semiconductors than insulators. Photoconductivity of anthracene, with its three conjugated benzene

rings, intrigued researchers from the beginning of the 20th century [25.1]. The feature that light is emitted from anthracene crystals under the absorption of high-energy radiation such as neutrons or x-rays has been widely used in scintillation detectors [25.2]. Later, research began to explore whether organic semiconductors may be suitable for applications where inorganic semiconductors were already established. Such research required organic semiconductors in thin-film form for applications, and in single-crystal form mostly for basic research. Studies that focus on physical properties resulting from weak intramolecular bonds, high symmetry of molecules, and anisotropy of physical properties require measurements on single crystals. Therefore, many well-established crystal growth methods for inorganic materials have been adapted to the growth of organic semiconductor crystals and are discussed in this chapter.

Semiconductors composed from van der Waals bonded molecules, especially those comprising small organic molecules, may be soluble in numerous organic solvents, even at room temperature. This fact allows for low-temperature processing such as printing, spraying, casting, laminating, etc. to mention just a few. Low-temperature solubility distinguishes significantly organic semiconductors from covalently bonded inorganic semiconductors, which often can only be dissolved in high-temperature fluxes. Organic semiconductors therefore seem to be the perfect components for devices where the active materials, as well as the electrodes and conduction paths, may simply be printed by various techniques. Printing semiconducting elements on plastic foils promises large-scale production of inexpensive electronic devices such as bendable displays, field-effect transistor based circuits or large solar cell arrays [25.3,4].

The power of organic molecular synthesis and crystal engineering allows the formation of new semiconductor materials through systematic variation of crystalline and molecular structure for structure-properties investigations. Optimization of structural, electrical or optical characteristics through chemical design of molecules may then result in improved electronic devices. Furthermore, new properties may give rise to novel applications and devices. However, understanding the relationship between the molecular composition, the packing of molecules into crystals, and the physical properties of the resulting organic semiconductors still presents a challenge.

Often, studies of physical properties of organic semiconductors were performed on polycrystalline or

amorphous thin-film devices due to their ease of fabrication and good control over physical dimensions. However, grain boundaries, inhomogeneous distribution of impurities, and high defect densities make thin-film devices unattractive for studies of intrinsic properties [25.5,6].

In contrast, single crystals contain only small amounts of impurities and defects, due to the inherent purification during crystallization. Therefore, properties measured on single crystals tend to be more reproducible than those measured on amorphous or polycrystalline thin-film samples.

Historically, properties of inorganic semiconductors, such as silicon, germanium or III–V compounds, have been studied on single crystals or single-crystalline epitaxial thin films. It is therefore reasonable to assume that the intrinsic properties of organic semiconductors can also be studied following the same path. Contrary to inorganic semiconductors, where the growth units are atoms, the growth units in organic crystals are molecules. Such extended moieties, with their internal structure, require reorientation and alignment before incorporation into a crystalline lattice. These processes need to be considered by using a specific crystal growth technique for the growth of a particular organic semiconductor.

In general, organic semiconductors crystallize in low-symmetry unit cells. Therefore, all physical properties are tensorial properties with often large anisotropies and can only be properly evaluated on single crystals. The availability of high-purity and high-quality single crystals of organic semiconductors is thus crucial in exploring the physics of such materials and is very helpful in new material design and in building devices with novel functionality and high performance [25.7,8].

Single crystals of a series of organic semiconductors have been grown using well-described crystal growth techniques. Examples of monographs focused on the theory and practice of crystal growth are cited at the end of this chapter [25.9,10]. The weak van der Waals bonds between the growth units (in particular molecules) in organic crystals limit the methods applicable to the preparation of single-crystalline specimens [25.11,12]. In addition, the growth units may decompose relatively easily, thus contaminating the crystals. Since the properties of organic semiconductors, like their inorganic counterparts, are sensitive to low levels of impurities and defects, the growth of high-quality organic semiconductors needs to consider purification, contamination, and defect formation in every step of the preparation process.

In this chapter, we will therefore focus on practical approaches for purification and growth of high-quality molecular semiconductor single crystals. In the past, reviews concentrated either on melt growth [25.12] or gas-phase techniques [25.13, 14]. Here, we attempt to compare different crystal growth techniques in order to suggest their advantages and

disadvantages as well as practical criteria for the use of these techniques for organic semiconductors. We focus on technological differences between the growth of inorganic and organic semiconductors. We will further discuss defects and contaminants resulting from the use of particular crystal growth methods.

25.2 Theory of Nucleation and Crystal Growth

The growth kinetics of inorganic as well as organic materials are determined by their inherent parameters, such as the interaction between the individual species/units forming the crystals, and external parameters, such as the growth temperature or adsorption rate. Especially the set of external conditions such as the interaction between a substrate and the initial nucleation layer are often difficult to control, if at all. These parameters are critical for the initial step of nucleation and might even change during growth as a function of temperature.

Furthermore, a fundamental property of organics is the anisotropic extension of the electronic wavefunctions, meaning that the electron distribution shows strong spatial anisotropy of intermolecular overlap, in contrast to inorganic crystals with covalent or ionic bonding. The intention is to correlate the spatial anisotropy of the bonding strength with the tensorial properties, e.g., higher mobility values along certain crystallographic directions.

To characterize the influence of such external parameters on crystal preparation, it is helpful to highlight first the kinetics of crystal formation for the case of an ideal system. In this case it is appropriate to divide the crystal formation into two steps: the initial nucleation and the subsequent growth of the individual nuclei.

25.2.1 Stability Criteria for Nuclei

To initiate volume growth of the intended organic crystal, the formation of the initial nuclei on a given support is the essential step. Beside the optimization of nuclei density in the beginning of crystal formation, an important criterion is the smallest number of organic molecules forming a stable nucleus. As for their inorganic counterparts, stability is governed by the balance between loss in surface energy versus gain in volume energy upon incorporation of an additional molecular building block.

However, besides the van der Waals interaction, which was interpreted on the basis of temporary

ily fluctuating dipoles by London, the occurring internal degrees of freedom, e.g., the torsion of extended phenyl groups as in the case of 9,10-diphenylanthracene [25.15], might play a considerable role at the early stage of nucleation. Even thermally induced changes of the molecular shape in the gas phase can significantly influence the crystallinity of the molecular systems. For instance, the thermal energy during evaporation is not sufficient to planarize the tetracene backbone of rubrene, which is twisted due to pairwise repulsion of the attached phenyl rings. As a result, thin films of rubrene have proven to be amorphous without any indication of crystallinity [25.16, 17]. In contrast, growth from gradient sublimation under a constant gas flow provides sufficient energy to overcome the energy barrier of 210 meV and to planarize the molecule averaged over time [25.16]. In the latter case, rubrene shows defined crystal growth with spatial extensions of its growth planes in the centimeter range.

25.2.2 Thermodynamic Considerations of Crystal Growth

The thermodynamic quantities describing the energetics of crystal growth and especially of nucleation are the sublimation enthalpy and the entropy. Neglecting permanent dipoles, the bonding strength between molecular entities is governed by the weak van der Waals force, resulting in a distribution of sublimation enthalpies from 45 kJ/mol for benzene up to 215 kJ/mol for ovalene [25.18]. Normalizing the heat of sublimation divided by the number of intermolecular contacts reveals an average energy per contact of 50 J/mol for various polyaromatic hydrocarbon crystals, independent of the molecular packing [25.18]. However, for molecules offering additional degrees of freedom, e.g., due to twisted functional groups, the gain in entropy might add a significant amount of energy, determining the final crystalline structure.

25.2.3 Growth Morphology in Relation to Symmetry

In view of the anisotropic physical properties such as the tensor of charge carrier mobility or the optical indicatrix, one of the central aspects of crystal growth is the formation and stability of certain crystallographic facets, planes or axes. Similar to their inorganic equivalents, high-indices surfaces are unstable over time due to their higher growth velocities compared with low-index planes. However, for organic materials the crystal habit, defined as the relative size of the stable faces, proves to be more sensitive to the external growth conditions as a consequence of the weak van der Waals binding energies. Tetracene, and many other oligoacenes grown by plate sublimation, shows a distinct stable crystal habit depending on the environmental conditions. Under vacuum, a preferential growth along the (*ab*)-plane is observed. This mode is determined by the long-range diffusion and the gain of energy by incorporating the individual molecules in this plane under almost equilibrium conditions. In an atmosphere of 400 Torr N₂, however, the mean free path of the sublimed molecule is shorter than the traveling distance in the volume, and the crystal growth is governed by the material transport rather than by the diffusion atop the (*ab*)-crystal surface. The crystals emanating from this growth regime are needle shaped, preferentially oriented with the needle axis along the *c**-direction.

25.2.4 Structural Defects

The growth of organic molecular crystals, occurring in most cases in a temperature range between room

temperature up to about 700 K, is accompanied by the formation of structural defects, e.g., vacancies, dislocations, and growth sectors. According to Boltzmann's law, the density of vacancies *n* in a crystal is a function of the temperature *T* and the energy, *E_v*, required to form a vacancy: $n \sim \exp(-E_v/k_B T)$. Possible defects can be characterized by their dimensionality as vacancies (zero-dimensional, 0-D), dislocation lines or screw dislocations (one-dimensional, 1-D), or grain boundaries (two, dimensional 2-D). Even for high-quality anthracene crystals, thermal treatment might result in vacancy densities at room temperature of $10^{14} - 10^{16} \text{ cm}^{-3}$ after growth. Furthermore, due to the respective packing along the various crystallographic directions, an anisotropic distribution of defects has been observed. Especially in crystals with herringbone-type packing in the (*ab*)-plane and a (001) glide plane, enhanced formation of dislocation lines is observed along the (100)[010] Burgers vector. The quadratic scaling of the elastic energy with the respective Burgers vector makes the *b*-direction (the shortest distance between adjacent molecules) energetically favorable for the formation of dislocation lines.

In addition, the external conditions during crystal growth may have a significant impact on the defect density [25.19]. In melt-grown crystalline samples, the interaction of the crystal with the walls of the ampoule, especially during the cooling process, might induce dislocation densities three orders of magnitude higher compared with similar crystals grown from gas phase. However, subsequent thermal treatments might decrease the defect density by adding thermal energy to the system during annealing.

25.3 Organic Materials of Interest for Semiconducting Single Crystals

Organic semiconductors represent a large group of solids comprised of organic π -conjugated small molecules, oligomers or polymers. Since polymers are rarely available in single-crystalline form, the materials discussed in this chapter are limited to crystals of small molecules and oligomers.

Organic semiconductors are mostly used as active materials in field-effect transistors, light-emitting diodes or solar cells. These applications determine the selection of molecules of interest for research and production. Figure 25.1 presents examples of molecules with semiconducting properties used for research and applications.

Linear or planar fused-ring compounds, heterocyclic oligomers, and fullerenes are among the most studied molecules with semiconducting properties.

Single crystals of polycyclic aromatic hydrocarbons were among the first reported organic materials exhibiting small but measurable conductivity and photoconductivity. This suggested that these materials contain delocalized π -electrons and belong to the family of semiconducting compounds [25.20, 21].

These early studies required large single crystals for physical measurements. Therefore, the semiconductors selected for these measurements included molecules available in relative large quantity, stable at tempera-

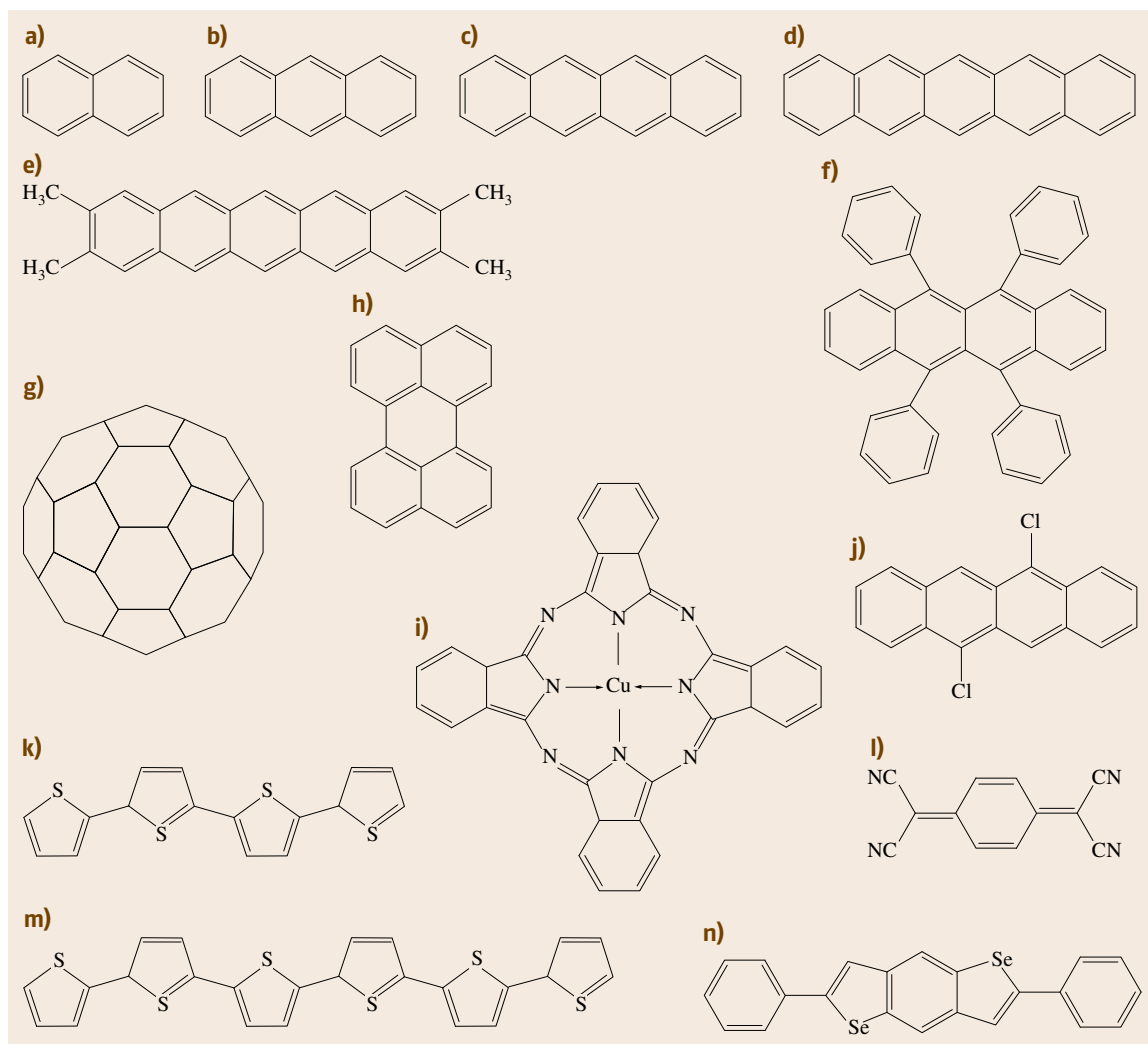


Fig. 25.1a–n Molecules of examples of the most studied organic semiconductors: **(a)** naphthalene, **(b)** anthracene, **(c)** tetracene, **(d)** pentacene, **(e)** 2,3,9,10-tetramethylpentacene (Me₄Pent), **(f)** rubrene, **(g)** fullerene (C₆₀), **(h)** perylene, **(i)** copper phthalocyanine, **(j)** 5,11-dichlorotetracene (DCT), **(k)** α -quaterthiophene (α -4T), **(l)** tetracyanoquinodimethane (TCNQ), **(m)** α -hexathiophene or α -sexithienyl (α -6T), **(n)** 2,6-diphenylbenzo[1,2-*b*:4,5-*b'*]diselenophene (DPH-BDS)

tures close to their melting point, and grown in the form of crystalline ingots from the melt. Some materials, such as naphthalene, anthracene, stilbene, terphenyl, diphenylacetylene or quaterphenyl, have been chosen for crystal growth due to their strong scintillation properties [25.22]. Others, such as naphthalene, anthracene, and perylene, were selected for melt growth and time-of-flight measurements [25.12].

Oligothiophenes decompose below their melting temperature and can only be grown from gas phase

in the form of small single crystals or thin films. These compounds are widely used in both single-crystal and thin-film forms for field-effect transistors [25.23, 24]. Hydrocarbons, such as rubrene, pentacene, and tetracene, are used to study the physical properties of organic semiconductors and for high-mobility transistors [25.8].

Fullerenes, such as C₆₀, and C₇₀, have received considerable attention due to their spherically delocalized π -electrons, yielding measurable conductivity

and even superconductivity in alkali metal- C_{60} compounds [25.25].

Another group showing promise for practical application are cofacially stacked phthalocyanine systems and, often with central 3d transition-metal atom, porphyrines [25.26]. These compounds are exceptional due to their broad chemical variability and excellent stability. These properties, and the fact that they are available in sufficient quantity and quality, make porphyrines and phthalocyanines prominent candidates for efficient photovoltaic energy conversion.

The observation of light emission from organic diodes and the field effect in transistor configurations stimulated the design and development of many new organic π -conjugated molecules with semiconductor properties [25.27]

Many were synthesized and used only in thin-film field-effect transistors by evaporation or solvent-growth techniques. However, only a limited number of these compounds were grown in single-crystal form and only a few examples are known where the electronic transport properties were optimized.

25.4 Pregrowth Purification

For research purposes, batches of organic semiconductor materials are typically purchased from chemical suppliers. Some special, commercially unavailable molecules are synthesized by individual chemists. In both cases, the syntheses involve multistep organic chemical reactions yielding the expected molecules. Because the yield of an organic synthesis may be low, the desired molecules are often mixed with numerous, not always well-characterized, contaminants. Contaminants may be the molecules introduced as starting material, molecules formed by side reactions or decomposition processes, as well as solvents used in the process. In comparison with classical inorganic semiconductors, such as silicon or GaAs, where 6N purity or better is available, organic semiconductors are significantly contaminated, with purity in the range of 95–98%. The contaminants are often not well defined and may form by reduction, oxidation, decomposition or photoinduced processes during storage. Therefore, before

crystals can be grown, the source materials need to be purified.

The purification methods may be the same as those used for inorganic compounds: zone refining, sublimation or distillation. Additional, due to the solubility of organic semiconductors in organic solvents, recrystallization from organic solvents, or purification by gas- or liquid-phase chromatography, is feasible. The product of such purification requires subsequent removal of traces of solvents. Moreover, some specific contaminants, which are difficult to remove by traditional purification methods, may be altered chemically for effective removal. For instance, removing β -methylnaphthalene and thionaphthalene from naphthalene by fusing naphthalene with molten potassium, which chemically modifies the solid/liquid and solid/gas distribution coefficients, may be an example of chemically altering contaminants prior to removing them via sublimation and zone refining [25.28].

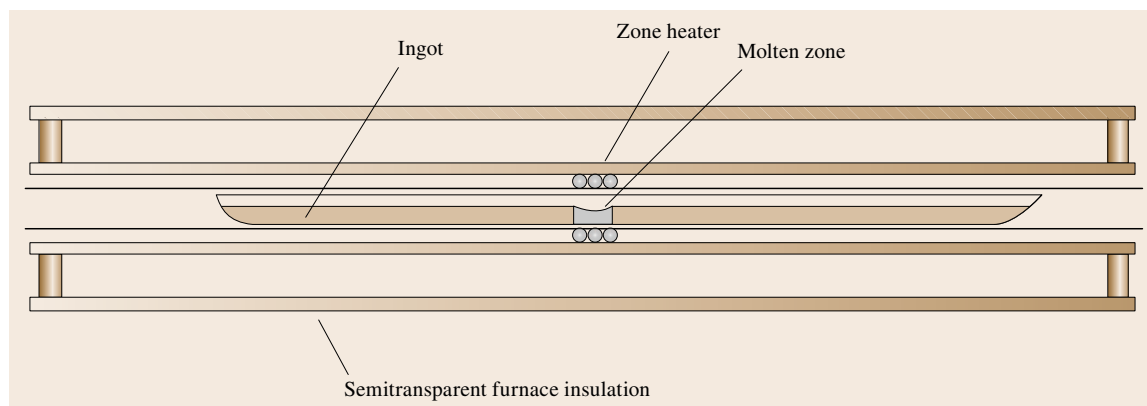


Fig. 25.2 Zone refining with one molten zone in a horizontal arrangement

Organic semiconductors, due to the peculiarity of the bonds, may not only decompose during storage but also dimerize and polymerize, especially if exposed to light. Anthracene is known to form dianthracene under illumination, but this dimer is not very stable and photolitically dissociates back to anthracene [25.29].

Pentacene, which has a mobility larger than $1 \text{ cm}^2/(\text{V s})$ in both thin-film and single-crystal field-effect transistors, easily oxidizes to 6,13-pentacenequinone [25.30], but also dimerizes and additionally reacts further to form a series of polycondensed aromatic hydrocarbons and undergoes a disproportionation reaction to 6,13-dihydropentacene [25.31].

25.4.1 Zone Refinement

Materials available in larger amounts, which can be melted without decomposition, such as anthracene, naphthalene or perylene, may be purified by repeated zone melting as the technique of choice. Established by *Pfann* for inorganic semiconducting materials [25.32], zone refinement was applied to anthracene [25.33, 34]. In this method, an ingot of about 20–50 cm length is formed and slowly dragged across a cylindrical heating zone of centimeter extension under an inert gas atmosphere. The inert gas on one hand protects the molten material from reaction with air and on the other hand reduces the evaporation of the material from the melted zone. The temperature of the heater is high enough to locally melt the material to form a short molten zone. Outside the heating zone the organic material remains in its solid phase (Figs. 25.2 and 25.3). A zone-refinement apparatus can be realized with an ingot fixed in either horizontal or vertical orientation. The heater moves along the fixed ingot, or alternatively, the ingot moves relative to fixed heater. To allow multiple melting and crystallization of zones along an ingot, a system with numerous heaters may be used (Fig. 25.4).

Due to the slow movement of the molten zone in one direction only, the purified material melts at one end of the zone and crystallizes at the other. Depending on the solubility of the respective impurities in the liquid and solid states, impurities with higher solubility in the melt than in the crystal are moved towards

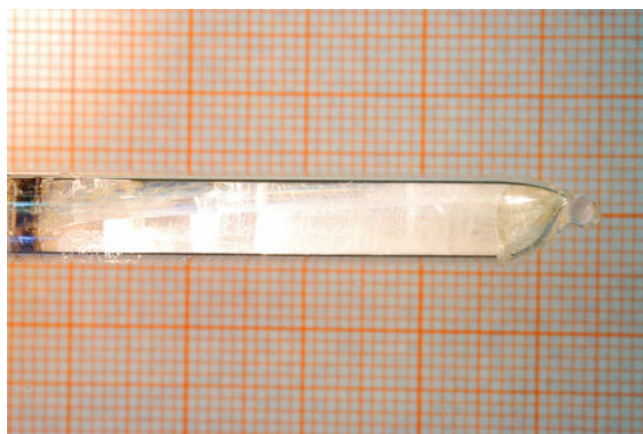


Fig. 25.3 Zone-refined anthracene. Contamination is moved to both ends of the ampoule, seen as a *dark* and a *light* part at each end of the anthracene ingot. Also, some cracks and crystal segments, formed due to crystal contraction during cooling, are seen

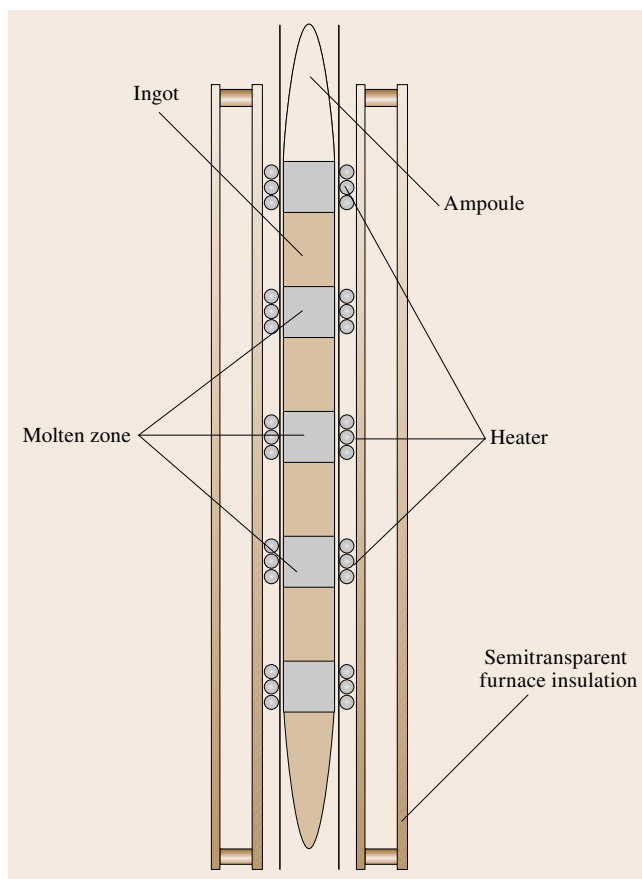


Fig. 25.4 Multizone refining system. To prevent evaporation of material from the melted zone, zone refining is run in vertical orientation. To decrease the time required for the process, a multizone furnace is used ►

the molten interface, while impurities with lower solubility move to the crystallization interface. Therefore, the former impurities are pulled with the zone whereas the others are transferred to the opposite end of the ingot. Repetition of this process up to several hundred cycles will accumulate impurities on both ends of the ingot and pure material is collected from its central part (Fig. 25.3).

In the case that impurities have equal solubility in the melt and the solid, they cannot be separated via zone melting and need to be removed using other techniques such as sublimation or chemical precipitation. Some success has been reported by using an additional material forming an eutectic with the impurity. In this way the distribution coefficient is changed from an unfavorable value close to 1.0, to a smaller value which simplifies moving the impurities with the eutectic to the end of an ingot. For instance, tetracene, for eutectic zone melting purification, has been mixed with 2-naphthoic acid, while anthracene has been melted with benzoic acid. The zone refinement of such an eutectic mixture allows removing otherwise hard-to-remove impurities [25.35].

The purified material does not need to be removed from the zone-refining apparatus after each run of the molten zone along the ingot. Therefore, the purification process may be automatically repeated many times in the same ampoule [25.36]. Additionally, subsequent purification steps may be performed only on material

collected from the central, purest part of the ingots. The purity of substances for which this method has been applied was superior, and low-temperature mobilities, evaluated by the time-of-flight method, were reported to be as high as a few hundred $\text{cm}^2/(\text{V s})$ at low temperature. Because zone melting requires a large amount of material (on the gram scale) and a specific, noncommercial apparatus, this method is preferred for large-scale purification and has been used only for a limited number of organic semiconductors.

25.4.2 Sublimation and Its Modifications

For studies of new organic semiconductors, laboriously synthesized in only milligram amounts, standard vacuum sublimation (with various modifications) has been commonly used. In this method, material sublimes in vacuum in a temperature gradient between evaporation and deposition zones. If only a very small amount of the material is available, the deposition temperature needs to be significantly lower than the evaporation temperature. Under such conditions, easily evaporated molecules, such as most solvents, evaporate into the vacuum and most of the molecules deposit on some form of cold finger. Heavy molecules do not sublime at all and remain in the evaporation zone.

Vacuum sublimation in a temperature gradient is very efficient, but it often lacks selectivity and most

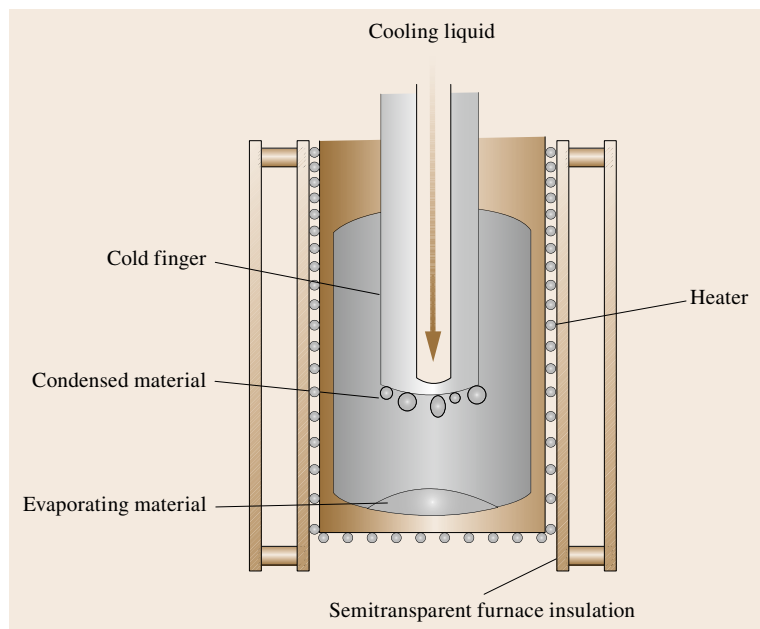


Fig. 25.5 Vacuum sublimation on a cold finger

molecules with comparable properties deposit simultaneously on cold surfaces.

Low-vapor-pressure molecules or solvents may be efficiently removed by sublimation. However, due to the weak van der Waals bonds between molecules, the volatility and evaporation enthalpies of organic molecules with comparable molecular mass are too close for efficient separation. It is worth mentioning at this point that this situation may become even more complex if the molecular species possess a permanent dipole moment, thereby significantly changing the sublimation enthalpies.

To improve the purification of organic semiconductors and change the mass transport kinetics, modified sublimation methods have been proposed. In one case, a carrier gas was introduced into the sublimation apparatus and a long deposition zone with a shallow temperature gradient from the evaporation zone to room temperature was used [25.13,37]. In this way, the heavy

impurity molecules, similar to vacuum sublimation, remain in the heating zone and the molecules with high vapor pressure (solvents, etc.) are removed from the deposition zone with the carrier gas stream. The carrier gas transports molecules with different molecular mass to different distances, allowing efficient separation of molecules with different mass.

This method is selective enough that it may even be used for separation of polymorphs or isomers. Polymorphs are crystalline substances formed from the same molecules but which crystallize in different structures and therefore possess different sublimation enthalpies.

Polymorphs of oligothiophenes, hexathiophenes, quaterthiophenes have been separated by this methods for crystal structure determinations.

Another modification of the sublimation technique is step sublimation. Here, the pristine material is placed in a boat at the end of a glass tube that is closed at

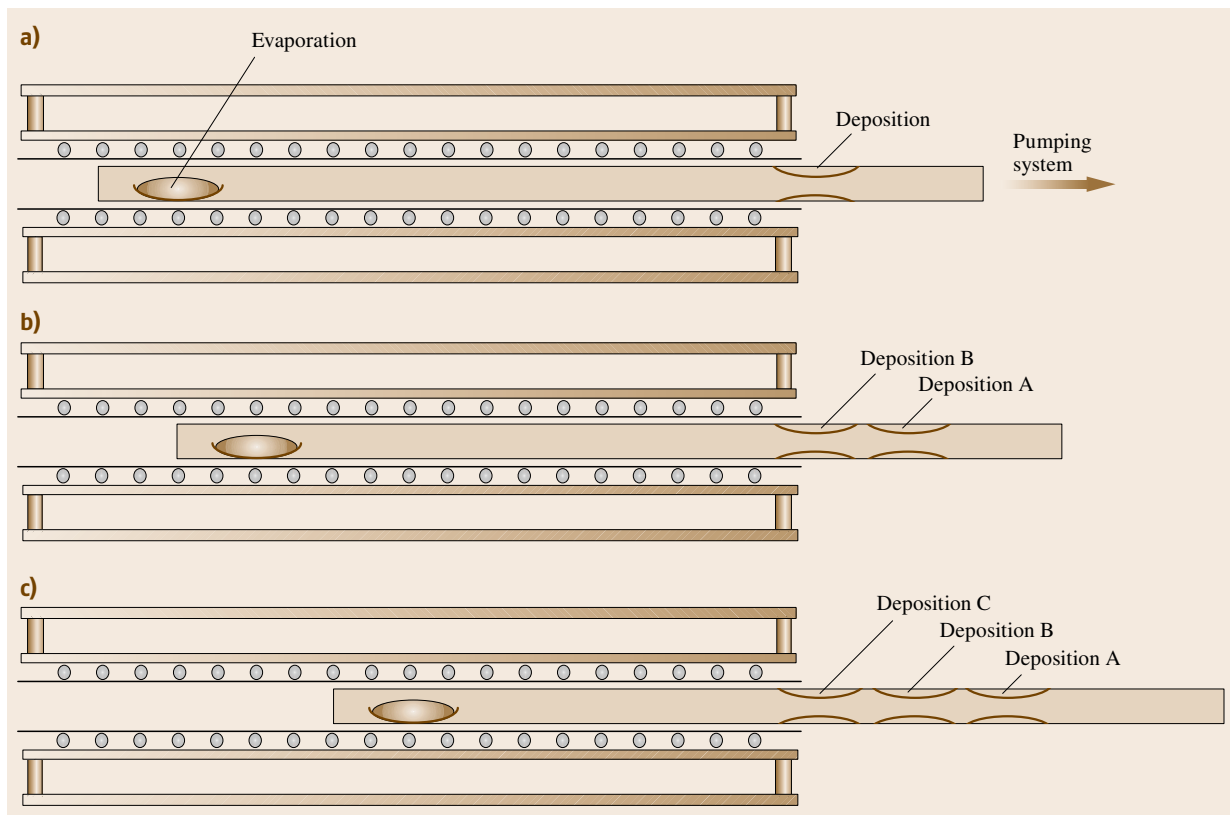


Fig. 25.6a–c The principle of step sublimation. The furnace is kept at constant temperature. The reaction tube is pulled from the furnace in such a way that material from the consecutive processes deposit at the positions marked A, B, C as depicted in (a–c)

one side. Connecting the open side to a pumping system, the tube is evacuated to pressures of 10^{-6} mbar and placed with the closed side into a transparent glass oven. Subsequent stepwise increases of the temperature, with the ingot partially translated out of the heated zone after each new temperature, allows for a detailed analysis of the respective contaminants subliming at different temperatures as well as the determination of the sublimation temperature of the intended material. Furthermore, the open arrangement of the setup allows for in situ optical investigations of the pristine material upon thermal treatment, e.g., for newly synthesized materials, changes between the solid and the liquid at a certain temperature can be observed. The technique can indicate changes in the chemical composition of the material as well as possible phase transitions. Due to its simplicity, this technique is well suited to estimate the thermal stability and sublimation conditions of newly synthesized molecules. Furthermore, this technique enables the purification of larger amounts of material compared with gradient sublimation and is

therefore ideal as a prepurification step in combination with zone refinement.

In both of the above-described modifications the purified material needs to be removed after one purification step. For consecutive purification steps, the material needs to be reloaded into a new clean apparatus and the purification process may be repeated. To avoid this laborious and expensive procedure, a vapor zone-refining technique has been developed [25.35]. In this method, tetracene in the form of a long ingot was sublimed in an apparatus similar to a zone-refining system. The temperature, however, was kept below the melting temperature at which tetracene decomposes. Due to the high vapor pressure of tetracene, it evaporates from the short heated zone. Because some impurities may have lower and others higher vapor pressure than tetracene, the impurities are concentrated at both ends of the vapor zone-refining ingot. The efficiency of this purification method was confirmed through liquid-phase chromatography, but no other physical properties sensitive to small quantities of contaminants have been reported.

25.5 Crystal Growth

Organic compounds may be grown from the gas phase, solution or melt. Many well-established methods used for crystal growth of elements, (metals and nonmetals) or compounds (oxides, semiconductors or insulators) may be modified for growth of single-crystal organic semiconductors. The relative weak van der Waals bonds between molecules, the large dimensions of growth units, and the limited thermal stability of organic materials impose specific limitations on the use of these well-established techniques. In comparison with inorganic materials, melting temperatures of organic compounds are relatively low. Many small molecules appear even at room temperature as liquids and cannot be considered as practical semiconductors for room-temperature applications.

Thiophene (C_4H_4S), for example, has a melting temperature of only -38°C and has not been reported as being used for electronic applications. Both 2,2'-bithiophene ($C_8H_6S_2$) and 2,2':5'2''-terthiophene are solids at ambient temperatures, with melting temperatures of 32 and 93°C , respectively. The larger oligothiophenes, i.e., quaterthiophene (four thiophene rings), quinquethiophene (five thiophene rings) [25.38], hexathiophene (sexithiophene, six thiophene rings) [25.24] or the longest synthesized octathiophene (eight thiophene rings), are all solid at room

temperature and numerous authors report the use of these oligothiophene for field-effect transistors. The longest oligothiophene, α -8T is difficult to synthesize, as it needs high temperatures for evaporation but is not very stable around the gas-phase growth temperature of 340°C [25.39]. However the polymer polythiophene, and its derivatives, are soluble and are again very popular as thin-film field-effect-transistor materials.

Similar relations exist in the polycyclic aromatic hydrocarbons. Benzene is a liquid at room temperature; naphthalene is a volatile solid, anthracene melts at 210°C , but photodimerizes under illumination. The longer hydrocarbons from the acene family, tetracene (naphthacene) and pentacene, are relatively stable solids with excellent semiconducting properties [25.40]. The next in the series, with six (hexacene) and seven (heptacene) conjugated benzene rings, are hard to synthesize and not very stable [25.41]. The polymer, an infinite linear chain of acenes or cyclic polyacenes, has not been synthesized [25.42].

The most frequently used single-crystal growth method for organic semiconductors are the numerous modifications of the vapor growth technique. Most organic molecules possess sufficient vapor pressure that the vapor growth method can be efficiently used. Some materials, such as anthracene, tetracene, pentacene, and

rubrene, have been crystallized in sealed ampoules in the form of needles, platelets or even large bulk single crystals. However, most organic semiconductors have been grown by evaporation and condensation in a carrier gas stream. Oligothiophenes and acenes, for example, have been grown from the vapor phase, and resulting single crystals have been used for physical measurements as well as device preparation. Many organic molecules, designed and synthesized for exploration of their semiconducting properties, have been evaporated during heating and crystallized in the form of small (only a few to tens of micrometers long) crystals. Such small crystals may have sufficient quality that the crystal structure can be determined by diffraction methods (where dimensions of the order of $50 \times 50 \times 5 \mu\text{m}^3$ are needed).

For some applications, such as scintillation detectors, where large crystals of a few cubic centimeters are required, the melt growth techniques are more practical. However, for other applications such as field-effect transistors, large crystals need to be cut and polished before preparing devices on their surfaces. Time-of-flight measurements revealed that the bulk quality of large organic crystals may be superior compared with at their surfaces. Unfortunately, due to the requirement for stability of the material up to the melting point, very few organic semiconductors have been grown from the melt.

Though the large molecules of oligothiophenes, acenes, and many others are excellent organic semiconductors, they have low vapor pressure, making it difficult to use them in gas-phase transport setups, and they often decompose before melting, excluding melt growth techniques. Additionally they show only limited solubility in solvents. These large molecules are sometimes functionalized with long alkane chains to improve solubility, but the substitution creates new molecules and therefore changes the physical properties of the semiconductor. Thus, due to their low solubility, crystals can only be grown from solvents by using high pressures and temperatures in a solvothermal method. However, to date, the quality of solvothermal-grown crystals was not optimized and the quality was insufficient for practical applications.

25.5.1 Melt Growth

Generally, materials that may be purified by zone melting may be crystallized from a melt by either the Bridgman or Czochralski method. In the Bridgman method, the material is melted in a container in a temperature gradient in such a way that crystallization starts

at the lowest point of a narrowed ampoule. In most practical Bridgman processes the ampoule is sealed; as a result, the vapor cannot escape from the system. The growth of crystals may be initiated spontaneously or on a small oriented single-crystalline seed.

In the Czochralski method, the material is melted in a crucible at a temperature slightly above the melting point. A seed crystal, which is just below the melting temperature, is pulled from the melt. The crystallization begins on an oriented monocrystalline seed. During the crystal growth process, the melt evaporates from the crucible during the crystal pulling and the vapors continuously escape from the crucible. There-

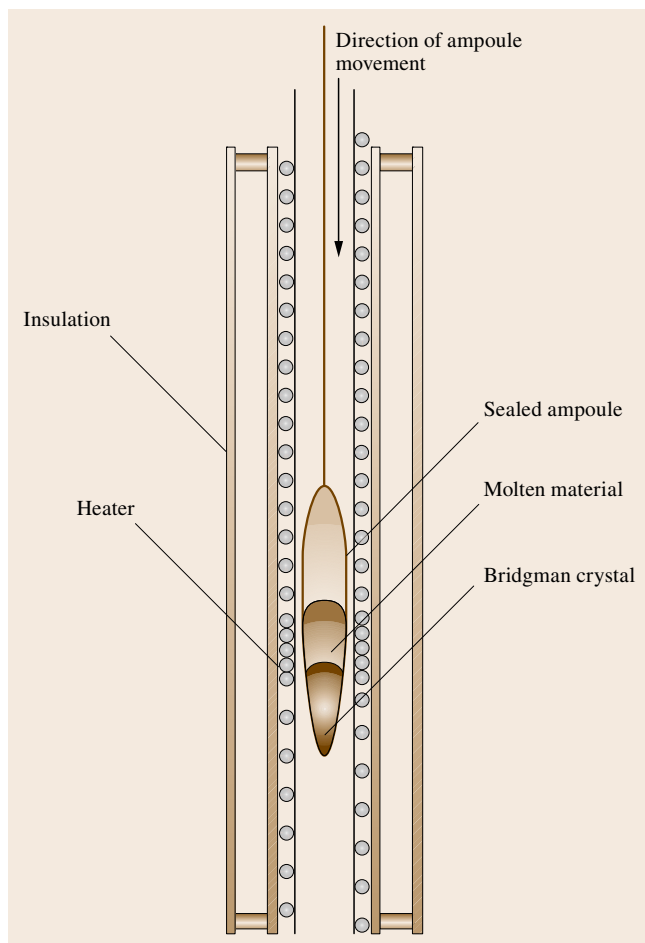


Fig. 25.7 The principle of the Bridgman crystal growth system in a sealed ampoule. A glass ampoule with molten material is moved through a temperature gradient. The crystal nucleates at the tip of the ampoule and grows from the melt when the lower part of the ampoule moves to the colder part of the furnace



Fig. 25.8 Anthracene crystal grown by the Bridgman method inside a glass ampoule; the crystal sticks to the ampoule wall and is shown before removal from the ampoule

fore this method is suitable only for low-vapor-pressure materials.

Organic Semiconductors Grown by the Bridgman Technique

Due to their thermal stability upon melting, low-weight acenes such as naphthalene, anthracene [25.43, 44], 2,3-dimethylnaphthalene [25.45], perylene [25.46], and phenanthrene [25.47] have been grown by the Bridgman technique. Similar to zone refinement, the material is placed in an ampoule sealed under vacuum or at a pressure slightly lower than ambient; for example, 400 Torr of N_2 , at room temperature, may be used. In a vertical oven with two different temperature zones, the organic compound is melted in the upper, hotter zone and then slowly lowered into the cooler region for crystallization. Depending on the organic materials, the growth speed can vary over a range from 0.1 mm/h to 0.1 mm/min.

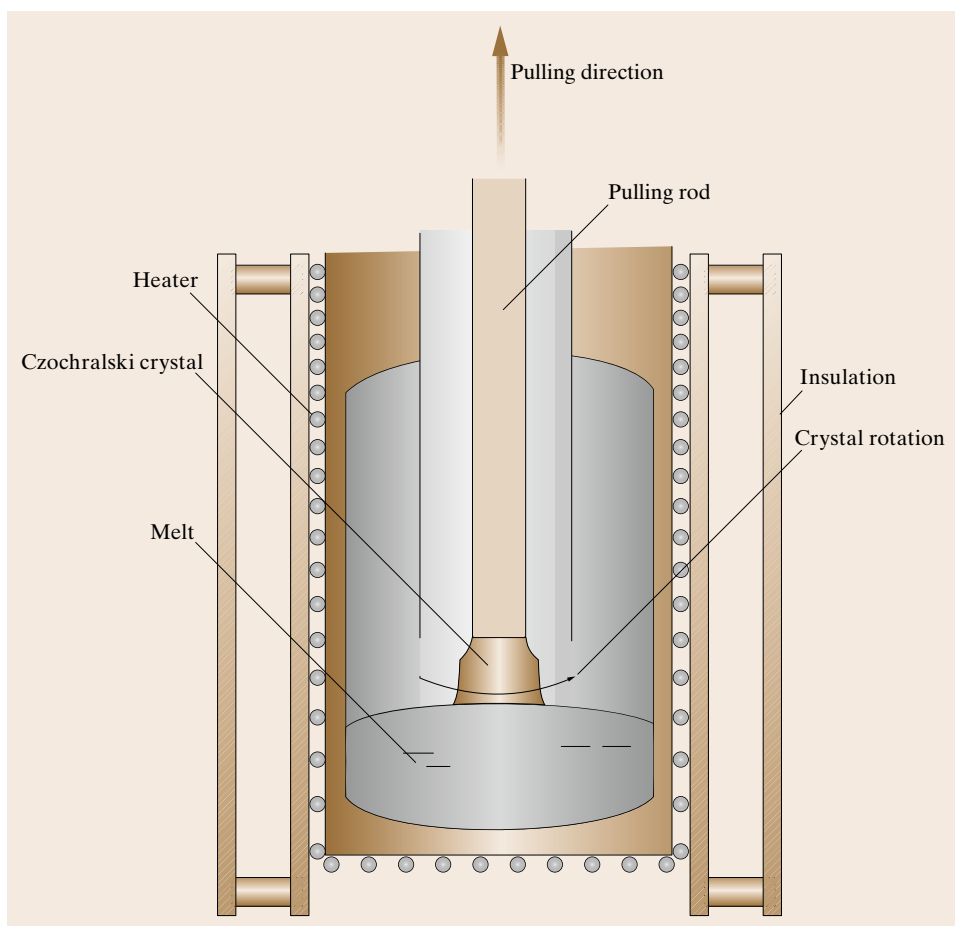


Fig. 25.9

A sketch of the Czochralski apparatus used for the growth of organic material. The pulling rod is slightly cooler than the melt. The heat is removed from the growing crystal through the pulling rod. The crystal is pulled from the melt. The vapor can escape during the growth process through the opening between pulling rod and the ampoule

To avoid possible formation of structural defects caused by mechanical vibrations during the process, the oven is moved instead of the ampoule. The resulting crystals are on the centimeter scale and provide a degree of purity that is as high as the pristine material, and sometimes even better due to the additional refinement cycle during growth.

A schematic diagram of the Bridgman crystal growth apparatus is shown in Fig. 25.7, and an anthracene single crystal grown by this method is shown in Fig. 25.8. A Pyrex or quartz glass ampoule containing a prepurified organic semiconductor is evacuated under vacuum, purged with inert gas, and sealed under vacuum or under reduced inert-gas pressure. The ampoule is heated slightly above the melting point of the material and then lowered through the temperature gradient.

Organic Semiconductors Grown by the Czochralski Technique

Crystals grown by the Bridgman method as well as ingots crystallized during zone refining suffer from cracks and stresses caused by contact with the walls of a container. To avoid this effect, the Czochralski technique was used for benzile, benzophenone, and stearic acid. The scheme of this method is presented in Fig. 25.9. A small seed crystal is slightly immersed into the melt and slowly rotated and pulled from the melt. The melt crystallizes on this seed, forming single crystals with the same orientation as the seed. The high vapor pressure of most organic compounds limits the usability of this method to a few organic semiconductors even though the quality of these crystals compares favorably with the perfection obtained by Bridgman or solution-grown crystals [25.48].

25.5.2 Growth from the Gas Phase

The most popular method of growing single crystals of many organic semiconductors is growth by gas-phase transport. The significant vapor pressure of van der Waals bonded materials [25.49] at moderate temperatures and the possible high purity and quality of vapor-grown crystals favor this method for the growth of single crystals for research purposes.

Even though the gas-phase growth technique is rather simple, the processes involved in evaporation and crystal formation are quite complex. The growth of crystals may be limited by processes occurring in the evaporating material, the gas-phase transport between evaporation and growth zone or on the surfaces of the crystal itself. Crystals may grow close to thermodynamic equilibrium within their own vapor, or far from equilibrium when the gas-phase transported molecules condense very fast or in the presence of an inert gas where molecules diffuse through the surface layer of adsorbed gas.

The growth unit of a molecular crystal is a single molecule, much larger than the growth unit of most inorganic crystals. Therefore, large molecules require additional energy to reorient, or even reconstruct, before incorporation into kinks or steps on the crystal surface.

For some molecules, the required rearrangement has been experimentally observed. Rubrene, which shows the highest charge carrier mobility at room temperature, crystallizes very poorly or as an amorphous layer if the growth temperature is low. The molecules strike a surface and stick to it where they hit, forming an amorphous conglomerate [25.16]. However, by increasing the growth temperature, the crystalline quality of thin films significantly improves [25.16]. To achieve a high enough growth temperature during condensation of rubrene thin film, a semiclosed method, i.e., hot-wall epitaxy, allowing growth at high vapor pressure, was used. Even higher growth temperatures are practical for rubrene and large well-formed rubrene single crystals are routinely obtained.

The presence of inert gas, in either an open or sealed system, radically changes the growth modus. Horowitz

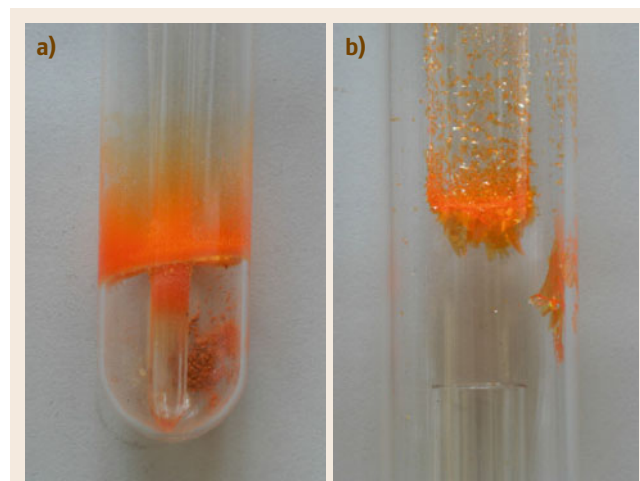


Fig. 25.10a,b α -Hexathiophene grown from the vapor phase. (a) Powder evaporated from the lower part of the ampoule, deposited in vacuum on the wall in the form of a fine crystalline powder. No crystals are observed. (b) When the ampoule was filled with 1 atm of an inert gas, up to centimeter-size crystals grew at the colder part of the ampoule

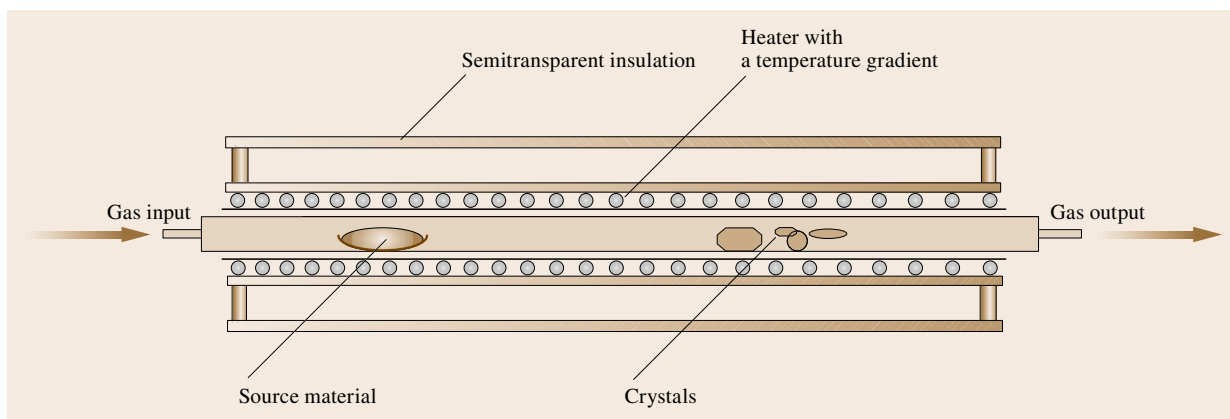
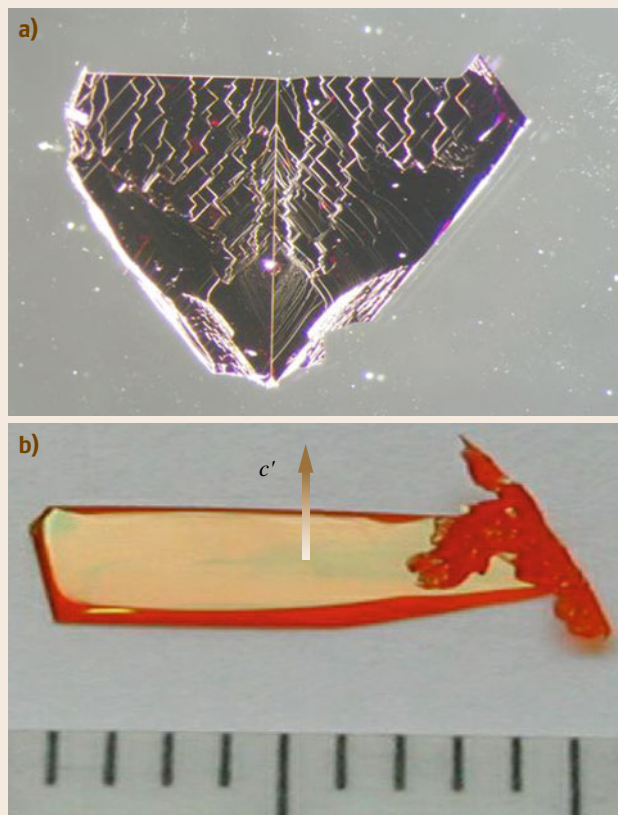


Fig. 25.11 The principle of a vapor-phase transport crystal growth system. The inert gas flows through the reactor, causing transport of molecules from high temperature, where the material evaporates, to the low temperature, where the material deposits. The high vapor pressure impurities are transported with the gas stream out of the furnace and the heavy contaminants remain at the evaporation zone. The presence of an inert gas modifies the surface processes, resulting in spontaneous formation of single crystals



et al. reported α -hexathiophene single crystals grown at a few mbar of argon [25.50].

However, α -hexathiophene, during evaporation in vacuum, deposits as a powder, independent of the temperature gradient. At higher temperature, the vacuum evaporation is very fast and molecules are not able to rearrange before attaching to the growth sides and thus form a powder rather than crystals. After introducing an inert gas into the ampoule or applying a gas flow in an open system, the evaporation rate was significantly reduced, allowing even higher temperatures for evaporation and crystal growth. The molecules gain additional thermal energy, allowing surface diffusion to the nearest growth steps. There the molecules rearrange before forming single-crystalline platelets with well developed faces [25.37]. The same improvement in crystal growth was observed for quaterthiophene [25.51,52].

At temperatures only slightly lower than the melting point, the occurrence of a rough or even quasiliquid surface layer is assumed. This layer influences the

Fig. 25.12a,b Examples of crystals grown from vapor phase. (a) Tetramethylpentacene grown in an inert gas stream: growth steps are visualized due to the use of illumination at shallow angle of incidence. (b) Tetracene grown in a closed ampoule: monolayer-high growth steps occur on the crystal surface (steps not visualized) ◀

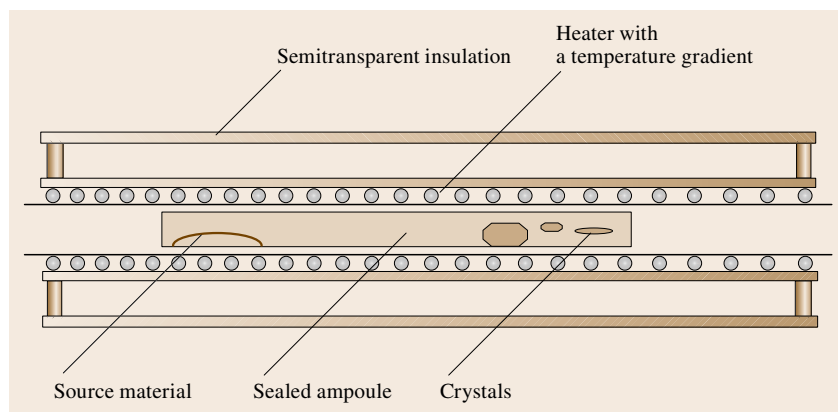


Fig. 25.13 Vapor-phase growth in a sealed glass ampoule. The ampoule may be filled with an inert gas under controlled pressure. The impurities cannot be removed from the ampoule during the growth process

adsorption, migration, surface diffusion, surface rearrangement, and nucleation of molecules and helps in the attachment of molecules to the crystal surface [25.53].

Various modifications of the gas-phase crystal growth technique have been described. They may be divided into processes run in sealed ampoules or in open tubes. Both processes, in a sealed or open tube, may run either in vacuum or in an inert gas atmosphere. In a sealed ampoule, the starting material is enclosed in a glass ampoule and the amount of the material is not changed during the process. However, due to chemical reactions, such as decompositions, photoreactions, polymerization, and others, the chemical composition of the material in a sealed ampoule may change. In an open tube system, a carrier gas is injected through one end of the tube and escapes from the other. The material for crystallization is located in the heated part of the tube, evaporates from there at elevated temperature, and condenses in the colder part of the tube [25.54]. The crystallizing material may undergo similar reactions as in the sealed ampoule. It may further react with the carrier gas and escape with it from the growth tube. The resulting composition and the amount of the material in the system may therefore change during the growth process.

Both variations of gas-phase crystal growth require only small quantities of the starting material. Therefore, many organic compounds have been grown in the form of small needles or platelets. These crystals, while often not large enough for device preparation, are large enough for x-ray diffraction analysis and structure determination. However to grow single crystals large enough for device fabrication, the process parameters need to be further optimized. To keep the temperature gradient between the evaporating and growing material

small, sealed ampoules have frequently been used. To lower the evaporation rate and run the growth processes at higher temperatures, an inert gas has been introduced in both sealed and open systems. To purify the material during growth, the open system is preferred, as impurities are carried away from the growing crystal by a stream of inert gas.

Sublimation in sealed ampoules filled with an inert gas has been efficiently used for growth of anthracene, chrysene, diphenyl, *p*-terphenyl, acridine, pyrene, naphthalene, phenanthrene, and benzanthracene. Fluorescence measurements have been performed on such crystals [25.55].

Rubrene and pentacene crystals have been grown in a small temperature gradient formed in a vacuum sealed glass ampoule [25.31, 56]. In both cases growth temperatures were lower than the corresponding temperatures for growth in the gas stream. Also, the crystals produced by vacuum growth were much thicker because the surface migration of adsorbed molecules was limited at lower temperatures. However, the same

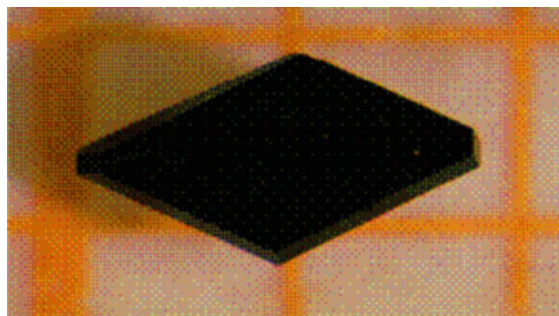


Fig. 25.14 C₆₀ crystal grown in a sealed quartz-glass ampoule

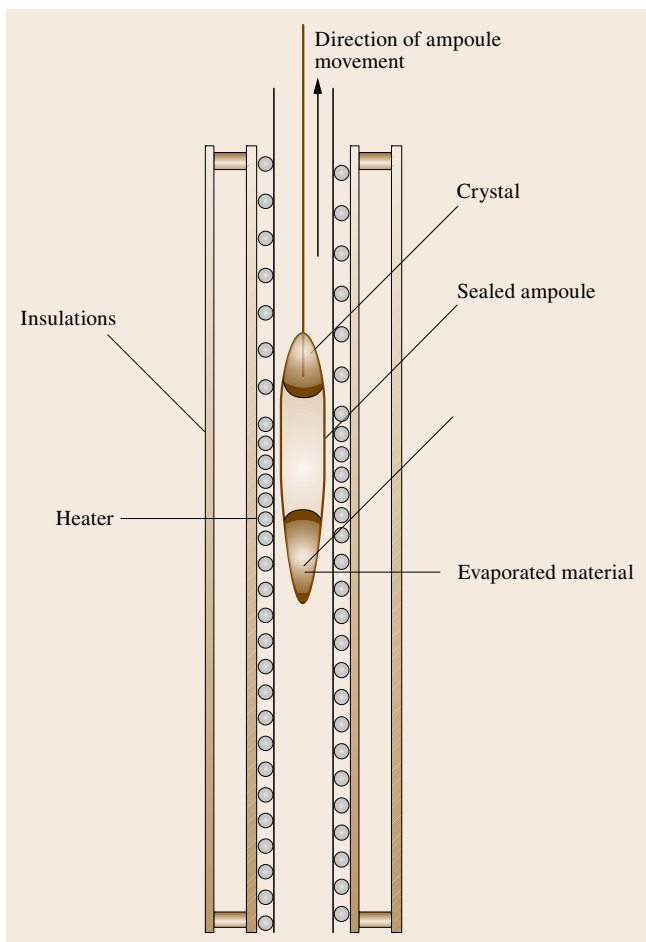


Fig. 25.15 Schematic diagram of the gas-phase growth of crystals while pulling the ampoule through a temperature gradient. Crystal nucleates in the narrow tip of the ampoule during pulling of the ampoule from the high-temperature zone in the lower part of the furnace to the colder, upper part of the furnace

growth technique was absolutely inadequate for oligothiophenes, where a gas flow is required to keep a high temperature and to remove impurities from the system.

Larger crystals may be obtained from the gas phase by pulling a sealed glass ampoule up through a temperature gradient (the inverse of the Bridgman technique). In this technique, the material evaporates from the lower, hotter part of the ampoule and condenses at a narrow tip of an ampoule pulled into the colder part of the furnace. The conical tip of the ampoule is filled by the growing crystal. Tetracene single crystals have been



Fig. 25.16 Tetracene crystal formed in the tip of an ampoule while pulling the ampoule through a temperature gradient

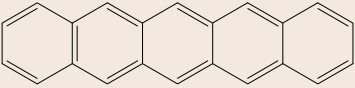
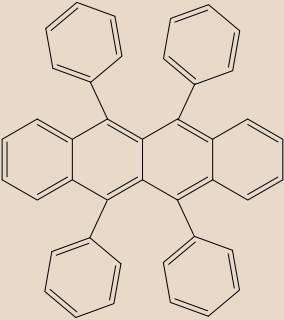
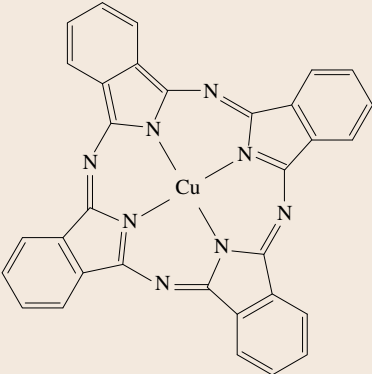
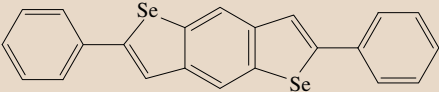
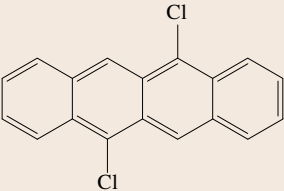
successfully grown by pulling the ampoule with a speed of 5 mm/day [25.57].

During the growth in a sealed ampoule, even if pre-purified materials are used, some impurity molecules may be formed by decomposition, and some impurity molecules intercalated in the source material may be discharged during heating. To avoid contamination of the growing crystals, a part of the vapor may be removed through a small effusion hole placed close to the conical tip of the ampoule. This method, known as semi-open physical vapor transport, has been successfully used to grow nonlinear optical crystals [25.58, 59], but has not been explored for organic semiconductors.

One of the striking features of sublimation-grown crystals is their morphological habit. Many of the polyacenes, rubrene, and perylene derivatives show a preferred two-dimensional growth with aspect ratio between lateral extension and height of the order of 10^2 – 10^4 . Such crystals are most suitable for transport studies carried out in field-effect transistor (FET) geometry by preparing metal contacts by thermal evaporation after growth. Since these measurements are governed by the charge carrier transport along the topmost layers of the crystal surface, contamination after growth by, for instance, photo-oxidation, has to be minimized by sample handling in a glovebox, under controlled lighting, etc.

The results of some field-effect transistor studies on organic single crystals with mobility values equal to or larger than $1 \text{ cm}^2/(\text{V s})$ are presented in Table 25.1.

Table 25.1 Organic semiconductors with a single-crystal field-effect transistor mobility above $1 \text{ cm}^2/(\text{V s})$

Structure	Mobility [$\text{cm}^2/(\text{V s})$]	Reference
 Pentacene	2.2	<i>Roberson et al.</i> [25.31]
 Rubrene	13	<i>Zeis et al.</i> [25.56]
 Copper phthalocyanine	1.0	<i>Zeis et al.</i> [25.60]
 2,6-Diphenylbenzo[1,2- <i>b</i> :4,5- <i>b'</i>]diselenophene	1.3	<i>Zeis et al.</i> [25.61]
 Dichlorotetracene	1.6	<i>Moon et al.</i> [25.62]

25.5.3 Solvent-Based Growth Methods

The solubility, vapor pressure, and stability of molecules declines with increasing mass of the organic semiconductor. Therefore melt or gas-phase crystal growth methods are unsuitable for large molecules, since the molecules tend to break apart before melting or evaporation. The only growth method available in such cases is solution growth close to room temperature. In analogy to inorganic materials, the solubility may be increased by high pressure and moderate temperatures below the melting point, similar to quartz crystals, which are grown by the hydrothermal method a few hundred degrees below the melting point of SiO_2 .

This concept has been used for organic materials [25.63], where a pressurized solvent (instead of water), was used. With this solvothermal method, it was shown that the practically insoluble material, hexathiophene, is well soluble in benzyl phenyl sulfide sealed in a glass ampoule. During cooling, hexathiophene precipitates to form small platelets. The crystal growth process has not been optimized, and resulting crystals were only a few hundred micrometers in dimensions, insufficient for transistor fabrication or transport measurement.

Small or polar molecules were successfully grown from organic solvents. During solvent evaporation or during cooling of saturated solutions, the material precipitates in the form of crystalline powders or, sometimes, small crystals. This is the method of choice for growth of small crystals for x-ray crystal structure determination. However, the solvent may intercalate or even form ordered mixed crystals. Larger crystals of or-

ganic semiconductors, such as anthracene and pyrene, were also grown from solvents by solvent evaporation or by temperature lowering and have been used for semiconducting parameter evaluation. Anthracene and pyrene crystals of a few millimeters, formed by slow evaporation of a solvent, were successfully used for dark conductivity and photoconductivity measurements [25.46].

Anthracene crystals with up to 2 cm^2 in area have been grown while suspended in a solvent. The essential feature of this method is the choice of the solvent, ethylene dichloride, with a density that is slightly greater than the density of anthracene at room temperature. Since the density of the solvent decreases faster than the density of anthracene upon heating, it is possible to find a temperature at which both solvent and anthracene density are equal and the crystal can be suspended and grown in solution. Additionally, a layer of xylene (a poor solvent for anthracene) was placed on the top of the anthracene/ethylene chloride solution. Xylene prevents ethylene dichloride from evaporating and further diffuses slowly into the ethylene dichloride and causes a decrease in anthracene solubility, thus creating supersaturation. Under such conditions, crystals can grow undisturbed while suspended in the solvent [25.64].

Further, large crystals of organic materials for nonlinear optics applications have been grown from solvents [25.65]. However, these crystals are transparent large-gap insulators and do not show properties typical of organic semiconductors; they are therefore not discussed in this chapter.

25.6 Quality of Organic Semiconducting Single Crystals

To understand the electronic properties of organic semiconductors, high-quality single crystals are required. In the past the structural quality of gas-phase-grown anthracene and Bridgman-grown 2,3-dimethyl naphthalene were studied with x-ray topography [25.19]. Because anthracene grew in the form of very thin platelets that were strongly warped, x-ray topography was severely hampered. Large, ultrapure Bridgman-grown anthracene as well as 2,3-dimethyl naphthalene single crystals were used for time-of-flight measurement of charge carrier mobilities. The x-ray topographs of these crystals revealed that defects were formed after the crystal growth process, during cooling of the crystals from the growth temperature to room temperature, during removal from ampoules, and during sample

preparation for measurements. However, if properly and carefully handled, the quality of cleaved lamellae prepared from Bridgman-grown ingots displayed a highly perfect mosaic with only a few dislocations appearing, mostly at the side where the cleavage process caused stress and glide dislocations [25.19].

Double-crystal x-ray topography was performed on rubrene single crystals grown from the vapor phase [25.66]. In comparison with other organic semiconductors that crystallize in lower symmetries (monoclinic or triclinic), rubrene crystallizes in the orthorhombic system. Besides thin platelets, rubrene forms also thicker crystals suitable for structure analysis. The thermal expansion is not very anisotropic. The rocking curve width of a few crystals (selected

under polarized light from a large batch grown in numerous growth runs) revealed a full-width at half-maximum (FWHM) of the (12 0 0) reflection of 0.013° for the best samples. Such a narrow rocking curve was also observed for the (004) reflection, but the FWHM was twice as large for the (020) reflection. Such a low mosaic spread is among the best exhibited by organic crystals. However, many other measured rubrene crystals displayed larger FWHMs of the order of 0.15° . The mechanism of forming such mosaic spreads in these crystals is not known. Furthermore, it

is assumed that both the growth process and, more probably, any temperature gradient formed during the crystal cooling are responsible for defect formation in these crystals, often with an inhomogeneous distribution of dislocations.

Rubrene single crystals show high charge carrier mobility, close to ten times larger than values seen in other organic semiconductors such as tetracene or pentacene. However, the mechanisms by which defects, impurities, and intra- and intermolecular structure impact on charge carrier mobility is not clear as of today.

25.7 Organic Single-Crystalline Field-Effect Transistors

At the foundation of organic semiconductors as an active element of plastic electronics is the ability to use assemblies of molecules in FETs. Charge carrier transport has attracted attention for decades and was often studied using thin-film FET structures. In contrast, only a limited number of groups have focused on intrinsic electronic properties of single-crystal organic semiconductors. While the measurements on thin films, which are the configurations used for applications, are useful and indicate the potential of a particular organic compound, the presence of grain boundaries, impurities, and defects obscures the intrinsic performance that one can expect to achieve from a specific material. The alternative approach for evaluation and selection is the fabrication of an FET structure directly on a single crystal. In this way, the most efficient π -conjugated molecules can be selected from among the many commercially available organic compounds. The latter method allows better evaluation of intrinsic properties of organic

semiconductors because the optical, electrical, and other properties are directly dependent on molecular properties of individual molecules that self-assemble (crystallize) on a nanoscale into well-ordered oriented grains, macroscopically defining a single crystal.

FET structures prepared on the natural surfaces of single crystals were described previously [25.8]. Two general variations are used. In the first, the source and drain electrodes, dielectric layer, and gate electrodes are fabricated by different techniques on a silicon wafer or plastic foil, and the single crystal is *stamped* (placed) onto such a device structure. In the second variation, the source and drain contacts are evaporated or printed onto the natural surface of a single crystal, then the dielectric is spun on or evaporated onto the crystal, and finally the gate electrode is fabricated on the dielectric layer. In the first method a strongly doped silicon wafer covered by an insulating layer of silicon oxide (SiO_2) with deposited metallic (mostly gold) electrodes

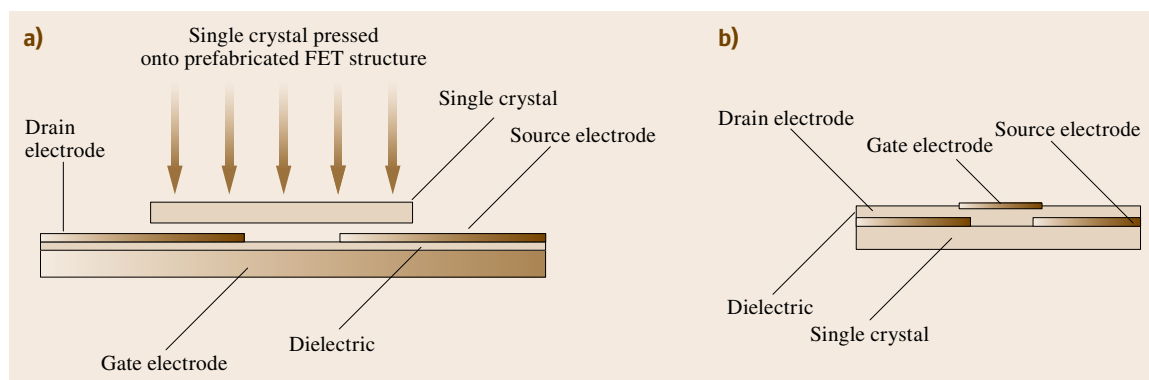


Fig. 25.17a,b Schematic diagram of two types of single-crystal field-effect transistor fabrication. (a) The FET electrodes and dielectric are prefabricated and a single crystals is attached by adhesion to the FET structure. (b) Electrodes and dielectric are built up step by step on the natural surface of a single crystal

is used as a support for crystals, which are gently affixed by adhesion to form the channel region between the source and gate electrodes. Good adhesion between the prefabricated FET support and crystal is crucial for proper operation of such a device. A similar concept of a prefabricated FET structure has been realized by using either a transparent indium oxide gate on glass or flexible foil and spun-on polymers as a gate dielectric. Again, strong adhesion between the electrodes, polymers, and crystals is crucial and may be controlled through chemical treatment of the polymer. An interesting modification of the last structure is an elastomeric stamp where the gate dielectric is replaced by an air gap. Since no direct contact between the dielectric (here air, inert gas or vacuum) and semiconductor surface occurs, the natural surface of the semiconductor may be studied and effects of the atmosphere on the FET properties may be observed.

For the second method, contact metals for p-type semiconductors are preferably gold or silver or low-work-function metals such as magnesium in the case of n-type materials. The lowest contact resistance on rubrene was obtained with painted contacts from a water-based solution of colloidal graphite. The gate insulation layer may consist of 0.5–2 μm of parylene, prepared from the dimer Parylene N or C. The dimer is evaporated at 160 °C and cracked to a monomer at 680 °C that subsequently polymerizes on the surface of a crystal kept at room temperature. The gate electrode may either be evaporated or painted (colloidal graphite) directly on the parylene layer over the channel area between source and drain contacts.

In both FET structures, the semiconductor properties are tested only in the very thin surface layer of

the single crystals (or thin films in a thin-film FET). However, this surface layer may be easily affected by intercalation/adsorption of gases present in the transistor environment. In this way, chemical sensors may be constructed, where the molecules are introduced into the channel area of the FET. Additionally, with the exception of the air-gap structure, the channel area may be modified/affected by the direct contact with a gate dielectric.

The highest FET mobility of 20 $\text{cm}^2/(\text{V s})$ in p-type rubrene or 1.6 $\text{cm}^2/(\text{V s})$ in n-type tetracyanoquinodimethane (TCNQ) [25.67] has been obtained in such devices. However, since FET structures probe only the top surface layers, the charge carrier mobility obtained in this way is not necessarily identical to the mobilities measured in the bulk.

The surface charge transport mobility generally decreases with decreasing temperature, an effect attributed to trapping states present at the surface. The bulk charge transport values of electrons and holes may be much higher, as was demonstrated by time-of-flight measurements in naphthalene, anthracene or perylene at low temperatures. In these cases the superior transport properties were attributed to meticulous purification and bulk crystal growth optimization as well as the insensitivity of the bulk properties on chemically poorly defined surface states.

In any case, electronic transport measurements are indispensable tools in evaluating the electronic traps affecting the charge transport in organic semiconductors. Together with optical methods and x-ray topography and diffraction to measure structural quality and elemental/molecular purity, the overall crystal quality of organic semiconductors can be efficiently assessed.

25.8 Conclusions

Single crystals of organic semiconductors have been grown mostly for basic research studies, for structure evaluation as well as for evaluation of maximum performance of organic semiconductor devices. Many purification and crystal growth methods have been applied to organic single crystals. Gas-phase transport is often used for growth of crystals used for field-effect transistors and x-ray structure determinations, whereas the Bridgman method dominates the growth of large crystals. So far, the highest electron and hole mobilities measured by the time-of-flight method have been achieved on crystals purified by extensive zone refining and grown from the melt by the Bridgman method.

However, the highest field-effect mobilities have been achieved on crystals purified by sublimation and grown from the vapor phase. The difference in mobilities between the bulk and surface measurements is attributed to different types of defects and contamination in the bulk and on the surfaces. These measurement values still reflect extrinsic effects and do not yet measure the intrinsic properties of organic semiconductor.

As of today, there are not enough studies of quality, purity, defect concentration, and optical and electrical properties on the same material grown by different methods. On the one hand this is a result of the instability of organic compounds and associated changes of

their properties with time, while on the other hand it is challenging to use specific analysis methods for precise characterization of brittle crystals where defects alter with aging. Organic semiconductors need defect and impurity evaluation at part-per-million levels, similar to inorganic semiconductors. Even though organic semiconductors are much less studied than their inorganic counterparts, it seems that organic semiconductors will

be an important component of future microelectronics. Organic light-emitting diodes (OLEDs) and displays are already commercially available. However, progress in organic material characterization is needed to guide improvements in purification and crystal growth that will consequently lead to the development of new, better organic semiconductors and higher-performance devices.

References

- 25.1 A. Byk, H. Borck: Photoelektrische Versuche mit Anthracen, *Verh. Dtsch. Phys. Ges.* **12**(15), 621–651 (1910)
- 25.2 J.B. Birks: *Scintillation Counters* (Pergamon, London 1953)
- 25.3 S.R. Forrest: The path to ubiquitous and low-cost organic electronic applications on plastic, *Nature* **428**, 911–918 (2004)
- 25.4 E. Reichmanis, H. Katz, C. Kloc, A. Maliakal: Plastic electronic devices: from materials design to devices applications, *Bell Labs Tech. J.* **10**, 87–105 (2005)
- 25.5 G. Horowitz, M. Hajlaoui: Mobility in polycrystalline oligothiophene field-effect transistors dependent on grain size, *Adv. Mater.* **12**, 1046–1050 (2000)
- 25.6 T.W. Kelley, C.D. Frisbie: Gate voltage dependent resistance of a single organic semiconductor grain boundary, *J. Phys. Chem. B* **105**, 4538–4540 (2001)
- 25.7 N. Karl: Charge-carrier mobility in organic crystals. In: *Organic Electronic Materials, Springer Series in Material Science*, Vol. 41, ed. by R. Farchioni, G. Grosso (Springer, Berlin Heidelberg 2001) pp. 283–326, Part II: Low Molecular Weight Organic Solids
- 25.8 M.E. Gershenson, V. Podzorov, A.F. Morpurgo: Colloquium: Electronic transport in single-crystal organic transistor, *Rev. Mod. Phys.* **78**, 973–989 (2006)
- 25.9 D.T.J. Hurle (Ed.): *Handbook of Crystal Growth* (Elsevier, Amsterdam 1994)
- 25.10 R.A. Laudise: *The Growth of Single Crystals* (Prentice-Hall, Englewood Cliffs 1970)
- 25.11 F.R. Lipsett: On the production of single crystals of naphthalene and anthracene, *Can. J. Phys.* **35**, 284–298 (1957)
- 25.12 N. Karl: High purity organic molecular crystals. In: *Crystals Growth, Properties and Applications*, Vol. 4, ed. by H.C. Freyhardt (Springer, Berlin Heidelberg 1980) pp. 1–100
- 25.13 R.A. Laudise, C. Kloc, P.G. Simpkins, T. Siegrist: Physical vapour growth of organic semiconductors, *J. Cryst. Growth* **187**, 449–454 (1998)
- 25.14 R.W.I. de Boer, M.E. Gershenson, A.F. Morpurgo, V. Podzorov: Organic single-crystal field-effect transistors, *Phys. Status Solidi (a)* **201**, 1302–1331 (2004)
- 25.15 A.T. Tripathi, M. Heinrich, T. Siegrist, J. Pflaum: Growth and electronic transport in 9,10-diphenyl-anthracene single crystals – An organic semiconductor of high electron and hole mobility, *Adv. Mater.* **19**(16), 2097–2101 (2007)
- 25.16 D. Käfer, G. Witte: Growth of crystalline rubrene films with enhanced stability, *PhysChemChemPhys* **7**, 2850–2853 (2005)
- 25.17 M.-C. Blüm, E. Čavar, M. Pivetta, F. Patthey, W.-D. Schneider: Conservation of chirality in a hierarchical supramolecular self-assembled structure with pentagonal symmetry, *Angew. Chem. Int. Ed.* **44**, 5334–5337 (2005)
- 25.18 A. Gavezotti, G.R. Desiraju: A systematic analysis of packing energies and other packing parameters for fused-ring aromatic hydrocarbons, *Acta Cryst. B* **44**, 427–434 (1988)
- 25.19 H. Klapper: X-ray topography of organic crystals, *Growth Cryst.* **13**, 109–162 (1991)
- 25.20 O.H. LeBlanc: Hole and electron drift mobilities in anthracene, *J. Chem. Phys.* **33**, 626 (1960)
- 25.21 R.G. Kepler: Charge carrier production and mobility in anthracene crystals, *Phys. Rev.* **119**, 1226–1229 (1960)
- 25.22 J.B. Birks: *Scintillation Counters* (Pergamon, London 1953)
- 25.23 G. Horowitz, D. Fichou, X.Z. Peng, Z.G. Xu, F. Garnier: A field-effect transistor based on conjugated alpha-sexithienyl, *Solid State Commun.* **72**, 381–384 (1989)
- 25.24 G. Horowitz, F. Garnier, A. Yassar, R. Hajlaoui, F. Kouki: Field-effect transistor made with a sexithiophene single crystal, *Adv. Mater.* **8**, 52–54 (1996)
- 25.25 G.S. Hammond, V.J. Kuck (Eds.): *Fullerenes, Synthesis, Properties, and Chemistry of Large Carbon Clusters* (ACS, Washington 1992)
- 25.26 F.H. Moser, A.L. Thomas (Eds.): *The Phthalocyanines, Properties* (CRC, Boca Raton 1983)
- 25.27 A. Facchetti, H.E. Katz, T.J. Marks, J. Veinot: Organic semiconductor materials. In: *Printed Organic and Molecular Electronics*, ed. by D. Gamota, P. Brazis, K. Kalyanasundaram (Kluwer, Dordrecht 2004)

- 25.28 W. Warta, R. Stehle, N. Karl: Ultrapure, high mobility organic photoconductors, *Appl. Phys. A* **36**, 163–170 (1985)
- 25.29 E.A. Chandross, J. Ferguson: Photodimerization of crystalline anthracene. The photolytic dissociation of crystalline dianthracene, *J. Chem. Phys.* **45**, 3564–3567 (1966)
- 25.30 O.D. Jurchescu, J. Baas, T.M. Palstra: Effect of impurities on the mobility of single-crystal pentacene, *Appl. Phys. Lett.* **84**, 3061–3063 (2004)
- 25.31 L.B. Roberson, J. Kowalik, L.M. Tolbert, C. Kloc, R. Zeis, X. Chi, R. Fleming, C. Wilkins: Pentacene disproportionation during sublimation for field-effect transistors, *J. Am. Chem. Soc.* **127**, 3069–3075 (2005)
- 25.32 G. Pfann: Principles of zone-melting, *J. Metals* **4**, 747–753 (1952)
- 25.33 K.H. Probst, N. Karl: Energy levels of electron and hole traps in the band gap of doped anthracene crystals, *Phys. Status Solidi (a)* **27**, 499–508 (1975)
- 25.34 K.H. Probst, N. Karl: Energy levels of electron and hole traps in the band gap of doped anthracene crystals, *Erratum, Phys. Status Solidi (a)* **31**, 793 (1975)
- 25.35 G.J. Sloan, A.R. McGhie: Purification of tetracene: vapor zone refining and eutectic zone melting, *Mol. Cryst. Liq. Cryst.* **18**, 17–37 (1972)
- 25.36 M. Brissaud, C. Dolin, J. Le Duigou, B.S. McArdle, J.N. Sherwood: The purification and growth of large ultra-pure plastic single crystals of trimethylacetic acid, *J. Cryst. Growth* **38**, 134–138 (1977)
- 25.37 C. Kloc, P.G. Simpkins, T. Siegrist, R.A. Laudise: Physical vapor growth of centimeter-sized crystals of α -hexathiophene, *J. Cryst. Growth* **182**, 416–427 (1997)
- 25.38 M. Melucci, M. Gazzano, G. Barbarella, M. Cavallini, F. Biscarini, P. Maccagnani, P. Ostojic: Multiscale self-organization of the organic semiconductor α -quinoxithiophene, *J. Am. Chem. Soc.* **125**, 10266–10274 (2003)
- 25.39 D. Fichou, B. Bachet, F. Demanze, I. Billy, G. Horowitz, F. Garnier: Growth and structural characterization of the quasi-2-D single crystal of α -octithiophene, *Adv. Mater.* **8**, 500–504 (1996)
- 25.40 J. Cornil, J.P. Calbert, J.L. Bredas: Electronic structure of pentacene single crystal: relation to transport properties, *J. Am. Chem. Soc.* **123**, 1250–1251 (2001)
- 25.41 W.J. Bailey, C.-W. Liao: Cyclic dienes XI. New syntheses of hexacene and heptacene, *J. Am. Chem. Soc.* **77**, 992–993 (1955)
- 25.42 S. Kivelson, O.L. Chapman: Polyacene and a new class of quasi-one-dimensional conductors, *Phys. Rev. B* **28**, 7236–7243 (1983)
- 25.43 H. Mette, H. Pick: Elektronenleitfähigkeit von Anthracen-Einkristallen, *Z. Phys.* **134**, 566–575 (1953), in German
- 25.44 H. Pick, W. Wissman: Elektronenleitung von Naphthalin-Einkristallen, *Z. Phys.* **138**, 436–440 (1954), in German
- 25.45 M. Tachibana, K. Kono, M. Shimizu, K. Kolima: Growth and dislocation characteristics of organic molecular crystals: 2,3-Dimethylnaphthalene, *J. Cryst. Growth* **198/199**, 665–669 (1999)
- 25.46 H. Inokuchi: Semi- and photo-conductivity of molecular single-crystals. Anthracene and pyrene, *Bull. Chem. Soc. Jpn.* **29**, 131–133 (1956)
- 25.47 B.J. McArdle, J.N. Sherwood: The growth and perfection of phenanthrene single crystals, *J. Cryst. Growth* **22**, 193–200 (1974)
- 25.48 J. Bleay, R.M. Hooper, R.S. Narang, J.N. Sherwood: The growth of single crystals of some organic compounds by the Czochralski technique and the assessment of their perfection, *J. Cryst. Growth* **43**, 589–596 (1978)
- 25.49 C. Kloc, R.A. Laudise: Vapor pressures of organic semiconductors: α -hexathiophene α -quaterthiophene, *J. Cryst. Growth* **193**, 563–571 (1998)
- 25.50 G. Horowitz, B. Bachet, A. Yassar, P. Lang, F. Demanze, J. Fave, F. Garnier: Growth and characterization of sexithiophene single crystals, *Chem. Mater.* **7**, 1337–1341 (1995)
- 25.51 T. Siegrist, C. Kloc, R.A. Laudise, H.E. Katz, R.C. Haddon: Crystal growth, structure, and electronic band structure of α -4t polymorphs, *Adv. Mater.* **10**, 379–382 (1998)
- 25.52 L. Antolini, G. Horowitz, F. Kouki, F. Garnier: Polymorphism in oligothiophenes with an even number of thiophene subunits, *Adv. Mater.* **10**, 382–385 (1998)
- 25.53 T. Kuroda: Vapor growth mechanism of a crystal surface covered with a quasi-liquid layer – Effect of self-diffusion coefficient of the quasi-liquid layer on the growth rate, *J. Cryst. Growth* **99**, 83–87 (1990)
- 25.54 H. Meng, M. Bendikov, G. Mitchell, R. Helgeson, F. Wudl, Z. Bao, T. Siegrist, C. Kloc, C. Chen: Tetramethylpentacene: Remarkable absence of steric effect on field effect mobility, *Adv. Mater.* **15**, 1090–1093 (2003)
- 25.55 L.E. Lyons, G.C. Morris: Photo- and semi-conductance in organic crystals. Part III. Photo-effects in dry air with eleven organic compounds, *J. Chem. Soc. August*, 3648–3660 (1957)
- 25.56 R. Zeis, C. Besnard, T. Siegrist, C. Schlockermann, X. Chi, C. Kloc: Field-effect studies on rubrene and impurities of rubrene, *Chem. Mater.* **18**, 244–248 (2006)
- 25.57 J. Niemax, A.K. Tripathi, J. Pflaum: Comparison of the electronic properties of sublimation- and vapor-Bridgman-grown crystals of tetracene, *Appl. Phys. Lett.* **86**, 122105 (2005)
- 25.58 G. Zuccalli, M. Zha, L. Zanotti, C. Paorici: Vapour growth of organic crystals by a semi-open Piz-

- zareello (SOP) technique, *Mater. Sci. Forum* **203**, 35–38 (1996)
- 25.59 R.S. Fiegelson, R.K. Route, T.-M. Kao: Growth of urea crystals by physical vapor transport, *J. Cryst. Growth* **72**, 585–594 (1985)
- 25.60 R. Zeis, T. Siegrist, C. Kloc: Single-crystal field-effect transistors based on copper phthalocyanine, *Appl. Phys. Lett.* **86**, 022103 (2005)
- 25.61 R. Zeis, C. Kloc, K. Takimiya, Y. Kunugi, Y. Konda, N. Niihara, T. Otsubo: Single-crystal field-effect transistors based on organic selenium-containing semiconductor, *Jpn. J. Appl. Phys.* **44**(6A), 3712–3714 (2005)
- 25.62 H. Moon, R. Zeis, E.-J. Borkent, C. Besnard, A.J. Lovinger, T. Siegrist, C. Kloc, Z. Bao: Synthesis, crystal structure, and transistor performance of tetracene derivatives, *J. Am. Chem. Soc.* **126**, 15322–15323 (2004)
- 25.63 A.R. Laudise, P.M. Bridenbaugh, C. Kloc, S.L. Jouppi: Organo-thermal crystal growth of $\alpha 6$ thiophene, *J. Cryst. Growth* **178**, 585–592 (1997)
- 25.64 H. Kallman, M. Pope: Preparation of thin anthracene single crystals, *Rev. Sci. Instrum.* **29**, 993–994 (1958)
- 25.65 L. Zeng, M. Zha, M. Curti, L. Zanotti, C. Paorici: Solution growth for high anisotropy organic crystals, *Mater. Sci. Forum* **203**, 39–42 (1996)
- 25.66 B.D. Chapman, A. Checco, R. Pindak, T. Siegrist, C. Kloc: Dislocations and grain boundaries in semiconducting rubrene single crystals, *J. Cryst. Growth* **290**, 479–484 (2006)
- 25.67 E. Menard, V. Podzorov, S.-H. Jur, A. Gaur, M.E. Gershenson, J.A. Rogers: High performance n- and p-type single-crystal organic transistors with free-space gate dielectrics, *Adv. Mater.* **16**(22/23), 2097–2101 (2004)

Growth of III-Nitrides with Halide Vapor Phase Epitaxy (HVPE)

Carl Hemmingsson, Bo Monemar, Yoshinao Kumagai, Akinori Koukitu

III-nitrides can be grown by employing several different techniques, such as molecular-beam epitaxy (MBE), metalorganic vapor-phase epitaxy (MOVPE), halide vapor-phase epitaxy (HVPE), high-pressure solution growth, and sputtering. Each of these are suited for a particular application; the specific property of HVPE is a much larger growth rate, which makes this technique the natural choice for growth of very thick layers that can be used as high-quality native substrates for subsequent growth of device structures using other techniques. Such substrates will be needed for certain devices with high current density or high voltage load, where the high defect density caused by growth on foreign substrates (heteroepitaxy) cannot be tolerated. The HVPE technology is still under development, and below we present the present situation with emphasis on GaN. The thermodynamic limitations of HVPE growth are discussed first, including the high-temperature chemistry in both the source zone and growth zone of a growth reactor. Examples of the design of growth systems are given; in particular, issues such as flow patterns, parasitic growth, and growth rates are discussed. Methods to reduce the defect density for growth on foreign substrates are discussed, as well as various lift-off techniques to prepare free-standing GaN wafers. Common characterization techniques are mentioned, and important physical properties of high-quality GaN wafers are given. The ongoing developments of HVPE growth for AlN and InN are also briefly summarized.

26.1	Growth Chemistry and Thermodynamics	869
26.2	HVPE Growth Equipment	872
26.3	Substrates and Templates for Bulk GaN Growth	875
26.3.1	Sapphire	875
26.3.2	Silicon Carbide	876
26.3.3	GaAs	876
26.3.4	Lattice-Matched Substrates	877
26.3.5	Growth on Templates	877
26.3.6	Basic 1S-ELO Structures	877
26.3.7	2S-ELO	878
26.4	Substrate Removal Techniques	879
26.4.1	Laser Lift-Off	879
26.4.2	Self-Separation	880
26.4.3	Mechanical Polishing	881
26.4.4	Plasma Etching	881
26.4.5	Chemical Etching and Spontaneous Self-Separation	881
26.5	Doping Techniques for GaN in HVPE	882
26.5.1	n-Type Doping of GaN	882
26.5.2	p-Type Doping of GaN	882
26.6	Defect Densities, Dislocations, and Residual Impurities	883
26.7	Some Important Properties of HVPE-Grown Bulk GaN Material	887
26.8	Growth of AlN by HVPE: Some Preliminary Results	888
26.9	Growth of InN by HVPE: Some Preliminary Results	890
	References	891

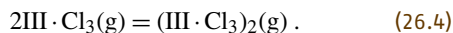
26.1 Growth Chemistry and Thermodynamics

Commonly, a HVPE reactor for growing group III nitrides (GaN, AlN or InN) consists of two main zones: the source zone for forming chloride gas of a group III

metal (Ga, Al or In) and the growth zone where the chloride of a group III metal and NH_3 are mixed to grow the nitride film. Therefore, understanding of the chemistry

at both source zone and growth zone is essential to grow nitrides by HVPE.

In the source zone of a reactor, the group III metal is placed and maintained at a certain temperature. HCl gas is commonly used to form chloride gas of the group III metal. Therefore, the gaseous species formed at the source zone and their equilibrium partial pressures when HCl gas is introduced over the group III metal are important issues. Principally, gaseous species at the source zone are $\text{III} \cdot \text{Cl}$, $\text{III} \cdot \text{Cl}_2$, $\text{III} \cdot \text{Cl}_3$, $(\text{III} \cdot \text{Cl}_3)_2$, HCl, H_2 , and inert gas (IG: N_2 , He, Ar, etc.). The following chemical reactions occur simultaneously



Equilibrium partial pressures of the gaseous species in the source zone can be calculated by a thermodynamic calculation [26.1]. It should be noted that a low source-zone temperature, a high HCl input partial pressure or a small surface area of group III metal might cause insufficient reactions in the source zone, i. e., the reactions will be kinetically limited.

Figure 26.1 shows equilibrium partial pressures of the gaseous species P_i in the source zone under a to-

tal pressure of the source zone ($\sum P_i$) of 1.0 atm, an input partial pressure of HCl (P_{HCl}^0) of 6×10^{-3} atm, and a mole fraction of hydrogen in the carrier gas (F^0) of 0.0 (inert carrier gas), calculated for Ga, Al, and In source zones. The source-zone temperature ranges from 300 to 1000 °C. In the Ga source zone, the major gaseous species of Ga is GaCl and its equilibrium partial pressure is almost equal to P_{HCl}^0 at temperatures above 500 °C. This means that the predominant reaction at the Ga source zone is (26.1), and almost all HCl introduced into the source zone reacts with Ga metal. The In source zone shows the same tendency as the Ga source zone. Only the Al source zone shows a change of the predominant reaction with increase of the source-zone temperature. At low temperatures, the major gaseous species of Al is AlCl_3 , with an equilibrium partial pressure one-third of P_{HCl}^0 , whereas it is AlCl at high temperatures, above 800 °C. Although the carrier gas used in Fig. 26.1 is IG, the equilibrium partial pressures of group III chlorides do not vary when H_2 is used as a carrier gas ($F^0 = 1.0$).

Figure 26.2 shows the values of equilibrium constants K of the growth reactions of GaN, AlN, and InN using $\text{III} \cdot \text{Cl}$ or $\text{III} \cdot \text{Cl}_3$ and NH_3 as a function of the reciprocal of the reaction (growth-zone) temperature.

The equilibrium constants can be calculated using thermochemical tables [26.2, 3]. As seen in Fig. 26.1, the group III chloride formed at the source zone is $\text{III} \cdot \text{Cl}$ (monochloride) when the source-zone temperature is sufficiently high. However, with decreasing

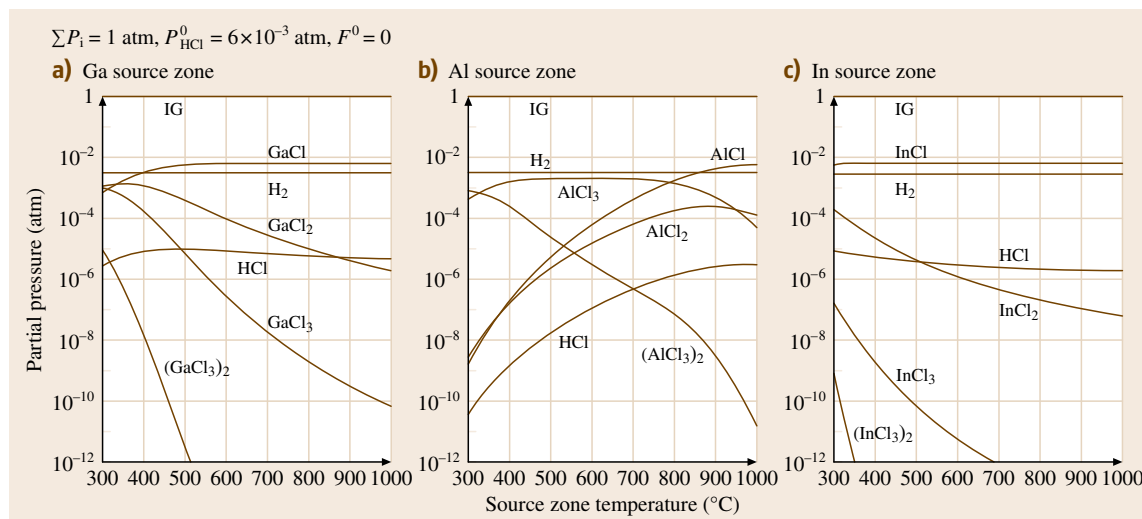


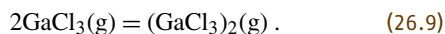
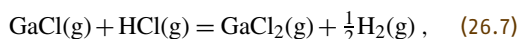
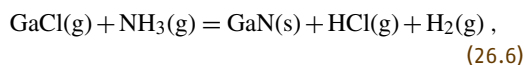
Fig. 26.1a–c Equilibrium partial pressures of gaseous species over group III metals placed in the source zone as a function of temperature calculated for (a) Ga, (b) Al, and (c) In source zones

source-zone temperature, the equilibrium partial pressure of $\text{III} \cdot \text{Cl}_3$ usually increases. Also, GaCl_3 , AlCl_3 , and InCl_3 are available commercially in powder form, which makes it possible to sublime them for growth of nitrides, as an alternative to the use of HCl . Therefore, equilibrium constants of growth reactions using trichlorides are also shown. In the figure, the following order of equilibrium constants K for growing nitrides is seen

$$K_{\text{AlN}} \gg K_{\text{GaN}} > K_{\text{InN}}. \quad (26.5)$$

In general, this order corresponds to the growth rate of nitrides using group III chlorides. For the growth reactions of GaN , the equilibrium constants are close to zero in both reactions using GaCl and GaCl_3 . Therefore, growth of GaN is possible using GaCl or GaCl_3 . In the AlN growth, the values of equilibrium constants are extremely large in both reactions using AlCl and AlCl_3 , indicating high-speed growth of AlN . On the other hand, in the case of InN growth, the value of $\log K$ using InCl is significantly small and negative. Consequently, growth of InN is possible only using InCl_3 as an In source. Another point expected from the figure is the influence of H_2 on the growth of nitrides, since the growth reactions contain H_2 as a product when monochlorides are used. Therefore, thermodynamic analysis for the growth zone of a HVPE system is meaningful as well as that for source zone, since growth is commonly performed under mass-transportation-limited or thermodynamically controlled conditions.

Thermodynamic analysis of the HVPE growth zone has been performed and reported for GaN [26.4, 5], AlN [26.6], and InN [26.7]. In the literature the influence of various growth conditions on the driving force of growth is described. Here thermodynamic analysis of the conventional GaN growth zone is described as an example. When GaCl formed at the source zone and NH_3 are separately introduced into the growth zone with a carrier gas mixture of H_2 and IG , the following chemical reactions occur simultaneously



Equation (26.6) is the main reaction producing GaN growth and the others (26.7–26.9) are secondary reactions. Then, gaseous species coexisting at the growth

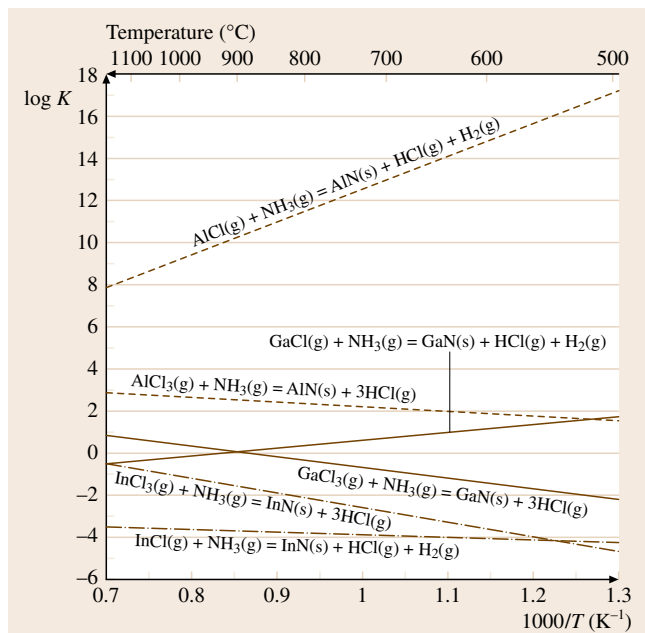
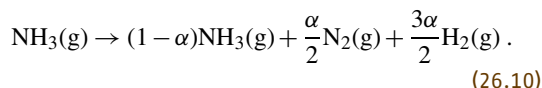


Fig. 26.2 Values of $\log K$ as a function of reciprocal of temperature calculated for growth reactions of GaN , AlN , and InN using mono- or trichloride of group III metals and NH_3

zone are GaCl , GaCl_2 , GaCl_3 , $(\text{GaCl}_3)_2$, NH_3 , HCl , H_2 , and IG . Figure 26.3 shows equilibrium partial pressures of gaseous species at the growth zone as a function of growth-zone temperature. Calculation of equilibrium partial pressures was performed after a procedure developed by Koukitu and Seki [26.8] for HVPE growth of arsenide and phosphide of Ga and In. The growth conditions are as follows: total pressure of the reactor ($\sum P_i$) of 1.0 atm, input partial pressure of GaCl (P_{GaCl}^0) of 6.0×10^{-3} atm, input V/III ratio ($P_{\text{NH}_3}^0/P_{\text{GaCl}}^0$) of 50, and mole fraction of hydrogen in the carrier gas (F^0) of 1.0 (H_2 carrier gas). An additional parameter α which denotes the mole fraction of decomposed NH_3 before GaN growth is introduced as follows



The value of α is difficult to determine exactly since it depends on the growth conditions, equipment, and temperature. In Fig. 26.3, the value is fixed at 0.03 according to the literature [26.9], and agreement between the calculated and experimental results [26.4–7]. It is seen that NH_3 , GaCl , IG (N_2), and HCl are major gaseous species as well as H_2 used as the carrier gas.

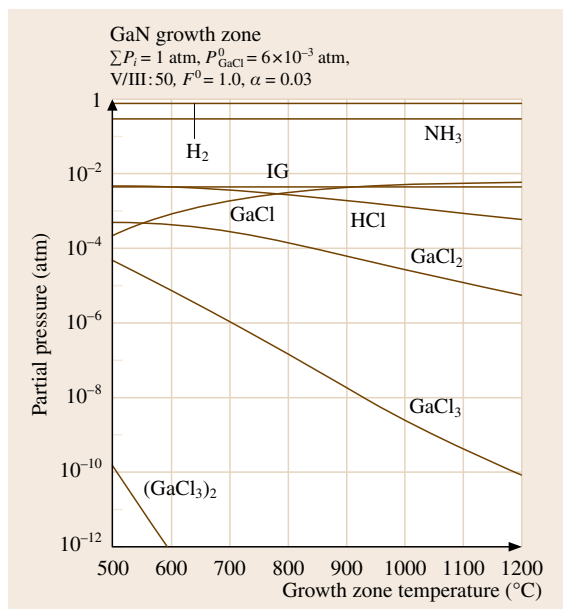


Fig. 26.3 Equilibrium partial pressures of gaseous species over GaN as a function of growth temperature

The equilibrium partial pressure of HCl decreases with increase of growth-zone temperature, while that of GaCl increases with increase of growth-zone temperature and approaches a value nearly equal to P_{GaCl}^0 . This means that the growth rate of GaN becomes smaller at high growth temperatures. It is of interest to calculate the driving force for growth as functions of various growth conditions. The driving force ΔP_{Ga} is given by

$$\Delta P_{\text{Ga}} = P_{\text{GaCl}}^0 - (P_{\text{GaCl}} + P_{\text{GaCl}_2} + P_{\text{GaCl}_3} + 2P_{(\text{GaCl}_3)_2}), \quad (26.11)$$

i. e., the difference between the number of Ga atoms put in and the amount of Ga atoms remaining in the vapor phase. Figure 26.4 shows the driving force for GaN growth using GaCl and NH_3 as a function of

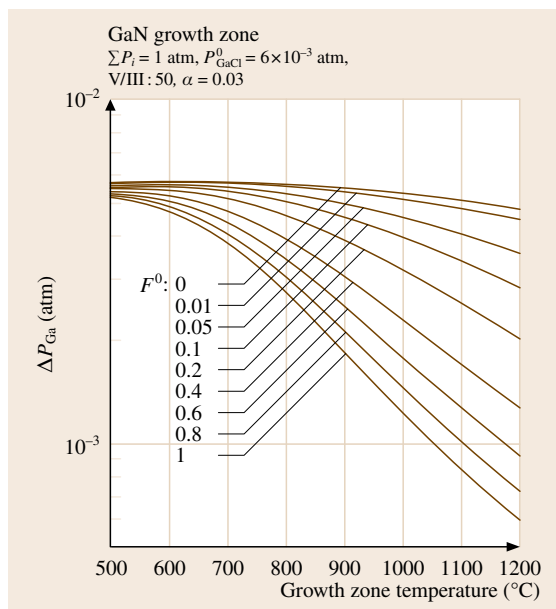


Fig. 26.4 Driving force for growth of GaN as a function of growth-zone temperature calculated for several values of F^0

growth temperature calculated for several values of F^0 . It is seen that the driving force decreases with increase of the growth temperature and F^0 . Furthermore, the influence of H_2 on the decrease of the driving force is more significant at high growth temperatures. It has also been clarified that the driving force decreases with increase of H_2 in the carrier gas in GaN and InN growths using trichlorides [26.5, 7]. By contrast, growth of AlN using mono- or trichloride of Al does not depend on the presence of H_2 , which is due to the extremely large equilibrium constants of the growth reactions, as can be seen in Fig. 26.2. Consequently, for high-speed and high-temperature growth of GaN by HVPE, use of inert carrier gas or mixed carrier gas of H_2 and IG with a small amount of H_2 is quite effective.

26.2 HVPE Growth Equipment

A schematic picture of a typical horizontal hot-walled HVPE growth system, which is the most commonly used geometry, is shown in Fig. 26.5. The reaction chamber is normally a quartz tube that is heated either with a multizone oven or by radiofrequency (RF)

induction. The reactor has one low-temperature region where the halides are formed by letting high-purity HCl or Cl_2 gas flow over a melt of a group III metal. The temperature is normally kept about 800–900 °C in this section of the reactor. The precursors are reacting

on the substrate, which is kept at a temperature about 1000–1100 °C. In order to minimize parasitic growth in the inlet of the growth zone and on the walls of the reactor, it is important that the ammonia and the halide are not mixed before they reach the substrate. Inert gases such as nitrogen (N_2), helium (He), argon (Ar) or hydrogen (H_2) and mixtures of these gases are used as carrier gases. In terms of the flow pattern, gases with lighter molecules, such as He or H_2 , are more favorable, i.e., the laminar flow condition is obtained more easily.

In HVPE, a huge amount of ammonium chloride (NH_4Cl) is formed downstream of the growth zone due to the reaction between HCl and ammonia. Thus, care has to be taken in order to avoid clogging of the exhaust. The growth system has to be equipped with some type of trap at the outlet. The deposition of ammonium chloride can also be avoided by heating the outlet pipes above ≈ 150 °C. Growth of boules requires very long growth runs, thus it may be necessary to change the trap during the process.

The growth takes place under excess ammonia conditions and in a growth regime where the growth rate is mass transport limited by the vapor pressure of the halide precursor. Thus, in a horizontal system such as shown in Fig. 26.5, it is difficult to achieve a uniform deposition of high-quality material over a large-area substrate since the halide easily becomes depleted over the substrate. Using an inlet geometry where the halide

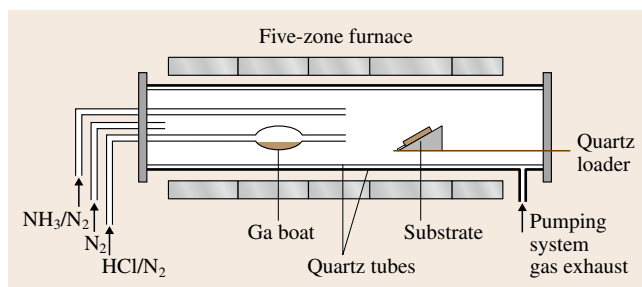


Fig. 26.5 Conventional horizontal HVPE system with a five-zone furnace

precursor is dispersed uniformly across the deposition zone by a showerhead can solve this problem. The proximity of the showerhead to the susceptor, on which the wafer is placed, minimizes premature reactions between the ammonia and the halide, which leads to good chemical efficiency. A showerhead in combination with rotation of the susceptor is suited to the deposition of uniform layers, allowing scalability to be combined with ease of operation. This type of reactor is normally used commercially in order to produce layers up to typically 300–500 μm . In order to grow thicker layers, this type of reactor is not suitable, mainly because of limitations due to parasitic deposition, which will create particle problems and changes of growth conditions during the growth run.

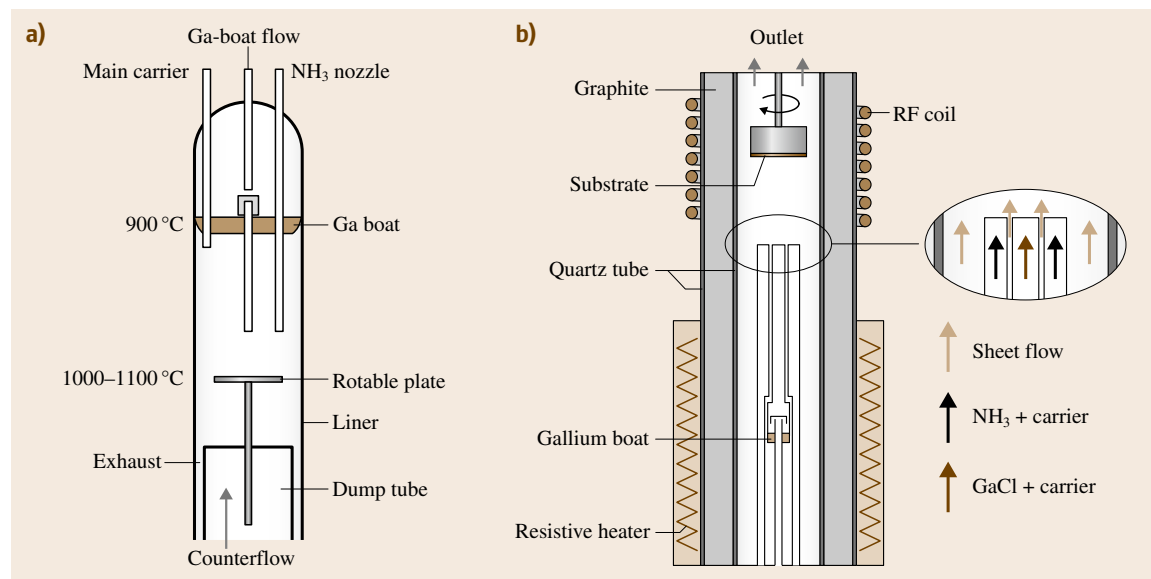


Fig. 26.6 (a) Top-fed vertical reactor geometry. The geometry is taken from [26.10] and (b) bottom-fed vertical HVPE reactor with a concentric inlet in order to minimize parasitical growth in the inlet

An alternative reactor geometry is a vertical setup, as shown in Fig. 26.6. The precursors can be introduced either from the top (Fig. 26.6a) or from the bottom (Fig. 26.6b). In the geometry where the gases are introduced from the top, the gas flow has to be controlled by adjusting the downward forced-convective flow to balance it with the upward buoyancy-driven convection. The problem with this geometry is a possible particle contamination over the substrate due to particles released from the parasitic growth upstream of the substrate. These particles may fall down and induce defect nucleation centers that degrade the quality of the grown crystal. By introducing the precursors from the bottom, this kind of problems can be minimized since the surface of the growing crystal is facing downwards. Figure 26.6b shows a schematic picture of a hot-walled vertical growth system where the precursors are introduced from the bottom. This system is designed for the growth of boules crystals (layers up to several millimeters). In order to avoid premature reactions between the GaCl and the ammonia, which will cause parasitic deposition at the inlet of the reactor, the inlet is designed with concentric tubes where the GaCl and the ammonia are separated using a sheet flow. In addition to the inlet sheet flow, a sheet flow close to the reactor walls prevents parasitic growth on the walls. The reactor is equipped with rotation of the sample holder, and the distance between the growing surface and the inlet can be kept constant by pulling of the holder.

In a vertical system one problem is to stabilize a high and constant conversion ratio of HCl to GaCl due to the small Ga area. This will affect the reactions (26.1–26.4). A reduction of the GaCl vapor pressure will reduce the growth rate, and the increase of the HCl vapor pressure increases the etching component in the growth process. Thus, it is important to design the Ga container in such a way that the HCl volume over the liquid Ga in the Ga container is kept approximately constant over time. Early work established that the GaCl conversion in a horizontal reactor with a large liquid Ga area was typically stabilized at a high value: the conversion efficiency to GaCl was above 95% [26.9]. By careful design of the Ga container, it has been shown that the conversion efficiency can be up to 98% in a vertical reactor [26.12], which is close to chemical equilibrium at 850 °C [26.13].

To achieve a desirable mass transport behavior, it is important to establish a stable, vortex-free flow field in the reactor. Any recirculating flow can create a nonuniform growth rate over the substrate, less control of the parasitic growth, and increased impurity incorporation.

Since the decay of ammonia is a slow process [26.9] which can be accelerated by catalytic effects, a recirculating flow where the gas may be in contact with the walls is especially severe in HVPE, since the parasitic growth on the walls can accelerate the decomposition of the ammonia and, consequently, change the growth conditions. It has been shown that, by minimizing the recirculation flows in the reactor, run-to-run reproducibility is improved drastically [26.14].

The flow pattern in a HVPE reactor is influenced by several mechanisms, such as reactor geometry, heat transfer characteristic, flow boundary conditions, and choice of carrier gases. With respect to recirculation flow, a bottom-fed vertical configuration where the colder gases are flowing upwards towards the normally hotter substrate is preferred because the buoyancy effect has a tendency to stabilize the flow. The use of a hot-walled system will also reduce the recirculation flows generated by natural convection since the precursors are efficiently heated and the thermal gradients are small in such a system. However, since the substrate is oriented perpendicular to the flow direction some care has to be taken in the choice of carrier gases and gas velocities. Figure 26.7 shows an example of modeling using different gas velocities and gas compositions in

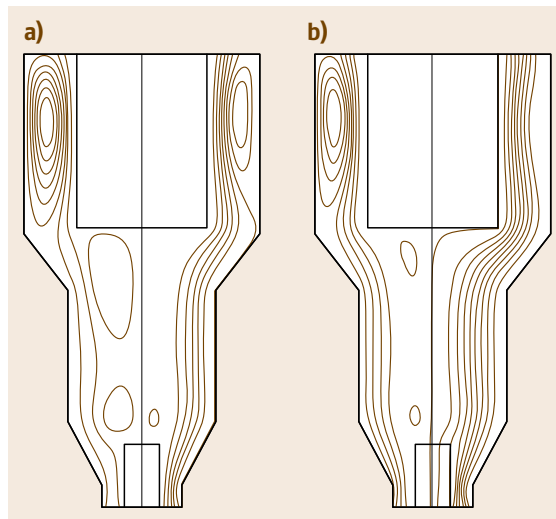


Fig. 26.7 (a) Streamline plots using N₂ as a carrier gas. The left side shows the streamlines using 0.51/min of carrier gas and the right side shows the situation when using 51/min of carrier gas and (b) shows the streamlines using 31/min of N₂ (left side) and 31/min of He (right side). The GaCl and NH₃ flow was 20 and 500 ml/min, respectively, in all cases (after [26.11])

a bottom-fed vertical configuration [26.11]. With a low total N_2 carrier gas flow ($< 11/\text{min}$), the growth is turbulent, with a vortex pattern in the middle of the substrate. At higher total flow the pattern evolves to an approximately laminar flow in the range $3\text{--}101/\text{min}$. N_2 is an attractive choice for carrier gas, since it is in-

ert during the growth conditions, and does not affect the growth chemistry. However, in terms of the flow pattern, gases with lighter molecules, such as He or H_2 , are more favorable, i. e., the laminar flow condition can be obtained using lower gas velocities, as clearly shown from Fig. 26.7b.

26.3 Substrates and Templates for Bulk GaN Growth

The ideal way of producing bulk GaN crystals is homoepitaxial growth on a GaN seed crystal. However, due to the lack of commercially available GaN wafers, the use of GaN substrates for HVPE bulk growth is not yet commonly employed. In the few reported experiments on homoepitaxial growth using HVPE, high-pressure grown platelets [26.15] have been used. The dislocation density is low ($< 100\text{ cm}^{-2}$) in this type of substrate; however, the lateral size and thickness are limited to about 1 cm and $100\text{ }\mu\text{m}$, respectively, and the carrier concentration is very high ($\approx 10^{19}\text{ cm}^{-3}$). The high carrier concentration expands the lattice parameters compared with the relatively low-doped HVPE GaN, which results in stress and cracking problems for layers thicker than $\approx 100\text{ }\mu\text{m}$ [26.16, 17]. Thus, due to the lack of commercial bulk GaN substrates, the growth of bulk crystals is mostly performed on foreign substrates (heteroepitaxy). Several different types of substrate are used or have been used for growth of thick GaN layers using HVPE, such as sapphire (Al_2O_3), SiC, GaAs, Si, MgO, ZnO, TiO_2 and $MgAl_2O_4$ [26.18], to mention a few.

Among these Al_2O_3 is the most commonly employed substrate material for bulk GaN growth, mainly due to the possibility of obtaining large-area sapphire wafers (2 inches) at relatively low cost. Most often, heteroepitaxial growth gives rise to numerous defects such as threading dislocations (TD), stacking faults, voids, and hexagonal pits due to the lattice mismatch and

difference in thermal expansion between the substrate and the grown material. Table 26.1 summarizes these properties for some of the most important substrate materials used today. A nonpolar substrate can also give rise to inversion domains and mixed polarities in the grown layer. These defects are detrimental to device performance, causing high device leakage current, short minority-carrier lifetime, reduced thermal conductivity, etc. Other important properties of the substrate that have to be considered are those related to the surface, such as surface roughness, step height, terrace width, and wetting behavior.

26.3.1 Sapphire

Heteroepitaxial growth on sapphire involves several problems. The large difference in lattice constant between sapphire and GaN gives rise to a high density of TDs, and the larger thermal expansion coefficient of sapphire compared with GaN causes a biaxial compressive stress in the GaN layer as it is cooled from growth temperature. For thicker films ($> 50\text{ }\mu\text{m}$), the stress can cause cracking of both the GaN epilayer and the substrate. GaN epitaxy on *c*-plane (0001) sapphire, which is the most common orientation, results in *c*-plane-oriented films, but with a 30° rotation of the in-plane GaN crystal directions with respect to the same directions in the sapphire. Without the in-plane rotation, the lattice mismatch between the GaN and the sapphire is

Table 26.1 Surface lattice parameters and thermal expansion coefficients of some technologically important substrate materials for GaN growth

Substrate	Crystal structure	Growth plane for wurtzite GaN	Surface lattice parameter (\AA)	In-plane lattice mismatch to GaN (%)	Thermal expansion coefficient (10^{-6} K^{-1})
GaN	Wurtzite	(0001)	3.189		5.6
Al_2O_3	Wurtzite	(0001)	4.758	16.1	7.5
6H-SiC	Wurtzite	(0001)	3.08	3.54	4.2
GaAs	Zincblende	(111)	2.54	20.2	6.03

about 30%. However, the in-plane rotation of the GaN minimizes the lattice difference between the GaN and the sapphire to about 16%. The good morphological, crystallographical, and electrical properties of *c*-plane-grown GaN is mostly responsible for the widespread use of the *c*-orientation.

Nevertheless, in some cases it is beneficial to use growth on planes other than the *c*-plane. In *c*-plane nitrides, we have a built-in electrostatic field in the [0001] direction due to the spontaneous and piezoelectric polarization [26.19]. This field is undesirable for optoelectronics devices since it results in an uncontrollable shift of the emission peak and/or a reduction of the emission efficiency. The influence of this field can be avoided by the use of GaN with other orientations. Thus, other orientations such as *r*-plane ($1\bar{1}02$), *a*-plane ($11\bar{2}0$), and *m*-plane ($10\bar{1}0$) sapphire have been used in order to grow nonpolar *a*-plane GaN [26.20] or to facilitate cleavage of the structure to form edge-emitting lasers [26.21].

By using a miscut sapphire wafer it has been shown that the GaN quality can be improved in MOVPE [26.22, 23]. In HVPE an improvement in the morphology has been observed. Using a slightly miscut *c*-plane substrate with an $\approx 0.3^\circ$ off-orientation against the *a*-plane or the *m*-plane, a reduction in hillocks is observed [26.24]. It has been shown that *a*-plane off-oriented substrates suppress the hillock formation more efficiently than other directions.

Growth on sapphire requires a pretreatment of the sapphire to improve the wetting properties and the crystal quality. One pretreatment step is nitridation, which is done by exposing the sapphire substrate to ammonia at typical growth temperatures (1000–1100°C). It is believed that a thin AlN or AlN–Al₂O₃ layer forms on the surface, which facilitates nucleation [26.25]. This type of pretreatment is also employed in MOVPE [26.26–29] and MBE [26.30] growth of GaN on sapphire substrates. A second step, which is commonly employed and has been shown to reduce the pit density and improve the crystal structure [26.31, 32] is GaCl pretreatment. The GaCl pretreatment is done just before the growth of GaN commences, by exposing the sapphire to GaCl for ≈ 10 –20 min at the growth temperature. It is believed that the GaCl pretreatment supplies nucleation centers for GaN islands and the promotion of the coalescence of the GaN layer in the early stages of growth.

The crystal quality has been shown to improve by the use of a low-temperature-grown GaN buffer layer (LT-GaN). This technique is used for MOVPE

growth of GaN on sapphire and has also been shown to be useful for HVPE growth. This LT-GaN layer greatly improves the surface morphology and reduces the dislocation density of the subsequently grown high-temperature GaN layer. Initially, a thin GaN film on the order of 100 nm is grown at ≈ 550 –650°C. This layer can serve as a starting layer for growth [26.33]. However, it has been shown that annealing of the LT-GaN layer in ammonia before commencing the high-temperature growth reduces the TD density further [26.34]. Upon annealing of the LT buffer, relatively large grains are formed that can serve as nucleation centers for the subsequent high-temperature growth.

26.3.2 Silicon Carbide

SiC is widely used for growth of device structures using MOVPE and MBE due to the fact that it has several advantages to sapphire such as a smaller lattice mismatch (3.1%), a higher thermal conductivity (3.8 W/cm K), it is conductive, SiC has a polarity which facilitates control of polarity of the GaN, and there is no in-plane rotation between the GaN and the SiC, which makes it possible to cleave the crystal for laser facet formation. However, it has also several disadvantages, i.e., it requires in most cases a buffer layer of AlN or AlGaIn due to its poor wetting properties, and the surface roughness is one order of magnitude larger than that of sapphire. The cost of SiC is also much higher than that of sapphire. Most of the above-mentioned favorable properties are not very important for bulk growth and, consequently, SiC substrates are not commonly employed for bulk growth.

26.3.3 GaAs

GaAs is an interesting substrate material since it is brittle and can easily be mechanically removed after growth. It can also be easily removed by etching in aqua regia. Furthermore, it has a thermal expansion coefficient closer to that of GaN than any other foreign substrate material (Table 26.1). GaAs substrates can be used both for growth of zincblende GaN and wurtzite GaN depending on the orientation of the substrate. GaAs(001) gives zincblende GaN while GaAs(111) is used for growth of wurtzite GaN. In principle, zincblende GaN has better electronic properties for device applications, such as isotropic properties, higher mobility, and high optical gain; however, the quality of the zincblende GaN grown on GaAs is very poor due to coexistence between the two phases. Thus, hereafter

we only consider growth of wurtzite GaN grown on GaAs(111).

One problem with growth of GaN on GaAs is the fact that GaAs is decomposed in ammonia ambient at a temperature where the growth of GaN normally takes place (above 1000 °C). This may lead to problems with a degraded GaAs surface before the growth starts and autodoping of As [26.35]. Thus, it is necessary to grow a buffer layer to protect the GaAs surface. One way to do that is to grow a thin protective GaN layer at lower temperatures [26.36, 37]. Using the epitaxial lateral overgrowth (ELO) technique in combination with a low-temperature GaN buffer, 2 inch free-standing GaN layers with a thickness of about 500 μm have been demonstrated [26.28].

26.3.4 Lattice-Matched Substrates

There exist several other potential substrate materials such as LiAlO_2 , LiGaO_2 , and NdGaO_3 with closer lattice matching to GaN than the substrate materials discussed above. Among these, γ -lithium aluminum oxide (LiAlO_2) has shown potential as a substrate material for growth of thick GaN using HVPE [26.38]. The orientation between the LiAlO_2 and the GaN is $\text{GaN}(0001)||\text{LiAlO}_2(110)$ and $\text{GaN}(0001)||\text{LiAlO}_2(001)$ with a lattice mismatch of -1.4% and -6.3% , respectively.

Lithium gallate (LiGaO_2) has the best lattice matching of all, with only 0.9% lattice mismatch in the basal plane, and has been used for growth of thick GaN [26.39]. However, the poor chemical and thermal stability of these substrate materials in the HVPE growth environment makes the growth conditions very critical. In order to avoid decomposition of the substrate surface before growth, elaborate starting procedures have to be applied, with pretreatment steps and low-temperature GaN buffer layers before growth can commence. However, due to a partial decomposition of the substrate during growth, the grown GaN layer is very often spontaneously separated from the substrate during cooling after growth.

26.3.5 Growth on Templates

A very common growth procedure in HVPE is to start the growth on a starting layer of GaN [26.40], AlN [26.41–43] or ZnO [26.25, 44–46] in order to facilitate the initial nucleation process. The starting layer is normally grown heteroepitaxially with MOVPE (GaN) or by sputtering (AlN, MgO). Among these different

types of starting layer, MOVPE-grown GaN is the most frequently used. With the state of the art of the MOVPE GaN heteroepitaxial growth technique today, the starting layers have a TD density typically in the 10^9 cm^{-2} range. In order to reduce the TD density further, the ELO technique can be used. However, this reduction is obtained at the expense of several additional process steps.

26.3.6 Basic 1S-ELO Structures

As mention above, one way to reduce the TD density is the ELO process. This technique has been used in growth of GaAs and has also been successfully used for growth of GaN. A one-step ELO structure (1S-ELO) is fabricated as follows, as depicted in Fig. 26.8: A substrate is covered with a dielectric film (Fig. 26.8a), normally SiN or SiO_2 , and patterned by conventional photolithography to form on its whole area a grating of mask-free seeding windows, as shown in Fig. 26.8b. The orientation of the stripes is normally in the $\{1100\}$

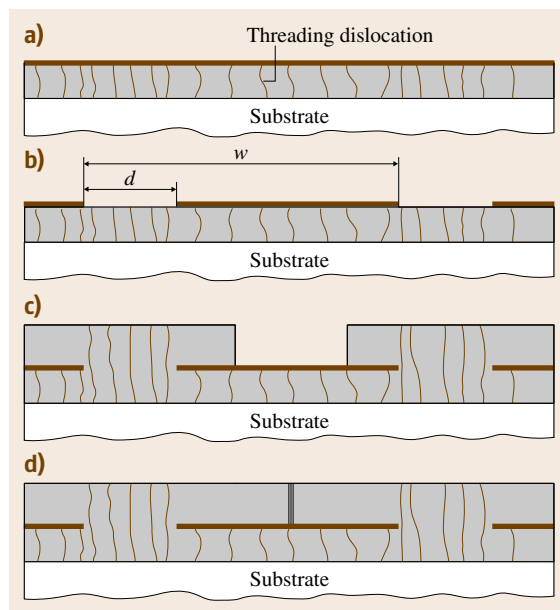


Fig. 26.8a–d Cross-sectional view perpendicular to the $[1100]$ direction showing the different steps in the fabrication of a 1S-ELO structure. Black thin vertical lines represent threading dislocations. (a) Deposition of dielectric film, (b) after etching of the dielectric film, where d is the width of the stripes while w is the period of the stripes, (c) growth in the lateral direction over the film and (d) fully coalesced structure

direction of the GaN layer since it has been shown that lateral expansion is easier in this direction [26.47–50]. The width of the windows (d) in the mask and the periodicity of the lines (w) in the grating is typically about 3 and 10 μm , respectively, and the thickness of the dielectric film is typically about 100 nm. The dielectric is deposited using well-established techniques such as chemical vapor deposition (CVD) or plasma-enhanced CVD (PECVD). Then, an epitaxial layer is deposited on such a substrate. Initially, there is no nucleation on the dielectric stripes; however, as soon as the crystallization front passes the top layer of the mask, growth in the lateral direction over the film starts (Fig. 26.8c), which finally leads to coalescence of the layer, as shown in Fig. 26.8d, and a smooth (0001) surface suitable for further processing is formed.

The basic idea of the ELO technique is that the dielectric mask filters dislocations present in the substrate since defects cannot penetrate through the mask. Thus, in areas above the dielectric stripes where the GaN has grown laterally (wing region), the GaN should be dislocation free. However, in the region where the two laterally grown crystallization fronts meet on the mask, defects are created. Thus, using this technique, two regions with a higher defect density are formed, one in the region without mask and the other in the region where the two laterally growing parts meet on the mask. By using the 1S-ELO technique, the TD density can be reduced by about two orders of magnitude [26.47].

26.3.7 2S-ELO

To reduce the TD density further, double-layer ELO (or 2S-ELO) can be used, where a second dielectric mask layer is processed on a fully coalesced ELO structure. The idea is to cover the remaining regions where the TD is still high with a second dielectric mask. Thus, the remaining TDs are prevented from propagating to the second ELO layer. The mask can either be rotated by 60 or 90° [26.51] in order to keep the orientation along another equivalent $\langle 1\bar{1}00 \rangle$ orientation, or be displaced [26.52] from the first array of openings so that the second mask covers the coherent GaN over the window region of the first mask layer. From the theory of image dislocations and image forces [26.53], it is known that dislocations near a free surface bend towards the free surface. In the case of TDs in GaN, they can be bent 90° and start to propagate along the basal plane [26.47, 54, 55]. This phenomenon can be used to reduce the TDs over larger areas. A mask is formed in a similar way as for the conventional ELO

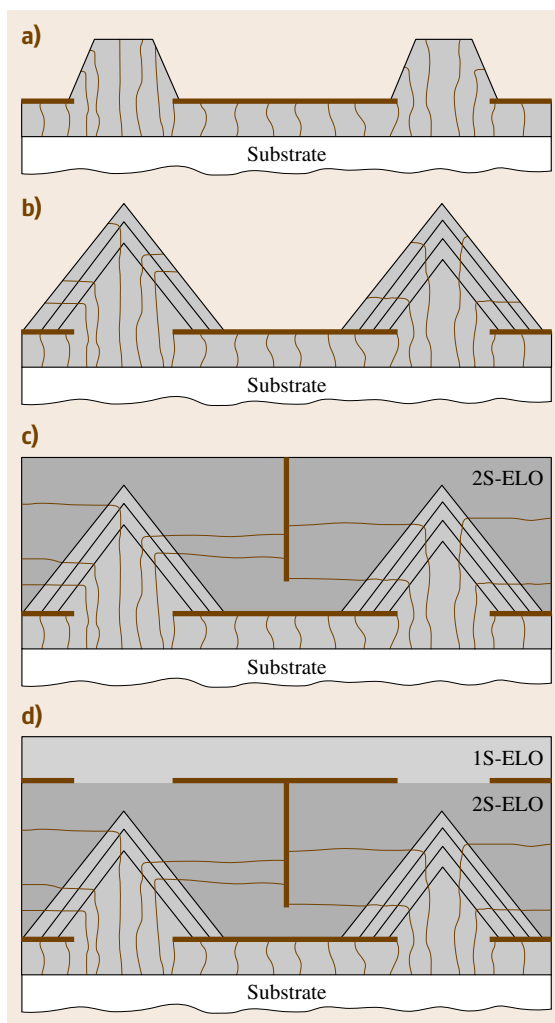


Fig. 26.9a–d Cross-sectional view perpendicular to the $[1\bar{1}00]$ direction showing the different steps in the fabrication of a 2S-ELOG structure (a–c) and a layered ELO structure (d). Black thin vertical lines represent threading dislocations. (a,b) The evolution of the formation of triangular stripes with $\{11\bar{2}2\}$ lateral facets, (c) fully coalesced 2S-ELOG structure and (d) additional 1S-ELO on 2S-ELO structure

process as described above. However, initially during the first step of growth, growth parameters that favor vertical expansion are selected, as shown in Fig. 26.9a. By tuning the process parameters, the stripes will adopt a triangular shape in cross section with $\{11\bar{2}2\}$ lateral facets. Thus, since the TDs are propagating perpendicular to the growing surface, they are bent 90°. This

growth mode is kept until the (0001) top facet vanishes completely (Fig. 26.9b). In the second step, the growth condition is changed to promote lateral growth in order to fully coalesce the layer. This can be done either by adding Mg or increasing the growth temperature. The bent TDs from the neighboring window regions meet each other in the middle of the dielectric mask layer, as shown in the Fig. 26.9c. Thus, the TDs pile up above the middle of the mask and start to grow in the *c*-direction.

26.4 Substrate Removal Techniques

The development of advanced III-nitride devices, such as laser diodes (LDs) or some high-power lamps for general illumination, will require the growth of device structures on high-quality III-nitride substrates with a low TD density ($< 10^6 \text{ cm}^{-2}$). These types of substrates are very difficult to produce by using heteroepitaxial growth on sapphire or SiC substrates, which is the common technique today. Thus, there is a strong need for free-standing GaN substrates with low TD density in order to fully exploit the III-V nitride materials.

Two major routes have appeared towards the production of bulk GaN wafers. One possibility is growing a thick boule followed by slicing and polishing. The alternative is growing a thick GaN layer on some foreign substrates, followed by substrate removal and proper polishing. Among these, the most attractive way to produce GaN substrates is directly by slicing of a GaN boule and polishing. However, despite many years of development and research, the process control and technical issues are not yet fully solved. Instead, several techniques using thick GaN layers grown by HVPE on foreign substrates followed by substrate removal have been developed.

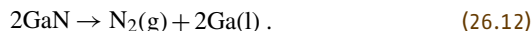
26.4.1 Laser Lift-Off

The most used substrate material in HVPE is sapphire, which is very hard and chemical inert. This makes it very difficult to remove the substrate mechanically or chemically. Instead, a technique which relies on thermal decomposition of the GaN at the interface between the sapphire and the GaN film has attracted most attention in recent years. Using this so-called laser lift-off process (LLO) [26.58], large-area crack-free GaN substrates up to 2 inches in diameter

To further reduce the TDs, a 1S-ELO can be processed on a 2S-ELO with the mask located exactly above the first structure [26.56]. Thus, the TDs originating from the coalesced region on the 2S-ELO structure are efficiently prevented from propagating to the top GaN layer, as shown in Fig. 26.9d. Using this technique with several ELO structures stacked on each other, it has been shown that the TD density can be reduced down to or even below the 10^6 cm^{-2} range [26.57].

with a thickness of about $300 \mu\text{m}$ have been demonstrated [26.59].

The idea behind the LLO process is to irradiate the GaN-sapphire substrate through the sapphire with a laser beam with an energy that is less than the bandgap of sapphire but larger than the bandgap of GaN. Thus, the laser beam will be absorbed at the GaN-sapphire interface, as shown in Fig. 26.10. If the power density of the laser beam is sufficient, a thin layer (of the order 100 nm) of GaN at the interface to the sapphire will decompose into liquid Ga and N_2 gas according to



The decomposition rate of GaN rapidly increases for elevated temperatures [26.60] and a high-power laser beam can easily obtain the onset of thermal decomposition. By scanning the beam, the GaN at the interface can be completely decomposed and, consequently, the GaN layer is delaminated from the sapphire.

Figure 26.11 shows a schematic picture of an LLO setup. It consists of a high-power laser with photon energy larger than the bandgap of GaN (3.43 eV). A suitable energy of 3.49 eV (355 nm) is obtained from the third harmonic of a neodymium-doped yttrium alu-

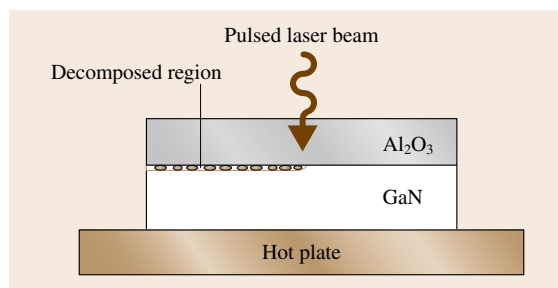


Fig. 26.10 Drawing of the principle of the LLO process

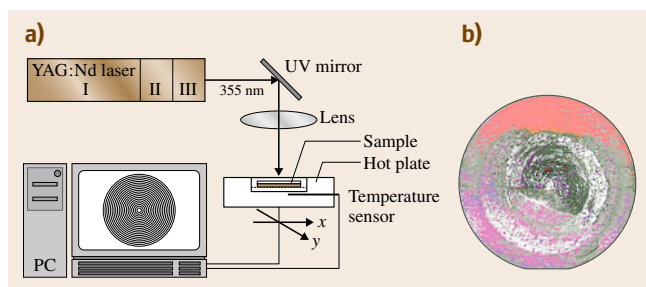


Fig. 26.11 (a) Schematic drawing of a laser lift-off setup. The movement of the wafer on the hot plate is done with a computer-controlled x - y stage tool. (b) Transmission light image of a 300 μm thick 2 inch free-standing GaN layer. On the backside of the wafer, traces from the laser lift-off process can be observed

minum garnet (Nd:YAG) laser. Another type of laser system that can be used is, for example, a KrF laser with an energy of 5 eV (248 nm). The laser beam is directed and focused on the backside of the sample. In order to reduce the stress due to the difference in thermal expansion coefficients between the substrate and the GaN layer and facilitate the thermal decomposition process, the sample is heated to about 700 °C. The entire sample holder is connected to an x - y stage, which is moved in a controlled fashion via a computer. The laser spot is moved in a spiral pattern from the perimeter to the center of the wafer. An example of a 300 μm thick 2 inch GaN wafer removed from the substrate by this technique is shown in Fig. 26.11b. The wafer is shown in transmitted light with the top surface up, and the spiral pattern from the scanning of the laser beam over the wafer can be observed as a circular pattern on the backside of the wafer. The process is very sensitive to the focusing of the laser beam and the laser output energy. Too high a power density generates cracks in the interface that can propagate through the layer and cause cracking of the wafer, while too small a power density might cause local islands where the layer has not separated. These islands create a strong nonuniform stress in the material during cool down after LLO, which may result in cracking of the layer. Another cause for incomplete separation is parasitic GaN growth on the backside of the substrate. The parasitic GaN absorbs the laser light and prevents the decomposition of the GaN at the interface.

The free-standing layers obtained after LLO are practically strain free. The main problem with free-standing GaN wafers is the substantial bowing of the wafers typically observed. Figure 26.12a shows an example of bowing of a 250 μm thick 2 inch layer residing

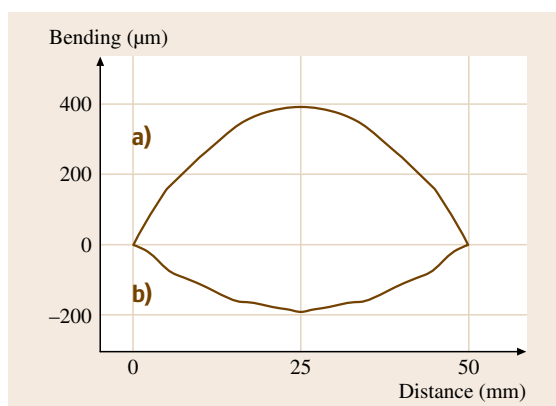


Fig. 26.12a,b Experimentally observed bow for two GaN layers. (a) 250 μm thick layer residing on sapphire and (b) 300 μm thick free-standing GaN layer. A convex bow of the GaN layer is observed when the GaN layer is residing on sapphire. When the sapphire is removed, the bow switches to a concave bow (after [26.12], with permission from Elsevier)

on sapphire and a 300 μm thick free-standing GaN layer obtained by LLO. As can be seen, the bowing can be quite large, in this example 400 μm before LLO and 200 μm after LLO. The sign of the bow is changed after LLO. Before LLO, the wafer is convex due to the larger thermal expansion coefficient of the sapphire, while afterwards the layer adopts a concave shape due to the defective interfacial region with large dislocation density and microcracks between the sapphire and the GaN, as shown in Fig. 26.12b. The layer shown in the example has too large a bow for further processing. Thus, in order to reduce the bowing, further processing such as annealing and/or removal of the highly defective region by etching is necessary.

26.4.2 Self-Separation

Many alternative techniques to LLO are under development since the LLO process normally has a relatively low yield. Several of these techniques use the stress that is built up in the GaN layer during cooling due to the difference in thermal expansion of the substrate and the GaN layer. By making a weak link that is provided by cavities between the substrate and the GaN layer, the separation of the substrate and the layer can be done spontaneously during cool down from the growth temperature.

Using ELO structures, voids can intentionally be created. By adjusting the growth process, the size and

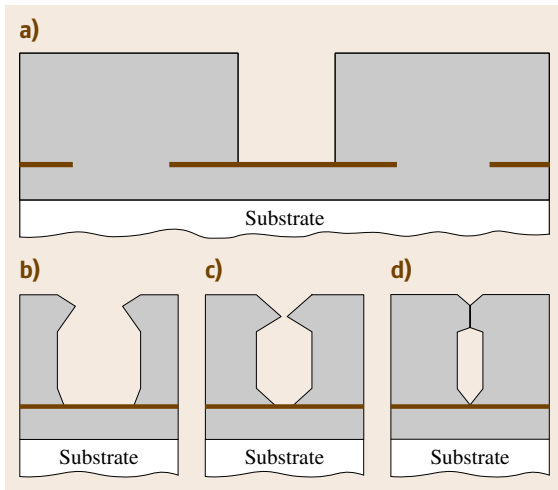


Fig. 26.13a–d Example of using ELO and mass transport in order to create voids at the substrate–GaN interface. (a) 1S-ELO structure with not fully coalesced wing region. (b–d) Evolution of the void under mass-transport conditions

shape of the voids can be engineered to facilitate separation during cooling [26.54, 61]. Figure 26.13 shows an example of a structure created by using mass transport. A conventional ELO structure with a SiO₂ or SiN mask is used as a starting template. During growth, in the stage when the lateral growth starts, the growth conditions are tuned such that the lateral facet becomes {11 $\bar{2}$ 0} (Fig. 26.13a). The growth is interrupted when the distance between the two lateral facets is a couple of microns. Then, by increasing the temperature to about 1100 °C under ammonia, mass transport will occur, as shown in Fig. 26.13b, c. At the end of the mass transport process, a vertical cavity has been created (Fig. 26.13b), which will facilitate the separation of the GaN layer from the substrate.

One of the more successful techniques that rely on self-separation is the so-called void-assisted separation (VAS) technique. The idea is basically the same as using ELO structures with cavities in the interface. Using this technique, high-quality free-standing substrates of both *c*-oriented [26.62] and *a*-oriented [26.63] GaN have been demonstrated. A thin layer of suitable metal (≈ 20 nm), generally Ti or Al, is deposited onto a thin MOVPE-grown GaN template prepared on a sapphire substrate. Subsequent annealing at ≈ 1050 °C of the metal-coated GaN template in a mixture of hydrogen and ammonia causes the metal to break up and form a nanonet-like metal nitride structure with

many nanoscale holes with a typical diameter of about 20–30 nm. During the subsequent growth of the thick GaN layer, additional etching of the mask and the underlying GaN occurs, creating multiple voids at the substrate–GaN interface. If these voids exceed a critical size, it is found that the GaN layer is spontaneously separated from the substrate during cooling after growth. For a 250 μ m thick GaN layer it was estimated that the critical void size is about 20 μ m [26.63]. The nanonet-like metal nitride structure layer also serves as a growth mask, which efficiently blocks the propagation of threading dislocations along the growth axis.

26.4.3 Mechanical Polishing

Using mechanical polishing with diamond slurry, 30 \times 30 mm² free-standing GaN substrates have been demonstrated from 400–450 μ m thick GaN layers [26.64] grown on sapphire. However, this technique will be difficult to use for large-area wafers due to the strong convex bow of the layers that normally occurs after heteroepitaxial growth on foreign substrates. The bow makes it difficult to achieve uniform removal of the substrate by polishing.

26.4.4 Plasma Etching

Free-standing GaN wafers with a thickness of 200 μ m and diameter of 30 mm have been demonstrated using reactive-ion etching (RIE) to remove the substrate. The GaN layer was grown on a SiC substrate and the substrate was removed by RIE in an SF₆-containing mixture gas [26.65, 66]. The main disadvantage with this technique is the long plasma processing times. Considering a typical etching rate of ≈ 100 nm/min for SiC, for a 300 μ m thick SiC substrate an etching time of about 50 h is required.

26.4.5 Chemical Etching and Spontaneous Self-Separation

Sapphire and SiC are very hard and chemically inert and are difficult to etch chemically. However, for other types of substrates, which are softer and less chemically inert, the removal process can be done more easily. Growth of GaN on GaAs(111) has been shown to be a possible route to fabricate free-standing GaN. The substrate can most easily be removed by wet etching in aqua regia after growth. Using GaAs as the substrate, 2 inch free-standing GaN layers with thickness of about 500 μ m

have been demonstrated [26.28]. Chemical etching has also shown to be useful for separation of GaN grown on LiGaO₂. LiGaO₂ can be rapidly etched in a buffered basic solution at 50 °C [26.67] with an etch rate of about 0.25 μm/min.

GaN layers grown on softer and less chemically inert substrates have shown in many cases to be spontaneously separated from the substrate after growth. Examples are HVPE-grown GaN on NdGaO₃ [26.68, 69], LiGaO₂ [26.39] or LiAlO₂ [26.38].

26.5 Doping Techniques for GaN in HVPE

Doping in HVPE can be done either by introducing a diluted dopant gas, mixing of the dopant in the Ga melt or using a separate doping source exposed to HCl in order to form gaseous metal halides.

26.5.1 n-Type Doping of GaN

Nitride semiconductors can easily be n-type doped; in fact they often exhibit unintentional n-type conductivity. This background doping has mainly been attributed to unintentionally introduced impurities, such as oxygen or silicon, which can be introduced from quartz parts within the reactor or from the process gases. For intentional n-type doping, silicon is the most suitable doping element. Silicon can, in principle, act as both an acceptor and a donor, depending on whether it is substituting a gallium atom or a nitrogen atom. However, the silicon atom mainly replaces a gallium atom due to the low covalent radii difference between Si and Ga compared with the radii difference from nitrogen.

Both gaseous sources and solid silicon sources have been used in growth of n-type HVPE GaN. The most commonly used doping gas for n-type doping of MOVPE-grown GaN is silane (SiH₄) or disilane (Si₂H₆). Silane has also been reported to be a useful source for HVPE growth of GaN [26.70]. However, the entrance zone where the Ga boat is situated is rather far away in most HVPE systems, which may result in problems with decomposition of the silane (or disilane) before it reaches the substrate, since the decomposition of the silane (disilane) starts already at temperatures below the temperature of the Ga boat. This problem can be solved by using more stable gases such as dichlorosilane (SiH₂Cl₂) that decomposes at higher temperatures. Using dichlorosilane, doping levels up to $8 \times 10^{18} \text{ cm}^{-3}$ have been reported [26.71].

Solid Si can also be used as a Si source by exposing the Si to HCl to form SiCl_x. Using this technique, a free electron concentration in GaN up to 10^{18} cm^{-3} has been reported [26.72]. The temperature of the Si source can control the doping level. By changing the tem-

perature in the range 200–400 °C the Si concentration was controlled in the range 1.0×10^{17} – $2.5 \times 10^{19} \text{ cm}^{-3}$. However, only 30–50% of the Si atoms were activated as donors.

Bulk growth requires a stable well-controlled doping source. This can be a problem with a solid Si source, as pointed out in [26.71]. These authors observed that controllability was poor using a solid Si source due to changes of the exposed Si area and morphology during growth.

Other n-type dopants that have been used in MOVPE growth of GaN are O, Ge, and Sn. However, there are no reports on intentional doping of HVPE-grown GaN using these dopants.

26.5.2 p-Type Doping of GaN

One of the major challenges associated with growth and development of III–V nitride-based materials is to understand and control the p-type doping. Today, magnesium (Mg) is the only element that has been shown to be a relatively efficient and controllable p-type impurity. Other elements such as Zn and Cd have too large activation energies to be useful as a p-type dopant for GaN due to a very low activation of these dopants at room temperature. Be introduces a shallow acceptor, but suffers from self-compensation problems, so p-type material is not obtained with Be doping [26.73]. However, despite Mg being the most suitable acceptor, it still has a relatively high thermal activation energy ($E_a \approx 0.17 \text{ eV}$, after [26.74]). The high ionization energy results in only a few percent of the Mg acceptors being ionized at room temperature. One additional problem with Mg doping, which was for a long time the bottleneck for the development of III-nitride technology, is that hydrogen can passivate the Mg dopants by forming an Mg–H complex. The Mg dopant can be activated by removing the hydrogen either by postgrowth annealing in N₂ or an electron irradiation treatment using low-energy electron-beam irradiation (LEEBI) [26.75, 76]. For thick bulk-like material, thermal annealing is the

only useful technique for activation of the acceptors since the penetration depth of low-energy electrons is small. This treatment is normally done in situ, directly after the growth. However, despite the thermal post-growth treatments, the acceptor thermal activation efficiency is still only a few percent. Thus, obtaining a suitably high hole concentration ($> 10^{18} \text{ cm}^{-3}$ at 300 K) in p-doped GaN using Mg is not an easy task. The upper limit of Mg acceptors that can be incorporated into the lattice is about 10^{20} cm^{-3} , which gives a hole concentration only in the low 10^{18} cm^{-3} range in *c*-plane GaN. Increasing the Mg concentration does not improve the conductivity; in fact, it has been reported that it leads to an even lower hole concentration [26.77]. It has been suggested that the solubility of Mg is limited due to competing formation of Mg_3N_2 [26.78]. Increasing the Mg concentration in GaN beyond this limit may result in precipitation of Mg_3N_2 , which leads to a reduction in the hole concentration and a decrease in crystal quality.

Doping of Mg in HVPE can be done by either using a separate boat for the doping species or mix-

ing it with the Ga source. The HCl gas is reacted with the Mg, forming its halide MgCl , which is transported to the growth zone by some suitable carrier gas. A second technique, which has been used both for Zn and Mg doping [26.79], is to thermally evaporate the dopant and transport the species in a suitable carrier gas to the growth zone. To avoid passivation of the acceptors by formation of Mg-H complexes, the rationale would be to avoid using hydrogen as carrier gas. However, it has been suggested that hydrogen is actually beneficial for p-type doping [26.80–83] compared with the hydrogen-free case. It has been proposed that the hydrogen passivates the Mg acceptors during growth and, consequently, represses formation of native donors to compensate for the acceptors. However, despite the technological breakthroughs in growth and development of GaN-based devices, many properties of this material system are not well understood. Doping of bulk growth of GaN using HVPE is not well documented and only a few scientific reports have been presented.

26.6 Defect Densities, Dislocations, and Residual Impurities

Thick HVPE-grown GaN layers are typically developed for the purpose of later use as thick high-quality substrates for epitaxial growth of device structures. Such substrates need lapping and chemical polishing to obtain a suitable surface finish for later epitaxy with other growth techniques. Defects such as minor surface features will be removed during these processing steps, and will therefore not be discussed here. Important problems are wafer bowing, dislocations and stacking faults, impurities, and localized bulk defects.

A major problem already discussed above is the bowing of bulk GaN wafers produced by HVPE on a foreign substrate, which is removed by some lift-off techniques. It is important to reduce the original bowing before lift-off as much as possible; some techniques involving ELO structures with cavities are successful in this respect. Another technique to accomplish this is to grow under conditions where an O-rich defective layer is present close to the substrate. This layer can absorb the deformation during growth and cooling, and give a low-strain (and low-bowing) GaN layer prior to lift-off [26.84]. For substrates suitable for epitaxy the bowing should ideally not be larger than about $10 \mu\text{m}$ (measured as the elevation of the middle of a 2 inch wafer compared with the perimeter). If the grown free-

standing wafer has a substantially larger bowing, the subsequent polishing may produce a variable lattice tilt across the final wafer, i.e., a variable miscut. This in turn might cause a variable growth morphology across the wafer in a later epitaxial growth process for a device structure. If the wafers are prepared from boules, these boules are usually grown with a length of about 10 mm. In this case the memory of a bowing is typically very much reduced, but these properties are not well documented in the literature to date.

A problem related to bowing is cracking. For thick layers on sapphire, cracking typically already occurs in situ during the first tens of microns of growth, due to the tensional strain developed in this initial growth process [26.85]. This cracking helps relax the strain during growth. These cracks typically overgrow (Fig. 26.14) and are generally not seen after growth of a $300 \mu\text{m}$ layer. Their presence in the interior of the material may well initiate more severe cracking during cool down after growth or during the polishing step. When GaN buffer layers are used for the growth it seems that this initial cracking behavior can be avoided, and the strain in the layer accumulates during growth, increasing the bowing of the wafer. Cracking during cool down is then a more critical issue, depending on the wafer thickness.

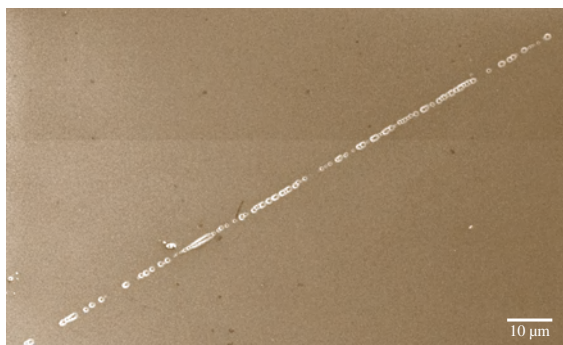


Fig. 26.14 Scanning electron microscopy (SEM) image of a HVPE-grown GaN layer on sapphire, showing an array of pits along a partly overgrown crack

Dislocations threading up through the wafer are severe defects in substrates, since they are typically replicated in the device structure epitaxially grown on top of the wafer. Dislocations are known to have a serious influence on carrier recombination in semiconductors; in GaN it seems that screw dislocations and mixed dislocations are most severe in terms of causing nonradiative recombination [26.86]. The threading dislocation density can be studied in several ways. Upon surface etching they typically form pits, which have a specific shape and size depending on the type of dislocations, and on the etch procedure used. This was studied by Hino et al. with HCl etching at 600 °C, where different pit shapes were produced by screw, mixed, and edge dislocations, respectively [26.86].

The dislocation types were established from separate transmission electron microscopy (TEM) studies. Complementary studies by cathodoluminescence (CL) topography reveal a different dark contrast, usually interpreted as due to nonradiative recombination, with strong contrast for screw and mixed dislocations, and quite a weak contrast for edge dislocations [26.86]. Similar results are observed from comparison of a different etching procedure (H_3PO_4 at 180 °C for 45 min) in Fig. 26.15. Here different sizes of pits observed by atomic force microscopy (AFM) (Fig. 26.15a) are observed [26.12]. The large pits are supposed to correspond to dislocations with a screw component, while the small pits correspond to edge dislocations. Figure 26.15b shows a CL topograph of another sample, showing mainly the high-contrast screw and mixed dislocations.

If the etching times are tuned to avoid overlap between different pits, the TD density of a layer can thus be determined by a simple etch pit count, a convenient method for a quick evaluation. The reliability of this technique can be tested by comparison of the dislocation count via etch pits and TEM studies of the same wafer, as reported in [26.86]. Obviously etch pit counting will omit dislocations that are running parallel to the surface, but these are usually not replicated in the overgrown epitaxial structure anyway.

The experience from HVPE growth of thick GaN layers is that the dislocation density is reduced with thickness in a manner that looks like a linear relation in a log–log plot, as seen in Fig. 26.16, where

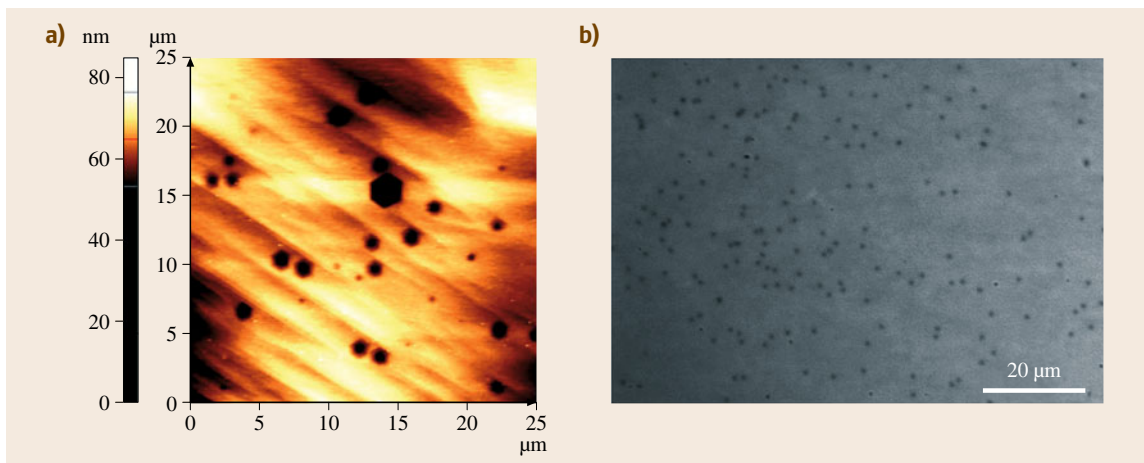


Fig. 26.15 (a) AFM pictures of a 250 μm thick layer after etching in H_3PO_4 at 180 °C for 45 min and (b) CL image of a 400 μm thick layer

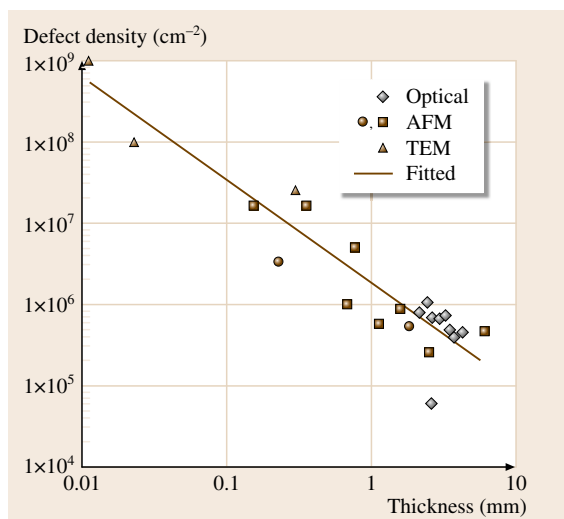


Fig. 26.16 Threading dislocation density as a function of thickness of thick HVPE-grown GaN layers. Points labeled (\diamond), (\square), and (Δ) are taken from [26.89], while (\bullet) from [26.87]

data from different groups are collected. For a thickness of 500 μm the TD density is typically at or below 10^7 cm^{-2} , while for a thickness of several millimeters a TD density of the order of 10^5 cm^{-2} is expected [26.87]. The mechanism for this has been investigated and suggested to be dislocation annihilation by recombination, driven by the dislocation strain fields and a certain mobility of dislocations at the growth temperature [26.88].

Stacking faults (SFs) are not abundant in GaN grown in the conventional polar (0001) direction. The situation is quite different in the case of growth of non-polar wafers, such as *a*-plane and *m*-plane GaN on foreign substrates. *a*-Plane GaN can be grown on *r*-plane sapphire, and the defect density in such thick layers has been investigated [26.90]. Apart from dislocations a high density of stacking faults is observed, as shown in Fig. 26.17. These stacking faults thread up through the entire wafer, and are clearly undesirable defects, since they will propagate into an overgrown epitaxial structure [26.91]. The defects are found to be important recombination centers, and have a radiative emission characteristic for each type of SF (Fig. 26.18). This figure shows the low-temperature photoluminescence (PL) spectrum of an *a*-plane GaN layer grown by HVPE, with SF defects as shown in Fig. 26.17. The near-bandgap emission peak (NBE) is due to donor-

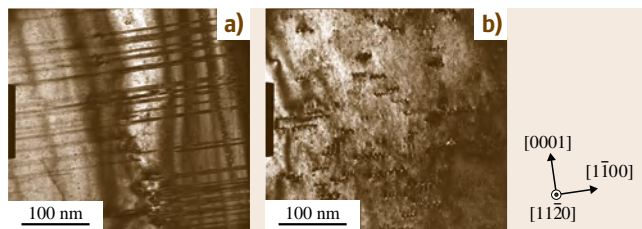


Fig. 26.17a,b Bright-field plan-view TEM images of an *a*-plane GaN film grown by HVPE with an MOVPE-GaN template layer taken close to the $[11\bar{2}0]$ zone axis, slightly tilted: (a) along the $[0001]$ direction, visualizing stacking faults formed in the basal plane of GaN by parallel lines, and (b) around the $[0001]$ direction, visualizing partial dislocations having a nonzero $[0001]$ component

bound excitons, while the broad peak at 3.43 eV is related to basal-plane SFs [26.92].

Growth employing ELO techniques has been attempted to reduce the SF density in thick HVPE GaN layers [26.93]. In this way part of the wafer surface can be free from SFs. However, efficient methods to eliminate these defects over an entire nonpolar wafer have not yet been developed.

X-ray diffraction (XRD) is a standard technique to obtain an overall characteristic of the structural quality of a semiconductor sample. The presence of internal defects such as microcracks and wafer bowing strongly affects the XRD characteristics of thick GaN wafers produced in the way discussed above. The coherence length along the growth direction increases as the TD

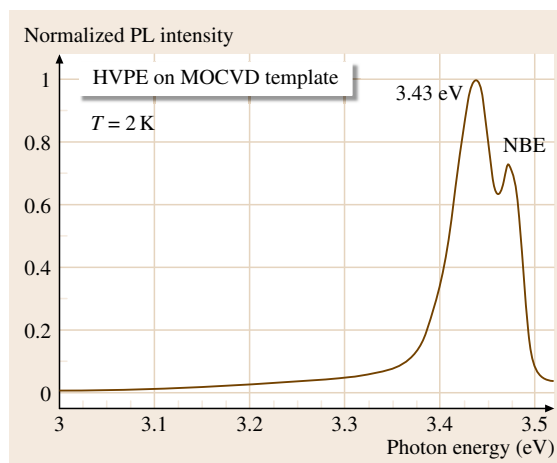


Fig. 26.18 Low-temperature PL spectra of an *a*-plane GaN layer grown by HVPE on an MOCVD-GaN template on *r*-plane sapphire

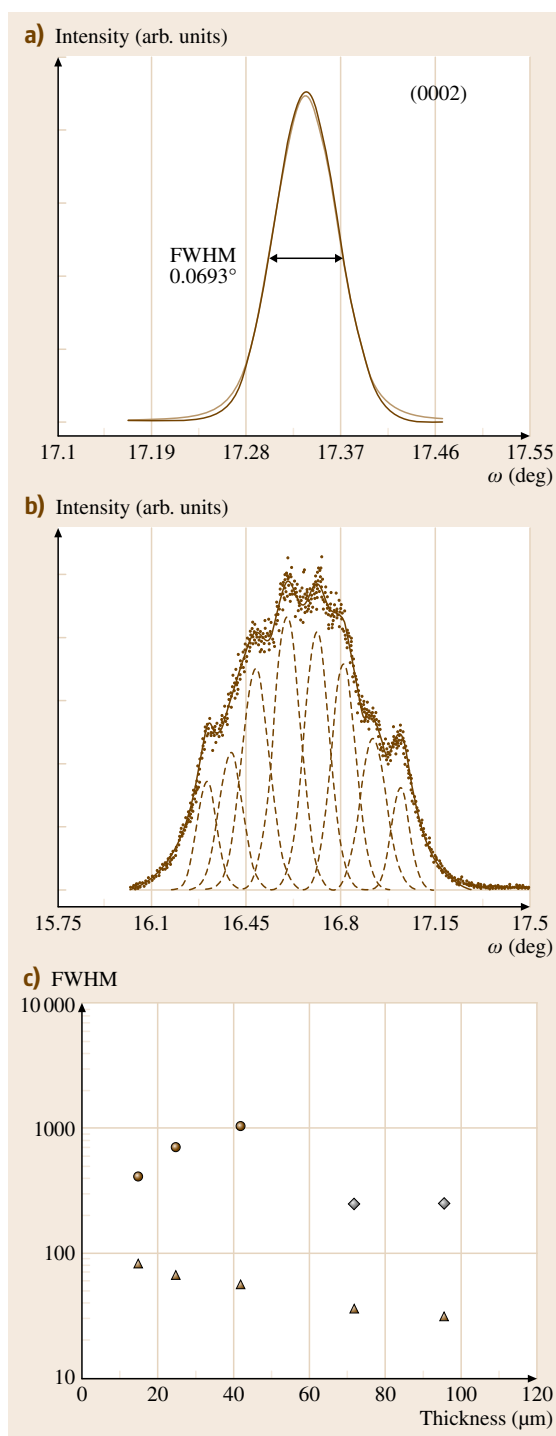
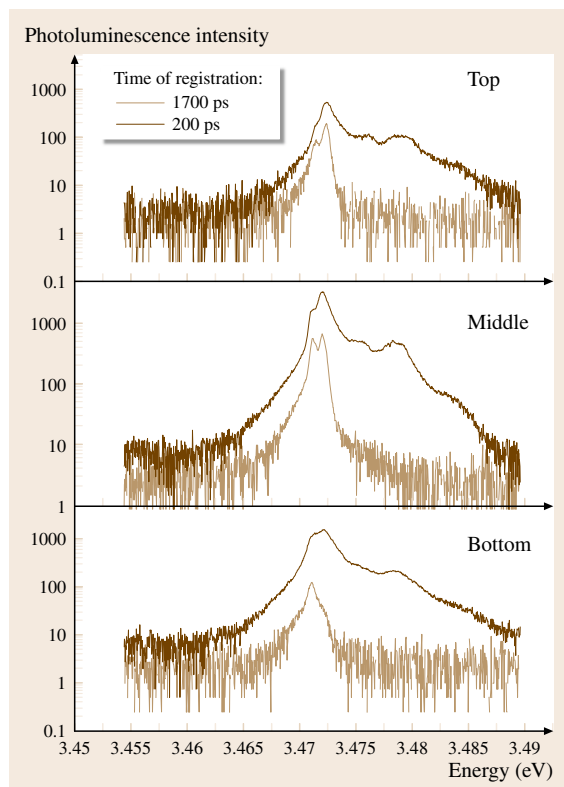


Fig. 26.19a–c Measured XRD line widths versus thickness for HVPE-grown GaN layers on sapphire. **(a)** Shows the line shape of a single rocking curve for a rather thin layer, while a thicker layer in **(b)** shows clear evidence of a mosaic substructure. **(c)** Shows a typical dependence of the line width on thickness for both rocking curve and the radial scan ◀

density is reduced. The full-width at half-maximum (FWHM) value of ω - 2θ scans then decreases as the GaN film grows thicker, as seen in Fig. 26.19c for a set of moderately thick HVPE layers on sapphire. These data are consistent with those for another set of much thicker samples (about 300 μm), all having ω - 2θ values of about 1 arcmin. The ω -scans show dramatically larger FWHM values, reflecting the presence of domain formation after a certain thickness (Fig. 26.19a,b), the residual bowing, and perhaps to some extent the internal cracks, and these effects are expected to contribute to the lattice tilt of the layers [26.94].

The characteristic XRD data for much thicker free-standing layers typically show much lower line widths. As an example, the FWHM for the ω -rocking curve of a 2 mm thick free-standing layer for the (002) reflection is 187 arcsec and the corresponding 2θ - ω peak has a FWHM of 36 arcsec, measured from the top Ga face [26.12].

Another class of defects of decisive importance for the quality of the material is impurities and point defects such as vacancies and interstitials. Residual impurities are introduced in the material during growth, and the density of such defects is critical mainly in the case of high-resistive material. The two common shallow donors in GaN are Si and O, both of which are easily introduced during growth, for different reasons. The Si contamination may strongly depend on the purity of the ammonia gas used; high-purity ammonia will minimize the Si contamination. There may also be some contribution from the attack on the quartz by parasitic growth upstream and in the growth zone. This process will depend on the proximity of the quartz walls to the substrate during growth. It has been shown that, with extended growth time, Si becomes the dominant residual impurity, while at the beginning of growth O is typically the dominant impurity incorporated. This is natural since O and water vapor are present, e.g., adsorbed or chemisorbed on quartz walls, or on the surface of the Ga source, and will gradually be released during a growth run, so that the amount of O contamination finally de-



creases as the source of O is depleted. O can of course also be introduced via small air leaks in the system. An example is shown in Fig. 26.20, where the PL spectrum from the cross section of a 2 mm thick GaN wafer is dominated by the O bound exciton (BE) spectrum close to the N-side, but dominated by Si at the Ga side (grown

Fig. 26.20 Spatially resolved PL spectra at 2 K measured from different spots at the cross section of a 2 mm thick bulk GaN layer grown by HVPE, measured at two different delay times after the excitation pulse. The lower-energy O-related bound-exciton line (at about 3.471 eV) clearly dominates at the N face, while at the Ga face (grown last) Si is the dominant donor species (the peak at about 3.4725 eV)

last). The ultimate value of Si contamination in a system not used for Si doping is presumably below 10^{15} cm^{-3} , but this has not been well documented to date.

Other important impurities are metal contaminants, in particular those from the iron group. These create deep levels in GaN, and thus act as compensation centers which decrease the efficiency of doping. The main source of these contaminants are the metal parts of the growth setup (tubing, manifolds, cylinders). Compounds including these metals may transport to the growth zone as particles, although these can be eliminated via particle filters. A more severe process is the transport of chloride molecules of these metals, promoted by the rather high vapor pressure they have already at room temperature. Such contaminants can easily be detected by optical spectroscopy, since these metals have characteristic spectra (typically sharp lines in the range 0.8–1.3 eV) related to the internal transitions in the ions [26.95]. Other important defects are vacancies. In n-type and undoped GaN the main vacancy defect is the $V_{\text{Ga}}\text{-O}$ complex, with the so-called yellow luminescence (YL) as the optical signature [26.96]. These defects are deep acceptors, and can be eliminated by carefully excluding O from entering the material during growth.

26.7 Some Important Properties of HVPE-Grown Bulk GaN Material

At present, HVPE is the only method that can produce high-purity ($< 10^{16} \text{ cm}^{-3}$) strain-free GaN material with low dislocation density ($< 10^6 \text{ cm}^{-2}$). Such material is therefore the prime choice for establishing the most relevant properties of bulk GaN. Such properties are lattice parameters, thermal expansion coefficients, thermal conductivity, and electron and hole mobilities. The lattice parameters obviously depend significantly on strain [26.97], but also on defect density and doping [26.98, 99], and values in the literature are therefore dependent on the material used. Recent studies on a 2 mm thick nominally undoped, free-standing GaN

bulk layer with a residual doping of about 10^{16} cm^{-3} and a dislocation density of about 10^6 cm^{-2} probably represent the most accurate values of the lattice parameters for pure bulk GaN (Table 26.2). The lattice parameters as a function of temperature were also measured recently on a free-standing GaN layer, and thermal expansion coefficients were established with improved accuracy [26.100]. The thermal conductivity is another important property that depends strongly on the quality of the material. Early determinations of this quantity on rather defective HVPE GaN layers gave a value of 1.3 W/(cm K) [26.101].

Table 26.2 Some important material parameters for strain-free bulk GaN

Lattice parameter a (Å)	Lattice parameter c (Å) [26.105]	Thermal expansion coefficient α_a (10^{-6} /K) at 300 K	Thermal conductivity 300 K (W/(cm K))	Electron mobility 300 K ($\text{cm}^2/(\text{V s})$) $n < 10^{16} \text{ cm}^{-3}$	Hole mobility 300 K ($\text{cm}^2/(\text{V s})$) $p \approx 10^{18} \text{ cm}^{-3}$
3.18943 ± 0.00015	5.18501 ± 0.00015	4.3	2.3	1350	10

A more recent study on HVPE material with low dislocation density and low doping indicates that the phonon-scattering-limited thermal conductivity at room temperature is much higher, about 2.3 W/(cm K), i. e., considerably better than Si [26.102]. The best electron mobilities in GaN has been obtained in nominally undoped free-standing thick HVPE grown samples; a value of 1350 cm²/(V s) has been reported [26.103]. The hole mobilities have so far been measured only

in highly doped and highly defective GaN; no reliable data are available for low-doped HVPE-grown bulk p-GaN to our knowledge. Extrapolated values for such material indicate a limiting hole mobility above 200 cm²/(V s) [26.104], to be confirmed in the future. In Mg-doped epitaxially grown device structures with a typical Mg concentration close to 10²⁰ cm⁻³, the hole mobility is at best about 10 cm²/(V s) [26.104] (see also Table 26.2).

26.8 Growth of AlN by HVPE: Some Preliminary Results

High-quality and large-scale AlN wafers are recently in increasing demand as substrates for ultraviolet (UV)

light-emitting devices and high-power high-frequency electronic devices. There have been several reports on growth of AlN by the sublimation–recondensation method [26.106, 107] and by solution growth [26.108]. Although AlN crystals with extremely low dislocation densities can be grown by these methods, expanding the size of the grown crystals is a challenging problem.

On the other hand, high-speed growth of thick AlN layers by HVPE followed by separation of the grown layers from the starting substrates is an interesting approach to prepare AlN wafers. As is widely known, GaN wafers of 2 inch diameter have been mass-produced by HVPE using GaAs [26.109] or sapphire [26.59, 62, 110, 111] as starting substrates. However, investigations concerning HVPE of AlN have been limited [26.1, 112–115] due to the fact that the molten Al or hot AlCl gas reacts violently with the quartz (SiO₂) reactor of the HVPE system, damaging the reactor. On the other hand, there are other Al chlorides such as AlCl₂, AlCl₃, and (AlCl₃)₂. Figure 26.21 shows the values of the equilibrium constants K of the thermodynamically feasible reactions between gaseous AlCl, AlCl₂, AlCl₃ or (AlCl₃)₂ and quartz as a function of the reciprocal of the reaction temperature [26.1]. The following order of the equilibrium constants K of the reactivity of Al chlorides is seen

$K_{\text{AlCl}} > K_{\text{AlCl}_2} > K_{(\text{AlCl}_3)_2} > K_{\text{AlCl}_3} . \tag{26.13}$

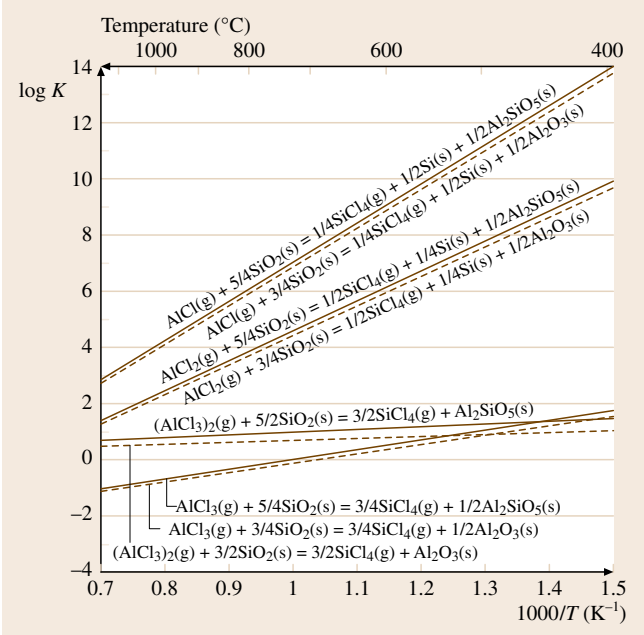


Fig. 26.21 Equilibrium constants (K) as a function of the reciprocal of reaction temperature for reactions between Al chlorides and quartz

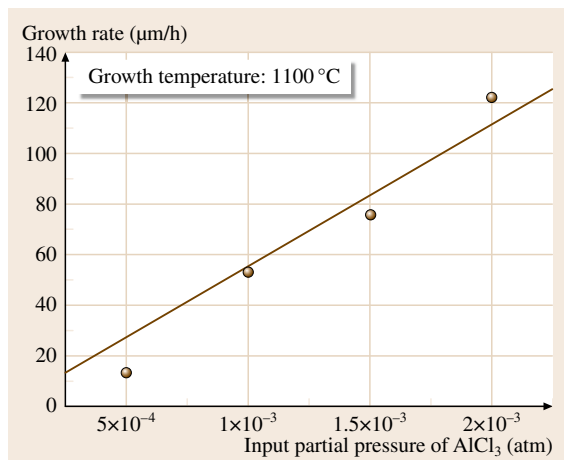


Fig. 26.22 Dependence of AlN growth rate on the AlCl₃ input partial pressure at 1100 °C

The reactions between AlCl and quartz have extremely large values of K . On the contrary, reactions between AlCl₃ and quartz have small values of K , and negative values of $\log K$ at 700 °C or above. Therefore, the reaction between AlCl₃ and the quartz reactor is negligible, and AlCl₃ is suitable as an Al source in AlN HVPE.

It has already been reported that preferential generation of AlCl₃ is possible [26.1] at the Al source zone of a conventional HVPE system by decreasing the source-zone temperature to about 500 °C (Fig. 26.1b). Exploiting this fact, several groups have grown AlN using a conventional hot-walled quartz reactor. In Fig. 26.22, the dependence of AlN growth rate on the AlCl₃ input partial pressure is shown [26.114]. Al metal pellets (6 N grade) were placed in the source zone to enlarge the surface area and maintained at 500 °C. AlCl₃ was formed by the reaction between the Al metal and HCl gas and mixed with NH₃ in the growth zone where a (0001) sapphire substrate was placed. The input V/III ratio (NH₃/AlCl₃) was fixed at 2. Growth was performed at 1100 °C under atmospheric pressure using H₂ as a carrier gas. A linear increase of the growth rate with increase of AlCl₃ input pressure is seen in the figure. With an AlCl₃ input partial pressure of 2×10^{-3} atm, the growth rate exceeds 100 μm/h. Therefore, high-speed growth of AlN by HVPE is possible just as in the HVPE growth of GaN.

Figure 26.23 shows the FWHM of the x-ray diffraction (XRD) rocking curves of (0002) (tilt component)

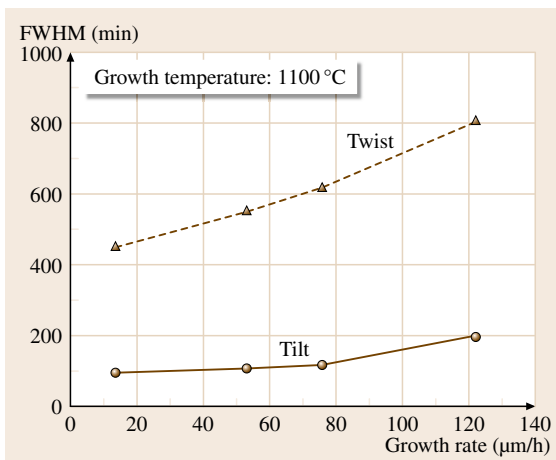


Fig. 26.23 FWHM of XRD rocking curves of the (0002) (tilt component) and the (10 $\bar{1}$ 0) (twist component) of AlN layers grown at 1100 °C with various growth rates

and (10 $\bar{1}$ 0) (twist component) of AlN layers grown at 1100 °C with various growth rates [26.114]. Although high-speed growth of AlN is possible at 1100 °C, the FWHM of the (0002) and the (10 $\bar{1}$ 0) increase with increasing growth rate. In order to grow high-quality AlN layers with a high growth rate, it is considered that a higher growth temperature will be required.

The result of absorption measurements for a 2 μm thick AlN layer grown at 2 μm/h on a sapphire substrate

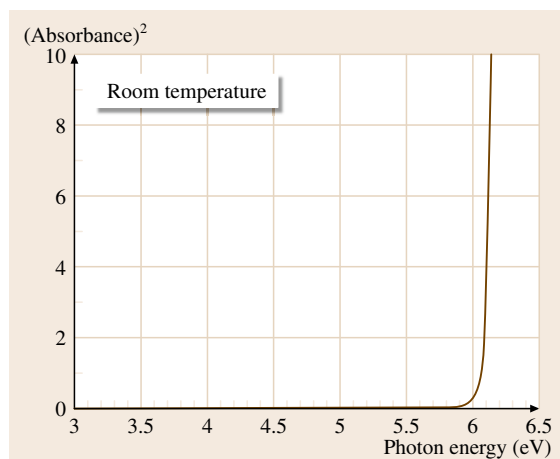


Fig. 26.24 Absorbance squared versus photon energy of an AlN layer measured at room temperature

is shown in Fig. 26.24, where absorbance squared is plotted as a function of photon energy. Extrapolation of the linear region to the horizontal axis gives the bandgap of AlN to be just above 6.0 eV (somewhat influenced by strain).

26.9 Growth of InN by HVPE: Some Preliminary Results

Recent progress in the growth of InN by MBE and MOVPE has clarified that the bandgap of InN is around 0.7 eV [26.116–118]. However, growth of thick InN layers remains difficult due to poor thermal stability, low growth rate of InN, and the lack of a suitable substrate material for epitaxy.

Although HVPE is a useful method for high-speed growth of GaN [26.47] and AlN [26.114] without formation of metal droplets, HVPE of InN is complicated: InN growth does not occur when InCl is used as an In source [26.119], while appreciable growth of InN occurs when InCl₃ powder is sublimated and transported by a carrier gas other than H₂ [26.119–121]. This is due to the fact that the equilibrium constant of the reaction between InCl₃ and NH₃ is larger than that between InCl and NH₃ (Fig. 26.2), and a suppression of InN growth in the presence of H₂ [26.7]. However, in order to grow high-quality InN layers without contamination, formation of InCl₃ gas in the source zone of a conventional HVPE system is needed, since commercially available InCl₃ powder inevitably contains water due to its hygroscopic nature. According

From the results shown above, the next challenges for AlN HVPE are thought to be high-temperature (> 1100 °C) growth and reduction of dislocation density in the grown layer using AlN templates, ELO structures, etc.

to the thermodynamic analysis of the In source zone, where Cl₂ gas is introduced over the In metal, the equilibrium partial pressure of InCl₃ increases with decreasing source-zone temperature [26.122]. Here, it is essential to use Cl₂ instead of HCl to form InCl₃ because the reaction between In metal and HCl produces H₂, which suppresses the growth of InN at the growth zone [26.7].

We report preliminary results for successful HVPE growth of InN. Figure 26.25 shows the dependence of InN growth rate on the In source-zone temperature [26.122]. Cl₂ with an input partial pressure of 3.0×10^{-3} atm was introduced over the In metal using N₂ carrier gas, and NH₃ with an input partial pressure of 1.5×10^{-1} atm was separately introduced into the growth zone using N₂ carrier gas. Single-crystalline InN layers *c*-axis oriented without In droplets can be grown on a (0001) sapphire substrate at a growth zone temperature of 500 °C. It is seen that the growth rate increases with decreasing source-zone temperature above 450 °C. This is due to the increase of the InCl₃ equilibrium partial pressure at the In source zone. On the other

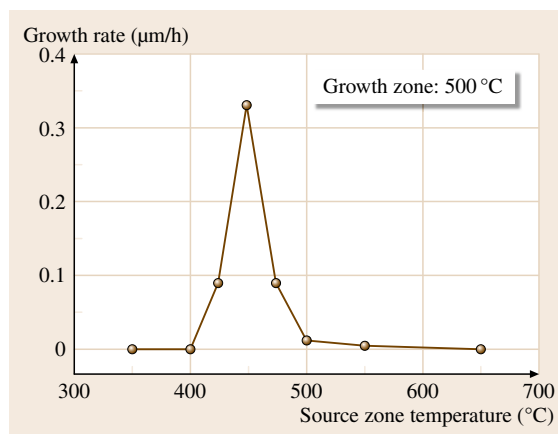


Fig. 26.25 Dependence of InN growth rate on the In source-zone temperature. Growth-zone temperature was fixed at 500 °C

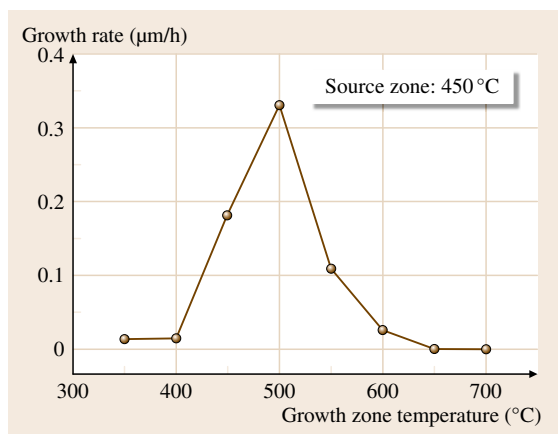


Fig. 26.26 Dependence of InN growth rate on the growth-zone temperature. In source-zone temperature was fixed at 450 °C

hand, with the source-zone temperature below 450 °C, the growth rate dropped rapidly because of insufficient reaction between Cl_2 and In metal.

As for the growth-zone temperature, InN growth is obtained within a narrow temperature range. Figure 26.26 shows the dependence of InN growth rate on the growth-zone temperature. The temperature of the In source zone was fixed at 450 °C. At growth temperature above 500 °C, the growth rate decreases as the growth-zone temperature increases. The growth rate also decreases with decrease of the growth-zone temperature below 500 °C due to insufficient reaction between InCl_3 and NH_3 . Therefore, either an increase of Cl_2 input into the In source zone or an increase of the total gas flow rate in the reactor will be required to increase the growth rate of InN.

A room-temperature cathodoluminescence spectrum of the InN layer grown at 500 °C is shown in Fig. 26.27. An emission peak is seen at around 0.7 eV. Hall-effect measurements revealed that the InN layer had n-type conductivity with a carrier concentration of $3 \times 10^{19} \text{ cm}^{-3}$ and a carrier mobility of $890 \text{ cm}^2/(\text{Vs})$.

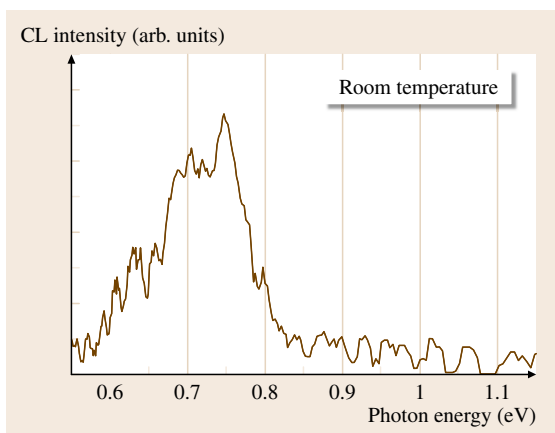


Fig. 26.27 Room-temperature CL spectrum of an InN layer grown at 500 °C by HVPE

The carrier concentration obtained is in agreement with that estimated from the dependence of the bandgap on electron concentration due to the Burstein–Moss effect [26.123].

References

- 26.1 Y. Kumagai, T. Yamane, T. Miyaji, H. Murakami, Y. Kangawa, A. Koukitu: Hydride vapor phase epitaxy of AlN: thermodynamic analysis of aluminum source and its application to growth, *Phys. Status Solidi (c)* **0**, 2498–2501 (2003)
- 26.2 M.W. Chase Jr. (Ed.): *NIST-JANAF Thermochemical Tables*, 4th edn. (National Institute of Standards and Technology, Gaithersburg 1998)
- 26.3 I. Barin (Ed.): *Thermochemical Data of Pure Substances* (Wiley, New York 1989)
- 26.4 A. Koukitu, S. Hama, T. Taki, H. Seki: Thermodynamic analysis of hydride vapor phase epitaxy of GaN, *Jpn. J. Appl. Phys.* **37**, 762–765 (1998)
- 26.5 Y. Kumagai, K. Takemoto, T. Hasegawa, A. Koukitu, H. Seki: Thermodynamics on tri-halide vapor-phase epitaxy of GaN and $\text{In}_x\text{Ga}_{1-y}\text{N}$ using GaCl_3 and InCl_3 , *J. Cryst. Growth* **231**, 57–67 (2001)
- 26.6 Y. Kumagai, K. Takemoto, J. Kikuchi, T. Hasegawa, H. Murakami, A. Koukitu: Thermodynamics on hydride vapor phase epitaxy of AlN using AlCl_3 and NH_3 , *Phys. Status Solidi (b)* **243**, 1431–1435 (2006)
- 26.7 Y. Kumagai, K. Takemoto, A. Koukitu, H. Seki: Thermodynamics on halide vapor-phase epitaxy of InN using InCl and InCl_3 , *J. Cryst. Growth* **222**, 118–124 (2001)
- 26.8 A. Koukitu, H. Seki: Thermodynamic analysis of the vapor growth of GaAs: the inert gas–hydrogen mixed carrier system, *Jpn. J. Appl. Phys.* **16**, 1967–1971 (1977)
- 26.9 V.S. Ban: Mass spectrometric studies of vapor-phase crystal growth. II. GaN, *J. Electrochem. Soc.* **119**, 761–765 (1972)
- 26.10 R.J. Molnar, W. Götz, L.T. Romano, J.M. Johnson: Growth of gallium nitride by hydride vapor-phase epitaxy, *J. Cryst. Growth* **178**, 147–156 (1997)
- 26.11 B. Monemar, H. Larsson, C. Hemmingsson, I.G. Ivanov, D. Gogova: Growth of thick GaN layers with hydride vapour phase epitaxy, *J. Cryst. Growth* **281**, 17–31 (2005)
- 26.12 C. Hemmingsson, P.P. Paskov, G. Pozina, M. Heuken, B. Schineller, B. Monemar: Growth of bulk GaN in a vertical hydride vapour phase epitaxy reactor, *Superlattices Microstruct.* **40**, 205–213 (2006)
- 26.13 V.S. Ban: Mass spectrometric and thermodynamics studies of the CVD of some III–V compounds, *J. Cryst. Growth* **17**, 19–30 (1972)
- 26.14 E. Richter, C. Hennig, M. Weyers, F. Habel, J.-D. Tsay, W.-Y. Liu, P. Brückner, F. Scholz, Y. Makarov, A. Segal, J. Kaeppler: Reactor and growth process optimization for growth of thick GaN layers on sapphire substrates by HVPE, *J. Cryst. Growth* **277**, 6–12 (2005)
- 26.15 S. Porowski: High pressure growth of GaN – New prospects for blue lasers, *J. Cryst. Growth* **166**, 583–589 (1996)
- 26.16 I. Grzegory, B. Łuczniak, M. Boćkowski, B. Pastuszka, G. Kamler, G. Nowak, M. Krysko,

- S. Krukowski, S. Porowski: Crystallization of GaN by HVPE on pressure grown seeds, *Phys. Status Solidi (a)* **203**, 1654–1657 (2006)
- 26.17 B. Łuczniak, B. Pastuszka, I. Grzegory, M. Boćkowski, G. Kamler, E. Litwin-Staszewska, S. Porowski: Deposition of thick GaN layers by HVPE on the pressure grown GaN substrates, *J. Cryst. Growth* **281**, 38–46 (2005)
- 26.18 L. Liu, J.H. Edgar: Substrates for gallium nitride epitaxy, *Mater. Sci. Eng. Rep.* **37**, 61–127 (2002)
- 26.19 O. Ambacher, J. Majewski, C. Miskys, A. Link, M. Hermann, M. Eickhoff, M. Stutzmann, F. Bernardini, V. Fiorentini, V. Tilak, B. Schaff, L.F. Eastman: Pyroelectric properties of Al(In)GaN/GaN hetero- and quantum well structures, *J. Phys. Condens. Matter* **14**, 3399–3434 (2002)
- 26.20 T. Paskova, P.P. Paskov, E. Valcheva, V. Darakchieva, J. Birch, A. Kasic, B. Arnaudov, S. Tungasmita, B. Monemar: Polar and nonpolar GaN grown by HVPE: Preferable substrates for nitride-based emitting devices, *Phys. Status Solidi (a)* **201**, 2265–2270 (2004)
- 26.21 W.A. Melton, J.I. Pankove: GaN growth on sapphire, *J. Cryst. Growth* **178**, 168–173 (1997)
- 26.22 B. Pécz, M.A. Di Forte-Poisson, F. Huet, G. Radnóczy, L. Tóth, V. Papaioannou, J. Stoemenos: Growth of GaN layers onto misoriented (0001) sapphire by metalorganic chemical vapor deposition, *J. Appl. Phys.* **86**, 6059–6067 (1999)
- 26.23 K. Hiramatsu, H. Amano, I. Akasaki, H. Kato, N. Koide, K. Manabe: MOVPE growth of GaN on a misoriented sapphire substrate, *J. Cryst. Growth* **107**, 509–512 (1991)
- 26.24 P. Brückner, M. Feneberg, K. Thonke, F. Habel, F. Scholz: High quality GaN layers grown on slightly miscut sapphire wafers, *Mater. Res. Soc. Symp. Proc.* **892**, 511–516 (2006)
- 26.25 R.J. Molnar, P. Maki, R. Aggarwal, Z.L. Liao, E.R. Brown, I. Melngailis, W. Götz, L.T. Romano, N.M. Johnson: Gallium nitride thick films grown by hydride vapor phase epitaxy, *Mater. Res. Soc. Symp.* **423**, 221–226 (1996)
- 26.26 S. Keller, B.P. Keller, Y.F. Wu, B. Heying, D. Kapolnek, J.S. Speck, U.K. Mishra, S.P. DenBaars: Influence of sapphire nitridation on properties of gallium nitride grown by metalorganic chemical vapor deposition, *Appl. Phys. Lett.* **68**, 1525–1527 (1996)
- 26.27 S. Fuke, H. Teshigawara, K. Kuwahara, Y. Takano, T. Ito, M. Yanagihara, K. Ohtsuka: Influences of initial nitridation and buffer layer deposition on the morphology of a (0001) GaN layer grown on sapphire substrates, *J. Appl. Phys.* **83**, 764–767 (1998)
- 26.28 K. Motoki, T. Okahisa, S. Nakahata, N. Matsumoto, H. Kimura, H. Kasai, K. Takemoto, K. Uematsu, M. Ueno, Y. Kumagai, A. Koukitu, H. Seki: Growth and characterization of freestanding GaN substrates, *J. Cryst. Growth* **237–239**, 912–921 (2002)
- 26.29 M. Ishida, T. Hashimoto, T. Takayama, O. Imafuji, M. Yuri, A. Yoshikama, K. Itoh, Y. Terakoshi, T. Sugino, J. Shirafuji: Growth of GaN thin films on sapphire substrate by low pressure MOCVD, *Mater. Res. Soc. Symp.* **468**, 69–74 (1997)
- 26.30 F. Widmann, G. Feuillet, B. Daudin, J.L. Rouviere: Low temperature sapphire nitridation: A clue to optimize GaN layers grown by molecular beam epitaxy, *J. Appl. Phys.* **85**, 1550–1555 (1999)
- 26.31 K. Naniwae, S. Itoh, H. Amano, K. Itoh, K. Hiramatsu, I. Akasaki: Growth of single crystal GaN substrate using hydride vapor phase epitaxy, *J. Cryst. Growth* **99**, 381–384 (1990)
- 26.32 R.J. Molnar, K.B. Nichols, P. Maki, E.R. Brown, I. Melngailis: The role of impurities in hydride vapor phase epitaxial grown gallium nitride, *Mater. Res. Soc. Symp. Proc.* **378**, 479–484 (1995)
- 26.33 J. Lee, H. Paek, J. Yoo, G. Kim, D. Kum: Low temperature buffer growth to improve hydride vapor phase epitaxy of GaN, *Mater. Sci. Eng. B* **59**, 12–15 (1999)
- 26.34 P.R. Tavernier, E.V. Etzkorn, Y. Wang, D.R. Clarke: Two-step growth of high-quality GaN by hydride vapor-phase epitaxy, *Appl. Phys. Lett.* **77**, 1804–1806 (2000)
- 26.35 H. Tsuchiya, K. Sunaba, M. Minami, T. Suemasu, F. Hasegawa: Influence of As autodoping from GaAs substrates on thick cubic GaN growth by halide vapor phase epitaxy, *Jpn. J. Appl. Phys.* **37**, L568–L570 (1998)
- 26.36 F. Hasegawa, M. Minami, K. Sunaba, T. Suemasu: Thick and smooth hexagonal GaN growth on GaAs (111) substrates at 1000 °C with halide vapor phase epitaxy, *Jpn. J. Appl. Phys.* **38**, L700–L702 (1999)
- 26.37 Y. Kumagai, H. Murakami, H. Seki, A. Koukitu: Thick and high-quality GaN growth on GaAs (111) substrates for preparation of freestanding GaN, *J. Cryst. Growth* **246**, 215–222 (2002)
- 26.38 E. Richter, C. Hennig, U. Zeimer, M. Weyers, G. Tränkle, P. Reiche, S. Ganschow, R. Uecker, K. Peters: Freestanding two inch c-plane GaN layers grown on (100) γ -lithium aluminium oxide by hydride vapour phase epitaxy, *Phys. Status Solidi (c)* **3**, 1439–1443 (2006)
- 26.39 O. Kryliouk, M. Reed, T. Dann, T. Anderson, B. Chai: Large area GaN substrates, *Mater. Sci. Eng. B: Solid-State Mater. Adv. Technol.* **66**, 26–29 (1999)
- 26.40 T. Paskova, S. Tungasmita, E. Valcheva, E. Svedberg, B. Arnaudov, S. Evtimova, P. Persson, A. Henry, R. Beccard, M. Heuken, B. Monemar: Hydride vapour phase homoepitaxial growth of GaN on MOCVD-grown 'templates', *MRS Internet J. Nitrid. Semicond. Res.* **5**, W3.14 (2000)
- 26.41 H. Lee, M. Yuri, T. Ueda, J.S. Harris, K. Sin: Growth of thick GaN films on RF sputtered AlN buffer layer by hydride vapor phase epitaxy, *J. Electron. Mater.* **26**, 898–902 (1997)

- 26.42 E. Valcheva, T. Paskova, S. Tungasmita, P.O. Å. Persson, J. Birch, E.B. Svedberg, L. Hultman, B. Monemar: Interface structure of hydride vapor phase epitaxial GaN grown with high-temperature reactively sputtered AlN buffer, *Appl. Phys. Lett.* **76**, 1860–1862 (2000)
- 26.43 T. Paskova, E. Valcheva, J. Birch, S. Tungasmita, P.O. Å. Persson, P.P. Paskov, S. Evtimova, M. Abrashev, B. Monemar: Defect and stress relaxation in HVPE-GaN films using high temperature reactively sputtered AlN buffer, *J. Cryst. Growth* **230**, 381–386 (2001)
- 26.44 T. Detchprohm, K. Hiramatsu, H. Amano, I. Akasaki: Hydride vapor phase epitaxial growth of a high quality GaN film using a ZnO buffer layer, *Appl. Phys. Lett.* **61**, 2688–2690 (1992)
- 26.45 T. Ueda, T.-F. Huang, S. Spruytte, H. Lee, M. Yuri, K. Itoh, T. Baba, J.S. Harris Jr: Vapor phase epitaxy growth of GaN on pulsed laser deposited ZnO buffer layer, *J. Cryst. Growth* **187**, 340–346 (1998)
- 26.46 S. Gu, R. Zhang, J. Sun, L. Zhang, T.F. Kuech: The nature and impact of ZnO buffer layers on the initial stages of the hydride vapor phase epitaxy of GaN, *MRS Internet J. Nitrid. Semicond. Res.* **5**, W3.15 (2000)
- 26.47 A. Usui, H. Sunakawa, A. Sakai, A.A. Yamaguchi: Thick GaN epitaxial growth with low dislocation density by hydride vapor phase epitaxy, *Jpn. J. Appl. Phys.* **36**, L899–L902 (1997)
- 26.48 K. Hiramatsu, H. Matsushima, T. Shibata, N. Sawaki, K. Tadatomo, H. Okagawa, Y. Ohuchi, Y. Honda, T. Matsue: Selective area growth of GaN by MOVPE and HVPE, *Mater. Res. Soc. Symp. Proc.* **482**, 257–268 (1998)
- 26.49 G. Nataf, B. Beaumont, A. Bouillé, S. Haffouz, M. Vaille, P. Gibart: Lateral overgrowth of high quality GaN layers on GaN/Al₂O₃ patterned substrates by halide vapour-phase epitaxy, *J. Cryst. Growth* **192**, 73–78 (1998)
- 26.50 O. Parillaud, V. Wagner, H.J. Bühlmann, M. Illegems: Localized Epitaxy of GaN by HVPE on patterned Substrates, *MRS Internet J. Nitrid. Semicond. Res.* **3**, 40 (1998)
- 26.51 Y. Zhonghai, M.A.L. Johnson, J.D. Brown, N.A. El-Masry, J.F. Muth, J.W. Cook Jr, J.F. Schetzina, K.W. Haberern, H.S. Kong, J.A. Edmond: Epitaxial lateral overgrowth of GaN on SiC and sapphire substrates, *MRS Internet J. Nitrid. Semicond. Res.* **4S1**, G4.3 (1999)
- 26.52 R. F. Davis, O. H. Nam, T. Zheleva, M. Bremser: Methods of fabricating gallium nitride semiconductor layers by lateral overgrowth through masks, and gallium nitride semiconductor structures fabricated thereby, Patent W09944224 (1999)
- 26.53 J. Hirth, J. Lothe: The theory of straight dislocations. In: *Theory of Dislocations* (Wiley, New York 1982) pp. 55–95
- 26.54 P. Gibart, B. Beaumont, P. Vennéguès: Epitaxial lateral overgrowth of GaN. In: *Nitride Semiconductors, Handbook on Materials and Devices*, ed. by P. Ruterana, M. Albrecht, J. Neugebauer (Wiley, New York 2003) pp. 45–106
- 26.55 Z. Liliental-Weber, M. Benamara, W. Swider, J. Washburn, J. Park, P.A. Grudowski, C.J. Eiting, R.D. Dupuis: TEM study of defects in laterally overgrown GaN layers, *MRS Internet J. Nitrid. Semicond. Res.* **4S1**, G4.6 (2000)
- 26.56 H. Miyake, H. Mizutani, K. Hiramatsu, Y. Iyechika, Y. Honda, T. Maeda: Fabrication of GaN layer with low dislocation density using facet controlled ELO technique, *Mater. Res. Symp. Proc.* **639**, G5.3.1. (2001)
- 26.57 S.-I. Nagahama, N. Iwasa, M. Senoh, T. Matsushita, Y. Sugimoto, H. Kiyoku, T. Kozaki, M. Sano, H. Matsumura, H. Umemoto, K. Chocho, T. Mukai: High-power and long-lifetime InGaN multi-quantum-well laser diodes grown on low-dislocation-density GaN substrates, *Jpn. J. Appl. Phys.* **39**, L647–L650 (2000)
- 26.58 W.S. Wong, T. Sands, N.W. Cheung: Damage-free separation of GaN thin films from sapphire substrates, *Appl. Phys. Lett.* **72**, 599–601 (1998)
- 26.59 M.K. Kelly, R.P. Vaudo, V.M. Phanse, L. Gorgens, O. Ambacher, M. Stutzmann: Large free-standing GaN substrates by hydride vapor phase epitaxy and laser-induced liftoff, *Jpn. J. Appl. Phys.* **38**, L217–L219 (1999)
- 26.60 O. Ambacher, M.S. Brandt, R. Dimitrov, T. Metzger, M. Stutzmann, R.A. Fischer, A. Miehr, A. Bergmaier, G. Dollinger: Thermal stability and desorption of group III nitrides prepared by metal organic chemical vapor deposition, *J. Vac. Sci. Technol. B* **14**, 3532–3542 (1996)
- 26.61 D. Gogova, A. Kasic, H. Larsson, C. Hemmingsson, B. Monemar, F. Toumisto, K. Saarinen, L. Dobos, B. Pécz, P. Gibart, B. Beaumont: Strain-free bulk-like GaN grown by hydride-vapor-phase-epitaxy on two-step epitaxial lateral overgrown GaN template, *J. Appl. Phys.* **96**, 799–806 (2004)
- 26.62 Y. Oshima, T. Eri, M. Shibata, H. Sunakawa, K. Kobayashi, T. Ichihashi, A. Usui: Preparation of freestanding GaN wafers by hydride vapor phase epitaxy with void-assisted separation, *Jpn. J. Appl. Phys.* **42**, L1–L3 (2003)
- 26.63 P.R. Tavernier, B. Imer, S.P. DenBaars, D.R. Clarke: Growth of thick (1120) GaN using a metal interlayer, *Appl. Phys. Lett.* **85**, 4630–4632 (2004)
- 26.64 H.M. Kim, J.E. Oh, T.W. Kang, H.M. Kim, J.E. Oh, T.W. Kang: Preparation of large area free-standing GaN substrates by HVPE using mechanical polishing liftoff method, *Mater. Lett.* **47**, 276–280 (2001)
- 26.65 Y.V. Melnik, K.V. Vassilevski, I.P. Nikitina, A.I. Babanin, V.Y. Davydov, V.A. Dmitriev: Physical

- properties of bulk GaN crystals grown by HVPE, MRS Internet J. Nitrid. Semicond. Res. **2**, 39 (1997)
- 26.66 Y. Melnik, A. Nikolaev, I. Nikitina, K.V. Vassilevski, V.A. Dmitriev: Properties of free-standing GaN bulk crystals grown by HVPE, Mater. Res. Soc. Symp. Proc. **482**, 269–274 (1998)
- 26.67 T.J. Kropewnicki, W.A. Doolittle, C. Carter-Coman, S. Kang, P.A. Kohl, N.M. Jokerst, A.S. Brown, S. April: Selective wet etching of lithium gallate, J. Electrochem. Soc. **145**, L88–L90 (1998)
- 26.68 O. Oda, T. Inoue, Y. Seki, K. Kainosho, S. Yaegashi, A. Wakahara, A. Yoshida, S. Kurai, Y. Yamada, T. Taguchi: GaN bulk substrates for GaN based LEDs and LDs, Phys. Status Solidi (a) **180**, 51–58 (2000)
- 26.69 A. Wakahara, T. Yamamoto, K. Ishio, A. Yoshida, Y. Seki, K. Kainosho, O. Oda: Hydride vapor phase epitaxy of GaN on NdGaO_3 substrate and realization of freestanding GaN wafers with 2-inch scale, Jpn. J. Appl. Phys. **39**, 2399–2401 (2000)
- 26.70 R. P. Vaudo, V. M. Phanse, J. Jayapalan, D. Wang, B.J. Skromme: Si-doping of GaN grown on sapphire by HVPE, abstract book, MRS fall meeting, (1997) D16.3
- 26.71 E. Richter, C. Hennig, U. Zeimer, L. Wang, M. Weyers, G. Tränkle: n-Type doping of HVPE-grown GaN using dichlorosilane, Phys. Status Solidi (a) **203**, 1658–1662 (2006)
- 26.72 A.V. Fomin, A.E. Nikolaev, I.P. Nikitina, A.S. Zubrilov, M.G. Mynbaeva, N.I. Kuznetsov, A.P. Kovarsky, B.J. Ber, D.V. Tsvetkov: Properties of Si-doped GaN layers grown by HVPE, Phys. Status Solidi (a) **188**, 433–437 (2001)
- 26.73 C. G. Van de Walle, S. Limpijumnong, J. Neugebauer: First-principles studies of beryllium doping of GaN, Phys. Rev. B **63**, 245205–1–245205–17 (2001)
- 26.74 W. Götz, N.M. Johnson, J. Walker, D.P. Bour, R.A. Street: Activation of acceptors in Mg-doped GaN grown by metalorganic chemical vapor deposition, Appl. Phys. Lett. **68**, 667–669 (1996)
- 26.75 H. Amano, M. Kito, K. Hiramatsu, I. Akasaki: p-Type conduction in Mg-doped GaN treated with low-energy electron beam irradiation (LEEBI), Jpn. J. Appl. Phys. **28**, L2112–L2114 (1989)
- 26.76 S. Nakamura, T. Mukai, M. Senoh, N. Iwasa: Thermal annealing effects on p-type Mg-doped GaN films, Jpn. J. Appl. Phys. **31**, L139–L142 (1992)
- 26.77 D.P. Bour, H.F. Chung, W. Götz, L. Romano, B.S. Krusor, D. Hofstetter, S. Rudaz, C.P. Kuo, F.A. Ponce, N.M. Johnson, M.G. Craford, R.D. Bringans: Characterization of OMVPE-grown AlGaInN heterostructures, Mater. Res. Soc. Symp. Proc. **449**, 509–518 (1997)
- 26.78 J. Neugebauer, C.G. Van de Walle: Theory of point defects and complexes in GaN, Mater. Res. Soc. Symp. Proc. **395**, 645–656 (1996)
- 26.79 A. Usikov, O. Kovalenkov, V. Ivantsov, V. Sukhoveev, V. Dmitriev, N. Schmidt, D. Poloskin, V. Petrov, V. Ratnikov: p-Type GaN epitaxial layers and AlGaIn/GaN heterostructures with high hole concentration and mobility grown by HVPE, Mater. Res. Soc. Symp. Proc. **831**, 453–457 (2005)
- 26.80 J.A. Van Vechten, J.D. Zook, R.D. Horning, B. Goldenberg: Defeating compensation in wide gap semiconductors by growing in H that is removed by low temperature de-ionizing radiation, Jpn. J. Appl. Phys. **31**, 3662–3663 (1992)
- 26.81 J. Neugebauer, C.G. Van de Walle: Atomic geometry and electronic structure of native defects in GaN, Phys. Rev. B **50**, 8067–8070 (1994)
- 26.82 J. Neugebauer, C.G. Van de Walle: Hydrogen in GaN: Novel aspects of a common impurity, Phys. Rev. Lett. **75**, 4452–4455 (1995)
- 26.83 J. Neugebauer, C.G. Van de Walle: Gallium vacancies and the yellow luminescence in GaN, Appl. Phys. Lett. **69**, 503–505 (1996)
- 26.84 A. Kasic, D. Gogova, H. Larsson, I.G. Ivanov, C. Hemmingsson, R. Yakimova, B. Monemar, M. Heuken: Characterization of crack-free relaxed GaN grown on 2" sapphire, J. Appl. Phys. **98**, 073525–1–073525–6 (2005)
- 26.85 E.V. Etzkorn, D.R. Clarke: Cracking of GaN films, J. Appl. Phys. **89**, 1025–1034 (2001)
- 26.86 T. Hino, S. Tomiya, T. Miyajima, K. Yanashima, S. Hashimoto, M. Ikeda: Characterization of threading dislocations in GaN epitaxial layers, Appl. Phys. Lett. **76**, 3421–3423 (2000)
- 26.87 R.P. Vaudo, X. Xu, C. Loria, A.D. Salant, J.S. Flynn, G.R. Brandes: GaN boule growth: A pathway to GaN wafers with improved material quality, Phys. Status Solidi (a) **194**, 494–497 (2002)
- 26.88 M. Albrecht, I.P. Nikitina, A.E. Nikolaev, V.Y. Melnik, V.A. Dmitriev, H.P. Strunk: Dislocation reduction in AlN and GaN bulk crystals grown by HVPE, Phys. Status Solidi (a) **176**, 453–458 (1999)
- 26.89 CREE homepage: www.cree.com/products/gan_tech.asp (24-Sep 2008)
- 26.90 T. Paskova, V. Darakchieva, P.P. Paskov, J. Birch, E. Valcheva, P.O.A. Persson, B. Arnaudov, S. Tungasmita, B. Monemar: Properties of nonpolar a -plane GaN films grown by HVPE with AlN buffers, J. Cryst. Growth **281**, 55–61 (2005)
- 26.91 T. Paskova, R. Kroeger, P.P. Paskov, S. Figge, D. Hommel, B. Monemar, B. Haskell, P. Fini, J.S. Speck, S. Nakamura: Microscopic emission properties of nonpolar a -plane GaN grown by HVPE, Proc. SPIE **6121**, 47 (2006)
- 26.92 P.P. Paskov, T. Paskova, B. Monemar, S. Figge, D. Hommel, B.A. Haskell, P.T. Fini, J.S. Speck, S. Nakamura: Optical properties of nonpolar a -plane GaN layers, Superlattices Microstruct. **40**, 253–261 (2006)
- 26.93 B.A. Haskell, F. Wu, M.D. Craven, S. Matsuda, P.T. Fini, T. Fujii, K. Fujito, S.P. DenBaars, J.S. Speck, S. Nakamura: Defect reduction in (11 $\bar{2}$ 0) a -plane gallium nitride via lateral epitaxial overgrowth by

- hydride vapor-phase epitaxy, *Appl. Phys. Lett.* **83**, 644–646 (2003)
- 26.94 B. Monemar, T. Paskova, C. Hemmingsson, H. Larsson, P.P. Paskov, I.G. Ivanov, A. Kasic: Growth of thick GaN layers by hydride vapor phase epitaxy, *J. Ceram. Process. Res.* **6**, 153–162 (2005)
- 26.95 J. Baur, U. Kaufmann, M. Kunzer, J. Schneider, H. Amano, I. Akasaki, T. Detzprohm, K. Hiramatsu: Characterization of residual transition metal ions in GaN and AlN, *Mater. Sci. For.* **196–201**, 55–60 (1995)
- 26.96 K. Saarinen, T. Laine, S. Kuisma, J. Nissilä, P. Hautajärvi, L. Dobrzynski, J.M. Baranowski, K. Pakula, R. Stepniewski, M. Wojdak, A. Wyszomolek, T. Suski, M. Leszczynski, I. Grzegory, S. Porowski: Observation of native Ga vacancies in GaN by positron annihilation, *Phys. Rev. Lett.* **79**, 3030–3033 (1997)
- 26.97 M. Leszczynski, H. Teisseyre, T. Suski, I. Grzegory, M. Boćkowski, J. Jun, S. Porowski, K. Pakula, J.M. Baranowski, C.T. Foxon, T.S. Cheng: Lattice parameters of gallium nitride, *Appl. Phys. Lett.* **69**, 73–75 (1996)
- 26.98 V. Darakchieva, P.P. Paskov, T. Paskova, E. Valcheva, B. Monemar, M. Heuken: Lattice parameters of GaN layers grown on *a*-plane sapphire: Effect of in-plane strain anisotropy, *Appl. Phys. Lett.* **82**, 703–705 (2003)
- 26.99 C. G. Van de Walle: Effects of impurities on the lattice parameters of GaN, *Phys. Rev. B* **68**, 165209–1–165209–5 (2003)
- 26.100 C. Roder, S. Einfeldt, S. Figge, D. Hommel: Temperature dependence of the thermal expansion of GaN, *Phys. Rev. B* **72**, 085218–1–085218–6 (2005)
- 26.101 E.K. Sichel, J.I. Pankove: Thermal conductivity of GaN, 25–360 K, *J. Phys. Chem. Solids* **38**, 330 (1977)
- 26.102 A. Jezowski, P. Stachowiak, T. Plackowski, T. Suski, S. Krukowski, M. Boćkowski, I. Grzegory, B. Danilchecenko, T. Paszkiewicz: Thermal conductivity of GaN crystals grown by high pressure method, *Phys. Status Solidi (b)* **240**, 447–450 (2003)
- 26.103 D.C. Look, J.R. Sizelove: Predicted maximum mobility in bulk GaN, *Appl. Phys. Lett.* **79**, 1133–1135 (2001)
- 26.104 J.W. Orton, C.T. Foxon: Group III nitride semiconductors for short wavelength light-emitting devices, *Rep. Prog. Phys.* **61**, 1–75 (1998)
- 26.105 V. Darakchieva, private communication, 2006
- 26.106 J.C. Rojo, G.A. Slack, K. Morgan, B. Raghothamachari, M. Dudley, L.J. Schowalter: Report on the growth of bulk aluminum nitride and subsequent substrate preparation, *J. Cryst. Growth* **231**, 317–321 (2001)
- 26.107 R. Schlessler, R. Dalmau, Z. Sitar: Seeded growth of AlN bulk single crystals by sublimation, *J. Cryst. Growth* **241**, 416–420 (2002)
- 26.108 M. Boćkowski, M. Wróblewski, B. Łuczniak, I. Grzegory: Crystal growth of aluminum nitride under high pressure of nitrogen, *Mater. Sci. Semicond. Process.* **4**, 543–548 (2001)
- 26.109 K. Motoki, T. Okahisa, N. Matsumoto, M. Matsushima, H. Kimura, H. Kasai, K. Takemoto, K. Uematsu, T. Hirano, M. Nakayama, S. Nakahata, M. Ueno, D. Hara, Y. Kumagai, A. Koukitu, H. Seki: Preparation of large freestanding GaN substrates by hydride vapor phase epitaxy using GaAs as a starting substrate, *Jpn. J. Appl. Phys.* **40**, L140–L143 (2001)
- 26.110 S.S. Park, I.-W. Park, S.H. Choh: Free-standing GaN substrates by hydride vapor phase epitaxy, *Jpn. J. Appl. Phys.* **39**, L1141–L1142 (2000)
- 26.111 D. Gogova, H. Larsson, A. Kasic, G.R. Yazdi, I. Ivanov, R. Yakimova, B. Monemar, E. Aujol, E. Frayssinet, J.-P. Faurie, B. Beaumont, P. Gibart: High-quality 2" bulk-like free-standing GaN grown by hydride vapour phase epitaxy on a Si-doped metal organic vapour phase epitaxial GaN template with an ultra low dislocation density, *Jpn. J. Appl. Phys.* **44**, 1181–1185 (2005)
- 26.112 A. Nikolaev, I. Nikitina, A. Zubrilov, M. Mynbaeva, Y. Melnik, V. Dmitriev: AlN wafers fabricated by hydride vapor phase epitaxy, *Mater. Res. Soc. Symp. Proc.* **595**, W6.5 (2000)
- 26.113 O.Y. Ledyayev, A.E. Cherenkov, A.E. Nikolaev, I.P. Nikitina, N.I. Kuznetsov, M.S. Dunaevski, A.N. Titkov, V.A. Dmitriev: Properties of AlN layers grown on SiC substrates in wide temperature range by HVPE, *Phys. Status Solidi (c)* **0**, 474–478 (2002)
- 26.114 Y. Kumagai, T. Yamane, A. Koukitu: Growth of thick AlN layers by hydride vapor-phase epitaxy, *J. Cryst. Growth* **281**, 62–67 (2005)
- 26.115 Y.-H. Liu, T. Tanabe, H. Miyake, K. Hiramatsu, T. Shibata, M. Tanaka, Y. Masa: Growth of thick AlN layer by hydride vapor phase epitaxy, *Jpn. J. Appl. Phys.* **44**, L505–L507 (2005)
- 26.116 V.Y. Davydov, A.A. Klochikhin, R.P. Seisyan, V.V. Emtsev, S.V. Ivanov, F. Bechstedt, J. Furthmüller, H. Harima, A.V. Mudryi, J. Aderhold, O. Semchinova, J. Graul: Absorption and emission of hexagonal InN. Evidence of narrow fundamental band gap, *Phys. Status Solidi (b)* **229**, R1–R3 (2002)
- 26.117 J. Wu, W. Walukiewicz, K.M. Yu, J.W. Ager III, E.E. Haller, H. Lu, W.J. Schaff, Y. Saito, Y. Nanishi: Unusual properties of the fundamental band gap of InN, *Appl. Phys. Lett.* **80**, 3967–3969 (2002)
- 26.118 T. Matsuoka, H. Okamoto, M. Nakao, H. Harima, E. Kurimoto: Optical bandgap energy of wurtzite InN, *Appl. Phys. Lett.* **81**, 1246–1248 (2002)
- 26.119 N. Takahashi, J. Ogasawara, A. Koukitu: Vapor phase epitaxy of InN using InCl and InCl₃ sources, *J. Cryst. Growth* **172**, 298–302 (1997)
- 26.120 L.A. Marasina, I.G. Pichugin, M. Tlaczala: Preparation of InN epitaxial layers in InCl₃–NH₃ system, *Krist. Tech.* **12**, 541–545 (1977)
- 26.121 N. Takahashi, R. Matsumoto, A. Koukitu, H. Seki: Growth of InN at high temperature by halide vapor

- phase epitaxy, Jpn. J. Appl. Phys. **36**, L743–L745 (1997)
- 26.122 Y. Kumagai, J. Kikuchi, Y. Nishizawa, H. Murakami, A. Koukitu: Hydride vapor phase epitaxy of InN by the formation of InCl_3 using In metal and Cl_2 , J. Cryst. Growth **300**, 57–61 (2007)
- 26.123 J. Wu, W. Walukiewicz, S.X. Li, R. Armitage, J.C. Ho, E.R. Weber, E.E. Haller, H. Lu, W.J. Schaff, A. Barcz, R. Jakiela: Effects of electron concentration on the optical absorption edge of InN, Appl. Phys. Lett. **84**, 2805–2807 (2004)

27. Growth of Semiconductor Single Crystals from Vapor Phase

Ramasamy Dhanasekaran

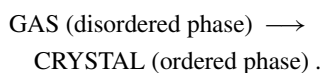
Growth of single crystals from the vapor phase is considered to be an important method to obtain stoichiometric crystalline materials from inexpensive and readily available raw materials. Elements or compounds which are relatively volatile can be grown from vapor phase. Most II–VI, I–III–VI₂, and III–N compounds are high-melting-point materials which may be grown as single crystals by careful use of vapor phase. The chemical vapor transport (CVT) method has been widely used as an advantageous method to grow single crystals of different compounds at temperatures lower than their melting points. This method is quite useful for the growth of II–VI and I–III–VI₂ compounds, which generally have high melting point and large dissociation pressure at the melting point. In addition, they undergo solid-state phase transition during cooling or heating processes, which makes the growth of these compounds by some other methods, such as from the melt, difficult. In addition, the low growth temperature involved reduces defects produced by thermal strain, pollution from the crucible, and the cost of the growth equipment. II–VI compound semiconductors cover a very broad range of electronic and optical properties due to the large range of their energy gaps. These materials in the form of bulk single crystals or thin films are used in light emitters, detectors, linear and nonlinear optical devices, semiconductor electronics, and other devices. The development of growth technology for II–VI compound semiconductors from the vapor phase with the necessary theoretical background is important. I–III–VI₂ chalcopyrite compounds are of technological interest since they show promise for application in areas of visible and infrared light-emitting diodes, infrared detectors, optical parametric oscillators, upconverters, far-infrared generation, and solar energy conversion.

27.1	Classifications of Vapor Growth	899
27.2	Chemical Vapor Transport – Transport Kinetics	901
27.2.1	Transport Models	901
27.2.2	Physical Chemistry of Chemical Transport Reactions...	902
27.2.3	Factors Affecting the CVT Reaction	903
27.2.4	Choice of Transporting Agents	904
27.2.5	Advantages and Limitations of CVT Method	904
27.3	Thermodynamic Considerations	905
27.3.1	Estimation of Optimum Growth Parameters for the ZnSe–I ₂ System by CVT	905
27.3.2	Fluctuations in the Transport Rates	906
27.3.3	Supersaturation Ratios in the ZnS _x Se _{1-x} System	908
27.4	Growth of II–VI Compound Semiconductors by CVT	912
27.4.1	Apparatus	912
27.4.2	Preparation of Starting Materials..	913
27.4.3	Growth of ZnSe Single Crystals	914
27.4.4	Growth of CdS Single Crystals	915
27.5	Growth of Nanomaterial from Vapor Phase	916
27.6	Growth of I–III–VI₂ Compounds	917
27.6.1	Growth of Undoped and Doped Crystals of CuAlS ₂	918
27.6.2	Growth of Undoped and Doped Crystals of CuAlSe ₂	919
27.6.3	Growth of CuGaS ₂ –Based Single Crystals ...	921
27.6.4	Growth of AgGaS ₂ and AgGaSe ₂ Single Crystals	923
27.7	Growth of GaN by VPE	925
27.7.1	Vapor–Phase Epitaxy (VPE)	925
27.7.2	VPE GaN Film Growth	925
27.7.3	Strength of HVPE Method	926
27.7.4	Development of VPE System for the Growth of GaN	926

27.7.5 Growth of GaN by HVPE	927	27.8 Conclusion	929
27.7.6 Characterization of GaN Films	928	References	930

A great deal of interest in these materials is generated by their chalcopyrite structure, which is noncentrosymmetric and makes them useful for second-harmonic generation. III-nitride semiconductors are of great interest to industry and the military due to their optoelectronic and mechanical properties, permitting the development of devices operating in the blue and ultraviolet regions of the spectrum and at high temperatures. Gallium nitride has particularly attracted considerable attention in this regard. Despite the progress recently achieved, some fundamental properties of GaN and its related compounds, such as InGaN and AlGaN, are still not fully understood. Epitaxial methods continue to lead the field of crystal growth by exploring new physics, materials science, and fabrication of novel devices. Good-quality GaN layers have been grown by employing vapor-phase epitaxy systems, the technical details of which are presented in detail herein.

During recent decades, ternary, quaternary, and more recently multinary semiconductor materials have been widely investigated because of their importance for solid-state device applications. However, their crystal growth technology is far from well understood. Due to practical difficulties involved in growing single crystals of most of these materials by melt techniques, regular production of small samples perfect enough and of good enough quality almost always depends upon the availability of vapor-phase (VP) chemical transport reactions (usually *iodine* transport) in closed tubes. One of the common drawbacks of these VP methods is the high level of supersaturation, and hence uncontrolled primary nucleation, which can give rise to many small-sized (often submillimeter) crystals. This high supersaturation is also responsible for various instability patterns (dendrites, overgrowths, etc.) that show up in the final crystals. Crystal growth from the vapor phase is in principle a flexible method of growing single crystals. This potential flexibility has occasionally been exploited, but more often the principles have been poorly understood [27.1]. Preparation of a crystal from the gas phase requires the general reaction



The gas phase may consist of molecules of the crystal substance, or of its separate constituents, if they are all volatile. Otherwise, the constituents may be reacted with a transporting agent to provide volatile species. In all cases, an inert gas is added to modify the transport kinetics. The basic reaction results in an increase in atomic order.

Important research efforts have been focused on II–VI compounds since the late 1950s. Because of their superiority over rival materials, these compounds are becoming of more importance day by day in research into electronic materials. Many experimental procedures have been improved, and theoretical models have been developed. However, in spite of their positive properties, the crystallographic properties of some II–VI semiconductor materials (e.g., ZnS and ZnSe) have hindered their application in the electronic industry due to polytypism.

Currently, I–III–VI₂ compounds (chalcopyrite ternary semiconductor), such as copper indium diselenide (CuInSe₂), copper indium disulfide (CuInS₂), and copper gallium diselenide (CuGaSe₂), are the most promising low-cost thin-film materials for solar cell applications due to their high absorption coefficient and excellent thermal stability. Photovoltaic (PV) cells based on these materials have potentials to be used on the Earth as well as in various space applications. Scientists from the US National Renewable Energy Laboratory (NREL), have achieved efficiency of about 19.2% with CuInSe₂ absorber in laboratory cells. The best efficiency of a thin-film solar cell up to now is 19.5%, by using Cu(In,Ga)Se₂ as absorber [27.2], which is comparable to that for polycrystalline Si solar cells. In view of their potential low cost and light weight, these solar cells have been expected to be useful in space applications in addition to the terrestrial domain. Thus, there is strong demand for improvement of the efficiency of PV cells based on these chalcopyrite materials.

The demonstration of blue light-emitting diodes (LEDs) and blue laser diodes (LDs) [27.3] has led to the emergence of III–V nitrides as a suitable material for high-power, high-temperature electronic and optoelectronic device production. The development of

high-quality nitride-based devices is still restricted by the lack of suitable epitaxial substrates materials. Nitride-based structures are most commonly deposited on sapphire (Al_2O_3) substrates. The lattice mismatch of about 15% to GaN causes formation of threading dislocations (TDs) in the sapphire interface and device layers [27.4]. In order to improve GaN epitaxial layers, a two-step deposition process is often applied in both metalorganic chemical vapor deposition (MOCVD) [27.5, 6] and hydride vapor-phase epitaxy (HVPE) [27.7] systems. The application of HVPE tech-

nology assures high growth rates of about 500 nm/min for growth of GaN. Hence, sufficiently thick layers can be deposited in a relatively short time. This makes HVPE an advantageous fabrication option for freestanding GaN substrates.

In this chapter, growth of semiconductor single crystals from the vapor phase is explained in general, and the chemical vapor transport technique in particular. Growth of II–VI and I–III–V₂ compounds is reviewed, and growth of GaN thin films using vapor-phase epitaxy is presented.

27.1 Classifications of Vapor Growth

The growth of crystal from vapor phase can be divided [27.7] into various categories:

1. *Sublimation or evaporation*, in which the vapor is obtained from the pure condensed phase at an appropriate temperature;
2. A compound may highly dissociate in the growth system, namely *dissociative sublimation*;
3. If a transporting reaction is used for one or more of the constituents of the crystal, the process is termed either *chemical vapor transport (CVT)* or *physical vapor transport (PVT)*, distinguished on the basis of the conditions over the growing crystal. A comparison between PVT, physical vapor deposition (PVD), chemical vapor deposition (CVD), and CVT is shown in Table 27.1

PVT is a closed-tube technique that can be used to grow crystals if the vapor pressure of the material exceeds 10^{-2} Torr at some feasible temperature. Typically in these processes, the source is a solid which must be sublimed (dissociatively or similarly) to provide the vapor. The process by which vapor is obtained from the pure condensed phase at an appropriate temperature and transported to a deposition zone at a lower temperature is called physical vapor transport. The vapor atoms impinge on the substrate surface and become adsorbed, releasing part of their latent heat of condensation and migrating across the crystal surface. They become incorporated into the crystal lattice, releasing their remaining heat of condensation; otherwise they evaporate. This is a relatively high-temperature method.

In the CVT process, as shown in Table 27.1, vapor atoms or molecules are chemically different from

those of the growing crystal. Chemical transport reactions are those in which a solid or liquid substance A reacts with a gas to form exclusively volatile products, which in turn undergo the reverse reaction at a different place in the system, resulting in the formation of A. The process appears to be sublimation; however, it does not possess appreciable vapor pressure at the temperatures applied. In addition to a reversible heterogeneous reaction, a concentration gradient must be established. The latter can be the result of a temperature difference, changes in the relative pressures, or the difference in free energy of formation of two substances.

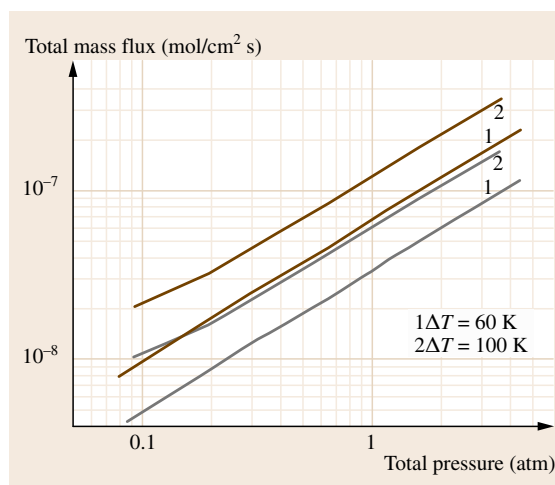


Fig. 27.1 Variation of total mass flux as a function of total pressure in the CdSe–I₂ system for the given two temperature differences between the source zone and growth zone and for the given diameter of 15 cm and length of 14 cm of the growth ampoule

Table 27.1 Comparison between PVT, CVT, PVD, and CVD

Parameters	Physical vapor transport (PVT)	Chemical vapor transport (CVT)	Physical vapor deposition (PVD)	Chemical vapor deposition (CVD)
Growth mechanism and bond energy	Monatomic, associative or dissociative sublimation Direction always from hot to cold ($T_s \rightarrow T_g$)	Reversible chemical reaction migration from hot to cold ($T_s \rightarrow T_g$) as well as from cold to hot ($T_g \rightarrow T_s$) possible	Direction always from hot to cold Nonconformal deposition Highly directional deposition Bonding energy is weak, less than 10 kcal/mol or 0.434 eV/atom	Conformal deposition Multidirectional deposition Bonding energy is strong compared with physical bond, up to 200 kcal/mol
Transport (carrier) gas	Without transport agent or inert gas	Needs a transporting agent such as I_2 , Cl_2 , etc.	Not necessary	Needs a transporting agent such as nitrogen, argon, etc.
Temperature difference (ΔT)	1–10 K	3–500 K	≈ 50 K to Several 100 K	≈ 50 –100 K
Total system pressure (P)	High vacuum (or) inert gas of 0.01–0.5 atm	Up to 3 atm	1 atm	Atmospheric pressure to very low pressure
Thermophysical parameter	Constant	Varying	Constant	Varying
Compressible effect	Insignificant	Significant	Insignificant	Significant
Aspect ratio (l/d)	Typically 5	Typically 10	–	–
Possible flow pattern	Diffusion/advective and solutal convection	Diffusion/advective and thermal convection	Diffusion/advective and solutal convection	Diffusion/advective, thermal convection and laminar for HVPE GaN

The stationary temperature profile (STP) technique has been successfully applied for growing crystals since the growth of crystals by chemical vapor transport was initiated several decades ago. In the STP procedure, the source temperature (T_s) and growth temperature (T_g) are fixed at particular values after keeping a reverse temperature profile for the first few hours in order to clean the crystallization zone. As T_s and T_g are kept at constant values, the supersaturation remains unchanged during the whole growth period. Though this procedure can be adopted to obtain single crystals of many compounds, it may not be the most suitable technique for obtaining large-size single crystals. Also in most cases one ends up with too many crystals as the supersaturation is maintained constant throughout the growth experiment.

In the time-varying temperature profile (TVTP) method, the source temperature is increased linearly with time from a value below the growth temperature, while the growth temperature is kept constant. Hence the supersaturation increases from a negative value (i. e., at $T_s < T_g$) to positive values at which the formation of primary nuclei is possible. After the formation of primary nuclei, although T_s continues to increase, the

supersaturation drops due to the decrease of the vaporized mass, which is consumed in producing the first crystal. Then, for a certain length of time depending on the particular vaporization kinetics of the charge, supersaturation remains sufficiently low that the first crystal can be further grown by secondary nucleation. After this, supersaturation increases again, enabling primary nucleation to take place. This TVTP procedure was adopted for growing ternary chalcopyrite crystals. It enables the growth of crystals much larger than those grown by the STP procedure. Also the quality of the crystals has been reported to be superior to those grown by adopting the STP procedure.

One of the drawbacks of the STP procedure is often the onset of constitutional undercooling from the very beginning of the growth process. In this respect, the TVTP procedure is an improvement because, in the first part of the growth period, this cause of instability is avoided. Constitutional undercooling appears as a result of both large supersaturation and the presence of mass convection in the vapor. Supersaturation can practically be reduced by working with small T_s and T_g differences, possibly at temperatures and pressures where thermody-

namics predict low supersaturation. Mass convection, which can be reduced by working at suitably small values of the Grashof number, induces constitutional undercooling through the reduction of the diffusion boundary layer at the growing interface. It is concluded that the time-varying temperature profile method described above can be used to increase the size of the crystals of some ternary compounds. Enlargements of about two- to threefold were obtained by this procedure, as compared with the usual **STP** technique. Time-varying temperature profile methods have been applied by various researchers to improve the size of CdS [27.8], CdIn₂S₄, and CuInS₂ [27.9] single crystals grown by **CVT** technique.

In **PVD** there is a transfer of subliming molecules/atoms A by (saturated) carrier gas to a colder growth area.

In chemical vapor deposition gaseous compounds of the materials to be deposited are transported to a substrate surface, where a thermal reaction/deposition occurs. Reaction byproducts are then exhausted out of the system.

The other vapor growth methods are:

1. Metalorganic chemical vapor deposition (**MOCVD**)
2. Vapor-phase epitaxy (**VPE**)
3. Metalorganic vapor-phase epitaxy (**MOVPE**)
4. Organometallic vapor-phase epitaxy (**OMVPE**).

27.2 Chemical Vapor Transport – Transport Kinetics

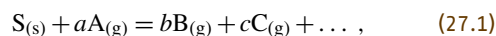
Crystal growth from the melt using the classical methods of Czochralski, Kyropoulos or Bridgman becomes difficult if the compounds to be grown have high melting points. Additional difficulties arise if the compounds show appreciable dissociation at the melting point or melt only under elevated pressure. To obtain single crystals of such compounds, they are sublimed (either in vacuum or in a stream of carrier gas or vapor of its constituents) and allowed to react in the crystallization chamber [27.10–12]. The temperature required for these processes is high, in the vicinity of the sublimation point. Instead of directly vaporizing a solid at high temperature it may be vaporized at much lower temperature by forming highly volatile chemical intermediates and reacting back the resulting gas mixture at a different temperature, utilizing the temperature dependence of the chemical equilibrium involved [27.12–16]. By properly adjusting the two temperatures, the departure from chemical equilibrium in the vicinity of the growing seeds can be made small enough to avoid nucleation but large enough to make the seeds grow, i.e., appropriate supersaturation can be maintained.

27.2.1 Transport Models

In general transport models have been developed based on the following experimental conditions:

1. The system is one dimensional and the length of the growth ampoule is L units, with the source at $x = 0$, transported to a deposit at $x = L$.

2. The transport mechanism involves a chemical equilibrium which can be written as



associated with an equilibrium constant K and an enthalpy change ΔH , where $S_{(s)}$ is the crystalline source materials, A is the transporting agent, and B and C are the gaseous products.

3. Diffusion is the only means of transport through the vapor phase; turbulent flow and thermal diffusion are ignored.
4. The mean free path is much smaller than the dimension of the system. As a consequence, a total pressure gradient cannot be considered. Impedance to the flow due to total pressure gradients is so small that we can ignore these gradients relative to partial pressure gradients.
5. The surface rate of the reaction is infinitely fast, so local equilibrium is essentially established in the neighborhoods of the source and the substrate.
6. The change of the equilibrium constant upon moving from $x = 0$ to $x = L$, leads to a difference in temperature between the source and growth zones ΔT , which is much smaller than T_g . An equivalent statement is $\Delta T = T_s - T_g \ll (RT_g T_s / \Delta H)$, according to the usual thermodynamic relationship between ΔH and ΔT .
7. $|\Delta H| \gg RT \cong \frac{1}{2} R(T_g + T_s)$. This also implies $\Delta T \ll T_g$.
8. All gases behave ideally.

Following *Schäfer's* model [27.12], a transport reaction is defined as a reaction of a solid or liquid with a gaseous component in a temperature gradient to form exclusively gaseous products. For chemical transport caused only by diffusion, such as in a sealed silica ampoule, *Schäfer* [27.12] obtained a transport equation for the migration of a solid in a one-dimensional system. *Lever* [27.14] described the chemical transport of a solid involving several simultaneous heterogeneous and homogeneous equilibria [27.17, 18]. *Arizumi* and *Nishinaga* [27.19–21] proposed transport equations for the transport of materials (semiconductors) in closed tubes, assuming a one-dimensional system and considering diffusion and laminar flow as the fundamental transport mechanism (AN model).

Following the model of *Factor* and *Garrett* [27.22, 23] in a one-dimensional transport system, the flux rate J (mol/cm² s) of a component i caused by diffusion and Stefan flow can be described. The variation of total mass flux as a function of total pressure in the CdSe–I₂ system for various growth temperatures for given dimensions of the growth ampoule (diameter 15 cm and length 14 cm) is shown in Fig. 27.1.

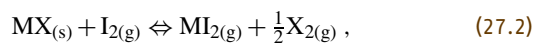
Using the flux function method of *Richardson* and *Nöling*, it is possible to calculate the net fluxes J_k (mol/cm² s) based on an equilibrium model [27.24–26]. The flux function takes into account the Stefan flow, as well as the temperature and total pressure variation of the diffusion coefficient. Thus it becomes possible to compute the transport rates of the simultaneous migration of several condensed phases. A flux function Φ takes into account the temperature dependency of the diffusion coefficient. The advantage of this flux function is that different transport systems with different transporting agents, temperature gradients, and diffusion coefficients can be compared with each other [27.27–29].

27.2.2 Physical Chemistry of Chemical Transport Reactions

Partial Pressure

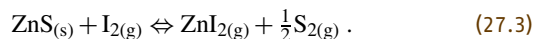
Consider a closed system containing $n + 1$ components, all of which are in chemical equilibrium with one other [27.30]. The temperature is chosen such that only one component is solid, whereas the other n components are in gaseous state. For $n = 1$, the trivial case of sublimation of a solid via its gaseous atoms or molecules results. In the following, the case $n = 3$ is considered, which applies to the transport of metal chalcogenides by halogens. The equilibria involved

are [27.12]



where $M = \text{Cd, Zn}$ and $X = \text{S, Se}$.

A specific example is [27.13, 18, 31]



In a CVT system, a solid substance MX reacts with a gaseous transporting agent I_2 (chalcogenides) at a higher temperature T_s to form exclusively vapor-phase products MX and $\frac{1}{2}\text{X}$ at the source zone. The vapor products in turn undergo the reverse reaction at the growth zone at a lower temperature T_g



The corresponding equilibrium constants of (27.2) and (27.4) are

$$K_{(27.2)} = \frac{p_{\text{MI}_2} \left(\frac{1}{2} p_{\text{MX}_2} \right)^{\frac{1}{2}}}{p_{\text{I}_2}}, \quad (27.5)$$

$$K_{(27.4)} = \frac{p_{\text{I}}^2}{p_{\text{I}_2}}, \quad (27.6)$$

respectively.

The total pressure of the system is given by

$$P = p_{\text{I}_2} + p_{\text{I}} + 1.5 p_{\text{MI}_2}. \quad (27.7)$$

The equilibrium constant $K_i(T)$ ($i = 3, 2, 4$) as a function of temperature T can be evaluated using the relations (27.2) and (27.4–27.6) [27.27–29]

$$\log K_i(T) = a_i - b_i T^{-1} - c_i T^{-2} - d_i \log(T) - e_i T. \quad (27.8)$$

If the temperature T and total pressure p are fixed and the value of $K_i(T)$ is known, then the partial pressure of species MI_2 , X_2 , I_2 , and I can be determined by using (27.2) and (27.4–27.8). A graph showing the partial pressure of various gaseous species as a function of total pressure of the CdSe–I₂ system is shown in Fig. 27.2; for ZnSe–I₂ and other systems, refer to literature [27.13, 31–34].

Thermophysical Parameters

The diffusion coefficient of a binary gas mixture is based on the well-known Chapman–Enskog formula [27.29, 32, 35, 36]

$$D_{ij} = 1.858^{-27} \frac{\sqrt{T^3(1/M_i + 1/M_j)}}{P \sigma_{ij}^2 \Omega_{D_{ij}}}. \quad (27.9)$$

In (27.9) σ_{ij} is the characteristic length expressed in Å and Ω_D is the dimensionless diffusion collision integral. The binary collision integral was estimated from individual collision diameters σ_A and σ_B using the expression

$$\sigma_{ij} = \frac{\sigma_i + \sigma_j}{2}, \quad (27.10)$$

where Ω_D is a function of $k_B T / \varepsilon_{ij}$, where k_B is the Boltzmann's constant, $\varepsilon_{ij} = (\varepsilon_i \varepsilon_j)^{1/2}$, and ε_i and ε_j are the Lennard–Jones energy values for species i and j , respectively. The complete expression for Ω_D can be given as

$$\Omega_D = \frac{A}{T^{*B}} + \frac{C}{\exp(DT^*)}, \quad (27.11)$$

where $T^* = k_B T / \varepsilon_{ij}$ is the reduced temperature and the values of A , B , C , and D can be calculated from reported data. The diffusion collision integral and diffusion coefficients for various species are presented in Table 27.2.

The molecular viscosity μ and thermal conductivity k_T of the species can be calculated from Chapman–Enskog and Lennard–Jones potential theory [27.29, 37, 38]

$$\mu = 2.669 \times 10^{-26} \frac{\sqrt{MT}}{\sigma_{ij}^2 \Omega_\mu} \text{ [kg/(m s)]} \quad (27.12)$$

and

$$k_T = 8.324 \times 10^{-22} \frac{\sqrt{(T/M)}}{\sigma_{ij}^2 \Omega_\mu} \text{ [W/(m K)]}, \quad (27.13)$$

where M is the molecular weight (kg/mol), T is the average temperature (K), σ_{ij} is the collision diameter, and Ω_μ is the viscosity collision integral.

Table 27.2 Characteristic length and diffusion collision integral of different species

ij	σ_{ij} (Å)	Ω_{D-ij} at $T = 1173$ K	ij	σ_{ij} (Å)	Ω_{D-ij} at $T = 1173$ K
I ₂ -S ₂	4.051	0.914	ZnI ₂ -Se ₂	5.278	0.945
I-S ₂	3.538	0.903	ZnI ₂ -I ₂	4.955	0.954
I ₂ -Se ₂	4.189	0.967	Cd-I ₂	3.512	0.981
I-Se ₂	4.409	0.935	Cd-S ₂	3.422	0.914
I ₂ -I	4.253	0.938	Cd-Se ₂	3.762	1.040
Zn-I ₂	4.081	1.007	CdI ₂ -Cd	4.248	0.977
Zn-S ₂	4.597	1.175	CdI ₂ -I ₂	5.534	1.262
Zn-Se ₂	4.323	0.946	CdI ₂ -Se ₂	5.431	1.232
ZnI ₂ -S ₂	4.673	1.189	CdI ₂ -S ₂	5.072	1.129

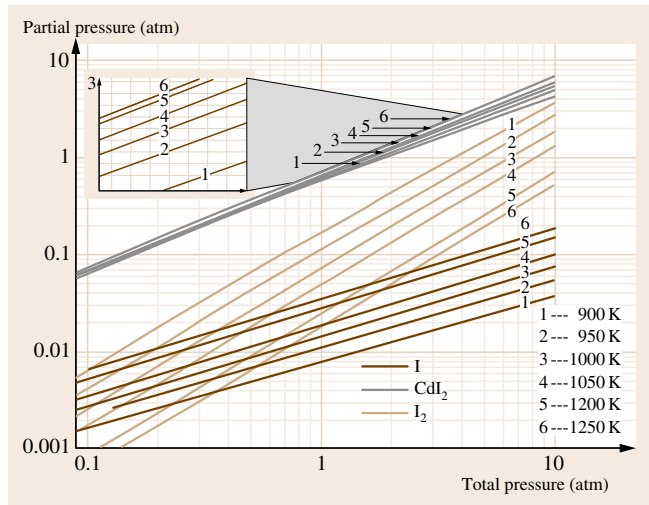


Fig. 27.2 Partial pressures of various gaseous species as a function of total pressure of the CdSe–I₂ system for different temperatures

27.2.3 Factors Affecting the CVT Reaction

Influence of Chemical Parameters on CVT Growth of Crystals

Generally chemical vapor transport reactions depend on chemical parameters such as the free energy change (ΔG), the concentration of the transporting agent (C_T), the temperatures at the source and growth zones (T_s and T_g), etc. [27.29, 39–42]. The free energy change for a reaction depends to a considerable extent on the partial pressures of the chemical species used in the reactions. The amount of material transportation from the source to the growth zone depends strongly on C_T . Also it has been observed by many authors that there is a strong dependence of the size and quality of the resulting crystals on C_T .

If one is concerned only about the rate of transportation and not the quality of the crystals, the absolute values of the temperatures T_s and T_g can be varied over a relatively wide range.

Influence of Geometrical Parameters on CVT Growth of Crystals

The amount of material transported decreases linearly with the length of the tube due to the increase in flow resistance [27.13]. If several seeds are to be formed and to grow in one experiment then the crystallization chamber should not be too small, to avoid intergrowth between the crystals. The distribution of the temperature in the deposition zone must be as uniform as possible in order to avoid reevaporation of crystals from warmer parts during the experiment. The use of a tapered growth zone is advantageous for this purpose, and it induces nucleation at the corner of the tube where the temperature is low. The most important geometrical parameter is the tube cross-section q , which influences the transport rate decisively [27.12, 39, 43, 44].

27.2.4 Choice of Transporting Agents

The choice of transporting agent generally depends on the thermodynamics of the transport reaction and the volatility of the compounds involved [27.1, 22]. In selecting the transporting agents, the following conditions should be taken into consideration [27.40–42, 45–51]:

1. The transporting agent should be chosen such that all species that will be formed by reaction with the solid to be transported have adequate volatility. Moreover there should be good knowledge of the volatility and stability of all the vapor species formed in the reaction and their solubility in the growing crystal.
2. If it is assumed that element M is transported by halogen I through the transport reaction (27.2), the equilibrium constant for this reaction is given by (27.4). To obtain efficient transport, the equilibrium constant for the reactions must not be extreme and should have suitable magnitude at a convenient temperature.
3. The knowledge on the various components of the substances to be transported which have sizable va-

por pressures in the temperature range selected for growth.

4. It should be known to the extent of the substance to be transported as undissociated, uncombined molecules in the vapor phase.

27.2.5 Advantages and Limitations of CVT Method

Advantages of Chemical Vapor Transport

1. The growth process is normally carried out at temperatures much lower than the melting point of the material, which is useful for the growth of materials with high melting points and those that exhibit appreciable dissociation at their stoichiometry melting points.
2. Decrease in contamination from the crucible due to the reduced growth temperature.
3. Allotropic crystalline forms can be grown.
4. Good stoichiometry control is possible.
5. Growth of epitaxial layers is possible.
6. In situ chemical vapor cleaning of the substrate/system is possible.
7. The solid–vapor interfaces exhibit higher interfacial morphological stability during growth than in the case of solid–liquid interfaces.

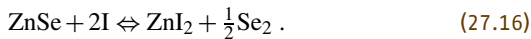
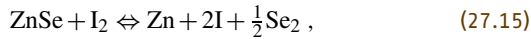
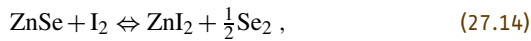
Limitations of Chemical Vapor Transport

1. Thermodynamics and kinetics are complex and poorly understood.
2. Deposition occurs on the substrate as well as on the walls of the container.
3. The reactive gases involved are dangerous in some cases and need special handling procedures.
4. Controlling nucleation is difficult, and growing several crystals due to primary nucleation will result in a decrease in their sizes for a given amount of charge materials.
5. Transporting agents will incorporate into the growing crystals during the growth process and alter the physical properties of the grown crystals.
6. There are difficulties incorporating some doping elements (e.g., Ga, In, Al) into the growing crystals because of their low vapor pressures.

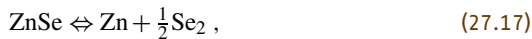
27.3 Thermodynamic Considerations

27.3.1 Estimation of Optimum Growth Parameters for the ZnSe–I₂ System by CVT

The partial pressures inside the tube during growth, the temperature, the iodine concentration, and the tube dimensions have been taken into account for these calculations (Fig. 27.3). The vapor-phase chemical transport of ZnSe with iodine has been considered to consist of three equilibria



Neglecting dissociation of ZnSe via



and dissociation of ZnI₂ via



it was assumed that, as a first approximation, the vapor phase contains only four components (I, I₂, ZnI₂, and Se₂) and also the law of mass conservation of iodine at equilibrium was considered

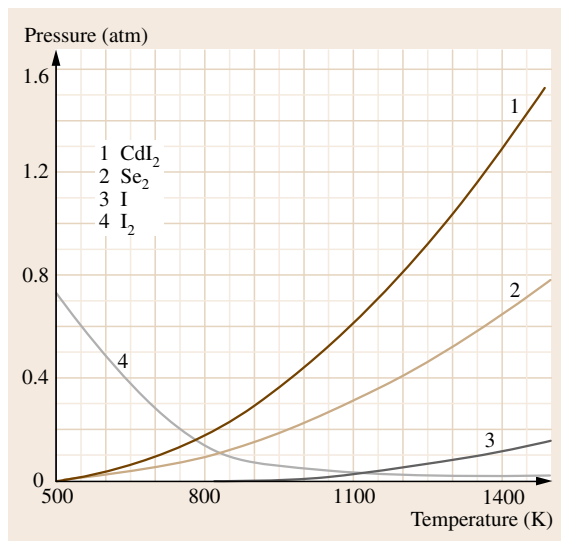


Fig. 27.3 Partial pressures of various species as a function of temperature for various iodine concentration

The partial pressures in terms of initial iodine concentration can be expressed by

$$p_{\text{I}_2}^0 = p_{\text{I}_2} + 0.5p_{\text{I}} + p_{\text{ZnI}_2}. \quad (27.20)$$

The exact stoichiometry of the ZnSe source materials gives the equation

$$p_{\text{ZnI}_2} = 2p_{\text{Se}_2}, \quad (27.21)$$

where $p_{\text{I}_2}^0$ is the partial pressure of iodine concentration initially taken into account for the calculations, and the other p symbols are the partial pressures of the corresponding components at a given temperature. The equilibrium constants for the reactions (27.14) and (27.19) are given by

$$K_{(27.14)} = \frac{(p_{\text{ZnI}_2} p_{\text{Se}_2}^{0.5})}{p_{\text{I}_2}}, \quad (27.22)$$

$$K_{(27.19)} = \frac{p_{\text{I}}^2}{p_{\text{I}_2}}. \quad (27.23)$$

The values can be calculated as a function of temperature from [27.52]

$$K_{(27.14)} = 7.64 - 5849T^{-1} - 4154T^{-2} - 0.83 \log T - 1.5 \times 10^{-4}T, \quad (27.24)$$

$$K_{(27.19)} = 4.34 - 7879T^{-1} + 4264T^{-2} + 0.33 \log T + 2 \times 10^{-5}T. \quad (27.25)$$

Using (27.20–27.25), the following equation can be derived

$$2 \frac{p_{\text{I}}^2}{K_{2.6}} + \left(4 \frac{K_{(27.14)}}{K_{(27.19)}} \right)^{\frac{2}{3}} p_{\text{I}}^{\frac{4}{3}} + p_{\text{I}} - 2 \frac{CRT}{M} = 0, \quad (27.26)$$

where p_{I} is the partial pressure of atomic iodine, C is the initial concentration of iodine, R is the universal gas constant, T is temperature, and M is the molar mass of iodine.

It was assumed that iodine behaves as an ideal gas in these calculations. From (27.26), the partial pressures of the components inside the tube during growth were calculated for iodine concentration in the range 0.5–10 mg/cm³ and for temperatures in the range 500–1200 °C. The partial pressures of I, I₂, ZnI₂, and Se₂ for temperatures of 500–1200 °C are plotted in Fig. 27.4 for iodine concentration of 2 mg/cm³.

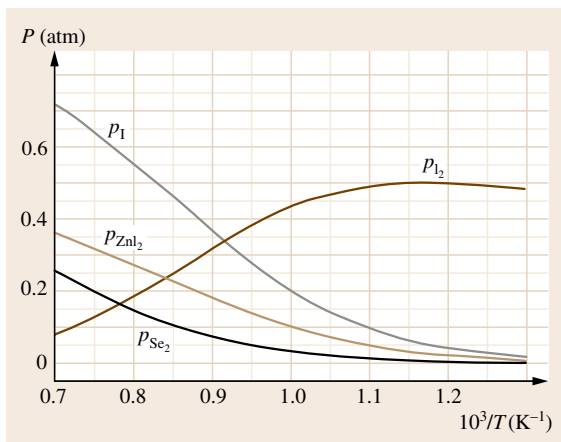


Fig. 27.4 Partial pressure of components for 2 mg/cm³ iodine

The amount of ZnI₂ formed with respect to the initial concentration of I₂ can be described by the ratio α

$$\alpha = \frac{p_{\text{ZnI}_2}}{p_{\text{I}_2}^0} \quad (27.27)$$

The variation in the ratio α for different iodine concentrations at different temperatures is shown in Fig. 27.5. The transport rate of ZnI₂ determines the size and quality of the crystal grown at the growth zone. It can be considered as the difference in α between the source and growth zones for given temperature. It can be approximated by

$$\Delta\alpha = \frac{\Delta p_{\text{ZnI}_2}}{p_{\text{I}_2}^0} \quad (27.28)$$

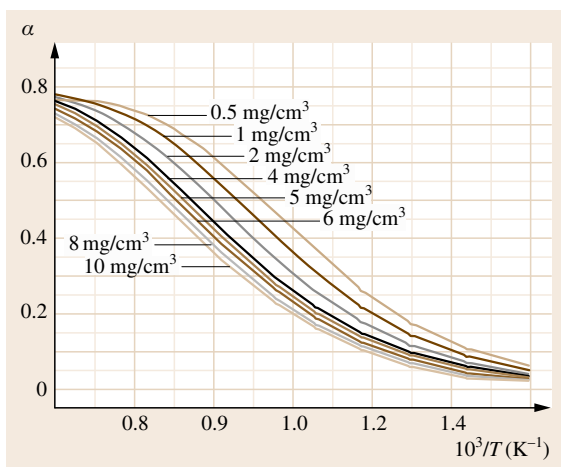


Fig. 27.5 Variation in the ratio α for different iodine concentrations at different temperatures

The temperature difference between two zones was fixed at 50 °C in the calculations. The number of moles of ZnSe transported from the source to the growth end as ZnI₂ in time t is given by

$$n_{\text{ZnSe}} \propto \Delta\alpha x t \quad (27.29)$$

The diffusion-limited transport rates (J_D) can be calculated using the formula [27.15,53]

$$J_D = \frac{2D_{\text{ZnI}_2} p_T}{RTL} \ln \left(\frac{(2p_T - p_{\text{ZnI}_2(\text{g})})}{(2p_T - p_{\text{ZnI}_2(\text{s})})} \right) \quad (27.30)$$

where D_{ZnI_2} is the diffusion coefficient of the component ZnI₂, p_T is the total pressure at the temperature T , $p_{\text{ZnI}_2(\text{g})}$ is the partial pressure of ZnI₂ at the growth zone, $p_{\text{ZnI}_2(\text{s})}$ is the partial pressure of ZnI₂ at the source zone, R is the universal gas constant, T is temperature, and L is the distance between the sublimed source and growing crystals in the ampoule.

27.3.2 Fluctuations in the Transport Rates

The iodine concentration of 2 mg/cm³ is considered for the present investigation. The partial pressure of the components I, ZnI₂, and Se₂ increases with increasing temperature. The partial pressure of I₂ decreases with increasing temperature. The ratio (α) between the partial pressure of ZnI₂ and that of initial iodine pressure is found to decrease with increasing iodine concentration at a given temperature. Also, at higher iodine concentrations, the change in partial pressures of ZnI₂ is found to be minimum. Hence it can be concluded that increase in iodine concentration has little effect on the partial pressure of ZnI₂. From (27.29), the transport rate of ZnI₂ is proportional to the difference in α values of source and deposition zones, i.e., $\Delta\alpha$. The variation of $\Delta\alpha$ with respect to temperature for the various iodine concentrations is shown in Fig. 27.6. For a given iodine concentration the value of $\Delta\alpha$ is found to increase gradually, reach a maximum, and then decrease with increasing temperature. As the iodine concentration increases, the maximum of the curve positions shifts to higher temperatures and also the curves become broadened. From the figure, it can be observed that, for each iodine concentration, there is an optimum temperature region near the peak position where the change in $\Delta\alpha$ is minimum. Hence the fluctuations in transport rates will be minimum in that region. The change in transport rate is proportional to Δp_{ZnI_2} , i.e., the difference between the partial pressures of ZnI₂

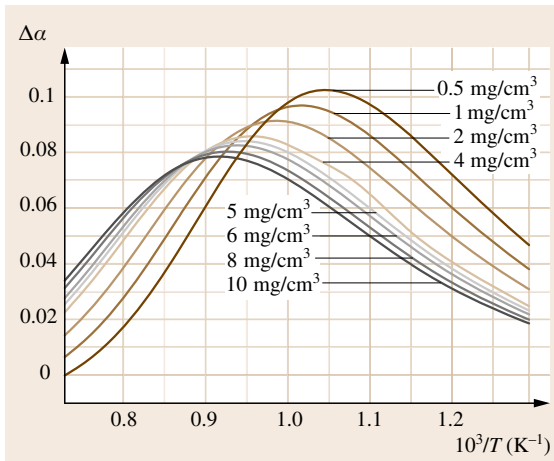


Fig. 27.6 Change in the value of $\Delta\alpha$ with respect to temperature for a given iodine concentration

in the source and deposition zones. So, it can be assumed that, without considering the type of migration along the ampoule, the growth rate is proportional to $\Delta\alpha$.

The fluctuation in transport rates affects the quality of the crystals grown. The fluctuation in transport rates should be minimum to achieve good-quality crystals. Hence it is essential to find the optimum conditions for which the fluctuation is minimum. However a slight drop in temperature at the deposition zone during the growth process causes multinucleation of crystals, which leads to intergrowth and changes in the com-

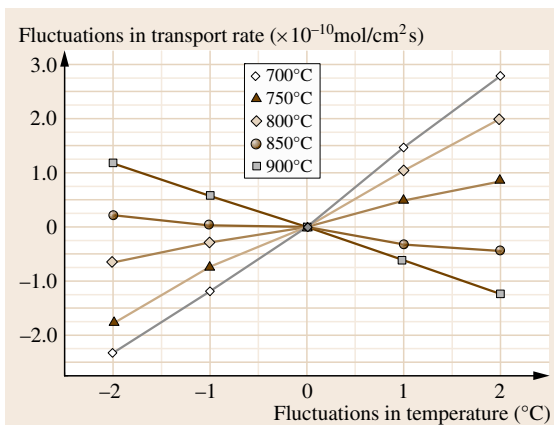


Fig. 27.7 Fluctuation in transport rates at different temperatures for $\Delta T = 50^\circ\text{C}$ and for iodine concentration of 2 mg/cm^3

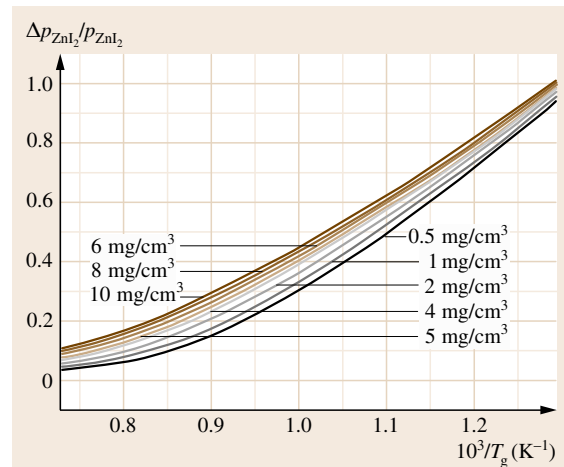


Fig. 27.8 Change in supersaturation ratio as a function of growth temperature for undercooling of 50 K and various iodine concentrations

position of the crystals. The flow of the material is highly dependent on temperature, and control of temperature at the growth interface is always poorer than the accuracy shown by the temperature controllers in the furnace. Temperature variation up to $\pm 2\text{ K}$ can normally be expected inside the quartz ampoule during the growth process. The fluctuation in transport rates has been calculated for temperature fluctuation up to $\pm 2\text{ K}$ using (27.30), considering an iodine concentration of 2 mg/cm^3 and a constant temperature difference between the two zones of 50 K; the results are shown in Fig. 27.7. It can be observed from the figure that the temperature range of 800–850°C was found to have minor fluctuations in the transport rates. Somewhere in this temperature range, one can find a line nearly parallel to the x -axis and close to zero on the y -axis, for which the fluctuation in transport rate is expected to be minimum. It was therefore concluded that one could obtain good-quality crystals in the temperature range 800–850°C.

The change in supersaturation ratio $\Delta p_{\text{ZnI}_2}/p_{\text{ZnI}_2}$ as a function of growth temperature for undercooling of 50 K and various iodine concentrations is shown in Fig. 27.8. It can be seen from the figure that an increase in iodine concentration produces only a small change in supersaturation at given temperature. It can be concluded that the iodine concentration has very little influence on the supersaturation ratio at a given temperature and thus the growth of the crystals.

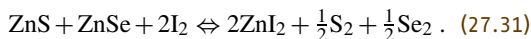
Nucleation Calculations for the Growth of $\text{ZnS}_x\text{Se}_{1-x}$ Single Crystals by CVT

The binary nucleation theory was applied to find the critical radius and free energy for the formation of the critical nucleus. The formation and composition of $\text{ZnS}_x\text{Se}_{1-x}$ single crystals by CVT was found to be affected by the supersaturation ratios of S_2 and Se_2 and hence by the corresponding partial pressure values. The partial pressures of the components in the $\text{ZnS}_x\text{Se}_{1-x}$ - I_2 system by CVT were found with the thermodynamic model as applied to the case of ZnSe in the previous section.

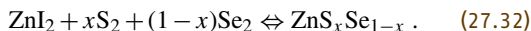
27.3.3 Supersaturation Ratios in the $\text{ZnS}_x\text{Se}_{1-x}$ System

The formation of $\text{ZnS}_x\text{Se}_{1-x}$ by iodine transport may take place by the following chemical equilibrium reactions.

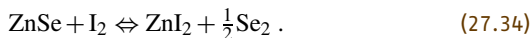
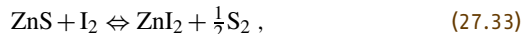
At the source zone



At the growth zone



It is assumed that the vapor phase contains only I , I_2 , ZnI_2 , S_2 , and Se_2 . The vapor-phase chemical transport of ZnS and ZnSe with I_2 in a closed tube follows the individual reaction steps as given below



Also, considering the mass conservation of iodine at the equilibrium



the partial pressures in terms of initial iodine concentration can be given by

$$p_{\text{I}_2}^0 = p_{\text{I}_2} + 0.5p_{\text{I}} + p_{\text{ZnI}_2}. \quad (27.36)$$

The equilibrium constants for (27.33–27.35) are given by

$$K_{(27.33)} = 8.8 - 7539T^{-1} + 8745T^{-2} - 1.19 \log T + 2.18 \times 10^{-6}T, \quad (27.37)$$

$$K_{(27.34)} = 7.64 - 5849T^{-1} - 4154T^{-2} - 0.83 \log T - 1.5 \times 10^{-4}T, \quad (27.38)$$

$$K_{(27.35)} = 4.34 - 7879T^{-1} + 4264T^{-2} + 0.33 \log T + 2 \times 10^{-5}T. \quad (27.39)$$

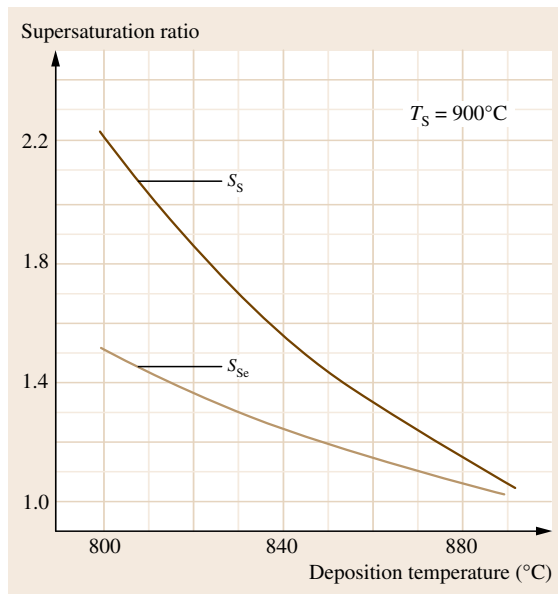


Fig. 27.9 Variation in supersaturation ratios of S_2 and Se_2 with deposition temperature

The partial pressures of the components inside the growth ampoule were calculated using these equations. The partial pressures of S_2 and Se_2 were found to affect the composition of $\text{ZnS}_x\text{Se}_{1-x}$ even when an ideal solid solution of ZnS and ZnSe (1 : 1) was assumed. Therefore the supersaturation ratios of S_2 and Se_2 have been obtained as a function of deposition temperature for a fixed source temperature and iodine concentration. The supersaturation ratio of the S_2 component in closed-tube vapor transport of $\text{ZnS}_x\text{Se}_{1-x}$ is given by

$$\frac{p_{\text{S}_2}}{p_{\text{S}_2}^*} = \frac{(p_{\text{S}_2})_s}{(p_{\text{S}_2})_d}, \quad (27.40)$$

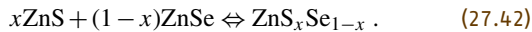
where p_{S_2} is the partial pressure of sulphur at a given temperature, $p_{\text{S}_2}^*$ is the equilibrium partial pressure of sulphur, $(p_{\text{S}_2})_s$ is the partial pressure of sulphur at the source zone, and $(p_{\text{S}_2})_d$ is the partial pressure of sulphur at the deposition zone. Similarly, the supersaturation ratio of selenium can be calculated using

$$\frac{p_{\text{Se}_2}}{p_{\text{Se}_2}^*} = \frac{(p_{\text{Se}_2})_s}{(p_{\text{Se}_2})_d}. \quad (27.41)$$

Figure 27.9 shows the change in supersaturation ratios of S_2 and Se_2 with respect to varying growth zone temperature for fixed source temperature (900 °C).

Homogeneous Nucleation in the Growth of $\text{ZnS}_x\text{Se}_{1-x}$ Single Crystals

The spontaneous formation of a nucleus of another supersaturated phase is called homogeneous nucleation. The simple theory of homogeneous nucleation brings out two essential features of the nucleation process: (1) The vapor must be supersaturated with respect to the bulk condensate for small clusters to have any stability; the greater the supersaturation, the smaller the cluster which stands an even chance of increasing in size. (2) The rate of nucleation is strongly dependent on the size of the critical nucleus and hence on the supersaturation. In the present study, binary nucleation theory (capillarity approximation) was applied to the $\text{ZnS}_x\text{Se}_{1-x}$ system containing 1 : 1 ZnS and ZnSe



The free energy of formation of a nucleus is given by

$$\Delta G = -ak_B T \ln \frac{p_S}{x p_S^*} - bk_B T \ln \frac{p_{Se}}{(1-x)p_{Se}^*} + (aV_{\text{ZnS}} + bV_{\text{ZnSe}})^{2/3} (36\pi)^{1/3} \sigma, \quad (27.43)$$

where p_S/p_S^* is the supersaturation ratio of sulfur, p_{Se}/p_{Se}^* is the supersaturation ratio of selenium, a the number of ZnS molecules in the nucleus, b is the number of ZnSe molecules in the nucleus, x is the mole fraction of ZnS, $(1-x)$ is the mole fraction of ZnSe, V_{ZnS} is the molecular volume of ZnS, V_{ZnSe} is the molecular volume of ZnSe, σ is the interfacial tension (assumed to be constant at 1000 erg/cm^2), k_B is Boltzmann's constant, and T is temperature.

The free energy of formation of a nucleus corresponding to the saddle point can be obtained from

$$\left(\frac{\partial \Delta G}{\partial a} \right)_{T,P} = 0, \quad \left(\frac{\partial \Delta G}{\partial b} \right)_{T,P} = 0. \quad (27.44)$$

Applying this condition to (27.43) yields

$$-k_B T \ln \frac{p_S}{x p_S^*} + \frac{2}{3} V_{\text{ZnS}} (36\pi)^{1/3} \times \sigma (a^* V_{\text{ZnS}} + b^* V_{\text{ZnSe}})^{-1/3} = 0, \quad (27.45)$$

and

$$-k_B T \ln \frac{p_{Se}}{(1-x)p_{Se}^*} + \frac{2}{3} V_{\text{ZnSe}} (36\pi)^{1/3} \times \sigma (a^* V_{\text{ZnS}} + b^* V_{\text{ZnSe}})^{-1/3} = 0. \quad (27.46)$$

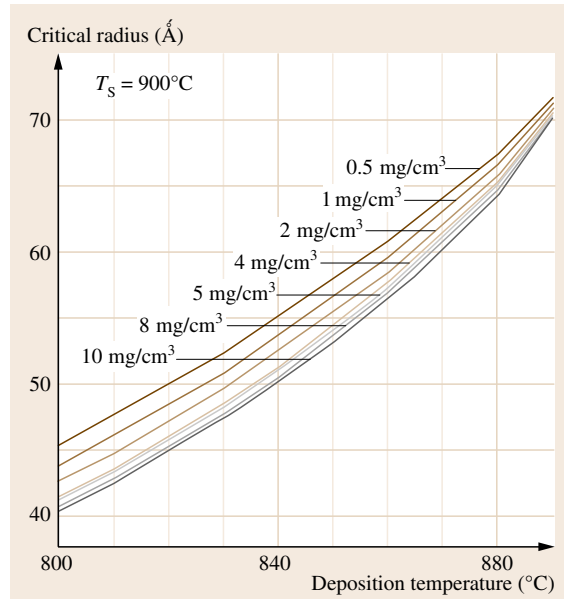


Fig. 27.10 Change in critical radius with deposition temperature

Assuming the shape of the nucleus to be spherical, one has

$$\frac{4}{3}\pi r^{*3} = (a^* V_{\text{ZnS}} + b^* V_{\text{ZnSe}}), \quad r^* = \left(\frac{3(a^* V_{\text{ZnS}} + b^* V_{\text{ZnSe}})}{4\pi} \right)^{1/3}, \quad (27.47)$$

solving (27.45) and (27.46) to

$$r^* = \frac{2\sigma V_{\text{ZnS}}}{k_B T \ln \left(\frac{p_S}{x p_S^*} \right)}. \quad (27.48)$$

The value of the critical radius has been calculated for iodine concentration of $0.5\text{--}10 \text{ mg/cm}^3$ and deposition temperature of $800\text{--}890^\circ\text{C}$ with a constant source temperature of 900°C . The variation of the critical radius of the $\text{ZnS}_x\text{Se}_{1-x}$ nucleus is shown in Fig. 27.10 with respect to deposition temperature.

The free energy of formation of the critical nucleus is given by

$$\Delta G^* = \frac{16\pi\sigma^3}{3(\Delta G_v)^2}, \quad (27.49)$$

$$\Delta G^* = \frac{16\pi\sigma^3}{3k_B^2 T^2 \ln^2 \left(\frac{p_S}{x p_S^*} \right)}. \quad (27.50)$$

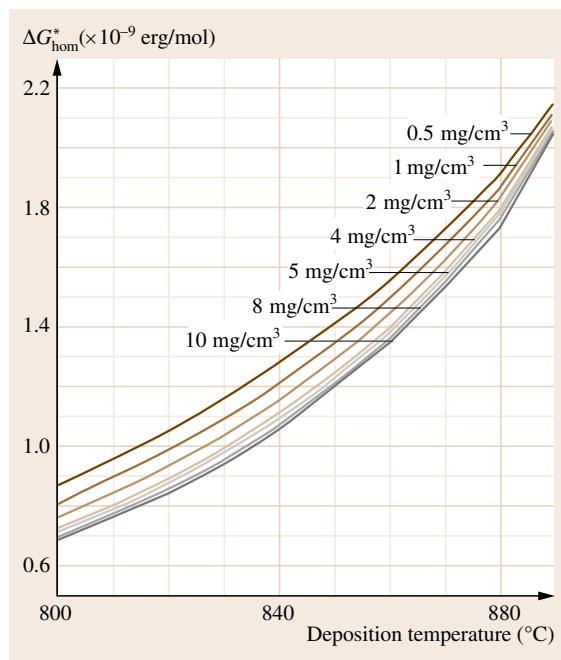


Fig. 27.11 Free energy change for the formation of a critical nucleus with deposition temperature under homogeneous nucleation condition

The value of the free energy has been calculated as a function of deposition temperature for various iodine concentrations and is shown in Fig. 27.11.

Heterogeneous Nucleation of $\text{ZnS}_x\text{Se}_{1-x}$ Single Crystals

The nucleation of a condensed phase on the surface of a foreign body is called heterogeneous nucleation. The nucleation rate depends on the presence of available sites on the surface on which growth can take place to a considerable extent. For example, kinks, steps on a surface, inclusions, etc. facilitate the process of nucleation. In chemical vapor transport, deposition may occur on the ampoule wall so that transported vapor components react to form the crystal. Since the presence of a suitable surface induces nucleation at supersaturations lower than that required for spontaneous nucleation, the free energy associated with the formation of such a critical nucleus must be less than the corresponding free energy change. It is given by

$$\Delta G_{\text{het}}^* = \phi(\theta) \Delta G_{\text{hom}}^*, \quad (27.51)$$

where the factor $\phi(\theta)$ is less than 1. In treating such nucleation, a spherical cap-shaped embryo of radius r of

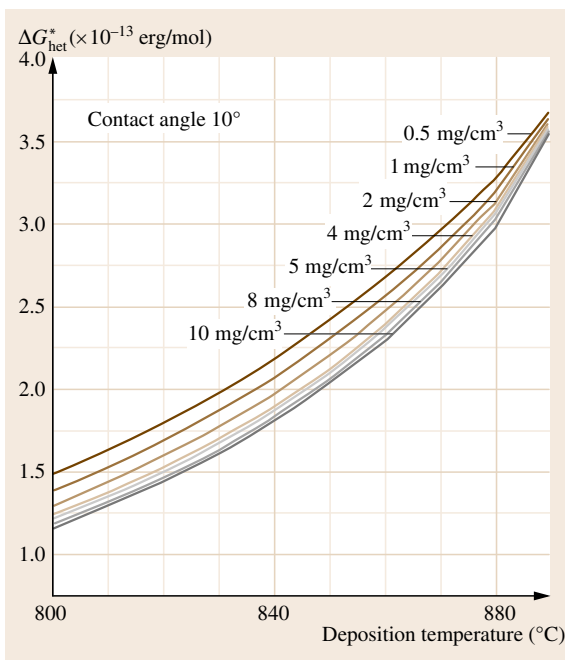


Fig. 27.12 Change in free energy for the formation of a critical heterogeneous nucleus (for contact angle 10°) with deposition temperature

solid phase S deposited on a substrate is considered. The contact angle between the cap and the substrate is θ . The ΔG_{het}^* for a critical nucleus is given by

$$\Delta G_{\text{het}}^* = \frac{16\pi\sigma_{13}^3\phi(\theta)}{3\Delta G_v^2}, \quad (27.52)$$

where σ_{13} is the interfacial tension between the vapor and solid

$$\phi(\theta) = \frac{(2 + \cos\theta)(1 - \cos\theta)^2}{4}. \quad (27.53)$$

The contact angle θ varies between 0° and 180° . In this case, ΔG_{het}^* has been calculated for θ values of 10° , 30° , and 50° at different deposition zone temperatures, as shown in Figs. 27.12–27.14, respectively.

Variation in Composition with Growth Temperature

In vapor growth, the composition of the growing compound is controlled by the composition of the vapor over it. The undercooling or supersaturation plays the dominant role in determining the composition of the growing crystals. It has been found that the partial pressures of S_2 and Se_2 affect the formation and composition of

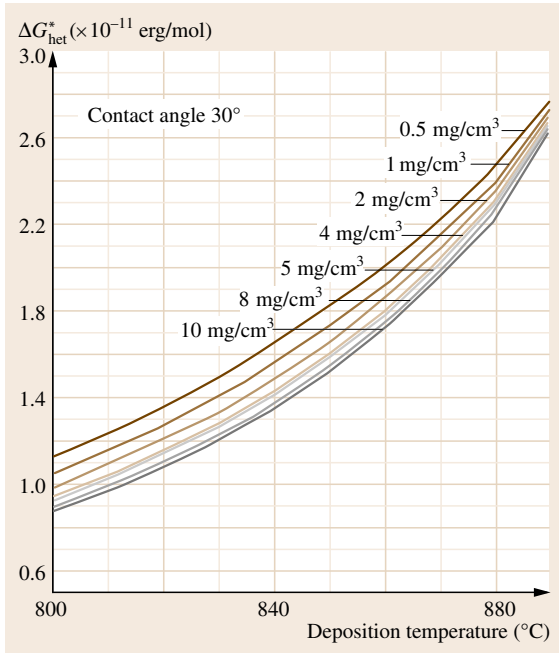


Fig. 27.13 Change in free energy for the formation of a critical heterogeneous nucleus (for contact angle 30°) with deposition temperature

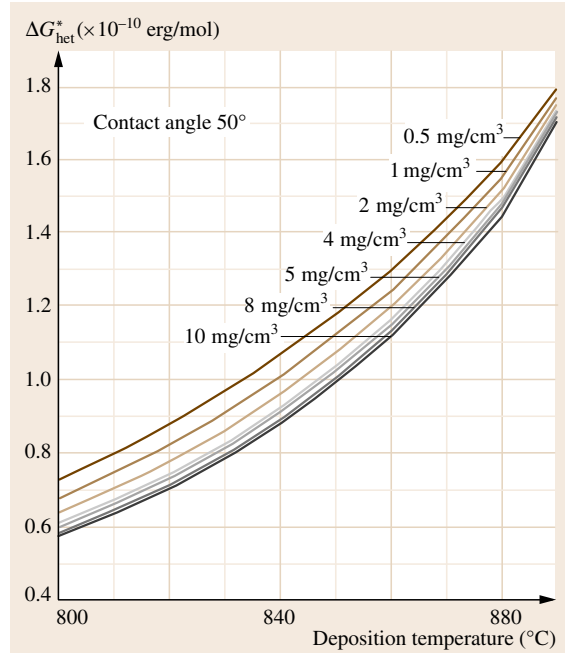


Fig. 27.14 Change in free energy for the formation of a critical heterogeneous nucleus (for contact angle 50°) with deposition temperature

$\text{ZnS}_x\text{Se}_{1-x}$ even when the ideal solid solution of ZnS and ZnSe was assumed [27.54]. The mole fraction ratio of ZnS and ZnSe is proportional to corresponding partial pressure ratios, given by

$$\frac{x_{\text{ZnS}}}{x_{\text{ZnSe}}} = \frac{K_{\text{ZnSe}}}{K_{\text{ZnS}}} \left(\frac{p_{\text{S}_2}}{p_{\text{Se}_2}} \right)^{1/2}, \quad (27.54)$$

where K_{ZnS} is the dissociation constant of ZnS, K_{ZnSe} is the dissociation constant of ZnSe, x_{ZnS} is the mole fraction of ZnS, x_{ZnSe} is the mole fraction of ZnSe, and p_i is the partial pressure of the corresponding component ($i = \text{S}_2$ or Se_2). By considering this fact, in the present investigation, the supersaturations ratios of S_2 and Se_2 were taken into account for the calculation of the critical radius and free energy of formation. From Fig. 27.9, it was observed that the supersaturation decreases with decreasing undercooling (ΔT). Under conditions of smaller undercooling, the supersaturations of S_2 and Se_2 were found to be close enough; on the other hand, for large undercooling, the difference in the supersaturations of S_2 and Se_2 was large. So one could expect correct stoichiometry of the supersaturated vapor for the case of lower undercooling, resulting in crystal with equal x and $(1-x)$ values for an initial 1 : 1 solid

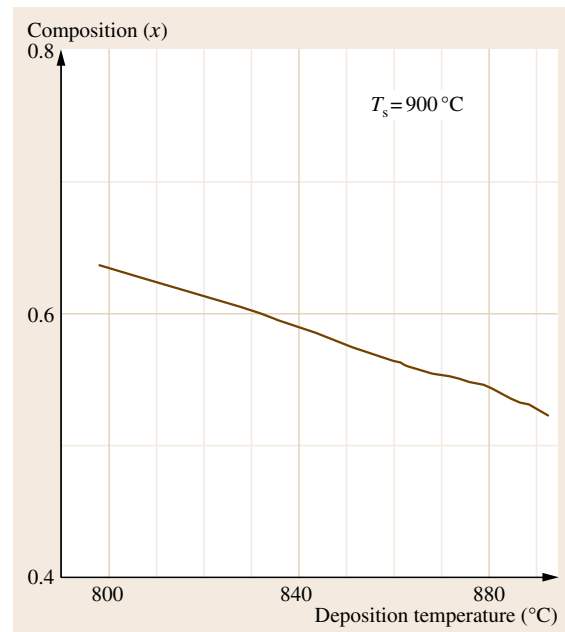


Fig. 27.15 Change in the composition of the grown crystal as a function of deposition temperature

source. For larger undercooling, the crystal would have an S-rich composition as the supersaturation of S will be high compared with that of Se. The calculated change of composition with deposition temperature is shown in Fig. 27.15. As the difference supersaturation ratio of S_2 and Se_2 increases, a crystal with sulfur-rich composition may be obtained.

The deposition temperature was varied from 800 °C to 890 °C for a fixed source zone temperature of 900 °C. The range of iodine concentrations used was 0.5–10 mg/cm³. The critical radius was found to be high under conditions of smaller undercooling, and remained the same irrespective of iodine concentration. Under conditions of larger undercooling, the critical radius was found to decrease with increasing iodine

concentration. The partial pressure of ZnI_2 increased with increasing iodine concentration (and hence supersaturation), resulting in the formation of large number of primary nuclei in the growth zone so that spurious nucleation occurred and hence the size of the critical nucleus decreased. The free energy of formation of a critical nucleus was calculated using (27.49) for different growth zone temperatures and iodine concentrations. As discussed earlier, ΔG_{het}^* was calculated for different contact angles between the substrate or ampoule wall and the crystal using classical nucleation theory. As the contact angle increased, the free energy also increased. The results are similar to that of ΔG_{hom}^* with respect to deposition temperature and iodine concentration.

27.4 Growth of II–VI Compound Semiconductors by CVT

This section deals in detail with the apparatus generally used for growth of II–VI compound single crystals by CVT technique and the preparation of starting materials for the growth process [27.54–68].

27.4.1 Apparatus

Double-zone or multizone furnaces are generally used for crystal growth by CVT technique [27.17, 54–59]. Depending on the required temperature profile and maximum operating temperature, the design and material used in fabrication of these furnaces will be different. Figure 27.16 shows a schematic of a double-zone horizontal furnace.

The muffles are made from ceramic materials or quartz tube of different lengths and diameters depending on the design of the furnace. The gap between the outer casing and muffle is packed with bricks and

nonconducting materials such as asbestos powder in order to avoid heat loss. The ampoule is placed above the brick support. The two temperature zones must be considered as two different furnaces, and there is a gap between the two zones called the dead zone, which provides a smooth temperature gradient between the source and growth zone. The length of the dead zone is normally a few centimeters, depending on the required profile. The temperature of each zone is controlled by separate temperature controllers. Each zone has its own temperature sensors. For various regions, the temperature field in a typical cylindrical furnace is not radially symmetrical. If the axis of the furnace is horizontal, then the top part is usually a few degrees hotter than the bottom. If the furnace is set with its axial vertical, this effect is removed as far as the radial distributaries is concerned, but the heat field still depends on the configuration of the heating elements, etc.

In chemical vapor transport growth, the most common temperature measurement and control techniques are based on thermocouples. Chromel–alumel thermocouples can be used to measure up to 1273 K. The essential requirement for this is purity, which should be 99.999% of the individual metal or alloy. An alumina sheath has to be provided to protect the thermocouple to a considerable extent of its diameter. Generally these temperature sensors will give a very weak signal, on the order of mV. The weak signal will be amplified and used to control the power input of the furnace. The requirements of crystal grower are not fulfilled by

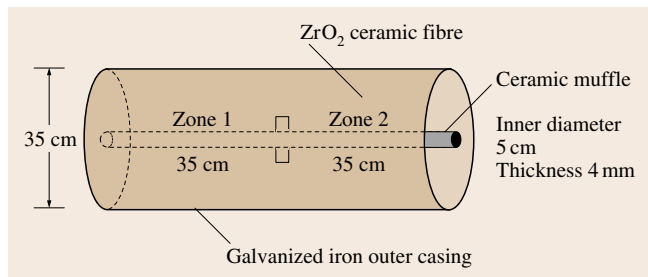


Fig. 27.16 Schematic diagram of a double-zone horizontal furnace for CVT growth

mechanical regulators and on–off controllers and nowadays they have been replaced by electronic controllers. To achieve a stable temperature without a setting error in real systems, proportional–integral–differential (PID) or Eurotherm controllers are used. Since the weak signals obtained from thermocouples are passed to the controllers, they must be carefully shielded. Otherwise stray voltages may be introduced by direct or capacitive coupling. Extension wires used to connect thermocouple outputs to the controller must be prepared from the same alloys with similar thermoelectric characteristics. Such cables are referred to as compensating cables. However these compensating cables can only minimize the error.

The ampoule may be made of any material which does not melt, soften or react appreciably with the species in the system at the operating temperature [27.13]. At temperature up to about 450 °C, Pyrex glass is suitable for many systems. At higher temperature silica is very commonly used, but aluminosilicates can be used as alternatives. Generally a cylindrically shaped ampoule is used to grow the crystals, although different shapes of growth and ampoule have been studied. The effect of changing the shape of the growth end of the ampoule has been investigated by many researchers. A rounded end usually results in distributions of crystallites over several centimeters. A tapered, pointed end defines the cold region much better. The next stage was to extend the end of the ampoule by a narrow tube. Nucleation takes place inside the tube at several places, and after a time the crystallites grow together. The final stage of evolution was to provide a crystallite seed, rather than wait for nucleation. A convenient way of doing this is to trap a crystallite at the end of the ampoule by inserting a stopper above it. Generally it is considered that a rounded end to the ampoule gives the lowest possibility of developing unwanted nuclei, assuming that there is initially just one nucleus located centrally at the end of the ampoule.

Vacuum systems are used to evacuate the reaction tubes after filling with the charge materials and transporting agents. This is done for the following reasons:

1. It reduces the chance of explosion of the tube at operating temperature due to the increased vapor pressure of the elements.
2. It enables easy access to the growth zone as the mean free path of the gaseous particles becomes greater than or comparable to the size of the ampoule at lower total pressure.

3. It is advantageous for materials which exhibit a tendency for thermal decomposition and affinity for oxygen.

Oil rotary with diffusion pumps generally provide a vacuum level down to 10^{-6} Torr for loaded transporting agent and feed material within the ampoule.

Before loading the charge materials, the ampoules should be properly cleaned. Cleaning of the ampoule is one of the most important aspects of the growth of crystals by chemical vapor technique. If the ampoules are not cleaned properly, impurities may get into the growing crystal or serve as sites for heterogeneous nucleation and affect crystal quality. The general cleaning procedures include washing and etching (50 : 50 concentrated HNO_3 and 40% HF) and flame polishing. The polycrystalline of the material to be grown is taken in one tube (A) and the other tube (B) is loaded with transporting agent with the use of stopper D while it is cooled with Dewar flask to minimize sublimation of iodine. Then tube A will be cooled while B is heated gently. The iodine which has sublimed from tube B will be condensed in tube A, which will be sealed off in vacuum.

27.4.2 Preparation of Starting Materials

Purification

Whenever the impurity content of the starting elements is higher than desired, a careful check should be made to determine whether a purification step will effectively improve the situation. If one is dealing with an already high-purity semiconductor-grade material, one runs the risk that impurities will be introduced during handling or processing of the material. It is also possible that, even though multiple purification steps may sufficiently decrease certain impurity concentrations, one or two less desirable impurity elements may at the same time be incorporated into the material. Thus, it can occur that, after purification, the overall purity may be better, but the material may be of lesser quality with regards to a specific application. The above comments are not to be taken as a discouragement towards purification steps, but rather as a caution that, during the purification procedure and in the handling of high-purity material in general, great care must be taken to avoid unnecessary contamination. There are two types of purification steps which can often be incorporated during preparation and therefore deserve special mention. The removal of surface oxide is readily achieved by firing the metal compounds, i. e., Zn or Cd, in a stream of pure H_2 just

prior to use. The other step is distillation of the elemental compounds into apparatus.

Preparation of the Starting Compounds

If it is possible to prepare large quantities of the starting compounds in a single sealed system, the chance of obtaining high-purity or controlled impurity-doped material is greatly improved. There are several methods used to prepare ZnSe. In one procedure, ZnO, ZnS, and Se are reacted to yield ZnSe, which probably contains some residual sulfide and oxide.

The most direct method is rapid heating of Zn and Se under argon pressure of 200 atm in an autoclave to the melting point of ZnSe, followed by rapid quenching of the system. The reactor has been designed [27.69] along with a temperature profile for synthesizing ZnSe powder of ≈ 0.9 crystal density from the reaction of 5 N pure elemental zinc and H_2Se in the gas phase by means of H_2 carrier gas. The gas flow rates are: H_2 carrier at $100 \text{ cm}^3/\text{min}$, H_2 over zinc boat at $90 \text{ cm}^3/\text{min}$, and H_2 mixed with H_2Se at $20 \text{ cm}^3/\text{min}$ with H_2 -to- H_2Se ratio of 40 : 1. The zinc boat is loaded with 10 g zinc before each run, and used entirely to prevent cracking of the quartz upon cooling. ZnSe is controlled as a granular yellow powder both on the liner and attached in a solid chunk to the $\text{H}_2/\text{H}_2\text{Se}$ nozzle. The rate of collection is 1.0 g/h with 50% yield. This powder is then vapor transported under a dynamic vacuum of 10^{-5} Torr out of a furnace at 850°C using a 20 mm-diameter tube. Again a high-density ZnSe powder is collected at the mouth of the tube furnace while unused Zn and Se are transported further downstream. The approximate weight loss is 10%. All impurities usually detected by spectroscopic analysis are present at less than 0.1 ppm, including copper. This material is then collected and used for crystal growth.

27.4.3 Growth of ZnSe Single Crystals

Increasing attention has been focused on the growth of ZnSe single crystals for application as a substrate for blue light-emitting diodes [27.70, 71]. Growth of ZnSe single crystals was initiated in 1958, but no report of the size of the grown crystals was made in the early literature. The first report on the growth of ZnSe single crystals with mention of their size came from *Nitsche* [27.72], who used the CVT method for growth of these crystals with size of up to $4 \times 4 \times 3 \text{ mm}^3$. Since 1960 there have been a lot of reports on growth of ZnSe single crystals, mostly by vapor methods and in limited

cases by other methods such as melt [27.69, 73], solution [27.74], and solid-state recrystallization [27.75]. The high melting point (1520°C), multitwin patterns produced during phase transitions from hexagonal to cubic at 1425°C , and other defects produced at high temperatures have made growth of ZnSe from the melt difficult [27.76]. Attempts have been made by various researchers to use CVT with iodine as a transporting agent to grow ZnSe single crystals with larger size and improved properties suitable for device applications [27.77].

By using seed methods and applying smaller undercooling ($\Delta T = 7 \text{ K}$), ZnSe single crystals with dimensions of $20 \times 15 \times 15 \text{ mm}^3$ were grown [27.78]. Later it was shown that the grain size of the grown crystals depends strongly on the undercooling and growth ampoule geometry, and growth of ZnSe with dimensions of $24 \times 14 \times 14 \text{ mm}^3$ with undercooling as small as 7°C using an ampoule with a steep conical tip was reported [27.79]. Later there was no further improvement in the size of ZnSe single crystals grown by CVT, and attempts were oriented towards growth of these crystals with more attention to their morphological perfection and improved electrical and optical properties. *Kaldis* [27.80] discussed that the morphology of crystals grown from the vapor phase depends on the mechanism that is rate determining. Very recently, it has been shown that changes in experimental variables such as the system pressure, the temperature conditions, and the concentration of the transporting agent will affect the contribution of mass transport through the convection and diffusion mechanisms and affect the crystallographic perfection and morphological stability of ZnSe single crystals grown by the CVT method [27.81]. The growth aspect of ZnSe single crystals grown by CVT has been studied with special emphasis placed on the formation of different micromorphological patterns formed on the surface of crystals grown under different experimental conditions [27.58].

Pretreatment of starting material for the growth process was carried out by mixing a stoichiometric ratio of ZnSe elements with 5 N purity and loading them into a quartz ampoule. The mixture was heated in vacuum at a temperature of 850°C for 10 h in order to remove volatile impurities and obtain homogenized polycrystalline ZnSe. The formation of ZnSe was verified by x-ray diffractography. Ampoules with length of 23 cm and diameter of 1 cm were filled with 3 g heat-treated ZnSe polycrystalline powder along with iodine at concentration of 3 mg/cm^3 of the empty space of

the ampoule. The ampoules, cooled by ice, were evacuated to 2×10^{-6} Torr and sealed off. The capsules were placed into a double-zone horizontal furnace controlled by Eurotherm controllers with accuracy of ± 0.1 K. PID controllers with accuracy of ± 5 K were also used in one of the growth runs. A reverse temperature profile was developed across the ampoule, with the growth zone at high temperature for 24 h to remove powders sticking to the deposition zone of the ampoules and diminish the active sites. Growth runs were carried out for different undercooling (ΔT) values using various compositions of starting materials and ampoule geometries while keeping the temperature of the growth zone constant at 890°C . Each growth run was carried out for a week. At the end of each growth process, the furnace was slowly cooled to room temperature at a rate of 50°C/h to prevent thermal strain. The grown crystals have been characterized for their structure and morphology [27.80–85].

27.4.4 Growth of CdS Single Crystals

There has been a long-standing interest in CdS because of its optical and electrical properties. Due to its large bandgap (≈ 2.5 eV) and high quantum efficiency, CdS is used for applications from window material for solar cells to coloring plastics [27.86]. Single crystals of CdS have been grown largely by vapor and in limited cases by melt [27.87], solution, and flux methods [27.88]. Vapor growth of CdS at low temperatures was first achieved by Nitsche [27.72], who utilized the chemical vapor technique with iodine as the transporting agent. The growth of CdS by CVT technique was continued by various researchers, and crystals with different morphological habits and sizes were grown under different experimental conditions. Paorici [27.89] reported growth of CdS single crystals in the form of hollow prismatic rods in an iodine-rich atmosphere. Kaldis [27.90] has extensively studied the growth of CdS single crystals by CVT under different experimental conditions such as source temperature ($750^\circ\text{C} < T_2 < 1120^\circ\text{C}$), undercooling ($5^\circ\text{C} < T < 200^\circ\text{C}$), and iodine concentration ($0.1 \text{ mg/cm}^3 < c < 12 \text{ mg/cm}^3$) in order to find suitable conditions for control of nucleation and to improve the size of the grown crystals. These studies showed that, using the vertical pulling method with iodine transport, controlled nucleation was possible only at iodine concentration less than 0.2 mg/cm^3 and critical undercooling less than 15°C . However, applying these conditions resulted in growth of crystals with cadmium deficiency. It was also reported that CdS grown

under different experimental conditions exhibited different morphological habits (e.g., hexagonal platelets, hollow conical, and pyramidal) due to random nucleation and when using seed and undercooling of 5°C . Change in morphology of CdS crystals with change in growth temperature and iodine concentration was also reported by other researchers. Matsumoto et al. [27.91] observed that CdS crystals grown at different temperatures and with different iodine concentrations showed different morphological habits such as needles, polyhedron, prisms, pyramids, rods, platelets, dendrites, and irregular shapes. Attolini et al. [27.8] improved the perfection of CdS single crystals grown by CVT by adopting the time-increasing supersaturation method, showing that crystals grown under small supersaturation do not exhibit skeletal and hollow forms. Later it was reported that using hydrogen as the transporting agent improved the size of the CdS single crystals and has several other advantages such as better control of nucleation, up to the point of obtaining large crystals and lack of contamination of grown crystals by the transporting agent [27.92]. Paorici and Pelosi [27.36] extensively studied closed-tube CVT techniques for the Cd:I₂ system from the thermodynamical as well as hydrodynamical point of view and calculated the mass transport rate as a function of overall pressure inside the tube, considering the contribution of thermal convection. Attolini et al. [27.93] applied the multidirectional productivity function for predicting the maximum transport efficiency as well as some other CVT features such as the relative importance of the various chemical reactions and the effect of inert gas on transport performance in the CdS:I₂ system.

CdS single crystals grown by CVT in closed tubes using iodine as the transporting agent show different morphological habits and degree of perfection when changing experimental conditions such as the growth temperature and iodine concentration. The growth temperature and iodine concentration have been changed over wide ranges to find empirically the most suitable growth conditions which yield CdS crystals of higher quality and large size. However the optimal growth temperature for a particular concentration of transporting agent for the growth of nearly perfect CdS single crystals remains to be determined. Hence the growth of CdS single crystals under different growth conditions has been studied to proof the agreement of theoretically predicted optimum conditions with experimental observations [27.94].

The experimental details for the growth of CdS single crystals followed at Crystal Growth Centre, Anna

University, are as follows: The starting material was cadmium sulfide of spectroscopic grade (5N purity). Before use, the powder was heat-treated at 200–300 °C for several hours in vacuum. Three grams of heat-treated powder was filled into quartz ampoule having length of 20 cm and diameter of 1 cm, along with iodine. Due to the high vapor pressure of CdS, the ampoules were made from quartz tubes with thickness of 2 mm for safety reasons. The ampoule, cooled by ice, was evacuated to 2×10^{-6} Torr and sealed off. The capsule was placed into a double-zone horizontal furnace controlled by Eurotherm controllers. A reverse temperature profile was developed across the ampoule over several hours to remove the powder sticking to the tip or deposition zone of the ampoule. The growth temperature (T_g) was varied from 600–950 °C. The concentration of the transporter was varied from 1 to 10 mg/cm³ and the difference in temperature of the source and deposition was kept constant at ($\Delta T = 50$ K) for all growth runs. Each growth run was carried out for 1 week. After that, the furnace was cooled at room temperature in 20 h.

Crystals grown at different growth temperatures with the same amount of iodine concentration showed different habits and optical quality. The crystals were orange, red, and pale yellow in color, with average dimensions of $3 \times 2 \times 1$ mm³. The experimental results observed are in good agreement with the theoretical calculations. Crystals grown at growth temperature of 750 °C had complete faces, and their habits were mostly pyramidal and platelet. They were found to be more transparent compared with CdS crystal grown at other temperatures for the same transporter concentration. In general, the quality of the grown crystals was found to be good. This could be due to the stability of the flow of the materials transported from the source to the growth zone and the growth at the temperature of 750 °C predicted to be optimum for the iodine concentration of

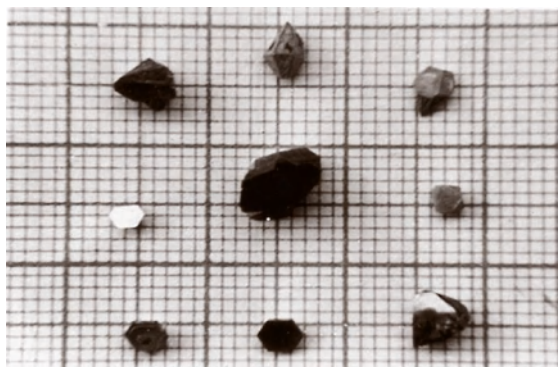


Fig. 27.17 CdS crystals grown at growth temperature of 750 °C

5 mg/cm³. At the growth temperature of 600 °C, due to the higher partial supersaturation, more crystals, of smaller size, with needle and irregular habits, and of poor quality were grown. Crystals grown at 950 °C were found to have poorly developed faces in most cases and showed less transparency. The deficiency in the surface perfection and optical quality of CdS crystals grown at 600 °C and 950 °C compared with CdS crystals grown at 750 °C may be due to variations of the transfer rate caused by small fluctuations in the temperature of the deposition zone where the slope of the $\Delta\alpha$ curve is large. Since the optical transmission measurements were carried out for crystalline samples of the same thickness (2 mm) and equally polished surfaces, the difference in transmission could be due to scattering from defect centers. Because of the temperature fluctuation at the growth interface, defects such as precipitates, inclusions, and dislocations may get into the lattice of the growing crystals and affect their optical quality. Figure 27.17 shows some of the CdS single crystals grown at 750 °C for $c = 5$ mg/cm³ and $\Delta T = 50$ K.

27.5 Growth of Nanomaterial from Vapor Phase

ZnSe can be used in optoelectronic devices such as LED and LDs in the blue wavelength region [27.95]. ZnS:Mn and ZnSe:Mn are known to be good luminescent materials [27.96, 97]. The recent interest in these semiconductors is due to the magnetic properties when transition metals are doped at lower concentrations, forming a separate class of research identified as diluted magnetic semiconductors [27.98]. The sp-d exchange interaction between ZnSe and Mn

makes it possible to obtain magnetic character in nonmagnetic semiconductor, as applicable in magnetooptical devices [27.99]. Nanocrystalline growth of ZnS:Mn- and ZnSe:Mn-based semiconductors has attracted substantial interest in recent years [27.100, 101]. Nanocrystals and nanostructures of these materials were grown from aqueous solutions [27.102, 103]. Vapor growth methods such as MOVPE and MOCVD have also been used to synthesize nanostructures of

ZnSe [27.104, 105]. Magnetron sputtering has been used to deposit SiO₂/CdTe/SiO₂ nanocrystalline thin films [27.106]. A few II–VI compound nanocrystallites were grown on glassy matrix [27.107]. Sol–gel synthesis of ZnS was carried out in SiO₂ gels [27.108]. These nanostructures have usually been analyzed by characterizations techniques such as transmission electron microscopy (TEM), photoluminescence, Raman and ultraviolet–visible spectroscopy (UV-vis), etc. Electron spin resonance (ESR) has been used as a tool to analyze paramagnetic impurities in ZnS nanocrystals and quantum dots [27.109].

SiO₂ aerogels were obtained by sol–gel synthesis followed by annealing at high temperatures up to 400 °C. This matrix has been used to deposit nanocrystalline ZnSe:Mn on its pores by the chemical vapor transport method using iodine as transporting agent. ZnSe doped with 0.2 mol % Mn powder synthesized by vapor transport has been used in the experiment. The growth temperature was 800 °C and the temperature difference was 50 K. The experimental procedure has been discussed in detail [27.26]. The characterization details have been reported in the literature [27.104–115].

27.6 Growth of I–III–VI₂ Compounds

Nonvolatile solid substances can be transported through a vapor phase by chemical vapor transport (CVT) when suitable reactive gases are provided in the presence of a temperature gradient, such as when transforming solid substances into gaseous compounds via heterogeneous chemical reactions and vice versa. Vapor-phase chemical transport methods, as first described by Schäfer [27.12] and Nitsche et al. [27.116], are widely used in closed-tube arrangements for growing crystals. These vapor-grown crystals are often perfect enough and of good enough quality to be used in solid-state physics experiments.

Honeyman and Wilkinson [27.117] have grown CuGaS₂, CuAlTe₂, AgGaS₂, AgAlS₂, AgAlSe₂, and AgAlTe₂ single crystals from polycrystalline materials by chemical vapor transport using iodine as the transporting agent to form single crystals. Table 27.3 gives

the details of the growth conditions used, such as temperatures, ampoule dimension, and transporting time, and the crystals obtained.

In all cases 5 mg/cm³ iodine per unit volume of ampoule was used as the transporting agent. The silver compounds required much longer growth times than the copper compounds. This is probably due to the vapor pressure of silver iodide, which is approximately 30 times less than that of copper iodide at the same temperature. The tellurium compounds were also very difficult to grow and gave a low crystal yield. This may be due to the formation of TeCl₄, which would prevent the normal iodide vapor transport.

Paorici et al. [27.9] have grown CuGaS₂, CuInS₂, CuAlS₂, and AgIn₅S₈ single crystals using a temperature-variation method of the chemical vapor transport technique and iodine as the transporting agent. Larger

Table 27.3 Growth parameters of some I–III–VI₂ compounds by CVT method and their results

Compound	Ampoule diameter (mm)	Length of ampoule (cm)	Source–growth zone temperature (°C)	Transport time	Crystals obtained
CuGaS ₂	18	20	800–700 850–750	3 days	High yield, yellow–green crystals stable in atmospheres
CuAlTe ₂	18	20	780–650	5 months	Very low yield, red hexagonal platelets
AgGaS ₂	18	20	840–740	2 weeks	Moderate yield straw-yellow transparent crystals
AgAlS ₂	15	14	800–600	3 weeks	Colorless crystals, very unstable in air
AgAlSe ₂	18	20	750–630	3 months	Low yield, yellow–black crystals
AgAlTe ₂	18	20	830–630	2 weeks	No crystals

crystals were obtained by means of a time-varying temperature profile method. The principle of the method involves a gradually increase of the source temperature, which allows firstly reduced primary nucleation and secondly the avoidance of constitutional undercooling during the first stages of nucleus growth. The source temperature (at the hot end of the ampoule) T_s is slowly raised as a function of time, while the growth temperature T_g is kept constant. Initially, the ampoule is placed such that T_s is lower than T_g by about 100 °C (temperature inversion). This temperature inversion is a very important feature of the method, because of its cleaning effect on the quartz wall of the deposition zone. After 2–3 days of temperature inversion, T_s is adjusted to about 10 °C lower than T_g . Qualitatively, the growth mechanism can be described as follows. By increasing T_s , when T_s reaches some value, the supersaturation reaches a value for which primary nucleation has a high probability of occurring on some active sites of the quartz walls. If careful quartz treatment is performed, only a few primary nuclei are found. Since now the growth process of these primary nuclei will result in a more probable process, their development into large single crystals is expected. The two alternative methods, i. e., stationary temperature profile (STP) and time-varying temperature profile (TVTP), were used and the sizes of the crystal grown were compared.

27.6.1 Growth of Undoped and Doped Crystals of CuAlS₂

CuAlS₂ is a wide-bandgap (3.49 eV) member of the ternaries, which has been found to emit strong green and blue photoluminescence (PL) and therefore is considered a candidate material for blue and green light-emitting device realization [27.118,119]. Single crystals were grown by chemical vapor transport technique from

polycrystalline CuAlS₂, which was prepared by direct melting of the constituent elements in a BN crucible. The resulting crystals, which were typically plate-like with dimensions of 20×10×0.5 mm³, were then annealed in evacuated and sealed quartz ampoules in the presence of 100 mg Zn metal placed at one end of the ampoule with the CuAlS₂ crystals placed at the other end. Thermal treatments were carried out for 50 h at different temperatures in the range 973–1173 K.

Shirakata et al. [27.120] have grown CuAlS₂ single crystals by chemical vapor transport using iodine as the transporting agent. Growth conditions of source and growth temperatures were 800–650 °C and iodine concentration was 5 mg/cm³. PL measurements were carried out at low temperatures (77 and 10 K). Most of the crystals exhibited a strong, orange PL band peaking at 2.1 eV and weak peaks at 2.9 and 3.55 eV. These results can be explained by considering that a large concentration of antisite disorder defects should be expected in Cu- and Al-rich crystals, being acceptors such as Cu_{Al} defects in Cu-rich samples and donors such as Al_{Cu} defects in Al-rich samples. Thermal treatment in sulfur vapor will result in a decrease of the concentration of sulfur vacancies and an increase of the concentration of the cation vacancies V_{Cu} and V_{Al}. Since the former defects are donor-like while the latter are acceptor-like the degree of compensation under sulfur annealing will be reduced, which was observed experimentally as an increase of *p*-type conductivity. The results for the sharp, near-bandgap PL lines are summarized in Table 27.4, where peak energies and assignment of the exciton PL lines in CuAlS₂ crystals are given. The crystals under consideration are as-grown ones of stoichiometric, Al-rich, and Cu-rich compositions as well as crystals annealed in sulfur and in vacuum. Strong lines are indicated by (++), weak lines by (+), and missing lines by (–).

Table 27.4 Summarized PL results on CVT-grown CuAlS₂ single crystals

Energy	Crystals			Annealed		Assignment
	As grown			In sulfur	In vacuum	
	Stoichiometric	Al-rich	Cu-rich			
3.376	+	–	+	–	–	–
3.567	+	Broad	+	+	+	–
3.550	++	–	++	++	++	Free exciton
3.540	++	–	++	+	++	Bound exciton
3.532	++	Broad	++	+	++	Bound exciton
3.500	+	–	–	++	–	Bound exciton
3.475	+	–	–	++	–	Bound exciton

Aksenov et al. [27.121] recorded PL spectra for CuAlS₂ single crystals doped with Zn by adding metallic zinc into the starting composition of the constituent elements prior to synthesis of the CuAlS₂ compound. Zn doping was carried out by using different techniques:

1. Zn dopant was added into the starting composition of constituent elements prior to synthesis of CuAlS₂ by direct melting. In this case the concentration of Zn in CVT-grown crystals was found to be equal to the nominal one.
2. Undoped CVT-grown crystals were annealed in evacuated and sealed quartz ampoules in the presence of ZnS and S at 973–1073 K for 60 h, the S pressure being 1–3 atm.
3. The undoped crystals were annealed at 873 K for 20–120 h in the presence of Zn, the Zn metal being placed at one end of the ampoule and the crystals to be doped at the other.

Aksenov et al. [27.122] have grown Cd-doped CuAlS₂ single crystals by CVT using iodine as the transporting agent, with grown crystal annealed under different atmospheres such as Cd. Annealing of the crystals in the presence of Cd at 700 °C did not result in any significant change in the PL properties of the crystals, the resulting PL spectrum being essentially the same for as-grown crystals. In the case of annealing at 900 °C for 50 h, an intense yellow–green photoluminescence band peaking at 565 nm was observed. This emission is interpreted as originating from donor–acceptor pair recombination, involving deep levels, formed by Cd-introduced defects.

27.6.2 Growth of Undoped and Doped Crystals of CuAlSe₂

CuAlSe₂ is one of the wide-bandgap ternary compounds with chalcopyrite-type structure and is promising as an optical application in the blue wavelength region. Kurposhi et al. [27.123] have grown single crystals of CuAlSe₂ by chemical vapor transport, which were plate-like and transparent with yellowish color. Relatively large single crystals with a well-developed (112) face and typical dimensions of 9 × 5 × 0.45 mm³ were obtained at source and growth temperatures of 1263 K and 1223 K and iodine concentration of 2–3 mg/cm³. It was found that the light transmittance of the crystals decreased with during the days after growth. This may be due to surface oxidation of CuAlSe₂ crystals after growth, which is a serious problem for optical applications of this compound.

Chichibu et al. [27.124] have studied the resistivities, carrier concentrations, optical absorption, and PL of undoped and Cd- and Zn-doped CuAlSe₂ single crystals grown by CVT. The electrical and optical properties were almost unchanged after annealing under Se pressure. However, resistivity increased about seven orders of magnitude after annealing in vacuum. Resistivity also increased with Cd or Zn doping. The samples showed p-type conduction even with Cd or Zn doping. It was seen in all samples that the reduction of transmittance began from about 2.4 eV. A binding state such as a deep donor level which accompanies a lattice relaxation acts as an optical absorption center that needs more than 2.4 eV for its excitation. The assumed binding state appears to be related to a vacancy at the Se site because the absorption edge was almost unchanged after annealing in a Se atmosphere and shifted after annealing in vacuum. Therefore, taking into account that the absorption edge did not shift with Zn doping but did shift with Cd doping, the binding state may be a complex center consisting of the cation atoms and the nearest X_{Se}, where X is an atom or vacancy.

CuAlSe₂ single crystals were grown by CVT method using an ingot synthesized by a melt-grown technique in a rotating horizontal furnace using the elements Cu, Al, and Se with excess Se of 3 mol % form the stoichiometry. A concentration of iodine of 5 mg/cm³ was used [27.125]. The crystal growth was carried out for 7 days at constant temperature of 850 °C for the source region and 700 °C for the growth zone. As-grown crystals had platelet and needle shape, with typically dimensions of about 9 × 6 × 0.5 mm³, and showed a greenish yellow color. In PL spectra measured at 80 K, two independent, broad emission bands with peak energies of 1.77 and 1.93 eV were observed.

Prabukanthan and Dhanasekaran [27.126] reported the growth of CuInTe₂ single crystal by CVT method. A polycrystalline ingot of stoichiometric CuInTe₂ was synthesized from copper, indium, and tellurium elements with 4N purity. The stoichiometric ternary mixture was taken into a quartz ampoule and sealed in a quartz ampoule under vacuum of 2 × 10^{−6} Torr (0.3 mPa). The ternary mixture was gradually heated to 1323 K at a heating rate of 20 K/h. The ampoule was maintained at this temperature for 2 days until the reaction was complete. Then the furnace was cooled at a rate of 50 K/h. The ampoule was opened and the synthesized polycrystalline CuInTe₂ material was analyzed using powder x-ray diffraction (XRD). Single-phase polycrystalline CuInTe₂ powder showed a well-defined chalcopyrite structure. Two

grams of synthesized CuInTe_2 polycrystalline material and 5 mg/cm^3 of high-purity iodine were taken into a quartz ampoule. The ampoule, cooled by ice, was evacuated to 2×10^{-6} Torr and then sealed off. The ampoule was placed into a double-zone horizontal electrical furnace controlled by Eurotherm temperature controller. During the first stage, the furnace was slowly heated. The temperatures of the source and the growth zones were allowed to reach 873 and 923 K, respectively, in order to remove the material and also to clean the growth zone of the ampoule. The duration was 20 h. After this, the temperatures of the source and growth zones were maintained at 923 and 873 K, respectively. After growth lasting 14 days, the furnace was slowly cooled at a rate of about 20 K/h. When the temperature of the ampoule reached room temperature it was opened to obtain CuInTe_2 crystals. The crystals were then cleaned in an ultrasonic bath containing a mixture of acetone and methanol, and then rinsed with deionized water. The CuInTe_2 single crystals obtained were black in color with mirror-like upper surface; the maximum dimensions of the crystals obtained was $15 \times 5 \times 3 \text{ mm}^3$. Similarly, single crystals of CuInTe_2 were also grown by maintaining source and growth temperatures of 923–823 K and 923–773 K, respectively, for a period of 14 days. The dimensions of the crystals grown at 823 and 773 K were $7 \times 3 \times 5 \text{ mm}^3$ and $4 \times 3 \times 3 \text{ mm}^3$, respectively. The single crystals of CuInTe_2 grown at growth zone temperatures of 873, 823, and 773 K are shown in Fig. 27.18a–c. Single-crystal x-ray diffraction studies of CuInTe_2 single crystals carried out on crystals grown at different growth zone temperatures indicated tetragonal (chalcopyrite phase) structure.

Gombia et al. [27.127] have grown CuGaTe_2 and CuInTe_2 single crystals by chemical vapor transport technique and considered thermodynamically the growth parameters. The behavior of all gaseous species, the formation of spurious phases, i.e., liquid Te and solid TeI_4 , and transport conditions were discussed. Polycrystalline CuGaTe_2 and CuInTe_2 ingots were prepared by fusion of the constituents, weighed in stoichiometric ratio. The mixture was sealed in a quartz ampoule under vacuum of 10^{-6} Torr and heated at a rate of about 10°C/min up to 420°C (below the Te melting point) for several hours, then kept at a temperature of 900°C for CuInTe_2 and 950°C for CuGaTe_2 for several hours to ensure complete reaction and homogenization. Finally the samples were cooled slowly to 650°C , annealed at this temperature for 3 days, and quenched to room temperature.

A vapor transport method in a closed tube, using iodine as transport agent and polycrystalline CuGaTe_2 and CuInTe_2 as the starting source, was employed. To produce single crystals of significant size it is necessary to limit the number of potential sites for crystallization nuclei. Experimentally this can be done by thoroughly cleaning the quartz ampoule and using a low starting temperature gradient to assure a small supersaturation. To ensure the latter condition, a tubular eight-zone furnace permitting different gradients and profiles to establish conditions as close as possible to the theoretical ones was used. Inversion of the temperature profile between the source and crystallization zones reduced the number of nuclei. This process was performed automatically by means of an electronic programmer. The grown crystals were characterized and the resistivity,

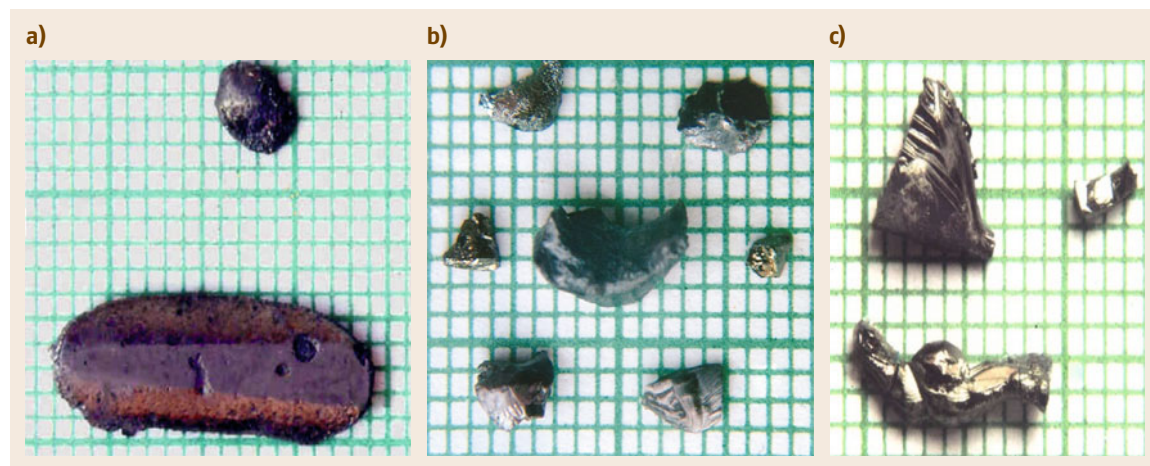


Fig. 27.18a–c CuInTe_2 crystals grown at growth temperature of (a) 873 K, (b) 823 K, and (c) 773 K

carrier mobility, and carrier concentration were determined in the temperature range between 80 and 300 K. CuInTe₂ crystal grown in this way and annealed under Cd atmosphere changes from p-type to n-type and also exhibits increased mobility.

27.6.3 Growth of CuGaS₂-Based Single Crystals

Yu et al. [27.128] have grown CuGaS₂ single crystals by two different methods: melt-growth and chemical vapor-phase transport. In the CVT technique iodine was used as a transporting agent. The crystals were synthesized from the constituent elements (Cu, Ga, and S of 6N purity) in stoichiometric proportions in an evacuated quartz ampoule. The material was held in the temperature range 1050–1100 °C. It was cooled slowly at a rate of 2 °C/h to 700 °C and then cooled at a faster rate to room temperature. Crystals obtained from the melt varied in color from red to yellow–green. The crystals grown from the melt were crushed into powder and used as the initial charge for the vapor transport. This method involved placing the reacted material together with a small amount of iodine in an evacuated quartz ampoule, and heating it in a temperature gradient. The volatile iodine serves as the transporting agent. The temperature difference between the charge and crystallization zones was kept at 50 °C. The temperature of the charge zone was 1000 °C. The grown crystals were homogeneous and showed yellow–green color. The typical crystal dimensions obtained were 1 × 3 × 0.4 mm³.

Shirakata et al. [27.129] have grown CuGaS₂ single crystal by chemical vapor transport method using iodine as the transporting agent. Stoichiometric quantities of the elements Cu, Ga, and S (6N) with total weight of 0.5 g were sealed into an evacuated quartz ampoule (10 mm inner diameter, 15 cm length) together with 3–25 mg/cm³ iodine. The ampoule was placed in a two-zone horizontal furnace with temperature gradient of 900–700 °C and maintained for 4 days. With more than 10 mg/cm³ iodine all source materials were transported to the other end of the ampoule, and plate-like crystals (5 × 5 × 0.2 mm³ typical dimensions) with well-developed (112) plane were grown. With less than 5 mg/cm³ iodine, some of the source materials remained and crystals were typically yellow–green, but the color became greenish as the quantity of iodine was increased. PL measurements have been carried out on CuGaS₂ single crystals at 4.2 and 77 K. At 4.2 K, high-quality single crystals grown by CVT method show sharp PL lines.

Prabukanthan and Dhanasekaran [27.130] have grown CuGaS₂ (CGS) single crystal by CVT method. Single crystals of CGS were grown by chemical vapor transport method using iodine as the transporting agent. The CGS crystals were grown at three different growth temperatures with 10 mg/cm³ iodine concentration and temperature difference of 50, 100, and 150 K. The purity of the elements used for these experiments was 4N. A mixture of the elements Cu, Ga, and S was taken into a quartz ampoule of length 18 cm and diameter 1 cm along with iodine at a concentration of 10 mg/cm³. The ampoule, cooled by ice, was evacuated to around 2 × 10^{−6} Torr and sealed off. The ampoule was placed into a double-zone horizontal furnace controlled by temperature controllers with accuracy of ±0.1 K. A reverse temperature profile was developed across the ampoule over several hours to clean the quartz walls of the growth zone. The duration was 20 h [27.131, 132]. After this, the temperatures of the source and growth zones were maintained at 1173 K and 1123 K, respectively. The growth duration was 7 days, after which the furnace was slowly cooled at a rate of about 10 K/h to 773 K and then at the rate of 60 K/h. The CGS single crystals obtained were yellow in color with maximum dimensions of 6 × 4 × 6 mm³. Similarly single crystals of CGS have been grown with the same iodine concentration and source zone temperature of 1173 K. Temperature differences of 100 and 150 K were maintained between source and growth zones, i. e., the temperature of the growth zone was maintained at 1073 and 1023 K, respectively. Growth was carried out for a period of 7 days in each case. The CGS single crystals obtained with growth zone temperature of 1073 and 1023 K were orange and green in color, respectively. The maximum dimensions of orange-colored CGS single crystals were 4 × 2 × 3 mm³ and of green-colored crystals were 15 × 0.4 × 1.2 mm³ (needle like) and 3 × 2.5 × 3 mm³.

Single crystals of CGS grown with growth zone temperature of 1123, 1073, and 1023 K are shown in Fig. 27.19. The temperature difference between the source and growth zones affects the quality and color of the resulting crystals. The crystal nucleation rate depends on the magnitude of supersaturation of the gas phase, which is proportional to the temperature difference between the source and growth zones. Normally the temperature difference between the source and growth zones is very low so that the formation of primary nucleation is controlled to form large-size crystals [27.17]. To initiate the crystallization processes, crystal nuclei have to be formed in the crystallization

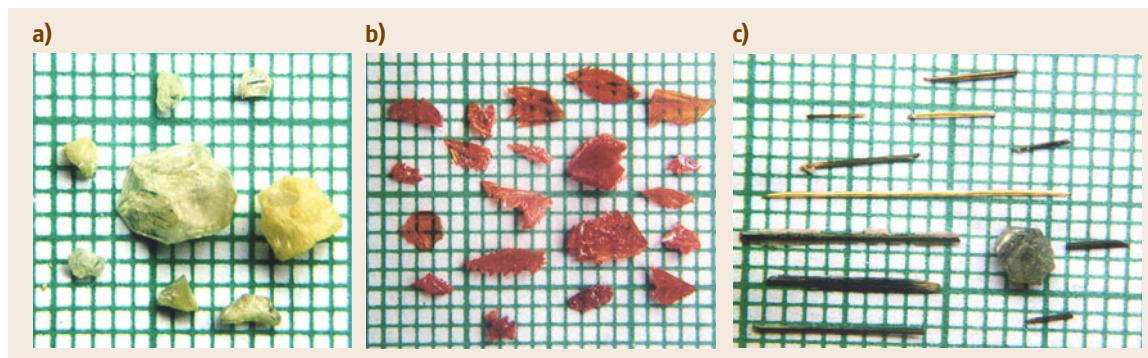


Fig. 27.19a–c As-grown single crystals of CuGaS_2 at different growth temperatures: (a) 1123 K, (b) 1073 K, and (c) 1023 K

zone. This is possible only if the gas phase is sufficiently supersaturated (i.e., the gas phase is in the unstable state). In the unstable state of high supersaturation, the rate of crystal nucleation is high and crystal nuclei are formed spontaneously in a short period of time. In the case of our experimental observations at growth temperature of 1023 K, the crystals grown were small in size due to high supersaturation ratio. However, at 1123 K, the crystals grown were larger in size due to the low supersaturation of the gas phase. Under chemical vapor transport conditions, the partial pressures of noble-metal iodides (CuI and GaI_3) are high compared with the partial pressure of sulfur. So controlling the stoichiometric composition is difficult. It is concluded from our experimental observations that, during the growth of CGS single crystal by CVT method with temperature difference between source and growth zones of 50 and 100 K, sulfur may play the main role in the transport process. The formation of other phases such as Cu_2S and Ga_2S_3 takes place during the growth of CGS single crystals at 1123 and 1073 K, respectively. However, when the temperature difference is maintained at 150 K, iodides such as CuI and GaI_3 may be the dominant gas species to form stoichiometric CGS single crystals.

Prabukanthan and Dhanasekaran [27.133] have grown Mn-doped CuGaS_2 single crystal by CVT method. Stoichiometric compositions of Cu, Ga, and S with 1 mol % Mn as precursor materials were taken into a quartz ampoule with iodine concentration of 10 mg/cm^3 (total weight 1 g, including Mn concentration). The quartz ampoule, cooled by ice, was evacuated to around 2×10^{-6} Torr and sealed off. The ampoule was placed into a double-zone horizontal electrical furnace. The furnace was controlled by Eurotherm tem-

perature programmer and controller. The source and growth zones temperature were 1173 and 1023 K, respectively. The growth period was 7 days. The furnace was slowly cooled at a rate of 10 K/h to 873 K, after which it was cooled rapidly at a rate of 60 K/h. Similar growth conditions were used for growth of 2 mol % Mn-doped CuGaS_2 crystals. CuGaS_2 single crystals grown with 1 mol % and 2 mol % Mn doping were green and orange in color with dimensions of $2.5 \times 3 \times 4 \text{ mm}^3$ and $4 \times 3 \times 3 \text{ mm}^3$, respectively. Single crystals of 1 mol % and 2 mol % Mn-doped CuGaS_2 are shown in Fig. 27.20a,b. The Mn-doped CuGaS_2 single crystals were determined to be paramagnetic in nature. The increase of bulk conductivity of the Mn-doped CuGaS_2 single crystals at room temperature indicates an increase of hole concentration, and p-type conductivity was also found.

Tanaka et al. [27.134] have grown $\text{CuGaS}_{2-2x}\text{Se}_{2x}$ single crystal by CVT method. First, in order to prepare CuGaS_2 powder, Cu, Ga, and S were weighed in stoichiometric portions and sealed into evacuated silica tubes; then the tubes were heated in a furnace. The temperature was increased gradually to 1200°C for about 24 h. CuGaSe_2 powders were also prepared in a similar way. Subsequently $\text{CuGaS}_{2-2x}\text{Se}_{2x}$ crystals were prepared by iodine transport method. CuGaS_2 and CuGaSe_2 powders were weighed in certain proportions, crushed, mixed, and then sealed in evacuated silica tubes (12 mm inner diameter, 10 cm length) with about 18 mg/cm^3 iodine. These ampoules were placed in a two-zone furnace. The source and growth zone temperatures were kept at $850\text{--}900^\circ\text{C}$ and $650\text{--}700^\circ\text{C}$, respectively. Under these conditions all starting materials were transported by iodine within several days, and crystals of dimensions $3 \times 10 \times 0.5 \text{ mm}^3$ were yielded.

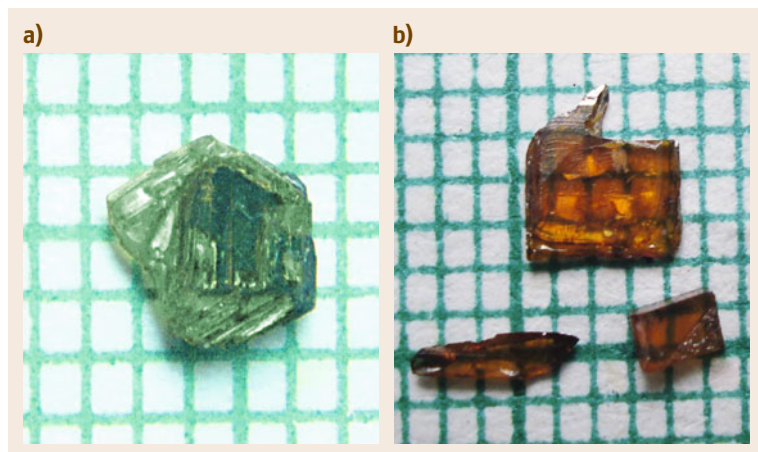


Fig. 27.20a,b As-grown single crystals of (a) 1 mol % Mn-doped and (b) 2 mol % Mn-doped CuGaS₂

The color of the crystals obtained varied continuously with composition: from dark green ($x = 0$), through red, to black ($x = 1$).

Sato et al. [27.135] have grown Fe-doped single crystals of CuAl_{1-x}Ga_xS₂ by CVT method using iodine as the transporting agent. Polycrystalline powders of CuAlS₂ and CuGaS₂ prepared by sintering were used as source materials. The source material and a transporting agent was sealed in vacuum in a silica ampoule with inner diameter of 13 mm and length of 20 cm. The iodine concentration was 25 mg/cm³. The silica ampoule was placed in a double-zone electrical furnace. Then the temperature of the source and growth zones were kept at 900 °C and 700 °C, respectively. The dimensions of the crystals were 3 × 4 × 2 mm³. All of these undoped bulk crystals were black. Crystals with composition in the vicinity of CuAlS₂ were colored blue when polished to less than 0.5 mm, while those with the composition near CuGaS₂ were colored green, indicating the presence of trace impurity of iron. Crystals intentionally doped with Fe were also prepared with Fe concentrations of 0.1 mol % and 0.3 mol %. The grown crystals were characterized by PL. In addition, several researchers have grown CuGaS₂ single crystals, described in the literature [27.130, 132].

27.6.4 Growth of AgGaS₂ and AgGaSe₂ Single Crystals

Prabukanthan and Dhanasekaran [27.136] have reported the growth of AgGaS₂ single crystal by CVT method. The 1 : 1 : 2 mole ratio of Ag, Ga, and S with excess 0.5% sulfur as precursor materials, and 10 mg/cm³ of high-purity iodine as the transporting

agent, were taken into a quartz ampoule. In order to prevent deviation from stoichiometry resulting from possible volatile loss of sulfur during initial steps, it was found necessary to add excess sulfur. The starting materials were taken into a quartz ampoule (15 mm diameter, 180 mm length) evacuated to 2×10^{-6} Torr and then sealed off. The ampoule was placed into a double-zone (source and growth zones) horizontal electrical furnace. During the first stage the furnace was slowly heated at the rate of 10 K/h. The temperatures of the source and growth zones were allowed to reach 1023 and 1073 K, respectively, in order to clean the wall of the ampoule. The duration was 20 h. After this, the temperature of the source and growth zones were maintained at 1073 and 1023 K, respectively, for the next 15 days, after which the furnace was slowly cooled at a rate of 20 K/h. When the temperature of the ampoule reached room temperature it was opened to obtain yellow-colored AgGaS₂ crystals. Similarly single crystals of AgGaS₂ were grown with the same iodine concentration and source zone temperature of 1073 K. A temperature differences of 100 K was maintained between source and growth zones, so that the temperature of the growth zone was maintained at 973 K. The growth was carried out for a period of 15 days. The AgGaS₂ single crystals obtained were yellow in color. AgGaS₂ single crystals grown at growth zone temperatures of 1023 and 973 K are shown in Fig. 27.21a,b. Cut and polished AgGaS₂ single crystal grown at 1023 K is shown in Fig. 27.21c. Single-crystal XRD and powder XRD studies indicate that the as-grown AgGaS₂ crystals belong to the tetragonal (chalcopyrite) system with (112) plane as the dominant peak. The full width at half-maximum (FWHM) of the x-ray rocking curve

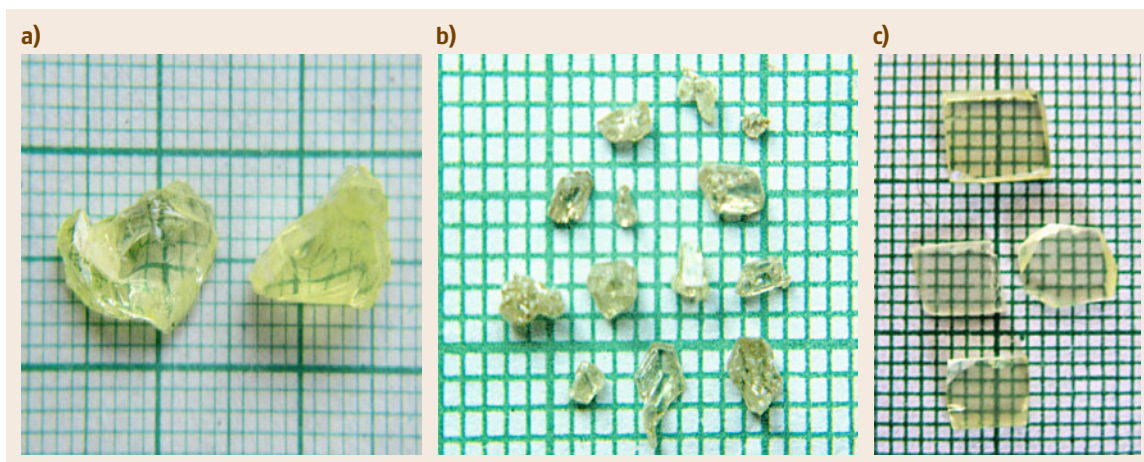


Fig. 27.21a–c AgGaS₂ crystals grown at (a) 1023 K, (b) 973 K, and (c) cut and polished AgGaS₂ crystals grown at 1023 K

for the as-grown AgGaS₂ single crystal was 5 arcsec. The quality of the crystals obtained with both temperature differences (100 and 50 K) between the source and growth zones was found to be good.

Noda et al. [27.137] have measured the transport rate for CVT growth of AgGaS₂ single crystal. The transport rate was measured by weighing the total amount of AgGaS₂ crystals grown in the growth zone. The important parameters affecting crystal growth were the amount of iodine, source temperature, and the temperature difference between the source and growth zones. The observed transport rate tends to increase with increasing ΔT at fixed T_s , but a higher transport rate does not necessarily mean larger single crystals. The other parameters affecting crystal growth is the presence of a maximum transport rate with increasing T_s at fixed ΔT . This indicates that condensation of the atoms at the growth zone was delayed with increasing growth temperature. All the as-grown crystals were transparent and yellowish in color and had rod and plate morphologies. The rod forms of single crystals were obtained when the growth temperature was more than 1173 K and the transport rate less than 10 mm/day. The biggest plate-type crystal ($7 \times 5 \times 2 \text{ mm}^3$) was obtained under the conditions of $T_s = 1248 \text{ K}$ and $\Delta T = 75 \text{ K}$ for 1 week. The habit plane of the rod was (112) and the growth direction was nearly in the (112) direction. The PL spectra of the crystals were dependent on the amount of iodine used, and excitonic emission was observed, which means that good-quality crystals were obtained.

Polycrystalline AgGaS₂ was prepared by synthesis from its constituent elements Ag, Ga, and S with 5 N

purity taken into a quartz tube. Polycrystalline powder (2 g) as a source, was sealed with iodine as the transporting agent at concentration of 5 mg/cm^3 into a quartz ampoule of length 20 cm and inner diameter 1 cm. The as-grown AgGaS₂ single crystals were transparent and yellowish in color.

Single crystals of AgGaS₂ [27.56] have been successfully grown from 2.5 g polycrystalline powder AgGaS₂ as source, sealed with iodine at concentration of 5 mg/cm^3 into a quartz ampoule of length 20 cm and inner diameter 1 cm.

Nigge et al. [27.138] have grown single crystals of AgGaSe₂ by CVT method using iodine as the transporting agent. Growth temperature of 770°C and concentrations of the transporting agent of $1.6\text{--}1.7 \text{ mg I}_2/\text{cm}^3$ yielded compact single crystals with dimensions up to $8 \times 5 \times 5 \text{ mm}^3$.

Tafreshi et al. [27.57] have grown single crystals of $\text{Cu}_{0.5}\text{Ag}_{0.5}\text{InSSe}$ for the first time by chemical vapor transport technique using iodine as the transporting agent. A stoichiometric mixture of the constituent elements with 5 N purity was taken, and polycrystalline $\text{Cu}_{0.5}\text{Ag}_{0.5}\text{InSSe}$ ingots were synthesized in a vertical furnace in vacuum at 900°C . The polycrystalline synthesized powder of 2.5 g together with 5 mg/cm^3 5 N purity iodine was placed in a quartz ampoule with length 16 cm and diameter 1 cm. The ampoule, cooled by ice, was evacuated to $2 \times 10^{-6} \text{ Torr}$ and sealed off. The capsule was then placed into a double-zone horizontal furnace controlled by Eurotherm controllers. A reverse temperature profile was developed across the ampoule over several hours to

remove the powder sticking at the tip or deposition zone of the ampoule. The source and growth zone temperatures were kept at 937 °C and 849 °C, respectively. The growth run was carried out for 1 week. After that, the furnace was cooled to room temperature in 20 h. The grown crystals were in the form of small platelets with dimensions of $1 \times 2 \times 0.5 \text{ mm}^3$, joined to-

gether with mirror-like upper faces. X-ray analysis, surface analysis, and microindentation studies were carried out on the grown crystals to determine structure and lattice parameters, the growth mechanism, and mechanical properties, respectively. $\text{Cu}_{0.5}\text{Ag}_{0.5}\text{InSSe}$ was found to crystallize in tetragonal chalcopyrite structure.

27.7 Growth of GaN by VPE

Epitaxial growth can be achieved by solid-phase, liquid-phase, vapor-phase, and molecular-beam deposition. Vapor-phase growth is by far the most widely used technique for semiconductors. It consists of oriented crystal growth of a material transported from the gas phase onto a suitable solid substrate.

27.7.1 Vapor-Phase Epitaxy (VPE)

VPE systems are particularly employed in mass production of electronic devices because of their proven low cost and high throughput, in addition to their capability to grow advanced epitaxial structures. The fundamental reason for their success is due to the ease of dealing with low- and high-vapor-pressure elements. This is achieved by using specific chemical precursors, in the form of vapor, containing the desired elements. These precursors are brought into the reactor by a suitable carrier gas and normally mix shortly before reaching the substrate, giving rise to the nutrient phase for the crys-

tal growth [27.139]. The release of the gas elements necessary for the construction of the crystalline layer may occur at the solid–gas interface or directly in the gas phase, depending on the type of precursors and the thermodynamic conditions.

In vapor-phase epitaxy with open flow systems a carrier gas containing the reactive species is forced to flow past the substrate crystal. At the crystal surface the species undergo a sequence of chemical reactions leading to extension of the substrate crystal lattice and formation of products which must leave the vicinity in order for the process to continue.

The sequence of steps which is generally assumed to occur is shown schematically in Fig. 27.22. The factors which influence the growth rate and material composition are the vapor pressure and the temperature, both of which can be precisely controlled. Depending upon the sources and the reactor type, one can distinguish between two special cases of VPE, namely hydride vapor-phase epitaxy (HVPE) and metalorganic vapor-phase epitaxy (MOVPE). The former uses inorganic sources and a hot-wall reactor, whereas the latter uses fully or partly organic sources and a cold-wall reactor.

27.7.2 VPE GaN Film Growth

Since the earliest pioneering work on growth of epitaxial films by VPE [27.140] until the early 1980s, VPE was a popular method for the growth of epitaxial layers of gallium nitride [27.141]. However, this technique was largely abandoned in the early 1980s because of its apparent inability to reduce the native defect concentration to nondegenerate levels and thus achieve p-type doping. This was presumed to be due to nitrogen vacancy defects, which would be thermodynamically favored at the high growth temperatures typically used in HVPE GaN growth. This interpretation predominated in spite of reports of nondegenerate films grown by HVPE [27.141] and careful growth stud-

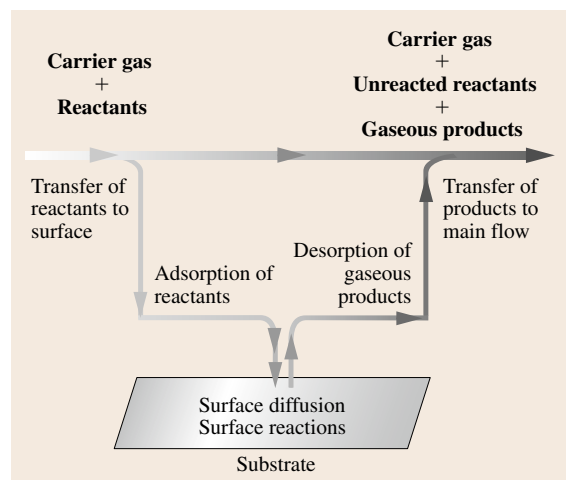
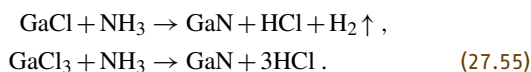


Fig. 27.22 The sequence of steps in a VPE process

ies which suggested that the incorporation behavior of this donor was inconsistent with a nitrogen vacancy defect [27.142]. With the advent of high-purity source materials and improved heteronucleation schemes, the growth of nondegenerate material has been reported by several groups.

The nature of the chemistry involved in GaN growth by HVPE technique differs from that of other III–V semiconductors. For instance, in GaAs growth by halide vapor-phase epitaxy, which uses the halide of the group V precursor AsCl₃ instead of its hydride AsH₃, thermal dissociation of the arsenic compounds results in the formation of As₄ and As₂ molecules, which typically remain volatile and chemically reactive and thus participate in film growth. In GaN HVPE, NH₃ is used as a source of nitrogen rather than nitrogen halide, NCl₃, which is highly explosive and highly unstable. In this process the thermal dissociation of NH₃ results in the formation of N₂ molecules, which are extremely stable and essentially unreactive at temperatures of interest [27.143–145].

Hydride VPE (HVPE) and chloride VPE (Cl-VPE) operate in a very similar manner and can be described by the final reaction as



However, the precursor for generating gallium chloride is different in both techniques. In HVPE of GaN, the gallium source is gallium monochloride (GaCl), which is stable only at temperatures above 600 °C and is produced by the reaction of liquid gallium with HCl gas [27.146–149]. The supply of GaCl is controlled by the gallium cell temperature and the flow rates of HCl gas and H₂ carrier gas. Several researchers have chosen presynthesized GaCl₃ instead of HCl gas [27.134, 143–145]. In Cl-VPE, gallium trichloride (GaCl₃) is used as the Ga source, due to its high vapor pressure. The use of monohalide (GaCl) or trihalide is the main difference between HVPE and Cl-VPE, respectively.

27.7.3 Strength of HVPE Method

It is important to analyze the importance of HVPE with respect to the other techniques. Shaw [27.150] has demonstrated that the Cl-VPE technique is an equilibrium process. The other epitaxial techniques (MOVPE and MBE) operate far from equilibrium conditions [27.151–153]. The near-equilibrium nature arises because of the reversible processes occurring at

the interface due to the volatility of group III at the operating temperatures; shift from equilibrium is caused by kinetic factors mainly due to ammonia decomposition. Based on this description it is easy to enumerate the strengths of VPE:

1. In VPE, being a near-equilibrium process, the growth rates are in principle uniquely determined by the mass input rate of the reactants; hence, unlike in nonequilibrium processes (MOVPE and MBE), very high growth rates (> 10 μm/h) can be easily achieved;
2. The lack of carbon incorporation into the film;
3. Cost effectiveness.

In the following, the details of the system and the process of chloride VPE for the growth of GaN layers are described. Furthermore, the optimum conditions for the growth of gallium nitride have been established. Based on our experimental investigations on the influence of the different growth parameters on the quality of the layer, it has been identified that the growth temperature plays a dominant role in the growth of GaN as compared with other parameters such as the flow rate, deposition time, etc.

27.7.4 Development of VPE System for the Growth of GaN

The development of experimental apparatus for the growth of GaN at our university is described [27.153]. The vapor-phase epitaxy (VPE) system mainly consists of a reaction chamber, single-zone furnace, GaCl₃ cell assembly, process control, and ammonia gas purifier assembly. The schematic diagram of the system is shown in Fig. 27.23.

As the film growth involves a high-temperature process, the reaction chamber is made out of a quartz tube of length 90 cm, wall thickness 2 mm, and diameter 70 mm. Both ends of the tube are made of stainless steel and the assembly consists of two ports on one end and three ports on the other. Integral structures are made to hold the quartz tube rigidly at either end. One end of the quartz is used for the transport of GaCl₃ vapor with nitrogen as carrier gas, and another inlet is used for another stream of nitrogen gas for diluting the reacting species, as the reaction is a dilute reaction. The other end of the reactor tube is used for an ammonia gas input port, exhaust line, and substrate holder setup.

The single-zone furnace consists of heating arrangements surrounded by metal boxes. A ceramic muffle of length 80 cm has been used for winding the heating

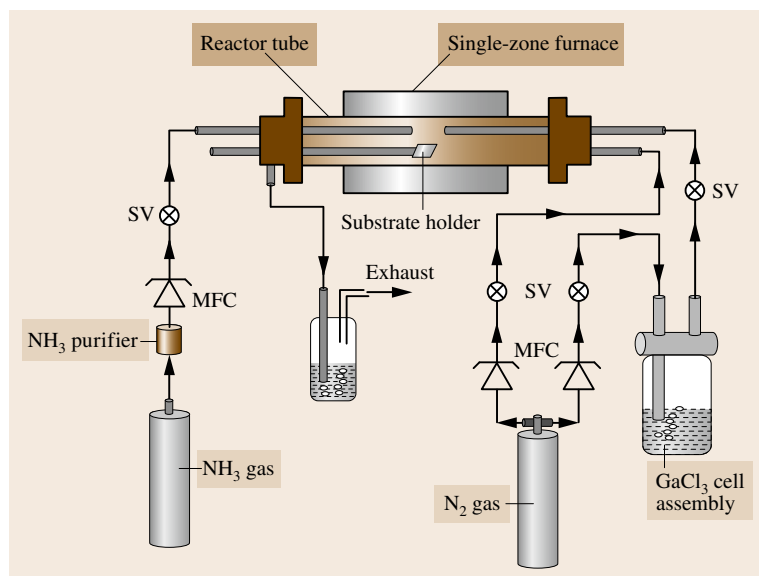


Fig. 27.23 Schematic diagram of the GaN vapor-phase epitaxy system

element (Al Kanthal wire: SWG 18 type). The windings were done in such a way that the space between them gradually becomes narrow at the ends compared with at the center of the tube in order to compensate for heat losses at the ends of the tube to a certain extent. The windings were insulated by applying a paste of corundum cement and silica gel mixture (the silica gel provides a binding action to the refractory cement). The tube is then packed inside a stainless-steel container using a zirconia-grade fiber blanket of density 128 kg/m^3 , which acts as a heat shield. Two thermocouples are used: one to control the furnace temperature, placed at the middle of the ceramic tube, i.e., near the growth zone; and another mounted inside the quartz tube, very close to the boat, so that the growth temperature could be monitored correctly.

The GaCl_3 cell assembly is made of quartz tube and a special Teflon assembly. The crystalline GaCl_3 in the cell is melted by a liquid-paraffin bath in which it is immersed. An electric heater maintains the paraffin bath at a suitable temperature in the range $80\text{--}150^\circ\text{C}$. GaCl_3 vapor was transported to the reactor by nitrogen carrier gas. The partial pressure of GaCl_3 could be controlled by both the GaCl_3 cell temperature and the flow rate of the N_2 gas. A mass flow controller and solenoid valves were used to control the flow rate of the carrier gas. A separate nitrogen gas line is used to dilute the ammonia gas to the required partial pressure. This nitrogen gas flow is measured by a float-type flow meter. The flow rate is varied by a needle valve. A computer pro-

gram controls the temperature of both the furnace and the GaCl_3 bath. The entire growth scheme can be pre-programmed. The program also enables the heating and cooling cycle to be programmed and data to be acquired during the growth cycle.

The purifier system consists of molecular sieves, which is a palladium- and silica-based compound, to remove moisture, carbon monoxide, and carbon dioxide from the ammonia gas. The purified ammonia is expected to be of analytical grade. After this online purification of the ammonia gas, its flow is monitored by a gas flow (float-type) meter.

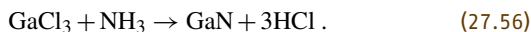
27.7.5 Growth of GaN by HVPE

The experimental conditions for growth of high-quality GaN layers using GaCl_3 precursor are discussed in this section. In view of the high-quality GaN growth, it is understood that careful cleaning of substrates prior to loading into the growth furnace is an important issue, because the quality of the grown layer (desired morphology and good optical properties) depends on this process, as does the reproducibility of the results. Sapphire ($\text{Al}_2\text{O}_3(0001)$) substrates were degreased in trichloroethylene (TCE), acetone, methanol, and deionized water in sequence for about 10 min. After completing the organic cleaning processes, in order to remove residual damage and scratches on the surface, substrates were chemically etched with $\text{HCl} + \text{H}_3\text{PO}_4$ (3 : 1) solution heated at 80°C for 15 min. Etched

sapphire substrates were again rinsed thoroughly in deionized water.

A quartz plate of 8 cm² area was used as the substrate holder, located at an optimized distance from the GaCl₃ : NH₃ mixing zone. Substrates of 1 cm² area are used per run and are placed lengthwise along the deposition zone. Considerable variation of the amount and quantity of deposition was observed between layers grown in a single run with respect to the position of the substrate. It was observed that GaN layer always deposits in regions closer to the GaCl₃ : NH₃ mixing zone. Initially the substrates are placed close to the mixing zone to find the exact position of uniform deposition. The substrate position has been varied further downstream from the mixing zone. It is observed that the layer thickness decreases rapidly with distance from the mixing zone. Growth ceases completely at distances from 6 to 10 cm downstream of the mixing zone.

After loading the substrates, the reactor was purged with nitrogen gas. Subsequently, the substrate was heated to the desired growth temperature and GaCl₃ was supplied using nitrogen carrier gas. The nitrogen source, NH₃, is not stable at high temperature and will thermally decompose to nitrogen and hydrogen gases. At the typical growth temperature (1200 K) the equilibrium value is about 0.1. Hence most of the ammonia will decompose to nitrogen and hydrogen at that elevated temperature in thermodynamic equilibrium. However, it is not easy to reach thermodynamic equilibrium in such an open system. The actual value depends on the NH₃ temperature, partial pressure, residence time, and surface conditions. Both NH₃ partial pressure and residence time can be changed by varying the NH₃ and N₂ flow rates. The H₂ gas, produced from the thermal decomposition of ammonia, will promote the reduction of GaCl₃ to GaCl. If hydrogen reduction of GaCl₃ is not complete, the remaining GaCl₃ can react with ammonia via the following reaction:



No low-temperature buffer layer was used in these experiments. Typical N₂ flow rate for GaCl₃ transport was 0.11/min. During the process, 1.0–2.01/min NH₃ and 1.0–2.01/min of N₂ were introduced into the reactor zone. The growth temperature was varied in the range 925–1050 °C. Ambient pressure inside the reactor was maintained at 1 atm for all the experiments.

Under typical growth conditions, reaction (27.56) is thermodynamically favorable. A thick deposition of GaCl₃ is always observed on the exhaust side of the re-

actor, which implies that unreacted GaCl combines with HCl and forms GaCl₃, which is a more stable form of gallium chloride at lower temperature (< 600 °C).

27.7.6 Characterization of GaN Films

Following the development of the growth technique described previously, the next most important element aspect is characterization of the materials grown. Characterization of a material can be defined as complete description of its physical and chemical properties. A thorough and extensive characterization of an epilayer is very difficult because this would require a variety of tests using a number of sophisticated instruments. It is obvious that there are no ideal crystals in reality and all crystals grown by any technique contain some defects, impurities, and inhomogeneities. Most physical properties are therefore sensitive to deviation from ideality, and generally the characterization of the grown crystals is necessary.

The assessment of crystalline perfection is essential to interpret the structure-dependent properties. Postgrowth analysis of an epitaxial layer provides information on the processes that occurred during growth. Feedback from the analysis can be used to modify the growth process in order to improve the quality of the layers. Moreover, characterization of the grown epilayers forms an integral part of the growth studies performed by the crystal grower. The demand for layers of the highest quality is increasing, and only systematic characterization enables the crystal grower to optimize growth parameters in order to obtain better results.

An epitaxial layer may be characterized by a description of its chemical composition, its structure, its defects, and the spatial distribution of these three features. It is crucial to know the degree of purity and perfection of epilayers in order to interpret structure-dependent properties and determine whether the material can be successfully employed in experiments or for device fabrication.

GaN, being a technologically important material, has elicited a large number of characterization studies [27.154–159]; further optimization of device performance requires that the fundamental mechanisms upon which these devices operate be better understood. Optimization of GaN growth to reduce defect density is of paramount importance for achieving high-quality GaN layers. The grown epilayers were subjected to the following characterization studies that provide a basic understanding of the GaN material properties:

1. Crystal structure analysis by x-ray powder diffraction and high-resolution x-ray diffraction (HRXRD) techniques
2. Molecular structural analysis by Raman scattering studies
3. Determination of the bandgap of the film by UV–vis absorption spectra
4. Identification of excitonic transitions by both room- and low-temperature photoluminescence (PL) spectra
5. Surface morphology by scanning electron microscope (SEM) studies
6. Electrical transport properties and Hall-effect measurements.

X-ray diffraction was used to determine the crystallinity and orientation of the GaN films. GaN films grown under different experimental conditions were characterized for crystalline quality and phase formation by using powder x-ray diffractometer with Cu K_α radiation; the recorded XRD patterns are shown in Fig. 27.24. It is clear from this figure that films grown at 950 °C and 990 °C exhibit a high degree of c -axis orientation nature, which indicating that basal planes of the GaN film and sapphire substrate are parallel to each other. However, the XRD pattern for the film grown at 925 °C shows polycrystalline nature. When the temperature is increased to 950 °C and 990 °C, the polycrystalline nature of the film is suppressed and the single-crystalline nature dominates. It is observed from the XRD results that decomposition of NH_3 is very low at those temperatures and hence the amount of atomic nitrogen for the reaction is also very low.

From XRD analysis, it has been observed that GaN layers are single-phase wurtzite structure. For GaN grown at 925 °C and 950 °C, XRD spectra exhibit a sharp peak of wurtzite GaN (0002) at 34.25°

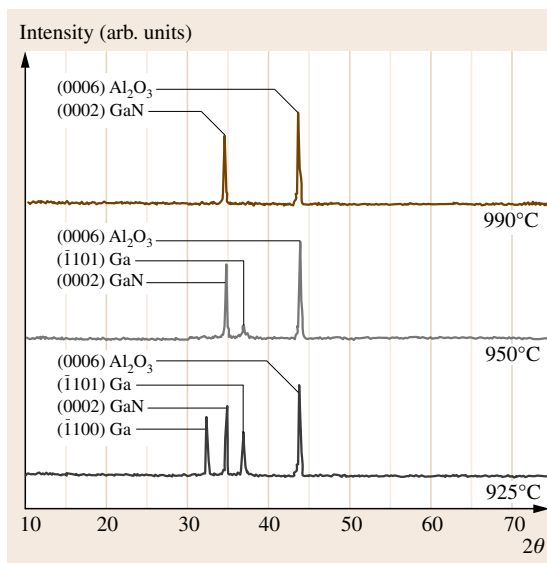


Fig. 27.24 XRD pattern of GaN grown on (0001) sapphire substrate at different growth temperatures

with blunt peaks for GaN ($\bar{1}011$) and GaN ($\bar{1}100$) at $2\theta = 36.60^\circ$ and 32.24° , respectively. However the XRD spectrum for GaN grown at 990 °C shows diffraction only from the c -plane of GaN and the sapphire substrate. This indicates that preferentially oriented GaN layer is realized when the growth temperature is kept at 990 °C [27.152]. The lattice parameters have also been calculated from the XRD data as $a = 3.186 \text{ \AA}$ and $c = 5.184 \text{ \AA}$, which are in very good agreement with reported values. The results of the other characterization studies are available in the literature [27.160–162]. Single-crystalline GaN nanowires on C- Al_2O_3 substrates have been synthesized by vapor-phase epitaxy process with the help of a Ni catalyst [27.163].

27.8 Conclusion

The growth of single crystals of II–VI and I–III–VI₂ compounds from vapor phase is a field of active research, with many researchers. The theoretical and thermodynamical background for the growth of these crystals have been given. The partial pressures of different components inside the growth ampoule during CVT growth of ZnSe single crystals were calculated using a thermodynamic model. Iodine was considered as the transporting agent. From the calculations, the optimum

conditions for the growth of good-quality ZnSe single crystals were determined. The optimum temperature range was found to be 800–850 °C for an iodine concentration of 2 mg/cm^3 . The undercooling and hence supersaturation ratios of S_2 and Se_2 were the factors determining the composition of $\text{ZnS}_x\text{Se}_{1-x}$ single crystals grown in closed-tube vapor transport when ZnS and ZnSe were taken as source materials in 1 : 1 ratio. These values were calculated as a function of deposition

temperature and iodine concentrations. The partial pressures were calculated using a thermodynamic model. The critical radius and free energy of formation were calculated using the supersaturation ratios by classical nucleation theory. Undercooling was found to have an influence on the supersaturations of S_2 and Se_2 , and hence on the composition of the resulting crystals. Conditions of larger undercooling were found to favor S-rich composition whereas smaller undercooling was found to favor ZnS_xSe_{1-x} composition near to that of the source. $ZnSe:Mn$ nanocrystals have been synthesized by chemical vapor transport method using iodine as the transporting agent on a matrix of SiO_2 aero-

gel. The cubic structure has been confirmed based on powder XRD results. The size of the nanocrystals calculated using Debye–Scherrer formula was ≈ 60 nm. This result is supported by TEM and electron diffraction pattern. A well-resolved ESR spectrum containing six lines corresponding to the Mn^{2+} ion in the $ZnSe$ nanocrystal lattice was obtained and attributed to the presence of a low concentration of Mn. The luminescence spectrum shows the band-edge emission at around 466 nm and Mn-related emission at 570 nm. The growth of I–III–VI₂ compounds has been described. Our recent results on vapor-phase epitaxial growth of GaN have been presented.

References

- 27.1 M.M. Faktor, I. Garrett, R. Hecklingbottom: Diffusional limitations in gas phase growth of crystals, *J. Cryst. Growth* **9**, 3–11 (1971)
- 27.2 M.A. Contreras, B. Egaas, K. Ramanathan, J. Hiltner, A. Swartzlander, F. Hasoon: Progress toward 20% efficiency in $Cu(In,Ga)Se_2$ polycrystalline thin-film solar cells, *Prog. Photovolt.* **7**, 311–316 (1999)
- 27.3 S. Nakamura, T. Mukai, M. Senon: Candela-class high-brightness $InGaN/AlGaIn$ double-heterostructure blue-light-emitting diodes, *Appl. Phys. Lett.* **64**, 687–689 (1994)
- 27.4 T. Lang, M. Odnoblyudov, V. Bougrov, S. Suihkonen, M. Sopanen, H. Lipsanen: Validating gallium nitride growth kinetics using a precursor delivery showerhead as novel chemical reactor, *J. Cryst. Growth* **292**, 26–32 (2006)
- 27.5 I. Akasaki, H. Amano, Y. Koide, K. Hiramatsu, N. Sawaki: Effects of an buffer layer on crystallographic structure and on electrical and optical properties of GaN and $Ga_{1-x}Al_xN$ ($0 < x \leq 0.4$) films grown on sapphire substrate by MOVPE, *J. Cryst. Growth* **98**, 209–219 (1989)
- 27.6 M. Sumiya, N. Ogusu, Y. Yotsuda, M. Itoh, S. Fuke, S. Nakamura: Systematic analysis and control of low-temperature GaN buffer layers on sapphire substrates, *J. Appl. Phys.* **131**, 1311–1319 (2003)
- 27.7 G.H. Westphal: Convective transport in vapor growth systems, *J. Cryst. Growth* **65**, 105–123 (1983)
- 27.8 G. Attolini, C. Paorici, P. Ramasamy: Skeletal and hollow crystals of cadmium sulphide grown under time-increasing supersaturation, *J. Cryst. Growth* **78**, 181–184 (1986)
- 27.9 C. Paorici, L. Zanotti, G. Zuccalli: A temperature variation method for the growth of chalcopyrite crystals by iodine vapor transport, *J. Cryst. Growth* **43**, 705–710 (1978)
- 27.10 R.F. Lever, G. Mandel: Diffusion and the vapor transport of solids, *J. Phys. Chem. Solids* **23**, 599 (1962)
- 27.11 H. Hartmann: Vapor-phase epitaxy of II–VI compounds: A review, *J. Cryst. Growth* **31**, 323–332 (1975)
- 27.12 H. Schäfer: *Chemical Transport Reactions* (Academic, New York 1964)
- 27.13 R. Zuo, W. Wang: Theoretical study on chemical vapor transport of $ZnS-I_2$ system. Part II. Numerical modelling, *J. Cryst. Growth* **236**, 695–710 (2002)
- 27.14 R.F. Lever: Solid transport rate in the vapor–solvent growth system $ZnS:I$, *J. Chem. Phys.* **37**, 1078–1082 (1962)
- 27.15 G. Mandel: Diffusion and the vapor-transport of solids, *J. Chem. Phys.* **37**, 1177–1198 (1962)
- 27.16 G. Mandel: Vapor transport of solids by vapor phase reactions, *J. Phys. Chem. Solids* **23**, 587–598 (1962)
- 27.17 E. Lendvay: Growth of structurally pure cubic and hexagonal ZnS single crystals, *J. Cryst. Growth* **10**, 77–84 (1971)
- 27.18 R. Zuo, W. Wang: Theoretical study on chemical vapor transport of $ZnS-I_2$ system. Part I: Kinetic process and one-dimensional model, *J. Cryst. Growth* **236**, 687–694 (2002)
- 27.19 T. Arizumi, T. Nishinaga: Transport reaction in closed tube process, *Jpn. J. Appl. Phys.* **4**, 165–172 (1965)
- 27.20 T. Arizumi, T. Nishinaga: Thermodynamics of vapor growth of $ZnSe-Ge-I_2$ system in closed tube process, *Jpn. J. Appl. Phys.* **5**, 21–28 (1966)
- 27.21 H. Watanabe, T. Nishinaga, T. Arizumi: Vapor transport equations for III–V compound semiconductors, *J. Cryst. Growth* **17**, 183–188 (1972)
- 27.22 M.M. Faktor, I. Garrett: *Growth of Crystals from the Vapor* (Chapman and Hall, London 1974)

- 27.23 K. Noda, N. Mastsumura, S. Otsuka: Chemical-vapor-transport rate of ZnS in closed Tube, J. Electrochem. Soc. **137**, 1281–1294 (1990)
- 27.24 B.I. Nöläng, M.W. Richardson: The transport flux function – A new method for predicting the rate of chemical transport in closed systems: I. Theory, J. Cryst. Growth **34**, 198–204 (1976)
- 27.25 B.I. Nöläng, M.W. Richardson: The transport flux function – a new method for predicting the rate of chemical transport in closed systems: II. A theoretical study of systems and experimental conditions for the chemical transport of SnO₂, J. Cryst. Growth **34**, 205–214 (1976)
- 27.26 M.W. Richardson, B.I. Nöläng: Predicting the rate of chemical transport using the flux function method, J. Cryst. Growth **42**, 90–97 (1977)
- 27.27 K. Klosse: A new productivity function and stability criterion in chemical vapor transport processes, J. Solid State Chem. **15**, 105–116 (1975)
- 27.28 K. Klosse, P. Ullersma: Convection in a chemical vapor transport process, J. Cryst. Growth **18**, 167–174 (1973)
- 27.29 S.R. Brodkey, H.C. Hershey: *Transport Phenomena. A Unified Approach* (McGraw-Hill, New York 1988)
- 27.30 R. Nitsche, D.F. Sargent, P. Wild: Crystal growth of quaternary 1₂246₄ chalcogenides by iodine vapor transport, J. Cryst. Growth **1**, 52–53 (1967)
- 27.31 O. Senthil Kumar, S. Soundeswaran, R. Dhanasekaran: Thermodynamic calculations and growth of ZnSe single crystals by chemical vapor transport technique, Cryst. Growth Des. **2**, 585–589 (2002)
- 27.32 C. Paorici, C. Pelosi, G. Attolini, G. Zuccalli: Closed-tube chemical-transport mechanisms in the Cd:Te:H:Cl:N system, J. Cryst. Growth **28**, 358–364 (1975)
- 27.33 C. Paorici, G. Attolini, C. Pelosi, G. Zuccalli: Chemical transport mechanisms in the Cd:Te:H:I system, J. Cryst. Growth **21**, 227–234 (1974)
- 27.34 C. Paorici, L. Zecchina: The productivity function for multi-reaction chemical vapor transport in closed tubes, J. Cryst. Growth **97**, 267–272 (1989)
- 27.35 C. Paorici, L. Zecchina: Note on the productivity function in closed tube chemical vapor transport, J. Cryst. Growth **83**, 453–455 (1987)
- 27.36 C. Paorici, C. Pelosi: Kinetics of vapor growth in the system CdS:I₂, J. Cryst. Growth **35**, 65–72 (1976)
- 27.37 R.C. Reid, J.M. Prausnitz, T.K. Sherwood: *The Properties of Gases and Liquids*, 3rd edn. (McGraw-Hill, New York 1977)
- 27.38 K. Böttcher, H. Hartmann, D. Siche: Computational study on the CVT of the ZnSe–I₂ material system, J. Cryst. Growth **224**, 195–203 (2001)
- 27.39 B.I. Nöläng, M.W. Richardson: The transport flux function – A new method for predicting the rate of chemical transport in closed systems: I. Theory, J. Cryst. Growth **34**, 198–204 (1976)
- 27.40 S. Fiechter, K. Eckert: Crystal growth of HfS₂ by chemical vapor transport with halogen (Cl, Br, I), J. Cryst. Growth **88**, 435–441 (1988)
- 27.41 O. Senthil Kumar, S. Soundeswaran, D. Kabiraj, D.K. Avasthi, R. Dhanasekaran: Effect of heat treatment and Si ion irradiation on ZnS_xSe_{1–x} single crystals grown by CVT method, J. Cryst. Growth **275**, e567–e570 (2005)
- 27.42 H. Ogawa, M. Nishio: Epitaxial growth and chemical vapor transport of ZnTe by closed-tube method, J. Cryst. Growth **52**, 263–268 (1981)
- 27.43 J.O. Hirschfelder, C.F. Curtiss, R.B. Bird: *Molecular Theory of Gases and Liquids* (Wiley, New York 1954)
- 27.44 F. Rosenberger, M.C. DeLong, J.M. Olson: Heat transfer and temperature oscillations in chemical vapor transport crystal growth I, J. Cryst. Growth **19**, 317–328 (1973)
- 27.45 H. Watanabe, T. Nisi-iinaga, T. Arezume: Vapor transport equations for III–V compound semiconductors, J. Cryst. Growth **17**, 183–188 (1972)
- 27.46 M. Nishio, H. Ogawa: Chemical vapor transport in the ZnTe–HCl closed-tube system and its thermodynamic analysis, J. Cryst. Growth **78**, 218–226 (1986)
- 27.47 M. Lenz, R. Gruehn: Developments in measuring and calculating chemical vapor transport phenomena demonstrated on Cr, Mo, W, and their compounds, Chem. Rev. **97**, 2967–2994 (1997)
- 27.48 Y.-G. Sha, C.-H. Su, F.R. Sofrari: Thermodynamic analysis and mass flux of the HgZnTe–HgI₂ chemical vapor transport system, J. Cryst. Growth **131**, 574–588 (1993)
- 27.49 D.W. Mackowski, V.R. Rao, R.W. Knight: Effect of solid phase heat transfer and wall deposition on crystal growth in physical vapor transport ampoules, J. Cryst. Growth **165**, 323–334 (1996)
- 27.50 A. Nadarajahk, F. Rosenberger, D. Alexander, J. Iwan: Effects of buoyancy-driven flow and thermal boundary conditions on physical vapor transport, J. Cryst. Growth **118**, 49–59 (1992)
- 27.51 M. Shiloh, J. Gutman: Growth of ZnO single crystals by chemical vapor transport, J. Cryst. Growth **11**, 105–109 (1971)
- 27.52 H. Hartmann, R. Mach, B. Selle: *Current Topics in Material Science*, Vol. 9, ed. by E. Kaldis (North-Holland, Amsterdam 1982)
- 27.53 K. Böttcher, H. Hartmann: Zinc selenide single crystal growth by chemical transport reactions, J. Cryst. Growth **146**, 53–58 (1995)
- 27.54 K. Mochizuki: Vapor growth and stoichiometry control of zinc sulfo-selenide, J. Cryst. Growth **58**, 87–94 (1982)
- 27.55 O. Senthil Kumar: Growth of pure and doped single crystals and nanocrystals of ZnSe and ZnS_xSe_{1–x} semiconductors by chemical vapor transport and their characterization, Ph.D. Thesis (Anna University, Chennai 2005)

- 27.56 M.J. Tafreshi: Growth of II–VI. I–III–VI₂ and CdIn₂S₄ single crystals by CVT method and their characterizations, Ph.D. Thesis (Anna University, Chennai 1996)
- 27.57 M.J. Tafreshi, K. Balakrishnan, R. Dhanasekaran: Growth and characterization of pentenary Cu_{0.5}Ag_{0.5}InS₂ crystals grown by chemical vapor transport technique, *Mater. Res. Bull.* **30**, 1371–1377 (1995)
- 27.58 M.J. Tafreshi, K. Balakrishnan, R. Dhanasekaran: Micromorphological studies on the ZnSe single crystals grown by chemical vapor transport technique, *J. Mater. Sci.* **32**, 3517–3521 (1997)
- 27.59 W. Palosz: Vapor transport of ZnO in closed ampoules, *J. Cryst. Growth* **286**, 42–49 (2006)
- 27.60 D.W. Greenwell, B.L. Markham, F. Rosenberger: Numerical modeling of diffusive physical vapor transport in cylindrical ampoules, *J. Cryst. Growth* **51**, 413–425 (1981)
- 27.61 J.N. Butler, R.S. Brokaw: Thermal conductivity of gas mixtures in chemical equilibrium, *J. Chem. Phys.* **26**, 1636–1645 (1957)
- 27.62 G.T. Kim, J.T. Lin, O.C. Jones, M.E. Glicksman, W.M.B. Duval, N.B. Singh: Effects of convection during the physical vapor transport process: application of laser Doppler velocimetry, *J. Cryst. Growth* **165**, 429–437 (1996)
- 27.63 B.M. Bulakh, G.S. Pekar: The CdS crystal synthesis from vapors of the component elements, *J. Cryst. Growth* **8**, 99–103 (1971)
- 27.64 J.M. Ntep, S. Said Hassani, A. Lusson, A. Tromson-Carli, D. Ballutaud, G. Didier, R. Triboulet: ZnO growth by chemical vapor transport, *J. Cryst. Growth* **207**, 30–34 (1999)
- 27.65 G.R. Patzke, S. Locmelis, R. Wartchow, M. Binnewies: Chemical transport phenomena in the ZnO–Ga₂O₃ system, *J. Cryst. Growth* **203**, 141–148 (1999)
- 27.66 H. Wiedemeier, W. Palosz: Physical vapor transport of cadmium telluride in closed ampoules, *J. Cryst. Growth* **96**, 933–945 (1989)
- 27.67 T. Yamauchi, Y. Takahara, M. Naitoh, N. Narita: Growth mechanism of ZnSe single crystal by chemical vapor transport method, *Physica B: Condens. Matter* **376/377**, 778–781 (2006)
- 27.68 C.S. Fang, Q.T. Gu, J.Q. Wei, Q.W. Pan, W. Shi, J.Y. Wang: Growth of ZnSe single crystals, *J. Cryst. Growth* **209**, 542–546 (2000)
- 27.69 W.N. Holton, R.K. Watts, R.D. Stinedurf: Synthesis and melt growth of doped ZnSe, *J. Cryst. Growth* **6**, 97–100 (1969)
- 27.70 R. Nishizawa, K. Itoh, Y. Okuno, F. Sakurai: Blue light emission from ZnSe p–n junctions, *J. Appl. Phys.* **57**, 2210–2214 (1985)
- 27.71 N. Krasnov, Y. Purtov, F. Vaksman, V.V. Serdyuk: ZnSe blue-light-emitting diode, *J. Cryst. Growth* **125**, 373–374 (1995)
- 27.72 R. Nitsche: The growth of single crystals of binary and ternary chalcogenides by chemical transport reactions, *J. Phys. Chem. Solids* **17**, 163–165 (1960)
- 27.73 P. Rudolph, K. Umetsu, H.J. Koh, T. Fukuda: Growth of twin reduced ZnSe bulk crystals from the melt, *J. Cryst. Growth* **143**, 359–361 (1994)
- 27.74 H. Unuma, M. Higuchi, Y. Yamakawa, K. Kodaira, Y. Okano, K. Hoshikawa, T. Fukuda, T. Koyama: Liquid encapsulated flux growth of ZnSe single crystals from Se solvent, *Jpn. J. Appl. Phys.* **31**, L383–L384 (1992)
- 27.75 H.H. Woodbury, R.B. Hall: Diffusion of the chalcogens in the II–VI compounds, *Phys. Rev.* **157**, 641–645 (1967)
- 27.76 M. Shone, B. Greenberg, M. Kaczinski: Vertical zone growth and characterization of undoped and Na, P and Mn doped ZnSe, *J. Cryst. Growth* **86**, 132–137 (1988)
- 27.77 R.N. Bhargava: Materials growth and its impact on devices from wide band gap II–VI compounds, *J. Cryst. Growth* **86**, 873–879 (1990)
- 27.78 E. Kaldis: Crystal growth and growth rates of CdS by sublimation and chemical transport, *J. Phys. Chem. Solids* **26**, 1701–1732 (1965)
- 27.79 S. Fujita, H. Mimoto, H. Takebe, T. Noguchi: ZnO-based thin films synthesized by atmospheric pressure mist chemical vapor deposition, *J. Cryst. Growth* **47**, 326–334 (1979)
- 27.80 E. Kaldis: The chemistry of imperfect crystals, preparation, purification, crystal growth and phase theory by F.A. Kruger, *J. Cryst. Growth* **24**, 24–39 (1974)
- 27.81 K. Böttcher, H. Hartmann: Zinc selenide single crystal growth by chemical transport reactions, *J. Cryst. Growth* **146**, 53–58 (1995)
- 27.82 A.A. Simanovskii, N.N. Sheftal, E.I. Givargizov: Effect of crystallization condition on the morphology of ZnSe crystals, *Growth Cryst.* **9**, 225–229 (1975)
- 27.83 I. Nakada, E. Bauser: Origin of multiple steps in vapor growth of NbSe₄I_{0.33}, *J. Cryst. Growth* **96**, 243–257 (1989)
- 27.84 A.A. Simanovskii, N.N. Sheftal, E. Givargizov: Production of ZnSe single crystals via transport reaction, *Growth Cryst.* **7**, 224–229 (1969)
- 27.85 M.H.J. Hottenhuis, C.B. Lucasius: The influence of impurities on crystal growth: In situ observation of the (010) face of potassium hydrogen phthalate, *J. Cryst. Growth* **78**, 379–388 (1986)
- 27.86 Z. Sobiesierski, I.M. Dharmadasa, R.H. Williams: Photoluminescence as a probe of semiconductor surfaces: CdTe and CdS, *J. Cryst. Growth* **101**, 599–602 (1990)
- 27.87 W.E. Metcalf, R.H. Fahrig: High-pressure, high-temperature growth of cadmium sulfide crystals, *J. Electrochem. Soc.* **105**, 719–723 (1958)
- 27.88 M. Rubenstein: Solution growth of some II–VI compounds using tin as a solvent, *J. Cryst. Growth* **3**, 309–312 (1968)

- 27.89 C. Paorici: Iodine-doped hollow CdS crystals, *J. Cryst. Growth* **5**, 315–316 (1969)
- 27.90 E. Kaldis: Crystal growth and growth rates of CdS by sublimation and chemical transport, *J. Cryst. Growth* **5**, 376–390 (1969)
- 27.91 K. Matsumoto, K. Takagi, S. Kaneko: Kinetics of the cubic to hexagonal transformation of cadmium sulfide, *J. Electrochem. Soc.* **62**, 389–393 (1983)
- 27.92 G. Attolini, C. Paorici, L. Zanoti: Growth of cadmium sulphide single crystals by vapor-phase hydrogen transport, *J. Cryst. Growth* **56**, 254–258 (1982)
- 27.93 G. Attolini, C. Paorici, L. Zecchina: Productivity function for multireactional CVT and its application to iodine transport of cadmium sulphide, *J. Cryst. Growth* **99**, 731–736 (1990)
- 27.94 M.J. Tafreshi, K. Balakrishnan, R. Dhanasekaran: Growth, electrical conductivity and microindentation studies of CuInS_2 single crystals, *J. Mater. Sci. Mater. Electron.* **7**, 243–245 (1996)
- 27.95 S. Itoh, K. Nakano, A. Ishibashi: Raman studies of phosphorus-doped ZnSe, *J. Cryst. Growth* **214/215**, 1029–1034 (2000)
- 27.96 E. Chimczak, J.W. Allen: Energy transfer in the electroluminescence of ZnS:Mn and ZnSe:Mn driven by short voltage pulses, *J. Phys. D: Appl. Phys.* **18**, 951–957 (1985)
- 27.97 G. Jones, J. Woods: The luminescence of manganese-doped zinc selenide, *J. Phys. D: Appl. Phys.* **6**, 1640–1651 (1973)
- 27.98 C. Jin, B. Zhang, Z. Ling, J. Wang, X. Hou, Y. Segawa, X. Wang: Growth and optical characterization of diluted magnetic semiconductor $\text{Zn}_{1-x}\text{Mn}_x\text{Se}/\text{ZnSe}$ strained-layer superlattices, *J. Appl. Phys.* **81**, 5148–5153 (1997)
- 27.99 J.K. Furdyna, N. Samranth: Magnetic properties of diluted magnetic semiconductors: A review, *J. Appl. Phys.* **61**, 3526–3593 (1987)
- 27.100 J.F. Suyver, J.J. Kelly, A. Meijerink: Temperature-induced line broadening, line narrowing and line shift in the luminescence of nanocrystalline ZnS:Mn^{2+} , *J. Lumin.* **104**, 187–196 (2003)
- 27.101 H. Heulings IV, X. Huang, J. Li, T. Yuen, C.L. Lin: Mn-substituted inorganic-organic hybrid materials based on ZnSe: Nanostructures that may lead to magnetic semiconductors with a strong quantum confinement effect, *Nano Lett.* **1**, 521–525 (2001)
- 27.102 C. Wang, W.X. Zhang, X.F. Qian, X.M. Zhang, Y. Xie, Y.T. Qian: An aqueous approach to ZnSe and CdSe semiconductor nanocrystals, *Mater. Chem. Phys.* **60**, 99–102 (1999)
- 27.103 C. De Mello Donega, A.A. Bol, A. Meijerink: Time-resolved luminescence of ZnS:Mn^{2+} nanocrystals, *J. Lumin.* **96**, 87–93 (2002)
- 27.104 D. Sarigiannis, J.D. Peck, G. Kioseoglou, A. Petrou, T.J. Mountziaris: Characterization of vapor-phase-grown ZnSe nanoparticles, *Appl. Phys. Lett.* **80**, 4024–4027 (2002)
- 27.105 X.T. Zhang, K.M. Ip, Z. Liu, Y.P. Leung, Q. Li, S.K. Hark: Structure and photoluminescence of ZnSe nanoribbons grown by metal organic chemical vapor deposition, *Appl. Phys. Lett.* **84**, 2641–2647 (2004)
- 27.106 S.K. Bera, S. Choudhuri, A.K. Pal: Electron transport properties of CdTe nanocrystals in $\text{SiO}_2/\text{CdTe}/\text{SiO}_2$ thin film structures, *Thin Solid Films* **415**, 68–77 (2002)
- 27.107 A.A. Lipovskii, E.V. Kolobkova, V.D. Petrikov: Formation of II–VI nanocrystals in a novel phosphate glass, *J. Cryst. Growth* **184/185**, 365–369 (1998)
- 27.108 P. Yang, M.K. Lu, C.F. Song, G.J. Zhou, Z.P. Ai, D. Xu, D.R. Yuan, X.F. Cheng: Strong visible-light emission of ZnS nanocrystals embedded in sol-gel silica xerogel, *Mater. Sci. Eng. B* **97**, 149–153 (2003)
- 27.109 P.A. Gonzalez Beerman, B.R. McGarvey, S. Muralidharan, R.C.W. Sung: EPR spectra of Mn^{2+} -doped ZnS quantum dots, *Chem. Mater.* **16**, 915–918 (2004)
- 27.110 N. Taghavinia, T. Yao: ZnS nanocrystals embedded in SiO_2 matrix, *Physica E* **21**, 96–102 (2004)
- 27.111 K. Manzoor, S.R. Vadera, N. Kumar, T.R.N. Kutty: Synthesis and photoluminescent properties of ZnS nanocrystals doped with copper and halogen, *Mater. Chem. Phys.* **82**, 718–725 (2003)
- 27.112 C. Liu, J. Liu, W. Xu: The g-factor-shift in ZnS:Mn^{2+} nanocrystals/pyrex glasses composites, *Mater. Sci. Eng. B* **75**, 78–81 (2000)
- 27.113 K. Kawano, R. Nakata, M. Sumita: Electron spin resonance study of laser-annealed $(\text{Zn,Mn})\text{O}$ ceramics, *Appl. Phys. Lett.* **58**, 1742–1745 (1991)
- 27.114 M. Tanaka: Do triboluminescence spectra really show a spectral shift relative to photoluminescence spectra?, *J. Lumin.* **100**, 115–126 (2002)
- 27.115 V.J. Leppert, S. Mahamuni, N.R. Kumbhojkar, S.H. Risbud: Structural and optical characteristics of ZnSe nanocrystals synthesized in the presence of a polymer capping agent, *Mater. Sci. Eng. B* **52**, 89–92 (1998)
- 27.116 R. Nitsche, H.U. Bölsterli, M. Lichtensteiger: Crystal growth by chemical transport reactions I. Binary, ternary, and mixed-crystal chalcogenides, *J. Phys. Chem. Solids* **21**, 199–205 (1961)
- 27.117 W.N. Honeyman, K.H. Wilkinson: Growth and properties of single crystals of group I–III–VI₂ ternary semiconductors, *J. Phys. D: Appl. Phys.* **4**, 1182–1185 (1971)
- 27.118 I. Aksenov, K. Sato: Visible photoluminescence of Zn-doped CuAlS_2 , *Appl. Phys. Lett.* **61**, 1063–1066 (1992)
- 27.119 O. Madelung, V. Rössler, M. Schulz: Optical properties of I–III–VI₂ compounds, *Phys. Status Solidi* **115**, K113–K118 (1989)
- 27.120 S. Shirakata, I. Aksenov, K. Sato, S. Isomura: Photoluminescence studies in CuAlS_2 crystals, *Jpn. J. Appl. Phys.* **31**, L1071–L1074 (1992)

- 27.121 I. Aksenov, T. Yasuda, Y. Seawa, K. Sato: Violet photoluminescence in Zn-doped CuAlS₂, J. Appl. Phys **74**, 2106–2110 (1993)
- 27.122 I. Aksenov, T. Yasuda, T. Kai, N. Nishikawa, T. Ohgoh, K. Sato: Visible photoluminescence in undoped and Zn-doped CuAlS₂, Jpn. J. Appl. Phys **32**, 1068–1072 (1993)
- 27.123 N. Kuroishi, K. Mochizuki, K. Kimoto: Surface oxidation of CVT-grown CuAlSe₂, Mater. Lett. **57**, 1949–1954 (2003)
- 27.124 S. Chichibu, M. Shishikura, J. Ino, S. Matsumoto: Electrical and optical properties of CuAlSe₂ grown by iodine chemical vapor transport, J. Appl. Phys **70**, 1648–1654 (1991)
- 27.125 M.-S. Jin, C.-S. Yoon, H.-G. Kim, W.-T. Kim: Growth and characterization of CuAlSe₂ single crystals, J. Korean Phys. Soc. **26**, 628 (1993)
- 27.126 P. Prabukanthan, R. Dhanasekaran: Growth of CuInTe₂ single crystals by iodine transport and their characterization, Mater. Res. Bull. **43**, 1996–2004 (2008)
- 27.127 E. Gombia, F. Leccabue, C. Pelosi, D. Seuret: Vapor growth, thermodynamical study and characterization of CuInTe₂ and CuGaTe₂ single crystals, J. Cryst. Growth **65**, 391–396 (1983)
- 27.128 P.W. Yu, D.L. Downing, Y.S. Park: Electrical properties of CuGaS₂ single crystals, J. Appl. Phys. **45**, 5283 (1974)
- 27.129 S. Shirakata, K. Saiki, S. Isomura: Excitonic photoluminescence in CuGaS₂ crystals, J. Appl. Phys. **68**, 291–297 (1990)
- 27.130 P. Prabukanthan, R. Dhanasekaran: Growth of CuGaS₂ single crystal by chemical vapor transport and characterization, Cryst. Growth Des. **7**, 618–623 (2007)
- 27.131 S. Chichibu, S. Shirakata, A. Ogawa, R. Sudo, M. Uchida, Y. Harada, T. Wakiyama, M. Shishikura, S. Matsumoto, S. Isomura: Growth of Cu(Al_xGa_{1-x})S₂ pentenary alloy crystals by iodine chemical vapor transport method, J. Cryst. Growth **140**, 388–397 (1994)
- 27.132 K. Sugiyama, K. Mori, H. Miyake: Growth of epitaxy layer of CuAlS₂ on CuGaS₂ and characterization, J. Cryst. Growth **113**, 390–395 (1991)
- 27.133 P. Prabukanthan, R. Dhanasekaran: Influence of Mn doping on CuGaS₂ single crystals grown by CVT method and their characterization, J. Phys. D: Appl. Phys. **41**, 115102 (2008)
- 27.134 S. Tanaka, S. Kawami, H. Kobayashi, H. Sasakura: Luminescence in CuGaS_{2-2x}Se_{2x} mixed crystals grown by chemical vapor transport, J. Phys. Chem. Solids **38**, 680–681 (1977)
- 27.135 K. Sato, K. Tanaka, K. Ishii, S. Matsuda: Crystal growth and photoluminescence studies in Fe-doped single crystals of CuAl_{1-x}Ga_xS₂, J. Cryst. Growth **95**, 772–775 (1990)
- 27.136 P. Prabukanthan, R. Dhanasekaran: Stoichiometric single crystal growth of AgGaS₂ by iodine transport method and characterization, Cryst. Res. Technol. **43**, 1292–1296 (2008)
- 27.137 Y. Noda, T. Kurasawa, N. Sugai, Y. Furukawa, K. Masumoto: Growth of AgGaS₂ single crystals by chemical transport reaction, J. Cryst. Growth **99**, 757–761 (1990)
- 27.138 K.M. Nigge, F.P. Baumgartner, E. Bucher: CVT-growth of AgGaSe₂ single crystals: Electrical and photoluminescence properties, Sol. Energy Mater. Sol. Cells **43**, 335–343 (1996)
- 27.139 R. Fornari: Vapor phase epitaxial growth and properties of III-nitride materials, Proc. Int. School Cryst. Growth Technol. Important Electron. Mater., ed. by K. Byrappa (2003) pp. 367–390
- 27.140 H.P. Maruska, J. Tietjen: The preparation and properties of vapor deposited single crystalline GaN, J. Appl. Phys. Lett. **15**, 327–329 (1969)
- 27.141 M. Illegems: Vapor epitaxy of gallium nitride, J. Cryst. Growth **13/14**, 360–364 (1972)
- 27.142 W. Seifert, G. Fitzl, E. Butter: Study on the growth rate in VPE of GaN, J. Cryst. Growth **52**, 257–262 (1981)
- 27.143 R.J. Molnar, W. Gotz, L.T. Romano, N.M. Johnson: Growth of gallium nitride by hydride vapor-phase epitaxy, J. Cryst. Growth **178**, 147–156 (1997)
- 27.144 H. Lee, J.S. Harris: Observation of superstructure in high-quality pseudomorphic films of NiAl grown on GaAs, J. Cryst. Growth **169**, 689–693 (1996)
- 27.145 F. Dwikusuma, J. Mayer, T.F. Kuech: Nucleation and initial growth kinetics of GaN on sapphire substrate by hydride vapor-phase epitaxy, J. Cryst. Growth **258**, 65–74 (2003)
- 27.146 A. Shintani, S. Minagawa: Kinetics of the epitaxial growth of GaN using Ga, HCl and NH₃, J. Cryst. Growth **22**, 1–5 (1974)
- 27.147 G. Jacob, M. Boulou, M. Furtado: Effect of growth parameters on the properties of GaN:Zn epilayers, J. Cryst. Growth **42**, 136–143 (1977)
- 27.148 R. Fornari, M. Bosi, N. Armani, G. Attolini, C. Ferrari, C. Pelosi, G. Salviati: Hydride vapor phase epitaxy growth and characterisation of GaN layers, Mater. Sci. Eng. B **79**, 159–164 (2001)
- 27.149 X. Xu, R.P. Vaudo, C. Loria, A. Salant, G.R. Brandes, J. Chaudhuri: Growth and characterization of low defect GaN by hydride vapor-phase epitaxy, J. Cryst. Growth **246**, 223–229 (2002)
- 27.150 D.W. Shaw: *Mechanisms in Vapor Phase Epitaxy in Crystal Growth*, ed. by C.H.L. Goodman (Plenum Press, New York 1974) p. 25
- 27.151 G.B. Stringfellow: Fundamental aspects of vapor growth and epitaxy, J. Cryst. Growth **115**, 1–11 (1991)
- 27.152 G.B. Stringfellow: Fundamentals of thin film growth, J. Cryst. Growth **137**, 212–223 (1994)
- 27.153 E. Varadarajan, J. Kumar, R. Dhanasekaran: Fabrication of vapor-phase epitaxy system for the growth of gallium nitride, Proc. 6th Int. Conf. Optoelectron. Photonics **1**, 236–237 (2002)

- 27.154 I. Akasaki, H. Amano: Widegap column-III nitride semiconductors for UV/blue light emitting devices, *J. Electrochem. Soc.* **141**, 2266–2269 (1994)
- 27.155 S. Nakamura, M. Senoh, S. Nagahama, N. Iwasa, Y. Yamada, T. Matsushita, Y. Sugimoto, H. Kiyoku: Large conductance anisotropy in a novel two-dimensional electron system grown on vicinal (111) B GaAs with multiatomic steps, *Appl. Phys. Lett.* **69**, 3034–3041 (1996)
- 27.156 I. Akasaki, S. Sota, H. Sakai, T. Tanaka, M. Koike, H. Amano: Shortest wavelength semiconductor laser diode, *Electron. Lett.* **32**, 1105–1106 (1996)
- 27.157 S.J. Pearton, J.C. Zolper, R.J. Shul, F. Ren: GaN: Processing, defects, and devices, *J. Appl. Phys.* **86**, 1–6 (1999)
- 27.158 H. Morkoc: Comprehensive characterization of hydride VPE grown GaN layers and templates, *Mater. Sci. Eng. R* **33**, 135–207 (2001)
- 27.159 R. Fornari, M. Bosi, D. Bersani, G. Attolini, P.P. Lot-tici, C. Pelosi: Characterization of HVPE GaN layers by atomic force microscopy and Raman spectroscopy, *Semicond. Sci. Technol.* **16**, 776–782 (2001)
- 27.160 E. Varadarajan, P. Puviasu, J. Kumar, R. Dhanasekaran: On the chloride vapor-phase epitaxy growth of GaN and its characterization, *J. Cryst. Growth* **260**, 43–49 (2004)
- 27.161 E. Varadarajan, J. Kumar, R. Dhanasekaran: Growth of GaN films by chloride vapor phase epitaxy, *J. Cryst. Growth* **268**, 475–477 (2004)
- 27.162 E. Varadarajan, R. Dhanasekaran, D.K. Avasthi, J. Kumar: Structural, optical and electrical properties of high energy irradiated Cl-VPE grown gallium nitride, *Mater. Sci. Eng. B* **129**, 121–125 (2006)
- 27.163 T.I. Shin, H.J. Lee, W.Y. Song, H. Kim, S.-W. Kim, D.H. Yoon: High quality GaN nanowires synthesized from Ga₂O₃ with graphite powder using VPE method, *Colloids. Surf. A* **313/314**, 52–55 (2008)

Epitaxial

Part E

Part E Epitaxial Growth and Thin Films

**28 Epitaxial Growth of Silicon Carbide
by Chemical Vapor Deposition**

Ishwara B. Bhat, Troy, USA

**29 Liquid-Phase Electroepitaxy
of Semiconductors**

Sadik Dost, Victoria, Canada

**30 Epitaxial Lateral Overgrowth
of Semiconductors**

Zbigniew R. Zytkiewicz, Warszawa, Poland

31 Liquid-Phase Epitaxy of Advanced Materials

Christine F. Klemenz Rivenbark, Titusville, USA

32 Molecular-Beam Epitaxial Growth of HgCdTe

James W. Garland, Bolingbrook, USA
Sivalingam Sivananthan, Chicago, USA

**33 Metalorganic Vapor-Phase Epitaxy of Diluted
Nitrides and Arsenide Quantum Dots**

Udo W. Pohl, Berlin, Germany

**34 Formation of SiGe Heterostructures
and Their Properties**

Yasuhiro Shiraki, Tokyo, Japan
Akira Sakai, Osaka, Japan

**35 Plasma Energetics in Pulsed Laser
and Pulsed Electron Deposition**

Mikhail D. Strikovski, Beltsville, USA
Jeonggoo Kim, Beltsville, USA
Solomon H. Kolagani, Beltsville, USA

28. Epitaxial Growth of Silicon Carbide by Chemical Vapor Deposition

Ishwara B. Bhat

The properties of silicon carbide materials are first reviewed, with special emphasis on properties related to power device applications. Epitaxial growth methods for SiC are then discussed with emphasis on recent results for epitaxial growth by the hot-wall chemical vapor deposition method. The growth mechanism for maintaining the polytype, namely *step-controlled epitaxy*, is discussed. Also described is the selective epitaxial growth carried out on SiC at the author's laboratory, including some unpublished work.

28.1 Polytypes of Silicon Carbide	941
28.2 Defects in SiC	942
28.2.1 Micropipes	942
28.2.2 Screw Dislocations	942
28.2.3 Growth Pits and Triangular Inclusions	943
28.3 Epitaxial Growth of Silicon Carbide	944
28.3.1 Substrates for Silicon Carbide Growth	944

28.3.2 How to Control the Polytypes in SiC Homoepitaxy	945
28.3.3 SiC Epitaxial Growth Techniques ...	946
28.3.4 Chemical Vapor Deposition	946

28.4 Epitaxial Growth on Patterned Substrates	952
28.4.1 Selective Epitaxial Growth	953
28.4.2 Selective Epitaxial Growth of 4H-SiC Using TaC Mask	954
28.4.3 Orientation Dependence of SiC Selective Growth	956
28.4.4 Effects of Mask-to-Window Ratio ($M:W$) on SiC Selective Growth	957
28.4.5 Effects of C/Si Ratio on SiC Selective Growth	959
28.4.6 Mechanism of Selective Etching and Effect of Atomic Hydrogen	960
28.4.7 Fabrication of 4H-SiC p-n Junction Diodes Using Selective Growth	960
28.5 Conclusions	961
References	961

Advanced Si technology has brought about the very large-scale integrated circuits (VLSI) that are available today, and still further development of Si VLSI technology is expected. However, Si is approaching its performance limit due to intrinsic material properties, especially in applications related to high-power, high-temperature, and high-frequency devices. Thus, the development of new materials and technologies useful in this area is crucial.

SiC is an extremely hard and inert IV-IV compound material having a lot of attractive features, in particular electrical properties which are suitable for advanced electronic devices that cannot be achieved using Si. An appreciation of the potential of SiC for electronics can be gained by examining Table 28.1, which compares the relevant material properties of

SiC with Si and GaAs. As can be seen, SiC has large bandgaps (2.4–3.3 eV) [28.1–4], high breakdown fields ($\approx 3 \times 10^6$ V/cm) [28.5], high saturation electron velocities (2.7×10^6 cm/s) [28.6, 7], and high thermal conductivity (3.2–4.9 W/(cm K)) [28.8]. Owing to these excellent electrical and physical properties, SiC has been regarded as able to function well under high-temperature, high-power, and high-radiation conditions at which conventional semiconductors cannot perform adequately. This ability is expected to enable significant improvements for a wide variety of applications and systems. These applications range from greatly improved high-voltage switching for energy savings in public electric power distribution and electric vehicles, to more powerful microwave electronics for radar and communications, to sensors and controls for cleaner-

Table 28.1 Physical properties of 3C-, 6H-, 4H-SiC, Si, and GaAs at 300 K [28.1]

Properties	3C-SiC	6H-SiC	4H-SiC	Si	GaAs
Crystal structure	ZB	Hex.	Hex.	Dia.	ZB
Lattice constant (Å)	4.36	$a = 3.09$ $c = 15.12$	$a = 3.09$ $c = 10.08$	5.43	5.65
Band structure	Indirect	Indirect	Indirect	Indirect	Direct
Bandgap (eV)	2.4	3.0	3.3	1.11	1.43
Electron mobility ($\text{cm}^2/(\text{V s})$)	900	350 ^a 50 ^b	720 ^a 650 ^b	1400	8500
Breakdown field 10^6 (V/cm)	1.2	2.0	2.4	0.3	0.4
Thermal conductivity (W/(cm K))	3.2	4.9	3.7	1.5	0.5
Saturation drift velocity $\times 10^7$ (cm/s)	2.0	2.0	2.0	1	2
Dielectric constant	9.6	9.7	10	11.8	12.8

^a mobility along a -axis, ^b mobility along c -axis

burning more fuel-efficient jet aircraft and automobile engines.

Theoretical simulations have indicated that SiC power metal-oxide semiconductor field-effect transistors (MOSFETs) and diode rectifiers would operate over higher voltage and temperature ranges, have superior switching characteristics, and yet have die sizes nearly 80% smaller than correspondingly rated silicon-based devices [28.9]. Hence, realization of practical SiC power devices will greatly impact the power electronics field.

The development of SiC for electronic applications has been a subject of study for more than 40 years. During the early years, a significant amount of fundamental research was performed, but the development of commercially viable SiC-based devices was limited by the low quality of bulk materials and inadequate epitaxial process. During the late 1980s, significant improvements in bulk and epitaxial process enabled commercial availability of device-quality wafers from Cree Research, Inc. Together, these factors have enabled the fabrication of higher quality device structures and have generated increased research activities in SiC electronic devices. A large number of devices, such as high-voltage Schottky rectifiers [28.10, 11], power metal-oxide semiconductor field-effect transistors [28.9], microwave and millimeter-wave devices [28.12], and high-temperature, radiation-resistant junction FETs (JFETs) [28.13], have been fabricated. However, SiC devices with quality sufficient for large-scale industrial applications were not available until

recently. This is primarily due to the fact that the crystal growth and device fabrication technologies for SiC were not sufficiently developed to the degree required for reliable incorporation into electronic systems. Recent commercial availability of SiC Schottky diodes (up to 1200 V and 20 A) from Infineon Technology AG and Cree, Inc., should accelerate the introduction of SiC in commercial systems [28.14]. However, bipolar and power MOSFETs remain commercially elusive.

As for SiC epitaxial growth, homoepitaxial growth of SiC epitaxial layers on SiC substrates has been achieved by so-called *step-controlled growth* [28.15]. The quality of the epilayer and controllability of growth are improving with the improvement of the substrate quality and growth technology. However, abundant defects, including micropipes, screw dislocations, growth pits, step bunching, and 3C inclusions can still be found even in today’s commercial wafers. Among these, growth pits, step bunching, and 3C inclusions can be caused by an unoptimized growth process while others are mainly due to defects propagated from the substrate. It is believed that these structural and surface morphological features are the major cause of poor device yield and premature device failure. Thus, these issues have to be addressed in order to advance the widespread commercial introduction of SiC-based systems, especially for high-power applications.

In this chapter, some basic properties of SiC that are relevant for good epitaxial growth are described. Recent progress on thick epitaxial growth as well as on selective growth of SiC will also be described.

28.1 Polytypes of Silicon Carbide

In this section, a concise review of the physical and electrical properties of SiC are presented. This is by no means complete, and further information can be found in the references of this chapter.

SiC has a large number of crystal structures (more than 200) [28.16], which are called polytypes. Considering close-packed structure, each layer of atoms along the c -axis can occupy three different positions, denoted by A, B, and C (Fig. 28.1). For SiC, a Si–C pair should be considered as one unit for atoms in close-packed structure. Variation of occupation sites along the c -axis brings about different crystal structures. They are usually represented by Ramsdell notation, which is denoted by the number of layers in the unit cell and a crystal system (C for cubic, H for hexagonal,

R for rhombohedral). From ABCABCABC... stacking, we generate the 3C-SiC lattice, and from ABABAB... stacking, we generate the 2H-SiC lattice. Depending on the stacking order, the bonding between Si and C atoms in adjacent bilayer planes is of either zincblende (cubic) or wurtzite (hexagonal) nature. Zincblende bonds are rotated 60° with respect to nearest neighbors while hexagonal bonds are mirror images (Fig. 28.2). Each type of bond provides a slightly altered atomic environment, making some lattice sites inequivalent in polytypes. This also results in different ionization energy for dopants when substituted at these two different sites. Bonds in 3C-SiC are all cubic whereas bonds in 2H-SiC are all hexagonal. All of the other polytypes are mixtures of the fundamental zincblende and wurtzite bonds. Some common hexagonal polytypes with more

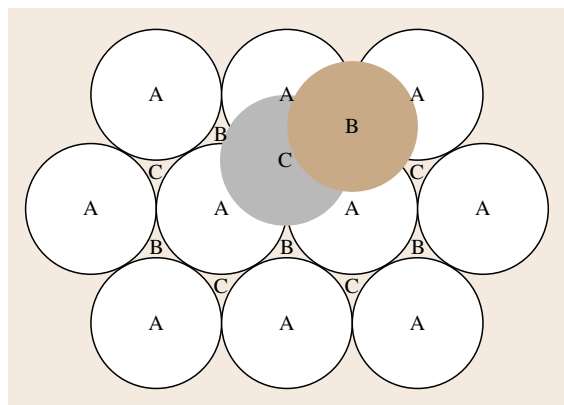


Fig. 28.1 Hexagonal close-packed structure

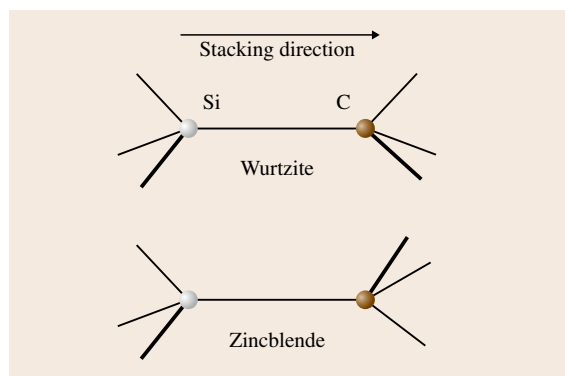


Fig. 28.2 Wurtzite bonding and zincblende bonding between Si and C atoms in adjacent planes. The three tetrahedral bonds are rotated 60° in the cubic case and mirror images in the hexagonal phase

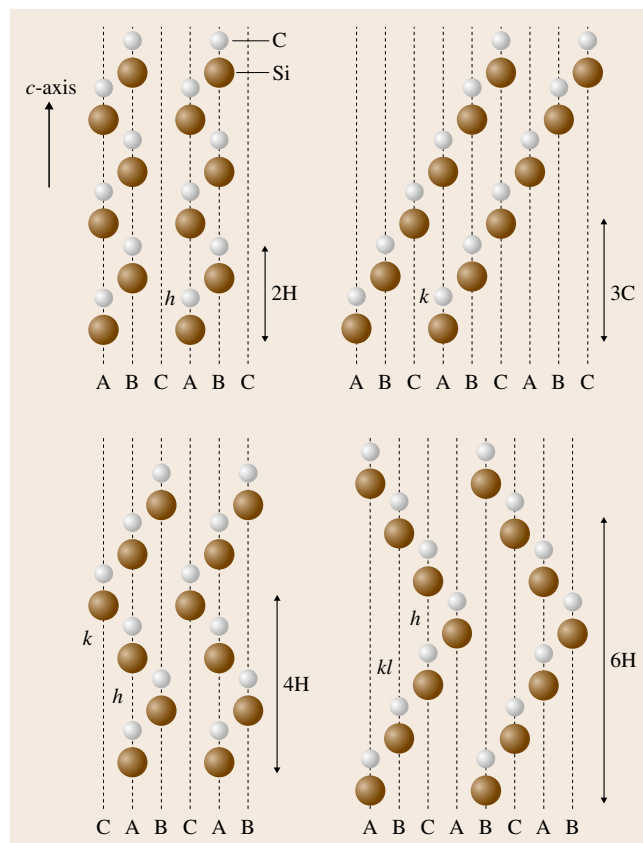


Fig. 28.3 Stacking sequences of different SiC polytypes projected on the $[11\bar{2}0]$ plane. Examples of hexagon-stacked bilayers are labeled with h , while cubic-stacked bilayers are labeled with k

complex stacking sequences are 4H-SiC and 6H-SiC. 4H-SiC is composed equally of cubic and hexagonal bonds, whereas 6H-SiC is two-thirds cubic and one-third hexagonal. Despite the cubic elements, each has overall hexagonal crystal symmetry. The family of hexagonal and rhombohedral polytype is sometimes referred to as α -SiC, whereas 3C-SiC is referred to as β -SiC.

Figure 28.3 shows the stacking sequences for 3C-, 4H-, and 6H-SiC [28.16]. As can be seen, cubic SiC has a lattice constant of $a = 0.4349$ nm at room temperature. For hexagonal SiC, a is approximately 0.3080 nm for all polytypes whereas c varies with the number of layers in the unit cell, one single atomic layer being approximately 0.252 nm for all polytypes.

Why are there so many polytypes? The simplest level of understanding is that the formation energy difference between different polytypes is small. As

calculated by Park et al. [28.17], the total energy difference for various polytypes is within 4.3 meV/atom. Hence, the temperature and other crystal growth conditions significantly affect the stability of the polytype. The occurrence probability of polytypes depends on the temperature. Generally, 3C-SiC is stable at temperature below 1900 °C, and 6H-SiC is stable at temperature above 1900 °C. A 3C-to-6H solid-phase transformation has been observed at temperature above 2150 °C [28.18, 19]. 4H-SiC also sometimes occurs in the high-temperature region, but the probability is low compared with 6H-SiC [28.20]. The 2H polytype is typically unstable because it can transform to a mixture of 3C and 6H polytypes at typical crystal growth temperatures [28.21]. Powell and Will have reported that the phase transformation away from 2H polytype can happen at temperatures as low as 400 °C [28.22].

28.2 Defects in SiC

Quality of materials is essential to the performance of the devices. As the development of devices proceed, demands on the quality of the bulk and epitaxial SiC wafers are increasing. Commercially available SiC wafers still contain a large number of various defects, including impurities, micropipes, growth pits, dislocations etc. Understanding the nature and properties of these defects is important to improve both the material quality and device performance. Since structural defects are currently limiting the introduction of commercial SiC devices, these defects are briefly reviewed.

SiC bulk and epitaxial wafers contain a large number of crystal structural defects, including micropipes, screw dislocations, growth pits, triangular inclusions, etc. Table 28.2 summarizes the properties of these defects and their impacts on device operation. More detailed descriptions of some of these defects are given below. Over the last few years, the concentrations of these structural defects have come down significantly, but their density is still high enough to cause problems in devices.

28.2.1 Micropipes

Among the various defects that exist in SiC crystals, screw dislocations lying along the [0001] axis are the most significant and are generally accepted to be one of the major factors limiting the extent of the successful applications of SiC [28.23]. These screw

dislocations have been shown to have Burgers vector equal to nc (where c is the lattice parameter and n is an integer), with hollow cores becoming evident with $n \geq 2$ for 6H-SiC and $n \geq 3$ for 4H-SiC. These latter hollow-core dislocations are generally referred to as micropipes. The diameter of micropipes ranges from a few tens of nanometers to several tens of micrometers. Their density has come down in recent years, and micropipe-free wafers have been announced by commercial vendors [28.14]. Figure 28.4 shows an optical microscope picture of a micropipe in a typical 6H substrate used for our epitaxial growth. Using proper growth initiation procedure, it has been possible to close these micropipes during epitaxial growth [28.24]. However, this closure of the micropipe results in a group of elementary screw dislocations in its vicinity.

28.2.2 Screw Dislocations

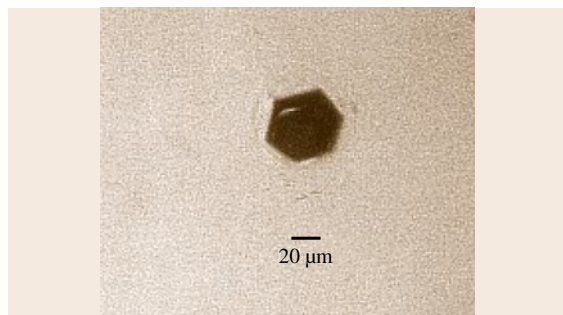
When the Burgers vector of a SiC screw dislocation is small enough, hollow-core formation is avoided [28.25]. Nevertheless, the screw dislocation possesses many properties similar to micropipes, starting with an undesirable propensity to propagate through the entire thickness of bulk crystals and epilayers. These defects are present in average densities on the order of several thousands to around ten thousand per cm^2 in commercial wafers [28.21]. Because they have not declined in density over time as fast as micropipes, it

Table 28.2 Properties of SiC epilayer extended structural defects [28.29–31]

SiC epilayer defect	Density (/cm ²)	Observed defect source	Observed impact on high-field junction	Summary (comments)
Micropipe	< 30 (commercial) < 1 (best)	Substrate micropipes that propagate into epilayer	> 50% breakdown voltage reduction Microplasmas Increased leakage current	Improved in recent years such that the density is less than $\approx 1 \text{ cm}^{-2}$ so, large-area power devices possible
Closed-core screw dislocation	≈ 3000 to 10 000	Substrate screw dislocations that propagate into epilayer	≈ 10 –30% breakdown voltage reduction Softened breakdown Microplasmas	Density slowly improving, but will be present and affect $\approx 1 \text{ cm}^2$ power devices
Triangular 3C inclusions	< 5	Wafer preparation and epitaxial growth process	> 50% breakdown voltage reduction Increased leakage current	Density improving to where these may not be present in most $\approx 1 \text{ cm}^2$ power devices
Carrots and comet tails	< 5	Undetermined	Increased leakage current Nonsmooth surface seems likely to impact on Schottky rectifying properties	Density improving to where these may not be present in most $\approx 1 \text{ cm}^2$ power devices
Small growth pits	> 3000	Screw dislocations Wafer preparation and epitaxial growth	Nonsmooth surface seems likely to impact on Schottky rectifying properties	Density improving, but screw dislocation density may represent a limiting floor for these defects

would appear that all devices manufactured on mass-produced wafers will contain these defects for the foreseeable future. While not as detrimental to device characteristics as micropipes, experimental evidence is emerging that screw dislocations somewhat negatively impact on the electrical properties of high-field SiC junctions. One study that used x-ray topography to map

screw dislocations demonstrated that elementary dislocations are detrimental to the reverse leakage and breakdown properties of low-voltage (< 250 V) 4H-SiC p⁺n diodes [28.26]. Similar observations of increased reverse leakage, soft breakdown, and microplasma not associated with micropipes are reported in [28.27, 28]. The physical mechanisms and models for the electrical behavior of these dislocations remain to be further studied.


Fig. 28.4 Optical microscope image of a micropipe in a 6H-SiC substrate

28.2.3 Growth Pits and Triangular Inclusions

Besides screw dislocations, other defects, such as growth pits, triangular inclusions, etc., have also been observed in SiC epilayers [28.32, 33]. Unlike micropipes and closed-core screw dislocations, which generally extend through the whole wafer, growth pits and triangular inclusions are primarily present in the epilayer. They are believed to be primarily caused by nonoptimized wafer preparation and epitaxial growth

processing. *Powell* and *Larkin* [28.33] also demonstrated that many morphological imperfections in the as-grown SiC epilayer surface are greatly impacted by surface polishing as well as the epitaxial growth initiation process. However, a recent study by *Schnabel* et al. [28.32], in which electron-beam-induced current (EBIC) measurements were correlated with x-ray screw dislocation mapping and surface growth pit mapping on a 6H-SiC epitaxial layer, revealed that all closed-core screw dislocations on the substrate mapped by x-ray resulted in a corresponding small growth pit on the as-grown epilayer. This suggested that epilayers process improvements may not be able to reduce small growth pit densities below bulk wafer screw dislocation densities.

The quality and smoothness of the semiconductor surface are well known to critically control the electrical

properties of Schottky diode junctions. The presence of nonsmooth surface features, such as growth pits and triangular inclusions, could perturb the local electric field and thermionic carrier emission properties, which could result in locally increased current under both forward and reverse bias [28.21]. It is plausible that p–n junction devices are perhaps less affected by SiC surface defects, primarily due to the fact that the peak electric field occurs at the junction buried within the semiconductor. However, p–n junction characteristics can be expected to track surface imperfections in those cases where a surface defect arises due to an extended defect that actually runs through the thickness of the epilayer to intersect the p–n junction. For example, 3C triangular inclusions have been found to greatly increase leakage current and decrease breakdown voltage for kV-class epitaxial p–n junction diodes [28.34].

28.3 Epitaxial Growth of Silicon Carbide

To improve the quality of materials for use in devices and to produce complicated device structures, epitaxial growth techniques are necessary. This section contains a summary of several aspects of SiC epitaxial growth technology, including the SiC growth mechanism, commonly used reactors, SiC precursor sources, substrate materials, and dopant incorporation control. Also discussed are some recent advancements in SiC epitaxial growth.

28.3.1 Substrates for Silicon Carbide Growth

The majority of earlier chemical vapor deposition (CVD) crystal growth research was focused on determining the appropriate processes for obtaining low-defect-density single-crystal SiC films for the advancement of SiC-based devices. The first available substrates for SiC epitaxial growth were mainly small ($\approx 5 \text{ mm}^2$) and irregularly shaped Lely and Acheson-derived SiC substrates that were only suitable for some epilayer physical property studies and limited prototype SiC-based devices. Therefore, dissimilar substrate materials of regular shapes and larger areas were usually chosen for CVD SiC epitaxial growth.

Motivated by the potential for Si–SiC device integration [28.35–37], many workers have attempted to grow SiC heteroepitaxially on Si. Since the growth temperature is limited by the melting point of the Si wafer ($< 1412^\circ\text{C}$), only cubic SiC can generally be

grown on Si substrates, whether the substrate used is (100) or (111). This is because the more stable polytype at these temperatures is cubic. Large thermal and lattice mismatches between Si and SiC have limited the resultant material quality. Many defects such as antiphase boundaries (APBs), stacking-fault (SF) defects, and threading dislocations usually existed in these films and contributed to electrically leaky p–n junctions. APBs are the result of polar SiC growth on nonpolar Si substrate. In addition, other novel substrates such as silicon-on-insulator (SOI) [28.38], twist-bonded universal compliant (UC) substrates [28.38], porous silicon [28.39], and free-standing 3C-SiC (made by removing silicon substrates from thick SiC heteroepitaxial layers) [28.40] have been investigated. Epilayers with improved quality on these substrates have been reported, but p–n junctions built on these layers still show very high leakage current. Recently, a group in Japan has used *undulating* Si substrates to grow thick cubic SiC, followed by the removal of the Si substrates to obtain large-area 3C-SiC wafers [28.41, 42]. Using this undulating Si substrate, they succeeded in reducing the stacking fault density compared with films grown on a planar substrate. However, the large-scale commercial use of this 3C-SiC appears years away, as high-field device performance has remained relatively poor.

TiC has been used as an alternative to Si to grow 3C-SiC, since TiC is more closely lattice-matched to SiC [28.43]. Although 3C-SiC epitaxial layers on TiC

were somewhat superior to those grown on Si, lack of high-quality TiC substrate material and high defect densities in the resulting SiC epitaxial layers have limited advancement of device research using 3C-SiC on TiC substrates.

As (0001)-oriented SiC substrates have become commercially available, more researchers started choosing SiC to grow SiC homoepitaxially. For epitaxial growth on (0001)SiC, typically the Si face has been the preferred surface, partly because of the superior epitaxial surface morphology and well-understood doping behavior compared with the C face. For 6H-SiC, the Si-face substrates are typically polished 3° off-axis from the basal plane, which increases the number of crystallographic steps on the surface to ensure SiC homoepitaxial growth (see the next section). In general, this homoepitaxial growth using off-axis SiC substrates proceeds by a step-controlled crystal growth process, as reported by Itoh and Matsunami [28.20]. Now the focus of much epitaxial crystal growth research has turned to 4H, mainly because of superior intrinsic properties such as higher bandgap, higher electron mobility, and lower dopant ionization energies. Similar to its off-axis 6H-SiC substrate predecessors, 4H-SiC substrates were initially polished 3° off-axis from the basal plane. However, researchers discovered that, compared with epitaxial growth on 6H-SiC substrates, 4H-SiC growth produces more triangular defects, which were later identified as 3C polytype inclusions [28.44, 45]. With the use of in situ pregrowth surface treatments, the occurrence of these 3C inclusions can be significantly reduced. Subsequently, the incidence of 3C inclusions was eliminated by increasing the 4H step density by using 8° off-axis substrates [28.46].

28.3.2 How to Control the Polytypes in SiC Homoepitaxy

As mentioned in the previous section, the best way to obtain a high-quality epilayer is *homoepitaxy*, which is effectively free from lattice mismatch between the epilayers and the substrates. To ensure the growth of single polytypes, a method commonly called *step-controlled growth* has been employed in which the substrates are miscut a few degrees off from the (0001)Si face [28.20, 47]. Miscut SiC(0001) crystal surfaces consist of terraces and steps, and these steps reflect the substrate crystal structure, either 4H or 6H. According to the classical growth theory, adsorbed species migrate on the surface and are incorporated into the crystal at steps where the surface potential is low. Another competi-

tive growth process of nucleation takes place on the terraces when the supersaturation is high enough. On the slightly misoriented (0001) plane, the step density is low and vast terraces exist. Then, crystal growth may occur on the terrace through two-dimensional nucleation due to the high supersaturation on the surface. In this case, the polytype of grown layers is determined by the growth conditions, mainly the growth temperature. At temperatures below 1800°C , 3C-SiC is usually formed because it is stable at low temperature [28.48]. The growth of 3C-SiC can take two possible stacking orders, ABCABC... and ACBACB..., which leads to the formation antiphase boundaries (Fig. 28.5a). On off-oriented substrates, the step density is high and the terrace width is narrow enough for adsorbed species to reach steps. At a step, the incorporation site is uniquely determined by bonds from the step (Fig. 28.5). Hence, homoepitaxy can be achieved through lateral growth from the steps, inheriting the stacking order of the substrate. Hence, epitaxy is usually carried out on (0001) face of SiC (usually Si face) misoriented either 3.5° for 6H or 8° for 4H towards (11 $\bar{2}$ 0) surface. In recent years, the emphasis has been to use reduced miscut wafers, such as 4° -off (0001) wafers, since they provide several advantages, such as reduction of crystal wastes while slicing wafers from the ingots and reduction of basal plane dislocations [28.49]. It is still possible to replicate substrate polytypes with SiC wafers with smaller off-cut, but the optimum growth window for good growth

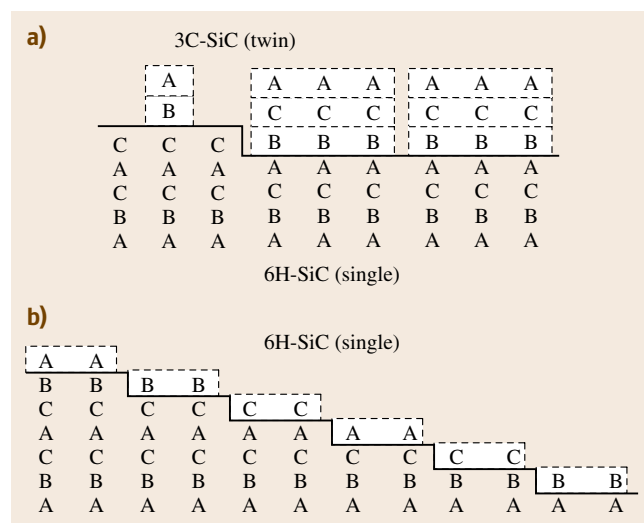


Fig. 28.5a,b Growth modes and polytypes on 6H-SiC substrate. **(a)** 3C-SiC growth by two-dimensional terrace nucleation, **(b)** homoepitaxy of 6H-SiC by step-flow growth (after [28.20])

is much narrower. In addition, increased step bunching is observed when the offcut angle is reduced, thus resulting in increased surface roughness.

28.3.3 SiC Epitaxial Growth Techniques

The purpose of epitaxy is to create a high-quality layer of desired thickness with controlled doping concentration, such as the abrupt p–n junction structure. Various epitaxial growth techniques have been used to achieve this goal. In this section, several important non-CVD epitaxial growth techniques that have been used for growing SiC are presented.

Liquid-phase epitaxy (LPE) is appealing since it is a growth process carried out at or close to equilibrium and thus produces high-quality materials [28.50]. During the LPE process, a SiC wafer, fixed on a graphite holder, is dipped into Si-based melt, which is heated to between 1000 and 2000 °C in a graphite crucible [28.50–54]. Growth takes place due to mass transfer from the crucible acting as the C source to the SiC wafer (seed) in the established temperature gradient. One of the most promising advantages of this method for SiC epitaxial growth is the potential to close micropipes emerging from the substrate. LPE epitaxial layer grows at low supersaturation compared with the physical vapor transport (PVT) growth technique, in which supersaturation is much higher and temperature fluctuations may easily result in local deviations from optimal growth conditions, leading to defect formation. LPE of SiC was shown to be an effective technique to overgrow micropipes in SiC wafers prepared by the physical vapor transport (PVT) technique [28.50–54]. Micropipe closing efficiency of > 80% has been demonstrated, and the growth rate ranges from several micrometer to millimeter per hour. LPE of SiC requires accurate control of thermal equilibrium conditions to avoid growth of different polytypes at the same time. It is difficult to control the doping concentration by LPE. Also the surface morphology of LPE SiC is rough, and terraces and steps are usually observed on the surface, which needs to be avoided for device fabrication.

Molecular-beam epitaxy (MBE) is an ideal technique for thin epitaxial layer deposition. Gas-source MBE (GSMBE) has been used for SiC homoepitaxial growth [28.55, 56]. It was found that low substrate temperature (< 1000 °C) resulted in deposition of 3C-SiC instead of replication of the stack sequences of the substrate. The growth rate is typically several nm/h. MBE has also been used for growing SiC on Si at relatively

low temperature [28.57, 58] to avoid the formation of the voids that are usually observed in Si substrates at the SiC/Si interface when CVD techniques are used. Single-crystal 3C-SiC could be obtained by GSMBE at temperatures as low as 800–900 °C. MBE is suitable for low-dimensional modulation-doped structures or heterostructures of different SiC polytypes in the quantum regime due to its low growth temperature and growth rate. However, the thick epilayers required by high-voltage power device are unlikely to be obtained by MBE.

28.3.4 Chemical Vapor Deposition

The most common epitaxial growth technique for SiC is chemical vapor deposition (CVD), which has the advantages of precise control of the epitaxial layer thickness and impurity doping combined with a reasonable growth rate and good surface morphology. The growth temperatures for typical SiC CVD processes range from 1200 to 1800 °C, while the growth pressures vary from several tens of Torr to atmospheric pressure.

Precursors for SiC CVD Epitaxial Growth

Typical CVD techniques for SiC epitaxial layer growth employ separate sources of Si and C. Silane is the commonly used silicon source, while various choices of hydrocarbons have been used as carbon source. Both are introduced into the reactor with a high-purity H₂ carrier gas. Propane has been the most popular among the hydrocarbon choices, probably because of its association with the first successful demonstration of large-area epitaxial SiC on Si substrates [28.35], while methane, ethylene, and acetylene have been used less extensively. Methane is of interest because of the increased purity available from commercial sources compared with that of propane, although the larger thermal stability results in a smaller C source cracking efficiency [28.59].

Chlorine-based silicon sources, such as SiH₂Cl₂ and Si₂Cl₆, have been used to grow 3C-SiC on Si [28.60, 61]; one advantage is that Cl in the reactor could help to suppress silicon codeposition. Also, as reported by Yagi and Nagasawa [28.61], the supplied SiH₂Cl₂ is decomposed into SiCl₂ and H₂ at the growth temperature. The in situ generated SiCl₂ absorption is thought to be self-limited. Thus, atomic-layer epitaxial growth can be achieved by alternating supply of SiH₂Cl₂ and hydrocarbon. Using this method, Yagi and Nagasawa [28.61] have grown high-uniformity 3C-SiC on 6 inch Si substrates. The thickness deviation of the SiC film (4215 Å in thickness) was less than 1.3% over the substrate. Re-

cently, *Miyagi* and *Nishino* [28.62] used Si_2Cl_6 as a silicon source material to grow 4H-SiC. Si_2Cl_6 is a safer material than SiH_4 , but large numbers of etching pits and scratch-like defects were seen on the resulting epilayers.

Single-source SiC precursors, such as hexamethyldisilane (HMDS) [28.63] and tetramethylsilane [28.64], have also been studied because they usually have much lower cracking temperature than that of multiple-source precursors, which could make lower-temperature ($< 1100^\circ\text{C}$) SiC CVD possible. However, these chemicals are not available in sufficiently high purity, so their use will not result in layers with low background carrier concentration. Also it is impossible to adjust the C/Si ratio with a single-source precursor, which makes optimization of growth conditions difficult. One possible solution is to use an additional carbon source such as propane to control the C/Si ratio and hence the background doping concentration [28.65]. In addition, a few examples of their use in obtaining reproducible growth of high-quality SiC epitaxial layer have been reported. Hence, use of higher-purity chemicals such as silane and propane offers the best possible routes for growing layers for high-voltage applications. These chemicals can be further purified in situ in the reactor using resin-based purifiers [28.66].

CVD Reactor Configurations

The most commonly used simple reactor configuration for SiC CVD has been the quartz horizontal reactor operating at atmospheric or low pressure (Fig. 28.6). These reactors can be warm-walled or water-cooled. Researchers from the National Aeronautics and Space Administration (NASA) and Kyoto University have shown that high-quality SiC epilayers can be achieved using this type of reactor [28.33,67]. The gases used are

silane (SiH_4) and propane (C_3H_8) with a large amount of H_2 carrier gas. Figure 28.6 shows the schematic of the reactor. The growth rate is determined by the flow of silane gas, whereas the layer quality and the density of defects such as cubic SiC inclusions, dopant incorporations etc. are strongly dependent on the growth temperature and the flow rate of propane for a given growth rate. If the silane flow is increased beyond a certain value, the morphology of the grown layer deteriorates quickly. Growth rates of a few $\mu\text{m/h}$ have been obtained using this type of system. *Nakamura* et al. [28.68] reported epitaxial growth in a horizontal cold-wall system with growth rates of up to $6\mu\text{m/h}$ at 1500°C by improving the initial growth conditions. Procedures to minimize doping and thickness nonuniformities include increasing the carrier gas flow (decreasing the residence time of the precursor), reducing the deposition pressure, and tilting the susceptor with respect to the gas flow. More importantly, the limited growth rate and parasitic deposits falling from the ceiling of the reactor wall make it difficult to grow thick ($> 50\mu\text{m}$) SiC epilayers with good surface morphology.

Vertical cold-wall reactors have also been built and used to grow SiC with high purity and crystal quality [28.69–71]. Precursor gases were introduced from the top of the reactor and the particles falling from the ceiling in the horizontal cold-wall reactor were avoided. The susceptor and attached sample were rotated at up to 1500rpm to increase uniformity and prevent recirculation of the gases in the chamber. This fast rotation provides a pumping action for the gas flow. A background impurity level below 10^{14}cm^{-3} was obtained with a growth rate of 5–6 $\mu\text{m/h}$. Although a similar growth rate was obtained to that achieved in the horizontal cold-wall reactor, longer growth times could be

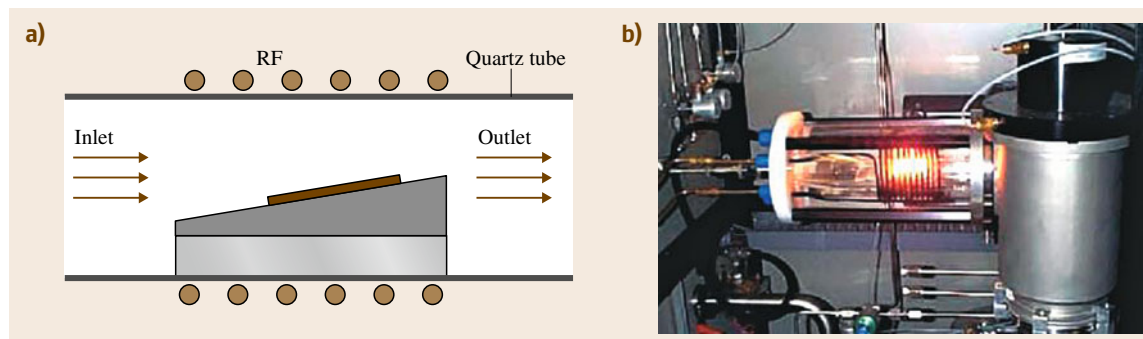


Fig. 28.6a,b Schematic drawing of a typical horizontal cold-wall SiC CVD reactor (a) and a horizontal water-cooled cold-wall reactor in operation at Rensselaer Polytechnic Institute (RPI) (b) (RF – radiofrequency)

used with the vertical reactor. Thick epilayers up to 50 μm have been obtained using this type of reactor.

In order to reproducibly grow thick, high-quality epilayers for power device applications, horizontal hot-wall reactors were proposed by Kordina and coworkers [28.72]. The idea of the hot wall was to obtain very good heating efficiency together with a high cracking efficiency of the precursors since gases could be much more efficiently heated in a hot-wall reactor. Also, since the system is heated more uniformly, Si droplet formation just above the sample surface may be suppressed, and hence a much higher silane flow can be used for growing SiC. This has been discussed as one of the problems that limit the growth rate in cold-wall reactors. Since the reactor walls are all heated (Fig. 28.7), the parasitic deposits on the reactor walls are polycrystalline SiC, which tends to stick to the wall more strongly than the amorphous SiC or byproducts that stick to the reactor wall in cold-wall reactors. Due to all these reasons, it is possible to grow SiC in a hot-wall reactor at a much higher rate and also for longer time without creating the *dusting* and surface morphology degradation that usually occur in cold-wall reactors. Several researchers have adapted this hot-wall process to grow SiC, and currently this appears to be the commonest process to grow SiC epitaxial films. For example, Kimoto et al. [28.73] have improved on this process, and have reported very high-purity SiC growth using this type of reactor. Epilayers with 50 μm thickness and n-type background doping in the low 10^{13} cm^{-3} range have been achieved reproducibly at 1550 $^{\circ}\text{C}$ and 80 Torr. With additional mechanical rotation, excellent thickness uniformity (1% standard deviation over mean value) and doping uniformity (6% standard deviation over mean value) have been achieved on 2 inch wafers

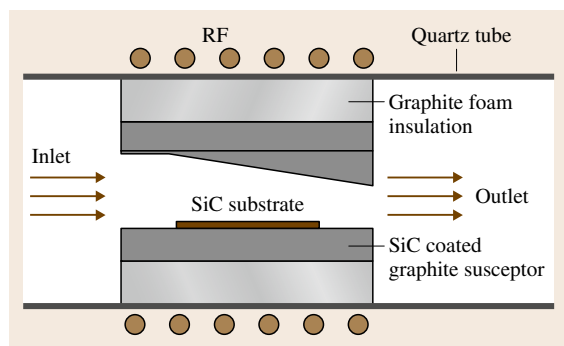


Fig. 28.7 Schematic drawing of a typical horizontal hot-wall SiC CVD reactor. The cross section of graphite wall is rectangular in shape

using a horizontal hot-wall reactor [28.74]. Recently, Thomas and Hecht [28.75] reported a planetary horizontal hot-wall reactor with handling capacity of seven 2 inch or five 3 inch wafers. High-quality epilayers were grown by optimizing the process conditions. Excellent intrawafer homogeneity (thickness uniformity standard deviation of 2% of mean, doping uniformity standard deviation of 9% of mean) as well as wafer-to-wafer (thickness uniformity standard deviation of 1.6% of mean, doping uniformity standard deviation of 3.3% of mean) on 3 inch wafers have been achieved using this system. These horizontal hot-wall reactors with multiple-wafer capability are becoming industry-standard for growing epitaxial films for commercial production.

The vertical hot-wall reactor (also called the *chimney CVD* reactor) has also been developed as a high-temperature CVD technique in order to increase growth rates further [28.76–78]. The epitaxial growth of SiC in this geometry is investigated mainly for the purpose of growing thick epitaxial layers for high-power applications. In the chimney reactor, the high-temperature (1600–1900 $^{\circ}\text{C}$) growth process enables epitaxial rates of 10–50 $\mu\text{m}/\text{h}$. Under optimum conditions, mirror-like SiC epilayers with low background doping of low 10^{13} cm^{-3} can be obtained. Recently, Danno et al. reported fast epitaxial growth (14–19 $\mu\text{m}/\text{h}$) on 4H-SiC(0001) substrate using a chimney-type reactor [28.79]. High-quality epilayers with 100% micropipe closing have been grown at 1750 $^{\circ}\text{C}$ at C/Si ratio of 0.6. Fujiwara et al. reported the reduction of stacking faults in fast epitaxial growth by optimizing initial growth conditions during the heating process [28.80]. Stacking fault density could be dramatically reduced from 1000–9000 cm^{-2} to 0–5 cm^{-2} . The vertical hot-wall reactor has also been used in the author's own laboratory [28.81] for growing thick epitaxial films with high growth rate ($> 20 \mu\text{m}/\text{h}$).

Another type of epitaxial growth, termed *sublimation epitaxy*, was developed to grow bulk-like thick SiC, and was one of the first techniques to produce SiC epitaxial layers. This growth process is based on heating polycrystalline SiC source material to 1700–2000 $^{\circ}\text{C}$ under conditions at which it sublimates into the vapor phase and subsequently condenses onto a cooler SiC seed crystal. This is similar to the bulk growth process. It is possible to achieve high epitaxial growth rate ($> 2 \text{ mm}/\text{h}$) with a stable mechanism, resulting in high-quality SiC. Thick homoepitaxial growth of 4H-SiC (50–100 μm) [28.82] and 3C-SiC (300 μm) [28.83] with high growth rates of 100 $\mu\text{m}/\text{h}$

and 50 $\mu\text{m}/\text{h}$, respectively, have been demonstrated using this technique. Specular surface and better quality layers (compared with substrate) were obtained by this technique. Recently, Sveinbjornsson et al. reported higher field-effect channel mobility ($208\text{ cm}^2/(\text{Vs})$) in 4H-SiC MOSFETs fabricated on sublimation-grown epilayer compared with that ($125\text{ cm}^2/(\text{Vs})$) fabricated on a commercial CVD epilayer [28.84]. The mobility enhancement is attributed to better surface morphology of the sublimation epilayer, resulting in less surface scattering and lower density of interface states [28.85] as compared with the reference CVD epilayers. However, good results by sublimation epitaxy can only be obtained when the growth parameters are carefully controlled within a narrow window. One of the remaining challenges is to avoid the introduction of impurities from the growth environment into the epilayers. The purity of the solid polycrystalline SiC source material is the most critical issue in the growth of low-doped SiC by this method.

Recently, a new epitaxial growth process by introducing chlorinated silicon precursors or simply HCl addition was proposed to achieve high growth rate of SiC [28.86–88]. A high growth rate of 90 $\mu\text{m}/\text{h}$ has been obtained using methyltrichlorosilane (MTS) as a precursor [28.86], while growth rates of up to 49 $\mu\text{m}/\text{h}$ have been reported using standard silane–propane–hydrogen growth chemistry with incorporation of HCl into the gas mixture [28.87]. No significant difference has been observed in terms of defects, doping uniformity or thickness uniformity compared with the standard process without HCl (or chlorinated silicon precursor). Although the growth mechanism is not fully understood, it is proposed that the addition of chlorine suppresses Si cluster formation in the gas phase, which is thought to be responsible for limiting the growth rate in horizontal cold-wall reactors. Therefore, epitaxial growth with both high growth rate and specular surface morphology is possible using this process. A complete investigation of this process is still ongoing to obtain high-quality SiC epilayers with even higher growth rates.

Doping Incorporation Technology

In order to ensure reproducible and reliable SiC semiconductor device characteristics, well-controlled dopant incorporation must be accomplished. Unlike the doping technology routinely used in the silicon semiconductor industry, SiC cannot be efficiently doped by diffusion at SiC growth temperature due to its low diffusion coefficient. Doping of SiC epitaxial layers of a device

structure is accomplished either by flowing a dopant source into the reactor during growth or by implanting the dopant atoms.

Nitrogen is the most common n-type source for in situ doping. Since the atomic size of nitrogen (0.74 \AA) is closer to that of carbon (0.77 \AA), nitrogen tends to substitute at C sites to a first approximation, consistent with the reported experimental results [28.20]. As discussed previously, the bonding between Si and C atoms in adjacent bilayer planes can be of either zincblende (cubic) or wurtzite (hexagonal) nature. Each type of bond provides a slightly altered atomic environment, making some lattice sites inequivalent in polytypes. In 6H-SiC, three inequivalent sites are available (two cubic sites and one hexagonal site), whereas two inequivalent sites are available in 4H-SiC (one cubic site and one hexagonal site). The ionization energy will be different when a dopant is incorporated into different inequivalent sites. The ionization energies for nitrogen have been reported by several authors, but the values differ a lot. In general, measurements on epitaxial layers with higher donor concentration typically yield lower ionization energy due to Coulombic interactions with neighboring impurities [28.89]. Also, experimentally, it was found that the ionization energies of nitrogen in 4H-SiC are shallower than the corresponding values in 6H-SiC.

In situ nitrogen doping can be realized by passing nitrogen or ammonia into the reactor during the growth. However, control of net dopant incorporation by simply increasing or decreasing the flow of the dopant source is limited in terms of both reproducibility and doping range. This doping range is typically limited to 2×10^{16} – $5 \times 10^{18}\text{ cm}^{-3}$ for a nitrogen-doped n-type layer. If one increases the nitrogen flow further, either the growth rate is found to reduce or the surface morphology is found to deteriorate significantly [28.90]. So, an alternative method, termed *site-competition growth*, is used to increase the doping concentration [28.91]. It was found that nitrogen incorporation was very sensitive to the C/Si ratio employed during the growth and increased when C/Si decreased for growth on Si-face substrate (Fig. 28.8b). This was explained by site competition between nitrogen and carbon during the growth: since nitrogen and carbon occupy the same sites in SiC, decreasing C/Si will produce more C vacancies in SiC, which will in turn increase nitrogen incorporation. Use of this technique has enabled large expansion of the reproducible doping range, which as a result, now spans from 10^{14} to $5 \times 10^{19}\text{ cm}^{-3}$.

Phosphorous is another n-type dopant in SiC. However, phosphorous appears to have limited potential as a replacement for nitrogen, especially considering its larger atomic size and similar ionization energy to the nitrogen donor [28.91]. Understanding of the location of phosphorous in the SiC lattice as an isolated impurity, phosphorous-related complexes, and corresponding electronic levels is still poor. Hall measurements on phosphorous-implanted SiC epilayers have yielded two ionization energies: 80 ± 5 and 110 ± 5 meV for 6H-SiC [28.92] and 53 and 93 meV for 4H-SiC [28.93], which were assigned to the hexagonal and quasicubic sites of silicon, respectively. Recent research on phosphorous-implanted SiC indicates that the sheet resistance in high-dose phosphorous-implanted 4H-SiC is as much as an order of magnitude lower than those measured in nitrogen-implanted 4H-SiC with comparable doping and thermal processing [28.94]. Thus, there are some advantages in replacing nitrogen with phosphorous for applications where low sheet resistance is required.

Very little has been reported on in situ doping of phosphorous in CVD. The phosphorous donor ionization energy is also only available on phosphorous-implanted SiC, which generally contains lots of N or Al background. In one report [28.88] on the site-competition effect for phosphorous doping, *Larkin* reported that phosphorous substitutes at the Si site due to its similar atomic size (1.10 \AA) to Si (1.17 \AA). However, our own experimental results seem to be different from this conclusion, and it appears that phosphorous occupies both Si and C sites [28.95].

Aluminum serves as a shallow acceptor dopant in SiC and can be introduced during growth, or afterwards by implantation. In contrast to nitrogen, the aluminum acceptor resides at the Si lattice sites. Its ionization energy is only weakly dependent on polytype or to lattice sites h , k . The scatter of published data ranges from 190 meV [28.96] to 280 meV [28.97]. The in situ incorporation of Al strongly depends on the C/Si ratio during growth. Increasing C/Si will increase the Al doping concentration.

Boron is another acceptor dopant in SiC. During epitaxial growth, a considerable amount of hole-passivating hydrogen is simultaneously incorporated into the growing B-doped CVD epilayer. Postannealing at 1700°C in Ar is usually used to dissociate B–H and better activate the B acceptors [28.91]. Although the atomic size of boron (0.82 \AA) is closer to that of C (0.77 \AA), B–H has an atomic size (1.10 \AA) more closely matched with that of Si (1.17 \AA) and therefore should occupy Si sites. Experiments have also shown that boron incorporation increases with C/Si [28.91], which is in agreement with the site-competition theory. However, this does not imply that boron substitutes exclusively at Si sites. Experiments have shown that a small amount of boron can also occupy C sites and form an energetically deep complex termed a D-center. The energy level for the boron at the Si site is about 300 meV, as measured from the top of the valence band. The deeper center is about 600–700 meV above the valence band and manifests itself optically by producing donor–acceptor pair spectra at low temperature [28.97]. Its existence was also confirmed by deep-level transient

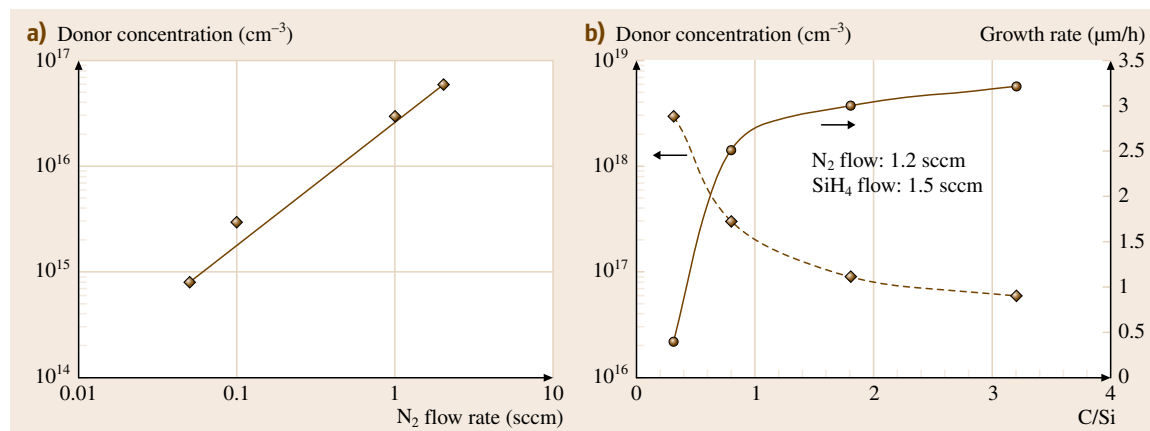


Fig. 28.8 (a) Carrier concentration versus N_2 flow for CVD of SiC. Increasing C/Si ratio can decrease the carrier concentration further as shown in (b) (after [28.95])

spectroscopy (DLTS) spectra [28.96]. The formation of shallow boron acceptors and deep D-centers can be adjusted during the doping process by the site-competition effect. Use of higher C/Si during growth will reduce the carbon vacancies, thus producing more shallow boron acceptors.

Epitaxial Growth on Nonstandard Crystal Orientations

After the success of epitaxial growth on off-axis (0001)Si-face substrate, growth on many other crystallographic faces of SiC has also been investigated. Most of the epitaxial growth studies on nonstandard crystal planes have focused on 4H-SiC due to its electronic properties advantages over 6H-SiC. Figure 28.9 shows schematics of several selected 4H-SiC lattice planes.

Epitaxial growth on (000 $\bar{1}$)C-face substrate has been carried out by CVD and compared with growth on (0001)Si face. SiC (000 $\bar{1}$)C face has a different surface atom configuration from (0001)Si face, and the electronegativity of Si and C atoms is different. This brings about various polarity dependences in chemical reactivity, growth kinetics, impurity incorporation efficiency, thermal oxidation rate, and oxide-SiC interface properties. SiC (000 $\bar{1}$)C face has shown superior properties of faster oxidation rate [28.98] and low surface roughness [28.96] compared with Si(0001) face. Therefore, it shortens the extremely time-consuming oxidation process on SiC(0001) and it is possible to obtain higher channel mobility of SiC MOSFETs due to reduced surface roughness scattering. Although it was found that the growth window on (000 $\bar{1}$)C face is narrower and the background doping level is higher compared with growth on (0001)Si face [28.97], high-quality epilayer with a background doping of mid- 10^{14} cm $^{-3}$ has been obtained following the development of the hot-wall CVD reactor [28.99]. The nitrogen donor incorporation efficiency has been found to be higher on (000 $\bar{1}$)C face, while the aluminum acceptor incorporation efficiency on (000 $\bar{1}$)C is lower compared with on (0001)Si face [28.100–102].

Epitaxial growth of 4H-SiC on (1 $\bar{1}$ 00) and (11 $\bar{2}$ 0) faces has also been investigated with the motivation to improve the SiC MOSFET channel mobility [28.103]. Both faces are perpendicular to the (0001) face, as shown in Fig. 28.9b,c, respectively, and no intentional off-angles are required for these faces to realize homoepitaxy of 4H-SiC, owing to the appearance of stacking information on the surface. The surface morphology of epitaxial layers grown on (1 $\bar{1}$ 00) face was found to be very poor, whereas the resulting SiC(11 $\bar{2}$ 0)

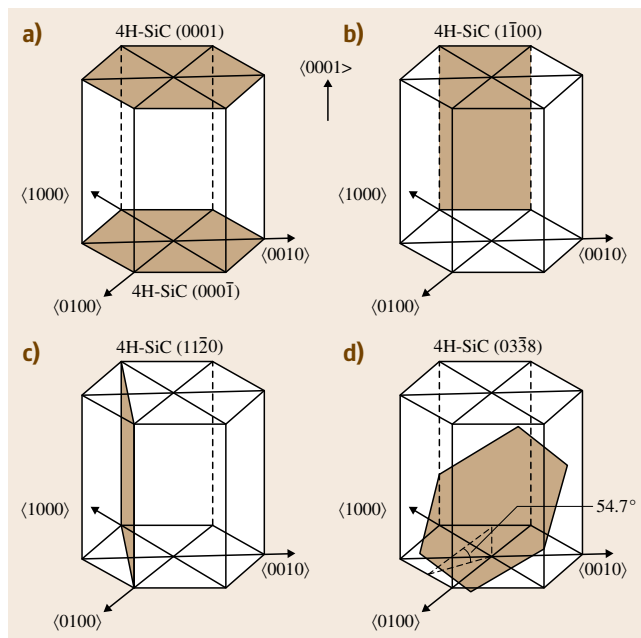


Fig. 28.9a–d Schematic of the selected lattice planes of 4H-SiC. (a) 4H-SiC(0001) and (000 $\bar{1}$), (b) 4H-SiC(1 $\bar{1}$ 00), (c) 4H-SiC(11 $\bar{2}$ 0), and (d) 4H-SiC(03 $\bar{3}$ 8)

epitaxial surface morphology was comparable to or even better than those grown on off-axis (0001)Si face. Although threading screw dislocations and edge dislocations parallel to the c -axis are present in (11 $\bar{2}$ 0) substrate, they are found not to propagate into epilayers. Extremely smooth and micropipe-free layers have been obtained by epitaxial growth on (11 $\bar{2}$ 0) substrate [28.104, 105]. Growth rates on (1 $\bar{1}$ 00) and (11 $\bar{2}$ 0) faces are almost the same as that on off-axis (0001) under the same conditions. The C/Si ratio dependence of dopant incorporation has been observed for epitaxial growth on (11 $\bar{2}$ 0) substrate [28.102, 105]. When nitrogen was introduced, epitaxial layers grown on (11 $\bar{2}$ 0) always showed higher donor concentration than on off-axis (0001). Although nitrogen incorporation was suppressed by increased C/Si ratio on (11 $\bar{2}$ 0), the C/Si dependence was weaker on (11 $\bar{2}$ 0) epilayers. A background doping concentration of low- 10^{14} cm $^{-3}$ for (11 $\bar{2}$ 0) epilayers can be achieved by increasing the C/Si ratio. In contrast to nitrogen doping, the acceptor (both Al and B) concentration of (11 $\bar{2}$ 0) epitaxial layers was lower than that of off-axis (0001) epitaxial layers under identical growth conditions.

To avoid propagation of defects along growth direction, SIXON Ltd., Japan, [28.106] developed crystal

growth of 4H-SiC along the $\langle 03\bar{3}8 \rangle$ direction which is inclined to the c -axis by 54.7° as shown in Fig. 28.9d. During the bulk growth, defects along the $\langle 0001 \rangle$ direction propagate diagonally and terminate to the side of ingot. Epitaxial growth on $\langle 03\bar{3}8 \rangle$ 4H-SiC has shown improved surface morphology [28.105, 107]. Microsteps and triangular defects have not been observed on the surface, and almost perfect micropipe closing has been realized in 4H-SiC($03\bar{3}8$) epitaxial growth. Growth rate on $\langle 03\bar{3}8 \rangle$ is the same as on an off-axis $\langle 0001 \rangle$ Si face under the same conditions. Similar dopant incorporation efficiency as that on $\langle 11\bar{2}0 \rangle$ has been found for epilayers on $\langle 03\bar{3}8 \rangle$. The C/Si ratio dependence of impurity incorporation is intermediate between the case of the $\langle 0001 \rangle$ Si face and the $\langle 000\bar{1} \rangle$ C face. A background doping of low 10^{14} cm^{-3} can be achieved on $\langle 03\bar{3}8 \rangle$, similar to that on $\langle 11\bar{2}0 \rangle$.

Based on the experimental results, impurity incorporation in SiC growth is believed to be dominated mainly by surface bond configuration. Since both Al and B atoms occupy Si sites to form acceptors in SiC, the doping efficiency of these impurities may depend on the number of chemical bonds available from the surface C atoms. On $\langle 0001 \rangle$ Si plane, three bonds are available from neighboring C atoms on the surface, while two bonds are available from surface C atoms on $\langle 11\bar{2}0 \rangle$ and $\langle 03\bar{3}8 \rangle$. On $\langle 000\bar{1} \rangle$ C face, only one bond is available from the top C atom. This difference may be the reason why the doping efficiency of Al or B on $\langle 11\bar{2}0 \rangle$ and $\langle 03\bar{3}8 \rangle$ faces is lower than on $\langle 0001 \rangle$ Si face but higher than on $\langle 000\bar{1} \rangle$ C face. In a similar manner, N doping may be influenced by the number of chemical bonds from the surface Si atoms, as N atoms substitute at C sites. Therefore, nitrogen incorporation on $\langle 11\bar{2}0 \rangle$ and $\langle 03\bar{3}8 \rangle$ faces is more efficient than on $\langle 0001 \rangle$ Si face and less efficient than on $\langle 000\bar{1} \rangle$ C face.

The MOS interface properties of these nonstandard faces have also been studied to explore potential advantages for SiC power MOSFET applications. Although

the interface state density (D_{it}) of the 4H-SiC(0001) MOS structure exhibits a rapid increase near the conduction-band edge, those on the other faces exhibit a rather flat D_{it} distribution. $\langle 000\bar{1} \rangle$, $\langle 11\bar{2}0 \rangle$, and $\langle 03\bar{3}8 \rangle$ have about one order of magnitude lower interface density near the conduction-band edge than $\langle 0001 \rangle$ [28.108]. As known, the extremely high D_{it} near the band edge causes trapping of electrons induced in the inversion layer and significantly reduces the channel mobility of SiC MOSFETs [28.109]. Planar MOSFETs fabricated on 4H-SiC(0001), $\langle 000\bar{1} \rangle$, $\langle 11\bar{2}0 \rangle$, and $\langle 03\bar{3}8 \rangle$ faces have shown that the effective channel mobility of those nonstandard faces is 2–3 times higher than that on $\langle 0001 \rangle$ face. Although the reason for this crystal face dependence is unclear, bond configurations and the polarity of nonstandard surfaces might lead to an intrinsic difference in chemical reactivity during oxidation and to a reduced number of electrically active states near the band edge. Recently, Kimoto et al. reported a new oxidation process using N_2O to reduce the interface state density [28.110]. The interface state density near the conduction-band edge was found to be much lower on 4H-SiC($000\bar{1}$) and $\langle 11\bar{2}0 \rangle$ ($\approx 3 \times 10^{11} \text{ (/cm}^2 \text{ eV)}$) than on 4H-SiC(0001) ($\approx 1 \times 10^{12} \text{ (/cm}^2 \text{ eV)}$) with N_2O oxidation. A significant improvement of the channel mobility in SiC MOSFETs fabricated on $\langle 000\bar{1} \rangle$ ($> 30 \text{ cm}^2 \text{/(V s)}$), and $\langle 11\bar{2}0 \rangle$ ($> 70 \text{ cm}^2 \text{/(V s)}$) epilayers has been achieved [28.111, 112]. 4H-SiC(0001), $\langle 11\bar{2}0 \rangle$, and $\langle 03\bar{3}8 \rangle$ faces are promising for MOS-based devices owing to the superior properties of the MOS interface. Note that research on $\langle 03\bar{3}8 \rangle$ epitaxial growth and device applications is still limited due to the lack of substrates. All results have been reported by SIXON Ltd. and Kyoto University. Even though these orientations may have better device properties, the lack of availability of these wafers at lower cost may limit widespread use, and most epitaxial work will still be carried out on $\langle 0001 \rangle$ Si wafers.

28.4 Epitaxial Growth on Patterned Substrates

Epitaxial growth of SiC provides in situ doping of as-grown layers and better crystal quality as compared with ion implantation. Step-controlled epitaxy has been used at lower temperature ($< 1800^\circ\text{C}$) for high-quality crystal growth, avoiding SiC sublimation and surface roughening during growth. Therefore, if selective doping of SiC can be achieved via epitaxial growth, then

it provides a promising alternative to ion implantation in SiC processing. There are two essential means to realize selective doping by epitaxial growth. One is to apply blanket growth on a patterned substrate, followed by a polishing process to remove excess epilayers on the mesas. The other is to use selective growth with a high-temperature mask that could be selectively re-

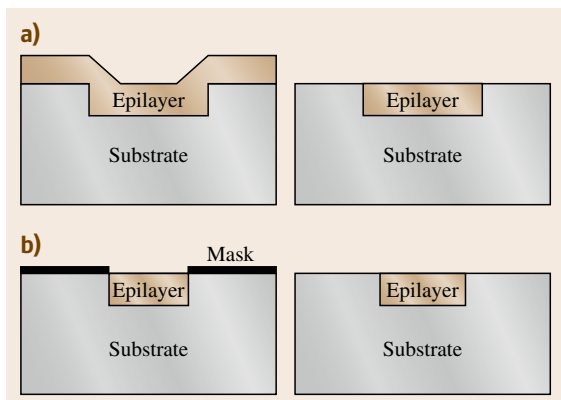


Fig. 28.10a,b Schematic of selective doping of SiC by epitaxial growth. (a) Blanket epitaxial growth followed by polishing to remove excess epilayers, (b) selective epitaxial growth followed by mask removal

moved after growth. These two processes are illustrated schematically in Fig. 28.10.

A few trials of homoepitaxial CVD growth of SiC on a trenched substrate have been reported. Nordell et al. [28.113] investigated the growth behavior at various C/Si ratios and temperatures. It was found that a low C/Si ratio gave smooth growth and small differences in growth rates between different lattice planes. A larger C/Si ratio gave more faceted growth, and the growth rate was lower in the $\langle 1\bar{1}00 \rangle$ direction than in the $\langle 11\bar{2}0 \rangle$ direction. Chen et al. [28.114] also carried out homoepitaxial CVD growth on trenched 4H-SiC substrate. Similar growth behavior was observed near trenches. It was found that the growth rate on trench side walls was usually lower than that on the bottom of a trench and on the top surface, and this difference became smaller with decreasing C/Si ratio. Growth on mesas oriented parallel to the substrate miscut direction showed clear step-flow growth, while growth on mesas oriented perpendicular to the miscut direction revealed the formation of (0001) plane. These studies focus more on crystal growth behavior; applications on device fabrication have hardly been reported.

Epitaxial growth on patterned substrates, specifically, 4H-SiC mesas, has been carried out at NASA [28.115–118]. 4H-SiC substrates were patterned with a series of mesas of various shapes and sizes (such as squares and hexagons) by dry etching techniques. When epitaxial growth is carried out on these substrates, step-free surfaces are obtained provided that the mesas do not contain any screw dislocations. Such techniques have been used to provide step-free large-size

mesas up to $200\text{ }\mu\text{m} \times 200\text{ }\mu\text{m}$. Such mesas have been used for growth of cubic SiC or hexagonal GaN layers. The results from these studies have been reviewed before [28.117] and will not be repeated here.

28.4.1 Selective Epitaxial Growth

Selective epitaxial growth is a well-established technique for Si [28.119] and GaN [28.120, 121]. However, only a few works have been reported on selective growth of SiC. This is not surprising since high growth temperature above 1450°C is generally required to grow high-quality epilayers of SiC by chemical vapor deposition. This high growth temperature makes it a challenge to identify an appropriate mask for selective epitaxial growth of SiC.

Several groups [28.122, 123] have demonstrated low-temperature ($\approx 1000\text{--}1200^\circ\text{C}$) selective deposition of 3C-SiC on Si substrate using SiO_2 and Si_3N_4 as the mask. Two conflicting requirements became apparent: high growth temperatures were needed to produce the best crystal quality 3C-SiC films, but low growth temperatures were needed to minimize damage to the mask. Polycrystalline 3C-SiC was usually deposited in unmasked window when the temperature was lowered to avoid significant damage to the mask. In addition, delamination of dielectric mask was often observed. To improve selectivity, HCl was sometimes added to the carrier gas [28.124]. Lateral epitaxial overgrowth (LEO) has also been studied, and it was found that defect density in the LEO region was significantly reduced compared with films grown directly on Si substrate [28.125, 126].

Selective growth at higher temperature requires masks that can withstand the growth temperature of $> 1500^\circ\text{C}$. One such mask is graphite. Recently, homoepitaxial selective growth of SiC has been reported using graphite mask [28.127–129]. Chen et al. investigated selective homoepitaxial growth of 4H-SiC on off-axis (0001) and $(11\bar{2}0)$ substrate at 1500°C [28.128]. Polycrystalline 3C-SiC was observed on the graphite mask, and laterally overgrown polytype was identified as 3C-SiC in contrast to the 4H-SiC grown in window openings. Local epitaxy and lateral epitaxial overgrowth of SiC were even studied by using physical vapor transport (PVT) [28.129]. A lateral/vertical growth rate ratio of 6 was achieved. It was found that dislocations in the substrate propagated only into epilayers grown above the seed regions but not into the lateral overgrown region. The apparent disadvantage of the graphite mask is that the mask itself could act as

a carbon source during high-temperature SiC epitaxial growth. This results in local variation in the C/Si ratio, which affects local crystal growth behavior and the doping concentration of grown layers. Also, polycrystalline SiC deposition on the mask interferes with the lateral growth. Because of these limitations, it is better to identify another mask that will withstand the high growth temperature but that will not cause contamination of the layer itself.

28.4.2 Selective Epitaxial Growth of 4H-SiC Using TaC Mask

At RPI, we have used TaC as the high-temperature mask for growing SiC selectively. Some salient features of this selective growth will now be presented, followed by some device results.

The mask to be used for selective epitaxial growth of SiC essentially needs to be stable under high tem-

perature ($> 1400^{\circ}\text{C}$) in hydrogen ambient. Silicon oxide and silicon nitride are commonly used masks for selective growth of silicon and III-V compound semiconductors [28.119, 130, 131]. However, they are etched very quickly in hydrogen ambient under high temperatures and can be used only at relatively low temperature ($\approx 1000^{\circ}\text{C}$). TaC is a well-known refractory material with high melting point and high chemical resistance. TaC-coated components have been used with success in conventional vapor-phase epitaxy (VPE) of SiC [28.132]. In addition, TaC has been successfully used as a coating of the graphite susceptor in SiC epitaxy [28.95, 133].

A TaC mask was prepared by converting Ta to TaC in a CVD reactor. Specifically, high-purity Ta metal (99.999%) was first evaporated by electron-beam evaporation and patterned. Ta-coated SiC wafers were then placed in the CVD reactor, and the chamber was pumped down to 5×10^{-6} Torr using a turbo pump be-

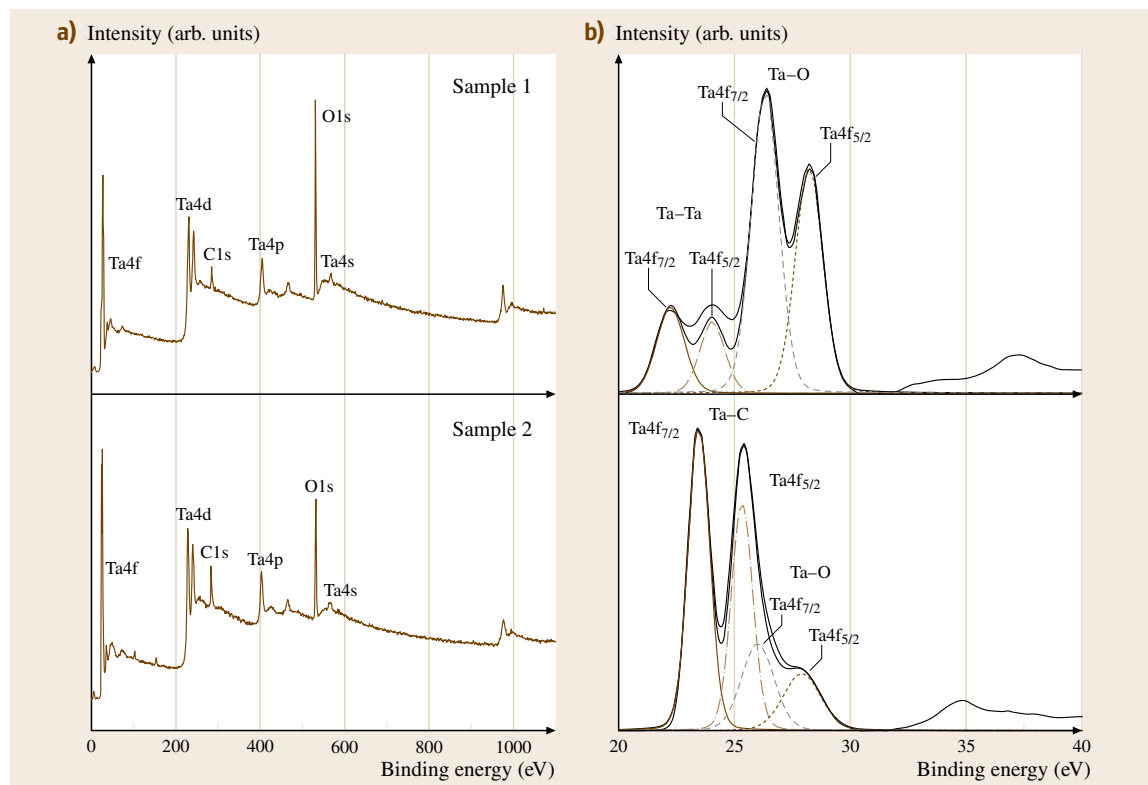


Fig. 28.11a,b XPS spectra of the Ta- and TaC-coated SiC wafer. (a) Wide-scan XPS spectra for sample 1 and 2 which have as-deposited 600–700 Å Ta film on the SiC. Sample 2 has been kept in $\text{C}_3\text{H}_8/\text{H}_2$ ambient at 1300°C for 15 min. (b) XPS spectra from Ta4f for sample 1 and 2. They are fitted with Gaussian peaks which are assigned to Ta (Ta4f_{7/2}: 22.4 eV, Ta4f_{5/2}: 24.0 eV) Ta₂O₅ (Ta4f_{7/2}: 26.3 eV, Ta4f_{5/2}: 28.2 eV), TaC (Ta4f_{7/2}: 23.5 eV, Ta4f_{5/2}: 25.3 eV)

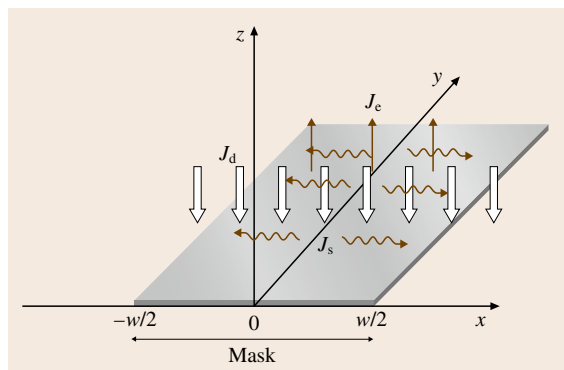


Fig. 28.12 Schematic of reactant species motion on the mask surface, taking into account surface diffusion

fore the susceptor was heated up. The wafers were then kept at 1300 °C in 180 ppm C_3H_8 diluted in H_2 ambient under 100 Torr pressure for 15 min. After the carburization process, the color of the mask changed from grey to golden yellow. X-ray photoelectron spectroscopy (XPS) has been used to confirm the formation of TaC, as shown in Fig. 28.11. Sample 1 has as-deposited Ta on the surface whereas the carburization process was carried out on sample 2. Figure 28.11a shows wide-scan XPS spectra of the samples. The main peaks correspond to tantalum (Ta4s, Ta4p, Ta4d, and Ta4f), carbon (C1s), and oxygen (O1s). It is clear that the carbon fraction (18 and 31.5% for samples 1 and 2, respectively) increases after the carburization process. Also notice that some oxygen is present on the top surface of the films and that the amount of oxygen decreases after the carburization process. The same analysis was carried out for both samples at a depth of 100 Å below the surface (materials near the surface were removed by Ar^+ ion sputtering). The analysis shows that the amount of oxygen decreases significantly with depth. It is likely that

the oxygen near the surface of the film is from natural oxidation.

Figure 28.11b shows high-resolution XPS spectra from Ta4f for samples 1 and 2. They are fitted with six Gaussian peaks, which are assigned to Ta (Ta4f_{7/2}: 22.2 eV, Ta4f_{5/2}: 24.0 eV), Ta₂O₅ (Ta4f_{7/2}: 26.2 eV, Ta4f_{5/2}: 28.0 eV) and TaC (Ta4f_{7/2}: 23.4 eV, Ta4f_{5/2}: 25.4 eV). The binding energies are close to those reported elsewhere [28.134, 135]. Particularly, comparing the results with the work by Gruzalski and Zehner [28.134], who determined core-level binding energies of TaC_x over the range $0.5 < x < 1.0$, the carburized film here corresponds in composition to TaC_{1.0}.

The growth selectivity with a TaC mask is significantly dependent on the growth conditions. Polycrystalline film deposition occurs on the mask under nonoptimized conditions. The polycrystalline deposition on the masks is closely related to the surface concentration of the reactant species. Figure 28.12 shows a schematic diagram of the motion of reactant species on the mask region, taking account of surface diffusion. The reactant species arrive on the mask region with a flux density of J_d , migrate on the mask surface during a mean surface lifetime of τ_s , and then desorb from the mask surface and re-evaporate with a flux density of J_e . In general, the surface concentration of reactant species on the SiC surface could be assumed to be negligibly small due to the homoepitaxial incorporation of the species.

However, the surface concentration on the mask area cannot be neglected because the reactant species arriving on the mask surfaces are difficult to be incorporated into adsorption sites. Thus, the reactant species that arrive on the mask within a diffusion length (λ_s) of the edge of the window opening are incorporated into the substrate during epitaxial growth, and the surface concentration distribution across the mask is dependent

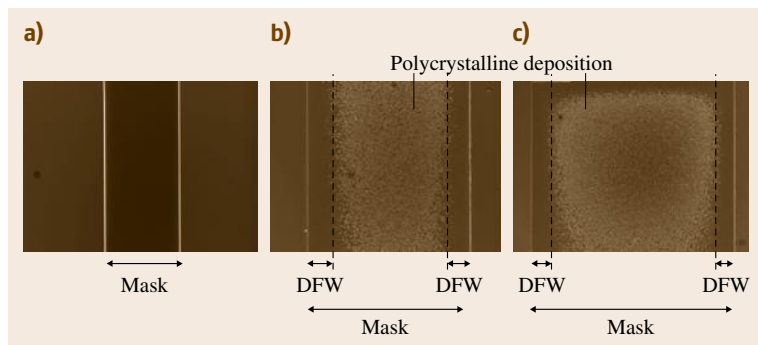


Fig. 28.13a–c SEM viewgraph of SiC polycrystal deposition on TaC mask at 1833 K. Flow rate is 2.24 sccm for both SiH_4 and C_3H_8 . Growth pressure is 80 Torr. Width of the mask is (a) 100 μm, (b) 500 μm, (c) 1000 μm, while $M : W = 1$

on the surface diffusion length, which determines the profile of polycrystalline deposition.

Figure 28.13 shows the polycrystalline growth on a mask and the defect free width (DFW) when the mask widths are very large; this experiment gives an approximate surface diffusion length of the growth species on the TaC mask.

28.4.3 Orientation Dependence of SiC Selective Growth

A circular pattern was first used to study the orientation dependence of the selective growth of SiC. The circular pattern consists of 5 μm wide mask windows spaced every half degree as spokes of a wheel. The patterned sample was then carburized and SiC was grown in the CVD reactor. The flow rates were 1.2 and 1.2 sccm for C_3H_8 and SiH_4 , respectively, using H_2 as the carrier gas. The epilayers were grown at 1550 $^\circ\text{C}$ under 80 Torr pressure, which would result in nominal planar growth rate of 3–4 $\mu\text{m}/\text{h}$. The growth lasted for 1 h.

Figure 28.14 shows tilted top views of selectively grown SiC window stripes along different directions. When the window stripes are parallel to the $\langle 11\bar{2}0 \rangle$ miscut direction, the growth on the exposed area followed the substrate orientation, and the top surface was smooth and specular (Fig. 28.14a). However, when

the window stripes were aligned along $\langle 1\bar{1}00 \rangle$, the growth on the window stripes developed (0001) facet (Fig. 28.14c). For window stripes along a direction between $\langle 11\bar{2}0 \rangle$ and $\langle 1\bar{1}00 \rangle$, (0001) facet intersected the 8 $^\circ$ off (0001) fronts and the extent of (0001) facet depended on the angle between the stripe orientation and the $\langle 11\bar{2}0 \rangle$ miscut direction.

To explain the formation of the (0001) facets, the effect of substrate offcut orientation has to be taken into account. As mentioned above, off-axis 4H-SiC(0001) 8 $^\circ$ miscut towards $\langle 11\bar{2}0 \rangle$ was used in this work. When the stripe direction is along $\langle 11\bar{2}0 \rangle$ miscut, there is no restriction on the step-flow growth. New steps are continuously available and facet develops starting from the edges of the selective epitaxial layer. However, when the selective growth opening is along the $\langle 1\bar{1}00 \rangle$ direction, step flow was restricted within the opening window and pure step-flow growth makes all steps to move out of the edge, as depicted in Fig. 28.15. Cross-sectional scanning electron microscopy (SEM) of selectively grown films in $\langle 1\bar{1}00 \rangle$ strip openings indicated good agreement of w/h ratio with the schematic shown in Fig. 28.15. When the growth opening window is aligned between $\langle 1\bar{1}00 \rangle$ and $\langle 11\bar{2}0 \rangle$ with an angular displacement larger than 20 $^\circ$ from these two orientations, step-flow growth is dominant, although partially restricted due to the angu-

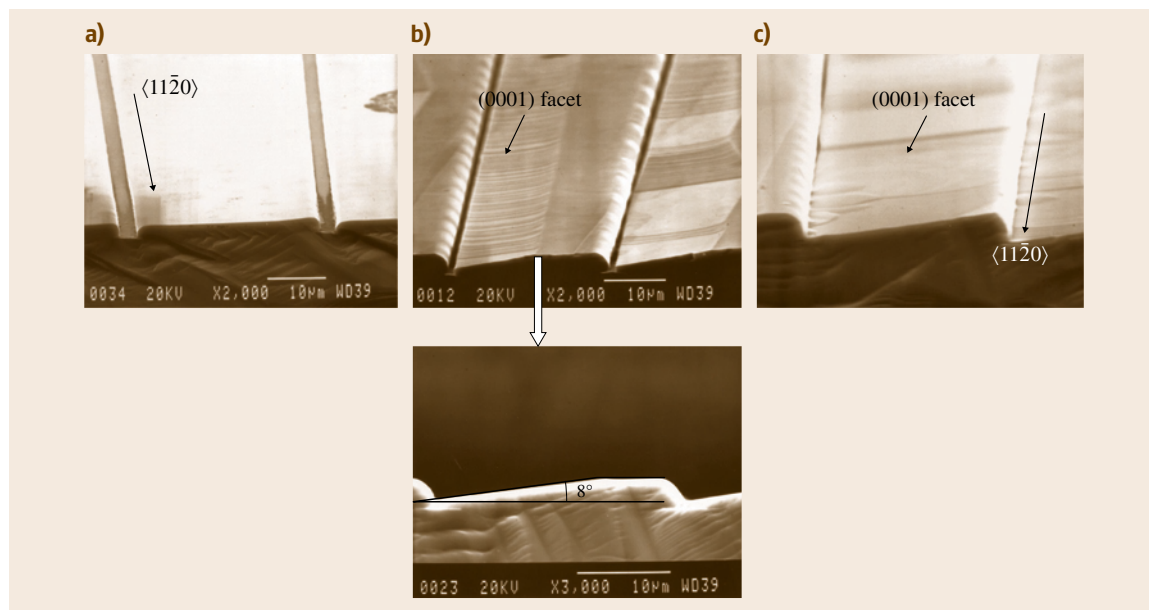


Fig. 28.14a–c Top view of the selective growth of 4H-SiC when window openings are along: (a) $\langle 11\bar{2}0 \rangle$ miscut direction, (b) direction between $\langle 11\bar{2}0 \rangle$ and $\langle 1\bar{1}00 \rangle$, (c) $\langle 1\bar{1}00 \rangle$ direction

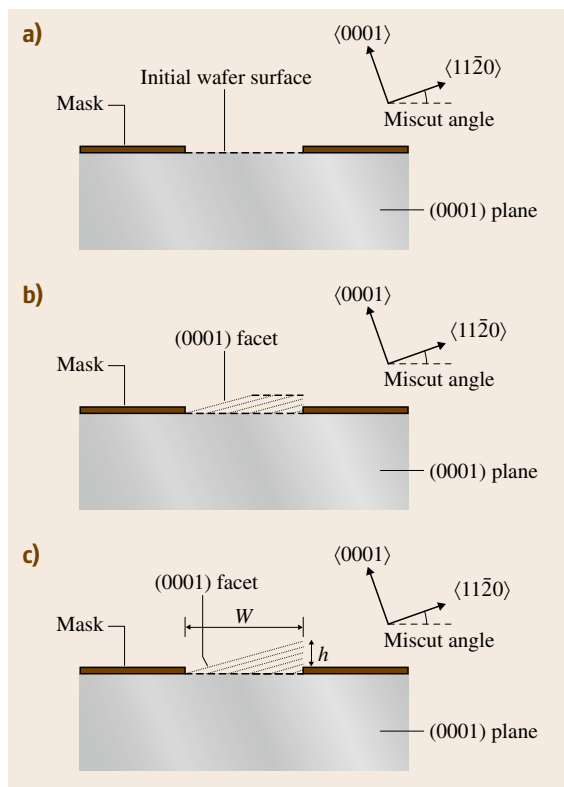


Fig. 28.15a–c Schematic images of the (0001) facet formation on 4H-SiC off (0001) axis towards $\langle 11\bar{2}0 \rangle$ substrate: (a) after selective growth, (b) after selective growth for a short time, (c) after selective growth for a longer time

lar displacement between step orientation and opening window orientation. Therefore, (0001) facet was formed within the growth window, whereas the percentage of the window occupied by (0001) facet does not increase significantly with increasing angular displacement from $\langle 11\bar{2}0 \rangle$.

The morphology of growth on (0001) facet was rougher, whereas smoother surface was observed on 8° off-axis growth front (Fig. 28.14a–c). It is likely that some 3C-SiC may have also nucleated on (0001) facet at relatively low temperature ($\approx 1550^\circ\text{C}$). Similar facet formation was also reported by Chen et al. [28.136] during SiC deposition on mesa structures of 4H-SiC(0001) substrate. Since step-flow growth dominated on the off-axis SiC surface, the flat and specular epilayers without 3C-SiC were grown on the off-axis surface. Therefore, when selective epitaxial growth on planar off-axis substrate is designed for device fabrication, growth

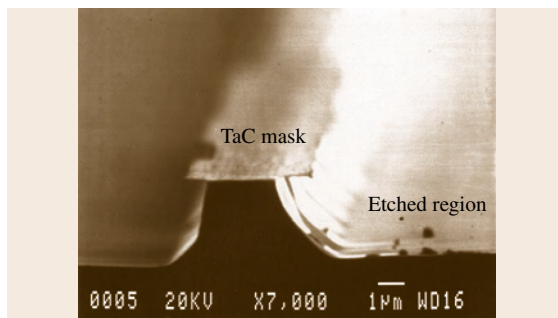


Fig. 28.16 In situ etching, instead of growth, occurs if SiH_4 flow is reduced by half compared with that used for Fig. 28.14. Note that the mask is intact after etching. SiH_4 flow rate: 0.6 sccm

window openings should be aligned along the miscut orientation.

It is worth mentioning that the TaC mask can also act as an in situ etching mask instead of a selective growth mask. When the silane flow rate was reduced to half that used in Fig. 28.14 under otherwise identical conditions, $3\ \mu\text{m}/\text{h}$ etching was obtained in unmasked region (Fig. 28.16). The mask itself was not etched, and etching of SiC under the mask left the mask hanging over the edge of the mesa. The mask peeled off during dicing for SEM observation, indicating that it was intact after etching. In situ etching studies using various gases have been carried out previously [28.95], and it was pointed out that the etch rate increases with increasing temperature under otherwise identical conditions. On the other hand, reactive atomic hydrogen is concluded to play a key role in etching of SiC. Therefore, the most plausible reasons for selective etching of SiC are: (1) the local temperature of the window opening region is higher than the nominal measured temperature of the susceptor since the conditions resulting in the etching of TaC-coated wafer are still within the growth window for a bare SiC substrate in our horizontal cold-wall CVD system, and (2) Ta at high temperature may produce atomic hydrogen that may enhance the etching rate of SiC.

28.4.4 Effects of Mask-to-Window Ratio ($M:W$) on SiC Selective Growth

As mentioned previously, selective in situ etching occurred with lower SiH_4 flow, even though the same conditions result in growth when a bare SiC substrate is used. It is evident that the mask itself has an influence on the selective growth and/or etching. In order

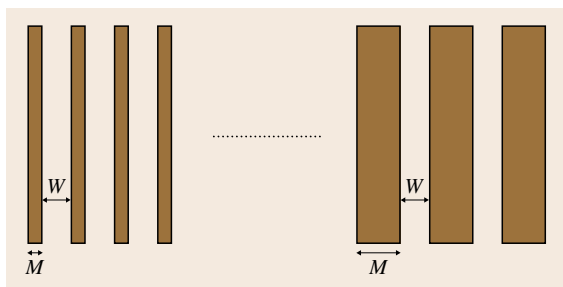


Fig. 28.17 Schematic of the linear pattern with varied mask (M) and window opening (W) width. M and W varied from 2 to 1000 μm . Pitch width (P) = mask width (M) + window opening width (W)

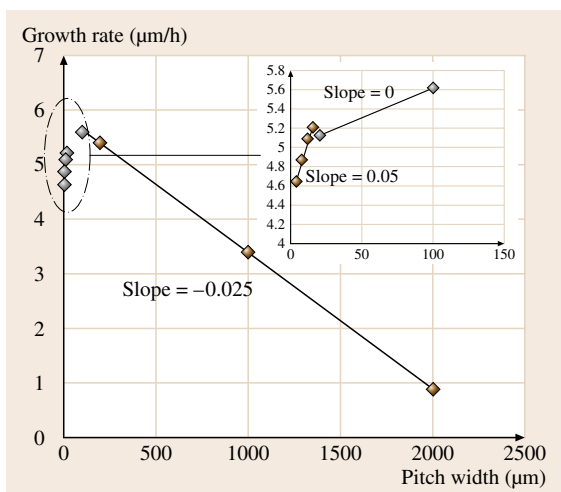


Fig. 28.18 Plot of selective growth rate as a function of pitch width. Pitch width (P) = mask width (M) + window width (W). $M : W = 1$. Flow rate is 2.24 sccm for both SiH_4 and C_3H_8 . Growth temperature and pressure are 1833 K and 80 Torr, respectively. The insert shows an expanded plot for pitch width $\leq 100 \mu\text{m}$

to identify the effects of the mask during the process, a linear pattern with varied mask and window opening width (Fig. 28.17) was made on the same substrate. This assures that the local conditions, such as temperature, precursor flow, pressure etc., for each window opening are the same. Therefore, different growth and/or etching behaviors, if any, are basically due to the existence of the mask. The growth was carried out on such a patterned substrate at temperature of 1560 $^\circ\text{C}$ under 80 Torr while the flow rate was kept at 2.24 sccm for both SiH_4 and C_3H_8 . Figure 28.18 shows a plot of selective growth rate versus pitch width (pitch width = mask width (M) + window width (W)) when the mask width-to-window width ratio ($M : W$) was kept at 1. As can be seen, the selective growth rate increases with increasing pitch width when the pitch width is below 100 μm , indicating that the growth process rather than etching is dominant under these conditions and is enhanced by diffusion of species from the mask.

The enhanced growth due to the supply of the reactants from the mask is also illustrated by the ridge growth at the edges of the mask, as shown in Fig. 28.19. Since the window stripes were patterned along the $\langle 11\bar{2}0 \rangle$ miscut direction, miscut steps were provided continuously. Excess species supplied laterally from the mask could be easily incorporated at step sites near the edge. Therefore, the step-flow growth velocity became higher than that at the center area of the window opening. Figure 28.20 shows a schematic diagram of the vicinal surface and ridge growth due to the diffusion of species from the mask to the window. Step-flow growth occurs not only along but also perpendicular to the miscut direction.

However, the selective growth rate decreases with further increasing of the pitch width ($\geq 200 \mu\text{m}$). The growth rate reduces from 5.5 to 0.9 $\mu\text{m}/\text{h}$ when the pitch width increases from 200 to 2000 μm . As is well known, both growth and etching process exist during SiC epitaxy and the etching process could be dominant under certain circumstances (e.g., higher temperature or lower precursor flow). In this experiment, the growth conditions were identical for all window openings since they were patterned on the same substrate and growth was carried out in the same run. It is believed that the decreased growth rate with increasing mask width is due to the enhanced etching by the mask. The enhanced etching process is probably caused by the production of atomic hydrogen by tantalum at high temperature, similar to the well-known hydrogenation catalysis by metals such as palladium [28.137]. Therefore, a larger area of the mask results in more atomic hydrogen and thus more

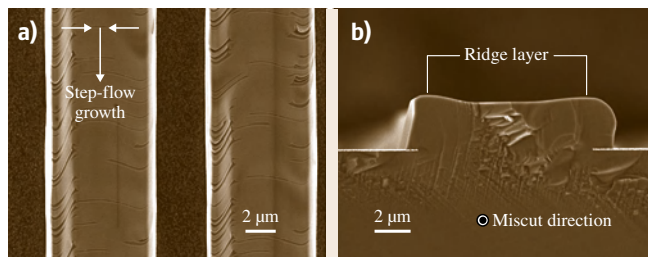


Fig. 28.19 (a) Top and (b) cross-sectional views of ridged layer grown on a 4H-SiC(0001) substrate miscut towards $\langle 11\bar{2}0 \rangle$ direction. Stripes are along $\langle 11\bar{2}0 \rangle$ miscut direction

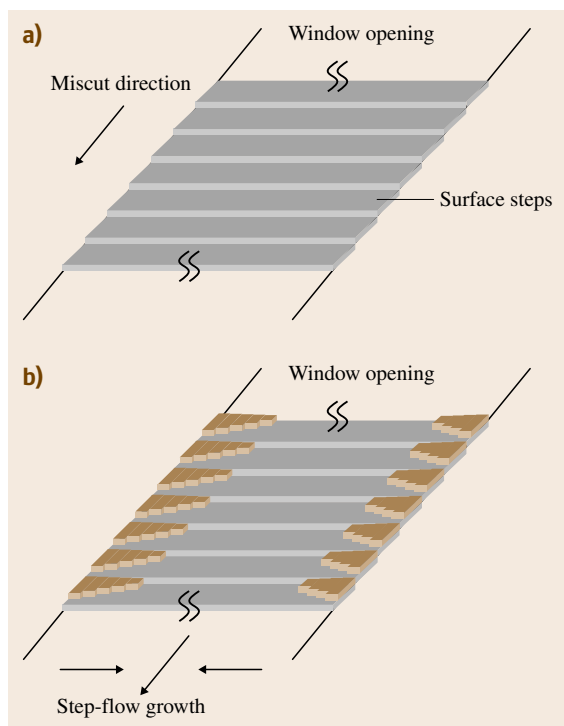


Fig. 28.20a,b Schematic of (a) (0001) vicinal surface and (b) ridge growth of the edge of the mask. Note that step-flow growth is along the directions parallel and perpendicular to miscut direction due to excess supply of species from the mask to the edge of window openings

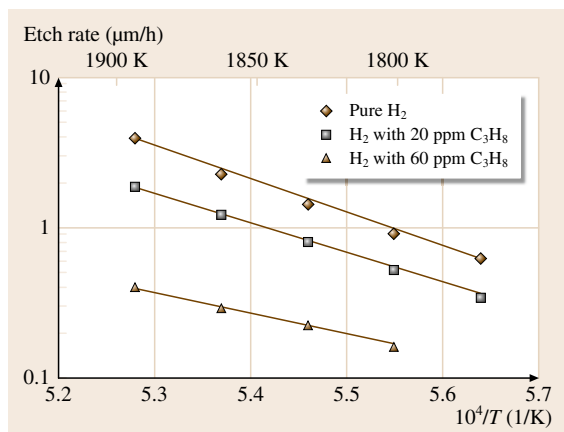


Fig. 28.21 Arrhenius plot of the etch rate of 4H-SiC as a function of temperature at different C_3H_8 flows. Reactor pressure is 100 Torr

etching of SiC in the vicinity. It is worth mentioning that significant etching of about $30\mu m$ in 30 min has been obtained when growth was carried out on a patterned substrate with $> 90\%$ of the surface covered by the mask [28.90].

Based on the studies of growth rate as a function of mask layout, it is evident that the growth process is dominant and that growth is enhanced by reactant diffusion from the mask when the mask is narrow ($< 100\mu m$ in this study). This increase in growth rate is limited by the surface diffusion rate of reactant species on the mask. However, the etching process competes with the growth process when the mask area becomes larger, and the growth rate decreases (or even etching occurs) with further increases in mask width.

28.4.5 Effects of C/Si Ratio on SiC Selective Growth

It has been found from in situ etching study of SiC [28.95] that adding a small amount of C_3H_8 increases the hydrocarbon pressure and hence suppresses the etching of SiC. Figure 28.21 shows the variation of etch rate of a bare 4H-SiC substrate at different C_3H_8 flows, for etching carried out at temperature range of 1800–1900 K in hydrogen ambient. Therefore, changing the C_3H_8 flow during the growth with fixed SiH_4 flow would change the formation of hydrocarbon in the chamber and hence the etching of SiC. Figure 28.22 shows the dependence of selective growth rate on C/Si ratio at different pitch widths and $M : W$ ratios. When the C/Si ratio is low ($= 1$), the etching process is dominant and no mask-enhanced growth is observed for narrow mask width ($\leq 100\mu m$), as observed previously. The selective growth rate decreases with increasing mask width, and almost no growth is obtained when the mask width was increased to $1000\mu m$. On a nonmasked wafer, such growth conditions would result in about $3\mu m/h$ growth rate. With increasing of the C/Si ratio, as expected, the growth rate increases for all investigated pitch widths. Mask-enhanced growth for pitch width $\leq 100\mu m$ is observed for C/Si ratio of both 3 and 6, and the growth rate saturates with further increasing of the mask width.

Decreased growth rate with increasing $M : W$ ratio for pitch width of $500\mu m$ is obtained for a C/Si ratio of 1 and 3, as shown in Fig. 28.22. However, mask-enhanced growth, instead of etching, is achieved for pitch width of $500\mu m$ for a C/Si ratio of 6, indicating

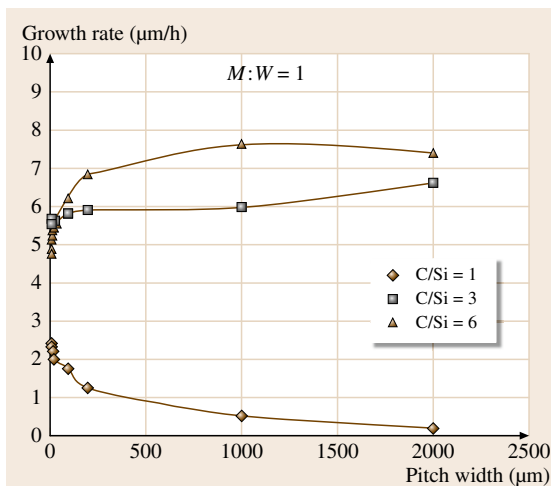


Fig. 28.22 Plot of selective growth rate as a function of pitch width at various C/Si ratios. Pitch width P = mask width (M) + window width (W). $M : W = 1$. Flow rate of SiH_4 is kept at 2.24 sccm. Growth temperature is 1813 K. Growth pressure is 80 Torr

that the etching process during epitaxy is suppressed by additional C_3H_8 flow.

28.4.6 Mechanism of Selective Etching and Effect of Atomic Hydrogen

It is worth pointing out that growth is obtained (Fig. 28.23) for extreme $M : W = 1000 \mu\text{m} : 5 \mu\text{m}$ at a C/Si ratio of 6 with SiH_4 flow of 2.24 sccm, while selectivity is insignificantly deteriorated. It is evident from the experiment that in situ selective etching is enhanced by atomic hydrogen produced by the mask under high

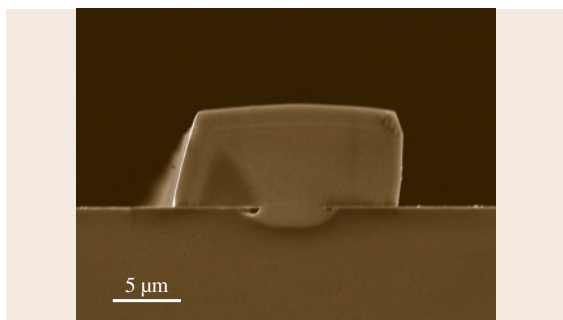


Fig. 28.23 Cross-sectional view of selective growth with $M : W = 1000 \mu\text{m} : 5 \mu\text{m}$ at C/Si = 6. Flow rate of SiH_4 is kept at 2.24 sccm. Growth temperature is 1813 K. Growth pressure is 80 Torr

temperature, which could be suppressed by increasing the C_3H_8 flow. Increasing the C_3H_8 flow is believed to be the most effective way to suppress in situ etching of SiC using a TaC mask without greatly deteriorating selectivity.

28.4.7 Fabrication of 4H-SiC p-n Junction Diodes Using Selective Growth

To illustrate the efficacy of selective growth for device fabrication, p-n junction diodes have been fabricated using selectively grown SiC. The starting wafer is commercial 8° off (0001)Si face, p-epitaxial layer grown on p^+ 4H-SiC substrate from CREE Research Inc. The nominal thickness and Al doping of the p-epilayer are $12 \mu\text{m}$ and $9.3 \times 10^{15} \text{ cm}^{-3}$, respectively. Fabrication was started by cleaning the wafers using a standard solvent degrease, Piranha clean, and RCA clean. Alignment marks were then trenched using CHF_3/O_2 plasma through a titanium/nickel transfer mask while the metal mask was prepared using a lift-off process. Next, refill regions were formed by reactive ion etch (RIE) through an oxide mask. In this step, $\approx 600 \text{ \AA}$ tantalum was first deposited using an e-beam evaporator and a masking oxide was then deposited, patterned, and etched using a combination of dry and wet processes to open the refill window. Two etch steps followed to form refill trench. Tantalum and SiC trench were etched using CF_4/O_2 and CHF_3/O_2 plasma, respectively. The etched trenches were about $1.5 \mu\text{m}$ deep. After the trench etching, the masking oxide was stripped using buffered oxide etch (BOE). Since both tantalum and SiC are inert to BOE at room temperature, it is safe to use BOE for oxide removal. Next, the wafer was loaded into the horizontal cold-wall reactor and tantalum film was then converted to tantalum carbide by exposing the wafer in propane/hydrogen ambient at 1300°C for 15 min as described previously. Epitaxial growth of SiC was carried out at temperature in the range of $1500\text{--}1600^\circ\text{C}$. Silane, propane, and nitrogen were used as the precursors with hydrogen as the carrier gas. The flow rates of silane, propane, nitrogen, and hydrogen were kept at 2.2, 3.7, 8 sccm, and 12.5 slm, respectively, during the growth. The RIE-etched trenches were refilled by nitrogen-doped n-type epitaxial film grown by selective epitaxy. The doping concentration was measured by mercury probe capacitance-voltage (C-V) using an epilayer grown on planar substrate under the same conditions. The TaC mask was then removed after selective growth using wet etchant. Subsequently, diodes were fabricated using standard contact procedure.

The forward and reverse current–voltage (I – V) characteristics of a square-trench ($250\text{ }\mu\text{m} \times 250\text{ }\mu\text{m}$) re-filled diode were first compared with those of a mesa etched PIN circular diode. Similar I – V characteristics were observed for both diodes, indicating that damage from the RIE etching might have been cured during epi-

taxial growth and that the junction interface is as good as that in a PIN diode fabricated by planar epitaxial growth. The difference in the forward I – V characteristic at higher current is possibly due to the higher series resistance of the p-type base of the trench refilled diode.

28.5 Conclusions

In this chapter, some basic properties of SiC and its epitaxial growth process have been described. Most of the early epitaxial growth was carried out using propane and silane in a horizontal cold-wall reactor. In recent years, hot-wall reactors have been developed for SiC growth, allowing much higher growth rate with very good surface morphology and very low background doping concentration. High-voltage ($> 10\text{ kV}$) power devices have been demonstrated. Epitaxial growth of SiC on bulk SiC substrates has advanced significantly

during the last decade, and commercial SiC devices have been introduced by several manufacturers. Further refinement of the basic reactor geometry and the growth process will be necessary to fully exploit the advantages of SiC over Si in devices. One such improvement may be the introduction of chlorine-containing precursors in addition to the more conventional silane and propane precursors. Some aspects of selective growth of SiC using TaC masks developed at the author's laboratory (mostly unpublished) are also reviewed.

References

- 28.1 T.P. Chow: SiC and GaN high voltage power switching devices, *Mater. Sci. Forum* **338–342**, 1155–1160 (2000)
- 28.2 R.G. Humphreys, D. Bimberg, W.J. Choyke: Wave-length modulated absorption in SiC, *Solid State Comm.* **39**, 163–167 (1981)
- 28.3 W.J. Choyke, L. Patrick: Exciton recombination radiation and phonon spectrum of 6H-SiC, *Phys. Rev.* **127**, 1868–1877 (1962)
- 28.4 W.V. Münch, I. Pfaffeneder: Breakdown field in vapor grown silicon carbide p–n junctions, *J. Appl. Phys.* **48**, 4831–4833 (1977)
- 28.5 D.K. Ferry: High field transport in wide band gap semiconductors, *Phys. Rev. B* **12**, 2361–2369 (1975)
- 28.6 R.P. Joshi: Monte Carlo calculations of the temperature and field dependent electron transport parameters for 4H-SiC, *J. Appl. Phys.* **78**, 5518–5521 (1995)
- 28.7 E. Moruan, O. Noblanc, C. Dua, C. Brylinski: SiC microwave power devices, *Mater. Sci. Forum* **353–356**, 669–674 (2001)
- 28.8 G.A. Slack: Thermal conductivity of pure and impure silicon, silicon carbide, and diamond, *J. Appl. Phys.* **35**, 3460 (1964)
- 28.9 M. Bhatnagar, B.J. Baliga: Comparison of 6H-SiC, 3C-SiC and Si power devices, *IEEE Trans. Electron. Dev.* **40**(3), 645–655 (1993)
- 28.10 T. Kimoto, T. Urushidani, S. Kobayashi, H. Matsunami: High voltage SiC Schottky barrier diodes with low on-resistances, *IEEE Electron. Dev. Lett.* **14**, 548–550 (1993)
- 28.11 D. Alok, B.J. Baliga, P.K. Mclarty: A simple edge termination for silicon carbide devices with nearly ideal breakdown voltages, *IEEE Electron. Dev. Lett.* **15**, 394–395 (1994)
- 28.12 R.J. Trew, J.-B. Yan, P.M. Mock: The potential of diamond and SiC electronic devices for microwave and millimeter wave power applications, *Proc. IEEE* **79**(5), 598–620 (1991)
- 28.13 J.M. McGarrity, F.B. McLean, W.M. DeLancey, J. Palmour, C. Carter, J. Edmond, R.R. Oakley: SiC JFET radiation response, *IEEE Trans. Nucl. Sci.* **39**(6), 1974–1981 (1992)
- 28.14 See for example, <http://www.cree.com/> and <http://www.infineon.com/>
- 28.15 H. Matsunami, T. Kimoto: Step controlled epitaxial growth of SiC: High quality homoepitaxy, *Mater. Sci. Eng.* **R20**(3), 125–166 (1997)
- 28.16 W.J. Choyke, G. Pensl: Physical properties of SiC, *MRS Bull.* **22**(3), 25–29 (1997)
- 28.17 C.H. Park, B.H. Cheong, K.H. Lee, K.J. Chang: Structural and electronic properties of cubic, 2H, 4H and 6H SiC, *Phys. Rev. B* **49**(7), 4485–4493 (1994)
- 28.18 W.S. Yoo, H. Matsunami: Polytype-controlled single crystal growth of silicon carbide using 3C–6H solid state phase transformation, *J. Appl. Phys.* **70**(11), 7124–7131 (1991)

- 28.19 W.S. Yoo, H. Matsunami: Solid state phase transformation in cubic silicon carbide, *Jpn. J. Appl. Phys. Part I (regular papers and short notes)* **30**, 545–553 (1991)
- 28.20 A. Itoh, H. Matsunami: Single crystal growth of SiC and electronic devices, *Crit. Rev. Solid State Mater. Sci.* **22**(2), 111–197 (1997)
- 28.21 P.G. Neudeck: Electrical impact of SiC structural defects on high electric field devices, *Mater. Sci. Forum* **338–342**, 1161–1166 (2000)
- 28.22 J.A. Powell, H.A. Will: Low temperature solid state phase transformations in 2H SiC, *J. Appl. Phys.* **43**(4), 1400–1408 (1972)
- 28.23 M. Dudley, X. Huang: Characterization of SiC using synchrotron white beam x-ray topography, *Mater. Sci. Forum* **338–342**, 431–436 (2000)
- 28.24 I. Kamata, H. Tsuchida, T. Jikimoto, K. Izumi: Structural transformation of screw dislocation via thick 4H-SiC epitaxial growth, *Jpn. J. Appl. Phys.* **39**, 6496–6500 (2000)
- 28.25 P. Pirouz: On micropipes and nanopipes in SiC and GaN, *Philos. Mag. A* **78**, 727–736 (1998)
- 28.26 P.G. Neudeck, H. Wei, M. Dudley: Study of bulk and elementary screw dislocation assisted reverse breakdown in low-voltage (< 250 V) 4H-SiC pn junction diodes: DC properties, *IEEE Trans. Electron. Dev.* **46**(3), 478–484 (1999)
- 28.27 U. Zimmermann, A. Hallen, A.O. Konstantinov, B. Breitholtz: Investigation of microplasma breakdown in 4H SiC, *Mater. Res. Soc. Symp. Proc.* **512**, 151–156 (1998)
- 28.28 A.O. Konstantinov, Q. Wahab, N. Nordell, U. Lindefelt: Study of Avalanche breakdown and impact ionization in 4H SiC, *J. Electron. Mater.* **27**(4), 335–341 (1998)
- 28.29 P.G. Neudeck, J.A. Powell: Performance limiting micropipe defects in SiC wafers, *IEEE Electron. Dev. Lett.* **15**, 63–65 (1994)
- 28.30 W. Si, M. Dudley, R. Glass, V. Tsvetkov, C. Carter Jr: Hollow core screw dislocations in 6H-SiC single crystals: A test of Frank's theory, *J. Electron. Mater.* **26**, 128–133 (1997)
- 28.31 W. Si, M. Dudley: Experimental studies of hollow core screw dislocations in 6H- and 4H-SiC single crystals, *Mater. Sci. Forum* **264–268**, 429–432 (1998)
- 28.32 C.M. Schnabel, M. Tabib-Azar, P.G. Neudeck, S.G. Bailey, H.B. Su, M. Dudle, R.P. Raffaele: Correlation of EBIC and SWBXT imaged defects and epilayer growth pits in 6H-SiC Schottky diodes, *Mater. Sci. Forum* **338–342**, 489–492 (2000)
- 28.33 J.A. Powell, D.J. Larkin: Process induced morphological defects in epitaxial CVD silicon carbide, *Phys. Status Solidi (b)* **202**, 529–548 (1997)
- 28.34 T. Kimoto, N. Miyamoto, H. Matsunami: Performance limiting surface defects in SiC epitaxial pn junction diodes, *IEEE Trans. Electron. Dev.* **46**(3), 471–477 (1999)
- 28.35 S. Nishino, J.A. Powell, W. Will: Production of large area single crystal of 3C-SiC for semiconductor devices, *Appl. Phys. Lett.* **42**, 460 (1983)
- 28.36 S. Nishino, K. Matsumoto, Y. Chen, Y. Nishio: Epitaxial growth of 4H-SiC by sublimation close space technique, *Mater. Sci. Eng. B* **61/62**, 121–124 (1999)
- 28.37 H. Nakazawa, M. Suemitsu, S. Asami: Formation of high quality SiC on Si(001) at 900 °C using monomethylsilane gas source MBE, *Mater. Sci. Forum* **338–342**, 269–272 (2000)
- 28.38 M.E. Okhuysen, M.S. Mazzola, Y.-H. Lo: Low temperature growth of 3C-SiC on silicon for advanced substrate development, *Mater. Sci. Forum* **338–342**, 305–308 (2000)
- 28.39 M.-A. Hasan, A. Faik, D. Purser, D. Lieu: Heteroepitaxy of 3C-SiC on Si (100) using porous Si as a compliant seed crystal, *Tech. Dig. Int. Conf. SiC Relat. Mater. ICSCRM2001 (Tsukuba 2001)* pp. 492–493
- 28.40 Y. Ishida, K. Kushibe, T. Takahashi, H. Okumura, S. Yoshida: 3C-SiC homoepitaxial growth by chemical vapor deposition and Schottky barrier junction characteristics, *Mater. Sci. Forum* **389–393**, 275–278 (2002)
- 28.41 H. Nagasawa, K. Yagi, T. Kawahara: 3C-SiC heteroepitaxial growth on (001) Si undulant substrates, *J. Cryst. Growth* **237–239**, 1244–1249 (2002)
- 28.42 H. Nagasawa, K. Yagi, T. Kawahara, N. Hatta, G. Pensl, W.J. Choyke, T. Yamada, K.M. Itoh, A. Schoner: *Silicon Carbide: Recent Major Advances* (Springer, Berlin, Heidelberg 2004) p. 207
- 28.43 F.R. Chien, S.R. Nutt, J.M. Carulli Jr., N. Bunchan, C.P. Beetz Jr., W.S. Yoo: Heteroepitaxial growth of beta SiC films on TiC substrates: Interface structure and defects, *J. Mater. Res.* **9**(8), 2086–2095 (1994)
- 28.44 C. Hallin, A.O. Konstantinov, O. Kordina, E. Janzen: Mechanism of cubic SiC nucleation on off-axis substrates, *Proc. 6th Int. Conf. SiC Relat. Mater. 1995, Inst. Phys. Conf. Ser.* **142**, 85–88 (1996)
- 28.45 J.A. Powell, D.J. Larkin, P.B. Abel, L. Zhou, P. Pirouz: Effect if tilt angle on the morphology of SiC epitaxial films grown on vicinal (0001) SiC substrates. In: *Silicon Carbide and Related Materials*, *Inst. Phys. Conf. Ser.*, Vol. 142 (1995) pp. 77–80
- 28.46 V.F. Tsvetkov, S.T. Allen, H.S. Kong, C.H. Carter Jr.: Recent progress in SiC crystal growth, *Proc. 6th Int. Conf. SiC Relat. Mater. 1995, Inst. Phys. Conf. Ser.* **142**, 17–22 (1996)
- 28.47 D.J. Larkin: An overview of SiC epitaxial growth, *MRS Bulletin* **22**(3), 36–41 (1997)
- 28.48 V. Heine, C. Cheng, R.J. Needs: The preference of SiC for growth in the metastable cubic form, *J. Am. Ceram. Soc.* **74**, 2630–2633 (1991)
- 28.49 K. Wada, T. Kimoto, K. Nishikawa, H. Matsunami: Epitaxial growth of 4H-SiC on 4° off-axis (0001) and (000-1) substrates by hot wall CVD, *Mater. Sci. Forum* **527–529**, 219–222 (2006)

- 28.50 S. Rendakova, V. Ivantsov, V. Dmitriev: High quality 6H- and 4H-SiC pn structures with stable electric breakdown grown by liquid phase epitaxy, *Mater. Sci. Forum* **264–268**, 163–166 (1998)
- 28.51 D.H. Hofmann, M.H. Muller: Prospects of the use of liquid phase techniques for the growth of bulk silicon carbide crystals, *Mater. Sci. Eng. B* **61/62**, 29–39 (1999)
- 28.52 R. Yakimova, M. Syväjärvi, S. Redankova, V.A. Dimitriev, A. Henry, E. Janzen: Micropipe healing in liquid phase epitaxial growth of SiC, *Mater. Sci. Forum* **338–342**, 237–240 (2000)
- 28.53 A. Tanaka, T. Ataka, E. Ohkura, H. Katsuno: Growth modes of silicon carbide in low-temperature liquid phase epitaxy, *Jpn. J. Appl. Phys.* **43**(11A), 7670–7671 (2004)
- 28.54 O. Filip, B. Epelbaum, M. Bickermann, A. Winacker: Micropipe healing in SiC wafers by liquid-phase epitaxy in Si-Ge melts, *J. Cryst. Growth* **271**, 142–150 (2004)
- 28.55 T. Hatayama, S. Nakamura, K. Kurobe, T. Kimoto, T. Fuyuki, H. Matsunami: High-temperature surface structure transitions and growth of alpha-SiC (0001) in ultrahigh vacuum, *Mater. Sci. Eng. B* **61/62**, 135–138 (1999)
- 28.56 S. Nakamura, T. Hatayama, T. Kimoto, T. Fuyuki, H. Matsunami: Growth of SiC on 6H-SiC (0114) substrates by gas source molecular beam epitaxy, *Mater. Sci. Forum* **338–342**, 201–204 (2000)
- 28.57 T. Sugii, T. Aoyama, T. Ito: Low-temperature growth of beta-SiC on Si by gas-source MBE, *J. Electrochem. Soc.* **137**(3), 989–992 (1990)
- 28.58 H. Nakazawa, M. Suemitsu, S. Asami: Formation of high quality SiC on Si (001) at 900 °C using monomethylsilane gas-source MBE, *Mater. Sci. Forum* **338–342**, 269–272 (2000)
- 28.59 C. Hallin, I.G. Ivanov, T. Egilsson, A. Henry, O. Kordina, E. Jansen: The material quality of CVD grown SiC using various precursors, *J. Cryst. Growth* **183**, 163 (1998)
- 28.60 Y. Gao, J.H. Edgar: Selective epitaxial growth of SiC: Thermodynamic analysis of the Si-C-Cl-H and Si-C-Cl-H-O systems, *J. Electrochem. Soc.* **144**(5), 1875–1880 (1997)
- 28.61 K. Yagi, H. Nagasawa: 3C-SiC growth by alternate supply of SiH₂Cl₂ and C₂H₂, *J. Cryst. Growth* **174**, 653–657 (1997)
- 28.62 T. Miyanagi, S. Nishino: Hotwall CVD growth of 4H-SiC using Si₂Cl₆-C₃H₈-H₂ system, *Mater. Sci. Forum* **389–393**, 199–202 (2002)
- 28.63 C. Sartel, V. Souliere, Y. Monteil, H. El-Harrouni, J.M. Bluet, G. Guillot: Epitaxial growth of 4H-SiC with hexamethyldisilane, *Mater. Sci. Forum* **389–393**, 263–266 (2002)
- 28.64 R. Rodriguez-Clemente, A. Figueras, S. Garelik, B. Armas, C. Combsure: Influence of temperature and tetramethylsilane partial pressure on the beta SiC depositin by cold wall chemical vapor deposition, *J. Cryst. Growth* **125**, 532–542 (1992)
- 28.65 T. Hatayama, H. Yano, Y. Uraoka, T. Fuyuki: High purity SiC epitaxial growth by chemical vapor deposition using CH₃SiH₃ and C₃H₄ sources, *Mater. Sci. Forum* **527–529**, 203–206 (2006)
- 28.66 See for example, <http://www.saespuregas.com/>
- 28.67 H. Matsunami, T. Kimoto: Step controlled epitaxial growth of SiC: High quality homoepitaxy, *Mater. Sci. Eng.* **R20**(3), 125–166 (1997)
- 28.68 S. Nakamura, T. Kimoto, H. Matsunami: Fast growth and doping characteristics of SiC in a horizontal cold wall CVD, *Mater. Sci. Forum* **389–393**, 183–186 (2002)
- 28.69 R. Rupp, A. Wiedenhofer, P. Friedrichs, D. Peters, R. Schorner, D. Stephani: Growth of SiC epitaxial layers in a vertical cold wall reactor suited for high voltage applications, *Mater. Sci. Forum* **264–268**, 89–96 (1998)
- 28.70 C. Sartel, J.M. Bluet, V. Souliere, I. El-Harrouni, Y. Monteil, M. Mermoux, G. Guillot: Characterization of homoepitaxial 4H-SiC layer grown from silane/propane system, *Mater. Sci. Forum* **433–436**, 165–168 (2003)
- 28.71 B. Thomas, W. Bartsch, R. Stein, R. Schorner, D. Stephani: Properties and suitability of 4H-SiC epitaxial layers grown at different CVD systems for high voltage applications, *Mater. Sci. Forum* **457–460**, 181–184 (2004)
- 28.72 O. Kordina, C. Hallin, A. Henry, J.P. Bergman, I. Ivanov, A. Ellison, N.T. Son, E. Janzen: Growth of SiC by hot-wall, CVD and HTCVD, *Phys. Status Solidi (b)* **202**, 321–334 (1996)
- 28.73 T. Kimoto, S. Nakazawa, K. Fujihira, T. Hirao, S. Nakamura, Y. Chen, H. Matsunami: Recent achievement and future challenges in SiC homoepitaxial growth, *Mater. Sci. Forum* **389–393**, 165–170 (2002)
- 28.74 A. Shoner, A. Konstantinov, S. Karlsson, R. Berge: Highly uniform epitaxial SiC-layer growth in a hot wall CVD reactor with mechanical rotation, *Mater. Sci. Forum* **389–393**, 187–190 (2002)
- 28.75 B. Thomas, C. Hecht: Epitaxial growth of n-type 4H-SiC on 3, wafers for power devices, *Mater. Sci. Forum* **483–485**, 141–146 (2005)
- 28.76 A. Ellison, J. Zhang, J. Peterson, A. Henry, Q. Wahab, J.P. Bergman, Y.N. Makarov, A. Vorob'ev, A. Vehanen, E. Janzen: High temperature CVD growth of SiC, *Mater. Sci. Eng. B* **61/62**, 113–120 (1999)
- 28.77 H. Fujiwara, K. Danno, T. Kimoto, T. Tojo, H. Matsunami: Fast epitaxial growth of thick 4H-SiC with specular surface by chimney-type vertical hot-wall chemical vapor deposition, *Mater. Sci. Forum* **457–460**, 205–208 (2004)
- 28.78 E. Janzén, J.P. Bergman, Ö. Danielsson, U. Forsberg, C. Hallin, J. ul Hassan, A. Henry, I.G. Ivanov, A. Kakanakova-Georgieva, P. Persson, Q. ul Wa-

- hab: SiC and III-nitride growth in a hot-wall CVD reactor, *Mater. Sci. Forum* **483–485**, 61–66 (2005)
- 28.79 K. Danno, T. Kimoto, K. Asano, Y. Sugawara, H. Matsunami: Fast epitaxial growth of high-purity 4H-SiC(0001) in a vertical hot-wall chemical vapor deposition, *J. Electron. Mater.* **34**(4), 324–329 (2005)
- 28.80 H. Fujiwara, T. Kimoto, T. Tojo, H. Matsunami: Reduction of stacking faults in fast epitaxial growth of 4H-SiC and its impacts on high-voltage Schottky diodes, *Mater. Sci. Forum* **483–485**, 151–154 (2005)
- 28.81 I. Bhat, Canhua Li: High growth rate epitaxy of SiC in a vertical hotwall reactor, unpublished
- 28.82 M. Syvajarvi, R. Yakimova, H. Jacobsson, M.K. Linnarsson, A. Henry, E. Janzén: High growth rate epitaxy of thick 4H-SiC layers, *Mater. Sci. Forum* **338–342**, 165–168 (2000)
- 28.83 T. Furusho, T. Miyanagi, Y. Okui, S. Ohshima, S. Nishino: Homoepitaxial growth of cubic silicon carbide by sublimation epitaxy, *Mater. Sci. Forum* **389–393**, 279–282 (2002)
- 28.84 E.O. Sveinbjornsson, H.O. Olafsson, G. Gudjonsson, F. Allerstam, P.A. Nilsson, M. Syvajarvi, R. Yakimova, C. Hallin, T. Rodle, R. Jos: High field effect mobility in Si face 4H-SiC MOSFET made on sublimation grown epitaxial material, *Mater. Sci. Forum* **483–485**, 841–844 (2005)
- 28.85 D. Ziane, J.M. Bluett, G. Guillot, P. Godignon, J. Monserrat, R. Ciechonski, M. Syvajarvi, R. Yakimova, L. Chen, P. Mawby: Characterizations of SiC/SiO₂ interface quality toward high power MOSFETs realization, *Mater. Sci. Forum* **457–460**, 1281–1286 (2004)
- 28.86 R.C. Glass, P. Lu, J.H. Edgar, O.J. Glembocki, P.B. Klein, E.R. Glaser, J. Perrin, J. Chaudhuri: High-speed homoepitaxy of SiC from methyltrichloro-silane by CVD, *Int. Conf. Silicon Carbide Relat. Mater.* (Pittsburgh 2005)
- 28.87 R. Myers, O. Kordina, Z. Shishkin, F. Yan, R.P. Devaty, S.E. Saddow: Effects of HCl additive on the growth rate of 4H-SiC in a hot wall CVD reactor, *Int. Conf. Silicon Carbide Relat. Mater.* (Pittsburgh 2005)
- 28.88 A. Veneroni, F. Omarini, M. Masi: Silicon carbide growth mechanisms from SiH₄, SiHCl₃ and nC₃H₈, *Cryst. Growth Technol.* **40**(10/11), 967–971 (2005)
- 28.89 G. Pensl, W.J. Choyke: Electrical and optical characterization of SiC, *Physica B* **185**, 264–283 (1993)
- 28.90 R. Wang, I. Bhat, unpublished results
- 28.91 D.J. Larkin: SiC dopant incorporation control by site competition CVD, *Phys. Status Solidi (b)* **202**, 305–320 (1997)
- 28.92 T. Troffer, C. Peppermüller, G. Pensi, K. Rottner, A. Schoner: Phosphorus-related donors in 6H-SiC generated by ion implantation, *J. Appl. Phys.* **80**(7), 3739–3743 (1996)
- 28.93 M.A. Capano, J.A. Cooper Jr., M.R. Melloch, A. Saxler, W.C. Mitchel: Ionization energies and electron mobilities in phosphorous and nitrogen implanted SiC, *J. Appl. Phys.* **87**(12), 8773–8777 (2000)
- 28.94 S. Rao, T.P. Chow, I. Bhat: Dependence of the ionization energy of phosphorous donor in 4H-SiC on doping concentration, *Mater. Sci. Forum* **527–529**, 597–600 (2006)
- 28.95 R. Wang: SiC epitaxial growth for power device applications. Ph.D. Thesis (Rensselaer Polytechnic Institute, Troy 2002)
- 28.96 M.H. Anikin, A.A. Lebedev, A.L. Syркин, A.V. Suvorov: Investigation of deep levels in SiC by capacitance spectroscopy methods, *Sov. Phys. Semicond.* **19**, 69–71 (1985)
- 28.97 W. Suttrop, G. Pensi, P. Lanig: Boron related deep centers in SiC, *Appl. Phys. A* **51**, 231–237 (1990)
- 28.98 A. Golz, G. Horstmann, E. Stein von Kamienski, H. Kurz: Oxidation kinetics of 3C, 4H and 6H silicon carbide, *Proc. Sixth Int. Conf. Silicon Carbide Relat. Mater.* (1996) pp. 633–636
- 28.99 K. Wada, T. Kimoto, K. Nishikawa, H. Matsunami: Improved surface morphology and background doping concentration in 4H-SiC (0001) epitaxial growth by hot-wall CVD, *Mater. Sci. Forum* **483–485**, 85–88 (2005)
- 28.100 T. Yamamoto, T. Kimoto, H. Matsunami: Impurity incorporation mechanism in step-controlled epitaxy growth temperature and substrate off-angle dependence, *Mater. Sci. Forum* **264–268**, 111–116 (1998)
- 28.101 U. Forsberg, Ö. Danielsson, A. Henry, M.K. Linnarsson, E. Janzén: Nitrogen doping of epitaxial silicon carbide, *J. Cryst. Growth* **236**(1–3), 101–112 (2002)
- 28.102 U. Forsberg, Ö. Danielsson, A. Henry, M.K. Linnarsson, E. Janzén: Aluminium doping of epitaxial silicon carbide, *J. Cryst. Growth* **253**(1–4), 340–350 (2003)
- 28.103 T. Kimoto, T. Yamamoto, Z.Y. Chen, H. Matsunami: 4H-SiC (1120) epitaxial growth, *Mater. Sci. Forum* **338–342**, 189–192 (2000)
- 28.104 T. Kimoto, K. Hashimoto, K. Fujihira, K. Danno, S. Nakamura, Y. Negoro, H. Matsunami: Epitaxial growth and characterization of 4H-SiC(1120) and (0338), *Mater. Res. Soc. Symp. Proc.* **742**, 3–13 (2003)
- 28.105 Z. Zhang, Y. Gao, A.C. Arjunan, E.Y. Toupitsyn, P. Sadagopan, R. Kennedy, T.S. Sudarshan: CVD growth and characterization of 4H-SiC epitaxial film on (1120) as-cut substrates, *Mater. Sci. Forum* **483–485**, 113–116 (2005)
- 28.106 K. Nakayama, Y. Miyanagi, H. Shiomi, S. Nishino, T. Kimoto, H. Matsunami: The development of 4H-SiC {0338} wafers, *Mater. Sci. Forum* **389–393**, 123–127 (2002)
- 28.107 T. Kimoto, K. Danno, K. Fujihira, H. Shiomi, H. Matsunami: Complete micropipe dissociation in 4H-SiC (03–38) epitaxial growth and its impact on reverse characteristics of Schottky barrier diodes, *Mater. Sci. Forum* **433–436**, 197–200 (2003)

- 28.108 T. Kimoto, K. Danno, K. Fujihira, H. Shiomi, H. Matsunami: SiC epitaxy on non-standard surfaces, *Mater. Sci. Forum* **433–436**, 125–130 (2003)
- 28.109 E. Arnold, D. Alok: Effect of interface states on electron transport in 4H-SiC inversion layers, *IEEE Trans. Electron. Dev.* **48**, 1870–1877 (2001)
- 28.110 T. Kimoto, Y. Kanzaki, M. Noborio, H. Kawano, H. Matsunami: Interface properties of metal-oxide-semiconductor structures on 4H-SiC {0001} and {1120} formed by N₂O oxidation, *Jpn. J. Appl. Phys.* **44**(3), 1213–1218 (2005)
- 28.111 K. Fukuda, J. Senzaki, K. Kojima, T. Suzuki: High inversion channel mobility of MOSFET fabricated on 4H-SiC C(0001) face using H₂ post-oxidation annealing, *Mater. Sci. Forum* **433–436**, 567–570 (2003)
- 28.112 T. Kimoto, H. Kawano, J. Suda: 1200V-class 4H-SiC RESURF MOSFETs with low on-resistances, *Proc. 17th Int. Symp. Power Semicond. Devices IC's* (2005) pp. 159–162
- 28.113 N. Nordell, S. Karlsson, A.O. Kenstantinov: Growth of 4H and 6H SiC in trenches and around stripe mesas, *Mater. Sci. Forum* **264–268**, 131–134 (1998)
- 28.114 Y. Chen, T. Kimoto, Y. Takeuchi, R.K. Malhan, H. Matsunami: Homoepitaxy of 4H-SiC on trenced (0001) Si face substrates by chemical vapor deposition, *Jpn. J. Appl. Phys.* **43**(7A), 4105–4109 (2004)
- 28.115 P.G. Neudeck, J.A. Powell, G.M. Beheim, E.L. Benavage, P.B. Abel, A.J. Trunek, D.J. Spry, M. Dudley, W.M. Vetter: Enlargement of step-free SiC surfaces by homoepitaxial web growth of thin SiC cantilevers, *J. Appl. Phys.* **92**, 2391–2400 (2002)
- 28.116 P.G. Neudeck, A.J. Trunek, D.J. Spry, J.A. Powell, H. Du, M. Skowronski, N.D. Bassim, M.A. Mastro, M.E. Twigg, R.T. Holm, R.L. Henry, C.R. Eddy Jr.: Recent results from epitaxial growth on step free 4H-SiC mesas, *Mater. Res. Soc. Symp. Proc.* **911**, B08–03 (2006)
- 28.117 P.G. Neudeck, A.J. Powell: Homoepitaxial and heteroepitaxial growth on step-free SiC mesas. In: *Silicon Carbide: Recent Major Advances*, ed. by W.J. Choyke, H. Matsunami, G. Pensi (Springer, New York 2003) p. 179
- 28.118 N.D. Bassima, M.E. Twigg, M.A. Mastro, C.R. Eddy Jr., T.J. Zega, R.L. Henry, J.C. Culbertson, R.T. Holm, P. Neudeck, J.A. Powell, A.J. Trunek: Dislocations in III-nitride films grown on 4H-SiC mesas with and without surface steps, *J. Cryst. Growth* **304**, 103–107 (2007)
- 28.119 M.R. Goulding: Selective epitaxial growth of silicon, *Mater. Sci. Eng. B* **17**(1–3), 47–67 (1993)
- 28.120 D. Kapolnek, S. Keller, R. Vetry, R.D. Underwood, P. Kozodoy, S.P. Den Baars, U.K. Mishra: Anisotropic epitaxial lateral growth in GaN selective area epitaxy, *Appl. Phys. Lett.* **71**(9), 1204–1206 (1997)
- 28.121 O. Nam, T.S. Zheleva, M.D. Bremser, R.F. Davis: Lateral epitaxial overgrowth of GaN films on SiO₂ areas via metalorganic vapor phase epitaxy, *J. Electron. Mater.* **27**(4), 233–237 (1998)
- 28.122 Y. Ohshita: Low temperature and selective growth of β -SiC using the SiH₂Cl₂/i-C₄H₁₀/HCl/H₂, *Appl. Phys. Lett.* **57**(6), 605–607 (1990)
- 28.123 J.H. Edgar, Y. Gao, J. Chaudhuri, S. Cheema, P.W. Yip, M.V. Sidorov: Selective epitaxial growth of silicon carbide on SiO₂ masked Si(100): The effects of temperature, *J. Appl. Phys.* **84**(1), 201–204 (1998)
- 28.124 K. Teker: Selective epitaxial growth of 3C-SiC on patterned Si using hexamethyldisilane by APCVD, *J. Cryst. Growth* **257**(3/4), 245–254 (2003)
- 28.125 S. Nishino, C. Jacob, Y. Okui, S. Ohshima, Y. Masuda: Lateral over-growth of 3C-SiC on patterned Si(111) substrates, *J. Cryst. Growth* **237–239**(2), 1250–1253 (2002)
- 28.126 A.R. Bushroa, C. Jacob, H. Saijo, S. Nishino: Lateral epitaxial overgrowth and reduction in defect density of 3C-SiC on patterned Si substrates, *J. Cryst. Growth* **271**(1/2), 200–206 (2004)
- 28.127 E. Eshun, C. Taylor, M.G. Spencer, K. Kornegay, I. Ferguson, A. Gurray, R. Stall: Homoepitaxial and selective area growth of 4H and 6H silicon carbide using a resistively heated vertical reactor, *Mater. Res. Soc. Symp.* **572**, 173–178 (1999)
- 28.128 Y. Chen, T. Kimoto, Y. Takeuchi, H. Matsunami: Homoepitaxial mesa structures on 4H-SiC (0001) and {1120} substrates by chemical vapor deposition, *J. Cryst. Growth*, **254**, 115–122 (2003)
- 28.129 Y. Khlebnikov, I. Khlebnikov, M. Parker, T.S. Sudarshan: Local epitaxy and lateral epitaxial overgrowth of SiC, *J. Cryst. Growth* **233**, 112–120 (2001)
- 28.130 R. Zhang, I. Bhat: Atomic force microscopy studies of CdTe films grown by epitaxial lateral overgrowth, *J. Electron. Mater.* **30**(11), 1370–1375 (2001)
- 28.131 B.A. Haskell, T.J. Baker, M.B. McLaurin, F. Wu, P.T. Fini, S.P. DenBaars, J.S. Speck, S. Nakamura: Defect reduction in *m*-plane gallium nitride via lateral epitaxial overgrowth by hydride phase epitaxy, *Appl. Phys. Lett.* **86**(11), 111917–1–111917–3 (2005)
- 28.132 A.A. Burk Jr., M.J. O'Loughlin, H.D. Nordby Jr.: SiC epitaxial layer growth in a novel multi-wafer vapor-phase epitaxial (VPE) reactor, *J. Cryst. Growth* **200**, 458–466 (1999)
- 28.133 L.B. Rowland, G.T. Dunne, J.A. Freitas Jr.: Initial results on thick 4H-SiC epitaxial layers grown using vapor phase epitaxy, *Mater. Sci. Forum* **338–342**, 161–164 (2000)
- 28.134 G.R. Gruzalski, D.M. Zehner: Defect states in sub-stoichiometric tantalum carbide, *Phys. Rev. B* **34**(6), 3841–3848 (1986)
- 28.135 A.K. Dua, V.C. George: TaC coatings prepared by hot filament chemical vapour deposition: Characteri-

- zation and properties, Thin Solid Films **247**, 34–38 (1994)
- 28.136** Y. Chen, T. Kimoto, Y. Takeuchi, H. Matsunami: Selective homoepitaxy of 4H-SiC on (0001) and (11 $\bar{2}$ 0) masked substrates, J. Cryst. Growth **237–239**, 1224–1229 (2002)
- 28.137** Y. Fukai: *The Metal-Hydrogen System*, 2nd edn. (Springer, Berlin, Heidelberg 2005)

29. Liquid-Phase Electroepitaxy of Semiconductors

Sadik Dost

Part E | 29

The chapter presents a review of the growth of single-crystal bulk semiconductors by liquid-phase electroepitaxy (LPEE). Following a short introduction, early modeling and theoretical studies on LPEE are briefly introduced. Recent experimental results on LPEE growth of GaAs/GaNAs single crystals under a static applied magnetic field are discussed in detail. The results of three-dimensional numerical simulations carried out for LPEE growth of GaAs under various electric and magnetic field levels are presented. The effect of magnetic field nonuniformities is numerically examined. Crystal growth experiments show that the application of a static magnetic field in LPEE growth of GaAs increases the growth rate very significantly. A continuum model to predict such high growth rates is also presented. The introduction of a new electric mobility in the model, i. e., the *electromagnetic* mobility, allows accurate predictions of both the growth rate and the growth interface shape. Space limitation required the citation of a limited number of references related to LPEE [29.1–73]. For details of many aspects of the LPEE growth process and its historical developments, the reader is referred to these references and also others cited therein.

29.1 Background	967
29.1.1 Liquid-Phase Electroepitaxy	968
29.1.2 Natural Convection	970
29.1.3 Applied Magnetic Fields	970
29.1.4 Observation of Growth Rate	970
29.2 Early Theoretical and Modeling Studies ..	971
29.2.1 Peltier-Induced Growth Kinetics: Electromigration Mechanism	971
29.2.2 A One-Dimensional Model	973
29.2.3 Source-Current-Controlled (SCC) Growth	975
29.3 Two-Dimensional Continuum Models	977
29.4 LPEE Growth Under a Stationary Magnetic Field	978
29.4.1 Experiments	979
29.5 Three-Dimensional Simulations	981
29.5.1 Simulation Model	982
29.5.2 Numerical Method	983
29.5.3 Effect of Magnetic Field Strength ..	984
29.5.4 Evolution of Interfaces	989
29.5.5 Effect of High Electric and Magnetic Field Levels	990
29.6 High Growth Rates in LPEE: Electromagnetic Mobility	992
29.6.1 Estimation of the Electromagnetic Mobility Value	993
29.6.2 Simulations of High Growth Rates in a GaAs System	994
References	996

29.1 Background

Liquid-phase electroepitaxy (LPEE) is a solution growth technique by which layers of single crystals are grown at relatively low temperatures. It has great potential for producing high-quality, thick crystals of compound and alloy semiconductors. The LPEE growth technique was developed through the use of electric current for dopant modulation in LPE [29.1], and there-

after became a solution growth technique for growth of binary and ternary semiconductor crystals [29.1–11].

Growth in LPEE is initiated and sustained by passing an electric current through the substrate–solution–source system while the overall furnace temperature is kept constant. Since growth takes place at constant furnace temperature, LPEE has a number of advantages

Table 29.1 Potential applications of alloy semiconductors [29.12]

Semiconductor alloy	Applications
Ga _{0.96} In _{0.04} As	Substrates lattice matched to blue diodes and lasers (ZnSe)
Ga _x In _{1-x} As, InAs _{1-x} P _x	Substrates suitable for OEICs operating in the 1.3–2 μm region
Ga _x In _{1-x} P, GaAs _{1-x} P _x , Al _x Ga _{1-x} As	Substrates for diodes and lasers operating in the visible range
Hg _{1-x} Cd _x Te, Ga _{1-x} In _x Sb, InAs _x Sb _{1-x}	Substrates for mid- and far-infrared detectors and lasers
Si _{1-x} Ge _x	Substrates for n-channel field-effect transistors (FETs) and efficient optoelectronic devices, solar cells, photodetectors
Cd _x Zn _{1-x} Te	Substrates for γ- and x-ray detectors

such as steady and controlled growth rate, controlled doping, improved surface morphology and defect structure, low dislocation density, and improved electronic characteristics. In addition, the method is suitable for growing ternary and quaternary alloy crystals with desired compositions. This feature of LPEE has attracted interest in the growth of high-quality semiconductor crystals since the availability of such thick alloy substrates may solve the problems arising from lattice mismatch encountered in the integration of different material layers, and may open new horizons in the fabrication technology of optoelectronic devices and integrated circuits (OEICs). Due to the technological importance of LPEE, a number of experimental and modeling studies have been carried out in recent years.

Alloy semiconductors, such as GaInAs, GaInSb, GaInP, and CdZnTe, grown on commercially available GaAs, GaSb, GaP, and CdTe substrates, are of interest as lattice-matched substrates for novel semiconductor devices in optoelectronics (see [29.12] for more information). For instance, Ga_{0.47}In_{0.53}As ternary alloy grown epitaxially on the lattice-matched InP substrate has been used as an active layer in lasers and photodetectors in optical communication systems [29.12–14]. It is a very good candidate for high-speed transistors because of its high carrier mobility. GaInAs epitaxial layers grown on GaAs substrates have also been used for high-electron-mobility transistors (HEMT) structures with significantly improved performance, and for strained-layer lasers, modulators, and detectors operating in the near-infrared region [29.15]. For this ternary material, however, only thin layers can be grown due to the lattice mismatch. As a result, many problems have been observed in lasers fabricated on such substrates, which are therefore restricted to the 0.8–1.1 μm region [29.16].

High-performance semiconductor lasers operating in the 2–5 μm range are highly desirable in optical-fiber communication systems employing low-loss fluoride-based fibers, laser radar, remote sensing of atmospheric

gases, and molecular spectroscopy [29.17–19]. The availability of InAsP, GaInAs, and GaInSb substrates with desired thicknesses and quality would overcome this difficulty. These materials and many other desired alloy semiconductors either cannot be grown commercially, or are grown with inadequate thickness and quality, or cannot be grown reproducibly. LPEE has proven to have the potential for growing such crystals with the desired properties. The alloy materials that can be grown by LPEE are summarized in Table 29.1.

Semiconductors grown by LPEE show advantages over crystals grown by melt growth techniques, namely, lack of detectable electron traps [29.20], low vacancy densities [29.21], low dislocation densities [29.22], and high luminescence efficiency [29.23]. The distinct feature of the LPEE growth process is its capability to grow crystals with uniform crystal compositions. For example, millimeter-thick ingots of GaInAs [29.23–27], AlGaSb [29.28], and AlGaAs [29.29–32] exhibit remarkable compositional uniformity.

The above-mentioned features along with its low hardware cost make LPEE quite attractive for growth of high-quality alloy semiconductors in the form of both bulk crystals and buffer layers. However, reproducible growth of such crystals requires good understanding and control of the key mechanisms governing this process.

29.1.1 Liquid-Phase Electroepitaxy

In a typical LPEE growth system, graphite electrodes are placed at the top and bottom of the growth cell (Fig. 29.1). The substrate is placed at the bottom of the solution and the source material is placed between the solution and the upper electrode. The liquid contact zone located below the substrate provides a uniform, low-resistance electrical contact between the lower face of the substrate and the lower electrode, which is essential for satisfactory growth. The boron nitride jacket around the horizontal sandwich layers forms the cell

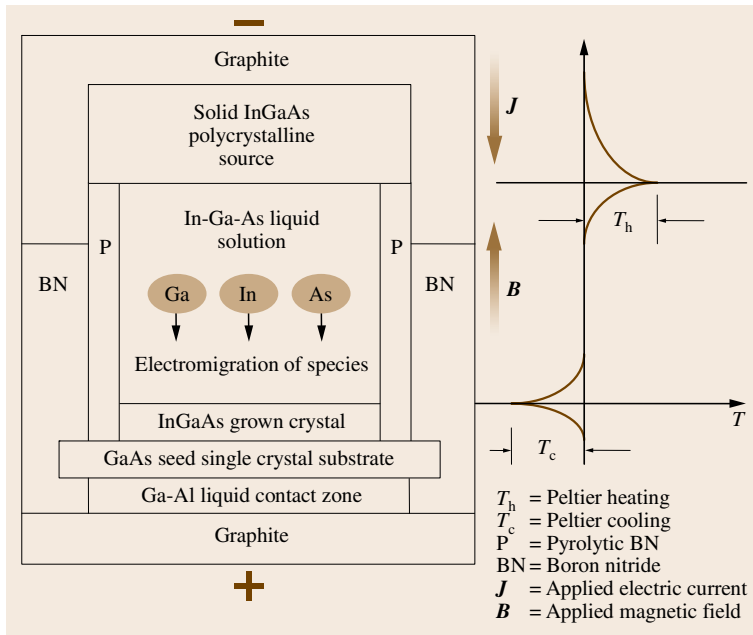


Fig. 29.1 Schematic view of an LPEE crucible for a GaInAs system. Note that the temperature distribution shown is not the actual one; it describes symbolically the Peltier cooling/heating at the interfaces

and acts as both a heat conductor and an electrical insulator. The growth temperature is typically in the range of 650–900 °C, depending on the material to be grown. After the system reaches thermodynamic equilibrium, the electric current is turned on and growth is initiated. During the growth process, the furnace temperature is kept constant. The applied electric current is the sole external driving force and the controlling element of the growth, and makes it possible to achieve a high growth rate and precise control of the process. The electric current passes through the lower electrode, contact zone, and substrate, but may bypass the source material into the upper electrode. A static magnetic field may also be used in LPEE. We discuss below some of the factors playing roles in the LPEE growth process.

Thermoelectric Effects

In a well-designed LPEE apparatus, vertical and horizontal external temperature gradients are effectively minimized. Thermal effects that may lead to temperature gradients in the solution may then be assumed to be solely due to the Peltier cooling/heating at the solid-liquid interfaces and the Joule heating in the grown crystal.

Peltier Cooling/Heating is a thermoelectric effect caused by the electric current passing across the solution-substrate (growth interface) and the substrate-

contact zone interfaces. The electric current causes heat absorption or evolution at the interfaces, depending on the direction of the electric current and type of electrical conductivity of the crystal (n-type or p-type). In an equilibrated LPEE system with a positive polarity of the n-type lower electrode crystal, Peltier cooling occurs at the growth interface and is accompanied by Peltier heating at the substrate-contact zone interface. Thus, heat transport across the substrate affects the amount of cooling at the growth interface. Indeed, the amount of cooling at the growth interface increases with increasing substrate thickness. If the current passes through the solution-n-type source (dissolution) interface, Peltier heating occurs at this interface.

Being a semiconductor, the substrate has high electrical resistivity. The electric current passing through the substrate induces Joule heating proportional to the square of the current density and electrical resistivity (Joule heating produced in the solution and graphite electrodes is at least an order of magnitude lower because of the low electrical resistivity). The effect of Joule heating in the substrate increases with increasing substrate thickness and becomes significant for bulk crystals. A one-dimensional model presented in [29.32] suggests that the Joule heating may present itself as a thermal limiting factor (barrier) in the growth of very thick crystals, particularly in the growth of high-resistivity materials.

Growth Mechanisms

The main growth mechanism of LPEE is the transport mechanism known as *electromigration*. In the growth of compound and alloy semiconductors, the solutions are metallic conductors. In such solutions, electromigration takes place due to electron momentum exchange and electrostatic field forces [29.5, 9]. Under the influence of the electric field induced by the applied electric current, solute species migrate towards the anode with a velocity proportional to the solute mobility and electric field. Thus, when the substrate has positive polarity, the solution becomes supersaturated with solute near the substrate–solution interface, resulting in epitaxial growth.

The combined effect of Peltier cooling/heating and Joule heating results in an axial temperature gradient in the solution. This temperature gradient supersaturates the solution in the vicinity of the growth interface, leading to a further contribution to epitaxial growth. This is the second main growth mechanism of LPEE. Either electromigration or Peltier cooling can become dominant, depending on the particular growth conditions [29.8, 9, 33]. However, these contributions can be affected by the presence of natural convection in the solutions, as shown numerically in [29.34].

A typical growth rate in the LPEE growth of GaAs at a 3 A/cm^2 electric current density is about 0.5 mm/day . For the growth of thick crystals (several millimeters), mass transport in the liquid solution is mainly due to electromigration. The contribution of molecular diffusion is very small, as shown experimentally in [29.26, 27], and also numerically in [29.35, 36]. The growth rate increases with increasing electric current density. However, at higher electric current densities, for instance 10 A/cm^2 or higher, the growth becomes unstable [29.26, 27].

29.1.2 Natural Convection

The effect of natural convection has been observed in various experiments [29.26, 27, 37, 38]. It enhances the overall transport processes, and thus increases the growth rate, which is desirable. However, convection often has an adverse influence on growth kinetics, and on the structure and quality of grown crystals [29.37]. It has been observed that convective flow, resulting from both thermal and solutal gradients, leads to the growth of GaAs/GaInAs layers with nonuniform thickness profiles [29.8, 10, 26, 27]. Furthermore, convection has been found to limit the maximum achievable thickness in bulk crystal growth experiments [29.23], due to the loss

of surface quality caused by unstable growth conditions [29.26, 27].

In the growth of alloy semiconductors, convection adds another dimension to the difficulty of the problem. In most alloys, the densities of the components are significantly different. This difference gives rise to inhomogeneity in the composition of the liquid solution during growth. In other words, gravity makes it difficult to maintain the solution with a uniform liquid composition. Less dense components move upwards, leading to the depletion of the required component(s) in the vicinity of the growth interface. This results in unsatisfactory growth. For example, in the case of GaInP, phosphorus, with the smallest density, tends to float.

29.1.3 Applied Magnetic Fields

In order to suppress convection, a static, external applied magnetic field has also been used in LPEE [29.26, 27]. As we will see later, the application of a vertical static magnetic field (perfectly aligned with the growth direction and the applied electric field) indeed suppresses convection significantly. However, it was also observed, unexpectedly, that the applied magnetic field increases growth rate very significantly. For instance, a field of 4.5 kG increases the growth rate about tenfold. Experimental [29.26, 27] and modeling [29.35, 36, 40, 41] studies have shown that the growth rate is also proportional to the intensity of the applied magnetic field; however its contribution to mass transport is about twice that of the applied electric current.

29.1.4 Observation of Growth Rate

One of the most significant advantages of the LPEE growth technique is the possibility of monitoring in situ the evolution of the growth interface. Although the subject of this chapter is the modeling and numerical simulations of the LPEE growth process, due to its significance we wanted to mention a great experimental technique developed in [29.74]. The technique is based on resistance measurements of the growth cell during LPEE growth. When scaled with the use of the technique of dopant modulation by current pulses (time markers) [29.1], the in situ monitoring allows the study of growth rate (averaged over the cross-section area of the crystal).

The literature on the experimental studies carried out on LPEE growth of various semiconductors is rich (for a detailed account of the subject, see [29.41]). In the following sections, we first present a short re-

view of the early modeling and theoretical studies. Then, due to its significance, we give a short summary of the results of the recent experimental study of [29.26], carried out for LPEE growth of GaInAs under a strong static magnetic field. We also present

a summary of the three-dimensional simulations carried out for LPEE growth of binary systems. Finally, a continuum model developed to predict the high growth rates observed in the LPEE growth of GaAs is introduced.

29.2 Early Theoretical and Modeling Studies

A number of conceptual/modeling studies have been carried out to have a better understanding of the relative contributions of electromigration, Peltier cooling, diffusion, and convection. These early studies contributed significantly to understanding of the LPEE growth process. Here, we present a summary of some of those early contributions.

29.2.1 Peltier-Induced Growth Kinetics: Electromigration Mechanism

An analytical treatment of the Peltier-induced growth kinetics in the LPEE growth of GaAs was presented in the absence of the effect of natural convection [29.10]. In this model, the growth rate was examined by considering diffusion and electromigration of As in a Ga-rich solution (Fig. 29.2). The mass balance for the solution and the grown layer is written as

$$\rho_L C_L(T_0) L = \rho_S C_S R(t) + \rho_L \int_R^L C(x, t) dx. \quad (29.1)$$

The distribution of solute $C(x, t)$ in the solution is expressed by writing the conservation of mass for the ionized species as

$$\frac{\partial C}{\partial t} = D_C \frac{\partial^2 C}{\partial x^2} - Z_{\text{eff}} \mu_E \frac{\partial}{\partial x} (EC), \quad (29.2)$$

where

$$\mu_E = \frac{FD_C}{RT} \quad (29.3a)$$

and

$$Z_{\text{eff}} = Z - Z_0 \frac{\sigma^{-1}(C) - \sigma^{-1}(0)}{C\sigma^{-1}(0)}, \quad (29.3b)$$

and μ_E , F , and σ_E are the electric mobility, the Faraday number, and the conductivity of the solution, respectively, Z and Z_0 represent the valences of solute and solvent ions, Z_{eff} is the effective charge of solute

species, and D_C is the diffusion coefficient. Differentiating (29.1) with respect to time and using (29.2), we obtain the growth rate as

$$V(t) = \rho_L \frac{D_C (\partial C / \partial x)|_{x=R} - \mu_E Z_{\text{eff}} E(R) C_L(T_1)}{\rho_S C_S - \rho_L C_L(T_1)}. \quad (29.4)$$

As can be seen, the calculation of the growth rate requires the electric field intensity E to be known, defined by the charge distribution in the solution and the solute concentration $C(x, t)$. Since the Ga (or Ga-rich) solution exhibits metallic properties, the participation of free electrons in the electric conductivity is much greater than that of the ionized solute (arsenic in this case) atoms. One may then assume that the electric field intensity E is constant across the solution and its value can be estimated from the expression $J = \sigma_E E$, which is simply the constitutive equation used for the electric

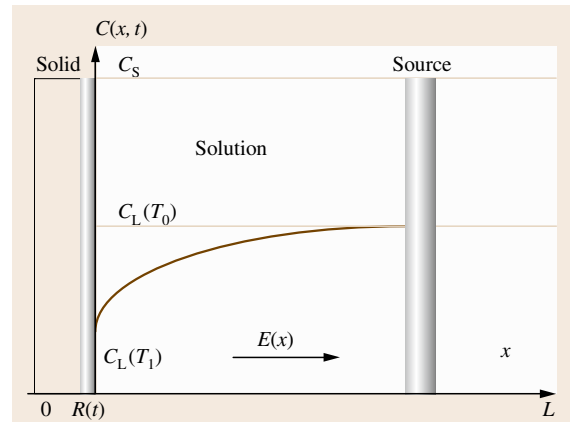


Fig. 29.2 Distribution of the solute concentration $C(x, t)$ in the solution (liquid) and solid: C_L = equilibrium composition of the solution, R = thickness of the grown layer, L = solution height, t = time, E = electric field intensity. In this setup electric current bypasses the source material (distribution of arsenic concentration in the solution after a very long time; after [29.10])

current with the conductivity σ_E of the solution [29.41]. In this case, the growth expression reduces to that given in [29.41, 63] with the assumption $E = Z_{\text{eff}} E$. Then, (29.2) reduces to the one-dimensional mass transport equation, which can be deduced from that given in [29.41, 63] as

$$\frac{\partial C}{\partial t} = D_C \frac{\partial^2 C}{\partial x^2} - \mu_E E \frac{\partial C}{\partial x}. \quad (29.5)$$

Equation (29.2) can be solved numerically under the following conditions (in the absence of Peltier effect at the source)

$$\begin{aligned} C(x, 0) &= C_L(T_0), \\ C(R, 0) &= C_L(T_1), \\ C(L, t) &= C_L(T_0), \\ \left. \frac{\partial C}{\partial x} \right|_{x=L} &= 0. \end{aligned} \quad (29.6)$$

One can see that, in order to calculate the growth rate in (29.4), one must know the values (or functions) of $D_C(T)$, $C_L(T)$, $\Delta T \equiv T_1 - T_0$, $\sigma_E(C)$, and also Z_{eff} . Some of these values can be determined experimentally (such as $D_C(T)$, $\sigma_E(C)$, and Z_{eff}) and some of them (such as $C_L(T)$ and $\Delta T \equiv T_1 - T_0$) can be estimated through calculations (or numerical simulations). These values were estimated in [29.10] as follows.

The temperature difference $\Delta T \equiv T_1 - T_0$ was estimated directly by taking into account the fact that the growth of an epitaxial layer without the source on the solution surface occurs until the following condition is

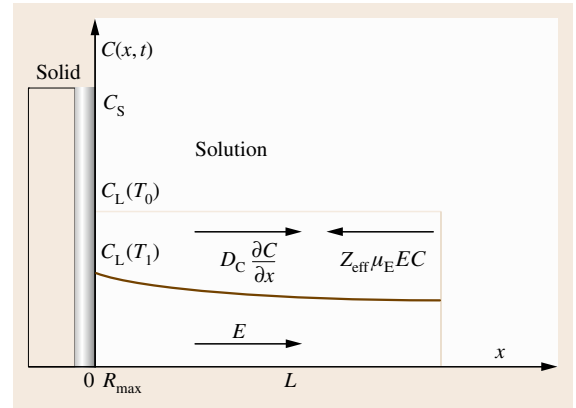


Fig. 29.3 Distribution of arsenic concentration in the solution after a very long time (after [29.10])

fulfilled (Fig. 29.3)

$$D_C \frac{\partial C}{\partial x} = Z_{\text{eff}} \mu_E E C, \quad (29.7)$$

which means that the diffusion, electromigration, and electrotransport streams balance each other. Solving (29.7) and substituting into (29.2) yields (see [29.10] for details)

$$C_L(T_1) = \frac{C_L(T_0) - (C_S \rho_S R_{\text{max}}) / (\rho_L L)}{1 - (\mu_E L Z_{\text{eff}} E) / (2 D_C)}, \quad (29.8)$$

where R_{max} is the maximum thickness of the layer. Equation (29.8) and the exact knowledge of the liquidus curve $C_L(T)$ will determine $\Delta T \equiv T_1 - T_0$.

The electric conductivity of the Ga solution and the parameter Z_{eff} were estimated in [29.10] as follows. The product $E Z_{\text{eff}}$, which is linearly dependent on current density, was treated as the parameter to fit the experimental data of the growth rates obtained (see [29.10] for the experimental data) as

$$\frac{J}{Z_{\text{eff}} E} = \text{const.}, \quad \text{at } T_0 = \text{const.} \quad (29.9)$$

It follows that the fitting parameter $Z_{\text{eff}} E$ has to be proportional to the current density J . Agreement within $\pm 20\%$ between the calculated and measured values can be achieved, as suggested in [29.10] (Fig. 29.4). Actually in the growth of very thick crystals (during prolonged growth periods), as will be seen later [29.26], this agreement is very close, within a very small margin.

Once the values of $Z_{\text{eff}} E$ are known from the fitting procedure, the electrical conductivity σ_E , the effective charge Z_{eff} , and the electric field intensity E can be

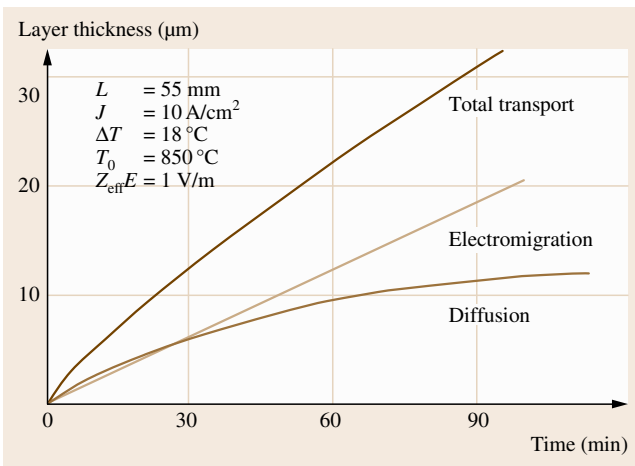


Fig. 29.4 Layer thickness versus time, and the relative contributions of electromigration and diffusion (after [29.10])

estimated. Using $J = \sigma_E E$, and (29.3b) we obtain

$$\sigma^{-1}(C) = \sigma^{-1}(0) \left(1 + \frac{ZC}{Z_0}\right) \frac{1 + (1 - \Pi)^{1/2}}{2} \quad (29.10)$$

and

$$Z_{\text{eff}} = Z - Z_0 \frac{\left(1 + \frac{ZC}{Z_0}\right) [1 + (1 - \Pi)^{1/2}] - 2}{2C} \quad (29.11a)$$

with

$$\Pi \equiv \frac{4Z_{\text{eff}}EC}{Z_0\sigma^{-1}(0)J \left(1 + \frac{ZC}{Z_0}\right)^2}. \quad (29.11b)$$

Using (29.10) and (29.11a,b) the calculated values of Z_{eff} are tabulated in Table 29.2.

These results showed that mass transport in the LPEE growth of GaAs is due to both diffusion and electromigration of solute (As) in the liquid towards the seed substrate. The high value of the effective charge, estimated by fitting the theoretical values to those measured ones, justifies the conclusion that *the migration of arsenic species in the liquid solution is realized mainly due to collisions with electrons flowing across the solution*.

Indeed, this conclusion given in [29.10] for the mechanism of electromigration established the understanding of the electromigration process. As we will discuss it later, the high growth rates achieved under an applied magnetic field in the LPEE growth of GaAs [29.26] can only be explained by such a mechanism, as suggested in [29.61–63]:

The resistance during the collision of electrons with the species of the solution determines the mobility of the species and in turn the growth rate. This resistance is very much reduced under an applied static magnetic field due to the possibility that the charged species are aligned along the magnetic field lines

Table 29.2 Estimated values of electrical conductivity and effective charge [29.10]

T_0 (°C)	$C_L(T_0)$ (at. %)	$(Z_{\text{eff}}E/J)$ $\times 10^3$ ($\Omega \text{ cm}$)	$\sigma^{-1}(C)$ $\times 10^5$ ($\Omega \text{ cm}$)	Z_{eff} (As^{3-})
750	1.38	−1.2	5	−24
800	2.23	−1.2	5.2	−23
850	2.75	−1.2	5.5	−22

(which are almost uniform along the growth direction in the growth system used in [29.26]), and leads to a very high mobility.

Thus, the mass transport due to electromigration increases tremendously and the total mobility of species depends not only on the electric mobility coefficient which is measured in the absence of an applied magnetic field, but also on the magnetic field intensity and a new material coefficient that is called the *magnetic mobility* in [29.61–63]. This understanding supports the earlier definition of electromigration in LPEE.

29.2.2 A One-Dimensional Model

Based on the conservation of species mass, a one-dimensional model for the LPEE growth process was given in [29.8, 9], where the contributions of the Peltier effect at the solid–solution interfaces and that of solute electromigration in the solution to the overall growth process were defined. According to this one-dimensional model, the contribution of electromigration to growth is dominant in the absence of convection, and the contribution of the Peltier effect can be dominant in the presence of convection. (The relative contributions of electromigration and the Peltier effect have been determined more clearly through two-dimensional numerical simulation models developed by the author; the reader is referred to [29.34, 48–50] for details.)

The one-dimensional mass transport equation was written as

$$\frac{\partial C}{\partial t} + V^g \frac{\partial C}{\partial x} = D_C \frac{\partial^2 C}{\partial x^2} - \mu_E E \frac{\partial C}{\partial x}. \quad (29.12)$$

The following boundary conditions were considered

$$-D_C \left. \frac{\partial C}{\partial x} \right|_0 + \mu_E E C_L = (C_S - C_L) V^g, \quad (29.13)$$

$C = C_0$ at $t = 0$ for all x , and
at $t > 0$ for $x = \infty$ (absence of convection), or
 $C = C_0$ at $t > 0$ for $x > \delta$ (presence of convection),
 $C = C_L$ at $t > 0$ and $x = 0$ (growth follows the liquidus line).

Equation (29.12) was solved analytically with the assumption of a small growth velocity so that the second term on the left-hand side of (29.12) was neglected. The growth velocity was obtained for two cases: (i) for an infinitely long boundary layer ($\delta = \infty$, no convection), and (ii) for a finite boundary layer (with convection),

which are given respectively as

$$V_T^g = \frac{\Delta T_p}{C_S - C_L} \frac{dC}{dT} \bigg|_L \left(\frac{D_C}{\pi t} \right)^{1/2} + \mu_E E \frac{C_L}{C_S - C_L} \quad (29.14)$$

and

$$V_T^g = \frac{\Delta T_p}{C_S - C_L} \frac{dC}{dT} \bigg|_L \frac{D_C}{\delta} + \mu_E E \frac{C_L}{C_S - C_L} \quad (29.15)$$

In (29.14) and (29.15) the first terms represent the contribution of the Peltier effect and the second terms represent the contribution of electromigration to the growth velocity. Both terms depend linearly on the electric current through ΔT_p and E , respectively. Equation (29.14) was solved for LPEE growth of GaAs from a Ga/As solution at 800°C growth temperature and using $J = 10 \text{ A/cm}^2$, $\Delta T_p = -3^\circ\text{C}$, $D_C = 6.0 \times 10^{-5} \text{ cm}^2/\text{s}$, and $\mu_E E = 10^{-5} \text{ cm/s}$. The results are plotted in Fig. 29.5.

Equation (29.15) was also solved for various boundary layer thicknesses. It was shown that, as the boundary layer gets thinner, the contribution of Peltier cooling to the growth rate increases. The contribution of Peltier cooling to the growth rate also increases with increasing Peltier cooling at the growth interface (see [29.8, 9] for details).

According to the model presented above the relative contributions of Peltier cooling at the growth interface and electromigration of solute species in the liquid towards the interface depend on the experimental conditions. On the basis of this model, a quantitative criterion was given in [29.8, 9] to determine the relative contributions of the Peltier effect and electromigration. A critical substrate thickness d_c was defined, for which the contributions of the Peltier effect and electromigration are equal. When the substrate thickness is greater than the critical thickness, the Peltier effect dominates, and when the thickness is smaller than the critical thickness, electromigration dominates. Their conclusion then was that, in the growth of thick crystals and in the presence of significant convection, electromigration is dominated by Peltier cooling. On the other hand, with thin substrates and in the absence of significant convection, electromigration dominates electroepitaxial growth.

In order to verify the predictions of the one-dimensional model, specific LPEE experiments were devised in [29.8, 9]. Under specific growth conditions, using n- and p-type seed substrates, it was shown that the growth in the case of the p-type substrate was smaller than in the case of the n-type substrate. From the difference in growth rates, it was concluded that the contribution of Peltier cooling to the growth rate is less than 15%. The almost linear relationship between growth rate and electric current density observed experimentally is consistent with theoretical predictions (Fig. 29.6).

It was shown experimentally that the growth rate is also proportional (almost linearly) to current density for all growth temperatures used, and that, for a given cur-

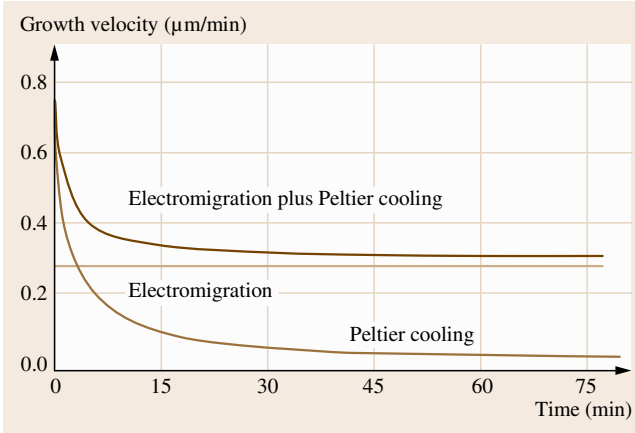


Fig. 29.5 Growth velocity of GaAs calculated from (29.14) (after [29.8, 9])

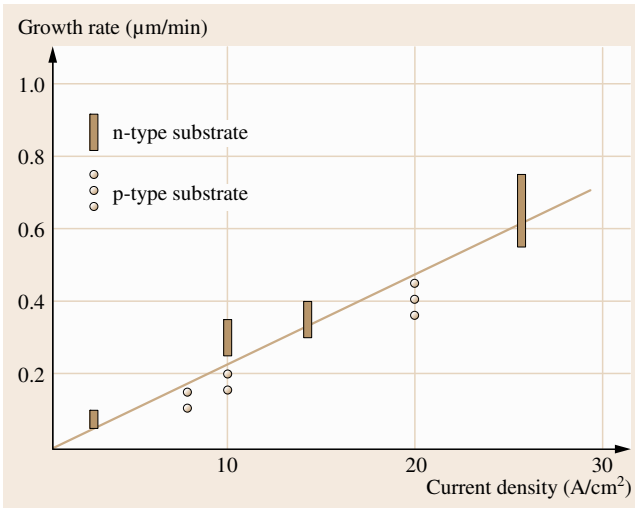


Fig. 29.6 Growth rate versus electric current density: 800 °C with a substrate thickness of 300 μm (after [29.8, 9])

rent density, the growth rate increases with temperature. Results are summarized in Fig. 29.7 for LPEE growth of GaAs on a 0.3 mm thick n-type substrate.

Another important issue is the selection of a proper solution height when an LPEE crucible is designed since it influences the growth rate, among of course other growth parameters. LPEE experiments designed for the growth of GaAs at 800 °C using an n-type substrate showed that growth rate is linearly proportional to solution height up to a certain height (about 10 mm), above which the growth rate remains constant. The results of experimental measurements in [29.8, 9] are presented in Fig. 29.8. Naturally, the relative contribution of the Peltier effect to the growth rate varies with solution height due to the contribution of convection in the solution. Experiments carried out in [29.8, 9] (at 25 A/cm² electric current density and 900 °C) show that the contribution of Peltier cooling increases with solution height (Fig. 29.9).

29.2.3 Source-Current-Controlled (SCC) Growth

The source-current-controlled (SCC) method is a version of LPEE with the difference that the furnace temperature is lowered gradually during growth similar to in liquid-phase epitaxy (LPE) while the electric current is simultaneously used to generate a temperature gradient and supply additional solute to the

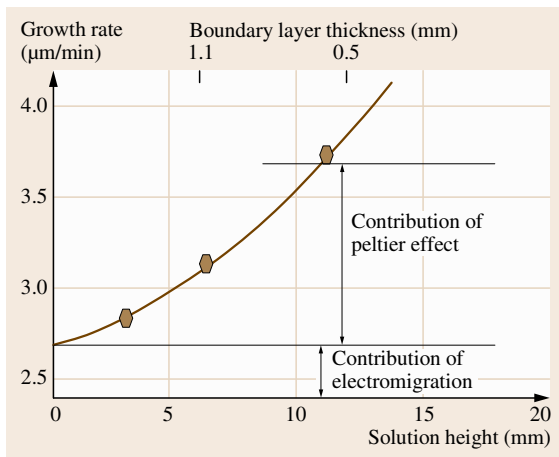


Fig. 29.9 Growth rate of GaAs from a Ga/As solution (at 900 °C and 25 A/cm²) as a function of solution height. Substrates were Cr-doped and 0.3 mm thick. The estimated boundary layer thicknesses are also indicated at the top (after [29.8, 9])

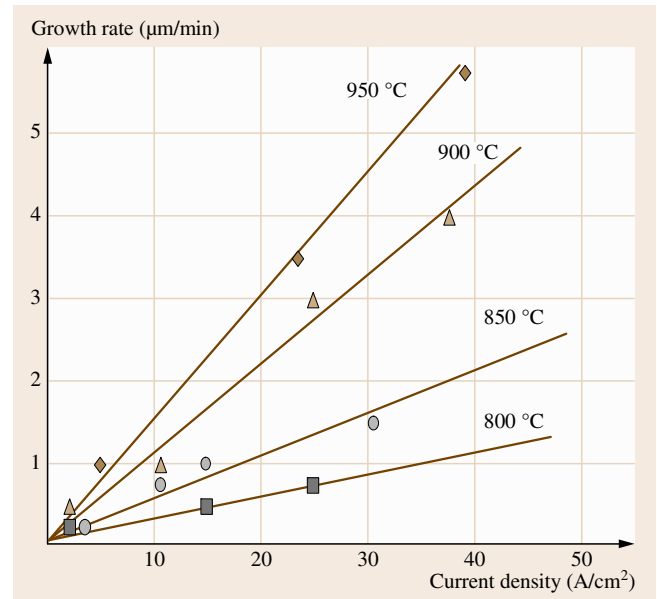


Fig. 29.7 Growth rate versus current density at various growth temperatures (after [29.8, 9])

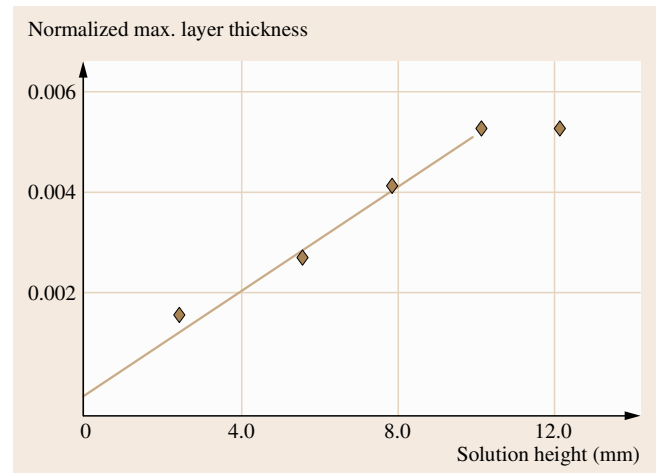


Fig. 29.8 Normalized maximum GaAs layer thickness as a function of solution height under the experimental conditions of 800 °C growth temperature, 0.3 mm thick n-type substrate (after [29.8, 9])

liquid [29.64–67]. In this setup the applied electric current passes through the source, the solution, and then through the graphite on top, but bypasses the substrate (Fig. 29.10). Due to the passage of electric current through the source the temperature T_1 just above the

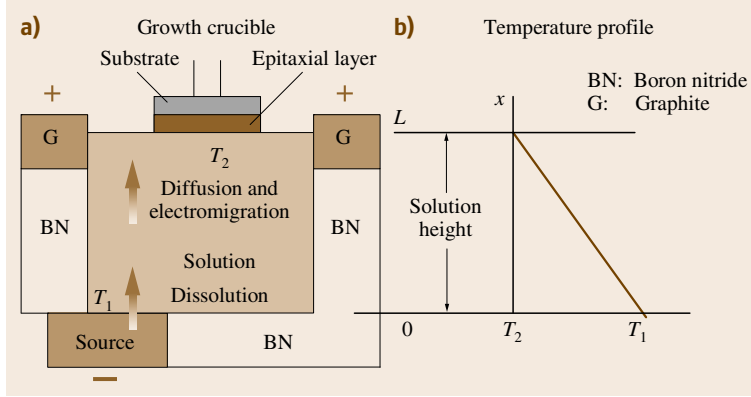


Fig. 29.10a,b Schematic view of the SCC (LPPE) growth crucible (a) domain and temperature profile (b) used in the model (after [29.64])

source is higher than that (T_2) just below the substrate. This temperature difference generates a temperature gradient between the source and the substrate. For this system, the thickness of the grown layer is calculated by solving the one-dimensional mass transport equation given in (29.5) (where we assume the mobility to be positive for current flow from source to substrate, opposite to the sign convection used in [29.64]: $\mu_E \equiv -\mu$) under the boundary conditions

$$\begin{aligned} C(0, t) &= C_0 - (R_0/m_0)t, \\ C(L, t) &= C_L - (R_L/m_L)t, \\ C(x, 0) &= C_0 + (C_L - C_0)(x/L), \end{aligned} \quad (29.16)$$

where C_0 and C_L are the initial solution concentration in the vicinity of the growth interface and the source, respectively, and R_0 and R_L represent, respectively, the cooling rates at the growth and dissolution interfaces. The solution height is denoted by L , and m_0 and m_L are the slopes of the liquidus curves near the growth and dissolution interfaces, given by

$$m_0 \equiv \frac{1}{w_L} \left. \frac{dT}{dX^L} \right|_{x=0},$$

and

$$m_L \equiv \frac{1}{w_L} \left. \frac{dT}{dX^L} \right|_{x=L}, \quad (29.17)$$

where X^L represents the atomic fraction of the solute, and w_L is the solution density. Through an approximate analytical solution to (29.5), an expression for the layer thickness was given as

$$L = M_t/C_S, \quad (29.18)$$

where

$$\begin{aligned} M_t &= D_C \left(\frac{\mu E}{2D_C} - \frac{1}{L} \right) \left(C_0 - \frac{R_0 t}{2m_0} \right) t \\ &+ \frac{D_C}{L} \exp \left(\frac{\mu E}{2D_C} \right) \left(C_L - \frac{R_L t}{2m_L} \right) t \\ &- \left[\frac{\pi}{L} \sum_{n=1}^{\infty} \frac{n T_n(0)}{A} + \frac{2}{L} \sum_{n=1}^{\infty} \frac{B C_L - C_0}{A} \right] \\ &\times [\exp(-D_C A t) - 1] \\ &+ \left(\frac{\pi}{L^3} \sum_{n=1}^{\infty} \frac{2n^2 \pi}{A^2} \right) \left(\frac{R_0}{m_0} - B \frac{R_L}{m_L} \right) \\ &\times \left[t + \frac{1}{D_C A} \exp(-D_C A t) - \frac{1}{D_C A} \right] \end{aligned} \quad (29.19)$$

and C_S is the concentration of C atoms per unit volume of the grown layer. For an $A_x B_{1-x} C$ system, C_S is given by $C_S = 4/d^3$, where d is the lattice constant of the ternary compound. The layer thickness for diffusion- and electromigration-limited growth in a temperature-graded solution can be calculated using (29.18) and (29.19) [29.64].

The thickness of the grown layers of an $\text{In}_{0.53}\text{Ga}_{0.47}\text{As}$ system was calculated in [29.64] and various numerical data were given for the dependence of concentration on growth time, layer thickness as a function of temperature and cooling rate, the relative contributions of electromigration and diffusion to growth rate, and the composition of the grown crystal along the growth direction. These calculations were made using the value $\mu E = 0.1-0.001$ cm/min for the mobility of As in the Ga/As solution. It was stated in [29.64] that *the real value of μ can be determined through a comparison of experimental layer thicknesses with computed ones*. Indeed, as shown

in [29.26, 62, 63] the mobility was calculated using experimental results of LPEE of a GaInAs system with and without the application of an external magnetic field.

The above analysis was extended in [29.68, 69] to a $\text{Ga}_x\text{In}_{1-x}\text{As}$ system to determine the composition variation in the grown crystals. In this model, for the first time, phase equilibrium between the crystal and the solution is maintained while having consistency be-

tween the transported and incorporated mass or solute atoms at the growth interface. The comparison of experiments with computed results revealed that in the Ga/In/As solution the diffusion coefficient of Ga is about twice that of As, and the electric mobility of Ga is larger than that of As. The above results were instrumental in the development of future two-dimensional (2-D) and three-dimensional (3-D) numerical models and simulations for such systems.

29.3 Two-Dimensional Continuum Models

As mentioned earlier, the growth process of LPEE is quite complex and involves the interactions of various thermomechanical and electromagnetic fields. These include fluid flow, heat and mass transfer, electric and magnetic fields, various thermoelectric effects and their interactions in the liquid phase, and heat and electric conduction with various thermoelectric effects in the solid phase. In addition, the moving growth and dissolution interfaces with possible finite mass transport rates complicate the process further. One-dimensional and simple models are not sufficient for a full understanding of the various aspects of the LPEE growth process. To gain a better understanding of the growth process of LPEE, over the past 10 years a number of numerical simulation modeling studies have been carried out by the author's research group [29.34–36, 39–41, 46, 48–50, 61–63, 70–73].

For the first time, a two-dimensional computer simulation model for the LPEE growth process of GaAs was introduced in [29.70]. This simulation model was based on the rational mathematical model given for a binary system in [29.71]. The objective of this diffusion model was to examine the relative contributions of electromigration and Peltier cooling without introducing the additional complexity of natural convection. The model includes heat transfer, diffusive mass transport, electromigration, and Peltier and Joule effects. The governing equations are solved numerically using a finite volume method. Simulations are presented for three different growth cell configurations to investigate: (i) temperature and concentration distribution in the growth cell, (ii) the effect of applied electric current density and substrate thickness, and (iii) the contribution of electromigration and Peltier cooling to the overall growth rate.

Based on the simplifying assumptions used in this work, the simulation results showed that the magnitude of the relative temperature at the growing interface is

controlled mainly by Peltier cooling for thin substrates (less than 2 mm) and small electric current densities (less than 20 A/cm^2). As expected, Joule heating becomes significant only for thick substrates and high electric current densities. For all configurations investigated, electromigration is found to be the dominant growth mechanism. In critical regions of the growth cell, relatively small changes in the configuration are found to have a significant impact on the process, and on the degree of nonuniformity of the grown crystal.

This diffusion model has been followed by a number of numerical simulation models specific to particular growth cell configuration. As an extension of the diffusion model in [29.70], the effect of natural convection in LPEE was introduced for the first time in [29.34]. In this work, the effect of thermosolutal convection in LPEE growth of GaAs was investigated through a two-dimensional numerical simulation model that accounts for heat transfer and electric current distribution with Peltier and Joule effects, diffusive and convective mass transport including the effect of electromigration, and fluid flow coupled with temperature and concentration fields. Simulations were performed for two growth cell configurations and the results are analyzed to determine growth rates, substrate shape evolution, and relative contributions of Peltier cooling and electromigration. The simulations predicted and helped explain a number of experimentally observed features, which previous diffusion-based models failed to reproduce. As we will see later in detail, in general, electromigration is found to be the dominant growth mechanism, but the contribution of Peltier cooling to the overall growth rate is found to be significantly enhanced by thermosolutal convection in the solution, and Peltier cooling can in fact become the dominant growth mechanism for certain growth conditions and growth cell configuration. The overall growth rate is found to increase with increasing

furnace temperature and applied electric current density. This thermosolutal convection model predicts an increased nonuniformity of the grown layers compared with the pure diffusion model in [29.70]. The shape of the grown layers is also shown to be very sensitive to changes in growth cell configuration.

The LPEE growth of ternary alloys was numerically simulated in [29.50] using a diffusion model for the growth of AlGaAs, and in [29.73] including the effect of convection in growth of GaInAs. The growth of $\text{Al}_x\text{Ga}_{1-x}\text{As}$ is considered from a Ga-rich solution. The solution is dilute, with 0.345% Al and 2.445% As. The growth temperature is 850 °C, the electric current density is 10 A/cm², and the solid composition is up to $x = 0.4$. Simulations are carried out in the absence of convection [29.50].

In the simulations carried out for LPEE growth of $\text{Ga}_x\text{In}_{1-x}\text{As}$ ($x = 0.94$), the computational domain covered one-half of the crucible geometry, assuming symmetry of the geometric and boundary conditions with respect to the y -axis [29.73]. The initial temperature was chosen as 780 °C, corresponding to the experimental growth conditions. The solution compositions, determined from the Ga/In/As phase diagram for growth at 780 °C, were assumed to be uniformly distributed in the liquid zone. In this experimental setup the Ga/In/As solution is nondilute, with 29.85% Ga and 7.07% As.

Two-dimensional simulation models have also been developed for LPEE growth of crystals under magnetic fields [29.72]. The feasibility of using a magnetic field for suppressing convection in LPEE was first studied

through a model for the growth of GaAs in [29.49]. The LPEE growth process of GaAs was numerically simulated under an applied static magnetic field using the finite element method based on the penalty function formulation [29.49]. It was found that this formulation is more robust and efficient than a mixed velocity–pressure formulation. The results of these early simulations have shown that the effect of natural convection can be reduced significantly by the application of an external static magnetic field. For the crucible selected, the uniformity of grown layers improves with increasing magnitude of the applied magnetic field. Results also showed that complete elimination of natural convection in the liquid phase requires the application of a very large magnetic field (about and more than 20 kG). However, this prediction is numerical, based on the model assumptions and simplifications made, and as we will see later in growth of bulk crystals by LPEE, the strong interaction between the applied magnetic and electric fields does not allow the use of a magnetic field intensity above a critical (maximum) value. For instance, this value was about 4.5 kG in LPEE growth of GaAs in experiments [29.26], and growth at higher field intensities led to unstable growth.

However, this early simulation model in [29.49] shed light on a number of issues in LPEE growth under magnetic field and laid the foundation for further experimental and numerical simulation studies in LPEE. It also provided a valuable insight into the use of the finite element technique for future studies. (A comprehensive review of the two-dimensional simulations carried out for LPEE can be found in [29.41].)

29.4 LPEE Growth Under a Stationary Magnetic Field

In spite of many significant advantages, LPEE has suffered historically from mainly three *shortfalls* towards its commercialization. The first is the achievable crystal thickness, which is relatively small, on the order of a few millimeters. This is mainly due to the combined effect of Peltier and Joule heating in the system, leading to higher temperature gradients and relatively strong natural convection in the liquid solution zone that cause unsatisfactory and unstable growth. This puts a limit on the achievable crystal thickness, particularly in the growth of bulk crystals, and providing less useful material. The second issue in LPEE has been its low growth rate. The growth rate in LPEE is almost linearly proportional to the applied electric current density,

and increases with increasing electric current density. For instance, it is about 0.5 mm/day at 3 A/cm². For higher electric current density levels, the growth rate will increase, but in the growth of thick (bulk) crystals the combined effect of temperature gradients and natural convection may lead to unstable growth. The third shortfall is the need for a single-crystal seed of the same composition as the crystal to be grown. Small compositional differences, on the order of 4% depending on the crystal lattice parameters, can be tolerated, but higher compositional differences may lead to unsatisfactory growth.

The first two shortfalls of LPEE have recently been addressed in [29.26]. By optimizing the growth param-

eters of LPEE, and also using a static external applied magnetic field, a number of thick, flat GaAs single crystals and $\text{In}_{0.04}\text{Ga}_{0.96}\text{As}$ single crystals of uniform compositions were grown, and the growth rate of LPEE was increased more than tenfold for a selected electric current density. The crystals grown under magnetic field or no magnetic field were all single crystals, and the results were reproducible in terms of crystal thickness, growth rate, and compositional uniformity. The addressing of the third shortfall has been attempted in [29.42–45] by utilizing the liquid-phase diffusion (LPD) technique.

A comprehensive experimental study of LPEE growth of GaAs and $\text{Ga}_{0.96}\text{In}_{0.04}\text{As}$ single crystals has been carried using the facility in the Crystal Growth Laboratory (CGL) of the University of Victoria. The LPEE experiments under no magnetic field have led to the growth of a large number of GaAs and $\text{Ga}_{0.96}\text{In}_{0.04}\text{As}$ single crystals of thicknesses up to 9 mm. It was possible to apply electric current densities of 3, 5, and 7 A/cm^2 . The corresponding growth rates in these experiments were about 0.57, 0.75, and 1.25 mm/day , respectively. Growth interfaces were very flat, and the growth experiments were reproducible in terms of crystal thickness and growth rate. Experiments at higher electric current intensities were not successful.

Experiments at the 3, 5, and 7 A/cm^2 electric current density levels were repeated under various applied static magnetic field levels, starting at 3 A/cm^2 electric current density and 20 kG magnetic field level (based on an earlier initial numerical estimation in [29.49]). The LPEE experiments at the 4.5 kG and lower magnetic field levels were successful, but those under higher magnetic field levels were not. These experiments indicate that for the LPEE system used in [29.26] the 4.5 kG field level is the maximum (*critical*) field intensity above which the growth is not stable. The numerical simulations conducted under the same conditions yielded a lower *critical* magnetic field level of 2.0–3.0 kG [29.35]. In addition, the experimental LPEE growth rates under a magnetic field are much higher than those under no magnetic field. For instance, as we will see later, the growth rate at 4.5 kG magnetic field level was about ten times higher than that under no magnetic field (at $J = 3 \text{ A/cm}^2$). The experiments performed at the $B = 1.0$ and 2.0 kG field levels (at $J = 3 \text{ A/cm}^2$) were also successful, and the growth rates were also higher at 1.62 and 2.35 mm/day , respectively. Experiments showed that the application of an external magnetic field is very beneficial in increas-

ing the growth rate in LPEE to a level competitive with other bulk crystal growth techniques.

At the higher magnetic field levels (even at the $J = 3 \text{ A/cm}^2$ electric current density level), and the higher electric current density levels ($J = 10 \text{ A/cm}^2$ or higher), the experiments did not lead to successful growth, but showed very interesting outcomes. Although very thick crystals were grown, even up to a 9 mm thickness, the growth processes were unstable and led to uneven grown crystals. From visual inspection of the grown crystals, the adverse effects of natural convection and strong electromagnetic interactions were obvious, causing either one-sided growth or, particularly in four experiments, to holes in the grown crystals [29.27]. It was considered that such growth (one-sided and with holes) is because of strong and unstable convection in the liquid zones (solution and contact zones) due to the strong interaction between the magnetic field and the applied electric current. Such predictions were confirmed qualitatively by numerical simulations [29.35, 36].

29.4.1 Experiments

In the initial LPEE experiments, a 20 kG magnetic field level was used based on the predictions in [29.49]. It was realized that this level of magnetic field was very strong, and the growth results were not successful. The applied magnetic field intensity was gradually lowered, and successful growth was first achieved at 4.5 kG.

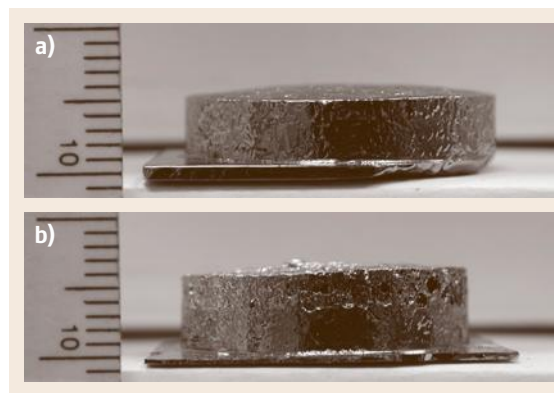


Fig. 29.11a,b Two sample GaAs crystals grown without magnetic field. (a) All the material put into the solution well was depleted. (b) The growth has been stopped before the depletion of the solution in order to measure the growth rate accurately, and the upper part is the secondary growth during cooling (after [29.26])

A number of experiments were performed at this level. Experiments were also performed at 1.0 and 2.0 kG field levels to study the effect of the applied magnetic field on the growth rate. Details of the experimental results can be found in [29.26].

In the LPEE setup used, the grown crystal and the liquid solution could not be separated at the end of an experiment. Therefore, a secondary growth (like an LPE growth) occurs during the cooling period in the experiments that were stopped earlier (before depleting all the solution put in the growth well). Some experiments were stopped before depleting the solution for the purpose of determining the growth rate accurately. Most of the crystals were grown under low current density levels (3, 5, and 7 A/cm²). Two sample GaAs crystals are shown in Fig. 29.11.

Attempts at these electric current density levels failed. This may be attributed to the strong convection

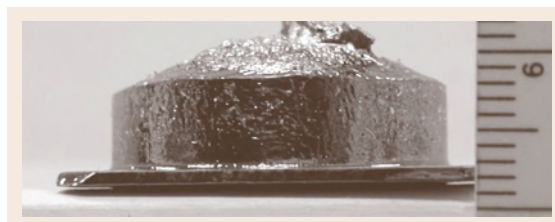


Fig. 29.13 Sample GaAs crystal grown at the $J = 3 \text{ A/cm}^2$ electric current density and $B = 4.5 \text{ kG}$ magnetic field level (after [29.26])

in the solution at these levels of applied current during the prolonged growth periods in growth of *bulk* crystals. It must be mentioned that it is possible to use higher electric current densities (higher than 7 A/cm²) in the growth of thin layers, as reported in the literature (e.g., [29.47]).

Experiments were conducted for various growth periods (from 1 to 8 days) at a temperature of 800 °C. The results are summarized in Fig. 29.12. As can be seen, the average thickness of the grown crystals is proportional to the applied electric current density. As expected, the thickness increases with time. It was concluded previously that the growth rate in LPEE is a linear function of the applied electric current density [29.12, 23]. The results shown in Fig. 29.12a indicate that this is approximately the case at the low electric current density levels, but that there is slight deviation from linearity (with a higher rate) at the higher electric current density levels. This deviation can be attributed to the enhanced natural convection in the solution. The increase of electric current density up to 7 A/cm² in the growth of *bulk* crystals by LPEE has been a significant contribution. This was possible due to the novel design features of the LPEE setup in [29.26].

Crystals were grown at 3 A/cm², without magnetic field, for various periods of time to determine the growth rate. Crystals were grown with thicknesses between 1.5 and 4.5 mm, with an average growth rate of 0.57 mm/day, as shown in Fig. 29.12b. In one of the experiments a thickness of 4.5 mm was achieved in 8 days. A number of crystals were also successfully grown under the electric current densities of 5 and 7 A/cm². The growth rates were 0.75 mm/day (2.25 mm thickness in 3 days) and 1.25 mm/day (3.75 mm thickness in 3 days), respectively. It must be mentioned that some of the growth thicknesses were not representative for calculating the growth rate since in such experiments the source material put into the well was completely depleted before stopping the growth (Fig. 29.12a). Those

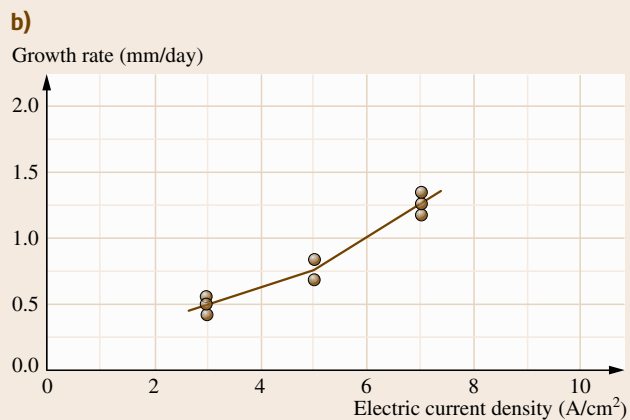
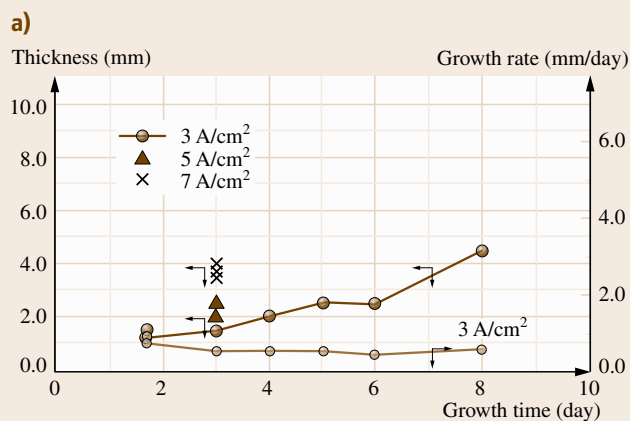


Fig. 29.12a,b Summary of the LPEE growth rates (b) and thickness (a) in the absence of applied magnetic field (after [29.26])

experiments were not included in the calculation of growth rates.

As mentioned earlier, in order to suppress the natural convection in the liquid solution for the purpose of prolonging and stabilizing the LPEE growth process for growing bulk single crystals (thicker crystals), an applied static magnetic field was used. A sample grown GaAs crystal is shown in Fig. 29.13.

The static applied magnetic field induces a magnetic body force acting on the moving particles of the liquid solution. The combined effect of the magnetic and gravitational body forces suppresses convection and prolongs growth. This beneficial effect of an applied magnetic field was the initial intention of the research program at UVic CGL. This goal was successfully achieved, by growing thick single crystals. However, the unexpected effect (a very positive effect of course) of the applied magnetic (at 4.5 kG and lower field levels) was the significant increase in the growth rate (about ten times at the 4.5 kG level, Fig. 29.14). The average growth rates were calculated at specific electric current density levels based on the selected representative

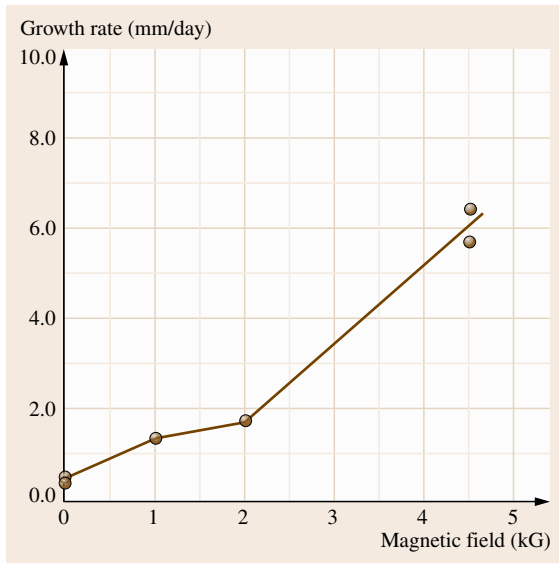


Fig. 29.15 Growth versus magnetic field intensity at $J = 3 \text{ A/cm}^2$ (after [29.26])

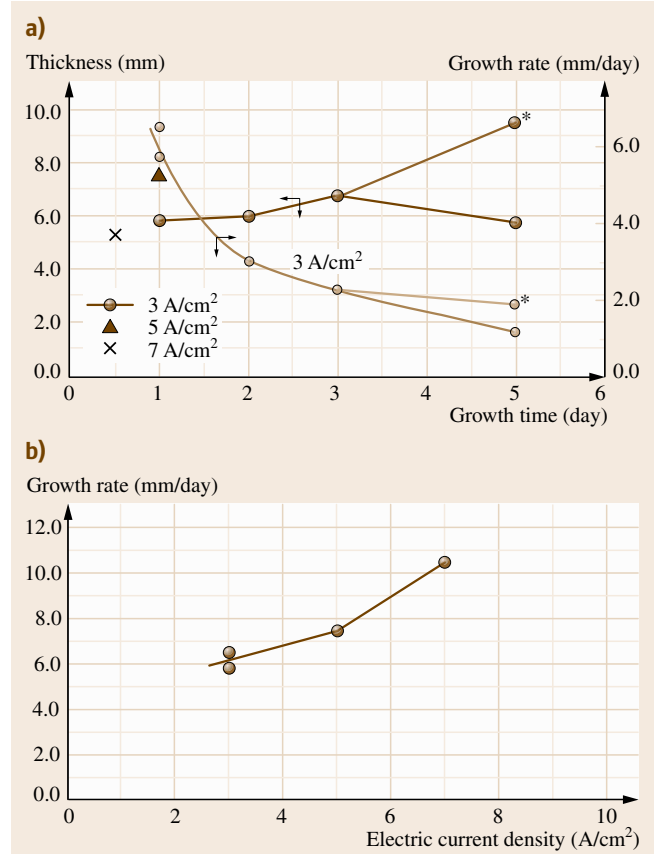


Fig. 29.14 Summary of the growth rates at the $B = 4.5 \text{ kG}$ magnetic field level (after [29.26])

experiments, those that were stopped deliberately before depleting the source material. This increase in the growth rate was almost the same at each of three electric current density levels, namely about 6.1, 7.8, and 10.5 mm/day at $J = 3, 5$, and 7 A/cm^2 . Such a drastic increase in the growth rate elevates the LPEE growth process to the category of a bulk growth. Growth rates at the $B = 1.0$ and 2.0 kG levels were also higher, about 1.62 and 2.35 mm/day, respectively. Results show that the growth rate is also proportional to the applied magnetic field level (Fig. 29.15).

29.5 Three-Dimensional Simulations

The earlier two-dimensional simulation results have shown that the level of applied magnetic field has a significant effect on natural convection in the solu-

tion, both in intensity and structure [29.46]. A stronger applied magnetic field leads to weaker convection in the solution, and more uniform interfaces. These

two-dimensional numerical simulations have shed light on various aspects of the applied magnetic field in LPEE. However, these models, being two dimensional, have naturally neglected the contributions of the circumferential velocity and magnetic body force components. Therefore, the results presented earlier were qualitative and did not include information about three-dimensional effects such as deviations from axisymmetry, variations of the magnetic field components, and mixing in the solution.

In order to shed light on these three-dimensional effects, three-dimensional models were developed in [29.35, 36] for the LPEE growth of a binary system. To the best of our knowledge, these were the first three-dimensional simulation models developed for LPEE. Here, we present the key features of these models.

29.5.1 Simulation Model

The three-dimensional simulation studies carried out in [29.35, 36] were focused on the growth of a binary system (GaAs) for computational simplicity. In addition, the inclusion of the third component (In) in the analysis would not have a significant effect on the flow structures of the solution. The effect of magnetic field nonuniformity was also investigated. Below we present the model and the simulation results of [29.35, 36].

The growth cell selected for simulation is shown in Fig. 29.1. The governing equations are written explicitly in cylindrical coordinates for a binary system as follows

Continuity

$$\frac{1}{r} \frac{\partial}{\partial r} (ru) + \frac{1}{r} \frac{\partial v}{\partial \varphi} + \frac{\partial w}{\partial z} = 0. \quad (29.20)$$

Momentum

$$\begin{aligned} & \frac{\partial u}{\partial t} + u \frac{\partial u}{\partial r} + \frac{v}{r} \frac{\partial u}{\partial \varphi} + w \frac{\partial u}{\partial z} - \frac{v^2}{r} \\ &= v \left(\nabla^2 u - \frac{u}{r^2} - \frac{2}{r^2} \frac{\partial v}{\partial \varphi} \right) - \frac{1}{\rho_L} \frac{\partial p}{\partial r} - \frac{\sigma_E B^2 u}{\rho_L}, \end{aligned} \quad (29.21)$$

$$\begin{aligned} & \frac{\partial v}{\partial t} + u \frac{\partial v}{\partial r} + \frac{v}{r} \frac{\partial v}{\partial \varphi} + w \frac{\partial v}{\partial z} + \frac{uv}{r} \\ &= v \left(\nabla^2 v - \frac{v}{r^2} + \frac{2}{r^2} \frac{\partial u}{\partial \varphi} \right) - \frac{1}{r \rho_L} \frac{\partial p}{\partial \varphi} - \frac{\sigma_E B^2 v}{\rho_L}, \end{aligned} \quad (29.22)$$

$$\begin{aligned} & \frac{\partial w}{\partial t} + u \frac{\partial w}{\partial r} + \frac{v}{r} \frac{\partial w}{\partial \varphi} + w \frac{\partial w}{\partial z} \\ &= v \nabla^2 w - \frac{1}{\rho_L} \frac{\partial p}{\partial z} - g \beta_t (T - T_0) + g \beta_c (C - C_0). \end{aligned} \quad (29.23)$$

Mass transport

$$\begin{aligned} & \frac{\partial C}{\partial t} + (u + \mu_E E_r) \frac{\partial C}{\partial r} + \frac{v}{r} \frac{\partial C}{\partial \varphi} \\ &+ (w + \mu_E E_z) \frac{\partial C}{\partial z} = D_C \nabla^2 C. \end{aligned} \quad (29.24)$$

Energy

$$\frac{\partial T}{\partial t} + u \frac{\partial T}{\partial r} + \frac{v}{r} \frac{\partial T}{\partial \varphi} + w \frac{\partial T}{\partial z} = \alpha \nabla^2 T. \quad (29.25)$$

Electric charge balance

$$\frac{\partial^2 \phi}{\partial r^2} + \frac{1}{r} \frac{\partial \phi}{\partial r} + \frac{\partial^2 \phi}{\partial z^2} = 0, \quad (29.26)$$

where the gradient operator is defined as

$$\nabla^2 = \frac{1}{r} \frac{\partial}{\partial r} \left(r \frac{\partial}{\partial r} \right) + \frac{1}{r^2} \frac{\partial^2}{\partial \varphi^2} + \frac{\partial^2}{\partial z^2}. \quad (29.27)$$

The associated boundary and interface conditions are given as follows. Along the vertical wall

$$\begin{aligned} & u = 0, \quad v = 0, \quad w = 0, \quad T = T_g - \frac{z - z_0}{H} \Delta T, \\ & \frac{\partial \phi}{\partial r} = 0, \quad \frac{\partial C}{\partial r} = 0. \end{aligned} \quad (29.28)$$

Along the growth interface

$$\begin{aligned} & u = 0, \quad v = 0, \quad w = 0, \\ & k_S \frac{\partial T}{\partial z} - k_L \frac{\partial T}{\partial z} = -\pi J, \\ & -\sigma_E \frac{\partial \phi}{\partial r} = J, \quad C = C_1. \end{aligned} \quad (29.29)$$

Along the dissolution interface

$$\begin{aligned} & u = 0, \quad v = 0, \quad w = 0, \\ & k_S \frac{\partial T}{\partial z} - k_L \frac{\partial T}{\partial z} = +\pi J, \quad \phi = 0, \quad C = C_2. \end{aligned} \quad (29.30)$$

Initial conditions at $t = 0$

$$C = C_0, \quad u = 0, \quad v = 0, \quad w = 0, \quad T = T_g, \quad (29.31)$$

where u , v , and w are the velocity components in the r -, φ -, and z -directions, respectively, T is temperature, C is solute concentration, T_0 and C_0 are the reference values, H is solution height, and C_1 and C_2 are the concentrations on the growth and dissolution interfaces, respectively. Definitions of other symbols used here are given in Tables 29.3 and 29.4.

Table 29.3 Physical properties of the GaAs system [29.34]

Parameter	Value
Growth temperature T_g	800 °C
Current density J	10 A/cm ²
Peltier coefficient π	0.3 V
Solution electric conductivity σ_E	25 000 Ω^{-1} cm ⁻¹
Solid (crystal and source) electric conductivity σ_S	40 Ω^{-1} cm ⁻¹
Thermal diffusivity α	0.30 cm ² /s
Solutal diffusion coefficient D_C	4.0 $\times 10^{-5}$ cm ² /s
Solution kinematic viscosity ν	1.21 $\times 10^{-3}$ cm ² /s
Solution density ρ^L	5.63 g/cm ³
Solute electric mobility μ_E	0.027 cm ² /V s
Thermal expansion coefficient β_t	9.85 $\times 10^{-5}$ K ⁻¹
Solutal expansion coefficient β_c	-8.4 $\times 10^{-2}$
Thermal conductivities k	
Graphite	0.225 W/cm K
Ga-As solution and contact zone	0.526 W/cm K
GaAs substrate	0.082 W/cm K
Boron nitride: the r -direction	0.282 W/cm K
Boron nitride: the z -direction	0.440 W/cm K
Crystal radius	6.0 mm
Furnace radius	36.0 mm
Graphite height	19.0 mm
Solution height	6.0 mm
Substrate thickness	0.3 mm
Source thickness	5.0 mm
Contact zone height	2.0 mm

Table 29.4 Parameters of the GaAs system [29.35]

Parameter	Symbol	Value
Crystal radius	R_c	12.0 mm
Solution height	H	10.3 mm
Magnetic field intensity	B	0–12 kG
Nonuniformity coefficient	A	0–4
Thermal Grashof number	Gr_T	6.84 $\times 10^4$
Solutal Grashof number	Gr_C	7.10 $\times 10^3$
Hartmann number	Ha	0–871.5
Prandtl number	Pr	4.00 $\times 10^{-3}$

flow field only, the evolution of the growth and dissolution interfaces is not included in the computations. The mass transport equation in the solution is solved simultaneously in order to take into account the influence of concentration field on the flow field (through the solutal Grashof number); however, the concentration field is not presented here for the sake of brevity. Transient terms are considered in the energy, mass transport, and momentum equations in order to account for possible unsteady flows and their influence. The simulation results are presented at $t = 1$ h since the flow field has fully developed by that time.

The required physical and growth parameters of the GaAs system are given in Tables 29.3 and 29.4. The Hartmann number is defined by

$$Ha = BH\sqrt{\sigma_E/\rho_L\nu}. \quad (29.32)$$

The simulations are carried out for half of the cylindrical cell domain for computational efficiency. However, to ensure that the half-domain solution represents fully the flow structure of the full domain, a full-domain solution was carried out for a case for which asymmetry was assured (under a large magnetic field, $B = 4$ kG). Results demonstrated that the half-plane treatment is reliable.

29.5.2 Numerical Method

The commercial CFX software was used to solve the field equations. The computation mesh in the liquid is $120 \times 40 \times 80$ in the r -, φ -, and z -directions, respectively, which was demonstrated to be sufficient for an accurate and stable solution. Since the focus is on the

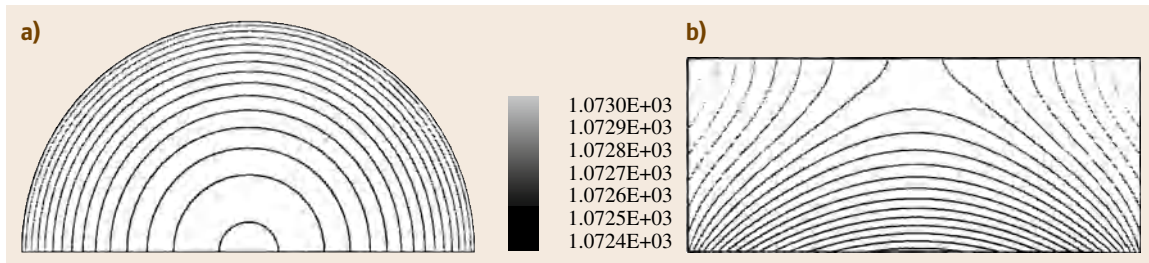


Fig. 29.16a,b Temperature distribution (K): (a) near the growth interface in the horizontal plane, (b) in the vertical plane at $\varphi = 0$ (after [29.35, 36])

Computed temperature distributions in the horizontal plane near the growth interface and also in the vertical plane at $\varphi = 0$ are given in Fig. 29.16. Temperature distributions agree with earlier 2-D solutions [29.34, 49, 50]. In addition, since the electric current is passing through the source in this setup, the computed isotherm patterns indicate that the shape of the growth interface will be single-humped (concave towards the crystal), as expected.

29.5.3 Effect of Magnetic Field Strength

For a better visualization, the simulation results for the flow field in the growth cell are presented in three distinct planes: the vertical (r - z) plane at $\varphi = 0$ that represents typical flow structures along the growth direction, the horizontal (r - φ) plane at the middle of the growth cell ($z = 5.15$ mm) where the changes in the flow field will be more prominent for radial and circum-

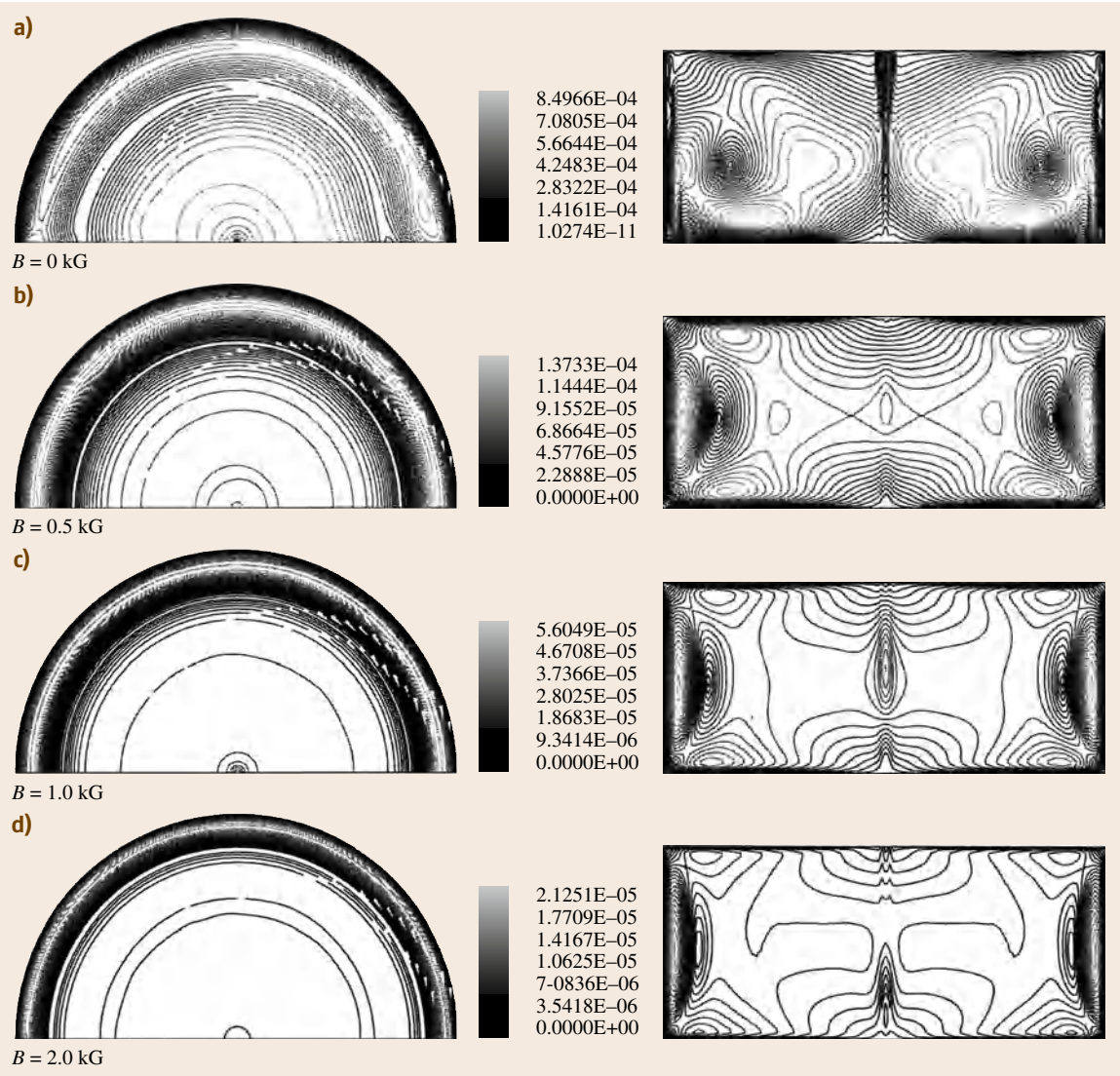


Fig. 29.17a-d Flow field in the horizontal plane in the middle of the solution zone (left column) and in the vertical plane at $\varphi = 0$ (right column) (after [29.35, 36])

ferential velocity components representing mixing, and finally the horizontal plane (r - φ) near the growth interface ($z = 0.4$ mm) where the flow field is often closely related to the quality of the grown crystals.

Figure 29.17 presents the simulation results for the flow field presented in the horizontal plane at the middle of the growth cell (left column) and in the vertical plane at $\varphi = 0$ (right column) for four levels of mag-

netic field strengths ($B = 0.0, 0.5, 1.0$, and 2.0 kG), while Fig. 29.18 shows the results for the flow field in the horizontal plane near the growth interface (left column) and in the vertical plane at $\varphi = 0$ (right column) for intermediate magnetic field intensities ($B = 2.5$ and 3.0 kG), and in the horizontal plane at the middle of the growth cell (left column) and in the vertical plane at $\varphi = 0$ (right column) for higher field levels ($B = 4.0$

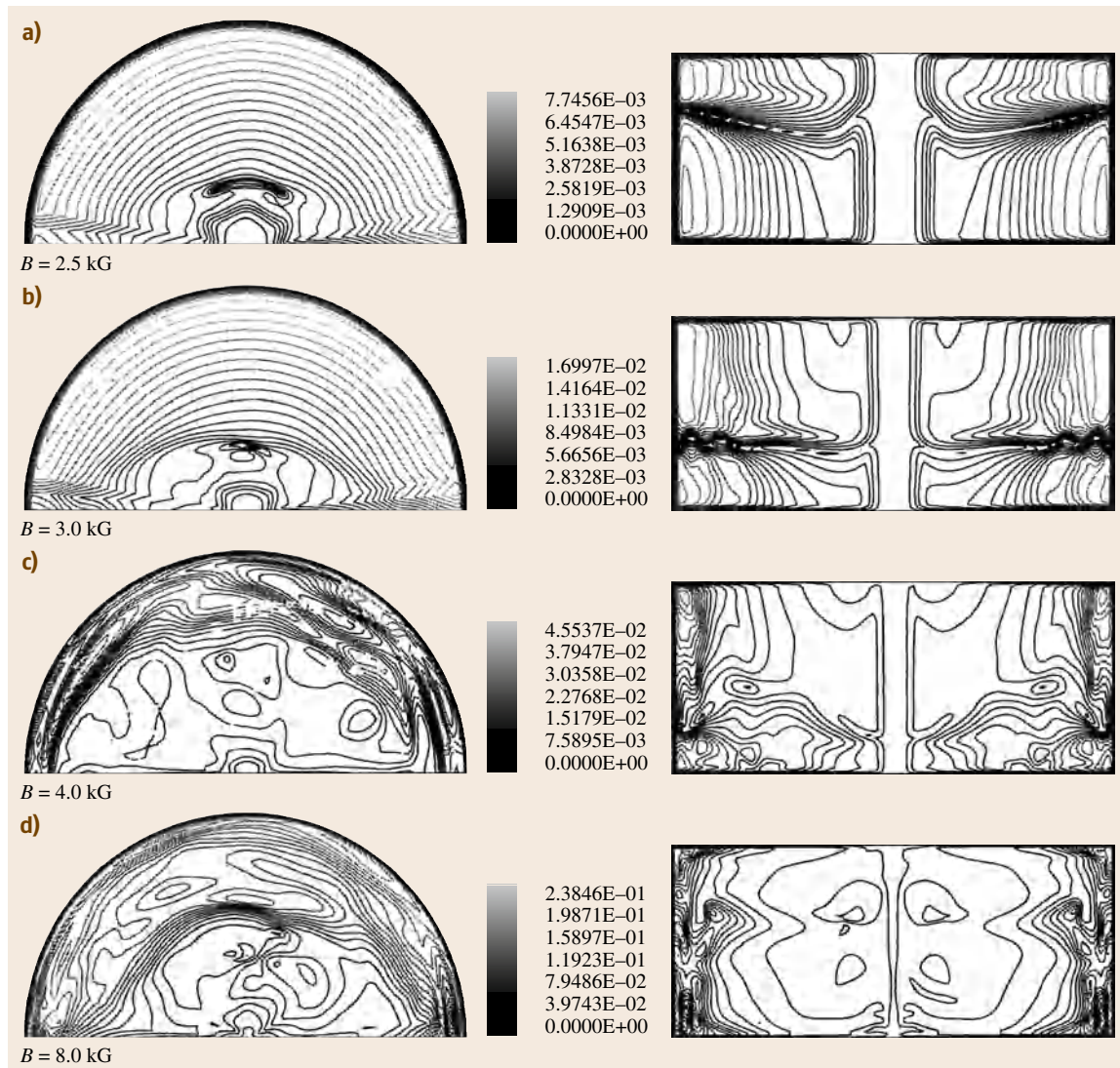


Fig. 29.18a-d Flow field in the horizontal plane near the growth interface at $z = 0.4$ mm (left column) and in the vertical plane at $\varphi = 0$ (right column) for (a) $B = 2.5$ kG, and (b) $B = 3.0$ kG, and in the horizontal plane at the middle of the growth cell (left column) and in the vertical plane (right column) for (c) $B = 4.0$ kG, and (d) $B = 8.0$ kG (after [29.35,36])

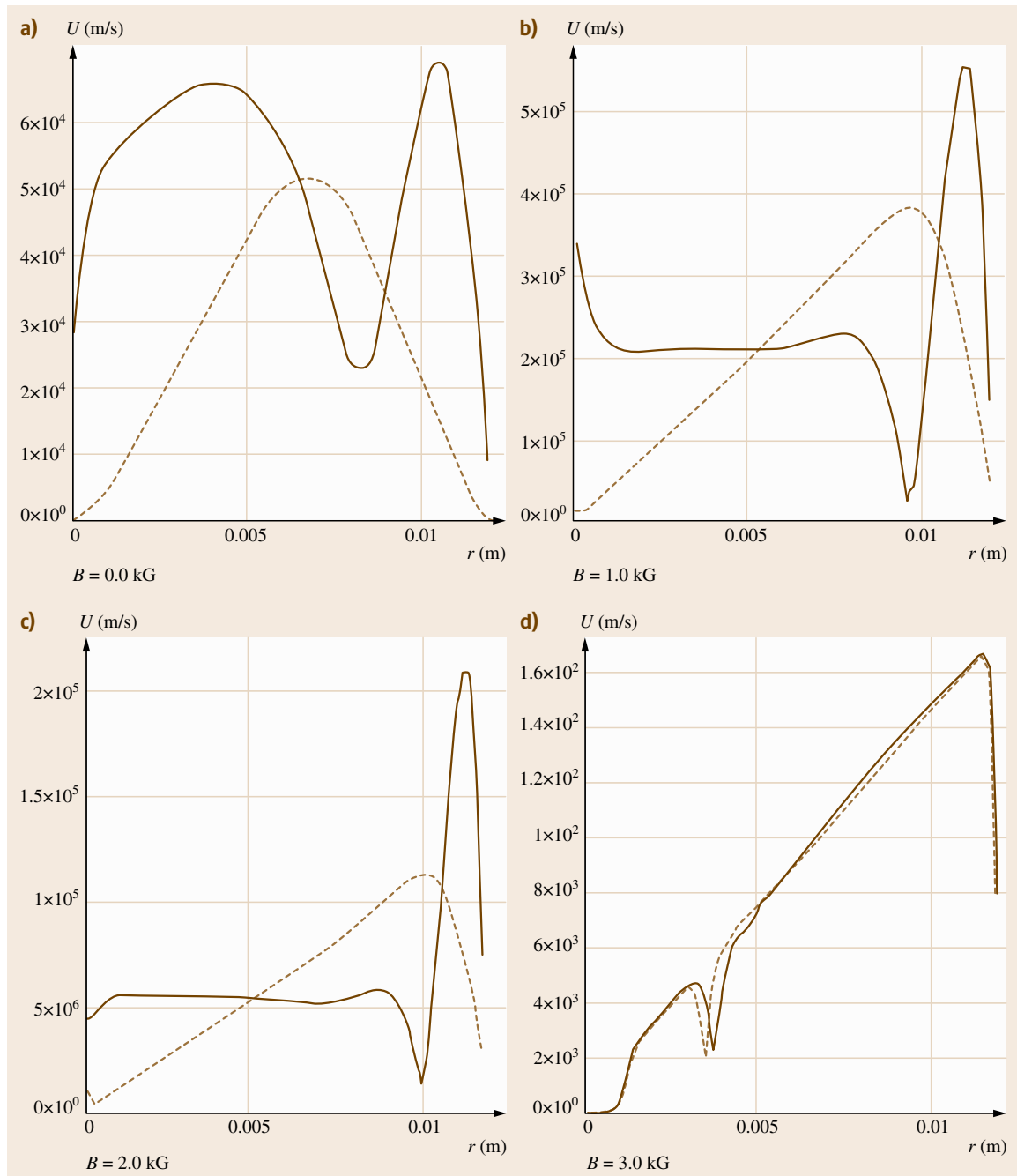


Fig. 29.19a–d Variation of the flow strength $U = (u^2 + v^2 + w^2)^{1/2}$ along the radial direction at $\varphi = \pi/2$ under various magnetic field strengths: **(a)** $B = 0.0$ kG, **(b)** $B = 1.0$ kG, **(c)** $B = 2.0$ kG, and **(d)** $B = 3.0$ kG. Solid lines at $z = 5.05$ mm (in the middle of the growth cell), and dashed lines at $z = 0.4$ mm (near the growth interface) (after [29.35, 36])

and 8.0 kG). Local magnitudes of the flow velocity $U = \sqrt{u^2 + v^2 + w^2}$ (which will be referred to as the *flow strength*) are computed in m/s, and the scales of flow strengths are shown in each figure.

The computed flow patterns in the vertical plane appear more complex than those of the 2-D simulations presented for the same LPEE growth system. This complexity can be attributed mainly to the inclusion of the contribution of the circumferential velocity component. In addition, the size of the growth crucible used in this study is twice that of the one used in [29.34,49,50]; this might have also contributed towards these differences. Such differences in the flow field of 2-D and 3-D models have also been observed in [29.39,52,53]. The strongest flow is seen in the lower part of the crucible cell, near the center of the half-domain along the r -direction. This is similar to what was observed in [29.34]. A weak flow cell forms just above the strongest flow cell. The flow in the horizontal planes is nearly homocentric. The flow in the horizontal plane near the growth interface is stronger in the middle region along the radial direction and becomes weaker and weaker near the growth cell wall or the axial center (Fig. 29.17a, left column). On the other hand, in the horizontal plane at the middle of the growth cell (Fig. 29.17a, right column) there are two maximum points for the flow intensity along the radial direction, with a relatively strong flow in the central region.

Note that the flow field in Fig. 29.17a is not strictly axisymmetric, especially in the middle of the growth cell, although the flow is stable. This result suggests that the present system is near the Grashof number that is a little bit lower than the critical Grashof number (2.5×10^5) under the same conditions (Prandtl number and geometry aspect ratio) given in [29.60] in the analysis of axisymmetry breaking of natural convection in a vertical Bridgman growth configuration.

Results are also summarized in Figs. 29.19 and 29.20 for various aspects of the flow field. Simulation results show three distinct characteristics depending on the level of applied magnetic field: (a) the *weak* magnetic field, with intensities from 0.0 to 2.0 kG, (b) the *intermediate* magnetic field, with levels from 2.0 to 3.0 kG, and (c) the *high* magnetic field, with intensities above 3.0 kG. Flow characteristics are quite different at each of these field levels.

Let us first focus on Fig. 29.17b–d, which represents results for magnetic field levels from 0.5 to 2.0 kG. In this category, the weak magnetic field level, an increase in the applied magnetic field strength results in signifi-

cant reduction in the flow strength, which is, in general, desirable for a stable and controlled crystal growth. Flow cells are the strongest near the vertical wall and forms the so-called Hartmann layer [29.51–54]. At higher magnetic field strengths, the relative strength of these flow cells becomes increasingly stronger compared with the flow in the rest of the growth cell domain, and the Hartmann layer becomes thinner, which is in accordance with the scaling analysis given in [29.51, 52]. Furthermore, the strongest flow cells appearing in the lower part of the growth cell (Fig. 29.17a) move further down towards the growth interface with increasing strength, and new flow cells form near the dissolution interface. These strong flow cells form very visible boundary layers near the growth and dissolution interfaces (the so-called *end layers* [29.51, 52, 54]), and hence give rise to strong vertical velocity gradients in the vicinity of the growth interface, which may have an adverse effect on the crystal growth process.

One may state that the application of a magnetic field may not always be beneficial for the growth process [29.40, 54]. It was shown in [29.54] that the radial nonuniformity in vertical Bridgman is the most

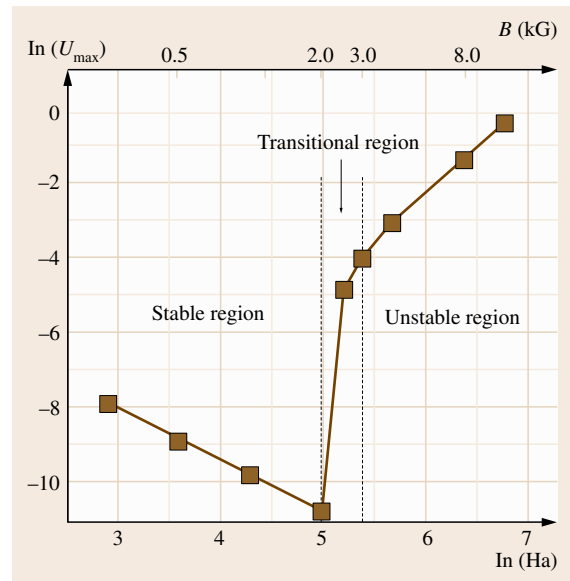


Fig. 29.20 Variation of the maximum velocity with magnetic field intensity: three distinct regions of stability of the flow field are obvious. The flow field is stable up to $Ha = 150$; in the region between $Ha = 150$ and 220 the flow is transitional; and above $Ha = 220$ the flow is unstable (after [29.35, 36])

significant at intermediate levels of magnetic field strength.

Flow fields become perfectly homocentric (and hence axisymmetric) with the increase of magnetic field strength, and hence the flow strength decreases. The flow velocities in the central region of the cell (in both the r - and z -directions) become more uniform at higher magnetic field levels, and form a core region of the uniform flow field, leading to a domain in which the flow is suppressed with the application of an applied magnetic field [29.51, 52, 54]. Indeed, an applied magnetic field at weak intensity levels can suppress fluid flows in a growth system, as shown in Fig. 29.17.

To the best of our knowledge, a magnetic field level higher than 8.0 kG is very strong for LPEE growth of thick crystals, due to the strong interaction between the applied magnetic and electric fields. Thus far, it was not possible to exceed the level of 4.5 kG in experiments, as higher magnetic field levels led to unsatisfactory growth [29.26]. The issue of LPEE growth under higher magnetic field levels and also the higher growth rates observed under an applied static magnetic field will be further discussed in the next section.

Figure 29.18 represents the simulation results for the intermediate magnetic intensity levels selected as $B = 2.5, 3.0, 4.0$, and 8.0 kG. In this case, flow strength increases with magnetic field intensity. This result has not been widely reported in the relevant literature. It is possible that it is numerical in nature, and can be fixed by some innovative numerical treatments [29.56], but it is also possibly physically, as was observed experimentally in the LPEE growth of GaAs in [29.27].

Some experimental and numerical studies indeed demonstrated the enhancement of heat transfer (and hence flow strength) in a melt under a stationary magnetic field [29.57–59]. As can be seen from Fig. 29.18, the flow patterns show dramatic changes, as two flow cells were formed in each half of the vertical plane, with the upper cells getting larger and lower cells getting smaller with increasing magnetic field intensity. In the vertical plane, some strong unidirectional flows appear in the middle region along the r -direction, and some with very weak intensity in the middle, forming a small cylindrical region where the flow is nearly stationary. The flow fields are no longer axisymmetric and homocentric. Such an axisymmetry breaking may be caused by the unsteadiness of the flow field according to [29.60].

The flow stability was also examined at $B = 2.5$ and 3.0 kG levels. Comparing the results at different times, it was found that the flow field is essentially

stable in spite of some small changes with time. One can then speculate that the reason for the axisymmetry breaking of the flow field at these magnetic field levels may be physical and due to a very delicate balance between the buoyancy and magnetic forces, even though the flow still remains stable. The variation of the flow strength along the radial direction for $B = 0.0, 1.0, 2.0$, and 3.0 kG levels are shown in Fig. 29.19. Solid and dashed lines represent, respectively, the values at the middle and the lower regions of the solution zone. As can be seen, the flow strength fluctuates and shows differences in these regions. However, at higher magnetic field levels, the difference becomes less obvious. The variation of the flow strength in the radial direction near the growth interface is almost symmetric in the absence of a magnetic field. However, this symmetry is broken at higher magnetic field intensity levels.

Although higher magnetic field intensity levels, higher than 4.5 kG, appear not to be practical for LPEE growth of thick crystals [29.26], for the sake of completeness and also for the purpose of comparison with other studies, higher magnetic field intensity levels of $B = 4.0$ and 8.0 kG were also considered. The flow patterns become dramatically different and show large fluctuations with time, and temperature distributions show asymmetric behavior.

The maximum flow strength (the maximum magnitude of the local velocity vector) values U_{\max} are presented in Fig. 29.20 for all magnetic field levels. As seen, the variation of the maximum flow strength shows three distinct regions of stability. The flow strength decreases with increasing magnetic field in the stable region (up to $Ha = 150$), but in the intermediate and unstable regions (between $Ha = 150$ and 220, and above $Ha = 220$, respectively) the flow strength increases. If one examines the logarithmic plot of U_{\max} as a function of the Hartmann number Ha given in Fig. 29.20, we can see that within the stable region, the relationship between U_{\max} and Ha obeys a power law of

$$U_{\max} \propto Ha^{-5/4}, \quad (29.33)$$

which has been demonstrated by many authors [29.51–55], although the index of the power law is slightly different due to different system parameters and conditions. In the unstable region, this relationship becomes

$$U_{\max} \propto Ha^{5/2}. \quad (29.34)$$

In the transitional (intermediate) region, on the other hand, as one expects, the change of the maximum strength (U_{\max}) of the flow field with the Hartmann

number is so dramatic that the power law is not suitable. The results given here for the intermediate and unstable regions were obtained for the first time in [29.35], and to the best of our knowledge, are not corroborated by anyone else in the literature.

29.5.4 Evolution of Interfaces

As mentioned earlier, the simulation results above were given at the end of a 1 h growth period ($t = 1.0$ h) and also for a *stationary* interface, for computational efficiency. This was sufficient for examining the flow field and the effect of a magnetic field on the flow structures. However, in order to draw meaningful conclusions for future experiments, and also examining the concentration fields in the solution and the evolution of interfaces, simulations were carried for a longer period of growth ($t = 20.0$ h) for three levels of magnetic fields, namely $B = 0.0$ kG (no applied magnetic field), $B = 1.0$ kG (the

mid-field level in the stable region), and $B = 3.0$ kG (a field at the beginning of the unstable region), and also the evolution of growth and dissolution interfaces are included. Higher magnetic field levels are not considered since the reliability of computations for concentrations in the unstable region may be questionable.

Figure 29.21 summarizes the computed results for the flow field in the horizontal plane at the middle of the growth cell (left column) and in the vertical plane at $\varphi = 0$ (right column) for three levels of magnetic field intensities ($B = 0.0, 1.0$, and 3.0 kG). Flow strengths are computed in m/s, and the scales are shown in each figure. The inclusion of the evolution of growth and dissolution interfaces affected the flow patterns to a certain extent, although it is not significant in terms of magnitudes. The effect of the magnetic field in the stable region is obvious in suppressing the natural convection in the solution. At the $B = 3.0$ kG level, however, the flow patterns show signs of unstable flows.

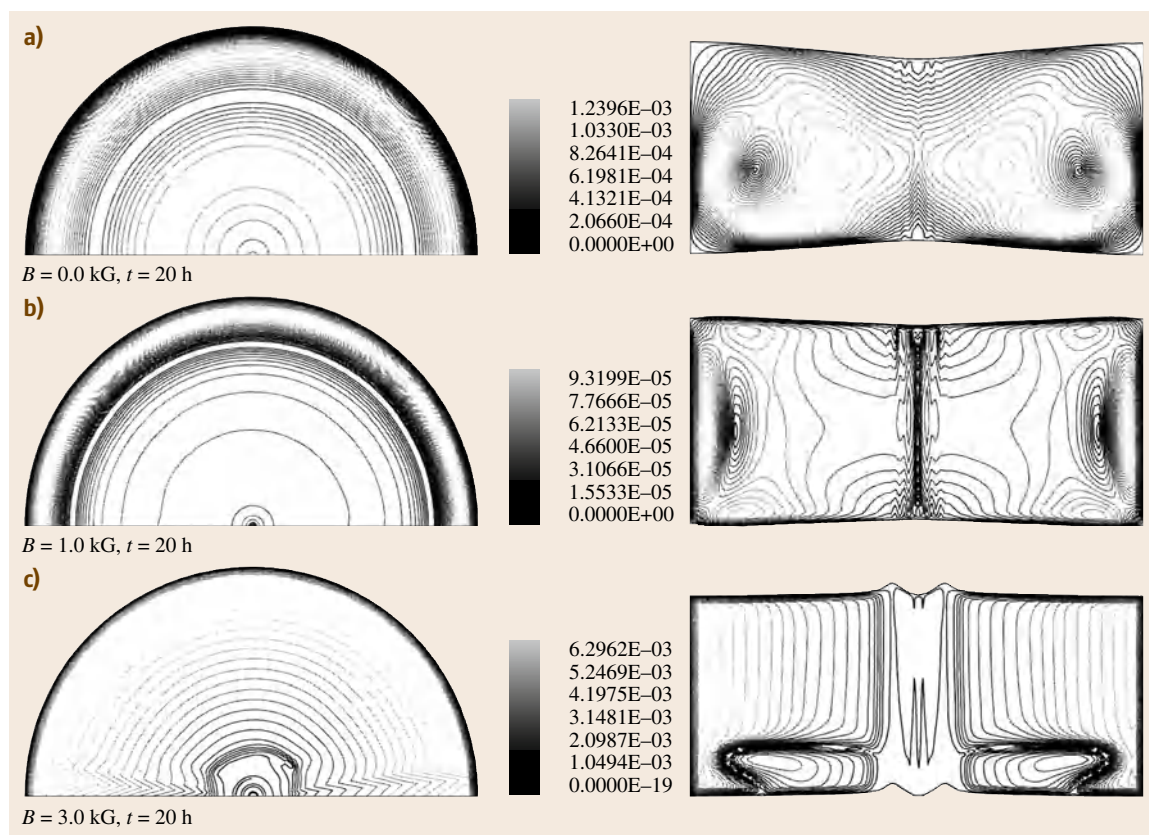


Fig. 29.21a–c Flow field in the horizontal plane in the middle of the growth cell (*left column*) and in the vertical plane at $\varphi = 0$ (*right column*) (after [29.35, 36])

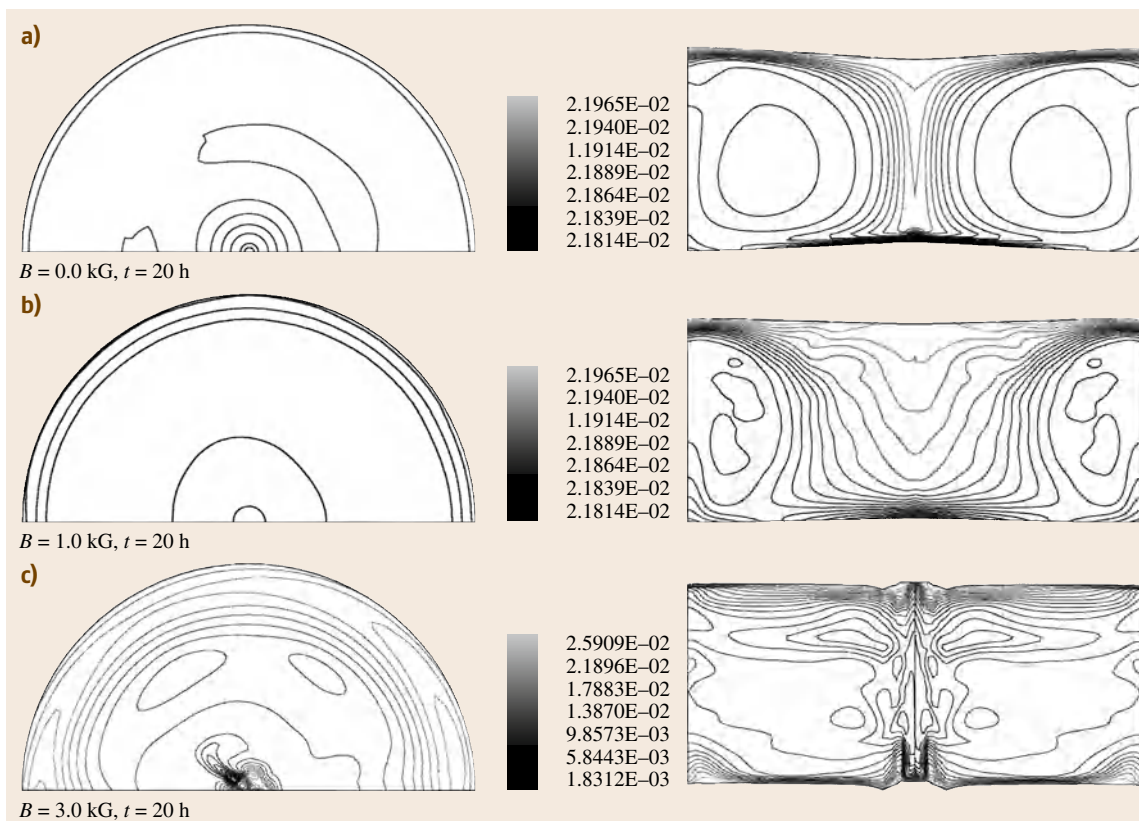


Fig. 29.22a–c Concentration distributions in the horizontal plane near the growth interface (left column) and in the vertical plane (right column) (after [29.35, 36])

The concentration distributions at the $B = 0.0$, 1.0 , and 3.0 kG magnetic field levels are presented in Fig. 29.22 at $t = 20$ h. Comparing Fig. 29.22a,b one can see that the concentration gradients near the center of the growth interface and near the growth cell wall in the vicinity of the dissolution interface decrease with the increasing magnetic field levels. This is due to the reduction in flow strength, resulting in slower mass transfer towards the growth interface, consequently slowing down both the growth and dissolution rates. The concentration vortices in Fig. 29.22a nearly disappear in Fig. 29.22b. At the $B = 3.0$ kG level (Fig. 29.22c), concentration distributions exhibit significant changes compared with those of Fig. 29.22a,b. The concentration vortices near the center of the symmetric axis, in the vicinity of the growth interface, form strong concentration gradients and lead to fast growth rates in that region. Concentration layers are formed in the vicinity of both the growth and dissolution interfaces.

The computed growth rates obtained from simulations [29.35] under magnetic field do not predict the experimental growth rates [29.40]. We will discuss this issue later in detail.

29.5.5 Effect of High Electric and Magnetic Field Levels

The flow field was also numerically simulated under various electric current densities in [29.36]. The maximum flow strength shows the same trend at $J = 3$, 5 , and 7 A/cm² electric field levels. The time evolution of the flow field was computed for various magnetic field intensity levels, and the one corresponding to $B = 4.0$ kG and $J = 7$ A/cm² is shown in Fig. 29.23. As can be seen, the flow patterns change with time and begin to become localized after 120 s of growth. This localization point is near the growth interface and is approximately at about a distance of a quarter of

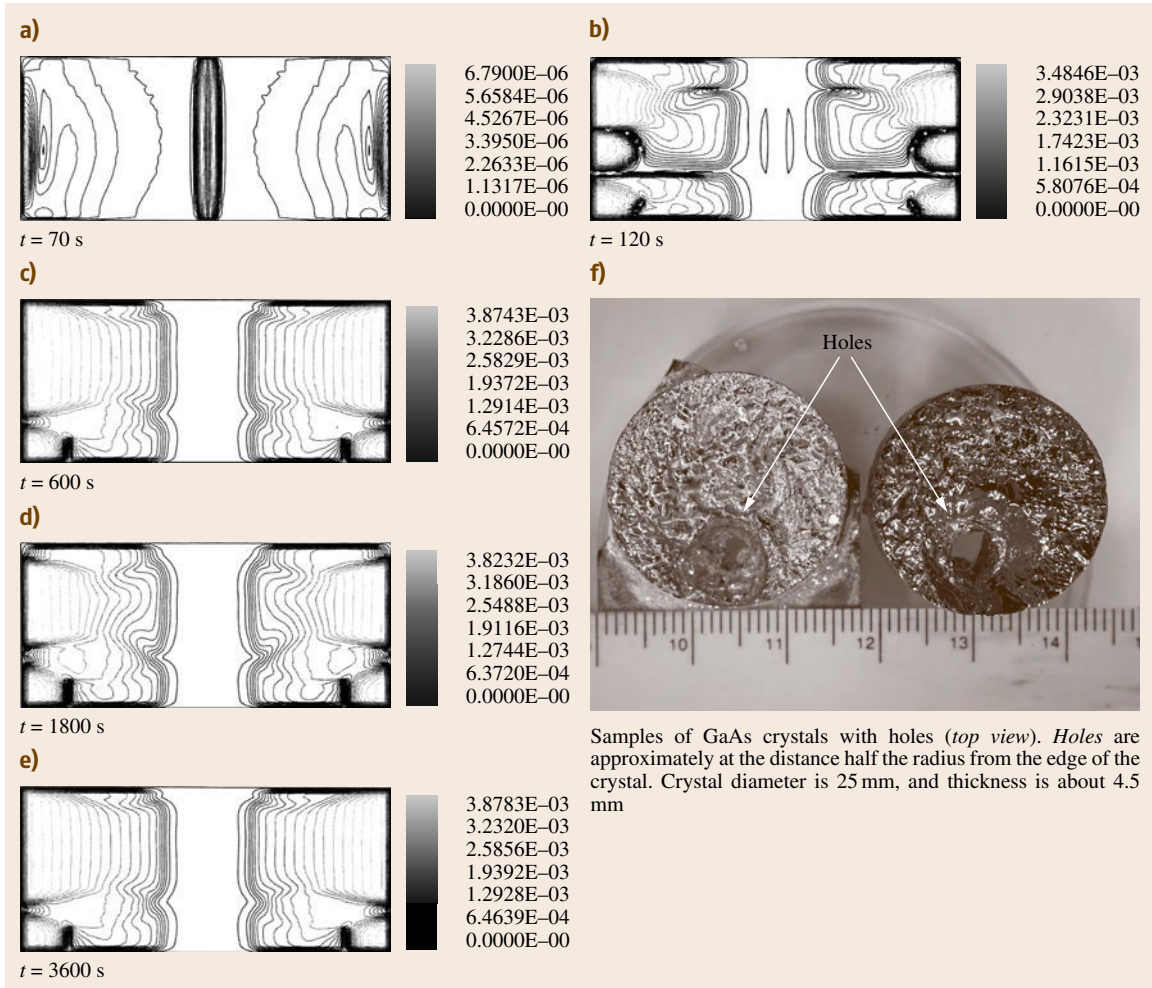


Fig. 29.23a–f Time evolution of the flow field (isostrength contours). The flow field is localized near the growth interface at about a distance of half of the crystal radius where approximately holes are observed (after [29.39]), samples from [29.27]

the diameter of the crystal from the edge. This point is almost at the locations where the holes (or damages) were observed in crystals grown under high fields in [29.27]. Simulations are shown in Fig. 29.23 for the liquid solution zone, but it is possible that similar flow patterns can also be computed in the liquid contact zone below the seed crystal. The flow patterns computed for $B = 3.0$ kG and $J = 5$ A/cm² show similar patterns [29.36]. The numerical simulations are in qualitative agreement with experiments, but do not agree quantitatively on the critical value of the magnetic field. Numerical simulations predict a lower value (just over 2 kG) than the maximum experimental value of 4.5 kG.

Crystals were grown in [29.26] at field values up to $B = 4.5$ kG, and $J = 7$ A/cm². However, experiments at higher fields failed (two samples of such crystals are shown in Fig. 29.23f).

Three-dimensional numerical simulation results have shown that magnetic field intensities up to 2.0 kG suppress the flow structures in the solution, and the flow structures are stable and get weaker with the increasing magnetic field level. These levels of magnetic field are beneficial in suppressing the natural convection. However, field intensities higher than 2.0 kG change the flow patterns significantly, and at intensities higher than 3.0 kG the flow structures become unstable.

As mentioned earlier, the LPEE growth system developed in [29.26] allowed the growth of a large number of GaAs and $\text{Ga}_{0.96}\text{In}_{0.04}\text{As}$ single crystals of thicknesses up to 9 mm. It was possible to apply electric current densities of 3, 5, and 7 A/cm², and the corresponding growth rates in these experiments with no magnetic field were, respectively, about 0.57, 0.75, and 1.25 mm/day. Growth interfaces were very flat, and the growth experiments were reproducible in terms of crystal thickness and growth rate. Experiments at higher electric current intensities were not successful. Experiments at 3, 5, and 7 A/cm² electric current densities were repeated under various applied static magnetic field levels. Results showed that LPEE experiments at the 4.5 kG and lower magnetic field levels were success-

ful, but those under higher magnetic field levels were not.

In fact the experimental study of the LPEE growth of GaAs and $\text{Ga}_{0.96}\text{In}_{0.04}\text{As}$ single crystals supported qualitatively the results of the three-dimensional numerical simulations [29.26]. It seems that the 4.5 kG field intensity level is a maximum (*critical*) value above which the growth is not stable. This experimental *critical* magnetic field level is higher than that predicted from the numerical simulations performed under the same growth conditions, which was somewhere between 2.0 and 3.0 kG [29.35]. Considering the complexity of the LPEE growth process, this is a good qualitative agreement.

29.6 High Growth Rates in LPEE: Electromagnetic Mobility

The LPEE experiments conducted in [29.26] yielded a very significant result that was not predicted from the modeling studies conducted earlier: the experimental LPEE growth rates under magnetic field were much higher than the predicted values. For instance, the growth rate at the 4.5 kG magnetic field level (at $J = 3 \text{ A/cm}^2$) was about 6.1 mm/day, which is about 12 times higher than that with no magnetic field. Experiments performed at $B = 1.0$ and 2.0 kG field levels (at $J = 3 \text{ A/cm}^2$) were also successful, and the growth rates were also higher: 1.62 and 2.35 mm/day, respectively. One more interesting observation of the LPEE experiments was that the direction of the applied magnetic field, either up or down, was not relevant. The growth rate was almost the same, being about 5–6% less when the magnetic field was in the direction of the applied electric field. As predicted from the three-dimensional models, at higher magnetic field levels (even with the $J = 3 \text{ A/cm}^2$ electric current density level), and higher electric current density levels ($J = 10 \text{ A/cm}^2$ or higher), experiments did not lead to successful growth, but showed very interesting outcomes [29.26, 36].

Although very thick crystals were grown, even up to 9 mm thickness, the growth processes were unstable, and led to uneven growth (Figs. 29.23 and 29.24). From visual inspection of the grown crystals, the adverse effect of natural convection was obvious, causing either one-sided growth or leading to holes in the grown crystals. It was considered that such growth (one-sided and with holes) is because of the strong and unsta-

ble convection in the liquid zones (solution and contact zones) due to the strong interaction between the applied magnetic field and the applied electric current. Such predictions were also confirmed qualitatively by the numerical simulations carried out by considering field nonuniformities in [29.35], and also by using a newly defined electromagnetic mobility in [29.40, 61, 62] and a new model in [29.63]. The simulated flow structures show the possibility of causing such nonuniform growth of crystals.

The contribution of electromigration under magnetic field was obtained through a nonlinear model in [29.63] (for the binary GaAs system, in the absence of the Soret effect) as

$$\dot{\mathbf{c}} = \rho_L D_C \nabla C + \rho_L (D_{EC} + D_{ECB} B) C \mathbf{E}. \quad (29.35)$$

The second term in (29.35) represents the contribution of the applied electric current density to mass transport under the effect of a static external magnetic field. This term represents electromigration in the mass transport equation. Its coefficient, which is called the *total mobility* [29.61–63], is written in the following form for convenience

$$\mu_T \equiv D_{EC} + D_{ECB} B \equiv \mu_E + \mu_B B, \quad (29.36)$$

where the material constant μ_E (a second-order material coefficient) is the classical electric mobility of the solute (As) in the liquid solution (Ga/As solution) due to the applied electric current in the absence of an applied magnetic field. The constant μ_B is a third-order

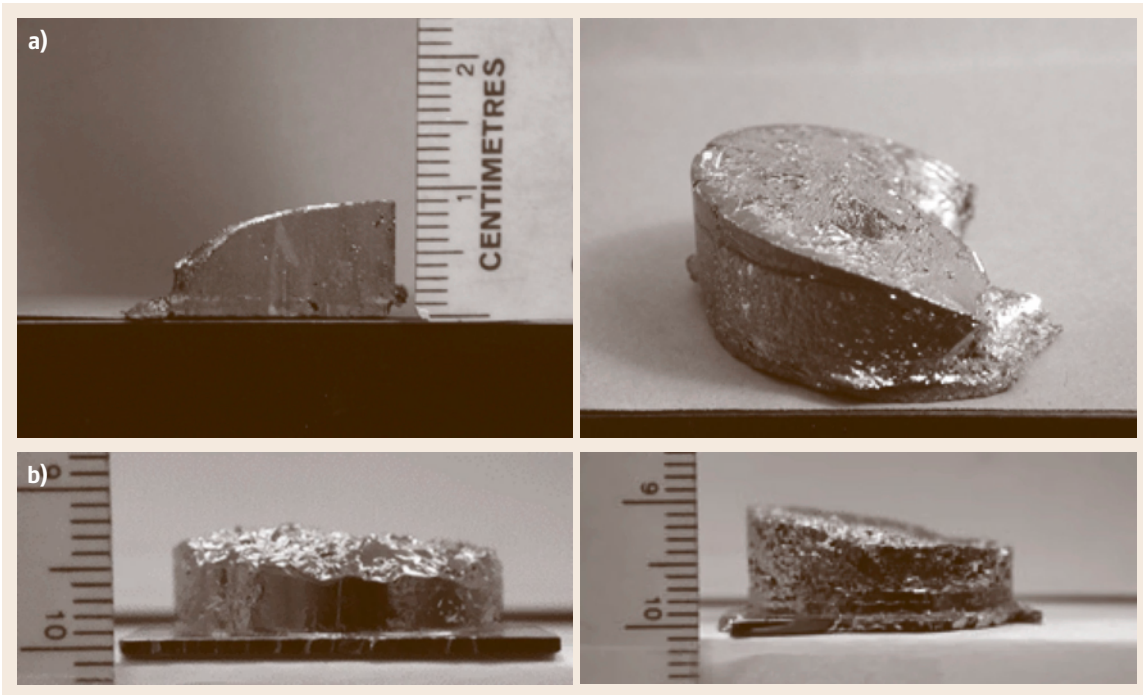


Fig. 29.24a,b Samples of LPEE-grown GaAs crystals under high fields: grown under (a) $B = 20$ kG and $J = 3$ A/cm², and (b) $B = 0$, and $J = 10$ A/cm² (after [29.26])

material coefficient that represents the contribution of the applied magnetic field intensity to the electromigration of species. It is zero (or insignificant) in the absence of an applied electric current. This term is called the electromagnetic mobility of solute [29.63]. Its value is determined using the data of [29.26]. The mass transport equation then becomes

$$(\mu_E + \mu_B B) (\mathbf{E} \cdot \nabla C) + D_C \nabla^2 C = \frac{\partial C}{\partial t} + \mathbf{v} \cdot \nabla C. \quad (29.37)$$

29.6.1 Estimation of the Electromagnetic Mobility Value

Experiments show that the growth rate is proportional to the applied electric current density, and we have evaluated the value of μ_E in the Ga/As solution in the absence of an applied magnetic field. The numerical simulations based on this value verify the experimental growth rates at all three electric current levels ($J = 3, 5$, and 7 A/cm²). Of course, diffusion (the second term in (29.37)) and also natural convection (the last term on the right-hand side of (29.37)) contribute to the growth

rate. However, as shown many times numerically, in LPEE the contribution of the first term (electromigration) is dominant, and the growth rate can be assumed approximately proportional to this term.

Experiments also show that the growth rate increases significantly in the presence of a static magnetic field, and is also proportional to the field intensity level as long as the field level is below a critical value, above which the growth is not stable [29.27]. Numerical values of the mobilities are calculated using the results of a large number of experiments in [29.26] in which the magnetic field vector B was applied both upward and downward. The growth rates in these experiments were almost the same whether B was up or down. In other words the mass transport due to electromigration was only dependent on the magnetic field intensity but not on its direction. This is also in compliance with the defined constitutive equations in [29.63]. Using the measured growth rates, the mobility values were computed (Table 29.5).

The dimensionless mobility is defined as

$$\mu = \frac{\mu_T}{\mu_E} = 1 + \frac{\mu_B}{\mu_E} \cong 1 + 2B, \quad (29.38)$$

Table 29.5 Numerical values of mobilities [29.26, 61, 63]

Experimental values				
Magnetic field (kG)	0.0	1.0	2.0	4.5
Electric current density (A/cm ²)	3.0	3.0	3.0	3.0
Growth rate (mm/day)	0.50	1.62	2.35	6.10
Computed values				
Electric mobility constant μ_E (m ² /V s)	0.7×10^{-5}	0.7×10^{-5}	0.7×10^{-5}	0.7×10^{-5}
Total mobility $\mu_T = \mu_E + \mu_B B$ (m ² /V s)	0.7×10^{-5}	2.3×10^{-5}	3.4×10^{-5}	7.1×10^{-5}
Electromagnetic mobility $\mu_B B$ (m ² /V s)	0.0	1.6×10^{-5}	2.7×10^{-5}	6.4×10^{-5}
Electromagnetic mobility constant μ_B (m ² /V s kG)	–	1.4×10^{-5}	1.4×10^{-5}	1.4×10^{-5}
Dimensionless mobility $\mu = \mu_T / \mu_B \cong 1 + 2B$	1	3	5	10

and is plotted in Fig. 29.25. As seen, the total mobility is almost linearly dependent on the magnetic field intensity, of course, within the limit of experimental measurements.

The first term in the mass transport equation reads explicitly

$$(\mu_E + \mu_B B) (\mathbf{E} + \mathbf{v} \times \mathbf{B}) \cdot \nabla C, \quad (29.39)$$

where the term $(\mathbf{v} \times \mathbf{B}) \cdot \nabla C$ is the contribution of the applied magnetic field due to the motion of the fluid particles (coupling term). Its contribution was found to be very small compared with that of $\mathbf{E} \cdot \nabla C$ (on the order of 3% based on a maximum velocity of 0.01 m/s and a 10 kG field level [29.35, 39]). Therefore, its con-

tribution can be neglected in the model for computer simulations. Then, the electromigration term in the mass transport equation is written as

$$(\mu_E + \mu_B B) \mathbf{E} \cdot \nabla C = \mu_T \mathbf{E} \cdot \nabla C, \quad (29.40)$$

and the growth rate is computed by

$$V_n^g = \frac{\rho_L}{\rho_S} \left(D_C \frac{\partial C}{\partial n} + \mu_T C E_n \right) \frac{1}{C_S - C}, \quad (29.41)$$

or simply by, for the purpose of evaluating the mobility constants,

$$V^g = \frac{\rho_L}{\rho_S} \left(D_C \frac{\partial C}{\partial n} + \mu_T C E_z \right) \frac{1}{C_S - C}. \quad (29.42)$$

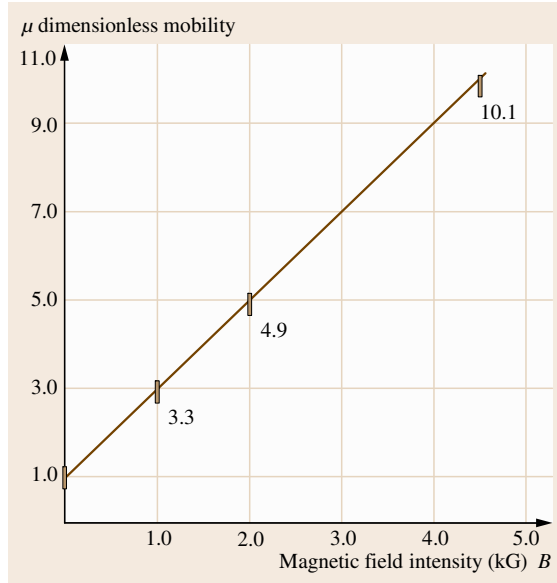


Fig. 29.25 Dependence of the total As mobility on magnetic field intensity (after [29.61, 63])

29.6.2 Simulations of High Growth Rates in a GaAs System

Simulations presented in the previous sections were repeated using the total mobility values in the mass transport equation (29.37). In earlier simulations only the electric mobility μ_E was used. A summary of the growth rates from these numerical simulations is presented in Fig. 29.26a. The values under no magnetic field are the experimental growth rates and are used to compute the value of μ_E . Naturally, they are coincident with the computed values. As seen, the growth rate decreases first with the magnetic field level and then increases with the magnetic field above the critical value. This pattern is similar to the pattern of experimental growth rates under various magnetic field levels, and also agrees with the numerical simulation results.

In order to predict the high experimental growth rates under an applied magnetic field, the mass transport equation in (29.24) was replaced with (29.37), and

Fig. 29.26 (a) Computed growth rates are presented versus applied magnetic field with the use of constant electric mobility μ_E . Squares represent the values at $J = 3 \text{ A/cm}^2$ and circles denote for the values at $J = 7 \text{ A/cm}^2$. **(b)** Growth rates computed using the total mobility, $\mu_T = \mu_E + \mu_B B$, are represented by full circles. These values are in agreement with the experimental growth rates (hollow circles, invisible as coincident with the full circles). The growth rates under no magnetic field are also shown (squares) for comparison (after [29.36]) ►

then the 3-D simulations were repeated using the total electromagnetic mobility $\mu_T = \mu_E + \mu_B B$ values given in Table 29.5. The growth rates computed using the total mobility μ_T are presented in Fig. 29.26b (full circles), and agree with those of experiments. The growth rates using only the electric mobility μ_E are also given in Fig. 29.26b for comparison (empty squares). For the sake of completeness and for comparison, the experimental growth rates under a magnetic field are also

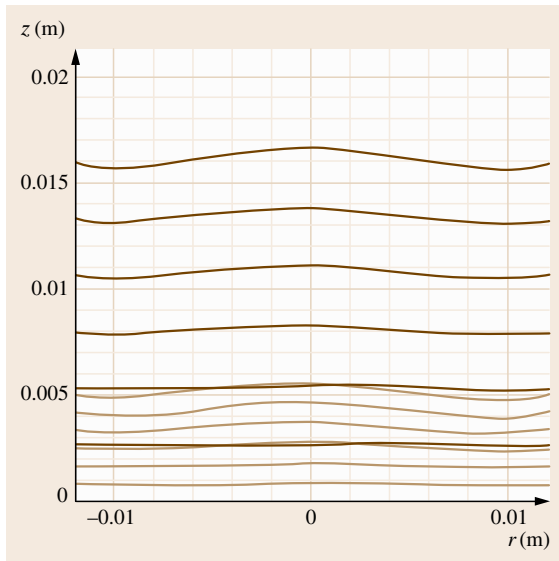
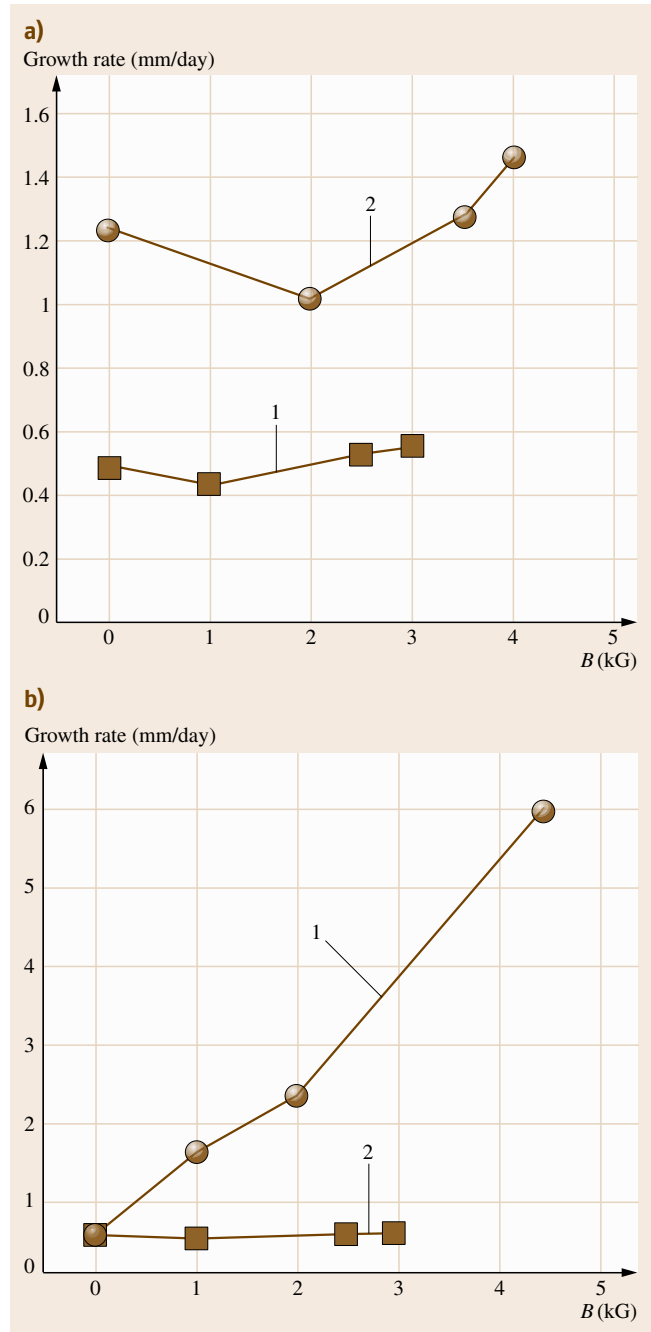


Fig. 29.27 Evolution of the computed growth interface using the total mobility $\mu_T = \mu_E + \mu_B B$ (thick lines) and using only the electric mobility μ_E (thin lines). Time increment between lines is 40 h. The shapes of the computed interfaces are in excellent agreement with those of experiments with and without magnetic field (see sample GaAs crystals in Fig. 29.11). It must be noted that the numerical simulations were let go until 15 mm growth thickness just to show that the interface remains flat. Thicknesses of the grown GaAs and GaInAs crystals were less than this value



presented in Fig. 29.26b (note that the full and empty circles are coincident).

The above results show that the inclusion of the new total mobility that includes the contributions of both

the applied electric current and also its interaction with the applied magnetic field provide much more accurate predictions for growth rates in LPEE under a magnetic field.

When only the electric mobility is used in simulations, not only the growth rates but also the shapes of the evolving growth interface were not predicted accurately. However, when the total mobility was introduced, in addition to better predictions for growth rates, the growth interface shapes were also much closer to those of experiments.

In Fig. 29.27 the evolution of computed growth interface is presented. As seen, the computed interfaces are flatter and agree with the shapes of the interfaces of

the crystals grown in [29.26], which are almost perfectly flat.

These results show that the introduction of a bulk constitutive coefficient representing the total electromagnetic mobility due to electromigration under magnetic fields in LPEE (the nonlinear model for LPEE under magnetic field in [29.63]) is a step in the right direction. It is by no means complete, since the interaction of electric and magnetic fields must also affect mass transport at the growth interface. Therefore, in addition to this model in the bulk (solution), a closer look may also be needed at various surface phenomena under the combined effect of applied electric and magnetic fields, in order to obtain better predictions from modeling.

References

- 29.1 M. Kumagawa, A.F. Witt, M. Lichtensteiger, H.C. Gatos: Current-controlled growth and dopant modulation in liquid-phase epitaxy, *J. Electrochem. Soc.* **120**, 583/584 (1973)
- 29.2 J.J. Daniele: Peltier-induced LPE and composition stabilization of GaAlAs, *Appl. Phys. Lett.* **27**, 373 (1975)
- 29.3 J.J. Daniele: Experiments showing absence of electromigration of As and Al in Peltier LPE of GaAs and $\text{Ga}_{1-x}\text{Al}_x\text{As}$, *J. Electrochem. Soc.* **124**, 1143 (1977)
- 29.4 V.A. Gevorkyan, L.V. Golubev, S.G. Petrosyan, Y.A. Shik, Y.V. Shmatsev: *Sov. Phys. Tech. Phys.* **22**, 750–755 (1977)
- 29.5 L. Jastrzebski, H.C. Gatos, A.F. Witt: Electromigration in current-controlled LPE, *J. Electrochem. Soc.* **123**, 1121 (1976)
- 29.6 L. Jastrzebski, H.C. Gatos: Current-controlled growth, segregation and amphoteric behavior of Si in GaAs from Si-doped solutions, *J. Cryst. Growth* **42**, 309–314 (1977)
- 29.7 L. Jastrzebski, H.C. Gatos, A.F. Witt: Current-induced solution growth of garnet layers, *J. Electrochem. Soc.* **124**, 633 (1977)
- 29.8 L. Jastrzebski, Y. Imamura, H.C. Gatos: Thickness uniformity of GaAs layers grown by electroepitaxy, *J. Electrochem. Soc.* **125**, 1140 (1978)
- 29.9 L. Jastrzebski, J. Lagowski, H.C. Gatos, A.F. Witt: Determination of carrier concentration distribution in semiconductors by IR absorption – Si, *J. Appl. Phys.* **49**, 5909 (1978)
- 29.10 T. Bryskiewicz: Peltier-induced growth kinetics of liquid-phase epitaxial GaAs, *J. Cryst. Growth* **43**, 567–571 (1978)
- 29.11 A.F. Witt, H.C. Gatos, M. Lichtensteiger, C.J. Herman: Crystal-growth and segregation under zero gravity – Ge, *J. Electrochem. Soc.* **125**, 1832 (1978)
- 29.12 T. Bryskiewicz, A. Laferriere: Growth of alloy substrates by liquid-phase electroepitaxy – theoretical considerations, *J. Cryst. Growth* **129**, 429–442 (1993)
- 29.13 Y.H. Lo, R. Bhat, P.S.D. Lin, T.P. Lee: Long-wavelength optoelectronic integrated circuit transmitter, *Proc. SPIE* **1582**, 60–70 (1992)
- 29.14 W.P. Hong, G.K. Chang, R. Bhat, C. Nguyen, H.P. Lee, L. Wong, K.R. Runge: InP-based MSM-HEMT receiver OEICs for long-wavelength light wave systems, *Proc. SPIE* **1582**, 134–144 (1992)
- 29.15 W.J. Schaff, P.J. Tasker, M.C. Foisy, L.F. Eastman: Device applications of stained layer epitaxy. In: *Semiconductors and Semimetals*, Vol. 33, ed. by T.P. Pearsall (Academic, New York 1991) pp. 73–133
- 29.16 L.F. Eastman: In: *Optoelectronic Materials and Devices Concepts*, ed. by M. Razeghi (SPIE Optical Engineering Press, Bellingham 1991) p. 41
- 29.17 A. Andaspaeva, A.N. Baranov, A. Guseinov, A.N. Imenkov, L.M. Litvak: *Sov. Tech. Phys. Lett.* **14**, 377 (1988)
- 29.18 H.K. Choi, S.J. Eglash: High-efficiency high-power GaInAsSb-AlGaAsSb double-heterostructure lasers emitting at 2.3 μm , *IEEE J. Quantum Electron.* **27**, 1555 (1991)
- 29.19 S.J. Eglash, H.K. Choi: MBE growth, material properties, and performance of GaSb-based 2.2 μm diode-lasers, *Inst. Phys. Conf. Ser.* **120**(10), 487 (1992)
- 29.20 T. Bryskiewicz, C.F. Boucher Jr., J. Lagowski, H.C. Gatos: Bulk GaAs crystal-growth by liquid-phase electroepitaxy, *J. Cryst. Growth* **82**, 279–288 (1987)
- 29.21 S. Dannefear, P. Mascher, D. Kerr: Annealing of grown-in defects in GaAs, *Proc. MRS* **104**, 471 (1978)
- 29.22 C.F. Boucher Jr., O. Ueda, T. Bryskiewicz, J. Lagowski, H.C. Gatos: Elimination of disloca-

- tions in bulk GaAs crystals grown by liquid-phase electroepitaxy, *J. Appl. Phys.* **61**, 359–364 (1987)
- 29.23 T. Bryskiewicz, M. Bugajski, J. Lagowski, H.C. Gatos: Growth and characterization of high quality LPE GaAs bulk crystals, *J. Cryst. Growth* **85**, 136–141 (1987)
- 29.24 T. Bryskiewicz, M. Bugajski, B. Bryskiewicz, J. Lagowski, H.C. Gatos: LPE growth and characterization of In(V)Ga/As(V) crystal, *Proc. Inst. Phys. Ser.* **91**(3), 259 (1988)
- 29.25 B. Bryskiewicz, T. Bryskiewicz, E. Jiran: Internal strain and dislocations in $\text{In}_x\text{Ga}_{1-x}\text{As}$ crystals grown by liquid phase electroepitaxy, *J. Electron. Mater.* **24**, 203 (1995)
- 29.26 H. Sheibani, S. Dost, S. Sakai, B. Lent: Growth of bulk single crystals under applied magnetic field by liquid phase electroepitaxy, *J. Cryst. Growth*, **258**(3–4), 283–295 (2003)
- 29.27 H. Sheibani, Y.C. Liu, S. Sakai, B. Lent, S. Dost: The effect of applied magnetic field on the growth mechanisms of liquid phase electroepitaxy, *Int. J. Eng. Sci.* **41**, 401–415 (2003)
- 29.28 G. Bischofink, K.W. Benz: THM growth of $\text{Al}_x\text{Ga}_{1-x}\text{Sb}$ bulk crystals, *J. Cryst. Growth* **128**, 466–470 (1993)
- 29.29 J.J. Daniele, A.J. Hebling: Peltier-induced liquid-phase epitaxy and compositional control of mm-thick layers of (Al,Ga)As, *J. Appl. Phys.* **52**, 4325–4327 (1981)
- 29.30 Z.R. Zytkeiwicz: Influence of convection on the composition profiles of thick GaAlAs layers grown by liquid phase electroepitaxy, *J. Cryst. Growth* **131**, 426–430 (1993)
- 29.31 Z.R. Zytkeiwicz: Liquid phase electroepitaxial growth of thick and compositionally uniform AlGaAs layers on GaAs substrates, *J. Cryst. Growth* **146**, 283–286 (1995)
- 29.32 Z.R. Zytkeiwicz: Joule effect as a barrier for unrestricted growth of bulk crystals by liquid phase electroepitaxy, *J. Cryst. Growth* **172**, 259–268 (1997)
- 29.33 C. Takenaka, K. Nakajima: Effect of electric-current on the LPE growth of InP, *J. Cryst. Growth* **108**, 519 (1991)
- 29.34 N. Djilali, Z. Qin, S. Dost: Role of thermosolutal convection in liquid phase electroepitaxial growth of gallium arsenide, *J. Cryst. Growth* **149**, 153–166 (1995)
- 29.35 Y.C. Liu, Y. Okano, S. Dost: The effect of applied magnetic field on flow structures in liquid phase electroepitaxy – A three-dimensional simulation model, *J. Cryst. Growth* **244**, 12–26 (2002)
- 29.36 Y.C. Liu, S. Dost, H. Sheibani: A three dimensional numerical simulation for the transport structures in liquid phase electroepitaxy under applied magnetic field, *Int. J. Trans. Phenom.* **6**, 51–62 (2004)
- 29.37 R.W. Wilcox: Influence of convection on the growth of crystals from solution, *J. Cryst. Growth* **65**, 133 (1983)
- 29.38 S. Ostrach: Fluid mechanics in crystal growth – The 1982 Freeman scholar lecture, *J. Fluids Eng.* **105**, 5–20 (1983)
- 29.39 S. Dost, Y.C. Liu, B. Lent: A numerical simulation study for the effect of applied magnetic field in liquid phase electroepitaxy, *J. Cryst. Growth* **240**, 39–51 (2002)
- 29.40 S. Dost, B. Lent, H. Sheibani, Y.C. Liu: Recent developments in liquid phase electroepitaxial growth of bulk crystals under magnetic field, *C. r. Mec.* **332**(5/6), 413–428 (2004)
- 29.41 S. Dost, B. Lent: *Single Crystal Growth of Semiconductors from Metallic Solutions* (Elsevier, Amsterdam 2007)
- 29.42 M. Yildiz, S. Dost, B. Lent: Growth of bulk SiGe single crystals by liquid phase diffusion, *J. Cryst. Growth* **280**(1–2), 151–160 (2005)
- 29.43 M. Yildiz, S. Dost: A continuum model for the liquid phase diffusion growth of bulk SiGe single crystals, *Int. J. Eng. Sci.* **43**, 1059–1080 (2005)
- 29.44 E. Yildiz, S. Dost, M. Yildiz: A numerical simulation study for the effect of magnetic fields in liquid phase diffusion growth of SiGe single crystals, *J. Cryst. Growth* **291**, 497–511 (2006)
- 29.45 M. Yildiz, S. Dost, B. Lent: Evolution of the growth interface in liquid phase diffusion growth of bulk SiGe single crystals, *Cryst. Res. Technol.* **41**(3), 211–216 (2006)
- 29.46 S. Dost, Z. Qin: A model for liquid phase electroepitaxial growth of ternary alloy semiconductors – 1. Theory, *Int. J. Electromagn. Mech.* **7**(2), 109–128 (1996)
- 29.47 Y. Imamura, L. Jastrzebski, H.C. Gatos: Defect structure and electronic characteristics of GaAs layers grown by electroepitaxy and thermal LPE, *J. Electrochem.* **126**(8), 1381–1385 (1979)
- 29.48 Z. Qin, S. Dost, N. Djilali, B. Tabarrok: A finite element model for liquid phase electroepitaxy, *Int. J. Numer. Methods Eng.* **38**(23), 3949–3968 (1995)
- 29.49 Z. Qin, S. Dost, N. Djilali, B. Tabarrok: A model for liquid phase electroepitaxy under an external magnetic field – 2. Application, *J. Cryst. Growth* **153**, 131–139 (1995)
- 29.50 Z. Qin, S. Dost: A model for liquid phase electroepitaxial growth of ternary alloy semiconductors – 2. Application, *Int. J. Appl. Electromagn. Mech.* **7**(2), 129–142 (1996)
- 29.51 H. Ben Hadid, D. Henry: Numerical study of convection in the horizontal Bridgman configuration under the action of a constant magnetic field. Part 1. Two-dimensional flow, *J. Fluid Mech.* **333**, 23–56 (1996)
- 29.52 H. Ben Hadid, D. Henry: Numerical study of convection in the horizontal Bridgman configuration under the action of a constant magnetic field. Part 2. Three-dimensional flow, *J. Fluid Mech.* **333**, 57–83 (1996)

- 29.53 H. Ben Hadid, S. Vaux, S. Kaddeche: Three-dimensional flow transitions under a rotating magnetic field, *J. Cryst. Growth* **230**, 57–62 (2001)
- 29.54 D.H. Kim, P.M. Adornato, R.A. Brown: Effect of vertical magnetic field on convection and segregation in vertical Bridgman crystal growth, *J. Cryst. Growth* **89**, 339 (1988)
- 29.55 L. Davoust, M.D. Cowley, R. Moreau, R. Bolcato: Buoyancy-driven convection with a uniform magnetic field – Part 2. Experimental investigation, *J. Fluid Mech.* **400**, 59 (1999)
- 29.56 V. Kumar, S. Dost, F. Durst: Numerical modeling of crystal growth under strong magnetic fields: An application to the travelling heater method, *Appl. Math. Modell.* **31**(3), 589–605 (2006)
- 29.57 T. Tagawa, H. Ozoe: Enhancement of heat transfer rate by application of a static magnetic field during natural convection of liquid metal in a cube, *J. Heat Transf.* **119**, 265 (1997)
- 29.58 T. Tagawa, H. Ozoe: Enhanced heat transfer rate measured for natural convection in liquid gallium in a cubical enclosure under a static magnetic field, *J. Heat Transf.* **120**, 1027 (1998)
- 29.59 K. Terashima, J. Nishio, S. Washizuka, M. Watanabe: Magnetic field effect on residual impurity concentrations for LEC GaAs crystal growth, *J. Cryst. Growth* **84**, 247 (1987)
- 29.60 A.Y. Gelfgat, P.Z. Bar-Yoseph, A. Solan: Axisymmetry breaking instabilities of natural convection in a vertical Bridgman growth configuration, *J. Cryst. Growth* **220**, 316 (2000)
- 29.61 S. Dost, H. Sheibani, Y.C. Liu, B. Lent: Recent developments in modelling of liquid phase electroepitaxy under applied magnetic field, *Cryst. Res. Technol.* **40**(4/5), 313 (2005)
- 29.62 S. Dost, H. Sheibani, Y.C. Liu, B. Lent: On the high growth rates in electroepitaxial growth of bulk semiconductor crystals in magnetic field, *J. Cryst. Growth* **275**(1–2), e1–e6 (2005)
- 29.63 S. Dost, H. Sheibani: A mathematical model for solution growth of bulk crystals under magnetic field, *Philos. Mag.* **85**(33–35), 4331–4351 (2005)
- 29.64 K. Nakajima: Liquid phase epitaxial growth of very thick $\text{In}_{1-x}\text{Ga}_x\text{As}$ layers with uniform composition by source-current-controlled method, *J. Appl. Phys.* **61**(9), 4626 (1987)
- 29.65 K. Nakajima, S. Yamazaki, I. Umebu: A new growth method using source current control to supply solute elements—demonstration of $\text{In}_{1-x}\text{Ga}_x\text{As}$ case, *Jpn. J. Appl. Phys.* **23**(1), L26–L28 (1984)
- 29.66 K. Nakajima, S. Yamazaki: A new method to supply solute elements into growth solutions – Demonstration by liquid phase epitaxial growth of $\text{In}_{1-x}\text{Ga}_x\text{As}$, *J. Electrochem. Soc.* **132**, 904 (1985)
- 29.67 K. Nakajima, S. Yamazaki: Growth of very thick $\text{In}_{1-x}\text{Ga}_x\text{As}$ layers by source-current-controlled method, *J. Cryst. Growth* **74**, 39–47 (1986)
- 29.68 K. Nakajima: Calculation of composition variation of $\text{In}_{1-x}\text{Ga}_x\text{As}$ ternary crystals for diffusion and electromigration limited growth from a temperature graded solution with source material, *J. Cryst. Growth* **110**, 781–794 (1991)
- 29.69 K. Nakajima: Calculation of stresses in $\text{In}_{0.12}\text{Ga}_{0.88}\text{As}$ ternary bulk crystals with compositionally graded $\text{In}_{1-x}\text{Ga}_x\text{As}$ layers on GaAs seeds, *J. Cryst. Growth* **113**, 477–484 (1991)
- 29.70 S. Dost, N. Djilali, Z. Qin: A two-dimensional diffusion model for liquid-phase electroepitaxial growth of GaAs, *J. Cryst. Growth* **143**(3/4), 141–154 (1994)
- 29.71 S. Dost, H.A. Erbay: A continuum model for liquid phase electroepitaxy, *Int. J. Eng. Sci.* **33**(10), 1385–1402 (1995)
- 29.72 S. Dost, Z. Qin: A model for liquid-phase electroepitaxy under an external magnetic field. Part 1. Theory, *J. Cryst. Growth* **153**, 123–130 (1995)
- 29.73 S. Dost, Z. Qin: A numerical simulation model for liquid phase electroepitaxial growth of GaInAs , *J. Cryst. Growth* **187**, 51–64 (1998)
- 29.74 A. Okamoto, S. Isozumi, J. Lagowski, H.C. Gatos: In situ monitoring of liquid phase electroepitaxial growth, *J. Electrochem. Soc.* **129**, 2095–2098 (1982)

30. Epitaxial Lateral Overgrowth of Semiconductors

Zbigniew R. Zytewicz

The state of the art and recent developments of lateral overgrowth of compound semiconductors are reviewed. First we focus on the mechanism of epitaxial lateral overgrowth (ELO) from the liquid phase, highlighting the phenomena that are crucial for growing high-quality layers with large aspect ratio. Epitaxy from the liquid phase has been chosen since the equilibrium growth techniques such as liquid-phase epitaxy (LPE) are the most suitable for lateral overgrowth. We then present numerous examples for which the defect filtration in the ELO procedure is very efficient and leads to significant progress in the development of high-performance semiconductor devices made of lattice-mismatched structures. Structural perfection of seams that appear when layers grown from neighboring seeds merge is also discussed. Next, we concentrate on strain commonly found in various ELO structures and arising due to the interaction of ELO layers with the mask. Its origin, and possible ways of its control, are presented. Then we show that the thermal strain in lattice-mismatched ELO structures can be relaxed by additional tilting of ELO wings while still preserving their high quality. Finally, recent progresses in the lateral overgrowth of semiconductors, including new mask materials and liquid-phase electroepitaxial growth on substrates coated by electrically conductive masks, are presented. New versions of the ELO technique from solution and from the vapor (growth from ridges and pendeo-epitaxy) are described and compared with standard ELO. A wide range of semiconductors, including III-V compounds grown from solution and vapor-grown GaN, are used to illustrate phenomena discussed. Very often, the similar behavior of various ELO structures

30.1 Overview.....	1000
30.2 Mechanism of Epitaxial Lateral Overgrowth from the Liquid Phase	1002
30.2.1 Choice of Substrate Geometry for Growth of ELO Layers	1004
30.2.2 Optimization of Liquid-Phase Lateral Overgrowth Procedure	1007
30.3 Dislocations in ELO Layers.....	1011
30.3.1 Filtration of Substrate Dislocations in ELO....	1011
30.3.2 Structural Perfection of Coalescence Front in Fully Overgrown ELO Structures.	1014
30.4 Strain in ELO Layers.....	1016
30.4.1 Mask-Induced Strain in Homoepitaxial ELO Layers	1017
30.4.2 Thermal Strain in ELO Layers	1024
30.5 Recent Progress in Lateral Overgrowth of Semiconductor Structures	1026
30.5.1 Developments in Liquid-Phase ELO Growth	1027
30.5.2 New Concepts of ELO Growth.....	1030
30.6 Concluding Remarks	1034
References	1035

reveals that the phenomena presented are not related to a specific group of compounds or their growth techniques, but have a much more general nature.

30.1 Overview

Modern micro- and optoelectronic devices consist of thin layers grown epitaxially on a substrate. These layers must be of high crystallographic quality. Very often however, there are no substrates available for lattice-matched epitaxy, and dislocations are generated at the layer–substrate interface to relax the lattice-mismatch strain. Segments of these dislocations thread to the surface of the epilayer, and then to the next-grown layers of the structure, deteriorating parameters of the device and leading to its fast degradation. To reduce the density of threading dislocations in lattice-mismatched heteroepitaxial structures a buffer layer with a graded or abrupt composition profile is usually deposited on an available substrate to obtain a layer with the required lattice parameter value. Strained layer superlattices are often inserted into the buffer to bend threading dislocations and partially prevent them from propagating to the surface [30.1]. In situ or ex situ annealing of buffers has also been employed to induce mutual reactions between threading dislocations that eventually lead to their annihilation [30.2]. In addition, for heterostructures with large lattice mismatch, buffer growth is usually initiated at relatively low temperature, and is then continued at a higher temperature (so-called two-step growth) [30.3]. All these sophisticated methods of buffer layer engineering have been proven to reduce significantly density of defects in lattice-mismatched heterostructures. However, despite the progress made, the best modern buffers still contain dislocations with a density of $\approx 10^6 \text{ cm}^{-2}$, which is often too high for device applications. Therefore, the epitaxial lateral overgrowth (ELO) technique has been developed to block dislocations threading from the substrate or substrate/buffer structure to the next-grown epitaxial layers.

Figure 30.1 schematically illustrates the principle of epitaxial lateral overgrowth. First the substrate or substrate with a suitable buffer is covered by a thin amorphous masking film. Dielectrics, such as SiO_2 or Si_3N_4 , are commonly used to mask the substrate, but other materials such as tungsten [30.4, 5], zirconium nitride [30.6] or graphite [30.7] have also been successfully applied for the ELO of III–V semiconductors. In the next step the substrate is patterned by conventional photolithography and etching to form on its whole area a grating of mask-free seeding windows of width W separated by masked areas of width M (Fig. 30.1a). The ELO growth starts by a selective-area epitaxy, i. e., nucleation takes place exclusively in narrow windows (Fig. 30.1b). When the layer becomes thicker than the masking film the growth proceeds also in a lateral direction over the mask. Finally, a new epitaxial layer fully covers the patterned substrate if the growth time is sufficiently long for coalescence of ELO stripes grown from neighboring seeds. The main advantage of the ELO process is that dislocations can thread from the substrate into the epitaxial layer through the very narrow windows, so respective etch pits should be visible only in the part of the ELO layer grown vertically from the seed (Fig. 30.1b). Since there is no continuity of crystal lattice at the interface between monocrystalline substrate and the amorphous mask, substrate dislocations cannot propagate into the mask and must vanish at the substrate surface. In this way the mask efficiently blocks dislocations and their density in the laterally grown parts (wings) of the layer should be significantly reduced. Indeed, there are many experimental evidences showing that the density of dislocations in the wings area is orders of magnitude lower than that observed in standard planar epilayers (Sect. 30.3.1). Thus the ELO process

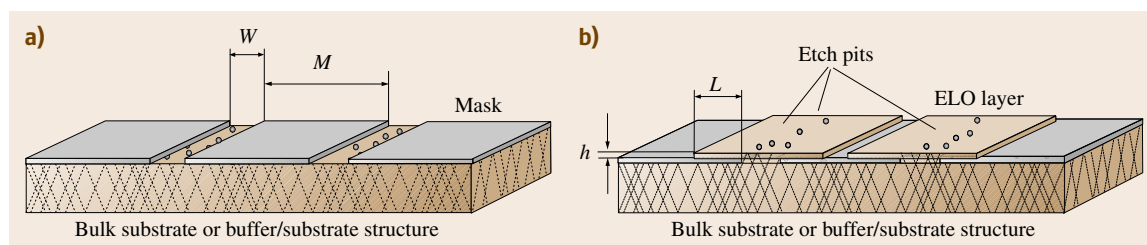


Fig. 30.1a,b Principle of epitaxial lateral overgrowth. (a) A substrate or substrate with a suitable buffer is covered by a thin amorphous masking film. Seeding windows of width W separated by masked areas of width M are opened up in the mask. (b) The ELO growth begins exclusively inside the seeding windows. Then the growth proceeds laterally over the mask. Note that substrate dislocations, marked by dotted lines, propagate to the ELO layer through the openings in the mask, only. L and h denote the width of the laterally grown part (wing) of the layer and its thickness, respectively

is a powerful method to grow epilayers with a low density of dislocations on heavily dislocated substrates such as the relaxed buffers deposited on lattice-mismatched substrates. When combined with well-developed methods of buffer layers engineering the ELO technique offers the possibility of producing high-quality substrates with adjustable value of lattice constant required by modern electronics. If ternary buffers are used the value of the lattice parameter might be controlled by choosing the proper composition of the buffer. Next, homoepitaxial lattice matched lateral overgrowth would be employed to remove the buffer dislocations.

A more detailed discussion on the dislocation filtration processes in ELO together with some examples will be presented in Sect. 30.3. However, it must be mentioned here that, according to the ELO concept presented in Fig. 30.1, the number of dislocations propagating into the layer should decrease as the width W of the seeding window decreases. In particular, the growth of a completely dislocation-free layer might be possible if the window width is smaller than the average distance between dislocations in the substrate. This means that for the density of dislocations of $\approx 10^{10} \text{ cm}^{-2}$ the condition $W \ll 100 \text{ nm}$ should be fulfilled. In principle, windows a few nanometers wide should be sufficient for the transfer of information on the lattice parameter from the substrate to the epilayer, i.e., for epitaxial growth. Due to technical reasons, however, windows a few micrometers wide are usually applied. Note also that in many epitaxial systems dislocations threading through the seeding windows are inclined at some angle to the epilayer surface, so the width of dislocated area on the surface increases as the layer grows thicker [30.8]. Thus, the ELO layers should be as wide and as thin as possible in order to maximize dislocation-free wing area available for devices. In other words, the largest value of the aspect (width/thickness) ratio AR , defined in this work by the equation $AR = (2L + W)/h$, is required.

Besides the use for defect filtration during the heteroepitaxy of lattice-mismatched systems, the ELO technique in its homoepitaxial version has also found practical applications in the production of silicon-on-insulator structures [30.9], metal-oxide-semiconductor (MOS) transistors [30.10], field-effect transistors [30.11], solar cells [30.12], pressure sensors [30.13], and for three-dimensional device integration [30.14]. If metallic masks are applied they may be further used as buried electrical contacts to devices produced by ELO [30.11]. Finally, if the windows opened up in the insulating mask are so narrow that electrical conductance of ELO-substrate connec-

tions becomes small, the ELO process can be used for growing layers electrically separated from the substrate. This might be the way to obtain electrically insulated epilayers of semiconductors for which lattice-matched semi-insulating substrates are not available (e.g., GaSb).

To the best of our knowledge, the ELO process was initiated in 1980 when McClelland and his coworkers applied vapor-phase epitaxy (VPE) to grow GaAs epitaxial layers on masked-GaAs substrate [30.15]. Since the ELO layer was easily separable from its host substrate by cleaving, the technique was designed as an efficient way of producing GaAs epitaxial films on reusable substrates. Tsaur et al. were probably the first to report (in 1982) an efficient reduction of dislocation density in GaAs layers grown by VPE lateral overgrowth on Ge-coated Si substrates [30.16]. Then the ELO technique was used by Jastrzebski's [30.9] and Bauser's [30.17] groups to produce silicon-on-insulator structures by VPE and liquid-phase epitaxy (LPE), respectively. Finally, the efficient filtration of substrate dislocations has been reported in a series of papers on the growth of SiGe, GaAs, GaP, InP, InGaAs, and InGaP ELO layers on lattice-mismatched substrates [30.18–22]. However, the most spectacular recent achievement of the ELO technique was the breakthrough in the development of long-lifetime GaN/InGaN blue lasers, partly being due to the high efficiency of defects filtration during the lateral growth of GaN on sapphire [30.23].

Nowadays, a large body of ELO research concentrates on the lateral overgrowth of GaN epilayers on sapphire or SiC substrates using metalorganic VPE (MOVPE) or hydride VPE (HVPE) techniques. This is a result of the market demand for low-dislocation-density GaN substrates. GaN ELO activity is so dominant that sometimes the technique is called ELOG, which stands for epitaxial lateral overgrowth of gallium nitride. Apparently this is not correct since the principle of the ELO process is much more general and is not limited to either a specific group of materials or to a single epitaxial growth technique. In parallel, a great deal of increase in research on the lateral overgrowth of zincblende III–V epilayers on various substrates is observed.

The aim of this chapter is to present recent developments in the lateral overgrowth of compound semiconductors and review its present state. The chapter is organized as follows. In Sect. 30.2 we will focus on the mechanism of the ELO growth of zincblende III–V compounds from the liquid phase, highlighting the phenomena that are crucial for growing high-quality

layers with large aspect ratio. Epitaxy from the liquid phase has been chosen since, as will be discussed in that section, the equilibrium growth techniques such as LPE are the most suitable for lateral overgrowth. The issue of defect filtration in the ELO procedure is widely addressed in Sect. 30.3.1. Numerous examples which are instrumental in showing that the defect filtration mechanism schematically shown in Fig. 30.1 is very efficient and leading to significant progresses in the development of high-performance semiconductor devices made of lattice mismatched structures, are presented. In Sect. 30.3.2 structural perfection of seams that appear when layers grown from neighboring seeds merge in fully overgrown ELO structures will be discussed. Strain in epitaxial layers may lead to the generation of new defects if it is too large. Therefore, the issue of strain in ELO layers will be extensively addressed in Sect. 30.4. First, we will concentrate on strain arising due to interaction of ELO layers with the mask underneath. This phenomenon leads to tilting of ELO wings and is commonly found in various ELO structures. The origin of mask-induced wing tilting and possible ways of its control will be presented. Then, the thermal strain in lattice-mismatched ELO structures will

be discussed (Sect. 30.4.2). We will show that in ELO structures thermal strain can be relaxed by additional tilting of ELO wings while still preserving their high quality. Finally, in Sect. 30.5 the recent progress made in the lateral overgrowth of semiconductor structures is presented. New developments in the ELO growth from the liquid phase include new mask materials and liquid-phase electroepitaxial growth on substrates coated by electrically conductive masks. Then, the new versions of ELO technique from solution and from the vapor phase, namely growth from ridges and pendeo-epitaxy, will be discussed and compared with the standard ELO. Since the author's intention was to present the ELO growth of a wide range of compound semiconductors, both the zincblende III–V compounds grown from the liquid solution as well as the vapor-grown GaN will be used to illustrate the phenomena discussed. In particular, in Sects. 30.3 and 30.4 it will be shown that a quite similar behavior is observed in various ELO systems despite the large differences in their properties and the variety of growth techniques applied. This, in turn, clearly indicates that the phenomena presented are not related to a specific group of compounds or their growth techniques, but have much more general nature.

30.2 Mechanism of Epitaxial Lateral Overgrowth from the Liquid Phase

An efficient ELO procedure requires a large growth rate anisotropy, i.e., growth conditions are necessary at which the lateral growth of the epilayer is much faster than that in the direction normal to the substrate. This can be achieved by taking advantage of the natural growth anisotropy of various crystal faces.

Figure 30.2 schematically shows growth rate versus interface supersaturation for three types of crystal faces. On a perfect singular face, atoms can be incorporated into solid in the form of two-dimensional nuclei only. If the face is singular but imperfect, the surface imperfections (e.g., dislocations) supply steps necessary for its growth. Due to the limited rate of the surface processes involved, larger surface supersaturation is required in these two growth modes to get a notable growth velocity. On the other hand, atoms can be added to an atomically rough crystal face in a random way and the growth rate of such a face varies linearly with the interface supersaturation. As discussed by Nishinaga [30.18] the basic idea of ELO lies in fundamental dissimilarities between those growth modes. If a slowly grown facet covers the upper plane of ELO while the sidewalls are rough, then for low supersaturation, growth rates in ver-

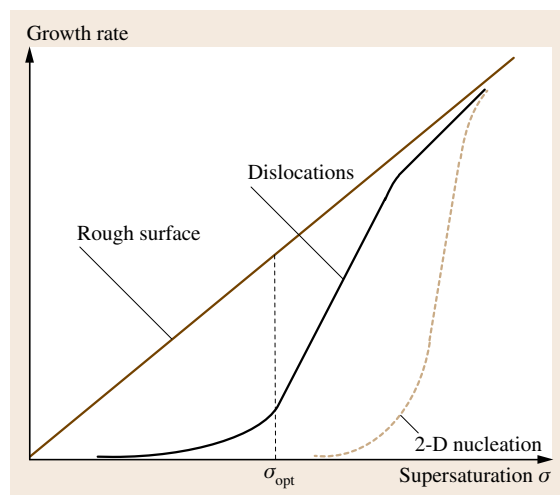


Fig. 30.2 Growth rate versus surface supersaturation for various crystal faces: perfect singular (brown dashed line), imperfect singular (thin central line), and atomically rough face (solid line). Dashed line schematically marks the surface supersaturation σ_{opt} that is optimal for large growth anisotropy in ELO

tical and horizontal directions differ significantly (see the vertical dashed line in Fig. 30.2 that schematically marks the optimal supersaturation σ_{opt}). Consequently, a large anisotropy of shape of ELO layers can be obtained.

Figure 30.2 indicates that there are two conditions necessary for successful lateral overgrowth. First, a proper geometry of the substrate must be chosen to keep the upper surface of the layer singular while the sidewalls of ELO remain atomically rough. Next, the growth conditions must be carefully adjusted for precise control of the surface supersaturation. These issues will be discussed in detail in Sects. 30.2.1 and 30.2.2. To illustrate that the mechanism of ELO growth presented above works in practice and to study the relative importance of various physical phenomena occurring during growth, we have conducted numerical simulations of ELO growth by LPE [30.24].

Figure 30.3 illustrates conceptually the solute movement in the liquid solution occurring during an ELO growth by LPE. Due to symmetry, only half of the substrate and liquid zone is shown. During LPE growth, the temperature of the system is slowly lowered to supersaturate the liquid solution. Since there is no nucleation on the mask, solute species diffuse exclusively towards the seeding area and are then incorporated into the growing ELO layer. Sidewall of the ELO layer is atomically rough, so there is no barrier there for incorporation of arriving species into the solid. Therefore, the solute con-

centration in the liquid zone near the side ELO face is equal to C_{eq} , the equilibrium concentration, a value that is determined by the phase diagram and actual temperature (Fig. 30.3). However, the upper ELO layer is faceted and the surface solute concentration there C_{in} is larger than the equilibrium concentration. This gives rise to a horizontal solute concentration gradient and so-called near-surface diffusion [30.25] in the liquid of solute species from upper ELO surface to its sidewall. It is obvious that the presence of near-surface diffusion significantly enhances lateral growth of ELO layers.

In the model [30.24], we consider a computational domain such as that shown in Fig. 30.3 and compute the change in the solute concentration field in the liquid zone as the system is cooled to force epitaxial growth on masked substrate. As discussed before, we assume a linear surface kinetic law to calculate the solute concentration C_{in} in the vicinity of the upper ELO surface while the solid–liquid phase equilibrium condition is used at the sidewall of the ELO layer. Moreover, the possible contribution of the Gibbs–Thomson effect is also considered to take into account the dependence of local equilibrium solute concentration on the surface curvature of the growing layer. Finally, the evolution of the solid–liquid interface shape with time is obtained using the growth velocity calculated from the solute concentration field in the vicinity of the growing layer. The results of calculations are discussed below, taking the GaAs/GaAs ELO system as an example due to its technological importance and the availability of the required input data.

Figure 30.4a shows the computed distribution of As concentration in the Ga/As solution after 2.5 h of ELO growth with an initial growth temperature of 650 °C and a cooling rate of 0.5 °C/min. In the far field, isoconcentration contours are circular since at this length scale ELO crystal looks like a point located in the lower left corner of the computational domain. Close to the crystal, however, the As concentration distribution shows additional features. In particular, a solute concentration gradient appears along the upper ELO surface, leading to near-surface diffusion of As towards the ELO sidewall (compare Fig. 30.3) and enhancing lateral growth rate. Furthermore, the As concentration gradient close to sidewall of ELO is much larger than that at the upper face. This indicates that the layer grows faster laterally than in the vertical direction.

Figure 30.4b presents the cross section of GaAs ELO layer calculated for the same input parameters. As seen, the shape of the upper ELO surface is very flat, which closely agrees with experimental observa-

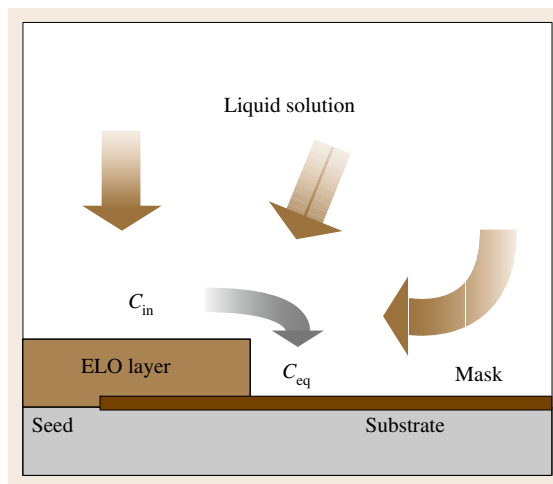


Fig. 30.3 Solute flow during LPE growth of ELO layer. The arrow from C_{in} to C_{eq} marks diffusion of solute in the liquid phase from upper surface of ELO to its sidewall (near-surface diffusion)

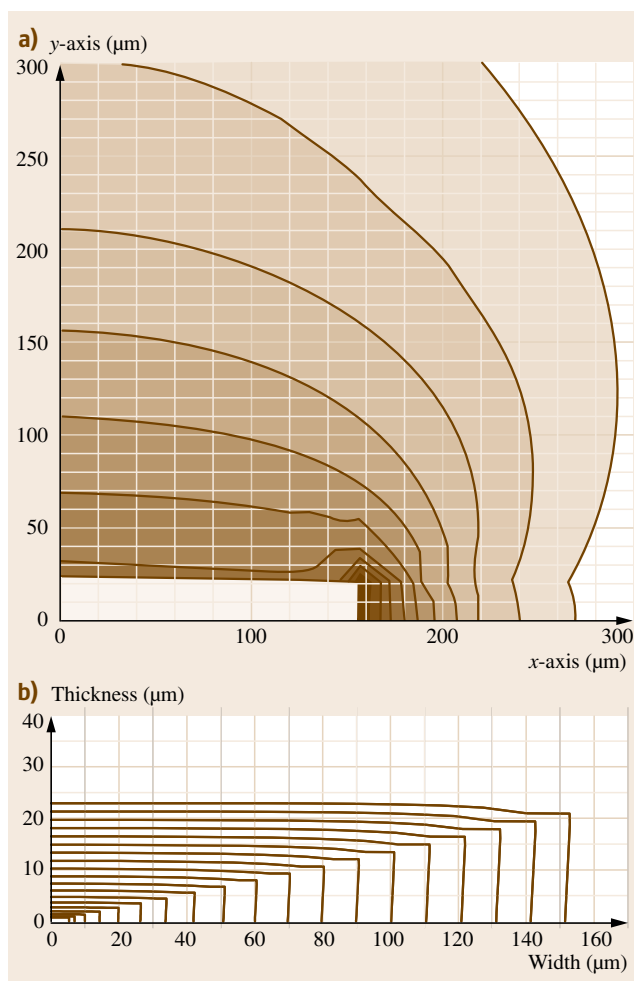


Fig. 30.4a,b Computed distribution of As concentration in the Ga-As solution (a) and cross section of GaAs ELO layer (b) after 2.5 h LPE growth with initial growth temperature of 650 °C and cooling rate of 0.5 °C/min

tions. Moreover, the lateral growth rate is much larger than that in the vertical direction, resulting in a thin and wide layer. A similar shape of layer was obtained by Yan et al. in their two-dimensional simulations of InP ELO growth by LPE [30.26]. However, in our case the prediction of a flat top face is a *result* of surface kinetics and diffusion processes included in the model, while in their approach the vertical growth rate is *assumed* to be the same along the whole upper surface. It is also noteworthy to mention that our model provides a good prediction for the dependence of ELO aspect ratio on surface kinetic coefficient and cooling

rate [30.24]. Therefore, it can be successfully used to optimize the LPE growth procedure. In addition, we have shown that a spiky growth starts from the ELO corner, which is not observed in real experiments, if the dependence of solid–liquid equilibrium on surface curvature is not taken into account. This demonstrates the importance of Gibbs–Thomson effect in growth of ELO layers.

Having presented the mechanism of lateral overgrowth it is now worth to discuss which epitaxial growth technique is most suitable for ELO growth. As was mentioned earlier the surface supersaturation must be kept low to grow ELO layers with large aspect ratio. Otherwise, two-dimensional nucleation takes place on the upper ELO surface leading to higher vertical growth rate and consequently less growth anisotropy. Therefore the equilibrium growth techniques such as LPE should be chosen, if possible, for lateral overgrowth. Indeed, as will be shown later, ELO layers with aspect ratio as large as 130 can be grown from a liquid phase. Solution or melt growth of group III nitrides is extremely complicated due to low solubility of nitrogen in liquid metals (Sect. 30.5.2). Therefore, MOVPE or HVPE is commonly used nowadays to grow ELO structures of these compounds. Then, however, large supersaturation at the growing face makes control of growth anisotropy difficult, so lateral structures of GaN with aspect ratio up to 6 are usually obtained [30.27]. Molecular beam epitaxy (MBE) growth of ELO layers is even more complicated. The ELO technique requires that growth proceeds from the seeding areas only while deposition of polycrystalline material on the mask is hard to avoid during MBE [30.28, 29]. Sophisticated systems with molecular beams oriented at low angle to the substrate, low growth rate, and precise temperature control [30.30, 31] or special substrate preparation and growth procedures [30.32] are necessary to get the growth started selectively from the seeds. Even then, however, MBE-grown ELO layers are usually very narrow, which makes their application in devices production very difficult.

30.2.1 Choice of Substrate Geometry for Growth of ELO Layers

As noted above, large anisotropy of ELO growth rate can be obtained if the upper surface of the layer is faceted while the sidewalls of ELO remain atomically rough. In practice, for zincblende III–V semiconductors this can be achieved using (111)- or (100)-oriented substrate and by twisting the line openings in the mask by

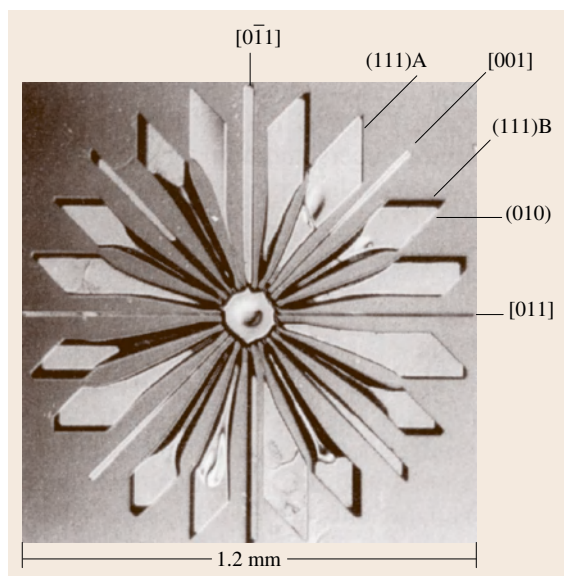


Fig. 30.5 Microphotograph of a GaAs ELO layer grown by LPE on a (100) GaAs substrate with a star-like pattern of seeds cut in the SiO₂ mask

some degrees off from the main crystallographic directions. Usually, optimal orientations of seeding lines in the substrate plane are determined experimentally by growing an ELO layer on a masked substrate with a star-like pattern of the seeds and by studying lateral growth rate versus seed orientation.

Figure 30.5 shows a plane view of a GaAs epilayer grown by LPE on a (100) GaAs substrate with a star-like pattern of openings cut in the SiO₂ mask [30.33]. The growth was forced by cooling the system from the temperature of 750 °C with a rate of 0.2 °C/min for 50 min. From Fig. 30.5 the dependence of lateral growth rate on the orientation of the seeds can be easily found. The width of the ELO is the largest when the stripe is ± 15 and $\pm 30^\circ$ off-oriented from the [011] direction or its equivalent orientations, while it is the smallest for the [011] and [001] directions. From simple geometrical considerations the facets on the side walls of ELO layers can be identified as the slowly grown {111} and {100} planes. Their formation proceeded much faster when the stripe was oriented in the (011) and (001) directions, which slowed down the lateral development of the ELO layer. Therefore, on the (100) substrate the line seeds oriented 15, 30, 60 or 75° off from the (011) direction should be used to obtain a large value of the lateral-to-normal growth rate ratio. Note that the angular dependence of the lateral

growth rate is centrosymmetric. As will be discussed later this is no longer true if slightly misoriented substrate is used. Note also that the width of ELO stripes shown in Fig. 30.5 increases with the distance r from the star center. As shown by Zhang and Nishinaga [30.34] this is due to the fact that the effective sink area for the growth units, and thus also the surface supersaturation, varies with r . For lateral overgrowth of GaSb on (100)-oriented GaSb substrates by LPE we have found the same dependence of ELO lateral growth rate on seed orientation. Results shown in Fig. 30.5 are in agreement with those published by Zhang and Nishinaga [30.34] and by Naritsuka and Nishinaga [30.35] for liquid-phase homoepitaxial lateral overgrowth of GaAs and InP, respectively. Similar angular dependence of lateral overgrowth has also been reported for ELO growth of GaAs by MOVPE [30.36] and for InP by VPE [30.37]. For (111)-oriented substrates analogous dependences can be found in [30.38, 39] for LPE ELO growth of GaAs and GaP, respectively.

In the case discussed thus far, the vertical growth of ELO was possible due to surface steps supplied by dislocations present in the substrates. However, sometimes dislocation-free substrates are used, for example, in silicon homoepitaxy. They must be slightly misoriented to provide steps necessary for crystal growth if uncontrolled two-dimensional nucleation is to be avoided. Then, the size and shape of ELO layer becomes dependent on the angle between seeding line and the substrate miscut directions. This issue has been discussed in detail by Bergmann et al. [30.40] and then by Bergmann [30.41] for lateral overgrowth of silicon on perfect Si substrates. On off-oriented imperfect substrates additional restriction applies for optimal direction of seed orientation. Sakawa and Nishinaga [30.42] have shown that, in such case, from many equivalent seed directions that are optimal on the (100) plane (Fig. 30.5), the one that should be chosen is that for which the density of misorientation steps inside the seeding area is the smallest.

The discussion above indicates that the presence of dislocations significantly affects the ELO growth mode. To present this issue in more detail Fig. 30.6 shows a sketch of the ELO layer grown from a line window on a misoriented, dislocation-free substrate. Direction of seeding line perpendicular to substrate miscut direction is assumed. As long as two-dimensional nucleation does not take place, the layer grows by flow of steps according to the misorientation direction (i.e., to the right side). Then the ELO growth is self-limited, i.e., it stops as soon as all the steps reach the edge of the layer

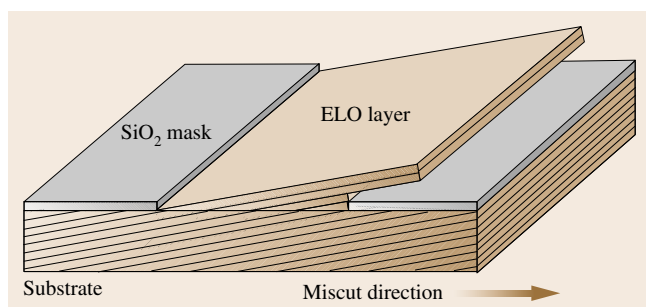


Fig. 30.6 Schematic illustration of **ELO** growth on misoriented, dislocation-free substrates; the seeding line is set perpendicular to the substrate miscut direction

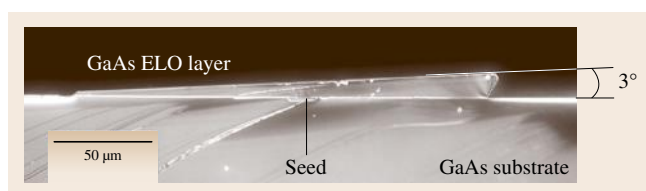


Fig. 30.7 Cross section of a GaAs **ELO** layer grown on a GaAs substrate with the surface misoriented by 3° from the (100) plane; substrate is miscut in the right-hand side direction

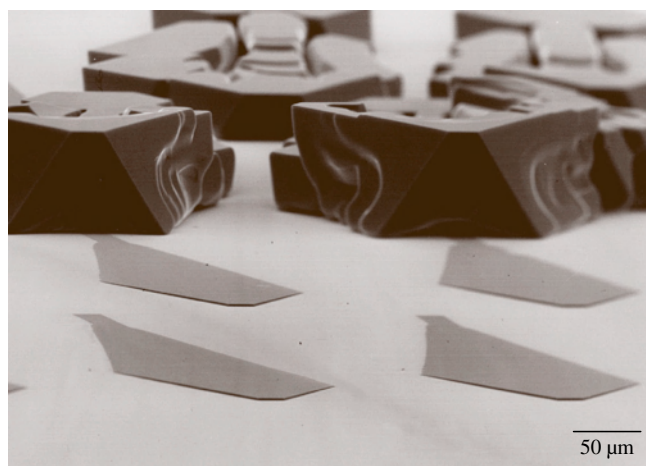


Fig. 30.8 Scanning electron microscopy image of Si **ELO** layers grown by **LPE** on a SiO_2 -masked Si substrate. Perfectly grown, defect-free layers are visible in the *foreground*; irregular-shaped defective layers are seen in the *background* (courtesy of Banhart)

and the sidewall is covered by a slowly grown facet. In particular, this means that no growth should take place to the left of the seeding line. Indeed, such behavior has been observed during **LPE** growth of silicon **ELO** layers on perfect silicon substrates [30.41]. Note also

in Fig. 30.6 that, for small substrate misorientation angles, substrate steps are partly in the shade of the mask edge and the **ELO** layer cannot get out of the seeding area if the mask is too thick. This prediction is also in agreement with experimental observations [30.40].

On the other hand, the situation is quite different if substrate dislocations contribute to the **ELO** growth. Figure 30.7 shows a cross section of a GaAs **ELO** layer grown on a GaAs substrate with the surface miscut by 3° from the (100) plane [30.43]. The seeds were oriented 15° off from the $[0\bar{1}1]$ direction for fast lateral overgrowth, and were nearly perpendicular to the direction of substrate miscut. It is seen that, similar to the case shown in Fig. 30.6, the thickness of the **ELO** layer is not uniform. The reason for this is the same as before: substrate steps lead to the layer growth to the right-hand side. This time, however, growth to the left of the window (i.e., in the direction opposite to substrate miscut axis) is also observed. Such growth can be explained by considering dislocations (with a density of $1.5 \times 10^3 \text{ cm}^{-2}$) present in our GaAs substrate. These dislocations provided steps that made an additional contribution to epitaxial growth and led to continuous growth of the layer to both sides of the seeding line. It is noteworthy that the surface of the layer is inclined to the substrate surface by an angle of $\approx 3^\circ$ (Fig. 30.7). Simple geometrical considerations of sample geometry show that this is the angle at which the (100) plane intersects with the substrate plane in the $(1\bar{1}0)$ cleavage section. This indicates that, despite substrate misorientation, the upper surface of the **ELO** layer forms the exact (100) plane, which is in agreement with our explanation.

As the final example of the essential role played by dislocations in the growth of **ELO** layers, Fig. 30.8 shows a scanning electron microscopy (SEM) image of silicon **ELO** layers grown by **LPE** on SiO_2 -masked Si substrate [30.44]. Perfectly grown flat **ELO** layers of thickness around $2\text{--}3 \mu\text{m}$ are seen in the foreground. Studies by transmission electron microscopy (TEM) showed that they were entirely free of crystallographic defects. However, as shown in the background of the figure, some **ELO** layers of thickness exceeding $20 \mu\text{m}$ and quite different shape were also found on the same substrate wafer. They showed deep grooves and were about twice as wide as perfectly grown layers. TEM analysis revealed that those layers contained a regular arrangement of dislocations generated during **ELO** growth in the vicinity of SiO_2 mask edge. The origin of these dislocations is not fully clarified but it is believed that their formation is influenced by stresses caused

by thermal oxidation of substrate wafer, the shape of the oxide edge, and nonuniform supersaturation of liquid solution volume. Once dislocations are generated they govern further development of the growth process. Instead of flow of steps supplied by substrate misorientation as illustrated in Fig. 30.6, dislocations become the dominant growth step source that leads to significant enhancement of vertical growth rate and worse surface morphology.

30.2.2 Optimization of Liquid-Phase Lateral Overgrowth Procedure

Having presented the effect of substrate geometry on the ELO growth process, in this section we will show examples of how parameters of an LPE procedure should be adjusted to optimize supersaturation near the crystal faces and obtain high growth anisotropy. In LPE, surface supersaturation reflects the relative magnitude of the solute supply from bulk of the liquid phase and solute consumption at the surface of growing crystal. Thus, the main parameters controlling these processes are the LPE growth temperature, the initial supercooling of the liquid phase, and the cooling rate.

Figure 30.9 shows lateral $V_{lat} = L/t$ and vertical $V_{ver} = h/t$ growth rates versus LPE growth temperature T_0 for nominally undoped GaAs ELO layers grown on SiO_2 -masked GaAs substrates. Figure 30.10 presents values of the aspect ratio (AR) for the same layers [30.43]. As seen, for high LPE temperature the vertical ELO growth rate is large since some thermal roughening of the upper crystal face takes place. Moreover, surface kinetic processes are very fast, which leads to an additional increase in the vertical growth rate. This results in ELO layers with a small value of the aspect ratio. On the other hand, for very low growth temperatures the sidewalls cannot be considered as ideally rough. Most probably surface kinetic processes start to play a role there and lateral growth rate decreases, which leads again to a decrease of the aspect ratio. Thus, there is an optimum growth temperature T_{opt} at which ELO layers have the largest aspect ratio. As shown by Yan et al. [30.25] for InP ELO layers T_{opt} corresponds to the temperature at which the interface supersaturation at the upper ELO face is the smallest. For other growth temperatures surface supersaturation is larger than σ_{opt} (compare Fig. 30.2). It is obvious that the optimum ELO growth temperature depends on many parameters such as the slope of the liquidus curve of the phase diagram, the geometry of the LPE system, etc., so it must be determined experimen-

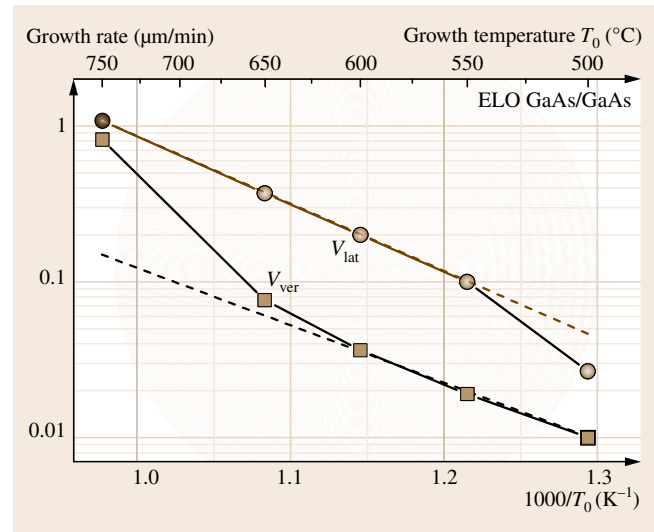


Fig. 30.9 Lateral V_{lat} (dots) and vertical V_{ver} (squares) growth rates versus LPE growth temperature T_0 for undoped GaAs ELO layers grown on GaAs substrates masked by SiO_2 film; seeding windows and masked area were 10 and 100 μm wide, respectively. The dashed lines guide the eye along the $V \propto \exp(-1/T_0)$ dependence

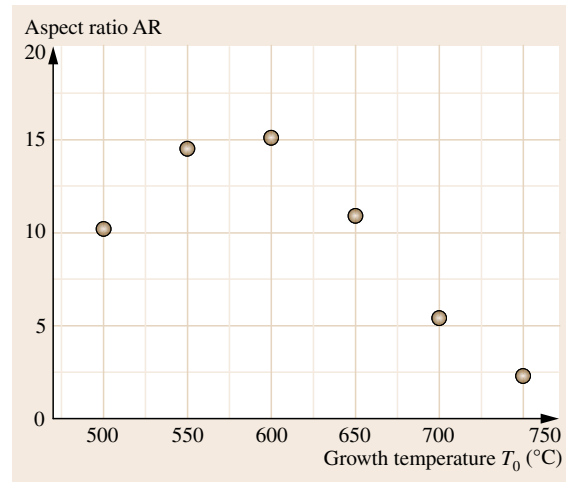


Fig. 30.10 Aspect ratio (AR) of undoped GaAs ELO layers versus LPE growth temperature T_0

tally for each particular case under study. Values of T_{opt} equal to 500, 580, and 530 $^{\circ}\text{C}$ have been reported for LPE growth of InP/InP [30.25], GaAs/GaAs [30.43], and GaAs/Si [30.45] ELO systems, respectively. For homoepitaxial GaSb ELO layers grown by LPE the optimal growth temperature $T_{opt} \leq 350$ $^{\circ}\text{C}$ has been found [30.46].

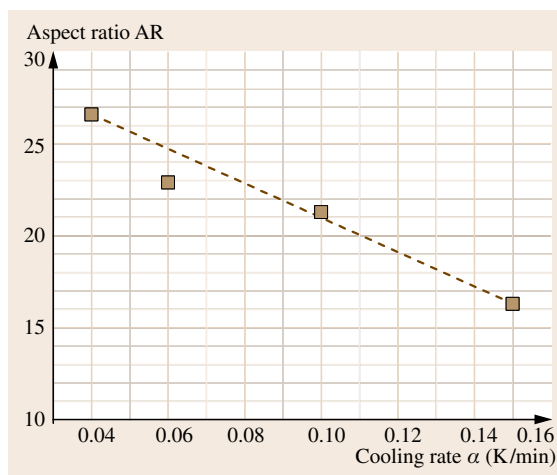


Fig. 30.11 Aspect ratio of Si-doped GaAs ELO layers grown at $T_0 = 575^\circ\text{C}$ versus cooling rate; silicon concentration in the Ga-As solution was $[\text{Si}] = 0.5 \text{ at. } \%$

To keep surface supersaturation at a low value, the cooling rate during LPE should be as low as possible. This is illustrated in Fig. 30.11, which shows the aspect ratio of Si-doped GaAs ELO layers versus cooling rate α [30.43]. The main idea behind that is to supply solute to the surface of the growing layer slowly enough that it can be transported by near-surface diffusion from upper to side walls of ELO and be incorporated there without any significant increase in surface supersaturation at the upper face. Similar dependence of aspect ratio on cooling rate has been found for InP [30.26] and GaSb [30.46] ELO systems. Also numerical simulations of ELO growth by LPE predict AR versus α dependence similar to that shown in Fig. 30.11 [30.24, 26].

Optimal choice of initial solution supercooling during ELO growth by LPE requires some additional effects to be taken into account. It is apparent that supercooling of the solution should be as small as possible. Then, the initial supersaturation of bulk of the liquid, and consequently that at the ELO surface, can be kept low. Indeed, we have found experimentally that, for the LPE growth of GaSb ELO structures, smaller values of initial melt supercooling lead to larger values of aspect ratio [30.46]. There are ELO systems, however, which require some initial supercooling of the liquid solution to initiate growth. Otherwise, the Gibbs–Thomson effect hinders the layer from growing out from the opening in the mask. In particular, this is the case for LPE growth of Si ELO layers on defect-free silicon substrates. Then the ELO layer grows only by flow of

steps supplied by substrate miscut as shown in Fig. 30.6. Sidewall of the layer beginning to grow laterally is strongly curved, and due to the Gibbs–Thomson effect, it requires higher equilibrium solute concentration than the planar face. Thus, instead of growing laterally the layer is dissolved and cannot get out of the opening in the mask as long as the liquid phase is not supersaturated sufficiently [30.47].

The situation is different if dislocations enhancing vertical ELO growth are present in the substrate. To illustrate this point Fig. 30.12a shows a cross section of silicon-doped GaAs ELO layer grown on GaAs substrate by LPE without any initial supersaturation of the liquid solution [30.48]. As we have already reported [30.49], by proper chemical etching, boundaries between vertically and laterally grown parts of the layer can be revealed, allowing analysis of the temporal development of ELO shape. These boundaries are sketched in Fig. 30.12b by dashed black lines, while dashed brown lines schematically mark their shape that would be observed without the contribution of the Gibbs–Thomson effect. Note that the Gibbs–Thomson

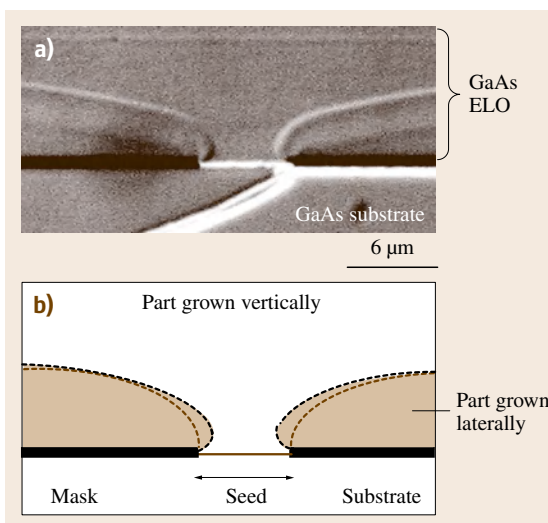


Fig. 30.12a,b Microphotograph (a) and schematic drawing (b) of the cross section of Si-doped GaAs ELO layer grown on GaAs substrate by LPE without initial supersaturation of the liquid solution. Boundaries between vertically and laterally grown parts of the layer are marked by *black dashed line* while their shape that would be observed without contribution of the Gibbs–Thomson effect are drawn by the *brown dashed lines* in (b). Note dissolution in the lateral direction induced by the Gibbs–Thomson effect at the beginning of growth

effect induces *dissolution* in the lateral direction instead of *growth* at the beginning of epitaxy. This is clearly visible as initial narrowing of the vertically grown part of **ELO**. However, during continuous cooling of the system, steps supplied by substrate dislocations still allow for vertical growth of the layer in the middle of the seed despite slow dissolution induced by the Gibbs–Thomson effect taking place in the direction parallel to the substrate. As soon as the layer grows thicker, curvature of the solid–liquid interface at the **ELO** sidewall decreases. Consequently, the contribution of the Gibbs–Thomson effect decreases and lateral overgrowth along the mask begins. We have proved that this explanation

is correct by showing that the magnitude of lateral dissolution caused by the Gibbs–Thomson effect can be reduced if slightly supersaturated liquid solution is used to grow the layer [30.33]. This example again illustrates the important role of dislocations in the growth of **ELO** layers.

Doping has been found to be a useful way to reduce the vertical growth rate, leading to thin and wide **ELO** layers. Figure 30.13a shows an image of a GaAs **ELO** layer grown from a nominally undoped solution by **LPE** on SiO_2 -masked GaAs substrate at 750°C [30.49]. Since the growth temperature was much higher than the optimal temperature, the cross section of the layer has

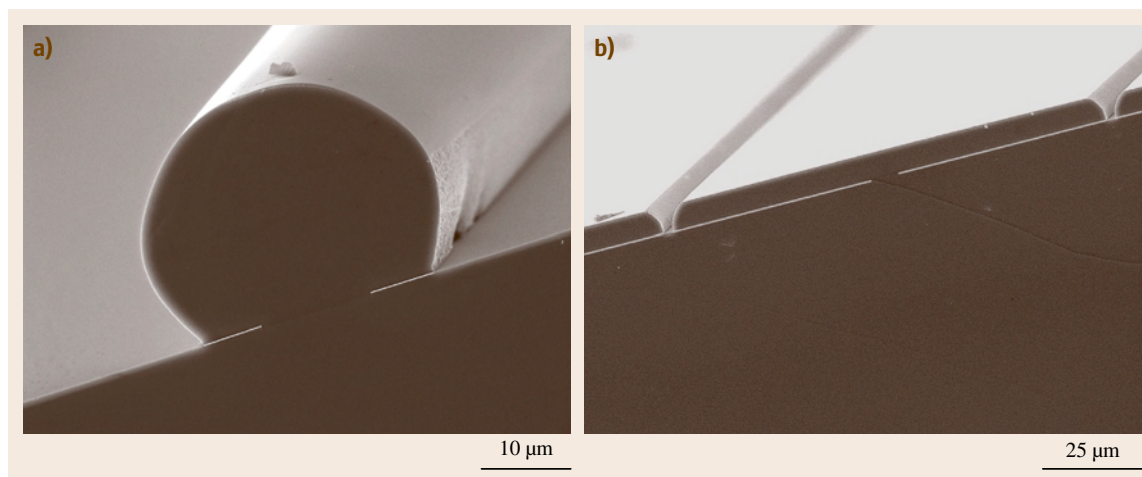


Fig. 30.13a,b Scanning electron microscopy images of undoped (a) and Si-doped (b) GaAs **ELO** layers grown at 750°C on SiO_2 -masked GaAs substrates. Besides doping, all the other growth parameters were the same for both layers

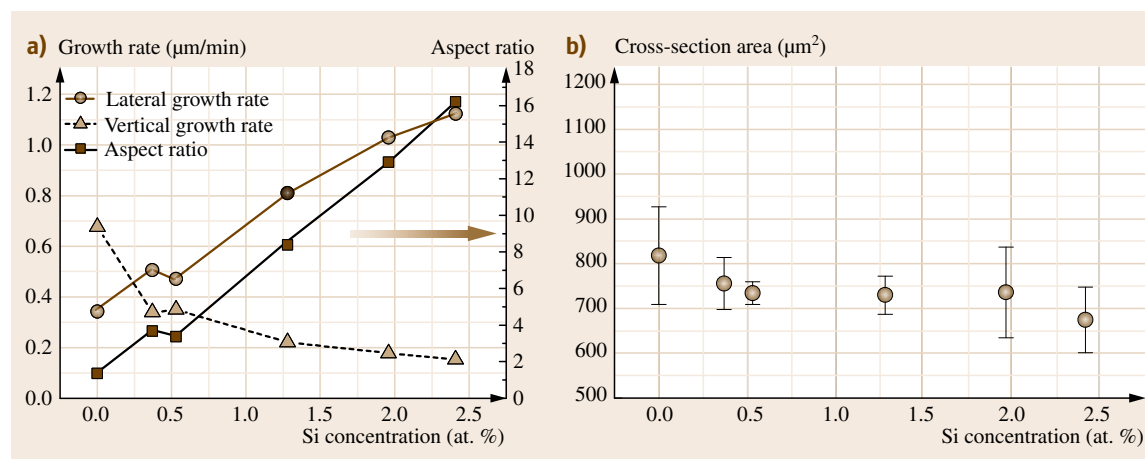


Fig. 30.14 (a) Lateral and vertical growth rates, and aspect ratio of GaAs **ELO** layers grown on GaAs substrates at 750°C versus Si concentration [Si] added to the Ga–As liquid solution; (b) the cross sectional area of the same layers versus [Si]

a circular shape and the aspect ratio is small (compare Fig. 30.10). A noticeable improvement of ELO shape has been achieved by adding 2.4 at. % Si to the Ga/As solution (Fig. 30.13b). As a result, the upper surface of the layer becomes very flat and the aspect ratio increases.

In order to study the effect in more detail, Fig. 30.14a shows a plot of lateral and vertical growth rates, and of the ELO aspect ratio of Si-doped GaAs layers versus the silicon concentration in the liquid phase. As seen, the vertical growth rate continuously decreases while the lateral one increases for higher dopant concentration in the liquid solution. As a result the ELO aspect ratio increases significantly with the doping level. It is important to emphasize that, whereas ELO layers become thinner and wider owing to the Si doping, within the limits of experimental error their cross sectional areas, being a measure of the amount of material deposited on the substrate, do not change (Fig. 30.14b). This means that the presence of Si has a negligible influence on the phase equilibrium, and a possible change of the liquid-zone supersaturation with doping cannot explain the effect presented. Thus, other processes affecting the redistribution of the growth units on the ELO surfaces should be considered.

The phenomenon of crystal habit modification by impurities is well known [30.50]. It might be attributed to hindering of the smooth step flow on the crystal face [30.51, 52]. The possible mechanism involves steps that are forced to squeeze between immobile impurity atoms tightly adsorbed on the surface. Thus, the steps have a local large curvature, which results in a decrease of their flow velocity. When applied to ELO growth this model leads us to the following interpretation of the data shown in Fig. 30.14: silicon atoms, when introduced to the liquid solution, are adsorbed on the upper ELO surface and render the steps there less operative, reducing in this way the vertical growth rate. On the other hand, the doping should have no direct influence on the random incorporation of growth units on atomically rough ELO faces. Since solute atoms cannot be easily incorporated onto the upper surface they are efficiently transported to the sidewalls by the near-surface diffusion. In that way the lateral growth rate increases at the expense of vertical one, while the total amount of material deposited on the substrate does not change.

It is worth mentioning that we have found a similar effect for Sn and Te dopants, although the reduction in the GaAs vertical growth rate caused by these impurities was much smaller than that for Si [30.49]. The reason

is still unclear, but different values of the surface mobility of Si, Sn, and Te might be responsible. We have also observed the same increase of ELO aspect ratio by Si dopant during LPE growth of Si-doped GaSb ELO layers [30.46]. Change of ELO shape with doping similar to that shown in Fig. 30.13 has been observed during ELO growth of GaAs on GaAs-coated Si substrates by LPE [30.8]. Kim and Lee reported that selenium is even more efficient than silicon in reducing vertical growth rate of ELO GaAs [30.53], but our experiments do not confirm their conclusion. It is important to point out that, in principle, similar phenomenon should be expected in other epitaxial systems in which the upper ELO face grows by the flow of surface steps. Indeed, a strong influence of magnesium doping on the growth habit of the GaN ELO layers grown by MOVPE on sapphire was found recently [30.54]. The effect of Si doping was negligible in that case. This shows that the phenomenon of vertical growth rate reduction by doping is not a specific attribute of ELO layers grown by LPE and has much more general nature, although its magnitude depends on growth conditions and the most effective impurity must be found for each particular system under study. Basic research is still needed to obtain a deeper insight into the effect of impurities on the growing crystal and to indicate which best suits the growth of thin and wide ELO layers.

Finally it should be noted that in some systems the value of the ELO aspect ratio is much more sensitive to the presence of dopants in the liquid solution than to the LPE growth temperature. One may try to increase the aspect ratio by growing ELO layers at a relatively low optimal temperature T_{opt} as discussed earlier. However, the dopant solubility at this temperature might be too low to increase further the aspect ratio. Alternatively, some increase in the growth temperature over T_{opt} with a simultaneous increase of doping might be a reasonable way to grow thin and wide ELO layers. This procedure can give satisfactory results only if the aspect ratio increase due to higher doping is larger than its decrease caused by higher LPE growth temperature. We have found that this is the case for Si-doped GaSb ELO layers [30.46]. However, care is advised when trying this approach since heavy doping may lead to a worse surface morphology of the layers.

To summarize this section, Fig. 30.15 presents a scanning electron microscopy cross section image of a GaAs ELO layer grown in our laboratory by LPE on SiO₂-masked GaAs substrate. The layer was doped with silicon and the LPE growth conditions were carefully adjusted according to the rules discussed above to get

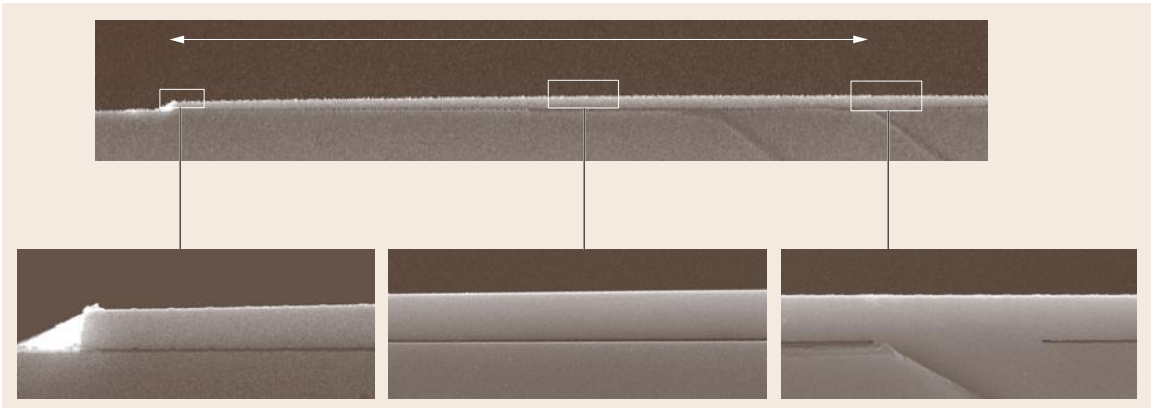


Fig. 30.15 Cross-section of Si-doped GaAs ELO layer grown by LPE on SiO₂-masked GaAs substrate. The thickness of the layer in its central part is 2.8 μm . The wing (marked by the *white arrow*) is 172 μm wide, yielding an aspect ratio of 126

the largest value of aspect ratio. The layer is 2.8 μm thick while its wings are 172 μm wide, which gives an aspect ratio as large as 126. Note that the thickness of

the layer continuously decreases from the center to the edge. This is evidence of bending of the layer towards the mask as will be discussed in Sect. 30.4.1.

30.3 Dislocations in ELO Layers

As discussed in Sect. 30.1 the unique advantage of growing epitaxial layers by the ELO technique is that substrate dislocations are efficiently filtered during the growth, so low-dislocation-density epitaxial layers can be obtained on heavily dislocated substrates. In the following subsections this issue will be addressed in more detail. First, we will focus on the distribution of dislocations in lattice-mismatched ELO layers, showing examples where the process illustrated schematically in Fig. 30.1 is really observed in laboratory practice. In Sect. 30.3.2, the structural perfection of seams that appear when layers grown from neighboring seeds merge in fully overgrown ELO structure will be discussed.

30.3.1 Filtration of Substrate Dislocations in ELO

Figure 30.16a shows a cross section of a GaAs ELO layer grown by LPE on a silicon substrate. The structure consists of Si(100) substrate with 2 μm -thick GaAs buffer grown by MBE and coated with the SiO₂ masking film. Width and thickness of the layer are 85 and 11 μm , respectively. More growth details can be found elsewhere [30.55]. Figure 30.16b shows a plane view

of the same layer with etch pits revealed by etching in molten KOH. It is noteworthy that the density of etch pits on the buffer surface is very high ($\approx 10^8 \text{ cm}^{-2}$). On the contrary, wings of the layer are nearly dislocation free, and only the dislocations threading through the seeding window from the buffer are seen on the upper ELO surface. In agreement with the model presented in Fig. 30.1 these dislocations are confined in a narrow area above the seed. The same behavior is seen in Fig. 30.17, which presents a cross section (Fig. 30.17a) and plane view (Fig. 30.17b) of GaSb ELO layer grown by LPE on GaAs substrate coated by MBE-grown GaSb buffer [30.43]. These examples show that substrate defect filtration during ELO procedure is very efficient, and low-dislocation-density epilayers can be obtained by this technique despite high dislocation density in the seeding area.

Figure 30.18a presents a cross sectional TEM image of a GaAs ELO layer grown by LPE on a GaAs-coated Si substrate [30.56]. Note the large density of dislocations at the bottom of the figure, i.e., close to the GaAs/Si interface. Density of these defects decreases with thickness of the buffer and finally all of them are blocked by the SiO₂ film. Thus, no dislocation is

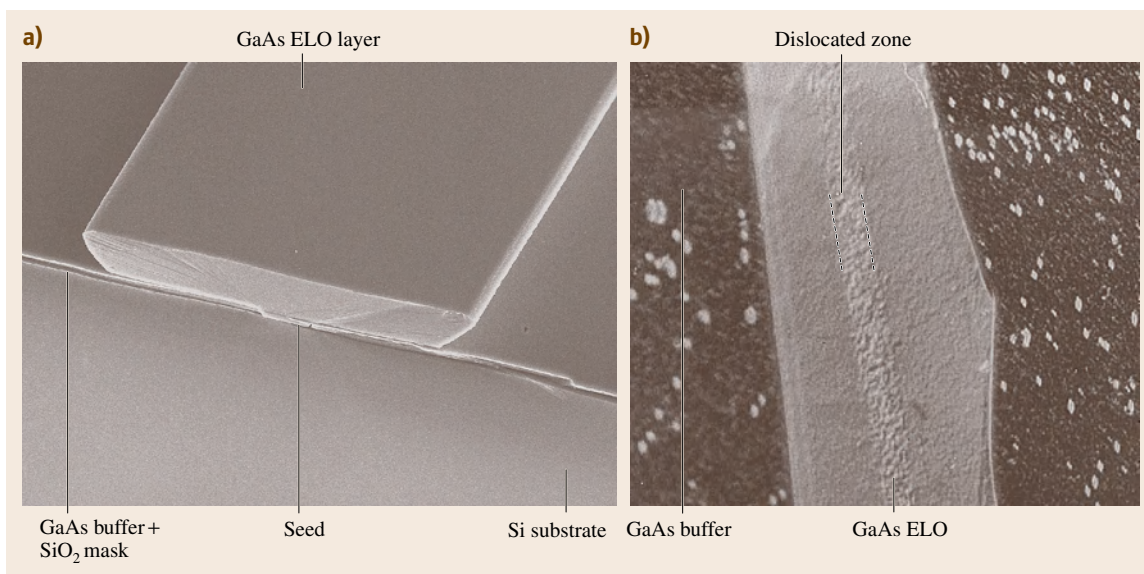


Fig. 30.16a,b SEM image of LPE-grown GaAs on Si ELO structure (a) and its plane view after etching in KOH to reveal the etch pit distribution (b). The layer is 85 μm wide

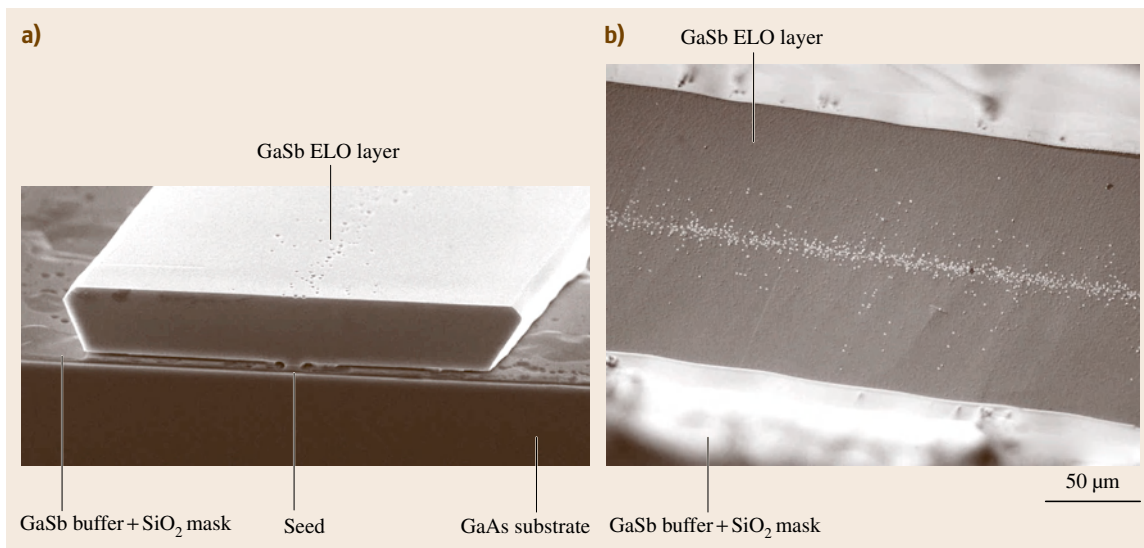


Fig. 30.17a,b Cross-section (a) and plane view (b) of a GaSb ELO layer grown by LPE on a GaAs substrate coated by 2 μm-thick GaSb buffer and SiO₂ mask; in (b) etch pits are revealed by chemical etching

seen in the GaAs wing area above the mask (compare Fig. 30.18b), which agrees with results shown in Figs. 30.16 and 30.17. Dislocations propagate to the ELO layer only through the opening in the mask. They are aligned on {111} planes, so the width of the defective area on the layer surface increases with the

thickness of the layer. This is exactly the behavior postulated in Sect. 30.1 when explaining the ELO concept with the use of Fig. 30.1.

As the last example of an efficient filtration of substrate dislocations in ELO, Fig. 30.19 shows the distribution of dislocations analyzed by cross sectional

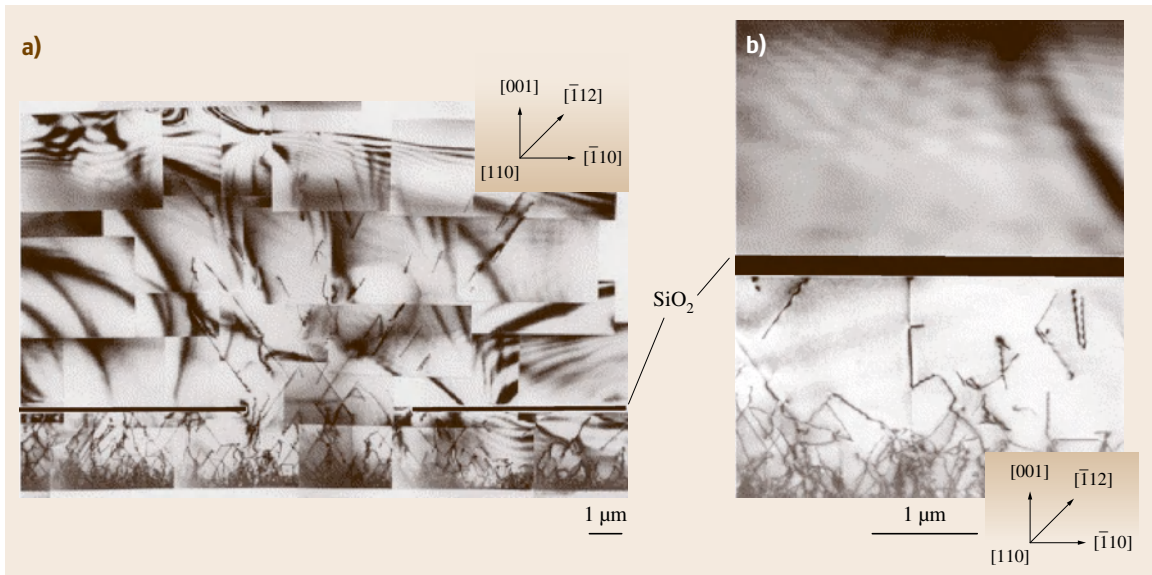


Fig. 30.18 (a) TEM cross sectional image of a GaAs ELO layer grown by LPE on a GaAs-coated Si substrate; (b) larger magnification of the ELO GaAs/SiO₂/GaAs buffer area; the mask position is marked by solid black lines for better visibility (courtesy of Tamura)

TEM in 140 μm-thick GaN ELO layers grown by HVPE on sapphire substrates [30.57]. The efficient blocking of buffer dislocations by the 1 μm-wide mask is clearly visible. Note also that some of the dislocations threading to the layer through the opening in the SiO₂ mask change their direction close to the mask edge and propagate parallel to the mask surface without reaching the upper ELO face. Sakai et al. claim that this phenomenon, instead of mechanical blocking of dislocations by the mask, gives the main contribution to the reduction of threading dislocation density in HVPE GaN films [30.58]. The mechanism of bending of threading dislocations in GaN ELO layers is not yet fully understood, although there are suggestions that it may be closely related to the change of the growth front direction and appearance of crystal facets at the very beginning of lateral overgrowth [30.58]. Probably, stress present during growth of the layers may play a role as well. It is worth mentioning that, to the best of our knowledge, there are no reports on similar behavior of dislocations in ELO structures of zincblende III–V materials. Actually, no evidence of dislocation bending in GaAs ELO layer grown on Si substrate is seen in Fig. 30.18. Some of the dislocations threading from the GaN buffer propagate through the GaN ELO layer without any change of direction, creating a defect zone on the surface above the seed, similar to those shown

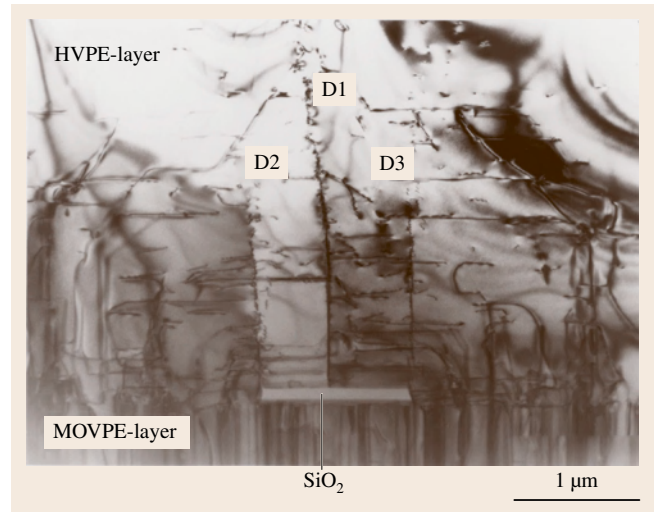


Fig. 30.19 TEM cross sectional image of a GaN ELO layer grown by HVPE on a GaN-coated sapphire substrate. Note that some dislocations threading from the buffer bend in the vicinity of the SiO₂ mask edge and propagate along the mask surface to ELO side-wall (courtesy of Sakai)

in Figs. 30.16b and 30.17b. In GaN these dislocations are aligned parallel to the *c*-axis, i. e., perpendicular to the substrate surface. Consequently, the width of the de-

fect zone on the upper ELO surface does not change significantly with layer thickness. Again, this behavior is quite different from that observed in ELO structures of zincblende compounds (compare Fig. 30.18a). Note also that two additional types of defects, denoted by D1 and D2, aligned along the [0001] direction, are visible in Fig. 30.19: the D1 defect originates approximately from the center of the SiO₂ mask while the D2 defect originates from both edges of the mask. Their origin will be discussed in the following sections.

Finally, let us mention that high crystallographic perfection of ELO wings results in their better optical and electrical properties than those of planar buffers. In particular, we have shown that cathodoluminescence intensity is much higher in the wing area of the GaAs on Si ELO structure than that from the material grown vertically above the seed, and even higher than that from the MBE-grown GaAs buffer [30.20]. This should be expected, as dislocations are known to behave like centers of effective nonradiative recombination of excited carriers. A similar distribution of cathodoluminescence intensity has also been observed across surfaces of GaN on sapphire [30.59] and SiGe on Si [30.60] ELO structures. The advantage of using ELO layers for devices was first demonstrated by Nakamura et al., who reported in 1997 continuous-wave (CW) room-temperature operation of a blue, InGaN/GaN laser diode with a lifetime longer than 1000 h when deposited on GaN/sapphire ELO substrate [30.23]. Since then the lifetime of these diodes has been significantly increased, so they are commercially available at present. This remarkable improvement was due to a significant reduction of the threshold current density of the laser diodes fabricated on low-dislocation-density GaN ELO substrates. Similar behavior has been re-

ported for GaAs-based lasers grown on GaAs/Si ELO substrate [30.61]. Kozodoy et al. have shown that the use of lateral overgrowth to eliminate dislocations leads to better electrical properties of GaN p-n junctions [30.62]. Reverse-bias leakage current was reduced by three orders of magnitude for diodes located on low-dislocation-density ELO wings. This has led to improved performance of light-emitting diodes [30.63,64]. Moreover, large reduction of dark current and sharper cutoff have been found for AlGaIn solar-blind photodetectors fabricated on ELO substrates [30.65]. These examples provide the best evidence that the application of ELO technology led to significant progresses in the development of high-performance semiconductor devices made of lattice-mismatched epitaxial structures.

30.3.2 Structural Perfection of Coalescence Front in Fully Overgrown ELO Structures

In order to ensure high quality of ELO layers special care must be taken to avoid the generation of new defects during lateral overgrowth. The areas above the mask edges and fronts of coalescence of layers grown from neighboring seeds are the most sensitive since stress is the largest there. Therefore, factors influencing the structural perfection of ELO layers at these particular points will be briefly discussed.

Figure 30.20 shows a TEM image of the seeding area of the GaAs ELO layer grown by LPE on a SiO₂-masked GaAs substrate [30.66]. It is seen that the layer sticks closely to the SiO₂ mask. Contrast in the ELO image is very homogeneous, indicating that the overgrowth at the seed level is nearly stress free. Note that no dislocation is visible around the mask edge. As mentioned earlier, regular arrangements of dislocations generated during LPE growth in the vicinity of SiO₂ mask edge are sometimes observed in Si ELO layers [30.44]. Their creation leads to the growth of defective layers such as those shown in Fig. 30.8. It seems, however, that in this particular case defects originated due to specific LPE growth conditions used and that their generation can be completely avoided if the growth parameters are carefully adjusted. Indeed, the same group of authors has reported LPE growth of completely defect-free Si ELO layers [30.40]. A quite different behavior is observed in GaN ELO structures, in which dislocations above the mask edge are commonly found (see the D2 defect in Fig. 30.19). They are related to tilting of ELO wings as will be discussed in Sect. 30.4.1.

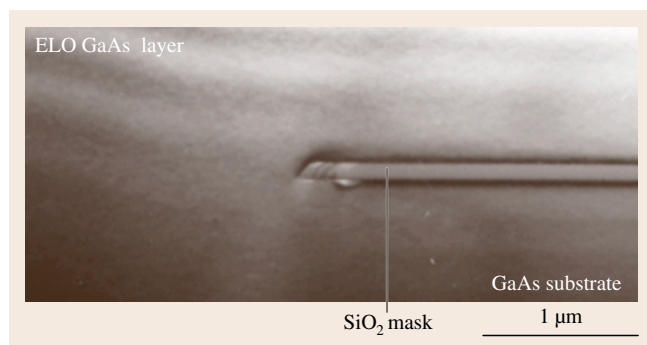


Fig. 30.20 TEM image of GaAs ELO/GaAs substrate interface at the edge of the SiO₂ mask. Note that no dislocation is seen above the mask edge

Coalescence fronts (seams) of ELO layers grown from adjacent seeding windows in fully overgrown ELO structures are other points where large mechanical stresses might be present. Thus, nucleation of dislocations is likely to occur there. Figure 30.21 presents a front of partial coalescence of two GaAs ELO layers grown from neighboring seeds by LPE on SiO₂-masked GaAs substrate [30.66]. From geometrical considerations the sidewalls of ELO layers were identified as close to the {232} planes. When approaching each other these planes separated mask area from the solution, thus the growth just above the mask terminated and a small void remained at the front of coalescence. Then the upper hollow filled up and the continuous ELO layer with a flat upper surface was finally obtained.

Creation of voids can significantly deteriorate the perfection of ELO layers. During their liquid-phase growth the solution is likely to be trapped inside the void. Since the thermal expansion coefficients of metallic inclusion and surrounding crystal are usually different this may lead to stresses that extend from the inclusion into the epitaxial layer and eventually to the formation of dislocations. This issue was extensively studied by Nagel et al. [30.67] and Banhart et al. [30.68] for LPE growth of Si ELO layers on thermally oxidized

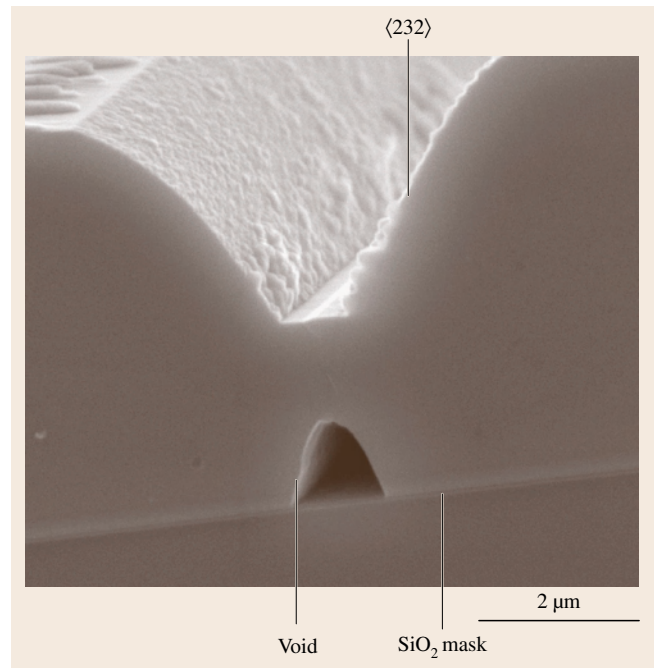
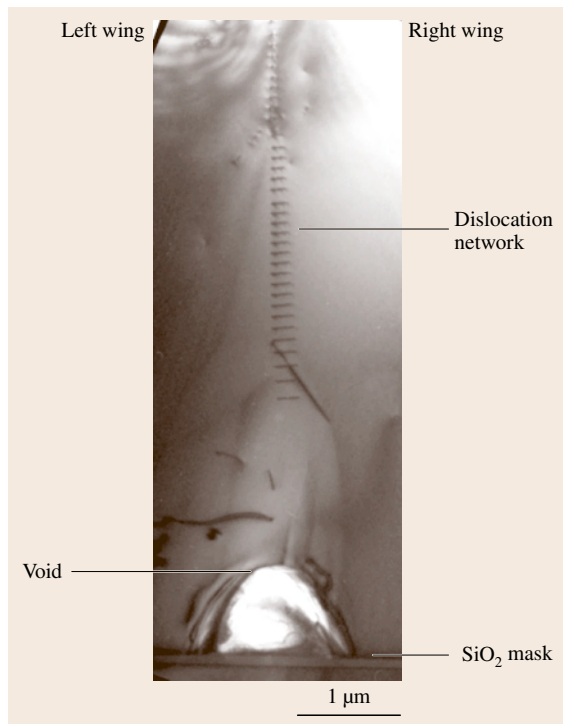


Fig. 30.21 SEM image of the front of partial coalescence of two GaAs ELO layers grown by LPE on SiO₂-masked GaAs substrate. Note the presence of inclined $\langle 232 \rangle$ sidewalls of ELO



Si substrates. They found that shape, size, orientation, and arrangements of seeding windows must be carefully designed for high quality of coalescence front. In particular, they have shown that 150 μm-long defect-free seams can be achieved in silicon lateral overgrowth by LPE if advancing layers start to join at only one point. Then the process should proceed in a zipper-like way in the direction of the seeding line. It is important that the growth solution could flow away along the window direction from the space between advancing growth fronts. When the merging layers join at two or more different points of the seam and coalescence proceeds inwards, solute inclusion and related dislocations are observed at the last point of coalescence. This usually happens if parallel seeding windows are used. Therefore, the application of nonparallel seeds has been advised to facilitate the zipper-like mechanism. This approach has been successfully employed

Fig. 30.22 TEM image of the front of coalescence of two GaAs ELO layers grown on SiO₂-masked GaAs substrate. Note the void at the mask surface and a well-organized network of dislocations separated by a distance of about 100 nm ◀

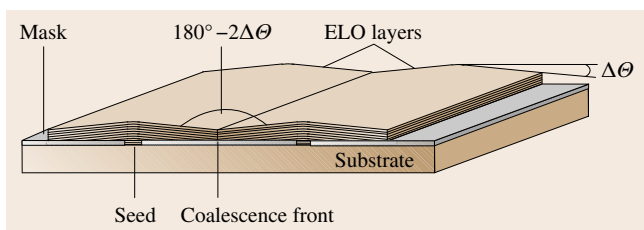


Fig. 30.23 Schematic drawing of merged ELO layers with their laterally grown parts tilted towards the mask. Since wings are tilted in opposite directions, the misorientation of the lattice planes at the seam is $2\Delta\Theta$, where $\Delta\Theta$ is the tilt angle of each wing

for defect-free coalescence of GaAs/GaAs [30.69] and InP/InP [30.70] ELO layers by LPE.

Figure 30.22 shows a TEM image of a coalescence front of two GaAs ELO layers grown by LPE on a SiO₂-masked GaAs substrate [30.66]. A void at the mask surface, similar to that seen in Fig. 30.21, is clearly visible. Probably, it was originally filled with gallium solvent that was later removed during the ion milling of the specimen. This might explain why some single dislocations surrounding the void are seen in its vicinity. The most important feature, however, is a well-organized set of dislocations starting at a distance of about 1 μm from the void and creating a low-angle grain boundary at the seam plane. These dislocations are parallel to the (010) direction with a Burgers vector of $\frac{1}{2}[110]$, both included in the (001) plane that is parallel to the surface of the substrate. Creation of the grain boundary at the seam can be explained as follows: very often laterally grown sections of ELO layers are tilted towards the mask with the tilt axis aligned parallel to the seeding window direction. This situation is schematically illustrated in Fig. 30.23 where the wing tilt angle is marked by $\Delta\Theta$. The phenomenon of wing tilting will be extensively discussed in Sect. 30.4.1. However, it must be noted here that it creates significant problems for coalescence of neighboring ELO layers as they tilt

in opposite direction. Since the sense of bending must be reversed at the seam the crystal lattice is heavily stressed in this region and dislocations appear as soon as the critical shear stress is reached. As discussed by Banhart et al. [30.68] for LPE growth of Si ELO layers on thermally oxidized Si substrates the stress at the seam increases with the thickness of merging layers and the value of the tilt angle $\Delta\Theta$. They have found defect-free coalescence for Si ELO layers thinner than 3–4 μm and tilted less than 0.1°. For larger thicknesses and/or values of the tilt angle $\Delta\Theta$ generation of a low-angle grain boundary similar to that shown in Fig. 30.22 was observed.

The dislocation network created in our GaAs ELO layers is similar to the D1 defect found at the center of the mask in GaN ELO layers (Fig. 30.19). Sakai et al. claim that this grain boundary consists of dislocations that had propagated laterally in the GaN wing area and had changed their direction again in the seam area [30.57]. On the contrary, the density of threading dislocations in GaAs ELO layers is very low. Therefore, in our case new dislocations must have been generated and rearranged into the low-angle grain boundary at the seam to accommodate the mutual tilt of merging wings. A similar behavior has been reported by Shih et al. for fully overgrown Si ELO layers grown by chemical vapor deposition on SiO₂-masked Si substrates [30.71]. The result they found, i.e., that the number of seam defects increases with increasing buried oxide width, can be explained by larger tilt angles $\Delta\Theta$ for wider overgrowths.

The geometry of the dislocation network shown in Fig. 30.22 can be used to measure the relative misorientation of merging ELO lattice planes [30.66]. The value of the tilt angle $\Delta\Theta \approx 0.1^\circ$ obtained in this way is nearly ten times smaller than that determined for the GaN on sapphire ELO layer shown in Fig. 30.19. Possible reasons and consequences of that will be discussed in the next section.

30.4 Strain in ELO Layers

All examples presented thus far prove that ELO layers are of much higher quality than the reference planar structures. Even if new dislocations are created at the fronts of coalescence the overall density of dislocations is still significantly reduced. However, ELO layers are not free of strain. In particular, there is a question about strain induced by the mask itself and/or its possible in-

teraction with the overgrown epitaxial layer. Moreover, the lattice mismatch and thermal strain induced by different thermal expansion coefficients of various parts of ELO structure may result in large deformations of the layers. Although in real heteroepitaxial ELO structures all these phenomena take place simultaneously, for clarity of presentation we will first focus on the

problem of interaction of ELO layers with the mask underneath (Sect. 30.4.1). Then, the issue of thermal strain in ELO structures will be addressed (Sect. 30.4.2). It is important to point out that ELO samples have a specific geometry. They consist of separated or coalesced monocrystalline stripes grown from line seeds cut in the mask, so different properties in the directions parallel and perpendicular to seeding lines may be expected. Therefore, before proceeding further a brief introduction will be given, presenting how the x-ray diffraction (XRD) technique is used to study a strain field in ELO layers.

Figure 30.24 shows the geometry commonly used for analysis of ELO layers by XRD. First, x-ray diffraction measurements are taken for the sample position in which the scattering plane (defined by the incident and diffracted wavevectors) is perpendicular to the seeding line direction. This corresponds to the axis of sample rotation during the ω scan being parallel to the seeds ($\varphi = 0^\circ$). Next, the sample is rotated around the substrate normal and the measurements are repeated for the x-ray scattering plane being parallel to the seeds (i. e., for $\varphi = 90^\circ$). Reciprocal space maps and/or x-ray diffraction curves (so-called *rocking curves*) are recorded for each sample positions.

Usually ELO layers are much narrower than the x-ray beam used in the standard x-ray diffraction experiments. Therefore, the diffraction pattern obtained contains information integrated over many stripes illuminated by the beam. To analyze strain distribution in a more detail we have developed a XRD technique in which the sample is moved in small steps and the x-ray beam, being much narrower than the ELO width, illuminates in sequence various parts of a single ELO stripe. For each position of the beam the diffraction pattern originating from a precisely defined area of the stripe is recorded. This allows us to analyze strain field *locally* inside a particular ELO stripe chosen. As will be shown later, this procedure allows the most characteristic features of the strain field in the samples to be determined.

30.4.1 Mask-Induced Strain in Homoepitaxial ELO Layers

Figure 30.25 shows x-ray rocking curves of GaAs ELO layer grown by LPE on SiO₂-masked GaAs substrate [30.7]. The layer was 10 μm thick and 90 μm wide. Both, the as-grown sample and that cut from the same wafer and etched to remove selectively the SiO₂ mask have been studied. The rocking curves presented

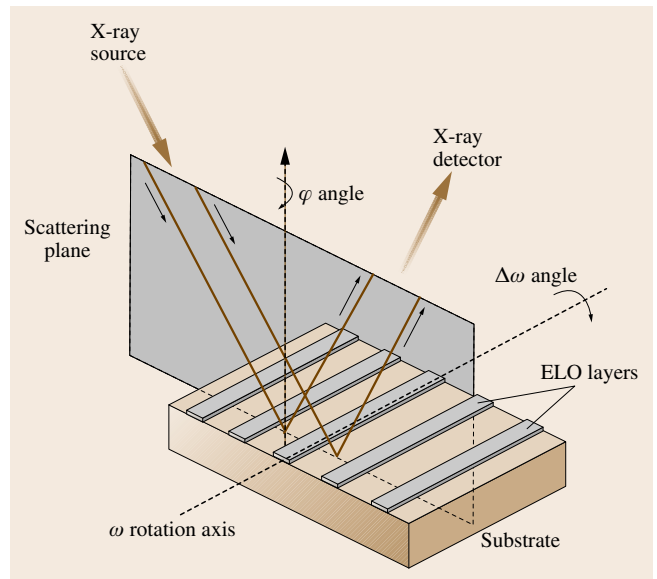


Fig. 30.24 Sketch of the geometry used for x-ray diffraction studies of ELO samples. The scattering plane is defined by the incident and diffracted vectors. φ is the angle between the direction of the seeds and the axis of sample rotation during the ω scan; $\varphi = 0^\circ$ for the geometry shown

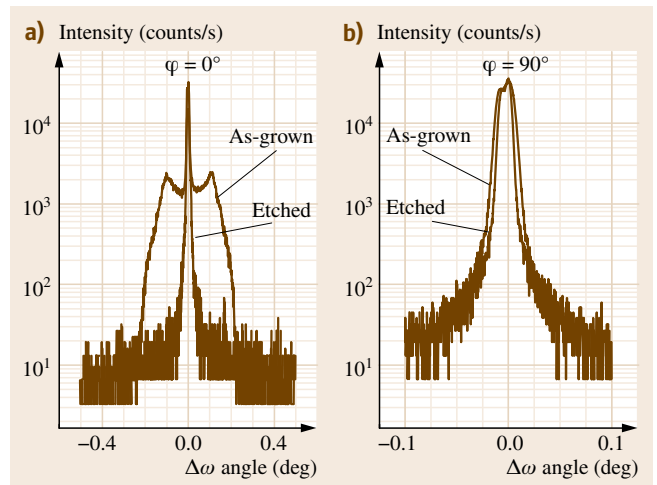


Fig. 30.25a,b X-ray rocking curves of (400) $\text{CuK}\alpha_1$ reflection from the as-grown and etched GaAs ELO layer on the SiO₂-covered GaAs substrate measured with the ω -axis parallel (a) and perpendicular (b) to the seeding lines

in Fig. 30.25a,b have been measured with the $\varphi = 0^\circ$ and $\varphi = 90^\circ$ sample orientation, respectively. As can be seen from Fig. 30.25a the rocking curve of the as-grown

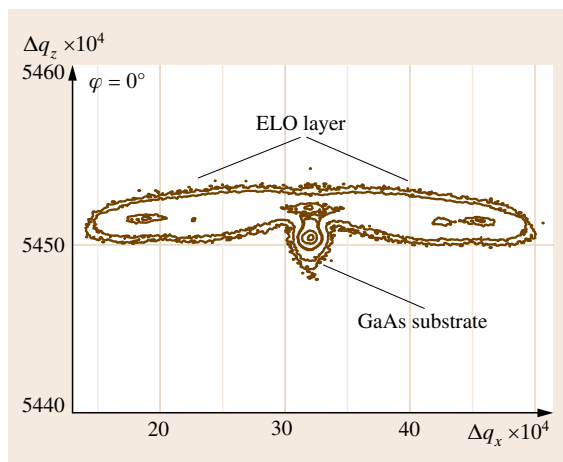


Fig. 30.26 Reciprocal-space map of (400) $\text{CuK}\alpha_1$ reflection from the as-grown GaAs ELO layer on a SiO_2 -covered GaAs substrate with the ω -axis parallel to the seeding lines. Both axes are marked in units of $\lambda/2d$, where λ is the wavelength of the x-ray radiation and d is the GaAs lattice spacing

sample is very broad. However, it becomes much narrower after the SiO_2 mask has been removed. On the contrary, for $\varphi = 90^\circ$ the rocking curve is quite narrow and etching causes only a slight change of its shape (Fig. 30.25b). It is worth mentioning that during rocking curve measurements the x-ray diffraction is sensitive mainly to the distortion of the crystal planes in the scattering plane. Therefore, the large width of the rocking

curve shown in Fig. 30.25a indicates that a significant deformation of the as-grown ELO takes place in the cross section plane perpendicular to the seeds.

Figure 30.26 shows the reciprocal space map of the same ELO layer. This map has been constructed for the same sample geometry as that used to measure the rocking curves presented in Fig. 30.25a. The distribution of the diffracted x-ray intensity proves that the reason for the large width of the rocking curve is the ELO stripe deformation in the direction perpendicular to the seeding line. This deformation is elastic since a narrow well-concentrated diffraction picture has been observed on the reciprocal lattice map if this is taken for the sample with the SiO_2 removed [30.72]. There are also slightly different positions of the ELO and substrate peaks visible in Fig. 30.26 that indicates some lattice misfit ($\approx 7 \times 10^{-5}$) between the heavily Si-doped ELO layer and undoped GaAs substrate [30.7].

When developing our ELO growth technology, occasionally we found GaAs ELO layers with an air gap between their laterally grown parts and the mask [30.73]. A cross section of such a layer is shown in Fig. 30.27a. Note the wings hanging over the substrate without any contact with the mask surface. Note also that the (400) $\text{CuK}\alpha_1$ rocking curves of the layer are very narrow for both positions of the scattering plane (Fig. 30.27b), which means that deformation of the ELO wings, if any, is negligible. Comparison of the data shown in Figs. 30.25a and 30.27b proves that deformation of GaAs ELO wings must be due to their interaction with the mask surface.

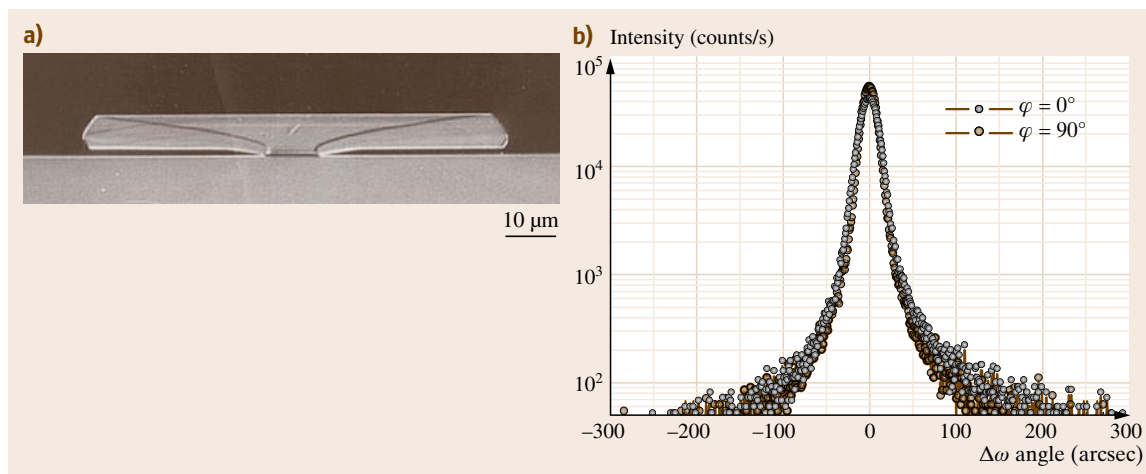


Fig. 30.27a,b Cross-section image (a) and x-ray rocking curves of (400) $\text{CuK}\alpha_1$ reflection (b) of a GaAs ELO layer on a SiO_2 -masked GaAs substrate. Note the air gap between the mask and the ELO wings

The results presented above allow us to present a picture of deformation of the ELO layer that is schematically illustrated in Fig. 30.28: During the growth the layer is bent towards the SiO₂ mask in the direction perpendicular to the seeding line (Fig. 30.28a). When the SiO₂ mask is removed by selective etching the ELO stripe behaves like a released spring and the wings tilt disappears (Fig. 30.28b). This corresponds to a narrowing of the curve shown in Fig. 30.25a. From a comparison of the rocking curves shown in Fig. 30.25b it can be concluded that similar deformation does not occur along the ELO stripe.

In the model presented in Fig. 30.28a it is postulated that the ELO wings are tilted towards the mask. Note, however, that the direction of tilt, upward or downward, cannot be directly determined from the shape of the rocking curve shown in Fig. 30.25a. Therefore, we have applied a spatially resolved XRD (SRXRD) technique in which the ELO stripe is moved in small steps, so the x-ray beam, being much narrower than the ELO width, illuminates in sequence various parts of the layer (see the geometry of the experiment sketched in Fig. 30.29c). For each position of the beam on the sample a local x-ray rocking curve originating from a precisely defined area of the stripe is recorded. The results of such a procedure are presented in Fig. 30.29b, which shows the set of x-ray rocking curves measured locally at various parts of a 304 μm -wide and 16.8 μm -thick GaAs ELO layer grown on SiO₂-masked GaAs substrate [30.74]. The standard rocking curve measured for the same sample with a 500 μm -wide x-ray beam is included in Fig. 30.29a for comparison. The diffraction plane was perpendicular to the seeds in these experiments. For the positions $x = -184 \mu\text{m}$ and $x = 230 \mu\text{m}$ the beam was out of the ELO area. Therefore, only narrow substrate peaks are visible. As soon as the beam approached the ELO stripe ($x = -138 \mu\text{m}$) a strong side-maximum, apparently due to radiation diffracted by the ELO edge, appeared in the curve. For $x = 0 \mu\text{m}$ only the middle part of the stripe was illuminated by x-rays. As a result, the side-maxima are missing whereas the intensity of the substrate peak is significantly reduced. When the beam starts to move out of the stripe surface ($x = 138 \mu\text{m}$) the intensity in the central part of the curve decreased again, the side-maximum due to the edge reflection remained, while the intensity of the substrate peak increased. The data shown in Fig. 30.29b explains the origin of all the features visible in the standard rocking curve presented in Fig. 30.29a. In particular, this proves that the side-maxima are due to diffraction from the edges of the

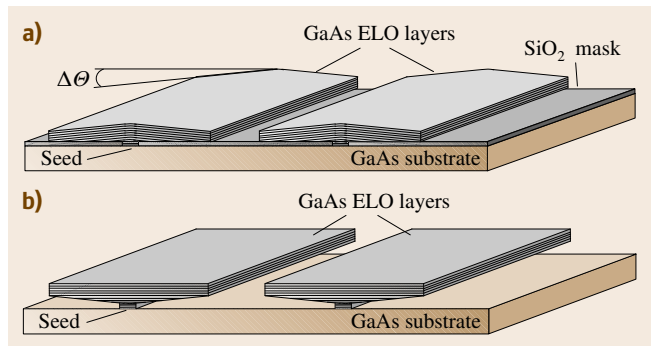


Fig. 30.28a,b Schematic drawing of the GaAs on GaAs ELO cross section. Bent layers are shown in the as-grown state (a), deformation of ELO disappears when the SiO₂ mask is removed by etching (b). $\Delta\Theta$ is the tilt of (100) crystal planes between the edge and the central part of ELO

ELO stripe. Therefore, the misorientation of ELO crystal planes must be the largest there. Consequently, half of the angular separation of the side-peaks on the standard rocking curve can be used as a good measure of the maximum tilt angle $\Delta\Theta$ of ELO lattice planes (compare Fig. 30.28a). Moreover, using a simple geometry of the diffraction system and analyzing the order in which the side-maxima appear while the beam moves across the stripe the direction of ELO tilt can be unambiguously determined. For example, the x-ray rocking curves of Fig. 30.29b show that the left wing diffracts x-rays at larger Bragg angle than the right one. This is clear evidence that the wings are tilted towards the mask [30.74]. It is worth mentioning that, improving the technique of spatially resolved x-ray diffraction presented above, we have employed it successfully for analysis of ELO layers using an x-ray beam as narrow as 20 μm [30.66]. Subsequently, even a 10 μm -wide beam moved in steps as small as 3 μm was applied, which allowed us to create x-ray rocking curve maps of bent ELO stripes [30.75]. Despite this progress the technique cannot be easily applied for GaN ELO layers. Since their widths are usually much smaller, electron diffraction [30.76] or synchrotron x-ray diffraction [30.77] must be used to determine the local magnitude and direction of the GaN wing tilt.

Additional evidence of the downward tilt of ELO wings comes from our studies of similar GaAs ELO samples by synchrotron x-ray topography (SXRT) [30.78, 79]. The basic idea of the experiment was to analyze how a white-beam synchrotron x-ray radiation collimated with the use of very narrow slits reflects back from the surface of the GaAs ELO sam-

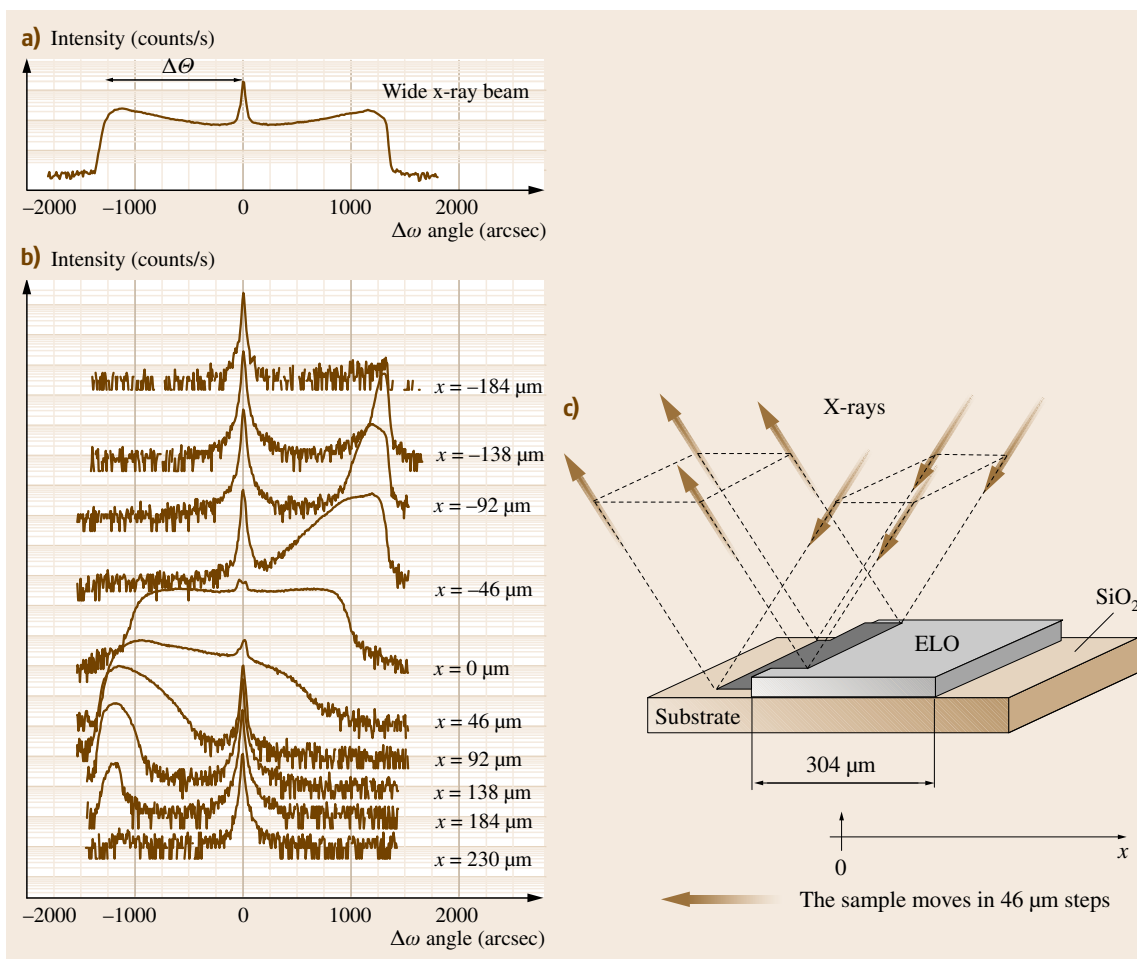


Fig. 30.29a–c X-ray rocking curves of a 304 μm -wide as-grown GaAs ELO layer on a GaAs substrate measured with the scattering plane perpendicular to the seeding lines with the use of a 500 μm -wide x-ray beam (a) and 90 μm -wide x-ray beam scanned across the ELO stripe in 46 μm steps (b). x denotes the position of the beam on the ELO. The $x = -184$ and 230 μm curves correspond to reflections from the substrate outside the ELO stripe. (c) Schematic geometry of the experiment

ple. More details on experimental conditions can be found in the source publications. The topograph obtained is shown in Fig. 30.30a where “w,” “s,” and “e” mark images of window seed, substrate, and ELO layer areas, respectively. The shape of the ELO layer image directly indicates a downward tilt of the GaAs ELO wings. Additionally, the image was simulated numerically (Fig. 30.30b) to gain information on the distribution of the (100) lattice plane tilt angle versus position across the single ELO stripe. This data allowed us to calculate the shape of (100) lattice planes in the sample as shown in Fig. 30.30c together with the ex-

perimental profile of ELO layer thickness determined by surface stylus profilometer. As seen, the numerical results agree very well with the experimental results.

It should be noted in Fig. 30.30c that the curvature of the (100) lattice planes is the largest in the central part of the ELO stripe. This finding has allowed us to postulate that bending of the ELO stripes starts at the very beginning of growth when the laterally overgrown parts are thin and flexible. Then, the bent crystal planes might be reproduced during subsequent growth, although retaining their shape [30.78]. As will be shown later, this is exactly the behavior observed experimentally.

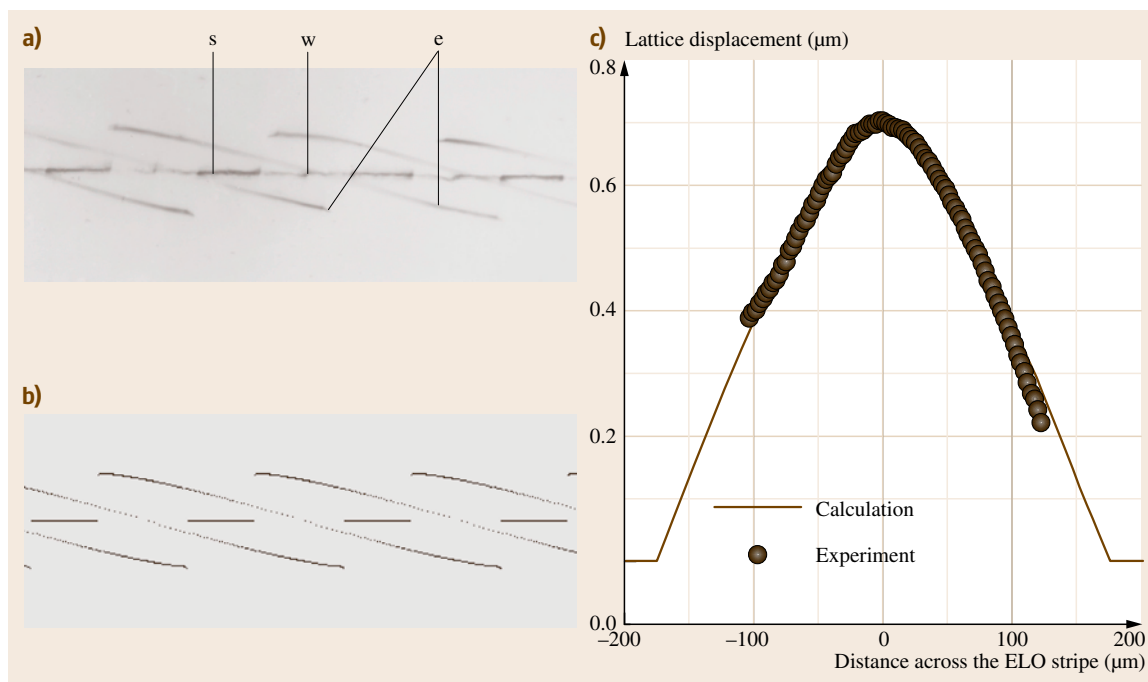


Fig. 30.30a–c 206 back-reflection section synchrotron x-ray topograph measured (a) and calculated (b) for GaAs ELO layer grown by LPE on SiO₂-masked GaAs substrate; “w,” “s,” and “e” mark topographic images of window seed, substrate and ELO layer, respectively; calculated (solid line) and measured (dots) displacements of ELO lattice planes across the single ELO stripe are shown in (c)

Note also that the data shown in Fig. 30.30c indicates a continuous decrease of layer thickness from the center of the layer to its edge, being due to the wing tilt. Indeed, this effect is observed experimentally as, for example, is clearly seen in the cross section image presented in Fig. 30.15. Its magnitude, namely the thickness change of $\approx 0.9 \mu\text{m}$ on a $\approx 170 \mu\text{m}$ -wide wing, also agrees with data shown in Fig. 30.30c. A similar phenomenon has been reported for LPE-grown Si ELO layers. Since the upper ELO surface was a singular, atomically smooth face, tilting of the wings should lead to the presence of monoatomic steps at the Si/SiO₂ interface where silicon crystal planes terminate (see the sketch in Fig. 30.28a). Indeed, analysis of Si ELO layers by high-resolution transmission electron microscopy revealed the presence of such steps at the interface between the epitaxial layer and the SiO₂ film [30.17].

The tilting of ELO wings towards the mask has also been found for many other ELO systems, including Si layers grown by LPE on oxidized Si substrates [30.68] and GaN ELO layers grown by HVPE or MOVPE on sapphire or SiC substrates coated by SiO₂ or Si₃N₄

masks [30.57, 80–82]. Fini and coworkers used x-ray diffraction to observe the time evolution of lattice planes bending in GaN on sapphire ELO layers [30.83]. The scans in reciprocal space through the (10 $\bar{1}$ 3) diffraction peak of GaN obtained in situ, during growth of the structures by MOVPE, are shown for various growth times in Fig. 30.31a. Prior to epitaxy only the central peak, due to the diffraction from the GaN buffer, is visible. Emergence of the side-maximum is evident for the growth times ≈ 100 s, and by ≈ 300 s, distinct side-peaks have evolved, indicating wing tilt of $\approx 0.9^\circ$. Postgrowth SEM studies of layer cross sections have shown that a significant lateral overgrowth started just at that moment. The wing peak narrows during subsequent growth while its position changes slightly, reaching a tilt of $\approx 1.19^\circ$ after 3600 s of growth. The data collected during this elegant experiment are direct evidence that wing tilt must be due to interaction of the wing with the mask and that it starts at the very beginning of lateral overgrowth, in agreement with our earlier suggestion presented above when discussing the results shown in Fig. 30.30c [30.78].

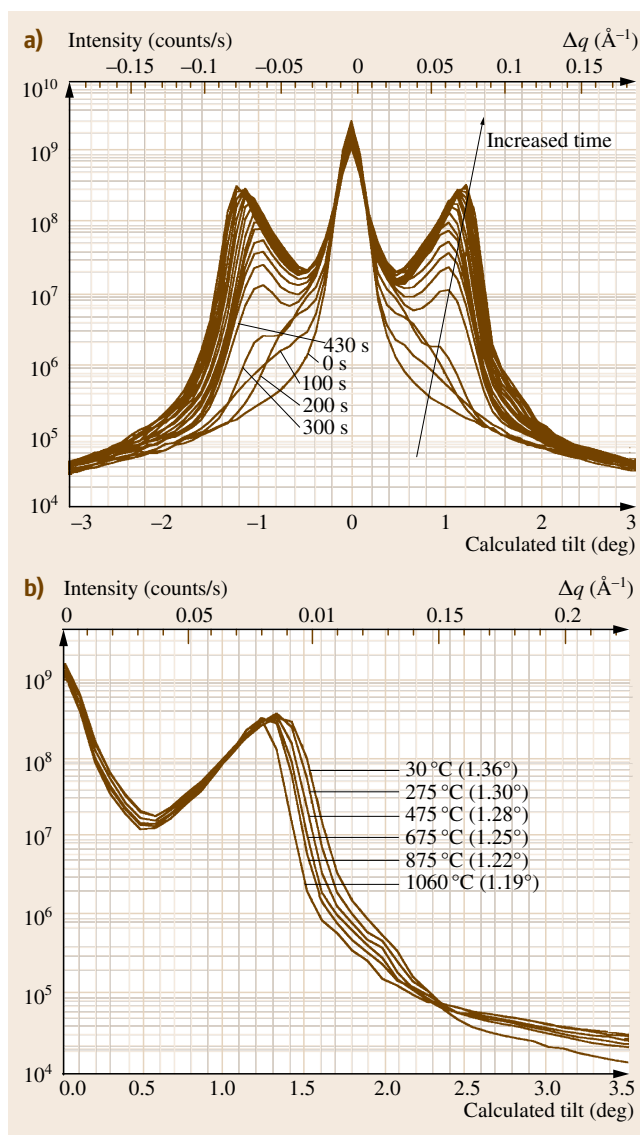


Fig. 30.31a,b Scans in reciprocal space trough the $(10\bar{1}3)$ x-ray diffraction peak obtained for various growth times during MOVPE growth of GaN on sapphire ELO structures (a) and on cooling to room temperature (b). The scans in (b) are shown over half of the range measured (courtesy of Fini)

The difference between the GaN and GaAs or Si ELO structures is the magnitude of wing tilt and the mechanism of its relaxation. As discussed earlier, tilt angles $\Delta\theta \approx 0.1^\circ$ are commonly found in LPE-grown GaAs ELO layers (Fig. 30.25a). Thus, the bending strain at the seed-mask edges is small enough to be

accommodated elastically. Generation of dislocations in the layer does not take place and deformation of the wings disappears completely when the mask is removed by postgrowth etching. Consequently, no defects above the mask edge (compare Fig. 30.20) and narrow x-ray rocking curve of the sample with the mask removed (Fig. 30.25a) are observed. On the contrary, tilt angles up to $\approx 1.5^\circ$ are reported in literature for GaN ELO layers (Fig. 30.31a and [30.57, 80]). So large tilts cannot be accommodated elastically and the strain above the mask edge partially relaxes via the creation of a low-angle grain boundary. This relaxation process is energetically favorable if the ELO structure contains dislocations threading from the buffer. In such a case, the grain boundary can be easily formed from bent threading dislocations that pile up near the mask-seed edges. Indeed, as shown already in Fig. 30.19, cross sectional TEM studies of GaN on sapphire ELO structures have revealed additional low-angle tilt boundaries (the D2 defects) above the edges of the SiO_2 mask. Consequently, when the mask is etched away after the growth, similarly to our approach for GaAs/GaAs layers, only the elastic component of the bending strain is released. The plastic deformation of the crystal lattice above the mask edge remains, and as a result, only partial narrowing of the x-ray rocking curve takes place. This is exactly the behavior observed experimentally [30.81].

All the arguments presented up to now indicate that downward tilt of ELO wings originates from an interaction between laterally grown material and the mask. The nature of this interaction is still not fully clarified. Kohler with coworkers have suggested that an attractive van der Waals force starts to be active during LPE growth when the mutual distance between Si ELO wing and the upper surface of the SiO_2 mask falls below a certain value [30.84]. The surface tension of the solution should also be taken into account as a source of wing tilting during ELO growth from the liquid phase [30.47]. However, the tilt of GaN ELO wings seems to be too large to be related to adhesion or weak van der Waals forces. Therefore, a chemical reaction of laterally overgrown GaN with the SiO_2 underneath and/or densification of the oxide being due to a high temperature and chemically aggressive conditions (e.g., presence of ammonia) during vapor phase epitaxy of GaN have been considered as possible reasons of the tilt [30.83].

As discussed in Sect. 30.3.2, tilting of ELO wings towards the mask creates a significant problem for coalescence of neighboring stripes as they tilt in the opposite direction (Fig. 30.23). Therefore, there is no

doubt that for ELO layers of high crystallographic quality tilting of their wings should be reduced as much as possible.

We have proposed the following recipe for reduction of the mask-induced bending of the ELO layers: The initial vertical growth rate of ELO must be increased to start the lateral overgrowth at some microscopic distance from the upper surface of the mask [30.74]. Then the chance of ELO wings capture by attractive force and their interaction with the mask should be reduced. We have found that this recipe works efficiently in practice. In particular, tilting of the wings has been efficiently tailored by controlling the ratio of vertical to lateral growth rates at the beginning of ELO growth. This has been achieved by growing GaAs ELO layers on SiO₂-coated GaAs substrates with increasing density of dislocations. Then, the ratio of vertical to lateral growth rates at the beginning of the growth was increased due to the higher density of surface steps, which in turn led to reduction of the mask-induced tilt of ELO wings [30.73, 74]. In the limiting case of heavily dislocated GaAs substrates, namely on GaAs buffers grown by MBE on Si substrates, the vertical growth of GaAs ELO was so fast that air-bridged structures without any interaction with the mask were obtained [30.55]. Basically the same approach has been used by *Fini et al.* [30.86]. They have shown that the crystallographic quality of coalescence of neighboring ELO GaN stripes can be improved if vertical development of ELO stripes is forced at the beginning of the growth, followed by a change

of growth conditions and fast lateral overgrowth of the structure.

If thermally activated processes during the growth itself are considered as origins of wing tilt, reduction of the ELO growth temperature might be helpful. Indeed, *Silier* with coworkers have reported negligible adhesion to the SiO₂ mask of Si ELO layers grown by LPE at 450 °C, in contrast to their previous growth experiments performed at high temperature of ≈ 900 °C [30.17]. Also replacement of commonly used dielectric films by other mask materials seems to be a promising way of reduction of mask-induced wing tilt. In particular, we have found that bending of GaAs ELO layers grown by LPE is negligible when the SiO₂ mask is replaced by a thin graphite film [30.7]. This finding has been explained by delayed beginning of lateral growth due to a change of the shape of the liquid solution in the vicinity of the ELO edge when the SiO₂ was replaced by graphite film not wetted by the gallium melt [30.73]. Similarly, tungsten has been found to be a promising mask material for MOVPE growth of GaN ELO structures with very low tilt of the wings [30.4]. In principle, however, it is difficult to predict a priori the mask material that would be the most suitable for each particular ELO case.

The most natural way to eliminate the mask-induced strain would be to grow the ELO structures with their wings having no contact with the mask surface. An example of such a GaAs structure grown by LPE was shown in Fig. 30.27. Another example is shown

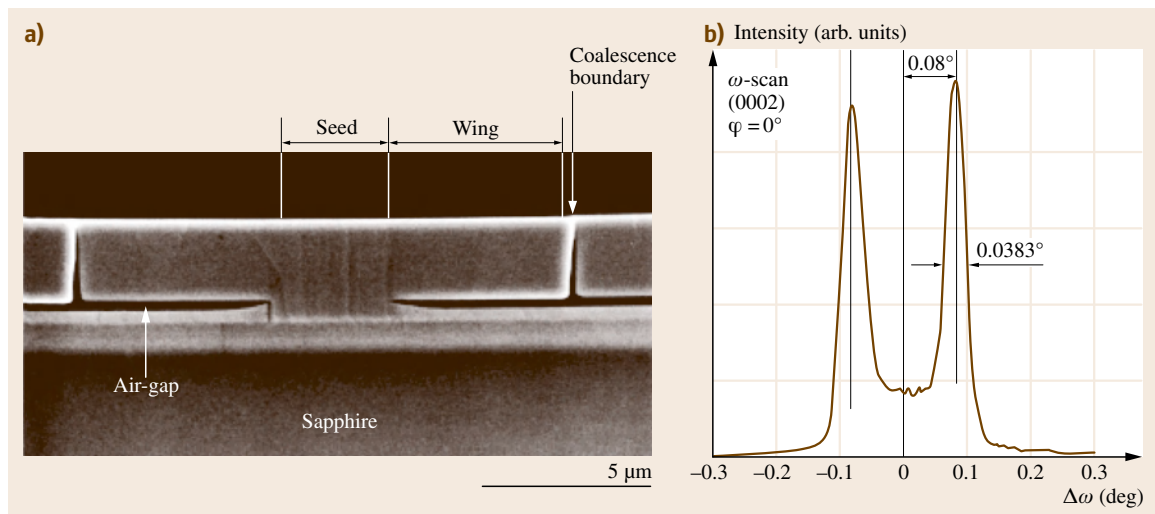


Fig. 30.32a,b Cross-sectional SEM image (a) and x-ray rocking curve measured for the scattering plane perpendicular to the seeding lines (b) of the air-bridged GaN on sapphire layers (after [30.85], © AIP 2000)

in Fig. 30.32a, which presents a cross section of air-bridged GaN layers grown by MOVPE on sapphire substrates coated by GaN buffer and silicon nitride mask [30.85]. Note that, due to profiling of the GaN buffer thickness, an air gap is formed during the growth above the mask and a free-standing laterally grown GaN is obtained. In this way, direct interaction of ELO wing with the mask is eliminated. Figure 30.32b shows the x-ray rocking curve of the layer measured with the x-ray scattering plane perpendicular to the seed direction. Two peaks originating from ELO wings are clearly visible. Each of them is much narrower than that obtained for standard GaN ELO layer (compare Fig. 30.31a), which means that the mask-induced bending of GaN wings is significantly suppressed. However, the different angular position of both peaks indicates that some residual tilt ($\approx 0.08^\circ$) of the c -axis in the wing area relative to the underlying GaN is still present. Its origin is explained in the next section.

30.4.2 Thermal Strain in ELO Layers

Besides the mask-induced strain an additional deformation of ELO lattice planes may arise when the sample experiences a large stress upon cooling from the growth to room temperature due to the different thermal expansion coefficients of its components. This effect is commonly observed in planar heterostructures. In the following we will show that in the ELO structures ther-

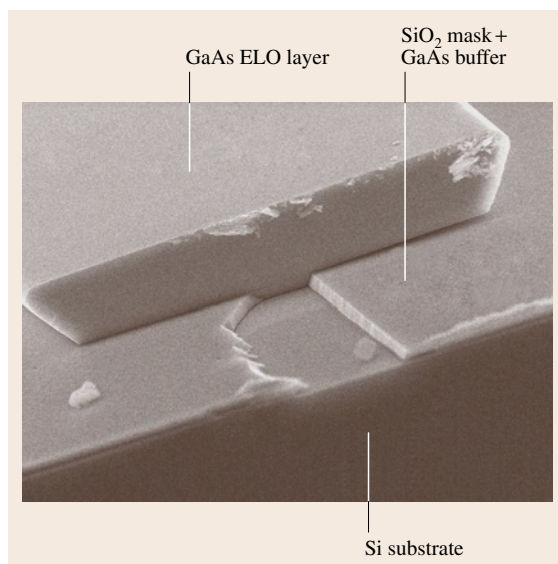


Fig. 30.33 Cross-sectional SEM image of the as-grown GaAs ELO layer on GaAs-coated Si substrate; the layer is $62\ \mu\text{m}$ wide and $9.2\ \mu\text{m}$ thick. Note that ELO wings overhang the mask

mal strain can be relaxed via additional tilting of the wings while still preserving their high quality.

Figure 30.33 shows a SEM image of a GaAs ELO layer grown by LPE on a silicon substrate coated by

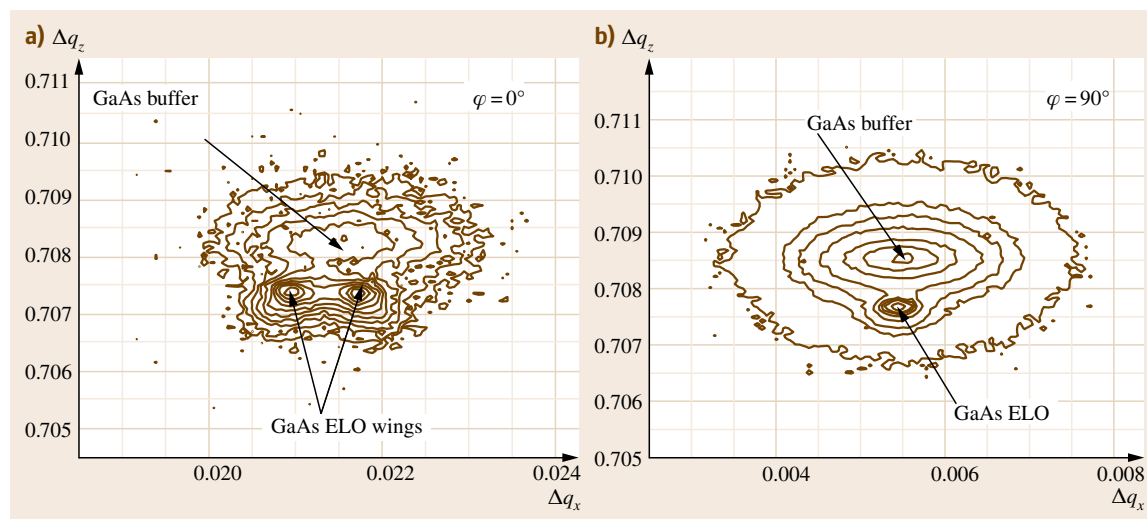


Fig. 30.34a,b Reciprocal-space map of (400) $\text{CuK}\alpha_1$ reflection of the as-grown GaAs ELO layer on GaAs-coated Si substrate measured with the scattering plane perpendicular (a) and parallel (b) to the seeding lines. Axes are marked in units of $\lambda/2d$, where λ is the wavelength of the x-rays and d is the lattice spacing

a MBE-grown GaAs buffer layer and a SiO₂ mask. The layer was grown at 540 °C and was 62 μm wide and 9.2 μm thick. More details of the growth procedure can be found in the source publication [30.55]. Note that the layer does not stick to the substrate and its wings overhang the mask surface. This is the result of a fast vertical growth rate caused by buffer dislocations supplying surface steps as discussed in the previous section. Reciprocal-space maps measured for the same sample with the x-ray scattering plane perpendicular and parallel to the seeds are presented in Fig. 30.34a,b, respectively. The broad Bragg peak from the GaAs buffer as well as narrow, well-separated reflections originating from ELO wings are clearly visible. Note that, for $\varphi = 0^\circ$, reflection from the layer consists of two peaks, whereas a single Bragg peak is visible only for $\varphi = 90^\circ$. This is a quite similar behavior to that observed for our GaAs/GaAs ELO samples (compare Fig. 30.25) and indicates tilt of ELO wings in the plane perpendicular to the direction of the seeds.

Figure 30.35 shows x-ray rocking curves of the same sample before and after etching to remove selectively the SiO₂ mask. Note that the full-width at half-maximum of the reflection from the wing equals 94 arcsec, only. This is much less than that of the MBE-grown buffer (≈ 435 arcsec) and confirms the very high structural quality of laterally overgrown parts of the layer. However, the whole curve is so wide that tilt of ELO wings caused by their interaction with underlying

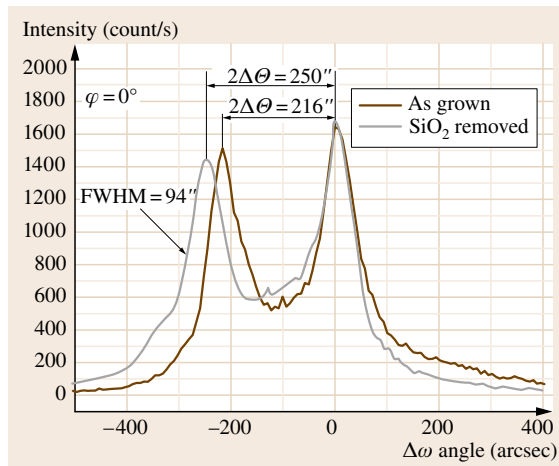


Fig. 30.35 X-ray rocking curves of (400) CuK α_1 reflection for the as-grown (solid line) and etched (dashed line) GaAs ELO layer on the SiO₂-coated Si substrate with GaAs buffer, with the x-ray scattering plane perpendicular to the direction of the seeding lines

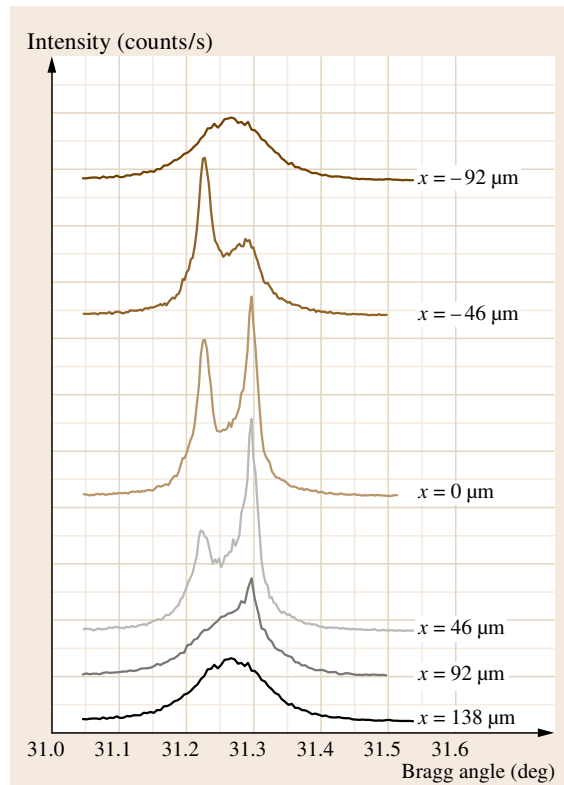


Fig. 30.36 (400) CuK α_1 rocking curves from as-grown GaAs on a Si ELO layer measured with a 90 μm-wide x-ray beam moved across the ELO stripe in 46 μm steps. The $x = -92$ and 138 μm positions correspond to reflections from the GaAs buffer outside the ELO stripe

SiO₂, similar to that presented for homoepitaxial GaAs ELO layers, might be suspected. It is worth noticing, however, that this time behavior of the system is quite different. The wing tilt angle increases when the mask is removed. Moreover, the wings hang over the mask, so the mask-induced strain, if any, should be negligible.

We have checked the direction of the tilt of the GaAs wings using the SRXRD technique described earlier (Fig. 30.29c). The set of x-ray rocking curves obtained from precisely defined areas of the GaAs stripe is shown in Fig. 30.36. The geometry of the experiment was exactly the same as before, i.e., the beam illuminated the left ELO wing first ($x = -46$ μm), then the central part of the ELO stripe ($x = 0$ μm), and finally left the sample on its right-hand side ($x = 92$ μm). Note the order in which ELO diffraction peaks appeared when the beam was illuminating subsequent parts of the stripe. The left ELO wing diffracted x-rays at smaller Bragg an-

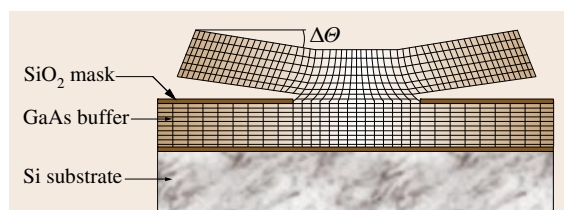


Fig. 30.37 Schematic drawing of the cross section of the as-grown GaAs ELO layer on a Si substrate. The tilt of the ELO wing is $\Delta\theta$, where $2\Delta\theta$ is the angular separation of the diffraction peaks, as marked in Fig. 30.35

gle than the right one. This is the opposite behavior to that observed for the GaAs/GaAs ELO system (compare Fig. 30.29) and indicates upward tilt of laterally overgrown parts of the layer [30.55]. All these findings indicate that processes other than wing adhesion to the mask must be involved.

We have explained the results presented above by taking into account the thermal strain that appears in the ELO structure during its postgrowth cooling to room temperature. This is illustrated in Fig. 30.37, which schematically shows deformation of lattice planes in the cross section plane of GaAs on Si ELO layer. A biaxial tensile strain caused by the different thermal contraction of epilayer and substrate is commonly observed in planar GaAs layers grown on Si substrates [30.87]. This strain disappears when the GaAs/Si structure is heated to $\approx 500^\circ\text{C}$ [30.88]. Therefore, at the LPE growth temperature, the GaAs ELO layer grows essentially stress free. At room temperature, the basal plane of ELO layer should have the same tensile deformation in the direction perpendicular to the line seed as the upper surface of the buffer GaAs. We have shown that the ELO layer stands free and does not adhere to the mask. Therefore, unrestricted strain relaxation and free contraction of vertically grown volume of ELO should take place in its upper part, as shown in Fig. 30.37. This, in turn, must lead to the upward bending of ELO wings. Note, however, that this process does not affect the structural perfection of ELO wings, and the high crystallographic

quality of laterally overgrown parts of the layer is preserved.

Finally, the shift of diffraction pattern seen in Fig. 30.35 for the etched sample should be explained. The thermal expansion coefficient of silicon oxide is much smaller than that for zincblende III–V semiconductors. Therefore, the SiO_2 film exerts a tensile stress on GaAs underneath and a compressive strain is present in oxide-free GaAs seeding windows [30.72]. In the GaAs/Si ELO system the thermal tensile strain in the GaAs seeding area exerted by the substrate is partially compensated by the mask-induced compression [30.55]. Therefore, deformation of ELO at its base, and consequently the ELO wings tilt angle, increase when the SiO_2 mask is etched away. This leads to increase of the angular separation of x-ray reflections, as shown in Fig. 30.35.

It is worth noting that our model of thermal strain relaxation in ELO layers predicts that the direction of wing tilt is correlated with the sign of the strain in the buffer. In particular, downward wings tilt should be observed if the buffer layer is under compressive thermal stress, which is usually the case for GaN ELO layers grown on SiC or sapphire substrates. This is exactly the behavior presented in Fig. 30.31 for the GaN on sapphire ELO system. At the growth temperature GaN ELO wings are tilted downward due to their interaction with the mask. Upon cooling to room temperature, the position of the wing peak increases from 1.19° to 1.36° (Fig. 30.31b), which means that an additional downward tilt induced by thermal stress has occurred. Qualitatively, the same phenomenon can be inferred from simulations via finite-element analysis of strain in ELO structures [30.89]. Most likely, the residual tilt found in GaN air-bridged structures illustrated in Fig. 30.32b might also be explained in a similar way by the thermal strain in the GaN buffer. All these examples prove that our model is correct. Moreover, they show that the phenomenon of thermal strain relaxation via tilting of ELO wings is not a specific attribute of GaAs/Si ELO structures grown by LPE but has much more general nature.

30.5 Recent Progress in Lateral Overgrowth of Semiconductor Structures

There is continuous progress in the application of the lateral overgrowth technology, and new versions of the ELO technique are being tested. In this section, we first present the recent progress made in liquid-phase ELO

growth, including new mask materials and ELO growth by the liquid-phase electroepitaxy. Then, new concepts of ELO growth will be briefly reviewed and compared with the conventional ELO technique. Liquid-phase

epitaxy of InGaAs bridge layers and pendeo-epitaxy of GaN layers from vapor and liquid phase will be used as examples.

30.5.1 Developments in Liquid-Phase ELO Growth

Recent developments in liquid-phase ELO growth include the application of novel mask materials. In particular, electrically conductive masking films are interesting since they can be used in photovoltaic and thermophotovoltaic devices as back mirrors for photon recycling and/or as buried electrical contacts. However, the main problem is to find mask material that adheres strongly to the substrate and is thermally and chemically stable to remain undamaged during the aggressive conditions of epitaxial growth. Moreover, it is of prime importance that no nucleation takes place on the mask during the growth since in ELO technique the layer should start growing exclusively from the opening in the mask.

We have applied tungsten for substrate masking in lateral overgrowth of GaAs by LPE [30.5]. Tungsten masks were already successfully used to grow GaN ELO layers on sapphire by MOVPE and dramatic reduction of strain in the layers was found when tungsten film instead of common dielectrics was used to mask the substrate [30.4]. However, MOVPE growth conditions for GaN are quite different from those for solution growth of zincblende III–V compounds, so applicability of a W mask for selective growth of GaAs by LPE has to be verified experimentally.

Figure 30.38 shows a SEM image of GaAs layer grown at 600 °C on a tungsten-masked GaAs substrate. As seen, the epitaxial growth is perfectly selective, i. e., the layer starts growing from the line seed without any nucleation of GaAs on the mask. However, the tungsten mask peels off from the substrate, which often leads to cracking of the ELO layer. This effect is attributed to a large grain size and the strain built into the metallic film sputtered onto the bare GaAs. It has been reported that the application of a AuZn wetting layer between the substrate and the tungsten film helps to reduce the tungsten grain size, and consequently leads to lower strain inside the mask [30.90]. Indeed, we have found that use of a AuZn interlayer significantly improves adhesion of the W mask to the GaAs substrate during LPE growth of GaAs and cracking of ELO layers by the mask peeling off from the substrate is avoided [30.5]. Unfortunately, sometimes a melt removal from W-masked substrate after growth was incomplete since tungsten is well wetted

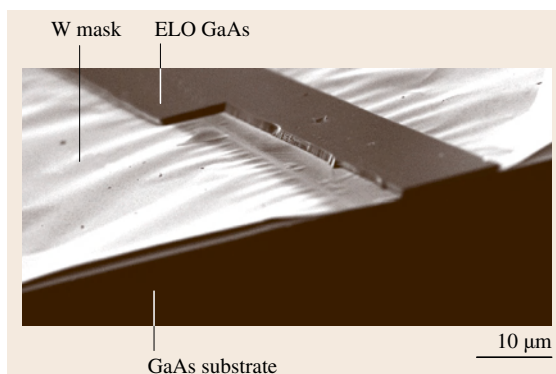


Fig. 30.38 SEM image of a GaAs ELO layer grown at 600 °C by LPE on a tungsten-masked GaAs substrate; mask deposited on bare GaAs substrate. Note that the mask peels off from the substrate, which leads to cracking of the layer

by gallium-rich solution. Consequently, local polycrystalline deposits from melt droplets left on the mask surface are often observed. This encouraged us to look for alternative mask materials.

We have found zirconium nitride films promising for electrically conductive masking in ELO technique [30.6]. This material has interesting properties resulting from its both metallic and covalent bonding characteristics. The covalent crystalline properties are: high melting point, extreme hardness and brittleness, and excellent thermal and chemical inertness. The metallic characteristics are high electrical conductivity and metallic reflectance [30.91]. Moreover, ZrN film when sputtered on a substrate usually has a fine-grained microstructure, thereby exhibiting a low strain level.

Figure 30.39 shows SEM image of a GaAs ELO layer grown at 750 °C by LPE on a ZrN-masked GaAs substrate. As seen from the figure, perfect growth selectivity is obtained. Moreover, the masking film is mechanically stable, adheres strongly to the substrate, and does not show any signs of mechanical degradation even at LPE growth temperature as high as 750 °C. A similar behavior can be seen in Fig. 30.40, which shows SEM image of a GaSb ELO layer grown at 480 °C on ZrN-masked GaSb substrate. This indicates that, due to the high stability of zirconium nitride, long time contact of the mask with Ga – As or Ga – Sb melts does not lead to degradation of its mechanical properties. Moreover, we have found that ZrN forms a low resistivity ohmic contact to n-type GaAs, which is important if the mask is to be further used as a buried electrical contact. Unfortunately, our experiments show

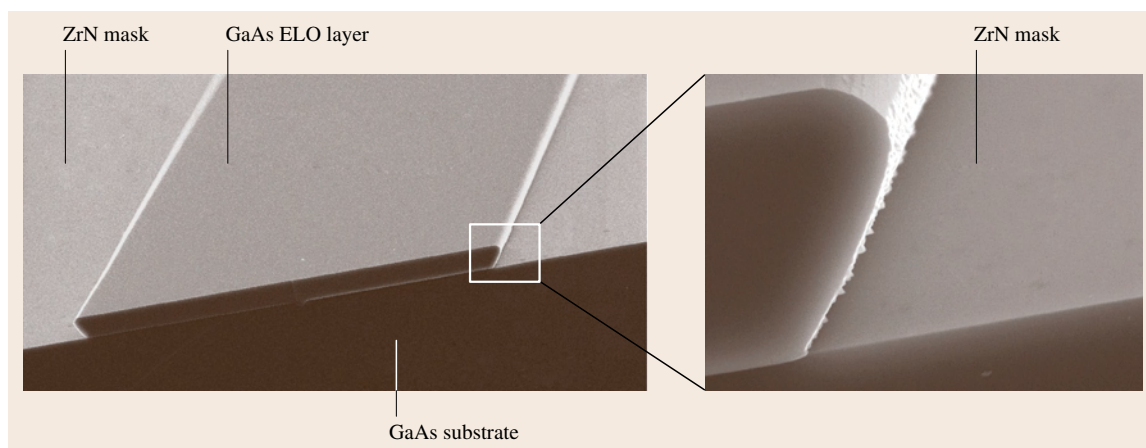


Fig. 30.39 SEM image of a GaAs ELO layer grown at 750 °C by LPE on a ZrN-masked GaAs substrate

that at temperatures higher than $\approx 580^\circ\text{C}$ the ZrN masks become highly resistive when they are heat-treated in hydrogen atmosphere during LPE growth. Most likely, ZrN is converted into insulating zirconium hydrides, though more work is needed to clarify this issue. This phenomenon sets an upper limit for LPE growth temperature if ZrN masks are to be used as electrical contacts. Thus, the ELO growth of GaAs becomes more difficult, though still possible. For ELO of GaSb layers however, typical LPE growth temperature is about 480°C , which allowed us to grow high-quality GaSb ELO layers by LPE still preserving the high electrical conductivity of the ZrN mask.

As illustrated above, a proper choice of mask material is crucial for successful lateral overgrowth. However, masks that survive undamaged during a long growth process are difficult to find if extreme crystallization conditions are required. This is the case in solution growth of GaN. Since at typical conditions solubility of nitrogen in gallium is low, very high temperatures ($\approx 1450^\circ\text{C}$) and very high nitrogen pressure ($\approx 1\text{ GPa}$) are necessary to achieve a reasonable growth rate of GaN from Ga-N solution. Bockowski et al. have found that under such conditions silicon nitride, SiO_2 , nickel, and molybdenum masks dissolve in the hot gallium while iridium reacts with Ga forming IrGa [30.92]. They have also found that tungsten platelets do not react with the Ga-N solution, so tungsten seemed to them a promising mask material for solution growth of GaN ELO layers. However this argument is not convincing enough since W films sputtered on a substrate have not been tested and other effects such as reduced chemical stability of thin films and cracking caused

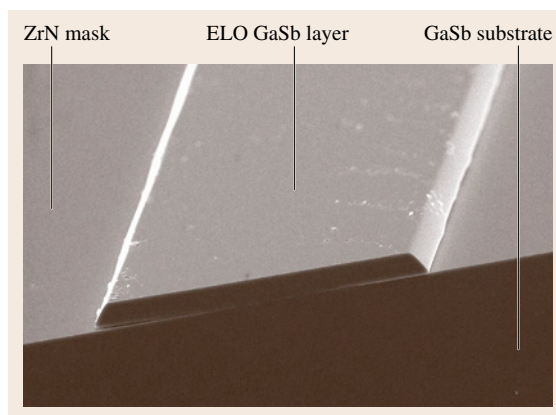


Fig. 30.40 SEM image of a GaSb ELO layer grown at 480°C by LPE on a ZrN-masked GaSb substrate

by built in strain or weak adhesion to the substrate (compare Fig. 30.38) might cause problems during ELO growth.

Recently there has been increasing interest in lateral overgrowth of semiconductor layers by the liquid-phase electroepitaxy (LPEE) technique – a solution growth method in which layer crystallization is achieved by passing an electric current through the solid–liquid interface while the furnace temperature of the system is kept constant (see [30.93] for a review). The main mechanisms of solute transport toward the substrate during LPEE are diffusion due to the Peltier-effect-induced temperature gradient and electromigration of species (i. e., momentum exchange between free charge carriers and solute species). Technical realization of LPEE is slightly more complicated than that of LPE.

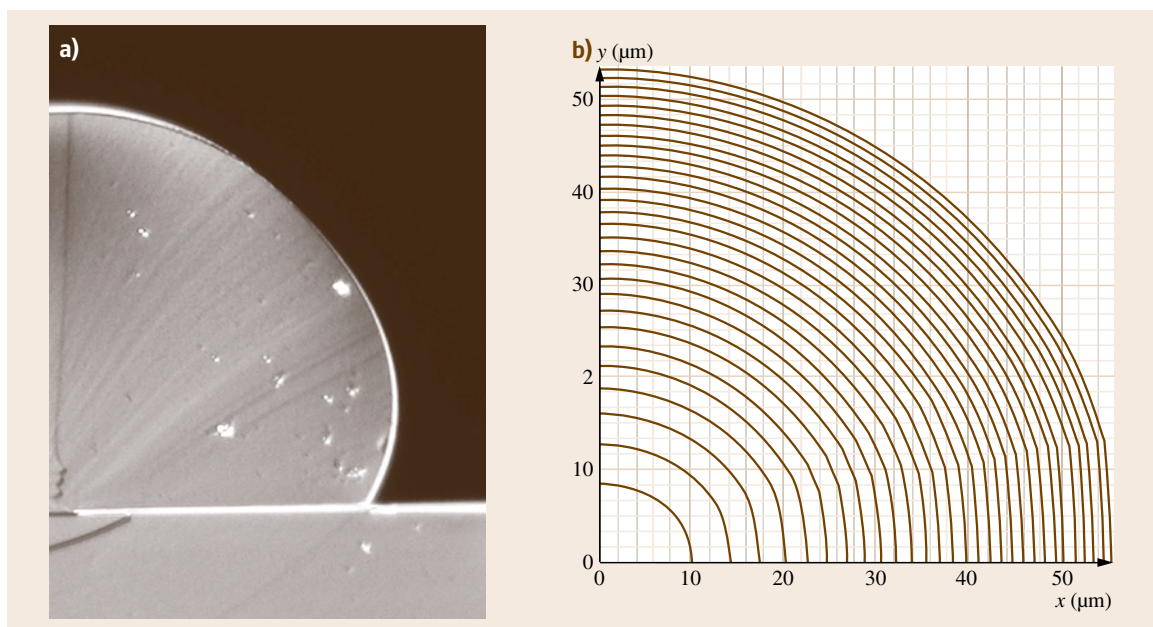


Fig. 30.41a,b SEM image of cross section (a) and calculated shape (b) of undoped GaAs ELO layer grown at 700 °C by LPEE on a SiO₂-masked GaAs substrate. The scale in both figures is the same for easier comparison. The time interval in (b) is 8 min

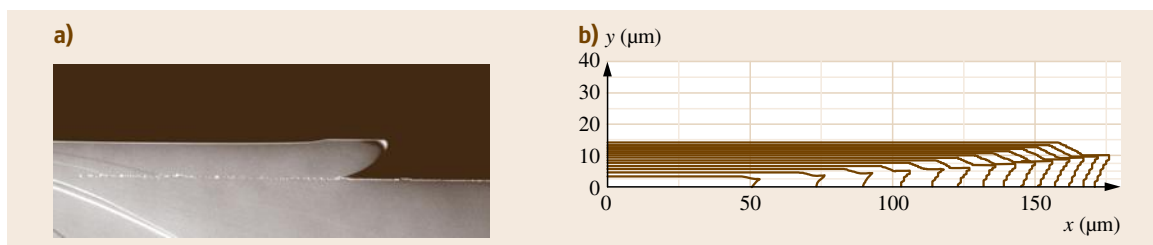


Fig. 30.42a,b SEM image of cross section (a) and calculated shape (b) of undoped GaAs ELO layer grown at 700 °C by LPEE on a GaAs substrate coated by electrically conductive (tungsten) mask. The scale in both figures is the same for easier comparison. The time interval in (b) is 16 min

However, electroepitaxy offers unique possibility to control the growth kinetics and properties of crystals produced. In particular, since the electric current flow affects the solute distribution in the liquid solution, by controlling the electrical current distribution areas with *local* supersaturation in the liquid zone can be produced, which is crucial for selective epitaxy techniques such as ELO. The progress achieved with the application of substrates coated by metallic masks has allowed a novel approach to ELO growth by LPEE.

Figures 30.41a and 30.42a show cross sections of undoped GaAs ELO layers grown at 700 °C by LPEE on (100) GaAs substrates. The difference between them

is that they were grown on substrates masked by SiO₂ and tungsten films, respectively, while the growth parameters were kept the same in both cases (see [30.5] for more details). As seen, the ELO growth on the SiO₂-masked substrate is nearly isotropic while under the same conditions a wide and thin ELO layer is grown on the tungsten-masked substrate. This means that the shape and dimensions of the ELO layers grown by LPEE can be efficiently tailored by varying the electrical conductivity of the mask.

We have developed a simple mathematical model for LPEE growth of ELO layers, which predicts the electric current intensity and solute concentration dis-

tributions in the liquid zone under various LPEE growth conditions [30.94]. Moreover, the model allows for direct simulation of the evolution of the growth interface with time. Calculated shapes of the GaAs ELO layers grown by LPEE on GaAs substrates are plotted in Figs. 30.41b and 30.42b. They are shown on the same scale as the experimental images for easier comparison. As seen, the numerical results are in very good quantitative agreement with the experimental ones. The model allows us to postulate the following mechanism for ELO growth of semiconducting layers by LPEE: During growth on substrate masked by electrically insulating film electromigration of solute towards the seed dominates growth kinetics. Since the electric current distribution in the liquid zone around the seed is isotropic, this leads to a rounded shape of layers and to a low value of their aspect ratio despite surface kinetic processes on the upper ELO surface. On the other hand, if the substrate is coated by an electrically conductive mask and the resistivity of its contact to the substrate is low, after some initial ELO growth more electric current passes to the substrate directly through the melt-mask interface than through the ELO crystal and the seeding area. Here, the main role of electromigration is to supersaturate the solution just above the mask between the adjacent seeds. Then diffusion dominates ELO growth by supplying solute from these supersaturated areas directly to side-walls of growing layers. In agreement with our experiments, this mechanism significantly increases the lateral growth rate, thereby producing thin and wide ELO layers with flat upper facets. It is worth mentioning that a similar increase in the lateral growth rate in LPEE has been reported by *Mauk* and *Curran* for ELO of silicon from Si-Bi melt [30.95].

30.5.2 New Concepts of ELO Growth

The most characteristic feature of the ELO process presented so far is the change of the predominant growth

direction – from vertical in the growth window to lateral in the regions over the masking film. In principle, however, it is possible to start lateral overgrowth from seeds oriented perpendicular to the substrate surface, so change of the growth direction is not necessary. If the substrate (bare substrate or substrate covered by a suitable buffer layer) is etched to create on its surface a pattern of ridges or elongated columns oriented similar to that of windows in ELO, conditions are provided such that the side-walls of the columns provide the crystallographic template for lateral growth.

As an example, Fig. 30.43 shows the geometry of a silicon substrate used for the LPE lateral overgrowth of Si from ridge seeds [30.17,96]. A thin SiO₂ mask has been deposited in the trenches to avoid direct epitaxy on the substrate. During LPE, the growth starts from the sidewalls of the ridges and proceeds laterally over the mask. The top surface of the ridge is the dislocation-free Si(111) facet, so it contains no step sources. Therefore, under proper growth conditions the vertical growth is completely eliminated and the layer grows laterally without any change of its thickness. As the thickness of the layer is determined by the ridge height, it can be easily controlled. However, very thin layers are difficult to obtain. When the thickness of the layer decreases the radius of curvature of its side-wall decreases as well (Fig. 30.43). This leads to an increase in the equilibrium concentration of the solute around this wall due to the Gibbs–Thomson effect (compare discussion in Sect. 30.2.2). Therefore, a higher melt supersaturation must be used to grow thinner layers. Then, however, the vertical growth may be initiated if the supersaturation is large enough for two-dimensional nucleation at the top surface of the ridge. Using this technique 18.8 μm wide and as thin as 0.23 μm, i. e., with L/h ratio up to 82, Si layers have been grown laterally upon SiO₂-coated Si substrates by LPE [30.96].

In contrast with the case of homoepitaxy, in lattice-mismatched heterostructures the top surface of the columns is not dislocation free and must be covered by an additional mask to avoid excessive vertical growth. Figure 30.44a shows schematically how this approach has been applied by *Iida* et al. to grow by LPE InGaAs bridge layers on GaAs substrates [30.21]. First, the substrate covered by the SiN mask has been processed by photolithography and etching to fabricate on its surface a pattern of deep circular trenches. Then, an In_xGa_{1-x}As ($x \approx 0.06$) layer has been grown on such substrate by LPE. It is worth noting that no InGaAs buffer is used in this case. The layer grew inwards from the side-wall of the trench, forming a bridge over the

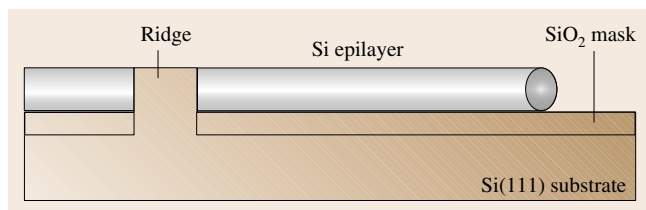


Fig. 30.43 Schematic illustration of the cross section of a Si epilayer grown by LPE on a SiO₂-masked Si substrate from a ridge seed

trench. Some growth over the mask outside the trench area was observed as well. Analysis of the layer surface revealed presence of dislocated zone with etch pits density $\approx 10^6 \text{ cm}^{-2}$ only above the small area where the layer was in direct contact with the GaAs substrate (Fig. 30.44b). The rest of the layer, having diameter above 1 mm, was of very high quality with dislocation density below 10^4 cm^{-2} (Fig. 30.44c), so it could be used as substrate for further deposition of device layers. The same authors have tested the bridge growth from maskless trenches. Then the lateral growth from the trench wall shown in Fig. 30.44a is accompanied by additional growth of InGaAs from the trench bottom. As a result, new dislocations are found in the InGaAs bridge layer at the places where the heavily dislocated material growing from the trench bottom comes in contact with the bridge. If GaAs substrates are used the presented technique allows for growth of $\text{In}_x\text{Ga}_{1-x}\text{As}$ layers with very low In concentrations ($x \approx 0.06$). For a higher indium content ($x \approx 0.20$), InAs wafer converted into InGaAs instead of GaAs has been used as the substrate [30.97]. The technology of LPE growth of bridge layers over the trenches seems to be very promising due to its simplicity, very high efficiency, and high quality of layers produced.

The method of lateral overgrowth that has received much attention recently is pendeo- (from the Latin: to hang or to be suspended from) epitaxy (PE). To grow PE GaN layers, a thin AlN wetting layer and GaN buffer are grown first on an available substrate as shown in Fig. 30.45a. Next, trenches deep enough to reach the substrate surface (or even slightly deeper) are etched in the structure. The bottoms of trenches and top surfaces of GaN columns are then covered by a suitable masking film, so the GaN column side-walls are the only surfaces exposed for subsequent GaN regrowth. During pendeo-epitaxy, the GaN layers overflow the trenches growing laterally from the column side-walls (Fig. 30.45b). Also some vertical growth takes place followed by lateral growth over the mask covering the top of GaN mesas. After sufficiently long growth time the PE layers starting from adjacent seeds merge at the fronts marked A and B in Fig. 30.45c, so a continuous PE GaN layer is formed. As mentioned earlier, dislocations thread in the GaN buffer mainly along the c -axis (i. e., perpendicular to the surface). Thus, only a very small part of them intersect the side-wall of GaN columns and propagate into the PE GaN layer. Therefore, the regrown material contains four to five orders of magnitude lower density of dislocations than that in the buffer [30.98]. Moreover, in contrast to the standard ELO case, also the disloca-

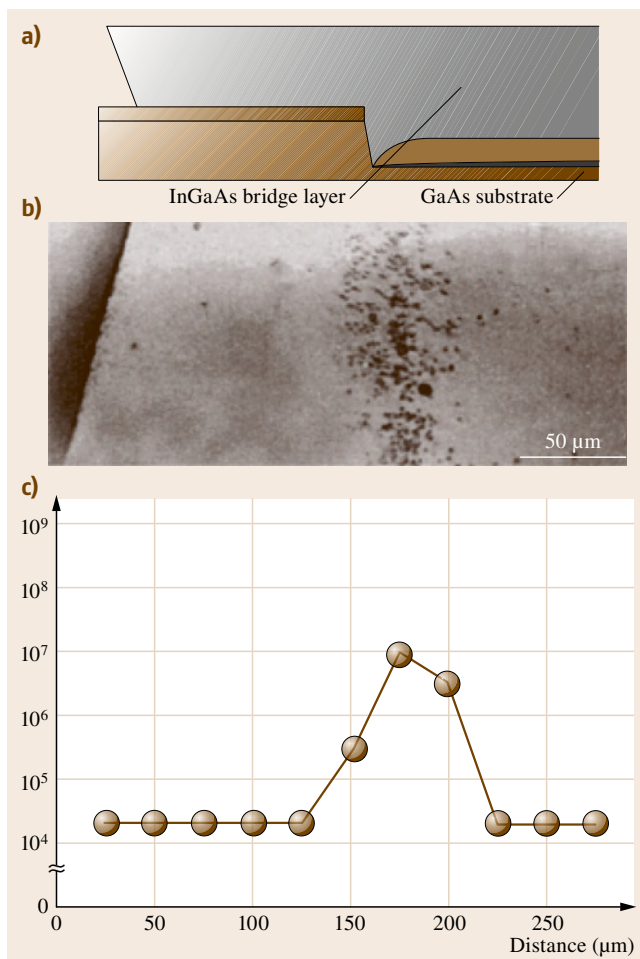


Fig. 30.44a–c Schematic illustrations of the layer cross section (a), photographs of the etched surface (b), and the profiles of etch pits density (c) in an InGaAs bridge layer grown by LPE on a SiO_2 -masked (111) GaAs substrate (courtesy of Hayakawa)

tions originally present in the buffer (marked as TDs in Fig. 30.45) are prevented from reaching the PE layer if the GaN columns are capped by the mask. Thus, in principle, the density of dislocations should be reduced over the whole area of the substrate and the need to locate devices only in the laterally overgrown parts of the structures (as was in the case of ELO; see Sect. 30.3) could be eliminated. The PE technique in its version shown in Fig. 30.45 has been used by Chen et al. to grow by MOVPE GaN layers on SiO_2 -masked sapphire substrates [30.99]. Studies of the layers with the use of transmission electron microscopy have proved that laterally overgrown parts of the layers are nearly dislo-

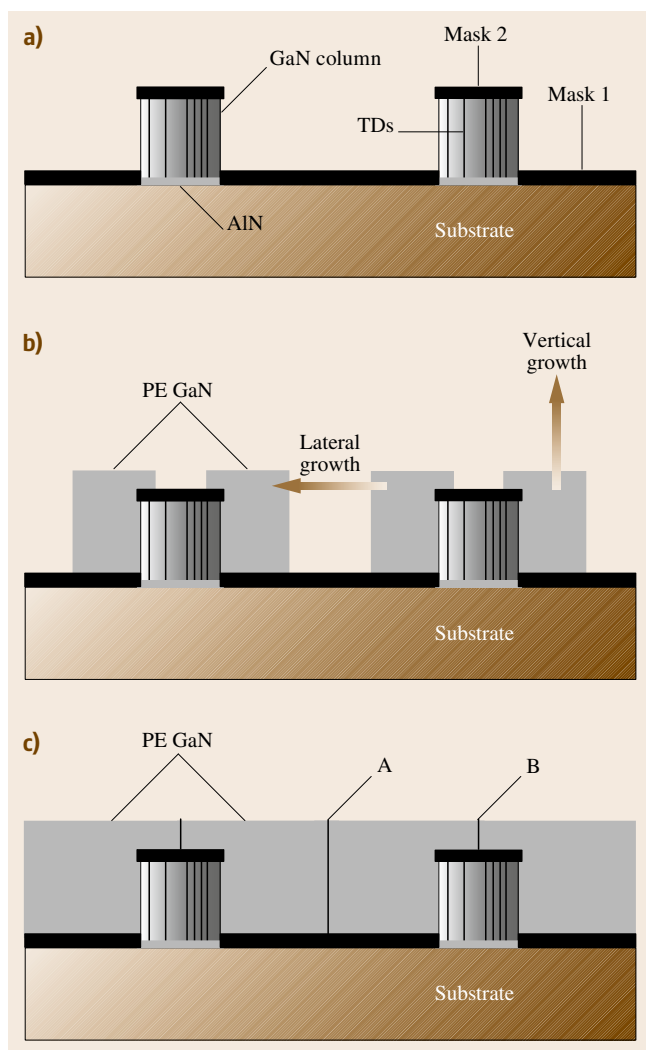


Fig. 30.45a–c Schematic of the process steps for pendeo-epitaxy of GaN: **(a)** etching of elongated columns in GaN buffer layer followed by masking of the substrate (mask 1) and the top column surfaces (mask 2); **(b)** epitaxial growth of GaN starts from exposed side-walls of GaN columns and proceeds laterally to fill the trenches; also some vertical growth occurs; **(c)** PE layers merge over the trenches (seam A) and over the capped GaN columns (seam B), so continuous PE GaN film is formed. TDs are the dislocations threading to the surface of the GaN column

cation free. However, new dislocations have been found at the fronts where the layers merge (marked A and B in Fig. 30.45c) as well as over the edges of masked GaN columns. In the light of what has been written in Sect. 30.4 above, this finding is not surprising. Most

probably, interaction of the laterally overgrown parts of the layers with the SiO_2 mask has occurred, leading to their relative misorientation and defect creation above the mask edges and at the coalescence fronts. Thus, this is the same phenomenon as we have discussed already.

These results, as well as the whole discussion in Sect. 30.4, clearly show that properties of laterally overgrown layers are strongly influenced by the presence of a mask. In particular, the strain introduced by the mask and poisoning by impurities diffusing out from the mask at high temperature have negative impact on quality of the layers. Therefore, processes are needed in which layers can be grown laterally without any masking film. It is important to note that each mask requires additional technological steps. Thus, a maskless version of selective epitaxy would result in significant simplification of the whole procedure, which is especially important if the growth process under development is to be applied on industrial scale. Zheleva et al. have found that under proper MOVPE conditions neither GaN nor free Ga accumulate on 6H-SiC (0001) surface [30.98]. Thus, pendeo-epitaxy of GaN without a mask between the GaN columns (mask 1 in Fig. 30.45) became possible by replacement of sapphire by SiC. As before, PE growth started from the side-walls of the GaN columns and proceeded laterally at some distance from the SiC surface. Transmission electron microscopy showed that neither tilting nor low-angle tilt boundaries were present at the coalescence boundary over the trench (seam A in Fig. 30.45c). However, tilting of 0.2° and defects at seam B were still found in the portion of the coalesced GaN layer that interacted with the mask covering the GaN column [30.100]. This tilt can be further eliminated if a completely mask-free PE process (i.e., without masks 1 and 2) is employed, as has been reported for GaN [30.98] and AlGaIn [30.101] on SiC systems. Then, defect-free coalescence can be obtained at both coalescence fronts [30.98]. The price paid for that, however, is enhanced vertical growth of the PE layer and free propagation into regrown GaN of threading dislocations originally present in the GaN buffer.

The next step towards commercialization of pendeo-epitaxy of GaN would be to replace SiC substrates, which are expensive and available with low diameters, by large-area silicon wafers. However, direct epitaxy of GaN on Si is difficult and usually results in polycrystalline films, most likely due to the prior formation of SiN_x film on the Si surface. Therefore, Davis et al. have employed a procedure in which Si(111) substrates

are first covered by an epitaxial film of SiC, followed by their transfer to the MOVPE system for deposition of an AlN wetting layer and a GaN buffer [30.100]. Next, they could make use of the process route elaborated earlier for PE of GaN on bulk SiC, namely, substrate etching to define GaN columns and PE regrowth. The quality of the GaN layers they obtained was quite similar to that on bulk SiC substrates. The problem, however, was the thermal stress arising due to the large difference of thermal expansion coefficients between subsequent layers, which resulted in cracking of the structures on cooling if the SiC transition layer was too thin.

As the final example of new developments in lateral overgrowth, successful liquid-phase growth of GaN layers will be briefly presented. Solution growth is preferred for ELO of GaN since supersaturation at the crystal surface can be kept lower than that during vapor-phase epitaxy. Moreover, the growth velocity along the *c*-axis of GaN is usually much smaller than in perpendicular directions [30.102], so fast lateral growth is expected if (0001)-oriented substrates are used. Unfortunately, as discussed in the Sect. 30.5.1, mask materials that survive undamaged extreme conditions of GaN growth from liquid solution are difficult to find. Therefore, for ELO of GaN Bockowski with coworkers [30.103] have used unmasked sapphire substrate with GaN ridges cut from 3 μm -thick GaN buffer grown by MOVPE (Fig. 30.46a). Basically, this is the maskless version of the substrate drawn schematically in Fig. 30.45a. Figure 30.46b shows a plane view of the epilayer grown on such substrate from Ga-N solution at 1430 $^{\circ}\text{C}$ and nitrogen pressure of 1 GPa. The GaN stripes increased their width from 20 to 60 μm and grew $\approx 20 \mu\text{m}$ high during 5 h-long crystallization. Unfortunately, simultaneous direct crystallization of GaN on unprotected sapphire took place too, so small GaN grains are visible between the stripes. These grains disturbed lateral growth by consuming solute arriving from the bulk solution. Moreover, dislocations were generated in the layer when grains came into contact with laterally grown GaN, in the similar way to that observed in InGaAs bridge layers (compare Sect. 30.5.1). As the result, quite high dislocation density of $\approx 10^6 \text{ cm}^{-2}$ was found in the GaN wing area, though it was much smaller than the $\approx 10^8 \text{ cm}^{-2}$ dislocation density in the areas above the GaN ridges. It has been expected that parasitic GaN nucleation on bare sapphire might be reduced by decreasing the distance between neighboring GaN ridges [30.92]. It is not clear if this has really happened since decrease of ridges spacing from 300 to 60 μm did

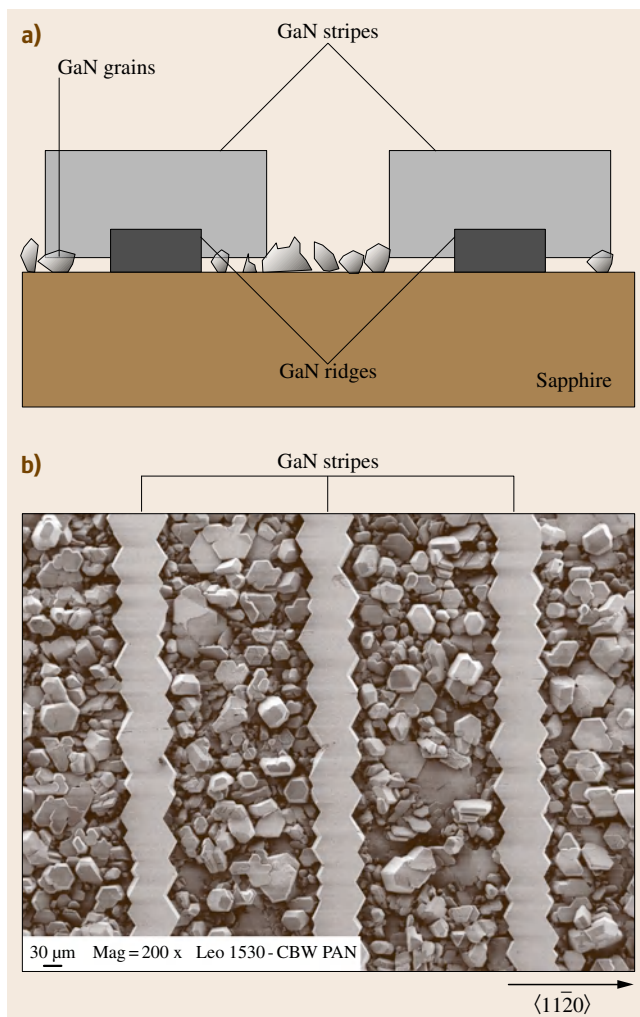


Fig. 30.46a,b Schematic cross section (not to scale) (a) and plane-view SEM image (b) of GaN layers grown from the Ga-N solution at high nitrogen pressure on sapphire substrate with 20 μm -wide 3 μm -high GaN ridges cut from 3 μm -thick MOVPE-grown GaN buffer. Spacing between the ridges was 300 μm (courtesy of Boćkowski)

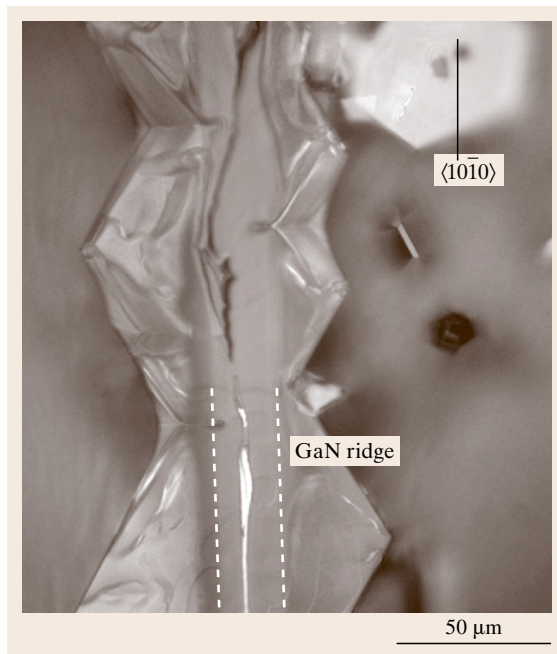
not lead to a significant reduction of dislocation density in laterally grown GaN.

Another mode of lateral growth of GaN from Ga-N solution at high nitrogen pressure was found when $\approx 800 \mu\text{m}$ -thick free-standing GaN substrate grown by HVPE was patterned to create on its surface 5–10 μm -high GaN ridges [30.104]. During GaN growth at 1425 $^{\circ}\text{C}$ and nitrogen pressure of 1 GPa some growth took place directly from the unprotected HVPE sub-

Fig. 30.47 SEM image of GaN layers grown from Ga-N solution at high nitrogen pressure on free-standing HVPE GaN substrate with 20 μm -wide 10 μm -high GaN ridges (dashed lines). Spacing between the ridges was 300 μm (courtesy of Boćkowski) ►

strate as in the previous case. However, due to the specific distribution of solution supersaturation at the substrate surface, preferential lateral overgrowth from ridge edges was also observed. A plan view of such a sample is shown in Fig. 30.47. An important finding by Bockowski et al. was that laterally overgrown parts hang over the substrate if the ridge height was increased to 10 μm . This resulted in their better crystallographic quality. Indeed, analysis of the sample by defect-selective etching has shown that ELO wing areas were dislocation free.

These initial results obtained in lateral overgrowth of GaN from high-temperature Ga-N solution at high nitrogen pressure are very promising. Note that the widths of GaN wings are much larger than those commonly obtained by vapor growth techniques. However, it seems that for further progress application of a suitable mask will be needed to avoid direct crystallization on the substrate. If such a mask is found, much wider wings with lower dislocation density could be grown. Also, im-



provement of upper surface morphology is required for free-standing layers, similar to that shown in Fig. 30.47.

30.6 Concluding Remarks

A review of epitaxial lateral overgrowth is provided. The main idea behind lateral overgrowth techniques is selective epitaxy of a homoepitaxial layer on a relaxed buffer having a required lattice parameter. The seeds can be defined by patterning of the mask covering the buffer layer (ELO) or the growth starts from the exposed side-walls of ridges etched in the buffer (PE). Selective nucleation of the layer in the narrow seeds allows information on buffer lattice spacing to pass through, while blocking all (or the main part of) defects created due to lattice misfit between the buffer and its substrate. We have shown numerous examples in which this procedure works efficiently. Usually, practical realization of the idea above depends on the system considered. Quite often specific properties of the materials and growth technique used determine the way in which laterally overgrown structures are produced (*vide* maskless pendeo-epitaxy of GaN on SiC, solution growth of GaN, etc.). There are, however, some basic phenomena typical for all laterally overgrown structures. These

include some general rules that should be followed to obtain wide and thin laterally overgrown layers (i.e., choice of optimal direction of the seeds, high quality of the buffer, low growth rate, use of doping to enhance lateral growth, etc.). Efficient filtration of dislocations originally present in the buffer is well evidenced in all laterally overgrown structures. Tilt of wings caused by their interaction with the mask underneath is commonly observed in both ELO and PE layers, independently of the growth technique used. If the tilt angle is small the accompanied strain can be accommodated elastically (e.g., in GaAs/GaAs ELOs). Otherwise, arrays of dislocations creating low-angle boundaries appear above the mask edges (e.g., in GaN ELO structures). Tilting of laterally grown parts of the layer leads to the generation of new defects at the coalescence front where two layers grown from neighboring seeds and having opposite tilt direction merge. Growing the layers standing free above the mask seems to be the best way to improve the quality of the coalescence front, although there are no gen-

eral recipes for how to grow such structures. Thermal strain due to different thermal expansion coefficients of subsequent layers is also commonly found in laterally overgrown heterostructures. However, if the layer is attached to the buffer through the narrow seeds only, this strain is usually much smaller than in reference planar structures.

It is difficult to predict future developments in the ELO technology. From a scientific point of view there are still many questions to be answered. In particular, understanding of the microscopic interaction of ELO wings with the mask, identification of mechanisms leading to bending of dislocations threading in a seed area, and many other issues require further work. Basic crystal growth research including process modeling is

needed to increase the width of laterally overgrown layers, improve the quality of coalescence fronts, develop technology for lateral overgrowth of ternary layers on binary substrates, find new mask materials, and simplify the whole growth procedure to meet industrial standards. Application of laterally overgrown layers will depend on progress in these areas. Market demands for novel semiconductor devices will decide if and which techniques of lateral epitaxy will find their permanent position in industrial practice. Nowadays there is great demand for group III nitride substrates, so lateral overgrowth of these compounds is most studied in many laboratories worldwide. It is believed that the importance of lateral overgrowth of *traditional* zincblende III–V ternary substrates will increase in the near future.

References

- 30.1 T. Kawai, H. Yonezu, Y. Ogasawara, D. Saito, K. Pak: Segregation and interdiffusion of In atoms in GaAs/InAs/GaAs heterostructures, *J. Appl. Phys.* **74**, 1770–1775 (1993)
- 30.2 N. Chand, R. People, F.A. Baiocchi, W.K. Wecht, A.Y. Cho: Significant improvement in crystalline quality of molecular beam epitaxially grown GaAs on Si (100) by rapid thermal annealing, *Appl. Phys. Lett.* **49**, 815–817 (1986)
- 30.3 N. Gopalakrishnan, K. Baskar, H. Kawanami, I. Sakata: Effects of the low temperature grown buffer layer thickness on the growth of GaAs on Si by MBE, *J. Cryst. Growth* **250**, 29–33 (2003)
- 30.4 Y. Honda, Y. Iyechika, T. Maeda, H. Miyake, K. Hiramatsu, H. Sone, N. Sawaki: Crystal orientation fluctuation of epitaxial–lateral–overgrown GaN with W mask and SiO₂ mask observed by transmission electron diffraction and x-ray rocking curves, *Jpn. J. Appl. Phys.* **38**, L1299–L1302 (1999)
- 30.5 D. Dobosz, Z.R. Zytewicz, T.T. Piotrowski, E. Kaminska, E. Papis, A. Piotrowska: Application of tungsten films for substrate masking in liquid phase epitaxial lateral overgrowth of GaAs, *Cryst. Res. Technol.* **38**, 297–301 (2003)
- 30.6 D. Dobosz, K. Golaszewska, Z.R. Zytewicz, E. Kaminska, A. Piotrowska, T.T. Piotrowski, A. Barcz, R. Jakiela: Properties of ZrN films as substrate masks in liquid phase epitaxial lateral overgrowth of compound semiconductors, *Cryst. Res. Technol.* **40**, 492–497 (2005)
- 30.7 Z.R. Zytewicz, J. Domagła, D. Dobosz, J. Bak-Misiuk: Microscopic bending of GaAs layers grown by epitaxial lateral overgrowth, *J. Appl. Phys.* **84**, 6937–6939 (1998)
- 30.8 S. Sakawa, T. Nishinaga: Effect of Si doping on epitaxial lateral overgrowth of GaAs on GaAs-coated Si substrate, *Jpn. J. Appl. Phys.* **31**, L359–L361 (1992)
- 30.9 L. Jastrzebski, J.F. Corboy, R. Soydan: Issues and problems involved in selective epitaxial growth of silicon for SOI fabrication, *J. Electrochem. Soc.* **136**, 3506–3513 (1989)
- 30.10 R. Bergmann, E. Czech, I. Silier, N. Nagel, E. Bauser, H.J. Queisser, R.P. Zingg, B. Hofflinger: MOS transistors with epitaxial Si, laterally grown over SiO₂ by liquid phase epitaxy, *Appl. Phys. A* **54**, 103–105 (1992)
- 30.11 H. Asai, S. Adachi, S. Ando, K. Oe: Lateral GaAs growth over tungsten gratings on (001) GaAs substrates by metalorganic chemical vapor deposition and applications to vertical field-effect transistors, *J. Appl. Phys.* **55**, 3868–3870 (1984)
- 30.12 J.M. Olchowik, A. Fave, B. Semmache, A. Laugier, A. Kaminski, W. Sadowski: Crystallisation of Si epitaxial lateral overgrowth layers for photovoltaic structures, *Proc. 16th Eur. Photovolt. Sol. Energy Conf.*, Vol. 2 (2000) pp. 1286–1288
- 30.13 J.J. Pak, G.W. Neudeck, A.E. Kabir, D.W. DeRoo, S.E. Staller, J.H. Logsdon: A new method of forming a thin single-crystal silicon diaphragm using merged epitaxial lateral overgrowth for sensor applications, *IEEE Electron. Dev. Lett.* **12**, 614–616 (1991)
- 30.14 G.W. Neudeck, P.J. Schubert, J.L. Glenn Jr., J.A. Friedrich, W.A. Klaasen, R.P. Zingg, J.P. Denton: Three dimensional devices fabricated by silicon epitaxial lateral overgrowth, *J. Electron. Mater.* **19**, 1111–1117 (1990)
- 30.15 R.W. McClelland, C.O. Bozler, J.C.C. Fan: A technique for producing epitaxial films on reusable substrates, *Appl. Phys. Lett.* **37**, 560–562 (1980)
- 30.16 B.-Y. Tsaur, R.W. McClelland, J.C.C. Fan, R.P. Gale, J.P. Salerno, B.A. Vojak, C.O. Bozler: Low-dislocation-density GaAs epilayers grown on Ge-coated Si substrates by means of lateral epi-

- taxial overgrowth, *Appl. Phys. Lett.* **41**, 347–349 (1982)
- 30.17 I. Silier, A. Gutjahr, N. Nagel, P.O. Hansson, E. Czech, M. Konuma, E. Bauser, F. Banhart, R. Kohler, H. Raidt, B. Jenichen: Solution growth of epitaxial semiconductor-on-insulator layers, *J. Cryst. Growth* **166**, 727–730 (1996)
- 30.18 T. Nishinaga: Epitaxial lateral overgrowth of III–V compounds for obtaining dislocation free layers, *Cryst. Prop. Prep.* **31**, 92–99 (1991)
- 30.19 P.O. Hansson, A. Gustafsson, M. Albrecht, R. Bergmann, H.P. Strunk, E. Bauser: High quality $\text{Ge}_x\text{Si}_{1-x}$ by heteroepitaxial lateral overgrowth, *J. Cryst. Growth* **121**, 790–794 (1992)
- 30.20 Z.R. Zytckiewicz: Laterally overgrown structures as substrates for lattice mismatched epitaxy, *Thin Solid Films* **412**, 64–75 (2002)
- 30.21 Y. Hayakawa, S. Iida, T. Sakurai, H. Yanagida, M. Kikuzawa, T. Koyama, M. Kumagawa: Epitaxial lateral overgrowth of InGaAs on patterned GaAs substrates by liquid phase epitaxy, *J. Cryst. Growth* **169**, 613–620 (1996)
- 30.22 S. Nakayama, M. Kaneko, S. Aizawa, K. Kashiwa, N.S. Takahashi: InGaP lattice-mismatched LPE growth on GaAs substrates by epitaxial lateral overgrowth technique, *J. Cryst. Growth* **236**, 132–136 (2002)
- 30.23 S. Nakamura, M. Senoh, S. Nagahama, N. Iwasa, T. Yamada, T. Matsushita, H. Kiyoku, Y. Sugimoto, T. Kozaki, H. Umemoto, M. Sano, K. Chocho: InGaN/GaN/AlGaIn-based laser diodes with modulation-doped strained-layer superlattices, *Jpn. J. Appl. Phys.* **36**, L1568–L1571 (1997)
- 30.24 Y.C. Liu, Z.R. Zytckiewicz, S. Dost: Computational analysis of lateral overgrowth of GaAs by liquid-phase epitaxy, *J. Cryst. Growth* **275**, e953–e957 (2005)
- 30.25 Z. Yan, S. Naritsuka, T. Nishinaga: Interface supersaturation in microchannel epitaxy of InP, *J. Cryst. Growth* **203**, 25–30 (1999)
- 30.26 Z. Yan, S. Naritsuka, T. Nishinaga: Two-dimensional numerical calculation of solute diffusion in microchannel epitaxy of InP, *J. Cryst. Growth* **209**, 1–7 (2000)
- 30.27 B. Beaumont, P. Vennegues, P. Gibart: Epitaxial lateral overgrowth of GaN, *Phys. Status Solidi (b)* **227**, 1–43 (2001)
- 30.28 R.J. Matyi, H. Shichijo, T.M. Moore, H.-L. Tsai: Microstructural characterization of patterned gallium arsenide grown on (001) silicon substrates, *Appl. Phys. Lett.* **51**, 18–20 (1987)
- 30.29 J.T. Torvik, J.I. Pankove, E. Iliopoulos, H.M. Ng, T.D. Moustakas: Optical properties of GaN grown over SiO_2 on SiC substrates by molecular beam epitaxy, *Appl. Phys. Lett.* **72**, 244–245 (1998)
- 30.30 G. Bacchin, T. Nishinaga: A new way to achieve both selective and lateral growth by molecular beam epitaxy: Low angle incidence microchannel epitaxy, *J. Cryst. Growth* **208**, 1–10 (2000)
- 30.31 S.C. Lee, K.J. Malloy, L.R. Dawson, S.R.J. Brueck: Selective growth and associated faceting and lateral overgrowth of GaAs on a nanoscale limited area bounded by a SiO_2 mask in molecular beam epitaxy, *J. Appl. Phys.* **92**, 6567–6571 (2002)
- 30.32 H. Tang, J.A. Bardwell, J.B. Webb, S. Moisa, J. Fraser, S. Rolfe: Selective growth of GaN on a SiC substrate patterned with an AlN seed layer by ammonia molecular-beam epitaxy, *Appl. Phys. Lett.* **79**, 2764–2766 (2001)
- 30.33 Z.R. Zytckiewicz: Epitaxial lateral overgrowth of GaAs: Principle and growth mechanism, *Cryst. Res. Technol.* **34**, 573–582 (1999)
- 30.34 S. Zhang, T. Nishinaga: Epitaxial lateral overgrowths of GaAs on (001) GaAs substrates by LPE: Growth behavior and mechanism, *J. Cryst. Growth* **99**, 292–296 (1990)
- 30.35 S. Naritsuka, T. Nishinaga: Epitaxial lateral overgrowth of InP by liquid phase epitaxy, *J. Cryst. Growth* **146**, 314–318 (1995)
- 30.36 R.P. Gale, R.W. McClelland, J.C.C. Fan, C.O. Bozler: Lateral epitaxial overgrowth of GaAs by organometallic chemical vapor deposition, *Appl. Phys. Lett.* **41**, 545–547 (1982)
- 30.37 J. Park, P.A. Barnes, C.C. Tin, A. Allerman: Lateral overgrowth and epitaxial lift-off of InP by halide vapor-phase epitaxy, *J. Cryst. Growth* **187**, 185–193 (1998)
- 30.38 T. Nishinaga, T. Nakano, S. Zhang: Epitaxial lateral overgrowth of GaAs by LPE, *Jpn. J. Appl. Phys.* **27**, L964–L967 (1988)
- 30.39 S. Zhang, T. Nishinaga: LPE lateral overgrowth of GaP, *Jpn. J. Appl. Phys.* **29**, 545–550 (1990)
- 30.40 R. Bergmann, E. Bauser, J.H. Werner: Defect-free epitaxial lateral overgrowth of oxidized (111) Si by liquid phase epitaxy, *Appl. Phys. Lett.* **57**, 351–353 (1990)
- 30.41 R. Bergmann: Model for defect-free epitaxial lateral overgrowth of Si over SiO_2 by liquid phase epitaxy, *J. Cryst. Growth* **110**, 823–834 (1991)
- 30.42 S. Sakawa, T. Nishinaga: Faceting of LPE GaAs grown on a misoriented Si(100) substrate, *J. Cryst. Growth* **115**, 145–149 (1991)
- 30.43 D. Dobosz, Z.R. Zytckiewicz: Epitaxial lateral overgrowth of semiconductor structures by liquid phase epitaxy, *Int. J. Mater. Prod. Technol.* **22**, 50–63 (2005)
- 30.44 F. Banhart, R. Bergmann, F. Phillipp, E. Bauser: Dislocation generation in silicon grown laterally over SiO_2 by liquid phase epitaxy, *Appl. Phys. A* **53**, 317–323 (1991)
- 30.45 Y.S. Chang, S. Naritsuka, T. Nishinaga: Optimization of growth condition for wide dislocation-free GaAs on Si substrate by microchannel epitaxy, *J. Cryst. Growth* **192**, 18–22 (1998)

- 30.46 D. Dobosz, Z.R. Zytewicz, E. Papis, E. Kaminska, A. Piotrowska: Epitaxial lateral overgrowth of GaSb layers by liquid phase epitaxy, *J. Cryst. Growth* **253**, 102–106 (2003)
- 30.47 H. Raidt, R. Kohler, F. Banhart, B. Jenichen, A. Gutjahr, M. Konuma, I. Silier, E. Bauser: Adhesion in growth of defect-free silicon over silicon oxide, *J. Appl. Phys.* **80**, 4101–4107 (1996)
- 30.48 Z.R. Zytewicz, D. Dobosz, Y.C. Liu, S. Dost: Recent progress in lateral overgrowth of semiconductor structures from the liquid phase, *Cryst. Res. Technol.* **40**, 321–328 (2005)
- 30.49 Z.R. Zytewicz, D. Dobosz, M. Pawlowska: Epitaxial lateral overgrowth of GaAs: Effect of doping on LPE growth behaviour, *Semicond. Sci. Technol.* **14**, 465–469 (1999)
- 30.50 J.C. Brice: *The Growth of Crystals from Liquids* (North-Holland, Amsterdam 1973)
- 30.51 M. Ohara, R.C. Reid: *Modelling Crystal Growth Rates from Solution* (Prentice-Hall, Englewood Cliffs 1973)
- 30.52 W.J.P. van Enckevort, A.C.J.F. van den Berg: Impurity blocking of crystal growth: a Monte Carlo study, *J. Cryst. Growth* **183**, 441–455 (1998)
- 30.53 D.-K. Kim, B.-T. Lee: Heteroepitaxial growth of GaAs on (100) GaAs and InP by selective liquid phase epitaxy, *Jpn. J. Appl. Phys.* **33**, 5870–5874 (1994)
- 30.54 B. Beaumont, S. Haffouz, P. Gibart: Magnesium induced changes in the selective growth of GaN by metalorganic vapor phase epitaxy, *Appl. Phys. Lett.* **72**, 921–923 (1998)
- 30.55 Z.R. Zytewicz, J. Domagala: Thermal strain in GaAs layers grown by epitaxial lateral overgrowth on Si substrates, *Appl. Phys. Lett.* **75**, 2749–2751 (1999)
- 30.56 T. Nishinaga: Microchannel epitaxy: an overview, *J. Cryst. Growth* **237–239**, 1410–1417 (2002)
- 30.57 A. Sakai, H. Sunakawa, A. Usui: Transmission electron microscopy of defects in GaN films formed by epitaxial lateral overgrowth, *Appl. Phys. Lett.* **73**, 481–483 (1998)
- 30.58 A. Sakai, H. Sunakawa, A. Usui: Defect structure in selectively grown GaN films with low threading dislocation density, *Appl. Phys. Lett.* **71**, 2259–2261 (1997)
- 30.59 Z. Yu, M.A.L. Johnson, T. McNulty, J.D. Brown, J.W. Cook, J.F. Schetzina: Study of the epitaxial lateral overgrowth (ELO) process for GaN on sapphire using scanning electron microscopy and monochromatic cathodoluminescence, *MRS Internet J. Nitride Semicond. Res.* **3**, 6 (1998)
- 30.60 A. Gustafsson, P.O. Hansson, E. Bauser: Cathodoluminescence from relaxed $\text{Ge}_x\text{Si}_{1-x}$ grown by heteroepitaxial lateral overgrowth, *J. Cryst. Growth* **141**, 363–370 (1994)
- 30.61 Z.I. Kazi, P. Thilakan, T. Egawa, M. Umeno, T. Jimbo: Realization of GaAs/AlGaAs lasers on Si substrates using epitaxial lateral overgrowth by metalorganic chemical vapor deposition, *Jpn. J. Appl. Phys., Part 1* **40**, 4903–4906 (2001)
- 30.62 P. Kozodoy, J.P. Ibbetson, H. Marchand, P.T. Fini, S. Keller, J.S. Speck, S.P. DenBaars, U.K. Mishra: Electrical characterization of GaN p-n junctions with and without threading dislocations, *Appl. Phys. Lett.* **73**, 975–977 (1998)
- 30.63 T. Mukai, K. Takekawa, S. Nakamura: InGaN-based blue light-emitting diodes grown on epitaxially laterally overgrown GaN substrates, *Jpn. J. Appl. Phys., Part 2* **37**, L839–L841 (1998)
- 30.64 C. Sasaoka, H. Sunakawa, A. Kimura, M. Nido, A. Usui, A. Sakai: High-quality InGaN MQW on low-dislocation-density GaN substrate grown by hydride vapor-phase epitaxy, *J. Cryst. Growth* **189/190**, 61–66 (1998)
- 30.65 G. Parish, S. Keller, P. Kozodoy, J.P. Ibbetson, H. Marchand, P.T. Fini, S.B. Fleischer, S.P. DenBaars, U.K. Mishra, E.J. Tarsa: High-performance (Al,Ga)N-based solar-blind ultraviolet p-i-n detectors on laterally epitaxially overgrown GaN, *Appl. Phys. Lett.* **75**, 247–249 (1999)
- 30.66 Z.R. Zytewicz, J.Z. Domagala, D. Dobosz, L. Dobaczewski, A. Rocher, C. Clement, J. Crestou: Tilt and dislocations in epitaxial laterally overgrown GaAs layers, *J. Appl. Phys.* **101**, 013508 (2007)
- 30.67 N. Nagel, F. Banhart, E. Czech, I. Silier, F. Phillipp, E. Bauser: The coalescence of silicon layers grown over SiO_2 by liquid-phase epitaxy, *Appl. Phys. A* **57**, 249–254 (1993)
- 30.68 F. Banhart, N. Nagel, F. Phillipp, E. Czech, I. Silier, E. Bauser: The coalescence of silicon layers grown over SiO_2 by liquid-phase epitaxy, *Appl. Phys. A* **57**, 441–448 (1993)
- 30.69 W. Huang, T. Nishinaga, S. Naritsuka: Microchannel epitaxy of GaAs from parallel and nonparallel seeds, *Jpn. J. Appl. Phys.* **40**, 5373–5376 (2001)
- 30.70 Z. Yan, Y. Hamaoka, S. Naritsuka, T. Nishinaga: Coalescence in microchannel epitaxy of InP, *J. Cryst. Growth* **212**, 1–10 (2000)
- 30.71 Y.-C. Shih, J.-C. Lou, W.O. Oldham: Seam line defects in silicon-on-insulator by merged epitaxial lateral overgrowth, *Appl. Phys. Lett.* **65**, 1638–1640 (1994)
- 30.72 Z.R. Zytewicz, J. Domagala, D. Dobosz, J. Bak-Misiuk: Strain in GaAs layers grown by liquid phase epitaxial lateral overgrowth, *J. Appl. Phys.* **86**, 1965–1969 (1999)
- 30.73 Z.R. Zytewicz, J. Domagala, D. Dobosz: Control of adhesion to the mask of epitaxial laterally overgrown GaAs layers, *J. Appl. Phys.* **90**, 6140–6144 (2001)
- 30.74 Z.R. Zytewicz, J. Domagala, D. Dobosz: Mask-induced strain in GaAs layers grown by liquid phase epitaxial lateral overgrowth, *Mater. Res. Soc. Symp. Proc.* **570**, 273–278 (1999)
- 30.75 J.Z. Domagala, A. Czyzak, Z.R. Zytewicz: Imaging of strain in laterally overgrown GaAs layers by spatially resolved x-ray diffraction, *Appl. Phys. Lett.* **90**, 241904 (2007)

- 30.76 I.-H. Kim, C. Sone, O.-H. Nam, Y.-J. Park, T. Kim: Crystal tilting in GaN grown by pendeoepitaxy method on sapphire substrate, *Appl. Phys. Lett.* **75**, 4109–4111 (1999)
- 30.77 D. Lubbert, T. Baumbach, P. Mikulik, P. Pernot, L. Helfen, R. Kohler, T.M. Katona, S. Keller, S.P. DenBaars: Local wing tilt analysis of laterally overgrown GaN by x-ray rocking curve imaging, *J. Phys. D Appl. Phys.* **38**, A50–A54 (2005)
- 30.78 R. Rantamaki, T. Tuomi, Z.R. Zytkeiwicz, J. Domagala, P.J. McNally, A.N. Danilewsky: Synchrotron x-ray topographic and high-resolution diffraction analysis of mask-induced strain in epitaxial laterally overgrown GaAs layers, *J. Appl. Phys.* **86**, 4298–4303 (1999)
- 30.79 R. Rantamaki, T. Tuomi, Z.R. Zytkeiwicz, J. Domagala, P.J. McNally, A.N. Danilewsky: Comparative analysis of synchrotron x-ray transmission and reflection topography techniques applied to epitaxial laterally overgrown GaAs layers, *J. X-ray Sci. Technol.* **8**, 277–288 (2000)
- 30.80 P. Fini, H. Marchand, J.P. Ibbetson, S.P. DenBaars, U.K. Mishra, J.S. Speck: Determination of tilt in the lateral epitaxial overgrowth of GaN using x-ray diffraction, *J. Cryst. Growth* **209**, 581–590 (2000)
- 30.81 M.H. Kim, Y. Choi, J. Yi, M. Yang, J. Jeon, S. Khym, S.J. Leem: Reduction in crystallographic tilting of lateral epitaxial overgrown GaN by removal of oxide mask, *Appl. Phys. Lett.* **79**, 1619–1621 (2001)
- 30.82 K. Hiramatsu, H. Matsushima, T. Shibata, Y. Kawaguchi, N. Sawaki: Selective area growth and epitaxial lateral overgrowth of GaN by metalorganic vapor phase epitaxy and hydride vapor phase epitaxy, *Mater. Sci. Eng. B* **59**, 104–111 (1999)
- 30.83 P. Fini, A. Munkholm, C. Thompson, G.B. Stephenson, J.A. Eastman, M.V. Ramana Murthy, O. Auciello, L. Zhao, S.P. DenBaars, J.S. Speck: In situ, real-time measurement of wing tilt during lateral epitaxial overgrowth of GaN, *Appl. Phys. Lett.* **76**, 3893–3895 (2000)
- 30.84 R. Kohler, B. Jenichen, H. Raidt, E. Bauser, N. Nagel: Vertical stress in liquid-phase epitaxy Si layers on SiO₂/Si evaluated by x-ray double-crystal topography, *J. Phys. D Appl. Phys.* **28**, A50–A55 (1995)
- 30.85 I. Kidoguch, A. Ishibashi, G. Sugahara, Y. Ban: Air-bridged lateral epitaxial overgrowth of GaN thin films, *Appl. Phys. Lett.* **76**, 3768–3770 (2000)
- 30.86 P. Fini, L. Zhao, B. Morgan, M. Hansen, H. Marchand, J.P. Ibbetson, S.P. DenBaars, U.K. Mishra, J.S. Speck: High-quality coalescence of laterally overgrown GaN stripes on GaN/sapphire seed layers, *Appl. Phys. Lett.* **75**, 1706–1708 (1999)
- 30.87 S.F. Fang, K. Adomi, S. Iyer, H. Morkoc, H. Zabel, C. Choi, N. Otsuka: Gallium arsenide and other compound semiconductors on silicon, *J. Appl. Phys.* **68**, R31–R58 (1990), and references therein
- 30.88 N. Lucas, H. Zabel, H. Morkoc, H. Unlu: Anisotropy of thermal expansion of GaAs on Si(001), *Appl. Phys. Lett.* **52**, 2117–2119 (1988)
- 30.89 T.S. Zheleva, W.M. Asmawi, K.A. Jones: Pendeo-epitaxy versus lateral epitaxial overgrowth of GaN: A comparative study via finite element analysis, *Phys. Status Solidi (a)* **176**, 545–551 (1999)
- 30.90 E. Kaminska, A. Piotrowska, E. Mizera, M. Guziewicz, A. Barcz, E. Dynowska, S. Kwiatkowski: Rapid thermal nitridation of tungsten-capped shallow ohmic contacts to GaAs, *Mater. Res. Soc. Symp. Proc.* **337**, 349–354 (1994)
- 30.91 L.E. Toth: *Transition Metals Carbides and Nitrides* (Academic, New York 1971)
- 30.92 M. Boćkowski, I. Grzegory, G. Nowak, G. Kamler, B. Łuczniak, M. Wróblewski, P. Kwiatkowski, K. Jasik, S. Krukowski, S. Porowski: Growth of GaN on patterned GaN/sapphire substrates with various metallic masks by high pressure solution method, *Proc. SPIE* **6121**, 612103–1–612103–9 (2006)
- 30.93 T. Bryskiewicz: Liquid phase electroepitaxy of semiconductor compounds, *Prog. Cryst. Growth Charact.* **12**, 29–43 (1986), and references therein
- 30.94 Y.C. Liu, Z.R. Zytkeiwicz, S. Dost: A model for epitaxial lateral overgrowth of GaAs by liquid-phase electroepitaxy, *J. Cryst. Growth* **265**, 341–350 (2004)
- 30.95 M.G. Mauk, J.P. Curran: Electro-epitaxial lateral overgrowth of silicon from liquid-metal solutions, *J. Cryst. Growth* **225**, 348–353 (2001)
- 30.96 Y. Suzuki, T. Nishinaga: Si LPE lateral overgrowth from a ridge seed, *Jpn. J. Appl. Phys.* **29**, 2685–2689 (1990)
- 30.97 K. Balakrishnan, S. Iida, M. Kumagawa, Y. Hayakawa: A novel method to grow high quality In_{1-x}Ga_xAs ELO and bridge layers with high indium compositions, *J. Cryst. Growth* **237–239**, 1525–1530 (2002)
- 30.98 T.S. Zheleva, S.A. Smith, D.B. Thomson, K.J. Linthicum, P. Rajagopal, R.F. Davis: Pendeoepitaxy: A new approach for lateral growth of gallium nitride films, *J. Electron. Mater.* **28**, L5–L8 (1999)
- 30.99 Y. Chen, R. Schneider, S.Y. Wang, R.S. Kern, C.H. Chen, C.P. Kou: Dislocation reduction in GaN thin films via lateral overgrowth from trenches, *Appl. Phys. Lett.* **75**, 2062–2063 (1999)
- 30.100 R.F. Davis, T. Gehrke, K.J. Linthicum, E. Preble, P. Rajagopal, C. Ronning, C. Zorman, M. Mehregany: Conventional and pendeo-epitaxial growth of GaN(0001) thin films on Si(111) substrates, *J. Cryst. Growth* **231**, 335–341 (2001)
- 30.101 R.F. Davis, T. Gehrke, K.J. Linthicum, T.S. Zheleva, E.A. Preble, P. Rajagopal, C.A. Zorman, M. Mehregany: Pendeo-epitaxial growth of thin films of gallium nitride and related materials and their

- characterization, *J. Cryst. Growth* **225**, 134–140 (2001)
- 30.102 I. Grzegory: High pressure growth of bulk GaN from solutions in gallium, *J. Phys. Condens. Matter* **13**, 6875–6892 (2001)
- 30.103 M. Boćkowski, I. Grzegory, J. Borysiuk, G. Kamler, B. Łuczniak, M. Wróblewski, P. Kwiatkowski, K. Jasik, S. Krukowski, S. Porowski: Growth of GaN on patterned GaN/sapphire substrates by high pressure solution method, *J. Cryst. Growth* **281**, 11–16 (2005)
- 30.104 M. Boćkowski, I. Grzegory, G. Nowak, B. Łuczniak, B. Pastuszka, G. Klamer, M. Wróblewski, P. Kwiatkowski, K. Jasik, W. Wawer, S. Krukowski, S. Porowski: Growth of GaN on patterned thick HVPE free standing GaN substrates by high pressure solution method, *Phys. Status Solidi (c)* **3**, 1487–1490 (2006)

31. Liquid-Phase Epitaxy of Advanced Materials

Christine F. Klemenz Rivenbark

The performance of many electronic and optoelectronic devices critically depends on the structural quality and homogeneity of the base material, which is often an epitaxial film grown by either vapor-phase epitaxy (VPE) or liquid-phase epitaxy (LPE).

This chapter presents the state of the art in LPE growth of selected advanced materials:

1. High-temperature superconductors
2. Calcium gallium germanates (langasite-type materials)
3. III-V wide-bandgap nitrides.

It is not the aim, herein, to present LPE growth of more *traditional* III-V semiconductors (Si, Ge, GaAs, GaP, InP, GaP) and garnets, which have already been described extensively in the literature since about 1960. Instead, some of the most relevant literature references are given in the historical overview, which also provides a very good insight into the potential of LPE growth of newer materials. Despite the fact that LPE growth has gained less attention over the past decades, mainly due to the development of VPE growth techniques, there is a silver lining which clearly indicates that the highest-quality epitaxial films, for most efficient electronic and optoelectronic devices, will ultimately be achieved from liquid-assisted or LPE-grown films.

31.1	Historical Development of LPE	1042
31.2	Fundamentals of LPE and Solution Growth	1042
31.3	Requirements for Liquid-Phase Epitaxy ..	1044
31.4	Developing New Materials: On the Choice of the Epitaxial Deposition Method	1044
31.5	LPE of High-Temperature Superconductors ...	1046
31.5.1	Phase Relations, Solvent System, and Solubility Curves	1046
31.5.2	Heat of Solution	1048
31.5.3	Supersaturation and Driving Force for LPE.....	1048
31.5.4	Substrates and Epitaxial Relationship	1049
31.5.5	LPE Growth System and Film Growth Procedure	1051
31.5.6	Growth Mechanisms and Growth Parameters: Theory Versus Experiment.....	1052
31.6	LPE of Calcium Gallium Germanates	1055
31.6.1	Solvent System.....	1055
31.6.2	Substrates for Homoepitaxial LGT LPE Film Growth	1056
31.6.3	LPE growth of LGS, LGT, and LGN.....	1057
31.6.4	Structural and Chemical Characterization of Doped LGT LPE Films.....	1057
31.7	Liquid-Phase Epitaxy of Nitrides	1059
31.7.1	Developments and Trends in LPE of GaN and AlN	1060
31.7.2	Substrates for Epitaxy of Nitrides....	1061
31.7.3	Growth System and Optimization ...	1062
31.7.4	Morphological Evolution of LPE-Grown Nitride Films.....	1062
31.8	Conclusions	1063
	References	1064

Liquid-phase epitaxy (LPE) is a growth process where a film of crystalline material is deposited from a supersaturated solution onto a single-crystal substrate. This

method was first described by *Nelson* in 1963 [31.1], who used a tipping LPE apparatus for the fabrication of GaAs laser diodes. Since then, the LPE tech-

nique has been widely investigated and applied to a variety of materials, among others II–V and III–

V semiconductors, carbides, nitrides, and a variety of oxides.

31.1 Historical Development of LPE

Liquid-phase epitaxy has traditionally been the optimal method of choice for the synthesis of highest-quality material. However, this method present also challenges. Today, more *flexible* vapor growth techniques are generally preferred, especially when film defects are not a limiting factor for a given device application.

The potential of LPE to yield low-defect material has been documented in many instances, following the path of the development of technologically important materials. In LPE, the driving force (or supersaturation) for epitaxy is very low. Hence, growth occurs near to thermodynamic equilibrium. The atoms can migrate efficiently on the growing surface until they find the most energetically favorable position where they will incorporate. If supersaturation and other requirements are sufficiently met, the LPE growth process may result in single-crystalline films with very high homogeneity and purity. This was best demonstrated with the development of light-emitting diodes (LEDs), with compound semiconductors such as GaAs [31.2] and GaP [31.3]. Films grown by LPE contain inherently a very low concentration of point defects, which is often orders of magnitude lower than material grown by any other growth technique. Most relevant evidence is found in the research and development of green GaP LEDs. Due to an extremely low concentration of nonstoichiometric point defects in GaP LPE films, even at room temperature, the dominant emission transition mechanism is free exciton recombination. This enables a highly efficient nitrogen-free pure-green light emission (550 nm) [31.4] that cannot be obtained from GaP produced by other growth techniques.

As early as in 1974, studies on selective LPE growth of GaAlAs led to the discovery of the epitaxial lateral overgrowth (ELO) technique [31.5]. The combination of ELO and LPE [31.6] enabled dislocation-free films of many semiconductors, such as Si, GaAs, GaP, GaAs/Si, and InP [31.7–10]. In view of this, one may wonder why LPE growth is only marginally studied today. For example, research on wide-bandgap nitride semiconductors could highly profit from dislocation-free LPE films to be used as substrates. Often, the potential of a growth technique is evaluated from its commercialization perspective. Without contest, the broadest commercialization to report for films grown by LPE resides in the field of optoelectronic devices. Even today, the highest-efficiency red GaAs LEDs are commercially produced by LPE. Films grown by LPE are also used in other applications, such as γ -ray [31.11] and high-end infrared (IR) detectors based on CdHgTe/CdTe [31.12], for example, where low-defect films are required.

The LPE growth technique has been applied to oxides as early as 1968 by Linares [31.13], who was able to demonstrate high-quality yttrium iron garnet (YIG) films for the first time. Different magnetic garnet compositions were studied for their use in bubble domain devices, and this led to extensive studies on many fundamental and experimental aspects of LPE of oxides, including the development of different LPE growth techniques, which are summarized in excellent review papers [31.14–16]. The LPE growth method has been successfully applied for the growth of many oxides, among which one can also cite high-temperature superconductors (HTSCs), optical, nonlinear optical, and electrooptical materials, and ferroelectric and dielectric materials.

31.2 Fundamentals of LPE and Solution Growth

The fundamental mechanisms for LPE growth are similar to the growth of free-standing crystals from a solution (or flux), or to the growth of larger crystals by top-seeded solution growth (TSSG). Usually, the same solution can be used for the three methods. In growth

from solutions, a supersaturation is created either by cooling or by solvent evaporation of the saturated solution. Another method that can be used is the transport of the growth species through a temperature gradient in the solution. In each case, the growth is controlled by the

diffusion of growth species towards the growing interface and the counterdiffusion of solvent species towards the bulk of the solution.

In the initial stages of crystallization from solutions, some degree of supersaturation, or driving force, has to be established for nucleation to take place. A crystal can only develop once a nuclei has reached a critical size and thus is stable. In the phase diagram, the region between the liquidus temperature and the temperature at which nucleation proceeds spontaneously is called the metastable or Ostwald–Miers region. Within this region, heteronucleation is possible, for example, on the crucible, on a substrate or seed, or on an impurity. The width of the metastable region can vary greatly for different solvent–solute systems. It depends on many factors, such as the nature and complexity (number of components) of the crystallizing material, the viscosity of the solution, additives/dopants, and hydrodynamic flows. For oxides, undercoolings up to 150 °C are possible [31.17], whereas metallic semiconductor solutions allow only a few degrees or less of undercooling. When a seed or a substrate is used, the initial supersaturation required for crystallization is less than that required for spontaneous and free nucleation in the solution. This means that, in LPE, nucleation starts within a range between the liquidus temperature and the temperature for spontaneous homogeneous nucleation.

The relative supersaturation is expressed by

$$\sigma = \frac{x - x_e}{x_e}, \quad (31.1)$$

where x and x_e represent the actual and equilibrium concentration of the solution.

The undercooling $\Delta T = T_e - T$ is related to the respective concentrations through the specific phase diagram of the system considered.

During the LPE film growth, a boundary layer of thickness δ is created at the growth front, in which a temperature and a concentration gradient exist. At the growth interface, two processes are determining: hydrodynamic flow and diffusion. For mass transport, flow is far more effective than diffusion. However, the growth is governed by the slowest process. In addition, the hydrodynamic flow decreases from the bulk of the solution to become negligible at the growth interface. Thus, at the growing interface, within the boundary layer, the process is solely controlled by diffusion, and the thickness of the boundary layer will be determined by the hydrodynamic flow. As a consequence, for a given system at a given supersaturation, the thickness of the

boundary layer will ultimately determine the growth rate, which in turn can be adjusted through the substrate rotation rate.

In the case of LPE growth, for systems with relatively large Schmidt number ($Sc = \nu/D$), the thickness of the diffusion boundary layer on the rotating substrate interface can be estimated from

$$\delta = 1.61 \left(\frac{\nu}{\omega} \right)^{1/2} \left(\frac{D}{\nu} \right)^{-1/3}, \quad (31.2)$$

where ν is the kinematic viscosity, ω is the rotation rate of the substrate, and D is the diffusion coefficient of the solute [31.18].

In LPE, the growth rate will not only be determined by the mass transport process of the growth species to the growing interface, but also by the incorporation of the solute atoms on the growing surface. Thus, supersaturation and surface kinetics should both be considered, and *Ghez* and *Giess* [31.19] developed a model for the growth of garnets that includes surface kinetic terms. However, in most growth rate studies, it is generally assumed that surface diffusion can be neglected [31.20]. For supersaturations σ below a critical value σ_c , the dependence between growth rate and supersaturation is quadratic, with $r \sim \sigma^2$ for $\sigma < \sigma_c$, and linear above, with $r \sim \sigma$ for $\sigma > \sigma_c$. High growth rates can be achieved when a continuous source of steps is present on the growing surface, for example, when growth spirals are present [31.20, 21].

In solution growth or LPE of complex crystals, the solute usually has a different composition than the solution, and the tendency for the incorporation of specific growth species in the growing crystals is expressed by the distribution coefficient k . The equilibrium distribution coefficient k_0 can be determined from the phase diagram. The effective distribution coefficient describes the concentration ratio between an element in the solution and in the crystal, as $k_{\text{eff}} = c_{\text{crystal}}/c_{\text{solution}}$. The relation describing the dependence of the effective segregation coefficient on the diffusion boundary layer δ and growth rate r has been derived by *Burton* et al. [31.22] as

$$k_{\text{eff}} = \frac{k_0}{k_0 + (1 - k_0) \exp - \left(\frac{cr\delta}{D} \right)}. \quad (31.3)$$

In this equation, c is a constant for the ratio of the mass density between the whole system and the element in the solution. The effective distribution coefficient is an extremely important parameter. If k_{eff} for a certain element is known, it is possible to adjust its concentration in a thin film or crystal, thereby opening the possibil-

ity to *engineer* the properties of a given material, which is important, for example, for the development of laser materials. For $k_{\text{eff}} < 1$, the concentration of the element

considered will be smaller in the crystal than in the solution. Hence, this can be used in purification processes by crystallization.

31.3 Requirements for Liquid-Phase Epitaxy

For **LPE** growth of a new material, the greatest challenge is usually to find a suitable solvent system in which the material crystallizes first and as a single phase. This requires sufficient knowledge of the phase relations in the system considered. Unfortunately, complex phase diagrams are often not available, therefore the first choice is usually made empirically, based on experience with similar material systems.

Besides the solvent, the substrate has to fulfill several requirement, and not only for the epitaxial deposition itself, but there are also requirements depending on foreseen applications. If heteroepitaxy is considered, the growth of layers by **LPE** is very demanding. Since **LPE** is a near-equilibrium process, it is very sensitive to all parameters. Basic substrate requirements are low misorientation, low misfit at growth temperature, similar thermal expansion coefficients, and excellent chemical/thermal stability. An important factor for control of the growth mode is the misfit between substrate and film. In the case of **LPE** of garnets [31.13, 23] it has been demonstrated that the misfit Δa ($= a_{\text{substrate}} -$

a_{film}), with a being the lattice constant, had to be less than 0.01\AA in order to avoid cracking. In **LPE**, there are three major parameters that govern the film growth mode: the supersaturation, the substrate misfit, and the substrate misorientation. Extremely flat surfaces can only be obtained if all three values are extremely low; for example, in the case of c -oriented $\text{YBa}_2\text{Cu}_3\text{O}_{7-x}$ (**YBCO**) films grown by **LPE** on $(110)\text{NdGaO}_3$, it has been demonstrated that surfaces with interstep distances of $10\text{ }\mu\text{m}$ between monosteps of $12\text{ }\text{\AA}$ can only be achieved if the following conditions are jointly met: substrate misfit of $\leq 0.08\%$, substrate misorientation of $\leq 0.02\%$, and relative supersaturation of $\leq 0.18\%$ [31.24]. Even if values will vary for other material systems, these values can be taken as order-of-magnitude requirements.

There exist three major methods commonly used for **LPE** growth: the tipping, dipping, and sliding boat techniques. They have been extensively described in the literature [31.1, 14–16, 23, 25], and will not be reviewed herein, except for the specific materials discussed further below.

31.4 Developing New Materials: On the Choice of the Epitaxial Deposition Method

Deposition methods can be divided into two categories: growth from the vapor phase, and growth from the liquid phase. In vapor growth, or vapor-phase epitaxy (**VPE**), deposition occurs under vacuum conditions. **VPE** techniques include radiofrequency (**RF**) sputtering, laser ablation, thermal and electron-beam evaporation, ion-beam deposition, molecular-beam epitaxy (**MBE**), atomic layer epitaxy (**ALE**), chemical vapor deposition (**CVD**), metalorganic chemical vapor deposition (**MOCVD**), and plasma-assisted processes. These methods either create a vapor or molecular nutrient by thermal or electron beam evaporation, or the effusion of gas atoms from a Knudsen cell. The growth species are transported to the heated substrate, where nucleation and growth occur. Vapor-phase epitaxy is

a very powerful method for the growth of semiconductors. In particular, **VPE** has the flexibility needed to grow and explore a variety of p/n-multilayer and quantum well structures, and allows the growth and control of the deposition process down to atomic scale. Thus, over the past decades, **VPE** growth techniques have constantly improved and become widely applied, whereas interest in **LPE** growth declined.

The successes of **VPE** growth techniques, however, resides mainly in the field of conventional semiconductors, such as InGaAsSb and similar systems. Surprisingly, **VPE** growth of oxides and nitrides exhibits much lower performance, yielding rather defect-rich films that often contain secondary phases and numerous grain boundaries.

In oxides, difficulties typically arise due to the complexity of the material [31.25], the high melting point of constituent oxides, complex phase diagrams, and also often a limited temperature–pressure stability range which restricts the growth conditions that can be applied. Especially important is also the low mobility of growth species under vacuum conditions, which limits surface diffusion of adatoms. Thus, oxide films grown by VPE typically show two-dimensional nucleation of small islands that spread over the growing surface and coalesce. This *birth-and-spread* growth mechanism results in films with numerous grain boundaries, and surfaces with high density of steps with small interstep distances (typically < 50 nm) [31.26]. Surface nucleation can be suppressed by large misorientation angles of the substrates, thereby providing kinks and steps. However, films grown on misoriented substrates show a very high step density with very small interstep distances, and hence are rough. With increasing thickness of oxide VPE films, a columnar structure often develops, which is not desirable for most applications [31.27]. Similar behavior has been observed for nitride VPE films. In VPE, near-equilibrium conditions may exist very close to the growth steps, and kinetics is the dominant factor that governs the deposition. In contrast, in LPE, the low driving force is maintained over a much larger extensions, and when all substrate and growth parameters are sufficiently met, the layer-by-layer growth mechanism can proceed over macroscopic dimensions. In LPE, extremely flat surfaces may develop, and interstep distances of several microns are not uncommon [31.28, 29].

For the achievement of high structural film perfection, it is essential that growth and decomposition reactions coexist at the growing interface. It is postulated that the high stability of nitrides, combined with a low mobility of growth species under vacuum (VPE) conditions, limits the surface mobility of atoms and thereby also reversible reactions associated with surface diffusion. This could also tentatively explain the experimental limit to the minimum dislocation density observed in vapor-grown nitride films, where dislocations can only be reduced to about 10^5 cm^{-2} despite the use of ELO techniques [31.30–33]. The nucleation and growth kinetic processes are extremely complex, and the reasons for this experimentally observed limit are not well understood.

The achievable surface flatness, density of defects (point defects, dislocations), and film homogeneity/perfection are three aspects where the LPE technique

may surpass VPE, and the choice of the deposition method should also be based on such consideration.

The growth system required for LPE growth (in any configuration) is very inexpensive compared with the equipment required for VPE growth. However, the achievement of high-quality LPE layers of complex oxides, nitrides or carbides can be very challenging, because this requires a multidisciplinary approach and high degree of expertise, especially in solution chemistry and thermodynamics, phase diagrams, and an excellent knowledge of the fundamentals of crystal growth and epitaxy. Like any other growth method, LPE presents advantages and disadvantages. Among the advantages, we can mention:

1. Films with highest structural perfection (low dislocation density, low concentration of point defects)
2. Automatic stoichiometry control
3. Dopant incorporation can be extremely homogeneous
4. Extremely flat surfaces (facets) can develop
5. Upscaling and mass production are possible.

Among the disadvantages, we can mention:

1. Usually thick films: minimum achievable is about 500 nm (atomic layer epitaxy not possible)
2. Not practical for the growth of heterostructures/quantum/multilayers
3. Rough interfaces frequent, due to back-dissolution
4. Very sensitive to substrate surface defects and parameters (misfit, misorientation)
5. Three major conditions have to be satisfied for the highest-quality LPE films:
 - Very small misfit
 - Misorientation
 - Supersaturation.

Only a few aspects were discussed in this introductory section. In the following sections, this paper discusses these challenges more precisely, with examples from recent studies on LPE growth of three different advanced materials, developed for different applications:

1. High-temperature superconductors, for flat (Josephson-junction) tunnel-device technology
2. Nitrides, for optoelectronic and high-power electronic devices
3. Novel frequency-agile piezoelectrics, for high-precision resonators and oscillators.

31.5 LPE of High-Temperature Superconductors

In 1986, the discovery of superconductivity at 35 K in a La-Ba cuprate [31.35], above the 23 K of Nb_3Ge , initiated the search for other cuprates with a higher critical temperature T_c . One year later, Wu et al. [31.36] found $\text{YBa}_2\text{Cu}_3\text{O}_7$ (YBCO) with a T_c of 90 K. This superconductivity above the boiling point of liquid nitrogen (77 K) stimulated worldwide research on this new group of superconducting materials (ceramics), and numerous applications based on tunneling were envisaged assuming that a timely solution of the material and crystal growth problems could be found. A new technological era seemed to be born, and this discovery initiated a race for the identification of new ceramic compounds with even higher critical temperatures. Among all high-temperature superconductors (HTSC), the so-called 123-cuprates became the most investigated. In particular, $\text{YBa}_2\text{Cu}_3\text{O}_{7-x}$ (YBCO) and $\text{NdBa}_2\text{Cu}_3\text{O}_{7-x}$ (NdBCO) attracted significant attention.

Due to their complexity and limited thermal and chemical stability, the growth process parameters that can be used for the synthesis of HTSCs are limited; for example, YBCO and NdBCO compounds melt incongruently below 1100 °C, and their oxygen content will depend on the growth conditions. In most cases, YBCO is grown as tetragonal $\text{YBa}_2\text{Cu}_3\text{O}_{6.2}$, which has to be oxidized at high temperature to be transformed to the superconducting orthorhombic $\text{YBa}_2\text{Cu}_3\text{O}_{6.93}$ phase with the highest T_c . This structural phase tran-

sition results in twinning, which in epitaxial layers depends on the substrate misfit and on the film thickness. Most thin-film growth efforts were concentrated on vapor-phase epitaxy (VPE), with more than 500 groups worldwide exploring chemical and physical vapor deposition of HTSCs. These VPE films typically show two-dimensional (2-D) nucleation and localized step flow, or spiral-island formation [31.37, 38]. Thus, step densities were very high, with interstep distances typically between 10 and 30 nm. For planar tunnel device technology, due to the very short coherence length in HTSCs, extremely flat film surfaces and interfaces were required. Thus, despite the challenges, researchers started to investigate liquid-phase epitaxy (LPE) growth of HTSCs. Early attempts in LPE growth of YBCO, NdBCO, $\text{Bi}_2\text{Sr}_2\text{CaCu}_2\text{O}_y$ (2212), and $\text{Tl}(\text{1223})/(\text{1324})$ can be found in [31.39–52].

31.5.1 Phase Relations, Solvent System, and Solubility Curves

Phase Relations

Knowledge of phase relations and solubilities is of fundamental importance for crystal growth and liquid-phase epitaxy of a given compound. In order to avoid the crystallization of competing secondary phases, the growth has to occur in the primary crystallization field (PCF) of the material to be grown, where it crystallizes

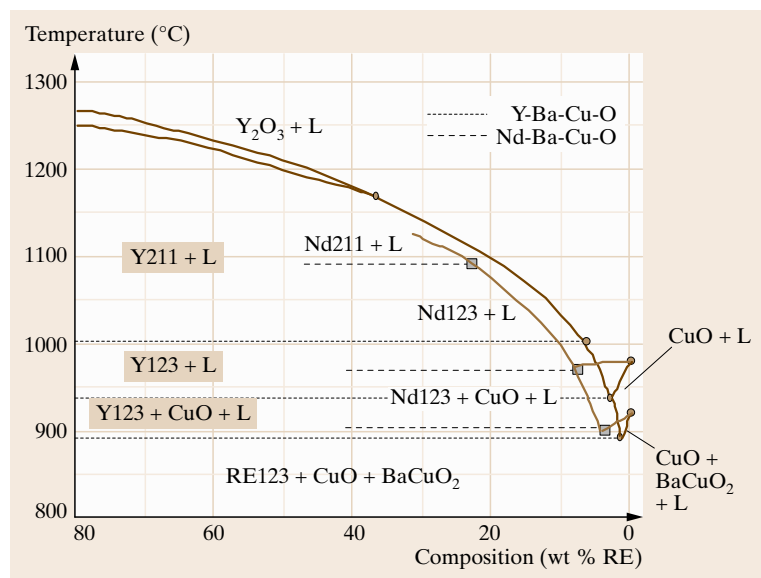


Fig. 31.1 Pseudobinary cut in the phase diagram of YBCO compared with NdBCO (after [31.34])

first, as a single phase, upon cooling. Due to the chemical and structural complexity of YBCO and NdBCO, this turned out to be very challenging [31.53,54].

YBCO and NdBCO are incongruently melting in air, i.e., they decompose upon melting. Therefore, it is not possible to grow YBCO and NdBCO substrate crystals directly from their melt, for example, by Czochralski or Bridgman techniques. Therefore, they have to be grown from high-temperature solutions.

Solvent System

Finding a suitable solvent for a given crystal may sometimes represent a real challenge. The old concept *similia similibus solvuntur*, (Latin: similar is dissolved in similar) is the basic criterion to be followed. The optimum choice is a solvent which is chemically similar (in the type of bonding) to the solute, but which has sufficient crystal-chemical differences between the solvent and solute constituents in order to prevent the incorporation of solvent species into the solute structure. For example, for the growth of metals, metallic solutions can be used. For high-melting oxide compounds, oxides or fluorides (or a mixture of both) are generally used.

In the case of YBCO and NdBCO, attempts to use solvents traditionally applied to other oxides, for example, lead oxide and lead fluoride, were not successful [31.55]. Hence, a self-flux was chosen. Since the lowest possible growth temperature is desired, a solution composition near the binary eutectic between BaCuO₂ and CuO, which is at about 29 ± 1.5 mol % BaO at a temperature of 910 ± 10 °C in air [31.54], is used as solvent.

The two systems, NdBCO and YBCO, are not fundamentally different. Compared with YBCO, NdBCO

has two advantages: a higher thermal stability reaching nearly 1100 °C in air, and a much wider PCF allowing concentrations up to approximately 20 wt % for single-phase growth. Figure 31.1 shows a pseudobinary cut in the phase diagrams of YBCO compared with NdBCO [31.34].

Thus, YBCO LPE films (or crystals) can be grown from about 920 to 1000 °C from the BaCuO/CuO eutectic solvent; for NdBCO, temperatures up to 1100 °C can be applied. Crystals and films grown from this solvent are not superconducting, because they are depleted in oxygen. They have to be annealed in oxygen after the growth to become superconducting. This will be discussed in detail below.

Solubility Curves

In order to adjust the supersaturation, knowledge of the solubility of the solute in the solution is essential. In the case of YBCO and NdBCO, solubility studies were performed by observation of the formation of crystals on the top of the solution, and by crystallization experiments on nonpolished seeds dipped into the saturated solution [31.34]. Figure 31.2 shows the solubility data obtained (our work) compared with the data published by other authors.

There is a strong scatter in the published solubility data shown in Fig. 31.2, which can be tentatively explained by the difficulties of HTSCs and the quite different methods, solution compositions, chemicals, and crucibles used by the different authors [31.56,57].

Observation of the formation and dissolution of crystals on top of a solution is usually not sufficiently accurate for the determination of the solubility curve. Indeed, due to the metastable (Ostwald-Miers) region,

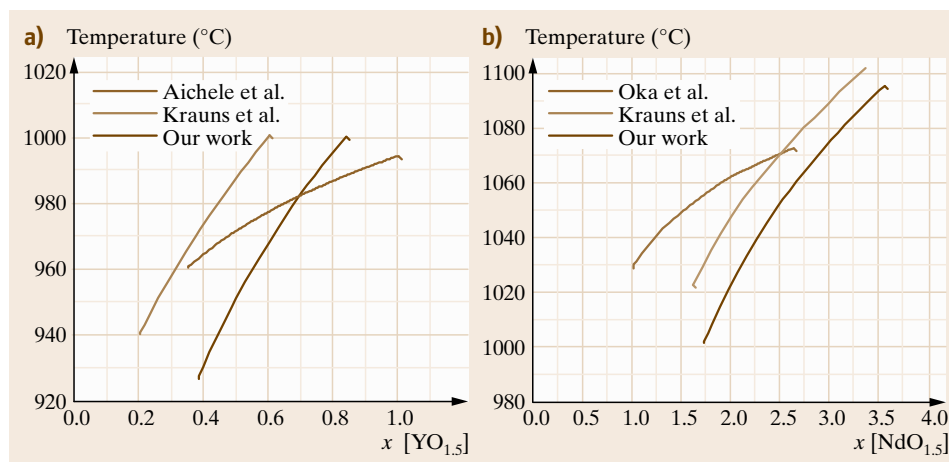


Fig. 31.2a,b
Solubility of
YBCO (a) and
NdBCO (b) in
the BaO/CuO
flux at 31 mol %,
compared with
data published
by other authors
(after [31.34])

spontaneous crystallization does not necessarily occur at the liquidus temperature, because a stable nucleus of critical size needs to be formed first. Thus, the solution can be supersaturated by several degrees before a visible crystallite is observed. The use of a seed may allow the supersaturation required for nucleation and growth to be reduced, and may thus give a better estimate of the liquidus temperature. This became clear during our investigations, and our values shown in Fig. 31.2 were mainly obtained using seeds, and were further confirmed by the LPE experiments.

31.5.2 Heat of Solution

In an ideal solution there are no attraction forces between the chemical species in solution, and there is no change in internal energy upon mixing. Thus, all the chemical potentials can be expressed as

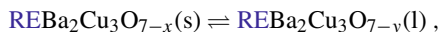
$$\mu_j = \mu_{0j} + RT \ln x_j, \quad (31.4)$$

where μ_{0j} is a function of temperature and pressure only, x_j is the mole fraction of the component j , and each component's chemical potential is a linear function of $\ln x_j$.

In the case of nonideal solutions, the mole fractions in (31.1) have to be replaced by the activities a_j , which are related to the concentrations by the activity coefficients γ_j according to

$$a_j = \gamma_j x_j. \quad (31.5)$$

For YBCO and NdBCO, there exist different possibilities to express the heat of solution. One may use a one-particle model by considering the reaction



with the solid (s), liquid (l), and with RE = Y, Nd.

For an ideal solution, the relationship between the concentration, expressed in mole fraction, x_1 and x_2 at the temperatures T_1 and T_2 , respectively, is then given by

$$\ln \left(\frac{x_2}{x_1} \right) = -\frac{\Delta H_{\text{fus}}}{R} \left(\frac{1}{T_2} - \frac{1}{T_1} \right), \quad (31.6)$$

where ΔH_{fus} represents the enthalpy of fusion. For an ideal solution, a linear plot of $\ln(x)$ versus $1/T$ is obtained. This Arrhenius-type relation allows the whole solubility curve to be extrapolated based on the melting point of the solute and a few solubility points. A deviation from linearity would indicate nonideal solution behavior. Since the volume change on melting is small,

ΔH_{fus} may be approximated by the heat of solution L_{sol} [31.58, 59]. Then the heat of solution can be related to the saturation concentration of the solute in the solvent by the relationship

$$L_{\text{sol}} = RT^2 \frac{d \ln x_{\text{sat}}}{dT} \quad (31.7)$$

or

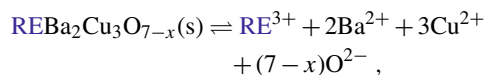
$$L_{\text{sol}} = 4.574 T_1 T_2 \frac{\log x_{\text{sat}1} - \log x_{\text{sat}2}}{T_1 - T_2}, \quad (31.8)$$

where $x_{\text{sat}1}$ and $x_{\text{sat}2}$ are the saturation concentrations at temperatures T_1 and T_2 .

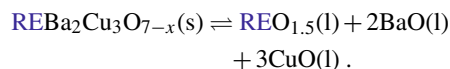
By using the above expressions and according to our refined experimental solubility curve, for $\text{YBa}_2\text{Cu}_3\text{O}_{7-x}$ crystals with $x \approx 0.8$, grown in air ($P_{\text{O}_2} \approx 0.2$ atm) in a flux with Ba-to-Cu ratio of 31 : 69, a value of $L_{\text{sol}} = 34.7$ kcal/mol at 1273 K is obtained [31.34], which is in good agreement with the calculations of Tsagareisvili et al. [31.60, 61], who obtained an enthalpy of melting of ΔH_{melt} of 36.44 and 41.03 kcal/mol for $\text{YBa}_2\text{Cu}_3\text{O}_6$ at 1446 K and $\text{YBa}_2\text{Cu}_3\text{O}_7$ at 1503 K, respectively.

For $\text{Nd}_{1.1}\text{Ba}_{1.9}\text{Cu}_3\text{O}_{7+x}$ crystals grown in air, at 1060 °C, from the same flux composition, a heat of solution of $L_{\text{sol}} = 28.1$ kcal/mol at 1333 K [31.34] is obtained.

The heat of solution can also be expressed by using a multiparticle model, similar to the eight-particle model used for garnets [31.62–64]. In this case, it is assumed that the REBCO molecule splits into several particles or molecules upon dissolution according to



or



31.5.3 Supersaturation and Driving Force for LPE

An important condition to achieve high-quality films and flat surfaces by LPE is the control of supersaturation. Knowledge of the solubility curve of a system allows one to estimate the supersaturation and the driving force for epitaxy for given growth conditions.

Crystals grow when the total free energy of the system can be decreased. Thus, the driving force for

crystallization is the free energy difference

$$\Delta G = \Delta H - T \Delta S \quad (31.9)$$

between the solid and the supersaturated solution. Here, ΔH and ΔS are the differences in enthalpy and entropy of the crystalline and fluid phase, respectively.

For near-equilibrium conditions, we can write

$$\Delta G = \Delta H \left(1 - \frac{T}{T_e}\right) \approx \Delta H \left(\frac{\Delta T}{T_e}\right), \quad (31.10)$$

with $\Delta T = T_e - T$ being the difference between the equilibrium and actual temperature.

When we cool a solution that is at equilibrium, the concentration of solute x becomes greater than the equilibrium concentration x_e . Then, the free energy difference at the solid-liquid interface can be written as

$$\Delta G = RT \ln \left(\frac{x}{x_e}\right) = RT \ln \left(1 + \frac{x - x_e}{x_e}\right). \quad (31.11)$$

For small values of supersaturation σ , we have

$$\ln \left(1 + \frac{x - x_e}{x_e}\right) \approx \frac{x - x_e}{x_e} = \sigma. \quad (31.12)$$

Substitution into (31.11) yields

$$\Delta G = RT\sigma. \quad (31.13)$$

and by using (31.10), the following relation is obtained

$$\sigma = \frac{x - x_e}{x_e} = \Delta H \frac{\Delta T}{RT T_e}, \quad (31.14)$$

where σ is the relative supersaturation, x and x_e are the actual and equilibrium concentrations, and ΔH is the enthalpy of solution.

Besides σ , other expressions are often used

$$\alpha = \frac{x}{x_e} \quad \text{the supersaturation ratio,}$$

$$\Delta T = T_e - T \quad \text{the undercooling.}$$

From the solubility curve of YBCO, if we assume an undercooling of $\Delta T = 0.5$ K, the Gibbs free energy difference (driving force) would then be $\Delta G(\Delta T = 0.5) = 13.6$ cal/mol, and for $\Delta T = 2.5$ K, $\Delta G(\Delta T = 2.5) = 68.1$ cal/mol.

31.5.4 Substrates and Epitaxial Relationship

For the growth of high-quality LPE films, the substrate has to fulfill several requirements: low misfit at the

growth temperature, similar thermal expansion coefficients to film material, high chemical stability in the solvent, and excellent thermal stability, from the film growth to the application temperature. In the case of YBCO and NdBCO, the considered temperature range is from about 1100 °C down to 77 K (liquid nitrogen). Furthermore, in LPE, a very low supersaturation has to be applied during film growth. Since all these requirements have to be satisfied for best results, it is evident that homoepitaxy would represent the best choice. In heteroepitaxy, there is generally no substrate material fulfilling all requirements, and compromises are necessary. Often, buffer layers (also called templates) of the same or a similar film material are used for better lattice matching. In the case of LPE of YBCO and NdBCO, the gallates LaGaO₃ (LGO) and NdGaO₃ (NGO) were extensively explored as substrate materials, as they present a better lattice match compared with other substrates such as SrTiO₃ or MgO. Both gallates and their solid solutions can be grown by Czochralski technique.

Due to the severe misfit requirements in LPE [31.65], precise knowledge of the lattice constants and thermal expansion coefficients of the substrate and HTSC film material is essential [31.66]. High-temperature lattice constant data available in the literature can vary significantly. This is not necessarily due to different determination methods or experimental inaccuracies, but can also be due to the crystal material itself. Indeed, the lattice constants of the same oxide material grown by Czochralski in different laboratories can vary, depending on the starting oxides and growth conditions applied. In addition, radial and longitudinal compositional variations are frequently observed in oxides grown by Czochralski technique. In the case of HTSCs, it was found more accurate to perform high-temperature x-ray measurements on film and specific substrate material used for LPE growth, using the same diffractometer/method [31.66]. For the measurements, single-crystalline film and substrate samples were ground into powder. A Philips Xpert diffractometer with CuK α -radiation was used for the θ -2 θ scans between 20 and 75° in the temperature range of about 35–1000 °C. The Bühler heating chamber HDK was equipped with a tightening tunable electrode for compensation of heat expansion of the Pt-strip heater, keeping the sample in focusing position. The samples were fixed with a Pt/Rh net with mesh size 200 μ m \times 200 μ m, length 20 mm, and thickness 100 μ m, attached to the strip heater, reducing existing lateral temperature gradients over the sample. Lattice parameters

were refined by Rietveld analysis. The most challenging aspect during such measurements (and also the greatest source of error) is usually lack of knowledge of the exact temperature of the sample. The use of an internal standard for calibration allows more accurate determinations. The thermal expansion behavior of alumina (Al_2O_3) and its chemical stability is well established. Therefore, Al_2O_3 reference powder was mixed with the gallates for calibration of the temperature [31.66].

The lattice parameters and lattice angles of the orthorhombic, tetragonal, and rhombohedral rare-earth gallates and cuprates (YBCO and NdBCO) can be transformed into a pseudocubic system. The pseudocubic cell of orthorhombic REGaO_3 (with $\text{RE} = \text{Y}, \text{Nd}$) consists of two $[110]/2$ axes, of which the distance is $0.5(a^2 + b^2)^{1/2}$, and the orthogonal axis $c/2$. The pseudocubic angle $\gamma = 2 \arctan(a/b) \neq 90^\circ$ exists between the $[110]$ directions. The substrate gallate planes (001)

and (110) fit the film lattice parameters a , b , and $c/3$, depending on film orientation [31.65]. The epitaxial relations, in terms of pseudocubic lattice parameters, are shown schematically in Fig. 31.3, for c -oriented YBCO films on (001) and (110)NGO, on the left, compared with a -oriented films on (110)NGO, on the right. For epitaxy on the (001) gallate plane, both $d/2$ axes include the pseudocubic angle γ which slightly deviates from the cubic angle by $\Delta\gamma = 90^\circ - \delta$. Thus, in-plane shear strains in the orthogonal film cell are introduced. For epitaxy on (110) planes the $[110]$ direction pointing out of the (110) plane is inclined by $\Delta\gamma$, leading to *out-of-plane* shear strains in the film. The values of $\Delta\gamma$ at 1000 and 25 °C are 0.24 and 0.32° (LaGaO_3), and 0.34 and 0.74° (NdGaO_3).

Both compounds, YBCO and NdBCO, undergo a structural phase transition when they are cooled to room temperature after the growth. They are tetragonal ($a = b, c$) at LPE growth temperature of about

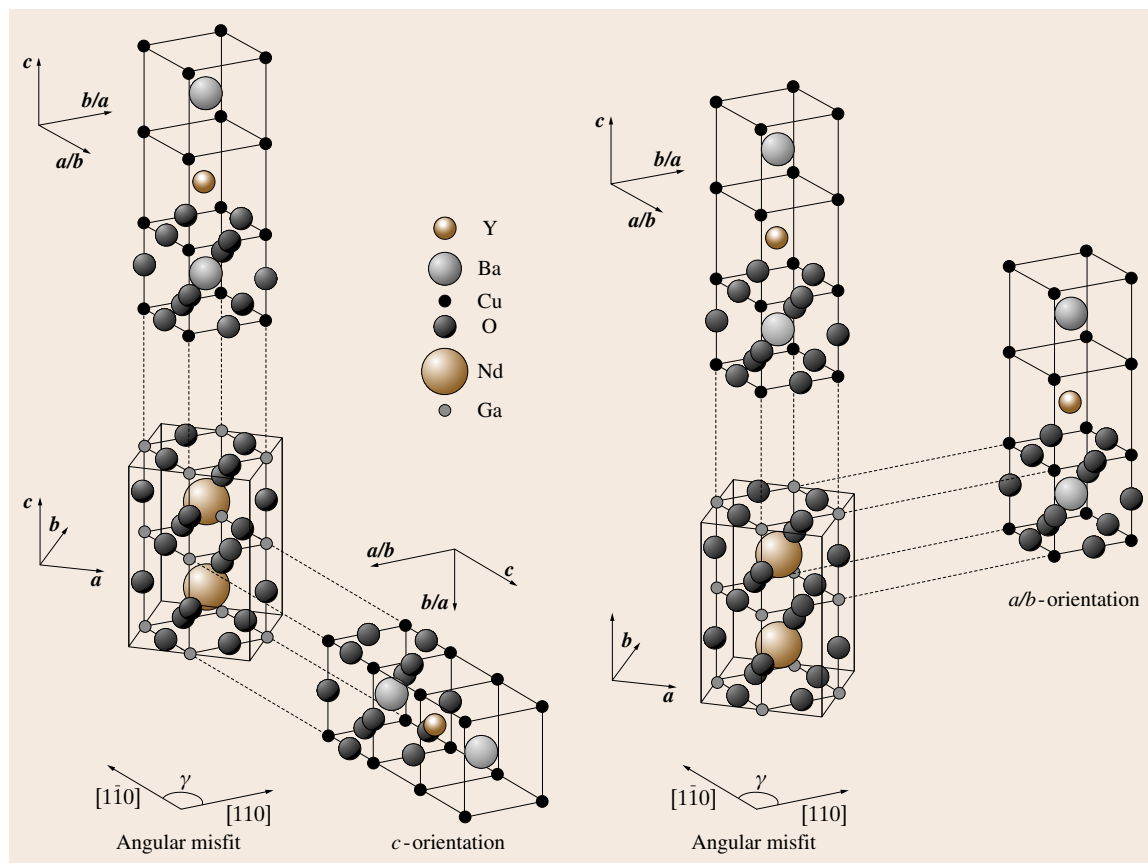


Fig. 31.3 Substrate–film orientations observed in epitaxial growth of YBCO on NGO

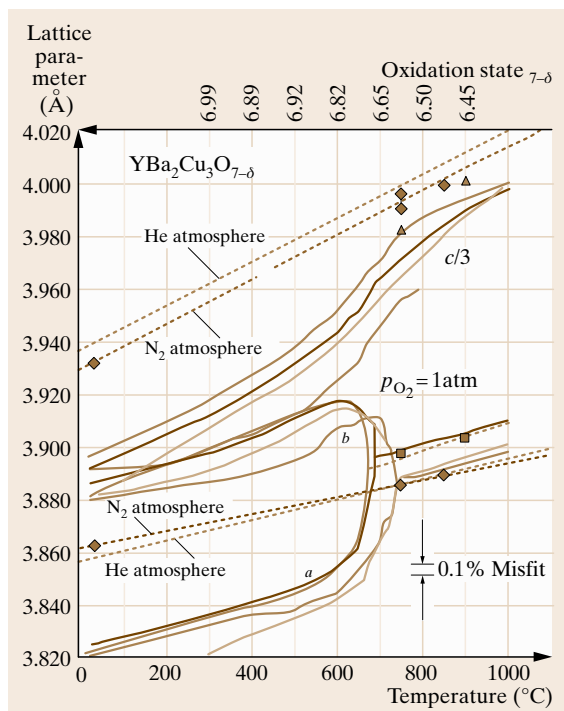


Fig. 31.4 Thermal expansion and oxidation behavior for **YBCO** according to different authors at $p_{O_2} = 1$ atm (after [31.66])

1000°C, and orthorhombic ($a \neq b, c$) once at room temperature. For **YBCO**, the splitting of the tetragonal a -axis into two a - and b -axes during this phase transition occurs at a temperature of about 600°C, depending on the oxidation state of the material, as shown in Fig. 31.4. Since **YBCO** and **NdBCO** cannot directly be grown as orthorhombic phase, they have to be annealed in oxygen after the growth to become superconducting. This poses a formidable challenge for **LPE** growth of high-quality films, and will be discussed in detail in the film morphology section later.

The misfit relations between **YBCO** and (110) **NdGaO₃** and **PrGaO₃** at room temperature and at 1000°C (approximate film growth temperature) [31.65, 66] are shown in Fig. 31.5. In this figure, assuming a rigid substrate, one can conclude that for a - and b -films at growth temperature the in-plane c -axis of the film, $c_L \parallel d_S$ (where “L” indicates film and “S” indicates substrate), is under high compressive strain of 2.5%, whereas the tetragonal a -axis (= b -axis) of the

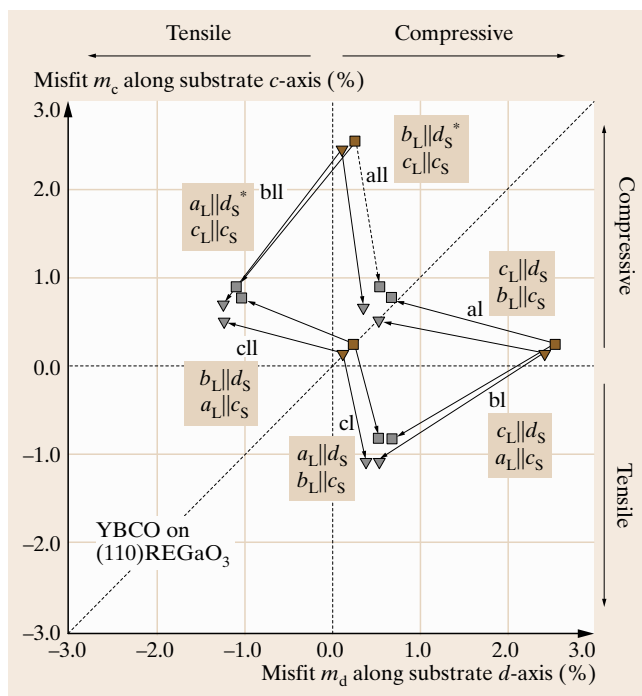


Fig. 31.5 Misfit relations of **YBCO** on (001)**NdGaO₃** (\square) and **PrGaO₃** (∇) at 1000°C (full symbols) and room temperature (open symbols). Arrows mark the path of cooling (and oxidation) after growth. Films are a -, b - or c -oriented (after [31.65])

film shows only a small misfit of 0.15 and 0.2% for **PrGaO₃** and **NdGaO₃**, respectively.

31.5.5 LPE Growth System and Film Growth Procedure

An important requirement for the achievement of high-quality **LPE** layers is precise control of the supersaturation σ . The supersaturation has to be small enough to prevent spontaneous three-dimensional nucleation, to prevent step bunching (described by the kinematic wave theory), and for layer-by-layer growth. The achievable growth mode depends also on substrate parameters, as discussed previously. Technically, precise control of supersaturation requires a corresponding precision of temperature control and programming, in combination with homogenization of the solution by forced convection. For preliminary **LPE** growth experiments, a chamber furnace can be sufficient. For highest-quality oxide films, low-gradient platinum-wound three-zone vertical **LPE** furnace systems allow

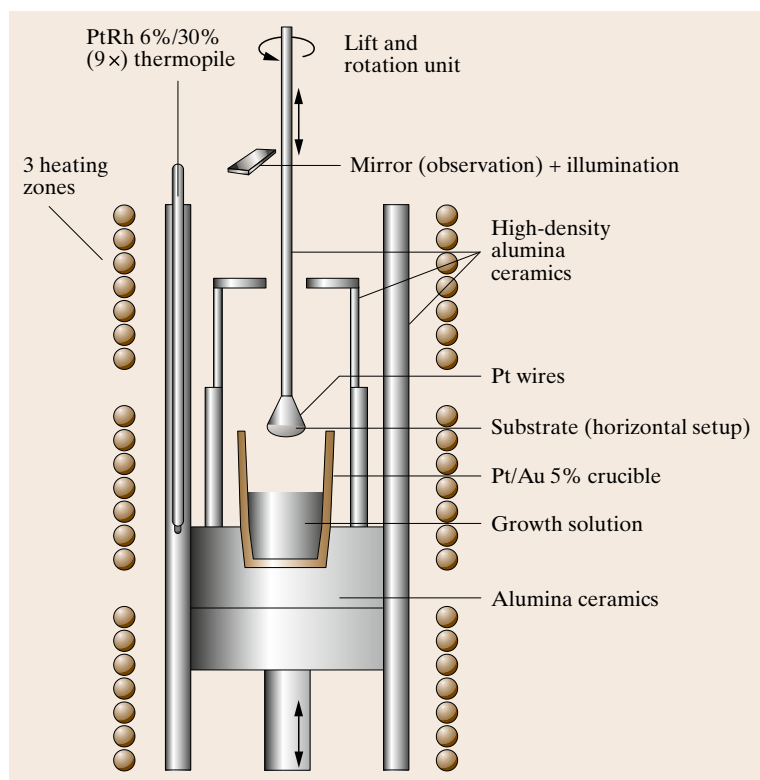


Fig. 31.6 Vertical three-zone LPE growth furnace system

the required control of temperature gradients [31.15, 16]. A typical three-heating-zone LPE growth furnace system is shown schematically in Fig. 31.6.

Such platinum LPE growth system can be used for LPE growth of a variety of oxides, up to 1200 °C. It is equipped with lift and rotation mechanisms. Optical-fiber illumination and mirror are used to observe the surface of the solution and for precise substrate dipping.

In a typical YBCO LPE growth experiment, high-purity starting chemicals (BaO_2 , CuO , and Y_2O_3) are well mixed and introduced into the ceramic crucible. The crucible is placed in the furnace and heated to about 1010 °C during 9 h. After soaking for 7 h, the temperature is increased to 1040 °C and reduced to 1000 °C within 90 min. The equilibration to the liquidus temperature is done by the dipping of nonpolished test substrates into the solution. Then, several YBCO films are successively grown on (110)NGO by slow cooling of the solution. The substrates can be mounted in vertical or horizontal position, and the substrate rotation rate is typically between 15–30 and 100–120 rpm, for each configuration, respectively.

31.5.6 Growth Mechanisms and Growth Parameters: Theory Versus Experiment

The primary motivation for using the LPE growth technique for film growth has traditionally been the need for extremely homogeneous crystal material and/or flat surfaces for a given application. In the case of HTSCs, due to their short coherence length (≈ 4 and 12 \AA , for a -oriented and c -oriented films, respectively), extremely flat film surfaces are required for planar tunnel-device applications. For c -oriented YBCO films, this represents one c -axis monostep height of 12 \AA , separated from another monostep by $10 \mu\text{m}$ lateral distance. This formidable requirement can be better understood if we consider, for example, a step with a height of 1 m that would need to be separated from another step by a distance of 10 km . From this, it is obvious that only a growth mechanism providing a continuous source of steps, such as the layer-by-layer or spiral growth mode, would allow such surfaces to be obtained over macroscopic dimensions. This requirement leads to unprecedented challenges in film synthesis, and therefore

precise evaluation of the tolerances on all substrate and growth parameters is required.

Besides substrate misfit and misorientation, knowledge of the supersaturation is especially critical. Supersaturation can be calculated from the phase diagram, for a given undercooling applied during the film growth. However, the values that are obtained are, at best, indicative only. Growth features, such as spirals, reflect the real conditions existing at the growing interface, and can thereby provide important fundamental data on growth parameters that cannot be measured. The approach discussed below can be applied to other materials as well, and the reader is encouraged to look into the original literature for full details.

In LPE of YBCO on (110)NdGaO₃ the film orientation depends on the supersaturation. It was found experimentally that the transition from *a*-oriented to mixed *a/c* to *c*-oriented films occurs with decreasing undercooling (supersaturation), with a threshold at about $\Delta T \approx 3$ K ($\sigma \approx 0.03$) [31.28].

Screw dislocations provide a continuous source of steps, which can propagate over macroscopic distances. It has been shown [31.20], that the distance between steps originating from a single dislocation is proportional to the size of the 2-D nucleus at a given supersaturation. For an Archimedean spiral, the

relationship between supersaturation σ and interstep distance y_0 can be expressed by [31.67]

$$y_0 = 19\rho_c = \frac{19\gamma_m a}{k_B T \vartheta}, \quad (31.15)$$

with the relative supersaturation $\sigma = (n - n_e)/n_e$, where n and n_e represent the actual and equilibrium concentration of the solute, and a is the length of a growth unit. In the case of solution growth, the energy per growth unit (or molecule) γ_m on the edge of the critical nucleus is of the order of 1/6 of the heat of solution per molecule. The anisotropy of γ_m , which will be higher for low-energy planes, is neglected in the following development.

In the case of YBCO, with $\gamma_m = 4.01 \times 10^{-20}$ J/molecule, $a = 3.9$ Å ($a = b$ for tetragonal YBCO at the growth temperature of 996 °C), and $T = 1269$ K, we can estimate the achievable interstep distances as a function of undercooling. This is shown in Fig. 31.7, for an Archimedean, monostep, single-source spiral. From this, the size of the critical nucleus was estimated to be about 23 nm for this surface. This is one order of magnitude larger than observed for YBCO films grown by VPE [31.68].

In this figure, we recognize that the undercooling has to be smaller than 0.17 °C in order to obtain interstep distances larger than 10 μm, as required for the specific application discussed herein. Such small under-

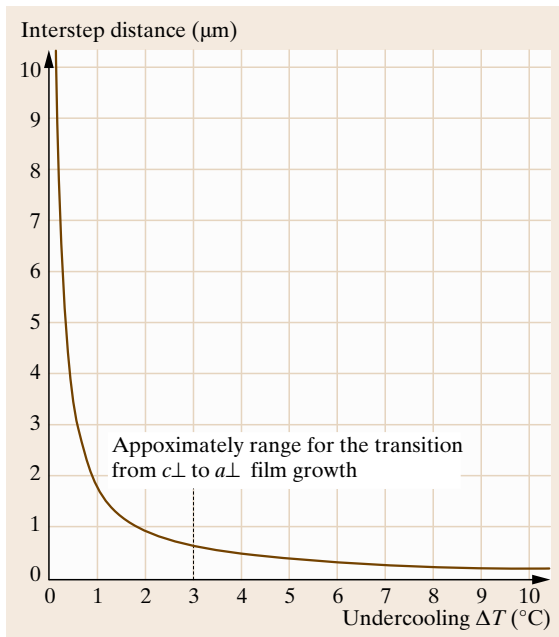


Fig. 31.7 Interstep distances as a function of undercooling (after [31.28])

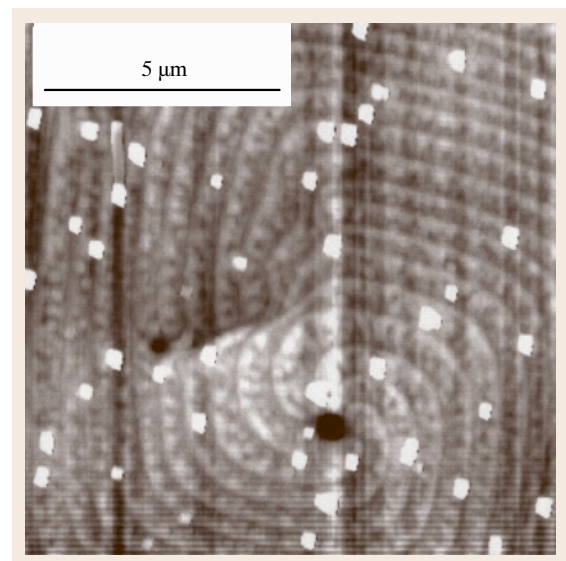


Fig. 31.8 AFM image of a complex YBCO spiral ($m = 2$ and $S = 6$) observed on a LPE film surface (after [31.29])

cooling sets stringent requirements on the temperature stability of the growth process.

Growth spirals can also emerge from groups of dislocations. In this case, the interstep distance is given by $y_0 = 4\pi r_c/\varepsilon$ [31.20], where r_c is the radius of the critical nucleus. For a group of dislocations of the same sign, ε can be as large as the number of dislocations contained in it. A group of S dislocations of the same sign, arranged on an array of length L , has an activity of ε times that of a single dislocation. Accordingly [31.20]

$$\begin{aligned} \text{If } 2\pi r_c \gg L, & \quad \text{then} & \varepsilon = S, \\ 2\pi r_c = L, & & \varepsilon = \frac{S}{2}, \\ 2\pi r_c \ll L, & & \varepsilon = 2\pi r_c \frac{S}{L}. \end{aligned}$$

A comparison was made with complex growth spirals observed on c -oriented YBCO films grown on (110)NGO [31.29]. Figure 31.8 shows a typical YBCO spiral where six double steps ($2 \times 12 \text{ \AA}$) emerge from the core region.

Interstep distances and step height of several complex growth spirals observed on single film surface

of $1 \text{ mm} \times 1 \text{ mm}$, were measured by atomic force microscopy (AFM), and the following relation was found

$$y_0 = \frac{19\gamma_m am}{\varepsilon k_B T \vartheta}, \quad (31.16)$$

with $2\pi r_c S/L < \varepsilon < S/2$, and where m represents the number of monosteps of the step source.

The high nucleus density in vapor-grown films results in high screw dislocation densities of typically 10^9 cm^{-2} [31.68–70] and high grain boundary densities due to the coalescence of misaligned islands [31.71]. High critical current densities are generally observed for such defect-rich films. Island formation can be prevented and a pure step flow mode achieved when the substrate misorientation, which is $3\text{--}5^\circ$ for physical vapor deposition (PVD) and chemical vapor deposition (CVD) [31.71], is adapted to the size of the critical nucleus. In contrast, in LPE, the nucleus density is lower.

With increasing radius of critical nuclei at low supersaturations, the substrate parameters misfit and misorientation become crucial for the initial growth stage and the growth mode of the films. Hence, in LPE, to understand the a/c -transition of YBCO on (110)NdGaO₃, the substrate strain energy contribution must be taken into account. Furthermore, the surface energy between a liquid and its solid is lower than the surface energy between a vapor and its solid. Therefore, in LPE, the strain energy is not negligible with respect to surface energy terms. In order to estimate the influence of substrate misfit and misorientation on the thermodynamically determined equilibrium size of the nucleus, characteristic substrate parameters were compared [31.24]. A relationship between misfit, relative supersaturation, radius of critical nucleus, and film orientation could be established, as shown in Fig. 31.9.

For the achievement of large interstep distances of $y_0 \approx 10 \mu\text{m}$ between monosteps of 12 \AA height for c -oriented YBCO layers on (110)NGO, the estimated corresponding undercooling is $\Delta T \approx 0.17 \text{ K}$. From Fig. 31.8, one can see that the maximum tolerable misfit with the substrate would then be 0.08% . For thin, strained c -YBCO films on (110)NGO with average misfit of 0.28% , it follows that a maximum interstep distance of $y_0 \approx 2.5 \mu\text{m}$ between monosteps of 12 \AA height can be obtained. It is also found that the substrate misorientation has to be smaller than 0.02° to avoid step bunching [31.24].

Only selected aspects were discussed in this section on HTSCs, to demonstrate the challenges and also

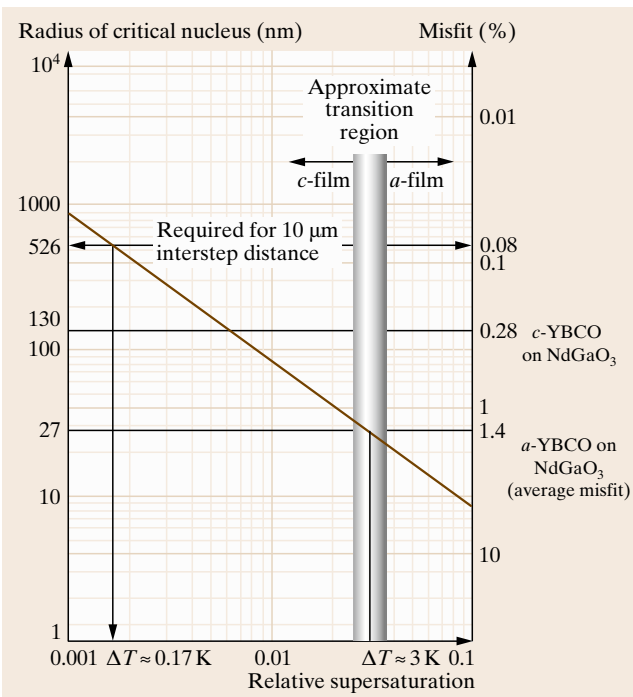


Fig. 31.9 Radius of critical nucleus as a function of misfit and supersaturation in LPE of YBCO (after [31.24])

the potential of this growth technique for the development of high-quality complex oxide films. Cracking and twinning of high-quality LPE REBCO films are further challenges to their application in devices. Whereas the T_c of LPE HTSC films was found comparable, after

oxidation, to that of VPE-grown material, the critical current density was usually lower due the high quality of the LPE films (lack of pinning centers). The interested reader should refer to the specific literature for additional details.

31.6 LPE of Calcium Gallium Germanates

Langasite-type materials represent a family of trigonal acentric crystals whose structure was found to be similar to that of calcium gallium germanate, $\text{Ca}_3\text{Ga}_2\text{Ge}_4\text{O}_{14}$, (CGG, space group D_3^2-P321). They were first investigated as laser hosts [31.72], and rediscovered later for their outstanding piezoelectric properties [31.73]. So far, the most investigated ternary compositions have been $\text{La}_3\text{Ga}_5\text{SiO}_{14}$ (LGS), $\text{La}_3\text{Ga}_{5.5}\text{Ta}_{0.5}\text{O}_{14}$ (LGT), and $\text{La}_3\text{Ga}_{5.5}\text{Nb}_{0.5}\text{O}_{14}$ (LGN). Langasite-type materials are the first real competitors to quartz in high-precision resonators and high-temperature high-pressure sensors and displace a quartz technology that has been dominant over the past 50 years [31.74–76]. The advantages of langasites over quartz include lower acceleration sensitivity; higher piezoelectric coupling, which enables devices to be made smaller; and higher Q (quality factor), which reduces phase noise and enables higher-frequency operation. Unlike quartz, these materials have no phase transition below the melting point, which enables devices capable of high-temperature operation.

Ternary langasites LGS, LGT, and LGN, can be grown by Czochralski technique. However, due to inherent materials properties (phase relations/stability) and particularities of the growth process, these crystals and wafers show a defect structure and inhomogeneities [31.77] that lead to nonreproducibility in surface acoustic wave (SAW) device parameters [31.78] and discrepancies in fundamental measurements. Recently, high-quality 2 inch diameter LGT crystals have enabled the achievement of high Q -values [31.79] and overall better reproducibility in resonator parameters. It is also acknowledged that better values would probably be possible if the crystal quality could be further improved. In particular, better ordering of atoms in the LGT lattice and lower density of point defects could be beneficial.

Ternary langasites can be described as a mixed framework consisting of an octahedra (1a), and two types of tetrahedra, a small (2d) and a larger (3f). The holes of the Thomson cubes are occupied by large

cations (3e) [31.80,81]. Due to the presence of four sites for cations, the CGG-type crystal structure accommodates a wide spectrum of ions. Structure-forming ions, dopant ions, and their radii range (tolerance factor) for corresponding coordination number have been determined [31.81], and a stability diagram derived [31.82]. In ternary CGG-type materials, the four sites can be populated by more than one kind of cation, and this leads to a disordered structure of these materials. In LGT, the Ga and Ta ions share the same octahedral site, which leads to compositional inhomogeneities. Best ordering of atoms, and hence, highest Q -value, is expected from crystals grown near thermodynamic equilibrium. This was one of the reasons to investigate LPE growth of langasite materials. In addition, as we know from semiconductor studies (Sect. 31.1), the concentration of native intrinsic (point) defects is very low in crystal material grown by LPE or from solutions. From fundamental thermodynamics, for the same material, the point defect concentration will be lower if a growth process is used that allows a lower growth temperature. In Czochralski growth of ternary langasites, the growth temperature is about 1450 °C, whereas the same materials can be grown from solutions at about 950 °C [31.83–85]. This growth temperature difference results in a remarkable reduction in the concentration of intrinsic point defects. This may result in higher Q -values, and hence this was a further motivation to investigate LPE growth of langasites.

31.6.1 Solvent System

Finding a suitable solvent for the growth of such complex materials represents one of the major challenges. A first selection of possible fluxes is always done according to chemical and structural aspects, and through systematic studies of available respective or related phase diagrams. Compared with the solute, the solvent should be chemically similar in the type of bonding, but it should have components that present sufficient

crystal-chemical differences to avoid incorporation of solvent species into the crystal.

In langasites, with decreasing temperature, the following crystallization sequence of possible phases is expected from respective melting points and considerations of the complexity of the corresponding oxide. Simple oxides (R_2O_3 ; $R = A, B$) have the highest melting temperature, followed by the perovskite (ABO_3) phase at a lower melting temperature, then the garnet ($A_3B_5O_{12}$) phase could be expected, and finally the langasite phase at the lowest temperature. However, when $A = La^{3+}$, the garnet phase does not exist, because La^{3+} is too large for the garnet crystal structure. Hence, in ternary langasites, $LaGaO_3$ is the phase likely to crystallize in a temperature region above the langasite liquidus. Hence, an ideal solvent should present sufficient solubility for the langasite phase below this temperature.

Alkali vanadates, molybdates, and tungstates were widely used as fluxes for crystal growth of silicates and germanates. $Li_2MoO_4:MoO_3$ readily dissolves many oxides, and was used for the growth of BeO , GeO_2 , SiO_2 , TiO_2 , Be_2SiO_4 , Y_2SiO_5 , as well as for emerald ($Be_3Al_2Si_6O_{18}$). Early attempts to crystallize the langasite phase from $Li_2MoO_4:MoO_3$ flux were not successful [31.85].

Another typical solvent for oxides is PbO . $PbO-B_2O_3$ fluxes as well as $BaO-BaF_2-B_2O_3$ ternary solvent systems were successfully applied for the flux and LPE growth of perovskites and garnets [31.16]. Bi_2O_3 -based fluxes have similarities to PbO -based fluxes, and were explored as lead-free alternates for the growth of magnetic garnets. However, two major problems were reported: a flux difficult to remove after the growth, leaving usually a rough film surface after cleaning, and a growth-induced anisotropy of about one order of magnitude lower than with a $PbO-B_2O_3$ flux [31.16]. Due to the valence state of Bi^{3+} , bismuth-based solvents cannot be used for the growth of many oxides containing large rare-earth ions such as La^{3+} , because of possible substitution, therefore they were not investigated in those studies.

For the growth of LGS, LGT, and LGN, PbO -based solvent systems with various solute ion ratios and concentrations were tested by flux-growth experiments. In preliminary experiments performed between 950 and 1000 °C, lanthanum gallate was often obtained as secondary phase, and it became evident that the growth temperature had to be lower. However, PbO has a melting point of 886 °C and becomes very viscous around 900 °C. Thus, a eutectic-forming additive was sought

to lower the growth temperature towards the expected stability field of the ternary langasites. The addition of MoO_3 was found to be beneficial, and LPE films could then be successfully grown in a lower temperature range from a solvent with PbO -to- MoO_3 ratio of 12 : 1 [31.85].

31.6.2 Substrates for Homoepitaxial LGT LPE Film Growth

In LPE, the substrate misfit is a determining factor in the achievable growth mode and film quality. The availability of Czochralski-grown LGS, LGN, and LGT substrates to be used as substrates for homoepitaxial LPE growth therefore represents an important advantage.

In case of homoepitaxy (LPE), the supersaturation required to initiate nucleation is extremely small. Hence, substrate surface defects, scratches, as well as residual strain due to the polishing process, will strongly affect the initial stages of film growth. Chemical etching is an efficient method that can be used to remove the damaged surface substrate layer prior to LPE. For LGT, similarly to perovskites and garnets, hot orthophosphoric acid was found to be particularly suitable, also to reveal substrate defects [31.77]. In langasites, striations can be revealed by etching the substrate in H_3PO_4 at 130 °C during 2–3 h, as shown in Fig. 31.10.

In ternary langasites, striations are likely due to the solid solubility between Si-Ga in LGS (tetrahedral site, CN IV), between Nb-Ga in LGN, and between Ta-Ga in LGT (octahedral site CN VI), associated with temperature fluctuations at the growth interface during Czochralski growth. These striations cause periodic (three-dimensional, 3-D) variations of lattice parameters and inhomogeneous dopant/impurity incorporation. In Czochralski growth of LGT, striations can be strongly reduced, below the detection limit of x-ray synchrotron topography, when all growth parameters are properly optimized [31.79].

When a film is grown by LPE on a striated substrate of same composition (homoepitaxy), the first monolayers of the film will try to adapt their composition to minimize the misfit strain. This phenomenon is well known, especially in semiconductor heteroepitaxy where it has been documented as the lattice pulling effect. A film grown on a striated substrate will show a variation of composition as a function of its thickness, which in turn may affect the film properties. It is therefore important to investigate such defects in the substrates used for epitaxial deposition.

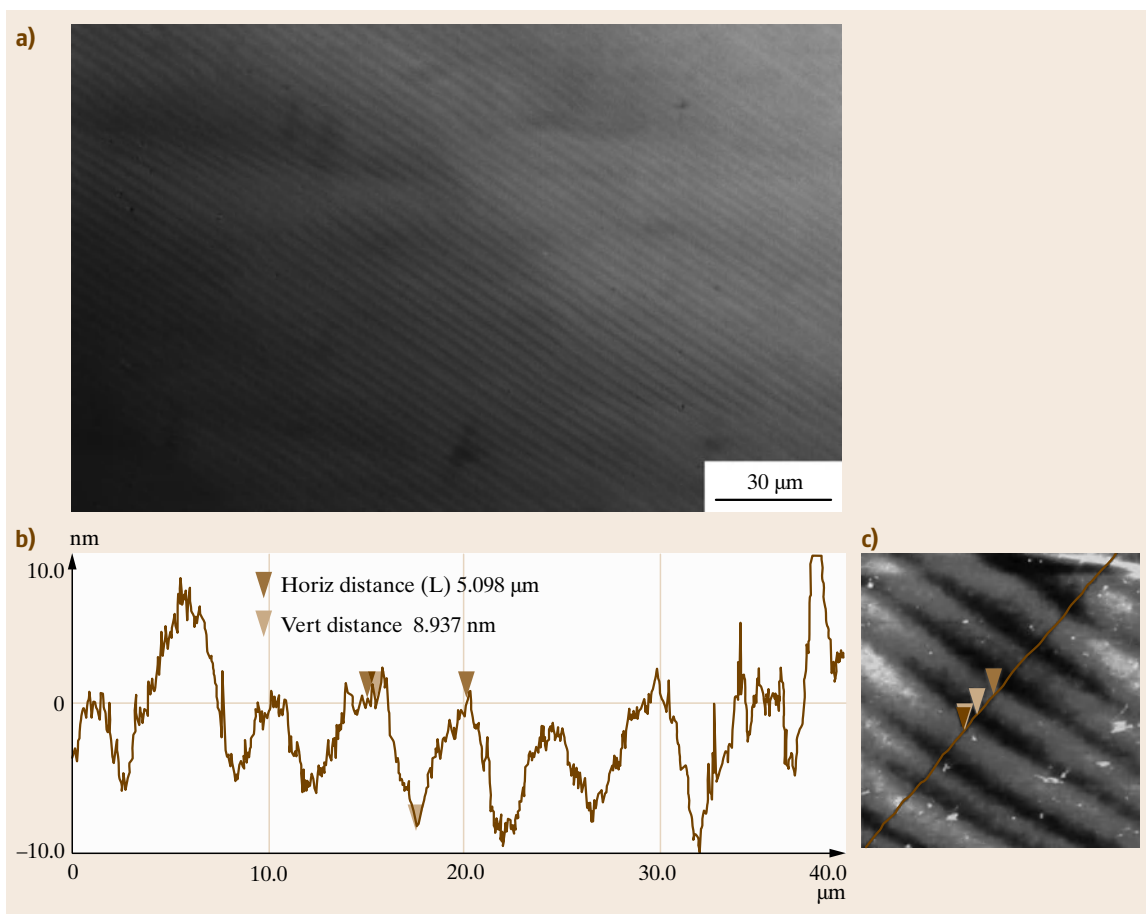


Fig. 31.10a–c Striations on *x*-cut LGT substrates after chemical etching in hot H_3PO_4 . (a) Nomarski microphotography, (b,c) AFM profile

31.6.3 LPE growth of LGS, LGT, and LGN

Langasite LPE films are grown in a similar vertical furnace system to that previously described. In a typical experiment [31.84, 85], the starting oxides and dopants, consisting of 10–15 wt % stoichiometric LGT (or LGN) in the PbO solvent, are hand-mixed, introduced in a Pt crucible of about 45 cm^2 , and covered with a lid. The crucible is placed in the furnace, and the furnace is heated to 980°C in 5 h, followed by 24–48 h soaking at this temperature. Once during this time, the flux is gently mixed by using a fork made of Pt stripes mounted on an alumina rod. After soaking, the lid is removed and the temperature progressively is lowered to 900°C and kept there for 5–10 h. The search for the liquidus is then carried out by slowly cooling the furnace while

dipping unpolished LGT seeds and analyzing the phases that crystallize onto them by x-ray diffraction (XRD). Several LPE films are then grown in a temperature range of typically 900 – 850°C . After the growth, the residual flux can easily be removed by cleaning the film in diluted nitric acid at room temperature.

31.6.4 Structural and Chemical Characterization of Doped LGT LPE Films

Various techniques have been used for the structural and chemical characterization of high-quality LPE films, and the best way to evaluate the films is usually to compare their quality with the substrates. In the following, only selected methods are discussed.

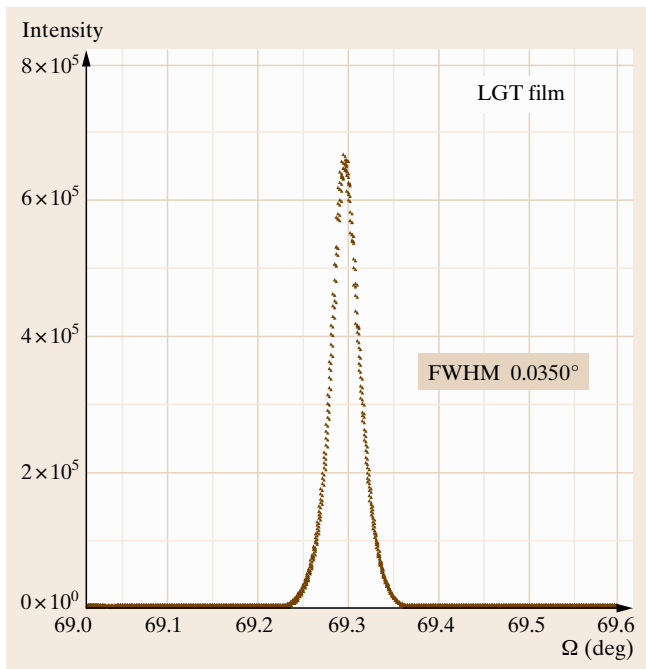


Fig. 31.11 Rocking curve of *x*-LGT film, (004) reflection (after [31.86])

Rocking Curve Measurements

The structural characterization of high-quality crystals and films can be done by rocking curve measurements. During such measurements, the crystal is rotated (rocked) through the Bragg angle, and the reflected beam is measured by a fixed counter. Each potentially slightly misoriented subgrain comes into reflection as the crystal is rotated. Hence, the width of a rocking curve is a direct measure of the range of orientation present in a crystal. For a perfect crystal, the theoretical full-width at half-maximum (FWHM) is on the order of 0.003°. Very few natural crystals reach this value, and most single-crystals have FWHM 10–100 times larger.

In the case of LGT, films and substrates with different orientation were analyzed [31.86]. For *x*-oriented LGT substrates, typical value of about FWHM of 0.044° was obtained for the (004) rocking curve. The rocking curve of an *x*-oriented Al:Ti:LGT film is shown in Fig. 31.11. A FWHM of 0.035° was obtained, which indicates its very high structural perfection, better than that of the substrate.

The structural perfection of *x*-oriented LGT films was consistently better than that of LGT substrates. Also, the surface of *x*-LGT films is usually extremely

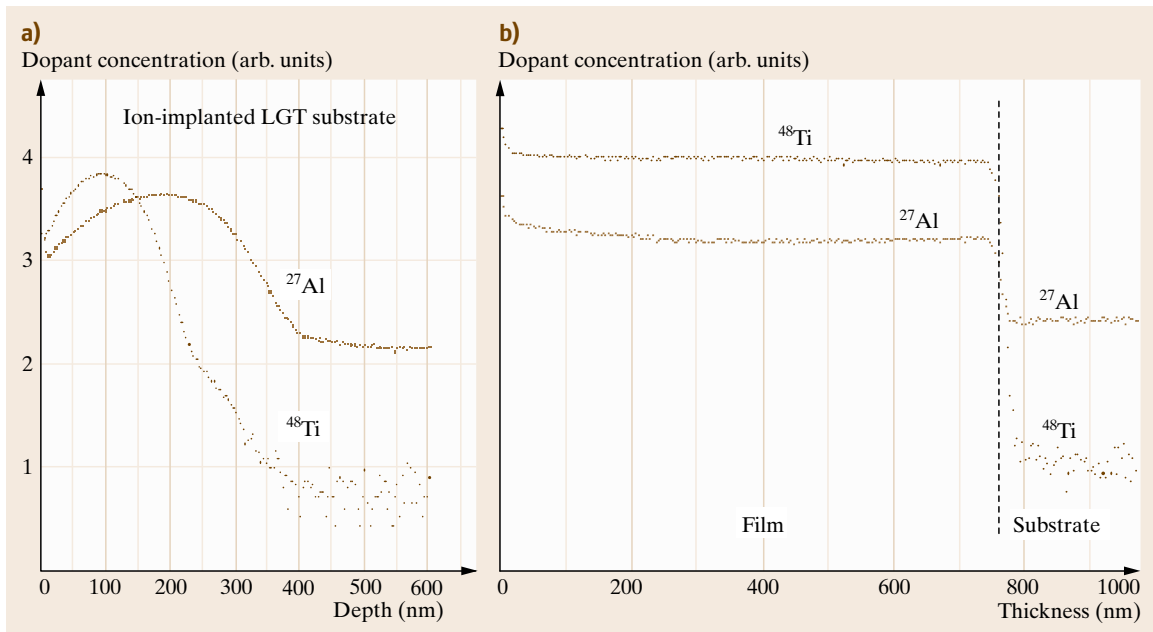


Fig. 31.12a,b Dopant concentration SIMS profile of: Al:Ti ion-co-implanted LGT substrate (a), and in situ codoped Al:Ti:LGT LPE film (b)

smooth, whereas y -oriented LGT films traditionally show a stepped surface [31.83]. Consequently, we obtained FWHM values slightly larger for y -oriented LGT LPE films, typically around 0.0465° . These values are quite remarkable for oxide films.

Quantitative Estimation of Dopant Concentration by SIMS

Secondary-ion mass spectroscopy (SIMS) is an analytical technique used for near-surface and small-area analysis. Depth profiling from about 1 nm to a few microns is possible. All elements and their isotopes can be detected by SIMS. Dynamic SIMS is used for bulk compositional analysis and depth profiles of trace elements. Several dopants were explored. Herein we focus on Al:Ti:LGT LPE films [31.86]. For quantitative measurement of the dopants concentration films by SIMS, standards are needed. Hence, Al and Ti ion-(co)implanted LGT substrates were used as standards. Figure 31.12a shows the SIMS profile of an Al:Ti ion-(co)implanted x -LGT substrate. The curved shape of the depth distribution is typical for ion-implanted samples, and demonstrate the inhomogeneous dopant concentration obtained by ion implantation. This should be compared with Fig. 31.12b, which is the SIMS

profile obtained for an x -oriented Al:Ti:LGT LPE film.

One can see that the Al and Ti dopants are extremely homogeneously distributed through the whole thickness of the LGT LPE film, with almost constant value, and a very abrupt decrease at the film-substrate interface. The SIMS profile also allows a precise measurement of the thickness of the films, which is challenging to measure by other techniques in the case of almost perfect lattice match with the substrate (homoeopitaxy).

The thickness of this film is about 770 nm. For a growth time of 30 min, these LGT films had typically thickness of 0.3–4 μm , depending on applied growth parameters. This also demonstrates that, in principle, relatively thin films can be grown by LPE technique. The mean dopant concentration values obtained for this film from the SIMS profile are: $^{48}\text{Ti}(100\text{--}700\text{ nm}) \approx 2.72 \times 10^{19} \text{ atoms/cm}^3$, and $^{27}\text{Al}(200\text{--}700\text{ nm}) \approx 5.67 \times 10^{18} \text{ atoms/cm}^3$ within the film depth given in brackets. If one assumes that the isotopic abundance is preserved, the corrected value for Ti is $3.69 \times 10^{19} \text{ atoms/cm}^3$. These are equilibrium concentrations for the applied film growth temperature and conditions.

31.7 Liquid-Phase Epitaxy of Nitrides

Group III nitrides such as AlN, GaN, InN, and their alloys are the focus of intense research for their high potential in optoelectronic devices and high-power high-temperature electronics. These nitrides form ternary and quaternary solid solutions which enable the energy bandgap of the devices to be tuned from about 0.7 eV (InN) to 3.45 eV (GaN), to 6.2 eV (AlN). Hence, they are excellent candidates for engineering of materials with a specific bandgap. The III–V nitrides and their solid solutions are suitable for a wide range of applications, for example, for high-temperature piezoelectric and pyroelectric applications, surface acoustic wave (SAW) devices, light-emitting diodes (LEDs), laser diodes (LDs), and ultraviolet (UV) detectors and sensors.

Wide-bandgap nitride semiconductors have been successfully commercialized as LEDs for solid-state lighting/illumination, compact laser sources for digital versatile disk (DVD) heads, and even high-power electronics in the form of high-electron-mobility transistors (HEMTs). However, doping issues, the lack of lattice-

matched substrates, and high film defect density are currently major obstacles for the reliable development of high-performance devices.

The field of nitrides would highly profit from the availability of bulk GaN and AlN single crystals. However, their synthesis is faced with several difficulties. They cannot be grown from the melt by Czochralski or Bridgman technique due to their extremely high decomposition temperature of about 45 000 atm for GaN at a (theoretical) melting temperature of about 2500 $^\circ\text{C}$. Various methods have been applied to synthesis of bulk nitrides, but none of them has yet provided substrates of sufficient quality and/or sufficient yield to be successfully implemented in device technology.

Interest in nitrides as semiconducting materials in the blue/UV range dates back to early 1970, with the first studies on epitaxial deposition of GaN with promising electrical and optical properties. However, the material showed strong n -type character, and p -type doping could not be achieved. Thus, interest in GaN faded until 1989, when p -type conduction could be

demonstrated for the first time by low-energy electron-beam irradiation (LEEBI) of Mg-doped films [31.87]. The majority of GaN layers are grown from the vapor phase, by MOVPE, MBE, or HVPE, on mismatched substrates. On sapphire and SiC, the layers present a columnar structure consisting of many small hexagonal grains [31.88], which are tilted and rotated within the GaN film and which give rise to very high dislocation densities of about 10^9 – 10^{10} cm $^{-2}$. In spite of this, very bright LEDs and LDs have been demonstrated [31.89]. The highest brightness and lifetimes are reported for layers grown by the epitaxial lateral overgrowth (ELO) technique on sapphire [31.90] and SiC [31.91], which is due to the reduction of the dislocation density to about 10^5 cm $^{-2}$ that can be obtained using ELO. This clearly demonstrates the impact of the crystalline perfection of the GaN layer on device performance.

Aluminum nitride has great potential in UV sensor devices. It also presents the required attributes for high-temperature high-power applications, where a high bandgap energy, high thermal and chemical stability, low leakage currents, high breakdown currents, high dielectric constant, and high resistance are required. In particular, AlN has emerged as a potential candidate for high-energy-density capacitors. Film defects such as low-angle grain boundaries (LAGBs), threading dislocations (TDs), and the development of a columnar structure are responsible for leakage currents. Hence, despite its potential, this material has not yet found broad application in such devices. Improving the quality of AlN films (and single crystals) is a critical challenge towards applications of AlN.

The case of InN and InGa N solid solutions is particularly interesting. This material received less attention than AlN and GaN until recently, when the energy gap of wurtzite InN was found to be about 0.7 eV [31.92–94] instead of the previously reported value of 1.9 eV [31.95]. This has extended the range of the energy gaps of group III nitride alloys from the deep-ultraviolet to the near-infrared spectral region. It has been shown that the bandgap of InGa N solid solutions can be varied continuously from 0.7 to 3.4 eV [31.96], providing a full-solar-spectrum material system for multijunction solar cells. In addition, a much greater radiation resistance has been reported for InGa N alloys compared with materials such as GaAs and GaInP. This makes them particularly suitable for radiation-hard high-efficiency solar cells for space exploration [31.97]. Here also, the highest photovoltaic cell efficiencies are expected from low-defect films and

lattice-matched high-quality substrates, and this is a further area where LPE growth is particularly important to explore.

Today, the majority of AlInGa N devices rely on vapor-phase growth, often on highly mismatched substrates such as sapphire and SiC, leading to epilayers with large density of defects. As can be recognized from above, almost all applications of nitrides would greatly benefit from high-quality crystal/film nitride material. It is therefore surprising that LPE growth of nitrides is only marginally studied by a few groups.

31.7.1 Developments and Trends in LPE of GaN and AlN

LPE growth of GaN has been explored as early as 1972, by Logan and Thurmond [31.98], with the successful growth of GaN films on sapphire from Ga and Ga + Bi solvents, and ammonia gas as nitrogen source. A low solubility of $x_{\text{GaN}} \approx 3 \times 10^{-5}$ at 1150 °C at 1 atm pressure was reported. LPE growth of GaN on highly mismatched sapphire substrates (misfit $\approx 1.6\%$) turned out to be very challenging, and n-type material was obtained, similarly to vapor-grown films. GaN and InGa N films were successfully grown by LPE on a variety of substrates: sapphire, LiGaO $_2$ (LG), LiAlO $_2$ (LAO), and on MOVPE/HVPE buffer layers [31.99]. The kinetics of GaN formation from Ga solvent in ammonia atmosphere was investigated [31.100]. In 1964, Glemser [31.101] showed that Li $_3$ N dissolves in melts based on lithium halides. Li $_3$ N is one of the few nitrides that can be grown by Czochralski technique, and the solubility of nitrogen in molten Li $_3$ N has been investigated [31.102]. Later, Li and Li $_3$ N [31.103] fluxes were applied for the growth of GaN. Other solvent systems were investigated for the synthesis of nitride single crystals. Solutions based on Ga with Na have been successfully applied to the growth of GaN [31.104, 105], and dislocation densities as low as 2.3×10^5 cm $^{-2}$ were reported [31.106]. Considering the fact that the LPE growth process that can be applied is very inexpensive compared with the multistep VPE growth technology necessary for similar film quality, there is significant potential in this approach. A remarkable aspect of LPE of GaN is that films with dislocation densities as low as 10^4 cm $^{-2}$ can be grown on MOCVD GaN templates that have a much higher dislocation density (10^7 – 10^8 cm $^{-2}$) [31.107]. Most GaN LPE and flux-growth experiments were performed at pressure of about 40–50 atm in sealed crucibles [31.106, 107]. In such systems, not only the

temperature but also the pressure becomes a variable. Besides challenges in nucleation control, growth stability is difficult to achieve in such systems. Hence, the use of solvents and LPE methods that allow the growth of GaN at atmospheric pressure may represent a better choice for the growth of thin high-quality LPE GaN films. From the low defect densities already obtained despite the use of nonideal templates [31.107] and nonoptimal LPE growth conditions, we can certainly predict that lowest dislocation (defects) densities will some day be reported for LPE-grown nitride films.

In the case of AlN, Dugger was the first to demonstrate the growth of AlN crystals of about 1 mm length from AlN-Ca₃N₂ solutions [31.108]. Recent studies with similar fluxes were only marginally successful, and the growth of AlN single crystals and LPE films from such solutions represents still a challenge.

31.7.2 Substrates for Epitaxy of Nitrides

Under near-equilibrium growth conditions, the substrate parameters misfit, misorientation, as well as the substrate surface structure after polishing/cleaning play a fundamental role. Only at practically zero misfit and low supersaturation can the layer-by-layer or Frank-van der Merwe growth mode, yielding films with highest structural perfection, be expected. Besides sapphire, MgO, SiC, MgAl₂O₄, and Si have been investigated as substrate material for nitrides, but all of them have too high a misfit for coherent overgrowth and layer-by-layer growth by LPE. Promising substrate materials such as LiGaO₂ (LGO) and LiAlO₂ (LAO) have emerged. However, their low chemical and thermal stability (about 900 °C) limits the growth parameters to be applied for any growth technique. Zinc oxide is actually the best lattice-matched substrate for nitrides, available at high yield [31.109]. The combination of ZnO and GaN in multilayer device structures would also be of particular interest to optoelectronic devices. However, ZnO has limited chemical stability with respect to halogenides at high temperature, and therefore cannot be used in chloride-HVPE nitride growth processes. This does not represent a major issue in LPE growth, where the substrate is immersed in the (metallic) solvent and the process is performed in such a way that the substrate never comes into direct contact with the reactive atmosphere.

Among all choices, homoepitaxial deposition provides the best possible conditions for highest-quality GaN LPE-grown films [31.99]. Hence, thick GaN films

or GaN substrate crystals would be of greatest interest, also as base structure for the fabrication of devices by VPE. Among all methods, the ammonothermal is actually the most promising method for obtaining large-size (≥ 2 inch) GaN at high yield. In 1997/1998 Dwilinski et al. demonstrated ammonothermal growth of GaN and AlN from supercritical ammonia and lithium and potassium amides [31.110]. The excellent properties reported led to intensive research in this area by different groups. It was found that GaN show a retrograde solubility when basic mineralizers are used, and quite high pressures (100–300 MPa) have to be applied [31.111, 112]. In acid mineralizers, the solubility behavior of GaN is conventional, and the process can be carried out at lower pressures (≤ 150 MPa) [31.113], which makes growth stability easier to achieve. The increasing availability of near-lattice-matched substrates will be very significant for major advances in the field.

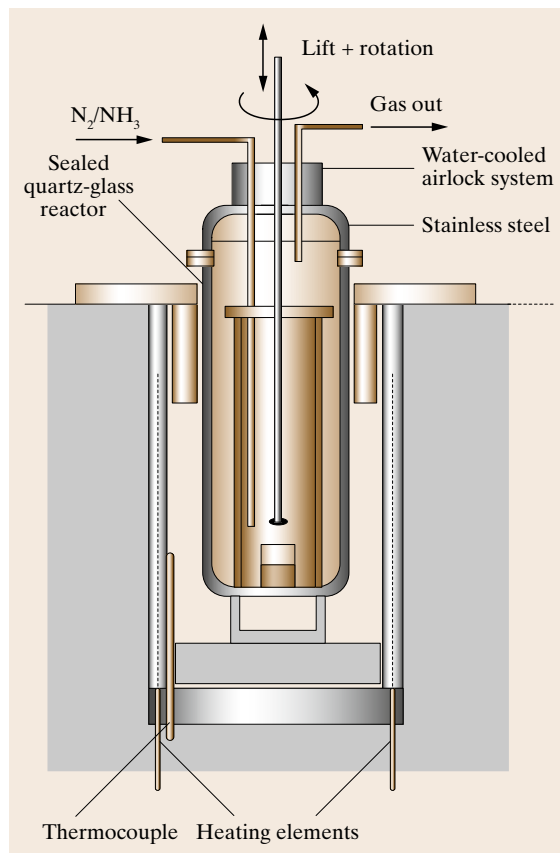


Fig. 31.13 Schematic view of the nitride LPE growth system (after [31.99])

31.7.3 Growth System and Optimization

In the following, a relatively simple growth system and method is presented, which was successfully used for the growth of GaN and InGaN films from Ga or Ga + Bi solutions, using NH_3 nitrogen source [31.99]. The film growth was performed in a sealed quartz glass reactor placed in a chamber furnace schematically shown in Fig. 31.13.

The crucible is placed in an appropriate temperature gradient in the middle of the reactor. A quartz liner is placed between the crucible and the reactor wall, with quartz glass plates placed on its top. This arrangement allows to reduce the convection of the gases above the crucible and is beneficial to prevent contamination of the solution by impurities/contaminants from the quartz reactor and/or airlock system.

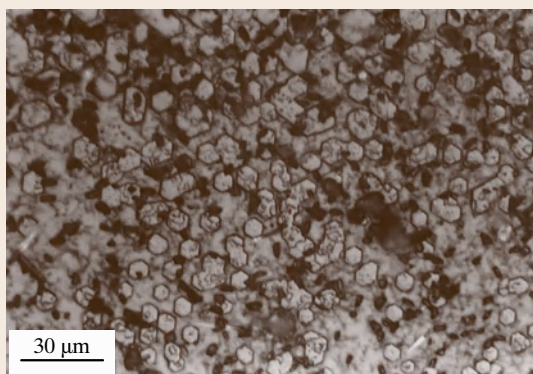


Fig. 31.14 Typical surface morphology of GaN LPE film on sapphire (basal plane). A large lattice mismatch results in the Volmer–Weber growth mode with development of hexagonal GaN islands

In a typical experiment, the reactor with empty crucible is evacuated and cleaned several times with nitrogen gas and heated to about 850°C . The liquid gallium or other (liquid/preheated) solvent can be introduced into the crucible from the top of the reactor, through the airlock system. The suitability of this method depends on the solvent used. If it is applied, this procedure has to be done under nitrogen overpressure, to prevent oxygen contamination. The temperature is then raised to the growth temperature. The substrate is fixed on an alumina or graphite substrate holder in horizontal, vertical or inclined position, and introduced into the reactor through the airlock system. The substrate is dipped into the solution, rotated, and the reactive gas mixture is then introduced into the reactor. This procedure allows the use of substrates that would not withstand the reactive gas atmosphere without degradation, for example, ZnO. In principle, various reactive gases can be applied. In the specific experiments described herein [31.99], a gas mixture of NH_3 and N_2 with ratio 1 : 4 was used. After the growth, before removing the substrates from the solution, pure nitrogen is introduced and the temperature reduced to about 800°C while removing the film from the solution. Growth times of 10–72 h were applied, and several films were grown successively.

31.7.4 Morphological Evolution of LPE-Grown Nitride Films

Sapphire substrates (basal plane) have a lattice mismatch of -13.7% with GaN along the a direction, which leads to the Volmer–Weber (or islands) film growth mechanism. GaN LPE films grown directly on sapphire typically present hexagonal islands, which may spread over the entire substrate surface by coalescence, resulting in grain-boundary-rich films. Figure 31.14 shows a Nomarski microphotography of a GaN LPE on sapphire during the coalescence phase.

When GaN LPE films are grown on GaN templates, growth starts preferentially on existing defects. Etch back and regrowth mechanisms can easily take place, as growth proceeds near thermodynamic equilibrium, with very low supersaturation. Hence, surface mobility of atoms is high, which leads to the smoothing effect on growth hillocks present on GaN buffer layer. This is shown in the Nomarski microscopy images of Fig. 31.15. On the left, we can see the surface morphology of a GaN HVPE seed layer grown on sapphire before LPE. Conical islands and overall roughness along the macrosteps are clearly visible. On the right,

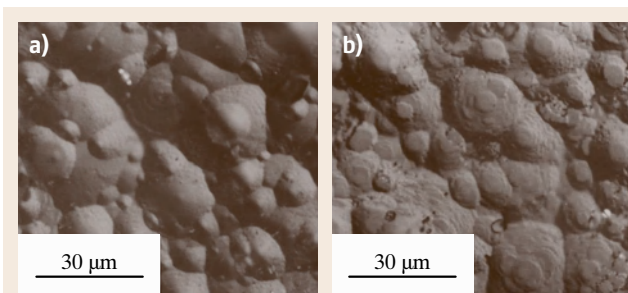


Fig. 31.15 (a) Nomarski microphotography of the surface of a HVPE GaN template before LPE growth. (b) GaN film morphology at the early stage of LPE growth on the GaN HVPE template

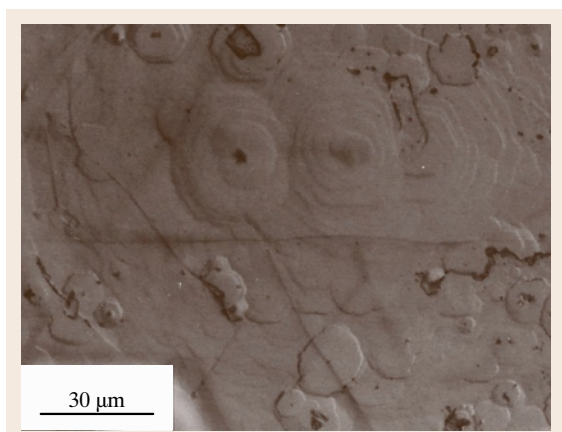


Fig. 31.16 Nomarski microphotograph of the surface of a GaN LPE film, grown on a HVPE MOVPE seed layer on sapphire (after [31.99])

after LPE growth, we recognize the overgrown regions, with smooth regions that start to develop from the pre-existing islands. For longer growth time, such film may evolve into a smooth surface, with large flat areas.

Improved surface morphology can be obtained by using better-quality GaN templates, as shown in Fig. 31.16. The overgrown regions develop to rather flat areas already in the early stages of LPE film growth, when using a multilayer HVPE GaN template grown on a MOVPE GaN buffer layer on sapphire [31.99].

InGaN LPE films could be successfully grown [31.114] using the same growth system described above. However, the film morphologies that were obtained for films grown on sapphire, without a buffer layer, were quite surprising. In contrary to GaN LPE films, island growth was largely suppressed, and smooth surfaces did develop despite the lattice mismatch. Rather smooth, rounded hillocks developed and steps

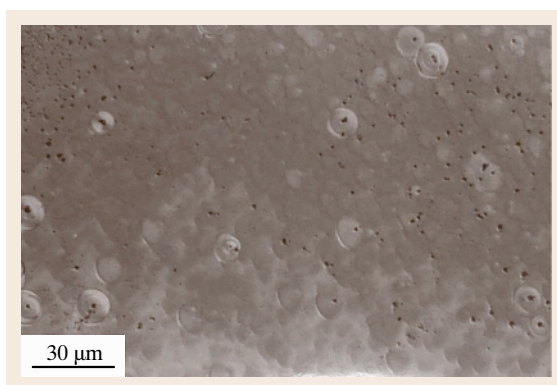


Fig. 31.17 InGaN film grown by LPE on *c*-sapphire, without a buffer layer. The lattice pulling effect can tentatively explain the (partial) suppression of the island growth mechanism that would be expected from the large lattice mismatch with the substrate

propagated over large surface area. This can be recognized in the Nomarski microphotographs of InGaN LPE film, which is shown in Fig. 31.17.

The InGaN film shown in Fig. 31.17 was grown from liquid Ga and ammonia reactive gas atmosphere by the procedure previously described. Growth conditions were similar to those applied for LPE of GaN [31.99], and film thickness was typically a few microns (GaN and InGaN). This significant difference in growth morphology can tentatively be explained by a possible lattice pulling effect that would minimize the lattice mismatch and hence reduce or suppress the island growth mechanism. Further investigations are needed to confirm this. However, this preliminary result is very promising, and LPE-grown high-quality InGaN solid-solution films may become a valuable approach in the fabrication of high-efficiency radiation-hard photovoltaic solar cells.

31.8 Conclusions

Liquid-phase epitaxy has been a major technique for the development of many materials, and for a variety of applications. The challenges of this technique, and especially the stringent requirements in all substrate and growth process parameters, have often been critical limiting factors. This has been shown especially in Sect. 31.5, where some aspects of LPE growth of high-temperature superconductors were presented. However, the structural perfection and homogeneity of the films

that can potentially be achieved is the highest possible, when compared with any other melt or thin-film growth techniques. This is not only true for the case of semiconductors (for example, GaP; Sect. 31.1) but also in the case of complex oxides. There is a misconception that only thick films can be grown by LPE. Though this has been true for a majority of compounds investigated by LPE so far, the recent results presented in Sect. 31.6 on the LPE growth of langasites demonstrates that thin

films of the order of a few hundred nanometers can also be grown by LPE.

The technologically important field of nitrides could greatly benefit from LPE-grown low-defect films, and this was discussed in Sect. 31.3. Several nitride applications actually hinge on the high density of film defects, and the lack of lattice-matched substrates. Despite the use of sophisticated multistep deposition methods and epitaxial lateral overgrowth, and the significant amount of research by several groups in this area over the past 10 years, the lower limit for the dislocation density achieved is about 10^5 cm^{-2} , which is two or three orders of magnitude too high for many applications. Especially here, the LPE technique could possibly lead to major advances, enabling material with lower dislocation density that could also be used as ideal substrates for growth of multilayer structures by VPE. In fact, LPE GaN films

with low dislocation densities of the order of 10^2 cm^{-2} have already been demonstrated, and they can be grown without the need of any external patterning or the ELO technique. Besides GaN, AlN and InN could also benefit from LPE studies; for example, one would expect highest efficiencies for In-rich InGaN photovoltaic cells based on LPE-grown material.

Despite its challenges, the LPE technique offers the unique possibility to explore fundamental structure–property relations in a variety of doped and undoped materials grown under equilibrium conditions. This technique allows the study of incongruently melting materials with potentially interesting properties that are not investigated because they cannot be grown by any other (melt) growth technique. In conclusion, there is significant margin for the discovery and study of novel materials using the LPE growth technique.

References

- 31.1 H. Nelson: Epitaxial growth from the liquid state and its application to the fabrication of tunnel and laser diodes, *RCA Review* **24**, 603 (1963)
- 31.2 L.R. Dawson: High-efficiency graded band-gap $\text{Ga}_{1-x}\text{Al}_x\text{As}$ light-emitting diodes, *J. Appl. Phys.* **48**, 2485–2492 (1977)
- 31.3 J.I. Nishizawa, Y. Okuno: Liquid-phase epitaxy of GaP by a temperature difference method under controlled vapor-pressure, *IEEE Trans. Electron. Dev.* **22**, 716–721 (1975)
- 31.4 J. Nishizawa, Y. Okuno, M. Koike, F. Sakurai: Bright pure green emission from N-free GaP LEDs, *Jpn. J. Appl. Phys.* **19**, 377–382 (1980)
- 31.5 M. Konagi, K. Takahashi: Formation of GaAs–(GaAl)As heterojunction transistors by liquid-phase epitaxy, *Trans. IEEE J.* **94-C**, 141 (1974)
- 31.6 E. Bauser, D. Kass, M. Warth, H.P. Strunk: *Mater. Res. Soc. Symp. Proc.* **54**, 267 (1986)
- 31.7 T. Nishinaga, T. Nakano, S. Zhang: Epitaxial lateral overgrowth of GaAs by LPE, *Jpn. J. Appl. Phys.* **27**, L964–L967 (1988)
- 31.8 Y. Suzuki, T. Nishinaga: Epitaxial lateral overgrowth of Si by LPE with Sn solution and its orientation dependence, *Jpn. J. Appl. Phys.* **28**, 440–445 (1989)
- 31.9 S. Kinoshita, Y. Suzuki, T. Nishinaga: Epitaxial lateral overgrowth of Si on non-planar substrate, *J. Cryst. Growth* **115**, 561–566 (1991)
- 31.10 T. Kochiya, Y. Oyama, T. Kimura, K. Suto, J.I. Nishizawa: Dislocation-free large area InP ELO layers by liquid-phase epitaxy, *J. Cryst. Growth* **281**, 263–274 (2005)
- 31.11 S.H. Shin, G.T. Niizawa, J.G. Pasko, G.L. Bostrup, F.J. Ryan, M. Khoshnevisan, C.I. Westmark, C. Fuller: P–I–N CdTe gamma-ray detectors by liquid phase epitaxy (LPE), Presented at the Nucl. Sci. Symp., Orlando (1984)
- 31.12 G. Bostrup, K.L. Hess, J. Ellsworth, D. Cooper, R. Haines: LPE HgCdTe on sapphire: Status and advancements, *J. Electron. Mater.* **30**, 560–566 (2001)
- 31.13 R.C. Linares: Epitaxial growth of narrow linewidth yttrium iron garnet films, *J. Cryst. Growth* **314**, 443–446 (1968)
- 31.14 H.J. Levinstein, S. Licht, R.W. Landorf, S. Blank: Growth of high-quality garnet thin films from supercooled melts, *Appl. Phys. Lett.* **19**, 486–488 (1971)
- 31.15 S.L. Blank: Crystal growth: Magnetic garnets by liquid-phase epitaxy, *J. Educ. Modules Mater. Sci. Eng.* **2**, 357–390 (1980)
- 31.16 M.H. Randles: Crystals for magnetic applications. In: *Crystals: Growth, Properties, and Applications*, Vol.1, ed. by C.J.M. Rooijmans (Springer, Berlin, Heidelberg 1978) pp. 71–96
- 31.17 D. Elwell, H.J. Scheel: *Crystal Growth from High-Temperature Solutions* (Academic, London 1975)
- 31.18 W. van Erk: The growth kinetics of garnet liquid-phase epitaxy using horizontal dipping, *J. Cryst. Growth* **43**, 446–456 (1978)
- 31.19 R. Ghez, E.A. Giess: Liquid phase epitaxial-growth kinetics of magnetic garnet films grown by isothermal dipping with axial rotation, *Mater. Res. Bull.* **8**, 31–42 (1973)
- 31.20 W.K. Burton, N. Cabrera, F.C. Frank: The growth of crystals and the equilibrium structure of their surface, *Philos. Trans. R. Soc. Lond. Ser. A* **243**, 299–358 (1951)
- 31.21 A.A. Chernov: Crystal growth from the solution and from the melt, *Sov. Phys. Usp.* **4**, 129 (1961)

- 31.22 J.A. Burton, R.C. Prim, W.P. Slichter: The distribution of solute in crystals grown from the melt, *J. Chem. Phys.* **21**, 1987–1991 (1953)
- 31.23 G. Winkler: *Magnetic Garnets* (Vieweg, Braunschweig 1981)
- 31.24 C. Klemenz, I. Utke, H.J. Scheel: Film orientation, growth parameters and growth modes in epitaxy of $\text{YBa}_2\text{Cu}_3\text{O}_x$, *J. Cryst. Growth* **204**, 62–68 (1999)
- 31.25 D.P. Norton: Science and technology of high-temperature superconducting films, *Annu. Rev. Mater. Sci.* **28**, 299–347 (1998)
- 31.26 H. Hilgenkamp, J. Mannhart: Grain boundaries in high- T_c superconducting films, *Rev. Mod. Phys.* **74**, 485–549 (2002)
- 31.27 K.H. Wu, S.P. Chen, J.Y. Juang, T.M. Uen, Y.S. Gou: Investigation of the evolution of $\text{YBa}_2\text{Cu}_3\text{O}_{7-d}$ films deposited by scanning pulsed laser deposition on different substrates, *Physica C* **289**, 230–242 (1997)
- 31.28 C. Klemenz, H.J. Scheel: Flat $\text{YBa}_2\text{Cu}_3\text{O}_{7-\delta}$ layers for planar tunnel-device technology, *Physica C* **265**, 126–134 (1996)
- 31.29 C. Klemenz: Hollow cores and step bunching effects on (001)YBCO surfaces grown by liquid-phase epitaxy, *J. Cryst. Growth* **187**, 221–227 (1998)
- 31.30 A. Chakraborty, K.C. Kim, F. Wu, J.S. Speck, S.P. DenBaars, U.K. Mishra: Defect reduction in nonpolar a -plane GaN films using in situ SiN_x nanomask, *Appl. Phys. Lett.* **89**, 041903 (2006)
- 31.31 K.A. Dunn, S.E. Babcock, D.S. Stone, R.J. Matyi, L. Zhang, T.F. Kuech: Dislocation arrangement in a thick LEO GaN film on sapphire, *MRS Internet J. Nitride Semicond. Res.* **5**, W2.11 (2000)
- 31.32 B.A. Haskell, T.J. Baker, M.B. McLaurin, F. Wu, P.T. Fini, S.P. DenBaars, J.S. Speck, S. Nakamura: Defect reduction in (1100) m -plane gallium nitride via lateral epitaxial overgrowth by hydride vapor phase epitaxy, *Appl. Phys. Lett.* **86**, L1197–L1199 (2005)
- 31.33 B.A. Haskell, F. Wu, M.D. Craven, S. Matsuda, P.T. Fini, T. Fujii, K. Fujito, S.P. DenBaars, J.S. Speck, S. Nakamura: Defect reduction in (1120) a -plane gallium nitride via lateral epitaxial overgrowth by hydride vapor-phase epitaxy, *Appl. Phys. Lett.* **83**, 644–646 (2003)
- 31.34 C. Klemenz, H.J. Scheel: Solubility of $\text{YBa}_2\text{Cu}_3\text{O}_{7-\delta}$ and $\text{Nd}_{1-x}\text{Ba}_2-x\text{Cu}_3\text{O}_{7+\delta}$ in the BaO/CuO flux, *J. Cryst. Growth* **200**, 435–440 (1999)
- 31.35 J.G. Bednorz, K.A. Müller: Possible high- T_c superconductivity in the Ba-La-Cu-O system, *Z. Phys. B* **64**, 189–193 (1986)
- 31.36 M.K. Wu, J.R. Ashburn, C.J. Torng, P.H. Hor, R.L. Meng, L. Gao, Z.J. Huang, Y.Q. Wang, C.W. Chu: Superconductivity at 93 K in a new mixed-phase Y-Ba-Cu-O compound system at ambient pressure, *Phys. Rev. Lett.* **58**, 908–910 (1987)
- 31.37 M. Hawley, I.D. Raistrick, J.G. Beery, R.J. Houlton: Growth mechanism of sputtered films of $\text{YBa}_2\text{Cu}_3\text{O}_7$ studied by scanning tunneling microscopy, *Science* **251**, 1587–1589 (1991)
- 31.38 C. Gerber, D. Anselmetti, J.G. Bednorz, J. Mannhart, D.G. Schlom: Screw dislocations in high- T_c films, *Nature* **350**, 279–280 (1991)
- 31.39 R.F. Belt, J. Ings, G. Diercks: Superconductor film growth on LaGaO_3 substrates by liquid-phase epitaxy, *Appl. Phys. Lett.* **56**, 1805–1807 (1990)
- 31.40 G. Balestrino, V. Foglietti, M. Marinelli, E. Milani, A. Paoletti, P. Paroli: Epitaxial films of BSCCO grown from liquid KCl solutions onto several substrates, *IEEE Trans. Magn.* **27**, 1589–1591 (1991)
- 31.41 G. Balestrino, V. Foglietti, M. Marinelli, E. Milani, A. Paoletti, P. Paroli, G. Luce: Structural and electrical properties of epitaxial films of BSCCO grown from liquid phase epitaxy, *Solid State Commun.* **76**, 503–505 (1990)
- 31.42 S. Narayanan, K.K. Raina, R.K. Pandey: Thin film growth of the 2122-phase of BCSCO superconductor with high degree of crystalline perfection, *J. Mater. Res.* **7**, 2303–2307 (1992)
- 31.43 H. Takeya, H. Takei: Preparation of high- T_c Bi-Sr-Ca-Cu-O films on MgO substrates by the liquid phase epitaxial (LPE) method, *Jpn. J. Appl. Phys.* **28**, L229–L232 (1989)
- 31.44 R.S. Liu, Y.T. Huang, P.T. Wu, J.J. Chu: Epitaxial growth of high- T_c Bi-Ca-Sr-Cu-O superconducting layer by LPE process, *Jpn. J. Appl. Phys.* **27**, L1470–L1472 (1988)
- 31.45 R.S. Liu, Y.T. Huang, J.M. Liang, P.T. Wu: Epitaxial growth of high- T_c superconducting Ti-Ca-Ba-Cu-O films by liquid phase epitaxial process, *Physica C* **156**, 785–787 (1988)
- 31.46 A.S. Yue, W.S. Liao, H.J. Choi: LPE growth of high- T_c $\text{Bi}_2\text{Sr}_2\text{Ca}_1\text{Cu}_2\text{O}_x$ films, *Cryogenics* **32**, 596–599 (1992)
- 31.47 J.S. Shin, H. Ozaki: Superconducting Bi-Sr-Ca-Cu-O films prepared by the liquid phase epitaxial method, *Physica C* **173**, 93–98 (1991)
- 31.48 L.H. Perng, T.S. Chin, K.C. Chen, C.H. Lin: Y-Ba-Cu-O superconducting films grown on (100) magnesia and sapphire substrates by a melt growth method without crucible, *Supercond. Sci. Technol.* **3**, 233–237 (1990)
- 31.49 C. Klemenz, H.J. Scheel: Liquid-phase epitaxy of high- T_c superconductors, *J. Cryst. Growth* **129**, 421–428 (1993)
- 31.50 C. Dubs, K. Fischer, P. Gönert: Liquid phase epitaxy of $\text{YBa}_2\text{Cu}_3\text{O}_{7-x}$ on NdGaO_3 and LaGaO_3 substrates, *J. Cryst. Growth* **123**, 611–614 (1992)
- 31.51 H.J. Scheel, C. Klemenz, F.-K. Reinhardt, H.P. Lang, H.-J. Güntherodt: Monosteps on extremely flat $\text{YBa}_2\text{Cu}_3\text{O}_{7-\delta}$ surfaces grown by liquid-phase epitaxy, *Appl. Phys. Lett.* **65**, 901–903 (1994)
- 31.52 T. Kitamura, M. Yoshida, Y. Yamada, Y. Shiohara, I. Hirabayashi, S. Tanaka: Crystalline orientation of $\text{YBa}_2\text{Cu}_3\text{O}_x$ film prepared by liquid-phase epitaxial growth on NdGaO_3 substrate, *Appl. Phys. Lett.* **66**, 1421–1423 (1995)

- 31.53 H.J. Scheel, F. Licci: Phase diagrams and crystal growth of oxide superconductors, *Thermochim. Acta* **174**, 115–130 (1991)
- 31.54 F. Licci, H.J. Scheel, P. Tissot: Determination of the eutectic composition by crystal growth and flux separation: example $\text{BaCuO}_2\text{--CuO}_x$, *J. Cryst. Growth* **112**, 600–605 (1991)
- 31.55 H.J. Scheel, F. Licci: Crystal growth of $\text{YBa}_2\text{Cu}_3\text{O}_{7-x}$, *J. Cryst. Growth* **85**, 607–614 (1987)
- 31.56 T. Aichele, S. Bornmann, C. Dubs, P. Görnert: Liquid-phase epitaxy (LPE) of $\text{YBa}_2\text{Cu}_3\text{O}_{7-x}$ high T_c superconductors, *Cryst. Res. Technol.* **32**, 1145–1154 (1997)
- 31.57 C. Krauns, M. Sumida, M. Tagami, Y. Yamada, Y. Shiohara: Solubility of RE elements into Ba–Cu–O melts and the enthalpy of dissolution, *Z. Phys. B* **96**, 207–212 (1994)
- 31.58 P. Bennema, J.P. van der Eerden: Crystal graphs, connected nets, roughening transition and the morphology of crystals. In: *Morphology of Crystals*, ed. by I. Sunagawa (Terra Scientific, Tokyo 1987), Chap. 1
- 31.59 G.H. Gilmer, K.A. Jackson: Computer simulation of crystal growth. In: *Crystal Growth and Materials*, ed. by E. Kaldis, H.J. Scheel (North Holland, Amsterdam 1977) pp. 80–114
- 31.60 D.S. Tsagareishvili, G.G. Gvelesiani, I.B. Baratashvili, G.K. Moiseev, N.A. Vatolin: Thermodynamic functions of $\text{YBa}_2\text{Cu}_3\text{O}_7$, $\text{YBa}_2\text{Cu}_3\text{O}_6$, Y_2BaCuO_5 and BaCuO_2 , *Russ. J. Phys. Chem.* **64**, 1404–1406 (1990)
- 31.61 G.K. Moiseev, N.A. Vatolin, S.I. Zaizeva, N.I. Ilyinych, D.S. Tsagareishvili, G.G. Gvelesiani, I.B. Baratashvili, J. Sesták: Calculation of thermodynamic properties of the phases in the Y–Ba–Cu–O system, *Thermochim. Acta* **198**, 267–278 (1992)
- 31.62 W. van Erk: The growth kinetics of garnet liquid-phase epitaxy using horizontal dipping, *J. Cryst. Growth* **43**, 446–456 (1979)
- 31.63 W. van Erk: A solubility model for rare-earth iron garnets in a $\text{PbO/B}_2\text{O}_3$ solution, *J. Cryst. Growth* **46**, 539–550 (1979)
- 31.64 W. van Erk: Growth of a mixed crystal from an ideal dilute solution, *J. Cryst. Growth* **57**, 71–83 (1982)
- 31.65 I. Utke, C. Klemenz, H.J. Scheel, M. Sasaura, S. Myazawa: Misfit problems in epitaxy of high- T_c superconductors, *J. Cryst. Growth* **174**, 806–812 (1997)
- 31.66 I. Utke, C. Klemenz, H.J. Scheel, P. Nüesch: High-temperature x-ray measurements of gallates and cuprates, *J. Cryst. Growth* **174**, 813–820 (1997)
- 31.67 N. Cabrera, M.M. Levine: On the dislocation theory of evaporation of crystals, *Philos. Mag.* **1**, 450–458 (1956)
- 31.68 H.P. Lang, H. Haefke, G. Leemann, H.J. Güntherodt: Scanning tunneling microscopy study of different growth stages of $\text{YBa}_2\text{Cu}_3\text{O}_{7-d}$ thin films, *Physica C* **194**, 81–91 (1992)
- 31.69 M. Hawley, I.D. Raistrick, J.G. Beery, R.J. Houlton: Growth mechanism of sputtered films of $\text{YBa}_2\text{Cu}_3\text{O}_7$ studied by scanning tunnelling microscopy, *Science* **251**, 1587–1589 (1991)
- 31.70 C. Gerber, D. Anselmetti, J.G. Bednorz, J. Mannhart, D.G. Schlom: Screw dislocations in high- T_c films, *Nature* **350**, 279–280 (1991)
- 31.71 T. Nishinaga, H.J. Scheel: Crystal growth aspect of high- T_c superconductors. In: *Advances in Superconductivity VIII*, ed. by H. Hyakawa, Y. Enomoto (Springer, Tokyo 1996) pp. 33–38
- 31.72 A.A. Kaminskii, B.V. Mill, G.G. Khodzhabyan, A.F. Konstantinova, A.I. Okorochkov, I.M. Silvestrova: Investigation of trigonal $(\text{La}_{1-x}\text{Nd}_x)_3\text{Ga}_5\text{SiO}_{14}$ crystals: I. Growth and optical properties, *Phys. Status Solidi (a)* **80**, 387–398 (1983)
- 31.73 Y.V. Pisarevski, P.A. Senushencov, P.A. Popov, B.V. Mill: New strong piezoelectric $\text{La}_3\text{Ga}_{5.5}\text{Nb}_{0.5}\text{O}_{14}$ with temperature compensation cuts, *Proc. IEEE Int. Freq. Control Symp.* (1995) pp. 653–656
- 31.74 S. Kück: Laser-related spectroscopy of ion-doped crystals for tunable solid-state lasers, *Appl. Phys. B* **72**, 515–562 (2001)
- 31.75 Y. Kim, A. Ballato: Force-frequency effects of Y-cut langanite and Y-cut langatate, *IEEE Trans. Ultrason. Ferroelectr. Freq. Control* **50**, 1678–1682 (2003)
- 31.76 J.A. Kosinski, R.A. Pastore Jr., X. Yang, J. Yang, J.A. Turner: Stress-induced frequency shifts in langasite thickness-mode resonators, *Proc. IEEE Int. Freq. Control Symp.* (2003) pp. 716–722
- 31.77 C. Klemenz, M. Berkowski, B. Deveaud-Pledran, D.C. Malocha: Defect structure of langasite-type crystals: a challenge for applications, *Proc. IEEE Int. Freq. Control Symp.* (2002) pp. 301–306
- 31.78 R. Fachberger, T. Holzheu, E. Riha, E. Born, P. Pongratz, H. Cerva: Langasite and langatate nonuniform material properties correlated to the performance of SAW-devices, *Proc. IEEE Int. Freq. Control Symp.* (2001) pp. 235–239
- 31.79 C.F. Klemenz, J. Luo, D. Shah: High-quality 2 inch $\text{La}_3\text{Ga}_{5.5}\text{Ta}_{0.5}\text{O}_{14}$ and $\text{Ca}_3\text{TaGa}_3\text{Si}_2\text{O}_{14}$ crystals for oscillators and resonators, *Adv. Electron. Ceram. Mater. Ceram. Eng. Sci. Proc.* **26**, 169–176 (2005)
- 31.80 B.V. Mill, Y.V. Pisarevshy, E.L. Belokoneva: Synthesis, growth, and some properties of single crystals with the $\text{Ca}_3\text{Ga}_2\text{Ge}_4\text{O}_{14}$ structure, *Proc. Jt. Meet. Eur. Freq. Time Forum IEEE Int. Freq. Control Symp.* (1999) pp. 829–834
- 31.81 B.V. Mill, M.V. Lomonosov: Two new lines of langasite family compositions, *Proc. IEEE Int. Freq. Control Symp.* (2001) pp. 255–262
- 31.82 V.I. Chani, K. Shimamura, Y.M. Yu, T. Fukuda: Design of new oxide crystals with improved structural stability, *Mater. Sci. Eng. R* **20**, 281–338 (1997)
- 31.83 C. Klemenz: Liquid-phase epitaxy of $\text{La}_3\text{Ga}_5\text{SiO}_{14}$, *Proc. Eur. Freq. Time Forum* (2001) pp. 42–45

- 31.84 C. Klemenz: High-quality langasite films grown by liquid-phase epitaxy, *J. Cryst. Growth* **237**, 714–719 (2002)
- 31.85 C. Klemenz: High-quality $\text{La}_3\text{Ga}_{5.5}\text{Ta}_{0.5}\text{O}_{14}$ and $\text{La}_3\text{Ga}_{5.5}\text{Nb}_{0.5}\text{O}_{14}$ LPE films for oscillators and resonators, *J. Cryst. Growth* **250**, 34–40 (2003)
- 31.86 C.F. Klemenz, A. Sayir: In-situ Al:Ti-co-doped $\text{La}_3\text{Ga}_{5.5}\text{Ta}_{0.5}\text{O}_{14}$ films for high-Q resonators, *Proc. IEEE Int. Freq. Control Symp.* (2006) pp. 676–680
- 31.87 H. Amano, M. Kito, K. Hiramatsu, I. Akasaki: P-type conduction in Mg-doped GaN treated with low-energy electron beam irradiation (LEEBI), *Jpn. J. Appl. Phys.* **28**, L2112–L2114 (1989)
- 31.88 F.A. Ponce: Defects and interfaces in GaN epitaxy, *MRS Bull.* **22**, 51–57 (1997)
- 31.89 S. Nakamura, M. Senoh, S. Nagahama, N. Iwasa, T. Yamada, T. Matsushita, Y. Sugimoto, H. Kiyoku: Subband emissions of InGaN multi-quantum-well laser diodes under room-temperature continuous wave operation, *Appl. Phys. Lett.* **70**, 2753–2755 (1997)
- 31.90 T. Detchprohm, T. Kuroda, K. Hiramatsu, N. Sawaki, H. Goto: The selective growth in hydride vapor phase epitaxy of GaN, *Inst. Phys. Conf. Ser.* **142**, 859–862 (1996)
- 31.91 T.S. Zheleva, O. Nam, M.D. Bremser, R.F. Davis: Dislocation density reduction via lateral epitaxy in selectively grown GaN structures, *Appl. Phys. Lett.* **71**, 2472–2474 (1997)
- 31.92 V.Y. Davydov, A.A. Klochikhin, R.P. Seisyan, V.V. Emtsev, S.V. Ivanov, F. Bechstedt, J. Furthmüller, H. Harima, V. Mudryi, J. Aderhold, O. Semchinova, J. Graul: Absorption and emission of hexagonal InN. Evidence of narrow fundamental band gap, *Phys. Status Solidi (b)* **229**, R1–R3 (2002)
- 31.93 J. Wu, W. Walukiewicz, K.M. Yu, J.W. Ager, E.E. Haller, H. Lu, W.J. Schaff, Y. Saito, Y. Nanishi: Unusual properties of the fundamental bandgap of InN, *Appl. Phys. Lett.* **80**, 3967 (2002)
- 31.94 J. Wu, W. Walukiewicz, W. Shan, K.M. Yu, J.W. Ager, E.E. Haller, H. Lu, W.J. Schaff: Effects of the narrow band gap on the properties of InN, *Phys. Rev. B* **66**, 201403 (2002)
- 31.95 T.L. Tansley, C.P. Foley: Optical bandgap of indium nitride, *J. Appl. Phys.* **59**, 3241–3244 (1986)
- 31.96 J. Wu, W. Walukiewicz, K.M. Yu, J.W. Ager, E.E. Haller, H. Lu, W.J. Schaff: Small band gap bowing in $\text{In}_{1-x}\text{Ga}_x\text{N}$ alloys, *Appl. Phys. Lett.* **80**, 4741–4743 (2002)
- 31.97 J. Wu, W. Walukiewicz, K.M. Yu, W. Shan, J.W. Ager, E.E. Haller, H. Lu, W.J. Schaff, W.K. Metzger, S. Kurtz: Superior radiation resistance of $\text{In}_{1-x}\text{Ga}_x\text{N}$ alloys: Full-solar-spectrum photovoltaic material system, *J. Appl. Phys.* **94**, 6477–6482 (2003)
- 31.98 R.A. Logan, C.D. Thurmond: Heteroepitaxial thermal gradient solution growth of GaN, *J. Electrochem. Soc.* **119**, 1727–1734 (1972)
- 31.99 C. Klemenz, H.J. Scheel: Crystal growth and liquid-phase epitaxy of GaN, *J. Cryst. Growth* **211**, 62–67 (2000)
- 31.100 G. Sun, E. Meissner, P. Berwian, G. Müller, J. Friedrich: Study on the kinetics of the formation reaction of GaN from Ga-solutions under ammonia atmosphere, *J. Cryst. Growth* **305**, 326–334 (2007)
- 31.101 O. Glemser, M. Field, K. Kleine-Weischeide: *Z. Anorg. Chem.* **332**, 257–259 (1964)
- 31.102 R.M. Yonco, E. Veleckis, V.A. Maroni: Solubility of nitrogen in liquid lithium and thermal decomposition of solid Li_3N , *J. Nucl. Mater.* **57**, 317–324 (1975)
- 31.103 W.J. Wang, X.L. Chen, Y.T. Song, W.X. Yuan, Y.G. Cao, X. Wu: Assessment of Li-Ga-N ternary system and GaN single crystal growth, *J. Cryst. Growth* **264**, 13–16 (2004)
- 31.104 M. Yano, M. Okamoto, Y.K. Yap, M. Yoshimura, Y. Mori, T. Sasaki: Growth of nitride crystals, BN, AlN and GaN by using a Na flux, *Diam. Relat. Mater.* **9**, 512–515 (2000)
- 31.105 H. Yamane, M. Shimada, S.J. Clarke, F.J. DiSalvo: Preparation of GaN single crystals using a Na flux, *Chem. Mater.* **9**, 413–416 (1997)
- 31.106 F. Kawamura, T. Iwahashi, M. Morishita, K. Omae, M. Yoshimura, Y. Mori, T. Sasaki: Growth of transparent: Large size GaN single crystal with low dislocations using Ca-Na flux system, *Jpn. J. Appl. Phys.* **42**, L729–L731 (2003)
- 31.107 F. Kawamura, H. Umeda, M. Kawahara, M. Yoshimura, Y. Mori, T. Sasaki, H. Okado, K. Arakawa, H. Mori: Drastic decrease in dislocations during liquid-phase epitaxy growth of GaN single crystals using Na flux method without any artificial processes, *Jpn. J. Appl. Phys.* **45**, 2528–2530 (2006)
- 31.108 C.O. Dugger: The synthesis of aluminum nitride single crystals, *Mater. Res. Bull.* **9**, 331–336 (1974)
- 31.109 T. Fukuda, D. Ehrentraut: Prospects for the ammonothermal growth of large GaN crystal, *J. Cryst. Growth* **305**, 304–310 (2007)
- 31.110 R. Dwiliński, R. Doradziński, J. Garczyński, L. Sierzputowski, J.M. Baranowski, M. Kamińska: AMMONO method of GaN and AlN production, *Diam. Relat. Mater.* **7**, 1348–1350 (1998)
- 31.111 T. Hashimoto, K. Fujito, M. Saito, J.S. Speck, S. Nakamura: Ammonothermal growth of GaN on an over-1-inch seed crystal, *Jpn. J. Appl. Phys.* **44**, L1570–L1572 (2005)
- 31.112 B. Wang, M.J. Callahan, K.D. Rakes, L.O. Bouthillette, S.-Q. Wang, D.F. Bliss, J.W. Kolis: Ammonothermal growth of GaN crystals in alkaline solutions, *J. Cryst. Growth* **287**, 376–379 (2006)

- 31.113 D. Ehrentraut, N. Hoshino, Y. Kagamitani, A. Yoshikawa, T. Fukuda, H. Itoh, S. Kawabata: Temperature effect of ammonium halogenides as mineralizers on the phase stability of gallium nitride synthesized under acidic ammonothermal conditions, *J. Mater. Chem.* **17**, 886–893 (2007)
- 31.114 C. Klemenz: unpublished

32. Molecular-Beam Epitaxial Growth of HgCdTe

James W. Garland, Sivalingam Sivananthan

Epitaxial HgCdTe grown by molecular-beam epitaxy (MBE) is the material of choice for advanced infrared (IR) detection and imaging devices. Its bandgap is easily tunable over the entire IR range with only very small changes in lattice constant, offering the possibility of multilayer device structures and thus an unlimited choice of device designs, and it yields devices with quantum efficiencies as high as 0.99. Despite a number of unresolved challenges in achieving its ultimate promise for industrial application, the great achievements in the MBE growth of HgCdTe are made evident by its routine use in the industrial manufacture of focal-plane arrays (FPAs). MBE growth can be continuously monitored in situ by reflection high-energy electron diffraction, spectroscopic ellipsometry (SE), and other characterization tools, providing instantaneous feedback on the influence of growth conditions on film structure. This allows the growth of a large range of unique structures such as superlattices (SLs), quantum well devices, lasers, and advanced design devices such as multicolor and high-operating-temperature IR sensors and focal-plane arrays. This chapter considers the theory and practice of MBE growth of HgCdTe and HgTe/CdTe superlattices and the use of HgCdTe in IR devices, emphasizing such incompletely resolved issues as the choice and preparation of substrates, dislocation reduction, p-doping, and the uses of SE.

The theory of MBE growth is summarized briefly in Sect. 32.2, followed by a lengthy discussion of substrate-related issues in Sect. 32.3, including a summary of the relative merits and demerits of different substrate materials. The growth hardware is discussed very briefly in Sect. 32.4, followed by a discussion of the in situ characterization tools used for monitoring and control of the growth in Sect. 32.5 and of the growth procedure for HgCdTe in Sect. 32.6. A discussion of the doping of HgCdTe, including the serious issues still surrounding

p-type doping, is given in Sect. 32.7. The properties achievable in MBE-grown HgCdTe are summarized in Sect. 32.8, with emphasis on the types of defects common in MBE-grown material, their effects on device performance, and possible methods to reduce the present defect densities. The use of MBE-grown HgTe/CdTe SLs for IR absorbers in lieu of HgCdTe alloy material is considered in Sect. 32.9. Finally, a brief discussion of the devices enabled by the MBE growth of HgCdTe and of their fabrication is given in Sects. 32.10 and 32.11, and a brief concluding summary of the chapter is given in Sect. 32.12.

32.1 Overview	1070
32.1.1 Why HgCdTe Is Important	1071
32.1.2 Why MBE Is the Preferred Method of Growth for HgCdTe IR Detectors and Imagers	1072
32.1.3 General Description of the MBE Growth Technique	1072
32.2 Theory of MBE Growth	1073
32.2.1 Pseudo-Equilibrium Theories	1074
32.2.2 Kinetic Theories	1075
32.3 Substrate Materials	1076
32.3.1 Substrate Orientation	1077
32.3.2 CdZnTe Substrates	1077
32.3.3 Si-Based Substrates	1084
32.3.4 Other Substrates	1087
32.4 Design of the Growth Hardware	1088
32.4.1 Mounting of the Substrate	1088
32.4.2 Valving of the Effusion Cells	1089
32.5 In situ Characterization Tools for Monitoring and Controlling the Growth	1090
32.5.1 Spectroscopic Ellipsometry (SE): Basic Theory and Experimental Setup	1090
32.5.2 SE Data Analysis	1092

32.5.3	SE Study of Hg Absorption and Adsorption on CdTe	1098	32.8	Properties of HgCdTe Epilayers Grown by MBE	1107
32.5.4	Correlation Between the Quality of MBE-Grown HgCdTe and the Depolarization and Surface Roughness Coefficients Measured by in situ SE	1099	32.8.1	Electrical and Optical Properties ..	1107
32.5.5	Surface Characterization by in situ RHEED	1100	32.8.2	Structural Properties	1110
32.5.6	Other in situ Tools for Controlling the Growth	1101	32.8.3	Surface Defects	1110
32.6	Nucleation and Growth Procedure.....	1101	32.9	HgTe/CdTe Superlattices.....	1112
32.6.1	Nucleation and Growth of CdTe or ZnTe on Si.....	1101	32.9.1	Theoretical Properties	1113
32.6.2	Substrate Preparation and Growth of HgCdTe	1102	32.9.2	Growth	1114
32.7	Dopants and Dopant Activation	1104	32.9.3	Experimentally Observed Properties	1114
32.7.1	Extrinsic n-Type Doping	1104	32.10	Architectures of Advanced IR Detectors ..	1115
32.7.2	Extrinsic p-Type Doping	1105	32.10.1	Reduction of Internal Detector Noise	1116
32.7.3	In situ Group I Dopant Incorporation	1106	32.10.2	Increasing Detector Response	1116
32.7.4	In situ Group V Dopant Incorporation	1106	32.10.3	High-Speed IR Detectors	1117
32.7.5	As Activation.....	1106	32.10.4	High-Operating-Temperature (HOT) IR Detectors	1118
			32.11	IR Focal-Plane Arrays (FPAs)	1118
			32.12	Conclusions	1119
			References	1121

Molecular-beam epitaxy (MBE) is a process for growing thin epitaxial films of a wide variety of materials, ranging from oxides to semiconductors to metals. Because of their high technological value, its first and still most common application is for the growth of compound semiconductors and their alloys. In MBE beams of atoms or molecules are incident in an ultra-high vacuum upon a heated crystal processed to produce a nearly atomically clean, smooth surface. The arriving atoms form a crystalline layer in registry with the substrate, i. e., an epitaxial film. MBE allows doping levels and alloy compositions to be controlled precisely and changed rapidly, producing almost atomically abrupt homojunctions or heterojunctions. In 1969 *Cho* [32.1] published landmark results reporting the first in situ observations of the MBE growth process using high-energy electron diffraction. He demonstrated that MBE growth could produce atomically flat, ordered layers; thus these studies marked the beginning of the use of MBE for practical device fabrication. This structural

analysis capability proved to be crucial for characterizing MBE epitaxy because it provided instantaneous feedback on the influence of growth conditions on film structure. That allowed the growth of a large range of unique structures such as superlattices (SLs), quantum well devices, lasers, and advanced design devices such as multicolor and high-operating-temperature IR sensors and focal-plane arrays.

MBE-grown HgCdTe is the material of choice for advanced infrared (IR) detection and imaging devices. Its bandgap is easily tunable over the entire IR range with only very small changes in lattice constant, it offers the possibility of multilayer device structures and thus an unlimited choice of device designs, and it yields devices with quantum efficiencies as high as 0.99. Despite a number of unresolved challenges in achieving its ultimate promise for industrial application, the great achievements in the MBE growth of HgCdTe are made evident by its routine use in the industrial manufacture of focal-plane arrays (FPAs).

32.1 Overview

The MBE growth technique for HgCdTe, the in situ characterization techniques used in its growth, the

present status of achievable HgCdTe material quality, and its applications to IR detection are reviewed here.

Particular emphasis is placed on the issues remaining to be solved before MBE-grown HgCdTe can reach its full potential as an ideal material for IR devices. These issues include substrate choice and preparation, the p-doping of HgCdTe, and the reduction of material defect densities. Recent progress in addressing those issues is discussed, as are techniques still under investigation for addressing those issues. Except for points not documented elsewhere, detailed discussions are left to the references.

32.1.1 Why HgCdTe Is Important

Infrared detectors fall into two broad categories: photon and thermal detectors. Photon detectors offer much higher detection speeds and sensitivities as well as the ability to differentiate between objects at different temperatures using multicolor or hyperspectral detectors and to form high-resolution images using FPAs. These properties are essential for almost all military and space applications. Mercury cadmium telluride has been of great interest as a material for infrared (IR) detection since it was first grown almost 50 years ago and has dominated the market for more than two decades [32.2]. It is the only semiconductor system in which the optical absorption edge can be made to vary across the entire IR spectrum with an almost constant lattice parameter. The 300 K lattice constant changes only from 6.4614 Å for HgTe with a -0.14 eV bandgap to 6.4825 Å for CdTe with a 1.56 eV bandgap. This allows the high performance of photodiodes over a much larger range than InGaAs, for example, and allows the epitaxial growth of layers with different optical cutoffs on top of one another with very little strain, $\approx 0.1\%$, which in turn, along with the low-temperature MBE growth method, allows the fabrication of advanced detectors and FPAs, such as multicolor and high-operating-temperature (HOT) FPAs, and allows the growth of HgTe/CdTe SLs, either for very long-wavelength infrared (VLWIR) detection or as buffer layers. In addition to this great advantage, HgCdTe offers two other overwhelming advantages that explain its dominance in the IR marketplace. Both the thermal generation rate per unit volume of material and the quantum efficiency for photon absorption in the IR are higher in HgCdTe than in any competing material. From a fundamental point of view only the diffusion-limited operation of a photovoltaic diode need be considered. In that case only these two properties are important in determining the maximum useful operating temperature, as discussed by Kinch [32.3] and outlined below.

The following four different types of materials systems have been serious players in the IR systems marketplace:

1. Direct-bandgap semiconductors (minority-carrier transport):
 - a) Binary III–V alloys such as InSb-based alloys
 - b) Ternary II–VI alloys (tunable-bandgap HgCdTe)
 - c) II–VI tunable-bandgap type I SLs (HgTe/CdTe)
 - d) Type II and III SLs such as InAs/GaInSb.
2. Extrinsic semiconductors such as Si:Ga or Ge:Hg (majority-carrier transport)
3. Type I SL quantum-well infrared photodetectors (QWIPs) such as GaAs/AlGaAs QWIPs (majority-carrier transport)
4. Silicon Schottky barriers such as PtSi or IrSi (majority-carrier transport).

For the reasons discussed in the previous paragraph, HgCdTe is the dominant direct-bandgap semiconductor material for applications in all regions of the IR spectrum except the VLWIR. Even there, either HgCdTe or HgTe/CdTe SLs are expected to become strong or even dominant players.

In the long-wavelength IR (LWIR) spectral band the normalized detector dark current is four orders of magnitude smaller for direct-bandgap semiconductors such as HgCdTe than for any of the other three types of systems, so that direct-bandgap semiconductors such as HgCdTe give the highest background-limited performance (BLIP) operating temperature by far. This is extremely important because cryogenic cooling is expensive and greatly increases the weight and bulk of IR detection and imaging systems. The sensitivity of a detector can be expressed in a variety of ways, but the limiting factor in all of them is the fluctuation in the relevant carrier concentration, as this determines the minimum observable signal. Ideally, neglecting the background incident flux, the most commonly used measure of the detectivity D^* depends only on the properties of the IR material in the detector. It is two or more orders of magnitude higher for HgCdTe than for any of the other three types of systems. Although material growth issues have prevented HgCdTe from reaching its full potential, it is the material of choice for most detector systems. The only important advantage of III–V alloys and SL QWIPs is their lower cost arising from the preexisting large industrial infrastructure in III–V materials and device growth, processing, and packaging. For military systems, which dominate the market, the increasing requirements of succeeding generations of IR detection and imaging systems will further enhance

the dominance of HgCdTe in the IR materials marketplace. No other material, even in principle, will be able to meet the requirements for higher operating temperatures (and ultimately totally uncooled operation), larger-area FPAs, faster frame rates, and multispectral operation with no increase, or even a reduction, in cost.

32.1.2 Why MBE Is the Preferred Method of Growth for HgCdTe IR Detectors and Imagers

Since the growth of HgCdTe by MBE was first reported in 1982 [32.4], more than 15 groups have been established worldwide for the growth of Hg-based alloys and SLs by MBE or metalorganic MBE (MOMBE) for IR device applications. Since that time enormous progress has been made in reducing defect densities, increasing growth areas, improving the control of alloy compositions and doping levels, and demonstrating increasingly sophisticated and powerful IR electrooptical devices, as discussed in later sections of this chapter. Molecular-beam epitaxy has many advantages over other methods for the epitaxial growth of HgCdTe [32.5]:

1. The MBE growth temperature for HgCdTe is only $\approx 185^\circ\text{C}$, far below the liquid-phase epitaxy (LPE) and metalorganic vapor-phase epitaxy (MOVPE) (also called metalorganic chemical vapor deposition (MOCVD)) growth temperatures of $\approx 450^\circ\text{C}$ and $300\text{--}400^\circ\text{C}$, respectively. This offers several great advantages. It greatly reduces impurity outdiffusion from the substrate, it allows the formation of precisely controlled, atomically sharp or graded hetero- or homojunctions, and it allows the growth of SLs.
2. MBE is ideally suited for the deposition of multilayer structures; in addition to having only diffuse junctions, heterostructures grown by LPE usually are limited to two or three layers because different melts are required for the growth of layers having different compositions or dopings. MBE is the only technique suited to the growth of SLs and the only technique allowing in situ growth of CdTe and ZnS passivation layers for devices.
3. MBE growth allows the use of spectroscopic ellipsometry (SE), reflection high-energy electron diffraction (RHEED), and other in situ analytical characterization techniques to monitor and control the growth.
4. Unlike LPE, no aggressive medium is present in MBE growth. Combined with the low growth temperature and analytical facilities for surface control,

this allows the use of alternative lower cost, more robust, larger size, more attainable substrates such as CdTe/Si with improved matching of the substrate and readout system thermal expansion coefficients.

5. In MBE no contamination of interfaces occurs because one can grow different compounds in the same growth run in the same system under ultrahigh vacuum.

In 1983 the first photovoltaic device fabricated from MBE-grown HgCdTe was reported [32.6]. By 1985 the quality of MBE-grown HgCdTe layers was comparable to that of the best layers grown by other techniques [32.7]. By 1997 the performance of IR FPAs made from MBE-grown material was comparable to that of those made from LPE materials [32.8]. Although materials-related HgCdTe problems remain, progress in MBE technology continues to outstrip that in more mature techniques such as LPE. Meanwhile, techniques closely related to conventional MBE and at first appearing to offer advantages have largely been abandoned: metalorganic MBE (MOMBE) [32.9, 10] because of its higher growth temperature and because of the ease of carbon contamination and void formation, and photo-assisted MBE (PAMBE) [32.11], which offered higher-quality growth and the as-grown activation of dopants with no self-compensation [32.12], because it was limited to extremely small-area growth.

32.1.3 General Description of the MBE Growth Technique

The reader is referred to [32.13, 14] for detailed and extensive reviews of the physical principles, equipment, and general procedures of MBE growth. Only a very brief general description is given here; specifics of the MBE growth of HgCdTe are discussed in Sects. 32.3–32.7. MBE uses localized beams of atoms or molecules in an ultrahigh-vacuum (UHV) environment as the source of the constituents to the growing surface of a substrate crystal. The UHV environment minimizes contamination of the growing surface. The beam atoms and molecules travel in nearly collision-free paths until arriving either at the substrate or at chilled walls of the chamber, where they condense and are effectively removed from the system. The substrate is kept at a moderately elevated temperature to provide sufficient thermal energy to the arriving atoms for them to migrate over the surface to lattice sites. When a shutter is interposed in a beam, the beam is effectively turned off almost instantly. These features make it possible

to grow the films very slowly without contamination, and to change the composition of the arriving stream of atoms very abruptly; in fact, the composition of the flux can be changed in times much shorter than that needed to grow a single atomic layer of the film.

The vacuum environment surrounding the growing crystal must be kept as low as possible to avoid contamination that might affect surface morphology and the electrical properties of the epilayer grown. Because the growth rate is low, $\approx 1\text{--}3\text{ ML/s}$, to keep the arrival rate of a background species at 10^{-6} of the growth rate would require a partial pressure of $\approx 10^{-12}$ Torr; however, fortunately many of the background species have low reactivities (low sticking coefficients). For III–V growth, the best background pressures achievable are $\approx 10^{-11}$ Torr (except in brand-new growth chambers), and pressures commonly are $\approx 10^{-10}$ Torr; for HgCdTe growth the achievable pressures are ≈ 100 times higher because of Hg contamination. Typically substrates are loaded into the growth chamber via a load-lock chamber, where they are outgassed while the growth chamber

remains under vacuum. Then, the vacuum is broken only in the small loading chamber, so only it needs to be evacuated. II–VI and III–V semiconductors should not be grown in the same chamber because the residual pressure from one would dope the other.

The growth chamber must include source ovens, beam shutters and their actuating mechanisms, a substrate holder and heater, in situ growth characterization tools, beam flux monitors, and cryopanels to act as cryopumps and to condense unused beam flux. All of these must be designed to minimize outgassing. The chamber must be designed to keep the substrate at a uniform well-controlled temperature, to provide uniform well-controlled fluxes to the substrate, to avoid temperature transients on the growth surface due to the shuttering and unshuttering of the atomic beams. Variations in the flux ratios and/or the temperature of the growing surface lead to compositional variations and even nonstoichiometry, which can destroy the crystalline quality of the growth. Typically, chambers are custom-designed for each type of material to be grown.

32.2 Theory of MBE Growth

Theories of MBE growth can be classified either as quasi-equilibrium thermodynamic theories or as kinetic growth theories. Although MBE growth typically is a far-from-equilibrium process, quasi-equilibrium theories have been found to yield valuable results even in cases in which desorption is negligible, so that the solid and vapor phases are far from equilibrium with one another. Only a partial equilibrium of the solid phase, not a global quasi-equilibrium, is required for the validity of most quasi-equilibrium theories. On the other hand kinetic theories are necessary to understand important aspects of MBE growth such as the surface morphology, as well as in determining the limits of validity of quasi-equilibrium thermodynamic theories. The structural quality of MBE-grown films depends largely on whether partial, or at least local, thermodynamic equilibrium is established on a time scale appropriate to the growth. If local thermodynamic equilibrium is established, one may use the usual notions of absolute rate theory and the resulting rate expressions for kinetic processes when describing MBE growth [32.15, 16]. However, whether the combined effect of individual kinetic processes is able to move the growing film toward a partial equilibrium state and to reach this state in a time scale relevant to the growth depends on the growth conditions and the specific nature of the material

being grown. Under some conditions, local thermodynamic equilibrium may exist during the growth, but the kinetics may not be fast enough to ensure partial equilibrium across the entire growth surface or even macroscopic areas of that surface. The microstructural and even the chemical properties of a film grown under only local equilibrium conditions can be very different from those of the film if it were grown under partial equilibrium conditions.

The basic MBE growth models have been reviewed in detail by Tsao [32.14]. The driving forces for MBE growth are the difference $\Delta\mu^\alpha$ between the chemical potential μ^α of the vapor of the α element and its equilibrium chemical potential for sublimation μ_{eq}^α . For many elements desorption is negligible in MBE; on the other hand, the desorption rate of Hg is orders of magnitude higher than its absorption rate in the MBE growth of HgCdTe. This implies that $\Delta\mu^{\text{Hg}} \ll k_{\text{B}}T$ at the growth temperature. For growth on a planar surface there exist three basic MBE growth modes. First, there is the layer-by-layer, two-dimensional or Frank–van der Merwe growth mode, in which each atomic layer tends to be completed before the next layer is started. Second, there is the three-dimensional or Volmer–Weber mode, in which hillocks and cavities form on the surface. Third is Stranski–Krastanov growth, in which the

growth begins as two dimensional and then becomes three dimensional. In fact, MBE growth of HgCdTe occurs on vicinal surfaces, with a well-defined miscut to a surface with low Miller indices. In this mode the growth surface is characterized by an array of steps between smooth terraces. The adatoms preferentially bond at the bottoms of the steps and the crystal grows as the steps advance across the growth surface with a velocity proportional to $\Delta\mu$ for the controlling chemical species (Te for HgCdTe) (step-flow growth).

A phenomenon of particular interest is the self-assembly of islands to form a regular array of quantum dots. To a first approximation, this can be understood as a form of growth in the Stranski–Krastanov regime. According to this point of view, based on general thermodynamic arguments, the deposited material starts to grow as a homogeneous wetting layer, because it has a lower surface energy than the substrate. After a critical thickness, the growth of three-dimensional islands that allow for partial elastic strain relaxation becomes energetically preferable to the two-dimensional film growth. These three-dimensional islands grow until they have reached an optimum size [32.17, 18]. Kinetics enters in this theory only as an external parameter, the island density, which is determined during the nucleation phase and assumed to remain constant during three-dimensional growth of the islands.

32.2.1 Pseudo-Equilibrium Theories

The general principles of the quasichemical thermodynamic theory were presented as early as the 1930s [32.19–24]. The formalism usually used was first given in 1956 [32.25]. The validity of the theory, which rests almost solely on the law of mass action, is unquestioned for thermodynamic equilibrium. However, by definition, thermodynamic equilibrium does not exist during crystal growth. Therefore, it is interesting to consider the past successes and failures of the theory in modeling MBE growth in terms of the degree of equilibrium of the growth. In the theory, one derives from any existing equilibrium condition a corresponding relationship between the probability of occurrence of some configuration of atoms, vacancies, etc. in the solid and the partial pressures of the gases with which the solid is approximately in equilibrium. For approximate global equilibrium during growth two requirements must be met. First, the sticking coefficient of that species must be very small, so that the ratio of the incident flux to the exeunt flux is very nearly

one. Second, any intermediate-state reactions must either be sufficiently fast not to hinder thermodynamic equilibrium or so slow that they take place only after absorption is complete, i. e., in the bulk below the growth surface. These two requirements suffice for the valid application of the theory to MBE growth. However, it has been shown that the application of the theory to MBE growth correctly describes the growth even in the absence of global equilibrium, provided that the second requirement holds.

As early as 1958, equilibrium thermodynamic arguments were used [32.26] to explain the different modes of epitaxial growth in terms of the surface energies at the epilayer–vacuum (σ), the epilayer–substrate (σ_i), and the substrate–vacuum (σ_s) layer interfaces. In partial equilibrium, layer-by-layer growth should be expected when $\sigma_s > \sigma + \sigma_i$, that is, when the change in the surface energy $\Delta\sigma = \sigma + \sigma_i - \sigma_s$ accompanying the deposition process is negative. When $\sigma_s < \sigma + \sigma_i$, or $\Delta\sigma > 0$, the film will grow as isolated islands. Stranski–Krastanov growth takes place when $\Delta\sigma$ changes sign from negative to positive because of strain energy after some characteristic thickness. This theory of course requires the atoms on the growing surface to have a high enough mobility to find the lowest-energy sites to occupy. Thus, it typically is valid only at the high end of the window of desirable growth temperatures.

Many authors have given first-principles thermodynamic treatments of the MBE growth of III–V compounds and alloys in agreement with experiment, even though their MBE growth is far from equilibrium for all chemical species involved. For example, the dependence of the desorption rate of Ga in $\text{Ga}_{1-x}\text{Al}_x\text{As}$ on x and on the growth temperature was established [32.27], and it was shown [32.28–30] that dopant incorporation in the MBE growth of GaAs occurs in accord with the theory. Also, the growth rates and compositions of a series of III–V compounds and alloys have been calculated, and results in agreement with experiment were found [32.31]. Additionally, the In desorption rate in MBE-grown AlInAs alloys has been calculated as a function of the As beam flux and substrate induced strain, again in agreement with experiment [32.32, 33]. Finally, the surface segregation of base elements and impurities in MBE-grown II–V compounds has been described [32.34].

Of more interest for this review, several authors have applied equilibrium thermodynamic theory to the growth of HgCdTe with useful results. Gaillard [32.35] found that MBE growth of CdTe, HgTe, and HgCdTe

is correctly described by the theory, and successfully calculated growth rates and compositions, as well as determining the range of acceptable growth conditions, all with no adjustable parameters. *Colin and Skauli* [32.36] used the theory to construct a general model for the optimization of the MBE growth conditions for HgCdTe. They calculated an optimal growth temperature as a function of Hg flux, Cd concentration, and growth rate. They also suggested that the growth of HgCdTe is improved by growing on a Te-rich surface, which is now common practice. *Vydyanath et al.* [32.37] used equilibrium thermodynamics to determine the Cd composition in In-doped HgCdTe as a function of the In and Te source temperatures. *Piquette et al.* [32.38] modified the results of Colin and Skauli by forcing the population of Hg atoms on the growth surface to be proportional to the HgTe fractional growth rate, finding a new formula for the optimized growth temperature that experimentally led to consistently lower defect densities. *Chang et al.* [32.39] have used that result to show that all thermodynamically equivalent growth conditions near optimized conditions lie on a straight line with slope -5385 in a graph of $\ln[p_{\text{Hg}}/\nu(1-x)]$ versus T^{-1} , where p_{Hg} is the pressure read by the Hg flux gauge, ν is the growth rate, and x is the Cd concentration. Equilibrium thermodynamics has also been applied to study the density of Te-condensation-related voids as a function of Hg flux [32.10] and to determine that As dopants from an uncracked source are incorporated primarily as As_4 molecules [32.40], rather than being dissociated on the growth surface.

32.2.2 Kinetic Theories

The MBE growth of semiconductors is performed at relatively low temperatures and slow growth rates in comparison with LPE and vapor-phase epitaxy (VPE). Low growth temperatures result in growth mechanisms that are strongly dominated by surface kinetics and chemistry. As the source molecular beams are introduced into the MBE chamber some of these molecular species reach the substrate and become physisorbed or weakly chemisorbed to the surface. The adsorbed molecules can then migrate to energetically favorable lattice sites, step edges, nucleated islands, etc. and bond there. A thermodynamic redistribution near the surface layers then establishes the final configuration.

MBE growth depends on the sticking coefficients and surface kinetics of atomic or molecular beams impinging on a suitable substrate. The importance of kinetics in the MBE growth of HgCdTe is demonstrated by the strong dependence of the Hg sticking coefficient [32.41–43] and the quality of growth [32.43, 44] on substrate orientation. One can identify a number of parameters relating to the kinetics of growth; they include the flux F of the impinging species, the sticking coefficient S , the desorption rate R , substrate orientation, substrate temperature, etc. A variety of kinetic rate equation atomistic models [32.45] have been explored for growth from the vapor phase on a planar substrate. In the case of epitaxial HgCdTe MBE growth, surface kinetics place strict boundaries on optimal deposition conditions. It has been found [32.46] that surface kinetics limits the Hg flux, the substrate orientation, and the substrate temperature during MBE HgCdTe growth.

Various kinetics problems have been treated; a few examples follow. A model for the evolution of the profile of a growing interface and a Langevin equation (the Kardar–Parisi–Zhang (KPZ) equation) for the local growth of the profile have been proposed [32.47]. It has been argued [32.48] that the KPZ equation is not the relevant continuum equation for MBE growth at intermediate temperatures, where overhangs and bulk defects can be neglected. A new nonlinear growth equation was suggested as the relevant dynamical equation for ideal MBE growth at intermediate to high temperatures. When desorption and overhangs occur, the KPZ equation remains the relevant equation describing MBE growth.

The effect of finite size on smooth layer-by-layer MBE growth has been examined, and it was concluded that, for finite system sizes, growth can always be smooth as long as the diffusion length is comparable to the system size even though the asymptotic growth may be rough in the thermodynamic limit [32.49]. The heteroepitaxy of InAs on GaAs(001) has been discussed, and first-principles density-functional theory calculations for In diffusion on the strained GaAs substrate have been presented [32.50]. In particular, the effect of heteroepitaxial strain on the growth kinetics of coherently strained InAs islands was considered. The strain field around an island was found to cause a slowing down of material transport from the substrate towards the island, and thus to help achieve more homogeneous island sizes.

32.3 Substrate Materials

As with all epitaxial systems and techniques, the structural quality of HgCdTe epilayers deposited by MBE is inextricably linked to the quality of the substrate. The absence of any substrate material satisfactory in all respects for the MBE growth of HgCdTe is perhaps the primary factor limiting the performance of IR detectors and FPAs. In 1993 Triboulet et al. [32.51] compared the basic properties and the advantages and disadvantages of different substrate materials. Here, we summarize and update that discussion and consider the question of substrate orientation. Special attention is paid to growth on CdZnTe and CdTe/Si substrates. For CdZnTe emphasis is placed on the nature of substrate bulk and surface imperfections, on their effect on MBE-grown epilayers, and on methods to ameliorate those effects and screen out bad substrate wafers before growth. For CdTe/Si, emphasis is placed on possible methods to overcome or ameliorate the effects of the large lattice mismatch between Si and CdTe, including new methods

being developed or under consideration. Several characteristics of the substrates in common use are compared in Table 32.1.

The first MBE growth of HgCdTe [32.4] was performed on a CdTe(111) substrate; early growths also were performed on CdTe(100) [32.6]. However, even the small lattice mismatch between CdTe and $\text{Hg}_{1-x}\text{Cd}_x\text{Te}$ with $x < 0.5$ caused threading dislocations and other crystalline defects. Also the growth on high-symmetry planes allowed the formation of a high density of microtwins in the HgCdTe [32.6]. The twinning can be eliminated by growth on higher-index planes or miscut surfaces, but bulk CdTe was abandoned as a substrate material because of a combination of factors, including the lattice mismatch, its low thermal conductivity, its poor crystalline quality, its brittleness, and its cost. $\text{Cd}_{0.96}\text{Zn}_{0.04}\text{Te}$ has become the substrate of choice for the growth of the highest-quality HgCdTe epilayers because of its in-principle

Table 32.1 Characteristics of the types of substrates currently used for MBE growth of HgCdTe

	$\text{Cd}_{1-y}\text{Zn}_y\text{Te}$ ($y = 0.04$)	GaAs	Si
Cost per cm^2	US\$ 400 (high-pressure Bridgman growth)	US\$ 0.71 (vertical gradient freeze growth) (US\$ 28.00 w/CdTe buffer)	US\$ 0.56 (float zone growth) (US\$ 27.86 w/CdTe buffer)
Largest commercially available size (cm^2)	49	182.4	5228
Robustness of material	Brittle	Moderately robust	Strong
Vickers hardness (kg/mm^2 at 300 K)	60	360	1150–1330
Thermal conductivity ($\text{mW}/(\text{cm K})$)	55	500	1235
Surface preparation	Difficult, sometimes poor	Standardized by large III–V industry	Standardized by large Si industry
Substrate surface defect density (cm^{-2})	10^4	5×10^3 (10^5 on CdTe buffer)	10^2 (10^5 on CdTe buffer)
Lattice mismatch with HgCdTe ($x = 0.2$ at 300 K)	$< 1\%$ ($< 1\%$ w/CdTe)	13.6% ($< 1\%$ w/CdTe)	19.47%
Substrate etch pit density (cm^{-2})		< 500 on CdTe buffer	< 5000 on CdTe buffer
Thermal mismatch with HgCdTe ($x = 0.2$ at 300 K)	3.53%	27.04% (1.85% w/CdTe)	51.85% (1.85% w/CdTe)
Valence issues	None	Minor	Severe
Other	Impurities, crystalline defects, compositional uniformity problem, large thermal mismatch with Si ROIC	In situ surface preparation may cause contamination	Allows monolithic integration Requires buffer layer

perfect lattice match to IR HgCdTe, but is plagued with many problems. Composite substrates consisting of epilayers of CdTe or $\text{Cd}_{0.96}\text{Zn}_{0.04}\text{Te}$ grown on InSb, sapphire, Ge, GaAs, and Si have been used because of their greater robustness, much lower cost, higher thermal conductivity, greater lateral uniformity, and larger possible areas in comparison with $\text{Cd}_{0.96}\text{Zn}_{0.04}\text{Te}$ substrates. Of these substrates, two are still in common use: CdTe/GaAs and CdTe/Si. However, the very large lattice and thermal mismatches between the underlying substrate material and the top epilayer in these substrates lead to serious problems. Great progress has been made in solving these and other problems associated with each type of substrate still in common use, but for no substrate have the problems yet been completely solved.

32.3.1 Substrate Orientation

Substrate orientation is of primary importance in MBE growth, as was recognized very early for growth on CdTe substrates by noting the strong dependence of the Hg sticking coefficient on orientation [32.41–43] and as is seen from the strong dependence of the quality of growth on substrate orientation [32.43, 44]. It was recognized from the beginning that growth on a low-index CdTe plane such as the (100) or (111) planes led to microtwinning. On alternative substrates such as GaAs or Si growth on the (100) plane led to twinning and double domains rotated by 90° from one another due to the equivalence of different CdTe orientations on such planes. Two approaches were taken to reduce the symmetry of the substrate surface and thus eliminate this problem:

1. To slightly miscut the substrate away from a low-index surface plane [32.52–57]
2. To grow on higher-index planes containing steps between (100) or (111) flat terraces [32.58–61].

Today almost all growth is carried out on (211) substrates. However, the question of the preferred substrate orientation is not as clear for lattice-matched substrates as for alternative substrates. A brief review of the results for growth on substrates with various orientations is given here. In 1988 a study [32.46] of growth on (100), (111)B, (211)A, and (211)B substrates revealed that (211)B growth gives the best surface morphology, suppresses twinning, and gives higher Hg sticking coefficients and thus better control of composition than any other orientation studied except (111)B. In

1994 simultaneous growth was conducted [32.62] on (111)B substrates miscut by 4° towards (110) (labeled (776)) and on (211)B-oriented substrates. These orientations were described as (111)B surfaces tilted 19° towards and 4° away from (100), respectively. The primary difference between these two orientations was the width of the (111) terraces between steps: 53 and 10.6 \AA , respectively. It was found that the (776) orientation with broader terraces was more susceptible to twinning at lower growth temperatures. In 2000 it was found [32.63] that growth on (211)B and (311)B surfaces under optimized conditions gives material of comparable quality. Recently, simultaneous MBE growth was conducted [32.44] in the (511)B, (311)B, (211)B, (111)B, and (255)B orientations tilted 15.8 , 25.2 , 35.3 , 54.7 , and 74.2° away from the (100) surface in the (011) direction. Over a nominal range of growth temperatures from 180 to 187°C the x-ray rocking curve full-width at half-maximum (FWHM), and etch pit density (EPD) were measured for all samples, and surface defect densities were measured using Nomarski microscopy. Under the best growth conditions comparable results were obtainable for all orientations, although the (255) orientation allowed the lowest-temperature growth.

32.3.2 CdZnTe Substrates

A golden rule of epitaxial growth is to match the lattice parameter of the substrate to that of the epitaxial layer in order to avoid strain and dislocation formation in the epilayer. Although, because of its lattice match to HgCdTe, bulk CdZnTe is the substrate of choice for the MBE growth of the highest-quality material, especially for LWIR and VLWIR detection, it suffers from both intrinsic limitations and quality concerns, as listed in Table 32.1. Many of the intrinsic limitations – the very high cost, limited area, brittleness and large thermal mismatch with the Si readout integrated circuit (ROIC) in devices – do not affect the quality of MBE growth but do impact the practicality of use of the HgCdTe layers grown for device applications. The poor thermal conductivity and quality concerns – crystalline defects, impurities, nonuniform composition, surface roughness, imperfect surface flatness, and stoichiometry – all impact the quality of the HgCdTe grown on the substrates. Furthermore, all are amplified in importance by great variations in quality from substrate to substrate. These variations introduce great variations in HgCdTe material and thus both significantly lower yield in device production and make it difficult to identify optimal

growth conditions; see, for example, [32,44]. For those reasons it is desirable to develop and use methods to screen substrates before the MBE growth of HgCdTe.

Effects of Poor Thermal Conductivity on HgCdTe Growth

Because the growth is highly noncongruent, the temperature window for the optimal growth of HgCdTe is very narrow, and the composition obtained for a given flux ratio is strongly temperature dependent. However, it is very important to have compositional and crystalline

uniformity across HgCdTe epilayers to be used for FPAs. Thus, it is very important to keep the temperature as nearly uniform as possible across a growing HgCdTe layer. On the other hand, in MBE growth the outside edges, and especially the corners, of a growing epilayer become hotter than the central region. For that reason, it is highly desirable to use a substrate with a high thermal conductivity to minimize thermal gradients across a growing HgCdTe epilayer so as to minimize compositional gradients and pixel-to-pixel cutoff wavelength gradients in FPAs.

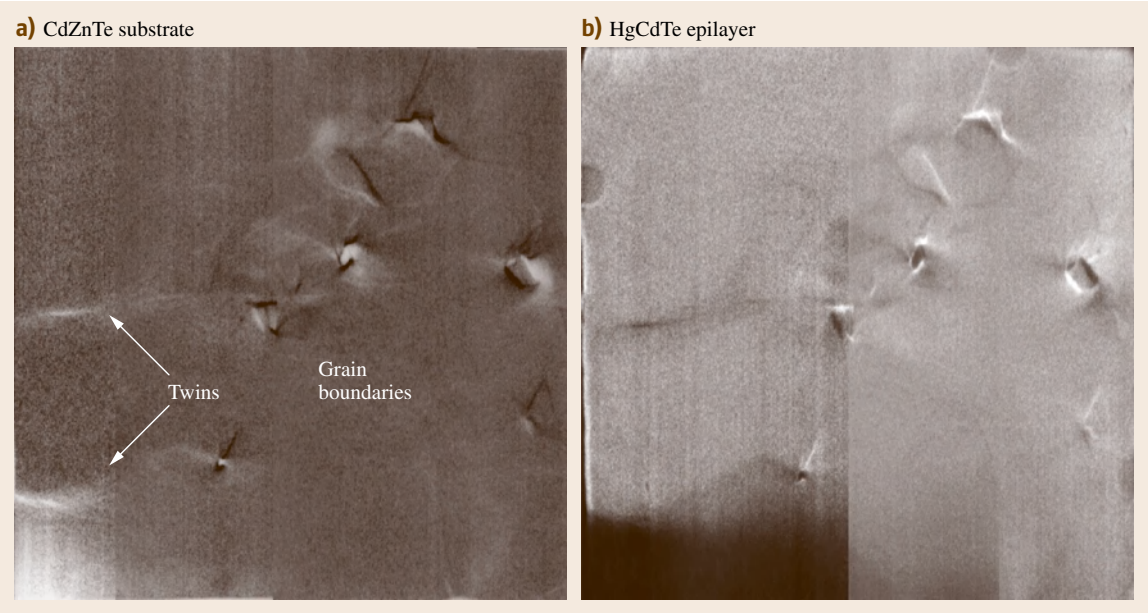


Fig. 32.1a,b Effects of (a) substrate twins and grain boundaries on defect formation in (b) HgCdTe epilayers

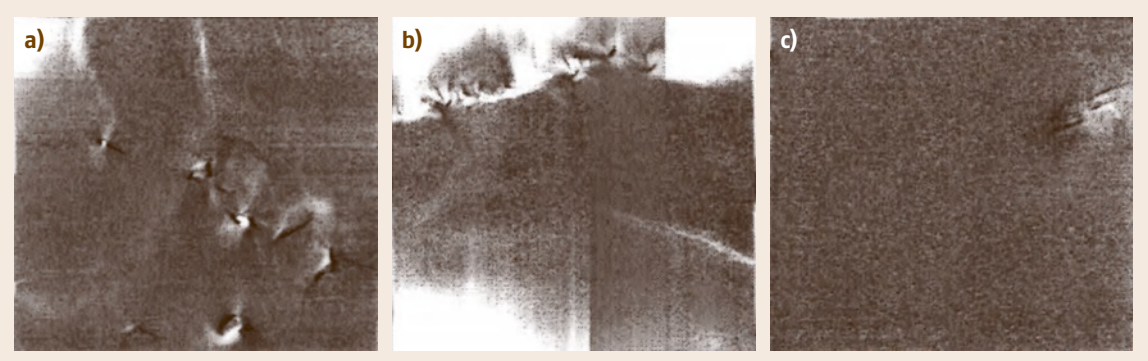


Fig. 32.2a–c Typical x-ray topographic mapping results from commercially purchased wafers with (a) and (b) large-area surface crystalline imperfections and (c) a moderate area of surface crystalline imperfection

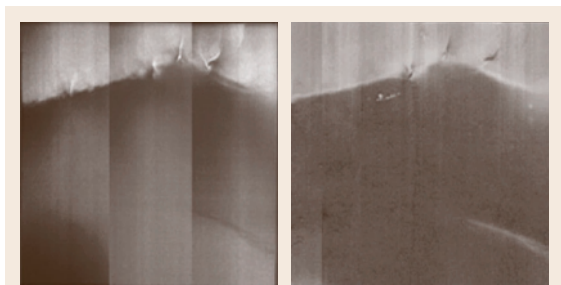


Fig. 32.3 X-ray topographic mapping results from HgCdTe epilayers grown on the substrates shown in Fig. 32.2a,b again showing that the defective features on the substrate are transferred to the HgCdTe epilayer

Effects of Substrate Crystalline Defects on HgCdTe Growth

Irrespective of the choice of substrate material, the crystalline quality of an MBE-grown HgCdTe epilayer depends on the crystalline quality of the substrate on which it is grown. The absence of a large quantity of substrate structural defects is a necessary, although not sufficient, condition for the MBE growth of a HgCdTe layer of high structural quality. The effects of substrate twins and grain boundaries on defect formation in HgCdTe epilayers is strikingly shown in Fig. 32.1; the HgCdTe surface defects form an exact map of

the underlying CdZnTe defects. Of 12 commercially obtained substrates recently screened at the US Army Night Vision and Electronic Sensors Directorate, five showed large-area crystalline imperfections, as shown in Fig. 32.2a,b, three showed moderate areas of crystalline imperfections, as shown in Fig. 32.2c, and only four showed reasonably good surface crystalline perfection as revealed by x-ray topographic mapping, FWHM maps, and Fourier-transform IR (FTIR) transmittance maps. Results on others of these samples are given by Carini et al. [32.64]. When HgCdTe epilayers were grown on these substrates, the defective structures were transferred to the epilayers as shown in Fig. 32.3. Also, a high density of threading dislocations was found in the epilayers above the imperfections and very short carrier recombination lifetimes were measured [32.65]. These threading dislocations also can lead to microtwinning by allowing nucleation on the (111) terraces during growth as well as at the bottom of steps, thus giving three-dimensional rather than step-flow growth. This in turn leads to surface hillocks such as those shown in Fig. 32.4. More recently it was reported [32.44] that some substrates of a recently purchased batch had FWHM values of 15–25 arcsec, whereas others had values of 10–12 arcsec, with CdTe epilayers grown on the substrates having FWHM values limited by the substrate values.

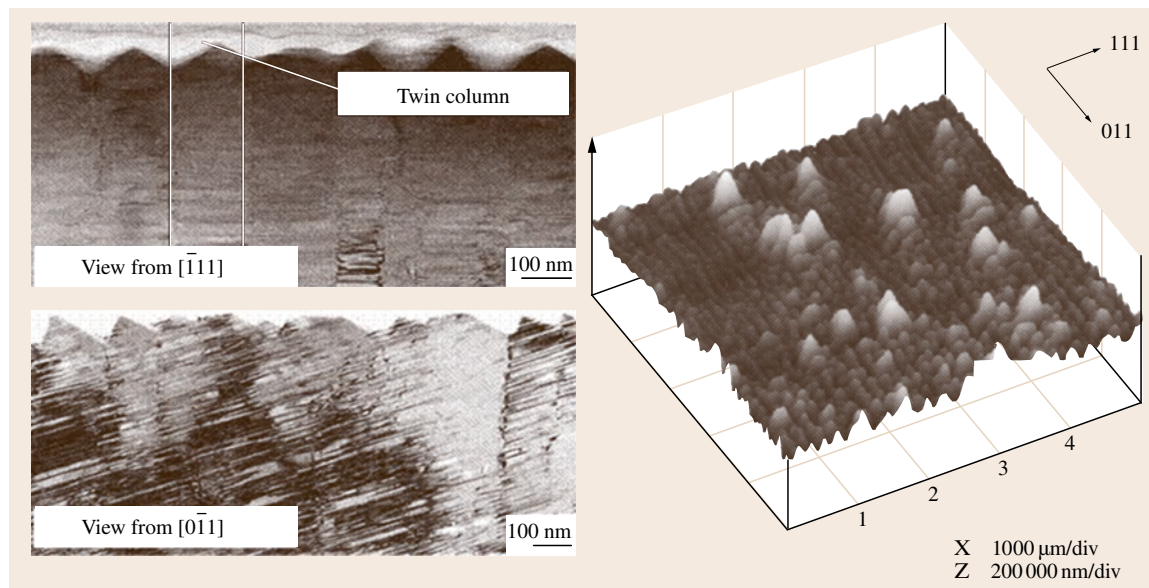


Fig. 32.4 Scanning electron microscopy (SEM) and atomic-force microscopy (AFM) images showing hillocks due to the formation of adjacent columns of twins

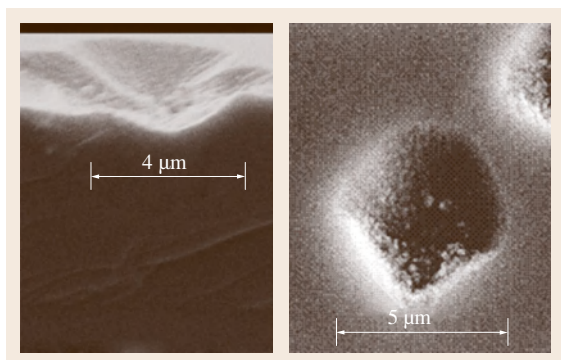


Fig. 32.5 SEM photographs of small voids

Another type of bulk defect found in CdZnTe substrates is Te precipitates. A large density of Te precipitates is unavoidable in as-grown CdZnTe boules because there is a large deviation from stoichiometry at the growth temperature. As the CdZnTe is cooled to room temperature, the excess Te forms precipitates from $< 1 \mu\text{m}$ to $\approx 25 \mu\text{m}$ in size. Much attention has been paid to elimination of these defects [32.66, 67], yet they remain a problem. These substrate precipitates create dislocation clusters [32.68] and induce Te precipitates [32.66, 69] in epilayers grown on the substrates and crater or void defects on the epilayer surfaces [32.70]. These voids can short p–n junctions and hence blind pixels in FPAs. Scanning electron microscopy (SEM) images of typical voids are shown in Fig. 32.5. The Te precipitates also give rise to high hole concentrations in HgCdTe layers grown by LPE on the substrates [32.69].

Effects of Substrate Impurities

For best performance of LWIR HgCdTe FPAs, it is necessary to minimize low-temperature leakage currents. At temperatures such as 40 K the major sources of dark current crossing the p–n junction are believed to be tunneling and generation in the depletion region. These mechanisms involve trap sites that most likely are due to impurities. Some impurities also act as unwanted dopants. For these reasons, it is necessary to minimize impurities in the HgCdTe layers. For growth on CdZnTe substrates, one origin of impurities is the substrate, from which they diffuse during layer growth [32.71] and device fabrication. A well-known example is Cu [32.72, 73], which diffuses rapidly from substrate to epilayer, has been shown [32.74] to be preferentially attracted to HgCdTe over CdZnTe, and harms devices by shortening the carrier lifetime and

converting weakly n-type material to p-type. Methods to extract mobile impurities from CdZnTe before MBE growth [32.75] and to getter and localize Cu at Te precipitates in CdZnTe [32.60] have been proposed, but Cu impurities remain a possible problem.

Effects of Nonuniform Composition

Zn segregation along the growth axis in the vertical Bridgman growth of CdZnTe leads to a gradual decrease in Zn composition from the bottom of a boule to the top, so that different wafers do not have the same lattice constant, allowing only part of a boule to be lattice-matched to a given composition of HgCdTe. More importantly, the Zn composition typically varies by about 1% from the center to the outside of a nominally 4% wafer, and that variation creates a variation in lattice constant equal to that caused by a 0.2% change in the composition of HgCdTe. Although small, that variation can cause a lateral variation in the density of threading dislocations in HgCdTe epilayers grown on CdZnTe substrates that is sufficient to cause significant lateral variations in the responsivity of LWIR and VLWIR FPAs. It also induces cross-hatch defects [32.76, 77] on the surface of MBE-grown HgCdTe epilayers, such as those shown in Fig. 32.6. Assuming CdZnTe and HgCdTe to relax with $a/2 \langle 011 \rangle$ Burger's vectors which propagate on the $\{111\}$ family of glide planes \mathbf{g} , the resultant dislocation lines would be $\{\mathbf{u}\} = \{[01\bar{1}], [\bar{2}13], [0\bar{1}1], [2\bar{3}\bar{1}]\}$. Misfit dislocations from the small lattice mismatch

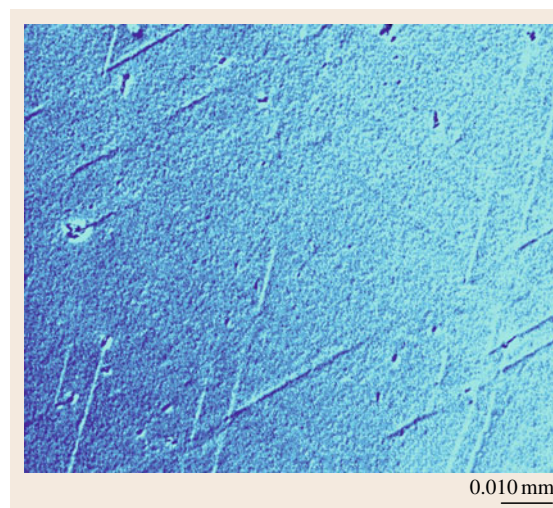


Fig. 32.6 Nomarski micrograph showing crosshatches on defect etched MBE-grown HgCdTe epilayers

and later from the thermal mismatch would allow threading dislocations to propagate on the {111} glide planes and close their dislocations along the u directions, resulting in the observed cross-hatch defects. Thus, these cross-hatch defects result from dislocations, but only when the dislocation density is low.

Effects of Substrate Roughness

Substrate surface roughness may be present on commercial substrates as received or may arise from imperfect surface preparation by the MBE grower. AFM surface roughness measurements on HgCdTe layers grown on substrates with smooth or rough surfaces show a direct correlation between substrate surface roughness and the surface roughness of the HgCdTe epilayer (Table 32.2). A high epilayer surface roughness on any lateral scale leads to imperfections in device fabrication and can lead to dead pixels in FPAs. High-frequency substrate roughness on a lateral scale of ≈ 100 Å or less inhibits the mobility of atoms on the epilayer growth surface and thus can lead to three-dimensional growth and poor crystalline quality. It has been observed that, for growth on moderately rough substrates (> 10 Å of roughness as measured by SE), the epilayer surface roughness increases in the initial growth stage [32.78] consistent with three-dimensional growth.

It also has been observed that high densities of elongated *needle* defects oriented in a preferred direction occur on the surfaces of HgCdTe epilayers grown on rough CdZnTe substrates. As shown in Fig. 32.7, the density of these defects was found to increase exponentially with increasing substrate surface roughness as measured by SE [32.78]. However, the MBE deposition of an 80 Å CdTe buffer layer before HgCdTe growth reduces the final needle defect density by an order of magnitude or more, as shown in Fig. 32.7. Needle defects occur only for growth on CdZnTe, their density does not correlate to the CdZnTe bulk qual-

Table 32.2 Correlation of substrate surface roughness and epilayer surface roughness

	Smooth substrate (Å)	Rough substrate (Å)
Substrate surface roughness	8	50
HgCdTe epilayer surface roughness	8	58

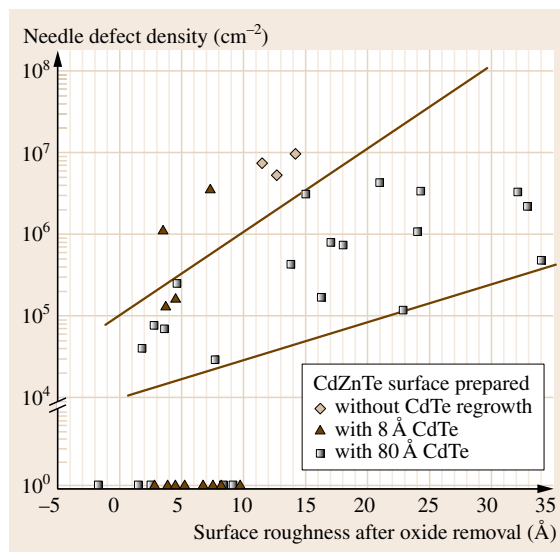


Fig. 32.7 Plot of the HgCdTe needle defect density versus surface roughness as measured by in situ SE with and without CdTe buffer layers. The straight lines are upper and lower limits of the defect density with an 80 Å CdTe buffer layer

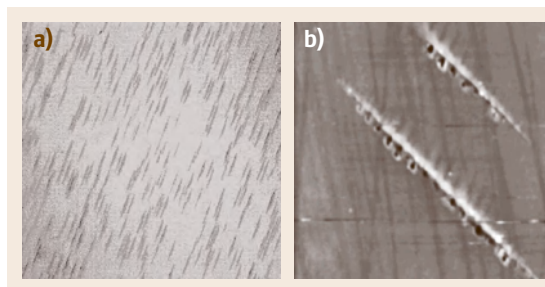


Fig. 32.8 (a) A Nomarski picture (1000×) of needle defects on a HgCdTe epilayer and (b) an AFM image of two needle defects (5 μm × 5 μm)

ity, and their connection to the surface roughness is not well understood. It also is not known how they affect device quality or how they correlate with surface preparation technique. It is possible that they could be eliminated by using plasma etching rather than wet chemical etching followed by thermal desorption of contaminants, the common practice. The length of the needle defects varies from a few micrometers to > 10 μm in different samples, their width is only 0.2–0.3 μm, and their height is ≈ 100 Å. Figure 32.8 shows (a) a Nomarski picture (1000×) of needle de-

fects on a HgCdTe epilayer and (b) an AFM image of two needle defects. The HgCdTe epilayers grown on these substrates also were characterized by temperature-dependent, photoconductive-decay lifetime data. Fits to the data indicate the presence of mid-gap recombination centers, which were not removed by 250 K/24 h annealing under a Hg-rich atmosphere. The strong correlation observed between the substrate roughness measured by SE and the density of these centers leads us to believe that they originate from bulk defects related to the substrate roughness rather than from Hg vacancies.

Effects of Substrate Surface Curvature

Substrate surface curvature can have two deleterious effects. First, any deviation in surface flatness $\approx 0.5 \mu\text{m}$ or more can give problems in bonding to the flat Si ROIC surface for device fabrication. Second, the curvature will yield a surface orientation which is not constant across the wafer; that, in turn, may lead to epilayer MBE growth problems for a substrate which is only slightly miscut off a principal crystal axis, although it should have no effect on the usual growth on (211) surfaces.

Effects of Surface Nonstoichiometry and Contaminants

The surfaces of substrates must be prepared for MBE growth, i.e., polished and cleaned. The surfaces must be atomically clean, ordered, and have, at least approximately, the stoichiometry of the underlying wafer. The surfaces of commercially obtained wafers typically are covered with $\approx 1.5 \text{ ML}$ of contaminants (mostly oxygen, carbon, and chlorine) [32.79]. The usual wet chemical preparation of the surface typically employs a 0.5% bromine in methanol solution that leaves behind an amorphous Te layer and residual carbon contamination, both of which must be removed for satisfactory nucleation of HgCdTe growth, although improved chemical polishing and cleaning procedures are under investigation [32.80, 81]. The substrate is then heated to 300–340 °C to remove the amorphous Te and residual contaminants such as carbon and oxygen to obtain a crystalline surface. This surface preparation procedure has been shown to leave $\approx 1/4$ of a monolayer of carbon as well as either excess Te or excess Zn [32.79, 82]. Incompletely removed amorphous Te leads to three-dimensional growth and microtwinning, and residual contaminants degrade the electrical properties of any HgCdTe epilayer grown on the substrate. Alternative wet chemical treatments lead to similar problems. An alternative electron cyclotron resonance Ar/H₂ plasma cleaning technique has been shown to

leave the CdZnTe surface free of contaminants and with a roughness of only 4 Å as measured by interferometric microscopy [32.79]. However, HgCdTe epilayers grown by MBE on plasma-cleaned substrates were not found to be noticeably better than those grown on substrates cleaned by conventional wet chemical methods followed by annealing [32.79].

Characterization and Screening of CdZnTe Substrates

Many experimental methods have been used to characterize the crystalline quality, purity, and surface characteristics of CdZnTe substrate wafers. Poor crystalline quality – the presence of grain boundaries, low angle microcrystals, microtwinning, precipitates, and voids – can be examined in detail using cross-sectional SEM and TEM; however, those measurements are expensive, destructive, and can only be used to image microscopic sections of a substrate. X-ray topographic mapping measurements, which produce images such as those shown in Figs. 32.1 and 32.2, also require very expensive equipment and are not as detailed, but are nondestructive and capable of mapping an entire substrate wafer [32.64]. More detailed structural information, such as small variations in lattice spacing and the existence of regions of the substrate tilted only 0.011°, can be obtained by reciprocal-space mapping (RSM) and triple-axis x-ray diffractometry [32.83]. A simple gross quantitative measure of the substrate crystal structural perfection is given by the full-width at half-maximum (FWHM) of the x-ray double crystal rocking curve and by the existence or nonexistence of multiple peaks. The IR transmittance at wavelengths $< 6 \mu\text{m}$ [32.64] and χ , the ratio of channel counts to random counts in Rutherford backscattering spectroscopy [32.66], also give qualitative measures of the crystal structural perfection, with the IR transmittance being higher and χ being smaller for better crystals.

Individual Te precipitates and other extended defects can be seen by relatively simple non-destructive optical measurements: IR transmission microscopy [32.66, 69, 70], light-scattering IR tomography [32.84], and scanning photoluminescence (PL) [32.84]. Also, the presence of Te precipitates or excess Te atoms is revealed by an A(Te) peak in the Raman scattering spectra at $\approx 127 \text{ cm}^{-1}$ [32.67] and IR transmittance gives at least a qualitative measure of the density of Te precipitates, falling off rapidly with increasing wavelength for wafers having a high density of Te precipitates [32.67]. A general rule of thumb is that, for wavelengths well above the cutoff wavelength,

the transmittance should be $> 63\%$ in the absence of antireflection coatings. Reflection high-energy electron diffraction (RHEED), which is installed on all HgCdTe MBE growth chambers and is discussed in Sect. 32.5, gives yet another nondestructive qualitative description of the substrate crystalline perfection. Etch pit density (EPD) measurements reveal threading dislocations and Te precipitates at the substrate surface and are nondestructive except for the requirement of a surface etch, usually either an Everson [32.85] or a Nakagawa etch [32.86]; EPDs in the mid 10^4 cm^{-2} are desirable.

Quantitative measurements of substrate impurity dopant concentrations require destructive techniques. The most common are glow-discharge mass spectroscopy [32.73, 75, 87], sputter-initiated resonance ionization spectroscopy [32.70, 74], and secondary-ion mass spectroscopy (SIMS) [32.67, 88–90]. However, a qualitative measure can be obtained from the IR transmittance; for high impurity dopant levels the transmittance decreases by an amount proportional to $\ln(N_D - N_A)$ as the wavelength increases in the LWIR and VLWIR [32.84].

The Zn concentration and its lateral variations usually are measured by FTIR or spectral photometry, measuring the cutoff in the FTIR transmission in the near IR, because this is a very simple nondestructive measurement. However, the shape of the FTIR transmission curve is affected by crystalline imperfections, in particular by Te precipitates, in a way that can make the determination of the Zn concentration uncertain by as much as ± 0.015 [32.81]. It can be determined somewhat more accurately by SE using a high-resolution ellipsometer such as the M2000, as discussed in Sect. 32.5. A much more accurate method of determining the Zn concentration and its lateral variation is low-temperature PL mapping. Measurement of the reabsorption dip at the free exciton energy is capable of determining the Zn concentration within a precision of ± 0.0005 [32.81, 82]. The depth variation of the Zn concentration also can be measured, but only by destructive techniques: Auger electron spectroscopy (AES) or atomic absorption spectroscopy (AAS) on beveled edges or vertical slices of a substrate [32.88].

The surface roughness can be nondestructively and easily measured directly by Nomarski microscopy, Zygo interferometry, and AFM with increasing resolution but over decreasing areas, and indirectly by SE, as discussed in Sect. 32.5. Surface contamination also can be measured nondestructively by x-ray photoelectron spectroscopy (XPS), directly by measuring the photoelectron peak intensities corresponding to the different

possible contaminants or indirectly by measuring the decrease in the intensity of the CdTe peak [32.82]. In screening substrates, the substrate should first be thermally cleaned in vacuum in the XPS chamber and then transferred in vacuum to the growth chamber after the XPS measurement. AES also can be used to verify the absence of contaminants on substrate surfaces [32.79] but is not as easily used to measure amounts of contamination.

Use of Buffer Layers on Substrates

The use of buffer layers to block the propagation of defects originating in substrates or at the substrate–epilayer interface has proven useful and is being optimized. The various commercial manufacturers of FPAs use buffer layers in the growth of HgCdTe, but the details of their growth procedures remain proprietary. Thin interfacial CdTe layers have proven effective in reducing the surface roughness, evening out variations in strain, and improving the quality of HgCdTe layers grown on the substrates [32.78]. However, in order to be fully effective in smoothing out the surface and reducing the dislocation density, these layers must be grown to a thickness exceeding the critical layer thickness, so that the lattice match to HgCdTe is lost. This suggests the use of HgTe/CdTe SLs as buffer layers. They are more effective at blocking dislocations and can be grown more nearly lattice matched to the HgCdTe epilayer to be grown. Cross-sectional TEM micrographs such as those shown in Fig. 32.9 show that the substrate microscopic roughness is smoothed out after several periods of SL growth (a) and that threading dislocations terminate (b) or bend (c) at the HgTe/CdTe interfaces in the SL, despite the small (0.32%) lattice mismatch between HgTe and CdTe which would normally be considered insufficient to induce the motion of threading dislocations [32.91, 92]. After growth, the SLs are interdiffused by annealing to produce a short-wavelength IR (SWIR) HgCdTe layer which serves as a window for backside-illuminated devices and typically has a lattice mismatch of $\leq 0.09\%$ with the final HgCdTe epilayer to be grown. It has been shown [32.91, 92] that the use of HgTe/CdTe SL buffer layers leads to reproducibly high-quality MBE-grown HgCdTe layers with EPDs $\approx 10^5 \text{ cm}^{-2}$ with values as low as $4 \times 10^4 \text{ cm}^{-2}$ and minority-carrier lifetimes close to the theoretical limits for perfect material. It also has been found that, even aside from the improvement of material characteristics, the presence of an SWIR buffer layer improves device quality by reducing the back-surface recombination velocity.

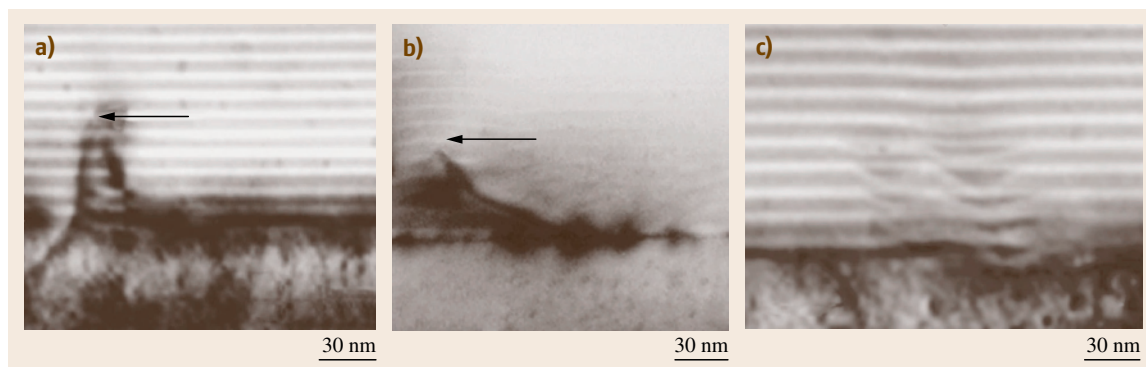


Fig. 32.9a–c Cross-sectional TEM micrographs showing the (a) bending and (b) termination of threading dislocations by HgTe/CdTe SL buffer layers, and (c) the smoothing of substrate roughness by SL buffer layers

32.3.3 Si-Based Substrates

There has been great interest in alternatives to CdZnTe as a substrate for the reasons outlined in Table 32.1 and detailed in Sect. 32.3.2 above. Of the many possible alternative substrate materials for the MBE growth of HgCdTe, Si has captured the greatest interest. HgCdTe was first grown on Si substrates in 1989 [32.93], and the growth of HgCdTe on Si having properties as good as those of HgCdTe grown on CdZnTe was reported in 1995 [32.94]. Although many factors favor Si over all other possible substrate materials, one factor in particular singles out Si uniquely – only Si offers the possibility of fabricating truly monolithic detectors and FPAs. Because the readout integrated circuit (ROIC) in all IR devices is based on Si, the use of any material other than Si for the substrate necessitates a hybrid-array technology wherein the detector and ROIC arrays are fabricated on separate manufacturing lines and subsequently indium-bump bonded to each other pixel by pixel. The functions of detection and charge readout would be monolithically integrated onto a single Si wafer in the ultimate IRFPA. This has been demonstrated by the epitaxial deposition of HgCdTe in selected areas of a Si ROIC [32.95].

Aside from the ultimate goal of monolithic integration, Si-based substrates offer many short-term benefits over all other possible substrate materials. First, Si wafers are commercially available in far larger sizes. This allows either much larger focal planes for greater resolution or greater numbers of smaller FPAs for reduced production costs. Second, in conjunction with that advantage, Si offers perfect thermal matching of its lattice to that of the ROIC, and thus no thermal mismatch limit on the size of FPAs. With other substrates,

the thermal mismatch between substrate and Si ROIC creates a strain upon cycling down to cryogenic operating temperatures which could destroy the bump bonding for very large-area FPAs. Third, Si substrates allow the use of automated Si processing technology for increased efficiency in device fabrication. Fourth, Si is the most robust and durable possible substrate material, leading to less breakage and a higher device yield. Fifth, Si has the highest thermal conductivity, leading to the highest lateral uniformity of MBE-grown HgCdTe composition and thickness. Sixth, Si offers the lowest level of impurity migration into the HgCdTe. Finally, it has by far the lowest density of surface defects, although that advantage is overwhelmed by the problems associated with the large lattice and thermal mismatches between Si and HgCdTe. In summary, in every way that CdZnTe is a poor substrate, Si is clearly the best.

On the other hand, Si has the worst lattice and thermal mismatches with HgCdTe of any substrate material considered. The lattice parameter of HgCdTe ($\approx 6.46 \text{ \AA}$) is $\approx 19\%$ larger than that of Si ($\approx 5.43 \text{ \AA}$). The lattice mismatch is so extreme that HgCdTe does not even grow epitaxially on Si, so that a buffer layer is required. The buffer layers chosen have been $\text{Cd}_{0.96}\text{Zn}_{0.04}\text{Te}$ [32.96], CdSeTe [32.97], CdZnSeTe [32.98], and CdTe . Also, a first buffer layer of ZnTe, originally found to be necessary to preserve the substrate orientation [32.93], usually is grown before the deposition of the final buffer layer. Although $\text{Cd}_{0.96}\text{Zn}_{0.04}\text{Te}$ and CdZnSeTe buffer layers offer the advantage of an almost perfect lattice match to the HgCdTe to be grown, they have largely been abandoned because of the difficulty of obtaining epilayers of sufficient crystalline quality; the best values obtained for the x-ray diffraction (XRD) FWHM for lattice

match to HgCdTe have been > 150 arcsec. Even CdTe buffer layers have a relatively poor crystalline quality because of their large lattice mismatch with Si. Even with special growth procedures involving the predeposition of ZnTe films on As-terminated Si surfaces [32.99, 100], CdTe buffer layers exhibit etch pit densities of 2×10^5 – 5×10^5 cm $^{-2}$, indicative of threading dislocation densities of the order of 2×10^5 – 5×10^5 cm $^{-2}$. This in turn leads to dislocation densities in the mid 10^6 cm $^{-2}$ in the HgCdTe layers grown on these substrates by MBE. Although otherwise excellent material quality has been achieved [32.101–104], little success was achieved in lowering the dislocation density in HgCdTe grown on Si substrates without undesirable high-temperature cyclic annealing.

For dislocation densities $< 10^5$ cm $^{-2}$ the dislocation density has little effect on the minority-carrier recombination time for $T > 77$ K, even for LWIR HgCdTe, because carrier recombination is dominated by intrinsic Auger mechanisms. However, for dislocation densities above the mid 10^5 cm $^{-2}$ range and $T \leq 77$ K, carrier recombination is dominated by Shockley–Read–Hall (SRH) recombination due to the dislocations, and the minority-carrier recombination time for LWIR HgCdTe for is roughly inversely proportional to the dislocation density [32.105]. Also, dislocations can locally short out p–n junctions in devices, considerably increasing the dark current [32.106]. The MBE growth of HgCdTe on CdTe/Si substrates yields SWIR and mid-wavelength infrared (MWIR) photodiodes having performances similar to those grown on CdZnTe substrates at operating temperatures above 77 K [32.102, 103, 107, 108]. However, to date it has been incapable of yielding LWIR or VLWIR devices having similar performances (similar R_0A values) to the best devices grown on CdZnTe substrates [32.103, 109], except for devices with very small junction areas (< 180 μm^2) [32.110] or for high background operation at temperatures ≥ 77 K [32.104]. LWIR FPAs fabricated from HgCdTe grown on Si give near-ideal performance even at 40 K if the junction sizes are sufficiently small to have no more than ≈ 5 threading dislocations passing through each junction area. This limits the ideal pixel pitch for LWIR FPAs to pixel sizes < 25 – 30 μm [32.110].

There exist in principle two general ways to ameliorate the effects of the large lattice and thermal mismatches between Si and HgCdTe:

1. Reduce the as-grown dislocation density
2. Passivate the dislocations so as to reduce their effect on device properties.

Buffer Layers to Reduce the As-Grown Dislocation Density

If the as-grown dislocation density could be reduced by an order of magnitude, growth on composite Si-based substrates would be the clear choice for the MBE growth of HgCdTe. The use of improved buffer layers is expected to yield quantitative, but not qualitative, improvements. The authors have briefly explored the use of strained-layer CdTe/ZnTe SLs to lower the dislocation density and improve the crystal quality of the final CdTe buffer layer, but with only moderate success. Also, the growth of CdSeTe buffers on top of the usual CdTe buffers has been suggested. More recently, preliminary results [32.111] have shown that nanometer-thick perovskite oxide buffer layers tend to smooth the surface of the final CdTe buffer layer and may offer a promising approach to reducing the dislocation density. In particular, under certain growth conditions, an amorphous silicate layer forms between the perovskite and the Si, making the perovskite a potentially compliant buffer and thus potentially greatly reducing the dislocation density for growth on Si [32.112]. Another approach [32.113] would be the epitaxial growth of insulating Be chalcogenides and then BeCdTe or BeMgTe with a graded lattice parameter, initially lattice matched to Si (BeSe $_{0.45}$ Te $_{0.55}$) and ending with a layer lattice matched to CdTe or HgCdTe. These layers could be grown in the same MBE reactor as a CdTe buffer layer, and the final HgCdTe epilayer would be grown in as part of one continuous growth run. They should grow with relatively few defects because the Be chalcogenides have very high stacking fault energies – more than ten times that of ZnS, which suppress the formation of dislocations. Also, the Be chalcogenides have a much higher thermal stability than CdTe or ZnTe. Alternatively, one could just use a single BeTe layer, which shows [32.114] good two-dimensional growth on Si:As and has an intermediate lattice constant. However, Be would be a very difficult contaminant to remove from the MBE growth chamber.

Thermal Cycling to Reduce the Dislocation Density

It has been shown that the thermal cycling of HgCdTe grown by MBE or MOCVD on CdTe/GaAs and CdTe/Si substrates can greatly reduce the HgCdTe dislocation density. Dislocation densities as low as 2.3×10^5 , almost as low as those obtained for growth on CdZnTe, have been obtained by thermal cycling between 300 and 490 °C [32.115]. The reduction in the

HgCdTe dislocation density was accompanied by an increase in the CdTe dislocation density by two to three orders of magnitude. This effect was explained as due to the large thermally induced stresses between the CdTe and the Si or GaAs. The problem with this approach is that high-temperature annealing can cause substantial diffusion and destroy the sharpness of the hetero- and homojunctions required by many modern detector designs.

Growth on Si-Based Compliant Substrates

Growth on compliant substrates was first suggested by *Lo* [32.116]. Compliant substrates either take up most of the strain associated with a lattice mismatch or getter the dislocations formed at the epilayer–substrate interface. A compliant substrate is made much thinner than the epilayer grown on it and is free to slide against a thicker *handle* substrate. The most common example of a compliant substrate is a Si-on-insulator (SOI) structure with a Si layer ≈ 10 nm thick floating on an SiO₂ layer on a Si handle. Modification of the relaxation behavior in lattice-mismatched films due to growth on SOI compliant substrates is well documented. TEM measurements for SiGe grown on such films have shown dislocation densities reduced by more than five orders of magnitude [32.117]. AFM measurements have shown a factor of four reduction in surface roughness, and the XRD FWHM was shown to be reduced from 270 to 155 arcsec [32.118]. It has been shown that in this case the compliant thin Si layer does not deform elastically to absorb the strain due to the lattice mismatch, but rather facilitates a net downward image force on the dislocations so that they grow into the thin Si layer rather than the SiGe epilayer [32.117, 118]. In preliminary studies CdTe has been grown on an SOI substrate 20 nm thick. As opposed to the tensile strain found for growth on the usual Si substrates, the CdTe was found to be under compressive strain due to the difference between its thermal contraction and that of Si during the cooldown from its growth temperature to room temperature. However, the fact that CdTe has lower energies of formation for stacking faults and dislocations than does SiGe will make it more difficult to grow dislocation free CdTe on an SOI substrate. Ge/SiO₂/Si would be an attractive alternative compliant substrate because Ge is more nearly lattice matched to CdTe than is Si and has even been used as a bulk substrate for the growth of HgCdTe. This substrate and a method for its growth are suggested in [32.113].

Selective-Area Growth on Patterned Substrates

There are two basic approaches to patterned heteroepitaxial growth. The first involves selective-area growth on a prepatterned substrate followed by lateral epitaxial overgrowth (LEO). The second involves the standard planar growth of a buffer layer followed by patterning of the buffer, annealing and then LEO. Both have been used with great success. The first approach has been used with MOCVD to grow GaAs on Si (4% lattice mismatch) [32.119] and GaN on Si (22% lattice mismatch) [32.119–121], as well as CdTe on Si (19% lattice mismatch) [32.122, 123], with dislocation densities much lower than those for planar growth in all cases. Patterned growth and LEO by MBE have been published only for GaAs on a patterned GaAs substrate [32.124] and for GaN on patterned Si [32.125] and has not been considered possible for CdTe. However, using nanopatterning with a CdTe seed layer, Bommena now has achieved the selective growth of CdTe on Si and LEO with MBE. Although much remains to be demonstrated, this work may open the door to finally overcoming the lattice mismatch between Si and CdTe. If nanopatterning does not sufficiently reduce the dislocation density at the CdTe surface, a further reduction could be achieved by patterning compliant SOI rather than Si.

The second approach has been used to remove almost all threading dislocations from patterned ZnSe epitaxial layers grown on GaAs by MOCVD by bending them over along glide planes to the pattern sidewalls [32.126, 127]. The activation energy for the glide process (≈ 0.7 eV) requires a high-temperature anneal, 400–600 °C, making this approach less desirable for MBE growth of CdTe.

Passivation of Dislocations

A possible alternative to achieving an order of magnitude reduction in the dislocation density would be to achieve a partial reduction in the dislocation density and attempt to passivate the remaining dislocations, i.e., eliminate the trap states normally introduced by dislocations. The hydrogen passivation of both shallow and deep levels has been well studied in many major semiconductors, particularly Si and GaAs. Perhaps, its most prominent application is in α -Si:H solar cells. Notably, it has been found to significantly reduce leakage currents through dislocation cores in GaN [32.128]. Atomic hydrogen has been found to passivate shallow donors and acceptors in virtually all semiconductors. The exact mechanisms by which hydrogen passivates

deep levels are poorly understood, in part due to the lack of a clear understanding of the microscopic nature of many deep levels. The passivation of shallow and deep levels in CdTe and has received some attention; hydrogen was found to be an effective passivant when introduced in either molecular or atomic form, improving both electrical and optical properties [32.129–131].

The effects of hydrogen in HgCdTe still are not clear. Early research on the hydrogen passivation of HgCdTe involved electrochemical methods of introducing hydrogen into $\text{Hg}_{0.5}\text{Cd}_{0.5}\text{Te}$, followed by deep-level transient spectroscopy to determine its influence on deep levels [32.132, 133]. The dominant deep levels at approximately $E_g/2$ and $3E_g/4$ were significantly reduced in concentration after hydrogenation. Unfortunately, annealing at 70 °C restored their activity. Two more recent papers [32.134, 135] examine the effects of the hydrogenation of mercury-vacancy-doped MWIR and LWIR HgCdTe. Reference [32.134] concludes that electron cyclotron resonance (ECR) plasma hydrogenation is effective in passivating surface trap states, whereas [32.135] concludes that its only role is to passivate mercury vacancies.

Recently [32.136], attempts have been made to passivate the dislocations in HgCdTe grown on Si with hydrogen introduced via an ECR plasma. The dangling bonds formed along the dislocations give rise to states in the bandgap that act as Shockley–Read–Hall recombination centers. However, the attachment of hydrogen to the dangling bonds would be expected to eliminate the gap states, forming bonding states in the valence band and antibonding states in the conduction band. Hall mobility and minority-carrier lifetime data indicated that the incorporated hydrogen did passivate both scattering and recombination centers. It also was found that dislocations act as atomic diffusion channels both for outdiffusion, observed during annealing, and for indiffusion during ECR hydrogenation. Therefore it is reasonable to conclude that dislocations would be among the first type of defects to be passivated when samples are exposed to ECR plasmas, and that this passivation of dislocations was primarily responsible for the observed increases in mobilities and minority-carrier lifetimes. Preliminary stability studies indicated that the beneficial effects of hydrogenation remain after 3 months shelf storage and after heating to 80 °C.

Te and As Monolayers on Si

The growth of an As monolayer on Si before the growth of a CdTe or ZnTe buffer layer has been shown to be crucial [32.137]. First-principles density-functional

calculations of Te adsorption on Si(100) [32.138] and pseudopotential density-functional calculations of the electronic and atomic structure of monolayers of Te and As on Si(211) [32.139] have been performed. Te-covered surfaces were found not to have any definitive reconstruction, explaining conflicting experimental results for the reconstruction [32.138]. Both As and Te surfaces were found to be metallic [32.139]. More importantly, the effects of Te passivation and As passivation of the Si surface before CdTe growth have been compared experimentally [32.137]. The CdTe film grown on a substrate treated with a Te flux was found to exhibit a rough film–substrate interface and to have very poor crystalline quality with a $\approx (111)\text{A}$ orientation. In contrast, the CdTe film grown under identical conditions except that the Si substrate was treated with an As flux was found to have an atomically abrupt film–substrate interface and a single-domain structure in the technologically preferred (111)B orientation. On the As-passivated surface the CdTe growth is initiated with Cd atoms having one bond to an As atom and three bonds with Te atoms from the incoming Te flux, producing an initial smooth Te stabilized growth surface. Recently, the structure of the As and Te atoms on As-passivated Si(211) surfaces after the early stages of ZnTe growth has been investigated [32.140] by x-ray photoelectron spectroscopy (XPS) and ion-scattering spectroscopy (ISS). It was found that the Si(111) terraces are completely covered by a monolayer of As, but that the step edges were left free to be covered by the first layer of Te atoms, allowing optimum nucleation of either a ZnTe or a CdTe buffer.

32.3.4 Other Substrates

As seen in Table 32.1, the characteristics of GaAs are intermediate between those of CdZnTe and Si. GaAs was the first substrate commonly used as a substitute for CdTe, is still the most commonly used substrate for the LPE growth of HgCdTe, and is still used for the MOMBE and MBE growth of HgCdTe by some groups. Although the lattice mismatch between GaAs and HgCdTe is 13.6%, high-quality HgCdTe can be grown on CdTe/GaAs substrates. However, growth on GaAs does limit the growth area to $\approx 1/30$ of that allowed for growth on Si, does not allow monolithic integration, and allows the outdiffusion of Ga and As into the HgCdTe, which can seriously affect the electrical properties of the HgCdTe. To bring the diffused Ga and As in the HgCdTe down to background levels, one must grow either CdTe/ZnTe SL buffer layers [32.51]

or thick (3–8 μm) CdTe buffer layers [32.51, 141]. The dislocation density of HgCdTe grown on CdTe/GaAs is similar to that of HgCdTe grown on CdTe/Si : As.

Ge also is still used as a substrate for the MBE growth of HgCdTe with CdTe buffer layers. As in the case of Si, large-area Ge substrates are available. Two-color MWIR FPAs fabricated from HgCdTe grown on Ge substrates displayed responsivities, noise characteristics, and operabilities matching those of detectors fabricated from HgCdTe grown on CdZnTe substrates, although the HgCdTe grown on Ge substrates was of lower quality [32.142, 143]. Because Ge is a more homogeneous substrate than CdZnTe, the XRD FWHM of the HgCdTe grown on CdTe/Ge was more uniform; however, it was $\approx 50\%$ larger than that of the HgCdTe grown on the better CdZnTe substrates. Also, the dislocation density was two orders of magnitude higher in the HgCdTe grown on CdTe/Ge, indicating that CdTe/Ge substrates would not be suitable for LWIR or VLWIR material. In summary, Ge would appear to have most of the advantages and disadvantages of Si as a substrate material, with easier to prepare growth surfaces, but without quite as large a possible area, quite as high a crystal quality, or the great potential advantage of being used for monolithic detectors.

In the past, sapphire also has been extensively used as a substrate for the MBE, VPE, and LPE growth of HgCdTe and the fabrication of MWIR photodiodes [32.144], although it is no longer used for MBE growth. It has high crystalline quality, high electrical resistivity and thermal conductivity, and low cost, and is robust. However, like GaAs, sapphire substrates are available only with areas $\approx 1/30$ of that allowed for

growth on Si. Also, CdTe buffers grown on sapphire exhibit a high density of dislocations, although that density is rather uniform, allowing the fabrication of highly uniform devices. Also, sapphire is not transparent in the LWIR and VLWIR, and thus cannot be used as a substrate for back-illuminated devices in those spectral ranges.

The final possible substrate material we consider is InSb. The physical properties of InSb suggest it as an almost ideal substrate for the epitaxial growth of HgCdTe. InSb and IR HgCdTe have almost identical lattice constants and coefficients of thermal expansion, and HgCdTe has been grown on InSb with XRD FWHM values as low as 18–22 arcsec [32.145]. Also, InSb wafers are available with diameters up to 4 inches. However, a number of difficult issues must be solved before InSb can be developed as a substrate material for the growth of HgCdTe. First, InSb has a low melting point (527 °C) and a tenacious native oxide, precluding thermal desorption as a wafer cleaning technique. The oxide can be removed in situ by Ar sputtering, and the induced damage partially removed by thermal annealing, but some surface and subsurface damage remains. Second, In_2Te_3 forms readily at the interface, creating structural defects that degrade any following CdTe or HgCdTe epitaxial growth, although this effect can be partially suppressed by using a Cd-enhanced flux during the initial CdTe growth. Finally, both In and Sb diffuse rapidly into CdTe and HgCdTe, where they strongly affect the electrical properties. Thus, appropriate diffusion blocking buffer layers would be required with the use of InSb substrates unless the substrates are removed before any annealing.

32.4 Design of the Growth Hardware

The reader is referred to [32.13] for a comprehensive review of the growth hardware for MBE growth. Here we discuss only two more recent growth hardware issues of importance for the MBE growth of HgCdTe: the mounting of the substrate on which the HgCdTe is to be grown, and the valving of the effusion cells which supply the growth materials.

32.4.1 Mounting of the Substrate

The standard mounting geometries for MBE substrates include contact and contactless configurations. In the contact configuration the substrate is bonded to a dif-

fusion plate using a mounting or bonding medium such as In or Ga. Contactless configurations were introduced to reduce the risk of contamination from the mounting media such as In or Ga; thus they are referred to as free or In-free mounting configurations. Another advantage of contactless configurations is the smaller thermal mass, allowing more rapid substrate temperature adjustments. In contactless configurations, the substrate is sandwiched between a diffuser plate and either a Mo retaining spring plate for a square substrate such as CdZnTe or a Mo ring for round substrates such as Si. The diffusion plate can be just a Mo plate; however, to achieve a constant growth temperature with only

a Mo plate one must severely ramp the nominal thermocouple temperature during growth [32.146]. Moreover, for a fixed thermocouple reading, the actual growth temperature depends strongly on the exact position of the thermocouple and on the mounting geometry, and its run-to-run variation was found to be $> 10^\circ\text{C}$, as measured by optical pyrometry and by SE. As an improvement, the diffuser plate can be replaced by a Mo plate and a graphite disk in contact with the substrate. It also was found to be beneficial to put a sapphire disk between the Mo plate and the graphite disk because the flat sapphire disk offers better mechanical support to the soft graphite plate. The use of a diffuser plate with a graphite plate in contact with the sample increases thermal conduction, decreasing the importance of irradiation, thereby allowing much better temperature run-to-run reproducibility. Another mounting problem is that the substrate must be rotated at a constant rapid angular velocity to ensure a uniform beam flux across a growth wafer, and with a wobble as small as possible to avoid excessive noise in the SE data.

The temperature ramping recipe that has to be employed to keep the growth temperature constant depends on the substrate area compared with the area of the diffusion plate. For example, for the growth of large-area samples, the substrate can be either (i) directly exposed to the heater and heated by irradiation, or (ii) juxtaposed to a diffuser plate and heated mainly by conduction. Case (iii) is that of smaller-area substrates such as CdZnTe, which are mounted using a molybdenum spring plate that holds the substrate in contact with a diffuser plate facing the heater. The heating power is determined by a closed-loop feedback involving a thermocouple, which floats in the gap between the heater and the substrate. Its readings are related to both the heater and substrate temperatures, and in some cases even to the temperature of the cell walls. Thus, the grower of HgCdTe faces a serious temperature stabilization problem during growth, since it has a very small growth window in comparison with other MBE-grown materials. It has been experimentally observed that in case (i) the heater temperature must be ramped down [32.146], whereas in cases (ii) and (iii) (which have some similarity to mounting on a full molybdenum block) a temperature increase is necessary to keep the growth temperature constant [32.147]. Case (i) has been the most widely investigated, especially for III–V MBE-grown materials [32.148, 149]. Here the temperature transient is believed to stem from the fact that the substrate is largely transparent to infrared radiation, whereas the growing material is not. Thus the thermal

absorptivity increases during growth, which results in an increase of the temperature. If the sample heating mechanism is conduction rather than irradiation, as in cases (ii) and (iii), material deposition results in a temperature decrease. This is because the emissivity of the front face increases without any substantial change in the heat conducted through the sample, as the substrate is much thicker than the epilayer being grown. Also radiative energy from the effusion cells can increase the substrate temperature, especially at nucleation, when temperature stability is essential to achieving good crystalline quality [32.150].

For these reasons, several optical methods have been used to measure the HgCdTe temperature in situ, such as (a) SE [32.151], (b) in situ FTIR spectroscopy [32.152], (c) dynamic reflectance spectroscopy (DRS) [32.153], and (d) absorption-edge spectroscopy (ABES) [32.154], on both II–VI and III–V materials. It has been shown that good reproducibility can be obtained from SE even though it gives no direct information on the growth temperature (Sect. 32.5.1). In the case of HgCdTe, DRS measurements must be carried out from the back face of the sample and generally require the deposition of a reflecting intermediate layer. For FTIR and ABES the HgCdTe must be optically thick to obtain reliable readings, so they are not applicable during the early stages of growth. However, information provided by RHEED spectra also can be used to indirectly analyze the growth surface temperature stability. In fact, RHEED and SE so far are the only measurements capable of characterizing growth nucleation in situ.

The employment of spring plates coated with materials with infrared emissivities similar to that of the HgCdTe to be grown allows the temperature ramping to be dramatically reduced or even eliminated for the growth of small-area samples. By employing a graphite plate in addition to a diffusion plate and coating the spring plates with an appropriate material, a dramatic improvement in growth yield was found. So long as substrates with similar characteristics were used, thermocouple run-to-run errors as low as $\pm(2-3)\text{K}$ were found for samples mounted with graphite plates and appropriately coated spring plates.

32.4.2 Valving of the Effusion Cells

Valved cells were introduced in the MBE growth of III–V materials as early as 1993 [32.155]. For the growth of HgCdTe a valved Hg source was introduced at the Microphysics Laboratory (MPL) of the Univer-

sity of Illinois at Chicago in 1998 and a valved Te source was introduced at the Rockwell Science Center in 1999 [32.156]. The use of a valved As cracker cell also recently has become common. The different valved cells share the same design concept, but with the Hg cell having a tube connected to the Hg reservoir to ease the Hg supply and the As cell having a high-temperature cracker to increase the ratio of As and As₂ to As₄ in the exent flux. The Hg and As fluxes can be precisely controlled and optimized by adjusting the computer-controlled needle valve for nearly continuous or abrupt flux changes with rapid flux stabilization, quick shutoff, and improved growth reproducibility. Also, the exit orifices of the valves can be customized to obtain excellent flux uniformity in any MBE systems. All these supe-

rior flux control capabilities are extremely desirable to maintain the optimized MBE growth of HgCdTe heterojunction material with complicated design architectures, which is impossible to achieve using conventional thermally controlled sources.

An As-valved cracker cell provides the convenience of a gas source with the safety of a solid source, which is beneficial to optimize flux profiles in time, reduce As consumption, and eliminate unintentional As incorporation into heterojunction structures. The source's cracking zone temperature can be adjusted to generate either As₄- or As₂-dominated flux beams. Such a valved cracker design also offers great flexibility to adjust the charge capacity and obtain optimized cracking efficiency.

32.5 In situ Characterization Tools for Monitoring and Controlling the Growth

Because the sticking coefficient of Hg is very much lower than those of Cd and Te, the growth window for MBE growth of HgCdTe is very small. The window in growth temperature for the growth of optimal epilayers has been reported to be as low as $\pm 0.5^\circ\text{C}$, and that for the Hg flux $\pm 2.5\%$, which corresponds to $\pm 0.5^\circ\text{C}$ in the temperature of the Hg cell [32.71]. This precise a degree of control is not possible, but it is very desirable to be able to control the growth temperature within $\pm 3^\circ\text{C}$ and the Hg flux within $\pm 5\%$. Furthermore, to obtain a desired cutoff wavelength or cutoff energy $\pm 6\%$ in a device, one must control the Cd composition x within ± 0.002 . Thus, excellent in situ monitoring and controlling of the growth are necessary, requiring multiple methods for monitoring and controlling the growth.

32.5.1 Spectroscopic Ellipsometry (SE): Basic Theory and Experimental Setup

Due to its simplicity, intrinsic accuracy and noninvasiveness, spectroscopic ellipsometry (SE) is widely used as an in situ tool to monitor, control, and characterize the MBE growth of Hg_{1-x}Cd_xTe alloys. The growth temperature, alloy composition, and presence of defects, overlayers or roughness at the surface in principle all are measurable by in situ SE, if the appropriate data analysis technique is used. Here, greatest attention is given to:

1. The use of SE to determine the temperature and surface roughness of substrates and the composi-

tion and surface roughness of the HgCdTe during growth

2. The principal methods of analysis of SE data, pointing out the strengths and weaknesses of each method.

Various specialized applications of SE in the study of the MBE growth of Hg_{1-x}Cd_xTe also are given.

Since shortly after its introduction [32.157] as an in situ characterization tool in 1991, ellipsometry has been applied primarily to find the Hg_{1-x}Cd_xTe alloy composition x . Single-wavelength ellipsometers were first used for this purpose [32.158, 159]. In 1964 44-wavelength SE was used to determine x to within ± 0.01 during MOCVD growth of Hg_{1-x}Cd_xTe and feedback control was established to force x to converge faster to its targeted value [32.160, 161]. Growth rate control and monitoring of the CdZnTe preparation procedure, its surface roughness, and its temperature were reported in 1996 [32.162]. By 1998 SE was mature enough to be introduced in a production environment, as the run-to-run precision in x had improved to ± 0.001 or ± 0.002 [32.163]. Now SE has entered the realm of standard use for compositional control, even in industry. In actuality, the capabilities of SE go well beyond the determination of x , although little work has been done to explore other applications.

Introduction to Ellipsometry

Ellipsometry is a polarimetric technique that uses the change of polarization of light upon reflection for

the characterization of surfaces, interfaces, and thin films [32.164]. If the analyzed surface is homogeneous, isotropic, and not contaminated by the presence of overlayers, and neglecting the difference between the electronic structure at the surface, a single ellipsometric measurement with light of wavelength λ yields the complex optical dielectric function $\varepsilon_s(\lambda)$ of the material at that wavelength

$$\varepsilon_s(\lambda) = \varepsilon_a(\lambda) \left[\sin^2 \phi + \sin^2 \phi \tan^2 \phi \left(\frac{1-\rho}{1+\rho} \right)^2 \right], \quad (32.1)$$

where $\varepsilon_a(\lambda)$ is the dielectric function of the ambient, ϕ is the angle of incidence, and ρ is the complex reflectance ratio $r_s/r_p = \tan \Psi e^{i\Delta}$, where r_s and r_p are the Fresnel coefficients, i. e., the ratios between the incident and reflected electric fields for s- and p-polarized light, respectively. If $n > 1$ layers are optically accessible, $\varepsilon_s(\lambda)$ is replaced by a pseudodielectric function $\langle \varepsilon_s(\lambda) \rangle$ that depends on the dielectric function of each layer and the thickness of the first $n - 1$ layers.

Multiwavelength ellipsometry (SE) provides the frequency-dependent dielectric function $\varepsilon_s(\omega)$, which is intimately connected to the semiconductor band structure and in particular to its critical-point (CP) energies. At these energies E_i there are discontinuities or infinite first derivatives in the joint density of states and thus, in the absence of line broadening, in the probability of photon absorption and hence in $\varepsilon_2(\omega)$, the imaginary part of $\varepsilon(\omega)$. Great effort has been devoted to the precise determination of the CP energies and line widths because they reflect any changes in temperature, composition, and other physical parameters. Given an ellipsometer with sufficient resolution and low noise, accurate determinations of the CP energies can be achieved by higher-order differentiation of the experimentally measured dielectric function [32.165], which greatly enhances the CP structure.

The actual measured quantities are the Fresnel coefficients of the sample, which usually are organized into Jones matrices of the form

$$\mathbf{J} = \begin{pmatrix} r_{pp} & r_{ps} \\ r_{sp} & r_{ss} \end{pmatrix} = r_{ss} \begin{pmatrix} \rho_{pp} & \rho_{ps} \\ \rho_{sp} & 1 \end{pmatrix}. \quad (32.2)$$

The Jones matrix of a stack of layers is just the product of the Jones matrices of the layers in the stack. For isotropic materials, such as HgCdTe and its substrates, the Jones matrices reduce to diagonal form. Since no existing in situ ellipsometer can measure all four Fresnel coefficients in one reading at a single azimuthal angle,

surface anisotropy due to oriented surface defects or the morphology of high-index surfaces can only be treated in an approximate fashion as a source of uncertainty.

The polarizing properties of any sample are given by its Mueller matrix, which relates the Stokes vector \mathbf{S} of the exiting reflected, transmitted or scattered light to that of the incident light \mathbf{S}_0 . For a homogeneous, isotropic semiconductor, the Mueller matrix can be represented as the product of an ideal linear polarizer with transmission axis ψ and an ideal retarder of retardance Δ

$$\mathbf{M} = \begin{pmatrix} 1 & -\cos 2\psi & 0 & 0 \\ -\cos 2\psi & 1 & 0 & 0 \\ 0 & 0 & \sin 2\psi \cos \Delta & \sin 2\psi \sin \Delta \\ 0 & 0 & -\sin 2\psi \sin \Delta & \sin 2\psi \cos \Delta \end{pmatrix} = \begin{pmatrix} 1 & -N & 0 & 0 \\ -N & 1 & 0 & 0 \\ 0 & 0 & C & S \\ 0 & 0 & -S & C \end{pmatrix}. \quad (32.3)$$

The final form in (32.3) holds even with depolarization; in general, $C^2 + S^2 + N^2 = p^2$, where $p = 1$ for nondepolarizing samples and $p = 0$ for completely depolarizing samples. C , S , and N completely characterize all isotropic, homogenous materials, even depolarizing ones. If the further assumption is made that a sample is nondepolarizing, then the knowledge of any two of C , S , and N suffices to calculate the pseudodielectric function.

Ellipsometer Designs

The primary ellipsometer designs in use for in situ SE are the rotating compensator ellipsometer (RCE) and the rotating analyzer ellipsometer (RAE). These designs differ in how fully they characterize the Mueller matrix. In the RAE [32.166], light generated by the source is first linearly polarized by a polarizer, then reflected by the sample, goes through an analyzer, and finally enters the photodetector. The presence of the first polarizer makes the measurement immune from polarization by the source optics. The analyzer is continuously rotated to generate a modulation of the detected signal, which is Fourier-analyzed to extract C and N . This design cannot measure S because that would require circularly polarized light. A simple calculation shows that the irradiance at the detector is given by

$$I = I_{dc} + I_s \sin 2\omega t + I_c \cos 2\omega t,$$

where

$$\frac{I_s}{I_{dc}} = \frac{C \sin 2\theta_p}{1 - N \cos 2\theta_p}, \quad \frac{I_c}{I_{dc}} = \frac{\cos 2\theta_p - N}{1 - N \cos 2\theta_p}. \quad (32.4)$$

The azimuthal angle of the polarizer θ_p can be determined through a calibration procedure [32.167, 168]. Because S does not appear in these equations, even in the absence of depolarization only S^2 is determined, and the sign of Δ is undetermined. Also, the sensitivity of the **RAE** ellipsometer is zero for $\varepsilon_2(\omega) = 0$, hence, at or below the optical energy gap of semiconductors. In particular, **RAE** ellipsometers designed for the characterization of HgCdTe in the region around the E_1 **CP** (2–3.5 eV) do not perform well for CdTe or Si in the same energy range.

The **RCE** was introduced to circumvent these limitations. A compensator is inserted between the polarizer and the sample. In the most common design, the compensator is rotated continuously, whereas the analyzer and the polarizer remain fixed. The output irradiance at the detector has extra Fourier components, of angular frequency 4ω ,

$$I(t) = I_{dc} + I_c^{(2)} \cos(2\omega t) + I_s^{(2)} \sin(2\omega t) \\ + I_c^{(4)} \cos(4\omega t) + I_s^{(4)} \sin(4\omega t),$$

which allows C , S , and N to be calculated without ambiguity. Thus, the **RCE** determines the sign of Δ , gives accurate readings even for $\varepsilon_2(\omega) = 0$, and can measure depolarization. Several other ex situ designs which have been proposed can measure the anisotropic dielectric function and the depolarization at a single azimuthal angle, taking only two separate measurements, for example that by *Jellison and Modine* [32.169], but no applications to in situ measurements of HgCdTe have been proposed.

Retrofitting the MBE Chamber

The setup for in situ experiments is complicated by many constraints, and the data are subject to more sources of uncertainty than in an ex situ setup. Constraints are for example posed by the availability of ports for the windows, the window type, the intrinsic characteristics of the substrate manipulator, etc. The effect of windows on accuracy is very large for most ellipsometers [32.170]. Different ellipsometers measure different linear combinations of the Mueller matrix elements, and therefore differ in how fully they characterize and hence can correct for window imperfections. The **RAE** cannot measure even the out-of-plane component of birefringence during an experiment, while the

RCE can. It is not possible with any instrument to separate the in-plane window retardation from that of the sample, even when the entire Mueller matrix is measured. To determine the in-plane window retardation one must resort to measurements with well-known samples, such as Si oxide of known thickness. Low-strain bakeable windows, guaranteed to have a birefringence of less than 1° , are commercially available, but even run-to-run variations of the order of 0.1° , which may occur when the windows are baked out, can be important. Also, the measured $\varepsilon_2(\omega)$ is extremely sensitive to changes in the angle and plane of incidence, so that much care must be taken to minimize wobble using wobble-free manipulators and a proper substrate mounting procedure. Unfortunately, substrate rotation cannot be avoided. Thus, it is common to equate the data acquisition time to the total rotation time of the substrate.

32.5.2 SE Data Analysis

To interpret ellipsometric results, the complex reflection coefficients must be computed from a model of the sample surface. In the general case, one constructs a model for the dielectric function which depends on the parameters to be determined. This is fitted to the experimental data using the standard Levenberg–Marquardt algorithm. The function itself and possibly its first, second or third derivatives, or a combination of them, are fitted. There are two principal approaches to parameterizing the optical constants of a bulk semiconductor, based either on the construction of calibrated libraries of optical dielectric functions or on the determination of their **CP** parameters. Library models are commonly used to find the composition and surface roughness of HgCdTe during growth, and the temperature and surface roughness of CdZnTe or CdTe before growth. Their main advantage is their ease of use. Unfortunately, when growth conditions are changed, such models can suffer from large run-to-run uncertainties, due to changes in surface morphology, small changes in temperature, and changes in window retardation and birefringence. The use of **CP** models for the dielectric function has been introduced to reduce these uncertainties.

Multilayer Models and the Virtual Interface Approximation

The most common multilayer model for HgCdTe, CdZnTe, and CdTe characterization is a three-layer model, comprised of epilayer or substrate, a surface roughness layer, and the ambient, normally vacuum. If the optical constants of the growing layer are un-

known, the virtual interface approximation [32.171, 172] and dynamic algorithms can be used to extract them, the growth rates, and in some cases even the surface roughness of the growing layer at the beginning of growth. Exact expressions for the dielectric function ε_0 of a virtual surface located at the physical surface can be found as a function of the measured pseudodielectric function $\langle\varepsilon\rangle$. These expressions can be fitted to the experimental data to obtain estimates for both the near-surface composition and the growth rate, as shown [32.150] for MOCVD-grown HgCdTe. The virtual interface approximation has attained great importance for the characterization of HgCdTe, as it provides a way to monitor growth nucleation.

Surface Roughness

Surface roughness results in reflectance loss, polarization of the specularly reflected light, and the introduction of stray light reflected at near-specular angles. Most of the specularly reflected light is reflected coherently and stays polarized. Part is reflected incoherently and is depolarized, but the depolarization caused by a small degree of microscopic roughness is minimal and needs to be taken into account only for moderately to very rough surfaces. In that case, near-specular scattering may also play a role [32.173]. For roughness on a scale smaller than the wavelength of the reflected light, the changes in the coherent, polarized part of the reflected beam can be described by the Bruggeman effective medium theory (EMA) [32.174, 175]. That theory is derived from the Clausius–Mossotti expression [32.176] for the dielectric response of a heterogeneous medium of point-like microstructures embedded in a host for the case of an aggregate of two types of microstructures in which the volume fractions of the two types are comparable, so that the host must be chosen as some self-consistently chosen effective medium. In the EMA the dielectric function of the effective medium is chosen to be

$$\varepsilon = \frac{\varepsilon_a \varepsilon_b + \bar{\varepsilon}(f_a \varepsilon_a + f_b \varepsilon_b)}{\bar{\varepsilon} + (f_a \varepsilon_b + f_b \varepsilon_a)}, \quad (32.5)$$

where ε_a and ε_b are the dielectric functions of the two types of microstructures, $\bar{\varepsilon} = (q^{-1} - 1)\varepsilon_b$, and q is a screening parameter between zero and one. The thickness t of the roughness layer is related to the mean-square roughness by $t = 2\sqrt{2}\sigma_z$ [32.177]. The void fraction in the roughness layer is commonly taken to be 50%, so that (32.5) reduces to the form $\varepsilon = [2\varepsilon_b + \bar{\varepsilon}(1 + \varepsilon_b)]/[2\bar{\varepsilon} + (1 + \varepsilon_b)]$.

Analysis Based on Dielectric Function Libraries

Libraries of dielectric functions are acquired at a set of values of one or more parameters, e.g., the temperature and/or the alloy composition, and interpolated between those values. In the simplest case, libraries are used in conjunction with multilayer models for the dielectric function. A typical model valid only for optically thick layers consists of a composition-dependent epilayer or temperature-dependent substrate, surface roughness, and ambient. The surface roughness is described in the EMA. Hence, a fit to the experimental data yields the thickness t of the roughness layer and either temperature or composition. In most in situ environments, it is also necessary to leave the angle of incidence ϕ free in the fit, thus having three independent fitting parameters.

To obtain a meaningful library, one's ellipsometer must be accurately calibrated, the windows must be free of birefringence, the angle of incidence must be known, and the sample composition and temperature must be known. Also the surface one is measuring must be exactly known, and no undesired overlayer or unknown roughness should be present. These conditions are very hard to attain in situ, but they can be attained at least approximately. A full calibration of the ellipsometer before data acquisition can be performed ex situ, with the angle of incidence as well as the sample type perfectly known. Then, standard calibration procedures can be performed. For most commercially available RAEs or RCEs, these calibration procedures are executed automatically by software algorithms. The window birefringence must be minimized using *strain-free* windows. Residual in-plane birefringence can be estimated in situ using a thermally grown SiO₂/Si calibration sample, the optical constants of which are well known. Since the window birefringence is approximately constant on any given MBE system, if low-strain windows are used, a precision of about $\pm 0.1^\circ$ in the measured values of Δ is expected. The angle of incidence can be measured in situ in most cases, exploiting databases of room-temperature optical constants available in the literature.

Unfortunately, exact knowledge of a sample surface is very difficult to attain even in situ; submonolayer overlayers and roughness are always present, even in the cleanest in situ environment. Fortunately, they can be estimated by comparison with ex situ data at room temperature, and subtracted mathematically using the Jones formalism for multilayer analysis. The caveat here is that usually surface roughness and oxide layers are essentially indistinguishable in treating the effects

of a thin overlayer of unknown thickness [32.178–180]. Usually an oxide overlayer is subtracted from the data to obtain the bulk dielectric function.

Since all in situ SE measurements of epilayer and substrate properties are based on the dielectric function library used, the measuring accuracy and precision largely depends on that library. Bearing in mind the caveats discussed above, *Johs* [32.181] developed a procedure to measure dielectric function libraries of growing materials, in particular of HgCdTe during MBE growth. He confronted with great success the problem of determining a library of dielectric functions for different Cd molar fractions, from $x = 0.2$ to 0.5 , at the ideal growth temperature T_g . His paper discusses the difficulties that one encounters in measuring a compositional library $\langle \varepsilon(\omega; x, T_g) \rangle$ in great detail. Because $\varepsilon(\omega)$ depends strongly on T as well as x , the very narrow growth window for HgCdTe turns out to be very helpful in obtaining $\langle \varepsilon(\omega; x, T_g) \rangle$. Because of the very narrow growth window, the measured thickness of the surface roughness layer increases rapidly as the growth temperature departs from the ideal. This allows one to adjust the temperature to T_g even without knowing its value and thus to hold the uncertainty in the measured $\langle \varepsilon(\omega; x, T_g) \rangle$ to a minimum.

The compositional control of HgCdTe attained using the library developed by *Johs* has been excellent, as reported by a large number of authors [32.182–188]. Attention has not been focused on the real-time variations of the composition (which are inaccessible by routine FTIR measurements in any case), but only on its average value over the entire layer. This was obtained as follows: a set of 8–10 measured dielectric functions was suitably selected to span the entire growth process. A global fit was performed, treating the angle of incidence as a global parameter and leaving composition and surface roughness free to attain different values for each spectrum. Finally, the obtained x -values were averaged to get the average composition.

A fit to $\langle \varepsilon_2 \rangle$ yields average compositional values that are in good agreement with those obtained by FTIR. The fact that a fit to the measured values of $\langle \varepsilon_2 \rangle$ gives the best ellipsometric measurement of x is due to two factors:

1. $\langle \varepsilon_2 \rangle$ contains much more direct information on the joint density of states (JDS) than either $\langle \varepsilon_1 \rangle$ or Δ and Ψ
2. $\langle \varepsilon_2 \rangle$ is much less affected by variations in the window birefringence.

These two factors also assure that $\langle \varepsilon_2 \rangle$ gives a very accurate measurement of x when proper care is taken and when the library used is appropriate for the growth temperature and growth and SE measurement configurations used. However, it should be emphasized that the excellent results found for compositional monitoring and control require fully reproducible growth conditions. Changes in the geometry of the growth setup, the growth rate, the sample mounting, etc. have been shown to lead to substantial errors in the HgCdTe compositions measured using the library function of *Johs*. Also, in situ measurements of the composition y in CdZnTe as a function of temperature using a library of $\text{Cd}_{1-y}\text{Zn}_y\text{Te}$ dielectric functions have been performed for three samples with $z = 0.0, 0.045$, and 0.125 , starting at room temperature, going up to 350°C , and coming back down to 150°C . He found that the composition measured upon coming back down in temperature from 350°C was very different from that measured going up in temperature, ≈ 0.05 higher over the range $150\text{--}300^\circ\text{C}$ for the CdTe sample. He also measured the temperatures using the same library, and found errors in the measured temperatures from -10 to -30°C for the CdTe sample upon coming back down in temperature.

The acquisition of a two-dimensional (2-D) library $\langle \varepsilon(\omega; x, T) \rangle$ of HgCdTe pseudodielectric functions as a function of the two variables x and T is much more difficult than might be expected a priori. This is because high-quality HgCdTe only grows within a $\pm 5^\circ\text{C}$ window, so that to get a temperature library one must interrupt the growth and ramp the temperature to different values. This must be done leaving the layer under Hg flux to avoid irreparable damage to the surface. We have found no systematic dependence of the CP energies on T , in data taken with this procedure, probably because of Hg evaporation, which alters the composition near the surface, producing random changes in the dielectric function and in any measured CP energies. No alternative procedure has been proposed to date.

These difficulties may be overcome in the near future, for example by a more accurate control of the Hg flux. However, even if a two-dimensional library were obtained, one must still conclude that one could not obtain x and T simultaneously from such a library without SE data greatly improved over that provided by the 88-wavelength RAE now commonly used, which does not provide the resolution necessary to allow the accurate determination of CP energies through multi-

ple differentiation of the data. It has been shown that a fit to the undifferentiated data leaving four parameters free (x , T , t , and ϕ) yields a reasonably good estimate for T , but also substantially increases the uncertainty in x and t . A better approach would be based on the interplay of a 2-D library for $\langle \varepsilon(\omega; x, T) \rangle$ and a knowledge of the energy $E_1(x, T)$ obtained by multiply differentiating that library with respect to ω . The energy E_1 could be obtained very precisely and would be almost independent of any surface overlayer. One could find T as a function of x from a measured E_1 , reducing a two-dimensional fitting problem to a one-dimensional problem using the undifferentiated library. One cannot simultaneously determine x and T by measuring two CP parameters without an ellipsometer capable of simultaneously measuring E_0 and E_1 accurately. No such ellipsometer is available at present. Measurements of the other E_i do not give sufficient information; $E_1 + \Delta_1$ and $E_0 + \Delta_0$ cannot be measured sufficiently precisely, and $E_1 + \Delta_1$ moves almost in parallel with E_1 with changes in x or T . Also, the line widths Γ_i depend strongly on material quality and cannot be measured as precisely as the E_i .

A new set of libraries of $\varepsilon(\omega; T)$ for $\text{Cd}_{1-z}\text{Zn}_z\text{Te}$ for $z = 0.0, 0.045, 0.125$, and 1.0 is available from MPL. That library ranges from 75 to 300°C in increments of 25°C with increments of 15 \AA in wavelength from 1.2 to 5.0 eV and increments of 30 \AA from 0.7 to 1.2 eV . The library was obtained by ramping the temperature of each CdZnTe sample up in 25°C steps, pausing at each step to allow the sample to come to a steady state, and then measuring $\varepsilon(\omega)$ at that temperature. The following procedure [32.151] was used. Clean $\text{Cd}_{1-z}\text{Zn}_z\text{Te}$ was introduced in the MBE chamber after etching in a 0.5% bromine and methanol solution, and rinsing in methanol and deionized (DI) water. The surface oxide was desorbed at $\approx 250^\circ\text{C}$, the substrate was ramped to different temperatures, and its pseudodielectric function $\langle \varepsilon(\omega; T, \phi, t) \rangle$ was measured at each temperature T . The temperature at the surface was measured with a thermocouple, and the temperature measurements were calibrated according to the melting points of Sn and In. A fit to room-temperature data gave the angle of incidence ϕ and the thickness t of the surface roughness overlayer, using calibrated data acquired ex situ. This procedure allowed us to obtain a set of spectra $\varepsilon_{\text{CZT}}(\omega; T_1, \dots, T_n)$ with overlayer effects removed. The library was obtained using an M-2000 ellipsometer, which has 220 wavelengths from 1000 to

1700 nm , allowing the differentiation of the data to determine the E_0 and E_1 CP energies using a CP model, as discussed immediately below.

One can never ensure that one is measuring the optical constants of an abruptly terminated, clean, and smooth semiconductor surface. All that can be ensured is that our optical constants are reproducible, under the same conditions, on the same system. One cannot ensure the absolute accuracy of a library of measured optical constants, because of window birefringence and the presence of overlayers, but one can expect one's measurements to be reproducible from run to run on the same system. However, system-to-system portability of a library is never certain.

Analysis Based on Critical Point (CP) Models

An analysis of the dielectric function which includes a CP analysis in principle is superior to an analysis based on libraries, for the following reasons. First, much of the information obtainable from the derivatives of the pseudodielectric function is complementary to that obtainable from fits to the function itself and is not available from fits to the function itself. That information consists of the energies E_i and intrinsic line widths Γ_i of all band-structure CPs within the spectral range of the SE data. Second, the use of a parameterized theoretical model for the dielectric function allows us to measure directly the phase shift of the incoming light in SE as it passes through a surface overlayer and thus to measure directly the optical thickness of the overlayer, which is not otherwise possible. The E_i are virtually independent of surface overlayers and, given sufficiently good SE data, can be obtained very precisely.

High accuracy in the determination of the E_i and Γ_i is paramount in in situ applications. The problems with CP analyses are that the data fitting is more difficult and that low-noise, high-resolution SE data is required to perform the higher-order differentiation needed to obtain accurate values for the CP parameters. It has been found [32.189] that it is impossible to perform a useful CP analysis using only the 88 wavelengths available with an M-88 ellipsometer with the typical signal-to-noise ratio (SNR) of in situ data. However, the use of an M-2000 ellipsometer in situ has been found to yield sufficient resolution and a sufficiently small noise level to allow the profitable use of a CP model for data analysis.

Several CP models have been proposed, but only the Kim model [32.190] is capable of simultaneously fitting the optical dielectric function and its derivatives. The optical dielectric function is given by the fundamental

expression [32.191]

$$\begin{aligned} \varepsilon(\omega) = 1 + \frac{8\pi^2 e^2}{m^2} \\ \times \sum_{c,v} \int W_{cv}(E) dE \\ \times \{ [\Phi(\hbar\omega - E) - \Phi(\hbar\omega + E)] \}. \end{aligned} \quad (32.6)$$

In this expression, $W_{cv}(E) = P_{cv}(E)^2 J_{cv}(E)$ represents the product of the Brillouin-zone-average transition probability at the energy E and a joint density of states (**JDS**), $J_{cv}(E)$. $\Phi(\hbar\omega \pm E)$ is the broadening function and is equal to $|\hbar\omega \pm E + i\Gamma|^{-1}$ for Lorentzian broadening; in general, the broadening is intermediate between Lorentzian and Gaussian [32.192]. The **JDS** is given by the formula

$$J_{cv}(E) = \int_{\text{BZ}} \delta[E_c(\mathbf{k}) - E_v(\mathbf{k}) - E] d\mathbf{k}, \quad (32.7)$$

and counts the number of states per unit energy between a given pair of conduction (c) and valence (v) bands that differ by an energy E . The **JDS** and hence the $W_{cv}(E)$ are smoothly varying functions of energy away from the critical points.

The Kim model parameterizes the fundamental expression (32.6) by approximating the $W_{cv}(E)$ by low-order polynomials in energy multiplied by functions of energy having the proper analytic behavior at the **CPs**. Thus the model has two parameters for each **CP**, E_i and Γ_i , along with amplitude parameters with respect to which the dielectric function is linear. $W_{cv}(E)$ is divided into seven contributions, one for each pair of connected **CPs**. The resultant **JDS** is shown schematically in Fig. 32.10. The expression for each region

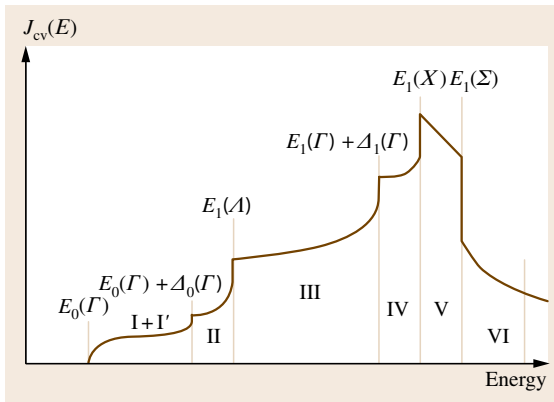


Fig. 32.10 Schematic diagram of the joint density of states of a zincblende semiconductor

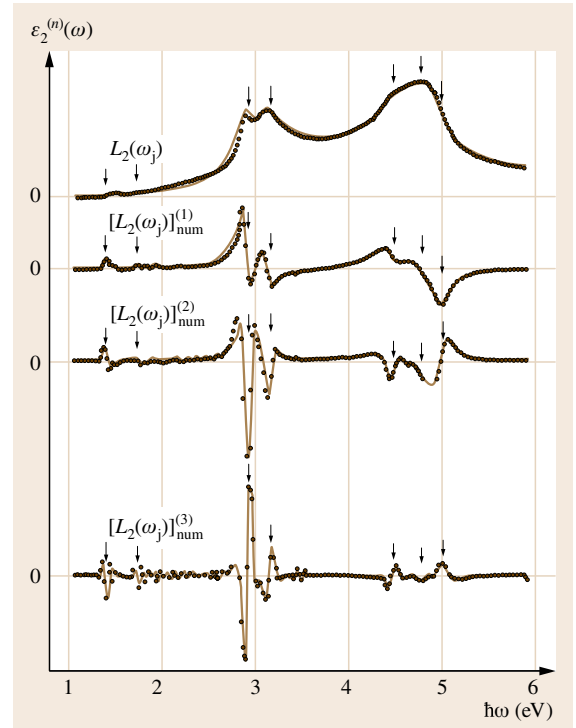


Fig. 32.11 Simultaneous fit of the Kim, et al. model to the experimental $\varepsilon_2(\omega)$ for GaAs and its first three numerical derivatives allowing a mixture of Lorentzian and Gaussian broadening for the four lowest-energy critical points. The arrows show the energies of the seven critical points used in the fit. The black dots show the experimental $\varepsilon_2(\omega)$ and its numerical derivatives; the red curves show the modeled $\varepsilon_2(\omega)$ and its numerical derivatives

in Fig. 32.10 is given in [32.190] and is fitted independently. The expressions for the seven contributions are substituted in (32.6) and integrated analytically. A proper harmonic oscillator is also added to account for out-of-range contributions to $\varepsilon_1(\omega)$.

The Kim model allows:

1. Predictions for the region below the fundamental gap, but above the onset of phonon transitions
2. The measurement of the true **JDS**
3. The measurement of the thickness of overlayers using the measured phase shifts at the **CPs**.

It was initially tested by simultaneously fitting $\varepsilon_2(\omega)$ for GaAs and its first three derivatives; the results are shown in Fig. 32.11; the fit to $\varepsilon_2(\omega)$ was good to 0.4%. It was later used to fit the dielectric functions of CdTe [32.193] and ZnSe [32.194] and their derivatives and to obtain

functional forms for the temperature-dependent dielectric functions of CdTe [32.195] and HgCdTe [32.196] and the composition dependent dielectric function of AlGaAs [32.197]. It was found that, with a total of 75 free parameters, the measured $\varepsilon_2(\omega)$ for $\text{Al}_{1-x}\text{Ga}_x\text{As}$ and its derivatives for all compositions could be fitted by functions of x and ω within a fractional root-mean-square (rms) error of only 1.2% in $\varepsilon_2(\omega; x)$. When measuring in situ, fewer parameters should be used because the data are affected by much larger uncertainties.

One value of using the Kim model is its failure to fit the measured $\varepsilon_2(\omega)$ for materials having poor crystalline quality or having overlayers not explicitly included in the fitting through the use of a multilayer model. This means that it cannot give incorrect CP energies to compensate for the effects of overlayers or poor crystalline quality, so the CP energies given are very reliable. This is illustrated by its failure to fit the alloy series $\text{Hg}_{1-y}\text{Zn}_y\text{Te}$ and $\text{Cd}_{1-y}\text{Zn}_y\text{Te}$. Fits to samples having different alloy compositions [32.198] failed to yield a systematic dependence of the room-temperature T_i on y over the compositional range $0 < y < 1$. The poor material quality of these alloy systems led to fluctuations in the CP line widths with alloy composition that made it impossible to obtain functional forms for their composition-dependent dielectric functions. That result highlights the sensitivity of this model to even small changes in CP parameters. To be able to monitor such changes opens new horizons for the in situ monitoring of HgCdTe growth.

Comparison of Results from Fitting to a Library and from CP Analysis Using the Kim Model

Consider a few cases in which both library functions and a CP analysis have been used in fitting data obtained from an M-2000 ellipsometer to measure composition or temperature. Abad found that the CP energies found for CdZnTe from the derivatives of the measured dielectric function are essentially unaffected by surface changes caused by annealing, even though those changes cause significant changes in the dielectric function itself. Also, *Badano et al.* [32.199] recently have studied the effect of surface roughness on the ellipsometric response from CdTe epilayers having up to ≈ 200 Å-thick surface roughness with a correlation length of several micrometers. SE data were taken ex situ at room temperature to reduce the noise in the data and the CP line widths, so as to improve the precision of measurement of the CP energies. Although the surface roughness introduced noticeable changes in the dielectric function, the CP energies found were unaffected

by the roughness. Since the sample surface temperature can be defined solely by the CP energy E_1 , this confirmed that the sample surface does not affect the temperature measured using the Kim model. These results, which argue in favor of using CP analysis, are not unexpected, because the dielectric function of a microscopically disordered surface does not have sharp derivatives.

Also, *Badano et al.* [32.200] recently have compared the use of library functions and the use of the Kim model for the measurement of the temperature of CdTe epilayers grown on Ge. The layers were ramped up and down in temperature as in the study by Abad, but only up to $\approx 250^\circ\text{C}$, and were measured under a Te flux and under no flux. The reproducibility obtained using the two different data analysis methods, upon ramping the temperature up and then back down, were similar, except that the Te flux affected the values obtained for T using library functions but not those obtained using the Kim model. An error analysis of the CP fitting procedure suggested that noise in the data should introduce a random error of approximately ± 5 K in the value of T found using the Kim mode. However, the values of T obtained using the Kim model were reproducible within ± 2 K, an outstanding result. The values for T found using a library were systematically higher than those found using the Kim model. Since values obtained using a library are much more subject to systematic error while those obtained from the Kim model are much more subject to random error, it would be reasonable to ascribe this systematic difference to systematic error arising from the use of library functions.

On the other hand, even with the use of an M-2000 ellipsometer, the noise in SE data induced random dispersions in y and T of the order of ± 0.005 in y and ± 4 K in T for $\text{Cd}_{1-y}\text{Zn}_y\text{Te}$. Those uncertainties are somewhat too large, although substantially better than those found using a library of dielectric functions. On the other hand, it suggests that by measuring y ex situ at room temperature and then, knowing y , measuring T in situ, one could obtain more precise values than are now available. The uncertainties would be substantially reduced by not having to determine y and T simultaneously, and the uncertainty in y would be further reduced by measuring it ex situ. However, the large variations in y which sometimes exist from point to point on a CdZnTe substrate would make this method problematic, because the in situ and ex situ measurement points on the CdZnTe may not be identical. Also, Abad found the Kim model to be substantially more difficult to use than library fitting with the software provided with the ellipsometer. This result is discouraging

with regard to the possibility of being able to measure x and T in situ simultaneously for HgCdTe, although the method proposed for HgCdTe is different, involving the determination of x from a library of dielectric functions and T from the determination of the CP energy E_1 .

In conclusion, the use of the Kim model eliminates errors arising with the use of library functions due to changes in incident flux, surface damage and surface states, window coatings, etc., but introduces uncertainties due to the relatively large amount of noise in in situ SE data. Although for measuring temperature those uncertainties appear to be smaller than the errors which easily can occur with the use of library functions, they may need to be reduced further for SE to become a valuable tool for measuring T . Also, the use of the Kim model entails fits that are not as robust and may converge slowly, a serious problem for the in situ control of growth. The use of the Kim model for the in situ determination of substrate temperature with an M-2000 ellipsometer is promising, but would require a more robust fitting procedure to be justified in a well-controlled production environment, in which the use of

library functions determines T reproducibly even if not accurately.

However, the use of the Kim model would have two other advantages, namely the determination of the CP line widths and, unlike fitting to library functions, the determination of absolute values for the surface roughness or the thickness of other overlayers. Results from Badano et al. show that the use of a CP model can pinpoint the presence of overlayers on a sample, and does not fit SE data unless a proper model for such an overlayer is adopted. We envision the possibility of acquiring libraries of true bulk dielectric functions, by eliminating the roughness overlayer from the data, and possibly also the effect of other overlayers due to the presence of the impinging fluxes. More work is being done in this field.

32.5.3 SE Study of Hg Absorption and Adsorption on CdTe

SE has been shown [32.201,202] to measure the relative abundance of chemisorbed and physisorbed monolayers of Hg on the CdTe substrate surface prior to growth nucleation. Data with submonolayer resolution were obtained. The substrate dielectric function was measured after the substrate was prepared using a standard procedure, but before subjecting it to Hg flux. Then, the Hg flux was opened and the dielectric function was remeasured. In the analysis of the change in the pseudodielectric function due to Hg deposition, two major approximations were made. First, the surface roughness and the chemisorbed and physisorbed Hg were treated as separate layers with the physisorbed Hg on top of the chemisorbed Hg, and, second, the three-dimensional (3-D) form of $\varepsilon(\omega; x)$ for $\text{Hg}_{1-x}\text{Cd}_x\text{Te}$ for large x was used to mimic the effect of chemisorbed Hg in the surface region. Thus, the data were interpreted using a five-layer model comprised of CdTe substrate, surface roughness, chemisorbed Hg, physisorbed Hg, and ambient. The quantities left free in the fit to the data were the thicknesses of the two Hg layers, that of the roughness layer, and the plasma frequency ω_p in the Drude form assumed for the dielectric function of the physisorbed Hg layer. The values found for the relative thicknesses of the chemisorbed and physisorbed layers are physically reasonable and show the expected dependence on the temperature and the Hg flux, as shown in Fig. 32.12. Although the absolute numbers provided by the analysis undoubtedly are not accurate, the results confirm our general ideas regarding the nature of the CdTe(211) surface under a Hg flux, and is valuable at least techno-

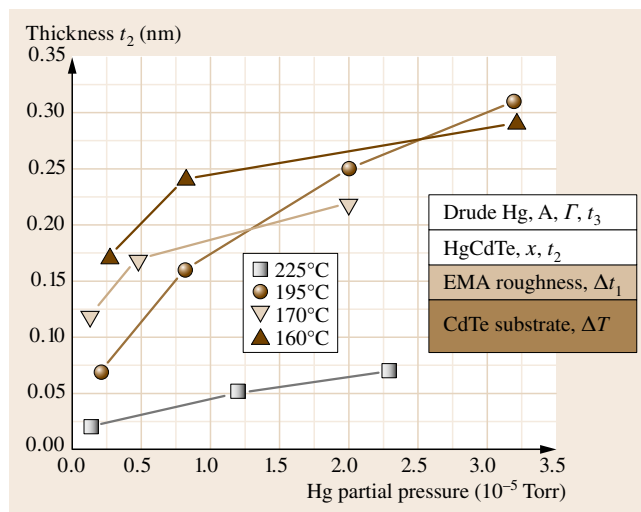


Fig. 32.12 Calculated thickness t_2 of the chemisorbed Hg layer, obtained as a function of the Hg flux for different substrate temperatures. The uncertainty in each thickness obtained from the correlation matrix is approximately ± 0.4 Å. The values for the Hg partial pressure are uncorrected N_2 pressure readings. The data at 195 °C were acquired during a separate run than the data taken at 225, 160, and 170 °C. In the 195 °C run, the sample was exposed to Te flux down to a lower temperature, thus it was likely to have a higher Te coverage. The inset shows the assumed structure and the fitting parameters used in fitting the SE data

logically to obtain a reliable run-to-run characterization of the surface before growth.


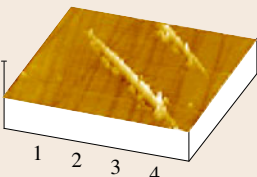
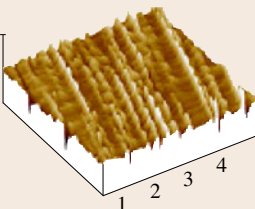
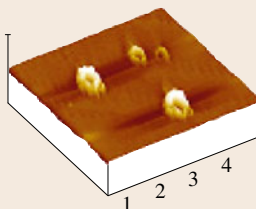
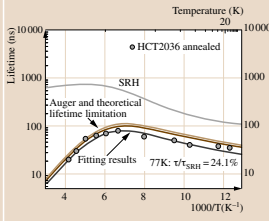
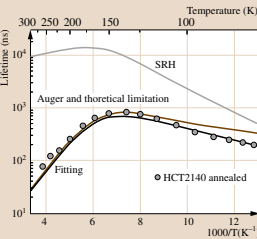
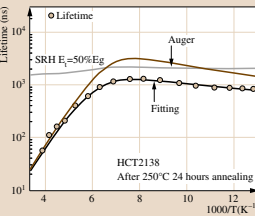
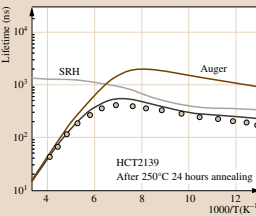
32.5.4 Correlation Between the Quality of MBE-Grown HgCdTe and the Depolarization and Surface Roughness Coefficients Measured in situ SE

The SE surface roughness thickness parameter t measured using an effective medium approximation (EMA) for the roughness is routinely used to monitor growth. The surface roughness measured by SE during growth is a good indicator of the final quality of HgCdTe layers. Substantive increases in t are always associated with the onset of 3-D growth and the degeneration of material quality, mostly associated with the formation of twins. In addition, the substrate submicroscopic roughness as

measured by SE correlates well with the qualitative roughness inferred from reflection high-energy electron diffraction (RHEED). Due to the nature of the EMA model, it is sensitive to roughness on an atomic scale and can give information about how small-scale defects form. However, it does not model roughness on a micrometer scale.

The evolution of surface roughness with increasing epilayer thickness for CdTe grown under nonideal conditions has been studied [32.199]. Both the use of the Kim model and the use of library functions gave surface roughness values which initially increased with increasing epilayer thickness and then decreased. It was found that the apparent decrease arose from the onset of macroscopic roughness, which could not be fitted by the EMA. For rough samples with roughness on much larger than a nanometer scale, the measured dielectric function departs significantly from the form

Table 32.3 Correlation between the depolarization coefficient \bar{u} , the surface morphology, the SRH contribution to the minority carrier recombination rate, the EMA surface roughness, and the etch pit density

Sample#	HCT2036			HCT2140			HCT2138			HCT2139		
Surface morphology												
Depolarization coefficient u	u_0	u_{end}	Δu	u_0	u_{end}	Δu	u_0	u_{end}	Δu	u_0	u_{end}	Δu
	-5	-5	± 5	-5	5	± 4	-5	18	± 4	-5	25	± 4
EMA t (Å)	t_0	t_{end}		t_0	t_{end}		t_0	t_{end}		t_0	t_{end}	
	0	2		0	2.5		0	5		0	5	
Temperature dependent lifetime												
τ/τ_{Auger} @77K (ns)	35/38			199/328			794/1361			188/778		
τ/τ_{SRH} @77K	24.1%			36.7%			56.2%			70.1%		
EPD (cm ⁻²)	2.0×10^5			9.1×10^5			2.7×10^6			4.9×10^6		

it takes with only atomic-scale roughness because the EMA is not suitable for describing larger-scale roughness with lower lateral spatial frequency. Because the RAE is very sensitive to depolarization effects, we have introduced a model for the analysis of RAE SE data, which contains a depolarization coefficient parameter.

The depolarization coefficient u for the RAE is defined by the equations

$$\begin{aligned}\cos 2\psi &= (1+u) \cos 2\psi' \quad \text{and} \\ \cos \Delta &= \cos \Delta' \left(1 + \frac{1}{\sin^2 \psi'} u \right),\end{aligned}\quad (32.8)$$

where ψ' and Δ' are the values of ψ and Δ measured by SE in the presence of depolarization, and ψ and Δ are the values in the absence of depolarization [32.203]. The quantity u is the ratio of the intensity of the light scattered incoherently to that of the specularly reflected light [32.204]. Obviously, u is a function of wavelength or frequency, $u = u(\omega)$, but no measurements of $u(\omega)$ are available in the literature for rough HgCdTe or CdZnTe. We define \bar{u} as the value of u averaged over the wavelength range of our SE data. It measures surface roughness on a scale larger than that of the EMA surface roughness, a lateral scale more nearly of order the wavelength of the incident polarized light.

We have discovered correlations between the minority-carrier recombination lifetime τ and \bar{u} . It correlates well enough with τ to be regarded as a useful predictor during growth. Typical results showing the correlation between \bar{u} measured in situ, the surface morphology, the EPD, and the relative importance of Shockley–Read–Hall recombination processes are shown in Table 32.3. This suggests that the measurement of \bar{u} can be developed as an in situ early warning of the degeneration of material quality, so that the MBE growth conditions can be reoptimized to stop the degeneration of layer quality, and hence improve the material growth yield.

eration of layer quality, and hence improve the material growth yield.

32.5.5 Surface Characterization by in situ RHEED

In general, reflection high-energy electron diffraction (RHEED) has been the most important analytical tool available to the MBE grower, although SE has now taken over that role for the growth of HgCdTe. RHEED employs electron guns and display units such as fluorescent screens and/or recording devices such as charge-coupled device (CCD) cameras to obtain information on the structure and/or morphology of crystal surfaces. It is installed on virtually all MBE systems, and various authors have given detailed discussions of applications of RHEED in MBE growth [32.205]. It is particularly well suited for the in situ characterization of the growth surface during MBE growth. MBE provides the high vacuum and clean surface required for RHEED measurements; in return, RHEED does not interfere with the incoming particle beams during growth and is particularly sensitive to the top few layers or even the top monolayer. It uses relatively high electron energies (5–100 keV, typically 20 keV for HgCdTe) and very low impact angles ($< 5^\circ$). The high energy of the electron beam makes the reflected image from an ordered surface sharp, and the low impact angle allows the electrons to pass only a few atomic layers into the crystal, giving an image that represents the structure of the surface instead of that of the whole crystal. RHEED signals from single-crystal surfaces that are flat on a nanometer scale produce a RHEED pattern with lines rather than dots because a 2-D array has a one-dimensional Fourier transform. Thus, the RHEED image of a smooth ordered surface shows sharp one-dimensional (1-D) rods, rather than zero-dimensional (0-D) dots. In contrast, an oxide substrate surface layer, being amorphous,

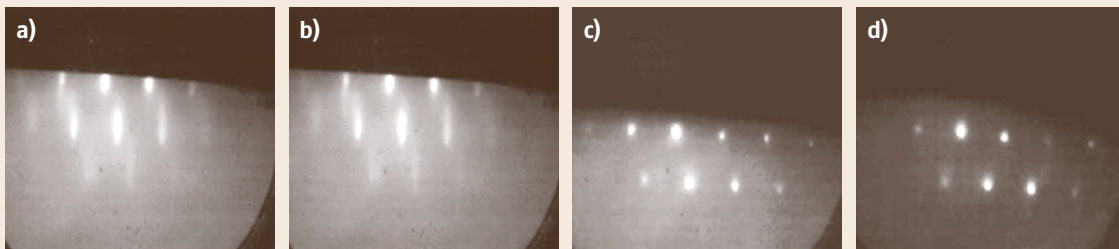


Fig. 32.13a–d RHEED patterns from CdZnTe substrates for different values of the surface roughness as measured by SE: (a) 3 Å, (b) 10 Å, (c) 20 Å, and (d) 30 Å

gives rise to a diffuse diffraction pattern, and relatively rough surfaces produce a **RHEED** pattern having dots rather than rods. The effect of CdZnTe substrate surface roughness is shown in Fig. 32.13. The HgCdTe (211)B **MBE** surface normally has several atomic layers of surface roughness, so the actual **RHEED** image normally has reflection and transmission contributions, which makes the quantitative analysis of the image very difficult. On the other hand, the analysis of **RHEED** data from 2-D growth on low-index surfaces has attracted great interest, with over 500 publications on oscillations in the **RHEED** intensity alone. Such oscillations, with a period equal to the growth period, were first observed in the early 1980s in the growth of GaAs [32.206–208], and in 1989 were observed in the (100) growth of HgTe/CdTe **SLs** [32.209]. They were first explained quantitatively in 1998 [32.210] and remain the subject of theoretical study even today [32.211].

32.5.6 Other in situ Tools for Controlling the Growth

Other commonly used in situ tools for controlling the growth include a heater and thermocouple behind the substrate to control the growth temperature and a thermocouple and/or ion flux gauge on each effusion cell to control the flux rates. The difficulty in determining the growth temperature from the thermocouple reading was discussed above in Sect. 32.4.1. Because of that difficulty, an optical pyrometer sometimes is used either to calibrate the thermocouple or to directly control the growth temperature. Because of the extreme sensitivity of the fluxes on effusion cell temperatures, the use of flux gages (and valved cells) is recommended for any fluxes which need to be well controlled. Finally, in situ **FTIR**, although not commonly used, can be used for temperature monitoring [32.152].

32.6 Nucleation and Growth Procedure

The nucleation of HgCdTe growth always occurs on either CdTe, CdZnTe with $\approx 4\%$ Zn or CdSeTe with $\approx 4\%$ Se. The more difficult nucleation process is the nucleation of CdTe, CdZnTe, CdSeTe or ZnTe on Si or another severely non-lattice-matched substrate material. We consider first the nucleation of CdTe or ZnTe on Si and then the nucleation and growth of HgCdTe.

32.6.1 Nucleation and Growth of CdTe or ZnTe on Si

The **MBE** growth of CdTe on Si has been studied for over a decade [32.54, 93, 97, 99, 212–215]. The primary issues to be faced when growing Te-based II–VI compounds on Si(211) are the high density of surface steps, which exacerbates the difficulty of removing oxygen and other contaminants from the surface, controlling the polarity of the II–VI layer to be grown, and finally reducing the dislocation density in that layer. Substrate preparation is a crucial step in the growth of Te-based II–VI compounds on Si. The two most important techniques for preparing silicon surfaces for low-defect epitaxy are oxidation and hydrogen passivation. Surface oxidation primarily serves to oxidize the adventitious surface contaminants to facilitate their low-temperature removal. Wet chemical techniques such as the RCA technique [32.216] or a modified RCA technique [32.217], which leave an oxide film ≈ 12 Å thick

on the surface, are effective in reducing contamination by metals and surface carbon contamination. One such technique is to clean the Si surface in a mixture of $\text{NH}_4\text{OH} : \text{H}_2\text{O}_2 : \text{H}_2\text{O}$ (1 : 1 : 5, 85 °C), etch the oxide in dilute **HF** (2%), and reoxidize the surface in a solution of $\text{HCl} : \text{H}_2\text{O}_2 : \text{H}_2\text{O}$ (1 : 1 : 5, 65 °C). However, these techniques require the oxide layer to be thermally desorbed in situ at temperatures ≥ 850 °C. Hydrogen passivation describes the formation of a self-protective layer on silicon surfaces upon exposure to **HF** acid. The hydrogen passivation layer has the important advantage of being volatile at ≈ 560 °C. A hydrogen passivation treatment has been developed [32.218] that greatly reduces the oxygen and carbon contamination of the Si surface without an extensive prebaking or the high-temperature thermal desorption required after RCA cleaning. This treatment allows the growth of epitaxial layers with reduced dislocation densities, but is substantially more difficult than the RCA treatment.

After thermal desorption of the passivant layer, the substrate is quickly cooled to ≈ 450 – 500 °C under an As_4 or cracked arsenic flux and then cooled to the nucleation temperature of ≈ 300 – 340 °C with either a Te_2 flux or no incident flux. This leaves a monolayer of As on the surface of the Si. The absorption of a precursor As layer has been shown to greatly reduce the sticking coefficient of Te on the Si surface and increase its surface mobility [32.219–221] and to

be essential to the MBE growth of ZnTe [32.219] or CdTe [32.220] with good growth morphology. A model has been proposed [32.221] for the effect of the As, and density-functional calculations of the geometrical and electronic structures of As and Te on Si(211) have been performed [32.222].

Different groups have developed a variety of recipes for the remainder of the growth procedure. Either a thin ZnTe buffer layer ($\approx 60\text{--}500\text{ \AA}$ thick) is grown by migration-enhanced epitaxy [32.96,97,99] at $230\text{--}300^\circ\text{C}$ or a thicker layer ($0.1\text{--}1\text{ }\mu\text{m}$) is grown by MBE at $\approx 220^\circ\text{C}$ and then annealed at $\approx 360\text{--}500^\circ\text{C}$ under a Te_2 flux before the final thick CdTe layer is grown at $\approx 300^\circ\text{C}$. The growth of an As precursor and a ZnTe buffer ensures the growth of CdTe (211)B on Si (211)B. To further enhance the quality of the final CdTe epilayer, a ZnTe/CdTe strained-layer SL buffer could be grown before the CdTe growth. It also has been reported [32.97, 223] that the quality of the CdTe growth is enhanced by periodically interrupting the growth and flash annealing at $\approx 530^\circ\text{C}$ or periodically annealing $\approx 10\text{ min}$ at $\approx 360\text{--}380^\circ\text{C}$ under a Te_2 flux. Reported CdTe growth rates vary from $0.7\text{ }\mu\text{m/h}$ at 300°C to $1.0\text{ }\mu\text{m/h}$ at 270°C . Both the desorption of the Si passivation layer and the subsequent growth are monitored by RHEED and SE.

32.6.2 Substrate Preparation and Growth of HgCdTe

The following nucleation and growth procedures are those followed at MPL and at EPIR Technologies; similar procedures are followed at other laboratories and production facilities. A 12 keV RHEED system and an SE system are used routinely to monitor the substrate preparation and HgCdTe growth in situ. All substrates are first degreased in two separately heated trichloroethylene baths followed by rinses in two methanol baths. They are then prepared for HgCdTe growth by etching in a bromine/methanol solution, followed by several methanol and DI water rinses. This leaves a Te-rich surface. For CdZnTe substrates, the etch is performed for 20 s in a 0.5 vol. % solution to remove the top $1000\text{--}2000\text{ \AA}$ of the CdZnTe, which may have polishing damage. For composite Si-based substrates, it is performed for 5 s in a 1 vol. % solution to remove $500\text{--}1000\text{ \AA}$ of the CdTe, CdSeTe or CdZnSeTe top layer. Finally, the substrate is dried with nitrogen and loaded into the MBE system. Then it is slowly heated to 300°C with no incident flux. At $\approx 135^\circ\text{C}$ the surface Te becomes mobile, decreasing

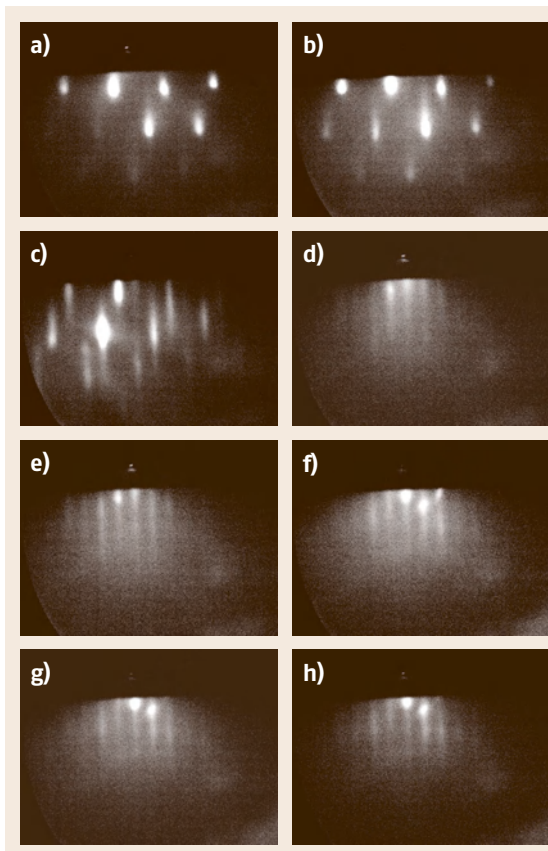


Fig. 32.14a–h In situ RHEED pictures of a HgCdTe sample grown on a CdZnTe substrate during MBE growth: (a) CdZnTe substrate as loaded, (b) after removal of Te and its oxide, (c) after CdTe regrowth and partial cooling towards the growth temperature, (d) at the moment HgCdTe growth is started, (e) 30 s of growth, (f) 1 h of growth, (g) about 2 h of growth, (h) after 3 h 45 min (end of growth)

the intensity of the rods in the RHEED pattern and causing dots to appear. At $195\text{--}205^\circ\text{C}$ the Te begins to evaporate, causing further changes in the RHEED pattern. At $\approx 220^\circ\text{C}$ the surface Te has evaporated, and the RHEED pattern again becomes streaky with rods. RHEED patterns taken during CdZnTe substrate preparation are shown in Fig. 32.14a–c. For the CdZnTe substrates, the Te shutter is opened at 300°C , and the temperature is increased to $\approx 320^\circ\text{C}$. The substrate is maintained at $\approx 320^\circ\text{C}$ for 5–10 min and then is slowly cooled down to 300°C , where $200\text{--}500\text{ \AA}$ of CdTe is grown to create a smooth surface. At 300°C an additional thin CdTe layer is grown on the Si-based

substrates and is annealed at $\approx 320^\circ\text{C}$. This procedure ensures a smooth and clean initial surface prior to HgCdTe nucleation.

After the final CdTe growth, all substrates are cooled to the HgCdTe growth temperature, $185 \pm 5^\circ\text{C}$, as measured by calibration of the thermocouple behind the substrate. Four temperatures can be used to calibrate the thermocouple readings:

1. The onset of Te surface mobility on CdTe at $\approx 135^\circ\text{C}$
2. The onset of Te evaporation at $\approx 195^\circ\text{C}$
3. The melting temperatures of In droplets on the surface of calibration substrates at 156°C
4. The melting temperatures of Sn droplets on the surface of calibration substrates at 232°C .

The growth of HgCdTe is then begun. A Hg flux is present even before the growth shutters are opened, so that the growth starts with a monolayer of Hg. The growth proceeds at a rate of $2\text{--}3\text{ }\mu\text{m/h}$ with $\approx 3 \times 10^{-4}\text{--}3.5 \times 10^{-4}$ Torr Hg flux, 10^{-6} Torr Te_2 flux, and 2×10^{-7} Torr CdTe flux. The growth temperature is continuously adjusted to minimize the roughness of the growing surface as measured by SE, and the CdTe flux is continuously adjusted to maintain the SE-measured composition at the targeted value. The evolution of the RHEED pattern during the MBE growth of a HgCdTe on CdZnTe substrate is shown in Fig. 32.14d–h. If the growth temperature and/or growth rate are too high, Te precipitates and crater defects (also

called voids) form due to the greatly reduced Hg sticking coefficient; if too low, microtwinning occurs and surface hillocks appear. To obtain lateral uniformity of the growth, the sample is continuously rotated and the growth fluxes are incident off center at an angle to the normal to the growth surface.

Due to initial island formation, the roughness of the growth initially increases up to a knee point corresponding to a critical growth thickness. Both the SE surface roughness and the RHEED intensity of a specular spot were studied at MPL during the early stages of growth at temperatures from 170 to 196°C . The knee was found to occur in the first minute of growth. At the lowest temperatures the increase in roughness continued beyond the knee, but much more slowly, at intermediate temperatures a very slow recovery was observed beyond the knee, and at higher temperatures an exponential decay with a time constant ≈ 3 min was observed. After the HgCdTe growth was paused, a recovery was observed under Hg flux at all temperatures. The critical thickness is plotted for two representative samples in Fig. 32.15, hct2352 having a higher growth rate than hct2387 at the same temperature. The critical thickness of layer hct2387 shows a much weaker dependence on temperature than layer hct2352. Their critical thicknesses are similar above 185°C , but layer hct2352 has higher critical thicknesses below 185°C . Those differences can be described in terms of the dimensionless ratio $\alpha = Jw^2/Dn_0$. This is the ratio of the input adatom flux J times the square of the (111) terrace width w to

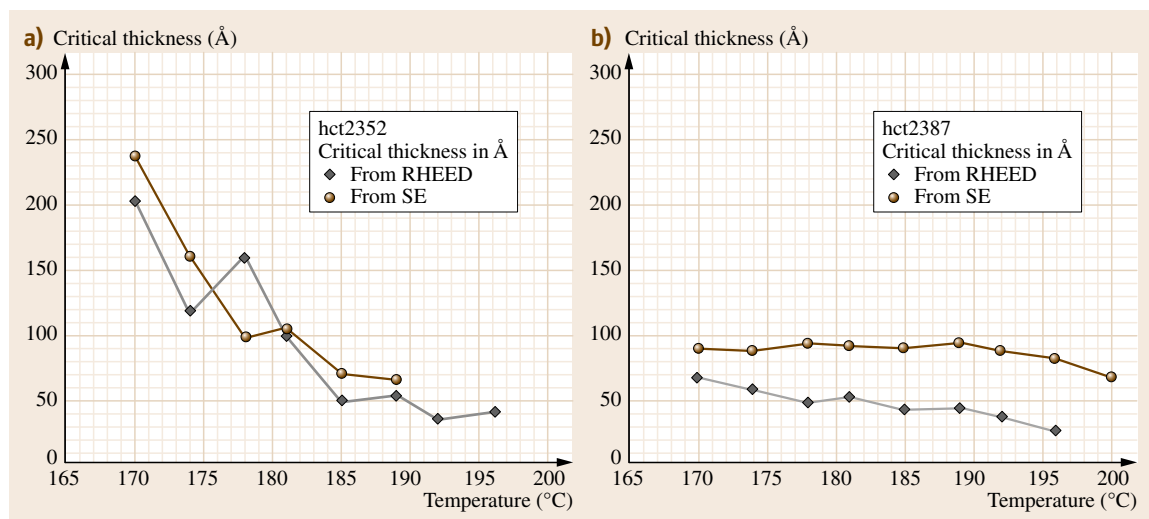


Fig. 32.15a,b Temperature dependence of the critical thickness during the initial stages of growth. The results shown in (a) are from a sample with a higher growth rate than that in (b)

the diffusion constant D times n_0 , the concentration of lattice sites for island formation. The results shown in Fig. 32.15 can be explained as follows:

1. At higher temperatures (small α), the rate of clustering is low, and growth proceeds largely by the incorporation of mobile adatoms into step edges. Because most nucleation occurs at the bottoms of step edges, the activation energies for nucleation and island formation are predominantly mechanical, temperature-insensitive energies. The critical thicknesses would be predicted to be of the same order as the step heights, $\approx 20 \text{ \AA}$.
2. At lower temperatures (large α), the adatoms are less mobile, so the island concentration builds up until the islands largely overlap. The lower the temperature, the lower the adatom mobilities, and thus the steeper the islands and the greater the island heights before overlapping becomes important. Therefore, the critical thickness increases rapidly as the temperature is decreased. The islands and
3. At very low temperatures (very large α), thermal diffusion is very low and hence the steepness of islands on the terraces is so large that the surface becomes extremely rough and continues to grow rougher even after reaching the critical thickness, eventually saturating and becoming time independent (3-D growth).

With a relatively small increase in temperature, 3-D growth turns into terraced hillock growth (modified S-K-M) and then into step-flow growth, as explained by the above discussion. It also explains why, as the input flux or the substrate roughness increases, step-flow growth requires a higher substrate temperature (lower α) due to a higher level of nucleation.

32.7 Dopants and Dopant Activation

The active components of both currently used and advanced IR photodetectors being developed, as well as other optoelectronic devices, use photovoltaic p-n junctions. In order to form sharp, precisely controlled interfaces and p-n junctions and to obtain well-controlled doping levels, it is essential to grow such junctions by MBE with extrinsic n- and p-type doping. Although the stable, well-controlled n-type extrinsic doping of as-grown HgCdTe and HgTe/CdTe SLs has been demonstrated by many authors, the p-type extrinsic doping of these materials has remained a problem. In particular, the reproducible p-type activation of As, the best low-diffusivity p-type dopant in these materials, has repeatedly been reported to occur reproducibly only at annealing temperatures sufficiently high to vitiate many of the advantages of MBE as a growth technique. Even though almost all device fabricators have demonstrated the ability to fabricate high-performance HgCdTe-based photovoltaic photodiodes using various p-doping techniques, interdiffusion across interfaces, dopant diffusion, and the formation of Hg vacancies all become problems at the high annealing temperatures required for the reproducible p-type activation of group V dopants. The absence of a reproducible p-type doping technique which does not require high-temperature annealing remains a major stumbling block

to successful implementation of high-yield fabrication of MBE-grown HgCdTe IR FPAs. This problem, attempts to solve it in the past, current progress, and alternative p-type dopants are reviewed briefly here.

32.7.1 Extrinsic n-Type Doping

Stable, well-controlled n-type extrinsic doping has not proven to be a major problem. The incorporation of In during MBE growth has been used to achieve this goal for as-grown HgCdTe [32.224–226] over a wide range of dopant concentrations (10^{14} – 10^{19} cm^{-3}) and for HgTe/CdTe SLs [32.227–229] over the somewhat smaller range from 10^{15} to 10^{18} cm^{-3} . A low-temperature postgrowth anneal can be used to optimize the structural and electronic properties of the doped material, but is not required for the n-type activation of the dopant In atoms. The only problem in achieving well-controlled n-type doping arises at very low doping levels from the intrinsic p-type doping which arises from Hg vacancies. For very small In concentrations, these vacancies can compensate the n-type conduction, lowering the mobility and destroying the otherwise precise control of the doping. However, Hg diffuses easily through interstitial sites in HgTe and IR-absorber HgCdTe material, even in perfect material, having an

activation energy of only about 0.67 eV for diffusion via interstitial sites [32.230], and diffuses even more rapidly along dislocation cores [32.231]. This allows the Hg vacancy density to be reduced to values below 10^{13} cm^{-3} by low-temperature annealing under a high Hg vapor overpressure, essentially eliminating this problem, although it could reoccur during subsequent device processing steps or during long-term storage.

32.7.2 Extrinsic p-Type Doping

Extrinsic doping is necessary:

1. Because intrinsic p-type doping by Hg vacancies is not stable against diffusion [32.230, 232, 233] from p- to n-type regions
2. Because the density profile of Hg vacancies cannot be well controlled
3. Because Hg vacancies significantly degrade carrier mobilities [32.234] and act as SRH recombination centers for minority carriers, shortening the carrier lifetimes [32.225, 235–239] and hence decreasing the quantum efficiency of detectors having p-type absorption layers.

On the other hand, achieving the stable, well-controlled extrinsic p-type doping of MBE-grown HgCdTe and HgTe/CdTe SLs without negating the advantages of MBE growth offers difficult and fundamental challenges. The primary problem arises because the MBE growth of HgCdTe is optimally performed under Te-rich conditions [32.226, 233, 240–242], so that Hg vacancies are the dominant native point defects in as-grown HgCdTe. Although their density typically [32.239] is only $\approx 10^{14} \text{ cm}^{-3}$, it is many orders of magnitude higher than the density of Te vacancies in as-grown HgCdTe [32.230, 232, 243–245]. Therefore, in equilibrium, group V atoms in as-grown HgCdTe are less likely to be located on anion (Te) sites than on cation (Hg or Cd) sites, where they form neutral complexes or act as donors rather than acceptors. This has been confirmed by both theory [32.230, 232, 243–245] and experiment [32.224, 225, 233, 241, 242, 246–251]. (Of course, even for very high As concentrations, the number of cation vacancy sites remaining to be filled by As atoms is essentially independent of the number already filled by As atoms.) On the other hand, group I atoms, which also are located primarily on cation sites, and thus are p-type activated, suffer from high diffusivities.

Postgrowth As Incorporation

Extrinsic p-type doping can be achieved either by the ex situ implantation or diffusion of dopant ions into n-type layers or by their in situ incorporation during MBE growth. As is the preferred p-type dopant for implantation or in situ incorporation during MBE growth. As implantation [32.252–255] is the key procedure of the planar device fabrication process, and has been employed in most IR FPA fabrications. However, ion implantation induces considerable damage, which reduces both minority-carrier lifetimes and carrier mobilities, and therefore is detrimental to device performance. A high-temperature ($\geq 425^\circ\text{C}$) anneal is usually performed after ion implantation. This anneal serves a dual purpose:

1. It activates the As as a p-type dopant
2. It reduces the residual implantation-induced damage.

This technology has been used successfully for the fabrication of mid-wave IR (MWIR) FPAs. However, such a high-temperature anneal itself is detrimental in several ways: it leads to the possibility of introducing a much higher density of Hg vacancies – at 500°C the equilibrium density of Hg vacancies has been calculated to be above 10^{18} cm^{-3} even under a 1 atm Hg partial pressure [32.244, 245] – and both interdiffusion across interfaces and dopant diffusion become problems, vitiating primary advantages of the MBE growth technique. Furthermore, even the residual damage remaining after annealing is severely detrimental to the performance of long-wavelength IR (LWIR) devices, due to their narrower bandgaps – bandgap states induce significant tunneling in devices with very narrow bandgaps, resulting in large dark currents. An alternative method [32.256, 257] for the postgrowth incorporation of As is to diffuse it in from the surface. However, that requires an even more deleterious thermal treatment. In addition, ion implantation and As indiffusion can be performed only in-plane, which dramatically limits the possible detector structure designs for which these techniques are applicable. The next generation of IR detectors, including single-focus multicolor detectors and high-operating-temperature LWIR detectors, cannot be fabricated in-plane. They will require in situ incorporation of extrinsic p-dopants during MBE growth and their activation as-grown or after only low-temperature ($< 250^\circ\text{C}$) annealing.

32.7.3 In situ Group I Dopant Incorporation

In principle, either group I or group V elements could act as acceptors in HgTe or HgCdTe – group I elements on cation (Hg or Cd) sites or group V elements on anion (Te) sites. However, unlike liquid-phase epitaxial growth, the MBE growth of HgTe and narrow-gap HgCdTe must be performed under Te-rich conditions [32.224, 233, 241, 242], so that during growth the number of cation vacancies is several orders of magnitude higher than the number of Te vacancies [32.230, 232]. Thus, group I dopant atoms in these materials reside almost entirely on cation sites and act as singly ionized p-dopants in the as-grown material, unlike group V dopant atoms. For this reason group I elements were the first to be tried as extrinsic p-dopants. The incorporation of Cu, Ag, Au, and Li as p-type dopants in HgCdTe epilayers and their diffusivities have been studied by many authors [32.224, 227, 233, 239, 258–269]. Even though the doped materials showed close to 100% activation and excellent transport properties and minority-carrier recombination times, all of these dopants proved to be unstable in HgCdTe, diffusing out of the doped region during further MBE growth or during the low-temperature postgrowth anneal. This behavior would appear to prevent their use in FPA technology and hence limit their usefulness as an acceptor dopant, especially for the abrupt junctions required for IR detectors. Thus, they suffered a period of relative neglect in the late 1980s. However, Au in particular is again being studied intensively as a p-type dopant, as its diffusivity may be able to be held within acceptable bounds. We have found no perceptible diffusion of Au dopants in a HgTe/CdTe SL after 3 years of storage at room temperature.

32.7.4 In situ Group V Dopant Incorporation

In recent years, because of the high diffusivities of group I elements and the damage caused by ion implantation, studies on the p-type doping of HgCdTe and of HgTe/CdTe SLs have focused on in situ doping with group V elements, especially with As [32.224, 229, 262, 270–286], because it is more easily activated than the other group V elements. The larger size of the group V atoms, and hence their lower diffusivity, allows the growth of stable, well-controlled p–n junctions, and thus sharp interfaces and/or precisely controlled dopant profiles. The incident As flux in most older experiments was uncracked and consisted almost entirely of As₄ tetramers, which are physisorbed

as tetramers or clusters of tetramers, not as single atoms [32.40], and which calculations suggest [32.270] remain as tetramers in as-grown HgCdTe. The use of cracked As has become common, so that the As is mostly chemisorbed in atomic or diatomic form, as happens with the use of a CdAs flux. This gives an As sticking coefficient orders of magnitude higher but appears not to ease the problem of obtaining p-type activation of the As without a high-temperature anneal.

32.7.5 As Activation

Because the As atoms in as-grown MBE-grown HgCdTe reside primarily on cation sites rather than Te sites, annealing under a Hg overpressure is required to activate the As as a p-dopant by transferring it to Te sites. Several authors have proposed models for the activation process and performed calculations [32.242, 244, 245, 271, 272], all assuming As incorporation as isolated atoms. The standard activation anneal is 10 min at $\approx 425^\circ\text{C}$ followed by 24 h at $\approx 250^\circ\text{C}$ under a Hg overpressure to fill the Hg vacancies created during the previous anneal. The anneal at a temperature well above 350°C induces Te evaporation, which allows the As atoms to move to the resultant Te vacancies in the second-stage anneal. This annealing procedure yields almost complete activation of the As up to concentrations of order 10^{18} – 10^{19} cm^{-3} depending on the temperature of the first-stage anneal [32.244, 245, 273, 274], with the doping abruptly saturating at that level, presumably due to all of the Te vacancies created during the first-stage anneal being filled.

Unfortunately, this annealing procedure introduces undesirable broadening of interfaces and dopant diffusion, and thus limits many of the advantages of MBE as a low-temperature growth technique. Therefore, a variety of approaches have been used in attempts to obtain the p-type activation of As either as-grown or after only a low-temperature anneal. Although each of these approaches has shown promise, none have consistently given full activation of the As. One approach [32.242, 247, 275, 276] is to use a two-stage anneal with $T \leq 300^\circ\text{C}$ in both stages, with Te vacancy–Te interstitial pairs formed in the first stage and As atoms filling the Te vacancies in the second stage. Another approach [32.250] is to force As atoms out of cation vacancy sites by using a high Hg overpressure in both stages of a two-stage low-temperature anneal. The lack of consistently reproducible results obtained using these approaches is not understood. A rather thorough study

of As incorporation, activation, and diffusion is given in [32.250].

Other approaches have involved either modified MBE growth methods or different methods of As incorporation. One approach [32.277–280] was to irradiate the growing HgCdTe with a laser beam (photo-assisted MBE, PAMBE), shifting the growth toward cation-rich conditions by causing Te desorption and thus allowing As incorporation on the vacant Te sites. This was combined with the idea of growing HgTe/CdTe SLs and then forming HgCdTe by annealing the SLs to interdiffuse the Hg and Cd. That allowed the As to be incorporated only during the CdTe growth, when the number of cation vacancies is much lower so that it is easier to incorporate the As on Te sites. This will yield almost complete p-activation of the As, but at a high price. PAMBE has been abandoned because it limits the growth to impractically small areas. Also, annealing the SL broadens any device interfaces. Another approach [32.281, 282] was to use a Te cracker cell so as to increase the Hg sticking coefficient and obtain As activation as-grown. Success was reported for (111) and (211) growth, but appears not to have been consistently reproducible.

An approach in which only the method of As incorporation is changed, not the growth technique, is

that of planar doping. In planar doping the As flux is shut off most of the time, but periodically the CdTe and Te fluxes are shut off and the As flux is turned on, along with the Hg flux, which is never shut off. This approach was originated [32.283] in 1995, has been used many times [32.255, 283–286] (and in unpublished results of the authors) and has been observed to give full p-activation of the As in the as-grown material [32.283, 284]. Although full activation in the as-grown material is not observed consistently, at least partial activation is observed, and full activation appears to be consistently obtainable by combining planar doping with anneals at $\leq 300^\circ\text{C}$. More consistent activation is obtainable in the planar doping of CdTe or of the CdTe layers of a HgTe/CdTe SL.

In conclusion, although progress is being made in solving the problem of obtaining well-controlled fully reproducible p-type doping of HgCdTe without the use of undesirable high-temperature anneals, this remains one of the major problems in the growth of material for advanced HgCdTe-based IR detectors and focal-plane arrays. The most promising avenue of attack on this problem appears to be planar doping with As coupled with the development of an optimal sequence of low-temperature anneals.

32.8 Properties of HgCdTe Epilayers Grown by MBE

The most important epilayer properties for detector and FPA performance are the minority-carrier lifetime, the carrier concentration and mobility, the perfection of the epilayer surface (to ensure the absence of dead pixels), and the lateral uniformity of the epilayer (to ensure uniformity of pixel response). Substrate imperfections, poor lattice matching and thermal matching between the substrate and the epilayer, and nonoptimal growth conditions all can degrade these properties. We consider first the electrical and optical properties.

32.8.1 Electrical and Optical Properties

Minority-carrier recombination processes in HgCdTe directly decrease photon detection and increase noise generation in photovoltaic infrared devices. Hence, it is especially important to maximize the minority-carrier lifetime τ . The three commonly recognized recombination mechanisms – Auger, radiative, and Shockley–Read–Hall (SRH) – are characterized by recombination lifetimes that are usually measured by

fitting photoconductive decay data, which measure the total recombination lifetime $\tau = (\tau_{\text{Auger}}^{-1} + \tau_{\text{radiative}}^{-1} + \tau_{\text{SRH}}^{-1})^{-1}$. One can determine each recombination rate separately by fitting the measured values of τ as a function of T . Of these three mechanisms, two (Auger and radiative recombination) are determined by intrinsic material properties, such as the composition and doping level, which can be precisely measured by other techniques, e.g., the Hall effect and infrared absorption mapping [32.287]. The Auger and radiative lifetimes can be calculated from those measured quantities using sets of semi-empirical formulas developed by Beattie, Landsberg, and Blackmore [32.288, 289] based on Kane's $k \cdot p$ model with several key parameters determined experimentally [32.290]. These intrinsic mechanisms establish upper limits on the lifetime. The differences between the calculated and measured lifetime values are attributed to SRH recombination, which arises from impurities or defects and can be fitted within the theoretical framework given by Shockley, Read, and Hall [32.291, 292]. A primary criterion for a high-

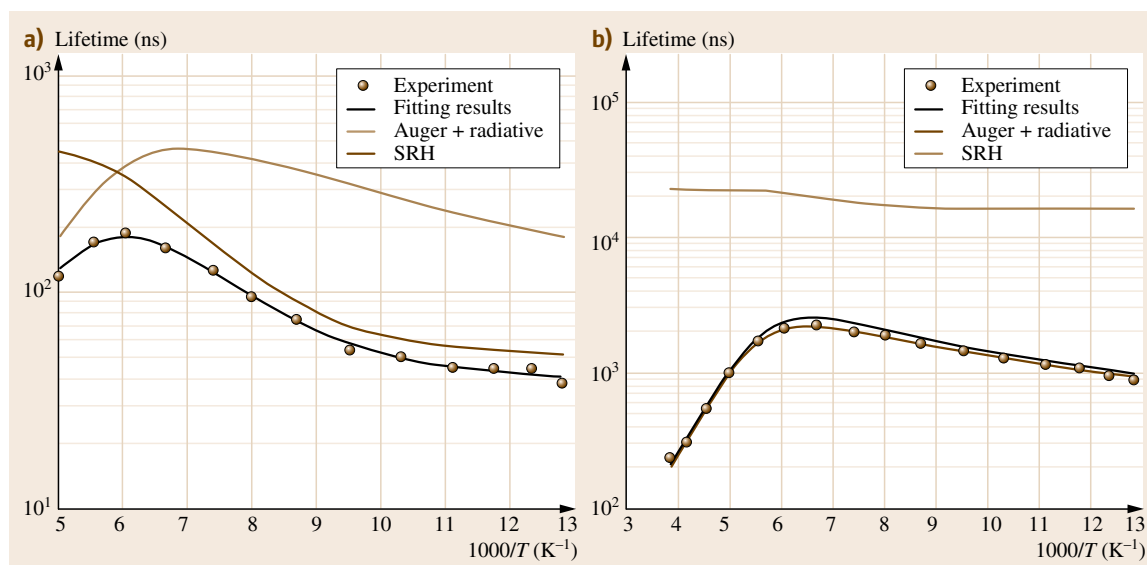


Fig. 32.16a,b Two fits to τ as a function of inverse temperature (T^{-1}) showing the measured values, the fitted intrinsic (dotted) and SRH (solid) lifetimes, and the fit to the measured values of τ ; (a) shows a case in which SRH recombination dominates below 150 K, and (b) shows a case in which the SRH recombination rate is small and hence less well determined

quality layer is $\tau_{\text{SRH}} \gg \tau$. Two fits to τ are shown in Fig. 32.16: (a) with SRH processes dominant below ≈ 150 K and (b) with SRH processes negligible. Note the difference in the dependence of τ on T^{-1} in the two cases. Also, note that in Fig. 32.16b τ_{SRH} is very poorly determined because SRH recombination is so unimportant in that case.

In general, it is found that, for growth on CdZnTe substrates, the strong Auger recombination dominates the determination of τ and thus limits detector performance for p-type layers. However, intrinsic lifetimes are much longer in n-type materials, so it is more difficult to achieve the condition $\tau_{\text{SRH}} \gg \tau$. Others [32.293] have found that SRH recombination is dominant for low In doping levels in n-type MWIR HgCdTe samples, but that τ increases with increasing doping, suggesting that In may passivate the SRH defects for MWIR HgCdTe. On the other hand, we have found at MPL that lifetimes ≈ 1 μs dominated by intrinsic recombination can be reproducibly achieved in n-type LWIR material with doping levels $\approx 10^{15} \text{ cm}^{-3}$ after annealing under a Hg-rich atmosphere to reduce the concentration of Hg vacancies, which act as SRH recombination centers.

Two other electrical characteristics of a grown HgCdTe epilayer are important: the carrier concentra-

tion and the mobility. In the absence of compensation (the presence of only n- or only p-type dopants) both are routinely determined from Hall-effect measurements. However, in the presence of compensation their determination requires Hall-effect measurements as a function of magnetic field as well as temperature [32.293]. For LWIR $\text{Hg}_{1-x}\text{Cd}_x\text{Te}$ layers with $x = 0.23$ grown on Si-based substrates, at 77 K mobilities $\mu \approx 10^5 \text{ cm}^2/\text{Vs}$ are consistently obtainable for n-type layers with $n \approx 10^{15} \text{ cm}^{-3}$, $\mu \approx 500 \text{ cm}^2/\text{Vs}$ for p-type layers with $p \approx 1.3 \times 10^{16} \text{ cm}^{-3}$, and $\mu \approx 200 \text{ cm}^2/\text{Vs}$ for p-type layers with $p \approx 2.0 \times 10^{16} \text{ cm}^{-3}$. For layers of the same composition grown on CdZnTe substrates the electron mobilities reported are lower by a factor of $\approx 2-3$.

The primary optical characteristic of HgCdTe epilayers is the IR transmittance or absorptivity, which is measured by FTIR spectroscopy. A general review of the IR optical characterization of HgCdTe and of FTIR spectroscopy in general is given elsewhere [32.294]; here we outline how FTIR measurements can be used to assess epilayer quality. Below the energy gap, impurity absorption can be measured and carrier concentrations can be measured by free carrier absorption. By scanning transmission/reflection mapping, the uniformity of composition and thickness across a wafer can be meas-

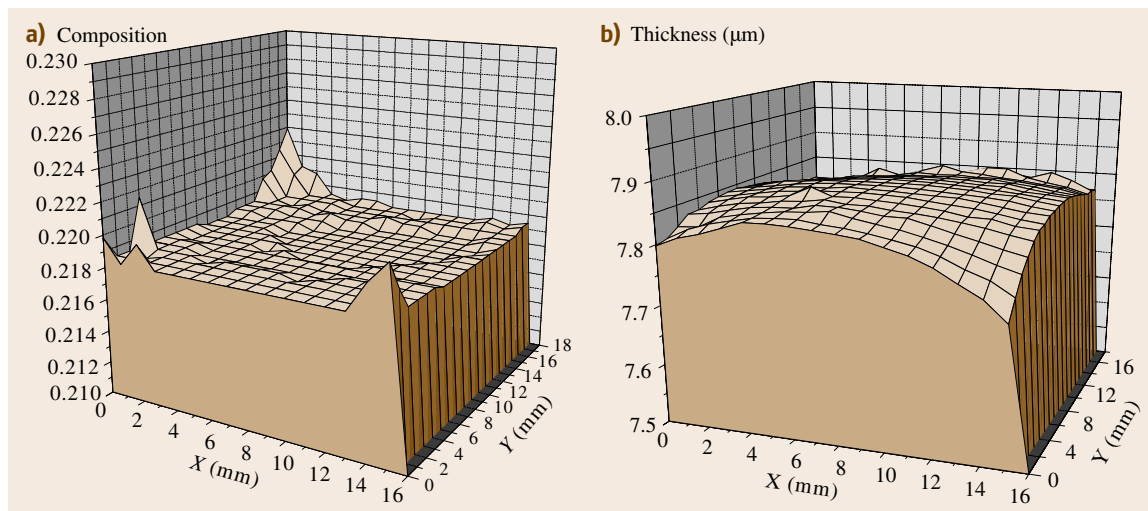


Fig. 32.17a,b Mapping results for a HgCdTe epilayer grown on CdZnTe: (a) composition and (b) thickness

ured. Typical results obtained at MPL for growth on square 20 mm × 20 mm CdZnTe substrates are shown in Fig. 32.17; the average HgCdTe composition was $x = 0.2182$ with a standard deviation of 0.0006, and the average thickness was $d = 7.84 \mu\text{m}$ with a standard deviation of $0.03 \mu\text{m}$ [32.287]. Higher compositions and thinner material was found in about $2 \times 2 \text{ mm}^2$ areas in each corner, presumably due to the low thermal conductivity resulting in a higher growth temperature in the corners and hence a lower Hg sticking coefficient there. This explanation is supported by the existence of a higher density of voids or crater defects near the corners; these are found primarily in Te-rich or higher- T growth. For growth on 3 inch-diameter Cd/Si substrates, there was no evidence of nonuniformity in T , and the nonuniformities in x and d over the central $20 \times 20 \text{ mm}^2$ area were much smaller than for growth on CdZnTe, although over the entire samples somewhat larger nonuniformities were observed, presumably due to flux nonuniformities.

Of greater importance, the Urbach tail energy, which arises primarily from electron–phonon interactions, alloy disorder, and structural disorder, has been shown to be useful in characterizing material quality [32.295]. The absorption coefficient below the energy gap can be expressed as [32.296, 297]

$$\alpha(\omega) = \alpha_0 \exp \left[\frac{\hbar\omega - E_0}{W(T)} \right], \quad (32.9)$$

where $W(T)$ is defined as the Urbach tail energy. It measures the steepness of the band tail and can be

obtained by fitting the the absorption data below the energy gap. We obtained values for $W(T)$ by measuring $\alpha(\omega)$ from 4 K to room temperature and fitting the logarithmically linear part of $\alpha(\omega)$ below the bandgap. Those samples with surface microtwin defects arising from low growth temperatures or with high dislocation densities were seen to consistently show relatively high Urbach tail energies having large standard deviations over small areas, suggesting that nonuniformly distributed structural disorder dominates the nonuniformity of device performance figures of merit in HgCdTe IR FPAs. Moreover, Urbach tail energy mapping measurements we have performed correlate strongly with Cd composition mappings and with crystalline defects revealed by x-ray topograph mappings. The contribution of the electron–phonon interaction was calculated and found to be much smaller than the contribution of alloy and structural disorder and to give the observed small temperature dependence of $W(T)$ [32.295]. We also calculated the contribution of alloy disorder, $W_{\text{alloy}} = x(1-x)\text{VBO}^2 m_{\text{HH}}^* L^2 / 7.2 \hbar^2$, where x is the alloy composition, VBO is the valence band offset, and L is the alloy disorder correlation length (estimated to be of the order of one interatomic spacing). It also was found to be much smaller than the contribution of structural disorder. $W(T)$ also was found to be only weakly dependent on T for CdZnTe substrates, for which the alloy contribution also is very small because of the small Zn concentration. Thus, $W(T)$ serves as a quantitative measure of structural disorder for both HgCdTe epilayers and CdZnTe substrates.

32.8.2 Structural Properties

The structural properties of HgCdTe depend greatly on the type of substrate used for its growth. For (211)B growth on CdZnTe, substrate defects are the primary cause of structural defects in the HgCdTe. For (211)B growth on CdTe/ZnTe/Si, the lattice and thermal mismatches at the ZnTe/Si and ZnTe/CdTe interfaces are primary causes of structural defects in the HgCdTe. The lattice mismatches are much greater than any mismatch resulting from thermal changes, but the thermal mismatches can cause strains much greater in magnitude than the residual lattice-mismatch strains remaining after relaxation by dislocation formation during growth. For simplicity consider a CdTe/Si interface. Following Carmody et al. [32.110], the equilibrium residual strain in a CdTe film of thickness h is $\varepsilon(h) = (h_c/h)\varepsilon_{\text{misfit}} \approx 10^{-4} \times \varepsilon_{\text{misfit}}$ for a film of thickness $5 \mu\text{m}$, where $h_c \approx 5 \text{ \AA}$ is the equilibrium critical thickness and $\varepsilon_{\text{misfit}} = -0.193$ is the lattice-mismatch strain, giving a residual stress $\sigma_{\text{resid}} \approx 1.4 \text{ MPa}$. Of course, the CdTe does not come to a complete equilibrium during growth, but even so the stress remaining at the growth temperature at the end of growth is much less than the thermal stress resulting from cooling to room temperature, which is $\approx 45 \text{ MPa}$. Also, the relaxation of the strain induced during cooldown will be much less complete than the relaxation of the lattice-mismatch strain because of the much shorter time at an elevated temperature. Thus, incomplete relaxation upon cooldown can be a greater source of strain than the large lattice mismatch.

The most common measure of crystalline perfection is the **XRD FWHM**. Under optimal growth conditions the **XRD FWHM** of HgCdTe grown on CdZnTe substrates is limited only by the substrate **FWHM**, at least for (112)B, (113)B, and (552)B orientations, and is $\approx 20 \text{ arcsec}$ [32.44]. However, the **XRD FWHM** is substantially larger for HgCdTe grown on CdTe/Si substrates. From 1991 to 1995 the best values obtained were reduced from 210 to 65 arcsec, but little progress has been made in achieving further reduction. In fact, typical values of the **FWHM** are still above 100 arcsec, and the best consistently obtainable value is $\approx 100 \pm 30 \text{ arcsec}$, limited by the **FWHM** of the underlying CdTe layer [32.96]. One possible source of the 65 arcsec **XRD** line broadening is incomplete lattice relaxation giving rise to changes in the lattice constant in the growth direction as one moves away from the surface. This possibility is supported by an anticorrelation between the density of threading dislocations and

the **FWHM**; if true, it would explain why no further significant decrease in the **FWHM** has been observed since 1995. The primary sources of the extra width observed before 1995 were microtwinning and low-angle grain boundaries due to growth at nonoptimal orientations and with nonoptimal buffer layers. The extra width above 65 arcsec still usually seen today probably arises in large part from low-angle grain boundaries.

Another measure is the etch pit density, which measures the density of threading dislocations at the HgCdTe surface. Dislocations adversely affect HgCdTe electrical properties and device performance in many ways [32.298]; the deleterious effects of dislocations were discussed briefly in Sect. 32.3.3. Threading dislocation densities below the mid 10^5 cm^{-2} are not a serious problem unless they form clusters or bend over to form misfit dislocations parallel to the surface under device contacts [32.298]. Growth on CdZnTe yields etch pit densities of order low 10^4 to low 10^6 cm^{-2} , depending primarily on the substrate defect density. Growth on CdTe/ZnTe/Si typically yields etch pit densities of order mid 10^6 to mid 10^7 cm^{-2} . As discussed in Sect. 32.3.3, this density of threading dislocations to date has prohibited the use of Si-based substrates for the growth of HgCdTe for **LWIR** and **VLWIR** detectors and **FPA**s.

Other structural defects commonly encountered before the last decade, such as two-phase growth, twinning and microtwinning, and low-angle grain boundaries, have been greatly reduced by choice of growth orientation, proper substrate preparation and the use of buffer layers, and improved control over growth conditions. However great care must be exercised to maintain the level of these defects at an acceptable level, especially twinning, which occurs at low growth temperatures T or high Hg flux, and can cause harmful surface defects. Under optimal growth conditions T is high enough that the surface diffusion length of incoming atoms is approximately the terrace width. Then, growth nucleation occurs at kinks or step edges, and step-flow growth occurs. If T is too low or in the presence of defects, growth can also nucleate on the terraces, so that growth from different points must coalesce, forming grain boundaries or laminar microtwins.

32.8.3 Surface Defects

The common surface defects are voids or crater defects, large triangle defects (like a type of void and treated here under the same heading), faceted microvoids or small triangle defects (similar to microvoids and in-

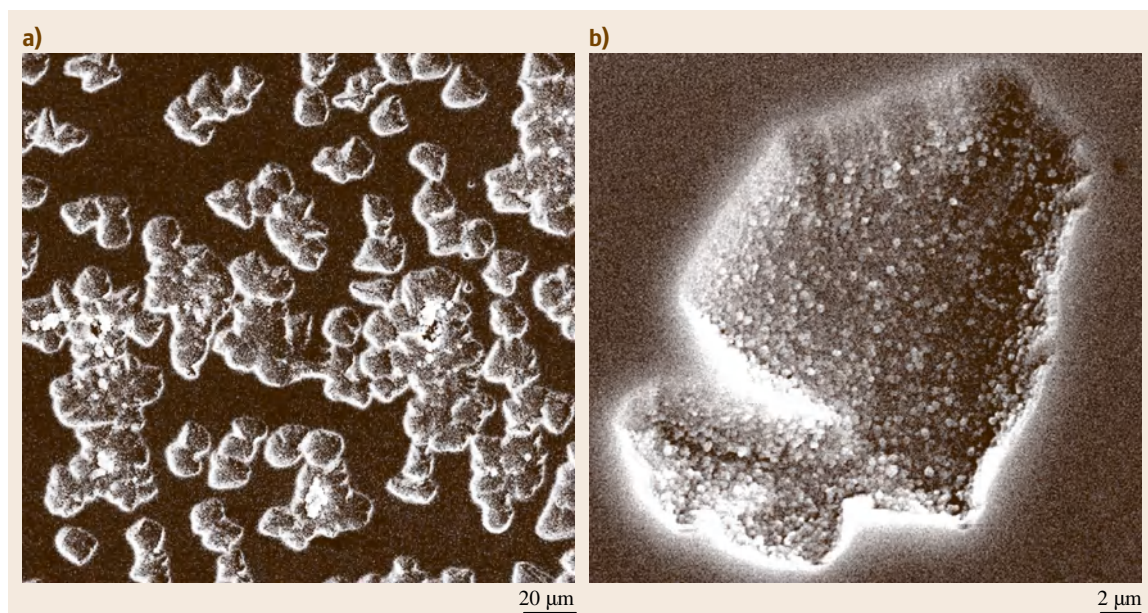


Fig. 32.18a,b SEM micrographs showing (a) large crater defects on a HgCdTe/CdZnTe (211)B epilayer grown on a poor substrate and (b) the typical morphology of a large crater defect

cluded here under the same heading), flakes, hillocks, needle defects, cross-hatching, and surface roughness. The reduction of the density of surface macroscopic defects (voids, microvoids of size 3–5 μm, and flakes) is one of the most serious challenges in MBE growth of HgCdTe. Voids or crater defects, discussed briefly in Sect. 32.3.2 and shown in Figs. 32.5 and 32.18, are the surface manifestations of threading defects associated with Te precipitates. Small and mid-size voids arise during growth from incomplete Te₂ dissociation (low *T*) or excess Te under Te-rich growth conditions (high *T*, low Hg flux or high growth rate) [32.39, 299–301]. For growth on CdZnTe substrates, large voids can arise from dust or other particulate matter on the substrate surface [32.183, 302] or Te precipitates in CdZnTe substrates [32.66, 69]. Detailed descriptions of their origin and morphology are given in [32.300] and [32.301]. They range in size from 2 to 40 μm [32.302] and can bypass p–n junctions and give premature reverse-bias breakdowns or even blind sensor elements [32.303]; hence, they are extremely harmful to FPA performance. They can be minimized by tight control of the growth conditions [32.39, 304] and by the proper preparation of CdZnTe substrates [32.66–70]. Typically, the void or crater density is mid to high 10² cm^{−2} for growth on Si-based substrates and low 10² to high 10³ cm^{−2}

for growth on CdZnTe substrates [32.38], depending strongly on both the substrate quality and the growth conditions. The minimum reproducible void density is high 10² cm^{−2} for growth on Si-based substrates and ≈ 10³ cm^{−2} for growth on CdZnTe substrates.

Faceted microvoids have a sharp triangular shape and smooth, slightly raised surfaces. For growth on Si-based substrates, they are typically 3–5 μm long, their density is ≤ low 10² cm^{−2}, and they almost always result in electrical shorts at 140 K, blinding sensor elements [32.303]. At EPIR Technologies, 1 μm-long faceted microvoids have been found on the ZnTe and CdTe epilayers in CdTe/ZnTe/Si substrates and have been identified with microtwinning. To the best of the authors' knowledge, there has been no report of faceted microvoids for HgCdTe grown on CdZnTe. It is reasonable to assume that the microvoids observed on the surface of HgCdTe epilayers grown on CdTe/ZnTe/Si arise from microvoids on the substrate surface.

Like faceted microvoids, flakes have been reported only for growth on Si-based substrates. They have been investigated at the US Army Research Laboratory [32.96], the Night Vision Electronic Sensors Directorate [32.96], and EPIR Technologies. A typical flake defect is shown in Fig. 32.19. Flakes on the HgCdTe epilayers are known to result from correspond-

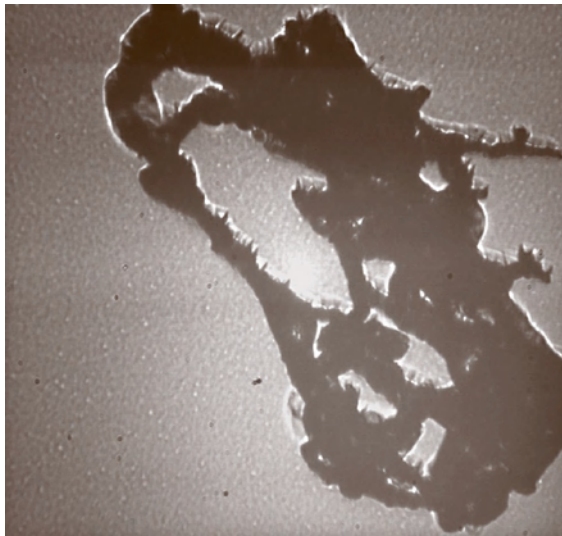


Fig. 32.19 An optical micrograph of a typical flake defect

ing flakes on the top CdTe layers of the substrates; they are completely a substrate problem. Unlike other defects, they have no known intrinsic origin. They arise primarily from sputtering from the CdTe cell during the substrate CdTe growth, but also from spitting from accumulated deposits in the growth chamber. They have irregular shapes, lateral dimensions ranging from several micrometers to > 1 mm and vertical dimensions ranging from $< 1 \mu\text{m}$ to $> 10 \mu\text{m}$. Their density can be reduced to $\approx 2 \text{ cm}^{-2}$ by reducing the CdTe growth

rate to $\leq 2 \mu\text{m/h}$ and taking care not to overheat the CdTe source, and has been reduced to $\approx 0.2 \text{ cm}^{-2}$ by EPIR Technologies by taking other measures. However, because of their very large sizes and 3-D nature, even one large flake is extremely deleterious to FPA performance. Large flakes must be completely eliminated for satisfactory FPA fabrication. They are the primary factor preventing the commercial success of HgCdTe grown on Si-based substrates, because the high dislocation density in HgCdTe grown on Si-based substrates is not harmful for most SWIR and MWIR applications.

Hillocks arise from structural defects – microtwinning or 3-D growth – and thus have largely been brought under control by the advent of (211)B growth and improved control of the growth conditions [32.305]. Needle defects were considered in Sect. 32.3.2. They occur only for growth on CdZnTe, and their density has been reduced to the range from mid 10^4 cm^{-2} to mid 10^5 cm^{-2} for better substrates and mid 10^6 cm^{-2} for the worst substrates. The densities of needle defects and threading dislocations have been found to be correlated, but not in a cause-and-effect manner. This correlation makes it difficult to see any effect of the needle defects on electrical properties, and no effect has been seen. They appear not to be a problem, at least not below the mid 10^5 cm^{-2} range. Cross-hatching is a sign of high-quality growth and is not detrimental to device performance. Surface roughness is an indicator of sub-optimal growth, but also is not in itself detrimental to device performance.

32.9 HgTe/CdTe Superlattices

HgTe/CdTe SLs were first proposed in 1979 [32.304]. Their first actual growth was performed in 1982 [32.306]. They possess several potential advantages over HgCdTe alloy material for use in IR detectors, especially for very long wavelengths, in particular:

1. Their bands can be engineered to suppress Auger recombination relative to that in comparable bulk detectors, and SRH lifetimes up to $20 \mu\text{s}$ have been measured [32.307].
2. The band-to-band tunneling currents are lower than those in comparable bulk detectors due to greater effective masses in the growth-axis direction.
3. Their optical cutoff energies E_c or wavelengths λ_c are sharper than those in comparable bulk detectors for well and barrier widths $\leq 90 \text{ \AA}$.

4. By doping only in the CdTe barrier layers, reproducible As activation can be achieved at lower temperatures than in MBE-grown HgCdTe alloys.
5. There is no alloy disorder scattering in HgTe wells such as that in HgCdTe alloys.
6. By doping only in the CdTe barrier layers, one can largely eliminate carrier scattering off dopant atoms. Also, their electrons and holes are in the same layers, resulting in strong optical absorption as compared with that in type II SLs.

However, the usefulness of HgTe/CdTe SLs as a narrow-bandgap optical material relies on the stability of the constituent Hg, Cd, and Te atoms to remain in place across the heterointerfaces of the SL structure. Interdiffusion in HgTe/CdTe SLs has been studied

since shortly after their first growth [32.308–315]. Significant interdiffusion would drastically decrease the cutoff wavelength of a SL and greatly reduce the potential advantages that SLs have over conventional bulk HgCdTe devices. The FTIR spectra and E_c values of HgTe/CdTe SLs change rapidly at even moderate annealing temperatures $T_{an} < 300^\circ\text{C}$ after growth, with the cutoff energies becoming higher. This has furthered serious concerns about the practicality of SLs for use as absorbers in the LWIR (8–12 μm) and VLWIR ($> 15 \mu\text{m}$) due to the presumed smearing out and further instability of the HgTe/CdTe interfaces during annealing, device processing, and possibly even after long storage times. On the other hand, we have found that the interdiffusion which takes place during growth and initially thereafter results in a sharpening of the initially rough SL interfaces.

The novel electrical and optical properties of these structures have been reviewed by many authors [32.308, 316–320]. The MBE growth of HgTe/CdTe SLs was initiated at many industrial and other research laboratories in the mid to late 1980s – Rockwell in 1983, Honeywell in 1984, North Carolina State University in 1985, Texas Instruments and Bell Labs in 1986, Hughes Research Laboratory in 1987, and McDonnell Douglas in 1988. Research on HgTe/CdTe SLs peaked in the late 1980s and early 1990s, when MBE was still a relatively new technology and the growth of HgTe-based materials was in its infancy. Because even better control over the growth is required to grow a high-quality HgTe/CdTe SL than to grow high-quality HgCdTe alloy material, for practical technological reasons, the great advantages possessed by HgTe/CdTe SLs in theory were not realized in practice despite rather comprehensive research efforts. Among the factors that hindered the growth of high-quality HgTe/CdTe SLs at that time were the poor design of the Hg cells used, the absence of computer controlled shutters on the MBE system cells, and the unavailability of consistently high-quality substrates. Thus, the interest in HgTe/CdTe SLs peaked well ahead of its time.

32.9.1 Theoretical Properties

Either inverted-band or normal HgTe/CdTe SLs can be grown. With 50 Å CdTe barrier thicknesses d_b , a SL has a normal band structure if the HgTe well thickness d_w is less than 90 Å and an inverted band structure if $d_w > 90 \text{ Å}$. SLs having $d_w < 70 \text{ Å}$ are preferred because SLs with a direct band structure have much longer Auger lifetimes τ_A . For a p-type 60 Å

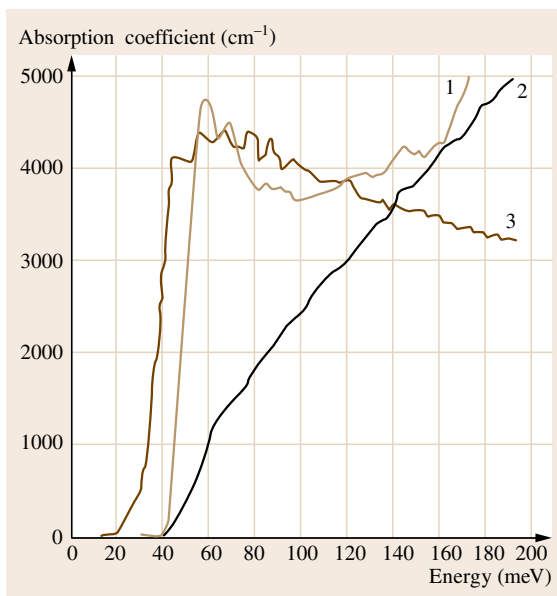


Fig. 32.20 Computed fundamental optical absorption spectra for two SLs (curve 1 for a normal-band-structure 60 Å HgTe/50 Å Hg_{0.05}Cd_{0.95}Te SL and curve 3 for an inverted-band-structure 110 Å HgTe/50 Å Hg_{0.05}Cd_{0.95}Te SL) and for bulk HgCdTe alloy (curve 2), all with optical bandgaps of approximately 40 meV at 40 K

HgTe/50 Å CdTe SL having a 28.8 μm optical cutoff and $p = 5 \times 10^{15} \text{ cm}^{-3}$, $\tau_A = 7 \text{ ns}$ at 40 K, whereas $\tau_A \ll 1 \text{ ns}$ at 40 K for a HgCdTe alloy having the same optical cutoff and doping level. For the same doping level, a 50 Å HgTe/50 Å CdTe SL having a 15 μm cutoff has an intrinsic lifetime of $\approx 1 \mu\text{s}$.

Another theoretical property of great interest is the sharpness of the optical absorption edge. Here, HgTe/CdTe SLs have a great advantage over HgCdTe alloys. As shown in Fig. 32.20 for a normal SL, an inverted-band SL, and bulk HgCdTe alloy, all having optical cutoffs of $\approx 29 \mu\text{m}$ (optical bandgaps of $\approx 40 \text{ meV}$), both the normal and the inverted band SLs have much sharper absorption edges than the alloy. Note that interfacial roughness, as long as it is uniform over lateral distances of order 1 μm and occupies no more than $\approx 1/2$ of the SL volume, does not significantly affect the sharpness of the SL absorption edges. Even a poorly grown SL will display a sharp absorption edge and other sharp structure from the SL subband structure.

For CdHgTe barrier layers containing $\leq 20\%$ Hg with $d_b \geq 50 \text{ Å}$, the normal-band SL energy gap and optical cutoff are almost independent of d_b and the Hg

concentration, and depend almost entirely on d_w and on the Cd concentration in the wells, with the dependence on Cd concentration being ≈ 0.9 times as large as that in the HgCdTe alloy with the same cutoff. If one could prevent Cd diffusion into the wells so that they would be pure HgTe, one could control d_w well enough to determine the optical cutoff more accurately in a SL than one could in the alloy by controlling the concentration. However, in reality the combination of interfacial roughness and diffusion make the determination of the optical cutoff less accurate in the SL than in the alloy.

32.9.2 Growth

The growth of HgTe/CdTe offers four challenges not present in the growth of HgCdTe alloy material:

1. The growth of CdTe is optimally performed at $\approx 270^\circ\text{C}$, $\approx 80^\circ\text{C}$ higher than the optimal growth temperature of HgTe or Hg-rich HgCdTe
2. The HgTe well widths must be precisely controlled within a fraction of a monolayer
3. The SL interfacial roughness must be minimized and made reproducible to obtain good control of the optical cutoff
4. p-Type doping must be activated as-grown or after only short anneals at temperatures $\leq 300^\circ\text{C}$.

The substrate preparation and in situ growth monitoring are the same as for the growth of HgCdTe. The growth temperature must be that for HgTe, so the CdTe growth cannot be performed under optimum conditions. Also, the Hg flux must be present at all times, so the barrier layers grown are $\text{Cd}_{1-y}\text{Hg}_y\text{Te}$ with $y \approx 0.05$ rather than $y = 0$. This small amount of Hg in the barrier

layers does not significantly affect the optical cutoff or the band structure.

For (211)B growth the control of the well widths must be achieved by precise control of the growth temperature and the Hg and Te fluxes or by using the virtual interface approximation [32.171, 172] and an ellipsometer capable of taking data below the SL optical energy gap. For (211)B growth, which is step-flow growth, one cannot measure the growth of each monolayer by monitoring RHEED oscillations as has been done in the past for (100) growth [32.209]. In step-flow growth the terraces remain unchanged during the growth except for moving laterally; there is no progression from an empty atomic layer to a layer randomly partially occupied to a full layer, and therefore no RHEED oscillations. To have RHEED oscillations one must grow on a surface conducive to the formation of grain boundaries and twinning.

Modulated doping with In in the barrier layers is used for in situ n-type doping, and planar doping with As in the barrier layers, as described in Sect. 32.7.5, is used for in situ p-type doping. The flux shutters are computer controlled and operate on the schedules shown in Fig. 32.21a,b for In and As doping, respectively.

32.9.3 Experimentally Observed Properties

The important observed properties of HgTe/CdTe SLs which do not correspond closely to HgCdTe alloy properties are the macroscopic and microscopic HgTe layer uniformities, the amount of interfacial roughness, and the amount of Cd interdiffused into the HgTe layers during growth. All other observed properties of HgTe/CdTe SLs match expectations based on the observed properties of MBE-grown HgCdTe al-

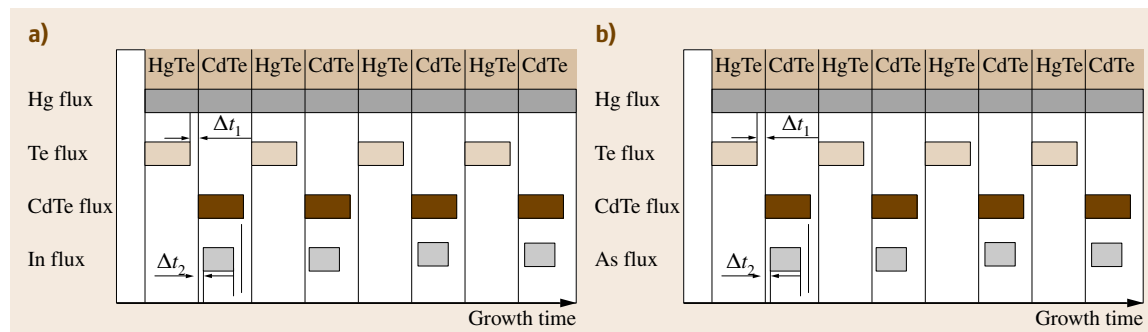


Fig. 32.21a,b MBE shutter sequences for HgTe/CdTe SL growth with: (a) In modulation doping and (b) As planar doping in the barrier layers

loys. Furthermore, As planar doping of the CdTe layers yields p-activation either as-grown or after only a short low-temperature anneal at $T \leq 300^\circ\text{C}$.

In situ **RHEED** and **SE** measurements indicate high-quality growth, and ex situ **XRD** measurements yield results indicative of high structural quality. Also, scanning **XRD** and **FTIR** measurements have shown the layer uniformities to be excellent. However, both interfacial roughness and Cd interdiffusion during growth pose serious problems. For early (100) growth on $\text{Hg}_{0.73}\text{Cd}_{0.27}\text{Te}/\text{Hg}_{0.15}\text{Cd}_{0.85}\text{Te}$ **SLs**, it was found by quantitative chemical mapping that the **FWHM** of the as-grown interfacial roughness is only ≈ 2 monolayers near the surface of an as-grown $0.75\text{ }\mu\text{m}$ -thick **SL** [32.313]. More recently, we have found by **TEM** that for (211)B growth the **FWHM** of the as-grown interfacial roughness can be as large as ≈ 7 monolayers (**ML**) at the surface of a $10\text{ }\mu\text{m}$ -thick **SL** and $\approx 5.5\text{ ML}$ at the substrate, with no evidence during growth of poor growth morphology. Much of this observed roughness arose from the step-flow nature of (211)B growth and the existence of (100) steps several monolayers high between successive (111) terraces.

In agreement with earlier calculations [32.311,314], our **TEM** results show that during growth and during subsequent annealing the CdTe layers become narrower and the HgTe layers wider. Cd atoms diffuse into the HgTe layers from the interfacial roughness region and later, more slowly, from the edges of the CdTe layers, with very little diffusion into the CdTe layers. We have shown that interdiffusion becomes unimportant once the Cd in the alloyed interfacial roughness layers diffuses throughout the HgTe well layers. This is because the diffusion coefficient for Cd in HgTe is much higher than that for Hg in CdTe and because the diffusion coefficient for Cd in HgCdTe increases rapidly with increasing Hg content [32.314]. For a **SL** of thickness $\approx 10\text{ }\mu\text{m}$, the growth time is sufficiently long, $\approx 10\text{ h}$, to induce considerable Cd diffusion far from the surface, but there is little diffusion near the surface, which was exposed to the growth temperature only briefly. Thus

a **SL** of thickness $\approx 10\text{ }\mu\text{m}$ displays a greatly broadened optical absorption edge, because the absorption edge moves to a much higher energy near the substrate than that at the surface, due to Cd diffusion during growth, which increases with increasing time exposed to the growth temperature. In order to avoid this problem, one must either:

1. Grow only thin **SL** epilayers, say $< 3\text{ }\mu\text{m}$ thick
2. Anneal away the as-grown interfacial roughness throughout the epilayer.

It is not a practical option to greatly broaden the HgTe wells or to reduce the height or thickness of the CdTe barriers; either of those options would result in the loss of the primary **SL** advantages.

The problem with growing only thin **SL** epilayers is that thin layers give less absorption and thus lower quantum efficiencies. However, this could be overcome by stacking layers on top of one another in a device as is done by DRS in their three-color detector. The problem with annealing away the as-grown interfacial roughness throughout the epilayer is that the resultant Cd concentration in the well layers can easily become too high to obtain an absorption edge in the **VLWIR**. At 40 K a (211)B $60\text{ }\text{\AA}$ HgTe/ $50\text{ }\text{\AA}$ CdTe **SL** has a $24.57\text{ }\mu\text{m}$ cutoff. Assuming an average Cd concentration of 0.5 in the roughness layers, to preserve a cutoff $\geq 14\text{ }\mu\text{m}$ one must anneal away $\leq 3\text{ ML}$ of interfacial roughness; to preserve a cutoff $\geq 10\text{ }\mu\text{m}$ one must anneal away $< 6\text{ ML}$ of interfacial roughness.

To make **SLs** practical for use in the **VLWIR**, one must greatly reduce the amount of as-grown interfacial roughness, possibly by growing on a slightly miscut (100) or (111) plane. On the other hand, going back to (100) or (111) growth would reintroduce all of the problems solved by (211)B growth, such as microtwinning, surface hillocks, and **3-D** growth. The achievement of well-controlled **SL** layer thicknesses with little interfacial roughness is essential to the practical use of **SLs** for **VLWIR** detection and possibly even for the **LWIR**.

32.10 Architectures of Advanced IR Detectors

The mechanisms that convert **IR** radiation to a device's electrical output and properties (current out, capacitance, etc.) are described by device physics. The reader is referred to [32.321] for a complete description of photon detector behavior. Here, we deal with photon detectors in which **IR** photons are absorbed by the detector

material, creating excess carriers that form an output current proportional to the photon intensity.

An **IR** detector is a multilayer structure. These layers include contact metal, photon absorbing material, substrates, etc. The architecture describes how the layers are assembled to form the desired structure as well

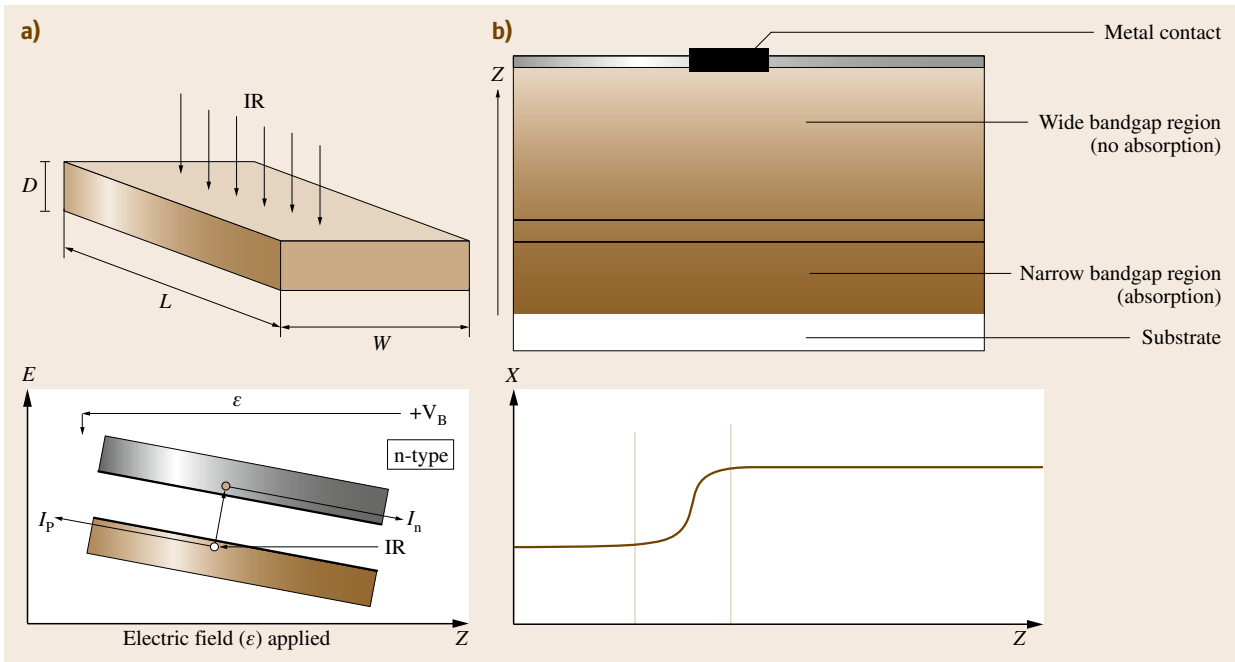


Fig. 32.22a,b Schematic diagrams of (a) a photoconductor and (b) a graded double-layer heterojunction

as the function of each layer. The two principal IR detectors used today are:

1. The photoconductor (PC), a resistor whose resistance changes under IR illumination, shown in Fig. 32.22a
2. The diode, a graded double-layer heterojunction (DLHJ) shown in Fig. 32.22b, which is a high-impedance minority-carrier device operating under reverse bias.

A detailed description of the performance of these two detector architectures is given in [32.321]. However, these two architectures are not adequate for all IR detector applications and under all external conditions. There are specific applications that require improvement in:

1. The performance at the upper end of the IR spectrum
2. The magnitude of the operating temperature
3. The speed of the detector response
4. The lowering of the detector internal noise.

In summary, there is a need to reduce power consumption, hence lowering cooling costs, to raise the operating temperature while keeping noise at a minimum, to increase the speed of detector response to rapidly changing targets, to increase the number of

photoelectrons created per IR photon in and hence to increase the output signal, and/or to increase the detector signal-to-noise ratio. To resolve some of these needs, new detector architectures have been introduced and/or advanced material growth technologies have been exploited.

32.10.1 Reduction of Internal Detector Noise

One of the problems with the graded DLHJ is that optimal performance depends on placing the p–n junction extremely accurately within the graded bandgap region. Optimal p–n junction placement allows the minimization of diode leakage and g-r noise, hence improving the performance. Device physics calculations [32.322] show that the p–n junction must be placed within a few hundred Angstroms of the optimal position; pushing the junction too far into the wider gap region will cause barriers to form, reducing the minority photocurrent. To perform the precise p–n junction placement requires MBE layer growth.

32.10.2 Increasing Detector Response

The response of a detector is determined partly by the quantum efficiency (QE), a measure of the number of

carriers generated per incident photon. For the standard PC or DLHJ, the QE is less than one, which results in an extremely low output current, of the order of nanoamperes. This means that an IR detector requires a preamplifier with a large amplification factor and extremely low noise. This is a tall order, especially if the preamplifier circuit must fit into an area roughly the size of current IR detectors, $\approx 30\text{--}50\text{ }\mu\text{m}$. It is desirable then to increase the number of current carriers produced per incident IR photon. In order to do so, one must take advantage of a process called impact ionization. Here, an incoming photon creates a free electron with energy well above the conduction-band energy. As the electron moves through the crystal lattice, if the photon-generated free carrier has sufficient energy, when it collides with a bound electron on an atom, that electron becomes a free carrier. At this stage, one photon has created two free carriers. This process will continue until no electron has sufficient energy to free a new electron. To preserve charge neutrality, a free hole is also created. The multiplication process leads to a $\text{QE} > 1$. The probability that a photon-created carrier will create another carrier via impact ionization is called the impact ionization coefficient for that carrier.

The problem with this process is ionization noise. Impact ionization noise is at a maximum if the impact ionization coefficients for electrons and holes are equal. To reduce the noise, one must turn to a more complex device architecture such as the sawtooth variation in concentration shown in Fig. 32.23. Here the teeth created by varying the Cd composition in HgCdTe cause one of the impact ionization coefficients, either

for electrons or for holes, to be small. Hence, the ratio of the two coefficients is large. This minimizes the impact ionization noise, resulting in a large multiplication factor (increased response) without increasing the noise, which would defeat the purpose. To create the desired sawtooth structure and maximize multiplication while minimizing impact ionization noise requires precise control of the MBE growth process.

32.10.3 High-Speed IR Detectors

A homojunction detector is a three-layer structure: a p-layer dominated by positively charged hole free carriers; a junction layer in which there is a large built-in electric field, hence the layer is depleted of free carriers; and an n layer dominated by negatively charged electrons. A photon-generated free carrier will diffuse to the edge of the junction and will drift at some rate to the opposite edge. In the absence of an external bias voltage, the junction crossing speed is not high for junction widths of $\approx 0.5\text{ }\mu\text{m}$. One can increase the transit speed by applying an external bias whose field is in the same direction as the built-in field. The applied field is a reverse-bias field, which will increase the junction width. So, with the increased width of the region that will support an electric field and with the added external field, the increased total field exerting a force on a carrier will cause the carrier to transit the junction more rapidly.

The transit speed is too low, hence the response time is too long, for many applications such as detecting the wavefront of an electromagnetic wave. To increase the transit speed, one needs to significantly increase the external bias. However, there is a limit to the reverse bias one can apply to the junction before the junction breaks down, avalanches, and behaves like a resistor. To get around this, a three-layer device can be built with the outer layers doped n-type and p-type, respectively. The middle layer is an undoped (intrinsic) layer that contains few free carriers, and hence can support a large electric field. Because the width of the intrinsic layer is much greater than the junction width, say 10–20 times larger, the device can support a very large external voltage, hence a very large external field without the device breaking down. This type of device is called a p-i-n diode, where i stands for intrinsic. To increase the speed of detector response, the effective width where there are few carriers, and hence which can support a large electric field junction, can be increased by at least a factor of 20 over the p-n junction width. Furthermore, the p- and n-side doping can be made much larger. Hence,

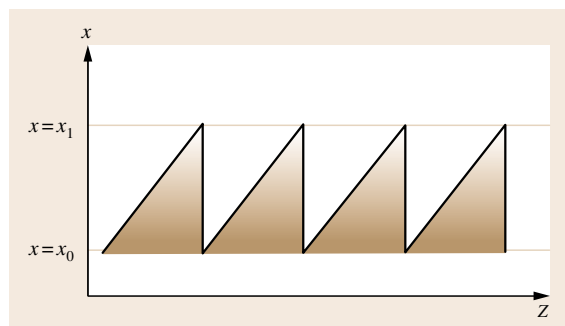


Fig. 32.23 Cd composition in HgCdTe versus distance from substrate for a potential avalanche photodiode (APD) design. This structure was proposed before it could be realized by MBE growth. The sawtooth significantly reduces one carrier's impact ionization coefficient compared with the other, which reduces the impact ionization coefficient

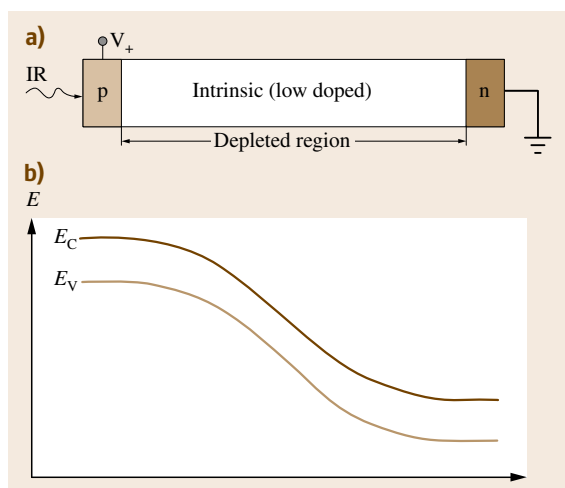


Fig. 32.24a,b Schematic diagram of a rapid-response p-i-n detector. (a) Device structure with a wide depleted region with no free carriers present. (b) Spatial band structure

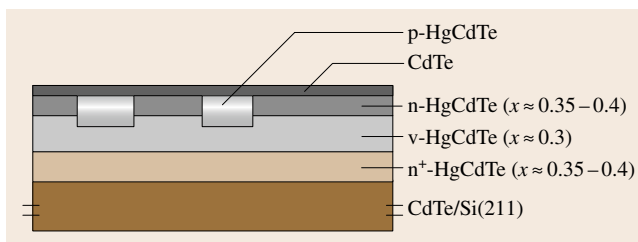


Fig. 32.25 Schematic diagram of a **HOT** detector architecture used at EPIR Technologies

the electric field in the junction is increased and acts over a longer distance. The carrier when it enters the field of the junction region will feel a very large force that will sweep the carrier to the opposite contact in an extremely short time. As a result, the p-i-n detector could fully respond to IR radiation in a time on the

order of a nanosecond or less. The actual structure and the spatial band structure of a p-i-n diode are shown schematically in Fig. 32.24.

32.10.4 High-Operating-Temperature (HOT) IR Detectors

Normally, an IR detector must be cooled so that the near-field IR radiation from its surrounding structure does not interfere with the IR signal coming from a few meters to a few thousand kilometers away. The reason for this is that a body produces IR radiation with a power which increases with increasing temperature T . The near-field radiation is a source of noise because there are mechanisms that generate random numbers of electron-hole pairs, which in turn contribute random fluctuations in the output current and thus noise. Therefore, the higher the operating temperature of the detector, the lower the signal-to-noise ratio (SNR). Depending on the cutoff wavelength, IR photon detectors are operated at anywhere from 4 to 77 K. This lays a heavy burden on the system due to the cooler's weight, power needs, and lifetime.

The ideal, to avoid the cost and weight of cooling, is a detector that yields a good SNR at room temperature, that is, a **HOT** detector. To achieve this, one must suppress the mechanisms that yield the random (thermal) generation of free carriers. A **HOT** detector is one that via a specific multilayer architecture suppresses one or more of the principal thermal generation mechanisms. While still in a very early stage of development, these structures promise operation near room temperature or at least at thermoelectrically cooled temperatures. One **HOT** architecture is shown in Fig. 32.25. Note that the structure requires precise control of layer thickness and doping, and hence is an ideal application of MBE growth technology. Recent references on **HOT** detectors include [32.323–325].

32.11 IR Focal-Plane Arrays (FPAs)

An IR FPA consists of four layers involving different kinds of materials. The top layer is the detector array, consisting of an array of HgCdTe detectors arranged in a linear or checkerboard pattern. The detector array is grown on a substrate, the second layer, which usually is CdZnTe, GaAs or Si based. Given a sufficiently large substrate and reasonable sized arrays, several detector arrays can be grown on a single substrate. The

output of an IR detector is very low, on the order of nA. Therefore, the detector array must be connected to a signal processor, which has a preamplifier for each detector plus various signal processing functions such as multiplexing and analogue-to-digital (A/D) conversion. This readout integrated circuit (ROIC) or multiplexor (MUX) is fabricated from silicon. The difference between the thermal coefficients of expansion of HgCdTe

or CdTe and Si is quite large. Therefore, each detector must be connected to its preamplifier on the ROIC by an In bump. Therefore, a 256×256 detector array requires more than 65 000 separate In bumps. Detector sizes typically are $20 \mu\text{m}$ on a side to $30 \mu\text{m}$ on a side, making the In bump cross section extremely small, perhaps $10 \times 10 \mu\text{m}^2$. In is used because it is a good conductor, is ductile, and can accommodate the strain introduced by the mismatched thermal coef-

ficients of expansion. The array of In bump electrical contacts forms the third layer. The Si ROIC is the fourth layer.

IR FPAs designed for astronomical investigations can be as large as 2000×2000 . This requires a very precise manufacturing process involving many steps of photolithography. Therefore, one becomes immediately concerned about yield versus cost versus quantity required for a given application.

32.12 Conclusions

The inherent properties of HgCdTe make this alloy the most preferred material for IR detection. During the past several decades HgCdTe alloys have been used as the primary material for IR detectors, which are most important for a variety of military and space applications. Significant advances in the MBE growth of HgCdTe alloys since the early 1980s have offered a new dimension in the ability to fabricate innovative detector structures, control multiple layer heterostructures, and use alternative substrates such as Si for large-format two-dimensional arrays. Today, the MBE of HgCdTe has emerged as a viable technology for research and development and the manufacture of high-performance IR FPAs.

Several factors have contributed to the growth and advancement of HgCdTe MBE technology. The large body of literature published by researchers studying various aspects of HgCdTe deposition experiments and theory has generated much useful information. Various advantages of the MBE technique such as the availability of SE, RHEED, and other in situ analytical characterization techniques to monitor and control the growth have enabled the verification of these experimental data and the related theories. The knowledge base has matured HgCdTe MBE technology in recent years to a point similar to that of III–V compound semiconductor MBE technology in the past. Unlike many III–V semiconductors, it took a while to understand the HgCdTe MBE process because of its stringent thermodynamic constraints. These constraints offer only a narrow window of parameter space for optimum epitaxy. These difficulties are further compounded by temperature changes in the growing HgCdTe layer due to its enhanced IR absorption. In situ tools, particularly SE and RHEED, helped to better understand MBE HgCdTe growth. In the past, and to a certain extent even today, LPE has been the preferred approach for HgCdTe

growth. Today, however MBE technology with its various advantages and advancement is becoming more attractive and is required for detectors with advanced architectures.

Abrupt p–n junctions and the control of layer thickness were first demonstrated in GaAs III–V semiconductor MBE technology. Recently, the maturation of the HgCdTe MBE process has also enabled fabrication of device structures with various architectures such as p^+/n , n^+/p , $p\text{--}i\text{--}n$, etc. Fabrication of these structures in HgCdTe is now possible because of the thin-film process available in MBE wherein HgCdTe layers can be controlled within submicrometer thicknesses. MBE also has facilitated multiple-layer heterostructure growth with various compositions of stacked HgCdTe layers. Unlike LPE, MBE allows the control of multiple heterostructure growth and thus allows for new device designs and optimization. This very feature also makes it suitable for superlattice structures, and adds the ability to implement bandgap engineering in this alloy. Therefore, MBE has been used to demonstrate both ion-implanted and in situ doped p–n junction devices, and various device designs including superlattice and multicolor detectors have been reported.

The low-temperature and ultrahigh-vacuum nature of MBE adds to its many advantages. Paramount among these is the ability to achieve abrupt material junctions with minimum interdiffusion or interface contamination, and the possibility of depositing HgCdTe on foreign substrates such as Si, GaAs or Al_2O_3 . Traditionally, bulk CdZnTe has been preferred as a substrate material for HgCdTe epitaxy. In the past, all three major growth techniques, LPE, MBE, and MOCVD, employed bulk CdZnTe substrates because of their close lattice and chemical match with HgCdTe alloys. During the past decade significant advances have occurred in the MBE of CdTe and HgCdTe on Si and

GaAs substrates. This has been possible due to the low temperature at which MBE occurs, where cross-contamination of the substrate material in the HgCdTe layer does not occur. The primary advantage of growing on Si or GaAs is the opportunity to produce very large-area HgCdTe epitaxial layers. Large-area growth is limited in bulk CdZnTe substrates because of the lack of high-quality large substrates and because of the large difference between the thermal coefficients of expansion of HgCdTe or CdTe and that of Si. The use of Si or GaAs offers more dies of IRFPAs per wafer, large-format IRFPAs, ease of device processing, and a low-cost option for manufacturing.

The challenge of HgCdTe MBE technology has been to produce material structures with structural, optical, and electrical characteristics better than or equivalent to the best LPE-grown materials. MBE technology has developed to the point at which MBE HgCdTe layers grown on bulk CdZnTe substrates have characteristics comparable to those of LPE material. The technology has reached the state at which the quality of MBE HgCdTe layers depends mostly on the characteristics of the substrate material. MBE is sensitive to even minute changes in substrate morphology, and tends to replicate those morphological defects in the growing HgCdTe layer. Various techniques have been developed to mitigate this problem so as to improve the crystalline quality of the HgCdTe layer. The use of buffer layers to block the propagation of defects originating in substrates or at the substrate–epilayer interface has proven useful and is being studied. A thin interfacial CdTe layer has proven effective in reducing substrate surface roughness, but has limitations. The most significant improvement is achieved by growing an interfacial HgTe/CdTe superlattice as a buffer layer. These superlattices are more effective at blocking dislocations and can be grown more nearly lattice matched to the HgCdTe epilayer to be grown.

Today the main challenge of HgCdTe MBE technology is to grow very high-crystalline-quality layers on Si. This epitaxial combination (HgCdTe/Si) creates an extreme 19.2% epitaxial mismatch. Thus growing HgCdTe layers with crystalline quality that is equivalent in characteristics to layers grown on bulk CdZnTe substrates is very difficult. Various techniques have been developed to reduce defect densities in HgCdTe layers grown on Si. Examples of these are variations of II–VI buffer layers such as CdTe and CdSeTe, and other techniques such as reduced-area growth, hydrogen passivation of defects, thermal anneal cycling, etc. Significant progress has been made in the MBE of

CdTe and CdSeTe on Si, and extended defect densities as low as $2 \times 10^5 \text{ cm}^{-2}$ have been achieved. However, progress in reducing defects in the HgCdTe layers grown on buffer/Si substrates is lagging. The best MBE HgCdTe layers grown on buffer/Si substrates achieved thus far exhibit defect densities of $2\text{--}5 \times 10^6 \text{ cm}^{-2}$. Clearly, more research and development is necessary to reduce the defect density by at least an order of magnitude.

Another remaining challenge in the MBE of HgCdTe is to be able to reproducibly grow layers with the desired levels of p-type doping stable against diffusion. In order to form sharp, precisely controlled interfaces and p–n junctions and to obtain well-controlled doping levels, it is essential to grow such junctions by MBE with extrinsic n- and p-type doping. Although stable, well-controlled n-type extrinsic doping of as-grown HgCdTe and HgTe/CdTe SLs has been demonstrated by many authors, p-type extrinsic doping of these materials has remained a problem. Unfortunately, As, which has a low diffusion coefficient, can be reproducibly activated in HgCdTe only at annealing temperatures significantly higher than the growth temperature. Annealing at such high temperatures limits many of the advantages of MBE as a growth technique. Even though high-performance HgCdTe-based photovoltaic photodiodes using various p-doping techniques (in situ and implantation) have been demonstrated, interdiffusion across interfaces, dopant diffusion, and the formation of Hg vacancies all become problems at the high annealing temperatures required for reproducible p-type activation of the preferred group V dopants. The absence of a reproducible p-type doping technique which does not require high-temperature annealing remains a major stumbling block to successfully implementing high-yield fabrication of MBE-grown HgCdTe IRFPAs. Much progress is needed in developing a reproducible in situ extrinsic p-type doping process for MBE technology to advance further.

It is worth noting that, despite the various difficulties faced by the HgCdTe MBE technology, the state of IRFPA technology can still be advanced significantly by further maturation of the MBE process. Considering the current military engagements, advancement of IRFPA technology is needed more than ever. MBE has the potential to emerge as a leading technique to develop innovative IR device architectures and other detector array designs that have not been possible in the past. Already, multicolor IRFPAs have been fabricated from HgCdTe grown by MBE. With more research it is potentially possible to use the HgCdTe MBE process to

develop very large-format **IRFPAs**. The advent of this technology will undoubtedly lead to important applications required to constantly monitor battlefields and borders. The progress of **MBE** in the area of alterna-

tive substrate technology would lead to more robust and low-cost **IRFPAs**. This will be most desirable in military applications, where more **IR** capability must be deployed.

References

- 32.1 A.Y. Cho: Morphology of epitaxial growth of GaAs by a molecular beam method: The observation of surface structures, *J. Appl. Phys.* **41**, 782–786 (1970)
- 32.2 S. Sivananthan, M.D. Lange, G. Monfroy, J.P. Faurie: New achievements in $\text{Hg}_{1-x}\text{Cd}_x\text{Te}$ grown by molecular-beam epitaxy, *J. Vac. Sci. Technol. B* **6**, 788–793 (1987)
- 32.3 M.A. Kinch: Fundamental physics of infrared detector materials, *J. Electron. Mater.* **29**, 809–817 (2000)
- 32.4 J.P. Faurie, A. Million: Molecular beam epitaxy of II–VI compounds $\text{Cd}_x\text{Hg}_{1-x}\text{Te}$, *J. Cryst. Growth* **54**, 582–585 (1982)
- 32.5 Y.G. Sidorov, S.A. Dvoretzky, M.V. Yakushev, N.N. Mikhailov, V.S. Varavin, V.I. Liberman: Peculiarities of the MBE growth physics and technology of narrow-gap II–VI compounds, *Thin Solid Films* **306**, 253–265 (1997)
- 32.6 J.P. Faurie, A. Million, R. Boch, J.L. Tissot: Latest developments in the growth of $\text{Cd}_x\text{Hg}_{1-x}\text{Te}$ and CdTe – HgTe superlattices by molecular beam epitaxy, *J. Vac. Sci. Technol. A* **1**, 1593–1597 (1983)
- 32.7 J.P. Faurie, M. Boukerche, J. Reno, S. Sivananthan, C. Hsu: Molecular beam epitaxy of alloys and superlattices involving mercury, *J. Vac. Sci. Technol. A* **3**, 55–59 (1985)
- 32.8 L. He, J.R. Yang, S.L. Wang, S.P. Guo, M.F. Yu, X.Q. Chen, W.Z. Fang, Y.M. Qiao, Q.Y. Zhang, R.J. Ding, T.L. Xin: A study of MBE growth and thermal annealing of p-type long wavelength HgCdTe, *J. Cryst. Growth* **175/176**, 677–681 (1997)
- 32.9 C.R. Abernethy: Compound semiconductor growth by metallorganic molecular beam epitaxy (MOMBE), *Mater. Sci. Eng. R* **14**, 203–254 (1995)
- 32.10 A. Parikh, S.D. Pearson, R.N. Bicknell-Tassius, L.H. Zhang, R. Benz, C.J. Summers: Optimization of the structural properties of $\text{Hg}_{1-x}\text{Cd}_x\text{Te}$ ($x = 0.18 - 0.30$) alloys: Growth and modeling, *J. Electron. Mater.* **26**, 524–528 (1997)
- 32.11 J.F. Schetzina: Photoassisted MBE growth of II–VI films and superlattices, *Appl. Surf. Sci.* **80**, 171–185 (1994)
- 32.12 R.N. Bicknell, N.C. Giles, J.F. Schetzina, C. Hitzman: Controlled substitutional doping of CdTe thin films grown by photoassisted molecular-beam epitaxy, *J. Vac. Sci. Technol. A* **5**, 3059–3063 (1987)
- 32.13 J.R. Arthur: Molecular beam epitaxy, *Surf. Sci.* **500**, 189–217 (2002)
- 32.14 J.Y. Tsao: *Materials Fundamentals of Molecular Beam Epitaxy* (Academic, Boston 1993)
- 32.15 A. Madhukar: Far from equilibrium vapour phase growth of lattice matched III–V compound semiconductor interfaces: some basic concepts and Monte-Carlo computer simulations, *Surf. Sci.* **132**, 344–374 (1983)
- 32.16 M.A. Herman: Approaches to understanding MBE growth phenomena, *Thin Solid Films* **267**, 1–14 (1995)
- 32.17 L.G. Wang, P. Kratzer, M. Scheffler, N. Moll: Formation and stability of self-assembled coherent islands in highly mismatched heteroepitaxy, *Phys. Rev. Lett.* **82**, 4042–4045 (1999)
- 32.18 L.G. Wang, P. Kratzer, N. Moll, M. Scheffler: Size, shape, and stability of InAs quantum dots on the GaAs(001) substrate, *Phys. Rev. B* **62**, 1897–1904 (2000)
- 32.19 C. Wagner, W. Schottky: Theory of controlled mixed phases, *Z. Phys. Chem. B* **11**, 163 (1931)
- 32.20 C. Wagner, W. Schottky: Theorie der geordneten Mischphasen II (Diffusionsvorgänge), *Z. Phys. Chem. Bodenst.-Festband*, 177 (1931), in German
- 32.21 C. Wagner: Theory of ordered mixture phases. III. Appearances of irregularity in polar compounds as a basis for ion conduction and electron conduction, *Z. Phys. Chem. B* **22**, 181 (1933)
- 32.22 C. Wagner: Errors in the classifications of crystalized polar compounds as basis for electron and ion conduction, *Z. Elektrochem.* **39**, 543 (1933)
- 32.23 W. Schottky: The mechanism of ion movement in solid electrolytes, *Z. Phys. Chem. B* **29**, 335 (1935)
- 32.24 W. Schottky: Statistics and thermodynamics of disorder states in crystals, especially in small disarranged states, *Z. Elektrochem.* **45**, 33 (1939)
- 32.25 F.A. Kröger, H.J. Vink: *Solid State Physics* Vol. 3, ed. by F. Seitz (Academic, New York 1956) p. 307
- 32.26 E. Bauer: Phänomenologische Theorie der Kristallabscheidung an Oberflächen I, *Z. Kristallogr.* **110**, 372–394 (1958), in German
- 32.27 R. Heckingbottom: Thermodynamic aspects of molecular beam epitaxy: high temperature growth in the GaAs/Ga_{1-x}Al_xAs system, *J. Vac. Sci. Technol. B* **3**, 572–575 (1985)
- 32.28 R. Heckingbottom, C.J. Todd, G.J. Davies: The Interplay of thermodynamics and kinetics in molecular beam epitaxy (MBE) of doped gallium arsenide, *J. Electrochem. Soc.* **127**, 444–450 (1980)

- 32.29 R. Heckingbottom, G.J. Davies: Germanium doping of gallium arsenide grown by molecular beam epitaxy – Some thermodynamic aspects, *J. Cryst. Growth* **50**, 644–647 (1980)
- 32.30 R. Heckingbottom, G.J. Davies, K.A. Prior: Growth and doping of gallium arsenide using molecular beam epitaxy (MBE): Thermodynamic and kinetic aspects, *Surf. Sci.* **132**, 375–389 (1983)
- 32.31 H. Seki, A. Koukitu: Thermodynamic analysis of molecular beam epitaxy of III–V semiconductors, *J. Cryst. Growth* **78**, 342–352 (1986)
- 32.32 F. Turco, J.C. Guillaume, J. Massies: Thermodynamic analysis of the molecular beam epitaxy of AlInAs alloys, *J. Cryst. Growth* **88**, 282–290 (1988)
- 32.33 J.Y. Shen, C. Chatillon: Thermodynamic analysis of molecular beam epitaxy of III–V compounds; application to the $\text{Ga}_y\text{In}_{1-y}\text{As}$ multilayer epitaxy, *J. Cryst. Growth* **106**, 553–565 (1990)
- 32.34 S.V. Ivanov, P.S. Kop'ev, N.N. Ledentsov: Thermodynamic analysis of segregation effects in MBE of $\text{A}^{\text{III}}\text{--B}^{\text{V}}$ compounds, *J. Cryst. Growth* **111**, 151–161 (1991)
- 32.35 J.P. Gailliard: A thermodynamical model of molecular beam epitaxy, application to the growth of II–VI semiconductors, *Rev. Phys. Appl.* **22**, 457–463 (1987)
- 32.36 T. Colin, T. Skauli: Applications of thermodynamical modeling in molecular beam epitaxy of $\text{Cd}_x\text{Hg}_{1-x}\text{Te}$, *J. Electron. Mater.* **26**, 688–696 (1997)
- 32.37 H.R. Vydyanath, F. Aqariden, P.S. Wijewarnasuriya, S. Sivananthan, G. Chambers, L. Becker: Analysis of the variation in the composition as a function of growth parameters in the MBE growth of indium doped $\text{Hg}_{1-x}\text{Cd}_x\text{Te}$, *J. Electron. Mater.* **27**, 504–506 (1998)
- 32.38 E.C. Piquette, M. Zandian, D.D. Edwall, J.M. Arias: MBE growth of HgCdTe epilayers with reduced visible defect densities: kinetics considerations and substrate limitations, *J. Electron. Mater.* **30**, 627–631 (2001)
- 32.39 Y. Chang, G. Badano, J. Zhao, C.H. Grein, S. Sivananthan, T. Aoki, D.J. Smith: Formation mechanism of crater defects on HgCdTe/CdZnTe (211)B epilayers grown by molecular beam epitaxy, *Appl. Phys. Lett.* **83**, 4785–4787 (2003)
- 32.40 J.W. Garland, C.H. Grein, B. Yang, P.S. Wijewarnasuriya, F. Aqariden: Evidence that arsenic is incorporated as As_4 molecules in the molecular beam epitaxial growth of $\text{Hg}_{1-x}\text{Cd}_x\text{Te:As}$, *Appl. Phys. Lett.* **74**, 1975–1977 (1999)
- 32.41 S. Sivananthan, X. Chu, J. Reno, J.P. Faurie: Relation between crystallographic orientation and the condensation coefficients of Hg, Cd and Te during molecular beam epitaxial growth of $\text{Hg}_{1-x}\text{Cd}_x\text{Te}$ and CdTe , *J. Appl. Phys.* **60**, 1359–1363 (1986)
- 32.42 S. Sivananthan, X. Chu, J.P. Faurie: Dependence of the condensation coefficient of Hg on the orientation and the stability of the Hg–Te bond for the growth of $\text{Hg}_{1-x}\text{M}_x\text{Te}$ ($\text{M} = \text{Cd}, \text{Mn}, \text{Zn}$), *J. Vac. Sci. Technol. B* **5**, 694–698 (1987)
- 32.43 J.P. Faurie: Developments and trends in MBE of II–VI Hg-based compounds, *J. Cryst. Growth* **81**, 483–488 (1987)
- 32.44 L.A. Almeida, M. Groenert, J.H. Dinan: Influence of substrate orientation on the growth of HgCdTe by molecular beam epitaxy, *J. Electron. Mater.* **35**, 1214–1218 (2006)
- 32.45 J.A. Venables: Kinetic studies of nucleation and growth at surfaces, *Thin Solid Films* **50**, 357–369 (1978)
- 32.46 R.J. Koestner, H.F. Schaake: Kinetics of molecular beam epitaxial HgCdTe growth, *J. Vac. Sci. Technol. A* **6**, 2834–2839 (1988)
- 32.47 M. Kardar, G. Parisi, Y. Zhang: Dynamic scaling of growing interfaces, *Phys. Rev. Lett.* **56**, 889–892 (1986)
- 32.48 P.I. Tamborenea, Z.–W. Lai, S. Das Sarma: Molecular beam epitaxial growth: Simulation and continuum theory, *Surf. Sci.* **267**, 1–4 (1992)
- 32.49 S. Das Sarma, Z.–W. Lai, P.I. Tamborenea: Crossover effects in models of kinetic growth with surface diffusion, *Surf. Sci. Lett.* **268**, L311–L318 (1992)
- 32.50 P. Kratzer, E. Penev, M. Scheffler: First-principles studies of kinetics in epitaxial growth of III–V semiconductors, *Appl. Phys. A* **75**, 79–88 (2002)
- 32.51 R. Triboulet, A. Tromson-Carli, D. Lorans, T. Nguyen Duy: Substrate issues for the growth of mercury cadmium telluride, *J. Electron. Mater.* **22**, 827–834 (1993)
- 32.52 R. Sporken, Y.P. Chen, S. Sivananthan, M.D. Lange, J.P. Faurie: Current status of direct growth of CdTe and HgCdTe on silicon by molecular-beam epitaxy, *J. Vac. Sci. Technol. B* **10**, 1405–1409 (1992)
- 32.53 R. Korenstein, P. Madison, J.P. Hallock: Growth of (111) CdTe on GaAs/Si and Si substrates for HgCdTe epitaxy, *J. Vac. Sci. Technol. B* **10**, 1370–1375 (1992)
- 32.54 Y.P. Chen, S. Sivananthan, J.P. Faurie: Structure of CdTe(111)B grown by MBE on misoriented Si(001) , *J. Electron. Mater.* **22**, 951–957 (1993)
- 32.55 Y.P. Chen, J.P. Faurie, S. Sivananthan, G.C. Hua, N. Otsuka: Suppression of twin formation in CdTe(111)B epilayers grown by molecular beam epitaxy on misoriented Si(001) , *J. Electron. Mater.* **24**, 475–481 (1995)
- 32.56 L.A. Almeida, Y.P. Chen, J.P. Faurie, S. Sivananthan: D.J. Smith, S.C.Y. Tsen: Growth of high quality CdTe on Si substrates by molecular beam epitaxy, *J. Electron. Mater.* **25**, 1402–1405 (1996)
- 32.57 M. Kawano, A. Ajisawa, N. Oda, M. Nagashima, H. Wada: HgCdTe and $\text{CdTe(}\bar{1}\bar{1}\bar{3}\text{)B}$ growth on Si(112)° off by molecular beam epitaxy, *Appl. Phys. Lett.* **69**, 2876–2879 (1996)
- 32.58 M.D. Lange, R. Sporken, K.K. Mahavadi, J.P. Faurie, Y. Nakamura, N. Otsuka: Molecular beam epi-

- taxy and characterization of CdTe(211) and CdTe(133) films on GaAs(211)B substrates, *Appl. Phys. Lett.* **58**, 1988–1990 (1991)
- 32.59 J.P. Faurie, R. Sporken, Y.P. Chen, M.D. Lange, S. Sivananthan: Heteroepitaxy of CdTe on GaAs and silicon substrates, *Mater. Sci. Eng. B* **16**, 51–56 (1993)
- 32.60 V.S. Varavin, S.A. Dvoretzky, V.I. Liberman, N.N. Mikhailov, Y.G. Sidorov: The controlled growth of high-quality mercury cadmium telluride, *Thin Solid Films* **267**, 121–125 (1995)
- 32.61 T.J. de Lyon, D. Rajaval, S.M. Johnson, C.A. Cockrum: Molecular-beam epitaxial growth of CdTe(112) on Si(112) substrates, *Appl. Phys. Lett.* **66**, 2119–2121 (1995)
- 32.62 T. Colin, D. Minsas, S. Gjoen, R. Sizmann, S. Lovold: Influence of surface step density on the growth of mercury cadmium telluride by molecular beam epitaxy, *Mater. Res. Soc. Symp. Proc.* **340**, 575 (1994)
- 32.63 F. Aqariden, H.D. Shih, A.M. Turner, D. Chandra, P.K. Liao: Molecular beam epitaxial growth of HgCdTe on CdZnTe(311)B, *J. Electron. Mater.* **29**, 727–728 (2000)
- 32.64 G.A. Carini, C. Arnone, A.E. Bolotnikov, G.S. Camarda, R. de Wames, J.H. Dinan, J.K. Markunias, B. Raghothamachar, S. Sivananthan, R. Smith, J. Zhao, Z. Zhong, R.B. James: Material quality characterization of substrates for HgCdTe epitaxy, *J. Electron. Mater.* **35**, 1495–1502 (2006)
- 32.65 H. Abad, J. Zhao, G. Badano, Y. Chang, S. Sivananthan: Correlation of pre-growth surface morphology of substrates with the quality of HgCdTe epilayers, *Mil. Sens. Symp. (Tucson 2004)*
- 32.66 H.R. Vydyanath, J. Ellsworth, J.J. Kennedy, B. Dean, C.J. Johnson, G.T. Neugebauer, J. Sepich, P.K. Liao: Recipe to minimize Te precipitation in CdTe and (Cd,Zn)Te crystals, *J. Vac. Sci. Technol. B* **10**, 1476–1484 (1992)
- 32.67 B. Li, J. Zhu, X. Zhang, J. Chu: Effect of annealing on near-stoichiometric and non-stoichiometric wafers, *J. Cryst. Growth* **181**, 204–209 (1997)
- 32.68 S.J.C. Irvine, A. Stafford, M.U. Ahmed: Substrate/layer relationships in II–VIs, *J. Cryst. Growth* **197**, 616–625 (1999)
- 32.69 E. Weiss, O. Klin, E. Benory, E. Kedar, Y. Juravel: Substrate quality impact on the carrier concentration of undoped annealed HgCdTe LPE layers, *J. Electron. Mater.* **30**, 756–761 (2001)
- 32.70 S. Sen, C.S. Liang, D.R. Rhiger, J.E. Stannard, H.F. Arlinghaus: Reduction of defects and relation to epitaxial HgCdTe quality, *J. Electron. Mater.* **25**, 1188–1195 (1996)
- 32.71 J.P. Faurie, S. Sivananthan, P.S. Wijewarnasuriya: Current status of the growth of mercury cadmium telluride by molecular beam epitaxy on (211)B HgCdTe substrates, *SPIE Proc.* **1735**, 141–150 (1992)
- 32.72 R. Korenstein, R.J. Olsen, D. Lee, P.K. Liao, C.A. Castro: Copper outdiffusion from substrates and its effect on the properties of metalorganic chemical-vapor deposition-grown HgCdTe, *J. Electron. Mater.* **24**, 511–514 (1995)
- 32.73 J.P. Tower, S.P. Tobin, M. Kestigian, P.W. Norton, A.B. Bollong, H.F. Shaake, C.K. Ard: Substrate impurities and their effects on LPE HgCdTe, *J. Electron. Mater.* **24**, 497–504 (1995)
- 32.74 J.P. Tower, S.P. Tobin, P.W. Norton, A.B. Bollong, A. Socha, J.H. Tregilgas, C.K. Ard, H.F. Arlinghaus: Trace copper measurements and electrical effects in LPE HgCdTe, *J. Electron. Mater.* **25**, 1183–1187 (1996)
- 32.75 S. Sen, D.R. Rhiger, C.R. Curtis, P.R. Norton: Extraction of mobile impurities from CdZnTe, *J. Electron. Mater.* **29**, 775–780 (2000)
- 32.76 D.R. Rhiger, J.M. Peterson, R.M. Emerson, E.E. Gordon, S. Sen, Y. Chen, M. Dudley: Investigation of the cross-hatch pattern and localized defects in epitaxial HgCdTe, *J. Electron. Mater.* **27**, 615–623 (1998)
- 32.77 M. Martinka, L.A. Almeida, J.D. Benson, J.H. Dinan: Suppression of strain-induced cross-hatch on molecular beam epitaxy (211)B HgCdTe, *J. Electron. Mater.* **31**, 732–737 (2001)
- 32.78 J. Zhao, Y. Chang, G. Badano, S. Sivananthan, J. Markunas, S. Lewis, J.H. Dinan, P.S. Wijewarnasuriya, Y. Chen, G. Brill, N. Dhar: Correlation of (211)B substrate surface morphology and HgCdTe(211)B epilayer defects, *J. Electron. Mater.* **33**, 881–885 (2005)
- 32.79 J.N. Johnson, L.A. Almeida, M. Martinka, J.D. Benson, J.H. Dinan: Use of electron cyclotron resonance plasmas to prepare (211)B substrates for HgCdTe molecular beam epitaxy, *J. Electron. Mater.* **28**, 817–820 (1999)
- 32.80 R. Singh, S. Velicu, J. Crocco, Y. Chang, J. Zhao, L.A. Almeida, J. Markunas, A. Kaleczyc, J.H. Dinan: Molecular beam epitaxy growth of high-quality HgCdTe LWIR layers on polished and repolished substrates, *J. Electron. Mater.* **34**, 885–890 (2005)
- 32.81 P. Moravec, P. Höschl, J. Franc, E. Belas, R. Fesh, R. Grill, P. Horodyský, P. Praus: Chemical polishing of substrates fabricated from crystals grown by the vertical-gradient freezing method, *J. Electron. Mater.* **35**, 1206–1218 (2006)
- 32.82 Y.S. Wu, C.R. Becker, A. Waag, R.N. Bicknell-Tassius, G. Landwehr: Thermal effects on (100) substrates as studied by x-ray photoelectron spectroscopy and reflection high energy electron diffraction, *Appl. Phys. Lett.* **60**, 1878–1880 (1992)
- 32.83 R.H. Sewell, C.A. Musca, J.M. Dell, L. Faraone, B.F. Usher, T. Dieing: High-resolution x-ray diffraction studies of molecular beam epitaxy-grown HgCdTe heterostructures and substrates, *J. Electron. Mater.* **34**, 795–803 (2005)

- 32.84 R. Triboulet, A. Durand, P. Gall, J. Bonnafé, J.P. Fillard, S.K. Krawczyk: Qualification by optical means of CdTe substrates, *J. Cryst. Growth* **117**, 227–232 (1992)
- 32.85 W.J. Everson, C.K. Ard, J.L. Sepich, B.E. Dean, G.T. Neugebauer, H.F. Shaake: Etch pit characterization of CdTe and CdZnTe substrates for use in mercury cadmium telluride epitaxy, *J. Electron. Mater.* **24**, 505–510 (1995)
- 32.86 K. Nakagawa, K. Maeda, S. Takeuchi: Observation of dislocations in cadmium telluride by cathodoluminescence microscopy, *Appl. Phys. Lett.* **34**, 574–575 (1979)
- 32.87 M. Kestigian, A.B. Bollong, J.J. Derby, H.L. Glass, K. Harris, H.L. Hettich, P.K. Liao, P. Mitra, P.W. Norton, H. Wadley: Cadmium zinc telluride growth, characterization, and evaluation, *J. Electron. Mater.* **28**, 726–731 (1999)
- 32.88 P. Capper, E.S. O'Keefe, C. Maxey, D. Dutton, P. Mackett, C. Butler, I. Gale: Matrix and impurity element distributions in CdHgTe (CMT) and (Cd,Zn)(Te,Se) compounds by chemical analysis, *J. Cryst. Growth* **161**, 104–118 (1996)
- 32.89 B. Li, J. Zhu, X. Zhang, J. Chu: Effect of annealing on near-stoichiometric and non-stoichiometric wafers, *J. Cryst. Growth* **181**, 204–209 (1997)
- 32.90 S.L. Price, H.L. Hettich, S. Sen, M.C. Currie, D.R. Rhiger, E.O. McLean: Progress in substrate producibility and critical drivers of IRFPA yield originating with substrates, *J. Electron. Mater.* **27**, 564–572 (1998)
- 32.91 Y. Chang, J. Zhao, H. Abad, C.H. Grein, S. Sivananthan, T. Aoki, D.J. Smith: Performance and reproducibility enhancement of HgCdTe molecular beam epitaxy growth on substrates using interfacial HgTe/CdTe superlattice layers, *Appl. Phys. Lett.* **86**, 131924 (2005)
- 32.92 Y. Chang, C.H. Grein, J. Zhao, S. Sivananthan, C.Z. Wang, T. Aoki, D.J. Smith, P.S. Wijewarnasuriya, V. Nathan: Improve molecular beam epitaxy growth of HgCdTe on (211)B substrates using interfacial layers of HgTe/CdTe superlattices, *J. Appl. Phys.* **100**, 114316–1–114316–6 (2006)
- 32.93 R. Sporken, S. Sivananthan, K.K. Mohavadi, G. Monfroy, M. Boukerche, J.P. Faurie: Molecular beam epitaxial growth of CdTe and HgCdTe on Si(100), *Appl. Phys. Lett.* **55**, 1879–1881 (1989)
- 32.94 S. Sivananthan, Y.P. Chen, P.S. Wijewarnasuriya, J.P. Faurie, F.T. Smith, P.W. Norton: Properties of $Hg_{1-x}Cd_xTe$ grown on CdZnTe and Si substrates, *Inst. Phys. Conf. Ser.* **144**, 239–244 (1995)
- 32.95 S. Velicu, T.S. Lee, C.H. Grein, P. Boieriu, Y.P. Chen, N.K. Dhar, J. Dinan, D. Lianos: Monolithically integrated HgCdTe focal plane arrays, *J. Electron. Mater.* **34**, 820–831 (2005)
- 32.96 L.A. Almeida, L. Hirsch, M. Martinka, P.R. Boyd, J.H. Dinan: Improved morphology and crystalline quality of MBE CdZnTe/Si, *J. Electron. Mater.* **30**, 608–610 (2001)
- 32.97 Y.P. Chen, G. Brill, N.K. Dhar: MBE growth of Cd–SeTe/Si composite substrate for long-wavelength IR HgCdTe applications, *J. Cryst. Growth* **252**, 270–274 (2004)
- 32.98 Y.P. Chen, G. Brill, E.M. Campo, T. Hierl, J.C.M. Hwang, N.K. Dhar: Molecular beam epitaxial growth of $Cd_{1-y}Zn_ySe_xTe_{1-x}$ on Si(211), *J. Electron. Mater.* **33**, 498–502 (2004)
- 32.99 N.K. Dhar, C.E.C. Wood, A. Gray, H.-Y. Wei, L. Salamanca, J.H. Dinan: Heteroepitaxy of CdTe on (211) Si using crystallized amorphous ZnTe templates, *J. Vac. Sci. Technol. B* **14**, 2366–2370 (1996)
- 32.100 S. Rujirawat, L.A. Almeida, Y.P. Chen, S. Sivananthan, D.J. Smith: High quality large-area CdTe(211)B on Si(211) grown by molecular beam epitaxy, *Appl. Phys. Lett.* **71**, 1810–1812 (1998)
- 32.101 J.M. Peterson, J.A. Franklin, M. Reddy, S.M. Johnson, E. Smith, W.A. Radford, I. Kasai: High-quality large-area MBE HgCdTe/Si, *J. Electron. Mater.* **35**, 1283–1286 (2006)
- 32.102 M.F. Vilela, A.A. Buell, M.D. Newton, G.M. Venzor, A.C. Childs, J.M. Peterson, J.J. Franklin, R.E. Bornfreund, W.A. Radford, S.M. Johnson: Growth and control of middle wave infrared (MWIR) $Hg_{(1-x)}Cd_xTe$ on Si by molecular beam epitaxy, *J. Electron. Mater.* **34**, 898–904 (2005)
- 32.103 M. Carmody, J.G. Pasko, D. Edwall, R. Bailey, J. Arias, S. Cabelli, J. Bajaj, L.A. Almeida, J.H. Dinan, M. Groenert, A.J. Stoltz, Y. Chen, G. Brill, N.K. Dhar: Molecular beam epitaxy grown long wavelength infrared HgCdTe on Si detector performance, *J. Electron. Mater.* **34**, 832–838 (2005)
- 32.104 M. Carmody, J.G. Pasko, D. Edwall, M. Daraselia, L.A. Almeida, J. Molstad, J.H. Dinan, J.K. Markunas, Y. Chen, G. Brill, N.K. Dhar: Long wavelength infrared, molecular beam epitaxy, HgCdTe-on-Si diode performance, *J. Electron. Mater.* **33**, 531–537 (2004)
- 32.105 K. Jówikowski, A. Rogalski: Effect of dislocations on performance of LWIR HgCdTe photodiodes, *J. Electron. Mater.* **29**, 736–741 (2000)
- 32.106 S.M. Johnson, D.R. Rhiger, J.P. Rosbeck, J.M. Peterson, S.M. Taylor, M.E. Boyd: Effect of dislocations on the electrical and optical properties of long-wavelength infrared HgCdTe photovoltaic detectors, *J. Vac. Sci. Technol. B* **10**, 1499–1506 (1992)
- 32.107 T.J. de Lyon, R.D. Rajavel, J.A. Vigil, J.E. Jensen, O.K. Wu, C.A. Cockrum, S.M. Johnson, G.M. Venzor, S.L. Bailey, I. Kasai, W.L. Ahlgren, M.S. Smith: Molecular beam epitaxial growth of HgCdTe infrared focal-plane arrays on Si substrates for midwave infrared applications, *J. Electron. Mater.* **27**, 550–555 (1998)
- 32.108 T.J. de Lyon, J.E. Jensen, I. Kasai, G.M. Venzor, K. Kosai, J.B. de Bruin, W.L. Ahlgren: Molecular-beam epitaxial growth and high-temperature

- performance of HgCdTe midwave infrared detectors, *J. Electron. Mater.* **31**, 220–226 (2002)
- 32.109 S.M. Johnson, A.A. Buell, M.F. Vilela, J.M. Peterson, J.B. Varesi, M.D. Newton, G.M. Venzor, R.E. Bornfreund, W.A. Radford, E.P.G. Smith, J.P. Rosbeck, T.J. de Lyon, J.E. Jensen, V. Nathan: HgCdTe/Si materials for long wavelength infrared detectors, *J. Electron. Mater.* **33**, 526–530 (2004)
- 32.110 M. Carmody, J.G. Pasko, D. Edwall, R. Bailey, J. Arias, M. Groenert, L.A. Almeida, J.H. Dinan, Y. Chen, G. Brill, N.K. Dhar: LWIR HgCdTe on Si detector performance and analysis, *J. Electron. Mater.* **35**, 1417–1422 (2006)
- 32.111 E.M. Campo, S. Nakahara, T. Hierl, J.C.M. Hwang, Y. Chen, G. Brill, N.K. Dhar, V. Vaithyanathan, D.G. Schlom, X.-M. Fang, J.M. Fastenau: Epitaxial growth of CdTe on Si through perovskite oxide buffers, *J. Electron. Mater.* **35**, 1219–1223 (2006)
- 32.112 Y. Liang, H. Li, J. Finder, C. Overgaard, J. Kulik, D. McCreedy, S. Shutthanandan: Mater. Res. Soc. Symp. (2004) p. 218
- 32.113 T.D. Golding, O.W. Holland, M.J. Kim, J.H. Dinan, L.A. Almeida, J.M. Arias, J. Bajaj, H.D. Shih, W.P. Kirk: HgCdTe on Si: Present status and novel buffer layer concepts, *J. Electron. Mater.* **32**, 882–889 (2003)
- 32.114 X. Zhou, S. Jiang, W.P. Kirk: Molecular beam epitaxy of BeTe on vicinal Si(100) surfaces, *J. Cryst. Growth* **175/176**, 624–631 (1997)
- 32.115 S.H. Shin, J.M. Arias, D.D. Edwall, M. Zandian, J.G. Pasko, R.E. DeWames: Dislocation reduction in HgCdTe on GaAs and Si, *J. Vac. Sci. Technol. B* **10**, 1492–1498 (1992)
- 32.116 Y. Lo: New approach to grow pseudomorphic structures over the critical thickness, *Appl. Phys. Lett.* **59**, 2311–2313 (1991)
- 32.117 Z. Yang, J. Alperin, W.I. Wang, S.S. Iyer, T.S. Kuan, F. Semendy: In situ relaxed $\text{Si}_{1-x}\text{Ge}_x$ epitaxial layers with low threading dislocation densities grown on compliant Si-on-insulator substrates, *J. Vac. Sci. Technol. B* **16**, 1489–1491 (1998)
- 32.118 P.D. Moran, D.M. Hansen, R.J. Matyi, L.J. Mawst, T.F. Kuech: Experimental test for elastic compliance during growth on glass-bonded compliant substrates, *Appl. Phys. Lett.* **76**, 2541–2543 (2000)
- 32.119 S.D. Hersee, D. Zubia, R. Bommena, X. Sun, M. Fairchild, S. Zhang, D. Burckel, A. Frauenglass, S.R.J. Brueck: Nanoheteroepitaxy for the integration of highly mismatched semiconductor materials, *IEEE J. Quantum Electron.* **QE-38**, 1017–1028 (2002)
- 32.120 S. Nakamura, M. Senoh, S.-I. Nagahama, N. Iwasa, T. Yamada, T. Matsushita, H. Kiyoku, Y. Sugimoto, T. Kozaki, H. Umemoto, M. Sano, K. Chocho: InGaN/GaN/AlGaIn-based laser diodes with modulation-doped strained-layer superlattices grown on an epitaxially laterally overgrown GaN substrate, *Appl. Phys. Lett.* **72**, 211–213 (1998)
- 32.121 H. Marchand, X.H. Wu, J.P. Ibbetson, P.T. Fini, P. Kozodoy, S. Keller, J.S. Speck, S.P. DenBaars, U.K. Mishra: Microstructure of GaN laterally overgrown by metalorganic chemical vapor deposition, *Appl. Phys. Lett.* **73**, 747–749 (1998)
- 32.122 R. Zhang, I. Bhat: Selective growth of CdTe on Si and GaAs substrates using metalorganic vapor phase epitaxy, *J. Electron. Mater.* **29**, 765–769 (2000)
- 32.123 I. Bhat, R. Zhang: Anisotropy in selective metalorganic vapor phase epitaxy of CdTe on GaAs and Si substrates, *J. Electron. Mater.* **35**, 1293–1298 (2006)
- 32.124 S.C. Lee, K.J. Malloy, L.R. Dawson: Selected growth and associated faceting and lateral overgrowth of GaAs on a nanoscale limited area bounded by a SiO_2 mask in molecular beam epitaxy, *J. Appl. Phys.* **92**, 6567–6571 (2002)
- 32.125 R. Bommena, C. Fulk, J. Zhao, T.S. Lee, S. Sivananthan, S.R.J. Brueck, S.D. Hersee: Cadmium telluride growth on patterned substrates for mercury cadmium telluride infrared detectors, *J. Electron. Mater.* **34**, 704–709 (2005)
- 32.126 X.G. Zhang, P. Li, G. Zhao, D.W. Parent, F.C. Jain, J.E. Ayers: Removal of threading dislocations from patterned heteroepitaxial semiconductors by glide to sidewalls, *J. Electron. Mater.* **27**, 1248–1253 (1998)
- 32.127 X.G. Zhang, A. Rodriguez, P. Li, F.C. Jain, J.E. Ayers: Patterned heteroepitaxial processing applied to ZnSe and $\text{Zn}_{0.02}\text{Se}_{0.98}$ on GaAs(001), *J. Appl. Phys.* **91**, 3912–3917 (2002)
- 32.128 Y. Dong, R.M. Feenstra, D.W. Greve, J.C. Moore, M.D. Sievert, A.A. Baski: Effects of hydrogen on the morphology and electrical properties of GaN grown by plasma-assisted molecular-beam epitaxy, *Appl. Phys. Lett.* **86**, 121914 (2005)
- 32.129 Y.F. Chen, C.S. Tsai, Y.H. Chang, Y.M. Chang, T.K. Chen, Y.M. Pang: Hydrogen passivation in $\text{Cd}_{1-x}\text{Zn}_x\text{Te}$ studied by photoluminescence, *Appl. Phys. Lett.* **58**, 493–495 (1991)
- 32.130 A.P. Jacobs, Q.X. Zhao, M. Willander, T. Baron, N. Magnea: Hydrogen passivation of nitrogen acceptors confined in CdZnTe quantum well structures, *J. Appl. Phys.* **90**, 2329–2332 (2001)
- 32.131 H.Y. Lee, T.W. Kang, T.W. Kim: Temperature dependence of the optical properties in p- $\text{Cd}_{0.96}\text{Zn}_{0.04}\text{Te}$ single crystals, *J. Mater. Res.* **16**, 2196–2199 (2001)
- 32.132 A.I. Evstigneev, V.F. Kuleshov, G.A. Lubochkova, M.V. Pashkovskii, E.B. Yakimov, N.A. Yarkin: Influence of hydrogen on the concentration of deep-level centers in $\text{Cd}_x\text{Hg}_{1-x}\text{Te}$ crystals, *Sov. Phys. Semicond.* **19**, 562 (1985)
- 32.133 S.P. Komissarchuk, L.N. Limarenko, E.P. Lopatinskaya: *Narrow Gap Semiconductors and Semimetals* (LVOV, Moscow 1983) p. 126
- 32.134 H. Jung, H. Lee, C. Kim: Enhancement of the steady state minority carrier lifetime in HgCdTe photodiode using ECR plasma hydrogenation, *J. Electron. Mater.* **25**, 1266–1269 (1996)

- 32.135 Y. Kim, T. Kim, D. Redfern, C. Musca, H. Lee, C. Kim: Characteristics of gradually doped LWIR diodes by hydrogenation, *J. Electron. Mater.* **29**, 859–864 (2000)
- 32.136 P. Boieriu, C.H. Grein, S. Velicu, J. Garland, C. Fulk, A. Stoltz, W. Mason, L. Bubulac, R. DeWames, J.H. Dinan: Effects of hydrogen on majority carrier transport and minority carrier lifetimes in LWIR HgCdTe on Si, *Appl. Phys. Lett.* **88**, 62106 (2006)
- 32.137 Y. Xin, S. Rujirawat, N.D. Browning, R. Sporken, S. Sivananthan, S.J. Pennycook, N.K. Dhar: The effect of As passivation on the molecular beam epitaxial growth of high-quality single-domain CdTe(111)B on Si(111) substrates, *Appl. Phys. Lett.* **75**, 349–351 (1999)
- 32.138 P. Sen, S. Ciraci, I.P. Batra, C.H. Grein, S. Sivananthan: Finite temperature studies of Te adsorption on Si(001), *Surf. Sci.* **519**, 79–89 (2002)
- 32.139 P. Sen, I.P. Batra, S. Sivananthan, C.H. Grein: Nabir Dhar, S. Ciraci, Electronic structure of Te- and As-covered Si(211), *Phys. Rev. B* **68**, 045314 (2003)
- 32.140 M. Jaime-Vazquez, M. Martinka, R.N. Jacobs, M. Groenert: In-situ spectroscopic study of the As and Te on the Si(112) surface for high-quality epitaxial layers, *J. Electron. Mater.* **35**, 1455–1460 (2006)
- 32.141 S.D. Chen, L. Lin, X.Z. He, M.J. Ying, R.Q. Wu: High quality HgCdTe epilayers grown on (211)B GaAs by molecular beam epitaxy, *J. Cryst. Growth* **152**, 261–265 (1995)
- 32.142 P. Ballet, F. Noël, F. Pottier, S. Plissard, J.P. Zanatta, J. Baylet, O. Gravrand, E. De Borniol, S. Martin, P. Castelain, J.P. Chamonal, A. Million, G. Destefanis: Dual-band infrared detectors made on high-quality HgCdTe epilayers grown by molecular beam epitaxy on or CdTe/Ge substrates, *J. Electron. Mater.* **33**, 667–672 (2004)
- 32.143 J.P. Zanatta, G. Badano, P. Ballet, C. Langeron, J. Baylet, O. Gravrand, J. Rothman, P. Castelain, J.P. Chamonal, A. Million, G. Destefanis, S. Mi-bord, E. Brochier, P. Costa: Molecular beam epitaxy growth of HgCdTe on Ge for third-generation infrared detectors, *J. Electron. Mater.* **35**, 1231–1236 (2006)
- 32.144 A.I. D'Souza, J. Bajaj, R.E. de Wames, D.D. Ed-wall, P.S. Wijewarnasuriya, N. Nayar: MWIR DLPH photodiode performance dependence on substrate material, *J. Electron. Mater.* **27**, 727–732 (1998)
- 32.145 A.J. Norieka, R.F.C. Farrow, F.A. Shirland, W.J. Takai, J. Gregg Jr., S. Wood, W.J. Choyke: Characterization of molecular beam epitaxially grown HgCdTe on CdTe and InSb buffer layers, *J. Vac. Sci. Technol. A* **4**, 2081–2085 (1986)
- 32.146 G. Brill, S. Velicu, Y. Chen, N.K. Dhar, T.S. Lee, Y. Selamet, S. Sivananthan: MBE growth and device processing of MWIR HgCdTe on large area Si substrates, *J. Electron. Mater.* **30**, 717–722 (2001)
- 32.147 S. Sivananthan: Experimental study on the prop-erties of HgCdTe grown by molecular beam epitaxy. Ph.D. Thesis (Department of Physics. Univ. Illinois, Chicago 1987) p.160
- 32.148 B.V. Shanabrook, J.R. Waterman, J.L. Davis, R.J. Wagner: Large temperature changes induced by molecular-beam epitaxial growth on radiatively heated substrates, *Appl. Phys. Lett.* **61**, 2338–2340 (1992)
- 32.149 B.V. Shanabrook, J.R. Waterman, J.L. Davis, R.J. Wagner, D.S. Katzer: Variations in substrate temperature induced by molecular-beam epitax-ial growth on radiatively heated substrates, *J. Vac. Sci. Technol. B* **11**, 994–997 (1993)
- 32.150 P. Thompson, Y. Li, J.J. Zhou, D.L. Sato, L. Flan-ders, H.P. Lee: Diffuse reflectance spectroscopy measurement of substrate temperature and tem-perature transient during molecular beam epitaxy and implications for low-temperature III–V epi-taxy, *Appl. Phys. Lett.* **70**, 1605–1607 (1997)
- 32.151 L.A. Almeida, N.K. Dhar, M. Martinka, J.H. Di-nan: HgCdTe heteroepitaxy on three-inch (112) CdZnTe/Si: Ellipsometric control of substrate tem-perature, *J. Electron. Mater.* **29**, 754–759 (2000)
- 32.152 M. Daraselia, C.H. Grein, R. Rujirawat, B. Yang, S. Sivananthan, F. Aqariden, S. Shih: In-situ mon-itoring of temperature and alloy composition of $Hg_{1-x}Cd_xTe$ using FTIR spectroscopic techniques, *J. Electron. Mater.* **28**, 743–748 (1999)
- 32.153 T.P. Pearsall, S.R. Saban, J. Booth, B.T. Beard Jr., S.R. Johnson: Precision of noninvasive temperature measurement by diffuse reflectance spectroscopy, *Rev. Sci. Instrum.* **66**, 4977–4980 (1995)
- 32.154 T.J. de Lyon, J.A. Roth, D.H. Chow: Substrate temperature measurement by absorption-edge spectroscopy during molecular beam epitaxy of narrow-band gap semiconductor films, *J. Vac. Sci. Technol. B* **15**, 329–336 (1997)
- 32.155 F.G. Johnson, G.W. Wicks, R.E. Viturro, R. LaForce: Molecular-beam epitaxial growth of arsenide/ phosphide heterostructures using valved, solid group V sources, *J. Vac. Sci. Technol. B* **11**, 823–825 (1993)
- 32.156 D.D. Edwall, D.B. Young, A.C. Chen, M. Zandian, J.M. Arias, B. Dlugosch, S. Priddy: Initial Evaluation of a valved Te source for MBE growth of HgCdTe, *J. Electron. Mater.* **28**, 740–742 (1999)
- 32.157 W.V. McLevige, J.M. Arias, D.D. Edwall, S.L. John-son: Ellipsometric profiling of HgCdTe heterostruc-tures, *J. Vac. Sci. Technol. B* **9**, 2483–2486 (1991)
- 32.158 D.R. Rhiger: Use of ellipsometry to characterize the surface of HgCdTe, *J. Electron. Mater.* **22**, 887–898 (1993)
- 32.159 K.K. Svitasev, S.A. Dvoretzky, Y.G. Sidorov, V.A. Shvets, A.S. Mardezhov, I.E. Nis, V.S. Varavin, V. Liberman, V.G. Remesnik: The growth of high-quality MCT films by MBE using in-situ ellipsometry, *Cryst. Res. Technol.* **29**, 931–937 (1994)

- 32.160 S.D. Murthy, I.B. Bhat, B. Johs, S. Pittal, P. He: Application of spectroscopic ellipsometry for real-time control of CdTe and HgCdTe growth in an OMCVD system, *J. Electron. Mater.* **24**, 445–449 (1995)
- 32.161 S. Pittal, B. Johs, P. He, J.A. Woollam, S.D. Murthy, I.B. Bath: In-situ monitoring and control of MOCVD growth using multiwavelength ellipsometry, *Compound Semiconductors*, *Inst. Phys. Conf. Ser.* **141**, 41–44 (1994)
- 32.162 J.D. Benson, A.B. Cornfeld, M. Martinka, K.M. Singley, Z. Derzko, P.J. Shorten, J.H. Dinan: In-situ spectroscopic ellipsometry of HgCdTe, *J. Electron. Mater.* **25**, 1406–1410 (1996)
- 32.163 B. Johs, C. Herzinger, J. Dinan, A. Cornfeld, J.D. Benson, D. Doctor, G. Olson, I. Ferguson, M. Pelcynski, P. Chow, C.H. Kuo, S. Johnson: Real-time monitoring and control of epitaxial semiconductor growth in a production environment by in situ spectroscopic ellipsometry, *Thin Solid Films* **313**, 490–495 (1998)
- 32.164 R.M.A. Azzam, N.M. Bashara: *Ellipsometry and Polarized Light* (Elsevier North-Holland, New York 1977)
- 32.165 J.W. Garland, C. Kim, H. Abad, P.M. Raccah: Determination of accurate critical-point energies, linewidths and line shapes from spectroscopic ellipsometry data, *Thin Solid Films* **233**, 148–152 (1993)
- 32.166 D.E. Aspnes, G.P. Schwartz, G.J. Gualtieri, A.A. Studna: Optical properties of gallium arsenide and its electrochemically grown anodic oxide from 1.5 to 6.0 eV, *J. Electrochem. Soc.* **128**, 590–597 (1981)
- 32.167 R.W. Collins: Automatic rotating element ellipsometers: calibration, operation, and real-time applications, *Rev. Sci. Instrum.* **61**, 2029–2062 (1990)
- 32.168 B. Johs: Regression calibration method for rotating element ellipsometers, *Thin Solid Films* **234**, 395–398 (1993)
- 32.169 G.E. Jellison, F.A. Modine: Two-modulator generalized ellipsometry: Theory, *Appl. Opt.* **36**, 8190–8198 (1997)
- 32.170 G.E. Jellison: Windows in ellipsometry measurements, *Appl. Opt.* **38**, 4784–4789 (1999)
- 32.171 D.E. Aspnes: Minimal-data approaches for determining outer-layer dielectric responses of films from kinetic reflectometric and ellipsometric measurements, *J. Opt. Soc. Am.* **10**, 974–983 (1993)
- 32.172 D.E. Aspnes: Optical approaches to determine near-surface compositions during epitaxy, *J. Vac. Sci. Technol. A* **14**, 960–966 (1996)
- 32.173 S.F. Nee: Polarization of specular reflection and near-specular scattering by a rough surface, *Appl. Opt.* **35**, 3570–3582 (1996)
- 32.174 D.A. Aspnes, J.B. Theeten, F. Hottier: Investigation of effective-medium models of microscopic surface roughness by spectroscopic ellipsometry, *Phys. Rev. B* **20**, 3292–3302 (1979)
- 32.175 H. Fujiwara, J. Koh, P.I. Rovira, R.W. Collins: Assessment of effective-medium theories in the analysis of nucleation and microscopic surface roughness evolution for semiconductor thin films, *Phys. Rev. B* **61**, 10832–10844 (2000)
- 32.176 J.D. Jackson: *Classical Electrodynamics* (Wiley, New York 1962), Sect. 6
- 32.177 S.F. Nee: Ellipsometric analysis for surface roughness and texture, *Appl. Opt.* **27**, 2819–2831 (1988)
- 32.178 D.E. Aspnes: *Optical Properties of Solids: New Developments*, ed. by O. Seraphin (North-Holland, Amsterdam 1976) p. 799
- 32.179 D.E. Aspnes, A.A. Studna: Optical detection and minimization of surface overlayers on semiconductors using spectroscopic ellipsometry, *SPIE Proc.* **276**, 227–232 (1981)
- 32.180 D.E. Aspnes, A.A. Studna: Chemical etching and cleaning procedures for silicon, germanium and some III–V compound semiconductors, *Appl. Phys. Lett.* **39**, 316–318 (1981)
- 32.181 B. Johs, C.M. Herzinger, J.H. Dinan, A. Cornfeld, J.D. Benson: Development of a parametric optical constant model for HgCdTe for control of composition by spectroscopic ellipsometry during MBE growth, *Thin Solid Films* **313/314**, 137–142 (1998)
- 32.182 J.D. Phillips, D.D. Edwall, D.L. Lee: Control of very-long-wavelength infrared HgCdTe detector-cutoff wavelength, *J. Electron. Mater.* **31**, 664–668 (2002)
- 32.183 L.A. Almeida, M. Thomas, W. Larsen, K. Spariosu, D.D. Edwall, J.D. Benson, W. Mason, A.J. Stolt, J.H. Dinan: Development and fabrication of two-color mid- and short-wavelength infrared simultaneous unipolar multispectral integrated technology focal-plane arrays, *J. Electron. Mater.* **31**, 669–676 (2002)
- 32.184 T.J. Delyon, G.L. Olson, J.A. Roth, J.E. Jensen, A.T. Hunter, M.D. Jack, S.L. Bailey: HgCdTe composition determination using spectroscopic ellipsometry during molecular beam epitaxy growth of near-infrared avalanche photodiode device structures, *J. Electron. Mater.* **31**, 688–693 (2002)
- 32.185 J. Phillips, D. Edwall, D. Lee, J. Arias: Growth of HgCdTe for long-wavelength infrared detectors using automated control from spectroscopic ellipsometry measurements, *J. Vac. Sci. Technol. B* **19**, 1580–1584 (2001)
- 32.186 D. Edwall, J. Phillips, D. Lee, J. Arias: Composition control of long wavelength MBE HgCdTe using in-situ spectroscopic ellipsometry, *J. Electron. Mater.* **30**, 643–646 (2001)
- 32.187 L.A. Almeida, J.H. Dinan: In situ compositional control of advanced HgCdTe-based IR detectors, *J. Cryst. Growth* **202**, 22–25 (1999)
- 32.188 L.A. Almeida, J.N. Johnson, J.D. Benson, J.H. Dinan, B. Johs: Automated compositional control of

- Hg_{1-x}Cd_xTe during MBE using in situ spectroscopic ellipsometry, *J. Electron. Mater.* **27**, 500–503 (1998)
- 32.189 G. Badano, J.W. Garland, S. Sivananthan: Accuracy of the in situ determination of the temperature by ellipsometry before the growth of HgCdTe by MBE, *J. Cryst. Growth* **251**, 571–575 (2003)
- 32.190 C.C. Kim, J.W. Garland, H. Abad, P.M. Raccah: Modeling the optical dielectric function of semiconductors – Extension of the critical-point parabolic-band approximation, *Phys. Rev. B* **45**, 11749–11767 (1992)
- 32.191 H. Ehrenreich, M.H. Cohen: Self-consistent field approach to the many-electron problem, *Phys. Rev.* **115**, 786–790 (1959)
- 32.192 J.W. Garland, H. Abad, M. Vaccaro, P.M. Raccah: Line shape of the optical dielectric function, *Appl. Phys. Lett.* **52**, 1176–1178 (1988)
- 32.193 C.C. Kim, S. Sivananthan: Modeling the optical dielectric function of II–VI compound CdTe, *J. Appl. Phys.* **78**, 4003–4010 (1995)
- 32.194 C.C. Kim, S. Sivananthan: Optical properties of ZnSe and its modeling, *Phys. Rev. B* **53**, 1475–1483 (1996)
- 32.195 C.C. Kim, M. Daraselia, J.W. Garland, S. Sivananthan: Temperature dependence of the optical properties of CdTe, *Phys. Rev. B* **56**, 4786–4797 (1997)
- 32.196 C.C. Kim, S. Sivananthan: Temperature dependence of the optical properties of Hg_{1-x}Cd_xTe, *J. Electron. Mater.* **26**, 561–566 (1997)
- 32.197 C.C. Kim, J.W. Garland, P.M. Raccah: Modeling the optical dielectric function of the aluminum gallium arsenide alloy system Al_xGa_{1-x}As, *Phys. Rev. B* **47**, 1876–1888 (1993)
- 32.198 O. Castaing, J.T. Benhlal, R. Granger: An attempt to model the dielectric function in II–VI ternary compounds Hg_{1-x}Zn_xTe and Cd_{1-x}Zn_xTe, *Eur. Phys. J. B* **7**, 563–572 (1999)
- 32.199 G. Badano, P. Ballet, J.P. Zanatta, X. Baudry, A. Million: Ellipsometry of rough CdTe(211)B–Ge(211) surfaces grown by molecular beam epitaxy, *J. Opt. Soc. Am. B* **23**, 2089–2096 (2006)
- 32.200 G. Badano, P. Ballet, X. Baudry, J.P. Zanatta, A. Million, J.W. Garland: Molecular beam epitaxy of BeTe on vicinal Si(100) surfaces, *J. Cryst. Growth* **296**, 129–134 (2006)
- 32.201 G. Badano, Y. Chang, J.W. Garland, S. Sivananthan: In-situ ellipsometry studies of adsorption of Hg on CdTe(211)B/Si(211) and molecular beam epitaxy growth of HgCdTe(211)B, *J. Electron. Mater.* **33**, 583–589 (2004)
- 32.202 G. Badano, Y. Chang, J.W. Garland, S. Sivananthan: Temperature-dependent adsorption of Hg on CdTe(211)B studied by spectroscopic ellipsometry, *Appl. Phys. Lett.* **83**, 2324–2326 (2003)
- 32.203 D.G.M. Anderson, R. Barakat: Necessary and sufficient conditions for a Mueller matrix to be derivable from a Jones matrix, *J. Opt. Soc. Am. A* **11**, 2305–2319 (1994)
- 32.204 S.F. Nee: Polarization of specular reflection and near-specular scattering by a rough surface, *Appl. Opt.* **35**, 3570–3582 (1996)
- 32.205 W. Braun: *Applied RHEED, Reflection High-Energy Electron Diffraction During Crystal Growth*, Springer Tracts in Modern Physics, Vol. 154 (Springer, Berlin 1999)
- 32.206 J.J. Harris, B.A. Joyce, P.J. Dobson: Oscillations in the surface structure of Sn-doped GaAs during growth by MBE, *Surf. Sci.* **103**, L90–L96 (1981)
- 32.207 C.E.C. Wood: RED intensity oscillations during MBE of GaAs, *Surf. Sci.* **108**, L441–L443 (1981)
- 32.208 J.M. van Hove, C.S. Lent, P.R. Pukite, P.I. Cohen: Damped oscillations in reflection high energy electron diffraction during GaAs MBE, *J. Vac. Sci. Technol. B* **1**, 741–746 (1983)
- 32.209 J. Arias, J. Singh: Use of cation-stabilized conditions to improve compatibility of CdTe and HgTe molecular beam epitaxy, *Appl. Phys. Lett.* **55**, 1561–1563 (1989)
- 32.210 W. Braun, L. Däweritz, K.H. Ploog: Origin of electron diffraction oscillations during crystal growth, *Phys. Rev. Lett.* **80**, 4935–4938 (1998)
- 32.211 M. Itoh, T. Ohno: Probing the submonolayer morphology change in epitaxial growth: A simulation study, *Appl. Phys. Lett.* **90**, 073111 (2007)
- 32.212 T.J. de Lyon, S.M. Johnson, C.A. Cockrum, O.K. Wu, W.J. Hamilton, G.S. Kamath: CdZnTe on Si(001) and Si(112): Direct MBE growth for large-area HgCdTe infrared focal-plane array applications, *J. Electrochem. Soc.* **141**, 2888–2893 (1994)
- 32.213 W.-S. Wang, I. Bhat: Growth of high quality CdTe and ZnTe on Si substrates using organometallic vapor phase epitaxy, *J. Electron. Mater.* **24**, 451–455 (1995)
- 32.214 P.S. Wijewarnasuriya, M. Zandian, D.D. Edwall, W.V. McLevige, C.A. Chen, J.G. Pasko, G. Hildebrandt, A.C. Chen, J.M. Arias, A.I. D'Souza, S. Rujirawat, S. Sivananthan: MBE p-on-n Hg_{1-x}Cd_xTe heterostructure detectors on silicon substrates, *J. Electron. Mater.* **27**, 546–549 (1998)
- 32.215 P. Boieriu, G. Brill, Y. Chen, S. Velicu, N.K. Dhar: Hg_{1-x}Cd_xTe(112) nucleation on silicon composite substrates, *SPIE Proc.* **4454**, 60–70 (2001)
- 32.216 W. Kern, D.A. Puotinen: Cleaning solutions based on hydrogen peroxide for use in silicon semiconductor technology, *RCA Review* **31**, 187 (1970)
- 32.217 A. Ishikawa, Y. Shiraki: Low temperature surface cleaning of silicon and its application to silicon MBE, *J. Electrochem. Soc.* **133**, 666–671 (1986)
- 32.218 P.J. Taylor, W.A. Jesser, M. Martinka, K.M. Singley, J.H. Dinan, R.T. Lareau, M.C. Wood, W.W. Clark III: Reduced carbon contaminant, low-temperature silicon substrate preparation for defect-free homoepitaxy, *J. Vac. Sci. Technol. A* **17**, 1153–1159 (1999)
- 32.219 N.K. Dhar, P.R. Boyd, M. Martinka, J.H. Dinan, L.A. Almeida, N. Goldsman: Heteroepitaxy on 3"

- (112)Si: Interface, surface, and layer characteristics, *J. Electron. Mater.* **29**, 748–753 (2000)
- 32.220 Y. Xin, S. Rujirawat, N.D. Browning, R. Sporken, S. Sivananthan, S.J. Pennycook, N.K. Dhar: The effect of As passivation on the molecular beam epitaxial growth of high-quality single-domain CdTe(111)B on Si(111) substrates, *Appl. Phys. Lett.* **75**, 349–351 (1999)
- 32.221 M. Jaime-Vasquez, M. Martinka, R.N. Jacobs, M. Groenert: In situ spectroscopic study of the As and Te on the Si(112) surface for high-quality epitaxial layers, *J. Electron. Mater.* **35**, 1455–1460 (2006)
- 32.222 P. Sen, I.P. Batra, S. Sivananthan, C.H. Grein, N.K. Dhar, S. Ciraci: Electronic structure of Te- and As-covered Si(211), *Phys. Rev. B* **68**, 045314 (2003)
- 32.223 Y.P. Chen, G. Brill, N.K. Dhar: MBE growth of Cd-SeTe/Si composite substrate for long-wavelength IR HgCdTe applications, *J. Cryst. Growth* **252**, 270–274 (2003)
- 32.224 M. Boukerche, P.S. Wijewarnasuriya, S. Sivananthan, I.K. Sou, Y.J. Kim, K.K. Mahavadi, J.P. Faurie: The doping of mercury cadmium telluride grown by molecular-beam epitaxy, *J. Vac. Sci. Technol. A* **6**, 2830–2833 (1988)
- 32.225 P.S. Wijewarnasuriya, M.D. Lange, S. Sivananthan, J.P. Faurie: Carrier recombination in indium-doped HgCdTe(211)B epitaxial layers grown by molecular beam epitaxy, *J. Appl. Phys.* **75**, 1005–1009 (1994)
- 32.226 M. Boukerche, P.S. Wijewarnasuriya, J. Reno, I.K. Sou, J.P. Faurie: Electrical properties of molecular beam epitaxy produced mercury cadmium telluride layers doped during growth, *J. Vac. Sci. Technol. A* **4**, 2072–2076 (1986)
- 32.227 M.L. Wroge, D.J. Peterman, B.J. Feldman, B.J. Morris, D.J. Leopold, J.G. Broerman: Impurity doping of mercury telluride-cadmium telluride superlattices during growth by molecular-beam epitaxy, *J. Vac. Sci. Technol. A* **7**, 435–439 (1989)
- 32.228 C.A. Hoffman, J.R. Meyer, F.J. Bartoli, Y. Lansari, J.W. Cook Jr., J.F. Schetzina: Electron mobilities and quantum Hall effect in modulation-doped mercury telluride/cadmium telluride superlattices, *Phys. Rev. B* **44**, 8376–8379 (1991)
- 32.229 K.A. Harris, T.H. Myers, R.W. Yanka, L.M. Mohnkern, N. Otsuka: A high quantum efficiency in situ doped midwavelength infrared p-on-n homojunction superlattice detector grown by photoassisted molecular-beam epitaxy, *J. Vac. Sci. Technol. B* **9**, 1752–1758 (1991)
- 32.230 A. Sher, M.A. Berding, M. Van Schilfgaarde, A.B. Chen: HgCdTe status review with emphasis on correlations, native defects and diffusion, *Semicond. Sci. Technol.* **6**, C59–C70 (1991)
- 32.231 P. Boieriu, C.H. Grein, S. Velicu, J. Garland, C. Fulk, S. Sivananthan, A. Stoltz, L. Bubulac, J.H. Dinan: Effects of hydrogen on majority carrier transport and minority carrier lifetimes in long wavelength infrared HgCdTe on Si, *Appl. Phys. Lett.* **88**, 062106 (2006)
- 32.232 M.A. Berding, A. Sher, A.B. Chen: Mercury cadmium telluride, defect structure overview, *Mater. Res. Soc. Symp. Proc.* **216**, 3–10 (1991)
- 32.233 M.A. Berding, A. Sher, M. Van Schilfgaarde: Behavior of p-type dopants in (Hg,Cd)Te, *J. Electron. Mater.* **26**, 625–628 (1997)
- 32.234 R. Balcerak: Infrared material requirements for the next generation of systems, *Semicond. Sci. Technol.* **6**, C1–C5 (1991)
- 32.235 P.A. Bakhitin, S.A. Dvoretiskii, V.S. Varavin, A.P. Korabkin, N.N. Mikhailov, I.V. Sabanina, Y.G. Sidorov: Effect of low-temperature annealing on electrical properties of n-HgCdTe, *Semiconductors* **38**, 1172–1175 (2004)
- 32.236 P.S. Wijewarnasuriya, M.D. Lange, S. Sivananthan, J.P. Faurie: Minority carrier lifetime in Indium-doped HgCdTe(211)B epitaxial layers grown by molecular beam epitaxy, *J. Electron. Mater.* **24**, 545–549 (1995)
- 32.237 D.L. Polla, R.L. Aggarwal, D.A. Nelson, J.F. Shanley, M.B. Reine: Mercury vacancy related lifetime in mercury cadmium telluride ($\text{Hg}_{0.68}\text{Cd}_{0.32}\text{Te}$) by optical modulation spectroscopy, *Appl. Phys. Lett.* **43**, 941–943 (1983)
- 32.238 M.E. d'Souza, M. Boukerche, J.P. Faurie: Minority-carrier lifetime in p-type (111)B mercury cadmium telluride grown by molecular-beam epitaxy, *J. Appl. Phys.* **68**, 5195–5199 (1990)
- 32.239 R. Fastow, Y. Nemirowsky: The excess carrier lifetime in vacancy-doped and impurity-doped HgCdTe, *J. Vac. Sci. Technol. A* **8**, 1245–1250 (1990)
- 32.240 M. Boukerche, S. Sivananthan, P.S. Wijewarnasuriya, I.K. Sou, J.P. Faurie: Electrical properties of intrinsic p-type shallow levels in HgCdTe grown by molecular-beam epitaxy in the (111)B orientation, *J. Vac. Sci. Technol. A* **7**, 311–313 (1989)
- 32.241 M. Zandian, A.C. Chen, D.D. Edwall, J.G. Pasko, J.M. Arias: p-type arsenic doping of $\text{Hg}_{1-x}\text{Cd}_x\text{Te}$ by molecular beam epitaxy, *Appl. Phys. Lett.* **71**, 2815–2817 (1997)
- 32.242 M. Zandian, E. Goo: TEM investigation of defects in arsenic doped layers grown in-situ by MBE, *J. Electron. Mater.* **30**, 623–626 (2001)
- 32.243 M.A. Berding, A. Sher, M. van Schilfgaarde, A.C. Chen: Model for As activation, *J. Electron. Mater.* **27**, 605 (1998)
- 32.244 M.A. Berding, A. Sher: Amphoteric behavior of arsenic in HgCdTe, *Appl. Phys. Lett.* **74**, 685–687 (1999)
- 32.245 M.A. Berding, A. Sher: Arsenic incorporation during MBE growth of HgCdTe, *J. Electron. Mater.* **28**, 799–803 (1999)

- 32.246 H.R. Vydynath: Amphoteric behavior of group V mass action constants for lattice site transfers, *Semiconductors* **5**, S231 (1990)
- 32.247 S. Sivananthan, P.S. Wijewarnasuriya, F. Aqariden, H.R. Vydynath, M. Zandian, D.D. Edwall, J.M. Arias: Mode of arsenic incorporation in HgCdTe grown by MBE, *J. Electron. Mater.* **26**, 621–624 (1997)
- 32.248 P. Boieriu, C.H. Grein, H.S. Jung, J.W. Garland, V. Nathan: Arsenic activation in molecular beam epitaxy grown, in situ doped HgCdTe(211), *Appl. Phys. Lett.* **86**, 212106 (2005)
- 32.249 P.S. Wijewarnasuriya, S. Sivananthan: Arsenic incorporation in HgCdTe grown by molecular beam epitaxy, *Appl. Phys. Lett.* **72**, 1694–1696 (1998)
- 32.250 A.C. Chen, M. Zandian, D.D. Edwall, J.M. Arias, P.S. Wijewarnasuriya, S. Sivananthan, M.A. Berding, A. Sher: MBE Growth and characterization of in situ arsenic doped HgCdTe, *J. Electron. Mater.* **27**, 595–599 (1998)
- 32.251 J. Wu, F.F. Xu, Y. Wu, L. Chen, Y.Z. Wang, M.F. Yu, Y.M. Qiao, L. He: As-doping HgCdTe by MBE, *SPIE Proc.* **5640**, 637–646 (2005)
- 32.252 L.O. Bubulac, W.E. Tennant, D.S. Lo, D.D. Edwall, J.C. Robinson, J.S. Chen, G. Bostrup: Ion implanted junction formation in mercury cadmium telluride ($\text{Hg}_{1-x}\text{Cd}_x\text{Te}$), *J. Vac. Sci. Technol. A* **5**, 3166–3170 (1987)
- 32.253 L.O. Bubulac, D.D. Edwall, C.R. Viswanathan: Dynamics of arsenic diffusion in metalorganic chemical vapor deposited mercury cadmium telluride on gallium arsenide/silicon substrates, *AIP Conf. Proc.* **235**, 1695–1704 (1991)
- 32.254 L.O. Bubulac, D.D. Edwall, S.J.C. Irvine, E.R. Gertner, S.H. Shin: P-type doping of double layer mercury cadmium telluride for junction formation, *J. Electron. Mater.* **24**, 617–624 (1995)
- 32.255 P.S. Wijewarnasuriya, S.S. Yoo, J.P. Faurie, S. Sivananthan: P-doping with arsenic in (211)B HgCdTe grown by MBE, *J. Electron. Mater.* **25**, 1300–1305 (1996)
- 32.256 M.C. Chen, L. Colombo, J.A. Dodge, J.H. Tregilgas: The minority-carrier lifetime in doped and undoped p-type $\text{Hg}_{0.78}\text{Cd}_{0.22}\text{Te}$ liquid-phase epitaxy films, *J. Electron. Mater.* **24**, 539–544 (1995)
- 32.257 S.H. Shin, J.M. Arias, M. Zandian, J.G. Pasko, L.O. Bubulac, R.E. DeWames: Annealing effect on the p-type carrier concentration in low-temperature processed arsenic-doped HgCdTe, *J. Electron. Mater.* **22**, 1039–1047 (1993)
- 32.258 C.A. Merilainen, C.E. Jones: Deep centers in gold-doped mercury cadmium telluride, *J. Vac. Sci. Technol. A* **1**, 1637–1640 (1983)
- 32.259 M. Brown, A.F.W. Willoughby: Diffusion of gold and mercury self-diffusion in n-type Bridgman-grown mercury cadmium telluride ($\text{Hg}_{1-x}\text{Cd}_x\text{Te}$) ($x = 0.2$), *J. Vac. Sci. Technol. A* **1**, 1641–1645 (1983)
- 32.260 L.O. Bubulac, W.E. Tennant, R.A. Riedel, J. Bajaj, D.D. Edwall: Some aspects of lithium behavior in ion-implanted mercury cadmium telluride, *J. Vac. Sci. Technol. A* **1**, 1646–1650 (1983)
- 32.261 P.S. Wijewarnasuriya, I.K. Sou, Y.J. Kim, K.K. Mahavadi, S. Sivananthan, M. Boukerche, J.P. Faurie: Electrical properties of lithium-doped mercury cadmium telluride ($\text{Hg}_{1-x}\text{Cd}_x\text{Te}$)(100) by molecular beam, *Appl. Phys. Lett.* **51**, 2025–2027 (1987)
- 32.262 D.J. Peterman, M.L. Wroge, B.J. Morris, D.J. Leopold, J.G. Broerman: p-on-n heterojunctions of mercury cadmium telluride by molecular-beam epitaxy, controlled silver doping and compositional grading, *J. Appl. Phys.* **63**, 1951–1954 (1988)
- 32.263 A. Uedono, K. Ozaki, H. Ebe, T. Moriya, S. Tanigawa, K. Yamamoto, Y. Miyamoto: A study of native defects in Ag-doped HgCdTe by positron annihilation, *Jpn. J. Appl. Phys.* **36**, 6661–6667 (1997)
- 32.264 N. Tanaka, K. Ozaki, H. Nishino, H. Ebe, Y. Miyamoto: Electrical properties of HgCdTe epilayers doped with silver using an AgNO_3 solution, *J. Electron. Mater.* **27**, 579–582 (1998)
- 32.265 M. Chu, S. Terterian, P.C. Wang, S. Mesropian, H.K. Gurgenian, D.-S. Pan: Au-doped HgCdTe for infrared detectors and focal plane arrays, *SPIE Proc.* **4454**, 116–122 (2001)
- 32.266 Y. Selamet, A. Ciani, C.H. Grein, S. Sivananthan: Extrinsic p-type doping and analysis of HgCdTe grown by molecular beam epitaxy, *SPIE Proc.* **4795**, 8–16 (2002)
- 32.267 Y. Selamet, R. Singh, J. Zhao, Y.D. Zhou, S. Sivananthan, N.K. Dhar: Gold diffusion in mercury cadmium telluride grown by molecular beam epitaxy, *SPIE Proc.* **5209**, 67–74 (2003)
- 32.268 A.I. D'Souza, M.G. Stapelbroek, E.R. Bryan, J.D. Beck, M.A. Kinch, J.E. Robinson: Au- and Cu-doped HgCdTe HDVIP detectors, *SPIE Proc.* **5406**, 205–213 (2004)
- 32.269 A.J. Ciani, S. Ogut, I.P. Batra, S. Sivananthan: Diffusion of gold and native defects in mercury cadmium telluride, *J. Electron. Mater.* **34**, 868–872 (2005)
- 32.270 C.H. Grein, J.W. Garland, S. Sivanantuan, P.S. Wijewarnasuriya, M. Fuchs: Arsenic Incorporation in MBE Grown $\text{Hg}_{1-x}\text{Cd}_x\text{Te}$, *J. Electron. Mater.* **28**, 789–792 (1999)
- 32.271 H.F. Schaaake: Kinetics of activation of group V impurities in $\text{Hg}_{1-x}\text{Cd}_x\text{Te}$ alloys, *J. Appl. Phys.* **88**, 1765–1770 (2000)
- 32.272 D. Chandra, H.F. Schaaake, M.A. Kinch, F. Aqariden, C.F. Wan, D.F. Weirauch, H.D. Shih: Activation of arsenic as an acceptor in $\text{Hg}_{1-x}\text{Cd}_x\text{Te}$ under equilibrium conditions, *J. Electron. Mater.* **31**, 715–719 (2002)
- 32.273 T.S. Lee, J.W. Garland, C.H. Grein, M. Sumstine, A. Jandeska, Y. Selamet, L.S. Sirem: Correlation of arsenic incorporation and its electrical activation in MBE HgCdTe, *J. Electron. Mater.* **29**, 869 (2000)
- 32.274 H.R. Vydyanath, L.S. Lichtman, S. Sivananthan, P.S. Wijewarnasuriya, J.P. Faurie: Annealing ex-

- perimenta in heavily arsenic-doped (Hg,Cd)Te, *J. Electron. Mater.* **24**, 625–634 (1995)
- 32.275 L.O. Bubulac, D.D. Edwall, C.R. Viswanathan: Dynamics of arsenic diffusion in metalorganic chemical vapor deposition HgCdTe on GaAs/Si substrates, *J. Vac. Sci. Technol. B* **9**, 1695–1704 (1991)
- 32.276 P. Boieriu, Y. Chen, V. Nathan: Low-temperature activation of As in $\text{Hg}_{1-x}\text{Cd}_x\text{Te}$ (211) grown on Si by molecular beam epitaxy, *J. Electron. Mater.* **31**, 694–698 (2002)
- 32.277 J.W. Han, S. Hwang, Y. Lansari, R.L. Harper, Z. Yang, N.C. Giles, J.W. Cook, J.F. Schetzina, S. Sen: p-type modulation-doped HgCdTe, *Appl. Phys. Lett.* **54**, 63–65 (1989)
- 32.278 R.L. Harper, S. Hwang, N.C. Giles, J.F. Schetzina, D.L. Dreifus, T.H. Myers: Arsenic-doped CdTe epilayers grown by photoassisted molecular beam epitaxy, *Appl. Phys. Lett.* **54**, 170 (1989)
- 32.279 J.M. Arias, S.H. Shin, D.E. Cooper, M. Zandian, J.G. Pasko, E.R. Gertner, R.E. DeWames, J. Singh: p-type arsenic doping of cadmium telluride and mercury telluride/cadmium telluride superlattices grown by photoassisted and conventional molecular-beam epitaxy, *J. Vac. Sci. Technol. A* **8**, 1025–1033 (1990)
- 32.280 J. Arias, M. Zandian, J.G. Pasko, S.H. Shin, L.O. Bubulac, R.E. DeWames, W.E. Tennant: Molecular-beam epitaxy growth and in situ arsenic doping of p-on-n HgCdTe heterojunctions, *J. Appl. Phys.* **69**, 2143–2148 (1991)
- 32.281 O.K. Wu, G.S. Kamath, W.A. Radford, P.R. Bratt, E.A. Patten: Chemical doping of HgCdTe by molecular-beam epitaxy, *J. Vac. Sci. Technol. A* **8**, 1034–1038 (1990)
- 32.282 O.K. Wu, D.N. Jamba, G.S. Kamath: Growth and properties of In- and As-doped HgCdTe by MBE, *J. Cryst. Growth* **127**, 365–370 (1993)
- 32.283 S. Sivananthan, P.S. Wijewarnasuriya, J.P. Faurie: Recent progress in the doping of MBE HgCdTe, *SPIE Proc.* **2554**, 55–68 (1995)
- 32.284 P.S. Wijewarnasuriya, F. Aqariden, C.H. Grein, J.P. Faurie, S. Sivananthan: p-type doping with arsenic in (211)B HgCdTe grown by MBE, *J. Cryst. Growth* **175**, 647–652 (1997)
- 32.285 P.S. Wijewarnasuriya, S. Sivananthan: Arsenic incorporation in HgCdTe grown by molecular beam epitaxy, *Appl. Phys. Lett.* **72**, 1694–1696 (1998)
- 32.286 F. Aqariden, P.S. Wijewarnasuriya, S. Sivananthan: Arsenic incorporation in HgCdTe grown by molecular beam epitaxy, *J. Vac. Sci. Technol. B* **16**, 1309–1311 (1998)
- 32.287 Y. Chang, G. Badano, E. Jiang, J.W. Garland, J. Zhao, C.H. Grein, S. Sivananthan: Composition and thickness distribution of HgCdTe molecular beam epitaxy wafers by infrared microscope mapping, *J. Cryst. Growth* **277**, 78–84 (2005)
- 32.288 A.R. Beattie, P.T. Landsberg: Auger effect in semiconductors, *Proc. R. Soc. Lond. Ser. A* **249**, 16–29 (1959)
- 32.289 J.S. Blakemore: *Semiconductor Statistics* (Pergamon, New York 1962), Chap. 6
- 32.290 V.C. Lopes, A.J. Syllaios, M.C. Chen: Minority carrier lifetime in mercury cadmium telluride, *Semicond. Sci. Technol.* **8**, 824–842 (1993), and ref. cit.
- 32.291 W. Shockley, W.T. Read: Statistics of the recombinations of holes and electrons, *Phys. Rev.* **87**, 835–842 (1952)
- 32.292 R.N. Hall: Electron-hole recombination in germanium, *Phys. Rev.* **87**, 387 (1952)
- 32.293 C.H. Swartz, S. Chandril, R.P. Tompkins, N.C. Giles, T.H. Myers, D.D. Edwall, E.C. Piquette, C.S. Kim, I. Vurgaftman, J.R. Meyer: Accurate measurement of composition, carrier concentration, and photoconductive lifetime in $\text{Hg}_{1-x}\text{Cd}_x\text{Te}$ grown by molecular beam epitaxy, *J. Electron. Mater.* **35**, 1360–1368 (2006)
- 32.294 Y. Chang, J.W. Garland, S. Sivananthan: Infrared optical characterization of the narrow gap semiconductor HgCdTe. In: *Advanced Materials in Electronics*, ed. by Q. Guo (Research Signpost, Trivandrum 2004) pp. 249–264
- 32.295 Y. Chang, G. Badano, J. Zhao, Y.D. Zhou, R. Ashokan, C.H. Grein, V. Nathan: Near-bandgap infrared absorption properties of HgCdTe, *J. Electron. Mater.* **33**, 709–713 (2004)
- 32.296 F. Urbach: The long-wavelength edge of photographic sensitivity and of the electronic absorption of solids, *Phys. Rev.* **92**, 1324 (1953)
- 32.297 C.H. Grein, S. John: Temperature dependence of the Urbach optical absorption edge: A theory of multiple phonon absorption and emission sidebands, *Phys. Rev. B* **39**, 1140–1151 (1989)
- 32.298 M. Carmody, D. Lee, M. Zandian, J. Phillips, J. Arias: Threading and misfit dislocation motion in molecular-beam epitaxy-grown HgCdTe epilayers, *J. Electron. Mater.* **32**, 710–716 (2003)
- 32.299 T. Aoki, D.J. Smith, Y. Y. J. Zhao, G. Badano, C.H. Grein, S. Sivananthan: Mercury cadmium telluride/tellurium intergrowths in HgCdTe epilayers grown by molecular beam epitaxy, *Appl. Phys. Lett.* **82**, 2275–2277 (2003)
- 32.300 I.V. Sabinina, A.K. Gutakovsky, Y.G. Sidorov, A.V. Latyshev: Nature of V-shaped defects in HgCdTe epilayers grown by molecular beam epitaxy, *J. Cryst. Growth* **274**, 339–346 (2005)
- 32.301 T. Aoki, Y. Chang, G. Badano, J. Zhao, C.H. Grein, S. Sivananthan, D.J. Smith: Electron microscopy of surface-crater defects on HgCdTe/CdZnTe(211)B epilayers grown by molecular beam epitaxy, *J. Electron. Mater.* **32**, 703–709 (2003)
- 32.302 M. Zandian, J.M. Arias, J. Bajaj, J.G. Pasko, L.O. Bubulac, R.E. DeWames: Origin of void defects in $\text{Hg}_{1-x}\text{Cd}_x\text{Te}$ grown by molecular beam epitaxy, *J. Electron. Mater.* **24**, 1207–1210 (1995)

- 32.303 J.B. Varesi, A.A. Buell, J.M. Peterson, R.E. Bornfreund, M.F. Vilela, W.A. Radford, S.M. Johnson: Performance of molecular-beam epitaxy-grown midwave infrared HgCdTe detectors on four-inch Si substrates and the impact of defects, *J. Electron. Mater.* **32**, 661–666 (2003)
- 32.304 J.N. Schulman, T.C. McGill: The CdTe/HgTe superlattice: Proposal for a new infrared material, *Appl. Phys. Lett.* **34**, 663–665 (1979)
- 32.305 D. Chandra, F. Aquariden, J. Frazier, S. Gutzler, T. Orent, H.D. Shih: Isolation and control of voids and void-hillocks during molecular beam epitaxial growth of HgCdTe, *J. Electron. Mater.* **29**, 887–892 (2000)
- 32.306 J.P. Faurie, A. Million, J. Piagnet: CdTe–HgTe multilayers grown by molecular beam epitaxy, *Appl. Phys. Lett.* **41**, 713–715 (1982)
- 32.307 K.A. Harris, R.W. Yanka, L.M. Mohnkern, A.R. Reisinger, T.H. Myers, Z. Yang, Z. Yu, S. Hwang, J.F. Schetzina: Properties of (211)B HgTe–CdTe superlattices grown by photon assisted molecular-beam epitaxy, *J. Vac. Sci. Technol. B* **10**, 1574–1581 (1992)
- 32.308 J.P. Faurie: Growth and properties of HgTe–CdTe and other Hg-based superlattices, *IEEE J. Quantum Electron.* **QE-22**, 1656–1665 (1986)
- 32.309 J.P. Faurie, J. Reno, M. Boukerche: II–VI semiconductor compounds: New superlattice systems for the future?, *J. Cryst. Growth* **72**, 111–116 (1985)
- 32.310 D.K. Arch, J.L. Staudenmann, J.P. Faurie: Layer intermixing in HgTe–CdTe superlattices, *Appl. Phys. Lett.* **48**, 1588–1590 (1986)
- 32.311 K. Zanio: The effect of interdiffusion on the shape of HgTe/CdTe superlattices, *J. Vac. Sci. Technol. A* **4**, 2106–2109 (1986)
- 32.312 D.J. Leopold, J.G. Broerman, D.J. Peterman, M.L. Wroge: Effect of annealing on the optical properties of HgTe–CdTe superlattices, *Appl. Phys. Lett.* **52**, 969–971 (1988)
- 32.313 Y. Kim, A. Ourmazd, M. Bode, R.D. Feldman: Nonlinear diffusion in multilayered semiconductor systems, *Phys. Rev. Lett.* **63**, 636–639 (1989)
- 32.314 S. Holander-Gleixner, H.G. Robinson, C.R. Helms: Simulation of HgTe/CdTe interdiffusion using fundamental point diffusion mechanisms, *J. Electron. Mater.* **27**, 672–679 (1998)
- 32.315 Y. Selamet, Y.D. Zhou, J. Zhao, Y. Chang, C.R. Becker, R. Ashokan, C.H. Grein, S. Sivananthan: HgTe/HgCdTe superlattices grown on CdTe/Si by molecular beam epitaxy for infrared detection, *J. Electron. Mater.* **33**, 503–508 (2004)
- 32.316 J.P. Faurie, S. Sivananthan, J. Reno: Present status of molecular beam epitaxial growth and properties of HgTe–CdTe superlattices, *J. Vac. Sci. Technol. A* **4**, 2096–2100 (1986)
- 32.317 T.C. McGill, G.Y. Wu, S.R. Hetzler: Superlattices: Progress and prospects, *J. Vac. Sci. Technol. A* **4**, 2091–2095 (1986)
- 32.318 C.A. Hoffman, J.R. Meyer, F.J. Bartoli, Y. Lansari, J.W. Cook Jr., J.F. Schetzina: Electron mobilities and quantum Hall effect in modulation-doped HgTe–CdTe superlattices, *Phys. Rev. B* **44**, 8376–8379 (1991)
- 32.319 J.M. Arias, S.H. Shin, D.E. Cooper, M. Zandian, J.G. Pasko, E.R. Gertner, R.E. DeWames: p-type arsenic doping of CdTe and HgTe/CdTe superlattices grown by photoassisted and conventional molecular-beam epitaxy, *J. Vac. Sci. Technol. A* **8**, 1025–1033 (1990)
- 32.320 C.R. Becker, L. He, M.M. Regnet, M.M. Kraus, Y.S. Wu, G. Landwehr, X.F. Zhang, H. Zhang: The growth and structure of short period (001) Hg_{1-x}Cd_xTe–HgTe superlattices, *J. Appl. Phys.* **74**, 2486–2493 (1993)
- 32.321 A. Rogalski, M. Kimata, V.F. Kocherov, J. Piotrowski, F.F. Sizov, I.I. Taubkin, N. Tubouchi, N.B. Zaletaev: *Infrared Photon Detectors* (SPIE Optical Engineering Press, Bellingham 1995)
- 32.322 P.R. Bratt, T.N. Casselman: Potential barriers in HgCdTe heterojunctions, *J. Vac. Sci. Technol. A* **3**, 238–245 (1985)
- 32.323 M.A. Kinch, F. Aqariden, D. Chandra, P.K. Liao, H.F. Schaaake, H.D. Shih: Minority carrier lifetime in p–HgCdTe, *J. Electron. Mater.* **34**, 880–884 (2005)
- 32.324 S. Velicu, R. Ashokan, C.H. Grein, S. Sivananthan, P. Boieriu, D. Rafol: High-temperature HgCdTe/CdTe/Si infrared photon detectors by MBE, *SPIE Proc.* **4454**, 180–187 (2001)
- 32.325 J.F. Piotrowski, A. Rogalski: *High-Operating-Temperature Infrared Photodetectors* (SPIE Optical Engineering, Bellingham 2007)

33. Metalorganic Vapor-Phase Epitaxy of Diluted Nitrides and Arsenide Quantum Dots

Udo W. Pohl

Metalorganic vapor-phase epitaxy offers the ability for controlled layer deposition down to the monolayer range. Versatile application in a wide range of materials and its upscaling ability has established this growth technique in industrial mass production, particularly in the field of semiconductor devices. A topic of current research is the extension of the well-developed GaAs-based technology to the near-infrared spectral range for optoelectronic applications. The complementary approaches of either employing dilute nitrides quantum wells or quantum dots have recently achieved significant advances in the field of laser diodes. This chapter introduces the basics of metalorganic vapor-phase epitaxy and illustrates current issues in the growth of InGaAsN/GaAs quantum wells and InAs/GaAs quantum dots. Section 33.1 gives a brief introduction to the growth technique, exemplified by the classical GaAs epitaxy. Sections 33.2 and 33.3 address two current topics of GaAs-related MOVPE, which are

33.1	Principle of MOVPE	1133
33.1.1	MOVPE Precursors	1133
33.1.2	Growth Process	1135
33.2	Diluted Nitride InGaAsN Quantum Wells ..	1137
33.2.1	Nitrogen Precursors	1138
33.2.2	Structural and Electronic Properties of InGaAsN	1139
33.2.3	Dilute Nitride Quantum Well Lasers ..	1141
33.3	InAs/GaAs Quantum Dots	1142
33.3.1	The Stranski-Krastanow 2-D-3-D Transition	1142
33.3.2	MOVPE of InAs Quantum Dots	1144
33.3.3	Quantum Dot Lasers	1147
33.4	Concluding Remarks	1148
	References	1148

intensely studied for, e.g., datacom laser applications: Epitaxy of dilute nitrides and InGaAs quantum dots.

33.1 Principle of MOVPE

Metalorganic vapor-phase epitaxy (MOVPE), also termed metalorganic chemical vapor deposition (MOCVD; sometimes O and M in the acronyms are exchanged), is the most frequently applied CVD technique for semiconductor device fabrication. Industrial large-scale reactors presently have the capacity for simultaneous deposition on 50 2-inch wafers, and the majority of advanced semiconductor devices are produced using this technique. Applications of MOVPE are not restricted to semiconductors, but also include oxides, metals, and organic materials. The technique emerged in the 1960s [33.1–4], when epitaxy was dominated by liquid-phase epitaxy and chloride vapor-phase epitaxy, and molecular-beam epitaxy (MBE) did not ex-

ist in its present form. Complex sample structures with abrupt interfaces and excellent uniformity may today be fabricated using either MOVPE or MBE, though application of MOVPE is advantageous in realizing graded layers or in As-P alloys and nitride materials.

33.1.1 MOVPE Precursors

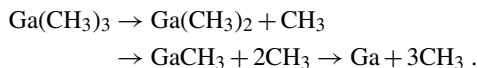
A common feature of chemical vapor-phase techniques is the transport of the constituent elements in the gas phase to the vapor-solid interface in the form of volatile molecules. In MOVPE these species consist of metalorganic compounds, and the transport is made by a carrier gas such as hydrogen at typically 100 mbar total pres-

sure. The gaseous species dissociate thermally at the growing surface of the heated substrate, thereby releasing the elements for layer growth. The dissociation at the surface is generally assisted by chemical reactions.

The net reaction for the MOVPE of GaAs using the standard source compounds trimethylgallium and arsine reads



The reaction is actually much more complicated and comprises many successive steps and species in the chemistry of deposition [33.6] such as, e.g., some steps of precursor decomposition



The source compounds employed for MOVPE must meet some basic requirements. Their stability is low to allow decomposition in the process, but still sufficient for long-term storage. Furthermore their volatility should be high, and a liquid state is favorable to provide a steady-state source flow. Most source molecules have the form MR_n , where M denotes the element used for MOVPE, and R are alkyls such as methyl CH_3 . By choosing a suitable organic ligand, the bond strength to a given element M can be selected to comply with the requirements of MOVPE for the solid to be grown. The metal–carbon bond strength depends on the electronegativity of the metal M and the size and configuration of the ligand R [33.7]. As a rule of thumb the bond strength decreases as the number of carbons bonded to the central carbon in the alkyl is increased. This trend is also reflected in the dissociation energy of the first carbon–hydrogen bond, given in Table 33.1 [33.8].

The organic radicals R most frequently used for MOVPE precursors are depicted in Fig. 33.1.

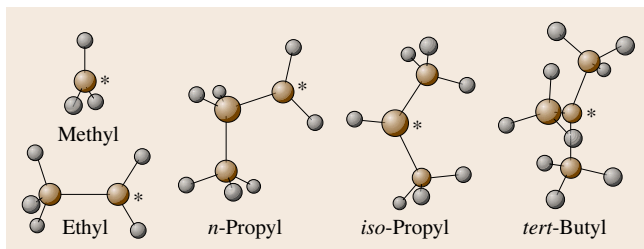


Fig. 33.1 Alkyl radicals used as organic ligands in MOVPE source molecules. Brown and gray spheres represent carbon and hydrogen atoms, respectively, and the location of a bond to an element M used for epitaxy is indicated by an asterisk

Table 33.1 Dissociation energy of the carbon–hydrogen bond for radicals R used in MOVPE source molecules

R	E (kJ/mol)	R	E (kJ/mol)
Methyl	435	iso-Propyl	398
Ethyl	410	tert-Butyl	381
n-Propyl	410	Allyl	368

Besides metalorganic sources also hydrides such as arsine are employed as precursors. Their use is interesting since they release hydrogen radicals under decomposition that can assist removal of carbon-containing radicals from the surface. A major obstacle is their high toxicity and their very high vapor pressure, requiring extensive safety precautions. To reduce the hazardous potential, hydrides are increasingly replaced by metalorganic alternatives, e.g., arsine by tertiarybutylarsine, where one of the three hydrogen radicals is replaced by a tertiarybutyl radical. Thereby the vapor pressure is strongly reduced, yielding usually liquids at ambient conditions. In addition the toxicity decreases significantly.

Partial pressures for some standard precursors used in the MOVPE of As-related III–V semiconductors are given in Table 33.2. The values are expressed in terms of the parameters a and b to account for the exponential temperature dependence of the vapor pressure according to

$$\log(P_{\text{eq MO}}) = a - b/T, \quad (33.2)$$

$P_{\text{eq MO}}$ and T given in Torr and K, respectively. Hydrides AsH_3 and PH_3 are stored at 20 °C as liquids under pressures of 11 250 and 26 250 Torr, respectively, and introduced as gases to the MOVPE setup.

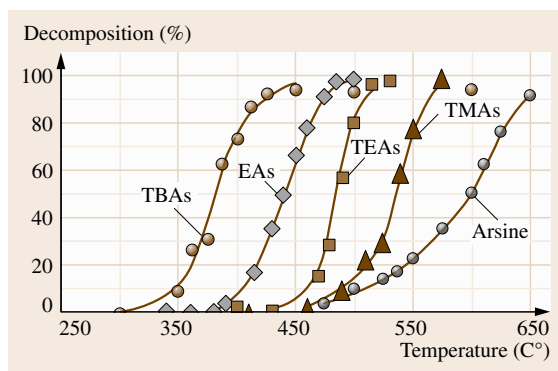


Fig. 33.2 Decomposition of As precursors; the labels TBAs, EAs, TEAs, and TMAs denote *tert*-butyl-As, ethyl-As, triethyl-As, and trimethyl-As, respectively [33.5]

Table 33.2 Equilibrium vapor pressure data of some metalorganic compounds used for III–V MOVPE. (Vapor pressure data taken from data sheets of several precursor suppliers.)

Element	Precursor	Vapor pressure		
		<i>a</i>	<i>b</i> (K)	<i>P</i> _{eq MO} (Torr) at 20 °C
Al	Trimethylaluminum	8.224	2135	8.7
Ga	Trimethylgallium	8.07	1703	182
	Triethylgallium	8.083	2162	5.1
In	Trimethylindium	10.520	3014	1.7
P	Tertiarybutylphosphine	7.586	1539	142 (10 °C)
As	Tertiarybutylarsine	7.243	1509	81 (10 °C)
Sb	Trimethylantimony	7.708	1697	83
	Triethylantimony	7.904	2183	2.9
N	Dimethylhydrazine	8.646	1921	123

Note: 1 Torr = 1.333 mbar

Precursor molecules may decompose by a number of pyrolytic mechanisms, the most simple being free-radical homolysis, i. e., simple bond cleavage. Since the M–H bond is generally stronger than the M–C bond, metalorganic alternatives of the stable hydrides decompose at lower temperatures – a further incentive for their use. Results of pyrolysis studies for various As precursors, performed in an isothermal flow tube, are given in Fig. 33.2. The bond strength rule of thumb noted above is well reflected in these curves.

33.1.2 Growth Process

Most metalorganic sources are liquids, which are stored in bubblers. For transport to the reactor a carrier gas with a flow Q_{MO} is introduced by a dip tube ending near the bottom. At a fixed temperature the metalorganic liquid forms an equilibrium vapor pressure $P_{\text{eq MO}}$ given by (33.2), and the bubbles saturate with precursor molecules. At the outlet port of the bubbler a pressure controller is installed, which acts like a pressure relief valve and allows to define a fixed pressure P_{bub} ($> P_{\text{eq MO}}$) in the bubbler, thereby decoupling the bubbler pressure from the total pressure P_{tot} in the reactor. The partial pressure of a metalorganic source in the reactor P_{MO} results from the mentioned parameters by

$$P_{\text{MO}} = \frac{Q_{\text{MO}}}{Q_{\text{tot}}} \times \frac{P_{\text{tot}}}{P_{\text{bub}}} \times P_{\text{eq MO}}. \quad (33.3)$$

The two fractions in (33.3) are employed to control the partial pressure of the source in the reactor. For sources used as dopants or compounds with very high vapor pressures an additional dilution by mixing with a controlled flux of carrier gas is applied. The gaseous

hydrides are directly controlled by their flux Q_{Hyd} , and (33.3) simplifies to

$$P_{\text{Hyd}} = \frac{Q_{\text{Hyd}}}{Q_{\text{tot}}} \times P_{\text{tot}}. \quad (33.4)$$

The total flux in the reactor Q_{tot} results from the sum of all component fluxes and the flux of the carrier gas, which is additionally introduced into the reactor by a separate mass flow controller. This flux is generally much higher than that of all sources, and the sum of all source partial pressures P_{MO} and P_{Hyd} is consequently much smaller than the total pressure in the reactor P_{tot} . The reactor pressure P_{tot} is controlled as an independent parameter by a control valve attached to an exhaust pump behind the reactor.

The complete treatment of the MOVPE growth process involves numerous gas-phase and surface reactions, in addition to hydrodynamic aspects. Such complex studies require a numerical approach, and solutions were developed for specific processes such as MOVPE of GaAs from trimethylgallium and arsine [33.6, 9]. We will draw a more general picture of the growth process and outline some relations of growth parameters.

Growth represents a nonequilibrium process. The driving force is given by a drop in the chemical potential μ from the input phase to the solid. For the discussion of the MOVPE process a description by consecutive steps as depicted in Fig. 33.3 is convenient. The reactants in the carrier gas represent the source. Near the solid surface a vertical diffusive transport component originates from reactions of source molecules and incorporation into the growing layer. All processes from adsorption at the surface to the incorporation are sum-

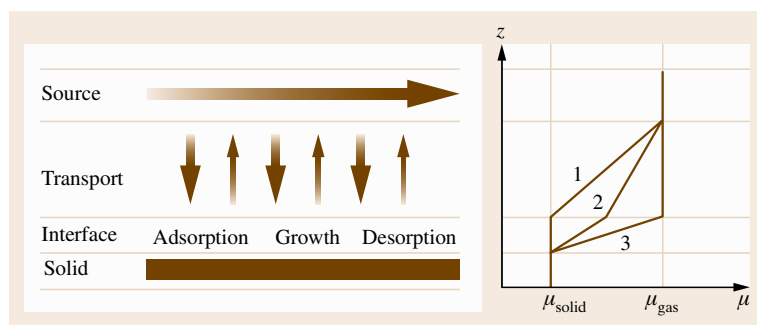


Fig. 33.3 Scheme of the chemical potential μ near the surface of the growing solid during MOVPE. Path 1 signifies growth controlled by mass transport, paths 3 and 2 denote growth being limited by interface reactions and the general case, respectively

marized by interface reactions. Finally excess reaction products desorb from the interface by diffusion.

The slowest process of the successive steps limits the growth rate. Without considering mechanisms of growth in detail, processes limited by either transport or kinetics can be well distinguished. Figure 33.4 shows on a logarithmic scale the dependence of the GaAs growth rate on the reciprocal substrate temperature. At low temperature, experiment and simulation show an exponential relation, indicating that thermally activated processes limit the growth rate. Precursor decomposition and interface growth reactions lead to a pronounced temperature dependence, the slope $\propto -\Delta E/(k_B T)$ yields an activation energy ΔE near

19 kcal/mole for the given process. This regime is referred to as *kinetically limited growth*. The gas phase supplies precursors to the surface at a rate well exceeding the rate of growth reactions. As the temperature is increased, the growth rate becomes nearly independent of temperature. In this range precursor decomposition and surface reactions are much faster than mass transport from the source to the interface of the growing solid. Since diffusion in the gas phase depends only weakly on temperature, this process is called *transport-limited growth*. Mass transport in this regime depends on the geometry of the reactor, because flow field and temperature profile above the substrate affect cracking and arrival of precursors at the interface; this accounts for the difference in the maximum growth rates in Fig. 33.4. In the high temperature range growth rates decrease due to enhanced desorption and parasitic deposition at the reactor walls, inducing a depletion of the gas phase.

MOVPE is usually performed in the mid-temperature range of transport-limited growth, where variations of the substrate temperature have only a minor effect on growth rate, composition of alloys, and doping. For III–V semiconductors the range is typically 500–800 °C.

Mass transport of the reactants from the gas source to the interface of the growing solid are essentially controlled by diffusion: The mass flow j_i of component i is given by the direct flow component v normal to the interface, the diffusion along the partial pressure gradient $\partial P_i / \partial r$, and the thermodiffusion, according to [33.11]

$$j_i = \frac{P_i v}{k_B T} - \frac{D_i}{k_B T} \left(\frac{\partial}{\partial r} P_i + \frac{\alpha_i}{T} P_i \frac{\partial}{\partial r} T \right), \quad (33.5)$$

where D_i and α_i are the diffusion constant and the thermodiffusion factor, respectively. The direct flow component normal to the interface should be negligible in a laminar gas flow. Also thermodiffusion is

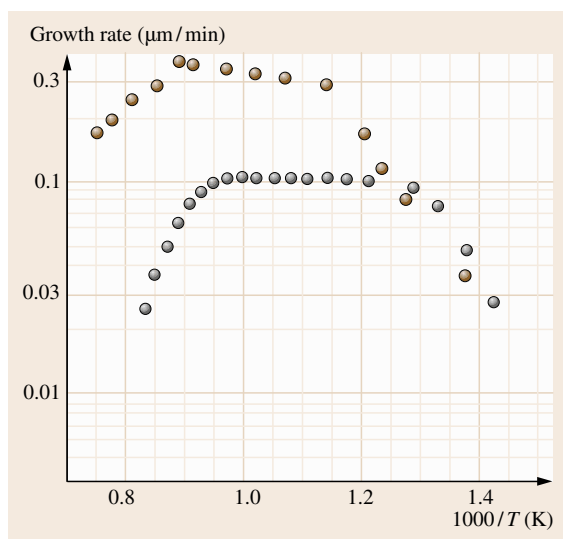


Fig. 33.4 Growth rate of (001)-oriented GaAs as a function of reciprocal temperature. Trimethylgallium and arsine are used as precursors. Brown and gray circles represent measured data [33.10] and model predictions [33.6], respectively

generally assumed to make no sizeable contribution. Equation (33.5) is hence reduced to the diffusion term.

A simplified one-dimensional model assumes that the partial pressures P_i drop over a so-called diffusion boundary layer of thickness d from their values in the source to values $P_i^{\text{interface}}$ at the interface to the solid [33.7]. Equation (33.5) then reduces to

$$j_i = \frac{D_i}{k_B T d} (P_i - P_i^{\text{interface}}). \quad (33.6)$$

The factor $D_i/(k_B T d)$ may be considered as an effective coefficient of mass transport for component i .

Due to the supersaturation set to induce growth, the partial pressures of the components at the inlet of the reactor P_i are much higher than the near-equilibrium values at the interface to the solid $P_i^{\text{interface}}$. For III–V compounds such as GaAs this means $P_{\text{III}} P_V \gg P_{\text{III}}^{\text{interface}} P_V^{\text{interface}}$. Furthermore, the group V precursors are far more volatile than the group III species (except for Sb sources); III–V semiconductors are hence usually grown with a large excess of group V species, i. e., $P_V/P_{\text{III}} \gg 1$. These conditions and the requirement of stoichiometric growth lead to the relations of the partial pressures at the interface and the reactor inlet $P_{\text{III}}^{\text{interface}} \ll P_{\text{III}}$, and $P_V^{\text{interface}} \approx P_V$. This means that the growth rate is limited by the flow of group III species, and all group III species arriving at the interface are incorporated into the solid. Equation (33.6) then further reduces to

$$j_{\text{III}} = \frac{D_{\text{III}} P_{\text{III}}}{k_B T d}. \quad (33.7)$$

The transport properties expressed by (33.7) may be related to other growth parameters by applying the *boundary-layer model*. Though being oversimplified, this model provides a reasonable description of basic relations. The model assumes a horizontal flow reactor and considers, that the velocity component of the gas

flow parallel to the substrate must be zero at the interface due to friction. In a distance δ above the substrate the velocity flow arrives at a constant value v . The range of δ was interpreted in terms of a stagnant layer for the mass transport to the interface δ may be written [33.7]

$$\delta \cong 5 \sqrt{\frac{D}{v}}. \quad (33.8)$$

Substituting d in (33.7) by δ and bearing in mind that the diffusion constant D in the gas phase is inversely proportional to the total pressure P_{tot} , yields for the growth rate

$$r = \text{const } P_{\text{III}} \sqrt{\frac{v}{P_{\text{tot}}}}. \quad (33.9)$$

The growth rate shows the proportional dependence on the partial pressure of the group III species already expressed by (33.7). According to (33.3), r is hence proportional to the flow of carrier gas through the bubbler Q_{MO} of the group III source. Equation (33.9) predicts a growth rate that is independent of the total reactor pressure, because both P_{III} (cf., (33.3)) and v (inversely proportional to P_{tot}) are functions of P_{tot} . Moreover, the model yields a square-root decrease of the growth rate as the total flow in the reactor Q_{tot} is increased. Deviations from these reasonable predictions are observed at low pressures and low flow velocities, where the boundary-layer thickness is in the range of the reactor height.

The outline of metalorganic vapor-phase epitaxy given above is intended to provide an insight into the basics of the growth technique. Albeit being established in many fields of materials fabrication, new areas of application are steadily developed. Even the classical GaAs-related materials are widely studied to further extend applications, and two current topics are considered in the following sections.

33.2 Diluted Nitride InGaAsN Quantum Wells

The quaternary dilute nitride alloy InGaAsN (or GINA, GaInNAs), which can be grown lattice-matched to GaAs substrates, has recently gained considerable attention as a promising material for laser diodes in the datacom wavelength range. The constituent binaries GaAs and GaN have large differences in electronegativities and lattice constants, leading to an extraordinary large bowing parameter in GaAsN alloys and a strong bandgap decrease for even small N compositions. The

same applies for the In-related binaries, cf. Fig. 33.5; in this connection it must be noted that the InN bandgap energy is still controversial, but serious indications exist for a gap near or below 1 eV [33.12–14]. Large band offsets between InGaAsN and GaAs provide the opportunity for good carrier confinement in quantum structures. The attractive quaternary compound is, however, metastable, and introduction of nitrogen is difficult due to a large miscibility gap. Furthermore, intrinsic

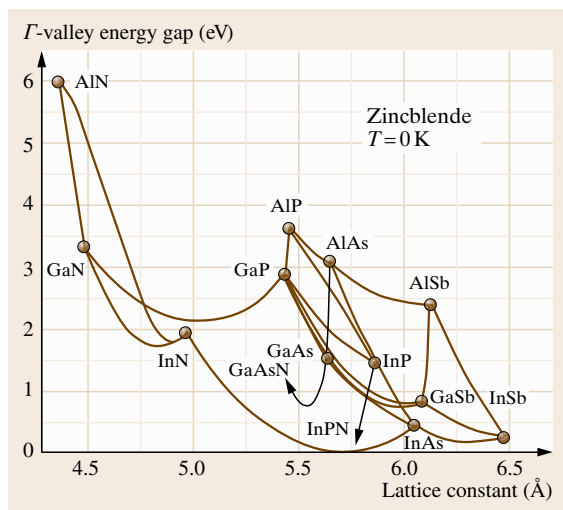


Fig. 33.5 Direct energy gap as a function of lattice constant for zincblende III–V compounds and their alloys; arrows indicate limits for predictions with any accuracy [33.15]. For InN more recently a value of 0.78 eV was given [33.13]

regions of high strain and strong localization result from the large differences in lattice parameters and the large energy range induced by statistical composition fluctuations. However, significant advances have been achieved by applying epitaxy at rather low temperatures. This section addresses the issue of suitable precursors for MOVPE of InGaAsN, the materials properties of epitaxial layers on GaAs substrate, and eventually the current state of laser device applications.

33.2.1 Nitrogen Precursors

The small covalent radius of nitrogen leads to very small solubilities in the conventional III–V compound semiconductors GaAs and InAs, predicted to be only 10^{14} cm^{-3} and 10^{17} cm^{-3} , respectively, at typical growth temperatures [33.17]. To increase the N concentration well above the equilibrium solubility limit, the temperature is lowered to achieve metastable nonequilibrium growth in the range between the concentrations of the spinodal and the stable binodal limit. The latter was determined to be below 2% at 800 K for GaN in GaAs [33.18].

The standard nitrogen source for GaN-related group III nitride semiconductors is ammonia (NH_3). Since dissociation of ammonia in MOVPE requires very high growth temperatures, alternative precursors

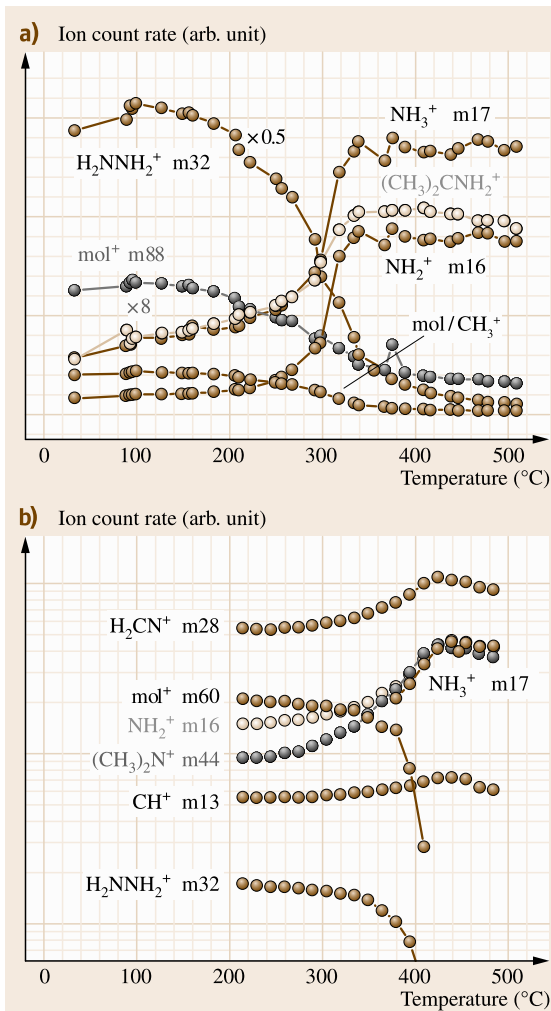


Fig. 33.6a,b Thermal decomposition of the nitrogen sources *tert*-butylhydrazine ((a), mass 88) and dimethylhydrazine ((b), mass 60), measured by mass spectrometry in an isothermal reaction tube [33.16]

are required for epitaxy of dilute nitride alloys. Hydrazine (H_2NNH_2) is much less stable than ammonia, has a convenient vapor pressure, and provides reactive nitrogen by N–N bond cleavage at temperatures as low as 400 °C. Though low-temperature growth of GaN was proved [33.19], this source is not used due to its toxicity and very high reactivity. Instead, derivatives with one [33.20] or two methyl [33.21, 22] or with tertiarybutyl [33.23, 24] ligands were introduced. Comparative pyrolysis studies of dimethylhydrazine $(\text{CH}_3)_2\text{NNH}_2$ and tertiarybutylhydrazine $(\text{C}_4\text{H}_9)(\text{H})\text{NNH}_2$ demon-

strated that both sources decompose below 400 °C by N–N bond cleavage, enabling low-temperature nitride growth [33.16]. As shown in Fig. 33.6, decomposition of both precursors produce reactive NH_2 radicals (mass 16) required for the growth process.

Dimethylhydrazine, more precisely (1,1)-dimethylhydrazine with both methyl radicals attached to one nitrogen (also referred to as unsymmetric UDMHy), has developed as the standard source for InGaAsN epitaxy. Pressure data are included in Table 33.2. Tertiarybutylarsine is generally employed as As source due to its favorable pyrolysis properties at low temperature, shown in Fig. 33.2. For the same reason triethylgallium is often used as Ga source instead of trimethylgallium employed for standard GaAs MOVPE, while the generally applied trimethylindium precursor for In supply is sufficiently unstable to be also used for InGaAsN growth.

Lattice-match of InGaAsN to GaAs requires an In/N ratio of about 3. Such a ratio cannot be maintained for a quaternary-alloy QW of 1.3 μm devices due to the low miscibility for N alloying. Instead *strained* QWs with $\approx 30\%$ In and up to 4% N are used. Even then, introduction of N is difficult, since In alloying strongly counteracts N incorporation into the solid. The dependence of the nitrogen content on the In concentration is shown in Fig. 33.7 for two growth temperatures, illustrating the benefit of low-temperature growth. For MOVPE of QWs deposition temperatures as low as 525 °C are used, while thicker layers are grown at slightly increased temperatures (e.g., 550 °C) to achieve a higher growth rate.

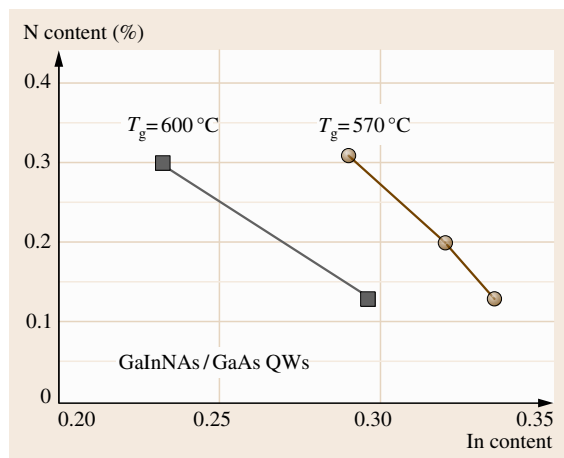


Fig. 33.7 Nitrogen content in InGaAsN/GaAs quantum wells as a function of In content for two deposition temperatures T_g [33.25]

Composition of the quaternary alloy also depends sensitively on other growth parameters. A high tertiarybutylarsine flow was found to favor N incorporation up to a maximum value near 4% [33.26], and higher In concentration was obtained for lower III/V ratios [33.25]. A particular issue of MOVPE is the incorporation of carbon and hydrogen. p-Type character of as-grown material was assigned to C incorporation, and a type conversion upon annealing was attributed to an N–H complex [33.27]. High C levels were ascribed to the strong N–C bond, and growth using various precursors indicated triethylgallium as a possible source [33.28]. Conditions to supply sufficient other radicals to the surface to prevent bonding of N radicals to C-containing groups are suggested to lower C contamination.

33.2.2 Structural and Electronic Properties of InGaAsN

The lattice parameter of GaAsN calculated from total energy minimum yields excellent agreement with Vegard's law despite the large lattice mismatch of more than 20% [33.18]. Due to the good miscibility with In such linear dependence on the composition also applies for the quaternary InGaAsN. Deviations were observed for high N concentrations exceeding 2.9% and were assigned to interstitial, i. e., nonsubstitutional incorporation [33.29]. In molecular-beam epitaxy Sb was used as a surfactant, significantly improving structural and optical properties of highly strained material [33.30–32].

In and also N were found to be randomly distributed on a large scale. While this applies for In also on a microscopic scale, a slightly enhanced number of nitrogen pairs oriented along the [001] growth direction was found in scanning tunneling micrographs of GaAsN [33.33] and InGaAsN layers [33.34, 35]. Calculations based on the pseudopotential method [33.36] and the Keating valence force field model [33.37] show that such N pairs reduce the strain compared with two isolated N atoms. Moreover, adding of further N atoms to a [001]-oriented chain is found to be energetically favorable. The ordering of nitrogen in the quaternary alloy leads to local nanometer-sized strain fields [33.37, 38]. Figure 33.8 shows a transmission electron microscopy (TEM) image taken from an as-grown QW under strain-sensitive imaging conditions. The apparent columnar structure along the [001] growth direction is also found in thick layers. It is not visible if chemically sensitive imaging conditions are used. The

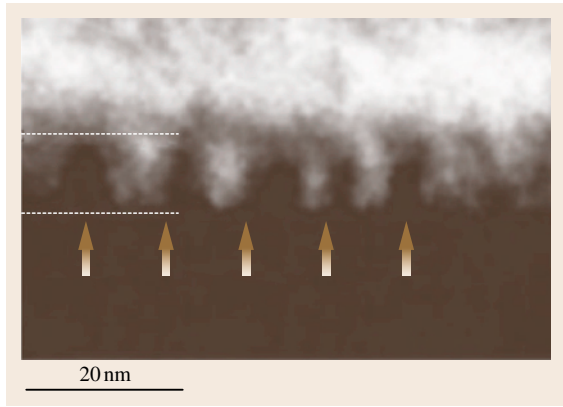


Fig. 33.8 Cross-sectional transmission electron micrograph of an as-grown InGaAsN/GaAs quantum well with 30% In and 2.7% N. Dashed lines depict QW boundaries; arrows indicate column-like strain fields [33.37]

density of the columns was shown to increase with the N content.

As-grown InGaAsN material with high N content generally shows poor luminescence efficiency, which strongly improves upon annealing. The strain fields visible in TEM images dissolve by annealing. Studies of the nearest-neighbor bonds using x-ray absorption fine structure show that the short-range ordering of the nitrogen chains largely disappears, accompanied by an increase of In–N bonds at the expense of Ga–N bonds [33.39–41]. While N chains build a stable configuration at the growth surface, the highly In-coordinated state of N was calculated to have a lower total energy in the bulk [33.37,42,43]. Strain in the layers does not significantly affect the nearest-neighbor bonding [33.40], but the optimum annealing temperature with respect to photoluminescence (PL) efficiency was found to decrease with strain [33.44]. The origin of the improved luminescence efficiency after anneal was assigned to the removal of nonsubstitutional nitrogen, which builds a complex weakly bonded to Ga and acts as a trap for photoexcited charge carriers [33.29].

Thermal annealing of as-grown InGaAsN induces a blue-shift of the bandgap due to the changed bond-

ing [33.40,45]. This finding agrees with the described reduction of N pairing and predictions of total energy calculations, which yield a reduced bandgap in case of clustering and also a reduced momentum matrix element (i. e., PL intensity) [33.36]. It was pointed out that the band structure of diluted nitride alloys shows an alloying mechanism different from that of conventional semiconductors [33.46]. Addition of nitrogen induces localized cluster states below the conduction band edge, which are gradually overtaken by states composed of both localized and delocalized states. These perturbed host states form the alloy conduction band edge and lead to the strong, composition-dependent bowing parameter. The effect of a few percent of nitrogen on the valence band is small and neglected in the generally accepted parameterized band anticrossing (BAC) model [33.47,48]. The splitting into a lower-lying E_- and an E_+ band can be considered as the interaction between the spatially localized N level and the delocalized conduction band states of the host semiconductor, and the respective dependence on the nitrogen fraction x reads

$$E_{\pm} = \frac{1}{2} \left((E_C + E_N) \pm \sqrt{(E_C - E_N)^2 + 4V^2 x} \right), \quad (33.10)$$

with E_C being the conduction band edge of the unperturbed host semiconductor, E_N the position of the N impurity level in this host, and V the interaction potential between the two bands. Respective model parameters for diluted nitride alloys are given in Table 33.3.

The offsets of valence and conduction bands are basic parameters for fabricating heterostructure devices. Data of InGaAsN/GaAs QW samples were particularly obtained from photoreflectance spectra by evaluating the splitting between the heavy-hole and light-hole ground state [33.49], and from photovoltage spectra by directly measuring the transition energy between confined and free states [33.50]. A type I band alignment is found for electron and heavy hole, with values for $Q_C = \Delta E_C / (\Delta E_C + \Delta E_V)$ of 55–70%. The light-hole valence band offset of a tensile-strained GaAsN QW

Table 33.3 Band anticrossing model parameters for dilute nitride semiconductors; the energy of the isoelectronic nitrogen impurity E_N is given with respect to the valence band maximum [33.15]

Alloy	E_N (eV)	V (eV)
GaAsN	1.65	2.7
InAsN	1.44	2.0
$\text{In}_x\text{Ga}_{1-x}\text{AsN}$	$1.65(1-x) + 1.44x - 0.38x(1-x)$	$2.7(1-x) + 2.0x - 3.5x(1-x)$

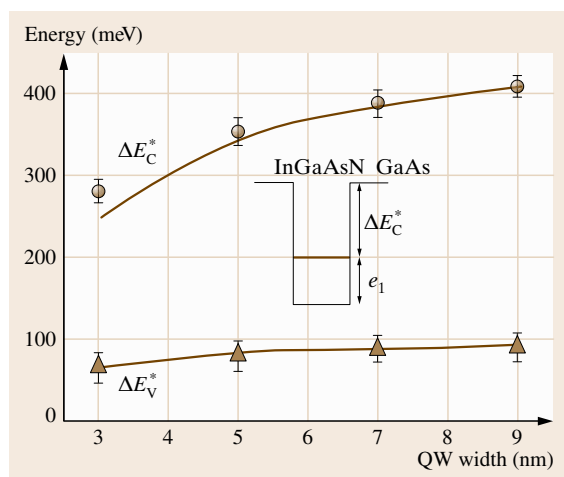


Fig. 33.9 Energy differences ΔE^* between confined states and band edges of $\text{In}_{0.3}\text{Ga}_{0.7}\text{As}_{0.98}\text{N}_{0.02}$ quantum wells with various widths, measured using photovoltage spectra; the continuous lines represent simulated values [33.50]

with 2% N was reported to be type II, and the counteracting strain introduced by 15% In was expected not to convert the type of alignment [33.49]. Introduction of Sb leads essentially to an increase of the hole QW depth [33.51]. Figure 33.9 shows measured energy differences between confined states and band edges for QWs with 2% N and 30% In. These values are of practical relevance and related to the band offsets by $\Delta E_C = \Delta E_C^* + e_1$, and $\Delta E_V = \Delta E_V^* + h_1$, with e_1 and h_1 being the energies of the first quantized states of electrons and holes, respectively.

33.2.3 Dilute Nitride Quantum Well Lasers

The ability to grow InGaAsN quantum wells lattice matched on GaAs substrates and the formation of a type I band alignment to confine both electrons and holes makes this dilute nitride alloy promising for device applications. Most work focused on fabrication of injection lasers emitting in the 1.3 and 1.55 μm wavelength windows of common datacom fibres, stimulated by the great commercial demand and the compatibility with the well-developed GaAs/AlAs technology. In fact, InP-based device structures used in optical networks suffer from poor thermal conductivity of the substrate material and low refractive index variation of alloys. InGaAsN also gained interest as a 1 eV subcell added to commercially available InGaP₂/GaAs/Ge multijunction solar cells. Inserted

between GaAs and Ge, conversion efficiencies exceeding 40% are expected [33.52]. In the following some aspects of the work related to edge-emitting lasers are discussed.

InGaAsN QWs for long-wavelength lasers were introduced in the mid 1990s using both gas-source MBE (GSMBE, also denoted metalorganic MBE, MOMBE) and MOVPE [33.53]. The first edge-emitting ridge waveguide lasers used single QWs and achieved emission wavelengths near 1.2 μm at 300 K with high threshold current densities exceeding 1 kA/cm^2 . Lasers grown using MOVPE have focused since then on the 1.3 μm range, while considerable progress in the 1.55 μm range was achieved with MBE by additionally introducing Sb as a surfactant during growth of the active quantum wells in lasers [33.30]. Most lasers have a single QW with a thickness of 6–8 nm. During the first years of research on diluted nitride lasers a general trend of increasing threshold current densities was found when the emission wavelength was increased to longer wavelengths, irrespective of the growth technique employed, MOVPE or MBE [33.28, 54–56]. Wavelength tuning beyond 1.2 μm requires a sizeable incorporation of nitrogen into InGaAs. This can be achieved by a decreased growth temperature, an increased growth rate, and an increased N/(N+As) ratio [33.54]. The latter is more easily achieved using a low As/(Ga+In) ratio rather than a high flow of the N source, another advantage of employing tertiarybutylarsine over AsH₃ as arsenic source [33.57].

Generally such wavelength tuning was accompanied by material deterioration. A direct correlation of the threshold current density to the concentration of carbon in the QWs was observed [33.28]. For lasers grown using MOVPE the finding could be related to C from the gallium source. The high levels were claimed to be a consequence of the strong C–N bond. A similar trend found in MBE-grown lasers indicated a respective issue also for this growth technique.

A high PL efficiency of the active QW is crucial to obtain a low lasing threshold. As noted in Sect. 33.2.2, the PL, which drops for high N incorporation, largely recovers by annealing. A major improvement of InGaAsN QW lasers was therefore obtained by adding an annealing step to the fabrication procedure [33.58]. This step can also be accomplished in situ during growth of the upper cladding layer at increased temperature [33.57]. Further improvements were achieved by engineering the confinement and strain in the quantum well. Cladding of the compressively strained QW by a strain-compensating tensile

GaAsP barrier layer led to a threshold current density as low as 211 A/cm^2 for lasing at 1295 nm [33.57]. Using tensile-strained GaAsN instead of GaAsP proved to be even more advantageous [33.59, 60]. The conduction band discontinuity from the quaternary QW to the GaAs waveguide is segmented into two steps, thereby reducing the quantum confinement of the electrons and hence inducing a red-shift of the emission. In addition, stronger hole confinement is achieved due to a larger valence band step from the QW to GaAsN with respect to GaAs, resulting in improved high-temperature characteristics of the device. The characteristic temperature T_0 was shown to increase by 15 K for lasers emitting near 1315 nm with thresholds of $210\text{--}270 \text{ A/cm}^2$ [33.59]. Using this approach, lasing at the longest wavelength reported to date of 1410 nm was achieved, with a threshold of 1.4 kA/cm^2 [33.60].

33.3 InAs/GaAs Quantum Dots

Semiconductor quantum dots (QDs) are nanometer-sized objects in which charge carriers are confined in all three spatial dimensions. Their size is in the range of the de Broglie matter wavelength of the confined particles, and the quantum size effect leads to a delta-function-like electronic density of states. The properties of such zero-dimensional structures resemble those of atoms. The unique electronic properties of QDs, the discovery of self-organization processes which control their coherent (i.e., defect-free) growth, and the ease of incorporating QDs into a semiconductor device led to rapid development in this field. This section focuses on InAs QDs in GaAs matrix material and provides an insight into the basics of their formation, structural, and electronic properties. Finally, results on recent applications in edge-emitting lasers with gain media comprising QDs are reported.

33.3.1 The Stranski–Krastanow 2-D–3-D Transition

Efforts to realize quantum dots in semiconductor heterostructures were initially devoted mainly to lithographic patterning of quantum wells, e.g., [33.65]. Such structures generally suffered from residual damage introduced by nanopatterning that affected the electronic and optical properties. In the 1990s the concept of exploiting the fundamental growth mode named after Stranski and Krastanow was introduced to form large

Shift of the lasing wavelength to $1.55 \mu\text{m}$ will certainly be difficult to achieve with InGaAsN QWs. The results obtained using MOVPE are largely comparable to those achieved using MBE of lasers with quaternary QWs [33.61–63]. The most striking difference is a substantially lower temperature during growth of the active QW, ranging between 350°C and 330°C in MBE compared with about 530°C in MOVPE. The longest wavelength reached to date, by applying a carefully adjusted low-temperature MBE, is 1510 nm , with a still very low threshold of 780 A/cm^2 [33.56]. Substantial progress beyond $1.5 \mu\text{m}$ was recently achieved with quinary quantum wells in MBE [33.64]. Using a single $\text{In}_{0.38}\text{Ga}_{0.62}\text{As}_{0.943}\text{N}_{0.03}\text{Sb}_{0.027}$ QW with cladding by strain-compensating $\text{GaAs}_{0.96}\text{N}_{0.04}$ barriers, lasing was observed at $1.55 \mu\text{m}$ with a low threshold of 579 A/cm^2 .

arrays of defect-free quantum dots in a self-organized (also called self-assembled or self-ordered) way. The original paper describes the formation of islands on a flat substrate surface in heteroepitaxy of lattice-matched ionic crystals with different charges [33.66]. Stranski–Krastanow growth can also be induced if a two-dimensional layer is deposited on a crystalline substrate which has a sufficiently large *mismatch* of the lateral lattice constant (typically $\Delta a/a > 2\%$). The layer adopts the lateral atomic spacing of the substrate and hence accumulates strain with increasing thickness. Above a critical layer thickness the strain is relaxed by introduction of misfit dislocations. Below this critical thickness, a considerable part of the strain can be relaxed *elastically*, i.e., without introduction of dislocations, by forming faceted surface structures. A precondition for this 2-D–3-D transition is a total energy gain of the heteroepitaxial system, expressed by the actual surface area A and the change of the areal energy density $\Delta\gamma$. This quantity is given by

$$\Delta\gamma = \gamma_{\text{surface}} + \gamma_{\text{interface}} - \gamma_{\text{substrate}}, \quad (33.11)$$

the three summands being the surface energy of the epitaxial layer, the energy of the interface between layer and substrate, and the surface energy of the substrate, respectively. If $\Delta\gamma < 0$, the layer wets the substrate surface and grows two-dimensionally in the Frank–van-der-Merve layer-by-layer growth mode. If $\Delta\gamma > 0$, the layer tries to leave the substrate uncovered and

grows three-dimensionally in the Volmer–Weber island growth mode. In the intermediate case of Stranski–Krastanow growth, $\Delta\gamma < 0$ applies for the first layer(s), which grow two-dimensionally, while $\Delta\gamma > 0$ for subsequently grown layers, e.g., due to accumulated strain. The driving force of the 2-D–3-D transition is therefore minimization of the total strain energy [33.67]. The total energy gain per volume of a single QD can be expressed by [33.68]

$$\frac{E_{\text{total}}}{V} = \varepsilon_{\text{QD}}^{\text{elast}} - \varepsilon_{\text{layer}}^{\text{elast}} + \frac{A\gamma_{\text{facet}} - L^2\gamma_{\text{layer}}(d_0)}{V} + \left(\frac{1}{\rho} - L^2\right) \frac{\gamma_{\text{layer}}(d) - \gamma_{\text{layer}}(d_0)}{V}, \quad (33.12)$$

$\varepsilon_{\text{QD}}^{\text{elast}}$ and $\varepsilon_{\text{layer}}^{\text{elast}}$ being the elastic energy densities of the QD and the uniformly strained layer. The third term describes the change in surface energy due to the QD, with γ_{facet} being the surface energy of the island facets, A their area and L the base length of the QD, which is assumed to have a pyramidal shape. The fourth term accounts for that part of the layer which converts to the

QD; ρ is the area density of QDs, $\gamma_{\text{layer}}(d_0)$ and $\gamma_{\text{layer}}(d)$ are the formation energies of the layer as a function of its thickness d . The sum of these contributions is the total energy density, which has an energy minimum for a particular dot size as shown in Fig. 33.10. This minimum causes preferential formation of dots around this size and a stability of the dot ensemble against Ostwald ripening in thermodynamic equilibrium. The ripening still observed in experiments indicates the presence of kinetic barriers under the usually applied growth conditions. It should be noted that, even under equilibrium conditions, the entire material of the two-dimensional layer does not entirely reorganize to QDs; rather, a thin 2-D layer, the wetting layer, remains.

Self-organized growth of InAs QDs on GaAs was first realized using MBE [33.70]. Since then InAs and $\text{In}_{1-x}\text{Ga}_x\text{As}$ [33.71] dots in GaAs matrix have become a model system for self-organized QD growth. The InAs lattice constant exceeds that of GaAs by $\approx 7\%$. Details of QD formation sensitively depend on growth parameters, particularly on temperature, growth rate, and arsenic partial pressure. The 2-D–3-D transition of InAs layers occurs on (001)-oriented GaAs between 1.5 and 1.8 monolayer thickness for typical deposition temperatures of 450–520 °C. Nucleation of 3-D dots starts on top of a 2-D InAs layer which exceeds some critical thickness d_c of coverage. The density ρ of the emerging dots was measured from atomic force microscopy (AFM) images of InAs layers with varied thickness, deposited on (001) GaAs at 530 °C using MBE, cf. Fig. 33.11.

The dot density ρ depicted in Fig. 33.11 follows a dependence on the InAs coverage similar to that of

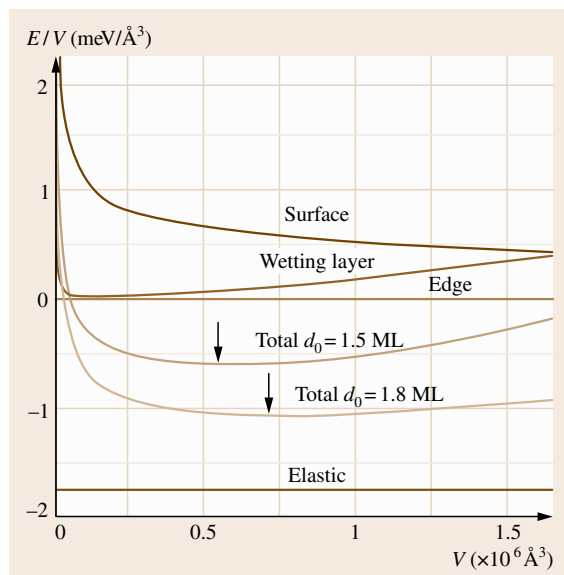


Fig. 33.10 Total energy gain by QD formation from $d_0 = 1.8$ monolayers (ML) and 1.5 monolayers InAs films deposited on GaAs. A QD area density of $\rho = 10^{10} \text{ cm}^{-2}$ is assumed; notations on the curves denote contributions from the surface, the wetting layer, the edges of the assumed pyramid shape of the QDs, and the elastic relaxation energy [33.68]. Arrows mark the minima of the curves

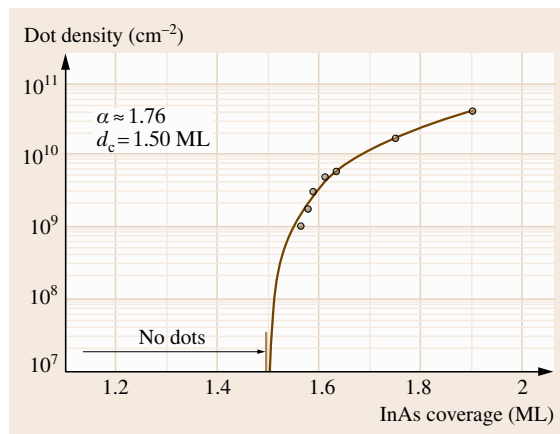


Fig. 33.11 Areal density of self-organized InAs dots on GaAs as a function of deposition thickness d [33.69]

a first-order phase transition [33.69]

$$\rho = \rho_0(d - d_c)^\alpha. \quad (33.13)$$

The least-squares fit represented by the solid line yields $\rho_0 = 2 \times 10^{11} \text{ cm}^{-2}$, $\alpha = 1.76$, and $d_c = 1.50 \text{ ML}$.

33.3.2 MOVPE of InAs Quantum Dots

Most studies on the MOVPE of quantum dots in the InGaAs system comprise ternary $\text{In}_x\text{Ga}_{1-x}\text{As}$ dots with In content x of 30–70% [33.73–75]. The reduced strain in the layer with respect to InAs retards the onset of dot nucleation, facilitating deposition control, and the tendency to form large, dislocated clusters is smaller [33.74]. The growth procedure is often varied in many respects, complicating a comparison of results: The dot material may be deposited on a thin InGaAs buffer layer with lower In content to obtain a high dot density, or overgrown by a respective thin InGaAs layer to induce a red-shift of the emission wavelength [33.76]. In addition, seeding or stacking of dot layers is applied to modify optical properties or increase the dot density in the matrix [33.72, 77], and also atomic layer epitaxy [33.78] or use of a surfactant [33.79] has been reported. Structural and electronic properties of InGaAs QDs were found to differ significantly from those of InAs dots. For InGaAs depositions a depletion of the effective In content in the wetting layer was found [33.80], and an inhomogeneous In distribution in the InGaAs dot was observed [33.81]. To treat a more concise situation, we focus on the MOVPE of binary InAs dots. The precursors used for QD growth are standard sources for III–V epitaxy, namely trimethylindium, trimethylgallium, and either arsine or tertiarybutylarsine.

The general procedure of self-organized QD fabrication starts with the preparation of the surface. The low deposition temperature of typically about 500°C , which is required for Stranski–Krastanow growth of InAs dots, is much lower than the temperature needed to grow GaAs matrix material with good quality at reasonable growth rate. Therefore first a GaAs buffer layer is grown at a suitable high temperature (e.g., 650°C), and then the surface is stabilized with arsenic partial pressure while setting up the lowered temperature and eventually adjusting the V/III ratio. Then InAs is deposited, and subsequently a growth interruption is applied. Finally a GaAs cap layer is grown on top. Each of these steps comprises some crucial issues to obtain defect-free structures.

The deposition of InAs must occur with some minimum rate to prevent the formation of large incoherent clusters, in contrast to MBE, where processes can largely be retarded by using very low temperatures. The QD properties depend sensitively on the InAs thickness and the As partial pressure during InAs deposition and the growth interruption. Figure 33.12 shows PL spectra of InAs/GaAs QD samples prepared at 485°C and 8 s growth interruption with different deposition thicknesses and V/III ratios [33.72]. The spectra were nonresonantly excited into the matrix and show the near-band-edge emission of GaAs above 1.4 eV, emission from the 2-D wetting layer (WL), and the luminescence of the QD ensemble. For a given InAs deposition thickness d_0 , Fig. 33.12a shows the emission from a 2-D wetting layer clad by GaAs (dark line)

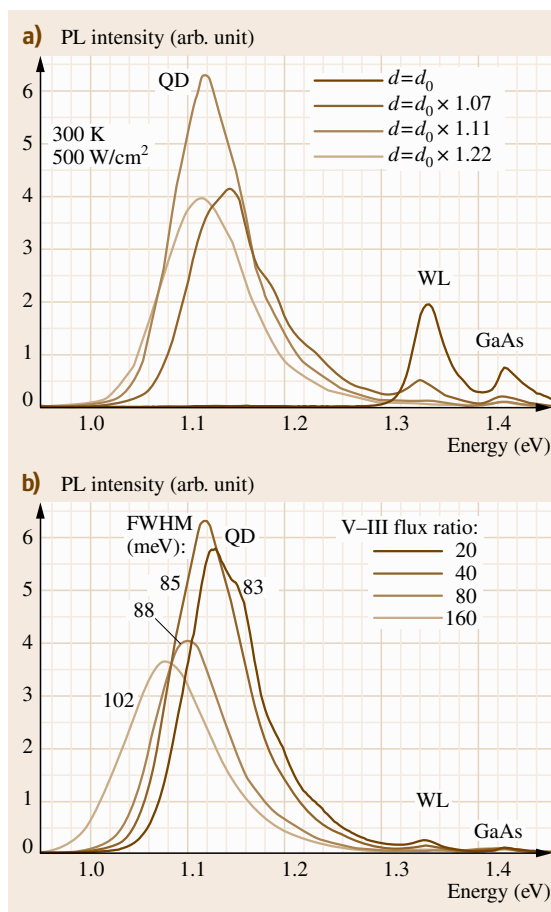


Fig. 33.12a,b PL spectra of InAs/GaAs quantum dot samples with different layer thicknesses (a) and different V/III ratios (b) applied during InAs deposition [33.72]

$d = d_0$); from the emission energy a thickness of 1.5 ML was evaluated. QDs are formed when this critical value is exceeded, and an optimum at $1.11 d_0$ was found for the given growth conditions. The decrease of PL intensity for thicker InAs depositions indicates the onset of plastic strain relaxation. Keeping the optimum thickness d_0 , the V/III ratio was varied in the series given in Fig. 33.12b by gradually changing the arsine partial pressure from 0.09 to 0.72 mbar. The PL shows a redshift, accompanied by a broadening of the full width at half maximum (FWHM) of the emission. Maximum efficiency and minimum FWHM are obtained for lowest V/III ratios. It must be noted that the effective V/III ratio at the growing surface is much lower than the quoted gas-phase ratios due to a quite incomplete decomposition of the stable arsine at 485 °C, cf. Fig. 33.2. A high V/III ratio apparently degrades the QDs. This applies also for the use of tertiarybutylarsine instead of arsine. Due to the high cracking efficiency, growth temperature and V/III ratio then become largely independent parameters [33.82], and a V/III ratio near unity is usually applied [33.79, 83].

The growth interruption conditions also strongly influence QD properties. In the sample series characterized in Fig. 33.13 the arsine flow was varied during a constant growth interruption (GRI) duration of 14 s [33.84]. Maximum PL efficiency is obtained when arsine is switched off during the first 12 s. In contrast, if the surface is stabilized under an As partial pressure during the entire growth interruption, the PL intensity drops by two orders of magnitude. AFM images of

such samples show a high density of large, dislocated clusters. The only slight drop in PL intensity for the intermediate case of 3 s without arsine supply (factor 2) shows that the first stage after InAs deposition is most critical. The presence of arsine during the growth interruption of QDs prepared using MOVPE may obviously affect QD properties. Such behavior is not reported for InAs dots grown using MBE. An enhanced In mobility in MOVPE was suggested to account for this finding [33.84].

A cap layer is deposited after the growth interruption, allowing for integration of QDs into a device structure. The temperature is kept unchanged at least during growth of the first few nanometers due to the unstable state of uncovered QDs. GaAs growth at such low temperatures favors the formation of defects, which affect the optical properties of QDs. Since buried InAs QDs are stable below 600 °C [33.85], an overgrowth procedure was established which maintains a high luminescence efficiency [33.86]. Here, the dots are buried by a thin (2–3 nm) GaAs cap at QD growth temperature, and further GaAs overgrowth is accomplished during a temperature increase to 600 °C. Besides an essential improvement of optical properties, a flat growth front is re-established at the otherwise corrugated surface above QDs. This is a precondition for continued QD growth in a stack, made to achieve an increased optical confinement factor and to overcome gain saturation in lasers with QD gain media. Furthermore, the flattening reduces interface roughness for subsequently deposited upper waveguide cladding, and thereby optical cavity losses in edge-emitting lasers.

Detailed insight into the dynamics of formation and evolution of InAs QDs was gained by studying ensembles with a multimodal size distribution [33.87, 88]. The particular feature of this kind of QDs is decomposition of the ensemble luminescence into individual lines as shown in Fig. 33.14. The QDs have the shape of a truncated InAs pyramid with a flat top facet, and the individual lines were shown to originate from subensembles which differ in height by an integer number of InAs monolayers. The clear detection of size quantization allows to trace redistribution of material among the QDs during the growth interruption.

InAs QDs with a multimodal size distribution form after a comparatively fast deposition of a rough, two-dimensional layer with a thickness close to the critical value for the 2-D–3-D transition [33.89]. If no growth interruption is applied, a quantum well is formed as shown in the inset of Fig. 33.14. The long exponential low-energy tail of the PL indicates significant thickness

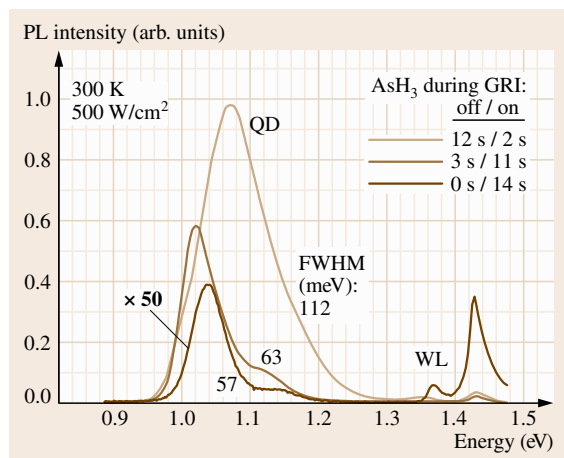


Fig. 33.13 PL spectra of InAs/GaAs QD samples with different arsine fluxes supplied during growth interruption after InAs deposition [33.84]

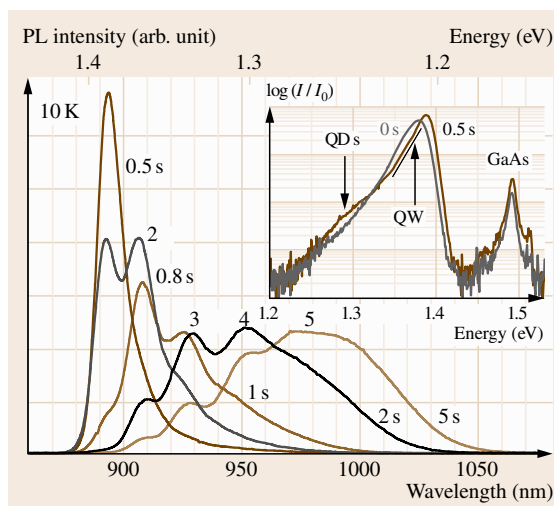


Fig. 33.14 PL spectra of QD samples grown with various growth interruptions (indicated in seconds on the curves); numbers denote QD heights in units of monolayers. Inset: spectra of samples grown without and with 0.5 s growth interruption [33.91]

fluctuations. Introduction of a short interruption leads to a blue-shift of the QW PL-maximum, i.e., a thinning of the QW, and the appearance of locally thicker regions (QDs). For longer interruptions (≥ 0.8 s) the emission of a multimodal QD ensemble with individual subensemble peaks evolves from shallow localizations in the density-of-states (DOS) tail of the rough QW. The material hence partially concentrates at some QD precursors. It must be noted that the thickness and composition of the wetting layer were found to remain constant during the entire duration of the growth in-

terruption [33.87, 88]. The PL of the QD ensemble experiences a red-shift for longer interruptions due to an increase of the average QD volume, a behavior generally reported for self-organized QDs, cf. Fig. 33.15a. The persistent shift also occurring for very long interruptions indicates the action of kinetic barriers which prevent the achievement of thermal equilibrium on the studied time scale. The drop of PL intensity at the longest growth interruption indicates the onset of plastic relaxation, as confirmed by TEM images. Interestingly, the subensemble peaks shift to the blue during QD evolution. This and the PL intensity decrease of a given subensemble peak with prolonged interruption time indicate that the ripening of the QDs is fed by dissolution of smaller QDs. The development of the integral subensemble PL intensities was considered a reasonable measure for the number of QDs with a specific corresponding height, showing directly the formation of subensembles with larger dots by dissolution of smaller QDs [33.90], cf. Fig. 33.15b. The subensemble with 5 ML QD height, e.g., grows during the initial 5 s growth interruption at the expense of those with 2–4 ML height. Then it starts to dissolve, feeding the 6 ML-high subensemble, which after 10 s interruption also starts to dissolve.

The optical study noted above is confirmed by structural data of the InAs QDs. Using strain and chemically sensitive {200} reflections, InAs dots appear as bright central areas in TEM images with a low aspect ratio and flat top and bottom interfaces, cf. Fig. 33.16. Side facets are steep, but less well resolved due to strain perturbations. Analysis of such images show that both the base and the top layer of the flat dots apparently consist of plain, continuous InAs layers [33.87, 88]. This yields QDs with a shape of a truncated pyramid, which

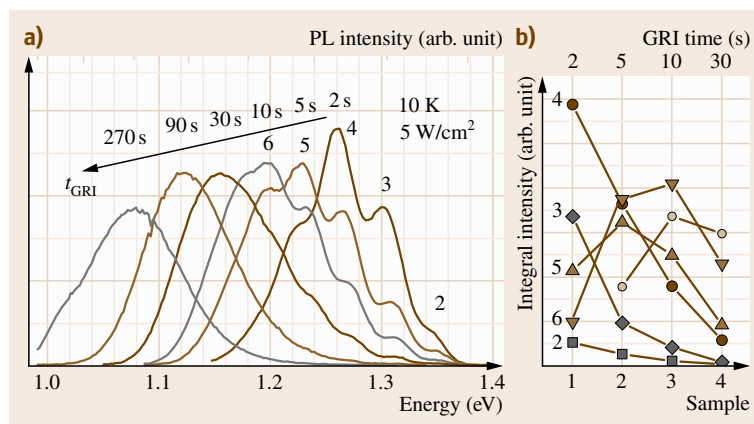


Fig. 33.15 (a) PL spectra of QD samples grown with long growth interruptions t_{GRI} . (b) Integral PL intensity of subensemble peaks as a function of growth interruption time. Numbers refer to QD heights as indicated in (a)

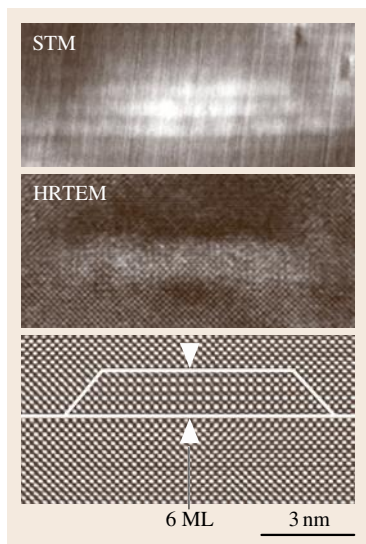


Fig. 33.16 Cross-sectional scanning tunneling micrograph (top, [33.92]) and high-resolution transmission electron micrograph [33.87] of InAs/GaAs QDs with 6 ML height; bottom: Fourier-filtered image of the transmission electron micrograph

differ in height by integer numbers of InAs monolayers. The same conclusions were drawn from recent scanning tunneling micrographs [33.92].

33.3.3 Quantum Dot Lasers

Work on InGaAs quantum dot lasers is a competing development to InGaAsN quantum well lasers to use GaAs-based laser technology for the long-wavelength datacom range. Zero-dimensional charge-carrier localization in the active region of a semiconductor laser was predicted two decades ago to lead to superior device performance, e.g., with respect to decreased threshold current and high-temperature stability [33.93, 94]. Furthermore, the reduction of lateral charge-carrier diffusion suppresses beam filamentation and strongly enhances robustness against facet degradation during high-power operation. The first realization of a QD injection laser using a single layer of MBE-grown self-organized $\text{In}_{0.5}\text{Ga}_{0.5}\text{As}$ QDs proved the fundamental validity of theoretical predictions [33.95]. A low lasing threshold of 120 A/cm^2 and a characteristic temperature T_0 as high as 350 K were achieved at liquid-nitrogen temperature. At room temperature, lasing occurred at a high threshold of 950 A/cm^2 from an excited state due to ground-state gain saturation. Generally the lasing threshold is reached if the modal gain g_{mod} just equilibrates the internal losses α_{int} and those of the cavity mirrors α_{mirr} ,

$$g_{\text{mod}} = \Gamma g_{\text{mat}} = \alpha_{\text{int}} + \alpha_{\text{mirr}}. \quad (33.14)$$

The material gain of QD gain media g_{mat} exceeds that of QWs by far [33.94, 96]. The optical confinement factor Γ of a QD layer is, however, much smaller than that of a QW, leading to a largely comparable modal gain of QD and QW lasers. Since the number of states in a QD layer is quite small compared with a QW, low lasing threshold and also a low gain saturation level are easily reached in single active layers. To increase both confinement factor and gain saturation level, actual QD lasers comprise a stack of QD layers. The spacers between the QD layers should preferably be thin to position the QDs near the optical field maximum. Further improvements of QD lasers aim to confine charge carriers efficiently in the QDs at energies well below that of the wetting layer.

The first MOVPE-grown QD lasers, reported in 1997, already used a threefold InAs QD stack [33.97] and a tenfold $\text{In}_{0.5}\text{Ga}_{0.5}\text{As}$ QD stack [33.98]. Both approaches achieved ground-state lasing at room temperature, and a T_0 of 385 K was demonstrated for the tenfold stack laser up to 50°C . The stacks were grown at the same low temperature for QD layers and GaAs spacers. Substantial progress in laser performance has been made since then, particularly by introducing temperature ramping to improve spacer quality and smoothen the interfaces [33.86]. For threefold stacked dot layers emitting at $1.16 \mu\text{m}$, threshold and transparency current densities of 110 and 18 A/cm^2 , respectively, with internal quantum efficiency exceeding 90% were achieved [33.99]. Also the internal loss below 1.5 cm^{-1} substantiates the benefit of temperature ramping. All these devices were grown using arsine as group V precursor. Good data were likewise reported for lasers grown using tertiarybutylarsine. Devices emitting at $1.1 \mu\text{m}$ showed a transparency current below 30 A/cm^2 , 91% internal quantum efficiency, and internal loss of 2.2 cm^{-1} [33.82].

Much work has been devoted to extending the emission wavelength towards $1.3 \mu\text{m}$. An efficient means is overgrowth of the $\text{In}(\text{Ga})\text{As}$ QDs by an InGaAs QW with lower In content to form a dot-in-a-well (DWELL) structure [33.76, 100]. Since this QW reduces the strain on the buried QD layer with respect to a GaAs cap, it is also referred to as a strain-reducing layer (SRL). Note that the overall strain in the QD stack is increased by the QW. Furthermore, the local strain at the large, In-rich QDs required for long-wavelength emission is rather high. This easily leads to formation of large In-rich incoherent clusters, which degrade device characteristics. Using the DWELL approach and carefully adjusting the growth parameters for each individual QD layer in the stack to avoid defect for-

mation, lasing at 1250 nm with a very low threshold current density of 66 A/cm² and 94% internal quantum efficiency was recently obtained [33.101]. In a complementary approach a DWELL laser was subjected to a postgrowth annealing procedure at moderate 560 °C, yielding 1280 nm lasing at high threshold [33.102]. As an alternative, strain-compensating GaP layers were introduced into the stacking sequence. Lasing at 1249 nm with a reasonable threshold of 550 A/cm² was reported for partial strain compensation using 4 ML-thick GaP layers [33.103]. The presently (2006) most ad-

vanced MOVPE-grown lasers used 1.5 nm-thick lattice-matched InGaP buffers below the stacked InGaAs QD layers, yielding 1280 nm lasing at 200 A/cm² threshold with $T_0 = 210$ K [33.104]. The target of 1.3 μm lasing has been accomplished to date with DWELL devices grown using MBE, a technique much more widely employed in the field. By applying temperature ramping comparable to that described above for the MOVPE, operation at 1307 nm with an extraordinary low threshold of 33 A/cm² (17 A/cm² with facet coating) was achieved [33.105].

33.4 Concluding Remarks

Metalorganic vapor-phase epitaxy has become established as a versatile technique for advanced fabrication of heterostructures with thickness control down to the monolayer range. Besides applications in industrial mass production, fast progress is being made in the development of new fields. This chapter intended to deliver an insight into the technique and selected problems. Just two topics on current issues in semiconductor MOVPE were highlighted: epitaxy of GaAs-related dilute nitrides and quantum dots. Both aim at extending the well-developed GaAs-based technology to the

long-wavelength spectral range and have recently achieved significant advances in the field of lasers. The performance of these demanding devices is comparable to the best fabricated devices using the complementary molecular-beam epitaxy described in Chap. 32. Both growth techniques presently provide the basis for novel low-dimensional structures in research and development. Note added in proof: Recently ground-state lasing at 1.35 μm and a threshold down to 328 A/cm² were accomplished by employing antimony-mediated MOVPE with tenfold stacked InAs/GaAs QDs [33.106].

References

- 33.1 W. Miederer, G. Ziegler, R. Dötzer: Verfahren zum tiegelfreien Herstellen von Galliumarsenidstäben aus Galliumalkylen und Arsenverbindungen bei niedrigen Temperaturen, German Patent 1176102, filed 25.9.1962; and: Method of crucible-free production of gallium arsenide rods from alkyl galliums and arsenic compounds at low temperatures, US Patent 3226270, filed 24.9.1963
- 33.2 H.M. Manasevit, W.I. Simpson: The use of metalorganics in the preparation of semiconductor materials on insulating substrates: I. Epitaxial III–V gallium compounds, J. Electrochem. Soc. **12**, 66C (1968)
- 33.3 R.W. Thomas: Growth of single crystal GaP from organometallic sources, J. Electrochem. Soc. **116**, 1449–1450 (1969)
- 33.4 H.M. Manasevit: The use of metalorganics in the preparation of semiconductor materials: Growth on insulating substrates, J. Cryst. Growth **13/14**, 306–314 (1972)
- 33.5 G.B. Stringfellow: Organometallic vapor phase epitaxy reaction kinetics. In: *Handbook of Crystal Growth*, ed. by D.R.T. Hurlé (Elsevier, Amsterdam 1994) pp. 491–540
- 33.6 T.J. Mountziaris, K.F. Jensen: Gas-phase and surface reaction mechanisms in MOCVD of GaAs with trimethyl-gallium and arsine, J. Electrochem. Soc. **138**, 2426–2439 (1991)
- 33.7 G.B. Stringfellow: *Organometallic Vapor-Phase Epitaxy*, 2nd edn. (Academic, New York 1999)
- 33.8 R.T. Morrison, R.N. Boyd: *Organic Chemistry*, 5th edn. (Allyn & Bacon, New York 1987)
- 33.9 K.F. Jensen: Transport phenomena in vapor phase epitaxy reactors. In: *Handbook of Crystal Growth*, ed. by D.R.T. Hurlé (Elsevier, Amsterdam 1994) pp. 541–599
- 33.10 D.H. Reep, S.K. Ghandhi: Deposition of GaAs epitaxial layers by organometallic CVD, J. Electrochem. Soc. **130**, 675–680 (1983)
- 33.11 R.B. Bird, W.E. Stewart, E.N. Lightfoot: *Transport Phenomena* (Wiley, New York 1962)

- 33.12 A.G. Bhuiyan, A. Hashimoto, A. Yamamoto: Indium nitride (InN): A review on growth, characterization, and properties, *J. Appl. Phys.* **94**, 2779–2808 (2003)
- 33.13 I. Vurgaftman, J.R. Meyer: Band parameters for nitrogen-containing semiconductors, *J. Appl. Phys.* **94**, 3675–3696 (2003)
- 33.14 M. Drago, T. Schmidtling, U.W. Pohl, S. Peters, W. Richter: InN metalorganic vapour phase epitaxy and ellipsometric characterization, *Phys. Status Solidi (c)* **0**(7), 2842–2845 (2003)
- 33.15 I. Vurgaftman, J.R. Meyer, L.R. Ram-Mohan: Band parameters for III–V compound semiconductors and their alloys, *J. Appl. Phys.* **89**, 5815–5875 (2001)
- 33.16 U.W. Pohl, C. Möller, K. Knorr, W. Richter, J. Gottfriedsen, H. Schumann, K. Rademann, A. Fielicke: Tertiarybutylhydrazine: A new precursor for the MOVPE of group III–nitrides, *Mater. Sci. Eng. B* **59**, 20–23 (1999)
- 33.17 I. Ho, G.B. Stringfellow: Solubility of nitrogen in binary III–V systems, *J. Cryst. Growth* **178**, 1–7 (1997)
- 33.18 J. Neugebauer, C.G. Van de Walle: Electronic structure and phase stability of $\text{GaAs}_{1-x}\text{N}_x$ alloys, *Phys. Rev. B* **51**, 10568–10571 (1995)
- 33.19 D.K. Gaskill, N. Bottka, M.C. Lin: Growth of GaN films using trimethylgallium and hydrazine, *Appl. Phys. Lett.* **48**, 1449–1451 (1986)
- 33.20 H. Tsuchiya, A. Takeuchi, M. Kurihara, F. Hasegawa: Metalorganic molecular beam epitaxy of cubic GaN on (100) GaAs substrates using triethylgallium and monomethylhydrazine, *J. Cryst. Growth* **152**, 21–27 (1995)
- 33.21 S. Miyoshi, K. Onabe, N. Ohkouchi, H. Yaguchi, R. Ito, S. Fukatsu, Y. Shiraki: MOVPE growth of cubic GaN on GaAs using dimethylhydrazine, *J. Cryst. Growth* **124**, 439–442 (1992)
- 33.22 H. Sato, H. Takanashi, A. Watanabe, H. Ota: Preparation of GaN films on sapphire by metalorganic chemical vapor deposition using dimethylhydrazine as nitrogen source, *Appl. Phys. Lett.* **68**, 3617–3619 (1996)
- 33.23 U.W. Pohl, K. Knorr, C. Möller, U. Gernert, W. Richter, J. Bläsing, J. Christen, J. Gottfriedsen, H. Schumann: Low-temperature metalorganic vapor phase epitaxy (MOVPE) of GaN using tertiarybutylhydrazine, *Jpn. J. Appl. Phys.* **38**, L105–L107 (1999)
- 33.24 U.W. Pohl, K. Knorr, J. Bläsing: Metalorganic vapor phase epitaxy of GaN on LiGaO_2 substrates using tertiarybutylhydrazine, *Phys. Status Solidi (a)* **184**, 117–120 (2001)
- 33.25 Z. Pan, T. Miyamoto, D. Schlenker, S. Sato, F. Koyama, K. Iga: Low temperature growth of GaInNAs/GaAs quantum wells by metalorganic chemical vapor deposition using tertiarybutylarsine, *J. Appl. Phys.* **84**, 6409–6411 (1998)
- 33.26 J. Derluyn, I. Moerman, M.R. Leys, G. Patriarche, G. Sek, R. Kudrawiec, W. Rudno-Rudziński, K. Ryczko, J. Misiewicz: Control of nitrogen incorporation in Ga(In)NAs grown by metalorganic vapor phase epitaxy, *J. Appl. Phys.* **94**, 2752–2754 (2003)
- 33.27 S. Kurtz, J.F. Geisz, D.J. Friedman, W.K. Metzger, R.R. King, N.H. Karam: Annealing-induced-type conversion of GaInNAs , *J. Appl. Phys.* **95**, 2505–2508 (2004)
- 33.28 K. Volz, T. Torunski, B. Kunert, O. Rubel, S. Nau, S. Reinhard, W. Stolz: Specific structural and compositional properties of $(\text{GaIn})(\text{NAs})$ and their influence on optoelectronic device performance, *J. Cryst. Growth* **272**, 739–747 (2004)
- 33.29 S.G. Spruytte, C.W. Coldren, J.S. Harris, W. Wampler, P. Krispin, K. Ploog, M.C. Larson: Incorporation of nitrogen in nitride–arsenides: Origin of improved luminescence efficiency after anneal, *J. Appl. Phys.* **89**, 4401–4406 (2001)
- 33.30 X. Yang, M.J. Jurkovic, J.B. Héroux, W.I. Wang: Molecular beam epitaxial growth of InGaAsN:Sb/GaAs quantum wells for long-wavelength semiconductor lasers, *Appl. Phys. Lett.* **75**, 178–180 (1999)
- 33.31 L.H. Li, V. Sallet, G. Patriarche, L. Largeau, S. Bouchoule, L. Travers, J.C. Harmand: Investigations on GaInNAsSb quinary alloy for 1.5 μm laser emission on GaAs, *Appl. Phys. Lett.* **83**, 1298–1300 (2003)
- 33.32 H.B. Yuen, S.R. Bank, H. Bae, M.A. Wistey, J.S. Harris: The role of antimony on properties of widely varying GaInNAsSb compositions, *J. Appl. Phys.* **99**, 093504 (2006)
- 33.33 H.A. McKay, R.M. Feenstra, T. Schmidtling, U.W. Pohl: Arrangement of nitrogen atoms in GaAsN alloys determined by scanning tunneling microscopy, *Appl. Phys. Lett.* **78**, 82–84 (2001)
- 33.34 H.A. McKay, R.M. Feenstra, T. Schmidtling, U.W. Pohl, J.F. Geisz: Distribution of nitrogen atoms in dilute GaAsN and InGaAsN alloys studied by scanning tunneling microscopy, *J. Vac. Sci. Technol. B* **19**, 1644–1649 (2001)
- 33.35 R. Duca, G. Ceballos, C. Nacci, D. Furlanetto, P. Finetti, S. Modesti, A. Cristofolio, G. Bais, M. Pecchin, S. Rubini, F. Martelli, A. Franciosi: In–N and N–N correlation in $\text{In}_x\text{Ga}_{1-x}\text{As}_{1-y}\text{N}_y/\text{GaAs}$ quasi-lattice-matched quantum wells: A cross-sectional scanning tunneling microscopy study, *Phys. Rev. B* **72**, 075311 (2005)
- 33.36 L. Bellaiche, A. Zunger: Effects of atomic short-range order on the electronic and optical properties of GaAsN , GaInN , and GaInAs , *Phys. Rev. B* **57**, 4425–4431 (1998)
- 33.37 O. Rubel, K. Volz, T. Torunski, S.D. Baranovskii, F. Grosse, W. Stolz: Columnar [001]-oriented nitrogen order in Ga(NAs) and $(\text{GaIn})(\text{NAs})$ alloys, *Appl. Phys. Lett.* **85**, 5908–5910 (2004)
- 33.38 K. Volz, T. Torunski, W. Stolz: Detection of nanometer-sized strain fields in $(\text{GaIn})(\text{NAs})$ alloys by specific dark field transmission electron microscopic imaging, *J. Appl. Phys.* **97**, 014306 (2005)
- 33.39 G. Ciatto, F. D'Acapito, L. Grenouillet, H. Mariette, D. De Salvador, G. Bisognin, R. Carboni,

- L. Floreano, R. Gotter, S. Mobilio, F. Boscherini: Quantitative determination of short-range ordering in $\text{In}_x\text{Ga}_{1-x}\text{As}_{1-y}\text{N}_y$, *Phys. Rev. B* **68**, 161201 (2003)
- 33.40 V. Lordi, H.B. Yuen, S.R. Bank, M.A. Wistey, J.S. Harris, S. Friedrich: Nearest-neighbor distributions in $\text{Ga}_{1-x}\text{In}_x\text{N}_y\text{As}_{1-y}$ and $\text{Ga}_{1-x}\text{In}_x\text{N}_y\text{As}_{1-y-z}\text{Sb}_z$ thin films upon annealing, *Phys. Rev. B* **71**, 125309 (2005)
- 33.41 K. Uno, M. Yamada, I. Tanaka, O. Ohtsuki, T. Takizawa: Thermal annealing effects and local atomic configurations in GaInNAs thin films, *J. Cryst. Growth* **278**, 214–218 (2005)
- 33.42 E.-M. Pavelescu, J. Wagner, H.-P. Komsa, T.T. Rantala, M. Dumitrescu, M. Pessa: Nitrogen incorporation into GaInNAs lattice-matched to GaAs: The effects of growth temperature and thermal annealing, *J. Appl. Phys.* **98**, 083524 (2005)
- 33.43 A.M. Teweldeberhan, S. Fahy: Effect of indium-nitrogen bonding on the localized vibrational mode in $\text{In}_y\text{Ga}_{1-y}\text{N}_x\text{As}_{1-x}$, *Phys. Rev. B* **73**, 245215 (2006)
- 33.44 H.B. Yuen, S.R. Bank, H. Bae, M.A. Wistey, J.S. Harris: Effects of strain on the optimal annealing temperature of GaInNAsSb quantum wells, *Appl. Phys. Lett.* **88**, 221913 (2006)
- 33.45 T. Kitatani, M. Kondow, M. Kudo: Transition of infrared absorption peaks in thermally annealed GaInNAs, *Jpn. J. Appl. Phys.* **40**, L750–L752 (2001)
- 33.46 P.R.C. Kent, A. Zunger: Evolution of III–V nitride alloy electronic structure: The localized to delocalized transition, *Phys. Rev. Lett.* **86**, 2613–2616 (2001)
- 33.47 J.D. Perkins, A. Mascarenhas, Y. Zhang, J.F. Geisz, D.J. Friedman, J.M. Olson, S.R. Kurtz: Nitrogen-activated transitions, level repulsion, and band gap reduction in $\text{GaAs}_{1-x}\text{N}_x$ with $x < 0.03$, *Phys. Rev. Lett.* **82**, 3312–3315 (1999)
- 33.48 W. Shan, W. Walukiewicz, J.W. Ager III, E.E. Haller, J.F. Geisz, D.J. Friedman, J.M. Olson, S.R. Kurtz: Effect of nitrogen on the band structure of GaInNAs alloys, *J. Appl. Phys.* **86**, 2349–2351 (1999)
- 33.49 J.B. Héroux, X. Yang, W.I. Wang: Photoreflectance spectroscopy of strained (In)GaAsN/GaAs multiple quantum wells, *J. Appl. Phys.* **92**, 4361–4366 (2002)
- 33.50 M. Galluppi, L. Geelhaar, H. Riechert, M. Hetterich, A. Grau, S. Birner, W. Stolz: Bound-to-bound and bound-to-free transitions in surface photovoltage spectra: determination of the band offsets for $\text{In}_x\text{Ga}_{1-x}\text{As}$ and $\text{In}_x\text{Ga}_{1-x}\text{As}_{1-y}\text{N}_y$ quantum wells, *Phys. Rev. B* **72**, 155324 (2005)
- 33.51 R. Kudrawiec, M. Motyka, M. Gladysiewicz, J. Misiewicz, H.B. Yuen, S.R. Bank, H. Bae, M.A. Wistey, J.S. Harris: Band gap discontinuity in $\text{Ga}_{0.9}\text{In}_{0.1}\text{N}_{0.027}\text{As}_{0.973-x}\text{Sb}_x/\text{GaAs}$ single quantum wells with $0 \leq x < 0.06$ studied by contactless electrophotoreflectance spectroscopy, *Appl. Phys. Lett.* **88**, 221113 (2006)
- 33.52 A.J. Ptak, D.J. Friedman, S. Kurtz, R.C. Reedy: Low-acceptor-concentration GaInNAs grown by molecular-beam epitaxy for high-current *p-i-n* solar cell applications, *J. Appl. Phys.* **98**, 094501 (2005)
- 33.53 M. Kondow, T. Kitatani, S. Nakatsuka, M.C. Larson, K. Nakahara, Y. Yazawa, M. Okai, K. Uomi: GaInNAs: A novel material for long-wavelength semiconductor lasers, *IEEE J. Sel. Top. Quantum Electron.* **3**, 719–730 (1997)
- 33.54 S. Sato, S. Sato: Metalorganic chemical vapor deposition of GaInNAs lattice matched to GaAs for long-wavelength laser diodes, *J. Cryst. Growth* **192**, 381–385 (1998)
- 33.55 F. Höhnsdorf, J. Koch, S. Leu, W. Stolz, B. Borchert, M. Druminski: Reduced threshold current densities of (GaIn)(NAs)/GaAs single quantum well lasers for emission wavelengths in the range 1.28–1.38 μm , *Electron. Lett.* **35**, 571–572 (1999)
- 33.56 G. Jaschke, R. Averbeck, L. Geelhaar, H. Riechert: Low threshold InGaAsN/GaAs lasers beyond 1500 nm, *J. Cryst. Growth* **278**, 224–228 (2005)
- 33.57 N. Tansu, N.J. Kirsch, L.J. Mawst: Low-threshold-current-density 1300-nm dilute-nitride quantum well lasers, *Appl. Phys. Lett.* **81**, 2523–2525 (2002)
- 33.58 W. Li, J. Turpeinen, P. Melanen, P. Savolainen, P. Uusimaa, M. Pessa: Growth of strain-compensated GaInNAs/GaAsP quantum wells for 1.3 μm lasers, *J. Cryst. Growth* **230**, 533–536 (2001)
- 33.59 N. Tansu, J.-Y. Yeh, L.J. Mawst: Low-threshold 1317-nm InGaAsN quantum-well lasers with GaAsN barriers, *Appl. Phys. Lett.* **83**, 2512–2514 (2003)
- 33.60 J.-Y. Yeh, N. Tansu, L.J. Mawst: Long wavelength MOCVD grown InGaAsN–GaAsN quantum well lasers emitting at 1.378–1.41 μm , *Electron. Lett.* **40**, 739–740 (2004)
- 33.61 Y.Q. Wei, M. Sadeghi, S.M. Wang, P. Modh, A. Larson: High performance 1.28 μm GaInNAs double quantum well lasers, *Electron. Lett.* **41**, 1328–1329 (2005)
- 33.62 B. Damilano, J. Barjon, J.-Y. Duboz, J. Massies, A. Hierro, J.-M. Ulloa, E. Calleja: Growth and in situ annealing conditions for long-wavelength (GaIn)(NAs)/GaAs lasers, *Appl. Phys. Lett.* **86**, 071105 (2005)
- 33.63 M. Hopkinson, C.Y. Jin, H.Y. Liu, P. Navaretti, R. Airey: 1.34 μm GaInNAs quantum well lasers with low room-temperature threshold current density, *Electron. Lett.* **42**, 923–924 (2006)
- 33.64 S.R. Bank, H.P. Bae, H.B. Yuen, M.A. Wistey, L.L. Goddard, J.S. Harris: Room-temperature continuous-wave 1.55 μm GaInNAsSb laser on GaAs, *Electron. Lett.* **42**, 156–157 (2006)
- 33.65 A. Forchel, H. Leier, B.E. Maile, R. Germann: Fabrication and optical spectroscopy of ultra small III–V compound semiconductor structure. In: *Advances in Solid State Physics*, Vol. 28, ed. by U. Rössler (Vieweg, Braunschweig 1988) pp. 99–119
- 33.66 I. N. Stranski, L. Krastanow: Zur Theorie der orientierten Ausscheidung von Ionenkristallen

- aufeinander. In: *Sitzungsberichte der Akademie der Wissenschaften in Wien, Math.-naturwiss. Klasse, Abt. IIB*, Vol. 146 (1937) pp. 797–810, in German
- 33.67 V.A. Shchukin, N.N. Ledentsov, P.S. Kop'ev, D. Bimberg: Spontaneous ordering of arrays of coherent strained islands, *Phys. Rev. Lett.* **75**, 2968–2971 (1995)
- 33.68 L.G. Wang, P. Kratzer, M. Scheffler, N. Moll: Formation and stability of self-assembled coherent islands in highly mismatched heteroepitaxy, *Phys. Rev. Lett.* **82**, 4042–4045 (1999)
- 33.69 D. Leonard, K. Pond, P. M. Petroff: Critical layer thickness for self-assembled InAs islands on GaAs, *Phys. Rev. B* **50**, 11687–11692 (1994)
- 33.70 L. Goldstein, F. Glas, J.Y. Marzin, M.N. Charasse, G. Le Roux: Growth by molecular beam epitaxy and characterization of InAs/GaAs strained-layer superlattices, *Appl. Phys. Lett.* **47**, 1099–1101 (1985)
- 33.71 D. Leonard, M. Krishnamurthy, C.M. Reaves, S.P. Denbaars, P.M. Petroff: Direct formation of quantum-sized dots from uniform coherent islands of InGaAs on GaAs surfaces, *Appl. Phys. Lett.* **63**, 3203–3205 (1993)
- 33.72 F. Heinrichsdorff, A. Krost, N. Kirstaedter, M.-H. Mao, M. Grundmann, D. Bimberg, A.O. Kosogov, P. Werner: InAs/GaAs quantum dots grown by metalorganic chemical vapor deposition, *Jpn. J. Appl. Phys.* **36**, 4129–4133 (1997)
- 33.73 J. Oshinowo, M. Nishioka, S. Ishida, Y. Arakawa: Area density control of quantum-size InGaAs/Ga(Al)As dots by metalorganic chemical vapor deposition, *Jpn. J. Appl. Phys.* **33**, L1634–L1637 (1994)
- 33.74 F. Heinrichsdorff, A. Krost, M. Grundmann, D. Bimberg, F. Bertram, J. Christen, A. Kosogov, P. Werner: Self-organization phenomena of InGaAs/GaAs quantum dots grown by metalorganic chemical vapour deposition, *J. Cryst. Growth* **170**, 568–573 (1997)
- 33.75 A.A. El-Emawy, S. Birudavolu, P.S. Wong, Y.-B. Jiang, H. Xu, S. Huang, D.L. Huffaker: Formation trends in quantum dot growth using metalorganic chemical vapor deposition, *J. Appl. Phys.* **93**, 3529–3534 (2003)
- 33.76 I.N. Kaiander, F. Hopfer, T. Kettler, U.W. Pohl, D. Bimberg: Alternative precursor growth of quantum dot-based VCSELs and edge emitters for near infrared wavelengths, *J. Cryst. Growth* **272**, 154–160 (2004)
- 33.77 N.N. Ledentsov, J. Böhrer, D. Bimberg, I.V. Kochnev, M.V. Maximov, P.S. Kop'ev, I.Z. Alferov, A.O. Kosogov, S.S. Ruvimov, P. Werner, U. Gösele: Formation of coherent superdots using metal-organic chemical vapor deposition, *Appl. Phys. Lett.* **69**, 1095–1097 (1996)
- 33.78 K. Mukai, N. Ohtsuka, M. Sugawara: Controlled quantum confinement potentials in self-formed InGaAs quantum dots grown by atomic layer epitaxy technique, *Jpn. J. Appl. Phys.* **35**, L262–L265 (1996)
- 33.79 K. Pötschke, L. Müller-Kirsch, R. Heitz, R.L. Sellin, U.W. Pohl, D. Bimberg, N. Zakharov, P. Werner: Ripening of self-organized InAs quantum dots, *Physica E* **21**, 606–610 (2004)
- 33.80 A. Krost, F. Heinrichsdorff, D. Bimberg, A. Darhuber, G. Bauer: High-resolution x-ray diffraction of self-organized InGaAs/GaAs quantum dot structures, *Appl. Phys. Lett.* **68**, 785–787 (1996)
- 33.81 A. Lenz, R. Timm, H. Eisele, C. Hennig, S.K. Becker, R.L. Sellin, U.W. Pohl, D. Bimberg, M. Dähne: Reversed truncated cone composition distribution of $\text{In}_{0.8}\text{Ga}_{0.2}\text{As}$ quantum dots overgrown by an $\text{In}_{0.1}\text{Ga}_{0.9}\text{As}$ layer in a GaAs matrix, *Appl. Phys. Lett.* **81**, 5150–5152 (2002)
- 33.82 R.L. Sellin, I. Kaiander, D. Ouyang, T. Kettler, U.W. Pohl, D. Bimberg, N.D. Zakharov, P. Werner: Alternative-precursor MOCVD of self-organized InGaAs/GaAs quantum dots and quantum dot lasers, *Appl. Phys. Lett.* **82**, 841–843 (2003)
- 33.83 L. Höglund, E. Petrini, C. Asplund, H. Malm, J.Y. Andersson, P.O. Holtz: Optimising uniformity of InAs/(InGaAs)/GaAs quantum dots by metal organic vapor phase epitaxy, *Appl. Surf. Sci.* **252**, 5525–5529 (2006)
- 33.84 F. Heinrichsdorff, A. Krost, D. Bimberg, A.O. Kosogov, P. Werner: Self-organized defect free InAs/GaAs and InAs/InGaAs/GaAs quantum dots with high lateral density grown by MOCVD, *Appl. Surf. Sci.* **123/124**, 725–728 (1998)
- 33.85 F. Heinrichsdorff, M. Grundmann, O. Stier, A. Krost, D. Bimberg: Influence of In/Ga intermixing on the optical properties of InGaAs/GaAs quantum dots, *J. Cryst. Growth* **195**, 540–545 (1998)
- 33.86 R. Sellin, F. Heinrichsdorff, C. Ribbat, M. Grundmann, U.W. Pohl, D. Bimberg: Surface flattening during MOCVD of thin GaAs layers covering InGaAs quantum dots, *J. Cryst. Growth* **221**, 581–585 (2000)
- 33.87 U.W. Pohl, K. Pötschke, A. Schliwa, F. Guffarth, D. Bimberg, N.D. Zakharov, P. Werner, M.B. Lifshits, V.A. Shchukin, D.E. Jesson: Evolution of a multimodal distribution of self-organized InAs/GaAs quantum dots, *Phys. Rev. B* **72**, 245332 (2005)
- 33.88 U.W. Pohl: InAs/GaAs quantum qots with multimodal size distribution. In: *Self-assembled Quantum Dots*, ed. by Z.M. Wang (Springer, New York 2008) pp. 43–66
- 33.89 U.W. Pohl, K. Pötschke, M.B. Lifshits, V.A. Shchukin, D.E. Jesson, D. Bimberg: Self-organized formation of shell-like InAs/GaAs quantum dot ensembles, *Appl. Surf. Sci.* **252**, 5555–5558 (2006)
- 33.90 U.W. Pohl, K. Pötschke, A. Schliwa, M.B. Lifshits, V.A. Shchukin, D.E. Jesson, D. Bimberg: Formation and evolution of multimodal size-distributions

- of InAs/GaAs quantum dots, *Physica E* **32**, 9–13 (2006)
- 33.91 U.W. Pohl, A. Schliwa, R. Seguin, S. Rodt, K. Pötschke, D. Bimberg: Size-tunable exchange interaction in InAs/GaAs quantum dots. In: *Advances in Solid State Physics*, Vol. 46, ed. by R. Haug (Springer, Berlin 2008) pp. 41–54
- 33.92 R. Timm, H. Eisele, A. Lenz, T.-Y. Kim, F. Streicher, K. Pötschke, U.W. Pohl, D. Bimberg, M. Dähne: Structure of InAs/GaAs quantum dots grown with Sb surfactant, *Physica E* **32**, 25–28 (2006)
- 33.93 Y. Arakawa, H. Sakaki: Multidimensional quantum well laser and temperature dependence of its threshold current, *Appl. Phys. Lett.* **40**, 939–941 (1982)
- 33.94 M. Asada, Y. Miyamoto, Y. Suematsu: Gain and the threshold of three-dimensional quantum-box lasers, *IEEE J. Quantum Electron.* **22**, 1915–1921 (1986)
- 33.95 N. Kirstaedter, N.N. Ledentsov, M. Grundmann, D. Bimberg, V.M. Ustinov, S.S. Ruvimov, M.V. Maximov, P.S. Kop'ev, I.Z. Alferov, U. Richter, P. Werner, U. Gösele, J. Heydenreich: Low threshold, large T_0 injection laser emission from (InGa)As quantum dots, *Electron. Lett.* **30**, 1416–1417 (1994)
- 33.96 N. Kirstaedter, O.G. Schmidt, N.N. Ledentsov, D. Bimberg, V.M. Ustinov, A.Y. Egorov, A.E. Zhukov, M.V. Maximov, P.S. Kop'ev, I.Z. Alferov: Gain and differential gain of single layer InAs/GaAs quantum dot injection lasers, *Appl. Phys. Lett.* **69**, 1226–1228 (1996)
- 33.97 F. Heinrichsdorff, M.-H. Mao, N. Kirstaedter, A. Krost, D. Bimberg, A.O. Kosogov, P. Werner: Room-temperature continuous-wave lasing from stacked InAs/GaAs quantum dots grown by metal-organic chemical vapor deposition, *Appl. Phys. Lett.* **71**, 22–24 (1997)
- 33.98 M.V. Maximov, I.V. Kochnev, Y.M. Shernyakov, S.V. Zaitsev, N.Y. Gordeev, A.F. Tsatsul'nikov, A.V. Sakharov, I.L. Krestnikov, P.S. Kop'ev, I.Z. Alferov, N.N. Ledentsov, D. Bimberg, A.O. Kosogov, P. Werner, U. Gösele: InGaAs/GaAs quantum dot lasers with ultrahigh characteristic temperature ($T_0 = 385$ K) grown by metal organic chemical vapour deposition, *Jpn. J. Appl. Phys.* **36**, 4221–4223 (1997)
- 33.99 R.L. Sellin, C. Ribbat, M. Grundmann, N.N. Ledentsov, D. Bimberg: Close-to-ideal device characteristics of high-power InGaAs/GaAs quantum dot lasers, *Appl. Phys. Lett.* **78**, 1207–1209 (2001)
- 33.100 L.F. Lester, A. Stintz, H. Li, T.C. Newell, E.A. Pease, B.A. Fuchs, K.J. Malloy: Optical characteristics of 1.24 μm InAs quantum-dot laser diodes, *IEEE Photon. Technol. Lett.* **11**, 931–933 (1999)
- 33.101 A. Strittmatter, T.D. Germann, T. Kettler, K. Posilovic, U.W. Pohl, D. Bimberg: Alternative precursor metal-organic chemical vapor deposition of InGaAs/GaAs quantum dot laser diodes with ultra-low threshold at 1.25 μm , *Appl. Phys. Lett.* **88**, 262104 (2006)
- 33.102 J. Tatebayashi, N. Hatori, M. Ishida, H. Ebe, M. Sugawara, Y. Arakawa, H. Sudo, A. Kuramata: 1.28 μm lasing from stacked InAs/GaAs quantum dots with low-temperature-grown AlGaAs cladding layer by metalorganic chemical vapor deposition, *Appl. Phys. Lett.* **86**, 053107 (2005)
- 33.103 N. Nuntawong, Y.C. Xin, S. Birudavolu, P.S. Wong, S. Huang, C.P. Hains, D.L. Huffaker: Quantum dot lasers based on a stacked and strain-compensated active region grown by metal-organic chemical vapor deposition, *Appl. Phys. Lett.* **86**, 193115 (2005)
- 33.104 S.M. Kim, Y. Wang, M. Keever, J.S. Harris: High-frequency modulation characteristics of 1.3 μm InGaAs quantum dot lasers, *IEEE Photon. Technol. Lett.* **16**, 377–379 (2004)
- 33.105 I.R. Sellers, H.Y. Liu, K.M. Groom, D.T. Childs, D. Robbins, T.J. Badcock, M. Hopkinson, D.J. Mowbray, M.S. Skolnick: 1.3 μm InAs/GaAs multilayer quantum-dot laser with extremely low room-temperature threshold current density, *Electron. Lett.* **40**, 1412–1413 (2004)
- 33.106 D. Giumard, M. Ishida, N. Hatori, Y. Nakata, H. Sudo, T. Yamamoto, M. Sugawara, Y. Arakawa: CW lasing at 1.35 μm from ten InAs-Sb:GaAs quantum-dot layers grown by metal-organic chemical vapor deposition, *IEEE Photon. Technol. Lett.* **20**, 827–829 (2008)

34. Formation of SiGe Heterostructures and Their Properties

Yasuhiro Shiraki, Akira Sakai

The Si/Ge system provides a lot of varieties of materials growth due to the lattice mismatch between Si and Ge. From the point of view of device applications, both pseudomorphic growth and strain-relaxed growth are important. Not only the layer growth but also dot formation is now attracting much attention from both the scientific community and for device applications. Comprehensive studies on the growth mechanisms have resulted in the development of novel formation techniques of SiGe heterostructures and enable us to implement strain effects in Si devices. It is obvious that the device applications largely depend on the material growth, particularly control of surface reaction and formation of dislocations and surface roughness that strongly affect device performances. Here we review the fabrication technology of SiGe heterostructures aiming at growth of high-quality materials. The relaxation of strain of SiGe buffer layers grown on Si substrates is discussed in detail, since many devices are formed on the strain-relaxed buffer layers that are sometimes called *virtual substrates*. Carbon incorporation and dot formation that are now studied to extend the possibilities of SiGe are discussed in this chapter too.

34.1	Background	1153
34.2	Band Structures of Si/Ge Heterostructures	1154
34.3	Growth Technologies	1156
34.3.1	Molecular-Beam Epitaxy	1156
34.3.2	Chemical Vapor Deposition	1157
34.4	Surface Segregation	1157
34.5	Critical Thickness	1161
34.6	Mechanism of Strain Relaxation	1163
34.7	Formation of Relaxed SiGe Layers	1165
34.7.1	Graded Buffer	1165
34.7.2	Low-Temperature Method	1166
34.7.3	Chemical-Mechanical Polishing Method	1167
34.7.4	Ion Implantation Method	1168
34.7.5	Ge Condensation Method	1169
34.7.6	Dislocation Engineering for Buffer Layers	1170
34.7.7	Formation of SiGeC Alloys	1172
34.8	Formation of Quantum Wells, Superlattices, and Quantum Wires	1173
34.9	Dot Formation	1177
34.10	Concluding Remarks and Future Prospects	1184
	References	1184

34.1 Background

SiGe heterostructures have great potential to improve state-of-the-art Si devices, particularly very large-scale integrated circuits (VLSIs), and add such new functions as optics. Moreover, they provide a new scientific field of materials growth and characterization related to the lattice mismatch between Si and Ge. Band modification due to the strain coming from the lattice mismatch brings about the increase of the mobility of both electrons and holes. Since heterostructure bipo-

lar transistors (HBTs) became commercially available, many people have become engaged in the research and development of field-effective transistor (FET)-type devices which have a much wider range of applications. SiGe-based optical devices including optical interconnection and optoelectronic integrated circuits (OEICs) will provide new possibilities to enhance the performance and functions of Si VLSIs. Heterostructures such as quantum wells and dots make it possible to real-

ize light-emitting devices even with indirect-bandgap materials. These fascinating applications obviously depend on the material growth, particularly the control of surface reaction and formation of dislocations and surface roughness, which strongly affect device performance.

In this chapter, we review the fabrication technology of SiGe heterostructures developed so far and discuss the physics and chemistry behind the process. The relaxation of strain of SiGe buffer layers grown on Si substrates is very important in this field, since many

devices are formed on the strain-relaxed buffer layers which are sometimes called *virtual substrates*. The formation and properties of these layers are discussed here in detail. To extend the possibilities of SiGe, carbon incorporation is applied, which is also very interesting from the point of view of material growth. The large lattice mismatch in this material system causes the formation of misfit dislocations as well as dot formation. The latter is now one of the hottest topics in semiconductor physics and technology and will be discussed in this chapter too.

34.2 Band Structures of Si/Ge Heterostructures

Since there exists about 4.2% lattice mismatch between Si and Ge, the strain induced by the lattice mismatch

modifies the band structures of SiGe layers [34.1–3]. The bandgap energy of SiGe layers grown on Si substrates is changed by the strain, as shown in Fig. 34.1 as a function of Ge composition. The bandgap is decreased from the bulk value under lateral compressive strain, and the lowest point of the conduction band of strained SiGe is the delta valley, as in Si crystals, over the whole composition range.

Figure 34.2 shows the change in the conduction and valence bands due to strain. The degenerate sixfold conduction bands are separated into two groups, that is, twofold degenerated bands and fourfold degenerated bands. The degenerated heavy-hole (HH) and light-hole (LH) bands are also separated, and the energy difference of the spin–orbit splitting band is changed. This change effectively modifies the transport properties of electrons and holes, providing opportunities to improve transistor performance. In particular, the mobility enhancement of both electrons and holes is highly attractive from the point of view of device applications such as complementary metal–oxide–semiconductor (MOS) FETs, i.e., CMOS circuits.

The band alignment at Si/Ge heterointerfaces is also significantly modified and type I and type II alignments are realized by changing the strain distribution, as illustrated schematically in Fig. 34.3, i.e., when $\text{Si}_{1-x}\text{Ge}_x$ ($x < 0.4$) layers are grown on Si substrates and are laterally compressed, the band alignment becomes type I and electrons and holes are confined to the same SiGe region. On the other hand, when Si layers are grown on unstrained SiGe layers and are under lateral tensile strain, type II alignment is realized and electrons and holes are confined sepa-

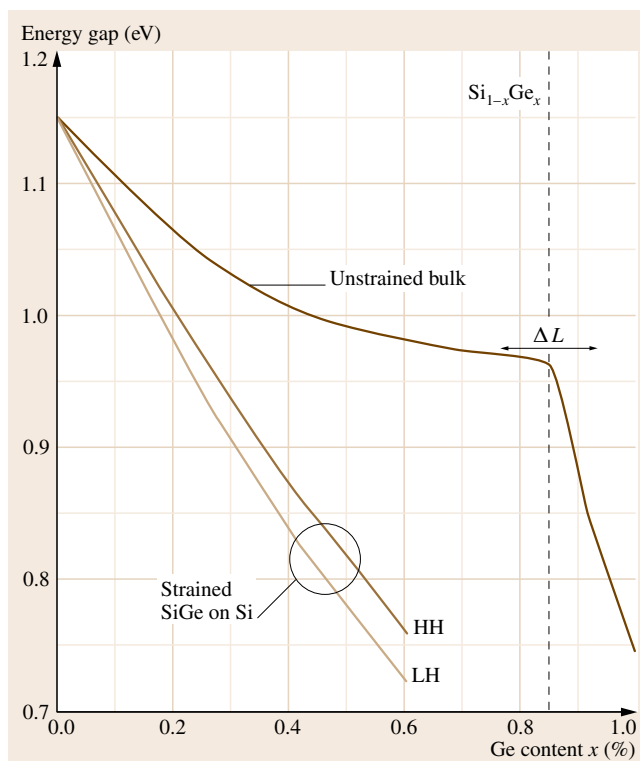


Fig. 34.1 Ge content dependence of the energy bandgap of strained SiGe grown on Si substrates. HH and LH represent bandgaps for heavy and light hole bands. That of unstrained SiGe is also shown as a reference

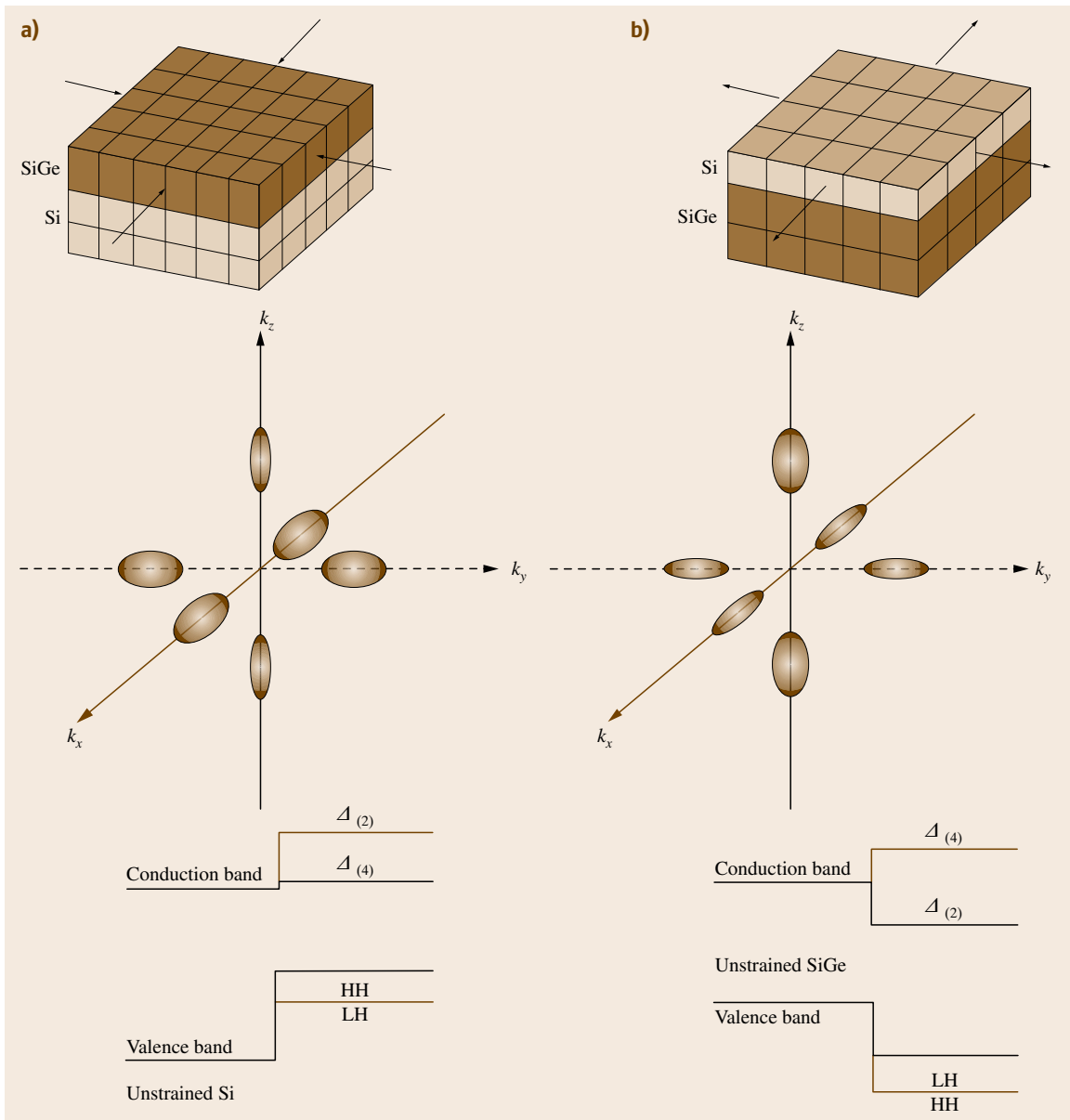


Fig. 34.2a,b Band modification of tensilely strained Si (a) and compressively strained SiGe (b)

ately. When Ge is laterally compressed by growth on SiGe layers, type II alignment also appears, as shown in the figure. Both band alignments are very useful from the point of view of device applications. Espe-

cially, since the band discontinuity at the conduction band of the former is very small, type II alignment is important when band engineering for electrons is intended.

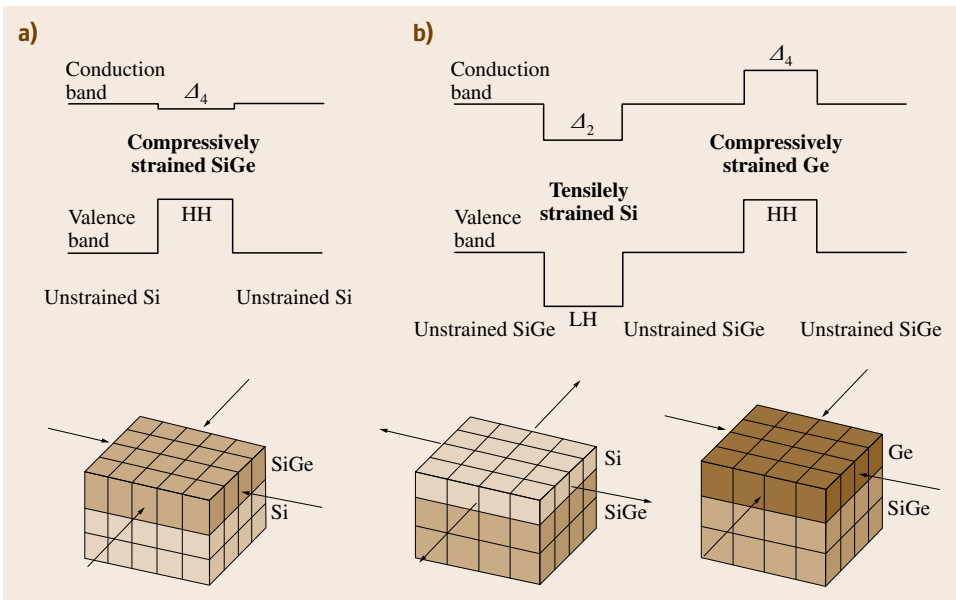


Fig. 34.3a,b Band alignment of Si/Ge heterostructures under various strains: (a) compressively strained SiGe on Si substrate (type I), (b) tensilely strained Si and compressively strained Ge on unstrained SiGe (type II)

34.3 Growth Technologies

34.3.1 Molecular-Beam Epitaxy

Molecular-beam epitaxy (MBE) is broadly used for depositing semiconductor and metallic materials to form thin films and multilayers. For the growth of Si films by MBE, a Si molecular beam is irradiated onto a clean surface of a Si substrate in a stainless-steel chamber in which the base pressure is reduced to the ultrahigh-vacuum (UHV) range, typically of the order 10^{-10} Torr.

An electron gun evaporator is usually used as a solid source of Si in order to achieve the vapor pressure required for practical growth. The evaporation of Ge is performed using a conventional Knudsen cell (K-cell), which is surrounded by liquid-nitrogen-cooled shrouds to condense unwanted evaporants and improve the vacuum in the sample region. The K-cell is also used for evaporating dopant materials: Ga and B for p-type doping, and Sb for n-type. Solid-source MBE is so simple and safe that it is also widely employed for fundamental research into thin-film growth mechanisms. Due to the reduced-pressure environment during growth, in situ and real-time diagnostic tools, such as reflection high-energy electron diffraction, scanning electron microscopy, and scanning tunneling microscopy, can be readily incorporated into the vacuum system to moni-

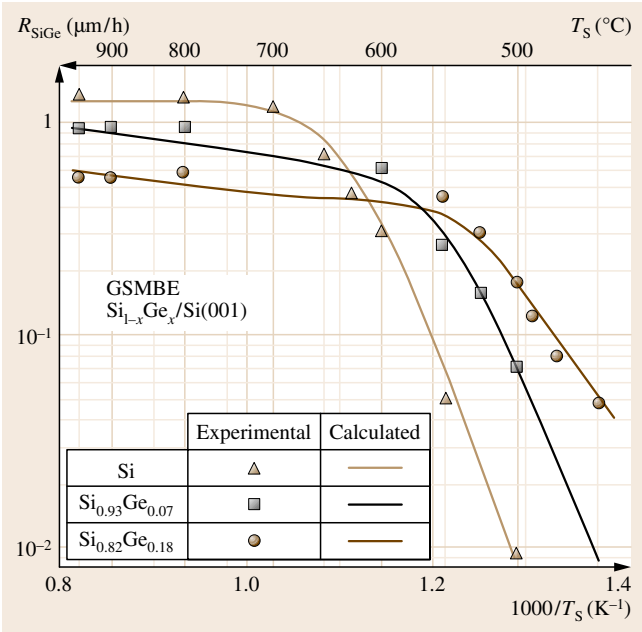


Fig. 34.4 Growth rate R_{SiGe} of GSMBE $\text{Si}_{1-x}\text{Ge}_x(001)$ layers with $x = 0, 0.07$, and 0.18 as a function of temperature T_s . The solid lines are calculated. For details, see [34.4]

tor the dynamics occurring on the surface of a growing film.

On the other hand, growth is often achieved using gas sources of Si and Ge, such as SiH_4 , Si_2H_6 , and GeH_4 , in the same type of UHV chambers as are used for solid-source MBE. An advantage of gas-source MBE is its ability for selective epitaxial growth on SiO_2 -mask-patterned Si substrates [34.5,6]. The growth kinetics of epitaxy on clean Si surfaces has been extensively studied for SiH_4 [34.7,8], Si_2H_6 [34.4,9–13], GeH_4 [34.11,13–15], Ge_2H_6 [34.4,14], and organosilanes [34.16–18]. Typical trends of SiGe growth on Si in gas-source MBE can be seen in Fig. 34.4 [34.4], which shows the growth rate of SiGe layers on Si(001) substrates as a function of substrate temperature when using Si_2H_6 and GeH_4 . In the low-temperature regime, surface-reaction-limited growth takes place and the growth rate increases with increasing Ge concentration. On the contrary, the growth rate saturates at high temperature, where impingement-flux-limited growth occurs, and decreases with increasing Ge concentration. These phenomena are also observed when using monohydride sources of SiH_4 and GeH_4 , and can be well modeled in terms of several kinetic parameters such as the sticking probability of gas species at adsorption sites, hydrogen desorption, and Ge segregation [34.4,19,20].

34.3.2 Chemical Vapor Deposition

Chemical vapor deposition (CVD) is most frequently used for the growth of semiconductor, metal, and insulator films for device production. In general, either a hot- or cold-wall reactor is used, with pumping and sophisticated gas control systems which enable exact supply of reactive gases onto heated substrates to produce thin,

epitaxial SiGe and SiGeC alloy films. CVD can ordinarily be categorized according to operating pressure into: UHV, low pressure (LP), reduced pressure (RP), and atmospheric pressure (AP) CVD.

UHV-CVD was firstly achieved by Meyerson et al. for growth of SiGe films on Si substrates using SiH_4 and GeH_4 [34.21]. They developed a hot-wall-type system consisting of a quartz reactor tube surrounded by an electrical heater with pumping systems to realize the UHV condition. Most commercially applicable processing is LP-CVD and RP-CVD, typically operating at pressures ranging from 1 Torr to a few tens of Torr. Gaseous sources of SiH_4 , SiH_2Cl_2 , SiH_3CH_3 , GeH_4 , CH_4 , and SiCH_3 are usually used for growth of Si, SiGe, and SiGeC films, and PH_3 and B_2H_6 for doping [34.22–25].

As mentioned earlier for gas-source MBE, during CVD growth of SiGe layers on Si, dramatic acceleration of the growth rate was also observed with the introduction of GeH_4 into the Si source gas, as compared with that of Si layer growth alone [34.21–23,25–27]. This is mainly due to the lowering of the hydrogen desorption energy caused by the presence of Ge on the Si surface. Selective epitaxial growth of Si and SiGe on Si surfaces has also been widely studied in CVD. For growth at pressure of more than 10 Torr, besides SiH_2Cl_2 and GeH_4 as gaseous sources, HCl was effectively used to control deposition selectivity with respect to SiO_2 -masked regions [34.28,29], whereas it was achieved without HCl in the case of very low pressure, less than 1 Torr [34.30,31]. Practical applications of selective epitaxial growth technology have mainly been the formation of SiGe channels for high-performance MOSFETs, elevated source/drain regions in shallow-junction electrode MOSFETs, and base regions of high-speed SiGe heterojunction bipolar transistors.

34.4 Surface Segregation

It is well known that the real heterointerface is not atomically flat and abrupt. There are several effects that deteriorate interface abruptness, of which surface segregation is considered to be the main one. Surface segregation is a reaction between impinging atoms and surface atoms of substrates, which then exchange positions to reduce the total energy of the system. This phenomenon was first recognized to be important when MBE layers were doped with some kinds of impurities [34.32,33]. It should be pointed out, however, that

surface segregation takes place not only in cases of doping, but also during heterointerface formation. Ge and In are well known to segregate when forming Si-on-(Si)Ge and GaAs-on-In(Ga)As heterostructures, respectively.

Figure 34.5 shows a typical example of the surface segregation phenomenon [34.34]. This figure shows secondary-ion mass spectroscopy (SIMS) profiles for the case when Si atoms are deposited on Si substrate covered with submonolayer Sb atoms. It is seen that Sb atoms do not remain at the original position and that

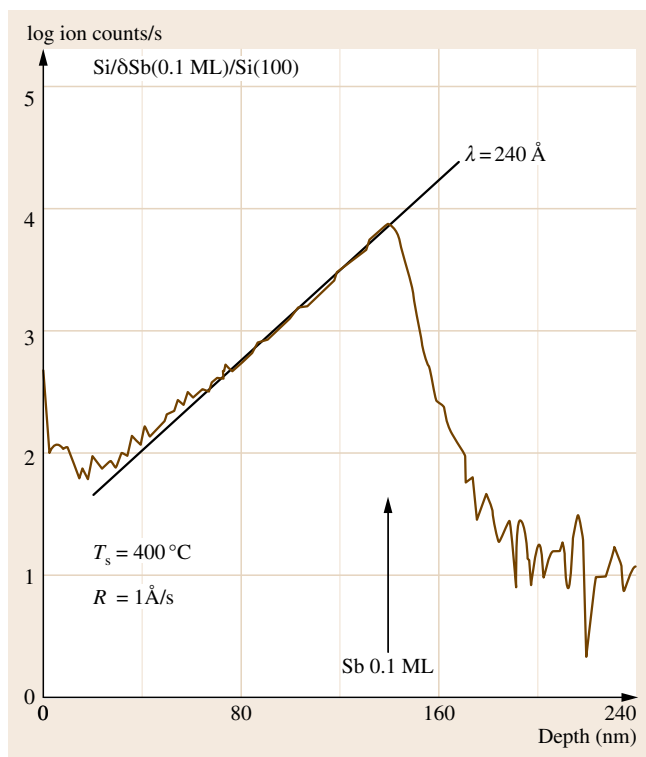


Fig. 34.5 SIMS profile of Sb atoms with 0.1 ML deposited on Si substrates measured after overgrowth of Si epitaxial layer. Due to surface segregation, the profile shows a tail with segregation length of $\lambda = 240$ Å towards the surface

they show an exponential distribution towards the surface with a characteristic parameter of the segregation length.

Another example is seen in Fig. 34.6, which shows how surface segregation occurs when Si overlayer is grown on the Ge layers [34.35]. If Ge atoms sat on their original sites and site exchange between Ge and impinging Si did not occur, the x-ray photoemission (XP) intensity of Ge atoms should decrease exponentially with increasing Si overlayer thickness, as shown by the dashed line. It is, however, seen that the x-ray photoemission spectroscopy (XPS) intensity does not follow the exponential decay but is much stronger even after growth of Si layers with thickness of 10 nm, which is much larger than the escape depth of photoexcited electrons.

Surface segregation of Ge is also clearly seen in photoluminescence (PL) of SiGe/Si quantum wells, the details of which will be described later. Due to the quantum confinement effect, the PL peak positions

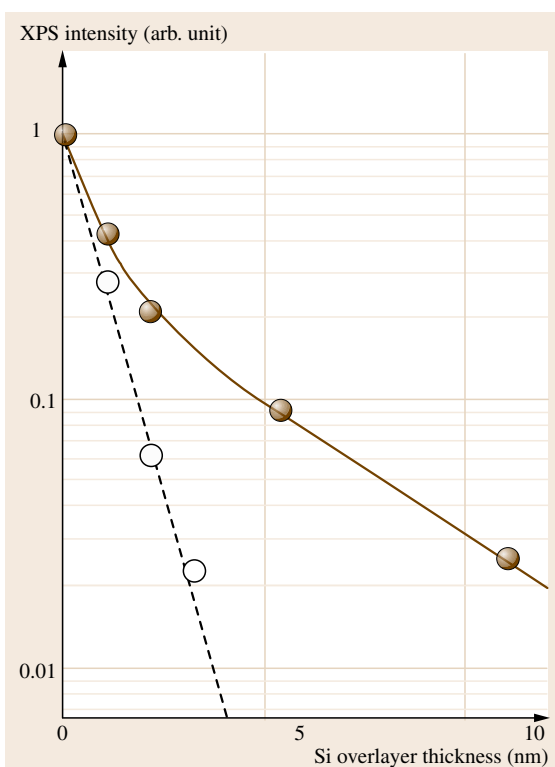


Fig. 34.6 XPS intensity of Ge atoms as a function of the thickness of overgrown Si layer. Filled circles are experimental results and the dotted line represents the calculated dependence without surface segregation. Open circles are for the case of surfactant-mediated growth

shift to higher energies with decreasing well width. The solid symbols in Fig. 34.7 show no-phonon (NP) and transverse optic (TO) phonon replica peak positions as a function of well width [34.34]. The dashed lines in the figure show the well width dependence of the peaks calculated based on the square well, that is, when surface segregation does not take place. It is seen that the peaks shift to higher energies from the expected positions. This is because the quantum levels are lifted by the deformation of the well shape due to Ge surface segregation.

It is confirmed [34.36] that only the topmost Ge atoms are mainly incorporated in the segregation and that we may neglect underlying atoms to a first approximation. The surface segregation phenomenon is therefore described in terms of a two-state exchange model where only exchange of atoms in surface and subsurface states is taken into account, as shown in

Fig. 34.8 [34.32, 37]. The exchange is described by the following rate equation

$$\frac{dn_1}{dt} = -pn_1 + qn_2, \quad (34.1)$$

$$\frac{dn_2}{dt} = -qn_2 + pn_1, \quad (34.2)$$

$$n_1 + n_2 = n_0,$$

where $p = p_0 \exp(-E_a/k_B T)$, $q = q_0 \exp[-(E_a + E_b)/k_B T]$, E_a is a potential for atoms to jump into the surface state from the underlying site and is less than the bulk thermal diffusion potential, E_b is the energy gain for the surface segregation and a measure of the segregation strength, and p_0 and q_0 are pre-exponential factors corresponding to the attempt frequency of atomic jumps and that may be considered to be on the order of the lattice vibration of 10^{12} – 10^{13} s^{-1} . Under the equilibrium condition, the equation can be numerically solved as

$$n_2(t) = n_0 \left[1 - \frac{1}{p+q} \left(q + e^{-(p+q)t} \right) \right]. \quad (34.3)$$

This solution shows the exponential distribution of atoms segregating towards the surface, well representing the results of SIMS experiments. Figure 34.9 shows a logarithmic plot of segregated atoms as a function of inverse temperature, in which the line labeled *equilibrium segregation* corresponds to the above solution. It

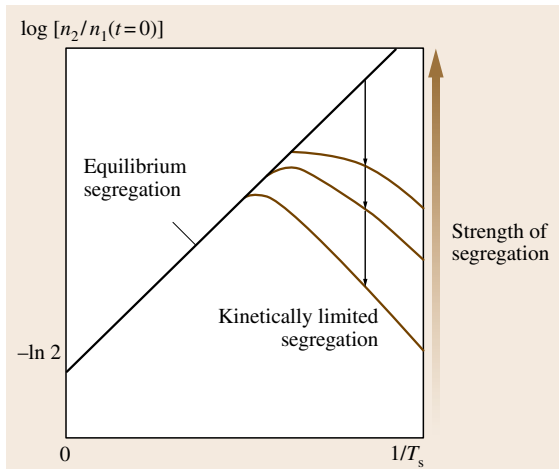


Fig. 34.9 Surface segregation (n_2/n_1) as a function of inverse temperature. Equilibrium segregation occurs under thermal equilibrium conditions and kinetically limited segregation occurs in the case of real crystal growth, particularly at low temperatures

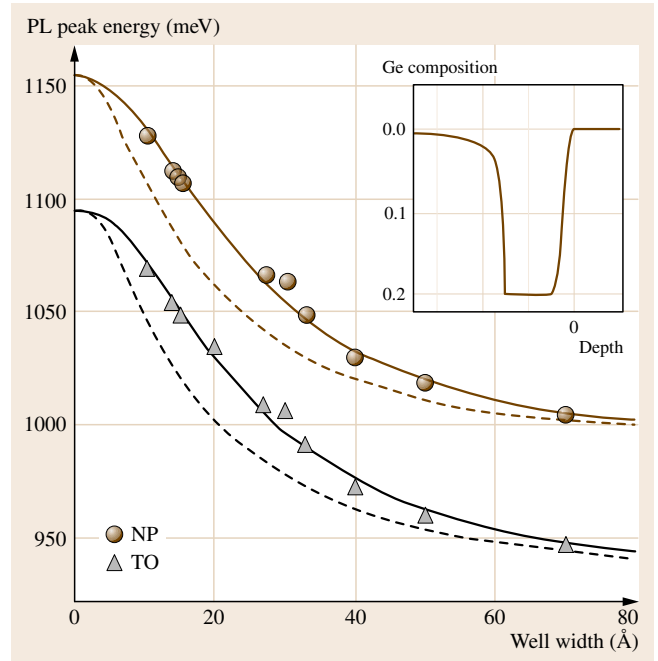


Fig. 34.7 Well width dependence of NP and TO peaks of PL from SiGe/Si quantum wells. Solid symbols are experimental results and the dotted lines represent the calculated well width dependence without surface segregation. The solid lines represent the dependence obtained by taking into account surface segregation in the two-state exchange model. The inset shows a schematic of the well shape distorted by surface segregation

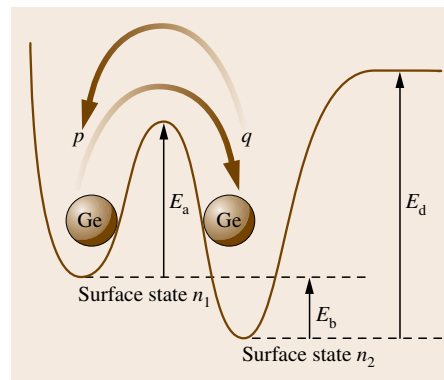


Fig. 34.8 Energy diagram of a two-state exchange model. E_a is the potential for atoms to jump from the subsurface position, and E_b is the energy gain for surface segregation. E_d is the desorption energy

is noted that segregation becomes smaller as the temperature increases. At first sight, this contradicts the observation that segregation is enhanced with increasing temperature. However, it should be pointed out that the experiments are not conducted under conditions of thermal equilibrium but under kinetically limited con-

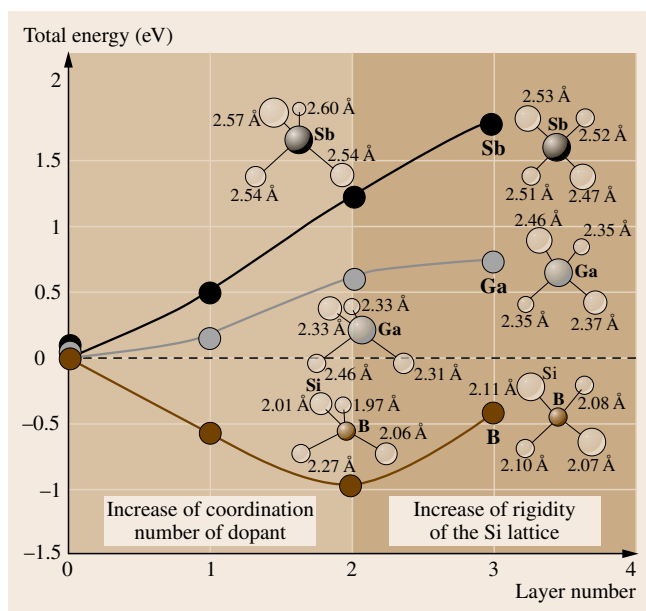


Fig. 34.10 Total energy of the system of Si with impurity atoms as a function of impurity position

ditions, that is, surface atoms are embedded before they reach the equilibrium as the crystal growth proceeds continuously. This situation is called kinetically limited segregation, as shown in Fig. 34.9, and segregation is largely suppressed at lower temperatures.

The solid line in Fig. 34.7 shows the well width dependence of quantum well (QW) edge emissions calculated by taking into account the distortion of the well shape based on the two-state exchange model. It is seen that the energy position is sufficiently represented by the calculation, indicating that the model describes the surface segregation well, even though it is phenomenological.

More microscopically, the local strain energy calculation is very useful to understand the segregation [34.38]. Figure 34.10 shows the total energy of the atomic arrangement in Si as a function of foreign atom site. In the case of Sb in Si, the energy is seen to increase as the site becomes deeper in the Si substrate. This indicates that Sb tends to move to the surface region to reduce the total energy, resulting in surface segregation. Interestingly, the energy minimum of B atoms is the third layer, and therefore B always tends to sit in this layer as crystal growth proceeds.

The trend for surface segregation can be predicted by considering the bond energy with Si atoms. The bond energy of Sb–Si, Ga–Si, and Ge–Si are smaller than that

of Si itself. These atoms are, therefore, rejected from the Si matrix to form strong chemical bonds and show surface segregation.

To avoid segregation and obtain abrupt heterointerfaces, low-temperature growth has been thought to be essential. However, low-temperature growth deteriorates crystal quality. Surfactant-mediated growth (SMG) is now well known to avoid interface smearing and obtain abrupt interfaces. In this method, a small amount of foreign atoms that show strong segregation, sometimes called segregants, are deposited before formation of heterointerfaces. For this purpose, As, Sb, Ga, Bi, and H are well known to suppress Ge segregation for the formation of Si/SiGe/Si structures. The principle of this method is as follows: before the Si overlayer of the Si/SiGe/Si heterostructure is grown, the SiGe layer is covered with strong segregants such as Sb so that Ge is no longer the topmost surface atom. When Si atoms are deposited on the Sb-covered Ge surface, the position of Sb becomes the subsurface site and Sb exchanges position with impinging Si atoms sitting at surface sites. However, site exchange between Si and Ge atoms does not follow. This is because Ge atoms do not occupy surface sites or subsurface site, that is, they are in bulk sites once Si is deposited. Between atoms in bulk sites, there is a high potential barrier that they cannot climb at the growth temperature, which is much lower than thermal diffusion temperatures, and therefore they do not exchange their positions.

In Fig. 34.6, the open circles show the XPS intensity of Ge atoms when 0.75 ML of Sb atoms are introduced as suppressors of segregation at the heterointerface before Si layers are overgrown [34.35]. It is seen that the XPS intensity follows the exponential decay and that surface segregation is effectively suppressed. Suppression of Ge segregation is also seen in SIMS profiles of Si/Ge superlattices and, once Sb atoms are deposited on Ge layers, the long tail towards the surface is seen to disappear [34.35]. The amount of Sb atoms required to suppress surface segregation is then an important question, and it was found that the effect becomes pronounced at around 0.5 ML and is optimized at 0.75 ML [34.34].

Gas-source MBE (GSMBE) is another important example of SMG, or pseudo-SMG where atomic hydrogen decomposed from hydrogenated gases such as Si_2H_6 and GeH_4 acts as a suppressor of Ge segregation. The well width dependence of the PL peak positions of QWs grown by GSMBE is found to coincide well with the square-well potential calculation, indicating that GSMBE provides heterostructures with-

out significant interfacial smearing [34.39]. It is also reported that Ge segregation is almost absent in UHV-CVD growth, in which hydrogen and/or hydrogenated compounds are speculated to act as suppressors [34.40]. It is, however, noted that hydrogen desorbs at high tem-

peratures such as those used in GSMBE. Therefore, hydrogen is thought to have a relatively long residence time on Si surfaces before desorption and can stay to act as a surfactant during a period of monolayer growth.

34.5 Critical Thickness

In epitaxial growth of overlayers that have a lattice parameter slightly different from that of the substrate, pseudomorphic (or coherent or commensurate) overlayers are formed when the thickness is not large. Since, in this case, the in-plane lattice constant of the pseudomorphic film is equivalent to that of the substrate, the film is elastically deformed according to Poisson's ratio to accommodate the lattice mismatch between the film and the substrate. The elastic energy due to the strain in the film increases linearly with increasing film thickness. However, there is a film thickness beyond which the introduction of misfit dislocations into the film becomes energetically favorable even though the energy increase due to the self-energy of the dislocations is taken into account. This minimum value of the film thickness is called the *critical thickness*.

Early theoretical works elucidating the critical thickness in lattice-mismatched heteroepitaxial growth were done by Frank [34.41–43] and van der Merwe [34.44, 45]. They gave a fundamental approach for predicting the critical thickness on the basis of the elastic energy and dislocation energy in strained epitaxial systems. The model proposed by van der Merwe was modified to be applied more practically to the diamond lattice in low-lattice-mismatch systems such as SiGe/Si [34.46–48]. Minimization of total energy given as a sum of the elastic energy stored in a homogeneously strained film and the energy associated with the misfit dislocations leads to the following equation for the critical thickness h_c

$$h_c = \frac{b}{8\pi(1+\nu)f} \left[1 + \ln \left(\frac{2h_c}{r} \right) \right]. \quad (34.4)$$

In (34.4), b is the magnitude of the active component of the misfit dislocation Burgers vector, ν is Poisson's ratio, and r is the inner cutoff radius of the misfit dislocation. Using the spacing between dislocations d and the elastic strain ε , the misfit of the overlayer with the substrate f is defined to be

$$f = |\varepsilon| + \frac{b}{d}. \quad (34.5)$$

In (34.5), when $d \rightarrow \infty$, $\varepsilon = f$. A more detailed expression including numerical values associated with a SiGe/Si(001) system is also given in [34.48]. On the other hand, a simple and helpful model was developed by Matthews and Blakeslee and has often been used for interpreting various types of lattice-mismatched epitaxial systems [34.49–51]. Contrary to the aforementioned energy balance model, they considered the balance of forces exerted on a propagated dislocation with misfit and threading segments in the strained film, as shown in Fig. 34.11. The physical concept of the derivation of critical thickness in the force balance model is essentially the same as that in the energy balance model. The critical thickness in this case is given as

$$h_c = \frac{b(1-\nu \cos^2 \alpha)}{8\pi(1+\nu)f \cos \theta} \left[1 + \ln \left(\frac{h_c}{b} \right) \right], \quad (34.6)$$

where α is the angle between the misfit dislocation line and its Burgers vector, and θ is the angle between the misfit dislocation Burgers vector and a line in the interface drawn perpendicular to the dislocation line direction.

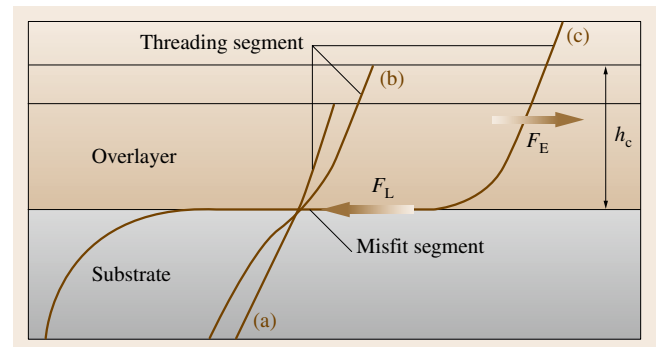


Fig. 34.11 Schematic illustration of the Matthews and Blakeslee model of critical thickness. A pre-existing threading dislocation in a coherent interface (a), critical interface (b), and incoherent interface (c). Critical thickness h_c is determined by the equality of the force exerted in the dislocation line by misfit stress F_E and the line tension in the dislocation line F_L .

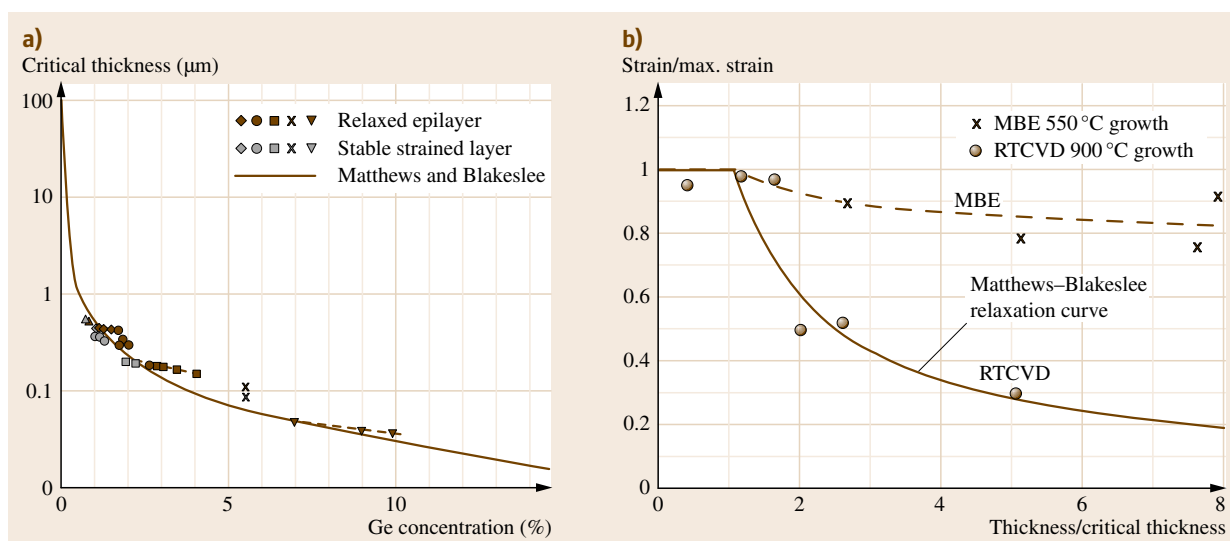


Fig. 34.12 (a) Experimentally determined critical values for thickness and composition obtained from annealed SiGe samples where the thickness and composition were laterally graded. An abrupt transition from a stable strained layer to a relaxed epilayer was detected to give a value of critical thickness at a certain composition. The solid curve is based on the Matthews and Blakeslee model, showing critical thickness as strain converted to Ge concentration in SiGe layers [34.56]. (b) Strain in the SiGe film divided by the theoretical maximum strain for that film versus film thickness divided by the critical thickness for that film grown by RTCVD. For comparison, the data of MBE-grown SiGe films [34.52] are also shown [34.57]

The discrepancy between theoretically predicted values and experimentally observed ones for the critical thickness has been reported in early works of molecular-beam epitaxy (MBE) of SiGe films on Si(001) substrates [34.52]. To explain the considerably larger critical thicknesses observed experimentally for SiGe films grown by MBE at 550 °C, *People and Bean* [34.53] firstly attempted to derive an expression of the critical thickness by taking into account the extra energy required for the generation of misfit dislocations. They obtained the critical thickness by setting the area density of strain energy associated with a film equal to the energy density of dislocations. Although this model showed quite good agreement with the experimental values of the critical thickness depending on the Ge content in the film, their interpretation is rather ad hoc, and the estimation of dislocation core energy is opposed to the elasticity treatment which is ordinarily employed for conventional semiconductor materials. On the other hand, it was pointed out that finite experimental resolution for detecting dislocation introduction in x-ray diffraction measurements for lattice parameters led to spurious results, and the critical thickness obtained by high-resolution measurements, such as stimulated-emission characteristics and photolumi-

nescence, approaches the equilibrium theory proposed by *Matthews and Blakeslee* [34.54]. High-sensitivity detection for misfit dislocations was also performed using electron-beam-induced current imaging in scanning electron microscopy (SEM) and transmission electron microscopy (TEM) [34.55]. The obtained critical thicknesses were revealed to be less than those determined in [34.52], although the SiGe films were grown under similar conditions.

For another dominant reason causing the discrepancy between the theory and experiment, nonequilibrium growth conditions for strain-relaxed SiGe films seemed to be responsible. High-temperature (900 °C) postgrowth annealing for SiGe films grown at 500–600 °C [34.56, 58] and rapid-thermal chemical vapor deposition (RTCVD) at 900 °C [34.57] led to excellent agreement of the experimental critical thickness with the predicted values of the Matthews and Blakeslee model, as shown in Fig. 34.12a,b, respectively. In general, the kinetic barrier for the formation or motion of misfit dislocations gives rise to nonequilibrium behavior of the critical thickness. This kinetic effect on strain-relaxation behavior was the focus of the early stage of development of the Matthews and Blakeslee theory, in which *Matthews et al.* proposed that Peierls stress

results in a friction force on the dislocation [34.59]. Contrary to this model, assuming only a velocity-dependent friction force, a model taking the static Peierls barrier into account was developed [34.60]. Other models including precise expression of arrays of misfit dislocations [34.61] and surface-relaxation effects [34.62] have been proposed so far. As mentioned

above, prediction of the critical thickness requires the consideration of kinetic effects relevant to practical growth conditions, such as growth temperature, initial dislocation density, and growth rate. This simultaneously means that strain relaxation of SiGe/Si(001) systems is strongly influenced by the kinetics, which will be explained in more detail in the next section.

34.6 Mechanism of Strain Relaxation

SiGe alloy films epitaxially grown on Si substrates have a maximum lattice mismatch of approximately 4.2% (when the film is pure Ge). This lattice mismatch induces strain mainly into the film, and elastic strain energy is accumulated with increasing film thickness. The relief of the elastic energy in the strained film occurs mainly through two mechanisms: elastic deformation accompanying surface evolution of the film, and plastic deformation with the introduction of misfit dislocations. In this section, to explain strain-relaxation mechanisms in SiGe/Si systems, we first mention the former process in which surface perturbation mainly contributes to the reduction of elastic energy and then the latter process including nucleation, propagation, and reaction/multiplication of dislocations.

It is well known that Ge grows on Si in Stranski–Krastanov mode in which layer-by-layer growth is followed by islanding of Ge. In practice, at the initial growth stage of Ge on Si(001) surfaces, dislocation introduction is preceded by the formation of dislocation-free (coherently strained) Ge islands [34.63] and/or *hut clusters* [34.64], i. e., {501}-faceted Ge islands, each of which was revealed by TEM and scanning tunneling microscopy (STM), respectively, and has a slightly different shape with respect to each other. Further TEM analysis revealed the hut cluster to be also a coherently strained Ge island and clarified the interplay between surface morphological variation and defect introduction concomitant with Ge islanding, which is critically dependent on the growth temperature [34.65, 66].

On the other hand, islanding phenomena occurring in SiGe/Si systems can be interpreted as strain relaxation based on Asaro–Tiller–Grinfeld instability in elastically stressed solids [34.67, 68]. The formation of perturbation on the stressed solid surface significantly reduces the stored elastic energy at the peak of perturbation but, at the same time, costs additional surface energy. Thus, the critical wavelength of the surface undulation can be drawn, which determines the sta-

bility of perturbation. The critical wavelength λ_c for a semi-infinite uniaxially stressed solid with a sinusoidal surface profile was derived as follows [34.69]

$$\lambda_c = \frac{\pi M \gamma}{\sigma^2}, \quad (34.7)$$

where M is the elastic modulus appropriate to the local surface orientation, γ is the surface tension, and σ is the mean stress in the solid. A more realistic model for the morphological instability of both growing and static epitaxially strained films was further developed, including differences in lattice parameters and elastic constants between the films and the substrate [34.70]. For experimental studies, wafer curvature measurements [34.71], direct observation using scanning transmission electron microscopy (STEM) [34.62], and STM [34.72] have been effectively applied to analyze the strain-related morphological evolution in SiGe/Si(001).

Surface evolution for elastic strain relaxation is generally followed by the introduction of misfit dislocations. A model describing total processes of strain relaxation in SiGe/Si systems was proposed by Dodson and Tsao [34.73]. On the basis of a phenomenological model of the dislocation dynamics and the plastic flow in bulk diamond-lattice semiconductors [34.74], they established a kinetic model of strain relaxation in which propagation and multiplication of pre-existing dislocations were treated systematically. In their model, a differential equation for the time-dependent degree of strain relaxation $\chi(t)$ is expressed as

$$\frac{d\chi(t)}{dt} = C\mu^2 [f_0 - \chi(t) - s(h)]^2 [\chi(t) + \chi_0]. \quad (34.8)$$

In this equation, f_0 is the misfit, μ is the shear modulus, $s(h)$ is the thickness-dependent homogeneous strain retained by the overlayer, and χ_0 is the dislocation source density. The choice of appropriate C and χ_0 values

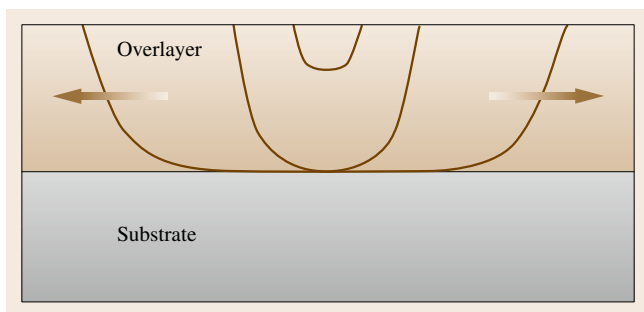


Fig. 34.13 Schematic illustration of nucleation and growth of a dislocation half-loop. Each threading part moves toward the edges of the sample, leaving a misfit segment at the interface, when the film thickness exceeds the critical thickness ◀

as fitting parameters resulted in remarkable agreement with the previous experimental results [34.52, 75]. Ac-

cording to the Dodson and Tsao model, even though the film thickness exceeds the critical thickness, both the effective stress exerted on the overlayer and the density of dislocations available for multiplication are small and this leads to initial slow relaxation of strain. Later on, the strain relaxation proceeds with the increase in the dislocation density exponentially with time, but then becomes sluggish due to the reduction of effective stress accompanied by the strain relaxation. They also explained when predicting the critical thickness that the initial slow relaxation combined with the later sluggish relaxation allows the growth of overlayers with a thickness considerably larger than the equilibrium critical thickness. Quantitative data obtained from in situ TEM analysis were also systematically applied to develop a model of strain relaxation including the effects of dislocation nucleation, propagation, and interaction [34.76].

Although detailed mechanisms for misfit dislocation nucleation in SiGe/Si systems are still controversial, the phenomena generally obey either heterogeneous or homogeneous nucleation mechanism. Earlier works looked for the source of heterogeneous nucleation, such as SiC precipitates formed by incomplete substrate cleaning [34.77], $a/4\langle 114 \rangle$ stacking fault regions [34.78, 79], surface half-loops, and faulted dislocation loops associated with metallic contamination [34.80, 81]. However, all of these heterogeneous sites appear dependently of the growth conditions and cannot account for the strain-relaxation behavior occurring in the initial stage because of their relatively low density. An activation barrier for homogeneous nucleation of surface dislocation half-loops was calculated for SiGe/Si(001) systems and was shown to be sensitively influenced by Ge contents, i.e., strain, and the dislocation core energy parameter [34.82]. A con-

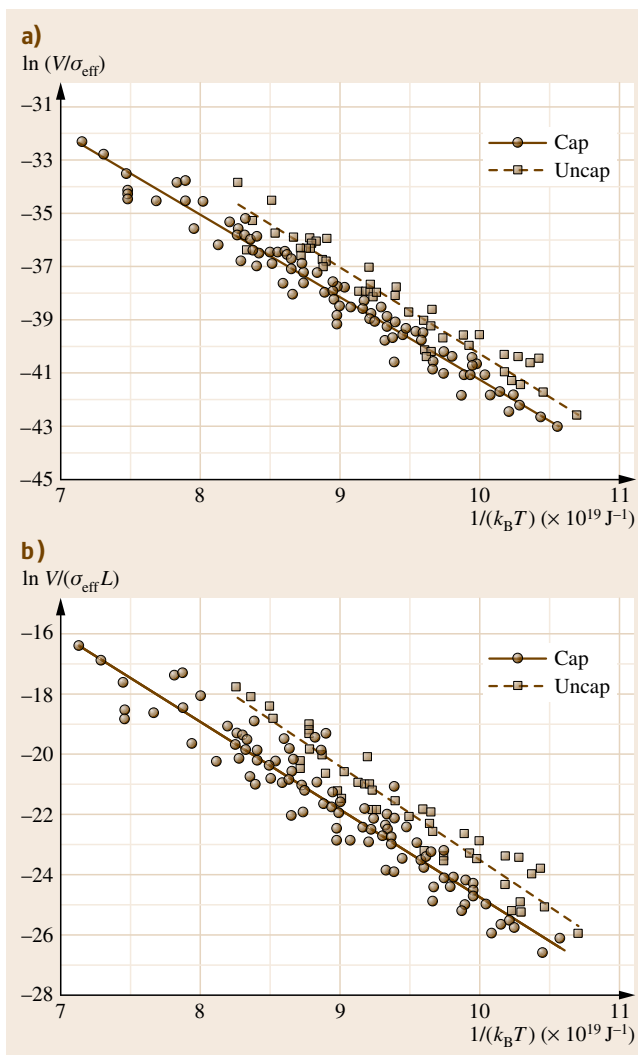


Fig. 34.14a,b Dislocation velocities in capped and uncapped (Si)/Si_{1-x}Ge_x/Si(001) heterostructures measured by TEM. The measured velocities V are normalized to equivalent velocities in pure Si by assuming a linear interpolation of the activation energy of Si and Ge, i.e., $E_a = (2.2 - 0.6x)$ eV. The velocities are also normalized to the effective stress σ_{eff} (a) and the product $\sigma_{\text{eff}}L$, where L is the length of the propagated dislocation line (b) ◀

sensus of qualitative arguments was reached in which homogeneous nucleation of half-loops is physically plausible at moderate and high mismatches, while heterogeneous nucleation relevant to a neighboring defect operates at low mismatch [34.83]. Furthermore, the aforementioned perturbation formed on the film surface plays a crucial role in dislocation nucleation. On the basis of STEM images showing SiGe cusp profiles, the condition that the local stress concentration at the surface cusp overcomes the nucleation barrier of half-loop dislocations was quantitatively discussed and the critical geometry for barrierless nucleation of 60° half-loops was derived [34.82, 84]. Similar analysis has been carried out for interfacial prismatic dislocation loops resulting from subnanometer-sized Ge-rich clusters as an efficient nucleation source [34.85].

As shown in Fig. 34.13, once half-loops nucleate on the film surface, they grow until they reach the substrate–overlayer interface. Then, each threading part of the dislocation moves toward the edges of the sample, leaving a misfit dislocation in the plane of the interface. The kinetics of such misfit dislocation propagation has been extensively investigated by two categorized methods: either direct observation of dislocation velocities by TEM or measurements of maximum length of dislocations by Nomarski interference microscopy of defect-etched surfaces [34.86–90]. These studies, irrespective of the difference in the measurements, show reasonable quantitative agreement with each other. In principle, the velocity of dislocation propagation V is

of the form of

$$V = V_0 \sigma_{\text{eff}} \exp\left(-\frac{E_a}{k_B T}\right), \quad (34.9)$$

where V_0 is a prefactor containing an attempt frequency, σ_{eff} is the effective stress acting on the threading dislocation arm, and E_a is an activation energy of dislocation glide [34.73]. Systematic measurements of dislocation velocities were achieved using in situ TEM [34.91]. Assuming a linear interpolation of the activation energies of Si and Ge, i. e., $(2.2-0.6x)$ eV, where x denotes the Ge content in $\text{Si}_{1-x}\text{Ge}_x$, the measured velocity was normalized to an equivalent velocity under a stress of 1 Pa in pure Si. Consequently, fairly good correlation is seen between samples across all ranges of epilayer composition and thickness (Fig. 34.14).

In the final stage of strain relaxation, dislocation multiplication events are dominant. The Hagen–Strunk source [34.92], which was first observed in orthogonal dislocation configurations in Ge/GaAs systems, is commonly cited for dislocation multiplication. However, later on, theoretical and experimental analyses showed that it seems an unlikely source [34.93, 94]. At present, several multiplication sources are proposed, such as so-called modified Frank–Read sources [34.95], cross-slip and pinning [34.96], and cross-slip for branch formation [34.97]; the latter two events are also followed by Frank–Read-type dislocation multiplication mechanisms.

34.7 Formation of Relaxed SiGe Layers

34.7.1 Graded Buffer

There are various types of strain-relaxed SiGe buffer layers developed so far for strained-layer channels in metal–oxide–semiconductor field-effect transistors (MOSFETs) and modulation-doped field-effect transistors (MODFETs). A compositionally graded SiGe buffer layer is most successfully applicable to such devices [34.98–102]. In the formation procedure, the Ge concentration x in the $\text{Si}_{1-x}\text{Ge}_x$ alloy gradually increases with increasing film thickness. The in-depth composition profile of Ge is generally set to be either linear or step-like. Since this structure is considered to be the sum of low-mismatch interfaces, misfit dislocations are successively introduced during growth, resulting in total strain relaxation of the film. Contrary to SiGe films without a gradi-

ent, since each atomic plane tends to have its own equilibrium lattice parameter, the dislocations accommodating the lattice parameter difference between the substrate and the top layer are distributed over the thickness of the graded region. This specific configuration of dislocations results in a much lower density of threading dislocations than that of the constant-composition film. Typically, a threading dislocation density on the order of 10^5 – 10^7 cm^{-2} is obtained, depending on the grading rate and final Ge concentration in the top layer. One of the reasons for the absence of threading dislocations in the top layer is high dislocation velocities at which the dislocation can bypass pinning points such as a site of dislocation intersection [34.95]. Since all dislocations are not attracted to only a single interface in the compositionally graded film, there is great freedom for a dislocation to move

onto another (001) plane reaching the edges of the wafers.

However, severe surface roughness, referred to as a cross-hatch pattern, has been pointed out from the beginning of the research on SiGe graded buffers [34.103–107]. Fitzgerald et al. have shown that such cross-hatch patterns are related to the strain field in the epilayer caused by an inhomogeneous distribution of misfit dislocations [34.106]. According to their calculation, the critical thickness h_{gc} for the introduction of dislocations into a graded layer is

$$h_{gc}^2 = \frac{3\mu b}{2\pi Y C_f (1-\nu)} \left(1 - \frac{\nu}{4}\right) \left[1 + \ln\left(\frac{h_{gc}}{b}\right)\right], \quad (34.10)$$

where C_f is the grading rate and Y is the Young's modulus. This formula clearly explains that larger grading rate leads to smaller h_{gc} , meaning that dislocations are introduced much closer to the surface and more strongly affect the evolution of the surface. On the other hand, a different mechanism was proposed, by which surface steps arising from the single and multiple 60° dislocations at the film–substrate interface directly influence the surface morphology of films [34.108]. Note that

these two cases employ different growth conditions: a steeper (slower) grading rate of 50% Ge μm^{-1} (10% Ge μm^{-1}) and a lower (higher) growth temperature of 560 $^\circ\text{C}$ (900 $^\circ\text{C}$) for the latter (former). Recently, a simulation study was performed to model the development of cross-hatch patterning on the basis of a combination of dislocation-assisted strain relaxation and surface steps during growth [34.109].

In graded buffers, there is a strong correlation between surface roughening and residual threading dislocation density. In general, the higher the final Ge concentration, the higher the threading dislocation density, despite the same grading rate. This results from a mechanism by which the combination of strain fields of underlying multiple misfit dislocations and the resultant surface roughness blocks the motion of a propagating threading dislocation, leading to dislocation pileups [34.110]. More recently, dislocation glide and blocking kinetics in compositionally graded SiGe buffers grown by UHV-CVD were reported and the dislocation density on the order of 10^4 cm^{-2} for 30% Ge was achieved at relatively high growth temperature of 900 $^\circ\text{C}$ [34.111].

In principle, graded buffers with low threading dislocation density require slow grading rate, which results in large thickness of the films and requires from time and material. Furthermore, poor thermal conductivity relevant to included Ge severely affects the performance of devices fabricated on graded buffers. Thus several techniques other than growth of graded buffers have also been attempted for strain-relaxed SiGe buffers on Si(001) substrates.

34.7.2 Low-Temperature Method

To reduce the layer thickness and improve the crystal quality of buffer layers, the low-temperature (LT) method was proposed [34.112, 113]. In this method, before growing relatively thin SiGe buffer layers (about 500 nm), a thin Si layer, e.g., 50 nm thick, is grown at a low temperature such as 400 $^\circ\text{C}$. Although the thickness of the SiGe buffer is much smaller than that required for the graded buffer method, it was found that the surface roughness is much better and the dislocation density is much smaller than those of the graded buffer method, while the relaxation ratio is almost equal, more than 80% [34.114]. That is, when the Ge composition is 30%, the surface roughness is about 1.5 nm and the dislocation density is around 10^5 cm^{-2} , while they are more than 10 nm and 10^7 cm^{-2} for the graded buffer method. It is known that surface roughness and re-

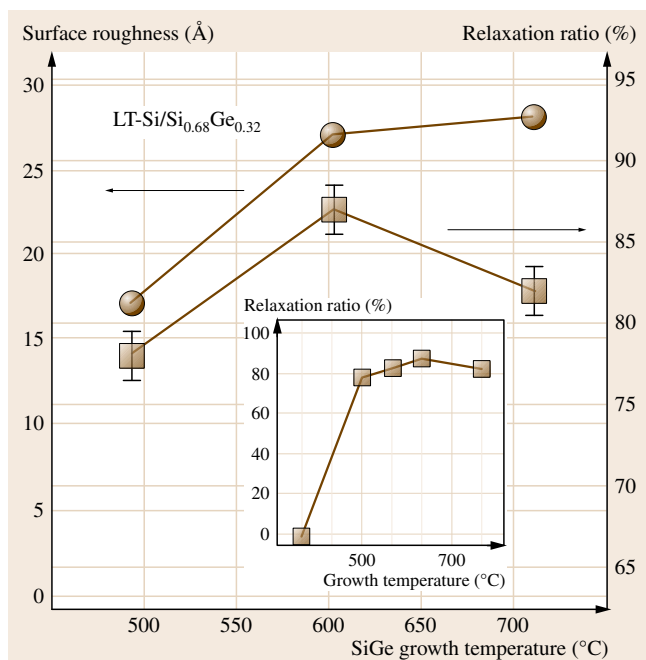


Fig. 34.15 Growth temperature dependence of surface roughness and relaxation ratio of Si_{0.68}Ge_{0.32} buffer layers grown on low-temperature-grown Si (LT-Si). The inset shows relaxation ratio in the wider temperature range

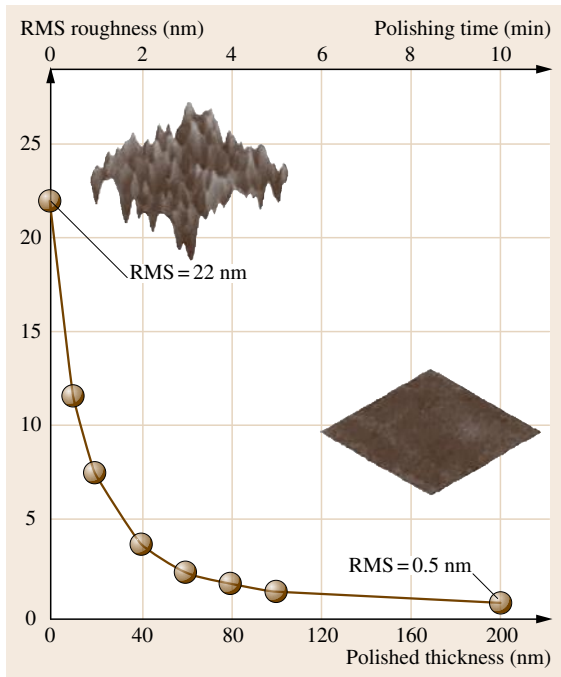


Fig. 34.16 CMP-polished thickness dependence of root-mean-square (RMS) surface roughness of relaxed SiGe buffer layers

laxation ratio do not change much when the growth temperature of **LT** Si layers is varied between 300 and 400 °C. However, the quality of buffer layers grown on **LT** Si largely depends on the buffer layer growth temperature. The relaxation ratio increases from 0 to 90% as the temperature increases from 400 to 700 °C and the roughness also increases, from 1 to 3 nm, with increasing temperature as shown in Fig. 34.15.

The quality of buffer layers largely depends on the Ge composition as well. Surface roughness as well as threading dislocation density increase with increasing Ge content up to 40% and then decrease.

From positron annihilation experiments, it is revealed that the Si layer grown at 400 °C contains a lot of defects, particularly vacancy clusters [34.115]. So, it is reasonably considered that these defects act as dislocation sources and confine dislocations in the vicinity of **LT** Si layers.

When high-Ge-content buffer layers are grown, the two-step growth of **LT** layers is found to provide strained overgrown layers with higher quality than the one-step growth method. Although the surface roughness of the buffer is hardly distinct between the two- and

one-step methods, short-period roughness is found to be superimposed in the case of the one-step method. This roughness may degrade the transport properties of the structures grown on it, and higher mobility was obtained in the case of the two-step method.

34.7.3 Chemical–Mechanical Polishing Method

Since obtaining high-quality relaxed SiGe buffer layers is a critical issue and the quality of the layers obtained by the methods described above is still not satisfactory for production, there have been a lot of attempts to develop better techniques. Chemical–mechanical polishing (**CMP**) of SiGe buffer layers with large roughness is one of the promising techniques [34.116–120]. **CMP** consists of mechanical polishing by small particles and chemical etching and is well established for preparation of Si wafers. The surface flatness of SiGe buffers after proper **CMP** polishing is almost equal to that of Si wafers, as shown in Fig. 34.16 where surface roughness is plotted as a function of polishing time [34.116]. It is demonstrated that the mo-

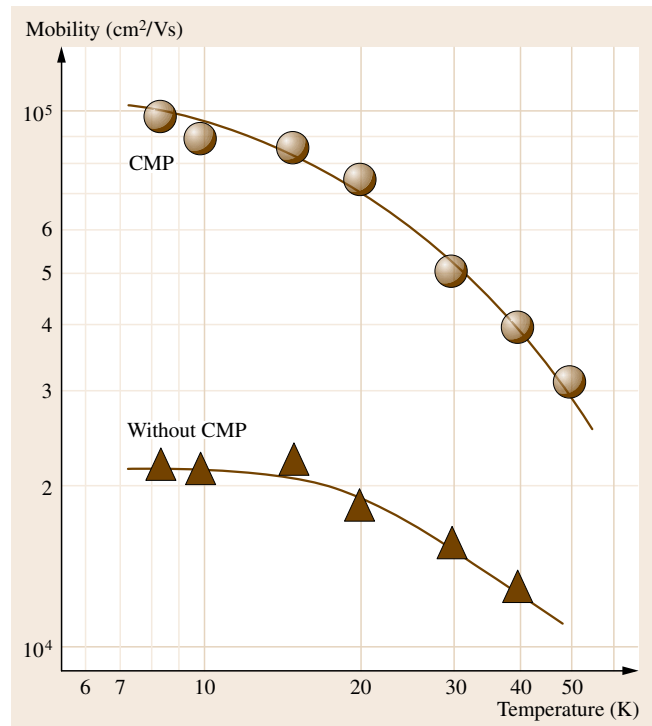


Fig. 34.17 Temperature dependence of electron mobility of SiGe/Si modulation-doped structures with and without **CMP** polishing

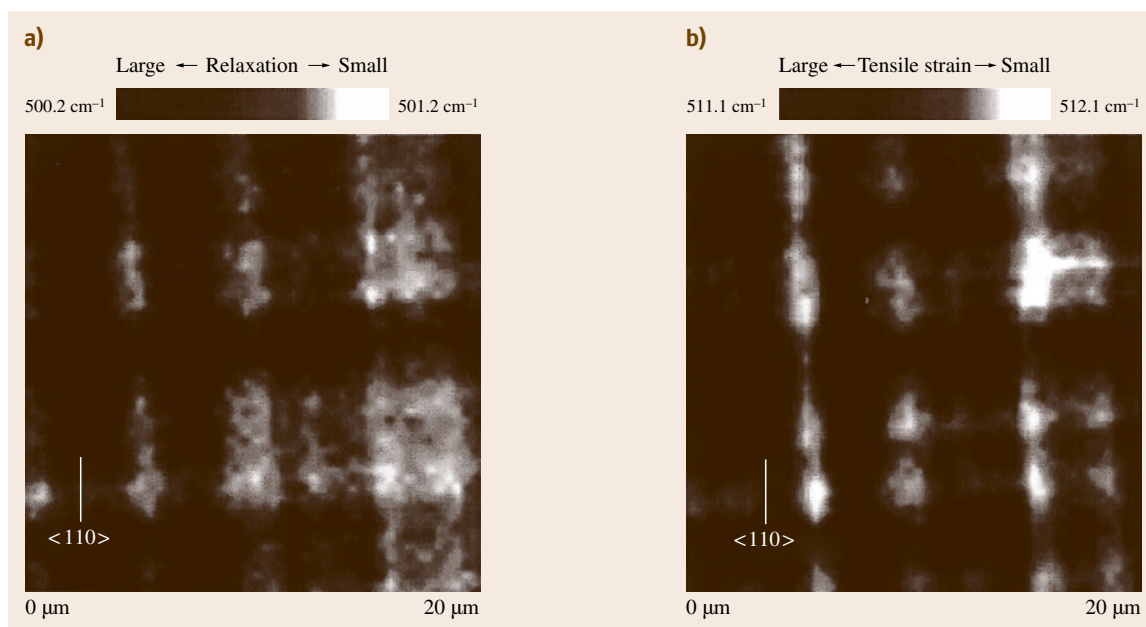


Fig. 34.18a,b Raman mapping of (a) relaxed SiGe buffer layer and (b) strained Si layer grown on SiGe buffers

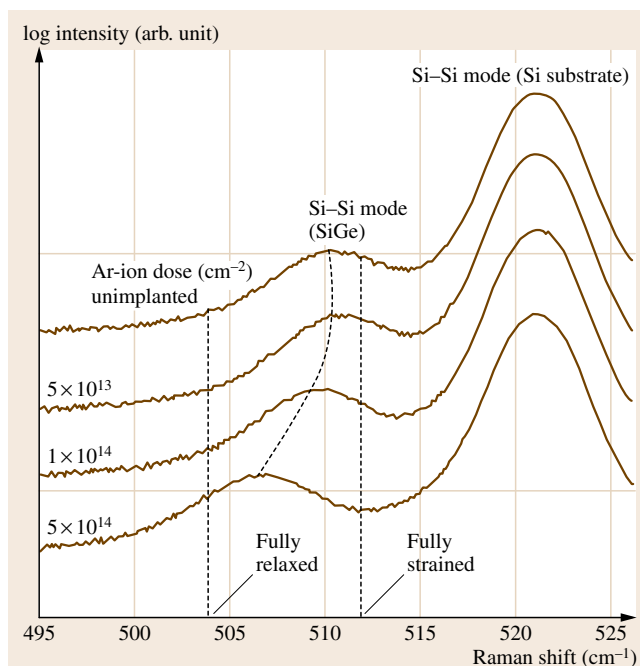


Fig. 34.19 Raman spectra of SiGe buffer layers grown on unimplanted and implanted Si substrates. Si-Si mode of SiGe layer is seen to shift to smaller wavenumber with increasing Ar-ion dose

bility of MOD structures formed on the flat surface is enhanced due to the reduction of interface scattering [34.117]. Figure 34.17 shows the temperature dependence of the mobility of the MOD structures formed on CMP polished and unpolished SiGe buffer layers. It is seen that the CMP sample provides an electron mobility four times higher than that of the unpolished sample. The mobility is shown to increase to about $600\,000\text{ cm}^2/(\text{V s})$ at very low temperatures. As for hole mobility, it has also been demonstrated recently that p-type Ge channel grown on CMP-polished SiGe buffers provides mobility eight times higher than that on unpolished ones [34.120].

However, it is noted that, even though CMP provides very flat surfaces, there still exists strain fluctuation coming from the underlying misfit dislocations in the SiGe buffer [34.121]. Figure 34.18 shows Raman mapping of SiGe buffer as well as strained Si grown on the buffer, from which it is clear that strain fluctuations similar to the cross-hatch pattern exist. It is also known that this strain fluctuation affects the growth rate of the overlayer and causes surface roughening [34.121].

34.7.4 Ion Implantation Method

Another interesting approach is ion bombardment of Si substrates. It was demonstrated [34.122–126] that

proton or helium ion implantation into Si substrates through epitaxially grown SiGe layers and annealing provided good strain relaxation of SiGe layers, and misfit dislocations were generated at the interface thanks to the defects introduced by the ion bombardment. To control defect formation well in the surface region of Si substrates, ion implantation with heavy ions such as Ar and Ge before epitaxial growth of SiGe layers has been shown to be very effective to relax the SiGe buffer layers [34.127–130]. Figure 34.19 shows Raman spectra of implanted and unimplanted samples, showing clearly that the implanted sample shows good strain relaxation, even though the SiGe buffer is much thinner than that produced by the conventional graded method. Many defects, mainly consisting of vacancy clusters, act as nucleation centers as well as dislocation absorbers similar to the role of the **LT** buffer layers. A thickness of only 100 nm is good enough to obtain fully relaxed SiGe buffer layers, which is attractive from the point of view of production. However, the surface roughness is not very low, being almost the same as that of the **LT** method.

Surface flatness comparable to that of Si wafers was found to be obtained when thin SiGe layers were pseudomorphically deposited at low temperatures on ion-implanted Si substrates and postannealing was carried out at relatively high temperatures [34.131]. As seen in Fig. 34.20, the surface of the SiGe buffer formed by this method is very smooth, almost the same as for Si wafers, and the relaxation ratio is more than 80%. It is also noted that the strain distribution is much more uniform and no cross-hatch-like pattern is observed. Since the cross-hatch pattern is not seen in this sample, uniform distribution of misfit dislocation without bunching or strain-relief mechanisms due to point defects, different from the conventional misfit dislocation formation, may occur in this sample.

This the ion implantation method is very useful for growth methods such as **CVD** and **GSMBE** where low-temperature growth cannot be performed to decompose source gases.

34.7.5 Ge Condensation Method

The ultimate application of strained Si may be as silicon-on-insulator (**SOI**). **SOI** has a lot of advantages over the bulk devices, such as suppression of short-channel effects and so on. To realize high-quality strained Si on relaxed SiGe-on-insulator (**SGOI**), a very unique and attractive method called the Ge condensation method was proposed [34.132–135]. The principle

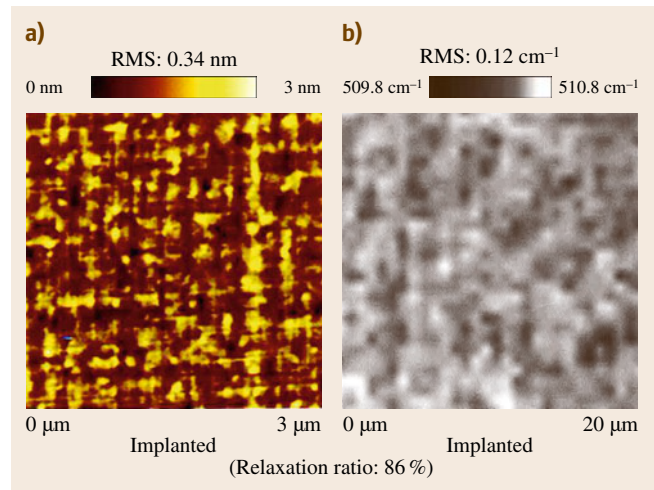


Fig. 34.20 (a) AFM image and (b) Raman mapping of SiGe buffers grown on ion-implanted Si substrate

of this method is shown in Fig. 34.21. When SiGe layers are oxidized, only Si atoms are consumed to form SiO_2 while Ge atoms are rejected from the oxide film. Therefore, when one deposits SiGe layers on **SOI** substrates and oxidizes the SiGe layers, the Ge content of the unoxidized SiGe layers is increased as the oxidation proceeds. It is also found that strain relaxation of SiGe grown on **SOI** simultaneously takes place during oxidation. As a result, relaxed SiGe layers with higher Ge content are formed on the buried oxide, that

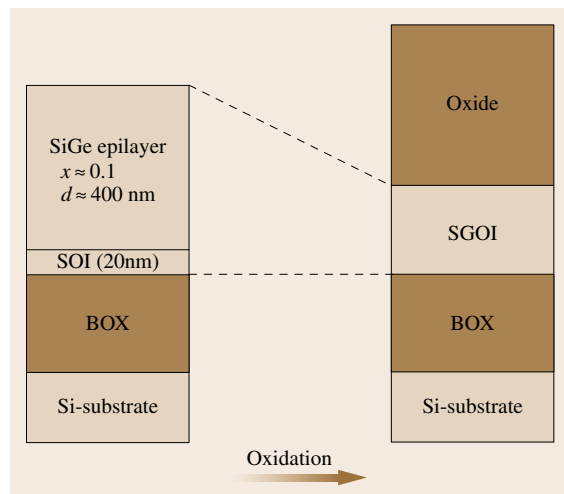


Fig. 34.21 Schematic illustration of Ge condensation method applied on SiGe epitaxial layer grown on **SOI** substrates. BOX is the buried oxide

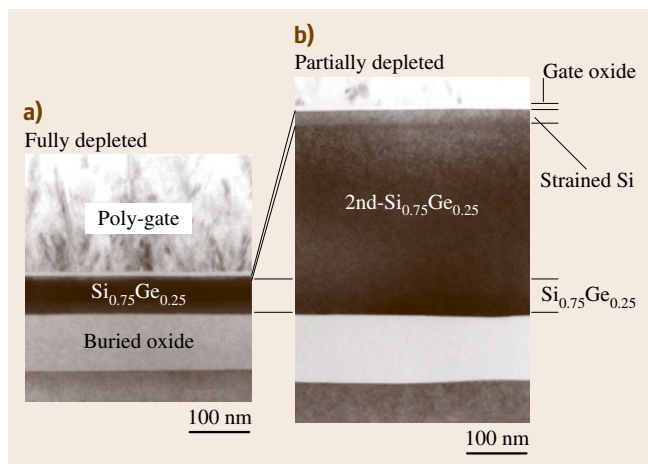


Fig. 34.22a,b TEM images of strained Si grown on (a) thin (fully depleted) and (b) thick (partially depleted) relaxed SiGe buffer layers formed by Ge condensation method

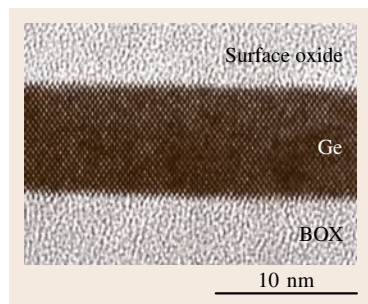


Fig. 34.23 TEM picture of Ge-on-insulator (GOI) structure fabricated by Ge condensation method

is, **SGOI** structures are formed. Strained Si layers can, therefore, be grown on this **SGOI**. Figure 34.22 shows TEM images of **SGOI** with strained Si layers; both fully (thin) and partially depleted **SGOI** (thick) structures are seen to be formed [34.136]. In the extreme case, pure Ge layers can be formed by this Ge condensation method and Ge-on-insulator (GOI) is realized, as shown in Fig. 34.23 where the Ge content of the layer on the insulator becomes almost 100% after complete oxidation of SiGe layers [34.137].

34.7.6 Dislocation Engineering for Buffer Layers

In general, glide dislocations, i. e., 60° dislocations, are predominantly introduced into the SiGe/Si(001) interface as a result of the operation of the $\langle 110 \rangle / \{111\}$ slip system. Although misfit strain is mainly relaxed by an edge component of the Burgers vector of the 60° dislo-

cation parallel to the interface, a screw component and components nonparallel to the interface simultaneously induce nonisotropic strain relaxation [34.138], as well as crystallographic tilting and rotation of SiGe. Such crystallographic inhomogeneity severely influences the lattice deformation of the channel Si and eventually leads to nonuniformity of the energy band structure. In this subsection, recent experimental results on epitaxial growth in which dislocation generation and propagation are precisely controlled during strain relaxation of SiGe are presented.

The two-step strain-relaxation procedure [34.139] was demonstrated to realize fully strain-relaxed thin buffer layers with low threading dislocation densities. This procedure consists of, first, annealing of a metastable pseudomorphic SiGe layer with a Si cap layer and, second, subsequent growth of SiGe on that layer. The thin cap layer effectively suppresses surface roughening during the annealing due to reduction of the surface stress of the film [34.140, 141]. More than 90% relaxation was achieved after growth of only a 100 nm thick second Si_{0.7}Ge_{0.3} layer. Figure 34.24 shows a representative cross-sectional TEM image of a sample having a Si_{0.7}Ge_{0.3}(200 nm)/Si-cap(5 nm)/Si_{0.7}Ge_{0.3}(50 nm)/Si(001) structure. Note that threading dislocations are almost absent from the observed area and almost all misfit dislocations are confined at the first SiGe/Si substrate interface. These dislocations tend to be dispersed at the interface and pileup of the dislocations, which is often observed in compositionally graded layers [34.108], is hardly observed. The observed periodic surface undulation comes



Fig. 34.24 Cross-sectional TEM image of a sample grown by the two-step strain-relaxation procedure. The sample has a Si_{0.7}Ge_{0.3}(200 nm)/Si-cap(5 nm)/Si_{0.7}Ge_{0.3}(50 nm)/Si(001) structure. Threading dislocations are almost absent from the observed area and almost all misfit dislocations are dispersively confined at the first SiGe–Si substrate interface. The observed periodic surface undulation comes from aligned SiGe islands formed at the earlier stage on the misfit dislocation network buried at the first SiGe–substrate interface as a template

from aligned SiGe islands formed at the earlier stage on the misfit dislocation network buried at the first SiGe–substrate interface as a template. Similar preferential nucleation over dislocation was reported by Xie et al. [34.142]. As mentioned in Sect. 34.6, since a cusp in the surface undulation acts as a preferential nucleation site for misfit dislocations [34.143], dislocation half-loops are likely introduced at every cusp on the surface to relax the strain during the growth of the second layer. Therefore, strain relaxation is dominated by the introduction of new dislocations from the surface, and a regular strain field created by the periodic undulation greatly enhances the propagation of the introduced dislocations so that the threading segments have the opportunity to travel long distances.

Due to the intrinsic structure of a 60° dislocation, a SiGe film strain-relaxed by 60° dislocations often exhibits mosaicity [34.144] and cross-hatch patterns [34.106, 108]. In order to prevent such degradation, the introduction of pure-edge dislocations is crucial. A novel approach based on strain relaxation predominantly by a pure-edge dislocation network buried at the SiGe/Si(001) interface was recently demonstrated [34.145]. Employing pure-Ge thin-film growth prior to SiGe formation effectively restrains the introduction of 60° dislocations; instead, a high density of pure-edge dislocations can be generated [34.146]. Figure 34.25a shows a plan-view TEM image of the Ge layer, which was grown at 200°C and then subjected to annealing at 700°C . A dislocation network, consisting of pure-edge dislocations aligned along two orthogonal $\langle 110 \rangle$ directions, can be clearly observed at the Ge–Si(001) interface. For forming SiGe layers, solid-phase

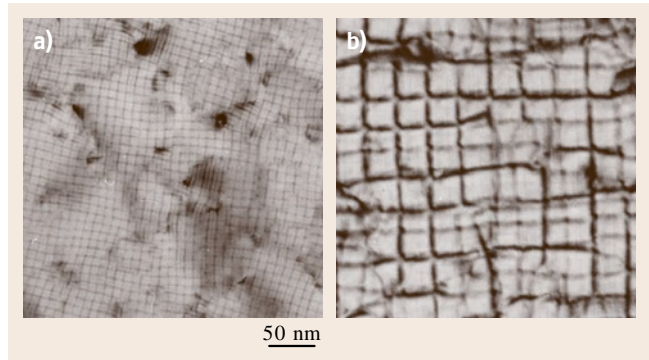


Fig. 34.25 (a) Plan-view TEM image of a Ge layer on Si(001), which was grown at 200°C and then subjected to annealing at 700°C , showing a dislocation network consisting of pure-edge dislocations aligned along two orthogonal $\langle 110 \rangle$ directions. (b) Plan-view TEM image of an a-Si (17 nm)/Ge(30 nm)/Si(001) sample annealed at 1100°C (the scale is the same as that in (a)). The morphology of the pure-edge dislocation network is retained even after the high-temperature annealing, but the dislocation spacing increases

intermixing of amorphous Si (a-Si) deposited on the Ge layer was performed. Figure 34.25b shows a plan-view TEM image of an a-Si (17 nm)/Ge(30 nm)/Si(001) sample annealed at 1100°C . Note that the morphology of the pure-edge dislocation network is explicitly retained even after the high-temperature annealing but the dislocation spacing is found to increase. Figure 34.26a shows an x-ray diffraction two-dimensional reciprocal-space map around a SiGe(115) diffraction peak of the sample annealed at 1100°C . From the peak position,

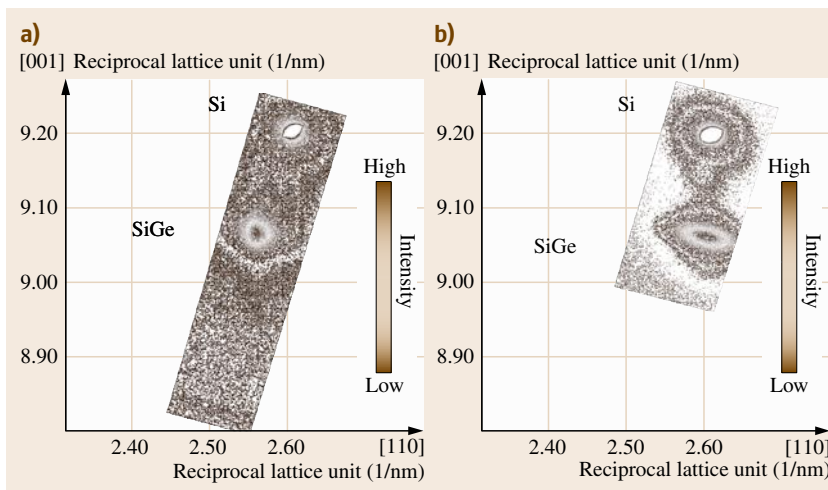


Fig. 34.26a,b XRD two-dimensional reciprocal maps around Si(115) and SiGe(115) diffraction peaks of (a) the sample annealed at 1100°C , which has a pure-edge dislocation network at the SiGe–Si(001) interface, and (b) the sample with 60° dislocations grown by the two-step strain-relaxation procedure

it is found that an in-plane lattice constant corresponding to that of a SiGe crystal with a Ge fraction of 0.48 is obtained, enabling practical use as a SiGe buffer. A remarkable feature is found in the peak shape being sharp and highly symmetric, in marked contrast to that of the reference sample shown in Fig. 34.26b, which is prepared by the two-step strain relaxation procedure and predominantly has 60° dislocations at the interface. This result clearly demonstrates that the mosaicity, such as lateral finite sizes and microscopic in-plane tilts of the SiGe crystal [34.147], is greatly reduced when introducing pure-edge dislocations.

34.7.7 Formation of SiGeC Alloys

Since the first epitaxial growth of high-quality $\text{Si}_{1-y}\text{C}_y$ and $\text{Si}_{1-x-y}\text{Ge}_x\text{C}_y$ films on Si(001) was reported in 1992 [34.148–150], the introduction of C into Si and SiGe films has attracted increasing interest for application of these films to electric and optoelectronic devices composed of group IV semiconductor materials. Due to the different covalent radius of Si, Ge, and C of 0.117, 0.122, and 0.077 nm, respectively, substitutional introduction of C atoms into SiGe lattice sites gives rise to a substantial decrease of the lattice parameter and a reduction of strain in SiGe layers on Si substrates [34.151–154]. The addition of C into $\text{Si}_{1-x}\text{Ge}_x$ films is, therefore, expected to yield several advantageous effects in terms of device performance. In Si/SiGe/Si HBTs, when C is incorporated into a SiGe base layer, the strain caused by the SiGe/Si lattice mismatch can be alleviated and thus the generation

of misfit dislocations can be prevented, realizing improved crystalline quality of the base layer and resultant reliability of the devices. Furthermore, C incorporation can significantly suppress boron outdiffusion from a p-type base layer due to the undersaturation of interstitial Si atoms [34.155–158]. On the other hand, it has been reported that the bandgap and band offsets with respect to the conduction band and valence band sensitively vary with C contents and strain in $\text{Si}_{1-x-y}\text{Ge}_x\text{C}_y$ films [34.159–169]. On the basis of the control over the band alignment in $\text{Si}_{1-x-y}\text{Ge}_x\text{C}_y$ heterostructures, $\text{Si}_{1-x-y}\text{Ge}_x\text{C}_y$ epitaxial films were applied to channel layers in MOSFET [34.170, 171], high-electron-mobility transistor (HEMT), and optical devices [34.172–174]. However, substitutional incorporation of C exceeding a few percent is very difficult to achieve. One dominant reason seems to be the thermal equilibrium solubilities of C into Si and Ge, of the order of 10^{17} and 10^8 atoms/cm³, respectively [34.175, 176]. The crystalline quality of the films is degraded with increasing C fraction and exhibits nonplanar morphology, SiC polytype precipitates, and extended defects such as stacking faults and dislocations. Therefore, film growth techniques in which the growth mode is governed not by thermodynamics but kinetics are now widely employed, such as MBE [34.150, 151, 177, 178], UHV-CVD [34.179, 180], and RT-CVD [34.181, 182]. However, this still remains an essential issue in the growth of high-quality epitaxial $\text{Si}_{1-x-y}\text{Ge}_x\text{C}_y$ films with a substitutional C content higher than 3% and this limits the potential of these films to be applied widely to various kinds of devices [34.178, 183]. Enhanced solubility of C was theoretically predicted [34.184], and it was experimentally demonstrated that $\text{Si}_{1-y}\text{C}_y$ layers with $y \approx 0.2$ can be grown pseudomorphically on Si(001) due to the formation of low-energy ordered structures [34.185]. In the case of $\text{Si}_{1-x-y}\text{Ge}_x\text{C}_y$ films, high repulsive interaction between Ge and C in the Si lattice plays a dominant role in determining the composition profiles of the film; both theoretical and experimental works on this matter have been performed [34.152, 186, 187]. Furthermore, attractive interaction between Si and C affects the final film morphology. Figure 34.27a shows an STM image of a surface of a $\text{Si}_{0.478}\text{Ge}_{0.478}\text{C}_{0.044}$ film with a thickness of four monolayers (ML) [34.188]. The surface exhibits the onset of three-dimensional (3-D) islanding, suggesting the local increase of Ge fraction around the island where the film locally exceeds the critical thickness for islanding. It should be noted that these islands are different from those

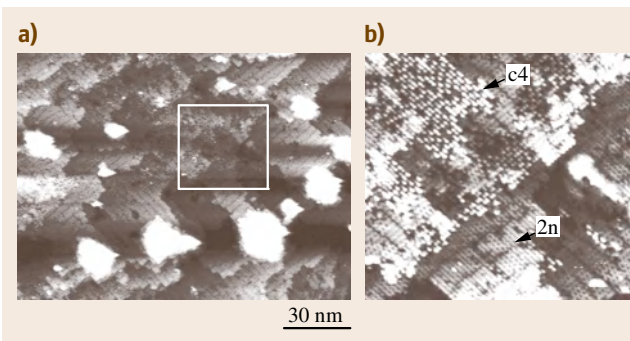


Fig. 34.27a,b STM images of a $\text{Si}_{0.478}\text{Ge}_{0.478}\text{C}_{0.044}$ film of 4 ML thickness grown on Si(001). (a) Islands with a height of about 2 nm on average are frequently observed on top of protruding regions of the terraces. (b) Magnified $30 \times 30 \text{ nm}^2$ image of the boxed area in (a). Examples of the $c(4 \times 4)$ and $(2 \times n)$ reconstructions are indicated by the labels “c4” and “2n,” respectively

due to C-induced Ge islanding [34.189, 190], since they were not formed at the beginning of the growth. As shown in Fig. 34.27b, a close-up of the fairly flat terraces reveals the $c(4 \times 4)$ reconstructed structure caused by significant C condensation on the growing surface [34.191–193] and the $(2 \times n)$ reconstruction consisting of buckled dimers and missing dimer rows. These results clearly show the formation of C-rich and Ge-rich regions in the film, which is presumably driven by the phase separation between Si-C and Si-Ge during growth when the film contains high concentration of C.

Control over the initial growth stage was performed to improve the film morphology [34.188, 193]. The addition of a thin (1–2 ML) SiGe interlayer between the $\text{Si}_{1-x-y}\text{Ge}_x\text{C}_y$ film and the Si substrate drastically improves the film structure, leading to a planar morphology even with large C fractions present in the film. Figure 34.28 shows an STM image of a sample which has a structure of $\text{Si}_{0.473}\text{Ge}_{0.473}\text{C}_{0.054}$ (6 ML)/ $\text{Si}_{0.5}\text{Ge}_{0.5}$ (1 ML)/Si(001). Note that a planar surface morphology consisting of a step and terrace structure is formed even though the film contains a 4.6% average C fraction. Three-dimensional islanding partially appears at the step edges with increasing $\text{Si}_{1-x-y}\text{Ge}_x\text{C}_y$ film thickness [34.194, 195] but no $c(4 \times 4)$ reconstructions were observable in any growth stage. This clearly demonstrates that the $\text{Si}_{1-x}\text{Ge}_x$ interlayer explicitly plays a role in suppressing C condensation and Si-C/Si-Ge phase separation during the film evolution.

More recently, sequential alternate deposition of 1 ML thick $\text{Si}_{0.793}\text{Ge}_{0.207}$ and 0.048 ML thick C layer on Si(001) was attempted in order to suppress local phase separation, 3-D island growth, and defect formation [34.196]. A comparison of the surface atomic morphologies between the 5 ML thick $\text{Si}_{0.769}\text{Ge}_{0.183}\text{C}_{0.048}$ layer formed by the codeposition of Si, Ge, and C and that by the alternate deposition is shown in Fig. 34.29. In Fig. 34.29a, the 3-D islands, with a height of approximately 2 nm, and a rough surface consisting of small terraces are observed. Many defects, observed as dark spots on the surface, which are sink sites of C atoms, seem to prevent conformal step-flow growth due to the positive (normal) Ehrlich–Schwoebel barrier [34.197–

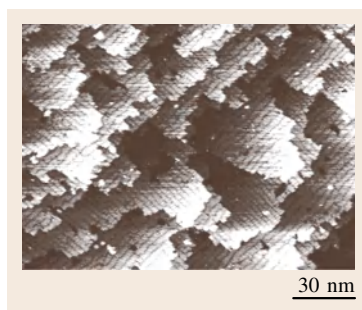


Fig. 34.28 STM image of a sample with a structure of $\text{Si}_{0.473}\text{Ge}_{0.473}\text{C}_{0.054}$ (6 ML)/ $\text{Si}_{0.5}\text{Ge}_{0.5}$ (1 ML)/Si(001). A planar surface morphology is realized by the formation of the SiGe interlayer, in spite of the large C fraction

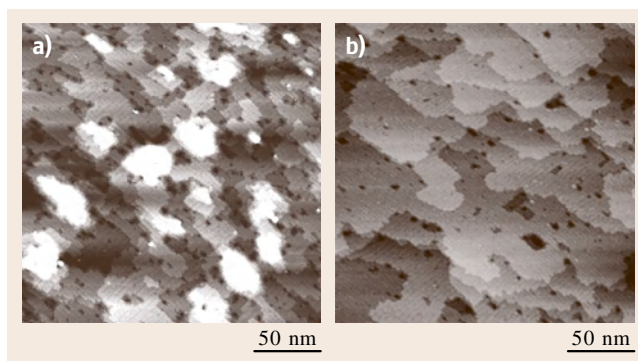


Fig. 34.29a,b STM images of the 5 ML thick $\text{Si}_{0.769}\text{Ge}_{0.183}\text{C}_{0.048}$ layer formed by (a) the codeposition of Si, Ge, and C; (b) the alternating deposition of 1 ML thick $\text{Si}_{0.793}\text{Ge}_{0.207}$ and 0.048 ML thick C layers. In the codeposition, 3-D islands with a height of approximately 2 nm, a rough surface consisting of small terraces, and defects as dark spots are observed on the surface, while no 3-D islands with reduced defects are seen in the case of the alternating deposition

[199]. On the other hand, in Fig. 34.29b, no 3-D islands are observed and aligned steps are still formed. The density of defects is relatively low compared with the codeposition case. In the alternate deposition case, the migration of C on the growing surface is effectively restrained because the Ge atoms, which give rise to the repulsive interaction force to the deposited C atoms, are uniformly distributed on the $\text{Si}_{1-x}\text{Ge}_x$ surface. This effect leads to suppression of defect formation at the initial stage of $\text{Si}_{1-x-y}\text{Ge}_x\text{C}_y$ growth and consequently increases the critical thickness of layer-by-layer growth of $\text{Si}_{1-x-y}\text{Ge}_x\text{C}_y$.

34.8 Formation of Quantum Wells, Superlattices, and Quantum Wires

The formation of double heterostructures results in quantum well (QW) formation. Type I QWs are eas-

ily realized by growing strained SiGe layers on Si substrates and sandwiching it with unstrained Si lay-

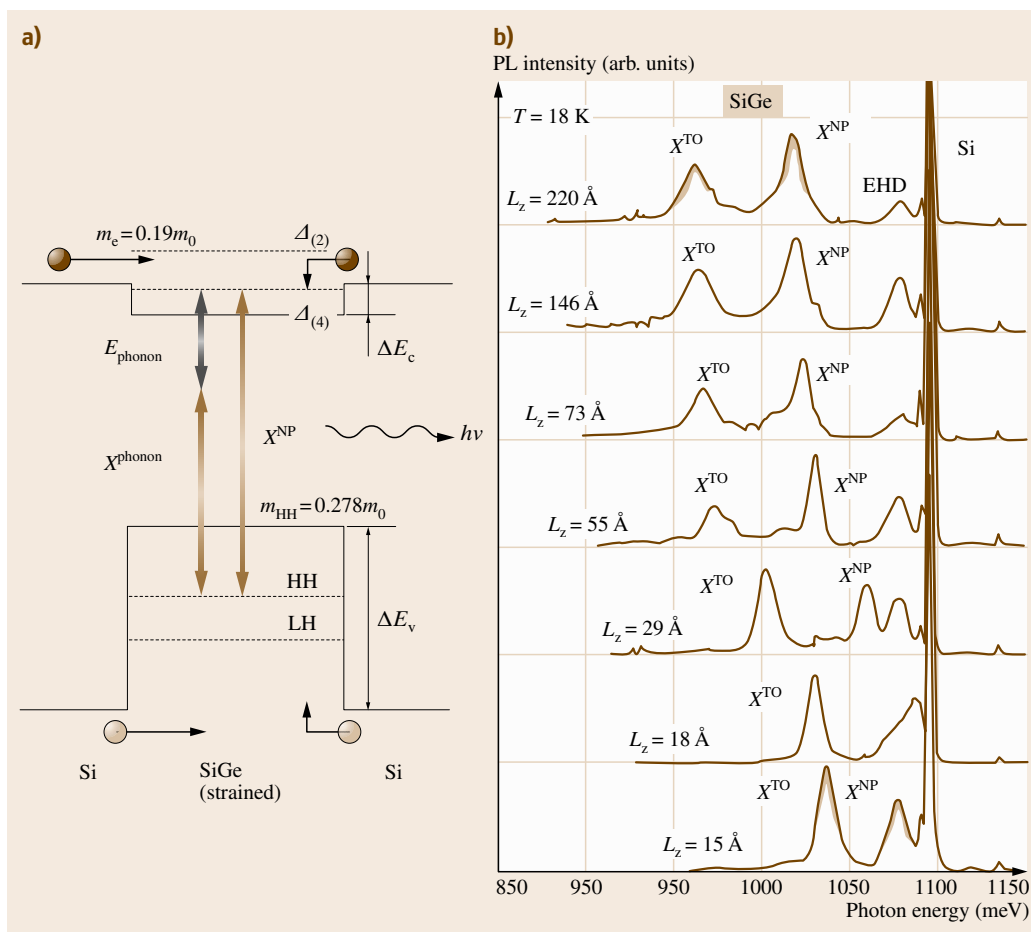


Fig. 34.30a,b Schematics of PL from strained SiGe/Si quantum well (a) and well width dependence of PL spectra of the quantum well (b). NP represents luminescence peaks without phonon assistance, and phonon and TO represent phonon replica peaks

ers. Peak shift due to the quantum confinement effect characteristic of QWs is clearly seen in the PL spectra of QWs grown by gas-source MBE, as shown in Fig. 34.30 [34.200]. There are two prominent PL peaks, no-phonon (NP) and the TO-phonon replica, which are characteristic of indirect-bandgap transition in this system, and both peaks shift to higher energies with decreasing well width. The theoretical calculation based on square QWs well represents the well width dependence of the quantum confinement energy.

Although the luminescence peaks become broader with increasing temperature, their integrated intensity is stable up to 100 K. Above 100 K, however, the intensity decreases rapidly with an activation energy of around 100 meV [34.34]. This activation energy corresponds to the energy difference between the valence band of Si barriers and the ground quantum level in the SiGe QW. That is, carrier confinement of QWs is quite

efficient at low temperatures but holes begin to escape from the well above the temperature corresponding to the confinement energy.

Since the band alignment changes depending on the strain condition, type II QWs are also formed. When tensile-strained Si layer is sandwiched by unstrained SiGe barrier layers, holes are trapped in the Si well layers while electrons are located in the SiGe barrier layers and therefore the transition is indirect in real space as well as in momentum space. However, luminescence, due to both NP and TO peaks, is clearly observed and the energy shift coming from the quantum confinement effect is confirmed [34.201].

Although the band alignment is type I when strained SiGe layers with Ge composition less than 30% is set between unstrained Si layers, the band discontinuity at the conduction band is too small to confine electrons well in the well region. To overcome this problem, there

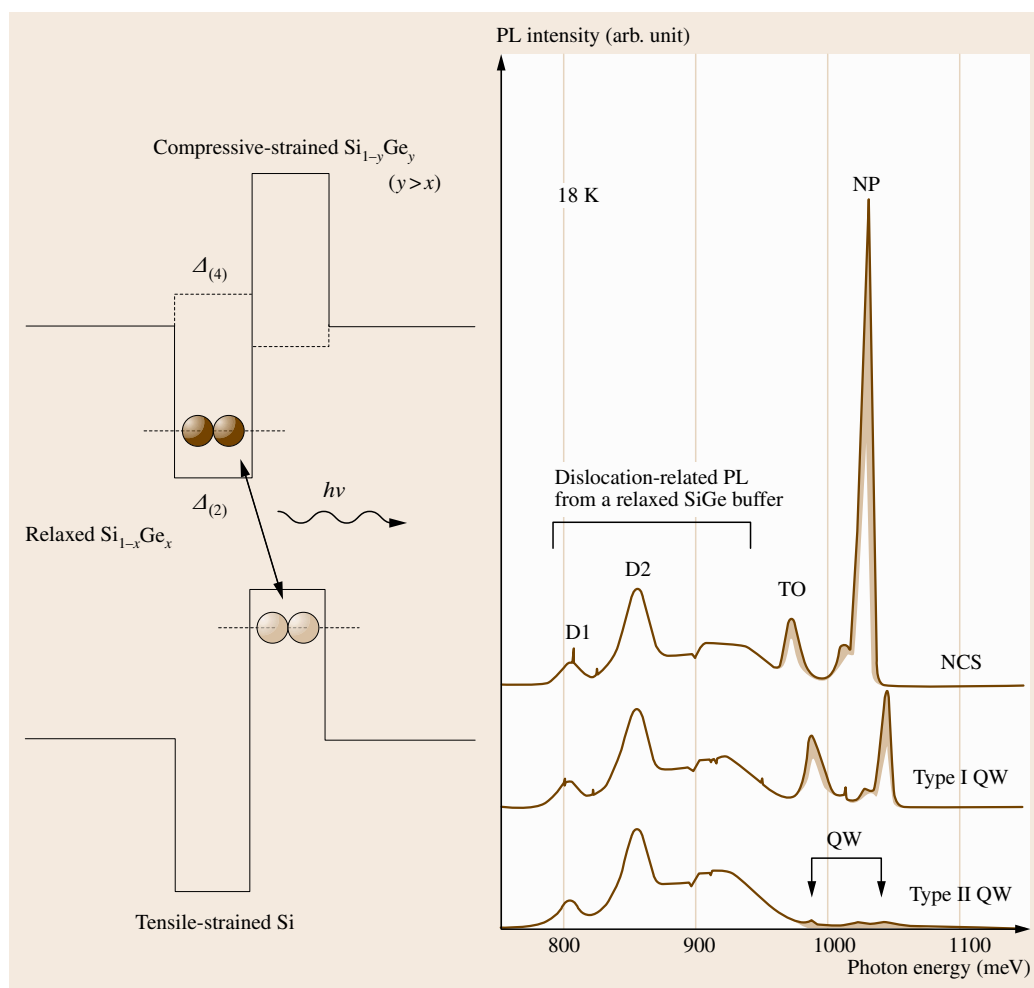


Fig. 34.31 Band structure of Si/SiGe neighboring confinement structure (NCS) and PL spectra of NCS, type I and type II quantum wells

are several ideas to improve the carrier confinement, one of which is the neighboring confinement structure (NCS), in which a pair of compressively strained and tensile-strained layers is sandwiched by strain-relaxed SiGe barrier layers, as shown in Fig. 34.31 [34.202]. Although electrons and holes are separately confined in the well region, the PL intensity, particularly the NP peak, is significantly enhanced in this structure and is stronger than that in conventional type I QWs. This comes from the significant wavefunction overlap between electrons in Si and holes in Ge layers, but it is noted here that the thickness of the pair layers should be thin to keep sufficient wavefunction overlap for the transition.

The coupling of QWs results in the formation of superlattices, which is seen in the energy shift of PL

peaks, with the peaks shifting to lower energies with decreasing distance between the QWs [34.203]. The peak energies of coupled QWs agree well with the calculated results based on ideal square-shaped wells, in accordance with the theoretical prediction [34.1] that the band alignment is type I when Ge content is lower than 0.3. This also indicates that wells without deformation due to surface segregation are formed by GSMBE.

The evolution of superlattices is seen when the number of coupled wells is increased [34.204]. Since the increase in the number of coupled wells lowers the ground-state energy and finally forms a miniband, the PL peak energy, corresponding to the miniband edge, decreases with increasing well number. The peak energy is found to follow a simple Kronig-Penny-type calculation for the superlattices [34.204].

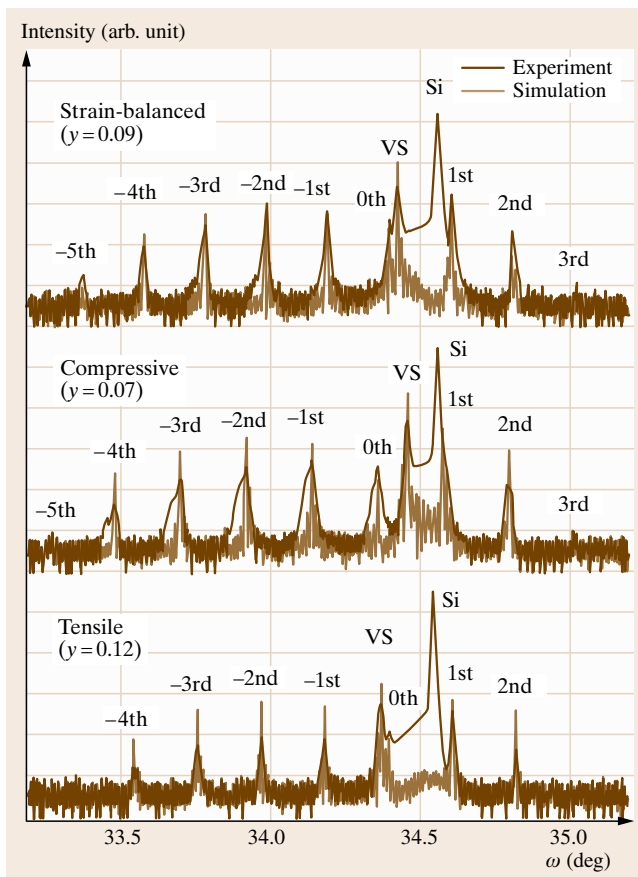


Fig. 34.32 XRD intensity profiles of SiGe/Si multilayers (DBR structures) grown under strain-balanced, compressive, and tensile conditions

Multilayer structures, in which each layer is much thicker than in superlattices, are also important from the point of view of optical device applications. The typical

example of such structures for optical applications is the distributed Bragg reflector (DBR) mirror, which consists of multilayers of materials with different refractive index, such as GaAs/AlAs and Si/Ge. Since the period of DBR structures should be comparable to the wavelength of light in semiconductors, the thickness of each layer is as large as ten times that in a superlattice. Therefore, the growth of such structures with a strained system is very difficult due to the limitation of the critical thickness. To overcome this problem, strain-balanced structures are very useful [34.205], and DBR mirrors consisting of Si and SiGe layers have been successfully fabricated [34.206–209]. In this method, a pair of layers with lattice constants a_1 and a_2 are grown on a substrate with lattice constant a_0 , where $a_1 < a_0 < a_2$. This condition is satisfied when a pair of Si layers with tensile strain and SiGe layers with compressive strain are grown on relaxed SiGe with Ge content less than that of the pair. The thickness and Ge composition are selected so that the strain energy of the structure is minimized.

Figure 34.32 shows x-ray diffraction measurements where the Ge content of the virtual substrate is changed. It is seen that the peak of the sample with $y = 0.09$ coincides well with the position of the strain-balanced condition, showing that strain-balanced structures are formed by carefully choosing the layer thickness and Ge contents. Figure 34.33 shows an SEM image of a DBR structure grown under the strain-balanced condition, and it is seen that high-quality structures without detectable defects are obtained.

Figure 34.34 shows the reflection spectrum of SiGe DBR mirrors fabricated by this method. In this structure, Si and SiGe layers with thickness of 94 and 90 nm, respectively, were grown on fully relaxed SiGe buffer layers to compensate the strain. Reflectivity of about 90%, which is quite large for the strained system, is obtained.

Selective epitaxial growth, which takes place in growth techniques such as gas-source MBE, leads to the formation of wire and dot structures. This occurs, for instance, between Si and SiO₂ substrates, and epitaxy occurs only on Si. When SiGe/Si QWs are formed on V-groove-patterned Si(100) substrates with (111) facets [34.210, 211], crescent-shaped SiGe features are grown in the bottom of the V-groove. This feature gives rise to PL with large blue-shift in the spectrum compared with the reference QW sample. It is also seen that the cross-sectional emission in the case of the wire

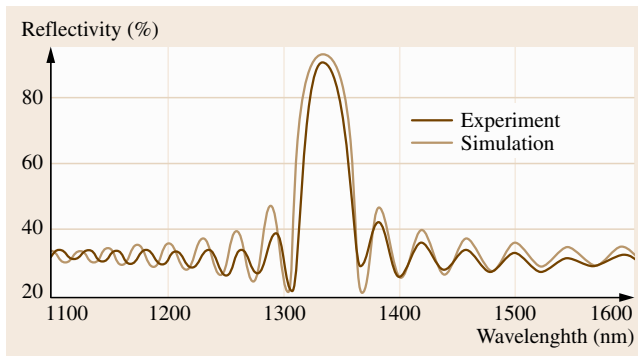


Fig. 34.34 Reflectivity spectrum of SiGe/Si DBR mirror formed by the strain-balanced method ◀

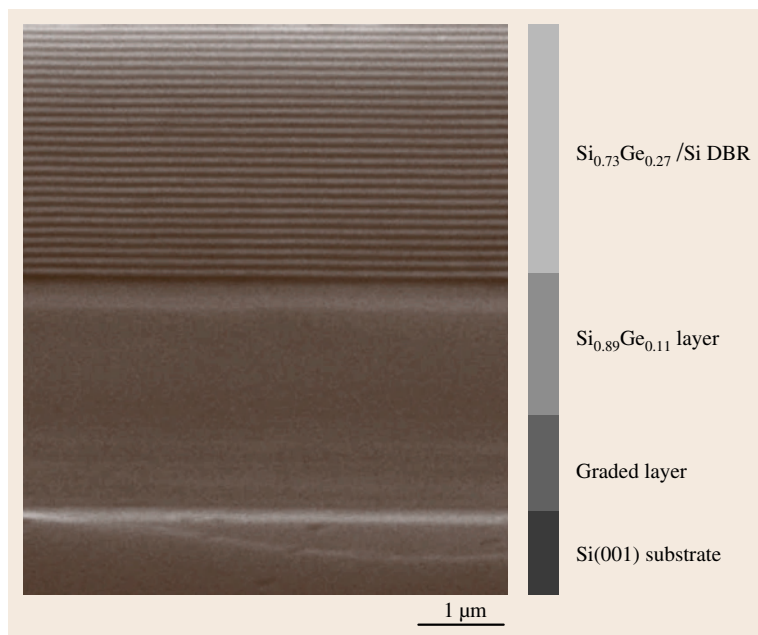


Fig. 34.33 Cross-sectional SEM image of $\text{Si}_{0.73}\text{Ge}_{0.27}/\text{Si}$ DBR mirror grown on $\text{Si}_{0.89}\text{Ge}_{0.11}$ buffer layers formed by the graded-buffer technique

structure shows polarization characteristics while no polarization is seen in the emission from the QWs. This result suggests that the wire structure in the V-grooved sample is likely to be a quantum wire. However, the energy shift in quantum wires is too large and does not agree with a simple estimation based on their size. The main cause of the energy shift may be the change in the

strain distribution. The wire surrounded by Si crystal is considered to be under hydrostatic-like pressure that causes bandgap broadening comparable to the observed energy shift. Since spatial variation of the Ge composition in the wire is also likely to occur, more detailed study is required to clarify the nature of quantum wires in the SiGe/Si system.

34.9 Dot Formation

There are a large number of studies on Ge and SiGe dot formation, which strongly depends on the growth methods and conditions. Since there are several good reviews [34.212–215] concerning Ge dot formation, some general features of the formation, which are observed in the case of gas-source MBE (GSMBE), are described here [34.216].

Figure 34.35 shows the thickness dependence of the PL spectrum from Si/pure-Ge/Si quantum-well structures grown by GSMBE [34.217]. Up to 3.7 ML, the PL spectrum shows a conventional quantum confinement effect of quantum wells and the peaks shift to lower energies with increasing Ge layer thickness. Above 3.7 ML, however, the peaks originating from QWs stop the energy shift and a new broad peak is seen to appear. The appearance of this broad peak corresponds

well to the formation of Ge islands observed by TEM measurements. That is, above the critical thickness, Ge begins to form islands on Ge wetting layers to release the strain energy as described in the previous section. It is remarkable that these Ge dots give rise to significant luminescence, and therefore their application as quantum dots is eagerly awaited.

The critical thickness in the case above is 3.7 ML and depends on the growth temperature, as shown in Fig. 34.36. It is seen from this figure that the critical thickness increases with decreasing growth temperature.

It is well known that Ge dot formation takes place in a bimodal fashion, that is, small pyramidal-shape and large dome-shape dots are formed simultaneously, as shown in Fig. 34.37, and that their relative numbers

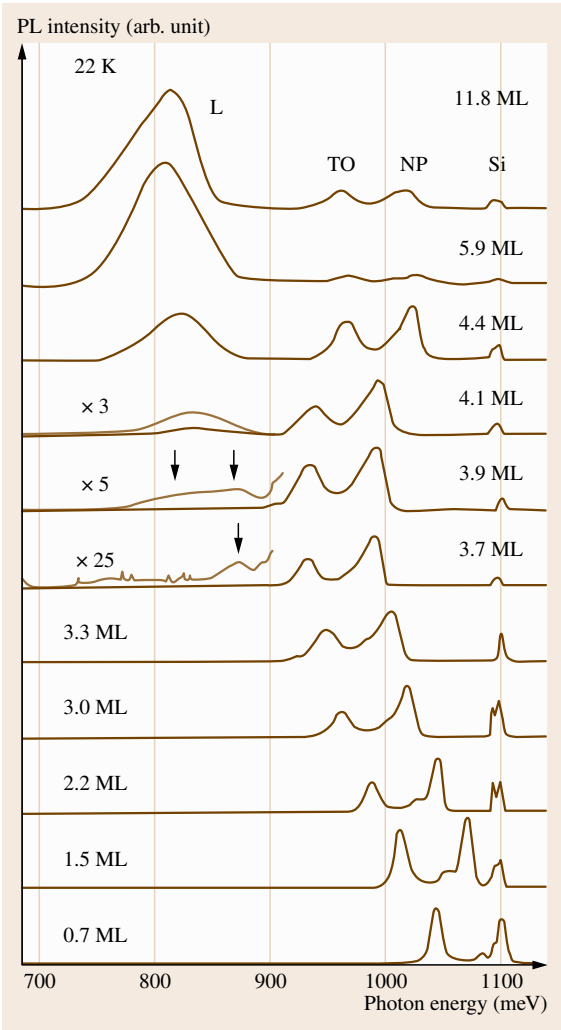


Fig. 34.35 Ge layer thickness dependence of PL spectrum of Si/pure-Ge/Si structures. Above 3.7 ML, a new broad PL peak (L) corresponding to Ge dot formation appears and grows with increasing Ge amount, while the peaks corresponding to quantum wells are seen to stop the energy shift once the dot is formed ◀

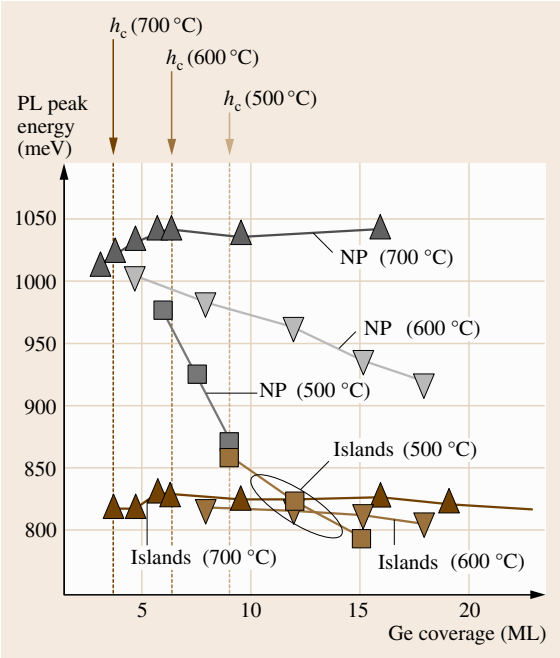


Fig. 34.36 Ge coverage dependences of NP and island PL peaks as a function of growth temperature. The critical thickness h_c of Ge dot formation is seen to increase with decreasing growth temperature

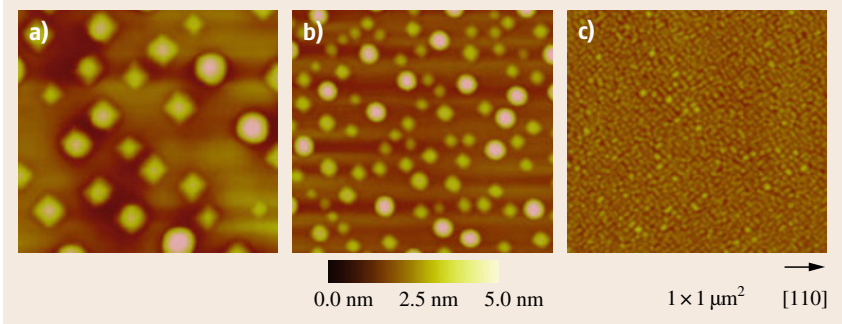


Fig. 34.37a–c AFM images of Ge dots grown at (a) 700 °C, (b) 600 °C, and (c) 500 °C. Scale is 1 × 1 μm²

change depending on the growth conditions. When the growth temperature is decreased, the number of dots becomes larger and their size becomes smaller; in particular, the density of pyramids becomes larger rather

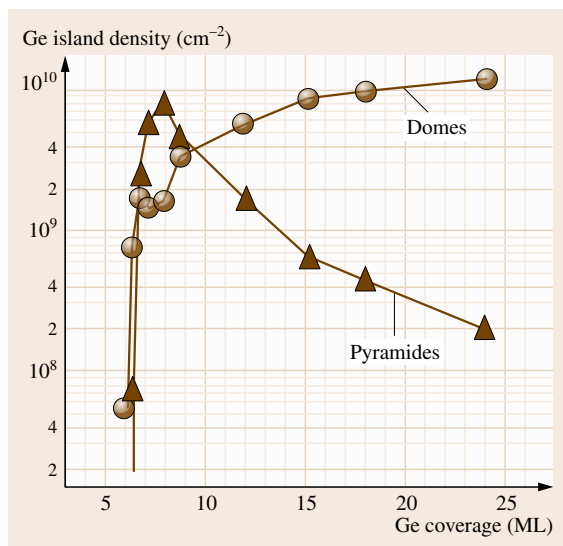


Fig. 34.38 Ge coverage dependence of island density. Morphological change is seen from pyramid to dome shapes when coverage exceeds about 8 ML.

than that of domes. At lower temperatures, that is, 500 °C, domes and pyramids disappear and quite a large number of small elongated dots known as *hut clusters* appear, as seen in Fig. 34.37c. Energetically, domes are stable, whereas pyramids are metastable and therefore appear at rather higher temperatures. When the growth temperature is low, atom migration is suppressed and unstable hut clusters are formed.

Figure 34.38 shows the Ge coverage dependence of dot formation. It is interesting that a morphological change from pyramidal to dome shape is observed with increasing coverage. This is probably due to accumulating strain. Since the domes have a much larger degree of strain relaxation than the pyramids, this shape change may occur to reduce the total energy, and it dominates at higher coverage.

The relative number of pyramids to domes is also dependent on the growth rate. The density of pyramids is drastically decreased by decreasing the growth rate, and it is also found that inserting growth interruption or annealing decreases the number of pyramids. This reflects the fact that the dome is energetically more stable than the pyramid, and that the shape change takes place more easily under near-equilibrium conditions.

The formation of SiGe alloy dots is quite different from the case of pure Ge dots at first sight. As seen in Fig. 34.39, a large number of pyramids are formed compared with pure-Ge islands, and domes are hardly

observed. The number of pyramids increases with increasing SiGe coverage, in contrast to the case of pure Ge, and the shape change does not take place. This feature is very similar to that of low-temperature growth of pure-Ge dots, in which hut clusters are formed and the shape change does not occur. This difference results from the growth mechanism. It is noted that, when the dots are formed at 600 °C by gas-source MBE with Si₂H₆ and GeH₄, the growth mode is in the reaction-limited regime, where the growth is strictly limited by the chemical reaction of impinging gases. In the reaction-limited regime, the surface migration of atoms is suppressed and the shape change from pyramid to dome hardly occurs since the energy barrier is too high compared to the surface migration energy. On the other hand, the growth of pure Ge proceeds in the supply-limited regime at this temperature, and the suppression of surface migration is quite small, which allows the formation of stable domes. If the growth of SiGe dots is performed in the supply-limited regime, that is, at higher growth temperatures, the situation changes greatly and very similar behavior to that of pure Ge dots is seen, as shown in Fig. 34.40. In this figure,

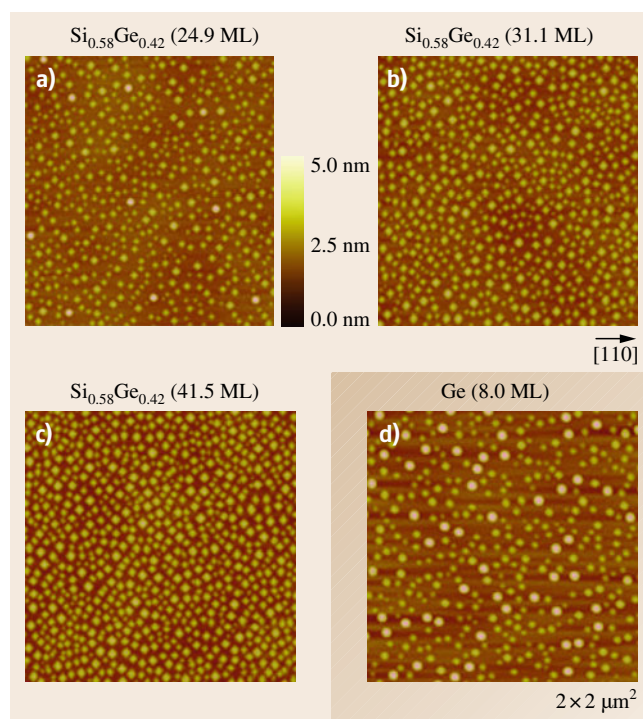


Fig. 34.39a–d Coverage dependence (a–c) of AFM images of Si_{0.58}Ge_{0.42} dots and (d) Ge dots with 8 ML. Scale is 2 × 2 μm²

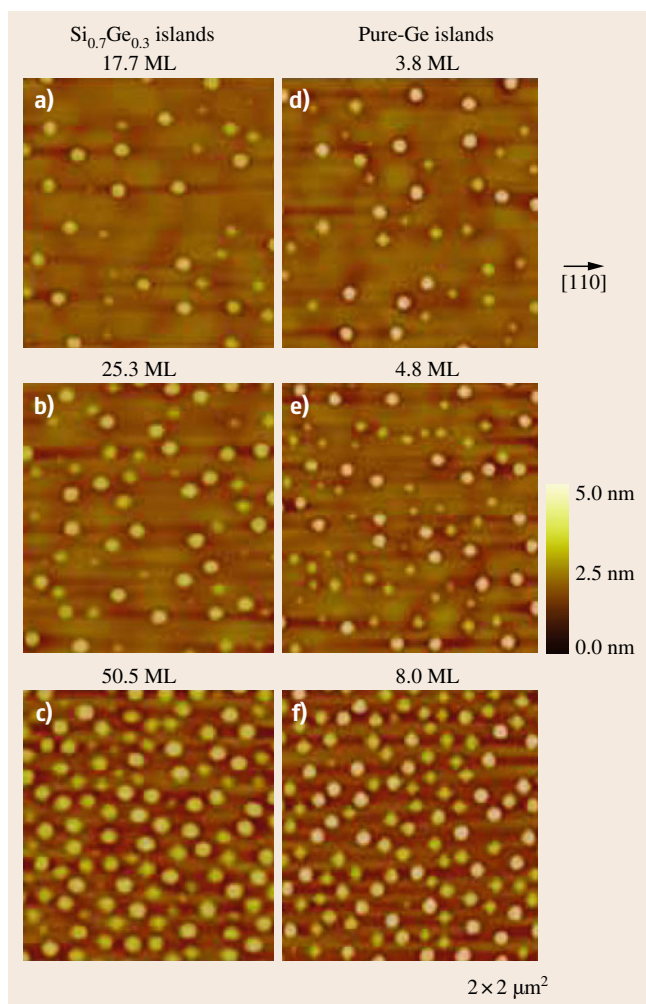


Fig. 34.40a–f Coverage dependence of AFM images of $\text{Si}_{0.7}\text{Ge}_{0.3}$ dots grown at high temperatures (a–c) and pure Ge dots grown at low temperatures (d–f). Scale is $2 \times 2 \mu\text{m}^2$

bimodal growth of islands and the shape change are clearly seen for SiGe islands. This similarity suggests intermixing of Si and Ge even for pure-Ge dot formation. It is now known that the intermixing effect of Si and Ge, particularly at high temperatures, is important for dot formation and reduces the formation barrier for dots, resulting in a smaller critical thickness than that for low-temperature growth.

The formation of Ge dots on a strained SiGe layer is also important from the device application point of view. Although the critical thickness for dot formation is different from that on Si substrates, the bimodal

growth and the shape change are very similar to those on Si. The Ge coverage dependence of the dot density is just shifted to lower coverage, which can be understood if we consider the strain energy of the two-dimensional (2-D) underlying strained layers. That is, the strain energy of the Ge thickness difference between SiGe and Si substrates for dot formation is almost equal to that of the underlying strained SiGe layer. This implies that the same dot formation mechanism is in operation and that the strain of the underlying layers contributes to dot formation.

Stacking of dot layers is attracting great attention from the point of view of crystal growth as well as device applications. As mentioned above, the strain originating from the underlying layer affects dot formation greatly. If the thickness of the separation layers is properly selected, it is well known that dots are aligned vertically, as shown in Fig. 34.41. This is because the strain coming from the underlying dots provides energetically favorable sites for dot formation. However, it should be noted that the kinetics is very complicated and that dot alignment does not always occur, that is, the dot formation strongly depends on the growth conditions, the dot distribution, and the distance to the underlying dot layer. As a typical example of dot alignment, the distance dependence is shown for high-temperature growth in Fig. 34.42 [34.218]. As seen in this figure, the distribution of dot size and position depends on the Si interlayer thickness. It is natural that the distribution is almost similar to that of single-layer formation when the Si spacer is thick, since the strain effect of the underlying layer does not reach the upper surface. In the sample with a thinner Si spacer layer, a very large size distribution and a drastic increase of dome size appear. However, in the case of intermediate thickness such as 39 nm, it is quite interesting that very uniform distribution and ordering of dots are realized. This tendency can also be understood in terms of the change of the strain distribution due to the underlying dots with spacer thickness.

To enhance the quantum effect of Ge dots, small island formation is favorable. For this purpose, the low-temperature growth where small hut-cluster dots are formed is suitable. However, crystal quality is sacrificed at lower growth temperatures. To overcome this problem, two-step growth or stacking of dots is proposed and highly luminescent dots with relatively small size are successfully formed, as seen in Fig. 34.43 [34.219]. Here, the first layer of Ge dots is formed at a low temperature of 500°C to obtain small dots and the second layer is grown at a higher temperature of 600°C

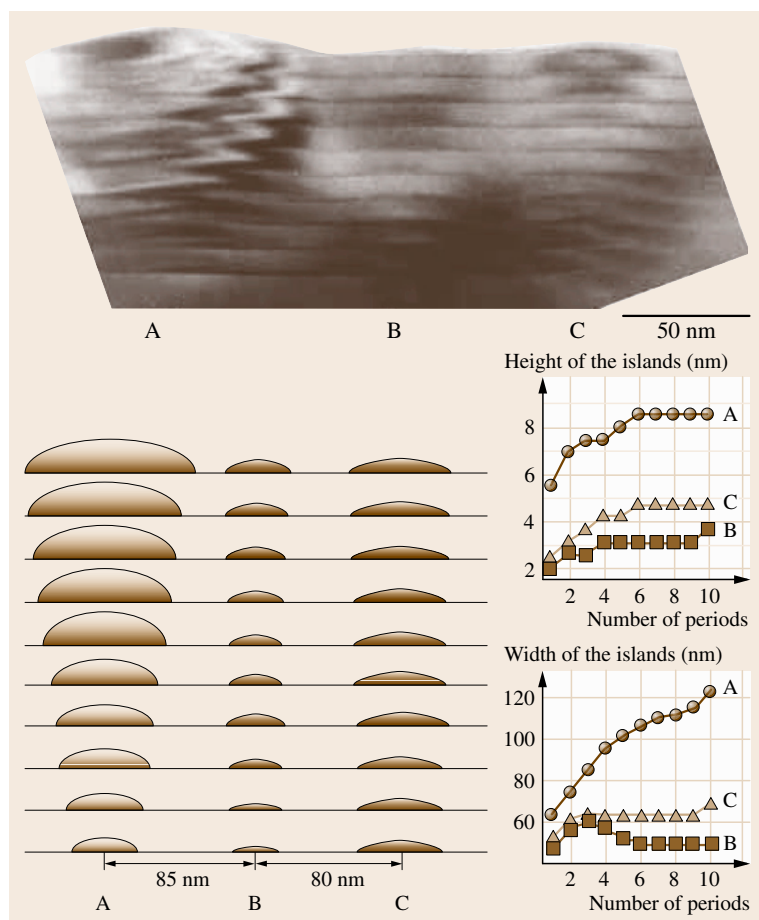


Fig. 34.41 TEM image of stacked Ge dots with 10 nm Si spacer and their schematic illustration. The right-hand side inset shows the height and width evolution of the dots as a function of the period number of the Ge layer

to obtain high-quality dots. Thanks to the strain field from the underlying small dots, the size and shape are almost repeated in the second layer, even though the growth is performed at higher temperatures where dome formation is favorable. It is confirmed that these dots have high luminescence efficiency, comparable to that of domes grown at higher temperatures. By using this method, relatively small dots with small size distribution and high luminescence efficiency can be obtained.

However, the size distribution is still large for device applications and the position is not perfectly controlled. Combination of selective epitaxial growth (SEG) and electron-beam (EB) lithography is a promising approach for sufficient control of the dots [34.220, 221]. As mentioned above, GSMBE has the advantage of providing selectivity between Si and SiO₂ surfaces and Ge dots can be grown only on Si surfaces. Therefore, when windows are opened in SiO₂ films on Si substrates, Ge

dots are formed only in the windows. If the window size is smaller than the Ge migration length, only one Ge dot grows in a window and the dot size decreases with decreasing window size, as shown in Fig. 34.44 [34.220]. It is noted that the Ge dot is formed on the Ge wetting layer, that is, by the SK growth mode, even in SEG. These controlled Ge dots give rise to luminescence, and two well-resolved peaks are observed in contrast to the disordered Ge dots.

In order to enhance the quantum effects, several attempts to reduce Ge dot size and increase the dot density are now under investigation. Predeposition of elements such as C [34.189] and B [34.222] has been shown to be very effective to reduce the size. Incorporation of C is also found to be effective when dots are formed by using GSMBE [34.223]. Figure 34.45 shows dot formation when (CH₃)₃SiH (TMS) is incorporated into the GeH₄ gas. There are some interesting features, different

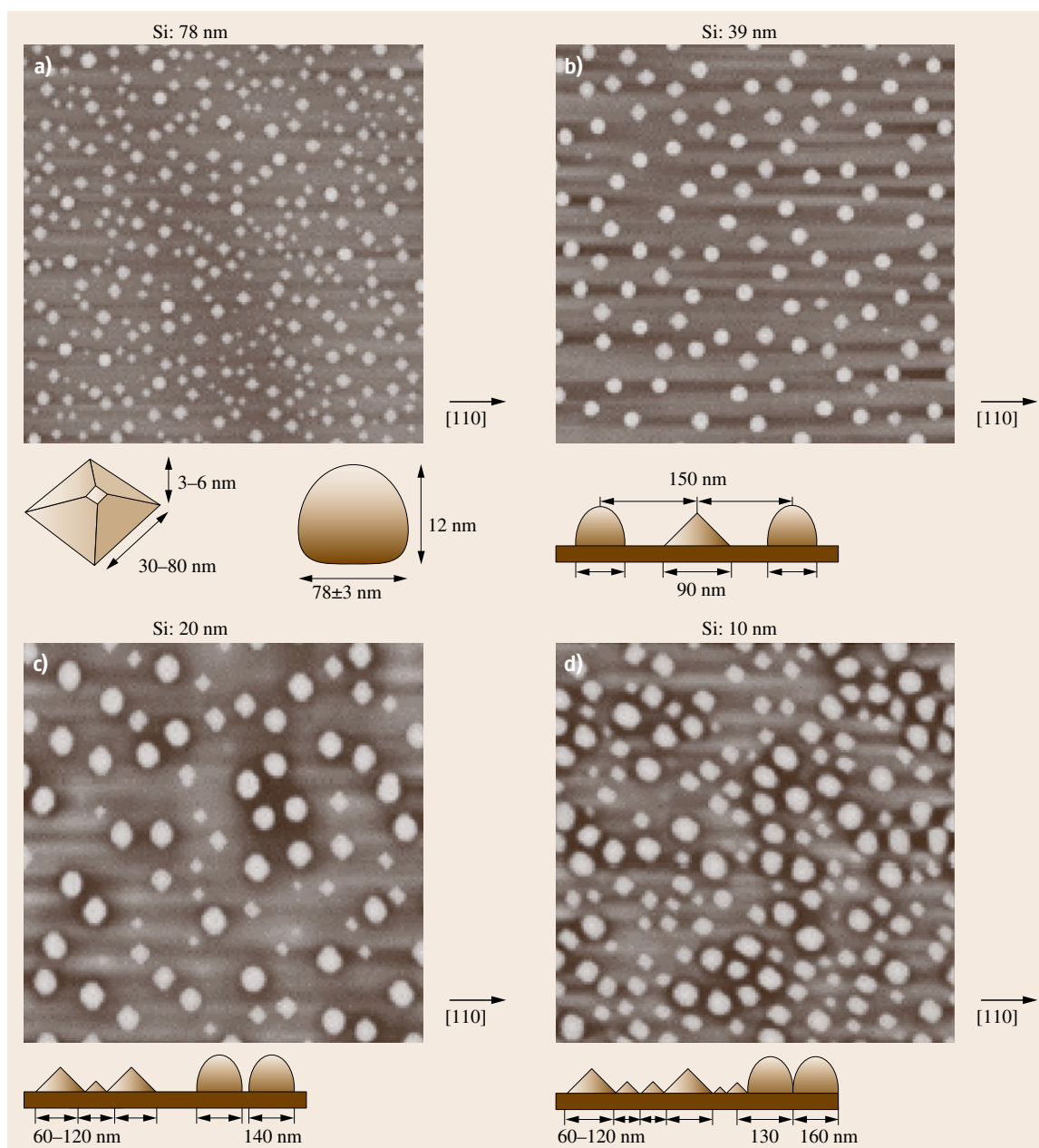


Fig. 34.42a–d AFM images of stacked Ge dots with Si spacer thickness as a parameter, from 78 nm (a) to 10 nm (d). Scale is $2 \times 2 \mu\text{m}^2$. Subfigures show schematics of formed Ge dots

from pure-Ge dot formation with GeH_4 : (1) the critical thickness for dot formation increases to 7.5 ML from about 4 ML, (2) the dots strongly reduce in size and increase in number by as much as three times that of pure-Ge dots and (3) monomodal formation of dome-

like dots occurs instead of the bimodal formation of pure-Ge dots. Dots with C provide luminescence as well, but the peak shift as a function of the deposition is different from that of Ge dots grown at the same growth temperature and very similar to the behavior of Ge dots

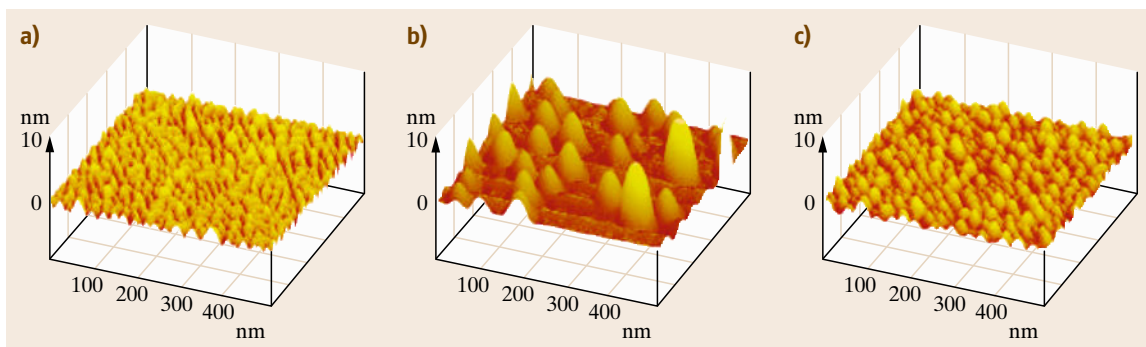


Fig. 34.43a–c AFM results of single Ge layers grown at (a) 500 °C and (b) 600 °C, and (c) stacked layer where the first and second layers are grown at 500 and 600 °C, respectively. The stacked one shows formation of small dots similar to the low-temperature growth one, even though the growth temperature is high ▲

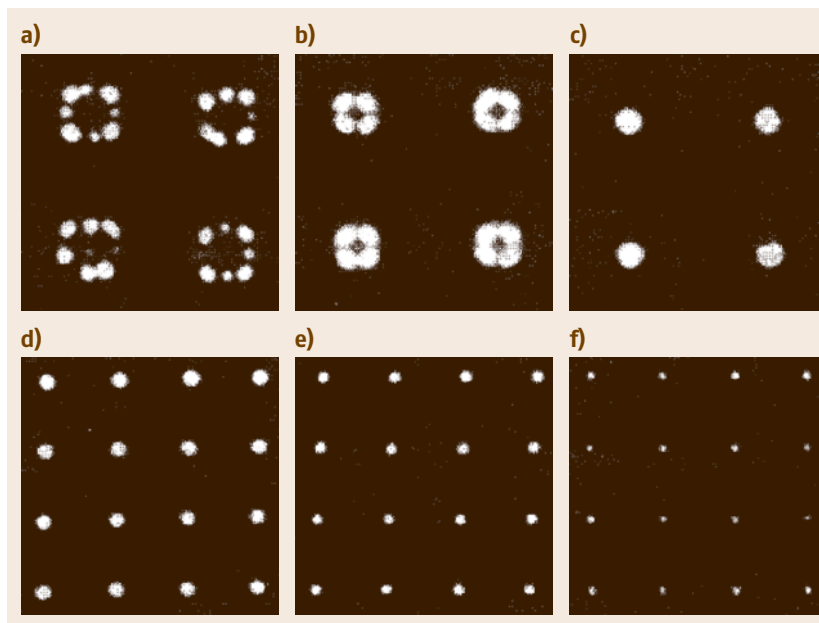


Fig. 34.44a–f SEM images of Ge dots formed in SiO₂ windows on Si substrates. The diameters of the windows are (a) 580 nm, (b) 440 nm, (c) 300 nm, (d) 180 nm, (e) 130 nm, and (f) 90 nm

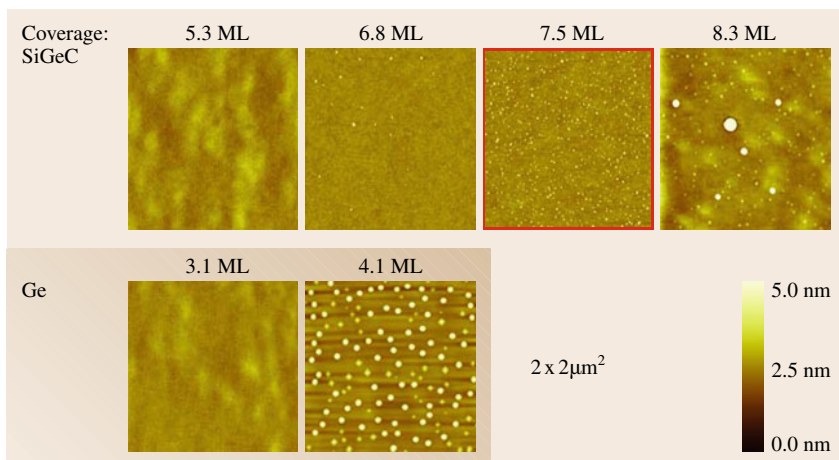


Fig. 34.45 AFM images showing the coverage dependence of dots grown with and without mixing of (CH₃)₃SiH in the GeH₄ gas. Scale is 2 × 2 μm²

grown at lower temperature. This indicates that migration of atoms is impeded by the presence of C atoms, and therefore the low-temperature growth mode occurs

even at higher temperatures. This corresponds well to the small dot formation resulting from the reduction of the migration length of atoms on the surface.

34.10 Concluding Remarks and Future Prospects

The Si/Ge system provides a lot of varieties of materials growth, from pseudomorphic growth and strain-relaxed growth to dot formation, and the strain coming from the lattice mismatch between Si and Ge plays an important role in the growth. Comprehensive studies on the growth mechanisms have resulted in the development of novel formation techniques for SiGe heterostructures and enable us to implement strain effects into Si devices.

It is now widely accepted that the performance of Si VLSIs is greatly improved with the aid of SiGe heterostructures and a lot of work on material growth and device design is being conducted. It is therefore forecast that SiGe heterostructures will be implemented in some important VLSI devices soon.

Recently, much attention has also been paid to the photonic properties of Si-related materials, particularly SiGe heterostructures. This is because the performance

of VLSIs is improved by adding optical functions such as optical interconnection and parallel signal processing. In order to realize optical functions in Si VLSIs, various kinds of optical elements based on Si, including light sources, should be developed. Among these, photonic crystals are now attracting much attention, since not only can light emission be well controlled but also light waveguides with high flexibility can be realized. If one can apply the photonic crystal to Si devices, waveguides for optical interconnection may be realized on Si VLSIs. Moreover, by combining VLSIs and sophisticated Si, new devices with optical functions and multiprocessing of signals, which is highly desired for such devices as image processors, can be realized based on Si. In this case, SiGe heterostructures will play the main role, and therefore, more intensive studies on new formation techniques for SiGe heterostructures are required.

References

- 34.1 C.G. Van de Walle, R.M. Martin: Theoretical calculations of heterojunction discontinuities in the Si/Ge system, *Phys. Rev. B* **34**, 5621–5634 (1986)
- 34.2 C.G. Van de Walle, R.M. Martin: Theoretical study of band offsets at semiconductor interfaces, *Phys. Rev. B* **35**, 8154–8165 (1987)
- 34.3 C.G. Van de Walle: Band lineups and deformation potentials in the model-solid theory, *Phys. Rev. B* **39**, 1871–1883 (1989)
- 34.4 H. Kim, N. Taylor, T.R. Bramblett, J.E. Greene: Kinetics of $\text{Si}_{1-x}\text{Ge}_x(001)$ growth on $\text{Si}(001) 2 \times 1$ by gas-source molecular-beam epitaxy from Si_2H_6 and GeH_4 , *J. Appl. Phys.* **84**, 6372–6381 (1998)
- 34.5 H. Hirayama, T. Tatsumi, A. Ogura, N. Aizaki: Gas source silicon molecular beam epitaxy using silane, *Appl. Phys. Lett.* **51**, 2213–2215 (1987)
- 34.6 H. Hirayama, T. Tatsumi, N. Aizaki: Selective growth condition in disilane gas source silicon molecular beam epitaxy, *Appl. Phys. Lett.* **52**, 2242–2243 (1988)
- 34.7 M. Suemitsu, F. Hirose, Y. Takakuwa, N. Miyamoto: Growth kinetics in silane gas-source molecular beam epitaxy, *J. Cryst. Growth* **105**, 203–208 (1990)
- 34.8 Y. Tsukidate, M. Suemitsu: Infrared study of SiH_4 -adsorbed $\text{Si}(100)$ surface: Observation and mode assignment of new peaks, *Jpn. J. Appl. Phys.* **40**, 5206–5210 (2001)
- 34.9 H. Hirayama, T. Tatsumi, N. Aizaki: Gas source silicon molecular beam epitaxy using disilane, *Appl. Phys. Lett.* **52**, 1484–1486 (1988)
- 34.10 D. Lubben, R. Tsu, T.R. Bramblett, J.E. Greene: Mechanisms and kinetics of Si atomic-layer epitaxy on $\text{Si}(001) 2 \times 1$ from Si_2H_6 , *J. Vac. Sci. Technol. A* **9**, 3003–3011 (1991)
- 34.11 S.H. Li, S.W. Chung, J.K. Rhee, P.K. Bhattacharya: Gas-source molecular-beam epitaxy using Si_2H_6 and GeH_4 and x-ray characterization of $\text{Si}_{1-x}\text{Ge}_x$ ($0 < x < 0.33$) alloys, *J. Appl. Phys.* **71**, 4916–4919 (1992)
- 34.12 T.R. Bramblett, Q. Lu, T. Karasawa, M.-A. Hasan, S.K. Jo, J.E. Greene: $\text{Si}(001) 2 \times 1$ gas-source molecular-beam epitaxy from Si_2H_6 : Growth kinetics and boron doping, *J. Appl. Phys.* **76**, 1884–1888 (1994)
- 34.13 R. Chelly, T. Angot, P. Louis, D. Bolmont, J.J. Koulmann: In situ monitoring of growth rate param-

- eters in hot-wire assisted gas source-molecular beam epitaxy using a quartz microbalance, *Appl. Surf. Sci.* **115**, 299–306 (1997)
- 34.14 A.M. Lam, Y.-J. Zheng, J.R. Engstrom: Gas-source reactivity in mixed-crystal systems: The reaction of GeH_4 and Ge_2H_6 on Si surfaces, *Surf. Sci.* **393**, 205–221 (1997)
- 34.15 T. Murata, M. Suemitsu: GeH_4 adsorption on Si(001) at RT: Transfer of H atoms to Si sites and atomic exchange between Si and Ge, *Appl. Surf. Sci.* **224**, 179–182 (2004)
- 34.16 M. Foster, B. Darlington, J. Scharff, A. Campion: Surface chemistry of alkylsilanes on Si(100) 2×1 , *Surf. Sci.* **375**, 35–44 (1997)
- 34.17 J. Xu, W.J. Choyke, J.T. Yates Jr.: Role of the $-\text{SiH}_3$ functional group in silane adsorption and dissociation on Si(100), *J. Phys. Chem. B* **101**, 6879–6882 (1997)
- 34.18 K. Senthil, H. Nakazawa, M. Suemitsu: Adsorption and desorption kinetics of organosilanes at Si(001) surfaces, *Jpn. J. Appl. Phys.* **42**, 6804–6808 (2003)
- 34.19 S. Gu, R. Wang, R. Zhang, Y. Zheng: Simulation model to very low pressure chemical vapor deposition of SiGe alloy, *J. Vac. Sci. Technol. A* **14**, 3256–3260 (1996)
- 34.20 D.J. Robbins, J.L. Gasper, A.G. Cullis, W.L. Leong: A model for heterogeneous growth of $\text{Si}_{1-x}\text{Ge}_x$ films from hydrides, *J. Appl. Phys.* **69**, 3729–3732 (1991)
- 34.21 B.S. Meyerson, K.J. Uram, F.K. LeGoues: Cooperative growth phenomena in silicon/germanium low-temperature epitaxy, *Appl. Phys. Lett.* **53**, 2555–2557 (1988)
- 34.22 J. Murota, S. Ono: Low-temperature epitaxial growth of Si/Si $_{1-x}\text{Ge}_x$ /Si heterostructure by chemical vapor deposition, *Jpn. J. Appl. Phys.* **33**, 2290–2299 (1994)
- 34.23 J. Murota, T. Matsuura, M. Sakuraba: Atomically controlled processing for group IV semiconductors, *Surf. Interface Anal.* **34**, 423–431 (2002)
- 34.24 V. Loup, J.M. Hartmann, G. Rolland, P. Holliger, F. Laugier, C. Vannuffel, M.N. Séméria: Reduced pressure chemical vapor deposition of Si $_{1-x-y}\text{Ge}_x\text{C}_y$ and Si $_{1-y}\text{C}_y$ /Si heterostructures, *J. Vac. Sci. Technol. B* **20**, 1048–1054 (2002)
- 34.25 J.M. Hartmann, V. Loup, G. Rolland, M.N. Séméria: Effects of temperature and HCl flow on the SiGe growth kinetics in reduced pressure-chemical vapor deposition, *J. Vac. Sci. Technol. B* **21**, 2524–2529 (2003)
- 34.26 P.M. Garone, J.C. Sturm, P.V. Schwartz, S.A. Schwartz, B.J. Wilkens: Silicon vapor phase epitaxial growth catalysis by the presence of germane, *Appl. Phys. Lett.* **56**, 1275–1277 (1990)
- 34.27 J.L. Hoyt, C.A. King, D.B. Noble, C.M. Gronet, J.F. Gibbons, M.P. Scott, S.S. Laderman, S.J. Roser, K. Kauka, J. Turner, T.I. Kamins: Limited reaction processing: Growth of Si $_{1-x}\text{Ge}_x$ /Si for heterojunction bipolar transistor applications, *Thin Solid Films* **184**, 93–106 (1990)
- 34.28 T.O. Sedgwick, D.A. Grutzmacher, A. Zaslavsky, V.P. Kesan: Selective SiGe and heavily As doped Si deposited at low temperature by atmospheric pressure chemical vapor deposition, *J. Vac. Sci. Technol. B* **11**, 1124–1128 (1993)
- 34.29 S. Bodnar, E. de Berranger, P. Bouillon, M. Mouis, T. Skotnocki, J.L. Regolini: Selective Si and SiGe epitaxial heterostructures grown using an industrial low-pressure chemical vapor deposition module, *J. Vac. Sci. Technol. B* **15**, 712–718 (1997)
- 34.30 W.-C. Wang, J.P. Denton, G.W. Neudeck, I.-M. Lee, C.G. Takoudis, M.T.K. Koh, E.P. Kvam: Selective epitaxial growth of Si $_{1-x}\text{Ge}_x$ /Si strained-layers in a tubular hot-wall low pressure chemical vapor deposition system, *J. Vac. Sci. Technol. B* **15**, 138–141 (1997)
- 34.31 L. Vescan, K. Grimm, C. Dieker: Facet investigation in selective epitaxial growth of Si and SiGe on (001) Si for optoelectronic devices, *J. Vac. Sci. Technol. B* **16**, 1549–1554 (1998)
- 34.32 J.J. Harris, D.E. Ashenford, C.T. Foxon, P.J. Dobson, B.A. Joyce: Kinetic limitations to surface segregation during growth of III–V compounds: Sn in GaAs, *Appl. Phys. A* **33**, 87–92 (1984)
- 34.33 R.A. Metzger, F.G. Allen: Evaporative antimony doping of silicon during molecular beam epitaxial growth, *J. Appl. Phys.* **55**, 931–940 (1984)
- 34.34 S. Fukatsu: Growth of group-IV semiconductor heterostructures with controlled interfaces and observation of band-edge luminescence from strained SiGe/Si quantum wells. Ph.D. Thesis (University of Tokyo, Tokyo 1992)
- 34.35 K. Fujita, S. Fukatsu, H. Yaguchi, T. Igarashi, Y. Shiraki, R. Ito: Realization of abrupt interfaces in Si/Ge superlattices by suppressing Ge surface segregation with submonolayer of Sb, *Jpn. J. Appl. Phys.* **29**, L1981–L1983 (1990)
- 34.36 K. Fujita, S. Fukatsu, H. Yaguchi, Y. Shiraki, R. Ito: Involvement of the topmost Ge layer in the Ge surface segregation during Si/Ge heterostructure formation, *Appl. Phys. Lett.* **59**, 2240–2241 (1991)
- 34.37 S. Fukatsu, K. Fujita, H. Yaguchi, Y. Shiraki, R. Ito: Self-limitation in the surface segregation of Ge atoms during Si molecular beam epitaxial growth, *Appl. Phys. Lett.* **59**, 2103–2105 (1991)
- 34.38 J. Ushio, K. Nakagawa, M. Miyao, T. Maruizumi: Surface segregation behavior of Ge in comparison with B, Ga, and Sb: Calculations using a first-principles method, *J. Cryst. Growth* **201/202**, 81–84 (1999)
- 34.39 S. Fukatsu, N. Usami, Y. Kato, H. Sunamura, Y. Shiraki, H. Oku, T. Ohnishi, Y. Ohmori, K. Okumura: Gas-source molecular beam epitaxy and luminescence characterization of strained Si $_{1-x}\text{Ge}_x$ /Si quantum wells, *J. Cryst. Growth* **136**, 315–321 (1994)

- 34.40 M. Copel, C. Reuter, E. Kaxiras, R.M. Tromp: Surfactants in epitaxial growth, *Phys. Rev. Lett.* **63**, 632–635 (1989)
- 34.41 F.C. Frank, J.H. van der Merwe: One-dimensional dislocations. I. Static theory, *Proc. R. Soc. Lond. Ser. A* **198**, 205–216 (1949)
- 34.42 F.C. Frank, J.H. van der Merwe: One-dimensional dislocation. II. Misfitting monolayers and oriented overgrowth, *Proc. R. Soc. Lond. Ser. A* **198**, 216–225 (1949)
- 34.43 F.C. Frank, J.H. van der Merwe: One-dimensional dislocation. III. Influence of the second harmonic term in the potential representation on the properties of the model, *Proc. R. Soc. Lond. Ser. A* **200**, 125–134 (1949)
- 34.44 J.H. van der Merwe: Crystal interface. Part I. Semi-infinite crystals, *J. Appl. Phys.* **34**, 117–122 (1963)
- 34.45 J.H. van der Merwe: Crystal interface. Part II. Finite overgrowths, *J. Appl. Phys.* **34**, 123–127 (1963)
- 34.46 E. Kasper, H.-J. Herzog: Elastic and misfit dislocation density in $\text{Si}_{0.92}\text{Ge}_{0.08}$ films on silicon substrates, *Thin Solid Films* **44**, 357–370 (1977)
- 34.47 E. Kasper: Growth and properties of Si/SiGe superlattices, *Surf. Sci.* **174**, 630–639 (1986)
- 34.48 E. Kasper, H.-J. Herzog, H. Daembkes, G. Abstreiter: Equally strained Si/SiGe superlattices on Si substrates, *Mater. Res. Soc. Proc.* **56**, 347–357 (1986)
- 34.49 J.W. Matthews, A.E. Blakeslee: Defects in epitaxial multilayers. I. Misfit dislocations, *J. Cryst. Growth* **27**, 118–125 (1974)
- 34.50 J.W. Matthews, A.E. Blakeslee: Defects in epitaxial multilayers. II. Dislocation pile-ups, threading dislocations, slip lines and cracks, *J. Cryst. Growth* **29**, 273–280 (1975)
- 34.51 J.W. Matthews, A.E. Blakeslee: Defects in epitaxial multilayers. III. Preparation of almost perfect multilayers, *J. Cryst. Growth* **32**, 265–273 (1976)
- 34.52 J.C. Bean, L.C. Feldman, A.T. Fiory, S. Nakahara, I.K. Robinson: $\text{Ge}_x\text{Si}_{1-x}/\text{Si}$ strained-layer superlattice grown by molecular beam epitaxy, *J. Vac. Sci. Technol. A* **2**, 436–440 (1984)
- 34.53 R. People, J.C. Bean: Calculation of critical layer thickness versus lattice mismatch for $\text{Ge}_x\text{Si}_{1-x}/\text{Si}$ strained-layer heterostructures, *Appl. Phys. Lett.* **47**, 322–324 (1985)
- 34.54 I.J. Fritz: Role of experimental resolution in measurements of critical layer thickness for strained-layer epitaxy, *Appl. Phys. Lett.* **51**, 1080–1082 (1987)
- 34.55 Y. Kohama, Y. Fukuda, M. Seki: Determination of the critical layer thickness of $\text{Si}_{1-x}\text{Ge}_x/\text{Si}$ heterostructures by direct observation of misfit dislocations, *Appl. Phys. Lett.* **52**, 380–382 (1988)
- 34.56 D.C. Houghton, C.J. Gibbings, C.G. Tuppen, M.H. Lyons, M.A.G. Halliwell: Equilibrium critical thickness for $\text{Si}_{1-x}\text{Ge}_x$ strained layers on (100) Si, *Appl. Phys. Lett.* **56**, 460–462 (1990)
- 34.57 M.L. Green, B.E. Weir, D. Brasen, Y.F. Hsieh, G. Hingashi, A. Feygenson, L.C. Feldman, R.L. Headrick: Mechanically and thermally stable Si-Ge films and heterojunction bipolar transistors grown by rapid thermal chemical vapor deposition at 900 °C, *J. Appl. Phys.* **69**, 745–751 (1991)
- 34.58 D.C. Houghton, D.D. Perovic, J.-M. Baribeau, G.C. Weatherly: Misfit strain relaxation in $\text{Ge}_x\text{Si}_{1-x}/\text{Si}$ heterostructures: The structural stability of buried strained layers and strained-layer superlattices, *J. Appl. Phys.* **67**, 1850–1862 (1990)
- 34.59 J.W. Matthews, S. Mader, T.B. Light: Accommodation of misfit across the interface between crystals of semiconducting elements or compounds, *J. Appl. Phys.* **41**, 3800–3804 (1970)
- 34.60 B.A. Fox, W.A. Jesser: The effect of frictional stress on the calculation of critical thickness in epitaxy, *J. Appl. Phys.* **68**, 2801–2808 (1990)
- 34.61 T.J. Gosling, S.C. Jain, J.R. Willis, A. Atkinson, R. Bullough: Stable configurations in strained epitaxial layers, *Philos. Mag. A* **66**, 119–132 (1992)
- 34.62 A. Fischer, H. Kuhne, M. Eichler, F. Hollander, H. Richter: Strain and surface phenomena in SiGe structures, *Phys. Rev. B* **54**, 8761–8768 (1996)
- 34.63 D.J. Eaglesham, M. Cerullo: Dislocation-free Stranski-Krastanov growth of Ge on Si(100), *Phys. Rev. Lett.* **16**, 1943–1946 (1990)
- 34.64 Y.-W. Mo, D.E. Savage, B.S. Swartzentruber, M.G. Lagally: Kinetic pathway in Stranski-Krastanov growth of Ge on Si(001), *Phys. Rev. Lett.* **65**, 1020–1023 (1990)
- 34.65 A. Sakai, T. Tatsumi: Defect-mediated island formation in Stranski-Krastanov growth of Ge on Si(001), *Phys. Rev. Lett.* **71**, 4007–4010 (1993)
- 34.66 A. Sakai, T. Tatsumi: Defect and island formation in Stranski-Krastanov growth of Ge on Si(001), *Mater. Res. Soc. Symp. Proc.* **317**, 343–348 (1994)
- 34.67 R.J. Asaro, W.A. Tiller: Interface morphology development during stress-corrosion cracking. Part I. Via surface diffusion, *Metall. Mater. Trans.* **3**, 1789–1796 (1972)
- 34.68 M.A. Grinfeld: Instability of the separation boundary between a non-hydrostatically stressed elastic body and a melt, *Sov. Phys. Dokl.* **31**, 831–834 (1986)
- 34.69 D.J. Srolovitz: On the stability of surfaces of stressed solids, *Acta Metall.* **37**, 621–625 (1989)
- 34.70 B.J. Spencer, P.W. Voorhees, S.H. Davis: Morphological instability in epitaxially strained dislocation-free solid films, *Phys. Rev. Lett.* **67**, 3696–3699 (1991)
- 34.71 J.A. Floro, G.A. Lucadamo, E. Chason, L.B. Freund, M. Sinclair, R.D. Twisten, R.Q. Hwang: SiGe island shape transition induced by elastic repulsion, *Phys. Rev. Lett.* **80**, 4717–4720 (1998)
- 34.72 G. Medeiros-Ribeiro, A.M. Bratkovski, T.I. Kamins, D.A.A. Ohlberg, R.S. Williams: Shape transition of germanium nanocrystals on a silicon (001) surface from pyramids to domes, *Science* **279**, 353–355 (1998)

- 34.73 B.W. Dodson, J.Y. Tsao: Relaxation of strained-layer semiconductor structures via plastic flow, *Appl. Phys. Lett.* **51**, 1325–1327 (1987)
- 34.74 H. Alexander, P. Haasen: Dislocations and plastic flow in the diamond structure, *Solid State Phys.* **22**, 22–158 (1968)
- 34.75 E. Kasper, H.J. Herzog, H. Kibbel: One-dimensional SiGe superlattice grown by UHV epitaxy, *Appl. Phys.* **8**, 199–205 (1975)
- 34.76 R. Hull, J.C. Bean, C. Büscher: A phenomenological description of strain relaxation in $\text{Ge}_x\text{Si}_{1-x}/\text{Si}(100)$ heterostructures, *J. Appl. Phys.* **66**, 5837–5843 (1989)
- 34.77 D.D. Perovic, G.C. Whetherly, J.M. Baribeau, D.C. Houghton: Heterogeneous nucleation sources in molecular beam epitaxy-grown $\text{Ge}_{1-x}\text{Si}_x/\text{Si}$ strained layer superlattices, *Thin Solid Films* **183**, 141–156 (1989)
- 34.78 D.J. Eaglesham, E.P. Kvam, D.M. Maher, C.J. Humphrey, J.C. Bean: Dislocation nucleation near the critical thickness in GeSi/Si strained layers, *Philos. Mag. A* **59**, 1059–1073 (1989)
- 34.79 C.J. Humphreys, D.M. Maher, D.J. Eaglesham, E.P. Kvam, I.G. Salisbury: The origin of dislocations in multilayers, *J. Phys. III* **1**, 1119–1130 (1991)
- 34.80 V. Higgs, P. Kightley, P. Goodhew, P. Augustus: Metal-induced dislocation nucleation for metastable SiGe/Si , *Appl. Phys. Lett.* **59**, 829–831 (1991)
- 34.81 M.D. de Coteau, P.R. Wilshaw, R. Falster: Gettering of copper in silicon – precipitation at extended surface-defects, *Inst. Phys. Conf. Ser.* **117**, 231–234 (1991)
- 34.82 R. Hull, J.C. Bean: Nucleation of misfit dislocations in strained-layer epitaxy in the $\text{Ge}_x\text{Si}_{1-x}/\text{Si}$ system, *J. Vac. Sci. Technol. A* **7**, 2580–2585 (1989)
- 34.83 U. Jain, S.C. Jain, A.H. Harker, R. Bullough: Nucleation of dislocation loops in strained epitaxial layers, *J. Appl. Phys.* **77**, 103–109 (1995)
- 34.84 D.E. Jesson, S.J. Pennycook, J.-M. Bribeau, D.C. Houghton: Surface stress, morphological development, and dislocation nucleation during $\text{Si}_{1-x}\text{Ge}_x$ epitaxy, *Scanning Microsc.* **8**, 849–857 (1994)
- 34.85 D.D. Perovic, D.C. Houghton: The introduction of dislocations in low misfit epitaxial systems, *Microsc. Semicond. Mater.* 1995, *Inst. Phys. Conf. Ser.* **146**, 117–134 (1995)
- 34.86 E.A. Stach, R. Hull, R.M. Tromp, M.C. Reuter, M. Copel, F.K. LeGoues, J.C. Bean: Effect of the surface upon misfit dislocation velocities during the growth and annealing of SiGe/Si (001) heterostructures, *J. Appl. Phys.* **83**, 1931–1937 (1998)
- 34.87 D.C. Houghton, C.J. Gibbings, C.G. Tuppen, M.H. Lyons, M.A.G. Halliwell: The structural stability of uncapped versus buried $\text{Si}_{1-x}\text{Ge}_x$ strained layers through high temperature processing, *Thin Solid Films* **183**, 171–182 (1989)
- 34.88 D.C. Houghton: Strain relaxation kinetics in $\text{Si}_{1-x}\text{Ge}_x/\text{Si}$ heterostructures, *J. Appl. Phys.* **70**, 2136–2151 (1991)
- 34.89 H. Hull, J.C. Bean, D. Bahnck, L.J. Petico-las, K.T. Short, F.C. Unterwald: Interpretation of dislocation propagation velocities in strained $\text{Ge}_x\text{Si}_{1-x}/\text{Si}(100)$ heterostructures by the diffusive kink pair model, *J. Appl. Phys.* **70**, 2052–2065 (1991)
- 34.90 Y. Yamashita, K. Maeda, K. Fujita, N. Usami, K. Suzuki, S. Fukatsu, Y. Mera, Y. Shiraki: Dislocation glide motion in heteroepitaxial thin-films of $\text{Si}_{1-x}\text{Ge}_x/\text{Si}(100)$, *Philos. Mag. Lett.* **67**, 165–171 (1993)
- 34.91 R. Hull, J.C. Bean: New insights into the microscopic motion of dislocations in covalently bonded semiconductors by in-situ transmission electron microscope observations of misfit dislocations in thin strained epitaxial layers, *Phys. Status Solidi (a)* **138**, 533–546 (1993)
- 34.92 W. Hagen, H. Strunk: New type of source generating misfit dislocations, *Appl. Phys.* **17**, 85–87 (1978)
- 34.93 R. Hull, J.C. Bean, D.J. Eaglesham, J.N. Bonara, C. Büscher: Strain relaxation phenomena in $\text{Ge}_x\text{Si}_{1-x}/\text{Si}$ strained structures, *Thin Solid Films* **183**, 117–132 (1989)
- 34.94 A. Lefebvre, C. Herbeaux, J. Di Persio: Interactions of misfit dislocations in $\text{In}_x\text{Ga}_{1-x}\text{As}/\text{GaAs}$ interfaces, *Philos. Mag. A* **63**, 471–485 (1991)
- 34.95 F.K. LeGoues, B.S. Meyerson, J.F. Morar, P.D. Kirchner: Mechanism and conditions for anomalous strain relaxation in grade thin films and superlattices, *J. Appl. Phys.* **71**, 4230–4243 (1992)
- 34.96 J. Washburn, E.P. Kvam: Possible dislocation multiplication source in (001) semiconductor epitaxy, *Appl. Phys. Lett.* **57**, 1637–1639 (1990)
- 34.97 C.G. Tuppen, C.J. Gibbings, M. Hockly, S.G. Roberts: Misfit dislocation multiplication processes in $\text{Si}_{1-x}\text{Ge}_x$ alloys for $x < 0.15$, *Appl. Phys. Lett.* **56**, 54–56 (1990)
- 34.98 Y.J. Mii, Y.-H. Xie, E.A. Fitzgerald, F.B.E. Weir, L.C. Feldman: Extremely high electron mobility in $\text{Si}/\text{Ge}_x\text{Si}_{1-x}$ structures grown by molecular beam epitaxy, *Appl. Phys. Lett.* **59**, 1611–1613 (1991)
- 34.99 J.J. Welser, J.L. Hoyt, S. Takagi, J.F. Gibbons: Strain dependence of the performance enhancement in strained-Si n-MOSFETs, *Tech. Dig. Int. Electron Device Meet.* (1994) pp. 373–376
- 34.100 K. Ismail, M. Arafa, K.L. Saenger, J.O. Chu, B.S. Meyerson: Extremely high electron mobility in Si/SiGe modulation-doped heterostructures, *Appl. Phys. Lett.* **66**, 1077–1079 (1995)
- 34.101 A.C. Churchill, D.J. Robbins, D.J. Wallis, N. Griffin, D.J. Paul, A.J. Pidduck: High-mobility two-dimensional electron gases in Si/SiGe heterostructures on relaxed SiGe layers grown at high temperature, *Semicond. Sci. Technol.* **12**, 943–946 (1997)

- 34.102 S. Bozzo, J.-L. Lazzari, C. Coudreau, A. Ronda, F. Arnaud d'Avitaya, J. Derrien, S. Mesters, B. Holländer, P. Gergaud, O. Thomas: Chemical vapor deposition of silicon-germanium heterostructures, *J. Cryst. Growth* **216**, 171–184 (2000)
- 34.103 K.H. Chang, R. Gibala, D.J. Srolovitz, P.K. Bhat-tacharya, J.F. Mansfield: Crosshatched surface morphology in strained III–V semiconductor films, *J. Appl. Phys.* **67**, 4093–4098 (1990)
- 34.104 A.J. Pidduck, D.J. Robbins, A.G. Cullis, W.Y. Leong, A.M. Pitt: Evolution of surface morphology and strain during SiGe epitaxy, *Thin Solid Films* **222**, 78–84 (1992)
- 34.105 J.W.P. Hsu, E.A. Fitzgerald, Y.-H. Xie, P.J. Silverman, M.J. Cardillo: Surface morphology of related $\text{Ge}_x\text{Si}_{1-x}$ films, *Appl. Phys. Lett.* **61**, 1293–1295 (1992)
- 34.106 E.A. Fitzgerald, Y.-H. Xie, D. Monroe, P.J. Silverman, J.M. Kuo, A.R. Kortan, F.A. Thiel, B.E. Weir: Relaxed $\text{Ge}_x\text{Si}_{1-x}$ structures for III–V integration with Si and high mobility two-dimensional electron gasses in Si, *J. Vac. Sci. Technol. B* **10**, 1807–1819 (1992)
- 34.107 S.Y. Shiryayev, F. Jensen, J.W. Petersen: On the nature of cross-hatch patterns on compositionally graded $\text{Si}_{1-x}\text{Ge}_x$ alloy layers, *Appl. Phys. Lett.* **64**, 3305–3307 (1994)
- 34.108 M.A. Lutz, R.M. Feenstra, F.K. LeGoues, P.M. Mooney, J.O. Chu: Influence of misfit dislocations on the surface morphology of $\text{Si}_{1-x}\text{Ge}_x$ films, *Appl. Phys. Lett.* **66**, 724–726 (1995)
- 34.109 A.M. Andrews, J.S. Speck, A.E. Romanov, M. Bo-beth, W. Pompe: Modeling cross-hatch surface morphology in growing mismatched layers, *J. Appl. Phys.* **91**, 1933–1943 (2002)
- 34.110 E.A. Fitzgerald, S.B. Samavedam: Line, point and surface defect morphology of graded, relaxed GeSi alloys of Si substrates, *Thin Solid Films* **294**, 3–10 (1997)
- 34.111 C.W. Leitz, M.T. Currie, A.Y. Kim, J. Lai, E. Robbins, E.A. Fitzgerald, M.T. Bulsara: Dislocation glide and blocking kinetics in compositionally graded SiGe/Si, *J. Appl. Phys.* **90**, 2730–2736 (2001)
- 34.112 H. Chen, L.W. Guo, Q. Cui, Q. Hu, Q. Huang, J.M. Zhou: Low-temperature buffer layer for growth of a low-dislocation-density SiGe layer on Si by molecular-beam epitaxy, *J. Appl. Phys.* **79**, 1167–1169 (1996)
- 34.113 J.H. Li, C.S. Peng, Y. Wu, D.Y. Dai, J.M. Zhou, Z.H. Mai: Relaxed $\text{Si}_{0.7}\text{Ge}_{0.3}$ layers grown on low-temperature Si buffers with low threading dislocation density, *Appl. Phys. Lett.* **71**, 3132–3134 (1997)
- 34.114 T. Ueno, T. Irisawa, Y. Shiraki: p-type Ge channel modulation doped heterostructures with very high room-temperature mobilities, *Physica E* **7**, 790–794 (2000)
- 34.115 T. Ueno, T. Irisawa, Y. Shiraki, A. Uedono, S. Tanigawa, R. Suzuki, T. Ohdaira, T. Mikado: Characterization of low temperature grown Si layer for SiGe pseudo-substrates by positron annihilation spectroscopy, *J. Cryst. Growth* **227–228**, 761–765 (2001)
- 34.116 K. Sawano, K. Kawaguchi, T. Ueno, S. Koh, K. Nakagawa, Y. Shiraki: Surface smoothing of SiGe strain-relaxed buffer layers by chemical mechanical polishing, *Mater. Sci. Eng. B* **89**, 406–409 (2002)
- 34.117 K. Sawano, Y. Hirose, S. Koh, K. Nakagawa, T. Hattori, Y. Shiraki: Mobility enhancement in strained Si modulation-doped structures by chemical mechanical polishing, *Appl. Phys. Lett.* **82**, 412–414 (2003)
- 34.118 K. Sawano, K. Arimoto, Y. Hirose, S. Koh, N. Usami, K. Nakagawa, T. Hattori, Y. Shiraki: Planarization of SiGe virtual substrates by CMP and its application to strained Si modulation-doped structures, *J. Cryst. Growth* **251**, 693 (2003)
- 34.119 K. Sawano, K. Kawaguchi, S. Koh, Y. Hirose, T. Hattori, K. Nakagawa, Y. Shiraki: Surface planarization of strain-relaxed SiGe buffer layers by CMP and post cleaning, *J. Electrochem. Soc.* **150**, G376–G379 (2003)
- 34.120 K. Sawano, Y. Abe, H. Satoh, K. Nakagawa, Y. Shiraki: Mobility enhancement in strained Ge heterostructures by planarization of SiGe buffer layers grown on Si substrates, *Jpn. J. Appl. Phys.* **44**, L1320–L1322 (2005)
- 34.121 K. Sawano, N. Usami, K. Arimoto, S. Koh, K. Nakagawa, Y. Shiraki: Observation of strain field fluctuation in SiGe relaxed buffer layers and its influence on overgrown structures, *Mater. Sci. Semicon. Process.* **8**, 177–180 (2005)
- 34.122 R. Hull, J.C. Bean, J.M. Bonar, G.S. Higashi, K.T. Short, H. Temkin, A.E. White: Enhanced strain relaxation in $\text{Si}/\text{Ge}_x\text{Si}_{1-x}/\text{Si}$ heterostructures via point-defect concentrations introduced by ion implantation, *Appl. Phys. Lett.* **56**, 2445–2447 (1990)
- 34.123 B. Holländer, S. Mantl, R. Liedtke, S. Mesters, H.-J. Herzog, H. Kibbel, T. Hackbarth: Enhanced strain relaxation of epitaxial SiGe layers on Si(100) after H^+ ion implantation, *Nucl. Instrum. Methods B* **148**, 200–205 (1999)
- 34.124 H. Trinkaus, B. Holländer, S. Rongen, S. Mantl, H.-J. Herzog, J. Kuchenbecher, T. Hackbarth: Strain relaxation mechanism for hydrogen-implanted $\text{Si}_{1-x}\text{Ge}_x/\text{Si}(100)$ heterostructures, *Appl. Phys. Lett.* **76**, 3552–3554 (2000)
- 34.125 M. Luysberg, D. Kirch, H. Trinkaus, B. Holländer, S. Lenk, S. Mantl, H.-J. Herzog, T. Hackbarth, P.F.P. Fichtner: Effect of helium ion implantation and annealing on the relaxation behavior of pseudomorphic $\text{Si}_{1-x}\text{Ge}_x$ buffer layers on Si (100) substrates, *J. Appl. Phys.* **92**, 4290–4295 (2002)
- 34.126 L.-F. Zou, Z.G. Wang, D.Z. Sun, T.W. Fan, X.F. Liu, J.W. Zhang: Characterization of strain relaxation in As ion implanted $\text{Si}_{1-x}\text{Ge}_x$ epilayers grown by gas

- source molecular beam epitaxy, *Appl. Phys. Lett.* **72**, 845–847 (1998)
- 34.127 K. Sawano, Y. Hirose, S. Koh, K. Nakagawa, T. Hattori, Y. Shiraki: Relaxation enhancement of SiGe thin layers by ion implantation into Si substrates, *J. Cryst. Growth* **251**, 685–688 (2003)
- 34.128 K. Sawano, Y. Hirose, Y. Ozawa, S. Koh, J. Yamanaka, K. Nakagawa, T. Hattori, Y. Shiraki: Enhancement of strain relaxation of SiGe thin layers by pre-ion-implantation into Si substrates, *Jpn. J. Appl. Phys.* **42**, L735–L737 (2003)
- 34.129 K. Sawano, Y. Hirose, S. Koh, K. Nakagawa, T. Hattori, Y. Shiraki: Formation of thin SiGe virtual substrates by ion implantation into Si substrates, *Appl. Surf. Sci.* **224**, 99–103 (2004)
- 34.130 K. Sawano, S. Koh, Y. Shiraki, Y. Ozawa, T. Hattori, J. Yamanaka, K. Suzuki, K. Arimoto, K. Nakagawa, N. Usami: Fabrication of high-quality strain-relaxed thin SiGe layers on ion-implanted Si substrates, *Appl. Phys. Lett.* **85**, 2514–2516 (2004)
- 34.131 K. Sawano, Y. Ozawa, A. Fukumoto, N. Usami, J. Yamanaka, K. Suzuki, K. Arimoto, K. Nakagawa, Y. Shiraki: Strain-field evaluation of strain-relaxed thin SiGe layers fabricated by ion implantation method, *Jpn. J. Appl. Phys.* **44**, L1316–L1319 (2005)
- 34.132 T. Tezuka, N. Sugiyama, S. Takagi: Fabrication of strained Si on an ultrathin SiGe-on-insulator virtual substrate with a high-Ge fraction, *Appl. Phys. Lett.* **79**, 1798–1800 (2001)
- 34.133 T. Mizuno, N. Sugiyama, T. Tezuka, S. Takagi: Relaxed SiGe-on-insulator substrates without thick SiGe buffer layers, *Appl. Phys. Lett.* **80**, 601–603 (2002)
- 34.134 T. Tezuka, N. Sugiyama, S. Takagi, T. Kawakubo: Dislocation-free formation of relaxed SiGe-on-insulator layers, *Appl. Phys. Lett.* **80**, 3560–3562 (2002)
- 34.135 N. Sugii, S. Yamaguchi, K. Washio: SiGe-on-insulator substrate fabricated by melt solidification for a strained-silicon complementary metal-oxide-semiconductor, *J. Vac. Sci. Technol. B* **20**, 1891–1896 (2002)
- 34.136 T. Mizuno, N. Sugiyama, T. Tezuka, T. Numata, S. Takagi: High performance CMOS operation of strained-SOI MOSFETs using thin film SiGe-on-insulator substrate, *Dig. Tech. Pap. Symp. VLSI Technology 2002*, pp. 106–107
- 34.137 S. Nakaharai, T. Tetsuka, N. Sugiyama, Y. Moriyama, S. Takagi: Characterization of 7-nm-thick strained Ge-on-insulator layer fabricated by Ge-condensation technique, *Appl. Phys. Lett.* **83**, 3516–3518 (2003)
- 34.138 T. Egawa, A. Sakai, T. Yamamoto, N. Taoka, O. Nakatsuka, S. Zaima, Y. Yasuda: Strain-relaxation mechanisms of SiGe layers formed by two-step growth on Si(001) substrates, *Appl. Surf. Sci.* **224**, 104–107 (2004)
- 34.139 A. Sakai, K. Sugimoto, T. Yamamoto, M. Okada, H. Ikeda, Y. Yasuda, S. Zaima: Reduction of threading dislocation density in SiGe layers on Si(001) using a two-step strain-relaxation procedure, *Appl. Phys. Lett.* **79**, 3398–3400 (2001)
- 34.140 A. Sakai, T. Tatsumi, K. Aoyama: Growth of strain-relaxed Ge films on Si(001) surfaces, *Appl. Phys. Lett.* **71**, 3510–3512 (1997)
- 34.141 N. Ikarashi, T. Tatsumi: Suppression of surface roughening on strained Si/SiGe layers by lowering surface stress, *Jpn. J. Appl. Phys.* **36**, L377–L379 (1997)
- 34.142 Y.H. Xie, S.B. Samavedam, M. Bulsara, T.A. Langdo, E.A. Fitzgerald: Relaxed template for fabricating regularly distributed quantum dot arrays, *Appl. Phys. Lett.* **71**, 3567–3568 (1997)
- 34.143 D.E. Jesson, S.J. Pennycook, J.-M. Baribeau, D.C. Houghton: Direct imaging of surface cusp evolution during strained-layer epitaxy and implications for strain relaxation, *Phys. Rev. Lett.* **71**, 1744–1747 (1993)
- 34.144 P.M. Mooney, F.K. LeGoues, J.O. Chu, S.F. Nelson: Strain relaxation and mosaic structure in relaxed SiGe layers, *Appl. Phys. Lett.* **62**, 3464–3466 (1993)
- 34.145 N. Taoka, A. Sakai, T. Egawa, O. Nakatsuka, S. Zaima, Y. Yasuda: Growth and characterization of strain-relaxed SiGe buffer layers on Si(001) substrates with pure-edge misfit dislocations, *Mater. Sci. Semicond. Process.* **8**, 131–135 (2005)
- 34.146 T. Yamamoto, A. Sakai, T. Egawa, N. Taoka, O. Nakatsuka, S. Zaima, Y. Yasuda: Dislocation structures and strain-relaxation in SiGe buffer layers on Si (001) substrates with an ultra-thin Ge interlayer, *Appl. Surf. Sci.* **224**, 108–112 (2004)
- 34.147 P.F. Fewster: *X-Ray Scattering from Semiconductors* (Imperial College Press, World Scientific, Singapore 2000)
- 34.148 S.S. Iyer, K. Eberl, M.S. Goorsky, F.K. LeGoues, J.C. Tsang, F. Cardone: Synthesis of Si_{1-y}Cy alloys by molecular beam epitaxy, *Appl. Phys. Lett.* **60**, 356–358 (1992)
- 34.149 K. Eberl, S.S. Iyer, J.C. Tsang, M.S. Goorsky, F.K. LeGoues: The growth and characterization of Si_{1-y}Cy alloys on Si(001) substrate, *J. Vac. Sci. Technol. B* **10**, 934–936 (1992)
- 34.150 K. Eberl, S.S. Iyer, S. Zollner, J.C. Tsang, F.K. LeGoues: Growth and strain compensation effects in the ternary Si_{1-x-y}Ge_xCy alloy system, *Appl. Phys. Lett.* **60**, 3033–3035 (1992)
- 34.151 B. Cordero, V. Gomez, A.E. Platero-Prats, M. Reves, J. Echeverria, E. Cremades, F. Barragan, S. Alvarez: Covalent radii revisited, *J. Chem. Dalton Trans.*, 2832–2838 (2008)
- 34.152 H.-J. Osten, E. Bugiel, P. Zaumseil: Growth of an inverse tetragonal distorted SiGe layer on Si(001) by adding small amounts of carbon, *Appl. Phys. Lett.* **64**, 3440–3442 (1994)

- 34.153 P.C. Kelires: Monte Carlo studies of ternary semiconductor alloys: Application to the $\text{Si}_{1-x-y}\text{Ge}_x\text{C}_y$ system, *Phys. Rev. Lett.* **75**, 1114–1117 (1995)
- 34.154 P.C. Kelires: Short-range order, bulk moduli, and physical trends in $\text{C-Si}_{1-x}\text{C}_x$ alloys, *Phys. Rev. B* **55**, 8784–8787 (1997)
- 34.155 M. Berti, D. De Salvador, A.V. Drigo, F. Romanato, J. Stangl, S. Zerlauth, F. Schäffler, G. Bauer: Lattice parameter in $\text{Si}_{1-y}\text{C}_y$ epilayers: Deviation from Vegard's rule, *Appl. Phys. Lett.* **72**, 1602–1604 (1998)
- 34.156 H.-J. Osten, B. Heinemann, D. Knoll, G. Lippert, H. Rücker: Effects of carbon on boron diffusion in SiGe: Principles and impact on bipolar devices, *J. Vac. Sci. Technol. B* **16**, 1750–1753 (1998)
- 34.157 H. Rücker, B. Heinemann, K.D. Bolze, D. Knoll, D. Krüger, R. Kurps, H.-J. Osten, P. Schley, B. Tillack, P. Zaumseil: Dopant diffusion in C-doped Si and SiGe: Physical model and experimental verification, *Tech. Dig. Int. Electron Device Meet.* (1999) pp. 345–348
- 34.158 A. Biswas, P.K. Basu: Estimated effect of germanium and carbon on the early voltage of a $\text{Si}_{1-x-y}\text{Ge}_x\text{C}_y$ heterojunction bipolar transistor, *Semicond. Sci. Technol.* **16**, 947–953 (2001)
- 34.159 K. Oda, E. Ohue, I. Suzumura, R. Hayami, A. Kodama, H. Simamoto, K. Washio: High performance self-aligned SiGeC HBT with selectively grown $\text{Si}_{1-x-y}\text{Ge}_x\text{C}_y$ base by UHV/CVD, *IEEE. Trans. Electron. Dev.* **50**, 2213–2220 (2003)
- 34.160 P. Boucaud, C. Francis, F.H. Julien, J.-M. Lourtioz, D. Bouchier, S. Bodnar, B. Lambert, J.L. Regolini: Band-edge and deep level photoluminescence of pseudomorphic $\text{Si}_{1-x-y}\text{Ge}_x\text{C}_y$ alloys, *Appl. Phys. Lett.* **64**, 875–877 (1994)
- 34.161 K. Brunner, W. Winter, K. Eberl: Spatially indirect radiative recombination of carriers localized in $\text{Si}_{1-x-y}\text{Ge}_x\text{C}_y/\text{Si}_{1-y}\text{C}_y$ double quantum well structure on Si substrates, *Appl. Phys. Lett.* **69**, 1279–1281 (1996)
- 34.162 B.A. Orner, J. Olowolafe, K. Roe, J. Kolodzey, T. Laursen, J.W. Mayer, J. Spear: Band gap of Ge rich $\text{Si}_{1-x-y}\text{Ge}_x\text{C}_y$ alloys, *Appl. Phys. Lett.* **69**, 2557–2559 (1996)
- 34.163 B.A. Orner, J. Kolodzey: $\text{Si}_{1-x-y}\text{Ge}_x\text{C}_y$ alloy band structures by linear combination of atomic orbitals, *J. Appl. Phys.* **81**, 6773–6780 (1997)
- 34.164 B.L. Stein, E.T. Yu, E.T. Croke, A.T. Hunter, T. Laursen, A.E. Bair, J.W. Mayer, C.C. Ahn: Band offsets in $\text{Si}/\text{Si}_{1-x-y}\text{Ge}_x\text{C}_y$ heterojunctions measured by admittance spectroscopy, *Appl. Phys. Lett.* **70**, 3413–3415 (1997)
- 34.165 O.G. Schmidt, K. Eberl: Photoluminescence of tensile strained, exactly strain compensated, and compressively strained $\text{Si}_{1-x-y}\text{Ge}_x\text{C}_y$ layers in Si, *Phys. Rev. Lett.* **80**, 3396–3399 (1998)
- 34.166 D.V. Singh, K. Rim, T.O. Mitchell, J.L. Hoyt, J.F. Gibbons: Admittance spectroscopy analysis of the conduction band offsets in $\text{Si}/\text{Si}_{1-x-y}\text{Ge}_x\text{C}_y$ and $\text{Si}/\text{Si}_{1-y}\text{C}_y$ heterostructures, *J. Appl. Phys.* **85**, 985–993 (1999)
- 34.167 C.L. Chang, L.P. Rokhinson, J.C. Sturm: Direct optical measurement of the valence band offset of $\text{p}^+\text{Si}_{1-x-y}\text{Ge}_x\text{C}_y/\text{p}^-\text{Si}(100)$ by heterojunction internal photoemission, *Appl. Phys. Lett.* **73**, 3568–3570 (1998)
- 34.168 H.-J. Osten: Band-gap changes and band offsets for ternary $\text{Si}_{1-x-y}\text{Ge}_x\text{C}_y$ alloys on $\text{Si}(001)$, *J. Appl. Phys.* **84**, 2716–2721 (1998)
- 34.169 K. Brunner, O.G. Schmidt, W. Winter, K. Eberl, M. Glück, U. König: SiGeC: Band gaps, band offsets, optical properties, and potential applications, *J. Vac. Sci. Technol. B* **16**, 1701–1706 (1998)
- 34.170 S. Galdin, P. Dollfus, V.A. Fortuna, P. Hesto, H.J. Osten: Band offset predictions for strained group IV alloys: $\text{Si}_{1-x-y}\text{Ge}_x\text{C}_y$ on $\text{Si}(001)$ and $\text{Si}_{1-x}\text{Ge}_x$ on $\text{Si}_{1-z}\text{Ge}_z(001)$, *Semicond. Sci. Technol.* **15**, 565–572 (2000)
- 34.171 S. John, S.K. Ray, E. Quinones, S.K. Oswal, K. Banerjee: Heterostructure P-channel metal-oxide-semiconductor transistor utilizing a $\text{Si}_{1-x-y}\text{Ge}_x\text{C}_y$ channel, *Appl. Phys. Lett.* **74**, 847–849 (1999)
- 34.172 E. Cassan, P. Dollfus, S. Galdin: Effect of doping profile on the potential performance of buried channel SiGeC/Si heterostructure MOS devices, *Physica E* **13**, 957–960 (2002)
- 34.173 M. Glück, U. König, W. Winter, K. Brunner, K. Eberl: Modulation-doped $\text{Si}_{1-x-y}\text{Ge}_x\text{C}_y$ p-type hetero-FETs, *Physica E* **2**, 768–771 (1998)
- 34.174 R.A. Soref: Silicon-based group IV heterostructures for optoelectronic applications, *J. Vac. Sci. Technol. A* **14**, 913–918 (1996)
- 34.175 A.S. Amour, L.D. Lanzerotti, C.L. Chang, J.C. Sturm: Optical and electrical properties of $\text{Si}_{1-x-y}\text{Ge}_x\text{C}_y$ thin films and devices, *Thin Solid Films* **294**, 112–117 (1997)
- 34.176 O. Madelung (Ed.): *Semiconductors-Basic Data*, 2nd edn. (Springer, Berlin 1996) p. 22
- 34.177 M. Okinaka, Y. Hamana, T. Tokuda, J. Ohta, M. Nunoshita: MBE growth mode and C incorporation of GeC epilayers on $\text{Si}(001)$ substrates using an arc plasma gun as a novel C source, *J. Cryst. Growth* **249**, 78–86 (2003)
- 34.178 M.W. Dashiell, L.V. Kulik, D.A. Hits, J. Kolodzey, G. Watson: Carbon incorporation in $\text{Si}_{1-y}\text{C}_y$ alloys grown by molecular beam epitaxy using a single silicon-graphite source, *Appl. Phys. Lett.* **72**, 833–835 (1998)
- 34.179 J.P. Liu, H.-J. Osten: Substitutional carbon incorporation during $\text{Si}_{1-x-y}\text{Ge}_x\text{C}_y$ growth on $\text{Si}(100)$ by molecular-beam epitaxy: Dependence on germanium and carbon, *Appl. Phys. Lett.* **76**, 3546–3548 (2000)
- 34.180 Y. Kanzawa, K. Nozawa, T. Saitoh, M. Kubo: Dependence of substitutional C incorporation on Ge content for $\text{Si}_{1-x-y}\text{Ge}_x\text{C}_y$ crystals grown by ul-

- trahigh vacuum chemical vapor deposition, Appl. Phys. Lett. **77**, 3962–3964 (2000)
- 34.181 V. LeThanh, C. Calmes, Y. Zheng, D. Bouchier, V. Fortuna, J.-C. Dupuy: In situ RHEED monitoring of carbon incorporation during SiGeC/Si(001) growth in a UHV-CVD system, Mater. Sci. Eng. B **89**, 246–251 (2002)
- 34.182 J. Mi, P. Warren, P. Letourneau, M. Judelewicz, M. Gailhanou, M. Dutoit, C. Dubois, J.C. Dupuy: High quality $\text{Si}_{1-x-y}\text{Ge}_x\text{C}_y$ epitaxial layers grown on (100) Si by rapid thermal chemical vapor deposition using methylsilane, Appl. Phys. Lett. **67**, 259–261 (1995)
- 34.183 W.K. Choi, J.H. Chen, L.K. Bera, W. Feng, K.L. Pey, J. Mi, C.Y. Yang, A. Ramam, S.J. Chua, J.S. Pan, A.T.S. Wee, R. Liu: Structural characterization of rapid thermal oxidized $\text{Si}_{1-x-y}\text{Ge}_x\text{C}_y$ alloy films grown by rapid thermal chemical vapor deposition, J. Appl. Phys. **87**, 192–197 (2000)
- 34.184 V. Loup, J.M. Hartmann, G. Rolland, P. Holliger, F. Laugier, M.N. Séméria: Growth temperature dependence of substitutional carbon incorporation in SiGeC/Si heterostructures, J. Vac. Sci. Technol. B **21**, 246–253 (2003)
- 34.185 J. Tersof: Enhanced solubility of impurities and enhanced diffusion near crystal surfaces, Phys. Rev. Lett. **74**, 5080–5083 (1995)
- 34.186 H. Rücker, M. Methfessel, E. Bugiel, H.-J. Osten: Strain-stabilized highly concentrated pseudomorphic $\text{Si}_{1-x}\text{C}_x$ layers in Si, Phys. Rev. Lett. **72**, 3578–3581 (1994)
- 34.187 P.C. Kelires: Theoretical investigation of the equilibrium surface structure of $\text{Si}_{1-x-y}\text{Ge}_x\text{C}_y$ alloys, Surf. Sci. **418**, L62–L67 (1998)
- 34.188 H. Jacobson, J. Xiang, N. Herbots, S. Whaley, P. Ye, S. Hearne: Heteroepitaxial properties of $\text{Si}_{1-x-y}\text{Ge}_x\text{C}_y$ on Si(001) grown by combined ion- and molecular-beam deposition, J. Appl. Phys. **81**, 3081–3091 (1997)
- 34.189 A. Sakai, Y. Torige, M. Okada, H. Ikeda, Y. Yasuda, S. Zaima: Atomistic evolution of $\text{Si}_{1-x-y}\text{Ge}_x\text{C}_y$ thin films on Si(001) surfaces, Appl. Phys. Lett. **79**, 3242–3244 (2001)
- 34.190 O.G. Schmidt, C. Lange, K. Eberl, O. Kienzle, F. Ernst: Formation of carbon-induced germanium dots, Appl. Phys. Lett. **71**, 2340–2342 (1997)
- 34.191 O. Leifeld, A. Beyer, E. Müller, K. Kern, D. Grützmacher: Formation and ordering effects of C-induced Ge dots grown on Si(001) by molecular beam epitaxy, Mater. Sci. Eng. B **74**, 222–228 (1999)
- 34.192 R.I.G. Uhrberg, J.E. Northrup, D.K. Biegelsen, R.D. Bringans, L.-E. Swartz: Atomic structure of the metastable $c(4 \times 4)$ reconstruction of Si(100), Phys. Rev. B **46**, 10251–10256 (1992)
- 34.193 H. Nörenberg, G.A.D. Briggs: The Si(001) $c(4 \times 4)$ surface reconstruction: a comprehensive experimental study, Surf. Sci. **430**, 154–164 (1999)
- 34.194 O. Leifeld, D. Grützmacher, B. Müller, K. Kern, E. Kaxiras, P.C. Kelires: Dimer pairing on the C-alloyed Si(001) surface, Phys. Rev. Lett. **82**, 972–975 (1999)
- 34.195 S. Ariyoshi, S. Takeuchi, O. Nakatsuka, A. Sakai, S. Zaima, Y. Yasuda: Influence of $\text{Si}_{1-x}\text{Ge}_x$ interlayer on the initial growth of SiGeC on Si(100), Appl. Surf. Sci. **224**, 117–121 (2004)
- 34.196 S. Zaima, A. Sakai, Y. Yasuda: Control in the initial growth stage of heteroepitaxial $\text{Si}_{1-x-y}\text{Ge}_x\text{C}_y$ on Si(001) substrates, Appl. Surf. Sci. **212–213**, 184–192 (2003)
- 34.197 S. Takeuchi, O. Nakatsuka, Y. Wakazono, A. Sakai, S. Zaima, Y. Yasuda: Initial growth behaviors of SiGeC in SiGe and C alternate deposition, Mater. Sci. Semicond. Process. **6**, 5–9 (2005)
- 34.198 G. Ehrlich, F. Hudda: Atomic view of surface self-diffusion: Tungsten on tungsten, J. Chem. Phys. **44**, 1039–1049 (1966)
- 34.199 R.L. Schwoebel, E.J. Shipsey: Step motion on crystal surfaces, J. Appl. Phys. **37**, 3682–3686 (1966)
- 34.200 J. Mysliveček, C. Schelling, G. Springholz, F. Schäffler, B. Voigtländer, P. Šmilauer: On the origin of the kinetic growth instability of homoepitaxy on Si(001), Mater. Sci. Eng. B **89**, 410–414 (2002)
- 34.201 S. Fukatsu, H. Yoshida, N. Usami, A. Fujiwara, T. Takahashi, Y. Shiraki, R. Ito: Quantum size effect of excitonic band-edge luminescence in strained $\text{Si}_{1-x}\text{Ge}_x$ /Si single quantum well structures grown by gas-source Si molecular beam epitaxy, Jpn. J. Appl. Phys. **31**, L1319–L1321 (1992)
- 34.202 D.K. Nayak, N. Usami, S. Fukatsu, Y. Shiraki: Band-edge photoluminescence of SiGe/strained-Si/SiGe type-II quantum wells on Si(100), Appl. Phys. Lett. **63**, 3509–3511 (1993)
- 34.203 N. Usami, Y. Shiraki, S. Fukatsu: Spectroscopic study of Si-based quantum wells with neighbouring confinement structure, Semicond. Sci. Technol. **12**, 1596–1602 (1997)
- 34.204 S. Fukatsu, Y. Shiraki: Interwell coupling in strained $\text{Si}_{1-x}\text{Ge}_x$ /Si quantum wells, Ext. Abs. 1993 Int. Conf. Solid State Devices Mater. (Makuhari, 1993) p. 895
- 34.205 S. Fukatsu: Luminescence investigation on strained $\text{Si}_{1-x}\text{Ge}_x$ /Si modulated quantum wells, Solid-State Electron. **37**, 817–823 (1994)
- 34.206 K. Kawaguchi, Y. Shiraki, N. Usami, J. Zhang, N.J. Woods, G. Breton, G. Parry: Fabrication of strain-balanced Si/Si $_{1-x}\text{Ge}_x$ multiple quantum wells on Si $_{1-y}\text{Ge}_y$ virtual substrates and their optical properties, Appl. Phys. Lett. **79**, 344–346 (2001)
- 34.207 K. Kawaguchi, S. Koh, Y. Shiraki, J. Zhang: Fabrication of strain-balanced Si $_{0.73}\text{Ge}_{0.27}$ /Si distributed Bragg reflectors on Si substrates, Appl. Phys. Lett. **79**, 476–478 (2001)
- 34.208 K. Kawaguchi, S. Koh, Y. Shiraki, J. Zhang: Fabrication of strain-balanced Si $_{0.73}\text{Ge}_{0.27}$ /Si-distributed Bragg reflectors on Si substrates for optical device applications, Physica E **13**, 1051–1054 (2002)

- 34.209 K. Kawaguchi, K. Konishi, S. Koh, Y. Shiraki, Y. Kaneko, J. Zhang: Optical properties of strain-balanced $\text{Si}_{0.73}\text{Ge}_{0.27}$ planar microcavities on Si substrates, *Jpn. J. Appl. Phys.* **41**, 2664–2667 (2002)
- 34.210 K. Kawaguchi, M. Morooka, K. Konishi, S. Koh, Y. Shiraki: Optical properties of strain-balanced SiGe planar microcavities with Ge dots on Si substrates, *Appl. Phys. Lett.* **81**, 817–819 (2002)
- 34.211 N. Usami, T. Mine, S. Fukatsu, Y. Shiraki: Realization of crescent-shaped SiGe quantum wire structures on a V-groove patterned Si substrate by gas-source Si molecular beam epitaxy, *Appl. Phys. Lett.* **63**, 2789–2791 (1993)
- 34.212 N. Usami, T. Mine, S. Fukatsu, Y. Shiraki: Optical anisotropy in wire-geometry SiGe layers grown by gas-source selective epitaxial growth technique, *Appl. Phys. Lett.* **64**, 1126–1128 (1994)
- 34.213 B. Teichert: Self-organization of nanostructures in semiconductor heteroepitaxy, *Phys. Rep.* **365**, 335–432 (2002)
- 34.214 Z. Zhang, M.G. Lagally: *Morphological Organization in Epitaxial Growth and Removal* (World Scientific, Singapore 1998)
- 34.215 K. Brunner: Si/Ge nanostructures, *Rep. Prog. Phys.* **65**, 27–72 (2002)
- 34.216 J.-M. Baribeau, N.L. Rowell, D.J. Lockwood: Self-assembled $\text{Si}_{1-x}\text{Ge}_x$ dots and islands. In: *Self-organized Nanoscale Materials*, ed. by M. Adachi, D.J. Lockwood (Springer, New York 2006)
- 34.217 M. Miura: Studies of formation process and optical properties of self-assembled Ge/Si nanostructures. Ph.D. Thesis (University of Tokyo, Tokyo 2001)
- 34.218 M. Miura, J.M. Hartmann, J. Zhang, B. Joyce, Y. Shiraki: Formation process and ordering of self-assembled Ge islands, *Thin Solid Films* **369**, 104–107 (2000)
- 34.219 H. Takamiya, M. Miura, J. Mitsui, S. Koh, T. Hattori, Y. Shiraki: Size reduction of the Ge islands by utilizing the strain fields from the lower-temperature-grown hut-clusters buried in the Si matrix, *Mater. Sci. Eng. B* **89**, 58–61 (2002)
- 34.220 E.S. Kim, N. Usami, Y. Shiraki: Control of Ge dots in dimension and position by selective epitaxial growth and their optical properties, *Appl. Phys. Lett.* **72**, 1617–1619 (1998)
- 34.221 E.S. Kim, N. Usami, Y. Shiraki: Selective epitaxial growth of dot structures on patterned Si substrates by gas source molecular beam epitaxy, *Semicond. Sci. Technol.* **14**, 257–265 (1999)
- 34.222 H. Takamiya, M. Miura, N. Usami, Y. Shiraki: Drastic modification of the growth mode of Ge quantum dots on Si by using boron adlayer, *Thin Solid Films* **369**, 84–87 (2000)
- 34.223 S. Koh, K. Konishi, Y. Shiraki: Small and high-density GeSiC dots stacked on buried Ge hut-clusters in Si, *Physica E* **21**, 440–444 (2004)

Plasma Energetics

35. Plasma Energetics in Pulsed Laser and Pulsed Electron Deposition

Mikhail D. Strikovski, Jeonggoo Kim, Solomon H. Kolagani

Surface bombardment by energetic particles strongly affects thin-film growth and allows surface processing under non-thermal-equilibrium conditions. Deposition techniques enabling energy control can effectively manipulate the microstructure of the film and tune the resulting mechanical, electrical, and optical properties. At the high power densities used for depositing stoichiometric films in the case of pulsed ablation techniques such as pulsed laser deposition (PLD) and pulsed electron deposition (PED), the initial energetics of the material flux are typically on the order of 100 eV, much higher than the optimal values (≤ 10 eV) required for high-quality film growth. To overcome this problem and to facilitate particle energy transformation from the original as-ablated value to the optimal value for film growth, one needs to carefully select the ablation conditions, conditions for material flux propagation through a process gas, and location of the growth surface (substrate) within this flux. In this chapter, we discuss the evolution of the material particles energetics during the flux generation and propagation in PLD and PED, and identify critical control parameters that enable optimum thin-film growth. As an example, growth optimization of epitaxial GaN films is provided.

PED is complementary to PLD and exhibits an important ability to ablate materials that are transparent to laser wavelengths typically used in PLD. Some examples include wide-bandgap

35.1 Energetic Condensation in Thin Film Deposition	1193
35.2 PLD and PED Techniques	1194
35.3 Transformations of Atomic Energy in PLD and PED	1195
35.3.1 Plasma Formation of Vaporized Material	1196
35.3.2 Plasma Formation in PED	1198
35.3.3 Expansion of Plasma and Particle Acceleration	1199
35.3.4 Deceleration of Plasma in Background Gas	1202
35.4 Optimization of Plasma Flux for Film Growth	1204
35.4.1 Ion Current of Plasma Propagating in Ambient Gas	1205
35.4.2 Optimization of Growth of GaN Films – A Materials Example	1206
35.5 Conclusions	1208
References	1209

materials such as SiO₂, Al₂O₃, and MgO. Both PLD and PED can be integrated within a single deposition module. PLD–PED systems enable in situ deposition of a wide range of materials required for exploring the next generation of complex structures that incorporate metals, complex dielectrics, ferroelectrics, semiconductors, and glasses.

35.1 Energetic Condensation in Thin Film Deposition

Thin-film deposition under energetic particle bombardment is well known. Originally suggested in 1938 for improving film density, the energetic process was fur-

ther developed as *ion plating* in 1963 [35.1]. A variety of techniques to produce energetic conditions are currently in practice [35.2]. These include plasma-assisted

film deposition techniques [35.3], magnetron sputtering [35.4], and ion-beam-assisted deposition [35.5, 6]. A common factor accompanying all energetic condensation processes is that the film growth surface is under constant bombardment by an energetic particle flux as it receives the desired material for film growth.

Under the bombardment by energetic particles, surfaces and subsurface layers of crystals are in an unusual (nonequilibrium) state controlled by the particle flux parameters rather than by deposition conditions such as substrate temperature. In this state, the equilibrium dynamics are no longer applicable to the dynamics of the crystal surface modification processes, which include implantation of atoms, radiation-enhanced diffusion, point-defect interaction, sputtering, ion mixing, adsorption, adatom movement, and film growth. The modified layers retain a *memory* of the conditions of their origin and exhibit unusual properties. This can be beneficial for some applications of the modified layers, and undesirable for others. Control of the bombardment conditions is critical for optimizing a specific process. In general, the particle energy of interest is in the range of 10–100 eV, which is well above the common processing temperature of < 0.1 eV (≈ 1200 K). In some sense, the particle bombardment substitutes for

the higher temperature that is problematic to achieve under equilibrium conditions.

Pulsed laser deposition (PLD) and pulsed electron deposition (PED) are relatively new energetic condensation techniques with unique plasma flux parameters. In PLD and PED, a pulsed laser or a pulsed electron beam rapidly vaporizes a thin section of a target material, providing a stream of energetic plasma flux under highly nonequilibrium conditions. This process is known as ablation. The film growth conditions are intricately linked to and controlled by the conditions of the flux generation and its propagation in an ambient process gas (or in vacuum). This chapter will consider and compare these two techniques, emphasizing the critical role of plasma energetics in thin-film formation. The objective is to follow the energy balance through the entire process sequence from flux generation at the target surface to flux arrival at the growth surface (substrate), and to draw conclusions on the possibilities of controlling and optimizing the deposition conditions in PLD and PED.

We limit our consideration to the most commonly used laser pulses of nanosecond duration. Also we leave beyond the scope of this chapter the subject of macrodefects (droplets) in deposited films.

35.2 PLD and PED Techniques

The idea of utilizing the exceptionally high power density of a laser beam for material processing has been

tested contemporarily with the development of lasers since the 1960s. The effects of heating a material to temperatures well above an *evaporation temperature* and transforming the vapor into a state of plasma have been studied extensively. In their pioneering work, *Smith and Turner* [35.7] explored plasma condensation to form a film layer on a substrate placed in a vacuum. Since then, a variety of PLD processes have been considered and summarized in several excellent reviews [35.6, 8–10]. In the conventional PLD process, shown schematically in Fig. 35.1, a high-power pulsed laser beam is used as an external energy source to rapidly vaporize the target material. When a pulse of submicrosecond duration is used (accomplished in Q-switched solid-state or excimer lasers, for example), the general process is not limited to evaporation but is accompanied by strong absorption of the laser beam in the vapor and its transformation into plasma. The interaction of the laser beam with the target and the generated plasma is a very complex physical process, and depends on the properties of both the target and the laser beam.

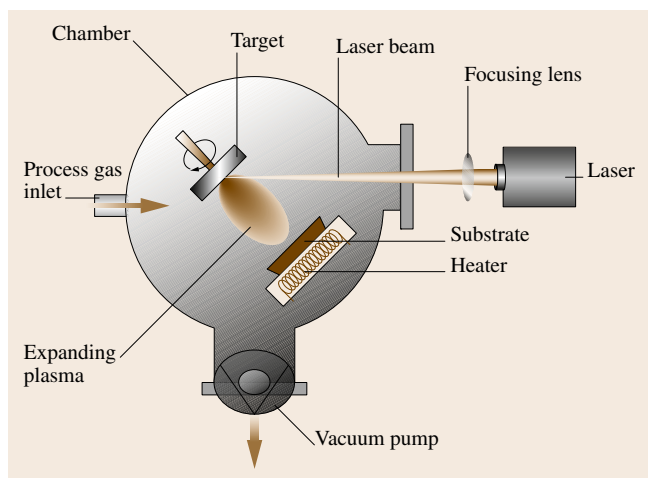


Fig. 35.1 Schematic representation of a conventional PLD process

In **PED**, the general scheme and ablation processes are very similar to in **PLD**, although a significant difference in the nature of the pulse energy source exists. In the **PED** process, the energy for ablation is delivered to the target by pulsed electrons rather than photons (as in **PLD**). The electron beam interacts differently with the target and the evaporant it generates. However, similarly

dense plasma is formed at the target surface by both the pulsed electron and the pulsed laser beam. This dense plasma is the primary precursor source material for film deposition. The dense, high-temperature, strongly ionized plasma layer at the target surface propagating in a direction perpendicular to the target surface is known as the *plasma plume* in the published literature.

35.3 Transformations of Atomic Energy in PLD and PED

In energetic deposition processes, atoms from the target surface pass through several energy transformation phases before arriving at a substrate surface. Starting from their evaporation, the atoms are involved in a series of energy transfer processes controlled by different mechanisms. These atoms experience significant changes in their temperature, ionization state, as well as kinetic energy. To evaluate the possibilities of controlling the energetics in the film deposition process, it is critical to follow the dynamics of the energetics of the atoms. For every phase, there are key parameters enabling control of the transient processes. Ultimately, this enables control over the energy of the atoms arriving at the substrate, which is important for the film growth. **PLD** and **PED** processes, viewed as a sequence of several phases, are shown schematically in Fig. 35.2.

The pulse width of the laser or electron beam defines the duration of phase 1 in Fig. 35.2. During this period, most of the beam energy is transformed into the internal energy (enthalpy) of the atoms in the plasma. This includes energies of evaporation and ionization, the thermal energy of material atoms, as well as the energy of electrons in the plasma. Typically, the thickness of the plasma layer near the target surface is below 0.1 mm during this phase.

Under the action of high internal pressure, the plasma layer ejects itself in a direction perpendicular to the target surface (phase 2, Fig. 35.2). The plasma pressure is orders of magnitude larger than any practical gas pressure in the process chamber. Thus, the plasma ejection is not affected by the presence of process gases. The plasma experiences continuous acceleration by the pressure gradient supported through recombination of atoms and electrons. During this phase, the original energy spectrum of the plasma flux is formed. A typical plasma size in this phase is on the order of several times the spot size on the target. A three-dimensional expansion begins within this distance. In a typical **PLD** or **PED** process, this expansion is ≈ 10 mm in length. If depo-

sition is carried out in a vacuum (10^{-6} Torr or below), the plasma expands and the original energy spectrum is *frozen*, and can be analyzed by an appropriate time-of-flight technique.

If deposition takes place in a background gas (phase 3, Fig. 35.2), the flux atoms collide with the gas atoms. As a result, the initial energetic spectrum of the atoms in the plasma evolves on a characteristic length scale related to the length scale of the mean free path at a given pressure. If the number of ablated atoms is sufficient to involve a comparable number of gas atoms in the mutual hydrodynamic movement, this *snowplow* effect drives most of the gas atoms towards the substrate, leaving behind a gas-rarefied region (shown pale brown in Fig. 35.2). Simultaneously, as the entire ensemble decelerates during this phase, the kinetic energy of both the target and gas atoms decreases.

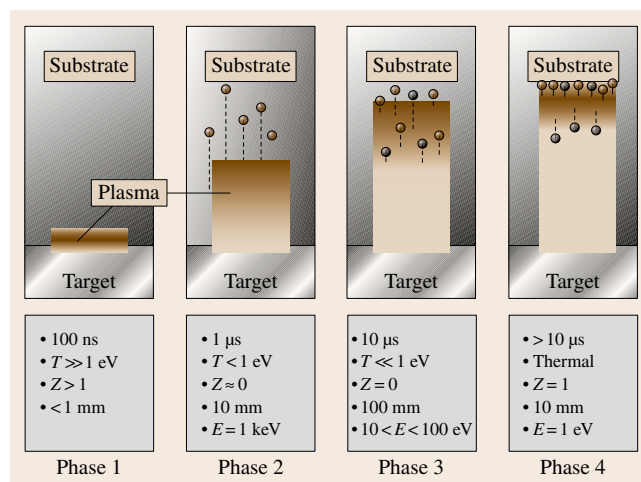


Fig. 35.2 Schematic representation of **PLD** and **PED** processes. Conventions: *brown circles*: fast atoms of target material, *black circles*: gas atoms, *pale brown area*: depleted gas volume behind the plasma front

In the next phase (phase 4, Fig. 35.2), the directional velocity of plasma flux becomes comparable to the thermal velocity of its particles (i.e., the flux transforms from supersonic to subsonic states). Plasma expansion nearly stops (seen as a range for its visible radiation *plume*), and becomes nearly isotropic. In most cases, an optimal substrate location for film growth can be found in the near vicinity of this range.

35.3.1 Plasma Formation of Vaporized Material

The dominant process in phase 1 is the evaporation and ionization of a small amount of material. First, at the typical beam power density used in ablation ($Q \approx 10^9 \text{ W/cm}^2$), the target surface is rapidly heated, attaining temperatures well above the common *evaporation* temperature of all the elements in the target. The evaporation can be so intense that the vapor density at the surface can approach the limiting value of the atomic concentration in a solid ($n_L \approx 5 \times 10^{22} \text{ cm}^{-3}$). Second, in the field of the intense laser beam, the vapor effectively ionizes (transforms into plasma) and absorbs the majority of the incoming energy from the laser, preventing further heating of the target. Several key parameters that control the process are, pulse duration τ , power density Q [W/cm^2], and energy density $Q\tau$ [J/cm^2]. The laser wavelength λ in *PLD* and the energy of each electron [keV] in *PED* define the ab-

sorption depth of the beam with respect to the target material.

The pulse energy is distributed in the target over a depth ($D + D_T$), and the rate of surface temperature rise can be expressed as

$$\frac{dT}{dt} \sim \frac{Q}{D + D_T}, \quad (35.1)$$

where D is the absorption length (photon or electron range) and D_T is the thermal diffusion length. D_T can be expressed as $D_T = 2(at)^{1/2}$, where a is the thermal diffusivity and t is the time. D_T is also the characteristic depth of exponential decay of the temperature distribution, $T(x, t) \propto \exp(-x^2/4at)$ for one-dimensional (x) heat diffusion from a surface source [35.12].

For $\tau = 10 \text{ ns}$, a pulse width typical in *PLD*, D_T is about $0.2 \mu\text{m}$ for most common dielectrics. This value is less than or comparable to the photon absorption depth D , and D_T can be neglected in (35.1). Thus the heating rate is controlled by the target optical properties at a given wavelength, and increases *proportionally* with the beam power.

This is not the case in *PED*. The penetration depth (or absorption range) of an electron in a solid depends on its energy. In *PED*, both the electron beam power Q and the electron range depend on the electron source voltage V . Since the number of electrons in the pulse is proportional to the total beam current density I , and since the average energy of each electron ($\sim \text{eV}$) is directly related to the pulsed electron beam source (*PEBS*) voltage V , the power density carried by the beam is $Q \approx IV$, where $I = I(V)$. The $I(V)$ relation characterizes a *PEBS* design. For 10–100 kV electrons, the range D changes with voltage as $D \propto V^2$, as shown in Fig. 35.3. If $D > D_T$, the $D \propto V^2$ dependence controls the denominator in (35.1), and thus strongly affects the heating rate in *PED*. In some sense, changing the voltage in the *PEBS* is equivalent to changing the laser wavelength (and absorption depth) in *PLD*. The interplay of $Q(V)$ and $D(V)$ controls the surface heating rate in *PED*. The expected heating rate for *PED* has been examined elsewhere [35.13]. Experiments show that the beam power is not able to increase as fast as the beam penetration length at $> 15 \text{ kV}$, which leads to a maximum in the heating rate at $\approx 15 \text{ kV}$ (Fig. 35.4). Therefore, it is not always beneficial to use the source at higher voltage (and accordingly with higher energy electrons). A more efficient way to improve the heating rate in *PED* is via a larger current density at the target surface by minimizing the beam cross-section. In order to increase the current density, the target has to

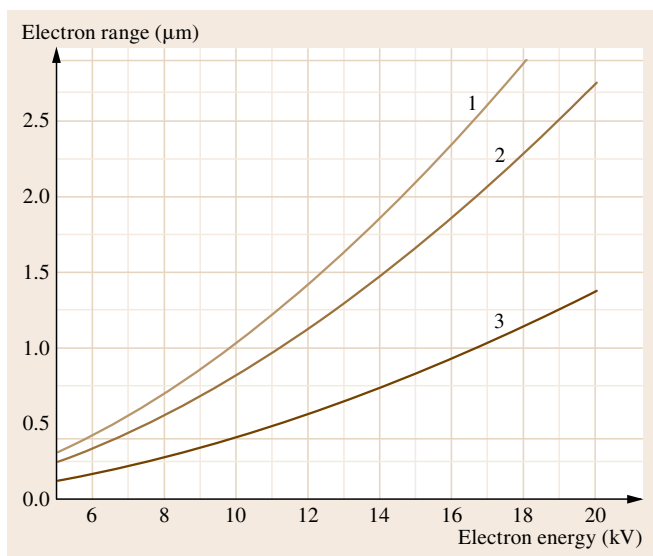


Fig. 35.3 Calculated penetration depth (range) of energetic electrons in Si (1), Al_2O_3 (2), and $\text{YBa}_2\text{Cu}_3\text{O}_x$ (3) (after [35.11])

be as close to the tube output as is practically possible since the electron beam diverges with distance from the output channel tube.

In both **PLD** and **PED**, once vapor with a sufficient density is formed at the target surface, the beam ionizes it. **PLD** differs from **PED** in the target surface heating dynamics and the mechanism of ionization. In **PLD**, free electrons gain energy in the oscillating electric field of a laser and ionize atoms by impact. This avalanche-like process is similar to the *optical breakdown* of gases by intense laser beams. The breakdown physically means that, once transformed into a strongly ionized plasma state, the plasma becomes nontransparent to the laser beam. The plasma shields the target material from the beam, and absorbs the majority of the pulse energy. This plasma shielding strongly affects the energy balance in **PLD** and **PED**, the primary topic of interest in this chapter. Well above the ablation threshold, the fraction of the beam energy used for target heating is relatively small. The majority of the beam energy is preserved within the plasma [35.14]. The net energy balance of the entire ablation process can be roughly understood as

$$Qt = E_1 N, \quad (35.2)$$

where E_1 is the *total* average energy per evaporated particle (ion or atom) and N is the total number of atoms or ions per unit area. The energy E_1 eventually transforms into kinetic energy $E \leq E_1$ of atoms ejected from the target. The balance indicates that higher particle energy E_1 is expected in an ablation process in which a smaller number (N) of ablated particles enables a strong shielding effect.

The total number N of atoms absorbing the beam energy can be estimated as $N \approx nL$, where n is the atomic concentration in the shielding plasma and L is the thickness of the plasma layer. Some understanding of $n(\lambda)$ scaling laws for different laser wavelength λ (frequency $\omega = c/\lambda$) can be gained by considering the conditions for optical breakdown of gases. Under a crude approximation, the gas concentration most favorable for developing the electron avalanche corresponds to the condition where the frequency Ω of electron collisions with atoms is on the same order as the beam frequency ω . The critical concentration $n = n_c$ can be found from the condition $\Omega(n_c) \approx \omega$. The physical reason for the optimum is that, for a given ω of the laser, the rate of electron energy gain in the electric field of the beam has a maximum at this value of collision frequency [35.15]. The gas ionization develops via inverse bremsstrahlung absorption. The

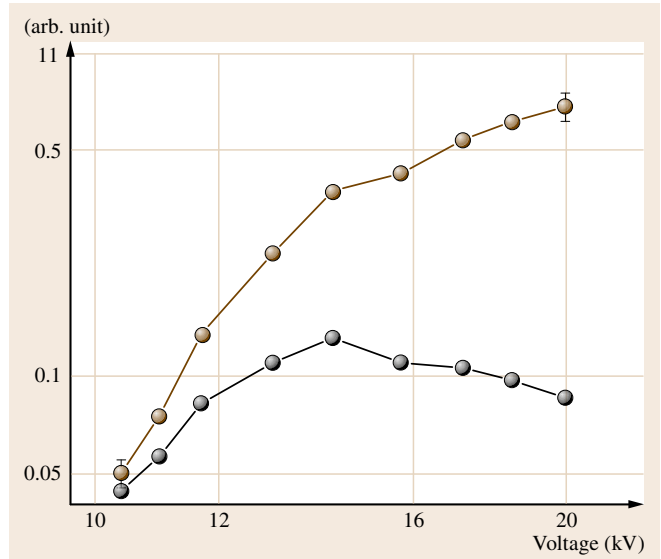


Fig. 35.4 Estimated surface heating rate (black circles) and measured beam power (brown circles) as functions of the electron energy

collision frequency relates directly to the gas (vapor) concentration as $\Omega = an$. As an example, for normal conditions of 760 Torr ($n = 2.47 \times 10^{19} \text{ cm}^{-3}$) of Ar gas ($\alpha = 1.6 \times 10^{-7} \text{ cm}^3 \text{ s}^{-1}$), one finds $\Omega = 4 \times 10^{12} \text{ s}^{-1}$, and $\lambda = 75 \mu\text{m}$ radiation would be optimal to create plasma.

As a wide range of atom concentration in the vapor is available in **PLD** at the prebreakdown stage, the above condition can be satisfied at least for λ down to $\approx 1 \mu\text{m}$.

The condition gives an estimate for the initial atomic concentration to develop the shielding plasma. It is inversely proportional to the laser wavelength, $n_c \propto \lambda^{-1}$. The relations above describe proper conditions to initiate plasma at microwave frequencies, where the pressure of ≈ 2 Torr is optimal for 2.8 GHz ($\lambda = 1.0 \text{ mm}$). It is also suitable for CO_2 laser with $\lambda = 10.6 \mu\text{m}$. The calculated value of 15 atm ($n_c = 3.8 \times 10^{20} \text{ cm}^{-3}$) as the optimal pressure for Xe gas plasma formation is close to the experimental value of 20 atm [35.15]. The breakdown threshold power density Q^* of the CO_2 pulsed laser is as low as $\approx 5 \times 10^7 \text{ W/cm}^2$. For radiation of an Nd:yttrium aluminum garnet (**YAG**) laser ($\lambda = 1.06 \mu\text{m}$), it can be estimated that the optimal vapor concentration is $n_c = 3.8 \times 10^{21} \text{ cm}^{-3}$. For a shorter-wavelength laser, the plasma starts to develop in a higher atomic concentration in the vapor. For the **PLD** process, this suggests that more material has to be evaporated before shielding occurs.

For much shorter wavelengths such as those of ultraviolet (UV) excimer lasers, the vapor breakdown condition and mechanism are more complex. Theoretical estimation from the above relations implies that the estimated optimal atomic concentration in a vapor of $n_c = 1.6 \times 10^{22} \text{ cm}^{-3}$ becomes unrealistically high at $\lambda = 248 \text{ nm}$ (KrF laser), for example. The vapor breakdown threshold intensity of the beam, according to the classical theory, should also increase sharply as $Q^* \propto \lambda^{-2}$ [35.16]. The scaling from $10.6 \mu\text{m}$ leads to $Q^* \approx 9 \times 10^{10} \text{ W/cm}^2$. These estimations, however, have not been supported by experimental results. Experimental values as low as $\approx 1 \times 10^8 \text{ W/cm}^2$ for Al and Cu targets has been found for 248 nm [35.17]. The suggested explanation of the reduced breakdown threshold for UV lasers is that a multiphoton photoelectric effect takes over from the atomic ionization process as the high energy of UV quantum becomes comparable to the atomic excitation and ionization potentials [35.15, 18]. The threshold can actually decrease with wavelength at $\lambda < 1 \mu\text{m}$. The low thresholds indicate that a very dense vapor is not needed to form UV laser plasma. Thus, the atomic concentration on the order of $n \approx 1 \times 10^{21} \text{ cm}^{-3}$ in the vapor may be a reasonable estimate for typical breakdown conditions for wavelengths in the range of $\lambda = 1.0\text{--}0.25 \mu\text{m}$ in PLD. However, the concentration does change with λ . Data for the laser wavelength dependence of the ablated material mass [35.19] indicate that the plasma can still be created in vapor with higher density for shorter-wavelength lasers. Following the considerations mentioned above, in this case the energy balance for the PLD process is shifted towards a smaller number of ablated atoms and a larger energy of ejected atoms/ions. This trend is indeed seen in the energy spectrum of ejected ions [35.20, 21].

Experiments suggest that, at $3 \times 10^8 \text{ W/cm}^2$ ($\lambda = 248 \text{ nm}$), breakdown starts at the beginning of a 30 ns pulse and takes just $\sim 5 \text{ ns}$ to develop a plasma absorbing $\approx 85\%$ of the beam intensity [35.17]. The majority of the beam energy is loaded into the vapor. The plasma thickness L can be estimated as $v_T t \approx 10^{-3} \text{ cm}$ where $v_T \approx 10^5 \text{ cm/s}$ is the thermal velocity of vapor expanding from the target surface. The plasma contains $nL \approx 1 \times 10^{18} / \text{cm}^2$ atoms, which would originally occupy a $\approx 2 \times 10^{-5} \text{ cm}$ deep layer in a solid target. Note that, for typical cohesive energy of $\approx 4 \text{ eV/atom}$ in solids, the evaporation of this number of atoms requires $\approx 0.8 \text{ J/cm}^2$. This is typically a small fraction of the beam energy in intensive ablation conditions ($> 3 \text{ J/cm}^2$). Most of the pulse energy is loaded into the total energy (enthalpy) of plasma, including the thermal

energy of ions and electrons as well as the ionization energy.

With increasing laser intensity Q , both N and E increase, as confirmed by numerous data on the Q dependence of evaporated materials, deposited film thickness, and ion/neutral atom kinetic energy. Although most of these data were obtained in conditions of one-dimensional plasma expansion (plasma layer thickness smaller than the focal spot size of the laser beam), the dependencies generally follow the scaling of the model [35.22] developed for the regime with partial target shielding by the flowing plasma. Such a self-regulating regime (*optical plasmatron*) is established once the laser pulse duration is much longer than the time of the plasma expansion to the characteristic scale of the ablation spot diameter, as has been observed in $\geq 1 \mu\text{s}$ long-pulse (transversely excited atmospheric pressure (TEA) CO_2 laser, [35.23, 24]) or small-spot nanosecond-pulse ablation [35.12, p. 243].

Based on mass and energy conservation laws and based on the assumption of a three-body plasma recombination process, the *steady-state* ablation model suggests that the ablation rate can be expressed as

$$\frac{dN}{dt} \propto \lambda^{-4/9} Q^{5/9}. \quad (35.3)$$

Accordingly, to satisfy the $E_1 dN/dt = Q = \text{const.}$ condition, the energy per atom can be expressed by

$$E_1 \propto \lambda^{4/9} Q^{4/9}. \quad (35.4)$$

These relations again point to the tendency of a shorter-wavelength laser beam to evaporate more material from a target, providing each atom with a lower energy. As a crude approximation, one can conclude that the average kinetic energy E of particles produced by laser ablation scales as $E \propto \lambda$ for $1.06\text{--}10.6 \mu\text{m}$ wavelength lasers and as $E \propto \lambda^{1/2}$ for $0.2\text{--}1.0 \mu\text{m}$ wavelength lasers. Choice of the laser is one of the possibilities to control the energy spectrum of the plasma flux in PLD.

35.3.2 Plasma Formation in PED

In PED, the electron beam energy of $5\text{--}15 \text{ keV}$ is well above the threshold potential for atomic excitations and ionizations. Fast electrons collide directly with the deep-level electrons of target material atoms, experience broad-angle scattering, and eventually stop at a certain depth from the target surface (electron range). This stopping at a certain depth requires a certain number of collisions to happen. This number is practically independent of the specific state of the atoms, with atoms in the solid lattice scattering

electrons as effectively as atoms in a gas phase (vapor). An important consequence of this fact is that, for the electron beam, there is no transition to the vapor plasma shielding effect that is characteristic for the laser ablation. Throughout the entire pulse length, the electron beam continues to interact with the same number of atoms as contained within the beam absorption range D in the target. As $D \propto 1/\rho$ (ρ [g/cm³] is the target material's density), the total mass ablated by the intense beam is expected to be independent of materials ablated, $m = \rho D = \text{const.}$ [35.11]. As mentioned above, the electron range is strongly dependent on the electron energy ε [keV]. The absorption range can be expressed as

$$D [\mu\text{m}] \approx 5.37\varepsilon \left(1 - \frac{0.9815}{1 + 0.0031\varepsilon} \right) \rho^{-1}.$$

Figure 35.3 shows the range of 0.5–2.0 μm for a typical PED electron beam energy of 10–15 keV. Even for dense materials (such as YBCO with a density of ≈ 6 g/cm³), the range of $\approx 1.0 \mu\text{m}$ is greater than the typical depth of $\approx 0.2 \mu\text{m}$ for laser ablation (using a 248 nm KrF laser at 5 J/cm²) [35.12]. If all the material within the penetration depth is PED-ablated, it follows, from (35.2), that the average kinetic energy of particles in the plasma flux can be smaller in PED than in PLD. For lower-density materials, a higher PED ablation rate and accordingly smaller energy per ablated atom could be expected. This is actually the case. However, the particle energy spectrum in PED is broader than in PLD due to the presence of a small amount of highly energetic ions, up to several keV. Some specific mechanism of ion acceleration could be responsible for the fast ion generation in PED.

35.3.3 Expansion of Plasma and Particle Acceleration

A dense layer of highly ionized high-pressure plasma is formed at the target surface by the focused laser pulse. The plasma expands and accelerates primarily in a direction normal to the target surface (Fig. 35.2, phase 2). During this process, the energy E_1 (the total energy per atom, i. e., the enthalpy per atom) is transformed into an asymptotic kinetic energy E of atoms [35.25], which is the energy of interest in the present discussion, as this flux of energetic particles arrives at the substrate for film formation (when PLD is carried out in vacuum). Gradient of plasma pressure is the driving force for the acceleration of particles. Note that, even when PLD is carried out in a typical pressure background gas, due

to the large difference between the plasma pressure at the ablation spot and the gas pressure, the initial energy spectrum of E is established at a distance of a few millimeters (≈ 3 times the spot diameter) from the target and is not affected by the presence of the process gas.

For a vacuum process (or at a low gas pressure), the ablation particle energy spectrum established soon after leaving the spot region remains mostly unchanged during the following geometrical expansion. The ion condition is *frozen* due to the low thermal energy of the plasma and the lack of efficient collisions. Laser-produced plasma retains a significant portion of the atoms in the ionized state. Film growth in vacuum is accompanied by the impact of particles of the largest possible energy. This feature also makes the laser flux an efficient source of ions for analytical laser plasma spectroscopy or for further acceleration of ions in special applications.

Specific conditions of the laser-produced plasma facilitate kinetic energy of particles well above the plasma temperature. At the end of the laser pulse, the total internal energy per plasma atom, $I + (1 + Z)T$, is stored in the thermal energy of the ion, Z electrons, and the total potential energy I of the atomic ionization. During the plasma expansion, electrons contribute to the acceleration pressure. The plasma temperature is also supported by release of the potential energy by three-body recombination. Thus the resulting kinetic energy of the flux particles can greatly exceed the original thermal energy of the plasma atom $\sim T$ [eV].

The model for the steady plasma flow regime (pulse length > 1000 ns) [35.22] predicts for the asymptotic particle energy

$$E = 5(1 + Z)T. \quad (35.5)$$

The functional relation $Z(I, T)$ can be used for atoms of a specific target material. As the beam energy stored per a plasma atom is ≈ 3 times greater than the target atom cohesion energy ≈ 4 eV (see before), a plasma temperature of > 10 eV can be estimated for a typical ablation with 3 J/cm². The potential energy of the first ionization I_1 is usually within the range 7–15 eV, and the $Z = 1$ ionization is already significant at temperature $T \approx I_1/5 = 1.4$ –3 eV [35.16]. At $T \approx 2$ –3 eV, the generation of $Z = 2$ ions is already possible. $Z = 2$ ions have been routinely observed under PLD ablation conditions. Equation (35.5) estimates $E = 30$ –45 eV for $Z = 2$ ions according to the model [35.22] for a steady flow ablation regime.

The steady regime is not usually realized in a practical excimer-laser-based PLD configuration with spot

sizes of ≈ 1 mm, where the ≈ 30 ns laser pulse is too short in comparison with the time to establish the steady regime. However, this regime has been realized in small-spot nanosecond-pulse ablation [35.12, p. 243], and ablation with a long TEA CO₂ laser ($\lambda = 10.6$ μ m) pulse of ≈ 2 μ s duration [35.23, 24]. Its specific features are an increased average ablation rate, and narrower energy spectrum $dN/dE = f(E)$ relative to the unsteady pulsed regime.

The narrow ion energy spectrum $dN/dE = f(E)$ observed [35.23, 24] can be explained by the fact that the majority of the registered ions have been generated under nearly similar, quasistationary evaporation–absorption–acceleration conditions during most of the pulse duration. The average particles energy is laser wavelength dependent. For a $\lambda = 10.6$ μ m CO₂ laser with $Q = 10^9$ W/cm², a narrow spectrum with a maximum at ≈ 400 eV was measured. This energy is about a factor of ≈ 2.5 larger than that observed for the $\lambda = 1.06$ μ m laser, and ≈ 5 times larger than that for 0.248 μ m radiation, in accordance with the prediction of (35.4). Another feature of the steady regime is that the average energy of neutrals is nearly as high as that of ions [35.23, 24]. This reflects the fact that both the neutrals and the ions experience the same acceleration conditions.

Thus, at the same beam energy density of a 11 ns duration excimer laser pulse, the ablation rate (μ m/pulse) increases by several times if the spot size is reduced from 83 to 24 μ m [35.12]. This can be explained by a transition to a steady regime with a plasma more transparent to the laser beam than in the case of one-dimensional expansion (large spot). In accordance with the energy balance, one can expect a lower average kinetic energy of ablated particles to result.

If the laser beam power density is high enough, such an important feature of PLD as congruent evaporation of complex materials is preserved in the quasistationary ablation regime. Indeed, the basic requirement for stoichiometric material removal is that the volume of ablated material is much greater than the volume of remaining heated material. That can be expressed as $v\tau \gg a/v$, where the ablation rate v is the velocity of the ablation surface propagation into a target, and a/v is the thickness of the heated material in front of it. As mentioned above, for a given power density, v is even higher in stationary than in pulsed ablation, and the condition is satisfied. Experimentally, for example, stoichiometric ablation in the quasistationary regime has been demonstrated by fabricating high-quality YBCO films using 2 μ s long pulses from a TEA CO₂ laser [35.26].

In an *unsteady* pulsed regime, the energy spectrum broadens in both directions compared with the energy spectrum for the steady flow regime. The leading ions on the front of the plasma layer are in favorable conditions to experience more effective acceleration, and attain greater energy. On the other hand, at the end of the laser pulse, the plasma pressure build up is terminated, and the ions at the surface created in this time are not able to accelerate. Thus, the leading ions with higher energy are present on the front of the expanding plasma stream. The effect is well known in classical gas dynamics in unsteady (abruptly started) gas flow in vacuum [35.16]. The energy of the leading particles E_{\max} is $\sim 2/(\gamma - 1)$ times larger than the energy from the steady flow. The additional kinetic energy is acquired at the expense of heat energy in the neighboring particles. For plasma at the ablation conditions, the exponent γ can be approximated to 1.3–1.4. The maximal energy of the accelerated particles is $E_{\max} = 10T(1 + Z)/(\gamma - 1) = 100$ –200 eV at $Z = 2$ and $T = 2$ –3 eV.

The velocity or energy of neutral components of the flux is generally somewhat lower, but still close to that of the ions. A possible explanation is that a significant number of the neutrals is in effect the former ions fraction, which has recombined. This fact makes it possible to apply the ion time-of-flight technique to probe the energetics of the laser-producing plasma fluxes. Data of the time-of-flight mass spectrometry and time-resolved emission spectroscopy applicable to trace the neutrals dynamics [35.27, 28] show a neutral's velocity of ≈ 0.6 –0.75 for ions (energy difference about a factor of 2–3). Still, the ion probe measurements are representative of the general flux energetics and represent a good estimate of the upper energy limit of the particles.

Films grow in vacuum under the impact of the particles of largest possible energy. The ion probe (Faraday cap) is a convenient and frequently used technique to characterize the dynamics of the plasma arriving at a point a distance L from the target. In this technique, a slightly negatively biased probe registers the current of the ions in the flux. For ablation in vacuum (or at low gas pressure), due to a large mean free path, the ions travel the distance ballistically, and the delay time t for ions arriving at the probe directly relates to their speed $v = L/t$ and kinetic energy $mV^2/2$. Thus, the ionic energy spectrum can be obtained as $dN/dE = f(E)$. The spectrum for $f(E)$ can be calculated from the ion probe current density $j = eZ(dN/dt)$ using the relation $dN/dE = (dN/dt)(dE/dt)^{-1}$, where $E = M(L/t)^2/2$

is the kinetic energy of an ion with mass M arriving at time t .

For ablation in an ambient background gas pressure, collisions with the gas alter the velocity of flux species and the probe signal. Since the relation $v = L/t$ is not valid any more due to the velocity change with distance, the probe signal cannot be used to extract the arriving ion's energy spectrum. The relation overestimates the ion's kinetic energy at distance L , as the original velocity is greater than L/t and as the velocity at arrival is smaller than L/t . A proper particle deceleration model can be used to describe the special evolution of their average energy.

A typical energy spectrum of Si ions is given in Fig. 35.5 for the plasma flux created by KrF laser pulse (wavelength 248 nm, 20 ns pulse, 2.5 J/cm² energy density) in vacuum. The insert shows the original ion current signal obtained at a distance of 11 cm. The median energy is ≈ 60 eV, large enough not only to significantly change the conditions of the surface movement of the arriving atoms but also to introduce property changes of the previously deposited layers of the growing film [35.29]. Characteristically, the spectrum exhibits an extended lip towards energies up to ≈ 200 eV. As discussed above, the fastest ions are those that are on the front of the expanding plasma cloud, where the largest pressure gradient exists for an extended time. Two additional factors can also contribute to the increased ion signal amplitude at the higher end of the spectrum and extending from the median energy value. First, multiple-ionized ions create a larger probe signal by a factor of Z (ion charge) than single-charged ones. Second, the energy of leading ions can be additionally increased by the effect of electrostatic acceleration of ions in a double layer of space charge existing at the front of the plasma [35.30].

Figure 35.6 compares the energy spectra of CeO₂ plasma flux ions obtained by PLD and PED at a distance of 14.5 cm at a similar energy density. The relatively small oxygen gas pressure of 1 mTorr does not alter the spectra significantly, at this distance, in comparison with the vacuum conditions. The spectra are normalized to probe signal maximum. A somewhat surprising result of this comparison is that the energy of the fastest ions in the PED-generated plasma flux is larger than in PLD. Possibly, some additional mechanism of ion acceleration exists in PED, the origin of which is not fully understood at the present time. One possible explanation is that the negative charging of the plasma cloud leads to a stronger expulsion of the electrons and to a stronger effect of electrostatic acceleration

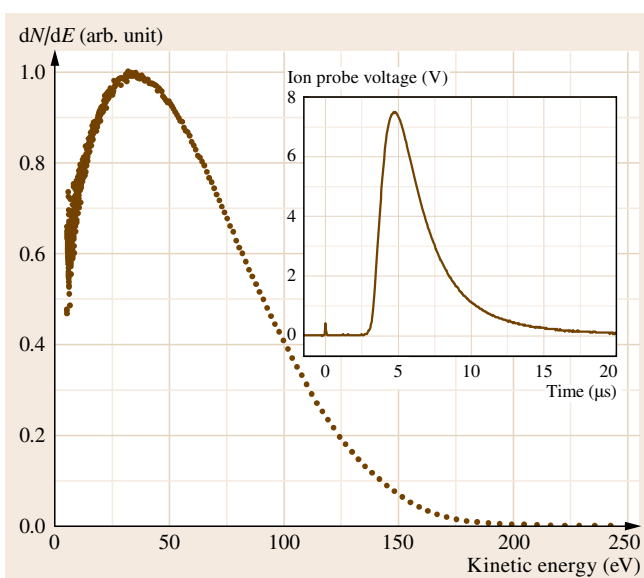


Fig. 35.5 Typical energy spectrum of Si ions generated by a KrF (248 nm) pulsed laser in vacuum. The *inset* shows the original ion probe signal at a distance of 11 cm from the Si target

of ions on the plasma front. At the same time, the PED spectrum is broader, and relatively more atoms with low energy are in ionized state. The average energy of the PED flux particles can be smaller than the

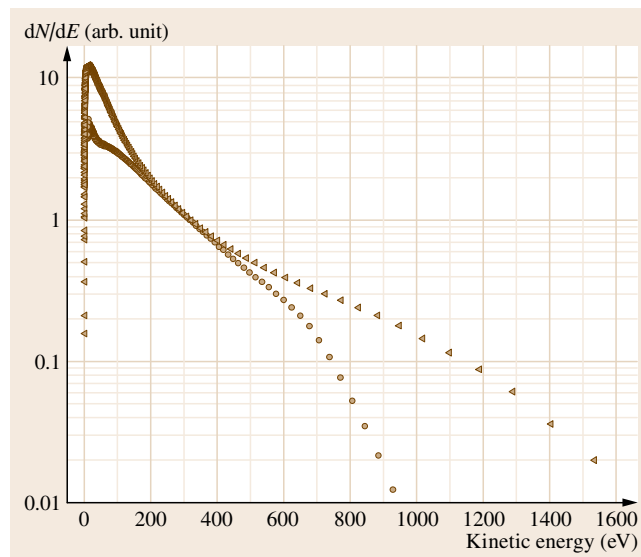


Fig. 35.6 Energy spectra of ions produced by pulsed laser (closed circles) and pulsed electron beam (open triangles) in oxygen pressure of 1 mTorr

energy in PLD. More studies are needed to fully understand the dynamics of PED-generated plasmas and their properties.

35.3.4 Deceleration of Plasma in Background Gas

In PED and PLD, the presence of background gases during ablation can significantly change both the average energy of the particles arriving at a substrate and the general attributes of the energy spectrum. When the mass of the evaporated atoms and of the incorporated gas atoms become comparable, hydrodynamic models can be used to describe deceleration of this ensemble and its thermalization. These are the phases 3 and 4 shown in Fig. 35.2. Introduction of a reactive or inert buffer gas into the deposition chamber is an effective tool to control the energy of species during film growth. Unlike vacuum PLD, plasma flux parameters change drastically with distance L from the target, which is critical for film growth. At a characteristic distance L_0 , the flux loses its unidirectional velocity, as it undergoes scattering, thermalization, and finally deceleration. It has been experimentally discovered that optimum

conditions for film growth exist in the vicinity of this distance [35.31–33].

In the presence of background gases, the ion probe signal is not useful to calculate the arriving particles' energy as their velocity changes with distance. If calculated as the ratio L/t , the velocity (and the energy) would be overestimated. A simple model has been suggested to describe the dynamics of plasma deceleration, the average particle energy at a distance L_0 , and the scaling of L_0 as a function of ablation and gas parameters [35.34]. In this model, the ensemble of initially ablated N_0 atoms, with an average velocity v_0 , is considered as a piston, incorporating and driving the gas atoms as it propagates. The essential processes here are energy transfer from the initial kinetic energy of the N_0 atoms to the thermal energy of the atom and the gas cloud (i. e., deceleration and thermalization). From the conservation of momentum and energy in an adiabatic process, the following dependencies are obtained for the velocity v of the directed movement of the ensemble and the characteristic thermal velocity $v_T = (k_B T/M)^{1/2}$ of the particles.

$$\frac{v}{v_0} = (1 + x^3)^{-1},$$

$$\frac{v_T}{v_0} = x^{3/2} [3(1 + x^3)(1 + \mu x^3)]^{-1/2},$$

where $\mu = M/m$ is the atomic mass ratio between the target material and the gas, and $x = L/R$ is the normalized distance. R has a clear physical meaning: after the ensemble covers the distance R , the total mass of the gas atoms becomes equal to the mass of ejected N_0 atoms.

Comparison of the velocities $v(x)$ and $v_T(x)$ (Fig. 35.7) shows that there is a characteristic distance L_0 where the thermal expansion rate of the ensemble exceeds its forward movement rate. It is reasonable to view the distance L_0 as the *range* of the flux defined according to the condition

$$v(L_0) = v_T(L_0).$$

By the definition of v_T , half of the ensemble atoms are not moving towards the substrate at a distance L_0 . The optimal position of the substrate for growth of high-quality films is usually found experimentally to be at around the end of the luminous flux area (*plume*). It is reasonable to associate this position with the characteristic range L_0 of the plasma flux. Let us consider three issues regarding this location important for film growth: the average particle energy $E(L_0) = Mv^2(L_0)/2$ at the distance L_0 , the dependence of the distance L_0 on the gas pressure and intensity of ablation N_0 , and the deposition rate $h(L_0)$ [nm/pulse] at this location.

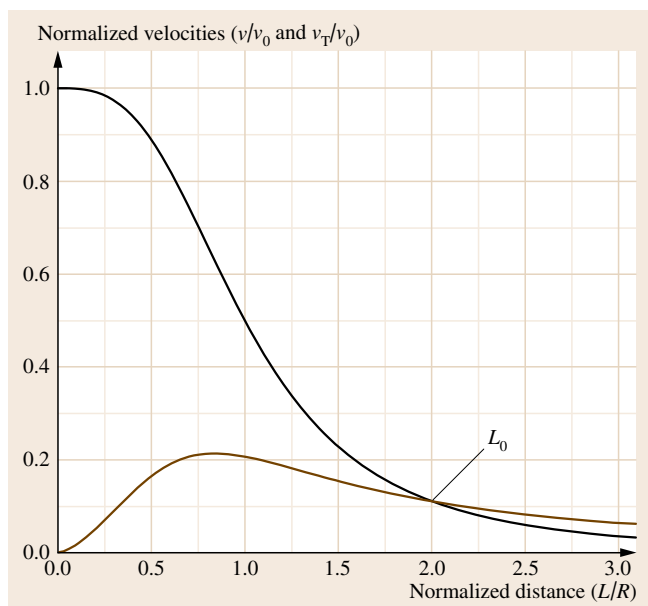


Fig. 35.7 Evolution of the directional v and thermal v_T velocities of plasma flux particles as a function of normalized distance L/R from the target. Velocities are normalized to the initial velocity v_0 of particles. L_0 indicates the location of the plasma range, where $v(L_0) = v_T(L_0)$

Note that the flux range L_0 does not depend on the initial velocity v_0 . However, an increase in the initial energy $E_0 = (Mv_0^2)/2$ of ejected atoms makes the process faster and increases the kinetic and thermal energies of particles at distance L_0 . As can be seen from Fig. 35.7, the ensemble velocity in the vicinity of the flux range drops to $\approx 10\text{--}20\%$ of the initial velocity, i.e., $E(L_0) \approx (0.01\text{--}0.04)E_0$ at this point. Thus, for a flux with an average initial energy of particles of $\approx 200\text{ eV}$, the expected energy of particles arriving at the substrate surface at the distance L_0 is $2\text{--}8\text{ eV}$. Particles with this energy are acceptable for film growth as they are able to nonthermally activate the film surface without damaging it.

The distance L_0 itself is controlled by the ratio of the ablated material amount to the background gas concentration n_g (gas pressure $P \propto n_g$)

$$L_0 \propto \left(\frac{N_0}{n_g} \right)^{1/3}.$$

To maintain the substrate in the optimal position, the ejected material amount N_0 should be changed proportionally with the changing pressure. The parameter N_0 characterizes a specific PLD system and can be easily measured. To do so, it is sufficient to measure the thickness (per pulse) h of the film deposited with the system (at some target-to-substrate distance d) in a vacuum or at a pressure low enough to assure that all the ejected atoms reach the substrate. By definition, N_0 is directly related to h as $N_0 = hn_L d^2$, where n_L is the concentration of deposited atoms ($n_L \approx 5 \times 10^{22} \text{ cm}^{-3}$ for most solids). Numerically, $N_0 = 5 \times 10^{16}$ for a system delivering $h = 0.1 \text{ nm/pulse}$ at $d = 10 \text{ cm}$. For typical PLD and PED of dielectric materials, the deposition rates at 5 cm distance are within the range $0.01\text{--}0.1 \text{ nm/pulse}$. The dependence $L_0(n_g)$ of the range on gas pressures is shown in Fig. 35.8. The process pressure for PED (in the range $1\text{--}10 \text{ mTorr}$) is about two orders of magnitude lower than that for PLD in the case of several dielectrics. This leads to larger target-to-substrate distances that are expected to be optimal in PED relative to PLD.

The deposition rate at the optimum distance $h(L_0)$ turns out to be only weakly dependent on the ablation intensity N_0

$$h(L_0) \propto n_g^{2/3} N_0^{1/3}. \quad (35.6)$$

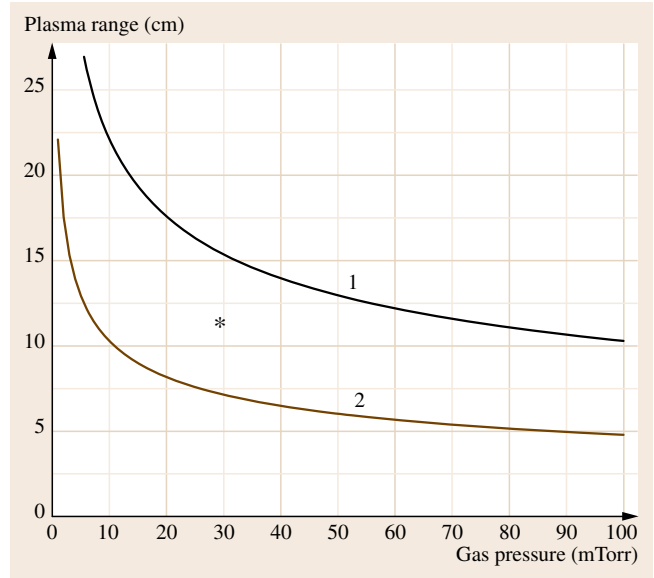


Fig. 35.8 Plasma propagation range L_0 as a function of gas pressure for ablation intensities N_0 of 0.1 nm/pulse (1) and 0.01 nm/pulse (2) at 10 cm distance. The asterisk represents an experimental optimal condition for PED growth of YBCO films

This result is remarkable, since it explains why different PLD systems (with different N_0 values) exhibit quite similar optimal deposition rates. Indeed, the reported deposition rates of YBCO films were close to 0.1 nm/pulse in a number of publications [35.35–39]. Thus, that deposition rate could be considered typical for PLD in a background gas pressure of $100\text{--}200 \text{ mTorr}$.

On the other hand, as follows from (35.6), the deposition rate at an optimal distance scales rather strongly with the gas pressure. The optimal deposition rates in PED (at 5 mTorr) are expected to be about ten times lower than in PLD (at 150 mTorr). Note here that all these differences follow from the difference in operational pressures. The dynamics of the deceleration of plasmas produced with pulsed lasers and pulsed electron beams is the same. Lower-pressure operation generally leads to a longer flux range, larger optimal film deposition distance, and larger deposition area. The overall productivity of the film fabrication (grams of material per second) is controlled by the average power of the beam (pulsed laser or pulsed electron).

35.4 Optimization of Plasma Flux for Film Growth

As the models predict, and experimental data confirm, the particle energy generated by lasers (not considering exotic high-power, subnanosecond pulse lasers) and intensive electron beams can cover a wide energy spectrum range of 3–3000 eV. Depending on the particle energy, their interaction with crystal surface can have very different results. Due to the significant dispersion of the spectrum, it is difficult to predict the cumulative integrated effect of the energetic particle flux on a crystal (substrate) surface. However, to fit the spectrum and the desired result for a particular application, an optimal type of laser (λ , τ), and beam intensity Q can be chosen accordingly to the discussions presented above.

High-energy (> 1000 eV) particles cause shallow implantation on a crystal surface, resulting in generally improved coating adhesion through ion mixing. Nonequilibrium generation of lattice vacancies promotes radiation-enhanced diffusion into the subsurface layer. Crystal surface compensation or doping by the laser-ablated materials can be realized [35.40].

When the incoming flux has a large fraction of energetic ions ≥ 200 eV, this can strongly affect the average deposition rate of metallic films where self-sputtering becomes significant. The effect is especially strong for large-atomic number metals such as Cu, Ag or Au [35.41]. For these materials, the self-sputtering coefficient of unity is reached at the ion energy as low as 100 eV [35.42, 43]. When the high-energy fraction in the deposition flux is large enough, no film can be formed. In some instances, much thinner film (or no film at all) is obtained on the axis of the deposition flux (where most of the higher-energy particles are concentrated) than in off-axis directions. Attempt to reduce the self-sputtering effect by adding a background gas leads to a maximum in the deposition rate (at ≈ 100 mTorr) dependence on pressure [35.44]. The effect can be understood as due to the interplay between two kinds of rate reductions. One is due to scattering or stopping of the flux material at higher pressures while the other is due to partial self-sputtering of films by the energetic portion of plasma flux ions at lower pressures. It is interesting that the maximum deposition rate was obtained in He background gas, which was able to decelerate fast ions without causing their effective large-angle scattering. The film stress also showed strong gas pressure dependence.

The concurrent bombardment of growing film promotes the growth of dense films. The increase in film density is a major factor in modifying film properties

such as hardness, electrical resistivity, optical properties, and corrosion resistance. At the same time, it can introduce high compressive stresses. Especially strong is the effect of stress level on the electrical properties of conducting oxide films where their charge carrier concentration and mobility critically depend on the film lattice parameters.

Enhancement of film growth and film properties by the energetic particle interaction with film surfaces is a well-known phenomenon. Low-energy (≈ 5 eV) bombardment promotes the surface mobility of adatoms that is used for epitaxial growth [35.45]. Properties of films grown from wide-energy-spectrum plasma fluxes are the integrated result of all the effects above. Especially important process parameters are the average energy of arriving atoms and the ratio of high- and low-energy particles. According to the well-known Thornton model, the energy per deposited atom should be about 20 eV to complete the disruption of the columnar morphology of the growing film for the maximum density [35.46, 47]. A variety of techniques have been developed to provide additional nonthermal activation at the film growth surface. In the low-pressure process of ion-beam-assisted deposition (IBAD), an auxiliary source of energetic ions is used to concurrently bombard the surface of the growing film. The effectiveness of IBAD combined with PLD has also been demonstrated elsewhere [35.48]. In plasma-based techniques such as direct-current (DC) or radiofrequency (RF) sputtering deposition, substrate biasing is used to extract and accelerate the energetic ions directly from the deposition plasma [35.29].

The above considerations show several means that can be used to control the energetics of the PLD- and PED-generated plasma flux for thin-film deposition. Accepting particles with energy of ≈ 10 eV as the most favorable for nonthermally activated film growth, one can see that most of the plasmas produced by laser or electron beam pulses are excessively energetic, especially at the higher-energetic end. The reason for this higher-energy tail is that, especially in the common non-steady pulsed ablation regime, much larger energy/atom than the target's atom cohesive energy of ≈ 5 –10 eV is loaded into the target. This is necessary to facilitate reproducible stoichiometric ablation, far from its threshold. The pulsed nature of the ablation leads to a broad energy spectrum that includes a significant portion of the extra-energetic particles generated at the front of generated plasma flux.

Film deposition with both the PLD and PED techniques includes two processes that are very different in their requirements, and yet both have to be facilitated. First is the ablation of the target material, which is necessarily a highly nonequilibrium process. Second is the film condensation process, which is desirable to be close to equilibrium (i. e., providing the surface with nonthermal excitation without causing surface damage). Thus, the general objective in optimizing the film deposition process is to transform the original energetic ablation plasma flux into a flux most suitable for the film growth.

As discussed above, some control over the initial particles' energy can be accomplished at the level of the energy source. Minimization of the particles energy leads to the choice of a shorter-wavelength laser (248 nm KrF excimer, for example) and energy density not too far above the ablation threshold. Another possibility is to thermalize the flux with ambient gases. Proper choices of gas pressure and target-to-substrate distance can also drastically improve the resultant film quality.

35.4.1 Ion Current of Plasma Propagating in Ambient Gas

The ion probe signal reflects the dynamics of the ionized component arriving at a substrate surface, regardless of whether it is in a vacuum or an ambient gas. Typically, the maximum intensity of the ion current is created by the relatively small amount of faster-moving ions on the front of the plasma flux. Therefore, the maximum probe signal represents the dynamics of this flux component rather than that of the bulk plasma. The probe signal from the relatively slow but numerous ions with a lower energy is small, especially for ablation in a background gas. Still, those particles contribute to most of the film formation. The average energy of the arriving particles cannot be obtained directly from the probe signal when measured in a background gas pressure. However, the dependence of the probe signal on the gas pressure provides useful information on the degree of interaction between the particles of the plasma flux and the background gas atoms.

A typical evolution of the probe signal is given in Fig. 35.9 for GaN film formation with a KrF laser at a distance of 17.5 cm from the target. The signal amplitude decreases with pressure, as expected. However, the energy of the faster ions (taken as the flight time of the ions contributing to the signal at half-maximum) is nearly independent of the pressure. This can be understood by considering that the number of the fastest

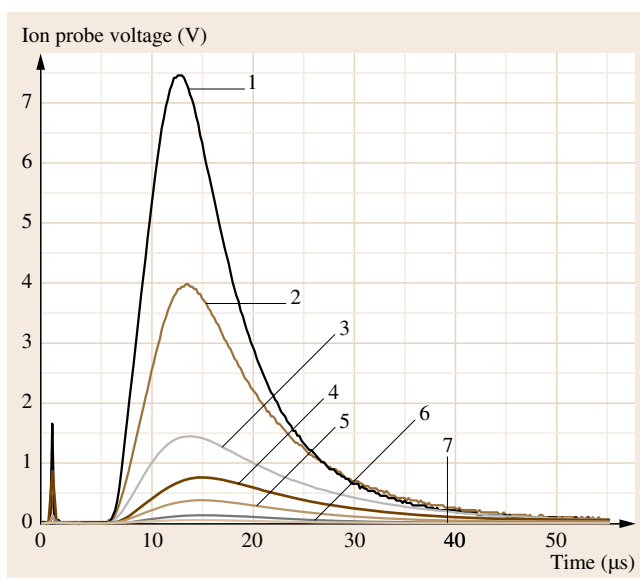


Fig. 35.9 Evolution of ion probe signal of ions propagating in a background gas with different pressure of 6 (1), 10 (2), 15 (3), 17 (4), 20 (5), 25 (6), and 30 mTorr (7) of N₂ (GaN target, KrF 248 nm laser, 17.5 cm target-to-probe distance)

ions is small, and they propagate individually, unable to create a hydrodynamic ensemble with gas atoms. The fraction of ions passing a distance L without a collision is $F \propto \exp(-\alpha PL)$, where the constant α is directly related to an effective cross-section of ion collisions with gas atoms. Evidently, the *surviving* ions arrive at the probe with their original energy. However their number exponentially decreases with pressure. The $F(P)$ dependence can be used to estimate the cross-section. This portion of ballistically moving ions is also seen as *fast components* in the emission studies of the plasma dynamics [35.49,50]. A single collision of a fast ion significantly reduces the energy, and most likely changes its direction away from the aperture of the ion probe.

From the viewpoint of film growth, this implies that the fast ions cannot be completely removed from the plasma flux arriving at the substrate. Their number can only be exponentially decreased by increasing the gas pressure and/or distance from the plasma source. At some degree of filtering out the fast ions by the ambient gas, their fraction in the film growth flux can become acceptably small.

Propagation of the bulk plasma becomes hydrodynamic as it incorporates a gas mass comparable to the plasma mass. Dynamics of the deceleration in this slow flux component can be seen in time-resolved emission

measurements [35.49]. Due to the much lower ion velocity (ion current), the probe signal generated by the bulk plasma is smaller than the first peak. However, at some conditions, the decelerated ions can be seen as a second peak in the probe signal (plume splitting) [35.51, 52]. The amount of ion energy lost per collision depends on the mass ratio of the ion and the gas atom. For heavier gases, a single collision can significantly drive down the ion energy and it appears in the slower, second peak. The bulk plasma propagation distance increases with time as $\sim t^{2/5}$ in a point-blast model [35.16, 53] or $\sim t^{1/4}$ in the simple model [35.34].

PLD and PED share the common feature of energetic particles in the as-generated plasma flux. Thus, both techniques require some *dumping* of the energy in a process gas of suitable pressure to adjust it for optimal film growth conditions. The main difference between the methods is in the dynamic range of the gas pressure, and the ability to ablate different materials. In contrast to PLD, with its very broad range of allowed gas pressures, PED operates in a rather narrow pressure interval of 5–10 mTorr. Accordingly, it requires more attention to optimizing target-to-substrate distance.

The main advantageous feature of PED is its ability to ablate materials based on wide-bandgap (SiO₂, Al₂O₃, MgO, etc.) dielectrics, which is difficult for PLD due to their transparency at (excimer) laser wavelengths. Due to strong absorption of electrons and relatively low thermal conductivity, PED ablation of these dielectrics results in films of higher quality and with fewer droplets. Furthermore, PED easily creates plasmas of polymers.

Thus, PLD and PED can be considered as complementary techniques, sharing a similar arrangement, and able to be explored in a unified deposition chamber. A PLD–PED deposition system enable in situ deposition of a wider range of materials, which is important the for exploration of complex structures, incorporating metals, complex dielectrics, ferroelectrics, semiconductors, glasses, etc.

35.4.2 Optimization of Growth of GaN Films – A Materials Example

Wide-bandgap GaN thin-film growth has been intensively researched due to this material’s excellent blue-light emitting characteristics. Solid-state lighting-based applications have fueled a large amount of research in this area. A variety of deposition techniques have been used, including chemical vapor deposition (CVD) [35.54], molecular-beam epitaxy

Table 35.1 PLD process parameters for AlN and GaN films on *c*-axis Al₂O₃ substrate

Parameter	AlN	GaN
Temperature	930 °C	950 °C
Target distance	20 cm	20 cm
Deposition rate	0.1 Å per pulse	0.08 Å per pulse
Energy density	2.5 J/cm ²	3.1 J/m ²
Gas pressure	0.5 mTorr NH ₃	1–50 mTorr N ₂

(MBE) [35.55], vapor-phase epitaxy (VPE) [35.56], pulsed laser deposition (PLD) [35.57], and sputtering (SP) [35.58]. PLD-produced GaN films have been reported with extremely high crystalline quality, but only a few groups have been successful in demonstrating photoluminescence in these films, usually at low temperature (\approx 12 K) only [35.57], or in films with an associated broadband *yellow* emissions indicative of impurity states in these films [35.59].

While PLD has the advantage of producing a very energetic plasma [35.60], the kinetic energy of particles in the plasma flux can be too high in the as-generated plasmas and could potentially deteriorate the electronic properties of the deposited films. To demonstrate the importance of controlling the plasma energetics in tailoring the electronic properties, a material example is presented in this section. The process optimization for the fabrication of GaN films, performed at Neocera, is presented. The plasma energy was optimized by a systematic variation of gas pressure at fixed ablation intensity and target-to-substrate distance. Room-temperature photoluminescence accompanied by excellent crystalline quality indicate that careful optimization of plasma energetics during film growth is critical for realizing optimum electronic and structural properties during PLD film growth.

GaN films by PLD were fabricated on single-crystalline *c*-axis-oriented Al₂O₃ substrates with an AlN buffer layer. A background of NH₃ and N₂ was used during depositions. For process optimization, the plasma energy was tailored to an optimal level by gas-phase collisions with the ambient gas. Excellent photoluminescence was observed at room temperature for GaN films fabricated under optimized conditions. The general PLD process conditions are presented in Table 35.1.

During optimization of film growth, increasing the nitrogen gas pressure during film growth systematically reduced the plasma energy. The best GaN films were obtained at nitrogen gas pressure of 30 mTorr. Both the AlN buffer layers and GaN layers were grown epi-

Table 35.2 Impact of gas pressure on GaN film parameters

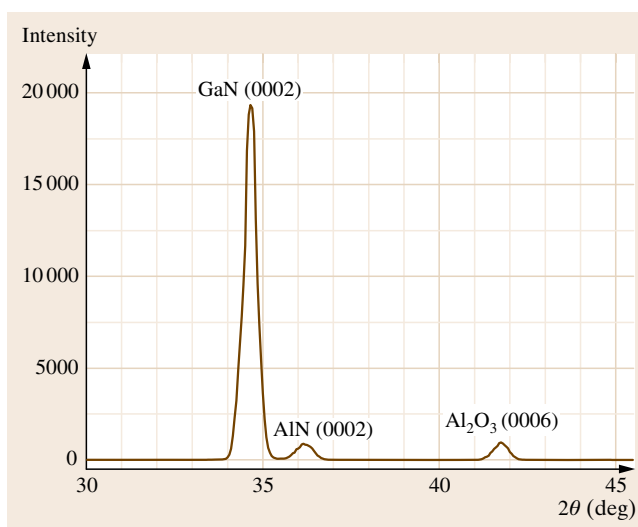
Process pressure (mTorr)	ω -Scan width (deg)	Room-temperature photoluminescence
1	0.47	no
15	0.45	no
30	0.38	yes
50	1.78	no

taxially on the c -axis-oriented single-crystalline Al_2O_3 substrates. For 450 nm thick GaN films with AlN buffer layers, the film crystal structures were measured by four-circle x-ray diffractometer; the θ - 2θ scan is illustrated in Fig. 35.10.

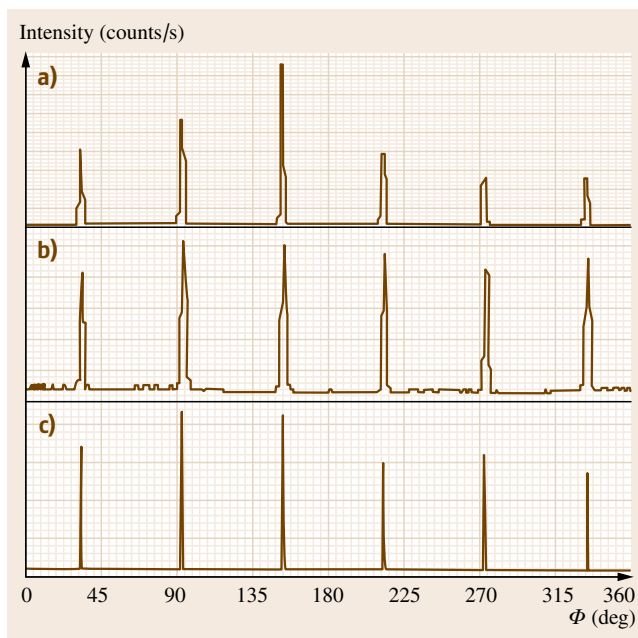
c -Axis-oriented GaN(0002) and AlN(0002) peaks were clearly visible at 2θ of 34.65 and 36.18°, respectively. Comparing with the Al_2O_3 single-crystal peak ($2\theta = 41.75^\circ$), the GaN and AlN peaks were strongly intensified, suggesting high quality of the GaN and AlN layers. In the optimized films deposited at 30 mTorr N_2 , full-width at half-maximum (FWHM) of 0.38 and 0.48° was obtained from ω -scans of GaN(0002) and AlN(0002) respectively, indicating highly c -axis-oriented layers. In addition, Φ -scans were performed for GaN($10\bar{1}1$), AlN($10\bar{1}1$), and $\text{Al}_2\text{O}_3(11\bar{2}3)$ peaks, as illustrated in Fig. 35.11. The repeated peak-to-peak 60° distance indicates the hexagonal structure of the film layers, and the clear matching peak positions of GaN, AlN, and Al_2O_3 confirm that GaN and AlN layers are epitaxial with regards to the (0001) Al_2O_3 substrate.

Photoluminescence (PL) was measured at room temperature and is illustrated in Fig. 35.12. A nitrogen laser with wavelength of 340 nm was used as the excitation source, and room-temperature PL intensity was plotted with respect to wavelength. For GaN films deposited at pressures lower than 30 mTorr excellent crystallinity was exhibited, but no PL was observed at room temperature. Room-temperature PL was only observed when the chamber pressure for GaN deposition was 30 mTorr. Blue luminescence was detected at 370 nm with significant peak intensity. The yellow emission at 545 nm was very weak, which was mainly attributed to structural imperfections such as grain boundaries or dislocations [35.59, 61]. The peak-to-peak ratio of blue emission to yellow emission is superior to other results from GaN films processed by CVD [35.61], MBE [35.55], VPE [35.62], SP [35.63], and in several nonoptimal PLD films [35.57, 59].

Table 35.2 summarizes the influence of ambient gas pressures on the GaN film quality as meas-


Fig. 35.10 θ - 2θ scan of GaN grown under the conditions of Table 35.1 on (0001) Al_2O_3 substrate with AlN buffer layer

ured by FWHM of ω -scans and room-temperature photoluminescence (RTPL). RTPL appears to be extremely sensitive to the energy of plasma particles, being observed only from films deposited at pressure


Fig. 35.11a-c Φ -scans for GaN/AlN/ Al_2O_3 structure: GaN($10\bar{1}1$) peak (a), AlN($10\bar{1}1$) peak (b), $\text{Al}_2\text{O}_3(11\bar{2}3)$ peak (c)

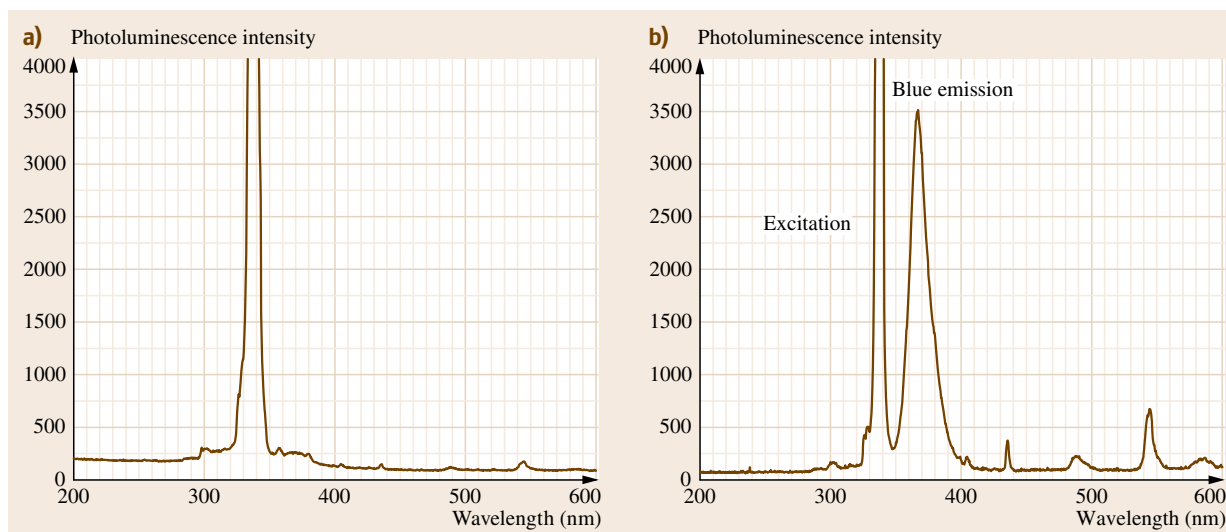


Fig. 35.12a,b Photoluminescence spectrum of PLD GaN films deposited at 14 mTorr (a), and 30 mTorr (b)

≈ 30 mTorr. There was no RTPL in GaN deposited at lower pressures. This can be related to the excessive energy of arriving particles. However, remarkably, room-temperature PL was not observed in film deposited at 50 mTorr. Thus, some degree of nonthermal activation (present in the 30 mTorr process) is indeed necessary to obtain optimal film properties, such as photoluminescence at room temperature. ω -Scan width is another parameter exhibiting the pressure dependence, with the best performance in the 30 mTorr process. As seen from the Table 35.2, ω -scan has the minimal FWHM at this pressure, implying that GaN crystallinity was significantly degraded at higher pressure of 50 mTorr.

Comparison of the optimal conditions with the expected range (Fig. 35.8, asterisk) of the plasma flux (Table 35.1) in 30 mTorr nitrogen shows that the substrate position of 20 cm corresponds to a distance from the target greater than the expected ≈ 12 cm. Thus, the optimal average energy of the arriving particles can be estimated as lower than expected from the model [35.34]. The initial mean energy of the Ga ions is ≈ 50 eV (from Fig. 35.9 data at low pressure). The mean energy at the 12 cm is $(0.02-0.04) \times 50 \text{ eV} \approx 1-2$ eV, according to the model. The estimated mean energy at the optimal 20 cm distance is lower but roughly agrees with that predicted by the model.

35.5 Conclusions

Thin-film deposition by condensation of energetic plasma combines two events. First, material from a target is ablated in a highly nonequilibrium process, resulting in the generation of particles with kinetic energies orders of magnitude above those observed in equilibrium evaporation. This rapid (pulsed) evaporation of material is critically needed to achieve a congruent, stoichiometric flux from a multicomponent target. The second event is the film formation on a substrate that requires critical control of the plasma energetics leading to an optimal material flux arriving at

the substrate. The optimal films can be deposited at energetic conditions that are not too far from equilibrium. Lower deposition rates and particle energies below the point-defect generation threshold seem to aid the formation of optimal films. In a vacuum process, these two contradicting requirements (high-energy ablation plasma near the target surface and a lower-energy materials flux at the substrate surface) can only be satisfied partially by choosing a shorter-wavelength laser (in the case of PLD) and lower beam intensity near the ablation threshold. A smaller material flux and particle energy

can be achieved in this way. An appropriate process gas in a deposition chamber can serve as a more effective tool for converting the high-density high-energy ablation plasma flux into the required low-density low-energy condensation flux. By controlling the deposition conditions, low-temperature film growth activated by particles with optimal energy can be achieved. Careful optimization of the entire deposition system design and process parameters facilitates growth of high-quality single- and multicomponent films by both **PLD** and **PED**. The main advantageous feature of **PED** is its abil-

ity to ablate materials based on wide-bandgap (SiO_2 , Al_2O_3 , MgO , etc.) dielectrics, which are difficult for **PLD** due to their transparency at (excimer) laser wavelengths. Thus, **PLD** and **PED** can be considered as complementary techniques, sharing a similar arrangement, and able to be explored in a unified deposition chamber. **PLD–PED** deposition systems enable in situ deposition of a wider range of materials, which is important for the exploration of complex structures that incorporate metals, complex dielectrics, ferroelectrics, semiconductors, and glasses.

References

- 35.1 D.M. Mattox, J.E. McDonald: Interface formation during thin film deposition, *J. Appl. Phys.* **34**, 2493–2496 (1963)
- 35.2 J.S. Colligon: Energetic condensation: processes, properties, and products, *J. Vac. Sci. Technol. A* **13**, 1649–1657 (1995)
- 35.3 H. Fehler: *Vacuum* **45**, 997–1000 (1994)
- 35.4 W.D. Sproul: *Mater. Sci. Eng. A* **163**, 187–190 (1993)
- 35.5 J.M.E. Harper, J.J. Kuomo, H.R. Kaufman: *J. Vac. Sci. Technol.* **21**, 737 (1982)
- 35.6 D.B. Chrisey, G. Hubler (Eds.): *Pulsed Laser Deposition of Thin Films* (Wiley, New York 1994)
- 35.7 H.M. Smith, A.F. Turner: Vacuum deposited thin films using a ruby laser, *Appl. Opt.* **4**, 147–148 (1965)
- 35.8 K.L. Saenger: Pulsed laser deposition, Part 1, *Process. Adv. Mater.* **2**, 1–24 (1993)
- 35.9 K.L. Saenger: Pulsed laser deposition, Part 2, *Process. Adv. Mater.* **3**, 63–82 (1993)
- 35.10 J. Schou: Laser beam–solid interactions: fundamental aspects. In: *Materials Surface Processing by Direct Energy Techniques*, ed. by Y. Pauleau (Elsevier, Oxford 2006) pp. 35–66
- 35.11 G. Müller, M. Konijnenberg, G. Krafft, C. Schultheiss: Thin film deposition by means of pulsed electron beam ablation. In: *Science and Technology of Thin Films*, ed. by F.C. Maticotta, G. Ottaviani (World Scientific, Singapore 1995) pp. 89–119
- 35.12 D. Bäuerle: *Laser Processing and Chemistry* (Springer, Berlin, Heidelberg 2000)
- 35.13 M. Strikovski, K.S. Harshavardhan: Parameters that control pulsed electron beam ablation of materials and film deposition processes, *Appl. Phys. Lett.* **82**, 853–855 (2003)
- 35.14 A. Bogaerts, Z. Chen: Effect of laser parameters on laser ablation and laser-induced plasma formation, *Spectrochim. Acta A* **60**, 1280–1307 (2005)
- 35.15 Y.P. Raizer: *Gas Discharge Physics* (Springer, Berlin, Heidelberg 1997)
- 35.16 Y.B. Zel'dovich, Y.P. Raizer: *Physics of Shock Waves and High-Temperature Hydrodynamic Phenomena* (Academic, New York 1966)
- 35.17 H. Schittenhelm, G. Callies, P. Berger, H. Hügel: Investigation of extinction coefficient during excimer laser ablation and their interpretation in terms of Rayleigh scattering, *J. Phys. D Appl. Phys.* **29**, 1564–1575 (1996)
- 35.18 V.I. Mazhukin, V.V. Nossov, M.G. Nickiforov: Optical breakdown in aluminum vapor induced by ultraviolet laser radiation, *J. Appl. Phys.* **93**, 56–66 (2003)
- 35.19 C. Geertsen, P. Mauchien: Optical spectrometry coupled with laser ablation for analytical applications on solids. In: *Application of Beams in Materials Technology*, ed. by P. Misaelides (Kluwer, Dordrecht 1995) pp. 237–258
- 35.20 S. Metev: Process characteristics and film properties in pulsed laser deposition. In: *Pulsed Laser Deposition of Thin Films*, ed. by D.B. Chrisey, G. Hubler (Wiley, New York 1994) pp. 255–264
- 35.21 L. Torrisi, S. Gammino, L. Ando, V. Nassisi, D. Doria, A. Pedone: Comparison of nanosecond laser ablation at 1064 and 308 nm wavelength, *Appl. Surf. Sci.* **210**, 262–273 (2003)
- 35.22 H. Puell, H.J. Neusser, W. Kaiser: Heating of laser plasma generated at plane solid targets, *Z. Naturforsch. A* **25**, 1807–1815 (1970)
- 35.23 S.V. Gaponov, M.D. Strikovski: Formation of plasma during vaporisation of materials by the radiation of a CO_2 TEA laser, *Sov. Phys. Tech. Phys.* **27**(9), 1127–1130 (1982)
- 35.24 N. Arnold, J. Gruber, J. Heitz: Spherical expansion of the vapor into ambient gas: an analytical model, *Appl. Phys. A* **69**, s87–s93 (1999), (suppl.)
- 35.25 J. Stevefelt, C.B. Collins: Modelling of a laser plasma source of amorphous diamond, *J. Phys. D Appl. Phys.* **24**, 2149–2153 (1991)
- 35.26 M. Strikovski: unpublished (1987)
- 35.27 R. Teghil, L. D'Alessio, A. Santagata, M. Zaccagnino, D. Ferro, D.J. Sordelet: Picosecond and femtosecond pulsed laser ablation and deposition of quasicrystals, *Appl. Surf. Sci.* **210**, 307–317 (2003)

- 35.28 L. D'Alessio, A. Galasso, A. Santagata, R. Teghil, A.R. Villani, P. Villani, M. Zaccagnino: Plume dynamics in TiC laser ablation, *Appl. Surf. Sci.* **208/209**, 113–118 (2003)
- 35.29 D.M. Mattox: *Handbook of Physical Vapor Deposition (PVD) Processing* (Noyes, Westwood 1998)
- 35.30 N.M. Bulgakova, A.V. Bulgakov, O.F. Bobrenok: Double layer effects in laser-ablation plasma plumes, *Phys. Rev. E* **62**, 5624–5635 (2000)
- 35.31 H.S. Kim, H.S. Kwok: Correlation between target substrate distance and oxygen pressure in pulsed laser deposition of $\text{YBa}_2\text{Cu}_3\text{O}_7$, *Appl. Phys. Lett.* **61**, 2234–2236 (1992)
- 35.32 P.E. Dyer, A. Issa, P.H. Key: An investigation of laser ablation and deposition of Y-Ba-Cu-O in an oxygen environment, *Appl. Surf. Sci.* **46**, 89–95 (1990)
- 35.33 H.S. Kwok, H.S. Kim, D.H. Kim, W.P. Chen, X.W. Sun, R.F. Xiao: Correlation between plasma dynamics and thin film properties in pulsed laser deposition, *Appl. Surf. Sci.* **109/110**, 595–600 (1997)
- 35.34 M. Strikovski, J. Miller: Pulsed laser deposition of oxides: Why the optimum rate is about 1 Å per pulse, *Appl. Phys. Lett.* **73**, 1733–1735 (1998)
- 35.35 C.C. Chang, X.D. Wu, R. Ramesh, X.X. Xi, T.S. Ravi, T. Venkatesan, D.M. Hwang, R.E. Muenchausen, S. Foltyn, N.S. Nogar: Origin of surface roughness for c-axis oriented Y-Ba-Cu-O superconducting films, *Appl. Phys. Lett.* **57**, 1814–1816 (1990)
- 35.36 A. Gupta, B.W. Hussey: Laser deposition of $\text{YBa}_2\text{Cu}_3\text{O}_{7-x}$ films using a pulsed oxygen source, *Appl. Phys. Lett.* **58**, 1211–1213 (1991)
- 35.37 S.J. Pennycook, M.F. Chisholm, D.E. Jesson, R. Feenstra, S. Zhu, X.Y. Zheng, D.J. Lowndes: Growth and relaxation mechanisms of $\text{YBa}_2\text{Cu}_3\text{O}_{7-x}$ films, *Physica C* **202**, 1–11 (1992)
- 35.38 A.T. Findikoglu, C. Doughty, S.M. Anlage, Q. Li, X.X. Xi, T. Venkatesan: DC electric field effect on the microwave properties of $\text{YBa}_2\text{Cu}_3\text{O}_7/\text{SrTiO}_3$ layered structures, *J. Appl. Phys.* **76**, 2937–2944 (1994)
- 35.39 W. Zhang, I.W. Boyd, M. Elliott, W. Herrenden-Harkerand: Transport properties and giant magnetoresistance behavior in La-Nd-Sr-Mn-O films, *Appl. Phys. Lett.* **69**, 1154–1156 (1996)
- 35.40 Y.A. Bityurin, S.V. Gaponov, E.B. Klyuenkov, M.D. Strikovsky: GaAs compensation by intense fluxes of low energy particles, *Solid State Commun.* **45**, 997–1000 (1983)
- 35.41 S. Fähler, K. Sturm, H.U. Krebs: Resputtering during the growth of pulsed-laser-deposited metallic films in vacuum and in ambient gas, *Appl. Phys. Lett.* **75**, 3766–3768 (1999)
- 35.42 A. Anders: Observation of self-sputtering in energetic condensation of metal ions, *Appl. Phys. Lett.* **85**, 6137–6139 (2004)
- 35.43 Oak Ridge National Laboratory: *Atomic Data for Fusion*, Vol. 3 (1985), <http://www-cfadc.phy.ornl.gov/redbooks/three/a/3a18.html>
- 35.44 T. Scharf, J. Faupel, K. Sturm, H.-U. Krebs: Pulsed laser deposition of metals in various inert gas atmospheres, *Appl. Phys. A* **79**, 1587–1589 (2004)
- 35.45 T. Ohmi, T. Shibata: Advanced scientific semiconductor processing based on high-precision controlled low-energy ion bombardment, *Thin Solid Films* **241**, 159–162 (1993)
- 35.46 J.A. Thornton: The influence of bias sputter parameters on thick copper coatings deposited using a hollow cathode, *Thin Solid Films* **40**, 335–340 (1977)
- 35.47 D.R. Brighton, G.K. Hubler: Binary collision cascade prediction of critical ion-to-atom arrival ratio in the production of thin films with reduced intrinsic stress, *Nucl. Instrum. Methods Phys. Res. B* **28**, 527–530 (1987)
- 35.48 K.S. Harshavardhan, H.M. Christen, S.D. Silliman, V.V. Talanov, S.M. Anlage, M. Rajeswari, J. Claasen: Low-loss $\text{YBa}_2\text{Cu}_3\text{O}_7$ films on flexible, polycrystalline-yttria-stabilized zirconia tapes for cryoelectronic applications, *Appl. Phys. Lett.* **78**, 1888–1890 (2001)
- 35.49 S.S. Harilal, C.V. Bindhu, M.S. Tillack, F. Najmabadi, A.C. Gaeris: Internal structure and expansion dynamics of laser ablation plumes into ambient gases, *J. Appl. Phys.* **93**, 2380–2388 (2003)
- 35.50 S.S. Harilal, B. O'Shay, Y. Tao, M.S. Tillack: Ambient gas effects on the dynamics of laser-produced tin plume expansion, *J. Appl. Phys.* **99**, 083303–1–083303–10 (2006)
- 35.51 R.F. Wood, J.N. Leboeuf, K.R. Chen, D.B. Geohegan, A.A. Puzos: Dynamics of plume propagation, splitting, and nano-particle formation during pulsed-laser ablation, *Appl. Surf. Sci.* **127–129**, 151–158 (1998)
- 35.52 S. Amoroso, B. Toftman, J. Schou: Broadening and attenuation of UV laser ablation plumes in background gases, *Appl. Surf. Sci.* **248**, 323–328 (2005)
- 35.53 N. Arnold, J. Gruber, J. Heitz: Spherical expansion of the vapor into ambient gas: An analytical model, *Proc. COLA'99, 5th Int. Conf. Laser Ablation*, Göttingen (Springer, Berlin, Heidelberg 1999)
- 35.54 J. Han, M.H. Crawford, R.J. Shul, J.J. Figiel, M. Banas, L. Zhang, Y.K. Song, H. Zhou, A.V. Nurmikko: AlGaIn/GaN quantum well ultraviolet light emitting diodes, *Appl. Phys. Lett.* **73**, 1688–1690 (1998)
- 35.55 D. Doppalapudi, E. Iliopoulos, S.N. Basu, T.D. Moustakas: Epitaxial growth of gallium nitride thin films on a-plane sapphire by molecular beam epitaxy, *J. Appl. Phys.* **85**, 3582–3589 (1999)
- 35.56 T. Nishida, H. Saito, N. Kobayashi: Efficient and high-power AlGaIn-based ultraviolet light-emitting diode grown on bulk GaN, *Appl. Phys. Lett.* **79**, 711–712 (2001)

- 35.57 M. Cazzanelli, D. Cole, J.F. Donegan, J.G. Lunney, P.G. Middleton, K.P. O'Donnell, C. Vinegoni, L. Pavesi: Photoluminescence of localized excitons in pulsed-laser-deposited GaN, *Appl. Phys. Lett.* **73**, 3390–3392 (1998)
- 35.58 M.P. Chowdhury, R.K. Roy, S.R. Bhattacharyya, A.K. Pal: Stress in polycrystalline GaN films prepared by R.F. Sputtering, *Eur. Phys. J. B* **48**, 47–53 (2005)
- 35.59 T. Venkatesan, K.S. Harshavardhan, M. Strikovski, J. Kim: Recent advances in the deposition of multi-component oxide films by pulsed energy deposition. In: *Thin Films and Heterostructures for Oxide Electronics*, ed. by S.B. Ogale (Springer, New York 2005) pp.385–413
- 35.60 S. Ito, H. Fusioka, J. Ohta, H. Takahshi, M. Oshima: Effect of AlN. Buffer Layers on GaN/MnO Structure, *Phys. Status Solidi (c)* **0**, 192–195 (2002)
- 35.61 A.N. Red'kin, V.I. Tatsii, Z.I. Makovei, A.N. Gruzintsev, E.E. Yakimov: Chemical vapor deposition of GaN from gallium and ammonium chloride, *Inorg. Mater.* **40**, 1049–1053 (2004)
- 35.62 P.R. Tavernier, P.M. Verghese, D.R. Clarke: Photoluminescence from laser assisted debonded epitaxial GaN and ZnO films, *Appl. Phys. Lett.* **74**, 2678–2680 (1999)
- 35.63 T. Miyazaki, K. Takada, S. Adachi, K. Ohtsuka: Properties of radio-frequency-sputter-deposited GaN films in a nitrogen/hydrogen mixed gas, *J. Appl. Phys.* **97**, 093516–093518 (2005)

Modeling

Part F

Part F Modeling in Crystal Growth and Defects

36 Convection and Control in Melt Growth of Bulk Crystals

Chung-Wen Lan, Taipei, Taiwan

37 Vapor Growth of III Nitrides

Dang Cai, Ronkonkoma, USA
Lili Zheng, Beijing, China
Hui Zhang, Beijing, China

38 Continuum-Scale Quantitative Defect Dynamics in Growing Czochralski Silicon Crystals

Milind S. Kulkarni, St. Peters, USA

39 Models for Stress and Dislocation Generation in Melt Based Compound Crystal Growth

Vishwanath (Vish) Prasad, Denton, USA
Srinivas Pendurti, Cincinnati, USA

40 Mass and Heat Transport in BS and EFG Systems

Thomas F. George, St. Louis, USA
Stefan Balint, Timisoara, Romania
Liliana Braescu, Timisoara, Romania

36. Convection and Control in Melt Growth of Bulk Crystals

Chung-Wen Lan

During melt growth of bulk crystals, convection in the melt plays a critical role in the quality of the grown crystal. Convection in the melt can be induced by buoyancy force, rotation, surface tension gradients, etc., and these usually coexist and interact with one another. The dominant convection mode is also different for different growth configurations and operation conditions. Due to the complexity of the hydrodynamics, the control of melt convection is nontrivial and requires a better understanding of the melt flow structures. Finding a proper growth condition for optimum melt flow is difficult and the operation window is often narrow. Therefore, to control the convection effectively, external forces, such as magnetic fields and accelerated rotation, are used in practice. In this chapter, we will first discuss the convections and their effects on the interface morphology and segregation for some

36.1 Physical Laws for Transport Processes	1217
36.1.1 Conservation Equations	1217
36.1.2 Boundary Conditions	1218
36.2 Flow Structures in the Melt	1219
36.2.1 ZM Configuration	1219
36.2.2 Bridgman Configuration	1225
36.3 Flow Control by External Forces	1228
36.3.1 Steady Magnetic Field	1229
36.3.2 Rotation	1233
36.3.3 Vibration	1237
36.4 Outlook	1238
References	1238

melt growth configurations. The control of the flows by external forces will also be discussed through some experimental and simulation results.

Bulk crystals used in electronic and optoelectronic devices require low defects and good composition uniformity, and melt convection during growth of bulk crystals plays a crucial role. The growth interface, which is critical to defect formation, is significantly affected by heat flow. Dopant incorporation and distribution on both macroscopic and microscopic scales are affected by melt convection as well. Therefore, the control of melt flow is necessary for crystal growth in practice. This chapter aims to provide a basic understanding of melt convection and its control through a few heuristic experimental and simulation examples, focusing on the effects of melt convection on the growth interface and composition uniformity.

Various melt growth techniques have been used for the growth of semiconductor and oxide bulk crystals. They can be grouped into three categories: namely, the Czochralski, Bridgman, and zone-melting configurations,

as illustrated in Fig. 36.1. The Czochralski (CZ) configuration shown in Fig. 36.1a (*left*) is the most popular growth process, especially for silicon and compound semiconductors. Dislocation-free single crystals up to 16 inch in diameter have been grown, while 8–12 inch-diameter silicon has been produced routinely for integrated-circuit applications. Due to its practical importance, research into melt convections and their control has been very extensive [36.1–4]. The melt flow in the CZ melt is dauntingly complicated. The rising buoyancy flow from the heated crucial wall turns inwards radially and joins the thermocapillary (Marangoni) flow at the melt surface. On the other hand, the rotating crystal sucks up the melt axially at the center of the melt, spinning it up in a thin Ekman layer. The radially outward flow meets the buoyancy and Marangoni flows, leading to a complicated flow structure [36.5]. The rotation of the crucible further

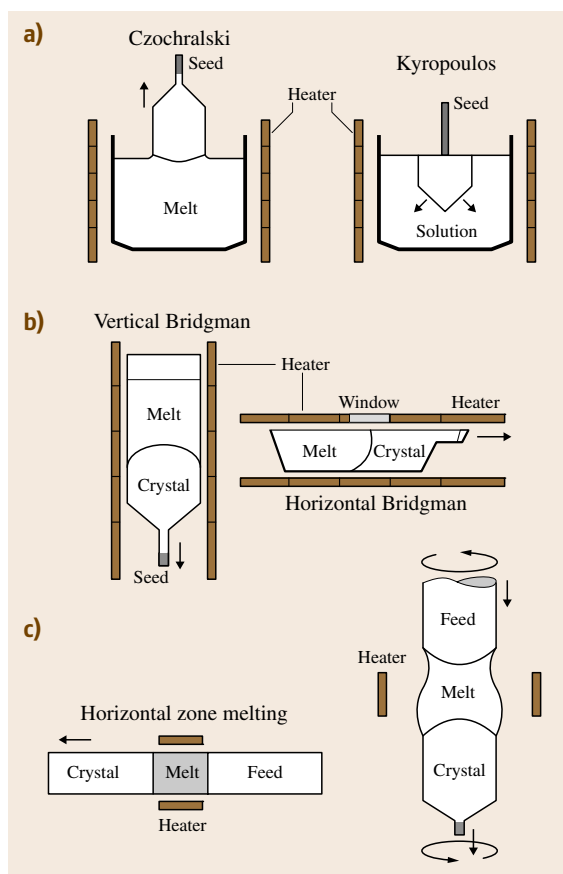


Fig. 36.1a–c Schematic of some configurations for bulk crystal growth from the melt: (a) Czochralski (left) and Kyropoulos configurations; (b) vertical (left) and horizontal Bridgman configurations; (c) zone melting (left) and floating zone configurations

complicates the flow, and a Taylor–Proudman column appears under the crystal, while outside this column the melt rotates with the crucible. Such a flow easily becomes nonaxisymmetric [36.6]. Furthermore, in commercial large-scale silicon growth, the melt flow is usually turbulent. With the advance of computing power, by using the large-eddy simulation (LES), Lukanin et al. [36.7] successfully simulated 300 mm-diameter CZ silicon growth. The calculated thermal fields and the growth front shape are in good agreement with the measured ones. The Kyropoulos method is a variant of the CZ configuration, but its crystal growth is carried out by slow cooling, usually without crystal pulling. The Bridgman and zone-melting (ZM) configurations, as depicted in Fig. 36.1b,c, respectively, are also

important in applications, but the crystal size that can be grown, as compared with that from the CZ configuration, is much smaller. Nevertheless, 6 inch-diameter GaAs ingots grown by the vertical Bridgman (VB) configuration are now commercially available. Beside the general impression, their applications in compound semiconductors and oxides have increased rapidly in recent years because of the ease of operation and the lower cost in mass production. Furthermore, due to the use of the ampoule, especially for VB, very low thermal gradients are allowed and thus the thermal stress in the grown crystal is greatly reduced. Due to the thermally stable configuration, the buoyancy convection in the melt for VB growth is much weaker and simpler. The buoyancy convection is usually generated by the radial thermal gradients caused by the interface deformation or the radial heating from the furnace. Some reviews of earlier research can be found elsewhere [36.8–12]. In particular, the convections in the melt are discussed in detail by [36.10].

For the Bridgman and ZM configurations, the growth orientation can be vertical or horizontal. For the horizontal configuration [on the right of Fig. 36.1b and on the left of Fig. 36.1c for the horizontal Bridgman (HB) and horizontal ZM (HZM) configurations, respectively], an open boat is usually used due to the ease of observation. As we will discuss shortly, due to gravity being perpendicular to the thermal gradient, buoyancy convection, as well as the Marangoni convection due to the free surface, is much stronger as compared with that in the vertical configuration [36.13, 14]. Similarly, due to the radial heating, the buoyancy convection in the ZM configuration (Fig. 36.1c) is also strong. For both horizontal configurations, the growth interface is often significantly affected by the melt convection [36.14, 15]. Another variation for the ZM configuration is the so-called floating-zone (FZ) process, as illustrated on the right of Fig. 36.1c. In the FZ configuration, because the molten zone is supported by its surface tension, contamination from the ampoule material can be avoided. However, due to the limitation of the zone stability, the grown crystal size is usually small, being less than 1 cm for most materials. Nevertheless, FZ growth has been a popular process for research [36.16–21]. Moreover, visualization is easy, and power consumption and material usage are small. Meanwhile, the heat flow phenomena in FZ growth are complicated and interesting. The interplay of the heat flow and the interfaces, as well as the crystal quality, can be investigated effectively. Therefore, much attention has been paid to the flow instability, especially the Marangoni flow, for the

past 20 years [36.17,20]. For the growth of silicon using induction-heated FZ method, the needle-eye configuration is used. Due to the stabilization by the magnetic force, the grown silicon crystal diameter can be up to 8 inch. The convection in the molten zone has also been investigated in detail [36.22,23].

In general, to grow crystal with good quality, careful control of convections is necessary, so that heat and mass transport are favored for dopant segregation and the shape of the growth interface. For example, a flat or slightly convex growth front toward the melt is desired to minimize parasitic nucleation. Dopant uniformity, both radial and axial, is also a major concern to ensure product quality. Therefore, the basic understanding of the role of the convections in the growth interface and the segregation is important for crystal growth. In addition, these flows affect the growth in many different ways. For the VB configuration, the convection in the melt is usually quite weak and stable. Therefore, the interface shape is mainly determined by global heat transfer and solidification [36.9,12]. Although the convection is weak, due to the low diffusivity of dopants added to the melt, dopant uniformity is influenced dramatically by the flow. Therefore, manipulating the melt flow to obtain a desired dopant distribution has become a key issue in VB growth. On the contrary, for the ZM (both vertical and horizontal) or HB configurations, the buoyancy convection or the Marangoni flow is usually strong, so that dopant can be well mixed, but the interface shape is strongly affected.

Besides the understanding of melt convections, finding an effective strategy for better growth control is also important. Tuning the temperature profile through furnace design to achieve a desired condition is typical, but this approach is laborious, rather inflexible, and not always very successful. Thus, the use of external forces to assist in controlling crystal growth is becoming popular. Examples include magnetic fields [36.24–33],

accelerated crucible rotation (ACRT) [36.34–38], vibration [36.39–47], centrifugation [36.48–58], and reduced gravity [36.59]. Again, we will briefly discuss the results for achieving better growth control, in terms of both interface and dopant distribution, through the use of external forces. Although the introduction is not extensive, we shall illustrate some important concepts that help improve understanding and control of melt convections. Particularly, we shall discuss the origin of the convections through the basic conservation equations and boundary conditions for mass, momentum, energy, and species first. From the basic equations, the mechanisms for flow control by external forces can be easily understood. As discussed by Müller and Ostrogorsky [36.10], for buoyancy convection, the growth configurations can be characterized by the orientation of the body force with respect to the thermal gradients, which mainly depend on the way of heating. The crystal or crucible rotation and the Marangoni flow are imposed from the boundaries. Therefore, the governing equations and boundary conditions are indeed necessary in understanding and further controlling the convections.

In the next section, the basic governing equations and some boundary conditions are summarized. Since these equations govern the physical laws, the mechanisms and driving forces for melt convections can be easily realized; the control of melt flows by external forces can be better realized as well. In Sect. 36.2, we discuss the basic flow structures of the crystal growth processes through flow visualization experiments using a transparent material and simulation results. In Sect. 36.3, how to control the melt convections through external forces is discussed. The discussion will be focused on the Bridgman and ZM configurations. Due to space limitation, the CZ configuration is not discussed. An outlook is given in Sect. 36.4, where some recent research in melt convection and its control is briefly discussed.

36.1 Physical Laws for Transport Processes

36.1.1 Conservation Equations

The heat flow and dopant transport in crystal growth from the melt are governed by the conservation of momentum, energy, and mass. In the melt, one can consider in general an incompressible heat problem in a rotational field having a constant angular speed Ω and a uniform magnetic field \mathbf{B} ; the crystal is rotating at a speed Ω_c . In a dimensionless form, the conservation

laws for mass, momentum, energy, and dopant based on the Boussinesq approximation for laminar flow can be expressed by the following equations in a rotating frame [36.51,56]:

$$\nabla \cdot \mathbf{v} = 0, \quad (36.1)$$

$$\frac{\partial \mathbf{v}}{\partial \tau} + \mathbf{v} \nabla \cdot \mathbf{v} = -\nabla P + \text{Pr} \nabla^2 \mathbf{v} + \mathbf{F}, \quad (36.2)$$

$$\frac{\partial T}{\partial \tau} + v \nabla T = \nabla^2 T + q, \quad (36.3)$$

$$\frac{\partial C}{\partial \tau} + v \nabla C = \frac{\text{Pr}}{\text{Sc}} \nabla^2 C, \quad (36.4)$$

where the dimensionless body force \mathbf{F} is given as

$$\begin{aligned} \mathbf{F} = & -\text{Pr} [\text{Ra}_T (T - T_{\text{ref}}) + \text{Ra}_S (C - C_{\text{ref}})] \\ & \times [\mathbf{e}_g - \text{Fr} \mathbf{e}_c] + \text{Ha}^2 \text{Pr} (-\nabla \Phi + v \mathbf{e}_B) \\ & \times \mathbf{e}_B - \text{Ta}^{1/2} \text{Pr} \mathbf{e}_\Omega \times v, \end{aligned}$$

where v , τ , P , T , and C are dimensionless velocity, time, pressure, temperature, and dopant concentration, respectively; \mathbf{e}_g , \mathbf{e}_c , \mathbf{e}_Ω , and \mathbf{e}_B are unit vectors in the gravitational, centrifugal, angular rotational, and magnetic field directions, respectively; and T_{ref} and C_{ref} are the dimensionless reference temperature and dopant concentrations, respectively. The dimensionless thermal Rayleigh Ra_T , Hartmann Ha , Taylor Ta , and Froude Fr numbers and their physical meaning are summarized as

$$\begin{aligned} \text{Ra}_T &= \frac{\beta_T g \Delta T L^3}{\nu_m \alpha_m} = \frac{\text{Buoyancy force}}{\text{Viscous force}}, \\ \text{Ta} &= 4 \Omega^2 L^4 / \nu_m^2 = \frac{\text{Coriolis force}}{\text{Viscous force}}, \\ \text{Ha} &= |\mathbf{B}| L (\sigma / \mu_m)^{1/2} = \frac{\text{Lorentz force}}{\text{Viscous force}}, \\ \text{Fr} &= \Omega^2 L / g = \frac{\text{Centrifugal force}}{\text{Gravitational force}}, \end{aligned}$$

where L is the characteristic length, σ is the electrical conductivity, μ_m is the melt viscosity, and g is the gravitational acceleration. Additional dimensionless parameters are the Prandtl number $\text{Pr} = \nu_m / \alpha_m$ and the Schmidt number $\text{Sc} = \nu_m / D$, where ν_m is the kinematic viscosity and α_m and D are the thermal and dopant diffusivities, respectively. Also, Ra_S is the solutal Rayleigh number, similar to the thermal one but where the driving force is based on $\beta_S \Delta C$, where β_S is the solutal expansion coefficient, and ΔC the concentration difference. For molten oxides, Pr is about unity and the thermal field can be affected easily by convection. However, for molten semiconductors or metals, $\text{Pr} \ll 1$ and the effect of flow on the heat transfer and the interface shape is much less. On the other hand, for most dopants in the melts, $\text{Sc} \gg 1$, indicating that the dopant field and thus segregation are dominated by convection rather than by molecular diffusion.

36.1.2 Boundary Conditions

To solve the above equations, a set of proper boundary conditions is necessary [36.55]. For crystal growth, the energy and solute balances at the interfaces are particularly important and cannot be ignored. Taking the Bridgman configuration as an example, if the dimensionless ampoule moving speed is v_{amp} , the balances for energy (ignoring internal radiation) and dopant (ignoring solid-state diffusion) at the growth front are

$$0 = Q_c - Q_m + \gamma \text{St} \times \left[\left(v_{\text{amp}} - \frac{dh_c}{d\tau} \right) \mathbf{n} \mathbf{e}_z + r \Omega_c \mathbf{n} \mathbf{e}_\phi \right], \quad (36.5)$$

$$0 = \mathbf{n} \nabla C|_m + \frac{\text{Sc}}{\text{Pr}} (1 - K) C \times \left[\left(v_{\text{amp}} - \frac{dh_c}{d\tau} \right) (\mathbf{n} \mathbf{e}_z) + r \Omega_c^* (\mathbf{n} \mathbf{e}_\phi) \right], \quad (36.6)$$

respectively, where Q_c and Q_m are the normal heat fluxes in the crystal and melt sides, respectively, γ_c is the density ratio of the crystal and the melt, St is the Stefan number scaling the heat of fusion by the sensible heat of the melt ($\text{St} = \Delta H / C p_m \Delta T$), h_c is the dimensionless interface position, \mathbf{e}_z is the unit vector in the axial direction, K is the segregation coefficient of the dopant, \mathbf{e}_ϕ is the unit vector in the azimuthal direction, and \mathbf{n} is the unit normal vector. If the interface shape is not axisymmetric ($\mathbf{n} \mathbf{e}_\phi \neq 0$), the freezing rate may oscillate and melt-back may even occur ($\mathbf{n} \mathbf{e}_\phi > 0$) during rotation if the growth rate is very small [36.15].

For the FZ and HB configurations, the free surface requires normal and tangential shear stress balances for the momentum equations. At the free surface, the shear stress balance is imposed ([36.60])

$$\tau : \mathbf{n} \mathbf{s} = \text{Ma} \partial T / \partial s, \quad (36.7)$$

where $\tau : \mathbf{n} \mathbf{s}$ is the shear stress at the n - s plane of the free surface; \mathbf{n} and \mathbf{s} are the unit normal and tangential vectors at the free surface, respectively. Also, Ma is the Marangoni number, which is defined as

$$\text{Ma} = \frac{|\partial \gamma / \partial T| T_m L}{\rho_m \nu_m \alpha_m},$$

where $\partial \gamma / \partial T$ is the surface tension-temperature coefficient of the melt. Two tangential directions need to be considered for the stress balance. In addition, the kinematic condition ($\mathbf{n} \mathbf{v} = 0$) at the free surface and the normal stress balance (the Young-Laplace equation) are also satisfied, i. e.,

$$\tau : \mathbf{n} \mathbf{n} = (2H) \text{Bo} + \lambda_0, \quad (36.8)$$

where $2H$ is the mean curvature scaled by $1/L$ and $Bo = \gamma/(\rho_m g_0 L^2)$ is the static Bond number, where γ is the surface tension of the melt. The detailed procedure for calculating the mean curvature can be found elsewhere [36.61]. Also, λ_0 is a reference pressure head that needs to be determined to satisfy the growth angle constraint for a steady growth.

The governing equations and the associated boundary conditions can be solved by numerical methods. For example, *Lan and Liang* [36.62] have developed a multiblock three-dimensional (3-D) finite-volume method with multigrid acceleration to solve the above equations. In each block, a structure mesh is adopted. During iterations, the interface is found by locating the

melting temperature. The iterations continue until all the variables converge.

In the following sections, we will discuss first the flow structures and their effect on crystal growth through a few examples, focusing on the Bridgman and ZM configurations. These examples provide a heuristic introduction of melt flow structure and its effects on interface shape and segregation. Much more complicated cases exist for large-scale Czochralski growth of silicon, where the melt flow is usually turbulent [36.1, 7, 63]. However, due to space limitation, we do not attempt to touch on this topic. This introduction is not extensive, and the interested reader can find further discussion in the related references [36.5, 9, 10].

36.2 Flow Structures in the Melt

Flow structures in the melt have significant influence on interface morphology and dopant segregation. Oscillatory melt flows can also cause growth striations, as a result of microscopic composition nonuniformity [36.5]. Therefore, understanding the basic flow structures in the melt is important for growth control. Furthermore, beside the flow structures, the heat of fusion released during crystal growth (the Stefan effect) could significantly affect the interface shape. Therefore, the interaction of the heat flow and solidification is the key factor for the interface shape. In this section, typical convection structures in the ZM and Bridgman configurations will be discussed. The buoyancy, Marangoni, and forced convections are illustrated. Solutal effects on the melt convection will be discussed as well.

36.2.1 ZM Configuration

For the ZM configuration, if the molten zone generated by a resistance heater is confined in the ampoule, the buoyancy convection is caused by radial heating. The typical buoyancy flow is like that in Fig. 36.2a, observed during the ZM growth of a 11 mm-diameter sodium nitrate (NaNO_3) crystal [36.64]. As shown, due to radial heating, the hotter and lighter melt near the ampoule floats upward, while the cooler and heavier melt near the centerline sinks, thus producing the flow loop. Because NaNO_3 is a high-Prandtl-number material ($Pr = 9.2$), the heat transfer in the molten zone is significantly enhanced. As a result, the growth interface is also affected, having a gull-wing shape.

On the other hand, with the presence of the free surface for the FZ configuration, the flow structure is

dramatically changed due to the Marangoni flow. The Marangoni flow is induced by the nonuniform surface tension due to temperature variation at the free surface. For small-scale growth, the Marangoni flow could be dominant in the molten zone. Figure 36.2b shows a visualized Marangoni flow in a floating molten zone of a 4 mm-diameter NaNO_3 rod [36.65]. As shown, there are four flow cells near the free surface, induced by the surface-tension difference along the free surface; the surface tension is higher near the solid side with a lower temperature. Due to the flow, the heat absorbed from the heater is brought toward to the melt–solid interfaces, leading to very convex interfaces. Compared with that in Fig. 36.2a, the interface convexity is significantly larger than the buoyancy-flow induced one. The effects of buoyancy and Marangoni convections can be better understood from the simulation results shown

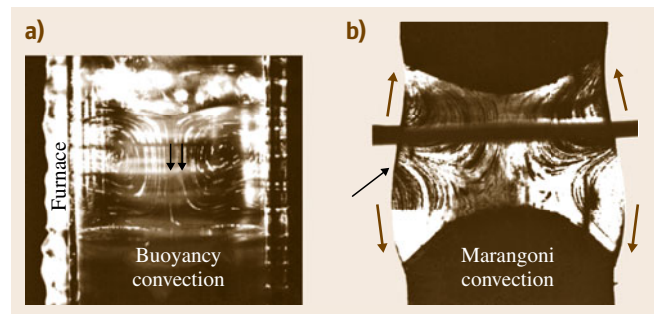


Fig. 36.2a,b Observed flow structures and zone shapes in (a) zone-melting growth of NaNO_3 (11 mm diameter, growth rate of 1 cm/h); (b) observed flow patterns in a stationary floating zone of NaNO_3 (4 mm diameter)

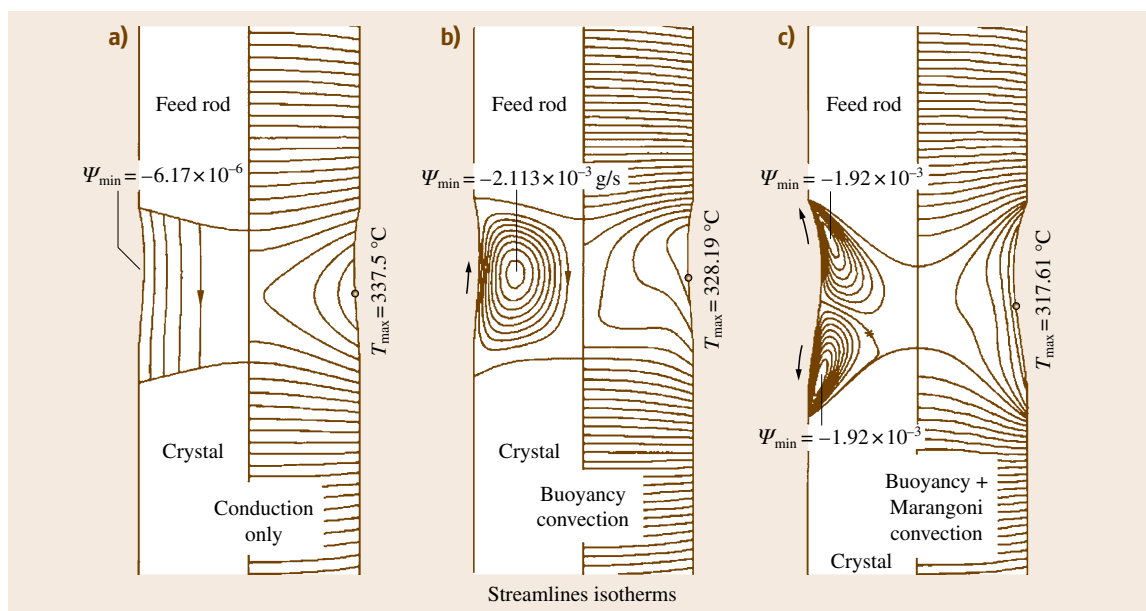


Fig. 36.3a–c Effect of convection modes on the interface shapes for FZ growth of a 4 mm-diameter NaNO₃ crystal: (a) conduction mode; (b) buoyancy convection; (c) buoyancy and Marangoni convections; the *left-hand side* shows the flow patterns and the *right-hand side* the isotherms

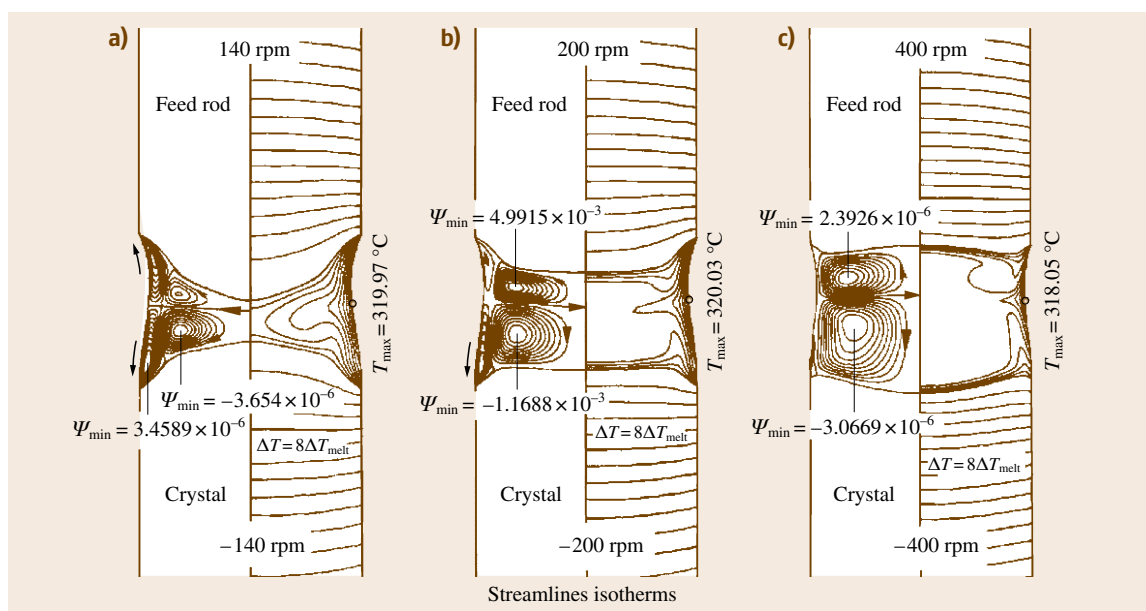


Fig. 36.4a–c Effect of counter-rotation on the flow structures and interface shapes for FZ growth of a 6 mm-diameter NaNO₃ crystal: (a) 140 rpm; (b) 200 rpm; (c) 400 rpm

in Fig. 36.3 [36.66]. In Fig. 36.3a, the streamlines are due to the rod feeding and crystal pulling (downwards).

With the buoyancy flow in Fig. 36.3b, the flow structure and the resulted interface shape are similar to the ones

in Fig. 36.2a. As the Marangoni effect is considered, the interface shape becomes very convex, consistent with that observed in Fig. 36.2b.

Forced convection can also be introduced for FZ growth through rotation. In general, counter-rotating the feed and crystal rods is often used, but usually below 30 rpm. Lan and Kou [36.66] proposed an extreme situation by using high-speed rotation, say 200 rpm, for zone shape control. Figure 36.4 shows the effects of counter-rotation for a FZ growth of a 6 mm-diameter NaNO_3 crystal. As shown, the flow structures due to the forced convection are also very different from the previous ones. The counter-rotating rods act as a centrifugal fan, sucking the melt axially toward the solid and spinning outward radially in the thin Ekman boundary layer near the solid. Thus, the induced convection cells are near the center core of the molten zone. Because their flow directions are different from the Marangoni cells, the Marangoni flow is suppressed with increasing rotation speed. The photograph of the visualized flow at 200 rpm is shown in Fig. 36.5a. Due to the lens effect of the melt as a result of its different reflective index from the air, the Marangoni flow cannot be seen. From this side view, it can be imagined that the heat absorbed from the heater can be brought into the zone center effectively. As a result, the interfaces become flat and the zone can be kept very short by using a smaller heating power. This idea has been applied to the growth of 1 cm-diameter NaNO_3 crystal with a very short and stable zone [36.67]. A photograph of the growth is shown in Fig. 36.5b. Computer simulation has also been carried out, and good agreement with experimental observation has been obtained.

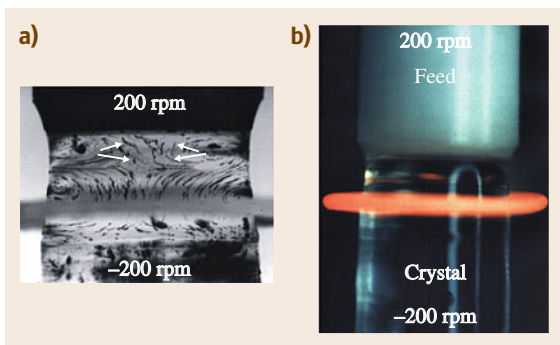


Fig. 36.5 (a) Observed flow patterns in FZ growth (6 mm-diameter rod) under 200 rpm counter-rotation; (b) FZ growth of a 1 cm-diameter NaNO_3 crystal under 200 rpm counter-rotation

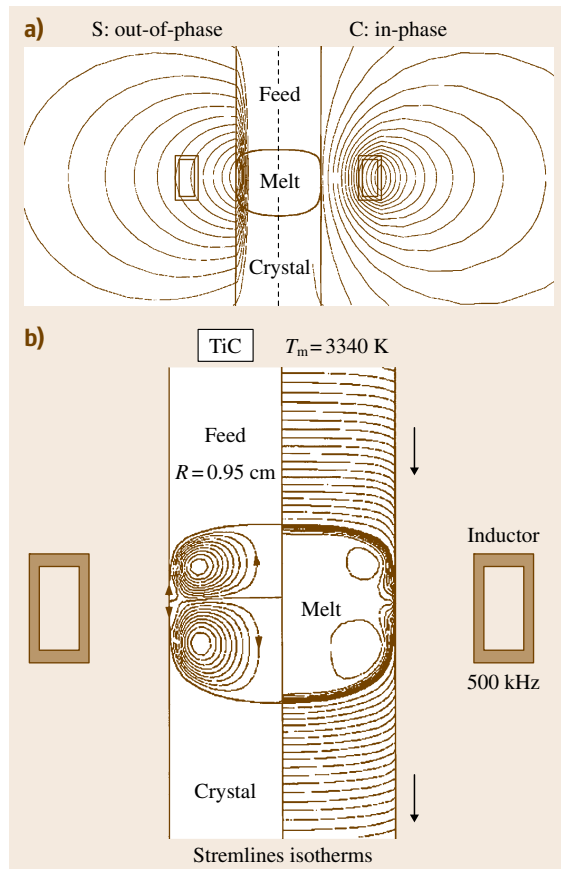


Fig. 36.6a,b Effect of induction heating for FZ growth of 2 cm-diameter TiC: (a) calculated in-phase (right) and out-of-phase (left) magnetic components; (b) calculated flow patterns (left) and isotherms (right) and the zone shape

Furthermore, for electrically conductive melt, the molten zone can also be produced by an induction coil; the heat is generated by the Joule heating of the induced eddy current. In addition, the Lorentz force can induce significant magnetic stirring and this leads to a severe distortion of the molten zone. Especially, if no insulation is used for the zone, the significant radiative heat loss from the molten zone causes a very concave growth front. Figure 36.6a shows calculated magnetic fields for FZ growth of a 2 cm-diameter TiC rod, and Fig. 36.6b shows the calculated flow (right) and thermal fields (left) as well as the zone shape. From the distortion of the isotherms, the magnetic stirring inside the molten zone is quite vigorous. The Marangoni flow in this case is weak as compared with the flow generated by the magnetic stirring. Increasing the coil frequency

reduces the skin depth and magnetic stirring. The interface concavity can be reduced as well. However, a more effective way for interface control is to reduce the radiation heat loss, for which the use of insulation or a secondary heater is helpful [36.68]. In addition, the power (induction current) required and also the magnetic stirring can be significantly reduced.

The flow structures in the previous examples are axisymmetric. However, in reality, several factors can cause symmetry breaking. Imperfect heating or alignment can cause asymmetric zone as well. Inherent nonlinear bifurcation is also typical. *Lan* and *Liang* [36.69] have demonstrated through numerical simulation the nonlinear symmetry breaking leading to three-dimensional (3-D) flows for a *ZM* growth for a 2 cm-diameter GaAs crystal in a quartz ampoule (wall thickness 2 mm). The bifurcation diagrams for the zone length and surface temperature differences using the heater temperature (T_p) as the parameter are illustrated in Fig. 36.7a and b, respectively. Some plots for thermal and flow fields indicated in Fig. 36.7 are further illustrated in Fig. 36.8. First, we start the solution at 1500 °C, as shown in Figs. 36.7 and 36.8a, the solution is axisymmetric and stable. On further increasing the heater temperature, we can observe a subcritical bifurcation at about 1513 °C. However, the new mode that bifurcates from the axisymmetric ($m0$) mode is an $m2$ mode instead of an $m1$ mode. Two stable solutions b and c at 1510 °C are shown in Fig. 36.8b,b', respectively. The $m2$ mode c has a twofold symmetry, which can be clearly seen from the cut of the isotherms at the middle section of the molten zone ($z = L/2$). As shown at the bottom of Fig. 36.8b', although they are both symmetric with respect to the centerline, the results are quite different. By comparing the interface shapes from the two cuts, one may also get a 3-D view of the interface shapes. Further increasing the heater temperature, as shown in Fig. 36.7, we encounter a secondary bifurcation, and the $m2$ mode becomes unstable. The new mode branching from $m2$ is the $m1$ mode again. This bifurcation is subcritical as well. Two stable solutions c and c' are further illustrated in Fig. 36.8c,c', respectively.

It is believed that the existence of the $m2$ mode at lower T_p is due to the much smaller aspect ratio of the molten zone. As the zone length is increased by increasing the heating power, the $m1$ mode becomes dominant. Furthermore, the subcriticality is due to the existence of the deformable interfaces. The bifurcation becomes supercritical if we fix the interfaces. Such an observation is similar to that in the two-phase Rayleigh–Bernard

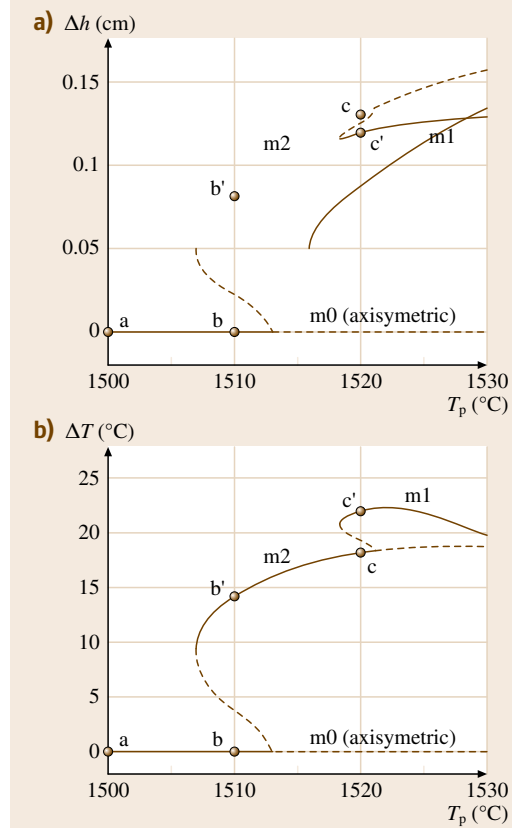


Fig. 36.7a,b Bifurcation diagrams of *ZM* growth of 1 inch-diameter GaAs using the heater temperature as the parameter of: (a) the zone length deviation and (b) the surface temperature deviation

problem discussed by *Lan* and *Wang* [36.70]. Again, although Ra_w [$Ra_w = (\beta_T g_0 \Delta T L^3) / (\nu_m \alpha_m)$; $\Delta T = T_w - T_m$, where T_w is the wall temperature] is up to 5.78×10^5 ($\Delta T = 63.33$ K is the maximum temperature in the molten zone) for the $m1$ mode at $T_p = 1530$ °C, the solution is still stable. Similar observations were found by *Baumgartl* et al. [36.71].

Besides the symmetry breaking, the bifurcation to unsteady state is often encountered, and this time-dependent flow is often related to growth striation; for example, in *ZM* growth of GaAs single crystals at $Ra_w \approx 4 \times 10^5$, 3-D striation patterns were found [36.71]. In the previous experiment, a steady axisymmetric mode bifurcated to a 3-D toroidal mode first at $Ra_w \approx 3 \times 10^4$ and then to a time-dependent mode at a higher Ra_w ($\approx 4 \times 10^4$) for a parabolic thermal profile at the melt surface. A steady one-roll

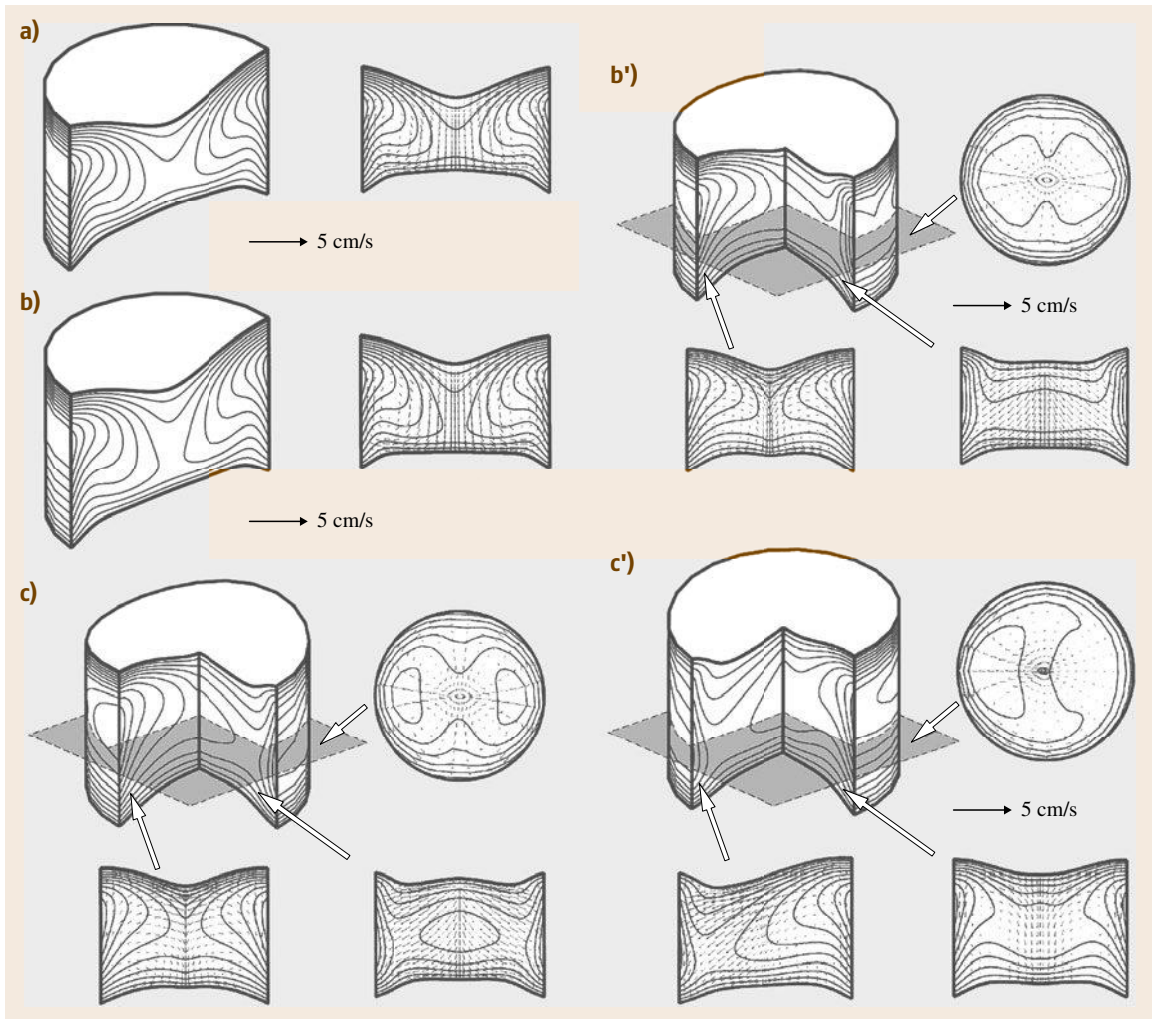


Fig. 36.8a–c Some solutions of Fig. 36.7: **(a)** 2-D solution at $T_p = 1500\text{ }^{\circ}\text{C}$; **(b)** 2-D solution at $T_p = 1510\text{ }^{\circ}\text{C}$; **(b')** 3-D m_0 solution at $T_p = 1510\text{ }^{\circ}\text{C}$; **(c)** 3-D m_2 solution at $T_p = 1520\text{ }^{\circ}\text{C}$; **(c')** 3-D m_1 solution at $T_p = 1520\text{ }^{\circ}\text{C}$

(m_1) mode was found for 8×10^4 ($Ra_w \approx 1.85 \times 10^5$). Beyond $Ra_w \approx 1.85 \times 10^5$, the m_1 flow became time dependent.

Similar to the nonlinear bifurcations in the **ZM** configuration in an ampoule, the **FZ** configuration also has a similar behavior. Indeed, the flow bifurcation is caused by Marangoni flow, and extensive studies have been made of this subject [36.17, 20, 21, 56].

In addition to the vertical configuration, the horizontal **ZM** (**HZM**) configuration is also used in bulk crystal growth and material purification [36.72]. The observed flow structure for a horizontal molten zone of succinonitrile (**SCN**) is shown in Fig. 36.9a. Due to the buoyancy

force, there are two flow cells in the melt. The melt flows upwards at the center, and downwards near the interfaces. The upward melt (lighter) is also heated at the top wall and then flows to the two sides to melt back the interfaces. As a result, the upper part of the zone becomes wider. The downward melt (heavier) from the interfaces is warmed up again from the bottom wall at the center and then flows upwards. Although the picture shown in Fig. 36.9a appears to be two dimensional, the flow structure is fully 3-D. However, the flow patterns at other light-cut planes are much more difficult to observe. The trapezoidal zone shape in Fig. 36.9a is caused by the buoyancy flow and is consistent with

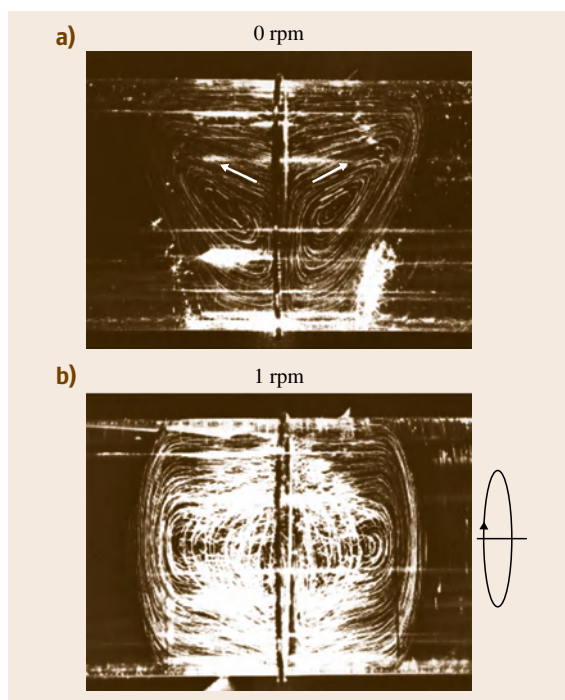


Fig. 36.9a,b Flow patterns in horizontal zone-melting growth of SCN: (a) without rotation; (b) with 1 rpm rotation

that reported [36.72]. Interestingly, if we impose only 1 rpm ampoule rotation, a significant change of the zone shape is observed, as shown in Fig. 36.9b. As shown, the zone shape becomes much more symmetric, and the upper and lower zone lengths are about the same. As compared with Fig. 36.9a, the rotation reduces the upper zone length, while widens the lower part; the zone length seems to be averaged by the rotation. The flow structure is also changed quite significantly. In fact, due to rotation, the flow visualization became much more difficult. The tracer particles (aluminum powder) are heavier than the melt. As a result, larger particles tended to settle down, as shown by the bright area at the melt bottom in Fig. 36.10a.

Computer simulation has also been conducted for the observed flows and interface shape [36.73], as shown in Fig. 36.10. Indeed, the simulation captures the key features of the experiments shown in Fig. 36.9: both the flow structures and the interface shapes. For the case without rotation, as shown in Fig. 36.10a, the flow patterns and interface shapes are in good agreement with Fig. 36.9a. Due to the buoyancy force, the hotter (lighter) melt at the bottom floats upwards. It is warmed up again at the top wall, and flows to the two sides, leading to a significant back melting of the interfaces at the top. The downward melt near the interfaces is cooler and heavier, but it is heated up again by the heater at the bottom wall and floats up at the center. One can also get a better picture from the distorted isotherms, which are consistent with the flow directions. The right-hand side view of Fig. 36.10a also illustrates the buoyancy convection; the melt near the wall is heated and flows upward. One cannot see a downward flow from this plane, because the major downward flows appear near the interfaces. With 1 rpm rotation, as shown in Fig. 36.10b, the zone shape becomes much more axisymmetric, which agrees well with the observation in Fig. 36.9b. The flow structure shown in Fig. 36.10b is also similar to that in Fig. 36.9b as well. One shall pay more attention on the flow shapes and vortices. The right figure of Fig. 36.10b also indicates that, although the effect of rotation becomes more obvious, the change of the flow and isotherms is small.

The success of the full model calculation in Fig. 36.10b is due to consideration of the interface energy balance. As shown in (36.5), for steady rotation without ampoule translation, the term $\gamma_c St(r\Omega_c n e_\phi)$ plays a crucial role. During rotation, solidification at the interface occurs at $\gamma_c St(r\Omega_c n e_\phi) < 0$, while melting occurs at $\gamma_c St(r\Omega_c n e_\phi) > 0$; for example, for the left interface, at the front side, $\gamma_c St(r\Omega_c n e_\phi) < 0$ and solid-

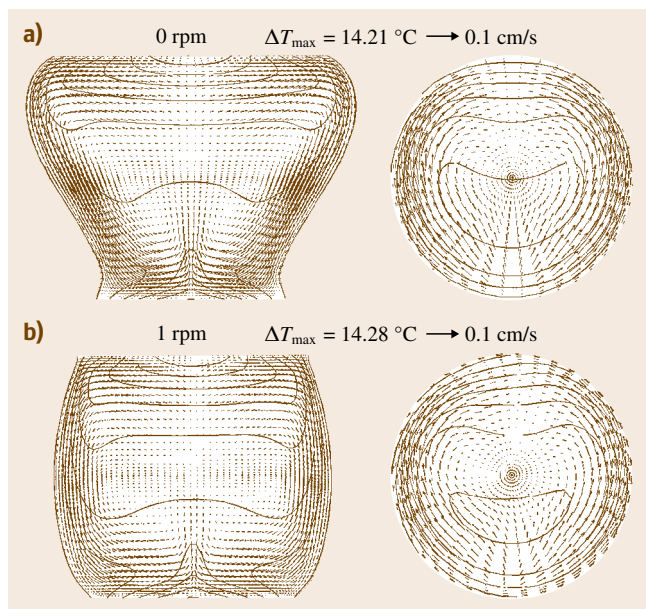


Fig. 36.10a,b Simulated flow and thermal fields: (a) 0 rpm; (b) 1 rpm rotation

ification dominates. The heat of fusion is released to the melt and it distorts the interface toward the rotational direction. Meanwhile, the melting occurs at the back side, and the heat of fusion is extracted from the melt, making the solid interface intrude toward the melt in the rotational direction there. As a result, the zone length is averaged out with the period of rotation. This mechanism (the Stefan effect) is dominant for the interface shapes here and cannot be ignored in the simulation.

36.2.2 Bridgman Configuration

The Bridgman configuration is also widely adopted for melt growth of bulk crystals. Unlike the ZM configuration, in which significant superheating is necessary to form a stable zone, the Bridgman configuration is suitable for growth that requires low superheating or thermal gradients. For the HB configuration using an open boat, due to the free surface, the Marangoni convection is also important. Nevertheless, due to the much larger melt volume, the buoyancy flow is also strong. To understand its basic flow structure, we take the HB growth of NaNO_3 as an example. The top view of the growth in a transparent furnace is shown in Fig. 36.11a [36.53]. During growth, the interface is always concave, due to the release of heat of fusion and the effect of melt convection, although the latter factor is much more significant. As will be discussed shortly, the Marangoni flow is responsible for the sharp contact angle between the interface and the crucible [36.13]. Such an acute angle often induces parasitic nucleation from the crucible wall, leading to a polycrystalline growth. The visualized flow is shown in Fig. 36.11b. As shown, the buoyancy and Marangoni flows are in the same direction, and the hot melt near the surface flows from the left to the right, pushing the interface to the crystal side. Meanwhile, because of the no-slip boundary condition at the solid wall, the isotherms at the solid wall are nearly pinned by the energy balance there with the conduction in the ampoule. Accordingly, the interface becomes very concave. The calculated flow patterns and isotherms, shown in Fig. 36.11b and c, respectively, further explain the situation.

Further understanding of the flow structures can be obtained from the numerical simulation of HB growth of GaAs by Lan and Liang [36.61]. Figure 36.12 shows the effects of convection modes on the thermal and velocity fields (on the planes at $z = 0$ and $y = 0$) and the growth front (crucible pulling speed is 5 mm/h). As shown in Fig. 36.12a, without any driving forces for convection, the growth front is only slightly concave;

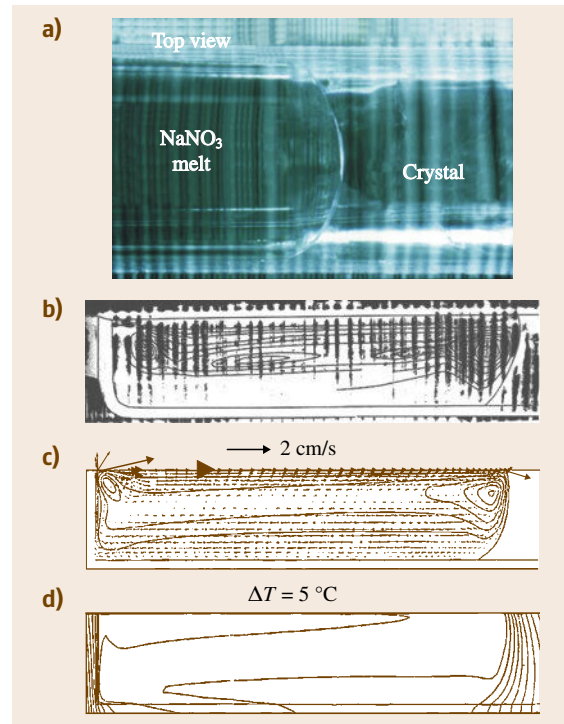


Fig. 36.11a–d Effect of buoyancy and Marangoni flows on the HB growth of NaNO_3 crystals: (a) observed interface seen from the top; (b) observed flow patterns; (c) calculated flow patterns; (d) calculated isotherms and interface shape

it is quit flat viewed from the top. When buoyancy force is considered in Fig. 36.12b, as shown in the side view of the flow fields, a clockwise natural convection is induced. Although the maximum melt velocity is less than 1.5 cm/s, the isotherms in the melt are highly distorted by the convection. As a result, the interface shape becomes highly distorted and very concave. The interface position at the bottom is not affected much, but the upper interface is melted backward significantly. A 3-D view of the growth front shape is illustrated on the right-hand side for comparison. Clearly, the effect of buoyancy convection on the growth front shape is significant.

When the Marangoni effect is included, as shown in Fig. 36.12c, the flow structures are not changed much; the flow in the side view is still clockwise in direction. However, the melt velocity near the free surface and the growth interface becomes much higher; the maximum velocity is about 5 cm/s. The isotherms near the free surface are thus further affected, even though the overall view of the isotherms is not changed much. As

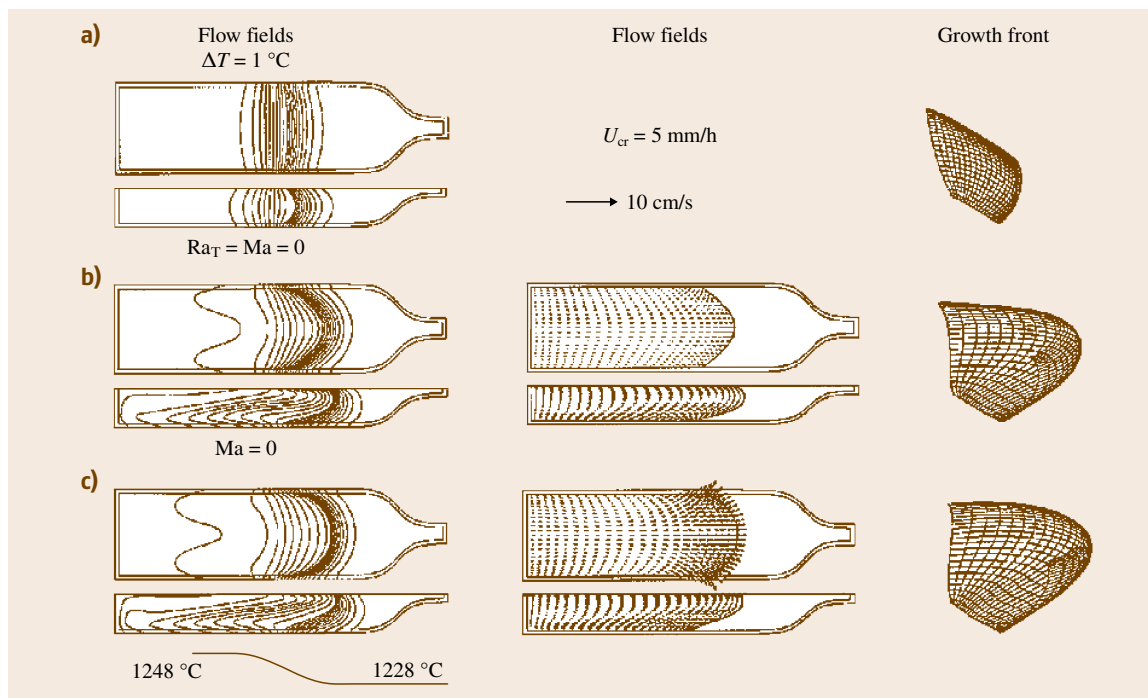


Fig. 36.12a–c Effects of buoyancy and Marangoni flows on the flow, thermal fields, and the interface shape for the HB growth of GaAs single crystal: (a) conduction mode; (b) buoyancy convection; (c) buoyancy and Marangoni convection

a result, the growth front near the top surface is melted back more. As shown in the side view, the growth interface also becomes sharper. Because the driving force for the Marangoni convection is proportional to local

thermal gradients at the free surface, the flow near the interface is thus stronger, where the thermal gradients are higher. In addition, the flow direction there becomes more perpendicular to the isotherms, leading to a diverged flow near the interface, as shown in the top view of the flow fields. This diverged flow also melts back the interface toward the crucible and results in a rounder interface shape at the free surface when viewed from the top. More importantly, the interface–crucible contact angle becomes much smaller as well, which from the crystal growth point of view, is more likely to induce parasitic nucleation and the formation of polycrystals. This is consistent with the observation in Fig. 36.11a.

In practice, control of the growth front shape is important for crystal quality. The results in Fig. 36.12 clearly illustrate the significance of the buoyancy and Marangoni convections for the growth interface. However, since the direction of driving forces for both convection modes is not likely to be changed, the room for modulating the convection and thus controlling the interface is not great. The convections can be reduced with smaller thermal gradients, but the smaller thermal gradients also cause other problems. With a fixed growth rate, the heat of fusion will cause a more de-

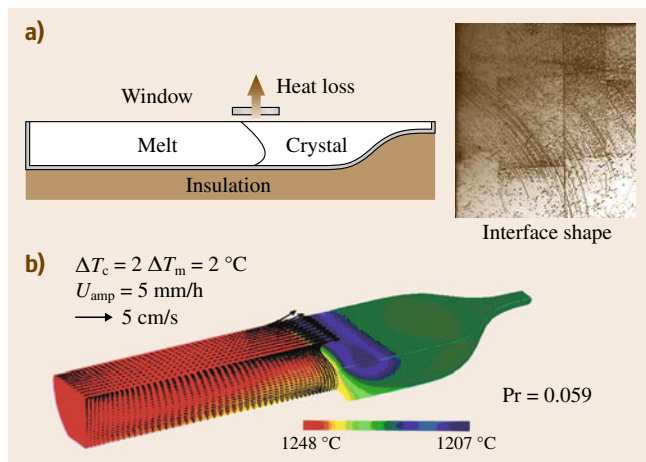


Fig. 36.13 (a) Schematic of HB growth of GaAs with a viewing window for local radiation cooling; on the right is the observed interface shape (cross section); (b) simulated flow and thermal fields

formed interface shape for lower thermal gradients. Constitutional supercooling [36.73] is a concern as well.

For this configuration, an effective approach is to provide local cooling at the top interface. This concept has been adopted for the growth of GaAs using a view window above the interface, as shown on the left of Fig. 36.13a [36.61]; the observed interface shape [36.74] is shown on the right of Fig. 36.13a. This window provides local radiative cooling and thus controls the interface shape. In addition to the top radiative cooling, booster heating (through the center zone) at the bottom of the interface is also useful, and this further reduces the interface concavity of the lower interface. Computer simulation based on these ideas has been conducted [36.61] and the result is shown in Fig. 36.13b. As shown, the temperature is greatly reduced near the window and the temperature gradients are also increased significantly there; the isotherm spacing in the crystal is increased to 2 °C, which is twice that in the melt. Because the quartz crucible has a higher emissivity than GaAs, the lowest temperature beneath the window is located at the crucible surface. Interestingly, although the interface is still slightly concave, its shape is reversed; the upper interface becomes closer to the hot zone. The growth interface is now more perpendicular to the crucible wall. A similar interface shape was also observed in crystal growth experiments [36.75]. A flatter interface is possible by reducing the heat loss through the window. Local cooling using an air jet was applied to the HB growth of NaNO₃, and a convex interface was successfully obtained [36.14].

Unlike the previous examples with large radial thermal gradients, the vertical Bridgman (VB) configuration is thermally stable and the radial thermal gradients are small. Accordingly, the thermally driven buoyancy convection is significantly weaker; for example, if the furnace thermal profile is linear, the buoyancy flow is only induced by the interface deformation. When stationary, the interface deflection is mainly due to the difference in the thermal conductivity between the melt and the crystal. If the thermal conductivity of the melt is larger than that of the crystal, the interface is concave. The concave interface induces radial thermal gradients and thus buoyancy flow. The concavity increases with the crystal growth speed due to the release of the heat of fusion. The buoyancy convection due to the interface concavity appears near the growth interface and affects the radial segregation significantly [36.76–78].

Figure 36.14a shows the simulated buoyancy flow and solute fields in VB growth of gallium-doped germa-

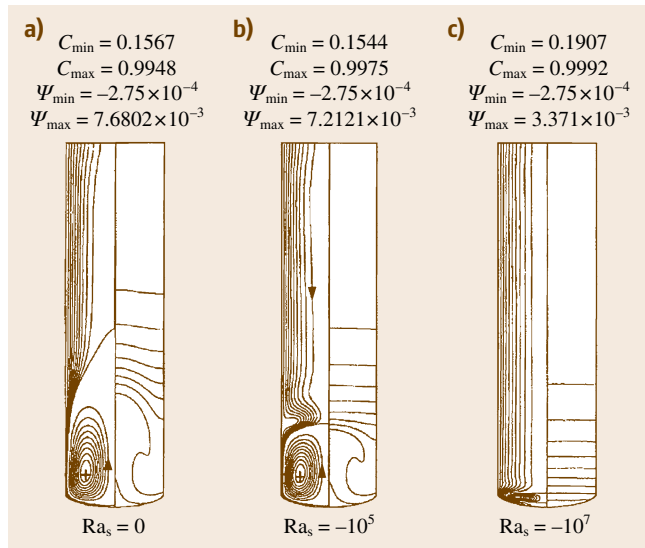


Fig. 36.14a–c Solutal effect on the buoyancy convection for VG growth of gallium-doped germanium: (a) $Ra_s = 0$; (b) $Ra_s = -10^5$; (c) $Ra_s = -10^7$; in each figure on the left-hand side of the simulated results is the flow fields and on the right-hand side the solute fields

nium in a small graphite ampoule at $Ra_T = 10^7$ [36.78]; $Ra_T = 2.489 \times 10^8$ for normal gravity at a thermal gradient of 50 K/cm. Because the ampoule is pulled downward, the streamlines in the bulk melt indicate the material flow due to the ampoule translation. Also, the interface concavity is here is due to the larger thermal conductivity of the melt than that of the crystal. In addition to the thermal convection, the solutal effect can also affect the flow; for example, if a solute is added to germanium, solute segregation causes density variation in the melt, leading to solutal convection. Figure 36.14b,c show the effect of solute (silicon), in terms of solutal Rayleigh number Ra_s , on the flow. Because silicon dissolves more in the germanium solid than in the melt, silicon is depleted near the interface during crystal growth. Due to the less and lighter silicon near the interface, the melt density near the interface increases and this suppresses the thermal convection. As shown in Fig. 36.14c, the buoyancy convection is almost suppressed due to the solutal effect.

Through the visualization experiments of SCN containing acetone (lighter) or salol (heavier), the thermal–solutal convection can be better understood. Figure 36.15a,b shows the interface shape evolution during Bridgman growth of SCN containing 0.064 wt % acetone and 0.15 wt % salol, respectively; the pulling speed is 1.6 $\mu\text{m/s}$ [36.47]. The simulated results are

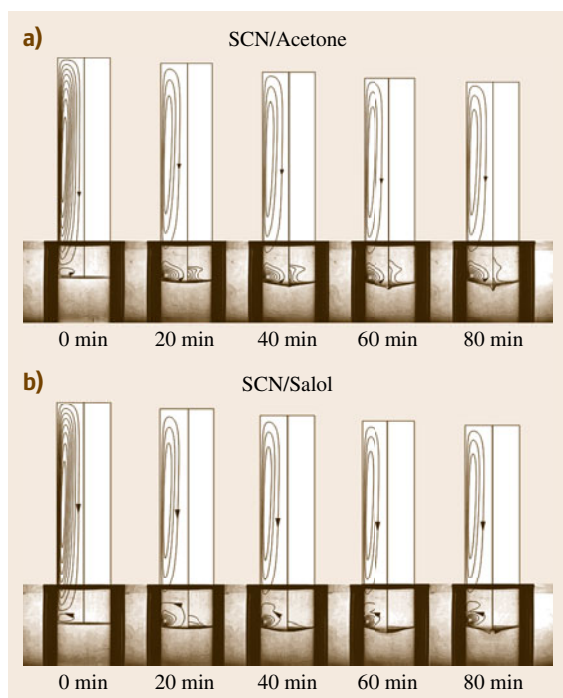


Fig. 36.15a,b Double diffusive convections in VB crystal growth of SCN: (a) SCN/acetone; (b) SCN/salol; in each figure on the *left-hand side* of the simulated results is the flow fields and on the *right-hand side* the solutal fields

also shown for comparison. In each simulated result, the left-hand side shows the streamlines, and the right-hand side the acetone fields. As shown in Fig. 36.15a for SCN/acetone stationary, the interface is flat and the convection near the interface is extremely weak. The upper cell is caused by the radial heating from the hot zone. As the solidification starts, the interface becomes concave and the flow cell near the interface is enhanced. As a result, the acetone rejected during solidification is redistributed by the flow, with increasing acetone concentration toward the center of the interface. Because acetone is lighter than SCN, the radial acetone gradients also enhance the flow, leading to a highly localized

solute distribution at the center of the interface. The local acetone accumulation further causes a depression of the interface there, which becomes obvious at about 40 min. As the supercooling is built up, morphological breakdown can occur when the supercooling overcomes the interfacial energy. The simulated results at 60 and 80 min show a deep depression (pit) at the center of the interface, where high constitutional supercooling exists. The convection in the bulk melt remains about the same during crystal growth.

The evolution of interface morphology for SCN/Salol shows a similar behavior. However, as shown in Fig. 36.15b, the depression shape is wider. The morphological breakdown occurs at about the same time, i.e., about 40 min. The bottom of the breakdown area is much flatter than that for SCN/acetone. The convection near the interface is much weaker than that for SCN/acetone, as shown in Fig. 36.15b. Such a weaker flow is due to the heavier solute, which suppresses the flow. In other words, the radial density due to thermal gradients is counterbalanced by the solutal gradients; one can observe this contribution from the source term of (36.1). In addition, the flow cell near the interface is closer to the ampoule wall as compared with that in Fig. 36.15a. More importantly, the concentration profile is quite uniform near the interface, as shown by the much flatter isoconcentration lines. This also indicates that the convective effect on the solute transport is much weaker.

Because the convection in the VB configuration in the previous examples is rather weak, nonlinear flow bifurcation to symmetry breaking or oscillatory flows is not likely. Nevertheless, in reality, a perfect axisymmetric growth condition is hard to achieve. An asymmetric furnace thermal profile or slight ampoule tilting can lead to significantly 3-D convections [36.79]. As a result, the segregation behavior predicted by an axisymmetric numerical model is often erroneous. Nevertheless, since the convection is rather weak, flow suppression by using rotation or magnetic field could be quite effective. We will thus briefly discuss its flow control by using external forces.

36.3 Flow Control by External Forces

So far, we have illustrated the convections in the ZM and Bridgman configurations. As just discussed, for the FZ configuration, crystal rotation is an effective way to introduce forced convection. However, in many cases, the suppression of unstable flows to avoid growth stri-

ations and the manipulation of local flow to reduce segregation are necessary. The use of external forces is particularly effective for such purposes. Various external forces have been considered for use in the melt growth of bulk crystals. The static magnetic field is one

of the most popular ones, and has been used widely for flow suppression [36.24, 27, 31], but it is restricted to electrically conductive melt. Rotation, steady or unsteady, can also be used, and its applications have no special limitations. In the following sections, we will discuss flow control through a few examples.

36.3.1 Steady Magnetic Field

A steady magnetic field is an effective way to suppress the flow if the melt is electrically conductive. Two examples for FZ and VB configurations are given here.

As discussed previously, in the FZ configuration, the free surface of the molten zone often induces significant Marangoni flow, and it often lead to unstable heat flows, striations, and distorted interfaces, even in microgravity environment [36.21]. The control of the unsteady Marangoni flow has been an important topic in crystal growth, and has attracted extensive research over the years [36.19]. For silicon growth, magnetic fields have been known useful for suppressing unsteady flows, so that steady growth can be obtained and the grown crystal is striation free [36.18, 21]. Both axial [36.18, 21] and transversal magnetic fields [36.28, 80] have been investigated. In the FZ Si growth experiments by Dold et al. [36.18], a striation-free core in the grown crystal was found, and the core size increased with increasing magnetic field. It was believed that the melt inside the core was significantly suppressed by the magnetic

field. Lan [36.81] made the first attempt to simulate the growth using an axisymmetric model. The results on the core size and dopant (phosphorous) distribution are shown in Fig. 36.16a,b, respectively. As shown in Fig. 36.16a, the streamlines are stretched along the direction of the applied magnetic field. Also, the radius of the suppressed core increases with increasing magnetic field strength, and the calculated core sizes at different axial magnetic field strengths are consistent with the measured ones. In addition, the calculated phosphorous distributions in Fig. 36.16b are consistent with the measured ones as well. Although the results based on the axisymmetric model are consistent with the experimental observations, the oscillatory and 3-D behavior cannot be seen in the simulation.

Further 3-D numerical simulations have been carried out recently [36.60]. Figure 36.17 shows the calculated results for an axial magnetic field of 0.5 T. At this condition, a steady-state result is obtained. However, as shown in Fig. 36.17, the result is not exactly axisymmetric but has a fourfold symmetry, which can be seen from the thermal and velocity fields on the z - y plane (growth direction is in the x -axis). The results on the x - y and x - z planes also show that the flow in the core region is greatly suppressed, but the thermocapillary flow is still quite strong near the melt surface. This is consistent with previous 2-D simulations shown in Fig. 36.16 [36.81]. In Fig. 36.17, the flow and thermal fields on the x - z and x - y planes happen

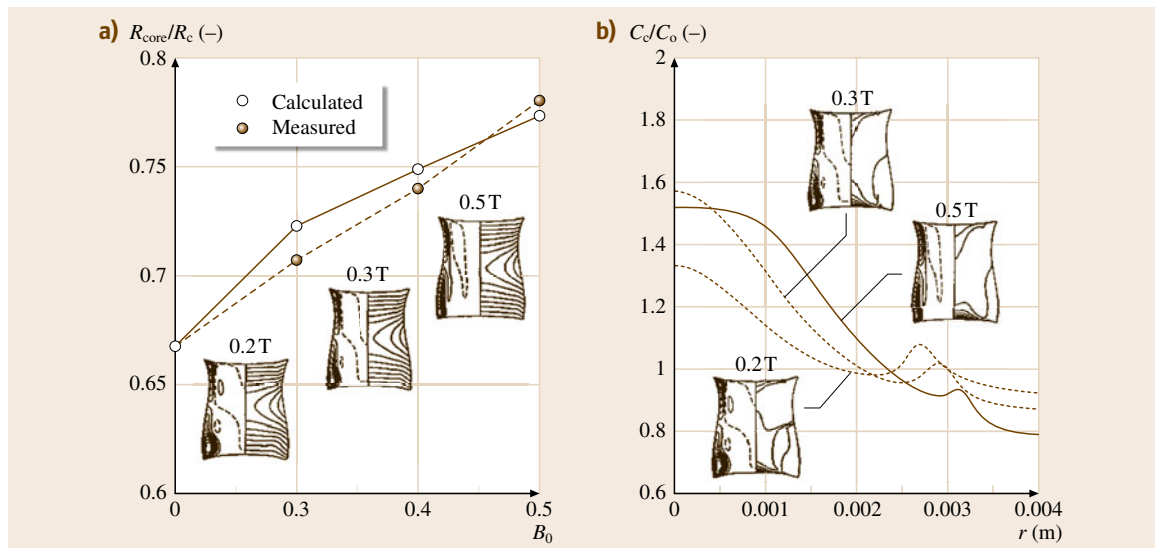


Fig. 36.16a,b Effect of axial magnetic fields on FZ silicon crystal growth: (a) the core size of the suppressed flow; (b) the radial phosphorous distribution; the simulated flow and solutal fields are also shown in (a) for comparison

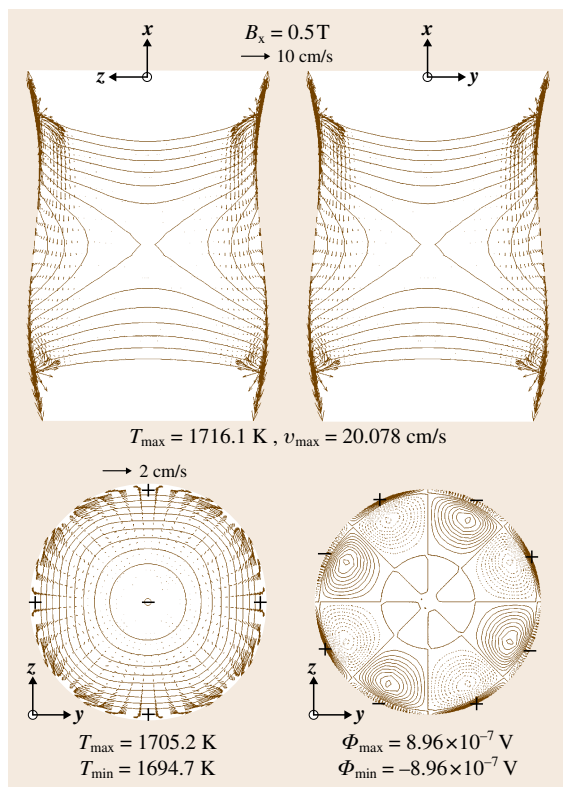


Fig. 36.17 Three-dimensional simulated flow, thermal, and potential fields in a FZ silicon growth under an axial magnetic field of 0.5 T

to be identical due to symmetry. However, if we examine the result at $x = 4.1$ cm (the middle of the molten zone) on the y - z plane, the temperature is lower at the

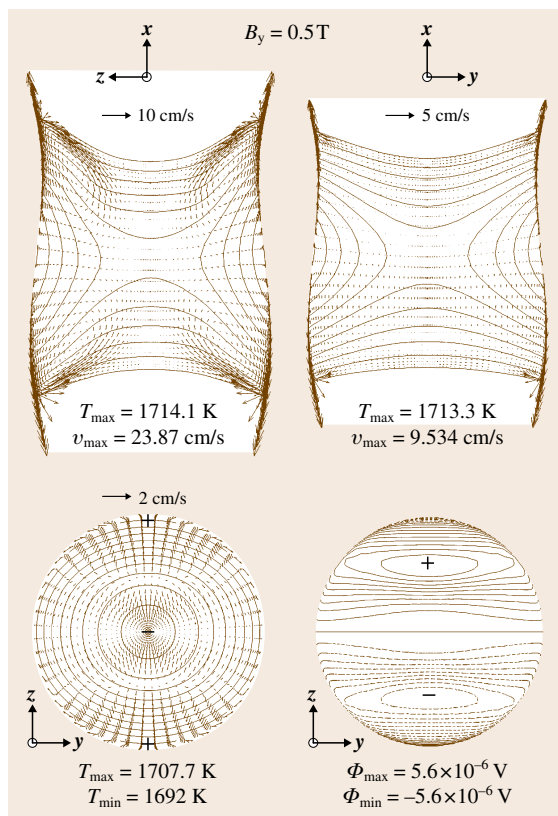


Fig. 36.18 Three-dimensional simulated flow, thermal, and potential fields in a FZ silicon growth under a transversal magnetic field of 0.5 T

four corners. Due to such nonuniform thermal gradients, there are eight flow vortices caused by the thermocapillary force. As a result, the induced electrical potential distribution on the same plane also has an eight-cell structure.

When the magnetic field strength is less than 0.46 T, the symmetry disappears and the result becomes 3-D and time dependent. In the experiments by [36.18], a magnetic field strength greater than 0.24 T was found to be necessary to obtain nearly striation-free crystals. In fact, even at 0.5 T, irregular striation patterns were visible near the crystal surface. Therefore, our results are still in reasonable consistency with the observations.

With a transversal field, the steady-state result is obtained at a much lower magnetic field strength of 0.15 T. The calculated result for 0.5 T is shown in Fig. 36.18; the velocity scales at different planes are different for clarity. As shown, the results are asymmetric, but have a twofold symmetry when viewed from the y - z plane.

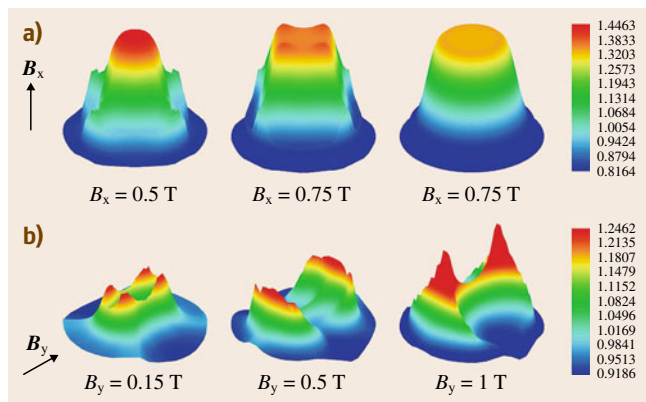


Fig. 36.19a,b Effect of axial (a) and transversal (b) magnetic fields on the dopant distribution in the growth crystal

The surface zone length on the plane (x - z plane) perpendicular to the magnetic direction is much longer than that on the parallel plane. If we examine the flow fields, clearly, as mentioned previously, the melt flow on the plane perpendicular to the magnetic field is not as suppressed as that on the parallel plane, leading to a longer zone length there. If we view the results at the y - z plane (at $x = 4.1$ cm), the isotherms have an ellipsoid shape, while the maximum temperature appears at the surface of the x - z plane.

The dopant distribution is also significantly affected by the flow. Figure 36.19 summarizes the dopant distributions obtained from previous results with more results added. As shown, under axial fields, the segregation increases with increasing magnetic field strength due to flow damping. At 0.5 and 0.75 T of the axial field, the fourfold distribution is caused by flow such as that shown in Fig. 36.17. Under transversal fields, two concentration peaks align parallel to the field direction at 0.5 and 1 T. This is simply due to the poorer mixing

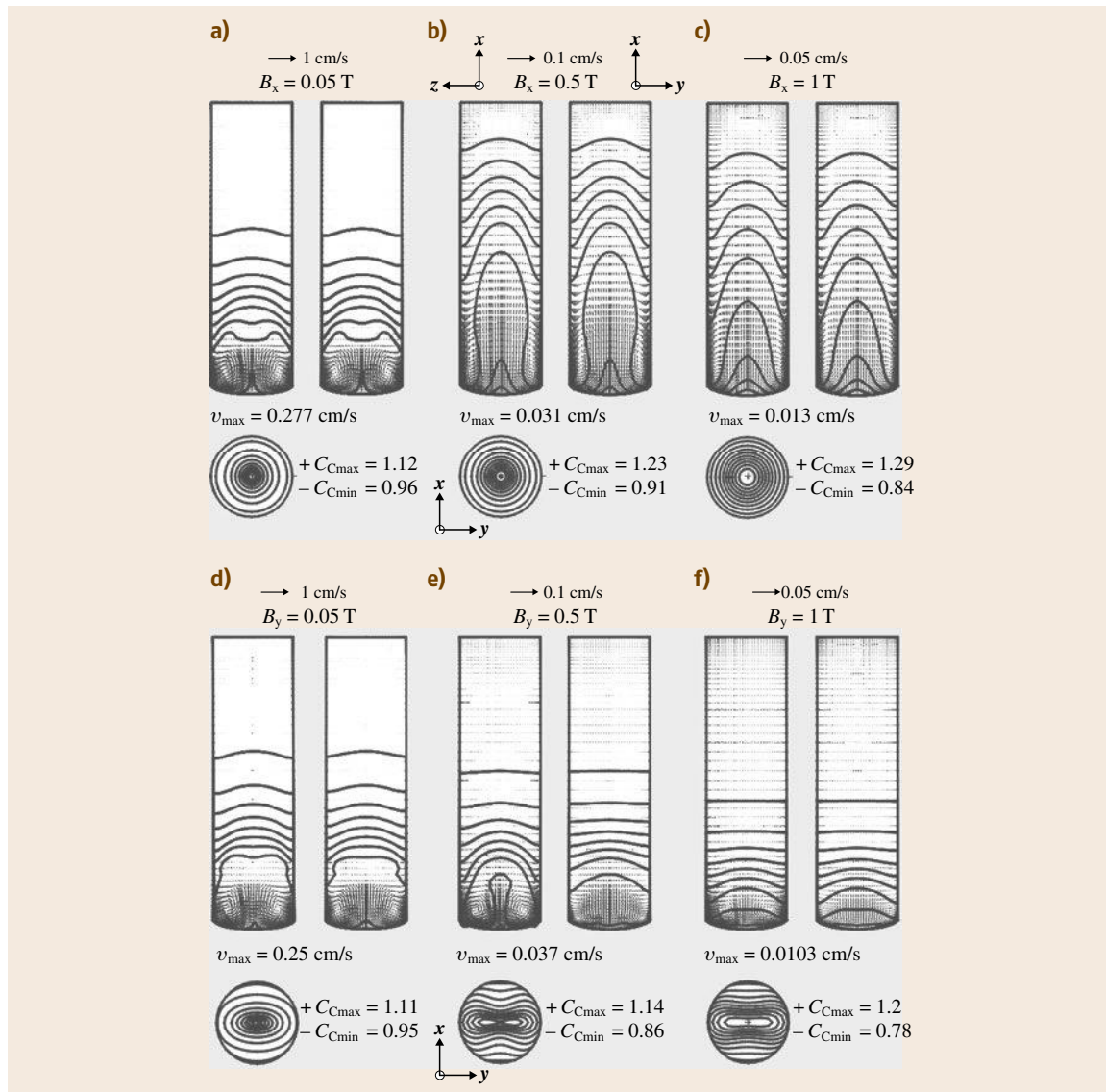


Fig. 36.20a-f Effect of axial and transversal magnetic fields on the flow and dopant fields

in the x - y plane, where the flow is suppressed more. On the other plane, the convection remains strong, so that the segregation is less. If we compare the segregation under both magnetic configurations, it is clear that the radial segregation is much less in the transversal field, even though it is highly asymmetric. Besides, as mentioned earlier, the minimum magnetic field strength to suppress the unsteady thermocapillary flow is also lower for the transversal field. Therefore, in real applications, it is believed that the transversal field may still be useful. If rotation is applied, the asymmetry may be reduced. The effect of rotation for the VB configuration has been investigated by Lan and Yen [36.60]. The effect of centrifugal pumping has also been discussed, where the conductivity of the crystal is important.

Flow suppression by static magnetic fields in the Bridgman configuration is even more effective, as could be clearly illustrated through numerical simulation. Again the gallium-doped germanium growth in a graphite ampoule discussed previously is used for illustration, with $Ra_T = 2.489 \times 10^8$. Figure 36.20 shows some flow structures and dopant fields for several axial and horizontal fields. For the case of axial magnetic fields (Fig. 36.20a-c), two lower cells induced by radial thermal gradients are stretched in the axial direction by the axial magnetic field. Because the flow tending to across the magnetic lines will be suppressed, the flow cells are elongated by the axial magnetic field. Interestingly, as the cell is stretched axially, the solute

penetrates more into the bulk melt. As will be shown shortly, for the case of $B_x = 0.5$ T, the bulk mixing is much enhanced. With the same magnetic strength, the horizontal field (Fig. 36.20d-f) is slightly more effective in suppressing the flow in terms of the maximum melt velocity. This is because the axial melt motion on the x - y plane is greatly suppressed; the axial melt motion is induced by radial thermal gradients. Although the flow on the plane (x - z plane) perpendicular to the magnetic direction is not suppressed effectively, the overall flow penetration into the upper bulk melt is significantly reduced. One can compare the dopant distributions in the x - z plane and the x - y plane to get a better idea of this. In addition, it is also clear that the solute mixing decreases monotonically with increasing magnetic field. Nevertheless, the flow and solute fields become asymmetric. One can further examine the solute concentration in the crystal ($C_c = KC$) at the interface; the solute field is stretched in the applied magnetic direction.

To illustrate the bulk solute mixing and the radial segregation, we have also calculated the effective segregation coefficient K_{eff} from the pseudo-steady-state results for various magnetic fields, $K_{\text{eff}} = \langle C \rangle / C_0$ [36.82, 83], where $\langle C \rangle$ is the average solute concentration in the melt. Figure 36.21a shows the effect of field strength (in terms of Ha number) on K_{eff} . As shown, the diffusion growth can be reached more quickly by applying a transversal field. However, for the axial field, there is a decrease in K_{eff} , i. e., better global dopant mixing, at

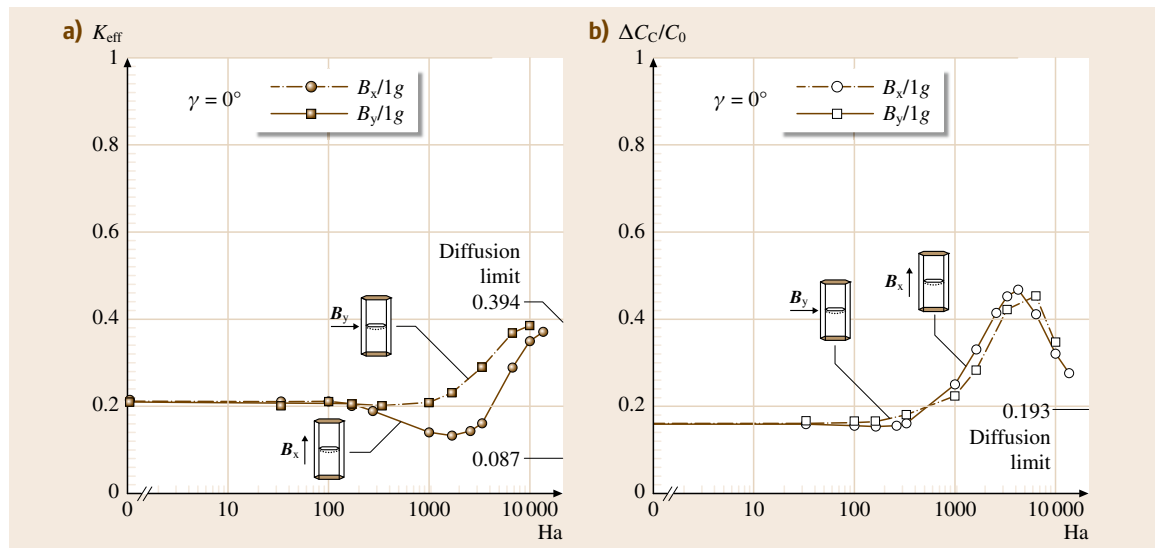


Fig. 36.21a,b Effect of axial and transversal magnetic fields: (a) effective segregation coefficient K_{eff} ; (b) radial dopant segregation

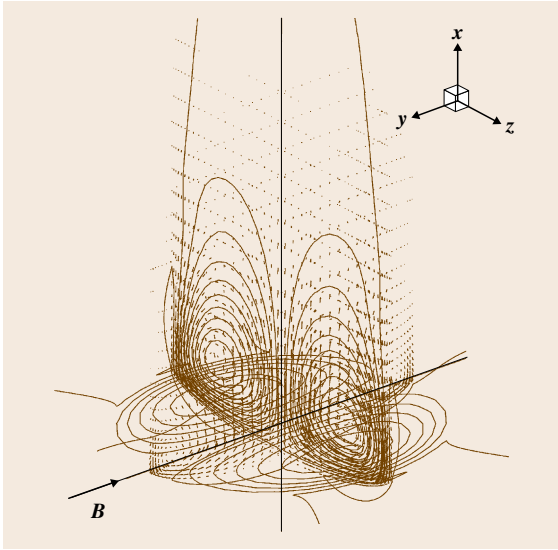


Fig. 36.22 Induced electrical potential and flow fields under a transversal magnetic field (1 T)

$Ha \approx 2000$. Again, as discussed regarding Fig. 36.20b, the flow cells are stretched axially by the axial field and penetrate deeply into the bulk melt, leading to better bulk dopant mixing. The amount of radial segregation by both types of fields in Fig. 36.21b remains similar; $\Delta C = C_{c\max} - C_{c\min}$ is the maximum dopant concentration difference at the interface.

Apparently, even though the magnetic field is quite effective in terms of flow damping, it is clear that to suppress the flow completely is also difficult. It should be noticed that the damping effect is effective only for the flow in the plane parallel to the magnetic field. The flow damping in the plane perpendicular to the magnetic field is much less effective. This could be explained by a buildup of the electric potential that reduces the induced electric current for the Lorentz force. Fig. 36.22 illustrates the flow and the induced electric potential fields due to the transversal field at 0.5 T. As shown, the potential gradients build up due to the thermal toroidal cells and the transversal fields. The potential contour surfaces look like a pair of kidneys (with one positive and one negative potential value), with a symmetry plane at $z = 0$. In other words, due to the potential gradients, the net currents, $\mathbf{j} = \sigma(-\nabla\Phi + \mathbf{v} \times \mathbf{e}_B)$, for the Lorentz force ($\mathbf{j} \times \mathbf{e}_B$) become smaller. Accordingly, the flow suppression becomes less effective. It can also be seen from the previous case for the FZ configuration that the flow perpendicular to the magnetic field cannot be suppressed effectively.

36.3.2 Rotation

Beside a static magnetic field, the use of rotation has been popular for crystal growth. There are a few ways of using rotation. The use of a centrifuge [36.51, 84], i. e., so-called centrifugal or high-gravity processing,

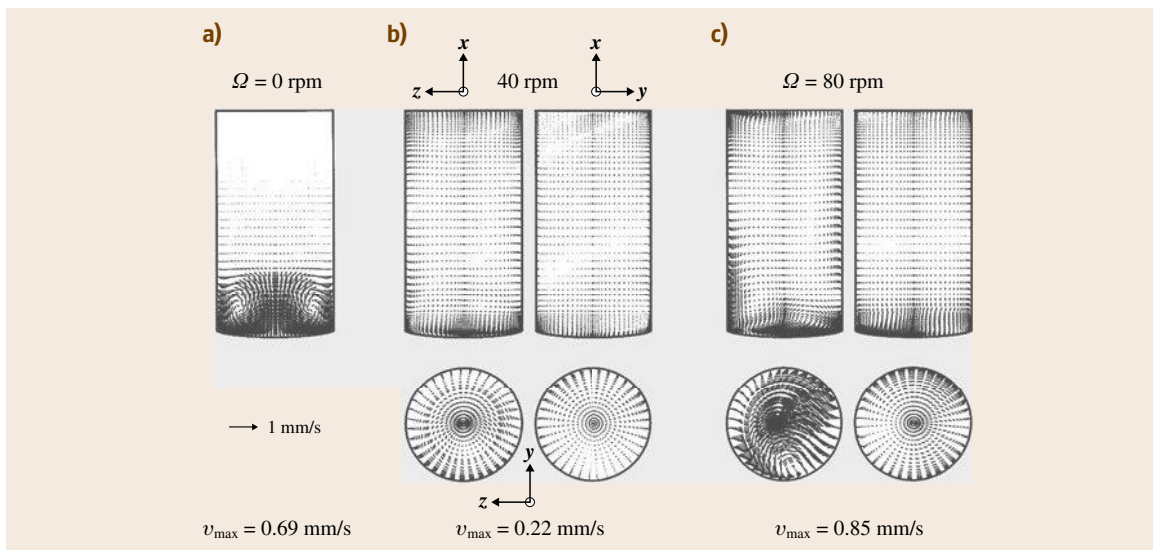


Fig. 36.23a–c Effect of free-swing rotation on the flow fields for a gradient freeze growth of GaAs: (a) 0 rpm; (b) 40 rpm; (c) 80 rpm

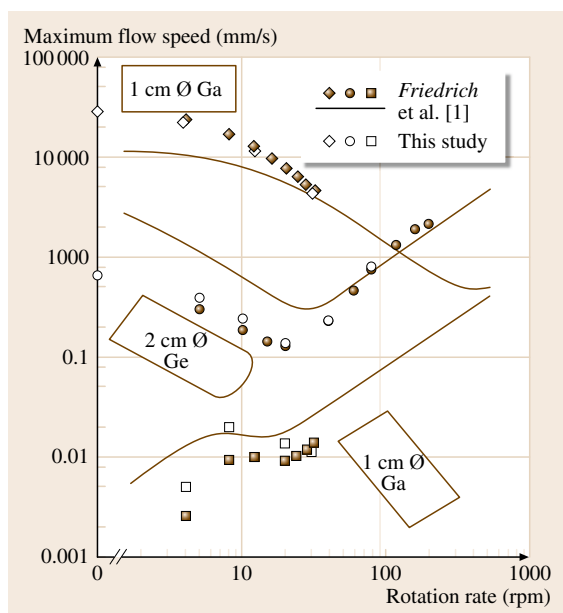


Fig. 36.24 Effect of rotation rate on the maximum melt velocity for various growth orientations

is particularly interesting. ACRT has also been widely used [36.34, 36–38]. The way of using the centrifuge in crystal growth has always been in the free-swinging configuration, in which the sample is placed at the end of a rotating arm. In such a case, the resultant acceleration is antiparallel to the axial thermal gradient, which is thus intuitively thermally stable. Accordingly, the convection can be suppressed at a certain rotation rate, or the so-called magic- g level [36.84], where the Coriolis force balances the gravitational acceleration. Beyond the magic- g level, the centrifugal acceleration becomes important and the centrifugal thermal convection increases. Figure 36.23 shows simulated flow patterns of Bridgman growth of germanium in a free-swing centrifuge at different rotation speed [36.51, 56]. For 0 rpm (Fig. 36.23a) the flow is axisymmetric and its structure is typical for the VB configuration, with a concave interface; the heating temperature profile is linear. At 40 rpm the flow near the growth interface is significantly suppressed by the Coriolis force and the flow structure is also changed dramatically. Although the averaged resultant gravity direction is still antiparallel to the growth axis, the centrifugal acceleration and the Coriolis force in the melt are asymmetric, leading to the 3-D flow. Due to the nonuniform forces, the global convection increases slightly away from the interface. As the rotation speed is further increased to 80 rpm, the centrifugal force becomes dominant and the convection increases, as can be seen from the larger velocity vectors. The flows in the x - y plane are also shown, but are in general featureless except for the flow near the growth interface.

We also present two flow patterns in the y - z plane, shown at the bottom of the figures for 40 and 80 rpm, respectively. One is at $x = 4.2$ cm and the other at 4.9 cm. The edge of the interface is at about $x = 4.0$ cm. As shown, near the interface the flow is mostly counterclockwise, but at some places the flow may be in the opposite direction. Interestingly, at 80 rpm, the flow pattern at $x = 4.9$ cm shows two cells with different flow directions. Therefore, the flow seen from the top does not have a well-defined structure. Closer to the growth interface, the counterclockwise flow seems to be clearer. Nevertheless, as the interface becomes flat, the flow pattern is also changed.

The maximum melt velocity as a function of rotation speed is further illustrated in Fig. 36.24 (open symbols), where the results of Friedrich et al. [36.51] (filled symbols and solid lines) are also included for comparison. We also performed calculations for gallium

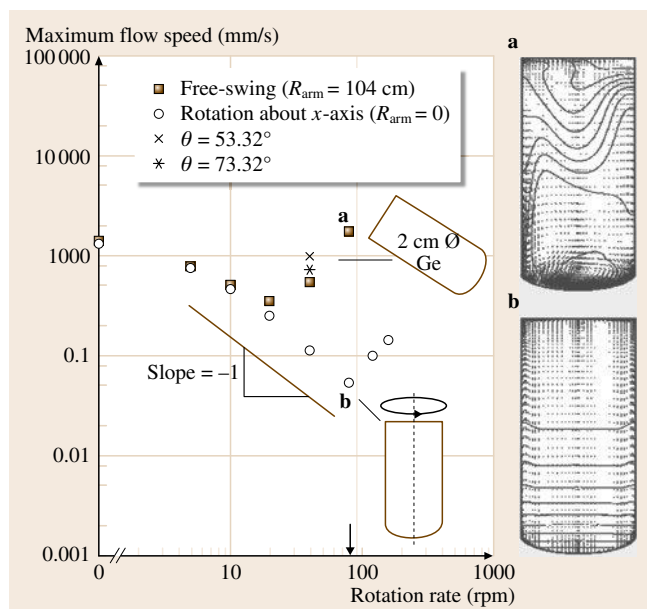


Fig. 36.25a,b Effect of rotation rate on the maximum melt velocity for rotation about the growth axis and the free-swing configuration. The flow and dopant fields for the free-swing (a) and rotation about growth axis (b) configurations are shown on the right

melt (in both the free-swing and horizontal configurations). The comparison with the previous study is also shown in Fig. 36.24. As shown, they are all in good agreement. The solid lines in Fig. 36.24 are from the scaling analysis of Friedrich et al. [36.51]. As shown for the free-swing case of germanium, there is a minimum of convection at about 20 rpm. This is supposed to be the so-called magic- g level, having the least axial dopant segregation. At this critical rotation rate, the Coriolis force balances the two gravitational forces. Beyond this value, the centrifugal force becomes dominant and enhances the convection.

Interestingly, in a recent numerical study by Lan and Tu [36.85], rotation about the growth axis could give a much better result. As shown in Fig. 36.25, the melt flow can be suppressed more effectively by this configuration, and its flow and dopant fields are still axisymmetric. On the contrary, the free-swing, or near, configuration at the magic- g level generates 3-D flows and severe dopant nonuniformity; a side view of the flow and dopant fields at 80 rpm is shown in Fig. 36.25. Lan [36.55] also performed a numerical simulation for a similar system and found that the flow direction (thermal convection) near the solidification front could be reversed at high speeds. As a result, an inversion of radial dopant distribution was found, clearly due to the centrifugal acceleration. In fact, in some of the earlier numerical studies of Bridgman crystal growth in a rotating ampoule [36.53, 54, 86], the centrifugal acceleration was ignored. As a result, the convection decreases monotonically with increasing rotation speed. This is correct only at low rotation rate (small Fr number). When the rotation speed is higher than the magic- g level, the convection is enhanced by centrifugal acceleration. Clearly, the centrifugal force is perpendicular to the axial gradient, and the buoyancy flow due to the centrifugal force is generated. This flow direction happens to be in the opposite direction to that near the interface due to the concave interface.

To validate the idea proposed by Lan and Tu [36.85], visualization experiments on a rotating table using SCN doped with a small amount of ethanol or acetone were performed by Lan et al. [36.57, 58]. Figure 36.26 shows the effect of rotation on the interface morphology after 3 h of growth (the growth rate was $2.5 \mu\text{m/s}$ with 0.07 wt % of acetone). Before the critical rotation speed was reached (Fig. 36.26a–c), the breakdown location from a planar to a cellular interface was a good indication of the acetone accumulation at the center of the interface; the initial stage of the growth also showed pit formation, as illustrated in Fig. 36.15a (60 min). Again,

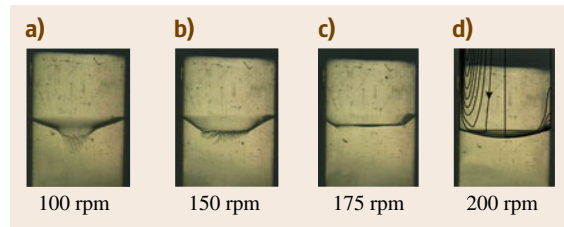


Fig. 36.26a–d Effect of rotation speed (about the growth axis) on interface morphology for the VB growth containing 0.007 wt % (after 3 h of crystal growth); the ampoule translation speed is $2.5 \mu\text{m/s}$; (a) 100 rpm; (b) 150 rpm; (c) 175 rpm; (d) 200 rpm

the morphological breakdown of the interface was due to constitutional supercooling. With a high enough ro-

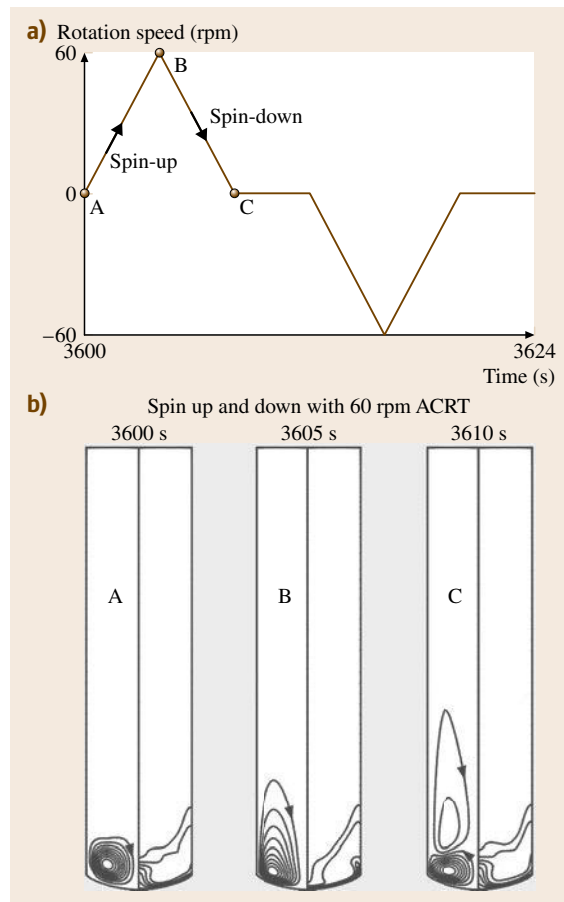


Fig. 36.27a,b Effect of ACRT on the flow and solute fields: (a) ACRT rotation cycle pattern; (b) instantaneous flow and solute fields at the moments indicated in (a)

tation speed, as shown in Fig. 36.26d at 200 rpm, the acetone was pushed outward to the edge of the interface, while the growth interface remained smooth. The calculated flow and solute fields near the growth interface are also illustrated in Fig. 36.26d. Therefore, by using an appropriate rotation rate, rotation about the growth axis is believed to be a useful approach for growth control, and this is not restricted to electrically conductive materials.

Beside steady rotation, ACRT is also a useful technique. Both the rotation cycle pattern and the period are critical to the flow control. Again, we take SCN as an example. The ACRT cycle pattern is shown in Fig. 36.27a, and some instantaneous flow patterns and acetone concentrations corresponding to the stages A, B, and C indicated in Fig. 36.27a are shown in Fig. 36.27b. The spin-up flows at 3600 and 3605 s near the interface are counterclockwise in direction. The spin-down flow at 3605 s is in the opposite flow direction. The acetone fields are significantly affected by the instantaneous flow as well. Similarly, the isotherms (not shown here) near the interface are found to be distorted toward the center of the interface. As a result,

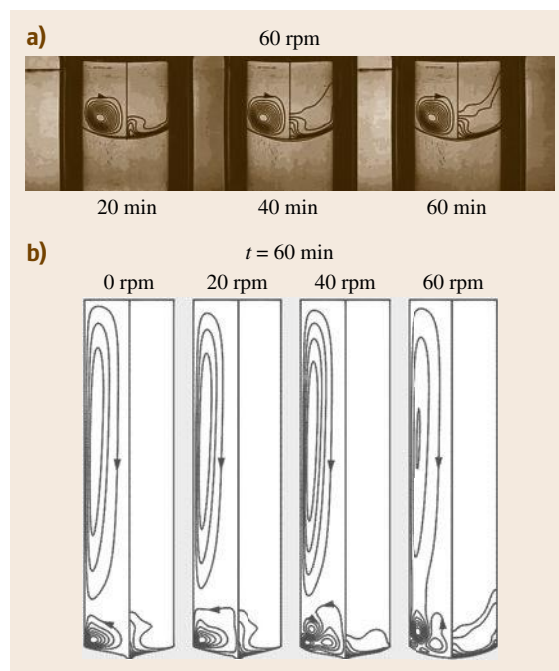


Fig. 36.28 (a) Flow and solute fields and the interface shapes at different growth periods for 60 rpm ACRT. (b) Average flow and solute fields and interface shapes for different maximum rotation magnitudes in ACRT

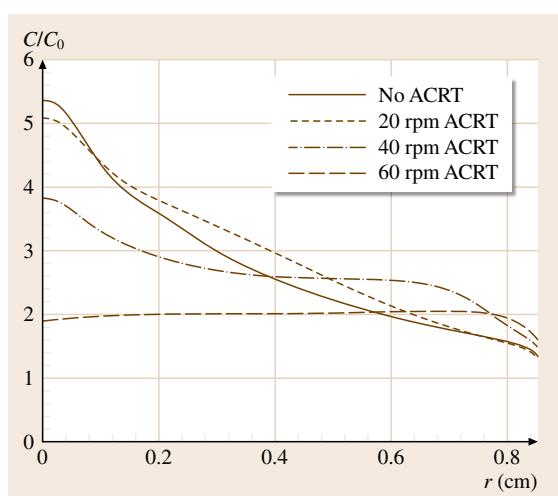


Fig. 36.29 Effect of the rotation amplitude in ACRT on the averaged radial acetone distribution

the interface becomes significantly concave at 60 rpm. The comparison of the calculated and observed interface shapes at different growth period for 60 rpm ACRT is shown in Fig. 36.28a. As shown, they are in good agreement. In addition, the interface when stationary is flat and it takes about 20 min to reach a steady shape.

The averaged flow and acetone fields for different ACRT amplitudes at 60 min after solidification are shown in Fig. 36.28b, from which the acetone concentration profiles at the interface are plotted in Fig. 36.29. As shown in Fig. 36.28b, it is clear that the original upper cell is not affected much by ACRT, except at 60 rpm. In other words, the solute mixing is confined to the region near the interface. However, at 60 rpm, the global mixing is slightly enhanced due to the connection of the lower and upper flow cells. Therefore, the maximum acetone concentration is significantly lower for 60 rpm. On the other hand, the lower cell is significantly affected by ACRT and this significantly affects the radial acetone segregation. As shown in Fig. 36.28, in general, as the rotation amplitude increases, except for 20 rpm, the acetone accumulation at the interface center decreases and the radial uniformity increases for the acetone concentration at the interface. From Fig. 36.29 it is thus clear that ACRT improves radial acetone uniformity and lowers its concentration due to improved mixing by ACRT. Particularly, at 60 rpm, the much slower acetone accumulation, as a result of better global mixing, reduces supercooling and enhances morphological stability.

36.3.3 Vibration

The ACRT mentioned previously usually requires a rotation cycle having a period long enough to develop Ekman flows. The Ekman time scale can be estimated by $R_c/\sqrt{\Omega\nu}$ [36.87], where R_c is the crystal radius, Ω is the rotation speed, and ν is the kinematic viscosity of the melt. For growth of SCN in small to medium-sized vertical Bridgman systems, the Ekman time scale is up to a few seconds. An alternative approach to applying ACRT is to use a cycle time that is much shorter than the Ekman time. This method is known as the angular vibration technique (AVT) [36.45]. In this technique the ampoule is vibrated at a frequency greater than 1 Hz in the rotational direction to generate a radial outward Schlichting flow near the growth front [36.45, 47].

Figure 36.30a,b shows some simulated results for AVT with different frequencies for SCN/acetone and SCN/salol, respectively. The observed interface shapes after 1 h growth are put together for comparison. As shown, the simulated interface concavity for both cases agrees quite well with the experiments. It should be noticed that the interface is at the upper boundary of the breakdown area. More importantly, from 0 to 5 Hz, the interface concavity decreases with frequency, while from 5 to 20 Hz the concavity increases with frequency. The reason is quite clear from the simulation. From 0 to 5 Hz, the flow above the interface is weakened by vibration because of the radial outward streaming flow induced by the angular vibration. As a result, the solute distribution becomes more uniform and this reduces the interface concavity caused by the local solute accumulation. On the other hand, from 5 to 20 Hz, the Schlichting flow becomes dominant. Since the flow is in the clockwise direction and the isotherms are distorted with the

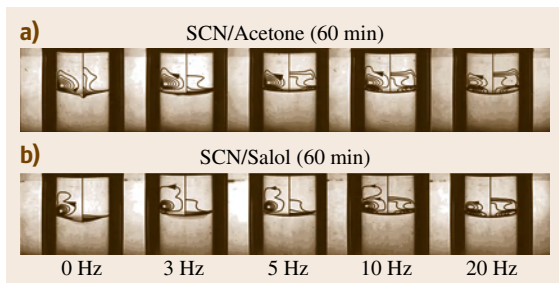


Fig. 36.30a,b Effect of angular vibration frequency on the flow and solute fields and the interface shape for VB growth of SCN: (a) containing 0.064 wt % acetone; (b) 0.15 wt % salol

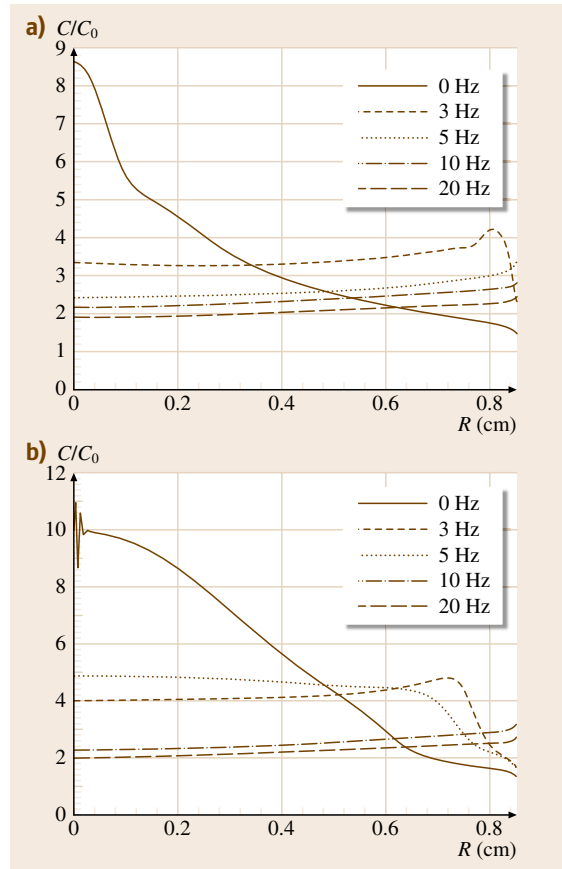


Fig. 36.31a,b Effect of angular vibration on the radial solute distributions for VB growth of SCN: (a) containing 0.064 wt % acetone; (b) 0.15 wt % salol

flow, the interface concavity increases with the vibration intensity (frequency).

The radial solute concentrations extracted from the simulated results in Fig. 36.30 are plotted in Fig. 36.31 for SCN/acetone and SCN/salol, respectively. As shown, for both cases, the radial segregation reverses from 0 to 3 Hz. This indicates that the Schlichting streaming flow is strong enough to overcome the buoyancy force and is able to push the solute from the interface center to the rim. From both Figs. 36.30 and 36.31, it is clear that, when the frequency is greater than 10 Hz, the Schlichting flow dominates and the solutal effect becomes insignificant, which can be seen from the solutal fields as well as the radial solute segregation profiles.

Besides angular vibration, vibration can also be applied axially. However, as discussed by Lan [36.68], the

thermovibration requires radial gradients, and the effect is not as significant as that by angular vibration. Further

discussion on flow control by vibration for crystal growth has been given by *Lyubimov et al.* [36.40].

36.4 Outlook

So far, we have discussed melt convection and its control for **ZM** and Bridgman bulk crystal growth through a few examples. As illustrated, the interface shape, which is a key factor for crystal quality, and the composition uniformity are significantly affected by the convective heat and mass transports due to the flow. We have introduced the basic flow structures through flow visualization experiments and numerical simulations. From these, one can better understand the interplay of the transport processes and the interface in crystal growth processes. The melt flow is affected by body forces, which can be the buoyancy (gravitational and centrifugal), Coriolis, and Lorentz forces. With a free surface, the thermocapillary force can also drive the melt flow. Thermal and solutal gradients are the sources for the buoyancy convection. Therefore, if these gradients are antiparallel to the gravitational or centrifugal acceleration, the convection can be minimized, and this is typically the case for vertical Bridgman growth in normal gravity or growth in a centrifuge under a free-swing configuration. In such a configuration, the flow is much more stable. Nevertheless, the residual flow can induce significant composition nonuniformity. The use of microgravity, magnetic fields, rotation or vibration is useful in manipulating the flow and thus improving crystal uniformity. Furthermore, suppressing the flow also helps improve axial composition uniformity, and a static magnetic field is particularly effective if the melt is electrically conductive.

Although we have not been able to discuss the flow and its control for Czochralski crystal growth, the concepts learned from previous examples are still useful. For example, similar to that in the **FZ** growth, in Czochralski growth of oxide crystals, the interface inversion can be easily controlled by crystal rotation [36.88]. However, the convection in the **CZ** configuration is much more complicated and hard to elucidate. For example, the buoyancy instability lead-

ing to spoke patterns at the melt surface [36.6, 89] and its coupling with rotation leading to baroclinic instability [36.90–92] are also typical in **CZ** oxide growth. The baroclinic instability has also been reported for **CZ** silicon growth [36.93]. Moreover, in large-scale **CZ** silicon growth, the flow is often turbulent. To suppress the turbulent flow, magnetic fields have been widely used in practice [36.27].

In contrast to flow damping, generating a favorable flow is also useful in bulk crystal growth. This includes the use of rotating and traveling magnetic fields [36.35, 94], as well as dynamic and alternating magnetic fields [36.4]. Recently, *Watanabe et al.* [36.30] proposed the electromagnetic Czochralski (**EMCZ**) method, in which the Lorentz force was used to generate a controlled melt flow. To generate this controlled melt flow, they created a Lorentz force by combining static magnetic fields with an electric current passing through the melt from a growing crystal. The controlled melt flow in the **EMCZ** method makes it easy to control the temperature distribution around the crystal, so that the growth interface can be better controlled [36.95]. Since the rotating flow washing over the crucible's inner surface can be adjusted, the oxygen content in the grown crystal can be controlled as well [36.32].

Over the years, extensive research has been applied to the investigation of melt flows, and many techniques have been proposed for their control. Still, with the increasing demands for crystal quality for advanced electronic and optoelectronic applications, this research will continue. Especially, their connection to as-grown defects and crystal quality still requires much more research to obtain deeper understanding. On the other hand, computer modeling has become an indispensable tool in the analysis and design of bulk crystal growth systems. Convection structures and their control in melt growth have been well stimulated and better understood [36.60, 96].

References

- 36.1 K. Kakimoto, M. Watanabe, M. Eguchi, T. Hibiya: Ordered structure in non-axisymmetric flow of silicon melt convection, *J. Cryst. Growth* **126**, 435–440 (1993)
- 36.2 K. Kakimoto, H. Ozoe: Oxygen distribution at a solid–liquid interface of silicon under transverse magnetic fields, *J. Cryst. Growth* **212**, 429–437 (2000)

- 36.3 I.Y. Evstratov, V.V. Kalaev, A.I. Zhmakin, Y.N. Makarov, A.G. Abramov, N.G. Ivanov, A.B. Korsakov, E.M. Smirnov, E. Dornberger, J. Virbulis, E. Tomzig, W. von Ammon: Numerical study of 3D unsteady melt convection during industrial-scale CZ Si-crystal growth, *J. Cryst. Growth* **237–239**, 1757–1761 (2002)
- 36.4 E. Tomzig, J. Virbulis, W. von Ammon, Y. Gelfgat, L. Gorbunov: Application of dynamic and combined magnetic fields in the 300mm silicon single-crystal growth, *Mater. Sci. Semicond. Process.* **5**, 347–351 (2003)
- 36.5 D.T.J. Hurle: *Crystal Pulling from the Melt* (Springer, Berlin Heidelberg 1993)
- 36.6 A.D.W. Jones: An experimental model of the flow in Czochralski growth, *J. Cryst. Growth* **61**, 235–244 (1983)
- 36.7 D.P. Lukanin, V.V. Kalaev, Y.N. Makarov, T. Wetzel, J. Virbulis, W. von Ammon: Advances in the simulation of heat transfer and prediction of the melt-crystal interface shape in silicon CZ growth, *J. Cryst. Growth* **266**, 20–27 (2004)
- 36.8 R.A. Brown: Theory of transport processes in single crystal growth from the melt, *AIChE J.* **34**, 881–911 (1989)
- 36.9 F. Dupret, N. van den Bogaert: Modeling Bridgman and Czochralski growth. In: *Handbook of Crystal Growth: Growth Mechanisms and Dynamics*, Vol.2b, ed. by D.T.J. Hurle (North-Holland, Amsterdam 1994)
- 36.10 G. Müller, A.G. Ostrogorsky: Convection in melt growth. In: *Handbook of Crystal Growth Growth Mechanisms and Dynamics*, Vol.2b, ed. by D.T.J. Hurle (North-Holland, Amsterdam 1994)
- 36.11 Y.F. Zou, G.-X. Wang, H. Zhang, V. Prasad: Mechanisms of thermo-solutal transport and segregation in high-pressure liquid-encapsulated Czochralski crystal growth, *J. Heat Transf.* **121**, 148–159 (1999)
- 36.12 C.W. Lan: Recent progress of crystal growth modeling and growth control, *Chem. Eng. Sci.* **59**, 1437–1457 (2004)
- 36.13 M.C. Liang, C.W. Lan: Three-dimensional thermocapillary and buoyancy convections and interface shape in horizontal Bridgman crystal growth, *J. Cryst. Growth* **180**, 587–596 (1997)
- 36.14 C.W. Lan, M.C. Su, M.C. Liang: A visualization and computational study of horizontal Bridgman crystal growth, *J. Cryst. Growth* **208**, 717–725 (1999)
- 36.15 C.W. Lan, J.H. Chian, T.Y. Wang: Interface control mechanisms in horizontal zone-melting with slow rotation, *J. Cryst. Growth* **218**, 115–124 (2000)
- 36.16 C.W. Lan: Heat Transfer, Fluid Flow, and Interface Shapes in Floating-Zone Crystal Growth. Ph.D. Thesis (University of Wisconsin, Madison 1991)
- 36.17 M. Levenstam, G. Amberg: Hydrodynamical instabilities of thermocapillary flow in a half-zone, *J. Fluid Mech.* **297**, 357–372 (1995)
- 36.18 P. Dold, A. Cröll, K.W. Benz: Floating-zone growth of silicon in magnetic fields. I. Weak static axial fields, *J. Cryst. Growth* **183**, 545–553 (1998)
- 36.19 S. Nakamura, T. Hibiya, K. Kakimoto, N. Imaishi, S. Nishizawa, A. Hirata, K. Mukai, S. Yoda, T.S. Morita: Temperature fluctuations of the Marangoni flow in a liquid bridge of molten silicon under microgravity on board the TR-IA-4 rocket, *J. Cryst. Growth* **186**, 85–94 (1998)
- 36.20 M. Prange, M. Wanschura, H.C. Kuhlmann, H.J. Rath: Linear stability of thermocapillary convection in cylindrical liquid bridges under axial magnetic fields, *J. Fluid Mech.* **394**, 281–302 (1999)
- 36.21 M. Schweizer, A. Croll, P. Dold, T. Kaiser, M. Lichtensteiger, K.W. Benz: Measurement of temperature fluctuations and microscopic growth rates in a silicon floating zone under microgravity, *J. Cryst. Growth* **203**, 500–510 (1999)
- 36.22 A. Mühlbauer, A. Muiznieks, J. Virbulis, A. Lüdge, H. Riemann: Interface shape, heat transfer and fluid flow in the floating zone growth of large silicon crystals with the needle-eye technique, *J. Cryst. Growth* **151**, 66–79 (1995)
- 36.23 G. Ratnieks, A. Muiznieks, A. Mühlbauer: Modelling of phase boundaries for large industrial FZ silicon crystal growth with the needle-eye technique, *J. Cryst. Growth* **255**, 227–240 (2003)
- 36.24 H.F. Utech, M.C. Flemming: Elimination of solute banding in indium antimonide crystals by growth in a magnetic field, *J. Appl. Phys.* **37**, 2021–2023 (1966)
- 36.25 K.M. Kim, P. Smetana: Oxygen segregation in CZ silicon crystal-growth on applying a high axial magnetic-field, *J. Electrochem. Soc.* **133**, 1682–1686 (1986)
- 36.26 K.M. Kim: Suppression of thermal convection by transverse magnetic field, *J. Electrochem. Soc.* **129**, 427–429 (1982)
- 36.27 D.T.J. Hurle, R.W. Series: Use of a magnetic field in melt growth. In: *Handbook of Crystal Growth*, Vol.2a, ed. by D.T.J. Hurle (North-Holland, Amsterdam 1994)
- 36.28 F.M. Herrmann, G. Müller: Growth of 20 mm diameter GaAs crystals by the floating-zone technique with controlled As-vapour pressure under microgravity, *J. Cryst. Growth* **156**, 350–360 (1995)
- 36.29 P. Dold, K.W. Benz: Rotating magnetic fields: fluid flow and crystal growth applications, *Prog. Cryst. Growth Charact. Mater.* **38**, 7–38 (1999)
- 36.30 M. Watanabe, M. Eguchi, T. Hibiya: Silicon crystal growth by the electromagnetic Czochralski (EMCZ) method, *Jpn. J. Appl. Phys.* **38**, L10–L13 (1999)
- 36.31 M. Watanabe, K.W. Yi, T. Hibiya, K. Kakimoto: Direct observation and numerical simulation of molten silicon flow during crystal growth under magnetic fields by x-ray radiography and large-scale computation, *Progr. Crystal Growth Charact. Mater.* **38**, 215–238 (1999)

- 36.32 M. Watanabe, M. Eguchi, W. Wang, T. Hibiya, S. Kuragaki: Controlling oxygen concentration and distribution in 200 mm diameter Si crystals using the electromagnetic Czochralski (EMCZ) method, *J. Cryst. Growth* **237–239**, 1657–1662 (2002)
- 36.33 A. Mitric, T. Duffar, C. Diaz-Guerra, V. Corregidor, L.C. Alves, C. Garnier, G. Vian: Growth of $\text{Ga}_{1-x}\text{In}_x\text{Sb}$ alloys by vertical Bridgman technique under alternating magnetic field, *J. Cryst. Growth* **287**, 224–229 (2006)
- 36.34 H.J. Scheel: Accelerated crucible rotation: a novel stirring technique in high-temperature solution growth, *J. Cryst. Growth* **13/14**, 560–565 (1971)
- 36.35 P. Capper, J.J. Gosney: Method of growing crystalline cadmium mercury telluride grown by method, UK Patent 2098879 (1982)
- 36.36 P. Capper, J.J.G. Gosney, C.L. Jones: Application of the accelerated crucible rotation technique to the Bridgman growth of $\text{Cd}_x\text{Hg}_{1-x}\text{Te}$: simulations and crystal growth, *J. Cryst. Growth* **70**, 356–364 (1984)
- 36.37 P. Capper, J.C. Brice, C.L. Jones, W.G. Coates, J.J.G. Gosney, C.K. Ard., I. Kenworthy: Interfaces and flow regimes in ACRT grown $\text{Cd}_x\text{Hg}_{1-x}\text{Te}$ crystals, *J. Cryst. Growth* **89**, 171–176 (1988)
- 36.38 W.G. Coates, P. Capper, C.L. Jones, J.J.G. Gosney, C.K. Ard, I. Kenworthy, A. Clark: Effect of ACRT rotation parameters on Bridgman grown $\text{Cd}_x\text{Hg}_{1-x}\text{Te}$ crystals, *J. Cryst. Growth* **94**, 959–966 (1989)
- 36.39 A.V. Anilkumar, R.N. Grugel, R.N. Shen, T.G. Wang: Control of thermocapillary convection in a liquid bridge by vibration, *J. Appl. Phys.* **73**, 4165–4170 (1993)
- 36.40 D.V. Lyubimov, T.P. Lyubimova, S. Meradji, B. Roux: Vibrational control of crystal growth from liquid phase, *J. Cryst. Growth* **180**, 648–659 (1997)
- 36.41 W.S. Liu, M.F. Wolf, D. Elwell, R.S. Feigelson: Low frequency vibrational stirring: a new method for radial mixing solutions and melts during growth, *J. Cryst. Growth* **82**, 589–597 (1987)
- 36.42 W. Yuan, M. Banan, L.L. Regel, W.R. Wilcox: The effect of vertical vibration of the ampoule on the direction solidification of InSb – GaSb alloy, *J. Cryst. Growth* **151**, 235–242 (1995)
- 36.43 V. Uspenski, J.J. Favier: High frequency vibration and natural convection in Bridgman-scheme crystal growth, *Int. J. Heat Mass Transf.* **37**, 691–698 (1994)
- 36.44 C.W. Lan: Effect of axisymmetric magnetic fields on heat flow and interface in floating-zone silicon crystal growth, *Model. Simul. Mater. Sci. Eng.* **6**, 423–445 (1998)
- 36.45 W.C. Yu, Z.B. Chen, W.T. Hsu, B. Roux, T.P. Lyubimova, C.W. Lan: Reversing radial segregation and suppressing morphological instability during Bridgman crystal growth by angular vibration, *J. Cryst. Growth* **271**, 474–480 (2004)
- 36.46 W.C. Yu, Z.B. Chen, W.T. Hsu: Effects of angular vibration on the flow, segregation, and interface morphology in vertical Bridgman crystal growth, *Int. J. Heat Mass Transf.* **50**, 58–66 (2007)
- 36.47 Y.C. Liu, W.C. Yu, B. Roux, T.P. Lyubimova, C.W. Lan: Thermal-solutal flows and segregation and their control by angular vibration in vertical Bridgman crystal growth, *Chem. Eng. Sci.* **61**, 7766–7773 (2006)
- 36.48 W.A. Arnold, W.R. Wilcox, F. Carlson, A. Chait, L.L. Regel: Transport modes during crystal growth in a centrifuge, *J. Cryst. Growth* **119**, 24–40 (1992)
- 36.49 G. Müller, G. Neumann, W. Weber: The growth of homogeneous semiconductor crystals in a centrifuge by the stabilizing influence of the Coriolis force, *J. Cryst. Growth* **119**, 8–23 (1992)
- 36.50 W.R. Wilcox, L.L. Regel: Influence of centrifugation on transport phenomena, 46th Int. Astronaut. Congr. (Oslo 1995)
- 36.51 J. Friedrich, J. Baumgartl, H.J. Leister, G. Müller: Experimental and theoretical analysis of convection and segregation in vertical Bridgman growth under high gravity on a centrifuge, *J. Cryst. Growth* **167**, 45–55 (1996)
- 36.52 W.R. Wilcox, L.L. Regel, W.A. Arnold: Convection and segregation during vertical Bridgman growth with centrifugation, *J. Cryst. Growth* **187**, 543–558 (1998)
- 36.53 C.W. Lan: Effects of ampoule rotation on flows and segregation in vertical Bridgman crystal growth, *J. Cryst. Growth* **197**, 983–991 (1999)
- 36.54 A. Yeckel, F.P. Doty, J.J. Derby: Effect of steady ampoule rotation on segregation in high-pressure vertical Bridgman growth of cadmium zinc telluride, *J. Cryst. Growth* **203**, 87–102 (1999)
- 36.55 C.W. Lan: Effects of centrifugal acceleration on flows and segregation in vertical Bridgman crystal growth, *J. Cryst. Growth* **229**, 595–600 (2001)
- 36.56 C.W. Lan, C.H. Chian: Three-dimensional simulation of Marangoni convection in floating-zone crystal growth, *J. Cryst. Growth* **230**, 172–180 (2001)
- 36.57 C.W. Lan, Y.W. Yang, C.Y. Tu: Reversing radial segregation and suppression morphological instability in directional solidification by rotation, *J. Cryst. Growth* **235**, 619–625 (2002)
- 36.58 C.W. Lan, Y.W. Yang, H.Z. Chen, I.F. Lee: Segregation and morphological instability due to double diffusive convection in rotational directional solidification, *Metal. Mater. Trans. A* **33**, 3011–3017 (2002)
- 36.59 A.F. Witt, H.C. Gatos, M. Lichtensteiger, M.C. Lavine, C.J. Herman: Crystal growth and steady state segregation under zero gravity, *J. Electrochem. Soc.* **122**, 276–283 (1975)
- 36.60 C.W. Lan, B.C. Yeh: Three-dimensional analysis of flow and segregation in vertical Bridgman crystal growth under a transversal magnetic field with ampoule rotation, *J. Cryst. Growth* **266**, 200–206 (2004)
- 36.61 M.C. Lan, M.C. Liang: A three-dimensional finite-volume/Newton method for thermal-capillary

- problems, *Int. J. Numer. Methods Eng.* **40**, 621–636 (1997)
- 36.62 C.W. Lan, M.C. Liang: Multigrid methods for incompressible heat flow problems with an unknown interface, *J. Comput. Phys.* **152**, 55–77 (1999)
- 36.63 A. Lipchin, R.A. Brown: Hybrid finite-volume/finite-element simulation of heat transfer and melt turbulence in Czochralski crystal growth of silicon, *J. Cryst. Growth* **216**, 192–203 (2000)
- 36.64 C.W. Lan, D.T. Yang: A numerical study on heat flow and interface of the vertical zone-melting crystal growth, *Numer. Heat Transf., Part A* **129**, 131–145 (1996)
- 36.65 C.W. Lan: Newton's method for solving heat transfer, fluid flow and interface shapes in a floating molten zone, *Int. J. Numer. Method Fluids* **19**, 41–65 (1994)
- 36.66 C.W. Lan, S. Kou: Heat-transfer, fluid-flow and interface shapes in floating-zone crystal-growth, *J. Cryst. Growth* **108**, 351–366 (1991)
- 36.67 S. Kou, C.W. Lan: Contactless heater floating zone refining and crystal growth, US Patent 5217565 (1993)
- 36.68 C.W. Lan: Heat transfer, fluid flow, and interface shapes in zone melting processing with induction heating, *J. Electrochem. Soc.* **145**, 3926–3935 (1998)
- 36.69 C.W. Lan, M.C. Liang: Three-dimensional simulation of vertical zone-melting crystal growth: Symmetry breaking to multiple states, *J. Cryst. Growth* **208**, 327–340 (2000)
- 36.70 C.W. Lan, C.H. Wang: Three-dimensional bifurcations of a two-phase Rayleigh–Benard problem in a cylinder, *Int. J. Heat Mass Transf.* **44**, 1823–1838 (2001)
- 36.71 J. Baumgartl, W. Budweiser, G. Müller, G. Neumann: Studies of buoyancy driven convection in a vertical cylinder with parabolic temperature profile, *J. Cryst. Growth* **97**, 9–17 (1989)
- 36.72 W.G. Pfann: *Zone Melting* (Wiley, New York 1958)
- 36.73 C.W. Lan: Effects of axial vibration on vertical zone-melting processing, *Int. J. Heat Mass Transf.* **43**, 1987–1997 (2000)
- 36.74 W.W. Mullins, R.F. Sekerka: The stability of a planar interface during solidification of a dilute binary alloy, *J. Appl. Phys.* **35**, 444–451 (1964)
- 36.75 K.H. Lie, J.T. Hsu, Y.D. Guo, T.P. Chen: Influence of through-window radiation on the horizontal Bridgman process for rectangular shaped GaAs crystals, *J. Cryst. Growth* **109**, 205–211 (1991)
- 36.76 P.M. Adornato, R.A. Brown: Convection and segregation in directional solidification of dilute and non-dilute binary alloy: effects of ampoule and furnace design, *J. Cryst. Growth* **80**, 155–190 (1987)
- 36.77 D. Hofmann, T. Jung, G. Müller: Growth of 2 inch Ge:Ga crystals by the dynamic vertical gradient freeze process and its numerical modeling including transient segregation, *J. Cryst. Growth* **128**, 213–218 (1992)
- 36.78 C.W. Lan, F.C. Chen: A finite-volume method for solute segregation in directional solidification and comparison with a finite-element method, *Comput. Methods Appl. Mech. Eng.* **31**, 191–207 (1996)
- 36.79 M.C. Liang, C.W. Lan: Three-dimensional convection and solute segregation in vertical Bridgman crystal growth, *J. Cryst. Growth* **167**, 320–332 (1996)
- 36.80 G.D. Robertson, D.J. O'Connor: Magnetic field effects on float-zone Si crystal growth: strong axial fields, *J. Cryst. Growth* **76**, 111–122 (1986)
- 36.81 C.W. Lan: Effect of axisymmetric magnetic fields on radial dopant segregation of floating-zone silicon growth in a mirror furnace, *J. Cryst. Growth* **169**, 269–278 (1996)
- 36.82 J.A. Burton, R.C. Prim, W.P. Slichter: The distribution of solute in crystals grown from the melt. Part I. Theoretical, *J. Chem. Phys.* **21**, 1987–1991 (1953)
- 36.83 D.H. Kim, P.M. Adornato, R.A. Brown: Effect of vertical magnetic field on convection and segregation in vertical Bridgman crystal growth, *J. Cryst. Growth* **89**, 339–356 (1988)
- 36.84 L.L. Rodot, M. Rodot, W.R. Wilcox: Material processing in high gravity—proceedings of the 1st international workshop on material processing in high gravity, *J. Cryst. Growth* **119**, R8 (1992)
- 36.85 C.W. Lan, C.Y. Tu: Three-dimensional analysis of heat flow, segregation, and interface shape of gradient-freeze growth in a centrifuge, *J. Cryst. Growth* **226**, 406–418 (2001)
- 36.86 M.R. Foster: The effect of rotation on vertical Bridgman growth at large Rayleigh number, *J. Fluid Mech.* **409**, 185–221 (2000)
- 36.87 A. Yeckel, J.J. Derby: Effect of accelerated crucible rotation on melt composition in high-pressure vertical Bridgman growth of cadmium zinc telluride, *J. Cryst. Growth* **209**, 734–750 (2000)
- 36.88 S.H. Lee, Y.J. Kim, S.H. Cho, E.P. Yoon: The influence of the Czochralski growth parameters on the growth of lithium niobate single crystals, *J. Cryst. Growth* **125**, 175–180 (1992)
- 36.89 Q. Xiao, J.J. Derby: Three-dimensional melt flows in Czochralski oxide growth: High-resolution, massively parallel, finite element computations, *J. Cryst. Growth* **152**, 169–181 (1995)
- 36.90 M.P. Gates, B. Cockayne: Purification of sodium tungstate, *Nature* **207**, 855 (1965)
- 36.91 C.D. Brandle: Flow transitions in Czochralski oxide melts, *J. Cryst. Growth* **57**, 65–70 (1982)
- 36.92 C.J. Jing, N. Imaishi, T. Sato, Y. Miyazawa: Three-dimensional numerical simulation of oxide melt flow in Czochralski configuration, *J. Cryst. Growth* **216**, 372–388 (2000)
- 36.93 M. Watanabe, M. Eguchi, K. Kakimoto: The baroclinic flow instability in rotating silicon melt, *J. Cryst. Growth* **128**, 288–292 (1993)
- 36.94 P. Dold, K.W. Benz: Modification of fluid flow and heat transport in vertical Bridgman configurations

by rotating magnetic fields, Cryst. Res. Technol. **32**, 51–60 (1997)

36.95 M. Watanabe, D. Vizman, J. Friedrich: Large modification of crystal–melt interface shape during Si crystal growth by using electromagnetic Czochral–

ski method (EMCZ), J. Cryst. Growth **292**, 252–256 (2006)

36.96 G. Müller, J. Friedrich: Challenges in modeling of bulk crystal growth, J. Cryst. Growth **266**, 1–19 (2004)

Vapor Growth of III Nitrides

Dang Cai, Lili Zheng, Hui Zhang

Good understanding of transport phenomena in vapor deposition systems is critical to fast and effective crystal growth system design. Transport phenomena are complicated and are related to operating conditions, such as temperature, velocity, pressure, and species concentration, and geometrical conditions, such as reactor geometry and source–substrate distance. Due to the limited in situ experimental monitoring, design and optimization of growth is mainly performed through semi-empirical and trial-and-error methods. Such an approach is only able to achieve improvement in the deposition sequence and cannot fulfill the increasingly stringent specifications required in industry. Numerical simulation has become a powerful alternative, as it is fast and easy to obtain critical information for the design and optimization of the growth system. The key challenge in vapor deposition modeling lies in developing an accurate simulation model of gas-phase and surface reactions, since very limited kinetic information is available in the literature. In this chapter, GaN thin-film growth by iodine vapor-phase epitaxy (IVPE) is used as an example to present important steps for system design and optimization by the numerical modeling approach. The advanced deposition model will be presented for multi-component fluid flow, homogeneous gas-phase reaction inside the reactor, heterogeneous surface reaction on the substrate surface, heat transfer, and species transport. Thermodynamic and kinetic analysis will be presented for gas-phase and surface reactions, together with a proposal for the reaction mechanism based on experiments. The prediction of deposition rates is presented. Finally, the surface evolution of film growth from vapor is analyzed for the case in which surface diffusion determines crystal grain size and morphology. Key control parameters for film instability are identified for quality improvement.

37.1 Overview of Vapor Growth of III Nitrides	1244
37.1.1 Various GaN/AlN Vapor-Growth Systems	1244
37.1.2 Modeling of AlN/GaN Vapor Deposition	1246
37.2 Mathematical Models for AlN/GaN Vapor Deposition	1248
37.2.1 Transport Equations	1248
37.2.2 Growth Kinetics	1249
37.2.3 Numerical Solution	1251
37.3 Characteristics of AlN/GaN Vapor Deposition	1251
37.3.1 Theoretical Analysis of Heat and Mass Transfer	1251
37.3.2 Thermodynamic and Kinetic Analysis of Chemical Reactions	1254
37.4 Modeling of GaN IVPE Growth – A Case Study	1258
37.4.1 Scaling Analysis	1258
37.4.2 Computational Issues	1258
37.4.3 Gas-Phase and Surface Reactions Analysis	1259
37.4.4 Geometrical and Operational Conditions Optimization	1264
37.4.5 Effect of Total Gas Flow Rate on Substrate Temperature	1264
37.4.6 Effect of Substrate Rotation on Deposition Rate and Deposition Uniformity	1269
37.4.7 Quasi-equilibrium Model for Deposition Rate Prediction	1270
37.4.8 Kinetic Deposition Model	1271
37.5 Surface Evolution of GaN/AlN Film Growth from Vapor	1274
37.6 Concluding Remarks	1275
References	1276

37.1 Overview of Vapor Growth of III Nitrides

Chemical vapor deposition (CVD) systems have been widely used to grow thin-film and bulk GaN/AlN crystals, which have a broad range of industrial applications, especially in the field of optoelectronics. For example, they have been used to manufacture optoelectronic devices such as light-emitting diodes (LEDs), laser diodes (LDs), and detectors [37.46, 47]. Due to their wide bandgap and high breakdown field, they have become important materials for high-temperature/high-power electronics [37.48–51].

In this section, GaN/AlN vapor-growth systems are briefly introduced first. An iodine vapor deposition system for GaN bulk growth is taken as an example to explain the modeling of comprehensive transport phe-

nomena and chemical reactions in crystal growth from vapor. Different numerical models, their limitations, and future trends are then reviewed. GaN thin-film growth by the iodine vapor-phase epitaxy (IVPE) technique is presented in this chapter as an example for discussion.

37.1.1 Various GaN/AlN Vapor-Growth Systems

For conventional semiconductors such as silicon, the Bridgman or Czochralski methods are usually used to grow ingots from a melt. However, the high vapor pressure of nitrogen at the melting temperature

Table 37.1 Research groups of GaN/AlN growth

Researchers	Growth techniques	Substrate	Growth conditions	Size	Maximum growth rate
Speck et al. (1997–2006)	MBE [37.1–8]	MOCVD GaN/sapphire template (0001)	GaN: 10 ^{−11} Torr 650–800 °C	–	750 nm/h
Karpov et al. (1998–2004)	HVPE [37.9, 10] Sublimation growth [37.11–15]	–	GaN: 760 Torr 900–1100 °C	–	GaN: 40 μm/h
		GaN:6H-SiC AlN:SiC	GaN: 1100–1250 °C AlN: 760 Torr; > 1700 °C	GaN: 15 × 15 × 0.5 mm ³ AlN: 10 × 10 × 0.08 mm ³	GaN: 1 mm/h AlN: 1 mm/h
Edgar et al. (2000–2006)	MOCVD [37.16–18] Sublimation growth [37.19–24]	GaN:3C-SiC/ Si(100)	GaN: 76 Torr; 950 °C	–	GaN: 1.5 μm/h
		AlN:6H-SiC	AlN: 100–800 Torr; 1700–1900 °C	–	AlN: 1 mm/h
Bliss et al. (1999–2005)	CVRP [37.25] IVPG [37.26, 27] HVTE [37.28, 29]	GaN:quartz	GaN: 1 atm; 900 °C	GaN: 9 × 2 mm ² × 100 μm	GaN: 25–100 μm/h
		GaN:sapphire	GaN: 75–750 Torr; 910–1025 °C	GaN: 32 μm thickness 0.05–1 mm diameter	GaN: 10–11 μm/h
		GaN:sapphire	AlN: 3.5–760 Torr, 1100–1300 °C	AlN: 75 μm thickness 2.5–5 mm diameter	AlN: 40 μm/h
Sitar (2001–2006)	IVPE [37.30] Sublimation growth [37.31–37]	GaN/AlN:sapphire	GaN: 400–800 Torr, 1000–1200 °C	GaN: 50 mm in diameter	GaN: 75 μm/h
		AlN/SiC	AlN: 500–900 Torr; 2200–2300 °C	AlN: 18 mm in diameter	AlN: 5 mm/h
Slack et al. (2000–2005)	Sublimation growth [37.38–40]	–	AlN: ≈ 1800 °C (Rojo et al., 2001)	AlN: 150 mm ²	AlN: 0.9 mm/h
Spencer et al. (1993–2004)	MOCVD [37.41–45]	4H-SiC or 6H-SiC	AlN: 10 Torr, 1160–1190 °C		AlN: 1 μm/h

of GaN/AlN hampers melt growth of the materials. Other growth techniques were developed to fabricate GaN/AlN thick films at lower temperature. Metalorganic chemical vapor deposition (MOCVD) [37.52–55] and molecular-beam epitaxy (MBE) [37.56–59] technologies have been extensively used to grow high-quality GaN/AlN films for device applications. Both methods, however, have the drawback of high cost. Owing to its cost effectiveness, the halide vapor-phase epitaxy (HVPE) technique has gained more attention for depositing thick AlN/GaN layers [37.25, 26, 60–63]. In HVPE, the growth rate is mainly determined by the mass flow rate of the reactants, since surface reactions inside the reactor are close to equilibrium due to high temperature on the substrate. High growth rates ($> 20 \mu\text{m/h}$) can easily be achieved in HVPE. Besides HVPE, sublimation methods [37.11, 31, 64–69] have also been used for AlN/GaN growth. In sublimation growth, high growth rate and good quality crystal are achieved [37.70] as the results of using high growth temperature ($\approx 2000^\circ\text{C}$) and employing the repeated seeding method [37.65]. Different AlN/GaN vapor-growth systems are summarized in Table 37.1.

HVPE method has been used to produce GaN thick films or ingots with growth rates of up to $50 \mu\text{m/h}$ and acceptable thickness uniformity [37.73, 74]. In the process, GaN is grown from the reactions of NH_3/GaCl or $\text{NH}_3/\text{GaCl}_3$. The use of HCl gas to obtain GaCl_x in the reactor creates contamination due to its corrosive effects. To prevent this problem, Bliss et al. [37.26, 27] developed an iodine vapor-phase epitaxy (IVPE) growth

system for the first time, in which solid iodine is vaporized and reacts with gallium source to form GaI_x . Using a horizontal IVPE system, GaN film at growth rate on the order of $10 \mu\text{m/h}$ has been obtained, and a low level of yellow luminescence of thus-produced GaN film has been observed, indicating the beneficial effect of reduced contamination in the process gases. To investigate the feasibility of higher GaN growth rate and better deposition quality, a vertical up-flow IVPE system for GaN has been designed and built at North Carolina State University to grow GaN thick film on a squared SiC substrate [37.30, 71, 72].

A schematic of the vertical reactor is presented in Fig. 37.1a. Iodine vapor is used to transport Ga from source to substrate to grow GaN. Ammonia gas is introduced to provide the nitrogen source for GaN growth. The reactor consists of four concentric tubes: furnace tube, reactor tube, outer silica tube, and inner silica tube. Iodine is carried by N_2 and H_2 gases flowing upwards through the inner silica. At the top of the inner silica tube is the gallium source within a BN holder. The iodine reacts with Ga melt to form GaI_x . A silica nozzle is placed above the gallium source to enhance Ga replacement. The gas flowing out of the silica nozzle is, therefore, a mixture of nitrogen, iodine, hydrogen, GaI_x , and gallium. N_2 gas flows between the inner and outer silica tubes to shield the Ga from the ammonia in the gas phase and enhance reactions on the substrate. Finally, the ammonia and nitrogen mixture flows through the space between the reactor tube and the outer silica tube. The system is heated by a re-

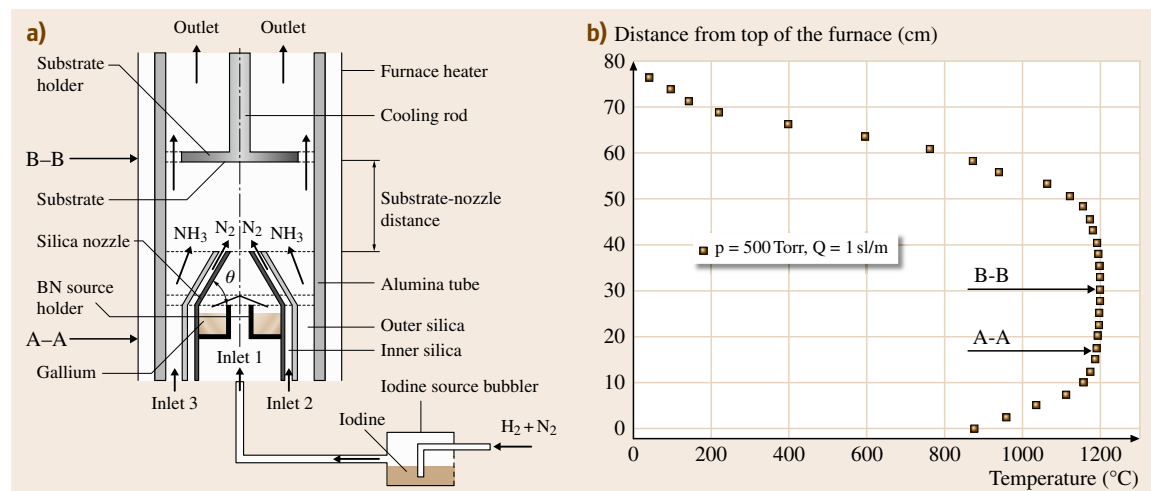


Fig. 37.1 (a) Schematic of the reaction chamber and (b) measured temperature profile from top to bottom along the furnace wall (after [37.30, 71, 72])

Table 37.2 List of simulation models for CVD process

Model	Length scale	Function
Ab initio methods, density function theory (DFT) [37.75, 76]	Electronic scale: 10^{-13} – 10^{-9} m	Calculate transition state structures, surface reaction pathways, etc.
Molecular dynamics [37.75, 77, 78]	Atomic scale: 10^{-10} – 10^{-6} m	Simulate the real atomic motion
Kinetic Monte Carlo (KMC) [37.79–84]	Microstructure scale: 10^{-9} – 10^{-5} m	Bridge atomic scale and microscopic scale in dynamic simulations
Level-sets or hybrid models [37.77, 85, 86]	Film scale 10^{-7} – 10^{-3} m	Simulate grain growth, recrystallization, etc.
Continuum models [37.87, 88]	Reactor scale 10^{-5} – 10 m	Simulate heat and mass transport in the CVD reactor

sistant heater. Calibration of the furnace temperature has been conducted under reactor pressure of 500 Torr and N₂ flow rate of 1 slm. Figure 37.1b shows the temperature profile measured by a thermocouple along the furnace wall. By setting the growth temperature at 1200 °C, the uniform-temperature zone achieved is about 37.1 cm. The gallium source (position A–A) and the substrate (position B–B) are both positioned in the uniform-temperature zone. The gallium source is positioned close to the bottom of the zone to ensure that the entire growth area is located in the uniform-temperature zone.

37.1.2 Modeling of AlN/GaN Vapor Deposition

Physics-based theoretical modeling and simulation are widely used for better understanding of growth mechanisms and identifying the important issues related to growth processes, material characteristics, and dopant incorporation. Advanced models integrating the key aspects in the growth process can help identify the material stability limits, define the ideal parametric window(s), and improve crystal perfection. In addition, the physical mechanisms that limit the growth process can be determined.

Vapor deposition modeling presents challenges in two aspects. First, except for some well-studied important reactions such as homogeneous and heterogeneous pyrolysis of silane, the kinetic data of gas-phase and surface reactions are limited. In this chapter, combined with experimental observation, theoretical methods are used to obtain insight into the chemical mechanisms and reaction kinetics of IVPE. Second, vapor deposition involves complex transport phenomena occurring on different length and time scales. The characteristic

length and time for atomic surface diffusion and relaxation and chemical reactions are approximately 10^{-10} m and 10^{-12} s, respectively. The typical reactor size is about 10^{-1} m and the deposition time is 10^3 – 10^5 s. A simulation model accurately describing both the microscale molecular motion and the macroscale species transport remains elusive due to the tremendous memory and extremely fast central processing unit (CPU) required for such a model. Currently, most numerical models have focused only on particular scales, either macroscale or microscale. Different models and their corresponding scales are summarized in Table 37.2.

Among the various models, only continuum models have been extensively used for vapor-growth reactor design. More advanced models tend to predict

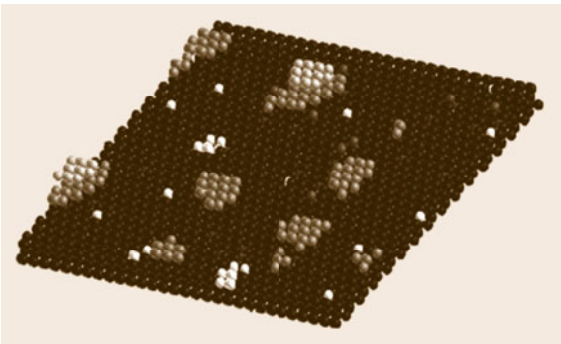


Fig. 37.2 Simulated Si(111) surface after deposition of 12% of C monolayer. Black and white spheres denote substrate atoms and vacancies created by thermal fluctuations, respectively. Dark grey spheres denote carbon atoms incorporated into the substrate. Atoms that are combined into the clusters are shown in light grey (lighter tint is used for upper cluster layers) (after CMS, with permission from Elsevier)

Table 37.3 Researchers and their models of GaN/AlN vapor growth

Authors	Models
Liu and Edgar [37.90,91]	AlN sublimation growth: 2-D thermal convection; Stefan flow model; surface kinetics model
Karpov et al. [37.9–11, 14,92,93]	GaN sublimation growth: 2-D gas dynamics and gaseous species model AlN sublimation growth: Diffusive and transport kinetic model GaN MBE growth: Surface kinetic model GaN HVPE growth: 3-D gas flow and growth rate model GaN MOCVD growth: Surface kinetic model
Safvi et al. [37.94,95]	GaN HVPE growth: Effects of flow rate, V/III ratio, and geometry on growth rate GaN MOCVD growth: Growth rate model
Theodoropoulos et al. [37.96]	GaN MOCVD growth: 2-D transport model; kinetic model
Aujol et al. [37.97]	GaN HVPE growth: Thermodynamic and kinetic model of growth rate
Dollet et al. [37.98]	AlN HVPE growth: Gas-phase and surface reaction analysis of AlCl_3 with NH_3 ; 2-D species transport modeling
Zhang et al. [37.29,37,72,99–101]	AlN sublimation growth: 2-D induction heating and vapor transport; growth morphology and growth rate prediction AlN HVPE growth: Gas-phase and surface reactions modeling; growth optimization of geometric and operating conditions GaN IVPE growth: Thermodynamic and kinetic analysis and modeling of gas-phase and surface reactions; growth rate prediction

the microstructure and properties of materials. Figure 37.2 shows three-dimensional SiC clusters on a Si substrate modeled by the kinetic Monte Carlo (KMC) method [37.89]. Parameters used in the KMC model are estimated from molecular-dynamics simulation and by fitting data to experimental transmission electron microscopy (TEM) results. Formation of three-dimensional clusters and pits in the surface is successfully demonstrated.

These models, however, are still under development and their use is still limited to research purposes because of numerous approximations used in the models. A model combining two or more of the aforementioned models is called a multiscale model. A few reviews of multiscale modeling of vapor deposition thin-film growth are available in the open literature [37.102–106]. It is difficult for this method to consider the effect of

feedback from the lower-scale model on the results of the upscale model [37.102].

Due to the lack of detailed reaction mechanisms, simulations of AlN/GaN vapor growth have been focused on the continuum modeling and solved gas flow, heat transfer, species diffusion, and chemical reactions in a vapor deposition reactor. A summary of the relevant research groups and their models is given in Table 37.3.

The continuum model will be used here to study the transport phenomena in the vapor-growth reactors for AlN/GaN growth. Gas-phase and surface reactions in the reactor will be studied and modeled to predict the species concentrations above the surface of the substrate accurately. The information obtained from the model will then be passed onto a surface deposition model to predict the AlN/GaN deposition rate distribution on the substrate.

37.2 Mathematical Models for AlN/GaN Vapor Deposition

Characteristics of chemical vapor deposition process are determined by gas hydrodynamics and chemical kinetics, which are affected by reactor geometry and process conditions. To reduce the complexity, the following assumptions are usually made for simulations:

1. The gas mixture is treated as a continuum
2. An ideal gas law is used
3. Gas flow is laminar
4. Gas mixture in the CVD reactor is radiative-transparent
5. Viscous dissipation of gas mixture is neglected.

It should be noted that these assumptions do not essentially limit the accuracy of the model for a wide range of vapor deposition process conditions.

37.2.1 Transport Equations

Based on these assumptions, the following equations can be used to describe the vapor deposition process:

$$\text{Continuity} \quad \frac{\partial \rho}{\partial t} + \nabla \cdot (\rho \mathbf{V}) = 0. \quad (37.1)$$

$$\text{Momentum} \quad \frac{\partial}{\partial t}(\rho \mathbf{V}) + \nabla \cdot (\rho \mathbf{V} \mathbf{V}) = -\nabla p + \rho \mathbf{g}. \quad (37.2)$$

$$\begin{aligned} \text{Energy} \quad \frac{\partial}{\partial t}(\rho h) + \nabla \cdot (\rho \mathbf{V} h) \\ = \nabla \cdot \left(\frac{k}{C_p} \nabla h \right) + \tau_{ij} \frac{\partial u_i}{\partial x_j} \\ + q_{\text{latent}}''' + q_{\text{radi}}''' + q_{\text{eddy}}''' \\ + q_{\text{react}}'''. \end{aligned} \quad (37.3)$$

Species transport (in mass fractions Y_i)

$$\frac{\partial}{\partial t}(\rho Y_i) + \nabla \cdot (\rho \mathbf{V} Y_i) = \nabla \cdot (\rho D \nabla Y_i) + \dot{w}_i. \quad (37.4)$$

$$\text{Ideal gas law} \quad p = \rho R T \sum_i \frac{Y_i}{W_i}. \quad (37.5)$$

Here ρ is the density, \mathbf{g} is the gravitational acceleration vector, \mathbf{V} is the gas velocity, p is the pressure, τ is the viscous stress tensor, T is the temperature, k is the thermal conductivity, D is the binary diffusion coefficient of reactant in carrier gas, Y_i is the mass fraction of species i , \dot{w}_i is the gas-phase reaction rate of species i , W_i is the molecular weight of species i , and R is the gas constant. $q_{\text{latent}}''' = \Delta H_{\text{vs}} \dot{M}_{\text{vs}}$ is the latent heat of phase change with ΔH_{vs} as the specific latent heat and \dot{M}_{vs} as

the deposition rate; q_{radi}''' is the heat exchange rate due to radiation; $q_{\text{eddy}}''' = \frac{1}{2} \sigma_c \omega A_0 A_0^*$ is the power dissipation rate due to an induced eddy current in the susceptor, in which σ_c is the electrical conductivity of the susceptor, ω is the alternate current frequency in the induction coils, and A_0 is the induced magnetic potential; q_{react}''' is the heat release or absorption due to reactions. Calculation of q_{radi}''' will be detailed in the radiative heat transfer model.

Critical Condition for Radiation Dominance. Radiative heat transfer becomes important when temperature is high ($\approx 1000^\circ\text{C}$). Heat fluxes transferred between the hot and cold walls due to heat conduction, convection, and radiation are calculated analytically to show the importance of radiative heat transfer. Considering a typical reactor for GaN/AlN growth, the distance between two walls d is chosen as 0.1016 m (5 inches), and the length of the walls is 0.508 m (20 inches). The radiative emissivity of the walls is 0.25 (if the reactor is made of metal). Temperature for the cold wall is 300 K, and the hot-wall temperature varies from 300 to 2000 K. Nitrogen is running between the walls with a Reynolds number of 100. Such a system can be approximated as a one-dimensional (1-D) problem for a first analysis. Heat flux due to heat conduction, convection, and radiation can then be calculated. The conductive heat flux is

$$q'' = k \frac{\Delta T}{d} = k \frac{T_{\text{hot}} - T_{\text{cold}}}{d}. \quad (37.6)$$

The convective heat flux is [37.107]

$$\begin{aligned} q'' &= h \Delta T = \frac{k \text{Nu}}{d} \Delta T \\ &= 0.46 k \text{Re}_f^{0.5} \text{Pr}_f^{0.43} \left(\frac{\text{Pr}_f}{\text{Pr}_w} \right)^{0.25} \\ &\quad \times \left(\frac{d}{L} \right)^{0.4} (T_{\text{hot}} - T_{\text{cold}}) / d. \end{aligned} \quad (37.7)$$

The radiative heat flux is

$$q'' = \frac{\sigma (T_{\text{hot}}^4 - T_{\text{cold}}^4)}{\frac{2(1-\varepsilon)}{\varepsilon} + \frac{1}{F_{\text{h-c}}}}, \quad (37.8)$$

where k is the thermal conductivity of nitrogen, h is the convective heat transfer of cold nitrogen on the hot wall surface, Nu is the Nusselt number, Re_f is the Reynolds number of the nitrogen flow, Pr_f is the Prandtl number with the reference temperature of the gas, Pr_w

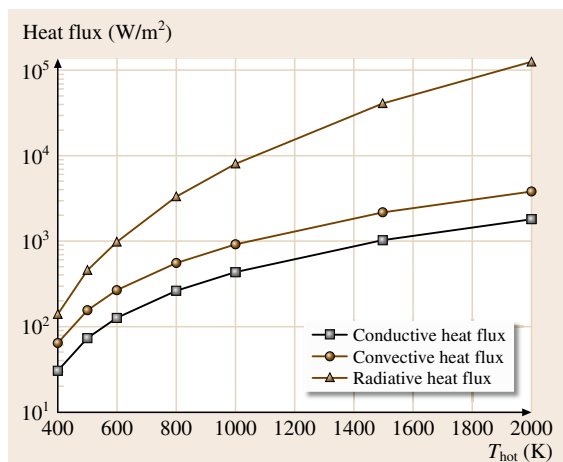


Fig. 37.3 Comparison of heat flux due to conduction, convection, and radiation

is the Prandtl number with the reference temperature of the hot wall, σ is the Stefan-Boltzmann constant ($5.672 \times 10^{-8} \text{ W/m}^2 \text{ K}^4$), and F_{h-c} is the view factor between the hot and cold walls, which is calculated to be 0.82. The heat fluxes calculated from (37.6–37.8) are summarized in Fig. 37.3.

It is found that the radiative heat flux is an order of magnitude higher than conduction or convection when the hot-wall temperature is 1000 K. Radiation will therefore be dominant when the temperature is higher than 1000 K.

The integro-differential radiative heat transfer equation for calculating the radiative heat flux can be written as follows

$$\frac{dI(\mathbf{r}, s)}{ds} = -(\alpha_a + \sigma_s)I(\mathbf{r}, s) + \alpha_a I_b(\mathbf{r}) + \frac{\sigma_s}{4\pi} \int_0^{4\pi} I(\mathbf{r}, s') \Phi(s \cdot s') d\Omega', \quad (37.9)$$

where I is the radiation intensity, \mathbf{r} is the position vector, s is the direction vector, α_a is the absorption coefficient, and σ_s is the scattering coefficient. I_b is the intensity of the black body, Φ is the phase function of energy transfer, and Ω' is the solid angle of the radiation beam.

Thermal radiation can be transported by the following four mechanisms:

1. From surface to surface
2. From surface to volume

3. From volume to surface
4. From volume to volume.

Equation (37.9) is applicable for an absorbing, emitting, and scattering medium. For some media, a simplified model can be used instead of (37.9). For inert gases, which can be considered as totally transparent to radiation, only surface-to-surface radiation should be considered instead of solving (37.9). It is therefore important to select an appropriate radiation model for a certain radiation problem to save calculation time. Optical thickness is usually used as a critical parameter to determine which radiation model should be used. The optical thickness L is defined as follows:

$$L = \alpha R, \quad (37.10)$$

where α is the absorption coefficient and R is the characteristic length of the medium. Some of the most commonly used radiation models and their applicable regimes in reference to optical thickness are summarized in Table 37.4, together with the radiation transportation considered in the model and the property of the radiative surface.

The first three models in Table 37.4 do not require (37.9) to be solved. The discrete ordinate model that needs to solve (37.9) will be used in most calculations presented in this chapter.

37.2.2 Growth Kinetics

In a typical chemical vapor deposition system, a thin film is formed by deposition from surface chemical reactions. Reactive molecules that contain atoms of the material to be deposited are introduced as a mixture of gases (usually diluted with inert carrier gases such as argon and nitrogen) into the temperature- and pressure-controlled environment of the reacting chamber in which the targets (wafers) on which deposition takes place are located. Heterogeneous reactions take place on the substrate. For example, in the case of epi-silicon production from silane pyrolysis, some initial portions of the overall reaction may occur in the gas phase, but the final stage of the reaction forming elemental silicon occurs on the wafer surface. Homogeneous gas-phase reactions may also occur, either preceding, parallel with, or in competition with the heterogeneous surface reactions. As the precursor gas approaches the wafer surface, it may react in the gas phase due to the high temperature ($> 400^\circ \text{C}$ at 1 atm). The reactions may form intermediate species, such as SiH_2 , or a series of reactions may proceed to form el-

Table 37.4 Summary of radiation models

Radiation model	Optical thickness (m)	Radiation transport mechanisms	Radiation surface
P1 model [37.108,109]	$L > 1$	(a) (c)	Gray
Rosseland model [37.108]	$L > 3$	(a) (c)	Gray
Surface-to-surface model [37.110]	$L \ll 1$	(c)	Gray
Discrete exchange factor model [37.111]	$0 < L < +\infty$	(a) (b) (c) (d)	Gray or non-gray
Discrete ordinate mode [37.112]	$0 < L < +\infty$	(a) (b) (c) (d)	Gray or non-gray
Discrete transfer model [37.113]	$0 < L < +\infty$	(a) (b) (c) (d)	Gray

emental silicon. In the latter case, silicon atoms may form small silicon grains in the gas phase. These grains then flow out of the system (sometimes causing an additional problem) or migrate to the wafer surface, where they form an irregular porous deposit, as well as loosely adherent particles. This gas-phase or homogeneous reaction does not form the dense uniform films needed for integrated-circuit applications and is usually suppressed in favor of heterogeneous reactions.

The sequence of events that may take place during vapor deposition process is shown in Fig. 37.4. It includes:

1. Reactant gases enter the reaction area inside the reactor by convection and diffusion.
2. Homogeneous gas-phase reactions take place, and intermediate species may be formed.
3. Species diffuse trough the boundary layer onto the surface.
4. Adsorption and diffusion of these species occur on the surface.
5. Heterogeneous reaction, nucleation, and lattice incorporation take place on the surface, leading to the formation of a solid film.

6. Desorption of adsorbed species away from the surface through the boundary layer.
7. Byproduct is transferred away from the reaction area in the reactor chamber.

Among these steps, the slowest will determine the deposition rate. A species concentration layer only exists when the reactor pressure is relatively high. If the gases pressure inside the reactor is low (i.e., in the range of mTorr), the species concentration boundary layer is no longer applicable, since the species transportation speed due to diffusion is much faster than the speed due to convection.

It is clear that many of the steps involved are transport related. The extent and role of the transport phenomena are, however, determined by process parameters such as substrate temperature, flow rate, and reactant partial pressure, as well as the chemistries involved. Depending on which of these is the dominant factor, the deposition process may be thermodynamical, diffusion or kinetics controlled.

In a thermodynamically controlled process, the mass transfer of species to and from the deposition zone is much slower than either mass transfer between the main flow and the substrate or mass transfer from the surface processes. Steps 1 and 7 are therefore rate-controlling steps. The process is assumed to proceed under thermodynamic equilibrium, and the deposition rate is generally determined by the equilibrium values of the partial pressures of species in the system.

In a diffusion- or mass-transport-controlled process, the rate-determining step is the diffusion or transport of the reactant gases to the substrate surface. The gas flow, heat transfer, and species diffusion play the dominant roles in determining the deposition characteristics.

Finally, in a kinetics-controlled system, the surface processes are not as fast as steps 1 and 7, nor 3 and 6. The rate-determining step is therefore the slowest of steps 4 and 5. Substrate temperature then

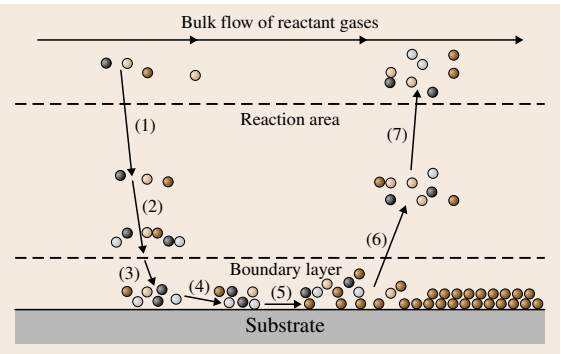


Fig. 37.4 Sequence of events during vapor deposition

plays an important role whereas the flow field has only a marginal influence. For some combinations of temperature and concentration, the homogeneous gas-phase reaction plays an important role and determines the deposition rate.

37.2.3 Numerical Solution

The simulation procedures are summarized as follows:

1. Grids are generated for calculating the electromagnetic field and heat and mass transfer, respectively.
2. The electromagnetic potentials are calculated. If the electrical/magnetic properties are dependent on temperature, this procedure will be repeated at a certain time interval until a steady-state temperature

distribution is achieved. The calculated power dissipation distribution will be used as a source term for the energy transport calculation.

3. Pressure and velocity fields are calculated.
4. Energy transport and radiative heat transfer equations are solved iteratively at each time step until convergence is reached.
5. The species transport equations are solved for every species.
6. The thermoelastic stress distribution in the crystal may be solved based on the temperature field obtained in the crystal.

It should be noted that, in the program, steps 2–5 have to be repeated in an iterative way until the final variable fields stabilize.

37.3 Characteristics of AlN/GaN Vapor Deposition

The purpose of studying the characteristics of transport phenomena in a CVD system is to achieve fast and effective design of CVD reactors. In this section GaN growth using an IVPE system will be used as an example to identify the critical transport parameters. Heat and mass transfer will be analyzed theoretically for the following two reasons. First, this can provide useful information for the control of the transport process. Second, analytical results can be used to validate the accuracy of numerical simulation. Gas-phase and surface reactions will be analyzed thermodynamically and kinetically. Based on this analysis, a model for gas-phase and surface reactions can be provided.

37.3.1 Theoretical Analysis of Heat and Mass Transfer

Important Dimensionless Groups

An order-of-magnitude study provides a basic understanding of the complex heat and mass transport phenomena in a vapor-growth system. The important dimensionless groups and their definitions are listed in Table 37.5.

For a typical vapor deposition system, the Reynolds number (Re) is usually in the range of 1–100, which corresponds to laminar flow. The Grashof number is usually kept below 10^5 . A large value of Gr indicates strong natural convection in the system, leading to a complicated flow pattern in the growth chamber. The ratio of the Grashof number Gr to the Reynolds number squared, Re^2 , is used to quantify whether heat

transfer is mainly controlled by natural or forced (inertia) convection. The regimes for natural convection, forced convection, and mixed convection are shown in Table 37.6 [37.114].

The value of the Prandtl number (Pr) is usually in the range of 0.1–0.7 for gas. The Schmidt number (Sc) is in the range of 0.01–1.0, depending strongly on pressure. At low pressure the species exhibits strong diffusion and the Schmidt number will lie towards the low end of this range. The thermal and mass Péclet numbers (Pe^T and Pe^M) are usually in the range of 1–100. The Damköhler numbers (Da) for the gas phase and surface are reaction dependent. A small value ($\ll 1$) means that the gas-phase or surface reactions are negligible. These dimensionless groups, along with the governing equations and appropriate boundary conditions, can provide the entire picture of a vapor deposition process.

Analytical Analysis of Gas Flow

For a conventional vapor-growth reactor, one of the key issues is maintaining a suitable growth environment near the substrate area, which is usually achieved by controlling the flow, temperature, and species concentration. To achieve an appropriate gas flow environment in the reactor, the relationship between the reactor diameter, total gas flux, and Reynolds number is studied. The Reynolds number can have the form

$$Re = \frac{\rho Q d}{A \mu}, \quad (37.11)$$

Table 37.5 Important dimensionless groups in a CVD reactor

Dimensionless group	Definition	Physical interpretation
Reynolds (Re)	$\frac{\rho_0 V_0 L_c}{\mu_0}$	Inertial forces/ viscous forces
Grashof (Gr)	$g \rho_0^2 L_c^2 (T_w) - \frac{T_{in}}{(\mu_0^2 T_0)^2}$	Buoyancy forces/ viscous forces
Prandtl (Pr)	$\frac{\mu_0 C_{p0}}{k_0}$	Momentum diffusivity/ thermal diffusivity
Schmidt (Sc)	$\frac{\mu_c}{\rho_0 D}$	Momentum diffusivity/ species diffusivity
Thermal Péclet (Pe ^T)	Re · Pr	Convective heat transfer/ conductive heat transfer
Mass Péclet (Pe ^M)	Re · Sc	Convective mass transfer/ conductive mass transfer
Gas-phase Damköhler (Da ^g)	$\frac{r_0^g L_c}{V_0}$	Typical time for flow/ typical gas-phase reaction time
Surface Damköhler (Da ^s)	$\frac{r_0^s L_c}{V_0}$	Typical time for flow/ typical surface reaction time

ρ_0 , μ_0 , k_0 , C_{p0} , D_0 , and β_0 are the values of ρ , μ , k , C_p , D , and β ($\beta = 1/T_0$ for ideal gas) at the average process gas temperature $T_0 = (T_w + T_{in})/2$, where T_w and T_{in} are the temperature on the reactor wall and the temperature at inlet of the reactor, respectively. L_c is the characteristic length, defined as the diameter of the reactor, V_0 is the characteristic velocity, defined as the inlet process gas velocity, r_0^g is the gas-phase reaction constant, and r_0^s is the surface reaction constant.

where ρ is the density of the mixing gases, Q is the total volume flow rate, d is the diameter of the reactor, A is the area, and μ is the dynamic viscosity. In the GaN growth system presented here, nitrogen and ammonia are the mass-dominant species in the reactor, and their molar ratio is assumed to be 1 : 1. The dynamic viscosities of nitrogen and ammonia are very similar. Sutherland’s law is used to determine the dynamic viscosity $\mu = (AT^{3/2})/(B + T)$, where the coefficients are

Table 37.6 Criteria for natural and forced convection

Convection	Gr/Re ² criteria
Natural	> 16
Mixed	∈ [0.3, 16]
Forced	∈ [0, 0.3]

$A = 1.461 \times 10^6$ and $B = 79.96$. The relationships of the volume flow rate and density with temperature and pressure can be expressed as $Q = Q_0(T/T_0)(P_0/P)$ and $\rho = \rho_0(T_0/T)(P/P_0)$, respectively.

Equation (37.11) can be rewritten as

$$\text{Re}_D = \frac{0.907 \rho_0 Q_0 (111.5 + T)}{dT^{3/2}}, \tag{37.12}$$

where ρ_0 (1.005 kg/m³) and Q_0 are the density and flow rate of the mixture under standard conditions (0 °C and 1 atm). For a typical vapor-growth system, the Reynolds number is usually kept in the range 1–100 to maintain a stable, laminar flow environment, which allows a sufficient residence time of reactants on the substrate for surface deposition. Figure 37.5 shows the relationship between the volume flow rate and reactor diameter at different Reynolds numbers. Experimental operating temperature of 1050 °C and pressure of 200 Torr are used in the calculation. It is shown in Fig. 37.5 that the total flow rate should be controlled at about 1 slm in order to achieve a Reynolds number of 10 for a reactor diameter of 5 cm.

Analytical Analysis of Heat and Mass Transfer

Besides forming a laminar-flow condition, a uniform species concentration distribution on the substrate is also preferred, as this is essential for deposition quality. Since gas flow is laminar in the reactor, there is no direct mixing. The transport of NH₃ from the near wall to the substrate surface will be mainly achieved through molecular diffusion in the stream. It is therefore impor-

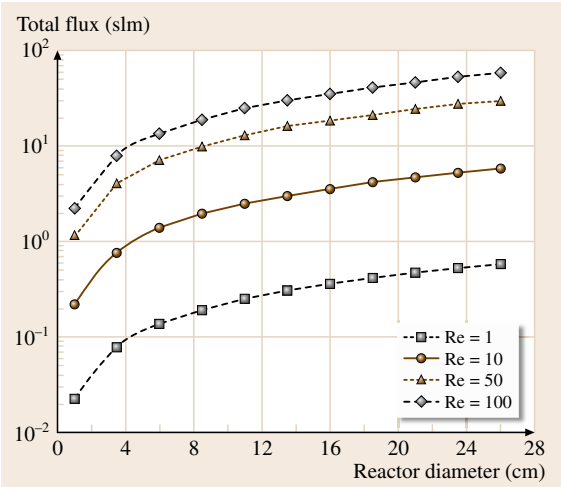


Fig. 37.5 Relationship between chamber diameter and gas flow rate with different Reynolds numbers

tant to allow ammonia sufficient time to diffuse to the substrate surface. This can be controlled by the total flow rate Q , the diameter of the reactor d , the diffusion coefficient of NH_3 in N_2 D , the distance between the substrate and the silica nozzle L , and the temperature and pressure in the reactor. To estimate the mixing time needed, or to select an appropriate substrate–nozzle distance (Fig. 37.1a) at different flow rates, it is assumed that the reactor tube is filled with N_2 with a flow rate of Q , and at $t = 0$ an NH_3 concentration of C_s is added on the wall of the reactor. According to [37.115], by solving the diffusion problem for a laminar flow in a rounded tube, the dimensionless average NH_3 concentration can be expressed as

$$\Delta' = \frac{C_s - C_{av}}{C_s - C_0} = 0.819e^{-14.6272\beta''} + 0.0976e^{-89.22\beta''} + 0.0135e^{-212.2\beta''} + \dots \quad (37.13)$$

where C_{av} is the averaged NH_3 concentration at a certain axial position X , $\beta'' = DX/4r^2\bar{U}_{av}$, D is the binary diffusion coefficient, r is the radius of the cylinder, \bar{U}_{av} is the averaged gas velocity, and $C_0 = 0$ is the initial concentration of NH_3 in the tube. According to (37.13), when $\beta'' = 0.2$, $C_{av} = 0.95C_s$ with an exposure length of X . It is therefore concluded that, when $\beta'' = 0.2$, different species have been mixed very well due to molecular diffusion. In the growth reactor, $\bar{U}_{av} = Q/A$, and the total exposure length, or the substrate–nozzle distance, is L . The following equation has to be satisfied for a uniform species concentration distribution on the substrate surface

$$\beta'' = 0.2 = DL \frac{A}{4r^2Q}. \quad (37.14)$$

The diffusion coefficient of NH_3 in N_2 can be estimated from [37.90]

$$D = D_0 \left(\frac{T}{T_0} \right)^n \left(\frac{P_0}{P} \right), \quad (37.15)$$

with $D_0 = 2.3 \times 10^{-5} \text{ m}^2/\text{s}$, $T_0 = 298 \text{ K}$, $P_0 = 760 \text{ Torr}$, and $n = 1.8$. The influence of species concentration on the diffusion coefficient can be neglected. Equation (37.14) can therefore be rewritten as

$$Q_0 = \frac{\pi D_0 \left(\frac{T}{T_0} \right)^{0.8}}{4\beta''} L, \quad (37.16)$$

with $\beta'' = 0.2$ and $T = 1373 \text{ K}$. The relationship between the standard flow rate and the substrate–nozzle distance is given by

$$Q_0 = 1.62L. \quad (37.17)$$

According to (37.17), when the total flow rate increases, a larger substrate–nozzle distance is required to achieve a uniform species concentration distribution on the substrate. For a typical flow rate of 3 slm, the corresponding substrate–nozzle distance for complete mixing is about 11.9 cm.

Temperature control in a vapor-growth system is critical. To obtain sufficiently high activation energy, reactants have to be preheated before they reach the substrate. The analytical method can be used to calculate the temperature variation of gases in the tubular reactor subject to different operational conditions such as flow rate, pressure and temperature of the furnace, and geometric conditions such as the diameter of the reactor. For the resistance heating system discussed here, we assume a constant temperature of $T_w = 1373 \text{ K}$ on the reactor wall and that the inlet gas mixture is composed of N_2 and NH_3 with a molar ratio of 1 : 1 and a temperature of $T_{in} = 300 \text{ K}$.

The analytical solution of the problem can be shown to be [37.116]

$$T_{m(x)} = T_w - (T_w - T_{in}) \exp\left(-\frac{\alpha \text{Nu}}{r^2 \bar{U}_{av}} z\right), \quad (37.18)$$

where $T_{m(x)}$ is the bulk longitudinal average temperature at position z , $\alpha_T = (k/(\rho C_p))$ is the thermal diffusion coefficient of the mixture, and $\text{Nu} = hd/k$ is the Nusselt number. Solution of the above problem gives $\text{Nu} = 3.66$. Since the average velocity in the round tube is $\bar{U}_{av} = Q/A = Q_0(T_{av}/T_0)(P_0/P)/(\pi r^2)$,

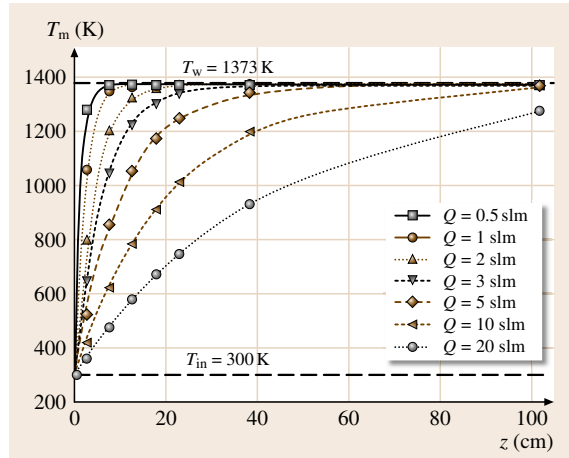


Fig. 37.6 Bulk mean temperature along the z -axis

(37.18) can be rewritten as

$$T_{m(z)} = T_w - (T_w - T_{in}) \times \exp\left(-\frac{3.66\alpha}{Q_0\left(\frac{T_{av}}{T_0}\right)\left(\frac{P_0}{P}\right)z}\right). \quad (37.19)$$

Equation (37.19) indicates that temperature is independent of the reactor diameter. With a reference pressure of 200 Torr and $T_{av} = 1000$ K, the thermal diffusion coefficients for NH_3 and N_2 are 8.49×10^{-4} and 6.22×10^{-4} m²/s, respectively. We used the averaged thermal diffusion of 7.36×10^{-4} m²/s in (37.19) to calculate the mean temperature distribution.

Figure 37.6 shows the bulk mean temperature variation along the z -axis, i.e., the distance from the gas inlet in the axial direction, under different total flow rates. The inlet gas temperature in this case is 300 K and the wall temperature is 1373 K (dashed line). For a reactor tube length of 102 cm, the gas can be heated to the reactor wall temperature at a flow rate of less than 10 slm. For a typical flow rate of 3.0 slm, the temperature of mixed gas can reach 1300 K within a heating length of 17.8 cm.

In experiments, a uniform temperature distribution on the substrate surface is essential to achieve uniform deposition and reduce the thermal stress in thick films. Numerical simulations can be conducted to optimize operating and geometric conditions.

37.3.2 Thermodynamic and Kinetic Analysis of Chemical Reactions

Thermodynamic and kinetic analysis of reactions allows us to predict the growth rate on the substrate in order to improve geometric and operating conditions for fast and uniform deposition. Assuming that reactions are in quasithermodynamic equilibrium, reaction constants can be calculated, and the quasi-equilibrium partial pressures of the reactants and products can be determined. The rate of the gas-phase reaction and surface deposition can be calculated. Thermodynamic calculations, however, only provide an upper limit. For the situation with high flow rate and limited reaction space, reactions in a vapor deposition system could be far from the equilibrium status. Kinetic analysis is therefore needed to understand how fast the reactions can proceed in the system. Kinetic data for gas-phase and surface reactions required for numerical simulations can be obtained from experiments. By solving the gas-phase reaction as a volumetric term and the surface reaction as a boundary condition on the substrate surface, the dis-

tributions of species concentration in the CVD reactor and the deposition rate on the substrate surface can be predicted under various operating conditions.

Thermodynamic Analysis of Gas-Phase and Surface Reactions

Prediction of Gas-Phase Reactions. Gas-phase reactions can be analyzed thermodynamically under different species concentrations, temperatures, and pressures. There are two methods to predict gas-phase reactions. In the first method, the species present in the system have to be specified, however no reaction step will be assigned. The concentration of difference species will be determined by minimizing the Gibbs energy of the system. In the second method, reaction steps will be assigned, and the reaction constants will be used to determine the reaction rates.

In the first method, chemical equilibrium is reached at constant temperature and pressure when the Gibbs energy is minimized. The Gibbs energy per unit mass of a system with N species can be written as follows:

$$G = \sum_{i=1}^N n_i \mu_i = \sum_{i=1}^N n_i \left(\mu_i^0 + RT \ln \frac{p_i}{p_0} \right), \quad (37.20)$$

where p_0 is the reference pressure of 1 atm and n_i is the molar amount of species i . Since the chemical potential μ_i is a function of temperature and pressure, the Gibbs energy is minimized at constant T and p for the correct combination of n_i . Elements must be conserved by the change in composition, which adds additional constraints to the system of the form

$$\sum_{i=1}^N a_{ji} n_i = b_j \quad \text{for } j = 1, \dots, M, \quad (37.21)$$

where a_{ji} is the number of atoms of element j in species i , M is the total number of elements in the system, and b_j is the total number of moles of element j per unit mass.

The composition that minimizes the Gibbs energy while satisfying the element balances is obtained by introducing the function

$$\Theta = G + \sum_{j=1}^M \lambda_j \left(\sum_{i=1}^N a_{ji} n_i - b_j \right). \quad (37.22)$$

The quantities λ_j are termed Lagrangian multipliers. Since (37.21) must be satisfied to conserve elements, the second term on the right-hand side vanishes and the composition that minimizes Θ also minimizes G .

Differentiating (37.22) with respect to n_i gives

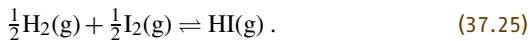
$$\frac{\partial \Theta}{\partial n_i} = \mu_i - \sum_{j=1}^M a_{ji} \lambda_j \quad \text{for } i = 1, \dots, N. \quad (37.23)$$

Differentiating (37.22) with respect to λ_i gives

$$\frac{\partial \Theta}{\partial \lambda_i} = b_i - \sum_{j=1}^N a_{ji} n_j \quad \text{for } i = 1, \dots, N. \quad (37.24)$$

Setting (37.23) and (37.24) to zero generates $N + M$ equations which can be solved to give the composition at the chemical equilibrium.

Thermodynamic gas-phase reaction analysis in the second method makes calculations simpler than in the first method since the reaction steps are already known. The gas-phase reaction from I_2 and H_2 will be used as an example to demonstrate the analysis process. The gas-phase reaction from I_2 and H_2 is given by



The following equations can be obtained according to the above reaction

$$K = \exp\left(-\frac{\Delta G_r^0}{RT}\right) = \frac{P_{\text{HI}}^e}{\sqrt{P_{\text{I}_2}^e P_{\text{H}_2}^e}}, \quad (37.26)$$

$$P_{\text{H}_2}^0 - P_{\text{H}_2}^e = P_{\text{I}_2}^0 - P_{\text{I}_2}^e, \quad (37.27)$$

$$P_{\text{HI}}^e = 2(P_{\text{I}_2}^0 - P_{\text{I}_2}^e), \quad (37.28)$$

where $P_{\text{H}_2}^0$ and $P_{\text{I}_2}^0$ are the initial partial pressures of H_2 and I_2 ; $P_{\text{H}_2}^e$, $P_{\text{I}_2}^e$, and P_{HI}^e are the equilibrium partial

pressures of H_2 , I_2 , and HI ; K is the reaction equilibrium constant; and ΔG_r^0 is the Gibbs free energy change. The dependence of ΔG_r^0 on temperature is shown in Fig. 37.7 [37.117, 118].

With the given reaction temperature, the Gibbs free energy change can be obtained. The equilibrium constant K can, therefore, be calculated. The reaction equilibrium pressure of each species in reaction (37.25) can be solved from (37.26–37.28) when the initial partial pressures of H_2 and I_2 are given.

Thermodynamic Prediction of Surface Reactions

Based on the assumption that surface kinetic limitations occur at the stage of species adsorption/absorption on the substrate surface, a quasithermodynamic approach can be used to predict the surface deposition rate with different sticking coefficients, growth temperatures, and gas supersaturations [37.92]. Surface deposition of GaN from GaI and NH_3 is used as an example to predict the deposition rate

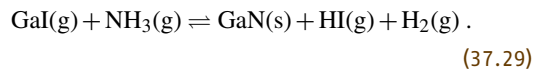


Figure 37.8a and b show a schematic of GaN deposition on the substrate surface and a typical reactant species concentration boundary layer formed on the substrate due to surface reactions, respectively. The concentration of GaI before the mixing gas reaches the substrate area is defined as $C = C_0$. Due to the surface reaction of GaI with NH_3 on the substrate, the GaI concentration decreases to $C = C_w$ on the substrate surface. The concentration boundary layer χ is defined as the distance where the GaI concentration changes from C_0 in the bulk gas to C_w on the substrate surface.

Species are transported to the concentration boundary layer by the concentration gradient due to the surface deposition. Assuming that the decrease of species concentration from the bulk gas to the substrate surface is linear with the concentration boundary-layer thickness, a species mass flux in the gas phase can be expressed as

$$J_i = D_i M_i \frac{\partial C}{\partial n} = \frac{D_i M_i}{\chi} (C_i^0 - C_i^w) \quad [\text{kg/m}^2 \text{s}], \quad (37.30)$$

where n is the coordinate normal to the substrate surface, C_i^0 and C_i^w are the species molar concentration in the bulk gas and on the deposition surface at the interface temperature, respectively, D_i is the

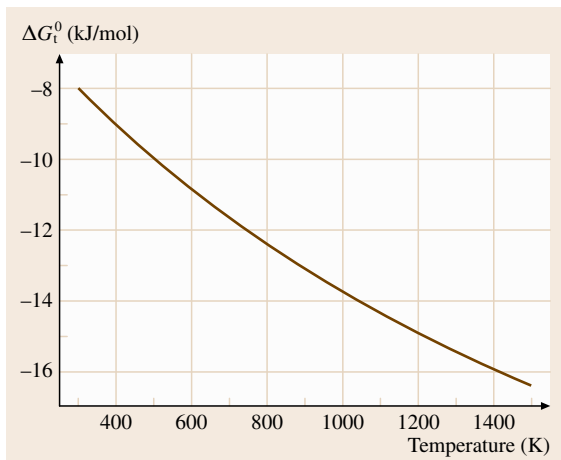


Fig. 37.7 Free energy change of reaction (37.25)

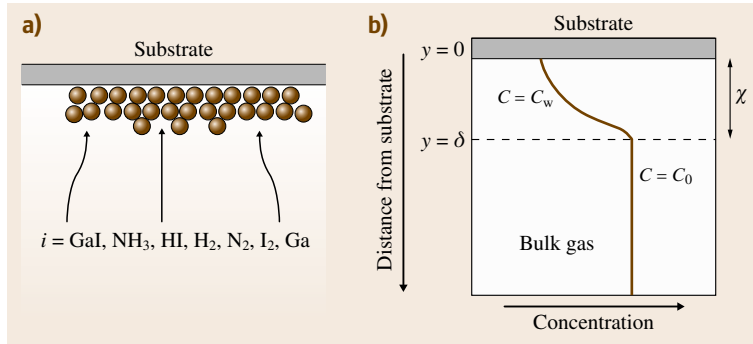


Fig. 37.8 (a) Schematic of GaN deposition on a substrate and (b) concentration boundary formed on the substrate due to surface reactions

diffusion coefficient of species i , M_i is the molecular weight of species i , and χ is the concentration boundary-layer thickness. According to the ideal gas law, $P_i = C_i RT$, (37.30) can be rewritten as

$$J_i = \frac{D_i M_i}{RT \chi} (P_i^0 - P_i^w) \quad [\text{kg/m}^2\text{s}], \quad (37.31)$$

where P_i^0 and P_i^w are the species partial pressure in the bulk gas and on the deposition surface. At the substrate surface, according to the Hertz–Knudsen law, the interface mass flux of species i is given by

$$J_i = \alpha_i \beta_i (P_i^w - P_i^e) \quad [\text{kg/m}^2\text{s}], \quad (37.32)$$

where α_i ($0 \leq \alpha_i \leq 1$) is the sticking coefficient of species i which accounts for all interfacial kinetics controlled by step and kink density, provided by two-dimensional nucleation and dislocations in the modern version of the Burton–Cabrera–Frank theory [37.119]; $\beta_i = \left(\frac{M_i}{2\pi RT}\right)^{1/2}$ is the thermodynamic factor of species i and P_i^e is the equilibrium partial pressure of species i on the substrate surface.

The following equations can be obtained according to reaction (37.29)

$$\frac{J_{\text{GaI}}}{M_{\text{GaI}}} = \frac{J_{\text{NH}_3}}{M_{\text{NH}_3}} = \frac{\rho_{\text{GaN}} V_g}{M_{\text{GaN}}}, \quad (37.33)$$

$$\frac{J_{\text{GaI}}}{M_{\text{GaI}}} + \frac{J_{\text{HI}}}{M_{\text{HI}}} = 0, \quad (37.34)$$

$$\frac{J_{\text{GaI}}}{M_{\text{GaI}}} + \frac{J_{\text{H}_2}}{M_{\text{H}_2}} = 0, \quad (37.35)$$

$$P_{\text{HI}}^e P_{\text{H}_2}^e = k_1 P_{\text{GaI}}^e P_{\text{NH}_3}^e. \quad (37.36)$$

According to (37.33–37.36), there are four unknowns, i.e., P_{HI}^e , P_{GaI}^e , $P_{\text{NH}_3}^e$, and $P_{\text{H}_2}^e$, and four equations. Given the wall partial pressures P_{HI}^w , P_{GaI}^w , $P_{\text{NH}_3}^w$, and $P_{\text{H}_2}^w$ and the sticking probabilities α_i of the species HI, GaI, NH₃, and H₂ on the substrate surface, the reaction rate can be obtained by solving (37.33–37.36).

Modeling of Gas-Phase

and Surface Reactions Kinetically

Kinetic Modeling of Gas-Phase Reactions. A system that has a number N_r of gas-phase reactions involving a number N_{sp} of species can be expressed in general notation by

$$\sum_{i=1}^{N_{\text{sp}}} v'_{ij} \Lambda_i = \sum_{i=1}^{N_{\text{sp}}} v''_{ij} \Lambda_i, \quad j = 1, \dots, N_r, \quad (37.37)$$

where v'_{ij} and v''_{ij} are the forward and backward stoichiometric coefficients for the i th species in the j th reaction. The above equation can be written more compactly as

$$\sum_{i=1}^{N_{\text{sp}}} v_{ij} \Lambda_i = 0, \quad j = 1, \dots, N_r, \quad (37.38)$$

where $v_{ij} = v'_{ij} - v''_{ij}$. The stoichiometric coefficients are integers for elementary reactions and are normally 0, 1 or 2.

The molar production rate of species i due to gas-phase reaction is

$$\omega_i^g = \sum_{j=1}^{N_r} v_{ij} q_j, \quad (37.39)$$

where q_j is the rate-of-progress variable for the j th reaction, which can be expressed as

$$q_j = (k_f)_j \prod_{i=1}^{N_{\text{sp}}} c_i^{a'_{ij}} - (k_r)_j \prod_{i=1}^{N_{\text{sp}}} c_i^{a''_{ij}}, \quad (37.40)$$

where $(k_f)_j$ and $(k_r)_j$ are temperature-dependent forward and backward rate coefficients, c_i is the concentration of species i , and a'_{ij} and a''_{ij} are constants. For elementary reactions which obey the mass action law,

Table 37.7 An example of gas species, adsorbed species, and bulk species

Surface reactions	Gas species	Adsorbed species	Deposited species
$\text{NH}_3(\text{g}) \rightleftharpoons \text{NH}_{3\text{ ads}}$	NH_3	$\text{NH}_{3\text{ ads}}$	None
$\text{GaI}(\text{g}) + \text{NH}_{3\text{ ads}} \rightleftharpoons \text{GaN}(\text{s}) + \text{HI}(\text{g}) + \text{H}_2$	$\text{GaI}, \text{HI}, \text{H}_2$	$\text{NH}_{3\text{ ads}}$	GaN
$\text{AlCl}_3(\text{g}) + \text{NH}_3(\text{g}) \rightleftharpoons \text{AlN}(\text{s}) + 3\text{HCl}(\text{g})$	$\text{AlCl}_3, \text{NH}_3, \text{HCl}$	None	AlN

$a'_{ij} = v'_{ij}$ and $a''_{ij} = v''_{ij}$, the rate coefficients are assumed to have the Arrhenius form of

$$k_f = AT^n \left(\frac{p}{p_{\text{atm}}} \right)^m e^{\frac{-E_{\text{af}}}{RT}}, \quad (37.41)$$

$$k_r = AT^n \left(\frac{p}{p_{\text{atm}}} \right)^m e^{\frac{-E_{\text{ar}}}{RT}}, \quad (37.42)$$

where A is pre-exponential constant, n indicates the temperature dependence, m is the exponent of the pressure dependency, E_{af} is the activation energy for the forward reaction, and E_{ar} is the activation energy for the backward reaction. All these constants are provided by experiment results of kinetic reaction analysis. For a typical reaction of the form



the rate of the gas-phase reaction is expressed as

$$\begin{aligned} \dot{\omega}_g &= A_p T^n \exp\left(\frac{-E_a}{RT}\right) \left(\frac{p}{p_{\text{atm}}}\right)^m \\ &\times C_A^\alpha C_B^\beta \quad [\text{kmol/m}^3\text{s}], \end{aligned} \quad (37.44)$$

where C_A and C_B are the molar concentrations of reactants A and B , and α and β are the concentration exponents of A and B , respectively.

Kinetic Modeling of Surface Reactions. The general form of the surface reaction is

$$\begin{aligned} &\sum_{i=1}^{N_g} a'_{ij} A_i + \sum_{i=1}^{N_s} b'_{ij} B_i(s) + \sum_{i=1}^{N_b} c'_{ij} C_i(b) \\ &= \sum_{i=1}^{N_g} a''_{ij} A_i + \sum_{i=1}^{N_s} b''_{ij} B_i(s) + \sum_{i=1}^{N_b} c''_{ij} C_i(b), \end{aligned} \quad (37.45)$$

where a_{ij} is the gas species stoichiometric, b_{ij} is the adsorbed species stoichiometric, c_{ij} is the bulk species stoichiometric, N_g is the total number of gas-phase species, N_s is the total number of adsorbed species, and N_b is the total number of deposited species. For example, in Table 37.7 the gas species, adsorbed species, and bulk species are listed for each reaction.

The surface reaction rate corresponding to reaction (37.43) may be expressed as

$$\begin{aligned} \dot{\omega}_{sj} &= k_{fj} \prod_{i=1}^{N_g} C_{aiw}^{a'_{ij}} \prod_{i=1}^{N_s} C_{bi(s)}^{b'_{ij}} \\ &- k_{rj} \prod_{i=1}^{N_g} C_{aiw}^{a''_{ij}} \prod_{i=1}^{N_s} C_{bi(s)}^{b''_{ij}} \quad [\text{kmol/m}^2\text{s}], \end{aligned} \quad (37.46)$$

where k_{fj} and k_{rj} are the forward and backward reaction rates, C_{aiw} is the gas-phase concentrations of species i at the surface and can be expressed as $C_{aiw} = \rho_w Y_i^w / M_i$, where ρ_w is the gas-phase mass density, Y_i^w is the gas-phase mass fraction of species i near the wall, and M_i is the molecular weight of gas species i . $C_{bi(s)}$ is the surface concentration of adsorbed species i and can be expressed as $C_{bi(s)} = \rho_s X_i$, where ρ_s is the surface site density and X_i is the surface site fraction of adsorbed species i . It is seen from (37.46) that the concentration dependence of bulk species is neglected.

Two different approaches, the sticking probability (or sticking coefficient) method and finite rate method, are usually used to estimate the surface reaction rate in numerical simulations. The sticking probability method calculates the reaction rate based on sticking probability and precursor thermal flux, while the finite rate chemistry uses the kinetic expression to evaluate the reaction rate. When using the sticking probability method, the surface rate becomes

$$\dot{\omega}_{sj} = \gamma_j J_A \prod_{i=1}^{N_s} (X_i)^{b'_{ij}}, \quad (37.47)$$

where the sticking probability γ_j is described in Arrhenius form as

$$\gamma_j = f(\theta^s)_j \exp\left(\frac{-E_{aj}(\theta^s)}{RT}\right), \quad (37.48)$$

where $f(\theta^s)_j$ is the function of the existing surface coverage of adsorbed species j , θ^s is the Langmuir definition of surface coverage of certain species or the fraction of sites that are occupied on the substrate surface, and E_{aj} is the activation energy for adsorption of species j .

The thermal flux of precursor A, or the incident rate of precursor onto the substrate (Hertz–Knudsen law) can be expressed as

$$J_A = \left(\frac{RT_w}{2\pi M_A} \right)^{1/2} C_{Aw}, \tag{37.49}$$

where C_{Aw} is the concentration of precursor A near the wall.

For the finite rate method, the surface reaction rate is the same as (37.47). For example, the reaction rate using a finite rate method can be expressed as

$$\dot{\omega}_s = A_s T^n \exp\left(\frac{-E_{as}}{RT}\right) \left(\frac{p}{p_{atm}}\right)^m C_{Aw}^\alpha C_{B(s)}^\beta, \tag{37.50}$$

for the reaction $\alpha A(g) + \beta B_{ads} \rightarrow C(s) + D(g)$.

37.4 Modeling of GaN IVPE Growth – A Case Study

In this section, a case study is presented to demonstrate optimization of GaN IVPE growth by computer modeling. In this example, the growth surface evolution mechanism will be presented and thermodynamic and kinetic methods will be used to predict gas-phase and surface reactions.

37.4.1 Scaling Analysis

The important dimensionless groups, their physical definitions, and calculated values in the vapor-growth reactor are listed in Table 37.8.

The values of ρ_0 , μ_0 , k_0 , C_{p0} , and D_0 obtained from simulation results are $6.0 \times 10^{-2} \text{ kg/m}^3$, $4.8 \times 10^{-5} \text{ kg s/m}$, $1.3 \times 10^{-1} \text{ J s/m K}$, 1740.0 J K/kg , and $1.0 \times 10^{-3} \text{ m}^2/\text{s}$, respectively. L_c is selected as the diameter of the furnace reactor, which is 0.045 m, and V_0 is estimated as 0.67 m/s based on a total flow rate of 3.0 slm and a reactor pressure of 200 Torr.

According to Table 37.8, the flow is mainly laminar in the reactor; heat and mass transfer due to convection is much more important than conduction/diffusion. The ratio of the Grashof number Gr to the Reynolds number squared Re^2 is used to examine whether heat

transfer is mainly controlled by natural convection, forced convection, or both. For the case presented here $Gr/Re^2 = 0.66$, indicating that both forced convection and natural convection are important.

37.4.2 Computational Issues

To better understand the heat and mass transfer inside the system, numerical simulations are conducted by solving governing equations together with gas-phase and surface reactions. A schematic of the system and numerical grids is shown in Fig. 37.9.

Since the growth cell is positioned in a uniform-temperature region, a constant temperature was as-

Table 37.8 Important dimensionless groups in the IVPE reactor

Dimensionless group	Value
Reynolds (Re)	37.7
Grashof (Gr)	940.0
Prandtl (Pr)	0.64
Schmidt (Sc)	0.73
Thermal Péclet (Pe ^T)	24.2
Mass Péclet (Pe ^M)	27.4
Gas-phase Damköhler (Da ^g)	–
Surface Damköhler (Da ^s)	–

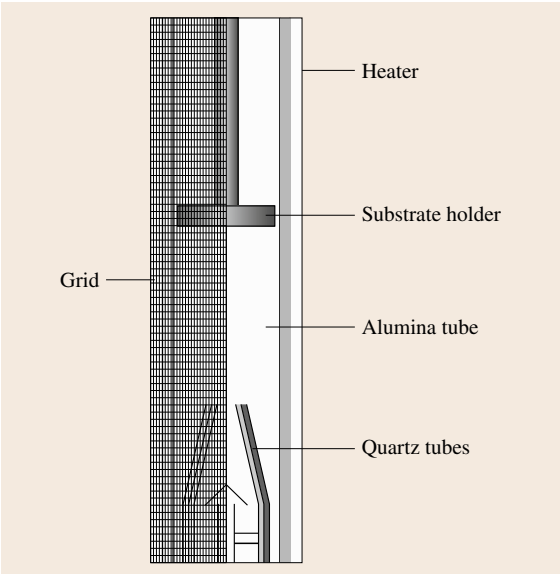


Fig. 37.9 Schematic of the calculation domain and grids for the system designed by Mecouch et al. [37.30, 72, 120]

Table 37.9

Wall on the graphite heater:	$V = 0, T = 1323 \text{ K}, \varepsilon = 1.0$
Wall on the substrate holder:	$V = 0, \varepsilon = 0.65$
Top surface of the gallium source:	$\dot{w}_{\text{gallium}} = \dot{w}_1, T = 700 \text{ K}, \varepsilon = 0.2;$
Wall on the surface of the substrate:	$V = 0, J_i = M_i \dot{w}_i^s, \varepsilon = 0.65$
Wall on the alumina tube:	$V = 0, \varepsilon = 0.7$
Wall on the quartz surface:	$V = 0, \varepsilon = 0.14$
Inlet carrier gas ($\text{NH}_3 + \text{N}_2$):	$V = V_1, T = 700 \text{ K}, P_{\text{in}} = P_{\text{ref}}, Y_{\text{NH}_3} = Y_1, Y_{\text{N}_2} = Y_2, \varepsilon = 0.15$
Inlet I_2, N_2 , and H_2 :	$V = V_2, T = 700 \text{ K}, P_{\text{in}} = P_{\text{ref}}, Y_{\text{I}_2} = Y_3, Y_{\text{N}_2} = Y_4, Y_{\text{H}_2} = Y_5, \varepsilon = 0.15$
Shield gas at the inlet (N_2):	$V = V_3, T = 700 \text{ K}, P_{\text{in}} = P_{\text{ref}}, Y_{\text{N}_2} = Y_6, \varepsilon = 0.15$
Outlet:	$T = 300 \text{ K}, P_{\text{out}} = P_{\text{ref}}, \varepsilon = 1.0$

signed to the surface of the furnace wall with emissivity of unity. The experimentally measured weight losses of iodine and Ga sources are converted to mass flow rates that are used as inlet gas flow rates. The surface reaction rate \dot{w}_i^s after being converted to the mass flux J_i can be incorporated into the simulation as boundary conditions on the substrate surface.

General boundary conditions are prescribed as in Table 37.9.

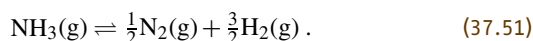
37.4.3 Gas-Phase and Surface Reactions Analysis

Gas-Phase Reaction Analysis

In the GaN epitaxy growth system, the carrier gas mixture of N_2 and H_2 enters the I_2 source bubbler, where liquid I_2 , heated by a jacket heater, vaporizes and will be transported to the reactor chamber by the carrier gas. H_2 and I_2 react to form HI. The gas mixture flowing over the gallium source surface includes $\text{N}_2, \text{H}_2, \text{I}_2$, and HI. Both I_2 and HI may react with Ga to form GaI_x , with $x = 1$ or 3. From [37.26], it is deduced that GaI is the main product of the reactions between gallium and iodine gas in the reactor chamber being studied. It is found that GaI_3 is more stable thermodynamically at the operational conditions of $T = 1323 \text{ K}$ and $P = 200 \text{ Torr}$. On the substrate surface, NH_3 will be adsorbed and cracked to form activated nitrogen atoms that will react with GaI_x to grow GaN [37.121]. It is important to control the concentrations of NH_3 and GaI_x achieved on the substrate surface in experiments. Gas-phase species

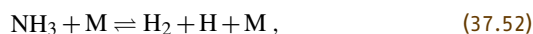
reaching the substrate area include $\text{NH}_3, \text{HI}, \text{H}_2, \text{N}_2, \text{GaI}, \text{GaI}_3$, and maybe I_2 and Ga. The gas pathways can be found in Fig. 37.1a.

Due to the high-temperature environment in the growth reactor ammonia may decompose to nitrogen and hydrogen gases before it reaches the substrate area. This will reduce the amount of ammonia reaching the substrate. The global equation for the ammonia gas phase decomposition can be expressed as



This reaction is a mildly endothermic process ($\Delta H = 46 \text{ kJ/mol}$). Thermodynamically, almost all NH_3 is decomposed into N_2 and H_2 at temperature higher than 300°C . In the actual experiments, the NH_3 is decomposed slowly and the decomposition rate strongly depends on the growth conditions and the equipment. This reaction is, in fact, far from the kinetic equilibrium state.

The Damköhler number of the gas phase is calculated for the ammonia gas-phase decomposition reaction to determine its importance under the aforementioned operational conditions. The physical interpretation of the gas-phase Damköhler number is the ratio of the gas-phase reaction time to the gas flow residence time. The gas flow residence time can be estimated from $t_F = L_F / \bar{U}_{\text{av}}$, where L_F is the distance between the gas inlet and the substrate, which is about 0.16 m . The averaged velocity is about 0.67 m/s with a typical flow rate of 3.0 slm under a pressure of 200 Torr and a furnace wall temperature of 1323 K . The fluid flow residence time is about 0.24 s . The comprehensive mechanism for NH_3 pyrolysis can be found in [37.122]. The controlling step of the reactions is found to be



where M is the third-party molecule that serves as a catalyst. Reaction (37.52) is a second-order reaction with a reaction coefficient of $k_r = A \exp(-E_a/RT)$ and a reaction rate of $\dot{w}_g = k_r[\text{NH}_3][\text{M}]$, where the pre-exponential coefficient (molecular collision frequency) A is 2.2×10^{10} , and the reaction activation energy E_a is $3.93 \times 10^5 \text{ J/mol}$ [37.122]. $k_r = 2.55 \times 10^{-5} \text{ m}^3/(\text{mol s})$ is calculated with the reference temperature of 1323 K . The third-party molecular concentration at temperature of 1323 K and pressure of 200 Torr is 1.17 mol/m^3 , if the molar ratio of the mixing gas of NH_3 and N_2 is assumed to be $1 : 1$. The reaction rate is calculated as $r_0^g = k_r[\text{M}] = 2.98 \times 10^{-5} \text{ s}^{-1}$. The gas-phase Damköhler number (Da) for ammonia pyrolysis is 7.12×10^{-6} ,

which is much smaller than 1. Based on this analysis, it can be concluded that ammonia gas-phase decomposition can be neglected under the discussed operational conditions. It should be noted that ammonia also tends to decompose on reactive solid surfaces. The heterogeneous reaction rate under the current operating conditions is, however, expected to be very low according to [37.9].

As well as the substrate surface, ammonia may also react with GaI_x in the gas phase. To reduce gas-phase reactions between NH_3 and GaI_x before their mixture reaches the substrate, shield gas N_2 runs between the inner and outer silica nozzle to prevent mixing in the area above the silica nozzle (Fig. 37.1a) in order to increase the NH_3 and GaI_x concentrations on the substrate surface. The gas-phase reactions of NH_3 and GaI_x are expected to be weak and can therefore be neglected due to the effect of the shield gas and short residence time of the reacting gases.

If the equilibrium vapor pressure of iodine has been reached in the iodine source bubbler, the molar concentration fraction of iodine $[\text{I}_2]$ can be written as

$$[\text{I}_2] = \frac{P_{\text{I}_2}^0}{P_{\text{total}}} . \quad (37.53)$$

The total mass reduction rate of I_2 in the source can be expressed as

$$\dot{m}_{\text{I}_2} = \rho_{\text{I}_2} Q_{\text{total}} \frac{P_{\text{I}_2}^0}{P_{\text{total}}} , \quad (37.54)$$

where Q_{total} is the total flow rate of the carrier gas.

The gas-phase reaction in the iodine source bubbler has been given in reaction (37.25). No reaction between N_2 and other gases are expected. Before reaction (37.25) starts, the initial partial pressures of H_2 , I_2 , HI , and N_2 are $P_{\text{H}_2}^0$, $P_{\text{I}_2}^0$, P_{HI}^0 , and $P_{\text{N}_2}^0$, respectively, where the initial partial pressure of HI obviously equals zero. When the reaction equilibrium is reached in the source bubbler, the equilibrium partial pressure of the species can be expressed as $P_{\text{H}_2}^e$, $P_{\text{I}_2}^e$, P_{HI}^e , and $P_{\text{N}_2}^e$. The total pressure inside the bubbler is maintained at 1 atm and remains unchanged since the partial pressure reduction of H_2 and I_2 due to reaction equals the partial pressure production of HI in reaction (37.25). The partial pressure of N_2 will not change during reaction. Controlled by the mass flow controller, the molar ratio of H_2 and N_2 in the carrier gas is 9 : 91, and it is assumed to be the same in the bubbler. Therefore, at time

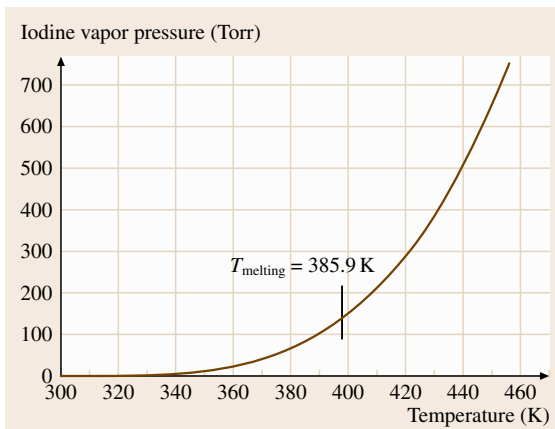


Fig. 37.10 Temperature dependence of iodine vapor pressure

zero, the follow equations can be obtained:

$$\sum P_i^0 = 1 = P_{\text{H}_2}^0 + P_{\text{I}_2}^0 + P_{\text{N}_2}^0 , \quad (37.55)$$

$$\frac{P_{\text{H}_2}^0}{P_{\text{N}_2}^0} = \frac{9}{91} , \quad (37.56)$$

$$\frac{P_{\text{I}_2}^0}{\sum P_i^0} = [\text{I}_2] . \quad (37.57)$$

The initial vapor pressure of iodine over the source surface $P_{\text{I}_2}^0$ can be obtained using Fig. 37.10 [37.123].

The equilibrium expression of the reaction (37.25) and two additional equations obtained from reaction (37.25) are provided in (37.26–37.28).

Given the initial partial pressure of iodine vapor (or the source bubbler temperature), the reaction equilibrium pressure of each species in reaction (37.25) can be solved from (37.26–37.28) and (37.56–37.64).

Figure 37.11a shows the equilibrium partial pressures of different species at the inlet of the reactor under different iodine concentrations in the source. The highest iodine vapor pressure that can be achieved in the source bubbler is limited by the temperature of the valve connected to the bubbler. Gas temperature cannot exceed 150 °C for a regular needle valve, so the highest I_2 vapor pressure is about 300 Torr in the bubbler. When the equilibrium for reaction (37.25) is established before the mixture flows over the gallium source, the HI gas concentration will be around 0.1. When the I_2 concentration in the source is larger than 0.3, I_2 will be the main species to react with gallium, through GaI_x formation.

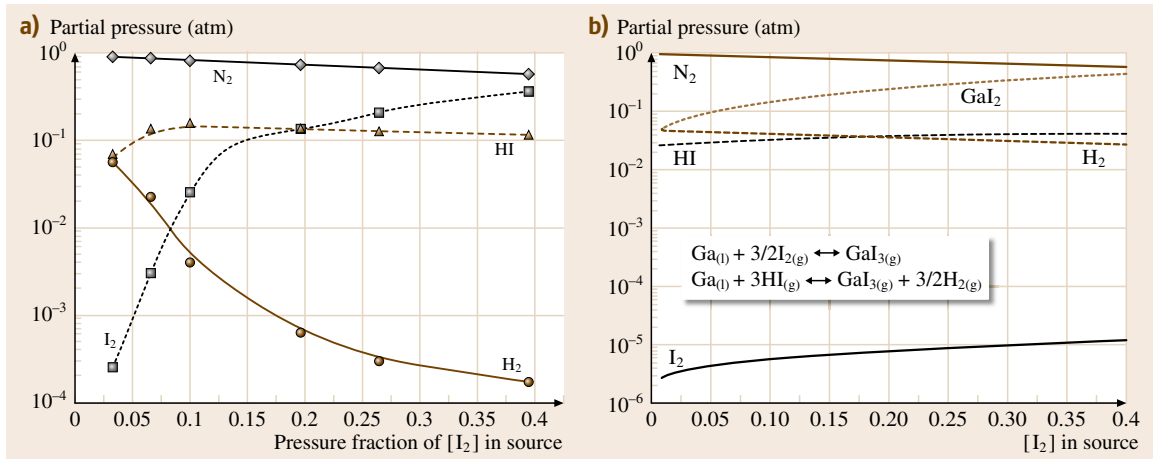
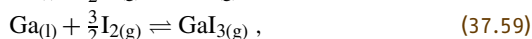
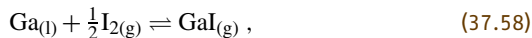
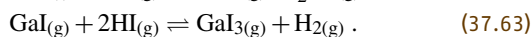
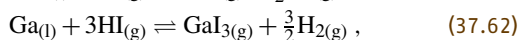
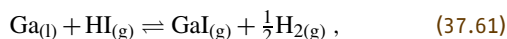


Fig. 37.11 (a) Equilibrium partial pressures with [I₂] in the source, and (b) equilibrium partial pressures above the liquid gallium at 1050 °C

The gas mixture coming out of the iodine source bubbler enters the reactor through the inner silica tube and reacts with gallium at the operating pressure of 200 Torr and growth temperature of 1050 °C. Instead of reacting with Ga vapor, both I₂ and HI will mainly react with gallium on its liquid surface, due to the very low gallium vapor pressure of 0.01 Torr under the given operating conditions. The reactions between I₂ and gallium can be written as



The reactions between gallium and HI can be written as



At a typical growth temperature of 1050 °C, the calculated reaction equilibrium constants for reactions (37.58–(37.60)) are 8900, 840 000, and 50, respectively. The equilibrium reaction constants are 3400, 13 000, and 4 for reactions (37.61–37.63), respectively. The formation of GaI₃ in both cases is strongly favored thermodynamically. It is, therefore, assumed that only GaI₃ will be formed at equilibrium. A group of equations similar to the formation of HI can be derived and the equilibrium partial pressure of species above the gallium source calculated.

Figure 37.11b shows the calculated partial pressures on the gallium source. Comparing Fig. 37.11a with Fig. 37.11b, it is revealed that the partial pressure of GaI₃ is seen to track the initial partial pressure of iodine.

The favorability of reactions (37.59) and (37.62) indicates that any GaI formed will further react either with I₂ or HI to form GaI₃ under equilibrium conditions. However, the thermodynamic calculation only provides an upper limit for what to expect. Given the small surface area of the gallium source (1.1 × 10⁻⁴ m²) and the relatively high velocity of the carrier gas over the gallium source (on the order of 0.1 m/s), it is unlikely that there is sufficient time for equilibrium condition to be established above the gallium source. The thermodynamic model describing transport of iodine and gallium species has to be compared with the experimental data to evaluate its accuracy.

Reported by *Mecouch* et al. [37.72, 120], Fig. 37.12a shows the measured gallium loss rate compared with the measured iodine loss rate. The data points indicated by the diamond and square correspond to a carrier gas mixture of 9% H₂/91% N₂, whereas the triangle and circle correspond to carrier gas of pure hydrogen. The data were measured based on 20 h growth runs. Also two lines represent iodine transport as GaI (Ga : I₂ = 2 : 1) and GaI₃ (Ga : I₂ = 2 : 3), respectively. It is revealed that the measured iodine loss rate falls between the values calculated based on the two transport species. This indicates that there is enough iodine loss to account for GaI transport, but not enough iodine is lost to account for GaI₃ transport. It is concluded that the dominant trans-

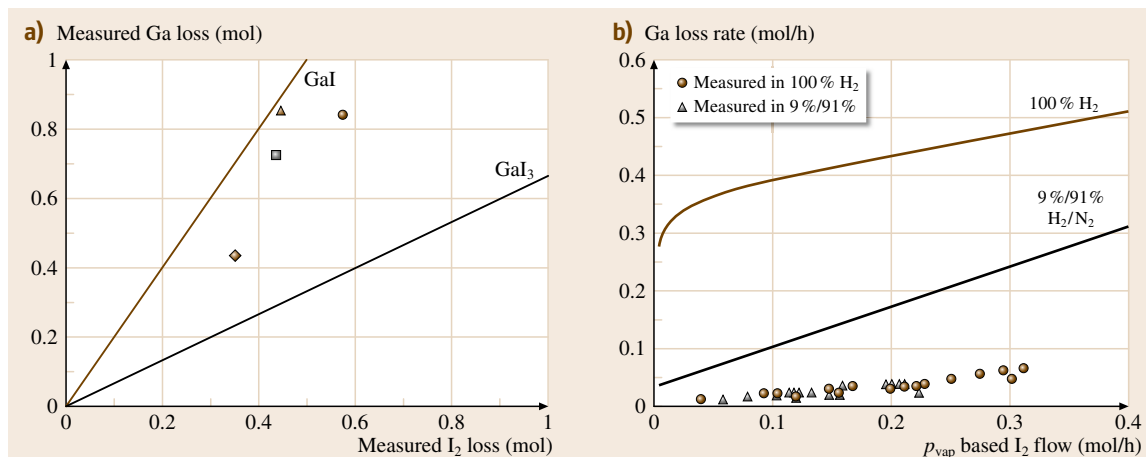


Fig. 37.12 (a) Measured gallium loss rate versus measured iodine loss rate and (b) gallium loss rate predicted from GaI₃-based thermodynamic equilibrium (lines) and measured during experiment growth runs (bullets and triangles) (after [37.72, 120])

port species is GaI, with some GaI₃ formed either on the Ga surface, or through subsequent reaction with the excess iodine species.

Figure 37.12b shows the predicted and measured rates of gallium loss versus the flow rates of I₂ [37.72, 120]. The solid lines represent the results obtained based on the thermodynamic equilibrium of the GaI₃ reaction, and diamonds and triangles represent the measured Ga loss with a pure H₂ carrier gas and a carrier gas mixture of 9% H₂/91% N₂, respectively. The experimental values fall well below the equilibrium prediction, and show no difference in measured loss rate of Ga between a carrier gas of pure H₂ and 9% H₂/91% N₂ mixture. This indicates that the source does not operate near the equilibrium as predicted by thermodynamics, and the reaction of HI formation does not significantly increase the transport of iodine. Thermodynamically calculated iodine loss rate is about 10–30 times greater than the measured iodine loss. Even if iodine is assumed to be transported from the source at the vapor equilibrium without any reaction to form HI, the calculated iodine flow rate is still 6–9 times higher than the observed loss rate from the iodine source. It is likely that the high flow rate of carrier gas and the crystal shape change in the iodine source as temperature fluctuates will both contribute to the difficulty in achieving equilibrium iodine vapor pressure in the source bubbler.

Based on the direct measurement of weight loss from both iodine and gallium sources after each experiment run, *Tassev* [37.26] reported that transport species in their reactor was GaI, with a slight excess of I₂. Fur-

thermore, *Rolsten* [37.124] reported that GaI can be formed by heating either GaI₃ or the reaction product of gallium and iodine. With respect to these data and the relatively high flow rate of carrier gas and small volume for the reaction, it is assumed that the measured gallium loss was transported as GaI.

In the numerical model, only reaction (37.58) is therefore used to describe the gas-phase reaction for GaI_x formation. Measured iodine and gallium mass reduction rates will be converted to the flow rate of I₂ and Ga, respectively. The gas-phase reaction rate of (37.58) can be described as

$$\dot{\omega}_g = A_p T^n \exp\left(\frac{-E_a}{RT}\right) \left(\frac{p}{p_{\text{atm}}}\right)^m \times [A]^\alpha [B]^\beta \quad [\text{kmol/m}^3 \text{ s}], \quad (37.64)$$

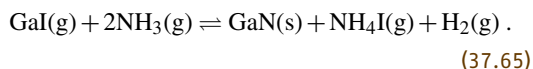
where $[A]$ and $[B]$ are the molar concentrations of reactants Ga and I₂, and α and β are the concentration exponents of $[A]$ and $[B]$, respectively. $E_a/R = 0 \text{ K}$ and $n = m = 0$ are assumed in the simulation. The value of A_p is used to determine the reaction rate and it is estimated as 4×10^8 , corresponding to more than 95% conversion of experimentally weighed Ga loss to GaI. $\alpha = 1$ and $\beta = 0.5$ are assigned, corresponding to the stoichiometric coefficients of the reactants.

Surface Reaction Analysis

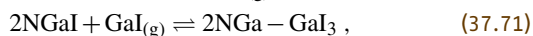
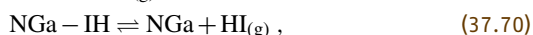
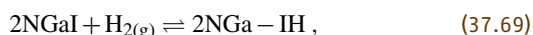
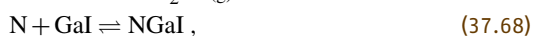
The overall surface reaction rate depends on the partial pressures of gas species such as GaI and NH₃, available free sites on the surface, surface concentrations of adsorbed species, surface diffusion coefficients, rate

constants of individual reaction step, and surface characteristics. Unlike the gas-phase reactions, predicting reaction paths and rate constants is more difficult for the heterogeneous surface reactions since the interactions between gas-phase and surface entities are more complicated than those between gas-phase molecules. A semi-empirical approach is usually used to simulate the surface mechanisms and kinetics.

Tassev et al. [37.26] discussed surface reactions from GaI/NH₃. Based on the byproducts detected in the GaN reactor, the rate-limiting step for the growth of GaN is given as



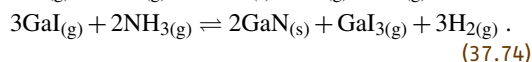
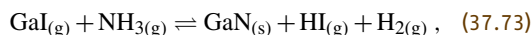
However, NH₄I detected in the cold reaction zone might be formed from NH₃ and HI at a temperature lower than 800 K since NH₄I decomposes above 800 K [37.118]. In the growth zone from silica nozzle to the substrate, the gas temperature will be close to 1323 K. It is therefore unlikely that NH₄I will be present. Considering different product gases which are stable at a temperature around 1323 K, the following analogs of element reactions to GaN growth from GaCl/NH₃ mixture in a halide vapor-phase epitaxy system [37.121] can be expressed:



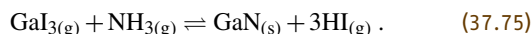
where *V* is the vacant surface site of ammonia adsorption.

Since a very large NH₃ partial pressure is maintained over the substrate in the experiments, reaction (37.66) is close to thermodynamic equilibrium, which means that the NH_{3ads} concentration on the substrate will be close to constant. The GaN deposition rate is mostly limited by reaction (37.68). This is supported by the experimental results that show the independence of GaN growth rate from the NH₃ partial pressure, but strong dependence on the GaI concentration. Since it is difficult to obtain the reaction constant for each elemental step, simplified overall surface reactions will be used in the simulations. Two overall reactions corresponding

to the above element reactions are obtained as follows, corresponding to the most energetically favorable reactions for the iodine vapor-growth system:



The following reaction might also be energetically favorable since GaI₃ is thermodynamically preferred



Reaction (37.75) will also be considered in our numerical simulation model, though the thermodynamics analysis shows that the contribution of reaction (37.75) to the GaN deposition rate will be less than 2%.

Figure 37.13 shows the free energy of reaction for the above three surface reactions on the substrate surface. Since GaI is assumed to be the dominant species for gallium transport, reactions (37.73) and (37.74) are expected to be more important than reaction (37.75). It is revealed that the reaction free energies of the above three reactions are all positive at a typical growth temperature of 1323 K, which means that the equilibrium reaction constants are all smaller than 1, and none of the reactions are spontaneous. An appropriate effective supersaturation, however, can still be achieved by controlling the reactants' partial pressure on the substrate, which serves as the driving force for GaN deposition. Supersaturation of a typical vapor-growth system is

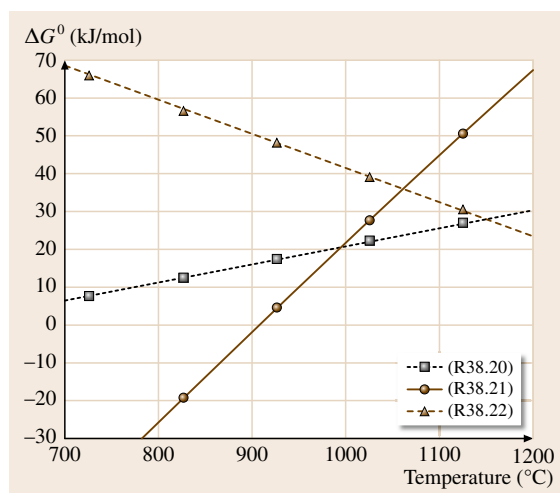


Fig. 37.13 Free energy of reaction for GaN surface deposition

about 5. For reaction (37.73), it can be expressed as

$$\sigma = \ln \left(\frac{P_{\text{GaI}} P_{\text{NH}_3}}{P_{\text{HI}} P_{\text{H}_2} K_{20}} \right), \quad (37.76)$$

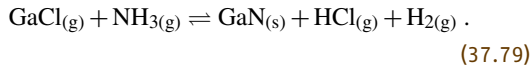
where K_{20} is the equilibrium constant. At a growth temperature of 1323 K, this can be calculated as

$$K_{20} = \frac{P_{\text{HI}}^e P_{\text{H}_2}^e}{P_{\text{GaI}}^e P_{\text{NH}_3}^e} = \exp \left(\frac{-\Delta G_r^0}{RT} \right) = 0.12. \quad (37.77)$$

Since reactions (37.74) and (37.75) can be combined to form reaction (37.73), reaction (37.73) will therefore be used as the overall surface deposition step at first in the numerical model. The surface reaction rate for reaction (37.73) is determined by

$$\dot{\omega}_s = \delta A_p T^n \exp \left(\frac{-E_a}{RT} \right) \left(\frac{p}{p_{\text{atm}}} \right)^m \times [A]^\alpha [B]^\beta \quad [\text{kmol/m}^2 \text{ s}], \quad (37.78)$$

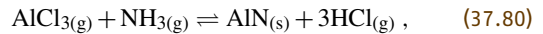
where δ is the deposition coefficient of GaN on the substrate surface. The rate constant r^s for reaction (37.73) has not been reported in the literature. An activation energy of 103 000 J/mol is reported in reference to the data from *Shintani* et al. [37.125] for the following surface reaction of GaN HVPE growth:



The temperature range of their data is 860–1020 °C, which is similar to the IVPE growth temperature (1050–1100 °C). The activation energy of 1.03×10^5 J/mol is estimated for the reaction (37.73). $n = m = 0$ is assumed here. $\alpha = x$ and $\beta = 0$ are assigned for the concentration coefficients of GaI and NH_3 . The value of α is set as undetermined since the concentration dependency of GaI should be 13 according to reactions (37.73–37.75). The ammonia concentration dependence is set to zero due to the fact that ammonia is always in excess on the substrate surface in the experiment. By matching the experimental data for the deposition rate with simulation results under different NH_3/GaI molar ratios, the value of δA_p and α can be determined using an optimization procedure, the detail of which will be covered in Sect. 37.4.8.

To determine the importance of reactions (37.73–37.75) in the GaN deposition rate, all three equations are included in the simulation. The contribution from individual reaction to the GaN growth rate will be

determined under the assumption that all of the reactions are stoichiometric. No kinetic data for reactions (37.74–37.75) are available in the literature. *Shaw* et al. [37.126] reported that the activation energy of GaAs epitaxial growth is between 6.18×10^4 J/mol and 1.648×10^5 J/mol in the Ga–As– Cl_3 system due to surface adsorption, surface reaction, and surface diffusion. The activation energy for reaction (37.74) is therefore chosen as $E_a = 1.133 \times 10^5$ J/mol, which is the medium value of the above energy range. For reaction (37.74), $n = m = 0$, $\alpha = 3$, and $\beta = 0$, and the value of δA_p is again determined by matching the simulation results with the experiment ones. $E_a = 116\,396$ K is reported by *Dollet* et al. [37.98] for the following surface reaction of AlN epitaxial growth:



which is used in the simulation as the activation energy for reaction (37.75). Also for reaction (37.75), we use $n = m = 0$, $\alpha = 1$, and $\beta = 0$, and $\delta A_p = 0.36$, as reported by *Cai* [37.29] for the reaction (37.80) of AlN epitaxial growth with a temperature of 1100 °C and pressure of 760 Torr.

Finally the GaN deposition rate can be calculated as

$$G = \frac{\dot{\omega}_s M_A}{\rho_A} \quad [\text{m/s or } 3.6 \times 10^9 \mu\text{m/h}], \quad (37.81)$$

where M_A and ρ_A are the molecular weight (84 kg/kmol) and density (6.15×10^3 kg/m³) of GaN, respectively.

37.4.4 Geometrical and Operational Conditions Optimization

Many parameters pertinent to reactor geometry and mixed gas injection are important to optimal design of the vapor-growth reactor. In this section, the effects of geometrical configurations such as the diameter of the substrate holder and operating conditions such as the process and shield gas flow rate on mixing process, deposition rate distribution, and deposition uniformity on the substrate are studied.

37.4.5 Effect of Total Gas Flow Rate on Substrate Temperature

A uniform and sufficient high temperature on the substrate is required to achieve high growth rate, uniform film thickness, and good film quality. In the experiments conducted by *Mecouch* et al. [37.30, 72, 120], the temperature on the furnace wall is monitored using thermocouples. In situ observation of temperature achieved

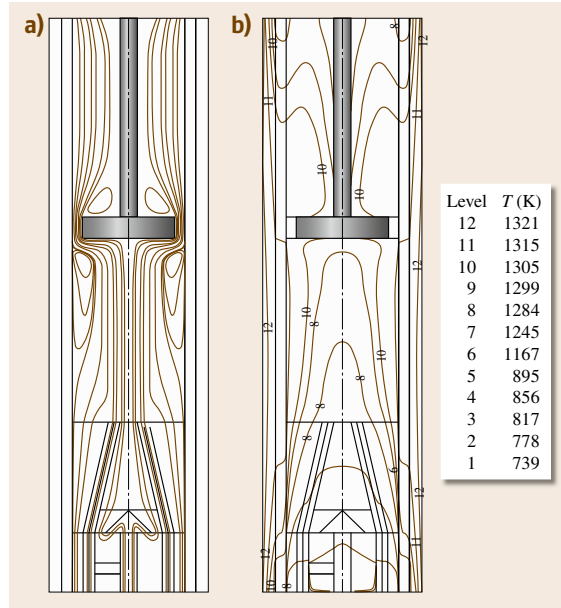
Table 37.10 Inlet gas conditions for an experiment run by Mecouch et al. [37.30, 72, 120]

Inlet	Species	Initial volume flow rate (slm)	Adjusted volume flow rate (slm)
1	I ₂	0.008	0.008
	H ₂	0.026	0.026
	N ₂	0.5	0.25
2	N ₂	1.0	0.62
3	NH ₃	2.0	1.0
	N ₂	–	1.25

on the substrate surface, however, is difficult to realize. Temperature difference between the substrate surface and furnace wall, and the effect of total gas flow rate on the temperature achieved on the substrate surface will be investigated numerically. Gas species at each inlet and their flow rates used are listed in Table 37.10.

The initial inlet gas conditions are tested both experimentally and numerically. The measured gallium weight reduction rate of 0.0133 slm is used in the simulation. This flow rate corresponds to a molar ratio of Ga : I₂ = 1.7 : 1, which favors the formation of GaI in the gas phase. The temperature (1050 °C) of the heating unit and the reactor pressure (200 Torr) remain unchanged for all the simulations presented here. Gas-phase and surface reactions are not activated in the simulation unless stated, since they are expected to have insignificant influence on the gas flow and heat transfer in the reactor. Thermodynamic properties of different substances are listed in Table 37.11.

Figure 37.14 shows the streamline and temperature distributions in the simulated system. Figure 37.14a shows that a reverse flow is formed near the alumina tube wall, which means that the radial mixing of different species is enhanced. The gas-phase reactions of GaI/NH₃ in the center part and the GaN deposition on the alumina tube wall will therefore increase, and the GaN deposition rate will decrease on the substrate. In addition, the reverse flow might be unstable in the experiment, which could be larger or smaller

**Fig. 37.14a,b** Distributions of (a) streamlines and (b) temperature inside the VPE reactor designed by Mecouch et al. [37.30, 72, 120]

as time progresses. The GaN deposition quality on the substrate could therefore be worsened. For the above reasons, it is necessary to make sure that no big reverse flow is formed in the reactor. Figure 37.14b shows the temperature distribution for the simulated system. The temperature of the gas mixture will be heated to more than 1200 K above the silica nozzle. Attributed to such high temperature, chemical deposition may occur on the surfaces of the reactor wall, substrate, and substrate holder.

The velocity ratio of NH₃ from inlet 3, shield gas N₂ from inlet 2, and carrier gas from inlet 1 is 1 : 11 : 13 at the height of the silica nozzle outlet. It is concluded that the reverse flow is formed mainly due to a large gas velocity difference at the silica nozzle outlet. To prevent the reverse flow, adjusted inlet gas flow rates are

Table 37.11 Thermodynamic properties used in the simulation

Properties	All gases	Al ₂ O ₃	GaN	Silica	BN
Specific heat (J/(kg K))	Mix JANAF method	900	490	710	1610
Density (kg/m ³)	Ideal gas law	3900	6150	2198	1900
Thermal conductivity (W/(m K))	Mix kinetic theory	30	130	1.38	28
Dynamic viscosity (kg/(m s))	Mix kinetic theory	–	–	–	–
Diffusivity	Sc = 0.72	–	–	–	–
Adsorption coefficient	0	1	1	0.145	1

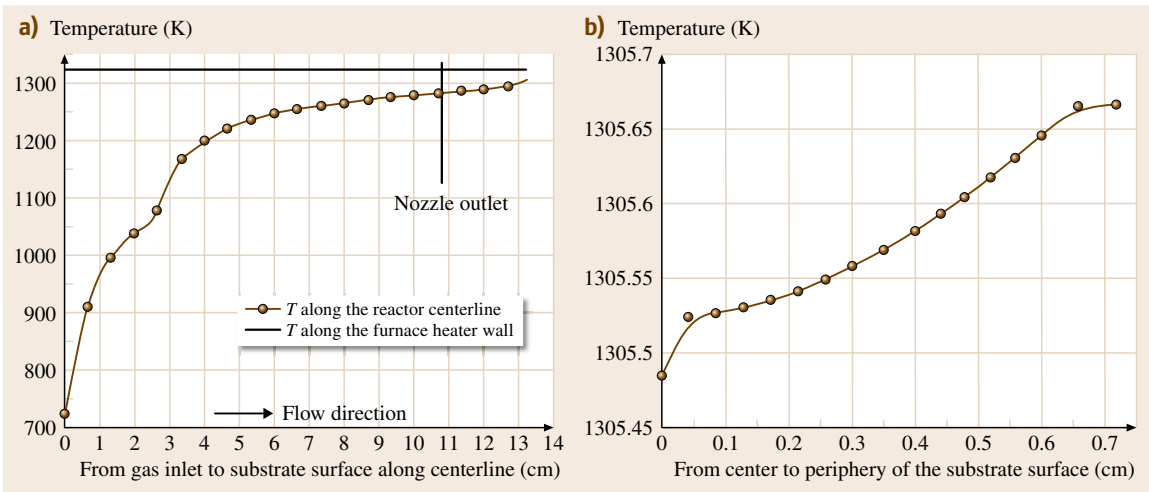


Fig. 37.15a,b Temperature distributions (a) along the reactor centerline and furnace heater wall and (b) from the periphery to the center on the substrate surface in the VPE reactor designed by Mecouch et al. [37.30, 72, 120]

used in the experiment (Table 37.10). The velocity ratio under the new inlet conditions is 1 : 6 : 6. Simulation results show that the reverse flow is eliminated under this condition.

Figure 37.15a shows the temperature distributions from inlet to the substrate surface along the reactor centerline and along the substrate surface, based on the adjusted inlet gas conditions. It is revealed that the mixing gases can be heated to about 1250 K when reaching the nozzle outlet, which further increases to 1300 K at

the substrate area. Figure 37.15b shows the temperature distribution from the periphery to the center of the substrate surface. It is found that the temperature on the substrate surface will be high at the periphery but low in the middle. The temperature difference along the substrate surface is only about 0.18 °C, and the substrate temperature is about 17 °C lower than the temperature on the furnace heater.

By reducing or increasing the flow rate at each gas inlet with the same ratio, the effect of the total flow rate on the temperature achieved on the substrate was investigated. Figure 37.16 shows the averaged temperature and the largest temperature difference achieved on the substrate with different total flow rates. It is revealed that the substrate temperature drops from 1307 °C to 1283 °C as the flow rate changes from 1 to 10 slm. Temperature nonuniformity on the substrate also changes with total flow rate. The largest temperature difference is defined as the highest minus the lowest temperature on the substrate. It is revealed that a total flow rate of 3 slm gives the lowest temperature difference, or the best uniformity, on the substrate surface. In the experiments, the total flow rate is controlled to around 3 slm [37.72, 120].

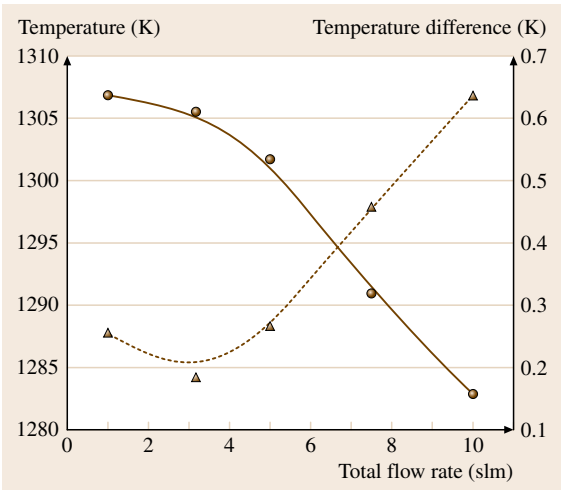


Fig. 37.16 Averaged temperature (solid line) and largest temperature difference (dashed line) on the substrate as functions of total flow rate

Effect of the Shield Gas Flow Rate

The shield gas, N_2 , is used to prevent Ga from mixing with NH_3 directly in the area above the silica nozzle in order to reduce the gas-phase reactions of GaI and NH_3 . Four shield gas flow rates of 0.5, 0.8, 1.2, and 1.5 slm were studied. The only reaction activated is (37.58).

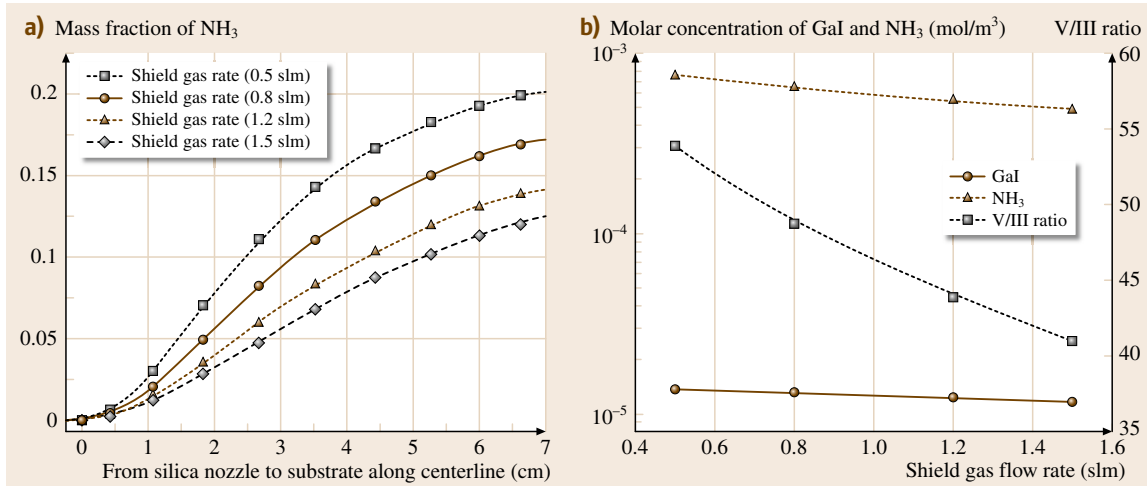


Fig. 37.17 (a) Mass fraction distribution of NH_3 along the centerline from the silica nozzle to the substrate and (b) averaged concentrations of GaI and H_3 on the substrate and V/III ratio achieved on the substrate as functions of the shield gas flow rate

Figure 37.17a shows the mass fraction change of NH_3 with the shield gas flow rate along the reactor centerline from the outlet of the silica nozzle to the substrate surface. It is seen that, at the silica nozzle outlet, the NH_3 concentration is zero, and then increases gradually with distance. The concentration of NH_3 with 1.5 slm shield gas flow rate is about half of that with 0.5 slm shield gas flow rate along the centerline. Figure 37.17b shows the averaged concentrations of GaI and NH_3 and the V/III ratio on the substrate surface. It is shown that the concentrations of GaI and NH_3 decrease as the shield gas flow rate increases. It is also observed that the effect of the shield gas flow rate on the NH_3 concentration is more significant than its effect on GaI concentration. When the shield gas flow rate increases from 0.5 to 1.5 slm, concentrations of GaI and NH_3 drop by 17% and 34%, respectively. This is attributed to the increase of the N_2 concentration on the substrate surface as the result of the increase of the shield gas flow rate. Furthermore, increasing the shield gas flow rate can reduce the residence time for NH_3 to diffuse into the center area, causing reduction of the NH_3 concentration and the V/III ratio.

Experiments were conducted to study the effect of the shield gas flow rate on the GaN deposition rate by Mecouch et al. [37.30]. Shield gas flow rates of 0.62 slm and 1.0 slm were used in their experiments. The flow rate of 0.62 slm corresponds to a velocity ratio of 1 : 1 between the shield gas and other gases at the outlet of the silica nozzle. It is revealed that the shield gas

flow rate of 0.62 slm produces a higher GaN growth rate under different iodine concentrations in the source bubbler compared with the shield gas flow rate of 1.0 slm. A shield gas flow rate of 0.62 slm was therefore used in the subsequent experiments. Figure 37.18a,b shows the mass fraction distributions of GaI and NH_3 in the growth reactor. The gas-phase reaction between Ga and

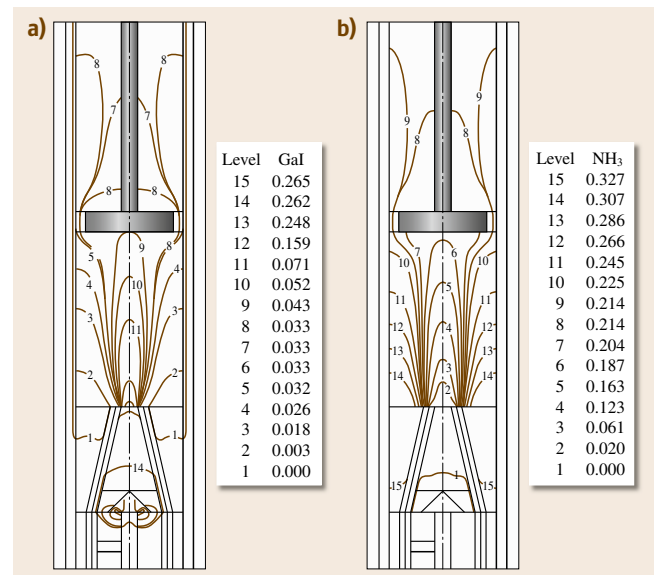


Fig. 37.18a,b Mass fraction distributions of (a) GaI and (b) NH_3 inside the VPE reactor designed by Mecouch et al. [37.30, 72, 120]

Table 37.12 Species concentrations on the substrate

	Ga	GaI	H ₂	I ₂	N ₂	NH ₃
<i>Y_i</i>	2.4 × 10 ^{−6}	0.042575	0.000855	0.005494	0.760977	0.190096
<i>C_i</i> (kmol/m ³)	2.16 × 10 ^{−9}	1.36 × 10 ^{−5}	2.69 × 10 ^{−5}	1.36 × 10 ^{−6}	1.71 × 10 ^{−3}	7.02 × 10 ^{−4}
<i>P_i</i> (Torr)	1.76 × 10 ^{−4}	1.11 × 10 ⁺⁰	2.19 × 10 ⁺⁰	1.11 × 10 ^{−1}	1.39 × 10 ⁺²	5.73 × 10 ⁺¹

I₂ takes place mainly inside the inner silica nozzle. Since the gas flow in the reactor is laminar (Fig. 37.18b), the NH₃ has been transferred into the center area of the reactor by mass diffusion.

The mass fraction *Y_i*, the molar concentration *C_i*, and the partial pressure *P_i* of species *i* on the substrate are listed in Table 37.12 for the shield gas flow rate of 0.62 slm. It is seen that the partial pressure of Ga is close to zero, and the achieved partial pressure of GaI is around 1 Torr on the substrate at a reactor pressure of 200 Torr.

Effect of Silica Nozzle Angle

The GaN growth rate is directly proportional to the partial pressure of GaI achieved on the substrate. A silica nozzle is used in experiments to force more GaI to the substrate area [37.30]. Adding a silica nozzle will also help prevent ammonia from diffusing towards the gallium source area because ammonia reacts with Ga directly on the liquid gallium surface to form polycrystalline GaN through the following reaction:



This reaction (37.82) could terminate the transport of gallium and stop the GaN growth on the substrate.

Design of silica nozzle angle *θ* (Fig. 37.1a) is an important task. To test the effect of nozzle angle on concentration distributions of NH₃ and GaI between the outlet of silica nozzle and substrate surface, growth systems with four nozzle angles of 77°, 81°, 86°, and 90° were simulated. Figure 37.19a shows the mass fraction distribution of NH₃ along the reactor centerline from the silica nozzle outlet to the substrate surface. It is found that, at the silica nozzle outlet, the NH₃ concentration is close to 0 when using a nozzle with angle < 81°. The ammonia mass fraction is up to 0.03 at the outlet of the inner silica nozzle when its angle is > 81°, indicating that ammonia may diffuse into the inner silica tube. Using a nozzle with small angle, such as 77°, can significantly reduce the NH₃ concentration in the area above the silica nozzle. This influence will be weakened when the mixed gas approaches the substrate. Thus, the concentration of NH₃ on the substrate can be maintained at an appropriate level even with a small nozzle angle. Figure 37.19b shows the average molar concentrations of GaI and NH₃ on the substrate surface. The concentra-

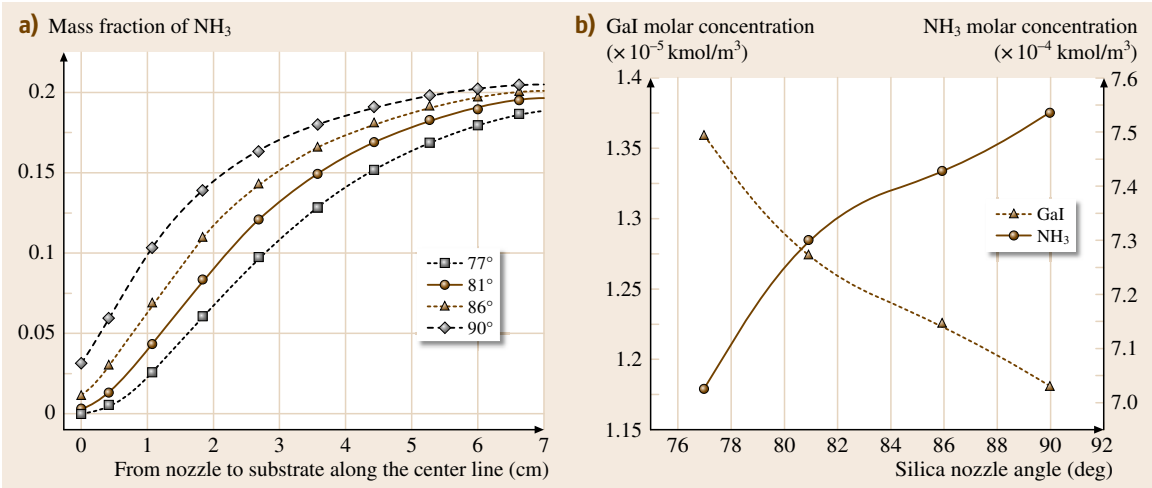


Fig. 37.19 (a) Mass fraction distribution of NH₃ along the centerline from the silica nozzle to the substrate and (b) averaged concentrations of GaI and NH₃ on the substrate under different silica nozzle angles

tion of NH_3 increases with the nozzle angle, while that of GaI decreases with the nozzle angle.

The silica nozzle used in the experiment has an angle of 77° [37.72]. This design can reduce the NH_3 concentration in the area above the silica nozzle outlet significantly, subsequently preventing NH_3 from diffusing into the inner silica nozzle and increasing the GaI concentration on the substrate. The simulation shows that using a nozzle angle of 77° can increase the GaI concentration on the substrate by about 10% compared with a silica nozzle angle of 90° .

Effect of Substrate–Nozzle Distance

The substrate–nozzle distance is one of the key parameters that affect the GaN growth rate and deposition quality. It controls the length and time allowed for different gases to mix with each other. An appropriate substrate–nozzle distance corresponds to a suitable V/III ratio above the substrate for fast and uniform GaN growth. The simulated substrate–nozzle distance ranges from 6.35 to 17.8 cm. Figure 37.20a shows the molar concentrations of GaI and NH_3 as a function of substrate–nozzle distance. The concentration of GaI decreases with substrate–nozzle distance until the mixing is completed at a substrate–nozzle distance of 13.0 cm. The error bars in Fig. 37.20a indicate the GaI concentration variation across the substrate surface. It is seen that, for a substrate–nozzle distance of 6.35 cm, the variation of GaI concentration on the substrate surface is small (around 0.6%). This indicates that species uniformity is not a problem. The concentration of NH_3 increases

with the distance since more time is available for ammonia to diffuse into the center area of the reactor. The variation of the V/III ratio with substrate–nozzle distance is shown in Fig. 37.20b. When the substrate–nozzle distance is less than 13.0 cm, an increase of substrate–nozzle distance of about 2.5 cm corresponds to a V/III ratio increase of 10.

It is concluded that complete mixing of different species needs a substrate–nozzle distance larger than 13.0 cm. The species concentrations across the substrate surface is fairly uniform even with a small substrate–nozzle distance such as 6.35 cm. To achieve uniform GaN deposition with high growth rate, the substrate–nozzle distance of 6.35 cm is used. This distance can achieve uniform species concentrations across the substrate surface and a high GaI concentration of $1.4 \times 10^{-5} \text{ kmol/m}^3$. The V/III ratio in this case will be about 50. For the growth of GaN from $\text{GaI}_{1-3}/\text{NH}_3$ or $\text{GaCl}_{1-3}/\text{NH}_3$, the concentration of NH_3 is maintained at a high value on the substrate, resulting in an appropriate supersaturation as the driving force for the surface deposition. For the current GaN vapor-growth system, the V/III ratio is kept above 50 for most experiments [37.30, 72, 120].

37.4.6 Effect of Substrate Rotation on Deposition Rate and Deposition Uniformity

In the experiment, the substrate is rotated by revolving the substrate holder to improve deposition uniformity,

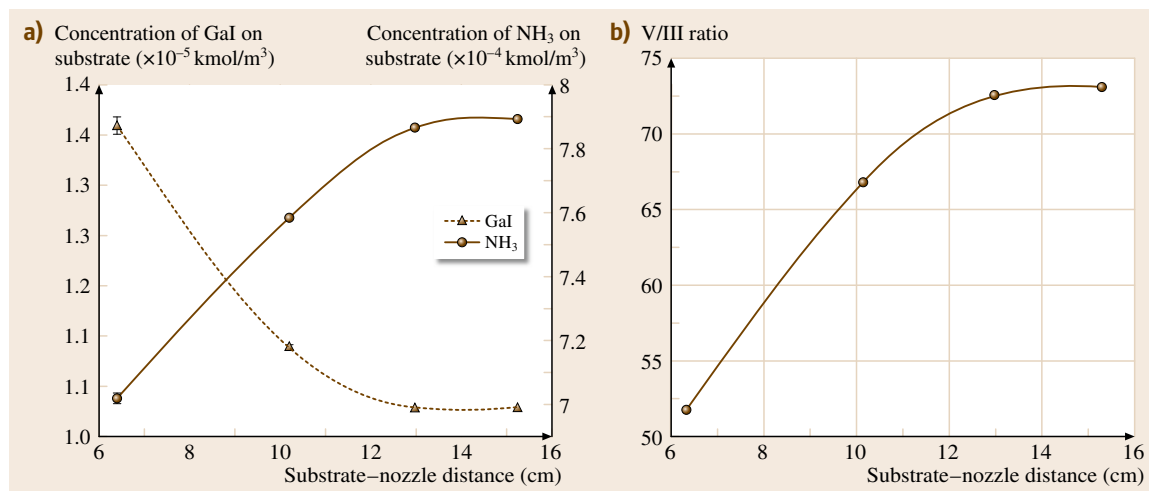


Fig. 37.20 (a) Averaged molar concentrations of GaI and NH_3 and (b) the V/III ratio achieved on the substrate under different substrate–nozzle distances

and consequently to improve deposition quality. It is shown by the simulation that temperature and species concentration distributions on the substrate are fairly uniform under the current geometrical and operational conditions. It is expected that the deposited GaN layer will be uniform. Experiments have been conducted using the gas inlet conditions listed in Table 37.10 for a growth time period of 1 h [37.30]. This experiment shows that the thickness of deposited GaN crystal layer varies from 35 to 75 $\mu\text{m/h}$ on the substrate surface. To improve the deposition uniformity, the substrate was rotated in the experiments. The instantaneous GaN deposition rate distribution on the substrate will be averaged due to rotation and the deposition uniformity will be improved. Cross-sectional scanning electron microscopy (SEM) images of GaN layer with a substrate rotation speed of 1 rpm show that the deposition uniformity is significantly improved since the thickness difference in the GaN layer is reduced from 40 to 2 $\mu\text{m/h}$ [37.30].

It should be noted that, in the simulation, since the entire system is assumed to be perfectly axisymmetric, the calculated temperature and species concentration distributions will be axisymmetric. In the experiment, the components in the growth reactor are mostly not axisymmetric. It is found experimentally that the deposition nonuniformity is mainly attributed to misalignment between the inner and outer silica nozzles and the seed holder. Deposition uniformity could therefore be improved by improving these alignments.

Another factor that could cause deposition nonuniformity across the substrate is reactant depletion in the species concentration boundary layer formed on the substrate due to surface reactions. Figure 37.8b shows that a typical boundary layer of the reactant species concentration is formed on the substrate due to surface reactions. The concentration of GaI before the mixing gas reaching the substrate area is defined as $C = C_0$. Due to the surface reactions (37.73–37.75) of GaI with NH_3 on the substrate, the GaI concentration drops to $C = C_w$ on the substrate surface. The concentration boundary layer thickness χ is defined as the distance where the GaI concentration changes from C_0 in the bulk gas to C_w on the substrate surface. The low-concentration layer will gradually accumulate as the gases flow from the center to the perimeter of the substrate. The growth rate is therefore expected to be low in the periphery area. To improve the deposition uniformity, one may reduce the concentration boundary-layer thickness. Substrate rotation can be used to reduce the thickness of the low-concentration layer. To estimate

the rotation speed at which the boundary-layer thickness will be affected, the following equation is used to calculate the ratio of the Reynolds number due to forced convection and rotation:

$$\frac{\text{Forced convection}}{\text{Rotation}} = \frac{\text{Re}_d}{\text{Re}_\theta} = \frac{UD/v}{\omega d^2/v} = \frac{1500}{\varpi}, \quad (37.83)$$

where ω and ϖ are the rotation frequency in units of rps and rpm, respectively.

It is revealed that the rotation speed has to be on the order of 10^3 rpm for rotation to affect the boundary-layer thickness. Such a high rotation speed will cause the growth environment to become unstable near the substrate. In experiments, only a small rotation speed (1 rpm) is recommended in order to even out the instantaneous deposition rate on the periphery of the substrate.

37.4.7 Quasi-equilibrium Model for Deposition Rate Prediction

Predicting the GaN deposition rate is the most important issue for modeling. A thermodynamic surface reaction model (local model) combined with a numerical simulation model (global model) for mass transfer in the growth reactor are used to calculate the GaN deposition rates under different substrate temperatures. Since reactions (37.74–37.75) can be combined to form reaction (37.73), reaction (37.73) is assumed to prevail on the substrate when reaction equilibrium is reached.

Figure 37.8a shows a schematic of GaN deposition on the substrate surface. Species on the substrate include GaI, NH_3 , HI, H_2 , N_2 , I_2 , and Ga. From the global heat and mass transfer model, we can calculate the concentration of these seven species, which will be used as the initial species conditions. As shown in Fig. 37.8b, the transport of species into the concentration boundary layer is driven by the concentration gradient due to surface deposition.

According to (37.33–37.36), there are four unknowns, i.e., P_{HI}^e , P_{GaI}^e , $P_{\text{NH}_3}^e$, and $P_{\text{H}_2}^e$, and four equations. The partial pressures of each species, P_{HI}^w , P_{GaI}^w , $P_{\text{NH}_3}^w$, and $P_{\text{H}_2}^w$, can be obtained using the global simulation model, whereas the sticking probabilities of each species α_i are required. NH_3 will crack on the substrate surface to provide nitrogen atoms for GaN growth. The sticking coefficient of NH_3 on the substrate is defined as the ratio of the NH_3 flux incorporated as GaN to the total NH_3 flow rate incident on the substrate. This definition assumes that all NH_3 flux incident on the substrate is involved in the reaction process, i.e.,

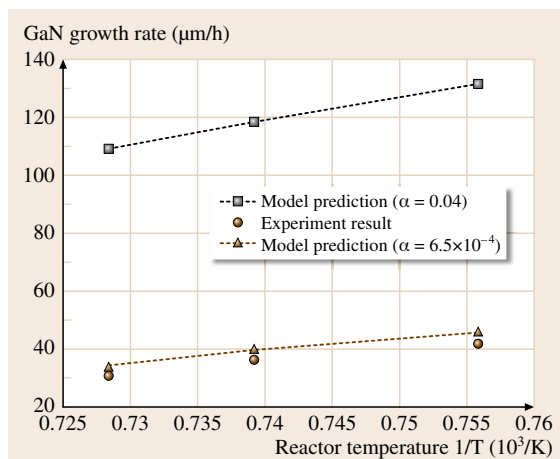


Fig. 37.21 Predicted and experimental results of GaN growth rate with ammonia sticking coefficient of 0.04 or 6.5×10^{-4} (after [37.72])

no saturation of surface sites occurs on the substrate. Mesrine et al. studied the efficiency of NH_3 as the nitrogen source for GaN molecular-beam epitaxy [37.127]. It was found that, at temperature of $830^\circ C$ and pressure of 10^{-5} Torr, the sticking coefficient of NH_3 , α_{NH_3} is about 0.04. The sticking coefficient at temperature of $1050^\circ C$ is expected to be slightly higher, therefore 0.04 is used as the sticking coefficient of NH_3 in the simulation. The sticking coefficient of GaI is assumed to be unity. The sticking probabilities of H_2 and HI are also assumed to be unity, considering the high reactivity of these species under high growth temperature. In Fig. 37.21 the square line and the black dots indicate the experimental and predicted GaN deposition rates, respectively. The predicted results are 3–4 times the experiment ones. The difference between the experiments and simulations is attributed to overprediction of the sticking coefficient of ammonia in the modeling, which is due to several reasons. First, the assumption that all the incident ammonia flux on the substrate is involved in the reaction process is not correct for the current GaN growth system. To study the ammonia sticking coefficient in the MBE system, Mesrine et al. [37.127] controlled the ammonia flow rate low enough to ensure that the above assumption is valid. However, in the GaN growth system, the ammonia flow rate is high and it is found experimentally that the GaN deposition rate is independent of the ammonia flow rate, as discussed in the next section. The efficiency of the ammonia deposition coefficient will be lowered greatly in this case. Second, since a much higher pressure, 200 Torr, is used in the

current system, the available surface sites for nitrogen atoms to deposit will be further reduced since it has to compete with other atoms on the substrate surface. The sticking coefficient will therefore be reduced further. Finally, since a much higher growth temperature is used, GaN decomposition on the substrate surface will be enhanced, causing the sticking coefficient of ammonia to drop further. By adjusting the ammonia sticking coefficient, it is found that, when the value is lowered to the order of 10^{-4} , the GaN growth rate from prediction and experiment matches very well, as shown in Fig. 37.21 for an ammonia sticking coefficient of 6.5×10^{-4} .

37.4.8 Kinetic Deposition Model

Combined with the experimental data, the GaN deposition rate at a constant growth temperature of $1050^\circ C$ was tested numerically while the flow rates at the inlet were changed to obtain different reactant concentrations and V/III ratios on the substrate. More importantly, simulations were performed to test the surface reaction pathway of GaN growth and the contribution of different reactions to the final GaN growth rate.

The energetically preferred surface reactions on the substrate for GaN deposition have been obtained previously. Reaction (37.73) was first used as the overall surface reaction step on the substrate in the simulation. Figure 37.22 shows the experimental data for the GaN deposition rate at different ammonia flow rates and iodine vapor fractions [37.30, 72]. The highest growth rate

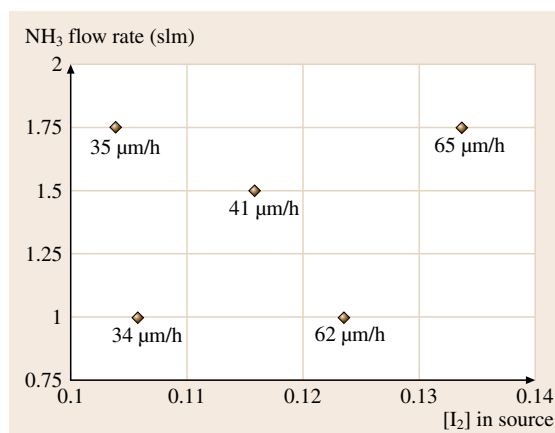


Fig. 37.22 Effect of ammonia flow rate and iodine vapor fraction in the source on the GaN deposition rate (after [37.30, 72])

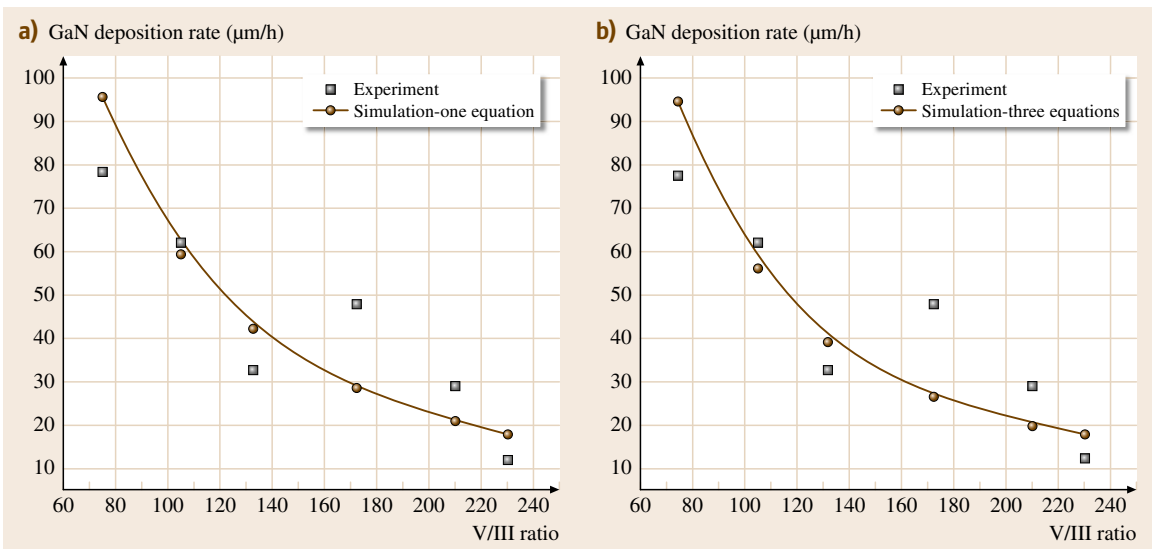


Fig. 37.23a,b GaN deposition rate as a function of the V/III ratio for (a) one surface reaction and (b) three surface reactions (after [37.72])

achieved is 65 μm/h. It is found that the GaN growth rate is independent of the NH₃ flow rate but dependent on the GaI concentration.

Experiments were conducted to examine the effect of V/III ratio on the GaN deposition rate [37.72, 120]. The V/III ratio was varied by maintaining the NH₃ flow rate at 1 slm while changing the I₂ concentration in the source. Using the same operating conditions as in the experiment, simulations were performed with reaction (37.73) as the boundary condition. The surface reaction rate coefficient δA_p and the concentration dependency of GaI α were determined by fitting the simulation results to the experimental data. Figure 37.23a shows the variation of the GaN deposition rate with the V/III ratio.

The surface reaction rate of reaction (37.73) used to obtain the numerical results in Fig. 37.23a is determined by the following equation

$$\dot{w} = 6.5 \times 10^9 \exp\left(\frac{-12\,390}{T}\right) [\text{GaI}]^{2.2} . \tag{37.84}$$

It is concluded that, when one overall surface reaction step is used to predict the GaN deposition rate, the reaction rate coefficient is 6.5×10^9 and the GaI concentration dependency is 2.2.

When reactions (37.73–37.75) are used, the reaction rate coefficient of each reaction step is determined by matching the simulation results to the experimental data. Figure 37.23b shows the GaN deposition rate calculated using all three surface reactions and the deposition rates from the experiment. The surface reactions and their reaction rates used here are summarized in Table 37.13.

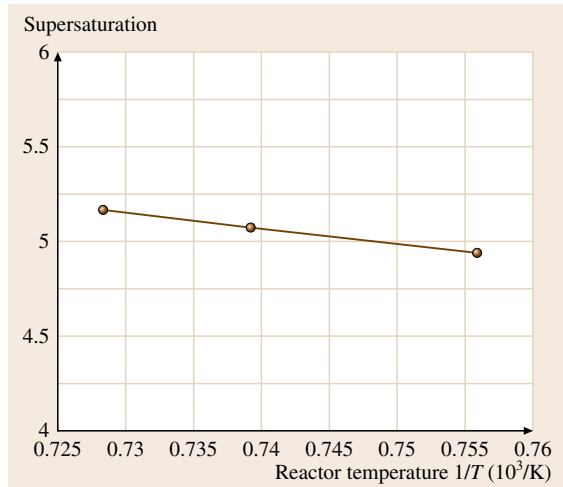
The calculated GaN deposition rate with reactions (37.73) and (37.74) is presented in Table 37.14. Since GaI is considered as the only medium for Ga source transport, the contribution of reaction (37.75) to the deposition rate is found to be less than 0.1% for all cases and is therefore not listed in Table 37.14. In the experiment, the contribution of reaction (37.75) to the GaN deposition rate might be larger. It is, however, not expected to be as significant as reactions (37.73)

Table 37.13 Surface reaction rates obtained by matching the simulation data with the experimental data

Reaction	Rate expression (kmol/m ² s)
(37.73) GaI(g) + NH ₃ (g) ⇌ GaN(s) + HI(g) + H ₂ (g)	$0.07 \exp(-12\,390/T) [\text{GaI}]$
(37.74) 3GaI(g) + 2NH ₃ (g) ⇌ 2GaN(s) + GaI ₃ (g) + 3H ₂ (g)	$5.88 \times 10^9 \exp(-13\,630/T) [\text{GaI}]^3$
(37.75) GaI ₃ (g) + NH ₃ (g) ⇌ GaN(s) + 3HI(g)	$0.36 \exp(-14\,000/T) [\text{GaI}_3]$

Table 37.14 GaN deposition rate and rate contribution from reactions (37.73) and (37.74)

V/III ratio	GaN deposition rate ($\mu\text{m/h}$)		Growth rate contribution (%)	
	Reaction (37.73)	Reaction (37.74)	Reaction (37.73)	Reaction (37.74)
75	21.80	73.10	22.97	38.03
105	17.62	38.61	31.33	68.67
132	15.04	24.01	38.52	61.48
172	12.54	13.89	47.41	52.59
210	10.86	9.03	54.60	45.40
230	10.16	7.40	57.86	42.14

**Fig. 37.24** Supersaturation of GaN growth under different reactor temperatures

and (37.74). The contribution of reaction (37.73) to the total GaN deposition rate increases with the V/III ratio, while for reaction (37.74) it decreases with the V/III ratio.

The supersaturation of GaN growth on the substrate can be calculated once the partial pressure of each species is obtained. Figure 37.24 shows the calculation results for the supersaturation with different reactor

Table 37.15 Sticking probability of reactant i with different V/III ratios

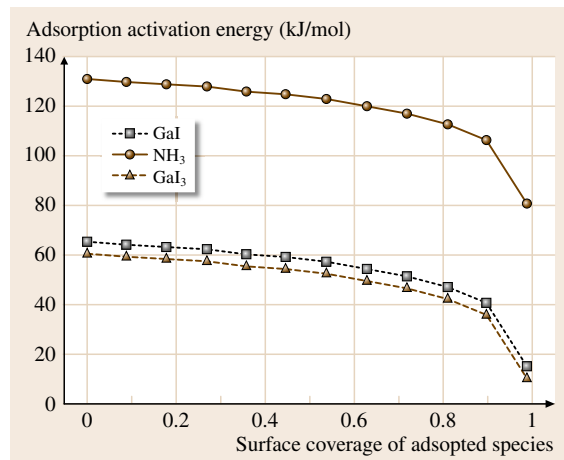
V/III ratio	Sticking probability		
	GaI ($\times 10^{-3}$)	NH ₃ ($\times 10^{-6}$)	GaI ₃ ($\times 10^{-3}$)
75	2.66	6.50	4.15
105	2.07	4.10	3.12
132	1.75	3.02	2.69
172	1.43	2.08	2.07
210	1.22	1.55	1.86
230	1.13	1.38	1.77

temperatures. The supersaturation is around 5. This is typical for an epitaxy growth system that needs a relatively low supersaturation to prevent the reactant partial pressures from deviating excessively from their equilibrium values. The supersaturation decreases only slightly with temperature, which means that the GaN deposition is diffusion controlled under the current operating conditions.

Table 37.15 summarizes the sticking probability of the reacting species deduced from various simulations. The calculated sticking probabilities of the order of 10^{-3} – 10^{-6} are reasonable for the saturated compound. The sticking probability of species i is defined by

$$S_i = f(\theta^s)_i \exp\left[\frac{-E_{ai}(\theta^s)}{RT}\right] = \frac{R_i}{F_i}, \quad (37.85)$$

where $f(\theta^s)_i$ is the function of the existing surface coverage of adsorbed species i , θ^s is the Langmuir definition of surface coverage of certain species, or the fraction of sites which are occupied on the substrate surface, E_{ai} is the activation energy for adsorption of species i ,

**Fig. 37.25** Activation energy of adsorption with surface coverage of 0–0.99

R_i (kmol/m²s) is the rate of adsorption of species i chemically, and $F_i = P_i^w(2\pi RTM_i)^{1/2}$ [kmol/m²s] is the incident flux rate of species i onto the substrate.

It is observed that the sticking probability decreases with increasing V/III ratio. When the I₂ concentration decreases in the source, the species reaction rate decreases more significantly compared with its incident flux onto the substrate. The sticking probability of ammonia is three orders of magnitude smaller than that of GaI or GaI₃, because the ammonia concentration is kept much higher than that of GaI on the substrate.

To determine the activation energy for adsorption of species i , it is assumed that the sticking probability is directly proportional to the concentration of vacant

surface sites $(1 - \theta^s)$. This assumption is a reasonable first approximation for nondissociative adsorption. The activation energy of adsorption is assumed to be independent of the surface coverage. The sticking probability is, thus, revised as

$$S_i = (1 - \theta^s) \exp\left(\frac{-E_{ai}}{RT}\right). \quad (37.86)$$

Figure 37.25 shows the calculated activation energy of adsorption for the three species for surface coverage of 0–0.99. The activation energy drops as the surface coverage increases. The averaged activation energies of adsorption for GaI, NH₃, and GaI₃ by calculation are 5.72×10^4 , 1.24×10^5 , and 5.28×10^4 J/mol, respectively.

37.5 Surface Evolution of GaN/AlN Film Growth from Vapor

In this section, sublimation and HVPE growth of AlN will be used as an example to investigate the surface evolution of thin film during growth. Since large-diameter AlN single crystal is not available in nature, the goal of research is to find a way to produce large, thick AlN films/ingots, which can then be sliced for use as substrates. The growth conditions of two systems are compared in Table 37.16. Figure 37.26 shows the AlN crystals grown by sublimation and HVPE techniques.

Srolovitz et al. [37.128] studied the surface evolution of film growth in which surface diffusion determines the crystal grain size and morphology. Figure 37.27 shows the deposition geometry in which a one-dimensional partial differential equation describes the evolution of an arbitrary initial surface profile $h(x, 0)$ under the joint influence of constant uniform deposition flux rate J of finite-size atoms of radius r and surface diffusion. C_k is the surface curvature and V_s is the velocity of surface diffusion.

By assuming a sinusoidal perturbation, i.e., $h(x, t) = \sin(x, t)$, the surface profile can be described as

$$h(x, t) = e^{(rJk^2 - D_e k^4)t} \sin(kx), \quad (37.87)$$

where $D_e = (D_s \sigma_s \Omega^2 \varepsilon) / (k_B T)$, D_s is the surface diffusivity of the atoms, σ_s is the isotropic surface energy density, Ω is the atomic volume, ε is the number of atoms per unit area, $k_B T$ is the thermal energy, and k is the wavenumber, relating to the wavelength λ by $\lambda = 2\pi/k$. It is revealed by (37.88) that, if $\delta Jk^2 - D_e k^4 > 0$, $e^{(rJk^2 - D_e k^4)t} > 1$ is obtained, and the initial sinusoidal perturbation will be enlarged, which means that the growth will be unstable and growth quality will be deteriorated. For stable growth, the wavelength of the initial perturbation λ has to be smaller than the effective diffusion length λ_e , which is defined as

$$\lambda_e = \sqrt{\frac{4\pi D_e}{rJ}}. \quad (37.88)$$

Table 37.16 Growth comparison for sublimation and HVPE systems

Growth system	Sublimation	HVPE
Surface reaction	$\text{Al(g)} + \frac{1}{2} \text{N}_2(\text{g}) \rightleftharpoons \text{AlN(s)}$	$\text{AlCl}_3(\text{g}) + \text{NH}_3(\text{g}) \rightleftharpoons \text{AlN(s)} + 3\text{HCl(g)}$
Substrate	AlN seed	Sapphire/SiC
Growth temperature	2240 °C	900–1200 °C
Growth rate	0.2–0.5 mm/h along c axis	5–75 $\mu\text{m/h}$
Crystal property	Transparent, DCRC 20 arcsec	Opaque, DCRC 1000 arcsec

Fig. 37.26 (a) An AlN crystal grown by sublimation method (after [37.70]). (b) An AlN crystal grown by HVPE method (after [37.130]) (with permission from Elsevier) ►

To obtain stable growth, one can either reduce the initial perturbation wavelength or increase the effective diffusion wavelength. The initial perturbation wavelength is related to the substrate and supersaturation. The effective diffusion length is proportional to the effective diffusion coefficient D_e and inversely proportional to the atom radius r and the growth flux rate. Collazo et al. [37.129] studied the effect of process conditions such as surface temperature T and the growth flux rate J on the effective diffusion length λ_e and the effect of process conditions such as supersaturation on the initial perturbation wavelength λ . They found that changing the process conditions cannot significantly affect the values of λ_e and λ .

It is concluded here that the substrate plays a critical role in determining the quality of AlN crystal when the crystal is grown large and thick. For HVPE growth using a foreign substrate such as sapphire or silicon carbide, the wavelength of the surface perturbation will be larger than the effective surface diffusion length due to the lattice mismatch between the AlN crystal and substrate when the thickness of the crystal is large.

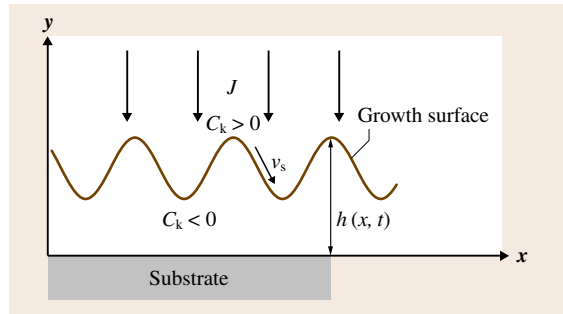
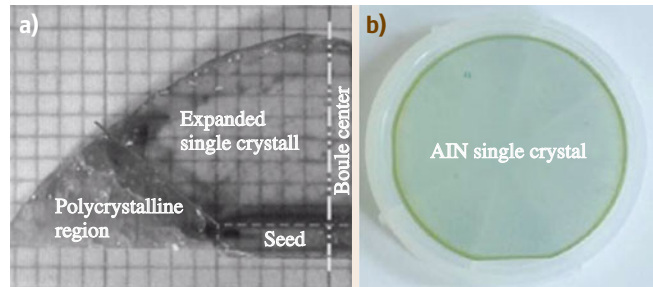


Fig. 37.27 Deposition geometry (after [37.128])

Therefore the film growth will be unstable, and consequently, low-quality crystals will be obtained.

37.6 Concluding Remarks

Transport phenomena in chemical vapor deposition of III nitrides are complicated due to gas flow, coupled convection and radiation, conjugate heat and mass transfer, homogeneous gas-phase and heterogeneous surface reactions, and the coexistence of multiple length and time scales. The multiplicity of governing parameters, complex geometric configurations, complicated boundary conditions, and the lack of information on gas-phase and surface reaction mechanisms make this process difficult to predict and control.

It is the authors' intention to provide a systematical procedure for those who are new to the field of vapor-growth process modeling. In this chapter an attempt has been made to present a comprehensive description of the fundamental theory as well as an extensive overview of the state of the art in vapor-growth process modeling. The main focus has been on continuum modeling of macroscopic gas flow, homogeneous gas-phase reactions inside the reactor chamber, heterogeneous surface reactions on the substrate surface, heat transfer, and

species transport in reactors for GaN/AlN vapor crystal growth.

Gas velocity, temperature and pressure, and species concentration distributions in a CVD reactor are correlated. The main difficulty in accurately predicting species concentration lies in the lack of detailed information for gas-phase and surface reactions. By using GaN IVPE growth as an example, mathematic models for thermodynamic and kinetic gas-phase and surface reactions have been described. Thermodynamic models can be used to predict gas-phase and surface reactions with or without detailed reactions steps. The results, however, only give the upper limit of what one can expect. By comparing the results with available experiment observations, one may determine the extent to which the gas-phase and surface reactions deviate from the equilibrium assumption. Empirical models were used in this chapter to simulate gas-phase and surface reaction kinetically. The detailed multistep gas-phase and surface reaction

mechanisms can only be obtained from the experiments. The current models can be used to predict species transport in the reactor in order to identify the critical controlling parameters for fast and uniform deposition.

Film instability during GaN/AlN growth has been analyzed, in which surface diffusion determines the crystal grain size and morphology. The key parameters,

such as the lattice mismatch between the substrate and deposited film, the effective diffusion length, and the supersaturation above the substrate, have been identified and their effects on film instability during growth quantified. It is found that, for growth of GaN/AlN bulk crystals, use of native substrate is the key for high deposition quality when the deposited film thickness becomes very large.

References

- 37.1 E.J. Tarsa, B. Heying, X.H. Wu, P. Fini, S.P. DenBaars, J.S. Speck: Homoepitaxial growth of GaN under Ga-stable and N-stable conditions by plasma-assisted molecular beam epitaxy, *J. Appl. Phys.* **82**, 5472–5479 (1997)
- 37.2 C.R. Elsass, I.P. Smorchkova, H.Y. Ben, E. Haus, C. Poblenz, P. Fini, K. Maranowski, P.M. Petroff, S.P. DenBaars, U.K. Mishra, J.S. Speck, A. Saxler, S. Elhamri, W.C. Mitchel: Electron transport in AlGaIn/GaN heterostructures grown by plasma-assisted molecular beam epitaxy, *Jpn. J. Appl. Phys. Part 2–Letters* **39**, L1023–L1025 (2000)
- 37.3 A. Hierro, A.R. Arehart, B. Heying, M. Hansen, J.S. Speck, U.K. Mishra, S.P. DenBaars, S.A. Ringel: Capture kinetics of electron traps in MBE-grown n-GaN, *Phys. Status Solidi b* **228**, 309–313 (2001)
- 37.4 R.F. Davis, A.M. Roskowski, E.A. Preble, J.S. Speck, B. Heying, J.A. Freitas, E.R. Glaser, W.E. Carlos: Gallium nitride materials – progress, status, and potential roadblocks, *Proc. IEEE* **90**, 993–1005 (2002)
- 37.5 P. Waltereit, H. Sato, C. Poblenz, D.S. Green, J.S. Brown, M. McLaurin, T. Katona, S.P. DenBaars, J.S. Speck, J.H. Liang, M. Kato, H. Tamura, S. Omori, C. Funaoka: Blue GaN-based light-emitting diodes grown by molecular-beam epitaxy with external quantum efficiency greater than 1.5%, *Appl. Phys. Lett.* **84**, 2748–2750 (2004)
- 37.6 C. Poblenz, P. Waltereit, J.S. Speck: Uniformity and control of surface morphology during growth of GaN by molecular beam epitaxy, *J. Vac. Sci. Technol. B* **23**, 1379–1385 (2005)
- 37.7 A. Corrión, F. Wu, T. Mates, C.S. Gallinat, C. Poblenz, J.S. Speck: Growth of Fe-doped GaN by RF plasma-assisted molecular beam epitaxy, *J. Cryst. Growth* **289**, 587–595 (2006)
- 37.8 A. Corrión, C. Poblenz, P. Waltereit, T. Palacios, S. Rajan, U.K. Mishra, J.S. Speck: Review of recent developments in growth of AlGaIn/GaN high-electron mobility transistors on 4H-SiC by plasma-assisted molecular beam epitaxy, *IEICE Trans. Electron.* **E89C**, 906–912 (2006)
- 37.9 A.S. Segal, A.V. Kondratyev, S.Y. Karpov, D. Martin, V. Wagner, M. Illegems: Surface chemistry and transport effects in GaN hydride vapor phase epitaxy, *J. Cryst. Growth* **270**, 384–395 (2004)
- 37.10 S.Y. Karpov, D.V. Zimina, Y.N. Makarov, B. Beaumont, G. Nataf, P. Gibart, M. Heuken, H. Jurgensen, A. Krishnan: Modeling study of hydride vapor phase epitaxy of GaN, *Phys. Status Solidi a* **176**, 439–442 (1999)
- 37.11 A.S. Segal, S.Y. Karpov, Y.N. Makarov, E.N. Mokhov, A.D. Roenkov, M.G. Ramm, Y.A. Vodakov: On mechanisms of sublimation growth of AlN bulk crystals, *J. Cryst. Growth* **211**, 68–72 (2000)
- 37.12 M.V. Bogdanov, S.E. Demina, S.Y. Karpov, A.V. Kulik, M.S. Ramm, Y.N. Makarov: Advances in modeling of wide-bandgap bulk crystal growth, *Cryst. Res. Technol.* **38**, 237–249 (2003)
- 37.13 E.N. Mokhov, A.D. Roenkov, Y.A. Vodakov, S.Y. Karpov, M.S. Ramm, A.S. Segal, Y.A. Makarov, H. Helava: Growth of AlN bulk crystals by sublimation sandwich method. In: *Silicon Carbide and Related Materials*, ed. by P. Bergman, E. Janzén (Trans Tech, Zurich 2002) pp. 979–982
- 37.14 S.Y. Karpov, D.V. Zimina, Y.N. Makarov, E.N. Mokhov, A.D. Roenkov, M.G. Ramm, Y.A. Vodakov: Sublimation growth of AlN in vacuum and in a gas atmosphere, *Phys. Status Solidi a* **176**, 435–438 (1999)
- 37.15 P.G. Baranov, E.N. Mokhov, A.O. Ostroumov, M.G. Ramm, M.S. Ramm, V.V. Ratnikov, A.D. Roenkov, Y.A. Vodakov, A.A. Wolfson, G.V. Saparin, S.Y. Karpov, D.V. Zimina, Y.N. Makarov, H. Jurgensen: Current status of GaN crystal growth by sublimation sandwich technique, *MRS Internet J. Nitride Semicond. Res.* **3**, 50 (1998)
- 37.16 C.H. Wei, Z.Y. Xie, L.Y. Li, Q.M. Yu, J.H. Edgar: MOCVD growth of cubic GaN on 3C-SiC deposited on Si(100) substrates, *J. Electron. Mater.* **29**, 317–321 (2000)
- 37.17 Z.Y. Xie, C.H. Wei, L.Y. Li, J.H. Edgar, J. Chaudhuri, C. Ignatiev: Effects of surface preparation on epitaxial GaN on 6H-SiC deposited via MOCVD, *MRS Internet J. Nitride Semicond. Res.* **4S1**, G3.39 (1999)
- 37.18 B.S. Sywe, J.R. Schlup, J.H. Edgar: Fourier-transform infrared spectroscopic study of pre-deposition reactions in metalloorganic chemical

- vapor-deposition of gallium nitride – Part II, *Chem. Mater.* **3**, 1093–1097 (1991)
- 37.19 J.H. Edgar, L.H. Robins, S.E. Coatney, L. Liu, J. Chaudhuri, K. Ignatiev, Z. Rek: A comparison of aluminum nitride freely nucleated and seeded on 6H-silicon carbide, *Silicon Carbide Relat. Mater.* **338–3**, 1599–1602 (2000)
- 37.20 Y. Shi, B. Liu, L.H. Liu, J.H. Edgar, E.A. Payzant, J.M. Hayes, M. Kuball: New technique for sublimation growth of AlN single crystals, *MRS Internet J. Nitride Semicond. Res.* **6**, 1–10 (2001)
- 37.21 J.H. Edgar, L. Liu, B. Liu, D. Zhuang, J. Chaudhuri, M. Kuball, S. Rajasingam: Bulk AlN crystal growth: self-seeding and seeding on 6H-SiC substrates, *J. Cryst. Growth* **246**, 187–193 (2002)
- 37.22 B. Liu, J.H. Edgar, Z. Gu, D. Zhuang, B. Raghothamachar, M. Dudley, A. Sarua, M. Kuball, H.M. Meyer: The durability of various crucible materials for aluminum nitride crystal growth by sublimation, *MRS Internet J. Nitride Semicond. Res.* **9**, 6 (2004)
- 37.23 Z. Gu, L. Du, J.H. Edgar, E.A. Payzant, L. Walker, R. Liu, M.H. Engelhard: Aluminum nitride-silicon carbide alloy crystals grown on SiC substrates by sublimation, *MRS Internet J. Nitride Semicond. Res.* **10**, 5 (2005)
- 37.24 Z. Gu, J.H. Edgar, D.W. Coffey, J. Chaudhuri, L. Nyakiti, R.G. Lee, J.G. Wen: Defect-selective etching of scandium nitride crystals, *J. Cryst. Growth* **293**, 242–246 (2006)
- 37.25 M. Callahan, M. Harris, M. Suscavage, D.F. Bliss, J. Bailey: Synthesis and growth of gallium nitride by the chemical vapor reaction process (CVRP), *MRS Internet J. Nitride Semicond. Res.* **4**, 10 (1999)
- 37.26 V. Tassev, D.F. Bliss, M. Suscavage, Q.S. Paduano, S.Q. Wang, L. Bouthillette: Iodine vapor phase growth of GaN: dependence of epitaxial growth rate on process parameters, *J. Cryst. Growth* **235**, 140–148 (2002)
- 37.27 M. Suscavage, L. Bouthillette, D.F. Bliss, S.Q. Wang, C. Sung: New iodide method for growth of GaN, *Phys. Status Solidi a* **188**, 477–480 (2001)
- 37.28 D.F. Bliss, V.L. Tassev, D. Weyburne, J.S. Bailey: Aluminum nitride substrate growth by halide vapor transport epitaxy, *J. Cryst. Growth* **250**, 1–6 (2003)
- 37.29 D. Cai, L.L. Zheng, H. Zhang, V.L. Tassev, D.F. Bliss: Modeling of aluminum nitride growth by halide vapor transport epitaxy method, *J. Cryst. Growth* **276**, 182–193 (2005)
- 37.30 W.J. Mecouch, B.J. Rodriguez, Z.J. Reitmeier, J.S. Park, R.F. Davis, Z. Sitar: Initial stages of growth of gallium nitride via iodine vapor phase epitaxy, *Mater. Res. Soc. Symp. Proc.* **831**, E3.23.1. (2005)
- 37.31 R. Schlesser, Z. Sitar: Growth of bulk AlN crystals by vaporization of aluminum in a nitrogen atmosphere, *J. Cryst. Growth* **234**, 349–353 (2002)
- 37.32 D. Zhuang, Z.G. Herro, R. Schlesser, B. Raghothamachar, M. Dudley, Z. Sitar: Seeded growth of AlN crystals on nonpolar seeds via physical vapor transport, *J. Electron. Mater.* **35**, 1513–1517 (2006)
- 37.33 D. Zhuang, Z.G. Herro, R. Schlesser, Z. Sitar: Seeded growth of AlN single crystals by physical vapor transport, *J. Cryst. Growth* **287**, 372–375 (2006)
- 37.34 R. Dalmau, R. Schlesser, B.J. Rodriguez, R.J. Neumanich, Z. Sitar: AlN bulk crystals grown on SiC seeds, *J. Cryst. Growth* **281**, 68–74 (2005)
- 37.35 V. Noveski, R. Schlesser, B. Raghothamachar, M. Dudley, S. Mahajan, S. Beaudoin, Z. Sitar: Seeded growth of bulk AlN crystals and grain evolution in polycrystalline AlN boules, *J. Cryst. Growth* **279**, 13–19 (2005)
- 37.36 V. Noveski, R. Schlesser, S. Mahajan, S. Beaudoin, Z. Sitar: Growth of AlN crystals on AlN/SiC seeds by AlN powder sublimation in nitrogen atmosphere, *MRS Internet J. Nitride Semicond. Res.* **9**, 2 (2004)
- 37.37 B. Wu, R.H. Ma, H. Zhang, M. Dudley, R. Schlesser, Z. Sitar: Growth kinetics and thermal stress in AlN bulk crystal growth, *J. Cryst. Growth* **253**, 326–339 (2003)
- 37.38 E. Silveira, J.A. Freitas, G.A. Slack, L.J. Schowalter, M. Kneissl, D.W. Treat, N.M. Johnson: Depth-resolved cathodoluminescence of a homoepitaxial AlN thin film, *J. Cryst. Growth* **281**, 188–193 (2005)
- 37.39 J.C. Rojo, G.A. Slack, K. Morgan, B. Raghothamachar, M. Dudley, L.J. Schowalter: Report on the growth of bulk aluminum nitride and subsequent substrate preparation, *J. Cryst. Growth* **231**, 317–321 (2001)
- 37.40 L.J. Schowalter, J.C. Rojo, N. Yakolev, Y. Shusterman, K. Dovidenko, R.J. Wang, I. Bhat, G.A. Slack: Preparation and characterization of single-crystal aluminum nitride substrates, *MRS Internet J. Nitride Semicond. Res.* **5**, W6.7 (2000)
- 37.41 G. Koley, M.G. Spencer: Scanning Kelvin probe microscopy characterization of dislocations in III-nitrides grown by metalorganic chemical vapor deposition, *Appl. Phys. Lett.* **78**, 2873–2875 (2001)
- 37.42 I. Jenkins, K.G. Irvine, M.G. Spencer, V. Dmitriev, N. Chen: Growth of solid-solutions of aluminum nitride and silicon-carbide by metalorganic chemical vapor-deposition, *J. Cryst. Growth* **128**, 375–378 (1993)
- 37.43 K. Wongchotigul, N. Chen, D.P. Zhang, X. Tang, M.G. Spencer: Low resistivity aluminum nitride: Carbon (AlN:C) films grown by metal organic chemical vapor deposition, *Mater. Lett.* **26**, 223–226 (1996)
- 37.44 C.M. Zetterling, M. Ostling, K. Wongchotigul, M.G. Spencer, X. Tang, C.I. Harris, N. Nordell, S.S. Wong: Investigation of aluminum nitride grown by metal-organic chemical-vapor deposition on silicon, *J. Appl. Phys.* **82**, 2990–2995 (1997)
- 37.45 K. Wongchotigul, S. Wilson, C. Dickens, J. Griffin, X. Tang, M.G. Spencer: Growth of aluminum nitride with superior optical and morphological properties. In: *Silicon Carbide, III–Nitrides and Related*

- Materials, Parts 1 and 2*, ed. by G. Pensl, H. Morkoç, B. Monemar, E. Janzén (Trans Tech, Zurich 1998) pp. 1137–1140
- 37.46 H. Hirayama: Quaternary InAlGa_N-based high-efficiency ultraviolet light-emitting diodes, *J. Appl. Phys.* **97**, 091101 (2005)
- 37.47 S. Krukowski, C. Skierbiszewski, P. Perlin, M. Leszczynski, M. Bockowski, S. Porowski: Blue and UV semiconductor lasers, *Acta Phys. Polonica B* **37**, 1265–1312 (2006)
- 37.48 T.P. Chow, R. Tyagi: Wide bandgap compound semiconductors for superior high-voltage unipolar power devices, *IEEE Trans. Electron. Dev.* **41**, 1481–1483 (1994)
- 37.49 S.J. Pearton, C.R. Abernathy, B.P. Gila, A.H. Onstine, M.E. Overberg, G.T. Thaler, J. Kim, B. Luo, R. Mehandru, F. Ren, Y.D. Park: Recent advances in gate dielectrics and polarized light emission from GaN, *Optoelectron. Rev.* **10**, 231–236 (2002)
- 37.50 S.H. Kim, J.H. Ko, S.H. Ji, Y.S. Yoon: Crystallinity effect of AlN thin films on the frequency response of an AlN/IDT/Si surface acoustic wave device, *J. Korean Phys. Soc.* **49**, 199–202 (2006)
- 37.51 K. Katahira, H. Ohmori, Y. Uehara, M. Azuma: ELID grinding characteristics and surface modifying effects of aluminum nitride (AlN) ceramics, *Int. J. Mach. Tool. Manuf.* **45**, 891–896 (2005)
- 37.52 Y.G. Gao, D.A. Gulino, R. Higgins: Effects of susceptor geometry on GaN growth on Si(111) with a new MOCVD reactor, *MRS Internet J. Nitride Semicond. Res.* **4S1**, G3.53 (1999)
- 37.53 M. Morita, S. Isogai, N. Shimizu, K. Tsubouchi, N. Mikoshiba: Aluminum nitride epitaxially grown on silicon – orientation relationships, *Jpn. J. Appl. Phys.* **20**, L173–L175 (1981)
- 37.54 J.D. Brown, R. Borges, E. Piner, A. Vescan, S. Singhal, R. Therrien: AlGa_N/Ga_N HFETs fabricated on 100 mm GaN on silicon (111) substrates, *Solid-State Electron.* **46**, 1535–1539 (2002)
- 37.55 K. Kim, S.K. Noh: Reactor design rules for GaN epitaxial layer growths on sapphire in metal-organic chemical vapour deposition, *Semicond. Sci. Technol.* **15**, 868–874 (2000)
- 37.56 R.P. Parikh, R.A. Adomaitis: An overview of gallium nitride growth chemistry and its effect on reactor design: application to a planetary radial-flow CVD system, *J. Cryst. Growth* **286**, 259–278 (2006)
- 37.57 W.E. Hoke, A. Torabi, R.B. Hallock, J.J. Mosca, T.D. Kennedy: Reaction of molecular beam epitaxial grown AlN nucleation layers with SiC substrates, *J. Vac. Sci. Technol. B* **24**, 1500–1504 (2006)
- 37.58 R.M. Feenstra, Y. Dong, C.D. Lee, J.E. Northrup: Recent developments in surface studies of GaN and AlN, *J. Vac. Sci. Technol. B* **23**, 1174–1180 (2005)
- 37.59 S.H. Cho, K. Hata, T. Maruyama, K. Akimoto: Optical and structural properties of GaN films grown on c-plane sapphire by ECR-MBE, *J. Cryst. Growth* **173**, 260–265 (1997)
- 37.60 A. Usui, H. Sunakawa, A. Sakai, A.A. Yamaguchi: Thick GaN epitaxial growth with low dislocation density by hydride vapor phase epitaxy, *Jpn. J. Appl. Phys. Part 2 – Letters* **36**, L899–L902 (1997)
- 37.61 A. Dollet, Y. Casaux, M. Matecki, R. Rodriguez-Clemente: Chemical vapour deposition of polycrystalline AlN films from AlCl₃–NH₃ mixtures: II – surface morphology and mechanisms of preferential orientation at low-pressure, *Thin Solid Films* **406**, 118–131 (2002)
- 37.62 M. Callahan, B.G. Wang, K. Rakes, D.F. Bliss, L. Bouthillette, M. Suscavage, S.Q. Wang: GaN single crystals grown on HVPE seeds in alkaline supercritical ammonia, *J. Mater. Sci.* **41**, 1399–1407 (2006)
- 37.63 Y. Kumagai, T. Yamane, A. Koukitu: Growth of thick AlN layers by hydride vapor-phase epitaxy, *J. Cryst. Growth* **281**, 62–67 (2005)
- 37.64 M. Tanaka, S. Nakahata, K. Sogabe, H. Nakata, M. Tobioaka: Morphology and x-ray diffraction peak widths of aluminum nitride single crystals prepared by the sublimation method, *Jpn. J. Appl. Phys. Part 2 – Letters* **36**, L1062–L1064 (1997)
- 37.65 C.M. Balkas, Z. Sitar, T. Zheleva, L. Bergman, R. Nemanich, R.F. Davis: Sublimation growth and characterization of bulk aluminum nitride single crystals, *J. Cryst. Growth* **179**, 363–370 (1997)
- 37.66 S. Kurai, K. Nishino, S. Sakai: Nucleation control in the growth of bulk GaN by sublimation method, *Jpn. J. Appl. Phys. Part 2–Letters* **36**, L184–L186 (1997)
- 37.67 Y. Naoi, K. Kobatake, S. Kurai, K. Nishino, H. Sato, M. Nozaki, S. Sakai, Y. Shintani: Characterization of bulk GaN grown by sublimation technique, *J. Cryst. Growth* **190**, 163–166 (1998)
- 37.68 I.K. Shmagin, J.F. Muth, J.H. Lee, R.M. Kolbas, C.M. Balkas, Z. Sitar, R.F. Davis: Optical metastability in bulk GaN single crystals, *Appl. Phys. Lett.* **71**, 455–457 (1997)
- 37.69 L.J. Schowalter, J.C. Rojo, G.A. Slack, Y. Shusterman, R. Wang, I. Bhat, G. Arunmozhi: Epitaxial growth of AlN and Al_{0.5}Ca_{0.5}N layers on aluminum nitride substrates, *J. Cryst. Growth* **211**, 78–81 (2000)
- 37.70 D. Zhuang, Z.G. Herro, R. Schlesser, Z. Sitar: Seeded growth of AlN single crystals by physical vapor transport, *J. Cryst. Growth* **287**, 372–375 (2006)
- 37.71 W.J. Mecouch: Preparation and characterization of thin, tomically clean GaN(0001) and AlN(0001) films and the deposition of thick GaN films via iodine vapor phase growth, *Mater. Sci. Eng. Dep. (North Carolina State Univ.)* 2005
- 37.72 D. Cai, W.J. Mecouch, L.L. Zheng, H. Zhang, Z. Sitar: Thermodynamic and kinetic study of transport and reaction phenomena in gallium nitride epitaxy growth, *Int. J. Heat Mass Transf.* **51**, 1264–1280 (2008)

- 37.73 R.J. Molnar, W. Gotz, L.T. Romano, N.M. Johnson: Growth of gallium nitride by hydride vapor-phase epitaxy, *J. Cryst. Growth* **178**, 147–156 (1997)
- 37.74 T. Paskova, E.M. Goldys, B. Monemar: Hydride vapour-phase epitaxy growth and cathodoluminescence characterisation of thick GaN films, *J. Cryst. Growth* **203**, 1–11 (1999)
- 37.75 K. Ohno, K. Esfarjani, Y. Kawazoe: *Computational Materials Science: From ab Initio to Monte Carlo Methods* (Springer, Berlin 1999)
- 37.76 W. Hergert, A. Ernst, M. Däne: *Computational Materials Science: From Basic Principles to Material Properties* (Springer, Berlin 2004)
- 37.77 D. Raabe: *Computational Materials Science: The Simulation of Materials Microstructures and Properties* (Wiley-VCH, Weinheim 1998)
- 37.78 C.R.A. Catlow: *Computational Materials Science* (NATO Science, Amsterdam 2003)
- 37.79 M.A. Gosálvez, R.M. Nieminen: Target-rate kinetic Monte Carlo method for simulation of nanoscale structural evolution, *J. Comput. Theor. Nanosci.* **1**, 303–308 (2004)
- 37.80 C.C. Battaile, D.J. Srolovitz, J.E. Butler: A kinetic Monte Carlo method for the atomic-scale simulation of chemical vapor deposition: application to diamond, *J. Appl. Phys.* **82**, 6293–6300 (1997)
- 37.81 C.C. Battaile, D.J. Srolovitz: Kinetic Monte Carlo simulation of chemical vapor deposition, *Annu. Rev. Mater. Res.* **32**, 297–319 (2002)
- 37.82 C. Cavallotti, A. Barbato, A. Veneroni: A combined three-dimensional kinetic Monte Carlo and quantum chemistry study of the CVD of Si on Si(100) surfaces, *J. Cryst. Growth* **266**, 371–380 (2004)
- 37.83 C. Cavallotti, M. DiStanislao, D. Moscatelli, A. Veneroni: Materials computation towards technological impact: The multiscale approach to thin films deposition, *Electrochem. Acta* **50**, 4566–4575 (2005)
- 37.84 Y. Akiyama: Modeling thermal CVD, *J. Chem. Eng. Jpn.* **35**, 701–713 (2002)
- 37.85 L.C. Musson, P. Ho, S.J. Plimpton, R.C. Schmidt: Feature length-scale modeling of LPCVD and PECVD MEMS fabrication processes, *Microsystem Technol. Micro. Nanosyst. Info. Storage Proc. Syst.* **12**, 137–142 (2005)
- 37.86 H.A. Al-Mohssen, N.G. Hadjiconstantinou: Arbitrary-pressure chemical vapor deposition modeling using direct simulation Monte Carlo with nonlinear surface chemistry, *J. Comput. Phys.* **198**, 617–627 (2004)
- 37.87 K.F. Jensen: Transport phenomena in vapor phase epitaxy reactors. In: *Handbook of Crystal Growth*, ed. by F.J.T. Hurler (Elsevier, Amsterdam 1994) pp. 541–
- 37.88 C.R. Kleijn: Chemical vapor deposition processes. In: *Computational Modeling in Semiconductor Processing*, ed. by M. Meyyappan (Artech House, Northwood 1995) pp. 97–216
- 37.89 A.A. Schmidt, V.S. Kharlamov, K.L. Safonov, Y.V. Trushin, E.E. Zhurkin, V. Cimalla, O. Ambacher, J. Pezoldt: Growth of three-dimensional SiC clusters on Si modelled by KMC, *Comput. Mater. Sci.* **33**, 375–381 (2005)
- 37.90 L.H. Liu, J.H. Edgar: Transport effects in the sublimation growth of aluminum nitride, *J. Cryst. Growth* **220**, 243–253 (2000)
- 37.91 L.H. Liu, J.H. Edgar: A global growth rate model for aluminum nitride sublimation, *J. Electrochem. Soc.* **149**, G12–G15 (2002)
- 37.92 S.Y. Karpov, V.G. Prokofyev, E.V. Yakovlev, R.A. Talalaev, Y.N. Makarov: Novel approach to simulation of group-III nitrides growth by MOVPE, *MRS Internet J. Nitride Semicond. Res.* **4**, 4 (1999)
- 37.93 S.Y. Karpov, R.A. Talalaev, Y.N. Makarov, N. Grandjean, J. Massies, B. Damilano: Surface kinetics of GaN evaporation and growth by molecular-beam epitaxy, *Surf. Sci.* **450**, 191–203 (2000)
- 37.94 S.A. Safvi, N.R. Perkins, M.N. Horton, R. Matyi, T.F. Kuech: Effect of reactor geometry and growth parameters on the uniformity and material properties of GaN/sapphire grown by hydride vapor-phase epitaxy, *J. Cryst. Growth* **182**, 233–240 (1997)
- 37.95 S.A. Safvi, J.M. Redwing, M.A. Tischler, T.F. Kuech: GaN growth by metallorganic vapor phase epitaxy – a comparison of modeling and experimental measurements, *J. Electrochem. Soc.* **144**, 1789–1796 (1997)
- 37.96 C. Theodoropoulos, T.J. Mountziaris, H.K. Moffat, J. Han: Design of gas inlets for the growth of gallium nitride by metalorganic vapor phase epitaxy, *J. Cryst. Growth* **217**, 65–81 (2000)
- 37.97 E. Aujol, J. Napierala, A. Trassoudaine, E. Gil-Lafon, R. Cadoret: Thermodynamical and kinetic study of the GaN growth by HVPE under nitrogen, *J. Cryst. Growth* **222**, 538–548 (2001)
- 37.98 A. Dollet, Y. Casaux, G. Chaix, C. Dupuy: Chemical vapour deposition of polycrystalline AlN films from AlCl₃ – NH₃ mixtures: analysis and modelling of transport phenomena, *Thin Solid Films* **406**, 1–16 (2002)
- 37.99 B. Wu, R.H. Ma, H. Zhang, V. Prasad: Modeling and simulation of AlN bulk sublimation growth systems, *J. Cryst. Growth* **266**, 303–312 (2004)
- 37.100 B. Wu, H. Zhang: Isotropic and anisotropic growth models for the sublimation vapour transport process, *Model. Simul. Mater. Sci. Eng.* **13**, 861–873 (2005)
- 37.101 D. Cai, L.L. Zheng, H. Zhang, V.L. Tassev, D.F. Bliss: Modeling of gas phase and surface reactions in an aluminum nitride growth system, *J. Cryst. Growth* **293**, 136–145 (2006)
- 37.102 A. Dollet: Multiscale modeling of CVD film growth – a review of recent works, *Surf. Coat. Technol.* **177**, 245–251 (2004)
- 37.103 A.V. Vasenkov, A.I. Fedoseyev, V.I. Kolobov, H.S. Choi, K.H. Hong, K. Kim, J. Kim, H.S. Lee,

- J.K. Shin: Computational framework for modeling of multi-scale processes, *J. Comput. Theor. Nanosci.* **3**, 453–458 (2006)
- 37.104 S.T. Rodgers, K.F. Jensen: Multiscale modeling of chemical vapor deposition, *J. Appl. Phys.* **83**, 524–530 (1998)
- 37.105 K.F. Jensen, S.T. Rodgers, R. Venkataramani: Multiscale modeling of thin film growth, *Curr. Opin. Solid State Mater. Sci.* **3**, 562–569 (1998)
- 37.106 H.N.G. Wadley, A.X. Zhou, R.A. Johnson, M. Neerock: Mechanisms, models and methods of vapor deposition, *Prog. Mater. Sci.* **46**, 329–377 (2001)
- 37.107 W.M. Rohsenow, J.P. Hartnett: *Handbook of Heat Transfer* (McGraw-Hill, New York 1975)
- 37.108 P. Cheng: 2-dimensional radiating gas flow by a moment method, *AIAA Journal* **2**, 1662–1664 (1964)
- 37.109 R. Siegel, J.R. Howell: *Thermal Radiation Heat Transfer* (Hemisphere, Washington 1992)
- 37.110 M.F. Modest: *Radiative Heat Transfer* (McGraw-Hill, New York 1993)
- 37.111 M.H.N. Naraghi, J.C. Huan: An N-bounce method for analysis of radiative-transfer in enclosures with anisotropically scattering media, *J. Heat Transf. Trans. ASME* **113**, 774–777 (1991)
- 37.112 G.D. Raithby, E.H. Chui: A finite-volume method for predicting a radiant-heat transfer in enclosures with participating media, *J. Heat Transf. Trans. ASME* **112**, 415–423 (1990)
- 37.113 M.G. Carvalho, T. Farias, P. Fotes: Predicting radiative heat transfer in absorbing, emitting, scattering media using the discrete transfer method. In: *Fundamentals of Radiation Heat Transfer*, ed. by W.A. Fiveland (ASME HTD, New York 1991) pp. 17–26
- 37.114 L.S. Yao: Free and forced-convection in the entry region of a heated vertical channel, *Int. J. Heat Mass Transf.* **26**, 65–72 (1983)
- 37.115 T.K. Sherwood, R.J. Pigford, C.R. Wilke: *Mass Transfer* (McGraw-Hill, New York 1975)
- 37.116 A. Bejan: *Convective Heat Transfer* (Wiley-Interscience, Hoboken 2004)
- 37.117 O. Knacke, O. Kubaschewski, K. Hesselmann: *Thermochemical Properties of Inorganic Substances I* (Springer, Berlin 1991)
- 37.118 I. Barin: *Thermochemical Data of Pure Substances* (VCH, Weinheim 1989)
- 37.119 A.A. Chernov: *Modern Crystallography III. Crystal Growth* (Springer, Berlin 1984)
- 37.120 W.J. Mecouch: Preparation and characterization of thin, atomically clean GaN(0001) and AlN(0001) films and the deposition of thick GaN films via iodine vapor phase growth, Ph. D. Thesis (North Carolina State Univ. 2005)
- 37.121 R. Cadoret, E. Gil-Lafon: GaAs growth mechanisms of exact and isoriented {001} faces by the chloride method in H₂: Surface diffusion, spiral growth, HCl and GaCl₃ desorption mechanisms, *J. Phys. I France* **7**, 889–907 (1997)
- 37.122 D.F. Davidson, K. Kohse-Hoinghaus, A.Y. Chang, R.K. Hanson: A pyrolysis mechanism for ammonia, *Int. J. Chem. Kinetics* **22**, 513–535 (1990)
- 37.123 D.R. Stull: Vapor pressure of pure substances – organic compounds, *Ind. Eng. Chem.* **39**, 517–540 (1947)
- 37.124 R.F. Rolsten: *Iodide Metals and Metal Iodides* (Wiley, New York 1961)
- 37.125 A. Shintani, S. Minagawa: Kinetics of epitaxial-growth of GaN using Ga, HCl and NH₃, *J. Cryst. Growth* **22**, 1–5 (1974)
- 37.126 D.W. Shaw: Influence of substrate temperature on GaAs epitaxial deposition rates, *J. Electrochem. Soc.* **115**, 405 (1968)
- 37.127 M. Mesrine, N. Grandjean, J. Massies: Efficiency of NH₃ as nitrogen source for GaN molecular beam epitaxy, *Appl. Phys. Lett.* **72**, 350–352 (1998)
- 37.128 D.J. Srolovitz, A. Mazor, B.G. Bukiet: Analytical and numerical modeling of columnar evolution in thin-films, *J. Vac. Sci. Technol. A* **6**, 2371–2380 (1988)
- 37.129 R. Collazo, R. Dalmau, Z. Herro, D. Zhuang, Z. Sitar: Is HVPE fundamentally inferior to PVT of AlN, ONR MURI: III-nitride crystal growth and wafering meeting (Arizona 2006)
- 37.130 O. Kovalenkov, V. Soukhoveev, V. Ivantsov, A. Usikov, V. Dmitriev: Thick AlN layers grown by HVPE, *J. Cryst. Growth* **281**, 87–92 (2005)

38. Continuum-Scale Quantitative Defect Dynamics in Growing Czochralski Silicon Crystals

Milind S. Kulkarni

The vast majority of modern microelectronic devices are built on monocrystalline silicon substrates produced from crystals grown by the Czochralski (CZ) and float-zone (FZ) processes. Silicon crystals inherently contain various crystallographic imperfections known as microdefects that often affect the yield and performance of many devices. Hence, quantitative understanding and control of the formation and distribution of microdefects in silicon crystals play a central role in determining the quality of silicon substrates. These microdefects are primarily aggregates of intrinsic point defects of silicon (vacancies and self-interstitials) and oxygen (silicon dioxide). The distribution of microdefects in a CZ crystal is determined by the complex dynamics, influenced by various reactions involving the intrinsic point defects and oxygen, and their transport. The distribution of these microdefects can also be strongly influenced and controlled by the addition of impurities such as nitrogen to the crystal. In this chapter, significant developments in the field of defect dynamics in growing CZ and FZ crystals are reviewed. The breakthrough discovery of the *initial point defect incorporation* in the vicinity of the melt-crystal interface, made in the early 1980s, allows a simplified quantification of CZ and FZ defect dynamics. Deeper insight into the formation and growth of microdefects was provided in the last decade by various treatments of the aggregation of oxygen and the intrinsic point defects of silicon. In particular, rigorous quantification of the aggregation of intrinsic point defects using the classical nucleation theory, a recently developed lumped model that captures the microdefect distribution by representing the actual population of microdefects by an equivalent population of identical microdefects, and another rigorous treatment involving the Fokker-Planck equations are discussed in detail.

The industrially significant dynamics of growing CZ crystals free of large microdefects is also reviewed. Under the conditions of large microdefect-free growth, a moderate vacancy supersaturation develops in the vicinity of the lateral surface of a growing crystal, leading to the formation of oxygen clusters and small voids, at lower temperatures. The vacancy incorporation near the lateral surface of a crystal, or the *lateral incorporation of vacancies*, is driven by the interplay among the Frenkel reaction, the diffusion of the intrinsic point defects, and their convection.

A review of CZ defect dynamics with a particular focus on the growth of large microdefect-free crystals is presented and discussed.

38.1	The Discovery of Microdefects	1283
38.2	Defect Dynamics in the Absence of Impurities	1284
38.2.1	The Theory of the Initial Incorporation of Intrinsic Point Defects	1284
38.2.2	The Quantification of the Microdefect Formation	1290
38.3	Czochralski Defect Dynamics in the Presence of Oxygen	1304
38.3.1	Reactions in Growing CZ Crystals...	1304
38.3.2	The Model	1305
38.3.3	Defect Dynamics in One-Dimensional Crystal Growth..	1308
38.3.4	Defect Dynamics in Two-Dimensional Crystal Growth .	1310
38.4	Czochralski Defect Dynamics in the Presence of Nitrogen	1313
38.4.1	The Model	1313
38.4.2	CZ Defect Dynamics in One-Dimensional Crystal Growth..	1316

38.4.3 CZ Defect Dynamics in Two-Dimensional Crystal Growth .	1318	38.6 Conclusions	1328
38.5 The Lateral Incorporation of Vacancies in Czochralski Silicon Crystals	1321	38.6.1 CZ Defect Dynamics in the Absence of Impurities.....	1329
38.5.1 General Defect Dynamics: A Brief Revisit	1322	38.6.2 CZ Defect Dynamics in the Presence of Oxygen	1330
38.5.2 Defect Dynamics Under Highly Vacancy-Rich Conditions	1323	38.6.3 CZ Defect Dynamics in the Presence of Nitrogen	1330
38.5.3 Defect Dynamics Near the Critical Condition.....	1324	38.6.4 The Lateral Incorporation of Vacancies	1331
		References	1332

In modern microelectronics industry, the majority of devices are fabricated on silicon substrates produced from silicon crystals grown by the Czochralski (CZ) process. The float-zone (FZ) process is also used to produce a small fraction of the silicon substrates used in the modern industry. In the CZ process, a silicon crystal is continuously pulled from a silicon melt placed in a quartz crucible, as shown in Fig. 38.1. A CZ crystal has a conical top called the *crown*, a conical bottom called the *endcone*, and a cylindrical section called the *body*, which provides substrates for the fabrication of devices. In the FZ process, a molten silicon zone is allowed to form and solidify along the entire length of a polycrystalline silicon body to form a silicon single crystal. Silicon crystals

grown prior to the late 1950s contained thermomechanically induced dislocations. A breakthrough discovery by Dash in the late 1950s allowed crystal growth free of these dislocations [38.2, 3]. In modern crystals, free of thermomechanically induced dislocations, various crystallographic imperfections known as microdefects, aggregated defects, and grown-in bulk defects can form and grow [38.4–15]. Microdefects vary in size from a few nanometers to > 200 nm. Microdefects of this size significantly affect the performance of the continuously shrinking modern microelectronic devices. This chapter addresses key developments in the crystal growth industry in the understanding and quantification of the physics of the formation of microdefects, popularly termed *defect dynamics*.

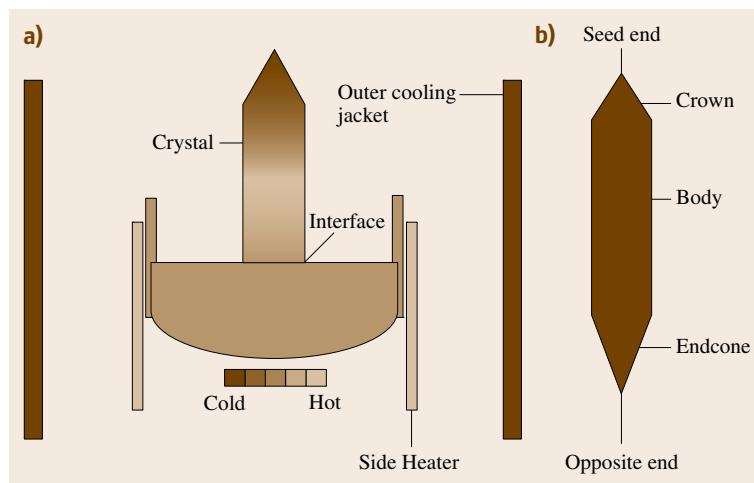


Fig. 38.1 (a) A schematic representation of the Czochralski (CZ) crystal growth process, (b) a grown CZ crystal (after [38.1])

38.1 The Discovery of Microdefects

Various types of microdefects are formed in CZ and FZ crystals. However, two types of microdefects commonly occur and hence are of critical significance. These are the aggregates of the intrinsic point defects of silicon: self-interstitials and vacancies. Vacancies are formed by silicon atoms missing from the silicon crystal lattice, whereas self-interstitials are silicon atoms that are not part of the lattice. Self-interstitial aggregates in

FZ crystals were first observed in the 1960s and were termed *A defect swirls* (*A defects*) and *B defect swirls* (*B defects*), although the origin of these defects was not clearly known [38.4, 6–9]. Later, A defects were identified as dislocation loops and B defects were presumed to be globular self-interstitial aggregates [38.10–13]. In the 1980s, vacancy aggregates in FZ crystals were first reported and later termed *D defects* [38.14, 15]. More recent studies have identified D defects as octahedral voids [38.17, 18].

The discovery of the described microdefects was followed by various attempts to explain their formation. The dependence of the type of microdefects formed on the crystal growth rate was reported in various papers [38.6, 8, 14, 15]. A and B defects were observed at lower growth rates while D defects were observed at higher growth rates (Fig. 38.2). A unifying and acceptable analysis of the microdefect distribution in silicon crystals, however, was not available until 1982, when Voronkov provided the first groundbreaking explanation of defect dynamics in both FZ and CZ growth [38.19].

Various impurities present in a silicon crystal can influence the defect dynamics. CZ crystals are grown

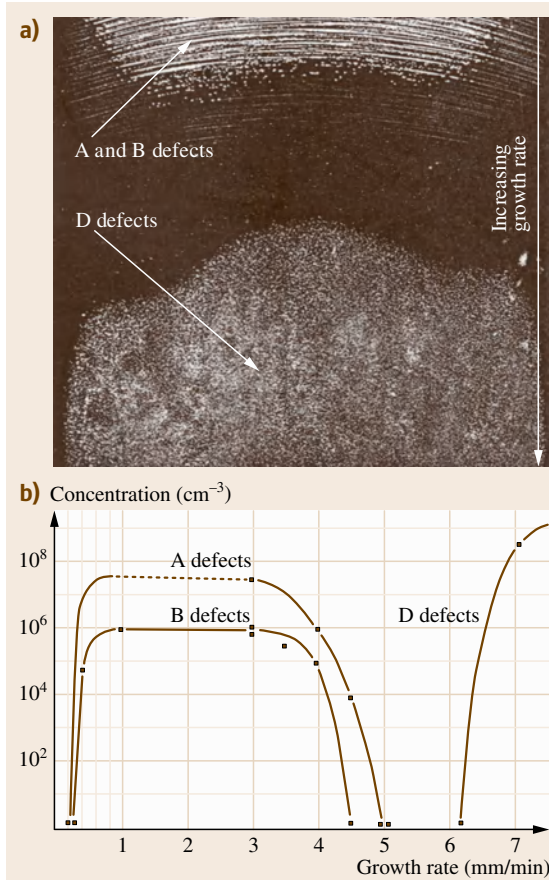


Fig. 38.2 (a) X-ray transmission topograph of a copper-decorated longitudinal section of a pedestal-pulled crystal, showing the dependence of the microdefect type on the growth rate. The growth rate varies from 4 to 7 mm/min from top to bottom. Note that the morphological details of microdefects are not revealed by the decoration of microdefects by the precipitation of copper. (b) The dependence of the type and density of microdefects on the crystal growth rate (after [38.14], © Elsevier 1981)

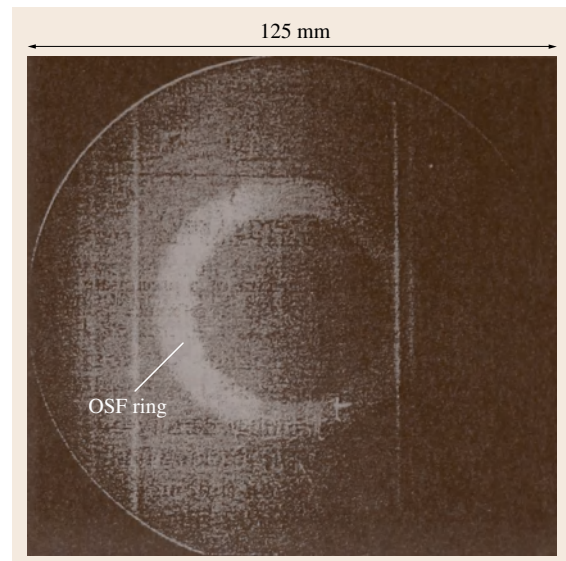


Fig. 38.3 An x-ray topograph (positive image) of a wafer showing the annular region containing OSFs. The wafer was sliced from a CZ crystal and treated at 1100 °C for 1 h in steam (after [38.16] © Jpn. J. Appl. Phys.)

from a melt contained in a quartz crucible, which is a source of oxygen. Hence, CZ crystals contain oxygen, unlike FZ crystals. Oxygen in CZ crystals typically precipitates as particles of silicon dioxide, which are popularly termed *oxygen precipitates* or *oxygen clusters*. Oxygen clusters in a growing CZ crystal are typically very small. These clusters facilitate the formation of stacking faults in crystals subjected to selective heat treatments that generate self-interstitials. Hence, oxygen clusters are typically identified by these stacking faults, known as oxidation-induced stacking faults

(OSFs) (Fig. 38.3) [38.16]. As microdefects in silicon substrates produced from CZ crystals can adversely affect the performance of devices built on them, the development of crystal growth processes that reduce the size of microdefects in growing crystals is of industrial significance. Various studies have shown that the microdefect distribution in CZ crystals can be influenced in the presence of nitrogen, in general, and that the size of D defects (voids) can be reduced, in particular [38.20]. Dopants such as boron also affect CZ defect dynamics [38.21–24].

38.2 Defect Dynamics in the Absence of Impurities

Considering the complexity of CZ defect dynamics, first CZ and FZ defect dynamics in the absence of impurities are discussed in this chapter, followed by CZ defect dynamics in the presence of nitrogen and oxygen.

38.2.1 The Theory of the Initial Incorporation of Intrinsic Point Defects

Voronkov was the first to provide a satisfactory and well-accepted explanation for the quality of the microdefect distributions observed in silicon crystals [38.19]. According to Voronkov's theory, an interplay between the transport of the intrinsic point defects in a growing crystal in the vicinity of the melt–crystal interface and the Frenkel reaction involving the mutual annihilation or the recombination of vacancies and self-interstitials plays a key role in determining the final microdefect distribution. Voronkov analyzed this interplay by quantifying the Frenkel reaction dynamics and the intrinsic point defect balances in a growing crystal. His groundbreaking work is briefly discussed below.

The Frenkel Reaction Dynamics in a Growing Crystal

The Frenkel reaction involves the reversible annihilation of vacancies and self-interstitials by their recombination and the spontaneous generation of vacancies and self-interstitials from silicon lattice atoms



where i is a self-interstitial, v is a vacancy, and Si is a silicon lattice atom. The net rate of recombination of vacancy and self-interstitial pairs is equal and opposite to the net rate of formation of self-interstitials or

vacancies, which is given by

$$-r_i = -r_v = k_{i \leftrightarrow v}(C_i C_v - C_{i,e} C_{v,e}), \quad (38.2)$$

where r is the net rate of formation of any species per unit volume, C is the concentration of any species, and $k_{i \leftrightarrow v}$ is the reaction rate constant known as the recombination constant. The subscript “ i ” denotes self-interstitials, “ v ” vacancies, “ e ” equilibrium conditions, and “ $i \leftrightarrow v$ ” the interaction between self-interstitials and vacancies. The intrinsic point defects are assumed to exist at equilibrium at the melt–crystal interface. The concentration of the intrinsic point defects, however, drops significantly in a crystal near the interface, as the decreasing temperature in the crystal facilitates rapid recombination of self-interstitials and vacancies. Hence, the intrinsic point defects diffuse from the interface into the crystal. In addition, the continuous growth of the crystal, or the crystal pulling, facilitates the transport of the intrinsic point defects by their convection. Compared with the timescale of the transport, the Frenkel reaction can be assumed to be instantaneous and, hence, in equilibrium. Thus, the following relationship remains valid

$$C_i C_v = C_{i,e} C_{v,e}. \quad (38.3)$$

The equilibrium concentrations of the intrinsic point defects are functions of the crystal temperature and are expressed as

$$C_{i,e} = C_{i,0} \exp\left(-\frac{E_{\text{form},i}}{k_B T}\right), \quad (38.4)$$

$$C_{v,e} = C_{v,0} \exp\left(-\frac{E_{\text{form},v}}{k_B T}\right), \quad (38.5)$$

where E_{form} is the formation energy (the subscript “form” denotes the formation energy) and k_B is the

Boltzmann constant. The temperature profile in a crystal, in the vicinity of the melt–crystal interface and at a fixed radial location, is reasonably represented by a linear approximation of the inverse of the temperature

$$\frac{1}{T} = \frac{1}{T_{s/l}} + \frac{1}{T_{s/l}^2} Gz, \quad (38.6)$$

where T is the temperature, G is the magnitude of the axial temperature gradient at the interface at any radial location, and z is the distance from the interface. The subscript “s/l” represents the conditions at the interface. Using (38.6), (38.4) and (38.5) can be written as

$$C_{i,e} = C_{i,e}(T_{s/l}) \exp\left(-\frac{E_{\text{form},i} Gz}{k_B T_{s/l}^2}\right), \quad (38.7)$$

$$C_{v,e} = C_{v,e}(T_{s/l}) \exp\left(-\frac{E_{\text{form},v} Gz}{k_B T_{s/l}^2}\right). \quad (38.8)$$

Thus, (38.3) describing the Frenkel reaction equilibrium takes the form

$$C_i C_v = C_{i,e}(T_{s/l}) C_{v,e}(T_{s/l}) \exp\left(\frac{-2z}{l}\right), \quad (38.9)$$

where the *characteristic recombination length* l is expressed as

$$l = \frac{2k_B T_{s/l}^2}{(E_{\text{form},i} + E_{\text{form},v})G}. \quad (38.10)$$

The discussed Frenkel reaction dynamics can be coupled with the overall intrinsic point defect balance in a growing crystal to describe the microdefect distributions observed in CZ and FZ crystals.

The Intrinsic Point Defect Balance and the Initial Incorporation

Driven by the Frenkel reaction, the concentrations of both the intrinsic point defect species dramatically drop in the vicinity of the melt–crystal interface. This intrinsic point defect concentration drop, in turn, drives the diffusion of both species from the interface, where they exist at equilibrium, into the crystal. In addition, the intrinsic point defects are also transported by the physical growth of the crystal, with respect to a fixed coordinate system. Crystal growth at a fixed rate and through a fixed temperature field with respect to a fixed coordinate system can be assumed to take place under a steady state. The excess intrinsic point defect flux, defined as the difference between the flux of vacancies and the flux of self-interstitials, is not explicitly affected by the Frenkel reaction. This excess flux is fixed for a given

crystal growth condition

$$j_{iv} = \left(-D_v \frac{dC_v}{dz} + VC_v\right) - \left(-D_i \frac{dC_i}{dz} + VC_i\right), \quad (38.11)$$

where j_{iv} is the excess intrinsic point defect flux, D is the diffusivity, and V is the magnitude of the axial crystal pull rate. The effects of radial diffusion are ignored in (38.11).

When the vacancy flux is greater than the self-interstitial flux or when the excess intrinsic point defect flux is positive, vacancies are the surviving dominant species in the growing crystal and self-interstitials are annihilated to very low concentrations, within a short distance from the melt–crystal interface. Vacancy supersaturation increases at lower temperatures to drive the formation of D defects. Vacancies are termed the *incorporated dominant intrinsic point defects* under this condition. When the self-interstitial flux is greater than the vacancy flux or when the excess intrinsic point defect flux is negative, self-interstitials are the dominant species in the crystal and vacancies are annihilated to very low concentrations, within a short distance from the interface. The crystal becomes supersaturated with self-interstitials, leading to the formation of B and A defects by the aggregation of self-interstitials at lower temperatures. Self-interstitials are termed the *incorporated dominant intrinsic point defects* under this condition.

When the vacancy flux is equal to the self-interstitial flux or when the excess intrinsic point defect flux is equal to zero, both the intrinsic point defect species remain in comparable concentrations in the growing crystal and annihilate each other to very low concentrations. Under this condition, defined as the *critical condition*, no detectable microdefects are formed in the crystal at any temperature. At the critical condition, (38.11) is satisfied when both the intrinsic point defect concentrations show the same dependence on z , if the diffusivities of both the species are fixed and temperature independent. This assumption is approximate but acceptable within a narrow range of temperatures close to the interface. Then, using (38.9), the intrinsic point defect concentrations in a crystal growing under the critical condition are defined as

$$C_i = C_{i,0} \exp\left(\frac{E_{\text{form},i} + E_{\text{form},v}}{2k_B T_{s/l}} - \frac{E_{\text{form},i}}{k_B T_{s/l}} - \frac{E_{\text{form},i} + E_{\text{form},v}}{2k_B T}\right), \quad (38.12)$$

$$C_v = C_{v,0} \exp \left(\frac{E_{\text{form},i} + E_{\text{form},v}}{2k_B T_{s/l}} - \frac{E_{\text{form},v}}{k_B T_{s/l}} - \frac{E_{\text{form},i} + E_{\text{form},v}}{2k_B T} \right). \quad (38.13)$$

Using (38.11–38.13), the critical condition is analytically derived as

$$(V/G)_c = \frac{E_{\text{form},i} + E_{\text{form},v}}{2k_B T_{s/l}^2} \times \frac{D_i(T_{s/l})C_{i,e}(T_{s/l}) - D_v(T_{s/l})C_{v,e}(T_{s/l})}{C_{v,e}(T_{s/l}) - C_{i,e}(T_{s/l})}, \quad (38.14)$$

where the subscript “c” denotes the critical value at zero excess intrinsic point defect flux.

Using this analysis, Voronkov explained the dependence of the microdefect distribution in a crystal on its growth rate (Fig. 38.2). At very high V , the convection dominates the diffusion. He hypothesized that the flux of vacancies into the crystal is higher than the flux of self-interstitials when the species convection is relatively appreciable, because the concentration of vacancies is higher than the concentration of self-interstitials at the interface. The crystal remains vacancy rich as the temperature drops. At very low V , the diffusion dominates the convection; Voronkov hypothesized that the flux of self-interstitials is greater than the flux of vacancies when the species diffusion is relatively appreciable, because self-interstitials diffuse faster than vacancies at higher temperatures. Thus, self-interstitials become the dominant incorporated species within a short distance from the interface, while vacancies are effectively annihilated. The dominant incorporated species eventually nucleates to form the appropriate microdefects at lower temperatures.

The competition between the intrinsic point defect convection and the intrinsic point defect diffusion is quantified not just by the crystal pull rate, but by the ratio of the crystal pull rate to the magnitude of the axial temperature gradient V/G . The convection of the intrinsic point defects increases with the crystal pull rate. The diffusion flux of an intrinsic point defect species increases with the increasing magnitude of its concentration gradient, which is driven by the temperature gradient near the interface. Thus, vacancies become the dominant incorporated intrinsic point defect species at higher V/G and self-interstitials become the dominant incorporated species at lower V/G . At the critical V/G , the flux of vacancies is equal

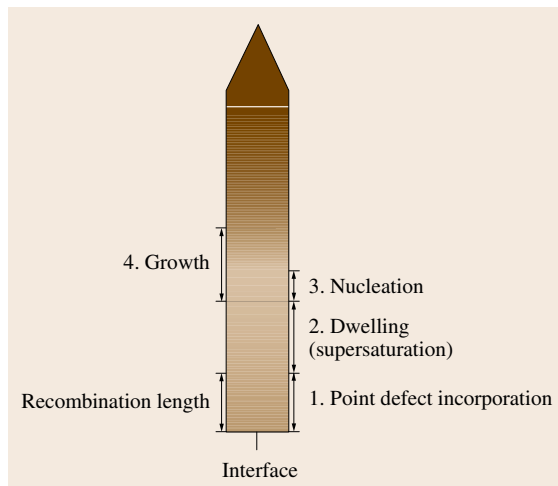


Fig. 38.4 The phases of defect dynamics in a growing crystal according to Voronkov's theory (not to scale) (after [38.25])

to the flux of self-interstitials and there is no dominance of either intrinsic point defect species as both species mutually annihilate each other to very low concentrations.

Table 38.1 Key properties of various species participating in reactions in growing CZ crystals and the recombination rate constant (after [38.1])

Property set I	
D_i (cm ² /s) = 0.19497 exp $\left(\frac{-0.9 \text{ (eV)}}{k_B T} \right)$	
D_v (cm ² /s) = 6.2617 × 10 ⁻⁴ exp $\left(\frac{-0.4 \text{ (eV)}}{k_B T} \right)$	
$C_{i,e}$ (cm ⁻³) = 6.1859 × 10 ²⁶ exp $\left(\frac{-4.0 \text{ (eV)}}{k_B T} \right)$	
$C_{v,e}$ (cm ⁻³) = 7.59982 × 10 ²⁶ exp $\left(\frac{-4.0 \text{ (eV)}}{k_B T} \right)$	
$k_{i \leftrightarrow v}$ (cm ³ /s) = 1.2 × 10 ⁻⁶ [$D_i(T) + D_v(T)$] × exp $\left[-\frac{0.61 + (-2.30 + 7.38 \times 10^{-3} T) k_B T}{k_B T} \right]^*$	
λ_i (eV) = 2.95**	
λ_v (eV) = 1.85	
* Reported by Sinno et al. [38.26]; the enthalpic barrier (0.61) is ignored in the simulations discussed in this chapter [38.1, 27]. An accurate estimation of this parameter is not necessary, because the Frenkel reaction dynamics is fast	
** For two-dimensional (2-D) simulations, a value of 2.85 eV is used	

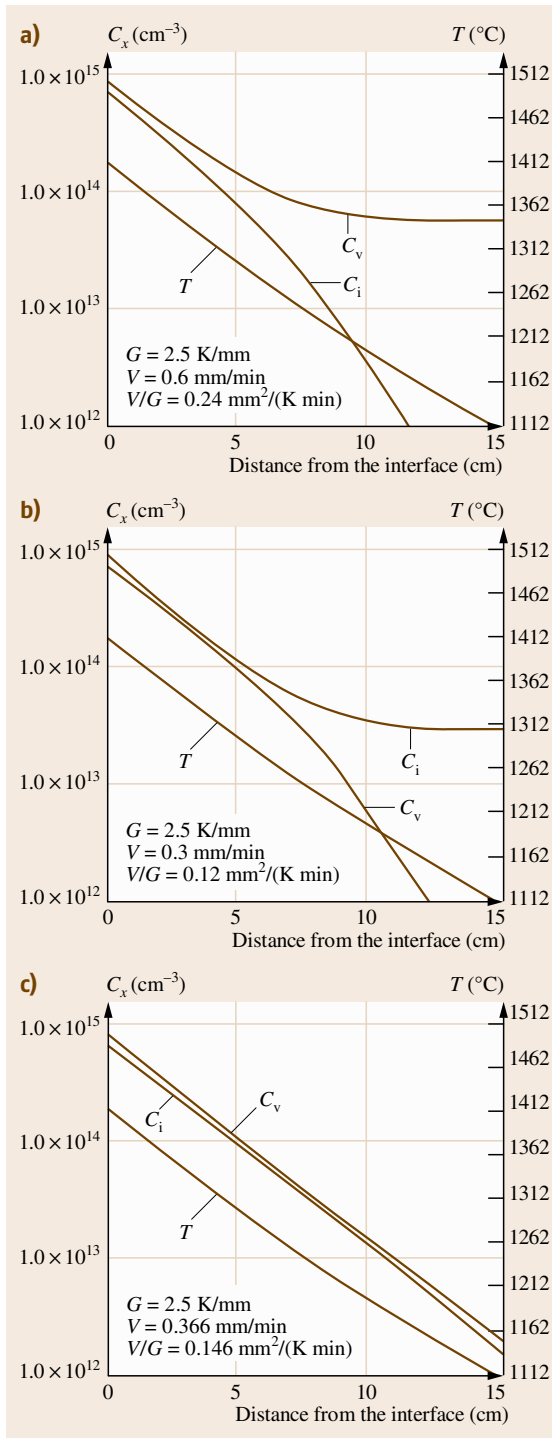


Fig. 38.5a–c The profiles of the vacancy concentration, the self-interstitial concentration, and the temperature in a Czochralski crystal growing at (a) a higher V/G , (b) a lower V/G , (c) close to the critical V/G (after [38.25])

The process of establishing the key intrinsic point defect concentration field in a growing CZ crystal in the vicinity of the melt–crystal interface is termed the *initial incorporation*. The initial incorporation takes place within a short distance from the interface, which scales with the characteristic recombination length l . When the operating V/G is either higher or lower than the critical V/G , the dominance of one intrinsic point defect species is established within the recombination length; when the operating V/G is closer to the critical V/G , however, both the intrinsic point defect species are incorporated in comparable concentrations and continue to recombine and annihilate each other beyond the recombination length, without forming large microdefects. A schematic representation of Voronkov’s theory is shown in Fig. 38.4. Voronkov’s theory can be verified by quantifying the intrinsic point defect concentration profiles ($C_x(z)$, x denoting either i or v) in a CZ crystal growing at various V/G , as shown in Fig. 38.5a–c. These computations were accomplished by assuming that both the diffusivities and the equilibrium concentrations of the intrinsic point defects vary with the temperature and by accounting for the Frenkel reaction kinetics [38.25]. The properties of the intrinsic point defects used in these simulations are listed in Table 38.1. There is significant uncertainty in the estimation of the properties of the intrinsic point defects. The parameters describing the Frenkel reaction kinetics, in particular, are not well known. An accurate estimation of the kinetic parameters is not necessary because the Frenkel reaction dynamics is very fast and, hence, reaction equilibrium prevails. It must be noted that the intrinsic point defect concentration profiles computed assuming the constant (fixed) intrinsic point defect diffusivities give slightly different results.

The evolution of the concentrations of the intrinsic point defects in a growing crystal strongly depends on the properties of the intrinsic point defects, especially the formation and migration energies. As shown by (38.12) and (38.13), at the critical V/G , the concentration of each intrinsic point defect species is equal to its equilibrium concentration at any axial location z , when the formation energy of a vacancy is equal to

the formation energy of a self-interstitial, the migration energies of both species are zero, and the temperature profile in the crystal is given by (38.6). Deviations from these conditions establish the nonequilibrium intrinsic point defect concentrations in a crystal growing at the critical V/G . The dynamics of crystal growth near the critical condition and the effects of the properties of the intrinsic point defects on this dynamics are discussed in detail in Sect. 38.5.

The significance of the discussed discovery of the initial intrinsic point defect incorporation in growing silicon crystals extends beyond the field of CZ and FZ defect dynamics; it remains valuable in the prediction of the properties of the intrinsic point defects of silicon by requiring that the difference $C_{v,e}(T_{s/l}) - C_{i,e}(T_{s/l})$ and the difference $D_i(T_{s/l})C_{i,e}(T_{s/l}) - D_v(T_{s/l})C_{v,e}(T_{s/l})$ be positive.

Validation and Limits of the Theory of One-Dimensional Initial Incorporation

Voronkov's theory of the intrinsic point defect incorporation has been validated by many experimental observations reported before and after its publication, in spite of a few initial questions raised by Tan and Gösele, among others [38.28]. The dependence of the microdefect type in FZ crystals on the crystal growth rate was reported in [38.6, 8, 14, 15]. By varying the pull rate of various CZ crystals, Sadamitsu et al. showed that the microdefect quality in the crystals shifted from vacancy type (vacancy aggregates) to self-interstitial type (self-interstitial aggregates) [38.29]. This study also revealed a radial variation in the microdefect distribution. This was explained by the radial variation in the temperature field, or the radial variation of G . In a typical CZ crystal, G monotonically increases and V/G monotonically decreases along the radial position. Thus, the central regions in many CZ crystals exhibit D defects and the peripheral regions exhibit A defects, as determined by V/G . The narrow microdefect-free region between the region of vacancy aggregates and the region of self-interstitial aggregates is known as the v/i boundary. The microdefect distributions in CZ crystals showing the v/i boundary were reported by many in the last decade [38.30–33].

The surface of a growing CZ crystal acts as a source or a sink of the intrinsic point defects and, hence, induces their radial diffusion; in addition, the radial variation in the temperature field also causes radial diffusion of the intrinsic point defects. The microdefect distributions away from the surfaces in rapidly pulled crystals in which the radial diffusion effects can be ignored, how-

ever, are very well explained by the one-dimensional initial incorporation theory. In a silicon crystal, the region containing abundant vacancies or vacancy aggregates is termed the *v-rich region* and the region containing abundant self-interstitials or the self-interstitial aggregates is termed the *i-rich region*. The position of the boundary between the *v-rich region* and the *i-rich region* established after the initial incorporation remains essentially the same even after the aggregation of the intrinsic point defects in a rapidly pulled CZ crystal. Hence, by following the v/i boundary separating the vacancy aggregates and the self-interstitial aggregates, in such crystals, the critical V/G can be experimentally determined. Typically, a narrow annular region inside the *v-rich region* of a CZ crystal near the v/i boundary exhibits another type of microdefects known as oxidation-induced stacking faults (OSFs), after a treatment with selective heat cycles. These OSFs are formed by the oxides of silicon, formed during the crystal growth, in the regions grown at V/G slightly above the critical V/G (Figs. 38.3 and 38.6). The incorporated vacancies in this region are too low in concentration to nucleate at higher temperatures ($\approx 1100^\circ\text{C}$) to form D defects during crystal growth; they survive at lower temperatures ($\approx 1000\text{--}850^\circ\text{C}$) to facilitate the formation of silicon oxide (primarily silicon dioxide) particles. Oxygen required for this oxidation in CZ crystals comes from the quartz crucible used in the CZ process. The specific volume of an oxide particle is greater than the specific volume of silicon. Hence, the formation and growth of the oxide particles generates compressive stresses. Relief of this stress can take place by the consumption of vacancies and the ejection of self-interstitials from the silicon lattice. During crystal growth, the oxide particles in the OSF region are formed essentially by facilitation by vacancies. The growth of the oxide particles by the ejection of self-interstitials can take place after the depletion of free vacancies at lower temperatures. These compressed oxide particles in a silicon wafer facilitate the growth of stacking faults or OSFs after selective heat treatments that inject self-interstitials into the silicon wafer. Hasebe et al. were among the first to report the presence of the annular region of OSFs termed the *OSF ring* in CZ crystals (Fig. 38.3) [38.16]. Often the location of the *OSF ring*, because of its vicinity to the v/i boundary, is used to mark the critical V/G . The CZ defect dynamics in the presence of oxygen describing the formation and growth of oxygen clusters is discussed later in this chapter.

The radial diffusion of the intrinsic point defects in a CZ crystal, both driven by the variation in the crys-

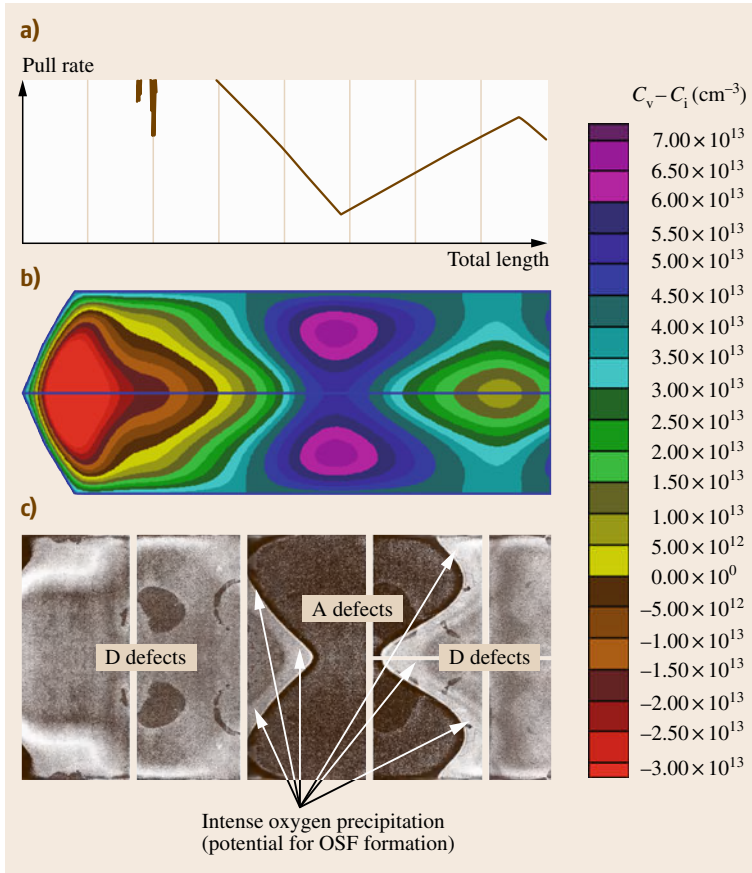


Fig. 38.6 (a) The pull-rate profile used to pull the experimental crystal. (b) The predicted excess intrinsic point defect concentration field in the crystal. (c) The experimentally observed microdefect distribution. The radial variation of G at the interface was more than 140%. Note: The simulation results are not completely mesh insensitive (after [38.25])

tal temperature field and induced by the lateral surface of the crystal, cannot be ignored in modern CZ growth. Thus, a more complete picture of the intrinsic point defect dynamics is described by considering the transport of the intrinsic point defects in an axisymmetric crystal growing through a temperature field at pseudo-steady state

$$\frac{\partial C_i}{\partial t} + V \frac{\partial C_i}{\partial z} = \nabla (D_i \nabla C_i) - k_{i \leftrightarrow v} (C_i C_v - C_{i,e} C_{v,e}), \quad (38.15)$$

$$\frac{\partial C_v}{\partial t} + V \frac{\partial C_v}{\partial z} = \nabla (D_v \nabla C_v) - k_{i \leftrightarrow v} (C_i C_v - C_{i,e} C_{v,e}). \quad (38.16)$$

Nakamura et al. and Sinno et al. were among the first to solve the two-dimensional intrinsic point defect dynamics in growing CZ crystals to clearly define the final microdefect distributions [38.26, 34].

The equations describing the intrinsic point defect distributions in a CZ crystal can be further simplified by assuming the Frenkel reaction equilibrium. The

evolution of the excess intrinsic point defect concentration $C_v - C_i$ is described without an explicit use of the Frenkel reaction kinetics as

$$\begin{aligned} \frac{\partial (C_v - C_i)}{\partial t} + V \frac{\partial C_v}{\partial z} - V \frac{\partial C_i}{\partial z} \\ = \nabla (D_v \nabla C_v) - \nabla (D_i \nabla C_i). \end{aligned} \quad (38.17)$$

The intrinsic point defect concentration field is then predicted by the solution of (38.17) and (38.3). The concentrations of the intrinsic point defects at the boundary of the crystal including the melt-crystal interface can be assumed to be at equilibrium. The excess intrinsic point defect concentration field can be mapped to the final microdefect distribution. A comparison between the predicted excess intrinsic point defect concentration field and the experimentally observed microdefect distribution in a crystal pulled by a varying rate in MEMC Electronic Materials is shown in Fig. 38.6 [38.25]. The crystal temperature field used in the simulation was

first predicted by the commercial software MARC and then corrected using the experimentally measured interface [38.35–37]. The heat transport dynamics was assumed to be very fast, and the melt was assumed to be an effective solid [38.35–37]. The shape of the interface changes with the crystal pull rate. It is reasonable, however, to assume that the interface remains fixed when the pull rate variation is moderate or that there exists a locally fixed effective interface when the pull rate variation is significant. Typically, a representative interface measured in the center of the region of interest suffices. The simulation was performed using one such experimentally measured interface. The properties of the intrinsic point defects used in the simulation are listed in Table 38.1. Figure 38.6a shows the actual crystal pull rate profile, and Fig. 38.6b shows the predicted excess intrinsic point defect concentration field in the crystal. The positive excess intrinsic point defect concentration represents vacancy aggregates or D defects, and the negative excess intrinsic point defect concentration represents self-interstitial aggregates (A and B defects). The experimental microdefect distribution is determined by the method of copper decoration and Secco etching and is shown in Fig. 38.6c. The reader is referred to Kulkarni et al. for the details of the microdefect decoration by the employed characterization technique [38.38–40]. The excess intrinsic point defect concentration field shown in Fig. 38.6 is influenced by the varying pull rate, the temperature field in the crystal, and the radial intrinsic point defect diffusion, to some extent. The v/i boundary in the crystal is clearly identified. The intensity of the oxygen precipitation is very high very close to the v/i boundary, indicating the potential for OSF formation. In rapidly pulled crystals, the observed microdefect distribution, the location of the OSF region, and the location of the v/i boundary can be quantified by the radial variation of G and the axial variation of the pull rate. Several studies [38.30–33] have directly or indirectly quantified the location of the v/i boundary in CZ crystals. It must be noted that the simulation results shown in Fig. 38.6 are not completely mesh insensitive at the level of discretization used. This inaccuracy is corrected in the computations discussed in the later sections of this chapter.

38.2.2 The Quantification of the Microdefect Formation

The quantification of the intrinsic point defect concentration field in a CZ crystal provides only a qualitative

information of the final microdefect distribution [38.19, 26, 34, 41–45]. As microelectronic devices are very sensitive to the size of microdefects, an accurate quantification of the microdefect distribution in CZ crystals is essential. Capturing the distribution of microdefects in a CZ crystal is quite rigorous and involves the solution of a set of complex equations. The formation and growth of microdefects in an element of silicon takes place over a finite period of time; thus, a population of the microdefects formed at various moments of the elapsed time period exists in the element. Hence, various approximations are made in capturing the entire microdefect distribution in a growing CZ crystal [38.1, 27, 46–54].

Based on the research reported in the literature, three broad approaches for the quantification of the microdefect distribution in a CZ crystal can be identified. The first approach involves the application of the classical nucleation theory for the formation of stable nuclei of microdefects followed by their diffusion-limited growth, the second approach involves representing the population of microdefects present at any location by an equivalent population of identical microdefects, and the third approach involves the application of the Fokker–Planck equation to create a continuum of the microdefect size. Voronkov and Falster were the first to publish the first approach [38.46]. For the sake of simplicity, however, they ignored axial and radial diffusion of the intrinsic point defects during the formation and growth of microdefects. Thus, in effect, the formation of microdefects was treated in an isolated element of silicon following a predetermined decrease in the temperature. Kulkarni et al. [38.1] augmented this model and quantified the CZ defect dynamics including the axial diffusion effects [38.1]. A detailed two-dimensional treatment of the CZ defect dynamics to capture the microdefect distribution by the approach of Kulkarni et al. [38.1] remains computationally unattractive. To address this shortcoming, Kulkarni and Voronkov [38.53] developed the *lumped model*, which represents a population of microdefects of varying sizes at any location in a CZ crystal by an equivalent population of identical microdefects and captures the two-dimensional distribution of microdefects.

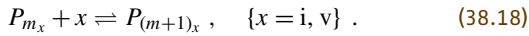
The quantification of the CZ defect dynamics by a more rigorous approach can be accomplished by a direct treatment of the reactions between the nucleating monomers and microdefects of various sizes. This approach is computationally impractical, considering the size of mature microdefects. The Fokker–Planck equations (FPE) are popularly used to address the

quantification of such systems. By the Fokker–Planck approach, a microdefect population at any location in a CZ crystal is quantified by a *size* coordinate. Sinno and Brown [38.47], Mori [38.27], Wang and Brown [38.48], and Brown et al. [38.49] accomplished the quantification of the defect dynamics in CZ crystals using the Fokker–Planck formulation.

For the sake of continuity, the quantifications of the defect dynamics in CZ crystals by the first and the second approach are discussed first in this chapter. The third approach, employing the Fokker–Planck equations, is discussed last.

First Approach: CZ Defect Dynamics Using the Classical Nucleation Theory

All microdefects are treated as clusters of the intrinsic point defects. The formation of microdefects takes place by a series of reactions of the following type [38.55–57]:



In reaction (38.18), P is a cluster of monomers or an intrinsic point defect species x . A cluster of m intrinsic point defects of type x is represented by P_{m_x} . At a given temperature and intrinsic point defect concentration, the total free energy change associated with the formation of a cluster containing m intrinsic point defects from a supersaturated solution is given by

$$\Delta F_x(m_x) = -m_x k_B T \ln \frac{C_x}{C_{x,e}} + \lambda_x m_x^{2/3}, \quad (38.19)$$

where F is the free energy and λ is the surface energy coefficient for the cluster. Note that the subscript x (for i and v) denotes the intrinsic point defect x (as in C_x) as well as the clusters containing the intrinsic point defect x (as in F_x and λ_x), depending on the variable. The first term on the right-hand side of (38.19) is the bulk (volume) free energy change (per m intrinsic point defects) associated with the intrinsic point defect supersaturation, and the second term is the cluster surface energy associated with the formation of the new cluster surface. The number of intrinsic point defects in the so-called *critical cluster* is obtained by maximizing the free energy change with respect to m

$$m_x^* = \left(\frac{2\lambda_x}{3k_B T \ln \frac{C_x}{C_{x,e}}} \right)^3. \quad (38.20)$$

The maximum free-energy change associated with the formation of the critical clusters containing m^* intrinsic

point defects is interpreted as the nucleation barrier and is given by the substitution of m^* into (38.19)

$$\Delta F_x(m_x^*) = \Delta F_x^* = \frac{4}{27} \frac{\lambda_x^3}{(k_B T \ln \frac{C_x}{C_{x,e}})^2}. \quad (38.21)$$

The classical nucleation theory gives the rate of formation of stable supercritical nuclei or clusters per unit volume, defined as the *nucleation rate*, as a function of various properties of the critical clusters and the intrinsic point defects as [38.57]

$$J_x = \eta_{x \leftrightarrow x}^* \times Z_x \times \phi_{x,e}^*, \quad (38.22)$$

where J_x is the nucleation rate of clusters of type x , or x -clusters, $\eta_{x \leftrightarrow x}^*$ is the attachment frequency of monomer x to the critical clusters of x , $\phi_{x,e}^*$ is the equilibrium density of the critical clusters, and Z_x is the Zheldovich factor. Clusters are assumed to be spherical in shape. The relevance and accuracy of this assumption are discussed in the following section. Using the classical expressions for the Zheldovich factor and the equilibrium concentration of the critical clusters, the nucleation rate is given as

$$J_x = [4\pi D_x C_x \times R_x(m_x^*)] \times \left[\{12\pi k_B T \times \Delta F_x(m_x^*)\}^{-\frac{1}{2}} \left(k_B T \ln \frac{C_x}{C_{x,e}} \right) \right] \times \left[\rho_x \exp \left(-\frac{\Delta F_x(m_x^*)}{k_B T} \right) \right]. \quad (38.23)$$

Here R is the radius (size) of a cluster, D is the diffusivity of any species, and ρ is the site density for nucleation. The first term in the square brackets on the right-hand side of (38.23) is the diffusion-limited intrinsic point defect attachment frequency to a critical cluster, the second term is the Zheldovich factor, and the third term is the equilibrium concentration of the critical clusters.

The Model. In this study, all microdefects are treated as spherical aggregates of either vacancies or self-interstitials and are termed *clusters*. Vacancy aggregates are termed v -clusters and represent D defects; self-interstitial aggregates are termed i -clusters and represent A and B defects. Since D defects are known to be octahedral voids, their approximation as spherical clusters is reasonably accurate [38.17, 18]. A defects are dislocation loops [38.10–13]. They presumably form, however, from globular self-interstitial aggregates

such as B defects [38,12, 19]. Therefore, the approximation of A defects as spherical clusters provides their density with a representative accuracy; globular B defects are quite accurately approximated as spherical clusters. All clusters are assumed to be immobile. The effect of impurities is ignored in this treatment.

The microdefect distribution in a CZ crystal is symmetric about the axis of growth. Thus, it suffices to treat the CZ defect dynamics by an axisymmetric model using the cylindrical coordinates r and z , where r is the radial coordinate and z is the axial coordinate. At any location (r, z) in the crystal, at any given time t , a population of clusters formed at various locations (r, ξ) at various moments of the elapsed time τ exists. The size (radius) R of these clusters is then a function of r, z, τ , and t . The clusters, once formed, are assumed to grow by a diffusion-limited kinetics. The growth equations for i-clusters and v-clusters are thus given by

$$\frac{\partial R_i^2(r, z, \tau, t)}{\partial t} + V \frac{\partial R_i^2(r, z, \tau, t)}{\partial z} = \frac{2D_i}{\psi_i^i} (C_i - C_{i,e}), \quad (38.24)$$

$$\frac{\partial R_v^2(r, z, \tau, t)}{\partial t} + V \frac{\partial R_v^2(r, z, \tau, t)}{\partial z} = \frac{2D_v}{\psi_v^v} (C_v - C_{v,e}), \quad (38.25)$$

where ψ_x^x is the concentration of any intrinsic point defect species, denoted by the superscript, in a cluster of any type, denoted by the subscript. The relationship among z, ξ , and τ is determined by the pull rate profile

$$\xi = z - \int_{\tau}^t V d\tau', \quad (38.26)$$

where τ' is the time between τ and t . The *cross-interaction* between i-clusters and vacancies and between v-clusters and self-interstitials is ignored, because the cluster growth is affected primarily by the dominant intrinsic point defect species. The dynamics at moderately low temperatures is strongly influenced by oxygen, which is beyond the scope of this model. The rate of the consumption of the intrinsic point defects x by x -clusters at any location at any time, q_x^x , is obtained by integrating the contributions from all the clusters present at the

location

$$q_i^i = 4\pi D_i (C_i - C_{i,e}) \int_0^t R_i(r, z, \tau, t) J_i(r, \xi, \tau) d\tau, \quad (38.27)$$

$$q_v^v = 4\pi D_v (C_v - C_{v,e}) \int_0^t R_v(r, z, \tau, t) J_v(r, \xi, \tau) d\tau. \quad (38.28)$$

The balance of the intrinsic point defects must account for the change in the intrinsic point defect concentration by convection, diffusion, the Frenkel reaction, their consumption by the diffusion-limited growth of the formed clusters, and their consumption by their nucleation.

$$\begin{aligned} \frac{\partial C_i}{\partial t} + V \frac{\partial C_i}{\partial z} = & \nabla (D_i \nabla C_i) \\ & - k_{i \leftrightarrow v} (C_i C_v - C_{i,e} C_{v,e}) \\ & - 4\pi D_i (C_i - C_{i,e}) \\ & \times \int_0^t R_i(r, z, \tau, t) J_i(r, \xi, \tau) d\tau \\ & - J_i(r, z, t) m_i^*, \end{aligned} \quad (38.29)$$

$$\begin{aligned} \frac{\partial C_v}{\partial t} + V \frac{\partial C_v}{\partial z} = & \nabla (D_v \nabla C_v) \\ & - k_{i \leftrightarrow v} (C_i C_v - C_{i,e} C_{v,e}) \\ & - 4\pi D_v (C_v - C_{v,e}) \\ & \times \int_0^t R_v(r, z, \tau, t) J_v(r, \xi, \tau) d\tau \\ & - J_v(r, z, t) m_v^*. \end{aligned} \quad (38.30)$$

The consumption of intrinsic point defects by their nucleation events only is negligible, and is ignored. The nucleation rates of both vacancies and self-interstitials are given by the classical nucleation theory

$$\begin{aligned} J_i = & [4\pi R(m_i^*) D_i C_i] \\ & \times \left[\{12\pi k_B T \Delta F_i(m_i^*)\}^{-\frac{1}{2}} \left(k_B T \ln \frac{C_i}{C_{i,e}} \right) \right] \\ & \times \left[\rho_i \exp \left\{ -\frac{\Delta F_i(m_i^*)}{k_B T} \right\} \right], \end{aligned} \quad (38.31)$$

$$\begin{aligned}
 J_v = & \left[4\pi R_x (m_x^*) D_v C_v \right] \\
 & \times \left[\left\{ 12\pi k_B T \Delta F_v (m_x^*) \right\}^{-\frac{1}{2}} \left(k_B T \ln \frac{C_v}{C_{v,e}} \right) \right] \\
 & \times \left[\rho_v \exp \left\{ -\frac{\Delta F_v (m_x^*)}{k_B T} \right\} \right]. \quad (38.32)
 \end{aligned}$$

The discussed set of equations must be solved for a moving crystal. The transient domain of the computation is described by the shape of the crystal as a function of time

$$\Omega(r, z, t) = 0. \quad (38.33)$$

The initial height of the crystal is assumed to be either zero or negligible. Equilibrium conditions are assumed on all crystal surfaces, on the basis of a fast surface kinetics. This assumption is valid in most CZ growth conditions [38.26, 34]. The initial size of the clusters formed at any location (r, ξ) is approximately described by the size of the critical clusters.

The cumulative density of all x -clusters in a population present at any location, n_x , can be explicitly defined using the solution of the described equations

$$n_i = \int_0^t J_i(r, \xi, \tau) d\tau, \quad (38.34)$$

$$n_v = \int_0^t J_v(r, \xi, \tau) d\tau. \quad (38.35)$$

The volumetric average radius of the cluster population at any location is given by

$$R_{i,\text{avg},\text{vol}} = \left(\frac{\int_0^t R_i^3(r, z, \tau, t) J_i(r, \xi, \tau) d\tau}{\int_0^t J_i(r, \xi, \tau) d\tau} \right)^{1/3}, \quad (38.36)$$

$$R_{v,\text{avg},\text{vol}} = \left(\frac{\int_0^t R_v^3(r, z, \tau, t) J_v(r, \xi, \tau) d\tau}{\int_0^t J_v(r, \xi, \tau) d\tau} \right)^{1/3}. \quad (38.37)$$

The subscript “avg,vol” denotes the volumetric average value.

Typically, the described set of equations can be solved in a quasistationary temperature field at any

given height of the crystal. The CZ heat transport dynamics is much faster than the CZ defect dynam-

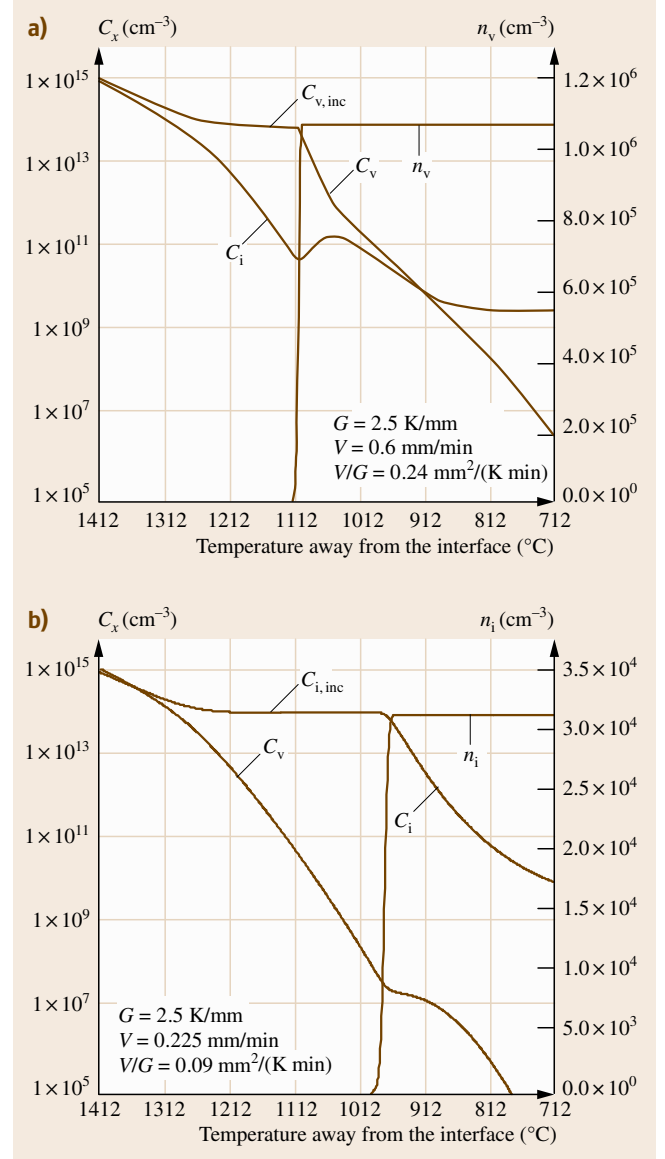


Fig. 38.7a,b The profiles of the concentrations of the intrinsic point defect species and the cluster densities as functions of the crystal temperature in a simulated (a) vacancy-rich crystal growing under steady state, (b) self-interstitial-rich crystal growing under steady state (after [38.1]). Note that the Frenkel reaction equilibrium remains valid until the cluster growth is complete and that the cross-interactions (i with v-clusters and v with i-clusters) are not included in the model

ics [38.26, 27, 34, 48, 49, 53, 54]. The temperature field in a growing crystal can be quantified accurately by the quasi-steady-state approximation [38.35–37]. In most cases, the assumption of one representative temperature field independent of the crystal height suffices [38.53, 54].

The accuracy of the model predictions strongly depends on the accuracy of the parameters describing the key properties of the intrinsic point defects. There is significant uncertainty in the reported values of the formation and migration energies of the intrinsic point defects. The parameters describing the Frenkel reaction kinetics, in particular, are highly approximate. Various studies have reported the acceptable parameters describing the CZ defect dynamics [38.1, 26, 34, 58–64]. In this section, the results obtained by Kulkarni et al. by solving the described equations using the properties of the intrinsic point defects listed in Table 38.1 are discussed [38.1]. The Frenkel reaction rate constant reported by Sinno et al. [38.26, 27] was used by Kulkarni and coworkers in their study [38.1]; the enthalpic barrier, however, was set to zero [38.1, 27]. An accurate estimation of this rate constant is not necessary, because the Frenkel reaction dynamics is very fast, lead-

ing to reaction equilibrium in the relevant temperature range.

It must be noted that the discussed model quantifies continuum-scale CZ defect dynamics. The effects of oxygen on the defect dynamics are also not included in the model.

Results and Discussion. Voronkov and Falster solved the described model by assuming that the effects of the axial and radial diffusion of the intrinsic point defects after the initial incorporation are negligible [38.46]. Kulkarni et al. solved the model describing both the steady-state and unsteady-state defect dynamics including axial diffusion effects [38.1]. The basic aspects of their study are discussed in this section.

Kulkarni et al. used a representative temperature profile described by (38.6) for their steady-state simulations [38.1]. A representative value for G of 2.5 K/mm was used. For the sake of simplicity, the units popularly applied in the crystal growth industry are used hereafter to describe key variables. Vacancies are incorporated as the dominant species at high V/G , as shown in Fig. 38.7a, and self-interstitials are the dominant incorporated species at low V/G , as shown in Fig. 38.7b. Figure 38.7 also shows that v-clusters and i-clusters are formed within a narrow range of temperature known as the nucleation temperature range. The nucleation temperature is defined as the temperature at which the nucleation rate is at its maximum. The predicted nucleation temperature of vacancies for the conditions studied is around 1100°C and that for self-interstitials is around 950°C. As reported by Kulkarni, the Frenkel reaction equilibrium prevails in the crystal until the cluster growth is complete [38.1]. At lower temperatures, when the intrinsic point defect concentrations are too low to affect the cluster distribution, the model predicts a deviation from the Frenkel reaction equilibrium. The model does not focus on an accurate quantification of the very low residual intrinsic point defect concentrations. Hence, it is not necessary to account for the Frenkel reaction kinetics in CZ growth. A set of simulations like this at a fixed G and varying V can capture the effect of V/G on the initial incorporation (Fig. 38.8). As shown in Fig. 38.8, the critical V/G is around 0.15 mm²/(K min). It must be noted that various other groups report slightly different values of the critical V/G [38.26, 30–33]. Figure 38.8 also shows that the nucleation temperature increases with

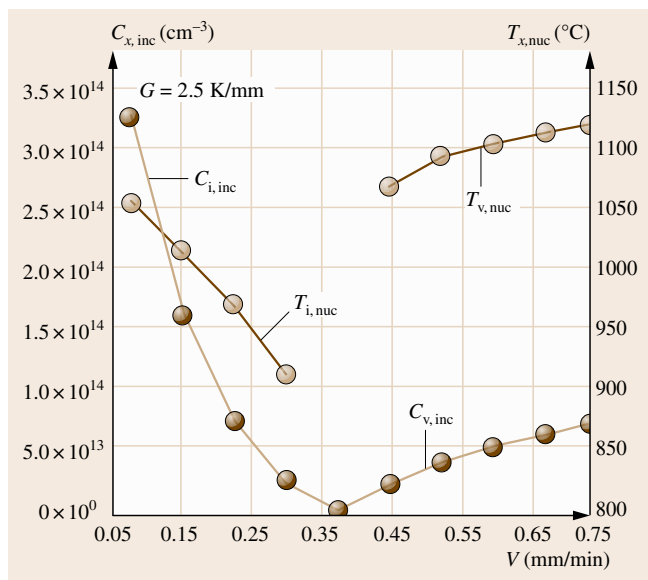


Fig. 38.8 Dependence of the concentration of the dominant incorporated point defect species and the nucleation temperature on the pull rate at a fixed G (subscript “inc” denotes the incorporated concentration and “nuc” denotes nucleation) (after [38.1])

increasing concentration of the incorporated dominant intrinsic point defect species, because the temperature at which the intrinsic point defect supersaturation is high enough to drive the nucleation events increases with increasing intrinsic point defect concentration. The cluster size distribution is influenced by an interplay between the formation of new clusters, which is driven by the dominant intrinsic point defect supersaturation, and the consumption of the intrinsic point defects by the existing clusters, which decreases the intrinsic point defect supersaturation. The conditions that allow the nucleation of the intrinsic point defects at a higher rate, before the intrinsic point defect concentration decreases by the cluster growth, lead to the formation of a large number of clusters, which remain very small in size; the conditions allowing the rapid growth of the formed clusters quickly reduce the intrinsic point defect concentration and the nucleation rate, leading to the formation of a small number of clusters that grow very large in size. More specifically, a higher cooling rate through the nucleation range leads to the evolution of smaller clusters at higher densities, whereas a higher incorporated intrinsic point defect concentration leads to the evolution of larger clusters at lower densities. This interplay is captured in the size distributions of the mature cluster populations in the simulated CZ crystals grown under varying conditions, as shown in Fig. 38.9. Using their simplified model, Voronkov and Falster quantified this interplay in terms of the cooling rate through the nucleation range and the concentration of the incorporated dominant intrinsic point defect species [38.46]

$$n_{x,\text{approx}} \propto \left(\frac{1}{D_x T_{\text{nuc},x}^2} \right)^{\frac{3}{2}} Q_{\text{nuc},x}^{\frac{3}{2}} C_{x,\text{nuc}}^{-\frac{1}{2}} \quad (38.38)$$

$$R_{x,\text{avg,approx}} \propto \left(D_x T_{\text{nuc},x}^2 \right)^{\frac{1}{2}} \left(\frac{C_{x,\text{nuc}}}{Q_{\text{nuc},x}} \right)^{\frac{1}{2}}, \quad (38.39)$$

where Q is the cooling rate, given by the product of the local pull rate and the magnitude of the axial temperature gradient. The subscript “nuc” denotes the conditions at nucleation, and the subscript “approx” denotes an approximate value. Kulkarni et al. showed that the predictions of (38.38) and (38.39) agree quite well with the predictions of their rigorous model [38.1].

Many modern CZ processes enforce unsteady-state conditions in crystal growth by varying the crystal pull rate. Kulkarni et al. [38.1] captured the salient fea-

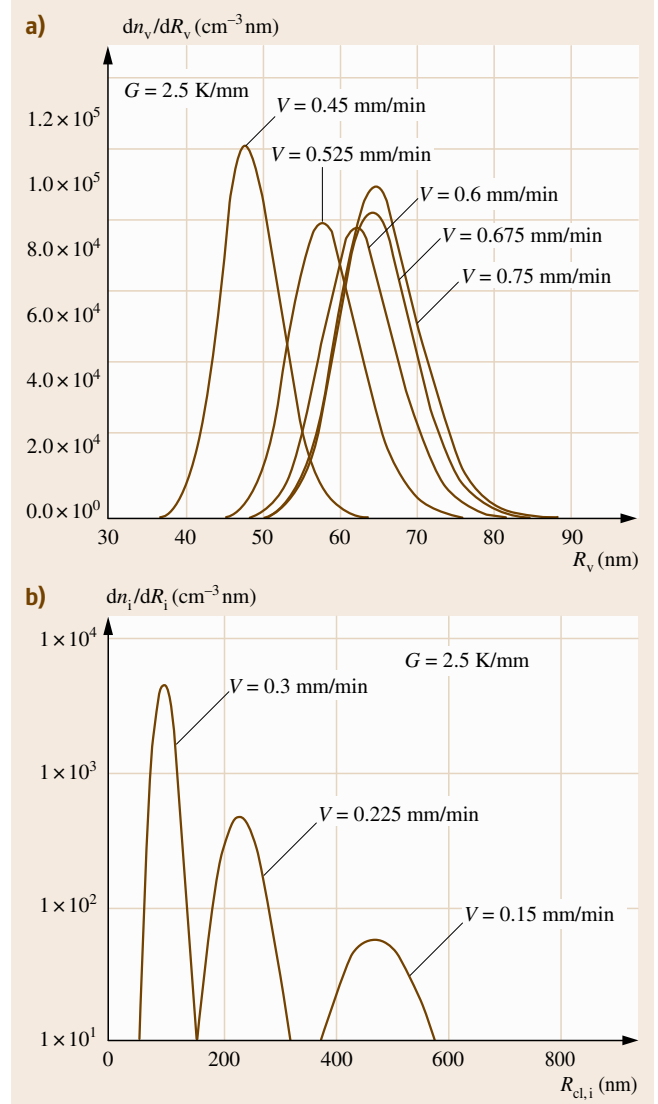


Fig. 38.9a,b The mature size distributions of (a) v-clusters and (b) i-clusters in various simulated crystals grown under steady states at various pull rates (after [38.1])

tures of unsteady-state CZ growth by simulating the growth of a crystal pulled at the varying rate shown in Fig. 38.10a. The body of the simulated crystal was grown first by continuously decreasing the pull rate and then continuously increasing the pull rate. The predicted cluster type and the cluster density variation are shown in Fig. 38.10b. Each element of the crystal undergoes

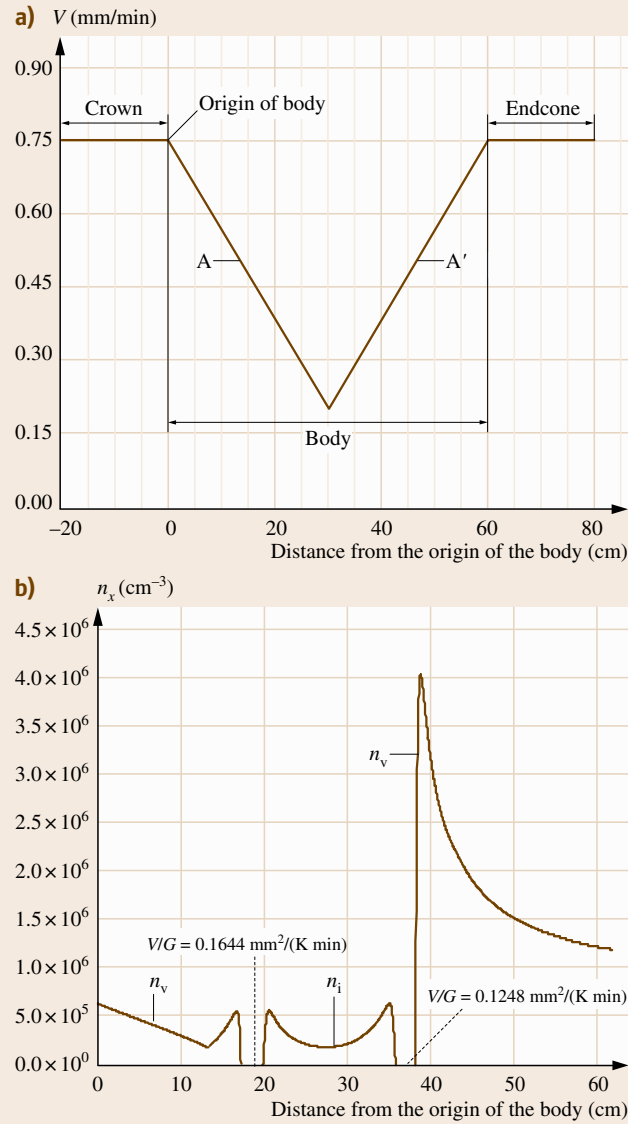


Fig. 38.10 (a) The crystal pull-rate profile used to understand the CZ defect dynamics under unsteady-state conditions. (b) The cluster density profile in the crystal grown using the pull-rate profile shown in (a) (after [38.1])

initial incorporation and nucleation under varying conditions, resulting in the interesting cluster distribution shown in Fig. 38.10. The most striking features of this study are the predicted shifts of the critical V/G , induced by the unsteady-state crystal growth. These shifts are caused by the variation of the excess intrinsic point

defect flux associated with the variation of the crystal pull rate. When the pull rate continuously decreases, an element of silicon moves away from the melt–crystal interface at a decreasing rate, allowing a more efficient diffusion of self-interstitials from the interface. In addition, at a given time and for a given pull rate, the driving force for self-interstitial diffusion at the interface is slightly higher than that for steady-state growth, and the driving force for the vacancy diffusion is slightly lower than that for steady-state growth; this dynamics is caused by the prior higher pull rate. Hence, the critical V/G increases when the pull rate continuously decreases. Conversely, the exact opposite effects explain the decrease of the critical V/G when the pull rate continuously increases. These shifts of the critical V/G were quantified by Kulkarni et al. for engineering applications as functions of the rate of the change of the pull rate with respect to crystal length [38.1]

$$\left(\frac{V}{G}\right)_{c,-\text{slope}} = \left(\frac{V}{G}\right)_c - 7.85 \text{ (mm}^2/\text{K)} \times \left(\frac{dV}{dL}\right) \text{ (min}^{-1}\text{)}, \quad (38.40)$$

$$\left(\frac{V}{G}\right)_{c,+\text{slope}} = \left(\frac{V}{G}\right)_c - 13.745 \text{ (mm}^2/\text{K)} \times \left(\frac{dV}{dL}\right) \text{ (min}^{-1}\text{)}. \quad (38.41)$$

The subscripts “–slope” and “+slope” indicate the decreasing pull rate and the increasing pull rate, respectively.

Finally, Kulkarni et al. [38.1] also showed that the predictions of the applied model agree reasonably well with experimental observations, as shown in Fig. 38.11. The D defect density was experimentally determined in a crystal grown under unsteady-state conditions by the method of copper decoration and Secco etching [38.38–40]. These studies clearly establish the validity of the applied model.

The model applied for the quantification of CZ defect dynamics discussed so far predicts the size distributions of all populations of clusters at all locations in a CZ crystal. The model requires the solution of the integro-differential equations for the intrinsic point defect concentration fields and of the cluster growth equations describing the evolution of the cluster populations at all locations in a CZ crystal. As this model provides rigorous quantification of the CZ defect dynamics, it is termed the *rigorous model*.

Fig. 38.11 (a) Comparison between the model predicted and experimentally determined approximate v-cluster density profiles in an experimental crystal. *Circles* indicate experimental data points. The profile of the volume-averaged v-cluster size in the crystal is also shown. **(b)** The v-cluster size distribution at two chosen axial locations in the crystal (after [38.1]) ►

Second Approach: The Quantification of the CZ Defect Dynamics by the Lumped Model

The rigorous model can be simplified by representing a population of clusters of varying sizes at any given location in a CZ crystal by an equivalent population of identical clusters, as first shown by *Kulkarni and Voronkov* [38.53]. Thus, the complex rigorous model is reformulated by explicitly introducing the density and the average size of clusters in a population

$$n_i(r, z, t) = \int_0^t J_i(r, \xi, \tau) d\tau, \quad (38.42)$$

$$n_v(r, z, t) = \int_0^t J_v(r, \xi, \tau) d\tau, \quad (38.43)$$

$$\langle R_i \rangle = \frac{\int_0^t R_i(r, z, \tau) J_i(r, \xi, \tau) d\tau}{n_i}, \quad (38.44)$$

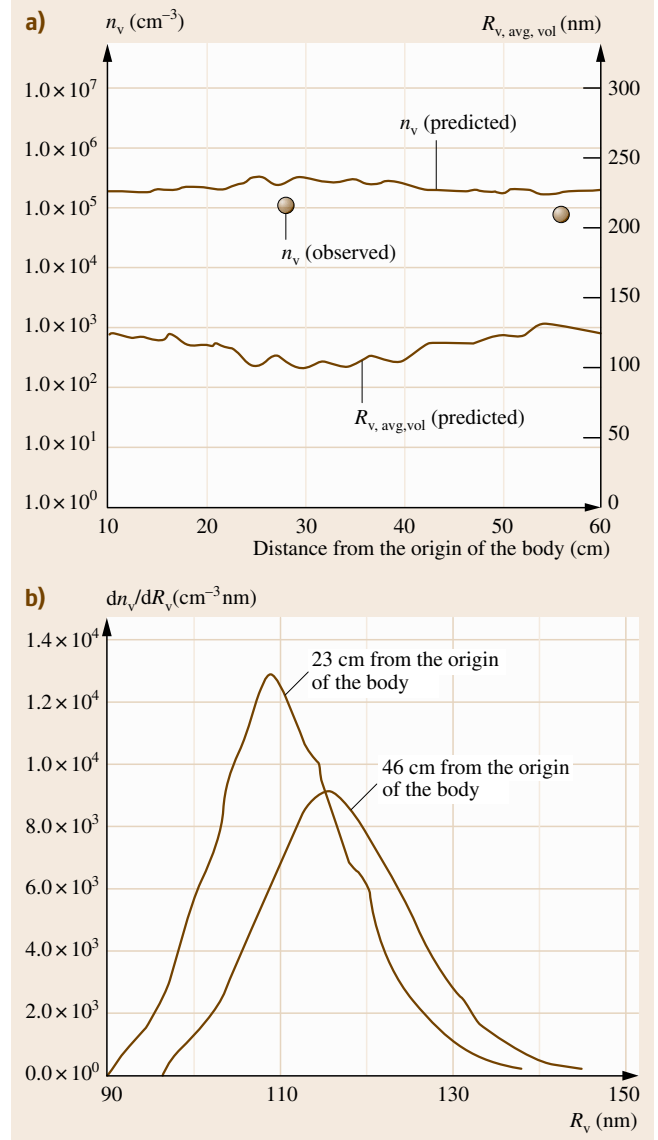
$$\langle R_v \rangle = \frac{\int_0^t R_v(r, z, \tau) J_v(r, \xi, \tau) d\tau}{n_v}, \quad (38.45)$$

where the brackets $\langle \dots \rangle$ indicate the average value. Note that these average radii are different from the volumetric average radii defined in (38.36) and (38.37). The total consumption rate (per unit volume) of the intrinsic point defects by this population is now given as

$$q_i^i = 4\pi D_i (C_i - C_{i,e}) \langle R_i \rangle n_i, \quad (38.46)$$

$$q_v^v = 4\pi D_v (C_v - C_{v,e}) \langle R_v \rangle n_v. \quad (38.47)$$

The essential aspect of the simplified model is to replace the average radius of the cluster population by the square root of the average of the squares of the radii of



all clusters in the population

$$\begin{aligned} \langle R_i \rangle &\approx \langle R_i^2 \rangle^{1/2} = \left(\frac{\int_0^t R_i^2(r, z, \tau) J_i(r, \xi, \tau) d\tau}{n_i} \right)^{1/2} \\ &= \left(\frac{U_i}{n_i} \right)^{1/2}, \end{aligned} \quad (38.48)$$

$$\begin{aligned} \langle R_v \rangle &\approx \langle R_v^2 \rangle^{1/2} = \left(\frac{\int_0^t R_v^2(r, z, \tau, t) J_v(r, \xi, \tau) d\tau}{n_v} \right)^{1/2} \\ &= \left(\frac{U_v}{n_v} \right)^{1/2}, \end{aligned} \quad (38.49)$$

where

$$U_i(r, z, t) = \int_0^t R_i^2(r, z, \tau, t) J_i(r, \xi, \tau) d\tau, \quad (38.50)$$

$$U_v(r, z, t) = \int_0^t R_v^2(r, z, \tau, t) J_v(r, \xi, \tau) d\tau. \quad (38.51)$$

The new auxiliary variable U is proportional to the total surface area of the cluster population. The intrinsic point defect consumption rate per unit volume is now rewritten as

$$\begin{aligned} q_i^i &= 4\pi D_i (C_i - C_{i,e}) \langle R_i^2 \rangle^{1/2} n_i \\ &= 4\pi D_i (C_i - C_{i,e}) (U_i n_i)^{1/2}, \end{aligned} \quad (38.52)$$

$$\begin{aligned} q_v^v &= 4\pi D_v (C_v - C_{v,e}) \langle R_v^2 \rangle^{1/2} n_v \\ &= 4\pi D_v (C_v - C_{v,e}) (U_v n_v)^{1/2}. \end{aligned} \quad (38.53)$$

The intrinsic point defect balances (38.29) and (38.30) are written using (38.52) and (38.53).

$$\begin{aligned} \frac{\partial C_i}{\partial t} + V \frac{\partial C_i}{\partial z} &= \nabla (D_i \nabla C_i) \\ &\quad - k_{i \leftrightarrow v} (C_i C_v - C_{i,e} C_{v,e}) \\ &\quad - 4\pi D_i (C_i - C_{i,e}) (U_i n_i)^{1/2}, \end{aligned} \quad (38.54)$$

$$\begin{aligned} \frac{\partial C_v}{\partial t} + V \frac{\partial C_v}{\partial z} &= \nabla (D_v \nabla C_v) \\ &\quad - k_{i \leftrightarrow v} (C_i C_v - C_{i,e} C_{v,e}) \\ &\quad - 4\pi D_v (C_v - C_{v,e}) (U_v n_v)^{1/2}. \end{aligned} \quad (38.55)$$

Thus the intrinsic point defect balances are described by (38.54) and (38.55) without the knowledge of the formation and growth histories of the cluster populations at any location. If the Frenkel reaction equilibrium is assumed, (38.54) and (38.55) are replaced by (38.3) and

(38.56), obtained by subtracting (38.54) from (38.55)

$$\begin{aligned} &\frac{\partial (C_v - C_i)}{\partial t} + V \frac{\partial (C_v - C_i)}{\partial z} \\ &= \nabla (D_v \nabla C_v) - \nabla (D_i \nabla C_i) \\ &\quad - 4\pi D_v (C_v - C_{v,e}) (U_v n_v)^{1/2} \\ &\quad + 4\pi D_i (C_i - C_{i,e}) (U_i n_i)^{1/2}. \end{aligned} \quad (38.56)$$

The evolution of the auxiliary variable U is derived using the cluster growth (38.24) and (38.25) with the definitions (38.50) and (38.51)

$$\frac{\partial U_i}{\partial t} + V \frac{\partial U_i}{\partial z} = \frac{2D_i n_i}{\psi_i^i} (C_i - C_{i,e}), \quad (38.57)$$

$$\frac{\partial U_v}{\partial t} + V \frac{\partial U_v}{\partial z} = \frac{2D_v n_v}{\psi_v^v} (C_v - C_{v,e}). \quad (38.58)$$

The initial size of the formed clusters is assumed to be zero in the derivation of (38.57) and (38.58). This assumption is accurate and does not affect the predictions of the model. The evolution of the density of clusters is directly obtained using the classical nucleation theory

$$\frac{\partial n_i}{\partial t} + V \frac{\partial n_i}{\partial z} = J_i, \quad (38.59)$$

$$\frac{\partial n_v}{\partial t} + V \frac{\partial n_v}{\partial z} = J_v. \quad (38.60)$$

The representative size of clusters at any location \mathcal{R} is given as

$$\mathcal{R}_i = \langle R_i^2 \rangle^{1/2} = \left(\frac{U_i}{n_i} \right)^{1/2}, \quad (38.61)$$

$$\mathcal{R}_v = \langle R_v^2 \rangle^{1/2} = \left(\frac{U_v}{n_v} \right)^{1/2}. \quad (38.62)$$

The defect dynamics in a **CZ** crystal is now quantified by the intrinsic point defect concentration C , the auxiliary variable U , and the cluster density n . These variables are described by a set of partial differential equations without the necessity to quantify the formation and growth histories of clusters. The simplified model eliminates the elapsed time, introduced in the rigorous model to describe the size distribution of a cluster population at any given location in a **CZ** crystal, as an independent variable. Hence, this simplified model is computationally attractive. As the simplified model represents the population of clus-

ters of varying sizes at a given location in the CZ crystal by an equivalent population of identical clusters, it is termed the *lumped model* by Kulkarni and Voronkov [38.53].

The accuracy of the lumped model is verified by a comparison of its predictions with the predictions of the rigorous model, for many different crystal growth conditions, as shown in Fig. 38.12a. In addition, the lumped model is validated by experimental observations (Fig. 38.12b). Finally, as shown in Fig. 38.13, the two-dimensional microdefect distribution in a crystal pulled at a varying rate is predicted reasonably well by the lumped model. It must be noted that the mesh discretization used for the computation is relatively coarse. The inaccuracies associated with the mesh discretization are reduced in the simulations discussed in Sect. 38.3. In the discussed simulations, the lumped model was solved assuming the Frenkel reaction equilibrium. The method of copper decoration and Secco etching was used for the experimental determination of the microdefect distribution [38.38–40]. These studies establish the lumped model as a valuable engineering tool for the development of new CZ crystal growth processes.

Third Approach: The Quantification of the CZ Defect Dynamics by the Discrete Rate Equations and the Fokker–Planck Equation

The models described in the previous sections apply the classical nucleation theory to predict the formation of stable clusters and a diffusion-limited growth kinetics to quantify the growth of these clusters. This approach works very well for Czochralski crystal growth. A more rigorous treatment of CZ defect dynamics, however, must account for all reactions involved in the intrinsic point defect aggregation, as described by reaction (38.18). Considering the large size of microdefects in CZ crystals, this approach requires the solution of an impractically large number of equations. Sinno and Brown [38.47], Mori [38.27], and Brown et al. [38.49] quantified the defect dynamics in CZ crystals by applying a mixed approach involving the solution of a set of equations derived treating smaller clusters as discrete particles and the solution of a set of Fokker–Planck equations derived from the discrete equations for larger clusters. In this section, the contributions of this work to the field of CZ defect dynamics are discussed.

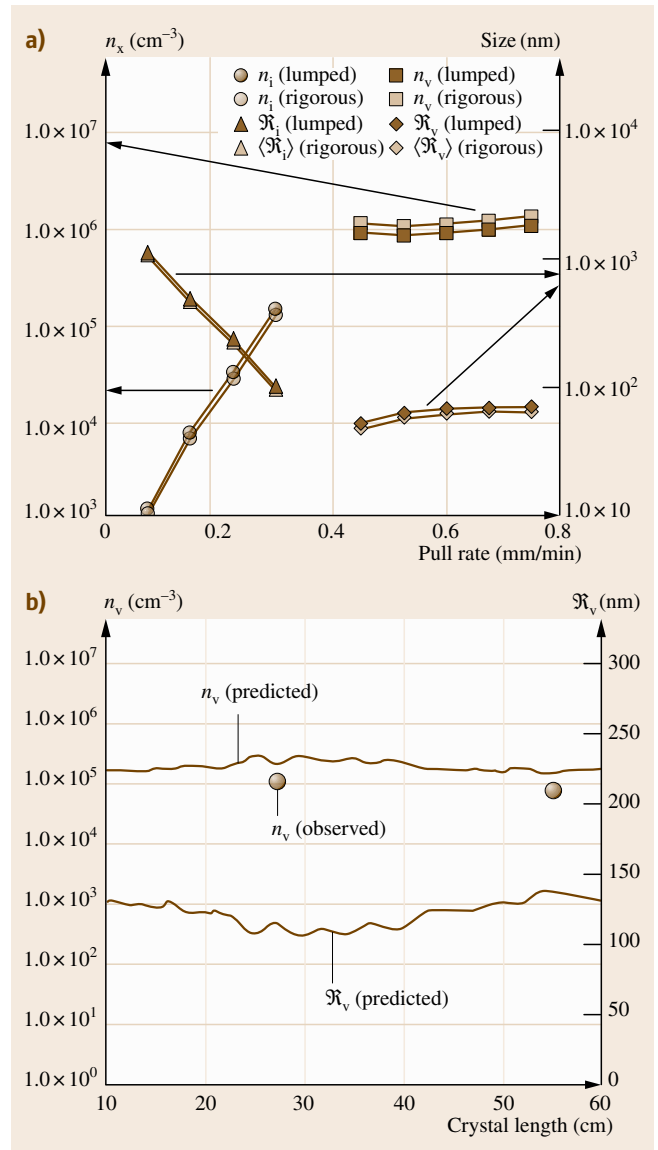


Fig. 38.12 (a) Comparison between the predictions of the rigorous model and the predictions of the lumped model. (b) Comparison between the predictions of the lumped model with the experimental observations (after [38.53])

The Discrete Rate Equations. Reaction set (38.18) defines the series of reactions driving the aggregation of vacancies and self-interstitials. In this reaction set, clusters of the same size and type are treated as a separate species. The cross-interactions between v-clusters and

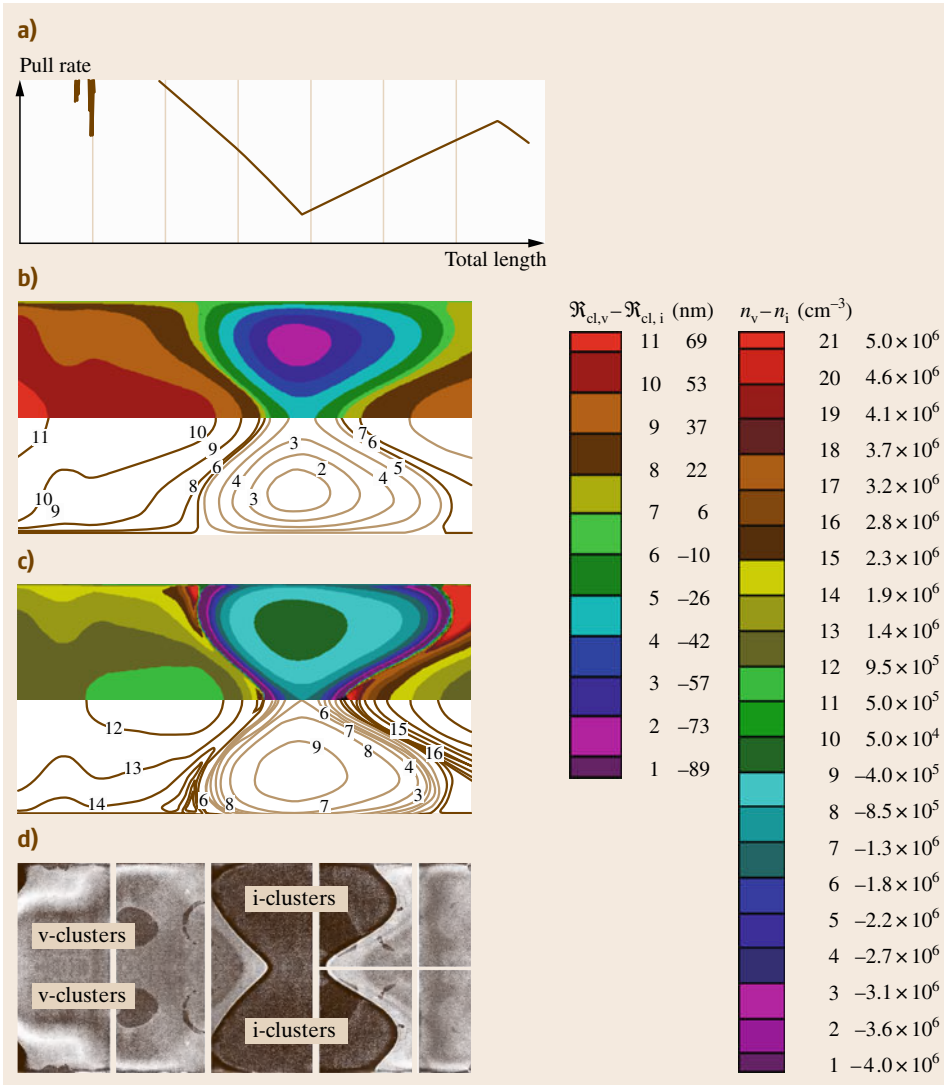


Fig. 38.13 (a) The pull-rate profile used to pull the experimental CZ crystal. (b) The predicted $\mathfrak{R}_v - \mathfrak{R}_i$. (c) The predicted $n_v - n_i$. (d) The observed defect distribution in the crystal. Positive values indicate the v-cluster size and density and the magnitudes of the negative values indicate the i-cluster size and density. v-clusters and i-clusters do not coexist (after [38.53])

self-interstitials and i-clusters and vacancies are ignored in this chapter.

In the previous sections, the size of a cluster was defined as its radius. In this section, the size of a cluster is defined by the number of intrinsic point defects in it rather than by its radius, following the work of *Simno* and *Brown* [38.47], *Mori* [38.27], *Wang* and *Brown* [38.48], and *Brown* et al. [38.49]. In an element of silicon, the overall rate of formation of clusters of size m , Φ_m , is given by the difference between the net volumetric flux coming from the clusters of size $m-1$ to the clusters of size m , I_m , and the net volumetric flux going from clusters of size m to clusters of

size $m+1$, $I_{(m+1)}$

$$\Phi_{m_x} = I_{m_x} - I_{(m+1)_x} \quad (38.63)$$

The subscript “ m_x ” indicates an x -cluster containing m intrinsic point defects of type x . Note that J_x defines the nucleation rate of stable x -clusters, as defined in the previous sections, and Φ_{m_x} defines the net formation rate of x -clusters of size m . The net volumetric flux coming from the clusters containing $m-1$ intrinsic point defects to the clusters containing m intrinsic point defects is defined by the growth rate of the former and the dissolution rate of the latter

$$I_{m_x} = g_{(m-1)_x} \phi_{(m-1)_x} - d_{m_x} \phi_{m_x} \quad (38.64)$$

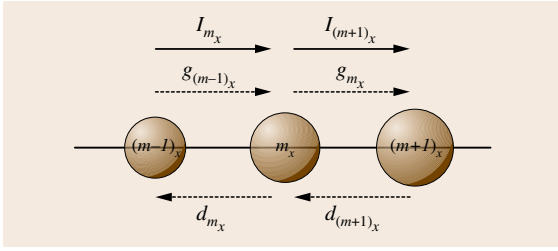


Fig. 38.14 The relationship among the nucleation flux I , the growth rate g , and the dissolution rate d (after [38.27])

where ϕ is the density of clusters, g is the growth rate of a cluster, and d is the dissolution rate. The relationship among I , g , and d is shown schematically in Fig. 38.14. Sinno and Brown [38.47], Mori [38.27], Wang and Brown [38.48], and Brown et al. [38.49] define the cluster growth rate and the dissolution rate by incorporating the kinetic interactions between monomers and clusters. In this section, these rates are defined assuming a diffusion-limited interaction between clusters and monomers, for the sake of consistency with the discussion in other sections of this chapter. The growth rate of a cluster containing m monomers of type x is given by the diffusion-limited attachment frequency of monomers to the cluster

$$g_{m_x} = 4\pi R_{m_x} D_x C_x, \quad (38.65)$$

where R_m is the radius of a cluster of size m . The cluster dissolution rate is given by its thermodynamic relationship with the cluster growth rate

$$d_{m_x} = \frac{g_{(m-1)_x} \phi_{(m-1)_x, e}}{\phi_{m_x, e}}. \quad (38.66)$$

The equilibrium concentration of clusters of size m , in a solution of a given composition, at a given temperature, is given by

$$\phi_{m_x, e} = \rho_x e^{-\left(\frac{\Delta F_{m_x}}{k_B T}\right)}. \quad (38.67)$$

The total free energy change associated with the formation of a cluster of size m , from a solution of a given composition, at a given temperature, is

$$\Delta F_{m_x} = -m_x k_B T \ln \frac{C_x}{C_{x, e}} + \Gamma_{m_x}, \quad (38.68)$$

where Γ_m is the formation energy of a cluster of size m . The formation energy of a large unstrained cluster of size m is simply approximated as $\lambda m^{2/3}$. Using (38.67) and (38.68), (38.66) is written as

$$d_{m_x} = \frac{g_{(m-1)_x}}{\left(\frac{C_x}{C_{x, e}}\right) e^{\frac{(\Gamma_{(m-1)_x} - \Gamma_{m_x})}{k_B T}}}. \quad (38.69)$$

These equations define the diffusion limited growth rates and dissolution rates of all clusters in a Czochralski crystal.

The Cluster Balance Using Discrete Rate Equations. With the discrete formulation, the cluster conservation equations in an axisymmetric CZ crystal are written as follows

$$\begin{aligned} \frac{\partial \phi_{m_x}(r, z, t)}{\partial t} + V \frac{\partial \phi_{m_x}(r, z, t)}{\partial z} \\ = I_{m_x}(r, z, t) - I_{(m+1)_x}(r, z, t), \end{aligned} \quad (38.70)$$

for $m_x \geq 2$.

In (38.70), the density of clusters of the same size and type is treated as a dependent variable. This equation must be solved with the intrinsic point defect balances. The quantification of the defect dynamics, in CZ crystals containing microdefects as large as 100–200 nm, using the discrete rate equations is computationally impractical. Therefore, reasonable approximations based on the discrete rate equations are necessary for a practical solution of the problem.

The Fokker–Planck Equation. The Fokker–Planck equation (FPE) is derived from the discrete rate equations by a Kramers–Moyal expansion treating m as a continuous independent variable [38.27, 47]. The FPE reduces the number of equations defining the CZ defect dynamics. By this formulation, the size distribution of clusters is written as a continuous function of m

$$\begin{aligned} \frac{\partial f_x(r, z, t, m_x)}{\partial t} + V \frac{\partial f_x(r, z, t, m_x)}{\partial z} \\ = -\frac{\partial}{\partial m_x} \left[A_x(r, z, t, m_x) f_x(r, z, t, m_x) \right. \\ \left. - B_x(r, z, t, m_x) \frac{\partial f_x(r, z, t, m_x)}{\partial m_x} \right]. \end{aligned} \quad (38.71)$$

The cluster density determined by the FPE is written as f and the subscript x defines the type of the cluster. A is termed the *drift coefficient* and B is termed the *diffusion coefficient* following the generalized transport equation written in m -space, and they are related to the discrete rate equations as

$$\begin{aligned} A_x(r, z, t, m_x) &= g_x(r, z, t, m_x) - d_x(r, z, t, m_x) \\ &\quad - \frac{\partial B_x(r, z, t, m_x)}{\partial m_x}, \end{aligned} \quad (38.72)$$

$$B_x(r, z, t, m_x) = \frac{g_x(r, z, t, m_x) + d_x(r, z, t, m_x)}{2}. \quad (38.73)$$

The Fokker-Planck equation thus reduces the number of equations describing the cluster growth. Using this formulation, a simplified model can now be developed.

The Model. The Fokker-Planck equation is accurate when clusters are large. Hence, an accurate model involves describing the **CZ** defect dynamics by the discrete rate equations for smaller clusters and by the Fokker-Planck equation for larger clusters. Thus, the cluster balances are written as follows

$$\begin{aligned} \frac{\partial \phi_{m_i}(r, z, t)}{\partial t} + V \frac{\partial \phi_{m_i}(r, z, t)}{\partial z} \\ = I_{m_i}(r, z, t) - I_{(m+1)_i}(r, z, t), \\ \text{for } (m_{\text{dis}} \geq m_i \geq 2), \end{aligned} \quad (38.74)$$

$$\begin{aligned} \frac{\partial \phi_{m_v}(r, z, t)}{\partial t} + V \frac{\partial \phi_{m_v}(r, z, t)}{\partial z} \\ = I_{m_v}(r, z, t) - I_{(m+1)_v}(r, z, t), \\ \text{for } (m_{\text{dis}} \geq m_v \geq 2), \end{aligned} \quad (38.75)$$

$$\begin{aligned} \frac{\partial f_i(r, z, t, m_i)}{\partial t} + V \frac{\partial f_i(r, z, t, m_i)}{\partial z} \\ = -\frac{\partial}{\partial m_i} \left[A_i(r, z, t, m_i) f_i(r, z, t, m_i) \right. \\ \left. - B_i(r, z, t, m_i) \frac{\partial f_i(r, z, t, m_i)}{\partial m_i} \right], \\ \text{for } (m_{\text{dis}} < m_i \leq m_{\text{max}}), \end{aligned} \quad (38.76)$$

$$\begin{aligned} \frac{\partial f_v(r, z, t, m_v)}{\partial t} + V \frac{\partial f_v(r, z, t, m_v)}{\partial z} \\ = -\frac{\partial}{\partial m_v} \left[A_v(r, z, t, m_v) f_v(r, z, t, m_v) \right. \\ \left. - B_v(r, z, t, m_v) \frac{\partial f_v(r, z, t, m_v)}{\partial m_v} \right], \\ \text{for } (m_{\text{dis}} < m_v \leq m_{\text{max}}). \end{aligned} \quad (38.77)$$

The subscript “dis” denotes the maximum cluster size treated by the discrete rate equations, and the subscript “max” denotes the maximum cluster size quantified by the Fokker-Planck equations. The intrinsic point defect balances following this approach are written as

$$\begin{aligned} \frac{\partial C_i}{\partial t} + V \frac{\partial C_i}{\partial z} = \nabla (D_i \nabla C_i) \\ - k_{i \leftrightarrow v}(C_i C_v - C_{i,e} C_{v,e}) - q_i^i, \end{aligned} \quad (38.78)$$

$$\begin{aligned} \frac{\partial C_v}{\partial t} + V \frac{\partial C_v}{\partial z} = \nabla (D_v \nabla C_v) \\ - k_{i \leftrightarrow v}(C_i C_v - C_{i,e} C_{v,e}) - q_v^v, \end{aligned} \quad (38.79)$$

where the intrinsic point defect consumption rates by clusters are given by

$$q_i^i = \left(\frac{\partial}{\partial t} + V \frac{\partial}{\partial z} \right) \times \left[\sum_{m_i=2}^{m_i=m_{\text{dis}}} m_i \phi_{m_i} + \int_{m_i=m_{\text{dis}}+1}^{m_i=m_{\text{max}}} m_i f_i dm_i \right], \quad (38.80)$$

$$q_v^v = \left(\frac{\partial}{\partial t} + V \frac{\partial}{\partial z} \right) \times \left[\sum_{m_v=2}^{m_v=m_{\text{dis}}} m_v \phi_{m_v} + \int_{m_v=m_{\text{dis}}+1}^{m_v=m_{\text{max}}} m_v f_v dm_v \right]. \quad (38.81)$$

The first term in the square brackets on the right-hand side of (38.80) accounts for the consumption of self-interstitials by the discrete i-clusters, and the second term accounts for the consumption of self-interstitials by the self-interstitial *FP-cluster*; (38.81) describes the vacancy consumption. The coupled model using the discrete rate equations for smaller clusters and the Fokker-Planck equation for larger clusters is still computationally expensive. As the model uses the described coupled approach, it is termed the *discrete-continuous* model in this chapter. For further details, the reader is referred to [38.27, 47–49]. As noted earlier, these researchers account for the kinetic interactions between monomers and clusters.

Results. Although the unsteady-state discrete-continuous model is described in this chapter, only the quantification of the steady-state **CZ** defect dynamics, at a fixed pull rate, involving the cluster growth has been reported in the literature thus far. The results obtained by the solution of the discrete-continuous model agree well with the results described by the rigorous model and the lumped model. The initial incorporation and the effects of the cooling rate and the incorporated dominant intrinsic point defect concentration on the cluster size distribution are captured very well. The evolution of the intrinsic point defect and the microdefect concentration profiles in a **CZ** crystal, as predicted by Wang and Brown, are shown in Fig. 38.15 [38.48]. The two-dimensional intrinsic point defect concentration fields and the microdefect distributions captured by the discrete-continuous model reported by Brown et al. are shown in Fig. 38.16 [38.49]. The physics of the **CZ** defect dynamics is quantified accurately by the applied model.

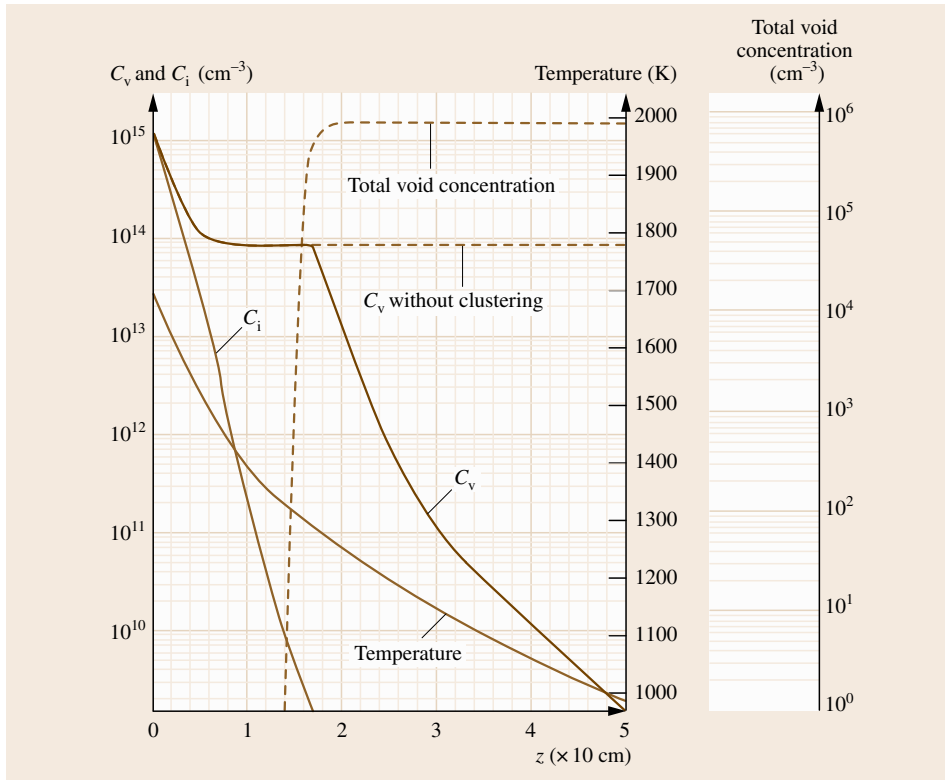


Fig. 38.15 The evolution of the intrinsic point defects and the microdefects as predicted by the discrete-continuous model (after [38.48], © Elsevier 2001)

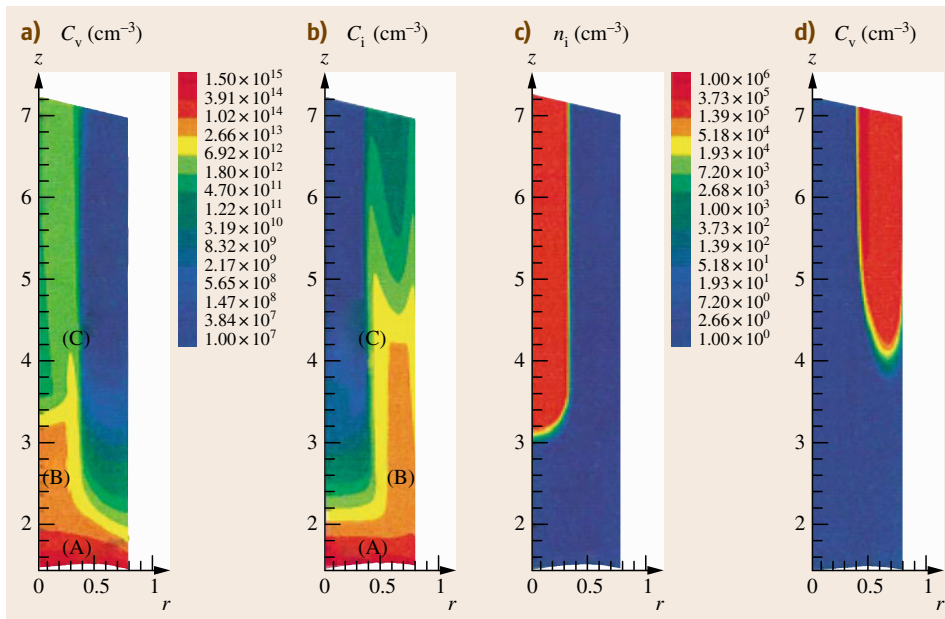


Fig. 38.16a-d Simulation results for steady-state crystal growth at $V = 0.6$ mm/min, showing (a) vacancy concentration, (b) self-interstitial concentration, (c) the total v-cluster density (> 50 nm diameter), and (d) the total i-cluster density (> 50 nm diameter). The *upper-case* letters in the figures are used by Brown et al. to describe the physics of the CZ defect dynamics and should not be mistaken for the figure labels, which are in lower case (after [38.49], © Elsevier 2001)

38.3 Czochralski Defect Dynamics in the Presence of Oxygen

As discussed so far, the aggregates of the intrinsic point defects commonly exist in silicon crystals grown by both the Czochralski process and the float zone (FZ) process. In addition, CZ crystals contain oxide particles, primarily silicon dioxide, termed oxygen clusters in this chapter. Oxygen clusters form only in CZ crystals, because CZ crystals, during their growth, incorporate oxygen in appreciable concentration from the crucible containing the silicon melt. Oxygen clusters in a growing CZ crystal are typically very small. These clusters facilitate the formation of stacking faults in the crystal subjected to selective heat treatments that generate self-interstitials (Fig. 38.3). Hence, oxygen clusters are popularly identified by these stacking faults known as oxidation-induced stacking faults (OSFs) [38.16].

The dynamics of the formation of various microdefects in CZ crystals is affected by many reactions involving the intrinsic point defects and oxygen, and their transport. This defect dynamics in the absence of oxygen has been discussed in detail in Sect. 38.2. The reported research on the direct quantification of the CZ defect dynamics in the presence of oxygen, in particular, and oxygen cluster formation in monocrystalline silicon, in general, are discussed in this section [38.48, 59, 65–70].

38.3.1 Reactions in Growing CZ Crystals

The essential aspect of understanding CZ defect dynamics is the quantification of the kinetics of all relevant reactions in a growing crystal. The Frenkel reaction involving the intrinsic point defects and silicon, the reactions involving vacancies and oxygen, and the aggregation reactions forming all microdefects influence the CZ defect dynamics.

Reactions Involving No Aggregation

The Frenkel reaction discussed in Sect. 38.1 and the reactions involving vacancies and interstitial oxygen (simply, oxygen) do not directly produce microdefects. The Frenkel reaction involves the mutual annihilation of a vacancy v and a self-interstitial i by their recombination to produce a silicon lattice atom Si and the backward production of a pair of a vacancy and a self-interstitial from a silicon lattice atom (reaction 38.1). Oxygen participates in a series of reversible reactions with vacancies and complexes of vacancies and oxygen in a growing CZ crystal. The following reactions

involving vacancies and oxygen are of primary importance [38.59]:

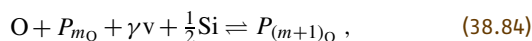


where vO and vO_2 are vacancy–oxygen complexes. Each forward or reverse reaction listed above is considered to be an elementary reaction. The net rate of formation of a reacting species is given by the summation of the rates of formation of the species by each elementary reaction. At equilibrium, the net rate of production of any species is zero.

The Nucleation of the Intrinsic Point Defects and Oxygen

Octahedral voids or D defects are formed by the aggregation of vacancies. Globular B defects are formed by the aggregation of self-interstitials. A defects presumably form by the transformation of B defects. These microdefects are modeled as clusters of intrinsic point defects. The thermodynamics and kinetics of the formation of these microdefects is discussed in Sect. 38.2.

Oxygen clusters (O-clusters) are modeled as spherical aggregates of oxygen (silicon dioxide) [38.70]. The specific volume of an oxygen cluster is greater than that of silicon. Thus, the formation of an oxygen cluster is associated with the generation of stress. In the presence of vacancies, however, the clusters relieve stress by the consumption of vacancies. Oxygen cluster formation proceeds through a series of reactions involving oxygen and vacancies. Hence, this series of reactions is written as



where γ is the number of vacancies absorbed per oxygen atom participating in the reaction. It must be noted that an oxygen cluster containing m oxygen atoms also contains $m/2$ silicon atoms.

The volume (bulk) free-energy change associated with the formation of an oxygen cluster containing m oxygen atoms in an isolated element of silicon at a fixed temperature and composition is given by the contributions from the oxygen supersaturation and the vacancy supersaturation. Thus, the total free-energy change associated with the formation of an oxygen clus-

ter containing m oxygen atoms is

$$\Delta F_O(m_O) = \left[-m_O k_B T \ln \frac{C_O}{C_{O,e}} - \gamma m_O k_B T \ln \frac{C_v}{C_{v,e}} \right] + \left[\lambda_O m_O^{2/3} \right]. \quad (38.85)$$

The first term in the square brackets on the right-hand side of (38.85) is the volume (bulk) free energy change, and the second term is the energy required to form the surface of an oxygen cluster containing m oxygen atoms. The subscript “O” denotes both oxygen and oxygen clusters depending on the variable.

The formation kinetics of oxygen clusters is quite complex. An oxygen cluster undergoes morphological changes as it grows. This chapter does not address the details of these morphological changes. A broad macroscopic understanding of the oxygen cluster distribution is obtained by assuming these clusters to be spherical. The number of oxygen atoms in the critical cluster is obtained by maximizing the free-energy change ΔF with respect to m . The net rate of formation of stable oxygen clusters is obtained using the classical nucleation theory. Typically, it is accurate to assume that the formation rate of stable oxygen clusters is described by the diffusion-limited attachment of oxygen atoms to the critical oxygen clusters. For the sake of completeness, however, the attachment frequency is described both by the oxygen diffusion-limited mechanism and the vacancy diffusion-limited mechanism, depending on the ratio of $D_v C_v$ to $D_O C_O$. Hence, the formation rate of stable oxygen clusters per unit volume of silicon, or the oxygen nucleation rate, is given as

$$J_O = [\eta_{O \leftrightarrow O}^*] \left[\left\{ 12\pi k_B T \times \Delta F_O(m_O^*) \right\}^{-1/2} \times \left(k_B T \ln \frac{C_O}{C_{O,e}} + \gamma k_B T \ln \frac{C_v}{C_{v,e}} \right) \right] \times \left[\rho_O \exp \left(-\frac{\Delta F_O(m_O^*)}{k_B T} \right) \right], \quad (38.86)$$

$$\eta_{O \leftrightarrow O}^* = \begin{cases} 4\pi R(m_O^*) D_O C_O & \left| D_v C_v \geq \gamma D_O C_O \right. \\ \frac{4\pi R(m_O^*) D_v C_v}{\gamma} & \left| D_v C_v < \gamma D_O C_O \right. \end{cases}, \quad (38.87)$$

where $\Delta F(m^*)$ is the free-energy change associated with the formation of a critical cluster containing m^*

monomers; the subscript “O” denotes oxygen or oxygen clusters and the superscript asterisk denotes the critical clusters. $\eta_{O \leftrightarrow O}^*$ is the attachment frequency of oxygen atoms to a critical oxygen cluster. The second term in the square brackets on the right-hand side of (38.86) is the Zheldovich factor and the third term is the equilibrium concentration of the critical oxygen clusters. The discussed kinetics can now be applied in the development of the equations governing the CZ defect dynamics.

38.3.2 The Model

The model quantifying the CZ defect dynamics must account for the balances of all species, cluster formation, and cluster growth. All microdefects are approximated as spherical clusters. As discussed before, D defects are termed v-clusters, A and B defects are termed i-clusters, and the aggregates of oxygen (silicon dioxide) are termed O-clusters. At any given location of a growing CZ crystal, at a given time, one or more than one population of clusters formed at various other locations during the elapsed time period can exist. The clusters are assumed to be immobile; thus, they are only carried convectively from one location to the next by the physical movement of the growing crystal. In addition, there is a spatial distribution of these populations. A rigorous treatment of the spatial distribution of these cluster populations is computationally expensive. Kulkarni and Voronkov developed a lumped model that represents a population of clusters at any given location by an equivalent population of identical clusters [38.53]. Later, Kulkarni applied this model to quantify the CZ defect dynamics in the presence of oxygen [38.70]. In this chapter, this research reported by Kulkarni is discussed in detail.

The Governing Equations

The balance of self-interstitials includes their transport and their consumption by the Frenkel reaction and i-clusters

$$\frac{\partial C_i}{\partial t} + V \frac{\partial C_i}{\partial z} = \nabla \cdot (D_i \nabla C_i) + [k_{i \leftrightarrow v}(C_{i,e} C_{v,e} - C_i C_v)] - q_i^i. \quad (38.88)$$

The term in the square brackets in (38.88) is the net rate of formation (negative consumption rate) of self-interstitials per unit volume by the Frenkel reaction.

Vacancies are consumed by both v-clusters and O-clusters. In addition, vacancies participate in reactions

with self-interstitials, oxygen, and vO. Hence, the vacancy balance is written as

$$\begin{aligned} \frac{\partial C_v}{\partial t} + V \frac{\partial C_v}{\partial z} = & \nabla (D_v \nabla C_v) \\ & + [k_{i \leftrightarrow v}(C_{i,e} C_{v,e} - C_i C_v) \\ & - k_{v \leftrightarrow O} C_v C_O + k_{vO} C_{vO}] \\ & - q_v^v - q_O^v. \end{aligned} \quad (38.89)$$

The rate constant for an elementary forward or an elementary reverse reaction is denoted by k . The subscripts of k indicate the reactants involved in a forward or a reverse reaction: “ k_x ” denotes the rate constant for the elementary reaction involving only x and “ $k_{x \leftrightarrow y}$ ” indicates the elementary reaction involving x and y , where x and y represent the reacting species. q_x^y is the volumetric consumption rate of species y , denoted by the superscript, by the clusters containing species x , denoted by the subscript. The term in the square brackets in (38.89) is the net rate of vacancy production by reactions (38.1) and (38.82). The species vO is considered to be immobile. It is not directly consumed by clusters. Thus, the vO species balance must account only for the convection and reactions (38.82) and (38.83)

$$\begin{aligned} \frac{\partial C_{vO}}{\partial t} + V \frac{\partial C_{vO}}{\partial z} = & (k_{v \leftrightarrow O} C_v C_O - k_{vO} C_{vO} \\ & - k_{vO \leftrightarrow O} C_{vO} C_O + k_{vO_2} C_{vO_2}). \end{aligned} \quad (38.90)$$

The species vO₂ is also considered to be immobile and it is also not directly consumed by clusters. It participates only in reaction (38.83)

$$\frac{\partial C_{vO_2}}{\partial t} + V \frac{\partial C_{vO_2}}{\partial z} = (k_{vO \leftrightarrow O} C_{vO} C_O - k_{vO_2} C_{vO_2}). \quad (38.91)$$

Oxygen is in abundance

$$\frac{\partial C_O}{\partial t} + V \frac{\partial C_O}{\partial z} = 0. \quad (38.92)$$

It is evident from (38.88–38.91) that the balance of the *excess total vacancy concentration*, defined as the difference between the sum of the concentrations of all species containing vacancies (v , vO, and vO₂) and the concentration of self-interstitials, $C_v + C_{vO} + C_{vO_2} - C_i$, is not explicitly affected by nonaggregation reactions (38.1), (38.82), and (38.83); this balance is written

as

$$\begin{aligned} & \frac{\partial (C_v + C_{vO} + C_{vO_2} - C_i)}{\partial t} \\ & + V \frac{\partial (C_v + C_{vO} + C_{vO_2} - C_i)}{\partial z} \\ & = \nabla (D_v \nabla C_v) - \nabla (D_i \nabla C_i) - q_v^v - q_O^v + q_i^i. \end{aligned} \quad (38.93)$$

Assuming the reaction equilibrium for reactions (38.1), (38.82), and (38.83), the species balances (38.88–38.91) are defined by (38.93), (38.3), and the reaction equilibria [38.59]

$$\frac{C_{vO}}{C_v} = \sqrt{\frac{C_{vO_2,e}}{C_{v,e}}}, \quad (38.94)$$

$$\frac{C_{vO_2}}{C_v} = \frac{C_{vO_2,e}}{C_{v,e}}. \quad (38.95)$$

In CZ crystals, only oxygen nucleation facilitated by vacancies is of primary interest. The formation of O-clusters by ejection of self-interstitials is negligible. Once formed in the presence of vacancies, O-clusters initially grow by consuming vacancies without ejecting self-interstitials; later, when the vacancy concentration decreases, O-clusters can grow by ejection of self-interstitials. For the sake of simplicity, the growth of O-clusters by ejection of self-interstitials is ignored. When the vacancy concentration is sufficiently high, the O-cluster growth is assumed to be limited by the consumption of oxygen by the clusters; when the vacancy concentration is relatively low, the O-cluster growth is assumed to be limited by the consumption of vacancies by the clusters. Thus, O-clusters do not grow when vacancies are at equilibrium concentration. These approximations accurately quantify the density of O-clusters but underpredict their size by ignoring their growth by ejection of self-interstitials under vacancy-lean conditions. The assumptions used in the model are self-consistent, however, and provide meaningful insights into the CZ defect dynamics. If desired, the upper limit of O-cluster size can be quantified by simply assuming oxygen diffusion-limited cluster growth under all conditions; this assumption is not used in the formulation of the discussed model, although it can be implemented without much effort.

The diffusion-limited volumetric consumption rates of vacancies, self-interstitials, and oxygen by various clusters are defined following the methodology devel-

oped by Kulkarni and Voronkov [38.53]

$$q_i^i = 4\pi D_i (C_i - C_{i,e}) (U_i n_i)^{1/2}, \quad (38.96)$$

$$q_v^v = 4\pi D_v (C_v - C_{v,e}) (U_v n_v)^{1/2}, \quad (38.97)$$

$$q_O^v = \begin{cases} \gamma 4\pi D_O (C_O - C_{O,e}) (U_O n_O)^{1/2} \\ |D_v (C_v - C_{v,e}) \geq \gamma D_O (C_O - C_{O,e})| \\ 4\pi D_v (C_v - C_{v,e}) (U_O n_O)^{1/2} \\ |D_v (C_v - C_{v,e}) < \gamma D_O (C_O - C_{O,e})| \end{cases}. \quad (38.98)$$

The evolution of the auxiliary variable U , which is proportional to the surface area of the cluster population, is described by the cluster growth equation

$$\frac{\partial U_i}{\partial t} + V \frac{\partial U_i}{\partial z} = \frac{2D_i n_i}{\psi_i^i} (C_i - C_{i,e}), \quad (38.99)$$

$$\frac{\partial U_v}{\partial t} + V \frac{\partial U_v}{\partial z} = \frac{2D_v n_v}{\psi_v^v} (C_v - C_{v,e}), \quad (38.100)$$

$$\frac{\partial U_O}{\partial t} + V \frac{\partial U_O}{\partial z} = \begin{cases} \frac{2D_O n_O}{\psi_O^O} (C_O - C_{O,e}) \\ |D_v (C_v - C_{v,e}) \geq \gamma D_O (C_O - C_{O,e})| \\ \frac{2D_v n_O}{\gamma \psi_O^O} (C_v - C_{v,e}) \\ |D_v (C_v - C_{v,e}) < \gamma D_O (C_O - C_{O,e})| \end{cases}. \quad (38.101)$$

The total cluster density is directly obtained by the classical nucleation theory

$$\frac{\partial n_i}{\partial t} + V \frac{\partial n_i}{\partial z} = J_i, \quad (38.102)$$

$$\frac{\partial n_v}{\partial t} + V \frac{\partial n_v}{\partial z} = J_v, \quad (38.103)$$

$$\frac{\partial n_O}{\partial t} + V \frac{\partial n_O}{\partial z} = J_O. \quad (38.104)$$

The representative radius of a cluster population at any location is given as

$$\mathcal{R}_i = \left(\frac{U_i}{n_i} \right)^{1/2}, \quad (38.105)$$

$$\mathcal{R}_v = \left(\frac{U_v}{n_v} \right)^{1/2}, \quad (38.106)$$

$$\mathcal{R}_O = \left(\frac{U_O}{n_O} \right)^{1/2}. \quad (38.107)$$

The domain of computation is transient, because a CZ crystal is continuously pulled. The equation describing this domain transience must be solved with the discussed equations. Vacancies and self-interstitials are assumed to exist at equilibrium on all crystal surfaces including the melt–crystal interface; the concentrations of the vO and vO_2 species are determined by the re-

Table 38.2 Key properties of various species, including oxygen and vacancy–oxygen complexes, participating in reactions in growing CZ crystals

Property set II	Property set III
$D_i \text{ (cm}^2/\text{s)} = 0.19497 \exp\left(\frac{-0.9 \text{ (eV)}}{k_B T}\right)$	$D_i \text{ (cm}^2/\text{s)} = 4 \times 10^{-3} \exp\left(\frac{-0.3 \text{ (eV)}}{k_B T}\right)$
$D_v \text{ (cm}^2/\text{s)} = 6.2617 \times 10^{-4} \exp\left(\frac{-0.4 \text{ (eV)}}{k_B T}\right)$	$D_v \text{ (cm}^2/\text{s)} = 2 \times 10^{-3} \exp\left(\frac{-0.38 \text{ (eV)}}{k_B T}\right)$
$D_O \text{ (cm}^2/\text{s)} = 1.3 \times 10^{-1} \exp\left(\frac{-2.53 \text{ (eV)}}{k_B T}\right)$	$D_O \text{ (cm}^2/\text{s)} = 1.3 \times 10^{-1} \exp\left(\frac{-2.53 \text{ (eV)}}{k_B T}\right)$
$C_{i,e} \text{ (cm}^{-1}) = 6.1759 \times 10^{26} \exp\left(\frac{-4.0 \text{ (eV)}}{k_B T}\right)$	$C_{i,e} \text{ (cm}^{-1}) = 4.725 \times 10^{27} \exp\left(\frac{-4.3492 \text{ (eV)}}{k_B T}\right)$
$C_{v,e} \text{ (cm}^{-1}) = 7.52 \times 10^{26} \exp\left(\frac{-4.0 \text{ (eV)}}{k_B T}\right)$	$C_{v,e} \text{ (cm}^{-1}) = 1.2 \times 10^{27} \exp\left(\frac{-4.12 \text{ (eV)}}{k_B T}\right)$
$C_O \text{ (cm}^{-1}) = 9 \times 10^{22} \exp\left(\frac{-1.52 \text{ (eV)}}{k_B T}\right)$	$C_O \text{ (cm}^{-1}) = 9 \times 10^{22} \exp\left(\frac{-1.52 \text{ (eV)}}{k_B T}\right)$
$C_{vO_2,e} \text{ (cm}^{-1}) = \frac{C_O^2}{5 \times 10^{22}} \exp\left(\frac{-0.5 \text{ (eV)}}{k_B T}\right)$	$C_{vO_2,e} \text{ (cm}^{-1}) = \frac{C_O^2}{5 \times 10^{22}} \exp\left(\frac{-0.5 \text{ (eV)}}{k_B T}\right)$
$\lambda_i \text{ (eV)} = 2.75 - 2.85^*$	$\lambda_i \text{ (eV)} = 2.75 - 2.85^*$
$\lambda_v \text{ (eV)} = 1.75$	$\lambda_v \text{ (eV)} = 1.75$
$\lambda_O \text{ (eV)} = 1.7$	$\lambda_O \text{ (eV)} = 1.7$
$\gamma = 0.42$	$\gamma = 0.42$

* Values between 2.75–2.85 eV give acceptable results. The simulations presented in this chapter were performed using $\lambda_i = 2.75 \text{ eV}$

action equilibria. As the final size of a cluster is far greater than its critical size, the initial size of clusters upon their formation is assumed to be zero. The initial length of a growing crystal is assumed to be finite but negligible. The discussed model describes the defect dynamics in CZ crystals growing under both steady as well as unsteady states.

There is a considerable uncertainty in the parameters describing the properties of many species participating in the CZ defect dynamics. Particularly, properties of self-interstitials are not very well known. Reported self-interstitial migration energies vary from 0.95 to 0.3 eV [38.1, 26, 34, 58–64]. As there are many parameters describing the properties of various species, a reasonably accurate prediction of the general characteristics of the observed microdefect distributions is possible for many different sets of values of these parameters. Two sets of properties, listed in Table 38.2, were used for simulations discussed in this section. The intrinsic point defect properties listed under property set II were derived from the property set proposed by Kulkarni et al., on the basis of further fine-tuning to fit experimental data [38.1, 70]. The intrinsic point defect properties proposed by Voronkov and Falster were fine-tuned to derive property set III [38.64, 70]. The for-

mation energy of vO_2 species and the surface energies of all clusters were tuned to predict experimental data and well-accepted nucleation ranges of self-interstitials, vacancies, and oxygen. Both property sets yield qualitatively similar results.

38.3.3 Defect Dynamics in One-Dimensional Crystal Growth

A CZ crystal growing at a fixed rate through a fixed temperature field remains in a steady state, with respect to a fixed coordinate system, far from the regions formed in the beginning of the growth. A solution of the one-dimensional version of the developed model assuming only axial variation of the microdefect distribution provides insights into the basics of the CZ defect dynamics in the presence of oxygen. For these simulations, the crystal is assumed to grow through a temperature profile described by the linear dependence of $1/T$ on z , according to (38.6).

As discussed in Sect. 38.2, Voronkov described the conditions leading to the formation of various microdefects in growing FZ and CZ crystals in the early 1980s, in the absence of oxygen [38.19]. In the interest of continuity and in the context of understanding the influence of oxygen on the CZ defect dynamics, salient features of this theory are discussed again in this section. According to Voronkov's theory, an interplay between the Frenkel reaction and the transport of the intrinsic point defects of silicon determines the concentration fields of the intrinsic point defects in the vicinity of the melt–crystal interface. Vacancies and self-interstitials are assumed to exist at equilibrium at the interface. The temperature drop in the crystal in the vicinity of the interface drives the recombination of vacancies and self-interstitials, decreasing their concentrations. The developed concentration gradients drive the diffusion of vacancies and self-interstitials from the interface into the crystal. The vacancy concentration at the interface is higher than the concentration of self-interstitials, whereas self-interstitials diffuse faster. Thus, when the convective transport is relatively appreciable, vacancies remain the dominant species in the crystal; when the diffusion is relatively appreciable, self-interstitials are replenished at a higher rate from the interface and become the dominant species. Voronkov approximately quantified the relative effect of the convection over the diffusion by the ratio of V to G (V/G). At higher V/G , convection is appreciable; at lower V/G , diffusion is appreciable; at the criti-

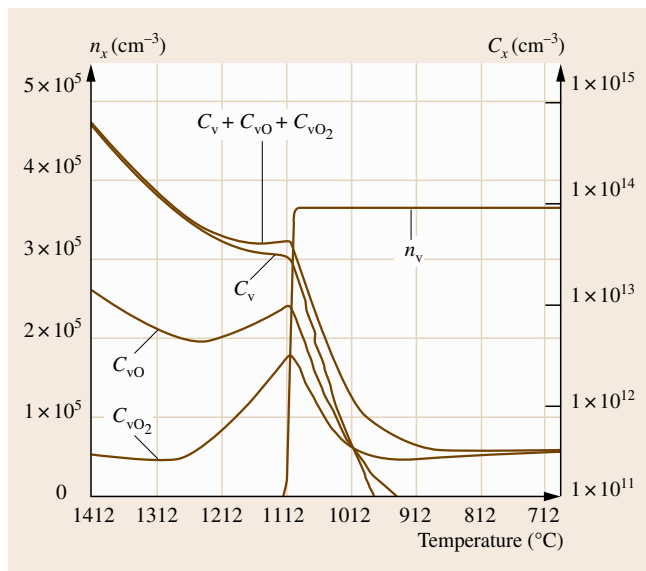


Fig. 38.17 Evolution of the concentrations of various reacting species and the density of v-clusters in a CZ crystal growing at a high rate ($G = 3.5$ K/mm, $V = 0.7$ mm/min, $C_O = 6.25 \times 10^{17}$ cm $^{-3}$ or 12.5 ppma) (after [38.70])

cal V/G , the flux of vacancies is equal to the flux of self-interstitials. This analysis does not take into account the effect of oxygen. Oxygen introduces reactions involving vacancies and oxygen into this dynamics. In the presence of oxygen, free vacancies for the recombination with self-interstitials are supplied from the dissociation of vO and vO_2 species as well as from the interface, which is an infinite source. Hence, the presence of oxygen shifts the balance of this dynamics in favor of vacancies.

The evolution of the concentrations of v , vO , and vO_2 species as functions of the temperature in a CZ crystal growing at very high V/G , or under highly vacancy-rich conditions, is shown in Fig. 38.17. Near the interface, where the recombination rate is significant, concentrations of all three species decrease, as both free vacancies (v) and bound vacancies (bound as vO and vO_2) participate in the recombination reaction; the participation of free vacancies in the recombination is direct, whereas the participation of bound vacancies results through the coupling of reactions (38.1), (38.82), and (38.83). Once the recombination rate decreases, the *total vacancy concentration*, $C_v + C_{vO} + C_{vO_2}$, remains essentially constant. The *bound vacancy concentration*, $C_{vO} + C_{vO_2}$, increases with decreasing temperature because of a shift in the reaction equilibrium. Free vacancies, however, remain dominant and nucleate at around 1100°C. The growth of voids predominantly consumes all vacancy species, as shown in Fig. 38.17. It must be noted, however, that the residual total vacancy concentration left at lower temperatures remains appreciable because of the binding between vacancies and oxygen.

At close to the critical yet moderately vacancy-rich condition, the free vacancy concentration does not remain high enough to form voids at higher temperatures, in a growing CZ crystal. As the temperature drops further, the concentration of bound vacancies increases. Under these conditions, free vacancies facilitate O-cluster formation at lower temperatures. The formation and growth of O-clusters predominantly consumes both free and bound vacancies, as shown in Fig. 38.18. The predicted total vacancy concentration at lower temperatures is approximate, because of the assumptions discussed in the previous section.

Conditions leading to the growth of crystals free of large v -clusters and i -clusters are desired in many microelectronic applications. Hence, the range of the pull rate within which a CZ crystal free of large clusters can be grown at different oxygen concentrations

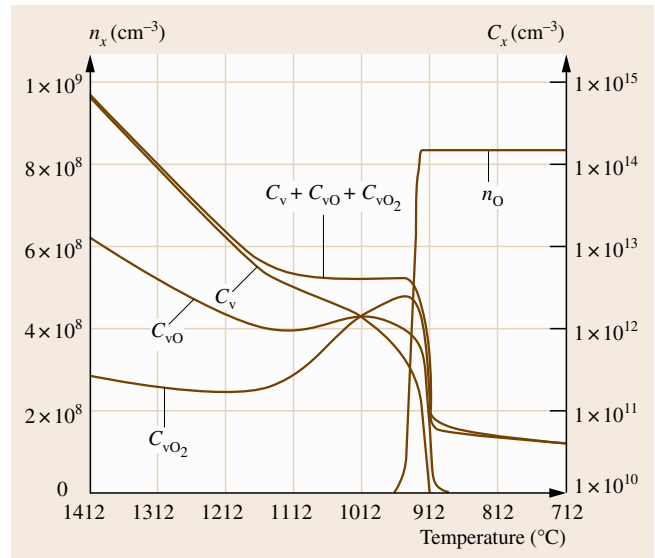


Fig. 38.18 Evolution of the concentrations of various reacting species and the density of O-clusters in a CZ crystal growing close to but moderately above the critical condition ($G = 3.5$ K/mm, $V = 0.48$ mm/min, $C_O = 6.25 \times 10^{17}$ cm $^{-3}$ or 12.5 ppma) (after [38.70])

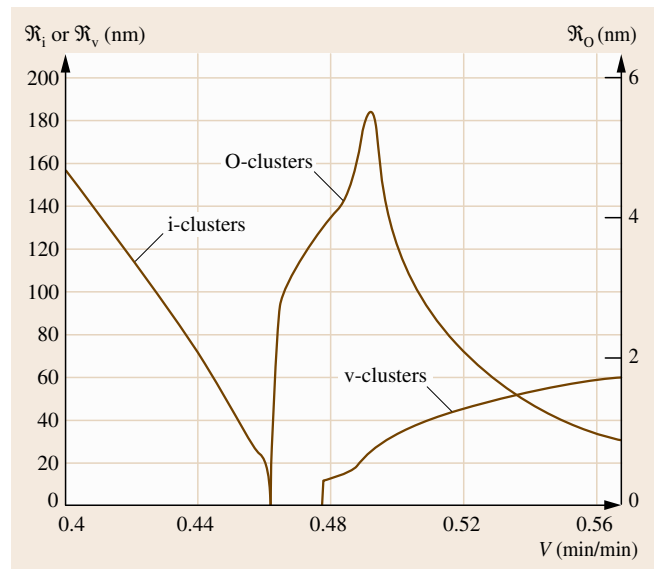


Fig. 38.19 The simulated sizes of various clusters as functions of the CZ crystal pull rate (after [38.70])

is of primary interest in industrial crystal growth. This range can be determined by a series of simulations at

different oxygen concentrations at different fixed pull rates. These simulations, however, are computationally expensive. An approximate pull rate range that allows the growth of a crystal without large v-clusters and i-clusters, at a given oxygen concentration, can be determined by simulating the growth at a continuously decreasing rate such that the microdefect distribution in the crystal continuously shifts as a function of the pull rate. A direct but approximate correlation between the microdefect distribution and the pull rate can thus be obtained. Figure 38.19 shows one such simulation, defining the microdefect distribution as a function of the pull rate for a given oxygen concentration and temperature profile. It must be noted that the region free of large v-clusters and i-clusters contains O-clusters. O-clusters are quite large in the vicinity of the boundary between v-clusters and O-clusters, as they are formed at higher temperatures in the presence of a relatively higher vacancy concentration. The size of O-clusters decreases as the vacancy concentration during their formation decreases. A series of such simulations at different oxygen concentrations shows how oxygen affects the range of the pull rate within which the growth of a crystal free of large v-clusters and i-clusters is possible. Oxygen clearly expands this range because of the binding be-

tween vacancies and oxygen, as shown in Fig. 38.20. In this figure, v-clusters greater than 20 nm in radius are defined as large. It must be noted that this definition is arbitrary. Figure 38.20 also shows how V/G defining the boundary between O-clusters and i-clusters, known as the v/i boundary, shifts with the oxygen concentration in the discussed one-dimensional crystals growing through the temperature profile defined by (38.6). As discussed before, the presence of vO and vO_2 species near the interface increases the total vacancy concentration available for the recombination with self-interstitials, thus decreasing the V/G marking the v/i boundary; in effect, the crystal becomes marginally more vacancy rich in the presence of oxygen. The surface energy of voids is assumed to be a constant and independent of the oxygen concentration in all these simulations.

The series of one-dimensional simulations discussed in this section establishes the salient effects of oxygen on the CZ defect dynamics. All simulations discussed in this section are performed using property set III.

38.3.4 Defect Dynamics in Two-Dimensional Crystal Growth

The radial variation of the temperature field in a growing CZ crystal and the radial diffusion of the intrinsic point defects, induced by the lateral surface of the crystal and the radial variation of the intrinsic point defect concentration, introduce a two-dimensional variation of the microdefect distribution in the crystal. In addition, variation of the crystal pull rate, commonly observed in modern CZ processes, introduces an axial variation of the microdefect distribution. Hence, it is necessary to validate the discussed model by a comparison of its predictions with the microdefect distribution observed in a crystal grown under an unsteady state representing a variety of possible conditions in modern CZ growth. An experimental crystal was pulled by the varying rate shown in Fig. 38.21. The crystal was cut longitudinally and the microdefect distribution was characterized by the method of copper decoration followed by etching [38.38–40]. The crystal was assumed to grow through a fixed temperature field predicted by the commercial software MARC, using the algorithm developed by Virzi [38.37]. As shown in Fig. 38.21, v-clusters are observed in the regions of crystal grown at higher rates, and i-clusters are observed in the regions grown at lower rates. The dense bands at the

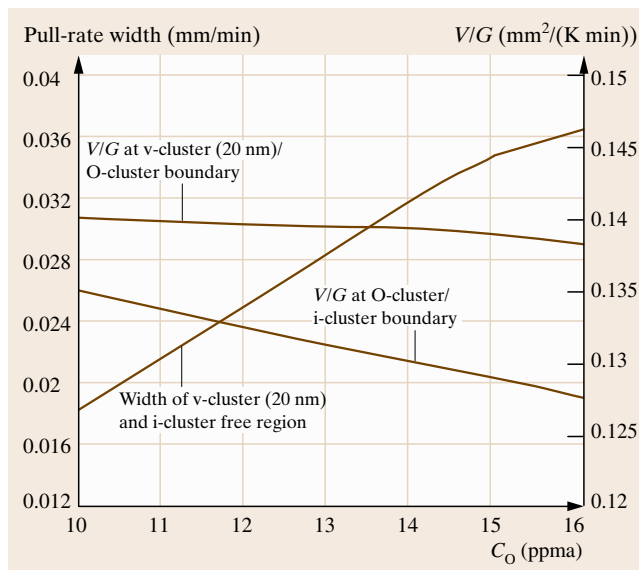


Fig. 38.20 The sensitivity of the microdefect distribution near the critical condition to the oxygen concentration. Note: The i-cluster and large v-cluster free region includes v-clusters smaller than 20 nm (radius) and O-clusters (after [38.70])

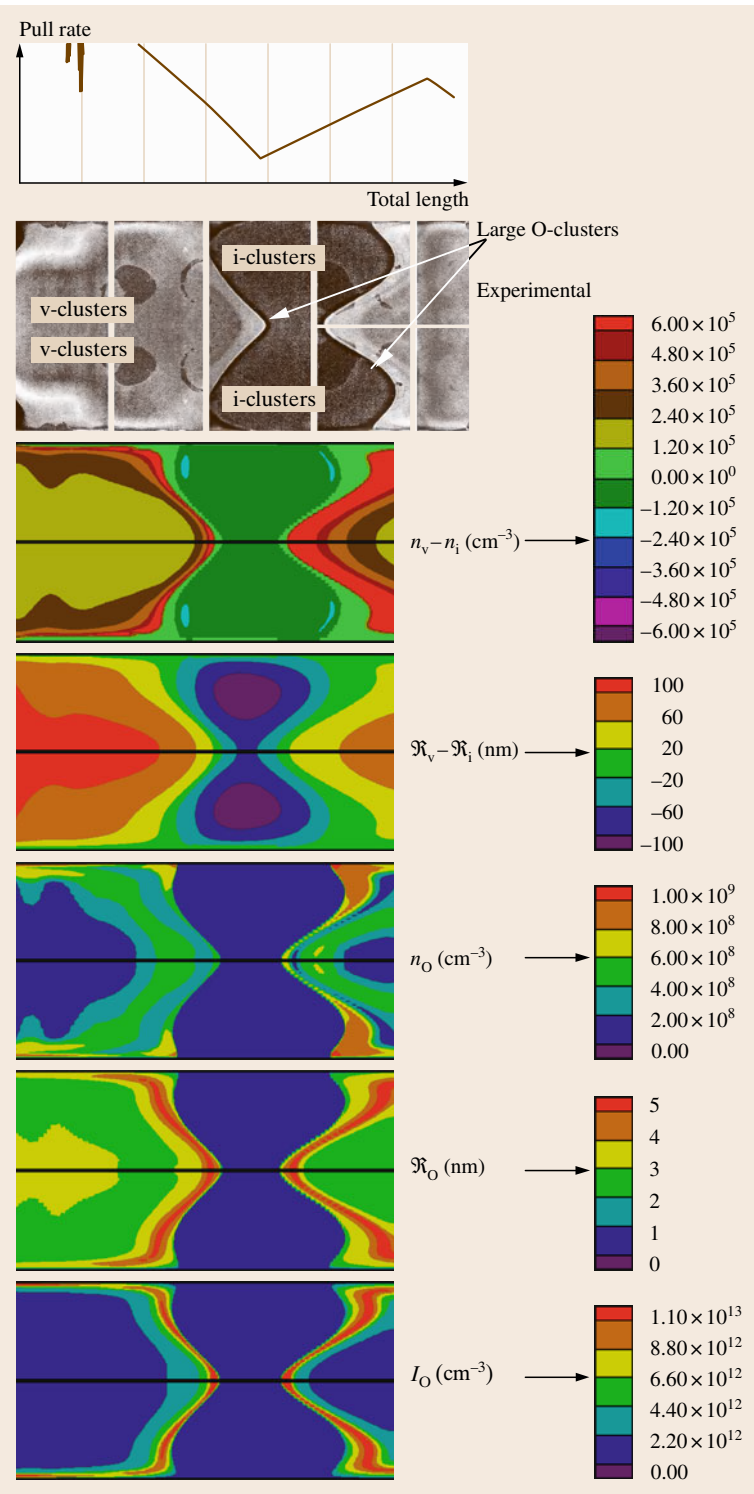


Fig. 38.21 Comparison of the predictions of the model, using property set III, with the experimental observations. The dense bands along the v/i boundary, near the edge of the region containing v-clusters, indicate intense oxygen precipitation (note: scales truncated for clarity) (after [38.70])

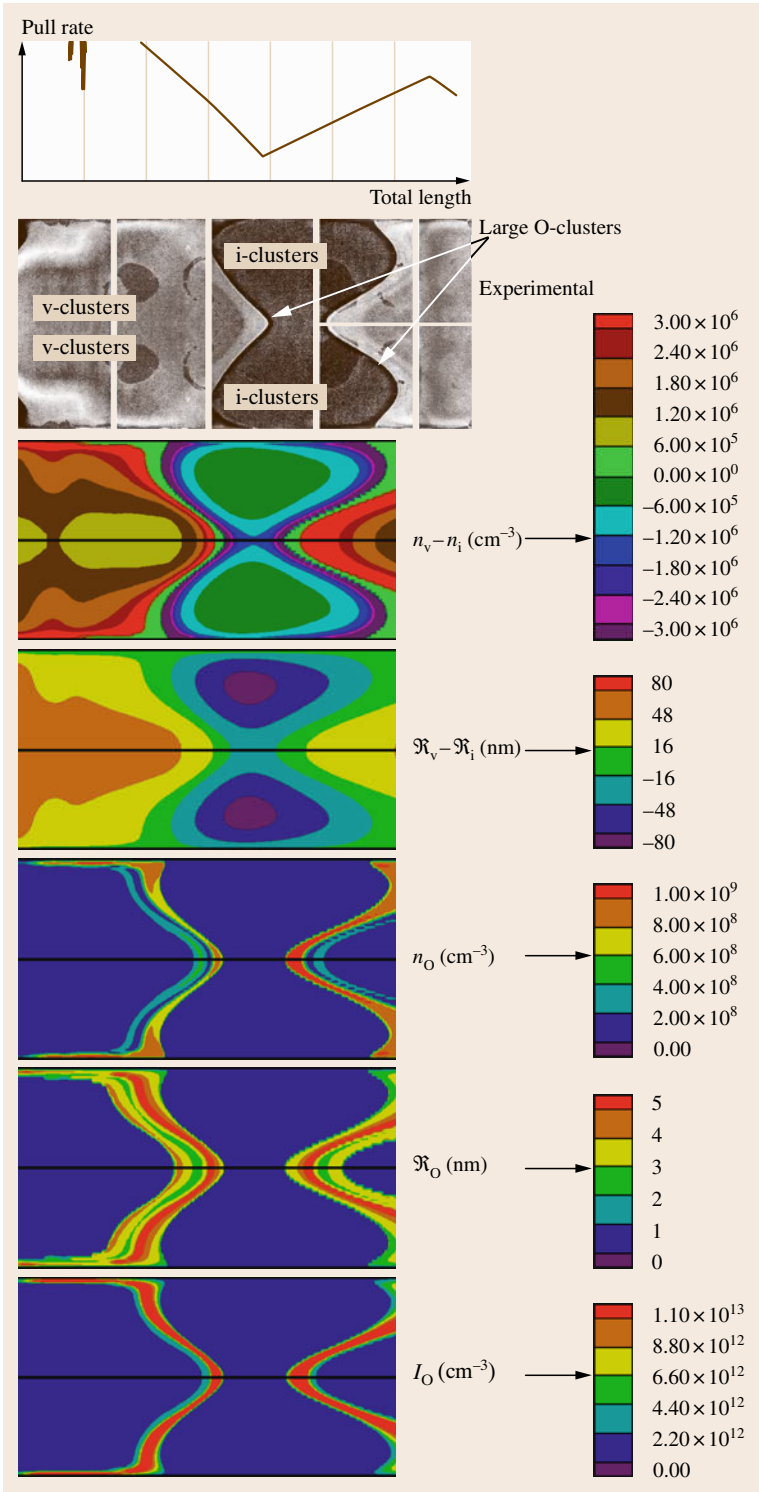


Fig. 38.22 Comparison of the predictions of the developed model, using property set II, with the experimental observations. The dense bands along the v/i boundary, near the edge of the region containing v-clusters, indicate intense oxygen precipitation (note: scales truncated for clarity) (after [38.70])

edge of the region containing large v-clusters, close to the featureless region in the vicinity of i-clusters, indicate the presence of large O-clusters at higher densities. This observation is only qualitative, as all O-clusters are not revealed by the applied characterization technique. The featureless band or region very close to the region of i-clusters can contain unobservable, small microdefects.

The microdefect distributions in the crystal, predicted using property set III, are also shown in Fig. 38.21. As i-clusters and v-clusters do not co-exist, a distribution of $\mathcal{R}_v - \mathcal{R}_i$ simultaneously shows the distribution of both types of clusters; a positive value of $\mathcal{R}_v - \mathcal{R}_i$ indicates the size of v-clusters and a negative value of $\mathcal{R}_v - \mathcal{R}_i$ indicates the size of i-clusters. Similarly, the distribution of the densities of i-clusters and v-clusters are quantified by the distribution of $n_v - n_i$. The size and density distribution of O-clusters are shown separately in Fig. 38.21. It must be noted that the lumped model predicts the representative size of an entire population of microdefects present at any given location. In crystal regions formed under the appreciable influence of the convection of the intrinsic point defects, the dominant clusters formed are v-clusters; in regions formed under the appreciable influence of the diffusion of the intrinsic point defects, the dominant clusters formed are i-clusters; near the critical but moderately vacancy-rich condition, O-clusters are dominant. Since the lumped model applies the continuum-scale kinetics and thermodynamics in the prediction of the representative size and density of any given cluster population, it typically predicts negli-

gible but finite oxygen precipitation even under highly vacancy-rich conditions. *Kulkarni* implemented various algorithms to ignore this negligible oxygen precipitation in the developed computer program that solves the model equations; but depending on the operating conditions and the species property set used for the simulation, a negligible but finite oxygen precipitation is predicted by the computer program even under highly vacancy-rich conditions [38.70]. This is evident in Fig. 38.21, which shows a negligible but definite presence of O-clusters in the regions grown under appreciable influence of convection of the intrinsic point defects. Both the size (radius) and density of O-clusters must be studied simultaneously to quantify the intensity of oxygen precipitation. The intensity of oxygen precipitation (I_O) can be measured by the amount of oxygen precipitated per unit volume of the crystal, which is given as

$$I_O = \frac{4}{3}\pi \mathcal{R}_O^3 \psi_O^O n_O. \quad (38.108)$$

As shown in Fig. 38.21, the intensity of oxygen precipitation is very high in the regions formed marginally above the critical condition and is negligible in the regions dominated by v-clusters and i-clusters.

The microdefect distributions, in the same crystal shown in Fig. 38.21, predicted using the property set II are shown in Fig. 38.22. The model captures the spatial distributions of various microdefects quite well. Although the predicted densities and sizes of various microdefects are not directly compared with the experimental data, the predictions are consistent with the reported experimental data [38.38, 39, 48].

38.4 Czochralski Defect Dynamics in the Presence of Nitrogen

As microdefects in silicon substrates produced from CZ crystals can adversely affect the performance of devices built on them, the development of crystal growth processes to reduce the size of the microdefects in growing crystals is of industrial significance. Various studies have shown that the microdefect distribution in CZ crystals can be influenced by the presence of nitrogen in general, and that the size of voids can be reduced, in particular [38.20, 71–75]. Various mechanisms to describe the effect of nitrogen on the CZ defect dynamics have been proposed [38.20, 72, 74, 75]. *Voronkov* and *Falster* quantified the effect of nitrogen on the void distribution in an isolated element of a growing CZ crystal [38.74]. An accurate model for the prediction of the effect of nitrogen on CZ defect dynamics, how-

ever, must account for the diffusion of mobile reacting species in a growing crystal. It must also incorporate reactions involving vacancies, self-interstitials, oxygen, and complexes of vacancies with oxygen and nitrogen, along with the formation of various microdefects in CZ crystals growing under both steady as well as unsteady states. This chapter discusses such a model, proposed and solved by *Kulkarni*, which quantifies both steady-state and unsteady-state CZ defect dynamics in the presence of nitrogen and oxygen [38.75].

38.4.1 The Model

An accurate quantification of CZ defect dynamics requires a treatment of a series of elementary reactions

describing the evolution of the populations of various clusters, which is computationally impractical. Therefore, reasonable approximations are required for the quantification of the microdefect distribution in a CZ crystal. The lumped model proposed by *Kulkarni* and *Voronkov* that approximates a population of microdefects of various sizes present at a given location in the crystal as an equivalent population of identical microdefects is adopted for the treatment of the growth of microdefects [38.53]. All microdefects are approximated as spherical clusters. The stable clusters are assumed to form according to the classical nucleation theory and to grow by diffusion-limited kinetics. The cluster formation and growth dynamics is treated simultaneously with the reactions involving vacancies, self-interstitials, oxygen, nitrogen, and complexes of oxygen and nitrogen.

Reactions in Growing CZ Crystals

The primary reaction influencing the CZ defect dynamics is the Frenkel reaction, which involves the mutual annihilation of a vacancy and a self-interstitial to produce a silicon lattice atom, and the generation of a pair of a vacancy and a self-interstitial from a lattice silicon atom, as shown in reaction (38.1). Oxygen participates in reactions with vacancies and the complexes of vacancies and oxygen, according to (38.82) and (38.83). Nitrogen exists as both a monomer and a dimer, and interacts with vacancies [38.74]



The microdefect distributions in CZ crystals are affected by defect dynamics at fairly higher temperatures, at which nitrogen predominantly exists as N, N₂, and vN; hence, the presence of any other species containing nitrogen can be ignored [38.74]. The species N and N₂ are assumed to exist in the interstitial form in silicon, and vN can be viewed to exist in the substitutional form. The equilibria for reactions (38.109) and (38.110) are given by

$$\frac{C_{\text{N}}^2}{C_{\text{N}_2}} = K_{\text{N} \leftrightarrow \text{N}_2}, \quad (38.111)$$

$$\frac{C_{\text{vN}}}{C_{\text{vN}}} = K_{\text{vN} \leftrightarrow \text{N}}, \quad (38.112)$$

where K is the equilibrium constant; the subscripts specify the reaction type.

The aggregation of the intrinsic point defects, vacancies and self-interstitials, and the aggregation of

oxygen proceed as discussed in Sects. 38.2 and 38.3, respectively. The thermodynamics and kinetics of formation of all clusters are also discussed in Sects. 38.2 and 38.3.

The Governing Equations

The governing equations describe the balances of all species participating in the CZ defect dynamics. The total vacancy concentration, defined as the sum of the concentration of free vacancies (v), and of the cumulative concentration of bound vacancies ($v\text{O}$, $v\text{O}_2$, and $v\text{N}$), is not affected by reactions (38.82), (38.83), (38.109), and (38.110); both free vacancies and self-interstitials are consumed by the Frenkel reaction at an equal rate and are generated at an equal rate. Hence, the rate of change of the *total excess vacancy concentration*, defined as the difference between the total vacancy concentration and the concentration of self-interstitials, is affected only by the transport of individual species, and their consumption by the clusters

$$\begin{aligned} & \frac{\partial (C_{\text{v}} + C_{\text{vO}} + C_{\text{vO}_2} + C_{\text{vN}} - C_{\text{i}})}{\partial t} \\ & + v \frac{\partial (C_{\text{v}} + C_{\text{vO}} + C_{\text{vO}_2} + C_{\text{vN}} - C_{\text{i}})}{\partial z} \\ & = \nabla (D_{\text{v}} \nabla C_{\text{v}}) - \nabla (D_{\text{i}} \nabla C_{\text{i}}) - q_{\text{v}}^{\text{v}} - q_{\text{O}}^{\text{v}} + q_{\text{i}}^{\text{i}}. \end{aligned} \quad (38.113)$$

All species except for vacancies and self-interstitials are assumed to be immobile. It must be noted that the formation of N₂ from N (reaction 38.109) requires N to be a mobile species. The diffusivity of N is implicitly assumed to be high enough to validate the assumption of equilibrium of reaction (38.109), but the diffusion flux of N is assumed to be negligible compared with the convective flux of N, in the overall species balance. These are reasonable simplifying assumptions. Equation (38.113) can also be derived from individual balances for all species. The overall nitrogen balance is given by

$$\begin{aligned} & \frac{\partial (C_{\text{N}} + 2C_{\text{N}_2} + C_{\text{vN}})}{\partial t} \\ & + v \frac{\partial (C_{\text{N}} + 2C_{\text{N}_2} + C_{\text{vN}})}{\partial z} = 0. \end{aligned} \quad (38.114)$$

The assumption of equilibrium of reactions (38.1), (38.82), (38.83), (38.109), and (38.110) does not necessitate the solution of the individual rate equations. Equations (38.3), (38.94), (38.95), (38.111), and (38.112), which describe the reaction equilibria, and equations (38.113), (38.114), and (38.92) define the balances of i, v, O, vO, vO₂, N, N₂, and vN.

As discussed before, O-clusters are formed in the presence of vacancies without the ejection of silicon atoms as self-interstitials. Once formed, the clusters grow by the consumption of vacancies. At higher vacancy concentrations, the O-cluster growth is assumed to be determined by the diffusion-limited consumption of oxygen by the clusters. At lower vacancy concentrations, the O-cluster growth is assumed to be determined by the diffusion-limited consumption of vacancies by the clusters. The growth of O-clusters by the ejection of silicon atoms as self-interstitials, at lower vacancy concentrations, is ignored in the model. These approximations accurately predict the density of O-clusters but underpredict their size. If desired, the upper limit on the size of O-clusters can be computed by assuming the oxygen diffusion-limited growth of the clusters under all conditions. This assumption is not made in the discussed model, although it can be incorporated without much effort. The volumetric consumption rates of different species by different clusters (i, v, and O), and the average sizes and densities of the cluster populations are given by (38.96–38.107) in Sect. 38.3, as per the methodology developed by *Kulkarni and Voronkov* [38.53].

The domain of the calculation is transient, because a CZ crystal is continuously pulled. The described equations must be solved with the equations defining the domain transience, the temperature field in the crystal, and the segregation of nitrogen between the melt and the crystal at the melt–crystal interface.

The heat transport dynamics is assumed to be faster than the defect dynamics. Hence, quasi-steady-state assumptions for the calculation of the temperature field suffice. The temperature field is first calculated by the commercial software MARC, using the algorithms developed by *Virzi*, and then corrected using the experimentally measured interface shape [38.37, 53, 54].

The concentration field of oxygen in a crystal is determined by the process conditions. Hence, the concentration of oxygen in a crystal at the melt–crystal interface is directly assigned on the basis of the process conditions. The concentrations of all vacancy–oxygen complexes are defined by the reaction equilibria, and the intrinsic point defects (vacancies and self-interstitials) are assumed to be at their respective equilibrium concentrations at the interface.

The concentration of nitrogen in a crystal at the melt–crystal interface can be computed by assuming the thermodynamic segregation of nitrogen between the crystal and a well-mixed melt. If it is assumed that nitro-

gen exists as a monomer in the melt, the thermodynamic segregation of monomeric nitrogen between the crystal and the melt defines its concentration in the crystal, and the concentrations of N_2 and vN species in the crystal are defined by the reaction equilibria (38.111) and (38.112), respectively. The evolution of the nitrogen concentration in the well-mixed melt as a function of time is calculated by following the loss of silicon by solidification and by recognizing that the melt is the only source of nitrogen in all forms (N , N_2 , and vN) in the crystal. It is a popular industrial practice, however, to define the relationship between the total nitrogen content in a crystal at the melt–crystal interface and the total nitrogen content in the melt (from which the crystal grows) using an apparent or effective segregation coefficient, which is just an engineering parameter that describes experimental observations. It is reiterated that this apparent segregation coefficient is not a thermodynamic parameter. This approach does not require any explicit assumptions on the state of nitrogen in a melt or a crystal and provides a simple yet reasonably accurate relationship between the total nitrogen content in the crystal and that in the melt. For a given total nitrogen content in the melt, the concentrations of all nitrogen-containing species in the crystal at the interface are defined by the apparent segregation of total nitrogen between the melt and the crystal, the stoichiometric relationship between the total nitrogen concentration and the concentrations of individual nitrogen containing species, and the reaction equilibria (38.111) and (38.112). The evolution of the nitrogen concentration in the well-mixed melt is quantified by following the silicon and nitrogen losses to the growing crystal across the interface. The results discussed in this section are generated using the apparent segregation coefficient, in accordance with popular industrial practice.

The accuracy of the predictions of the model depends on the accuracy of the parameters describing the properties of all reacting species and the parameters defining the thermodynamics of the discussed reactions. The parameters proposed by *Kulkarni et al.* for the simulation of the CZ defect dynamics in the presence of oxygen are used in this study [38.70]. The equilibrium constants defining the equilibria of reactions (38.109) and (38.110), $K_{N_2}^{N \leftrightarrow N}$ and $K_{vN}^{v \leftrightarrow N}$, are adopted from *Voronkov and Falster* [38.74]. The apparent segregation coefficient of nitrogen determining its segregation between a crystal and a melt is adopted from *Yatsurugi et al.* and others [38.20, 76, 77]. There is significant uncertainty in the parameters defining

the thermodynamics of the reactions and the properties of all species involved in the CZ defect dynamics.

Hence, the parameter set used must be interpreted as just a suggestion.

The developed model can capture the microdefect distributions in the presence of oxygen and nitrogen in CZ crystals growing under steady as well as unsteady states.

38.4.2 CZ Defect Dynamics in One-Dimensional Crystal Growth

The important effects of nitrogen on the CZ defect dynamics are better demonstrated by the simulation of the growth of one-dimensional crystals showing no radial variation in the microdefect distributions. Further simplification can be achieved by simulating steady-state crystal growth. A crystal growing at a fixed rate through a fixed temperature field reaches a steady state far from the regions formed in the beginning of the growth. For simulation of crystal growth at steady state, the crystal is assumed to grow through a fixed representative temperature profile.

Nitrogen affects the reaction dynamics near the melt–crystal interface by interacting with vacancies according to reaction (38.110). The vN species produced by this interaction provides free vacancies (v) by dissociation, for the annihilation of self-interstitials. As free vacancies are also available from the interface, which is an infinite source, the interaction of nitrogen with vacancies shifts the balance of this dynamics in favor of vacancies. The crystal becomes richer in vacancies in the presence of nitrogen. Oxygen also shifts this balance in favor of vacancies by producing vO and vO₂ species, which provide free vacancies by their dissociation; but the effect of oxygen is weaker than that of nitrogen [38.59, 70, 74, 75].

The evolution of the concentrations of key reacting species, when the convective transport is appreciable, as functions of the temperature along the length of a nitrogen-doped CZ crystal growing from a very large melt (effectively infinite), is shown in Fig. 38.23. Since the melt is very large, the total nitrogen concentration, $C_N + 2C_{N_2} + C_{vN}$ or $C_{N,total}$ in the crystal is effectively constant. Near the interface, all species containing vacancies participate in the recombination with self-interstitials; the participation of free vacancies is direct, and the participation of vN, vO, and vO₂ species is indirect through their dissociation. After the self-interstitial concentration drops significantly, the total vacancy concentration, $C_v + C_{vO} + C_{vO_2} + C_{vN}$ or $C_{v,total}$ remains essentially constant until v-clusters are formed in appreciable numbers at lower temperatures.

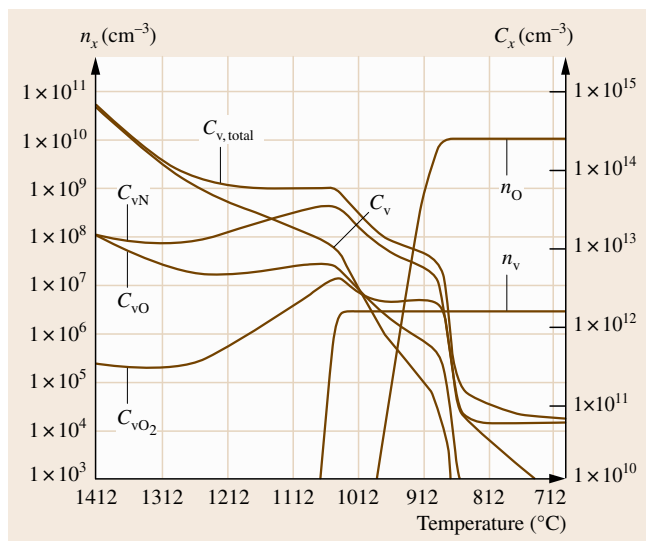


Fig. 38.23 Evolution of the concentrations of various reacting species in a nitrogen-doped CZ crystal growing at a high rate ($G = 3.9$ K/mm, $V = 0.8$ mm/min, $C_{N,total} = 2 \times 10^{14}$ cm⁻³, $C_O = 7 \times 10^{17}$ or 14 ppm)

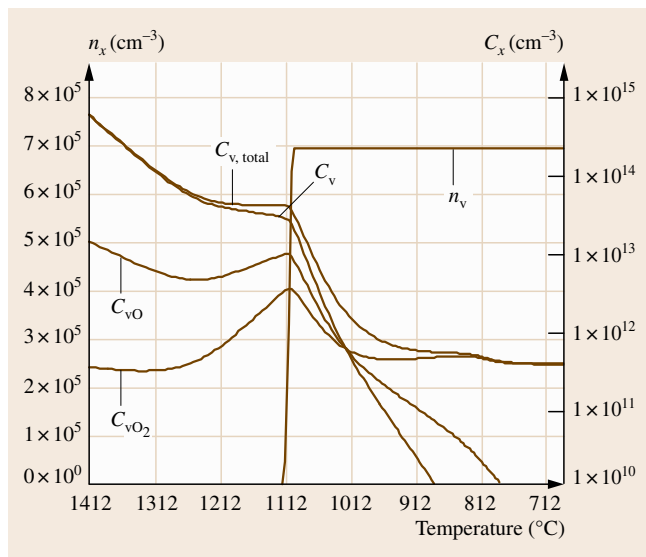


Fig. 38.24 Evolution of the concentrations of various reacting species in a CZ crystal growing at a high rate ($G = 3.9$ K/mm, $V = 0.8$ mm/min, $C_{N,total} = 0$ cm⁻³, $C_O = 7 \times 10^{17}$ or 14 ppm). Note the difference between the scale of the density axis in this figure and in Fig. 38.23

Free vacancies directly participate in the formation and growth of v-clusters; the bound vacancies, vO , vO_2 , and vN species, participate indirectly by their dissociation. The strong binding of vacancies with nitrogen reduces the free vacancy concentration before appreciable nucleation, compared with that in the absence of nitrogen, decreasing the vacancy nucleation temperature. The free vacancy consumption rate by v-clusters is low in the presence of lower vacancy concentration, facilitating their formation in appreciably higher densities. As the supply of total vacancies is fixed at the onset of the vacancy nucleation, the formation of v-clusters at higher densities reduces their size. The effect of nitrogen on the CZ defect dynamics is studied effectively by a comparison of the evolution of various reacting species in a growing CZ crystal in the presence of nitrogen (Fig. 38.23) with that in the absence of nitrogen (Fig. 38.24), under otherwise identical conditions.

A distinct effect of nitrogen is the facilitation of the formation of O-clusters in the presence of voids at appreciable densities. The strong binding between vacancies and nitrogen maintains appreciably high concentrations of bound and free vacancy species at lower temperatures at which vacancy-facilitated O-cluster formation and growth mark the CZ defect dynamics. After their formation, O-clusters become the dominant vacancy sinks compared with v-clusters, as shown in Fig. 38.23. In the absence of nitrogen, however, vN species is also absent, and both weakly bound (vO and vO_2) and free vacancies are consumed at higher temperatures primarily by v-clusters, suppressing the formation of O-clusters (Fig. 38.24). In a nitrogen-doped crystal exhibiting moderate dominance of vacancies near the interface, the free vacancy concentration does not remain high enough to form v-clusters at higher temperatures; at lower temperatures, however, O-clusters are formed in the absence of v-clusters (Fig. 38.25). It must be noted that the total vacancy concentration, even in the presence of clusters, remains negligible but finite in a fully grown CZ crystal because of the binding of vacancies with oxygen at lower temperatures.

The pull rate marking the boundary between O-clusters and i-clusters, known as the v/i boundary, represents the critical operating condition. The quantification of the variation of this critical pull rate with the nitrogen concentration, for otherwise fixed crystal growth conditions, is important. For a given temperature field in a crystal-puller, this pull rate can be quantified

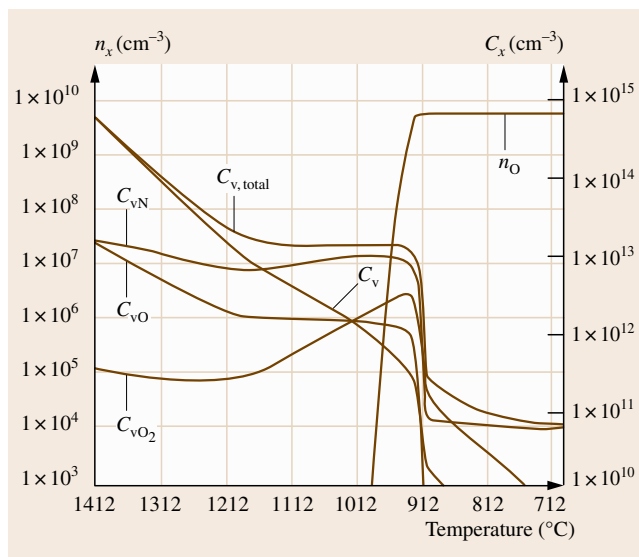


Fig. 38.25 Evolution of the concentrations of various reacting species in a nitrogen-doped CZ crystal growing close to the critical condition ($G = 3.9$ K/mm, $V = 0.50$ mm/min, $C_{N,total} = 2 \times 10^{14}$ cm $^{-3}$, $C_O = 7 \times 10^{17}$ or 14 ppma)

by a series of crystal growth simulations at various fixed or constant pull rates. These computations are numerous and can be expensive. An approximate variation of the cluster distribution in a crystal as a function of its pull rate can be captured by predicting this distribution in the crystal pulled by either continuously increasing or decreasing rate as shown in Fig. 38.26. One such simulation provides the approximate correlation between the cluster distribution in a crystal and its pull rate. The crystal growth conditions marking the v/i boundary can also be quantified in terms of the popular but approximate growth parameter V/G . The V/G marking this boundary, known as the critical V/G , continuously decreases with increasing nitrogen concentration (Fig. 38.27). The total vacancy concentration near the interface increases with increasing nitrogen concentration because of the strong binding between vacancies and nitrogen, resulting in a decrease in the critical V/G . This shift is particularly significant at higher nitrogen concentrations.

The conditions that allow the growth of CZ crystals in the absence of large clusters are also of interest in the crystal growth industry. Therefore, the quantification of the range of the crystal pull rate or V/G within which CZ crystals can grow free of large v-clusters and i-clusters is important. The large cluster-free range is

bracketed by the v/i boundary and the boundary between O-clusters and large v-clusters, arbitrarily defined

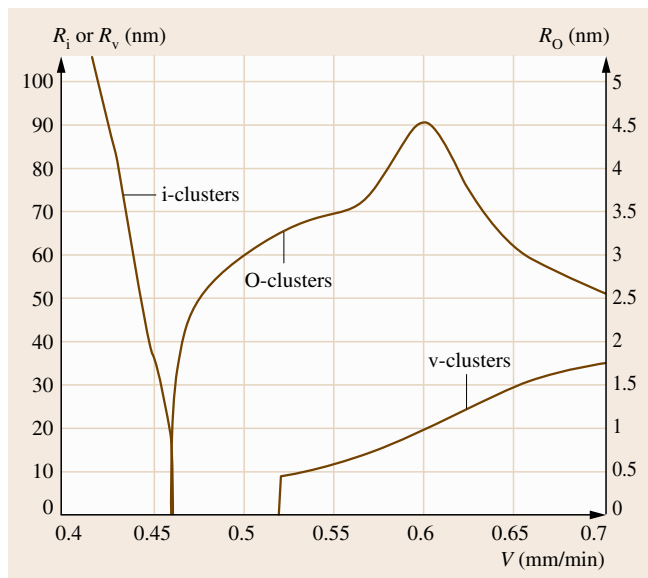


Fig. 38.26 The simulated sizes of various clusters as functions of the CZ crystal pull rate ($G = 3.9 \text{ K/mm}$, $C_{\text{N,total}} = 2 \times 10^{14} \text{ cm}^{-3}$, $C_{\text{O}} = 7 \times 10^{17}$ or 14 ppma)

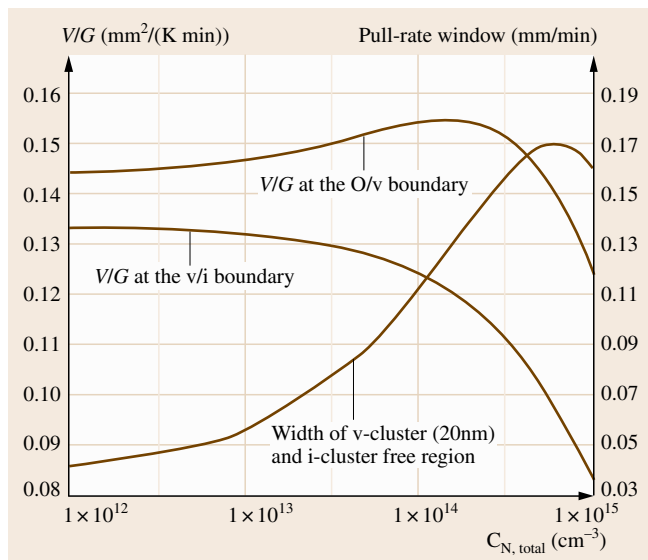


Fig. 38.27 The sensitivity of the cluster distributions near the critical condition to the nitrogen concentration. Note: The v-cluster and i-cluster free region includes v-clusters smaller than 20 nm ($G = 3.9 \text{ K/mm}$, $C_{\text{O}} = 7 \times 10^{17}$ or 14 ppma)

to be 20 nm large in radius; the latter boundary is termed the O/v boundary. It must be noted that the crystals free of such large clusters contain O-clusters, as discussed before. The size of O-clusters increases with increasing concentration of the free vacancies available during their formation, as shown in Fig. 38.26. The V/G marking the O/v boundary increases with the nitrogen concentration first, reaches a maximum, and then decreases; the increase in this V/G at lower nitrogen concentration, in spite of the decrease in the V/G marking the v/i boundary, is caused by the strong binding between v and N that reduces the free vacancy concentration near the vacancy nucleation temperature range. At moderately higher nitrogen concentrations, however, the shift in the V/G marking the v/i boundary is too strong because of a significant increase in the total vacancy concentration near the interface, forcing a decrease in the V/G defining the O/v boundary. The pull rate range and the V/G range allowing the large cluster-free crystal growth still increase until the nitrogen concentration is significantly high. In the presence of nitrogen at very high concentrations, the total vacancy concentration in the crystal near the interface dramatically increases with the nitrogen concentration such that the free vacancy concentration around the vacancy nucleation temperature increases. Hence, the pull rate range (as well as V/G range) within which crystals free of large clusters can be grown also marginally decreases with increasing nitrogen concentration, at very high nitrogen concentration, as shown in Fig. 38.27. This predicted increase in the size of v-clusters with increasing nitrogen concentration does not agree with reported data [38.75, 78]. Therefore, the model predictions are far less accurate at very high nitrogen doping levels.

The salient features of the CZ defect dynamics and the strengths and weaknesses of the discussed model are thus adequately described by the discussed simulations of one-dimensional crystal growth.

38.4.3 CZ Defect Dynamics in Two-Dimensional Crystal Growth

The observed microdefect distributions in a CZ crystal vary along its axis and radius. This radial variation is caused by the radial variation of the temperature field and the radial diffusion of the intrinsic point defects induced by the temperature field and the lateral surface of a growing crystal. Axial variations are primarily induced by the change in the pull rate

and, in the case of nitrogen-doped crystals, by the axial variation in the nitrogen concentration. Quantification of these two-dimensional microdefect distributions requires a solution of the discussed model for two-dimensional crystal growth.

Kulkarni predicted the microdefect distribution in a crystal, at the end of its growth, pulled at a fixed rate through a fixed temperature field, shown in Fig. 38.28 [38.75]. The oxygen concentration in the crystal is assumed to be 16 ppm. The nitrogen concentration varies from 8.25×10^{13} to $6.7 \times 10^{14} \text{ cm}^{-3}$, from one end (left-hand side) of the crystal to the other (right-hand side), and from 8.4×10^{13} to $3.9 \times 10^{14} \text{ cm}^{-3}$, along the central axis within the cylindrical body of the crystal. The crystal growth at a fixed rate well above the pull rate at the critical condition is assumed. The crystal grows under an appreciable influence of convection. The central region of the crystal contains larger v-clusters and relatively smaller O-clusters; the peripheral region is dominated by smaller v-clusters, relative to those in the center, and larger O-clusters, relative to those in the center. This variation, away from the lateral surface of the crystal, is primarily caused by the radial variation of the temperature field; the relative effect of the axial convection with respect to the axial diffusion becomes weaker along the radial position of the crystal, away from the lateral surface, because of the radial variation of the temperature field. The defect distribution in the crystal near the lateral surface is strongly influenced by the surface-induced diffusion of the intrinsic point defects, details of which will be discussed in Sect. 38.5. The vacancy-rich region, defined as the region marked by the presence of v-clusters, O-clusters or any vacancy containing species, expands in the crystal as the nitrogen concentration increases. It must be noted that the microdefect distributions in the crystal when the crystal is still in contact with the melt at the end of its growth are shown in Fig. 38.28. Hence, the vacancy nucleation

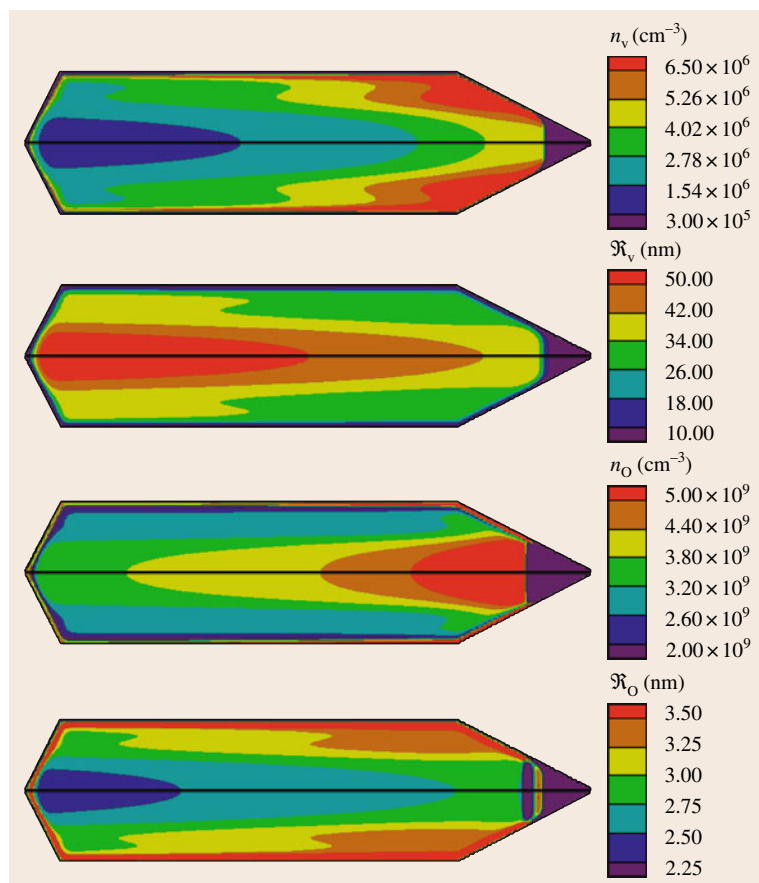


Fig. 38.28 The model predicted cluster distributions in a CZ crystal, pulled at a fixed rate well above the pull rate at the critical condition, at the end of its growth. Note: The melt–crystal interface is not flat. $C_{N,\text{total}}$ varies from 8.25×10^{13} to $6.7 \times 10^{14} \text{ cm}^{-3}$, from one end (left-hand side) of the crystal to the other (right-hand side), and from 8.4×10^{13} to $3.9 \times 10^{14} \text{ cm}^{-3}$, along the central axis within the cylindrical body of the crystal; $C_O = 16 \text{ ppm}$. The crystal cooling rates are moderate. The legend for each plot is shown to the right

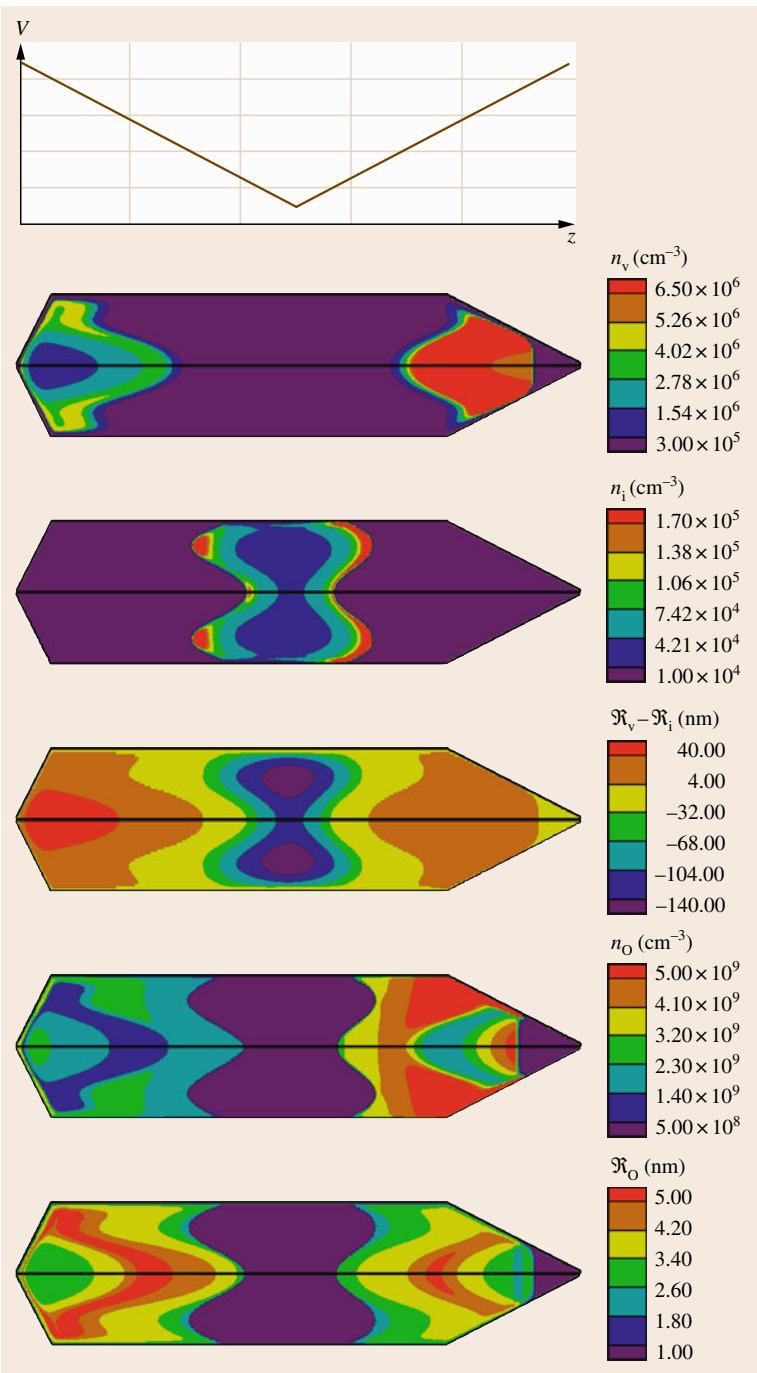


Fig. 38.29 The predicted cluster distributions in a simulated crystal at the end of its growth under transient conditions. Note: The melt–crystal interface is not flat. $C_{N,\text{total}}$ varies from 8.25×10^{13} to $6.7 \times 10^{14} \text{ cm}^{-3}$, from one end (*left-hand side*) of the crystal to the other (*right-hand side*), and from 8.4×10^{13} to $3.9 \times 10^{14} \text{ cm}^{-3}$, along the central axis within the cylindrical body of the crystal; $C_O = 16 \text{ ppma}$. The *legend* for each plot is shown on the *right*

front and the O-cluster formation front are also visible near the right end of the crystal.

The capability of the discussed model can be demonstrated by predicting the microdefect distribu-

tion in the crystal pulled at the varying rate shown in Fig. 38.29. The oxygen and nitrogen concentrations in the crystal were set at the same level as those set for the simulation of the crystal discussed in Fig. 38.28 [38.75]. Hence, the effect of varying pull rate can be observed by a comparison between the cluster distributions shown in Fig. 38.28 and those shown in Fig. 38.29. The varying pull rate generates a distribution of all discussed clusters in this chapter. As i-clusters and v-clusters do not coexist, the simultaneous distributions of these clusters can be quantified by the distributions of $\mathcal{R}_v - \mathcal{R}_i$ and $n_v - n_i$. Positive values indicate the distribution of v-clusters and negative values indicate the distribution of i-clusters. Considering their differences, however, the density distributions of i-clusters and v-clusters

are shown separately in Fig. 38.29. At a higher pull rate, v-clusters and O-clusters are formed; at a lower pull rate, i-clusters are formed; at a pull rate marking the moderate dominance of vacancies closer to the v/i boundary, only large O-clusters are formed. It must be noted that the microdefect distributions in the crystal at the end of its growth but still in contact with the melt are shown in Fig. 38.29. Hence, the vacancy nucleation front and the oxygen nucleation front are visible near the opposite end of the crystal.

The discussed model captures the salient features of the typical two-dimensional microdefect distributions observed in CZ crystals doped with nitrogen. In the presence of nitrogen at very high concentrations, however, the model predictions are less accurate.

38.5 The Lateral Incorporation of Vacancies in Czochralski Silicon Crystals

A crystal pulled at a very high rate, well above the critical condition, to meet industrial throughput goals, contains voids everywhere except very close to the lateral surface, where the surface-induced diffusion of both the intrinsic point defect species reduces the vacancy concentration at higher temperatures and allows the formation of oxygen clusters, during crystal growth (Fig. 38.30a). It must be noted that the Frenkel reaction couples the vacancy concentration with the self-interstitial concentration; hence, both vacancies that diffuse toward the lateral surface and self-interstitials that diffuse from the surface reduce the vacancy concentration near the surface. The temperature field of a typical growing CZ crystal shows significant radial variation; G increases significantly along the crys-

Fig. 38.30 (a) Typical microdefect distribution observed by copper precipitation followed by etching in a wafer produced from a CZ crystal grown at a very high rate well above the critical condition. (b) Typical microdefect distribution observed by copper precipitation followed by etching in a wafer produced from a CZ crystal grown through a radially highly nonuniform temperature field; note that a fraction of the crystal is grown above and the rest below the critical condition. (c) Typical microdefect distribution observed by copper precipitation followed by etching in a wafer produced from a CZ crystal grown close to the critical condition through a relatively radially uniform temperature field (Note: only $\frac{1}{4}$ of the wafer is shown) (after [38.79]) ▶



tal radius. Hence, many Czochralski crystals pulled at a moderate rate contain a central core of D defects and a peripheral region of A defects, as shown in Fig. 38.30b. The narrow detectable microdefect-free region close to the lateral surface of the crystal is also a result of the surface-induced diffusion of self-interstitials and vacancies, during its growth; while fast-diffusing self-interstitials dominantly contribute to their depletion near the surface, vacancies that diffuse from the surface also contribute to the depletion of self-interstitials through Frenkel reaction. Figure 38.30b also shows a very narrow detectable microdefect-free region termed the v/i boundary between the region of D defects and the region of A defects.

Recent advances in device industry demand either the reduction in the size of microdefects or their elimination from the CZ crystal. To address this requirement, many modern crystals are grown under a more radially uniform temperature field close to the critical condition. Hence, typical microdefects formed in these crystals are oxygen clusters and B defects. In practice, a perfect radial uniformity of the temperature field is not achieved; G marginally increases along the radius of a typical crystal. A crystal grown close to the critical condition, however, always exhibits a peripheral region, close to the surface, containing either oxygen clusters or both oxygen clusters and small voids, irrespective of the central microdefect distribution, as shown in Fig. 38.30c. Kulkarni described the physics of the evolution of microdefects in this region, known as the *edge ring* or the *peripheral ring* [38.79]. The peripheral ring loses its distinct appearance at higher crystal pull rates. This section addresses the evolution of the microdefect distribution in CZ crystals pulled at various rates, from the critical condition to highly vacancy-rich conditions.

38.5.1 General Defect Dynamics: A Brief Revisit

The theory of the initial point defect incorporation describes the defect dynamics in a growing crystal in the absence of oxygen [38.19]. According to this theory, the formation of microdefects in an oxygen-less crystal is driven by the supersaturation of crystal with either vacancies or self-interstitials. The concentrations of the intrinsic point defects in a growing crystal, away from its lateral surface, evolve primarily by an interplay between the species transport from the melt-crystal interface, both by convection and diffusion, and the Frenkel reaction. The intrinsic point defects of silicon exist at their respective equilibrium concentra-

tions at the interface. The recombination of vacancies and self-interstitials in a growing crystal, driven by the decreasing temperature with increasing distance from the interface, generates their concentration gradients, inducing their diffusion from the interface into the crystal. The species convection is induced by the physical growth of the crystal. Self-interstitials diffuse faster than vacancies near the interface at higher temperatures but the vacancy concentration is higher than the self-interstitial concentration at the interface, where the equilibrium conditions prevail. Thus, when the species diffusion is relatively appreciable, or *below the critical condition*, the self-interstitial flux into the crystal from the interface is greater than the vacancy flux and the concentration of self-interstitials increases, away from the interface, with increasing effect of diffusion relative to convection. When the species convection is relatively appreciable, or *above the critical condition*, the vacancy flux is greater than the self-interstitial flux and the concentration of vacancies, away from the interface, increases with increasing effect of convection relative to diffusion. The dominant intrinsic point defect species annihilates the other species to very low concentrations and aggregates to form microdefects, at lower temperatures. At the critical condition, the vacancy flux is equal to the self-interstitial flux and the two intrinsic point defect species annihilate each other to very low concentrations, without forming large microdefects. This dynamics, defined ignoring the radial diffusion of the reacting species and the effects of oxygen, essentially establishes the incorporated concentration fields of the intrinsic point defects in a growing crystal, prior to the formation of microdefects.

Vacancies also interact with oxygen present in CZ silicon, producing various vacancy-oxygen complexes. The sum of the concentrations of all vacancy-containing species ($C_{v,\text{total}}$), defined as the total vacancy concentration, is relevant in considering the interactions between vacancies and self-interstitials. Free vacancies (v) directly participate in the annihilation of self-interstitials through the Frenkel reaction; bound vacancies (vO and vO_2) are also available for the annihilation of self-interstitials by dissociation. Because the total vacancy concentration available for the annihilation of self-interstitials increases in the presence of oxygen, the crystal becomes richer in vacancies with increasing oxygen concentration. Bound vacancies are assumed to be immobile; hence they affect the CZ defect dynamics only through reactions and physical movement of the crystal.

The model discussed in Sect. 38.3 describes the CZ defect dynamics in the presence of oxygen, and, hence, was applied by Kulkarni in his study on the peripheral ring formation. The results of this study are discussed below [38.79].

38.5.2 Defect Dynamics Under Highly Vacancy-Rich Conditions

The simulation of the defect dynamics in a CZ crystal growing close to the critical condition through a radially uniform temperature field can provide insights into the formation of the peripheral ring. To understand the difference between the evolution of microdefects in a CZ crystal growing at a very high rate well above the critical condition and that in a crystal growing close to the critical condition, the simulations of defect dynamics under both conditions must be performed.

Figure 38.31a shows the radial concentration profiles of key reacting species (C_x) in a crystal growing at a very high rate through a radially uniform temperature field. In the interior or bulk of the crystal away from the lateral surface, vacancy supersaturation and self-interstitial undersaturation develop. Since the equilibrium conditions prevail on the lateral surface of the crystal, the self-interstitial concentration gradually increases and the vacancy concentration gradually decreases along the radius of the crystal in the vicinity of the surface, at a given axial location. Both the diffusion of vacancies toward the surface and the diffusion of self-interstitials from the surface into the crystal contribute to the depletion of vacancies near the surface; self-interstitials, which diffuse faster than vacancies at higher temperatures, reduce the vacancy concentration by recombining with vacancies. Although the coupled transport of all species and reactions involving all species determine the species concentration fields in the crystal, the Frenkel reaction and the transport of self-interstitials and vacancies primarily influence their concentration fields, at higher temperatures.

As the vacancy supersaturation increases in the crystal interior (bulk) with decreasing temperature, voids are formed at around 1100 °C. Very close to the lateral surface, however, the radial diffusion of the intrinsic point defects maintains a lower concentration of vacancies. Vacancies in lower concentrations escape consumption by void formation at higher temperatures; they facilitate the formation of oxygen clusters at lower temperatures, around 950 °C. Figure 38.31b shows the radial profile of the amount of vacancies absorbed by voids, per unit volume of the crystal ($C_{v-v-clusters}$), and

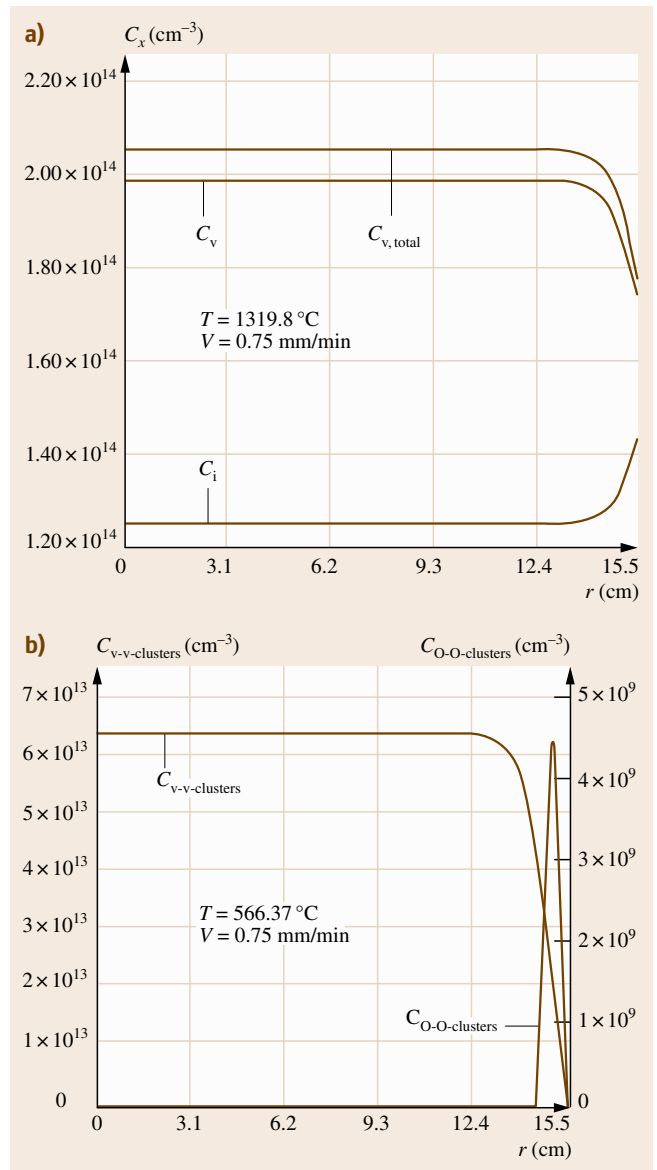


Fig. 38.31 (a) The radial profiles, close to the interface, of the concentrations of key reacting species in a CZ crystal growing well above the critical condition through a radially uniform temperature field. (b) The radial profiles of the concentration of vacancies in voids, per unit volume of crystal, and of oxygen in oxygen clusters, per unit volume of crystal, in a CZ crystal growing well above the critical condition through a radially uniform temperature field

of the amount of oxygen atoms absorbed by oxygen clusters, per unit volume of the crystal ($C_{O-O-clusters}$). There is negligible formation of oxygen clusters close

to the lateral crystal surface when the pull rate is very high, as shown in Fig. 38.31b.

38.5.3 Defect Dynamics Near the Critical Condition

A large microdefect-free crystal can be typically grown if the intrinsic point defect supersaturation in the crystal

prior to the onset of nucleation is very low and radially uniform. This is achieved by growing the crystal through a relatively radially uniform temperature field, at close to the critical condition, at which an acceptable balance between the total vacancy flux (convection and diffusion of total vacancies) and the self-interstitial flux (convection and diffusion of self-interstitials) is achieved, in the vicinity of the interface. This discussion

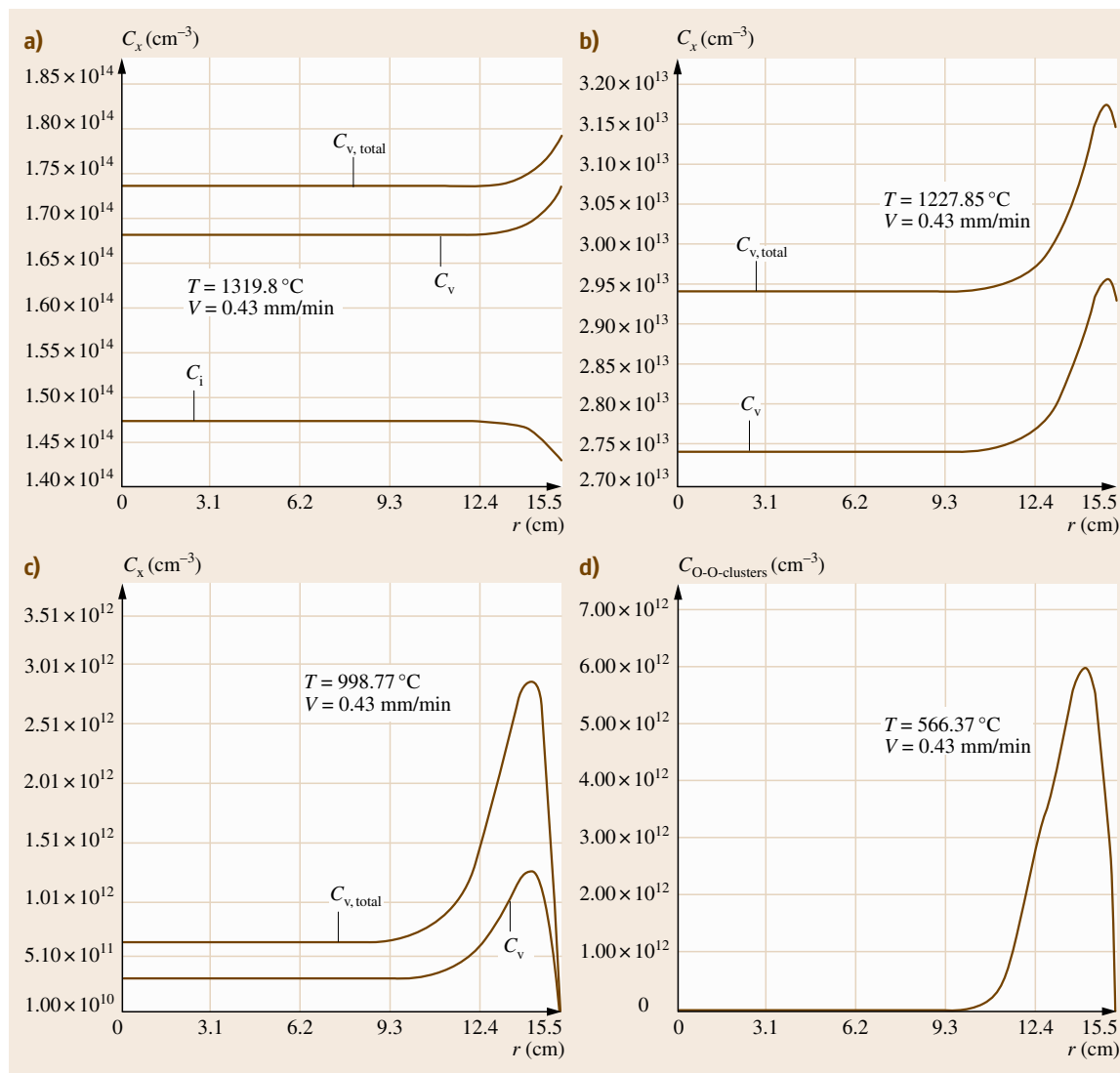


Fig. 38.32a-d The radial profiles of the concentrations of key reacting species in a CZ crystal growing close to the critical condition, through a radially uniform temperature field: (a) close to the interface, (b) at 1227.85°C , (c) and at 998.77°C . (d) The radial profiles of the concentration of oxygen in oxygen clusters, per unit volume of the crystal, in a CZ crystal growing close to the critical condition through a radially uniform temperature field

focuses on the growth of such marginally vacancy-rich or self-interstitial-rich crystals growing close to the critical condition. As total vacancies and self-interstitials remain in comparable concentrations under these growth conditions, the continuous interplay between the Frenkel reaction and the species transport remains relevant over the entire length of the crystal prior to the microdefect formation. Hence, the concentration fields of the intrinsic point defects and other species are sensitive to the relative shifts in their equilibrium concentrations and diffusivities with temperature.

Figure 38.32a shows the radial profiles of the concentrations of vacancies, self-interstitials, and total vacancies close to the interface of a crystal growing close to the critical condition through a radially uniform temperature field. The vacancy concentration in the bulk or the interior region of the crystal, away from the lateral surface, is higher than the self-interstitial concentration, but the crystal is marginally undersaturated with vacancies and marginally supersaturated with self-interstitials; the equilibrium conditions, however, prevail on the crystal surface. Therefore, self-interstitials diffuse towards the lateral surface from the crystal interior and vacancies diffuse from the lateral surface into the crystal. At higher temperatures, self-interstitials diffuse faster than vacancies and, hence, significantly affect the vacancy concentration field through the Frenkel reaction.

As the temperature decreases in the crystal, the diffusivities of both vacancies and self-interstitials decrease, along with their equilibrium concentrations, which prevail on the lateral surface. The Frenkel reaction remains at equilibrium, as shown by Kulkarni et al. [38.1]. All other homogeneous reactions are also assumed to be at equilibrium [38.70]. As the temperature decreases, the influence of the lateral surface-induced diffusion decreases and vacancies that were incorporated from the lateral surface at higher temperatures become the dominant species in the vicinity of the surface, annihilating self-interstitials to lower concentrations. Moreover, both the vacancy concentration at the lateral surface and the vacancy concentration in the crystal interior are lower than the vacancy concentration established in the vicinity of the surface. Hence, a relatively distinct vacancy supersaturation and a self-interstitial undersaturation in the vicinity of the lateral surface are established, as shown in Fig. 38.32b. In short, the interplay among decreasing equilibrium concentrations of all species, the decreasing effect of the species diffusion, and the fast reaction dynamics establishes a self-interstitial-lean and vacancy-rich ring near

the lateral surface. At the stage shown in Fig. 38.32b, self-interstitials diffuse to this region from the lateral

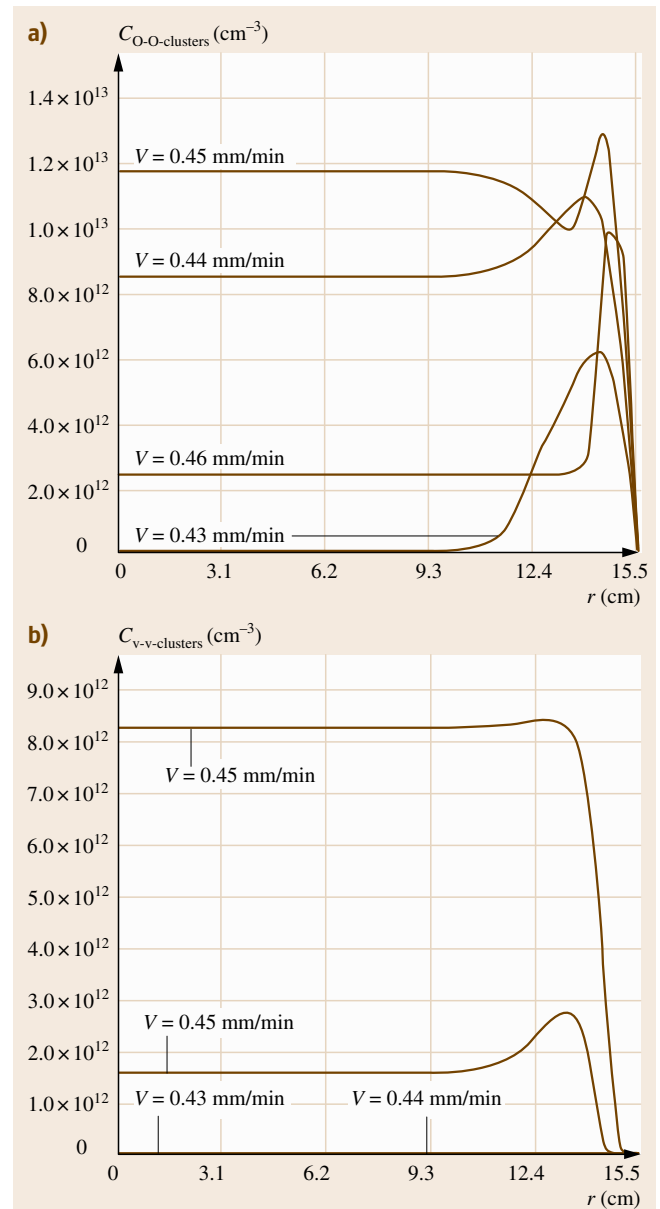


Fig. 38.33a,b The predicted radial profiles of the concentrations of (a) oxygen in oxygen clusters, per unit volume of crystal and (b) vacancies in voids, per unit volume of crystal, in CZ crystals growing close to the critical condition through a radially uniform temperature field, as functions of the pull rate. The predictions shown in this figure were generated using property set II

surface as well as from the crystal center and vacancies diffuse from this region, both radially inward and outward. Figure 38.32b shows that the interior (bulk) of

the crystal is still undersaturated with vacancies when the region near the lateral surface is supersaturated with vacancies at around 1228 °C.

As the temperature drops further, the vacancy undersaturation in the crystal interior (bulk) decreases, because of a fast reduction in the equilibrium vacancy concentration. Eventually, the crystal can become marginally supersaturated with vacancies in the interior. The region near the lateral surface, however, becomes distinctly more supersaturated with vacancies, as shown in Fig. 38.32c.

In essence, the equilibrium conditions prevail on the surface of the growing crystal; near the critical condition, in the first stage of cooling at higher temperatures, the difference between the vacancy concentration and the self-interstitial concentration on the lateral crystal surface is much higher than that in the crystal interior (bulk), driving the vacancy enrichment of the near-surface region relative to the crystal interior; the vacancy supersaturation builds in the near-surface region with the decreasing temperature, because of the decreasing intrinsic point defect diffusivities and equilibrium concentrations.

It must be noted that, as the temperature decreases, the ratio of the bound vacancy concentration to the free vacancy concentration increases. In spite of the vacancy supersaturation established by the lateral surface, the vacancy concentration is not high enough to form large voids. Free and bound vacancies survive high temperatures to facilitate the formation of oxygen clusters (and small voids, in a few cases) at lower temperatures. The radial profile of the concentration of oxygen clusters contained in oxygen clusters, per unit volume of the crystal, is shown in Fig. 38.32d. As can be observed, there is a distinct ring of oxygen clusters near the lateral surface of the crystal, which is the peripheral ring.

The peripheral ring becomes richer in vacancies but loses its distinct structure with increasing crystal pull rate. The microdefect distribution near the critical condition in a crystal as a function of the crystal pull rate is shown in Fig. 38.33. Figure 38.33a shows the radial profiles of $C_{O-O-clusters}$, and Fig. 38.33b shows the $C_{V-v-clusters}$ profiles. The competition between the void formation and the oxygen cluster formation for vacancies is evident as the pull rate increases. The peripheral ring cannot be formed when the relative effect of species convection is significant, because the vacancy supersaturation is maintained everywhere in the crystal under such condition, resulting in the diffusion of vacancies toward the lateral surface close to the interface, as already shown in Fig. 38.31. These results were generated

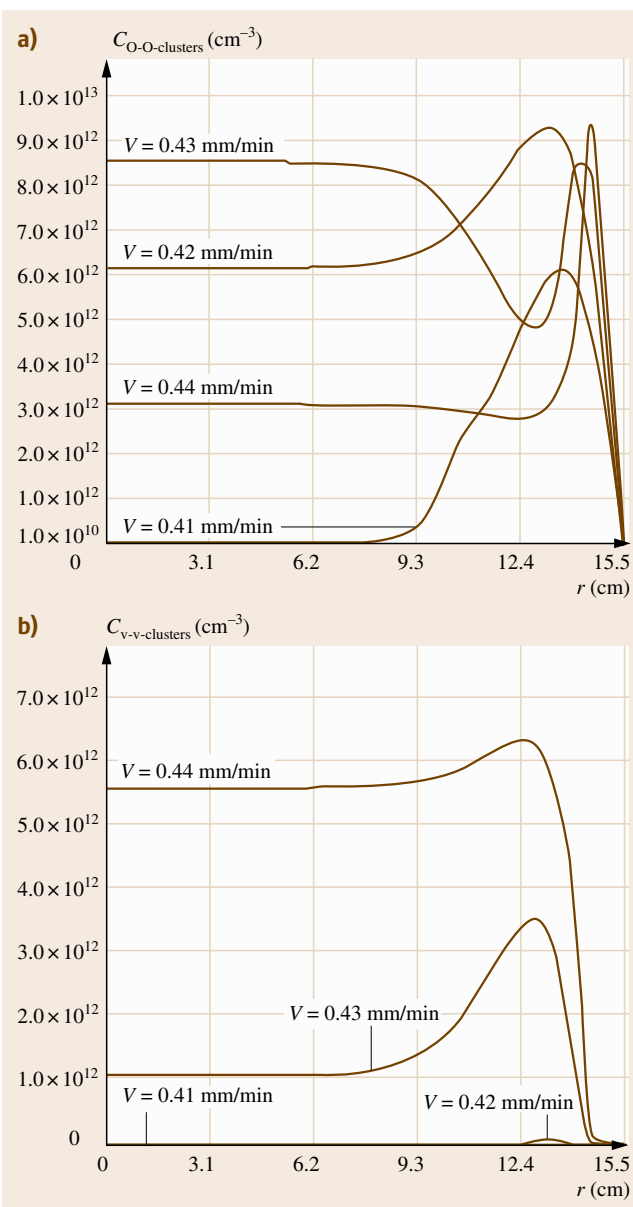


Fig. 38.34a,b The predicted radial profiles of the concentrations of (a) oxygen in oxygen clusters, per unit volume of crystal and (b) vacancies in voids, per unit volume of crystal, in CZ crystals growing close to the critical condition through a radially uniform temperature field, as functions of the pull rate. The predictions shown in this figure were generated using property set III

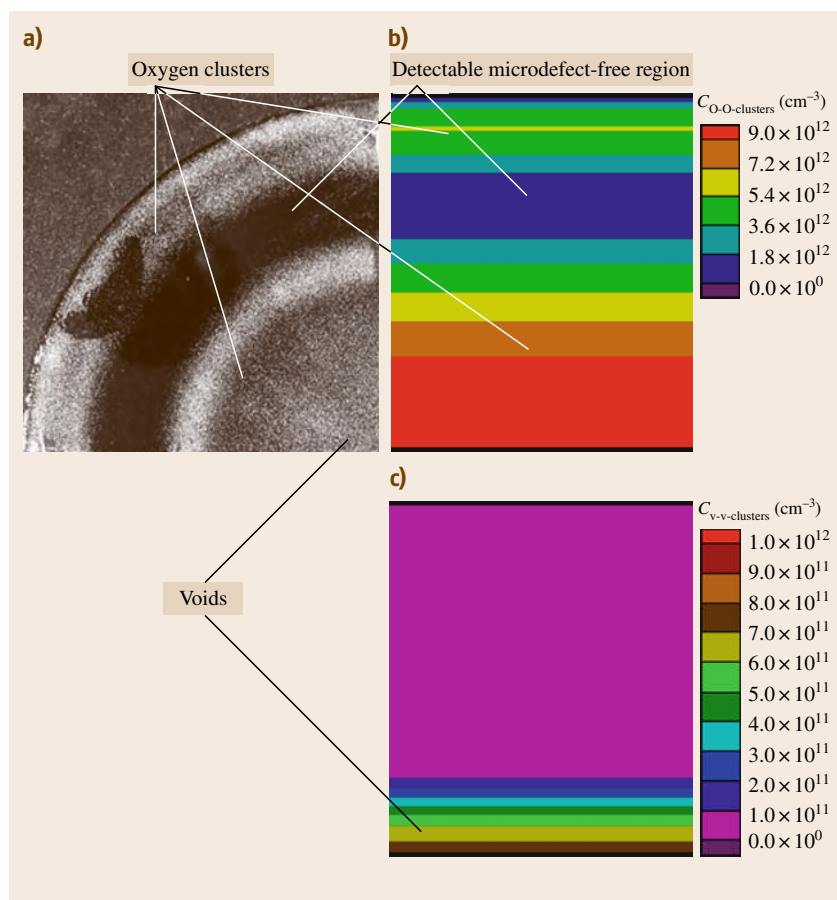


Fig. 38.35 (a) Observed microdefect distribution in a wafer showing a peripheral ring (Note: only 1/4 of the wafer is shown).

(b) Predicted $C_{O-O-clusters}$ distribution in a longitudinal cross-section of the crystal showing a peripheral ring. (c) Predicted $C_{v-v-clusters}$ distribution in a longitudinal cross-section of the crystal showing a peripheral ring. (Note: the central core of oxygen clusters and voids surrounded by the featureless region is a result of a marginal radial variation in the temperature field)

using property set II; qualitatively similar results were generated using property set III (Fig. 38.34).

A comparison between the predicted microdefect distribution and the observed microdefect distribution in a crystal containing a peripheral ring is shown in Fig. 38.35. The simulation was performed using property set III. The central region of the crystal contains oxygen clusters and small voids. There is a detectable microdefect-free region between the central region containing oxygen clusters and the peripheral ring. This distribution shows that the crystal growth occurred through a radially nonuniform temperature field. However, the presence of the peripheral ring implies that the temperature field was sufficiently uniform.

Influence of the Intrinsic Point Defect Properties on the Edge Ring

There is uncertainty in the properties of many species influencing the CZ defect dynamics. Although the de-

fect dynamics describing the evolution of the peripheral ring is driven by many parameters determining the properties of all participating species, the formation and migration energies of the intrinsic point defects have a particularly stronger influence.

The effect of the properties of the intrinsic point defects on the formation of the peripheral ring in a CZ crystal can be explained by considering the defect dynamics in the absence of oxygen, for simplicity. In the interior region of a CZ crystal growing through a uniform temperature field, the effects of radial species diffusion are negligible; thus, the evolution of the intrinsic point defect concentrations in this region near the melt-crystal interface is explained by the (axial) one-dimensional theory of initial incorporation [38.19]. According to this theory, the concentrations of the intrinsic point defects in an oxygen-less crystal growing at the critical condition through the temperature field approximated by a linear dependence of $1/T$ on z (38.6)

evolve according to (38.12) and (38.13), provided that the diffusivities of both species are temperature independent. In a narrow range of temperature near the interface, the assumption of constant species diffusivities, and a linear $1/T$ profile are acceptable, to some extent. Thus, (38.12) and (38.13) can be used as analytical guidelines for evaluating the evolution of the intrinsic point defect concentrations near the interface in a typical Czochralski crystal growing at the critical condition.

According to (38.4), (38.5), (38.12), and (38.13), both of the intrinsic point defect species are at their respective equilibrium concentrations in the interior of the crystal growing at the critical condition, if their formation energies are identical. The equilibrium conditions prevail on the crystal surface as well, because of the fast surface kinetics. Since there is no radial concentration gradient in the crystal under this condition, there is no surface-induced vacancy enrichment at the higher temperatures, which is required for the formation of the peripheral ring.

It is necessary to establish the vacancy undersaturation and self-interstitial supersaturation in the crystal interior (bulk) at higher temperatures to drive the near-surface vacancy enrichment. Moreover, the intensity of the peripheral ring increases with increasing difference between the equilibrium vacancy concentration and the vacancy concentration in the interior of the crystal, at higher temperatures, at the critical condition. This difference increases with decreasing vacancy formation energy, as given by (38.5) and (38.13). This difference also depends on the variation of the intrinsic point defect diffusivities with the temperature. Therefore, the assumption of constant diffusivities of the intrinsic point defects made by *Voronkov* must be relaxed [38.19]. At the critical condition, the self-interstitial flux is equal to the vacancy flux, i.e., the excess intrinsic point defect flux is zero.

When the self-interstitial migration energy is higher than the vacancy migration energy, the relative decrease in the self-interstitial diffusivity is higher than the relative decrease in the vacancy diffusivity, per unit length,

in the vicinity of the interface, relatively reducing the replenishment of self-interstitials by diffusion from the interface. Hence, the relative self-interstitial diffusion flux decreases, at any given location in the vicinity of the interface, with increasing self-interstitial migration energy. As the relative self-interstitial diffusion flux decreases, proper changes in the other components of the excess intrinsic point defect flux (38.11) are required to satisfy the necessary equality of the vacancy flux and the self-interstitial flux, at the critical condition. These changes involve a reduction in the vacancy flux by reductions in the critical pull rate (for a given temperature field) and the vacancy concentration. As a result, the established vacancy concentration decreases in the crystal interior with increasing self-interstitial migration energy.

The effect of the formation and migration energies of the intrinsic point defects on the peripheral ring dynamics is multifold. The difference between the vacancy concentration and the self-interstitial concentration on the lateral surface of the crystal at higher temperatures increases with decreasing vacancy formation energy. If the migration energy of a self-interstitial is higher than that of a vacancy, the lateral diffusion of self-interstitials from the surface into the near-surface crystal region, at a later stage of cooling, becomes less significant, which maintains a higher vacancy concentration within the peripheral ring. The near-surface vacancy concentration field is influenced by the diffusion of both self-interstitials and vacancies, coupled with the Frenkel reaction, and not by the vacancy diffusion alone. It must be noted that the migration energy of a self-interstitial is higher than the migration energy of a vacancy, according to property set II and that the formation energy of a vacancy is lower than that of a self-interstitial, according to property set III. It is also important to note that the presence of oxygen and a deviation from the assumed crystal temperature field described by the linear variation of $1/T$ along the crystal axis also influence the dynamics of the formation of the peripheral ring, in addition to the formation and migration energies of the intrinsic point defects.

38.6 Conclusions

The quality of modern microelectronic devices built on silicon substrates manufactured by the Czochralski (CZ) and float-zone (FZ) crystal growth processes is determined by the distribution of the crystallographic

imperfections known as microdefects present in the substrates. Microdefects are formed by the aggregation of the intrinsic point defects of silicon, vacancies (v) and self-interstitials (i), and by the vacancy-assisted aggre-

gation of oxygen (O) with silicon. Understanding the dynamics of the formation of these aggregates requires the quantification of this dynamics.

38.6.1 CZ Defect Dynamics in the Absence of Impurities

Early attempts at the quantification of defect dynamics were restricted to understanding the distribution of the intrinsic point defects in growing crystals, without accounting for the formation of microdefects, or the effects of oxygen. The theory of initial incorporation, proposed in 1982, explains and quantifies the conditions leading to the formation of microdefects [38.19]. According to this theory, in a growing CZ crystal, an interplay among the diffusion and convection of the intrinsic point defects and the Frenkel reaction driven by decreasing temperature near the vicinity of the melt–crystal interface establishes a dominant intrinsic point defect species, which nucleates at lower temperatures to form its aggregates. Vacancies, which exist at a higher concentration at the melt–crystal interface, remain dominant when the species convection is relatively appreciable; self-interstitials, which are fast diffusers in the higher temperature range, become the dominant species when the species diffusion is relatively appreciable. Vacancies form vacancy aggregates known as D defects; self-interstitials form self-interstitial aggregates known as A and B defects. This interplay is quantified in terms of the ratio of the crystal pull rate (V) to the magnitude of the axial temperature gradient at the interface (G), V/G , at any radial location of the crystal. Thus, D defects are formed at a radial location with higher V/G , A and B defects are formed at lower V/G , and no large microdefects are formed at V/G closer to its critical value. The radial distribution of microdefects in many crystals is reasonably explained by the radial variation of G .

The one-dimensional theory of initial incorporation does not effectively capture the effects of the radial diffusion of the intrinsic point defects induced by the radial variation in the temperature field and by the lateral surface of a crystal. Therefore, in the 1990s, many successful efforts were made to quantify the two-dimensional intrinsic point defect concentration fields in growing axisymmetric CZ crystals, to more accurately predict the microdefect distributions. These efforts, however, did not capture the effects of oxygen or the microdefect size distribution, as the actual events of the intrinsic point defect aggregation were not quantified.

Successful quantification of the microdefect distributions in CZ crystals, ignoring the effects of oxygen, was made only in and after the late 1990s. Capturing the CZ defect dynamics including the aggregation of the intrinsic point defects involves the quantification of the microdefect populations everywhere in a crystal. A microdefect population, at any given time and location in a crystal, consists of the microdefects formed at various locations during the elapsed time period. Therefore, a direct numerical treatment of the defect dynamics is impractical. Three popular approaches emerged to address the computational complexity of the CZ defect dynamics, in and after the late 1990s. All three approaches approximate the microdefects as spherical clusters; vacancy clusters or v-clusters represent D defects and self-interstitial clusters or i-clusters represent A and B defects.

The first approach, in its most rigorous form, requires the application of the classical nucleation theory to quantify the formation of the stable cluster nuclei and the prediction of the final microdefect distribution in a CZ crystal by quantifying the formation and growth histories of all clusters in the cluster populations everywhere in the crystal. Thus, the microdefect distribution is a function of location, time, and elapsed time. As the quantification of the CZ defect dynamics by the most rigorous form of this approach is computationally expensive, it is applied in its various reduced forms. An elegant treatment of the cluster formation and growth in an isolated element of a CZ crystal, cooled at a rate determined by its time–temperature history during the crystal growth, was first published in 1998. This treatment also quantifies the effect of the interesting interplay between the conditions facilitating the nucleation of the intrinsic point defects and the conditions facilitating the growth of the formed clusters on the final average size and the density of the clusters. This approximation, however, does not take into account the effect of the axial diffusion of the intrinsic point defects. The most elaborate model based on the first approach, reported in 2004, treats only the one-dimensional (axial) CZ defect dynamics. This model, however, is quite rigorous and addresses both the steady-state and unsteady-state defect dynamics. The shifts in the critical V/G associated with unsteady-state crystal growth were quantified for the first time by the unsteady-state model in 2004. The basic model used in the quantification of the defect dynamics by the first approach is termed the *rigorous model*.

The second approach followed in the quantification of the CZ defect dynamics approximates a population of

clusters present at any location in a crystal by another population of identical clusters. This is accomplished by approximating the average radius of the clusters in a population by the square root of the average of the squared radii of the clusters and by quantifying an auxiliary variable proportional to the total surface area of the clusters. The model based on this approach is termed the *lumped model*. The lumped model is computationally more attractive and effectively quantifies the two-dimensional microdefect distributions in CZ crystals.

The third approach followed in capturing the CZ defect dynamics couples the direct treatment of the reactions taking part in the aggregation events, for smaller clusters, and the Fokker–Planck formulation, for larger clusters. The formation of clusters and their growth is initially quantified by treating clusters of the same size and type as a species participating in the reactions. The discrete reaction rate equations derived by applying the classical nucleation theory are used for capturing the evolution of smaller clusters. The concentration (density) of all clusters of the same type exceeding a threshold size is treated as a continuous variable, which is a function of location, time, and the cluster size itself, by using the Fokker–Planck formulation. The Fokker–Planck equation (FPE) for larger clusters is derived from the discrete rate equations by a Kramers–Moyal expansion, treating the cluster size as a continuous independent variable. This approach is termed the *discrete–continuous approach* and is computationally very expensive.

38.6.2 CZ Defect Dynamics in the Presence of Oxygen

CZ crystals contain oxygen, which influences the defect dynamics. One-dimensional steady-state CZ defect dynamics in the presence of oxygen in a growing CZ crystal showing no radial variations has been modeled by both the Fokker–Planck formulation and the lumped model. The unsteady-state oxygen-influenced CZ defect dynamics accounting for the two-dimensional variations in microdefect distributions in growing CZ crystals, however, has been quantified only by the lumped model. The presence of oxygen primarily generates two bound vacancy species, vO and vO_2 , and the aggregates of oxygen. The aggregates of vacancies are modeled as spherical v -clusters; the aggregates of self-interstitials are modeled as spherical i -clusters; and the aggregates of oxygen, primarily silicon dioxide, are modeled as spherical O -clusters.

The key element of the model describing the oxygen-influenced CZ defect dynamics is the vacancy-assisted formation of O -clusters. Effectively, all large O -clusters in the CZ growth are formed by absorbing vacancies, as the specific volume of O -clusters is greater than that of silicon. The growing O -clusters directly consume only free vacancies (v); as the free vacancy concentration decreases, however, more free vacancies are generated by the disassociation of vO and vO_2 species. Thus, both free vacancies and vacancies bound in vO and vO_2 species are consumed.

The type of microdefect formed in a given region in a crystal depends on the concentration of the intrinsic point defects and of vO and vO_2 species established a short distance away from the melt–crystal interface. In the regions marked by a high free vacancy concentration, voids or v -clusters are formed at higher temperatures by the nucleation of vacancies. The v -cluster growth consumes both free and bound vacancies. In the regions marked by a moderate free vacancy concentration, v -cluster formation is suppressed at higher temperatures; free and bound vacancies are consumed by the formation and growth of O -clusters. The binding between vacancies and oxygen allows survival of vacancies in the bound form at very low concentrations at lower temperatures even in the presence of voids and O -clusters. In the regions marked by the dominance of self-interstitials, i -clusters are formed. The concentration fields of the intrinsic point defects in the vicinity of the interface are established primarily by the interplay between the Frenkel reaction and the intrinsic point defect transport. Oxygen increases the effective vacancy concentration available for the recombination with self-interstitials by increasing the concentration of vO and vO_2 species and marginally aids the conditions leading to the survival of vacancies as the dominant intrinsic point defect species, for fixed crystal growth conditions. The increase in the pull rate range within which crystals free of large v -clusters and i -clusters can be grown, with increasing oxygen concentration, is also predicted and explained by the reported lumped model. This behavior is caused by a strong binding between vacancies and oxygen.

38.6.3 CZ Defect Dynamics in the Presence of Nitrogen

The microdefect distribution in a CZ crystal is strongly influenced by impurities such as nitrogen. A reasonably good approximation of the dynamics of microdefect

formation in growing CZ crystals in the presence of nitrogen and oxygen requires the quantification of the Frenkel reaction, the interactions between oxygen and vacancies and between nitrogen and vacancies, along with the aggregation events. Vacancies and self-interstitials annihilated by the recombination near the interface are partly supplied by their transport from the interface and by the dissociation of different reacting species. Nitrogen binding with vacancies is much stronger than that of oxygen with vacancies. The complexes of vacancies with nitrogen in particular, and oxygen to some extent, provide free vacancies by dissociation for the annihilation of self-interstitials near the melt–crystal interface. These free vacancies are available in addition to the vacancies from the interface, which is an infinite vacancy source. This dynamics increases the total concentration of vacancies in all forms, defined as the total vacancy concentration, and establishes relatively vacancy-rich conditions compared with those in the absence of nitrogen. In addition, nitrogen reduces the free vacancy concentration by strong binding at lower temperatures, reducing the vacancy nucleation temperature. The formation of vacancy aggregates in the presence of lower vacancy concentration results in an increase in their density at the expense of their size. The strong binding between vacancies and nitrogen provides an appreciable supply of vacancies for the facilitation of the formation and growth of the aggregates of oxygen with silicon at lower temperatures. Hence, vacancy aggregates and oxygen aggregates coexist in a wide range of crystal growth conditions in the presence of nitrogen.

The defect dynamics in nitrogen-doped CZ crystals, showing two-dimensional variations in the microdefect distribution and growing under both steady and unsteady states, has been quantified by the lumped model. The model approximates all aggregates as spherical clusters. Classical nucleation theory captures the formation of all clusters with a reasonable accuracy. The formed clusters grow by diffusion-limited kinetics. Vacancy clusters and self-interstitial clusters are formed by homogeneous nucleation of vacancies and self-interstitials, respectively. Oxygen clusters, because of their higher specific volume, are formed by the facilitation by vacancies. The growth of oxygen clusters is limited by the diffusion of oxygen when vacancies are

in abundance and by the diffusion of vacancies when vacancies are scarce.

The conditions leading to the formation of different microdefects in CZ crystal growth have been quantified. The effects of varying pull rate and the nitrogen concentration are also captured. The model predictions agree well with the reported microdefect distributions in the presence of moderate and high nitrogen concentrations. In the presence of very high nitrogen concentrations, however, the model predictions are less accurate.

38.6.4 The Lateral Incorporation of Vacancies

A Czochralski crystal grown through a relatively radially uniform temperature field close to the critical condition is effectively free of large microdefects, but exhibits a prominent region of oxygen clusters (and small voids, in a few cases) near the lateral surface. Because of its ring-like appearance, the region is termed the peripheral ring. The peripheral ring is formed because of the vacancy supersaturation induced by the lateral surface of the crystal. The vacancies in moderate abundance facilitate the formation of oxygen clusters (and, possibly, small voids) at lower temperatures, giving the peripheral ring its characteristic appearance.

The equilibrium conditions prevail on the surface of a growing crystal; near the critical condition, in the first stage of cooling at higher temperatures, the difference between the vacancy concentration and the self-interstitial concentration on the lateral crystal surface is much higher than that in the crystal interior (bulk), driving the vacancy enrichment of the near-surface region relative to the crystal interior (bulk); the vacancy supersaturation builds in the near-surface region with the decreasing temperature, because of the decreasing intrinsic point defect equilibrium concentrations and diffusivities.

The moderate supersaturation of vacancies prior to the formation of oxygen clusters and small voids in the peripheral ring, when the bulk of the crystal is relatively vacancy lean, is driven by the Frenkel reaction, lateral surface-induced diffusion, and the crystal movement itself. This dynamics is termed the *lateral incorporation*. The lateral incorporation generates the *peripheral ring* only in crystals grown close to the critical condition.

References

- 38.1 M.S. Kulkarni, V.V. Voronkov, R. Falster: Quantification of unsteady-state and steady-state defect dynamics in the Czochralski growth of monocrystalline silicon, *J. Electrochem. Soc.* **151**, G663–G678 (2004)
- 38.2 W.C. Dash: Silicon crystals free of dislocations, *J. Appl. Phys.* **29**, 736–737 (1958)
- 38.3 W.C. Dash: Growth of silicon crystals free from dislocations, *J. Appl. Phys.* **30**, 459–474 (1959)
- 38.4 T. Abe, T. Samizo, S. Maruyama: Etch pits observed in dislocation free silicon crystals, *Jpn. J. Appl. Phys.* **5**, 458–459 (1966)
- 38.5 A.J.R. de Kock: Vacancy clusters in dislocation-free silicon, *Appl. Phys. Lett.* **16**, 100–102 (1970)
- 38.6 A.J.R. de Kock: The elimination of vacancy-cluster formation in dislocation-free silicon crystals, *J. Electrochem. Soc.* **118**, 1851–1856 (1971)
- 38.7 A.J.R. de Kock: Microdefects in dislocation-free silicon and germanium crystals, *Acta Electron.* **16**, 303 (1973)
- 38.8 A.J.R. de Kock, P.J. Roksnoer, P.G.T. Boonen: Effect of growth parameters on formation and elimination of vacancy clusters in dislocation-free silicon crystals, *J. Cryst. Growth* **22**, 311–320 (1974)
- 38.9 A.J.R. de Kock, P.J. Roksnoer, P.G.T. Boonen: Formation and elimination of growth striations in dislocation-free silicon crystals, *J. Cryst. Growth* **28**, 125–137 (1975)
- 38.10 P.M. Petroff, A.J.R. de Kock: Characterization of swirl defects in floating-zone silicon crystals, *J. Cryst. Growth* **30**, 117–124 (1975)
- 38.11 P.M. Petroff, A.J.R. de Kock: The formation of interstitial swirl defects in dislocation-free floating-zone silicon crystals, *J. Cryst. Growth* **36**, 4–12 (1976)
- 38.12 H. Föll, U. Gösele, B.O. Kolbesen: The formation of swirl defects in silicon by agglomeration of self-interstitials, *J. Cryst. Growth* **40**, 90–108 (1977)
- 38.13 A.J.R. de Kock, W.M. van de Wiljert: The effect of doping on the formation of swirl defects in dislocation-free Czochralski-grown silicon crystals, *J. Cryst. Growth* **49**, 718–734 (1980)
- 38.14 P.J. Roksnoer, M.M.B. van den Boom: Microdefects in a non-striated distribution in floating-zone silicon crystals, *J. Cryst. Growth* **53**, 563–573 (1981)
- 38.15 P.J. Roksnoer: The mechanism of formation of microdefects in silicon, *J. Cryst. Growth* **68**, 596–612 (1984)
- 38.16 M. Hasebe, Y. Takeoka, S. Shinoyama, S. Naito: Formation process of stacking faults with ringlike distribution in CZ-Si wafers, *Jpn. J. Appl. Phys.* **28**, L1999–L2002 (1989)
- 38.17 M. Kato, T. Yoshida, Y. Ikeda, Y. Kitagawara: Transmission electron microscope observation of “IR scattering defects” in As-grown Czochralski Si crystals, *Jpn. J. Appl. Phys.* **35**, 5597–5601 (1996)
- 38.18 T. Ueki, M. Itsumi, T. Takeda: Octahedral void defects observed in the bulk of Czochralski silicon, *Appl. Phys. Lett.* **70**, 1248–1250 (1997)
- 38.19 V.V. Voronkov: The mechanism of swirl defects formation in silicon, *J. Cryst. Growth* **59**, 625–643 (1982)
- 38.20 M. Iida, W. Kusaki, M. Tamatsuka, E. Iino, M. Kimura, S. Muraoka: Effects of light element impurities on the formation of grown-in defects free region of Czochralski silicon single crystal, *Proc. Electrochem. Soc.* **99-1**, 499–510 (2000)
- 38.21 E. Dornberger, D. Gräf, M. Suhren, U. Lambert, P. Wagner, F. Dupret, W. von Ammon: Influence of boron concentration on the oxidation-induced stacking fault ring in Czochralski silicon crystals, *J. Cryst. Growth* **180**, 343–352 (1997)
- 38.22 T. Sinno, H. Susanto, R.A. Brown, W. von Ammon, E. Dornberger: Boron-retarded self-interstitial diffusion in Czochralski growth of silicon crystals and its role in oxidation-induced stacking-fault ring dynamics, *Appl. Phys. Lett.* **75**, 1544–1546 (1999)
- 38.23 V.V. Voronkov, R. Falster: Dopant effect on point defect incorporation into growing silicon crystal, *J. Appl. Phys.* **87**, 4126–4129 (2000)
- 38.24 K. Terashima, H. Noguchi: The effects of boron impurity on the extended defects in CZ silicon crystals grown under interstitial rich conditions, *J. Cryst. Growth* **237-239**, 1663–1666 (2002)
- 38.25 M.S. Kulkarni: A selective review of the quantification of defect dynamics in growing Czochralski silicon crystals, *Ind. Eng. Chem. Res.* **44**, 6246–6263 (2003)
- 38.26 T. Sinno, R.A. Brown, W. von Ammon, E. Dornberger: Point defect dynamics and the oxidation-induced stacking-fault ring in Czochralski-grown silicon crystals, *J. Electrochem. Soc.* **145**, 302–318 (1998)
- 38.27 T. Mori: Modeling the Linkages Between Heat Transfer and Microdefect Formation in Crystal Growth: Examples of Czochralski Growth of Silicon and Vertical Bridgman Growth of Bismuth Germanate. Ph.D. Thesis (Massachusetts Institute of Technology, Massachusetts 2000)
- 38.28 T.Y. Tan, U. Gösele: Point defects, diffusion processes, and swirl defect formation in silicon, *Appl. Phys. A* **37**, 1–17 (1985)
- 38.29 S. Sadamitsu, S. Umeno, Y. Koike, M. Hourai, S. Sumita, T. Shigematsu: Dependence of the grown-in defect distribution on growth rates in Czochralski silicon, *Jpn. J. Appl. Phys.* **32**, 3675–3681 (1993)
- 38.30 W. von Ammon, E. Dornberger, H. Oelkrug, H. Weidner: The dependence of bulk defects on the

- axial temperature gradient of silicon crystals during Czochralski growth, *J. Cryst. Growth* **151**, 273–277 (1995)
- 38.31 E. Dornberger, W. von Ammon: The dependence of ring-like distributed stacking faults on the axial temperature gradient of growing Czochralski silicon crystals, *J. Electrochem. Soc.* **143**, 1648–1653 (1996)
- 38.32 E. Dornberger, W. von Ammon, N. Van den Bogaert, F. Dupret: Transient computer simulation of a CZ crystal growth process, *J. Cryst. Growth* **166**, 452–457 (1996)
- 38.33 R. Falster, V.V. Voronkov, J.C. Holzer, S. Markgraf, S. McQuaid, L. Mulétagno: Intrinsic point defects and reactions in the growth of large silicon crystals, *Proc. Electrochem. Soc.* **98**(1), 468–489 (1998)
- 38.34 K. Nakamura, T. Saishoji, T. Kubota, T. Iida, Y. Shimanuki, T. Kotooka, J. Tomioka: Formation process of grown-in defects in Czochralski grown silicon crystals, *J. Cryst. Growth* **180**, 61–72 (1997)
- 38.35 P.A. Ramachandran, M.P. Dudukovic: Simulation of temperature distribution in crystals grown by Czochralski method, *J. Cryst. Growth* **71**, 399–408 (1985)
- 38.36 R.K. Srivastava, P.A. Ramachandran, M.P. Dudukovic: Interface shape in Czochralski grown crystals: Effect of conduction and radiation, *J. Cryst. Growth* **73**, 487–504 (1985)
- 38.37 A. Virzi: Computer modelling of heat transfer in Czochralski silicon crystal growth, *J. Cryst. Growth* **112**, 699–722 (1991)
- 38.38 M.S. Kulkarni, J. Libbert, S. Keltner, L. Mulétagno: A theoretical and experimental analysis of macro-decoration of defects in monocrystalline silicon, *J. Electrochem. Soc.* **149**(2), G153–G165 (2002)
- 38.39 M.S. Kulkarni: A review and unifying analysis of defect decoration and surface polishing by chemical etching in silicon processing, *Ind. Eng. Chem. Res.* **42**, 2558–2588 (2003)
- 38.40 M.S. Kulkarni, H.F. Erk: Acid-based etching of silicon wafers: mass-transfer and kinetic effects, *J. Electrochem. Soc.* **147**, 176–188 (2000)
- 38.41 R.A. Brown, D. Maroudas, T. Sinno: Modelling point defect dynamics in the crystal growth of silicon, *J. Cryst. Growth* **137**, 12–25 (1994)
- 38.42 N.I. Puzanov, A.M. Eidenzon, D.N. Puzanov: Modelling microdefect distribution in dislocation-free Si crystals grown from the melt, *J. Cryst. Growth* **178**, 468–478 (1997)
- 38.43 E. Dornberger, W. von Ammon, J. Virbulis, B. Hanna, T. Sinno: Modelling of transient point defect dynamics in Czochralski silicon crystals, *J. Cryst. Growth* **230**, 291–299 (2001)
- 38.44 M. Okui, M. Nishimoto: Effect of the axial temperature gradient on the formation of grown-in defect regions in Czochralski silicon crystals; reversion of the defect regions between the inside and outside of the Ring-OSF, *J. Cryst. Growth* **237**, 1651–1656 (2002)
- 38.45 V.V. Kalaev, D.P. Lukanin, V.A. Zabelin, Y.N. Markarov, J. Virbulis, E. Dornberger, W. von Ammon: Calculation of bulk defects in CZ Si growth: impact of melt turbulent fluctuations, *J. Cryst. Growth* **250**, 203–208 (2003)
- 38.46 V.V. Voronkov, R. Falster: Vacancy-type microdefect formation in Czochralski silicon, *J. Cryst. Growth* **194**, 76–88 (1998)
- 38.47 T. Sinno, R.A. Brown: Modeling microdefect formation in Czochralski silicon, *J. Electrochem. Soc.* **146**, 2300–2312 (1999)
- 38.48 Z. Wang, R.A. Brown: Simulation of almost defect-free silicon crystal growth, *J. Cryst. Growth* **231**, 442–447 (2001)
- 38.49 R.A. Brown, Z. Wang, T. Mori: Engineering analysis of microdefect formation during silicon crystal growth, *J. Cryst. Growth* **225**, 97–109 (2001)
- 38.50 E. Dornberger, J. Virbulis, B. Hanna, R. Hölzl, E. Daub, W. von Ammon: Silicon crystals for future requirements of 300 mm wafers, *J. Cryst. Growth* **229**, 11–16 (2001)
- 38.51 E. Dornberger, D. Temmler, W. von Ammon: Defects in silicon crystals and their impact on DRAM device characteristics, *J. Electrochem. Soc.* **149**, G226–G231 (2002)
- 38.52 K. Kitamura, J. Furukawa, Y. Nakada, N. Ono, Y. Shimanuki, A.M. Eidenzon, N.I. Puzanov, D.N. Puzanov: Radial distribution of temperature gradients in growing CZ-Si crystals and its application to the prediction of microdefect distribution, *J. Cryst. Growth* **242**, 293–301 (2002)
- 38.53 M.S. Kulkarni, V.V. Voronkov: Simplified two-dimensional quantification of the microdefect distributions in silicon crystals grown by the Czochralski process, *J. Electrochem. Soc.* **152**, G781–G786 (2005)
- 38.54 M.S. Kulkarni, J.C. Holzer, L.W. Ferry: The agglomeration dynamics of self-interstitials in growing Czochralski silicon crystals, *J. Cryst. Growth* **284**, 353–368 (2005)
- 38.55 D. Turnbull, J.C. Fisher: Rate of nucleation in condensed systems, *J. Chem. Phys.* **17**, 71–73 (1949)
- 38.56 A.S. Michaels: *Nucleation Phenomena* (American Chemical Society, Washington 1966)
- 38.57 D. Kashchiev: *Nucleation, Basic Theory with Applications* (Butterworth-Heinemann, Oxford 2000)
- 38.58 V.V. Voronkov, R. Falster: Vacancy and self-interstitial concentration incorporated into growing silicon crystals, *J. Appl. Phys.* **86**, 5975–5982 (1999)
- 38.59 V.V. Voronkov, R. Falster: Intrinsic point defects and impurities in silicon crystal growth, *J. Electrochem. Soc.* **194**, G167–G174 (2002)
- 38.60 S.M. Hu: Nonequilibrium point defects and diffusion in silicon, *Mater. Sci. Eng.* **R13**(3/4), 105–192 (1994)

- 38.61 P.M. Fahey, P.B. Griffin, J.D. Plummer: Point defects and dopant diffusion in silicon, *Rev. Mod. Phys.* **61**, 289–384 (1989)
- 38.62 U. Gösele, D. Conrad, P. Werner, Q.Y. Tong, R. Gafiteanu, T.Y. Tan: Point defects, diffusion and gettering in silicon, *Mater. Res. Soc. Symp. Proc.* **469**, 13 (1997)
- 38.63 R. Falster, V.V. Voronkov, F. Quast: On the properties of the intrinsic point defects in silicon: a perspective from crystal growth and wafer processing, *Phys. Status Solidi (b)* **222**, 219–244 (2000)
- 38.64 V.V. Voronkov, R. Falster: Parameters of intrinsic point defects in silicon based on crystal growth, wafer processing, self- and metal-diffusion, *ECS Trans.* **2**(2), 61–75 (2006)
- 38.65 J. Esfandyari, C. Schmeiser, S. Senkader, G. Hobler, B. Murphy: Computer simulation of oxygen precipitation in Czochralski-grown silicon during HI–LO–HI anneals, *J. Electrochem. Soc.* **143**, 995–1001 (1996)
- 38.66 V.V. Voronkov, R. Falster: Grown-in microdefects, residual vacancies and oxygen precipitation bands in Czochralski silicon, *J. Cryst. Growth* **204**, 462–474 (1999)
- 38.67 V.V. Voronkov, R. Falster: Strain-induced transformation of amorphous spherical precipitates into platelets: application to oxide particles in silicon, *J. Appl. Phys.* **89**, 5965–5971 (2001)
- 38.68 V.V. Voronkov, R. Falster: Nucleation of oxide precipitates in vacancy-containing silicon, *J. Appl. Phys.* **91**, 5802–5810 (2002)
- 38.69 K. Sueoka, M. Akatsuka, M. Okui, H. Katahama: Computer simulation for morphology, size, and density of oxide precipitates in CZ silicon, *J. Electrochem. Soc.* **150**, G469–G475 (2003)
- 38.70 M.S. Kulkarni: Defect dynamics in the presence of oxygen in growing Czochralski silicon crystals, *J. Cryst. Growth* **303**, 438–448 (2007)
- 38.71 K. Nakai, Y. Inoue, H. Yokota, A. Ikari, J. Takahashi, K. Kitahara, Y. Ohta, W. Ohashi: Oxygen precipitation in nitrogen-doped Czochralski-grown silicon crystals, *J. Appl. Phys.* **89**, 4301–4309 (2001)
- 38.72 W. von Ammon, R. Hölzl, J. Virbulis, E. Dornberger, R. Schmolke, D. Gräf: The impact of nitrogen on the defect aggregation in silicon, *J. Cryst. Growth* **226**, 19–30 (2001)
- 38.73 A. Karoui, F.S. Karoui, G.A. Rozgonyi, M. Hourai, K. Sueoka: Structure, energetics, and thermal stability of nitrogen-vacancy-related defects in nitrogen doped silicon, *J. Electrochem. Soc.* **150**, G771–G777 (2003)
- 38.74 V.V. Voronkov, R. Falster: The effect of nitrogen on void formation in Czochralski crystals, *J. Cryst. Growth* **273**, 412–423 (2005)
- 38.75 M.S. Kulkarni: Defect dynamics in the presence of nitrogen in growing czochralski silicon crystals, *J. Cryst. Growth* **310**, 324–335 (2008)
- 38.76 Y. Yatsurugi, N. Akijama, Y. Endo, T. Nozaki: Concentration, solubility, and equilibrium distribution coefficient of nitrogen and oxygen in semiconductor silicon, *J. Electrochem. Soc.* **120**, 975–979 (1973)
- 38.77 V.V. Voronkov, M. Porrini, P. Collareta, M.G. Pretto, R. Scala, R. Falster, G.I. Voronkova, A.V. Batunina, V.N. Golovina, L.V. Arapkina, A.S. Guliaeva, M.G. Milvidski: Shallow thermal donors in nitrogen-doped silicon, *J. Appl. Phys.* **89**, 4289–4293 (2001)
- 38.78 J. Takahashi, K. Nakai, K. Kawakami, Y. Inoue, H. Yokota, A. Toshikawa, A. Ikari, W. Ohashi: Microvoid defects in nitrogen- and/or carbon doped Czochralski-grown silicon crystals, *Jpn. J. Appl. Phys.* **42**, 363–370 (2003)
- 38.79 M.S. Kulkarni: Lateral incorporation of vacancies in Czochralski silicon crystals, *J. Cryst. Growth* **310**, 3183–3191 (2008)

39. Models for Stress and Dislocation Generation in Melt Based Compound Crystal Growth

Vishwanath (Vish) Prasad, Srinivas Pendurti

A major issue in the growth of semiconductor crystals is the presence of line defects or dislocations. Dislocations are a major impediment to the usage of III–V and other compound semiconductor crystals in electronic, optical, and other applications. This chapter reviews the origins of dislocations in melt-based growth processes and models for stress-driven dislocation multiplication. These models are presented from the point of view of dislocations as the agents of plastic deformation required to relieve the thermal stresses generated in the crystal during melt-based growth processes. Consequently they take the form of viscoplastic constitutive equations for the deformation of the crystal taking into account the microdynamical details of dislocations such as dislocation velocities and interactions. The various aspects of these models are dealt in detail, and finally some representative numerical results are presented for the liquid encapsulated Czochralski (LEC) growth of InP crystals.

39.1 Overview	1335
39.2 Crystal Growth Processes	1336
39.2.1 Czochralski Technique.....	1336
39.3 Dislocations in Semiconductors Materials	1337
39.3.1 Deleterious Effects of Dislocations	1337
39.3.2 Origin of Dislocations.....	1338
39.4 Models for Dislocation Generation	1339
39.4.1 CRSS-Based Elastic Models.....	1340
39.4.2 Viscoplastic Models.....	1342

39.5 Diamond Structure of the Crystal	1343
39.6 Deformation Behavior of Semiconductors	1346
39.6.1 Stage of Upper and Lower Yield Points	1347
39.7 Application of the Haasen Model to Crystal Growth	1350
39.8 An Alternative Model	1351
39.8.1 Different Types of Dislocations	1351
39.8.2 Dislocation Glide Velocity	1352
39.8.3 Dislocation Multiplication.....	1355
39.8.4 Work Hardening.....	1357
39.8.5 The Initial Dislocation Density.....	1358
39.9 Model Summary and Numerical Implementation	1360
39.9.1 Summary of the Model.....	1360
39.9.2 Numerical Implementation.....	1361
39.10 Numerical Results	1362
39.10.1 Strength of Convection in the Melt and Gas.....	1362
39.10.2 Temperature Boundary Condition	1362
39.10.3 A Sample Case.....	1363
39.10.4 Effect of Gas Convection and Radiation	1368
39.10.5 Melt Convection and Rotation Reynolds Numbers	1369
39.10.6 Control of Encapsulation Height.....	1371
39.10.7 The Cool-Down Period	1371
39.10.8 The $[1\bar{1}1]$ Growth Axis.....	1372
39.10.9 Summary of the Calculations and Some Comparisons.....	1373
39.11 Summary	1374
References	1375

39.1 Overview

Semiconductors are the most important materials of our age. Currently, silicon-based technology accounts

for more than 95% of the total semiconductor market. In silicon technologies, high operating speed is

achieved primarily by scaling down device dimensions. Smaller dimensions enable greater packing on a single chip, which enhances its capability and efficiency. However, reducing the size of the device has many limitations. Firstly, the parasitic capacitance of the device does not scale down linearly with the device dimension. Secondly, interconnects may pose a problem, and lithographic techniques can place a limit on the size reduction as well. Lastly the minimum size of a device is ultimately limited by the induced electric fields, which cause the breakdown of the p–n junction. An alternative is the use of III–V materials in high-speed electronics. These materials have higher electron and hole mobilities than Si; for example, at room temperature, the electron mobility in GaAs is five times larger than that in Si, and hence it has a better high-frequency response. Therefore devices using III–V materials are expected to be faster than those using Si. Apart from high-frequency response, III–V-based devices have better thermal characteristics and lower threshold voltages than other devices. Better thermal characteristics would enable the manufacture of identical components in smaller form factors. For example, a power amplifier based on InP would be smaller, more compact, and more efficient than power amplifiers based on other technologies, and its lower threshold voltage would allow the amplifier to work at a lower supply voltage.

In the area of optoelectronics and photonics, III–V materials, particularly InP, are the industry leaders. The development of low-transmission-loss quartz optical fibers, with optimum transmission characteristics in the 1.1–1.6 μm wavelength region, has led to growing demand for InP bulk material, as InP is increasingly being used as the substrate material for GaInAsP lasers, which produce light of this wavelength. The high-speed and optoelectronic characteristics of InP facilitate integrating high-speed transistors, with photoreceivers and diodes, in close proximity on a single chip. This technology would eliminate interconnects and enable the creation of communications networks operating at 40 Gb/s and beyond. At such high speeds the monolithic integration of transistors and photoreceivers is crucial as the presence of even small interconnects would seriously degrade integrated circuit (IC) performance. Thus clearly, III–Vs are the materials of the future. The present limited use of InP is not due to limitations in device technology, but rather to the lack of availability of high-quality defect-free InP substrates of large diameter. Commercially, dislocation-free Si substrates are available up to a diameter of 300 mm. GaAs substrates are available up to 150 mm, and InP up to 75 mm; however, the GaAs and InP substrates suffer from a variety of defects, the most serious of which are line defects or dislocations.

39.2 Crystal Growth Processes

The bulk of modern-day requirements of Si and III–Vs are met by techniques involving pulling single crystals from their melt – Czochralski and its variants, Bridgman and its variations, float-zone melting, etc. A brief description of the Czochralski technique is provided below.

39.2.1 Czochralski Technique

This technique was developed by *Czochralski* [39.1] and later perfected by *Teal* and *Little* [39.2]. The required equipment consists of a rotating crucible (Fig. 39.1), which contains the charge material to be crystallized surrounded by a heater capable of melting the charge and maintaining it in a molten condition. A pull rod, with a seed crystal attached to its bottom and rotating, usually in an opposite direction to that of the crucible, is mounted coaxially, and lowered until the end of the seed touches the melt. The melt tempera-

ture is carefully adjusted until a meniscus is supported by the end of the seed. Once a thermal steady state is achieved the pull rod is carefully rotated and lifted, while the melt crystallizes on the seed. The diameter of the crystal is increased from that of the seed to a desired value by careful variation of the heater power and pulling rate. The crystal and the crucible are rotated during the whole process to maintain radial homogeneity. The whole crystal growth assembly is placed in a closed water-cooled chamber, which is evacuated and filled with an inert gas (generally argon) at low pressure; this is to ensure that the system is shielded from the effect of harmful atmospheric gases and temperature fluctuations of the ambient. III–V growth presents additional problems in the form of the decomposition of the melt, since the V element is volatile and escapes from the hot melt. The problem of decomposition has been overcome through a novel modification – the *LEC* technique (Fig. 39.2). If a high pressure is not required to maintain

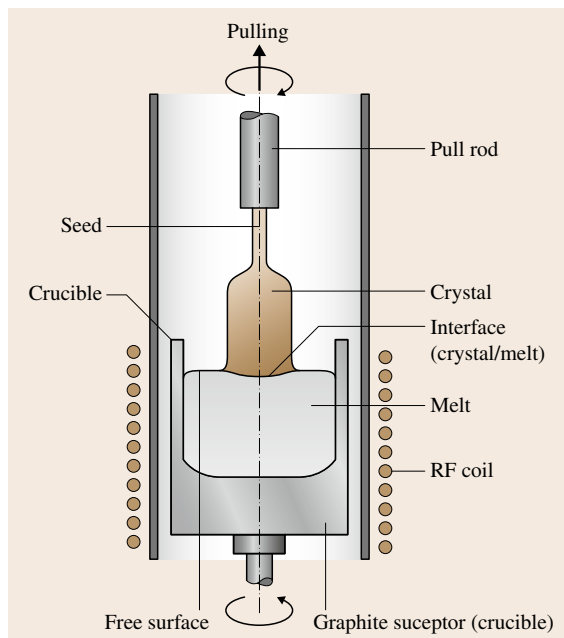


Fig. 39.1 Schematic of a low-pressure Czochralski system

the chemical equilibrium (i. e., the vapor pressure of the volatile component is not high), only minor modifications of the standard Czochralski system are required. In the case of GaAs, for example, it involves charging the crucible with a quantity of boric oxide, a low-melting-point glass, in addition to the polycrystalline gallium arsenide. On heating the crucible, the boric oxide softens and flows over the charge. Since it wets the crucible and is immiscible with and lighter than the melt, it encapsulates the charge. An inert gas is introduced into the growth chamber, at a pressure higher than the dissociation pressure of the GaAs melt, preventing loss of

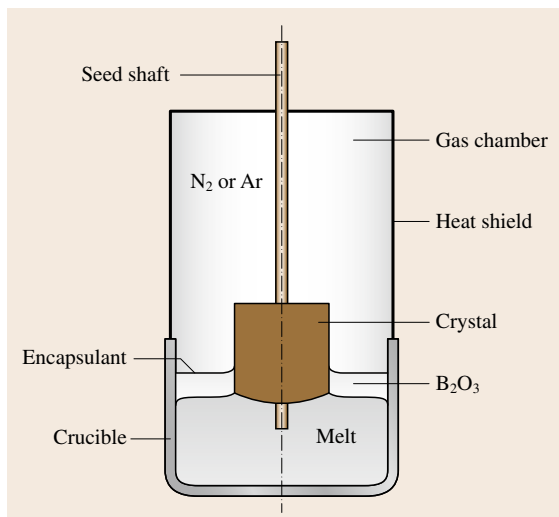


Fig. 39.2 Schematic of a high-pressure liquid-encapsulated Czochralski system

As from the melt surface. This suppresses arsenic bubble formation. Being essentially insoluble in the boric oxide, arsenic cannot diffuse through it. The crystal growing is performed in the usual manner by lowering the seed crystal through the encapsulant layer, until it contacts the melt interface; pulling is then initiated in the usual way.

The pressure of the inert gas in the growth chamber depends on the dissociation pressure of the melt and may range from about 1 atm for GaAs, through 40 atm for InP, to 70 atm for compounds such as GaP, and much higher pressures for ZnO, etc. The complexity and technological challenges associated with the LEC technique increase greatly with the pressure, which is high – 40 atm – for InP.

39.3 Dislocations in Semiconductors Materials

Dislocations are line defects in semiconductors, which adversely affect the characteristic semiconductor properties such as carrier density, mean lifetime of minority carriers, and carrier mean free path. Large single crystals of traditional elemental semiconductor materials such as Si and Ge can be grown virtually dislocation free using the necking technique pioneered by Dash [39.3]. However, growth of large-diameter single crystals of III–V and II–VI compound crystals is prone to the problem of dislocations regardless of the tech-

nique used. This problem is particularly severe in the growth of large crystals, and is one of the limiting factors in the growth of large-diameter high-quality GaAs and InP single crystals.

39.3.1 Deleterious Effects of Dislocations

The presence of dislocations introduces insurmountable problems in the use of such defective crystals for device applications. A high dislocation density in the crystal

introduces a large number of etch pits on the surfaces of wafers made from it. The use of wafers for device manufacture involves the etching and deposition of transistors, the dimensions of which are of the same order as that of the etch pits. If a transistor is engraved near an etch pit, its characteristic behavior is very different from that of a transistor etched in nondefective material. Hence it is imperative for device applications that wafers are uniform and largely free of defects.

Dislocations are detrimental for optoelectronic applications. Dislocations have been directly implicated in the case of degradation of GaAs-based light-emitting devices such as the GaAs–AlGaAs light-emitting diode (LED) [39.4]. The imperfect lattice near the dislocation core enhances nonradiative recombination between majority and minority carriers. Such recombinations near dislocation cores, instead of producing photons, only produce local lattice excitations and thermal energy, reducing luminescence. For example Roedel et al. [39.5] plotted luminescence efficiency versus dislocation density for 45 individual $\text{Al}_x\text{Ga}_{1-x}\text{As}:\text{Si}$ LEDs and obtained a curve directly documenting the decrease in efficiency with etch pit density on the original wafer from which the device was fabricated. The degradation is of three different broad categories, and the following are directly quoted from [39.4]

(1) A rapid degradation that occurs after a short duration of operation, (2) a slow degradation occurring during long term operation; and (3) a catastrophic degradation process that occurs at high optical power densities because of mirror facet damage.

The first two modes of degradation are closely linked to nonradiative recombination near the dislocation cores. Moreover the thermal energy generated during such recombinations leads to faster dislocation rearrangements and movements involving dislocation climb and glide, and leads to the development of more dislocation structure, more defective material, and degradation of luminescence with time. Reference [39.4] provides a more detailed discussion on this topic.

39.3.2 Origin of Dislocations

In most works thermal stresses are cited as the chief reason behind dislocations. This is because the stresses drive the multiplicative mechanisms of dislocations, which begin to operate as the small number of dislocations initially present begin to glide under the influence

of thermal stresses. While this is certainly true, this is a matter of dislocation multiplication from *existing dislocations* and does not explain the nucleation of the first *existing dislocations* from which others multiply. Hence one has to differentiate between *dislocation multiplication* and *dislocation nucleation*. Dislocation nucleation is not possible solely due to thermal stresses; it has been estimated that stresses of the order of $\mu/2\pi$, where μ is the theoretical shear modulus of the material, are required for the nucleation of dislocations solely under their influence. The crystal growth process does not involve thermal stresses of this magnitude. The nucleation of dislocations is generally attributed to the following mechanisms, many or all of which might be operating in tandem.

Agglomeration of Point Defects

During crystal growth, there exists a high equilibrium concentration of point defects in a given material element, when it is near the crystal–melt interface, because of the high temperature close to the melting point. During the growth process, the material element moves away from the interface, and cools down, giving rise to supersaturation of point defects. These point defects agglomerate into clusters, which in order to minimize their elastic strain energy collapse into various structures. Chapter 38 in this volume details the dynamics of the agglomeration and the defects formed therein, under various conditions, for Czochralski growth of Si. One of the minimum-energy structures into which the agglomerations of point defects can collapse is a planar disc in a (111) plane. Such a disc is equivalent to a stacking fault bound by a Frank partial dislocation loop. The disc grows by the climb of the bounding partial dislocation, and once it reaches a critical size, a Shockley partial may be spontaneously nucleated, removing the stacking fault and transforming the Frank partial into a loop of a perfect dislocation [39.6, Chap. 10]. For example, a Frank dislocation loop in the (111) plane dissociates as

$$\frac{a}{3}[111] + \frac{a}{6}[\bar{2}11] \rightarrow \frac{a}{2}[011].$$

The steps of point defect agglomeration – collapse into discs and Shockley nucleation – are governed by kinetics determined by the thermal history and the material. The perfect dislocation loop formed by the above process is not a glide dislocation, since its Burgers vector does not lie in the plane of the dislocation loop. However, a fraction of these loops become mobile glide dislocation loops by the escape of a segment onto a glide plane, which contains the Burgers vec-

tor. Refer to [39.7] for a more detailed explanation. In compound semiconductors, the situation is complicated by the sublattices of the diamond structure being occupied by atoms of different elements. In these compounds, the formation of a vacancy (interstitial) disc involves equal numbers of vacancies (interstitials) of both sublattices, which is difficult, since the concentration of point defects on the two sublattices is generally different, depending on factors such as stoichiometry, etc. *Lee et al.* [39.8] have identified mechanisms by which the above problem may be overcome, to nucleate glide dislocations. *Lagowski et al.* [39.9] have experimentally revealed the effect of doping on the nucleation of glide dislocations, through aggregation of point defects.

Surface Damage

Damage on the surface of the growing crystal due to indentation, scratching, grinding, and impingement of hard particles leads to the nucleation of dislocations. All of these processes involve the action of large local stresses causing the relative displacement of two layers of the crystal: the nucleation of a dislocation. This mode of nucleation might not be important in crystal growth, but it has been the experience of crystal growers that small particles from the melt on the surface of the growing crystal produce such dislocations [39.10].

Foreign Particles or Precipitates

The presence of a second phase in the form of foreign particles, precipitates, etc., leads to misfit due to differential thermal expansion of the particle and the surrounding matrix. This gives rise to very high local stresses and consequently misfit dislocations. Usually, these misfit dislocations are in the form of glide dislocations in the glide plane of maximum shear stress, as discussed by *Ashby and Johnson* [39.11] and *Alexander* [39.7]. *Ashby and Johnson* show that the radius of the original nucleated loop should be greater than $R_c = \mu b / \tau$, where τ is the effective shear stress and b is the Burgers vector, so that the loop can continue to grow and expand under the influence of the shear stress. In III–V compounds, inclusions from the B_2O_3 encapsulant or precipitates of one phase due to lack of

stoichiometry might act as foreign particles, thus nucleating glide dislocations.

Chemical Inhomogeneity

Chemical inhomogeneity may arise due to doping or impurity atoms and nonstoichiometry. These might lead to lattice mismatch, giving rise to misfit dislocations. Sometimes, the phenomenon of constitutional supercooling might arise in the melt near the solidification interface, giving rise to instabilities in the interface. In such cases, the planar interface splits into cells. Impingement of different parts of the interface (cells) might give rise to misfit dislocations. However, constitutional supercooling is expected to be rare in semiconductor single-crystal growth, due to the low concentration of impurity/dopant.

Use of a Defective Seed

If the seed crystal contains dislocations, these are likely to glide into the newly grown crystal. These seed dislocations would then multiply under the effect of thermal stresses. The use of a defective seed can be overcome by the use of a narrow necking (*Dash* process) [39.3].

Thermal Stresses

The most important cause for the presence of dislocations in as-grown semiconductor crystals is thermal stresses. Since the presence of temperature gradients in the crystal is necessary, crystal growth is an inherently nonequilibrium process, involving heat transfer through the crystal. The crystal acts as a medium through which heat, both released heat of fusion and that from the melt, is transferred to the ambient. The heat enters the crystal at the crystal–melt interface, and leaves through the external surfaces by radiation and convection. Thus the core of the crystal is hotter than the periphery, and the bottom of the growing crystal is hotter than the top. These temperature gradients give rise to differential expansion of different parts of the crystal, and consequently to thermal strains and stresses. These thermal stresses are the cause of plastic deformation, through the movement and multiplication of existing dislocations, resulting in unacceptable final dislocation densities in as-grown crystals.

39.4 Models for Dislocation Generation

Before we dwell on the mathematical models, a word on notation: vectors are represented as bold-face italic

and second-order tensors as bold-face upright; indicial notation for vectors and tensors and the Einstein sum-

mation convention are not used, except in Sect. 39.2 or unless specifically mentioned.

Since thermal stress in the growing crystal is considered as the primary reason for the presence of dislocations in as-grown crystals, models for dislocation generation take a solid mechanics approach. Towards this, efforts are made to characterize the mechanistic response of the crystal to loading through appropriate constitutive equations. Depending on the type of constitutive behavior, the modeling approach falls into two broad categories: the crystal is considered as (1) an elastic crystalline medium and (2) a viscoplastic crystalline medium.

39.4.1 CRSS-Based Elastic Models

In this approach the crystal is assumed to be a linear elastic continuum. The crystal usually being a cubic material, three elastic coefficients are prescribed to characterize its elastic behavior. Isotropic behavior is also assumed sometimes. The thermal loading during the growth is specified through a coefficient of thermal expansion and the consequent thermal strain. With the help of minimal boundary conditions designed to prevent rigid-body motion, the elastic problem can be solved at any given thermal loading (which can be obtained from the temperature field) during the growth of the crystal. Solution of the elastic problem yields information on the displacements, the total, thermal, and elastic strains, and the elastic stresses within the crystal. Once the elastic stresses are obtained, these are used to estimate the plastic deformation and whether a particular area of the crystal will have a high or low dislocation density.

Dislocations in III–V materials with zincblende structure glide in the family of four $\{111\}$ planes along the three $\langle 110 \rangle$ directions. Hence plastic deformation takes place along the 12 $\{111\} - \langle 110 \rangle$ slip systems. *Jordan et al.* [39.12] postulated that plastic deformation starts if the resolved elastic shear stress on any of these 12 systems exceeds a critical value, which they termed the critical resolved shear stress (CRSS). Thus this model is similar in spirit to the rate-independent non-hardening plasticity models, which have a fixed yield surface in stress space. The equations and the methodology applied by *Jordan et al.* [39.12] are summarized next.

The total strain (the symmetrical part of the gradient of the displacements) at any given instant in the growth history is split into an elastic component, which is a function of the stress, and a thermal component,

which is function of the temperature as follows

$$\boldsymbol{\varepsilon} = \boldsymbol{\varepsilon}(\boldsymbol{\sigma}, T) = \frac{1}{2} \left(\nabla \mathbf{u} + (\nabla \mathbf{u})^T \right), \quad (39.1)$$

and

$$\boldsymbol{\varepsilon}(\boldsymbol{\sigma}, T) = \boldsymbol{\varepsilon}^{\text{el}}(\boldsymbol{\sigma}) + \boldsymbol{\varepsilon}^{\text{th}}(T). \quad (39.2)$$

The elastic strain using the regular equations of linear elasticity is related to the stresses as

$$\boldsymbol{\sigma} = \mathbf{C} : \boldsymbol{\varepsilon}^{\text{el}}, \quad (39.3)$$

where \mathbf{C} is the fourth-order elastic modulus tensor. Similarly the thermal strain is expressed as

$$\boldsymbol{\varepsilon}^{\text{th}} = \alpha(T - T_0)\boldsymbol{\delta}, \quad (39.4)$$

where α is the coefficient of thermal expansion, T_0 is some reference temperature, and $\boldsymbol{\delta}$ represents the Kronecker delta tensor. The principle that completes the equations is the mechanical equilibrium in the crystal, which assuming negligible effects of body forces such as gravity is expressed as

$$\nabla \cdot \boldsymbol{\sigma} = 0. \quad (39.5)$$

For a given temperature field and assuming boundary conditions just sufficient to prevent rigid-body motion, (39.1–39.5) represent the familiar linear elastic problem and can be solved using any numerical technique to obtain the total strains, elastic strains, and stresses in the crystal.

The thermal–elastic stresses thus calculated are then resolved along the $\{111\}\langle 110 \rangle$ systems. These slip systems are summarized in Table 39.1, and are defined in

Table 39.1 Summary of the slip systems in elemental and III–V semiconductors

Slip system number (k)	$\sqrt{2}s_k$	$\sqrt{3}n_k$
1	[101]	[11 $\bar{1}$]
2	[011]	[11 $\bar{1}$]
3	[1 $\bar{1}$ 0]	[11 $\bar{1}$]
4	[110]	[1 $\bar{1}$ 1]
5	[011]	[1 $\bar{1}$ 1]
6	[10 $\bar{1}$]	[1 $\bar{1}$ 1]
7	[101]	[1 $\bar{1}$ $\bar{1}$]
8	[110]	[1 $\bar{1}$ $\bar{1}$]
9	[01 $\bar{1}$]	[1 $\bar{1}$ $\bar{1}$]
10	[10 $\bar{1}$]	[111]
11	[0 $\bar{1}$ 1]	[111]
12	[1 $\bar{1}$ 0]	[111]

terms of the slip plane normal vector \mathbf{n} and the slip direction vector \mathbf{m} , thus

$$\tau^i = \mathbf{m}_i \cdot \boldsymbol{\sigma} \cdot \mathbf{n}_i ,$$

where τ^i is the resolved shear stress on slip system i .

If the resolved shear stress along a slip system exceeds the critical resolved shear stress (CRSS), then that system is deemed active, contributing to the plastic deformation and multiplication of dislocation density. Towards this the *excess shear stress* on a given slip system can be calculated from

$$\tau_{\text{excess}}^i = |\tau^i| - \tau_{\text{CRSS}} . \quad (39.6)$$

Jordan et al. [39.12] postulated that the total dislocation density in a crystal is proportional to the sum of the excess shear stress on the first five slip systems, when the excess shear stresses are arranged in descending order. This follows from the fact that, although the plastic strain tensor has nine components, its symmetry and the incompressibility of the plastic strain mean that only five of the components are independent. Hence slip on five slip systems is sufficient to describe the plastic strain. In regions where this excess shear stress is zero, the dislocation density will be zero. Thus the total dislocation density N at a given location in the crystal is described as

$$N \propto \sum_{i=1}^5 \tau_{\text{excess}}^i . \quad (39.7)$$

Jordan et al. [39.12] presented the first detailed stress calculations after calculating the thermal field from a quasisteady heat transfer model. This analysis provided the first fundamental description of dislocation generation in III–V compounds. Jordan et al. in their heat transfer analysis made a few fundamental assumptions for the calculation of the temperature field, the most important of which are as follows:

1. The crystal is modeled as a cylindrical boule, which is pulled at a constant rate from the melt held at a constant temperature T_f .
2. The solid–liquid interface is planar and is at the temperature T_f .
3. The temperature of the ambient around the boule is a constant $T_a < T_f$.
4. Heat loss from the lateral and top surfaces by radiation and natural convection follows Newton's law of cooling.

An analytical solution for the temperature field in the crystal was obtained by solving the conduc-

tion equation in the crystal, along with the above assumptions. The plane-strain solution of classical thermoelasticity was then adopted to determine the stresses and calculate the dislocation densities. Jordan et al. [39.12] compared their calculated dislocation densities with a computerized scan of the etch pit density of a KOH-etched (100) GaAs wafer; the main feature of the dislocation distribution such as fourfold symmetry in the etch pit density, observed experimentally, was replicated by their calculations. Similar calculations were also performed for a (111) LEC-pulled InP wafer. In this case the sixfold defect distributions determined experimentally somewhat resembled the dislocation contours predicted by the model. These calculations firmly established the role of thermal stresses in dislocation generation and multiplication in crystals grown from the melt.

Following the pioneering work of Jordan et al. [39.12], Kobayashi and Iwaki [39.13] performed similar calculations without neglecting the axial displacements; their calculations are slightly closer to experimental data than the calculations of Jordan and coworkers. Duseaux [39.14] repeated the calculations with a more realistic geometry by including seed and shoulder regions of the growing crystal. These early calculations along with those by Lambropoulos [39.15], Schvezov et al. [39.16], and Meduoye et al. [39.17, 18] assumed a known geometry of the crystal, usually with a planar melt–crystal interface, and the thermal calculations were performed with an assumed convection coefficient for heat transfer from the melt to the crystal and from the crystal to the gas. Calculations by Motakef et al. [39.19], Dupret et al. [39.20], and Bornside [39.21], while still neglecting melt convection, used global radiation and conduction models which included both the melt and the crystal. The interface shape in these calculations was not assumed, but was obtained from the calculations. Zou et al. [39.22] coupled a finite element technique, performing an isotropic linear thermal–elastic analysis on the growing crystal, with a finite volume technique for the thermal and flow analysis of the growth process. This work incorporated a number of features, including convection in the melt and the gas, radiation, etc. It should be noted that most of these works treat the crystal as linear elastic and, after calculating the stresses, performed some sort of excess shear stress calculations, following Jordan et al. Thus, there is a large amount of literature devoted to calculating dislocation densities through a thermal–elastic model, using the approach of Jordan and coworkers.

This approach, though original and successful, has several shortcomings. For example, it treats the crystal as an elastic/perfectly plastic continuum, which is untenable for elemental and compound semiconductors. The deformation of semiconductors is a highly rate-dependent process; the response of such a material to stress is not instantaneous, but depends on the kinetics of the dislocation movement and multiplication, which are strong, time-dependent functions of temperature. The so-called **CRSS** proposed by Jordan is not a material property and is a function of the local dislocation configuration, temperature, doping, and other factors. The dislocation configuration and temperature are functions of growth history, and change within a given material element during its growth history. All the above analyses take one temperature field as an input; it is not very clear which temperature at which instant of the growth history is the appropriate one. It is however true that a **CRSS** such as locking stress does exist in certain materials such as GaAs [39.23] and Si due to the presence of impurities, which lock the dislocations. A certain minimum shear stress is then required to *unlock* these dislocations, but once the unlocking takes place the material again behaves in a rate-dependent manner.

39.4.2 Viscoplastic Models

The alternative approach to modeling dislocation density evolution is the use of viscoplastic constitutive equations. Once the thermal history of the crystal from seed to as-grown state is obtained, the procedure is to integrate these viscoplastic constitutive equations in time, while maintaining equilibration of stresses at all times to obtain the final dislocation density. The advantage of this approach is that the final dislocation densities and state of the as-grown crystal is a functional of the initial state of the seed, and the entire temperature history during the growth and the cool-down period of the crystal after growth. This approach also has the potential to give an estimate of the residual stresses in the cooled crystal.

While specific constitutive equations to be used will be discussed in the following sections, a brief description of the basic viscoplasticity formulation, described in detail in *Lubliner* [39.24], with some adaptations to present requirements is given here. As is customary in standard plasticity formulations, the internal structure, or the state of the crystal, at any point, is hypothesized as being represented by a set of internal variables denoted by ξ_α or the vector ξ . The mechanical strains at

a given position are completely determined by the troika of internal variables, stress components, and temperature at a given position.

$$\epsilon = \epsilon(\sigma, \xi, T) . \quad (39.8)$$

Additionally, for small-strain viscoplastic constitutive formulations, the following tenets are usually adapted.

Additive Decomposition of Strain Tensor

One assumes that the strain tensor can be decomposed into an elastic, plastic, and thermal part, according to the relation

$$\epsilon(\sigma, T, \xi) = \epsilon^{\text{el}}(\sigma) + \epsilon^{\text{pl}}(\xi) + \epsilon^{\text{th}}(T) , \quad (39.9)$$

where the elastic strain components are assumed to be a function of the stress tensor only, the plastic strain components are assumed to be a function of the internal variables only, and finally the thermal strain component is a function of temperature only.

(Elastic) Stress Response

The stress tensor σ_{ij} is related to the elastic strain $\epsilon_{ij}^{\text{el}}$ through the existence of a stored energy functional W , according to the hyperelastic relationship

$$\sigma = \frac{\partial W(\epsilon^{\text{el}})}{\partial \epsilon^{\text{el}}} .$$

For linear elasticity, the stored energy functional W assumes a quadratic form in the elastic strain, i.e., $W = \frac{1}{2} \epsilon^{\text{el}} : \mathbf{C} : \epsilon^{\text{el}}$, where \mathbf{C} is the fourth-order tensor of elastic moduli, which is assumed constant. Then the relations between the stress components and the elastic strain tensor reduce to

$$\sigma = \mathbf{C} : [\epsilon - \epsilon^{\text{pl}} - \epsilon^{\text{th}}] . \quad (39.10)$$

Evolution of Internal Variables and Plastic Strain

Evolution equations are proposed for the internal variables and plastic strain tensor over time. These evolution equations for $\{\epsilon^{\text{pl}}, \xi\}$ are termed the flow and hardening rules, respectively. The relations are of the form

$$\dot{\epsilon}^{\text{pl}} = \mathbf{r}(\sigma, \xi, T) , \quad (39.11a)$$

$$\dot{\xi} = \mathbf{h}(\sigma, \xi, T) . \quad (39.11b)$$

The relation (39.11b) is more basic and (39.11a) can be derived from it, because of the functional dependence of plastic strain solely on the internal variables according to (39.9).

Isotropic Thermal Strain Response

The thermal strain response is assumed to be isotropic and of the form

$$\epsilon^{\text{th}} = \alpha(T - T_0)\delta, \quad (39.12)$$

where α is the coefficient of thermal expansion, T_0 is some reference temperature, and δ is the Kronecker delta tensor.

Equations (39.9–39.12) form the outline of an internal-variable-based viscoplastic constitutive model, set in a small deformation framework, and assuming linear elastic response coupled with isotropic thermal expansion. If the internal variables adopted are some measures of dislocation densities, and the evolution

(39.11) is based on dislocation dynamics, the outline presented above has the potential to predict the final defect densities as integrated functions of the growth history. The procedure is essentially one of integrating (39.11) through the growth history, while ensuring the equilibration of stresses and fulfillment of boundary conditions on the surface of the crystal. Specific instances of constitutive relations to model the deformation behavior of semiconductor materials are presented in subsequent sections of this chapter. Prior to these, a brief description of the structure of the diamond crystal will be provided, as this has a great bearing on the deformation characteristics of semiconductor materials, at least, those that crystallize in this structure.

39.5 Diamond Structure of the Crystal

The peculiarities in the plasticity of elemental and III–V semiconductor materials arise from their structures. These materials crystallize in the diamond cubic structure or sphalerite structure for compound III–V semiconductors. These structures are illustrated in Figs. 39.3 and 39.4 (adapted from [39.25]), which show three-dimensional views of the diamond and sphalerite structure, respectively. It can be seen that each atom in these structures is tetrahedrally coordinated, i.e., each atom has exactly four neighbors, and the bonds between these neighbors are in the $\langle 111 \rangle$ directions. A projection of the three-dimensional structure on a $(1\bar{1}0)$ plane is shown in Fig. 39.5. In this view the (111) atomic planes are stacked in the sequence $AaB-bCCaAaBbCc\dots$. It can be seen from a straightforward comparison of Figs. 39.3 and 39.5 that the double and single lines in Fig. 39.5 mean one or two interatomic bonds. There are two different interatomic plane distances between the (111) planes – from the tetrahedral

geometry, it can be calculated that the perpendicular distance between the a and the A planes is thrice the distance between the A and the b planes. The diamond lattice can also be described as just two interpenetrating face-centered cubic (fcc) lattices, or alternatively as an fcc structure with a basis of two atoms per lattice point. If the stacking sequence in the first fcc lattice is $ABCABCABC\dots$, then the stacking sequence in the second interpenetrating lattice is $abcabcabc\dots$. Since the structure is just a doubled-up fcc lattice, the glide planes as in the fcc case, belong to the $\{111\}$ family, and the perfect dislocations have Burgers vector $\frac{1}{2}\langle 110 \rangle$. Due to the strong directional covalent bonding, the Peierls barrier in these materials is very high, and the resulting deep troughs in the Peierls barrier cause the dislocations to align primarily along the $\langle 110 \rangle$ directions, when the dislocation density is low. Thus the dislocations are primarily screw or 60° dislocations.

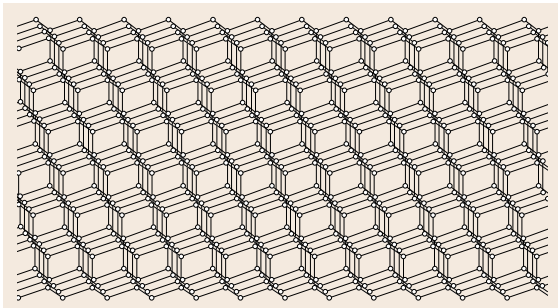


Fig. 39.3 The diamond lattice (after [39.25])

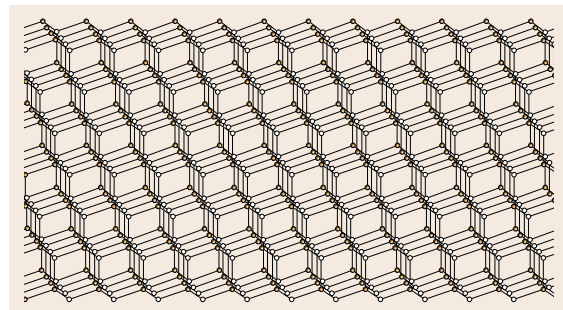


Fig. 39.4 The sphalerite lattice. Dark and light atoms show different species of atoms (after [39.25])

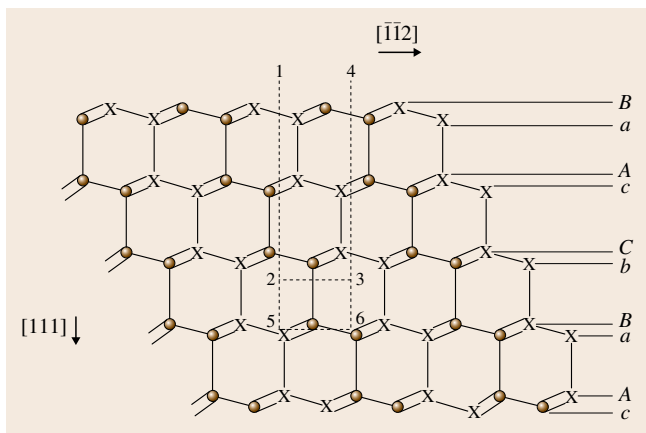


Fig. 39.5 The diamond lattice projected onto the $(1\bar{1}0)$ plane. *Bullets* represent atoms in the plane of the paper; *Xs* represents atoms below the plane of the paper (after [39.6])

Owing to the double-layered atomic arrangement of the diamond cubic lattice, there are two inherently different sets of dislocations, with one member of each having the same Burgers vector. These two different sets are termed the glide set and the shuffle set of dislocations. The difference is clarified by an examination of Fig. 39.5. A 60° dislocation of the glide set is formed by cutting out the material bounded by the surface 1–5–6–4, and then displacing the sides of the cut, until they are joined. The feature of these dislocations is that there is a dangling bond along surface 5–6, while all the other cut bonds on surfaces 1–5, 6–4 are made up after displacement. Thus the extra plane of atoms terminates between two layers of the different letter index, for example *a* and *B* in Fig. 39.5. Similarly, a 60° dislocation of the shuffle set is formed by cutting material along the surface 1–2–3–4 and then rejoining as before. In this case the dangling bond is along the

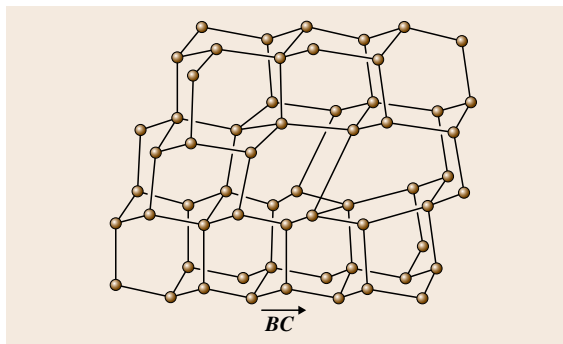


Fig. 39.6 The 60° glide dislocation (after [39.6])

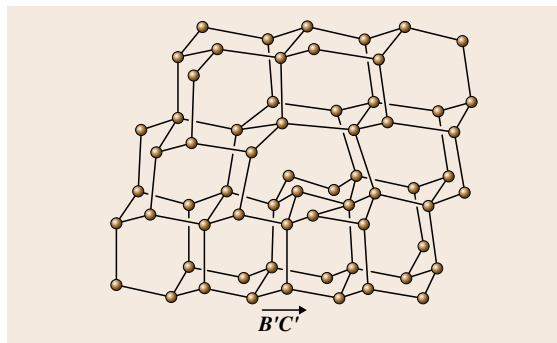


Fig. 39.7 The 60° shuffle dislocation (after [39.6])

surface 2–3, while all the bonds along surfaces 1–2 and 3–4 are filled after reconstruction. In this case the extra plane of atoms terminates between layers of the same index, such as *B* and *b* in Fig. 39.5. Three-dimensional views of the 60° glide (*BC*) and shuffle dislocations (*B'C'*) are given in Figs. 39.6 and 39.7, respectively. It can be seen that the shuffle and glide dislocations can transform into each other any time by the emission or absorption of point defects. The same distinction between glide and shuffle dislocations applies to dislocations of screw, edge, and intermediate orientations. To describe the dislocations the Thompson tetrahedron notation is used. Since there are two *fcc* lattices, there are two Thompson tetrahedrons used, one to describe the glide set (for example, dislocation *BC* above) and one to describe the shuffle set (for example, dislocation *B'C'* above).

Dislocations in the glide set can undergo dissociation into partial dislocations, in the same manner as dislocations in *fcc* metals. Figure 39.8 is a three-dimensional view of the glide dislocation *BC* dissociated into δC (30° partial) and $B\delta$ (90° partial). These partial dislocations in the glide set are glissile, and because the dislocation glides between the layers *b* and *C*, the dissociation into δC and $B\delta$ results in an intrinsic stacking fault between the two partials. The dissociation of shuffle dislocations in the set *A'B'C'D'* is not direct, because such dissociation would produce a high-energy fault of the type *CcAaB|aBbCc*.

Hornstra [39.26], and later Alexander [39.27], gave an alternate description of an extended shuffle dislocation, which may be described in two completely equivalent ways: either as an association of a stacking-fault ribbon to a shuffle dislocation, or as a dissociated glide dislocation that has emitted or absorbed a line of atoms in the core of one of its partials. This is consistent with the relationship between perfect shuffle and

glide dislocations that can be converted into each other by emission or absorption of point defects.

Dislocations of the screw, edge, and other intermediate types, of both the shuffle and glide variety, may be generated in ways equivalent to that of the 60° dislocation. For these configurations, dislocations of the glide and shuffle type may be dissociated into partial dislocations in equivalent ways. For example, a screw dislocation of the glide type may be dissociated into two 30° partial dislocations, with a stacking fault between them. These can be converted into the shuffle type by emission or absorption of point defects. A pertinent question in the literature is whether the dislocations are extended and, if so, whether they exist in the shuffle or the glide set. It was previously assumed that moving dislocations were undissociated and existed in the shuffle mode, since the number of covalent bonds to be broken is three times smaller than in the glide mode. However, it has been demonstrated that dislocations are dissociated when at rest in both the diamond and sphalerite structure [39.28,29], and remain dissociated while moving [39.30].

Since the movement of partial dislocations in the shuffle set is more difficult than those in the glide set, it is more probable that the glide set is prevalent. However, it must be pointed out that the coexistence of both sets is not ruled out in the literature, and sometimes the as yet unexplained generation of point defects during deformation of semiconductors is attributed to the existence of, and interchange between, both sets [39.31].

The situation is further complicated in the case of compound semiconductors such as InP, GaAs, InSb, and other III–V and II–VI compounds, which exist in the sphalerite or the zincblende structure (Fig. 39.4). The sphalerite structure is the same as the diamond structure, the only difference being that the two atoms at each lattice point are of two different elements in the sphalerite structure, while they are of the same element in the diamond structure. Identical to the diamond structure, the glide planes are $\{111\}$, the direction of closest packing, while the slip directions, or Burgers vector of the perfect dislocations, are again $\langle 110 \rangle$, the shortest translation vectors in the lattice. In the following paragraphs the chief differences between the two structures are illustrated.

α and β Dislocations

Apart from the complexities of the glide and shuffle sets already existing in the diamond cubic structure, there are further complexities in the sphalerite system, i.e., there are two different $\{111\}$ systems. For exam-

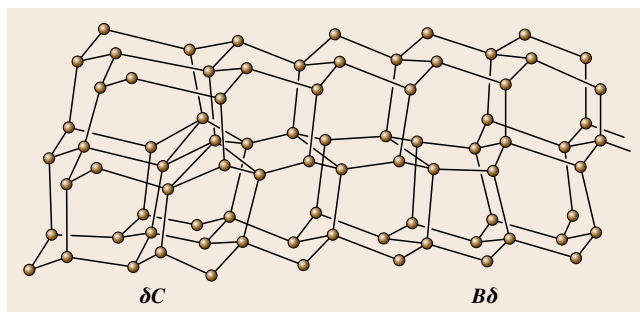


Fig. 39.8 Dissociation of a perfect 60° glide dislocation into 30° and 90° partials (after [39.6])

ple, in Fig. 39.5, the *A*, *B*, and *C* layers contain one atom, say In for InP, while the layers *a*, *b*, and *c* contain the P atoms. Opposite-sign dislocations in the sphalerite structure have the extra plane of atoms ending in different atoms. For example, in a 60° shuffle dislocation (Fig. 39.5), formed by removing material bounded by surface 1–2–3–4, the extra plane of atoms lies below the surface 2–3 and ends on the *B* layer in the diagram, which is an In layer. If instead a shuffle dislocation of exactly the opposite sign was formed at exactly the same place, the extra plane of atoms would lie above the surface 2–3, and end on the *b* layer, which is a P layer. Dislocations with the edge of their extra half-planes ending on In (atoms of lower valency) layers are called β dislocations, while those with the edge of their extra half-planes ending on P (atoms of higher valency) layers are called α dislocations. This terminology, although illustrated for the shuffle set, can also be applied to glide dislocations. Since, the core structures of α and β dislocations are different, they have different properties, the most important of which is the significant difference of mobility between the two.

As pointed out before, the dislocations in compound or elemental semiconductors lie along the $\langle 110 \rangle$ directions of the glide plane, at low dislocation densities. A perfect dislocation loop would thus consist of two screw dislocations and four 60° dislocations. The geometry of a typical loop is shown in Fig. 39.9a, which shows that a glide loop possesses two types of dislocation segments: screw and 60° dislocations (60° being the angle between the dislocation line and the Burgers vector). The 60° dislocations are of two different types, α and β , since the extra half-planes of these are respectively down and up. The screw dislocations are not classified since they do not have an extra half-plane. Figure 39.9b–d show the dissociation of the α , β , and screw dislocations into partial dislocations in the glide

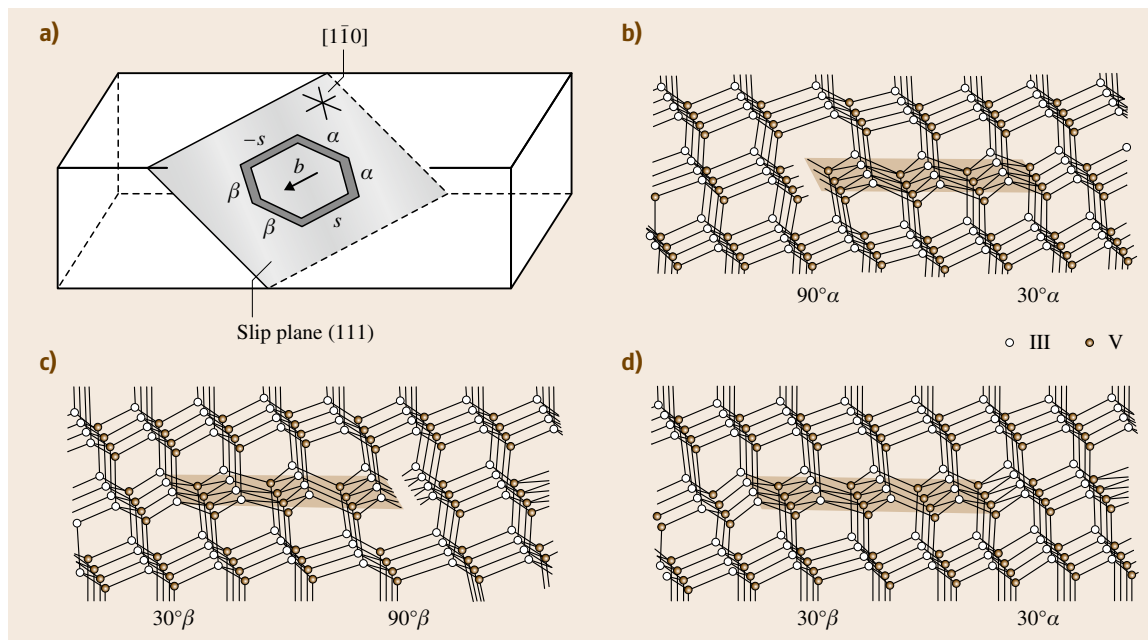


Fig. 39.9 (a) A hexagonal dislocation loop on a glide plane, (b) core structure of a $60^\circ \alpha$ dislocation, (c) $60^\circ \beta$ dislocation, and (d) screw dislocation. The shaded planes represent the stacking faults (after [39.25])

set, with 60° dislocations split into 30° and 90° partials, and each screw split into a 30° partial dipole. Each of

the partials can be associated with α or β character as shown.

39.6 Deformation Behavior of Semiconductors

Elemental and compound semiconductors are brittle at low temperatures, but acquire a substantial capacity for plastic deformation at temperatures above 30% of their melting point. The brittleness is a result of strong directional covalent bonds, which result in a deep Peierls potential. The plasticity of these materials is strongly strain rate and temperature dependent, again owing to the strong Peierls potential acting against dislocation movement. The dislocations glide in these materials at low speeds, in contrast to fcc metals whose plasticity is almost rate independent. The deformation behavior of these materials has been studied extensively through the stress-strain behavior of elemental and compound semiconductors such as Si, Ge, and InSb during uniaxial compression or tensile testing conducted at constant strain rate on a crystal oriented for single slip, and creep tests at constant stress for samples again oriented for single slip. The most common way of obtaining these curves is the constant-strain-rate compression test. This is done in a constant-displacement-rate ma-

chine, in which the specimen is kept between two rigid crossheads while one of them moves at a fixed speed. The axial force applied on the crosshead to compress the specimen is recorded at any instant. The force is recorded as a function of the crosshead displacement, which can then be converted into curves of shear stress versus shear strain based on the specimen dimensions. All elemental and compound semiconductors exhibit common behavior in uniaxial compression constant-strain-rate tests, oriented for single-slip conditions, when the tests are done at temperatures where the mobilities of the dislocations are similar for all materials. This commonality of behavior indicates that the underlying microscopic processes behind the deformation have a common origin. Figure 39.10 elucidates the generic features common to all elemental and III-V compound semiconductors. In this figure, the shear stress in the main slip system is plotted against the shear strain in the same system, as the deformation evolves. The striking feature of this curve is the presence of

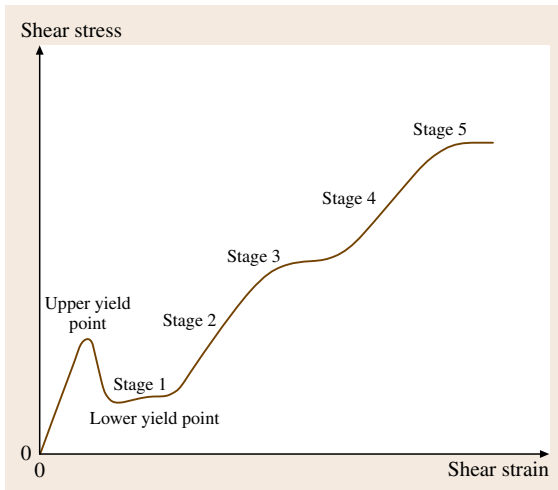


Fig. 39.10 Generic plot of shear stress versus shear strain for deformation of semiconductors in single slip

an upper and a lower yield point. The stress increases rapidly with strain at the beginning of the deformation, reaches a maximum, then decreases with increasing strain and reaches a minimum, from where the stress increases with increasing strain. The stress maximum and minimum are termed the upper and lower yield point, respectively. At low temperatures, three deformation stages following the upper and lower yield points are observed: a stage of low work hardening (I), a stage of strong work hardening (II), and a stage of increasing softening (III), where recovery processes operate in the crystals exposed to an external stress – dynamical recovery. At high temperatures, two further stages appear: a new hardening stage (IV) and a second recovery stage (V).

39.6.1 Stage of Upper and Lower Yield Points

The phenomena of upper and lower yield points was also observed in LiF. *Johnston and Gilman* [39.32] explained this phenomenon in terms of microscopic dislocation dynamics. In a constant-strain-rate uniaxial deformation test, the total strain rate can be split into its elastic and plastic components as

$$\dot{\epsilon} = \dot{\epsilon}_{pl} + \dot{\epsilon}_{el}.$$

At the beginning of the deformation, the plastic strain rate is low, due to the low initial dislocation density in semiconductors. The total strain rate is then mostly elas-

tic in origin, leading to a high initial rise in stress. This rising stress multiplies the dislocation density many-fold, leading to the plastic strain rate catching up and finally overtaking the total strain rate. As a result the stress actually falls, leading to a maximum: an upper yield point. The stress continues falling until dislocation interaction becomes important, leading to the hardening of the material, after a stress minimum: the lower yield point. *Alexander and Haasen* [39.33] reformulated the theory by Johnston, for semiconductors, to explain the yield phenomenon.

The central tenet of their theory is the introduction of a variable N to denote the dislocation density in the crystal. The plastic shear strain rate on the only active slip system is given by the Orowan relation

$$\frac{d\gamma_{pl}}{dt} = bNv, \quad (39.13)$$

where b is the Burgers vector of dislocations, v is the mean velocity of the dislocations, and γ_{pl} is the plastic shear strain on the only active slip system. Since there is only one active slip plane in the crystal, the axial component of the macroscopic plastic strain tensor, ϵ_{pl} , is given by $\epsilon_{pl} = \phi\gamma_{pl}$, where ϕ is a geometrical factor relating the shear and the axial strains.

The velocity of dislocations in the slip system v is dependent on the resolved shear stress on that system and has been found experimentally [39.34] to be of the form

$$v = v_0 \left(\frac{\tau_{eff}}{\tau_0} \right)^m \exp \left(-\frac{Q}{k_B T} \right), \quad (39.14)$$

where m , τ_0 , Q , and v_0 are empirical constants depending on the semiconductor material and its doping, k_B is the Boltzmann constant, τ_{eff} is the effective resolved shear stress on a dislocation and is given by

$$\tau_{eff} = \tau - A\sqrt{N}, \quad (39.15)$$

τ is the externally applied shear stress on the active slip system, and $A\sqrt{N}$ is the back-stress on a given dislocation due to the neighboring ones, which resist its movement through interaction. The square-root dependence of the back-stress on N is a classical one and was first derived by *Taylor* [39.35], based on an arrangement of parallel dislocations on a slip plane. Though the actual arrangement of the dislocations (the microstructure) was found to be much more complicated than that assumed by Taylor, this form of the back-stress has been found to be valid under a wide range of conditions and is widely used in work-hardening theory [39.36]. The

dislocations multiply as they move, resulting in evolution of the dislocation density. It is reasonable to assume that the multiplication rate is proportional to the dislocation density and the velocity of their movement. Thus the evolution of dislocation density can be modeled by

$$\frac{dN}{dt} = \delta N v. \quad (39.16)$$

Based on experimental evidence from [39.37] δ was assumed to be directly proportional to the effective stress τ_{eff} . *Alexander and Haasen* [39.33] opine that the multiplication mechanism is mainly due to the action of long jogs on screw dislocations, and the number of these jogs present is proportional to the effective stress, giving rise to the factor of τ_{eff} , therefore, $\delta = k\tau_{\text{eff}}$. Combining (39.13–39.16), the following two equations are obtained

$$\frac{d\varepsilon_{\text{pl}}}{dt} = \phi b N v_0 \left(\frac{\tau - A\sqrt{N}}{\tau_0} \right)^m \exp\left(-\frac{Q}{k_B T}\right), \quad (39.17)$$

and

$$\frac{dN}{dt} = k N v_0 \left(\frac{\tau - A\sqrt{N}}{\tau_0} \right)^{m+1} \exp\left(-\frac{Q}{k_B T}\right). \quad (39.18)$$

Equations (39.17) and (39.18) form a complete set of phenomenological models, which given the externally applied shear stress τ , can model the evolution of the plastic strain and dislocation density with time. They describe the yield region in the curve shown in Fig. 39.10 rather well, and can account for the occurrence of the upper and lower yield stress. In the stress–strain curve shown in Fig. 39.10, the total strain rate, which is the sum of elastic and plastic strain rates, is maintained constant. Hence

$$\dot{\varepsilon} = \phi \frac{\dot{\tau}}{G} + \dot{\varepsilon}_{\text{pl}} \quad \text{or} \quad \dot{\varepsilon} = \phi \frac{\dot{\tau}}{G} + \phi b N v \quad (39.19)$$

is held constant, where G is the shear modulus.

Equations (39.17–39.19) can be solved numerically to derive the stress–strain curve for constant-strain-rate compression tests. The results of these numerical solutions have confirmed the experimental observation that the upper and lower yield stresses are very sensitive to the strain rate, the temperature, and in some cases the initial dislocation density in the material. They replicate the experimental observation of the upper and lower yield stresses of the form

$$\tau_{\text{uy}} \propto \dot{\varepsilon}^{\frac{1}{n}} \exp\left(\frac{U}{k_B T}\right)$$

and

$$\tau_{\text{ly}} \propto \dot{\varepsilon}^{\frac{1}{n}} \exp\left(\frac{U_1}{k_B T}\right),$$

where τ_{uy} is the upper yield stress and τ_{ly} is the lower yield stress. *Alexander and Haasen* [39.33] through some approximations arrive at the results

$$\tau_{\text{uy}} \propto \dot{\varepsilon}^{\frac{1}{3}} \exp\left(\frac{Q}{3k_B T}\right) \left[\ln \dot{\varepsilon} + \left(\frac{Q}{k_B T}\right) - \frac{3}{2} \ln N_0 + \text{const.} \right]^{1/3}$$

and

$$\tau_{\text{ly}} \propto \dot{\varepsilon}^{\frac{1}{3}} \exp\left(\frac{Q}{3k_B T}\right) \left(A^2 b B_1 \right)^{1/3},$$

where $B_1 = v_0/\tau_0$, Q , A , v_0 , and τ_0 are parameters from (39.14) and (39.15) and m has been assumed to be 1. N_0 is the initial dislocation density. From the above analysis, the following conclusions can be drawn:

1. The numerical calculations from (39.17–39.19) predict the upper and lower yield stresses for a given deformation experiment. The predictions are quite accurate for a number of materials except that the lower yield stress is slightly underpredicted.
2. A log–log plot of the lower yield stress versus $1/T$, at constant strain rate, would yield a straight line, the slope of which is related to the quantity activation energy for dislocation velocity Q from (39.14). The same quantity Q can be estimated from dislocation velocity measurements and deformation tests. Values estimated independently from both methods have been shown to coincide for a number of semiconductor materials, thus giving an indirect validation of the above formulation [39.33].
3. The upper yield stress is shown to depend on the initial dislocation density. This is true for elemental semiconductors. In compound semiconductors such as InP and GaAs, the upper yield stress is experimentally seen to be independent of the initial dislocation density [39.38, 39]. This is because the dislocations present initially are locked in their position by impurities, and the surface acts as an effective source of dislocations. Hence the initial dislocation density does not play a big role in the deformation.
4. The lower yield stress is predicted to be independent of the initial dislocation density of the material. This is found to be true experimentally, with the

lower yield stress showing only weak dependence on the initial dislocation density. *Alexander* and *Haasen* [39.33] postulated that the state of the crystal at the lower yield point is a stationary state. In this state the dislocation density is at an optimum value, which gives a minimum stress for a given strain rate. The value of this optimum dislocation density was derived to be equal to $(4/9)\tau_{ly}^2/A^2$, which is independent of the initial dislocation density. Substituting the above result into (39.17), a state of plasticity of the form $f(\dot{\epsilon}, T, \tau_{ly}) = 0$ can be derived, independent of the state of the material at the beginning of the deformation.

5. The results of the uniaxial strain rate tests were compared with uniaxial, constant stress creep tests, with the material oriented for single slip. The generic shape of strain versus time is shown in Fig. 39.11. It can be seen that the inflexion point with strain ϵ_w has the largest strain rate. This again corresponds to a state of plasticity; the dislocation density at this point is again at the same optimum value, and the material is softest, corresponding to a maximum strain rate at this point. From the theory outlined above, this state of plasticity should satisfy the same relation as above: $f(\dot{\epsilon}_w, T, \tau) = 0$, as has been verified experimentally by *Völkl* [39.40].

Thus some level of understanding has been reached for the behavior in the yield regions, though there are still limitations to the theory as will be shown later. After the stage of the yield points, the stress-strain curve

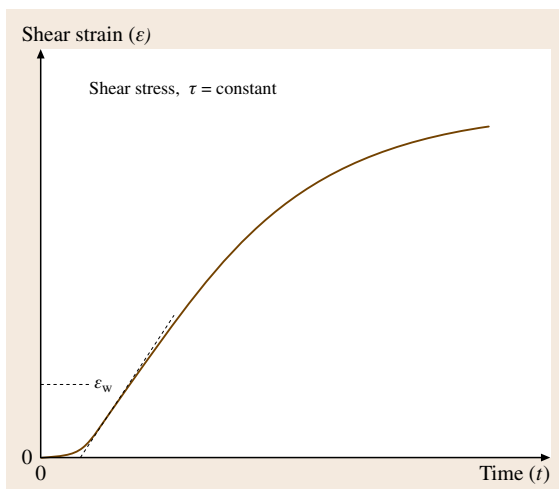


Fig. 39.11 Creep curve with specimen in single-slip orientation and constant applied stress

is followed by five more distinct stages at higher strains. Some of these stages are found only at higher temperatures and represent alternate stages of hardening and softening of the material due to phenomena such as cross-slip and climb of dislocations.

Stage I

This is also known as the stage of easy glide. In this stage, the dislocation structure changes from a predominance of screw dislocations in the yield regions to a predominance of edge dislocations, dipoles, and multipoles. This stage is characterized by low hardening.

Stage II

This stage is characterized by a constant hardening rate $\theta = d\tau/d\epsilon$, which is almost invariant with respect to temperature and strain rate changes. This value is also close to the hardening coefficients of stage II of fcc metals ($\approx 2.4 \times 10^{-3}G$, where G is the shear modulus of the material). The deformation in this region is characterized by inhomogeneity of dislocation distribution and a number of locally activated glide systems.

Stage III

This is characterized by the softening behavior of the crystal, during which the hardening coefficient decreases. This stage is also exhibited in fcc crystals, which might lead to assumptions about similar dislocation mechanisms operating in this range. However a detailed analysis of the temperature and strain rate dependence, together with metallographical investigations, reveals that stage III softening in semiconductors is due to climb of dislocations, while in metals it is due to cross-slip of dislocations. *Siethoff* and coworkers have extended the experimental data for this stage for Si and Ge [39.41], GaAs [39.42], and InP [39.43], and in [39.44] have fitted this data to the dislocation climb model of *Mukherjee* et al. [39.45] and the jog-dragging model of *Barret* and *Nix* [39.46]. They found the data to be more consistent with the jog-dragging model, which proposed the softening to be a consequence of interaction of point defects with dislocations when screw dislocations drag long jogs along with them. However, more light needs to be shed on this stage, before the final word can be said on deformation mechanisms of stage III.

Stages IV and V

These stages were discovered in Ge by *Brion* et al. [39.47] and occur only in a narrow tempera-

ture range below the melting point T_m . Stage IV, like stage II, is characterized by linear hardening, where the hardening coefficient is invariant with temperature and depends slightly on strain rate. Stage V is similar to stage III and is characterized by softening or dynamic recovery. Investigations have revealed the recovery to be due to the cross-slip of screw dislocations, and *Siethoff* [39.48] have fitted the data obtained for stage V to *Escaig's* theory for cross-slip of screw dislocations [39.49].

An important observation from experiment is the shrinkage of the stages with a rise in temperature.

Stages IV and V do not occur at low temperatures. As the temperature is raised, each of the stages begins earlier, i.e., at lower strain, in the deformation curves. This suggests that dislocation mechanisms that lead to stages II–V begin to operate earlier at high temperatures. The deformation, due to thermal stresses, in crystal growth processes is not expected to exceed stage I, but in areas of high temperature close to the melting point, such as the crystal–melt interface, mechanisms prevalent in the later stages such as cross-slip, climb, and interaction with point defects may be important.

39.7 Application of the Haasen Model to Crystal Growth

Völkl [39.40] was the first to use the above model to study dislocation generation in the Czochralski system. In this analysis, the entire thermal and thermal–elastic stress history of a given particle in the crystal, from the particle's evolution from the melt–crystal interface to the end of the growth process, is determined. The thermal–elastic stress history so determined is used to determine the resolved shear stress history on the highest stressed slip system; an unstated assumption by *Völkl* is that the same slip system is the most highly stressed throughout the growth history of the particle. The resolved shear stress history is designated $\tau_t^{\text{gs}}(t)$. *Völkl* assumes that, as the plastic deformation proceeds, the resolved shear stress relaxes or is dissipated by the plastic strain, and the residual elastic stress $\tau_{\text{er}}(t)$ is the driving force behind plastic deformation. The relaxation process can be described by

$$\frac{d\tau_{\text{er}}(t)}{dt} + \frac{G}{\varphi} \frac{d\varepsilon_{\text{pl}}}{dt} = \frac{d\tau_t^{\text{gs}}(t)}{dt}. \quad (39.20)$$

In conjunction with (39.20), (39.17), and (39.18) with τ replaced by $\tau_{\text{er}}(t)$ this leads to

$$\frac{d\varepsilon_{\text{pl}}}{dt} = \phi b N v_0 \left(\frac{\tau_{\text{er}}(t) - A\sqrt{N}}{\tau_0} \right)^m \exp\left(-\frac{Q}{k_B T}\right), \quad (39.21)$$

$$\frac{dN}{dt} = k N v_0 \left(\frac{\tau_{\text{er}}(t) - A\sqrt{N}}{\tau_0} \right)^{m+1} \exp\left(-\frac{Q}{k_B T}\right). \quad (39.22)$$

Since the thermal–elastic history $\tau^{\text{gs}}(t)$ has already been determined from the thermal history of the crystal, through a finite element code, (39.20–39.22) can be in-

tegrated simultaneously to obtain the final dislocation density N . The dislocation density, in the volume element, after it just emerges out from the melt is taken as a fixed constant N_0 , i.e., the initial condition

$$N|_{t=0} = N_0.$$

However, according to *Völkl* the final values of N are reasonably independent of the N_0 chosen. It is apparent that a choice of $N_0 = 0$ will lead to a singularity. *Völkl* justifies his assumption of single slip by observing that an exponential dependence of plastic deformation on stress will cause the most highly loaded slip system to act and thus release the stresses on all other slip systems. *Maroudas* and *Brown* [39.50] used an isotropic generalization of the plastic strain response in the Alexander–Haasen model and performed what they called an integrated analysis of crystal growth. *Tsai* [39.51] has also applied the Alexander–Haasen model to bulk crystal growth. He generalized the Alexander–Haasen model to an isotropic plastic response instead of assuming deformation on the most highly stressed slip system. *Tsai* et al. [39.52] later formulated a multislip generalization of the Alexander–Haasen model, involving all 12 slip systems active in the semiconductor crystal. *Lambropoulos* and *Wu* [39.53] applied the model to Czochralski growth of GaAs, and investigated the effect of the shape of the interface on the final dislocation generation, while *Miyazaki* and *Kuroda* implemented this model for Czochralski (CZ) growth, using a finite element technique [39.54].

The driving force behind deformation in the growing crystal is the thermal strain. Since thermal strains are small, the deformations are likely to fall within the yield region in Fig. 39.10, thus justifying the use

of the Alexander–Haasen model. However, there is no evidence that the thermal loading would favor the single-slip scenario. Moreover, as noted earlier, stages IV and V in Fig. 39.10 appear only at high temperatures. Higher temperatures are characterized by shrinkage of the stress–strain curves – the various stages occur at lower strains. This indicates that phenomena such as cross-slip and climb of dislocations, which dominate the later stages, become important at lower strains, for deformation at high temperatures. Thus, at tem-

peratures approaching the melting point of the crystal – for which little data is available – these phenomena might be important even in the yield-point region. A multislip generalization of the Alexander–Haasen model is therefore needed, with provisions for high-temperature phenomena such as cross-slip, climb, etc. A model by *Moosbrugger* [39.55] and *Moosbrugger* and *Levy* [39.56] considers several of these features for CdTe crystals, and is the most advanced of the Alexander–Haasen variants.

39.8 An Alternative Model

The Alexander–Haasen model, though impressive, suffers from certain drawbacks for its application to compound semiconductors, and even elemental semiconductors. It is well known that the structure of the lattice in semiconductors gives rise to different types of dislocations, for example, screw, α dislocations, β dislocations, etc. All of these have different mobilities, and each one of them is expected to follow a different relation of the type (39.14). Perhaps, the adoption of a single dislocation variable N and the characterization of the dislocation velocity by a single equation of the type (39.14) is insufficient. Moreover, equations of the type (39.14) have been experimentally verified only for certain range of temperatures and stresses, which do not quite cover the entire gamut of these occurring in the crystal growth process. The specification of the initial dislocation density N_0 is also problematic. What is N_0 in the growing crystal? *Völkl* [39.40] as well as other researchers, as mentioned in the previous section, assumed a certain low N_0 along with the claim that this does not affect the final result much. This claim might be true, but such a treatment means that the final grown crystal, even for Si, always contains dislocations, since the dislocations move and multiply even at small stresses. Such a situation is incompatible with daily experience, as silicon single crystals are grown without any dislocations.

The deformation experiments looked at so far are uniaxial creep or constant-strain-rate tests, where the crystal has been oriented for single slip. In multislip deformations, or in applications such as crystal growth, dislocations in many slip systems are expected to be active. Thus what is needed is a generalization of the Alexander–Haasen model, retaining the basic structure and ideas, but expanding it to include notions of multislip, different types of dislocations, modified mul-

tiplication laws, the possible effects of dopants, and some information on the initial dislocation sources in the crystal. Let us examine each of these issues to build a model.

39.8.1 Different Types of Dislocations

Semiconductors have a high Peierls energy, resulting in deep Peierls wells along the $\langle 110 \rangle$ directions. Consequently, the dislocations tend to align themselves along the $\langle 110 \rangle$ directions to minimize the energy. Thus typical dislocation loops tend to assume a hexagonal shape. Transmission electron microscopy (TEM) studies have shown that this condition holds when the dislocation density is low and the impurity concentration in the crystal is not too high [39.25, 27]. If the dislocation density is high, the local back-stresses between the dislocations will distort the hexagonal shape, and the dislocations may become curved, no longer lying in $\langle 110 \rangle$ directions. The conditions of low dislocation density might be expected to hold in crystal growth. X-ray topography by *Dudley* et al. [39.57, 58] shows long segments of screw dislocations aligned along the $\langle 110 \rangle$ directions, and hexagonal loops. The geometry

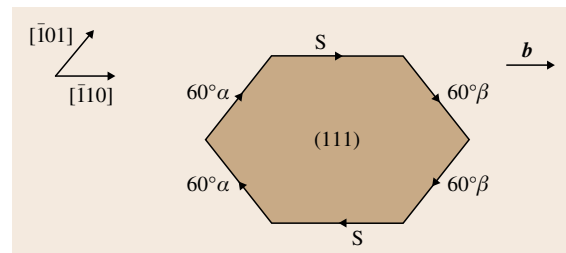


Fig. 39.12 Geometry of a hexagonal dislocation loop on the (111) plane.

of such a loop is shown in Fig. 39.12. Since there are three different dislocation types, the shear strain in this (111)[$\bar{1}10$] slip system is given by a straightforward extension of the Orowan equation

$$\dot{\gamma}_{\text{pl}} = (N_{\alpha}\bar{v}_{\alpha} + N_{\beta}\bar{v}_{\beta} + N_s\bar{v}_s)b, \quad (39.23)$$

where N_{α} , N_{β} , and N_s are the densities of α , β , and screw dislocations, respectively, in the (111) plane with the Burgers vector in the [$\bar{1}10$] direction. Here v_{α} , v_{β} , and v_s are the corresponding velocities, with the overbar representing an average. As the loop in the figure expands, it can be seen that the screw segments expand due to the movement of α and β segments, while these segments expand primarily by the movement of the screw dislocations. If the lengths of these segments are denoted by L_{α} , L_{β} , and L_s , their rate of change can be approximately given by

$$\dot{L}_{\alpha} = 2\bar{v}_s, \quad \dot{L}_{\beta} = 2\bar{v}_s \quad \text{and} \quad \dot{L}_s = 2(\bar{v}_{\alpha} + \bar{v}_{\beta}).$$

Since the evolution of the dislocation densities of α and β types are governed approximately by the same quantity, a good approximation would be

$$N_{\alpha} = N_{\beta}$$

and

$$\frac{N_{\alpha} + N_{\beta}}{N_s} = \frac{2\bar{v}_s}{\bar{v}_{\alpha} + \bar{v}_{\beta}}.$$

Substituting the above approximations into (39.23), we obtain the following approximation for the evolution of the shear strain

$$\dot{\gamma}_{\text{pl}} = 2N_s\bar{v}_sb.$$

Thus the evolution of the shear strain in a slip system is governed chiefly by the velocity and density of the screw dislocations in that system. Treatment similar to the above was first proposed by *Steinhardt* and *Haasen* [39.59] to explain results of creep experiments on GaAs, and was more clearly expounded by *Yonenaga* et al. [39.60], whom the above follows closely.

Since there are 12 {111}< $\bar{1}10$ > active in the lattice, the plastic shear strains on all of these have to be dyadically combined to get the total plastic strain rate, which is a second-order tensor. This can be expressed as

$$\dot{\epsilon}^{\text{pl}} = \sum_{i=1}^{12} N_s^i \bar{v}_s^i b (\mathbf{n}_i \otimes \mathbf{s}_i + \mathbf{s}_i \otimes \mathbf{n}_i) \text{sign}(\tau_i), \quad (39.24)$$

where index i represents the slip system, \mathbf{s}_i represents the slip direction of the slip system i , \mathbf{n}_i represents the

normal to the slip system i , N_s^i represents the density of screw dislocations on the slip system i , and \bar{v}_s^i is the average velocity of these dislocations. $\text{sign}(\tau_i)$ is the sign of the resolved shear stress along the slip system. Equation (39.24) represents a three-dimensional generalization of the Orowan equation (39.13), taking into account the geometry of a dislocation loop in compound semiconductors. The slip and slip plane normal vectors for the 12 slip systems are given in Table 39.1.

39.8.2 Dislocation Glide Velocity

The glide velocity of dislocations was investigated primarily for segments of the screw and 60° type mainly by the technique of producing dislocation half-loops through deliberate scratches on the surface of a semiconductor. Once the scratches are polished off, the material is subjected to loading (four-point bending, or tension or compression) and the glide velocities of the resulting dislocations are measured. This technique has been used for a wide range of temperature and stresses, and for various elemental and compound semiconductors. Following the work of *Chaudhuri* et al. [39.34] data has been collected for Si [39.61–63], and III–V semiconductors such as GaAs [39.59], InP [39.64–66], etc. A consensus exists regarding the results for measurements in the so-called central range of stress and temperature. *George* and *Rabier* [39.31] define this central range as

$$0.45T_m < T < 0.65T_m, \\ 5 \times 10^{-5} \mu < \tau < 10^{-3} \mu,$$

where T_m is the melting point of the material and μ is the shear modulus of the material.

The temperature and shear stress dependence of the glide velocity of screw and 60° segments is as follows.

In the central range of measurements, the temperature dependence of the dislocation velocities at constant stress is given by an Arrhenius-type law of the form

$$v \propto \exp\left(-\frac{Q(\tau)}{k_B T}\right),$$

where $Q(\tau)$ is a stress-dependent activation energy, τ is the shear stress acting on that slip system, and k_B is the Boltzmann constant. The activation energy Q is of the order of 1–2 eV in most semiconductors. The stress dependence of Q has been found to fall under two different regimes. For 60° dislocations in Ge, it is weakly stress dependent for stresses above 20 MPa, and is a strongly decreasing function of stress below this

stress. A similar transition stress of 10 MPa is found even for screw dislocations in Ge. In Si, the transition stress for 60° dislocations is 10 MPa, while none has been found for screw dislocations. The Arrhenius law has also been observed to breakdown in Si and Ge at some critical temperatures. *Farber* and *Nikitenko* measured 60° dislocation glide velocities up to temperatures of $0.9T_m$ in Si [39.63] and have observed some discrepancies. The velocities still depict an Arrhenius-type behavior, but the activation energy and prefactor are changed at temperatures above $0.75T_m$.

The dependence on stress of the dislocation glide velocity at constant temperature is conveniently described by a power law of the form

$$v \propto \exp(\tau^m).$$

Combining the above two dependencies, an overall dependence of the form

$$v = v_0 \left(\frac{\tau}{\tau_0} \right)^m \exp \left(-\frac{Q(\tau)}{k_B T} \right) \quad (39.25)$$

is obtained. This form is applicable for higher stresses, 20–100 MPa in Ge and > 30 MPa in Si, with constant m and Q . Below this range m and Q cannot be taken as constants. A double-logarithmic plot of v versus τ at constant temperature shows a bend. This is partly due to the stress dependence of $Q(\tau)$ below the critical stress mentioned above. *George et al.* [39.61] opine that, below the critical stress, Q can be expressed in the form

$$Q = Q_0 - E_i \ln \left(\frac{\tau}{\tau_0} \right).$$

Alexander [39.27] has explored the stress range above the critical stress for Si, and found that the parameter m depends not only on the type of dislocation but also on the glide system to which the dislocation belongs, and nonshear stress components etc. These complications are not well understood. However, *Sumino* [39.25] opines that the above complications are a result of impurities immobilizing the dislocations at low stresses, and also the many problem associated with the technique of measuring dislocation velocities described above. *Alexander* discusses these in reference [39.27]. *Imai* and *Sumino* [39.62] used a live x-ray topography technique to measure the velocity of dislocations in highly pure Si in the temperature range 600–800 °C and stress range 1–40 MPa. They found perfect agreement with (39.25), with $m = 1$, and $Q = 2.20$ eV for 60° dislocations and $Q = 2.35$ eV for screw dislocations.

Hence the use of (39.25) lies on shaky foundations with several opinions expressed regarding its form and range of usage for different materials. Several, theoretical models have been put forward to explain the phenomena of glide, a few of which will be reviewed, before a brief summary of literature about dislocation glide velocities in InP is presented.

Dislocation glide in diamond structured elemental and compound III–V semiconductors takes place through the formation and migration of double kinks. The theory has been formulated by *Hirth* and *Lothe* [39.6, Chap. 15]. They derived the nucleation rate of double kinks on a dislocation as

$$J = v_0 \frac{\tau b h}{k_B T} \frac{\exp(-2F_k - W_m)}{k_B T},$$

where v_0 is the Debye frequency, τ is the applied shear stress, $2F_k$ is the formation energy of a double kink under the action of a shear stress τ , W_m is the migration energy of the kink, b is the magnitude of the Burgers vector, and h is the kink height, or the distance between two Peierls valleys. For small kink densities or short dislocation segments, the double kinks traverse the entire length of the dislocation, without being annihilated, and the dislocation glide velocity is proportional to the length of the segment L . Hence

$$v = hLJ \text{ or } v = \frac{L\tau b h^2}{k_B T} \frac{v_0 \exp(-2F_k - W_m)}{k_B T}.$$

For long dislocation segments, the kinks are annihilated when they meet kinks of opposite sign, before they reach the ends of the segment. The mean free path X of the kinks in this case is given by

$$\frac{1}{\frac{X}{2}J} = \frac{X}{2v_k} \Rightarrow X = 2\sqrt{\frac{v_k}{J}},$$

where v_k is the kink velocity given by $v_k = (\tau b h)/(k_B T)v_0 a^2 \exp(-W_m/k_B T)$, where W_m is kink migration energy, and a is the jump distance of a kink.

In the case of long dislocation segments, the velocity is given as

$$v = hJX = 2h(Jv_k)^{\frac{1}{2}} = \frac{2v_0 \tau b h^2 a \exp(-F_k - W_m)}{k_B T}.$$

The above expressions suggest that the activation energy of dislocation glide would vary with the dislocation length; there exists a transition region between the two regimes. *Louchet* [39.67] confirmed this. He was able to observe that the velocity of long dislocation segments was independent of length, while the velocity

of short segments was proportional to their length. He determined the critical length for $\tau = 90$ MPa as $L_c = 0.4 \mu\text{m}$, which was interpreted as the mean free path of the kinks before annihilation. From these measurements, W_m and F_m were calculated separately, and both were of the magnitude of 1 eV. It was previously assumed that, analogously to fcc metals, the W_m in semiconductors was very small, and the presence of local obstacles along the dislocation was postulated to explain the discrepancy of a high W_m obtained. Theoretical treatments with this assumption presented by Celli et al. [39.68] and Rybin and Orlov [39.69] yield a very high density of obstacles, or a very high activation energy for dislocation glide velocities. The theory of local obstacles along the dislocation, opposing kink motion, is not accepted any longer, and it is now recognized that the high W_m is a result of a high secondary Peierls potential. The existence of a high Peierls means that migration of kinks is as difficult as their nucleation. This is related to the core structure of the partial dislocations, comprising the dislocation segment. It is believed that, in elemental semiconductors, the bonds on partial dislocations and kinks are reconstructed, except at certain defects along the core of the partials called solitons, or antiphase defects. It is only at these solitons that dangling bonds are present. The solitons play a direct role in the nucleation and migration of kinks, accounting for the same order of magnitude of the kink migration and nucleation energies.

Several analyses of the core structure of 90 and 30° partial dislocations, and estimates of W_m and F_k , have been performed [39.70, 71]. These analyses are based on atomistic simulations, using some empirical interatomic potentials, or ab initio methods, which are able to reproduce the quantum mechanical effects. These techniques, along with recently developed electron microscopy techniques [39.72] for the direct observation of movement and nucleation of kinks, should clarify W_m and F_k in the future. It should be pointed out that the above formalism is based on nucleation and migration of kinks in whole dislocations, while in reality the whole dislocation segments are split into partial dislocations. Möller [39.73] performed an analysis taking into account the presence of partial dislocations. He predicted the existence of a critical stress below which dislocation glide takes place through the correlated motion of the partials. At stresses above the critical stress, the glide took place with the movement of the two partials being independent. The correlated movement of partial dislocations has higher activation energy than the uncorrelated movement. This analysis somewhat repro-

duced the experimental observations in Ge and Si about the existence of two different regimes for the stress-dependence of the activation energy Q , described earlier in this section (Sect. 39.8.2). Möller's analysis was performed under the framework of local obstacles along the dislocation, and there is a need to adapt this to more recent ideas of a high secondary Peierls potential.

The influence of doping on the glide velocity of dislocations in semiconductors is well recorded. This is realized chiefly through electronic and metallurgical interaction. The metallurgical effect is classical and is relevant to any type of dopant or impurity in the semiconductor. It is a local effect and is due to the interaction between the impurity atom and the dislocation core. Another manifestation of this is the so-called locking stress, which certain impurities cause in certain semiconductors. At shear stresses below the locking stress, the dislocations are locked and do not glide and, once the shear stress exceeds the locking stress, the dislocations glide smoothly. Examples of this phenomenon are O, P, and S in Si. The electronic interaction is prevalent only for electrically active dopants or impurities when their concentration exceeds the intrinsic carrier concentration of the material. It has been found that III or V doping in elemental semiconductors affects the glide velocities in the same way irrespective of the size and chemical nature of the dopant. The primary influence of these electrically active dopants is that they change the Fermi energy level in the semiconductor. There are two classes of theories to explain the effect on dislocation glide velocity. Haasen [39.74] postulate that the line charge on a dislocation in a semiconductor depends on the position of the Fermi energy level. A charged dislocation has the formation energy of a double kink reduced, because of the electrostatic repulsion between the two kinks. This affects the dislocation glide velocity. Hirsch [39.75] postulated that the formation of a double kink leads to the generation of acceptor E_{ka} , or donor E_{kd} levels in the band gap. Charged as well as neutral kinks can exist on a dislocation, while the concentration of the neutral kinks is constant, the concentration of charged kinks depends on the position of the Fermi level (E_F), and the charged kink's own level in the spectrum. The concentrations of negatively and positively charged kinks are given by

$$\frac{C_k^+}{C_k^0} = \exp\left(\frac{(E_{kd} + eV) - E_F}{k_B T}\right)$$

and

$$\frac{C_k^-}{C_k^0} = \exp\left(\frac{E_F - (E_{ka} + eV)}{k_B T}\right),$$

where V is the gate voltage. The above formulae are derived by the application of Fermi–Dirac statistics. The concentration of neutral kinks is constant, and hence the dislocation glide velocity is directly dependent on the concentration of charged links. If the kink's level is near the middle of the energy gap – close to the Fermi level – increasing the n-type doping would raise the Fermi level and increase the concentration of negatively charged kinks and consequently dislocation velocity. Similarly increasing p-type doping will decrease the Fermi level and raise the concentration of positively charged kinks and consequently the dislocation velocity. Consequently both n-type as well as p-type materials will have higher dislocation velocity than the intrinsic material, as in the case of silicon. On the other hand, if the kink's level is near the valence band – much below the Fermi level – the intrinsic material will have negatively charged kinks. Increasing the n-type doping will raise the Fermi level and increase the concentration of negatively charged kinks raising the dislocation velocity, while a p-type doping will lower the Fermi level and decrease the concentration of negatively charged kinks and lower the dislocation velocity. Thus in materials where the kink's level is near the valence band, the velocity should increase from p-type to n-type material, as in Ge. This gives some understanding of the doping effect.

Finally the complications introduced by the splitting into partial dislocations and the existence of two different types of atomic species in compound semiconductors should be recognized. A 60° dislocation splits into a 30° and a 90° partial, and the mobility of each partial is different. The velocity of the whole 60° dislocation depends on which partial is leading in the direction of the movement. Thus the same dislocation might show asymmetry in velocity depending on the direction of the movement. In compound semiconductors, the velocity of α and β dislocations of the same type are expected to be different because of the different core structures. Thus, a review of the theoretical and experimental aspects of dislocation glide velocity reveals that, at this stage, the theory is not yet comprehensive enough to yield concrete relations for dislocation glide velocities that can be used in a microdynamical theory of plasticity. The best that can be done currently is to adapt an expression of the type (39.14), with constant m and Q , while recognizing its inherent limitations – that the parameters m and Q are stress and temperature dependent.

There is some data available on the direct measurement of the velocity of dislocations for InP. For undoped and sulphur-doped material, the velocity of

Table 39.2 Dislocation velocity data for undoped InP (after [39.64, 76])

Dislocation	v_0	m	Q (eV)
α	40 000	1.4	1.6
β	500 000	1.8	1.7
screw	40 000	1.7	1.7

α dislocations was reported by Nagai [39.65] in the temperature range 250 – 400°C . He fitted the velocities to a relation of the type (39.14), with $m = 2.7$, for both doped and undoped crystal. The value of Q was found to be constant, with $Q = 1.1$ eV for S-doped crystal ($6.5 \times 10^{18} \text{ cm}^{-3}$), and 1.0 eV for undoped InP. S doping was found to increase the velocity of α dislocations. Maeda and Takeuchi [39.66] set out to measure the effect of recombination-enhanced glide in InP crystal under the effect of minority carrier injection. In the course of their investigation, they measured the velocity dependence of β dislocations in S-doped crystal ($5 \times 10^{18} \text{ cm}^{-3}$) on temperature, in the range 220 – 410°C . They found a Q value of 1.6 eV. Yonenaga and Sumino [39.64, 76] investigated the velocity of all three types of dislocations in InP crystals – undoped, and with a variety of dopings. The temperature range of their measurements was 300 – 500°C , and stresses between 2 and 20 MPa. They fitted their data to an equation of type (39.14), with $\tau_0 = 1$ MPa. For undoped InP, they obtained the parametric fits presented in Table 39.2.

Yonnenaga and Sumino [39.64] have also obtained the corresponding parameters for material doped with Zn (p-doping), S (n-doping), and the isovalent impurities Ga and As. The dislocation velocity data in Table 39.2 is used in the modeling effort presented later.

39.8.3 Dislocation Multiplication

Dislocations being line defects, any movement of these will involve self-multiplication during motion and increase their lengths. If some parts of the dislocation loop are less mobile than others, the more mobile parts will move around in a spiral, increasing their length. In the loop shown in Fig. 39.12, the β segments are more mobile than the α segments, which are more mobile than the screw segments. Under the influence of stress, the β segments will move quickly through the material while screws will lag behind, resulting in an expansion of the screw segment's length. Another typical case is jogs, found on screw dislocation. These jogs are less mobile than the main dislocation; hence these lag behind,

Table 39.3 The type of interactions between dislocations of different slip systems (N: pair belong to cross-slip systems, G: pair form glissile junctions, H: Hirth locks, S: sessile junctions, C: pair belong to coplanar systems. The numbers in parentheses are f_{ij})

<i>i</i>	<i>j</i>	1	2	3	4	5	6	7	8	9	10	11	12
1			C(0)	C(0)	S(1)	G(0)	H(1)	N(0)	G(1)	G(1)	H(1)	S(1)	G(0)
2	C(0)			C(0)	G(1)	N(0)	G(1)	G(0)	S(1)	H(1)	S(1)	H(1)	G(0)
3	C(0)	C(0)			H(1)	G(0)	S(1)	G(0)	H(1)	S(1)	G(1)	G(1)	N(0)
4	S(1)	G(0)	H(1)			C(0)	C(0)	G(1)	N(0)	G(1)	G(0)	S(1)	H(1)
5	G(1)	N(0)	G(1)	C(0)			C(0)	S(1)	G(0)	H(1)	G(0)	H(1)	S(1)
6	H(1)	G(0)	S(1)	C(0)	C(0)			H(1)	G(0)	S(1)	N(0)	G(1)	G(1)
7	N(0)	G(1)	G(1)	G(0)	S(1)	H(1)			C(0)	C(0)	H(1)	G(0)	S(1)
8	G(0)	S(1)	H(1)	N(0)	G(1)	G(1)	C(0)			C(0)	S(1)	G(0)	H(1)
9	G(0)	H(1)	S(1)	G(0)	H(1)	S(1)	C(0)	C(0)			G(1)	N(0)	G(1)
10	H(1)	S(1)	G(0)	G(1)	G(1)	N(0)	H(1)	S(1)	G(0)			C(0)	C(0)
11	S(1)	H(1)	G(0)	S(1)	H(1)	G(0)	G(1)	G(1)	N(0)	C(0)			C(0)
12	G(1)	G(1)	N(0)	H(1)	S(1)	G(0)	S(1)	H(1)	G(0)	C(0)	C(0)		

while the more mobile part of the screw dislocation spirals around the jog, multiplying its length. Jogs can be formed either by the cross-slip mechanism, or by cutting of a screw dislocation by a forest dislocation in another slip plane. An example of this was shown by live topography of a dislocation multiplication process in silicon by *Sumino and Harada* [39.77], where a jog was formed on a screw dislocation by a 60° dislocation on a different slip plane cutting through it. The jog subsequently acted as a spiral center for multiplication. Dislocation multiplication can also occur by the Frank–Read mechanism, as was shown by an image of a Frank–Read source obtained by *Völkl et al.* [39.40]. The evolution of the dislocation density, through the dislocation multiplication, was modeled by the equation $dN/dt = k\tau_{\text{eff}}Nv$ in the Alexander–Haasen model. The basic premise of this equation was that the total length of dislocation created dN is proportional to:

1. The distance moved by the dislocation.
2. The length of already existing dislocations, since the longer the existing dislocations, the greater the probability of jogs forming on them.
3. The effective stress τ_{eff} in the equation is to represent the stress required by the spiraling segment in the parallel slip plane – which has been created by a jog – to pass the screw dislocation in the original slip plane.

Sumino and Yonenaga [39.76] retained the basic structure of the Haasen law and added to it features of multislip deformation and the different types of dis-

locations found in compound semiconductors. They introduced a dislocation multiplication law of the form

$$\frac{dN_s^i}{dt} = KN_s^i \bar{v}_f^i \tau_{\text{eff}}^i + K^* N_s^i \bar{v}_f^i \tau_{\text{eff}}^i \sum_{j \neq i} N_s^j, \tag{39.26}$$

where the index i represents one of the 12 slip systems, and the bar over the velocity denotes an average.

The above law models the evolution of screw dislocation density in all 12 possible slip systems in III–V compound semiconductors. The basic proportionality of the evolution rate to the dislocation density and velocity is retained. The average velocity of the fastest dislocation \bar{v}_f^i is used, since the expansion of a spiral and a loop is controlled by the velocity of the fastest segment, which in the case of InP is the β segment. The second term models the formation of jogs on screw dislocations and the consequent expansion through spiral formation. The rate of formation of jogs is proportional to the number of times dislocations in different slip systems cut each other, which can be modeled by a product of dislocation densities on the two slip systems.

Equation (39.26) can therefore be generalized as

$$\frac{dN_s^i}{dt} = KN_s^i \bar{v}_f^i \tau_{\text{eff}}^i + K^* N_s^i \bar{v}_f^i \tau_{\text{eff}}^i \sum_{j \neq i} f_{ij} N_s^j. \tag{39.27}$$

The f_{ij} are closely related to the formation of jogs. Following reference [39.78], the interaction between the dislocations of any pair of slip systems as categorized in Table 39.3 are:

1. Pairs belonging to two cross-slip systems such as 11 and 9, denoted by “N” in Table 39.3. When the dislocations of such systems cross each other, two kinks are formed, and no jogs result.
2. Pairs forming a Hirth lock. When the dislocations of such systems cross each other, jogs are formed on both dislocations. “H” denotes such interactions in Table 39.3.
3. Pairs that are in the same plane, and whose resulting Burgers vector is therefore on the same plane as the original ones. These interactions do not result in jogs on either system, and are denoted by “C” in Table 39.3.
4. Pairs forming glissile junctions, such as systems 1 and 12 in Fig. 39.1. The interaction between such systems produces a jog on one and a kink on the other. For example, if the dislocations of the two slip systems 1 and 12 pass, a jog is formed on slip system 12, while a kink is formed on slip system 1. The interactions between systems forming glissile junctions are denoted by “G” in Table 39.3.
5. Finally, the last type of interaction is between the pairs of systems forming sessile junctions, such as 4 and 1. When the dislocations of two such systems interact, they form stable Lomer–Cottrell locks, and impede the motion of both original dislocations. Such pairs are denoted by “S” in Table 39.3.

Alternatively, if the dislocations cross each other, a jog is formed on each one. The f_{ij} are assigned values of either 1 or 0 in Table 39.3 based on whether a jog is formed on a screw dislocation of system i when cut by a forest dislocation of system j . Equations (39.24) and (39.27) form a complete viscoplastic system with 12 internal variables. The meaning of the effective stress τ_{eff}^i is clarified next.

39.8.4 Work Hardening

The flow stress can be classically split into a rate-dependent term and a hardening term, independent of the strain rate and temperature. The rate-dependent part of the applied stress is used to overcome the frictional resistance of the lattice to the glide of a dislocation, which is temperature sensitive. The rate-independent part is the resistance from interaction with other dislocations, both in the same slip system as well as threading dislocations in other slip systems, and finally impurities. In the single-slip model described before, the work-hardening term was given by $A\sqrt{N}$. Taylor [39.35] first introduced this form, drawing from

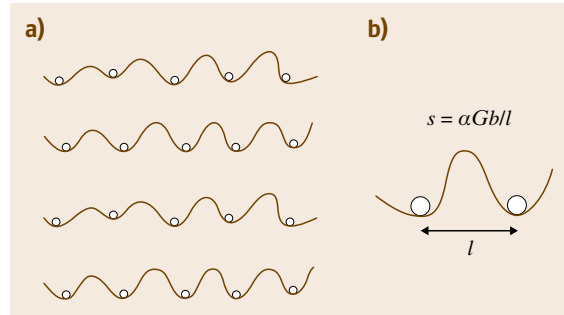


Fig. 39.13 (a) A series of dislocations facing barriers in the glide plane, and (b) a dislocation link stuck in an obstacle of strength s

theoretical treatment of the elastic interaction between parallel dislocations. The elastic theory of dislocations gives the magnitude of A as $Gb/(2\pi(1-\nu))$, where G is the shear modulus and ν is the Poisson ratio. Moulin et al. [39.79] conducted a mesoscopic simulation, using discrete dislocation dynamics, for the yield point of Si, in a single-slip framework. From a fit of their data, they found the work hardening to be adequately defined by an equation of the type $A\sqrt{N}$, but the value of A was $1.48Gb/(2\pi(1-\nu))$. Interaction between dislocations of different slip systems gives rise to complicated hardening behavior. Apart from long-range elastic interactions, stable locks may form between dislocations of noncoplanar slip systems. Hirth and Lothe [39.6] discuss different types of locks, the most prominent of which are the Lomer–Cottrell lock and the Hirth lock.

Franciosi and Zaoui [39.78] have classified the different types of locks formed, and their efficiency in locking. These locks act as obstacles to other dislocations in the glide plane. Figure 39.13 shows a dislocation stuck between such obstacles. If a link of dislocation is stuck between two such obstacles of distance l (Fig. 39.13b) the shear stress s in the glide plane required to release the dislocation is of the order $s = \alpha Gb/l$, where G is the shear modulus, b is the Burgers vector, and α is some numerical factor.

Hence the resistance offered to the dislocation motion on a given glide plane is inversely proportional to $1/l$. Since l is the distance between obstacles, it is inversely proportional to the number of obstacles on the glide plane. The number of obstacles on a glide plane, due to forest dislocations on another glide system, say the α glide system, is proportional to $\sqrt{N_\alpha}$. Hence the total rate-independent resistance offered to dislocation motion in glide system β can be denoted heuristically

as

$$\sum_{\alpha \neq \beta} a_{\beta\alpha} \sqrt{N_\alpha} + \frac{Gb}{2\pi(1-\nu)} \sqrt{N_\beta}, \quad (39.28)$$

where the second term is the self-hardening term of the Alexander–Haasen model. An equation of the type (39.28) has been used in the literature to justify experimental observations on latent hardening in Cu [39.78].

The coefficients $a_{\beta\alpha}$ are phenomenological and might depend on many factors including (1) the geometry of the forest dislocation configurations, which determines the distance between the intersections of these with the primary glide plane, and (2) the strength of the locks formed, which might depend on other factors such as the stacking fault energy. *Franciosi* and *Zaoui* [39.78] classified the $a_{\beta\alpha}$ based on the strength of the locks which are formed. They classify them according to whether the dislocations belong to the cross-slip systems (interaction coefficient a_1), form Hirth locks (interaction coefficient a_2), belong to coplanar systems (interaction coefficient a_3), form glissile junctions (interaction coefficient a_4), or form sessile Lomer–Cottrell locks (interaction coefficient a_5). They found the a coefficients to increase linearly with the stacking fault energy, and the anisotropy in the a coefficients to increase with decreasing stacking fault energy.

Alexander and *Crawford* [39.80] determined the interactions of different slip systems through latent hardening experiments. The procedure they used was as follows: A Ge single crystal was deformed at constant strain rate in single-slip orientation up to stage I. The lower yield stress was noted. The crystal sample was cut into smaller samples, which were then deformed at the same strain rate. Each sample was aligned for single slip, in such a way that the other secondary glide systems become the most stressed systems. The lower yield stress in each of these cases was noted, and compared with the lower yield stress in the initial sample. The results were then analyzed in the framework of the Alexander–Haasen model, with an equation similar to (39.28) adopted as the formula for the back-stress. Normalizing the $a_{\alpha\beta}$ by Gb , they found the normalized coefficients to be: 0.37 for systems forming Lomer–Cottrell locks, 0.24 for systems forming Hirth locks, 0.35 for glissile locks, and 0.64 for the cross-slip system. Thus, the cross-slip system was found to have the largest hardening coefficient. These results are at variance with those of *Franciosi* and *Zaoui* [39.78] cited above. *Alexander* and *Crawford* [39.80] explain their observation by noting that the structure in the primary glide system at the begin-

ning of easy glide consists primarily of edge dipoles, and from the geometry it can be deduced that these intersect the cross-slip plane most effectively. In the case of crystal growth, the deformation structure is dominated by long screws, hence these coefficients should be expected to differ from those determined by *Alexander* and *Crawford* [39.80]. Also the stacking fault energy of InP is nearly four times smaller than that of Ge, hence the values might be expected to be more asymmetric.

Summarizing, an equation of the form (39.29) can be used for the hardening. Since the interaction coefficients are not available, one hopes to determine them from fitting deformation data in multislip and single-slip experiments. The effective stress is thus given by

$$\tau_{\text{eff}}^i = |\tau^i| - \frac{Gb}{\beta} (N_s^i)^{1/2} - \frac{Gb}{\beta^*} \sum_{j \neq i} g_{ij} (N_s^j)^{1/2}. \quad (39.29)$$

The g_{ij} are set as a_1 , a_2 , a_3 , a_4 or a_5 , depending on whether the entry in Table 39.3 is N, H, C, G or S.

39.8.5 The Initial Dislocation Density

One of the main issues in the application of the Alexander–Haasen model to crystal growth is the specification of the initial dislocation densities. An important question is: what is the dislocation density in just-solidified, virgin material near the interface? Dislocations can arise at the interface due to certain phenomena at the crystal–melt interface, such as the formation of inclusions. Such dislocations are known as growth dislocations. The phenomena giving rise to them are manifestations of instability in the crystal–melt interface, and are described qualitatively in [39.81, Sect. 6.2]. Postgrowth analysis has shown that growth dislocations usually arise at inclusions formed at the growth interface, intersect the interface, and are propagated along with the movement of the interface. When the crystal is grown under stress-free conditions, the growth dislocations intersect the interface at certain specific angles, depending on their Burgers vector, in order to minimize their elastic energy. Thus growth dislocations arise from inclusions, and under stress-free conditions propagate in straight lines, intersecting the interface at a predetermined angle [39.82]. This configuration is disturbed under Czochralski growth at high temperatures, where stresses and considerable plastic deformation are prevalent. Postgrowth analysis of InP single crystals has shown the absence of growth dislo-

cations. X-ray topographs by *Dudley et al.* [39.57, 58] show that most of the dislocations are glide or slip dislocations intersecting the sides of the crystal. They rarely intersect the crystal–melt interface. This can be interpreted to be due to the absence of the generation of dislocations due to interfacial phenomena in InP.

As discussed before, another mode for the nucleation of dislocations is the condensation of excess point defects into prismatic dislocation loops, or voids. This effect is aggravated in compounds such as GaAs, InP, and other binary compounds due to the presence of a narrow homogeneity region. In these systems, the stoichiometric compounds do not have the highest melting point; hence the first to solidify composition would be rich in one of the components. Thus, in the case of GaAs, the first to form solid is As rich, this As precipitates out during cool down, and precipitates of As are formed. These precipitates can give rise to dislocations. The modeling of point defect dynamics, and the clustering of these defects, is a complex process with many issues still unresolved.

Another important source of dislocations is surface damage. When the growing InP crystal emerges from the boric oxide encapsulant, the volatile phosphorous species can escape from the sides of the crystal, leading to extensive surface damage. This surface damage is a local distortion of the lattice and is a good site for dislocation nucleation. Under the influence of thermal

stresses, the dislocations thus nucleated at the surface can move to the interior of the crystal and multiply. The rate of evaporation of the phosphorous vapor is closely related to the ambient pressure in the furnace.

Another source of dislocations is the initial seed crystal used in the CZ process. Dislocations present in the seed may move into the freshly formed material and multiply there under the influence of stresses. The necking process invented by *Dash* [39.3] prevents the movement of dislocations from the seed to the growing crystal. The term *necking* arises from the shape of the crystal being grown. The diameter of the growing crystal is decreased from the seed to a minimum value before increasing the diameter again. Thus the crystal has a neck of minimum diameter. Attempts have been made to extend the necking technique to sulfur-doped LEC-grown InP by *Dudley et al.* [39.83]. The InP crystals so grown were analyzed using synchrotron white-beam x-ray topography (SWBXT). Figure 39.14a,b presents the topographs of (110) wafers of two different as-grown InP crystals – sample A corresponding to a crystal grown with a narrow neck, and sample B corresponding to a crystal grown without necking. Figure 39.14c shows a geometric sketch of the dislocations in both the crystals. An analysis of these topographs reveals that most of the dislocations in LEC-grown InP crystals originate from the seed–crystal interface, propagate via slip planes, and

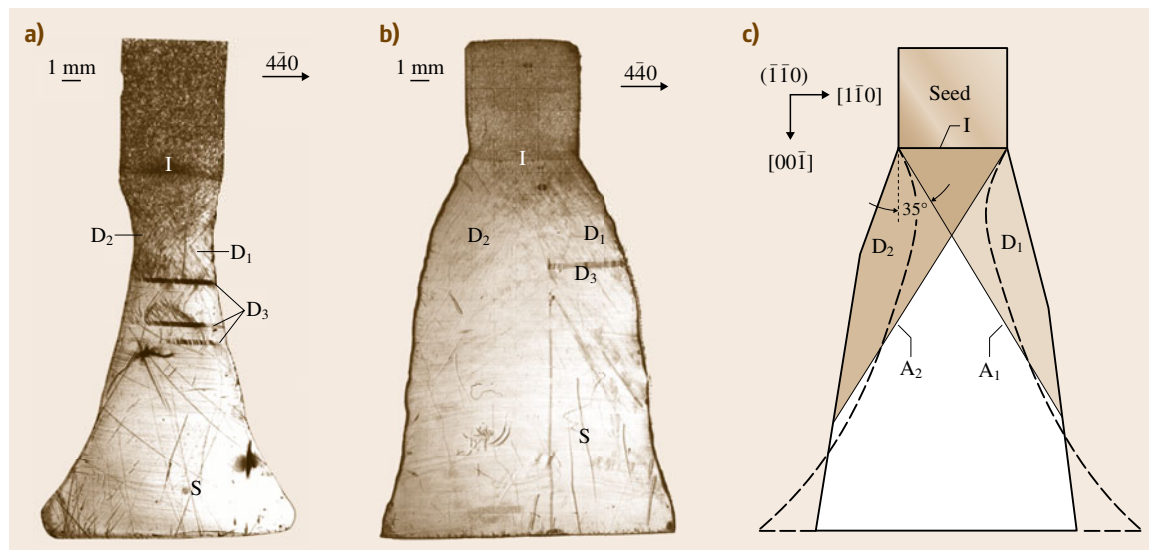


Fig. 39.14 (a) Sample A: X-ray topograph of (110) wafer of sulfur-doped InP crystal grown with a narrow neck. (b) Sample B: X-ray topograph of (110) wafer of sulfur-doped InP crystal grown without a narrow neck. (c) Schematic showing geometry and distribution of dislocations in as-grown crystals, for both shapes of crystals shown in (a,b) (after [39.83])

eventually exit the crystal through the periphery of the necked region. Based on this mechanism, dislocations exist only in the outer regions (dislocation regions) of the grown crystal separated by the four $\{111\}$ planes which are extended from the four edges of the seed bottom. In the cross-sectional view of Fig. 39.14c, two of these planes, $(11\bar{1})$ and $(1\bar{1}1)$, are represented by lines A_1 and A_2 , respectively. The regions of the crystal with dislocations are shaded, while those that are dislocation-free are unshaded.

As shown in Fig. 39.14c, the narrow necked portion of sample A makes the dislocation region much smaller than that of sample B. This means that the dislocations emerging from the seed-crystal interface in

sample A slipped out of the neck in much shorter distances than that in sample B. A pyramid-shaped crystal, which is nearly dislocation free, was quickly formed below the dislocation regions. The above experiment and conclusions show the necessity of considering the movement of dislocations from dislocated regions to regions containing no dislocations initially. Such a formulation can be established using the continuum theory of dislocations, and would resemble the strain-gradient theories in structure. Such a formulation would involve spatial gradients of internal variables, and is not amenable to solution on the length scales involving a typical crystal wafer. Hence this line has not been pursued.

39.9 Model Summary and Numerical Implementation

39.9.1 Summary of the Model

A complete set of equations for the boundary-value problem using the constitutive model derived are summarized here, followed by a brief description of the numerical procedure.

Equilibrium of forces

$$\nabla \cdot \boldsymbol{\sigma} = 0. \quad (39.30)$$

Compatibility

$$\boldsymbol{\varepsilon} = \frac{1}{2} \left(\nabla \mathbf{u} + (\nabla \mathbf{u})^T \right). \quad (39.31)$$

Split of total strain

$$\boldsymbol{\varepsilon} = \boldsymbol{\varepsilon}^{\text{el}} + \boldsymbol{\varepsilon}^{\text{pl}} + \boldsymbol{\varepsilon}^{\text{th}}. \quad (39.32)$$

Constitutive relation for thermal strain

$$\boldsymbol{\varepsilon}^{\text{th}} = \alpha \delta (T - T_0). \quad (39.33)$$

Constitutive relation for elastic strain

$$\boldsymbol{\varepsilon}^{\text{el}} = \mathbf{C}^{-1} : \boldsymbol{\sigma}. \quad (39.34)$$

Evolution equation for plastic strain and dislocation densities

$$\dot{\boldsymbol{\varepsilon}}^{\text{pl}} = \sum_{i=1}^{12} N_s^i \bar{v}_s^i b(\mathbf{n}_i \otimes \mathbf{s}_i + \mathbf{s}_i \otimes \mathbf{n}_i) \text{sign}(\tau_i), \quad (39.35)$$

$$\frac{dN_s^i}{dt} = K N_s^i \bar{v}_f^i \tau_{\text{eff}}^i + K^* N_s^i \bar{v}_f^i \tau_{\text{eff}}^i \sum_{j \neq i} f_{ij} N_s^j. \quad (39.36)$$

Auxiliary equations

$$\tau_{\text{eff}}^i = |\tau^i| - \frac{Gb}{\beta} (N_s^i)^{\frac{1}{2}} - \frac{Gb}{\beta^*} \sum_{j \neq i} g_{ij} (N_s^j)^{\frac{1}{2}}$$

and

$$\tau^k = \mathbf{n}_k \cdot \boldsymbol{\sigma} \cdot \mathbf{s}_k.$$

Related parameters

The values of K , K^* , β , β^* , and the interaction coefficients g_{ij} are obtained by fitting the data to results from the single-slip uniaxial compression tests at a constant strain rate. These tests were simulated using the model, and fitted to data in [39.76, 84]. The values obtained were: $K = 13 \times 10^{-6} \text{ Pa}^{-1} \text{ m}^{-1}$, $K^* = 8 \times 10^{-15} \text{ m/Pa}$, $\beta = 3.3$, $\beta^* = 1.0$, $a_1 = 0.33$, $a_2 = 0.33$, $a_3 = 0.33$, $a_4 = 1.2$, and $a_5 = 1.3$. More details can be found in [39.85].

The elasticity moduli C_{ijkl} (indicial notation is used here) are based on [39.86] with the assumption that the continuum behaves as a cubic crystal with only three independent parameters. The relevant values are $C_{ijkl} = 1.02 \times 10^{11} \text{ Pa}$ when $i = j = k = l$, $C_{ijkl} = 4.4 \times 10^{10} \text{ Pa}$ when $i = k \neq j = l$ or $i = l \neq j = k$, $C_{ijkl} = 5.7 \times 10^{10} \text{ Pa}$ when $i = j \neq k = l$, and $C_{ijkl} = 0.0$ in all other cases. The coefficient of thermal expansion α is assumed to vary in quadratic fashion from $4.869 \times 10^{-6} \text{ K}^{-1}$ at 0 K and $4.410 \times 10^{-6} \text{ K}^{-1}$ at 100 K to $5.75 \times 10^{-6} \text{ K}^{-1}$ at 1000 K [39.86]. The magnitude of the Burgers vector b is $4.15 \times 10^{-10} \text{ m}$ [39.87, Table 1].

39.9.2 Numerical Implementation

A finite element technique can be adopted to obtain solutions of the boundary-value problem described above (indicial notation is used in this section). Briefly, this task involves the integration of the constitutive equations over time while ensuring equilibration of stresses in the body. Reference [39.88] gives a good description of the numerical implementation of viscoplastic equations. Assume that, at time t_n , the body is at equilibrium and that the set of displacements at each of the finite element nodes $\{\mathbf{u}_i\}_n$, and stresses $\{\sigma_{ij}\}_n$, plastic strains $\{\epsilon_{ij}^{\text{pl}}\}_n$, and the 12 internal variables $\{N_s^i\}_n$ at the finite element Gaussian points are all known. However between time t_n and the subsequent time t_{n+1} , the temperature has changed and hence the thermal strain has changed. The task is now to find the new displacements, stresses, plastic strain, and dislocation densities at time t_{n+1} . This is accomplished by the following procedure:

1. The finite element technique runs either a global Newton–Raphson iteration or a quasi-Newton iteration for the updated displacements $\{\mathbf{u}_i\}_{n+1}$ at time t_{n+1} . This global iteration is based on a discretized version of (39.30).
2. A guess is made at every nodal point in the finite element domain for the set of updated displacements at the k -th global Newtonian iteration $\{\mathbf{u}_i\}_{n+1}^k$. The updated strains, at every Gaussian point in the finite element domain, for the k -th iteration can be calculated using the discretized version of (39.31), and the thermal strain at time t_{n+1} can be calculated from (39.33), using the thermal fields at time t_{n+1} .
3. To update the stresses, plastic strains, and the dislocation densities, (39.35) and (39.36) are integrated for the time step $\Delta t = (t_{n+1} - t_n)$ with the help of (39.31–39.34) and the auxiliary equations, at every Gaussian point. The integration method can be either an implicit Euler scheme, or any first-order ordinary differential equation (ODE) integration scheme such as one of the Runge–Kutta methods. The algorithmic elasto-plastic tangent modulus $\{D_{ijmn} = \partial \sigma_{ij} / \partial \epsilon_{mn}\}_{n+1}^k$ can also be obtained for a given integration scheme. Refer to [39.85] for a detailed development using an implicit Euler scheme and a (2)3 Fehlberg pair, which is an explicit integration scheme.
4. Once the integration is completed, one obtains the stresses $\{\sigma_{ij}\}_{n+1}^k$ and the algorithmic elasto-plastic tangent modulus at every Gaussian point in the finite element domain. These are then inserted into the

global Newton–Raphson iteration, and the displacements at the next iteration $\{\mathbf{u}_i\}_{n+1}^{k+1}$ are obtained.

5. Steps 3 and 4 are repeated until equilibrium is attained in the body to the desired tolerance level. The variables have now all been updated to time t_{n+1} .

Steps 1–5 are repeated at each new time point from the seed to the completely grown and cooled crystal. At each time point the thermal loading (strains) in the crystal has to be updated based on the temperature field prevailing in the crystal. This temperature data can be obtained either from experiment or more realistically through computational fluid dynamics (CFD) and heat-transfer-based computational models of the entire high-pressure Czochralski process.

A second complication that has been so far ignored is the addition of new material during the growth process. This addition of virgin material can be modeled as the addition of a new layer of finite elements at certain time points. The frequency of the addition of these elements depends on the general length scale of the finite element grid. If the length scale of the grid is say ‘1’ mm then a new layer of finite elements, with average dimension ‘1’ mm, can be added at time intervals corresponding to growth of ‘1’ mm of material. Figure 39.15 shows a layer of new elements that has just been added to the original grid. This new layer of elements corresponds to the material that has just crystallized. Now a relevant question is: what are the values of the plastic strains $\epsilon_{ij}^{\text{pl}}$ and the dislocation densities N_s^i in the newly crystallized material. Since the material has just crystallized, the obvious answer would be to set both the plastic strain components as well as the dislocation densities to zero. However, there are a couple of problems with this approach.

Firstly, setting the initial dislocation densities to zero would ensure that this material is always dislocation free, as the dislocation density evolution rate would always be zero according to (39.36). To resolve this, the approach of Völkl [39.40] is followed and the initial dis-

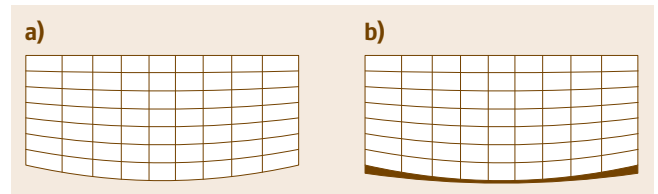


Fig. 39.15 (a) Two-dimensional projection of the grid system in the seed. (b) The grid system after 2 mm of growth. Shaded region represents the newly pulled material

location density is set to some finite but small positive value.

Secondly, setting the plastic strains to zero would give rise to huge stresses in the just-crystallized material, the reason being that nonfreshly crystallized (parent) parts of the crystal have significant plastic deformation, and the nodes on the interface between the two parts have significant displacement vectors to reflect this plastic strain. These displacements on the interface translate to large strains in the freshly crystallized material and large stresses, since this material behaves elastically due to the lack of plastic strain. This phenomenon as explained below is just a technicality. Before the crystallization of the new layer of elements, the present interface between the freshly crystallized material and the parent crystal was the crystal–melt interface, which is traction free. Hence the new layer of elements crystallize on a traction-free surface. Thus no stress from the parent crystal can propagate across this

surface into the freshly crystallized material. Hence if the thin layer of freshly crystallized elements is isothermal (which is a reasonable assumption) then the new layer of elements representing the freshly crystallized material should be stress free. So what leads to the high stresses described before? The answer is that the reference state corresponding to zero plastic strain for the freshly crystallized material is different from that for the parent crystal. Hence, in order to use the same reference state for the parent crystal as well as the freshly crystallized material, some plastic strain has to be added to the freshly crystallized material.

In conclusion, the freshly crystallized elements are added in a stress-free state. To accomplish this the plastic strains at the Gaussian integration points of the freshly added elements are set such that the stresses at these Gaussian integration points are zero. This approach has been used in all the results presented in Sect. 39.10.

39.10 Numerical Results

To be of any use, the viscoplastic model needs the complete thermal history of the crystal during the growth. Such detailed information has not yet been obtained experimentally for any specific case, hence the results have been derived from the temperature field history predicted by a CFD-based model of the high-pressure Czochralski process termed **MASTRAPP** (multizone adaptive scheme for transport and phase change processes) [39.89]. **MASTRAPP** is a two-dimensional axisymmetric CFD-based algorithm applied to a simplified domain of the furnace. It simulates the temperature and flow field history during the growth process; it includes phenomena such as heat conduction in the crystal, thermal radiation, convection in the melt and gas, radiation, moving crystal–melt interface, and latent heat generation, and can handle presence of different domains such as the gas, crystal, melt, and encapsulant, and the movement of the boundaries of these different domains during the growth process. The following inputs are required in **MASTRAPP** as macroscopic parameters specifying the growth process.

39.10.1 Strength of Convection in the Melt and Gas

The fluid flow and temperature distributions are a result of natural convection due to buoyancy forces, and forced convection due to the rotation of the crystal

and the crucible. The relevant nondimensional parameters for natural convection are the melt and gas Grashof numbers, and for forced convection are Re_s (the Reynolds number characterizing the crucible rotation) and Re_c (the Reynolds number characterizing the crystal rotation). For the Czochralski system shown in Fig. 39.2 with the diameter of the crucible being 100 mm and the height of the system – from the bottom of the crucible to the top of the heat shield – 170 mm, the Grashof numbers are of order 10^9 , and the Reynolds numbers are of order 10^4 . In papers dealing with numerical simulations of crystal growth, Grashof and Reynolds numbers an order of magnitude lower are used; the lower Grashof number can be justified by saying that they correspond to microgravity situations, and the lower Reynolds number to much lower revolution rates of the crystal and crucible than are typically used.

39.10.2 Temperature Boundary Condition

The reduced domain of Fig. 39.2 interacts with the other parts of the furnace through the specification of appropriate conditions at the boundaries of the reduced domain. Towards this the temperature on the crucible plus the heat shield is prescribed as a function of the distance from the base of the crucible in Fig. 39.2. The base of the crucible, and portions occupied by the melt, are maintained at 1435 K, and the temperature is lin-

early ramped down along the wall of the heat shield to a temperature of 427 K at the top. All the simulation results presented assume the boundary condition just described.

39.10.3 A Sample Case

A simulation of the growth of a flat-top 50 mm-diameter InP crystal from a height of 7–45 mm with a 20 mm height of encapsulation is used as a sample case. The gas and melt Grashof numbers are fixed at 10^6 , and the rotational Reynolds numbers at 500. The growth axis is along the [001] direction. The results presented below correspond to the end of the growth period, before the cooling of the crystal to room temperature.

Temperature Field in the Crystal

The primary reason for the thermal stress and the consequent plastic deformation is the incompatibility of the

thermal strain arising from the temperature field. The evolution of the axisymmetric temperature field and its gradients is shown in Figs. 39.16 and 39.17 respectively. At the beginning of the growth, when the seed has just thermally stabilized in the furnace, the isotherms show that heat enters the crystal from the sides and escapes from the top of the crystal. Hence the axial or vertical temperature gradient is higher in the upper parts of the crystal – of the order of 35 K/cm – than in the lower part. The radial temperature gradient is highest in the lower corners of the crystal, and is nearly zero in the central part of the crystal. As the crystal grows, the thickness of the encapsulant above the crystal decreases, thereby decreasing the thermal resistance to heat flow between the melt and the ambient gas; consequently the heat flux flowing through the crystal and the thermal gradients increase with growth.

The crystal just emerges out of the encapsulant at $t = 84$ min, and a direct pathway is established between

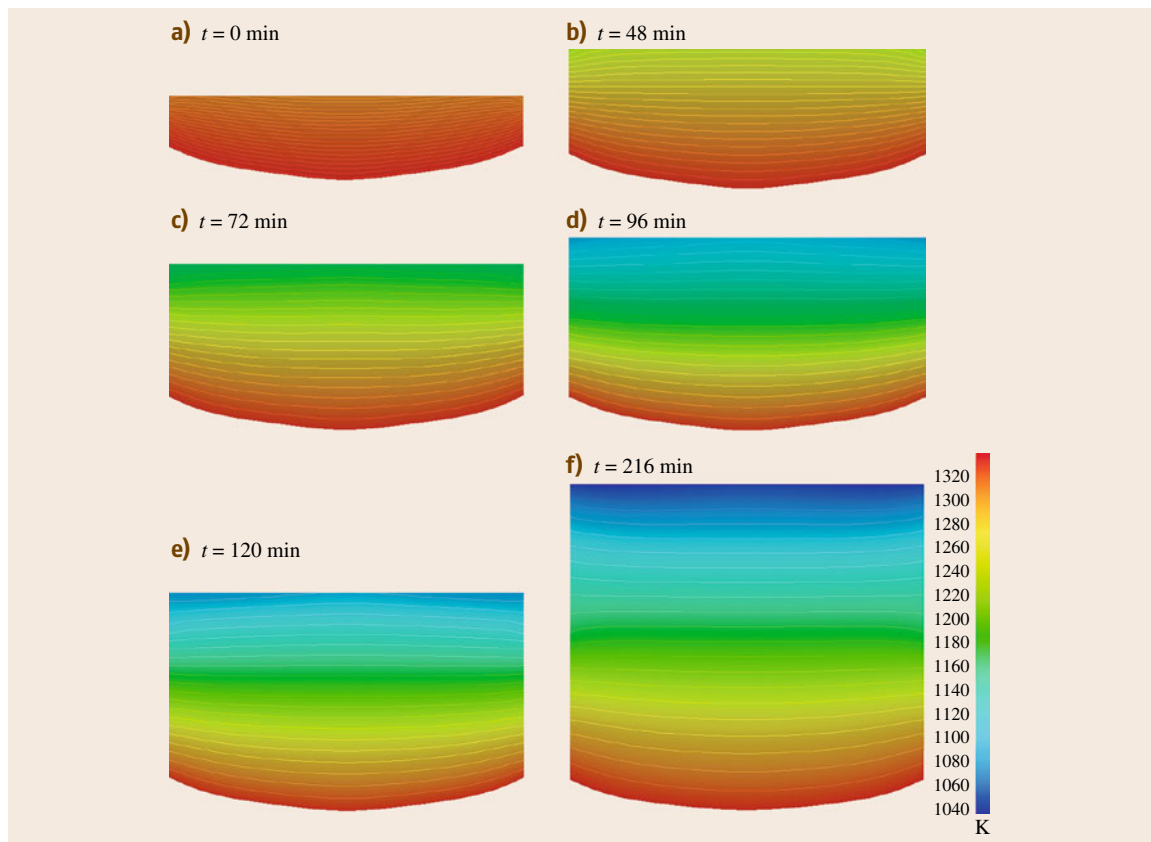


Fig. 39.16a–f Evolution of the temperature field in the growing crystal. The gas Grashof number is 10^6 , the melt Grashof number is 10^6 , the rotational Reynolds numbers are 500, and the encapsulant height is 20 mm

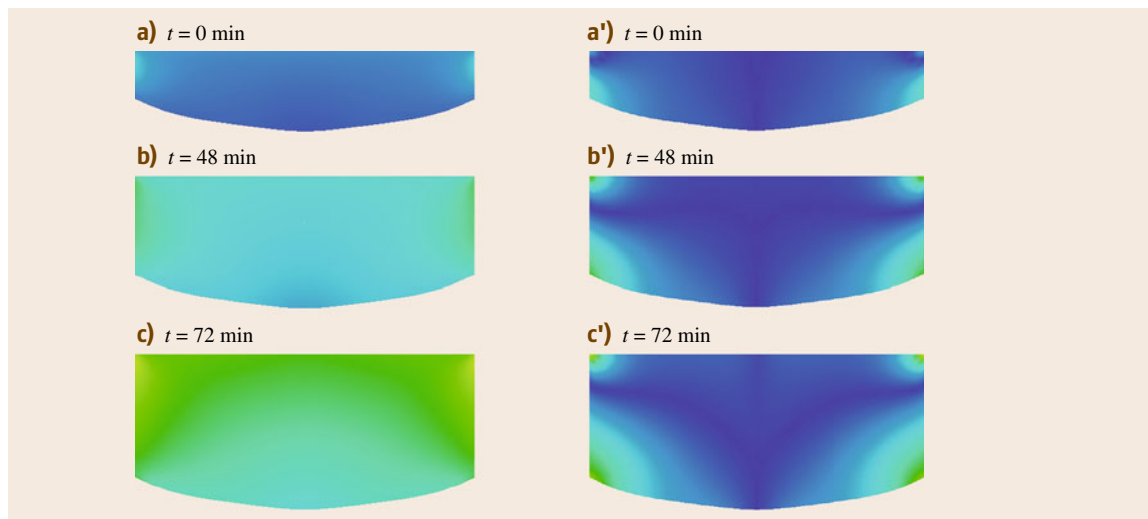


Fig. 39.17 History of thermal gradient field in the growing crystal. The gas Grashof number is 10^6 , the melt Grashof number is 10^6 , the rotational Reynolds numbers are 500, and the encapsulant height is 20 mm. Color scales for vertical and radial gradients are in (f) and (f'), respectively

the melt and the gas through the highly conducting crystal. Moreover, the lateral side of the part of the crystal above the encapsulant loses heat by convection and radiation to the cooler parts of the furnace, thus establishing a radially outward flow of heat, i.e., a radial temperature gradient. These give rise to a jump in the heat flux through the crystal. This is evident from comparing the frames at $t = 72$ min with the frames at $t = 96$ min in Fig. 39.17, when the top of the crystal is 1 mm below the encapsulant and 3 mm above the encapsulant respectively. In the latter frame the thermal gradients are appreciably higher. This change in the thermal profile and consequent high temperature gradients on emergence of the crystal from the encapsulant can be termed *thermal shock*.

As the crystal grows further, the length scale increases, while the temperature difference driving the heat flow between the melt and the gas remains the same; consequently vertical and radial temperature gradients decrease. The portion of the lateral surface of the crystal just above the encapsulant is hotter than the sidewalls of the furnace and loses heat by radiation and convection, leading to high radial temperature gradients in that region. Conversely, portions of the lateral surface of the crystal that are nearer to the top of the crystal are cooler than the side walls of the furnace and hence gain heat due to radiation from the sides of the furnace. Zou et al. report a similar behavior [39.22]. The radial temperature gradient is almost zero in most of

the crystal except on the lateral surface at three specific locations: the bottom corner of the crystal near the interface due to a radially inward flow of heat from the melt into the crystal, just above the encapsulant due to cooling by convection and radiation, and finally the top of the crystal due to heating of the lateral surface by radiation.

Summarizing, the thermal history of the crystal can be divided into three stages:

1. Low thermal gradients, when the crystal is below the encapsulant and the gradients increase with growth
2. The thermal shock, when the crystal grows out from beneath the encapsulant, resulting in a jump in the thermal gradients
3. The later stages of the growth, characterized by decreasing temperature gradients and practically zero radial gradients.

Except for in three regions on the lateral surface of the crystal: one near the interface, the other just above the encapsulant, and the third at the top of the crystal (Fig. 39.17f). The crystal experiences maximum temperature gradients when it has just emerged from the encapsulant. The vertical temperature gradients obtained from the simulation, in the range of 50–100 K/cm, are of the same order as those reported in experiments with both GaAs [39.90] and InP [39.91].

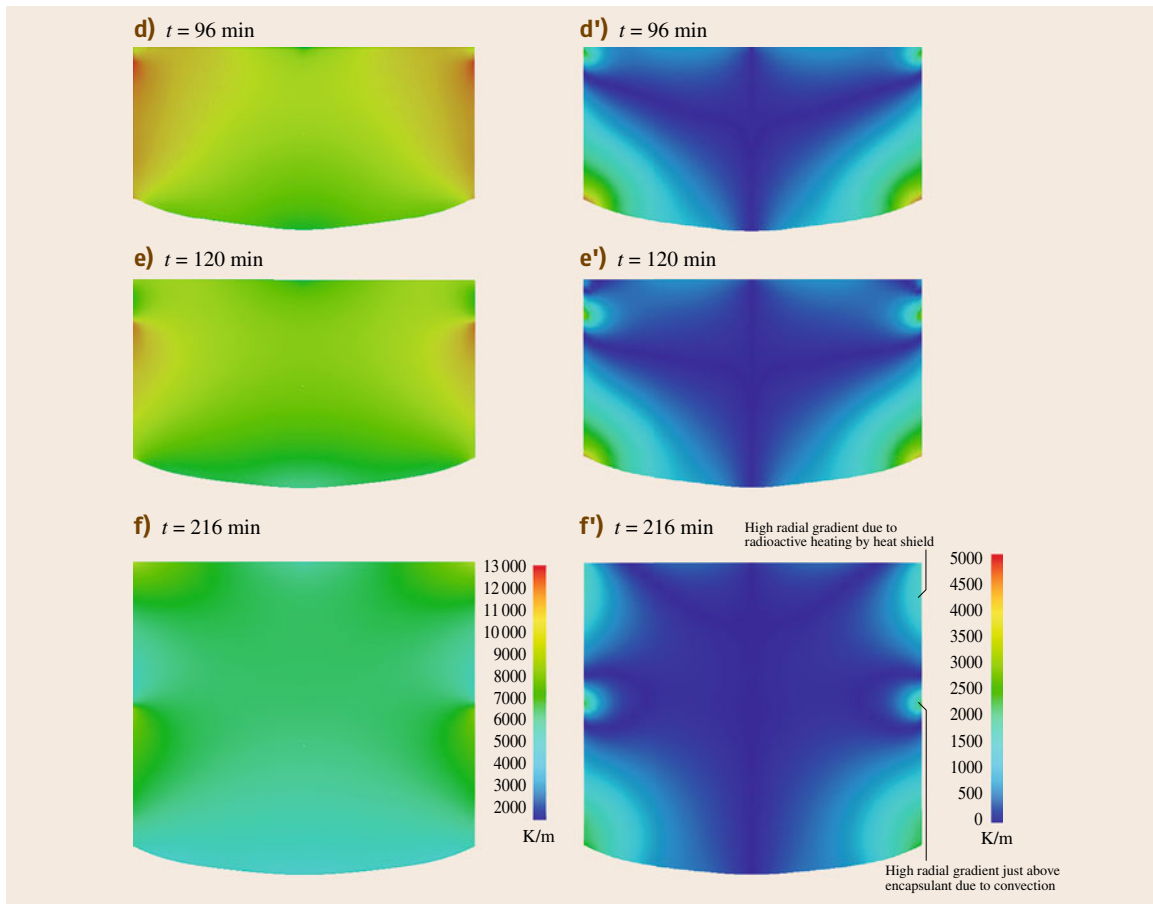


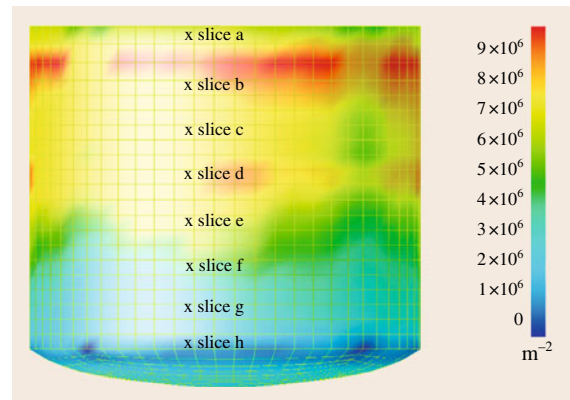
Fig. 39.17 (cont.)

Dislocation Densities after Growth Period

Figure 39.18 shows a fully grown crystal at the end of the growth period, with the colors representing the total dislocation density. The order of magnitude of the highest total dislocation density is around $1 \times 10^7 \text{ m}^{-2}$ and occurs near the top of the crystal. For a closer inspection of the total dislocation density, Fig. 39.19 shows the distribution on (001) slices, taken at various heights of the crystal, the position of each being indicated in Fig. 39.18. On all the slices, except slice h, the dislocation density is highest near the circumfer-

Fig. 39.18 Total dislocation density at the end of the growth period of a [001]-grown crystal. The vertical position of the various horizontal slices is indicated. The gas Grashof number is 10^6 , the melt Grashof number is 10^6 , the rotational Reynolds numbers are 500, and the encapsulant height is 20 mm ►

ence and lower towards the center. On slices a, f, and g (not shown) the dislocation density variation corresponds to the w-shaped variation mentioned often in



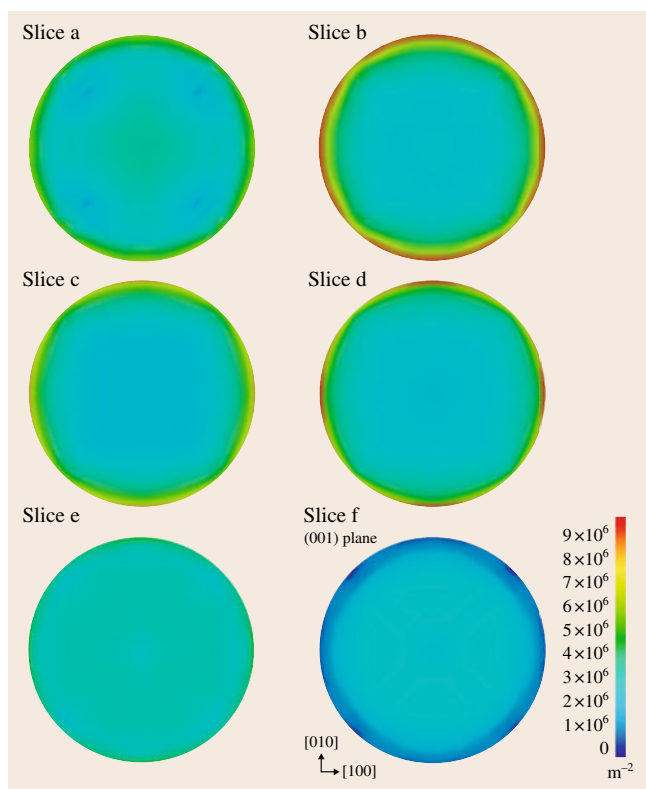


Fig. 39.19 Total dislocation densities at the end of the growth period projected on the (001) slices. The position of the various slices was indicated in Fig. 39.18. The gas Grashof number is 10^6 , the melt Grashof number is 10^6 , the Reynolds numbers are 500, and the encapsulant height is 20 mm

literature [39.12, 90, 92] – the dislocation density is highest on the circumference, initially decreases as one moves radially towards the center, and then increases. The dislocation density patterns on all the slices exhibit fourfold symmetry, and reflect the symmetry of the slip systems with respect to the [001] growth axis. All the slices, except slice h, exhibit distinct areas of low dislocation density aligned along the $\langle 110 \rangle$ directions and areas of highest density along the $\langle 100 \rangle$ directions, consistent with etch-pit observations [39.12, 93]. The values for total dislocation density are in the range $2 \times 10^6 - 1 \times 10^7 \text{ m}^{-2}$. It should be pointed out that the values of dislocation density are not those in the final crystal but only the fully grown crystal at the end of the growth period, with the cooling-down period still remaining. Figure 39.20 shows a KOH-etched LEC-grown GaAs(001) wafer from the work of Buchheit et al. [39.94]. The etch pit configuration in this figure is

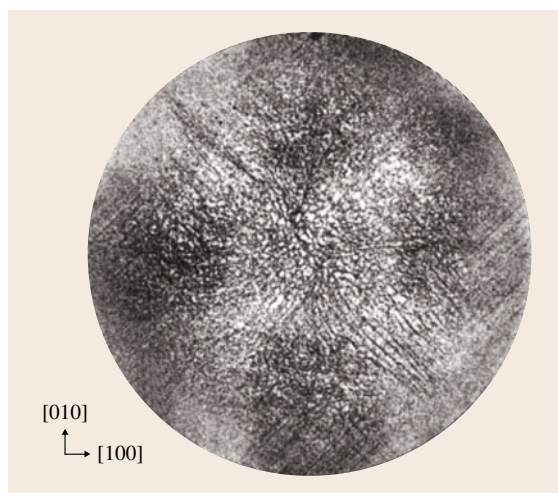


Fig. 39.20 KOH-etched (001) slice of GaAs (after [39.94], with permission)

similar to that of slice a in Fig. 39.19. A similar configuration can be seen in the work of Chung et al. [39.57, 58] from x-ray topographs of LEC-grown (001)InP wafers.

Distribution of Dislocation Density on the Individual Slip Systems

Due to the symmetry of the [001] growth axis [39.95, Fig. 1], the dislocation density distributions of slip systems 1, 2, 5, 6, 7, 9, 10, and 11 on a (001) cross-section are inherently the same and can be transformed from one to the other by simple operations such as reflection and rotation by some angle. Similarly, by symmetry considerations the dislocation density distributions of slip systems 3, 4, 8, and 12, on any (001) cross-section are identical except that they are rotated with respect to each other by multiples of 90° . Hence, the dislocation density on slip systems 1 and 3 is presented, as each is representative of the other systems with which it shares symmetry.

Figure 39.21a shows the density of dislocations belonging to slip system 1, projected onto slice b. Notice the location of the maximum on the circumference. It was found by inspection that the maximum occurs on the circumference and at the same angular orientation in a majority of the slices. Similarly, Fig. 39.21b shows the density of dislocations belonging to slip system 3 on slice b. In this case too, the dislocation density maxima always occur on the circumference and at the same angular locations for most of the slices. The angular orientations of the maxima might reveal the dominant stress component responsible for the multiplication of

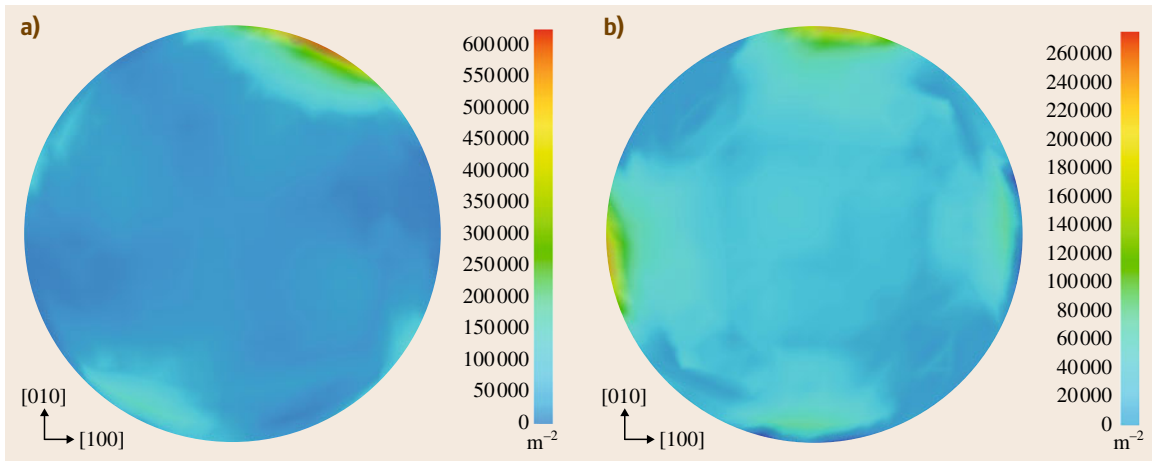


Fig. 39.21a,b Dislocation densities of slip systems 1 and 3 on slice b. The slip plane normal and slip direction for system 1 are $(11\bar{1})$ and $[101]$, and for system 3 are $(11\bar{1})$ and $[1\bar{1}0]$. **(a)** Density of dislocations belonging to slip system 1. **(b)** Density of dislocations belonging to slip system 3

dislocation densities. Since the temperature field is axisymmetric, an assumption of isotropy (for the purpose of analysis) would imply that the elastic strain field driving the deformation would be axisymmetric, and it would be appropriate to think in terms of axisymmetric stress components in cylindrical coordinates – σ_{rr} , $\sigma_{r\theta}$, σ_{rz} , $\sigma_{\theta\theta}$, $\sigma_{\theta z}$, and σ_{zz} . A useful exercise would be to isolate the effects of each of these components, by setting one of them to unity and the rest to zero, and plot the variation of the resolved shear stress on systems 1 and 3 with the polar angle. This might help explain the angular orientations of the location of the maxima for dislocation densities of slip systems 1 and 3. The results for slip system 1 are shown in Fig. 39.22a, while those for slip system 3 are shown in Fig. 39.22b. In both these figures $\sigma_{\theta\theta}$ is set to 1 and the rest to 0. A comparison of these figures with the distribution of dislocation densities on the (001) slice shown in Fig. 39.21a,b shows that the circumferential component $\sigma_{\theta\theta}$ dominates the deformation at least near the outer circumference of the slice. The reason for this is that the maxima in the resolved shear components on slip systems 1 and 3 due to $\sigma_{\theta\theta}$ occur at the same polar angles, where the dislocation density on these slip systems is high. The exercise was repeated with components other than $\sigma_{\theta\theta}$, but the polar angles of the maxima did not correspond to the polar angles of dislocation density maxima in those cases.

The deformation is multislip in some regions of the crystal. For example, consider the maximum in total dislocation density present on the circumference of slice b in the $[010]$ direction (Fig. 39.19). In this region slip

systems 1, 3, 4, and 6 are almost equally active and their dislocation densities are found to be of the order of $2.5 \times 10^6 \text{ m}^{-2}$ (Fig. 39.21a), $2 \times 10^6 \text{ m}^{-2}$ (Fig. 39.21b), $2 \times 10^6 \text{ m}^{-2}$, and $2.5 \times 10^6 \text{ m}^{-2}$, respectively. By symmetry, the other three maxima in total dislocation density present on the circumference are also composed of four, almost equally active slip systems. Similarly, multislip activity is present in the central parts of slice b. The total dislocation density here (Fig. 39.19) is of the order of $2.5 \times 10^6 \text{ m}^{-2}$. Dislocations belonging to each of the slip systems 1, 2, 5, 6, 7, 9, 10, and 11 have an approximate density of $2 \times 10^5 \text{ m}^{-2}$ and those belonging to each of slip systems 3, 4, 8, and 12 have a density of almost $2.5 \times 10^5 \text{ m}^{-2}$. Thus the total dislocation den-

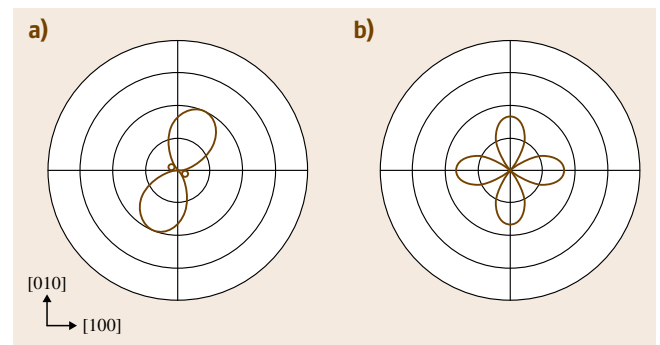


Fig. 39.22 Polar plot of resolved shear stress on slip systems 1 **(a)** and 3 **(b)**, with circumferential stress component set to 1 and all others to 0. The slip-plane normal and slip direction for system 1 are $(11\bar{1})$ and $[101]$, and for system 3 are $(11\bar{1})$ and $[1\bar{1}0]$.

sity in the central parts of slice b is due to almost equal activity on all the slip systems.

39.10.4 Effect of Gas Convection and Radiation

The effect of radiative interaction of the lateral walls of the crystal with the furnace walls on the dislocation generation was isolated by artificially setting the radiative term to zero. The final total dislocation density field was observed to be practically the same as the case without radiation.

The effect of gas convection was investigated by setting the gas Grashof number to zero, while retaining radiation. Figure 39.23a shows the total dislocation density projected on a (010) surface after the end of the growth for this simulation. The total dislocation density in the case without gas convection is less than that in the case with gas convection – Grashof number 10^6 (Fig. 39.23b) – by more than a factor of 2. Thus

a significant observation that can be made here is that radiation interaction of the sides of the crystal with the furnace does not significantly affect the dislocation density, while gas convection does.

Figure 39.23c shows a projection of the total dislocation density on the (010) plane at the end of the growth period (216 min) for a gas Grashof number of 10^7 . The maximum dislocation density is now in the range of $3 \times 10^7 \text{ m}^{-2}$. Similarly Fig. 39.23d shows the total dislocation density for the case of Grashof number 10^8 . It is interesting to note that the maximum dislocation density doubled from 4×10^6 to $9 \times 10^6 \text{ m}^{-2}$ for the case between no gas convection and Grashof number 10^6 , while a further tenfold increase in the gas Grashof number to 10^7 tripled the maximum dislocation density to $3 \times 10^7 \text{ m}^{-2}$, and another tenfold increase of the Grashof number to 10^8 further increased the maximum dislocation density to the range of $2 \times 10^8 \text{ m}^{-2}$. This confirms that gas convection plays a significant role in the evolution of the dislocation densities.

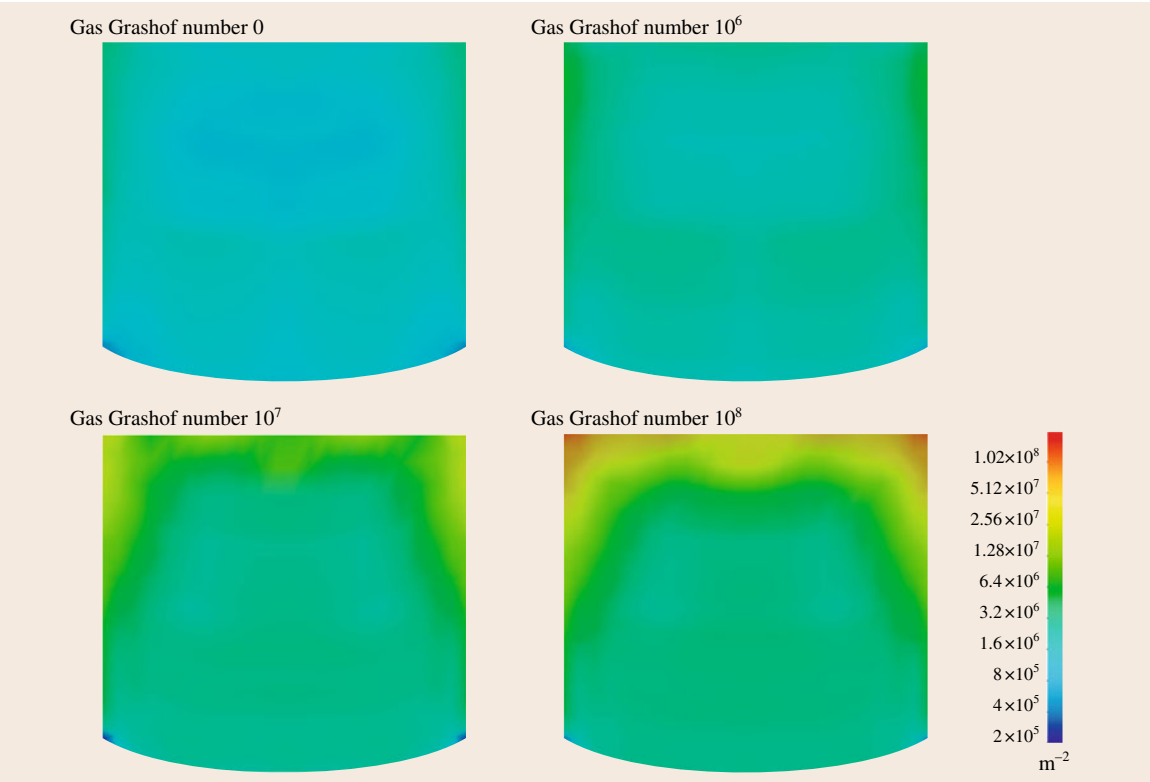


Fig. 39.23 Projection on the (010) plane passing through the growth axis, of the total dislocation density at the end of the growth period for different strengths of gas convection in the furnace. The melt Grashof number is 10^6 , the Reynolds numbers are 500, and the encapsulant height is 20 mm in all cases

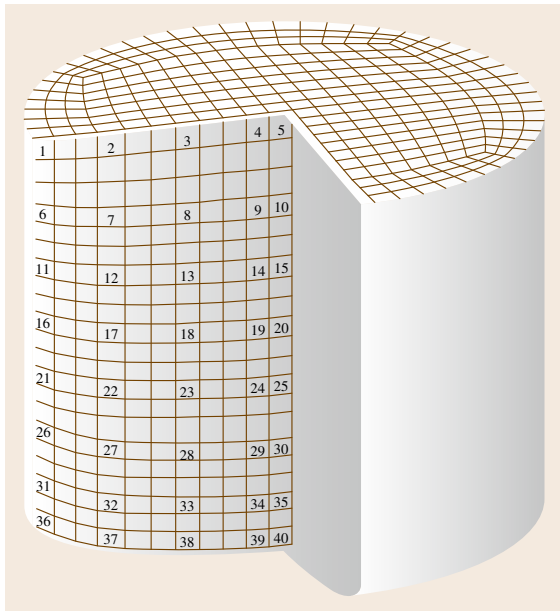


Fig. 39.24 Location of the various sample points, the history of which will be followed

The results for the total dislocation density at the end of the growth period for all the cases presented so far (growth with encapsulant height 20 mm with gas convection Grashof numbers of 0, 10^6 with radiation from the sides, 10^7 , and 10^8) are now analyzed on the grid of points 1–40 located as shown in Fig. 39.24. The total dislocation density evolution history at point 1, for the cases of no gas convection and for gas Grashof numbers 10^6 , 10^7 , and 10^8 , is presented in Fig. 39.25. The difference in dislocation density evolution history between the four cases again brings out the importance of gas convection. The dislocation density at point 1 is very low until a time of about 5500 s, and starts rising rapidly after this period. This timeframe corresponds to the period when the top of the crystal emerges from beneath the encapsulant (thermal shock).

39.10.5 Melt Convection and Rotation Reynolds Numbers

Melt Convection

In the calculations presented above, the Grashof number for melt convection was set at 10^6 , while in real life it is closer to 10^8 . Stronger melt convection might lead to increased heat flow through the crystal, and also affect the curvature of the crystal–melt interface. *Lambropou-*

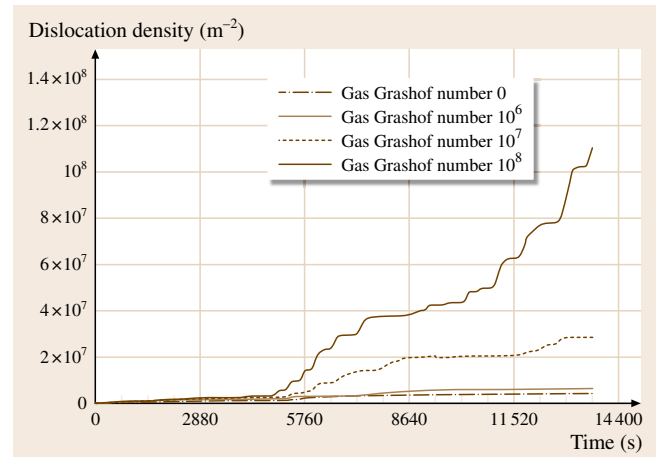


Fig. 39.25 Total dislocation density evolution for point 1, under different gas conditions. The melt Grashof number is 10^6 , the rotational Reynolds numbers are 500, and the encapsulant height is 20 mm

los [39.15], *Lambropoulos* and *Wu* [39.53], and *Chen et al.* [39.92] have proposed that the interface curvature will have a significant effect on the evolution of the total dislocation density.

The Grashof number in the melt was increased to 10^7 and then 10^8 to study the effect on the total dislocation density. In both of these simulations, the gas Grashof number was kept at 10^8 . It was found that, although the interface becomes highly convex towards the melt for a melt Grashof number of 10^8 , the final dislocation density does not change appreciably from the corresponding simulation when the melt Grashof number was 10^6 . This result differs from observations in literature, which suggest that a curved interface is dangerous since it leads to high stresses – the CRSS at the interface is very low and high stresses there will lead to a high dislocation density. The situation in these simulations is however more subtle. The high temperature (near the melting point) at the interface ensures that the strain (or stress) generated due to the curved interface is quickly dissipated as plastic strain due to the high velocity of the dislocations, and the resulting additional dislocation density due to the enhanced curvature is not high enough to show up in the final results at the end of the growth period, since later in its history the same material element goes through more strenuous loading at lower temperatures, thus masking the effect of the additional interface curvature.

Rotation of Crucible and Crystal

Another important factor might be the rotation of the crucible and the crystal. These are usually rotated in opposite senses, and typically the angular velocities of rotation are of the order of 5–10 rpm, which results in Re_c and Re_s of the order of 8000–16 000. The rotation

of the crucible creates a swirl component in the fluid motion, and as a result centrifugal and coriolis forces arise. The rotation of the crystal creates another forced convection term, and its effect on gas convection is akin to an Ekman flow above a rotating disk. The forces due to natural convection, crucible swirl, and crystal rotation

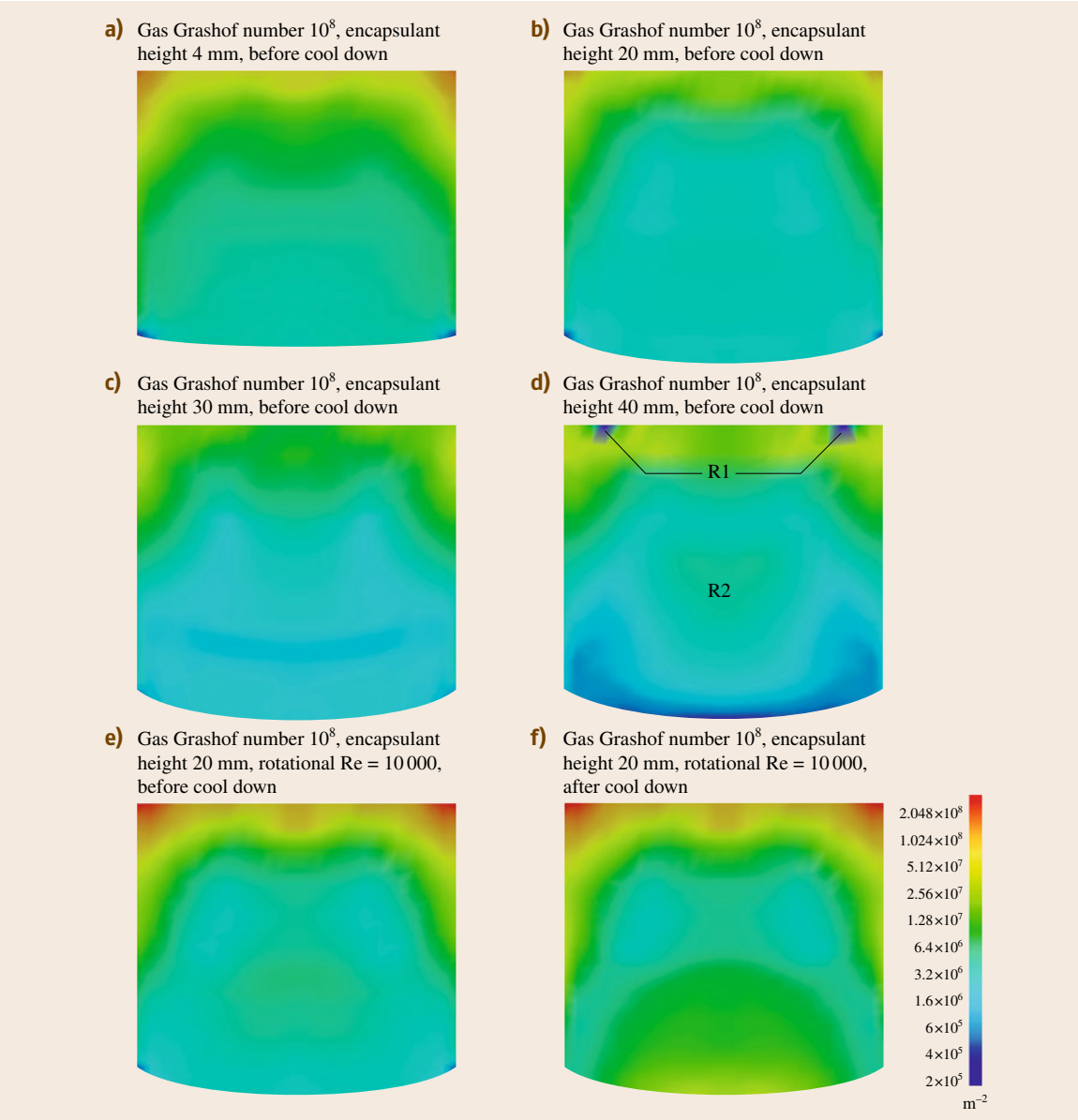


Fig. 39.26a–f Total dislocation densities projected on (010) plane passing through the growth axis. In all cases the melt Grashof Number is 10^6 , and the rotational Reynolds numbers are 500 unless otherwise indicated

create a complicated pattern of gas flow, which might be oscillatory and three dimensional in nature.

An increase of the rotation Reynolds number to 2500 and 5000 did not cause much difference in the total dislocation density from the corresponding case with rotation Reynolds number of 500. However, a further increase in the rotation Reynolds number to 10 000 caused a doubling of the maximum total dislocation density to $4 \times 10^8 \text{ m}^{-2}$, as can be seen in Fig. 39.26e. This might be consistent with the observations that at higher rotation rates the flow becomes unstable and promotes temperature and flow oscillations in the gas phase [39.96].

39.10.6 Control of Encapsulation Height

The height of encapsulation is expected to influence the total dislocation density by changing the temperature history. It will determine the instant at which the crystal will come out of the encapsulant and experience *thermal shock*, the duration of time for which the crystal is exposed to the hot gas, and the length of the crystal that is exposed to the gas. Figure 39.26a–d shows the total dislocation density projected on the (010) plane in the fully grown crystal for four different encapsulant heights (4, 20, 30, and 40 mm) with gas Grashof number of 10^8 , melt Grashof number of 10^6 , and rotational Reynolds numbers of 500. Though not shown in Fig. 39.26, a case for encapsulant height 50 mm under the same conditions was also simulated. This case corresponds to fully encapsulated growth, with the crystal remaining under the encapsulant throughout. The dislocation density in this case was one order of magnitude lower – less than $5 \times 10^6 \text{ m}^{-2}$. Elliot et al. [39.97] report very low dislocation densities for fully encapsulated growth. The 50 mm case is to be contrasted with the case of 40 mm encapsulant height. In this case too, the crystal is under the encapsulant for 204 of the 216 min of its entire growth history, and at the end of its growth period, only the top 3 mm of the 43 mm long crystal is exposed to the gas convection. However, the dislocation levels at the top in this case are an order of magnitude higher than in the fully encapsulated case. This is further proof of the dominant role played by exposure of the crystal to gas convection in dislocation multiplication, at least as predicted by the modeling effort.

The highest dislocation density occurs in the case of encapsulant height 4 mm. The maximum occurs in the top corner of the crystal, and is of the order of $2 \times 10^8 \text{ m}^{-2}$ in the case of 4 mm encapsulant, and decreases to around $8 \times 10^7 \text{ m}^{-2}$ in the case of en-

capsulant height of 40 mm. In every case, the crystal seems to be clearly demarcated into two different zones: an upper zone where the total dislocation density is of the order of 3×10^7 – $6 \times 10^7 \text{ m}^{-2}$, and a lower region where the dislocation density is of the order of 5×10^6 – $1 \times 10^7 \text{ m}^{-2}$. The dislocation density tends to be higher towards the edges of the crystal. The area of high dislocation density is greatest in the case of encapsulant height of 4 mm.

39.10.7 The Cool-Down Period

The results presented so far are those at the end of the growth process. After the growth is the process of cooling down the fully grown crystal to room temperature. The temperature field in the crystal during the cool-down period is a function of the environment in the furnace, the rate at which the heaters in the furnace are ramped down, and other such details. These features are not available in the MASTRAPP CFD model, for a realistic simulation of the cool-down period. Therefore a reasonable approximation to the cool-down process is to ramp the temperature field in the crystal at the end of the growth period down to room temperature over a length of time. What this means is that the temperature gradients and thermal loads on the fully grown crystal are ramped down to zero.

Consequently, as the thermal loading is withdrawn, stresses develop due to the incompatibility of the plastic strain, leading to additional plastic deformation and dislocation multiplication, and finally considerable residual stresses in the cooled-down crystal. An important issue is the length of time over which the temperature ramp-down should take place. In a real Czochralski furnace, the crystal ingot is cooled down to room temperature over a few hours. Integrating the viscoplastic equations over a few hours of real time is beyond the computational resources available. Hence, the strategy adopted was to ramp down the thermal fields to room temperature over 12 min. In certain cases, we used three times this period to check for differences in the results. A clear disadvantage of the shortness of the ramp-down period is that the exaggerated unloading rate might lead to an overestimation of the final total dislocation density and residual stresses.

Figure 39.26f shows the final dislocation density after the cool-down period on a (010) slice containing the centerline, for the case with encapsulant height of 20 mm, gas Grashof number of 10^8 , melt Grashof number of 10^6 , and rotational Reynolds number of 10 000. To contrast with the situation the dislocation density be-

fore the cool-down period is presented in Fig. 39.26e. It can be seen that the dislocation density in the lowest part of the crystal has doubled or even tripled during the cool-down period. In fact the highest dislocation density in the crystal now occurs in the bottom and top parts of the crystal, with a distinct low-dislocation-density region in the middle part of the crystal. This seems to coincide with the experimental observation by Chung et al. [39.57, 58]. Though the figures are not displayed here, the cool-down calculations were performed for every case discussed previously. The results have a common feature: while the total dislocation density at the top and sides of the crystal develops during the growth period, the bottom of the crystal acquires a high dislocation density during the cool-down period. This phenomenon occurs due to the large temperature difference between the top and bottom of the crystal – roughly 300 K. Due to this, by the middle of the cool-

ing period, the top portion of the crystal has cooled down sufficiently to be incapable of plastic deformation (since the threshold strain for plastic deformation is too high), and consequently generates considerable residual stresses. In contrast the bottom portion of the crystal is still hot (relative to the top portion) and is capable of plastic deformation. Since the crystal is a continuous medium, the residual stresses generated in the top part of the crystal generate a high loading in the lower part too, resulting in increased plastic deformation and dislocation generation there. Thus a new prediction by the modeling effort is that the dislocation density in the upper portions of the crystal develops during the growth period, while that in the lower part develops during the cool-down period. Though experimental data is scarce, this phenomenon has been reported by Neubert and Rudolph [39.98], in the context of vapor pressure controlled Czochralski (VCZ) growth of GaAs single crystals.

The cool-down period was tripled in the case of encapsulant height of 20 mm, gas Grashof number of 10^8 , melt Grashof number of 10^6 , and rotational Reynolds numbers of 500. A longer cool-down period means that parts of the crystal are at higher temperature for a longer time and capable of plastic deformation for a longer period. This gives rise to dislocation densities higher by a factor of 1.3 and slightly lower residual stresses at the end of the cool-down period than before.

39.10.8 The $[1\bar{1}1]$ Growth Axis

All the cases presented so far have been for growth along the $[001]$ axis. In this section, the case for growth along the $[1\bar{1}1]$ axis is presented. The main difference is in the geometry of the slip systems. While in the case of $[001]$ growth, the slip systems have fourfold symmetry with respect to the growth axis, in the case of $[1\bar{1}1]$ growth, threefold symmetry is expected.

Only one case is simulated for the $[1\bar{1}1]$ growth axis, with gas Grashof number of 10^8 , rotation Reynolds numbers of 500, melt Grashof number of 10^6 , and encapsulant height of 4 mm. Figure 39.27 presents the total dislocation density after growth and cool down in slices a–h (see Fig. 39.18 for locations of slices a–h) for the $[1\bar{1}1]$ case. The total dislocation density profiles in slices d and e exhibit threefold symmetry, and those in slices a, b, and c exhibit sixfold symmetry. Both of these symmetries are common in etch pit density observations on slices [39.40, 99]. A direct comparison of the slices showed that the total dislocation density after cool-down is slightly less for the $[1\bar{1}1]$ growth com-

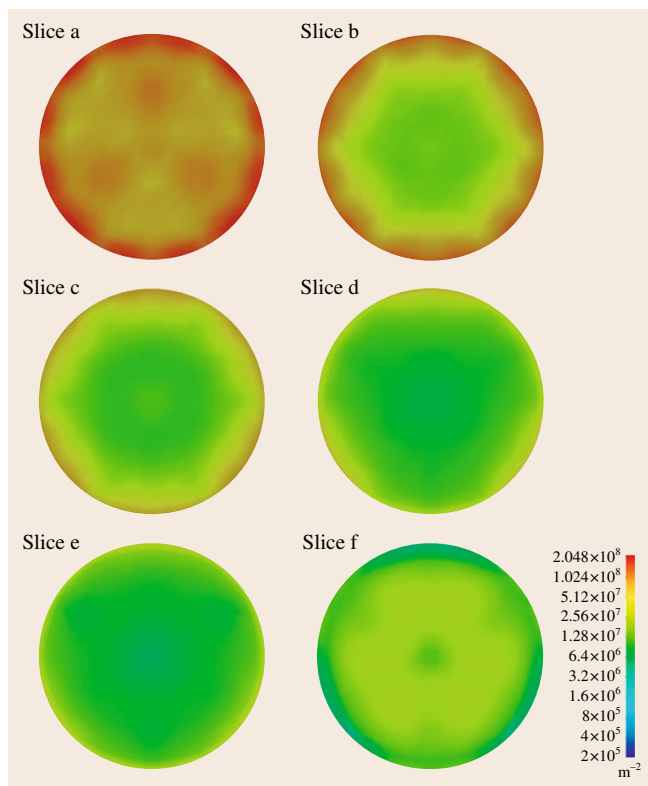


Fig. 39.27 Total dislocation density on $(1\bar{1}1)$ slices of a $[1\bar{1}1]$ -grown crystal after the growth and cool-down period. The gas Grashof number is 10^8 , the Reynolds numbers are 500, and the melt Grashof number is 10^6 . The encapsulant height is 4 mm. The position of the slices is as indicated in Fig. 39.18

pared with the [001] case. The explanation for this is not clear.

39.10.9 Summary of the Calculations and Some Comparisons

A CFD model for the high-pressure Czochralski growth of *InP* single crystals – **MASTRAPP** – was linked with the ABAQUS software to integrate the viscoplastic constitutive equations developed in previous sections under the thermal loading prevalent during the growth period and to predict the final total dislocation density and stress. After the growth period, the crystal temperature was ramped down from the temperature at the end of the growth period to room temperature to simulate the *cool-down* period of the crystal. A study was then conducted to delineate the effect of various parameters. The conclusions are summarized below:

1. The strength of gas convection has the most significant effect on the total dislocation density. The total dislocation density is very low – 400 cm^{-2} – for a gas Grashof number of zero, i. e., with no convection. On increasing the gas Grashof number to 10^6 , the total dislocation density approximately doubles, and a further increase of the gas Grashof number to 10^7 raises the maximum total dislocation density to the order of $2000\text{--}3000\text{ cm}^{-2}$; finally, an increase of the Grashof number to 10^8 raises the maximum total dislocation density to the order of $20\,000\text{ cm}^{-2}$. In a real furnace, the Grashof numbers are of the order of 10^9 , and hence dislocation densities one order of magnitude higher can be expected, and are found in commercial wafers. In contrast, thermal radiation was found not to play a significant role in dislocation generation.
2. The phenomenon of *thermal shock* has been delineated. The thermal shock is captured clearly in both the thermal and elastic stress histories. The total dislocation density in the crystal jumps multifold after the thermal shock.
3. An important finding is that the high dislocation density at the top of the crystal is developed during the growth process after exposure to gas convection, and that at the bottom of the crystal during the cool down.
4. The dislocation density pattern on select slices for [001]-grown crystal exhibits fourfold symmetry, and the total dislocation is higher at the edges of the wafer. The dislocation density is generally highest along the $\langle 010 \rangle$ directions and lowest along the

$\langle 110 \rangle$ directions, in agreement with experimental findings. Similarly, for $[1\bar{1}1]$ -grown crystal, the dislocation density pattern shows sixfold and threefold symmetry.

5. The effect of the height of encapsulation on the total dislocation density at the end of the growth period has been studied. Encapsulation heights of 4, 20, 30, 40, and 50 mm are used with gas Grashof number of 10^8 , melt Grashof number of 10^6 , and rotational Reynolds numbers of 500. The last case corresponds to fully encapsulated growth and the total dislocation density developed is only of the order of $2 \times 10^6\text{--}4 \times 10^6\text{ m}^{-2}$. This confirms experimental findings of fully encapsulated growth producing low-dislocation-density crystals.
6. Raising the melt Grashof number did not significantly affect the total dislocation density; however, an increase in the rotation Reynolds numbers increased the dislocation density.

If there is a common theme to the message from these calculations, it is that gas convection plays the most important role in dislocation multiplication. How does this square up with experimental observations? We report a few experimental papers which attempt to reduce the dislocation densities by adopting the same strategies explored numerically in the preceding sections – the reduction of thermal gradients – primarily achieved through certain artifices such as improving the design of the heat insulators and heaters, adjustment of the thickness of the boric oxide layer, reduction of the gas convection by reducing the ambient gas pressure as much as possible and design of appropriate baffles and convection shields, and finally stabilization of the melt flows. *Von Neida and Jordan* [39.100] achieved low thermal gradients in the LEC growth of GaAs by both adjusting the position of the heating source and modifying the B_2O_3 level. They noticed a reduction in dislocation densities by a factor of 10. *Elliot et al.* [39.101] achieved dislocation densities of 5000 cm^{-2} , in the LEC growth of GaAs, by reducing the thermal gradients to around 6°C/cm . *Katagiri et al.* [39.102] used a heat shield above the heater and crucible to decrease the axial temperature gradient from 100°C , in a conventional LEC method, to 40°C . The crystals grown in these conditions showed large areas free of dislocations. *Hirano and Uchida* [39.103] and *Hirano* [39.104] developed a new thermal baffle to obtain low-dislocation-density S-doped InP crystal of 50 mm diameter. The thermal baffle was designed to suppress gas convection. However, there are serious

problems associated with growth under low-thermal-gradient conditions – crystal diameter instability and instabilities at the crystal–melt interface, which might give rise to twinning. This problem is particularly severe in InP growth, which is prone to twinning because of the low stacking fault energy. These problems have been overcome by applying a vertical magnetic field to suppress the flow in the melt and stabilize the crystal–melt interface [39.105–108]. Another approach is to shield the crystal completely from gas convection by utilizing fully encapsulated growth. Kohda et al. [39.109] combined fully encapsulated growth and a vertical magnetic

field to obtain 50 mm-diameter completely dislocation-free semi-insulating GaAs crystals.

Thus there are close experimental precedents to the modeling results. A more detailed report of these modeling results can be found in [39.110]. With the rapid increase in computing power, and the greater availability of parallel clusters, a more detailed optimization study with better temperature histories – perhaps obtained from experiment or high-fidelity CFD models – has the potential to devise growth programs that completely minimize the dislocation densities in III–V as-grown crystals.

39.11 Summary

An effort has been made to present the state of the art in the theoretical and modeling aspects of dislocation generation in III–V compound semiconductors. Sections 39.1 and 39.2 set up and motivated the discussion. Section 39.3 discussed the need for the reduction of dislocation density, and traces the origin of these, the most important being the nucleation of dislocations from point defects. Section 39.4 described models for dislocation multiplication due to thermal stress; the popular Jordan model and also a more general and computationally intensive viscoplastic framework were introduced. Section 39.5 and beyond dealt with viscoplastic models in the literature, their main features, and their origins from microscopic dislocation dynamics. Section 39.5 gave an introduction to the structural aspects of common dislocations in diamond- and zincblende-type lattices. Section 39.6 discussed the deformation behavior of semiconductors and presents the Alexander–Haasen viscoplastic model. A brief description of the various components of the model is given. Section 39.7 gave a description of existing literature on the application of Alexander–Haasen-type models to the crystal growth problem. As a thorough examination of this class of models, Sect. 39.8 and the sections that follow discussed the development and application to crystal growth of a particular viscoplastic model. Section 39.8 described in great detail the various building blocks of the model, and the many limitations and assumptions that go into such models, as well as insights into future work that can be performed. Section 39.9 described briefly the numerical implementation of the model in a finite element framework and the methodology of its coupling with computational fluid dynamics and heat-transfer-based thermal models for crystal growth

processes. Section 39.10 presented the results of one such successful coupling, and various conclusions are drawn.

Finally, some open questions and avenues for research are now presented:

1. A question frequently posed is the reason for the growth of dislocation-free silicon. In view of the above conclusion, a bold hypothesis may be the absence of substantial gas convection in low-pressure Czochralski growth of silicon. It might be useful to make a viscoplastic model for silicon and investigate it further.
2. A substantial improvement can be made in the thermal models. With the advent of high-performance computing, it might be possible to develop a continuous, nonsteady, three-dimensional simulation of the entire growth process, instead of the present two-dimensional axisymmetric quasistatic series of simulations. Such a simulation would resolve instabilities in the gas flow, and the temperature and flow oscillations could be resolved with more certainty.
3. The viscoplastic model suffers from various difficulties. Firstly, the topological aspect of dislocations was neglected. Dislocations are continuous line defects and can either end at the surfaces of the material or form closed loops. Physically, this is reflected in a divergence-free dislocation density tensor. Present formulations ignore the topological aspects of dislocation density and simply model it as scalar variables. Again, it might be possible to formulate alternate models, with dislocation as line objects rather than scalar variables. This might lead to theories with a structure similar to strain gradient theories.

4. Instead of assuming an initially negligible but finite total dislocation density, a suitable alternative would be to model the initial dislocation density from condensation of point defects into Frank loops, and their subsequent transformation into glide dislocations. Such a model should necessarily be coupled with models for point defect dynamics in the crystal.
5. There is scope for a synergetic effort between experimentalists – TEM, constant-strain-rate tests – and theoreticians. There is a great deal of uncertainty in measurements of dislocation velocities and stress–strain curves. Often these experiments are done on materials from different sources; this gives

rise to great variations in the results. Furthermore, the virgin state of the material before the deformation, such as the initial dislocation density, is often not recorded. Hence a consistent set of experiments should be designed to measure quantities such as the dislocation density and stress–strain curves for material from the same set of sources. At the same time quantities such as the hardening coefficients and multiplication coefficients can be resolved with a mixture of atomistic quantum and mesoscopic discrete dislocation dynamics calculations. Such an effort will involve modeling on multiple scales along with the experimental data.

References

- 39.1 J. Czochralski: Ein neues Verfahren zur Messung der Kristallisationsgeschwindigkeit der Metalle, *Z. Phys. Chem.* **92**, 219–221 (1917), in German
- 39.2 G.K. Teal, J.B. Little: Growth of germanium single crystals, *Phys. Rev.* **78**, 647 (1950)
- 39.3 W.C. Dash: Dislocation free silicon crystals. In: *Growth and Perfection of Crystals*, ed. by R.M. Doremus, B.W. Roberts, D. Turnbull (Wiley, New York 1958)
- 39.4 V. Swaminathan, A.S. Jordan: Dislocations in III/V compounds, *Semicond. Semimet.* **38**, 293–341 (1993)
- 39.5 R.J. Roedel, A.R. Von Neida, R. Caruso, L.R. Dawson: The effect of dislocations in $\text{Ga}_{1-x}\text{Al}_x\text{As}:\text{Si}$ light-emitting diodes, *J. Electrochem. Soc.* **126**, 637–641 (1979)
- 39.6 J.P. Hirth, J. Lothe: *Theory of Dislocations* (Krieger, Malabar 1992)
- 39.7 H. Alexander: On dislocation generation in semiconductor crystals, *Radiat. Eff. Defects Solids* **112**(1/2), 1–12 (1989)
- 39.8 B.T. Lee, R. Gronsky, E.D. Bourret: Dislocation loops and precipitates associated with excess arsenic in GaAs, *J. Appl. Phys.* **64**(1), 114–118 (1988)
- 39.9 J. Lagowski, H.C. Gatos, T. Aoyama, D.G. Lin: Fermi energy control of vacancy coalescence and dislocation density in melt-grown GaAs, *Appl. Phys. Lett.* **45**(6), 680–682 (1984)
- 39.10 W. Zulehner: Czochralski growth of silicon, *J. Cryst. Growth* **65**(1–3), 189–213 (1983)
- 39.11 M.F. Ashby, L. Johnson: On the generation of dislocations at misfitting particles in a ductile matrix, *Philos. Mag.* **20**, 1009–1022 (1969)
- 39.12 A.S. Jordan, R. Caruso, A.R. Von Neida: A thermoelastic analysis of dislocation generation in pulled GaAs crystals, *Bell Syst. Technol. J.* **59**(4), 593–637 (1980)
- 39.13 N. Kobayashi, T. Iwaki: A thermoelastic analysis of the thermal stress produced in a semi-infinite cylindrical single crystal during the Czochralski growth, *J. Cryst. Growth* **73**, 96–110 (1985)
- 39.14 M. Duseaux: Temperature profile and thermal-stress calculations in GaAs crystals growing from the melt, *J. Cryst. Growth* **61**(3), 576–590 (1983)
- 39.15 J.C. Lambropoulos: Stresses near the solid–liquid interface during the growth of a Czochralski crystal, *J. Cryst. Growth* **80**, 245–256 (1987)
- 39.16 C.E. Schvezov, I.V. Samarasekera, F. Weinberg: Calculation of the shear stress distribution in LEC gallium arsenide for different growth conditions, *J. Cryst. Growth* **92**, 479–488 (1988)
- 39.17 G.O. Meduoye, K.E. Evans, D.J. Bacon: Modelling of the growth of the LEC technique II. Thermal stress distribution and influence of interface shape, *J. Cryst. Growth* **97**, 709–719 (1989)
- 39.18 G.O. Meduoye, D.J. Bacon, K.E. Evans: Computer modelling of temperature and stress distributions in LEC-grown GaAs crystals, *J. Cryst. Growth* **108**, 627–636 (1991)
- 39.19 S. Motakef, K.W. Kelly, K. Koai: Comparison of calculated and measured dislocation density in LEC-grown GaAs crystals, *J. Cryst. Growth* **113**, 279–288 (1991)
- 39.20 F. Dupret, P. Nécodeme, Y. Ryckmans: Numerical method for reducing stress level in GaAs crystals, *J. Cryst. Growth* **97**, 162–172 (1989)
- 39.21 D.E. Bornside, T.A. Kinney, R.A. Brown: Minimization of thermoelastic stresses in Czochralski grown silicon: Application of the integrated system model, *J. Cryst. Growth* **108**, 779–805 (1991)
- 39.22 Y.F. Zou, H. Zhang, V. Prasad: Dynamics of melt-crystal interface and coupled convection–stress predictions for Czochralski crystal growth processes, *J. Cryst. Growth* **166**, 476–482 (1996)

- 39.23 I. Yonenaga, K. Sumino: Impurity effects on the generation, velocity, and immobilization of dislocations in GaAs, *J. Appl. Phys.* **65**, 85–92 (1989)
- 39.24 J. Lubliner: *Plasticity Theory* (Macmillan, New York 1990)
- 39.25 K. Sumino: Mechanical behavior of semiconductors. In: *Handbook on Semiconductors*, Vol. 3a, ed. by S. Mahajan, T.S. Moss (Elsevier, Amsterdam 1994) pp. 73–181
- 39.26 J. Hornstra: Dislocations in the diamond lattice, *J. Phys. Chem. Solids* **5**, 129–141 (1958)
- 39.27 H. Alexander: Dislocations in covalent crystals. In: *Dislocations in Solids*, Vol. 7, ed. by F.R.N. Nabarro (North-Holland, Amsterdam 1986) pp. 113–234
- 39.28 D.J.H. Cockayne, A. Hons: Dislocations in semiconductors as studied by weak-beam electron-microscopy, *J. Phys.* **40**(6), 11–18 (1979)
- 39.29 H. Gottschalk, G. Patzer, H. Alexander: Stacking-fault energy and ionicity of cubic III–V compounds, *Phys. Status Solidi (a)* **45**(1), 207–217 (1978)
- 39.30 R. Meingast, H. Alexander: Dissociated dislocations in germanium, *Phys. Status Solidi (a)* **17**(1), 229–236 (1973)
- 39.31 A. George, J. Rabier: Dislocations and plasticity in semiconductors. I – Dislocation structures and dynamics, *Rev. Phys. Appl.* **22**, 941–966 (1987)
- 39.32 W.G. Johnston, J.J. Gilman: Dislocation velocities, dislocation densities, and plastic flow in lithium fluoride crystals, *J. Appl. Phys.* **30**, 129–144 (1959)
- 39.33 H. Alexander, P. Haasen: Dislocations and plastic flow in the diamond structure. In: *Solid State Physics*, Vol. 22, ed. by F. Seitz, D. Turnbull, H. Ehrenreich (Academic, New York 1968) pp. 28–158
- 39.34 A.R. Chaudhuri, J.R. Patel, L.G. Rubin: Velocities and densities of dislocations in germanium and other semiconductor crystals, *J. Appl. Phys.* **33**, 2736–2746 (1962)
- 39.35 G.I. Taylor: The mechanism of plastic deformation of crystals. Part I – Theoretical, *Proc. R. Soc. Lond. Ser. A* **145**, 362–387 (1934)
- 39.36 F.R.N. Babarro, Z.S. Basinski, D.B. Holt: The plasticity of pure single crystals, *Adv. Phys.* **13**, 193–323 (1964)
- 39.37 E. Peissker, P. Haasen, H. Alexander: Anisotropic plastic deformation of indium antimonide, *Philos. Mag.* **7**, 1279 (1962)
- 39.38 I. Yonenaga, K. Sumino: Effects of in impurity on the dynamic behavior of dislocations in GaAs, *J. Appl. Phys.* **62**(4), 1212–1219 (1987)
- 39.39 I. Yonenaga, K. Sumino: Mechanical properties and dislocation dynamics of GaP, *J. Mater. Res.* **4**(2), 355–360 (1989)
- 39.40 J. Völkl: Stress in the cooling crystal. In: *Handbook of Crystal Growth*, Vol. 2, ed. by D.T.J. Hurle (North Holland, Amsterdam 1994) pp. 823–874
- 39.41 H. Siethoff, W. Schröter: Work-hardening and dynamical recovery in silicon and germanium at high-temperatures and comparison with FCC metals, *Scr. Metall.* **17**(3), 393–398 (1983)
- 39.42 H. Siethoff, R. Behrensmeier: Plasticity of undoped GaAs deformed under liquid encapsulation, *J. Appl. Phys.* **67**(8), 3673–3680 (1990)
- 39.43 H. Siethoff, K. Ahlborn, H.G. Brion, J. Völkl: Dynamical recovery and self-diffusion in InP, *Philos. Mag. A* **57**(2), 235–244 (1988)
- 39.44 H. Siethoff, W. Schröter: New phenomena in the plasticity of semiconductors and FCC metals at high temperatures, *Z. Metall.* **75**(7), 475–491 (1984)
- 39.45 A.K. Mukherjee, J.E. Bird, J.E. Dorn: Experimental correlations for high temperature creep, *ASM Transactions* **62**, 155–179 (1969)
- 39.46 C.R. Barrett, W.D. Nix: A Model for steady state creep based on the motion of jogged screw dislocations, *Acta Metall.* **13**, 1247–1258 (1965)
- 39.47 H.G. Brion, H. Siethoff, W. Schröter: New stages in stress-strain curves of germanium at high-temperatures, *Philos. Mag. A* **43**(6), 1505–1513 (1981)
- 39.48 H. Siethoff: Cross-slip in the high-temperature deformation of germanium, silicon and indium-antimonide, *Philos. Mag. A* **47**(5), 657–669 (1983)
- 39.49 B. Escaig: Cross-slip processes in the fcc structure. In: *Dislocation Dynamics*, ed. by A.R. Rosenfield, R. Alan (McGraw-Hill, London 1968) pp. 655–677
- 39.50 D. Maroudas, R.A. Brown: On the prediction of dislocation formation in semiconductor crystals grown from the melt – Analysis of the Haasen model for plastic deformation dynamics, *J. Cryst. Growth* **108**, 399–415 (1991)
- 39.51 C.T. Tsai: On the finite-element modeling of dislocation dynamics during semiconductor-crystal growth, *J. Cryst. Growth* **113**, 499–507 (1991)
- 39.52 C.T. Tsai, A.N. Gulluoglu, C.S. Hertley: A crystallographic methodology for modeling dislocation dynamics in GaAs crystals grown from the melt, *J. Appl. Phys.* **73**, 1650–1656 (1993)
- 39.53 J.C. Lambropoulos, C.H. Wu: Mechanics of shaped crystal growth from the melt, *J. Mater. Res.* **11**, 2163–2176 (1996)
- 39.54 N. Miyazaki, Y. Kuroda: Dislocation density simulations for bulk single crystal growth process, *Met. Mater. Int.* **4**(4), 883–890 (1998)
- 39.55 J.C. Moosbrugger: Continuum slip viscoplasticity with the Haasen constitutive model – application to single-crystal inelasticity, *Int. J. Plast.* **11**, 799–826 (1995)
- 39.56 J.C. Moosbrugger, A. Levy: Constitutive modelling for CdTe single-crystals, *Metall. Mater. Trans. A* **26**(10), 2687–2697 (1995)
- 39.57 H. Chung, W. Si, M. Dudley, A. Anselmo, D.F. Bliss, A. Maniatty, H. Zhang, V. Prasad: Characterization of structural defects in MLEK grown InP single crystals using synchrotron beam x-ray topography, *J. Cryst. Growth* **174**(1–4), 230–237 (1997)
- 39.58 H. Chung, W. Si, M. Dudley, D.F. Bliss, R. Kalan, A. Maniatty, H. Zhang, V. Prasad: Characterization

- of defect structures in magnetic liquid encapsulated Kyropoulos grown InP single crystals, *J. Cryst. Growth* **181**(1–2), 17–25 (1997)
- 39.59 H. Steinhardt, P. Haasen: Creep and dislocation velocities in GaAs, *Phys. Status Solidi (a)* **49**, 93–101 (1978)
- 39.60 I. Yonenaga, U. Unose, K. Sumino: Mechanical properties of GaAs crystals, *J. Mater. Res.* **2**, 252–261 (1987)
- 39.61 A. George, C. Escaravage, G. Champier, W. Schröter: Velocities of screw and 60°-dislocations in silicon, *Phys. Status Solidi (b)* **53**, 483–496 (1972)
- 39.62 M. Imai, K. Sumino: In situ x-ray topographic study of the dislocation mobility in high-purity and impurity-doped silicon-crystals, *Philos. Mag. A* **47**(4), 599–621 (1983)
- 39.63 B.Y. Farber, V.I. Nikitenko: Change of dislocation mobility characteristics in silicon single-crystals at elevated-temperatures, *Phys. Status Solidi (a)* **73**(1), 1141–144 (1982)
- 39.64 I. Yonenaga, K. Sumino: Dislocation velocity in indium-phosphide, *Appl. Phys. Lett.* **58**(1), 48–50 (1991)
- 39.65 H. Nagai: Dislocation velocities in indium phosphide, *Jpn. J. Appl. Phys.* **20**(4), 793–794 (1981)
- 39.66 K. Maeda, S. Takeuchi: Recombination enhanced glide in InP single crystals, *Appl. Phys. Lett.* **42**(8), 664–666 (1983)
- 39.67 F. Louchet: On the mobility of dislocations in silicon by insitu straining in a high-voltage electron-microscope, *Philos. Mag.* **43**(5), 1289–1297 (1981)
- 39.68 V. Celli, M. Kabler, T. Ninoyama, R. Thomson: Theory of dislocation mobility in semiconductors, *Phys. Rev.* **131**(1), 58–72 (1963)
- 39.69 V.V. Rybin, A.N. Orlov: Theory of dislocation motion in low-velocity range, *Sov. Phys. Solid State* **11**, 2635–2641 (1970)
- 39.70 S. Öberg, P.K. Sitch, R. Jones, M.I. Heggie: First-principles calculations of the energy barrier to dislocation motion in Si and GaAs, *Phys. Rev. B* **51**(19), 13138–13145 (1995)
- 39.71 V.V. Bulatov, S. Yip, A.S. Argon: Atomic modes of dislocation mobility in silicon, *Philos. Mag. A* **72**(2), 453–496 (1995)
- 39.72 H.R. Kolar, J.C.H. Spencer, H. Alexander: Observation of moving dislocation kinks and unpinning, *Phys. Rev. Lett.* **77**(19), 4031–4034 (1996)
- 39.73 H.J. Möller: The movement of dissociated dislocations in the diamond-cubic structure, *Acta Metall.* **26**, 963–973 (1977)
- 39.74 P. Haasen: Kink formation in charged dislocation, *Phys. Status Solidi (a)* **28**(1), 145–155 (1975)
- 39.75 P.B. Hirsch: Mechanism for the effect of doping on dislocation mobility, *J. Phys.* **40**(6), 117–121 (1979)
- 39.76 K. Sumino, I. Yonenaga: Dislocation dynamics and mechanical behavior of elemental and compound semiconductors, *Phys. Status Solidi (a)* **138**, 573–581 (1993)
- 39.77 K. Sumino, H. Harada: In situ x-ray topographic studies of the generation and the multiplication processes of dislocations in silicon crystals at elevated temperature, *Philos. Mag. A* **44**(6), 1319–1334 (1981)
- 39.78 P. Franciosi, A. Zaoui: Multislip in fcc. crystals: A theoretical approach compared with experimental data, *Acta Metall.* **30**, 1627–1637 (1982)
- 39.79 A. Moulin, M. Condat, L.P. Kubin: Mesoscale modelling of the yield point properties of silicon crystals, *Acta Metall.* **47**(10), 2879–2888 (1999)
- 39.80 H. Alexander, J.J. Crawford: Latent hardening of germanium crystals, *Phys. Status Solidi (b)* **222**, 41–49 (2000)
- 39.81 A.A. Chernov: *Modern Crystallography III. Crystal Growth* (Springer, Berlin 1984)
- 39.82 H. Klapper: Generation and propagation of dislocations during crystal growth, *Mater. Chem. Phys.* **66**, 101–109 (2000)
- 39.83 G. Dhanaraj, B. Raghothamachar, J. Bai, H. Chung, M. Dudley: Synchrotron x-ray topographic characterization of defects in InP bulk crystals, *Proc. Int. Conf. Indium Phosphide Relat. Mater.* (2005) pp. 643–648
- 39.84 G.T. Brown, B. Cockayne, W.R. Macewan: Deformation behavior of single crystals of InP in uniaxial compression, *J. Mater. Sci.* **15**, 1469–1477 (1980)
- 39.85 S. Pendurti: Modeling Dislocation Generation in High Pressure Czochralski Growth of InP Single Crystals. Ph.D. Thesis (State University of New York, Stony Brook 2003)
- 39.86 A.S. Jordan: Some thermal and mechanical properties of InP essential to crystal growth modeling, *J. Cryst. Growth* **71**, 559–565 (1985)
- 39.87 H. Siethoff: The plasticity of elemental and compound semiconductors, *Semicond. Semimet.* **37**, 143–187 (1992)
- 39.88 J.C. Simo, T.J.R. Hughes: *Computational Inelasticity* (Springer, New York 1998)
- 39.89 H. Zhang, V. Prasad: A multizone adaptive process model for low and high pressure crystal growth, *J. Cryst. Growth* **155**, 47–65 (1995)
- 39.90 P. Rudolph, M. Jurisch: Bulk growth of GaAs – An overview, *J. Cryst. Growth* **199**(1), 325–335 (1999)
- 39.91 V.A. Antonov, V.G. Elsakov, T.I. Olkhovikova, V.V. Selin: Dislocations and 90°-twins in LEC-grown InP crystals, *J. Cryst. Growth* **235**(1–4), 35–39 (2002)
- 39.92 T.-C. Chen, H.-C. Wu, C.-I. Weng: The effect of interface shape on anisotropic thermal stress of bulk single crystal during Czochralski growth, *J. Cryst. Growth* **173**, 367–379 (1997)
- 39.93 J. Matsui: Study of strain variation in LEC-grown GaAs bulk crystals by synchrotron radiation x-ray, *Appl. Surf. Sci.* **50**, 1–8 (1991)
- 39.94 H.M. Buchheit, A. Khoukh, M. Bejar, S.K. Krawczyk, R.C. Blanchet: Residual strain mapping in III–V materials by spectrally resolving scanning pho-

- toluminescence, *Microelectron. J.* **30**(7), 651–657 (1999)
- 39.95 S. Pendurti, V. Prasad, H. Zhang: Modelling dislocation generation in high pressure Czochralski growth of InP single crystals: Part I. Construction of a visco-plastic deformation model, *Model. Simul. Mater. Sci. Eng.* **13**, 249–266 (2005)
- 39.96 V. Prasad, H. Zhang: Transport phenomena in Czochralski crystal growth processes, *Adv. Heat Transf.* **30**, 313–435 (1997)
- 39.97 A.G. Elliot, A. Flat, D.A. Vanderwater: Silicon incorporation in LEC growth of single-crystal gallium-arsenide, *J. Cryst. Growth* **121**(3), 349–359 (1992)
- 39.98 M. Neubert, P. Rudolph: Growth of semi-insulating GaAs crystals in low temperature gradients by using the vapour pressure controlled Czochralski method (VCZ), *Prog. Cryst. Growth Charact. Mater.* **43**(2/3), 119–185 (2001)
- 39.99 G. Müller, J. Völkl, E. Tomzig: Thermal analysis of LEC InP growth, *J. Cryst. Growth* **64**(1), 40–47 (1983)
- 39.100 A.R. Von Neida, A.S. Jordan: Reducing dislocations in GaAs and InP, *J. Met.* **38**, 35–40 (1986)
- 39.101 A.G. Elliot, C.L. Wei, R. Farraro, G. Woolhouse, M. Scott, R. Hiskes: Low dislocation density, large diameter, liquid encapsulated Czochralski growth of GaAs, *J. Cryst. Growth* **70**, 169–178 (1984)
- 39.102 K. Katagiri, S. Yamazaki, A. Takagi, O. Oda, H. Araki, I. Tsuboya: LEC growth of large diameter InP single crystals doped with Sn and with S, *Inst. Phys. Conf. Ser.* **79**, 67–72 (1986)
- 39.103 R. Hirano, M. Uchida: Reduction of dislocation densities in InP single crystals by the LEC method using thermal baffles, *J. Electron. Mater.* **25**, 347–351 (1996)
- 39.104 R. Hirano: Growth of low etch pit density homogeneous 2" InP crystals using a newly developed thermal baffle, *Jpn. J. Appl. Phys.* **38**(2B), 969–971 (1999)
- 39.105 K. Terashima, T. Fukuda: A new magnetic-field applied pulling apparatus for LEC GaAs single-crystal growth, *J. Cryst. Growth* **63**, 423–425 (1983)
- 39.106 H. Miyairi, T. Inada, M. Eguchi, T. Fukuda: Growth and properties of InP single crystals grown by the magnetic-field applied LEC method, *J. Cryst. Growth* **79**(1–3), 291–295 (1986)
- 39.107 J. Osaka, H. Kohda, T. Kobayashi, K. Hoshikawa: Homogeneity of vertical magnetic-field applied LEC GaAs crystal, *Jpn. J. Appl. Phys. Part 2 – Lett.* **23**(4), L194–197 (1984)
- 39.108 S. Ozawa, T. Kimura, J. Kobayashi, T. Fukuda: Programmed magnetic-field applied liquid encapsulated Czochralski crystal-growth, *Appl. Phys. Lett.* **50**(6), 329–331 (1987)
- 39.109 H. Kohda, K. Yamada, H. Nakanishi, T. Kobayashi, J. Osaka, K. Hoshikawa: Crystal-growth of completely dislocation-free and striation-free GaAs, *J. Cryst. Growth* **71**(3), 813–816 (1985)
- 39.110 S. Pendurti, H. Zhang, V. Prasad: Modeling dislocation generation in high pressure Czochralski growth of InP single crystals: Part II, *Model. Simul. Mater. Sci. Eng.* **13**, 267–297 (2005)

40. Mass and Heat Transport in BS and EFG Systems

Thomas F. George, Stefan Balint, Liliana Braescu

In this chapter several mathematical models describing processes which take place in the Bridgman–Stockbarger (BS) and edge-defined film-fed growth (EFG) systems are presented. Predictions are made concerning the impurity repartition in the crystal in the framework of each of the models. First, a short description of the real processes which are modeled is given, along with the equations, boundary conditions, and initial values defining the mathematical model. After that, numerical results obtained by computations in the framework of the model are provided, making a comparison between the computed results and those obtained in other models, and with the experimental data.

40.1 Model-Based Prediction of the Impurity Distribution – Vertical BS System	1380
40.1.1 Burton–Prim–Slichter Uniform–Diffusion–Layer Model (UDLM)	1380

40.1.2 Chang–Brown Quasi–Steady–State Model (QSSM)	1381
40.1.3 Adornato–Brown Pseudo–Steady–State Model (PSSM)	1383
40.1.4 Nonstationary Model (NSM)	1384
40.1.5 Modified Quasi–Steady–State Model (MQSSM) and Modified Nonstationary Model (MNSM)	1386
40.1.6 Larson–Zhang–Zheng Thermal–Diffusion Model (TDM)	1387
40.2 Model-Based Prediction of the Impurity Distribution – EFG System	1389
40.2.1 The Uniform–Diffusion–Layer Model (UDLM)	1389
40.2.2 Tatarchenko Steady–State Model (TSSM)	1389
40.2.3 Melt Replenishment Model (MRM)	1390
40.2.4 Melt Without Replenishment Model (MWRM)	1397
References	1400

The quality of the crystal being grown depends to a considerable extent on homogeneity and the distribution of both detrimental and specially added impurities. Variations of the concentration of impurities along the crystal length and cross section lead to variations of the mechanical, electrical, and optical properties in the mass of the crystal. The impurity repartition in the crystal is determined by the processes which take place in the melt during the growth and by mass transfer. Quantitative descriptions of these processes permit the prediction of such repartition in the crystal, which is a reason to build mathematical models in order to describe processes which take place during the growth. Consequently, computer modeling of the crystal growth processes has often been described as an art as well as a science, to acknowledge the seemingly endless

difficulties that arise in the application of numerical methods. Three core competencies are required for the effective use of modeling in crystal growth. One is a thorough grasp of the fundamentals of continuum transport phenomena. The second is the building of an appropriate mathematical model, and the third is a general understanding of the numerical methods necessary for solving the governing equations of transport phenomena.

The philosophy behind building the mathematical model is to provide a quantitative description of the mechanism by balancing what is wanted with what can be done. The quantitative description is made in terms of a certain number of variables (called the model variables) such that the mathematical model is a set of equations concerning these variables. The analysis of

a mathematical model leads to results or predictions that can be tested against observations. It is important to realize that all models are idealizations and hence are

limited in their applicability; experimental verification of the predictions can establish the authenticity of the model.

40.1 Model-Based Prediction of the Impurity Distribution – Vertical BS System

The prototype vertical BS crystal growth system (discussed here) consists of a crystal and melt contained in a cylindrical ampoule of radius R and length L pulled slowly through a vertically aligned furnace with hot and cold isothermal zones, as shown in Fig. 40.1.

The isothermal zones are separated by an adiabatic region of length L_g , designed to promote a steep axial temperature gradient and to maintain a flat solidification interface. A purpose of different mathematical models conceived to describe the processes which take place in such a system is the prediction of the distribution of detrimental and added impurities in the crystal being grown. The models discussed here describe one or several of the following processes: rejection of impurities at the melt–crystal interface, molecular diffusion, thermodiffusion, thermal convection, solutal convection, heat transfer between the furnace and ampoule walls, decrease of the melt in the ampoule, and melt–crystal interface morphology.

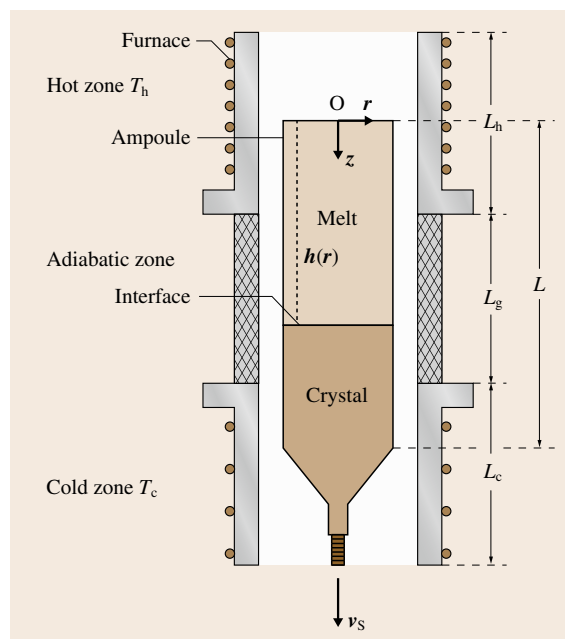


Fig. 40.1 Prototype BS crystal growth system

40.1.1 Burton–Prim–Slichter Uniform–Diffusion–Layer Model (UDLM)

For a large set of binary alloys, the rejection of impurities at the melt–crystal interface causes an unequal partitioning of the impurities between the melt and crystal during solidification. This leads to the accumulation of impurities in the melt and creates in the melt a nonuniform concentration field. A model to describe the above concentration field in the neighborhood of the melt–crystal interface (at the melt side) and the transfer of impurities in the crystal is the so-called uniform-diffusion-layer model (UDLM). The concept of an *axial boundary layer* evidently was introduced by Burton et al. [40.1]. Others [40.2–6] have extended this concept by introducing the notion of a *uniform diffusion layer* or *stagnant film*, without any picture for the fluid motion in the melt. Physically, the uniform diffusion layer is a thin layer masking the growing crystal which separates the crystal surface from the bulk melt [40.7].

According to UDLM, the isoconcentration lines of impurities are parallel to the interface, and the concentration decreases exponentially into the melt in this layer. The transport of impurities in the layer is molecular diffusion controlled, and the prediction is that, after an initial transient, the crystal exhibits a uniform (axial and radial) impurity distribution [40.8]. The effective partition coefficient k_{eff} , the equilibrium partition coefficient k , and the dimensionless diffusion-layer thickness $\delta = \tilde{\delta}/L$ are related by Fleming's formula

$$k_{\text{eff}} = \frac{k}{k + (1 - k) \exp\left(\frac{\text{Pe Sc}}{\text{Pr}} \delta\right)}, \quad (40.1)$$

where Pr is the Prandtl number, Pe is the Péclet number, and Sc is the Schmidt number [40.7]. The predicted impurity concentration in the crystal is given by

$$c_{\text{crys}} = k_{\text{eff}} c_0, \quad (40.2)$$

where c_0 represents the impurity concentration in the bulk melt.

This model is appropriate for the prediction of impurities in crystals grown from a quiescent melt. Thus, a reduction in the magnitude of the buoyancy forces when processing semiconductors, such as in a low-gravity environment, has been pursued over the past several decades. The effectiveness of space processing for the growth of chemically uniform crystals is supported by experimental and theoretical studies [40.9, 10]. For example, the InSb crystal reported in [40.11] exhibits axial distribution profiles that are characteristic of diffusion-controlled mass transfer growth. In [40.7] it is shown, based on modeling studies, that the low gravity levels achieved in space are sufficient to inhibit thermal convection in small-diameter Ge and Ga-Ge melts. At the same time, it is pointed out that UDLM is an oversimplified model for accurate prediction of the impurity distribution in the crystal [40.12].

40.1.2 Chang–Brown Quasi-Steady-State Model (QSSM)

An important process in a BS system is thermal convection, the effect of which is essentially neglected in UDLM. Thermal convection is driven by buoyancy differences induced by axial and radial temperature gradients, and it may be laminar, periodic or turbulent. When the melt is below the crystal, the axial temperature gradient places the hottest melt at the bottom of the ampoule and generates convection. Kim et al. [40.3] used gallium-doped germanium to identify the melt length at which three forms of convection were present. In [40.13–26], the melt was oriented above the crystal in order to produce a stable axial density gradient. Because radial temperature gradients cause lateral density variations [40.27], convection still exists in this configuration. Thermal convection in a BS system contributes to the distribution of the impurities in the crystal.

The QSSM is a simplified model of the thermal convection and of the heat and mass transport in a BS system. The real process is replaced by a quasi-steady-state process viewed from a stationary reference frame and described in the cylindrical polar coordinate system shown in Fig. 40.1. The translation of the ampoule is replaced by supplying melt into the ampoule at $z = 0$ with velocity $\tilde{v}_z = v_L$ and removing the crystal at the other end of the ampoule at the rate $v_S = (\rho_S/\rho_L) v_L$, where ρ_L represents the melt density and ρ_S the crystal density. Changes in the length of the melt are neglected in QSSM. The location of the melt–solid interface is represented as $z = h(r)$, $0 \leq r \leq \Lambda$, $\Lambda = R/L$, and the unit vectors normal \mathbf{n} and tangent \mathbf{t} everywhere to the

interface are

$$\mathbf{n} = \frac{\mathbf{e}_z - h_r \mathbf{e}_r}{(1 + h_r^2)^{1/2}}, \quad \mathbf{t} = \frac{\mathbf{e}_r + h_r \mathbf{e}_z}{(1 + h_r^2)^{1/2}}, \quad (40.3)$$

where $h_r = dh/dr$ and the set $(\mathbf{e}_r, \mathbf{e}_\theta, \mathbf{e}_z)$ are the unit vectors of the cylindrical polar coordinate system. According to [40.7], the equations governing the melt flow and heat and mass transport in the melt which define QSSM, in axisymmetric and dimensionless form, are

$$(\mathbf{v} \nabla) \mathbf{v} = -\nabla p + \text{Pr} \nabla^2 \mathbf{v} + \text{Ra}_T \text{Pr} \theta \mathbf{e}_z, \quad (40.4)$$

$$\nabla \mathbf{v} = 0, \quad (40.5)$$

$$\mathbf{v} \nabla \theta = \nabla^2 \theta, \quad (40.6)$$

$$\left(\frac{\text{Sc}}{\text{Pr}} \right) \mathbf{v} \nabla c = \nabla^2 c. \quad (40.7)$$

Here, $\nabla = \mathbf{e}_r \partial/\partial r + \mathbf{e}_z \partial/\partial z$ represents the gradient operator in cylindrical coordinates; Pr is the Prandtl number; Ra_T is the thermal Rayleigh number; Sc is the Schmidt number; \mathbf{v} is the dimensionless melt flow velocity; θ is the dimensionless melt temperature; c is the impurity concentration in the melt; and $0 \leq z \leq h(r)$, $0 \leq r \leq \Lambda$, $\Lambda = R/L$.

In the crystal, the velocity field \mathbf{v} is uniform at speed v_S

$$\mathbf{v} = v_S \mathbf{e}_z, \quad h(r) \leq z \leq 1, \quad 0 \leq r \leq \Lambda. \quad (40.8)$$

The heat transport in the crystal is described by

$$\text{Pe} \mathbf{e}_z \nabla \theta = \gamma \nabla^2 \theta, \quad h(r) \leq z \leq 1, \quad 0 \leq r \leq \Lambda, \quad (40.9)$$

where $\gamma = \alpha_S/\alpha_L$ represents the ratio of thermal diffusivities in crystal and melt, and $\text{Pe} = v_S L/\alpha_L$ is the Péclet number for convective heat transfer. The concentration of impurities in the crystal is given by

$$c_S(r) = kc(r, h(r)), \quad 0 \leq r \leq \Lambda. \quad (40.10)$$

Boundary conditions for the melt flow field \mathbf{v} at the interface ensure no slip tangential to the crystal and the solidification of the melt at rate v_S . The top surface and sidewall of the ampoule are assumed to be no-slip surfaces, i. e.,

$$v_r = 0, \quad v_z = \frac{\rho_S}{\rho_L} \text{Pe}. \quad (40.11)$$

This last condition dictates a jump in the velocity of the ampoule wall when $\sigma = \rho_S/\rho_L \neq 1$.

The axisymmetric boundary conditions for \mathbf{v} and θ at the axis of the cylinder are

$$v_r = \frac{\partial v_z}{\partial r} = \frac{\partial \theta}{\partial r} = 0, \quad r = 0, \quad 0 \leq z \leq 1. \quad (40.12)$$

The thermal boundary conditions incorporate the assumption that the ampoule has negligible thermal mass, the adiabatic region is a perfect insulator, and the ampoule has the temperature of the surrounding furnace; the ends of the ampoule are perfectly insulated. At the melt–crystal interface, the temperature satisfies

$$\theta(r, h(r)) = \frac{T_m - T_c}{T_h - T_c}, \quad 0 \leq r \leq \Lambda, \quad (40.13)$$

$$(n\nabla\theta)_L - K(n\nabla\theta)_S = \text{St Pe } n e_z; \quad z = h(r), \quad 0 \leq r \leq \Lambda, \quad (40.14)$$

where T_m is the melting temperature, K is the ratio of the thermal conductivities between crystal and melt, and St is the Stefan number. The boundary conditions for the impurity concentrations are

$$\frac{\partial c}{\partial z} = \left(\frac{\text{Pe Sc}}{\text{Pr}} \right) (c - 1); \quad z = 0, \quad 0 \leq r \leq \Lambda, \quad (40.15)$$

$$n\nabla c = \left(\frac{\text{Pe Sc}}{\text{Pr}} \right) (n e_z) (1 - k) c; \quad z = h(r), \quad 0 \leq r \leq \Lambda, \quad (40.16)$$

$$\frac{\partial c}{\partial r} = 0; \quad 0 \leq z \leq 1, \quad r = 0, \quad r = \Lambda. \quad (40.17)$$

These conditions express the following: a supply melt inlet at the top of the **BS** system; the rejected impurities at the melt–crystal interface; and the no-flux condition which is valid at the center line and at the side wall of the ampoule.

Using finite-element numerical methods for crystals and melts with thermophysical properties similar to gallium-doped germanium, the temperature field and dopant field in the melt and in the crystal were computed [40.7, 28] for several different Ra_T numbers in **QSSM**. Results are presented for two Bridgman configurations: vertically stabilized (melt on the top) and vertically destabilized (melt on bottom). Steady axisymmetric flows are classified according to Ra_T and are nearly equal to the growth velocity. Three distinct types of flow patterns were observed with changing Ra_T . At low Rayleigh numbers, the streamlines were rectilinear and only slightly distorted by buoyancy forces. Increasing the Rayleigh number developed first a cellular flow, and after that a weak secondary cell for stabilized configuration. The flows in these two configurations are in opposite directions. Calculations of the transport of

a dilute dopant by these flow fields reveal radial segregation levels as large as 60% of the mean concentration. Radial segregation is most severe at an intermediate value of the Rayleigh number, above which the dopant distribution along the interface levels increases. The complexity of the concentration field coupled with calculations of the effective segregation coefficient show the coarseness of the usual diffusion-layer approximation for describing the dopant distribution adjacent to the crystal.

The results reveal that **UDLM** is a gross oversimplification of the interactions between the complicated flow patterns and the concentration field of impurities. The diffusion-layer thickness δ considered in **UDLM** in the best case is an empirical fit to the effective segregation coefficient. Although the radially averaged diffusion-layer thickness computed in **QSSM** is of the same order of magnitude as those considered in **UDLM**, the actual concentration gradient adjacent to the crystal is far from being radially uniform. In the computations made in **QSSM**, the ratio of thermal conductivities K between the melt and the crystal and the length of the gradient zone L_g have emerged as important parameters for determining the interface shape and radial segregation. According to [40.7], the value of K sets the shape of the interface and determines the qualitative behavior of the radial segregation with increased convection, and L_g sets the degree of interaction between the cellular flow and the concentration gradient adjacent to the interface. For long enough gradient zones and moderate convection, the flow causes lower radial segregation. A critical issue not addressed in this chapter is the transition from the steady-state flow patterns predicted here to time-periodic flows observed in some experiments. Mathematically, these transitions occur as Hopf bifurcations from the steady flows and have been predicted theoretically by computer-aided bifurcation analysis for low-Prandtl-number melts in the horizontal boat geometry as studied experimentally by *Hurle et al.* [40.29]. Simulation of the crystal growth in the time-periodic regime requires a time-dependent solution of the Boussinesq equations.

The qualitative understanding of melt flow and impurities segregation offered by **QSSM** serves as a starting point for more refined and accurate calculations aimed at comparison with experimental data. These would require the inclusion in the model of the thermal interactions between the ampoule and the furnace, the solutal convection, the decrease of the melt in the ampoule, the thermal diffusion (Soret effect), and the effect of the precrystallization zone.

40.1.3 Adornato–Brown Pseudo–Steady–State Model (PSSM)

Thermosolutal convection which can occur in a BS system is driven by buoyancy differences induced by axial and radial temperature gradients and by concentration-dependent density differences. Convection driven by such density differences is initiated in the layer adjacent to the melt–crystal interface and is caused by the accumulation of impurities in this region. In nondilute alloy systems, the interaction of the solutal and thermal driving forces is so closely coupled through convection of the solute field that only a full numerical simulation can give a quantitative description of the flow [40.12]. PSSM is a simplified model of the real thermosolutal convection and of the heat and mass transport in a BS system which takes into account the heat transfer between the furnace and the ampoule. In PSSM, like in QSSM, the translation of the ampoule is replaced by supplying melt at the top of the ampoule with uniform velocity and composition, and removing crystal from the bottom of the ampoule at a certain growth rate. Transients in velocity, pressure, temperature, and concentration caused by the steady decrease of the length of the melt in the real ampoule, and the displacement of the ampoule in the furnace, are neglected in PSSM.

The equations (in axisymmetric and dimensionless form) governing the melt flow, and heat and mass transport in the melt, defining PSSM [40.12] are the following

$$(\mathbf{v} \nabla) \mathbf{v} = -\nabla p + \text{Pr} \nabla^2 \mathbf{v} + \text{Pr} (\text{Ra}_T \theta - \text{Ra}_S c) \mathbf{e}_z, \quad (40.18)$$

$$\nabla \mathbf{v} = 0, \quad (40.19)$$

$$\mathbf{v} \nabla \theta = \nabla^2 \theta, \quad (40.20)$$

$$\left(\frac{\text{Sc}}{\text{Pr}} \right) \mathbf{v} \nabla c = \nabla^2 c, \quad (40.21)$$

where ∇ , Pr , Ra_T , Sc , \mathbf{v} , θ , and c have the same meanings as in (40.4–40.7), and Ra_S represents the solutal Rayleigh number ($0 \leq z \leq h(r)$, $0 \leq r \leq \Lambda$). The velocity field \mathbf{v} in the crystal is uniform at speed v_S

$$\mathbf{v} = v_S \mathbf{e}_z; \quad h(r) \leq z \leq 1, \quad 0 \leq r \leq \Lambda. \quad (40.22)$$

The heat transport equations in the ampoule and in the crystal are

$$\text{Pe}_a \mathbf{e}_z \nabla \theta = \gamma_a \nabla^2 \theta; \quad h(r) \leq z \leq 1, \quad 0 \leq r \leq \Lambda \quad (40.23)$$

$$\text{Pe}_c \mathbf{e}_z \nabla \theta = \gamma_c \nabla^2 \theta; \quad h(r) \leq z \leq 1, \quad 0 \leq r \leq \Lambda, \quad (40.24)$$

where $\gamma_a = \alpha_a / \alpha_L$ and $\gamma_c = \alpha_c / \alpha_L$ are the ratios between the thermal diffusivities of each phase and the melt. The Péclet number Pe is the dimensionless transition rate of the ampoule scaled by the characteristic velocity for thermal diffusion. The shape of the melt–crystal interface is set by the shape of liquids curve $\theta_L(c)$ from the binary phase diagram as

$$\theta(r, h(r)) = \theta_L(c) = \theta_L^0 + m \left(c + 1 - \frac{1}{k} \right), \quad (40.25)$$

$$0 \leq r \leq \Lambda,$$

where the curve is approximated by a straight line with dimensionless slope m , and θ_L^0 is the melting temperature of the alloy with concentration c_0 . It is assumed that m and the partition coefficient k are independent of concentration.

The interfacial temperature and impurities field are related to the corresponding values in the bulk melt by the balances

$$(\mathbf{n} \nabla \theta)_L - K (\mathbf{n} \nabla \theta)_S = \text{St Pe } \mathbf{n} \mathbf{e}_z, \quad (40.26)$$

$$0 \leq r \leq \Lambda$$

$$\mathbf{n} \nabla c = \frac{\text{Pe Sc}}{\text{Pr}} (\mathbf{n} \mathbf{e}_z) (1 - k) c; \quad (40.27)$$

$$z = h(r), \quad 0 \leq r \leq \Lambda.$$

The boundary conditions for the melt flow field are the same as those presented for QSSM. The thermal boundary conditions along the ampoule wall are specified according to the heat transfer condition

$$\left. \frac{\partial \theta}{\partial r} \right|_a = \text{Bi}(z) \cdot (\theta - \theta_\infty(z)), \quad (40.28)$$

where $\text{Bi}(z) = h_a \cdot L / k_a$ is a dimensionless heat transfer coefficient defined to include radiative, conductive, and convective transport between the furnace and the ampoule, and $\theta_\infty(z)$ is the furnace temperature distribution. Perfect thermal contact at the melt–ampoule and crystal–ampoule interfaces are assumed, so that the conductive fluxes at the boundaries are equal

$$\left. \frac{\partial \theta}{\partial r} \right|_L = K_a \left. \frac{\partial \theta}{\partial r} \right|_a, \quad K_c \left. \frac{\partial \theta}{\partial r} \right|_c = K_a \left. \frac{\partial \theta}{\partial r} \right|_a; \quad (40.29)$$

$$r = \Lambda.$$

The top and bottom of the ampoule are assumed to be at the temperature of the hot and cold zones. The specification of the concentration field of impurities in the melt is completed by setting the diffusive flux of impurities through the inlet to be equal to Pe_c , and zero through

the ampoule wall. The concentration of the impurities in the crystal is given by

$$c_S(r) = kc(r, h(r)), \quad 0 \leq r \leq \Delta. \quad (40.30)$$

The axis of the ampoule is taken as a line of symmetry for all field variables.

Using finite-element numerical methods, computations in PSSM were performed for a binary alloy coupling heat transfer in the melt, crystal, and ampoule [40.12] with convection in the melt and segregation in the growing crystal, taking into account convection driven by both temperature and concentration gradients. Calculations presented for growth of gallium-doped germanium in ampoules of boron nitride, quartz, and graphite, along with a quartz/graphite composite ampoule, show the effects of ampoule conductivity on the flow structure and intensity. The thermal conductivity of the ampoule material and the thickness of the ampoule wall can be used as parameters to change the structure of the flow, as well as to modulate the flow intensity. The computations show that flow pattern and concentration fields have rich structures, depending on the furnace, either that constructed at Massachusetts Institute of Technology (MIT) by Wang and Witt (based on heat pipes for forming isothermal hot and cold regions separated by a nearly adiabatic zone; Fig. 40.1) or at Grenoble by Rouzaud and Favier (using a tapered heating element to establish a nearly linear temperature profile over the length of the ampoule). The vertical BS system used at MIT has a two-cell structure: one cell driven by the radial gradients at the junction of the adiabatic and hot zones of the furnace, and the other adjacent to the interface caused by the differences in the thermal conductivities of the melt, crystal, and ampoule. The constant-gradient furnace designed at Grenoble has only a single cell near the interface.

Impurities are transported mostly by diffusion between adjacent cells because the convective motion is laminar. The radial segregation is set primarily by the flow adjacent to the interface when this cell is long enough to completely contain the solute gradient for diffusion-controlled growth. The upper cell in the MIT furnace plays a small role in determining the solute distribution along the interface. Axial segregation depends on the intensity of the convective mixing through the ampoule, so that the cellular structure of the flow pattern is important. In the heat pipe system, solute transport between flow cells limits the effectiveness of this mixing and leads higher solute concentrations in the cell

next to the interface. The degree of axial segregation is set mainly by this cell.

The dependence of the degree of radial segregation on Ra_T studied in both the MIT and Grenoble systems is characterized by the following: (i) segregation is lowest for either diffusion-controlled growth (small Ra_T) or for when the intense laminar mixing is present (large Ra_T); (ii) segregation reaches a maximum for intermediate values of low intensity; (iii) the ampoule material, furnace design, and stabilizing solute all affect the values of segregation. This result is crucial for understanding the effects on solute segregation of microgravity solidification and of applied magnetic fields, and answers two questions which were not clarified before: (i) the way in which the reduced convection level affects the solute segregation, and (ii) the dependence of the segregation level on the ampoule size for the same Ra_T . In both situations the body forces acting on the melt are altered in an attempt to damp convection. Both approaches are clearly effective at eliminating time-periodic and chaotic convection present in large-size systems. If the reduced gravitational field has constant magnitude and is aligned with the crystal axis, then it is modeled exactly by reducing the thermal Rayleigh number. Thus, in [40.12], it is shown that the decrease in gravitational level needed to reach diffusion-controlled growth increases with a value which depend on the cube of the ampoule radius. This proves that the segregation effect is more severe for larger ampoules.

The prediction of the melt–crystal interface shape, radial impurity distribution, and effective segregation coefficient for the growth of dilute gallium-doped germanium obtained in [40.12] agrees reasonably well with the measurements by Wang [40.30].

40.1.4 Nonstationary Model (NSM)

NSM is a model of the unsteady thermoconvection, heat and impurity transport in a BS system which takes into account the decrease of the melt in the ampoule. The equations that govern such phenomena can be expressed in a mobile reference frame (Fig. 40.1) in axisymmetric and dimensionless form as [40.31]

$$\frac{\partial \mathbf{v}}{\partial t} + (\mathbf{v} \cdot \nabla) \mathbf{v} = -\nabla p + \text{Pr} \nabla^2 \mathbf{v} + \text{Pr} Ra_T \theta \mathbf{e}_z, \quad (40.31)$$

$$\nabla \cdot \mathbf{v} = 0, \quad (40.32)$$

$$\frac{\partial \theta}{\partial t} + \mathbf{v} \cdot \nabla \theta = \nabla^2 \theta, \quad (40.33)$$

$$\frac{\partial c}{\partial t} + \mathbf{v} \cdot \nabla c = \frac{\text{Pr}}{\text{Sc}} \nabla^2 c. \quad (40.34)$$

The meanings of the symbols which appear in the above equations correspond to those in (40.18–40.21). These equations are time dependent since the domain Ω_t occupied by the melt is time dependent. The boundary $\partial\Omega_t$ of Ω_t is decomposed as $\partial\Omega_t = (\partial\Omega_t)_{\text{top}} \cup (\partial\Omega_t)_w \cup (\partial\Omega_t)_i$, where $(\partial\Omega_t)_{\text{top}}$ and $(\partial\Omega_t)_w$ are the melt boundaries limited by the top and side walls of the ampoule, respectively, and $(\partial\Omega_t)_i$ is the melt boundary limited by the bottom of the ampoule for t satisfying $0 \leq t \leq L_g/(2v_p L)$ and by the melt–crystal interface for t satisfying $L_g/(2v_p L) \leq t \leq (1 + L_g/(2L))/v_p$, where v_p is the ampoule translation rate of the ampoule.

The boundary conditions for v , θ , and c are

$$v = 0 \quad \text{on} \quad \partial\Omega_t, \quad (40.35)$$

$$\frac{\partial\theta}{\partial z} = 0 \quad \text{on} \quad (\partial\Omega_t)_{\text{top}};$$

$$\theta = \theta_f \quad \text{on} \quad (\partial\Omega_t)_w;$$

$$\theta = \theta_i \quad \text{on} \quad (\partial\Omega_t)_i, \quad (40.36)$$

$$\frac{\partial c}{\partial z} = 0 \quad \text{on} \quad (\partial\Omega_t)_{\text{top}};$$

$$\frac{\partial c}{\partial r} = 0 \quad \text{on} \quad (\partial\Omega_t)_w;$$

$$\frac{\partial c}{\partial z} = \Phi_i \quad \text{on} \quad (\partial\Omega_t)_i. \quad (40.37)$$

Here, θ_f is the temperature of the surrounding furnace, θ_i is the temperature of the bottom of the ampoule for t satisfying $0 \leq t \leq L_g/(2v_p L)$, and temperature at the melt–crystal interface for t satisfying $L_g/(2v_p L) \leq t \leq (1 + L_g/(2L))/v_p$, $\Phi_i = 0$ for t sat-

isfying $0 \leq t \leq L_g/(2v_p L)$; and $\Phi_i = (\text{Pe Sc})/(\text{Pr})(1 - k)c$ for t satisfying $L_g/(2v_p L) \leq t \leq (1 + L_g/(2L))/v_p$. The initial conditions for the equations (40.31–40.34) are

$$\begin{aligned} v(0, r, z) &= 0; \\ \theta(0, r, z) &= 1; \\ c(0, r, z) &= 1. \end{aligned} \quad (40.38)$$

The impurity distribution in the crystal is given by

$$\begin{aligned} c_S(\xi, r) &= kc(t, r, h(r)) \\ &= kc\left(\frac{1}{v_p}\left(\xi + \frac{L_g}{2L}\right), r, h(r)\right), \end{aligned} \quad (40.39)$$

where ξ represents the solidified fraction

$$\begin{aligned} \xi &= v_p t - \frac{L_g}{2L} \\ \text{for } \frac{L_g}{2v_p L} &\leq t \leq \left(1 + \frac{L_g}{2L}\right)/v_p. \end{aligned} \quad (40.40)$$

Computations in NSM were made by the finite-element method using the software Cosmos/M [40.31] in a low-gravity environment ($\text{Ra}_T = 10^3$) for gallium-doped germanium. The results reveal that, during the growth process, $|v|_{\text{max}} = |v_z|_{\text{max}}$ is localized at $r = 0$ at the distance $1.25L_g/L$ from the top of the crystal, and $v_r|_{\text{max}}$ is localized at $r = 0.125$ at the distance $L_g/(2L)$ from the top of the crystal. In the first part of the growth process, $|v|_{\text{max}} = |v_z|_{\text{max}}$ increases from 0.1772 to 0.1817 and $|v_r|_{\text{max}}$ increases from 0.0598 to 0.0621. In the second part, $|v|_{\text{max}} = |v_z|_{\text{max}}$ decreases from 0.1817 to 0.0193

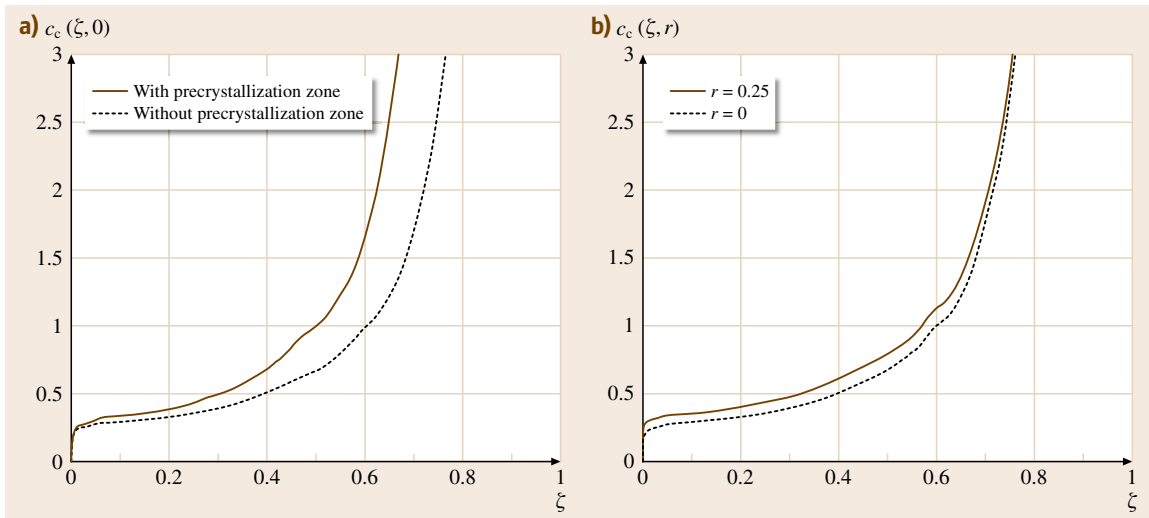


Fig. 40.2a,b Computed Ga concentration in the crystal versus ξ and r

and $|v_r|_{\max}$ decreases from 0.0621 to 0.0043. During the growth, at all points of the melt, the impurity concentration c increases but not uniformly. On the axis, parallel to the ampoule axis, c increases from the top towards the interface. In a transversal section of the ampoule, c increases from the axis towards the side wall. The impurity concentration on the axis of the crystal increases from kc_0 to c_0 in the solidified fraction $\xi \in (0; 0.6099)$, and the percent axial segregation defined by the formula $\Delta c_{\text{ax}} = |c_c(0, 0) - c_c(0.6099, 0)| \times 100/k$ is $\Delta c_{\text{ax}} = 854.5$ (Fig. 40.2a). The percent radial segregation, defined as $\Delta c_{\text{rad}} = |c_c(\xi, 0) - c_c(\xi, \Lambda)| \times 100/k$ for $\xi = 0.6099$, is $\Delta c_{\text{rad}} = 134$ (Fig. 40.2b).

Due to the decrease of the melt in the ampoule, the percent axial segregation in the crystal increases with the solidified fraction ξ . The percent radial segregation in the crystal increases for the first three-quarters and decreases thereafter. Finally, it has been shown [40.32] that, if the initial impurity distribution in the melt is not uniform like in [40.31], and if it is given by

$$c_0(r, z) = \frac{1}{\alpha(a)} \left\{ 1 + \frac{1-k}{k} \frac{\Lambda-r}{\Lambda} \times \exp \left[-\frac{v_p \text{Sc}}{\text{Pr}} (1-z) \right] - \frac{a \cdot r}{\Lambda} \right\}, \quad (40.41)$$

then the computed impurities distribution in the crystal (in the NSM) on the solidified fraction $\xi \in (0; 0.7)$ is a constant equal to the prescribed concentration $c_c = 1$.

40.1.5 Modified Quasi-Steady-State Model (MQSSM) and Modified Nonstationary Model (MNSM)

In order to evaluate the effect of the precrystallization zone on the impurity distribution in the crystal, two different models – MQSSM and MNSM – have been reported in the literature [40.28, 33–35]. In such models, it is assumed that the melt→solid phase transition does not take place on a flat mathematical surface like in UDL, QSSM, PSSM, and NSM, but rather in a thin region of width 10^{-9} m masking the crystal, where both phases coexists and there are periodically distributed solid inclusions (clusters) of size 10^{-10} m. This periodic microstructure is created by the crystal which, like a matrix, governs the arrangement of its own atoms from the melt into a specific crystalline lattice and creates periodically distributed clusters (solid inclusions). These clusters do not affect the melt flow but can influence the diffusion of impurities and the heat conductivity. In the isotropic case, for the impurities and heat transport, new diffusion and heat conductivity

coefficients appear, and in the anisotropic case, new diffusion and heat conductivity tensors appear. These new coefficients and tensors depend on the spatial coordinates, on the geometry of clusters, and on the volumetric concentration of the clusters.

In MQSSM presented in [40.28], it is assumed that in the precrystallization zone the new diffusion coefficient decreases with respect to the spatial coordinate z (Fig. 40.1). According to [40.36, 37], the clusters do not influence the flow near the interface (i.e., the computed flow fields are identical to those obtained in QSSM model), but have a very small influence (of order 10^{-4}) on the heat transport. For example, changing the Schmidt number in the impurity transport equation from QSSM, the effect of the precrystallization zone on the axial and radial impurity distribution in the neighborhood of the melt–crystal interface was computed for different volumetric concentration of the clusters (solid inclusions). Computations performed with this model show that the influence of the precrystallization zone on the repartition of impurities is relevant. The concentration of impurities in the precrystallization zone reaches values which can be as high as ten times those obtained with QSSM. Consequently, the axial impurity distribution is nonuniform. In MNSM presented in [40.34], it is assumed that the microstructure existing in the precrystallization zone does not influence the flow and the heat transport, but that the transport of impurities is governed by the equation

$$\Pi \frac{\partial c}{\partial t} + \mathbf{v} \nabla c = \frac{\text{Pr}}{\text{Sc}} (\mathbf{I} + \Phi) \nabla^2 c, \quad (40.42)$$

where Π is porosity, \mathbf{I} is the identity tensor, and Φ is a tensor defined by

$$\Phi_{kl} = -\varphi \left(\delta_{kl} - \frac{1}{|V|} \int_{\partial V} \gamma_k n_l dS \right). \quad (40.43)$$

In (40.43), φ represents the volumetric concentration of the clusters, $|V|$ represents the volume of a cluster, γ_k is the solution of the boundary-value problem, δ_{kl} is the Kronecker symbol, and dS represents the elementary surface [40.36]. In particular, if the clusters are spheres, the new diffusion tensor $\mathbf{D}(\mathbf{I} + \Phi)$ is diagonal, and the new diffusion coefficients are given by the Maxwell–Jeffries formula [40.38]

$$\frac{D_{11}}{D} = \frac{D_{22}}{D} = \frac{D_{33}}{D} = 1 - \left(\frac{3}{2} \right) \varphi. \quad (40.44)$$

in these conditions, (40.42) becomes

$$\Pi \frac{\partial c}{\partial t} + \mathbf{v} \nabla c = \frac{\text{Pr}}{\text{Sc}} \left(1 - \frac{3}{2} \varphi \right) \nabla^2 c. \quad (40.45)$$

Therefore, the dispersion of impurities in the precrystallization zone is governed by (40.45), and by (40.34) in the rest of the melt.

Numerical computations of the impurities concentration have been made for the melt and crystal with thermophysical properties similar to gallium-doped germanium [40.34]: $Ra_T = 10^3$; $\varphi = 0.00985, 0.0317, 0.0491, 0.055$; $Sc = 10$; $k = 0.1$; and replacing the true unsteady process by the quasi-steady-state process. Computations show that the impurity concentration in the crystal is larger than that obtained with QSSM. The axial impurity distribution is uniform, and the radial segregation of the impurities in the crystal, computed with MQSSM, is less than that computed with QSSM.

In [40.33], it was shown rigorously (from a mathematical point of view) that the assumption of the existence of a periodic structure in the precrystallization zone permits us to deduce MNSM starting from NSM in the framework of continuum mechanics. The obtained MNSM includes the effect of the precrystallization zone. This effect gives a decrease of the molecular diffusivity D of the impurities from D to $D_{\text{eff}} = 0.917D$, and a increase of the heat conductivity K to $K_{\text{eff}} = 1.1K$ in the precrystallization zone. Numerical computations made with MNSM using the quasi-steady-state approximation [40.33, 35] show that, due to the decrease of the molecular diffusivity D , the impurity concentration in the crystal is five times larger than that computed with QSSM. Computations made in [40.31] using MNSM and those presented for a low-gravity environment ($Ra_T = 10^3$) in [40.33] show that the impurity concentration on the axis and on the walls of the crystal increases faster than that computed with NSM. The ratio of the impurity concentrations computed with MNSM and NSM at $\xi = 0.5$ (on the axis and on the walls of the crystal) is 1.45. According to [40.39], this result is in agreement with the measurements of the samples grown on the Mir space station.

Finally, in [40.40] it is shown that, if the initial impurities distribution in the melt is not uniform like in [40.31], and it is given by the formula

$$c_0(r, z) = \frac{1}{\alpha(a)} \left\{ 1 + \frac{1-k}{k} \frac{\Lambda - r}{\Lambda} \times \exp \left[-\frac{v_p Sc}{Pr} (1-z) \right] - \frac{ar}{\Lambda} \right\}, \quad (40.46)$$

then the computed impurity distribution in the crystal (in the framework MNSM) on the solidified fraction $\xi \in (0; 0.7)$ is a constant equal to the prescribed concentration $c_c = 1$.

40.1.6 Larson–Zhang–Zheng Thermal-Diffusion Model (TDM)

Doped crystal grown in space in a BS system reported in [40.41, 42] exhibits significant axial compositional nonuniformities. Due to the fact that in these cases the thermosolutal convection can be neglected, the thermodiffusion of impurities is responsible for these nonuniformities. A one-dimensional mathematical model [40.43] has been developed to explain the impurity distribution in the sample presented in [40.41]. According to [40.43], for ampoules with small-diameter cross section and for a small impurity concentration, in a strictly zero-gravity environment, the mathematical model of the heat and impurities dispersion in the melt in a BS system is defined by the following dimensionless equations, boundary conditions, and initial conditions as written in a reference frame with the origin fixed at the interface

$$\frac{\partial \theta}{\partial t} = v_p \frac{\partial \theta}{\partial z} + \frac{1}{Pr} \frac{\partial^2 \theta}{\partial z^2} - \frac{2}{Pr} \frac{K_a}{K} \frac{L}{\delta} \frac{L}{R} (\theta - \theta_f), \quad \text{for } 0 < t < \frac{1}{v_p} \text{ and } 0 < z < 1 - v_p t, \quad (40.47)$$

$$\frac{\partial c}{\partial t} = v_p \frac{\partial c}{\partial z} + \frac{1}{Sc} \frac{\partial^2 c}{\partial z^2} + \frac{1}{Sc} \frac{\partial}{\partial z} \left(\sigma \Delta T c \frac{\partial \theta}{\partial z} \right), \quad \text{for } 0 < t < \frac{1}{v_p} \text{ and } 0 < z < 1 - v_p t, \quad (40.48)$$

$$\theta(t, z) = 0 \quad \text{for } 0 < t < \frac{1}{v_p} \text{ and } z = 0, \quad (40.49)$$

$$\frac{\partial \theta}{\partial z} = 0 \quad \text{for } 0 < t < \frac{1}{v_p} \text{ and } z = 1 - v_p t, \quad (40.50)$$

$$\frac{\partial c}{\partial z} + v_p Sc (1-k) c + \sigma c \Delta T \frac{\partial \theta}{\partial z} = 0, \quad \text{for } 0 < t < \frac{1}{v_p} \text{ and } z = 0, \quad (40.51)$$

$$\frac{\partial c}{\partial z} = 0 \quad \text{for } 0 < t < \frac{1}{v_p} \text{ and } z = 1 - v_p t, \quad (40.52)$$

$$\theta(0, z) = \begin{cases} 1 & \text{for } \frac{L_g}{2L} \leq z \leq 1 \\ \frac{2L}{L_g} z & \text{for } 0 \leq z \leq \frac{L_g}{2L} \end{cases}, \quad (40.53)$$

$$c(0, z) = c_0(z). \quad (40.54)$$

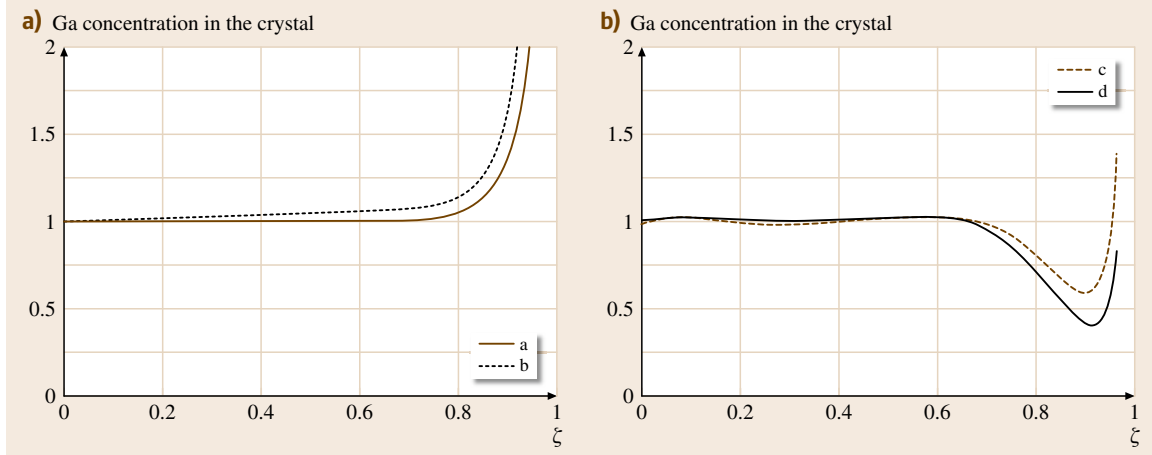


Fig. 40.3a,b Computed Ga concentration in the crystal versus ξ : **(a)** for the nonuniform case and **(b)** for the modified initial dopant repartition (after [40.44])

Equation (40.47) represents the dimensionless heat transport equation in the melt, which takes into account the heat dispersion due to the growth rate v_p , the thermal diffusivity in the melt $\lambda_L = \nu_L / \text{Pr}$, and the heat loss to the environment from the sample surface. Equation (40.48) represents the dimensionless impurities transport equation in the melt which takes into account the impurity dispersion due to the growth rate v_p , the molecular diffusion $D = \nu / \text{Sc}$, and the thermal diffusion σ (Soret effect). The boundary condition (40.49) expresses the melt–crystal interface as fixed at $z = 0$ and the dimensionless temperature at the interface equal to zero. In general, the shape of the melt–crystal interface is set by the conditions for the equilibrium melting temperature and the balance of conductive heat fluxes across the interface with the latent heat released there; for strictly zero gravity ($\text{Ra}_T = 0$) [40.7], computations show that the interface is flat and fixed. The boundary condition (40.50) represents the no-flux condition for the heat at the top of the ampoule, and the boundary condition (40.51) gives the dopant concentration near the melt–crystal interface on the melt side. The boundary condition (40.52) is for no flux of the impurities on the top of the ampoule. The initial condition (40.53) is the temperature distribution in the melt at the time when solidification begins, and the initial condition (40.54) represents the impurity repartition in the melt when solidification begins.

The solidified fraction ξ at time t is given by

$$\xi = v_p t, \quad (40.55)$$

and the impurity concentration in the crystal is given by

$$c_c(\xi) = kc \left(\frac{\xi}{v_p}, 0 \right) \quad \text{for } 0 \leq \xi \leq 1. \quad (40.56)$$

Numerical results obtained with TDM using a second-order central difference scheme [40.43] are in agreement with the experimental results reported in [40.41]. The same numerical method with TDM gives numerical results which are qualitatively in agreement with the results reported in [40.42], as shown in [40.45]. Moreover, in [40.45] it is shown that, if the initial impurity distribution in the melt is not uniform (Fig. 40.3a) like in [40.42], but if it is given by the formula

$$c_0(x) = \frac{v_p \text{Sc} L_g}{v_p \text{Sc} L_g + \sigma \Delta T 2L} \left\{ 1 + a_1 x + a_2 x^2 + \left(\frac{1-k}{k} + \frac{\sigma \Delta T 2L}{k v_p \text{Sc} L_g} \right) \times \exp \left[- \left(v_p \text{Sc} + \frac{\sigma \Delta T 2L}{L_g} \right) z \right] \right\}, \quad (40.57)$$

then the computed impurity concentration in the crystal on the solidified fraction $\xi \in (0; 0.7)$ is a constant equal to the prescribed concentration $c_c = 1$ (Fig. 40.3b).

40.2 Model-Based Prediction of the Impurity Distribution – EFG System

The prototype EFG system used in this work is presented in Fig. 40.4.

The central component of the system is a die which controls the heat and mass transfer from the crucible to the meniscus, i.e., the liquid bridge retained between the die and the crystal. Processes that take place in the melt (more precisely, in the meniscus melt) near the melt–crystal interface determine the impurity distribution in the crystal. During the past three decades, several mathematical models have been reported for predicting the impurity distribution in a crystal grown in such a system. Some of these models and the predictions obtained are presented below.

40.2.1 The Uniform-Diffusion-Layer Model (UDLM)

The UDLM presented for a BS system was extended for an EFG system considering that the effective partition coefficient k_{eff} is given by Fleming's formula [40.46]. If it is assumed that the uniform diffusion layer thickness is equal to the total height of the meniscus and the die has a long capillary channel, then the effective partition coefficient k_{eff} is equal to unity [40.47–53] for any impurity. Hence, according to UDLM, the impurity distribution in the crystal is uniform (i.e., no variations of the impurity concentration along the crystal length and cross section), and the value of the impurity concentration in the crystal is given by

$$c = k_{\text{eff}} c_{\infty} = c_{\infty}. \quad (40.58)$$

This prediction implies that the growth process in an EFG system has a low tolerance for rejected melt impurities, which definitively shows that UDLM is an oversimplified model. Impurities are generally trapped in the boundary layer within the meniscus melt. Interface-region convection in EFG can be manipulated through design of die capillaries to redistribute segregated impurities [40.50–53]

40.2.2 Tatarchenko Steady-State Model (TSSM)

TSSM is a model of impurity transport in the meniscus, which relates the values of k_{eff} to the parameters of capillary shaping and feeding, is presented in a book by Tatarchenko [40.46]. The stationary process is considered, and it is assumed that the meniscus and capillary melt have not been stirred, where the conditions of com-

plete stirring are maintained in the crucible. Impurity transport in the meniscus is described by the equation

$$D \left(\frac{d^2 c}{dr^2} + \frac{1}{r} \frac{dc}{dr} \right) = -v \frac{dc}{dr} \quad (40.59)$$

with the following boundary condition at the melt–crystal interface

$$-D \left. \frac{dc}{dr} \right|_{r=r_0} = v_0 (1-k) c(r_0). \quad (40.60)$$

Here, c represents the impurity concentration in the melt, D is the diffusion coefficient, k is the partition

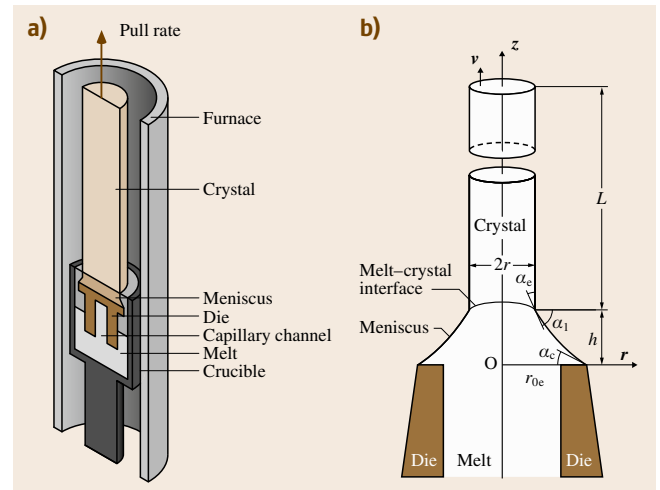


Fig. 40.4a,b Prototype EFG crystal growth system. (a) Prototype EFG system, (b) schematic EFG used in mathematical model

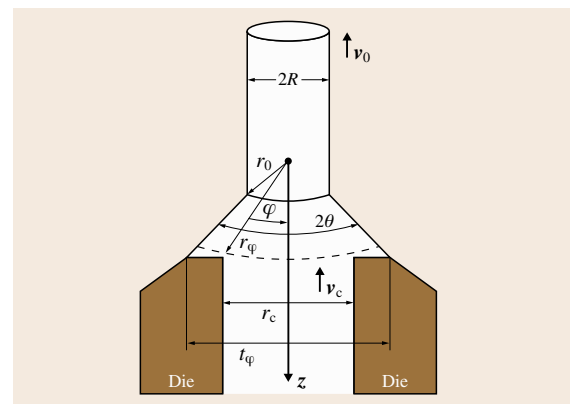


Fig. 40.5 EFG diagram for TSSM

coefficient at equilibrium, and the other notations are given in Fig. 40.5.

The melt flow rate in the meniscus is given by

$$v(r) = \frac{v_0 r_0}{r}. \quad (40.61)$$

Impurity transport in the capillary channel is described by the equation

$$D \frac{d^2 c}{dz^2} = -v_c \frac{dc}{dz} \quad (40.62)$$

with the following boundary condition

$$c \rightarrow c_\infty \quad \text{if} \quad z \rightarrow \infty. \quad (40.63)$$

Employment of these equations and boundary conditions gives the following expression describing the impurity concentration distribution in the meniscus

$$c(r) = (1 - k_{\text{eff}}) c(r_0) \left(\frac{r_0}{r} \right)^e + \frac{c_\infty - (1 - k) \left(\frac{r_0}{r_\phi} \right)^e (\cos \varphi - 1) c(r_0)}{1 + \left[\left(\frac{v_0 \theta r_0}{v_c \varphi r_\phi} - 1 \right) \right] \cos \varphi}, \quad (40.64)$$

where

$$\cos \varphi = \left(1 - \frac{r_c^2}{4r_\phi^2} \right)^{1/2} \quad \text{and} \quad e = \frac{v_0 R}{D \sin \theta}, \quad \varphi \in [0, \Phi]. \quad (40.65)$$

Taking into account the equalities $k = c_S/c(r_0)$, $k_{\text{eff}} = c_S/c_\infty$, from (40.64) for $r = r_0$ it follows that

$$k_{\text{eff}}^{-1} = 1 + \left(\frac{v_0 \theta r_0}{v_c \varphi r_\phi} - 1 \right) \cos \varphi + \frac{(1 - k)(1 - \cos \varphi) (r_0/r_\phi)^e}{k}. \quad (40.66)$$

Using the relations

$$2v_0 R = v_c r_c, \quad \frac{r_0}{r_\phi} = 2R/t_\phi, \quad r_0 = \frac{R}{\sin \theta}, \quad (40.67)$$

(40.66) becomes

$$k_{\text{eff}}^{-1} = 1 + \left(\frac{v_0 r_c}{\varphi t_\phi - 1} \right) \cos \varphi + \frac{(1 - k)(1 - \cos \varphi) (2R/t_\phi)^{v_0 R/D \sin \theta}}{k}. \quad (40.68)$$

Equation (40.68) relates the value of the effective coefficient of partition k_{eff} with the process parameters: v_0 , $2R$, t_ϕ , r_c , θ , D , and k .

When the capillary channel radius its maximum value, $r_c = t_\phi$, (40.68) becomes

$$k_{\text{eff}} = \frac{k}{k + (1 - k)(1 - \cos \varphi) \left(\frac{2R}{t_\phi} \right)^{\frac{v_0 R}{D \sin \theta}}}. \quad (40.69)$$

According to TSSM, the impurity distribution in the crystal is uniform (i.e., no variations of the impurity concentration along the crystal length and cross section), and the value of the impurity concentration in the crystal is given by

$$c_c = k_{\text{eff}} c_\infty, \quad (40.70)$$

where k_{eff} is given by (40.68).

In order to verify the above prediction for Al impurities in Si ($k = 0.002$, $D = 5.3 \times 10^{-4} \text{ cm}^2/\text{s}$, $2R = 0.03 \text{ cm}$, $t_\phi = 0.06 \text{ cm}$), the effective partition coefficient k_{eff} was computed. It was found that $k_{\text{eff}} \ll 1$, where k_{eff} increases as both the growth rate and the melt flow in the capillary channel increase [40.46]. Mass-spectrographic analysis of the impurity content in tapes grown from refined metallurgical silicon confirms that $k_{\text{eff}} \ll 1$. The sulfur distribution along the axis of a silicon tape obtained by laser emission analysis shows also that $k_{\text{eff}} \ll 1$, in agreement with the value of k_{eff} given by (40.68). According to [40.46], in order to verify the TSSM-based prediction, a series of 0.01 mass indium-doped silicon tapes was grown, where the predicted values of k_{eff} are in agreement with those obtained experimentally. The values of k_{eff} given by Fleming's formula are several orders of magnitude greater than the experimental values. For the variation of the impurity concentration observed experimentally along the crystal cross section in [40.46], the following explanation was given: For the case of a horizontal melt flow in the meniscus from the die edge towards the center, impurities with $k_{\text{eff}} < 1$ are driven off by the growing crystal and accumulate in the central part of the meniscus. Impurities may be moved away in order to improve the quality of the crystal. For this aim, the rejected impurities were studied using an axisymmetric or *displaced* die shape in an EFG system with melt replenishment [40.54, 55].

40.2.3 Melt Replenishment Model (MRM)

Recently, the influence of the die geometry and various growth conditions on the fluid flow and on the

solute distribution has been studied in an EFG system with melt replenishment (MR) using numerical simulation [40.56]. The nonuniform distribution of the voids (trapped gas bubbles) along the cross section of the sapphire rod was analyzed, assuming that the voids are impurities which are present in the melt and that their transport in the capillary channel and in the meniscus is governed by the stationary convection–diffusion equation. It was also assumed that the mechanism of transfer of the voids from the melt into the crystal is similar to the transfer of impurities. Two types of die designs were investigated: one with a central capillary channel (CCC) and another with an annular capillary channel (ACC). The fluid flow is characterized by a small Reynolds number (due to the small value of the fluid velocity and of the pulling rate) and consequently the fluid flow is laminar. Computations prove that, for both die geometries, the flow field near the meniscus free surface exhibits the same aspect, with only the velocity field values being different: for the ACC die, all the velocity values are higher than for the CCC die. For small Marangoni numbers (Ma), no loop or cell structure appears in the melt flow. As the Ma number increases, the loop position slightly migrates toward the crystallization interface. The isoconcentration field and solute concentration near the solidification interface are different for the two studied shaper designs. The solute fields for the CCC and ACC dies differ in aspect and concentration values: the concentration field for CCC die shows a single maximum close to the free meniscus surface; for the ACC die, a strong maximum that is two times higher appears near the symmetry axis. Moreover, the radial segregation is higher

for the ACC die than for the CCC die and increases if the Ma number increases. These numerical results with good agreement with the experiments show that the gas contained in the melt acts as a solute rejected at the interface and nucleates into bubbles at the more concentrated locations. The experimental fact that the outer bubbles are situated at a distance from the external surface of the order of the meniscus height demonstrates that Marangoni convection exists in a shaped sapphire meniscus. Finally, in order to reduce the concentration of voids, a CCC die is recommended as well as growth with low meniscus height and low pulling rate.

For optimization and control of the growth process, in order to concentrate the voids close to the crystal surface which can be removed by polishing, the dependences of the fluid flow and impurity distribution on some process parameters (e.g., the pulling rate, radius of the capillary channel, natural convection, Marangoni convection, and vertical temperature gradient) have been studied [40.44, 57–60]. First, the dependences of the melt flow and impurity distribution on the pulling rate and on the capillary channel radius were studied; the temperature variations and their consequences were completely neglected (no Marangoni convection) [40.57].

The equations which define the model are the incompressible Navier–Stokes equations and the conservative convection–diffusion equation

$$\rho_1 \frac{\partial \mathbf{u}}{\partial t} - \eta \nabla^2 \mathbf{u} + \rho_1 (\mathbf{u} \nabla) \mathbf{u} + \nabla p = \mathbf{F}, \quad (40.71)$$

$$\nabla \cdot \mathbf{u} = 0, \quad (40.72)$$

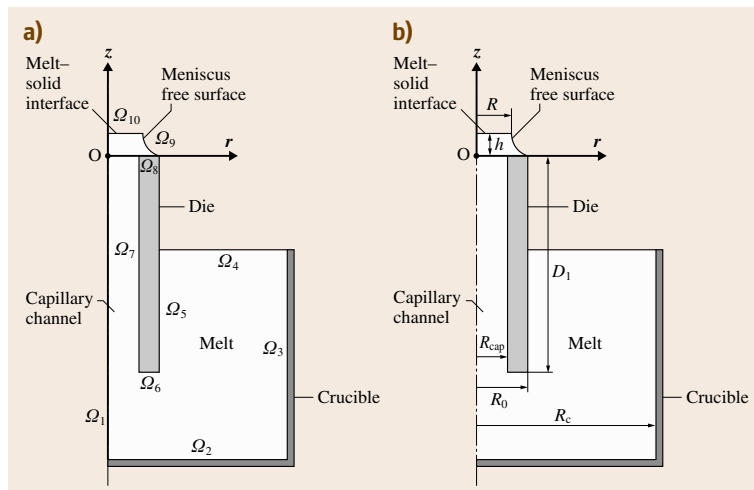


Fig. 40.6a,b EFG diagram in the case of MRM

$$\frac{\partial c}{\partial t} + \nabla(-D\nabla c + c\mathbf{u}) = 0, \quad (40.73)$$

written in a cylindrical polar coordinate system as shown in Fig. 40.4. In the above equations, $\mathbf{u} = (u_r, u_z)$ is the velocity vector, c is the impurity concentration; \mathbf{F} is the volume force field due to gravity, which for zero gravity is $\mathbf{F} = \mathbf{0}$ and for terrestrial conditions is $\mathbf{F} = \rho_l \mathbf{g}$ when: ρ_l is the melt density; \mathbf{g} is the gravitational acceleration; p is the pressure; η is the dynamical viscosity; t is time; and D is the impurity diffusion. Axisymmetric solutions are sought in a two-dimensional domain with boundaries $\Omega_1 - \Omega_{10}$, as shown in Fig. 40.6.

On the boundaries $\Omega_1 - \Omega_{10}$, the following conditions are considered:

1. For the incompressible Navier–Stokes equations:

- Axial symmetry on Ω_1

$$u_r = 0. \quad (40.74)$$

- Given inflow velocity on Ω_4

$$\mathbf{u} = -\frac{\rho_s}{\rho_l} \frac{R^2}{R_c^2 - R_0^2} v \mathbf{k}, \quad (40.75)$$

where \mathbf{k} represents the unit vector of the Oz -axis; this condition expresses continuous melt replenishment, i.e., the melt level in the crucible is maintained constant.

- Slip condition on Ω_9

$$\mathbf{un} = 0, \quad (40.76)$$

where \mathbf{n} is the unit normal vector of Ω_9 .

- Given outflow velocity on Ω_{10}

$$\mathbf{u} = v \mathbf{k}. \quad (40.77)$$

- Nonslip condition on $\Omega_2 U \Omega_3 U \Omega_5 U \Omega_6 U \Omega_7 U \Omega_8$

$$\mathbf{u} = \mathbf{0}. \quad (40.78)$$

2. For the conservative convection–diffusion equation

- Axial symmetry on Ω_1

$$\frac{\partial c}{\partial r} = 0. \quad (40.79)$$

- Impurity flux rejected into the melt on Ω_{10}

$$\frac{\partial c}{\partial \mathbf{n}} = -\frac{v}{D} (1 - K_0) c. \quad (40.80)$$

- No impurity flux, i.e., insulation on $\Omega_2 U \Omega_3 U \Omega_5 U \Omega_6 U \Omega_7 U \Omega_8 U \Omega_9$

$$\frac{\partial c}{\partial \mathbf{n}} = \mathbf{n} \nabla c = 0. \quad (40.81)$$

- Given concentration on Ω_4

$$c = C_0. \quad (40.82)$$

The system (40.71–40.73) has a unique stationary solution, i.e., $\partial \mathbf{u} / \partial t = 0$ and $\partial c / \partial t = 0$, which satisfies the above boundary conditions. This describes the steady-state process.

In order to identify a nonstationary solution of the system (40.71–40.73) which describes a transient process, beside the above boundary conditions, it is necessary to specify an initial melt flow velocity

$$u_r(t_0) = 0, \quad u_z(t_0) = 0, \quad (40.83)$$

and the initial impurity distribution

$$c(t_0) = C_0. \quad (40.84)$$

The significance of these quantities and their values for the considered EFG system are given in Table 40.1 for Al-doped Si.

According to MRM, the value of the impurity concentration in the crystal is given by

$$c_c = k c_{\text{interface}}. \quad (40.85)$$

Using the right-hand side of (40.85) and the stationary solution of the boundary-value problem (40.71–40.82),

Table 40.1 Nomenclature

Nomenclature		Value
c	Impurity concentration (mol/m ³)	
C_0	Initial alloy concentration (mol/m ³)	
D	Impurity diffusion (m ² /s)	5.3×10^{-8}
D_l	Die length (m)	0.04
g	Gravitational acceleration (m/s ²)	9.81
h	Meniscus height (m)	0.5×10^{-3}
K_0	Partition coefficient	0.002
η	Dynamical viscosity (kg/(m s))	7×10^{-4}
p	Pressure (Pa)	0
$Pe_{\text{mass}} = \frac{v R_{\text{cap}}}{D}$	Péclet number for mass transfer	
R	Crystal radius (m)	1.5×10^{-3}
R_{cap}	Capillary channel radius (m)	
R_c	Inner radius of the crucible (m)	23×10^{-3}
R_0	Die radius (m)	2×10^{-3}
ρ_l	Density of the melt (kg/m ³)	2500
ρ_s	Density of the crystal (kg/m ³)	2300
\mathbf{u}	Velocity vector	
v	Pulling rate (m/s)	
z	Coordinate in the pulling direction	

the following prediction can be obtained: constant impurity concentration along the crystal length and variation of the impurity concentration along the crystal cross section. The use of the right-hand side of (40.85) for a nonstationary solution of the boundary-value problem (40.71–40.84) leads to the prediction of the variation of the impurity concentration along the crystal length and along the crystal cross section during a transition period. In [40.44, 57], computations were

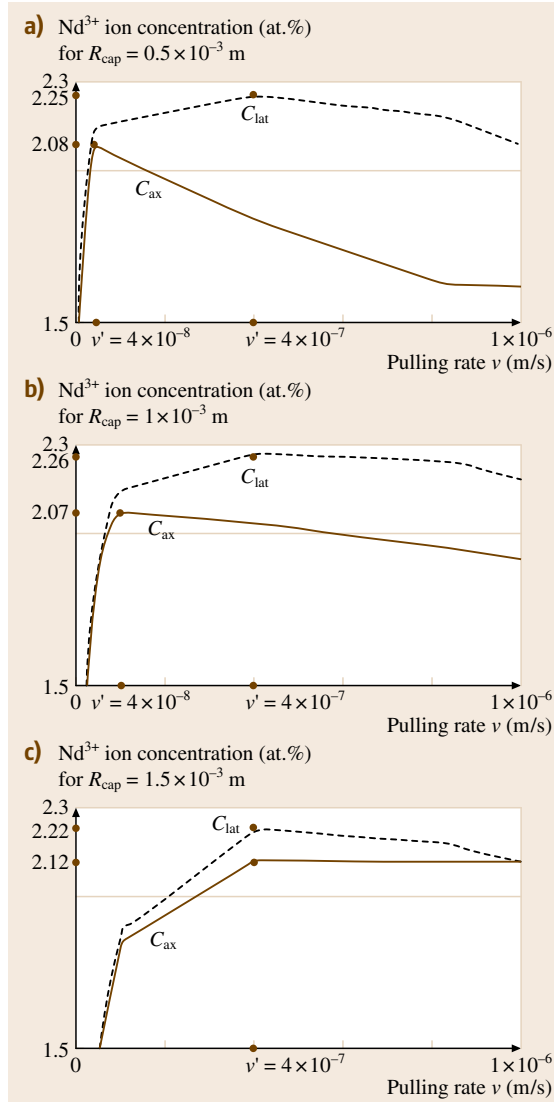


Fig. 40.7a–c Dependence of the Nd^{3+} ion concentration on the pulling rate v for (a) $R_{\text{cap}} = 0.5 \times 10^{-3}$ m, (b) $R_{\text{cap}} = 1 \times 10^{-3}$ m, and (c) $R_{\text{cap}} = 1.5 \times 10^{-3}$ m

made using COMSOL Multiphysics 3.2 software for zero gravity and for terrestrial conditions in the case of the following EFG system: crucible inner radius of $R_c = 23 \times 10^{-3}$ m, die radius of $R_0 = 2 \times 10^{-3}$ m, and die length of 40×10^{-3} m; two-thirds of the die immersed in the crucible melt; constant crucible melt height of 40×10^{-3} m; capillary channel radius of $R_{\text{cap}} = (0.5, 1, 1.5) \times 10^{-3}$ m; and pulling rate v in the range $10^{-10} \text{ m/s} \leq v \leq 10^{-6} \text{ m/s}$. The meniscus height was $h = 0.5 \times 10^{-3}$ m, and the single-crystal rod radius (being grown) was $R = 1.5 \times 10^{-3}$ m.

The computations reveal that, in the stationary case, for a given R_{cap} , there exist critical pulling rate values v' depending on R_{cap} at which the impurity concentration has a maximum. If v increases in the range $[1 \times 10^{-10}, v']$, the impurity concentration increases, and if v increases in $[v', 1 \times 10^{-6}]$, the concentration decreases slowly. Moreover, the impurity concentration on the axis and on the lateral surface of the crystal, and the absolute value of the difference between them – called the radial segregation – depend on the pulling rate and the capillary radius (Fig. 40.7). The optimal value of R_{cap} for which the crystal has the best homogeneity (radial segregation is minimum) is $R_{\text{cap}} = R = 1.5 \times 10^{-3}$ m.

Numerical results concerning a nonsteady state show that the nonstationary melt flow field and the impurity concentration field in the whole melt tend to the stationary melt flow field and to the stationary impurity concentration, respectively. The transition period, defined as that period of time after which the impurity concentration at the interface becomes equal to those obtained in the stationary case, depends on R_{cap} and v .

The impurity concentrations in the meniscus at three different instances of time $0 < t_1 < t_2 < t_3$ are presented in Fig. 40.8 for $R_{\text{cap}} = 1.5 \times 10^{-3}$ m and $v = 10^{-6}$ m/s.

These computed results are in agreement with experimental data reported by Cao et al. [40.53]: each impurity has a transient distance or crystal length until the steady-state segregation is established. The localization of the maximum of the dopant concentration on the free meniscus surface shows that the model is incomplete. More precisely, natural and Marangoni convections should be involved in order to move the maximum of the dopant concentration near the melt–solid interface, as was observed experimentally [40.56].

In [40.58–60] the combined effect of the buoyancy and Marangoni forces on the fluid flow and on the dopant distribution is analyzed in the stationary case. Thus, the growth process is described by the stationary incompressible Navier–Stokes equations written in the

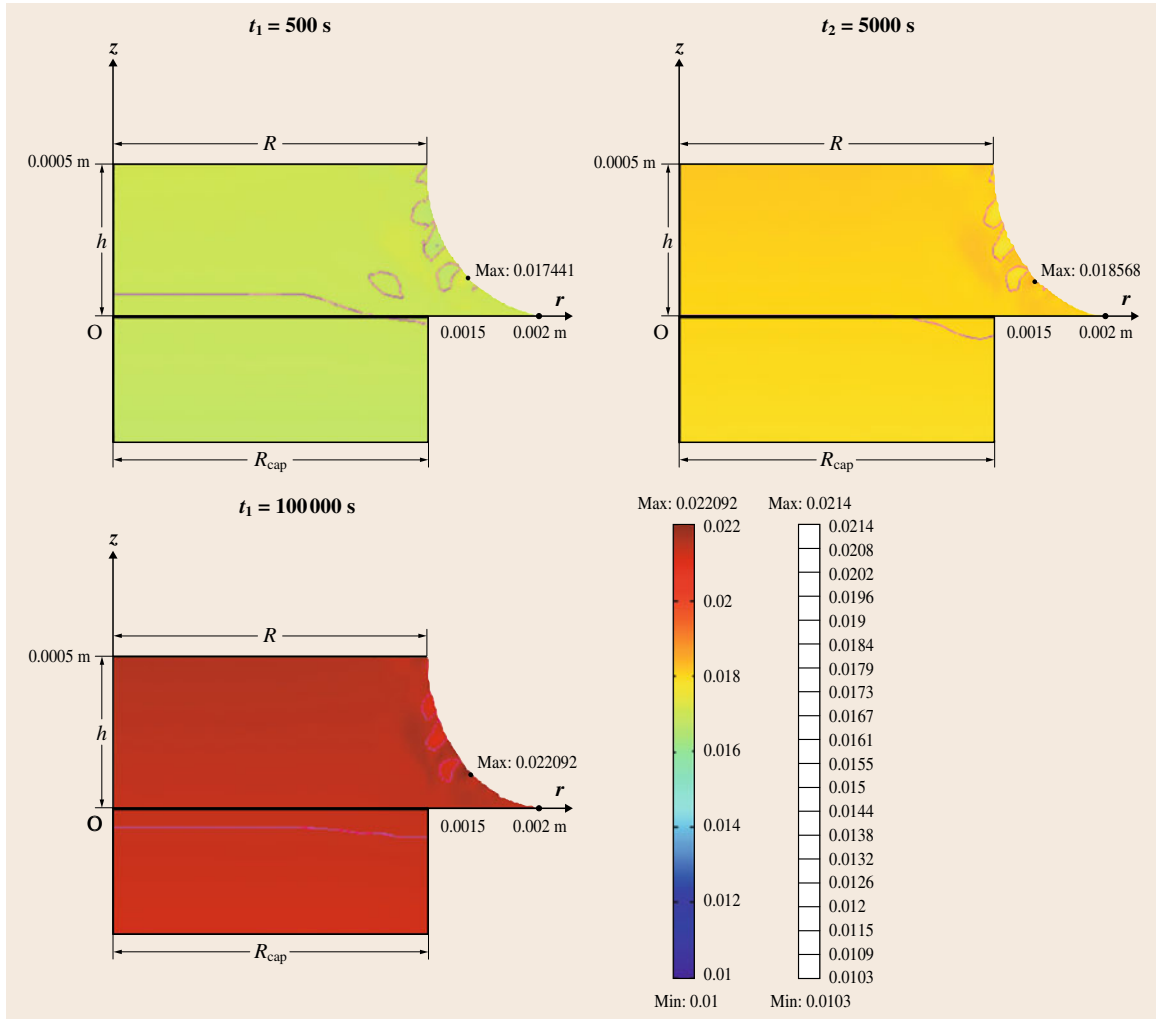


Fig. 40.8 Al concentration at three instances of time $t_1 < t_2 < t_3$, for $v = 10^{-6}$ m/s and $R_{\text{cap}} = 1.5 \times 10^{-3}$ m

Boussinesq approximation [i. e., $\mathbf{F} = \beta \rho_1 \mathbf{g}(T - \Delta T)$, where β is heat expansion coefficient and $\Delta T = (T_0 + T_m)/2$ is the reference temperature at the free surface], and the convection–conduction and conservative convection–diffusion equations. For implementation of the Marangoni effect, the weak form of the boundary application mode is employed. The fluid density is assumed to vary with temperature as $\rho(r, z) = \rho_1[1 - \beta(T(r, z) - \Delta T)]$, and the surface tension γ in the meniscus is assumed to vary linearly with temperature as $\gamma(r, z) = \gamma_1 + (d\gamma/dT)(T(r, z) - \Delta T)$, where γ_1 is the surface tension at the temperature ΔT , and $d\gamma/dT$ is the rate of change of surface tension with the temperature.

For implementation of the Marangoni effect, the boundary condition

$$\eta \begin{pmatrix} t_r & t_z \end{pmatrix} \begin{pmatrix} 2 \frac{\partial u}{\partial r} & \frac{\partial u}{\partial z} + \frac{\partial v}{\partial r} \\ \frac{\partial u}{\partial z} + \frac{\partial v}{\partial r} & 2 \frac{\partial v}{\partial r} \end{pmatrix} \begin{pmatrix} n_r \\ n_z \end{pmatrix} = \frac{d\gamma}{dT} \left(\frac{\partial T}{\partial r} + \frac{\partial T}{\partial z} \right), \quad (40.86)$$

is imposed on the free surface (meniscus). This expresses that the gradient velocity field along the meniscus is balanced by the shear stress, where $\mathbf{t} = (t_r, t_z)$ and $\mathbf{n} = (n_r, n_z)$. The sign of the rate $d\gamma/dT$, in general, depends on the material, with leading downward

($d\gamma/dT < 0$) or upward ($d\gamma/dT > 0$) flow on the free liquid surface.

The effect of the buoyancy and Marangoni forces on the fluid flow and on the impurity distribution were investigated numerically including both the cases of downward and upward flows on the liquid free surface (meniscus). Thus, two materials having negative and positive surface tension rates (Nd:Y₃Al₅O₁₂ (Nd:YAG) and Nd:LiNbO₃) were considered. The computed dopant distribution in the meniscus for different values of the Grashof and Marangoni numbers ($Gr = 0.00022$ and 0.02231 , $Ma = 0.049$ and 4.913 for Nd:YAG, and $Gr = 0.00252$ and 0.25222 , $Ma = 0.671$ and 67.072 for Nd:LiNbO₃), are illustrated in Figs. 40.9 and 40.10. Computations show that the dopant concentration increases from the initial value C_0 to a maximum value C_{max} situated at the level of the melt–crystal interface $z = h$, marked on Figs. 40.9 and 40.10. The maximum values of the Nd³⁺ ion concentration show that increases of the Marangoni and Grashof numbers lead to a decrease of C_{max} and can move it from the lateral surface of the crystal toward the axis. The effect of the Grashof number is smaller on the C_{max} localization and its values, and shows that the

Marangoni convection has a dominant effect on the natural convection.

The buoyancy- and surface-driven flows perturb the forced flow: the arrows presented in Figs. 40.9 and 40.10 denote the flow of the velocity field caused by the surface-tension-driven flow, with downward flow on the meniscus surface for Nd:YAG ($d\gamma/dT < 0$; Fig. 40.9), and upward flow on the meniscus surface for Nd:LiNbO₃ ($d\gamma/dT > 0$; Fig. 40.10). The maximum velocity of the fluid flow in the meniscus presents a linear dependence on the Marangoni number. More precisely, if the Marangoni number increases, then the maximum velocity of the fluid flow increases. Concerning the radial segregation, computations show that an increase of the Grashof or Marangoni number leads to a smaller radial segregation, clearly because of better mixing in these cases. The magnitude of the radial segregation is more sensitive to the Marangoni convection and less sensitive to the natural convection. The magnitude of the radial segregation changes are larger for larger Marangoni numbers.

Figure 40.10 shows a similar location of the maximum of the dopant distribution to those reported experimentally for sapphire [40.56]. The question here

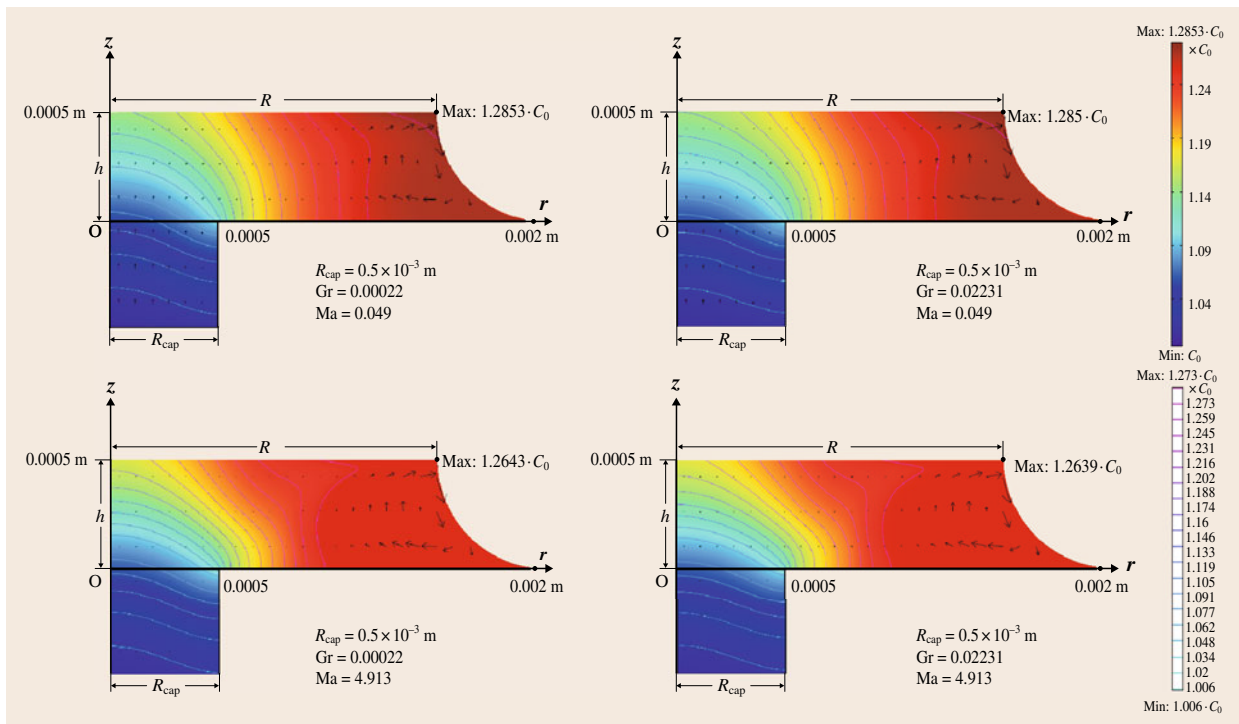


Fig. 40.9 Dependence of the dopant distribution on the Grashof and Marangoni numbers for Nd:YAG

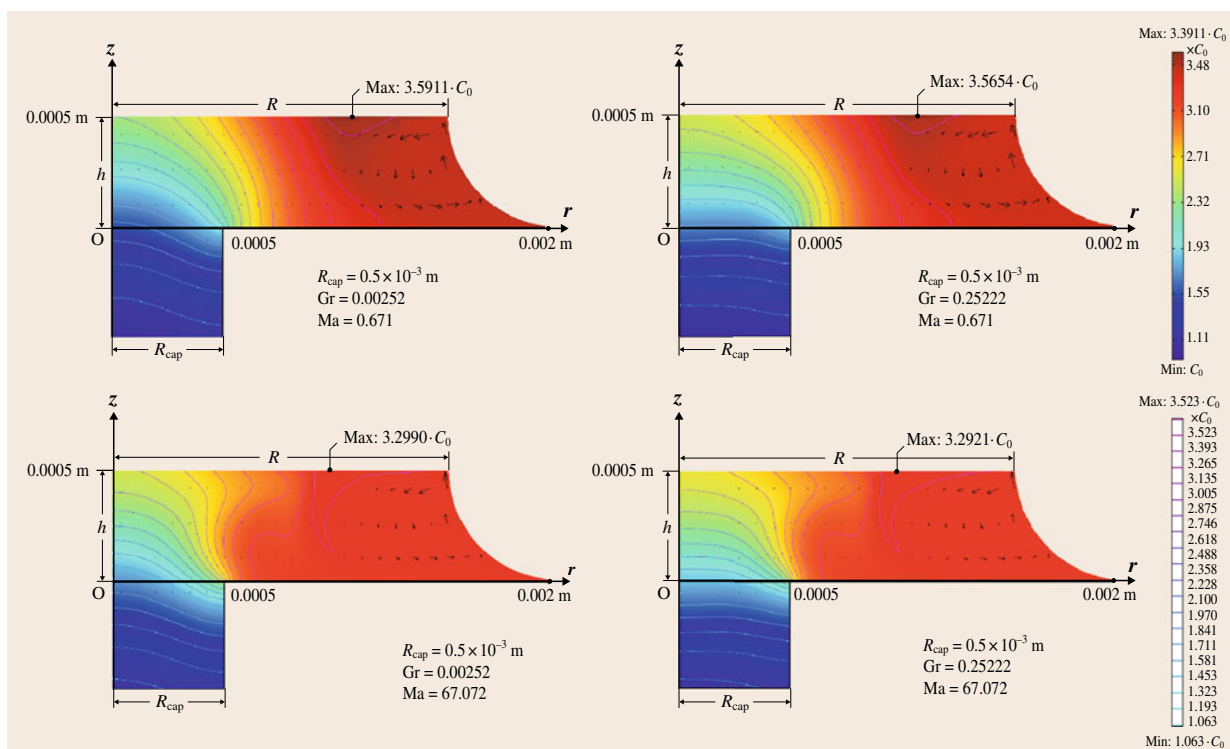


Fig. 40.10 Dependence of the dopant distribution on the Grashof and Marangoni numbers for Nd:LiNbO₃

is whether it is possible to determine conditions for which the maximum of the dopant distribution is located at the triple point, and at the distance from the lateral crystal surface equal to the meniscus height, respectively. There is also the question as to which case assures the best homogeneity of the crystal. The answers are found in the paper [40.60] in which the dependences of the Marangoni flow and impurity distribution on the vertical temperature gradient in sapphire (Al₂O₃) fibers are reported. Thus, for three representative values of the vertical temperature gradients k_g and for different Marangoni numbers Ma corresponding to the surface tension gradients $d\gamma/dT$ situated in the range $[-6 \times 10^{-5}, 0] \text{ N/(m K)}$, the impurity distributions are computed for two cases: (i) the buoyancy is taken into account (the heat expansion coefficient has the value reported in the literature, i. e., $\beta = 3 \times 10^{-5} \text{ 1/K}$); and (ii) the buoyancy is neglected ($\beta = 0$), revealing the existence of three critical Marangoni numbers – Ma_{c1} , Ma_{c2} , Ma_{c3} – as reported for two-dimensional containers, determined by the behavior of the fluid flow. For Ma in the range $[0, Ma_{c1})$, the downward flow ($d\gamma/dT < 0$) on the free liquid sur-

face leads to a steady flow, with a decrease of the maximum of the dopant concentration C_{max} located at the triple point if Ma increases. For Ma in the range $[Ma_{c1}, Ma_{c2})$, turbulence in the fluid flow appears, leading to an increase of C_{max} , still located at the triple point. For Ma in the range $[Ma_{c2}, Ma_{c3})$, this increased C_{max} is shifted inside the crystal from the melt–crystal interface at a distance on the same order as the meniscus height from the external crystal surface. If Ma is larger than Ma_{c3} , C_{max} is shifted into the center of the crystal.

We thus conclude that the best homogeneity of the crystal is assured in the range $[0, Ma_{c1})$ in which steady flow takes place (the maximum of the dopant distribution is located at the triple point). In this range, voids are situated at the lateral crystal surface and hence can be removed by polishing with minimum material loss. This range becomes larger if the vertical temperature gradient k_g and heat flux coefficient β decrease, which proves that a smaller vertical temperature gradient and a lower gravity, e.g., zero gravity, assures the best homogeneity of the crystal over a wide range of surface tension gradients. This suggests to practical crystal growers that a possible feedback control for delaying the Marangoni

convection can be obtained by decreasing the vertical temperature gradient in the furnace.

40.2.4 Melt Without Replenishment Model (MWRM)

In [40.61], a MWRM model in which the melt flow and impurity distribution are described in an EFG system without melt replenishment (the melt level in the crucible decreases during the growth process) is performed. It is assumed that temperature variations and their consequences in the system (no Marangoni convection) are negligible. The fluid flow and impurity distribution in the crucible, in the capillary channel, and in the meniscus are considered in a time-dependent domain $\Omega(t)$, $t \in [0, T]$ by the incompressible Navier–Stokes equations in terrestrial conditions (40.71–40.72) and the conservative convection–diffusion (40.73). For these equations, axisymmetric solutions are sought in the cylindrical polar coordinate system (rOz) (Fig. 40.11).

The evolution of $\Omega(t) = \{(r(R, Z, t), z(R, Z, t)) : (R, Z) \in \Omega(0)\}$ is described by the system of partial differential equations corresponding to the Laplace smoothing (Poisson equations)

$$\begin{cases} \frac{\partial^2}{\partial R^2} \left(\frac{\partial r}{\partial t} \right) + \frac{\partial^2}{\partial Z^2} \left(\frac{\partial r}{\partial t} \right) = 0, \\ \frac{\partial^2}{\partial R^2} \left(\frac{\partial z}{\partial t} \right) + \frac{\partial^2}{\partial Z^2} \left(\frac{\partial z}{\partial t} \right) = 0. \end{cases} \quad (40.87)$$

Here, R, Z represent the reference coordinates in the reference frame (ROZ), i.e., the fixed frame

used for the description of $\Omega(t)$ and of the mesh velocity, as depicted in Fig. 40.11a,b. The solution $(r(R, Z, t), z(R, Z, t))$ satisfies the condition $(r(R, Z, 0), z(R, Z, 0)) = (R, Z)$.

The coupled system (40.71–40.73, 40.87) is considered in the two-dimensional domain $\Omega(t)$ with boundaries $\Omega_1 - \Omega_{12}$, and for solving it, the arbitrary Lagrangian Eulerian (ALE) technique has been used. This technique for mesh movement [40.62, 63] is an intermediate between the Lagrangian and the Eulerian methods, combining the best features of both, i.e., it allows moving boundaries without the need for mesh movement to follow the material. The moving-mesh ALE application mode solves the system of partial differential equations (PDEs) (40.87) for the mesh displacement. This system smoothly deforms the mesh given by constraints on the boundaries. By the Laplace smoothing option (which has been chosen), the software introduces deformed mesh positions as degrees of freedom in the model.

In order to solve the system (40.71–40.73, 40.87), the following boundary conditions on the boundaries $\Omega_1 - \Omega_{12}$ are considered:

- For the incompressible Navier–Stokes (NS) equations:
 - Axial symmetry on Ω_1

$$u_r = 0. \quad (40.88)$$

- Given outflow velocity on Ω_3

$$\mathbf{u} = v\mathbf{k}. \quad (40.89)$$

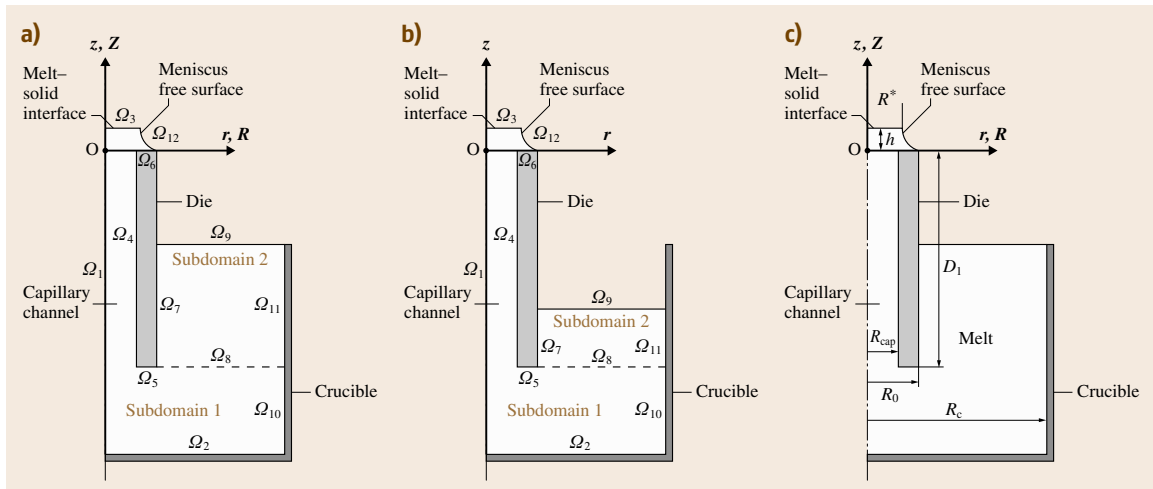


Fig. 40.11a–c EFG system and the boundary regions used in MWRM

- Nonslip condition on $\Omega_2 U \Omega_4 U \Omega_5 U \Omega_6 U \Omega_7 U \Omega_{10} U \Omega_{11} U \Omega_{12}$

$$\mathbf{u} = \mathbf{0} . \quad (40.90)$$

- Neutral condition on $\Omega_8 U \Omega_9$

$$[-p\mathbf{I} + \eta(\nabla \mathbf{u} + (\nabla \mathbf{u})^\top)]\mathbf{n} = 0 . \quad (40.91)$$

2. For the moving-mesh **ALE**:

The domain $\Omega(t)$ is divided in two subdomains, 1 and 2 (Fig. 40.11). Within subdomain 1 there is no displacement (i. e., no motion in this subdomain), whereas within subdomain 2 there are free displacements (i. e., motion is free in this subdomain). Hence, the mesh displacement takes place only in subdomain 2 and it is constrained by the boundary conditions on the surrounding boundaries of Ω_7 , Ω_8 , Ω_9 , and Ω_{11} . The displacement in subdomain 2 is obtained by solving the **PDEs** (40.87). The boundary conditions involve variables from the **NS** application mode. For convergence, it is important for the boundary conditions to be consistent. The usual pointwise constraints or ideal constraints for **ALE** cause unwanted modifications of the boundary conditions for the **NS** mode coupled with convection diffusion (**CD**). For this reason, nonideal weak constraints on the boundaries are used in the **ALE** application mode:

- The mesh displacements in the r - and z -directions on Ω_9 are the following

$$dr = 0 , \quad dz = v_n t , \quad (40.92)$$

where $v_n = -(\rho_S/\rho_l)R^{*2}/(R_c^2 - R_0^2)v$, and R^* is the crystal radius. (According to [40.62], the mesh velocity should be equal to the fluid velocity.)

- The mesh displacement in the r -direction on $\Omega_7 U \Omega_{11}$ is $dr = 0$; the mesh displacement dz in the z -direction is not specified, i. e., the mesh follows the fluid movement;
 - The mesh displacements dr and dz in the r - and z -direction are not specified on Ω_8 (the mesh follows the fluid flow).
3. For the conservative convection–diffusion equation:
- Axial symmetry on Ω_1 , i. e., $r = 0$.
 - Impurity flux rejected into the melt on Ω_3

$$\frac{\partial c}{\partial \mathbf{n}} = -\frac{v}{D}(1 - K_0)c . \quad (40.93)$$

- No impurity flux, i. e., insulation on $\Omega_2 U \Omega_4 U \Omega_5 U \Omega_6 U \Omega_7 U \Omega_9 U \Omega_{10} U \Omega_{11} U \Omega_{12}$

$$\frac{\partial c}{\partial \mathbf{n}} = \mathbf{n} \nabla c = 0 . \quad (40.94)$$

- Continuity on Ω_8

$$\mathbf{n}(N_1 - N_2) = 0, \quad N_i = -D_i \nabla c_i + c_i \mathbf{u}_i , \quad (40.95)$$

where $i = 1$ for subdomain 1 and $i = 2$ for subdomain 2. Besides the above boundary conditions, the followings initial conditions are also used:

- For the fluid flow

$$u(t_0) = 0, \quad v(t_0) = 0 \quad (40.96)$$

in subdomain 1, and

$$u(t_0) = 0, \quad v(t_0) = v_n \quad (40.97)$$

in subdomain 2 (according to [40.62] the fluid velocity should be equal to the mesh velocity).

- For the pressure

$$p(t_0) = P_0 = -\rho_l g z \quad (40.98)$$

in subdomain 1, and

$$p(t_0) = 0 \quad (40.99)$$

in subdomain 2.

- For the initial impurity distribution

$$c(t_0) = C_0 \quad (40.100)$$

in both subdomains.

- For the mesh displacement

$$r(t_0) = R , \quad z(t_0) = Z . \quad (40.101)$$

Numerical investigations were carried out for an Al-doped Si rod of radius $R^* = 1.5 \times 10^{-3}$ m, grown in terrestrial conditions with a pulling rate $v = 10^{-6}$ m/s. According to [40.57], for $R_{\text{cap}} = R^* = 1.5 \times 10^{-3}$ m, the radial segregation in the Si rod grown in terrestrial conditions is minimal over the range $[10^{-7}, 5 \times 10^{-6}]$ m/s of v . In order to evaluate the way in which the resulting fluid flow and deformed geometry determine the impurity distribution in the melt and in the crystal, COMSOL Multiphysics 3.2 software was used in order to solve the coupled **NS-ALE-CD** application modes in the **ALE** frame (rOz). COMSOL Multiphysics does the mathematics necessary to manipulate, move, and deform the mesh simultaneously with the boundary movement as required by the other coupled **NS-CD PDEs**. The computed impurity distributions at three different instances of time are presented in Fig. 40.12.

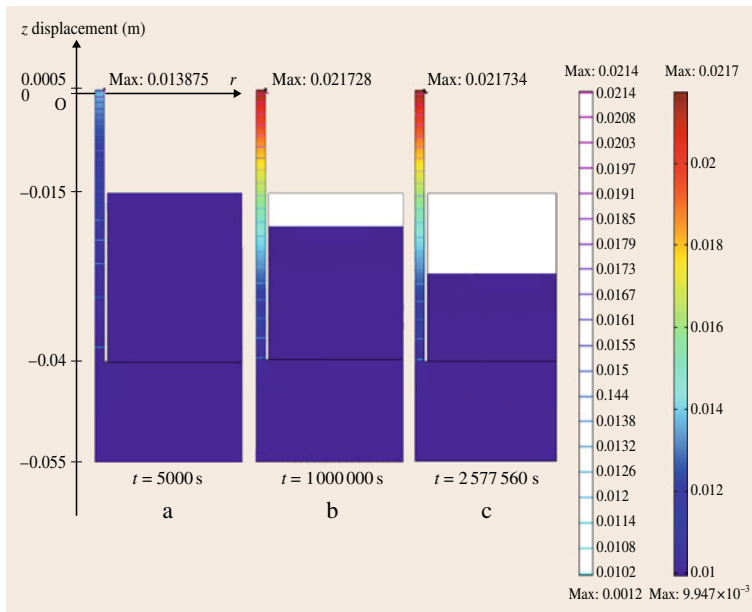


Fig. 40.12 Impurity distribution in the melt at three different instances of time $0 < t_1 < t_2 < t_3 < T$ for $R_{\text{cap}} = 1.5 \times 10^{-3}$ m and $v = 10^{-6}$ m/s for the case of no melt replenishment

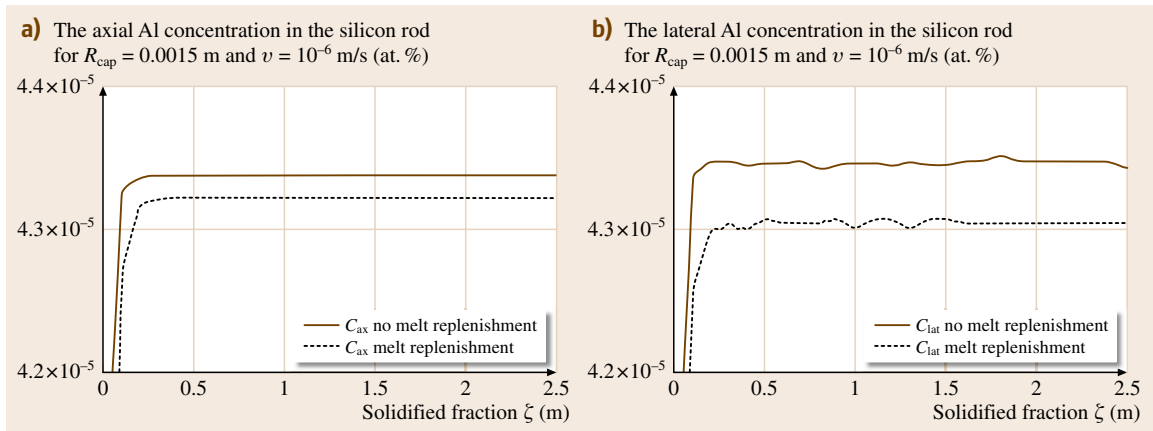


Fig. 40.13a,b Dependence of the impurity distributions on the axis (a) and on the lateral surface (b) of the crystal versus solidified fraction ξ for $R_{\text{cap}} = 1.5 \times 10^{-3}$ m and $v = 10^{-6}$ m/s, with and without melt replenishment

Figure 40.12a–c shows that, at the beginning, the concentration increases and there exists a certain time after which the impurity concentration becomes constant.

The computed impurity distributions versus solidified fraction along the crystal axis (C_{ax}) obtained with and without melt replenishment are presented in Fig. 40.13a. Similarly, the computed impurity distributions versus solidified fraction at the lateral surface (C_{lat}) of the crystal are presented in Fig. 40.13b.

Figure 40.13 shows that, after a transition period, the impurity distributions along the crystal axis

(C_{ax}) and on the lateral surface (C_{lat}), computed in MRM and MWRM, become constant. In the MWRM case these constants are larger than those obtained in the MRM case: the difference is on the order of 10^{-7} – 10^{-6} in the transition period, and after that, this difference is on the order of 1×10^{-7} on the crystal axis and 3×10^{-7} on the lateral surface. Moreover, Fig. 40.13 shows that the transition periods computed in MWRM are shorter. In MWRM the transition period for C_{ax} and C_{lat} is equal to 200 000 s. In MRM the transition period for C_{ax} is 300 000 s and for C_{lat} is 500 000 s.

References

- 40.1 J.A. Burton, R.C. Prim, W.P. Slichter: The distribution of solute on crystals grown from the melt, *J. Chem. Phys.* **21**, 1987–1996 (1953)
- 40.2 C. Wagner: Theoretical analysis of diffusion of solutes during the solidification of alloys, *J. Met.* **6**, 154–160 (1954)
- 40.3 K.M. Kim, A.F. Witt, M. Lichtensteiger, H.C. Gatos: Quantitative analysis of the thermo-hydrodynamic effects on crystal growth and segregation under destabilizing vertical thermal gradients: Ga-doped germanium, *J. Electrochem. Soc.* **125**, 475–480 (1974)
- 40.4 J.J. Favier: Macrosegregation-I: Unified analysis during non-steady state. Solidification, *Acta Metall.* **29**, 197–204 (1981)
- 40.5 J.J. Favier: Macrosegregation-II: A comparative study of theories, *Acta Metall.* **29**, 205–214 (1981)
- 40.6 D.E. Holmes, H.C. Gatos: Convective interference and "effective" diffusion-controlled segregation during directional solidification under stabilizing vertical thermal gradients; Ge, *J. Electrochem. Soc.* **128**, 429–437 (1981)
- 40.7 C.J. Chang, R.A. Brown: Radial segregation induced by natural convection and melt/solid interface shape in vertical Bridgman growth, *J. Cryst. Growth* **63**, 343–364 (1983)
- 40.8 W.A. Tiller, K.A. Jackson, J.W. Rutter, B. Chalmers: The redistribution of solute atoms during the solidification of metals, *Acta Metall.* **1**, 428–437 (1953)
- 40.9 P.R. Griffin, S. Motakef: Influence of non-steady gravity on natural convection during micro-gravity solidification of semiconductors. Part I. Time Scale Analysis, *J. Appl. Microgravity II* **3**, 121–127 (1989)
- 40.10 P.R. Griffin, S. Motakef: Influence of non-steady gravity on natural convection during micro-gravity solidification of semiconductors. Part II. Implications for crystal growth experiments, *J. Appl. Microgravity II* **3**, 128–132 (1989)
- 40.11 A.F. Witt, H.C. Gatos, M. Lichtensteiger, M.C. Lavine, C.J. Herman: Crystal growth and steady-state segregation under zero gravity, *J. Electrochem. Soc.* **122**, 276–283 (1975)
- 40.12 P.M. Adornato, R.A. Brown: Convection and segregation in directional solidification of dilute and non-dilute binary alloys, *J. Cryst. Growth* **80**, 155–190 (1987)
- 40.13 P.A. Clark, W.R. Wilcox: Influence of gravity on thermocapillary convection in floating zone melting of silicon, *J. Cryst. Growth* **50**, 461–469 (1980)
- 40.14 S.A.I. Nikitin, V. Polezhayev, A.I. Fedyushkin: Mathematical simulation of impurity distribution in crystals prepared under microgravity conditions, *J. Cryst. Growth* **52**, 471–477 (1981)
- 40.15 S.R. Coriell, R.F. Sekerka: Lateral solute segregation during unidirectional solidification of a binary alloy with a curved solid-liquid interface, *J. Cryst. Growth* **46**, 479–482 (1979)
- 40.16 S.R. Coriell, R.F. Boisvert, R.G. Rehm, R.F. Sekerka: Lateral solute segregation during unidirectional solidification of a binary alloy with a curved solid-liquid interface II. Large departures from planarity, *J. Cryst. Growth* **54**, 167–175 (1981)
- 40.17 H.M. Ettouney, R.A. Brown: Effect of heat transfer on melt/solid interface shape and solute segregation in edge-defined film-fed growth: Finite element analysis, *J. Cryst. Growth* **58**, 313–329 (1982)
- 40.18 J.P. Kalejs, L.Y. Chin, F.M. Carlson: Interface shape studies for silicon ribbon growth by the EFG technique I. Transport phenomena modeling, *J. Cryst. Growth* **61**, 473–484 (1983)
- 40.19 C.E. Chang, W.R. Wilcox: Control of interface shape in the vertical Bridgman-Stockbarger technique, *J. Cryst. Growth* **21**, 135–140 (1974)
- 40.20 T.W. Fu, W.R. Wilcox: Influence of insulation on stability of interface shape and position in the vertical Bridgman-Stockbarger technique, *J. Cryst. Growth* **48**, 416–424 (1980)
- 40.21 T.W. Clyne: Heat flow in controlled directional solidification of metals I. Experimental investigation, *J. Cryst. Growth* **50**, 684–690 (1980)
- 40.22 T.W. Clyne: Heat flow in controlled directional solidification of metals II. Mathematical model, *J. Cryst. Growth* **50**, 691–700 (1980)
- 40.23 P.C. Sukanek: Deviation of freezing rate from translation rate in the Bridgman-Stockbarger technique I. Very low translation rates, *J. Cryst. Growth* **58**, 208–218 (1982)
- 40.24 P.C. Sukanek: Deviation of freezing rate from translation rate in the Bridgman-Stockbarger technique II. Moderate translation rates, *J. Cryst. Growth* **58**, 219–228 (1982)
- 40.25 T. Jasinski, W.M. Rohsenow, A.F. Witt: Heat transfer analysis of the Bridgman-Stockbarger configuration for crystal growth I. Analytical treatment of the axial temperature profile, *J. Cryst. Growth* **61**, 339–354 (1983)
- 40.26 L.R. Morris, W.C. Winegard: The development of cells during the solidification dilute Pb-Sb alloy, *J. Cryst. Growth* **5**, 361–375 (1969)
- 40.27 A.F. Witt, H.C. Gatos, M. Lichtensteiger, C.J. Herman: Crystal growth and segregation under zero gravity, *J. Electrochem. Soc.* **125**, 1832–1840 (1978)
- 40.28 A.M. Balint, D.G. Baltean, T. Levy, M. Mihailovici, A. Neculae, S. Balint: The dopant fields in uniform-diffusion-layer, global-thermal-convection and precrystallization-zone models, *Mater. Sci. Semicond. Process.* **3**, 115–121 (2000)

- 40.29 D.T.J. Hurle, E. Jakeman, C.P. Johnson: Convective temperature oscillations in molten gallium, *J. Fluid Mech.* **64**, 565–576 (1974)
- 40.30 C.A. Wang, A.F. Witt: *Annual Report Material Processing Center* (Massachusetts Institute of Technology, Massachusetts 1984)
- 40.31 M.M. Mihailovici, A.M. Balint, S. Balint: The axial and radial segregation due to the thermo-convection, the decrease of the melt in the ampoule and the effect of the precrystallization-zone in the semiconductor crystals grown in a Bridgman–Stockbarger system in a low gravity environment, *J. Cryst. Growth* **237–239**, 1752–1756 (2002)
- 40.32 M.M. Mihailovici, A.M. Balint, S. Balint: On the controllability of the level of the dopant concentration and of the compositional uniformity of a doped crystal, grown in a low gravity environment by Bridgman–Stockbarger method, *Int. J. Theor. Physics, Group Theory Nonlin. Opt.* **10**, 425–436 (2003)
- 40.33 A.M. Balint, M.M. Mihailovici, D.G. Baltean, S. Balint: A modified Chang–Brown model for the determination of the dopant distribution in a Bridgman–Stockbarger semiconductor crystal growth system, *J. Cryst. Growth* **230**, 195–201 (2001)
- 40.34 A.M. Balint, M.M. Mihailovici, D.G. Baltean, S. Balint: Interface structure in the growth of semiconductor crystals using the Bridgman–Stockbarger method, *Thin Solid Films* **380**, 108–110 (2000)
- 40.35 M.M. Mihailovici, A.M. Balint, S. Balint: The dopant distribution computed in the modified Chang–Brown model using quasi-steady state approximation, *Comput. Mater. Sci.* **24**, 262–267 (2002)
- 40.36 D.G. Baltean, T. Levy, S. Balint: Transport de masse par convection et diffusion dans un milieu multiporeux, *C. r. Acad. Sci. Paris, Ser. IIB* **326**, 821–826 (1998)
- 40.37 K. Moutsopoulos, S. Bories: Dispersion en milieux poreux hétérogènes, *C. R. Acad. Sci. Paris, Ser. IIB* **316**, 1667–1672 (1993), in French
- 40.38 J.C. Maxwell: *Electricity and Magnetism* (Clarendon, Oxford 1873)
- 40.39 V.I. Avetisov, Mendeleev Institute Moscow (personal communication)
- 40.40 M.M. Mihailovici, A.M. Balint, S. Balint: Way to improve the compositional uniformity of doped crystals grown by Bridgman–Stockbarger method in a low gravity environment, *Int. J. Theor. Phys. Group Theory Nonlinear Opt.* **11**, 109–119 (2004)
- 40.41 D.J. Larson, J. Bethin, B.S. Dressler: *Shuttle Mission 51-G, Experiment MRS77F055, Flight Sample Characterization* (Grumman Corporate Research Center, Bethpage 1988), NASA Report RE-753
- 40.42 P.S. Dutta, A.G. Ostrogorsky: Segregation of Ga in Ge and InSb in GaSb, *J. Cryst. Growth* **217**, 360–365 (2000)
- 40.43 L.L. Zheng, D.J. Larson Jr., H. Zhang: Role of thermotransport (Soret effect) in macrosegregation during eutectic/off-eutectic directional solidification, *J. Cryst. Growth* **191**, 243–251 (1998)
- 40.44 L. Braescu: The dependence of the dopant distribution on the pulling rate and on the capillary channel radius in the case of a Nd:YVO₄ cylindrical bar grown from the melt by the EFG method, *Mater. Sci. Eng. B* **146**, 41–44 (2008)
- 40.45 E. Tulcan-Paulescu, A.M. Balint, S. Balint: The effect of the initial dopant distribution in the melt on the axial compositional uniformity of a thin doped crystal grown in strictly zero-gravity environment by Bridgman–Stockbarger method, *J. Cryst. Growth* **247**, 313–319 (2003)
- 40.46 V.A. Tatarchenko: *Shaped Crystal Growth* (Kluwer, Dordrecht 1993)
- 40.47 H.E. LaBelle Jr., A.I. Mlavsky, B. Chalmers: Growth of controlled profile crystals from the melt: Part I – Sapphire filaments, *Mater. Res. Bull.* **6**, 571–579 (1971)
- 40.48 H.E. LaBelle Jr., A.I. Mlavsky, B. Chalmers: Growth of controlled profile crystals from the melt: Part II – Edge-defined, film-fed growth (EFG), *Mater. Res. Bull.* **6**, 581 (1971)
- 40.49 B. Chalmers, H.E. LaBelle Jr., A.I. Mlavsky: Edge-defined, film-fed crystal growth, *J. Cryst. Growth* **13/14**, 84–87 (1972)
- 40.50 J.P. Kalejs: Impurity redistribution in EFG, *J. Cryst. Growth* **44**, 329–344 (1978)
- 40.51 J.P. Kalejs, G.M. Freedman, F.V. Wald: Aluminium redistribution in EFG silicon ribbon, *J. Cryst. Growth* **48**, 74–84 (1980)
- 40.52 B. Chalmers: Transient solute effects in shaped crystal growth of silicon, *J. Cryst. Growth* **82**, 70–73 (1987)
- 40.53 J. Cao, M. Prince, J.P. Kalejs: Impurity transients in multiple crystal growth from a single crucible for EFG silicon octagons, *J. Cryst. Growth* **174**, 170–175 (1997)
- 40.54 J.P. Kalejs: Interface shape studies for silicon ribbon growth by the EFG technique II. Effect of die asymmetry, *J. Cryst. Growth* **61**, 485–493 (1983)
- 40.55 J.P. Kalejs: Modeling contribution in commercialization of silicon ribbon growth from the melt, *J. Cryst. Growth* **230**, 10–21 (2001)
- 40.56 O. Bunoiu, I. Nicoara, J.L. Santailier, T. Duffar: Fluid flow and solute segregation in EFG crystal growth process, *J. Cryst. Growth* **275**, 799–805 (2005)
- 40.57 L. Braescu, S. Balint, L. Tanasie: Numerical studies concerning the dependence of the impurity distribution on the pulling rate and on the radius of the capillary channel in the case of a thin rod grown from the melt by edge-defined film-fed growth (EFG) method, *J. Cryst. Growth* **291**, 52–59 (2006)
- 40.58 L. Braescu, T.F. George, S. Balint: Evaluation and control of the dopant distribution in a Nd:LiNbO₃ fiber grown from the melt by the edge-defined

film-fed growth (EFG) method, Photonic Fiber and Crystal Devices: Advances in Materials and Innovations in Device Applications I (Optics and Photonics 2007), SPIE Proc. **6698**, 669803:1–8 (2007)

40.59 L. Braescu, T. Duffar: Effect of buoyancy and Marangoni forces on the dopant distribution in the case of a single crystal fiber grown from the melt by the edge-defined film-fed growth (EFG) method, J. Cryst. Growth **310**, 484–489 (2008)

40.60 T.F. George, L. Braescu: Sapphire fibers grown from the melt by the EFG technique: Dependence of the impurity distribution on temperature and surface tension gradients, Photonic Fiber and Crystal Devices: Advances in Materials and Innovations in Device Applications II (Optics and Photonics 2008), SPIE Proc. **7056**, 705603–1–705603–10 (2008)

40.61 L. Braescu, T.F. George: Arbitrary Lagrangian–Eulerian method for coupled Navier–Stokes and convection–diffusion equations with moving boundaries, Proc. 12th WSEAS Int. Conf. Appl. Math. – Math’07 (2007) pp. 33–36

40.62 F. Duarte, R. Gormaz, S. Natesan: Arbitrary Lagrangian–Eulerian method for Navier–Stokes equations with moving boundaries, Comput. Methods Appl. Mech. Eng. **193**, 4819–4836 (2004)

40.63 M. Fernandez, M. Moubachir: Sensitivity analysis for an incompressible aeroelastic system, Math. Models Methods Appl. Sci. **12**, 1109–1130 (2002)

Defects C

Part G

Part G Defects Characterization and Techniques

**41 Crystalline Layer Structures
with X-Ray Diffractometry**

Paul F. Fewster, Brighton, UK

**42 X-Ray Topography Techniques
for Defect Characterization of Crystals**

Balaji Raghothamachar, Stony Brook, USA
Michael Dudley, Stony Brook, USA
Govindhan Dhanaraj, Nashua, USA

43 Defect-Selective Etching of Semiconductors

Jan L. Weyher, Warsaw, Poland
John J. Kelly, Utrecht, The Netherlands

**44 Transmission Electron Microscopy
Characterization of Crystals**

Jie Bai, Hillsboro, USA
Shixin Wang, Boise, USA
Lu-Min Wang, Ann Arbor, USA
Michael Dudley, Stony Brook, USA

**45 Electron Paramagnetic Resonance
Characterization of Point Defects**

Mary E. Zvanut, Birmingham, USA

**46 Defect Characterization in Semiconductors
with Positron Annihilation Spectroscopy**

Filip Tuomisto, Espoo, Finland

Crystalline

41. Crystalline Layer Structures with X-Ray Diffractometry

Paul F. Fewster

X-ray scattering analysis and instrumentation has been evolving rapidly to meet the demands arising from the growth of sophisticated device structures. X-ray scattering is very sensitive to composition, thickness and defects in layered structures of typical present-day electronic device dimensions. Considerable information can be obtained from simple profiles, including an estimate of layer thickness and composition (by measuring peak separations) and a measure of the sample quality (from the peak broadening). The full simulation of the profiles takes this a stage further to interpret very complex structures and obtain more reliable parameter estimates. By obtaining two-dimensional scattering data the information becomes more extensive, including layer strain relaxation and defect analysis, quantum dot composition and shape. Generally the data is averaged over a few mm, however reducing the beam size can break this averaging to reveal inhomogeneities, isolating small regions and in some circumstances isolate individual quantum dots for analysis. This article gives an overview of the status, differentiating those methods that are easily accessible and those that require a collaborative approach because they are still being established.

41.1	X-Ray Diffractometry	1406
41.2	Basic Direct X-Ray Diffraction Analysis from Layered Structures	1407
41.2.1	Theory	1407
41.2.2	Interpretation of Data Collected from Planes Parallel to the Surface – the ω - 2θ Scan – an Example	1409
41.2.3	Interpretation of Data Collected from Several Reflections – The Reciprocal Space Map – An Example	1411
41.3	Instrumental and Theoretical Considerations	1412
41.3.1	The Instrument for Collecting X-Ray Diffraction Patterns	1412
41.3.2	Interpreting the Scattering by Simulation	1412
41.4	Examples of Analysis from Low to High Complexity	1413
41.4.1	Established Methods	1413
41.4.2	New Methods and New Analyses	1416
41.5	Rapid Analysis	1419
41.6	Wafer Micromapping	1420
41.7	The Future	1421
	References	1422

X-ray scattering offers a nondestructive method for determining phase composition in crystalline materials, layer thickness, interface details, shapes of crystallites and quantum dots, etc. The basic principles of the various techniques will be outlined in this chapter. Bulk materials are limited to their intrinsic properties, whereas composite materials of several thin layers extend this range, e.g., semiconductor light-emitting diodes and modern transistors. However these physical properties are influenced by the layer compositions, thickness, defect density, and other structural parameters.

X-ray scattering can be used very effectively for measuring all these structural parameters, some to very significant precision. The first part of this chapter discusses the general principles of the analysis, which is applicable to achieving an initial sample characterization by direct interpretation of the diffraction pattern. The limitations of this direct interpretation are also considered and how simulation of the scattering process gives more exact results. The advantages of simulation make the analysis of complex layer structures possible and also extend the applicability of x-ray scattering to

evaluating interface roughness, distortions, etc. Quantum dots are singled out as a particular area to illustrate the developments in x-ray scattering. Any analysis introduces some form of averaging, and approaches to

reduce the probed volume are discussed. This has enabled detailed mapping of lateral variations, yielding a wealth of information for detailed characterization and screening, as discussed in the penultimate section.

4.1.1 X-Ray Diffractometry

The measured x-ray intensity scattered from a sample, in terms of magnitude and distribution, is sensitive to the arrangement and type of atoms in a crystal. If the x-ray probe is very well collimated then the resulting *high-angular-resolution* mode, or more generally phrased *high-resolution x-ray diffraction*, is very sensitive to small changes in the atomic layer spacing and deposited layer thickness. This is a consequence of the angle through which x-rays are scattered, which is inversely related to the separation of the atomic layer planes and the deposited layer thickness. So the sensitivity of x-ray scattering is effectively very high for very thin layers. Fortunately this is the region of interest for many of today's device structures; however, this is only relevant if there is sufficient scattered intensity. This aspect of the compromise between scattered intensity and high resolution will be addressed in Sect. 4.1.5. To indicate the bounds, it is possible to measure the thickness of layers up to $\approx 4\ \mu\text{m}$ and down to single atomic layers or a single plane of quantum dots using conventional configurations and equipment. For example, a single 1 nm $\text{In}_{0.1}\text{Ga}_{0.9}\text{As}$ layer on GaAs can be observed as an asymmetry on the main substrate profile, and determined by simulation to within $\pm 0.1\ \text{nm}$; a layer thickness above this value begins to indicate distinctive oscillations, and below this it is possible to observe this asymmetry but in practice it requires considerable care to determine the thickness. If however the layer is buried, then thinner layers of 0.1 nm can be observed by virtue of the interference between the layers above and below. The measurement of the thickness, again by simulation, appears simple and sensitive, however the thickness is correlated with the composition, and so ideally a combination of profiles are required. Any increase in thickness at constant composition increases the amplitude of the interference oscillations. The positions of the main Bragg peaks give a measure of the interplanar spacing in a crystal that can be determined to within $\approx 1\ \text{ppm}$, i.e., considerably less than the classical radius of an electron. However extracting dilute composition information in alloy systems requires a combination of differences in covalent

radii and the concentration itself. So, to obtain the alloy composition of Al in GaAs, for example, where the difference in the covalent radius of Al to Ga is $\approx 2865\ \text{ppm}$, we require a method for differentiating the interatomic spacing to 28 ppm to achieve 1% precision in the concentration of Al in AlGaAs. With careful measurement and accounting for sample uncertainties this can be done routinely. For systems with larger differences in covalent radii, e.g., Ge in SiGe or In in GaN, the precision increases for the same amount of care in the measurement.

For obtaining the thickness of a layer, similar rules apply; as the thickness decreases, the width of the associated peak increases and the fringes associated with the interference of the scattering from the top and bottom surface of the layer become further apart. If the fringes are very close together and the central peak is narrow then the thickness measure becomes more problematic and requires higher-resolution instrumentation, up to the limit of the x-ray coherence length (typically $\approx 4\ \mu\text{m}$) or the layer perfection. Rough top and bottom surfaces reduce the intensity of the fringes and so can give a measure of the interface quality. As the thickness is reduced the peak broadens until eventually the scattering is indistinguishable from the inherent noise level of the instrument. If layers are stacked as in most device structures then thin layers modulate the overall pattern and appear more obvious again, e.g., interfacial layers in superlattice structures or single atomic layers separated by thicker layers. It is clear from this that x-ray scattering cannot simply be categorized in terms of what it can and cannot detect in terms of a single layer, for example, but rather the whole structure and the instrument are necessarily intertwined, and the route to extracting useful information generally comes down to simulating the scattering. However, some very useful analyses can be obtained quite directly from the measurements, although awareness of the pitfalls is important.

As far as instrument development is concerned, this can be a large and confusing subject, since as discussed above, the sample, the information to be extracted, and the instrument resolution are all linked. This has led to

instruments becoming more flexible for general materials research, and as the level of understanding or the improvement in control over the crystal growth develops, the resolution often needs to be increased. This allows more detailed information, deviations from perfection, etc., to be probed more easily. Similarly the analysis goes through a cycle of approximate quick interpretation, through to more precise simulation to understand the sample more fully, until eventually the analysis becomes a control feedback method that can be routine yet sophisticated and specific to the crystal properties of interest. When the growth of the material becomes too complex, in that there are many complex parameters to assess with high degrees of correlation, then some statistical significance is required. X-ray scattering can contribute here, since as illustrated above its high sensitivity to structural parameters can give some form of measure for obtaining correlations. A few examples of this will be given in this chapter.

As mentioned above x-ray scattering is very sensitive to structural changes and generally the probe is

large, usually mm and for some specialized applications down to μm . However, this does not mean that everything is averaged over that region. In fact the x-ray pattern contains the average and the fluctuations from the average for dimensions over which the x-rays are coherent, so for example, the onset of layer relaxation (the distortion around dislocations) and the existence of precipitates can be observed, both of which modify the scattering in quite characteristic ways. Examining the spatial distribution of the intensity in the scattered beam can also break this averaging effect. Chapter 42 in this volume, describe a very direct approach to obtaining defect information, and when combined with high-resolution reciprocal space mapping, the x-ray topographic contrast can be related to features in the scattering pattern [41.1,2].

This chapter will cover the rapid direct measures that give an indication of the material's properties. It will also show how far the analysis can be taken and finally the more systematic routine analysis methods for controlled crystal growth.

41.2 Basic Direct X-Ray Diffraction Analysis from Layered Structures

41.2.1 Theory

X-rays scatter strongly from electrons, principally those that are highly localized, i.e., core electrons. The scattering amplitude from an assembly of atoms at positions \mathbf{r} with individual scattering factors (or form factors) of f_r is given by

$$F_S = \int_r f_r e^{-2\pi i \mathbf{S} \cdot \mathbf{r}} d\mathbf{r}. \quad (41.1)$$

The scattering amplitude and therefore the consequent intensity is distributed but reaches a maximum for atom positions satisfying the condition

$$|\mathbf{S}| = \frac{1}{d}, \quad (41.2)$$

where d is the separation of the atomic planes. Any position in diffraction space \mathbf{S} can be probed by manipulating the incoming (\mathbf{k}_0) and the outgoing (\mathbf{k}_H) x-ray beam paths, where $|\mathbf{k}_0| = |\mathbf{k}_H| = 1/\lambda$, such that

$$\mathbf{S} = \mathbf{k}_H - \mathbf{k}_0, \quad (41.3)$$

which is Bragg's relation in vector form. It can be seen from the geometry of Fig. 41.1 that

$$S = \frac{1}{d} = \frac{2 \sin \theta}{\lambda}. \quad (41.4)$$

Therefore, to probe different regions of diffraction space, the incident beam direction with respect to the sample and the detector acceptance direction are manip-

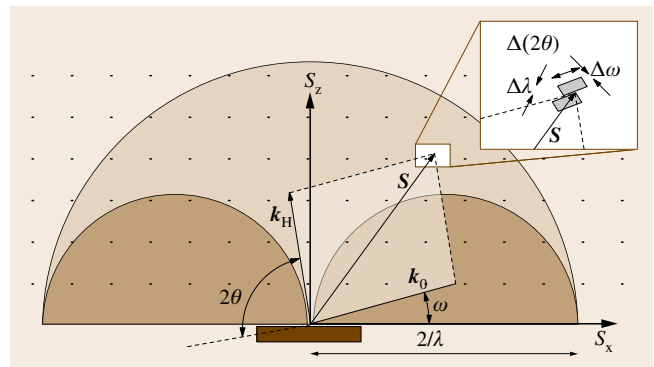


Fig. 41.1 The geometry of reciprocal space, indicating the incident and scattered beam vectors \mathbf{k}_0 and \mathbf{k}_H and the resultant position probed \mathbf{S} . The regular array of reciprocal lattice points represents the atomic plane spacings, and the limiting sphere for their observation is defined by the wavelength λ . The two smaller darker grey spheres are inaccessible regions to data collection in conventional reflection mode. The inset gives the detail of the size of the reciprocal space probe

ulated to map the distribution of intensity (Fig. 41.1). If the incident and scattered beam directions are very well defined, as with a high-angular-resolution diffractometer, then the length d can be measured very precisely as well as small differences in d . High resolution is very useful for studying closely lattice-matched semiconductor multilayers, for example.

The scattering amplitude F_S is complex, includes aspects of absorption, and is directly related to the refractive index. For most materials the refractive index for x-rays is less than one, and therefore x-rays total-externally reflect, and the actual Bragg scattering peaks are displaced to larger angles. The refractive index is $\approx (1 - 10^{-5})$, which has advantages in that for most measurements only small uncertainties are introduced, e.g., in thickness measurement from fringe spacings or lattice parameter determination. On the other hand the difference in refractive indices of layers from different materials creates modulations in the specular scattering (total external scattering), which offers another method for determining thickness and composition.

So the simplest information that can be extracted from an x-ray scattering experiment is the location of the peaks; this gives the crystal plane spacing, and their intensity relates to the atomic arrangement. The width of the peak relates to the number of contributing atomic planes, so in general for thin films the peaks become broadened normal to the surface direction, but very narrow parallel to the surface direction, so the term reciprocal space describes it all. This is the general guide relevant to the early stages of analyzing x-ray diffraction profiles.

Consider the early stages of crystal growth of a new material when little is known. Suppose that it consists

of some layers and the intention is to grow something epitaxially related to the thick substrate wafer. The structure could appear as in Fig. 41.2a, where some of the likely measurable features are illustrated. A reciprocal space map for a single-layer structure around a reflection close to $s_x = 0$ may appear as in Fig. 41.2b. If the substrate is a reasonable quality single crystal, then the scattering from this will be represented by a narrow peak, and if the layers are not too thick ($< 2 \mu\text{m}$), then this could be the highest peak and can be easily identified. Its position will give a value for the interplanar spacing, and the associated lattice parameter can be obtained if the reflection index H is known, since this relates the length scale d probed to that of the material lattice parameter. The layer peak is broader and wider and is not in line with the substrate peak. If the choice of reflection is from planes parallel to the surface (i.e., $\omega \approx \theta$, $s_x = 0$; Fig. 41.1), then this difference in angle $\delta\omega$ is indicative of layer planes being tilted with respect to the substrate planes by $\delta\omega$. The width of the layer peak in the direction normal to the surface (s_z) will be related to the layer thickness L_z or some variation of strain in the layer, the microstrain ε_{\perp} , or a combination of both. This width is obtained by scanning in ω and 2θ , coupled in a 1 : 2 ratio. If this width is purely due to the layer thickness then $L_z \equiv 1/\Delta s_z$, and from the geometry of Fig. 41.1

$$\frac{1}{\Delta s_z} = \frac{\lambda}{[\sin \omega_1 + \sin(2\theta_1 - \omega_1)] - [\sin \omega_2 + \sin(2\theta_2 - \omega_2)]} \quad (41.5)$$

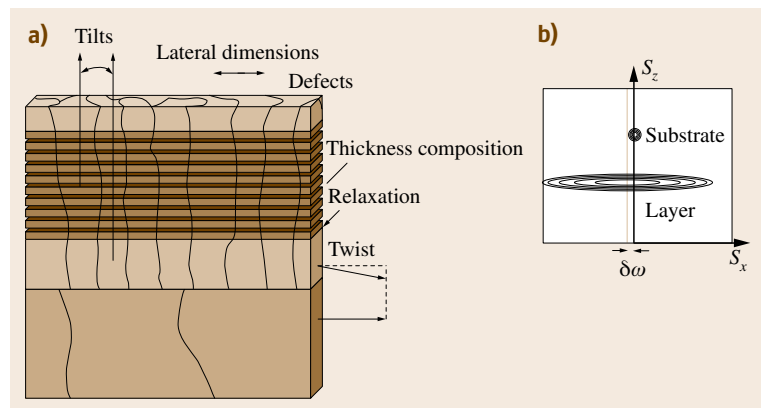


Fig. 41.2a,b The typical information that can be extracted from an x-ray scattering experiment (a), and a schematic of a reciprocal space map of an imperfect layer on a nearly perfect substrate (b)

In this case $2\theta_1 \approx 2\omega_1$ and $2\theta_2 \approx 2\omega_2$, $\Delta 2\theta = (2\theta_1 - 2\theta_2)$, and the chosen positions described by the subscripts correspond to the full-width at half-maximum (FWHM), hence

$$L_z \approx \frac{\lambda}{2\Delta\theta \cos \theta}, \quad (41.6)$$

which is the Scherrer equation [41.3]. If the peak is related to the microstrain then, from (41.2),

$$\frac{\Delta d}{d} = -\frac{\Delta S}{S}. \quad (41.7)$$

Hence for the scattering peak considered here

$$\frac{\Delta d}{d} = -\frac{\Delta s_z}{s_z} = -\frac{\lambda/(2 \sin \theta)}{\lambda/(2\Delta\theta \cos \theta)} = -\cot \theta \Delta\theta. \quad (41.8)$$

Separating these two influences on the peak width can either be judged by the acceptable ranges for the microstrain or layer thickness, or by combining several reflections (preferably along the same zone axis, i.e., 001, 002, 003, etc.), to separate the different dependency on θ [41.4].

The broadening normal to this also has two components. These two components are composed of local tilts and some lateral dimension: for mosaic layers these can be related to the Burgers vectors of the dislocations forming the mosaic blocks. If the layer is dominated by threading dislocations then the component of tilt is small and the width will give a good estimate of the mosaic block dimension, $L_x \equiv 1/\Delta s_x$, given by

$$\frac{1}{\Delta s_x} = \frac{\lambda}{[\cos \omega_1 - \cos(2\theta_1 - \omega_1)] - [\cos \omega_2 - \cos(2\theta_2 - \omega_2)]}, \quad (41.9)$$

where in this case $2\theta_1 \approx 2\theta_2$ and the peak width $\Delta\omega = (\omega_1 - \omega_2)$, thus

$$L_x \approx \frac{\lambda}{2\Delta\omega \sin \omega}. \quad (41.10)$$

If there is a high density of misfit dislocations that have Burgers vectors out of the plane of the interface, e.g., 60° dislocations in Si, then these will have a tilt component. The distribution of tilted regions and the size of these regions start to produce a more complex picture. However if the contribution is purely due to tilted regions of large dimensions then the spread of microscopic tilts is simply given by $\Delta\omega$.

41.2.2 Interpretation of Data Collected from Planes Parallel to the Surface – the ω - 2θ Scan – an Example

Consider the example of a GaN structure given in Fig. 41.3a and the reciprocal space map around the 0002 reflection (Fig. 41.3b). The reciprocal space map has many satellites associated with this periodic layer structure and two strong peaks having two very different widths along s_z and similar widths along s_x (Fig. 41.3c,d). A considerable amount of information can be extracted from this data. Firstly, the separation of the two peaks (Fig. 41.3c) relates to the difference in lattice parameter along s_z . The individual lattice parameter value along this direction is given by

$$a_z = d_z H_z = \frac{H_z}{s_z}, \quad (41.11)$$

where H_z is the index of the reflection along the surface normal direction, simply equal to 2 here. Therefore the most precise measure of the lattice parameter is obtained for larger values of s_z , as is also clear from (41.8). Referring to Fig. 41.3c, we could in the first instance assume that the underlying substrate, or a thick GaN buffer in this case, has a known lattice parameter (some database value) and therefore the layer lattice parameter $L a_z$ is simply given by combining (41.11) and (41.8) as

$$\begin{aligned} L a_z &= \frac{s a_z}{s H_z} \left(1 + \frac{\Delta d}{d} \right) L H_z \\ &\approx \frac{s a_z}{s H_z} (1 - \cot \theta \Delta\theta) L H_z, \end{aligned} \quad (41.12)$$

where $\Delta\theta$ is the difference in Bragg angle and $L H_z$ is the reflection index in the direction normal to the surface for the layer and $s H_z$ for the substrate. For the example $L H_z = s H_z = 2$, $s a_z = 0.51851$ nm for the 0002 reflection from GaN, $\theta_s = 17.284^\circ$ for an x-ray wavelength of $\lambda = 0.1540593$ nm, using (41.4). Since the measurement gives $\Delta\theta = 0.0777^\circ$, and if we assume that the layer has a good epitaxial relationship to the substrate or layer below, the lateral lattice parameter of the layer $L a_x$ is identical to $s a_x$ (0.31893 nm), so $L a_z = 0.52076$ nm.

Now the layer material would have a characteristic and usually unique set of lattice parameters, but in the undistorted state. The unstrained lattice parameters can be determined from taking the distorted unit cell (defined by the lattice parameters) and allowing it to relax to the expected shape. In this case InN and GaN and the phase mixture are hexagonal, such that certain unit cell parameters ($a, b, c, \alpha, \beta, \gamma$) are defined, i.e., $a = b$,

$\alpha = \beta = 90^\circ$, and $\gamma = 120^\circ$. The layer structure in the unstrained state is then just defined by the ratio c/a , which is 1.640 for InN and 1.626 for GaN. The way in which the distorted unit cell is transformed into the unstrained unit cell depends on the elastic coefficients that relate the stress and strains. The strain normal to the surface ε_{zz} is related to strains parallel to the surface, ε_{xx} and ε_{yy} , such that they can be related to a Poisson ratio ν

$$\begin{aligned} \left(\frac{\Delta d_z}{d_z} \right)_L &= \frac{Ld_z - Ld_{z0}}{Ld_{z0}} = \varepsilon_{zz} = \frac{-\nu}{1-\nu} (\varepsilon_{xx} + \varepsilon_{yy}) \\ &= \frac{-\nu}{1-\nu} \left(\frac{Ld_x - Ld_{x0}}{Ld_{x0}} + \frac{Ld_y - Ld_{y0}}{Ld_{y0}} \right), \end{aligned} \quad (41.13)$$

where Ld_{x0} , Ld_{y0} and Ld_{z0} are the lattice plane spacing for the layer parallel and normal to the surface in the unstrained state; these are parameters needed to identify the alloy composition. The Poisson ratio used in this way is dependent on the orientation, however this can be determined from the elastic coefficients or from tabulated values. Many typical semiconductors have values

$\nu \approx 0.3$, whereas maintaining constant volume $\nu \approx 0.5$. In our example in the first instance we are assuming $\varepsilon_{\parallel} = \varepsilon_{xx} = \varepsilon_{yy}$, i.e., that the strain is isotropic in the interface plane. Combining (41.13) with the c/a ratio ($= K$) of the expected unstrained state for the layer, we can isolate $c_L (= H_z Ld_{z0})$ in terms of the measurable (Ld_z or Δd_z) and known or tabulated values (H_z , K , ν , c_S , a_S) as

$$c_L = \left(\frac{2\nu}{1-\nu} \right) (Ka_S - Ld_z H_z) + Ld_z H_z, \quad (41.14)$$

where $Ld_z H_z = c_S + \Delta d_z H_z$, c_S is the lattice parameter of the underlayer or substrate normal to the surface, and a_S is the lattice parameter in the plane of the interface. Within the approximations in this example, the values of K and ν can be estimated, which can be iterated since they are composition dependent. It is assumed that a_S is a known or database value, then c_L can be derived and the phase composition can be obtained by the interpolation [41.5]

$$x = \frac{c_L - c_{\text{GaN}}}{c_{\text{InN}} - c_{\text{GaN}}}. \quad (41.15)$$

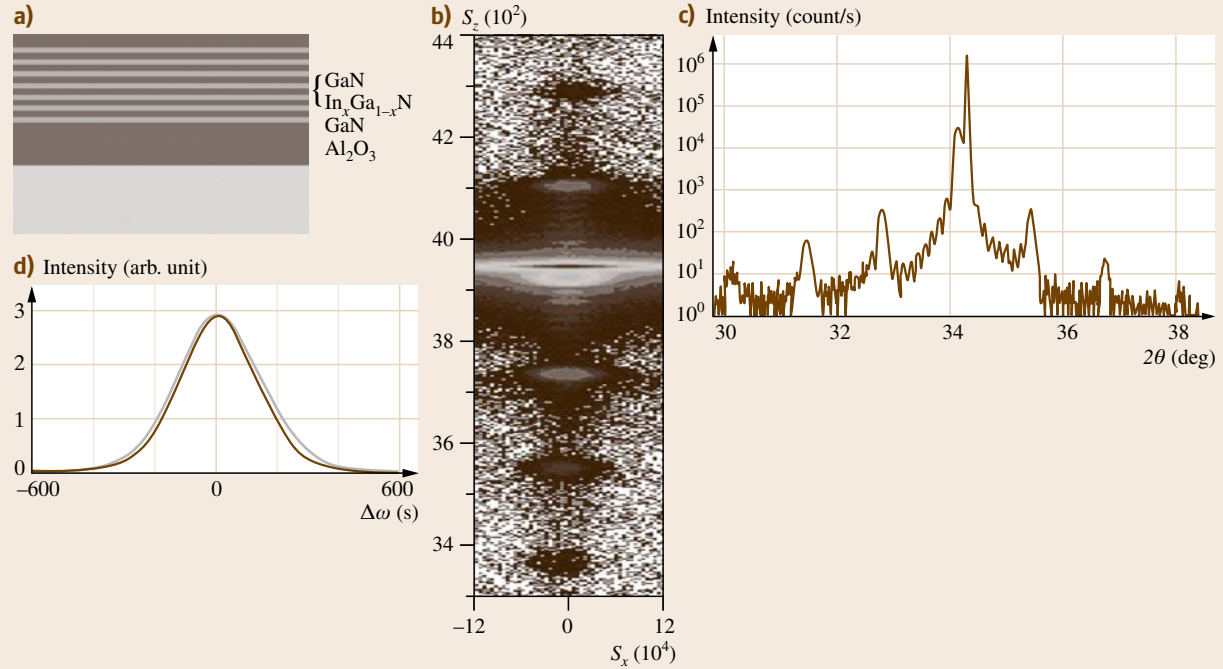


Fig. 41.3a–d The structure of an InGaN/GaN multilayer on a thick GaN buffer layer is given in (a), along with the reciprocal space map (b) and some extracted profiles along s_z (c) and along s_x (d). The intensities in (d) correspond to the GaN buffer (grey) and the superlattice (brown), indicating that they have similar microstructure, although the superlattice may be of better quality; the intensities are normalized for comparison

In the example discussed, $x = 2.2\%$. The purpose of the above derivations is to indicate some of the approximations required for a direct interpretation of the intensity distribution in reciprocal space. Before discussing a more rigorous approach, the influence of layer strain relaxation should be considered, since similar approaches are applicable.

41.2.3 Interpretation of Data Collected from Several Reflections – The Reciprocal Space Map – An Example

If the atom positions do not align from layer to substrate across the interface, then $Ld_x \neq Sd_x$ and $a_L \neq a_S$, and hence a_L should be substituted for a_S in (41.14). This dimension can be obtained from a reciprocal space map of a reflection having a component of this in-plane spacing (Fig. 41.4, compare with Fig. 41.2b). The distance in s_x between the layer peak of Fig. 41.4 and that of Fig. 41.2 gives the lateral plane spacings in the layer Ld_x by applying (41.9) and similarly for the substrate reflection Sd_x , so that $a_L = Ld_x \Delta H_x$. For example, when combining the $hkil$ reflections 0002 and $2\bar{1}\bar{1}4$, $\Delta H_x = \sqrt{4[h^2 + k^2 + hk]/3} = \sqrt{4[2^2 + 1^2 - 2]/3}$ for the hexagonal system with a (0001) surface plane. For the cubic system with a (001) surface, $\Delta H_x = \sqrt{[h^2 + k^2]}$. Alternatively if the substrate is unstrained and has known lattice parameters $a_L = a_S + \Delta d_x H_x$, where $\Delta d_x \equiv 1/\Delta s_x$, (41.9) the layer lattice parameter can be measured directly from the reciprocal space map of Fig. 41.4 (after accounting for any tilt). The tilt observed in the map of Fig. 41.2b changes $\omega_1 \rightarrow \omega_1 + \delta\omega$ for the layer, and ω_2 for the substrate is unchanged. This approach has been extended to the more general case, i. e., any space group, anisotropic relaxation or orientation [41.6].

From the discussion above a series of reciprocal space maps can yield a considerable wealth of information about the sample: the unit cell dimensions,

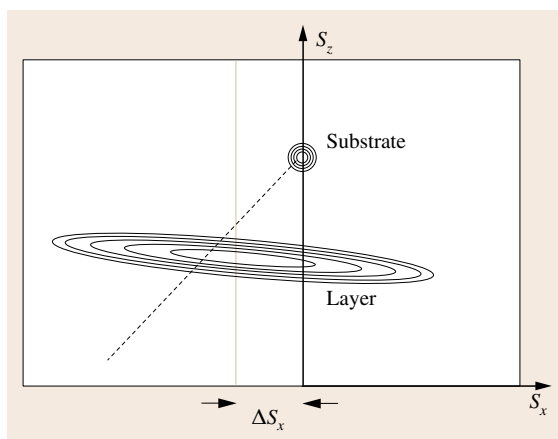


Fig. 41.4 A schematic of a reciprocal space map for a reflection from planes inclined to the surface plane. The lateral misalignment of the layer and substrate peak is indicative of differing lateral lattice parameters (layer strain relaxation) and/or relative lattice plane tilts

the distortion, and some characteristic dimensions (of mosaic blocks and thickness, for example) and their relationship to other layers or the substrate. The combination of several reflections or the shape of the peaks in reciprocal space can be used to isolate the contribution of the tilts, sizes, and strains [41.4, 6], using data as illustrated in Fig. 41.3b,d for the 0002 and 0004 reflections of GaN, for example. These direct approaches are very suitable for feedback during the early stages of crystal growth or for monitoring established growth procedures. However when there are several layers, and the material exhibits good crystal quality, the assumptions concerning the peak positions and the peak shapes become very approximate. This is because the simple interpretation assumes that each layer scatters independently, i. e., the scattering theory is represented very simply and it is assumed that the instrument and method of data collection create no artefacts.

41.3 Instrumental and Theoretical Considerations

The basics of the instrument for data collection and the appropriate scattering theories to use are discussed in this section. Many of these aspects will become clear in the examples.

41.3.1 The Instrument for Collecting X-Ray Diffraction Patterns

The reciprocal space maps of Figs. 41.2, 41.3, 41.4, etc., are a very small subset of Fig. 41.1. Referring to the expanded detail in the inset of Fig. 41.1, the representation of the angular divergence of the incident beam $\Delta\omega$, the angular acceptance of the scattered beam $\Delta 2\theta$, and the spread in wavelength of the source $\Delta\lambda$ all add to smearing of the x-ray probe [41.6]. The divergence $\Delta\omega$, the acceptance $\Delta 2\theta$, and the wavelength dispersion $\Delta\lambda$ vary throughout reciprocal space. If this capture volume is reduced too far, the intensity will be reduced significantly; however with recent advances in x-ray mirrors and lenses, and more significantly the availability of synchrotron sources, the expanding scope of x-ray scattering has not been diminished by insufficient intensity. The equipment is not significantly different from laboratory sources to synchrotron sources, but in terms of intensity differences the more exotic experiments only become feasible for synchrotron sources, especially if combinations of wavelengths are needed. However the long-term stability and convenience of laboratory sources make them the best choice for detailed analyses for most problems, and certainly for screening experiments prior to using a synchrotron source.

A good basic *workhorse* for many crystal growth studies is the instrument shown in Fig. 41.5 [41.7]. The monochromator and analyzer combination gives a very small reciprocal space probe over most of the accessible region available (defined by the wavelength used: the smaller the wavelength, the greater the accessible sphere). The intensity for laboratory sources is kept high by maintaining a reasonably large beam, $\approx 1 \times 10$ mm. The angular spread in the beam normal to Fig. 41.1 is the axial divergence, which is only restricted to $\approx 0.5^\circ$, compared with $\approx 0.001^\circ$ for $\Delta\omega$ and $\Delta 2\theta$, thus the measured reciprocal space map is a projection. Restricting the axial divergence creates a three-dimensional (3-D) reciprocal space map [41.8], yielding further information, but this approach will not be discussed further in this chapter. The resolution is a complex interplay between the instrument, the sample, the choice of reflection, the wavelength, and the alignment of the instrument and sample. Generally though, the sample is the determining factor and the probe is small compared with the structural features that influence the pattern, although the influence of the instrument should also be modeled.

These are only general comments on the resolution; methods of maintaining resolution and enhancing intensity will be addressed in Sect. 41.5.

41.3.2 Interpreting the Scattering by Simulation

The kinematical theory permits the basic interpretation summarized in Sect. 41.2 but is only valid for structures that are *ideally imperfect*. However, the majority of structures grown by highly controlled growth methods, e.g., molecular-beam epitaxy and metalorganic vapor-phase deposition, will result in crystal structures that are highly perfect. Also the substrate material is often Si, sapphire, MgO, GaAs, InP or SrTiO₃, which are nearly perfect. This level of perfection necessitates the application of dynamical theory [41.9], which includes extinction effects, the loss of incident intensity through scattering, interference with the multiply scattered wave, etc. [41.10, 11]. This can have a much more dramatic effect on the penetration depth than normal photoelectric absorption [41.12]. Also the peak positions, even for very simple structures, vary with layer thickness, creating uncertainties in the composition, thickness, and simple interpretation of periodic structures [41.13]. Perhaps the most important reason

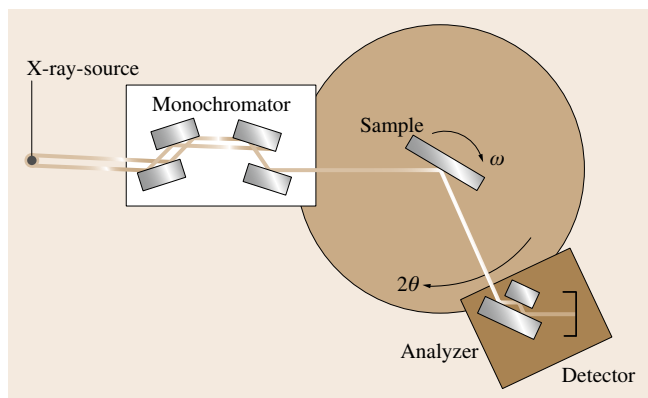


Fig. 41.5 The schematic of the high-resolution multiple-crystal diffractometer, which gives a small and well-defined reciprocal space probe over much of reciprocal space

for using dynamical theory is that, due to the increasing complexity of today's layer structures, the pattern is not a simple superposition of all the contributing layers, but a complex interference with peak shifts, beat frequencies, etc. Simulation also removes a few myths about direct interpretation, especially concerning superlattices, e.g., interfacial layers (roughening) that might appear as a loss of perfection can under some circumstances increase the satellite intensities [41.14]. Simulation has significant advantages in that the whole structure, thickness, and composition of each layer can now be analyzed simultaneously, and also all the iterative assumptions concerning the changing c/a ratio and Poisson ratio with composition, etc., are all included. The simulation of the profiles, or the reciprocal space maps, rely on the scattering amplitude (41.1), the unit cell parameters, and the elastic parameters, many of which are established database values, and of course some estimate of the structure to be simulated. The sensitivity to structural details is very high, so the need to have a good procedure for fitting the calculated to measured profiles by adjusting the model is evident. These procedures are becoming very sophisticated.

The simulation of more imperfect structures, for example, quantum dots within a perfect crystal matrix or rough interfaces in a period structure, is best achieved with the distorted-wave Born approximation (DWBA) [41.15]. This considers multiple scattering and is therefore dynamical and takes into account effects associated with the transmission of the beams. It is based on solving the scattering from a perfect

structure by the incident wave. This average scattered wave defines the local electric field of the wave, which is used to calculate the disturbed wave that results from quantum dots, precipitates, interfaces, and other disturbances. The combination of the undisturbed and disturbed waves gives the resultant scattering pattern. If the disturbance becomes too large then this perturbation method is not applicable and kinematical theory becomes more appropriate and can then be considered as a single scattering theory, i. e., the Born approximation (BA) [41.16].

The analytical approaches available and discussed in the following sections therefore have theoretical models that cover: perfect to nearly perfect structures (dynamical theory), imperfections giving rise to diffuse scattering (distorted-wave Born approximation), and highly imperfect or very small perfect regions (kinematical theory). If however an experiment is carried out when $S \approx 0$, i. e., with very small incident and scattering angles (specular scattering), then we see from (41.1) that the scattering amplitude is purely the sum of the scattering strength of individual atoms, independent of their position \mathbf{r} in the unit cell. It is then possible to consider the layers in a structure as consisting of a constant electron density, and therefore the interaction is analogous to light scattering from regions of constant refractive index; hence a much simpler, *optical* theory is valid [41.17]. Consequently specular reflectometry (close to the total external reflection condition) within a few degrees of the 000 reflection, is usually simulated with this optical theory.

41.4 Examples of Analysis from Low to High Complexity

The advances in x-ray scattering have been very rapid in recent years so this section will give a snapshot of the state of the art as well as the more established methods. Eventually the useful state-of-the-art analyses that are proven to be successful in revealing structural parameters, within a broad range of applications, will become established methods that are more accessible to more scientists. However, in the interim, these state-of-the-art methods are generally only accessible through collaboration with scientists in these fields, or through significant self-endeavor.

41.4.1 Established Methods

The interpretation of scattering profiles through simulation is now widely available for perfect and nearly

perfect structures, based on dynamical theory. A typical analysis is illustrated in Fig. 41.6a, for a GaAs-based structure. The approximate thickness and composition of each layer was known from the growth and this gave the starting model for its refinement through comparison of measured and simulated profiles. This is a two-layer sample so from the start we have to determine the composition and thickness for the InGaAs and the AlGaAs layers. The peak positions give some rough starting values, however with the limited number of parameters the fitting process can cope easily with the estimated values, which were within $\approx 20\%$ of the final fit values. The fit to the data was good with just this information included, i. e., two layers; however, the intensity of the fringes between -5000 and -4000 arcsec was significantly overestimated. The inclusion of some

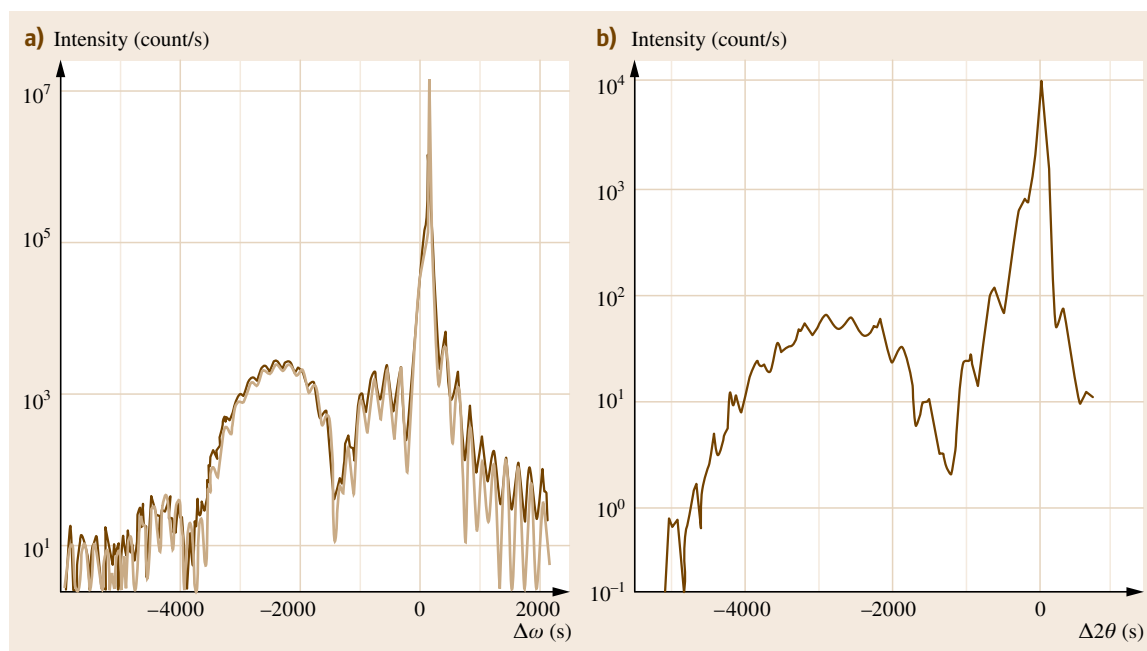


Fig. 41.6a,b The diffraction profile from an AlGaAs/InGaAs/GaAs structure obtained with the beam-selection diffractometer (brown) and simulated best fit profile (light brown) (a), and the static diffractometer, discussed in Sect. 41.5 (b). The data collected in (a) and (b) were collected in 7.3 min and 1 s, respectively

grading at the InGaAs to AlGaAs interface had a strong influence on this broad InGaAs layer fringe (with the AlGaAs thickness fringes superimposed). This grading reduced the intensity to achieve an improved fit (Fig. 41.6a). This additional graded layer is only observable with very high intensities or longer data collection times. This data was obtained with the beam-selection diffractometer, which is composed of an x-ray mirror, scattering from the 004 reflection of the sample to a 004 Ge analyzer in front of the detector [41.18]. This gives a substrate peak intensity of ≈ 30 Mcps, so the ω - 2θ scan data was collected in just over 7 min with a 0.005° step size. The final parameters were $0.0130\ \mu\text{m}$ of $\text{In}_{0.145}\text{Ga}_{0.855}\text{As}$, a $0.0059\ \mu\text{m}$ graded layer of InAlGaAs , and $0.0773\ \mu\text{m}$ of $\text{Al}_{0.258}\text{Ga}_{0.742}\text{As}$. These values compare with the best fit of $0.0157\ \mu\text{m}$ of $\text{In}_{0.145}\text{Ga}_{0.855}\text{As}$ and $0.0808\ \mu\text{m}$ of $\text{Al}_{0.258}\text{Ga}_{0.742}\text{As}$ when no interfacial grading was included, which would be the case if the broad InGaAs layer fringes were not observed.

For very complex samples the fitting process requires more persistence and time, mainly because of the high degree of correlation between parameters and the complicated interference in the scattering from individ-

ual layers. Typical structures that fall into this category are vertical-cavity surface-emitting lasers (VCSEL). This example is composed of quaternary AlGaInP layers flanking a ternary GaInP quantum well, which are surrounded by Bragg stacks of AlGaAs/AlGaAs periodic layers; the laser wavelength of the radiation generated in the quantum well is defined by its thickness and composition, and the efficiency of the cavity relies on the Bragg-stack composition modulation and thickness. There will be some interfacial grading and further layers making a total in excess of 450. This is quite a challenge, but possible to solve [41.19]. To add to the difficulty the surface is offset from the (001) crystal plane by 10° . Careful control of the fitting process and appropriate choice of reflections gives a very good indication of the sensitivity of certain parameters and some clear bounds that fit the x-ray data. The final fit compared with the experimental profile for the 006 reflection is shown in Fig. 41.7.

The sensitivity to composition and thickness is a clear advantage of x-ray scattering, and this is enhanced at increasing scattering angles (41.8). When the scattering angle is very small, the composition sensitivity from strain is negligible, but the scattering is still

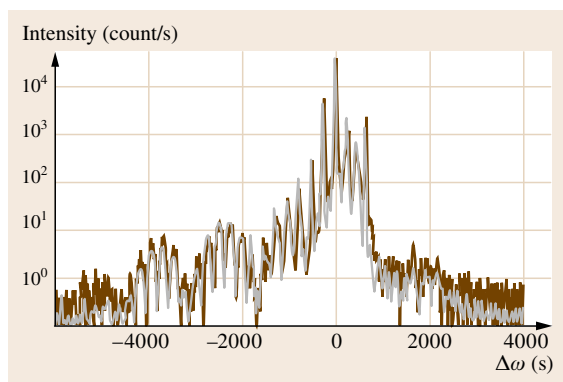


Fig. 41.7 The complex scattering from a VCSEL structure (brown) is shown along with the final fit to this profile (grey) (data courtesy of P. Kidd). The result gave bounds for the layer composition and thickness throughout this structure consisting of > 450 layers

sensitive to the composition because of the differences in scattering strength (41.1). This can be very useful for isolating the influence of compensating strain in structures such as $\text{Si}_{1-x-y}\text{Ge}_x\text{C}_y$ [41.20]. C has a very small covalent radius, but scatters very weakly, whereas Ge has a covalent radius closer to Si and scatters strongly. Since in this case Ge scatters strongly, the composition can be obtained from the reflectometry profile to within

$\approx 0.1\%$ in x , provided the C concentration is estimated to within $\approx 1\%$ in y . Since the typical C concentration is $< 1\%$, the Ge concentration can be determined to good precision; the reflectometry curve is given in Fig. 41.8a. The C concentration is then extracted from the 004 profile (Fig. 41.8b); however, this relies heavily on the assumptions concerning the C covalent radius. For the result to be consistent with secondary-ion mass spectrometry (SIMS), the covalent radius probably matches that in cubic SiC or the relationship between the lattice parameter and composition is far from linear.

From the above analyses it is clear that composition, thickness, and grading due to interdiffusion can be obtained quite directly. The interface roughness in the plane can also be estimated, although the theory does become a little more problematic. As with all the examples above, the structural model is derived via an iterative procedure by comparing simulated with measured profiles. Thickness, composition, and even interfacial grading are reasonably predictable, but lateral roughness is less clearly described. There are several models of interfaces, ranging from a truncated fractal [41.21], staircase for vicinal surfaces [41.22], and castellated surfaces, Holý within [41.6]. The resulting profiles are quite different and require estimates of the extent of the roughness replication layer to layer, i.e., none, partial, and full replication. The truncated fractal

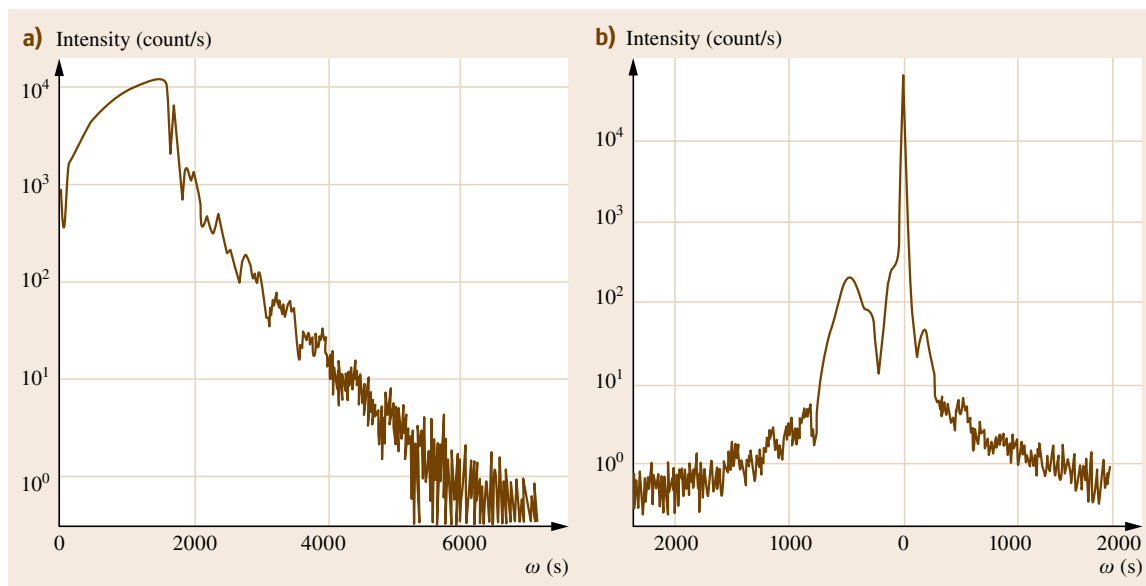


Fig. 41.8a,b The two profiles, close to the 000 (a) and the 004 (b) reflections, for a SiGeC structure used to break the correlation between parameters. By fitting the two profiles the composition of the Ge and C could be determined, because of their different influences on the two profiles

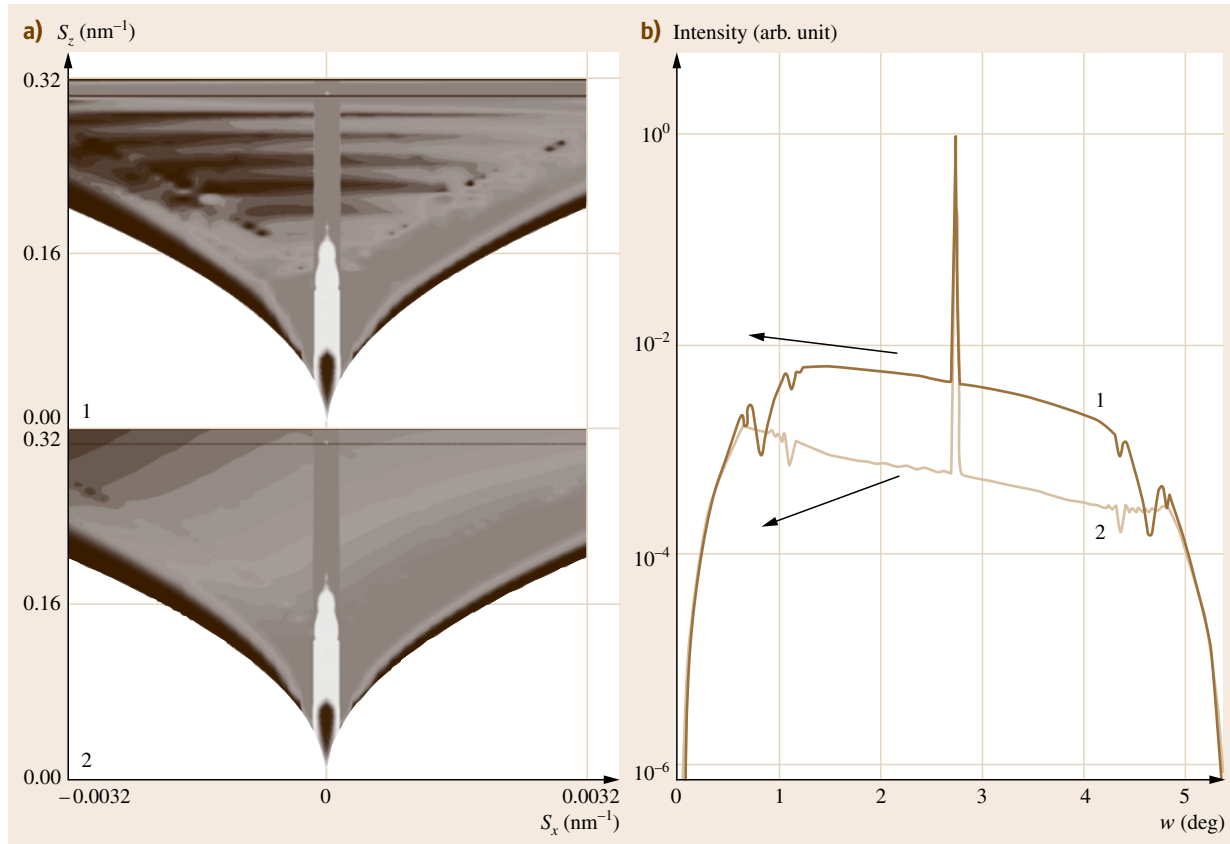


Fig. 41.9a,b The change in diffuse scattering close to the specular profile for various interface types: (1) castellated fully replicated and (2) unreplicated layer to layer for a periodic superlattice. The structure simulated is composed of (AlAs 50 nm + GaAs 50 nm) \times 10 on GaAs, all with raised regions of width 50 ± 50 nm and height 1 ± 0.2 nm

description has a maximum length that is often termed the lateral correlation length; however, this is not an easy parameter to visualize. The nature of the jaggedness is also described by a single parameter and the scattering is derived from the correlation between different heights across the interface. The staircase and castellated surfaces require a distribution of heights and widths, with the former having an inclination angle. The castellated surface will almost equate to a fractal surface at one extreme. It should be clear from this that a good physical model for the likely interface shape is required to obtain some significance in the results. If the roughness is not replicated from layer to layer then the distributed intensity around the specular profile is rather uniform and weak, whereas replicated roughness brings the diffuse scattering into bands (Fig. 41.9). The most appropriate theory for modeling the scatter-

ing is DWBA, but this is only applicable for small roughness and a limited s_z range. If the roughness becomes significant or the simulation is taken to large s_z , then the kinematic approach (BA) is more applicable. Making a decision on the cross-over of DWBA to BA depends on several aspects [41.23], but certainly interfaces that are comparable in width to the layer thickness itself should use the BA, although this will not reproduce the region close to the critical angle or Yoneda wings [41.24] associated with surface roughness and transmission factors.

41.4.2 New Methods and New Analyses

All the methods and analyses described above are generally available. However, because the science in this field is progressing rapidly, some of the most exciting

work requires considerable effort to reproduce. In many instances though, the equipment to undertake the work is either available commercially or for highly specialized experiments a synchrotron may be the only route. This section will consider some methods that extend the analysis beyond those discussed above; it does not pretend to be comprehensive, but rather picks out a few advances.

Dislocations are one of the significant defects that can destroy devices, and they influence the scattering, as will be clear from Chap. 42 on x-ray topography. Their influence is clear in reciprocal space maps, even at the very early stages of layer relaxation [41.25]. These misfit dislocations have a clear influence since they cause lattice plane rotation and strain that can be modeled [41.26]. The influence of threading dislocations is less clear since the Burgers vectors are not necessarily additive, but do contribute to a twist that is often interpreted purely in terms of peak broadening, although the influence of strain must also be considered [41.27]. Generally misfit dislocations, in GaN for example, are accompanied with threading dislocations, and obtaining the proportions of each requires analysis of the diffraction peak tails as well as the peak widths. A crucial aspect in this analysis is the correlation between dislocations, as this can have a profound influence on the FWHM [41.27, 28]. Holý et al. [41.29] are now taking this to the next stage, by reducing the probe volume to 1 μm or less, such that it is closer to the dislocation separation. It may then be possible to determine the threading dislocation densities in GaN epitaxial-lateral-overgrown structures, by averaging the diffraction profiles over several positions. However the simulation of these structures is not yet fully resolved.

The development in the analysis of quantum dots gives a good indication of what can be achieved by x-ray scattering experiments. The interpretation of scattering of buried dots can be based on DWBA. This is most appropriate in semiconductor systems where the dots form a region with a different lattice parameter and scattering strength. The distortion will then extend to the surface where the stress is relieved. The distribution of the dots can be measured by the lateral satellites associated with the Bragg peaks. For ordered arrays of dots these produce very strong effects [41.30]. However, for the more typical self-assembled dots, there may be only one broad satellite. This lateral spacing (41.9) between the satellite and the layer peak will give some measure of the dot spacing and its variation [41.31]. Combining spacings from planes inclined to the surface at several azimuths will give the average arrangement in

the plane. For dots on the surface, the best approach is to use grazing-incidence small-angle scattering [41.32] to give satellites either side of the specular scattered beam. To extract details of the shape of buried dots, in-plane scattering appears to be the most unambiguous route [41.33], by modeling the strain, which must be anisotropic [41.34]. Generally though, these approaches have been entirely concentrated at synchrotron sources, although the analysis of buried dots [41.34] was carried out with a standard laboratory instrument with a sealed x-ray source (Fig. 41.5) and has even been extended to the analysis of a single layer of quantum dots buried 100 nm below the surface [41.35].

As discussed in Sect. 41.4.1, the shape (thickness) and not the strain is obtained from scattering close to the 000 reflection condition, and therefore the grazing-incidence small-angle scattering configuration will only give the shape of the dots. However to obtain the strain state of surface dots one uses in-plane scattering, i.e., grazing-incidence and grazing-exit scattering close to Bragg peaks, as in the analysis of buried dots. If the dots are known to have a regular shape or the shape can be deduced, some estimate of the strain state (composition or strain relaxation) can be obtained [41.36], although this can lead to complications with uncertainties about the shape [41.37]. Extracting the dot shape is clearly an iterative method based on some initial guess, and this averaging of the diffraction process will result in a weighted average of the information. If the x-ray source is coherent and an individual dot can be isolated, then the resulting diffraction pattern can be directly inverted to reconstruct the dot shape [41.38]. In practice isolating one dot is difficult, as is having perfect coherence, however incorporating a few dots with a partially coherent beam gives adequate data to reconstruct the dot shapes [41.39]. The procedure uses the measured amplitudes and iteratively solves for the phase information using methods developed in optics. The scattering volume is so small that the kinematical (BA) scattering theory is sufficient. The typical data collected from an experiment with a sealed laboratory source, averaging over $\approx 10^7$ dots [41.35], compared with that collected from a coherent synchrotron source for a line of $\approx 10^1$ dots [41.39], is presented in Fig. 41.10. The former obtains the dot shape and composition indirectly from the strain distribution created by the dots, whereas the coherent diffraction experiment gives the scattered amplitudes, i.e., the Fourier coefficients for the shape of surface dots.

The arrangements of quantum dots can be either regular or self-assembled, and both can be studied

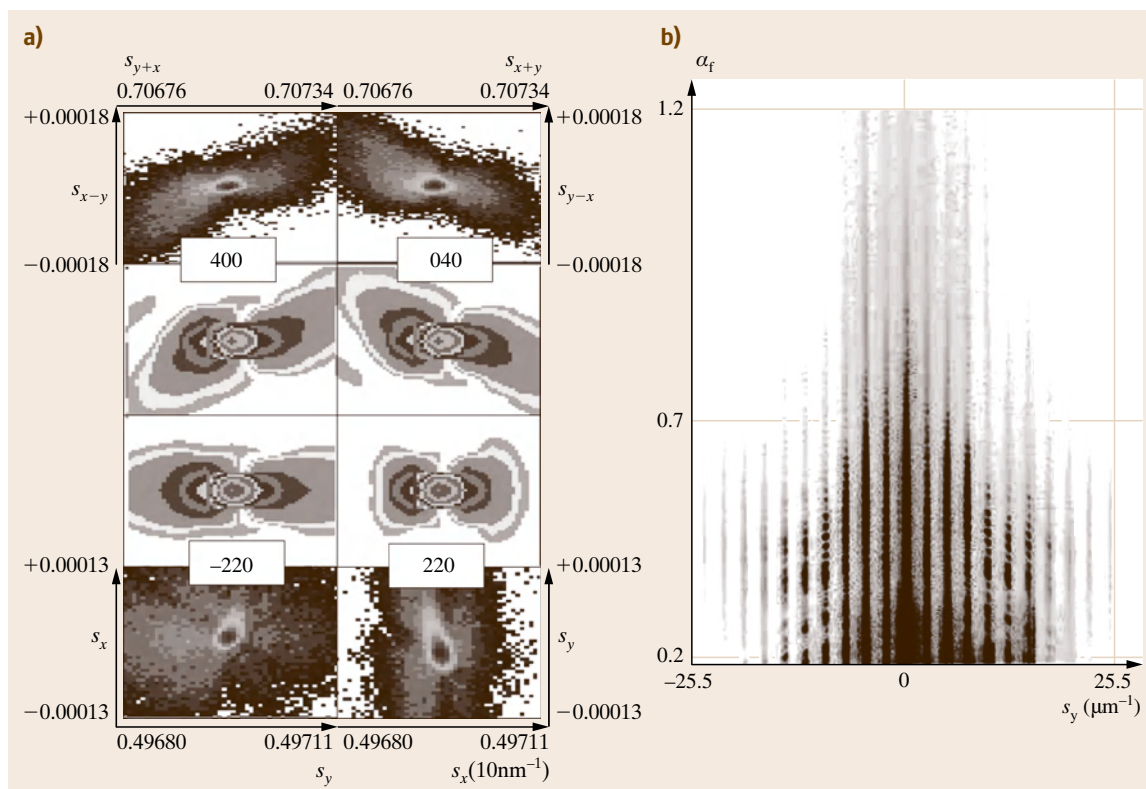
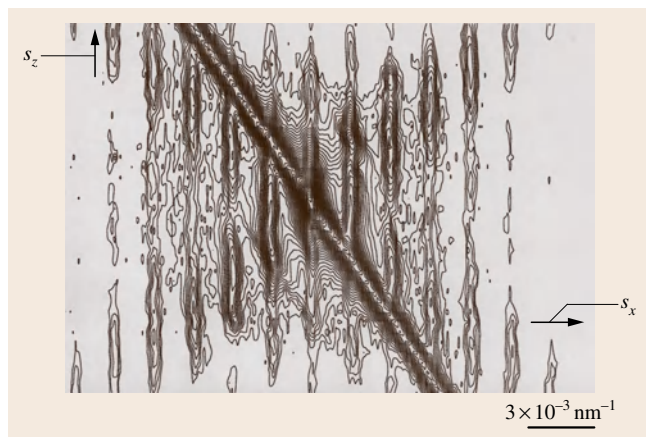


Fig. 41.10a,b Different experiments revealing different levels of information about dots: **(a)** buried dots using a sealed laboratory source, in-plane reciprocal space maps obtained just above the critical angle, for various reflections with their best-fit simulations, **(b)** the forward scattering, close to 000, from surface dots obtained with a coherent synchrotron source where the incident beam is below the critical angle for the substrate and the resultant scattering is purely from the dots (data courtesy of I. Vartanyants)

with x-ray scattering to yield useful information. Quantum wires on the other hand are nearly always regular

since their growth is governed by vicinal wafers or patterning. These structures give impressive scattering patterns (Fig. 41.11) that are easily observable with laboratory sources [41.40]. They also change depending on whether the quantum wires or Bragg gratings are parallel or perpendicular to the incident x-ray beam. A rather pragmatic approach to the analysis can be applied. Effectively the Fourier transform based on the BA (kinematical) theory of a trial model shape and period can be used to obtain some very useful shape parameters. This will not give reliable intensities or account for

Fig. 41.11 The scattering close to the 004 reflection for a laterally periodic grating on a GaAs substrate. The data was obtained with a high-resolution diffractometer (data courtesy of M. Gailhanou). The *long streak* comes from the analyzer that had insufficient channel bounces before reaching the detector ◀



the true shapes of the scattering peaks for detailed interpretation. All combinations of the beam paths need to be considered [those scattered directly from the grating, those transmitted (refracted) through the grating, etc.] and are coherently brought together to account for all the cross-hatching of intensity, etc. based on the DWBA [41.41]. Surface features, dots or wires, do have an added complication to the analysis in that the strain

influence is unlikely to be homogeneous and requires finite-element analysis to predict the strain distribution. However obtaining a good strain model can result in a high level of detail. Surface quantum wires studied with a detailed strain model suggest that SiGe/Si superlattice wires have an oxide coating [41.42]. For buried gratings the strains dominate the scattering [41.43], as with buried quantum dots.

41.5 Rapid Analysis

The methods discussed so far in this chapter have concentrated on analysis, both direct and simulation, and some specialized applications, with some discussion on the instrumentation. However it is largely the development in instrumentation that has made x-ray scattering so much more accessible. The instrumentation at synchrotron x-ray sources is very similar to how x-ray laboratories used to be, i.e., components are built specifically for the type of analysis required, so the set up time can be a significant factor. This does have the advantage in that some of the latest technology can be incorporated very rapidly, but the instruments do require highly trained specialists to set up the experiments, and it all becomes a significant team effort. Commercial laboratory machines are, on the other hand, rather versatile, with x-ray mirrors, lenses, and a plethora of monochromators, analyzers, and detectors. State-of-the-art laboratory equipment has exchangeable components that are precision-aligned so that several experimental configurations can be used without removing the sample. So in many ways the components, through significant cross-fertilization of ideas, are rather similar, although the intensity and wavelength choice at synchrotrons outstrips the laboratory source. However, with the use of mirrors, lenses, etc., the laboratory source gives sufficient intensity for the majority of applications. Some of the most interesting advances have been made in detector technology, which until recently were saturated by the high count rates. New developments in solid-state detectors, which are pixel-array single-photon counting detectors, will be a fascinating area to watch to create new opportunities.

Since the push is for increased speed and feedback in crystal growth there have been some interesting developments. In the quest for higher speed the intensity needs to be increased, or the data can be collected in parallel. Higher intensity usually comes at a cost to the

resolution, although this can be overcome by making the experiment much more specific to the analysis. The first example of this was given in Sect. 41.4.1, where the more specific beam-selection diffractometer gives a 30× increase in intensity compared with conventional instrumentation with an x-ray mirror (Fig. 41.5). This is still a scanning method, which cannot compete with parallel data collection. The discussion (Sect. 41.3.1) on the influence of the instrument considered only resolution in diffraction space. However, when this is combined with the *real* space resolution, it is possible to achieve high-resolution profiles instantaneously [41.44]. Consider the profile in Fig. 41.6a, which already has 30× the intensity of a conventional instrument (Fig. 41.5); it took ≈ 7 min to collect. However the profile given in Fig. 41.6b was collected in 1 s. This static diffractometer has rather simple components: an x-ray source, slit, and a linear position-sensitive detector. The simulation of the scattering profile requires modeling of the beam paths to account accurately for all the features. This method can be applied to all wafer-based samples, by finding a suitable reflection, or if that is not possible by choosing an alternative wavelength. The highest resolution relies on a high-quality sample; however, useful information can still be extracted from imperfect materials, as will be shown in Sect. 41.6.

There are several growth chambers at synchrotrons for in situ characterization. Some of the early work concentrated on analyzing the surface reconstruction [41.45], and the investigation of dislocations by topography [41.46]. Some of the methods discussed in Sect. 41.4.2 have been applied in situ at synchrotrons to study the evolving crystal growth, and it is possible to see features even when 0.5 monolayer has been deposited [41.47]. A laboratory source, with the advantage of bringing the x-ray experiment to the metalorganic chemical vapor deposition (MOCVD) growth

chamber, has been used for studying the growth of InGaN on GaN [41.48]. The source is used in combination with a Johansson monochromator to focus the beam onto the rotating sample, and despite the complications associated with rotation and wobbling, the evolution of the InGaAs on a GaN buffer layer is very clear. The integration time is $\approx 17\%$ of the rotation period. This is not high-resolution data, but perfectly sufficient to monitor the growing layer. This instrument is again relatively simple with a source and focusing Johansson crystal (which captures the divergent beam from the source and focuses it onto the sample);

the scattered wave is collected by a position-sensitive detector.

These rapid analyses could be very useful for either quick feedback during the initial stages of crystal growth or controlling an established process. However, there are some interesting possibilities associated with rapid data collection and high intensity that will be addressed in the next section. Although these examples are specific for the material of interest, they are easily adapted; the concentration at this stage is on composition and thickness measurement and some estimate of *quality*.

41.6 Wafer Micromapping

Lateral changes in the composition, thickness, and *quality* across a wafer can be very revealing to the crystal grower. Generally the x-ray probing beam is of the order of mm, and therefore can suffer from significant averaging, adding uncertainty to the interpretation. As an example, the influence of peak widths and peak shifts contribute to the measured peak widths. The benefit of rapid data collection is that the probing beam can be reduced and still achieve reasonable measurement times. The typical sizes of the beam of the beam-selection diffractometer and the static diffractometer are $100\text{ }\mu\text{m} \times 10\text{ mm}$ to achieve these high data collection rates, so reducing this to $100\text{ }\mu\text{m}$ double-pinholes reduces the intensity considerably ($> 100\times$). The intensity achieved is still very usable, although requiring longer count times or a compromise on counting statistics. As an example consider this far-from-perfect GaN sample, which is first probed with the beam-selection diffractometer using the $100\text{ }\mu\text{m}$ double-pinholes, to obtain an estimate of *quality*; this is achieved by centering on the 0002 GaN peak and scanning in ω (Fig. 41.12a). The width of this peak is related to small tilted regions or some finite lateral dimension, e.g., the distance between defects or mosaic block size. The resulting map over the $2.5 \times 5\text{ mm}$ sample at $50\text{ }\mu\text{m}$ intervals is given in Figs. 41.12b,c, where the peak positions and peak widths across the wafer are shown. Clearly the peak width varies on this $100\text{ }\mu\text{m}$ scale (Fig. 41.12b) and is most pronounced in one region that is between two areas that have quite different peak positions (Fig. 41.12c). These may be large mosaic blocks or regions of large curvature. If the measurement of the peak width was obtained on the mm scale then all these contributions

would be combined and may have led to a different interpretation.

A similar analysis has been performed with the static diffractometer, but for speed obtained with a $200\text{ }\mu\text{m}$ probe and stepping at $100\text{ }\mu\text{m}$ intervals. This analysis gave the variation in composition and period across the wafer. The satellites are very weak (Fig. 41.12d) from this structure (the In concentration was rather low), but still an indication of the period variations could be obtained and did not indicate any significant fluctuations. The composition, though, does vary significantly over the wafer, with the center-right region being 10% below that of the lower region of the wafer.

The variation in the composition and the period can probably be linked quite clearly to the growth of the structure. However, the material *quality* can help in screening wafers. Reducing the probe clearly begins to separate the peak width and the peak position, and since the width, rather than the position, is generally related to distorted regions this may correlate with the local defect density and hence optical emission in GaN lasers and light-emitting diodes (LEDs), for example. The reduction in the probe size has two effects, not only the isolation of small regions but also the variation in peak broadening effects is likely to become larger as the averaging effects are reduced [41.49]. In the extreme case when the probe is close to a micron, the effects of individual dislocations will be observed, as discussed in Sect. 41.4.2. Baumbach et al. [41.50] have extended micromapping towards this extreme, using an extension of their *rocking-curve imaging* technique [41.51], which requires a well-collimated monochromatic beam from a synchrotron source; the spatial resolution is

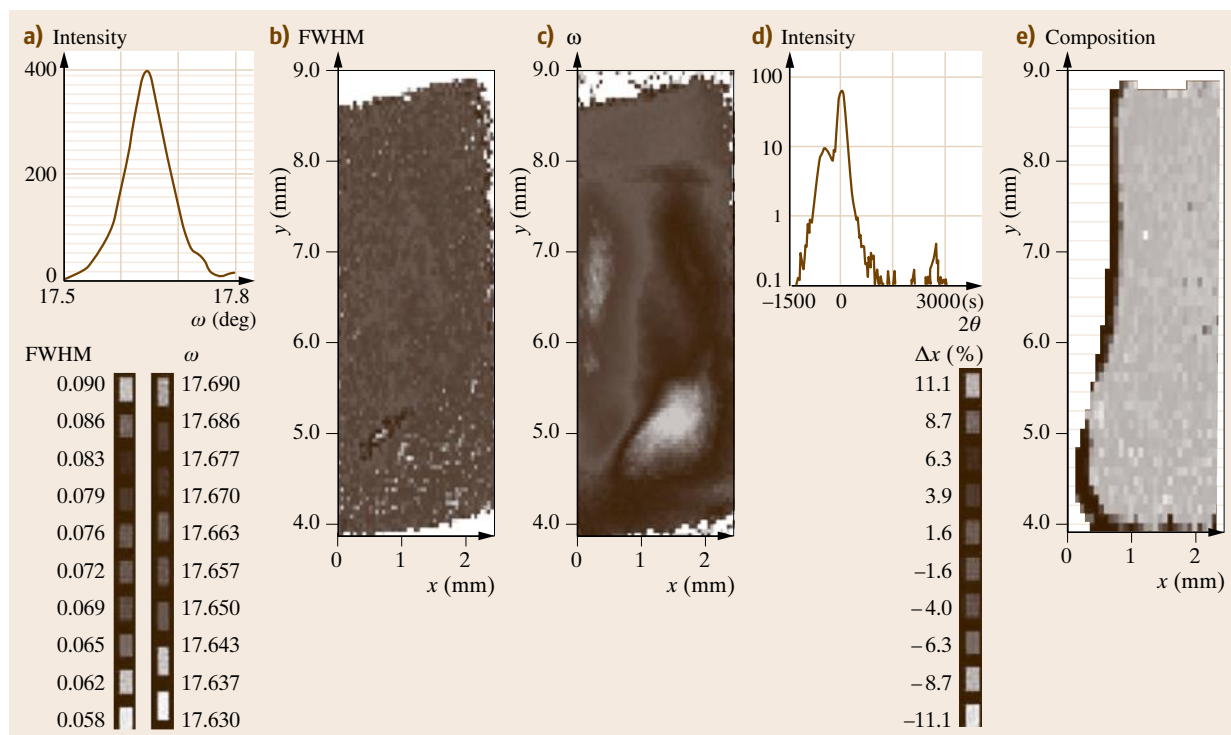


Fig. 41.12a–e Examples of wafer mapping on the 100 μm scale on a GaN wafer with an InGaN/GaN superlattice. Data collected with the beam-selection diffractometer: **(a)** a typical profile, **(b)** the distribution of the FWHM $\Delta\omega$, **(c)** the distribution of the peak position ω . The data collected with the static diffractometer; **(d)** a typical profile; and **(e)** the variation in composition across the wafer

defined by the pixel size of an area detector. By rocking the sample an array of profiles is achieved. An interesting aspect with this is the cross-over between topography and conventional high-resolution scattering, where the latter will not only break the averaging effect of larger probes but could provide ways of in-

terpreting the contrast in topography that can arise from several complicating aspects. This combination of microdiffraction or topography (real space) and reciprocal space has many advantages in unraveling the structural information that is not revealed on the mm scale.

41.7 The Future

There is little doubt that x-ray scattering is very sensitive to structural details, and these methods are pushing the technological, theoretical, and instrumental developments. The intensity and quality of x-ray sources is no longer a restriction, with many synchrotrons existing around the world. The possibilities from coherent x-ray sources will become clearer as these facilities become more widely available, e.g., not only at synchrotrons but at x-ray free-electron laser facilities. The improvements in detectors will also create many opportunities,

and are very necessary to cater for the large intensities now available.

Instrument development is benefiting from the cross-fertilization of laboratory and synchrotron-based work, with sophisticated optics being of use for both types of x-ray sources. Theoretical developments will also be a challenge as more scientists struggle to interpret the scattering from ever more exotic materials and structures. Enhanced computing power will benefit this field, for example, when modeling the diffuse scat-

tering or optimization for extracting parameters of very complex materials.

It is very difficult to pinpoint specific areas where the most significant method developments will occur, since there is a large range of possibilities: coherent

scattering, microtomography, micromapping, etc., but the most significant will be determined by the materials requiring analysis. The main aspect though, is that this whole field is moving very rapidly, creating an impressive toolset for materials characterization.

References

- 41.1 P.F. Fewster, N.L. Andrew: Interpretation of the diffuse scattering close to Bragg peaks by x-ray topography, *J. Appl. Cryst.* **26**, 812–819 (1993)
- 41.2 P.F. Fewster: Multicrystal x-ray diffraction of heteroepitaxial structures, *Appl. Surf. Sci.* **50**, 9–18 (1991)
- 41.3 P. Scherrer: Bestimmung der Grösse und der inneren Struktur von Kolloidteilchen mittels Röntgenstrahlen, *Nachr. Ges. Wiss. Göttingen* **2**, 98–100 (1918), in German
- 41.4 G.K. Williamson, W.H. Hall: X-ray line broadening from filed aluminium and wolfram, *Acta Metall.* **1**, 22–31 (1953)
- 41.5 L. Vegard: Die Konstitution der Mischkristalle und die Raumfüllung der Atome, *Z. Phys.* **5**, 17–26 (1921), in German
- 41.6 P.F. Fewster: *X-ray Scattering from Semiconductors*, 2nd edn. (Imperial College Press, London 2003)
- 41.7 P.F. Fewster: A high-resolution multiple-crystal multiple-reflection diffractometer, *J. Appl. Cryst.* **22**, 64–69 (1989)
- 41.8 P.F. Fewster: Reciprocal space mapping, *Crit. Rev. Solid State Mater. Sci.* **22**, 69–110 (1997)
- 41.9 P.P. Ewald: Zur Theorie der Interferenzen der Röntgenstrahlen in Kristallen, *Phys. Z.* **14**, 465–472 (1913), in German
- 41.10 C.G. Darwin: The theory of x-ray reflexion, *Philos. Mag.* **27**, 315–333 (1914)
- 41.11 C.G. Darwin: The theory of x-ray reflexion, *Philos. Mag.* **27**, 675–690 (1914)
- 41.12 J.A. Prins: Die Reflexion von Röntgenstrahlen an absorbierenden idealen Kristallen, *Z. Phys.* **63**, 477–493 (1930), in German
- 41.13 P.F. Fewster: X-ray diffraction from low dimensional structures, *Semicond. Sci. Technol.* **8**, 1915–1934 (1993), review article
- 41.14 J.M. Vandenberg, M.B. Panish, H. Temkin, R.A. Hamm: Intrinsic strain at lattice-matched $\text{Ga}_{0.47}\text{In}_{0.53}\text{As}/\text{InP}$ interfaces as studied with high-resolution x-ray diffraction, *Appl. Phys. Lett.* **53**, 1920–1922 (1988)
- 41.15 V. Holý, U. Pietsch, T. Baumbach: *High-Resolution X-ray Scattering from Thin Films and Multilayers* (Springer, Berlin, Heidelberg 1999)
- 41.16 M. Born, E. Wolf: *Principles of Optics*, 6th edn. (Cambridge Univ. Press, Cambridge 1980)
- 41.17 L.G. Parrat: Surface studies of solids by total reflection of x-rays, *Phys. Rev.* **95**, 359–369 (1954)
- 41.18 P.F. Fewster: A 'beam-selection' high-resolution x-ray diffractometer, *J. Appl. Cryst.* **37**, 565–574 (2004)
- 41.19 P. Kidd: Investigation of the precision in x-ray diffraction analysis of VCSEL structures, *J. Mater. Sci. Mater. Electron.* **14**, 541–550 (2003)
- 41.20 J. Zhang, J.H. Neave, X.B. Li, P.F. Fewster, H.A.W. El Mubarek, P. Ashburn, I.Z. Mitrovic, O. Buiui, S. Hall: Growth of SiGeC layers by GSMBE and their characterization by x-ray techniques, *J. Cryst. Growth* **278**, 505–511 (2005)
- 41.21 S.K. Sinha, E.B. Sirota, S. Garoff, H.B. Stanley: X-ray and neutron scattering from rough surfaces, *Phys. Rev. B* **38**, 2297–2311 (1988)
- 41.22 E.A. Kondrashkina, S.A. Stepanov, R. Opitz, M. Schmidbauer, R. Köhler, R. Hey, M. Wassermeyer, D.V. Novikov: Grazing-incidence x-ray scattering from stepped interfaces in AlAs/GaAs superlattices, *Phys. Rev. B* **56**, 10469–10482 (1997)
- 41.23 I.D. Feranchuk, S.I. Feranchuk, A.P. Ulyanenko: Self-consistent description of x-ray reflection and diffuse scattering from rough surfaces, unpublished work presented at XTOP 2006, Baden-Baden (2006)
- 41.24 Y. Yoneda: Anomalous surface reflection of x-rays, *Phys. Rev.* **131**, 2010–2013 (1963)
- 41.25 P. Kidd, P.F. Fewster, N.L. Andrew: Interpretation of the diffraction profile resulting from strain relaxation in epilayers, *J. Phys. D Appl. Phys.* **28**, A133–A138 (1995)
- 41.26 V. Kaganer, R. Köhler, M. Schmidbauer, R. Opitz, B. Jenichen: X-ray diffraction peaks due to misfit dislocations in heteroepitaxial structures, *Phys. Rev. B* **55**, 1793–1810 (1997)
- 41.27 V. Kaganer, O. Brandt, A. Trampert, K.H. Ploog: X-ray diffraction peak profiles from threading dislocations in GaN epitaxial films, *Phys. Rev. B* **72**, 045423–045434 (2005)
- 41.28 S. Daniš, V. Holý: Diffuse x-ray scattering from misfit and threading dislocations in $\text{PbTe}/\text{BaF}_2/\text{Si}(111)$ thin layers, *Phys. Rev. B* **73**, 014102–014107 (2006)
- 41.29 V. Holý, T. Baumbach, D. Lübbert, M. Elyyan, P. Mikulík: Diffuse x-ray scattering from dislocations in epitaxial layers – Beyond the ensemble

- averaging, unpublished work presented at XTOP 2006, Baden-Baden (2006)
- 41.30 V. Holý, J. Strangl, G. Springholz, M. Pinczoltis, G. Bauer, I. Kegel, T.H. Metzger: Lateral and vertical ordering of self-assembled PbSe quantum dots studied by high-resolution x-ray diffraction, *Physica B* **283**, 65–68 (2000)
- 41.31 A.A. Darhuber, P. Schittenhelm, V. Holý, J. Strangl, G. Bauer, G. Abstreiter: High-resolution x-ray diffraction from multilayered self-assembled Ge dots, *Phys. Rev. B* **55**, 15652–15663 (1997)
- 41.32 M. Schmidbauer, T. Wiebach, H. Raidt, M. Hanke, R. Köhler, H. Wawre: Self-organised ordering of $\text{Si}_{1-x}\text{Ge}_x$ nanoscale islands studied by grazing incidence small-angle x-ray scattering, *J. Phys. D Appl. Phys.* **32**, A230–A233 (1999)
- 41.33 J. Stangl, V. Holý, T. Roch, A. Daniel, G. Bauer, J. Zhu, K. Brunner, G. Abstreiter: Grazing incidence small-angle x-ray scattering study of buried and free-standing SiGe islands in a SiGe/Si superlattice, *Phys. Rev. B* **62**, 7229–7236 (2000)
- 41.34 P.F. Fewster, V. Holý, N.L. Andrew: Detailed structural analysis of semiconductors with x-ray scattering, *Mater. Sci. Semicond. Process.* **4**, 475–481 (2001)
- 41.35 P.F. Fewster, V. Holý, D. Zhi: Composition determination in quantum dots with in-plane scattering compared with STEM and EDX analysis, *J. Phys. D Appl. Phys.* **36**, A217–A221 (2003)
- 41.36 T.H. Metzger, I. Kegel, R. Paniago, J. Piesl: Grazing incidence x-ray scattering: an ideal tool to study the structure of quantum dots, *J. Phys. D Appl. Phys.* **32**, A202–A207 (1999)
- 41.37 D. Grigoriev, M. Hanke, M. Schmidbauer, P. Schäfer, O. Konovalov, R. Köhler: Grazing incidence x-ray diffraction at free-standing nanoscale islands: fine structure of diffuse scattering, *J. Phys. D Appl. Phys.* **36**, A225–A230 (2003)
- 41.38 I.A. Vartanyants, I.K. Robinson: Imaging of quantum array structures with coherent and partially coherent diffraction, *J. Synchrotron Rad.* **10**, 409–415 (2003)
- 41.39 I.A. Vartanyants, I.K. Robinson, J.D. Onken, M.A. Pfeifer, G.J. Williams, F. Pfeiffer, H. Metzger, Z. Zhong, G. Bauer: Coherent x-ray diffraction from quantum dots, *Phys. Rev. B* **71**, 245302.1–245302.9 (2005)
- 41.40 P. van der Sluis, J.J.M. Binsma, T. van Dingen: High resolution x-ray diffraction of periodic surface gratings, *Appl. Phys. Lett.* **62**, 3186–3188 (1993)
- 41.41 T. Baumbach, M. Gailhanhou: X-ray diffraction from epitaxial multilayered surface gratings, *J. Phys. D Appl. Phys.* **28**, 2321–2327 (1995)
- 41.42 Y. Zhang, V. Holý, J. Strangl, A.A. Darhuber, P. Mikulík, S. Zerlauth, F. Schäffler, G. Bauer, N. Darowski, D. Lübbert, U. Pietsch: Strain relaxation in periodic arrays of Si/SiGe quantum wires determined by coplanar high-resolution x-ray diffraction and grazing incidence diffraction, *J. Phys. D Appl. Phys.* **32**, A224–A229 (1999)
- 41.43 A. Ulyanenko, N. Darowski, J. Grenzer, U. Pietsch, H. Wang, A. Forchel: Evaluation of strain distribution in freestanding and buried lateral nanostructures, *Phys. Rev. B* **60**, 16701–16714 (1999)
- 41.44 P.F. Fewster: A 'static' high-resolution x-ray diffractometer, *J. Appl. Cryst.* **38**, 62–68 (2005)
- 41.45 M. Sauvage-Simkin, Y. Garreau, R. Pinchaux, M.B. Véron, J.P. Landesman, J. Nagle: Commensurate and incommensurate phases at reconstructed (In,Ga)As(001) surfaces: x-ray diffraction evidence for a composition lock-in, *Phys. Rev. Lett.* **75**, 3485–3488 (1988)
- 41.46 S.J. Barnett, C.R. Whitehouse, A.M. Keir, G.F. Clark, B. Usher, B.K. Tanner, M.T. Emeny, A.D. Johnson: X-ray topography of lattice relaxation in strained layer semiconductors: Post growth studies and a new facility for in-situ topography during MBE growth, *J. Phys. D Appl. Phys.* **26**, A45–A49 (1993)
- 41.47 D.K. Satapathy, B. Jenichen, W. Braun, V. Kaganer, L. Däweritz, K.H. Ploog: In situ grazing incidence x-ray diffraction study of strain evolution during growth and post growth annealing of MnAs on GaAs(113)A, *J. Phys. D Appl. Phys.* **38**, A164–A168 (2005)
- 41.48 C. Simbrunner, A. Navarro-Quezada, K. Schmidegg, A. Bonanni, A. Kharchenko, J. Bethke, K. Lishka, H. Sitter: In-situ x-ray diffraction during MOCVD of III-nitrides, *Phys. Status Solidi (a)* **204**, 2798–2803 (2007)
- 41.49 P.F. Fewster, G.A. Tye, N.L. Andrew, P. Kidd: Using the static diffractometer for micro-high-resolution x-ray scattering, unpublished work presented at XTOP 2006, Baden-Baden (2006)
- 41.50 T. Baumbach, D. Lübbert, V. Holý, P. Mikulík, L. Helfen, P. Pernot, M. Elyyan, S. Keller, B. Heskell, J. Speck: Epitaxial lateral overgrowth of GaN studied by x-ray micro-diffraction imaging, unpublished work presented at XTOP 2006, Baden-Baden (2006)
- 41.51 D. Lübbert, C. Ferrari, P. Mikulík, P. Pernot, L. Helfen, N. Verdi, D. Korytár, T. Baumbach: Distribution and Burgers vectors of dislocations in semiconductor wafers investigated by rocking-curve imaging, *J. Appl. Cryst.* **38**, 91–96 (2005)

42. X-Ray Topography Techniques for Defect Characterization of Crystals

Balaji Raghothamachar, Michael Dudley, Govindhan Dhanaraj

X-ray topography is the general term for a family of x-ray diffraction imaging techniques capable of providing information on the nature and distribution of structural defects such as dislocations, inclusions/precipitates, stacking faults, growth sector boundaries, twins, and low-angle grain boundaries in single-crystal materials. From the first x-ray diffraction image, recorded by Berg in 1931, to the double-crystal technique developed by Bond and Andrus in 1952 and the transmission technique developed by Lang in 1958 through to present-day synchrotron-radiation-based techniques, x-ray topography has evolved into a powerful, nondestructive method for the rapid characterization of large single crystals of a wide range of chemical compositions and physical properties, such as semiconductors, oxides, metals, and organic materials. Different defects are readily identified through interpretation of contrast using well-established kinematical and dynamical theories of x-ray diffraction. This method is capable of imaging extended defects in the entire volume of the crystal and in some cases in wafers with devices fabricated on them. It is well established as an indispensable tool for the development of growth techniques for highly perfect crystals (for, e.g., Czochralski growth of silicon) for semiconductor and electronic applications. The capability of in situ characterization during crystal growth, heat treatment, stress application, device operation, etc. to study the generation, interaction, and propagation of defects makes it a versatile technique to study many materials processes.

42.1 Basic Principles of X-Ray Topography	1426
42.1.1 Contrast	1426
42.1.2 Resolution	1427
42.2 Historical Development of the X-Ray Topography Technique	1428
42.3 X-Ray Topography Techniques and Geometry	1430
42.3.1 Conventional X-Ray Topography Techniques	1430
42.3.2 Synchrotron-Radiation-Based X-Ray Topography Techniques	1431
42.3.3 Recording Geometries	1435
42.4 Theoretical Background for X-Ray Topography	1435
42.4.1 Limitation of Kinematical Theory of X-Ray Diffraction	1436
42.4.2 Dynamical Theory of X-Ray Diffraction	1436
42.5 Mechanisms for Contrast on X-Ray Topographs	1440
42.5.1 Orientation Contrast from Subgrains and Twins	1440
42.5.2 Extinction Contrast	1441
42.6 Analysis of Defects on X-Ray Topographs	1445
42.6.1 Basic Dislocation Analysis	1445
42.6.2 Contrast from Inclusions	1446
42.6.3 Contrast Associated with Cracks	1448
42.7 Current Application Status and Development	1449
References	1450

The industrial demand for high-quality single crystals has increased manyfold following the inventions of the transistor and the laser, which led to a wide range of

applications [42.1]. In semiconductor technology the increasing density of devices on individual integrated circuits requires a high level of homogeneity in terms of

the chemical composition and structural perfection of crystals [42.2]. The presence of imperfections in crystals used in solid-state lasers, including semiconductor lasers, and nonlinear and electrooptical devices, negatively impacts on their reliable operation [42.3]. The study of such imperfections or defects is also important from the point of view of understanding the influence of imperfections on crystal growth processes, and conversely feedback can be used to develop higher-quality crystals [42.4]. Hence it is essential for process engineers and crystal growers to characterize and have knowledge of the amount, distribution, and nature of defects present in crystals. Even though there are several techniques based on optical, electron, and atomic force microscopy or x-ray imaging to reveal dislocations and other defects, none of these methods are ideal. These characterization methods have different ranges of capabilities and limitations, and hence should normally be used complementarily. However, compared with all other techniques, x-ray topography is powerful enough to image extended defects in the entire volume of the crystal and in some cases in wafers with devices fabricated on them. The capability of this technique to image both defects intersecting the wafer surface as well as those located in the bulk combines features specific to chemical etching and transmission electron microscopy (TEM), respectively. Using synchrotron radiation, the x-ray topography technique can be applied to study large wafers up to 300 mm diameter [42.5], crystal plates, and even as-grown boules weighing several kilograms [42.6]. Presently, x-ray topography has become a very important tool in fundamental research as well as in industrial applications, as described in detail in recent literature [42.7, 8].

X-ray topography is the general term for a family of x-ray diffraction imaging techniques capable of providing information on the nature and distribution of structural defects in single crystal materials. The complete name *x-ray diffraction topography* is slightly more informative, indicating that the technique is concerned with the topography of the internal diffracting

planes, i.e., local changes in the spacing and rotations of these planes, rather than with external surface topography. Even though the name *x-ray topography* does not articulate the correct meaning of the technique, it is commonly used by researchers, perhaps for convenience or as a continuation from its first usage in early literature [42.9]. This technique is usually nondestructive and suitable for studying single crystals of large cross-section with thickness ranging from hundreds of micrometers to several millimeters. It is superior to the complementary TEM technique in that it enables imaging of the entire crystal and displaying defects particularly at dislocation densities lower than 10^4 mm^{-2} . In x-ray diffraction topography, a collimated area-filling ribbon of x-rays is incident on the single-crystal sample, at a set Bragg angle, and the corresponding area-filling diffracted beam is projected onto a high-resolution x-ray film or detector. The two-dimensional diffraction spot thus obtained constitutes an x-ray topograph and precisely displays the variation of the diffracted intensity as a function of position depending upon the local diffracting power as well as the prevailing overall diffraction conditions. Local diffracting power is affected by the distorted regions surrounding a defect, leading to differences in intensities between these regions and the surrounding more perfect regions. This intensity variation gives rise to contrast, and different defect types can be characterized from the specific contrast produced by the way they distort the local crystal lattice and thereby the local diffracting power. The absence of magnification enables the correlation of the relative position of the image of a defect with its location inside the crystal. Quantitative information such as the line direction and Burgers vector of a dislocation can be obtained by detailed interpretation of the variations in contrast obtained under different diffraction conditions. Such interpretation requires an understanding of the mechanisms of contrast formation. These mechanisms are sensitive functions of the diffraction conditions and are derived from the kinematical and dynamical theories of x-ray diffraction [42.10].

42.1 Basic Principles of X-Ray Topography

42.1.1 Contrast

In general, the individual spots obtained from Laue diffraction patterns from crystals do not have uniform contrast. The localized variations in the intensity within

any individual diffracted spot arise from the deviation in structural uniformity in the lattice planes causing the spot, and this forms the basis for the x-ray topographic technique. The real information available in an x-ray topograph is manifested in the form of contrast within

the projected diffraction spot. This topographic contrast arises from differences in the intensity of the diffracted beam as a function of spatial coordinate inside the crystal. The diffracted intensity is a sensitive function of local crystal perfection. For example, under the correct diffraction conditions, highly mosaic regions of a crystal (i. e., those regions comprising small subgrains which are slightly tilted with respect to the perfect crystal) will diffract kinematically, whereas nearly perfect regions of the crystal will diffract dynamically. Kinematical diffraction is characterized by an absence of the primary extinction effects, which are the essence of dynamical diffraction. These primary extinction effects, created by the interference between diffracted waves and incident waves inside the crystal, lead to an overall reduction in diffracted intensity for a perfect crystal over the mosaic crystal. Conversely, there is an increase in diffracted intensity as the degree of mosaicity increases, eventually reaching the limit of the *ideally imperfect crystal* [42.11]. The difference between the intensities diffracted from one region of the crystal which diffracts kinematically and another which diffracts dynamically is one of the ways in which dislocations can be rendered visible in topography. However, the situation is not as simple as stated here. Even for a crystal which diffracts dynamically, the diffracted intensity is a sensitive function of the local distortion in the crystal. In addition, the type of contrast that arises from a particular type of distortion is also a function of the absorption conditions in the crystal. The effects of such conditions on contrast mechanism will be discussed in Sect. 42.5 with emphasis on mechanisms which give rise to dislocation images.

42.1.2 Resolution

The contrast from individual defects will only be clearly discernible if the spatial resolution is adequate. There is no magnification involved in topography and spatial resolution is controlled solely by geometrical factors. The Bragg law is defined as

$$\lambda = 2d \sin \theta_B, \quad (42.1)$$

where λ is the x-ray wavelength, d is the spacing between the diffracting planes, and θ_B is the Bragg angle, which is the angle between the incident rays and the diffracting planes. When the Bragg condition is satisfied, possible incident and diffracted beam directions lie, diametrically opposed, on the surface of a cone with semi-apex angle $90^\circ - \theta_B$, the axis of which is the active reciprocal lattice vector \mathbf{g} (i. e., the normal to the

diffracting planes). Therefore if an x-ray source has finite size, which it always does, the possibility arises that at a given point in the crystal the diffracting planes will receive radiation, at the correct Bragg angle, from several different points located at different positions on the source (which produce rays lying on the surface of the Bragg cone). The locus of these points on the source is the arc defined by the intersection between the operative Bragg cone and the source surface. This acceptance of rays with a finite vertical divergence imparts a finite vertical divergence to the diffracted beam, which emanates from the point of interest in the crystal, and hence gives rise to a blurring effect in the resultant *image* of the point. In fact the diffracted rays emanating from the point of interest in the crystal will lie on the arc defined by the intersection between the same Bragg cone and the detector plane (the length of this arc will, of course, be defined by the divergence angle of the accepted rays from the arc on the source). This is illustrated in Fig. 42.1, which shows how an image of a point P in the crystal, recorded with rays which emanate from points lying on the arc abc on the source, is spread over the arc a'b'c' on the detector. Therefore, the angle subtended by the longest dimension of the source in the direction perpendicular to the plane of incidence (defined by the incident and diffracted beam directions, and the active reciprocal lattice vector) is the crucial parameter, which should be minimized. The amount of blurring is proportional to the distance between the crystal and detector, and can be approximately written as

$$R = \frac{SD}{C}, \quad (42.2)$$

where R is the blurring (or the effective resolution), S is the maximum source dimension in the direction perpendicular to the plane of incidence, D is the specimen–film distance, and C is the source–specimen distance. In the plane of incidence, diffraction occurs over a finite range of angles determined by the acceptance angle of the crystal in that plane or the rocking curve width. This finite acceptance angle means that a given point in the crystal receives radiation from a finite width on the source (for the case of a horizontal plane of incidence). This width can be determined by back-projecting the fan of incident rays accepted at a point in the crystal to the source itself. Again a finite divergence, this time in the horizontal plane, can be attributed to the diffracted beam, and again a blurring effect will be evident. However, as can be verified by simple calculation, the limiting factor in determining spatial resolution is

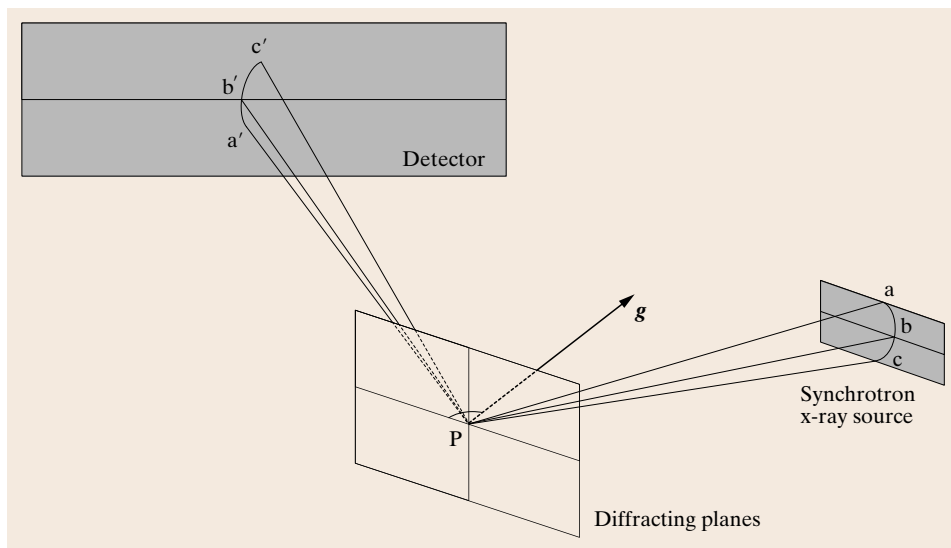


Fig. 42.1 Schematic diagram showing the effect of finite source dimension on resolution; g is the active reciprocal lattice vector. The angle bPg , which is the semi-apex angle of the Bragg cone, is $90^\circ - \theta_B$, where θ_B is the Bragg angle

the finite source height (i. e., the source dimension perpendicular to the incidence plane), rather than the finite effective source width (i. e., the dimension parallel to the incidence plane).

Since the spatial resolution is proportional to the distance between the crystal and detector, this distance should be minimized. However, the optimum spatial resolution of the photographic detectors typically uti-

lized in topography is limited, by photoelectron tracking between adjacent grains in the emulsion of the film, to around $1\ \mu\text{m}$. The specimen–film distance is usually set to yield a calculated spatial resolution which approximately coincides with this. It should be noted that, while this spatial resolution is greatly inferior to that of electron microscopy, it is more than sufficient for high-quality crystals of many materials currently grown.

42.2 Historical Development of the X-Ray Topography Technique

Even though the first topographic image of a single crystal was recorded as early as 1931 [42.12], the real potential of the technique was understood only in 1958 when *Lang* [42.13] demonstrated the imaging of individual dislocations in a silicon crystal. Different topographic geometries were developed independently during this period, namely, the *Berg–Barrett* reflection technique [42.12,14], the double-crystal technique [42.15], and the *Lang* technique [42.13] and its variant, the scanning oscillator technique [42.16].

In 1931, *Berg* carried out x-ray diffraction imaging on crystal surfaces using characteristic radiation falling at a very low angle to the crystal surface and obtained point-to-point variation of the reflected intensity resulting in a striated image on a photographic plate placed near the crystal. The striated images produced were attributed to plastic deformation in the crystals. Even though it was realized that x-rays could

be used as a powerful tool for studying inhomogeneities in crystals, no further attempt was made to use this tool until *Barrett* [42.14] recorded defect structure images from single crystals of silicon ferrite. *Barrett* improved *Berg's* reflection technique by minimizing the distance between the crystal and the photographic emulsion plate and also by using fine-grain high-resolution x-ray film. This technique is commonly known as *Berg–Barrett* reflection topography and is used to study large-size crystals. *Wooster* and *Wooster* [42.17] obtained topographic images revealing the defect structure from diamond surfaces using characteristic copper radiation. With further improvement in this technique, *Newkirk* [42.18] showed that individual dislocations could be resolved and their Burgers vectors could be experimentally determined. The *Schulz* technique [42.19] is another reflection topographic technique that uses white radiation from a point-focus x-ray generator.

The divergent x-ray beam diffracted by the crystal is recorded on a film. The white beam ensures diffraction from all the misoriented regions in the crystal. This simple technique can be used to reveal misorientations quickly in the form of separations and overlaps in the image.

Bond and *Andrus* [42.15] developed a high-resolution double-crystal technique for studying structural imperfections on the habit faces of natural quartz crystals. In this technique, x-rays from a line-focus source are Bragg-reflected from a highly perfect monochromator crystal and then diffracted from the specimen crystal in either reflection or transmission mode. High sensitivity is achieved in this technique because the first crystal further narrows the divergence of the slit-collimated beam, which subsequently probes the specimen crystal. This technique is highly sensitive to lattice misorientations: lattice tilts and lattice parameter changes down to 10^{-8} can be detected. The sensitivity can be increased further by introducing another monochromator or beam-conditioner crystal, and rocking curve measurements can also be carried out to assess the crystal quality.

Ramachandran [42.9] studied cleaved plates of diamond crystals using a white x-ray beam from a tungsten target in the transmission Laue geometry. He was the first to use the term *x-ray topograph* to describe the image contrast of full-size diffracted spots. The Laue spots were recognized as a topographic map of the crystal plate exhibiting variations in structure. He felt that the x-ray topographic technique might provide information on lattice perfection and compared the topographs with luminescence images. The term *x-ray topograph* became established in the literature when *Wooster* and *Wooster* [42.17] used the same term in describing diffraction images obtained from diamond surfaces revealing the defect structure. *Guinier* and *Tennevin* [42.20] studied both orientation and extinction contrast effects in aluminum in transmission mode using a polychromatic x-ray beam. *Tuomi* et al. [42.21] used a similar geometry and performed the first x-ray topography experiments using synchrotron radiation on silicon samples.

Important developments in x-ray topography took place in 1957–1958 when *Lang* developed a transmission technique to image the defects in crystals [42.13, 22]. He examined crystal sections using a narrow collimated characteristic radiation beam, a technique referred to as *section topography*. Linear and planar defects could be mapped with this technique by trans-

lating the specimen to known positions and taking a series of section topographs. Using this technique, low-angle boundaries in melt-grown metallic crystals were imaged [42.22]. By incorporating a linear traverse mechanism to translate the crystal plate and film cassette synchronously, *Lang* was able to image individual dislocations in an entire silicon crystal sample using projection topography, a milestone in the field of x-ray topography. In the *Lang* technique, an incident beam of narrow width and low horizontal divergence (about 4–5 arcmin) is obtained using a slit. The secondary slit placed on the other side of the sample blocks the direct beam while allowing the diffracted beam to pass through. It is possible to obtain an image on the film using K_{α_1} only. This technique can permit up to 1 μm resolution under optimized conditions. Coincidentally, during the same year, individual dislocations in silicon as well as germanium crystals were imaged by *Newkirk* [42.18] using the Berg–Barrett technique, and by *Bonse* and *Kappler* [42.23] using double-crystal topography, respectively. The tremendous development in x-ray topography during this period leading to resolving individual dislocations was also due to the fact that better-quality semiconductor crystals such as silicon and germanium were becoming available due to improved crystal growth technology. After *Lang*'s work [42.13, 22] on imaging of individual dislocations, x-ray topography has become an important quality control tool for assessment of semiconductor wafers before and after device fabrication. However, using this technique it is difficult to record topographs of crystals having elastic strains. Using the scanning oscillator technique developed by *Schwutke* [42.16], it is possible to record transmission topographs of large-size wafers up to 150 mm in diameter, containing appreciable amount of elastic and/or frozen-in strain. This technique is based on the *Lang* technique with provision to oscillate the crystal and film simultaneously when the crystal is scanned. The oscillation is chosen to cover the whole reflecting range of the crystal to obtain a complete image of the crystal. This technique was widely used to image dislocations in transmission mode in large-size silicon wafers.

While laboratory-based x-ray topography techniques continue to be used, in recent decades the availability of numerous synchrotron radiation facilities providing intense, low-divergence x-ray beams of wide spectral range has allowed the development of synchrotron x-ray topography techniques. This is discussed in detail in Sect. 42.3.2.

42.3 X-Ray Topography Techniques and Geometry

X-ray topographic techniques can be broadly classified into two types: conventional x-ray topographic techniques based on laboratory x-ray sources such as target tubes, rotating anodes, and similar sources; and synchrotron x-ray topographic techniques based on synchrotron radiation.

42.3.1 Conventional X-Ray Topography Techniques

Berg–Barrett Topography

This is one of the oldest x-ray topography technique and is usually based on Bragg (reflection) geometry. The basic experimental setup (Fig. 42.2a) uses an extended x-ray source and the crystal is aligned such that the diffracting conditions are satisfied for the characteristic K_α lines from a set of Bragg planes. The crystal is cut such that the incident beam makes a small angle to the specimen surface and the diffracted beam emerges almost normal to the specimen surface. The photographic film can be placed very close to the specimen surface (as near as 1 mm). This technique

is simple and uses low-cost equipment. The use of reflection geometry permits only imaging up to the x-ray penetration depth below the surface of the crystal, as determined by the extinction distance or absorption distance. This allows for the study of high-dislocation-density materials ($\approx 10^6 \text{ cm}^{-2}$). Limitations of this technique include image doubling due to the K_α doublet as well as significant loss of spatial resolution with increasing specimen–film distance. These limitations can be overcome by appropriate adjustments to the recording geometry. This technique is often used for initial assessment of crystals of new materials [42.24]. The transmission Berg–Barrett method [42.12, 14] (Fig. 42.2b) (also known as the Barth–Hosemann geometry) is similar to the Lang technique except that it suffers from high background scattered radiation that limits its use for studying dynamical images.

Lang X-Ray Topography

The Lang x-ray topography technique [42.13, 22] is the most widely used laboratory technique and is based on the transmission geometry. Figure 42.3 shows the basic experimental setup, where the x-ray source is collimated to allow diffraction from one K_α line (usually K_{α_1}). The diffracting planes are typically nearly perpendicular to the crystal surface and the diffracted beam passes through a secondary slit that blocks the direct beam before striking the photographic plate. When the incident beam width is small compared with the base of the Borrmann fan formed by the extremes of the diffracted and transmitted beams with the crystal surface (typically about $10 \mu\text{m}$), an image of a section through the crystal is obtained. This is the section topograph which allows the study of the three-dimensional defect distribution of defects. By translating both the crystal and film across the stationary beam, an image of the whole crystal can be obtained and this is the projection topograph. However, this results in loss of information available in the section topograph. The section topograph is therefore considered to be more fundamental. Usually, a much wider slit than that used in section topography is used when recording the projection topograph. Commercial Lang cameras consisting of a two-circle goniometer with precision translation stage and adjustable beam slits are available and widely used for laboratory-based x-ray topography [42.24].

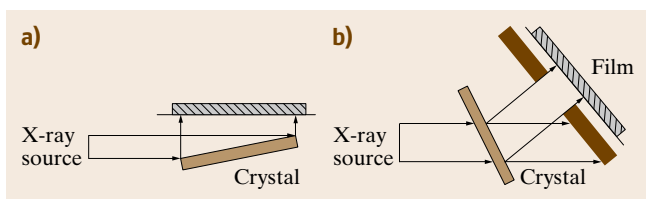


Fig. 42.2a,b Schematic diagrams of (a) reflection and (b) transmission Berg–Barrett techniques of topography

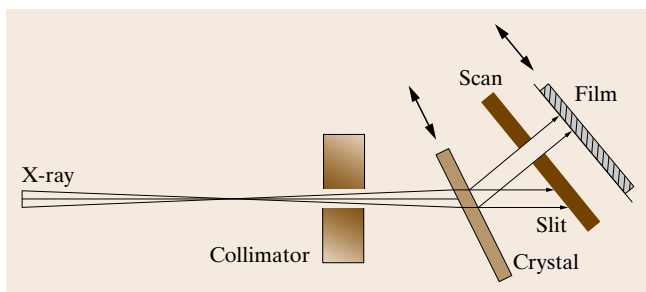


Fig. 42.3 Schematic diagram of the Lang projection technique. The topograph image due to K_{α_1} alone is recorded on the film. The secondary slit blocks the direct beam while allowing the diffracted beam to pass through. The crystal and film are translated synchronously and the whole image of the crystal is recorded

42.3.2 Synchrotron-Radiation-Based X-Ray Topography Techniques

The advent of dedicated sources of synchrotron radiation has enabled the development of a new realm of topography known as synchrotron topography. It has numerous advantages over conventional radiation techniques. These advantages derive from the high brightness, tunability, and natural collimation of synchrotron radiation.

White-Beam X-Ray Topography

One of the most important synchrotron topographic techniques developed is white-radiation topography [42.21, 25]. This technique is basically analogous to the Laue transmission technique, except with greatly enhanced capabilities which derive from the aforementioned natural collimation and high intensity of the synchrotron beam. The natural collimation (typically $\approx 2 \times 10^{-4}$ rad in the vertical plane coupled with an acceptance angle of typically a few milliradians in the horizontal plane) allows the use of very long beamlines (≈ 25 m) to maximize the area of the beam delivered at the sample without incurring significant losses in the total intensity originally available at the tangent point. This situation contrasts with that which would hold for isotropic emission from a conventional source. The large beam area delivered at the sample location allows studies to be carried out on relatively large-scale single crystals, and crystals as large as 150 mm or even 300 mm in diameter can be imaged by using precision translation stages similar to those used in the Lang technique (although exposure times are much shorter). Long beamlines also lead to small angles subtended by the source at points in the specimen, which in turn leads to excellent geometrical resolution capabilities. For example at the Stony Brook Topography Station, on beamline X-19C at the National Synchrotron Light Source (NSLS), the optimum theoretically attainable spatial resolution is $\approx 0.04 \mu\text{m}/\text{cm}$ of specimen–film distance.

If a single crystal is oriented in the beam, and the diffracted beams are recorded on a photographic detector, each diffraction spot on the resultant Laue pattern will constitute a map of the diffracting power from a particular set of planes as a function of position in the crystal with excellent point-to-point resolution (typically on the order of less than $1 \mu\text{m}$). In other words each diffraction spot will be an x-ray topograph (Fig. 42.4a,b). The excellent geometrical resolution capability has another important consequence since it

relaxes to a certain extent the requirement of having very small specimen–film distances (< 1 cm) in order to achieve good resolution. Thus, crystals can be surrounded with elaborate environmental chambers, necessitating considerable increases in specimen–detector distances (which would lead to intolerable resolution losses in conventional systems) without significant loss of resolution. The high intensity over the wide spectral range of the radiation emitted has several important advantages. Not only are the exposure times necessary to record a topograph drastically reduced from the order of days on conventional systems to seconds on a synchrotron, but since we have a white beam, a multiplicity of images is recorded simultaneously (Fig. 42.4c). This leads to great enhancement in the rate of data acquisition. The multiplicity of images also enables extensive characterization of strain fields present in the crystal. For example, instantaneous dislocation Burgers vector analysis can become possible by comparison of dislocation images obtained from several different Laue spots. Similarly, lattice rotation in the specimen can be characterized by analysis of the asterism (the spreading of a Laue spot) observed from several different Laue spots. In addition the good signal-to-noise ratios obtained associated with the high intensity also open up the possibility of direct imaging of topographs. Thus it becomes possible to conduct truly dynamic, quasi-real-time studies of crystals subjected to some kind of external stimulus such as applied fields, applied stress, heating, cooling, etc.

Synchrotron topography can also be used to image the surfaces of as-grown boules or large-size crystal plates in reflection geometry. This can reveal the overall distribution of defects and distortion around the cylindrical surface of these crystals. Investigating as-grown boules enables observation of the true microstructures and striations developed during growth and can substantially reduce the time and processing costs in cutting and polishing. Figure 42.5 shows reflection topographic images recorded from an as-grown boule grown by the Bridgman–Stockbarger method in microgravity. Topographs could be recorded covering the entire length of the boule in strips using the synchrotron beam. This boule revealed different defect structures depending on the amount of contact with the crucible wall.

Synchrotron x-ray topography in the reflection geometry can also be used to examine substrate/epilayer systems that have devices fabricated upon them. The features that make up the device topology typically provide contrast on x-ray topographs. The contrast usually

originates from the strain experienced by the crystal at the edges of growth mesas, or metallization layers, although some absorption contrast may also be superimposed on this. Topographs recorded from such structures provide an image of the defect microstructure superimposed on the backdrop of the device topology. Direct comparisons can be drawn between the performance of specific devices and the distribution of

defects within their active regions. This has made it possible to determine the influence of threading screw dislocations (closed and hollow core) on device performance [42.26, 27]. The back-reflection geometry is particularly useful here, since it gives a clear image of the distribution of screw dislocations on the background device topology that is imaged with sufficient clarity to unambiguously identify the device. An example of

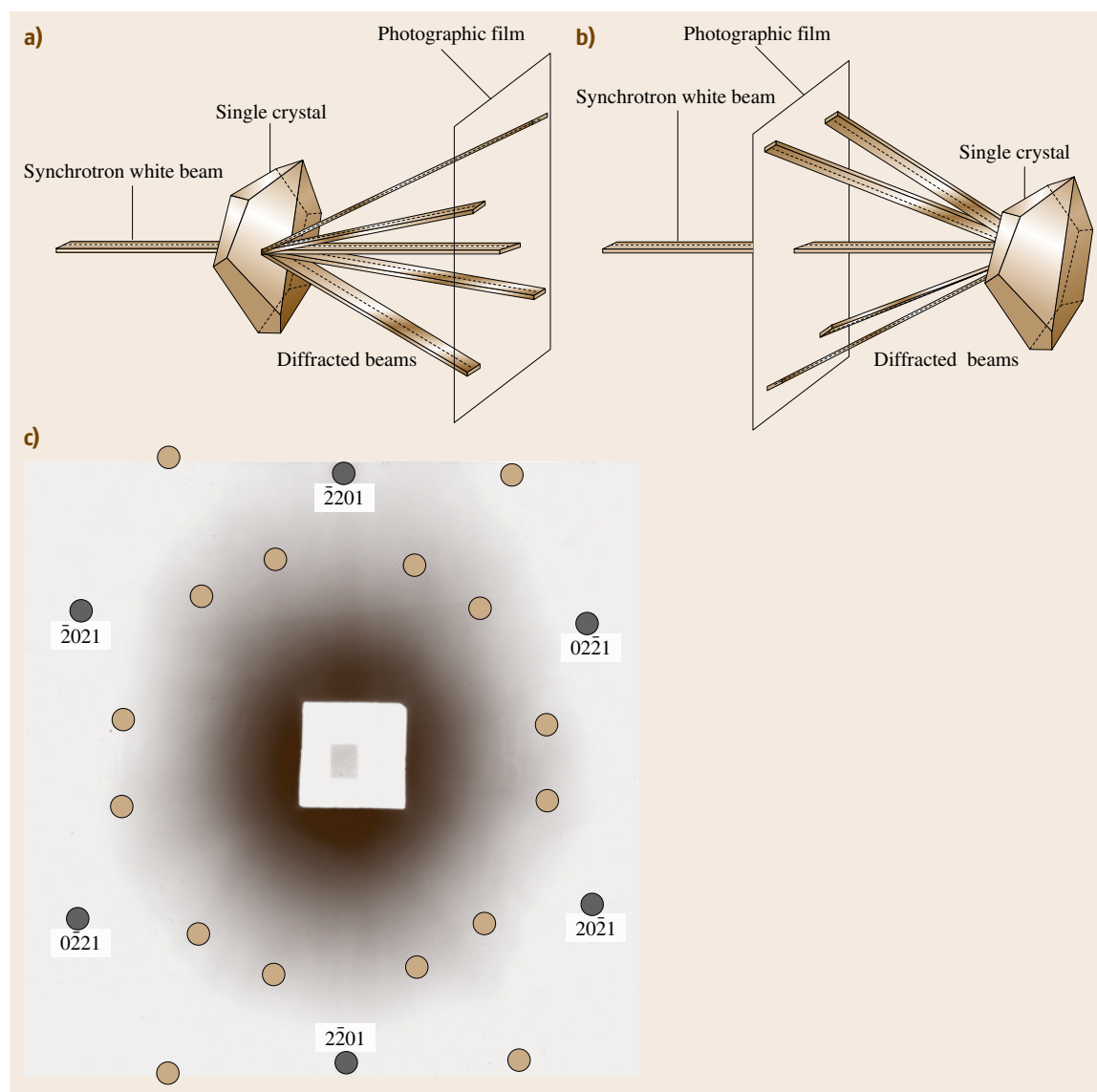


Fig. 42.4a–c Schematic diagram of the white-beam diffraction pattern recorded in (a) transmission geometry and (b) back-reflection geometry. (c) Actual transmission x-ray diffraction pattern recorded from an (0001) AlN single crystal on a SR-45 8" × 10" x-ray film

a back-reflection image recorded from a crystal with devices fabricated on it is shown in Fig. 42.6.

Another important advantage of the white-beam topographic technique over conventional topographic techniques is its enhanced tolerance of lattice distortion. The wide spectrum available in the synchrotron beam allows crystals which either exhibit a uniform range of lattice orientation (for example, uniformly bent by a small amount) or which contain several regions of distinctly different orientation (for example, containing subgrains, grains or twinned regions) or regions of different lattice parameter (for example, containing more than one phase or polytype) to be imaged in a single exposure. Analysis of Laue spot shape or Laue spot asterism (the deviation from the shape expected from an undistorted crystal) enables quantitative analysis of lattice rotation. Simultaneous measurement of the variation in diffracted wavelength as a function of position in the Laue spot, for example, using a solid-state detector, also enables determination of any variation in the spacing d of the particular diffracting planes. For those crystals that contain several regions of distinctly different orientations, so-called orientation contrast becomes evident whereby the two neighboring regions

of crystal separated by the boundary (a twin boundary or grain boundary, for example) each give rise to diffracted beams which travel in different directions in space, leading to image shifts on the detector. Analysis of the directions of these diffracted beams from the measured image shifts can enable the orientation relationships between the two regions of crystal to be established, leading to, for example, determination of twin laws. An example of a diffraction pattern recorded from a nominally (111) CdZnTe single crystal containing twins is shown in Fig. 42.7. Detailed analysis of the orientation relationships between the segments of the various diffraction spots enables the twin operation to be defined as a 180° rotation about [111].

By comparison, in the conventional topographic case, the maximum tolerable range of misorientation is defined by the convolution of the characteristic line width with the beam divergence. Since both of these quantities are small (typical line widths are of the order of 10^{-3} Å, equivalent to an angular divergence of ≈ 100 arcsec, and typically, beam divergences must be less than ≈ 20 arcsec in order to obtain the necessary angular resolution in the plane of incidence), misorientations greater than a few arcsec lead to the situation

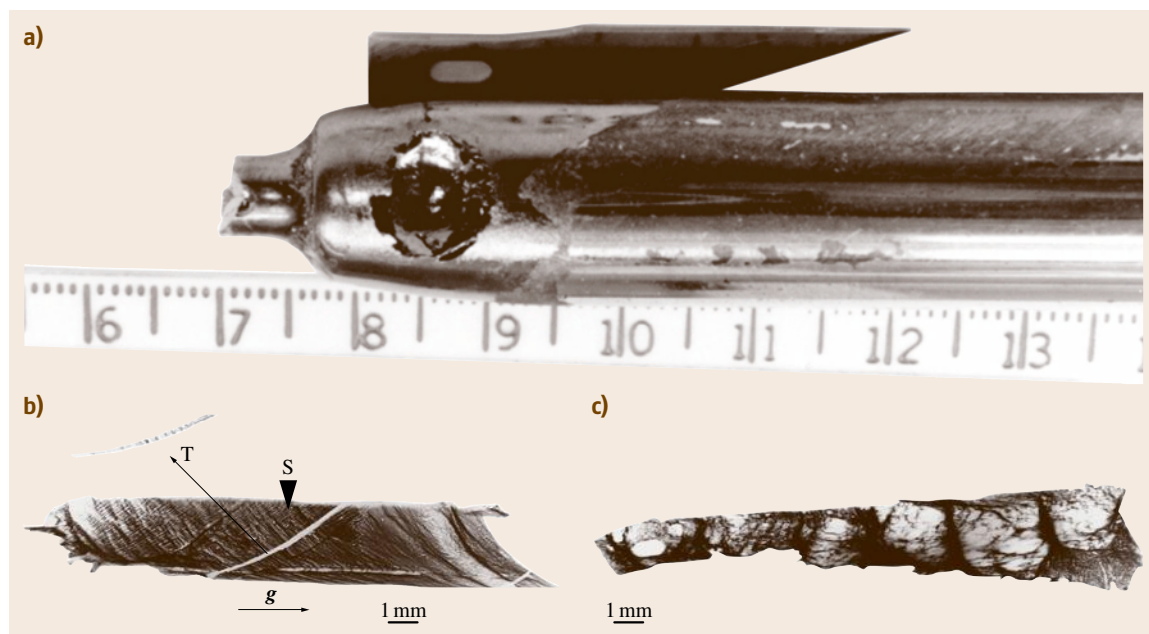


Fig. 42.5 (a) Optical picture of an as-grown CdZnTe boule grown in microgravity showing regions with different extent of wall contact. Reflection topographs recorded from the surface of as-grown CdZnTe boule grown in microgravity showing the defect structures. (b) Wall-contact region showing dense slip band networks and twins (S: slip bands, T: twin); (c) free-surface region showing a lower defect density and no twins

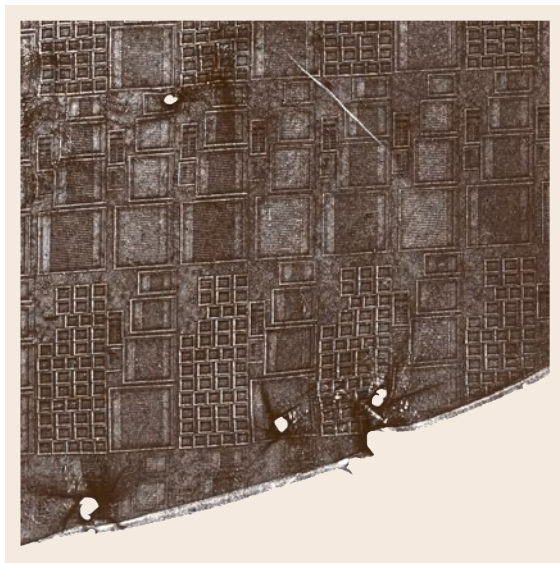


Fig. 42.6 Back-reflection white-beam x-ray topograph recorded from a 6H-SiC single crystal with thyristors fabricated upon it. The *small white spots* distributed over the image are 1c and larger screw dislocations. The location of these dislocations with respect to the device topology can be clearly discerned, enabling the influence of the defects on device performance to be determined. The *large white feature* corresponds to damage inflicted by a probe

where only part of the crystal fulfills the diffracting condition at a given time. In other words, Bragg contours are produced. These contours delineate those regions of the crystal which are in the diffracting condition from those which are not. Since their presence means that there are regions not set for diffraction, effectively there are blind spots in the crystal. Clearly this is a very undesirable situation if dynamic-type studies in large single crystals are to be conducted. Similar problems are encountered in monochromatic synchrotron-radiation topography.

Contrast mechanisms operative in white-beam topography are largely similar to those which are operative in Lang topography, with some notable subtle differences [42.28]. However, it has recently been demonstrated that many of these differences are attributable to the large difference in typical specimen–film distances for the two techniques (tens of centimeters for white-beam topography and ≈ 1 cm for Lang topography, see [42.29] for details). Some differences are also attributable to the added complication of harmonic contamination (the presence of several orders of

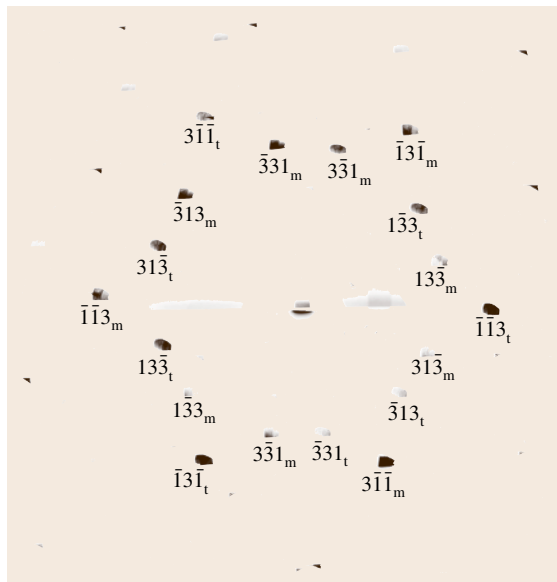


Fig. 42.7 Transmission x-ray diffraction pattern recorded from a CdZnTe crystal showing the presence of a twin. Detailed analysis of the orientation relationships between the segments of the various diffraction spots enables the twin operation to be defined as a 180° rotation about $[111]$

diffraction in a single diffraction spot), which becomes apparent in white-beam topography, potentially leading to a situation where more than one contrast mechanism operates in a single topograph. Harmonic contamination can, however, be avoided by judicious choice of diffraction geometry. In Sect. 42.5, a review of basic contrast mechanisms, pertinent to both Lang and white-beam topography, is presented.

Monochromatic-Beam X-Ray Topography

When a white synchrotron beam is passed through a monochromator, an x-ray topograph is obtained when the crystal is set to the Bragg angle for a specific set of lattice planes for the selected x-ray energy. Images from different atomic planes are acquired by orienting the sample to satisfy the Bragg condition for those planes and orienting the detector to the new scattering angle ($2\theta_B$) to record the image. With monochromatic radiation [42.30] only one topograph is recorded at a time, but the experimenter controls the energy or wavelength of the x-ray beam, the x-ray collimation, the energy or wavelength spread of the x-ray beam, and the size of the incident beam on the sample crystal. The synchrotron beam suffers significant loss of intensity on passing through the monochromator setup. This reduces

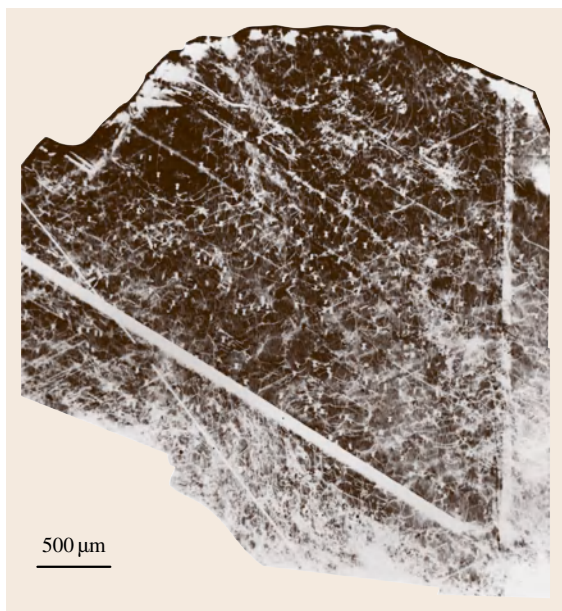


Fig. 42.8 Transmission x-ray topograph recorded from a CdZnTe crystal using a monochromatic synchrotron beam

the probability of radiation damage to the crystal. In addition to wavelength selection, the monochromator also improves angular collimation, and the plane-wave approximation is applicable. Monochromators used at synchrotron-radiation facilities can be either single- or multiple-crystal designs which can condition the x-ray beam to achieve optimal spatial and angular resolutions. An x-ray topograph (Fig. 42.8) recorded in transmission geometry from a CdZnTe single crystal shows dislocations, inclusions, and twinned regions.

42.3.3 Recording Geometries

X-ray topographs are acquired utilizing recording geometries based on either reflection (Bragg) from the surface, or transmission (Laue) through the bulk, of the sample crystal. In general, the reflection topograph geometry is employed for thick crystals or when absorption conditions and/or defect densities are too high

to permit the use of transmission geometry. Owing to its surface sensitivity, topography in reflection geometry is also useful for characterization of surface defect structures within semiconductor heterostructures and epitaxial thin films. In all reflection-type geometries, defect information can be obtained from the volume defined by the effective area of the incident beam on the crystal and the penetration depth of the x-ray beam. The penetration depth of x-rays is determined either by the kinematical penetration depth (in imperfect crystals) or by the dynamical penetration depth (in highly perfect single crystals). The kinematical penetration depth (t_p^k) can be determined simply by geometrical relations between the incident and diffracted beams and the sample surface, and is given by

$$t_p^k = \frac{\mu_0(\lambda)}{(\operatorname{cosec} \Phi_0 + \operatorname{cosec} \Phi_H)}, \quad (42.3)$$

where $\mu_0(\lambda)$ is the linear absorption coefficient and Φ_0 and Φ_H are the angles of the incident and diffracted beams with respect to the surface, respectively. The dynamical penetration depth (t_p^d) is defined to be equal to half the extinction distance ξ_g (42.15). In transmission topography, all the defects within the crystal volume are recorded, provided that the absorption is low enough to permit sufficient transmission through the crystal. Since the x-rays pass through the entire thickness of the sample, this technique is used to characterize the overall bulk defect content of a crystal, such as dislocation networks and inclusions. The high intensities from the synchrotron source enable one to record images from relatively thick specimens using this technique. Laue transmission technique finds limited application in studying crystals of low perfection and high absorption coefficients. The back-reflection technique, commonly used for orienting single crystals, can also be used to record x-ray topographs of crystals containing specific defects such as super-screw dislocations (micropipes) in SiC [42.31]. The grazing Bragg–Laue [42.32] and the grazing-incidence reflection geometries allow precise tuning of the penetration depth for depth profiling studies of epitaxial thin films.

42.4 Theoretical Background for X-Ray Topography

X-ray topography is an imaging technique based on x-ray diffraction. Understanding contrast formation on

x-ray topographs requires knowledge of the theory of x-ray diffraction in solids. In this section, the princi-

ples of the kinematical and dynamical theories of x-ray diffraction are briefly discussed with their implications for x-ray topography.

42.4.1 Limitation of Kinematical Theory of X-Ray Diffraction

In the kinematical theory of x-ray diffraction, initially developed to account for the intensities observed in x-ray diffraction studies, the amplitudes of the scattered waves are considered to be at all times small compared with the incident wave amplitude, and scattering from each volume element in the sample is treated as being independent of that from other volume elements. For small crystals, of dimensions less than a micrometer in diameter, and in heavily deformed crystals where the dislocations act to divide the crystal into a mosaic structure of independently diffracting cells, the kinematical theory may be employed satisfactorily to predict diffracted intensities. However, for large single crystals that are also highly perfect, significant discrepancies are found to exist between the measured and theoretically predicted intensities of diffracted beams. The diffracted intensity is predicted to increase continuously with increasing size of crystals and the diffracted intensity is actually predicted to become larger than the incident intensity beyond a certain size (about 1 μm). This is evidently incorrect since it violates the principle of conservation of energy. Under such conditions, the kinematical theory breaks down and the volume elements can no longer be treated as independent of one another. As one can recall from wave theory, x-rays diffracted

once from an atomic plane experience a phase change of $\frac{\pi}{2}$. When these waves are scattered again by the backside of the diffracting planes, they propagate in the same direction as the incident beam but are 180° out of phase. This gives rise to an attenuation of the incident intensity due to destructive interference between the primary incident and the secondary scattered beams, which in turn leads to a reduction in the total diffracted beam intensity. This is the so-called primary extinction effect, shown schematically in Fig. 42.9.

42.4.2 Dynamical Theory of X-Ray Diffraction

Breakdown of the kinematical theory in large, nearly perfect, single crystals is clearly demonstrated by the phenomenon of primary extinction. For a better understanding, it is necessary to take into account all the wave interactions within the crystal. The dynamical theory of x-ray diffraction considers the total wavefield inside a crystal while diffraction is taking place as a single entity.

The fundamental problem in the dynamical theory is to find solutions to Maxwell's equations in a periodic medium (i.e., the crystal) matched to solutions which are plane waves (the incident \mathbf{k}_0 and diffracted \mathbf{k}_h x-ray beams). These solutions must reflect the periodicity of the crystal, and such functions are known as Bloch or lattice functions and may be represented by a Fourier series with appropriate Fourier coefficients.

Maxwell's equations are

$$\nabla \times \mathbf{E} = -\frac{1}{c} \frac{\partial \mathbf{B}}{\partial t} \quad \text{and} \quad \nabla \times \mathbf{H} = -\frac{1}{c} \frac{\partial \mathbf{D}}{\partial t}, \quad (42.4)$$

where \mathbf{E} is the electric field, \mathbf{B} the magnetic induction, \mathbf{D} the electric displacement, \mathbf{H} the magnetic field, and c the velocity of light in vacuum, assuming that the electric conductivity is zero at x-ray frequencies. Properties of the crystal are introduced by representing the crystal as a medium with a periodic, anisotropic, complex dielectric susceptibility χ . Since χ is a Bloch function, it can be expressed as a Fourier sum over all the reciprocal lattice vectors \mathbf{R}_h as

$$\chi(\mathbf{r}) = \sum_h \chi_h \exp[-2\pi i(\mathbf{R}_h \cdot \mathbf{r})], \quad (42.5)$$

where the Fourier coefficients are given by

$$\chi_h = -\frac{r_e \lambda^2}{\pi V} \mathbf{F}_h,$$

where r_e is the classical electron radius, λ is the wavelength of the x-rays, V is the volume of the unit cell,

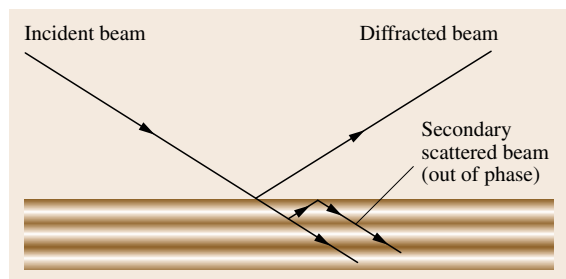


Fig. 42.9 Schematic diagram demonstrating the phenomenon of primary extinction in a perfect crystal. Diffracted beam (90° out of phase) is scattered by the backside of the diffracting planes to produce secondary scattered beam that is 180° out of phase with the incident beam, resulting in attenuation of the intensity of the incident beam, which in turn reduces the total diffracted beam intensity

\mathbf{R}_h is the reciprocal lattice vector, and F_h is the structure factor of the unit cell.

Inside the crystal, the allowed wavevectors should satisfy the Laue equation

$$\mathbf{K}_0 + \mathbf{R}_h = \mathbf{K}_h, \quad (42.6)$$

where \mathbf{K}_0 and \mathbf{K}_h are the incident and diffracted wavevectors inside the crystal.

Solutions for the electric displacement \mathbf{D} are Bloch or lattice functions of the type

$$\mathbf{D} = \sum \mathbf{D}_n \exp[2\pi i(\mathbf{v}t - \mathbf{K}_h \cdot \mathbf{r})]. \quad (42.7)$$

Using the expressions for \mathbf{D} (42.7) and χ (42.5) in Maxwell's equations, we obtain the fundamental equations of the dynamical theory that give the amplitudes of an infinite set of plane waves which together constitute a wavefield that satisfies the wave equation. In x-ray diffraction, only very rarely does more than one reciprocal lattice point provide a diffracted wave of appreciable amplitude. Thus, we need only consider two waves to have appreciable amplitude in the crystal: that associated with the incident wave and that associated with the diffracted wave from a reciprocal lattice vector \mathbf{h} . The solution of Maxwell's equations inside the crystal is then expressed in terms of the amplitudes \mathbf{D}_0 and \mathbf{D}_h of these two waves by

$$\left\{ \begin{aligned} [k^2(1 + \chi_0) - \mathbf{K}_0 \cdot \mathbf{K}_0] \mathbf{D}_0 + k^2 C \chi_h \mathbf{D}_h &= 0 \\ k^2 C \chi_h \mathbf{D}_0 + [k^2(1 + \chi_0) - \mathbf{K}_h \cdot \mathbf{K}_h] \mathbf{D}_h &= 0 \end{aligned} \right\}, \quad (42.8)$$

where C is the polarization factor and is unity for σ polarization (where vectors \mathbf{D}_0 and \mathbf{D}_h are perpendicular to the plane containing \mathbf{K}_0 and \mathbf{K}_h , and so are parallel) and $\cos(2\theta_B)$ for π polarization (where vectors \mathbf{D}_0 and \mathbf{D}_h lie in the plane containing \mathbf{K}_0 and \mathbf{K}_h , perpendicular to \mathbf{K}_0 and \mathbf{K}_h , respectively, but are not parallel to one another). Introducing the deviation parameters α_0 and α_h that express the deviation of the incident and diffracted wavevectors from the kinematic assumption

$$\left\{ \begin{aligned} \alpha_0 &= 1/2k [\mathbf{K}_0 \cdot \mathbf{K}_0 - k^2(1 + \chi_0)] \\ \alpha_h &= 1/2k [\mathbf{K}_h \cdot \mathbf{K}_h - k^2(1 + \chi_0)] \end{aligned} \right\}. \quad (42.9)$$

We can write the solution as

$$\alpha_0 \alpha_h = k^2 C^2 \chi_h \chi_{\bar{h}}. \quad (42.10)$$

The amplitude ratio R can be written as

$$R = \frac{D_h}{D_0} = \frac{2\alpha_0}{C \chi_{\bar{h}} k} = \frac{C \chi_h k}{2\alpha_h} = \left(\frac{\alpha_0 \chi_h}{\alpha_h \chi_{\bar{h}}} \right)^{1/2}. \quad (42.11)$$

Equations (42.10) and (42.11) are the fundamental equations of the two-beam dynamical theory that allow us to predict the wavefields and their intensities inside (and outside) the crystal.

Dispersion Surface

The wave equations satisfying Maxwell's equations can be represented geometrically by a construction known as the dispersion surface, illustrated in Fig. 42.10. In the kinematical condition, the center of the Ewald sphere is at the Laue point L which is at the intersection of spheres of radius k about the origin O and reciprocal lattice point H in the dispersion plane. In the dynamical condition, the wavevector inside the crystal is corrected for the mean refractive index resulting in a shorter wavevector and therefore the loci of these wavevectors are represented by spheres of diameter $k(1 + \chi/2)$ about O and H . This results in a shift of the intersection of these spheres and the dispersion plane from the Laue point L to the Lorentz point L_0 (Fig. 42.10a). Figure 42.10b shows the region around the Laue point at very high magnification ($\approx 10^6$). On the scale of the picture, the spherical sections $O'O''$ and $H'H''$ of the projections of the spheres can be approximated as planes. The deviation parameters α_0 and α_h are measured perpendicularly from the planes $O'O''$ and $H'H''$, respectively, and denote the *tie point* A at which the tails of wavevectors \mathbf{K}_0 from O and \mathbf{K}_h from H intersect and diffraction occurs.

Thus, the dispersion equation is the loci of all such tie points and is an equation of a hyperboloid of revolution with OH as its axis. At the diameter points $\alpha_0 = \alpha_h$ so that the semidiameter of the hyperbola is given by

$$d_h = \frac{1}{2} k C (\chi_h \chi_{\bar{h}})^{1/2} \sec \theta. \quad (42.12)$$

There are two independent dispersion surfaces for the two polarizations σ and π . The dispersion surface has two branches, the upper one denoted as branch 1 and the lower one as branch 2. Waves from the two branches are in antiphase. The direction of energy flow is described by the Poynting vector, parallel to $\mathbf{E} \times \mathbf{H}$, and it has been shown that this is perpendicular to the dispersion surface at the tie point [42.33, 34].

The boundary conditions at the crystal surface require that the tangential components of both \mathbf{E} and \mathbf{H} of the wavevectors should be continuous across the surface. The waves must be matched in amplitude at the crystal surface and in phase velocity parallel to the surface. The wavevectors inside the crystal differ from that

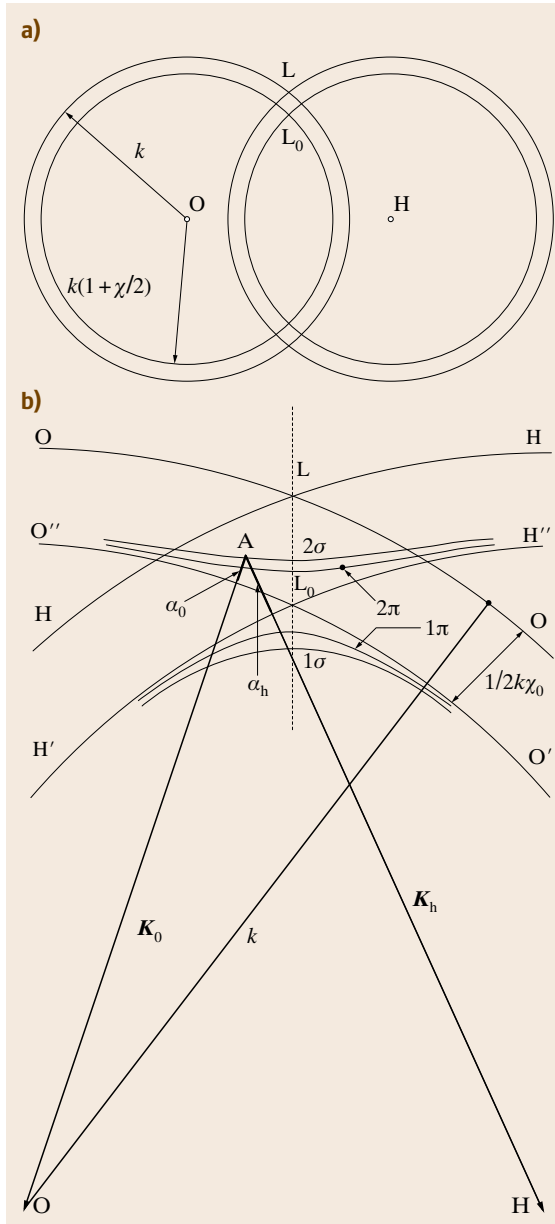


Fig. 42.10a,b Construction of the dispersion surface: (a) spheres of radius k and $k(1 + \chi/2)$ about the origin O and reciprocal lattice point H in reciprocal space showing the position of the Laue point L and Lorentz point L_0 ; (b) dispersion surface for σ and π polarization states

outside only by a vector normal to the crystal surface

$$\mathbf{K}_0 - \mathbf{k}_0 = \delta \mathbf{n}, \quad (42.13)$$

where \mathbf{n} is a unit vector normal to the surface and δ is a scalar variable. A normal drawn line from the tip of the incident wavevector \mathbf{k}_0 intersects the dispersion surface at the excited tie point and determines the tail of the wavevector \mathbf{K}_0 . In the Laue case (Fig. 42.11a), there are two points excited, one on each branch, labeled A and B. From each tie point, wavevectors directed towards O and H can be generated. There are thus four wavevectors generated in the crystal for each polarization, eight in all. At the exit surface of the crystal, the waves split up into diffracted and forward-diffracted beam and the boundary condition can be similarly determined. In the Bragg case (Fig. 42.11b), the normal from the surface intersects either two tie points on the same branch of the dispersion surface or none at all. The Poynting vectors associated with the two tie points are different; the energy flow from one point is directed into the crystal, but that from the other is directed outwards. The latter therefore does not generate any wavefields inside the crystal and can be ignored. Thus a single wavefield is generated for each polarization. When no tie points are selected, no wavefields are generated inside the crystal and total reflection occurs.

Borrmann Effect

The amplitudes of the wavefields are Bloch functions and modulated with the periodicity corresponding to the Bragg planes. The intensity I of each of this wavefields can be shown to be

$$I = D^2 = D_0^2 [1 + R^2 + 2RC \cos(2\pi \mathbf{h} \cdot \mathbf{r})]. \quad (42.14)$$

The intensity is modulated by the factor $\cos(2\pi \mathbf{h} \cdot \mathbf{r}) \cos(2\pi \mathbf{h} \cdot \mathbf{r})$, which has a maxima at $\mathbf{h} \cdot \mathbf{r} = n$ and minima at $\mathbf{h} \cdot \mathbf{r} = (2n + 1)/2$ for integer n (\mathbf{h} is the diffraction vector). That is, maxima and minima of the standing wavefield occur either at, or halfway between, atomic planes (Fig. 42.12). Analysis of (42.14) reveals that the sign of R is opposite for wavefields with tie points on opposite branches of the dispersion surface, and intensity maxima occurs at the atomic plane when R is positive and minima at the atomic plane when R is negative. Maximum modulation occurs when both R and C equal unity, i.e., in centrosymmetric crystal ($\chi_h = \chi_h^-$) for the σ polarized wave at the exact Bragg condition; i.e., when tie points excited on the two branches are at the diameter of the dispersion surface. Under such conditions, the wavefield with intensity maxima at the atomic planes (say branch 2) will suffer greater photoelectric absorption because the electron density is maximum at the atomic planes whereas the branch 1 wavefield, with intensity

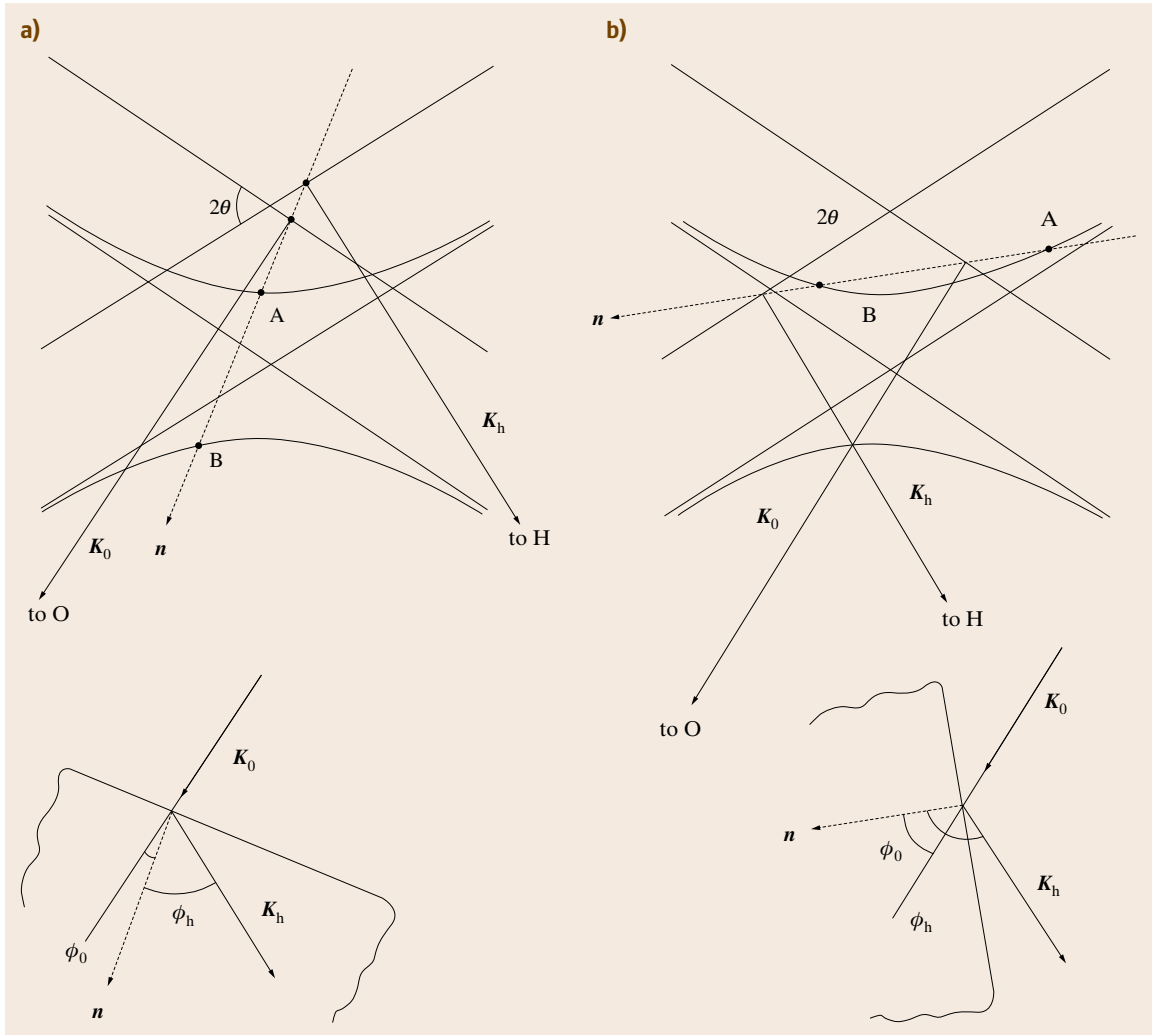


Fig. 42.11a,b Dispersion surface construction showing the tie points excited by an incident wave in (a) the Laue geometry: one tie point in each branch (A on branch 1 and B on branch 2) is excited (b) the Bragg geometry: two tie points (A and B) on the same branch are excited

maxima between the atomic planes, suffers minimum absorption. This effect is known as anomalous transmission or the Borrmann effect and was discovered by *Borrmann* in calcite [42.35, 36]. Presence of the Borrmann effect is indicative of crystal perfection.

Pendellösung Effect

An incident plane wave excites two tie points on the dispersion surface and generates two Bloch wavefields. The wavevectors associated with these tie points differ. The difference in wavevector leads to a difference

in the propagation velocity, and interference effects can occur between the Bloch waves. This gives rise to the production of beats, a phenomenon referred to as *Pendellösung*. The period of the beats is given by the extinction distance ξ_g , which is the reciprocal of the dispersion surface diameter d_h , for the case of exact fulfillment of the Bragg condition

$$\xi_g = d_h^{-1} = \frac{\cos \theta_B}{Ck(\chi_h \chi_{\bar{h}})^{1/2}} = \frac{\pi V \cos \theta_B}{r_e \lambda C(F_h F_{\bar{h}})^{1/2}}, \quad (42.15)$$

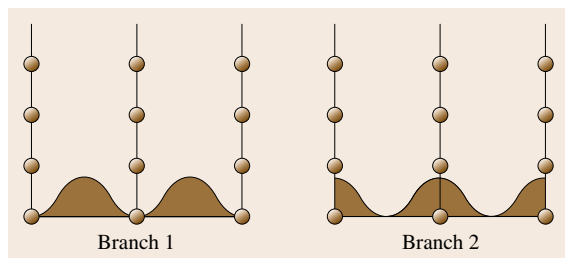


Fig. 42.12 Standing wavefields with a period corresponding to the spacing between the Bragg planes produced at the exact Bragg condition. Branch 1 waves, which have a minimum intensity at the atomic positions, suffer minimal absorption while branch 2 waves, which have a maximum intensity at the atomic positions, are strongly absorbed because of maximum electron density at the atomic planes

where F_h and $F_{\bar{h}}$ are the structure factors of (hkl) and $(\bar{h}\bar{k}\bar{l})$, respectively. When the Bragg condition is not exactly met, the extinction distance is given by

$$\xi'_g = \frac{\xi_g}{(1 + \eta^2)^{1/2}}, \quad (42.16)$$

where $\eta = \sin 2\theta_B / (C|\chi_h\chi_{\bar{h}}|)^{1/2} \Delta\theta$ is the deviation parameter expressing the departure $\Delta\theta$ of the tie points from the exact Bragg condition.

The above results can be extended to cover asymmetric reflections by the introduction of the terms γ_0 and γ_h , the cosines of the angles between the surface

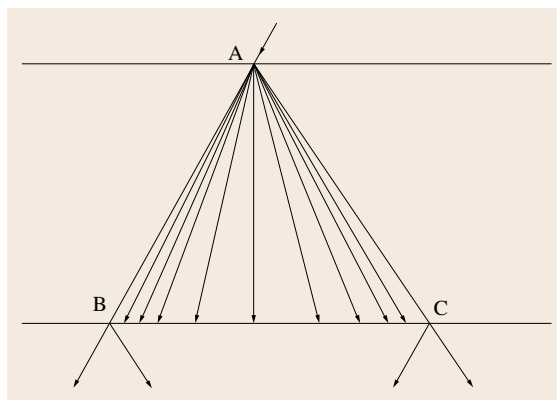


Fig. 42.13 Borrmann fan bounded by the incident (AB) and diffracted (AC) beams showing the distribution of energy for an incident spherical wave that excites all tie points along the dispersion surface

normal and the incident and diffracted beams, respectively, in the appropriate places.

The above analysis applies to an incident plane wave. However, in practice, laboratory sources used have a significant angular divergence because of which the entire dispersion surface is excited simultaneously. This gives rise to energy flow within the Borrmann fan bounded by the incident and diffracted beam directions (Fig. 42.13). Defects at any point within the Borrmann fan may contribute to the change of diffracted intensity at the exit surface of the crystal, and hence to image contrast.

42.5 Mechanisms for Contrast on X-Ray Topographs

Information from an x-ray diffraction topograph is obtained in the form of topographic contrast. As described earlier, local changes in orientation and spacing of crystal lattice planes give rise to local differences in either diffracted beam direction or intensity, which under the appropriate experimental conditions, are manifested as observable contrast on an x-ray topograph. There are two fundamental mechanisms for contrast in x-ray topographs:

1. Orientation contrast
2. Extinction contrast.

Extinction contrast can be further classified into three types:

1. Direct image contrast
2. Dynamical contrast
3. Intermediary contrast.

42.5.1 Orientation Contrast from Subgrains and Twins

Orientation contrast is explicitly defined as resulting from inhomogeneous intensity distributions arising purely from the overlap and/or separation of diffracted x-rays with varying directions. Orientation contrast is observed in crystals containing regions of different orientations such as grains, subgrains, and twins. Misorientations caused by dilations as well as rotations of the lattice can also lead to orientation contrast. Occur-

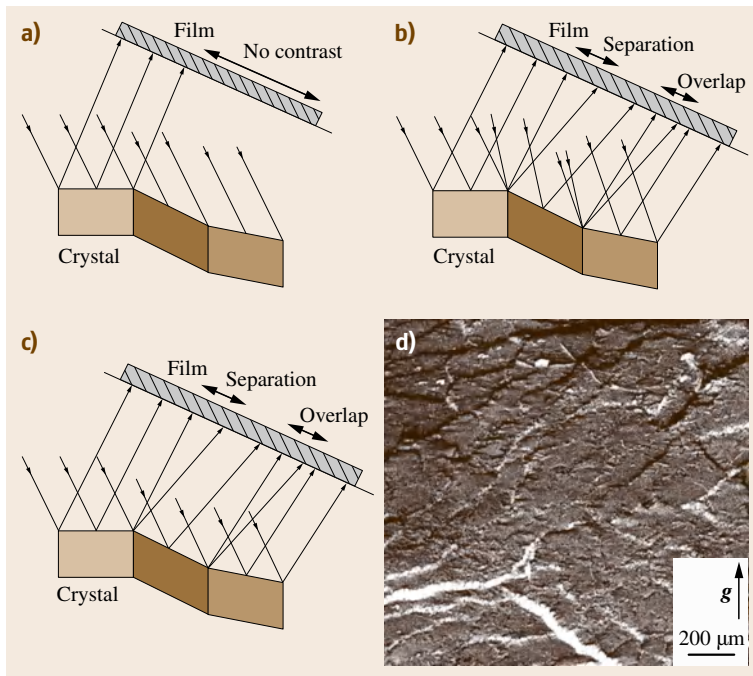


Fig. 42.14a–d Orientation contrast arising from misoriented regions: **(a)** monochromatic radiation (beam divergence < misorientation); **(b)** monochromatic radiation (beam divergence > misorientation); and **(c)** continuous radiation. **(d)** Reflection topograph from an HgCdTe single crystal. The *white bands* correspond to separation between images of adjacent subgrains, while the *dark bands* correspond to image overlap. The tilt angle is estimated at 1–4 arcsec

rence of orientation contrast depends on the nature of x-rays as well as on the nature of the misorientation, as illustrated in Fig. 42.14. If either the incident beam divergence or the range of wavelengths available in the incident x-ray spectrum is smaller than the misorientation between the blocks projected onto the incidence plane (Fig. 42.14a), then only one of the blocks can diffract at a given time. This produces one form of orientation contrast, i.e., the presence or absence of diffracted intensity. Under such conditions, one can adjust the diffraction geometry to bring the other block into the diffraction condition and thus obtain information on the mutual misorientation. However, if either the incident beam divergence or the range of wavelengths available in the incident spectrum allows each block to diffract independently (Fig. 42.14b or c), then the diffracted beams emanating from the individual blocks will travel in slightly different directions and give rise to image overlap if they converge, or separation if they diverge. This produces another form of orientation contrast. The degree of misorientation can be determined by measuring the image shifts (the amount of overlap or separation) as a function of specimen–detector distance on several different reflections. A white-beam x-ray topograph (Fig. 42.14d), recorded from a HgCdTe crystal that shows the overlap and separation of the subgrain images, clearly demonstrates orientation contrast.

42.5.2 Extinction Contrast

Extinction contrast arises when the scattering power around the defects differs from that in the rest of the crystal. Interpretation of this contrast requires understanding of the dynamical diffraction effects as discussed in the previous section (see also [42.37]). In this chapter, extinction contrast formation mechanisms are addressed with respect to images of dislocations on topographs since dislocations are among the most common defects studied by x-ray topography. Topographic contrast of dislocations (as well as other defects) consists of *direct*, *dynamic*, and *intermediary images* corresponding to the three different types of extinction contrast. In transmission geometry, which of the three types of image can be observed is determined by the absorption conditions. Absorption conditions are usually defined by the product of the linear absorption coefficient μ and the thickness of the crystal, t , traversed by the x-ray beam, i.e., μt . For topographs recorded under low absorption conditions ($\mu t < 1$), the dislocation image is dominated by the direct image contribution. Under intermediate absorption conditions, i.e., $5 > \mu t > 1$, all three components can contribute, while for high absorption cases ($\mu t > 6$), the dynamical contribution (in this case known as the Borrmann image) dominates.

The Direct Dislocation Image

The direct dislocation image is formed when the angular divergence or wavelength bandwidth of the incident beam is larger than the angular or wavelength acceptance of the perfect crystal [42.38]. Under this condition, only a small proportion of the given incident beam will actually undergo diffraction, with most of the incident beam passing straight through the crystal and simply undergoing normal photoelectric absorption. However, it is possible that the deformed regions around structural defects, such as dislocations and precipitates, present inside the crystal are set at the correct orientation for diffraction provided that their misorientation is larger than the perfect crystal rocking curve width and not greater than the incident beam divergence. The effective misorientation $\delta\theta$ around a defect is the sum of the tilt component in the incidence plane $\delta\varphi$ and the change in the Bragg angle θ_B due to dilation δd and is given by

$$\delta\theta = -\tan\theta_B \frac{\delta d}{d} \pm \delta\varphi. \quad (42.17)$$

Therefore, the distorted region will give rise to a new diffracted beam. Further, if the distorted region is small in size then this region will diffract kinematically and will not suffer the effective enhanced absorption associated with extinction effects to which the diffracted beams from the perfect regions of the crystal are subjected. The enhanced diffracted intensity from the distorted regions compared with the rest of the crystal gives rise to topographic contrast. This is known as direct or kinematical image formation. This form

of contrast dominates under low absorption conditions ($\mu t < 1-2$). Generally, the direct dislocation image formed by this extinction contrast model has been used to explain observed contrast features. Although the intensity increase for the direct image was in most cases qualitatively interpreted in a correct way [42.38], detailed measurements of dislocation image width made previously sometimes do not strictly coincide with the predictions of this theory [42.39].

From studies of the direct dislocation images of growth dislocations with large Burgers vectors (superscrew dislocations or micropipes) in x-ray topographs recorded from SiC single crystals, it was recently shown by Huang et al. [42.31, 40–42] that the extinction contrast theory alone is incapable of explaining the contrast features associated with superscrew dislocations on synchrotron topographs. By using a simple ray-tracing simulation method, it was demonstrated that the direct images of superscrew dislocations consist mainly of orientation contrast. Moreover, it was shown that this method is also applicable to elementary dislocations, indicating that it is a general phenomenon that orientation contrast makes a significant contribution to the direct dislocation image.

In the orientation contrast model, the mosaic region around the dislocation is divided into a large number of cubic diffraction units with their local misorientations coinciding with the long-range displacement field of the dislocation. These units diffract x-rays kinematically according to their local lattice orientation. Traces of the inhomogeneously diffracted x-rays are projected onto the recording plate to obtain the direct

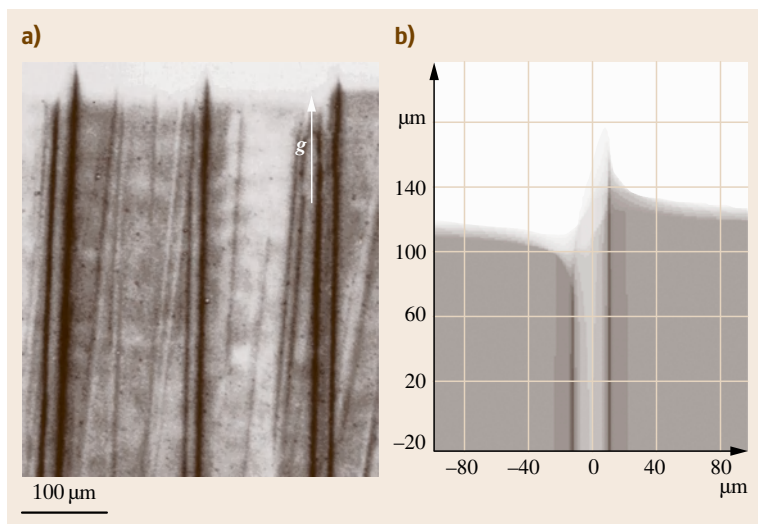


Fig. 42.15 (a) Synchrotron transmission topograph of superscrew dislocations in 6H-SiC ($g = 0006$, $\theta_B = 8.5^\circ$, sample–film distance $d = 20$ cm); (b) simulation of pure orientation contrast of a 5c superscrew dislocation. The simulation parameters are chosen to coincide with the experimental conditions of (a)

image. Thus the direct image here is due to orientation contrast arising from the overlap and separation of inhomogeneously diffracted x-rays with continuously varying directions. Figure 42.15a shows several images of giant screw dislocations in SiC recorded in transmission geometry. The Burgers vector of dislocation 1 was independently measured [using optical phase-contrast microscopy, atomic force microscopy (AFM), and other x-ray topography techniques] to be $5c$ ($|b| = 75.85 \text{ \AA}$). The full-width w of the image is around $40 \mu\text{m}$, and the separation between the maximum intensity peaks L_0 is around $24 \mu\text{m}$. The conventional misorientation contour model predicts an image width of several hundred micrometers, which is clearly not the case. On the other hand, a good correlation is clearly evident between the observed image and the image simulated using the orientation contrast model (Fig. 42.15b). The simulated image consists of pure orientation contrast resulting from the separation or overlap of the inhomogeneously diffracted x-rays. In a similar way, images of superscrew dislocations recorded in back-reflection geometry can be successfully simulated, as shown in Fig. 42.16. It has also been shown that, under low absorption conditions, the above orientation

contrast formation mechanism also applies to ordinary dislocations with Burgers vectors smaller than that of micropipes [42.7].

Origins of Dynamical Contrast from Dislocations

As discussed in Sect. 42.4, the dynamical theory of x-ray diffraction obtains solutions to Maxwell's equations in a periodic medium (i.e., the crystal) matched to solutions that are plane waves (the incident and diffracted x-ray beams). The wave equations satisfying Maxwell's equations can be represented geometrically by the dispersion surface [42.43], and a wavefield propagating in the crystal is represented by a tie point on the dispersion surface and comprises two waves corresponding to the incident and diffracted x-ray beams (Figs. 42.9 and 42.10). Dynamical contrast arises from the interaction of this wavefield with the dislocation distortion field (for a review see [42.37]). Under low absorption conditions this dynamical contribution to the dislocation contrast is mostly unobservable due to the fact that the image is dominated by the *direct image* contribution. Dynamical contrast becomes more observable as absorption increases, thereby attenuat-

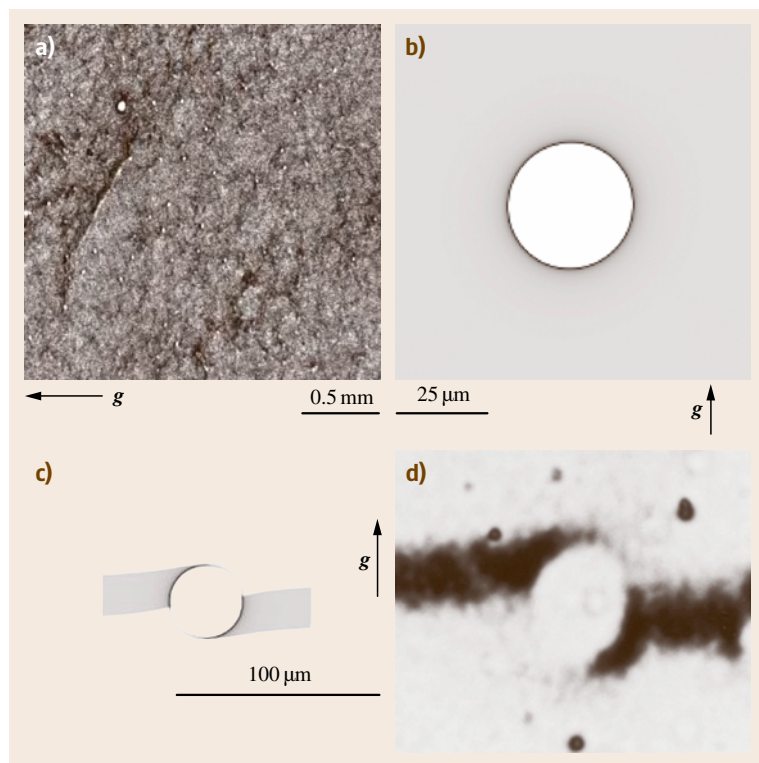


Fig. 42.16 (a) Back-reflection synchrotron topograph of a (0001) 4H-SiC wafer showing the circular images of superscrew dislocations ($g = 00016$, $\lambda = 1.25 \text{ \AA}$, sample-film distance $d = 20 \text{ cm}$); (b) enlargement of one of the circular images in (a); (c) computer-simulated white-beam back-reflection x-ray section topograph of a screw dislocation (Burgers vector magnitude $b = 3c$) simulated under the diffraction conditions of (a); (d) back-reflection x-ray section topograph of a screw dislocation ($b = 3c$)

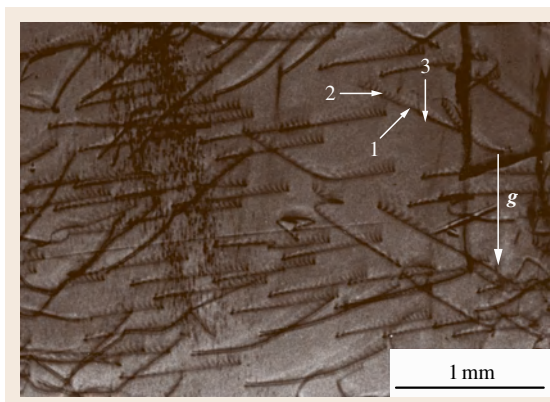


Fig. 42.17 SWBXT transmission topograph ($g = 10\bar{1}0$, $\lambda = 0.75 \text{ \AA}$) recorded from an AlN single crystal under intermediate absorption conditions ($\mu t = 8$) showing the direct (1), dynamical (2), and intermediary (3) images of a dislocation

ing the *direct image* contribution (the kinematically diffracted rays contributing to this image do not survive the absorption). Under these conditions, only wavefields associated with one branch of the dispersion surface (usually branch 1) which are close to the exact Bragg condition survive due to the Borrmann effect [42.35]. These wavefields can survive absorption even when the value of μt is significantly greater than unity.

For a perfect crystal, the incident boundary conditions determine the position of the tie point on the dispersion surface. However for an imperfect crystal, the local lattice distortion can modify the position of the tie point of a wavefield as it passes through the crystal. This can occur by two mechanisms depending on the nature of the distortion field. Tie point migration along the dispersion surface occurs when the wavefield encounters a shallow misorientation gradient upon passing through the crystal (e.g., regions away from the dislocation line). The variation of the misorientation should be less than the rocking curve width over an extinction distance, i. e.,

$$R_c \leq g\xi_g^2, \quad (42.18)$$

where R_c is the radius of the curvature of the reflecting plane and ξ_g is the extinction distance. Under these conditions, both the direction of propagation of the wavefield and the ratio of the amplitudes of its components are changed. This phenomenon can be treated using the so-called eikonal theory [42.44], analogous to its counterpart in geometrical optics, formulated for the case of light traveling through a region of varying

refractive index. As a wavefield approaches the long-range distortion field of a dislocation, rays will bend in opposite directions on either side of the core, potentially producing opposite contrast. However, if the dislocation is not located close to the crystal surface, the ray bending experienced above the defect may be compensated for by that experienced below the defect, suggesting that the contrast effects should cancel out. Net contrast is nevertheless observed, since any deviation of the wavefields from the direction of propagation corresponding to the perfect crystal region forces them to experience enhanced absorption, thereby producing a loss of intensity. Under these conditions, the dislocation image will appear white and diffuse. In cases where the dislocation is close to the exit surface of the crystal, the lattice curvature above and below the defect is asymmetric due to the requirements of surface relaxation. This means that the ray bending experienced above the defect is no longer compensated by that experienced below, with the result that opposite contrast is observed from regions either side of the defect.

On the other hand, when the wavefield encounters a sharp misorientation gradient upon passing through the crystal (e.g., regions close to a dislocation core), the strain field would completely destroy the conditions for propagation and force the wavefield to decouple into its component waves. When these component waves reach the perfect crystal on the other side of the defect, they will excite new wavefields (the so-called phenomenon of interbranch scattering). These newly created wavefields will have tie points which are distributed across the dispersion surface, and since only those wavefields with tie points close to the exact Bragg condition survive, they will be heavily attenuated, leading to a loss of intensity from the region surrounding the dislocation. Such images, known as Borrmann images, appear white on a dark background. An example is shown in Fig. 42.17, which is a detail from a white-beam x-ray topograph recorded from an AlN single crystal.

The Intermediary Image

The intermediary image arises from interference effects at the exit surface between the new wavefields created below the defect (as described in Sect. 42.4.2) and the undeviated original wavefield propagating in the perfect regions of crystal. Usually, these images often appear as a bead-like contrast along *direct* dislocation images on projection topographs. Under moderate absorption conditions when the defect (e.g., dislocation line) is inclined to the surface, the intermediary image forms a fan

within the intersections of the exit and entrance surface of the dislocation and has an oscillatory contrast with

depth periodicity over an extinction distance ξ_g . Again, this is illustrated in Fig. 42.17.

42.6 Analysis of Defects on X-Ray Topographs

Topography, both synchrotron and conventional, is well suited for analysis of low densities ($< 10^6 \text{ cm}^{-2}$) of dislocations in crystals. The restriction to low densities arises from the fact that topographic dislocation images can be anywhere from around 5 to around $15 \mu\text{m}$ wide, so that greater densities would lead to image overlap and therefore loss of information.

42.6.1 Basic Dislocation Analysis

Determination of Line Direction

For dislocations created by slip processes, knowledge of the line direction as well as detailed information on the Burgers vector of the dislocations is required to fully assign the active slip system. Knowledge of both line direction and Burgers vector of crystal-growth-induced dislocations is also very important in understanding their origin and for the development of strategies to reduce the density of such dislocations. The projected directions of direct images of growth dislocations have also been used very successfully to compare with line energy calculations designed to determine why particular line directions are preferred by such dislocations

in crystals (for a review see [42.45]). The line direction of a dislocation can be obtained by analyzing its direction of projection on two or more topographs recorded with different reciprocal lattice vectors. The use of analytical geometry enables the line direction to be determined either directly from the measured direction of projection [42.46] or indirectly by comparing calculated projected directions of expected dislocation line directions for the material of interest with the measured projection directions [42.47]. Such analysis is most readily carried out on direct images of dislocations since they are the most well defined, although similar analysis can be performed on dynamical or intermediary images.

Determination of Burgers Vector Direction

For sufficiently low dislocation densities, standard Burgers vector analysis, which enables the determination of the direction of the Burgers vector, is readily carried out in the low absorption regime, using the $\mathbf{g} \cdot \mathbf{b} = 0$ criterion for invisibility of screw dislocations, and the combination of $\mathbf{g} \cdot \mathbf{b} = 0$ and $\mathbf{g} \cdot \mathbf{b} \times \mathbf{l} = 0$ criterion for invisibility of edge or mixed dislocations (where \mathbf{b} is the dislocation Burgers vector and \mathbf{l} is the dislocation line direction). These criteria are also used in the analysis

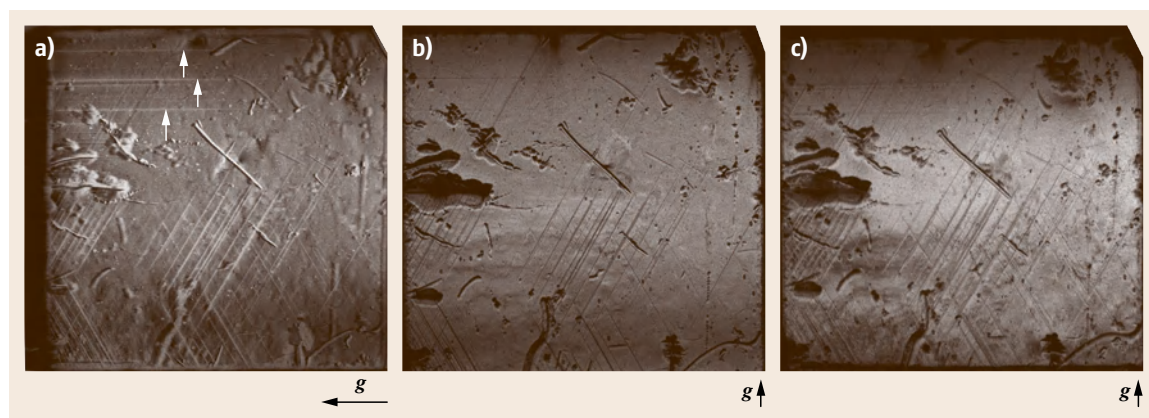


Fig. 42.18a–c Synchrotron white-beam topographs recorded in transmission geometry from a ZnO single crystal containing slip dislocations: (a) $\mathbf{g} = 11\bar{2}0$; (b) $\mathbf{g} = 1\bar{1}00$; (c) $\mathbf{g} = 2\bar{2}01$. Note the disappearance of dislocation segments (indicated by arrows on (a)) on (b) and the weak contrast on (c). The Burgers vector of these dislocations is determined to be $\frac{1}{3}[11\bar{2}0]$ and, from the line directions, it is determined that these are screw dislocations

of TEM images of dislocations. An example of dislocation analysis in a single crystal of zinc oxide (ZnO) is presented in Fig. 42.18. These dislocations were likely formed by deformation process during postgrowth cooling. These dislocations lie in the basal plane of the 2H crystal structure of ZnO and are visible in Fig. 42.18a ($g = 11\bar{2}0$) and invisible on the $1\bar{1}00$ (Fig. 42.18b) and the $2\bar{2}01$ (Fig. 42.18c) reflections, although weak contrast is observed. Application of the $g \cdot b = 0$ criterion to possible $\frac{1}{3}(11\bar{2}0)$ Burgers vectors which lie in the basal plane shows that the dislocations have Burgers vector $\frac{1}{3}[11\bar{2}0]$.

Determination of Burgers Vector Sense and Magnitude

The determination of the actual sense and magnitude of the Burgers vector of a dislocation, once the Burgers vector direction has been determined by $g \cdot b$ analysis, requires more detailed analysis. Chikawa [42.48] developed conventional-radiation divergent-beam techniques for the determination of the sense of both edge and screw dislocations through measurement of the sense of tilt of lattice planes surrounding the dislocation core. For the case of screw dislocations, Mardix et al. [42.49] subsequently further developed Chikawa's divergent-beam technique to enable the magnitude of this tilt to be measured as a function of distance from the core. This could then be fitted to the corresponding theoretical expression, enabling the Burgers vector magnitude to be determined. Si et al. [42.50] developed two methods, one section and one projection, which are analogous to those of Chikawa [42.48], and Mardix et al. [42.49], but which make use of synchrotron white radiation. In these techniques the lattice tilt surrounding dislocations of mainly screw character was measured with an accuracy that was significantly improved due to the relaxation of the requirement for short specimen–film distances which is inevitable in conventional radiation techniques. Chen, Dudley, and co-workers [42.51, 52] have similarly determined the dislocation sense of micropipes and closed-core threading screw dislocations in 4H-SiC by comparing grazing-incidence synchrotron white-beam x-ray topographic images of the dislocations with corresponding images simulated by the ray-tracing method.

42.6.2 Contrast from Inclusions

Individual point defects are not visible on x-ray topographs, but when such defects cluster to form a precipitate or inclusion, contrast can be observed. Under low absorption conditions, *direct* or kinematical

images of precipitates are formed on x-ray topographs and these typically consist of two dark half-circles separated by a line of no contrast perpendicular to the projection of the diffracted vector. This is simply due to the fact that distortions parallel to a given set of atomic planes are not discernible. An example is shown in Fig. 42.19, which is a transmission synchrotron white beam x-ray topography (SWBXT) image recorded from an AlN crystal. Under higher absorption conditions, dynamical contrast can be observed. When the precipitate is close to the x-ray exit surface, opposite contrast either side of the defect can usually be observed. This contrast will usually reverse with reversal of the sign of the reflection vector. The contrast is produced by tie point migration in the region above the defect. Since the defect is close to the exit surface, the reflecting planes rotate very sharply in order to meet the surface at the preferred angle, and so the curvature becomes too large for the eikonal theory to handle. Consequently, the contrast developed above the defect is *frozen-in*. The black–white contrast not only reverses with the sense of the reflection vector but also with the sense of the strain in the lattice. This can be used to determine the nature of the precipitate. If the contrast is enhanced on the side of positive g , then the lattice is under compression, and if reduced it is under tension. This empirical rule was first determined by Meieran and Blech [42.53].

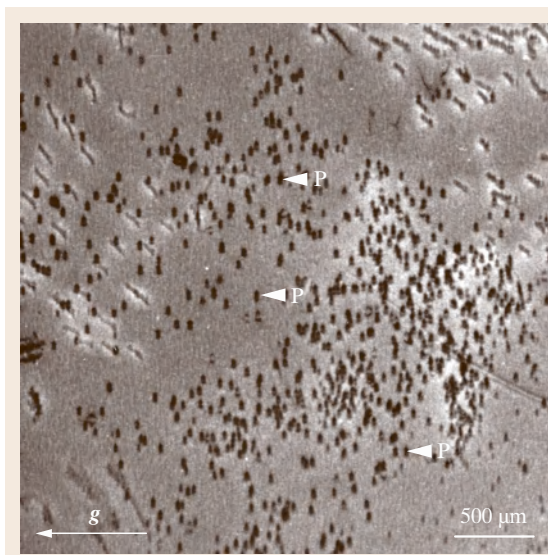
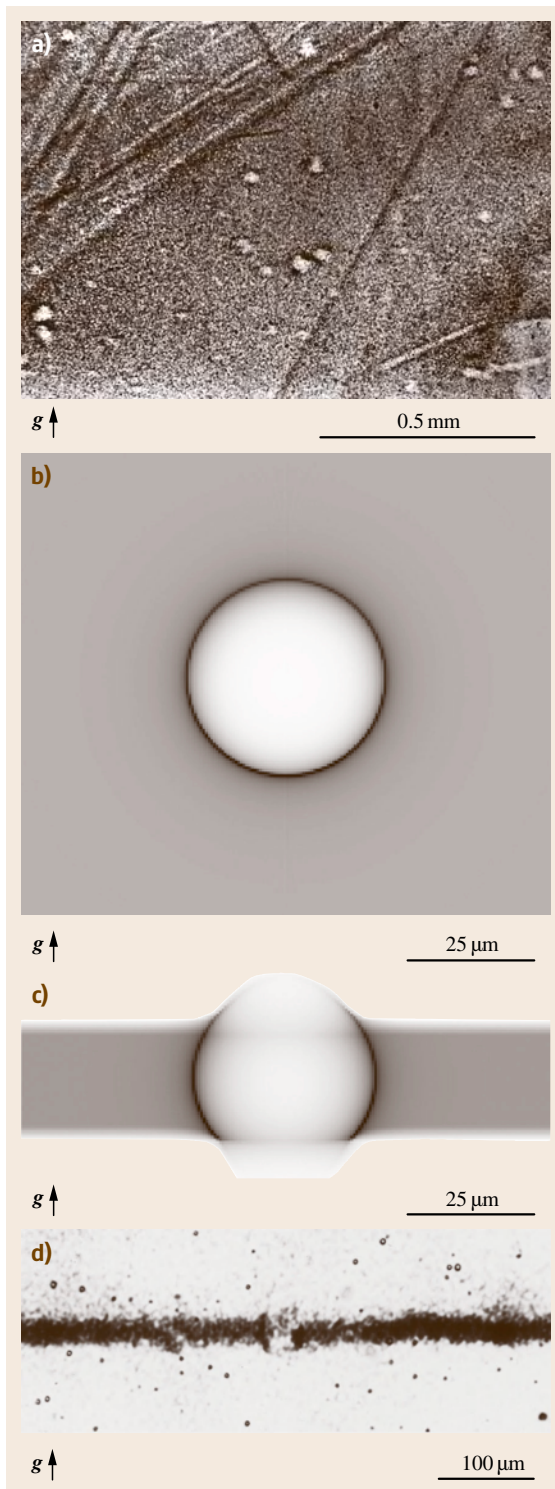


Fig. 42.19 Detail from a synchrotron white-beam topograph recorded in transmission from a AlN single crystal showing precipitate contrast (P) under low absorption conditions



Precipitates/inclusions may also be imaged using the back-reflection geometry, as shown in Fig. 42.20a for a 3C-SiC platelet containing inclusions near the surface [42.54]. The circular spots of inclusions are similar to the images of superscrew (micropipes) in 4H-SiC (Fig. 42.16) except the screw dislocation images have more distinct white contrast than the inclusion images, there being some diffracted intensity inside the inclusion spots making them appear gray rather than white.

Images of inclusions in back-reflection topographs can be understood by considering ray-tracing computer simulations based on the displacement field of a spherical inclusion. The ray-tracing concept is the same as the orientation contrast model (see Sect. 42.5.2). Figure 42.20b shows a simulated image of an inclusion with a diameter comparable to the white spots in Fig. 42.20a. The simulation a 3c axial screw dislocation in Fig. 42.16b and that of an inclusion in Fig. 42.20b are similar, in that intensity reflected from the area centered on their defects is concentrated into a dark ring. This effect is complete for the case of the screw dislocation of Fig. 42.16b with intensity being absent from the ring, whereas for the case of the inclusion the intensity within its dark ring is merely depleted.

The difference between the mechanisms of image formation in the back-reflection topography of axial screw dislocations and inclusions can be analyzed more intimately with section topographs. Simulated section topographs may be obtained by utilizing only the diffracting elements of the crystal that fall within the projected path of a narrow strip of incident rays. For a screw dislocation (Fig. 42.15c), on the section topograph, the strip of diffracted intensity is displaced downward and upward at either side of the white circular center of the simulated screw dislocation image to break into two tails. The upper tail originates from the left half of the illuminated dislocation core, while the lower tail corresponds to the right half. The presence of the tails stretching in directions out of their illuminated sides indicates that the diffracted rays are

Fig. 42.20 (a) Synchrotron white-beam back-reflection x-ray topographs from a 3C-SiC platelet ($g = 121212$, $\lambda = 1.24 \text{ \AA}$) showing inclusions; (b) computer-simulated back-reflection white-beam x-ray topograph ($\theta_B = 80^\circ$) of an inclusion $14 \mu\text{m}$ beneath the surface of a 3C-SiC sample; (c) computer-simulated white-beam back-reflection x-ray section topograph of an inclusion; (d) recorded synchrotron white-beam back-reflection x-ray section topograph of an inclusion $14 \mu\text{m}$ beneath the surface ($g = 121212$, $\lambda = 1.24 \text{ \AA}$) ◀

twisted from the incident beam direction. The twisting direction of the rays is opposite to the dislocation sense. Back-reflection section topography is then capable of discerning the senses of axial screw dislocations. The section topograph of an inclusion (Fig. 42.20d) lacks this two-tailedness.

Like the traverse topograph of Fig. 42.20a, the defect image again shows a gray center of depleted intensity bracketed by a dark perimeter. The diffracting planes in the vicinity of a spherical inclusion lack the helical twist that those in the core of a screw dislocation have. A spherical inclusion's strain field bulges the diffracting planes above it into convex curvatures, tilting them radially outward from the defect's center. In the simulated section topograph of an inclusion in Fig. 42.20c, the absence of twist is evident as the image is symmetrical about a line drawn through the center of the defect parallel to the g vector. Diffracted intensity is depleted from the central area of the defect image and concentrated at its edges, forming two curved bars of dark contrast. This is roughly what is seen in the section topograph of an inclusion in Fig. 42.20b.

42.6.3 Contrast Associated with Cracks

X-ray topography is also capable of discerning the deformation fields associated with cracks in single crystals. George et al. [42.55] have used x-ray topography to measure the extent of the plastic zone associated

with the stress concentrations that can arise at the tip of a crack. Raghoechamachar et al. [42.56] reported on deformation initiated at cracks in AlN crystals. This was achieved both in static mode using Lang topography [42.55] and synchrotron white-beam x-ray topography [42.56] and in dynamic mode using monochromatic synchrotron-radiation topography [42.57]. In a similar way, the elastic deformation field associated with crack tips can also be characterized. For example, for the case of *mud cracks*, which are often observed in GaN films grown on either SiC or sapphire substrates, the elastic field of the cracks can penetrate down into the substrate and be observable by x-ray topography. Itoh et al. [42.58] published an early report of such topographic observations in GaN films grown on sapphire. The presence of these mud cracks is evidence for the existence of tensile stresses in the films. For the case of SiC substrates, these tensile stresses may arise from thermal expansion mismatch, although this cannot explain their existence for the case of sapphire substrates. For the latter case, the tensile stresses are believed to be associated with grain coalescence [42.59]. TEM observation of the interface regions in the GaN/sapphire system indicates the absence of plastic deformation associated with the crack tips, rather just the presence of an elastic deformation field. This elastic deformation field (for both SiC and sapphire cases) behaves with respect to x-ray topographic observation like an edge dislocation, i.e., one can define a displacement vec-

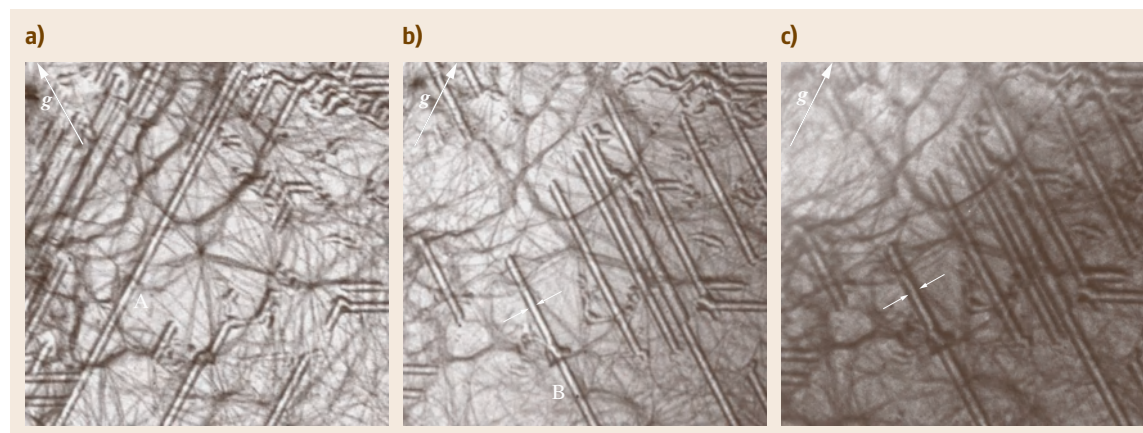


Fig. 42.21a–c SWBXT images recorded from a SiC substrate with GaN epilayers. (a) $g = \bar{2}110$, $d = 10$ cm; (b) $g = \bar{1}2\bar{1}0$, $d = 10$ cm; (c) $g = \bar{1}2\bar{1}0$, $d = 24.7$ cm. The pairs of dark parallel lines arise from the elastic deformation associated with *mud cracks* in the GaN film which penetrate into the SiC substrate (intensity from the GaN film is too low to be visible on this image). Crack images A are visible in (a) but invisible in (b), while the reverse is true for crack images B. This demonstrates the applicability of the $g \cdot u = 0$ and $g \cdot u \times l = 0$ criteria. The arrows on (b) and (c) highlight the increase in the separation between the two parallel components of the crack images as the specimen–film distance is increased

tor (\mathbf{u}) associated with the crack which is oriented in the plane of the interface and normal to the long axis (\mathbf{l}) of the crack. This means that the crack image disappears when the conditions $\mathbf{g} \cdot \mathbf{u} = 0$ and $\mathbf{g} \cdot \mathbf{u} \times \mathbf{l} = 0$ are simultaneously satisfied. Figure 42.21 shows topographs of a cracked GaN/SiC sample recorded under various diffraction conditions: $\mathbf{g} = \bar{2}110$ and $d = 10$ cm, where d is the sample–film distance (Fig. 42.21a), $\mathbf{g} = \bar{1}2\bar{1}0$ and $d = 10$ cm (Fig. 42.21b), and $\mathbf{g} = \bar{1}2\bar{1}0$ and $d = 24.7$ cm (Fig. 42.21c). All the topographs were taken with the GaN film on the x-ray exit surface. From these figures we can see that all the cracks running along $[2\bar{1}10]$ which have \mathbf{u} along $[01\bar{1}0]$ are invisible in Fig. 42.21a while all the cracks along $[\bar{1}2\bar{1}0]$ which have \mathbf{u} along $[\bar{1}010]$ are invisible in Fig. 42.21b, due to the

forementioned invisibility criteria. Ray tracing, carried out by recording SWBXT images of the crack deformation fields at different specimen–film distances, enables determination of the *sense* of the lattice rotation (i. e., on which side of the interface the *extra half-plane* would lie) as well as the exact location of the misoriented volume with respect to the core of the crack. This is demonstrated in Fig. 42.21b,c. The separation between the parallel components of the images in Fig. 42.21c is larger than that in Fig. 42.21b, indicating that the cracks open up towards the GaN film surface. Further quantitative ray-tracing analysis reveals that the misoriented volumes are located at a distance of $30\text{ }\mu\text{m}$ from the crack core and that the lattice rotations are of the order of 20 arcsec.

42.7 Current Application Status and Development

Photographic films continue to be the detectors of choice for recording x-ray topographs, although large-area charge-coupled device (CCD) detectors can be used when high resolution is not paramount. Currently, holographic films are capable of recording x-ray topographs with submicrometer resolution but require long exposure times even for an intense synchrotron beam. Nuclear emulsions (Ilford plates) which have a grain size below $1\text{ }\mu\text{m}$ are also suitable to record high-resolution x-ray topographs but they are expensive and require special handling and developing procedures. Single-side-coated high-resolution x-ray films (Agfa D3-SC, Kodak SR-45, Fuji IX20, etc.) which have a grain size on the order of $1\text{ }\mu\text{m}$ are usually adequate for recording most x-ray topographs. These have sufficient contrast and resolution and can be developed fast enough to allow real-time observation and feedback for recording multiple topographs. CCD detectors are used instead of films when quick imaging is needed in some dynamic studies; however, the results are somewhat limited due to the poor resolution ($25\text{--}40\text{ }\mu\text{m}$).

As an efficient technique to explore the microstructure of various materials, x-ray topography has been extensively applied in both the research and industrial fields. Through observation and analysis of structural features and defects, it plays a key role in the evaluation of materials quality, the investigation of defect forma-

tion mechanisms, and the processing–microstructure–properties correlation. For the development of the crystal growth process of any material, x-ray topography is a critical tool that goes hand in hand with the crystal growth technique employed. X-ray topography has also been used to characterize thin films and heterostructures. While conventional x-ray topography can be used as a laboratory tool for quick evaluation of materials, synchrotron-based techniques have the capability for a wide range of experimental modifications, including in situ studies of crystal growth, phase transformations, device performance, etc. Further advances in digitization and processing of images can allow for rapid and automated analysis of x-ray topographs.

Modifications to the x-ray topography technique have also been developed in recent years. One example is the technique of x-ray reticulography [42.60]. Based on this technique, a novel stress measurement procedure has been developed that is capable of non-invasively measuring the complete stress tensor of any single-crystal material. This technique can be applied to a wide range of materials, such as those used in the semiconductor industry for developing or improving the packaging processes for the ever-reducing dimensions of microprocessors, or to measure stresses in as-grown single-crystal materials for comparison with performance and simulations.

References

- 42.1 H.J. Scheel: The development of crystal growth technology. In: *Crystal Growth Technology*, ed. by H.J. Scheel, T. Fukuda (Wiley, New York 2003) pp. 1–14
- 42.2 C. Claeys, L. Deferm: Trends and challenges for advanced silicon technologies, *Solid State Phenom.* **47–48**, 1–16 (1993)
- 42.3 D.T.J. Hurle: *Handbook of Crystal Growth: Thin Films and Epitaxy* (Elsevier, New York 1994)
- 42.4 G. Dhanaraj, T. Shripathy, H.L. Bhat: Growth and defect characterization of L-arginine phosphate monohydrate, *J. Cryst. Growth* **113**, 456–464 (1991)
- 42.5 S. Kawado, S. Lida, Y. Yamaguchi, S. Kimura, Y. Hirose, K. Kajiwar, Y. Chikaura, M. Umeno: Synchrotron-radiation x-ray topography of surface strain in large-diameter silicon wafers, *J. Synchrotron. Radiat.* **9**, 166–168 (2002)
- 42.6 B. Raghothamachar, H. Chen, M. Dudley: Unpublished results (1998)
- 42.7 M. Dudley, X. Huang: X-ray topography. In: *Microprobe Characterization of Optoelectronic Materials*, ed. by J. Jimenez (Gordon Breach/Harwood Academic, Amsterdam 2003) pp. 531–594
- 42.8 G. Dhanaraj, X.R. Huang, M. Dudley, V. Prasad, R.H. Ma: Silicon carbide crystals – Part I: Crystal growth and characterization. In: *Crystal Growth Technology*, ed. by K. Byrappa, T. Ohachi (William Andrew/Springer, New York 2003) pp. 181–232
- 42.9 G.N. Ramachandran: X-ray topographs from diamond, *Proc. Indian Acad. Sci. A* **19**, 280–294 (1944)
- 42.10 A. Authier: Contrast of images in x-ray topography. In: *Diffraction and Imaging Techniques in Materials Science*, ed. by S. Amelinckx, R. Gevers, J. van Landuyt (North Holland, Amsterdam 1978) pp. 715–757
- 42.11 J.E. White: X-ray diffraction by elastically deformed crystals, *J. Appl. Phys.* **21**, 855–859 (1950)
- 42.12 V.W. Berg: Über eine röntgenographische Methode zur Untersuchung von Gitterstörungen an Kristallen, *Naturwissenschaften* **19**, 391–396 (1931), in German
- 42.13 A.R. Lang: Direct observation of individual dislocations by x-ray diffraction, *J. Appl. Phys.* **29**, 597–598 (1958)
- 42.14 C.S. Barrett: A new microscopy and its potentialities, *AIME Transactions* **161**, 15–65 (1945)
- 42.15 W.L. Bond, J. Andrus: Structural imperfections in quartz crystals, *Am. Mineral.* **37**, 622–632 (1952)
- 42.16 G.H. Schwuttke: New x-ray diffraction microscopy technique for study of imperfections in semiconductor crystals, *J. Appl. Phys.* **36**, 2712–2714 (1965)
- 42.17 W. Wooster, W.A. Wooster: X-ray topographs, *Nature* **155**, 786–787 (1945)
- 42.18 J.B. Newkirk: Method for the detection of dislocations in silicon by x-ray extinction contrast, *Phys. Rev.* **110**, 1465–1466 (1958)
- 42.19 L.G. Schulz: Method of using a fine-focus x-ray tube for examining the surfaces of single crystals, *J. Met.* **6**, 1082–1083 (1954)
- 42.20 A. Guinier, J. Tenevin: Sur deux variantes de la methode de luae et leurs applications, *Acta Cryst.* **2**, 133–138 (1949), in French
- 42.21 T. Tuomi, K. Naukkarinen, P. Rabe: Use of synchrotron radiation in x-ray-diffraction topography, *Phys. Status Solidi (a)* **25**, 93–106 (1974)
- 42.22 A.R. Lang: Point-by-point x-ray diffraction studies of imperfections in melt-grown crystals, *Acta Cryst.* **10**, 839 (1957)
- 42.23 U. Bonse, E. Kappler: Röntgenographische Abbildung des Verzerrungsfeldes einzelner Versetzungen in Germanium-Einkristallen, *Z. Naturforsch. A* **13**, 348 (1958), in German
- 42.24 D.K. Bowen, B.K. Tanner: *High Resolution X-ray Diffractometry and Topography* (Taylor Francis, London 1998) p. 174
- 42.25 J. Miltat: White beam synchrotron radiation. In: *Characterization of Crystal Growth Defects by X-ray Methods*, ed. by B.K. Tanner, D.K. Bowen (Plenum, New York 1980) pp. 401–420
- 42.26 P.G. Neudeck: Electrical impact of SiC structural defects on high electric field devices, *Mater. Sci. Forum* **338–342**, 1161–1166 (2000)
- 42.27 P.G. Neudeck, W. Huang, M. Dudley: Breakdown degradation associated with elementary screw dislocations in 4H-SiC p+n junction rectifiers. In: *Power Semiconductor Materials and Devices*, ed. by S.J. Pearton, R.J. Shul, E. Wolfgang, F. Ren, S. Tenconi (Materials Research Society, Warrendale 1998) pp. 285–294
- 42.28 M. Hart: Synchrotron radiation – Its application to high speed, high resolution x-ray diffraction topography, *J. Appl. Crystallogr.* **8**, 436–444 (1975)
- 42.29 X.R. Huang, M. Dudley, J.Y. Zhao, B. Raghothamachar: Dependence of the direct dislocation image on sample-to-film distance in x-ray topography, *Philos. Trans. R. Soc. Ser. A* **357**, 2659–2670 (1999)
- 42.30 D.R. Black, G.G. Long: X-ray Topography, Special Publication 0960-10 (National Institute of Standards and Technology (NIST), Washington 2004)
- 42.31 M. Dudley, S. Wang, W. Huang, C.H. Carter Jr., V.F. Tsvetkov, C. Fazi: White beam synchrotron topographic studies of defects in 6H-SiC single crystals, *J. Phys. D Appl. Phys.* **28**, A63–A68 (1995)
- 42.32 M. Dudley, J. Wu, G.-D. Yao: Determination of penetration depths and analysis of strains in single crystals by white beam synchrotron x-ray topography in grazing Bragg-Laue geometries, *Nucl. Instrum. Methods B* **40/41**, 388–392 (1989)

- 42.33 N. Kato: The flow of x-rays and materials waves in ideally perfect single crystals, *Acta Crystallogr.* **11**, 885–887 (1958)
- 42.34 N. Kato: The energy flow of x-rays in an ideally perfect crystal: comparison between theory and experiments, *Acta Crystallogr.* **13**, 349–356 (1960)
- 42.35 G. Borrmann: The extinction diagram of quartz, *Phys. Z.* **42**, 157–162 (1941)
- 42.36 G. Borrmann: Absorption of Röntgen rays in the case of interference, *Phys. Z.* **127**, 297–323 (1950)
- 42.37 B.K. Tanner: *X-ray Diffraction Topography* (Pergamon, Oxford 1976)
- 42.38 B.K. Tanner: Contrast of defects in x-ray diffraction topographs. In: *X-ray and Neutron Dynamical Diffraction: Theory and Applications*, ed. by A. Authier, S. Lagomarsino, B.K. Tanner (Plenum, New York 1996) pp. 147–166
- 42.39 J.E.A. Miltat, D.K. Bowen: On the widths of dislocation images in x-ray topography under low-absorption conditions, *J. Appl. Cryst.* **8**, 657–669 (1975)
- 42.40 X.R. Huang, M. Dudley, W.M. Vetter, W. Huang, C.H. Carter Jr.: Contrast mechanism in superscrew dislocation images on synchrotron back reflection topographs. In: *Applications of Synchrotron Radiation Techniques to Materials Science IV*, ed. by S.M. Mini, D.L. Perry, S.R. Stock, L.J. Terminello (Materials Research Society, Warrendale 1998) pp. 71–76
- 42.41 X.R. Huang, M. Dudley, W.M. Vetter, W. Huang, W. Si, C.H. Carter Jr.: Superscrew dislocation contrast on synchrotron white-beam topographs: An accurate description of the direct dislocation image, *J. Appl. Cryst.* **32**, 516–524 (1999)
- 42.42 X.R. Huang, M. Dudley, W.M. Vetter, W. Huang, S. Wang, C.H. Carter Jr.: Direct evidence of micropipe-related pure superscrew dislocations in SiC, *Appl. Phys. Lett.* **74**, 353–355 (1999)
- 42.43 B.W. Batterman, H. Cole: Dynamical diffraction of x-rays by perfect crystals, *Rev. Mod. Phys.* **36**, 681–717 (1964)
- 42.44 P. Penning, D. Polder: Anomalous transmission of x-rays in elastically deformed crystals, *Philips Res. Rep.* **16**, 419–440 (1961)
- 42.45 H. Klapper: Defects in non-metal crystals. In: *Characterization of Crystal Growth Defects by X-ray Methods*, ed. by B.K. Tanner, D.K. Bowen (Plenum, New York 1980) pp. 133–160
- 42.46 D. Yuan, M. Dudley: Dislocation line direction determination in pyrene single crystals, *Mol. Cryst. Liq. Cryst.* **211**, 51–58 (1992)
- 42.47 J. Miltat, M. Dudley: Projective properties of Laue topographs, *J. Appl. Cryst.* **13**, 555–562 (1980)
- 42.48 J.I. Chikawa: X-ray topographic observation of dislocation contrast in thin CdS crystals, *J. Appl. Phys.* **36**, 3496–3502 (1965)
- 42.49 S. Mardix, A.R. Lang, I. Blech: On giant screw dislocations in ZnS polytype crystals, *Philos. Mag.* **24**, 683–693 (1971)
- 42.50 W. Si, M. Dudley, C.H. Carter Jr., R. Glass, V.F. Tsvetkov: Determination of Burgers vectors of screw dislocations in 6H-SiC single crystals by synchrotron white beam x-ray topography. In: *Applications of Synchrotron Radiation to Materials Science*, ed. by L. Terminello, S. Mini, D.L. Perry, H. Ade (Materials Research Society, Warrendale 1996) pp. 129–134
- 42.51 Y. Chen, M. Dudley: Direct determination of dislocation sense of closed-core threading screw dislocations using synchrotron white beam x-ray topography in 4H silicon carbide, *Appl. Phys. Lett.* **91**, 141918 (2007)
- 42.52 Y. Chen, G. Dhanaraj, M. Dudley, E.K. Sanchez, M.F. MacMillan: sense determination of micropipes via grazing-incidence synchrotron white beam x-ray topography in 4H silicon carbide, *Appl. Phys. Lett.* **91**, 071917 (2007)
- 42.53 E.S. Meieran, I.A. Blech: X-ray extinction contrast topography of silicon strained by thin surface films, *J. Appl. Phys.* **36**, 3162 (1965)
- 42.54 W.M. Vetter, M. Dudley: The contrast of inclusions compared with that of micropipes in back-reflection synchrotron white-beam topographs of SiC, *J. Appl. Cryst.* **37**, 200–203 (2004)
- 42.55 G. Michot, K. Badawi, A.R. Halim, A. George: X-ray topographic study of crack-tip dislocation patterns in silicon, *Philos. Mag. A* **42**, 195–214 (1980)
- 42.56 B. Raghothamachar, M. Dudley, J.C. Rojo, K. Morgan, L.J. Schowalter: X-ray characterization of bulk AlN single crystals grown by the sublimation technique, *J. Cryst. Growth* **250**, 244–250 (2003)
- 42.57 G. Michot, A. George: In situ observation by x-ray synchrotron topography of the growth of plastically deformed regions around crack tips in silicon under creep conditions, *Scr. Metall.* **16**, 519–524 (1982)
- 42.58 N. Itoh, J.C. Rhee: Study of cracking mechanism in GaN/ α -Al₂O₃ structure, *J. Appl. Phys.* **58**, 1828–1837 (1985)
- 42.59 E.V. Etzkorn, D.R. Clarke: Cracking of GaN films, *J. Appl. Phys.* **89**, 1025–1034 (2001)
- 42.60 A.R. Lang, A.P.W. Makepeace: Synchrotron x-ray reticulography: principles and applications, *J. Phys. D Appl. Phys. A* **32**, 97–103 (1999)

43. Defect-Selective Etching of Semiconductors

Jan L. Weyher, John J. Kelly

In the present chapter we first briefly consider mechanisms for the etching of semiconductors (Sect. 43.1) and relate these principles to methods for controlling surface morphology and revealing defects (Sect. 43.2). Section 43.3 describes in some detail defect-sensitive etching methods. Results are presented for the classical (orthodox) method used for revealing dislocations in Sect. 43.3.1. More recently developed open-circuit (photo)etching approaches, sensitive to both crystallographic and electrically active inhomogeneities in semiconductors, are reviewed in Sect. 43.3.2. In particular, attention will focus on newly introduced etchants and etching procedures for wide-bandgap semiconductors.

43.1 Wet Etching of Semiconductors:	
Mechanisms	1454
43.1.1 Chemical Etching.....	1454
43.1.2 Electrochemical Etching	1454
43.1.3 Electroless Etching.....	1456
43.1.4 Photogalvanic Etching	1458
43.2 Wet Etching of Semiconductors:	
Morphology and Defect Selectivity	1459
43.2.1 Chemical Etching.....	1459
43.2.2 Electrochemical Etching	1459
43.2.3 Electroless Etching.....	1460
43.2.4 Photogalvanic Etching	1461
43.3 Defect-Selective Etching Methods	1461
43.3.1 Orthodox Etching	
for Revealing Dislocations	1461
43.3.2 Electroless Etching	
for Revealing Defects	1469
References	1473

Wet etching processes are widely used in the fabrication of semiconductors. There are three main application fields for this technique: device pattern formation, polishing, and visualization of damage or defects. This chapter is restricted to the description of defect-selective etching (DSE). Among the methods used for revealing and analyzing defects in semiconductors, such as x-ray topography and diffraction, transmission electron microscopy (TEM), cathodoluminescence (CL), electron-beam-induced current (EBIC), and laser scattering tomography (LST), etching has several favorable features that make the technique attractive for assessment of the quality of single crystals and device structures. These are: simple and relatively low-cost equipment, no limits to the size of samples to be examined, very quick data acquisition, and the broad range of defects that can be revealed and analyzed.

The rapid development of various etching systems and methods for different semiconductors began after

the discovery in the 1950s of a direct correspondence between the outcrops of dislocations and etch pits. Numerous review papers appeared in regular journals and books summarizing the current developments in this field [43.1–12]. Although for elemental and *classical* compound semiconductors different etching systems are well known, challenging problems arise due to the technological developments of the new generation of wide-bandgap compound semiconductors (group III nitrides and SiC). These materials are characterized by very high chemical resistance to the majority of the known acid-based etching systems, show strong polarity-related anisotropy of properties, and contain a very high density and diversity of defects, not occurring in classical compound semiconductors (e.g., inversion domains, macro- and nanopipes, pinholes, and extended stacking faults). New etching systems and more sophisticated etching methods as well as their calibration are therefore essential.

43.1 Wet Etching of Semiconductors: Mechanisms

For etching of semiconductors in solution (or in a melt) one can distinguish two mechanisms [43.7, 13]. In *chemical etching* valence electrons are exchanged *locally* between surface bonds of the semiconductor and an active agent in the etchant. When all back bonds are broken, the surface atom passes into solution. The other type of mechanism involves *free* charge carriers (valence-band holes or conduction-band electrons) which, when localized at the surface, cause rupture of surface bonds. If an electrochemical cell, with a voltage source and a counterelectrode, is used to supply charge carriers to the semiconductor, we speak of *electrochemical etching*. Both electrons and holes may cause decomposition of the solid. Alternatively, free charge carriers can be supplied from a chemical species in solution under open-circuit conditions: this is referred to as *electroless etching*. In addition, if minority carriers are required for etching, the semiconductor may be illuminated. In this case we can distinguish *photoelectrochemical etching* and *electroless photoetching*. Finally, there is a hybrid form of photoetching that requires a counterelectrode but no voltage source. This *photogalvanic etching* method has been used extensively for wide-bandgap semiconductors.

In this section we first briefly review the various etching mechanisms. This forms the basis for a consideration of defect-selective etching in Sect. 43.2, a theme that will be further developed in Sect. 43.3.

43.1.1 Chemical Etching

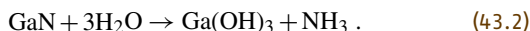
A typical example of a chemical etching reaction is that of InP in concentrated HCl solution [43.14]. By electron exchange In-P and H-Cl bonds are broken and InCl₃ and PH₃ are formed as products



The products are subsequently hydrolyzed in the aqueous solution. Etching of InP in HBr follows a similar mechanism [43.7]. The chemical etching of silicon in alkaline solution is another important reaction [43.15, 16]. These are complex, multistep processes. A general feature is that their rate is controlled by surface kinetics and, as a consequence, etching is strongly anisotropic. For example, the etch rate of the Si (111) face in KOH solution and of the (111) In face of InP in concentrated HCl solution is much lower than that of other crystallographic faces. Unlike electrochemical or electroless

etching, the kinetics of chemical etching is not dependent on the electrochemical potential of the sample.

For revealing defects in many semiconductors (Si, SiC, GaN) a NaOH/KOH eutectic is often used [43.12]. Despite the long and widespread application of this system, surprisingly little is known about the etching mechanism. In all these cases the semiconductor is oxidized, i. e., loses valence electrons, during etching. For example, GaN will be converted to Ga³⁺ (Ga(OH)₃ or Ga₂O₃) in the melt. OH[−] ions cannot act as a reducing agent, i. e., electron acceptor. We suggest that trace water in the eutectic is responsible for bond rupture and enhanced etching at defects. For example, in the case of GaN a possible reaction could be



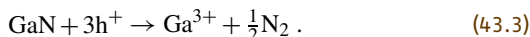
Water, strongly bound in the solvation shell of the cations and anions, is available for bond rupture. The product Ga(OH)₃ will dissolve in the melt.

43.1.2 Electrochemical Etching

For the kinetics of electrochemical etching one has to distinguish between reactions based on majority and minority carriers [43.7, 13]. In this section we first consider majority-carrier (holes in a p-type or electrons in an n-type semiconductor) and then minority-carrier reactions. To guide the reader we show in Fig. 43.1 a simple electrochemical cell with three electrodes: the semiconductor working electrode (WE), a platinum counterelectrode (CE), and a reference electrode (RE). With the aid of a voltage source (e.g., a potentiostat) the electrochemical potential V of the semiconductor can be varied with respect to that of the reference electrode. As a result, a current flows between the working electrode and the counterelectrode. This current j is measured as a function of V . The semiconductor can be illuminated to give photocurrent.

Majority-Carrier Reactions

If, in a p-type semiconductor, holes are localized at the surface (i. e., the bonding electrons are removed) the surface bonds will be broken. In the case of GaN, three holes are required to dissolve one formula unit of the solid in acidic solution [43.17].



The solid is *oxidized*; the Ga³⁺ ions dissolve and molecular nitrogen escapes to the gas phase. From (43.3)

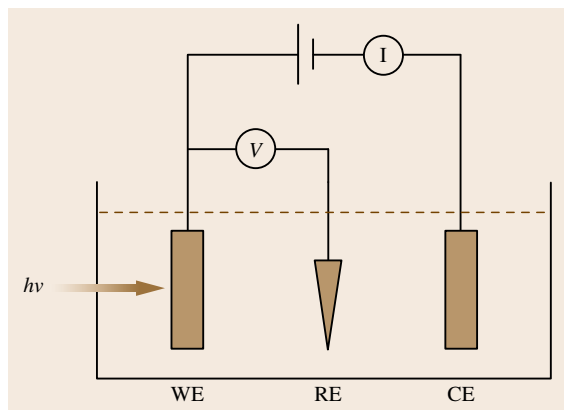


Fig. 43.1 A schematic view of a three-electrode electrochemical cell. The potential V of the semiconductor working electrode (WE) is regulated with respect to that of the reference electrode (RE) using a voltage source. As a result, a current j can flow between the working electrode and a counterelectrode (CE). In a typical experiment j is measured as a function of V either in the dark or under illumination. If electrons flow from WE to CE the current is *anodic* (j_a); an oxidation reaction occurs at the semiconductor. If electrons flow in the opposite direction (from CE to WE) the current is *cathodic* (j_c) and a reduction reaction occurs at the semiconductor

it follows that the rate of the reaction should depend on the surface hole concentration p_s , which is related to the hole concentration in the bulk p_b by

$$p_s = p_b \exp\left(\frac{eV_{sc}}{k_B T}\right), \quad (43.4)$$

where eV_{sc} is the band bending in the semiconductor at the interface with the solution. In an electrochemical experiment the band bending, and thus the reaction rate, can be varied by means of the applied potential V . A change in the applied potential can lead to a potential drop across the space-charge layer of the semiconductor (Fig. 43.2) and across the double layer (Helmholtz layer) in solution. For simplicity, we neglect the latter; this will not markedly affect the argument in this section [43.7, 13]. In that case the band bending is given by

$$eV_{sc} = e(V - V_{fb}), \quad (43.5)$$

where V_{fb} is the flat-band potential. At this potential, an important reference point in semiconductor electrochemistry, there is no space-charge layer or electric field present at the semiconductor surface (see the center

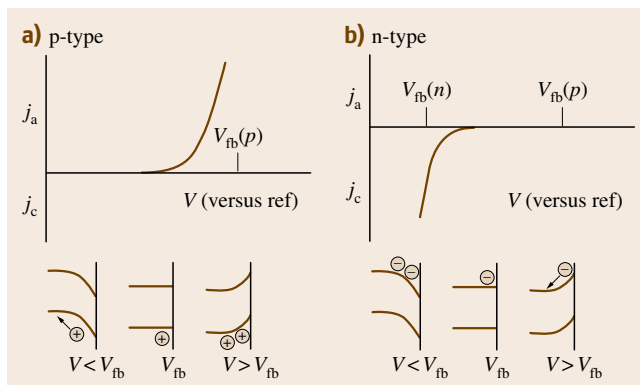


Fig. 43.2a,b Current-potential characteristics for majority-carrier reactions at (a) a p-type and (b) an n-type semiconductor. In case (a) accumulation of valence-band holes at the surface leads to oxidation of the electrode and an anodic current in the external circuit. The flat-band potential ($V_{fb}(p)$) is denoted, as well as energy-band schemes of the semiconductor at the interface with solution. In case (b) accumulation of electrons at the surface causes the reduction of H^+ ions or H_2O to hydrogen or, in some cases, the reduction of the semiconductor. Note: the difference in flat-band potential for n- and p-type forms of the same semiconductor corresponds to the difference in Fermi levels of the two types

picture at the bottom of Fig. 43.2a). At potentials considerably negative with respect to the flat-band potential of a p-type semiconductor ($V < V_{fb}(p)$) the surface hole concentration is very low ($p_s \ll p_b$): this corresponds to depletion. Oxidation reactions requiring holes cannot take place and no current flows in the external circuit. At potentials approaching $V_{fb}(p)$ an *anodic* current is measured which increases exponentially with increasing potential (Fig. 43.2a). For almost all semiconductors this process involves oxidation and dissolution of the solid: anodic etching (as in (43.3)). A reduction reaction at the counterelectrode (e.g., hydrogen evolution) provides the charge carriers required to oxidize the semiconductor. The anodic current density can be converted to an etch rate by applying Faraday's law [43.7]. It is clear that the etch rate can be simply regulated via the applied potential.

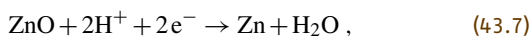
Because of the absence of holes in the valence band, anodic oxidation is not possible with an n-type semiconductor (in the dark). Instead reactions involving electrons via the conduction band can be expected. In aqueous solution this is generally the reduction of protons at low pH [43.18]



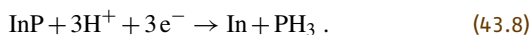
or of water at higher pH



giving hydrogen evolution. Since the surface electron concentration increases exponentially with decreasing potential, i.e., $n_s = n_b \exp(-eV_{sc}/k_B T)$, the rate of the cathodic current associated with these reactions also increases markedly (Fig. 43.2b). (In this case oxidation of water at the counterelectrode provides the electrons required at the semiconductor working electrode.) For a few semiconductors the presence of electrons at the surface can give rise to decomposition of the solid. For example, at negative potential the n-type semiconductor ZnO is electrochemically reduced



a reaction that competes with hydrogen evolution [43.18]. Another example is n-type InP [43.19]



Zinc and indium are reactive metals that dissolve readily in acidic and alkaline solution.

Minority-Carrier Reactions

Reactions requiring minority carriers (electrons in a p-type or holes in an n-type semiconductor) can be observed when the electrode is illuminated with

suprabandgap light. What is important for etching is the effective spatial separation of the photogenerated electrons and holes (the prevention of recombination) allowing the minority carriers to react at the surface.

In a p-type semiconductor electrons and holes generated by light are separated by the electric field of the space-charge layer at negative potentials (see inset in Fig. 43.3a). At the surface the electrons are used for the reduction of H^+ ions or H_2O (43.6a,b). In the case of p-type InP the semiconductor itself is decomposed under illumination (43.8). The photogenerated holes are swept to the back contact and registered as a cathodic photocurrent in the external circuit. The constant limiting photocurrent at negative potential generally depends on the light intensity. At more positive potentials going towards the flat-band condition the electric field at the surface decreases and electron-hole recombination competes with the electrochemical reaction of the electrons. Because of the importance of surface recombination at semiconductor electrodes in solution and the poor kinetics of reactions such as hydrogen evolution, the onset of photocurrent is generally at a potential considerably negative with respect to the flat-band value (up to 0.6 V), in contrast to a Schottky diode.

Holes created by suprabandgap light in an n-type semiconductor can give rise to photoelectrochemical oxidation of the solid (43.3). As in the case of the p-type electrode, electron-hole recombination generally dominates at potentials close to V_{fb} (Fig. 43.3b). The onset of photocurrent, anodic in this case, is at positive potentials where the electric field moves the holes to the surface, causing oxidation of the semiconductor: an anodic photocurrent is measured. For both cases, n- and p-type, the etch rate depends not only on the applied potential but also on the light intensity.

43.1.3 Electroless Etching

In electrochemical etching, the charge carriers are supplied to the semiconductor-solution interface via an external circuit. The disadvantage of this approach is the need for a counterelectrode, a voltage source, and, in well-defined experiments, a reference electrode (Fig. 43.1). Etching of semiconductors under open-circuit conditions is possible, in principle, if the charge carriers can be supplied from a redox species in solution [43.13]. While electron injection from solution into the conduction band of semiconductors can occur, this generally does not lead to decomposition. On the other hand, extraction of electrons from the valence band (i.e., *injection of holes* into the band) can be used for etching many semiconductors of both p- and n-type

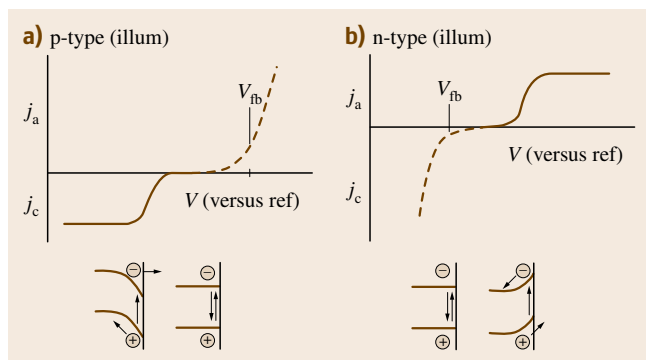
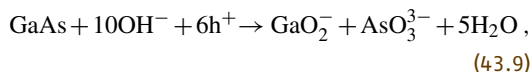


Fig. 43.3a,b The influence of suprabandgap illumination (illum) on the current-potential characteristics of (a) a p-type and (b) an n-type semiconductor. In case (a) the electric field of the space-charge layer drives the photogenerated minority carriers (electrons) to the surface, where a reduction reaction takes place. The holes are registered as a cathodic photocurrent in the external circuit. At positive potentials, electrons and holes recombine. In case (b) holes migrate to the surface, causing oxidation of the semiconductor: an anodic photocurrent is measured. In both cases the majority-carrier processes (Fig. 43.2) are shown as *dashed lines*

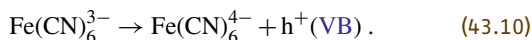
(see the next paragraph). There is another form of electroless etching in which minority carriers are generated by suprabandgap light. This will be dealt with in the paragraph *Electroless Photoetching*.

Electroless Etching in the Dark

The principle of electroless etching is shown in Fig. 43.4 for a p-type semiconductor, e.g., GaAs, in an alkaline solution containing an oxidizing agent (a strong electron acceptor) such as the $\text{Fe}(\text{CN})_6^{3-}$ ion [43.20]. Two electrochemical reactions occur: the oxidation of the semiconductor which, in the case of GaAs, requires six valence-band holes



and the reduction of the oxidizing agent by hole injection into the valence band (VB)



The potential dependence of the rates of these two reactions is shown in Fig. 43.4. The form of the anodic current–potential curve (a) for reaction (43.9) has been introduced before. Reduction of the oxidizing agent (43.10) starts at the equilibrium (Nernst) potential of the

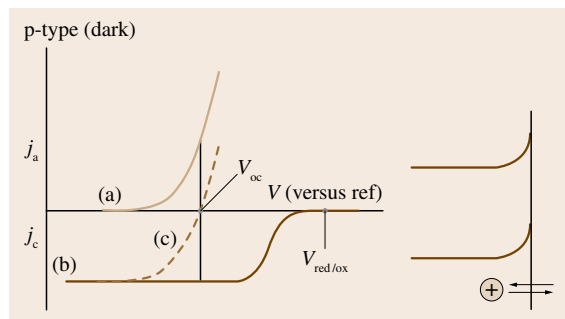


Fig. 43.4 The principle of electroless etching of a p-type semiconductor. Curve a is the anodic current–potential curve for oxidation/dissolution of the electrode. Curve b shows the cathodic current–potential curve for reduction of the oxidizing agent by hole injection into the valence band. This reaction starts at the equilibrium potential $V_{\text{red/ox}}$ and its rate becomes diffusion limited at negative potentials. The current measured with such a system, i.e., the sum of the anodic and cathodic contributions, is shown as a *dotted line*. At the open-circuit potential V_{oc} the two *partial* currents are equal ($j_a = j_c$). This is shown in the schematic diagram on the *right*. It is clear that at V_{oc} the semiconductor is etched

$\text{Fe}(\text{CN})_6^{3-}/\text{Fe}(\text{CN})_6^{4-}$ redox couple. The rate increases as the potential is made negative (curve b, Fig. 43.4). In the present case, the rate finally becomes diffusion controlled, i.e., the cathodic current is independent of the applied potential. In an electrochemical experiment, the measured current–potential curve (c) is the sum of the two *partial* curves a and b.

From Fig. 43.4 it is clear that at the open-circuit potential, indicated by V_{oc} , the two electrochemical reactions (43.9) and (43.10) occur at a significant rate; the anodic and cathodic currents are equal ($j_a = j_c$). For this system the electroless etch rate is determined by mass-transport-controlled hole injection (curve b). From this it follows that the etch rate can be enhanced by either increasing the concentration of the oxidizing agent in solution or by improving the hydrodynamics of the system.

In a similar way holes injected by $\text{Fe}(\text{CN})_6^{3-}$ into the valence band of n-type GaAs will give rise to etching at open-circuit potential. From this discussion it is clear that, for electroless etching of n-type and p-type materials, the oxidizing agent must be capable of extracting electrons from the valence band of the solid; the electron acceptor levels of the oxidizing agent must correspond in energy to the valence band of the solid. For wide-bandgap semiconductors such as GaN and SiC with an energetically low-lying valence band this is no longer possible. Even the strongest oxidizing agents fail to inject holes under normal conditions. Consequently, electroless etching is not possible for these materials.

Electroless Photoetching

As for photoelectrochemical etching that depends on minority carriers, electroless etching may also be promoted by illumination with suprabandgap light [43.21–23]. The principle is shown schematically in Fig. 43.5a. At open-circuit potential a photon generates an electron–hole pair. An electron acceptor in solution (Ox^+) captures the electrons very effectively from the conduction band, allowing the holes to break surface bonds and thus cause etching. The electron acceptor in this case is different from that required for electroless etching in the dark: its acceptor levels must correspond to the conduction band of the solid and thus be higher in energy. For electroless photoetching the rates of reaction of electrons and holes at the surface are equal and must be higher than the rate of electron–hole recombination.

Electroless photoetching can be understood in electrochemical terms on the basis of Fig. 43.5b for an n-type semiconductor. As in Fig. 43.4, the two partial

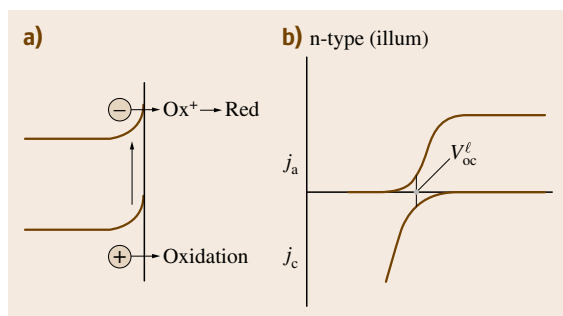


Fig. 43.5a,b The principle of electroless photoetching of an n-type semiconductor. Light generates electron-hole pairs (a). The electrons are captured by an electron acceptor (Ox^+) in solution. The holes cause oxidation and dissolution of the semiconductor. These reactions compete with electron-hole recombination. (b) Shows the current-potential characteristics of the two processes: photoanodic oxidation of the semiconductor (by minority carriers) and cathodic reduction of the oxidizing agent (by majority carriers). At the open-circuit potential under illumination (illum) V_{oc}^{ℓ} both reactions occur at the same rate ($j_a = j_c$) and the semiconductor is photoetched

current-potential curves are shown: (a) for the photoanodic oxidation of the semiconductor via the valence

band and (b) for the reduction of the electron acceptor via the conduction band (this reaction, involving majority carriers, can occur in the dark). At the open-circuit potential under illumination V_{oc}^{ℓ} both reactions occur and the semiconductor is photoetched. From this description it is clear that the systems shown in Fig. 43.3 will not give rise to photoetching. For example, the photocathodic reduction reaction at the p-type electrode (Fig. 43.3a) is only observed at negative potentials, a range in which the semiconductor cannot be oxidized (see anodic curve). In these cases the kinetics of the minority-carrier reaction is poor and electron-hole recombination dominates in the vicinity of the flat-band potential.

43.1.4 Photogalvanic Etching

For the case in which the rate of the majority-carrier reaction (e.g., electron transfer in the example of Fig. 43.5) is hindered by unfavorable kinetics, photoetching under open-circuit conditions may be promoted by short-circuiting the semiconductor to a noble metal in solution [43.24, 25]. A metal can be chosen that *catalyzes* the majority-carrier reaction (this may be the reduction of oxygen, naturally present in solution, or an added oxidizing agent). The principle is shown in Fig. 43.6a. Illumination creates in the semiconductor electrons and holes that are separated by the electric field of the space-charge layer. The holes react at the surface, causing oxidation and etching. The electrons, instead of having to react at the semiconductor-solution interface, now pass to the metal via the external circuit. Reduction of the oxidizing agent from solution occurs at the metal.

The corresponding electrochemical picture is shown in Fig. 43.6b. Curve a represents the potential dependence of the current of the illuminated n-type semiconductor electrode, while curve b is the cathodic current-potential curve measured in a separate experiment at the metal. Under open-circuit conditions (V_{oc1}^{ℓ}) the two currents must be equal ($j_a = j_c$). From Fig. 43.6 it is clear that photoetching will occur in this case. The ratio of the surface areas of semiconductor and metal exposed to solution is important for the photoetch rate. An increase in the area of the metal leads to an increase in the rate of reduction of the oxidizing agent (curve c). This causes a shift in the open-circuit potential to V_{oc2}^{ℓ} ($> V_{\text{oc1}}^{\ell}$) and an increase in the photoetch rate [43.25].

The principle shown in Fig. 43.6 is that of a galvanic cell (the semiconductor is the anode, the metal the

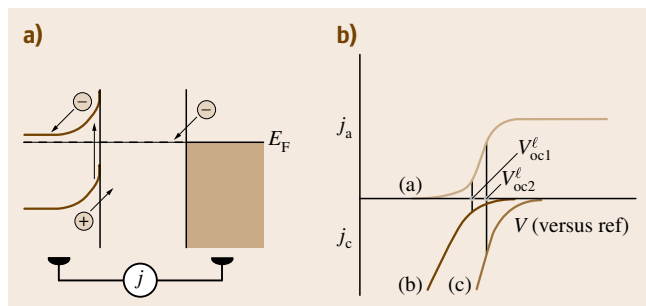


Fig. 43.6a,b The principle of photogalvanic etching. An n-type semiconductor is short-circuited to a metal in solution (without a voltage source). Electrons and holes generated by light (a) are separated by the electric field at the semiconductor surface. The holes cause etching. The electrons pass to the metal, where an oxidizing agent is reduced. Since the two electrodes are short-circuited, the Fermi level E_F is constant in the system. (b) shows the corresponding electrochemistry. Curve a gives the potential dependence of the minority-carrier reaction (photoanodic oxidation). Curve b describes reduction of the oxidizing agent (via majority carriers). The open-circuit potential is V_{oc1}^{ℓ} . If the surface area or the catalytic activity of the metal is increased (curve c) the open-circuit potential shifts to V_{oc2}^{ℓ} and the photoetch rate is significantly increased

cathode) that operates under illumination. It is, in fact, a solar cell that could supply electrical energy. This type of etching we refer to as *photogalvanic*.

Photogalvanic etching has an advantage over photoelectrochemical etching in that a voltage source is not required. However, the experiment is less well defined.

The open-circuit potential, and thus the photoetch rate, depend on what is happening at the metal, i.e., its active area, (catalytic) activity etc. An Ohmic resistance in the system, e.g., a poor contact to the semiconductor, complicates the picture [43.25] and can give rise to a considerable reduction in etch rate.

43.2 Wet Etching of Semiconductors: Morphology and Defect Selectivity

In the kinetics of wet etching of solids two types of limitation of the etch rate can be distinguished:

- **Surface kinetics:** an interfacial chemical step is rate limiting. In this case the crystallographic orientation of the surface is generally important (etching may be anisotropic). The activation energy, due to a chemical process, is high (> 40 kJ/mol). These are clearly conditions which may favor defect revealing.
- **Mass transport:** the rate-limiting step is convective diffusion of active etching species from solution to the surface, or of etching products away from the surface. The activation energy is considerably lower (< 20 kJ/mol), being due to the temperature dependence of the diffusion coefficient (i.e., of the solution viscosity). Etching in this case has a *polishing* effect: the concentration gradient responsible for dissolution is higher at protrusions and lower at recessed areas of the surface, thereby giving rise to surface leveling. This effect is enhanced if a soluble surface film is involved in the etching process.

In this section we consider briefly the surface morphology and the basis for defect selectivity in the etching systems described above.

43.2.1 Chemical Etching

The chemical etchants considered in Sect. 43.1.1 (concentrated HCl or HBr for InP, concentrated alkaline solution for Si) are kinetically controlled systems: they show strong anisotropy. The atomic structure of the surface is important in determining etching morphology; this is very clear in the Si case [43.15, 16]. Such etchants may be highly defect selective, e.g., HBr for InP [43.26]. Eutectic etching corresponds to this class. Since the etch rate at *disturbed* areas of the surface (e.g., at dislocations) is high, etch pits result in this case. In Sect. 43.3.1 defect revealing in these chemical etchants is considered in more detail.

Chemical etching, on the other hand, may also be mass-transport controlled. Etching of III–V semicon-

ductors (GaAs, InP) in aqueous solutions of halogens (chlorine, bromine, iodine) follows a chemical mechanism. The etch rate may be controlled by either kinetics or diffusion; this is also the case for etchants based on hydrogen peroxide [43.7]. Kinetic control gives defect selectivity [43.26]. Under mass-transport-controlled conditions these etchants are used for surface preparation and polishing. In the case of the halogens, water may be replaced as a solvent by an alcohol; bromine in methanol is a widely used etchant for GaAs.

43.2.2 Electrochemical Etching

The degree of defect selectivity in electrochemical etching depends on whether majority or minority carriers are responsible for etching.

Majority-Carrier Reactions

The kinetics of electrochemical etching of *p-type* semiconductors can be sensitive to surface structure: the rate constants of reactions such as those given by (43.3) may depend on surface properties, e.g., on whether the surface is Ga or N terminated. The defect selectivity of such anodic etching of *p-type* materials has not been studied much; it seems, however, in most cases to be inferior to that of other methods described in this chapter.

Anodic etching may be mass-transport limited. For example, for GaAs in alkaline solution the exponentially increasing current observed at positive potentials (Fig. 43.2a) levels off, becoming potential independent. This is due to limitation of the dissolution process by mass transport of OH^- ions in solution (43.9). The anodic etch rate depends on both the OH^- concentration and the hydrodynamics [43.20]. Another example is the anodic etching of *p-type* Si in acidic fluoride solution [43.27]. In both cases the semiconductor is *electropolished*.

Cathodic decomposition of *n-type* semiconductors via conduction-band electrons (as in (43.7)) is clearly not an attractive approach to etching. However, *de Wit* et al. [43.18] have shown that electrochemical reduction

of polycrystalline ZnO films reveals very clearly the grain boundaries. This indicates that, in certain cases, this approach could perhaps be interesting for defect revealing.

Minority-Carrier Reactions

Crystallographic and other defects usually give rise to electronic states in the bandgap of semiconductors. Such states can act as centers for very effective recombination of electrons and holes. In the onset of the anodic photocurrent–potential curve (Fig. 43.3b) surface recombination competes with the electrochemical reaction: holes required for dissolution of the solid are lost by recombination. This gives a significantly reduced etch rate at the surface defects, which show up as hillocks [43.7, 21, 28–31]. At positive potentials the photocurrent becomes independent of potential: the band bending at the surface is sufficient to separate effectively the photogenerated electrons and holes, thus preventing recombination. The limiting photocurrent can be determined by the light intensity or by mass transport in solution [43.25]. In the latter case electropolishing can be achieved.

43.2.3 Electroless Etching

As in Sect. 43.1.2 we must make a distinction here between electroless etching in the dark and under illumination. In this section we also consider an exceptional class of electroless system: Sirtl and adapted-Sirtl etchants.

Electroless Etching in the Dark

Since electroless etching requires strong oxidizing agents whose acceptor levels show a significant overlap with the valence band of the semiconductor, the rate of hole injection (e.g., (43.10)) is generally high and the etch rate is mass-transport controlled. In such a case one would not expect defect selectivity. However, in previous work [43.7, 20] we have shown that, since defects represent highly reactive areas on the surface, a galvanic cell can be formed between such areas and the more *noble* perfect surface: holes injected over the whole surface are used to etch preferentially defective areas, thus revealing defects as etch pits. This effect is expected when the etch rate is determined by the hole injection reaction (e.g., (43.10)). If, on the other hand, the oxidation reaction (43.9) is rate limiting and diffusion controlled, defects are not revealed. Instead polishing is observed. This subtle difference between the two cases can be understood on the basis of the electrochemistry

of the systems [43.20]. In chemical etching systems free charge carriers (holes in the valence band) are not involved. Consequently, galvanic effects are not observed with chemical etchants.

Electroless Photoetching

As in the case of photoelectrochemical etching, electron–hole recombination competes with open-circuit photoetching. Etchants with H_2O_2 as electron acceptor have been used successfully to reveal defects in III–V semiconductors such as GaAs, GaP, and GaAsP [43.7, 21, 32].

Sirtl-Type Etchants

In 1961 *Sirtl* and *Adler* developed an etchant for Si based on aqueous solutions of CrO_3 and HF [43.33]. This *Sirtl etchant* proved very effective in revealing crystallographic defects in various orientations of Si. In addition, the system has been used for the delineation of junctions between layers of different dopant concentration. Subsequently, a modified form of the Sirtl etch was proposed for GaAs [43.34]. This system, termed diluted Sirtl with light (**DSL**), was highly successful in the characterization of III–V semiconductors. With the appropriate choice of solution composition, all crystallographic defects could be revealed in n-type, p-type, and semi-insulating GaAs with high sensitivity. A special feature of this system is the exposure of defects as hillocks during etching, not only under illumination but also in the dark.

The electrochemistry of Si in Sirtl and of GaAs in **DSL** etchants has been studied thoroughly [43.35–39] and far-reaching conclusions could be drawn with regard to etching mechanisms. It was shown that, except at very high HF concentrations, the dissolution of both semiconductors follows an electroless mechanism: the holes required for oxidation of the semiconductor are supplied by a Cr VI complex in solution.

In the case of GaAs [43.35–37] three ranges of etchant composition could be defined on the basis of the concentration ratio of HF to CrO_3 . For $[\text{HF}]/[\text{CrO}_3]$ ratios below ≈ 10 and $[\text{HF}] < 10 \text{ M}$, the dissolution process is kinetically controlled (range A). In the dark p- and n-type etching kinetics are the same. Defects are revealed as hillocks and the defect sensitivity of n-type GaAs is higher. Illumination with suprabandgap light enhances both the etch rate and defect sensitivity of n-type GaAs but has no effect on p-type. For $[\text{HF}]/[\text{CrO}_3] > 20$ and $[\text{HF}] < 10$ (range B), etching is controlled by mass transport of the Cr VI complex in solution. Defect sensitivity is low for both p- and n-type

crystals. For solutions containing a HF concentration above 10 M (range C) a purely chemical attack on Si by HF species very likely occurs; this is analogous to the reaction between InP and HCl in (43.1).

An important feature of the electroless system is the formation of a passivating surface layer that contains both Cr VI and Cr III species. In range A the coverage by the surface film is high. Etching kinetics are determined by film formation (due to hole injection from Cr VI) and film removal (via intermediates of the semiconductor oxidation reaction with the aid of HF). In range B at relatively high HF concentration, the surface coverage decreases to low values. Hole injection by Cr VI, and thus GaAs oxidation/dissolution, are limited by mass transport of the oxidizing agent.

Defects are revealed as hillocks or ridges on the surface of p- and n-type GaAs crystals, both in the dark and under illumination. Defect sensitivity in the dark can be explained by assuming a reduced bond strength at the defect. This results in a local increase in surface coverage by the passivating film and, consequently, a reduction in etch rate. For n-type GaAs under illumination locally enhanced recombination at defects leads to a further decrease in etch rate and improved defect sensitivity. Other morphological features of the system which were explained include surface roughening and growth striations.

A subsequent study of the Si/SiO₂ system [43.38, 39] showed features very similar to those observed in DSL, including the importance of the formation of an adsorbed mixed-valence chromium complex during etching.

43.2.4 Photogalvanic Etching

Photogalvanic dissolution of an n-type semiconductor is, in many respects, similar to that of photoelectrochemical dissolution: in the latter, the photocurrent at fixed light intensity is regulated via the applied potential; in the former, the photocurrent is determined by the rate of reaction of the oxidizing agent at the metal electrode, which depends on concentration, and the electrode area and (catalytic) activity. In photogalvanic etching, conditions can be chosen to correspond to the rising part of the photocurrent–potential curve (Fig. 43.3b); in this case competition between dissolution and recombination gives defect selectivity in many systems. Alternatively, a photocurrent limited by mass transport in solution can be achieved by ensuring that the hole flux to the surface (dependent on light intensity) is much higher than the diffusion of a rate-determining species (e.g., OH[−] ions) in solution. In this case photogalvanic polishing is obtained [43.25].

43.3 Defect-Selective Etching Methods

In this section we consider in more detail methods for defect-selective etching (DSE). We distinguish two types of system, namely:

- Orthodox, also called classical or preferential, etchants (strong acids, molten bases); these are, in fact, the chemical systems described in Sects. 43.1.1 and 43.2.1.
- Newer systems based on electroless etching in the dark and under illumination, including photogalvanic etching.

43.3.1 Orthodox Etching for Revealing Dislocations

In this subsection, factors determining the kinetics of formation of pits and their morphology are described, as is the role of thermodynamics, i.e., the elastic energy of dislocations, as well as the calibration of these orthodox etchants and special applications.

Kinetics-Related Conditions

The mechanism of pit formation in semiconductors is governed by kinetically controlled, surface chemical reactions in both acidic and molten-salt etches. The details and some examples of etching systems have been described in Sects. 43.1.1 and 43.2.1. This etching method was discovered and used as early as the 19th century for disclosing the crystallographic symmetry of natural crystals, which was read from the shape of etch pits on the crystal faces. When the association between the pits and dislocations was found, the etch pit density (EPD) became a standard parameter describing the structural quality of semiconductor single crystals and substrates for device producers. Apart from the density of dislocations, much information can be obtained from the morphology of the etch pits, provided the basic requirements for formation of well-developed pits are fulfilled. These criteria were discussed in detail in earlier reviews [43.5, 6, 8] and are summarized in the following. The formation of pits proceeds via repeated nucleation

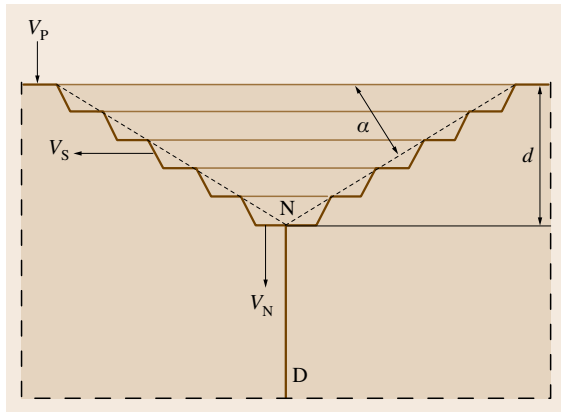


Fig. 43.7 Schematic drawing of an etch pit originating at a dislocation (D)

events at the emerging point of a dislocation on the etched surface, as shown in Fig. 43.7. Once the stable nucleus (N) is formed it grows further by horizontal step movement.

For practical applications, i. e., for obtaining clearly visible etch pits, the rate of formation of nuclei (V_N) must be larger than the step propagation velocity (V_S), while the rate of etching of the perfect surface (V_P) should be as low as possible (preferably zero). These criteria can be achieved by optimizing the etching temperature and the composition of the etchants, but the actual morphology of the etch pits, particularly the inclination angle of the side walls α , also depends on other factors such as the degree of decoration of dislocations (the presence of Cottrell atmospheres) and the type of dislocation. As an example, Fig. 43.8a shows the result of DSE of Ga-polar GaN in molten salts: deep pits

are formed with $\alpha = 25\text{--}50^\circ$ as derived from atomic force microscopy (AFM) section analysis in Fig. 43.8b. Etching of the same material in hot phosphoric acid or in a mixture of phosphoric and sulfuric acids (HH etch) yields very shallow pits with α below 10° . In the latter etch large shallow pits sweep away smaller neighboring pits, which might result in the erroneous estimation of the total density of dislocations. In order to avoid underestimation of the EPD in these acidic etches, the temperature and time have to be carefully optimized [43.40, 41]. Such optimization may allow edge and mixed/screw dislocations from the diverse size of pits to be distinguished [43.41], but from our experience it can be concluded that the procedure has to be repeated for samples grown in different conditions.

Factors Influencing Pit Morphology

There are a number of factors which may influence the morphology and relative size of etch pits formed on dislocations. These are:

- Crystallographic orientation (symmetry) of the etched surface
- Polarity of surfaces in compound semiconductors
- Composition of etching medium
- Changes of chemical composition around dislocations (Cottrell atmospheres) and in the matrix
- Position of dislocations with respect to the surface
- Elastic energy of dislocations represented by their Burgers vectors.

Symmetry. The correspondence between crystallographic symmetry and the shape of etch pits in single crystals is probably one of the best recognized and most

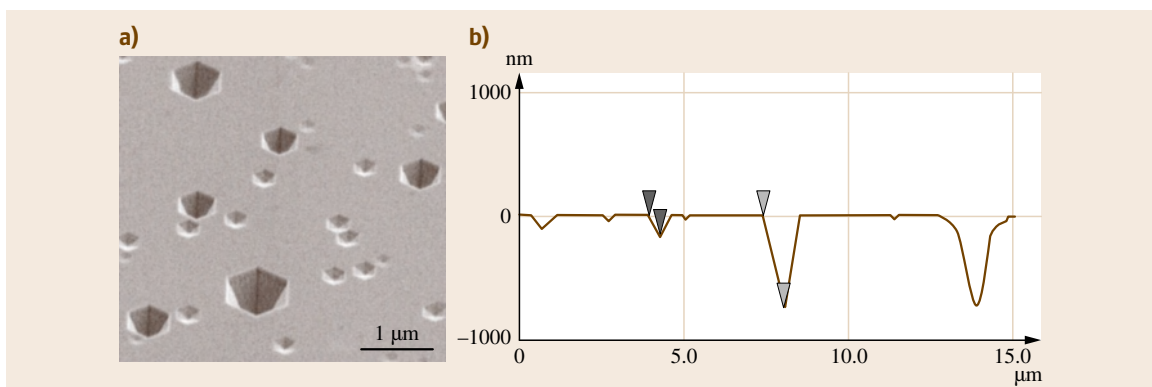


Fig. 43.8 (a) SEM image of deep pits formed on the Ga-polar surface of a GaN epitaxial layer during etching in molten KOH + NaOH eutectic. Sample tilt 45° . (b) AFM section profile across the pits from (a) (courtesy of G. Nowak)

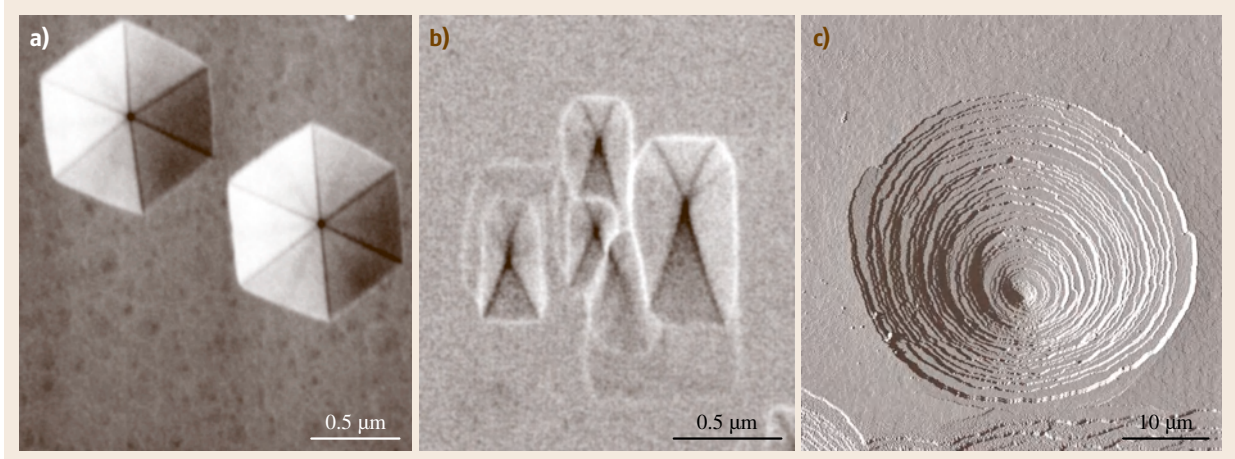


Fig. 43.9 (a,b) SEM and (c) AFM images of GaN single crystals etched on (a) (0001), (b) $(10\bar{1}0)$, and (c) $(000\bar{1})$ surfaces in molten salts (E-etch) (AFM image courtesy of S. Müller)

used advantages of the preferential etching method. Numerous etches are known for different semiconductors that show this characteristic, e.g., Sirtl etch for Si [43.33], molten KOH for GaAs [43.42], and several etching systems for InP [43.26, 43, 44]. A similar correlation has recently been shown for GaN in molten KOH + NaOH eutectic (E-etch after [43.12]) and is demonstrated in Fig. 43.9a,b: well-defined hexagonal and rectangular etch pits are formed during etching of (0001) Ga and $(10\bar{1}0)$ surfaces, respectively. It can be concluded that a properly calibrated etching method constitutes a fast and unambiguous tool for establishing the crystallographic orientation of semiconductor bulk crystals and epitaxial layers.

Polarity. Preferential etching is also sensitive to the bonding direction between atoms forming compound semiconductors. As a rule, polar surfaces show markedly different growth and etching behavior. In zincblende III–V materials (e.g., GaAs and InP) polar $\{111\}$ B surfaces are very reactive because the presence of the group V atom at this face gives a higher electron density than that of the $\{111\}$ A face. (In the extreme case the B face would have an electron pair in the dangling bond while this would be missing at the A face.) As a result of this difference it is easy to recognize the polar $\{111\}$ faces using well-known etches. The sensitivity of etching methods to the atomic configurations of the etched surfaces has an important practical application for recognition of nonequivalent $\langle 110 \rangle$ and $\langle \bar{1}\bar{1}0 \rangle$ directions on the nonpolar $\{001\}$ faces of III–V

compound semiconductors. For instance, the etch pits formed on the (001) surface of GaAs during etching in molten KOH are elongated in the $[0\bar{1}1]$ direction, as was unequivocally established by calibration with the x-ray Lang technique [43.45]. Consequently, the definition of the orientation and identification flats on the zincblende III–V substrates, given in standard commercial specifications, is based on the shape of the etch pits, as shown in Fig. 43.10.

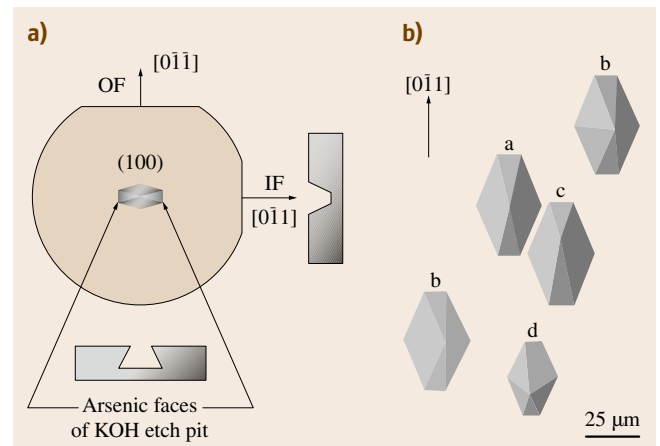


Fig. 43.10 (a) Example of commercial specification of a GaAs substrate with the description of orientation (OF) and identification flats (IF) on the basis of the shape of KOH-related etch pits. (b) Pits formed in molten KOH on the (001) surface of GaAs at dislocations differently inclined with respect to the surface

III–V materials with a wurtzite lattice (GaN, AlN) have very strong polarity-related anisotropy of properties, which shows up, for example, in markedly different chemical reactivity of (0001) Ga and (000 $\bar{1}$) N surfaces. Following standard assignment based on comparative hemispherically scanned x-ray photoelectron diffraction (HSXPD), TEM, and etching studies [43.46–48], it was shown that N-polar surfaces of GaN can be dissolved in dilute aqueous solution of KOH/NaOH even at room temperature, while Ga-polar surfaces remain intact in such etching conditions. Fast dissolution of the N-polar surface of GaN in KOH was explained by

adsorption of hydroxide ions at the negatively charged dangling bond of each nitrogen atom at this surface and subsequent formation and dissolution of gallium oxide [43.49]. As a result, numerous pyramids are formed on the (000 $\bar{1}$) N surface and, once the whole surface is covered by them, the etching process is terminated. As for Si (111) surfaces etched in concentrated KOH solution [43.15, 16], such pyramids are bounded by chemically stable low-index {1 $\bar{1}$ 01} planes and are not related to any specific defects (though for GaN this conclusion is still tentative). Similar behavior was reported for the nitrogen-polar surface of AlN [43.11] and this makes DSE of these surfaces more demanding. Dislocations on the N-polar surface of GaN single crystals can be revealed in molten eutectic [43.12] at relatively low temperatures as compared with the Ga-polar surfaces. In contrast to the Ga-polar surface, the resultant etch pits are circular, with a very irregular terraced morphology (Fig. 43.9a,c). The most convincing example of the difference of the polarity-dependent pit morphology was obtained by revealing dislocations in the vicinity of inversion domains (IDs) in Mg-doped homoepitaxial GaN [43.50]. The upper part of the image in Fig. 43.11a shows hexagonal pits formed on the Ga-polar surface while in the lower N-polar area circular pits are visible.

DSE of N-polar heteroepitaxial GaN layers is more difficult because, in addition to the high reactivity of this side, a higher density and variety of defects (e.g., inversion domains of different diameters, higher level of impurities, i. e., carrier concentration [43.51–53]) are inherent to these materials. Etching in molten salts results in fast dissolution of N-polar heteroepitaxial layers and overall roughness, without the possibility of attributing the tiny etch features to particular defects. It seems more promising to etch in hot acids, which reveals large and small inversion domains (IDs) in the form of protruding pyramidal etch features, as shown in Fig. 43.11b. However, evaluation of dislocation density in this material using orthodox etching methods does not seem to be viable.

Etchant Composition. The morphology of etch pits can be tailored by changing the ratio of constituents of the etching solution, etching conditions (e.g., temperature) or by adding so-called inhibitors. Theoretical considerations and rules were discussed and variable pit morphologies in different etching systems were demonstrated in earlier reviews [43.5, 6]. A very clear example of the dependence of the pit morphology on the etchant composition was found in the orthodox HBr–K₂Cr₂O₇ (BCA) etching system developed for InP [43.26]. In

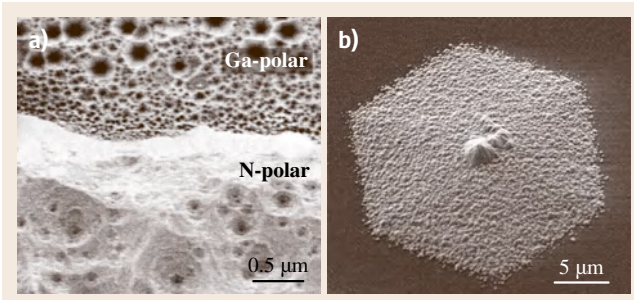


Fig. 43.11a,b SEM images of (a) GaN epitaxial layer with the neighboring Ga- and N-polar areas etched in molten E+M etch [43.45] (courtesy of G. Kamler) and (b) GaN N-polar epitaxial layer after etching in hot HH [43.46]

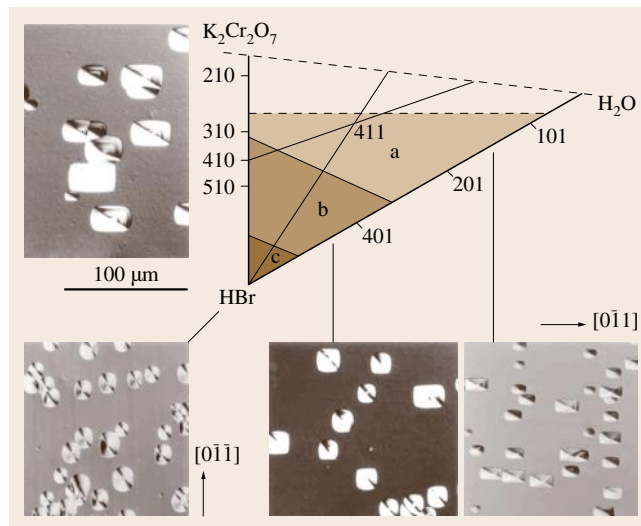


Fig. 43.12 HBr-rich corner of the BCA ternary etch system for InP. The differential interference contrast (DIC) optical images show the morphology of etch pits as a function of composition of etchants (with permission from [43.26])

the HBr-rich corner of the ternary BCA diagram there are three composition fields, denoted a, b, and c in Fig. 43.12. Etchants from these fields result in the formation of pits with different morphology: the pits formed in region b are square, while etchants from regions a and c yield rectangular pits, elongated in the $[0\bar{1}\bar{1}]$ and $[0\bar{1}1]$ directions, respectively.

The kinetics of DSE can be influenced by adding traces of ions (inhibitors) to the solution. Their role is to *poison* kinks and ledges inside the pits, which slows down horizontal movement of steps during etching (decrease of V_S in Fig. 43.7). This effect can have practical application when kinetics-related conditions of pit formation are not fulfilled, i. e., when the pits are too shallow as in etching of GaN in hot acids. It was recently shown that, by adding Al^{3+} and Fe^{3+} ions to H_3PO_4 , merging of pits on GaN heteroepitaxial layers can, indeed, be avoided and well-defined deep pits are formed [43.54].

Effect of Decoration and Composition. In semiconductors, foreign atoms (dopants, impurities) are attracted by dislocations due to the presence of a strain field and charge (Coulomb interaction). The resultant impurity (Cottrell) atmosphere may have a dual influence on the formation of etch pits:

1. By releasing the strain, the elastic energy of the dislocation is diminished, which should decrease the rate of nucleation (V_N in Fig. 43.7).
2. The chemical potential is changed and this may locally change the chemical reactivity in the given etching solution.

As was already pointed out by Amelinckx [43.2] it is difficult to predict which of these two factors will prevail. GaAs etching in molten KOH resulted in the formation of larger etch pits on so-called grown-in (i. e., strongly decorated) dislocations than on stress-induced dislocations [43.8]. A similar effect was observed in bulk GaN single crystals on which the size of pits formed on grown-in and indentation-induced dislocations was compared [43.55]. Morphology of pits can also be strongly influenced by heavy doping or alloying, as was shown for In-doped GaAs: the elongated hexagonal pits formed in molten KOH on nondoped GaAs (similar to these shown in Fig. 43.10b) were gradually transformed into regular hexagonal pits with increasing content of In [43.56].

Geometrical Position of Dislocations with Respect to the Surface. This effect seems to be obvious and was recognized already in the early 1960s [43.2] and subsequently well substantiated in numerous papers and reviews, e.g., [43.5, 8, 57, 58]. Most impressive was the work distinguishing five groups of etch pits and thereby five directions of dislocation lines in GaAs epitaxial layers after molten KOH etching [43.59]. These are: $a = \langle 001 \rangle$, $b = \langle 011 \rangle$ or $\langle 101 \rangle$, $c = \langle 112 \rangle$, $d = \langle 211 \rangle$, and $e = \langle 121 \rangle$ directions. Similar results were later obtained on bulk liquid-encapsulated Czochralski (LEC)-grown GaAs crystals and described in a review paper [43.8]. In Fig. 43.10b etch pits are shown in a GaAs substrate demonstrating the presence of four differently inclined dislocations (a – d types) in one place.

The majority of dislocations in GaN heteroepitaxial layers are perpendicular to the (0001) surfaces because

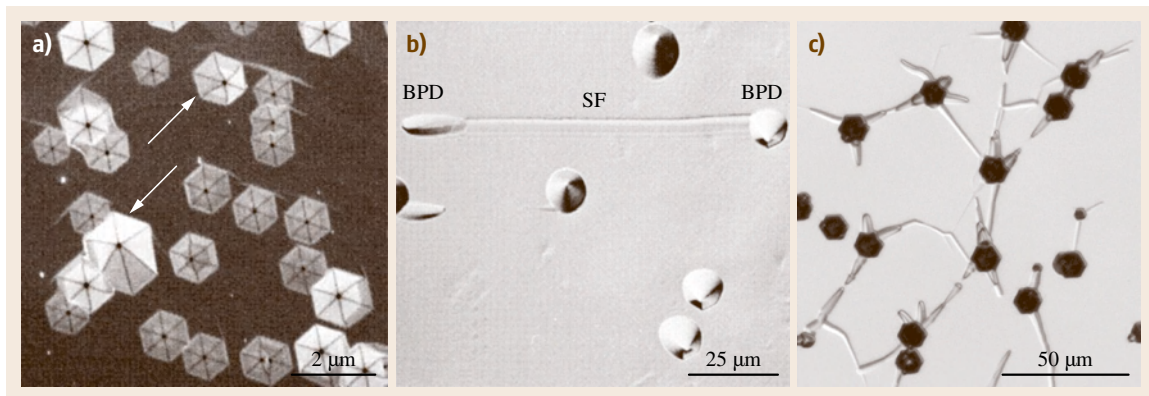


Fig. 43.13 (a) SEM image of thick HVPE-grown GaN layer after etching in molten E at 450 °C for 5 min. (b,c) DIC images of SiC substrate after etching in molten E at 520 °C for 5 min. The sample in (b) is 8° off axis

these are threading dislocations. The etch pits formed on them are, therefore, center-symmetrical, as shown in Fig. 43.9a. The same holds for bulk GaN single crystals and thick hydride vapor phase epitaxy (HVPE)-grown layers, though some inclined dislocations could be found (see two the non-center-symmetrical pits marked by arrows in Fig. 43.13a and the pit on the N-polar surface in Fig. 43.9c). In bulk and epitaxial SiC, so-called basal-plane dislocations are easily recognized from the characteristic morphology of shell-like etch pits. They are frequently observed both in SiC substrates and in 8° off-axis epitaxial layers [43.58, 60, 61]. The characteristic appearance of basal-plane dislocations (BPDs) and a bounding stacking fault (SF) in misoriented SiC is shown in Fig. 43.13b. In Fig. 43.13c, for comparison, pits are shown on an exactly (0001)-oriented SiC surface: hexagonal etch pits are on dislocations perpendicular to the surface (screw dislocations (SDs)), and grooves on dislocations almost parallel to the surface, i.e., basal plane dislocations (BPDs). In Fig. 43.13c the BPDs form dislocation nodes with SDs and a three-dimensional (3-D) network in the bulk of the material.

Thermodynamic Factors: Elastic Energy of Dislocations

From Cabrera's theory on the thermodynamics of pit formation [43.6] it follows that the critical value of the chemical potential difference ($\Delta\mu$) of a stable nucleus of a pit at the outcrop of a dislocation (N in Fig. 43.7) depends inversely on the elastic energy (E_{el}) of the dis-

location

$$\Delta\mu = 2\pi^2\Omega \frac{\gamma^2}{E_{el}}, \quad (43.11)$$

where γ is the edge free energy and Ω the molecular volume.

The elastic energy value differs for different types of dislocations [43.63]

$$E_s = Gb^2\alpha, \quad (43.12)$$

$$E_e = Gb^2\alpha \left(\frac{1}{1-\nu} \right), \quad \text{and} \quad (43.13)$$

$$E_m = Gb^2\alpha \left(1 - \nu \cos^2 \frac{\theta}{1-\nu} \right), \quad (43.14)$$

for screw, edge, and mixed dislocations, respectively (where G is the shear modulus, b the Burgers vector, α a geometrical factor, ν Poisson's constant, and θ the angle between screw and edge components of the Burgers vector of mixed dislocations). Heteroepitaxial layers of GaN are the best material for considering the influence of elastic energy of dislocations on the formation of pits during orthodox etching: in this material all three types of dislocations, including nanopipes, usually coexist. In addition, numerous TEM studies of cross-sectional specimens have showed that the vast majority of dislocations in epitaxial GaN layers are of the threading type and are perpendicular to the surface. As a result, the influence of the tilt of a dislocation line on the size and/or morphology of pits can be excluded. Figure 43.14a shows the typical surface morphology of a heteroepitaxial GaN sample after

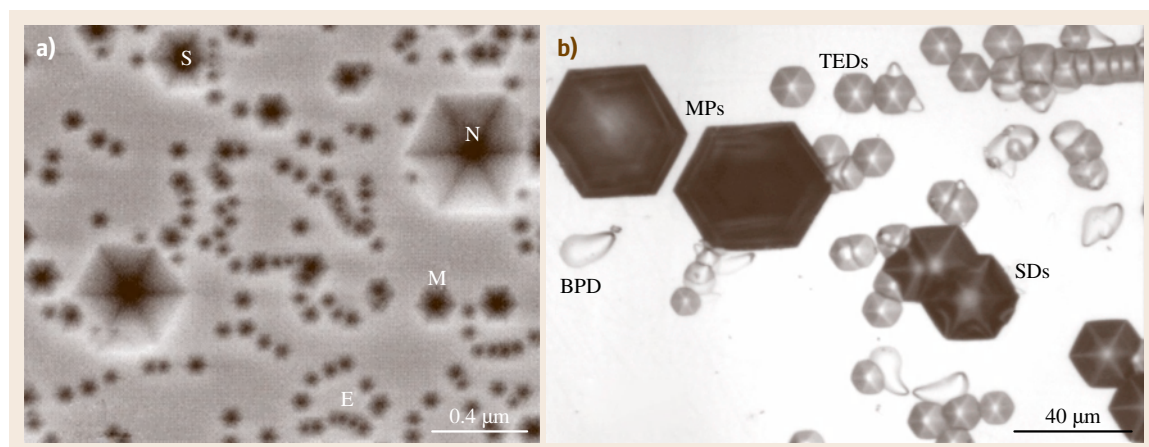


Fig. 43.14 (a) SEM image of heteroepitaxial GaN layer after etching in molten E+M. (b) Optical image of etch pits formed on different defects in 6H-SiC wafer during etching in molten KOH (with permission from [43.62])

etching in molten E+M orthodox etch (eutectic of KOH + NaOH + 10%MgO [43.64]). Four size grades (denoted N, S, M, and E) can be discerned in this material, representing nanopipes and screw-, mixed-, and edge-type dislocations, respectively. The assignment of the pit size to the type of dislocations was done on the basis of recent direct calibration of orthodox etching by TEM [43.64–66].

In the wurtzite lattice of GaN the Burgers vectors of dislocations are

$$\begin{aligned} \mathbf{b}_e &= \frac{1}{3} \langle 11\bar{2}0 \rangle, & (b_e = a, b_e^2 = a^2), \\ \mathbf{b}_m &= \frac{1}{3} \langle 11\bar{2}3 \rangle, & (b_m = \sqrt{c^2 + a^2}, \\ & & b_m^2 = 3.66a^2), \\ \mathbf{b}_s &= [0001], & (b_s = c, b_s^2 = 2.66a^2), \end{aligned}$$

$\mathbf{b}_{\text{nano}} = n \times \mathbf{b}_s$ where $n = 1, 2, \dots$, and a, c are the lattice parameters.

In the ideal lattice structure of an etched GaN sample, the size of pits should depend on the magnitude of the Burgers vector of dislocations, i.e., the largest pits should be formed on nanopipes and the smallest on the edge dislocations. This pit size sequence is indeed valid, with the exception of screw dislocations, on which the pits are usually larger than on the mixed ones. The arguments for explaining this seeming discrepancy have been discussed in recent work [43.66] and are based on the fact that both edge and mixed dislocations are characterized by a larger deformation of the lattice, i.e., the contribution of the Poisson-constant-related term in (43.12–43.14), than the screw dislocations. The resultant higher attractive forces may be responsible for more effective decoration of edge and mixed dislocations and,

in this way, for a release of strain around these defects. This, in turn, would result in a less favorable energetic condition for the formation of etch pits on edge and mixed dislocations.

The energy of defects has an even more pronounced effect on the size of pits in SiC. Very large differences between the size of pits formed on micropipes, screw, threading, and basal plane dislocations were found after an optimized etching procedure in molten KOH [43.62], as is obvious from Fig. 43.14b.

Calibration of Etching

Each new DSE system requires confirmation of its reliability in revealing all dislocations. Since the size and morphology of pits may vary depending on the type and status of dislocations, as was shown in the previous section, calibration by a direct method may allow one to identify the types of dislocation and provide an unequivocal interpretation of the etch features. Different approaches are used for this purpose, e.g., x-ray topography of etched samples [43.67] (suitable for dislocation density below 10^5 cm^{-2}), comparison with cathodoluminescence (CL) [43.68] or another calibrated etching method [43.40], sequential etching and calibration by TEM (e.g., [43.69, 70]). The latter is the most attractive because, apart from the direct association of the etch pit with the underlying defect, it yields information on the exact type of dislocation and on any additional characteristic features, such as decoration. The method became very popular especially after the introduction of the focused ion beam (FIB) technique, though the conventional cross-sectional approach is still used [43.71, 72]. Figure 43.15 shows a typical set of TEM images (specimen prepared by FIB) of the etch

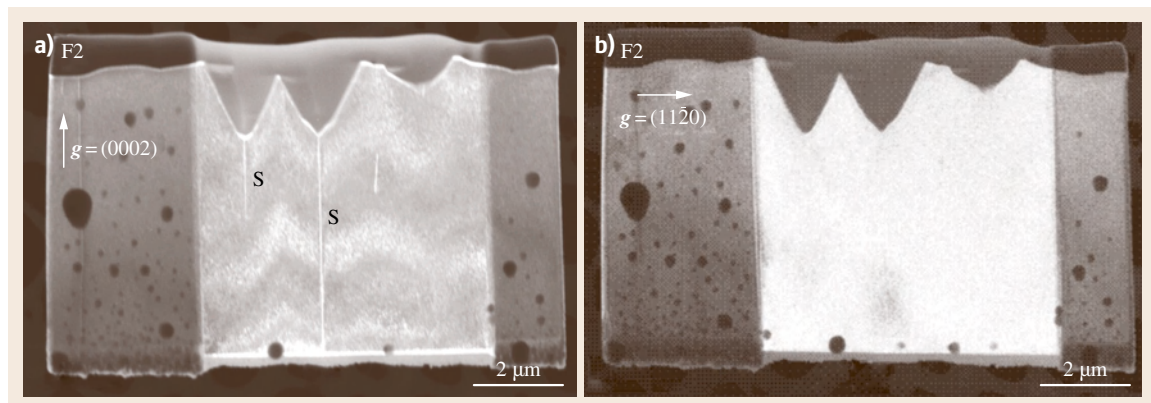


Fig. 43.15a,b Bright-field TEM images taken with different diffraction conditions showing the association of large etch pits with screw dislocations (with permission from [43.59])

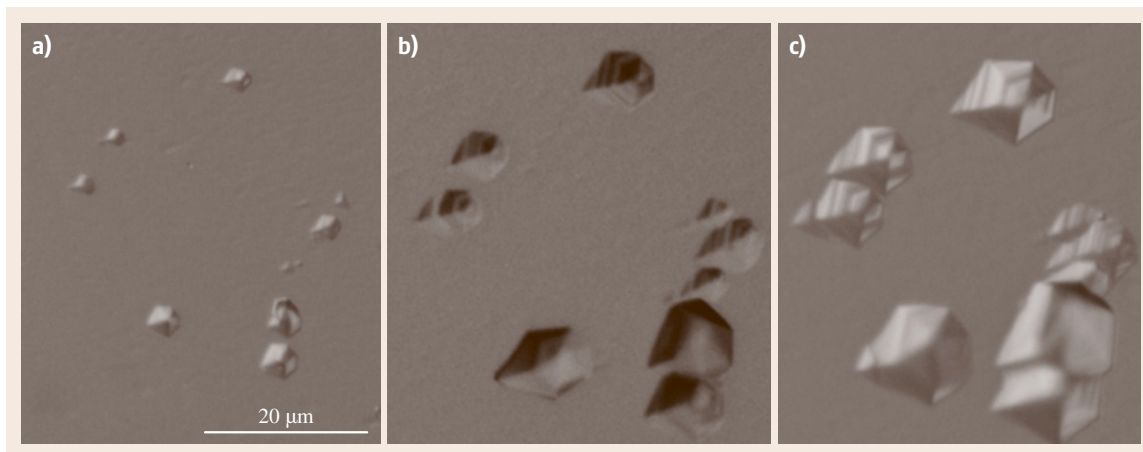


Fig. 43.16a–c DIC images of ZnO single crystal after sequential etching in 0.7% aqueous solution of HCl for (a) 30 s, (b) 60 s, and (c) 90 s

pits and underlying dislocations in thick HVPE-grown GaN. The method is particularly useful for samples with a moderate dislocation density, for which the conventional cross-sectional specimen preparation method is not effective because of the low probability of finding any defects in the thin foil.

The simplest way to verify the reliability of an orthodox etch for revealing dislocations is sequential etching: the pits formed on dislocations develop in size after each subsequent etching step and always have a point bottom indicating the position of the outcrop of the linear defect, as demonstrated by the set of images (made with the same magnification) in Fig. 43.16. Equally effective and simple is simultaneous etching of a two-sided polished sample. This method is, however,

limited to relatively thin samples (e.g., substrates for epitaxy) containing threading dislocations.

Special Applications of Orthodox Etching

Well-controlled orthodox etching has frequently been used for revealing the origin of defects in epitaxial layers and device structures. For this purpose multiple (sequential) etching and photography are employed, which allows in-depth tracing of the defects in the sample. The results presented in [43.73] illustrate well the potential of this method: the clusters of screw dislocations revealed on the top of thick SiC epitaxial layers (up to several micrometer) were shown to be formed as a result of the closing of micropipes from the substrate. A similar approach was used for tracking the origin of pairs of dislocations in SiC epitaxial layers [43.74] and conversion of BPDs from the substrates into threading edge dislocations (TEDs) in SiC epitaxial layers [43.75]. Application of orthodox etching for examination of device structures is also very attractive since it permits one to establish at which interface in multilayered samples the dislocations are nucleated. The principle of the method is based on the fact that the point-bottomed etch pits formed on dislocations are transformed into flat-bottomed pits when the interface at which nucleation occurred is reached [43.76]. The method was recently used for studying GaN-based laser structures [43.77] and was calibrated by TEM [43.78]. Figure 43.17a shows the result of etching in molten E of the laser structure similar to that from [43.78], in which the dislocations were nucleated at different interfaces (the depth of the flat-bottomed pits is different),

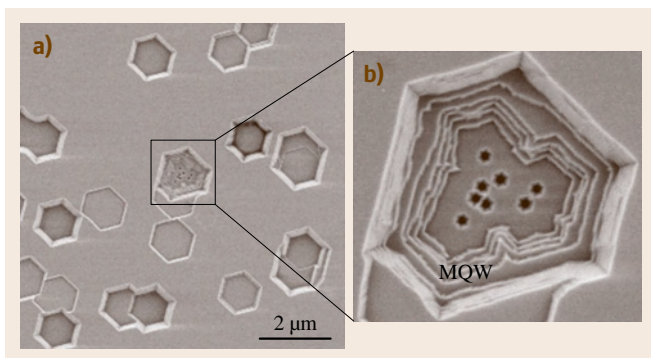


Fig. 43.17a,b SEM images of (a) MQW GaN-based laser structure after deep molten E+M etching. In (b) an enlarged fragment of image (a) is shown (etching and images: courtesy of G. Kamler)

with the exception of a cluster of dislocations propagating from the layers beneath the multiple quantum well (MQW) (see the enlarged central complex pit in Fig. 43.17b).

43.3.2 Electroless Etching for Revealing Defects

In another approach to etching, described in Sects. 43.1.2–43.1.4, free charge carriers (holes) localized at the surface cause the breaking of bonds. Holes can be supplied by an external voltage source (electrochemical etching), by an electron acceptor in solution (electroless etching) or by illumination (photoetching). Electrochemical etching has not been widely used for defect studies. Electroless etching, which operates under open-circuit conditions, has proved very successful. One of the most versatile electroless etchants for GaAs is the $\text{CrO}_3/\text{HF}/\text{H}_2\text{O}$ (DSL) system [43.37, 79]. This can be used for revealing dislocations both in the dark and under illumination. For wide-bandgap semiconductors such as GaN and SiC electroless etching in the dark is not possible (Sect. 43.1.3). In this case (photo)electrochemical or photogalvanic etching is an option. The latter is also described in the *Photogalvanic Etching* paragraph for revealing dislocations. These etching approaches can also be used for studying electrically active inhomogeneities in semiconductors. Special applications of electroless etching are dealt with in the final section.

Dislocations

We first consider the $\text{CrO}_3/\text{HF}/\text{H}_2\text{O}$ system in the dark and then two open-circuit photoetching approaches.

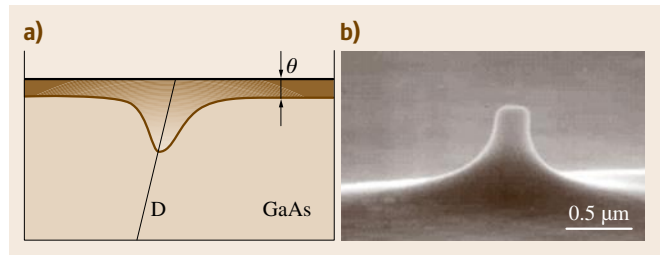


Fig. 43.18 (a) Hypothetical section profile of the thickness of the passivating layer θ formed on GaAs surface with an emerging dislocation D, immersed in $\text{CrO}_3/\text{HF}/\text{H}_2\text{O}$ etching solution. (b) SEM image of the protruding etch feature formed on a dislocation in GaAs during dark etching in the same solution

$\text{CrO}_3/\text{HF}/\text{H}_2\text{O}$ in the Dark. In this DS system (without light) the holes required for oxidation and dissolution of the semiconductor are injected into the valence band by hexavalent chromium ions in solution (Sect. 43.2.3). It has been shown that defect-selective etching in this case is determined by a surface passivating layer consisting of a Cr mixed-valence complex. The thickness of the passivating layer θ (or its coverage) determines the final morphological characteristics of the dislocation-related etch features [43.37]. The deformation field around dislocations reduces the Ga–As bond strength and, in this way, locally increases the thickness θ of the passivating layer (Fig. 43.18a). As a result during dark etching the outcrops of dislocations are revealed in the form of nanometer-size hillocks (tips), as shown in Fig. 43.18b. The surrounding Cottrell atmosphere has only a weak influence on the final shape of the etch features at the dislocation; it may contribute by diminishing the dislocation-related deformation field due to

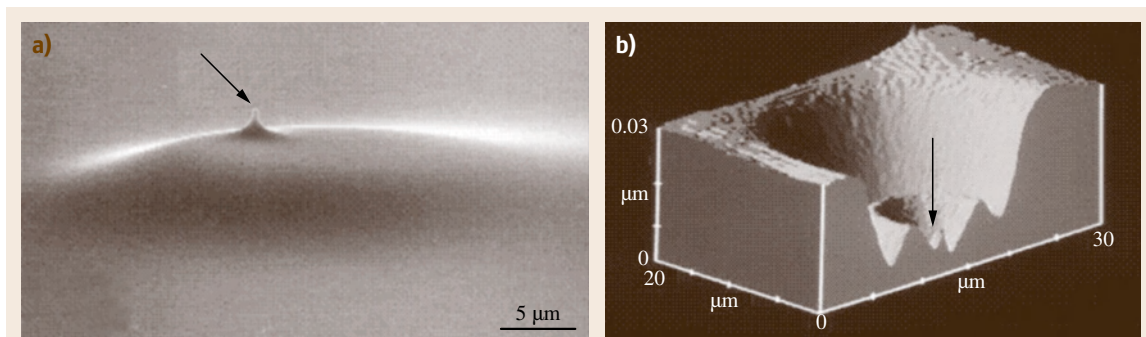


Fig. 43.19 (a) SEM and (b) phase-stepping microscopy (courtesy of P. Montgomery) images of dislocations and related Cottrell atmospheres, revealed by photoetching of n-type GaAs grown from: (a) slightly As-rich and (b) Ga-rich melt. The arrows indicate the etch features formed on dislocations

Table 43.1 Schematic representation of the surface profiles across the etch features formed on dislocations in GaAs after dark etching (DS) and photoetching (DSL) (with permission from [43.9]) (D: dislocations, dashed line: extent of electrically active zone with properties different from those of the dislocation-free matrix)

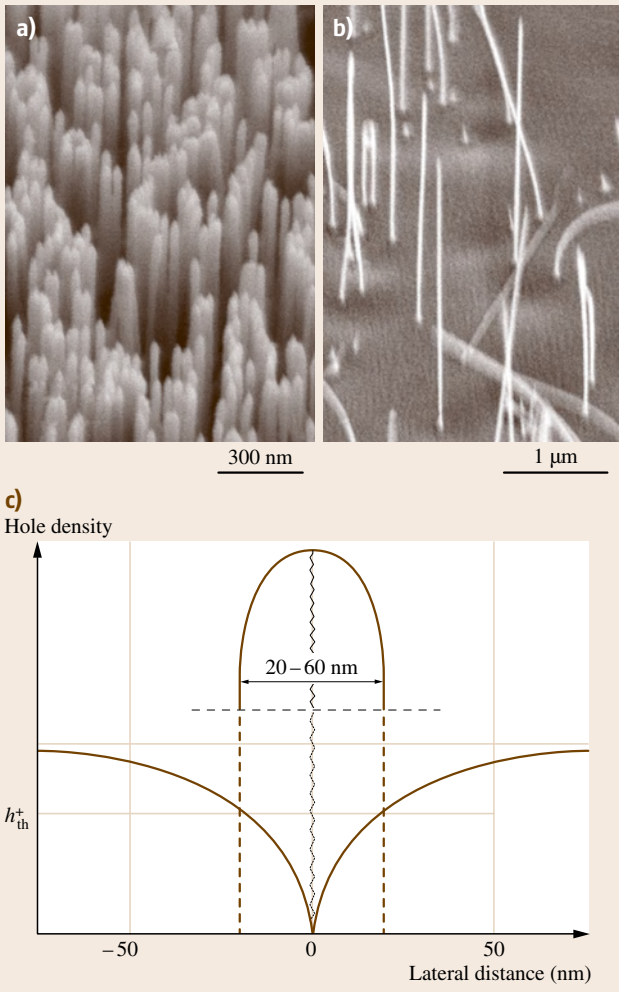
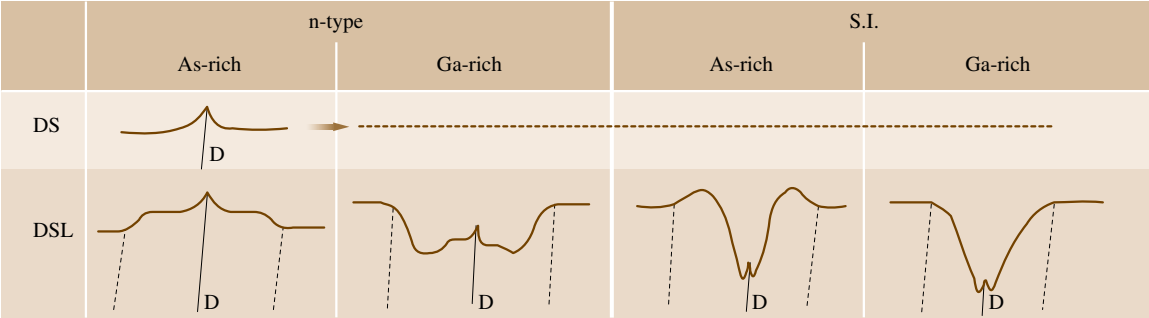


Fig. 43.20a–c SEM images of whisker-like features formed on dislocations during open-circuit photoetching of (a) high-dislocation-density MOCVD-grown and (b) low-dislocation-density HVPE-grown GaN layers. (c) Model of the formation of a whisker on a single dislocation during open-circuit photoetching of n-type GaN (with permission from [43.80]) ◀

the local increased concentration of foreign atoms or native point-type defects.

Photoetching

DSL System. When the surface of the semiconductor is illuminated with suprabandgap light during etching, complex etch features are formed on the dislocation sites. The final morphology of the etch features now depends on the electrical properties of both the dislocation and the surrounding atmosphere. Similar to etching in the dark, submicron protrusions are formed at the outcrops of dislocations (Fig. 43.19a), but now they reflect a cylindrical region depleted of carriers due to the recombination of electrons and holes at the dislocation. The dislocation-related atmospheres are revealed as either hillocks or depressions depending on their electronic nature: when the local recombination is stronger than in the matrix, the etch rate is locally decreased and large hillocks or ridges are formed [43.81] as can be recognized in Fig. 43.19a. On the other hand, the atmosphere containing excessive holes (as in GaAs grown from Ga-rich melt, in which Ga_{As}⁺⁺ double acceptors are present) locally increases the etch rate and depressions are formed around the dislocation-related protrusions (Fig. 43.19b). Such complex etch features are formed in As- and Ga-rich GaAs during DSL photoetching and the electronic nature of defects responsible for the influence

of atmospheres was disclosed by photoluminescence and EBIC studies [43.82, 83]. It was also shown that the section profile across the complex etch features around dislocations constitutes a fingerprint of the type of GaAs, as was discussed in [43.9] and demonstrated by the data in Table 43.1.

Photogalvanic Etching. Electroless etching of wide-bandgap semiconductors (GaN, SiC) can be performed only with the help of ultraviolet (UV) light and a supporting electrode (photogalvanic etching) for the reasons discussed in Sect. 43.1.4. The only widespread etching system used to date is based on aqueous solutions of KOH with dissolved oxygen as electron acceptor [43.24, 25], although more complex etching solutions containing a strongly oxidizing component ($K_2S_2O_8$) are emerging [43.85]. Since dilute KOH solutions (in the range 0.002–0.01 M KOH) are suitable for revealing dislocations, it is necessary to employ stirring during photoetching in order to ensure the supply of OH^- ions for the oxidation reaction at the surface. Other technical details and the limitations of this method have been discussed in several recent papers [43.11, 51, 52, 84, 86]. During etching of GaN in this system the recombination of electrons and holes at the dislocations is very effective; this leads to formation of whisker-like etch features with almost unlimited length (Fig. 43.20a,b). The diameter of the whiskers remains in the tens of nanometer range and represents a tube of the material from which holes are depleted due to recombination of photocarriers at the dislocation (see the model in Fig. 43.20c, in which h_{th}^+ describes the critical number of holes required for dissolution of a GaN molecule as follows from (43.3)). The fact that each whisker contains a dislocation was confirmed by direct TEM calibration of the photoetched samples [43.51, 53, 87–89].

Photogalvanic etching is also effective for revealing different defects in SiC. It was shown that dislocations, stacking faults, macropipes, and chemical inhomogeneities could be visualized in aqueous KOH solutions used with UV light [43.58]. Figure 43.21 shows a characteristic image of protruding features formed on dislocations parallel to the surface and pinned by two micropipes.

Electrically Active Inhomogeneities

Electroless photoetching constitutes an attractive tool for examination of extended electrically active inhomogeneities inherent to compound semiconductors, e.g., growth striations [43.90]. It was shown that well-



Fig. 43.21 SEM image of etch features formed on micropipes (M) and pinning dislocations (D) parallel to the (0001) Si surface of SiC substrate revealed by photoetching

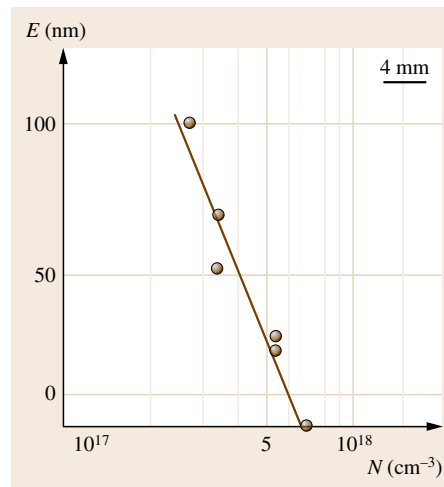


Fig. 43.22 Plot of relative etch depth E versus carrier concentration N for n-type GaAs photoetched in DSL (with permission from [43.84])

controlled photoetching is ultrasensitive to very small differences in carrier concentration both in n-type and in semi-insulating (SI) semiconductors and, after calibration by an appropriate method, can be used for quantitative evaluation of local differences in carrier concentration. Figure 43.22 shows a plot of the relative photoetch depth E of Si-doped GaAs as a function of the carrier concentration n ; the latter was determined by the EBIC method. This strong inverse dependence of E on n can be understood on the basis of the illuminated Schottky diode. Electron–hole pairs are generated by light to a depth determined by the absorption coefficient of the semiconductor. For photoetching to occur,

the valence-band holes must reach the surface. Two processes contribute. Holes created within the space-charge (depletion) layer are driven to the surface by the electric field. Since the thickness of the depletion is inversely proportional to the square root of the electron density ($W_{sc} \propto 1/n^{1/2}$), this contribution will decrease as the dopant density increases. Holes may also reach the edge of the space-charge layer by diffusion and then migrate to the surface. Photocurrent measurements on GaP Schottky diodes and p–n junctions [43.91] showed a strong inverse dependence of the apparent diffusion length of the minority carriers on the carrier concentration in the range of Fig. 43.22. As a result of these two effects, diffusion and migration, the hole flux to the surface of an illuminated SI or n-type semiconductor may be expected to decrease as the electron density increases. This, of course, will lead to a drop in photoetch rate, as shown for GaAs in Fig. 43.22.

A similar result was subsequently demonstrated for n-type GaN [43.92, 93]. The local photoetch rate again showed an inverse dependence on carrier concentration, determined in this case by Raman measurements. Very convincing experimental evidence of the general validity of this relationship has been found during etching of the N-polar heteroepitaxial GaN layer containing Ga-polar inversion domains (IDs). During simultaneous growth of areas of different polarities more impurities and doping element are incorporated into the N-polar material; it becomes more heavily doped, say

n^+ , while Ga-polar IDs have lower carrier concentration, say n . During photoetching the latter areas are etched more rapidly, i.e., deep craters are formed at IDs, as shown in Fig. 43.23a and explained by the model in Fig. 43.23b. The experimental details of such peculiar etching behavior have been discussed in recent papers [43.51–53].

Photoelectrochemical measurements on n-type GaN electrodes in the same KOH solution as used for electroless photoetching confirm the explanation given above. As the dopant density of the electrode is increased the onset for photocurrent is shifted to positive potential, i.e., the hole flux to the surface decreases. This trend can explain why bulk GaN single crystals, unintentionally doped (contaminated) with oxygen and carbon to the level of carrier concentration close to 10^{20} cm^{-3} , cannot be photoetched in aqueous KOH solutions.

The relationship between the etch depth and carrier concentration established for GaAs in the DSL etching system has recently been confirmed for photogalvanic etching of GaN in KOH solutions [43.92]. A quantitative correlation of the etch rate and carrier concentration was obtained by micro-Raman determination of the carrier concentration [43.93].

Special Application of Electroless Etching

There are some features of this method which allow analysis of specific defects occurring in compound semiconductors. It was shown that the popular Abra-

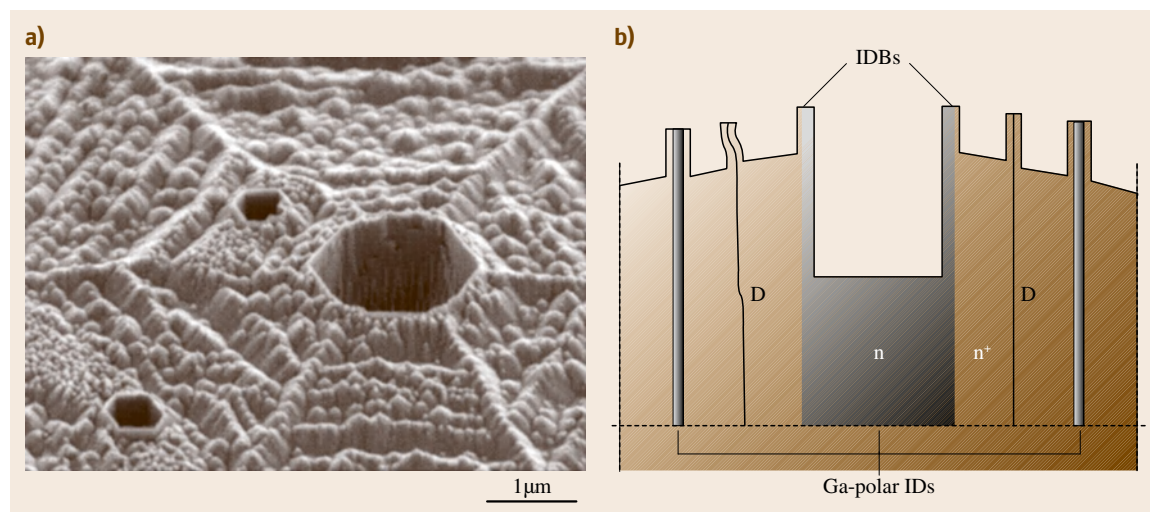


Fig. 43.23 (a) SEM image of etch features formed during photoetching of N-polar GaN heteroepitaxial layer containing inversion domains. (b) Schematic representation of a cross-section of the photoetched GaN layer from (a) (with permission from [43.53])

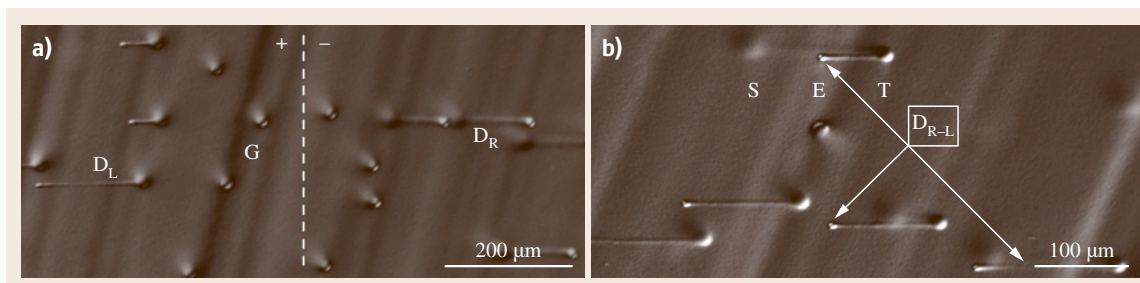


Fig. 43.24a,b DIC optical images of n-type GaAs after open-circuit photoetching

hams and Burocchi (AB) etch for GaAs is characterized by a so-called memory effect: the hillocks and ridges formed on defects remain intact even after very deep etching, even though the defects are no longer at the initial position [43.94]. On the basis of this result a projective etching method was developed and used for analysis of dislocations which moved in GaAs single crystals due to thermal stress during cooling after growth (G–S dislocations after [43.79]). This three-step etching procedure permits one to define the glide/climb system (glide/climb direction and plane) of any displaced dislocation. Numerous examples of these types of dislocations were shown and analyzed previously [43.8–10]. Figure 43.24 shows a set of images which illustrates the possibility offered by the photoetching method in analyzing the behavior of G–S dislocations. In Fig. 43.24a some dislocations moved to the left (denoted D_L) while others moved to the right (de-

noted D_R): most probably the strain was of the opposite sign, as indicated by “+” and “–” on the left and right side of the dashed line. The fact that in the central part of the image there are some dislocations that did not move [so-called grown-in dislocations (G), after [43.79]] supports this interpretation. In Fig. 43.24b some dislocations (denoted D_{R-L}) clearly *changed their mind* during the movement: first they moved from the starting position (S) to the right, stopped for some time (this can be recognized from the presence of the Cottrell atmosphere at the turning point (T) where the change of the direction of glide/climb occurred) and later moved to the left of the image, where they finally stopped at position E. Worth noting is the different size of the Cottrell atmospheres at positions S, T, and E, which is most probably the result of slower diffusion of decorating point defects due to decreasing temperature between the subsequent stop events of the D_{R-L} dislocations.

References

- 43.1 H.C. Gatos, M.C. Lavine: Characteristics of the {111} surfaces of the III–V intermetallic compounds, *J. Electrochem. Soc.* **107**, 427–433 (1960)
- 43.2 S. Amelinckx: *Direct Observation of Dislocations*, Supplement to Solid State Physics, Vol. 6 (Academic, New York 1964) pp. 15–50
- 43.3 D.J. Stirland, B.W. Straughan: A review of etching and defect characterization of gallium arsenide substrate material, *Thin Solid Films* **31**, 139–170 (1976)
- 43.4 D.C. Miller, G.A. Rozgonyi: Defect characterization by etching, optical microscopy and x-ray topography. In: *Handbook on Semiconductors*, Vol. 3, ed. by S.B. Keller (North-Holland, Amsterdam 1980) pp. 218–246
- 43.5 R.B. Heimann: Principles of chemical etching – the art and science of etching crystals. In: *Crystals: Growth, Properties and Applications*, Vol. 8, ed. by J. Grabmaier (Springer, Berlin, Heidelberg 1982) pp. 173–224
- 43.6 K. Sangwal: *Etching of Crystals* (North-Holland, Amsterdam 1987)
- 43.7 P.H.L. Notten, J.E.A.M. van den Meerakker, J.J. Kelly: *Etching of III–V Semiconductors: an Electrochemical Approach* (Elsevier, Oxford 1991)
- 43.8 J.L. Weyher: Characterization of compound semiconductors by etching. In: *Handbook on Semiconductors*, Vol. 3, ed. by S. Mahajan (Elsevier, Amsterdam 1994) pp. 995–1031
- 43.9 J.L. Weyher: Characterization of bulk as-grown and annealed III–Vs by photo-etching and complementary methods, *Inst. Phys. Conf. Ser.* **146**, 399–408 (1995)
- 43.10 J.L. Weyher, C. Frigeri, S. Müller: Selective etching and complementary microprobe techniques (SFM, EBIC). In: *Microprobe Characterization of Optoelectronic Materials*, Vol. 17, ed. by J. Jimenez (Taylor & Francis, New York 2003) pp. 595–689, Chap. 8
- 43.11 D. Zhuang, J.H. Edgar: Wet etching of GaN, AlN and SiC: a review, *Mater. Sci. Eng. R* **48**, 1–46 (2005)

- 43.12 J.L. Weyher: Characterization of wide-band-gap semiconductors (GaN, SiC) by defect-selective etching and complementary methods, *Superlattices Microstruct.* **40**, 279–288 (2006)
- 43.13 J.J. Kelly, D. Vanmaekelbergh: Chemical and electrochemical etching of semiconductors. In: *Semiconductor Micromachining*, Fundamental Electrochemistry and Physics, Vol. 1, ed. by S.A. Campbell, H.J. Lewerenz (Wiley, Chichester 1997), Chap. 2
- 43.14 P.H.L. Notten: The etching of InP in HCl solutions: a chemical mechanism, *J. Electrochem. Soc.* **131**, 2641–2644 (1984)
- 43.15 J.J. Kelly, H.G.G. Philipsen: Anisotropy in the wet-etching of semiconductors, *Curr. Opin. Solid State Mater. Sci.* **9**, 84–90 (2005)
- 43.16 R.A. Wind, M.A. Hines: Macroscopic etch anisotropies and microscopic reaction mechanisms: using microfabrication to unravel the complicated chemistry of KOH/Si etching, *J. Phys. Chem. B* **106**, 1557–1569 (2002)
- 43.17 I.M. Huygens, K. Strubbe, W.P. Gomes: Electrochemistry and photoetching of n-GaN, *J. Electrochem. Soc.* **147**, 1797–1802 (2000)
- 43.18 A.R. de Wit, M.D. Janssen, J.J. Kelly: Electrochemical characterization of polycrystalline ZnO layers, *Appl. Surf. Sci.* **45**, 21–27 (1990)
- 43.19 A. Gagnaire, J. Joseph, A. Etcheberry, J. Gautron: An ellipsometric study of the electrochemical surface modifications of n-InP, *J. Electrochem. Soc.* **132**, 1655–1658 (1985)
- 43.20 P.H.L. Notten, J.J. Kelly: Evidence for cathodic protection of crystallographic facets from GaAs etching profiles, *J. Electrochem. Soc.* **134**, 444–448 (1987)
- 43.21 J.J. Kelly, J.E.A.M. van den Meerakker, P.H.L. Notten: Electrochemistry of photoetching and defect-revealing in III–V materials, *Dechema-Monogr.* **102**, 453–464 (1986)
- 43.22 J. van de Ven, H.J.P. Nabben: Anisotropic photoetching of III–V semiconductors I. Electrochemistry, *J. Electrochem. Soc.* **137**, 1603–1610 (1990)
- 43.23 J. van de Ven, H.J.P. Nabben: Anisotropic photoetching of III–V semiconductors II. Kinetics and structural factors, *J. Electrochem. Soc.* **138**, 144–152 (1991)
- 43.24 C. Youtsey, I. Adesida, G. Bulman: Highly anisotropic photoenhanced wet etching of n-type GaN, *Appl. Phys. Lett.* **71**, 2151–2153 (1997)
- 43.25 L. Macht, J.J. Kelly, J.L. Weyher, A. Grzegorzczak, P.K. Larsen: An electrochemical study of photoetching of heteroepitaxial GaN: kinetics and morphology, *J. Cryst. Growth* **273**, 347–356 (2005)
- 43.26 J.L. Weyher, R. Fornari, T. Görög, J.J. Kelly, B. Ern : HBr–K₂Cr₂O₇–H₂O etching system for indium phosphide, *J. Cryst. Growth* **141**, 57–67 (1994)
- 43.27 V. Lehmann: *Electrochemistry of Silicon. Instrumentation, Science, Materials and Applications* (Wiley-VCH, Weinheim 2002)
- 43.28 M.M. Faktor, J.L. Stevenson: The detection of structural defects in GaAs by electrochemical etching, *J. Electrochem. Soc.* **125**, 621–629 (1978)
- 43.29 C.R. Elliott, J.C. Regnault: The detection of structural defects in indium phosphide by electrochemical etching, *J. Electrochem. Soc.* **128**, 113–116 (1981)
- 43.30 A. Yamamoto, S. Tohno, C. Uemura: Detection of structural defects in n-type InP crystals by electrochemical etching under illumination, *J. Electrochem. Soc.* **128**, 1095–1100 (1981)
- 43.31 R. Bhat: Photoelectrochemical defect delineation in GaAs using hydrochloric acid, *J. Electrochem. Soc.* **132**, 2284–2285 (1985)
- 43.32 L. Blok: Characterization of vapour grown (001) GaAs_{1–x}P_x layers by selective photo-etching, *J. Cryst. Growth* **31**, 250–255 (1975)
- 43.33 E. Sirtl, A. Adler: Cromas ure–Flu s ure als spezifisches System zur  tzgrubenentwicklung auf Silizium, *Z. Metallkd.* **52**, 529–531 (1961), in German
- 43.34 J. Weyher, J. van de Ven: Selective etching and photoetching of {100} Gallium Arsenide in CrO₃–HF aqueous solutions. Part I: Influence of composition on etching behaviour, *J. Cryst. Growth* **63**, 285–291 (1983)
- 43.35 J. van de Ven, J.E.A.M. van den Meerakker, J.J. Kelly: The mechanism of GaAs etching in CrO₃–HF solutions I. Experimental results, *J. Electrochem. Soc.* **132**, 3020–3026 (1985)
- 43.36 J.J. Kelly, J. van de Ven, J.E.A.M. van den Meerakker: The mechanism of GaAs etching in CrO₃–HF solutions II. Model and discussion, *J. Electrochem. Soc.* **132**, 3026–3033 (1985)
- 43.37 J. van de Ven, J.L. Weyher, J.E.A.M. van den Meerakker, J.J. Kelly: Kinetics and morphology of GaAs etching in aqueous CrO₃–HF solutions, *J. Electrochem. Soc.* **133**, 799–806 (1986)
- 43.38 J.E.A.M. van den Meerakker, J.H.C. van Vegchel: Silicon etching in CrO₃–HF solutions. I: High [HF]/[CrO₃] ratios, *J. Electrochem. Soc.* **136**, 1949–1953 (1989)
- 43.39 J.E.A.M. van den Meerakker, J.H.C. van Vegchel: Silicon etching in CrO₃–HF solutions. II: low [HF]/[CrO₃] ratios, *J. Electrochem. Soc.* **136**, 1954–1957 (1989)
- 43.40 P. Visconti, D. Huang, M.A. Reshchikov, F. Yun, R. Cingolani, D.J. Smith, J. Jasinski, W. Swider, Z. Liliental-Weber, H. Markoc: Investigation of defects and surface polarity in GaN using hot wet etching together with microscopy and diffraction techniques, *Mater. Sci. Eng. B* **93**, 229–233 (2002)
- 43.41 J. Chen, J.F. Wang, H. Wang, J.J. Zhu, S.M. Zgang, D.G. Zhao, D.S. Jiang, H. Yang, K.H. Ploog: Measurement of threading dislocation densities in GaN by wet chemical etching, *Semicond. Sci. Technol.* **21**, 1229–1235 (2006)

- 43.42 J. Angilello, R.M. Potemski, G.R. Woolhouse: Etch pits and dislocations in {100} GaAs, *J. Appl. Phys.* **46**, 2315–2316 (1975)
- 43.43 K. Akita, T. Kusunoki, S. Komiya, T. Kotani: Observation of etch pits produced in InP by new etchants, *J. Cryst. Growth* **46**, 783–787 (1979)
- 43.44 S.N.G. Chu, C.M. Jodluk, A.A. Ballman: New dislocation etchant for InP, *J. Electrochem. Soc.* **129**, 352–354 (1982)
- 43.45 S. Komiya, T. Kotani: Direct observation of dislocations in GaAlAs–GaAs grown by the LPE method, *J. Electrochem. Soc.* **125**, 2019–2024 (1978)
- 43.46 E.S. Hellman: The polarity of GaN: a critical review, *MRS Internet J. Nitride Semicond. Res.* **3**, 1–11 (1998)
- 43.47 M. Seelmann-Eggebert, J.L. Weyher, H. Obloh, H. Zimmermann, A. Rar, S. Porowski: Polarity of (00.1) GaN epilayers grown on a (00.1) sapphire, *Appl. Phys. Lett.* **71**, 2635–2637 (1997)
- 43.48 J.L. Rouvière, J.L. Weyher, M. Seelmann-Eggebert, S. Porowski: Polarity determination for GaN films grown on (0001) sapphire and high-pressure grown GaN single crystals, *Appl. Phys. Lett.* **73**, 668–670 (1998)
- 43.49 D. Li, M. Sumiya, S. Fuke, D. Yang, D. Que, Y. Suzuki, Y. Fukuda: Selective etching of GaN polar surface in potassium hydroxide solution studied by x-ray photoelectron spectroscopy, *J. Appl. Phys.* **90**, 4219–4223 (2001)
- 43.50 G. Kamler, J. Borysiuk, J.L. Weyher, R. Czarnecki, M. Leszczynski, I. Grzegory: Selective etching and TEM study of inversion domains in Mg-doped GaN epitaxial layers, *J. Cryst. Growth* **282**, 45–48 (2005)
- 43.51 J.L. Weyher, F.D. Tichelaar, H.W. Zandbergen, L. Macht, P.R. Hageman: Selective photoetching and transmission electron microscopy studies of defects in heteroepitaxial GaN, *J. Appl. Phys.* **90**, 6105–6109 (2001)
- 43.52 L. Macht, J.L. Weyher, P.R. Hageman, M. Zielinski, P.K. Larsen: Direct influence of polarity on structural and electro-optical properties of heteroepitaxial GaN, *J. Phys. Condens. Matter* **14**, 13345–13350 (2002)
- 43.53 J.L. Weyher, L. Macht, F.D. Tichelaar, H.W. Zandbergen, P.R. Hageman, P.K. Larsen: Complementary study of defects in GaN by photoetching and TEM, *Mater. Sci. Eng. B* **91/92**, 280–284 (2002)
- 43.54 M.G. Mynbaeva, Y.V. Melnik, A.K. Kryganovskii, K.D. Mynbaev: Wet chemical etching of GaN in H_3PO_4 with Al ions, *Electrochem. Sol.-State Lett.* **2**, 404–406 (1999)
- 43.55 J.L. Weyher, M. Albrecht, T. Wosinski, G. Nowak, H.P. Strunk, S. Porowski: Study of individual grown-in and indentation-induced dislocations in GaN by defect-selective etching and transmission electron microscopy, *Mater. Sci. Eng. B* **80**, 318–321 (2001)
- 43.56 H. Ono, J. Matsui: Influence of In atoms on the shape of dislocation etch pits in LEC In-doped GaAs crystals, *Jpn. J. Appl. Phys.* **25**, 1481–1484 (1986)
- 43.57 V. Gottschalch, W. Heinig, E. Butter, H. Rosin, G. Freydank: H_3PO_4 -etching of {001}-faces of InP, (GaIn)P, GaP, and Ga(AsP), *Krist. Tech.* **14**, 563–569 (1979)
- 43.58 J.L. Weyher, S. Lazar, J. Borysiuk, J. Pernot: Defect-selective etching of SiC, *Phys. Status Solidi (a)* **202**, 578–583 (2005)
- 43.59 T. Takenaka, H. Hayashi, K. Murata, T. Inoguchi: Various dislocation etch pits revealed on LPE GaAs{001} layer by molten KOH, *Jpn. J. Phys.* **17**, 1145–1146 (1978)
- 43.60 T. Ohno, H. Yamaguchi, S. Kuroda, K. Kojima, T. Suzuki, K. Arai: Direct observation of dislocations propagated from 4H-SiC substrate to epitaxial layer by x-ray topography, *J. Cryst. Growth* **260**, 209–216 (2004)
- 43.61 D. Siche, D. Klimm, T. Hölzel, A. Wohlfart: Reproducible defect etching of SiC single crystals, *J. Cryst. Growth* **270**, 1–6 (2004)
- 43.62 S.A. Sakwe, R. Müller, P.J. Wellmann: Optimization of KOH etching parameters for quantitative defect recognition in n- and p-type doped SiC, *J. Cryst. Growth* **289**, 520–526 (2006)
- 43.63 D. Hull, D.J. Bacon (Eds.): *Introduction to Dislocations* (Pergamon, Oxford 1984)
- 43.64 G. Kamler, J.L. Weyher, I. Grzegory, E. Jezierska, T. Wosinski: Defect-selective etching of GaN in a modified molten bases system, *J. Cryst. Growth* **246**, 21–24 (2002)
- 43.65 J.L. Weyher, P.D. Brown, J.L. Rouvière, T. Wosinski, A.R.A. Zauner, I. Grzegory: Recent advances in defect-selective etching of GaN, *J. Cryst. Growth* **210**, 151–156 (2000)
- 43.66 J.L. Weyher, S. Lazar, L. Macht, Z. Liliental-Weber, R.J. Molnar, S. Müller, V.G.M. Sivel, G. Nowak, I. Grzegory: Orthodox etching of HVPE-grown GaN, *J. Cryst. Growth* **305**, 384–392 (2007)
- 43.67 F. Secco d'Aragona: Dislocation etch for {100} planes in silicon, *J. Electrochem. Soc.* **119**, 948–951 (1972)
- 43.68 K. Motoki, T. Okahisa, S. Nakahata, N. Matsumoto, H. Kimura, H. Kasai, K. Takemoto, K. Uematsu, M. Ueno, Y. Kumagai, A. Koukitu, H. Seki: Growth and characterization of freestanding GaN substrates, *J. Cryst. Growth* **237–239**, 912–921 (2002)
- 43.69 J.L. Weyher, P.D. Brown, J.L. Rouvière, T. Wosinski, A.R.A. Zauner, I. Grzegory: Recent advances in defect-selective etching of GaN, *J. Cryst. Growth* **210**, 151–156 (2000)
- 43.70 M. Albrecht, H.P. Strunk, J.L. Weyher, I. Grzegory, S. Porowski, T. Wosinski: Carrier recombination at single dislocations in GaN measured by cathodoluminescence in a transmission electron microscope, *J. Appl. Phys.* **92**, 2000–2005 (2002)
- 43.71 K. Shiojima: Atomic force microscopy and transmission electron microscopy observations of KOH-

- etched GaN surfaces, *J. Vac. Sci. Technol. B* **18**, 37–40 (2000)
- 43.72 K. Engl, M. Beer, N. Gmeinwieser, U.T. Schwarz, J. Zweck, W. Wegscheider, S. Miller, A. Miler, H.-J. Lugauer, H. Brüderl, A. Lell, V. Härle: Influence of an in situ-deposited SiN_x intermediate layer inside GaN and AlGaN layers on SiC substrates, *J. Cryst. Growth* **289**, 6–13 (2006)
- 43.73 I. Kamata, H. Tsuchida, T. Jikimoto, K. Izumi: Structural transformation of screw dislocations via thick 4H-SiC epitaxial growth, *Jpn. J. Appl. Phys.* **39**, 6496–6500 (2000)
- 43.74 S. Ha, H.J. Chung, N.T. Nuhfer, M. Skowronski: Dislocation nucleation in 4H silicon carbide epitaxy, *J. Cryst. Growth* **262**, 130–138 (2004)
- 43.75 Z. Zhang, T.S. Sudarshan: Evolution of basal plane dislocations during 4H-silicon carbide homoepitaxy, *Appl. Phys. Lett.* **87**, 161917–1–161917–3 (2005)
- 43.76 G. Kamler, J. Borysiuk, J.L. Weyher, A. Presz, M. Wozniak, I. Grzegory: Application of orthodox defect-selective etching for studying GaN single crystals, epitaxial layers and device structures, *Eur. Phys. J. Appl. Phys.* **27**, 247–249 (2004)
- 43.77 J.L. Weyher, G. Kamler, G. Nowak, J. Borysiuk, B. Lucznik, M. Krysko, I. Grzegory, S. Porowski: Defects in GaN single crystals and homo-epitaxial structures, *J. Cryst. Growth* **281**, 135–142 (2005)
- 43.78 G. Kamler, J. Smalc, M. Wozniak, J.L. Weyher, R. Czarnecki, G. Targowski, M. Leszczynski, I. Grzegory, S. Porowski: Selective etching of dislocations in violet-laser diode structures, *J. Cryst. Growth* **293**, 18–21 (2006)
- 43.79 J.L. Weyher, J. van de Ven: Selective etching and photoetching of GaAs in CrO₃-HF aqueous solutions. Part III: Interpretation of defect-related etch figures, *J. Cryst. Growth* **78**, 191–217 (1986)
- 43.80 J.L. Weyher, L. Macht: Defects in wide band-gap semiconductors: selective etching and calibration by complementary methods, *Eur. Phys. J. Appl. Phys.* **27**, 37–41 (2004)
- 43.81 C. Frigeri, J.L. Weyher: Electron beam induced current and photoetching investigations of dislocations and impurity atmospheres in n-type LEC GaAs, *J. Appl. Phys.* **65**, 4646–4653 (1989)
- 43.82 J.L. Weyher, C. Frigeri, P.J. van der Wel: Complementary DSL, EBIC and PL study of grown-in defects in Si-doped GaAs crystals grown under Ga- and As-rich conditions by LEC method, *J. Cryst. Growth* **103**, 46–53 (1990)
- 43.83 J.L. Weyher, P.J. van der Wel, C. Frigeri: Spatially resolved study of dislocations in Si-doped LEC GaAs by DSL, PL and EBIC, *Semicond. Sci. Technol.* **7**, A294–A299 (1992)
- 43.84 J.L. Weyher, L. Macht, G. Kamler, J. Borysiuk, I. Grzegory: Characterization of GaN single crystals by defect-selective etching, *Phys. Status Solidi (c)* **0(3)**, 821–826 (2003)
- 43.85 J.A. Bardwell, J.B. Webb, H. Tang, J. Fraser, S. Moisa: Ultraviolet photoenhanced wet etching of GaN in K₂S₂O₈ solution, *J. Appl. Phys.* **89**, 4142–4149 (2001)
- 43.86 B. Yang, P. Fay: Etch rate and surface morphology controle in photoelectrochemical etching of GaN, *J. Vac. Sci. Technol. B* **22**, 1750–1754 (2004)
- 43.87 C. Youtsey, L.T. Romano, I. Adesida: Gallium nitride whiskers formation by selective photoenhanced wet etching of dislocations, *Appl. Phys. Lett.* **73**, 797–799 (1998)
- 43.88 C. Youtsey, L.T. Romano, R.J. Molnar, I. Adesida: Rapid evaluation of dislocation densities in n-type GaN films using photoenhanced wet etching, *Appl. Phys. Lett.* **74**, 3537–3539 (1999)
- 43.89 S. Lazar, J.L. Weyher, L. Macht, F.D. Tichelaar, H.W. Zandbergen: Nanopipes in GaN: photo-etching and TEM study, *Eur. Phys. J. Appl. Phys.* **27**, 275–278 (2004)
- 43.90 C. Frigeri, J.L. Weyher, L. Zanotti: Study of segregation inhomogeneities in GaAs by means of DSL photoetching and EBIC measurements, *J. Electrochem. Soc.* **136**, 262–266 (1989)
- 43.91 M.L. Young, D.R. Wight: Concentration dependence of the minority carrier diffusion length and lifetime in GaP, *J. Phys. D Appl. Phys.* **7**, 1824–1837 (1974)
- 43.92 J.L. Weyher, R. Lewandowska, L. Macht, B. Lucznik, I. Grzegory: Etching, Raman and PL study of thick HVPE-grown GaN, *Mater. Sci. Semicond. Process.* **9**, 175–179 (2006)
- 43.93 R. Lewandowska, J.L. Weyher, J.J. Kelly, L. Konczewicz, B. Lucznik: Calibration of the PEC etching of GaN by Raman spectroscopy, *J. Cryst. Growth* **307**, 298–301 (2007)
- 43.94 D.J. Stirland, R. Ogden: A dislocation “etch-memory” effect in gallium arsenide, *Phys. Status Solidi (a)* **17**, K1–K4 (1973)

Transmission

44. Transmission Electron Microscopy Characterization of Crystals

Jie Bai, Shixin Wang, Lu-Min Wang, Michael Dudley

Since the first observation of dislocations published in 1956, transmission electron microscopy (TEM) has become an indispensable technique for materials research. TEM not only provides very high spatial resolution for the characterization of microstructure and microchemistry but also elucidating the mechanisms controlling materials properties. The results of TEM analyses can also shed light on possible ways for improving the crystal quality. With the recent development of the electron exit wave reconstruction technique, the resolution of TEM has exceeded the typical Scherzer point resolution of ≈ 0.18 nm and observation of dislocation cores with an accuracy of 10 pm has been achieved. Most TEM studies are carried out in a static status; however, dynamic studies using in situ heating, in situ stressing, and even in situ growth can be conducted to study the development, interaction, and multiplication of defects.

44.1 Theoretical Basis of TEM Characterization of Defects	1477
44.1.1 Imaging of Crystal Defects Using Diffraction Contrast	1478
44.1.2 Phase-Contrast High-Resolution Transmission Electron Microscopy (HRTEM)	1482
44.1.3 Diffraction Techniques	1484
44.1.4 STEM, EELS, and EFTEM in Microanalysis	1489
44.1.5 FIB for TEM Sample Preparation	1493
44.2 Selected Examples of Application of TEM to Semiconductor Systems	1493
44.2.1 Studies of Conventional Heteroepitaxial Semiconductor Systems	1494
44.2.2 TEM Studies of Large-Mismatch Heteroepitaxial Systems	1500
44.2.3 Application of STEM, EELS, and EFTEM	1509
44.3 Concluding Remarks: Current Application Status and Development	1514
References	1515

44.1 Theoretical Basis of TEM Characterization of Defects

Modern TEM has three basic operation modes: imaging, diffraction, and spectroscopy analyses. In a transmission electron microscope, the objective lens takes the electrons emerging from the exit surface of the specimen, disperses them to create a diffraction pattern in the back focal plane, and recombines them to form an image in the image plane. When the lenses of the imaging system are adjusted so that the back focal plane of the objective lens coincides with the object plane of the intermediate lens, the diffraction pattern is projected onto the viewing screen. Alternatively, if the image plane of the objective lens works as the object plane of the intermediate lens, an image will be projected onto the viewing screen.

The contrast in the images recorded in imaging mode can be formed by several mechanisms:

1. Amplitude contrast (generally called diffraction contrast). The most commonly used bright field (BF) and dark field (DF) imaging techniques form images of dislocations with either the transmitted or diffracted beam under a two-beam condition. By excluding other beams, such images are formed by amplitude contrast.
2. Phase contrast and Z-contrast. When the transmitted and diffracted beams are made to combine, preserving both amplitude and phase information, a lattice image of the planes that are diffracting or even struc-

- tural images of the individual atom columns may be resolved directly (high-resolution TEM, HRTEM).
3. Mass thickness contrast. Incoherent (Rutherford) elastic scatter of electrons can form mass thickness contrast. Such contrast is generally weaker and overshadowed by the stronger effects of electron diffraction, except in cases where there are large differences in atomic number or when diffraction is weak. The investigation of microstructures of crystals mainly includes defects and interfaces. The imaging and analysis of defects are generally carried out with diffraction contrast under two-beam conditions while studies of interfaces are generally conducted under multibeam phase-contrast mode (HRTEM).

In diffraction mode, patterns such as selected-area diffraction patterns, Kikuchi patterns, and convergent beam diffraction patterns can provide crystallographic information such as the orientation, crystallographic symmetry, phase, strain, etc. When a nearly parallel electron beam illuminates the specimen and a particular area in the first image is selected by an aperture, a selected-area diffraction (SAD) pattern is formed; otherwise, if the beam converges onto a small area of the specimen, convergent-beam electron diffraction (CBED) consisting of diffraction discs will occur. On the other hand, large-angle convergent-beam diffraction (LACBED) is a relatively newly established technique which is extensively applied to the analysis of various defects. A LACBED image is formed by moving the specimen out of the object plane of a CBED setting and forming a combined image from both real space (the shadowed specimen image) and reciprocal space (diffracted Bragg lines).

The spectroscopy analyses in a modern analytical TEM include energy-dispersive x-ray spectroscopy (EDS) and electron energy-loss spectroscopy (EELS) that allow quick analysis of material chemistry on the nanoscale. With the newly developed energy-filtered TEM (EFTEM), quick elemental mapping not relying on the scanning technique is possible.

44.1.1 Imaging of Crystal Defects Using Diffraction Contrast

Defects in crystals can be described in terms of translational vectors which represent displacements of atoms from their regular positions in the lattice. Assuming the general displacement vector is \mathbf{R} , the Howie–Whelan equations describing the change in amplitude of the di-

rect beam ϕ_0 and the amplitude of the diffracted beam ϕ_g can be written as [44.1]

$$\frac{d\psi_0}{dz} = \frac{i\pi}{\xi_0} \phi_0 + \frac{i\pi}{\xi_g} \phi_g \exp(2\pi i s z + 2\pi i \mathbf{g} \cdot \mathbf{R}),$$

$$\frac{d\psi_g}{dz} = \frac{i\pi}{\xi_g} \psi_0 \exp(-2\pi i s z - 2\pi i \mathbf{g} \cdot \mathbf{R}) + \frac{i\pi}{\xi_g} \psi_g,$$

where ξ_0 and ξ_g are the extinction coefficients for the direct and diffracted beam, s is the deviation vector, z is the depth of the defect in the specimen, and \mathbf{g} is the reflecting vector.

When an objective aperture is used to exclude either the diffracted electrons or transmitted electrons under a two-beam condition, a bright-field (BF) or dark-field (DF) image is formed. By excluding other beams, such images are formed by amplitude contrast. The contrast can be used to determine the displacement field of the defect. Diffraction contrast and the appearance of features in BF and DF images depend sensitively on the deviation from the Bragg condition (deviation parameter s). Maximum transmission occurs in BF when s is small and positive, and it is under these conditions that most BF images are usually obtained [44.2].

Defects Characterized with Diffraction Contrast
Dislocations. In practical Burgers vector analysis of dislocations, the sample is tilted to a particular two-beam position with the deviation parameter s being set to a positive value. The presence of the dislocation bends the planes on one side into Bragg orientation and forms bright–dark line pair contrast in BF or DF images. A conventional technique to study the Burgers vector is $\mathbf{g} \cdot \mathbf{b}$ analysis (\mathbf{g} is the reflecting plane while \mathbf{b} is the Burgers vector of the dislocation) using their null-contrast properties. For dislocations with different nature, the $\mathbf{g} \cdot \mathbf{b}$ null-contrast rule works differently. Pure screw dislocations fully lose their contrast when the reflection plane satisfies $\mathbf{g} \cdot \mathbf{b} = 0$. For pure edge dislocations, $\mathbf{g} \cdot \mathbf{b} = 0$ and $\mathbf{g} \cdot (\mathbf{b} \wedge \mathbf{u}) = 0$ should be simultaneously satisfied to make the dislocation invisible. For mixed-type dislocations, $\mathbf{g} \cdot \mathbf{b}$, $\mathbf{g} \cdot \mathbf{b}_e$, and $\mathbf{g} \cdot \mathbf{b}_e \wedge \mathbf{u}$ are all required to be zero to minimize contrast (it is not possible to make it completely invisible). In practice, dislocations generally show faint contrast when $\mathbf{g} \cdot \mathbf{b} = 0$ even if $\mathbf{g} \cdot \mathbf{b}_e$ and $\mathbf{g} \cdot \mathbf{b}_e \wedge \mathbf{u}$ are not zero. Thus, the conventional method to determine the Burgers vector of dislocations is by finding two reflections \mathbf{g}_1 and \mathbf{g}_2 for which the invisibility criterion holds, and the Burgers vector may be determined using: $(\mathbf{g}_1 \wedge \mathbf{g}_2) \parallel \mathbf{b}$. It is recommended that at least three consistent cases of effective invisibility are found with $w < 1.0$ (where

w is the parameter describing the deviation from the Bragg condition $w = \xi_g s$ and using low-index reflections to avoid confusion. A detailed description of dislocation analysis is presented by Edington [44.3]. For strongly anisotropic materials, computer simulation must be used to determine both the direction and magnitude of the Burgers vector by employing variation of g , s , u , b and the foil normal.

Stacking Faults. A stacking fault is a planar defect at which the regular stacking sequence of the crystal is locally interrupted and a relative shift R of the top part of the crystal with respect to the lower part is introduced. For a column passing through the faults, a phase shift $2\pi g \cdot R$ is produced between the waves emitted by the two parts of the crystal located on each side of the fault. Therefore, a phase factor $\alpha = 2\pi g \cdot R$ is introduced into the main and diffracted beam amplitudes. When the fault is inclined to the specimen surface, contrast takes the form of light and dark fringes parallel to the line of intersection of the fault plane with the surface. Thus the observation and analysis of fringes formed by stacking faults inclined to the TEM foil normal can be used to determine the fault vector. This is the so-called $g \cdot R$ analysis used to characterize stacking faults. When $g \cdot R$ is zero or an integer, no contrast is presented and the fault is invisible. For other values of $g \cdot R$, however, the fault produces contrast. The precise form of the fringe contrast depends on the diffraction conditions employed, and this enables fault vector and type to be determined [44.5].

Polarity. Polarity is a consequence of the non-centrosymmetrical structure frequently encountered in compound semiconductors. Polarity reversal and symmetry of both (0001) wurtzite-type and (111) zincblende-type structures have been studied extensively [44.6]. One of the techniques to characterize polarity is the multiple dark-field TEM technique. Serneels et al. [44.7] conducted the theoretical calculations and predicted that, under multiple-beam conditions along a noncentrosymmetric zone axis, the inverted region of the crystal should be different in brightness from the surrounding matrix. The difference arises from the violation of Friedel's law. Taking GaN/AlN as an example, when multiple dark-field images are taken along a nonsymmetrical zone axis (say, $\langle 11\bar{2}0 \rangle$ or $\langle 10\bar{1}0 \rangle$) with $g = 0002$ and $g = 000\bar{2}$, an inversion domain will show either brighter or darker contrast than the matrix material [44.8]. Jasinski et al. applied this method to characterize the V-like inver-

sion domains in InN films [44.9]. Dark-field images recorded with (0002) and (000 $\bar{2}$) reflections under multiple diffraction conditions show a reversal defect-matrix contrast, as illustrated in Fig. 44.1. This method does not determine if the domain has Ga or N-polarity, but it may prove the presence of inversion.

High-Resolution Diffraction Contrast Imaging

For the characterization of crystal defects, the geometry and the character of the individual defects are two critical features of interest. In many studies, such as those involving the dissociation of dislocations, defects of high density without strain field overlap, defects with very small size etc., examination of images with high resolution is required. Apart from instrumental limits, the resolution is also determined by factors such as diffraction contrast. Two ways of achieving high-resolution diffraction contrast are described below.

Weak-Beam Dark-Field (WBDF) Technique. Since its first report by Cockayne et al. [44.4], the weak-beam dark-field (WBDF) technique has become a convenient and important method to achieve high-resolution diffraction contrast images of crystal defects. In par-

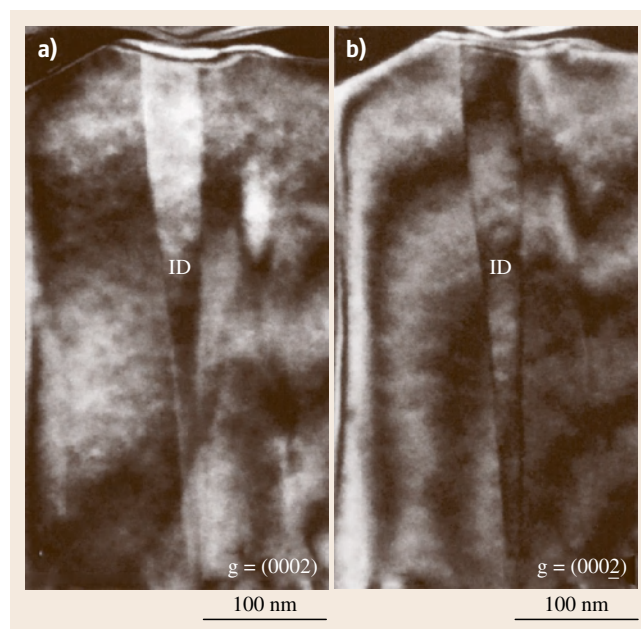


Fig. 44.1a,b Two-beam dark-field TEM images of an inversion domain in InN film ((a) recorded with $g = 0002$; (b) recorded with $g = 000\bar{2}$). A domain-matrix contrast reversal can be noticed (after [44.4], © AIP 1969)

ticular, it is widely employed to get sharp images of dislocation lines, resolving pairs of dislocations, and in precisely locating the positions of dislocation cores combined with simulation. The major advantage of the weak-beam approach over the two-beam dynamical technique lies in its improved resolution and the high contrast of the image. With the WBDF technique, only the diffraction contrast from the core of the defect contributes to the image. Consequently, systematic analysis of a given crystal defect is possible at a resolution approaching the limit of the microscope. Though the resolution of WBDF is not as high as the direct lattice resolution technique, it does have additional advantages such as allowing thicker specimens, reduced requirement of lens aberration, better contrast, and the validity of $\mathbf{g} \cdot \mathbf{b}$ analysis. In this technique, the TEM sample is tilted to a large, positive value of s , so that only the crystal planes close to the dislocation core are bent into a diffraction condition with $s \approx 0$ while neighboring lattice planes are away from the Bragg condition. By doing this, a sharp image of the near-core region of the dislocation can be recorded.

High-Order Reflection Method. The image width of a defect is approximately $\zeta_g/3$, where ζ_g is the extinction distance for the reflection \mathbf{g} [44.10]. Thus the image can be made narrower and the resolution increased by using high-order reflection with long extinction length. This technique was introduced by Bell and Thomas and is especially applicable at high voltages [44.11]. In this technique the specimen is tilted to put the high-order reflection into strong diffracting condition and form the image with transmitted beam. Compared with WBDF, this technique allows shorter exposure time and hence minimizes the risk of losing resolution because of mechanical or other instabilities. The disadvantage is that the image resolution is improved at the cost of contrast. If reflections of too high an order are employed, the defect will no longer be visible.

Quantitative Determination of the Indices of Line Features

Determination of the crystallographic direction of linear defects such as straight dislocation lines, needle-shaped precipitates, etc. can be very important when trying to understand their formation mechanisms. In a similar way, knowing the direction of the lines of intersection between planar defects or between inclined planar defects and the sample surface can also help in understanding their origins. For the case of a dislocation, in order to fully characterize this defect, both its line di-

rection and Burgers vector (magnitude and direction) need to be determined. TEM can be conveniently used to determine the line direction by tilting the specimen to at least two different orientations and measuring the angle, on the given micrograph, between the direction normal to the dislocation line direction and the trace of the reflecting plane (normal to \mathbf{g}). Stereographic projection analysis can then be used to deduce the line direction \mathbf{u} from these measurements as described by Edington [44.12]. This simply involves plotting the two (or three) normals to the dislocation line direction on a stereographic projection and the subsequent drawing of a great circle through these normals. The pole of this great circle is then the line direction of the dislocation in the crystal. Figure 44.2 is a schematic showing this stereographic analysis. The various points are plotted on a standard projection.

The dashed line shows the great circle corresponding to the trace of the plane perpendicular to the incident beam direction, $\mathbf{B}_1 \cdot \mathbf{g}_1$ is the \mathbf{g} vector used for this particular image, $\mathbf{g}_1 \times \mathbf{B}_1$ is the intersection of the trace of the reflecting plane on the image plane, and \mathbf{D}_1 is

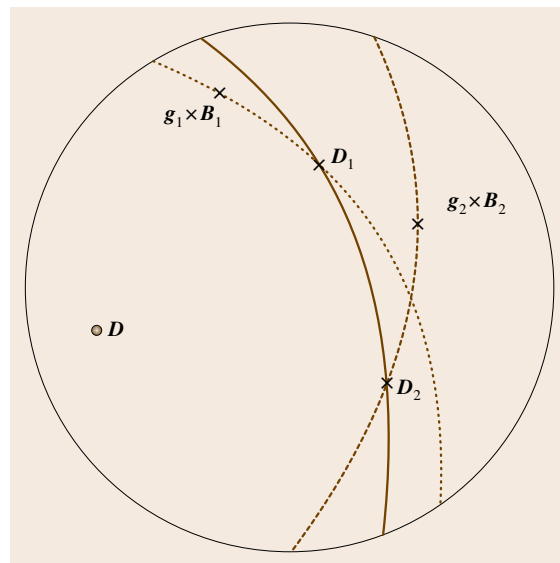


Fig. 44.2 Schematic showing the stereographic analysis. $\mathbf{g}_1 \times \mathbf{B}_1$ and $\mathbf{g}_2 \times \mathbf{B}_2$ are the intersections between the traces of the \mathbf{g} vectors utilized with the respective image planes (planes perpendicular to \mathbf{B}_1 and \mathbf{B}_2); \mathbf{D}_1 and \mathbf{D}_2 are the intersections between the traces of the planes perpendicular to the dislocation line direction observed on the two images. \mathbf{D} is the pole of the great circle containing \mathbf{D}_1 and \mathbf{D}_2

the intersection of the trace on the image plane of the plane normal with the dislocation line. δ_1 is the angle between $\mathbf{g}_1 \times \mathbf{B}_1$ and \mathbf{D}_1 measured from the TEM image and plotted on the great circle corresponding to the trace of the plane normal to \mathbf{B}_1 . The dotted line is the great circle corresponding to the trace of the plane normal to another incident beam direction \mathbf{B}_2 , with \mathbf{g}_2 being the reference \mathbf{g} vector and \mathbf{D}_2 being another observed direction normal to the dislocation line which is oriented at the measured angle δ_2 from $\mathbf{g}_2 \times \mathbf{B}_2$. The solid line is the great circle that runs through \mathbf{D}_1 and \mathbf{D}_2 ; the pole of this great circle is the dislocation line direction \mathbf{D} .

Unfortunately, such graphical techniques can be tedious, inconvenient, and imprecise. Bai [44.13] introduced an analytical, vector version of this technique wherein the trace of the \mathbf{g} vector on a given image is expressed as the vector $\mathbf{g} \times \mathbf{B}$. With suitably designed coordinate systems being defined, measurement of the angle (δ) between $(\mathbf{g} \times \mathbf{B})$ and the normal to the dislocation line direction enables it to be expressed as a vector \mathbf{D}_n . Repeating this measurement for a second image with different \mathbf{g} vector and beam direction \mathbf{B} generates another vector \mathbf{D}_n and the cross-product of two such vectors enables the line direction of the dislocation in the crystal to be determined.

The three coordinate systems utilized in the calculation (shown in Fig. 44.3) are defined as follows [44.14]:

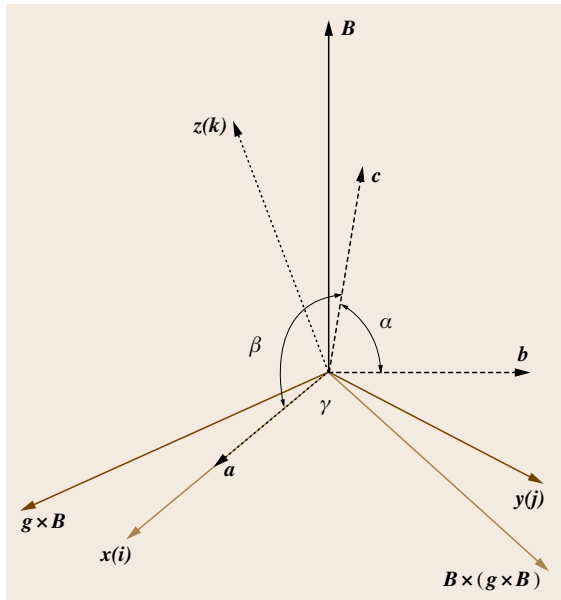


Fig. 44.3 Coordinate systems for the vector analysis of the determination of the line direction of a linear feature

1. A Cartesian coordinate system consisting of the beam direction (\mathbf{B}), $\mathbf{g} \times \mathbf{B}$, and $\mathbf{B} \times (\mathbf{g} \times \mathbf{B})$
2. The crystal coordinate system comprising the three basis vectors \mathbf{a} , \mathbf{b} , \mathbf{c} and three angular parameters α , β , γ of the unit cell for the crystal being studied
3. A Cartesian coordinate system \mathbf{x} , \mathbf{y} , and \mathbf{z} , in which the axis \mathbf{x} is along \mathbf{a} , \mathbf{b} lies in the \mathbf{xy} plane, and \mathbf{c} is in the upper half-space (since \mathbf{a} , \mathbf{b} , \mathbf{c} roughly form a right-handed relationship).

The normal of the line feature which lies at an angle δ to the trace of the \mathbf{g} vector can be represented as $\mathbf{D}_n = (\mathbf{g} \times \mathbf{B} / |\mathbf{g} \times \mathbf{B}|) \cos \delta + [\mathbf{B} \times (\mathbf{g} \times \mathbf{B}) / |\mathbf{B} \times (\mathbf{g} \times \mathbf{B})|] \sin \delta$. \mathbf{B} and \mathbf{g} are expressed as vectors in crystal system and therefore are the vectors $\mathbf{g} \times \mathbf{B}$ and $\mathbf{B} \times (\mathbf{g} \times \mathbf{B})$. All of these vectors then have to be expressed as vectors referred to the Cartesian coordinate system \mathbf{xyz} in order to carry out the necessary vector calculations.

The expressions enabling the basis vectors \mathbf{a} , \mathbf{b} , \mathbf{c} to be referred to the Cartesian coordinate system \mathbf{xyz} are

$$\mathbf{a} = a_x \mathbf{i} + a_y \mathbf{j} + a_z \mathbf{k} = a \mathbf{i},$$

$$a_x = a, \quad a_y = a_z = 0,$$

$$\mathbf{b} = b_x \mathbf{i} + b_y \mathbf{j} + b_z \mathbf{k} = b(\cos \gamma \mathbf{i} + \sin \gamma \mathbf{j}),$$

$$b_x = b \cos \gamma, \quad b_y = b \sin \gamma, \quad b_z = 0,$$

$$\mathbf{c} = c_x \mathbf{i} + c_y \mathbf{j} + c_z \mathbf{k},$$

$$c_x = c \cos \beta, \quad c_y = c \frac{(\cos \alpha - \cos \beta \cos \gamma)}{\sin \gamma},$$

$$c_z = \sqrt{c^2 - c_x^2 - c_y^2},$$

$$V_c = (\mathbf{a} \times \mathbf{b}) \cdot \mathbf{c} = abc \sin \gamma,$$

$$a_x^* = \frac{b_y c_z}{V_c}, \quad a_y^* = -\frac{b_x c_z}{V_c}, \quad a_z^* = (b_x c_y - b_y c_x),$$

$$b_x^* = \frac{a_x c_z}{V_c}, \quad b_y^* = -\frac{a_x c_y}{V_c},$$

$$c_z^* = \frac{a_x b_y}{V_c},$$

$$b_x^* = c_x^* = c_y^* = 0.$$

$\mathbf{B}_1(U_1, V_1, W_1)$ and $\mathbf{g}_1(h_1, k_1, l_1)$ can be expressed in the \mathbf{xyz} system as

$$\mathbf{B}_1 = B_x^1 \mathbf{i} + B_y^1 \mathbf{j} + B_z^1 \mathbf{k},$$

$$B_x^1 = U_1 a_x + V_1 b_x + W_1 c_x, \quad B_y^1 = V_1 b_y + W_1 c_y,$$

$$B_z^1 = W_1 c_z,$$

$$\mathbf{g}_1 = g_x^1 \mathbf{i} + g_y^1 \mathbf{j} + g_z^1 \mathbf{k},$$

$$g_x^1 = h_1 a_x^* + k_1 b_x^* + l_1 c_x^*,$$

$$g_z^1 = h_1 a_z^* + k_1 b_z^* + l_1 c_z^*.$$

Then $\mathbf{g}_1 \times \mathbf{B}_1$ and $\mathbf{B}_1 \times (\mathbf{g}_1 \times \mathbf{B}_1)$ can be written as

$$\begin{aligned}(\mathbf{g}_1 \times \mathbf{B}_1)_x &= g_y^1 B_z^1 - g_z^1 B_y^1, \\(\mathbf{g}_1 \times \mathbf{B}_1)_y &= g_z^1 B_x^1 - g_x^1 B_z^1, \\(\mathbf{g}_1 \times \mathbf{B}_1)_z &= g_x^1 B_y^1 - g_y^1 B_x^1, \\[\mathbf{B}_1 \times (\mathbf{g}_1 \times \mathbf{B}_1)]_x &= B_y^1 (\mathbf{g}_1 \times \mathbf{B}_1)_z - B_z^1 (\mathbf{g}_1 \times \mathbf{B}_1)_y, \\[\mathbf{B}_1 \times (\mathbf{g}_1 \times \mathbf{B}_1)]_y &= B_z^1 (\mathbf{g}_1 \times \mathbf{B}_1)_x - B_x^1 (\mathbf{g}_1 \times \mathbf{B}_1)_z, \\[\mathbf{B}_1 \times (\mathbf{g}_1 \times \mathbf{B}_1)]_z &= B_x^1 (\mathbf{g}_1 \times \mathbf{B}_1)_y - B_y^1 (\mathbf{g}_1 \times \mathbf{B}_1)_x.\end{aligned}$$

The normal of the dislocation line \mathbf{D}_1 in this case can be written as

$$\begin{aligned}\mathbf{D}_1 &= D_x^1 \mathbf{i} + D_y^1 \mathbf{j} + D_z^1 \mathbf{k}, \\D_x^1 &= \cos \delta_1 (\mathbf{g}_1 \times \mathbf{B}_1)_x + \sin \delta_1 [\mathbf{B}_1 \times (\mathbf{g}_1 \times \mathbf{B}_1)]_x, \\D_y^1 &= \cos \delta_1 (\mathbf{g}_1 \times \mathbf{B}_1)_y + \sin \delta_1 [\mathbf{B}_1 \times (\mathbf{g}_1 \times \mathbf{B}_1)]_y, \\D_z^1 &= \cos \delta_1 (\mathbf{g}_1 \times \mathbf{B}_1)_z + \sin \delta_1 [\mathbf{B}_1 \times (\mathbf{g}_1 \times \mathbf{B}_1)]_z.\end{aligned}$$

Similarly, we can get $\mathbf{D}_2 = D_x^2 \mathbf{i} + D_y^2 \mathbf{j} + D_z^2 \mathbf{k}$. Then the dislocation line $\mathbf{D} = \mathbf{D}_1 \times \mathbf{D}_2$ can be written as

$$\begin{aligned}\mathbf{D} &= D_x \mathbf{i} + D_y \mathbf{j} + D_z \mathbf{k}, \\D_x &= D_y^1 D_z^2 - D_z^1 D_y^2, \\D_y &= D_z^1 D_x^2 - D_x^1 D_z^2, \\D_z &= D_x^1 D_y^2 - D_y^1 D_x^2.\end{aligned}$$

Now the index of $\mathbf{D}(D_x, D_y, D_z)$ is in the Cartesian coordinate system xyz . We can convert this to a vector referred to the crystal system using the following relationships

$$\begin{aligned}U &= D_x \mathbf{p} + D_y \mathbf{p}' + D_z \mathbf{p}'', \\V &= D_y \mathbf{q}' + D_z \mathbf{q}'', \\W &= D_z \mathbf{r}'',\end{aligned}$$

where

$$\begin{aligned}\mathbf{p} &= \frac{1}{a}, \\\mathbf{p}' &= -\frac{b_x}{ab_y}, \\\mathbf{p}'' &= -\frac{1}{a} \left[-\frac{c_y b_x}{b_y c_z} + \frac{c_y}{c_z} \right], \\\mathbf{q}' &= \frac{1}{b_y}, \\\mathbf{q}'' &= -\frac{c_y}{b_y c_z}, \\\mathbf{r}'' &= \frac{1}{c_z}.\end{aligned}$$

The main source of error in this calculation relates to the accuracy of the determination of \mathbf{B} , the measurement of the angle δ , and the integralization of the decimal indices.

Generally, a \mathbf{g} vector in a low-index selected-area diffraction pattern with \mathbf{B} as zone axis is used in this process. The error in determination of \mathbf{B} and \mathbf{g} and hence δ can be avoided by carefully adjusting the zone axis \mathbf{B} along the electron beam. The 180° ambiguity does not create a problem because the coordinates $\mathbf{g} \times \mathbf{B}$ and $\mathbf{B} \times (\mathbf{g} \times \mathbf{B})$ go with the assigned \mathbf{g} . The critical point is the sense of δ . If \mathbf{D}_n is anticlockwise from $\mathbf{g} \times \mathbf{B}$, care must be taken regarding the sense of rotation sense of δ with respect to the trace of the known \mathbf{g} . An accurate calibration of the rotation between the image and the diffraction pattern is required for the application of this technique.

44.1.2 Phase-Contrast High-Resolution Transmission Electron Microscopy (HRTEM)

For dislocations in semiconductor materials, the individual dislocations exhibit significant deviations from average predictions due to various reasons and exhibit an unusual large data scattering that is commonly of unknown origin. Therefore, it is desirable to characterize individual dislocations with truly atomic resolution and to compare the results with theoretical calculations. Phase-contrast high-resolution TEM to date has broken the 0.1 nm barrier and it is possible to combine theory and experiment to accurately identify atomic column positions with better than 10 pm precision [44.15].

As opposed to the amplitude caused contrast observed in conventional TEM (where the image is formed by one beam), HRTEM images are formed with combined transmission and diffracted beams and the contrast is therefore a composite composed of both amplitude and phase information. There is no relative displacement between the location of a defect and the contrast variation caused by the defect in the HRTEM image, which is an advantage compared with diffraction imaging. However, there are limitations in direct interpretation of the HRTEM image in terms of the sample structure and composition. Since HRTEM images are sensitive to factors such as specimen thickness and orientation, objective lens defocus, spherical and chromatic aberration, etc., precise interpretation of the images may require extensive simulations. The effect of the interference between the beams can be predicted with the phase contrast transfer function (CTF) of the

objective lens and therefore a **HRTEM** image can be simulated. Since the **CTF** is focusing dependent, it is crucial to choose the optimum defocus to fully exploit the capabilities of electron microscopy in **HRTEM** mode. However, there is no simple optimized solution. Better experimental results can be achieved by conducting a specimen exit wave reconstruction with a series of through-focal images [44.16]. In this technique, a series of about 20 pictures is shot under the same imaging conditions with the exception of the focus, which is incremented between each take. Together with exact knowledge of the **CTF** the series allows for computation of the phase change. As mentioned earlier, amplitude change also contributes to image contrast. Consequently, sample thickness plays a critical role in the appearance of a lattice image. When the sample is thin enough that amplitude variations do not contribute to the image, the **HRTEM** image is formed purely by phase contrast and it shows directly a two-dimensional projection (down some low-index direction) of the crystal with defects and all.

A serious limitation to the interpretation of high-resolution images is the limited signal-to-noise ratio. By noise we refer to any contribution to image intensity which is not essentially a part of the signal, e.g., lattice image. Major contributions to noise are disordered surface layers, due to either contamination or specimen thinning damage, and shot noise in the electron beam or recording media. High noise-to-signal ratio could lead to errors in interpretation of crystal/amorphous interfaces.

There are two resolution limits in axial **HRTEM** which apply to imaging of the simple weak-phase object. The point-to-point resolution, attainable near the Scherzer defocus condition, is $d_{pp} \approx 0.66(C_s \lambda^3)^{1/4}$ (where C_s is the spherical aberration coefficient and λ is the electron wavelength). The information limit is $d_{in} \approx 2\sqrt{E/(C_c \lambda \Delta E)}$, where C_c is the coefficient of chromatic aberrations. For a totally unknown weak-phase object one can identify detail to d_{pp} simply and to d_{in} by careful image simulation or reconstruction from a through-focal series [44.17].

Dislocation Core Observation by HRTEM

Recent developments in electron microscopy have enabled microscopists to resolve the dislocation core structure down to the atomic level. For diamond cubic and zincblende semiconductors resolving dumbbell atom columns along the dislocation line requires resolution better than the typical Scherzer point resolution of ≈ 0.18 nm of most high-resolution transmission elec-

tron microscopes. By reconstructing an electron exit wave through-focal series, Xu et al. resolved a 30° partial dislocation in GaAs:Be with accuracy of the atomic position at the dislocation core region within 10 pm [44.18]. A modern aberration-corrected **TEM** can easily achieve point-to-point resolution of 0.1 nm.

Interfaces of Epitaxial Systems

HRTEM plays a valuable role in the characterization of interfaces in epitaxial systems. The investigation generally includes studies of the misfit dislocations, measurement of rigid shifts, and identification of the roughness and extent of the interface. The major requirement for characterization of interfaces is that both crystals should be well aligned on their appropriate zone axes and the interface should be aligned so that it is edge-on to the incident beam. The microscope should be well aligned and operate near the Scherzer focus and the thickness on both sides of the interface should be considerably less than half an extinction thickness (if possible).

For conventional epitaxial structures, e.g., SiGe on Si, low-index zones such as [100] and [110] are typically used, but [111] and [112] can provide further useful projections when three-dimensional views are required in order to specify the interface structures fully. For heterostructures of III–V compounds such as GaAs/Al_xGa_{1-x}As, it is extremely difficult to determine the location of the interface under the imaging conditions traditionally required for high-resolution imaging, namely, thin crystals and optimum defocus, and hence impossible to determine the interface sharpness. In order to highlight the compositional variations it is necessary to find thickness and defocus combinations which accentuate differences in the images from the two constituent materials. To get distinct interface, dark-field images formed by the 200 diffraction spot can be used to precisely determine the interface. This is due to the fact that, in the kinematical approximation, the intensity in the 200 diffraction beam is proportional to $(f_{III} - f_V)^2$, where f_{III} and f_V are the atomic scattering amplitudes of the group IIIA and group V elements, respectively. When this diffracted beam is strongly excited, the Al_xGa_{1-x}As layers appear much brighter than the GaAs layers. Such images provide an accurate measure of the layer thickness and of the flatness of the interface [44.19]. Another method to get distinct interface is to use the $\langle 100 \rangle$ projection rather than the $\langle 110 \rangle$ projection because the former has four chemically sensitive {002} beams compared with the latter with two of them [44.20]. The interfaces

of epitaxial systems can also be well studied by the high-resolution high-angle annular dark-field scanning TEM (HAADF-STEM) technique, which is extremely sensitive to the atomic number of the atoms in the high-resolution image (Sect. 44.1.4).

Polarity

Liliental-Weber et al. studied the atomic structure of Mg-rich hexagonal pyramids in GaN film which exhibit opposite polarity from the matrix material [44.21]. By taking a series of HRTEM images in a through-focal sequence, the electron wave exiting the specimen was reconstructed and atomic resolution was achieved. With such a high resolution, the exchange of Ga and N sublattices inside and outside the defect can be unambiguously determined. In this case a special crystal projection needs to be chosen, e.g., $[11\bar{2}0]$, such that two different atoms with different atomic numbers can be resolved. Figure 44.4 shows the reconstructed images

taken from different regions related to the pyramidal defect. The inversion of the polarity within the defect (BC) compared with the matrix (AB) can be clearly observed.

44.1.3 Diffraction Techniques

As mentioned previously, a parallel electron beam gives rise to diffraction patterns composed of sharp spots. Generally such a diffraction pattern is achieved by selecting a small region using an aperture inserted in the image plane of the objective lens, forming a selected-area diffraction (SAD) pattern. When the electron beam converges to image a small area of the specimen, a CBED pattern comprising diffraction discs forms. Compared with the limited spatial resolution of conventional SAD (usually down to a fraction of a micrometer), CBED gives resolution down to nanometer. Moreover, CBED discs contain more information than simple diffraction spots in SAD. The application of CBED includes phase identification, symmetry determination (point and space group), thickness measurement, strain and lattice parameter measurement, structure factor determination, etc.

Selected-Area Diffraction (SAD)

A SAD pattern can be treated as the magnified image of a planar section through the reciprocal lattice taken normal to the incident beam direction. It can be used to:

1. Identify the orientation of the specimen
2. Find the proper \mathbf{g} vector for defect analysis
3. Identify the structure of defects such as precipitates, twins, stacking faults, etc.
4. Determine the orientation relationship between phases
5. Determine the long-range order parameters.

The accuracy of analysis of a diffraction pattern depends upon the accuracy of measurement. Some factors of importance are:

1. The shape factor of the features, which determines the shape of the intensity distribution about the rel-points
2. Instrument alignment and beam divergence
3. Specimen perfection
4. Curvature of the reflecting sphere and relative orientation of the specimen
5. Double diffraction, giving rise to reflections of zero structure factor.

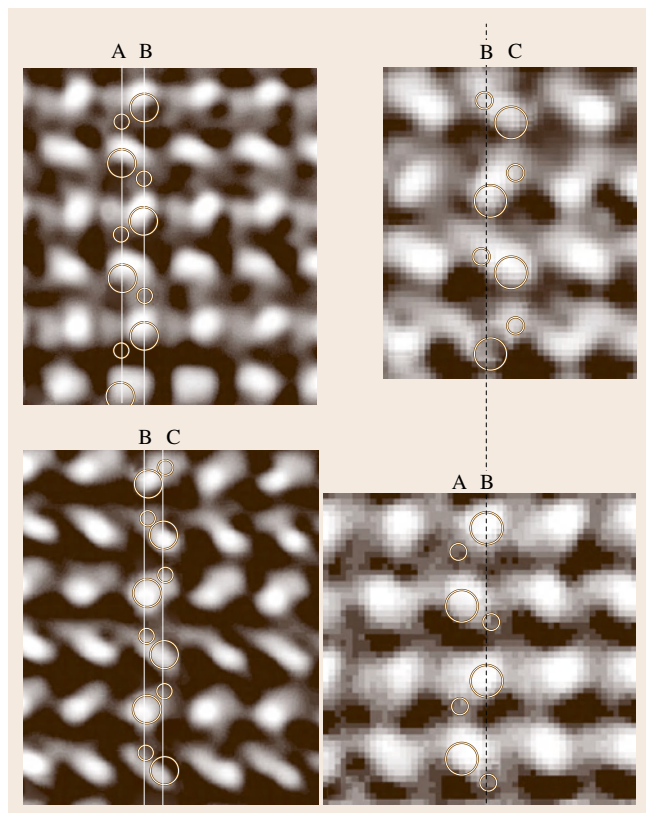


Fig. 44.4 Reconstructed exit wave phase of inversion domains in Mg-rich GaN. Note the change of polarity within the defect (BC) compared with the matrix (AB) (after [44.21], © Elsevier 2005)

Several examples of the application of the SAD technique are described in the following.

Twins in Diamond Cubic and Zincblende Structure Semiconductor Crystals. Twinning is a phenomenon which leads to the existence of domains in a crystal which have orientation relationships usually described by a simple symmetry operation. The most commonly observed type of symmetry operation involves a mirror image of the structure in the twinning plane, although the 180° (or equivalently 60°) rotation of the structure about the normal to the twin plane is also quite common in semiconductors with diamond cubic and zincblende structure. Twins can be produced either during growth or by mechanical deformation. The existence of twins can be discerned using the SAD technique, which is sensitive to the differences in orientation between a *twin* and *matrix*. If the twinned domains lay side by side with the untwinned *matrix* regions and the incident beam straddles both regions then a simple superposition of two diffraction patterns will occur, one from the matrix and one from the twin. For example, for a (110)-oriented diamond cubic crystal, a twin might be created by 180° rotation about the $(\bar{1}\bar{1}1)$ twin plane normal. This produces twin domains which have $(\bar{1}\bar{1}0)$ surface orientation (i.e., the same as the matrix) but which have different in-plane orientation. This is shown in the stereographic projections in Fig. 44.5, where it can be

seen that the orientation relationship between the two structures can not only be considered from the point of view of the 180° rotation about the $(\bar{1}\bar{1}1)$ twin plane normal but can also be considered either as a mirror across $(1\bar{1}2)$ or as a rotation by $70^\circ 32'$ about the (110) plane normal. The diffraction pattern associated with such side-by-side twins should therefore consist of the (110) matrix patterns with a second *twin* pattern being produced from the first by either a mirror operation across $(1\bar{1}2)$ or as a rotation by $70^\circ 32'$ about the (110) zone axis. However, if the twin and matrix domains overlap one another the diffraction pattern becomes slightly more complicated, with extra spots appearing at $1/3$ intervals along the $\langle 111 \rangle$ directions. Figure 44.6 shows an example SAD pattern of (110) Ge epilam with overlapping matrix and twin domains. Extra spots located at $n \times g/3$ can be clearly observed. Some of these extra spots can arise from multiple diffraction effects [44.22]. However, the full pattern can be understood by considering the tripling of the periodicity which occurs in this direction when the twin and matrix structures are overlapped [44.23]. Further details regarding analysis of twins can be found in the book by Edington [44.24].

Atomic Ordering of Semiconductor Alloys. For alloys containing different kinds of atoms which have attractive interactions, the desire to maximize the number of

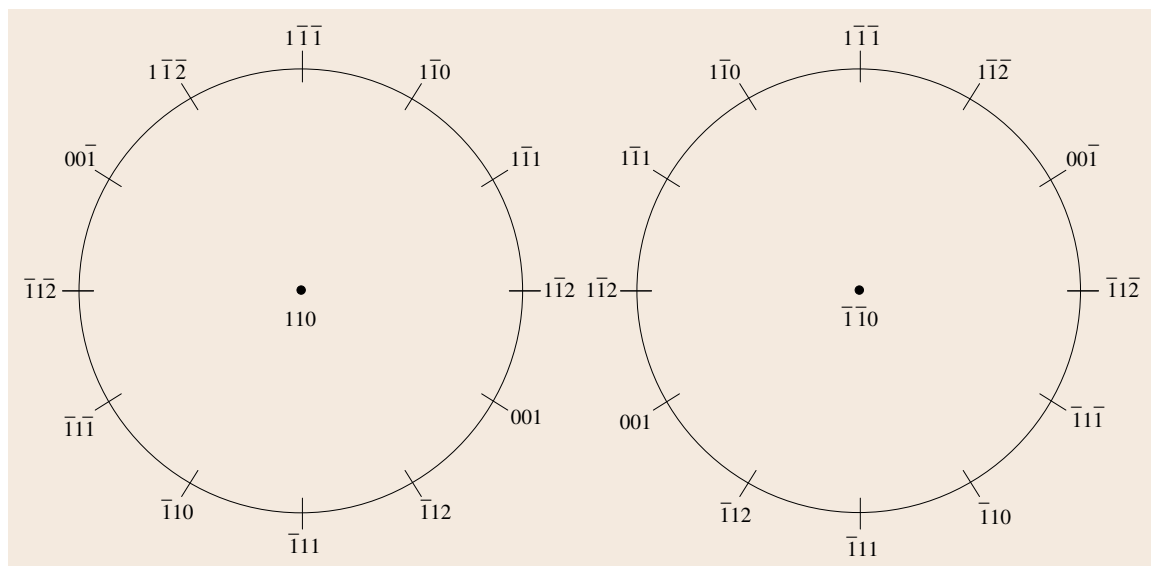


Fig. 44.5 Stereographic projections showing the orientation relationship between the original and twin structures

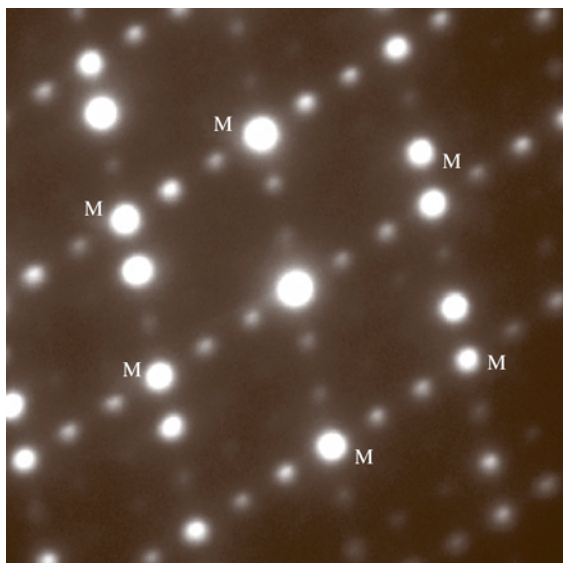


Fig. 44.6 SAD pattern of (110)Ge epilayer with overlapping matrix and twin domains, the main diffraction spots from matrix are indicated by “M”

unlike neighbors can lead to the formation of an ordered structure. Consequently, the usual structure factor rules determining the allowed reflections are relaxed and superstructure reflections in between the original Bragg reflections can be introduced. The intensity of such reflections is related to the difference between the atomic scattering factors of the atoms involved, as opposed to the intensity of fundamental reflections, which is related to their sum. A comprehensive review is given by Marcinkowski [44.25]. Studies of such long-range order structure can be carried out using the SAD technique to analyze the superstructure reflections. TEM specimens in various tilted orientations are required to obtain SAD patterns along different directions [44.26,27]. The extra diffraction spots are indexed and compared with those of the standard ordered structure in order to determine the long-range order. With the help of computer simulation, the structural ordering can be determined using smaller mutual tilts [44.28]. In various III–V alloy semiconductors such as AlGaAs, In(Al)GaP, InGaAsP, InAlAs, GaAsSb, GaAsP, and InAsSb, several types of ordered structures such as CuAu, CuPt, chalcopyrite, and famatinite, have been observed. In crystals grown on (001) substrates, observed ordered structure is mostly of CuPt type in which a doubling of the periodicity of the column III or V atoms occurs on the {111} plane [44.26].

Conventional Convergent-Beam Electron Diffraction (CBED)

When the incident electron waves impinging on the specimen comprise a convergent cone of rays, this generates a continuous range of Ewald spheres in reciprocal space. This causes higher-order Laue zones (HOLZs) to become visible in diffraction patterns, such that three-dimensional diffraction information is exhibited on the diffraction pattern. The fact that such information can be obtained from areas as small as a few nanometers in diameter is a major advantage of CBED. The diffraction discs in a CBED pattern are created exactly from the same area, and each disc contains the intensities determined by the orientation of the incident beam with respect to the (*hkl*) lattice plane. Several examples of the application of CBED are presented in the following sections.

Thickness Determination. CBED is a convenient method to determine the TEM specimen thickness. In this technique, the sample is tilted to form a two-beam condition. The intensity fringes (K-M fringes) in the diffracted discs due to various *s* are related to the sample thickness by $s_i^2/n_k^2 + 1/(\xi_g^2 n_k^2) = 1/t^2$ (where s_i is the diffraction deviation for the *i*-th fringe, n_k is an integer, ξ_g is the extinction length for the reflection, and *t* is the thickness of the sample). By choosing a proper n_k to plot a straight line of s_i^2/n_k^2 versus $1/n_k^2$, the thickness *t* can be determined by the intercept of the line [44.29]. For such measurement, the region of the foil selected should be flat without distortion and the beam must be focused at the plane of the specimen.

Polarity. There are several TEM methods for polarity determination: CBED, TEM-EDS, HRTEM, bend contour analysis, and EELS. Their relative capabilities to determine polarity depend strongly upon the species of crystal and the morphology of specimens to be examined. Since the CBED pattern is sensitive to both defects sample thickness in the illuminated area of the specimen, the use of this method is sometimes limited. Mitate et al. studied the polarity of GaN, ZnO, AlN and GaAs with both TEM-EDS (energy-dispersive x-ray spectroscopy) and the conventional CBED methods [44.30]. The results show that the CBED method is useful for ZnO and GaN, while the TEM-EDS method must be used for AlN and GaAs and can also be used for GaN and ZnO. It is clearly indicated that the TEM-EDS method is of use for the case where the difference in atomic scattering factor between the two constituent elements is small, while the CBED method is useful for

the case where the difference is large. In the presence of foil bending, it may be difficult to perform CBED experiments because any displacement of the electron beam on the sample is accompanied by a change of the local crystal orientation. In this case, the polarity can be determined from bend contours.

Sphalerite Structure. Taftø and Spence [44.31, 32] proposed a method of determining the deviations from centrosymmetry by taking advantage of the strong coherent multiple scattering normally present in CBED. In this technique, the TEM foil is tilted so that both the 200 reflection and two high odd-index reflections are simultaneously excited. When illuminating with a convergent electron beam, the effect of the dynamical interaction of these two weak reflections with the diffracted 200 beam is shown as cross-like contrast which intersects with the broad 200 Bragg line. Either bright or dark contrast suggests that the interference between the two weak reflections with the 200 reflection is either constructive or destructive and thus the type of the reflection hkl

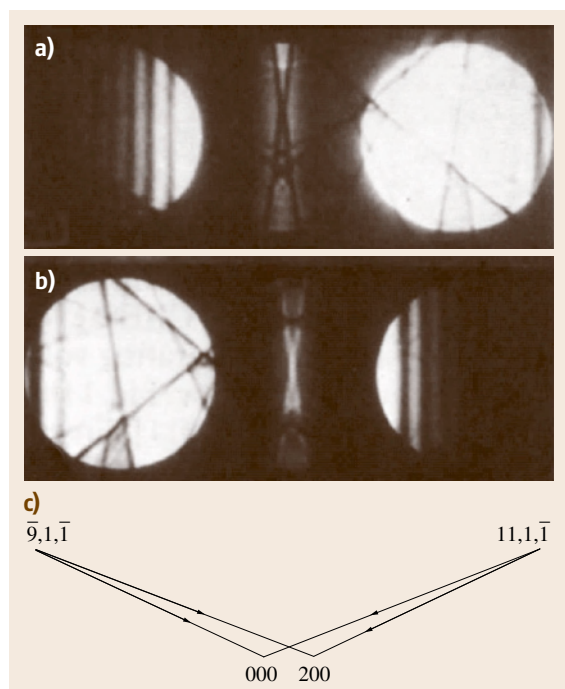


Fig. 44.7a-c $\bar{2}00$ (a) and 200 (b) diffraction discs showing the destructive and constructive interaction between the high-order odd reflections and $\bar{2}00/200$ reflection; (c) two double-scattering paths which contribute to the 200 reflection

can then be revealed. An example image showing the detailed features of the $\bar{2}00$ and 200 diffraction discs for a thickness of 100 nm is shown in Fig. 44.7a,b. Figure 44.7c shows the two double-scattering paths which contribute to the 200 reflection.

Wurtzite Structure. For polarity determination of wurtzite crystals such as GaN, conventional CBED is generally carried out along the $\langle 01\bar{1}0 \rangle$ axis. The intensity distributions within the $+\mathbf{g}$ and $-\mathbf{g}$ diffraction discs for polar directions such as $[0002]$ and $[000\bar{2}]$ are different and can be used for determination of atom distributions within the unit cell. To ensure the accurate determination of the polarity, the rotation angle and the 180° ambiguity between the image and the diffraction pattern need to be taken into account. Computer simulation of the intensity distribution taking into account the sample thickness, Debye–Waller factor, and absorption coefficient is necessary to verify the results. A good match between the experimental and simulated pattern is required for at least two different sample thicknesses to ensure that the interpretation is correct. Figure 44.8 shows a TEM image of an inversion domain boundary in an ammonothermally grown bulk GaN crystal [44.33]. The CBED patterns taken on either side of the boundary are shown as insets. An inversion

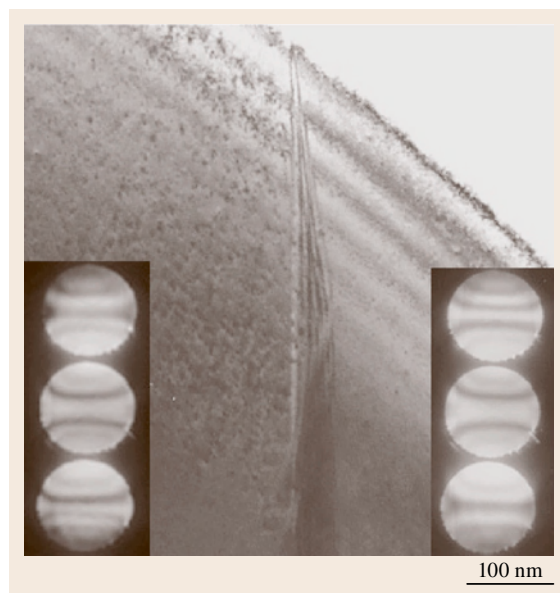


Fig. 44.8 TEM image showing an inversion domain boundary in a GaN bulk crystal; insets show the inversion of the intensity distribution in 0002 diffraction discs on either side of the boundary

of the intensity distribution in the 200 reflections on either side of the boundary can be clearly observed.

Lattice Parameter, Strain, and Composition. CBED has become a well-established technique to study lattice strain and composition in crystals with high spatial resolution and high accuracy [44.34, 35]. The high-order Laue zone (HOLZ) lines that arise from very high-order reflections are very sensitive to changes in lattice parameters. The geometry of HOLZ lines in the bright-field disc of a CBED pattern is also sensitive to the accelerating voltage. Hence, if the accelerating voltage of the incident electrons is maintained constant, changes in the angular position of the HOLZ lines can be directly correlated to variations in lattice parameter. The concept of effective accelerating voltage E_e is introduced in the pattern simulation to compensate for systematic shifts of HOLZ lines caused by dynamical effects [44.34]. The lattice parameters can be determined by matching the observed HOLZ pattern with computer simulations based on the kinematical theory of diffraction. Typically, the lattice parameter information can be obtained from a very small region defined by the incident probe size. The technique enables measurement of lattice parameter changes with a precision of approximately ± 0.0002 nm in many cases. Rozeveld and Howe conducted a detailed analysis of the lattice parameter error and developed a procedure to optimize the lattice parameter precision [44.36]. This method can be used to determine the six lattice parameters (a , b , c , α , β , and γ) from a single CBED pattern. Zipprich et al. [44.37] studied the strain and composition of Si/SiGe multilayer systems by analyzing the rocking curves in CBED patterns and comparing the experimental results with kinematical two-beam calculations. The resulting parameters are then further refined by dynamical simulations. The best accuracy for strain determination in this study is achieved by using perfectly flat specimen regions, recorded with the smallest possible beam diameter that yields sufficient signal intensity. The accuracy of this measurement can be greatly enhanced by application of the recently developed chromatic corrector for the modern TEM.

Strain determination methods using cross-sectional specimens, e.g., in HRTEM or in the measurement of the shift of Bragg lines in CBED patterns, are generally influenced by surface relaxation (i.e., *thin-foil effects*). Jacob et al. [44.38] studied the strained GaAs/In_xGa_{1-x}As/GaAs substrate structure with both finite-element calculation and experimental TEM imaging, showing that the surface strain relaxation of

cross-sectional TEM samples is significant regardless of the TEM foil thickness. Therefore, it is preferable to make strain measurements on plan-view samples.

Large-Angle Convergent-Beam Electron Diffraction (LACBED)

Large-angle convergent-beam electron diffraction (LACBED) is a relatively newly established TEM technique, first introduced by Tanaka et al. to overcome the limitations of conventional CBED that occur when the beam convergence becomes larger than the Bragg angle [44.39]. In the LACBED technique, the convergent electron beam is brought to a focus and the specimen is moved either above or below the object plane. Since the sample is defocused, a larger illuminated area forms shadow images in the diffraction discs. The transmitted beam is selected by means of the selected-area aperture and the disc pattern is made of deficiency lines. These Bragg lines are superimposed with the shadow image in the transmitted disc, i.e., information about reciprocal space (the Bragg lines) and direct space (the shadow image) are simultaneously present. In this way, a LACBED pattern can be considered as an image-diffraction mapping technique. There is no rotation between the shadow image and the diffraction pattern if the specimen is below the object plane, while there is a 180° rotation if the specimen is above. To a good approximation, the spatial resolution in the shadow image is given by the minimum probe size. Some examples of the application of LACBED are presented in the following sections.

Dislocation Analysis. LACBED was originally applied to the characterization of dislocation Burgers vectors by Cherns and Preston [44.40]. Since then, LACBED has evolved into a technique to investigate strain fields in materials. It can be used to unambiguously determine the magnitude and the sign of a dislocation Burgers vector and has been applied to the characterization of partial dislocations, stair-rod dislocations, grain boundary dislocations, etc. It is also an essential technique to study point defects, planar defects, and other crystalline phenomena [44.41].

It was found that splitting of HOLZ lines and Kikuchi lines occur when a convergent electron beam is brought close to a dislocation due to its long-range displacement, providing $\mathbf{g} \cdot \mathbf{b} \neq 0$ [44.42]. However since the displacement field of a dislocation varies from place to place, features in a CBED pattern are sensitive to the exact location of the probe, which is difficult to determine experimentally. This difficulty is overcome by the

use of LACBED, in which the specimen is defocused and a larger area including a segment of dislocation is illuminated. The displacement and the multiplicity of the splitting of a LACBED Bragg line when it intersects a dislocation may be simply related to the sign and magnitude of the dislocation under a wide range of diffracting conditions. Simple rules discovered by *Cherns* and *Preston* [44.43] can be summarized as follows, and a corresponding schematic is shown in Fig. 44.9:

1. The number (n) of interfringes present at a splitting is given by $n = |\mathbf{g} \cdot \mathbf{b}|$.
2. The sign of $\mathbf{g} \cdot \mathbf{b}$ is given by the characteristic twisting of the Bragg line: when $\mathbf{g} \cdot \mathbf{b} > 0$, then at $x > 0$, the contour is bent to the $s < 0$ side, and at $x < 0$, the contour is bent to the $s > 0$ side. On the other hand, when $\mathbf{g} \cdot \mathbf{b} < 0$, then the contour is bent in the opposite sense (s indicates the deviation vector, while x indicates the horizontal distance from the dislocation line).

The method requires the observation of at least three splittings in order to solve the set of three linear equations: $\mathbf{g}_1 \cdot \mathbf{b} = n_1$, $\mathbf{g}_2 \cdot \mathbf{b} = n_2$, and $\mathbf{g}_3 \cdot \mathbf{b} = n_3$.

Partial dislocations with small Burgers vectors, such as stair-rod dislocations with $\mathbf{b} = 1/6(110)$, are notoriously difficult to analyze directly in image mode. *Cherns* et al. successfully studied Shockley and Frank partial dislocations as well as stair-rod dislocations in Si, GaAs, and CdTe with LACBED [44.44].

Stacking Faults. LACBED can be employed to extract information on the type and the magnitude of the displacement associated with an inclined stacking fault [44.41, 45–47]. It also has the advantage of being applicable to in-plane stacking faults, in contrast to conventional imaging [44.41]. When the inclination of the fault is known, the LACBED technique can directly determine the fault type. The asymmetry of the LACBED pattern due to the fault indicates the sign of the fault. Also, with a more detailed comparison of theory and experiment, an estimate of the phase shift can be determined. In the case of $\{111\}$ intrinsic or extrinsic stacking faults present in face-centered cubic (fcc) structures, the phase shift α could be 0 or $\pm 2\pi/3$. As a result, the rocking curves are modified and the CBED lines with $\alpha = \pm 2\pi/3$ are split into a main line and a subsidiary one, the subsidiary line being on one side or on the other depending upon the sign of α and s . The best effect is observed when the incident beam is

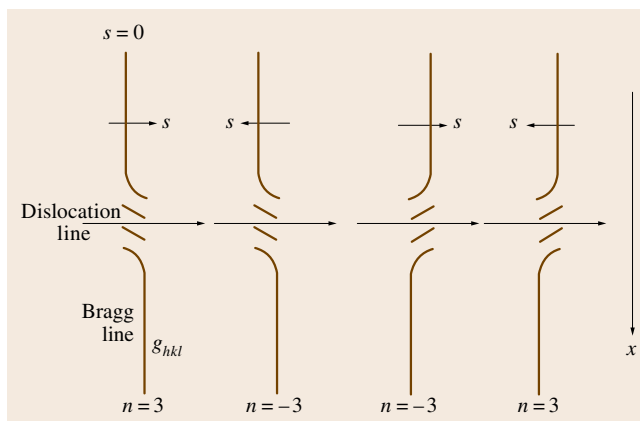


Fig. 44.9 Schematic showing the Cherns and Preston rules

located in the center of the stacking fault. From such a pattern, it is possible to identify \mathbf{R} [44.48].

Strain Measurement. The LACBED method enables examination of multilayers in plan view since rocking curves over a sufficient angle can be observed and allow for the analysis of the contributions from the component layers [44.41]. In the case of strained heterostructures, a shift of the ZOLZ or HOLZ lines in LACBED discs has been observed due to the relative misfit strain between epilayer and substrate. The strain in an epitaxial system may cause relative rotation of the individual planes in the epilayer and/or the substrate. Such a rotation can be observed as a splitting of the Bragg lines of medium- or high-index reflections. For large rotations, the peak splitting approximates to the relative angle of rotation resulting from the misfit stresses in bicrystals and multilayers. Misfit strains down to 0.1% can be measured by LACBED [44.41]. *Hovsepian* et al. studied the composition of GeSi quantum dots embedded in two Si layers with the LACBED technique [44.49]. The asymmetry of rocking curves of inclined planes (inclined to 001 growth direction) is caused by the phase shift $\mathbf{g} \cdot \mathbf{R}$, where \mathbf{R} is total normal displacement across the layer. By comparing to the two-beam kinematically calculated rocking curves, the composition of the Ge quantum dots can be determined.

44.1.4 STEM, EELS, and EFTEM in Microanalysis

Often combined with conventional TEM, scanning transmission electron microscopy (STEM), electron energy-loss spectroscopy (EELS), and energy-filtered

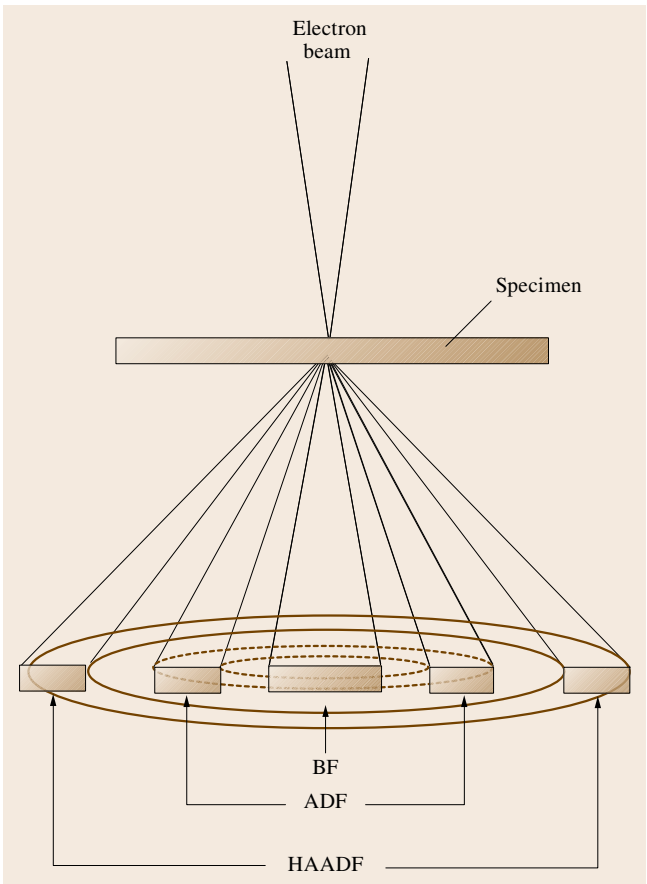


Fig. 44.10 Schematics showing different STEM detector arrangement

transmission electron microscopy (EFTEM) have found unique applications in a wide range of applications in

materials analysis. In many research areas, such as the semiconductor industry, STEM, EELS, and EFTEM have become essential tools to assist process development and defect analysis.

STEM Imaging

STEM has been used extensively in conjunction with conventional TEM, especially due to the advance in refining electron beam spot size by the availability of field-emission guns and lens aberration correctors [44.51, 52].

STEM image formation is achieved through scan synchronization of the electron beam and a television (TV) monitor with input signals from an electron detector. The electron detector is placed conjugate to the back focal plane of a microscope. Depending on the collection angle of the detector (Fig. 44.10), three major STEM methods are defined: bright field (BF), annular dark field (ADF), and high-angle annular dark field (HAADF). The BF detector is normally a circular disk which collects the transmitted electron beam and low-angle scattered electrons. Both ADF and HAADF detectors are annular disks with a hole in the middle, enabling a limited part of the scattered electrons to be collected for the STEM signal. Figure 44.11 shows examples of the same feature (TiN and TiSi_x crystal growth when forming a contact in a semiconductor device) viewed by three different STEM methods. With proper selection of camera lengths or by using an objective lens aperture, BF STEM gives essentially the same image as BF TEM. HAADF collects only high-angle (e.g., > 40 mrad) scattered electrons. The contrast is attributed to Rutherford scattering [44.53, 54], so the local intensity is proportional to $\sum n_i Z_i^2$, where Z is the atomic number and n_i is the number of elements of ele-

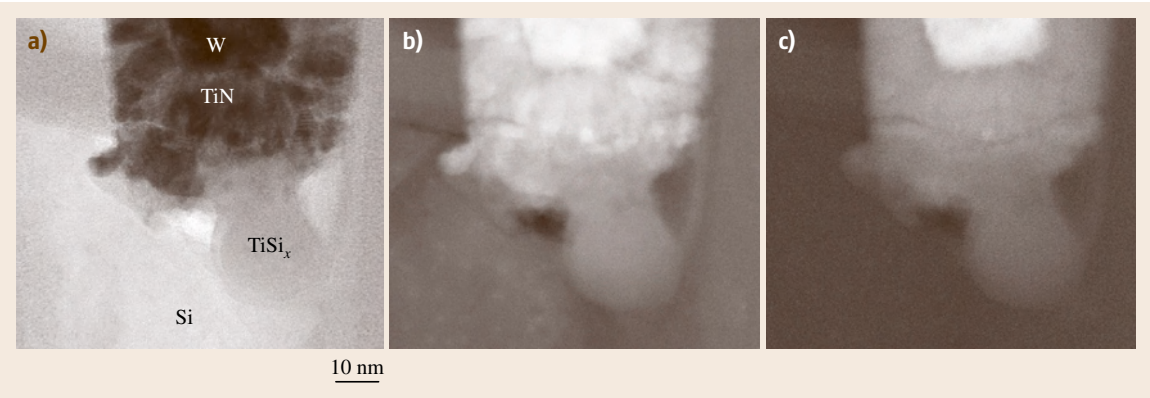


Fig. 44.11a–c Example STEM images (after [44.50]): (a) BF STEM, (b) ADF STEM, and (c) HAADF STEM

ment i present in an atom column. This simple approach gives a good explanation as to why the HAADF STEM is Z-contrast. Recent studies have found that HAADF STEM is better modeled by thermal diffuse scattering [44.55–57]. Using the thermal diffuse scattering model, the Z-dependent contrast HAADF STEM can be quantitatively analyzed. Because of its Z-dependency, HAADF STEM is also called Z-contrast STEM.

Positioned in the medium collection-angle range between BF and HAADF, the ADF collector collects diffracted electron beams as well as certain low-angle thermally scattered electrons. Thus the ADF image has mixed Z and diffraction contrasts, as shown in Fig. 44.11 [44.50]. Instrumentally, the ADF and HAADF often share the same detector, and the collection angle is normally controlled by camera length. Although different STEM methods have been used in different situations, the HAADF STEM has proven to be a unique and powerful tool by offering incoherent and Z-contrast imaging.

EELS Elemental Analysis

Recent advancements in instruments and software have made EELS a practical tool in various microanalysis applications. In combination with HAADF STEM imaging, EELS analysis offers rich information with regards to chemistry, chemical bonding, and thickness with high spatial resolution. When electrons pass through a specimen, some experience inelastic scattering. A magnetic spectrometer (either post-column or in column [44.58]) spreads the inelastically scattered electrons based on their energies. By plotting the number of electrons versus energy loss, we obtain an electron energy-loss spectrum.

The features of an EELS spectrum are illustrated in Fig. 44.12. The horizontal axis is the energy loss. However, it is often labeled *energy*, instead of *energy loss* ΔE , for simplicity. There are three general regions in a complete EELS spectrum: the zero-loss peak (ZLP), the low-loss region, and the core-loss edge. The zero-loss peak is formed by electrons that are not scattered

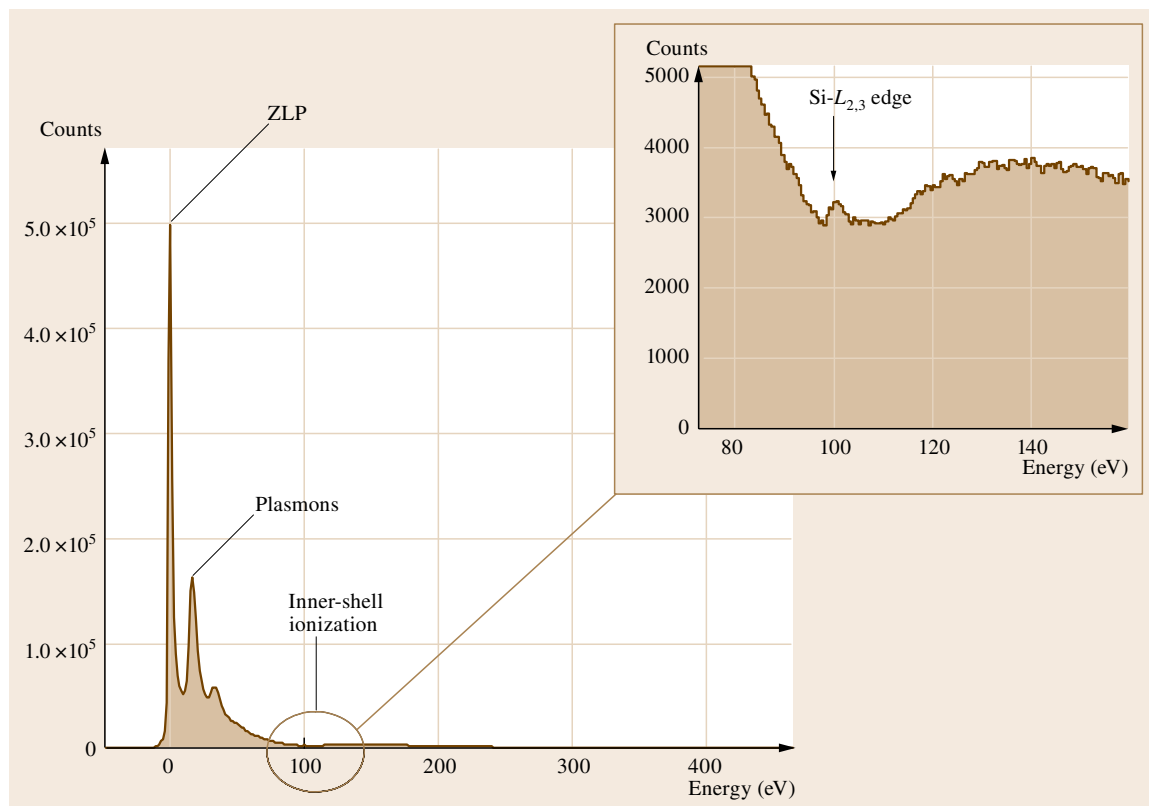


Fig. 44.12 An example EELS spectrum showing features of zero-loss peak (ZLP), low-loss region, and core-loss features (after [44.50])

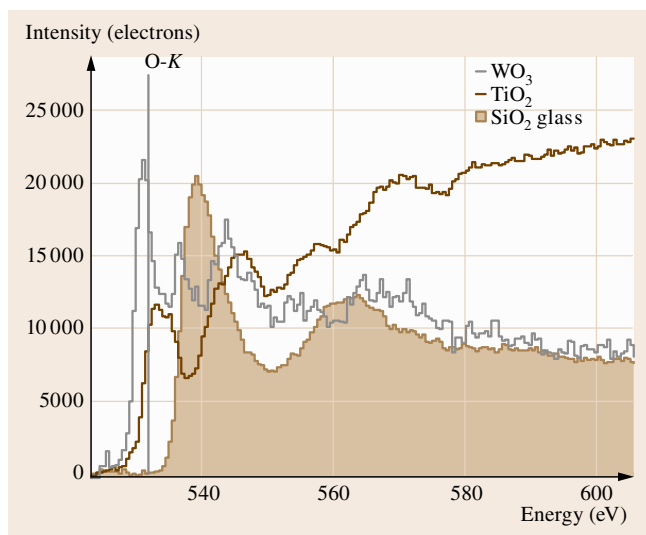


Fig. 44.13 Comparison of oxygen near edge fine structures from WO_3 , TiO_2 , and SiO_2 ◀

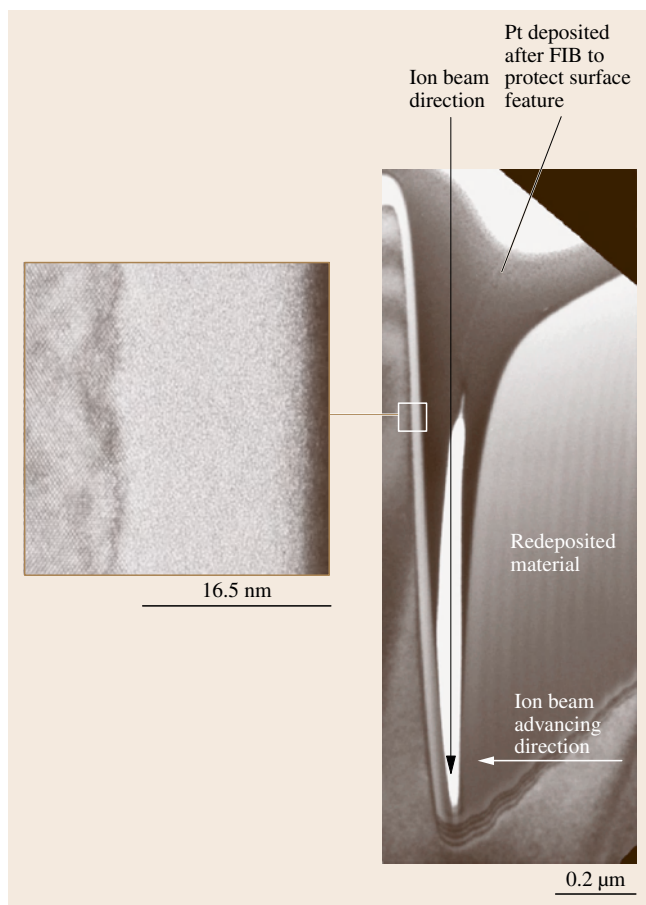
or scattered elastically in the specimen with negligible energy loss. A low-loss region is the energy loss range up to ≈ 50 eV. The signal in this region often includes plasmon excitation, due to collective excitation of valence electrons [44.58]. The core-loss edge in the spectrum occurs when an incident electron transfers sufficient energy to an orbital electron to move it to higher energy levels. The atom is said to be ionized. Thus, this process is also called inner-shell ionization loss. The character of the inner-shell energy loss is *edge*. The onset of the edge corresponds to the minimum energy for the ionization (the energy difference between the original energy level and the lowest available target level).

Important information often contained in **EELS** is the chemical bonding information. A bonding change can result in a variation of energy-loss near-edge structure (**ELNES**). Some examples of variation of near-edge fine structures are shown in Fig. 44.13, which compares the O-K edge (energy loss of K-shell electrons) for WO_3 , TiO_2 , and SiO_2 [44.50]. In these comparisons, we see pronounced differences in the shape of the O-K edge due to the difference of W-O, Ti-O and Si-O bonding. This valuable information is often of interest in microanalysis and helps to identify chemical information in certain ambiguous situations [44.60]. **EELS** and **EDS** are often complementary to each other in their efficiencies and accuracies of detecting certain elements [44.58, 61]. However, **EELS** generally offers higher spatial resolution and less signal overlapping than **EDS**. In **STEM** mode, the spatial resolution of **EELS** is essentially that of **STEM**. Nanoscale chemical analysis can be routinely obtained with a modern **STEM/EELS** system.

EFTEM

By combining an electron energy-loss spectrometer and imaging-forming lenses, it is possible to form an image with electrons of a selected energy. This technique is known as energy-filtered transmission electron

Fig. 44.14 A cross-sectional view of Si surface prepared by **FIB** using 30 keV Ga^+ . Note the amorphous layer caused by ion-beam damage. The milled surface is not parallel to the beam direction because of the radial intensity distribution of the ion beam (after [44.59]) ◀



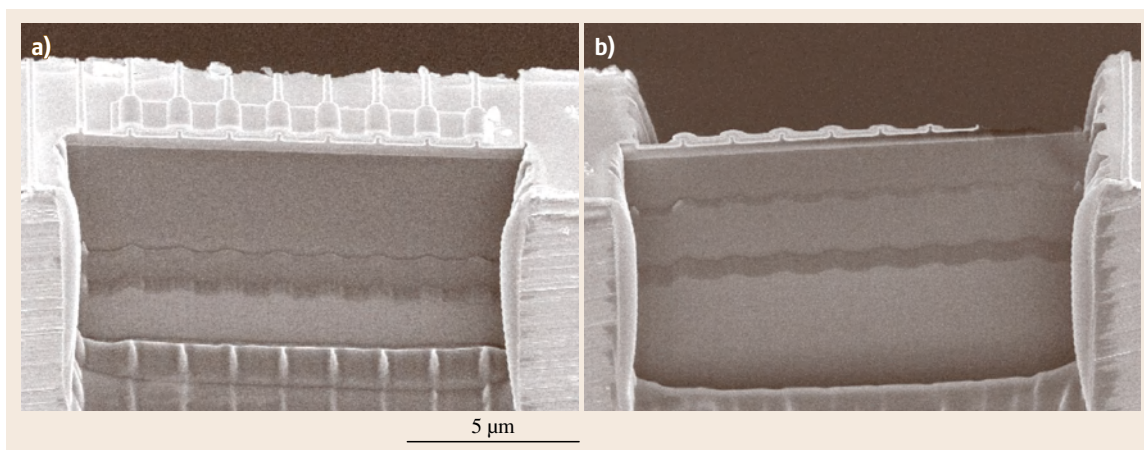


Fig. 44.15a,b Sample preparation for TEM using an FIB/SEM system. (a) The front side of the sample where the milling can be stopped at a desired location with monitoring by SEM. (b) Back-side view of the finished sample (after [44.50])

microscopy. EFTEM adds a new dimension to conventional TEM and its advantages include:

1. Cleaner imaging by the removal of inelastic scattered electrons (imaging using zero-loss energy window)
2. Element-specific mapping
3. Removal or suppression of diffraction contrast
4. Contrast enhancement.

Some examples from the application of EFTEM can be found in Sect. 44.2.3.

44.1.5 FIB for TEM Sample Preparation

The success of TEM analysis largely relies on the quality of the TEM sample. The development of the focused ion beam (FIB) system [44.62, 63] has greatly enhanced TEM sample preparation capabilities [44.59, 64]. In a FIB system, a focused ion beam (normally Ga^+) is used to micromachine the target material by ion beam sputtering. The emitted secondary electrons or ions can be used for in situ imaging. Direct ion-beam imaging makes the location control of FIB milling possible. Due to the capability of monitoring FIB milling process, combination of SEM and FIB has

become common and necessary for TEM sample preparation.

A cross-sectional view of a FIB-milled surface in Si is shown in Fig. 44.14 [44.65]. Figure 44.15 shows two SEM pictures of TEM sample preparation in a FIB/SEM system. The benefits offered by FIB in TEM sample preparation include:

1. The ability to be location specific with an accuracy of a few nanometers
2. The absence of mechanical damage to the sample
3. A similar cutting rate for different materials (because the milling front is controlled mostly by focused beam movement as opposed to sputtering rate)
4. The ability to isolate a small sample from a bulk material with a lift-out probe.

An undesirable artifact from FIB is the ion-beam damage to the sample prepared, as shown in Fig. 44.14. For many materials, such as crystalline Si, the structural damage can introduce certain problems with imaging and analysis, especially for thin samples. Low-energy ion-beam milling, either within FIB or with a conventional ion miller, can generally improve sample quality by reducing the thickness of the damaged layer [44.59].

44.2 Selected Examples of Application of TEM to Semiconductor Systems

In the following, TEM studies of defects, strain, interface, etc. of two kinds of semiconductor systems

will be detailed as examples: conventional heteroepitaxial systems and large-mismatch heteroepitaxial sys-

tems. Examples for the application of STEM, EELS, and EFTEM in semiconductor devices are given in Sect. 44.2.3.

44.2.1 Studies of Conventional Heteroepitaxial Semiconductor Systems

In low-mismatch systems, the theories of *van der Merwe* [44.66] and *Matthews* [44.67] describing the accommodation of lattice misfit are well established and have been experimentally verified. According to these theories, the epigrowth is assumed to follow a two-dimensional, layer-by-layer mode. When the thickness of the epilayer is lower than a critical thickness h_c , the film is pseudomorphic with the substrate and the mismatch is accommodated by elastic strain. At the critical thickness h_c , misfit dislocations form to accommodate the strain plastically as well as elastically. The formation of the misfit dislocations can occur in two ways:

1. Threading dislocations replicated from the substrate into the film are forced, under the influence of the mismatch stress, to glide leaving a trailing interfacial misfit segment connecting the original substrate threading segment and the mobile threading segment.
2. Dislocation half-loops nucleate at the surface of the film and glide toward the film–substrate interface, leaving a misfit segment and two threading segments (the surface nucleation will likely occur at some heterogeneity such as a step, surface sites where contamination is present, and possibly at the valleys of surface undulations caused by morphological instabilities) [44.68, 69].

This ultimately results in an interface composed of large coherent regions separated by rows of misfit dislocations. If the substrate is assumed to be rigid and the elastic strain is built up only on the film side, the lattice misfit is composed of two parts [44.67]

$$f_0 = \varepsilon_{pl} + \varepsilon_{el},$$

where ε_{pl} is the strain accommodated by dislocations and ε_{el} is the strain accommodated elastically, i.e.,

$$\varepsilon_{el} = \frac{(\langle a_0 \rangle - a_0)}{a_0},$$

$$\varepsilon_{pl} = \frac{b_f}{D_f},$$

where $\langle a_0 \rangle$ is the average lattice parameter of the grown film, b_f is the Burgers vector of the misfit dislocations,

and D_f is the average spacing between two misfit dislocations.

If the total misfit is relieved by plastic strain, the spacing between misfit dislocations should be $D = b_f / f_0$. However, this is difficult to achieve because the nucleation and glide of dislocations needs to overcome an energy barrier and its driving force presumes a sufficient amount of residual strain.

For metal films, the experimentally determined critical thickness agrees reasonably well with the value predicted using the equilibrium theory of *van der Merwe* and *Matthews*. For semiconductor films with diamond and zincblende structure, however, experimental observations revealed much larger values of the critical thickness and a slower relaxation of the elastic strain than would be expected from equilibrium calculations [44.70].

Misfit Dislocations

As aforementioned, epilayers which are mismatched with respect to the substrate due to either different structure or composition can be relaxed or partially relaxed by the formation of misfit dislocations with edge character once the epilayer exceeds a critical thickness. In most common cases of heteroepitaxial structures with diamond or zincblende-type structures with (001) orientation, the mismatch is accommodated by an orthogonal network of misfit dislocations along two perpendicular in-plane $\langle 110 \rangle$ directions. Figure 44.16 shows a plan-view TEM image taken along the [001] direction from a Si/Si_{0.85}Ge_{0.15} interface. Arrowed is a characteristic fingerprint of the Hagen–Strunk mechanism [44.71]. It has been always observed that the density of misfits along these two directions are different (i.e., not equally spaced). As the dislocation spacing approaches that needed to relax the layer fully the asymmetry between the two orthogonal arrays becomes less marked. This has been attributed to the differing mobilities of α and β dislocations which are more significant at lower stresses [44.72]. For small-mismatch systems, 60° misfit dislocations are dominant, although occasionally pure edge misfit dislocations can be observed in low-misfit systems; for example, *Fitzgerald* et al. [44.73] reported observation of such dislocations at the In_xGa_{1-x}As/GaAs ($x \approx 0.12$, mismatch = 0.085%) interface and attributed the generation of such sessile dislocations to the reaction of two glissile 60° dislocations with Burgers vectors in the same {111} glide plane. For higher-mismatch systems (misfit > 1.5–2%), the interfacial misfit dislo-

cations are predominantly of pure edge character with Burgers vectors $\pm a/2[1\bar{1}0]$ [44.74]. The explanation is the three-dimensional growth due to the high strain which occurs when the epitaxial deposit is very thin and the edge dislocations climb to the interface at the edge of the island. Figure 44.17 shows a HRTEM image taken from Ge/Si interface, showing that all three observed misfit dislocations are of 90° pure edge character.

For pure edge misfit dislocations, the reflections of $\{220\}$ can be easily applied to satisfy both the $\mathbf{g} \cdot \mathbf{b} = 0$ and $\mathbf{g} \cdot (\mathbf{b} \wedge \mathbf{u}) = 0$ criteria and make them invisible. However, the conventional Burgers vector analysis based on the simple $\mathbf{g} \cdot \mathbf{b} = 0$ invisibility criterion was not successful for the case of 60° misfit dislocations due to the strong residual contrast. Precise Burgers vector determination is difficult in (001) plan-view specimens because the reflections which give $\mathbf{g} \cdot \mathbf{b} = 0$ and $\mathbf{g} \cdot (\mathbf{b} \wedge \mathbf{u}) = 0$ ($\mathbf{g} = 422$, etc.) require high tilt angle. In practice, it is generally assumed that, if misfit dislocations lying along $[110]$ and $[\bar{1}\bar{1}0]$ cannot be made invisible with 220 and $2\bar{2}0$ reflections, then they are neither pure screw nor pure edge and therefore are likely to be 60°. Moreover, it is typical for 60° dislocations to show residual contrast in $\langle 400 \rangle$ diffraction. In addition, 60° dislocations show good contrast when the $\langle 220 \rangle \mathbf{g}$ vector is parallel to \mathbf{u} and stronger contrast when the $\langle 220 \rangle \mathbf{g}$ vector and \mathbf{u} are perpendicular. However, precise Burgers vector determination of 60° dislocations is still a problem. Nevertheless, several methods to analyze 60° misfit dislocations have been reported and are presented in the following.

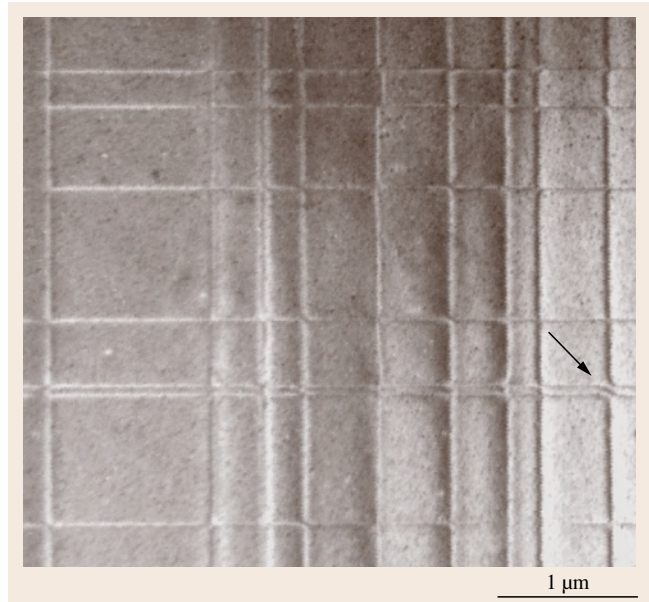


Fig. 44.16 Plan-view image taken along the $[001]$ growth direction showing the orthogonal misfit dislocation network at the strained Si/Si_{0.85}Ge_{0.15} interface; the arrow indicates a characteristic fingerprint of the Hagen–Strunk mechanism

One of the techniques of analyzing 60° dislocations is the $(\mathbf{g} \cdot \mathbf{b})_s$ criteria that has been utilized by Stach [44.75]. This is based on dynamical theory calculations of the electron scattering in the vicinity of dislocations, through which it can be shown that the position of the dislocation image with respect to its actual

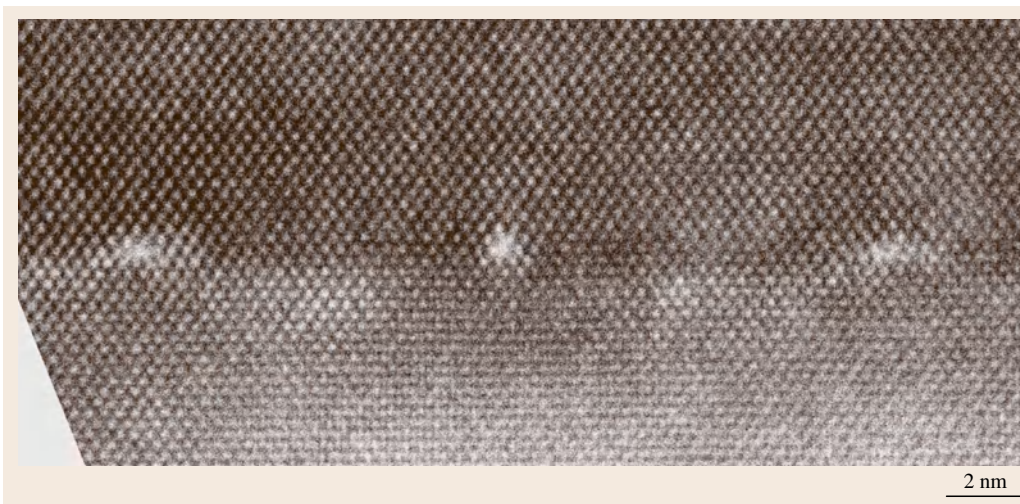


Fig. 44.17 HRTEM image showing the dominant misfit dislocations of pure edge character at the Ge/Si interface

core position varies with changes in deviation parameter as given by the quantity $(\mathbf{g} \cdot \mathbf{b})s$. Therefore, when $\mathbf{g} \cdot \mathbf{b} = 0$, the position of the dislocation core will not vary with changes of s . This means that, even when effective invisibility is not observed according to the usual $\mathbf{g} \cdot \mathbf{b} = 0$ condition, it is possible to determine the value of \mathbf{b} by tracking the position of the dislocation image as s is changed. This is done most efficiently using high magnification on the video screen on the TEM. In Stach's study, two-beam bright-field and dark-field images were recorded using 400, 040, 311, and $13\bar{1}$ diffractions and the position of the dislocation image was observed as the deviation parameter was varied from $s \ll 0$ to $s \gg 0$.

In another approach, bend contour analysis is used to investigate the 60° misfit dislocations. This technique was originally explored by Bollmann [44.76] and was recently revisited for large-area analysis of misfit arrays [44.77]. Basically, in a two-beam bright- or dark-field image, a characteristic splitting occurs when a dislocation crosses a bend contour with the number of splitting fringes given by $n = \mathbf{g} \cdot \mathbf{b}$. By evaluating the splitting of at least three bend contours from different reflections, the complete Burgers vector can be determined. In spite of the advantages that LACBED has (for example, controllable deviation error) for Burgers vector analysis, the bend contour technique is highly suitable for the analysis of misfit dislocations in small-mismatch semiconductor epistuctures (e.g., SiGe film grown on Si). Spiecker studied a large number of misfit dislocations simultaneously in SiGe/Si heterostructure plan-view samples by analyzing the splitting and displacement of the bend contour contrast that occurred as they were crossed by misfit dislocations.

For Burgers vector analysis, it is convenient to dissociate the 60° dislocation into three components, e.g., $a/2[101] = a/4[1\bar{1}0] + a/4[110] + a/2[001] = \mathbf{b}_{\text{misfit}} + \mathbf{b}_{\text{screw}} + \mathbf{b}_{\text{tilt}}$, as shown in Fig. 44.18. In this particular study, a dislocation with line direction $[110]$ was analyzed. The sign and the magnitude of the screw component is determined by the splitting and twisting of the 440 bend contour while the sign of $\mathbf{b}_{\text{misfit}}$ is determined by the displacement of the $4\bar{4}0$ bend contour. To determine the tilt component, the bend contours of higher-order Laue zone reflections $\bar{3}\bar{3}1$ and $\bar{3}\bar{3}3$ were used. The main advantage of this method is its applicability to simultaneous determination of the Burgers vectors of a large number of dislocations distributed over large sample regions.

Another technique capable of providing information of misfit dislocation Burgers vectors was reported by Dixon and Goodhew [44.78]. This method used detailed analysis of the interactions between orthogonal arrays of misfit dislocations to approximately estimate the distribution of possible Burgers vectors. Three types of interaction were considered:

1. Those where the dislocations have the same Burgers vectors (parallel or antiparallel), which leads to the formation of two L-shaped segments
2. Those where the Burgers vectors are oriented at 60° to each other, which leads to the formation of linking $1/2\langle 110 \rangle$ dislocation
3. Those where the Burgers vectors are perpendicular to each other, which are predicted to have no interaction.

For the case of an epitaxial interface where interfacial dislocations of 60° character are predominant, with edge character being also present in reduced number (screw character dislocations being absent) and assuming that the five possible Burgers vectors are present in equal numbers for each set of dislocations, there will be 25 types of interaction. By analyzing all the possibilities, it was found that 4/25 (16%) of intersections would be L-shaped, 16/25 (64%) would have links, and 5/25 (20%) would not react. For the case where no pure edge dislocations were found at the interface, only 16 reactions are possible, of which 4/16 (25%) intersections should be L-shaped, 8/16 (50%) would have links, and 4/16 (25%) would not have reacted. The linking segments formed at intersections are very short and assumed to be undistinguishable from the unreacted intersections. The reported observation showed that 18% of the intersections were L-shaped, implying that the in-

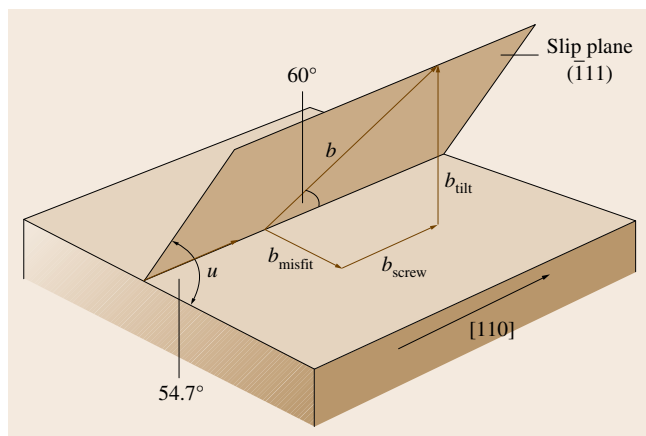


Fig. 44.18 Three components of a 60° misfit dislocations

terface probably contained dislocations of all four 60° types together with some pure edge dislocations.

Lattice imaging can, in principle, be used to distinguish between edge and 60° misfit dislocations. Both types of dislocation have the same Burgers vector magnitude ($a/2(110)$) but for edge-type dislocations the Burgers vector is oriented parallel to the interface while the 60° -type dislocations form a 45° angle with the interface. Therefore on $[110]$ lattice images, the edge dislocations should show two terminating $\{111\}$ planes at the core, while the 60° type should show only one terminating plane.

Critical Thickness

Extensive studies have been carried out by TEM to elucidate the practical critical thickness of the epilayers. Four general models have been identified defining critical thickness:

1. The Matthews and Blakeslee model [44.79] for the turnover of a single threading dislocation during the growth of a single epilayer
2. The Matthews and Blakeslee model for the turnover of a single threading dislocation in a multilayer structure which was subsequently pulled out into a half-loop by the internal stress in the layer
3. The Miles and McGill model [44.80], basically a modified and more sophisticated version of (1) and (2)
4. The People and Bean model [44.81], which concerns the critical thickness that allows the nucleation of fresh dislocation line.

Dixon et al. [44.82] performed a systematic study of the critical thickness in the $\text{In}_x\text{Ga}_{1-x}\text{As}/\text{GaAs}$ ($x < 0.25$) epistucture. In their study, two critical thicknesses are identified: threading dislocation are turned over, forming misfits at a thickness predicted by the Matthews and Blakeslee model; and, at larger thicknesses, fresh dislocations are nucleated at the interface and the critical thickness fits well with the predictions of the People and Bean model. Dixon et al. also concluded that some misfit dislocations were present which did not act to relieve misfit strain.

Stacking Faults and Partial Dislocations

The dissociation of 60° misfit dislocations and the existence of stacking faults are widely observed in conventional small-mismatch epistuctures. However, the geometry and the formation mechanism of the stacking faults have been the subject of extended research.

Theoretically [44.83], the order in which the partials can nucleate is determined by the atomic configuration on the $\{111\}$ glide planes. Under conditions of tensile stress, the first partial to nucleate is the 90° Shockley partial followed by the 30° partial. This order is reversed if the stress field is compressive. The resolved shear stress on the $\{111\}$ slip plane is, in both cases, in the same direction as the Burgers vector of the 90° partial. This means that the force exerted by the stress field on the 90° partial is twice as large as the force on the 30° Shockley partial. The consequence of this is that, in a tensile stress field, the 90° partial nucleates first, forming a stacking fault, since it experiences the largest force. On the other hand, the 30° partial, which would annihilate the stacking fault, feels a weaker force so that it may not nucleate until later in the growth process. As a result, stacking faults are very often observed extending from the interface to the film surface. In contrast, if the stress field is compressive, the 30° partial begins the nucleation process. Since this partial experiences a smaller force, a higher nucleation barrier results. Once the 30° partial is formed it will again be trailed by the 90° partial that is driven both by a higher force from the stress field and from a force associated with the stacking fault. This means that the extent of dissociation will be very small in a compressive field. An undissociated 60° perfect dislocation can then easily cross-slip, i. e., change from one $\{111\}$ glide plane to another. Such effects are observable if we compare misfit dislocation grids of a film under tensile and compressive strain; in the film under tensile strain, the misfit segments form straight lines and a number of stacking faults can be observed, whereas in the film under compressive strain the misfit dislocations exhibit higher curvature, evidence for cross-slip having occurred, and little evidence for the existence of stacking faults.

A variety of observations on different heterosystems have been reported. Kimura et al. [44.84] studied the development of defects in strained Si/SiGe heterostructures of supercritical thickness. TEM observations showed that, when the strain energy is increasing in the Si film, 60° misfit dislocations at the interface dissociate into Shockley partials with the 30° partial being located in the Si film and the 90° partial being located in the SiGe layer. The observed stacking faults are believed to form by the 30° partial gliding out to the surface of the Si film. Marshall et al. [44.85] reported that the predominant configuration of 60° misfit dislocations in low-misfit SiGe/Si films ($< 15\%\text{Ge}$ or 0.6% misfit) involves dissociation at the interface, with the stacking fault extending into the substrate. Zou and Cock-

ayne [44.86] studied the equilibrium geometries of the dissociated misfit dislocations in single-semiconductor heterostructures. They predicted that for, a tensile-strained layer grown on a (001) substrate, the 30°

partial is located in the strained layer and the 90° partial is located in the substrate. Their experimental observation in low-strained [001] $\text{In}_{0.1}\text{Ga}_{0.9}\text{As}/\text{GaAs}$ single heterostructures [44.87] showed that the dissociation of misfit dislocation is dominant in the structure, with the 90° partial being located above the strained interface and the 30° partial in the buffer layer. Hirashita et al. [44.88] reported the observation of stacking faults extending from a strained Si surface to a strained Si/SiGe interface, which are accompanied by 90° Shockley partials at the interface. These defects are increasingly formed in the strained Si layers on SGOI substrates while the strained layer thickness increases. It was concluded that the operative mechanism involved the generation of 90° partial dislocations at the Si surface which propagated on {111} planes towards the SiGe interface, relaxing the cumulative tensile strain in strained Si layers. Fitzgerald et al. [44.89] reported mechanisms for the reaction of partials in lattice-mismatched $\text{In}_x\text{Ga}_{1-x}\text{As}/\text{GaAs}$ heterostructures. In films which are under compression, the trailing partial which is closest to the epilayer surface is the 90° partial, while the leading partial is the 30° partial. Therefore, the two leading 30° partials can form a stair-rod dislocation ($\mathbf{b} = a/6\langle 1\bar{1}0 \rangle$), leaving two edge partials ($\mathbf{b} = a/6\langle 1\bar{1}2 \rangle$). In a tensile epilayer, the leading partials are edge partials, and the 30° partials are closer to the surface. In this case, the leading 90° partials would form an edge dislocation with $\mathbf{b} = a/3\langle 110 \rangle$.

Figure 44.19a is a cross-sectional image of two stacking faults formed at a strained Si/Si_{0.5}Ge_{0.5} interface. The reaction between stacking faults can be clearly observed. A stair-rod dislocation is formed at the junction and between two faults and leads to the annihilation of all the faults. The squared area is enlarged and shown in Fig. 44.19b. The stacking sequence can be clearly seen as CBACBCBA... as the stacking fault is crossed.

Graded Buffer and Insertion of Strained Layers

Compositionally graded buffers have been successfully employed in lattice-mismatched epitaxy to incorporate high-quality relaxed layers onto conventional semiconductor substrates [44.90, 91]. A typical example is the use of SiGe graded buffers as virtual substrates for the production of high-mobility complementary metal oxide semiconductor (CMOS) structures and for III–V integration on Si. Some of the major requirements for such application include: low threading dislocation density (TDD), low surface roughness, and high degree of relaxation of the 4% lattice mismatch between Si and Ge. The compositionally graded structure provides mul-

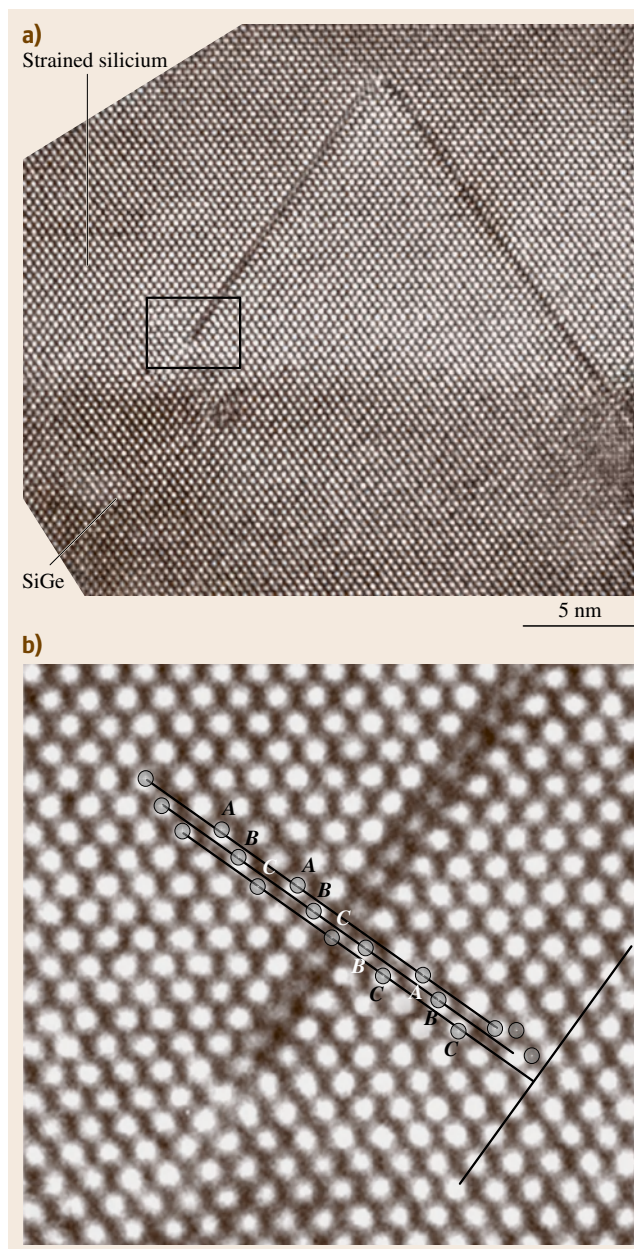


Fig. 44.19a,b A cross-sectional HRTEM image showing the stacking faults and their reaction at a strained Si/Si_{0.5}Ge_{0.5} interface (a) and a magnified image of the squared stacking fault (b)

multiple low-mismatch interfaces, preventing dislocation nucleation and facilitating the glide of existing threading dislocations at each interface to relieve mismatch strain. Such grading results in relaxed cap layers with threading dislocation densities in the 10^5 – 10^6 cm $^{-2}$ range, whereas direct growth of uniform composition relaxed layer with high lattice mismatch results in threading dislocation densities in the 10^8 – 10^9 cm $^{-2}$ range.

Another technique of filtering threading dislocations by the insertion of superlattice was reported by *Blakeslee* [44.92]. The study suggested that, by properly designing superlattice structures, multistrained interfaces are provided for threading dislocations to lie on. Such structure also reduces the harmful interactions between dislocations. The essential ingredients of the proper design include:

1. The superlattice thickness should be considerably larger than the equilibrium critical thickness in order to provide the necessary excess stress to move the dislocation.
2. The strain gradients should be as gentle as possible everywhere except in the superlattice itself.

Compared with the step-graded structure, the superlattice structure confines the dislocations better. However, in this study, the relaxation of the film was not discussed.

Park et al. [44.93] studied the effects on strain relaxation and threading dislocation density of the insertion of thin layers, strained in tension or compression, into compositionally graded SiGe. Figure 44.20 shows cross-sectional images of three samples for comparison. Figure 44.20a shows the sample grown as the control condition, having no inserted strained layers, consisting of a 2 μ m linearly graded SiGe buffer where the Ge content increased from 0 to 20% at a grading rate of 10 %/ μ m followed by a 0.5 μ m-thick Si $_{0.8}$ Ge $_{0.2}$ cap layer. The structure exhibits a quite uniform distribution of dislocations throughout the graded buffer. Figure 44.20b shows the case of two inserted layers of pure Si, strained in tension, the bottom layer being inserted at the 6% Ge location and the top layer being inserted at the 12% Ge location. Figure 44.20c shows the insertion of two SiGe layers strained in compression, the bottom layer with 12% Ge being inserted at the 6% Ge location and the top layer with 24% Ge being inserted at the 12% Ge location. Accumulation of dislocations was found at the bottom of the layers strained in compression and at the top of the layers strained in ten-

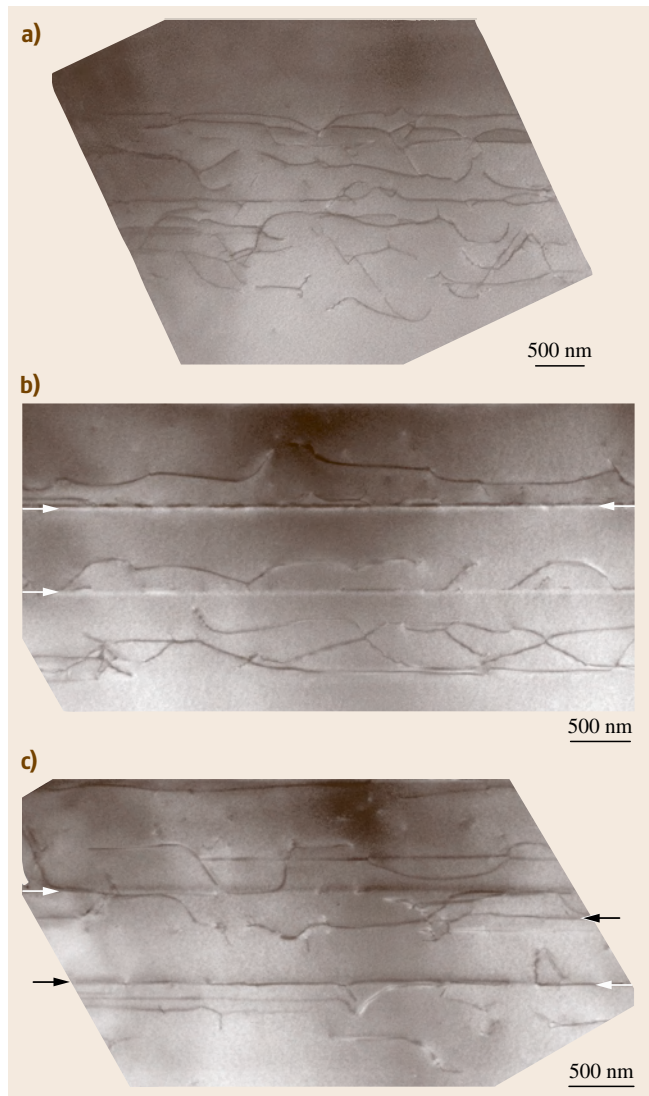


Fig. 44.20a–c Cross-sectional TEM images showing the dislocation behavior in the compositionally graded Si $_{0.8}$ Ge $_{0.2}$ buffer without/with insertion of tensile/compressed strained layers: (a) reference sample without insertion of layers; (b) insertion of two tensile layers; top layer (c) insertion of compression layer. Note: arrows indicate inserted layers

sion. This can be easily understood based on the sense of the dislocations. Compared with the sample with inserted compressive layers, the sample with tensile layers exhibits heavier accumulation of dislocations. Moreover, in the samples with inserted layers strained in tension, dislocations are pinned more heavily at the top

inserted tensile layer (0% Ge at 12% Ge) than at the lower inserted tensile layer (0% Ge at 6% Ge), whereas in the sample with layers strained in compression, dislocations were pinned more heavily at the lower inserted compressive layer (12% Ge at 6% Ge) than at the top inserted compressive layer (24% Ge at 12% Ge). The inserted strained layers in this study were always 20 nm thick, which is below the equilibrium critical thickness. Results showed that the relaxation in the cap layer is largely improved without significant increase of threading dislocations in the samples with inserted layers in compression compared with the control sample. Misfit dislocations are observed in the cap layer in both types of sample, in contrast to the control sample, indicating the disturbance of relaxation due to the insertion of stressed layers.

Observation of Dislocations in Aspect Ratio Trapping Epigrowth

Aspect ratio trapping (ART) is an epitaxial technique involving selective growth in patterned openings bounded by substantially vertical dielectric side-walls, enabling dislocations to be trapped if the aspect ratio (h/w) of the opening is sufficiently large. Recent research reported

by Park et al. [44.94] showed that ART could be effective for Ge grown on Si in trenches up to 400 nm wide and of arbitrary length. Figure 44.21 shows a plan-view TEM image recorded from such a sample that was thinned from the substrate side down to a thickness of ≈ 200 nm. Both the Si substrate and the first ≈ 300 nm of epilayer were removed, leaving only a defect-free Ge layer; this demonstrates the efficacy of the ART technique in eliminating threading dislocations in Ge films grown on Si substrates. Bai et al. [44.95] carried out analysis of the mechanisms by which dislocation elimination is achieved. Detailed TEM studies reveal that facets, when formed early on in the growth process, play a dominant role in determining the configurations of threading dislocations in the films. These dislocations are shown to behave as *growth dislocations*; during growth they are oriented approximately along the facet normal, and so are deflected out from the central regions of the trenches. This suggests a strategy of facet engineering by which the efficacy of threading dislocation trapping might be further improved. TEM images in Fig. 44.22 show the redirection of dislocations close to the normal of the encountered facets. The thin SiGe marker layers of approximately 10–15% Si content are periodically inserted to delineate the growth front.

44.2.2 TEM Studies of Large-Mismatch Heteroepitaxial Systems

Wurtzite polytypes of AlN, GaN, and InN and their alloys are suitable for numerous device applications such as short-wavelength light sources or detectors, and high-power and high-frequency devices. Due to the difficulty in obtaining GaN substrates, current GaN devices are fabricated on epitaxially grown films on various substrates. Most research on GaN epitaxy in the last two decades has been concentrated on growth on sapphire or SiC substrates. Sapphire is currently the most commonly used substrate for GaN epigrowth due to its relatively low cost. The large mismatch between GaN and sapphire (16%) leads to a very high density of interfacial dislocations. SiC is another candidate for the substrate which has smaller mismatch (3.4%). Si attracts attention as a substrate for GaN epigrowth since the first molecular-beam epitaxy (MBE) grown on GaN light-emitting diode (LED) on Si was demonstrated in 1998. The lattice mismatch between GaN and Si is -17% , yielding biaxial tensile stress in the GaN/Si interface. Owing to the high mismatch in lattice parameter and thermal properties between GaN and nonnative substrates, a high density of struc-

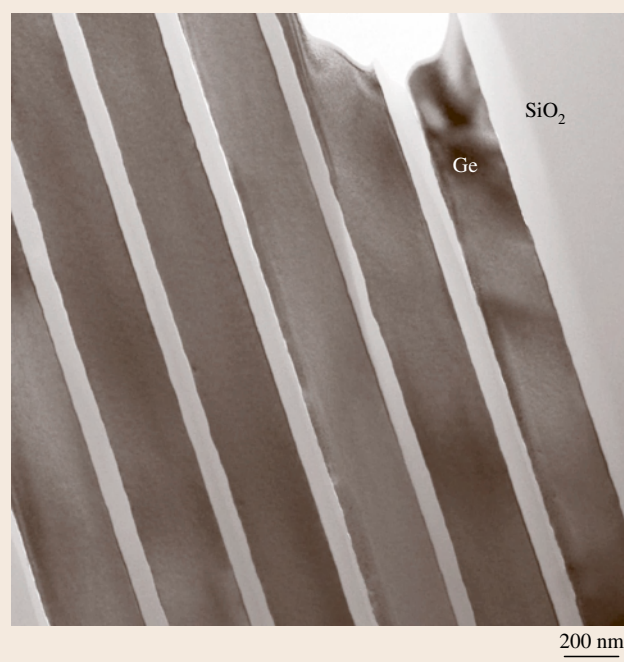


Fig. 44.21 Plan-view (along the [001] growth direction) TEM image of the top layer (≈ 200 nm from the film surface) of a Ge film grown with ART technique

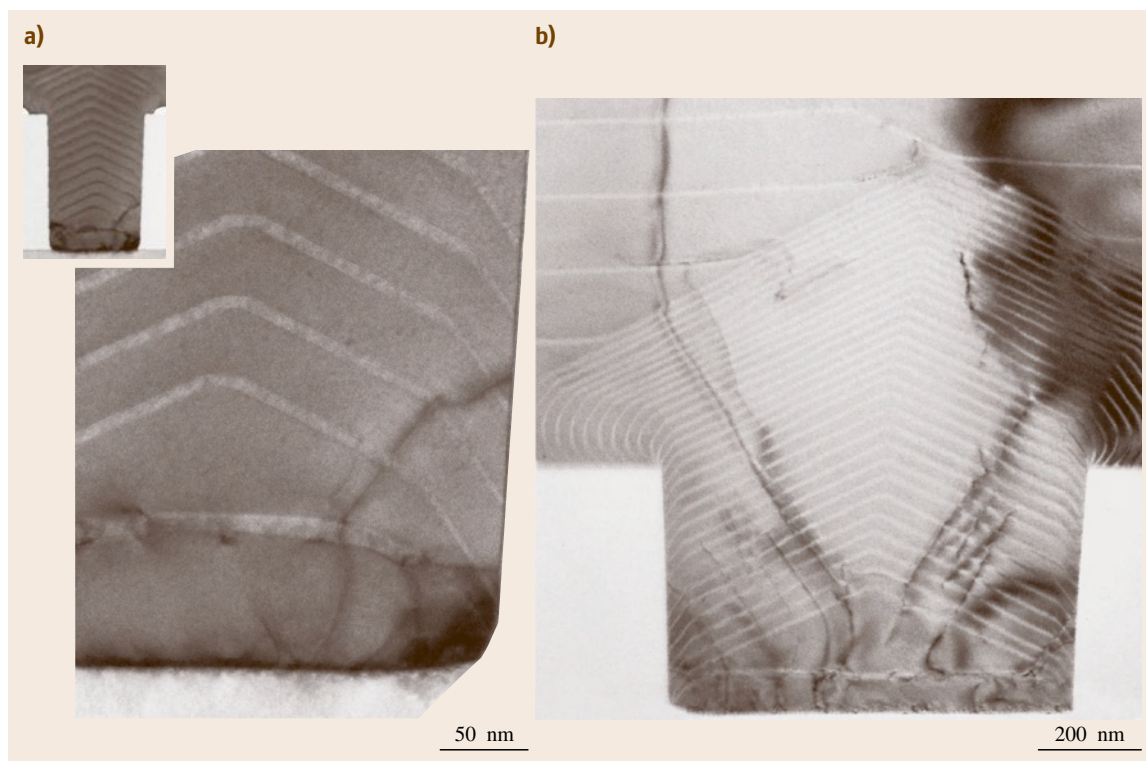


Fig. 44.22a,b Cross-sectional TEM images (viewed along the [110] trench direction) showing the redirection of threading dislocations under the influence of faceting **(a)** dislocation redirection in a trench of ≈ 300 nm wide (the linear white contrast features correspond to the inserted SiGe growth marker layers), where the *inset* shows the overview of the Ge film grown in the trench (the film was overgrown beyond the side wall); **(b)** dislocation redirection in a trench ≈ 800 nm wide

tural defects exists in GaN films. The large in-plane mismatch induces a high density of interfacial dislocations ($\approx 10^{13} \text{ cm}^{-2}$). Due to the three-dimensional (3-D) growth at the initial stage, a high density of threading dislocations ($\approx 10^8 - 10^{10} \text{ cm}^{-2}$) form in the GaN film to accommodate the twist between neighboring islands. The variations on the surface of substrates cause planar defects such as inversion domain boundaries (IDBs), stacking mismatch boundaries (SMBs), prismatic stacking faults (PSFs) or basal plane stacking faults (BSFs). Extensive research has been carried out to reduce the threading dislocation density in GaN epilayers. The employment of a low-temperature nucleation buffer layer before subsequent GaN growth was found to drastically improve epitaxial quality. Other strategies to improve the crystalline quality of III-nitride epilayers, such as lateral epitaxial overgrowth, vicinal surface epitaxy, insertion of low-temperature layers, use of porous substrates, etc., have been widely studied.

Interface

Unlike epitaxial systems with sphalerite structures (e.g., $\text{Si}_x\text{Ge}_{1-x}/\text{Si}$), large-mismatch systems such as GaN/SiC, GaN/sapphire, AlN/sapphire, etc., cannot occur by the formation and glide of dislocation half-loops to the interface producing misfit dislocation segments due to the absence of an effective slip system. As such the mechanisms of epilayer relaxation in these systems are far from understood. Furthermore, the stress caused by island coalescence and thermal processing as well as the high density of defects introduce further complexity into the relaxation mechanism. Some of the basic understanding of this topic can be summarized as follows.

Coincidence Lattice (Pseudosemicoherent Interfaces).

In large-mismatch systems which have mismatch parameters larger than $\approx 4-5\%$, the interface is incoherent, as shown in Fig. 44.23a, and there is no continuity

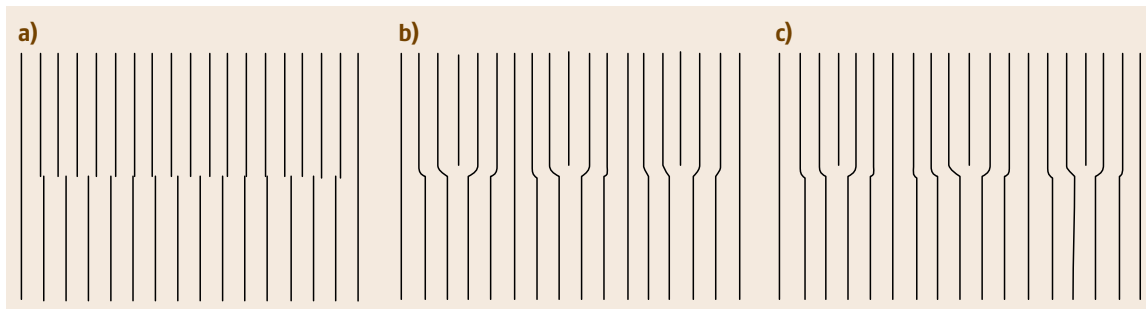


Fig. 44.23a–c Models for a large-mismatch interface: **(a)** perfect coincidence lattice with a lattice plane ratio of $m/n = 6/5$; **(b)** coincidence lattice with coherence relaxations within the unit cells; **(c)** as in **(b)**, but with a slight deviation of $1/80$, forming a new coincidence unit with $19/16 = 6/5 - 1/80$

between the lattice planes on the two sides of the interface [44.96]. However, the bonding between films and substrates in such systems suggest the appearance of coherency along some planes on the two sides of the interface separated by *geometrical misfit dislocations* (or *mismatch dislocations*), which separate these *pseudosemicoherent planes* (Fig. 44.23b). Perfect coincidence sites between the epilayer lattice a_e and substrate lattice a_s would occur when $a_s/a_e = m/n$, where m and n are positive integers. If $m = n + 1$, there is one extra lattice plane in each unit cell of the coincidence site lattice, i. e., a geometrical misfit dislocation is generated. The character of these dislocations depends on the symmetry of the coincidence lattice. In this sense, the Burgers vector of such a geometrical dislocation must not necessarily be an invariant vector as it is in the bulk lattices.

In contrast to the low-mismatch case, in which misfit dislocations are generally produced by lattice dislocations that may have Burgers vector not necessarily parallel to the interface, in large-mismatch systems the mismatch dislocations exist right from the start of film deposition and often have an in-plane Burgers vector.

Another difference between misfit dislocations in low-mismatch system and mismatch dislocations in high-mismatch system is that the latter lack long-range strain fields [44.97].

Near-Coincidence Lattice. An alternative model of generation of mismatch dislocations is that the deviation can also be accommodated by another type of secondary defect, as shown schematically in Fig. 44.23c [44.98]. Such secondary defects interrupt the periodicity of the original coincidence lattice and form a new coincidence unit.

Reported Models. Zheleva et al. suggested a domain-matching model for large-mismatch epitaxial systems [44.99]. In this model, a domain is defined by the minimum number of lattice planes that gives a value of unity for the difference between m (the number of epilayer lattice planes) and n (the number of substrate lattice planes). The residual domain strain can be calculated in both in-plane directions. Sun et al. suggested a concept of extended atomic distance mismatch (EADM) [44.100]. $EADM = (Id - I'd')/(I'd')$ (where I and I' are integers, d and d' are atomic distances of the epilayer and substrate, respectively. I and I' are determined in the following way: $d : d' \sim I : I'$, where $I : I'$ is the smallest irreducible integral ratio for $d : d'$. The difference between I and I' is one that introduces a periodic edge-type dislocation.)

TEM Observations of Large-Mismatch Interfaces. Kehagias et al. studied misfit relaxation at the AlN/Al₂O₃(0001) interface in both plan-view and cross-sectional geometry [44.101]. From moiré fringes shown in plan-view TEM images, a general case of a matching ratio of AlN:Al₂O₃ equal to 8 : 9 was observed, which is confirmed in the cross-sectional geometry. However, occasionally, AlN:Al₂O₃ ratios of 6 : 7 and 9 : 10 were also observed. Threading dislocation densities were also measured using the moiré fringes.

HRTEM performed on cross-sectional samples is generally used to observe interfaces and defects in the mismatched systems. In wurtzite structures, since the dominant slip system is $\{11\bar{2}0\}\{0001\}$, the $\{11\bar{2}0\}$ projection is generally used for investigation, with dislocation cores being viewed *end-on*, i. e., imaged along the line direction of the dislocation. This configuration is based on the presumption that the misfit disloca-

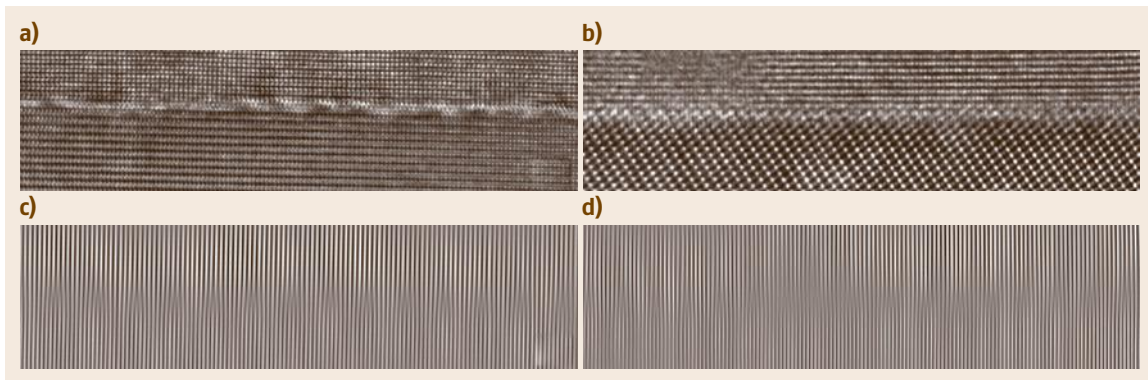


Fig. 44.24a–d HRTEM images taken at the AlN/sapphire interface: (a) along zone axis $[11\bar{2}0]_{\text{AlN}}$; (b) along zone axis $[1\bar{1}00]_{\text{AlN}}$; (c) reconstructed image from masked FFT of (a) showing the extra half-planes in the substrate; (d) reconstructed image from masked FFT of (b) showing the extra half-planes in the substrate

tions are of 60° mixed type with line direction along $\langle 11\bar{2}0 \rangle$ and Burger vector along another equivalent $\langle 11\bar{2}0 \rangle$ direction. However, studies of AlN film grown on sapphire substrate show extra half-planes along both $\langle 11\bar{2}0 \rangle_{\text{AlN}}$ and $\langle 1\bar{1}00 \rangle_{\text{AlN}}$ directions, as illustrated in Fig. 44.24 [44.13]. Further studies are required to reach any conclusive analysis.

Defects in AlN/GaN Films Originating from SiC Substrate Steps

One of the strategies that has been explored to reduce the defects in GaN epilayers grown on nonnative sub-

strates is the utilization of vicinal, offcut substrates. Offcut 6H-SiC substrates have been recently shown to reduce the stress level inside the films through the combined effects of mutual tilt between the epilayer and substrate, which helps to relax out-of-plane mismatch, and by the generation of geometric partial misfit dislocations (GPMDs) which serve both to relax in-plane mismatch and to accommodate stacking differences between the epilayer and substrate at some proportion of the steps at the substrate–film interface [44.102]. One of the critical factors in offcut epitaxy is the effect of the surface steps present on substrates on the quality of

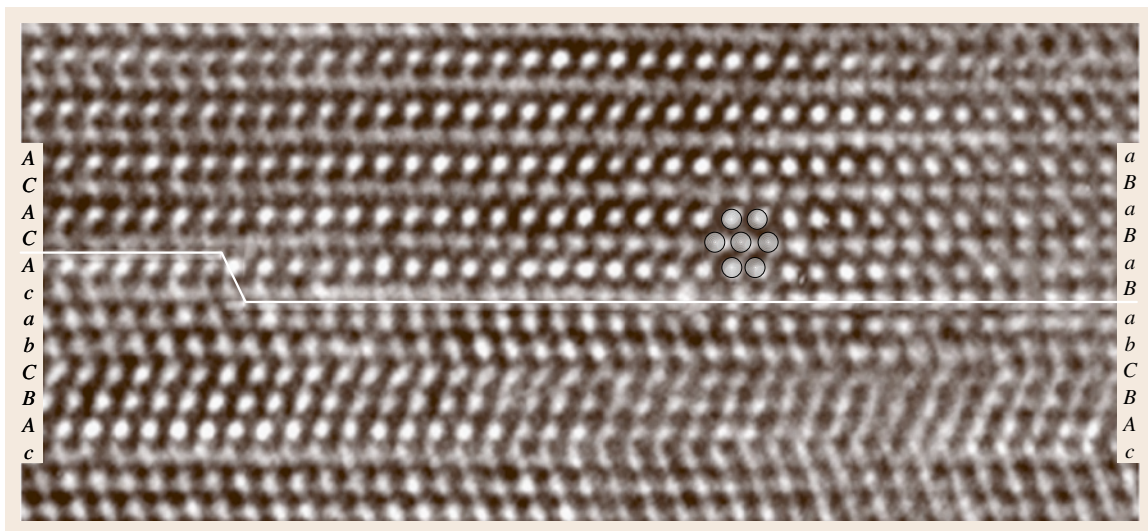
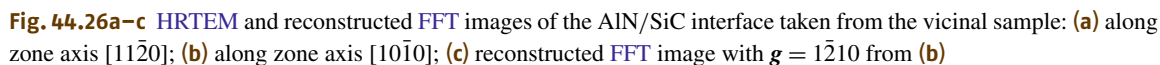


Fig. 44.25 HRTEM image taken at zone axis $[11\bar{2}0]$ showing a PSF forming at a I_1 -type step



Prismatic Stacking Faults (PSFs) Originating at I_1 Type Steps. Figure 44.25 shows a HRTEM image taken at an I_1 step region [44.104] along zone axis $[11\bar{2}0]$ (60° inclined to the offcut direction). The AlN/SiC interface is delineated by a white line separating SiC on the lower side from AlN on the upper side. The stacking sequences revealed in such HRTEM images can be un-

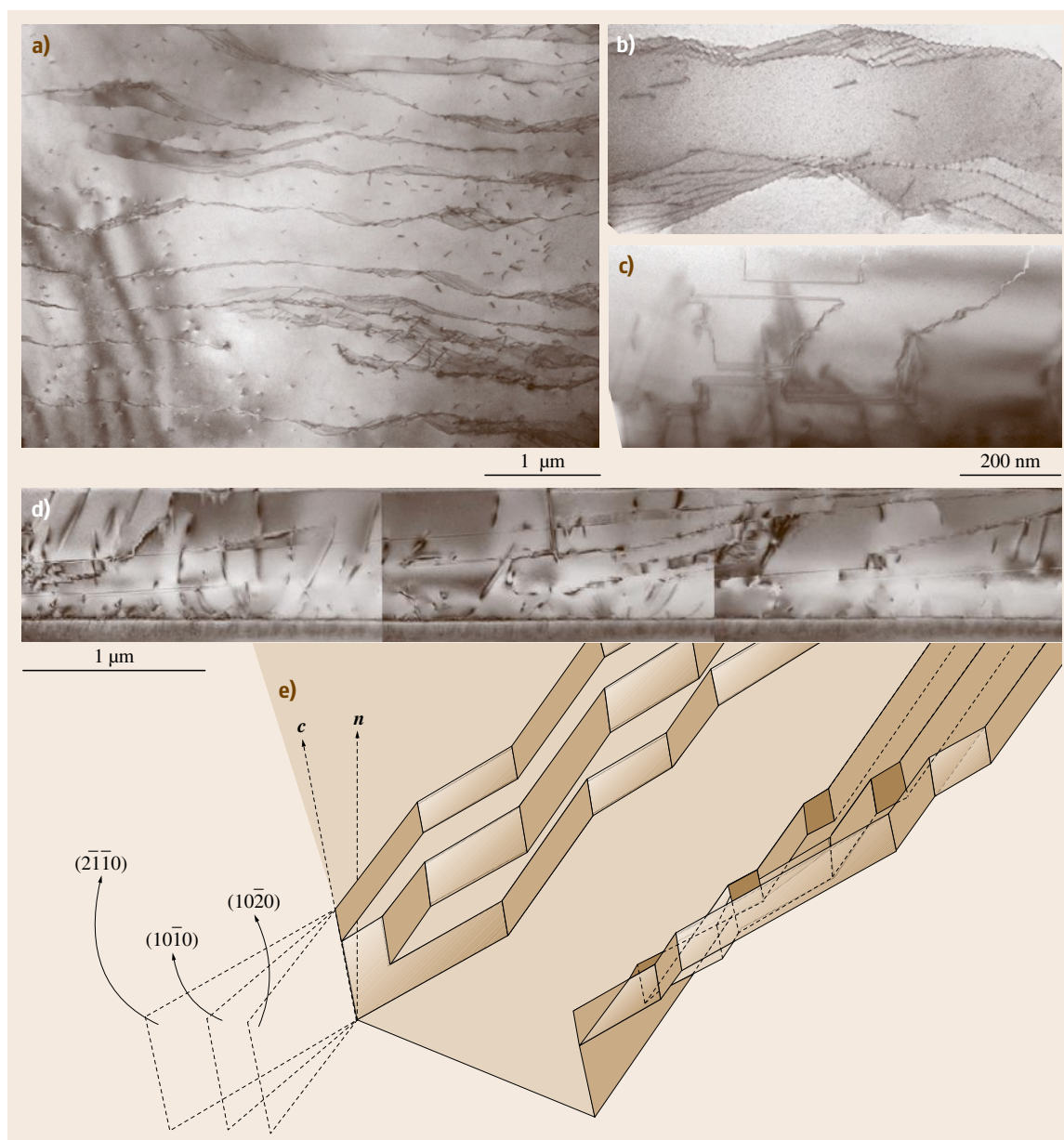


Fig. 44.27a–e TEM images taken from samples with various foil normals to show a three-dimensional view of the planar boundaries. **(a,b)** (0001) plan view of the defects with different magnification; **(c)** view along $[\bar{1}2\bar{1}0]$; **(d)** view along $[10\bar{1}0]$; **(e)** schematic representation of the *boat-shaped* walls created by the intersecting faults. The c -axis of the substrate is indicated along with the surface normal n

derstood with the aid of a notation system based on that introduced by Pirouz and Yang [44.105]. It can be seen that, in the vicinity of the two-bilayer-step riser, the first two AlN bilayers tend to duplicate the stacking posi-

tions exhibited to that step riser, i. e., cA . However, further out on the terrace, that stacking sequence changes to Ba (most probably under the influence of the stacking sequence under the terrace). The relationship between

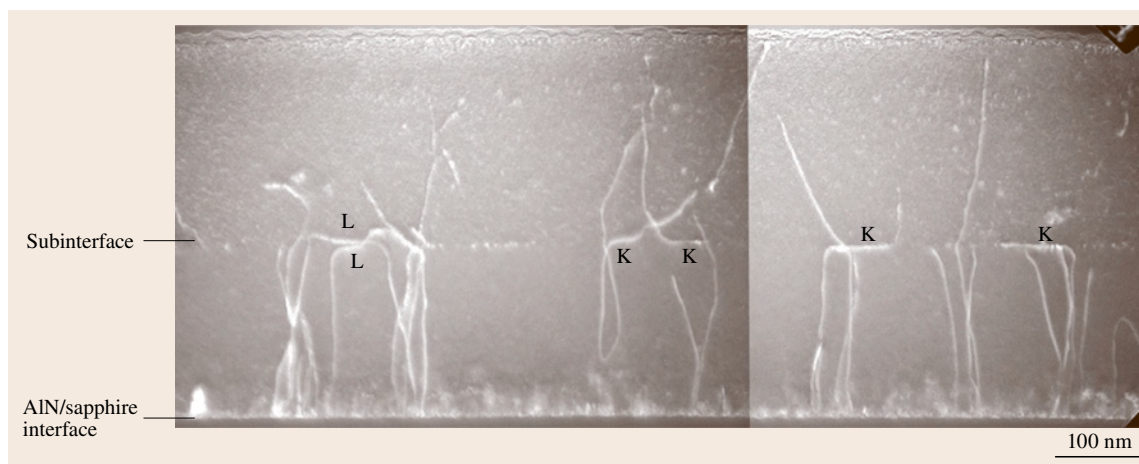


Fig. 44.28 A montage of two weak-beam dark-field images taken with $g = 0002$, showing the subinterface corresponding to when the V/III ratio and both fluxes were increased. Large kinks (indicated by K) or dipole half-loops (indicated by L) are formed at this subinterface

these two stacking sequences suggest a displacement vector of $1/6\langle 2\bar{2}03 \rangle$, which can be accommodated by a stacking mismatch boundary (SMB). However, observations reveal that the defects formed at such steps are predominantly PSFs, which add an additional lattice shift and have a displacement vector of $1/2\langle 1\bar{1}01 \rangle$. This might be due to the lower energy of PSFs than SMBs.

Geometrical Partial Misfit Dislocations (GPMDs) Formed at I_2 -Type Steps. Figure 44.26a shows a HRTEM image taken from an offcut sample along $[11\bar{2}0]$ zone axis (inclined to the offcut direction), showing two steps, S1 and S2 (in the same sense due to the offcut), at the substrate surface. Both steps S1 and S2 are of I_2 type [44.106] with dislocation vector $1/3\langle 10\bar{1}0 \rangle$. DI and DII are two regions exhibiting lattice distortion. It can be seen that, in the vicinity of S2, the first two AlN bilayers tend to duplicate the stacking positions exhibited by that step riser (on the higher side of the step), i.e., bC . However, further out on the terrace, the stacking sequence changes to cA through the distorted region DII (distorted region DI has similar features). Thus, it is clear that the distortions are confined close to the interface, and the stacking sequences above the distorted regions continuously overspan the step without interruption. Figure 44.26b shows an HRTEM image taken from the same sample along zone axis $[10\bar{1}0]$ (perpendicular to the offcut direction), and Fig. 44.26c is the corresponding reconstructed fast Fourier transform (FFT) image. Three dislocations are revealed with the extra half-planes on

the substrate side. Analysis shows that the Burgers vector has no out-of-plane component and its projection onto the $(10\bar{1}0)$ plane is $1/6\langle 11\bar{2}0 \rangle$. The localized dislocation core and well-defined extra half-plane imply that the dislocation line is along $[10\bar{1}0]$. These misfit dislocations can only be 30° complete dislocations (with Burgers vectors of $\pm 1/3\langle \bar{2}110 \rangle$ or $\pm 1/3\langle 11\bar{2}0 \rangle$) or 60° partial dislocations. Since the former is energetically unreasonable, the misfit dislocations (MDs) should be 60° partials. These *unpaired* partials, with line direction $\langle 10\bar{1}0 \rangle$ and Burgers vector $1/3\langle 1\bar{1}00 \rangle$, are suggested as geometrical partial misfit dislocations (GPMDs) that are formed at I_2 steps to accommodate both the lattice mismatch and stacking sequence mismatch simultaneously [44.102]. The distorted regions (DI and DII) shown in Fig. 44.26a may be due to the strain field associated with dislocations of this kind.

Intersecting Stacking Fault Structures in GaN/AlN/SiC Epitaxy

Bai et al. [44.104] conducted a systematic study of intersecting planar boundary structures observed in GaN epilayers grown on vicinal 6H-SiC substrates. These structures are shown to comprise stacking faults that fold back and forth from the basal plane. The prismatic stacking faults, with fault vector $1/2\langle 10\bar{1}1 \rangle$, nucleate at steps on the substrate surface as a consequence of the different stacking sequences exposed on either side of the step. Once nucleated, PSFs intersecting the vertical step risers in the AlN buffer and eventually in the GaN film are replicated during the predominantly step-

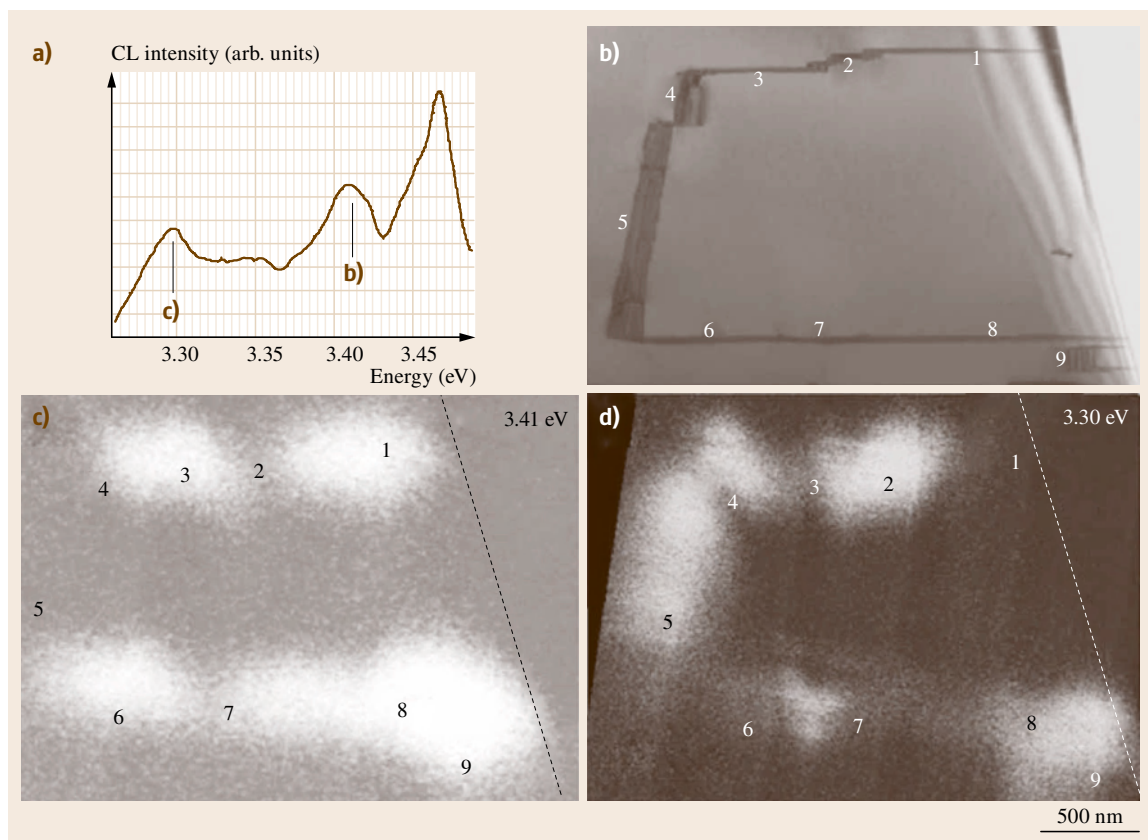


Fig. 44.29a–d TEM-CL observation of prismatic stacking faults. **(a)** A low-temperature CL spectrum acquired over a large area revealing three emission peaks. The luminescence intensity is plotted on a logarithmic scale. **(b)** Cross-section TEM image of the region of interest showing the presence of stacking faults. CL images from the same region corresponding to emission energies of **(c)** 3.41 eV and **(d)** 3.30 eV (after [44.107], © AIP 2006)

flow growth and propagate into the growing crystal. As a consequence of the different growth rates experienced on either side of the intersection of a PSF with a vertical step riser, the PSF may be redirected onto an equivalent $\{11\bar{2}0\}$ plane, leaving an I_1 BSF between the bottom of the redirected section of the PSF and the top of that portion of the original PSF which was below the terrace. This leads to the formation of folded PSF/BSF fault structures which exhibit various configurations. Such folded stacking fault configurations form walls which enclose domains of different stacking sequence. Figure 44.27 shows a series of TEM images recorded with foil normals parallel to $[0001]$, $[1\bar{2}10]$, and $[10\bar{1}0]$. These images reveal the existence of folded planar defect structures which thread diagonally through the epilayer and intersect the sample surface [44.104]. These complex configurations typi-

cally adopt *boat-like* shapes, as shown schematically in Fig. 44.27e. An unfolded or folded BSF forms the bottom of the boat while other folded BSFs/PSFs form the two side walls of the *boat*. These folded boundary configurations act as walls separating domains with different stacking sequence. Detailed contrast analysis confirms that domain walls consist of intersecting PSFs on equivalent $(11\bar{2}0)$ and $(2\bar{1}\bar{1}0)$ planes and I_1 BSFs on (0001) .

Dislocation Redirection in AlN/Sapphire Epilayer Driven by Growth Mode Modification

Bai et al. [44.108] reported TEM observation of redirection of threading dislocations in AlN epilayers grown on sapphire substrate. The threading dislocations experience redirection of their line orientation which is found to coincide with imposed increases in both of

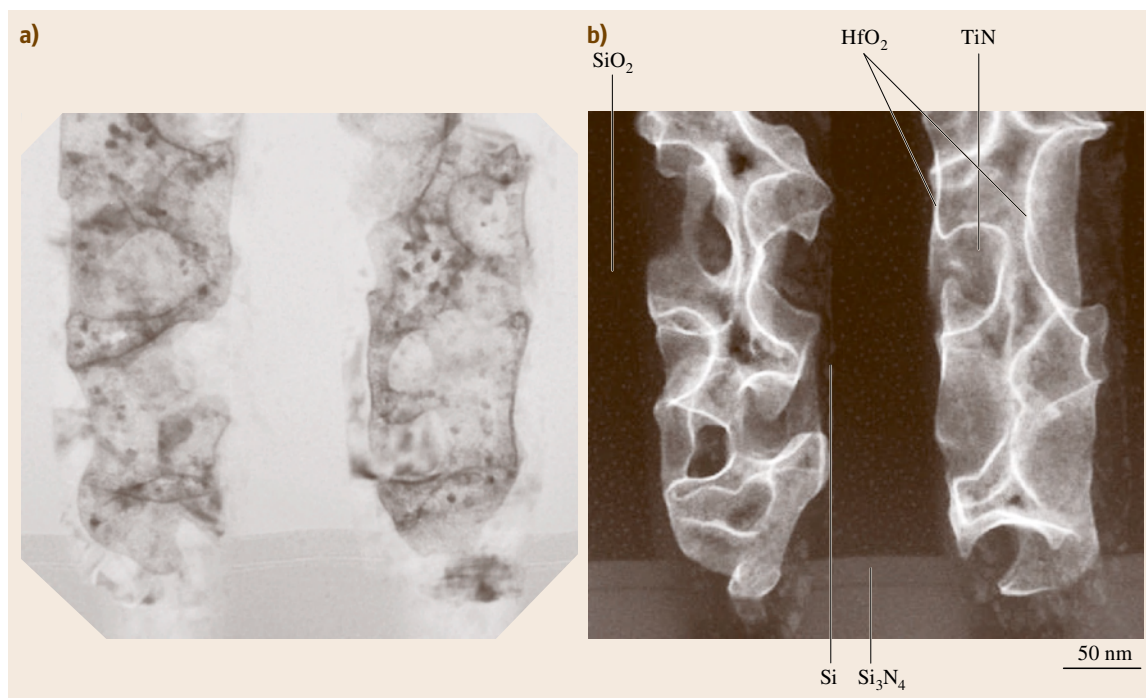


Fig. 44.30a,b The lower portion of two semiconductor memory capacitor cells. **(a)** Bright-field TEM image; **(b)** Z-contrast STEM image (after [44.50])

V/III ratio and overall flux rate leading to the formation of an internal subinterface delineated by the changes in dislocation orientation. Threading dislocations either experience large kinks and then redirect into threading orientation or form dipole half-loops via annihilation of redirected threading segments of opposite sign, with the latter leading to a significant dislocation density reduction. These phenomena can be accounted for by a transition of growth mode. At the point where the growth mode changes from atomic step-flow to two-dimensional (2-D) layer-by-layer growth, macrosteps sweep over dislocation outcrops, forcing the creation of large kinks and/or dipole half-loops as proposed by Klapper [44.109]. Figure 44.28 shows a weak-beam dark-field image taken with $g = 0002$, clearly portraying two phenomena:

1. Where a large kink forms in the dislocation line at this subinterface and the threading dislocations (TD) reorients back into approximately [0001] direction
2. Where two TDs are redirected towards each other forming a dipole half-loop.

The reorientation of the TDs upon increase of V/III ratio and flux magnitudes can be understood from the point of view of a transition in growth mode at this juncture of growth.

TEM-CL Observation of Prismatic Stacking Faults

Use of a TEM equipped with a scanning attachment and coupled with a cathodoluminescence (CL) light collector/spectrometer system offers the possibility of correlating microstructural information (diffraction contrast) with spatially resolved spectroscopy. This method is attractive for use with optoelectronic materials. Mei et al. [44.107] and Liu et al. [44.110] established a direct correlation between stacking faults in *a*-plane GaN epilayers and luminescence peaks in the 3.29–3.41 eV range. Combined TEM-CL allows the structural features of stacking faults to be determined by diffraction contrast, with the optical emission characteristics being observed by highly spatially resolved monochromatic cathodoluminescence in the exact same regions. Figure 44.29a shows a CL spectrum taken from the observing feature. There are two distinct peaks at 3.41 and 3.30 eV, besides the domi-

nant bulk GaN donor-bound exciton peak at 3.47 eV. Diffraction-contrast TEM analysis was performed in the same region where the localized emission was observed. By correlating the CL images in Fig. 44.29c,d with the TEM image in Fig. 44.29b, the location of the 3.41 eV emission can be identified as basal-plane stacking faults, while the emission at 3.30 eV is associated with prismatic stacking faults.

44.2.3 Application of STEM, EELS, and EFTEM

Z-Contrast STEM

A TEM and a HAADF STEM image of similar sections of two semiconductor memory capacitor cells are shown in Fig. 44.30. In the TEM image, the HfO_2 dielectric layer cannot be seen clearly because of the interference of diffraction contrast from TiN and Si. In comparison, the Z-contrast STEM gives a clean image, emphasizing materials differences. The continuity and thickness variation of the HfO_2 layer can be better studied in the Z-contrast STEM.

Figure 44.31 shows a HAADF STEM image of nano WN_x particles deposited on 100 nm-thick SiO_2 film. Due to the overlapping SiO_2 , the visibility and shape definition of particles are poor in conventional TEM, as shown by the HREM imaging (inset of Fig. 44.31). Here the Z-contrast STEM shows its advantage by giving high definition of nanoparticles and their low-density shells.

EELS Application in Microanalysis

EELS Study of Mn Diffusion. Figure 44.32 illustrates EELS elemental profiles across a magnetoresistive random-access memory (MRAM) stack ($\text{Ta}/\text{MnIr}/\text{NiFe}/\text{Al}_2\text{O}_3/\text{NiFe}/\text{Ta}$) as measured along the scan line [44.60]. From the Mn profile in Fig. 44.32b, diffusion of Mn through the FeNi layer into the Al_2O_3 layer due to thermal process is observed. In transition metals, L_3 and L_2 white lines ($2p^{3/2} \rightarrow 3d^{3/2}3d^{5/2}$, $2p^{1/2} \rightarrow 3d^{3/2}$) are observed in the energy-loss spectra [44.111]. The comparison of the Mn $L_{2,3}$ edges from the MnIr layer and $\text{NiFe}/\text{Al}_2\text{O}_3$ interface (Fig. 44.33) shows a significant difference in the fine structure, especially in the intensity ratio of $L_3 : L_2$ [44.60]. Studies have shown that the relative intensities of L_3 and L_2 of Mn are highly sensitive to the 3d occupancy and thus the valence state [44.112, 113]. The intensity ratio of white lines $I(L_3)/I(L_2)$ can be calculated from the spectra using the double-step background-fitting procedure with the step at the

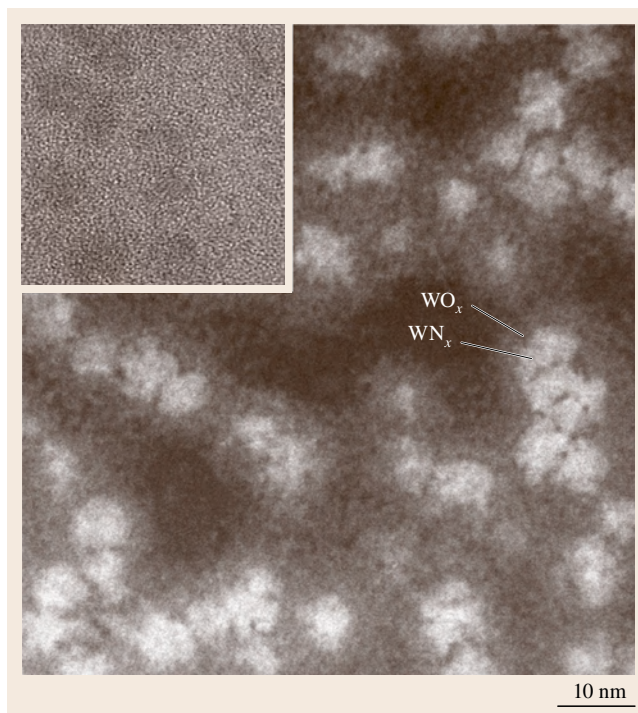


Fig. 44.31 Z-contrast STEM image of WN_x nanoparticles on 100 nm thick amorphous SiO_2 film. The particles are surrounded by low-density shells, possibly WO_x . The inset shows a HREM image of the particle (after [44.50])

peak [44.111, 112]. Figure 44.34 plots $I(L_3)/I(L_2)$ versus the Mn valence state for the reference data [44.112] and for the data from this MRAM study. Deduced from the correlation to the reference data, the valence state of Mn in Al_2O_3 is found to be around +2.2. Thus, Mn diffused into the Al_2O_3 layer and accumulated there in an oxidized state [44.60].

EELS Fine Edge to Study Interface Material. Figure 44.35 shows a HAADF STEM image of Al/WN_x interface with an EELS elemental line scan [44.50]. A nitrogen-rich interface is observed in the line scan profile. The interface is also observable in the STEM image. From the elemental profile, it is difficult to identify the phase of the interface material. The EELS fine edge structure can be strongly affected by chemical bonding variations. This fine structure allows us to probe the information beyond elemental identification. Figure 44.36 shows a comparison of $\text{Al}-L_{2,3}$ edge for the spectra from interface location and standard samples. The major difference in the fine edge structures of

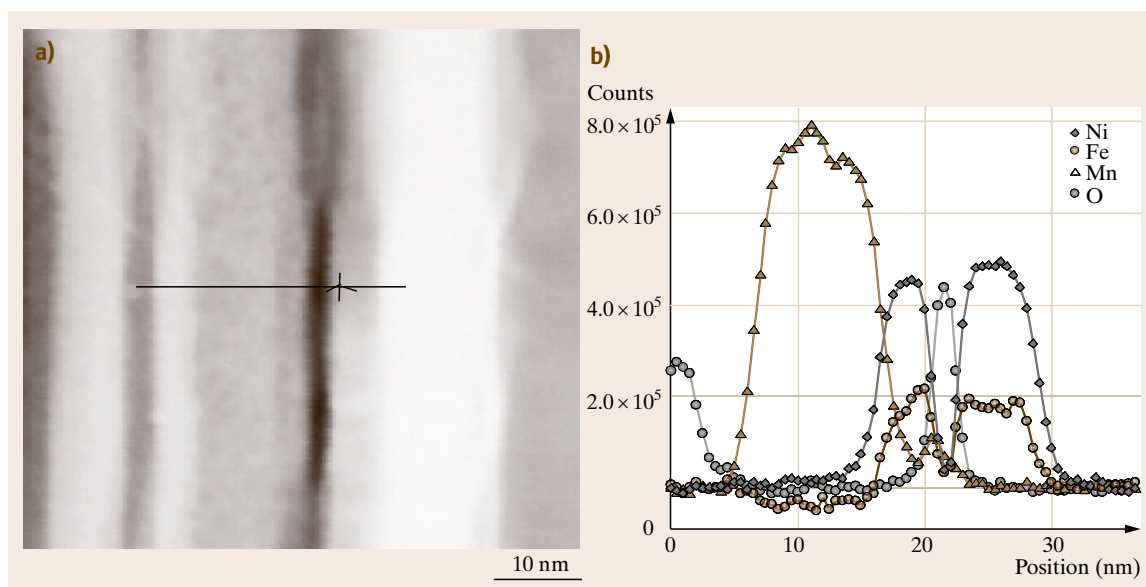


Fig. 44.32a,b EELS line scan across a MRAM stack. (a) STEM image showing the features and the scan line location. (b) Elemental profiles along the scan line as detected by EELS

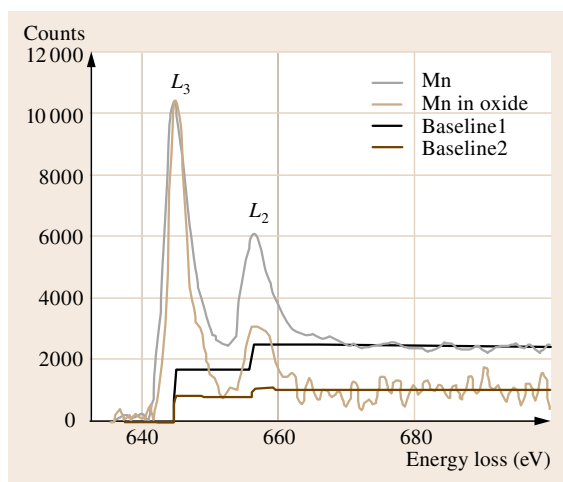


Fig. 44.33 Comparison of manganese $L_{2,3}$ edge spectra from Mn layer and from Al_2O_3 layer. The baselines are used for calculating the $L_3 : L_2$ ratio

Al and AlN is indicated by the three arrows (a, b, and c). Here we observe that the spectrum from interface is very similar to that of AlN, except for the small shoulder indicated by arrow a. In comparison with that of Al metal, we find this extra shoulder is most likely caused by overlapping Al metal. This analysis is further supported by comparison of EELS in the low-loss region

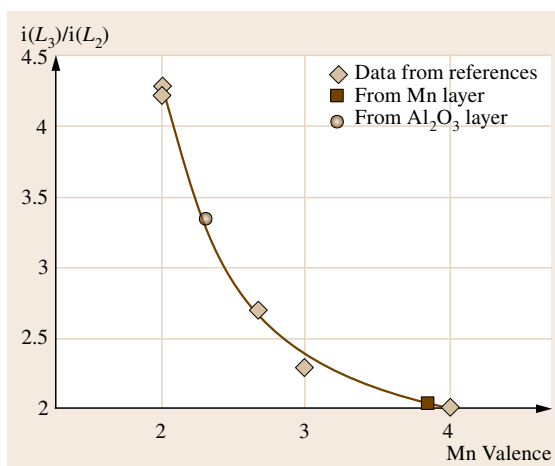


Fig. 44.34 A plot of white line intensity ratio $I(L_3)/I(L_2)$ versus the valence state of Mn (after [44.60])

(Fig. 44.37). In Fig. 44.37, we can see the distinguishing features for Al and AlN. The low-loss spectrum from the interface again resembles the summation of Al and AlN spectra. Thus, by combining the information from EELS line scan (elemental identification) and the fine edge structure comparison, we conclude that the interface layer between Al/ WN_x is AlN_x . The existence of Al metal at the interface is mostly likely caused by overlapping.

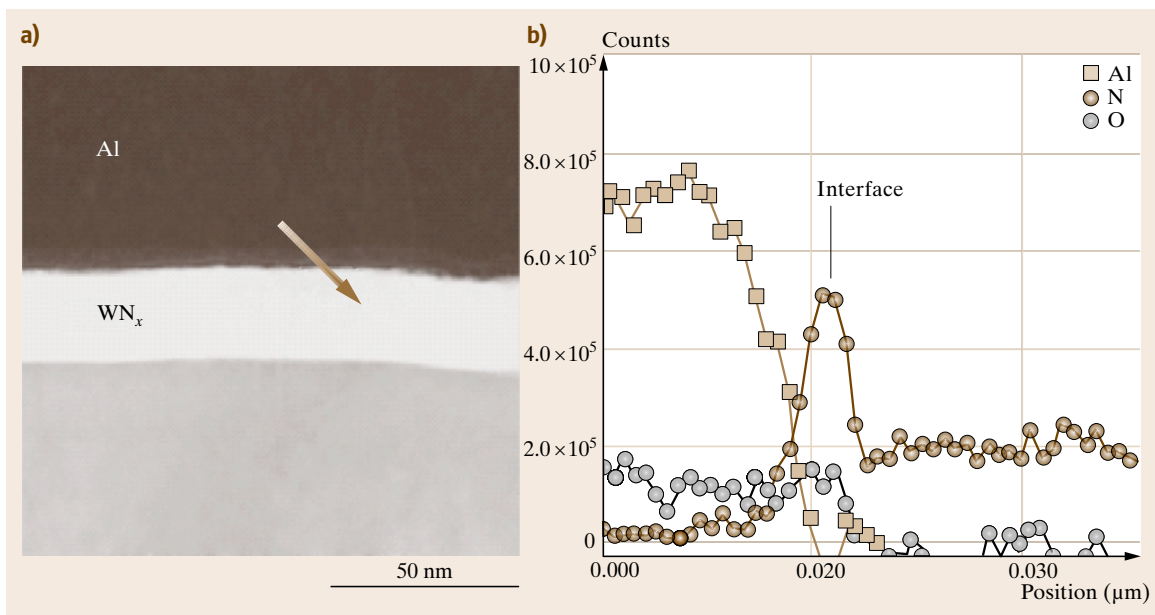


Fig. 44.35 EELS line scan across an Al/WN_x interface (after [44.50])

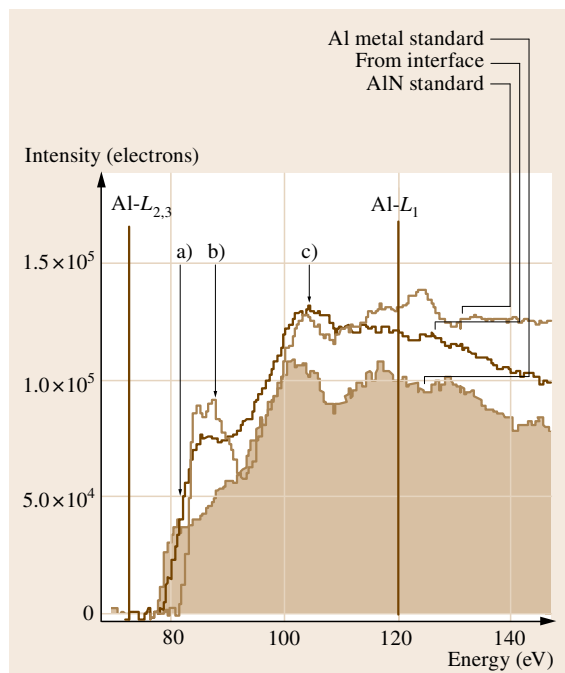


Fig. 44.36 Comparison of Al-L_{2,3} edges for interface in the study and standard sample (after [44.50])

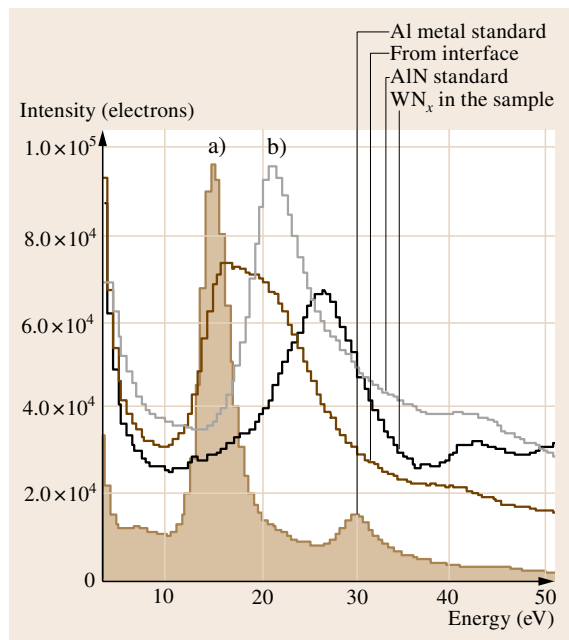


Fig. 44.37 Comparison of low-loss features for the locations in the study and the standard samples (after [44.50])

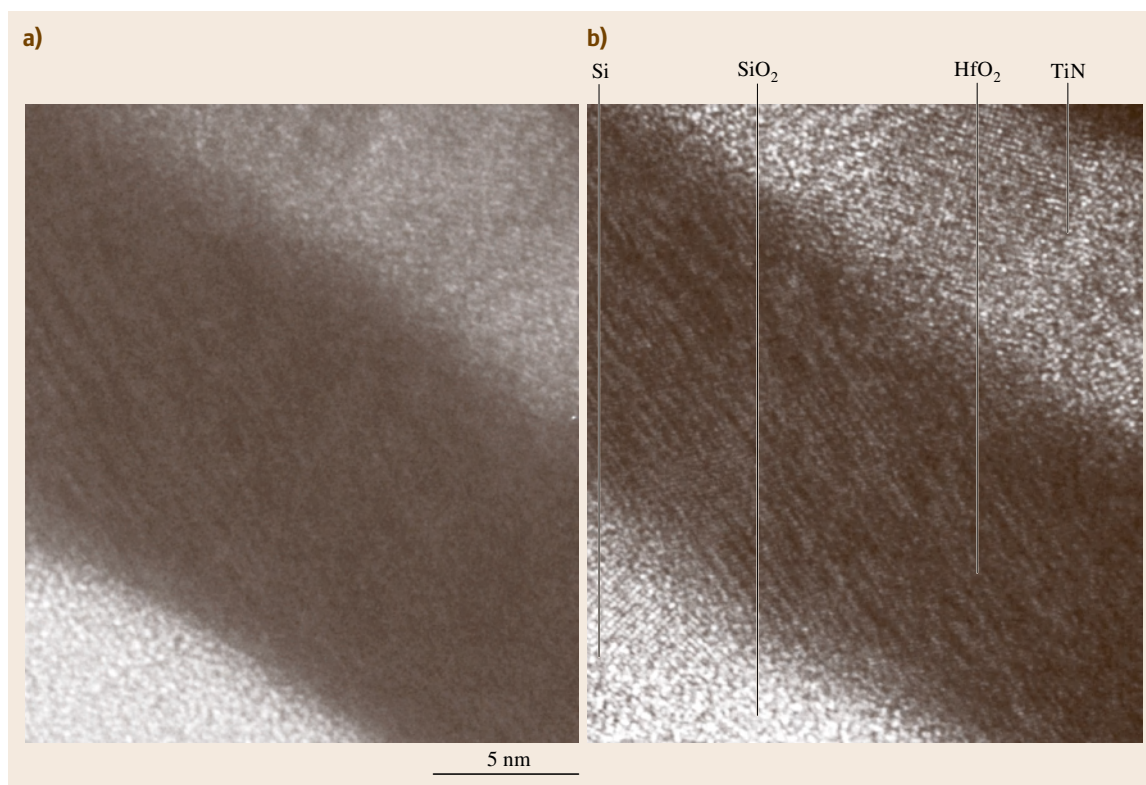


Fig. 44.38a,b Comparison of conventional HREM (a) and energy-filtered HREM (b)

EFTEM Applications

EFTEM to Image Thick Sample. Figure 44.38 shows a conventional HREM image of a crystalline HfO₂ layer in contact with Si and TiN. Because the sample is not sufficiently thin, part of the blurring of the HREM image is due to inelastic electrons. Figure 44.38b shows an energy-filtered (zero-loss) image of the same feature. The imaging improvement by energy filtering is obvious through the lattice images of the TiN, HfO₂, and Si regions.

EFTEM to Map Elemental Distributions. For many elements, EFTEM enables fast and distinctive elemental mapping. Figure 44.39 shows a series of elemental maps of a defect in a semiconductor device. The chemical distribution is clearly revealed. Compared with other elemental mapping techniques such as EDS elemental mapping, EFTEM elemental mapping can achieve much higher spatial resolution.

EFTEM to Enhance Contrast. EFTEM can be used to enhance contrast in situations when TEM would show low contrast. An example is given in Fig. 44.40. As indicated by the arrow, the Si low-loss image (using the Si plasma peak at about 15 eV) clearly reveals Si particles where the bright-field TEM image shows low or no contrast.

EFTEM to Reduce Diffraction Contrast. EFTEM can often be used as an alternative method to Z-contrast STEM to reduce diffraction contrast. This can be critical in situations such as electron tomography of crystalline materials where orientation-dependent contrast is to be avoided [44.114]. Most EFTEM, except zero-loss imaging, offers a certain reduction of diffraction contrast. The diffraction contrast reduction can be seen in both Figs. 44.38 and 44.39. EFTEM offers a wide variety of energy-filtering controls. Some EFTEM methods, such as jump-ratio imaging [44.114]

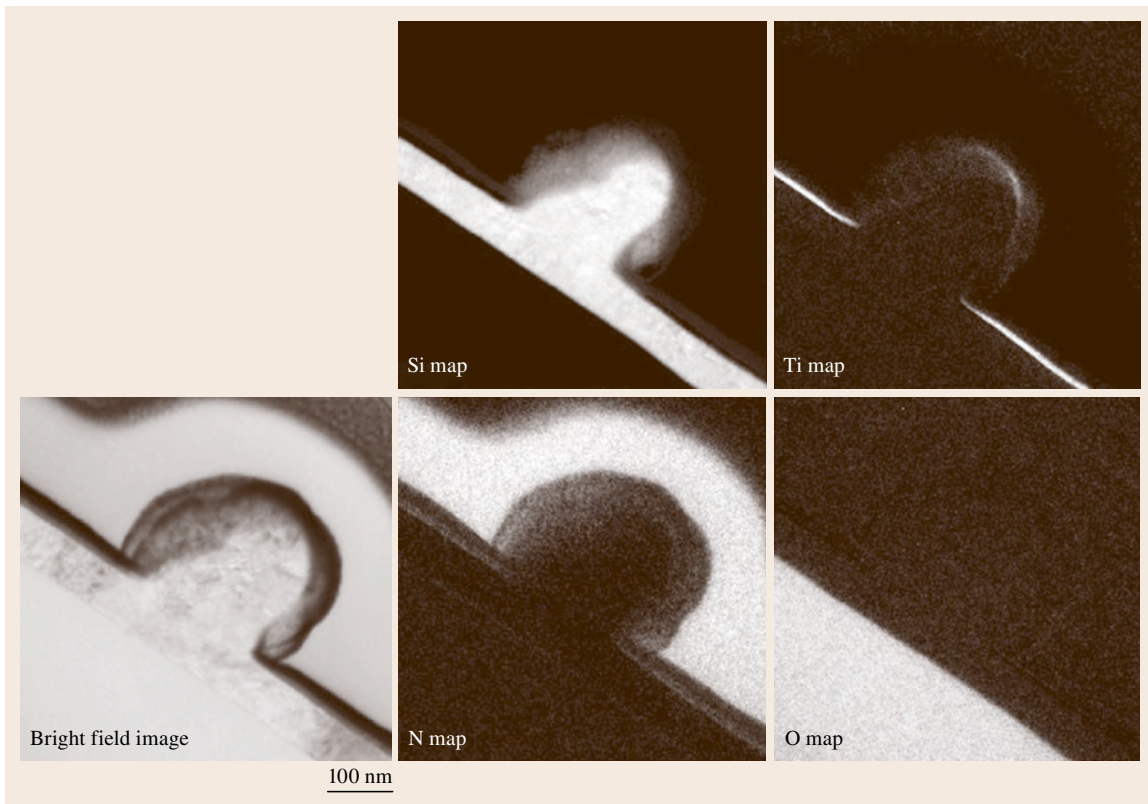


Fig. 44.39 Elemental maps of a defect in a semiconductor device obtained by EFTEM

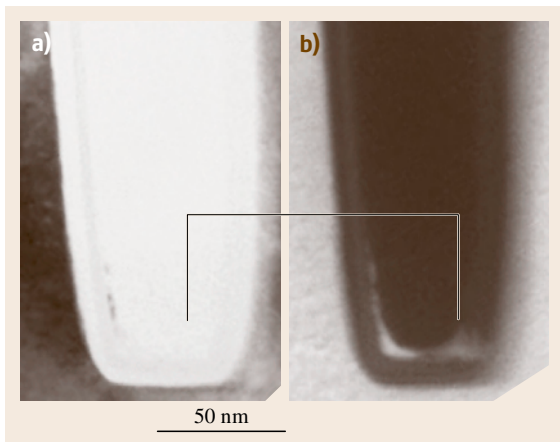


Fig. 44.40 (a) TEM image. (b) Si low-loss image. The arrow indicates equivalent area in the two images

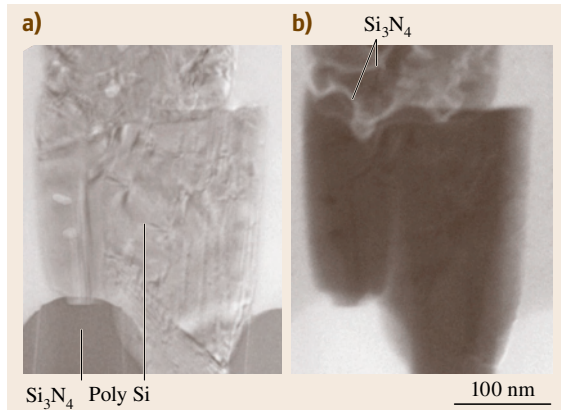


Fig. 44.41a,b The result of diffraction contrast reduction by EFTEM. (a) TEM bright-field image; (b) energy-filtered 74 eV low-loss (energy window width = 10 eV, centered at 74 eV) image (after [44.50])

(dividing the post-edge image by the pre-edge image) and certain low-loss-region imaging [44.115], are more effective in reducing diffraction contrast. Figure 44.41 shows a comparison of a **TEM** and the 74 eV low-loss

image. The prominent diffraction contrast in polycrystalline Si is effectively suppressed in the 74 eV low-loss image, where the majority contrast is due to material difference.

44.3 Concluding Remarks: Current Application Status and Development

As an efficient technique to explore the microstructure of various materials, **TEM** has been extensively applied in both the research and industrial fields. Through observation and analysis of structural features and defects, it plays a key role in the evaluation of materials quality, the investigation of defect formation mechanisms, and the correlation between processing and microstructural properties.

Conventional **TEM** techniques such as diffraction-contrast imaging, selected-area diffraction, convergent-beam electron diffraction, and large-angle convergent-beam electron diffraction are extensively used to characterize defects in both bulk and epitaxially grown crystals. Examples of such application include the study of threading dislocation density reduction in wurtzite-type epilayers, defects produced by composition variations in semiconductor alloys, and strain relaxation and dislocation behavior in strained Si/SiGe epilayers. LACBED has the advantage of being able to characterize most types of crystal defect (point defects, perfect and partial dislocations, stacking faults, antiphase boundaries, and grain boundaries). In addition to the aforementioned basic functions, many techniques, such as **EDS**, **EELS**, **STEM**, **EFTEM**, holography, and tomography, have been incorporated into the **TEM** system. The modern **TEM** system is a high-resolution probe with extensive capabilities for exploration of the internal structure of various materials.

In recent years, **TEM** has become even more important, as the structural dimensions in many research and industrial applications are rapidly approaching the nanometer scale. The high-resolution **TEM/STEM** with various analytical functions has become an indispensable tool for nanoscale defect analyses. Take the semiconductor industry as an example; the trend for ever-shrinking device dimension has demanded that defect analyses be localized to the nanometer scale. This has led to increased use of the **TEM** as an integral part of process development and failure analysis. Examples include distributions and density of crystalline defects at the thin-film metallization-silicon substrate interface, defect formation and involvement

during dopant implantation and thermal treatments, and measurement of local strains in the critical channel region of fully processed devices. The powerful sample preparation technique, **FIB**, providing accurate specimen thickness control over large area as well as being highly site specific, is especially useful in nanoscale devices. In addition to its importance in imaging nanoscale microstructures, **TEM** is also the only technique that can produce high count rates in diffraction patterns from individual nanotubes or other nanostructures. Capable of revealing small lattice-parameter changes, **CBED** strain analysis finds its application in the semiconductor industry in analyzing strain variations within device substrates. Furthermore, with the advances of nanotechnology, electron tomography has found an increasingly important role in the physical sciences. For materials with complex nanoscale structures, electron tomography offers a promising solution to overcome the difficulties caused by sample thickness limitations.

The progress of materials analysis by **TEM** largely relies on the advances of instrumentation. Various technologies have been applied to improve the spatial resolution of **TEM/STEM** imaging and the energy resolution of **EELS**. Recent progress includes lens aberration correctors to improve **TEM** and **STEM** resolution and monochromators for reducing energy spread of the electron beam. With the help of these new technologies, atomic-scale defect analysis will become more precise and convenient. The use of aberration correctors allows the relaxation of the tight spacing around the specimen. One benefit is naturally the easier accommodation of in situ apparatus within the **TEM**. The in situ experiments of interest to the readers may include in situ **TEM** observation of defects under the influence of mechanical and/or electrical stress. Meanwhile, the quality of electron microdiffraction has been greatly improved with the availability of energy-filtered imaging, field-emission guns, liquid-helium-cooled sample stages, charge-coupled device (**CCD**) cameras, monochromators, aberration correctors, and energy-loss spectrometers with parallel detec-

tion, together with much faster computers. It has now become possible to measure low-order structure factors from crystals of known structure using the quantitative convergent-beam diffraction method with accuracy equal to or better than that of the x-ray Pendellösung method. The well-developed analytical capabilities (EDS, EELS) of TEM provide compositional information with spatial resolution in the nanometer and subnanometer range. Combined with structural information from high-resolution phase-contrast imaging, such capabilities make TEM an indispensable tool for the development and application of new materials in the fields of semiconductors, ultrafine-grain materials or thin films. Energy-filtering TEM (EFTEM) has proven to be the key tool for nano-analytical applications, since it uses the rich information provided by the energy-loss spectrum in a spatially resolved manner with short acquisition times.

As with any analytical tools, TEM has its own limitations. The most notable ones are as follows:

1. TEM observation is very localized. It is not a suitable way for large-scale sampling.

2. Due to dynamical scattering, quantitative diffraction analysis can be difficult compared with x-ray and neutron diffraction.
3. TEM sample preparation is destructive.
4. There are possible surface effects, which become increasingly important with reduced sample thickness.
5. Electron-beam damage can be significant in some situations.
6. Structural defects can be generated or changed by sample preparation and electron-beam irradiation.

New developments in TEM instruments have enabled major improvements on two fronts: the ability to see ever smaller things and the ability to see the *unseeable*. Various contrasts with TEM/STEM have enabled various structural, defect, and chemical analysis with resolution as high as 0.1 nm. With improvements on both theoretical and instrumental fronts, we expect new advances in the field of transmission electron microscopy. At the same time, we may say that TEM itself has matured to be a premier research tool in materials analysis.

References

- 44.1 J.W. Edington: *Practical Electron Microscopy in Materials Science* (Van Nostrand Reinhold, New York 1976) pp. 113–116
- 44.2 J.W. Edington: *Practical Electron Microscopy in Materials Science* (Van Nostrand Reinhold, New York 1976) p. 63
- 44.3 J.W. Edington: *Practical Electron Microscopy in Materials Science* (Van Nostrand Reinhold, New York 1976) pp. 109–145
- 44.4 D.J.H. Cockayne, I.L.F. Ray, M.J. Whelan: Investigation of dislocation strain fields using weak beams, *Philos. Mag.* **20**, 1265–1270 (1969)
- 44.5 J.W. Edington: *Practical Electron Microscopy in Materials Science* (Van Nostrand Reinhold, New York 1976) pp. 145–149
- 44.6 D.B. Holt: Polarity reversal and symmetry in semiconducting compounds with the sphalerite and wurtzite structures, *J. Mater. Sci.* **19**(2), 439–446 (1984)
- 44.7 R. Serneels, M. Snykers, P. Delavignette, R. Gevers, S. Amelinckx: Friedel's law in electron diffraction as applied to the study of domain structures in non-centrosymmetrical crystals, *Phys. Status Solidi* (b) **58**, 277–292 (1973)
- 44.8 L.T. Romano, J.E. Northrup, M.A. O'Keefe: Inversion domains in GaN grown on sapphire, *Appl. Phys. Lett.* **69**(16), 2394–2396 (1996)
- 44.9 J. Jasinski, Z. Liliental-Weber, H. Lu, W.J. Schaff: V-shaped inversion domains in InN grown on c-plane sapphire, *Appl. Phys. Lett.* **85**(2), 233–235 (2004)
- 44.10 G. Thomas, M.J. Goringe: *Transmission Electron Microscopy of Materials* (Wiley, New York 1979) pp. 36–40
- 44.11 W.L. Bell, G. Thomas: *Electron Microscopy and Structure of Materials* (Univ. of California Press, Berkeley 1972) p. 23
- 44.12 J.W. Edington: *Practical Electron Microscopy in Materials Science* (Van Nostrand Reinhold, New York 1976) pp. 87–88
- 44.13 J. Bai: Studies of defects and strain relaxation in III-nitride epilayers. Ph.D. Thesis (State University of New York at Stony Brook, Stony Brook 2006)
- 44.14 M. Dudley: Lecture notes for ESM512, State University of New York at Stony Brook (2002)
- 44.15 C. Kisielowski, B. Freitag, X. Xu, S.P. Beckman, D.C. Chrzan: Sub-angstrom imaging of dislocation core structures: how well are experiments comparable with theory, *Philos. Mag.* **86**(29–31), 4575–4588 (2006)
- 44.16 A.H. Buist, A. van den Bos, M.A.O. Miedema: Optimal experimental design for exit wave reconstruction from focal series in TEM, *Ultramicroscopy* **64**, 137–152 (1996)

- 44.17 J.M. Gibson: High resolution electron microscopy of interfaces between epitaxial thin films and semiconductors, *Ultramicroscopy* **14**, 1–10 (1984)
- 44.18 X. Xu, S.P. Beckman, P. Specht, E.R. Weber, D.C. Chrzan, R.P. Erni, I. Arslan, N. Browning, A. Bleloch, C. Kisielowski: Distortion and segregation in a dislocation core region at atomic resolution, *Phys. Rev. Lett.* **95**, 145501 (2005)
- 44.19 B.C. de Cooman, N.-H. Cho, Z. Elgat, C.B. Carter: HREM of compound semiconductors, *Ultramicroscopy* **18**, 305–312 (1985)
- 44.20 D.J. Smith, Z.G. Li, P. Lu, M.R. McCartney, S.-C. Tsen: Characterization of thin films, interfaces and surfaces by high-resolution electron microscopy, *Ultramicroscopy* **37**, 169–179 (1991)
- 44.21 Z. Liliental-Weber, T. Tomaszewicz, D. Zakharov, M.A. O'Keefe: Defects in p-doped bulk GaN crystals grown with Ga polarity, *J. Cryst. Growth* **281**, 125–134 (2005)
- 44.22 H. Bender, A. Veirman, J. Landuyt, S. Amelinckx: HREM investigation of twinning in very high dose phosphorus ion-implanted silicon, *Appl. Phys. A* **39**, 83–90 (1986)
- 44.23 X.J. Wu, F.H. Li, H. Hashimoto: TEM study on overlapped twins in GaAs crystal, *Philos. Mag. B* **63**, 931–939 (1991)
- 44.24 J.W. Edington: *Practical Electron Microscopy in Materials Science* (Van Nostrand Reinhold, New York 1976) pp. 73–81
- 44.25 M.J. Marcinkowski: *Electron Microscopy and Strength of Crystals* (Univ. of California Press, Berkeley 1971) p. 333
- 44.26 O. Ueda, Y. Nakata, T. Fujii: Study on microstructure of ordered InGaAs crystals grown on substrates by transmission electron microscopy, *Appl. Phys. Lett.* **58**(7), 705–707 (1991)
- 44.27 T.-Y. Seong, A. G. Norman, G.R. Booker, A.G. Cullis: Atomic ordering and domain structures in metal organic chemical vapor deposition grown InGaAs (001) layers, *J. Appl. Phys.* **75**(12), 7852–7865 (1994)
- 44.28 N. Amir, K. Cohen, S. Stolyarova, A. Chack, R. Beserman, R. Weil, Y. Nemirovsky: Long-range order in CdZnTe epilayers, *J. Phys. D Appl. Phys.* **33**, L9–L12 (2000)
- 44.29 D.B. Williams, C.B. Carter: *Transmission Electron Microscopy* (Plenum, New York 1996) pp. 321–323
- 44.30 T. Mitate, Y. Sonoda, N. Kuwano: Polarity determination of wurtzite and zincblende structures by TEM, *Phys. Status Solidi (a)* **192**(2), 383–388 (2002)
- 44.31 J. Taftø, J.C.H. Spence: A simple method for the determination of structure-factor phase relationships and crystal polarity using electron diffraction, *J. Appl. Crystallogr.* **15**, 60–64 (1982)
- 44.32 K. Ishizuka, J. Taftø: Quantitative analysis of CBED to determine polarity and ionicity of ZnS-type crystals, *Acta Cryst. B* **40**, 332–337 (1984)
- 44.33 J. Bai, M. Dudley, B. Raghathamachar, P. Gouma, B.J. Skromme, L. Chen, P.J. Hartlieb, E. Michaels, J.W. Kolis: Correlated structural and optical characterization of ammonothermally grown bulk GaN, *Appl. Phys. Lett.* **84**(17), 3289–3291 (2004)
- 44.34 Y. Tomokiyo, S. Matsumura, T. Okuyama, T. Yasunaga, N. Kuwano, K. Oki: Dynamical diffraction effect on HOLZ-pattern geometry in Si-Ge alloys and determination of local lattice parameter, *Ultramicroscopy* **54**(2–4), 276–285 (1994)
- 44.35 A. Hovsepian, D. Cherns, W. Jäger: Analysis of ultrathin Ge layers in Si by large angle convergent beam electron diffraction, *Philos. Mag. A* **79**(6), 1395–1410 (1999)
- 44.36 S.J. Rozeveld, J.M. Howe: Determination of multiple lattice parameters from convergent-beam electron diffraction pattern, *Ultramicroscopy* **50**(1), 41–56 (1993)
- 44.37 J. Zipprich, T. Fuller, F. Banhart, O.G. Schmidt, K. Eberl: The quantitative characterization of SiGe layers by analyzing rocking profiles in CBED patterns, *J. Microsc.* **194**(1), 12–20 (1999)
- 44.38 D. Jacob, Y. Androussi, T. Benabbas, P. Francois, A. Lefebvre: Surface relaxation of strained semiconductor heterostructures revealed by finite-element calculations and transmission electron microscopy, *Philos. Mag. A* **78**(4), 879–891 (1998)
- 44.39 M. Tanaka, R. Saito, K. Ueno, Y. Harada: Large-angle convergent-beam electron diffraction, *J. Electron Microsc.* **29**(4), 408–412 (1980)
- 44.40 D. Cherns, A.R. Preston: Convergent beam diffraction studies of crystal defects, *Proc. 11th Int. Congr. Electron Microsc.*, Kyoto, Vol.1, ed. by T. Imura, S. Marusa, T. Suzuki (The Japanese Society of Electron Microscopy, Tokyo 1986) pp. 207–208
- 44.41 D. Cherns, A.R. Preston: Convergent beam diffraction studies of interfaces, defects, and multilayers, *J. Electron Microsc. Tech.* **13**, 111–122 (1989)
- 44.42 R.W. Carpenter, J.C.H. Spence: Three-dimensional strain-field information in convergent-beam electron diffraction patterns, *Acta Crystallogr. A* **38**, 55–61 (1982)
- 44.43 D. Cherns, A.R. Preston: Convergent beam diffraction studies of crystal defects, *Proc. 11th Int. Congr. Electron Microsc.*, Kyoto, Vol.1, ed. by T. Imura, S. Marusa, T. Suzuki (The Japanese Society of Electron Microscopy, Tokyo 1986) p. 721
- 44.44 D. Cherns, J.-P. Morniroli: Analysis of partial and stair-rod dislocations by large angle convergent beam electron diffraction, *Ultramicroscopy* **53**(2), 167–180 (1994)
- 44.45 K.K. Fung: Convergent-beam electron diffraction study of transverse stacking faults and dislocations, *Ultramicroscopy* **17**, 81–86 (1985)
- 44.46 C.T. Chou, L.J. Zhao, T. Ko: Higher-order Laue zone effects of stacking-faulted crystals, *Philos. Mag. A* **59**(6), 1221–1243 (1989)
- 44.47 D.E. Jesson, J.W. Steeds: Higher-order Laue zone diffraction from crystals containing transverse stacking faults, *Philos. Mag. A* **61**, 385–415 (1990)

- 44.48 J.P. Morniroli: CBED and LACBED characterization of crystal defects, *J. Microsc.* **223**(3), 240–245 (2006)
- 44.49 A. Hovsepien, D. Cherns, W. Jäger: Analysis of ultra-thin Ge layers in Si by large angle convergent beam electron diffraction, *Philos. Mag. A* **79**(6), 1395–1410 (1999)
- 44.50 S. X. Wang: EELS fine edge structure and quantification analyses, Internal report of Micron Technology (2005)
- 44.51 O.L. Krivanek, P.D. Nellist, N. Dellby, M.F. Murfitt, Z. Szilagy: Toward sub-0.5 Å electron beams, *Ultramicroscopy* **96**, 229–237 (2003)
- 44.52 D.A. Blom, L.F. Allard, S. Mishina, M.A. O’Keefe: Early results from an aberration-corrected JEOL 2200FS STEM/TEM at Oak Ridge National Laboratory, *Microsc. Microanal.* **12**, 483–491 (2006)
- 44.53 S.J. Pennycook, L.A. Boatner: Chemically sensitive structure-imaging with a scanning transmission electron microscope, *Nature* **336**, 565–567 (1988)
- 44.54 S.J. Pennycook, J. Narayan: Direct imaging of dopant distributions in silicon by scanning transmission electron microscopy, *Appl. Phys. Lett.* **45**, 385–387 (1984)
- 44.55 D.E. Jesson, S.J. Pennycook: Incoherent imaging of crystals using thermally scattered electrons, *Proc. R. Soc. Lond. Ser. A* **449**, 273–393 (1995)
- 44.56 S.J. Pennycook, D.E. Jesson: High-resolution incoherent imaging of crystals, *Phys. Rev. Lett.* **64**, 938–941 (1990)
- 44.57 P. Rez: Scattering cross sections in electron microscopy and analysis, *Microsc. Microanal.* **7**, 356–362 (2001)
- 44.58 R.F. Egerton: *Electron Energy-Loss in the Electron Microscope* (Plenum, New York 1986)
- 44.59 L.A. Giannuzzi, J.L. Drown, S.R. Brown, R.B. Irwin, F.A. Stevie: Focused ion beam milling and micro-manipulation lift-out for site specific cross-section TEM specimen preparation, *Mater. Res. Soc. Symp. Proc.* **480**, 19–27 (1997)
- 44.60 S.X. Wang, M.M. Kowalewski: TEM and PEELS study of Mn diffusion in an MRAM structure, *Microsc. Microanal.* **9**(Suppl. 2), 496–497 (2003)
- 44.61 C.C. Ahn, O.L. Krivanek: *EELS Atlas* (Gatan Inc./Arizona State Univ., Warrendal/Tempe 1983)
- 44.62 J. Orloff, L.W. Swanson: Optical column design with liquid metal ion sources, *J. Vac. Sci. Technol.* **19**, 1149–1152 (1981)
- 44.63 T. Ishitani, T. Ohnishi, Y. Madokoro, Y. Kawanami: Focused-ion-beam “cutter” and “attacher” for micromachining and device transplantation, *J. Vac. Sci. Technol. B* **9**, 2633–2637 (1991)
- 44.64 P. Gasser, U.E. Klotz, F.A. Khalid, O. Beffort: Site-specific specimen preparation by focused ion beam milling for transmission electron microscopy of metal matrix composites, *Microsc. Microanal.* **10**, 311–316 (2004)
- 44.65 S.X. Wang: TEM study of surface damage and profile of a FIB-prepared Si sample, *Microsc. Microanal.* **10**(Suppl. 2), 1158–1159 (2004)
- 44.66 J.H. van der Merwe: Strains in crystalline overgrowths, *Philos. Mag.* **7**(80), 1433–1434 (1962)
- 44.67 J.W. Matthews (Ed.): *Epitaxial Growth* (Academic, New York 1975) p. 559, Part B
- 44.68 D.E. Jesson, S.J. Pennycook, J.-M. Baribeau, D.C. Houghton: Direct imaging of surface cusp evolution during strained-layer epitaxy and implications for strain relaxation, *Phys. Rev. Lett.* **71**, 1744–1747 (1993)
- 44.69 D.D. Perovic, G.C. Weatherly, J.-M. Baribeau, D.C. Houghton: Heterogeneous nucleation sources in molecular beam epitaxy-grown $\text{Ge}_x\text{Si}_{1-x}/\text{Si}$ strained layer superlattices, *Thin Solid Films* **183**(1/2), 141–156 (1989)
- 44.70 P.M.J. Marée, J.C. Barbour, J.F. van der Veen, K.L. Kavanagh, C.W.T. Bulle-Lieuwma, M.P.A. Vieggers: Generation of misfit dislocations in semiconductors, *J. Appl. Phys.* **62**(11), 4413–4420 (1987)
- 44.71 W. Hagen, H. Strunk: New type of source generating misfit dislocations, *Appl. Phys.* **17**(1), 85–87 (1978)
- 44.72 K.R. Breen, P.N. Uppal, J.S. Ahearn: Interface dislocation structures in $\text{In}_x\text{Ga}_{1-x}\text{As}/\text{GaAs}$ mismatched epitaxy, *J. Vac. Sci. Technol. B* **7**, 758–763 (1989)
- 44.73 E.A. Fitzgerald, D.G. Ast, P.D. Kirchner, G.D. Pettit, J.M. Woodall: Structure and recombination in $\text{InGaAs}/\text{GaAs}$ heterostructures, *J. Appl. Phys.* **63**(3), 693–703 (1988)
- 44.74 E.A. Fitzgerald: Dislocations in strained-layer epitaxy-theory, experiment, and applications, *Mater. Sci. Rep.* **7**(3), 91 (1991)
- 44.75 E.A. Stach, R. Hull, R.M. Tromp, F.M. Ross, M.C. Reuter, J.C. Bean: In-situ transmission electron microscopy studies of the interaction between dislocations in strained $\text{SiGe}/\text{Si}(001)$ heterostructures, *Philos. Mag. A* **80**(9), 2159–2200 (2000)
- 44.76 W. Bollmann: Size and sign of the Burgers vector from transmission micrographs, *Philos. Mag.* **13**(125), 935–944 (1966)
- 44.77 E. Spiecker, W. Jäger: Quantitative large-area analysis of misfit dislocation arrays by bend contour contrast evaluation. In: *Microscopy of Semiconducting Materials*, Inst. Phys. Conf. Ser., Vol. 180, ed. by A.G. Cullis, P.A. Midgley (Institute of Physics, London 2003) pp. 259–264
- 44.78 R.H. Dixon, P.J. Goodhew: On the origin of misfit dislocations in $\text{InGaAs}/\text{GaAs}$ strained layers, *J. Appl. Phys.* **68**(7), 3163–3168 (1990)
- 44.79 J.W. Matthews, A.E. Blakeslee: Defects in epitaxial multilayers: I. Misfit dislocations, *J. Cryst. Growth* **27**, 118–125 (1974)
- 44.80 R.H. Miles, T.C. McGill: Structural perfection in poorly lattice matched heterostructures, *J. Vac. Sci. Technol. B* **7**(4), 753–757 (1989)

- 44.81 R. People, J.C. Bean: Calculation of critical layer thickness versus lattice mismatch for $\text{Ge}_x\text{Si}_{1-x}/\text{Si}$ strained-layer heterostructures, *Appl. Phys. Lett.* **47**(3), 322–324 (1985)
- 44.82 R.H. Dixon, P.J. Goodhew: On the origin of misfit dislocations in InGaAs/GaAs strained layers, *J. Appl. Phys.* **68**(7), 3163–3168 (1990)
- 44.83 P.M.J. Marée, J.C. Barbour, J.F. van der Veen, K.L. Kavanagh, C.W.T. Buile-Lieuwrna, M.P.A. Viegars: Generation of misfit dislocations in semiconductors, *J. Appl. Phys.* **62**(11), 4413–4420 (1987)
- 44.84 Y. Kimura, N. Sugii, S. Kimura, K. Inui, W. Hirasawa: Generation of misfit dislocations and stacking faults in supercritical thickness strained-Si/SiGe heterostructures, *Appl. Phys. Lett.* **88**, 031912–031914 (2006)
- 44.85 A.F. Marshall, D.B. Aubertine, W.D. Nix, P.C. McIntyre: Misfit dislocation dissociation and Lomer formation in low mismatch SiGe/Si heterostructures, *J. Mater. Res.* **20**(2), 447–455 (2005)
- 44.86 J. Zou, D.J.H. Cockayne: Theoretical consideration of equilibrium dissociation geometries of 60° misfit dislocations in single semiconductor heterostructures, *J. Appl. Phys.* **77**(6), 2448–2453 (1995)
- 44.87 J. Zou, D.J.H. Cockayne: Equilibrium dissociation configuration of misfit dislocations in low strained $\text{In}_{0.1}\text{Ga}_{0.9}\text{As}/\text{GaAs}$ single heterostructures, *Appl. Phys. Lett.* **63**(16), 2222–2224 (1993)
- 44.88 N. Hirashita, N. Sugiyama, E. Toyoda, S.-I. Takagi: Strain relaxation processes in strained-Si layer on SiGe-on-insulator substrates, *Thin Solid Films* **508**, 112–116 (2006)
- 44.89 E.A. Fitzgerald, D.G. Ast, P.D. Kirchner, G.D. Pettit, J.M. Woodall: Structure and recombination in InGaAs/GaAs heterostructures, *J. Appl. Phys.* **63**(3), 693–703 (1988)
- 44.90 Y.H. Xie, E.A. Fitzgerald, P.J. Silverman, A.R. Kortan, B.E. Weir: Fabrication of relaxed GeSi buffer layers on Si(100) with low threading dislocation density, *Mater. Sci. Eng. B* **14**, 332–335 (1992)
- 44.91 C.W. Leitz, M.T. Currie, A.Y. Kim, J. Lai, E. Robbins, E.A. Fitzgerald, M.T. Bulsara: Dislocation glide and blocking kinetics in compositionally graded SiGe/Si, *J. Appl. Phys.* **90**(6), 2730–2736 (2001)
- 44.92 A.E. Blakeslee: The use of superlattices to block the propagation of dislocations in semiconductors, *Mater. Res. Soc. Symp. Proc.* **148**, 217–227 (1989)
- 44.93 J.S. Park, M. Curtin, J. Bai, S. Bengtson, M. Carroll, A. Lochtefeld: Thin strained layers inserted in compositionally graded SiGe buffers and their effects on strain relaxation and dislocation, *J. Appl. Phys.* **101**, 053501 (2007)
- 44.94 J.S. Park, J. Bai, M. Curtin, B. Adekore, M. Carroll, A. Lochtefeld: Defect reduction of selective Ge epitaxy in trenches on Si(001) substrates using aspect ratio trapping, *Appl. Phys. Lett.* **90**, 052113 (2007)
- 44.95 J. Bai, J.S. Park, Z. Cheng, M. Curtin, B. Adekore, M. Carroll, A. Lochtefeld, M. Dudley: Study of the defect elimination mechanisms in aspect ratio trapping Ge growth, *Appl. Phys. Lett.* **90**(10), 101902 (2007)
- 44.96 Y. Ikuhara, P. Pirouz: High resolution transmission electron microscopy studies of metal/ceramics interfaces, *Microsc. Res. Tech.* **40**(3), 206–241 (1998)
- 44.97 A. Trampert: Private communication (2005)
- 44.98 A. Trampert, K.H. Ploog: Heteroepitaxy of large-misfit systems: Role of coincidence lattice, *Cryst. Res. Technol.* **35**(6/7), 793–806 (2000)
- 44.99 T. Zheleva, K. Jagannadham, J. Narayan: Epitaxial growth in large-lattice-mismatch systems, *J. Appl. Phys.* **75**(2), 860–871 (1994)
- 44.100 C.J. Sun, P. Kung, A. Saxler, H. Ohsato, K. Haritos, M. Razeghi: A crystallographic model of (00.1) aluminum nitride epitaxial thin film growth on (00.1) sapphire substrate, *J. Appl. Phys.* **75**(8), 3964–3967 (1994)
- 44.101 T. Kehagias, P. Komninou, G. Nouet, P. Ruterana, T. Karakostas: Misfit relaxation of the $\text{AlN}/\text{Al}_2\text{O}_3$ (0001) interface, *Phys. Rev. B* **64**, 195329 (2001)
- 44.102 X.R. Huang, J. Bai, M. Dudley, B. Wagner, R.F. Davis, Y. Zhu: Step-controlled strain relaxation in the vicinal surface epitaxy of nitrides, *Phys. Rev. Lett.* **95**, 086101 (2005)
- 44.103 P. Vermaut, P. Ruterana, G. Nouet, H. Morkoç: Structural defects due to interface steps and polytypism in III–V semiconducting materials: A case study using high-resolution electron microscopy of the $2\text{H-AlN}/6\text{H-SiC}$ interface, *Philos. Mag. A* **75**(1), 239–259 (1997)
- 44.104 J. Bai, X. Huang, M. Dudley, B. Wagner, R.F. Davis, L. Wu, E. Sutter, Y. Zhu, B.J. Skromme: Intersecting basal plane and prismatic stacking fault structures and their formation mechanisms in GaN, *J. Appl. Phys.* **98**(6), 063510 (2005)
- 44.105 P. Pirouz, J.W. Yang: Polytypic transformations in SiC: the role of TEM, *Ultramicroscopy* **51**(1–4), 189–214 (1993)
- 44.106 J. Bai, X. Huang, M. Dudley: High-resolution TEM observation of AlN grown on on-axis and off-cut SiC substrates, *Mater. Sci. Semicond. Process.* **9**, 180–183 (2006)
- 44.107 J. Mei, S. Srinivasan, R. Liu, F.A. Ponce, Y. Narukawa, T. Mukai: Prismatic stacking faults in epitaxially laterally overgrown GaN, *Appl. Phys. Lett.* **88**, 141912 (2006)
- 44.108 J. Bai, M. Dudley, W. Sun, H. Wang, M. Khan: Reduction of threading dislocation densities in AlN/sapphire epilayers driven by growth mode modification, *Appl. Phys. Lett.* **88**(5), 051903 (2006)

- 44.109 H. Klapper: Generation and propagation of dislocations during crystal growth, *Mater. Chem. Phys.* **66**, 101–109 (2000)
- 44.110 R. Liu, A. Bell, F.A. Ponce, C.Q. Chen, J.W. Yang, M.A. Khan: Luminescence from stacking faults in gallium nitride, *Appl. Phys. Lett.* **86**, 021908 (2005)
- 44.111 D.H. Pearson, C.C. Ahn, B. Fultz: *Phys. Rev. B* **47**, 8471–8478 (1993)
- 44.112 Z.L. Wang, J.S. Yin, Y.D. Jiang, J. Zhang: *Appl. Phys. Lett.* **70**, 3362–3364 (1997)
- 44.113 J.L. Mansot, P. Leone, P. Euzen, P. Palvadeau: *Microsc. Microanal. Microstruct.* **5**, 79–90 (1994)
- 44.114 P.A. Midgley, M. Wayland: 3-D electron microscopy in the physical sciences: the development of Z-contrast and EFTEM tomography, *Ultramicroscopy* **96**, 413–431 (2003)
- 44.115 L. Tsung, D. Matheson, C. Skelton, R. Turner, J. Ringnalda: Energy contrast from Si low loss at 74 eV for semiconductor devices, *Microsc. Microanal.* **9**(Suppl. 2), 490–491 (2003)

45. Electron Paramagnetic Resonance Characterization of Point Defects

Mary E. Zvanut

Electron paramagnetic resonance (EPR) spectroscopy identifies, counts, and monitors point defects in a wide variety of materials. Unfortunately, this powerful tool has faded from the literature in recent years. The present trend away from fundamental studies and towards technological challenges, and the need for fast diagnostic tools for use during and after materials growth has weakened the popularity of magnetic resonance tools. While admittedly the use of EPR in industrial laboratories for routine materials characterization is limited, EPR spectroscopy can be, and has been, successfully used to provide reams of information directly relevant to technologically significant materials.

The interpretation of EPR spectra involves an understanding of basic quantum mechanics and a reasonable investment of time. Once a defect is identified, however, the spectra may be used as a fingerprint that can be used in additional studies addressing the chemical kinetics, charge transport, and electronic energies of the defect and surrounding lattice. Numerous examples are provided in this chapter. In addition, the fundamental information extracted from EPR analysis should not be forgotten. Perhaps knowing the distribution of spin states about the core of a defect will not expedite the production of material X for use as device Y, but it may provide the seed of knowledge with which to build the 21st century's technological revolution. We must remember that the basic understanding of semiconductors developed in the middle of the last century

45.1	Electronic Paramagnetic Resonance	1522
45.2	EPR Analysis	1524
45.2.1	Zeeman Effect	1524
45.2.2	Nuclear Hyperfine Interaction	1526
45.2.3	Interactions Involving More than One Electron	1529
45.2.4	Total Number of Spins	1533
45.3	Scope of EPR Technique	1534
45.3.1	Defects in a Thin Film on a Substrate	1534
45.3.2	Defects at an Interface	1535
45.3.3	Defects at Surfaces	1536
45.3.4	Nondilute Systems	1537
45.4	Supplementary Instrumentation and Supportive Techniques	1538
45.4.1	Photo-EPR	1539
45.4.2	Correlation with Electrically Detected Trapping Centers and Defect Levels	1541
45.4.3	Heat Treatment and EPR	1543
45.5	Summary and Final Thoughts	1545
	References	1546

spawned the solid-state transistor, which unquestionably produced the computer revolution in the latter half of the 20th century.

This chapter will acquaint the reader with the fundamental methods used to interpret EPR data and summarize many different experiments which illustrate the applicability of the technique to important materials issues.

Electron paramagnetic resonance (EPR), or electron spin resonance (ESR), provides fundamental chemical and structural information about a point defect. For example, by detecting the unpaired (paramagnetic) electron on the nitrogen donor in SiC, EPR results show that

nitrogen substitutes for carbon and that the electron-nuclear hyperfine interaction differs by a factor of ten for the different symmetry sites in the 4H- and 6H-SiC polytypes. The total number of uncompensated nitrogen donors may also be determined. Note that EPR senses

specific charge states of the defect. For instance, in the case of nitrogen in SiC only neutral nitrogen with the donor electron *on* the nucleus is detected. Also, it is important to realize that EPR probes the ground state of a defect; thereby providing information about the *as-grown*, unperturbed defect. Illumination or heat may be used during a measurement to alter the charge state or produce the excited state, providing additional information. Ultimately, the electron wavefunction overlap with the core nucleus and surrounding neighbors may be determined. While this last bit of information may not be pertinent to most immediate applications, taken together the data paint a thorough picture of a specific center, enabling additional knowledge to be gleaned from the same defect in similar materials as well as other defects in the same host.

Having read other chapters in this Handbook, the reader may wonder how EPR compares with other techniques. EPR does *not* provide information about the lattice symmetry like x-ray diffraction or the overall chemical composition of the material as can be obtained from energy-dispersive x-ray analysis. Most importantly, the concentration of defects is not directly obtained from an EPR spectrum. The total number of a specific defect can be estimated, sometimes within a factor of two, but the distribution of centers is not sensed by magnetic resonance. Therefore, any concentration measurement must be inferred from etching studies or measurements of different sized samples. Finally, many readers may be familiar with nuclear magnetic resonance (NMR). Although the physical principle of NMR and EPR are the same, implementation of the techniques is entirely different, as a reader familiar with NMR will realize when they read this chapter. Unlike NMR, EPR has never been successfully adapted for scanning, as has NMR, where the technique has become the basis of magnetic resonance imaging. Whereas many of the methods discussed in this text provide the electronic or chemical identification of a defect, EPR can provide a complete picture – after great investment of time and analysis. Thus, while EPR provides a great deal of information, it cannot be used as a substitute for conventional characterization methods used routinely on a large volume of material. Rather, the technique provides many important details

about point defects that are not detectable by other means.

As with any technique, correlation with other experimental tools augments the information provided. The use of optical excitation, for example, sometimes enables one to extract defect levels (ionization energies) or probe the excited state of a defect. In addition, comparison of EPR spectra with optical absorption studies has enabled the identification of many optical absorption bands and the calculation of optical cross sections. Electrical measurements in tandem with EPR studies have also produced important scientific and technological information about trapping centers in electronic devices. In principle, comparison with secondary-ion mass spectroscopy (SIMS) or glow-discharge mass spectroscopy (GDMS) data could provide the fraction of impurities in a particular charge state or located at a specific lattice site.

Before closing this Introduction, the reader should be made aware that EPR measurements were first recorded in 1945, and have permeated the literature for the past 60 years, covering chemistry, biology, physics, and engineering journals. In addition to the defects in materials discussed here, the technique is widely used to study free radicals in solution and biological species. There is active work detecting the many complicated structures responsible for diseases, as well as the more benign moieties responsible for life. Within the framework of materials, there are studies in nanomaterials, amorphous solids, and interfaces, some of which will be mentioned in this chapter. Many texts and articles are available that cover the application of EPR to the multitude of fields mentioned [45.1–6].

The chapter will begin with a review of the EPR instrumentation, briefly explaining the significant parts of the spectrometer and detection system. This will be followed by a section outlining the heart of the analysis using examples to illustrate the many features extracted from EPR spectra. The next two sections will cover the scope of the technique as it applies to defects in solids and the typical correlation experiments involving EPR. Finally, the last section will summarize the material presented and outline the different types of magnetic resonance techniques amenable to the study of defects in materials.

45.1 Electronic Paramagnetic Resonance

Electron paramagnetic resonance is based on the absorption of energy between spin states induced by the

presence of an applied magnetic field [45.1, 7, 8]. In order to appreciate the technical aspects of the exper-

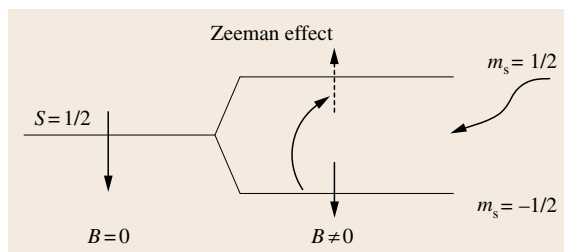


Fig. 45.1 Energy levels for a spin- $\frac{1}{2}$ electron in zero magnetic field (left) and nonzero applied field (right). The vertical arrows represent the spin of the electron; m_s is the magnetic spin quantum number

iment, one must understand the following. If there were no internal magnetic fields affecting the defect and if the defect contains a single unpaired electron (like that of a donor in a semiconductor), the absorbed energy is

$$h\nu = \Delta E = \mu_b g B, \quad (45.1)$$

where h is Planck's constant, ν is the frequency of the absorbed radiation, μ_b is the Bohr magneton, and B is the applied magnetic field. The term $\mu_b g B$ is the energy difference between the spin states shown in Fig. 45.1. We leave discussion of g until the next section. The point here is that, if you place your sample in a magnetic field while illuminating with different frequency radiation, you should be able to adjust the incident photon energy until absorption is detected, similar to an optical absorption measurement. However, because $g \approx 2$ and convenient magnetic fields are on the order of Tesla, ν is typically in the microwave region. Unfortunately, microwaves are not conveniently manipulated like optical photons; thus the actual situation requires placing a sample in a fixed microwave field and applying a series of magnetic fields. One then searches for the field that produces microwave absorption. The energy levels for the single unpaired electron in an applied magnetic field are shown schematically in Fig. 45.1 and a typical spectrum illustrating detection of the EPR signal is shown in Fig. 45.2.

The instrumentation for EPR was developed in the 1950s, and little has changed except for the addition of more sophisticated detection circuitry and data-acquisition electronics. Figure 45.3 illustrates the basic experimental setup. The spectrometer consists of the klystron or Gunn diode used to produce the microwave radiation, microwave bridge for setting the desired power, waveguides which transmit the radiation to the sample, and cavity resonator in which a particular mode of the microwave is stored. As stated above,

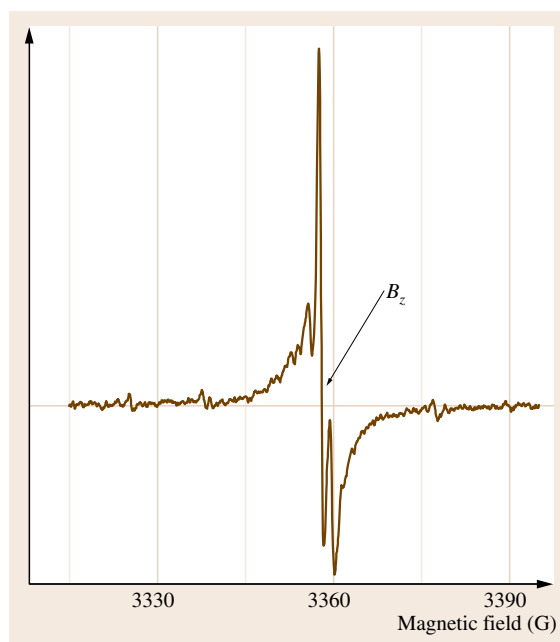


Fig. 45.2 Typical EPR spectrum illustrating the derivative line shape and zero-crossing B_z where the g value is calculated. The spectrum was obtained from 4H-SiC at 4 K with the magnetic field parallel to the c -axis of the crystal. The dotted line represents zero intensity

wavelengths in the microwave region are not easily varied, so a fixed frequency of 10 GHz is commonly used. The dimensions of the cavity establish a specific mode of the microwave frequency, in a similar way that a specific length of string determines the possible modes of a mechanical wave. The microwave energy stored in the standing wave is ultimately the energy absorbed by the sample when the resonance condition (45.1) is fulfilled. In order to produce an EPR signal, two more features must be understood: coupling of the microwaves in the

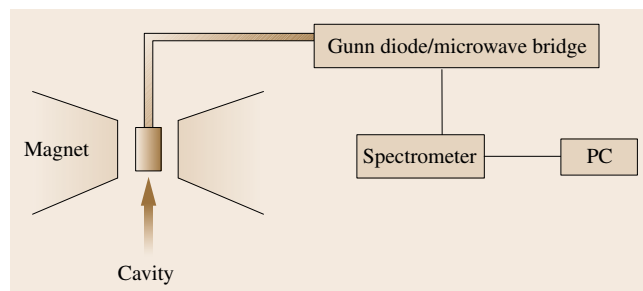


Fig. 45.3 Schematic diagram of EPR instrumentation; see text for description of the purpose for each component

cavity to the detection circuitry and the generation of the applied magnetic field. The former employs standard microwave electronics, as is discussed in detail in many texts [45.7]. The latter simply uses a standard magnet power supply and electromagnet that communicate with the spectrometer to set the magnetic field amplitude and ramp rate.

The instrumentation described above leads to the detection of microwave absorption at defects. However,

the reader familiar with spectroscopy will recognize that the spectrum in Fig. 45.2 is not a simple absorption; rather it reflects the derivative of the absorption. In order to detect the small amount of paramagnetic defects typical of most materials, a type of phase-sensitive detection is employed. In practice, an oscillating magnetic field is superimposed on the ramped field and the change in the absorption is detected. This AC detection method produces the derivative spectrum shown in Fig. 45.2.

45.2 EPR Analysis

The theory of EPR rests on the concept of the *spin Hamiltonian*, which sums all of the energy sources affecting the electron dipole moment at the defect. The most obvious contribution comes from the applied magnetic field, but there are many others, some of which can be much larger than the effect of the applied field. The only ones considered here are the nuclear magnetic field and the spin–spin interactions. Below, each effect is treated individually and is accompanied by examples reflecting the type of interaction described.

45.2.1 Zeeman Effect

If there were no internal fields affecting the defect, the absorbed energy may be described by the interaction of the applied magnetic field B with the electron spin at the defect. The appropriate Hamiltonian is the Zeeman term

$$H = \mu_b \mathbf{S} \cdot \mathbf{g} \cdot \mathbf{B}, \quad (45.2)$$

where μ_b is the Bohr magneton, \mathbf{S} is the total spin of the electron, and \mathbf{B} is the applied magnetic field. The \mathbf{g} -tensor is related to the proportionality factor between the quantized electron magnetic dipole moment and total angular momentum. In EPR \mathbf{g} takes on a significant role as will be seen later. Assuming simple spin- $\frac{1}{2}$ wavefunctions, $|\frac{1}{2}, \frac{1}{2}\rangle, |\frac{1}{2}, -\frac{1}{2}\rangle$, the energy solutions are

$$E = \mu_b g B m_s, \quad (45.3)$$

where m_s is the z -component of the spin angular momentum $\pm\frac{1}{2}$. (The “bra-ket” notation is a standard method for denoting the wavefunction of the electron where here we use only the spin part: $|s, m_s\rangle$ where s is the electron spin and m_s is the magnetic spin quantum number. In general, the spin wavefunction for a paramagnetic electron at a defect may be a linear combination of s, m_s states.) The energy difference between the two m_s states, $\mu_b g B \Delta m_s$, is $\mu_b g B$ as seen in (45.1). The two spin levels are illustrated in Fig. 45.1 for a fixed

value of magnetic field. Experimentally, the g -value is extracted from the magnetic field at which the intensity of the spectrum crosses zero intensity, as is indicated in Fig. 45.2 by B_z . In the simple case of a single electron free from the influence of any other magnetic fields, the g -value is the Lande free electron value. In a crystal, g is shifted by an amount that depends on the local environment of the defect. The shift is generally caused by a small amount of angular momentum that is not included in (45.2), but enters the theory as a perturbation and is incorporated into the g -value [45.1, 7–9]. Thus, each defect has a characteristic g -tensor determined by

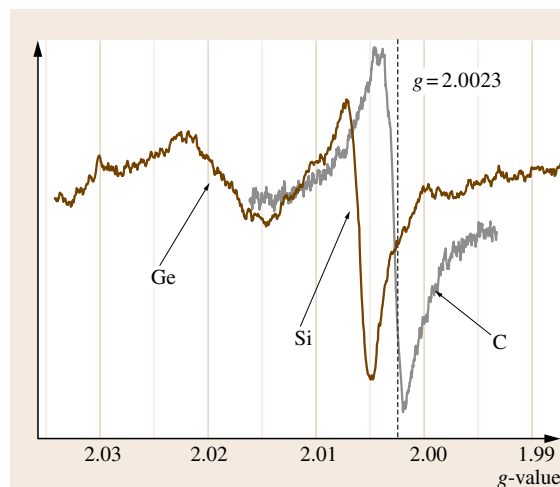


Fig. 45.4 EPR spectra illustrating the shift in the g -value as the mass of the central nucleus increases. Data was obtained from SiGe (brown) and SiC (grey) at 4 K. The elemental labeling (Ge, Si and C) indicates the central nuclei of the defects represented by the signal highlighted with an arrow. The vertical dashed line represents the g -value of a free electron. Note that the x -axis decreases to the right

its surroundings. Figure 45.4 illustrates the effect of the nearest neighbors on the g shift for a simple *dangling bond* center on a carbon atom in SiC (spectrum labeled “C”), silicon atom (Si) in SiGe and germanium (Ge) atom in SiGe (black spectrum). Here the x -axis is interpreted in terms of g through (45.1) with ΔE as the microwave energy; the free electron g -value, indicated by the dashed line, is used to approximate g for the defects. The EPR signal shifts to lower magnetic field (higher g) as the atomic number of the atom increases. Although by no means a hard rule, the shift is typical of this simple type of defect and reflects the change in the spin-orbit coupling parameter with increasing atomic number [45.9].

In the Zeeman term of (45.2), \mathbf{g} is a tensor that incorporates the angular dependence of the interaction between the magnetic field and electron spin angular momentum. Whereas the hyperfine tensor discussed next provides chemical information about the point defect, the \mathbf{g} -tensor provides structural details because it reflects the defect symmetry. The tensor is obtained from the g -value measured at each orientation of the sample with respect to the incident magnetic field. The interpretation of (45.2) in terms of the symmetry of \mathbf{g} and the method used to extract this information is described in many texts. Suffice it to say that in general \mathbf{g} may be written as

$$g^2 = g_X^2 \cos^2 \theta_X + g_Y^2 \cos^2 \theta_Y + g_Z^2 \cos^2 \theta_Z, \quad (45.4)$$

where θ_i is the angle between the i -th ($i = X, Y$, and Z) axes of the defect and the applied magnetic field. It is important to realize that X, Y , and Z are *not* necessarily the x -, y -, and z -axes of the crystal structure. Furthermore, the orientation of the defect axes with respect to, for example, the horizontal distance between the poles of the magnet, is not generally known. The procedure for extracting X, Y , and Z from angular measurements with respect to the known crystal axes is thoroughly described in [45.1].

To illustrate, consider a defect in a hexagonal material where measurements are made in a plane containing the c -axis. Measuring B_z for a series of spectra, calculating g , and plotting against the angle between B and the c -axis can produce the data shown in Fig. 45.5. The filled squares represent the g -values of the Mg-related acceptor signal in GaN and the solid line is a fit to the equation

$$g^2 = g_{\parallel}^2 \cos^2 \theta + g_{\perp}^2 \sin^2 \theta \quad (45.5)$$

where θ is the angle between the magnetic field and the principle axis of the defect. Note that (45.5) is a special case of (45.4) where $g_X = g_Y = g_{\perp}$ and $g_Z = g_{\parallel}$.

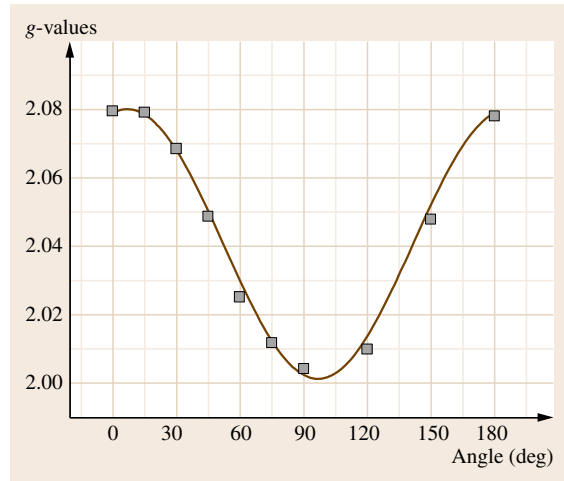


Fig. 45.5 Plot of the g -values calculated from EPR spectra obtained with the magnetic field in the plane of the c -axis and measured at selected angles with respect to the c -axis of a GaN film. The data (filled squares) were obtained from the Mg-related acceptor signal at 4 K. The fit to (45.5) is illustrated by the solid line

In the case of the Mg acceptor, θ_i is the same as the laboratory angle measured between B and the c -axis because the principle axis turns out to be the c -axis. A fit of (45.5) to the data in Fig. 45.5 shows that $g_{\parallel} = 2.096$ and $g_{\perp} = 2.008$. Although the specific values of g_{\parallel} and g_{\perp} provide some information, the main conclusion obtained from these data is the determination of the symmetry of the center. A defect exhibiting the angular dependence of (45.5) is said to have axial symmetry. In this case, the magnesium-related acceptor has axial symmetry about the c -axis. Confirmation of the axial symmetry requires rotation about two additional crystal axes. Specifically, rotation about the axis of symmetry, c -axis, should reveal spectra that do not depend on rotation angle. Unfortunately, this has not yet been possible for GaN because most samples are films grown in a predetermined orientation. Figure 45.6 shows measurements of the g -shift for the boron acceptor in bulk 6H-SiC, where results obtained from three rotation planes are plotted [45.10]. The Greek letters η , ξ , and ζ designate the high-symmetry cubic directions $[1\bar{1}0]$, $[112]$, and $[\bar{1}\bar{1}0]$, respectively. The sets of lines in each orientation plane represent data from the three different symmetry sites in 6H-SiC and the four possible bonding directions. Note that in the last panel, when the sample is rotated about the c -axis, one set of data forms a horizontal line. These results were obtained from the

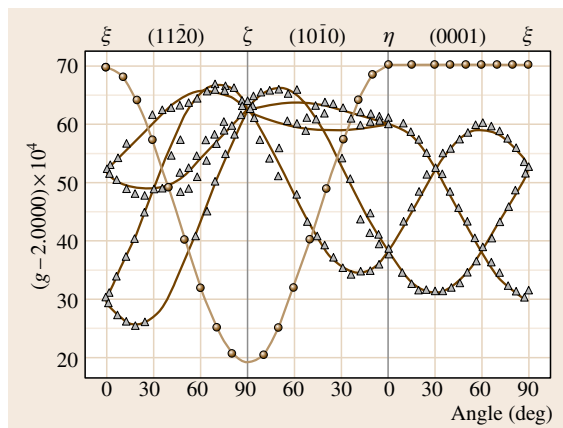


Fig. 45.6 The shift of the g -value from the free electron value when an EPR spectrum is measured in the rotation planes indicated above each panel in the graph: $(11\bar{2}0)$, $(10\bar{1}0)$, and (0001) . The vertical lines indicate the crystal directions in the cubic system: η , $[1\bar{1}0]$; ξ , $[112]$; ζ , $[\bar{1}\bar{1}0]$. Data were obtained from the shallow boron acceptor in 6H-SiC at 4 K (after [45.10], © IOP 1998)

hexagonal site where the defect axis is oriented along the c -axis of the crystal. When the data for this site is followed into the other two panels, the angular pattern illustrated in Fig. 45.5 is revealed, as expected for a site with axial symmetry about the c -axis.

At this point, it is not at all clear how the chemical identity of a defect is determined. One might guess that there are calculations relating the \mathbf{g} -tensor to specific types of point defects. Unfortunately, the \mathbf{g} -tensor is difficult to calculate accurately because the wavefunction must be known over the entire crystal space, a situation that is difficult to achieve using even the most powerful computers. However, the story does not end with the Zeeman term. The two remaining terms to be discussed in this chapter, the nuclear hyperfine and the fine-structure terms, provide a great deal more information about the chemical, structural, and electronic state of the defect.

45.2.2 Nuclear Hyperfine Interaction

When nuclei of nonzero spin are sufficiently close to a paramagnetic defect, an additional magnetic field must be considered, that of the nuclear magnetic moment. The term is written as

$$H = \sum_j \mathbf{S} \cdot \mathbf{A} \cdot \mathbf{I}_j, \quad (45.6)$$

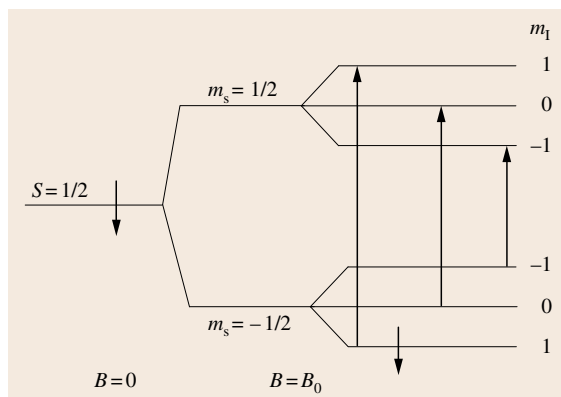


Fig. 45.7 Energy-level diagram from a spin- $\frac{1}{2}$ electron: in zero magnetic field (*leftmost*); applied field in absence of any other magnetic fields (*middle*); in the presence of a nuclear magnetic field (*rightmost*). m_I is the magnetic spin quantum number for the nucleus. The downward arrow represents the electron spin; the upward arrows represent allowed transitions

where \mathbf{A} is the hyperfine tensor and \mathbf{I} is the spin of the j -th nucleus surrounding the defect. This local nuclear magnetic field splits the electronic levels shown in Fig. 45.1, so that the situation becomes that shown in Fig. 45.7. Here m_I is the nuclear magnetic quantum number analogous to m_s . The size of the separation between the m_I levels A depends on the strength of the interaction. The nuclear hyperfine interaction may be different for the same defect in different materials as well as for different centers in the same material. However, I is a property of a given nucleus, so that it can be used to distinguish different defects, practically independent of the host. Specifically, the number of nuclear hyperfine lines originating from transitions between the different levels in Fig. 45.7 is proportional to I , thereby giving us the first clue into the chemical identity of the center. Since the selection rule allows only transitions with $\Delta m_s = \pm 1$ and $\Delta m_I = 0$ the Zeeman EPR line will divide into $2I + 1$ lines as shown by the upward arrows in Fig. 45.7. All the hyperfine lines will have the same intensity, and they will be spaced equally from the Zeeman EPR line. Because the intensity of a transition depends on the total number of defects causing the absorption, the isotopic abundance of the nonzero spin nuclei and the number of like nuclei determine the ratio of hyperfine line intensity to the intensity of the total spectrum. (Intensity here refers to the total integrated intensity of the hyperfine lines and the spectrum.)

Two examples are discussed to provide an understanding of the nuclear hyperfine portion of EPR spectra: the shallow nitrogen donor in SiC and the positively charged carbon vacancy in SiC. The former illustrates a 100% abundant nuclear spin entity and the latter is a case where the nuclear spin is much less than 100%. Although both examples are defects in SiC, the situations are quite general. The only effect of the environment is the strength and symmetry of the interaction, neither of which is critical to the basic understanding of the hyperfine term.

Figure 45.8 shows the characteristic EPR fingerprint of isolated N atoms in SiC: three evenly spaced lines of equal intensity. (Nitrogen has nuclear spin 1 and is 100% abundant.) The vertical arrows point to the three hyperfine lines arising from the interaction between the magnetic field and the nitrogen nuclei situated at the cubic sites in 4H-SiC. The large line marked with an arrow is a distorted spectrum of nitrogen on the hexagonal site in SiC. This site exhibits the three hyperfine lines as shown for the cubic site when different EPR parameters are used. Semiclassically, one could picture the origin of the three lines as follows: the Zeeman energy at which the paramagnetic electron absorbs the incident radiation E_z is shifted by the interaction between the hyperfine interaction between the electron and magnetic nucleus. Since almost all nitrogen atoms have a nuclear spin of 1, the Zeeman energy at each nitrogen has equal probability of being lowered ($m_I = -1$), increased ($m_I = +1$) or unaffected ($m_I = 0$), depending

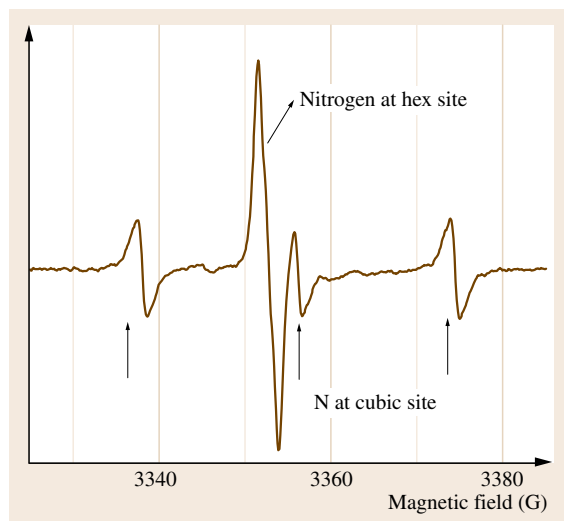


Fig. 45.8 EPR spectrum of nitrogen in 6H-SiC obtained at 30 K with the magnetic field parallel to the c -axis

on the relative orientations of the electron and nuclear magnetic dipole moments. Thus, three lines of equal intensity are produced: one representing $E_z - E_{\text{hf}}$, one $E_z + E_{\text{hf}}$, and one E_z , where E_{hf} is the hyperfine interaction energy. The magnetic field separation between the lines is proportional to E_{hf} . The hyperfine parameter A is proportional to this energy, and is often quoted in terms of magnetic field units T through the conversion A/gB , where g is the g -value for the spectrum and B_z is the magnetic field separation between the adjacent lines. The g -value is obtained from the average B_z of the outer two lines, or in this case, B_z of the central line. Exhaustive analysis of the nitrogen spectrum may be found in numerous papers [45.11, 12].

From the above, it should be apparent that observation of the nuclear hyperfine lines is the key to determining the chemical origin of an EPR center. Not all impurities have isotopes with 100% abundant nonzero nuclear spin. For example, only 4.5% of all Si atoms (^{29}Si) and a mere 1.1% of carbon atoms (^{13}C) are spin $\frac{1}{2}$. Therefore, any intrinsic defect in SiC has a very low probability of being situated near a nucleus of nonzero spin. In these cases, the spectrum consists of a strong Zeeman line due to defects involving spin-zero Si and C nuclei, and pairs of equally spaced smaller lines due to the very few defects involving spin- $\frac{1}{2}$ Si and C nuclei. Figure 45.9 shows an EPR measurement of V_c^+ . The satellite lines A and B arise from the spin- $\frac{1}{2}$ nearest-neighbor Si nuclei. The ratio of the relative integrated intensity of set A to the intensity of the entire spectrum is about 5% and that for set B is 15%. The outer set is attributed to those centers for which the spin- $\frac{1}{2}$ nucleus is located along the c -axis; the inner set to those in which any one of the three remaining Si neighbors is spin $\frac{1}{2}$. The darkest circle in the sketch in the upper right corner of the figure represents the single *unique* axial silicon (A lines), while the three lighter circles represent the other nearest neighbors (B lines). In summary, detection of two sets of hyperfine lines with intensity equivalent to interactions with four Si atoms distinguished by two different energies paints a picture of a carbon vacancy slightly distorted along the c -axis. The positive charge states is determined primarily from theoretical calculations as is discussed later. A complete analysis of this center along with that of the V_c^+ located on the other symmetry site of 4H-SiC is discussed in [45.13].

Hyperfine lines of low-atomic-abundance nuclear spins are often difficult to detect, particularly if the number of defects is also small. This is often the case for Si- and C-based semiconductors, where defect densities are below 10^{16} cm^{-3} and the abundance of the nonzero

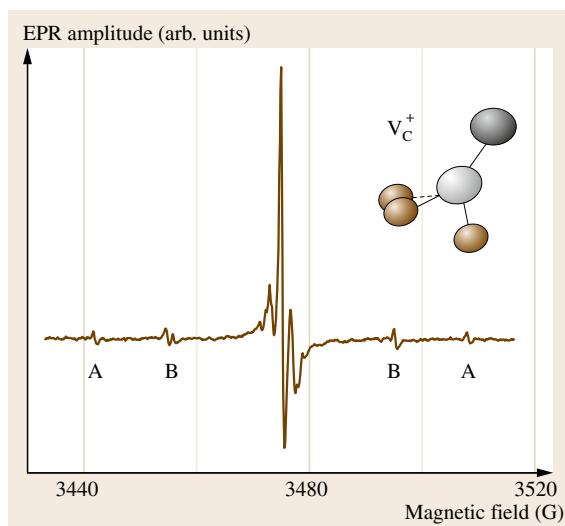


Fig. 45.9 EPR spectrum of the positively charged carbon vacancy in 4H-SiC obtained at 4 K with the magnetic field parallel to the c -axis. The lines marked A and B are the hyperfine lines due to neighboring Si atoms. The model in the upper-right corner shows the four Si neighbors of the carbon vacancy, where the brown circles produce the B lines and the dark gray circle produces the A lines. The light gray circle represents the carbon vacancy

spin isotopes is less than a few percent. In these cases, isotopic enrichment allows for enhanced hyperfine detection. For instance, recently isotopic enrichment was used to enhance the hyperfine of Se impurities in Si and intrinsic defects in SiGe alloys [45.14, 15].

The angular dependence of the hyperfine interaction allows one to map out the local spin density, or effectively determine the wavefunction of the paramagnetic electron. To understand this one has to appreciate that the type of spatial wavefunction will determine the relative directions of the electron–nuclear dipole coupling. Any orbital with $L > 0$ will be directionally dependent and therefore produce an angular-dependent hyperfine interaction. For example, a p_z -shell electron will have lobes along a specific axis, so that, if one measured an EPR signal along this axis, the hyperfine separation would be different from that measured along any other direction. Perhaps the more illuminating example is to consider $L = 0$, or an s -shell electron. Here, no angular dependence would be expected and the hyperfine parameter A should be isotropic, as is the case of phosphorus in Si. In many materials, a paramagnetic electron is a hybrid orbital containing contributions from s -, p -, and sometimes higher L -states. The separation be-

tween the hyperfine lines of nitrogen in Fig. 45.8 exhibit a small angular dependence. Contributions from s -like and p -like orbitals are deconvolved so that the percentage of the wavefunction that is s -like and p -like are determined. For the nearly isotropic nitrogen donor spectrum in 4H-SiC on the cubic site, the wavefunction at the impurity is found to be almost entirely s -like with less than 1% p -character [45.12]. The calculation of the amount of s - and p -character from angular-dependent hyperfine is straightforward and may be found in many texts [45.1]. Although not directly applicable to routine materials characterization, this type of information is extremely helpful to theorists calculating the strength of the hyperfine interaction because it provides a realistic starting function for determination of the hyperfine energies. It is these energies that refine the picture of the defect, particularly those involving nuclear spins common to many elements.

The nearest neighbors may not be the only nuclei contributing to the EPR spectra of a specific defect. When more distance neighbors are sensed, they often show up as sets of satellite lines more closely spaced than those of the nearest neighbors. For example, the pair of lines adjacent to the central line of the V_c^+ spectrum in Fig. 45.9 represents contributions from next-nearest-neighbor carbon atoms. Their intensity reflects the fact that any one of the 12 next nearest neighbors may be a ^{13}C nucleus. It should be pointed out that the analysis can eventually provide the probability that the paramagnetic electron resides on any one of the neighbors, effectively mapping out the spin density in the vicinity of the defect.

Theoretical Calculations of Hyperfine

As with any spectroscopic technique the experimental results may be compared with theory to extract additional information about the defect. In some cases, comparison with theory is the only means to interpret the EPR data in terms of a specific defect because the nuclear hyperfine is not detectable or is ambiguous. Luckily, unlike the g -tensor, the A -tensor is sensitive to at most the second or third nearest neighbors so that accurate calculations are feasible. Hyperfine calculations are particularly powerful tools to determine the defect structure because the strength of the nuclear spin–electron spin interaction is sensitive to the orientation and charge states of the environment. The entire A -tensor for different types of defects may often be predicted from density functional theory and the local spin-density approximation. The results produce an enormous amount of points that can be compared

with experimental data, thus reinforcing the interpretation of the data in terms of a specific defect structure. For example, the **A**-tensor for the positively charged carbon vacancy discussed above was calculated for the defect located at different symmetry sites of the two different polytypes of SiC (4H and 6H), as well as for different charge states [45.16]. The **A**-tensor was also extracted from the complete angular dependence of the EPR spectrum. Comparison of the two results showed that centers known as EI5 and EI6 are V_c^+ located at the hexagonal and cubic sites, respectively [45.13]. Similar comparison between theory and experiment revealed the spectra for HEI1 to be due to the negatively charged carbon vacancy [45.17]. Of course, not all defects in all materials are amenable to reasonable calculation. A large impurity atom and a low degree of symmetry can overwhelm the computational power of even the most modern computers. Nevertheless, comparison of EPR spectra to theoretical calculations of the nuclear hyperfine tensor has enabled the description of countless defects in innumerable types of materials.

To summarize, identification of nuclear hyperfine lines in EPR spectra is critical to determining the chemical origin of the center. The lines have the following characteristics:

1. Nearly equal intensity
2. Nearly equal separation and/or separated equally from the Zeeman line
3. The number of lines is $2I + 1$.

Also, all the lines should exhibit the same dependence on microwave power because they represent the same physical entity. Once the nuclear spin (I) is determined from the spectra, the possible types of nuclei contributing to the spectrum may be determined. Knowledge of the material composition and growth conditions often refines the type of nuclei expected to be involved in the defect. The angular dependence provides the basic components of the wavefunction, which can be used in theoretical calculations to determine the strength of the hyperfine interaction for different defect structures and charge states. Finally, comparison of the theoretically calculated **A**-tensor with the angular-dependent experimental data provides a reasonably definitive picture of the defect.

This section has emphasized the importance of the nuclear spin in detection of defects by magnetic resonance. However, too much of a good thing can create problems. In particular, difficulties arise when the crystal host is composed of atoms with 100% abundant nuclear spin. Depending on the strength of the inter-

action of the defect with host, the presence of many different sources of hyperfine interaction can lead to a series of barely resolved lines or even produce one broad EPR signal with all the powerful hyperfine information buried in its breadth. This is thought to be the cause of the limited information extracted from spectra in GaN because Ga has two isotopes, both with nuclear spin $\frac{3}{2}$, and nitrogen has one nearly 100% $I = 1$ isotope. The single broad line assigned to the Mg-related acceptor may be affected by unresolved hyperfine. The reader should be cautioned that the phrase *depending on the interaction with the host* is critical here. For instance the characteristic line pattern for Fe^{3+} and Mn^{2+} , transition metals that typically interact minimally with the host, are easily observed in GaN crystals [45.18, 19].

45.2.3 Interactions Involving More than One Electron

The above discussion suggests that theoretical calculations, which can predict the hyperfine interaction energy, can also be used to distinguish between the different charge states of a defect. However, in some cases, the charge state can be inferred from the experimental spectrum itself. This occurs if the number of electrons at a defect couple to a total spin greater than $\frac{1}{2}$. From the rules of adding spin angular momentum, it is known that n electrons can yield a total spin between 0 and $\frac{n}{2}$. In fact, Hund's rules tell us that the high spin is favored as the ground state; thus, all multiple electron defects should be paramagnetic. Of course Hund's rules do not strictly apply to a center surrounded by the many perturbing fields in a crystal lattice. Nevertheless, in some situations an EPR spectrum may best be described using a Hamiltonian of spin great than $\frac{1}{2}$. When this occurs, the term that must be included in the analysis is

$$H = \mathbf{S} \cdot \mathbf{D} \cdot \mathbf{S}, \quad (45.7)$$

where **D** is the fine-structure term, present only when $S > \frac{1}{2}$. Different physical situations can necessitate the use of this term including spin-orbit interaction and dipole-dipole coupling between different electrons. Here we will not be concerned with the origin of the term, but highlight two situations where the quadrupole term is used: an excited state of an $S = 0$ center and transition-metal impurities.

The EPR spectra discussed thus far represent the ground state of a defect. With the addition of optical illumination, one can populate the higher energy levels. This is particularly useful when the ground state of the center is an $S = 0$ EPR inactive state. Often, detection

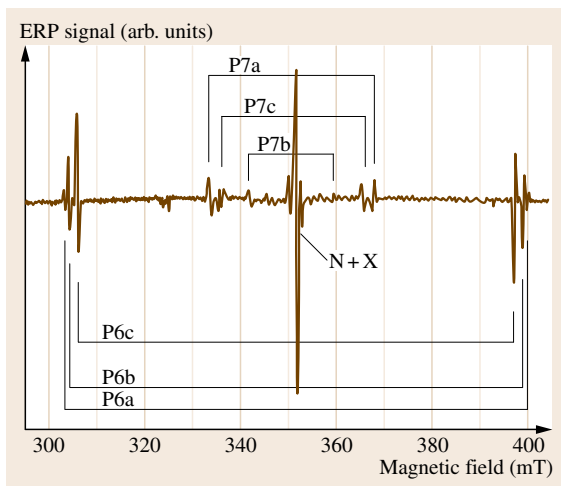


Fig. 45.10 EPR spectrum of P6 and P7 centers obtained from neutron-irradiated 6H-SiC with the magnetic field oriented parallel to the c -axis. The sharp lines in the center are due to nitrogen and an unidentified defect (after [45.20], © APS 2001)

of an excited state may be verified by the fact that, after removal of the light source, the spectrum immediately returns to its pre-illumination condition due to the inherently short lifetime of the excited state. The P6 and P7 centers in n-type 6H-SiC irradiated with neutrons provide an example [45.20]. Figure 45.10 shows the EPR spectrum obtained from neutron-irradiated 6H-SiC during illumination with white light from a halogen lamp. The two sets of paired lines highlighted by brackets represent two similar defects (P6 and P7) on the three different symmetry sites of 6H-SiC (a , b , c). Pertinent to this discussion is that each line of the pairs reflects EPR transitions between spin states $m_s = -1$ to $m_s = 0$ and $m_s = 0$ to $m_s = 1$ of the $S = 1$ center. These lines are often referred to as fine structure. P6 and P7 are thought to represent different orientations of the same defect, although the exact model for the defects remains under debate [45.20, 21]. Note that recent data indicate that the centers are observed in heavily N-doped material without illumination, implying that $S = 1$ is the ground state. Whatever the case, the presence of the paired lines identifies the center as $S = 1$.

The transition element vanadium provides an example of how both the type of impurity and its charge state are determined directly from observation of the spectrum. Figure 45.11 shows two spectra obtained from 4H-SiC: a multiplet of nearly equal intensity lines adjacent to a second set of lines with much lower intensity

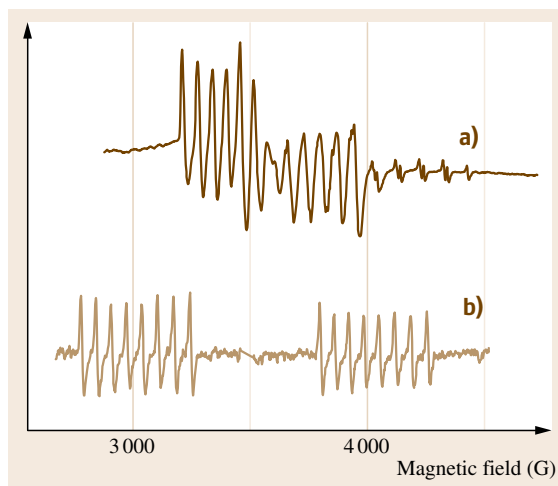


Fig. 45.11a,b EPR spectra of vanadium in 4H-SiC: (a) V^{4+} measured at 4 K with the magnetic field 10° from c -axis; (b) V^{3+} measured at 30 K with the magnetic field perpendicular to the c -axis

(Fig. 45.11a) and a pair of octets (Fig. 45.11b). According to the theory presented in the last section, the set of eight equally spaced lines in Fig. 45.11b indicates a 100% abundant $I = \frac{7}{2}$ nucleus. Checking the tables and considering typical unintentional impurities in SiC, it is concluded that the spectrum (Fig. 45.11b) arises from a vanadium atom on the cubic site [45.22]. A similar pair of octets, reflecting the hexagonal site, is found beyond the magnetic field range shown. Unfortunately, the spectrum in Fig. 45.11a is more complicated; suffice it to say that studies have shown that this spectrum also arises from a vanadium impurity, where the multiplet with high intensity arises from the cubic site and the set of low-intensity lines originate from the hexagonal site [45.23]. The presence of a single set of lines for each symmetry site in spectrum Fig. 45.11a and double set in Fig. 45.11b suggests that the former is an $S = \frac{1}{2}$ center while the latter is $S = 1$. V^{4+} in SiC has one unpaired electron, which would produce spin $\frac{1}{2}$, and V^{3+} has two, which could couple to spin 1. Thus, by simply examining the EPR line pattern, the impurity and its charge states are immediately determined.

How a high-spin defect produces a set of EPR lines at different magnetic fields is not immediately obvious from anything discussed thus far. Simply redrawing the $s = \frac{1}{2}$ energy diagram of Fig. 45.1 for $s = 1$ produces the levels shown in Fig. 45.12a, where the horizontal axis now represents a varying magnetic field and the verti-

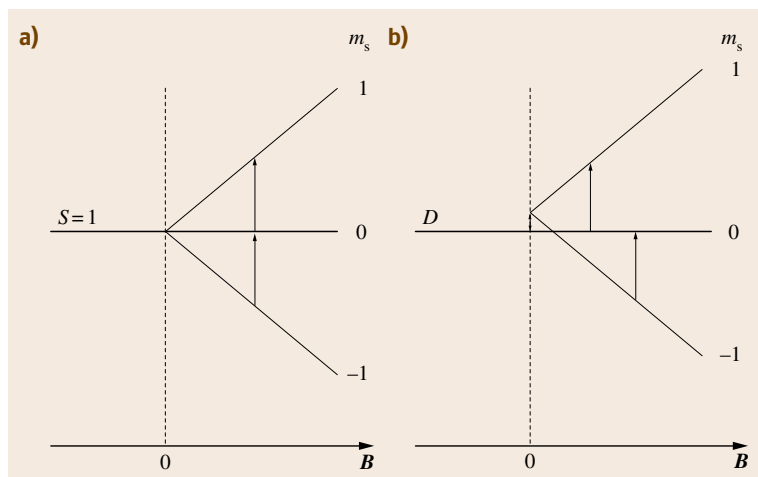


Fig. 45.12a,b Energy levels of a spin-1 electron system in a varying magnetic field: **(a)** in the absence of any zero-field splitting; **(b)** in the presence of a perturbing field causing a splitting of the spin states in zero magnetic field. The vertical arrows represent the fixed quanta of microwave energy available for the transitions

cal axis is energy. The equal sized arrows represent the fixed quantum of microwave energy available for the transitions. It is apparent that the transitions between the different m_s states occur at the same magnetic field. What then, produces the separated pattern of lines observed for high-spin defects? Basically, any perturbing field that removes the degeneracy of the $m_s = \pm 1$ and $m_s = 0$ states at zero magnetic field will yield noncoincident resonance absorptions. Figure 45.12b illustrates the resulting energy levels where the separation D on

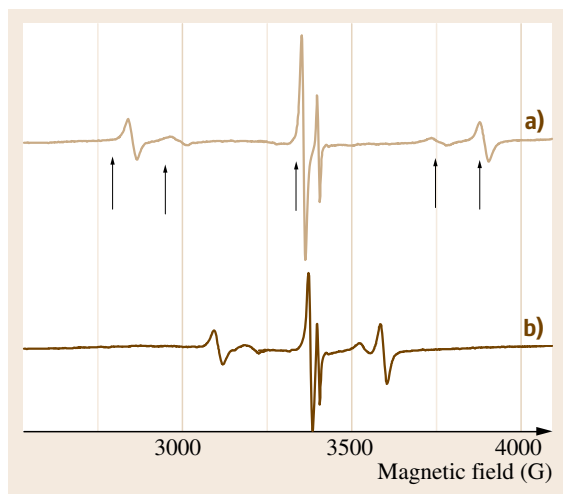


Fig. 45.13a,b EPR spectrum of Fe^{3+} in SrTiO_3 obtained at room temperature. The arrows point to the spin transitions that arise from Fe^{3+} ; the remaining EPR line is due to Cr^{3+} . Data were obtained with the magnetic field **(a)** at 0° and **(b)** at 30° with respect to the (100) direction

the vertical axis is referred to generally as the zero-field splitting. Once the states are separated at zero magnetic field, the $m_s = -1$ to $m_s = 0$ and $m_s = 0$ to $m_s = 1$ transitions no longer occur at the same magnetic field; thus, separate EPR lines will appear at each transition. In general $2S$ EPR resonances will occur. While several types of interactions can separate the energy of the degenerate spin states, the most common is the anisotropic magnetic dipole-dipole interaction. The calculation required to demonstrate the effect of the zero-field splitting is straightforward and is shown in many texts [45.1, 8].

The fine-structure lines produced by high-spin centers have different characteristics than those of hyperfine lines discussed at the end of the previous section. For example, the intensity of each EPR line is not the same. For any $S > 1$ center, the intensities of resonance lines from the various m_s transitions exhibit different, but predictable, variations. Figure 45.13a shows this for Fe^{3+} in SrTiO_3 measured with the magnetic field oriented along the c -axis of the sample. The five lines highlighted arise from the five transitions of the $S = \frac{5}{2}$ center. The remaining line represents Cr^{3+} . The relative integrated intensities of the Fe^{3+} lines, 5 : 8 : 9 : 8 : 5, follow from the transition-matrix element between the $\frac{5}{2}$ to $\frac{3}{2}$, $\frac{3}{2}$ to $\frac{1}{2}$, $\frac{1}{2}$ to $-\frac{1}{2}$, $-\frac{1}{2}$ to $-\frac{3}{2}$, and $-\frac{3}{2}$ to $-\frac{5}{2}$ spin states

$$g\mu_B B_x \left\langle \frac{5}{2}, m_s^i \left| S_x \right| \frac{5}{2}, m_s^f \right\rangle, \quad (45.8)$$

where B_x is the microwave magnetic field perpendicular to the applied field, m_s^i and m_s^f represents the magnetic spin quantum number for the initial and final states,

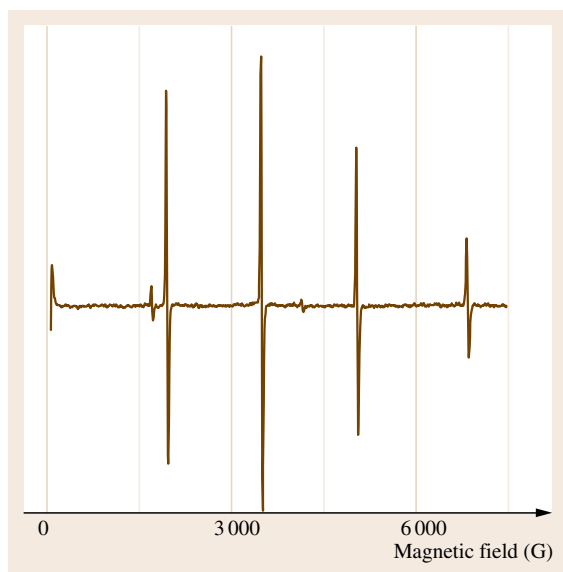


Fig. 45.14 EPR spectrum of Fe^{3+} in a GaN crystal obtained at 4 K

respectively, and S_x is the spin angular momentum operator that ultimately raises the electron from the lower state to the upper state. See [45.1, appendix C] for details. This intensity pattern would apply to any $S = \frac{5}{2}$ center with the simple $|s, m_s\rangle$ wavefunctions. Similar patterns may be predicted for other $S > \frac{1}{2}$ centers. For example, Fig. 45.14 shows that the line pattern for the $S = \frac{5}{2}$ impurity Fe^{3+} in GaN also consists of five lines of unequal intensity. The sharpness of the lines in GaN compared with those in SrTiO_3 most likely reflects a lower density of extended defects or less strain. The line width also explains why the relative amplitudes are different in the two samples; however, it is not obvious why certain transitions should be broadened more than others.

Not all situations involving high-spin defects are as straightforward as the two mentioned here. Sometimes the crystal field, the electric field generated by the ions or ligands surrounding the defect, dominant spin–spin and spin–orbit interactions ultimately producing wavefunctions which are linear combination of the simple spin states, $|s, m_s\rangle$. Crystal-field effects are exhaustively discussed in many texts [45.24]. For EPR, the only point is that the ground-state orbital wavefunction is determined by the field strength, thereby establishing the type of spin wavefunction appropriate for a particular defect. When the crystal field is much greater than other interactions, an EPR spectrum greatly different

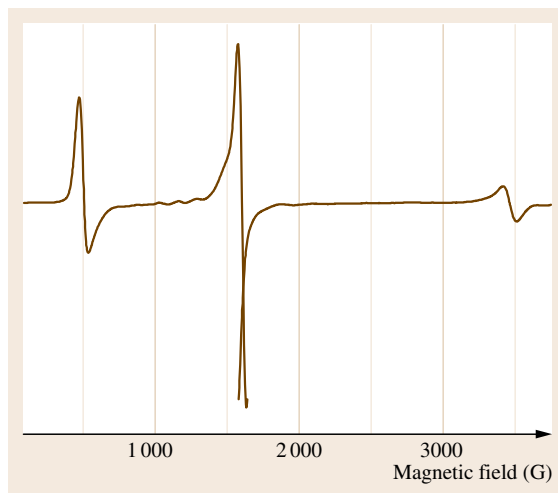


Fig. 45.15 EPR spectrum of Fe^{3+} in a LiNbO_3 crystal obtained perpendicular to the c -axis at room temperature

from the two iron spectra in Figs. 45.13 and 45.14 is produced. Figure 45.15, showing Fe^{3+} in LiNbO_3 , illustrates the point. Here, the trigonal crystal-field effect is of the same order of magnitude as the Zeeman effect, yielding an EPR signal significantly different from the five-line pattern seen previously. Additional interaction terms must be added to the Hamiltonian in order to unravel the meaning of the spectrum [45.25, 26].

Like the Zeeman and hyperfine terms, the fine-structure term can produce angular dependence. In some cases, a simple shifting of lines occurs as seen in Fig. 45.13b. However, often spectra dominated by D exhibit angular-dependent intensities. This occurs when the appropriate wavefunctions are linear combinations of the $|s, m_s\rangle$ states. Because the crystal field is directional, different wavefunctions are produced at different orientations of the sample with respect to the applied B field. The angular-dependent wavefunctions then lead to angular-dependent transition-matrix elements (45.8) and, therefore, varying spectral intensities. Note that high magnetic fields and high frequencies may be employed to avoid complications due to the large crystal field. However, using microwave frequencies larger than 10 GHz is tedious, involving different types of waveguides, cavities, and microwave bridges than those used for the lower frequencies. Often, it is easier to deconvolve the complicated experimental data using straightforward calculations than to execute an EPR measurement at sufficiently high frequency as to avoid the crystal-field effects.

To summarize, we have considered three energy contributions to a point defect in the presence of an applied magnetic field: the electronic Zeeman term (45.2), the nuclear hyperfine interaction (45.6), and the fine-structure term (45.7). In general, all three effects may be present, so that the appropriate Hamiltonian to begin analysis of a spectrum is

$$H = \mu_B S \cdot g \cdot B + \sum_j S \cdot A \cdot I + S \cdot D \cdot S. \quad (45.9)$$

For defects with $S > 1$, additional terms may be added depending on the nature of the defect and its surroundings. Because many of the defects typically encountered involve only two or more of the terms above, no discussion of the additional terms is presented here. Equation (45.9) is not the most *user-friendly* equation ever presented to the average reader. For those with peripheral interest in EPR, understanding how the number and separation of EPR lines are used to determine defect structure should be sufficient to appreciate the power of the technique. More interested readers will find the quantum-mechanical calculation techniques required for complete analysis in the many references referred to throughout this section, specifically [45.1, 8].

45.2.4 Total Number of Spins

In addition to a physical description, EPR data may provide the total number of centers of a specific defect. This is accomplished by comparing the spectrum of an unknown quantity of a defect with that obtained from a known quantity. Significantly, the EPR signal from the standard need not arise from the same defect or even a different defect in the same material. This convenience is afforded by the fact that the spin-flip probability is usually independent of the local environment. Common calibration standards include 2,2-diphenyl-1-picrylhydrazyl (DPPH) and the phosphorus signal in powdered, heavily doped, n-type Si. In principle, the comparison can lead to an absolute number of spins with an accuracy of 50% with sensitivity as low as 10^{10} spins [45.1]. However, the reader should be warned that the sensitivity depends strongly on line width and number of lines. The number quoted is based on a single resonance with 1 G line width. For a signal of 10 G line width composed of five lines, the minimum detectable spins increases by a factor of at least 50. Other factors

such as temperature and microwave saturation also limit sensitivity. Such issues are discussed in [45.1, appendix E].

A few items to remember regarding the absolute spin measurement are:

1. Only the paramagnetic state of any defect is being measured. For instance, the number of acceptor impurities may be calculated. However, the result is limited to acceptors that have captured the hole in the valence band. For this reason, EPR of acceptors (and donors) is often performed at low temperature to more closely reflect the total number. Compensation may further reduce the number of EPR-active acceptor sites. The amount of the impurity calculated from the acceptor signal will not include aggregates, complexes or other forms of the impurity; however, different EPR signals may be related to these entities and measured separately.
2. Only the total number of centers is determined. Additional experiments are needed to find the spatial distribution of defects. When concentration is given in an EPR study, the centers are assumed to be uniformly distributed throughout the material unless otherwise stated.
3. Defects arising from complex wavefunctions, such as high-spin centers in a strong crystal field, will exhibit intensities that are dependent on orientation. In these cases, one must first determine the various transition rates before the number of defects may be calculated.

Traditionally, the absolute number of spins is not the focus of an EPR study. This is partially because of the many caveats discussed above, as well as the difficulty of generating an accurate standard. One powerful aspect of the spectroscopy that is commonly employed, however, is determination of the variation in number of defects by measuring the relative amplitude of EPR signals. For a single EPR resonance that does not change shape during the course of a study, the amplitudes of a signal may be used to indicate varying defect densities. This is the approach used in many of the experiments discussed below. For the types of centers mentioned in item 3, however, careful alignment of the samples is required between measurements so that the amplitude changes truly reflect the number of spins and not angular-dependent transition probabilities.

45.3 Scope of EPR Technique

Having presented the basis for interpreting EPR spectra, without question the most challenging feature of EPR for most readers, the remainder of the chapter focuses on the power of EPR in terms of the types of defects detectable and typical correlation studies. All of the examples in the section above are simple point defects, either an intrinsic defect or single-atom impurity. Many other forms of defects are detected including substitutional, interstitial, antisite, vacancies, vacancy pairs, antisite–vacancy pairs, and impurity–vacancy pairs. The only requirement is that the defect be paramagnetic in the as-grown material or be able to be made paramagnetic with an external perturbation.

EPR was first used on bulk crystals, and indeed this is where the full power of the technique is realized. However, with the ongoing push towards miniaturization and increasing desire for a *chip-based* world, films less than one micrometer thick and particles with less than 100 nm diameter are typically encountered. While this has been the case in electronics for more than a generation, miniaturization of optical and even microwave devices is increasingly popular. Indeed, one of the most recent initiatives involves growing films using crystals with well-known microwave or magnetic properties. Ultimately, these will be deposited onto a full wafers with future integration into Si electronics as the goal.

The utility of applying EPR to films is not obvious because, although the technique is sensitive to as few as 10^{11} centers, for traditional defect analysis these defects must be isolated. A simple calculation shows that a micrometer-thick film with 10^{11} centers uniformly distributed yields 10^{15} cm^{-3} defects. While this is not an unrealistic number for the types of films of interest today, the calculation represents the most hopeful situation: the minimum spin detection limit and the thickest films of interest. Nevertheless, the example does show that studying films is not out of the question. Indeed many successful experiments are reported in the literature. Most take the advantage of stacking many film–substrate samples so that the signal intensity may be maximized. Careful alignment is required in these cases so that the crystallinity of the samples is not compromised. The examples below illustrate several different types of film–substrate studies:

1. Intrinsic defect in the *bulk* of a micrometer-thick film
2. Defect at a crystalline substrate–amorphous film interface
3. Near-surface impurities on a polycrystalline film.

45.3.1 Defects in a Thin Film on a Substrate

The first situation addressed is the study of a simple point defect in a film, a donor in GaN. The only difference between the film and bulk experiments in this case is the preparatory steps for the measurement. Usually, several film–substrate samples are stacked together to increase the total amount of GaN being studied. Furthermore, GaN is typically grown on sapphire or SiC. In either case, the substrate must be carefully studied to distinguish the substrate EPR signals from those of the film. The microwave absorption utilized in EPR detection completely penetrates most semiconductors and insulators, so that the technique senses the substrate and film equally. Luckily, the well-known EPR signatures of defects in sapphire are highly anisotropic, so that their contribution to the spectrum may often be minimized by prudent orientation of the sample with respect to the magnetic field. The only defect to be avoided in n-type SiC substrates is the nitrogen donor, which is easily resolved from the donor in GaN.

Most of the information about the donor EPR signal in GaN is contained within a work by Carlos and coworkers [45.27]. No hyperfine could be detected in the spectrum, leaving the chemical origin of the center uncertain, but several EPR characteristics suggest that the resonance represents an electron in a donor band. Work in our laboratory shows that the spectrum is found only in n-type samples, and that the signal intensity increases with increasing donor density for $n = 1 \times 10^{14} - 1 \times 10^{17} \text{ cm}^{-3}$ [45.28]. Carlos and coworkers concentrated on the spectroscopic characteristics of the EPR signal to demonstrate the donor assignment. Their measurements suggest that the *g*-value is typical of a donor electron and the angular dependence reflects that of the hexagonal lattice. Furthermore, the line width indicates that the paramagnetic electron is not *attached* to the donor atom, and the temperature dependence of the line width, shown in Fig. 45.16, eliminates a conduction-band electron. The different symbols represent data obtained from various thickness samples as indicated on the figure. The main point here is that all sets of data exhibit a decreasing line width until 20 K, followed by an increasing line width. The former region is

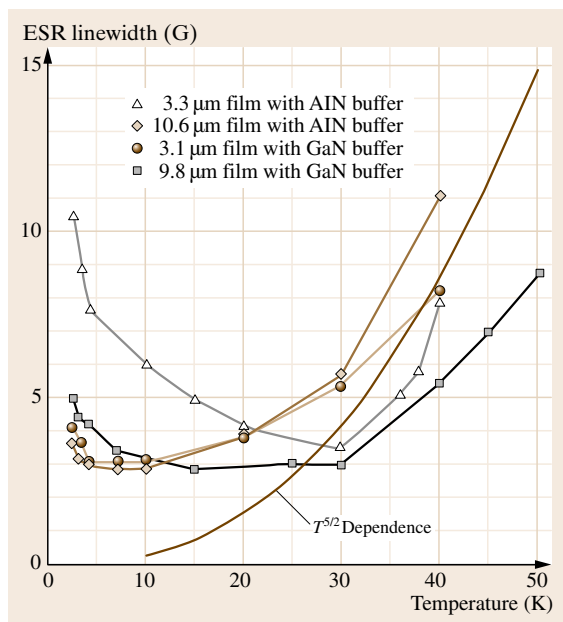


Fig. 45.16 Line width of the donor signal in GaN measured at selected temperatures. The smooth brown line is a $T^{5/2}$ fit to all of the data; other lines merely connect data points (after [45.27], © APS 1993)

thought to be due to motional effects and the latter due to coupling to acoustic phonons, neither of which should occur if conduction-band electrons were involved.

Although there are several other EPR studies of point defects in crystalline thin films, the small signal size inherent to the low sample volume limits the number of intensive investigations. Homoepitaxial films are highly unlikely to produce meaningful results about the film because the layer of interest cannot be separated spectroscopically from the bulk substrate. Consequently, many film studies were performed on amorphous material, the most common of which was SiO₂ films on Si substrates. Although many studies focused on oxide films irradiated by γ -rays or higher energy, several studies addressed the intrinsic defects in the oxide films [45.29–35]. In some cases, the defects, specifically an oxygen vacancy known as an E' center, was successfully correlated with many of the electrical trapping effects in metal–oxide–semiconductor field-effect transistor (MOSFET) devices [45.34, 35]. Other studies of film–substrate systems in which the point defect resides in the *bulk* of the film include diamond and MgO [45.36–38].

45.3.2 Defects at an Interface

The second type of center addressed in this section is one located at an interface, specifically the Si–SiO₂ interface. In Si devices, paramagnetic defects at the Si–oxide interface are known to be directly related to electrically active trapping sites that alter device performance [45.39, 40]. For this reason, much EPR work has concentrated on a dangling bond defect located at the semiconductor–oxide interface [45.39–44]. Several different types are found in pure silicon-based interfaces, each involving an unpaired electron on a Si atom located on the semiconductor side of the interface [45.40, 42]. Centers with a Ge dangling bond and C dangling bond are seen in SiGe–oxide and SiC–oxide interfaces, respectively [45.41, 43, 44]. The dangling-bond-like defects are referred to collectively as P_b centers.

In general, EPR cannot selectively detect centers at surfaces and interfaces because the microwave radiation penetrates the entire semiconductor substrate. However, for a perfectly flat surface, the angular dependence of the EPR resonance may provide enough information to deduce the surface nature of the center, as was done for the Si P_b center located at the interface between a (111) Si substrate and amorphous SiO₂ layer [45.42]. To understand the difference between interfacial and bulk angular dependence one must reconsider the discussion of the *g*-tensor presented earlier. *g* is a tensor because the absorbed energy depends on the orientation of the applied magnetic field and a preferred direction of the dipole moment. However, in a crystal a specific defect may be located at one of several different symmetry-related sites. For example, the simple dangling bond in bulk Si may be directed in any one of four (111) bonding directions, all of which may make a different angle with respect to the applied field depending on the orientation of the sample (Fig. 45.17). Since the defect may be any of the four (111) bonding directions of tetrahedral Si, the EPR spectrum should reveal four lines when the magnetic field is oriented at a general angle with respect to the surface normal of the sample. For special orientations, such as *B* rotated in a (111) plane,

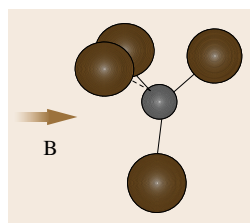


Fig. 45.17 Schematic model of a tetrahedrally coordinated atom (small circle) with the magnetic field directed at an arbitrary angle with respect to any one of the [111] directed bonds. The dangling bond could be any one of the four bonds with the large circle removed

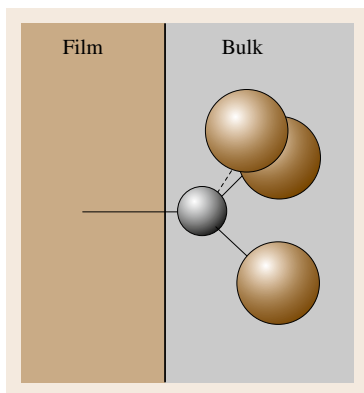


Fig. 45.18 Schematic model of a tetrahedrally coordinated atom at an interface, where one of the $[111]$ -directed bonds points perpendicular to the interfacial plane. The vertical solid line marks the ideal interface plane between the bulk and the substrate

the bond perpendicular to the plane should produce one isotropic line and the remaining three dangling bonds would generate one anisotropic line three times larger than the isotropic one.

Now perhaps the reader can see how an interface defect would be different. At an interface (or surface) not all of the four directions would be identical. The easiest case to imagine is the (111) surface, where one of the four bonds is perpendicular to the plane of the interface along a now unique (111) direction (Fig. 45.18). The other three possible bonds would be pointing into the *bulk* of the Si substrate, and if paramagnetic, would produce a different g -tensor than the interfacial defect. Since silicon is a perfected material, generally the back bonds are unbroken and do not contribute an EPR signal. Therefore, if the magnetic field were in the plane of the interface and perpendicular to the dangling bond, one would expect to see only a single isotropic EPR line due to the dangling bond at the interface. Unfortunately rotation in the plane of the interface is not realistic, but Poindexter and coworkers performed measurements with B in the $(11\bar{2})$ and $(1\bar{1}0)$ planes, revealing the expected angular dependence. Figure 45.19 shows the g -value versus angle with respect to the (100) direction for a P_b center in thermally oxidized (111) Si. The appearance of only a single g -value at each angle indicates that only one EPR line is observed at each angle. The coincidence of the unfilled and filled circles, which represent data obtained from two different planes of rotation, imply that the angular dependence of the spectrum is identical for the two different planes. Both observations are expected for a dangling bond between the (111) surface of Si and the overlying oxide film.

The relationship of the P_b center to Si was confirmed by observation of the nuclear hyperfine interaction. Detecting the hyperfine in this case is a heroic

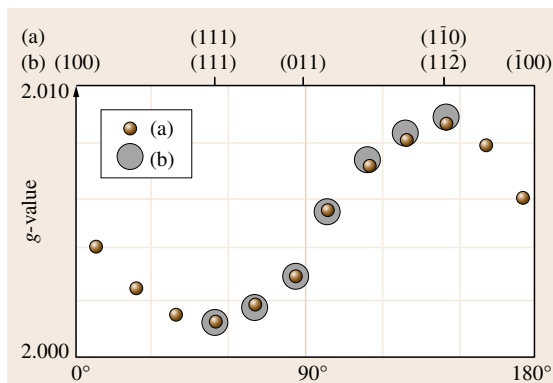


Fig. 45.19 g -values of the P_b center measured in oxidized Si with the magnetic field in the plane (a) (small circles) and plane (b) (large circles) (after [45.42], © AIP 1979)

experiment considering the low atomic abundance of ^{29}Si and small total number of defects at an interface. Nevertheless, Brower stacked 35 oxidized Si wafers together to observe the hyperfine lines, confirming that the nucleus associated with the dangling bond is Si [45.45]

As one might expect, other types of interfaces may be studied with EPR. However, to the author's knowledge, the only reports in the literature focus on the semiconductor–oxide system, specifically SiC–SiO₂ and SiGe–SiO₂ [45.41–44]. In both cases oxidized porous material or oxygen-implanted substrates were used, and the interfacial nature was confirmed through etching studies. The planar interfaces necessary for the angular-dependent studies are not achievable at this time for these types of materials. In principle, many other types of interfaces could be examined. The limitation, however, is always preparing the samples in such a way as to maximize the amount of interface in the EPR cavity. Multilayer heterostructures should make ideal samples for study, but the author is not aware of any attempts to date.

45.3.3 Defects at Surfaces

A surface may be thought of as a special case of an interface, one in which one side of the interface is the ambient atmosphere. In principle, the Si P_b center should be observable on bare Si. And indeed, one *should* be able to detect the center if one could do an EPR measurement in vacuum. Si oxidizes readily in air at room temperature, thus an unoxidized surface is virtually unobtainable under the conditions required for an EPR study. Nevertheless, many surface defects are

reported in the literature, but most relate to the roughened surface caused by cutting or polishing [45.46]. Such centers exhibit an isotropic g -value and are often passivated in the presence of hydrogen [45.47].

For single crystals, one may differentiate between bulk and surface defects in much the same way as was discussed for bulk and interface. However, for polycrystalline materials the situation is somewhat different, as is illustrated in the following example. Cr-doped polycrystalline SrTiO_3 films, 1700 nm and 350 nm thick, were grown on sapphire substrates [45.48]. The powder-pattern spectrum typical of a polycrystalline material was resolved into two separate spectra: one with a g -value of 1.977, typical of Cr^{3+} in SrTiO_3 , and a second center with $g = 1.974$. The authors show that the latter is consistent with a Cr^{3+} impurity located near the surface. As discussed earlier, the symmetry of a surface defect is inevitably lower than that of a bulk defect and angular-dependent measurements may be used to exploit the difference. However, the random nature of the polycrystallites requires a different data analysis than that of a pure crystal. Calculations by *Deigen* and *Glinchuck* show that the g -value for a surface defect should be shifted from that found in the bulk by an amount proportional to the angle between the applied field and the surface normal [45.49]. In the Cr-doped films, the EPR signal represented by $g = 1.974$ shifts as the sample is rotated in the magnetic field. The angular dependence of this portion of the signal agrees with the theory predicted for a surface center. Also, the authors point out that the ratio of the 1.974 signal intensity to that for the 1.977 signal is larger in the 350 nm films than in the 1700 nm ones, as expected for a surface center in a thinner sample.

The trapping of impurities within the bulk of sub- μm -sized particle is a well-known difficulty, and several studies have employed EPR to distinguish bulk and surface impurities in these nanoparticles. The Mn^{2+} impurity in ZnS provides just one example [45.50]. EPR of nanoparticles have also been used to address the relationship between the defects and ferromagnetic or ferroelectric behavior [45.51]. Si surface centers, not surprisingly, are often addressed in EPR studies of Si nanodimensional materials [45.52, 53].

45.3.4 Nondilute Systems

This chapter, as well as much of the EPR literature, focuses on low concentrations of isolated point defects separated by at least several atomic units. The interpretation of spectra requires a significantly dif-

ferent approach when the defect-defect distance gets smaller. More specifically, new terms such as the exchange interaction enter the Hamiltonian if nearby spins on separate defects begin to interact. *Ferher* et al. demonstrated this for P-doped Si [45.54] using samples with two different donor concentrations, 1×10^{17} and $4 \times 10^{17} \text{ cm}^{-3}$. The spectra reveal several pairs of EPR lines between the hyperfine lines from the isolated phosphorus atoms. *Ferher* demonstrated that the number of pairs increased as the concentration of phosphorus increased, suggesting that at sufficiently high density the spacing between some of the dopants is suitable for electron-electron exchange. The work was extended by *Maekawa* and *Kinoshita* studying Si doped with 10^{16} – 10^{19} cm^{-3} phosphorus atoms [45.55]. Temperature-dependent measurements confirmed the role of the exchange interaction suggested by *Ferher* for the most lightly doped samples and revealed the presence of electron-hopping and impurity-band conduction at the highest temperatures.

Bencini and *Gatteschi* discuss the role of the exchange interaction in EPR spectra for a variety of different circumstances ranging from transition-metal dopants to protein-based systems [45.56]. All cases including exchange and superexchange are discussed. The emphasis of these types of studies is distinctively different from that discussed above for the nondilute systems. For example, spin-spin correlation as well as spin-spin and spin-lattice relaxation times, are emphasized. Nuclear hyperfine may often be lost in the typically large line widths of exchange-dominated systems. Thus, the interaction of the defects with the local environment are the focus of the study, rather than the detailed atomic structure of a specific defect. Finally, the case of a nondilute system of a ferromagnetic material should be pointed out, in which the collection of spins creates a magnetic field without the application of an applied field. The magnetic resonance of such a system, referred to as ferromagnetic resonance, requires entirely different analysis from the paramagnetic resonance discussed in this chapter. The reader should consult [45.57, 58] for information on ferromagnetic resonance.

Much of the literature of nondilute systems is concerned with one- and two-dimensional systems of spins, reminiscent of dangling bonds at an extended defect. Unfortunately, sensitivity may present a limitation. In the case of strongly coupled spins, the minimum detectable number of spins would be severely crippled by the line width typical of dilute systems. Specifics are difficult to estimate, but most nondilute systems produce line widths hundreds of G wide, thereby de-

creasing EPR sensitivity from the typical 10^{11} spins to 10^{14} spins. Consider a material with 10^8 cm^{-2} line defects each $1 \mu\text{m}$ long, consisting of 1×10^3 defects. This yields 1×10^{11} defects in each cm^2 of material,

an amount on the edge of detectability for even a 1 G line width. However, in emerging materials where the concentration of extended defects may greatly exceed 10^8 cm^{-2} , EPR detection may not be unrealistic.

45.4 Supplementary Instrumentation and Supportive Techniques

As with any technique, correlation studies using data obtained from other techniques or the incorporation of additional instrumentation enhances the amount of information gained from the study. Many different types of techniques and layers of instrumentation have expanded the capabilities of EPR over the years. First, one example using additional instrumentation will be presented: photo-EPR. Then several correlation studies will be discussed, including electrical measurements and thermal annealing. Additional examples involving expanded instrumentation are briefly reviewed in the final section of the chapter.

In this section the term *defect level* is used extensively, so the reader must fully understand what it means. A defect level is similar to an ionization energy in that it represents the difference in energy between two charge states. In the case of ionization, however, the final state is represented by an electron infinitely far away from the ion. For a defect in a crystal, the electron is located in the conduction band after removal from the defect. The defect level is the energy necessary to remove an electron from a defect and place it in the conduction band. Similarly, a defect level may be viewed as the energy required to excite an electron from the valence band to the defect. The level is represented schematically as shown in Fig. 45.20. The lines labeled E_v and E_c are the valence- and conduction-band edges, respectively. The line labeled $X^{-/0}$ is the defect level, representing the energy required to change the charge

state of defect X from negative to neutral. The inverse, the energy required to change defect X from neutral to negative, is the same level. Since a defect level is always quoted with respect to a band edge, it is typically written as $E_c - E_x$ or $E_v + E_x$. From the discussion, it should be clear that a defect level has meaning only with respect to specific charge states. That is, the statement *the defect level of boron in SiC* is ambiguous. One should say *the defect level of boron from the neutral to negative charge state*, or $B^{-/0}$. However, for typical acceptor and donor impurities the charge states are well known and often omitted. For less common impurities the complete statement is imperative to avoid confusion.

Several different descriptive terms are used in conjunction with a defect level. *Shallow* and *deep* are used to distinguish the energy difference between the level and a band. The former generally refers a defect level that may be depopulated at room temperature; the latter implies any level sufficiently far from a band such that it is stable at room temperature. Recently a third descriptor, *mid-gap level*, has been introduced. This term applies to a level that is close to the center of the bandgap of a wide-bandgap semiconductor. Operationally, it generally refers to a level more than about 1 eV from either band edge, and one that is not easily detected by conventional thermal techniques such as deep-level transient spectroscopy.

Some defects have more than one level in the bandgap. The term *amphoteric* is used if the levels are $X^{0/+}$ and $X^{-/0}$, where the former is referred to as a donor level and the latter as an acceptor level. Confusion arises when one talks about transition-metal defects because the original work was performed on ionic insulators rather than semiconductors. Thus, the ionic notation is used. For example, for vanadium with five outer electrons in tetrahedrally bonded SiC, the neutral state is referred to as V^{4+} because four of the five outer electrons are transferred to the four *positive* C atoms surrounding the site. The $V^{4+/5+}$ level is referred to as the donor level because the vanadium becomes neutral (V^{4+}) after releasing an electron to the conduction band. Similar V^{3+} is negative and $V^{3+/4+}$ is the acceptor level.

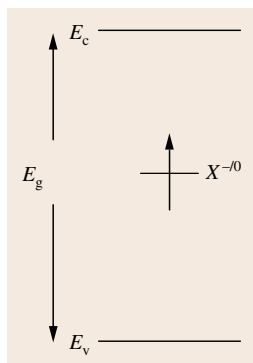


Fig. 45.20 Schematic energy diagram illustrating the concept of a defect level $X^{-/0}$ (see text)

Another confusion that may arise is the difference between a defect level measured using a standard thermal technique such as deep-level transient spectroscopy (DLTS) and an optical method, such as optical absorption. The former detects transitions between ground states, whereas in the latter measurement the final state may be an excited state of the optically induced charge state. In other words, using thermal methods one senses only zero-phonon transitions, whereas optical excitation induces the Franck–Condon (vertical) transition. By definition, a defect level is a thermally determined entity. The energy difference between the zero-phonon and Franck–Condon levels may be interpreted in terms of a structural relaxation of the defect, as is discussed by Godlewski et al. [45.59–61].

45.4.1 Photo-EPR

As mentioned earlier, optical illumination may excite the EPR active state of a defect in two different ways. Diamagnetic ($S = 0$) centers may be excited to their triplet ($S = 1$) state where the $\Delta m_s = 1$ transitions within the $S = 1$ manifold may be seen. An example involving the P6/P7 centers was presented. In this section, photo-EPR involving a change in charge state is discussed. Radiation such as near-infrared, visible or ultraviolet may ionize a defect by removing an electron to the conduction band or by exciting an electron from the valence band. This not only enables detection of previously nonparamagnetic centers, but may lead to determination of the electrical level of the defect [45.59–61]. For instance, the transition of vanadium from the $4+$ to $5+$ charge state $V^{4+/5+}$ was found to be 1.6 eV above the valence-band edge E_v using photo-EPR [45.22]. Several groups have presented studies for the defect level of the carbon vacancy V_c [45.62–64], and Son and coworkers used photo-EPR to address the levels of several different defects in SiC [45.65].

The technique consists of measuring the resonance signal during illumination with sub-bandgap light, usually from a 100 W-lamp monochromator system. Two different approaches may be used: steady-state and time-dependent photo-EPR. Almost all of the studies involve the former because the latter involves extensive time and is feasible only for defects with sufficiently long relaxation times. The typical time for an EPR scan, tens of seconds, limits the temporal resolution and the type of defects studied. Nevertheless, Godlewski and coworkers applied time-dependent EPR to impurities in ZnS and GaAs [45.59, 60]. Experimentally, the intensity of an EPR signal is monitored as a function of time

while illuminating the sample with a fixed photon energy, and the time dependence is fitted to one of many equations depending on the types of transitions involved. Cases involving interaction between acceptors, donors, and conduction/valence bands are thoroughly covered in a review article by Godlewski [45.61].

To understand the analysis, consider the simplest case of a single transition involving defect ionization of an electron to the conduction band. The time dependence of the signal intensity recorded at a specific wavelength should follow a first-order kinetic process

$$\Delta n(t) \propto 1 - \exp\left(\frac{-t}{\tau}\right), \quad (45.10)$$

where Δn represents the normalized change in defect concentration during illumination and τ is the time constant for the process. If the incident light intensity I can be measured, the cross section σ can be calculated from $\frac{1}{\tau} = I\sigma$. The intensity of light inside the sample may be estimated if all of the optical properties of the material are known. Typically samples are transparent to the illumination wavelengths used in photo-EPR, so the incident intensity serves as a good approximation to the intensity of light at the defect. Ideally, a plot of the cross section versus excitation wavelength produces a curve with a threshold reflecting the defect level of the center. Figure 45.21 illustrate some of these ideas, where the time evolution of the V_c^+ signal in 4H-SiC is shown for excitation energies of 1.73 eV (Fig. 45.21a) and 2.3 eV (Fig. 45.21b). The data represent two processes: one for ionization of an electron from V_c^0 to the conduction band (Fig. 45.21b) and the second for excitation of an electron from the valence band to V_c^+ (Fig. 45.21a). The good fit to a single exponential (solid line) supports a model based on a simple transition involving only one defect. When measurements are made with sufficiently low light intensity such that the number of V_c^+ defects generated by the light is proportional to I , the cross sections are shown to be on the order of 10^{-15} and 10^{-16} cm² for ionization to the conduction band and excitation from the valence band, respectively [45.64]. Unfortunately, the very long time constants typical of these samples precluded a detailed study of the energy dependence of the cross section. However, the two energies measured at the shortest time constants, 2.3 eV and 1.78 eV, may be used as estimates for the transitions energy from the defect to E_c and from E_v to the defect. The fact that they sum to a quantity larger than the bandgap of 4H-SiC (3.26 eV) suggests that some of the energy is consumed by relaxation of the defect upon capture or release of an electron. The value for

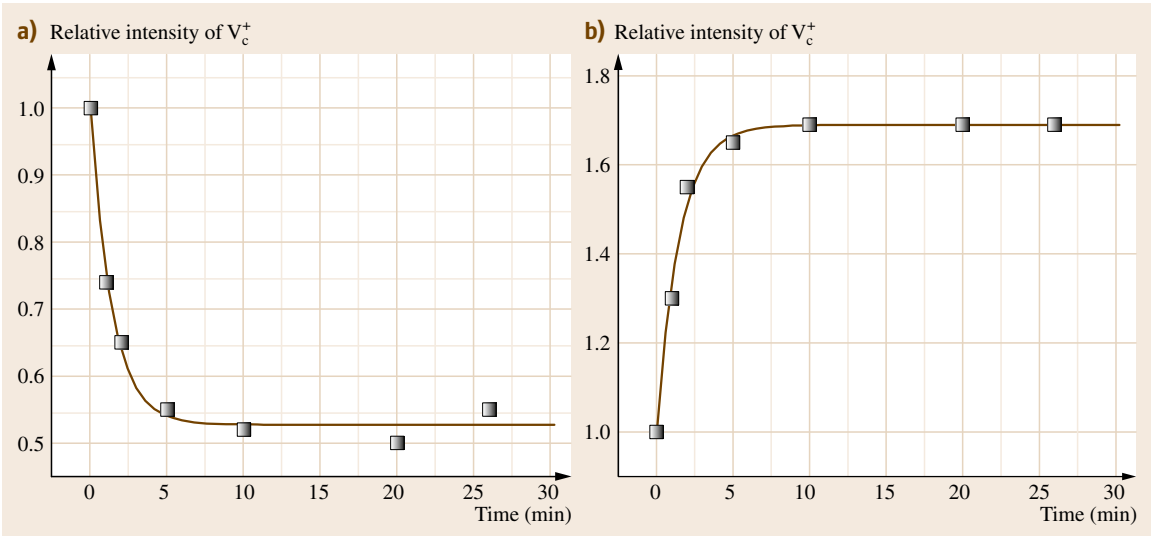


Fig. 45.21a,b Time-dependent photo-EPR data of V_c^+ measured in high-purity semi-insulating 4H-SiC. The photon energy used was (a) 1.78 and (b) 2.3 eV. The solid lines are exponential fits to the data

the relaxation energy extracted from the data, 0.8 eV, is consistent with that predicted by theory, supporting the simple interpretation of the results [45.66]. Analysis of steady-state photo-EPR data yields a similar result for the relaxation energy [45.66].

A more thorough application of time-dependent photo-EPR is presented by Godlewski [45.61]. Here, defect relaxation as well as phonon coupling and a model of the purely electronic cross section are included in the energy dependence of the photo-EPR optical cross section used to fit the data. Thermalization measurements are included along with the optically induced spectra to study the influence of defects with levels located very close to a band edge. The defect levels and relaxation energy are determined for $Cr^{+}/^{++}$ in ZnS and GaAs. These values, which compare favorably with those obtained from optical absorption studies, provide validity to the photo-EPR approach.

Although powerful, time-dependent photo-EPR requires that the transition times be long enough to be detected by the relatively slow EPR measurements and short enough to be measured within the lifetime of an experimentalist. The steady-state photo-EPR method provides a simpler approach to determining defect levels; however, the technique cannot distinguish the influence of multiple transitions and is therefore limited to pure materials in which a single dominant defect prevails. The term *steady state* photo-EPR refers to measuring the EPR signal after

a fixed period of illumination at a selected wavelength. Results obtained on high-purity SiC are shown in Fig. 45.22, for V_c^+ (brown circles), nitrogen (triangles), and boron (gray circles). In general, the threshold at 1.5 eV in the V_c^+ data is interpreted as the transition of the electron from E_v to the defect and the one at 1.7 eV is thought to represent the transition from the defect to the conduction band. The thresh-

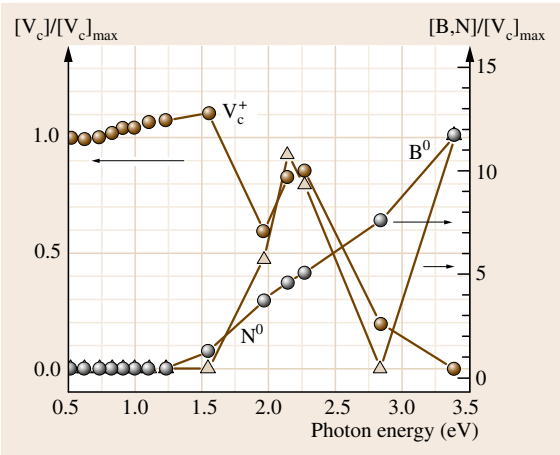


Fig. 45.22 Steady-state photo-EPR data obtained from high-purity semi-insulating 4H-SiC. The left vertical axis reflects the relative concentration of V_c^+ (brown circles); the right, boron (gray circles) or nitrogen (triangles)

olds are equivalent to transition energies obtained using thermal excitation in that they typically represent zero-phonon transitions. As such, the difference between each threshold value and the energy obtained from the time-dependent data of Fig. 45.21 is the difference between the Franck–Condon and zero-phonon transitions. In other words, the difference is a measure of the relaxation energy. However, as Fig. 45.22 shows, several other photoactive centers are detected, complicating this interpretation. Thus, while interpretation of the data shown in Fig. 45.22 provides a working model, many additional studies including comparison with other techniques need to be performed to completely understand the transitions.

45.4.2 Correlation with Electrically Detected Trapping Centers and Defect Levels

The importance of crystalline semiconductors to the electronics industry has spurred an overwhelming number of studies correlating charge-trapping centers and defect levels to impurities and intrinsic defects. For example, instabilities in metal–oxide–semiconductor field-effect transistors (MOSFETs) initiated numerous experimental programs linking charge-trapping centers in the thermally grown gate oxides with well-known EPR defects in quartz and glass [45.5, 6]. In crystalline materials, the electrical levels in semiconductors detected by deep-level transient spectroscopy (DLTS) and temperature-dependent Hall measurements (TDH) have been attributed to EPR-detected defects with similar thermal properties [45.68, 69]. Also, the interface defects discussed above were widely studied in terms of their electrically detected counterparts. Below, a few studies that employ electrical–EPR correlation measurements are summarized.

Before reading the examples, one must appreciate the limitations of comparisons between EPR and most electrical techniques. The same sample is seldom used for both measurements because the area required for an electrical method such as capacitance–voltage (C–V) or DLTS is often an order of magnitude less than that required for EPR. Besides, a metal contact is often necessary for electrical measurement, while a thick flat metal surface suitable for good electrical contact severely cripples the sensitivity of EPR. Several variations have been devised to avoid these difficulties, the most successful of which is described below, but in most cases separate pieces are used for the two different types of measurements.

Acceptor Activation and Passivation

In the bulk of semiconductors, many of the correlation studies focus on the identification of acceptors or donors and the mechanism by which they are passivated by hydrogen. The dominant GaN acceptor, magnesium, provides one example. Using samples with magnesium concentration in the range 10^{18} – 10^{19} cm^{−3} Glaser and coworkers studied a broad, axially symmetric signal found only in Mg-doped GaN. Additional work by others showed that the passivation of holes and the EPR defect followed the same trends [45.70, 71]. Activation by heat treatments in an inert environment produced similar results for the EPR signal and holes also [45.72]. Figure 45.23 shows a comparison of the resistivity measured by Nakamura and coworkers (gray squares) and the intensity of the Mg-related EPR signal (brown circles) observed in our laboratory during consecutive annealing treatments in dry N₂ [45.67]. In this comparison, not only are the samples different physical pieces, but they were grown by different groups using somewhat different methods. Nakamura's samples were grown by a metalorganic chemical vapor deposition (MOCVD) technique at 1035 °C on a GaN buffer layer using a sapphire substrate, while our samples were grown by organometallic CVD on an AlN buffer layer using an n-type 4H-SiC substrate. Nevertheless, the comparison is revealing: the resistivity decreases as the EPR signal intensity increases. This behavior is consistent with the release of hydrogen from an acceptor.

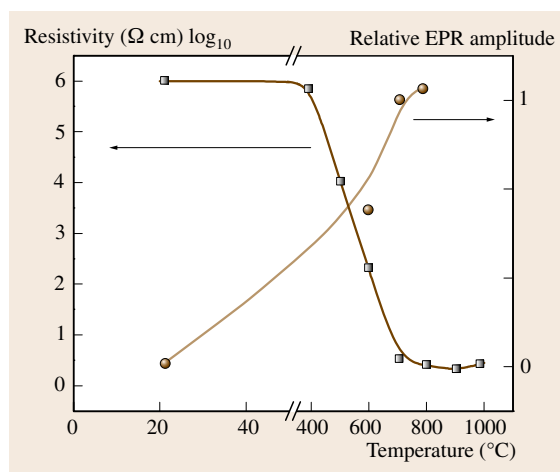


Fig. 45.23 Relative amount of Mg-related acceptors in GaN (brown circles) and resistivity (gray squares) after sequential annealing treatments in N₂ (after [45.67]). © Phys. Soc. Japan 1992)

Similar studies of samples grown by molecular-beam epitaxy and heat treatments in hydrogen are all consistent with the interpretation of acceptor activation by release of hydrogen [45.71]. Although the need to activate the CVD-grown GaN acceptor with a post-growth N_2 anneal was well accepted by the time of the EPR/annealing study, the spectroscopy confirms that the entity directly involved in the activation process is the acceptor. Observation of the behavior in only Mg-doped GaN suggests the relationship with magnesium, and infrared (IR) studies have indicated that the acceptor is a Mg–N complex, consistent with the broad EPR signal [45.71, 73, 74]. Other studies of acceptor and donor passivation are described by Gendron and coworkers, and separately Gerardi et al., studying N-doped (n-type) and Al-doped (p-type) SiC [45.75, 76].

Deep Levels: DLTS

Naturally, there is a desire to know the physical entity responsible for the deep levels in semiconductors. In the early days of Si, DLTS and EPR were often performed in the same laboratory in an effort to understand the nature of the deep levels. The C_iC_s (interstitial C–substitutional C pair) in Si provides one of the most complete examples linking a deep level to an EPR center [45.77, 78]. In this case the metastable properties of the center were monitored by several techniques, EPR, DLTS, photoluminescence, and optically detected magnetic resonance, allowing for strong correlations to be developed. The details are found in [45.78]. More recently, the concentration of the Z1/Z2 DLTS signal in 4H-SiC was shown to correlate with an EPR signal known as SI-5, a high-spin center thought to be a divacancy or V_c-C_{si} pair [45.68]. Figure 45.24 illustrates the comparison between the concentration of the SI-5 EPR signal and Z1/Z2. In addition to the one-to-one correspondence in the number of centers, it was pointed out that illumination was required to observe SI-5, consistent with the negative U character attributed to the DLTS signal. Once the model for SI-5 is confirmed, the DLTS/EPR study will provide a rare assignment of a physical entity in SiC to a deep level detected by DLTS.

Compensating Defects

The importance of semi-insulating semiconductor materials to the formation of high-power electronics has spurred investigations into the deep level, or more appropriately mid-gap level, responsible for compensation. The levels are detected with several techniques including optical DLTS, temperature-dependent Hall

measurements, and photo-EPR. A comparison of the latter two techniques has led to the assignment of vanadium and several different intrinsic defects as compensating centers in SiC [45.69]. However, the conclusions should be accepted with a great deal of caution. First, electrical measurements of these high-resistivity materials are crippled by the difficulty of making ohmic contacts. Also, temperature-dependent Hall measurements are often limited to resistivity measurements, from which the carrier density can be obtained only with an assumed model for the temperature dependence of the mobility. Finally, in some cases defect levels are extracted from steady-state photo-EPR, the limitations of which were outlined earlier. Nevertheless, the EPR and electrical studies of these compensating centers have generated a great deal of information on which to further advance the growth and characterization of SiC.

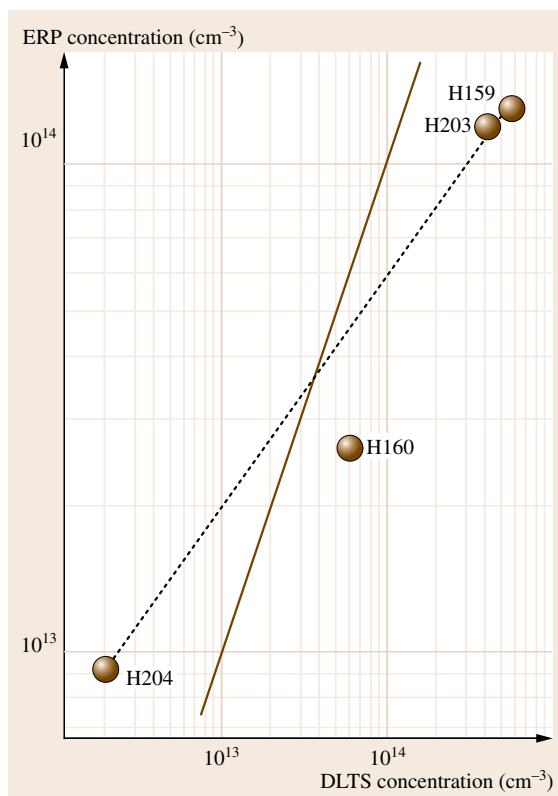


Fig. 45.24 Concentration of the P6, P7 centers versus concentration of the Z1/Z2 defect measured in the different samples indicated on the graph. The solid line represents a 1 : 1 correlation; the dashed line is a straight line fit (after [45.68])

With more time, the true nature of the compensating defect(s) may be revealed.

Interface Defects and Defect Level

One last study that deserves mention is the association of electrically detected states at the interface between Si and SiO₂ with the Si P_b center [45.39]. Unique among all the investigations described thus far, the interface

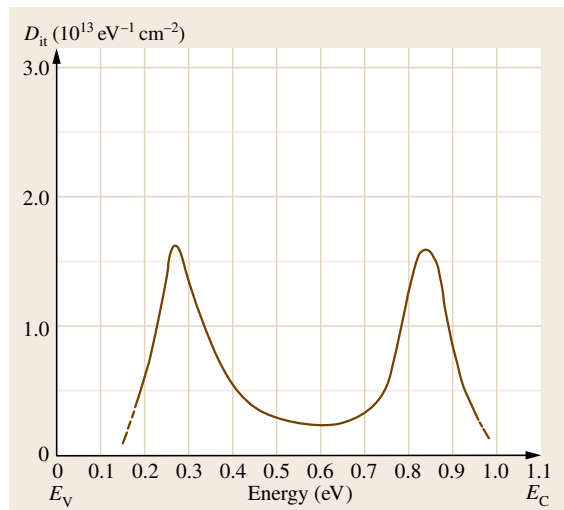


Fig. 45.25 Interface-state density peaks obtained from an oxidized Si sample measured in situ during an EPR measurement (after [45.39], © AIP 1984)

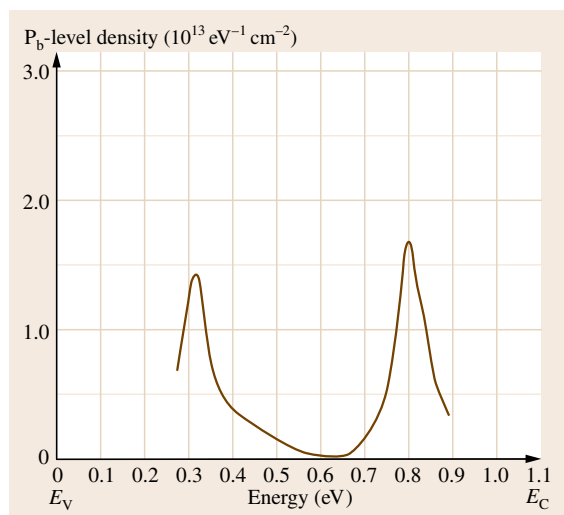


Fig. 45.26 Concentration of P_b centers obtained from EPR measurements made on the same sample as in Fig. 45.25 (after [45.39], © AIP 1984)

state–P_b center correlation was performed in situ. That is, the capacitance–voltage (C–V) measurements necessary to detect the interface states were measured on the EPR samples in the microwave cavity. In this way, sample-to-sample uncertainty was eliminated. The experiment requires special sample preparation because metal layers necessary for electrical contact severely reduce EPR sensitivity. The investigators soldered wires to a thick, 0.0028 cm² contact pad that was positioned adjacent a 0.53 cm² thin (50 nm) contact. As a varying electrical bias was applied, the small dot was used for the C–V measurement and the large area was used for EPR. The data of Figs. 45.25 and 45.26 show the interface state density and relative change in the number of P_b centers measured at selected values of the applied bias, respectively. The *x*-axes of both figures were derived from the applied gate voltage using standard analysis, and the *y*-axis of Fig. 45.26 was extracted from the derivative of the EPR signal intensity as a function of bandgap energy [45.39, 79]. The similarity of the two data sets clearly shows that the dangling bonds at the Si–SiO₂ interface are responsible for *D*_{it} located 0.3 and 0.8 eV above *E*_v. Many other electrical measurements and annealing studies have indirectly reaffirmed this conclusion.

45.4.3 Heat Treatment and EPR

Monitoring changes in the EPR signal during heat treatment may determine many interesting properties of defects. The changes may be simply intensity changes as the defect is gradually passivated by an external species introduced during the anneal or a complete transformation of the spectrum from one type of center to another. The heat treatment may be performed either in situ from 4 to 400 K or ex situ up to any temperature desired. Keeping the sample in the cavity is a tremendous advantage during an annealing study because it avoids uncertainties due to sample alignment; however, a typical cavity can withstand heat only slightly above room temperature. Special EPR cavities are available that can be used up to 1000 °C; however the cavities are extremely expensive and found mostly at user facilities. At the opposite extreme, temperatures approaching millikelvins are achievable in an EPR system, but not on a regular basis in a typical laboratory. Luckily, many centers are observable between the temperatures easily accessible in most facilities, 4–400 K.

The temperature range of ex situ annealing studies is limited only by the thermal properties of the sample and furnace availability. Since the sample must be re-

mounted in the cavity after each anneal, proper sample alignment is critical, but this is easily accomplished by thoughtful design of a sample holder. Another consideration in the annealing study is possible changes in the cavity quality factor Q , a measurement of the system sensitivity. The sample partially determines Q , so that any changes caused by heat treatments may change the sensitivity of the measurement and thus perturb the results. The most obvious concern is activation of shallow impurities that contribute to conductivity, one factor that affects the sensitivity of the cavity directly. To avoid confusion a standard can be mounted with the sample on the holder. The standard should contain a well-established isotropic signal with narrow line width and a g -value well separated from that of the sample. When EPR measurements are performed below the freeze-out temperature for carriers produced from shallow impurities, the sensitivity changes during the annealing study are less of a concern; nevertheless, it is good practice to include the standard during any experiment in which EPR intensities will be compared.

Another factor to consider when doing annealing studies is that the amplitude of an EPR signal is inversely proportional to the measurement temperature. This is a concern whenever spectra that are to be compared are measured at different temperatures. In this situation, one must account for the temperature dependence of the EPR signal by normalizing all spectra to a chosen temperature before analysis. The temperature dependence of an EPR signal, often referred to as the Curie law, originates from the statistical difference between spin populations in the initial and final energy levels producing the EPR transition. Boltzmann statistics states that this population difference is exponentially dependent on the temperature and the energy difference between the spin-up and spin-down states. The temperature dependence may often be approximated as $\frac{1}{T}$ because $k_B T$ is typically greater than the energy difference between the spin states. For measurements below 4 K, however, the exact expression should be used [45.1].

In situ EPR annealing studies have revealed information about the chemical kinetics among different charge states of defects as well as the mechanisms of charge transport in materials [45.54, 55, 75, 80]. The work of Merkle and Maier on the association of metal impurities with oxygen vacancies in SrTiO_3 provides an example where chemical kinetics are thoroughly analyzed using samples with different starting concentrations of impurities [45.80]. By monitoring the evolution of Fe^{3+} and Mn^{5+} with temperature, the au-

thors extracted the reaction enthalpies and entropies for the association of the metal impurities with oxygen vacancies. The EPR signals for Fe^{3+} , Mn^{5+} and the oxygen-vacancy-related species, Fe^{3+}V_0 and Mn^{5+}V_0 , were measured between room temperature and 170 K. Data analysis suggests that almost all the oxygen vacancies in Fe-doped material are bound to the iron impurities at 300 K, but the situation with the Mn is not as clear. In general, the results have interesting implications for those growing nominally pure titanate films. If the films are free of metal contaminants, will the chronic oxygen-deficiency problem associated with complex oxides be minimized or even eliminated? Such a question will remain unanswered until a sufficient quantity of films of repeatable quality is available for thorough materials characterization, including EPR.

Ex situ EPR/annealing studies range from simply noting the temperature at which an EPR signal intensity changes dramatically to a complete kinetic analysis of the chemical reactions involved in the thermal annealing process. The former do not need to be discussed here, but the latter is addressed below using the Si P_b center as an example.

A very thorough study of hydrogen release from a passivated P_b center is provided by Brower and Myer [45.81, 82]. Using (111) Si wafers oxidized to maximize the number of P_b centers, Brower measured the intensity of the EPR signal after isothermal vacuum heat treatments over a temperature range of 500 and 595 °C. The low signal-to-noise ratio prevented a more extensive temperature range. The data were found to fit a first-order kinetic equation that includes the temporal profile of the furnace and temperature-dependent rate constant. According to the model, the number of P_b centers remaining after an anneal at temperature T is

$$P_{b\text{-calc}} = N_0 \left(1 - \exp \left\{ -k_{d0} \int_{T_{\text{profile}}} \exp \left[-\frac{E_d}{k_B T}(t) \right] dt \right\} \right), \quad (45.11)$$

where k_{d0} is the first-order rate constant, E_d is the activation energy for dissociation, and N_0 is the maximum number of P_b centers measured by EPR. The analysis proceeded as follows. First, k_{d0} was obtained from a fit to the time evolution of the P_b center at a fixed temperature. The rate constants obtained from a range of temperatures were then fitted to a first-order kinetic equation to obtain E_d . The k_{d0} and E_d values were then used in (45.11) to determine $P_{b\text{-calc}}$. Figure 45.27 shows agreement between the values calculated us-

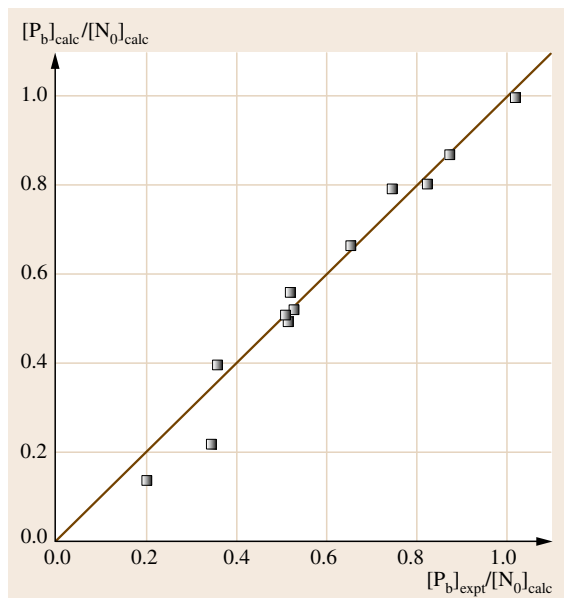


Fig. 45.27 Fraction of P_b centers calculated using (45.11) versus fractional P_b density measured after hydrogenation and subsequent vacuum annealing. The *straight line* represents a 1 : 1 correspondence (after [45.82])

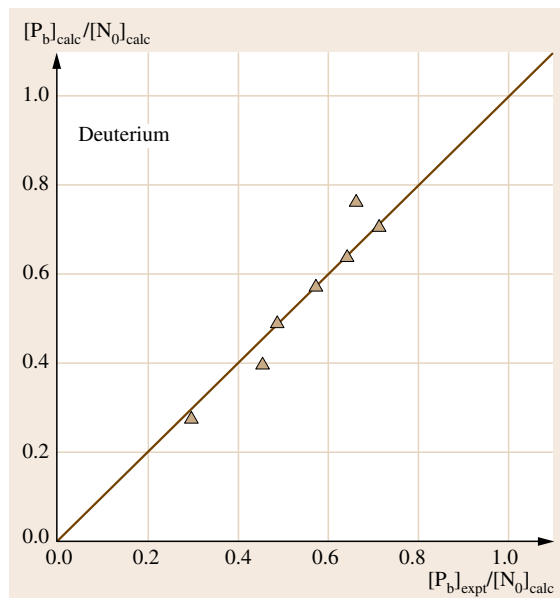


Fig. 45.28 Fraction of P_b centers calculated using (45.11) versus fractional P_b density measured after deuterium heat treatment and subsequent vacuum annealing. The *straight line* represents a 1 : 1 correspondence (after [45.82])

ing (45.11) and the experimental data points obtained between 500 and 595 °C. Figure 45.28 shows that similarly good agreement was obtained when D_2 instead of H_2 was released from the interface by the vacuum annealing process. The deuterium study provided support for the involvement of hydrogen in the annealing process in that the ratio of the k_{d0} values extracted from the H_2 and D_2 data agreed with that expected from the different vibrational frequencies for hydrogen and deuterium. Complete analysis of the data yields val-

ues of $k_{d0} = 1.2 \times 10^{12} \text{ s}^{-1}$ and $E_d = 2.56 \pm 0.06 \text{ eV}$ for the dissociation process $P_bH \rightarrow P_b + H$. Earlier studies of the passivation process $P_b + H \rightarrow P_bH$ had yielded $E_d = 1.66 \pm 0.06 \text{ eV}$. Brower used both sets of values to describe the dissociation of H_2 in semiconductors. Similar studies involving passivation of donors and acceptors in semiconductors exist in the literature [45.71, 75, 76]. Most are not as thorough as the one described here, but all provide insight into the chemical entities involved in the annealing treatments.

45.5 Summary and Final Thoughts

Electron paramagnetic resonance spectroscopy ultimately determines the spin wavefunction by probing the Δm_s transitions at paramagnetic defects. After intensive measurement and analysis, which often includes a comparison with theoretical calculations, a picture of a defect emerges including the identity of the nucleus (nuclei), symmetry, charge state, and absolute number of defects. The experimental procedure may be summarized as follows. A spectrum is obtained by placing a sample in a bath of 10 GHz microwaves situated between the poles of an electromagnet. The magnetic field

is ramped to remove the spin degeneracy of the ground state. When the energy difference between the m_s levels equals that of the microwave energy, the sample absorbs the microwaves and this absorption is detected by the external circuitry. The spectrum reflects the derivative of the absorption because the ramped magnetic field is modulated. Phase-sensitive detection is used to monitor the microwave intensity returned from the sample.

Once a spectrum is obtained, it can be interpreted in terms of the Zeeman, nuclear hyperfine, and nuclear

fine-structure terms as shown in (45.9). The g -value is determined from the first term and zero crossing of the EPR signal, and the angular dependence of g establishes the symmetry of the center. The second term relates directly to the nuclei that are involved in the defect. The number of hyperfine lines and their intensity is determined by the spin and isotopic abundance of the nucleus. This is often enough to identify the chemical elements forming the defect. Together with the angular dependence of the separation between the hyperfine lines, data may be compared with theory to establish the defect structure and charge state. Additional information is obtained from the fine-structure term, which reflects the spin multiplicity and can sometimes directly determine the charge state of the center. Although not every defect provides all this information, many may be thoroughly described by their electron paramagnetic resonance spectrum, as is illustrated many times throughout this chapter.

Throughout the past five decades, multitudes of intensive investigations have identified intrinsic defects and impurities in semiconductors and insulators. Often, a spectrum measured from a newly obtained sample is easily identified after a reasonable literature search. With the type of defect known, additional experiments may be performed to determine other parameters such as defect level, transport mechanisms or dissociation energy. Examples of such studies are discussed throughout this chapter.

Finally, the reader should be made aware of the many sophisticated versions of magnetic resonance that are not described in this chapter. The most powerful for determining defect structure is electron nuclear double resonance (ENDOR). Developed by Feher in the early 1950s, the technique allows for direct detection of the nucleus by monitoring the nuclear spin flips during an EPR experiment. The technique avoids the

ambiguity often encountered when measuring hyperfine line intensities by monitoring the nuclear resonance directly. Because the sensitivity of ENDOR is lower than that of EPR, films are rarely measured. On the other hand, a variation of magnetic resonance that monitors the change in luminescence when sweeping through the resonance field is ideal for studying small samples. Optically detected magnetic resonance (ODMR) combines the spectroscopic selectivity of EPR with the high sensitivity of photoluminescence. ODMR uses the applied magnetic field to flip the electron spin, so that previously spin-forbidden electronic transitions become allowed or allowed transitions become spin-forbidden. Basically, one excites the sample at a luminescence peak and ramps the magnetic field through resonance, causing the peak to increase or decrease depending on the exact nature of the transition. A second technique that is amenable to thin films is electrically detected magnetic resonance (EDMR). An electron-hole recombination current is monitored while the magnetic field is ramped through resonance. When the spins flip, the current changes because the electron-hole recombination transition is controlled by spin selection rules. Although most of the spectroscopic information is lost in the generally broadened signals, the high sensitivity of EDMR allows for studies of interfaces in a transistor-type structure. Thus, the technique is invaluable if direct comparison with electronic device characteristics is desired. Additional variations on EPR exist, including measurements in the time domain. However such pulsed-EPR techniques are seldom applied to crystals and are not typically classified as *materials characterization* techniques because of their inherent complexity and the fundamental nature of the information extracted. All of the magnetic resonance methods mentioned in this closing comment are outlined in [45.1], where further details may be obtained.

References

- 45.1 J.A. Weil, J.R. Bolton, J.E. Wertz: *Electron Paramagnetic Resonance* (Wiley, New York 1994)
- 45.2 C.P. Poole Jr., C.P. Poole, F.J. Owens: *Introduction to Nanotechnology* (Wiley, Hoboken 2003), Chap. 3
- 45.3 C. More, V. Belle, M. Asso, A. Fournel, G. Roger, B. Guigliarelli, P. Bertrand: EPR spectroscopy: a powerful technique for the structural and functional investigation of metalloproteins, *Biospectroscopy* **5**, S3–S18 (1999)
- 45.4 H.M. Swartz, N. Khan, J. Buckey, R. Corni, L. Gould, O. Grinberg, A. Hartford, H. Hopf, H. Hou, E. Hug, A. Iwasaki, P. Lesniewski, I. Salikhov, T. Walczak: Clinical applications of EPR: Overview and perspectives, *NMR Biomed.* **17**, 335 (2004)
- 45.5 D.L. Griscom: Electron spin resonance, *Glass Sci. Technol.* **4B**, 151–160 (1990)
- 45.6 D.L. Griscom: Defect structure of glasses, *J. Non-Cryst. Solids* **73**, 51 (1985)
- 45.7 C.P. Poole: *Electron Spin Resonance: A Comprehensive Treatise on Experimental Technique* (Interscience, New York 1967)

- 45.8 W. Gordy, W. West (Ed.): *Techniques of Chemistry*, Vol. 15 (Wiley, New York 1980)
- 45.9 M.H.L. Pryce: A modified perturbation procedure for a problem in paramagnetism, *Proc. Phys. Soc. A* **63**, 25 (1950)
- 45.10 S. Greulich-Weber, F. Feege, K.N. Kalabukhova, S.N. Lukin, J.-M. Spaeth, F.J. Adrian: EPR and EN-DOR investigations of B acceptors in 3C-, 4H- and 6H-silicon carbide, *Semicond. Sci. Technol.* **13**, 59 (1998)
- 45.11 H.H. Woodbury, G.W. Ludwig: Electron spin resonance studies in SiC, *Phys. Rev.* **124**, 1083 (1961)
- 45.12 N.T. Son, E. Janzen, J. Isoya, S. Yamasaki: Hyperfine interaction of the nitrogen donor in 4H-SiC, *Phys. Rev. B* **70**, 193207 (2004)
- 45.13 T. Umeda, J. Isoya, N. Morishita, T. Ohshima, T. Kamiya: EPR identification of two types of carbon vacancies in 4H-SiC, *Phys. Rev. B* **69**, 121201 (2004)
- 45.14 P.T. Huy, C.A.J. Ammerlaan, T. Gregorkiewicz, D.T. Dong: Hydrogen passivation of the selenium double donor in silicon: A study by magnetic resonance, *Phys. Rev. B* **61**, 7448 (2000)
- 45.15 H.J. von Bardeleben, M. Schoisswohl, J.L. Cantin: Electron paramagnetic resonance study of defects in oxidized and nitrided porous Si and Si_{1-x}Ge_x, *Colloids Surf. A Physicochem. Eng. Asp.* **115**, 277 (1996)
- 45.16 M. Bockstedte, M. Heid, O. Pankratov: Signature of intrinsic defects in SiC: Ab initio calculations of hyperfine tensors, *Phys. Rev. B* **67**, 193102 (2003)
- 45.17 T. Umeda, Y. Ishitsuka, J. Isoya, N.T. Son, E. Janzen, N. Morishita, T. Ohshima, H. Itoh: EPR and theoretical studies of negatively charged carbon vacancy in 4H-SiC, *Phys. Rev. B* **71**, 193202 (2005)
- 45.18 K. Maier, M. Kunzer, U. Kaufmann, J. Schneider, B. Monemar, I. Akasaki, H. Amano: Iron acceptors in gallium nitride (GaN), *Mater. Sci. Forum* **143-147**, 93-98 (1994)
- 45.19 P.G. Baranov, I.V. Il'yin, E.N. Mokhov, A.D. Roenkov: Identification of manganese trace impurity in GaN crystals by electron paramagnetic resonance, *Semicond. Sci. Technol.* **11**, 1843 (1996)
- 45.20 T. Lingner, S. Greulich-Weber, J.-M. Spaeth: Structure of the silicon vacancy in 6H-SiC after annealing identified as the carbon vacancy-carbon antisite pair, *Phys. Rev. B* **64**, 245212 (2001)
- 45.21 N.T. Son, P. Carlsson, J. ul Hassan, E. Janzen, T. Umeda, J. Isoya, A. Gali, M. Bockstedte: Divacancy in 4H-SiC, *Phys. Rev. Lett.* **96**, 055501 (2006)
- 45.22 K. Maier, J. Schneider, W. Wilkening, S. Leibenzeder, R. Stein: Electron spin resonance studies of transition metal deep level impurities in SiC, *Mater. Sci. Eng. B* **11**, 27-30 (1992)
- 45.23 K. Maier, H.D. Müller, J. Schneider: Transition metals in silicon carbide (SiC): Vanadium and titanium, *Mater. Sci. Forum* **81-87**, 1183-1194 (1992)
- 45.24 A. Abragam, B. Bleaney: *Electron Paramagnetic Resonance of Transition Ions* (Dover, New York 1986)
- 45.25 F. Mehran, B.A. Scott: Electron paramagnetic resonance of LiNbO₃:Fe³⁺, *Solid State Commun.* **11**, 15 (1972)
- 45.26 H.H. Towner, Y.M. Kim, H.S. Story: EPR studies of crystal field parameters in LiNbO₃:Fe³⁺, *J. Chem. Phys.* **56**, 3676 (1972)
- 45.27 W.E. Carlos, F.A. Freitas Jr., M. Asif Khan, D.T. Olson, J.N. Kuznia: Electron-spin-resonance studies of donors in wurtzite GaN, *Phys. Rev. B* **48**, 17878 (1993)
- 45.28 Haiyan Wang: unpublished data (2003)
- 45.29 A. Stesmans, K. Vanheusden: Generation of de-localized E' defects in buried Si oxide by hole injection, *J. Appl. Phys.* **76**, 1681 (1994)
- 45.30 A. Stesmans, F. Scheerlinck: Natural intrinsic EX center in thermal SiO₂ on Si:¹⁷O hyperfine interaction, *Phys. Rev. B* **50**, 5204 (1994)
- 45.31 W.L. Warren, P.M. Lenahan: Electron spin resonance study of high field stressing in metal-oxide-silicon device oxides, *Appl. Phys. Lett.* **49**, 1296 (1986)
- 45.32 M.E. Zvanut, T.L. Chen, R.E. Stahlbush, E.S. Steigerwalt, G.A. Brown: Generation of thermally induced defects in buried SiO₂ films, *J. Appl. Phys.* **77**, 4329 (1995)
- 45.33 M.E. Zvanut, F.J. Feigl, J.D. Zook: A defect relaxation model for bias instabilities in metal-oxide-semiconductor capacitors, *J. Appl. Phys.* **64**, 2221 (1988)
- 45.34 P.M. Lenahan, P.V. Dressendorfer: Hole traps and trivalent silicon centers in metal/oxide/silicon devices, *J. Appl. Phys.* **55**, 3495 (1984)
- 45.35 W.L. Warren, E.H. Poindexter, M. Offenberger, W. Müller-Warmuth: Paramagnetic point defects in amorphous silicon dioxide and amorphous silicon nitride thin films I. a-SiO₂, *J. Electrochem. Soc.* **139**, 872 (1992)
- 45.36 N. Mizuochi, M. Ogura, H. Watanabe, J. Isoya, H. Okuchi, S. Yamasaki: EPR study of hydrogen-related defects in boron-doped p-type CVD homoepitaxial diamond films, *Diam. Relat. Mater.* **13**, 2096 (2004)
- 45.37 M.E. Zvanut, W.E. Carlos, J.A. Freitas, K.D. Jamison, R.P. Hellmer: An identification of phosphorous in diamond thin films using electron paramagnetic resonance spectroscopy, *Appl. Phys. Lett.* **65**, 2287 (1994)
- 45.38 M. Sterrer, E. Fischbach, T. Risse, H.J. Freund: Geometric characterization of a singly charged oxygen vacancy on a single crystalline MgO (001) film by electron paramagnetic resonance spectroscopy, *Phys. Rev. Lett.* **94**, 186101 (2005)
- 45.39 E.H. Poindexter, G.J. Gerardi, M.-E. Rueckel, P.F. Caplan, N.M. Johnson, D.K. Biegelsen: Elec-

- tronic traps and P_b centers at the Si/SiO₂ interface: band-gap energy distribution, J. Appl. Phys. **56**, 2844 (1984)
- 45.40 E.H. Poindexter, P.J. Caplan: Interface states and electron spin resonance centers in thermally oxidized (111) and (100) silicon wafers, J. Appl. Phys. **52**, 679 (1981)
- 45.41 J.L. Cantin, H.J. von Bardeleben, Y. Shishkin, Y. Ke, R.P. Devaty, W.J. Choyke: Identification of the carbon dangling bond center at the 4H-SiC/SiO₂ interface by an EPR study of oxidized porous SiC, Phys. Rev. Lett. **92**, 015502 (2004)
- 45.42 P.J. Caplan, E.H. Poindexter, B.E. Deal, R.R. Razouk: ESR centers, interface states, and oxide fixed charge in thermally oxidized silicon wafers, J. Appl. Phys. **50**, 5847 (1979)
- 45.43 J.L. Cantin, M. Schoisswohl, H.J. von Bardeleben, V. Morazzani, J.J. Ganem, I. Trimaille: EPR study of the defects in porous Si/SiO_xN_y and Si_{0.80}Ge_{0.20}/SiGeO₂. In: *The Physics and Chemistry of SiO₂ and Si/SiO₂ Interfaces*, Proc., Vol.96-1, ed. by H.Z. Massoud, E.H. Poindexter, C.R. Helms (The Electrochemical Society, Pennington 1996) p. 28
- 45.44 M.E. Zvanut, W.E. Carlos, M.E. Twigg, R.E. Stahlbush, D.J. Godbey: Interfacial point defects in heavily implanted silicon germanium alloys, J. Vac. Sci. Technol. B **10**, 2026 (1992)
- 45.45 K.L. Brower: ²⁹Si hyperfine structure of unpaired spins at the Si/SiO₂ interface, Appl. Phys. Lett. **43**, 1111 (1983)
- 45.46 P.J. Macfarlane, M.E. Zvanut: Characterization of paramagnetic defect centers in three polytypes of dry heat treated, oxidized SiC, J. Appl. Phys. **88**, 4122 (2000)
- 45.47 P.J. Macfarlane, M.E. Zvanut: Reduction and creation of paramagnetic centers on surfaces of three different polytypes of SiC, J. Vac. Sci. Technol. B **17**, 1627 (1999)
- 45.48 M.D. Glinchuk, I.P. Bykov, A.M. Slipenyuk, V.V. Laguta, L. Jastrabik: ESR study of impurities in strontium titanate films, Phys. Solid State **43**, 841 (2001)
- 45.49 M.R. Deigen, M.D. Glinchuk: Theory of local electronic states on the surface of a non-metallic crystal, Surf. Sci. **3**, 243 (1965)
- 45.50 P.A.G. Beermann, B.R. McGarvey, B.O. Skadtchenko, S. Muralidharan, R.C.W. Sung: Cationic substitution sites in Mn²⁺-doped ZnS nanoparticles, J. Nanopart. Res. **8**, 235 (2006)
- 45.51 D. Pan, G. Xu, L. Lv, Y. Yong, X. Wang, J. Wan, G. Wang, Y. Sui: Observation and manipulation of paramagnetic oxygen vacancies in co-doped TiO₂ nanocrystals, Appl. Phys. Lett. **89**, 082510 (2006)
- 45.52 A.V. Brodovoi, S.G. Bunchuk, V.V. Polropivny, V.V. Skorokhod: Magnetic properties of nanoporous Si powder, Int. J. Nanotechnol. **3**, 57 (2006)
- 45.53 R.P. Wang: Defects in Si nanowires, Appl. Phys. Lett. **88**, 142104 (2006)
- 45.54 G. Feher, R.C. Fletcher, E.A. Gere: Exchange effects in spin resonance of impurity atoms in silicon, Phys. Rev. **100**, 1784 (1955)
- 45.55 S. Maekawa, N. Kinoshita: Electron spin resonance in phosphorous doped silicon at low temperatures, J. Phys. Soc. Jpn. **20**, 1447 (1965)
- 45.56 A. Bencini, D. Gatteschi: *EPR of Exchange Coupled Systems* (Springer, Berlin, Heidelberg 1990)
- 45.57 J.H. Van Vleck: Concerning the theory of ferromagnetic resonance absorption, Phys. Rev. **78**, 266 (1950)
- 45.58 C.E. Patton: Microwave resonance and relaxation. In: *Magnetic Oxides*, ed. by D.J. Craik (Wiley, London 1975), Chap. 10
- 45.59 M. Godlewski: Photoelectron paramagnetic resonance studies of ionization transitions of chromium impurities in ZnS and GaAs, J. Appl. Phys. **56**, 2901 (1984)
- 45.60 M. Godlewski, Z. Wilamowski, M. Kaminska, W.E. Lamb, B.C. Cavenett: Photo-EPR and ODMR investigations of radiative processes in ZnS:Cr,Sc, J. Phys. C Solid State Phys. **14**, 2835 (1981)
- 45.61 M. Godlewski: On the application of the photo-EPR technique to the studies of photoionization, DAP recombination, and non-radiative recombination processes, Phys. Status Solidi (a) **90**, 11 (1985)
- 45.62 N.T. Son, B. Magnusson, E. Janzen: Photoexcitation-electron-paramagnetic-resonance studies of the carbon vacancy in 4H-SiC, Appl. Phys. Lett. **81**, 3945-3947 (2003)
- 45.63 M.E. Zvanut, V.V. Konovalov: The level position of a deep intrinsic defect in 4H-SiC studied by photo-induced electron paramagnetic resonance, Appl. Phys. Lett. **80**, 410 (2002)
- 45.64 M.E. Zvanut, H. Wang, W. Lee, W.C. Mitchell, W.D. Mitchell: Deep level point defects in semi-insulating SiC. In: *Silicon Carbide and Related Materials*, ed. by R. Devaty, D. Larkin, S. Sadow (Trans Tech, Switzerland 2006) p. 517, or Mater. Sci. Forum **527-529**, 517 (2006)
- 45.65 N.T. Son, P. Carlsson, B. Magnusson, E. Janzen: Characterization of semi-insulating SiC, Mater. Res. Soc. Symp. Proc. **911**, 0911-B06-03 (2006)
- 45.66 H. Wang: Investigation of defect energy levels in SI 4H-SiC using EPR and photo-EPR. Ph.D. Thesis (Univ. of Alabama, Birmingham 2006)
- 45.67 S. Nakamura, T. Mukai, M. Senoh, N. Iwasa: Thermal annealing effects on P-type Mg-doped GaN films, Jpn. J. Appl. Phys. **31**, L139 (1992)
- 45.68 N.Y. Garces, W.E. Carlos, E.R. Glaser, S.W. Huh, H.J. Chung, S. Nigam, A.Y. Polyakov, M. Skowronski: Relationship between the EPR SI-5 signal and the 0.65 eV electron trap in 4H- and 6H-

- SiC polytypes, *Mater. Sci. Forum* **527–529**, 547–550 (2006)
- 45.69 M.E. Zvanut, W. Lee, W.C. Mitchel, W.D. Mitchell, G. Landis: The acceptor level for vanadium in 4H and 6H SiC, *Physica B* **376/377**, 346 (2006)
- 45.70 M. Palczewska, B. Suchanek, R. Dwilinski, K. Pakula, A. Wagner, M. Kaminska: Paramagnetic defects in GaN, *MRS Internet J. Nitride Semicond. Res.* **3**, 45 (1998)
- 45.71 D.M. Matlock, M.E. Zvanut, H. Wang, J.R. Di-Maio, R.F. Davis, J.E. Van Nostrand, R.L. Henry, D. Koleske, A. Wickenden: The effects of oxygen, nitrogen, and hydrogen annealing on Mg acceptors in GaN as monitored by electron paramagnetic resonance spectroscopy, *J. Electron. Mater.* **34**, 34 (2005)
- 45.72 M.E. Zvanut, D.M. Matlock, R.L. Henry, D. Koleske, A. Wickenden: Thermal activation of Mg-doped GaN as monitored by electron paramagnetic resonance spectroscopy, *J. Appl. Phys.* **95**, 1884–1887 (2004)
- 45.73 J. Neugebauer, C.G. Van de Walle: Hydrogen in GaN: Novel aspects of a common impurity, *Phys. Rev. Lett.* **75**, 4452 (1995)
- 45.74 V.J.B. Torres, S. Oberg, R. Jones: Theoretical studies of hydrogen passivated substitutional magnesium acceptor in wurzite GaN, *MRS Internet J. Nitride Semicond. Res.* **2**, 35 (1997)
- 45.75 G.J. Gerardi, E.H. Poindexter, D.J. Keeble: Paramagnetic centers and dopant excitation in crystalline silicon carbide, *Appl. Spectrosc.* **50**, 1428 (1996)
- 45.76 F. Gendron, L.M. Porter, C. Porte, E. Bringuier: Hydrogen passivation of donors and acceptors in SiC, *Appl. Phys. Lett.* **67**, 1253 (1995)
- 45.77 G.D. Watkins: Defect metastability and bistability, *Mater. Sci. Forum* **38–41**, 39 (1989)
- 45.78 L.W. Song, X.D. Zhan, B.W. Benson, G.D. Watkins: Bistable defect in silicon: The interstitial-carbon-substitutional-carbon pair, *Phys. Rev. Lett.* **60**, 460 (1988)
- 45.79 E.H. Nicollian, J.R. Brews: *MOS (Metal Oxide Semiconductor) Physics and Technology* (Wiley, New York 1982)
- 45.80 R. Merkle, J. Maier: Defect association in acceptor-doped SrTiO₃: Case study for Fe_{Ti}V₀ and Mn_{Ti}V₀, *Phys. Chem. Chem. Phys.* **5**, 2297 (2003)
- 45.81 K.L. Brower, S.M. Myers: Chemical kinetics of hydrogen and (111) Si-SiO₂ interface defects, *Appl. Phys. Lett.* **57**, 162 (1990)
- 45.82 K.L. Brower: Dissociate kinetics of hydrogen-passivated (111) Si-SiO₂ interface defects, *Phys. Rev. B* **42**, 3444 (1990)

46. Defect Characterization in Semiconductors with Positron Annihilation Spectroscopy

Filip Tuomisto

Positron annihilation spectroscopy is an experimental technique that allows the selective detection of vacancy defects in semiconductors, providing a means to both identify and quantify them. This chapter gives an introduction to the principles of the positron annihilation techniques and then discusses the physics of some interesting observations on vacancy defects related to growth and doping of semiconductors. Illustrative examples are selected from studies performed in silicon, III-nitrides, and ZnO.

A short overview of positron annihilation spectroscopy is given in Sect. 46.1. The identification of vacancies and their charge states is described in Sect. 46.2; this section also discusses how ion-type acceptors can be detected due to the positrons' shallow Rydberg states around negative ions. The role of vacancies in the electrical deactivation of dopants is discussed in Sect. 46.3, and investigations of the effects of growth conditions on the formation of vacancy defects are reviewed in Sect. 46.4. Section 46.5 gives a brief summary.

46.1 Positron Annihilation Spectroscopy	1552
46.1.1 Positron Implantation and Diffusion in Solids.....	1552

46.1.2 Positron States and Annihilation Characteristics...	1553
46.1.3 Positron Trapping at Point Defects	1556
46.1.4 Experimental Techniques	1557

46.2 Identification of Point Defects and Their Charge States

46.2.1 Vacancies in Si: Impurity Decoration	1560
46.2.2 Vacancies in ZnO: Sublattice and Charge State	1562
46.2.3 Negative Ions as Shallow Positron Traps in GaN..	1564

46.3 Defects, Doping, and Electrical Compensation.....

46.3.1 Formation of Vacancy–Donor Complexes in Highly n-Type Si	1566
46.3.2 Vacancies as Dominant Compensating Centers in n-Type GaN	1568

46.4 Point Defects and Growth Conditions

46.4.1 Growth Stoichiometry: GaN Versus InN	1570
46.4.2 GaN: Effects of Growth Polarity	1572
46.4.3 Bulk Growth of ZnO	1573

46.5 Summary

References	1576
-------------------------	------

Many techniques are applied to identify defects in semiconductors on the atomic scale. The role of the positron annihilation method is due to its ability to selectively detect vacancy-type defects. This is based on two special properties of the positron: it has a positive charge and it annihilates with electrons. An energetic positron which has penetrated into a solid rapidly loses its energy and then lives a few hundred picoseconds in thermal equilibrium with the environment. During its thermal motion the positron interacts with defects, which may lead to trapping into a localized state. Thus the final

positron annihilation with an electron can happen from various states.

Energy and momentum are conserved in the annihilation process, where two photons of about 511 keV are emitted in opposite directions. These photons carry information on the state of the annihilated positron. The positron lifetime is inversely proportional to the electron density encountered by the positron. The momentum of the annihilated electron causes an angular deviation from the 180° straight angle between the two 511 keV photons and creates a Doppler shift in their energy. Thus

the observation of positron annihilation radiation gives experimental information on the electronic and defect structures of solids.

The sensitivity of positron annihilation spectroscopy to vacancy-type defects is easy to understand. The free positron in a crystal lattice feels strong repulsion from the positive ion cores. An open-volume defect such as a vacant lattice site is therefore an attractive center where the positron gets trapped. The reduced electron density at the vacant site increases the positron lifetime. In addition, the missing valence and core electrons cause substantial changes in the momentum distribution of the annihilated electrons. Two positron techniques have been efficiently used in defect studies in semiconductors, namely the positron lifetime and the Doppler broadening of the 511 keV line. There are three main advantages of positron annihilation spectroscopy, which can be listed as follows. First, the identification of vacancy-type defects is straightforward. Second, the technique is strongly supported by theory, since the annihilation characteristics can be calculated from first principles. Finally, positron annihilation can be applied to bulk crystals and thin layers of any electrical conduction type.

The experimental and theoretical bases of the positron annihilation spectroscopy of vacancies in metals and alloys were developed in the 1970s. Its applications started gradually to widen to semiconductors in the beginning of the 1980s. At that time the low-energy positron beam was also developed and opened an avenue for defect studies of epitaxial layers and surface regions. The positron annihilation method

has had a significant impact on defect spectroscopy in solids by introducing an experimental technique for the unambiguous identification of vacancies. Native vacancies have been observed at high concentrations in many compound semiconductors, and their role in doping and compensation can now be quantitatively discussed.

In addition to vacancy defects, positrons may become confined to interesting regions of low-dimensional structures in semiconductors such as quantum wells, heterointerfaces and quantum dots due to favorable affinity or internal electric fields. The annihilation radiation carries information on the details of the electronic and atomic structures and the chemical composition of the annihilation site. We will, however, in this chapter concentrate on studies of vacancy defects which combined with, e.g., electrical measurements provide quantitative information on electrical compensation.

The aim of this chapter is twofold. We first want to introduce the principles of the positron annihilation techniques and then to discuss the physics of some interesting observations on vacancy defects related to growth and doping of semiconductors. For the sake of coherence, the illustrative examples are selected from the studies performed by the positron group of the Helsinki University of Technology in Si, III-nitrides, and ZnO. For full information on all the published works on positron annihilation in semiconductors, we refer to earlier review articles [46.1–4], books and book chapters [46.5–10], the proceedings of the International Conference on Positron Annihilation (ICPA), and other references therein.

46.1 Positron Annihilation Spectroscopy

In this section we review the principles of positron annihilation spectroscopy and describe the experimental techniques. Thermalized positrons in lattices behave like free electrons and holes. Analogously, positrons have shallow hydrogenic states at negative ions such as acceptor impurities. Furthermore, vacancies and other centers with open volume act as deep traps for positrons. These defects can be detected experimentally by measuring either the positron lifetime or the momentum density of the annihilating positron–electron pairs (Doppler broadening of the annihilation radiation). For the sake of clarity, we will concentrate on the measurements of those two quantities, as these two

methods are the most used in defect studies in semiconductors. Descriptions of other techniques can be found in, e.g., [46.9].

46.1.1 Positron Implantation and Diffusion in Solids

The basic principle of a positron experiment is shown in Fig. 46.1. Positrons are easily obtained from radioactive (β^+) isotopes such as ^{22}Na (other possible isotopes are, e.g., ^{58}Co , ^{64}Cu , and ^{68}Ge). The most commonly used isotope is ^{22}Na , where the positron emission is accompanied by a 1.27 MeV photon. This photon is used

in positron lifetime experiments as the time signal of the positron emission from the source. The stopping profile of positrons from the β^+ emission is exponential [46.6, 11]. For the ^{22}Na source, where the positron energy distribution extends to $E_{\text{max}} = 0.54 \text{ MeV}$, the positron mean stopping depth is about $110 \mu\text{m}$ in Si and $40 \mu\text{m}$ in GaN. The positrons emitted directly from a radioactive source thus probe the bulk of a solid.

Low-energy positrons are needed for studying thin overlayers and near-surface regions. Positrons from the β^+ emission are first slowed down and thermalized in a moderator. This is usually a thin film placed in front of the positron source and made of a material (e.g., Cu or W) that has a negative affinity for positrons. Thermalized positrons close to the moderator surface are emitted into the vacuum with energy of the order of 1 eV and a beam is formed using electric and magnetic fields. The positron beam is accelerated to a tunable energy of 0–40 keV, giving the possibility to control the positron stopping depth in the sample. The typical intensity of a positron beam created in this way is 10^4 – $10^6 \text{ e}^+ \text{ s}^{-1}$. Another way of producing a positron beam is through the electron–positron pair production process. This, however, requires a remarkably larger facility (e.g., a nuclear reactor) and hence not many such beams exist in spite of the advantage of obtaining a beam intensity several orders of magnitude higher than that of a conventional beam.

For monoenergetic positrons, the stopping profile can be described by a derivative of a Gaussian function, i.e., a Makhov profile, with a mean stopping depth [46.2, 11]

$$\bar{x} = 0.886x_0 = AE^n \text{ (keV)}, \quad (46.1)$$

where E is the positron energy, $A = (4/\rho)\mu\text{g}/\text{cm}^2$; $n \approx 1.6$, and ρ is the density of the material in g/cm^3 . The mean stopping depth varies with energy from 1 nm up to a few microns. A 20 keV energy corresponds to $2 \mu\text{m}$ in Si and $0.8 \mu\text{m}$ in GaN. The width of the stopping profile is rather broad and hence the positron energy must be carefully chosen so that, e.g., the signal from an overlayer is not contaminated by that from the substrate or the surface.

In a solid, the fast positron rapidly loses its energy through ionization and core electron excitation. Finally, the positron momentum distribution relaxes to a Maxwell–Boltzmann distribution through electron–hole excitation and phonon emission. The thermalization time at 300 K is 1–3 ps, i.e., much less than a typical positron lifetime of 200 ps [46.12, 13]. The

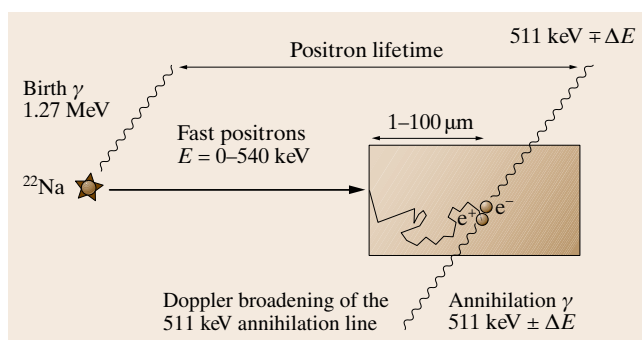


Fig. 46.1 Schematic figure of a positron experiment, where the positrons are implanted into a sample from a ^{22}Na source. The positron lifetime is determined as the time difference between the 511 keV annihilation photons and the 1.27 MeV photon emitted together with the positron from ^{22}Na . The Doppler shift ΔE results from the momentum of the annihilating electron–positron pairs

positron behaves thus as a fully thermalized particle in semiconductors.

The transport of thermalized positrons in solids can be described by diffusion theory. The positron diffusion coefficient has been measured in several semiconductors by implanting low-energy positrons at various depths and observing the fraction which diffuses back to the entrance surface [46.14–16]. The diffusion coefficient D_+ at 300 K is in the range 1.5 – $3 \text{ cm}^2 \text{ s}^{-1}$. The total diffusion length during the finite positron lifetime τ is

$$L_+ = (6D_+\tau)^{1/2} \approx 5000 \text{ \AA}. \quad (46.2)$$

If defects are present, the positron may get trapped before annihilation and this naturally reduces the effective diffusion length. On the other hand, the presence of an electric field, due to, e.g., charging of the sample surface, increases the effective diffusion length.

46.1.2 Positron States and Annihilation Characteristics

Positron Wavefunction and Lifetime, and the Momentum Distribution of the Annihilation Radiation

After implantation and thermalization positrons in semiconductors behave like free carriers (i.e., the positron state is a Bloch state in a defect-free lattice). Various positron states yield specific annihilation characteristics that can be experimentally observed in positron lifetime and Doppler broadening experiments. The positron wavefunction can be calculated from the

one-particle Schrödinger equation [46.3]

$$-\frac{\hbar^2}{2m}\nabla^2\Psi_+(\mathbf{r}) + V(\mathbf{r})\Psi_+(\mathbf{r}) = E_+\Psi_+(\mathbf{r}), \quad (46.3)$$

where the positron potential consists of two parts

$$V(\mathbf{r}) = V_{\text{Coul}}(\mathbf{r}) + V_{\text{corr}}(\mathbf{r}). \quad (46.4)$$

The first term is the electrostatic Coulomb potential and the second term takes into account the electron–positron correlation effects. Many practical schemes exist for solving the positron state Ψ_+ from the Schrödinger equation [46.3, 17].

A positron state can be characterized experimentally by measuring the positron lifetime and the momentum distribution of the annihilation radiation. These quantities can also be calculated once the corresponding electronic structure of the solid system is known. The positron annihilation rate λ , the inverse of the positron lifetime τ , is proportional to the overlap of the electron and positron densities

$$1/\tau = \lambda = \pi r_0^2 c \int d\mathbf{r} |\Psi_+(\mathbf{r})|^2 n(\mathbf{r}) \gamma[n(\mathbf{r})], \quad (46.5)$$

where r_0 is the classical electron radius, c is the velocity of light, $n(\mathbf{r})$ is the electron density, and $\gamma(n)$ is the enhancement factor that accounts for the pile-up of the electron density at the positron beyond the (average) density $n(\mathbf{r})$ [46.3]. The momentum distribution $\rho(\mathbf{p})$ of the annihilation radiation is a nonlocal quantity and requires knowledge of all the electron wavefunctions Ψ_i overlapping with the positron. It can be written in the form

$$\rho(\mathbf{p}) = \frac{\pi r_0 c}{V} \sum_i \left| \int d\mathbf{r} e^{-i\mathbf{p}\cdot\mathbf{r}} \Psi_+(\mathbf{r}) \Psi_i(\mathbf{r}) \sqrt{\gamma_i(\mathbf{r})} \right|^2, \quad (46.6)$$

where V is the normalization volume and $\gamma_i(\mathbf{r})$ may depend only on i or on \mathbf{r} . A Doppler broadening experiment measures the longitudinal momentum distribution along the direction of the emitted 511 keV photons, defined here as the z -axis

$$\rho(p_L) = \int_{-\infty}^{\infty} \int_{-\infty}^{\infty} dp_x dp_y \rho(\mathbf{p}). \quad (46.7)$$

It should be noted that the momentum distribution $\rho(\mathbf{p})$ of the annihilation radiation is mainly that of the annihilating electrons *seen by the positron*, because the momentum of the thermalized positron is negligible.

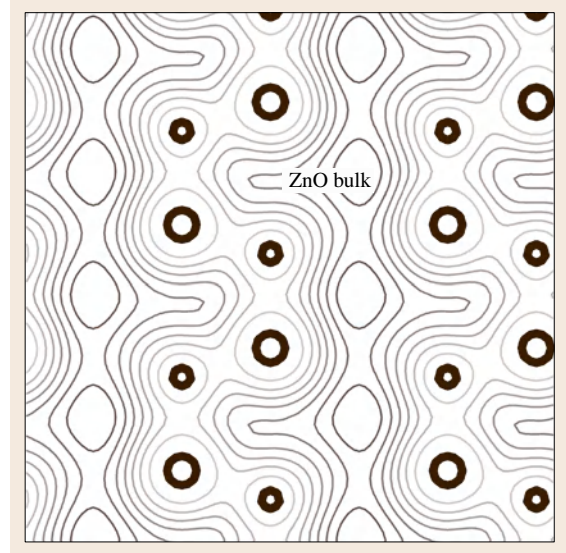


Fig. 46.2 Delocalized positron density in a perfect ZnO lattice according to theoretical calculations. The c -axis of the wurtzite structure is in the *vertical direction* in the figure plane. The positions of the Zn and O atoms are marked with *larger and smaller thick open circles*, respectively. The contour spacing is $1/7$ of the maximum value, the *darkest line denoting the highest value*

As an example, the calculated positron density in a perfect ZnO wurtzite lattice is shown in Fig. 46.2. For details of the calculations see [46.18]. The positron is delocalized in a Bloch state with $k_+ = 0$. Due to the Coulomb repulsion by positive ion cores, the positron wavefunction has its maximum at the interstitial space between the atoms. The positron energy band $E_+(\mathbf{k})$ is parabolic and free-particle-like with an effective mass of $m^* \approx 1.1 m_0$ [46.3].

Deep Positron States at Vacancy Defects

In analogy to free carriers, also the positron has localized states at lattice imperfections. At vacancy-type defects where ions are missing, the repulsion sensed by the positron is lowered and the positron feels these kinds of defects as potential wells. As a result, localized positron states at open-volume defects are formed. The positron ground state at a vacancy-type defect is generally deep: the binding energy is about 1 eV or more [46.3]. Figure 46.3 shows the calculated density of the localized positron at unrelaxed Zn and O vacancies in ZnO. The positron wavefunction is confined in the open volume formed at the vacancy. The localiza-

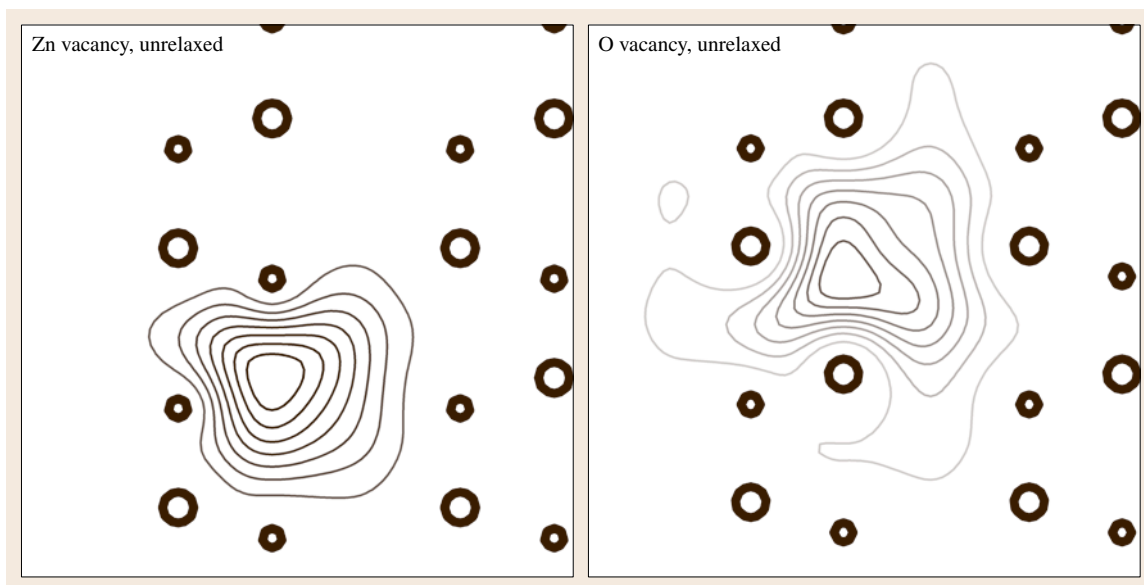


Fig. 46.3 Localized positron density in a perfect ZnO lattice according to theoretical calculations. The c -axis of the wurtzite structure is in the vertical direction in the figure plane. The positions of the Zn and O atoms are marked with larger and smaller thick open circles, respectively. The contour spacing is $1/7$ of the maximum value, the darkest line denoting the highest value

tion is clearly stronger in the case of the Zn vacancy because the open volume of V_{Zn} is much larger than that of V_{O} .

In a vacancy defect the electron density is locally reduced. This is reflected in the positron lifetimes, which are longer than in the defect-free lattice. For example, the calculated lifetimes in the unrelaxed Zn and O vacancies are 45 ps and 3 ps longer than in the perfect lattice. The longer positron lifetime at V_{Zn} is due to the larger open volume compared with that of V_{O} . The positron lifetime measurement is thus a probe of vacancy defects in materials. Positron annihilation at a vacancy-type defect leads also to changes in the momentum distribution $\rho(\mathbf{p})$ probed by the Doppler broadening experiment. The momentum distribution arising from valence electron annihilation becomes narrower due to a lower electron density. In addition, the localized positron at a vacancy has a reduced overlap with ion cores, leading to a considerable decrease in annihilation with high-momentum core electrons. In our model case of ZnO, where the dominant contribution to the high-momentum part of the distribution comes from the Zn 3d electrons, the changes in the momentum distribution are more pronounced when positrons are trapped at Zn vacancies.

The comparison of the measured positron lifetimes and Doppler broadening spectra with the theoretically calculated data for specific defects provides a very efficient tool for identification of the observed vacancy defects. Several *ab initio* approaches have been studied in recent years [46.17, and the references therein]. The agreement between theory and experiment is excellent in terms of differences or ratios between the data for defects and the perfect lattice. Also quantitative agreement has been obtained in many materials, but all the theoretical schemes applied so far seem to have problems with the treatment of 3d electrons, either under- or overestimating their contribution to the positron annihilation data. For example, in the case of ZnO, the calculated lifetimes in the perfect lattice range from about 140 to 180 ps [46.19, 20], depending on the scheme, while the experimentally determined bulk lifetime is 170 ps [46.20, 21]. On the other hand, the calculated differences in the lifetimes and the ratios of the momentum distributions between the defect and bulk states agree very well with experiments [46.17, 20, 22].

Shallow Positron States at Negative Ions

A negatively charged impurity atom or an intrinsic point defect can bind positrons at shallow states even if these

defects do not contain open volume [46.23, 24]. Being a positive particle, the positron can be localized at the hydrogenic (Rydberg) state of the Coulomb field around a negatively charged center. The situation is analogous to the binding of an electron to a shallow donor atom. The positron binding energy at the negative ion can be estimated from the simple effective-mass theory

$$E_{\text{ion},n} = \frac{13.6 \text{ eV}}{\varepsilon^2} \left(\frac{m^*}{m_0} \right) \frac{Z^2}{n^2} \approx 10\text{--}100 \text{ meV}, \quad (46.8)$$

where ε is the dielectric constant, m^* is the effective mass of the positron, Z is the charge of the negative ion, and n is the quantum number. With $m^* \approx m_0$, $Z = 1\text{--}3$, and $n = 1\text{--}4$, (46.8) yields typically $E_{\text{ion}} = 10\text{--}100 \text{ meV}$, indicating that positrons are thermally desorbed from the Rydberg states at 100–300 K.

The hydrogenic positron state around a negative ion has a typical extension of 10–100 Å and thus positrons probe the same electron density as in the defect-free lattice. As a consequence, the annihilation characteristics (positron lifetime, positron–electron momentum distribution) are not different from those in the lattice. Although the negative ions cannot be identified with the experimental parameters, information on their concentration can be obtained in the positron lifetime and Doppler broadening experiments when they compete with vacancies in positron trapping [46.23, 24].

46.1.3 Positron Trapping at Point Defects

Positron Trapping Rate and Trapping Coefficient

The positron transition from a free Bloch state to a localized state at a defect is called positron trapping. The trapping is analogous to carrier capture. However, it must be fast enough to compete with annihilation. The positron trapping rate κ onto a defect D is proportional to the defect concentration c_D

$$\kappa_D = \mu_D c_D. \quad (46.9)$$

The trapping coefficient μ_D depends on the defect and the host lattice. Since the positron binding energy at vacancies is typically $> 1 \text{ eV}$, the thermal escape (detrapping) of positrons from the vacancies can usually be neglected. Due to the Coulomb repulsion, the trapping coefficient at positively charged vacancies is so small that the trapping does not occur during the short positron lifetime of a few hundred picoseconds [46.25]. Therefore, the positron technique does

not detect vacancies or other defects in their positive charge states. The trapping coefficient at neutral vacancies is typically $\mu_D \approx 10^{14}\text{--}10^{15} \text{ s}^{-1}$ independently of temperature [46.25–27]. This value means that neutral vacancies are observed when their concentration is $\geq 10^{16} \text{ cm}^{-3}$.

The positron trapping coefficient at negative vacancies is typically $\mu_D \approx 10^{15}\text{--}10^{16} \text{ s}^{-1}$ at 300 K temperature [46.25–27]. The sensitivity to detect negative vacancies is thus $\geq 10^{15} \text{ cm}^{-3}$. The experimental fingerprint of a negative vacancy is the increase of μ_D with decreasing temperature [46.26, 27]. The $T^{-1/2}$ dependence of μ_D is simply due to the increase of the amplitude of the free positron Coulomb wave in the presence of a negative defect as the thermal velocity of the positron decreases [46.25]. The temperature dependence of μ_D allows to experimentally distinguish negative vacancy defects from neutral ones.

The positron trapping coefficient μ_{ion} at the hydrogenic states around negative ions is of the same order of magnitude as that at negative vacancies [46.24, 28]. Furthermore, the trapping coefficient exhibits a similar $T^{-1/2}$ temperature dependence. Unlike in the case of vacancy defects, the thermal escape of positrons from the negative ions plays a crucial role at usual experimental temperatures. The principle of detailed balance yields the following equation for the detrapping rate δ_{ion} from the hydrogenic state [46.3]

$$\delta_{\text{ion}} = \mu_{\text{ion}} \left(\frac{2\pi m^* k_B T}{h^2} \right)^{3/2} \exp \left(-\frac{E_{\text{ion}}}{k_B T} \right). \quad (46.10)$$

Typically ion concentrations above 10^{16} cm^{-3} influence positron annihilation at low temperatures ($T < 100 \text{ K}$), but the ions are not observed at high temperatures ($T > 300 \text{ K}$), where the detrapping rate (46.10) is large.

Kinetic Trapping Model

In practice the positron annihilation data is analyzed in terms of kinetic rate equations describing the positron transitions between the free Bloch states and localized states at defects [46.8–10]. Very often the experimental data show the presence of two defects, one of which is a vacancy and the other is a negative ion. The probability of a positron to be in the free state is $n_B(t)$, to be trapped at vacancies is $n_V(t)$, and to be trapped at ions is $n_{\text{ion}}(t)$. We can write the rate equations as

$$\frac{dn_B}{dt} = -(\lambda_B + \kappa_V + \kappa_{\text{ion}}) n_B + \delta_{\text{ion}} n_{\text{ion}}, \quad (46.11)$$

$$\frac{dn_V}{dt} = \kappa_V n_B - \lambda_V n_V, \quad (46.12)$$

$$\frac{dn_{ion}}{dt} = \kappa_{ion} n_B - (\lambda_{ion} + \delta_{ion}) n_{ion}, \quad (46.13)$$

where λ , κ , and δ refer to the corresponding annihilation, trapping, and detrapping rates.

Assuming that the positron at $t = 0$ is in the free Bloch state, (46.11–46.13) can be solved and the probability of a positron to be alive at time t is obtained as

$$n(t) = n_B(t) + n_V(t) + n_{ion}(t) = \sum_{i=1}^3 I_i \exp(-\lambda_i t), \quad (46.14)$$

indicating that the lifetime spectrum $-dn(t)/dt$ has three exponential components. The fractions of positron annihilations at various states are

$$\eta_B = \int_0^\infty dt \lambda_B n_B(t) = 1 - \eta_{ion} - \eta_V, \quad (46.15)$$

$$\eta_V = \int_0^\infty dt \lambda_V n_V(t) = \frac{\kappa_V}{\lambda_B + \kappa_V + \frac{\kappa_{ion}}{1 + \delta_{ion}/\lambda_{ion}}}, \quad (46.16)$$

$$\begin{aligned} \eta_{ion} &= \int_0^\infty dt \lambda_{ion} n_{ion}(t) \\ &= \frac{\kappa_{ion}}{(1 + \delta_{ion}/\lambda_{ion}) \left(\lambda_B + \kappa_V + \frac{\kappa_{ion}}{1 + \delta_{ion}/\lambda_{ion}} \right)}. \end{aligned} \quad (46.17)$$

These equations are useful because they can be related with the experimental average lifetime τ_{ave} (the center of mass of the lifetime spectrum), the positron–electron momentum distribution $\rho(p_L)$, and the shape parameters S and W of the Doppler-broadened annihilation line (representing annihilations with low-momentum valence electrons and high-momentum core electrons, respectively) as follows

$$\tau_{ave} = \eta_B \tau_B + \eta_{ion} \tau_{ion} + \eta_V \tau_V, \quad (46.18)$$

$$\rho(p_L) = \eta_B \rho_B(p_L) + \eta_{ion} \rho_{ion}(p_L) + \eta_V \rho_V(p_L), \quad (46.19)$$

$$S = \eta_B S_B + \eta_{ion} S_{ion} + \eta_V S_V, \quad (46.20)$$

$$W = \eta_B W_B + \eta_{ion} W_{ion} + \eta_V W_V. \quad (46.21)$$

Equations (46.15–46.21) allow the experimental determination of the trapping rates κ_V and κ_{ion} , and

consequently the defect concentrations can be obtained from (46.12). Furthermore, these equations enable the combination of positron lifetime and Doppler broadening results, and various correlations between τ_{ave} , $\rho(p_L)$, S , and W can be studied.

At high temperatures all positrons escape from the hydrogenic state of the negative ions and no annihilations take place at them. In this case the lifetime spectrum has two components

$$\tau_1^{-1} = \tau_B^{-1} + \kappa_V, \quad (46.22)$$

$$\tau_2 = \tau_V, \quad (46.23)$$

$$I_2 = 1 - I_1 = \frac{\kappa_V}{\kappa_V + \lambda_B - \lambda_D}. \quad (46.24)$$

The first lifetime τ_1 represents the effective lifetime in the lattice in the presence of positron trapping at vacancies. Since $\kappa_V > 0$ and $I_2 > 0$, τ_1 is less than τ_B . The second lifetime component τ_2 characterizes positrons trapped at vacancies, and it can be directly used to identify the open volume of the vacancy defect. When $\eta_{ion} = 0$ and $\delta_{ion}/\lambda_{ion} \gg 1$ the determination of the positron trapping rate and vacancy concentration is straightforward using (46.15–46.21)

$$\begin{aligned} \kappa_V &= \mu_V \kappa_V = \lambda_B \frac{\tau_{ave} - \tau_B}{\tau_V - \tau_{ave}} \\ &= \lambda_B \frac{S - S_B}{S_V - S} = \lambda_B \frac{W - W_B}{W_V - W}. \end{aligned} \quad (46.25)$$

Notice that in this case τ_{ave} , S , and W depend linearly on each other. The linearity of experimental points in (τ_{ave}, S) , (τ_{ave}, W) , and (S, W) plots thus provides evidence that positrons annihilate from two distinguishable states, indicating that they are trapped at only a single type of vacancy defect in the samples.

4.6.1.4 Experimental Techniques

Positron Lifetime Spectroscopy

Positron lifetime spectroscopy is a powerful technique in defect studies, because the various positron states appear as different exponential decay components. The number of positron states, and their annihilation rates and relative intensities can be determined. In a positron lifetime measurement, one needs to detect the start and stop signals corresponding to the positron entrance and annihilation times in the sample, respectively (Fig. 46.1). A suitable start signal is the 1.27 MeV photon that accompanies the positron emission from the ^{22}Na isotope. The 511 keV annihilation photon serves as the stop signal. The positron source is prepared by

sealing about $10\ \mu\text{Ci}$ (about $10^5\text{--}10^6\ \text{Bq}$) of radioactive isotope between two thin foils. The source is then sandwiched between two identical pieces (e.g., $5\times 5\times 0.5\ \text{mm}^3$) of the sample material. This technique is standard for bulk crystal studies. Pulsed positron beams have been constructed for lifetime spectroscopy in thin layers [46.29, 30], but so far they have not been used much in defect studies.

The conventional lifetime spectrometer consists of start and stop detectors, each of them made by coupling a fast scintillator to a photomultiplier. The timing pulses are obtained by differential constant-fraction discrimination. The time delays between the start and stop signals are converted into amplitude pulses, the heights of which are stored in a multichannel analyzer. Thanks to the development of fast analog-to-digital converters (ADCs), digital data readout techniques have recently become viable [46.31–34]. This allows direct digitization of the detector pulses and performance of the timing and energy windowing with software instead of the conventional analog electronics, simplifying the measurement setup significantly. About 10^6 lifetime events are recorded in 1 h. The experimental spectrum represents the probability of positron annihilation at time t and it consists of exponential decay components

$$-\frac{dn(t)}{dt} = \sum_i I_i \lambda_i \exp(-\lambda_i t), \quad (46.26)$$

where $n(t)$ is the probability for the positron to be alive at time t . The decay constants $\lambda_i = 1/\tau_i$ are called the annihilation rates and they are the inverses of the positron lifetimes τ_i . Each positron lifetime has intensity I_i . In practice the ideal spectrum of (46.26) is convoluted by a Gaussian resolution function which has a width of 200–250 ps (full-width at half-maximum, FWHM). About 5–10% of positrons annihilate in the source material and proper *source corrections* must be made. Due to the finite time resolution, annihilations in the source materials, and random background, typically only 1–3 lifetime components can be resolved in the analysis of the experimental spectra. The separation of two lifetimes is successful only if the ratio λ_1/λ_2 is $\geq 1.3\text{--}1.5$.

Figure 46.4 shows positron lifetime spectra recorded in as-grown and electron-irradiated high-quality ZnO bulk crystals [46.21, 35]. Positrons enter the sample and thermalize at time $t = 0$. The vertical axis of Fig. 46.4 gives the number of annihilations at a time interval of 25 ps. In the as-grown sample the positron lifetime spectrum has a single component of $170 \pm$

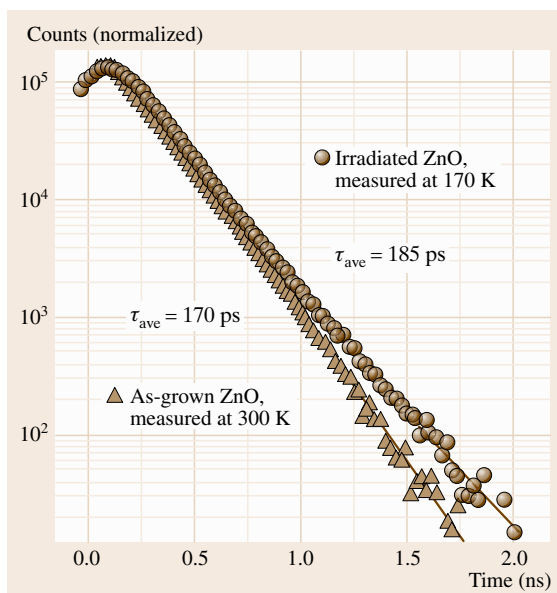


Fig. 46.4 Examples of positron lifetime spectra in as-grown and electron-irradiated high-quality ZnO samples. A constant background and annihilations in the source materials have been subtracted from the spectra, which consist of 2×10^6 recorded annihilation events. The *solid lines* are fits of the sum of exponential components convoluted with the resolution function of the spectrometer. The data in the as-grown sample was recorded at 300 K and has only a single component of 170 ± 1 ps. The spectrum in the electron-irradiated crystal was recorded at 170 K and can be decomposed into two components of $\tau_1 = 155 \pm 5$ ps, $\tau_2 = 230 \pm 10$ ps, and $I_2 = 38 \pm 5\%$

1 ps at 300 K corresponding to positron annihilations in the defect-free lattice. The electron-irradiated sample has two lifetime components, the longer of which ($\tau_2 = 230$ ps) is due to positrons annihilating when trapped at irradiation-induced Zn vacancies. For more discussion see Sect. 46.2.

The experimental results are often presented in terms of the average positron lifetime τ_{ave} , defined as

$$\tau_{\text{ave}} = \int_0^\infty dt \, t \left(-\frac{dn}{dt} \right) = \int_0^\infty dt \, n(t) = \sum_i I_i \tau_i. \quad (46.27)$$

The average lifetime is a statistically accurate parameter, because it is equal to the center of mass of the experimental lifetime spectrum. Hence it can be cor-

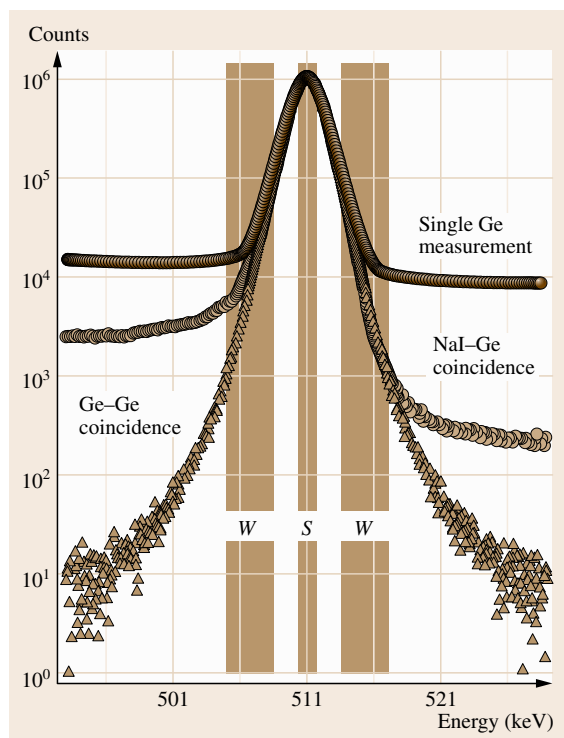


Fig. 46.5 Doppler broadening spectra obtained in different data collection modes. The definition of the shape parameters S and W is shown

rectly calculated from the intensity and lifetime values even if the decomposition only represents a good fit to the experimental data without any physical meaning. For example, the positron average lifetimes in the two spectra of Fig. 46.4 are 170 ps (as-grown ZnO) and 185 ps (electron-irradiated ZnO). The difference is very significant because changes below 1 ps in the average lifetime can be reliably observed in experiments.

Doppler Broadening Spectroscopy

Doppler broadening spectroscopy is often applied especially in the low-energy positron beam experiments, where lifetime spectroscopy is usually very difficult due to the missing start signal. The motion of the annihilating electron–positron pair causes a Doppler shift in the annihilation radiation (Fig. 46.1)

$$\Delta E_\gamma = \frac{1}{2} c p_L, \quad (46.28)$$

where p_L is the longitudinal momentum component of the pair in the direction of the annihilation photon emission. This causes the broadening of the 511 keV

annihilation line (Fig. 46.5). The shape of the 511 keV peak thus gives the one-dimensional momentum distribution $\rho(p_L)$ of the annihilating electron–positron pairs. A Doppler shift of 1 keV corresponds to a momentum value of $p_L = 3.91 \times 10^3 m_0 c$ (≈ 0.54 a.u.).

The Doppler broadening can be experimentally measured using a Ge gamma detector with a good energy resolution (Fig. 46.5). For measurements of bulk samples, the same source–sample sandwich is used as in the lifetime experiments. For layer studies, the positron beam hits the sample and the Doppler broadening is often monitored as a function of the beam energy. The typical resolution of a detector is around 1–1.5 keV at 500 keV. This is considerable compared with the total width of 2–3 keV of the annihilation peak, meaning that the experimental line shape is strongly influenced by the detector resolution. Therefore, various shape parameters are used to characterize the 511 keV line. Their definitions are shown in Fig. 46.5 as well.

The low-electron-momentum parameter S is defined as the ratio of the counts in the central region of the annihilation line to the total number of the counts in the line. In the same way, the high-electron-momentum parameter W is the fraction of the counts in the wing regions of the line. Due to their low momenta, mainly valence electrons contribute to the region of the S parameter. On the other hand, only core electrons have momentum values high enough to contribute to the W parameter. Therefore, S and W are called the valence and core annihilation parameters, respectively. The S parameter is integrated from the Gaussian part (given by the momentum distribution of the unbound or only weakly bound valence electrons) so that it includes roughly 50% of the total counts in the peak. The lower limit of the W parameter window is chosen so that the dominant contribution to that part of the spectrum comes from the exponential tails (linear in the semi-log plot) of the core electron distributions. In order to have as good statistics as possible, the upper limit is set as high as reasonable from the data scatter point of view. The proper choice of the lower limit of the W parameter window depends on the studied material.

The high-momentum part of the Doppler broadening spectrum arises from annihilations with core electrons which contain information on the chemical identity of the atoms. Thus detailed investigation of core electron annihilation can reveal the nature of the atoms in the regions where positrons annihilate. In order to study the high-momentum part in detail, the experimental background needs to be reduced. A second gamma detector is placed opposite to the Ge detector and the

only events that are accepted are those for which both 511 keV photons are detected [46.36, 37]. Depending on the type of the second detector, electron momenta

even up to $p \approx 60 \times 10^{-3} m_0 c$ (≈ 8 a.u.) can be measured with the coincidence detection of the Doppler broadening.

46.2 Identification of Point Defects and Their Charge States

The annihilation characteristics of trapped positrons serve as fingerprints in defect identification. The positron lifetime at a defect is a basic quantity for two reasons: it reflects the open volume of the defect and it can be predicted by theoretical calculations. However, the lifetime experiment alone is not enough for the direct identification of the sublattice of the vacancy in compound semiconductors or to determine whether the vacancy is isolated or complexed with impurity atoms, as it is insensitive to the chemical surroundings of the defect. Doppler broadening experiments provide information on the momentum distribution of the annihilating electrons. By the coincidence technique one can reveal the core electron momentum distribution that carries information about the type of atoms in the region of annihilation. In the case of a vacancy, the positron wavefunction is localized and overlaps predominantly with the core electrons of the neighboring atoms. Therefore, vacancies on different sublattices can be distinguished and impurities associated with vacancies may be identified. Finally, by varying the sample temperature during the experiments, one can distinguish between neutral and negative charge states of the vacancies due to the different thermal behavior of the positron trapping, and detect negatively charged non-open volume defects.

46.2.1 Vacancies in Si: Impurity Decoration

To illustrate how the positron lifetime together with Doppler broadening experiments can be used to identify vacancy defects, we review here results obtained in highly n-type Si doped with phosphorus (P) and arsenic (As). Electron irradiation with energies of the order of 1–2 MeV is a convenient experimental approach to produce a controlled concentration of vacancies. By changing the fluence one can vary the fraction of positrons annihilating at vacancies. Electron irradiation at 2 MeV creates vacancies and interstitials as primary defects, both of which are mobile in Si at 300 K [46.39]. Hence the vacancies produced in the irradiation disappear, e.g., by recombination with interstitials or by diffusion to the surface, or become stabilized by impuri-

ties or intrinsic defects, such as other vacancies. As both the vacancies and interstitials are mobile, the recombination and divacancy formation processes are not very efficient; in experiments about 1% of the primarily created vacancies have been observed to form divacancies when competing stabilizing defects, such as oxygen or dopant atoms (e.g., P or As), are not present [46.40].

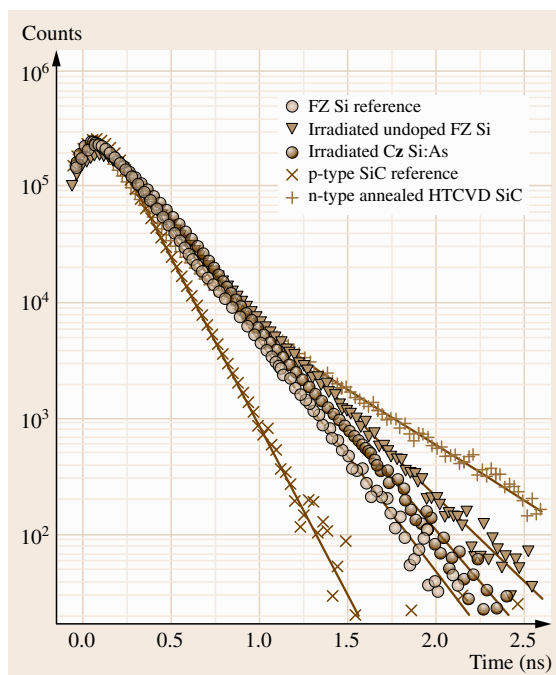


Fig. 46.6 Positron lifetime spectra in as-grown and 2 MeV electron-irradiated Si samples. Positrons annihilate in the as-grown sample with a single lifetime of 220 ps corresponding to delocalized positrons in the lattice. In the irradiated samples the experiments reveal vacancies with positron lifetimes of 250 ps (V–As pair in CZ Si:As sample doped with $[As] = 1020 \text{ cm}^{-3}$) and 300 ps (divacancy in undoped FZ Si sample) [46.38]. To illustrate the sensitivity of the lifetime measurement, data measured in a p-type SiC reference sample (single lifetime component of 150 ps) and a high-temperature-annealed n-type SiC sample (two components, of which the higher is 450 ps) are shown [46.38]

Figure 46.6 shows the positron lifetime spectra measured in unirradiated float-zone (FZ)-refined Si, electron-irradiated As-doped Czochralski (CZ)-grown Si ($[As] = 10^{20} \text{ cm}^{-3}$), and electron-irradiated FZ Si samples [46.38]. To illustrate the sensitivity of the lifetime measurement, data measured in a p-type SiC reference sample (single lifetime component of 150 ps) and a high-temperature-annealed n-type SiC sample (two components, of which the higher is 450 ps) are shown [46.41]. The unirradiated samples have only a single positron lifetime component of about 220 ps, which is practically constant as a function of temperature [46.40]. This behavior shows that no vacancies are observed by positrons and all annihilations take place at the delocalized state in the bulk lattice, with the lifetime $\tau_B = 220 \text{ ps}$. The presence of vacancy defects in the electron-irradiated FZ Si samples is evident in Fig. 46.6. The lifetime spectrum has two components, the longer of which, $\tau_2 = 300 \pm 5 \text{ ps}$, corresponds to positrons trapped at vacancy defects. The lifetime of $\tau_2 = 300 \pm 5 \text{ ps}$ is significantly larger than expected for a monovacancy but it is equal to the calculated lifetime for annihilation at divacancies [46.42]. Vacancy defects are clearly present in the electron-irradiated As-doped Si samples as well (Fig. 46.6). In this case the spectrum has only a single component due to the high concentration of vacancies, causing saturation trapping of positrons. This occurs when the vacancy concentration exceeds 10^{18} cm^{-3} , consistent with the expected introduction rate in electron-irradiated heavily n-type doped Si [46.26, 27, 39]. The lifetime component is $\tau_V = 250 \pm 5 \text{ ps}$, a lifetime characteristic of a single vacancy according to theoretical calculations [46.42]. The lifetime component $\tau_V = 250 \pm 5 \text{ ps}$ is detected in as-grown As-doped Si ($[As] = 10^{20} \text{ cm}^{-3}$) as well (not shown in the figure) [46.43], but the vacancy concentration is clearly smaller than in the electron-irradiated samples. The average lifetimes are $\tau_{ave} = 232 \text{ ps}$ and $\tau_{ave} = 250 \text{ ps}$ in the as-grown and irradiated samples, respectively [46.38, 41].

In order to identify the monovacancies in detail, Doppler broadening experiments using the two-detector coincidence technique have been performed. The lifetime results from above can be used to determine the fraction of positrons annihilating at vacancies $\eta = (\tau_{ave} - \tau_B)/(\tau_V - \tau_B)$ (Sect. 46.1). Since the momentum distribution in the lattice $\rho_B(p)$ can be measured in the reference sample, the distributions $\rho_V(p)$ at vacancies can be decomposed from the measured spectrum $\rho(p)$. They are shown in Fig. 46.7 for the monovacancies observed in as-grown Si ($[As] = 10^{20} \text{ cm}^{-3}$)

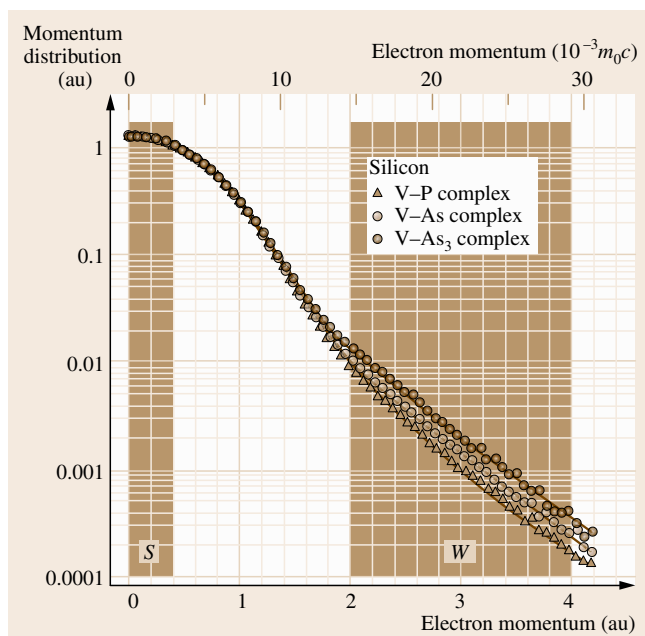


Fig. 46.7 The positron–electron momentum distribution at the various vacancy–impurity pairs, identified in electron-irradiated Si ($[P] = 10^{20} \text{ cm}^{-3}$) (full circles) and in as-grown (full circles) and irradiated (open triangles) Si ($[As] = 10^{20} \text{ cm}^{-3}$). The results of the theoretical calculations are shown by the solid curves

as well as in irradiated Si ($[As] = 10^{20} \text{ cm}^{-3}$) and Si ($[P] = 10^{20} \text{ cm}^{-3}$).

The momentum distributions $\rho_V(p)$ at vacancies indicate large differences at higher momenta ($p > 1.8 \text{ a.u.}$), where annihilation with core electrons is the most important contribution (Fig. 46.7). Since the core electron momentum distribution is a specific characteristic of a given atom, the differences between the spectra indicate different atomic environments of the vacancy in each of the three cases. Because in both Si ($Z = 14$) and P ($Z = 15$) the 2p electrons constitute the outermost core electron shell, the core electron momentum distributions of these elements are very similar. The crucial difference in the core electron structures of Si, P, and As is the presence of 3d electrons in As. The overlap of positrons with the As 3d electrons is much stronger than with the more localized Si or P 2p electrons. The large intensity of the core electron momentum distribution is thus a clear sign of As atoms surrounding the vacancy.

The 2 MeV electron irradiation creates vacancies and interstitials as primary defects, both of which are mobile at 300 K. In heavily n-type Si the donor atom may capture the vacancy and form a vacancy–impurity

pair [46.39]. The monovacancy detected in heavily P-doped Si is thus the V-P pair. Similarly, it is natural to associate the electron irradiation-induced vacancy in Si([As] = 10^{20} cm^{-3}) with a V-As pair. The influence of As next to the vacancy is clearly visible as the enhanced intensity in the high-momentum region (Fig. 46.7). An even stronger signal from As is seen in the as-grown Si([As] = 10^{20} cm^{-3}). A linear extrapolation of the intensity of the distribution shows that the native complex is V-As₃, i.e., the vacancy is surrounded by *three* As atoms.

The identifications are confirmed by theoretical results [46.42, 43], which are in very good agreement at both low and high momenta. The theory reproduces the linear increase of the intensity of the core electron momentum distribution with increasing number of As atoms surrounding the vacancy. For the V-As₃ complex the agreement with the experimental result is excellent (Fig. 46.7), whereas the intensities calculated for V-As₂ and V-As₄ are much too small or large, respectively. In the valence electron momentum range, the calculated curves for V-As and V-As₃ also fit very well with the experiment. To conclude, the theoretical calculations strongly support the experimental defect identifications that (i) vacancies complexed with a single donor impurities are detected in electron-irradiated P- and As-doped Si, and (ii) the native defect in Si([As] = 10^{20} cm^{-3}) is a vacancy surrounded by three As atoms.

46.2.2 Vacancies in ZnO: Sublattice and Charge State

The elemental sensitivity of the Doppler broadening spectrum demonstrated above can be helpful in the identification of the sublattice of a vacancy in a binary compound. Under certain conditions, vacancies complexed with impurities can be distinguished from isolated vacancies also in compound semiconductors [46.44]. In materials such as GaN and ZnO, where the group III–II element is significantly heavier (and larger) than the rather light group V–VI element, already the positron lifetime experiments often give conclusive identification of the group III–II vacancies, and the differences in the Doppler spectra are pronounced. On the other hand, it is not evident that the group V–VI vacancies are detected at all. In materials such as GaAs or ZnSe, in which the two elements are quite similar, vacancies on both sublattices are more likely to trap positrons, but the differences between the vacancy-specific parameters can be quite subtle [46.8].

The lifetime in the defect-free ZnO lattice has been measured to be about 170 ps. After 2 MeV electron irradiation at room temperature a longer lifetime component $\tau_2 = 230 \pm 10 \text{ ps}$ is detected in the measured spectrum (Fig. 46.4). In addition, the average lifetime increases to $\tau_{\text{ave}} = 178 \text{ ps}$ at room temperature and up to 185 ps at lower temperatures. The longer lifetime component can be directly associated with Zn vacancies based on comparison to theoretical calculations that predict a difference of 60 ps between the Zn vacancy and the bulk lifetimes, when lattice relaxations around the vacancy are taken into account [46.20]. On the other hand, the positron lifetime in the O vacancy, even with a strong outward relaxation, would be at most 20–25 ps longer than in the bulk [46.35]. In order to put the identification on an even firmer basis, the Doppler broadening results obtained in the irradiated ZnO samples can be compared with the theoretical ones. Figure 46.8 represents both the experimental and theoretically calculated ratios of the Zn-vacancy-specific momentum distribution to that of the defect-free lattice. The experimental data for the Zn vacancy are extracted from the spectrum measured at 170 K with the help of the annihilation fractions obtained from the lifetime measurements at the same temperature in the same way as in the case of the Si vacancies in Sect. 46.2.1. The data calculated for the O vacancy are similar to those in the defect-free lattice and are not shown in the figure. The agreement between the theoretically calculated and experimentally determined ratio curves is excellent, strengthening

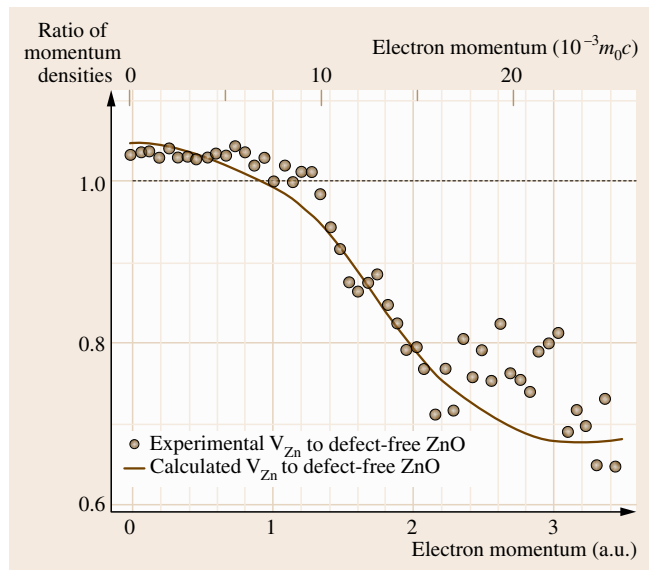


Fig. 46.8 Ratios curves of the experimental and theoretically calculated momentum densities specific to the Zn vacancy in ZnO

the identification of the irradiation-induced vacancy detected in ZnO as the Zn vacancy.

Figure 46.9 shows the positron lifetime measured as a function of temperature in as-grown and electron-irradiated high-quality (EaglePicher) n-type ZnO samples [46.35]. At 300–500 K the average positron lifetime in the as-grown sample is constant or very slightly increasing due to thermal expansion of the crystal lattice. It provides the lifetime of the positron in the delocalized state in the ZnO lattice, $\tau_B = 170$ ps at 300 K. The increase in the average positron lifetime with decreasing temperature at 10–300 K is a clear indication of the presence of negatively charged vacancies, the positron trapping coefficient of which increases with decreasing temperature (Sect. 46.1). A longer lifetime component of $\tau_2 = 265 \pm 25$ ps could be separated from the lifetime spectrum at 10 K, indicating that the vacancy in question is the Zn vacancy. The large un-

certainty in τ_2 is due to the fact that the increase in τ_{ave} is very small, only 3 ps (the vacancy signal is weak due to a low concentration). The same increase in the average positron lifetime with decreasing temperature at 10–300 K is observed in the data from the irradiated sample (Fig. 46.9). Here τ_{ave} is clearly above the bulk value τ_B and thus the decomposition of the lifetime spectra could be performed with much greater accuracy. The longer lifetime component is presented in the upper part of Fig. 46.9, and its average value is that specific to the Zn vacancy as discussed above, $\tau_2 = 230 \pm 10$ ps, within experimental accuracy the same as in the as-grown sample. The decrease in the average positron lifetime with decreasing temperature in the irradiated samples below 200 K is due to negative non-open volume defects (negative ions) acting as shallow traps for positrons and competing with the vacancies in trapping of positrons. Their effects are discussed in more detail in the next section.

The Doppler broadening parameters S and W , defined in Sect. 46.1, measured simultaneously with the positron lifetime fall on a line plotted against each other with temperature as the running parameter, which typically indicates the presence of only two distinguishable positron states (bulk and vacancy). The negative-ion-type defects (shallow traps) do not cause deviations from the straight line, since the annihilation parameters of positrons trapped at these defects coincide with those of the bulk. However, as can be seen in Fig. 46.10, the points measured at 90–190 K fall off the straight line determined by the annihilations in the defect-free lattice and the Zn vacancy in the (S, τ_{ave}) and (W, τ_{ave}) plots. This implies that a third positron state can be distinguished in the lifetime versus Doppler parameter data, although the Doppler data alone are linear. In order to cause a deviation from the straight line, the localization to this defect needs to be strong, implying that the defect has a distinguishable open volume. The open volume of this defect cannot be very large, since the independence of temperature of the longer lifetime component (Fig. 46.9) shows no evidence of possible mixing of several lifetime components. Hence, the lifetime specific to this defect needs to be sufficiently far from τ_2 (and closer to τ_1), below 200 ps. In addition, in order to produce the deviation from the straight line seen in Fig. 46.10, the defect-specific lifetime needs to be above τ_{ave} over the whole temperature range, i.e., above 185 ps. One additional aspect of the third type of defects is evident from the data. The fraction of positrons annihilating as trapped at this defect is vanishing at room temperature and clearly

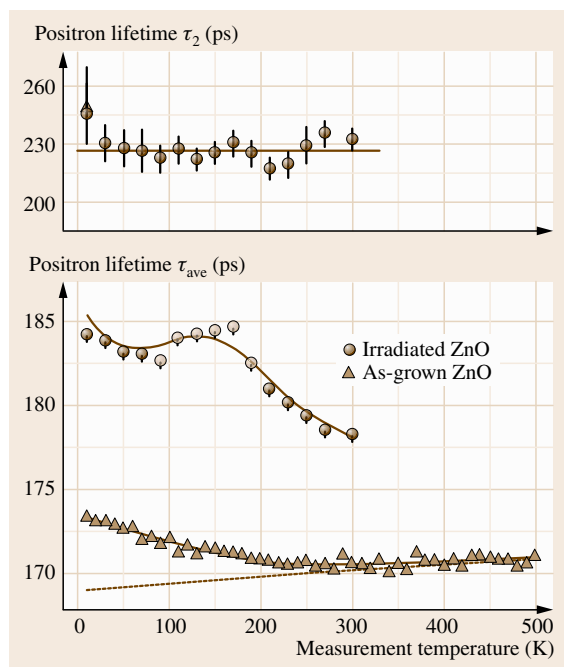


Fig. 46.9 The positron lifetime parameters of as-grown and electron-irradiated ZnO samples plotted as functions of measurement temperature. The data markers are drawn as open in the temperature range 90–190 K, where the effect of the O vacancies is the most visible. The *dashed line* shows the fitted bulk lifetime, where the temperature dependence is due to thermal expansion of the lattice. The *solid curves* represent the fitting of the temperature-dependent trapping model to the data [46.35]

smaller than the annihilation fractions at the Zn vacancies and negative-ion-type defects below 90 K, but larger at the intermediate temperature 90–190 K. This implies that the enhancement of positron trapping with decreasing temperature is larger at this defect at temperatures 190–300 K, but saturates around 150 K, where the Zn vacancies and the negative-ion-type defects become more important. This indicates that the third type of defect is neutral, and the temperature dependence of positron trapping observed at temperatures close to room temperature is due to either thermal escape from the defect or a change in the charge state (from neutral to positive) of the defect. Based on these considerations

and the lifetime value of 190–200 ps, a prominent candidate for this defect is the O vacancy that has a donor nature and would naturally have a smaller open volume than the Zn vacancy.

46.2.3 Negative Ions as Shallow Positron Traps in GaN

In addition to vacancy defects, negatively charged impurities and intrinsic defects with no open volume (called collectively negative ions), can trap positrons at shallow hydrogen-like states, as explained in Sect. 46.1. They can only be detected when they compete with vacancies in the trapping of positrons, and due to the weak localization of the positron at these defects they cannot be identified. However, their concentration can be estimated and compared with those (obtained by, e.g., secondary-ion mass spectrometry, SIMS) of the known impurities. Figure 46.11 shows a typical example of the temperature-dependent positron lifetime data when negative ions compete with vacancies in positron trapping. The data are measured in thick high nitrogen pressure (HNP)-grown bulk GaN crystals, with both the N and Ga polarity faces facing the positron source, and in thick homoepitaxial GaN layers grown with hydride vapor-phase epitaxy (HVPE) grown on both polarity faces of the bulk crystals [46.45]. All these samples are n-type.

The average positron lifetime is clearly above the bulk lifetime $\tau_B = 160 \pm 1$ ps in the HNP GaN and N-polar HVPE GaN samples (Fig. 46.11), indicating that positrons are trapped at vacancies. The lifetime spectra recorded at 300–500 K in those samples can be decomposed into two components. The positrons trapped at vacancies annihilate with the longer lifetime $\tau_V = \tau_2 = 235 \pm 10$ ps, characteristic of the Ga vacancy [46.44, 46, 47] that is negatively charged in n-type and semi-insulating GaN [46.44, 47, 48]. The average positron lifetime measured in the Ga-polar HVPE GaN samples coincides with the bulk lifetime $\tau_B = 160 \pm 1$ ps, indicating that the vacancy concentration in those samples is below the detection limit of about 10^{15} cm^{-3} .

At low temperatures the average positron lifetime in the HNP and N-polar HVPE GaN samples decreases and the lifetime at the Ga vacancy τ_V remains constant (Fig. 46.11). This behavior indicates that the fraction $\eta_V = (\tau_{\text{ave}} - \tau_B)/(\tau_V - \tau_B)$ of positrons annihilating at vacancies decreases. Since the positron trapping at negative Ga vacancies should be enhanced at low temperatures (Sect. 46.1), the decrease of η_V is due to other defects which compete with Ga vacancies as positron

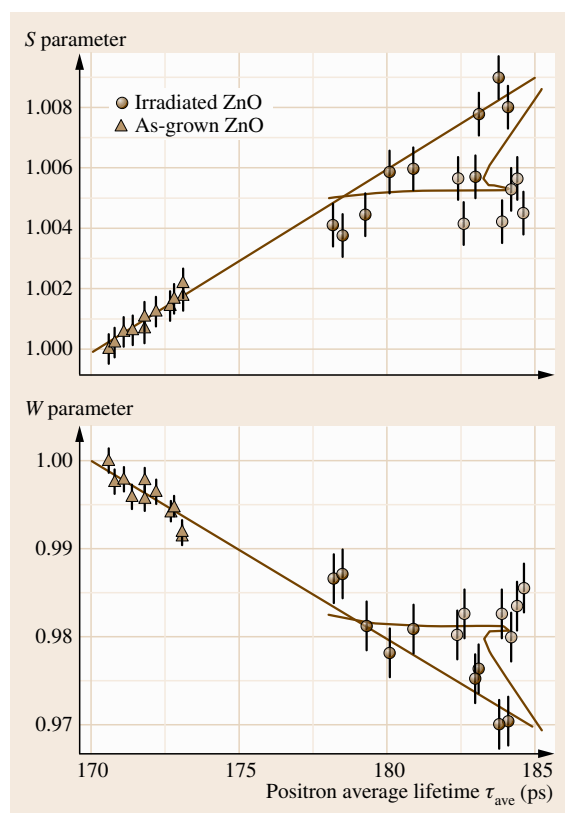


Fig. 46.10 The S and W parameters measured in as-grown and electron-irradiated ZnO samples plotted as functions of τ_{ave} with temperature as the running parameter. The data markers are drawn as open in the temperature range 90–190 K, where the effect of the O vacancies is the most visible. The solid lines connect the parameters of the bulk lattice to those (not shown) specific to the Zn vacancy. The solid curves are obtained from the fitting of the temperature-dependent trapping model [46.35]

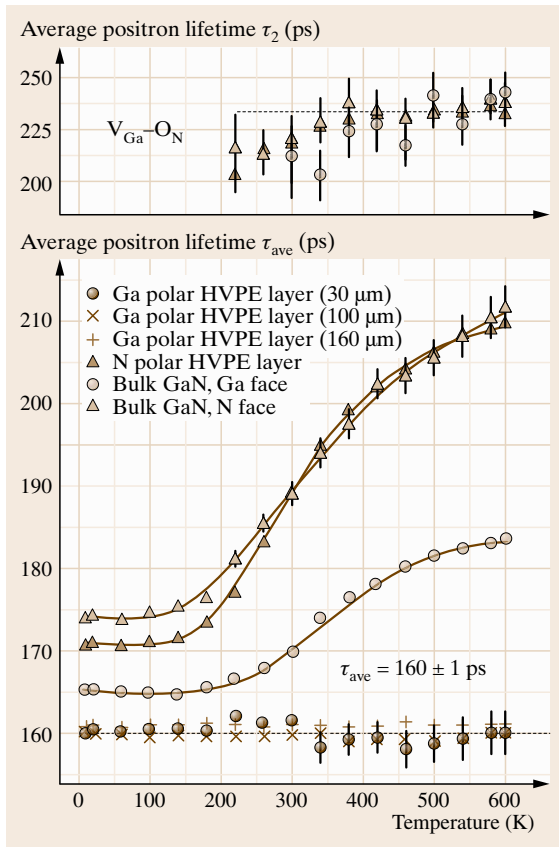


Fig. 46.11 Average positron lifetimes and the second lifetime components extracted from the lifetime spectra measured in HNP and HVPE GaN samples. The solid curves represent the fits of the temperature-dependent trapping model. The solid lines in the upper and lower parts of the figure show the average values of τ_{ave} and τ_2 in regions of no temperature dependence [46.45]

traps. Negative ions are able to bind positrons at shallow (< 0.1 eV) hydrogenic states in their attractive Coulomb field (Sect. 46.1). Since they possess no open volume, the lifetime of positrons trapped at them is the same

as in the defect-free lattice, $\tau_{\text{ion}} = \tau_{\text{B}} = 160 \pm 1$ ps. The average lifetime increases above 150 K when positrons start to escape from the ions and a larger fraction of them annihilates at vacancies.

The temperature dependence of the average lifetime can be modeled with the kinetic trapping equations introduced in Sect. 46.1. The positron trapping coefficients at negative Ga vacancies μ_{V} and negative ions μ_{ion} vary as $T^{-1/2}$ as a function of temperature [46.3,8]. The positron escape rate from the ions can be expressed as $\delta(T) \propto \mu_{\text{ion}} T^{-3/2} \exp(-E_{\text{ion}}/k_{\text{B}}T)$, where E_{ion} is the positron binding energy at the Rydberg state of the ions (46.10). The fractions of annihilations at Ga vacancies η_{V} and at negative ions η_{ion} are given in (46.16–46.17) and they depend on the concentrations $c_{\text{V}} = \kappa_{\text{V}}/\mu_{\text{V}}$ and $c_{\text{ion}} = \kappa_{\text{ion}}/\mu_{\text{ion}}$ of Ga vacancies and negative ions (46.9), respectively, as well as on the detrapping rate $\delta_{\text{ion}}(T)$ (46.10). We take the conventional value $\mu_{\text{V}} = 2 \times 10^{15} \text{ s}^{-1}$ for the positron trapping coefficient at 300 K [46.8, 9]. Inserting the annihilation fractions η_{B} , η_{ion} , and η_{V} from (46.15–46.17) into the equation for the average lifetime $\tau_{\text{ave}} = \eta_{\text{B}}\tau_{\text{B}} + \eta_{\text{ion}}\tau_{\text{ion}} + \eta_{\text{V}}\tau_{\text{V}}$ (46.18), the resulting formula can be fitted to the experimental data of Fig. 46.11 with c_{V} , c_{ion} , μ_{ion} , and E_{ion} as adjustable parameters. As indicated by the solid lines in Fig. 46.11, the fits reproduce well the experimental data with the positron binding energy of $E_{\text{ion}} = 60 \pm 10$ meV and trapping coefficient $\mu_{\text{ion}} = (7 \pm 4) \times 10^{16} (T/\text{K})^{-0.5}$. These values are close to those obtained previously in, e.g., GaAs and GaN [46.8,28,46].

Even though the negative ions cannot be identified based on the positron data alone, their concentrations can be determined and compared with acceptor impurity concentrations measured with SIMS. In as-grown GaN samples, the negative ion concentrations obtained from positron experiments correlate with the concentrations of magnesium (Mg) impurities in both HVPE- and HNP-grown samples [46.45,46]. This indicates that, as expected, the Mg impurities act as compensating defects in n-type GaN.

46.3 Defects, Doping, and Electrical Compensation

The concentrations of the defects detected by positrons can be estimated from their respective annihilation fractions. This can be done in a straightforward manner even when the exact defect structure such as the decoration by impurities of a vacancy remains unre-

solved. The experimental annihilation fractions depend on the trapping rates to the different defects through (46.16–46.17), and the trapping rate κ_{D} to a specific defect is directly proportional to the defect concentration c_{D} (46.9). The proportionality constant is called

the trapping coefficient μ_D (Sect. 46.1). The values and behavior as a function of temperature of the trapping coefficients depend on the type and charge state of the defect, and have been estimated both experimentally and by theoretical calculations [46.25–27]. Even though the absolute magnitude of the trapping coefficient may be off by a factor of two or three from the physically proper value, differences in vacancy concentrations in a given material can be detected with the high accuracy of the lifetime experiment: changes as low as 1 ps can be reliably detected in the average positron lifetime of about 200 ps. In this section studies of vacancy–donor complexes in Si and GaN are presented.

46.3.1 Formation of Vacancy–Donor Complexes in Highly n-Type Si

Doping levels up to 10^{20} cm^{-3} are used in current device technologies. In n-type doping of Si with arsenic, however, fundamental material problems start to appear when the impurity concentration increases above $\approx 3 \times 10^{20} \text{ cm}^{-3}$ [46.50, 51]. The concentration

of the free carriers (electrons) does not increase linearly with the doping concentration, indicating that inactive impurity clusters or compensating defects are formed. Furthermore, the diffusion coefficient of As starts to increase rapidly at $[\text{As}] > 3 \times 10^{20} \text{ cm}^{-3}$, demonstrating that new migration mechanisms become dominant [46.52].

Both the electrical deactivation of dopants and the enhanced As diffusion have often been attributed to the formation of vacancy–impurity complexes [46.51]. According to theoretical calculations, vacancies surrounded by several As atoms (V-As_n , $n > 2$) have negative formation energies, suggesting that these complexes are abundantly present at any doping level [46.53, 54]. The formation of these defects is however limited by kinetic processes such as the migration of As. The calculations predict that also the V-As_2 complex is mobile at relatively low temperatures, enabling the formation of higher-order V-As_n complexes [46.54, 55]. As shown in Sect. 46.2, the dominant structure of vacancy complexes has been identified as V-As_3 in Czochralski (CZ) Si doped up to $[\text{As}] = 10^{20} \text{ cm}^{-3}$ [46.43, 56].

In order to verify the formation mechanism of the V-As_3 complexes in highly As-doped Si, electron-irradiated Si ($[\text{As}] = 10^{20} \text{ cm}^{-3}$) samples, where V–As pairs were observed as dominant vacancy complexes defects, were subjected to thermal annealing experiments. Figure 46.12 shows the behavior of the average positron lifetime measured at room temperature as a function of the annealing temperature [46.49, 57]. For comparison, data obtained in P-doped Si ($[\text{P}] = 10^{20} \text{ cm}^{-3}$) samples subjected to similar irradiation and annealing are also shown in the figure. In Si ($[\text{As}] = 10^{20} \text{ cm}^{-3}$) the lifetime is around 242 ps up to 1100 K, indicating the presence of monovacancies. The peak at 500 K is due to the formation and annealing of divacancy defects [46.49, 57]. In the P-doped sample the average lifetime is initially higher due to a slightly higher concentration of divacancies, and decreases dramatically already after the annealing at 700 K, indicating that the vacancy concentration decreases at a lower temperature than in As-doped Si.

Coincidence Doppler broadening measurements were performed simultaneously with the lifetime experiments. As explained in Sect. 46.2.1, the vacancy defects observed after irradiation in As-doped Si are the V–As pairs (Fig. 46.7). After annealing at 600 K, the intensity of the high-momentum part (2–4 a.u.) has increased, and the defect in question can be identified as the V-As_2 complex by comparison with theoretical cal-

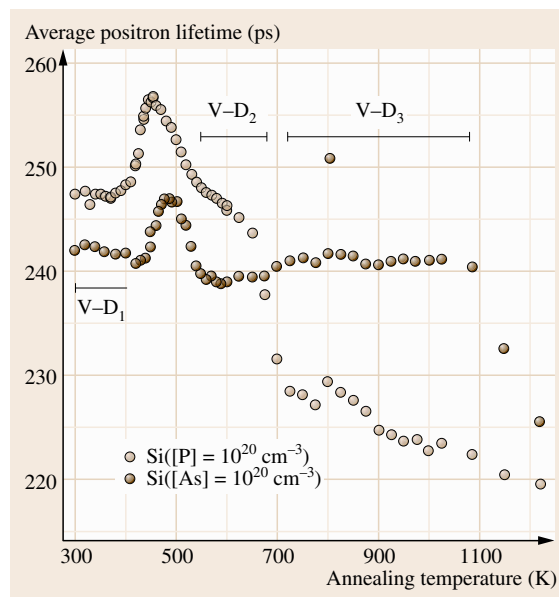


Fig. 46.12 Average positron lifetime measured at room temperature as a function of annealing temperature for the electron-irradiated Si samples. The annealings were performed isochronally (30 min at each temperature) in vacuum [46.49]. The regions where each of the vacancy–donor complex (V-D_n) is the dominant defect are also shown

culations. After annealing at 775 K, the intensity of the high-momentum part further increases up to the level of the V-As₃ complex (Fig. 46.7). The measurement after annealing at 1000 K gives the same Doppler-broadened spectrum, indicating that the defects are still the V-As₃ complexes formed around 700 K. After 1100 K the average lifetime (Fig. 46.12) starts to decrease, indicating that the vacancy defects are annealing away.

The average lifetime data in Fig. 46.12 suggests that similar dissociation and complexing of vacancy-donor pairs occurs in P-doped Si as well. It is worth noticing that the divacancy-related peak in the average lifetime is at a slightly lower temperature and the peak is slightly higher, demonstrating the fact that the V-P pairs formed in the irradiation are a slightly less stable than the V-As pairs. This, together with the initially higher average lifetime, shows that the formation of V₂ is more efficient in P-doped Si. In both the As- and P-doped samples no divacancies are observed (based on the separation of the lifetime components) after the annealing at 600 K. In P-doped Si, the high momentum part of the Doppler-broadened spectrum cannot be used in the identification of the complexes with different numbers of P atoms due to the similarity of the core electron distributions of P and Si (Sect. 46.2.1). On the other hand, the distribution in the valence region (momentum values below 0.5 a.u.) after the 600 K annealing is clearly broader than in the as-irradiated sample. This effect is observed in the case of As doping as well and is reproduced by theory. The broadening indicates the increased presence of positive P ions next to the vacancy causing increased valence electron density, leading to increased electron momentum. The valence region broadens further after 775 K annealing. Hence a similar conversion of V-P to V-P₂ and finally V-P₃ is observed in P-doped Si as for the V-As_n complexes in As-doped Si. However, the dissociations seem to be more dominant in P-doped Si, since only a small fraction of the V-P pairs are finally converted to V-P₃ by annealing. The difference may be related to the lower binding energy of the P-decorated vacancy complex as manifested by the lower annealing temperature of the V-P pairs compared with that of the V-As pairs [46.57].

In addition to particle irradiation, vacancies are formed in thermal equilibrium at relevant concentrations in highly doped Si when the sample temperature exceeds 650 K [46.58,59]. The vacancies are formed directly next to the dopant atoms, which reduces the high formation energy of the isolated vacancy of about 3 eV in highly n-type Si by the Coulomb binding energy and the ionization energy down to about 1 eV [46.58]. The

vacancy-donor pairs diffuse rapidly at these temperatures and finally form complexes with three donor atoms either already at the annealing temperature or during cooling down. These results have been obtained by both isochronal and isothermal annealing experiments, and positron measurements both at room temperature in between the annealings and in situ during the annealings. An interesting feature is that the detection of V-As₃ complexes at high temperatures is difficult due to positrons escaping from them above 500 K, indicating that the binding energy is about 0.25 eV [46.59], significantly lower than that typically observed (at least about 1 eV) for vacancy defects in semiconductors, as for example, in V-P₃.

The vacancy concentrations can be estimated in a straightforward manner when the vacancy-specific and bulk annihilation parameters are known. Equation (46.25) provides the relationship between the trapping rate and the experimental parameters. The vacancy concentration is proportional to the trapping coefficient, and can be obtained, e.g., from the Doppler data as

$$[V] = \frac{N_{\text{at}}}{\mu_V \tau_b} \frac{W - W_B}{W_V - W}, \quad (46.29)$$

where N_{at} is the atomic density. In the following, we have used the positron trapping coefficient $\mu_V = 10^{15} \text{ s}^{-1}$ for the Si vacancies and $\tau_b = 218 \text{ ps}$ for the positron lifetime in defect-free Si.

The concentration of the V-As₃ complexes in Czochralski-grown Si ([As] = 10^{20} cm^{-3}) is only 0.1% of the As concentration [46.43], and the material does not show substantial electrical deactivation. In addition, molecular-beam epitaxy (MBE) can be applied to achieve metastable n-type doping with Sb that becomes compensated only at 10^{21} cm^{-3} [46.60]. In order to illustrate the importance of vacancy defects in the compensation, selected electrical and positron results obtained with a slow positron beam in MBE-grown Si thin layers with [As] > 10^{20} cm^{-3} and [Sb] = 2.7×10^{19} – $3.7 \times 10^{21} \text{ cm}^{-3}$ [46.61, 62] are shown in Table 46.1. Here only the Doppler broadening spectra have been measured and the identification of the vacancy-donor complexes is based on the characteristic data acquired in the experiments on the electron-irradiated samples presented above.

The results show that the as-grown As-doped MBE Si layers are efficiently compensated, but the doping can be activated through rapid thermal annealing (RTA), a routinely used technique in device processing for this purpose. The total vacancy concentrations in these sam-

Table 46.1 Donor concentrations and electrical activities of highly As- and Sb-doped MBE Si samples. The total vacancy concentrations have been determined by combining electrical and positron experiments [46.61, 62]

Donor concentration (cm ⁻³)	Description	Electrical activity (%)	Total [V] (cm ⁻³)
[As] = 1.5 × 10 ²⁰	As-grown (720 K)	20	4 × 10 ¹⁹
[As] = 1.5 × 10 ²⁰	RTA 1170 K	98	1 × 10 ¹⁸
[As] = 3.5 × 10 ²⁰	As-grown (720 K)	2	1 × 10 ²⁰
[As] = 3.5 × 10 ²⁰	RTA 1170 K	85	1.5 × 10 ¹⁹
[Sb] = 2.7 × 10 ¹⁹	As-grown (550 K)	90	≤ 10 ¹⁹
[Sb] = 5.9 × 10 ²⁰	As-grown (550 K)	70	5 × 10 ¹⁹
[Sb] = 9.4 × 10 ²⁰	As-grown (550 K)	70	1.5 × 10 ²⁰
[Sb] = 3.7 × 10 ²¹	As-grown (550 K)	6	9 × 10 ²⁰

ples, which are high enough to be dominant in the compensation, are dramatically reduced in the RTA treatments. The vacancies in question are dominantly the V–As₃ complexes, but also more complicated defect structures such as V₂–As₅ give a nonvanishing contribution [46.61].

The highly Sb-doped MBE Si layers grown at low temperature, where the V–Sb₂ complex is stable [46.57], contain defects such as V–Sb₂ and V₂–Sb₂ instead of V–Sb₃ [46.62]. It is clearly seen from the total vacancy concentrations that they play an important role in the compensation of the Sb-doped layers as well. However, the electrical activity of the as-grown samples is far better than those grown at higher temperatures (and doped with As). This can be explained by the migration processes described above, i.e., the V–Sb₂ do not diffuse and form V–Sb₃ complexes, enabling a larger fraction of the dopants to be isolated and active.

46.3.2 Vacancies as Dominant Compensating Centers in n-Type GaN

Gallium nitride (GaN) is an important wide-band-gap semiconductor for optoelectronic and electronic applications. It can be grown by several methods, each of which have partially different impurity and defect characteristics. The oxygen and silicon impurities dope GaN to an n-type semiconductor. The conductivity of n-type GaN is partly compensated by Ga vacancies [46.46]. It is now possible to perform more exact and quantitative studies of defects in GaN due to the improved quality of the material over the past few years. In particular, GaN grown by hydride vapor-phase epitaxy (HVPE) has low residual impurity (10¹⁶ cm⁻³) and dislocation (< 10⁸ cm⁻²) densities. In such a material, the relation between intentional doping and compensating defects can be systematically studied.

The average positron lifetimes measured in free-standing HVPE GaN samples with different levels of intentional doping with oxygen are shown as a function of measurement temperature in Fig. 46.13 [46.44, 63]. Also data from an earlier study of nominally undoped but contaminated by O (concentration in the 10¹⁷ cm⁻³ range) 40 μm thick HVPE GaN on sapphire is shown for comparison [46.47]. The average lifetime is higher than in the defect-free GaN lattice (τ_B = 160 ps) in all the samples, indicating that positrons are trapped at vacancy defects. The vacancy defect present is related to V_{Ga}, since the decomposition reveals the component

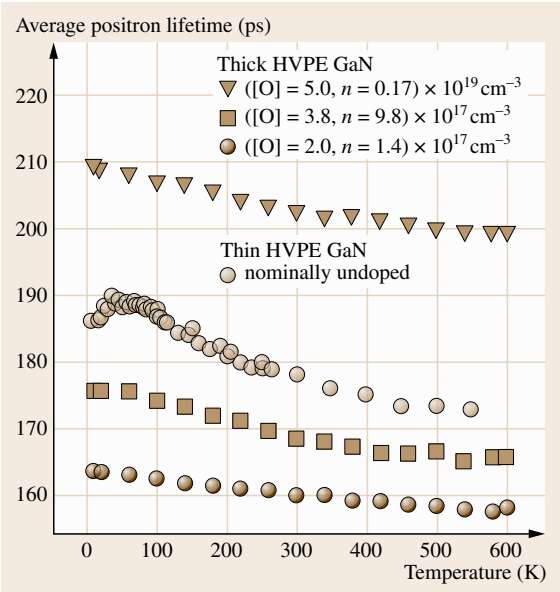


Fig. 46.13 Average positron lifetime as a function of measurement temperature in intentionally oxygen-doped free-standing HVPE GaN samples and one nominally undoped 40 μm thick HVPE GaN/Al₂O₃ sample

$\tau_2 = 235 \pm 5$ ps. There is a clear increasing trend of the average lifetime with the oxygen and free electron densities, indicating that the Ga vacancy concentration follows that of oxygen.

The increase of the average positron lifetime with decreasing temperature shows that the positron trapping rate increases at low temperatures. The temperature dependence of the average positron lifetime is totally reversible and reproducible, indicating that the concentration of Ga vacancies remains constant. Because the Fermi level is close to the conduction band, the charge states of acceptor-like defects such as V_{Ga} do not change with the measurement temperature. Hence, as explained in Sect. 46.1, this effect is a direct indication that the Ga vacancies are in the negative charge state. This is in excellent agreement with the results of theoretical calculations [46.64] that predict a charge state of 3− for the isolated Ga vacancy and 2− for $V_{\text{Ga}}\text{--O}_{\text{N}}$ and $V_{\text{Ga}}\text{--Si}_{\text{Ga}}$ complexes in n-type GaN.

The positron data show further that the defects involving Ga vacancies are the *dominant* negatively charged acceptors in the samples. The enhancement of positron trapping at low temperatures would not be observed if other negative centers competed with V_{Ga} as positron traps. For example, negative ions such as Mg_{Ga}^+ localize positrons at hydrogenic states at low temperatures, strongly decreasing the fraction of positron annihilations at vacancy defects and consequently the average positron lifetime (Sect. 46.2.3). The same behavior could be expected for possible neutral or negative charge states of the N vacancy, where the positron lifetime is very close to that of the GaN lattice.

The Ga vacancy concentrations in the GaN samples can be estimated from the positron results using (46.25). They range from $4 \times 10^{15} \text{ cm}^{-3}$ in the lowest-doped ($[\text{O}] = 2 \times 10^{17} \text{ cm}^{-3}$) to about 10^{17} cm^{-3} in the highest-doped sample ($[\text{O}] = 2 \times 10^{20} \text{ cm}^{-3}$), in correlation with the O concentration. According to electron irradiation studies, the isolated V_{Ga} is mobile already at 600 K [46.65], i. e., at much lower temperatures than applied in the HVPE growth. However, the Ga vacancies bound to defect complexes such as $V_{\text{Ga}}\text{--O}_{\text{N}}$ have a considerably higher thermal stability [46.45,65,66]. In

fact, recent detailed studies of the electron momentum density show that the dominant vacancy defect, responsible for the positron lifetime of 235 ps, is a complex of Ga vacancy and oxygen [46.44].

Unlike in the case of vacancy–donor pairs in highly n-type silicon (see previous section), the Ga vacancies are formed as isolated during growth of n-type GaN. They migrate fast at the high growth temperatures that are typically above 1300 K in the case of bulk or quasibulk crystals, and are stabilized (quenched) by donor impurities during cooling down. This is demonstrated by the fact that the $V_{\text{Ga}}\text{--O}_{\text{N}}$ concentrations are similar in materials grown by HVPE and the high-nitrogen-pressure method when the O concentrations are similar, in spite of the large difference of about 500 K in the growth temperatures [46.45]. In fact, it has been shown that the $V_{\text{Ga}}\text{--O}_{\text{N}}$ pairs are stable up to about 1300 K [46.66]. On the other hand, the concentration of Ga vacancies in Si-doped n-type GaN is significantly lower than in O-doped n-type GaN with similar free electron concentration due to the lower binding energy of the $V_{\text{Ga}}\text{--Si}_{\text{Ga}}$ pair originating from the larger distance between the individual acceptor (Ga vacancy) and donor (substitutional Si) defects [46.67].

The positron results show that Ga vacancies act as dominant compensating centers in n-type GaN. On the other hand, in p-type GaN, where the formation of Ga vacancies is energetically unfavorable due their acceptor nature, the natural question is whether N vacancies could compensate the doping. The detection of vacancy defects on the N sublattice with positrons is not evident due to the small open volume generated by the missing N atom. Nevertheless evidence of the existence N vacancies complexed with Mg ($V_{\text{N}}\text{--Mg}_{\text{Ga}}$) has been obtained with positrons in Mg-doped (p-type) GaN grown by metalorganic chemical vapor deposition (MOCVD) [46.68,69]. It is worth noting that, even though the vacancy concentrations are similar relative to the doping densities (a few percent at most) in both n- and p-type GaN, the vacancies are dominant compensating centers only in n-type GaN, while in p-type GaN other defects and impurities such as hydrogen play the most important role.

46.4 Point Defects and Growth Conditions

Compound semiconductor thin films can be epitaxially grown by several methods such as metalorganic chemical vapor deposition (MOCVD) or molecular-beam

epitaxy (MBE). There are many controllable growth parameters that affect the properties of the overgrown layers, such as the growth rate, stoichiometry, and tem-

perature. In addition, the layer properties may depend on the choice of the substrate material and the orientation of the substrate or the layer. Especially in the case of heteroepitaxy, the layer properties may vary significantly with the distance from the layer/substrate interface. The identities and quantities of both extended and point defects are affected by these parameters. In this section we will also describe how point defects can be studied in thin semiconductor layers by using a variable-energy positron beam.

46.4.1 Growth Stoichiometry: GaN Versus InN

The effect of the growth stoichiometry on the formation of cation vacancies in GaN and InN has been studied by measuring a set of samples grown by MOCVD employing different V/III molar ratios [46.70, 71]. The growth rate as well as the electrical and optical properties of the nitride samples change strongly with the V/III molar ratio [46.72, 73]. All the samples were investigated at room temperature as a function of the positron beam energy E . When positrons are implanted close to the sample surface with $E = 0$ –1 keV, the same S parameter of $S = 0.49$ is recorded in all the GaN and InN samples. These values characterize the defects

and chemical nature of the near-surface region of the samples at the depth 0–5 nm. S parameter data from selected GaN and InN samples are shown as a function of positron implantation energy in Fig. 46.14. In the GaN samples the S parameter is constant at 5–15 keV, indicating that all positrons annihilate in the GaN layer (Fig. 46.14), while in the InN samples the region of constant S is different from sample to sample due to the different thicknesses of the layers. The data recorded at the energies where S is constant can be taken as characteristic of the layer. In the case of GaN, the lowest S parameter is obtained in the Mg-doped reference layer [46.46], while for InN the reference value was obtained from a several microns thick layer grown by MBE [46.74]. The values in these samples correspond to positrons annihilating as delocalized particles in the defect-free lattice.

The S parameters in all the measured layers are larger than in the reference samples, as in Fig. 46.14. The increased S parameter indicates that the positron–electron momentum distribution is narrower than in the defect-free reference sample. The narrowing is due to positrons annihilating at vacancy defects, where the electron density is lower and the probability of annihilation with high-momentum core electrons is reduced compared with that of delocalized positrons in the lattice (Sect. 46.1). The increased S parameter is thus a clear sign of vacancy defects present in the measured layers.

The number of different vacancy defects trapping positrons can be investigated through the linearity between the low- and high-electron-momentum parameters S and W . If only a single type of vacancy is present, the W parameter depends linearly on the S parameter when the fraction of positron annihilations at vacancies η_V varies. The plot of the W parameter versus S parameter thus forms a line between the endpoints (S_B , W_B) and (S_V , W_V) corresponding to the defect-free lattice and the total positron trapping at vacancies, respectively. The S and W parameters of all the GaN and InN samples are plotted in Fig. 46.15. All the data points measured in GaN fall on the line connecting the parameters obtained in the Mg-doped GaN reference sample and those determined in earlier studies for the native Ga vacancy [46.46]. Hence Ga vacancies are found in all the GaN samples. Similarly the data points measured in the InN samples fall on the line connecting the parameters of the defect-free InN lattice and those of the In vacancy, also determined in an earlier study [46.74], indicating the presence of In vacancies in these samples. In GaN, the positron trapping fraction η_V and the

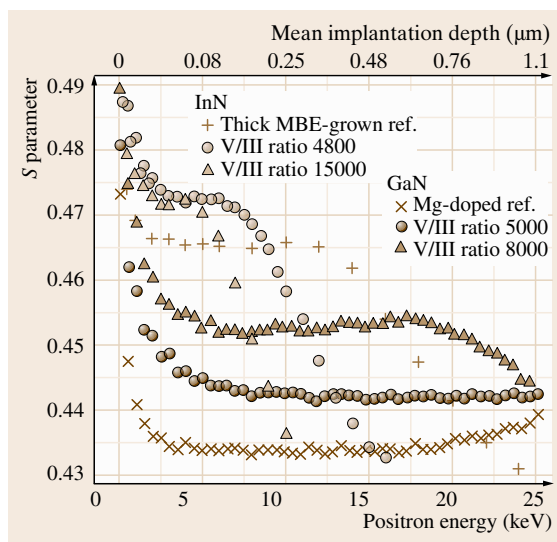


Fig. 46.14 The low-electron-momentum parameter S as a function of the positron implantation energy in three GaN and three InN samples. The *top axis* shows the mean stopping depth corresponding to the positron implantation energy

S parameter vary from one sample to another due to the different vacancy concentrations, while in InN the data indicates that the In vacancy concentrations are similar in all the samples. It is worth noticing that the data recorded in the InN samples are shifted with respect to that measured in the GaN samples by the differences in the parameter levels in the two materials: the S parameter is higher and W lower in defect-free InN than in defect-free GaN due to the differences in the electronic structures.

The presence of Ga vacancies is expected in n-type undoped GaN due to their low formation energy. The different levels of the S parameter in Figs. 46.14 and 46.15 indicate that the concentration of the Ga vacancies depends on the stoichiometry of growth. On the other hand, in InN the data are similar for all the samples with different V/III ratios, indicating that the In vacancy concentration is independent of the growth stoichiometry.

In order to quantify the concentration of V_{Ga} and V_{In} the S parameter data was analyzed with the positron trapping model. When the cation vacancies are the only defects trapping positrons, their concentration can be determined with the simple formula (46.25)

$$[V_{\text{Ga/In}}] = \frac{N_{\text{at}}}{\mu_V \tau_b} \frac{S - S_B}{S_V - S} \quad (46.30)$$

where $\tau_b = 160$ ps (185 ps) is the positron lifetime in the GaN (InN) lattice [46.46, 74], $\mu_V = 3 \times 10^{15} \text{ s}^{-1}$ is the positron trapping coefficient [46.8], and $N_{\text{at}} = 8.775 \times 10^{22} \text{ cm}^{-3}$ ($6.367 \times 10^{22} \text{ cm}^{-3}$) is the atomic density of GaN (InN). For the S parameter at the Ga and In vacancies we take $S_V/S_B = 1.050$ [46.46, 70, 71, 74].

The results in Fig. 46.16 indicate that the concentration of Ga vacancies in GaN is proportional to the stoichiometry of the growth conditions. Rather low $[V_{\text{Ga}}] \approx 10^{16} \text{ cm}^{-3}$ is observed for the sample with the V/III molar ratio of 1000. When the V/III molar ratio becomes 10 000, the V_{Ga} concentration increases by almost three orders of magnitude to $[V_{\text{Ga}}] \approx 10^{19} \text{ cm}^{-3}$. This behavior shows that empty Ga lattice sites are likely formed in the strongly N-rich environment. In contrast, the concentration of In vacancies in InN remains constant at the level of $[V_{\text{In}}] \approx 10^{17} \text{ cm}^{-3}$ over the whole range of V/III molar ratios from about 3000 to 24 000. The In vacancy concentration in these samples is on the same level as in samples of similar thickness grown by MBE where the growth conditions are much closer to being stoichiometric, suggesting that the In vacancy formation is dominated by thickness-dependent properties such as strain or dislocation

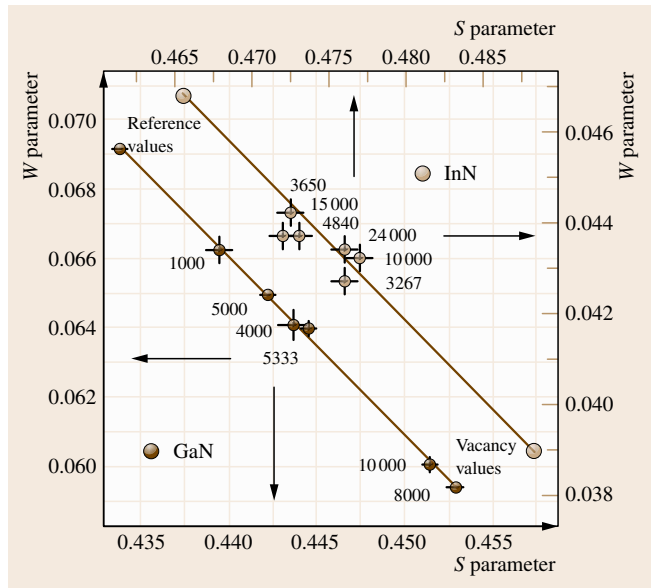


Fig. 46.15 The low- and high-momentum parameters S and W in various GaN and InN samples. The V/III molar ratio of each sample is indicated in the figure. The straight line indicates that the same vacancy defect (group III vacancy) is observed in all samples. Note the different scales on the left/right and top/bottom axes

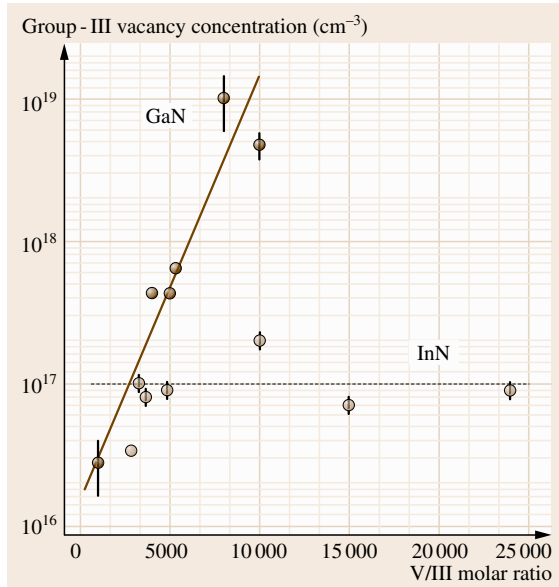


Fig. 46.16 The concentrations of Ga and In vacancies versus the V/III molar ratio in GaN and InN samples grown by MOCVD. The straight lines are drawn to emphasize the correlations [46.70, 71]

density. In fact, in MBE-grown InN, the In vacancy concentration drops by several orders of magnitude when the layer thickness increases from a few hundred nanometers to a few microns [46.74].

The difference in the behavior of the cation vacancies in GaN and InN as a function of the V/III molar ratio can be explained by the differences in the calculated vacancy formation energies and the temperatures of the MOCVD growth. In n-type material the calculated formation energy of the Ga vacancy is about 1.3 eV, while it is about 2.6 eV in InN [46.64, 75]. On the other hand, the growth temperature of the GaN samples was around 1000 °C, but only 550 °C in the case of InN samples [46.70, 71]. As the concentrations of the Ga and In vacancies are similar in the samples with low V/III ratios, the formation of the In vacancies must be dictated by other effects, such as strain or presence of dislocation, than the thermal formation (and subsequent stabilization by, e.g., impurities) of an isolated In vacancy in an otherwise perfect lattice. On the other hand, the observed Ga vacancy concentrations are of the same order of magnitude that could be expected from the growth temperature and the calculated formation energy, given that the vacancies (which are mobile already at relatively low temperatures) are stabilized by, e.g., O impurities close to the growth temperature. Hence it is understandable that the stoichiometric conditions affect the final Ga vacancy concentration in GaN more than the In vacancy concentration does in InN.

46.4.2 GaN: Effects of Growth Polarity

The wurtzite structure of GaN introduces effects related to the growth polarity of the layer. In the following, studies of both polar (Ga or N polarity) and nonpolar layers are reviewed [46.45, 47, 76]. The positron lifetime was measured in GaN layers grown by hydride vapor-phase epitaxy (HVPE) on dislocation-free high-pressure (HNP) bulk GaN crystals to thicknesses 30–160 μm [46.45]. Four of the layers were grown on the Ga face and one layer on the N face of the HNP GaN substrate. One of the Ga polar layers (30 μm) was grown in the same run with the N polar layer. Apart from the thickness, the properties of the Ga polar layers were similar to each other.

The average positron lifetimes measured as a function of temperature in the HVPE and HNP GaN samples are shown in Fig. 46.11. As shown in the figure, a second lifetime component of $\tau_2 = 235 \pm 10$ ps could be separated in the lifetime spectra, indicating that positrons annihilate as trapped at Ga vacancy related

defects when the average positron lifetime is above the bulk lifetime of 160 ps. On the other hand the decrease of the average positron lifetime with decreasing temperature in the samples (HNP GaN and N-polar HVPE GaN), where τ_{ave} is above τ_B , is a clear indication of the presence of negative ion defects trapping positrons at low temperature to hydrogenic states, where the positron lifetime is equal to τ_B .

Interestingly, the Ga vacancy concentrations ($7 \times 10^{17} \text{ cm}^{-3}$) coincide in the N-polar HVPE GaN and the N side of the HNP GaN samples, similarly as the impurity concentrations obtained from secondary-ion mass spectrometry (SIMS) experiments. On the other hand, the difference between the Ga-polar HVPE GaN ($[\text{V}_{\text{Ga}}] < 10^{16} \text{ cm}^{-3}$) and the Ga side of the HNP GaN bulk crystal ($[\text{V}_{\text{Ga}}] = 2 \times 10^{17} \text{ cm}^{-3}$) is significant. These observations support the idea proposed earlier [46.77], namely that the oxygen incorporation (and subsequent Ga vacancy formation) is stronger in the nonpolar directions, in which the N-polar growth mainly proceeds. The difference between the polarities is larger in the HVPE GaN samples than in the HNP bulk GaN crystals. This can be explained by the lower temperature and pressure in HVPE growth, which reduce the oxygen diffusion, and by the presence of more oxygen in the high-pressure growth.

In order to further study the role of growth polarity on the defect incorporation in GaN, *a*-plane GaN layers (thicknesses 1–25 μm) grown on sapphire were measured with a variable-energy positron beam [46.76]. The *S* parameter measured in these layers is shown as a function of positron implantation energy in Fig. 46.17. Ga vacancies complexed with oxygen were identified in the layers, and their concentrations are shown as a function of distance from the interface in Fig. 46.18. For comparison, also the data from the *c*-plane GaN [46.47] are reproduced here. The difference between the polar and nonpolar HVPE GaN layers is clear: the Ga vacancy concentration is constant in the *a*-plane HVPE GaN, whereas it decreases with increasing distance in *c*-plane HVPE GaN. SIMS results show that the O concentration is also constant in the HVPE GaN layers, as is the density of extended defects (observed with cross-sectional transmission electron microscopy).

These results give further support for the model based on growth-surface-dependent oxygen incorporation and subsequent Ga vacancy formation. In *c*-plane heteroepitaxial Ga-polar HVPE GaN, the O concentration profile is determined by the dislocation profile likely due to diffusion from the sapphire substrate. On the other hand, in homoepitaxial *c*-plane Ga-polar

HVPE GaN, in which the dislocation density is low and the amount of oxygen in the substrate is significantly lower, no vacancies are observed even in the thinnest layers, while in N-polar GaN both the Ga vacancy and O concentrations are high. Hence, as the growth modes are similar in the N-polar and nonpolar GaN, it is natural that the O incorporation from the growth ambient is effective in both, giving rise to a high O concentration and subsequent Ga vacancy concentration, independently of possible extended defects.

46.4.3 Bulk Growth of ZnO

Bulk ZnO crystals can be grown by various methods. In the following, we will compare the positron results [46.21] obtained in ZnO grown by the seeded vapor-phase (VP) [46.78], skull-melt [46.79], hydrothermal (HT) [46.80], and conventional and contactless chemical vapor transport techniques (CVT and CCVT) [46.81, 82]. The VP, skull-melt, CVT, and CCVT materials are all characterized by low (below 10^{17} cm^{-3}) impurity concentrations. In HT ZnO the concentration of the most abundant impurity, lithium, is in the 10^{18} cm^{-3} range in these samples. This is a general property of hydrothermally grown ZnO. All the studied samples were nominally undoped. ZnO grown by the HT method had high resistivity, likely due to Li, while the other materials were all slightly n-type due to residual impurities and/or intrinsic defects.

The average positron lifetimes measured as a function of temperature in all the different bulk ZnO crystals are collected in Fig. 46.19. As seen in the figure, the samples can be roughly divided into two groups, where in one the average lifetime τ_{ave} is very close to the bulk lifetime of $\tau_B = 170 \text{ ps}$ and in the other it is clearly above τ_B , in the 175–185 ps range. The ZnO crystals grown by the VP and skull-melt methods belong to the former and the crystals grown by the HT, CVT, and CCVT methods belong to the latter. As shown in the figure, a second lifetime component of $\tau_2 = 230 \pm 10 \text{ ps}$ (the same in all the samples) could be separated in the lifetime spectra, indicating that positrons annihilate as trapped at Zn vacancy related defects when the average positron lifetime is well above the bulk lifetime of 170 ps.

The ZnO crystals grown by the VP technique were obtained from Eagle-Picher (EP) and ZN-Technologies (ZNT), and the crystals grown by the skull-melt technique from Cermet. As explained in Sect. 46.2.2, the EP material contains Zn vacancies in the double-negative charge state, evident from the separation of

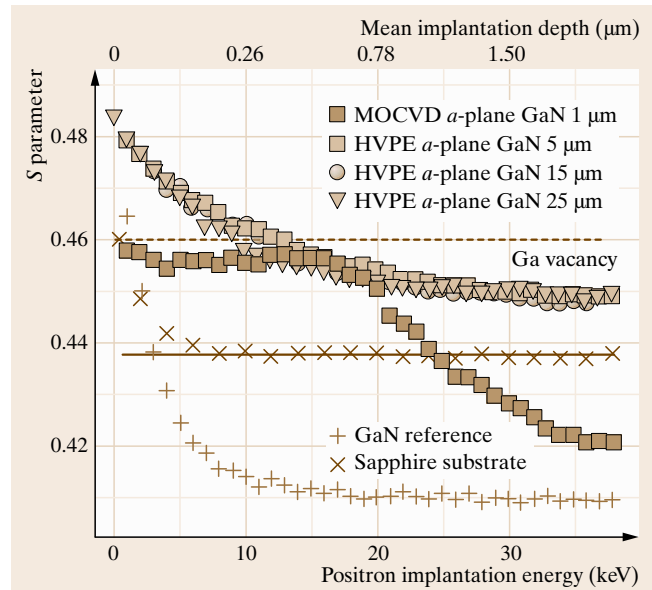


Fig. 46.17 The S parameter in the a -plane GaN layers as a function of positron implantation energy. The solid and dashed lines show the S parameter in the GaN lattice and at a Ga vacancy, respectively. Also the S parameters measured in the GaN reference and in the sapphire substrate are shown [46.21]

the lifetime components and the increase of the average lifetime with decreasing temperature. The average

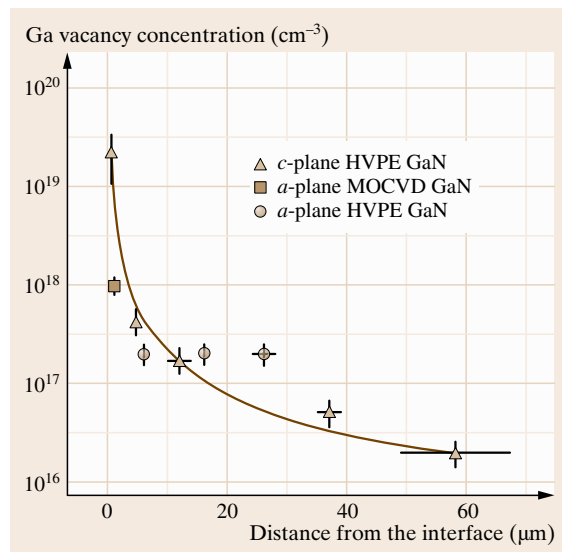


Fig. 46.18 Estimated Ga vacancy concentrations as a function of the distance from the sapphire interface [46.21, 47]

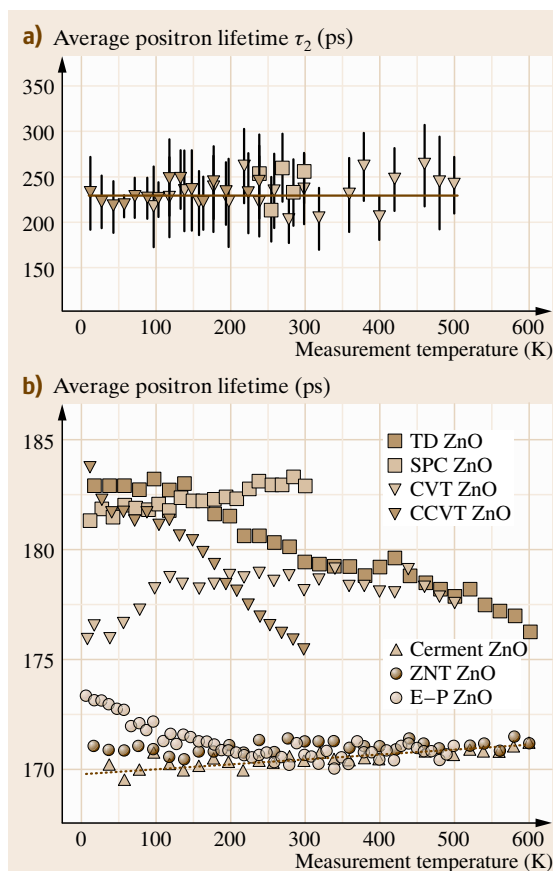


Fig. 46.19a,b The average positron lifetime (a) and the higher lifetime components separated from the annihilation spectra (b) as a function of measurement temperature in all the measured ZnO samples

lifetime of 173 ps at 20 K corresponds to a concentration of $[V_{\text{Zn}}] = 2 \times 10^{15} \text{ cm}^{-3}$. The positron lifetime representative of the pure ZnO lattice was fitted to the data obtained above 300 K, and is shown as the dotted line in Fig. 46.19. The slight increase with increasing temperature is due to the thermal expansion of the lattice. The ZNT ZnO is nominally identical to EP ZnO, and the average positron lifetimes in these two materials coincide above 300 K, but at lower temperatures the average lifetime is lower in the ZNT ZnO (about 171 ps at 20 K compared with 173 ps in EP ZnO), but still slightly above the fitted ZnO lattice lifetime. This indicates that a very small but measurable fraction of positrons annihilates at vacancy defects (concentration lower than in EP ZnO, about 10^{15} cm^{-3}), which are presumably Zn vacancies. However, the fraction is too

small for the lifetimes to be separable from the lifetime spectrum and hence the defects cannot be conclusively identified. Interestingly, the average positron lifetime measured in Cermet ZnO coincides with the lifetime of the ZnO lattice estimated from the EP ZnO data over the whole temperature range of the measurements, and no higher components could be separated from the lifetime spectra at any temperature. This indicates that the concentration of vacancy defects in this material is below the detection limit of positron annihilation spectroscopy, i. e., well below 10^{15} cm^{-3} .

The ZnO crystals grown by the HT method were obtained from Tokyo Denpa (TD) and the Scientific Production Company (SPC). The average positron lifetime is of similar magnitude (180–185 ps) in the TD and SPC ZnO crystals, about 10–15 ps above the lattice ZnO lifetime measured in the EP ZnO, in excellent agreement with earlier reports of positron lifetimes in ZnO crystals grown by the hydrothermal method [46.83, 84]. The main difference between the TD and SPC ZnO crystals is in the behavior of the average positron lifetime with measurement temperature: the average positron lifetime decreases with increasing temperature in TD ZnO, while it increases slightly in SPC ZnO. This indicates that positrons are trapped at negatively charged vacancy defects in TD ZnO, while the data in SPC ZnO suggest that the vacancy defects are neutral and that positrons are also trapped at negatively charged non-open volume defects (negative ions). The negatively charged vacancy defects in TD ZnO are likely to be Zn vacancies.

An average lifetime higher than that in the defect-free ZnO lattice indicates that a fraction of the annihilating positrons must be trapped at vacancy defects. An average lifetime value 10–15 ps different than that in the bulk is typically enough for the separation of lifetimes, as in, e.g., the case of electron-irradiated EP ZnO (Sect. 46.2.2). However, in these hydrothermal samples the separation was possible only in SPC ZnO at 250–300 K, indicating that Zn vacancies are present in the SPC ZnO as well. The problems in the separation of the lifetime components suggest that there is a relatively high intensity of some additional lifetime between the bulk and Zn vacancy lifetimes in the lifetime spectrum. Larger vacancy defects with higher lifetimes than those of the Zn vacancy are not present, as there would then be no problems in the separation. A natural cause for these problems would be the presence of a relatively high concentration of neutral O vacancies (whose specific positron lifetime is $\tau_{\text{VO}} = 195 \pm 15 \text{ ps}$). In order to create such problems in the separation of the lifetimes, the

concentration of these O vacancy related defects needs to be in the $[V_O] \cong 10^{17} \text{ cm}^{-3}$ range. On the other hand, the concentrations of the Zn-vacancy-related defects causing the increase of the average positron lifetime with decreasing temperature in TD ZnO and evident from the separation of the lifetime components in SPC ZnO must be in the low 10^{16} cm^{-3} range.

The ZnO samples grown by the CVT and CCVT methods were grown at the Institute of Physics of the Polish Academy of Sciences. The average lifetime is above the bulk lifetime $\tau_B = 170 \text{ ps}$ in both the CVT- and CCVT-grown samples throughout the whole temperature range, indicating the trapping of positrons at vacancy defects. The lifetime spectra measured in both materials could be separated into two components, of which the higher was the V_{Zn} -related lifetime $\tau_2 = 230 \pm 10 \text{ ps}$, as shown in Fig. 46.19. The increase of the average lifetime with decreasing temperature in CCVT ZnO is a clear indication that the Zn vacancies are in the negative charge state. On the other hand, the independence from temperature of the average positron lifetime in CVT-grown ZnO in the range 100–500 K indicates that the observed vacancies are in the neutral charge state. The decrease in the average lifetime below 100 K in the CVT ZnO sample and the flat region at 50–100 K in the CCVT ZnO sample are interpreted as positrons trapping at negative-ion-type defects, which have no open volume and hence produce the annihilation characteristics of the bulk lattice. This is observed only at low temperatures, since the negative-ion-type defects act as shallow traps for positrons, and the escape rate at elevated temperatures is faster than the annihilation rate. The effect of the negative-ion-type defects is small in the CCVT ZnO sample, and hence the Zn vacancies are the dominant negatively charged (acceptor-type) defect. The concentration of the negative Zn vacancies (or related complexes) in CCVT ZnO can be estimated as $[V_{\text{Zn}}] \cong 1.5 \times 10^{16} \text{ cm}^{-3}$. The concentration of the negative-ion-type defects can be estimated to be roughly one order of magnitude lower.

The first lifetime component τ_1 (not shown) is well below the bulk lifetime τ_B in CCVT-grown ZnO, indicating that the one-defect trapping model works. However, in CVT-grown ZnO the first lifetime component coincides with τ_B , indicating the mixing of the bulk component with a defect-specific component with a lifetime close to (but higher than) the bulk lifetime [46.85]. This can be interpreted as positrons trapping at O vacancies. The concentrations of the neutral Zn-vacancy-related complexes in CVT-grown ZnO

can be estimated as $[V_{\text{Zn}}] \cong 2 \times 10^{16} \text{ cm}^{-3}$, and the negative ion concentration can be estimated to be of the same order of magnitude. The concentration of the O vacancies in CVT-grown ZnO can be estimated with trapping rate analysis as $[V_O] \cong 10^{17} \text{ cm}^{-3}$ [46.35, 85].

Interestingly, the Zn vacancy concentrations in the bulk ZnO crystals grown by the chemical vapor transport and hydrothermal methods are very similar, in spite of the growth environment being Zn-rich in the former and O-rich in the latter. Further, the presence of a rather high concentration of O-vacancy-related defects in the ZnO crystals grown by the hydrothermal method is surprising, and is likely to be connected to the high Li concentration in the material. In fact, the possibility that the defects interpreted as O vacancies could instead be some complicated complexes of Zn vacancies with Li and/or H (another light element that is quite abundant in ZnO) cannot be completely ruled out. On the other hand, the O-rich skull-melt and Zn-rich seeded vapor transport methods also produce ZnO crystals that are very much alike from the vacancy point of view. Hence it seems that, in the case of the bulk growth techniques, the formation of the vacancy defects is not greatly affected by the stoichiometry or the partial pressures of the growth environment, but rather by the residual impurities and other intrinsic defects.

An important observation to be made from Fig. 46.19 is that the higher lifetime component separated from the measured lifetime spectra (where it could be performed) is the same in all the samples over the whole measurement temperature range, i.e., $\tau_2 \cong 230 \text{ ps}$. It also coincides with that obtained in electron-irradiated material, hence demonstrating that the Zn vacancies are important defects in ZnO and supporting the determination of their lifetime value. In as-grown ZnO, it is very likely that the Zn vacancies are complexed with either residual impurities or other intrinsic defects, as the irradiation-induced (likely isolated) vacancies have been shown to anneal out from the material already at rather low temperatures of about 500–600 K [46.35]. This applies to the O vacancies as well.

The results obtained for the EP ZnO and CCVT ZnO show that the Zn vacancies act as dominant acceptors in n-type ZnO, similarly to the Ga vacancies in n-type GaN (see Sect. 46.3.2). The situation is more complicated in the ZnO crystals grown by the other techniques due to either too low a concentration of vacancies in general, or too high a concentration of other types of vacancies, such as O vacancies. The Zn vacancies are most likely complexed with donor-type defects, and as they survive

the cooling down from the high growth temperatures of about 1000 °C, the stabilizing donors are likely to be located on the O sublattice. In the case of cation vacancies complexed with cation-sublattice-substitutional donor defects, the binding energy is prone to be too low for the vacancies to be effectively stabilized, as in the case of Si donors in GaN [46.67]. As the total open volume of the in-grown Zn vacancies is the same as that of the irradiated Zn vacancies, it is likely that these donor defects are residual impurities, the concentrations

of which are of the same order of magnitude as that of the Zn vacancies. On the other hand, the possibility of the Zn vacancies being bound to O vacancies as $V_{\text{Zn}}-V_{\text{O}}$ complexes cannot be completely ruled out, as the latter are very difficult to distinguish from the isolated Zn vacancies with positrons. It is important, however, to understand that the O vacancies possibly observed in the hydrothermal- and CVT-grown bulk ZnO crystals are not complexed with the Zn vacancies, as the positrons are sensitive to the total open volume of the defect.

46.5 Summary

Positron annihilation spectroscopy gives microscopic information about vacancy defects in the concentration range 10^{15} – 10^{19} cm⁻³. The positron lifetime is the fingerprint of the open volume associated with a defect. It is used to identify mono- and divacancies and larger vacancy clusters. The Doppler broadening of the annihilation radiation measures the momentum distribution of the annihilating electrons. It can be used to identify the nature of the atoms surrounding the vacancy. Consequently, vacancies on different sublattices of a compound semiconductor can be distinguished, and impurities associated with the vacancies can be identified. The charge state of a vacancy defect is determined by the temperature dependence of the positron trapping coefficient. Positron localization into Rydberg states around negative centers yields information about ionic acceptors that have no open volume.

Positron methods can be applied to study vacancies in both bulk crystals and epitaxial layers. The mea-

surements in bulk crystals are straightforward, as (fast) positrons obtained directly from the radioactive source can be used. The studies of epitaxial layers and near-surface regions of bulk crystals require slow positrons. Typically in these cases a monoenergetic positron beam is used, the energy tuning of which allows for depth profiling of the samples in the range from a few nanometers to several microns.

Applications of the technique to Si, GaN, and ZnO have been presented. The Si vacancies complexed with donor impurities have been identified in highly n-type Si and their role as electrically compensating centers has been discussed. Ga vacancies complexed with oxygen are observed as native defects in n-type GaN, while N vacancies complexed with magnesium are detected in p-type GaN. The effects of growth conditions on the formation of group III vacancies have been discussed for GaN and InN. In ZnO, vacancies on both sublattices have been identified and their presence in bulk ZnO crystals grown by various methods is discussed.

References

- 46.1 R.N. West: Positron studies of condensed matter, *Adv. Phys.* **22**, 263–383 (1973)
- 46.2 P.J. Schultz, K.G. Lynn: Interaction of positron beams with surfaces, thin films, and interfaces, *Rev. Mod. Phys.* **60**, 701–780 (1988)
- 46.3 M.J. Puska, R.M. Nieminen: Theory of positrons in solids and on solid surfaces, *Rev. Mod. Phys.* **66**, 841–897 (1994)
- 46.4 P. Asoka-Kumas, K.G. Lynn, D.O. Welch: Characterization of defects in Si and SiO₂-Si using positrons, *J. Appl. Phys.* **76**, 4935–4982 (1994)
- 46.5 P. Hautojärvi (Ed.): *Positrons in Solids*, Topics in Current Physics, Vol. 12 (Springer, Berlin Heidelberg 1979)
- 46.6 W. Brandt, A. Dupasquier (Eds.): *Positron Solid-State Physics* (North-Holland, Amsterdam 1983)
- 46.7 A. Dupasquier, A.P. Mills Jr. (Eds.): *Positron spectroscopy of solids*, Proc. Int. School Phys. Enrico Fermi, CXXV Course (IOS Press, Amsterdam 1995)
- 46.8 K. Saarinen, P. Hautojärvi, C. Corbel: Positron Annihilation Spectroscopy of Defects in Semiconductors. In: *Identification of Defects in Semiconductors*, Semiconductors and Semimetals, Vol. 51A, ed. by M. Stavola (Academic, New York 1998) pp. 209–285
- 46.9 R. Krause-Rehberg, H.S. Leipner: *Positron Annihilation in Semiconductors* (Springer, Berlin Heidelberg 1999)

- 46.10 K. Saarinen: Characterization of native point defects in GaN by positron annihilation spectroscopy. In: *III–V Nitride Semiconductors: Electrical, Structural and Defects Properties*, ed. by M.O. Manasreh (Elsevier, Amsterdam 2000) pp.109–163
- 46.11 S. Valkealahti, R.M. Nieminen: Monte Carlo calculations of keV electron and positron slowing down in solids. II, *Appl. Phys. A* **35**, 51–59 (1984)
- 46.12 R.M. Nieminen, J. Oliva: Theory of positronium formation and positron emission at metal surfaces, *Phys. Rev. B* **22**, 2226–2247 (1980)
- 46.13 K.O. Jensen, A.B. Walker: Positron thermalization and non-thermal trapping in metals, *J. Phys.: Condens. Matter* **2**, 9757–9776 (1990)
- 46.14 J. Mäkinen, C. Corbel, P. Hautojärvi, D. Mathiot: Measurement of positron mobility in Si at 30–300 K, *Phys. Rev. B* **43**, 12114–12117 (1991)
- 46.15 E. Soininen, J. Mäkinen, D. Beyer, P. Hautojärvi: High-temperature positron diffusion in Si, GaAs, and Ge, *Phys. Rev. B* **46**, 13104–13118 (1992)
- 46.16 Y.Y. Shan, P. Asoka-Kumar, K.G. Lynn, S. Fung, C.D. Beling: Field effect on positron diffusion in semi-insulating GaAs, *Phys. Rev. B* **54**, 1982–1986 (1996)
- 46.17 I. Makkonen, M. Hakala, J. Puska: Modeling the momentum distributions of annihilating electron-positron pairs in solids, *Phys. Rev. B* **73**, 035103:1–12 (2006)
- 46.18 M. Alatalo, B. Barbiellini, M. Hakala, H. Kauppinen, T. Korhonen, M.J. Puska, K. Saarinen, P. Hautojärvi, R.M. Nieminen: Theoretical and experimental study of positron annihilation with core electrons in solids, *Phys. Rev. B* **54**, 2397–2409 (1996)
- 46.19 G. Brauer, W. Anwand, W. Skorupa, J. Kuriplach, O. Melikhova, C. Moisson, H. von Weckstern, H. Schmidt, M. Lorenz, M. Grundmann: Defects in virgin and N^+ -implanted ZnO single crystals studied by positron annihilation, Hall effect, and deep-level transient spectroscopy, *Phys. Rev. B* **74**, 045208:1–10 (2006)
- 46.20 F. Tuomisto, V. Ranki, K. Saarinen, D.C. Look: Evidence of the Zn vacancy acting as a dominant acceptor in n -type ZnO, *Phys. Rev. Lett.* **91**, 205502–1–205502–4 (2003)
- 46.21 F. Tuomisto, D.C. Look: Vacancy defect distributions in bulk ZnO crystals, *Proc. SPIE* **6474**, 647413–1–647413–11 (2007)
- 46.22 I. Makkonen, M.J. Puska: Energetics of positron states trapped at vacancies in solids, *Phys. Rev. B* **76**, 054119–1–054119–10 (2007)
- 46.23 K. Saarinen, P. Hautojärvi, A. Vehanen, R. Krause, G. Dlubek: Shallow positron traps in GaAs, *Phys. Rev. B* **39**, 5287–5296 (1989)
- 46.24 C. Corbel, F. Pierre, K. Saarinen, P. Hautojärvi, P. Moser: Gallium vacancies and gallium antisites as acceptors in electron-irradiated semi-insulating GaAs, *Phys. Rev. B* **45**, 3386–3399 (1992)
- 46.25 M.J. Puska, C. Corbel, R.M. Nieminen: Positron trapping in semiconductors, *Phys. Rev. B* **41**, 9980–9993 (1990)
- 46.26 J. Mäkinen, C. Corbel, P. Hautojärvi, P. Moser, F. Pierre: Positron trapping at vacancies in electron-irradiated Si at low temperatures, *Phys. Rev. B* **39**, 10162–10173 (1989)
- 46.27 J. Mäkinen, P. Hautojärvi, C. Corbel: Positron annihilation and the charge states of the phosphorus-vacancy pair in silicon, *J. Phys.: Condens. Matter* **4**, 5137–5155 (1992)
- 46.28 K. Saarinen, S. Kuisma, J. Mäkinen, P. Hautojärvi, M. Törnqvist, C. Corbel: Introduction of metastable vacancy defects in electron-irradiated semi-insulating GaAs, *Phys. Rev. B* **51**, 14152–14163 (1995)
- 46.29 D. Schödlbauer, P. Sperr, G. Kögel, W. Triftshäuser: A pulsing system for low energy positrons, *Nucl. Instrum. Methods Phys. Res. B* **34**, 258–268 (1988)
- 46.30 R. Suzuki, Y. Kobayashi, T. Mikado, H. Ohgaki, M. Chiwaki, T. Yamazaki, T. Tomimatsu: Slow positron pulsing system for variable energy positron lifetime spectroscopy, *Jpn. J. Appl. Phys.* **30**, L532–L534 (1991)
- 46.31 K. Ryttsilä, J. Nissilä, K. Kokkonen, A. Laakso, R. Aavikko, K. Saarinen: Digital measurement of positron lifetime, *Appl. Surf. Sci.* **194**, 260–263 (2002)
- 46.32 H. Saito, Y. Nagashima, T. Kurihara, T. Hyodo: A new positron lifetime spectrometer using a fast digital oscilloscope and BaF_2 scintillators, *Nucl. Instrum. Methods Phys. Res. A* **487**, 612–617 (2002)
- 46.33 J. Nissilä, K. Ryttsilä, R. Aavikko, A. Laakso, K. Saarinen, P. Hautojärvi: Performance analysis of a digital positron lifetime spectrometer, *Nucl. Instrum. Methods Phys. Res. A* **538**, 778–789 (2005)
- 46.34 F. Bečvář, J. Čížek, I. Prochazka, J. Janotova: The asset of ultra-fast digitizers for positron-lifetime spectroscopy, *Nucl. Instrum. Methods Phys. Res. A* **539**, 372–385 (2005)
- 46.35 F. Tuomisto, K. Saarinen, D.C. Look, G.C. Farlow: Introduction and recovery of point defects in electron-irradiated ZnO, *Phys. Rev. B* **72**, 085206:1–11 (2005)
- 46.36 M. Alatalo, H. Kauppinen, K. Saarinen, M.J. Puska, J. Mäkinen, P. Hautojärvi, R.M. Nieminen: Identification of vacancy defects in compound semiconductors by core-electron annihilation: Application to InP, *Phys. Rev. B* **51**, 4176–4185 (1995)
- 46.37 P. Asoka-Kumar, M. Alatalo, V.J. Ghosh, A.C. Kruseman, B. Nielsen, K.G. Lynn: Increased Elemental Specificity of Positron Annihilation Spectra, *Phys. Rev. Lett.* **77**, 2097–2100 (1996)
- 46.38 K. Saarinen, V. Ranki: Identification of vacancy complexes in Si by positron annihilation, *J. Phys.: Condens. Matter* **15**, S2791–S2801 (2003)
- 46.39 G.D. Watkins: The Lattice Vacancy in Silicon. In: *Deep Centers in Semiconductors*, ed. by S.T. Pan-

- telides (Gordon and Breach, New York 1986) pp.177–214
- 46.40 H. Kauppinen, C. Corbel, J. Nissilä, K. Saarinen, P. Hautojärvi: Photoionization of the silicon divacancy studied by positron-annihilation spectroscopy, *Phys. Rev. B* **57**, 12911–12922 (1998)
- 46.41 R. Aavikko, K. Saarinen, F. Tuomisto, B. Magnusson, N.T. Son, E. Jánzén: Clustering of vacancy defects in high-purity semi-insulating SiC, *Phys. Rev. B* **75**, 085208:1–8 (2007)
- 46.42 M. Hakala, M.J. Puska, R.M. Nieminen: Momentum distributions of electron-positron pairs annihilating at vacancy clusters in Si, *Phys. Rev. B* **57**, 7621–7627 (1998)
- 46.43 K. Saarinen, J. Nissilä, H. Kauppinen, M. Hakala, M.J. Puska, P. Hautojärvi, C. Corbel: Identification of Vacancy–Impurity Complexes in Highly n-Type Si, *Phys. Rev. Lett.* **82**, 1883–1886 (1999)
- 46.44 S. Hautakangas, I. Makkonen, V. Ranki, M.J. Puska, K. Saarinen, X. Xu, D.C. Look: Direct evidence of impurity decoration of Ga vacancies in GaN from positron annihilation spectroscopy, *Phys. Rev. B* **73**, 193301:1–4 (2006)
- 46.45 F. Tuomisto, K. Saarinen, B. Lucznik, I. Grzegory, H. Teisseyre, T. Suski, S. Porowski, P.R. Hageman, J. Likonen: Effect of growth polarity on vacancy defect and impurity incorporation in dislocation-free GaN, *Appl. Phys. Lett.* **86**, 031915:1–3 (2005)
- 46.46 K. Saarinen, T. Laine, S. Kuisma, J. Nissilä, P. Hautojärvi, L. Dobrzynski, J.M. Baranowski, K. Pakula, R. Stępniewski, M. Wojdak, A. Wyszomolek, T. Suski, M. Leszczynski, I. Grzegory, S. Porowski: Observation of native Ga vacancies in GaN by positron annihilation, *Phys. Rev. Lett.* **79**, 3030–3033 (1997)
- 46.47 J. Oila, J. Kivioja, V. Ranki, K. Saarinen, D.C. Look, R.J. Molnar, S.S. Park, S.K. Lee, J.Y. Han: Ga vacancies as dominant intrinsic acceptors in GaN grown by hydride vapor phase epitaxy, *Appl. Phys. Lett.* **82**, 3433–3435 (2003)
- 46.48 D.C. Look, D.C. Reynolds, J.W. Hemsky, J.R. Sizelove, R.L. Jones, R.J. Molnar: Defect donor and acceptor in GaN, *Phys. Rev. Lett.* **79**, 2273–2276 (1997)
- 46.49 V. Ranki, J. Nissilä, K. Saarinen: Formation of vacancy–impurity complexes by kinetic processes in highly As-doped Si, *Phys. Rev. Lett.* **88**, 105506:1–4 (2002)
- 46.50 A. Lietoila, J.F. Gibbons, T.W. Sigmon: The solid solubility and thermal behavior of metastable concentrations of As in Si, *Appl. Phys. Lett.* **36**, 765–768 (1980)
- 46.51 P.M. Fahey, P. Griffin, J.D. Plummer: Point defects and dopant diffusion in silicon, *Rev. Mod. Phys.* **61**, 289–384 (1989)
- 46.52 A. Nylandsted Larsen, K. Kylesbech Larsen, P.E. Andersen, B.G. Svensson: Heavy doping effects in the diffusion of group IV and V impurities in silicon, *J. Appl. Phys.* **73**, 691–698 (1993)
- 46.53 K.C. Pandey, A. Erbil, I.G.S. Cargill, R.F. Boehme, D. Vanderbilt: Annealing of heavily arsenic-doped silicon: electrical deactivation and a new defect complex, *Phys. Rev. Lett.* **61**, 1282–1285 (1988)
- 46.54 M. Ramamoorthy, S.T. Pantelides: Complex dynamical phenomena in heavily arsenic doped silicon, *Phys. Rev. Lett.* **76**, 4753–4756 (1996)
- 46.55 J. Xie, S.P. Chen: Diffusion and clustering in heavily arsenic-doped silicon: discrepancies and explanation, *Phys. Rev. Lett.* **83**, 1795–1798 (1999)
- 46.56 D.W. Lawther, U. Myler, P.J. Simpson, P.M. Rousseau, P.B. Griffin, J.D. Plummer: Vacancy generation resulting from electrical deactivation of arsenic, *Appl. Phys. Lett.* **67**, 3575–3577 (1995)
- 46.57 V. Ranki, A. Pelli, K. Saarinen: Formation of vacancy–impurity complexes by annealing elementary vacancies introduced by electron irradiation of As-, P-, and Sb-doped Si, *Phys. Rev. B* **69**, 115205:1–12 (2004)
- 46.58 V. Ranki, K. Saarinen: Formation of thermal vacancies in highly As- and P-doped Si, *Phys. Rev. Lett.* **93**, 255502:1–4 (2004)
- 46.59 K. Kuitunen, K. Saarinen, F. Tuomisto: Positron trapping kinetics in thermally generated vacancy donor complexes in highly As-doped silicon, *Phys. Rev. B* **75**, 045210:1–5 (2007)
- 46.60 H.-J. Gossmann, F.C. Unterwald, H.S. Luftman: Doping of Si thin films by low-temperature molecular beam epitaxy, *J. Appl. Phys.* **73**, 8237–8241 (1993)
- 46.61 V. Ranki, K. Saarinen: Electrical deactivation by vacancy–impurity complexes in highly As-doped Si, *Phys. Rev. B* **67**, 041201:1–4 (2003)
- 46.62 M. Rummukainen, I. Makkonen, V. Ranki, M.J. Puska, K. Saarinen, H.-J.L. Gossmann: Vacancy–impurity complexes in highly Sb-doped Si grown by molecular beam epitaxy, *Phys. Rev. Lett.* **94**, 165501:1–4 (2005)
- 46.63 K. Saarinen, S. Hautakangas, F. Tuomisto: Dominant intrinsic acceptors in GaN and ZnO, *Phys. Scri. T* **126**, 105–109 (2006)
- 46.64 J. Neugebauer, C.G. Van de Walle: Gallium vacancies and the yellow luminescence in GaN, *Appl. Phys. Lett.* **69**, 503–505 (1996)
- 46.65 K. Saarinen, T. Suski, I. Grzegory, D.C. Look: Thermal stability of isolated and complexed Ga vacancies in GaN bulk crystals, *Phys. Rev. B* **64**, 233201:1–4 (2001)
- 46.66 F. Tuomisto, K. Saarinen, T. Paskova, B. Monemar, M. Bockowski, T. Suski: Thermal stability of in-grown vacancy defects in GaN grown by hydride vapor phase epitaxy, *J. Appl. Phys.* **99**, 066105:1–3 (2006)
- 46.67 J. Oila, V. Ranki, J. Kivioja, K. Saarinen, P. Hautojärvi, J. Likonen, J.M. Baranowski, K. Pakula, T. Suski, M. Leszczynski, I. Grzegory: The influence of dopants and substrate material on the forma-

- tion of Ga vacancies in epitaxial GaN layers, *Phys. Rev. B* **63**, 045205:1–8 (2001)
- 46.68 S. Hautakangas, J. Oila, M. Alatalo, K. Saarinen, L. Liskay, D. Seghier, H.P. Gislason: Vacancy defects as compensating centers in Mg-doped GaN, *Phys. Rev. Lett.* **90**, 137402:1–4 (2003)
- 46.69 S. Hautakangas, K. Saarinen, L. Liskay, J.A. Freitas Jr., R.L. Henry: Role of open volume defects in Mg-doped GaN films studied by positron annihilation spectroscopy, *Phys. Rev. B* **72**, 165303:1–10 (2005)
- 46.70 K. Saarinen, P. Seppälä, J. Oila, P. Hautojärvi, C. Corbel, O. Briot, R.L. Aulombard: Gallium vacancies and the growth stoichiometry of GaN studied by positron annihilation spectroscopy, *Appl. Phys. Lett.* **73**, 3253–3255 (1998)
- 46.71 A. Pelli, K. Saarinen, F. Tuomisto, S. Ruffenach, O. Briot: Influence of V/III molar ratio on the formation of In vacancies in InN grown by metal-organic vapor-phase epitaxy, *Appl. Phys. Lett.* **89**, 011911:1–3 (2006)
- 46.72 O. Briot, J.P. Alexis, S. Sanchez, B. Gil, R.L. Aulombard: Influence of the V/III molar ratio on the structural and electronic properties of MOVPE grown GaN, *Solid-State Electron.* **41**, 315–317 (1997)
- 46.73 O. Briot, B. Maleyre, S. Ruffenach: Indium nitride quantum dots grown by metalorganic vapor phase epitaxy, *Appl. Phys. Lett.* **83**, 2919–2921 (2003)
- 46.74 J. Oila, A. Kemppinen, A. Laakso, K. Saarinen, W. Egger, L. Liskay, P. Sperr, H. Lu, W.J. Schaff: Influence of layer thickness on the formation of In vacancies in InN grown by molecular beam epitaxy, *Appl. Phys. Lett.* **84**, 1486–1488 (2004)
- 46.75 C. Stampfl, C.G. Van de Walle, D. Vogel, P. Krüger, J. Pollmann: Native defects and impurities in InN: First-principles studies using the local-density approximation and self-interaction and relaxation-corrected pseudopotentials, *Phys. Rev. B* **61**, 7846–7849 (2000)
- 46.76 F. Tuomisto, T. Paskova, R. Kröger, S. Figge, D. Hommel, B. Monemar, R. Kersting: Defect distribution in a-plane GaN on Al₂O₃, *Appl. Phys. Lett.* **90**, 121915:1–3 (2007)
- 46.77 E. Frayssinet, W. Knap, S. Krukowski, P. Perlin, P. Wisniewski, T. Suski, I. Grzegory, S. Porowski: Evidence of free carrier concentration gradient along the c-axis for undoped GaN single crystals, *J. Cryst. Growth* **230**, 442–447 (2001)
- 46.78 D.C. Look, D.C. Reynolds, J.R. Sizelove, R.L. Jones, C.W. Litton, G. Cantwell, W.C. Harsch: Electrical properties of bulk ZnO, *Solid State Commun.* **105**, 399–401 (1998)
- 46.79 D.C. Reynolds, C.W. Litton, D.C. Look, J.E. Hoelscher, B. Clafin, T.C. Collins, J. Nause, B. Nemeth: High-quality, melt-grown ZnO single crystals, *J. Appl. Phys.* **95**, 4802–4805 (2004)
- 46.80 E. Ohshima, H. Ogino, I. Niikura, K. Maeda, M. Sato, M. Ito, T. Fukuda: Growth of the 2-in-size bulk ZnO single crystals by the hydrothermal method, *J. Cryst. Growth* **260**, 166–170 (2004)
- 46.81 A. Mycielski, L. Kowalczyk, A. Szadkowski, B. Chwalisz, A. Wyszomolek, R. Stępniewski, J.M. Baranowski, M. Potemski, A. Witowski, R. Jakiela, A. Barcz, B. Witkowska, W. Kaliszek, A. Jędrzejczak, A. Suchocki, E. Łusakowska, E. Kamińska: The chemical vapour transport growth of ZnO single crystals, *J. Alloys Compd.* **371**, 150–153 (2004)
- 46.82 K. Graszka, A. Mycielski: Contactless CVT growth of ZnO crystals, *Phys. Status Solidi (c)* **2**, 1115–1118 (2005)
- 46.83 S. Brunner, W. Puff, A.G. Balogh, P. Mascher: Characterization of radiation-induced defects in ZnO probed by positron annihilation spectroscopy, *Mater. Sci. Forum* **363–365**, 141–143 (2001)
- 46.84 Z.Q. Chen, S. Yamamoto, M. Maekawa, A. Kawasuso, X.L. Yuan, T. Sekiguchi: Postgrowth annealing of defects in ZnO studied by positron annihilation, x-ray diffraction, Rutherford backscattering, cathodoluminescence, and Hall measurements, *J. Appl. Phys.* **94**, 4807–4812 (2003)
- 46.85 F. Tuomisto, K. Saarinen, K. Graszka, A. Mycielski: Observation of Zn vacancies in ZnO grown by chemical vapor transport, *Phys. Status Solidi (b)* **243**, 794–798 (2006)

Part H

Special Topics

Part H Special Topics in Crystal Growth

47 Protein Crystal Growth Methods

Andrea E. Gutiérrez-Quezada,
Mexico City, Mexico
Roberto Arreguín-Espinosa,
Mexico City, Mexico
Abel Moreno, Mexico City, Mexico

48 Crystallization from Gels

S. Narayana Kalkura, Chennai, India
Subramanian Natarajan, Madurai, India

49 Crystal Growth and Ion Exchange in Titanium Silicates

Aaron J. Celestian, Bowling Green, USA
John B. Parise, Stony Brook, USA
Abraham Clearfield, College Station, USA

50 Single-Crystal Scintillation Materials

Martin Nikl, Prague, Czech Republic
Anna Vedda, Milano, Italy
Valentin V. Laguta, Prague, Czech Republic

51 Silicon Solar Cells: Materials, Devices, and Manufacturing

Mohan Narayanan, Gaithersburg, USA
Ted Cizek, Evergreen, USA

52 Wafer Manufacturing and Slicing Using Wiresaw

Imin Kao, Stony Brook, USA
Chunhui Chung, Stony Brook, USA
Roosevelt Moreno Rodriguez, Stony Brook, USA

Protein Cryst

47. Protein Crystal Growth Methods

Andrea E. Gutiérrez-Quezada, Roberto Arreguín-Espinosa, Abel Moreno

Nowadays, advances in genomics as well as in proteomics have produced thousands of new biological macromolecules for study in structural biology, biomedicine research, and drug design projects.

Novel and classical methods of protein crystallization as well as modern techniques for two-dimensional (2-D) and three-dimensional (3-D) characterization of different biomolecules are reviewed in this chapter. Production of high-quality single crystals will be analyzed in detail from classical approaches to modern, high-throughput crystal growth methods for x-ray diffraction, as will new strategies for reducing the amount of raw materials used, accelerating the work, and increasing success rates. It will be pointed out that this work on crystallization as well as characterization is multidisciplinary. These scientific efforts are also interrelated and require close collaboration between biochemists, biophysicists, microbiologists, and molecular biologists, as well as physicists and engineers to develop new strategies and equipment for structural purposes. Finally, some of the problems faced and plans for solving them by using x-ray diffraction, neutron diffraction, and electron microscopy will be revised.

47.1	Properties of Biomacromolecular Solutions	1584	47.3	Classic Methods of Crystal Growth	1587
47.2	Transport Phenomena and Crystallization	1587	47.4	Protein Crystallization by Diffusion-Controlled Methods	1588
			47.4.1	Crystallization in Microgravity Environments	1588
			47.4.2	Crystallization in Gels	1589
			47.4.3	Crystallization in Capillary Tubes ..	1590
			47.5	New Trends in Crystal Growth (Crystal Quality Enhancement)	1591
			47.5.1	Crystallization Under Electric Fields	1591
			47.5.2	Crystallization Under Magnetic Fields	1592
			47.5.3	Combining Electric and Magnetic Fields	1593
			47.5.4	Robotics and High-Throughput Protein Crystallization.....	1593
			47.6	2-D Characterization via Atomic Force Microscopy (Case Study) 1595	
			47.6.1	General Overview	1595
			47.6.2	Coupling AFM and Electrochemistry for Protein Crystal Growth	1596
			47.6.3	AFM Characterization by Protein Immobilization by Means of Polypyrrole Films Deposited on Different Electrodes (HOPG and ITO)	1597
			47.7	3-D Characterization via X-Ray Diffraction and Related Methods	1598
			References		1599

Progress made in the biological sciences (biology, biochemistry, and biomedicine) during the last 25 years has been deeply dependent on the structural knowledge of atomic or molecular resolution of different types of biological macromolecules: proteins, nucleic acids (DNA more than RNA), and a small number of polysac-

charides. Much effort has been made worldwide to stimulate the structural study of proteins and of the different conformations they adopt in nature. The final aim is to understand the diversity of protein structural families, their folding, and the relation that exists between their composition and structure/function. Up to now, the

redundancy in the motifs and structural elements found in nature suggests that the number of different conformations is finite and manageable. Once most of them are known, it will be possible to predict the function of new, unknown protein domains. In this way, the modeling of these biological macromolecules will become one of the most promising tools for protein structure predictions in the near future.

On the other hand, structural biology has also famously influenced the field of protein engineering. While recombinant DNA techniques are used as synthetic tools, structure elucidation is used as an analytical tool. Advances in genomics have allowed the expression of proteins in live systems, the study of their activities, and based on their structure, their genetic modification for any practical purpose, such as increasing their stability or affinity for a substrate, inhibitor, etc. All this will revolutionize human life in different aspects: economics, health sciences, food sciences (nutrition), as well as in the development of new biomaterials with tailored properties based on the structure of biological systems.

Beyond the impact that structural biology has had on biochemistry, the three-dimensional structures of macromolecules have been demonstrated to be of formidable value in biotechnology. Nowadays, structural biology promotes the pharmacology field, through rational drug design based on the high-resolution structure of target macromolecules. This will have great impact on such diverse problems as curing human diseases, solving veterinary problems, and attacking crop damages [47.1].

Advances in genomics as well as in proteomics have produced thousands of new proteins for study in structural biology and drug design projects. The complete sequencing of vertebrate and invertebrate genomes [47.2] has accelerated international efforts to develop high-throughput methods and technologies that allow fast, three-dimensional protein structure determination [47.3]. Since the number of new proteins will continue to increase, as well as the number of scientists who study them, the necessity for new, efficient, and effective methods of structure determination has emerged [47.4]. Up to now, and in the near future, x-ray

diffraction of single crystals of specific macromolecules has been the only technique that can provide structural data at atomic resolution for these purposes. Other techniques that generate structural and molecular dynamic data do exist, but they are not used for the purposes expressed previously [47.1].

Some public and private projects have emerged under the names of structural genomics and structural proteomics. More recently, new terms have been created such as crystallomics, crystallogenesis, and chemotronics (a new branch between science and technology, related to the creation of liquid electrochemical converters in which ions in solution instead of electrons perform the role of current carriers). These efforts need fast and efficient techniques for three-dimensional structure elucidation. They are focused on high-throughput crystal growth for x-ray diffraction, considering new strategies for reducing the amount of raw material used, accelerating the work, and increasing success rates. These efforts are multidisciplinary and interrelated, and need close collaboration between biochemists, biophysicists, microbiologists, and molecular biologists, as well as physicists and engineers to develop new strategies and equipment. Herein, some of the problems faced and plans for solving them will be reviewed.

For x-ray crystallography to be applied to crystals of adequate size and quality, precise data collection is required. This converts crystals into the key to the whole process, and their production into the bottleneck. The problem of growing adequate crystals involves diverse aspects; in this chapter some of them will be commented on, such as model biomolecules, in addition to some novel and ingenious approaches to solving them, as well as their growth in a high-quality crystalline state.

One of the difficulties in obtaining high-quality crystals is the natural convection that exists in every experiment performed under normal Earth gravity conditions. In addition, problems involved in protein crystallization from solution, transport phenomena, and methods of crystal growth will be carefully reviewed. This is the reason why protein crystallization is so difficult: because of the lack of understanding of many of their physicochemical properties.

47.1 Properties of Biomacromolecular Solutions

Since all chemical reactions in biological systems take place in aqueous solutions, the question is: What is a so-

lution? By solution we understand a single phase, or a homogeneous system of variable composition formed

by at least two independent components. A homogeneous system is characterized by the absence of an interphase between the component parts of the solution, and by uniform composition and properties throughout the entire volume.

The components of a solution are the individual chemical substances which can be isolated from the system and which can exist in an isolated state. For example, an aqueous solution of lysozyme (model protein) consists of water (or buffer solution) and molecules of lysozyme. The solution components are the solute (protein) and the solvent (in general, water, for biological systems). The solute is the component of the solution in which the state of aggregation in normal conditions differs from that of the solution. The other components of the solution are known as solvents. In the case of liquid solutions, solutes are substances that under normal conditions are solid or gaseous, while the solvents are liquids.

The composition of a solution, in contrast to the composition of definite chemical compounds, can vary continually within wide limits. In this respect solutions are similar to chemical mixtures, though differing from them in their homogeneity and the change of many properties on mixing. The properties of a solution depend on the interactions between the particles of the solute, on the interaction between the particles of the solvent, and on the interaction between the particles of the solute and the solvent [47.5].

In the particular case of biological macromolecules, solubility is defined according to the solvent properties or solution–crystal equilibrium. In general the solvent is water or a buffer solution, so that the protein will have a proper chemical composition to bond to the solution at a specific pH value, or ionic strength (given by salts), and finally some additives (detergents, divalent cations, etc.). All these factors will affect the properties of the protein solubility in a different way. For instance, all soluble proteins in water or buffer solutions will keep hydrophobic amino acids inside the internal structure. On the other hand the hydrophilic amino acids will be distributed around the protein, exposed to the solvent. This process gives stability to the protein molecule and keeps the biological system in equilibrium with the solvent. As a consequence, the stability of any biomolecule in a solution will depend on the interaction between solvent and solute. The balance of these interactions could be modified by chemical and physical parameters such as temperature, pH, salts, additives, organic solvents, etc. The appropriate way to look at the physical or chemical behavior of macromolecular solutions must

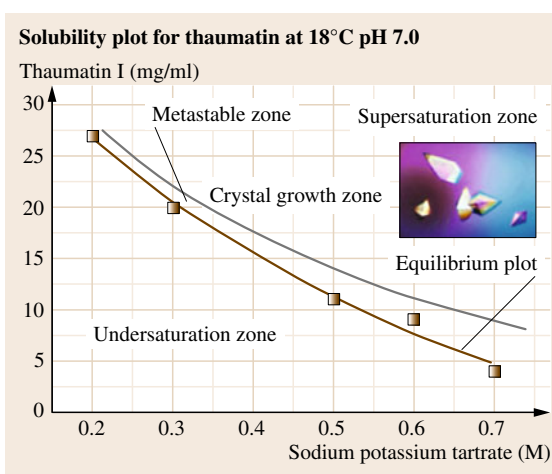


Fig. 47.1 Solubility plot for thaumatin experimentally obtained at 18 °C

be by means of a solubility plot showing the variation of the solubility of the protein versus the variation of the crystallization factor (the concentration of a precipitating agent, pH or temperature). A typical solubility curve shows different areas of the phase diagram where different types of phase separation take place. Figure 47.1 shows an example solubility curve for thaumatin, obtained at 18 °C.

This plot is divided into different zones where the crystal growth process takes place. In the area located under the equilibrium curve, the molecules of the protein are freely distributed throughout the solvent. This means that many biomolecules are needed to saturate the system. In the upper part of this equilibrium curve, there is a parallel line where a quasisteady state is obtained. This area is called the metastable zone, where nuclei are forming and dissolving at the same time and two types of forces are participating in the process: surface and volume forces. In the nucleation zone, the crystal growth process takes place, and larger crystals will grow at lower supersaturation values. However, at very high supersaturation, the system is highly supersaturated and protein–protein interactions will occur at high velocity, yielding amorphous precipitation. It is worth mentioning that everything is controlled by the driving force known as supersaturation. This is related to the differences in the chemical potential of the sample and connected to the Gibbs free energy. There is another way of investigating the solubility behavior of biomacromolecular solutions: by evaluating the solubility of protein molecules as a function of temperature. This physicochemical parameter will give us additional

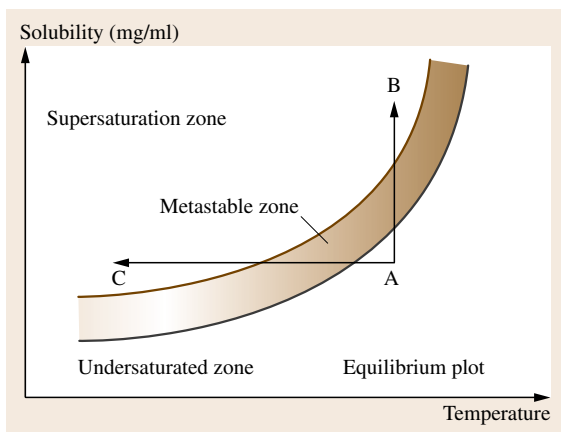


Fig. 47.2 Solubility plot as a function of temperature, the pathway from A to B is called isothermal growth and from A to C is called isotonic growth

information related to the stability of the protein molecule at a specific pH value. For instance, Fig. 47.2 shows a theoretical plot of solubility behavior versus temperature. This plot contains the same areas as those shown in Fig. 47.1.

From this curve it is possible to see two pathways which permit the solubility to be reduced: (1) traveling from the undersaturated region A to region B at constant temperature, (2) traveling from region A to region C while reducing the temperature. Both sides of this plot will permit the reduction of the solubility to obtain phase separation, and depending on the velocity, this solid phase could be a crystalline phase. We must take into account that there are several parameters that participate simultaneously in the crystallization process of a biological sample, and we must also take into account that understanding the nucleation step based on a solubility plot will give us the possibility of growing high-quality single crystals.

Nucleation is a major step in the crystallization process. It is primarily defined in terms of nuclei formation and size distribution. As soon as crystallites are detectable, the phenomenon is called crystal growth. During nucleation several events occur simultaneously on various time scales, namely: molecular conformation changes that take place in ≈ 0.01 ns, surface structure and defect displacements occurring within 1 ns, surface step displacement in 1 μ s, growth of one atomic layer in 1 ms, hydrodynamic transport in about 1 s, and finally homogenous nucleation, which needs no more than a few minutes [47.6]. Chemical and physical interactions between different molecules can be monitored,

but only some methods provide sufficient resolution in terms of particle size and time scale. Static and dynamic light-scattering methods have been employed to verify protein homogeneity and measure protein-protein interactions under precrystallization conditions. They have also been applied without a sophisticated data reduction scheme to predict protein solubility and crystallizability [47.7, 8]. As a consequence, the combination of spectroscopic and crystallographic data may provide an insight into the energetics of nucleation. The free-energy barrier of this process is controlled by the supersaturation value, which is normally the driving force and is related to the spontaneity of the system by (47.1).

$$\Delta G = - \left[\frac{\left(\frac{4}{3} \pi r^3 \right)}{\Omega} \right] k_B T \ln \beta + 4 \pi r^2 \gamma, \quad (47.1)$$

where Ω is the molar volume occupied by a unit in the crystal, r is the hydrodynamic radius of the macromolecule or the cluster, k_B and T are the Boltzmann constant and absolute temperature, respectively, and γ is the surface energy (expressed in units of J/cm²).

Supersaturation can be defined by its absolute value $\beta = C/C_e$, or its relative value, $\alpha = (C - C_e)/C_e$, where

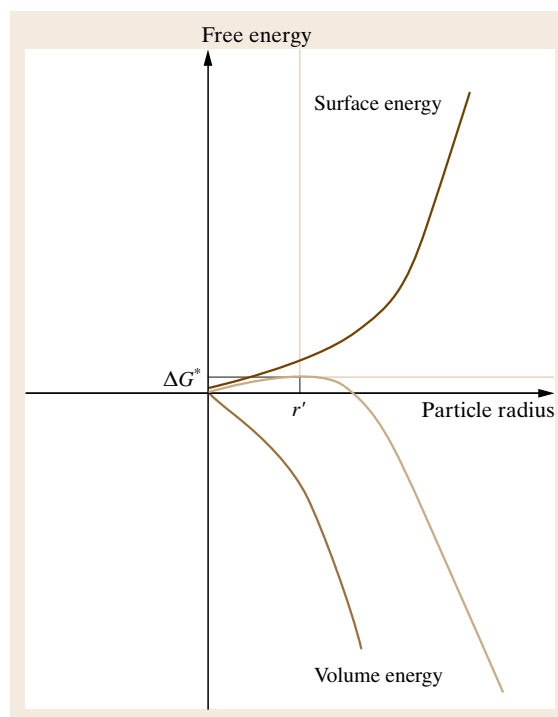


Fig. 47.3 Theoretical plot for the nucleation phenomena

C_e represents the actual value of solubility at certain concentrations of precipitant and protein, i.e., one of the (x, y) values of the plot shown in Fig. 47.1. Nucleation behavior can be easily computed if we have the values of Ω at which the molar volume is occupied by a unit in the crystal from x-ray diffraction, and the hydrodynamic radius (r) from the hydrodynamic properties of the solu-

tion as well as the surface energy (γ), both of which are usually obtained by dynamic light-scattering methods. Figure 47.3 shows the theoretical behavior of the nucleation process, where surface and volume forces are competing. The result of the summation of both plots will give us the variation of the Gibbs free energy versus the size in units of the monomer radius [47.9].

47.2 Transport Phenomena and Crystallization

Transport processes, and in particular mass transport, are very important for crystal growth from aqueous solutions [47.10–12]. Mass and heat transport processes are critical to the final quality and characteristics of the crystals [47.13]. Many crystallogensis techniques have been explicitly developed for controlling the relative contributions of convective and diffusive transport in crystal growth [47.14]. During the active incorporation of ions or molecules into the three-dimensional lattice, density differences are generated in the proximal area of the developing faces, leading to convective flux in the surroundings of the crystal [47.15–17]. Convective transport of molecules competes with pure diffusive transport, and the in-

teraction between them will determine the way and the kinetics of nutrient presentation of the growing crystal.

Transport phenomena not only affect the nutrients of the crystals but also the rate of adsorption and incorporation of impurities, which affects the size, morphology development, and perfection of the crystal [47.18]. On the other hand, convective transport only occurs in the presence of gravity. Only then can heavier fluids fall and lighter fluids rise, letting convective currents emerge in the bulk of the solution. Other types of convection do exist, such as convection due to surface tension [47.19], but they are not significant in the crystallization process of solutions.

47.3 Classic Methods of Crystal Growth

Medium-sized single crystals with near-to-perfect habits made of molecular arrangements with no defects that produce well-resolved and intense diffraction patterns are the dream of every protein crystallographer. Four basic crystallization methods are presently at the disposal of crystal growers to grow such crystals. Like half a century ago in chemistry laboratories, crystallization assays can be set up either (1) in batch mode, (2) by vapor diffusion between hanging (or sitting) droplets and a reservoir of precipitant, (3) by dialysis across a semipermeable membrane or (4) based on free-interface diffusion at the interface of two liquids [47.20–23].

In batch crystallization, nuclei can form and grow immediately in a constant volume once all ingredients, i.e., protein, buffer, precipitant, and additives, have been mixed. An automated version successfully employs microliter droplets that are deposited under a layer of oil [47.24]. In the vapor diffusion method, a small volume of macromolecular solution

is equilibrated against a larger volume of precipitant. Equilibration occurs with the transfer (at constant temperature) of a volatile compound (usually water) until isopiestic pressure is reached [47.25]. Its rate is viscosity and vapor pressure dependent, and the volume of the initial protein solution decreases proportionally to the precipitant concentration difference. Most commercial crystallization robots employed for high-throughput applications dispense a great number of submicroliter volume droplets onto dedicated crystallization plates [47.26]. On the other hand, dialysis permits us to approach the equilibrium differently, and can reach the supersaturation zone more smoothly and in a better controlled manner [47.27, 28]. Also samples can be reused as long as they are not irreversibly denatured. This technique is not so popular, probably because samples smaller than a few microliters are difficult to handle and because it has not yet been automated. Finally, in Earth-based laboratories, convectional flow triggered by density differences restricts

the use of diffusion at the interface between macromolecular and precipitant solutions to small sample volumes contained in capillary tubes [47.29]. Free-

interface diffusion has been successfully applied in quasiweightlessness, where solutal convection is naturally weak [47.30].

47.4 Protein Crystallization by Diffusion-Controlled Methods

47.4.1 Crystallization in Microgravity Environments

Many years of experimentation with diverse crystals has confirmed the notion that, by minimizing convective mass transport, better quality crystals can be obtained, with improved mechanical and optical properties, reduced density of defects, and larger size.

How is it possible to suppress the natural convection in crystallogenesis? Nowadays, different approaches have arisen for removing or at least reducing it. One of them is crystallization of macromolecules in space, where in the absence of gravity, convection disappears. In the last decade, a new approach that involves the use of magnetic fields has appeared. Magnetic forces opposed to gravity can reduce natural convection inside solutions [47.31, 32]. Also, methods for crystallizing macromolecules in gels are good and well-accepted alternatives for eliminating natural convection [47.33].

It is natural to think that, at zero or reduced gravity, crystals with superior properties can be grown [47.18]. Is this possible? Observations and experimental data support the hypothesis that convective flows can be related to the introduction of statistical disorder, defects, and dislocations on growing crystal surfaces [47.34–36]. Convective transport tends to be variable and random, producing variations in the supersaturation levels in the environment of the developing faces, exposing them permanently to high levels of nutrients, similar to those of bulk crystallization. On the contrary, under microgravity, convection is suppressed and the concentration of nutrients at the interface of the crystal is reduced. Mass transport is purely diffusive, which for proteins is very slow, and a region of depletion of nutrients is established around the nucleus. Thanks to the absence of gravity, this zone is quastable. We can imagine one crystal in the center and the gradient of nutrients on the right-hand side and on the left-hand side aggregates and large impurities. In the right-hand part, nutrient molecules diffuse very slowly because of their size, lengthening the effect. On the left, impure molecules diffuse more slowly than monomers

do. As a consequence, the depletion zone acts as a *diffusive filter*, avoiding the incorporation of impurities into the growing crystal. Apparently, this is the principal mechanism for improvement in crystal quality under microgravity. This hypothesis is not only supported by the experimental data but also by mathematical models that explain the mass transport process involved. It has also been shown (in a particular case) that up to a 40% reduction of nutrient molecules near the nucleus can be achieved in the absence of gravity, relative to the bulk concentration [47.37].

In the past, the aim of convection suppression was the inspiration for many scientists who devoted their work to developing new techniques and devices. The first serious experiment for crystallizing macromolecules under microgravity was done by a German team under the direction of Prof. Littke in 1978. On that occasion, lysozyme and β -galactosidase were successfully crystallized by the liquid–liquid diffusion method in a series of reactors [47.38–41].

The progression made in this crystal growth area was hard and slow, owing to the sparse literature on experiments performed in microgravity during the 1970s and 1980s. Moreover, many results were unavailable to the research community because they belonged to private companies or because of the lack of communication between Oriental and Western scientists [47.18]. It was not until 1989 that the first formal scientific paper was published in *Science*, in which x-ray diffraction analysis of many crystals grown in microgravity was reported. They presented higher intensity/estimated error ($I/\sigma(I)$) rates through the whole range of resolution, and higher resolution values [47.42]. This article provided tangible proof that crystals formed in microgravity environments generate more data of higher quality, producing more precise structures.

How are experiments performed in microgravity? Nowadays many devices exist, based primarily on two techniques: vapor diffusion and liquid–liquid diffusion [47.43], and the thermal-induced batch technique has also been successful in growing some large crystals that gave very high resolution [47.44]. The experiments are performed by governmental space agencies

or private consortia, such as Payload Systems (USA), Intospace (a European consortium, recently dissolved), and Bioserved (a center for commercial development sponsored by NASA). Each consortium has developed its own devices for its experiments [47.43]. Among the vapor diffusion devices, the vapor diffusion apparatus (VDA), designed and built by Bugg and collaborators from Alabama University at Birmingham, USA [47.45,46], is the most commonly used device, with more than 25 missions. Although originally the device was very simple, it was possible to crystallize many diverse proteins, such as lysozyme, canavaline, bovine serum albumin, and others. Presently, newer and more complex versions of microgravity devices exist, offering major advantages and possibilities for controlled experimentation.

As mentioned above, experiments done in space do not evolve in the same manner as those performed on Earth. For example, for vapor diffusion experiments done in both environments, the equilibrium kinetics is different, and this difference is stronger in liquid-liquid diffusion experiments. In spite of this, the superiority of crystals grown in space compared with those grown under Earth's gravity has been established by comparison according to four well-chosen criteria. First, a *visual examination* is fulfilled (this is a subjective analysis based on observation of the crystal under the microscope). Then, the *sizes and the distribution* of those values in the experiment are analyzed. *Morphology* is another evaluation criterion, as many protein crystals grow with different crystalline habits depending on whether the process was done on Earth or in space [47.42]. Finally, the properties of the x-ray diffraction pattern generated by a crystal must be considered (as the internal order of a crystal relies on the growth kinetics).

Following these criteria, a number of advantages found in crystals grown in microgravity can be summarized [47.42,47,48]:

- Visual superiority.
- Larger crystals, many orders of magnitude larger than the biggest crystals grown on Earth [47.18].
- Higher resolutions achieved in x-ray diffraction patterns.
- Better $I/\sigma(I)$ signals (Wilson plot); in the entire range of the resolution, higher values of $I/\sigma(I)$ for microgravity crystals were found. However, the physical properties responsible for this observation are as yet unknown. Apparently, the reason is a lower defect density.
- Sharper x-ray diffraction intensity peaks, showing quantitatively the better internal order and perfection of protein crystals grown in space.
- Not only proteins can be crystallized in the absence of gravity, but also other macromolecules such as viruses (satellite tobacco mosaic virus), DNA, pharmaceutical targets (HIV reverse transcriptase) or membrane proteins (bacteriorhodopsin).
- Under microgravity, the sedimentation effect disappears. In space, crystals keep their defined and stable positions over long periods of time. It is therefore a favorable environment for multiple crystal growth, minimizing the superposition of diffusive fields and assuring more or less uniform access to nutrients by all faces [47.49]. Besides, the incorporation of microcrystals or three-dimensional nuclei by sedimentation into the growing faces is avoided.

On the other hand, among its main disadvantages are the cost and the waiting time. It is an expensive method and requires a lot of time since the missions are not daily and they last for many days, especially when consecutive experiments are desired. Therefore, the disadvantages of microgravity protein crystallization are: high cost, low reproducibility, low reliability, lack of correspondence between Earth- and space-based observations, and lack of understanding of microgravity observations. Finally, based on these disadvantages, we could say that nowadays most protein crystallization programs have been abandoned by the respective space agencies.

47.4.2 Crystallization in Gels

As early as the end of the 19th century, inorganic compounds were crystallized in gelatin or gels made of siloxane [47.50, 51]. Once the actual role of the gel was recognized, it was added to crystallization media to reduce convective flow [47.52, 53], favor mass transfer by diffusion [47.54, 55], and immobilize crystal nuclei in the network and suppress gravity-driven sedimentation [47.50, 51, 56]. After the first report by Low and Richards in 1954 of the use of gelatin in the crystallization of albumin [47.57], it took a while before inorganic and organic gels were reintroduced for protein crystallization [47.55]. This led the way to the production of crystals having many fewer defects. Indeed, protein and virus crystals grown in such gels have enhanced diffraction properties, including sharper Bragg reflections, higher

diffraction intensities compared with background noise, or a higher diffraction limit compared with crystals grown in solution [47.58, 59]. Despite the discovery of these benefits, gels are largely underexploited by protein crystal growers. The same holds for counterdiffusion [47.60, 61], a crystallization method in which capillary forces exerted in cylindrical tubes of small diameter strongly reduce convection and stabilize the concentration gradients that exist around growing crystals [47.62, 63].

47.4.3 Crystallization in Capillary Tubes

The aim of this section is to summarize technically simple and efficient crystallization methods for optimizing the quality of crystals of a variety of biological particles, including proteins, nucleic acids, multimolecular assemblies, and viruses. Crystallization assays in microporous, chemical or physical hydrogels (as mentioned above) or inside capillary tubes (as described here) only require inexpensive chemicals and simple laboratory equipment. Conditions identified by a preliminary sparse-matrix approach in solution can be readily transferred to gels or capillaries in an attempt to enhance the diffraction properties of crystals. Gels and capillaries are also convenient for crystal storage and transport. In the course of this study, novel gel-forming compounds have been tested and a novel crystallization method for reducing convective flow has been implemented. Furthermore, crystal content analyses by mass spectrometry have been performed in order to determine the limits of the impurity-sieving effect of agarose on the incorporation of isoforms in thaumatin crystals. Crystallization and crystallographic results obtained with small model proteins and large enzymes involved in gene expression are presented. The contributions of diffusive media and of counterdiffusion methods are discussed and practical recommendations given. Another way to reduce the natural convection under Earth's gravity is to incorporate gelled media into the solutions. In 1968, Zeppezauer and coworkers described the use of microdialysis cells, made of capillary tubes sealed with gel stoppers (polyacrylamide), to reduce convection in crystallization solutions to obtain better crystals [47.64]. Then, in 1972, Salemmé also succeeded in the crystallization of proteins inside a glass capillary tube [47.29]. He put a protein solution into contact with a precipitant agent and let the system reach equilibrium by counterdiffusion [47.38]. Some years later, ribosomal

subunits were crystallized successfully with the same setup [47.65].

After many years of investigation, Prof. García-Ruiz proposed the use of gelled media for crystallizing macromolecules by counterdiffusion. This technique combined the principle of reduced convection and the advantage of having a wide range of conditions in a single experiment [47.66]. All this progress allowed García-Ruiz and colleagues in 1993 to develop of a new technique called the gel acupuncture method (GAME) [47.67, 68]. This novel technique consists of the permeation of the precipitating agent solution through the gel and the penetration by capillary force into the capillary tube, filled with a protein solution, allowing for crystallization [47.68]. This technique is well known today, and various types of gels, capillary tubes, additives, and precipitating agents have been evaluated for its use [47.68, 69]. A difference from other methods is that inside a capillary tube there is not only one supersaturation level, thus precipitation zones will be found in regions of very high supersaturation, nucleation will happen at high supersaturation levels, and the growth of those nuclei will be found in regions of lower supersaturation levels. This increases the probability of finding the right conditions for crystallization [47.70]. Other advantages are the possibility of crystallizing proteins inside capillary tubes ready for direct x-ray diffraction data collection, avoiding the usual physical manipulation of the crystals and thus reducing the risk of breakage at the moment of mounting them or transporting them to the synchrotron [47.71], or the use of cryoprotectors and/or heavy metals inside the crystallization solutions by using a counterdiffusion method in capillary tubes [47.72].

Through the counterdiffusion methods in capillary tubes it was possible to crystallize diverse proteins of different molecular weight and a wide range of isoelectric point, viruses, and protein–DNA complexes [47.73]. In addition, thanks to the advances in structural genomics, a new device was developed for executing multiple and independent experiments, which is appropriate for effective screening of crystallization conditions of biological macromolecules [47.71]. It combines the benefits of multiple conditions in one capillary, thereby increasing the chances of finding the optimal ones, with the possibility of direct x-ray diffraction analysis in the device. All these advantages have converted this device into the first totally all-inclusive system since the initial steps toward data collection for structural analysis [47.71].

47.5 New Trends in Crystal Growth (Crystal Quality Enhancement)

At the beginning of the new millennium, several structural projects were devoted to finding a cure for diseases based on knowledge of the three-dimensional structure of specific biological targets; the problem has been to obtain high-quality single biocrystals to be investigated by x-ray diffraction. There are several novel approaches to overcoming the poor quality usually obtained in biological crystals for high-resolution x-ray crystallography. Some of these are the application of an in-situ internal electric field in the crystal growth process [47.74–77], the use of external electric fields in protein crystallization [47.78–81], the application of strong magnetic fields and high pressure [47.82–84], the combination of electric and magnetic fields [47.80], the use of ultrasonic fields [47.77], the use of femtosecond laser irradiation (FSLI), and the solution-stirring (SS) method [47.85], as well as addition of nucleants to crystallization droplets [47.86–91]. Basically, the idea behind all of these approaches is related to placing the system in the nucleation regime in the solubility plot and providing the system energy for spontaneous first nucleation. In order to separate the nucleation phenomena and the crystal growth process, it is necessary to look for a precise technique to investigate the limits of these two processes. In this regard, dynamic light-scattering methods usually help to define those areas where nucleation is happening [47.8, 92–94] while atomic force microscopy or video microscopy is appropriate to investigate mechanisms of crystal growth (reviewed later).

47.5.1 Crystallization Under Electric Fields

The study of the effect of electric fields on protein crystallization had not been explored until the pioneering work on estradiol 17 β -dehydrogenase electrocrystallization [47.95]. Recent studies performed by Aubry and coworkers, with electric fields external to the crystallization solution, showed that it is possible to reduce lysozyme nucleation and increase the crystal growth rate. Then, the same group evaluated the crystal growth kinetics and found an increase in the protein concentration near drops that were close to the cathode [47.75]. Nanev and Penkova [47.76] came up with similar results when crystallizing lysozyme by batch method in the presence of an external electric field. They reported that lysozyme crystals grew with a definite orientation towards the cathode. Recently a full review of the ef-

fect of electric fields on protein crystallization has been published [47.77].

Biological macromolecule crystallization, in the presence of an internal electric field, uses a similar setup to that used by the gel acupuncture method, except that an inert electrode (Pt) is introduced into the capillary tube and comes into contact with the protein solution, and another electrode is set collinear to it, in the gel [47.74]. Protein molecules are charged since the pH solution is far from the protein's isoelectric point. When a small direct constant current is imposed on the system, a potential difference is established between the electrodes, provoking an orientation effect over the macroions (protein molecules). Lysozyme and thaumatin crystals were found to be firmly attached to the anode during the crystallization process.

To understand what is going on when the potential difference is established, it is important to comprehend how the solution is structured and the effects the electric field has on it. The proposed hypothesis for nucleation inside the capillary tube, in contact with an anode, considers the presence of an electric double layer in the surroundings of the electrode. When an electrode comes into contact with an electrolyte solution, the ions feel asymmetric forces and order themselves, forming an electric double layer. The first layer is composed of water molecules with their dipoles oriented, whereas the second layer is composed of counterions. Positively charged protein molecules need a negative ion for favorable protein–protein interactions, for example, CL^- for lysozyme [47.96] or potassium sodium tartrate for thaumatin [47.97]. The potential difference established in the cell allows the migration of anions of the precipitating agent into the capillary tube, encouraging interaction with the protein molecules in the solution, in the first instance. Then the counterions of the electric double layer will act as supports for positively charged protein molecules or nuclei, allowing the crystal grow over the anode. This behavior was not found when a cathode was placed inside the capillary tube [47.74].

This technique is very new and has only been evaluated with model proteins, such as lysozyme and thaumatin. However, it seems very promising as crystals with similar quality to those grown with the gel acupuncture method were obtained, but with shorter nucleation-induction times and without affecting three-dimensional growth rates [47.74]. This is

very interesting from a biotechnology point of view, since shortening the crystalline production time is desirable.

The reduction of the induction time in crystallization had also been observed by *Moreno* and *Sazaki* [47.79]. Lately, these scientists have studied the effect of an electric field with a different setup, using the batch method and with parallel electrodes. Despite these variations, they noticed an induction time three times shorter in the presence of an internal electric field, corroborating the results found with the gel acupuncture method plus an internal electric field [47.74]. Besides, for the same work, the benefit of nucleation control is remarkable, since they obtained fewer lysozyme crystals with homogeneous size distribution.

47.5.2 Crystallization Under Magnetic Fields

It is possible to reduce natural convection on the Earth with the help of magnetic fields. Depending on whether they are homogenous or inhomogeneous, the fields act upon a sample in different ways. Inhomogeneous magnetic fields are responsible for reducing the effective gravity that a solution feels through the action of a magnetization force [47.32]. If a magnetic field gradient is applied vertically, a magnetization force will be generated. When this force opposes gravitational force, a reduction of vertical acceleration (effective gravity) is obtained. Hence, a decrease in natural convection is accomplished.

With a mathematical model of a crystallization system under a magnetic field, the concentrations of macromolecules in the surroundings of a growing crystal were estimated [47.98, Fig. 2], verifying that a magnetic gradient of $-685 \text{ T}^2/\text{m}$ reduces convection by 50%, while a magnetic gradient of $-1370 \text{ T}^2/\text{m}$ practically eliminates convection, producing similar conditions to that of microgravity [47.98]. Experimentally, high-quality high-resolution crystals were obtained, in agreement with the mathematical model [47.99]. Moreover, *Wakayama* and colleagues found that, in the presence of a magnetizing force opposite to g , fewer lysozyme crystals were obtained than in the absence of the magnetic force [47.32].

When a homogeneous magnetic field is applied, high-quality crystals are also observed [47.100], even though the mechanism involved is different. An increase in viscosity near the growing crystal was observed when a magnetic field of 10 T was applied [47.101, 102]. This increase in viscosity means that there is a reduction of natural convection inside the solution. Furthermore,

an orientation effect was observed upon the crystals formed under high magnetic fields [47.31, 32].

More recently, in another study, the decrease of the diffusion coefficient of lysozyme inside a crystallization solution under a homogeneous magnetic field of 6 and 10 T was evaluated [47.103]. All these observations are interrelated and are the consequence of the orientation effect by the magnetic field at a microscopic level. In a supersaturated solution, proteinaceous nuclei are suspended in the solution bulk, and sediment upon reaching an adequate size, which depends on the magnitude of the magnetic field applied. These nuclei act as blocks, avoiding the free diffusion of monomers, turning the solution more viscous and as a result reducing convection [47.103].

The research field of crystal growth under magnetic fields is relatively new and needs more study. A lot of things still remain to be understood about the effects of magnetic fields (both homogeneous and inhomogeneous) on macromolecular solutions. Evidently, a strong external magnetic field induces a magnetizing force, increases the viscosity of the protein solution, orients the growing crystals, and affects the growth process in a complex manner. All these phenomena seem to favor the resulting crystal quality, although a more complete investigation is needed to understand the mechanism better [47.102].

Finally, it is worth mentioning that the use of strong magnetic fields is still very expensive to be performed only in crystallization experiments. Maintenance of the superconductive magnets and the magnet itself are limiting factors for economic reasons. However, there are recent publications that have demonstrated that applying only a strong magnetic field, coupled with growth in a gel, improves the resolution limit as well as the crystal quality [47.104]. The combined effects of a magnetic field and magnetic field gradients on convection in crystal growth were published by *Wakayama* and colleagues [47.103, 104].

More recently a novel experiment using a popular magnet usually used for nuclear magnetic resonance (NMR) commonly used in chemistry laboratories was published [47.105]. This combined the batch method in gels under the presence of strong magnetic fields of 7 and 10 T in capillary tubes inserted in silicon hydrogels. A significant effect on the orientation of the crystals was noticed after 48 h in the presence of a 10 T magnetic field. The size of the crystals of lysozyme, thaumatin, and ferritin was improved while the number of crystals was decreased compared with the control. For instance, the crystal quality of thaumatin reached 1.15 \AA resolu-

tion, compared with the control which produced crystals of the same thaumatin at 1.7–1.8 Å resolution.

47.5.3 Combining Electric and Magnetic Fields

The simultaneous effect of magnetic and electric fields is a new field of research. Depending on the configuration of the system, great advantages can be acquired, such as homogeneity in crystal size, thanks to apparent suppression of secondary nucleation events, permitting the continuous growth of previously formed nuclei [47.103, 106]. Also, an orientation effect is noticed when the magnetic field is parallel to the electrodes, having the same effect as described in previous works [47.79, 80].

47.5.4 Robotics and High-Throughput Protein Crystallization

In the last few years, genomic advances have encouraged high-throughput structural biology studies. So much so that it has received the name of structural genomics and many huge public grants have been given to academic laboratories and private enterprises, such as pharmaceutical industries, around the world. The projects are diverse and extend from the study of the structure–function relation of proteins, through the mechanisms involved in protein folding [47.107], to the more pragmatic approach of rational drug design based on the structure of target molecules [47.108]. X-ray diffraction crystallography is critical in these studies, being the battle-horse in such initiatives. In this way, the crystallogenes of biological macromolecules arises as a vital step in the whole process, although it is the most complicated and last understood step in structural biology. In this section some aspects involved in high-throughput crystal growth of biological macromolecules will be reviewed.

The growing of crystals of biological macromolecules in large quantities takes place in several steps: protein production in large amounts (by heterologous expression or from its natural source), purification, crystallization trials, and their corresponding inspections. Since many proteins are evaluated at the same time it is mandatory to have automated systems that accelerate the work, while at the same time they should be trustworthy since the efficiency of each step affects the next one.

Heterologous protein production is almost completely automated for massive aims. This includes

cloning, transformation, and gene expression. These stages involved DNA molecules and, thanks to their high stability, they can be automated easily [47.109, 110]. Nevertheless, there is not yet a totally automated system for protein purification on a large scale with applications in structural biology. Proteins differ in their expression levels, solubility, and physicochemical properties, so that most scientists prefer to adopt a combination of manual techniques to obtain pure proteins. Despite this, many biotechnological companies have developed more integral solutions for large-scale purification. For example, Syrrx (San Diego, USA) uses a purification system developed at the Genomics Institute of Novartis Research Foundation, which combines centrifugation and robotized sonication with a system of column chromatography arranged in parallel, which is able to purify 96–162 proteins per day [47.110]. Affinium Pharmaceuticals (Toronto) has also developed an integral purification system. Proteomax covers all the steps, from the cellular extract processing to the pure concentrated sample, ready for analysis. This equipment can clarify the lysate, perform column chromatography, and desalt and concentrate samples, giving in the best cases a pure protein ready for structural studies. So many automated steps results in very useful purification equipment for large-scale studies [47.108].

Structural biology laboratories are capable of handling more than 1000 different proteins in a month. As a consequence they require the maximum possible automation of every stage, including crystallogenesis. This is not such a big problem, particularly considering that the vapor diffusion and microbatch crystallization techniques are the most frequently used. Therefore, diverse robots that can perform these functions exist on the market. Decode Biostructures produces ROBO-HTC, composed of a robot that prepares all different conditions (Matrix Maker) and another robot that dispenses the drops. Douglas Instruments is responsible for ORIX 6, which performs vapor diffusion with sitting drops or microbatch assays. This robot can process about 240 cells per hour. Another commonly used robot is Mosquito, from Molecular Dimensions. Mosquito is built by TTP LabTech, of TTP Group plc, one of the most successful technology companies in the world. This robot contains a set of precision micropipettes mounted on a continuous band, which deposit small volumes from 50 nl to 1.2 µl. Moreover, the micropipettes are disposable, avoiding cross-contamination problems and exhaustive washing. The robot dispenses drops for microbatch or vapor diffusion, and hanging- or sitting-drop crystallization experiments. Also, it can

be used with 96-, 384-, and 1,536-well plates, and comes with an easy-to-use software system that can be programmed.

Once the assays are set for incubation, regular inspection is required in order to find the adequate conditions for obtaining high-quality crystals. This is the most arduous part of high-throughput crystallization. For any one protein 1000 experiments are needed, on average, to obtain an appropriate crystal for x-ray diffraction analysis [47.108]. Many companies use human inspection, a very tedious and laborious step, so the idea of designing an automated inspection system is very tempting. An ideal inspection system should have the following characteristics:

1. The identification and elimination of clear drops, with 0% error (without risk of losing any crystals)
2. The capture of kinetic data (of the growing process or precipitation versus time)
3. The ability to distinguish crystals from precipitates and to find crystals inside precipitates in most cases
4. The determination of size and form of the crystal
5. The ability to improve points 3 and 4 based on *internal learning* (databases)

Some promising advances in image technology have been made by Decode BioStructures, which offers the *Crystal Monitor Workstation*. This equipment has a stereoscopic microscope, digital camera, voice control, and a database interface and can be coupled with ROBOHTC (from the same company). There also exists *Crystal Score* by Diversified Scientific, which provides a microscope over a motorized plate. It comes with a device that counts and sizes the crystals. RoboDesign has two options on the market: RoboMicroscope II, which can localize the drops, focus them, capture a color image, and store them automatically, while CPXO can classify drops into clear, precipitated, with crystals, and other categories.

Some of the advantages of automated image capturing are the high frequency with which images are registered, at precise times, and the possibility of evaluating them with diverse computer software, and applying artificial intelligence. Although the equipment does not have human experience it can be trained to develop its own database. However, in the end, there is no system that can totally ignore human inspection. Crystals are very difficult to obtain and, as long as an automated system with 0% false negatives does not exist, the human eye will be indispensable [47.108].

So far the advances and problems of high-throughput structural biology have been mentioned in

a general way. However, most of those studies are on soluble proteins. Membrane proteins entail other kinds of problems, as previously mentioned (in the membrane crystallization section).

What are the specific challenges of membrane protein structural biology? Diverse stages can be mentioned, such as protein production, purification, and crystallogenesis. Unlike soluble proteins, where more than 90% of the new protein structures come from recombinant samples, membrane proteins obtained from molecular biology techniques make up less amount than 50% [47.111]. This is in part because the strategies developed for overexpressing proteins are designed for soluble ones and do not favor integral membrane proteins [47.109]. The synthesis of membrane proteins makes use of the cell's secretory system, certain directionality, and their insertion inside membranes [47.110, 112]. Besides, many cells are not equipped to withstand such a flux in new membrane proteins, which saturate their secretory pathways and generate inclusion bodies in the cytosol or toxic intermediates for those cells. So, the choice of the expression system is an important issue in the production of membrane proteins.

Prokaryotic integral proteins can be expressed in prokaryotic systems with promising results. Some examples are structures of ionic channels [47.113] and certain proteins from the outer membrane [47.114], among others. On the contrary, eukaryotic membrane proteins overexpressed in prokaryotic organisms have been harder to achieve [47.115], since prokaryotic membranes have a different lipidic composition and can have a hostile environment for heterologous proteins. Besides, posttranslational modifications are necessary for correct folding of eukaryotic proteins or their insertion into membranes, but these are absent in prokaryotic cells [47.116]. Despite this, some successful isolated examples do exist, such as the in case of an enzyme bound to mammal membranes overexpressed in *E. coli*, when it was crystallized [47.117] and its structure solved [47.118], or the overexpression of a eukaryotic receptor coupled to G-protein in *Halobacterium salinarum* [47.119]. On the other hand, yeasts are good overexpression systems for eukaryotic proteins since they are easy to handle and powerful genetics tools [47.120, 121]. Mammal cells are the best choice for preserving the structural and functional integrity of mammal membrane proteins. However they are expensive and very complex to use, and as a result they are the last choice.

With regard to purification, detergents are usually used to dissolve membrane proteins. The choice

of detergent is essential, especially when designing studies on a large scale. Ideally a detergent should solubilize the membrane protein without forming aggregates [47.122]. An appropriate detergent is one that can selectively stabilize the native structure of proteins [47.123]. Every protein behaves in a particular way, which means that a specific purification protocol is needed for each one. This concept is in opposition to a *unique measure for all*, the motto of *en masse* experiments. Diverse strategies have been thought up to resolve this, like fusing a protein which has a certain affinity for a ligand to the end of a membrane protein that one wants to overexpress in order to facilitate its purification [47.124, 125].

Once pure, integral proteins are ready for crystallizing. Two alternative paths can be applied:

- 1) Crystallize the protein–detergent complex directly
- 2) Incorporate the protein once again into a lipidic bilayer environment, previous to its crystallization

Most of the structures solved by x-ray diffraction analysis come from crystals formed by the first path, by vapor diffusion or microbatch techniques. The method is similar to that used on soluble proteins but in this case the solute is the detergent–protein complex [47.122]. The use of robots simplifies the handling of these mixtures. The other path consists of restoring the membrane

proteins to a lipidic bilayer environment, before setting the crystallization experiments. This approach has its major model in the lipidic cubic phases method, as explained previously [47.126]. Automated equipment that can use this criterion for high-throughput membrane protein crystallization is under construction [47.127].

Finally, we can understand how the advances in the processes involved and the automation achieved in recent years have influenced the development of structural biology throughout the world. Many laboratories can successfully clone, express, purify, and crystallize soluble proteins on a scale that was unthinkable years ago. Nevertheless, there is still much to control and predict in many different stages of the general process. In relation to soluble proteins, the process for integral membrane proteins has not been achieved. In the near future, the problem of the amount of protein available for crystallization must be overcome by increasing protein production levels and improving the system of purification, especially the detergent choice. All this will help to obtain more successful crystallization trials. Besides, studies of the mechanisms that rule the process will aid in its scaling up and automation. Moreover, so many crystallization experiments will enrich databases and in consequence it will be possible to extract the tendencies and crystallization patterns. This will be a valuable ability for structural genomics, particularly for the aim of crystallizing new proteins.

47.6 2-D Characterization via Atomic Force Microscopy (Case Study)

47.6.1 General Overview

Understanding the nucleation and crystallization processes and the control of size and quality of macromolecular crystals of different proteins for structural investigations in biology and biomedical sciences is still a challenge in many laboratories worldwide. Particularly, the mechanisms of crystal growth are important in order to understand the history of the crystallization process. The pioneering efforts devoted to this investigation of those mechanisms of crystal growth were done by using scanning electron microscopy methods, examining the surfaces of lysozyme crystals as well as model proteins and virus particles, and deducing recent mechanisms of crystal growth [47.128–141], as reviewed by McPherson et al. in 2000 [47.142]. These results showed that crystal growth occurred by a lattice defect mechanism at low supersaturation and by two-

dimensional nucleation at high supersaturation. Step velocities and two-dimensional nucleation rates were obtained, and their dependence on supersaturation was compared with theory. Preliminary results on the early stages of nucleation and the phenomenon of cessation of growth have been presented. More recently, atomic force microscopy (AFM) has become a common tool in biophysical studies of proteins (mainly due to its ability to perform characterizations near to physiological conditions) [47.143–151]. Tertiary and quaternary structures, forces driving folding–unfolding processes, and secondary structure elements can be studied in their native environments, allowing a high resolution level associated with small distortions. It is important to remark that surface characterization techniques are not limited to AFM. Several groups have carried out insightful electron microscopy characterizations. Another prolific method has been interferometry, in particular two-beam

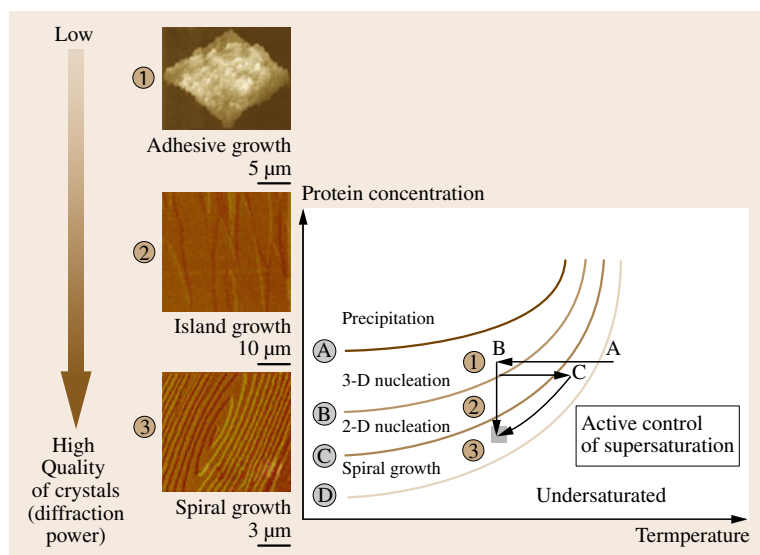


Fig. 47.4 Conceptual plot for protein crystal growth mechanisms observed by atomic force microscopy (designed by Dr. Gen Sasaki, Tohoku University Japan)

and phase-shifting methods, with several recent improvements. However, as a case study and reflecting the expertise of one of the authors, AFM methods coupled to electrochemical techniques will be revised in this chapter.

From the crystal growth viewpoint, we can use atomic force microscopy to show different areas where these crystal growth mechanisms are obtained on the solubility plot. Figure 47.4 shows those areas where high-quality single crystals can be obtained and their mechanisms of crystal growth can be studied by these atomic force microscopy methods. Knowledge of the limiting areas A, B, C, and D permits us to explain why a crystal that grows at high supersaturation will diffract the x-ray radiation poorly (due to adhesive crystal growth mechanism). On the contrary, crystals that grow at intermediate and low supersaturation values will diffract the x-ray radiation properly. The reason for this enhancement of crystal quality is that these crystals will grow by the following mechanisms of crystal growth: island growth or spiral growth. This plot also shows the best way to produce crystals of high quality by varying the temperature as a crystallizing parameter (as shown in Fig. 47.2). This overview image of the crystal growth mechanisms shown in Fig. 47.4 also explains why we can produce high-quality single crystals by microseeding methods. For instance, if one crystal nucleates at high supersaturation, the crystal growth cell will be filled with tiny, poorly shaped crystals. Most of the time these crystals will be poor scatterers of the x-ray diffraction due to the adhesive crystal growth

mechanism, which controls the crystal growth process at the beginning of the nucleation phenomena.

We can infer from Fig. 47.4 that the crystal will grow at the beginning by adhesive crystal growth at high supersaturation, and then the supersaturation will be reduced by the system itself (due to mass consumption). Then the crystal will continue to grow by island growth, finishing up with spiral growth at the end. This type of crystal is not available to diffract x-ray radiation (due to its poor internal crystalline order). However, since they finish growing by island or spiral growth mechanism, these crystalline species can be used as a source of microcrystals to be added to preequilibrated droplets by using the microseeding method, as pointed out by *Stura and Wilson* in 1991 [47.152].

47.6.2 Coupling AFM and Electrochemistry for Protein Crystal Growth

Nowadays, most atomic force microscopes are coupled to electrochemical devices (potentiostats and galvanostats). So, we can use these techniques from electrochemistry to produce electrocrystallization in different ways. The first is to produce compatible nuclei on the surface of various electrodes (mostly graphite). Then a potential difference can be applied to reduce the solubility of the solution of the biomolecule. Unfortunately, not all proteins are suitable for electrocrystallization. The most promising biological macromolecules are those which contain some metals as cofactors or that are covalently bonded to porphyrin groups, some amino

acids or certain disulfide bridges. There are only a few cases where the idea of electrocrystallization has been applied to some biological macromolecules. The pioneering work was performed on the crystallization of human placental estradiol 17 β -dehydrogenase, published by *Chin et al.* in 1976 [47.95]. There was another group who investigated the codeposition of electrocrystallized calcium phosphate and bovine serum albumin on the surfaces of titanium alloy (Ti-6Al-4V) under different conditions. Infrared (IR) and ultraviolet (UV) spectra showed that: (1) the content of the protein formed by electrochemical coprecipitation in the solution of calcium phosphate was higher than that formed by simple absorption; and (2) the protein formed at high direct current was more than that at low direct current. These results provided useful information about biocoating techniques of prosthetic implant materials [47.153]. The second approach focused on real electrocrystallization and was done by *Moreno and Rivera* [47.154]. They investigated the role of electrochemical processes on iron and CdSO₄ in the crystallization of horse spleen ferritin by using the cyclic voltammetry technique. It was found that, although both species exhibited important redox properties in the presence of an external applied potential, CdSO₄ played a leading role not only in the nucleation process but also in the growth behavior and morphology control of ferritin crystals.

47.6.3 AFM Characterization by Protein Immobilization by Means of Polypyrrole Films Deposited on Different Electrodes (HOPG and ITO)

Enzyme immobilization on electrode surfaces has been limited to soluble enzymes [47.155, 156]. However, recent developments in protein crystallization have created an important interest in the study of solid-state electrochemistry of protein single crystals in order to understand the mechanisms of crystal growth. Unfortunately, the fixation of these monocrystals to an electrode surface is difficult since the monocrystals break easily under mechanical pressure, and therefore they cannot be immobilized as other inorganic crystals [47.157, 158]. From this point of view, it is feasible to grow *ex situ* redox metalloprotein single crystals (such as catalases, ferritins, cytochromes, etc.) so that they can be introduced into the fluid cell of the atomic force microscope (AFM). In order to immobilize these crystals we can use polypyrrole (ppy) films deposited on highly oriented py-

rolytic graphite electrodes (HOPG) or indium-tin oxide electrodes (ITO) for structural investigations by AFM techniques. It is worth mentioning that ppy films are conductive and therefore their application as chemical cements will expand the number of future structural investigations into soft biological single crystals.

In general, we can fix any type of biocrystals by using the method of *Hernández-Pérez et al.* (2002) in which the polypyrrole film had been used as chemical glue for AFM investigations [47.159]. Figure 47.5 shows a case study in which we can see a ferritin monocrystal chemically fixed to a HOPG electrode by means of these ppy films. Recently, cytochrome c has been one of the most studied proteins in electrochemistry due to its electron-transfer properties and capability of being used as a solid-state electron-transfer device [47.160]. Even though only bovine cytochrome c is commercially available, its three-dimensional structure has recently been published at 1.5 Å resolution [47.161]. Therefore, in the near future this promising, natural electron-transfer protein can either be used for electrocrystallization investigations or as an electric biosensor component [47.160]. Pyrrole molecules can be polymerized in aqueous solutions by mixing 0.077 M pyrrole solution and 0.34 M LiClO₄ and applying a current of 50 mV/s in an electrochemistry AFM fluid cell (Veeco Co., Santa Barbara, USA). Figure 47.5a shows the surface of the HOPG electrode

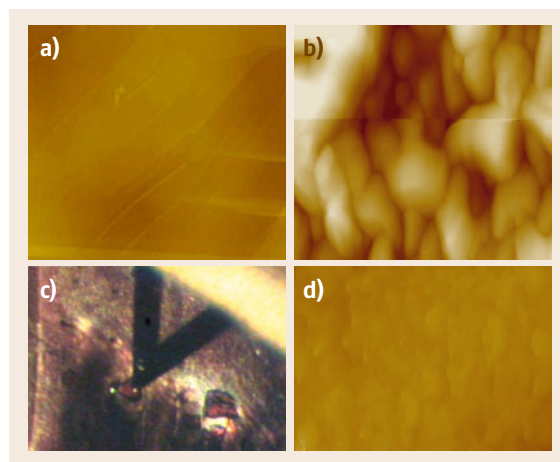


Fig. 47.5 (a) 12×12 μm² scanning AFM image of the HOPG surface. (b) 12×12 μm² AFM image of the HOPG surface after polymerization of the pyrrole. (c) Full optical image of the ferritin crystal when scanning and after polymerization of pyrrole. (d) 12×12 μm² scanning AFM image of the ferritin crystal surface

without polypyrrole films. On applying a potential difference, the pyrrole polymerizes and the morphology of the HOPG surface is changed (Fig. 47.5b). Figure 47.5c shows an overall image of ferritin crystals obtained by batch mixing method with 1 : 1 : 1 ratio 0.1 M cadmium sulfate/0.5 M ammonium sulfate, ferritin solution of 20 mg/ml, and pyrrole/LiClO₄ mixture as mentioned above for polymerization. This polymerization of pyrrole was performed by means of a fluid cell in an EC-AFM Nanoscope IIIa. Finally, the AFM image of the surface of this ferritin crystal is shown in Fig. 47.5d. This image is different when compared with the one containing the polypyrrole. This experiment is particularly important because we can see from that image that polypyrrole film will surround the crystal so as to fix it

properly onto the surface of the electrode. Later, after scanning the surface by AFM (Fig. 47.5d), we can see that there is no pyrrole on the surface of the biocrystal (ferritin), which means that the protein crystal has been fixed to the electrode by a chemical reaction with polypyrrole films (chemical glue) around it.

A novel idea is to grow large crystals on transparent electrodes (ITO for instance) by following the strategy previously described. Then a new solution of protein, precipitant, and additives can be added to the crystal fixed on the electrode. This tiny crystal can reach good sizes for structural research by neutron diffraction techniques. At the same time, having this type of fixed crystals on ITO or HOPG, we can say that an electron-transfer biosensor has been obtained.

47.7 3-D Characterization via X-Ray Diffraction and Related Methods

Protein crystallography is a part of the solid-state sciences which aims to solve the three-dimensional structure of biological macromolecules by means of the x-ray diffraction of single crystals [47.162–166]. The state of the art in the three-dimensional (3-D) structure of several proteins, nucleic acids, and polysaccharides is collected in the protein databank (PDB, initially administrated in Brookhaven National Laboratory, whose updated website is <http://www.rcsb.org>). This database is collecting all x-ray diffraction information for most of the biological macromolecules. A review of a variety and use of several databases has recently been presented by Einspahr [47.167].

The appropriate way to solve the 3-D structure begins by performing precise x-ray data collection. In order to perform this we must work with high-quality single crystals. As pointed out in Sect. 47.6, the better the crystal, the higher the resolution limit. The vast majority of proteins need to have a certain degree of purity to be crystallized. However, crystallization also depends on the molecular weight of the protein, the type of the protein, and even the method of crystal growth used to obtain the crystals. The first well-known case is the protein horse spleen ferritin. In order to produce wonderful cubic-octahedral single crystals, horse spleen ferritin must be purified to the extent of having just monomers in the solution (Fig. 47.6a,b). Otherwise the presence of a small amount of impurities will poison some crystal growth sectors, producing dendritic growth such as that shown in Fig. 47.6c. It is important to emphasize that nowadays we can also use twin

crystals in order to obtain the 3-D structure of almost any protein. It is clear that, using higher-quality single crystals, we can produce marvelous electron density maps or a wonderful structure (Fig. 47.7) of almost any protein. This figure shows the 3-D structure of cytochrome c from bovine heart obtained at 1.5 Å resolution [47.161]. It took that group nearly 2 years to crystallize this protein due to the existence of isoforms (which made the crystallization process difficult), only one of which was crystallized (native cytochrome). The only way in which we could produce suitable crystals of cytochrome c for x-ray diffraction was by means of the microseeding technique. The crystallization of membrane proteins, macromolecular complexes, and large assemblies is still a challenge.

Behind these beautiful structures is still a challenge: crystallization of membrane proteins and macromolecular complexes and assemblies. In this regard, in the near future, as mentioned in Sect. 47.5, the existence of robots and high-throughput techniques will help greatly. The real challenge will be how to predict accurate 3-D structure from de novo proteins, based on powerful databases of the three-dimensional structures of many biological macromolecules.

Finally, neutron-diffraction protein crystallography methods are also becoming promising powerful tools for 3-D structural characterization. Neutron diffraction provides an experimental approach for directly locating H atoms and hydration in proteins, a technique complementary to ultrahigh-resolution x-ray diffraction [47.168]. Recently, technical aspects as well as

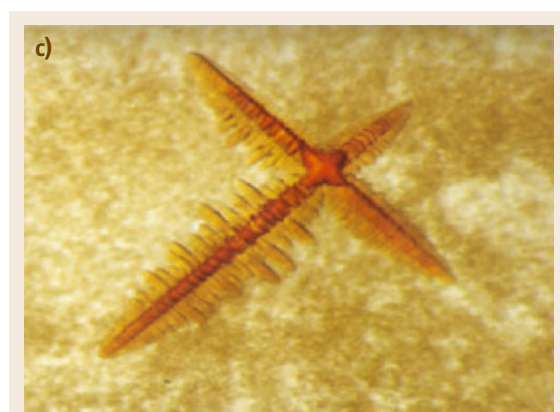
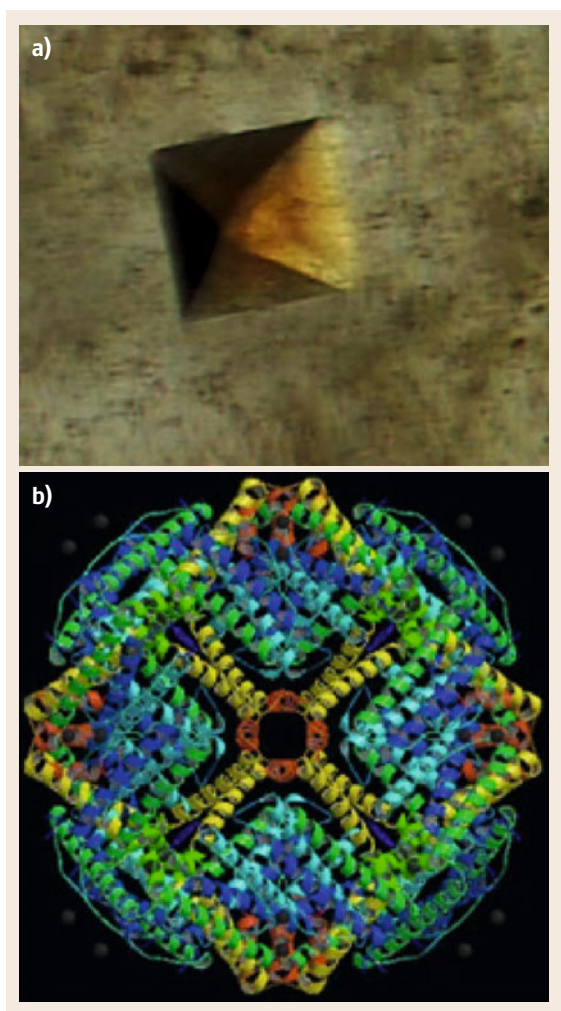


Fig. 47.6 (a) Crystal of ferritin grown by the batch method using only a purified fraction of monomers. (b) Three-dimensional structure of horse spleen ferritin showing the variety of cubic elements of the symmetry. (c) Dendrite of ferritin containing a mixture of oligomers ◀ ▲

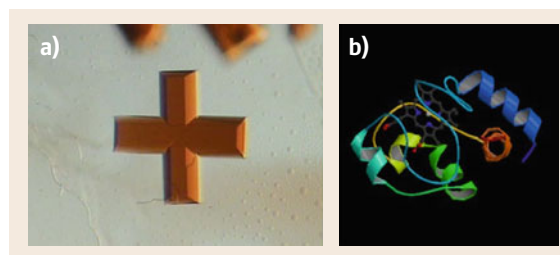


Fig. 47.7 (a) A perfect twin crystal of cytochrome c from bovine heart. (b) Image of the cytochrome structure obtained at high resolution (1.5 Å, PDB code: 2b4z) by Mirkin et al. 47.161

some potential applications and limitations of neutron protein crystallography have been reviewed [47.169].

New related methods coupling x-ray crystallography and scanning electron microscopy to obtain three-dimensional electron microscopy of macromolecular assemblies have also been published [47.170].

References

- 47.1 A. McPherson: Macromolecular crystallization in the structural genomics era, *J. Struct. Biol.* **142**, 1–2 (2003)
- 47.2 D. Roses: Genome-based pharmacogenetics and the pharmaceutical industry, *Nat. Rev. Drug Discov.* **1**, 541–549 (2002)
- 47.3 P. Kuhn, K. Wilson, M.G. Patch, R.C. Stevens: The genesis of high-throughput structure-based drug discovery using protein crystallography, *Curr. Opin. Chem. Biol.* **6**, 704–710 (2002)
- 47.4 J.L. Delucas, T.L. Bray, L. Nagy, K. McCombs, N. Chernov, D. Hamrick, L. Cosenza, A. Belgovskiy, B. Stoops, A. Chait: Efficient protein crystallization, *J. Struct. Biol.* **142**, 188–206 (2003)
- 47.5 R.J. Davey: The role of the solvent in crystal growth from solution, *J. Cryst. Growth* **76**, 637–644 (1986)
- 47.6 A.G.W. Wilson: Predicting protein crystallization from a dilute solution property, *Acta Crystallogr. D* **50**, 361–365 (1994)

- 47.7 V. Mikol, E. Hirsch, R. Giegé: Diagnostic of precipitant for biomacromolecule crystallization by quasi-elastic light-scattering, *J. Mol. Biol.* **213**, 187–195 (1990)
- 47.8 W.W. Wilson: Light scattering as a diagnostic for protein crystal growth – A practical approach, *J. Struct. Biol.* **142**, 56–65 (2003)
- 47.9 C.N. Nanev: Protein crystal nucleation, *Cryst. Res. Technol.* **42**, 4–12 (2007)
- 47.10 A.A. Chernov: *Modern Crystallography III, Crystal Growth* (Springer, Berlin Heidelberg 1984)
- 47.11 S. Sarig: *Handbook of Crystal Growth*, Vol. 2B, ed. by D.T.J. Hurle (North-Holland, Amsterdam 1994)
- 47.12 P. Bennema: Crystal growth from solution – Theory and experiment, *J. Cryst. Growth* **24**, 76–83 (1974)
- 47.13 D.T.J. Hurle: *Handbook of Crystal Growth*, Vol. 1B (North-Holland, Amsterdam 1994)
- 47.14 D.T.J. Hurle: *Handbook of Crystal Growth*, Vol. 2A (North-Holland, Amsterdam 1994)
- 47.15 F.E. Neumann: Über die optischen Eigenschaften der hemiprismatischen oder zwei- und eingliedrigen Krystalle, *Ann. Physik* **111**, 81–95 (1835), in German
- 47.16 F. Rosenberger: Inorganic and protein crystal growth – Similarities and differences, *J. Cryst. Growth* **76**, 618–636 (1986)
- 47.17 P.S. Cheng, P.J. Shlichta, W.R. Wilcox, R.A. Lefever: Convection phenomena during the growth of sodium chlorate crystals from solution, *J. Cryst. Growth*, **47**, 43–60 (1979)
- 47.18 A. McPherson: Macromolecular crystal growth in microgravity, *Crystallogr. Rev.* **6**, 157–308 (1996)
- 47.19 F. Rosenberger: *Fundamentals of Crystal Growth I, Macroscopic Equilibrium Concepts* (Springer, Berlin Heidelberg 1979)
- 47.20 T.M. Bergfors: Protein crystallization (Int. Univ. Line, La Jolla 1999)
- 47.21 A. Ducruix, R. Giegé: *Crystallization of Nucleic Acids and Proteins, a Practical Approach*, 2nd edn. (IRL, Oxford 1999)
- 47.22 A. McPherson: *Crystallization of Biological Macromolecules* (Cold Spring Harbor Laboratory, New York 1999)
- 47.23 R. Giegé, A. McPherson: General methods. In: *International Tables for Crystallography*, Vol. F, ed. by M.G. Rossmann, E. Arnold (IUCr, Kluwer Academic, Boston 2001)
- 47.24 A. D'Arcy, C. Elmore, M. Stihle, J.E. Johnston: A novel approach to crystallising proteins under oil, *J. Cryst. Growth* **168**, 175–180 (1992)
- 47.25 E.P.K. Hade, C. Tanford: Isopiestic compositions as a measure of preferential interactions of macromolecules in two-component solvents. Application to proteins in concentrated aqueous cesium chloride and guanidine hydrochloride, *J. Am. Chem. Soc.* **89**, 5034–5040 (1967)
- 47.26 J.R. Luft, J. Wolfley, I. Jurisica, J. Lasgow, S. Fortier, G.T. DeTitta: Macromolecular crystallization in a high throughput laboratory – The search phase, *J. Cryst. Growth* **232**, 591–595 (2001)
- 47.27 A. McPherson, J. Geller, A. Rich: Crystallographic studies on concanavalin B, *Biochem. Biophys. Res. Commun.* **57**, 494–499 (1974)
- 47.28 B.H. Weber, P.E. Goodkin: A modified microdiffusion procedure for the growth of single protein crystals by concentration-gradient equilibrium dialysis, *Arch. Biochem. Biophys.* **141**, 489–498 (1970)
- 47.29 F.R. Salemme: A free interface diffusion technique for the crystallization of proteins for X-ray crystallography, *Arch. Biochem. Biophys.* **151**, 533–539 (1972)
- 47.30 B. Lorber, R. Giegé: Nucleation and growth of thaumatin crystals within a gel under microgravity on STS-95 mission vs. under Earth's gravity, *J. Cryst. Growth* **231**, 252–261 (2001)
- 47.31 M. Ataka, E. Katoh, N.I. Wakayama: Magnetic orientation as a tool to study the initial stage of crystallization of lysozyme, *J. Cryst. Growth* **173**, 592–596 (1997)
- 47.32 N.I. Wakayama, M. Ataka, H. Abe: Effect of a magnetic field gradient on the crystallization of hen lysozyme, *J. Cryst. Growth* **178**, 653–656 (1997)
- 47.33 J.M.. García-Ruiz, M.L. Novella, R. Moreno, J.A. Gavira: Agarose as crystallization media for proteins. I: Transport processes, *J. Cryst. Growth* **232**, 165–172 (2001)
- 47.34 M. Pusey, W.K. Witherow, R. Naumann: Preliminary investigations into solutal flow about growing tetragonal lysozyme crystals, *J. Cryst. Growth* **90**, 105–111 (1988)
- 47.35 M. Beth, H. Broom, W.K. Witherow, R.S. Snyder, D.C. Carter: Preliminary observations of the effect of solutal convection on crystal morphology, *J. Cryst. Growth*, **90**, 130–135 (1988)
- 47.36 J.K. Baird, E.J. Meehan, A.L. Xidis, S.B. Howard: Convective diffusion in protein crystal growth, *J. Cryst. Growth* **76**, 694–700 (1986)
- 47.37 H. Lin, F. Rosenberger, J.L.D. Alexander, A. Nadarajah: Convective-diffusive transport in protein crystal growth, *J. Cryst. Growth* **151**, 153–162 (1995)
- 47.38 Y.P. Wang, Y. Han, J.S. Pan, K.Y. Wang, R.C. Bi: Protein crystal growth in microgravity using a liquid/liquid diffusion method, *Microgravity Sci. Technol.* **9**, 281–283 (1996)
- 47.39 W. Litke, C. John: Protein single crystal growth under microgravity, *Science* **225**, 203–204 (1984)
- 47.40 A. McPherson: *Methods of Biochemical Analysis*, Vol. 23, ed. by D. Glick (Academic, New York 1976)
- 47.41 A. McPherson: *The Preparation and Analysis of Protein Crystals* (Wiley, New York 1982)
- 47.42 J.L. DeLucas, C.D. Smith, H.W. Smith, V.K. Senagdi, S.E. Senadhi, S.E. Ealick, C.E. Bugg, D.C. Carter, R.S. Snyder, P.C. Weber, F.R. Salemme, D.H. Ohlen-dorf, H.M. Einspahr, L. Clancy, M.A. Navia, B. McKeever, T.L. Nagabhushan, G. Nelson, Y.S. Babu,

- A. McPherson, S. Koszelak, D. Stammers, K. Powell, G. Darby: Protein crystal growth in microgravity, *Science* **246**, 651–654 (1989)
- 47.43 R.S. Snyder, K. Fuhrmann, H.U. Walter: Protein crystallization facilities for microgravity experiments, *J. Cryst. Growth* **110**, 333–338 (1991)
- 47.44 M.M. Long, L.J. DeLucas, C. Smith, M. Carson, K. Moore, M.D. Harrington, D.J. Pillion, S.P. Bishop, W.M. Rosenblum, R.J. Naumann, A. Chait, J. Prah, C.E. Bugg: Protein crystals growth in microgravity—temperature induced large scale crystallization of insulin, *Microgravity Sci. Technol.* **7**, 196–202 (1994)
- 47.45 J.L. DeLucas, F.L. Suddath, R. Snyder, R. Naumann, M.B. Broom, M. Pusey, V. Yost, B. Herren, D. Carter, B. Nelson, E.J. Meehan, A. McPherson, C.E. Bugg: Preliminary investigations of protein crystal growth using the space shuttle, *J. Cryst. Growth* **76**, 681–693 (1986)
- 47.46 J.L. DeLucas, M.M. Long, K.M. Moore, W.M. Rosenblum, T.L. Bray, C. Smith, M. Carson, S.V.L. Narayana, D. Carter, A.D. Clark Jr., R.G. Nanni, J. Ding, A. Jacobo-Molina, G. Kamer, S.H. Hughes, E. Arnold, H.M. Einspahr, L.L. Clancy, G.S.J. Rao, P.F. Cook, B.G. Harris, S.H. Munson, B.C. Finzel, A. McPherson, P.C. Weber, F. Lewandowski, T.L. Nagabhushan, P.P. Trotta, P. Reichert, M.A. Navia, K.P. Wilson, J.A. Thomson, R.R. Richards, K.D. Bowersox, C.J. Meade, E.S. Baker, S.P. Bishop, B.J. Dunbar, E. Trinh, J. Prah, A. Sacco Jr., C.E. Bugg: Recent results and new hardware developments for protein crystal growth in microgravity, *J. Cryst. Growth* **135**, 183–195 (1994)
- 47.47 J.R. Helliwell, E. Snell, S. Weisgerber: Proc. 9th Europ. Symp. Gravity Depend. Phenom. Phys. Sci. (Berlin 1995)
- 47.48 E.H. Snell, S. Weisgerber, J.R. Helliwell: Improvements in lysozyme protein crystal perfection through microgravity growth, *Acta Crystallogr. D* **51**, 1099–1102 (1995)
- 47.49 R. Boistelle, J.P. Astier: Crystallization mechanisms in solution, *J. Cryst. Growth*, **90**, 14–30 (1988)
- 47.50 H.K. Henisch: *Crystals in Gels and Liesegang Rings* (Cambridge Univ. Press, Cambridge 1988)
- 47.51 K.-T. Wilke: *Kristallzüchtung* (Verlag Harri Deutsch, Frankfurt/Main 1988), in German
- 47.52 P.S. Chen, P.J. Schlichta, W.R. Wilcox, R.A. Lefever: Convection phenomena during the growth of sodium chlorate crystals from solution, *J. Cryst. Growth* **47**, 43–60 (1979)
- 47.53 M.C. Robert, F. Lefaucheux: Crystal growth in gels: Principle and applications, *J. Cryst. Growth* **90**, 358–367 (1988)
- 47.54 B. Rubin: The growth of single crystals by controlled diffusion in silica gel, *AIChE J.* **15**, 206–208 (1969)
- 47.55 M.C. Robert, F. Lefaucheux, B. Jannot, G. Godefroy, E. Garnier: A comparative study of gel grown and space grown lead hydrogen phosphate crystals, *J. Cryst. Growth* **88**, 499–510 (1988)
- 47.56 J.M. García-Ruiz, O. Fermín, M.L. Novella, J.A. Gavira, C. Sauter, O. Vidal: A supersaturation wave of protein crystallization, *J. Cryst. Growth* **232**, 149–155 (2001)
- 47.57 B.W. Low, F.M. Richards: Measurements of the density, composition and related unit cell dimensions of some protein crystals, *J. Am. Chem. Soc.* **76**, 2511–2518 (1954)
- 47.58 B. Lorber, C. Sauter, M.C. Robert, B. Capelle, R. Giegé: Crystallization within agarose gel in microgravity improves the quality of thaumatin crystals, *Acta Crystallogr. D* **55**, 1491–1494 (1999)
- 47.59 D. Maes, L.A. Gonzalez-Ramirez, J. Lopez-Jaramillo, B. Yu, H. De Bondt, I. Zegers, E. Afonina, J.M. García-Ruiz, S. Gulnik: Structural study of the type II 3-dehydroquinase dehydratase from *Actinobacillus pleuropneumoniae*, *Acta Crystallogr. D* **60**, 463–471 (2004)
- 47.60 J.M. García-Ruiz: Counterdiffusion methods for macromolecular crystallization, *Methods Enzymol.* **368**, 130–154 (2003)
- 47.61 F. Otálora, J.M. García-Ruiz, A. Moreno: Protein crystal quality studies using rod-shaped crystals, *J. Cryst. Growth* **168**, 93–98 (1996)
- 47.62 A. McPherson, A.J. Makin, Y.G. Kuznetsov, S. Koszelak, M. Wells, G. Jenkins, G. Howard, J. Lawson: The effects of microgravity on protein crystallization: evidence for concentration gradients around growing crystals, *J. Cryst. Growth* **196**, 572–586 (1988)
- 47.63 F. Otálora, J.M. García-Ruiz, L. Carotenuto, D. Castagnolo, M.L. Novella, A.A. Chernov: Lysozyme crystal growth kinetics in microgravity, *Acta Crystallogr. D* **58**, 1681–1689 (2002)
- 47.64 M. Zeppezauer, H. Eklund, E.S. Zeppezauer: Micro diffusion cells for the growth of single protein crystals by means of equilibrium dialysis, *Arch. Biochem. Biophys.* **126**, 564–573 (1968)
- 47.65 A. Yonath, J. Müssig, H.G. Witlmann: Parameters for crystal growth of ribosomal subunits, *J. Cell. Biochem.* **19**, 145–155 (1982)
- 47.66 J.M. García-Ruiz: The uses of crystal growth in gels and other diffusing-reacting systems, *Key Eng. Mater.* **58**, 87–106 (1991)
- 47.67 J.M. García-Ruiz, A. Moreno, C. Viedma, M. Coll: Crystal quality of lysozyme single crystals grown by the gel acupuncture method, *Mater. Res. Bull.* **28**, 541–546 (1993)
- 47.68 J.M. García-Ruiz, A. Moreno: Investigations on protein crystal growth by the gel acupuncture method, *Acta Crystallogr. D* **50**, 484–490 (1994)
- 47.69 V.M. Bolaños-García: The use of oil in a counter-diffusive system allows to control nucleation and coarsening during protein crystallization, *J. Cryst. Growth* **253**, 517–523 (2003)
- 47.70 J.M. García-Ruiz, A. Moreno, D. Rondón, F. Otálora, F. Zauscher: Teaching protein crystallization by the

- gel acupuncture technique, *J. Chem. Educ.* **75**, 442–446 (1998)
- 47.71 J.D. Ng, J.A. Gavira, J.M. García-Ruiz: Protein crystallization by capillary counterdiffusion for applied crystallographic structure determination, *J. Struct. Biol.* **142**, 218–231 (2003)
- 47.72 J.A. Gavira, D. Toh, J. Lopez-Jaramillo, J.M. García-Ruiz, J.D. Ng: *Ab initio* crystallographic structure determination of insulin from protein to electron density without crystal handling, *Acta Crystallogr. D* **58**, 1147–1154 (2002)
- 47.73 C. Biertümpfel, J. Basquin, D. Suck, C. Sauter: Crystallization of biological macromolecules using agarose gel, *Acta Crystallogr. D* **58**, 1657–1659 (2002)
- 47.74 N. Mirkin, B.A. Frontana-Urbe, A. Rodríguez-Romero, A. Hernández-Santoyo, A. Moreno: The influence of an internal electric field upon protein crystallization using the gel-acupuncture method, *Acta Crystallogr. D* **59**, 1533–1538 (2003)
- 47.75 M. Taleb, C. Didierjean, C. Jelsch, J.P. Mangeot, A. Aubry: Equilibrium kinetics of lysozyme crystallization under an external electric field, *J. Cryst. Growth* **232**, 250–255 (2001)
- 47.76 C. Nanev, A. Penkova: Nucleation of lysozyme crystals under external electric and ultrasonic fields, *J. Cryst. Growth* **232**, 285–293 (2001)
- 47.77 M.I. Al-Haq, E. Lebrasseur, H. Tsuchiya, T. Torii: Protein crystallization under an electric field, *Crystallogr. Rev.* **13**, 29–64 (2007)
- 47.78 E. Nieto-Mendoza, B. Frontana-Urbe, G. Sazaki, A. Moreno: Investigations on electromigration phenomena for protein crystallization using crystal growth cells with multiple electrodes, effect of the potential control, *J. Cryst. Growth* **275**, 1443–1452 (2005)
- 47.79 A. Moreno, G. Sazaki: The use of a new ad hoc growth cell with parallel electrodes for the nucleation control of lysozyme, *J. Cryst. Growth* **264**, 438–444 (2004)
- 47.80 G. Sazaki, A. Moreno, K. Nakajima: Novel coupling effects of the magnetic and electric fields on protein crystallization, *J. Cryst. Growth* **262**, 499–502 (2004)
- 47.81 A. Penkova, O. Gliko, I.L.D. Feyzim, V. Hodjaoglu, C. Nanev, P.G. Vekilov: Enhancement and suppression of protein crystal nucleation due to electrically driven convection, *J. Cryst. Growth* **275**, e1527–e1532 (2005)
- 47.82 G. Sazaki, E. Yoshida, H. Komatsu, T. Nakada, S. Miyashita, K. Watanabe: Effects of a magnetic field on the nucleation and growth of protein crystals, *J. Cryst. Growth* **173**, 231–234 (1997)
- 47.83 Y. Suzuki, S. Miyashita, G. Sazaki, T. Nakada, T. Sawada, H. Komatsu: Effects of pressure on growth kinetics of tetragonal lysozyme crystals, *J. Cryst. Growth* **208**, 638–644 (2000)
- 47.84 A. Kadri, G. Jenner, M. Damak, B. Lorber, R. Giegé: Crystallogensis studies of proteins in agarose gel—combined effect of high hydrostatic pressure and pH, *J. Cryst. Growth* **257**, 390–402 (2003)
- 47.85 Y. Mori, K. Takano, H. Adachi, T. Inoue, S. Murakami, H. Matsumura, T. Sasaki: Protein crystallization using femto-second laser irradiation and solution-stirring, *Proc. 11th Int. Conf. Cryst. Biol. Macromol.* (Quebec City 2006)
- 47.86 A. McPherson, P. Shlichta: The use of heterogeneous and epitaxial nucleants to promote growth of protein crystals, *J. Cryst. Growth* **90**, 47–50 (1988)
- 47.87 T.E. Paxton, A. Sambanis, R.W. Rousseau: Mineral substrates as heterogeneous nucleants in the crystallization of proteins, *J. Cryst. Growth* **198/199**, 656–660 (1999)
- 47.88 N.E. Chayen, E. Saridakis, R. El-Bahar, Y. Nemirovsky: Porous silicon: An effective nucleation-inducing material for protein crystallization, *J. Mol. Biol.* **312**, 591–595 (2001)
- 47.89 N.E. Chayen, L. Hench: (Imperial College Innovations Limited, UK) Mesoporous glass as nucleant for macromolecule crystallisation, Patent No. W02004041847 (2003)
- 47.90 R.P. Sear: Protein crystals and charged surfaces: Interactions and heterogeneous nucleation, *Phys. Rev. E* **67**, 061907/1–061907/7 (2003)
- 47.91 N.E. Chayen, E. Saridakis, R.P. Sear: Experiment and theory for heterogeneous nucleation of protein crystals in a porous medium, *Proc. Natl. Acad. Sci. USA* **103**, 597–601 (2006)
- 47.92 W.W. Wilson: Monitoring crystallization experiments using dynamic light scattering: Assaying and monitoring protein crystallization in solution, *Methods Companion Methods Enzymol.* **1**, 110–117 (1990)
- 47.93 G. Juárez-Martínez, C. Garza, R. Castillo, A. Moreno: A dynamic light scattering investigation of the nucleation and growth of thaumatin crystals, *J. Cryst. Growth* **232**, 119–131 (2001)
- 47.94 N. Chayen, M. Dieckmann, K. Dierks, P. Fromme: Size and shape determination of proteins in solution by a noninvasive depolarized dynamic light scattering instrument, *Ann. N. Y. Acad. Sci. (Transport Phenomena in Microgravity)*, **1027**, 20–27 (2004)
- 47.95 C. Chin, J.B. Dence, J.C. Warren: Crystallization of human placental estradiol 17 β -dehydrogenase. A new method for crystallizing labile enzymes, *J. Biol. Chem.* **251**, 3700–3705 (1976)
- 47.96 M.C. Vaney, I. Broutin, P. Retailleau, A. Douangmath, S. Lafont, C. Hamiaux, T. Prangé, A. Ducruix, M. Riès-Kautt: Structural effects of monovalent anions on polymorphic lysozyme crystals, *Acta Crystallogr. D* **57**, 929–940 (2001)
- 47.97 A. McPherson, J. Weickmann: X-ray analysis of new crystal forms of the sweet protein thaumatin, *J. Biomol. Struct. Dyn.* **7**, 1053–1060 (1990)

- 47.98 J. Qi, N.I. Wakayama, M. Ataka: Magnetic suppression of convection in protein crystal growth processes, *J. Cryst. Growth* **232**, 132–137 (2001)
- 47.99 S.X. Lin, M. Zhou, A. Azzi, G.J. Xu, N.I. Wakayama, M. Ataka: Magnet used for protein crystallization: novel attempts to improve the crystal quality, *Biophys. Res. Commun.* **275**, 274–278 (2000)
- 47.100 T. Sato, Y. Yamada, S. Saijo, T. Hori, R. Hirose, N. Tanaka, G. Sazaki, K. Nakajima, N. Igarashi, M. Tanaka, Y. Matsuura: Enhancement in the perfection of orthorhombic lysozyme crystals grown in a high magnetic field (10 T), *Acta Crystallogr. D* **56**, 1079–1083 (2000)
- 47.101 C.W. Zhong, N.I. Wakayama: Effect of a high magnetic field on the viscosity of an aqueous solution of protein, *J. Cryst. Growth* **226**, 327–332 (2001)
- 47.102 L. Wang, C.W. Zhong, N.I. Wakayama: Damping of natural convection in the aqueous protein solutions by the application of high magnetic fields, *J. Cryst. Growth* **237**, 312–316 (2002)
- 47.103 D.C. Yin, N.I. Wakayama, Y. Inatomi, W.D. Huang, K. Kuribayashi: Strong magnetic field effect on the dissolution process of tetragonal lysozyme crystals, *Adv. Space Res.* **32**, 217–223 (2003)
- 47.104 D. Lübbert, A. Meents, E. Weckert: Accurate rocking-curve measurements on protein crystals grown in a homogeneous magnetic field of 2.4 T, *Acta Crystallogr. D* **60**, 987–998 (2004)
- 47.105 A. Moreno, B. Quiroz-García, F. Yokaichiya, V. Stojanoff, P. Rudolph: Protein crystal growth in gels and stationary magnetic fields, *Cryst. Res. Technol.* **42**, 231–236 (2007)
- 47.106 T. Sato, Y. Yamada, S. Saijo, T. Hori, R. Hirose, N. Tanaka, G. Sazaki, K. Nakajima, N. Igarashi, M. Tanaka, Y. Matsuura: Improvement in diffraction maxima in orthorhombic HEWL crystal grown under high magnetic field, *J. Cryst. Growth* **232**, 229–236 (2001)
- 47.107 T. Terwillinger: Structural genomics in America, *Nat. Struct. Biol.* **7**, 935–939 (2000)
- 47.108 R. Hui, A. Edwards: High-throughput protein crystallization, *J. Struct. Biol.* **142**, 154–161 (2003)
- 47.109 J.-W. de Gier, J. Lührink: Biogenesis of inner membrane proteins in *Escherichia coli*, *J. Mol. Microbiol.* **40**, 314–322 (2001)
- 47.110 S.A. Lesley: High-throughput proteomics: Protein expression and purification in the postgenomic world, *Protein Expr. Purif.* **22**, 159–164 (2001)
- 47.111 Stephen White: http://blanco.biomol.uci.edu/Membrane_Proteins_xtal.html (2009)
- 47.112 R. Grishammer, C.G. Tate: Overexpression of integral membrane proteins for structural studies, *Q. Rev. Biophys.* **28**, 315–422 (1995)
- 47.113 A. Arora, D. Rinehart, G. Szabo, L.K. Tamm: Re-folded outer membrane protein A of *Escherichia coli* forms ion channels with two conductance states in planar lipid bilayers, *J. Biol. Chem.* **275**, 1594–1600 (2000)
- 47.114 M. Müller, H.G. Koch, K. Beck, U. Schäfer: Protein traffic in bacteria: Multiple routes from the ribosome to and across the membrane, *Prog. Nucleic Acid Res. Mol. Biol.* **66**, 107–157 (2001)
- 47.115 G. Chang, R.H. Spencer, A.T. Lee, M.T. Barclay, D.C. Rees: Structure of the MscL homolog from *Mycobacterium tuberculosis*: A gated mechanosensitive ion channel, *Science* **282**, 2220–2226 (1998)
- 47.116 C.G. Tate: Overexpression of mammalian integral membrane proteins for structural studies, *FEBS Letters* **504**, 94–98 (2001)
- 47.117 K.E.S. Matlack, W. Mothes, T.A. Rapoport: Protein translocation: Tunnel vision, *Cell* **92**, 381–390 (1998)
- 47.118 J.C. Otto, D.L. De Witt, W.L. Smith: N-glycosylation of prostaglandin endoperoxide synthases-1 and -2 and their orientations in the endoplasmic reticulum, *J. Biol. Chem.* **268**, 18234–18242 (1993)
- 47.119 M.P. Patricelli, H.A. Lashuel, D.K. Giang, J.W. Kelly, B.F. Cravatt: Comparative characterization of a wild type and transmembrane domain-deleted fatty acid amide hydrolase: Identification of the transmembrane domain as a site for oligomerization, *Biochemistry* **37**, 15177–15187 (1998)
- 47.120 M.H. Bracey, M.A. Hanson, K.R. Masuda, R.C. Stevens, B.F. Cravatt: Structural adaptations in a membrane enzyme that terminates endocannabinoid signaling, *Science* **298**, 1793–1796 (2002)
- 47.121 G.J. Turner, R. Reusch, A.M. Winter-Vann, L. Martínez, M.C. Betlach: Heterologous gene expression in a membrane-protein-specific system, *Protein Expr. Purif.* **17**, 312–323 (1999)
- 47.122 J.L. Cereghino, J.M. Cregg: Heterologous protein expression in the methylotrophic yeast *Pichia pastoris*, *FEMS Microbiol. Rev.* **24**, 45–66 (2000)
- 47.123 K. Sreekrishna, R.G. Brankamp, K.E. Kropp, D.T. Blankenship, J.T. Tsay, P.L. Smith, J.D. Wierschke, A. Subramaniam, L.A. Birkenberger: Strategies for optimal synthesis and secretion of heterologous proteins in the methylotrophic yeast *Pichia pastoris*, *Gene* **190**, 55–62 (1997)
- 47.124 P.J. Loll: Membrane protein structural biology: The high throughput challenge, *J. Struct. Biol.* **142**, 144–153 (2003)
- 47.125 J.P. Rosenbusch: Stability of membrane proteins: relevance for the selection of appropriate methods for high-resolution structure determinations, *J. Struct. Biol.* **136**, 144–157 (2001)
- 47.126 E.M. Landau, J.P. Rosenbusch: Lipidic cubic phases: A novel concept for the crystallization of membrane proteins, *Proc. Natl. Acad. Sci. USA* **93**, 14532–14535 (1996)
- 47.127 A. Cheng, B. Hummel, H. Qiu, M. Caffrey: A simple mechanical mixer for small viscous lipid-containing samples, *Chem. Phys. Lipids* **95**, 11–21 (1998)

- 47.128 S.D. Durbin, W.E. Carlson: Lysozyme crystal growth studied by atomic force microscopy, *J. Cryst. Growth* **122**, 71–79 (1992)
- 47.129 A.J. Malkin, Y.G. Kuznetsov, A. McPherson: Incorporation of microcrystals by growing protein and virus crystals, *Proteins* **24**, 247–252 (1996)
- 47.130 D.A. Walters, B.L. Smith, A.M. Belcher, G.T. Palocz, G.D. Stucky, D.E. Morse, P.K. Hansma: Modification of calcite crystal growth by abalone shell proteins: an atomic force microscope study, *Biophys. J.* **72**, 1425–1433 (1997)
- 47.131 H. Li, A. Nadarajah, M.L. Pusey: Determining the molecular-growth mechanisms of protein crystal faces by atomic force microscopy, *Acta Crystallogr. D* **55**, 1036–1045 (1999)
- 47.132 Y.F. Dufrene: Application of atomic force microscopy to microbial surfaces: From reconstituted cell surface layers to living cells, *Micron* **32**, 153–165 (2001)
- 47.133 M. Plomp, A. McPherson, A.J. Malkin: Repair of impurity-poisoned protein crystal surfaces, *Proteins* **50**, 486–495 (2003)
- 47.134 A.J. Malkin, R.E. Thorne: Growth and disorder of macromolecular crystals: Insights from atomic force microscopy and X-ray diffraction studies, *Methods* **34**, 273–299 (2004)
- 47.135 S. Hiroyuki: Modification, characterization and handling of protein molecules as the first step to bioelectronic devices, *Electron. Biotechnol. Adv. (EL.B.A.) Forum Ser.* **2**, 157–174 (1996)
- 47.136 I. Reviakine, W. Bergsma-Schutter, A. Brisson: Growth of protein 2-D crystals on supported planar lipid bilayers imaged in situ by AFM, *J. Struct. Biol.* **121**, 356–361 (1998)
- 47.137 S.-T. Yau, B.R. Thomas, P.G. Vekilov: Molecular mechanisms of crystallization and defect formation, *Phys. Rev. Lett.* **85**, 353–356 (2000)
- 47.138 A.P. Wheeler, C.S. Sikes: Proteins from oyster shell: biomineralization regulators and commercial polymer analogs, *Mater. Res. Soc. Symp. Proc.* **599**, 209–224 (2000)
- 47.139 H. Kim, R.M. Garavito, R. Lal: Atomic force microscopy of the three-dimensional crystal of membrane protein, OmpC porin, *Colloids Surf. B: Biointerfaces* **19**, 347–355 (2000)
- 47.140 A. Nadarajah, H. Li, J.H. Konnert, M.L. Pusey: New AFM techniques for investigating molecular growth mechanisms of protein crystals, *Proc. SPIE* **4098**, 31–39 (2000)
- 47.141 A. McPherson: Macromolecular crystal structure and properties as revealed by atomic force microscopy, *NATO Sci. Ser. I: Life Behav. Sci.* **325**, 1–8 (2001)
- 47.142 A. McPherson, A.J. Malkin, Y.G. Kuznetsov: Atomic force microscopy in the study of macromolecular crystal growth, *Annu. Rev. Biophys. Biomol. Struct.*, **29**, 361–410 (2000)
- 47.143 J. Yang, L.K. Tamm, T.W. Tillack, Z. Shao: New approach for atomic-force microscopy of membrane proteins. The imaging of cholera toxin, *J. Mol. Biol.* **229**, 286–290 (1993)
- 47.144 P. Hallett, G. Offer, M.J. Miles: Atomic force microscopy of the myosin molecule, *Biophys. J.* **68**, 1604–1606 (1995)
- 47.145 D. Pang, S. Yoo, W.S. Dynan, M. Jung, A. Dritschilo: Ku proteins join DNA fragments as shown by atomic force microscopy, *Cancer Res.* **57**, 1412–1415 (1997)
- 47.146 K.K. Chittur: Proteins on surfaces: methodologies for surface preparation and engineering protein function, *Surfact. Sci. Ser.* **75**, 143–179 (1998)
- 47.147 J. Cao, D.K. Pham, L. Tonge, D.V. Nicolau: Simulation of the force-distance curves of atomic force microscopy for proteins by the Connolly surface approach, *Proc. SPIE* **4590**, 187–194 (2001)
- 47.148 W. Huang, S. Taylor, K. Fu, Y. Lin, D. Zhang, T.W. Hanks, A.M. Rao, Y.-P. Sun: Attaching proteins to carbon nanotubes via diimide-activated amidation, *Nano Lett.* **2**, 311–314 (2002)
- 47.149 J. Torres, T.J. Stevens, M. Samso: Membrane proteins: the "Wild West" of structural biology, *Trends Biochem. Sci.* **28**, 137–144 (2003)
- 47.150 A. Tulpar, D.B. Henderson, M. Mao, B. Caba, R.M. Davis, K.E. Van Cott, W.A. Ducker: Unnatural proteins for the control of surface forces, *Langmuir* **21**, 1497–1506 (2005)
- 47.151 P.L. Silva: Imaging proteins with atomic force microscopy: An overview, *Curr. Protein Peptide Sci.* **6**, 387–395 (2005)
- 47.152 E.A. Stura, I.A. Wilson: Applications of the streak seeding technique in protein crystallization, *J. Cryst. Growth* **110**, 270–282 (1991)
- 47.153 Y. Zhang, T. Fu, H. Li, K. Xu, K. State: Co-deposition of electrocrystallized calcium phosphate and protein as biocoatings on the prosthetic materials, *Guisuanyan Xuebao* **28**, 379–380, 384 (2000), in Chinese
- 47.154 A. Moreno, M. Rivera: Conceptions and first results on the electrocrystallization behaviour of ferritin, *Acta Crystallogr. D* **61**, 1678–1681 (2005)
- 47.155 Y.H. Chen, J.Y. Wu, Y.C. Chung: Preparation of polyaniline-modified electrodes containing sulfonated polyelectrolytes using layer-by-layer techniques, *Biosens. Bioelectron.* **22**, 489–494 (2006)
- 47.156 J.P.H. Perez, E. Lopez-Cabarcos, B. Lopez-Ruiz: The application of methacrylate-based polymers to enzyme biosensors, *Biomol. Eng.* **23**, 233–245 (2006)
- 47.157 A. Baba, W. Knoll, R. Advincula: Simultaneous in situ electrochemical, surface plasmon optical, and atomic force microscopy measurements: Investigations of conjugated polymer electropolymerization, *Rev. Sci. Instrum.* **77**, 064101 (2006)
- 47.158 G.A. Álvarez-Romero, E. Garfías-García, M.T. Ramírez-Silva, C. Galán-Vidal, M. Romero-Romo,

- M. Palomar-Pardavé: Electrochemical and AFM characterization of the electropolymerization of pyrrole over a graphite-epoxy resin solid composite electrode, in the presence of different anions, *Appl. Surf. Sci.* **252**, 5783–5792 (2006)
- 47.159 T. Hernández-Pérez, N. Mirkin, A. Moreno, M. Rivera: In situ immobilization of catalase monocrystals on HOPG by the voltammetric growth of polypyrrole films for AFM investigations, *Electrochem. Solid-State Lett.* **5**, 37–39 (2002)
- 47.160 F. Acosta, D. Eid, L. Marín-García, B.A. Frontana-Urbe, A. Moreno: From cytochrome c crystals to a solid-state electron-transfer device, *Cryst. Growth. Des.* **7**, 2187–2191 (2008)
- 47.161 N. Mirkin, J. Jaconcic, V. Stojanoff, A. Moreno: High resolution X-ray crystallographic structure of cytochrome c from bovine heart and its application to the design of an electron transfer biosensor, *Proteins: Structure, Function, Bioinformatics* **70**, 83–92 (2008)
- 47.162 T.L. Blundell, L.N. Johnson: *Protein Crystallography* (Oxford Univ. Press, Oxford 1976)
- 47.163 C. Giacovazzo, C. Giazovazzo, H.L. Monaco, G. Artioli, D. Viterbo, G. Ferraris: *Fundamentals of Crystallography* (Oxford Univ. Press, Oxford 2002)
- 47.164 D.M. Blow: *Outline of Crystallography for Biologists* (Oxford Univ. Press, Oxford 2002)
- 47.165 A. McPherson: *Macromolecular Crystallography* (Wiley, New York 2002)
- 47.166 D.E. McRee: *Practical Protein Crystallography* (Academic, New York 1999)
- 47.167 H.M. Einspahr: A functioning crystallization database: What do we want and how do we get it? *Int. Sch. Biological Cryst. (Granada 2006)*
- 47.168 N. Niimura: *Neutron Protein Crystallography: Hydrogen and Hydration in Proteins. Neutron Scattering in Biology* (Springer, Berlin Heidelberg 2006) pp. 43–62
- 47.169 D.A.A. Myles: Neutron protein crystallography: current status and brighter future, *Curr. Opin. Struct. Biol.* **16**, 630–637 (2006)
- 47.170 R.M. Glaeser, K. Downing, D. DeRosier, W. Chiu, J. Frank: *Electron Crystallography of Biological Macromolecules* (Oxford Univ. Press, Oxford 2007)

Crystallization

48. Crystallization from Gels

S. Narayana Kalkura, Subramanian Natarajan

48.1 Gel Growth in Crystal Deposition Diseases1608	48.10 Dicalcium Phosphate Dihydrate (DCPD)1620
48.1.1 Gel Growth of Crystals..... 1608	48.10.1 Effect of Additives on Crystallization of Calcium Phosphates..... 1620
48.1.2 Types of Gels 1608	48.10.2 Effect of Some Extracts of Cereals, Plants, and Fruits and Tartaric Acid 1622
48.1.3 Mechanism of Gelling..... 1609	48.10.3 Calcium Hydrogen Phosphate Pentahydrate (Octacalcium Phosphate, OCP) 1622
48.2 Experimental Methods1609	48.10.4 Magnesium Ammonium Phosphate Hexahydrate (MAP) and Magnesium Hydrogen Phosphate Trihydrate (MHP) 1622
48.2.1 Chemical Reaction 1609	48.11 Calcium Sulfate1623
48.2.2 Complex Dilution 1609	48.12 Uric Acid and Monosodium Urate Monohydrate1623
48.2.3 Solubility Reduction 1610	48.13 L-Cystine1624
48.2.4 Chemical Reduction..... 1610	48.14 L-Tyrosine, Hippuric Acid, and Ciprofloxacin1625
48.2.5 Electrochemical/Electrolysis 1610	48.15 Atherosclerosis and Gallstones1625
48.2.6 Crystal Growth in the Presence of a Magnetic Field..... 1610	48.15.1 Crystal Growth in Bile 1625
48.2.7 Nucleation Control 1610	48.15.2 Cholesterol and Related Steroids 1626
48.3 Pattern Formation in Gel Systems1610	48.15.3 Cholic Acid 1627
48.4 Crystals Grown Using Gel Technique1611	48.16 Crystallization of Hormones: Progesterone and Testosterone1628
48.4.1 Advantages of Crystallization in Gels 1613	48.17 Pancreatitis1628
48.5 Application in Crystal Deposition Diseases1614	48.17.1 Calcium Carbonate 1629
48.5.1 Crystal Deposition Diseases 1614	48.18 Conclusions1629
48.5.2 Significance of In Vitro Crystallization 1614	References 1630
48.5.3 Crystallization of the Constituents of Crystal Deposits 1616	
48.6 Crystal-Deposition-Related Diseases1616	
48.6.1 Urinary Stone Disease 1616	
48.6.2 Theories of Urinary Stone Formation 1616	
48.6.3 Role of Trace Elements in Urinary Stone Formation 1617	
48.7 Calcium Oxalate1617	
48.7.1 Crystallization of Calcium Oxalate1617	
48.7.2 Effect of Trace Elements 1618	
48.7.3 Effect of Tartaric and Citric Acids. 1618	
48.7.4 Effect of the Extracts of Cereals, Plants, and Fruits 1618	
48.8 Calcium Phosphates1619	
48.9 Hydroxyapatite (HAP)1620	

Among the various crystallization techniques, crystallization in gels has found wide applications in the fields of biomineralization and macro-molecular crystallization in addition to crystallizing materials having nonlinear optical, ferroelectric, ferromagnetic, and other properties. Furthermore, by using this method it is possible to grow single

crystals with very high perfection that are difficult to grow by other techniques. The gel method of crystallization provides an ideal technique to study crystal deposition diseases, which could lead to better understanding of their etiology. This chapter focuses on crystallization in gels of compounds that are responsible for crystal deposition diseases. The introduction is followed by a description of the various gels used, the mechanism of gelling, and the fascinating phenomenon of Liesegang ring formation, along with various gel growth techniques. The importance and scope of study on crystal deposition diseases and the need for crystal growth experiments using gel media are stressed. The various crystal deposition diseases, viz. (1) urolithiasis, (2) gout or arthritis, (3) cholelithiasis and atherosclerosis, and (4) pancreatitis and details regarding the

constituents of the crystal deposits responsible for the pathological mineralization are discussed. Brief accounts of the theories of the formation of urinary stones and gallstones and the role of trace elements in urinary stone formation are also given. The crystallization in gels of (1) the urinary stone constituents, viz. calcium oxalate, calcium phosphates, uric acid, cystine, etc., (2) the constituents of the gallstones, viz. cholesterol, calcium carbonate, etc., (3) the major constituent of the pancreatic calculi, viz., calcium carbonate, and (4) cholic acid, a steroidal hormone are presented. The effect of various organic and inorganic ions, trace elements, and extracts from cereals, herbs, and fruits on the crystallization of major urinary stone and gallstone constituents are described. In addition, tables of gel-grown organic and inorganic crystals are provided.

48.1 Gel Growth in Crystal Deposition Diseases

48.1.1 Gel Growth of Crystals

Recently, there has been increasing interest in crystal growth in gels on account of its suitability to grow crystals of biological macromolecules and in studies involving biomineralization. The gel method of crystal growth is probably the most simple and versatile technique, compared with other methods of crystal growth from solutions under ambient conditions [48.1]. In 1896, *Liesegang* first observed the periodic precipitation of slightly soluble salts in gelatin [48.2]. Later, this technique was used extensively to crystallize many organic, inorganic, and even biological macromolecules in various colloidal media. The gel method of crystallization is well described by *Henisch* [48.1,3], *Arora* [48.4], and *Patel and Venkateswara Rao* [48.5] as well as by *Lefauchaux and Robert* [48.6]. The present chapter aims to review crystallization in gels with a special focus on crystallization of compounds causing crystal deposition diseases.

48.1.2 Types of Gels

Gel growth is a particular case of solution growth where the solution is trapped in a polymeric structure. The gel is a loosely linked polymer of a two-component sys-

tem formed by the establishment of a three-dimensional system of cross-linkages between molecules of one of the components. The system as a whole is permeated by the other component as a continuous phase, giving a semisolid, generally rich in liquid. Gels can be prepared by a variety of techniques and materials. The most commonly used ones for crystallization are gels of silica, agar, gelatin, clay (bentonite), and polyacrylamide.

Silica gel is prepared [48.1] by mixing aqueous solution of sodium metasilicate and mineral or organic acid. Gelation takes place in times ranging from a few seconds to a few months, depending on the pH, temperature, and concentration of the gel solution. To form agar gel [48.7], agar-agar is dissolved in water (1–2% by weight) and boiled. When this solution cools down, gelation takes place. Gelatin gel is prepared [48.8] by dissolving gelatin in water, stirring at a constant temperature of 50 °C for 1 h and cooling to room temperature. A small quantity of formaldehyde is added to strengthen the gel. To prepare clay gel, powdered clay is slowly sifted on rapidly stirred water making a blend until about 9% clay has been added; the gel sets immediately. Polyacrylamide gel [48.9] is prepared by dissolving 3.99 wt % acrylamide and 0.02 wt % of a cross-linking agent in water. The solution is bubbled

with nitrogen and degassed by lowering the pressure. This results in a rigid transparent gel. Crystallization has also been attempted using other gels such as pectin, polyethylene oxide (PEO), polyvinyl alcohol (PVA), and tetramethoxysilane (TMOS) [48.1, 3–7].

48.1.3 Mechanism of Gelling

Gels can be formed by cooling of a sol, by chemical reaction or by addition of a precipitating agent or incompatible solvents. The time taken for the gelling process varies from minutes to days, depending on the nature of the reagents and its temperature, pH, and history. The mechanical properties of fully developed gels can vary, depending on the gel density.

In the case of silica gels, when sodium metasilicate (Na_2SiO_3) is dissolved in water, monosilicic acid and sodium hydroxide are produced initially as per the

following reaction



Later on, monosilicic acid polymerizes with the liberation of water. The process of polymerization continues, until a three-dimensional network of Si-O links is established. The hydrogen ion concentration (pH) plays a vital role in the gelling process. During polymerization, it is known that two types of ions, viz. H_3SiO_4^- and $\text{H}_2\text{SiO}_4^{2-}$, are produced, whose relative amounts depend on the pH. The formation of the more reactive $\text{H}_2\text{SiO}_4^{2-}$ is favored at high pH values. However, higher charge implies a greater degree of mutual repulsion. H_3SiO_4^- is favored at low pH values and is responsible for the sharp increase in viscosity. Very high or very low pH values inhibit gelation. Gelling mechanism regarding agar and TMOS gels are reviewed by Lefaucheur and Robert [48.6].

48.2 Experimental Methods

Crystal growth methods in gels fall into the following classes: chemical reaction, complex dilution, reduction of solubility, chemical reduction, and electrochemical techniques [48.5].

48.2.1 Chemical Reaction

This method is suitable for crystals which are mostly insoluble or sparingly soluble in water and which decompose before melting. Here, two soluble reactants are allowed to react inside the gel medium by incorporation of one of the reactants (I) in the gel, whereas the other reactant (II), which is used as the supernatant, diffuses into the gel medium (Fig. 48.1). The reaction inside the gel leads to the formation of an insoluble or sparingly soluble crystalline product. The basic requirements of this method are:

1. The gel must remain stable in the presence of reacting solutions
2. It must not react either with the solutions or with the product.

U-tubes are used, where the two reactants are allowed to react by diffusion into an inactive gel. This technique can also be adopted to crystallize compounds which have poor aqueous and organic solubility (uric acid and cystine) using the displacement reaction method [48.10, 11].

48.2.2 Complex Dilution

In this method, the material to be crystallized is first complexed in some reagents which enhance its solubility. It is then allowed to diffuse into a gel which is free from active reagents. As the complex solution diffuses through the gel it gets diluted. This results in a high supersaturation of the material to be crystallized and

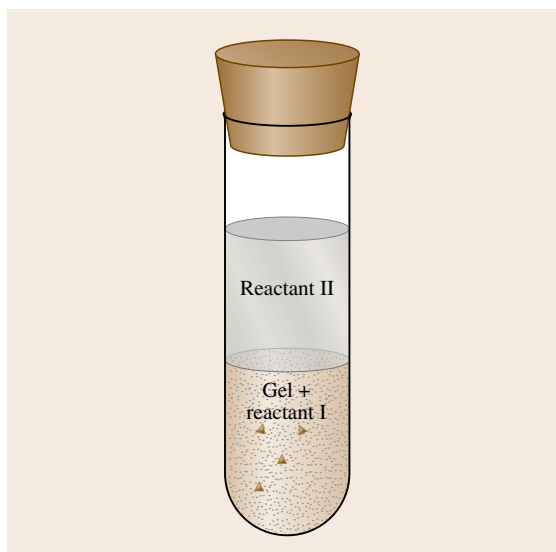


Fig. 48.1 Reaction method (single diffusion)

hence nucleation and subsequent crystallization occurs. Crystals of mercuric sulfide, cuprous, and silver halides and selenium have been grown using this method [48.5].

48.2.3 Solubility Reduction

This method is generally used for crystallization of highly water-soluble substances. The substance to be grown is dissolved in water and incorporated in the gel before gelation. After the gel has been set, a solution that reduces the solubility of the substance (solute) is added as a supernatant solution to induce crystallization. Compounds which have low aqueous solubility can also be crystallized using this technique. Steroids which have low aqueous solubility have been crystallized using this technique by reducing the water content in the gel by incorporating an organic solvent [48.12]. During this process of crystallization, crystals can be observed in the supernatant solution above the gel due to the reverse diffusion of the precipitating solvent [48.13, 14].

48.2.4 Chemical Reduction

This method is particularly suitable for growing metallic crystals (Cu, Au, and Ni). The metallic salt is incorporated with the gel and an aqueous solution of a reducing agent is slowly allowed to diffuse through the gel, where chemical reduction takes place to form metallic crystals [48.5].

48.2.5 Electrochemical/Electrolysis

Gels can be used to crystallize metals by electrolysis. *George and Vaidyan* [48.15] reported growth of single crystals and dendrites of silver. Recently, *Muzikar et al.* [48.16] reported crystallization of microcrystals of gold. Here, a small current was passed between two gold electrodes through a silica gel doped with HAuCl_4 . Single crystals of gold of sizes ranging from hundreds of nanometer to hundreds of micrometer were grown by

this technique. *Muzikar et al.* [48.17] have also crystallized platinum particles and a platinum complex by an identical procedure.

48.2.6 Crystal Growth in the Presence of a Magnetic Field

The effect of a magnetic field (up to 3 T) on the crystallization of calcium tartrate [48.18] and strontium tartrate [48.19] has been reported. The magnetic field has the effect of reducing the number of crystals formed but helps in the growth of a few, larger crystals. Crystallization of cholesterol in gels in a magnetic field was studied by *Sundaram et al.* [48.20, 21]; it was found that the presence of the magnetic field reduced the nucleation time and number of crystals but that there was an increase in the size of the crystals grown.

48.2.7 Nucleation Control

During crystallization in gels, the growing crystals compete with one another for the solute atoms, leading to a reduction in crystal size and perfection. Hence, nucleation has to be suppressed until only a few crystals are formed. The use of a particular combination of reactants, to grow the required crystals, has been found to reduce the nucleation density [48.22]. Acid-set gels, choosing a particular acid (based on experiments with various acids), is known to yield larger crystals [48.22]. It has been reported that changing the gel structure by varying one or more of the parameters, viz. pH and density, and by gel aging, can decrease the number of nucleation centers [48.1, 3–7]. The use of an intermediate neutral gel is also found to slow down the reaction and thereby reduce the number of nucleated crystals [48.23]. In another method, the concentration of the diffusing reactant is initially kept below the level at which nucleation is known to occur and then increased gradually in a series of small steps. Crystals grown by this method are more perfect and larger than those grown otherwise.

48.3 Pattern Formation in Gel Systems

Pattern formation is widespread in nature and can be found in structures ranging from agate rocks and gold veins to the growth of bacterial rings in agar and gallstones [48.24–26]. A specific example discussed below is the Liesegang ring structure, discovered in 1896 [48.2]. When coprecipitated ions interdiffuse in

a gelatinous medium, the sparingly soluble salt may precipitate discontinuously in a spectacular pattern of parallel bands. The pleasing appearance of Liesegang bands, as well as their spatiotemporal distribution, has elicited a steady proliferation of publications on the subject [48.3, 27–29]. It is quite easy to produce the

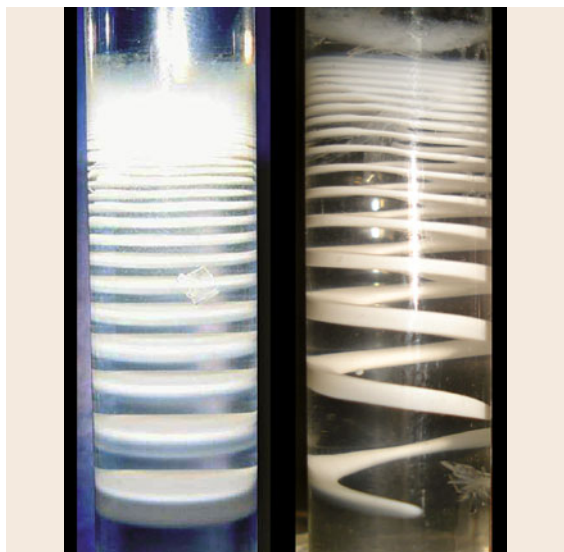


Fig. 48.2 Disc and helical Liesegang rings of calcium phosphates in silica gel (after [48.32])

patterns in the laboratory. Liesegang rings can be produced in gels by diffusing one of the reactants into an inert gel medium containing another reactant. The simplest and usual way to perform a Liesegang ring experiment is to fill a tube with an inert semisolid medium which contains one of the reactants (B), called the inner electrolyte. The other reactant (A), referred to as the outer electrolyte, is poured over the gel column as the supernatant solution. Usually the concentration level of the outer electrolyte is maintained high to minimize the possible loss of ions due to evaporation and other such transport mechanisms during the experimental processes. It involves the formation of concentric laminated rings or bands clearly separated in the direction perpendicular to the motion of the front [48.27]. The structures, which are often rings in circular geometries and bands in linear geometries, are formed by the nonuniform spatial distribution of crystals in a precipitation reaction in a gel [48.28, 29]. Recently, *George* and *Varghese* reported the formation of triplet Liesegang ring patterns [48.30]. *Terada* et al. [48.31] described the formation of sheets and helices of stron-

tium carbonate in silica gel. Helical rings of calcium phosphates (Fig. 48.2) were formed in silica gels by the diffusion of calcium ions into a phosphate-containing gel [48.32].

Though *in vivo* occurrence is rare, chemical concentration, geometry of the reactant containers or vessels, temperature, pH, and the presence of impurities are the main factors that influence the formation of Liesegang rings [48.33]. The role of the gel during the formation of Liesegang rings is essentially passive, i.e., to prevent convection of solutions and sedimentation of the precipitate. The dynamics of the banding are very complex, involving the coupling of diffusion and precipitation processes in a nonequilibrium regime.

Theoretical models explaining Liesegang patterns fall into two broad categories. The first one, called the prenucleation model, is based on the classical feedback cycle of supersaturation, precipitation, and depletion as originally proposed by *Ostwald* [48.34]. In the second theory, the so-called postnucleation or competitive particle growth model, it is assumed that competition between growing particles can, by itself, produce periodic precipitation structures, even in the absence of strong external gradients. It is worth mentioning that all the theories share the assumption that the precipitate appears as the system passes through some nucleation or coagulation thresholds. However, the theories differ in their pre- or postnucleation assumptions. The main unresolved problem in all these theories is the understanding of the mechanism behind the transformation of the diffusive reagents A and B into an immobile coagulant. *George* and *Varghese* proposed a new model [48.30, 35–38] based on the prime assumption that the boundary that separates the outer ions and the inner electrolyte virtually migrates in the positive direction of the advancement of the type A ions. *Izsák* and *Lagzi* [48.39] proposed a universal law, which is also valid in the case of various transport dynamics (purely diffusive, purely advective, and diffusion–advection cases). The mechanism responsible for these structures is not yet fully understood. The interest in precipitate patterning phenomena is growing because of the suitability of their underlying dynamics for modeling many self-organization processes [48.40, 41].

48.4 Crystals Grown Using Gel Technique

Recently, there have been several reports on the crystallization of inorganic, organic, organometallic compounds, and metals apart from biological macro-

molecules using gels. Some of the compounds (except biological macromolecules) which have been crystallized using gels are listed in Table 48.1a,b.

Table 48.1 (a) Organic/organometallic crystals grown in gels

Crystals grown	Gel used	Method adopted	Studies carried out	Reference
2-Amino-5-nitropyridinium dihydrogen phosphate	Silica	Single diffusion	Crystal growth and growth rate studies by holographic interferometry	[48.42]
Ammonium hydrogen D-tartrate	Silica	Single diffusion	Bulk growth, habit	[48.43]
Antimony thiourea-bromide	Silica	Single diffusion	Dielectric constant, refractive indices	[48.44]
Asparagine monohydrate	Agarose, carrageenan, gelatin	Single diffusion	Crystallization and habit modification	[48.45]
Barium oxalate	Agar-agar	Double diffusion	Growth and characterization	[48.46]
Benzil, phenyl phenol	Sephadex	Single diffusion	Growth and characterization	[48.47]
Bis-(1,3,5-benzenetricarboxylato) dipyridine, Zinc(II) nitrate	PEO	Double diffusion	Crystal growth	[48.48]
Cadmium tartarate	Silica	Double diffusion	Optical absorption	[48.49]
Calcium malate-decahydrate	Silica	Single diffusion	Growth and characterization	[48.50]
Calcium L-tartrate-tetrahydrate (Mn ²⁺ doped)	Silica	Single diffusion	Doping and dielectric studies	[48.51]
(Sr ²⁺ doped)			Growth and characterization	[48.52]
Cerium lanthanum-oxalate	Silica	Single diffusion	Growth and characterization	[48.53]
Cholic acid	Silica, TMOS	Single diffusion	Growth and characterization	[48.54]
Dysprosium-gadolinium oxalate	Silica	Single diffusion	Optical absorption and fluorescence studies	[48.55]
γ -Glycine	Silica	Single diffusion	NLO studies, dielectric constant, photoconductivity	[48.56]
Iron-manganese levo-tartrate (pure and mixed)	Silica	Single diffusion	Growth and characterization	[48.57]
Lead (II) <i>n</i> -octa-, <i>n</i> -nona- and <i>n</i> -decanoate	Silica	Double diffusion	Morphology	[48.58]
β -DL-Methionine	Silica	Single diffusion	Growth and characterization	[48.59]
3-Methyl-4-nitropyridine-1-oxide	TMOS	Single diffusion	X-ray topography, NLO experiments	[48.60]
L-Phenylalanine	Silica	Single diffusion	Growth and characterization	[48.61]
Rubidium hydrogen-tartrate, strontium tartrate-trihydrate and tetrahydrate	Silica	Single diffusion	Growth and characterization, effect of magnetic field, (Pb) ²⁺ doping laser scattering tomography, magnetic susceptibility measurements	[48.62] [48.19] [48.63]
Strontium malate trihydrate	Silica	Single diffusion	Growth and characterization	[48.64]

Table 48.1 (b) Inorganic crystals grown in gels

Crystals grown	Gel used	Method adopted	Studies carried out	Reference
Ammonium chloride	Agarose,	Single diffusion	Periodic roughening transitions, AFM, interference contrast microscopy	[48.65] [48.66]
	Agar, gelatin, pectin, PVA	Reduction of solubility by reducing the temperature	Morphology	
Barium nitrate, boric acid, potassium dichromate	Agar, gelatin, pectin, PVA	Reduction of solubility by reducing the temperature	Morphology	[48.66]
Barium iodate-monohydrate, calcium iodate (mono- and hexahydrates)	Silica	Single diffusion Double diffusion	Growth and characterization Growth, doping microtopography	[48.67] [48.68]
Calcium tungstate	Silica	Double diffusion	Nucleation behavior, crystal morphology	[48.69]
Copper iodide	Silica	Single diffusion (decomplexation)	Growth and characterization Influence of CuI-HI complex	[48.70] [48.71]
Gold	Silica	Electrochemical growth	Backscatter electron diffraction	[48.16]
Lead bromide	Silica	Double diffusion	Growth	[48.72]
Lead carbonate	Silica	Double diffusion	Topotactic relationships	[48.73]
Lead hydrogen-phosphate	TMOS	Single diffusion	Influence of a polycrystalline precipitation zone	[48.74]
Lead iodide	Silica	Single diffusion	Morphology, microstructure	[48.75]
β -Lithium ammonium-sulfate,	TMOS	Single diffusion	Morphology, epitaxial phenomena	[48.76]
β -Lithium sodium-sulfate, lithium sulfate-monohydrate	TMOS	Single diffusion	Epitaxial, intergrowth phenomena	[48.77]
Platinum, ammonium-hexachloroplatinate(IV)	Silica	Electrochemical	Growth	[48.17]
Potassium ferrocyanide-trihydrate	Silica	Solubility reduction	Growth and characterization	[48.78]
Sodium bromate	Agarose, gelatin, silica	Single diffusion	Habit changes in various gels	[48.79]
Sodium chlorate	Agarose	Single diffusion	Selective growth and distribution of crystalline enantiomers	[48.80]

48.4.1 Advantages of Crystallization in Gels

The gel is an ideal medium for diffusion reaction and it acts as a three-dimensional crucible holding the crystals in fixed positions without overlapping. It

is a chemically inert, transparent system for growing good-quality crystals. It is possible to observe the entire growth process and the grown crystals can be harvested easily. Gel method allows effective control over factors such as density, concentration, and pH

of the medium. Since crystals grow in the absence of convection, gel growth provides a good simulation of space growth experiments, as in the case of growth of protein crystals. To get valuable clues towards understanding the biomineralization process, extensive studies have been carried out on carbonates of calcium, barium, and strontium in silica gel

medium [48.81–84]. Crystal growth in gels has been used to simulate the crystal growth process in sedimentary environments [48.85]. The simulation of pathological biomineralization in human organs using gel technique and the crystallization of biological macromolecules using gels are some of the recent advancements in this field.

48.5 Application in Crystal Deposition Diseases

Quite a variety of materials occur as crystals in living tissues and plants. Biomineralization is found extensively among living systems (eggs, mollusks, shells, pearls, corals, bone, and teeth). Biomineralization leads to crystals of uniform size and morphology with specific crystallographic orientation and properties [48.86]. The use of sophisticated methods of crystal identification including analytical electron microscopy has led to the discovery of crystals in the human body system. In organisms, some tissues calcify while others do not. The control over their nucleation and growth patterns and their location developed during evolution. Many of the mineral deposits assist in the regulation of the levels of free cations and anions in cellular systems. The presence of crystals in the human body produces both beneficial and harmful effects. Bone and teeth are composed of oriented nanocrystals of hydroxyapatite (HAP, $\text{Ca}_{10}(\text{PO}_4)_6(\text{OH})_2$). Our sense of balance and acceleration is dependent upon the small calcite crystals present in the inner ear. Many crystal depositions in tissues are pathological, with unusual crystal forms and patterns of mineralization. The harmful effects of crystals result in the pathological deposition of crystals known as crystal deposition diseases.

48.5.1 Crystal Deposition Diseases

Crystal deposition diseases may be defined as pathological processes associated with the presence of microcrystals which contribute to tissue damage and cause pain and suffering [48.87]. The increasing incidence of crystal deposition diseases (Table 48.2) such as heart diseases, gout, gallstones, urinary stones, deposition in eyes, thyroid glands and bone marrow, etc., among our population has resulted in extensive research to understand their etiology and cure. Crystal nucleation frequently occurs in urinary tract, coronary artery tract, and gallbladder, resulting in formation of pathological urinary stones, atherosclerotic plaques, and gallstones, respectively. Although much technical advancements

have been made in the area of treatment of crystal deposition diseases, relatively little is known about the mechanisms involved in the process of pathological crystallization. Crystal deposition diseases are the result of a complex sequence of events that give rise to diseases through simple mechanical effects such as blocking ducts or hardening or weakening of flexible tissues. The formation of crystalline deposits in vivo is a multifactorial disorder, some of the significant factors being age, sex, occupation, diet, fluid intake, geographical location, and climate.

48.5.2 Significance of In Vitro Crystallization

Extensive research work is being carried out on the physicochemical aspects of compounds that are responsible for diseases such as atherosclerosis, gallstones, arthritis, urinary stones, etc., to study their growth mechanism and to find factors that can inhibit their growth in our body system [48.87–99]. One of the principal aims in this area is first to identify the mechanism of crystal growth conditions prevalent in biological systems and then to devise means of inhibiting the unwanted crystal growth. Despite the enormous research aimed at obtaining thorough knowledge of the genesis of pathological mineralization, the mechanism of crystal deposition remains largely unexplained. The main reason for this is the fact that mineralization in vivo cannot be observed directly. Also, in vivo experiments are possible only to a limited extent. Thus, the need to understand the situations that give rise to crystal deposition diseases has necessitated in vitro investigations of the crystalline components that lead to pathological deposits. The crystal growth process in gels is essentially like crystallization from solution and consists of the following three basic steps [48.81]:

1. Attainment of supersaturation of the salt to be deposited

Table 48.2 Location of stones/crystal deposits and the major crystals involved in crystal deposition diseases (*stones or crystal deposits are heterogeneous mixtures, some of them with more than one crystalline phase held together by a matrix)

Diseases	Location of the deposits	Major crystals involved*
Acute and chronic gouty arthritis	Joints of hands and feet	Monosodium urate monohydrate, uric acid
Acute pseudo gout	Knees, wrists, and pelvis	Calcium pyrophosphate dihydrate
Acute calcific periarthritis	Shoulders, hip, and spine	Hydroxyapatite (HAP)
Atherosclerotic arteries and veins	Arteries and veins	Cholesterol
Calcific pancreatitis	Pancreas	Calcium carbonate
Cholelithiasis	Gallbladder	Cholesterol
Urolithiasis	Stones in kidney, ureter, bladder, and urethra	Calcium oxalate-monohydrate (COM), calcium oxalate dihydrate (COD), dicalcium-phosphate dihydrate (DCPD), magnesium hydrogen phosphate-trihydrate (MHP), magnesium ammonium-phosphate hexahydrate (MAP), uric acid, urates, cystine, xanthine

Table 48.3 Constituents of crystal deposits grown in gel

Crystals grown	Gel used	Method adopted	References
Calcium carbonate	Silica, polyacrylamide	Double diffusion	[48.82, 90–94]
Calcium oxalate-monohydrate (COM) Calcium oxalate dihydrate (COD)	Agar-agar, agarose, gelatin, silica	Single, double diffusion	[48.89, 95–99]
Calcium sulfate dihydrate	Silica	Double diffusion	[48.100, 101]
Cholesterol	Silica	Single diffusion	[48.12, 102, 103]
Cholesteryl acetate	Silica	Solubility reduction	[48.12]
L-Cystine	Silica	Single, double diffusion	[48.11, 104]
Hippuric acid	Silica	Single, double diffusion	[48.98, 99, 105–110]
Hydroxyapatite (HAP)	Silica	Double diffusion	[48.111]
Magnesium hydrogen-phosphate trihydrate (MHP), magnesium ammonium-phosphate hexahydrate (MAP)	Silica	Single diffusion	[48.112, 113]
Monosodium urate-monohydrate (MSUM)	Silica, TMOS	Single diffusion	[48.114]
Octacalcium phosphate (OCP)	Polyacrylamide	Single diffusion	[48.115]
β -Sitosterol	Silica	Double diffusion	[48.116]
L-Tyrosine	Silica	Single diffusion	[48.12]
Uric acid	Silica, TMOS	Single diffusion	[48.117]
		Single diffusion	[48.10]

2. Nucleation
3. Subsequent crystal growth.

Investigations of either solution or solid-phase phenomenon will yield useful information regarding the etiology of calculi formation. The growth of crystals *in vivo* will be dependent on the same factors of solubility, nucleation, and growth rate as *in vitro*. It is also possible to study the effects of various inhibitors (covering a wide range of molecular weights) which are present in biological fluids, by knowing the growth and dissolution of the stones and stone mineral phases. The *in vitro* experiments simulate the conditions of stone formation artificially to infer the general principles of calculogenesis, which can shed some light on crystallogensis of pathological stones.

There is increasing interest in using gel as a crystallizing medium, as it acts as a medium for crystallization of biomolecules and to evaluate the processes of

biomineralization *in vitro* [48.6, 12, 32, 88, 89]. This is because of their viscous nature, providing simulation of synovial fluid, cartilage, and other biological fluids. This method also provides a convenient technique for assessing the effect of various compounds (present in the human body) in altering crystallization parameters such as aggregation of crystals and also the morphology of the insoluble particles. Hence, the gel method of crystal growth is considered ideal for studying crystal deposition diseases [48.88, 89].

48.5.3 Crystallization of the Constituents of Crystal Deposits

Table 48.3 lists references (1994–2006) related to the gel growth of materials that are constituents of calculi occurring in crystal deposition diseases. The references to earlier research contributions of this category are available in previous reviews [48.1, 3–6].

48.6 Crystal-Deposition-Related Diseases

48.6.1 Urinary Stone Disease

Generally, urinary stones are called renal stones, ureteral stones, bladder stones, or urethral stones, depending on their specific site of growth (Table 48.2). Variations in urine flow and tube blockage can cause local fluctuations in pH and concentration, leading to supersaturation of urine and subsequently crystal nucleation, growth, and aggregation resulting in the formation of calculi of different shapes and sizes (Fig. 48.3 [48.118, 119]).

The ultimate control of urolithiasis requires proper application of both approaches of stone removal and drug therapy. Drug therapy is mainly aimed at inhibi-

tion of growth and dissolution of the existing stone and prevention of stone recurrence. Hence, it is important to understand the mechanism of stone formation and identification of the inhibitors of different crystalline materials present in urinary calculi.

48.6.2 Theories of Urinary Stone Formation

There are various theories to explain the actual mechanism by which urinary calculi develop [48.89, 120–124]. *Randal*, in 1937 [48.125], reviewed all the existing theories and described that there must be some lesion in the renal pelvis to which a calculus could remain anchored during its period of growth. *Anderson and McDonald*, in 1946 [48.126], improved this theory by suggesting that the small crystalline deposits in the kidney reach renal papilla, come into contact with urine, and subsequently grow into stones by deposition of urinary salts. *Butt and Hauser*, in 1952 [48.127], concluded that crystalline constituents of the urine separate out of the urine because of the shortage of protective colloids. Crystalline deposits can also occur as a result of excessive excretion or abnormal pH of the urine. *Vermeulon and Lyon*, in 1968 [48.128], proposed an advanced theory by explaining the different stages such as supersaturation, nucleation, growth, aggregation, and retention involved in the formation of the

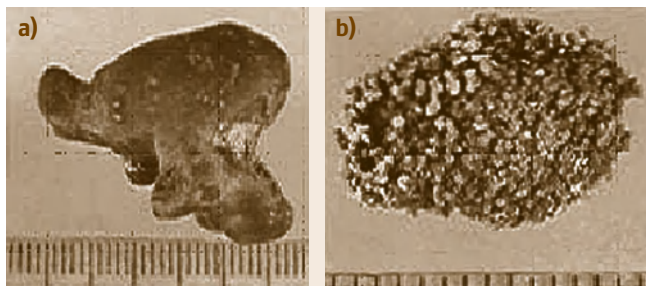


Fig. 48.3a,b COM urinary stones with (a) smooth surface (b) rough surface

stone. During the formation of urine, when it traverses the nephron, much of its water content is reabsorbed and urine gets supersaturated with respect to substances of limited solubility such as those found in stones. Molecular agglomerates of these substances having proper lattice orientation result in the formation of nuclei, or such nucleation can also be extraneous. When these nuclei attain critical size, they act as seeds and then grow into visible crystals. There are two different types of agglomeration, viz. primary and secondary agglomeration. Primary agglomeration is the growth of crystals on the surface or tips of crystals already formed. Secondary agglomeration is that which results from crystal-to-crystal collision. Primary agglomeration was recognized as a possible mechanism for the development of calculi [48.129, 130]. The conditions prevailing in the kidney are not conducive to the secondary agglomeration process, which is expected to play only a minor role in the formation of stones. The crystals, once formed, are retained inside the urinary tract and grow [48.89]. New small crystals originate upon the larger parent crystals and the matrix material binds crystalline material together, giving the stone its cohesive wholeness.

48.7 Calcium Oxalate

Calcium oxalate urolithiasis is the most common pathological condition associated with oxalate crystal deposition. Calcium oxalate crystalline deposits are also found in myocardium, bone marrow, and blood vessels. In urinary stones, calcium oxalate may exist as monohydrate (**COM**, $\text{Ca}(\text{COO})_2 \cdot \text{H}_2\text{O}$, 43%) or as dihydrate (**COD**, $\text{Ca}(\text{COO})_2 \cdot 2\text{H}_2\text{O}$, 20.5%). The formation of oxalate stone may be the result of supersaturation of the urine with its components, viz. calcium and oxalate, deficiency of inhibitors or the increase in concentration of promoters. Calcium oxalate forms mixed stones with calcium phosphates, uric acid, and magnesium ammonium phosphate hexahydrate (struvite, **MAP**, $\text{MgNH}_4\text{PO}_4 \cdot 6\text{H}_2\text{O}$).

48.7.1 Crystallization of Calcium Oxalate

COM was crystallized by *Girija et al.* [48.95] using calcium chloride and oxalic acid as the reactants in silica gel. Single-diffusion experiments yielded microcrystals of **COM** as seen in Fig. 48.4a. Crystallization using double diffusion yielded **COM** crystals of millimeter size. **COM** is a polymorphic crystal, and the crystals obtained

48.6.3 Role of Trace Elements in Urinary Stone Formation

The presence of certain trace elements may play a vital role in the formation of crystal deposition diseases. In recent years, the function of trace elements in the human body and the environment and their importance for medical practice have been increasingly recognized in the biomedical field. It has been suggested that some trace elements enhance the growth rate of deposits of crystalline compounds and that their high concentration in body fluids and tissues may be significant in this respect. One of the main problems is in determining whether nucleation is essentially homogeneous and takes place spontaneously from highly supersaturated fluids or whether it is heterogeneous and is initiated by some other agent such as trace elements (Mg, Pb, Ba, Fe, Sr, Zn, etc. [48.125, 127, 128, 131–133]). Impurities and diffusion limitations are suspected to play a major role in agglomeration. The process of aggregation through electrostatic forces would be expected to be controlled by the zeta potential of the particles, which is readily modified if any ion gets absorbed on the particles.

in this experiment were of prismatic (single, twinned, and bunched) morphology. These crystals enabled the measurement of Vicker's and Knoop microhardness and the values were found to be 192 and 73 kg/mm², re-

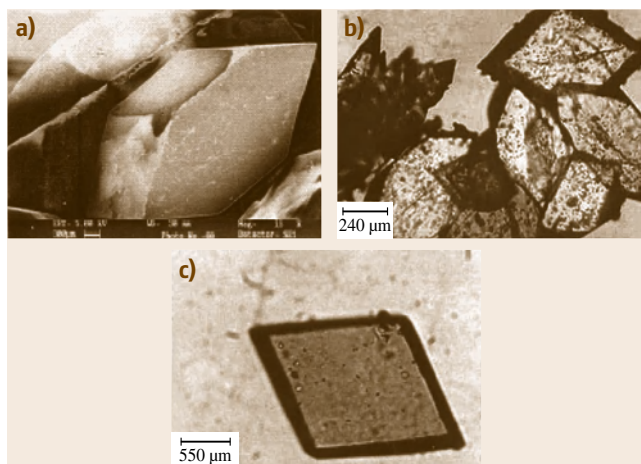


Fig. 48.4a–c **COM** single crystal in silica gel: (a) without any additives (b) in presence of cadmium, (c) in presence of zinc

spectively. *Achilles* et al. [48.89] designed a flow model of crystallization in gels, where crystal growth is performed from a flow of supersaturated urine at nearly constant supersaturation on **COM** particles in a gel matrix. Here, they used the discontinuous measurement of scattered light intensity by microphotometry to quantify various crystal growth parameters. These experiments to a large extent simulate the physiological conditions in which the pathological urinary crystals develop in vivo [48.134].

48.7.2 Effect of Trace Elements

Analyses of urinary stones showed the presence of more than 20 trace elements, and it is believed that these elements might play an important role in the formation of these stones [48.133]. *Girija* et al. [48.95] studied the effect of Mg, Cd, Zn, and Pb on the crystallization of **COM** at room temperature. There was significant influence of these ions on the process of primary agglomeration of **COM**.

The presence of the elements Mg and Zn, which are known to act as inhibitors of calcium oxalate urinary stones, was found to have less effect on crystal agglomeration and dendritic formation than the presence of the nephrotoxic elements Cd and Pb. Furthermore, Cd and Pb reduced the number of individual crystals and increased the tendency to form agglomerates of **COM** and dendrites of **COD** as seen in Fig. 48.4b. The incorporation of Cd and Pb was found to be high, the amount of incorporation following the order: Pb > Cd > Zn > Mg. The addition of Zn modified the morphology of the crystals from prismatic to rhombohedral (Fig. 48.4c [48.95]). Furthermore, *Petrova* et al. [48.97] crystallized **COM** in gelatin, agar-agar, agarose, and sodium silicate gels and studied the dissolution rates in the presence of Al and Fe. The rate of dissolution was found to increase in the presence of these ions, due to the adsorption of ions on the surface of the crystal, hindering further growth.

48.7.3 Effect of Tartaric and Citric Acids

Marickar and *Koshy* [48.135] crystallized **COM**, **COD**, dicalcium phosphate dihydrate (**DCPD**, brushite, $\text{CaHPO}_4 \cdot 2\text{H}_2\text{O}$), octacalcium phosphate (**OCP**, $\text{Ca}_8(\text{HPO}_4)_2(\text{PO}_4)_4 \cdot 5\text{H}_2\text{O}$), **HAP**, **MAP**, and magnesium hydrogen phosphate trihydrate (**MHP**, newberyite, $\text{Mg}(\text{PO}_3\text{OH}) \cdot 3(\text{H}_2\text{O})$) by reaction method in silica gel. The effect of known inhibitors of crystallization, viz. tartaric acid, citric acid, and human urine (affected and

unaffected), were studied. Tartaric and citric acid altered the crystal habit and inhibited growth. Urine from patients with stones modified the crystal habit. Normal urine samples produced reduction in the size of the crystals along with change in morphology. It is surmised from these observations that normal urine contains inhibitors of crystallization and that these were absent in the urine of certain patients affected by urinary stones.

48.7.4 Effect of the Extracts of Cereals, Plants, and Fruits

Natarajan et al. [48.99] grew crystals of **COM**, **DCPD**, and **MAP** in silica gel medium using reaction method, incorporating extracts of some cereals, plants, and fruits to screen these materials for their inhibitory role on crystallization of these compounds. Control experiments were carried out simultaneously to compare the growth of crystals without [48.98] and with the extracts. The concentration of the various substances incorporated in the gel was about 5 g/l. The generally expected inhibitory effects are the following:

1. No nucleation to lead to crystal growth (a powdery mass being produced)
2. Reduction in the number and size of the crystals
3. Change in the morphology of the crystals.

By carefully observing the shape, size, and approximate number of crystals obtained and also from the knowledge of their total mass, conclusions were derived regarding the inhibitory or promotive effect of the extracts incorporated. It was observed that the extracts of *Cocos nucifera*, *Citrus limon*, *Lycopersicon esculentum*, *Mimosa pudica*, *Musa sapientum*, *Hordeum vulgare*, *Tribulus terrestris*, and *Policos biflorus* produced very good inhibitory effects on **COM** crystallization. The extracts of *Mentha spicata*, *Raphanus sativus*, and *Vitis vinifera* had no effect on crystal growth. It was also interesting to observe that the extracts of *Borassus flabellifer* and *Ananas comosus* promoted the crystallization, producing larger crystals of **COM** crystals.

Irusan et al. [48.108] studied the effect of the herbal extracts *Phyllanthus niruri* and *Ocimum sanctum* on the crystallization of **DCPD** and found that, in the presence of these herbal additives, there was considerable reduction in the thickness of the crystals and also that the crystals became dendritic in nature. *Freitas* et al. [48.136] have also studied the effect of the aqueous extract of the folk medicinal plant *Phyllanthus niruri* on **COM** crystallization and concluded that the plant extract has an inhibitory effect on crystal

Table 48.4 Effect of cereal, plant, and fruit extracts on the crystallization of some urinary stone components

Cereal/plant/fruit		Effect of extracts on crystallization			Reference
Botanical name	Popular name	COM	DCPD	MAP	
<i>Ananas comosus</i>	Pineapple	Promoter	Inhibitor	No effect	[48.99]
<i>Bergenia ligulata</i>	Pashanbhed	Inhibitor	Not done	Not done	[48.137]
<i>Borassus flabellifer</i>	Palm juice	Promoter	Inhibitor	Inhibitor	[48.99]
<i>Citrus limon</i>	Lemon fruit	Inhibitor	Inhibitor	Inhibitor	[48.99]
<i>Cocos nucifera</i>	Tender coconut water	Inhibitor	Inhibitor	Inhibitor	[48.99]
<i>Hordeum vulgare</i>	Barley	Inhibitor	Inhibitor	Promoter	[48.99]
<i>Lycopersicon esculentum</i>	Tomato fruit	Inhibitor	Inhibitor	Inhibitor	[48.99]
<i>Mentha spicata</i>	Mint	No effect	Inhibitor	Inhibitor	[48.99]
<i>Mimosa pudica</i>	Touch-me-not plant	Inhibitor	Inhibitor	Inhibitor	[48.99]
<i>Musa sapientum</i>	Plantain stem	Inhibitor	No effect	Inhibitor	[48.99]
<i>Oscimum sanctum</i>	Thulasi	Not done	Inhibitor	Not done	[48.108]
<i>Phyllanthus niruri</i>	Kizhanelli	Not done	Inhibitor	Not done	[48.108]
		Inhibitor	Not done	Not done	[48.136]
<i>Policos biflorus</i>	Horsegram	Inhibitor	Promoter	No effect	[48.99]
<i>Rahanus sativus</i>	Radish	No effect	Inhibitor	Inhibitor	[48.99]
<i>Tamarindus indica</i>	Tamarind fruit pulp	Promoter	Inhibitor	Inhibitor	[48.99]
		Not done	Inhibitor	Not done	
<i>Tribulus terrestris</i>	Nerringi	Inhibitor	Inhibitor	Promoter	[48.98]
		Inhibitor	Not done	Not done	[48.138]
<i>Vitis vinifera</i>	Grapefruit	No effect	Inhibitor	No effect	[48.99]

growth. Recently, Joshi et al. [48.137] have shown the inhibitory effect of two herbs, viz. *Tribulus terrestris* and *Bergemia liuquolata*, on the growth of COM crystals, in vitro. *Bergemia liuquolata* was found to be a better inhibitor of COM than was *Tribulus terrestris*. They infer that the presence of some macromolecules in these

herbs seems to play an important role in inhibition of COM crystals. It may be pertinent to point out that the particular ingredient of the cereals/plants/fruits responsible for the inhibitory or promotive effect is yet to be identified. The observations of the various experiments described are summarized in Table 48.4.

48.8 Calcium Phosphates

Calcium phosphates are the major constituents of bone and teeth. Dental calculus, bursitis, arthritis etc. are the pathological conditions involving the deposition of calcium phosphate-like minerals. Calcium phosphate may mineralize in various phases, such as HAP, tricalcium phosphate (TCP, whitlockite, $\text{Ca}_3(\text{PO}_4)_2$), OCP, dicalcium phosphate (DCP, monetite), and DCPD, in order of increasing solubility. Investigations on the

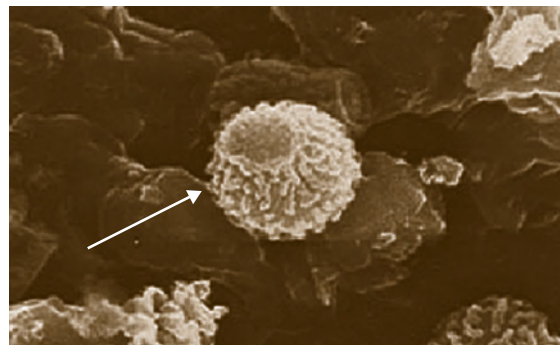


Fig. 48.5 Microstructure of a COM stone showing HAP as nidus of about 600 μm in diameter (indicated by an arrow)

nucleation and growth of calcium phosphates such as **DCPD**, **DCP**, **OCF**, **TCP**, and **HAP** have received considerable attention in connection with the formation of metabolic and nonmetabolic stones [48.138–140]. Among these, **DCPD** plays an important role in the formation of caries lesions under acidified conditions. Needles of **DCPD** crystals were reported in the outer layer of calculi [48.141]. It also forms the basis for the nucleation of calcium oxalate crystals.

Tiny crystals of **HAP** sometimes form in and around joints and can cause inflammation around the articular cartilage and periarticular connective tissues. They have been described as a cause of inflammations of the shoulder [48.87]. **HAP** is also a constituent of the urinary calculi and is sometimes found in the nidus of **COM** stones (Fig. 48.5 [48.142]). **HAP** has also been detected in atherosclerotic lesions [48.143].

48.9 Hydroxyapatite (HAP)

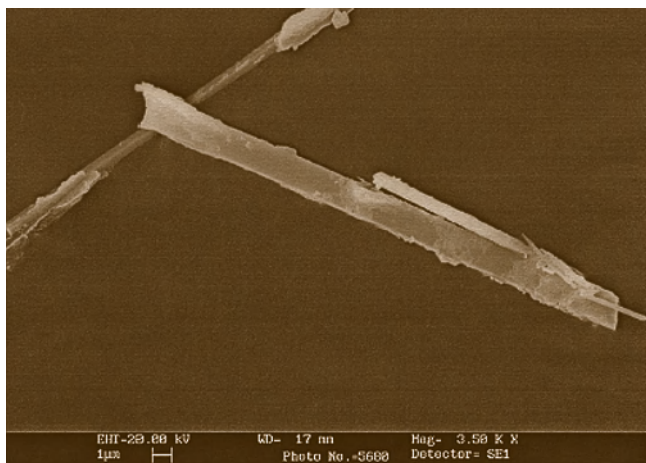


Fig. 48.6 Platy crystals of **HAP** grown in silica gel (after [48.144], © IOS) ◀

At present, there is no simple technique to crystallize large single crystals of **HAP** at ambient temperature. The crystal growth of **HAP** at ambient temperature and pressure conditions always yielded crystals of nanometer size. *Ashok* et al. [48.112] reported the crystallization of platy crystals of **HAP**, using single-test-tube diffusion technique in silica gel media at physiological temperature (37 °C). Discs of **HAP** containing platy crystals of size $27 \times 2 \mu\text{m}$ were obtained (Fig. 48.6, [48.112, 144]) using low-temperature crystallization techniques using gels. *Girija* et al. [48.113] also crystallized **HAP** biomimetically on collagen gel to evaluate the biomineralization process.

48.10 Dicalcium Phosphate Dihydrate (DCPD)

There are several reports on the crystallization of **DCPD** in gels [48.109]. Spherulitic **DCP** and **DCPD** of different morphologies which have close resemblance to

those found in pathological joints, stones, and dental calculi were crystallized in silica gel at physiological pH and temperature by *Sivakumar* et al. [48.107]. The crystals grown without any additives had characteristic platy and spherulitic morphology of **DCPD** and **DCP**, respectively (Figs. 48.7, 48.8a). Scanning electron photomicrographs of synthesized spherulitic **DCP** crystals revealed that the crystal consisted of radially arranged aggregation of rectangular rod-like spokes and rectangular platelets (Fig. 48.8b).

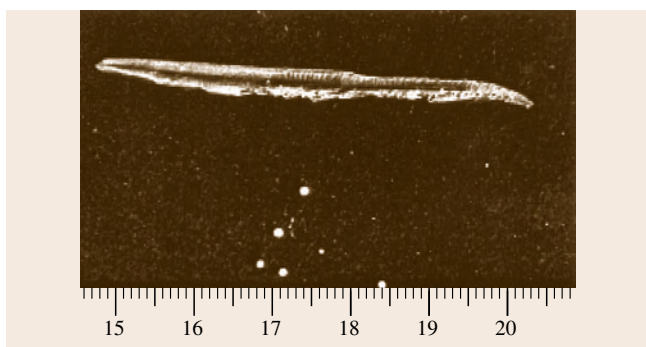


Fig. 48.7 Elongated platy crystals of **DCPD** grown in silica gel

48.10.1 Effect of Additives on Crystallization of Calcium Phosphates

The influence of organic and inorganic ionic species (Mg/Ca , Cd , Zn , Pb , $\text{P}_2\text{O}_7^{4-}$, and citrate) on crystal-

lization of DCP, DCPD, and magnesium phosphates have also been studied by Sivakumar et al. in silica gel [48.107, 114]. Incorporation of magnesium ions in the crystallizing medium led to a change in the size and morphology of crystals and the mechanical properties of the crystals (Fig. 48.9).

Even when the concentration of the calcium ions was considerably less than that of the magnesium ions, platy DCPD crystals were found to crystallize along with the MHP and MAP crystals (Fig. 48.10). The hardness of the MHP and MAP crystals increased with increasing calcium ions. The presence of magnesium ions in the crystallizing medium drastically reduced the hardness and also reduced the number of DCPD crystals. The magnesium ions decreased the hardness, whereas lead ions increased the hardness of the DCPD crystals. The incorporation of calcium in MHP and MAP crystals increased the hardness, whereas cadmium reduced the hardness. The presence of pyrophosphate and citrate ionic species in the crystallizing medium did not have any influence on the morphology, microstructure, and lattice parameters of DCP, DCPD, MHP, and MAP crystals. From in vitro crystallization using silica gels, it was concluded that Mg^{2+} , Zn^{2+} , $P_2O_7^{4-}$, and citrate ions inhibit growth of DCP, DCPD, and MAP crystals, whereas Cd^{2+} and Pb^{2+} accelerate the growth of crystals [48.107].

Anee et al. [48.110] studied the effect of Fe^{3+} ions on the crystallization of DCPD at various temperatures (27, 37, and 47 °C) using agarose gel medium. In these experiments, crystallization was inhibited in the absence of Fe^{3+} at 37 and 47 °C. Figure 48.11 shows iron-doped DCPD crystallized by single-diffusion technique at 27 °C. At 47 °C, spherulites of HAP were found to grow in the gel medium along with DCPD crystals. These crystals were of average length 1.33 mm

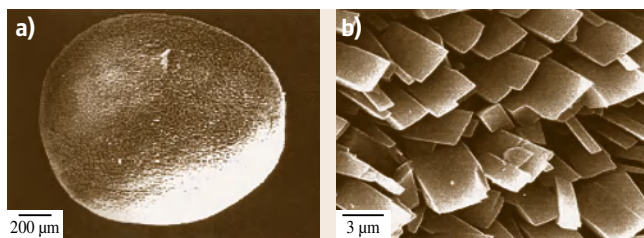


Fig. 48.8 (a) Spherulitic crystals of DCP and (b) its microstructure

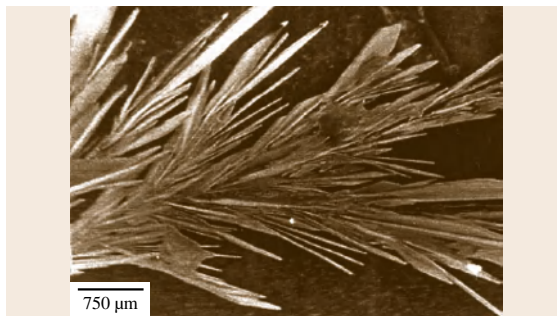


Fig. 48.9 Change in habit of DCPD when crystallized in silica gel with magnesium ions

and breadth of 4.28 μm , forming spherulites of more than 2.7 mm in diameter. Previous studies reported crystallization of needle-like morphology of HAP, of only micro- or nanometer size [48.111, 145, 146]. These studies [48.110] showed that Fe^{3+} played a significant role in the crystallization of phase-pure HAP at physiological pH. Furthermore, this technique provided an easier method to synthesize large crystals of HAP, at a low temperature.

Combined influence of an organic and an inorganic ion (cobalt and malic acid) on crystallization of DCPD

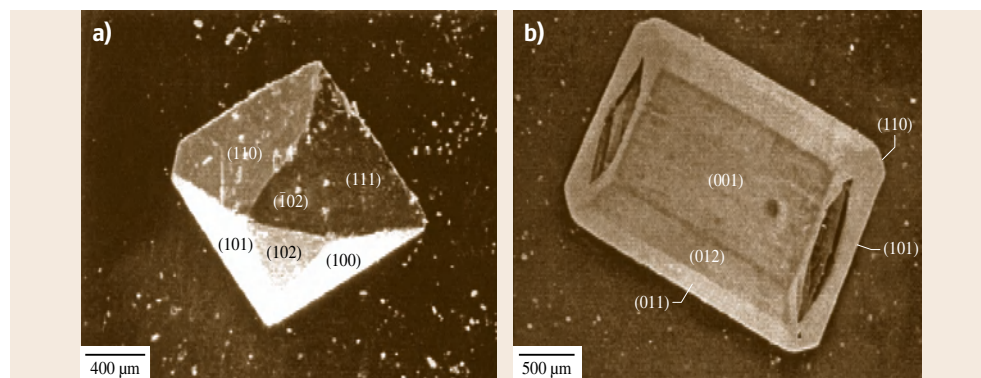


Fig. 48.10a,b Crystals of (a) newberyite (MHP) and (b) struvite (MAP) grown in silica gel

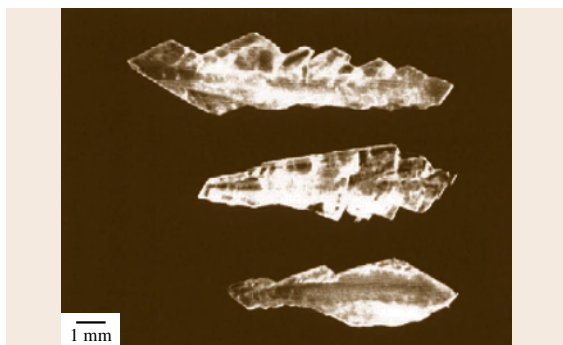


Fig. 48.11 DCPD crystals grown in agarose medium in presence of Fe^{3+}

in agarose gel was reported by Anee et al. [48.105]. Morphological changes were noticed when the growth assay was doped with cobalt and malic acid. Even at very low concentrations, malic acid exerted an influence on crystal morphology, producing elongated crystals. Increase in the malic acid concentration in the crystallization media promoted entry of Co^{2+} into the DCPD crystals. Hence, malic acid is expected to be a mediator for transporting Co^{2+} from the supernatant liquid into the gel where crystallization occurred. However, no crystallization occurred in the presence of malic acid alone. Presence of cobalt promoted crystallization, whereas malic acid modified the morphology of DCPD crystals. The molecules of organic additives can bind specifically to certain crystal planes during growth and modify the morphology of the crystals [48.147]. These types of studies help in understanding the process by which organic molecules control the biomineralization process leading to crystal deposition.

48.10.2 Effect of Some Extracts of Cereals, Plants, and Fruits and Tartaric Acid

Natarajan et al. [48.99] have also grown crystals of DCPD using reactants in silica gel and experimented with extracts of various cereals, plants, and fruits as possible inhibitors, as described in Table 48.4. It is of interest to observe that all the extracts tested, except *Policos biflorus* and *Musa sapientum*, inhibited crystallization of DCPD. The extract of *Policos biflorus* showed a promotive effect, whereas *Musa sapientum* had no effect on the crystal growth. Tartaric acid and tamarind (*Tamarindus indica*) were found to inhibit the

crystallization of DCPD in silica gels, due to the formation of calcium tartrate in preference to DCPD, as reported by Joseph et al. [48.138].

48.10.3 Calcium Hydrogen Phosphate Pentahydrate (Octacalcium Phosphate, OCP)

Iijima and Moriwaki [48.116] crystallized OCP in polyacrylamide gels; their experiments revealed that, in addition to other enamel extracellular matrix proteins, amelogenin nanospores are directly involved in controlling the morphology of crystals during enamel mineralization. Marickar and Koshy [48.135] also reported growth of OCP crystals in silica gel.

48.10.4 Magnesium Ammonium Phosphate Hexahydrate (MAP) and Magnesium Hydrogen Phosphate Trihydrate (MHP)

MAP and MHP are two major crystalline constituents of nonmetabolic or infection-induced urinary stones [48.139, 140]. These stones arise from infection produced by urea-splitting organisms such as *Proteus mirabilis*. The urease-catalyzed hydrolysis of urea generates ammonia, which elevates urine pH and causes precipitation of Mg^{2+} , as struvite. Though surgical treatment gives an immediate relief, it is usually followed by relapse of infection and recurrence of stone formation. The recurrence rate of struvite and newberry stone formation is high compared with other urinary stone constituents [48.148].

MAP and MHP were crystallized through the direct crystallization method in silica gel medium [48.114] as mentioned in Sect. 48.10.1; the presence of Mg/Ca , Zn , $\text{P}_2\text{O}_7^{4-}$, and citrate was found to inhibit the growth of MAP and MHP, whereas Pb and Cd promoted growth.

The effect of the extracts of several cereals, plants, and fruits on the crystallization of MAP was studied by Natarajan et al. [48.99]. As evident from the Table 48.4, all the extracts screened (except *Vitis vinifera*, *Policos biflorus*, *Ananas comosus*, *Hordeum vulgare*, and *Tribulus terrestris*) played inhibitory roles in the growth of MAP crystals. *Hordeum vulgare* and *Tribulus terrestris* promoted, whereas *Vitis vinifera*, *Policos biflorus*, and *Ananas comosus* had no effect on crystallization of MAP.

48.11 Calcium Sulfate

Naturally occurring mineral, gypsum (calcium sulfate dihydrate ($\text{CaSO}_4 \cdot 2\text{H}_2\text{O}$, CSD)) is one of the rare constituents of urinary stones. Gypsum also finds applications in dentistry and pottery, apart from its major use in the medical field to immobilize broken limbs after the bones have been set. Growth of gypsum crystals in silica

gel has been reported [48.100,101]. Kumareson and Devanarayanan [48.101] crystallized CSD using double-diffusion technique in silica gel and further studied the influence of additives such as citric acid, borax, and barium chloride. It was found that the presence of these additives increased the perfection of the grown crystals.

48.12 Uric Acid and Monosodium Urate Monohydrate

Uric acid ($\text{C}_5\text{H}_4\text{N}_4\text{O}_3$) is the major end-product of purine metabolism (Fig. 48.12). The classic example of a crystal deposition disease is gout. Gout is a very painful inflammatory condition associated with deposition of monosodium urate crystals [48.149] in various tissues of the body. Crystals of uric acid anhydrate and dihydrate as well as its sodium salts have been found in the renal tract, and interstitial tissues of the kidney and its collection ducts. Uric acid anhydrate and dihydrate are often found as a constituent of urinary calculi and have a high incidence in nephrolithiasis resulting in severe kidney damage [48.150, 151]. The solubility of uric acid changes dramatically with pH and, in acidic urine when supersaturated with uric acid, it is deposited as uric acid crystals [48.152]. It is found to occur in pure form or in association with calcium oxalates, HAP, struvite, and sodium and ammonium urates. In addition, it has been suggested that uric acid crystals could act as a support for heterogeneous nucleation of other crystalline species [48.153, 154].

Uric acid is insoluble in alcohol, ether, and most common organic solvents and, owing to its extremely low solubility in water, it would be difficult to prepare a pure specimen because of the large volume of solvent needed. As uric acid has very poor aqueous and organic solubility, it is very difficult to crystallize them in an aqueous medium such as silica gel. Kalkura et al. [48.10] crystallized uric acid dihydrate in TMOS

and silica gels using single- and double-diffusion techniques (Fig. 48.13). In this case, a solution of uric acid in sodium hydroxide was allowed to diffuse into the gel to produce a displacement reaction with dilute HCl inside the gel medium, producing uric acid crystals. These experiments showed that uric acid, which has a low aqueous and organic solubility, can be crystallized in an aqueous medium such as silica gel and in TMOS without the use of bulk solvents.

Monosodium urate monohydrate (MSUM) is the salt of singly ionized state of uric acid, and a component of urinary stones. It has also been identified in articular tissues of patients managed with long-term dialysis [48.155]. The presence of characteristic needle or spherulitic forms of MSUM in synovial fluid and within synovial leukocytes is recognized as a strong indication of the presence of gouty arthritis [48.156]. The synthetic crystals of MSUM were needle shaped, whereas the crystals grown in the presence of serum, synovial fluid, and components thereof closely resembled the morphology of the MSUM crystals present in the articular cartilage in vivo [48.157]. A saturated solution of

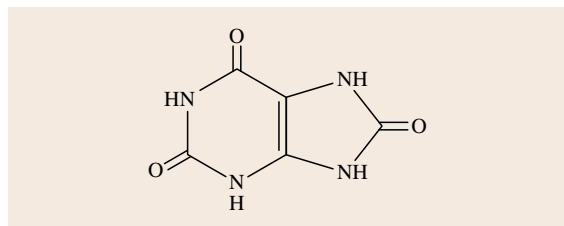


Fig. 48.12 Molecular structure of uric acid

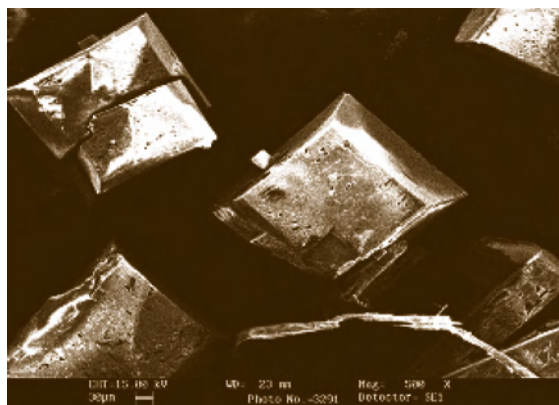


Fig. 48.13 Crystals of uric acid grown in TMOS gels

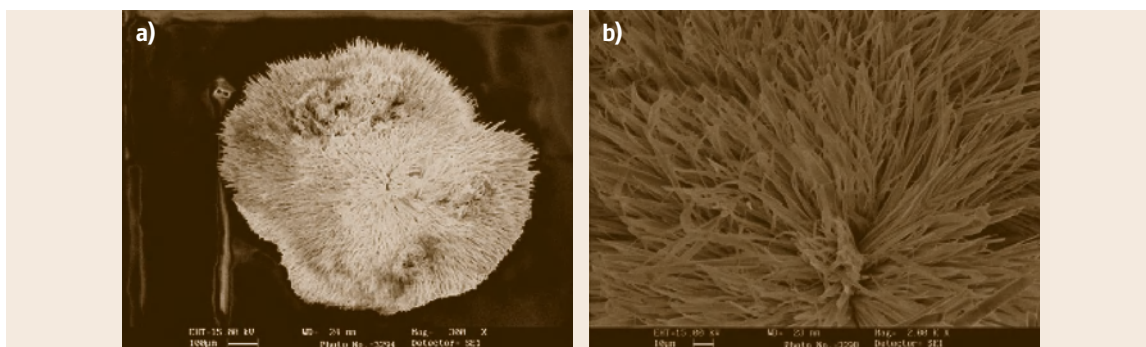


Fig. 48.14 (a) Spherulites of sodium urate monohydrate crystallized in **TMOS** gels, (b) magnified image

sodium urate in the presence of urate seeds at pH greater than 6.0 will form needle-shaped sodium urate crystals.

MSUM, which resembled the crystals found in synovial fluid of gouty patients, has been crystallized fairly easily by *Kalkura et al.* [48.115] without resorting to

any heating of the solutions in a wide range of pH (3–10) using **TMOS** and silica gels compared with the other existing standard method, viz. slow cooling of a NaOH–uric acid solution kept at pH of 8.9 from 60 to 4 °C, as seen in Fig. 48.14 [48.115, 154].

48.13 L-Cystine

Crystallization of cystine ($C_6H_{12}N_2O_4S_2$, Fig. 48.15), a dibasic sulfur-containing amino acid present in the body, results in disorders such as cystinuria and cystinosis. Cystinuria is characterized by excretion of large quantities of the above amino acid in urine. Cystinosis results in the formation of cystine calculi and could

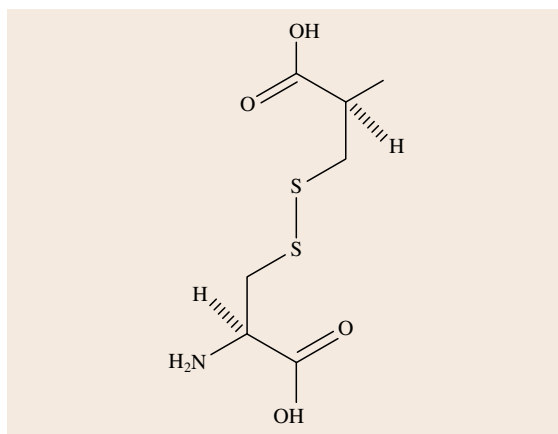


Fig. 48.15 Molecular structure of cystine

even lead to kidney damage. Cystine crystals could also occur in liver, spleen, thyroid glands, bone marrow, and ocular tissues [48.158]. Cystine can act as a seed and favors the crystallization of **MAP** [48.159], a urinary stone constituent with a high degree of recurrence [48.160].

Since cystine has low aqueous and organic solubility, it is difficult to crystallize using conventional methods of gel technique. Earlier, cystine crystallization was carried out in solution by dissolving it in an alkaline solution (ammonia) and then reducing it

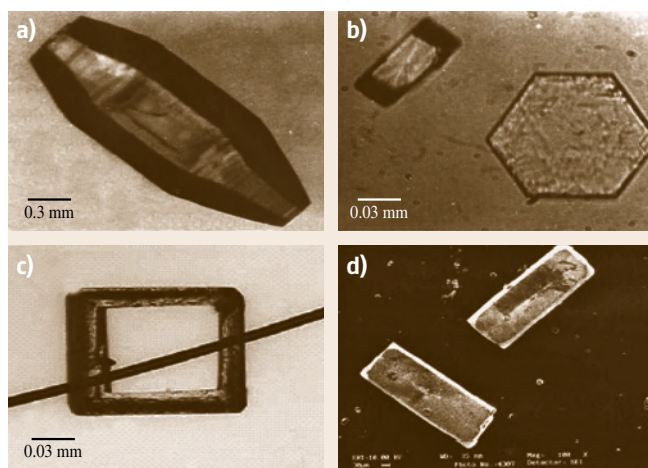


Fig. 48.16a–d Different morphologies of crystals of cystine crystallized from silica gels: (a) Bipyramidal (after [48.11], © Springer 1995), (b) hexagonal (after [48.11], © Springer 1995), (c) hollow crystal with a thread passing through it, (d) rectangular crystals

using a weak acid, such as acetic acid. In a novel technique, reported by *Girija et al.* [48.11], cystine was dissolved directly in silica gel and the crystals of cystine appeared without the diffusion of any supernatant solution into the gel medium. Here, acetic acid used for acidifying the silica gel also played the role of the reduction agent to produce crystals.

48.14 L-Tyrosine, Hippuric Acid, and Ciprofloxacin

Some components that are rarely found in urinary stones include L-tyrosine ($C_9H_{11}NO_3$), hippuric acid, and ciprofloxacin ($C_{17}H_{18}FN_3O_3$). Tyrosine is an amino acid present in living organisms. Hippuric acid ($C_6H_5CONHCH_2COOH$) is a colorless crystal obtained from urine of domestic animals and humans [48.162]. It is believed to be a natural regulator of urinary saturation with regard to calcium oxalate crystallization, which is the most frequent chemical constituent of all the urinary stones. Also, hippuric acid is a potential nonlinear optical (NLO) material. Ciprofloxacin is an antibiotic drug used for a wide range of infections. Drugs such as ciprofloxacin and triamterene induce calculi and they, along with many other drug metabolites, represent 1–2% of all renal calculi [48.160]. Ciprofloxacin crystals form rarely in humans. *Ramachandran and Natarajan* [48.111, 117, 163] reported

Single, twinned, and bunched hexagonal, cubic, rectangular, bipyramidal, and hollow morphologies of cystine crystals (Fig. 48.16a–d) were obtained by this technique [48.11, 104]. Cystine crystallized in the presence of ascorbic acid exhibited tetragonal structure and in addition had hourglass-type inclusion in crystals of rectangular morphology [48.161].

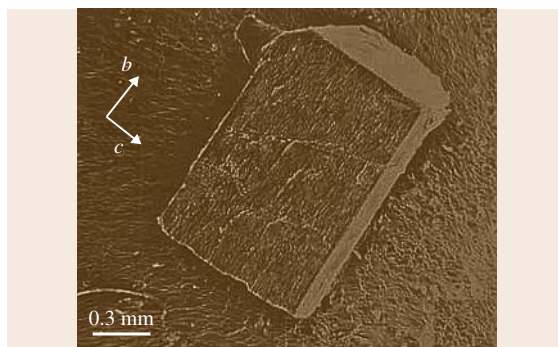


Fig. 48.17 Scanning electron micrograph of a crystal of ciprofloxacin

the crystal growth of L-tyrosine, hippuric acid, and ciprofloxacin (Fig. 48.17) in silica gel.

48.15 Atherosclerosis and Gallstones

Cardiovascular disease is one of the leading causes of death in humans. Cardiovascular diseases include such conditions as heart attacks, strokes, high blood pressure, and heart failure [48.165]. The main cause of these diseases is atherosclerosis (thickening of the artery due to the fatty deposits which are largely composed of cholesterol). Atherosclerotic plaques normally consist of lipids such as cholesterol, cholesteryl esters, and phospholipids [48.166]. These deposits interfere with normal blood flow and may result either in depriving some areas of adequate blood supply, in the formation of a blood clot or in the rupture of blood vessels.

48.15.1 Crystal Growth in Bile

Crystal growth frequently occurs in bile, usually resulting in the formation of gallstones. Generally, gallstones

Table 48.5 Constituents of gallstones and their relative abundance (%) (after [48.164], © Elsevier 1981)

Anhydrous cholesterol	$C_{27}H_{46}O$	52.3
Cholesterol monohydrate	$C_{27}H_{46}O \cdot H_2O$	16.0
Vaterite	$CaCO_3$	6.4
Calcium palmitate	$CH_3(CH_2)_{11}(COO)_2Ca$	5.9
Aragonite	$CaCO_3$	4.6
Calcite	$CaCO_3$	4.1
Cholesterol II	$C_{27}H_{46}O$	2.7
Apatite	$Ca_{10}(PO_4)_6(OH)_2$	2.4
Whitlockite	$\beta-Ca_3(PO_4)_2$	0.4
Palmitic acid	$CH_3(CH_2)_{14}COOH$	0.1
Artefacts, unidentified material	–	3.3

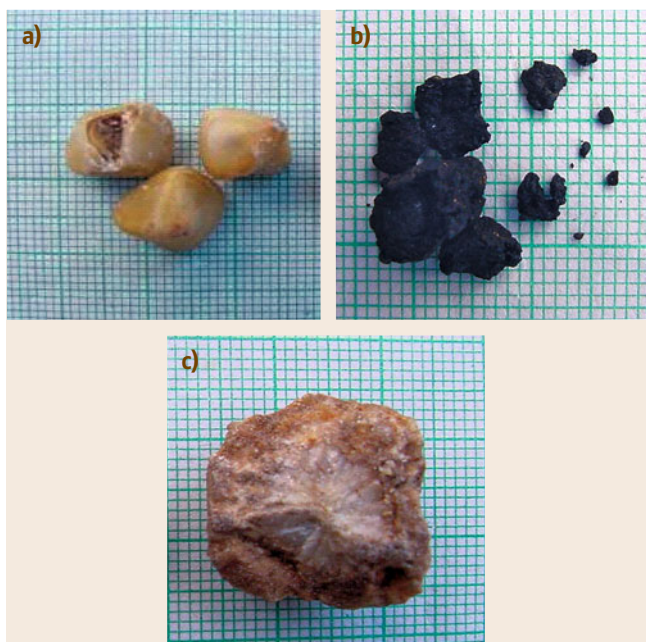


Fig. 48.18a–c Types of gallbladder stones: (a) cholesterol, (b) pigment, (c) mixed type

vary from patient to patient in number, size, color, and shape, as well as in composition (Fig. 48.18a–c, [48.164, 167]). Cholesterol is the most common constituent but certain calcium salts, notably calcium carbonate, are frequently present (Table 48.5). As cholesterol has low aqueous solubility, it is either solubilized in bile salt micelles or associated with different phospholipids, vesicles or with lipoprotein particles as free cholesterol or as cholesterol fatty-acid esters [48.168].

Bile secreted by the liver becomes supersaturated with cholesterol. Such abnormal bile contains an ex-

cess of cholesterol relative to the solubilizing agents, bile salts, and the phospholipid lecithin [48.169]. The liver, perhaps as a result of genetic programming, produces supersaturated bile by decreased secretion of bile salts or increased secretion of cholesterol, or both. The excess cholesterol precipitates out of the solution as solid monohydrated cholesterol microcrystals [48.170]. The cholesterol microcrystals precipitated from the bile are retained and subsequently aggregate and grow into macroscopic stones (Fig. 48.18a, [48.171]).

A possible explanation for the lack of cholesterol crystallization in some supersaturated bile is that a nucleating factor is required to seed crystal formation. Evidence has been obtained from bile-mixing experiments that gallbladder bile contains a nucleating factor that could be specific to the gallbladder or bile of cholesterol gallstone patients. Nucleation of cholesterol has been recognized as an important step in gallstone formation but few studies have been performed to examine the ability of potential nucleating agents to influence cholesterol crystal formation. Some of the factors which contribute to crystallization in bile may be crystal aggregation, overgrowth, and epitaxy [48.172].

48.15.2 Cholesterol and Related Steroids

Steroids are an important class of chemical compounds found in virtually all forms of plant and animal life. They are also extensively used in the treatment of ailments ranging from coronary insufficiency to endocrine hormone alterations. Cholesterol ($C_{27}H_{46}O$) is one of the most abundant steroids found in the animal kingdom. It is found in brain, nerve tissues, cell membranes, and gallstones. Plant sterols are structurally similar to cholesterol, and β -sitosterol ($C_{29}H_{50}O$) is the most common plant steroid. β -Sitosterol is a constituent of the gallbladder bile and gallstones. Cholesterol is supposed to be the causative agent for coronary heart diseases and gallstones. Cholesterol and similar compounds are the precursors of the steroid hormones, which play vital roles in human metabolism.

Cholesterol crystals are also seen in rheumatoid nodules, tophi, unicameral bone cysts, and even in isolated cholesterol granulomas of the skin [48.173]. When the cholesterol concentration exceeds the solubility limit in the lipid bilayers of micelles, deposition of cholesterol takes place. This leads to nucleation of crystalline cholesterol and subsequently to atherosclerosis and gallstones. The cholesterol has a ring system as illustrated in Fig. 48.19. It consists of three six-membered rings and a five-membered ring. The interesting fea-

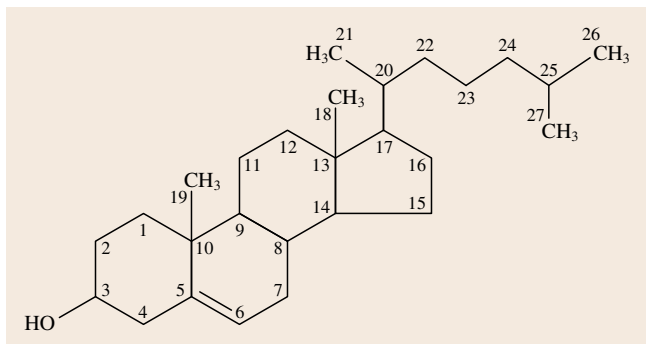


Fig. 48.19 Molecular structure of cholesterol ring

ture of the cholesterol crystals is the bilayer nature of its structure, with a molecular arrangement generally similar to that of cholesterol in biological membrane [48.174].

The physicochemical properties of cholesterol are important to its necessary functions on membranes. Many of the features of cholesterol are also found in its physiologically important derivatives. Cholesterol plays a significant role in the synthesis of essential steroids such as bile acids, sex hormones produced in special glands (ovaries, corpus leutum, placenta, and testis), adrenocortical hormones and vitamin D [48.158]. An esterified form of cholesterol plays an important role in atherosclerosis and cholelithiasis. Cholesteryl esters are precursors for the cyclic formation of free cholesterol synthesis. In addition to cholesterol monohydrate, anhydrous form of cholesterol is also present in freshly removed human gallstones, whereas atherosclerotic plaques contain only monohydrated cholesterol [48.103].

Kalkura and Devanarayanan have shown that cholesterol and related steroids such as cholesteryl acetate and β -sitosterol, which has a low aqueous solubility, can be crystallized in an aqueous silica gel medium without cholesterol being precipitated [48.12]. The single-test-tube diffusion method was employed to grow crystals of cholesterol in silica gel medium by solubility reduction technique. Cholesterol and cholesteryl acetate crystals grown in vitro are shown in Fig. 48.20 [48.12]. Cholesterol and β -sitosterol formed anhydrous crystals in the absence of water and monohydrated crystals in the presence of water. Platy and fibrous crystals of cholesterol monohydrate were obtained when crystallized in silica gels. This technique has also been used to study the effect of various solvents and the extracts from medicinal plants on the crystallization [48.102, 175]. The extracts of some Indian medicinal plants, viz. *Commiphora mughul*, *Aegle marmeleos*, *Cynoden dactylon*, *Musa paradisiaca*, *Polygala javana*, *Alphinia officinarum*, and *Solafoium* were used as additives to study their effect on the crystallization behavior of cholesterol. It was found that many of these herbs have an inhibitory effect on crystallization in terms of nucleation, crystal size or habit modification. Trace elements also seem to play an important role in the pathological mineralization of gallstones [48.176–178].

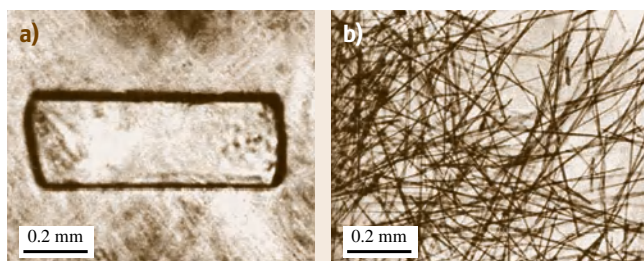


Fig. 48.20 (a) Cholesterol and (b) cholesteryl acetate crystallized in silica gel

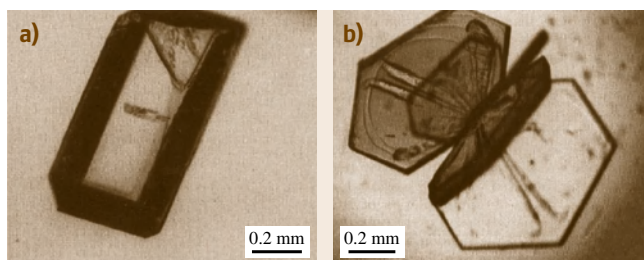


Fig. 48.21a,b Cholic acid crystallized in (a) silica, (b) TMOS gels (after [48.54], © Akademie Verlag 1997)

48.15.3 Cholic Acid

Cholic acid ($C_{24}H_{40}O_5$) is one of the bile acids and is responsible for many physiological functions, including promotion of lipid diffusion through intestinal mucosa, resorption of drugs, vitamins, and hormones, activation/inhibition of various enzyme reactions, and excretion of cholesterol [48.175]. Steroidal cholic acid and its derivatives can serve as host molecules to form inclusion compounds with a wide variety of organic substances. Cholic acid is also a promising candidate to be used as a building block in biomimetic/molecular recognition chemistry and in the construction of extended, preorganized molecular structures [48.179]. Kalkura et al. reported the crystallization of cholic acid in silica and TMOS gels. Crystals grew with different morphologies, and Liesegang rings were also seen in some cases. The grown crystals were found to be monohydrate in form (Fig. 48.21a,b, [48.54]). Since the bile salts have the ability to form inclusion compounds with a variety of molecules, these studies will be helpful in understanding the role played by cholic acid and its derivatives in cholesterol crystallization in gallbladder.

48.16 Crystallization of Hormones: Progesterone and Testosterone

Steroid hormones are derived from cholesterol, and a very small amount of these exerts potent physiological effects. Progesterone ($C_{21}H_{30}O_2$) is a naturally occurring mammalian hormone. It is known as the hormone of pregnancy because of its importance just prior to and during the gestation period. It is secreted by corpus luteum (material which surrounds the egg). The main functions of progesterone are the following:

1. Preparation of the uterine endometrium for the implantation of fertilized ovum
2. Maintenance of uterus during/after pregnancy
3. Inhibition of spontaneous contraction of the uterus
4. Participation in the development of breast
5. Inhibition of ovulation [48.180].

Progesterone is an important intermediate in biosynthesis of adrenocortical and gonadal steroid hormones. It also forms the basis for oral contraceptive agents.

Testosterone ($C_{19}H_{28}O_2$) belongs to a class of compounds called androgens. Androgens are responsible for the development of the male sex organs. Testosterone is the most active androgen and it is the functioning hormone found in the testes, ovary, and adrenal cortex. This most potent male sex hormone is isolated from testicular tissue and spermatic vein blood. The important function of this group is in the development

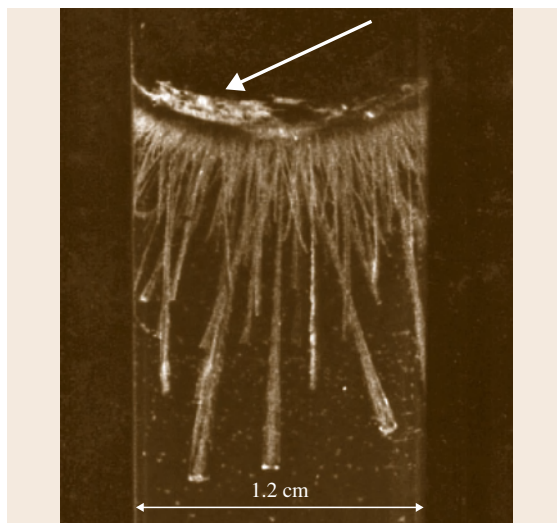


Fig. 48.23 Crystals of testosterone as grown in silica gel with crystals in the supernatant solution due to the reverse diffusion (arrow)

of masculine sexual characteristics such as deepening of voice, growth of a beard, and distribution of pubic hair. Their structure is similar to that of the female sex hormones, viz. estrogens [48.181]. Crystallization of the above hormones was carried out by Kalkura and Devanarayanan [48.12–14] by modifying the techniques of crystallization of steroids in gels. Crystals were obtained (Fig. 48.22a,b) when there was a slow diffusion of water into the gel medium containing sex hormones (progesterone and testosterone) in liquid phase. This suggests a possible mechanism for the growth of crystals. Water, while diffusing through the gel, supersaturates the sex hormone which is in a liquid phase in the gel medium, leading to nucleation of the crystals and their subsequent growth. In addition, crystals also appeared in the supernatant solution, due to the slow reverse diffusion of the precipitating solution from the gel medium into the supernatant solution, leading to the supersaturation of the hormones (Fig. 48.23).

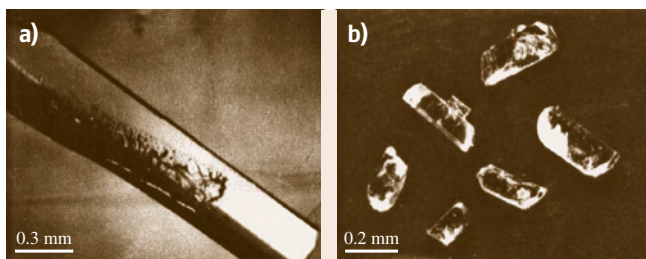


Fig. 48.22a,b Crystals of progesterone grown inside (a) silica gel, (b) crystallized in the supernatant due to reverse diffusion of the precipitating solvent

48.17 Pancreatitis

The pancreas in all mammalian species is an important gland located in the upper abdomen behind and below the stomach. The pancreas has both exocrine and

endocrine functions. Inflammation of the pancreas is known as pancreatitis. Chronic pancreatitis is a continuing inflammatory disease of the pancreas characterized



Fig. 48.24 Surgically removed pancreatic stones

by irreversible morphological changes that typically cause pain and permanent loss of pancreatic function. Initially, pain dominates, soon followed by the clinical complication of calcification, leading to stone formation (pancreatic calculi), in the main duct (Fig. 48.24). Biological fluids are generally supersaturated with respect to calcium salts such as oxalates in urine, phosphates in saliva, and carbonates in bile or pancreatic juice. It might become harmful if continuous crystal growth is allowed, leading to the formation of stones. Inhi-

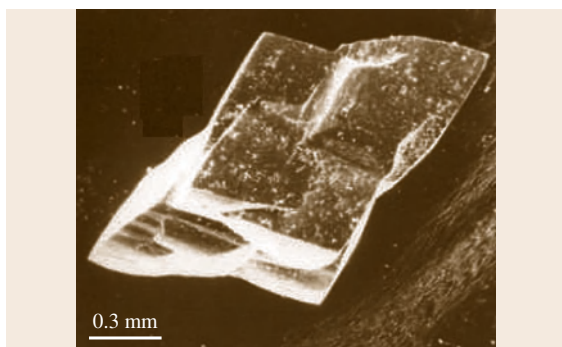


Fig. 48.25 Scanning electron micrograph of a bipyramidal calcite crystal

bition of stones is mainly done by protein inhibitors. In the pancreas, the stone formation is inhibited by a 144-amino-acid glycoprotein (15.5 kDa). However, the role of the pancreatic stone protein (PSP), called lithostathine, is controversial and is expected to contribute to the stone formation.

Studies on the composition of pancreatic stones using x-ray diffraction methods revealed calcium carbonate as the primary constituent [48.182, 183]. In addition, traces of nickel and fatty acids, organic matrix with desquamated epithelium, fibrin mucoid substances, and protein have also been reported [48.182]. Recent studies on pancreatic stones using x-ray diffraction, Fourier-transform infrared (FTIR) spectroscopy, and electron paramagnetic resonance (EPR) by *Narasimhulu et al.* [48.184] support the view that lithostathine has a role in the formation of pancreatic stones.

48.17.1 Calcium Carbonate

Calcium carbonate (CaCO_3) exists in three polymorphic forms: aragonite, vaterite, and calcite [48.185]. Calcite occurs as a biomineral and happens to be the major constituent of pancreatic calculi [48.186] and also a constituent of gallbladder and urinary stones [48.156, 159].

Gel method of crystallization has been used extensively to study calcium carbonate crystals to elucidate the biomineralization process. Double-diffusion technique using silica gel has been employed to study the effect of divalent cations Ba^{2+} , Sr^{2+} , Co^{2+} , and Mn^{2+} , in small concentrations (50, 200, and 600 ppm) [48.82]. Furthermore, calcite has also been crystallized using double-diffusion technique with polyacrylamide hydrogels incorporating carboxylate groups [48.93]. *Imai et al.* have crystallized porous aragonite crystals in silica gel [48.94]. *Ramachandran et al.* [48.91] have crystallized CaCO_3 in silica gel (Fig. 48.25) and studied the thermal parameters by photoacoustic method.

48.18 Conclusions

The *in vivo* processes leading to formation and growth of crystals in biological fluids are influenced by various factors which are very complex and not yet fully understood. Gel is the most suitable medium to study biomineralization because of its viscous nature, providing simulation of synovial fluid, cartilage, and other biological fluids where crystallization occurs. An ideal *in vitro* crystallization technique which mimics or sim-

ulates exactly the *in vivo* mineralization processes is yet to be developed. As described in this chapter, crystallization in gels is an ideal technique to study the pathological biomineralization *in vitro*, as this method provides a fairly simple technique which closely resembles crystallization *in vivo*. Furthermore, it can be extended to understand problems concerned with biological, medical, and geological aspects of biominerals.

Almost all major and minor constituents of pathological deposits which are responsible for diseases, such as atherosclerosis, gallstones, urinary stones, etc., can be crystallized in various gel media. Gel method of crystallization is also an ideal method to study the effect on crystallization of electric and magnetic fields, various drugs, herbal extracts, and the epitaxial relationship between the constituents in order to understand the anti- and pronucleating factors, which will help in finding factors that help in dissolution of pathological crystal deposits under physiological conditions. Once stones are formed in our body system, they rarely disappear and always grow in size. The factors responsible for this

are not clearly understood. Hence, suitable solvents and inhibitors could be applied to crystals in gel medium to determine the conditions under which already formed crystals can be dissolved, modified or inhibited from the viewpoint of devising new treatments and means to control crystal deposition diseases.

Intense research is going on into the pathogenesis and etiology of crystal deposition diseases. Medical treatment of crystal deposition diseases and prevention from further attacks are still at the experimental stage. Extensive research work is still needed to understand the factors that influence the formation and growth of various crystals in biological fluids.

References

- 48.1 H.K. Henisch: *Crystal Growth in Gels* (The Pennsylvania State Univ. Press, University Park 1973)
- 48.2 R.E. Liesegang: Über einige Eigenschaften von Gallerten, *Naturwiss. Wochenschr.* **11**, 353–362 (1896), in German
- 48.3 H.K. Henisch: *Crystals in Gels and Liesegang Rings* (Cambridge Univ. Press, Cambridge 1988)
- 48.4 S.K. Arora: Advances in gel growth: A review, *Prog. Cryst. Growth Charact.* **4**, 345–378 (1981)
- 48.5 A.R. Patel, A. Venkateswara Rao: Crystal growth in gel media, *Bull. Mater. Sci.* **4**, 527–548 (1982)
- 48.6 F. Lefaucheux, M.C. Robert: Crystal growth in gels. In: *Handbook of Crystal Growth*, ed. by D.T.J. Hurle (Elsevier Science, Amsterdam 1994)
- 48.7 B. Brezina, M. Havrankova: Growth of KH_2PO_4 single crystals in gel, *Mater. Res. Bull.* **6**, 537–543 (1971)
- 48.8 E. Banks, R. Chinanelli, F. Pintchovsky: The growth of some alkaline earth orthophosphates in gelatin gels, *J. Cryst. Growth* **18**, 185–190 (1973)
- 48.9 B. Brezina, M. Havrankova, K. Dusek: The growth of PbHPO_4 and $\text{Pb}_4(\text{NO}_3)_2(\text{PO}_4)_2 \cdot 2\text{H}_2\text{O}$ in gels, *J. Cryst. Growth* **34**, 248–252 (1976)
- 48.10 S. Narayana Kalkura, V.K. Vaidyan, M. Kanakavel, P. Ramasamy: Crystallization of uric acid, *J. Cryst. Growth* **132**, 617–620 (1993)
- 48.11 E.K. Girija, S. Narayana Kalkura, P. Ramasamy: Crystallization of cystine, *J. Mater. Sci. Mater. Med.* **6**, 617–619 (1995)
- 48.12 S. Narayana Kalkura, S. Devanarayanan: Crystallization of steroids in gels, *J. Cryst. Growth* **110**, 265–269 (1991)
- 48.13 S. Narayana Kalkura, S. Devanarayanan: Crystal growth of steroids in silica gel: Testosterone, *J. Cryst. Growth* **94**, 810–813 (1989)
- 48.14 S. Narayana Kalkura, S. Devanarayanan: Growth of progesterone crystals in silica gel and their characterization, *J. Mater. Sci. Lett.* **7**, 827–829 (1988)
- 48.15 M.T. George, V.K. Vaidyan: A new electrolytic method to grow silver dendrites and single crystals in gel, *J. Cryst. Growth* **53**, 300–304 (1981)
- 48.16 M. Muzikar, V. Komanicky, W.R. Fawcett: A detailed study of gold single crystal growth in a silica gel, *J. Cryst. Growth* **290**, 615–620 (2006)
- 48.17 M. Muzikar, P. Polkov, J.C. Fettinger, W.R. Fawcett: Electrochemical growth of platinum particle and platinum-containing crystals in silica gel, *Cryst. Growth Des.* **6**, 1956–1960 (2006)
- 48.18 K.V. Saban, T. Jini, G. Varghese: Influence of magnetic field on the growth and properties of calcium tartrate crystals, *J. Magn. Magn. Mater.* **265**, 296–304 (2003)
- 48.19 M.H. Rahimkuty, K.R. Babu, K.S. Pillai, M.R.S. Kumar, C.M.K. Nair: Thermal behaviour of strontium tartrate single crystals grown in gel, *Bull. Mater. Sci.* **24**, 249–252 (2001)
- 48.20 N.M. Sundaram, M. Ashok, S. Narayana Kalkura: Observation of cholesterol nucleation in magnetic field, *Acta Cryst. D* **58**, 1711–1714 (2002)
- 48.21 N.M. Sundaram: Investigations on the cholesterol, cholesteryl acetate, hydroxyapatite and lysozyme crystallization and the influence of magnetic field on the nucleation process. Ph.D. Thesis (Anna University, Chennai 2004)
- 48.22 A.R. Patel, A.V. Rao: Gel growth and perfection of orthorhombic potassium perchlorate single crystals, *J. Cryst. Growth* **47**, 213–218 (1979)
- 48.23 A.R. Patel, A.V. Rao: Modified gel technique to grow single crystals of KClO_4 , *Indian J. Pure Appl. Phys.* **16**, 544–545 (1978)
- 48.24 B. Sis, T. Canda, Ö. Harmancioglu: Liesegang rings in breast tissue: An unusual component of a for-

- eign body reaction, *Turk. J. Med. Sci.* **34**, 191–193 (2004)
- 48.25 T. Antal, M. Droz, J. Magnin, Z. Racz, M. Zrinyi: Derivation of the Matalon–Packter law for Liesegang patterns, *J. Chem. Phys.* **21**, 9479–9486 (1998)
- 48.26 Z. Racz: Formation of Liesegang patterns, *Physica A* **274**, 50–59 (1999)
- 48.27 D.S. Chernavskii, A.A. Polezhaev, S.C. Müller: A model of pattern formation by precipitation, *Physica D* **54**, 160–170 (1991)
- 48.28 J.H.E. Cartwright, J.M. Garcia-Ruiz, A.I. Villacampa: Pattern formation in crystal growth, *Comput. Phys. Commun.* **21**, 411–413 (1999)
- 48.29 G. Venzl, J. Ross: Comments on pattern formation in precipitation process, *J. Chem. Phys.* **77**, 1308–1313 (1982)
- 48.30 J. George, G. Varghese: Migrating triplet precipitation bands of calcium phosphates in gelatinous matrix, *J. Mater. Sci.* **40**, 5557–5559 (2005)
- 48.31 T. Terada, S. Yamabi, H. Imai: Formation process of sheets and helical forms consisting of strontium carbonate fibrous crystals with silicate, *J. Cryst. Growth* **253**, 435–444 (2003)
- 48.32 R.V. Suganthi, E.K. Girija, S. Narayana Kalkura, H.K. Varma, A. Rajaram: Self-assembled right handed helical ribbon of hydroxyapatite, *J. Mater. Sci. Mater. Med.* (2008) DOI 10.1007/s10856-008-3495-1
- 48.33 J.M. Garcia-Ruiz, D. Rondon, A. Garcia-Romero, F. Otalora: Role of gravity in the formation of Liesegang patterns, *J. Phys. Chem.* **100**, 8854–8860 (1996)
- 48.34 W. Ostwald: Besprechung (Rezension) der Arbeit von Liesegangs “A-Linien”, *Z. J. Phys. Chem.* **23**, 365 (1897), in German
- 48.35 J. George, G. Varghese: Formation of periodic precipitation patterns: A moving boundary problem, *Chem. Phys. Lett.* **362**, 8–12 (2002)
- 48.36 J. George, G. Varghese: Liesegang patterns: Estimation of diffusion coefficient and a plausible justification for colloid explanation, *Colloid Polym. Sci.* **280**, 1131–1136 (2002)
- 48.37 J. George, S. Nair, G. Varghese: Role of colloid dynamics in the formation of Liesegang rings in multi-component systems, *J. Mater. Sci. Lett.* **39**, 311–331 (2004)
- 48.38 J. George, I. Paul, P.A. Varughese, G. Varghese: Rhythmic pattern formation in gels and Matalon–Packter law: A fresh perspective, *Pramana J. Phys.* **60**, 1259–1271 (2003)
- 48.39 F. Izsák, I. Lagzi: A new universal law for the Liesegang pattern formation, *J. Chem. Phys.* **122**, 184707–1–184707–6 (2005)
- 48.40 B.A. Grzybowski, K.J.M. Bishop, C.J. Campbell, M. Fialkowski, S.K. Smoukov: Micro and nano-technology via reaction diffusion, *Soft Matter* **1**, 114–128 (2005)
- 48.41 A. Volford, F. Izsák, M. Ripszám, I. Lagzi: Systematic front distortion and presence of consecutive fronts in a precipitation system, *J. Phys. Chem. B* **110**, 4535–4537 (2006)
- 48.42 F. Lefaucheux, Y. Bernard, C. Vennin, M.C. Robert: Gel growth of 2-amino-5-nitropyridinium dihydrogen phosphate crystals followed by holographic interferometry, *J. Cryst. Growth* **165**, 90–97 (1996)
- 48.43 G. Sajeevkumar, R. Raveendran, B.S. Remadevi, A.V. Vaidyan: Growth feature of ammonium hydrogen D-tartrate single crystals, *Bull. Mater. Sci.* **27**, 323–325 (2004)
- 48.44 S.G. Bhat, S.M. Dharmaparakash: Crystal growth and characterization of antimony thiourea bromide, *J. Cryst. Growth* **181**, 390–394 (1997)
- 48.45 R.I. Petrova, R. Patel, J.A. Swift: Habit modification of asparagine monohydrate crystals by growth in hydrogel media, *Cryst. Growth Des.* **6**, 2709–2715 (2006)
- 48.46 P.V. Dalal, K.B. Saraf: Growth and study of barium oxalate single crystals in agar gel, *Bull. Mater. Sci.* **29**, 421–425 (2006)
- 48.47 M.C. Etter, D.A. John, B.S. Donahue: Growth and characterization of small molecule organic crystals, *J. Cryst. Growth* **76**, 645–655 (1986)
- 48.48 O.M. Yaghi, G. Li, H. Li: Crystal growth of extended solids by nonaqueous gel diffusion, *Chem. Mater.* **9**, 1074–1076 (1997)
- 48.49 S.K. Arora, A.J. Kothari, R.G. Patel, K.M. Chauhan, B.N. Chudasama: Optical absorption in gel grown cadmium tartrate single crystals, *J. Phys. Conf. Ser.* **28**, 48–52 (2006)
- 48.50 T. Jini, K.V. Saban, G. Varghese: Thermal and infrared studies of calcium malate crystals grown in diffusion limited medium, *Cryst. Res. Technol.* **40**, 1155–1159 (2005)
- 48.51 S.R. Suthar, M.J. Joshi: Growth and characterization of Mn^{2+} doped calcium L-tartrate crystals, *Cryst. Res. Technol.* **41**, 664–670 (2006)
- 48.52 X.S. Shajan, C. Mahadevan: On the growth of calcium tartrate tetrahydrate single crystals, *Bull. Mater. Sci.* **27**, 327–331 (2004)
- 48.53 M.V. John, M.A. Ittyachen: Growth and characterization of cerium lanthanum oxalate crystals grown in hydro-silica gel, *Cryst. Res. Technol.* **36**, 141–146 (2001)
- 48.54 S. Narayana Kalkura, M. Kanakavel, P. Ramasamy: Crystallization of an organic intercalation compound: cholic acid, *Cryst. Res. Technol.* **32**, 569–575 (1997)
- 48.55 A. Elizebeth, V. Thomas, G. Jose, G. Jose, N.V. Unnikrishnan, C. Joseph, M.A. Ittyachen: Studies on the growth and optical characterization of dyspro-

- sium gadolinium oxalate single crystals, *Cryst. Res. Technol.* **39**, 105–110 (2004)
- 48.56 K. Ambujam, S. Selvakumar, D. Prem Anand, G. Mohamed, P. Sagayaraj: Crystal growth, optical, mechanical and electrical properties of organic NLO material γ -glycine, *Cryst. Res. Technol.* **41**, 671–677 (2006)
- 48.57 S.J. Joshi, B.B. Parekh, K.D. Vohra, M.J. Joshi: Growth and characterization of gel grown pure and mixed iron–manganese levo–tartrate crystals, *Bull. Mater. Sci.* **29**, 307–312 (2006)
- 48.58 M.J. González-Tejera, S. López-Andrés, M.V. García, M.I. Redondo, J.A.R. Cheda: Single crystal growth of lead (II) *n*-octa-, *n*-nona- and *n*-decanoate, *J. Cryst. Growth* **152**, 330–333 (1995)
- 48.59 E. Ramachandran, S. Natarajan: Gel growth and characterization of gel grown DL-methionine, *Cryst. Res. Technol.* **41**, 411–415 (2006)
- 48.60 P. Andreazza, F. Lefaucheux, M.C. Robert, D. Josse, J. Zyss: Gel growth of 3-methyl-4-nitropyridine-1-oxide organic crystals: x-ray and nonlinear optics characterization, *J. Appl. Phys.* **68**, 8–13 (1990)
- 48.61 R. Mahalakshmi, S.X. Jesuraja, S. Jerome Das: Growth and characterization of L-phenylalanine, *Cryst. Res. Technol.* **41**, 780–783 (2006)
- 48.62 S. Selvakarapandian, K. Vivekanandan, P. Kolan-daivel: Vibrational studies of gel grown ferroelectric $\text{RbHfCl}_4\text{H}_4\text{O}_6$ and $\text{SrCl}_4\text{H}_4\text{O}_6 \cdot 4\text{H}_2\text{O}$ crystals, *Cryst. Res. Technol.* **34**, 873–880 (1999)
- 48.63 S.K. Arora, V. Patel, A. Kothari, B. Amin: Gel growth and preliminary characterization of strontium tartrate trihydrate, *Cryst. Growth Des.* **4**, 343–349 (2004)
- 48.64 T. Jini, K.V. Saban, G. Varghese: The growth, spectral and thermal properties of the coordination compound crystal–strontium malate, *Cryst. Res. Technol.* **41**, 250–254 (2006)
- 48.65 M. Wang, X.Y. Liu, C. Sun, N. Ming, P. Bennema, W.J.P. Van Enckevort: Periodic roughening transitions in diffusion-limited growth, *Europhys. Lett.* **41**, 61–66 (1998)
- 48.66 Y. Oaki, H. Imai: Experimental demonstration for the morphological evolution of crystals grown in gel media, *Cryst. Growth Des.* **2**, 711–716 (2003)
- 48.67 S.J. Shitole, K.B. Saraf: Growth and study of some gel grown group II single crystals of iodate, *Bull. Mater. Sci.* **24**, 461–468 (2001)
- 48.68 S.J. Shitole, K.B. Saraf: Growth, structural and microtopographical studies of calcium iodate monohydrate crystals grown in silica gel, *Cryst. Res. Technol.* **37**, 440–445 (2002)
- 48.69 C.M. Pina, L. Fernández-Díaz, J.M. Astilleros: Nucleation and growth of scheelite in a diffusing-reacting system, *Cryst. Res. Technol.* **35**, 1015–1022 (2000)
- 48.70 M. Gu, D.X. Wang, Y.T. Huang, R. Zhang: Growing CuI crystals with decomplexation method modified by concentration programming, *Cryst. Res. Technol.* **39**, 1104–1107 (2004)
- 48.71 M. Gu, Y.F. Li, X.L. Liu, D.X. Wang, R.K. Xu, G.W. Li, X.P.O. Yang: The influence of CuI–HI complex distribution on CuI crystal growth with decomplexation method in silica gel, *J. Cryst. Growth* **292**, 74–77 (2006)
- 48.72 H. Kusumoto, T. Kaito, S. Yanagiya, A. Mori, T. Inoue: Growth of single crystals of PbBr_2 in silica gel, *J. Cryst. Growth* **277**, 536–540 (2005)
- 48.73 C.M. Pina, L.F. Diaz, M. Prieto: Topotaxy relationships in the transformation phosgenite–cerussite, *J. Cryst. Growth* **158**, 340–345 (1996)
- 48.74 K. Mayer, D. Wörmann: Influence of a polycrystalline precipitation zone on the growth of single crystals using a gel method: Growth of single crystals of PbHPO_4 , *J. Cryst. Growth* **169**, 317–324 (1996)
- 48.75 D.S. Bhavsar, K.B. Saraf, T. Seth: Studies on growth and microstructure of lead iodide single crystals, *Cryst. Res. Technol.* **37**, 225–230 (2002)
- 48.76 C.M. Pina, L.F. Diaz, M. Prieto: Crystallization of $\beta''\text{-LiNH}_4\text{SO}_4$ and $(\text{NH}_4)_2\text{SO}_4$ in gels: Growth morphology and epitaxy phenomena, *J. Cryst. Growth* **177**, 102–110 (1997)
- 48.77 C.M. Pina, F.L. Diaz, J. Lopez-Gareia, M. Prieto: Growth of $\beta\text{-LiNaSO}_4$ and $\text{Li}_2\text{SO}_4 \cdot \text{H}_2\text{O}$: Epitaxy and intergrowth phenomena, *J. Cryst. Growth* **148**, 283–288 (1995)
- 48.78 R. Kanagadurai, R. Sankar, G. Sivanesan, S. Srinivasan, R. Jayavel: Growth and properties of ferroelectric potassium ferrocyanide trihydrate single crystals, *Cryst. Res. Technol.* **41**, 853–858 (2006)
- 48.79 R.I. Petrova, J.A. Swift: Habit changes of sodium bromate crystals grown from gel media, *Cryst. Growth Des.* **2**, 573–578 (2002)
- 48.80 R.I. Petrova, J.A. Swift: Growth of crystal enantiomers in hydrogels, *J. Am. Chem. Soc.* **126**, 1168–1173 (2004)
- 48.81 J.M. Garcia-Ruiz: On the formation of induced morphology crystal aggregates, *J. Cryst. Growth* **73**, 251–262 (1985)
- 48.82 L.F. Diaz, J.M. Astilleros, C.M. Pina: The morphology of calcite crystals grown in a porous medium doped with divalent cation, *Chem. Geol.* **225**, 314–321 (2006)
- 48.83 J.P. Reyes-Graveda, D. Jauregui-Zuniga, N. Batina, M. Salmon-Salazar, A. Moreno: Experimental simulations of the biomineralization phenomena in avian eggshells using BaCO_3 aggregates grown inside an alkaline silica matrix, *J. Cryst. Growth* **234**, 227–236 (2002)
- 48.84 M. Prieto, F. Diaz, L. Andres: Supersaturation evolution and first precipitate location in crystal growth in gels: application to barium and strontium carbonates, *J. Cryst. Growth* **98**, 447–460 (1989)

- 48.85 J.M. Garcia-Ruiz: Crystal growth in gels as a laboratory analogous of the natural crystallization, *Estud. Geol.* **38**, 209–225 (1982)
- 48.86 S. Mann, J. Webb, R.J.P. Williams (Eds.): *Biominer-alization* (VCH, New York 1989)
- 48.87 P. Dieppe, P. Calvert: *Crystals and Joint Disease* (Chapman Hall, New York 1983)
- 48.88 H. Iwata, Y. Abe, S. Nishio, A. Wakatsuki, K. Ochi, M. Takeuchi: Crystal-matrix interrelations in brushite and uric acid calculi, *J. Urol.* **135**, 397–401 (1986)
- 48.89 W. Achilles, R. Freitag, B. Kiss, H. Riedmiller: Quantification of crystal growth of calcium oxalate in gel and its modification by urinary constituents in a new flow model of crystallization, *J. Urol.* **154**, 1552–1556 (1995)
- 48.90 V.I. Katkova, V.I. Rakin: Bacterial genesis of calcite, *J. Cryst. Growth* **142**, 271–274 (1994)
- 48.91 E. Ramachandran, P. Raji, K. Ramachandran, S. Natarajan: Photoacoustic studies of the thermal properties of calcium carbonate – The major constituent of pancreatic calculi, *Cryst. Res. Technol.* **41**, 64–67 (2006)
- 48.92 O. Grassmann, R.B. Neder, A. Putnis, P. Lobmann: Biomimetic control of crystal assembly by growth in an organic hydrogel network, *Am. Mineral.* **88**, 647–652 (2003)
- 48.93 O. Grassmann, P. Lobmann: Biomimetic nucleation and growth of CaCO_3 in hydrogels incorporating carboxylate groups, *Biomaterials* **25**, 277–282 (2004)
- 48.94 H. Imai, T. Terada, T. Miura, S. Yamabi: Self-oriented formation of porous aragonite with silicate, *J. Cryst. Growth* **244**, 200–205 (2002)
- 48.95 E.K. Girija, S.C. Latha, S. Narayana Kalkura, C. Subramanian, P. Ramasamy: Crystallization and microhardness of calcium oxalate monohydrate, *Mater. Chem. Phys.* **52**, 253–257 (1998)
- 48.96 T. Jung, W.S. Kim, C.K. Choi: Crystal structure and morphology control of calcium oxalate using biopolymeric additives in crystallization, *J. Cryst. Growth* **279**, 154–162 (2005)
- 48.97 E.V. Petrova, N.V. Gvozdev, L.N. Rashkovich: Growth and dissolution of calcium oxalate monohydrate (COM) crystals, *J. Optoelectron. Adv. Mater.* **6**, 261–268 (2004)
- 48.98 N. Srinivasan, S. Natarajan: Growth of some urinary crystals and studies on inhibitors and promoters. I. Standardization of parameters for crystal growth and characterization of crystals, *Indian J. Phys.* **70A**, 563–568 (1996)
- 48.99 S. Natarajan, E. Ramachandran, D.B. Suja: Growth of some urinary crystals and studies on inhibitors and promoters. II. X-ray studies and inhibitory or promotory role of some substances, *Cryst. Res. Technol.* **32**, 553–559 (1997)
- 48.100 E. Ramachandran, S. Natarajan: XRD, thermal and FTIR studies on gel-grown gypsum crystals, *Indian J. Phys.* **79**, 77–80 (2005)
- 48.101 P. Kumareson, S. Devanarayanan: Growth of crystals of calcium sulphate in silica gel in presence of additive and their characterization, *Cryst. Res. Technol.* **22**, 1453–1458 (1987)
- 48.102 A. Elizabeth, C. Joseph, M.A. Ittyachen: Growth and micro-topographical studies of gel grown cholesterol crystals, *Bull. Mater. Sci.* **24**, 431–434 (2001)
- 48.103 C.R. Loomis, G.G. Shipley, D.M. Small: The phase behavior of hydrated cholesterol, *J. Lipid Res.* **20**, 525–535 (1979)
- 48.104 E. Ramachandran, S. Natarajan: Crystal growth of some urinary stone constituents: III. In-vitro crystallization of L-cystine and its characterization, *Cryst. Res. Technol.* **39**, 308–312 (2004)
- 48.105 T.K. Anee, N. Meenakshi Sundaram, D. Arivuoli, P. Ramasamy, S. Narayana Kalkura: Influence of an organic and an inorganic additive on the crystallization of dicalcium phosphate dihydrate, *J. Cryst. Growth* **285**, 380–387 (2005)
- 48.106 V.S. Joshi, M.J. Joshi: FTIR spectroscopic, thermal and growth morphological studies of calcium hydrogen phosphate dihydrate crystals, *Cryst. Res. Technol.* **38**, 817–821 (2003)
- 48.107 G.R. Sivakumar, E.K. Grija, S. Narayana Kalkura, C. Subramanian: Crystallization of calcium phosphates: Brushite and monetite, *Cryst. Res. Technol.* **33**, 197–205 (1998)
- 48.108 T. Irusan, S.N. Kalkura, D. Arivuoli, P. Ramasamy: Dendritic structures of brushite in silica gel, *J. Cryst. Growth* **130**, 217–220 (1993)
- 48.109 R.H. Plovnick: Crystallization of brushite from EDTA-chelated Ca in agar gels, *J. Cryst. Growth* **141**, 22–26 (1991)
- 48.110 T.K. Anee, M. Palanichamy, M. Ashok, N. Meenakshi Sundaram, S. Narayana Kalkura: Influence of iron and temperature on the crystallization of calcium phosphates at the physiological pH, *Mater. Lett.* **58**, 478–482 (2004)
- 48.111 E. Ramachandran, S. Natarajan: Crystal growth of some urinary stone constituents: II. In-vitro crystallization of hippuric acid, *Cryst. Res. Technol.* **37**, 274–279 (2002)
- 48.112 M. Ashok, N. Meenakshi Sundaram, S. Narayana Kalkura: Crystallization of hydroxyapatite at physiological temperature, *Mater. Lett.* **57**, 2066–2070 (2003)
- 48.113 E.K. Girija, Y. Yokogawa, F. Nagata: Bone like apatite formation on collagen fibrils by biomimetic method, *Chem. Lett.* **31**, 702–703 (2002)
- 48.114 G.R. Sivakumar: Investigations on crystallization and characterization of biominerals: Calcium and magnesium phosphates. Ph.D. Thesis (Anna University, Chennai 2000)

- 48.115 S. Narayana Kalkura, E.K. Girija, M. Kanakavel, P. Ramasamy: In-vitro crystallization of spherulites of monosodium urate monohydrate, *J. Mater. Sci. Mater. Med.* **6**, 577–580 (1995)
- 48.116 M. Iijima, Y. Moriwaki: Lengthwise and oriented growth of octacalcium phosphate crystal in polyacrylamide gel in a model system of tooth enamel apatite formation, *J. Cryst. Growth* **194**, 125–132 (1998)
- 48.117 E. Ramachandran, S. Natarajan: Crystal growth of some urinary stone constituents: I. In-vitro crystallization of L-tyrosine and its characterization, *Cryst. Res. Technol.* **37**, 1160–1164 (2002)
- 48.118 W.G. Robertson, M. Peacock: The pattern of urinary stone disease in Leeds and in the United Kingdom in relation to animal protein intake during the period 1960–1980, *Urol. Int.* **37**, 394–399 (1982)
- 48.119 R.L. Ryall: The scientific basis of calcium oxalate urolithiasis. Predisposition and precipitation, promotion and proscriptio, *World J. Urol.* **11**, 59–65 (1993)
- 48.120 X. Guan, R. Tang, G.H. Nancollas: The potential calcification of OCP on intraocular lenses, *J. Biomed. Mater. Res.* **71A**, 488–496 (2004)
- 48.121 S.R. Qui, A. Wierzbicki, C.A. Orme, A.M. Cody, J.R. Hoyer, G.H. Nancollas, J.J. De Yoreo: Molecular modulation of calcium oxalate crystallization by osteopontin and citrate, *Proc. Natl. Acad. Sci.* **101**, 1811–1815 (2004)
- 48.122 R. Tang, L. Wang, C.A. Orme, T. Bonstein, P. Bush, G.H. Nancollas: Dissolution at the nanoscale: Self-preservation of biominerals, *Angew. Chem. Int. Ed.* **43**, 2697–2701 (2004)
- 48.123 P. Spirnak, M.I. Resnick: Urinary stones. In: *Smith's General Urology*, ed. by E.A. Tangho, J.W. McAninch (Prentice-Hall International, San Francisco 1990)
- 48.124 A.D. Seftel, M.I. Resnick: Metabolic evaluation of urolithiasis, *Urol. Clin. North Am.* **17**, 159–170 (1990)
- 48.125 A. Randal: The origin and growth of renal calculi, *Ann. Surg.* **105**, 1009–1027 (1937)
- 48.126 L. Anderson, J.R. McDonald: The origin, frequency, and significance of microscopic calculi in the kidney, *Surg. Gynecol. Obstet.* **82**, 275–282 (1946)
- 48.127 A.J. Butt, E.A. Hauser: The importance of protective urinary colloids in the prevention and treatment of kidney stones, *Science* **115**, 308–310 (1952)
- 48.128 C.W. Vermeulon, E.S. Lyon: Mechanisms of genesis and growth of calculi, *Am. J. Med.* **45**, 684–692 (1968)
- 48.129 F. Grases, A. Costa-Bauza, M. Kroupa: Studies on calcium oxalate monohydrate crystallization: Influence of inhibitors, *Urol. Res.* **22**, 39–43 (1992)
- 48.130 A. Millan, F. Grases, O. Sönnel, I. Krivankova: Semi-batch precipitation of calcium oxalate monohydrate, *Cryst. Res. Technol.* **27**, 31–39 (1992)
- 48.131 J. Hofbauer, I. Steffen, K. Hobarth, G. Vujici, H. Schwetz, G. Reich, O. Zechner: Trace elements and urinary stone formation: New aspect of the pathological mechanism of urinary stone formation, *J. Urol.* **145**, 93–96 (1991)
- 48.132 I. Melnick, R.R. Landes, A.A. Hoffman, J.F. Burch: Magnesium therapy for recurring calcium oxalate urinary calculi, *J. Urol.* **105**, 119–122 (1971)
- 48.133 M. Ashok, S. Narayana Kalkura, V. Vijayan, P. Magudapathy, K.G.M. Nair: Investigations of the elemental concentration of kidney stones by PIXE analysis, *Int. J. PIXE* **11**, 21–25 (2001)
- 48.134 W. Achilles: In Vitro Crystallization systems for the study of urinary stone formation, *World J. Urol.* **15**, 244–251 (1997)
- 48.135 Y.M.F. Marickar, P. Koshy: Scanning electron microscopic study of effect of various agents on urinary crystal morphology, *Scanning Microsc.* **1**, 571–577 (1987)
- 48.136 A.M. Freitas, N. Schor, M.A. Boim: The effect of *Phyllanthus niruri* on urinary inhibitors of calcium oxalate crystallization and other factors associated with renal stone formation, *BJU Int.* **89**, 829–834 (2002)
- 48.137 V.S. Joshi, B.B. Parekh, M.J. Joshi, A.B. Vaidya: Herbal extracts of *Tribulus terrestris* and *Bergenia ligulata* inhibit growth of calcium oxalate monohydrate crystals in vitro, *J. Cryst. Growth* **275**, e1403–e1408 (2005)
- 48.138 K.C. Joseph, B.B. Parekh, M.J. Joshi: Inhibition of growth of urinary type calcium hydrogen phosphate dihydrate crystals by tartaric acid and tamarind, *Curr. Sci.* **88**, 1232–1238 (2005)
- 48.139 S.R. Khan, P.A. Glenton: Deposition of calcium phosphates and calcium oxalate crystals in the kidney, *J. Urol.* **153**, 811–817 (1995)
- 48.140 P.G. Werness, J.H. Bergert, L.H. Smith: Crystalluria, *J. Cryst. Growth* **53**, 166–181 (1981)
- 48.141 W.H. Boyce, J.S. King: Crystal-matrix interrelation in calculi, *J. Urol.* **3**, 351–365 (1959)
- 48.142 E.K. Girija: Investigations on biological crystals and analyses and epidemiological studies of urinary calculi. Ph.D. Thesis (Anna University, Chennai 1998)
- 48.143 D. Hirsch, R. Azoury, S. Sarig: DSC, x-ray and NMR properties of cholesterol crystals, *Clin. Chim. Acta* **174**, 65–82 (1988)
- 48.144 S. Narayana Kalkura, T.K. Anee, M. Ashok, C. Betzel: Investigations on the synthesis and crystallization of hydroxyapatite at low temperature, *J. Biomed. Eng.* **14**, 581–592 (2004)
- 48.145 S. Lazic: Microcrystalline hydroxyapatite formation from alkaline solutions, *J. Cryst. Growth* **147**, 147–154 (1995)
- 48.146 G. Morales, J.T. Burgues, R.R. Clemente: Crystal size distribution of hydroxyapatite precipitated in a MSMR reactor, *Cryst. Res. Technol.* **36**, 1065–1074 (2001)
- 48.147 A.L. Braybrook, B.R. Heywood, R.A. Jackson, K. Pitt: Parallel computational and experimental studies

- of the morphological modification of calcium carbonate by cobalt, *J. Cryst. Growth* **243**, 336–344 (2002)
- 48.148 D.B. Leusmann, H. Niggemann, S. Roth, H.V. Ahlen: Recurrence rate and severity of urinary calculi, *Scan. J. Urol. Nephron* **29**, 279–283 (1995)
- 48.149 R.J. Riese, K. Sakhaee: Uric acid nephrolithiasis: pathogenesis and treatment, *J. Urol.* **148**, 765–771 (1992)
- 48.150 D.J. Sutor, S. Scheidt: Identification standards for human urinary calculus components, using crystallographic methods, *Br. J. Urol.* **40**, 22–28 (1968)
- 48.151 F.L. Coe, A. Evan, E. Worcester: Kidney stone disease, *J. Clin. Invest.* **115**, 2598–2608 (2005)
- 48.152 C.Y.C. Pak, O. Waters, L.M. Arnold, K.H. Cox, C.D. Barilla: Mechanism of calcium urolithiasis among patients with hyperuricosuria: Supersaturation of urine with respect to monosodium urate, *J. Clin. Invest.* **59**, 426–431 (1977)
- 48.153 R. Boistelle, C. Rinaudo: Phase transition and epitaxies between hydrated orthorhombic and anhydrous monoclinic uric acid crystals, *J. Cryst. Growth* **53**, 1–9 (1981)
- 48.154 C. Rinaudo, R. Boistelle: The occurrence of uric acids and the growth morphology of the anhydrous monoclinic modification: $C_5H_4N_4O_3$, *J. Cryst. Growth* **49**, 569–576 (1980)
- 48.155 J.E.Z. Caner, J.L. Decker: Recurrent acute arthritis in chronic renal failure treated with periodic dialysis, *Am. J. Med.* **36**, 571–582 (1964)
- 48.156 J.F. Fiechtner, P.A. Simkin: Urate spherulites in gouty synovia, *J. Am. Med. Assoc.* **245**, 1533–1536 (1981)
- 48.157 N.W. McGill, P.A. Dieppe: The effect of biological crystals and human serum on the rate of formation of crystals of monosodium urate monohydrate in vitro, *Br. J. Rheum.* **30**, 107–111 (1991)
- 48.158 K.R. Murray, D.K. Granner, P.A. Mayers, V. Rodwell, O.K. Graner: *Lange Medical Book: Harper's Biochemistry* (Prentice Hall, New Jersey 1988)
- 48.159 D.S. Sutor, S.E. Wooley: The structure and formation of urinary calculi: oriented crystal growth, *Br. J. Urol.* **44**, 532–536 (1972)
- 48.160 M. Daudon, P. Jungers: Drug-induced renal calculi: epidemiology, prevention and management, *Drugs* **64**, 245–275 (2004)
- 48.161 R. Vani: Invitro crystallization and characterization of an amino acid: Cystine. M.Phil. Dissertation (Anna University, Chennai 1999)
- 48.162 B.L. Oser: *Hawk's Physiological Chemistry*, 14th edn. (Tata McGraw-Hill, New Delhi 1976)
- 48.163 E. Ramachandran: Investigations on certain chemical constituents of urinary stones and some amino acids. Ph.D. Thesis (Madurai Kamaraj University, Madurai 2006)
- 48.164 D.J. Sutor: Crystal growth in bile, *Prog. Cryst. Growth Charact.* **4**, 47–58 (1981)
- 48.165 D.M. Small, G.G. Shipley: Physical-chemical basis of lipid deposition in atherosclerosis, *Science* **185**, 222–229 (1974)
- 48.166 P. Libby, M. Aikawa, U. Schönbeck: Cholesterol and atherosclerosis, *Biochim. Biophys. Acta* **1529**, 299–300 (2000)
- 48.167 W.H. Admirand, D.M. Small: The physicochemical basis of cholesterol gallstone formation in man, *J. Clin. Invest.* **47**, 1043–1052 (1968)
- 48.168 R.P. Mensink, E.H.M. Temme, J. Plat: Dietary fats and coronary heart disease. In: *Food Lipids. Chemistry, Nutrition and Biotechnology*, ed. by C.C. Akoh, D.B. Min (Marcel Dekker, New York 1998) pp. 507–535
- 48.169 R.T. Holzbach: Factors influencing cholesterol nucleation in bile, *Hepatology* **4**, 1735–1765 (1984)
- 48.170 G.H. Nancollas: Crystallization in bile, *Hepatology* **4**, 1695–1725 (1984)
- 48.171 S.M. Strasberg: The pathogenesis of cholesterol gallstones – A review, *J. Gastrointest. Surg.* **2**, 109–125 (1998)
- 48.172 M.C. Frincu, S.D. Fleming, A.L. Rohl, J.A. Swift: The epitaxial growth of cholesterol crystals from bile solutions on calcite substrates, *J. Am. Chem. Soc.* **126**, 7915–7924 (2004)
- 48.173 A.J. Reginato, B. Kurnik: Calcium oxalate and other crystals associated with kidney diseases and arthritis, *Semin. Arthritis Rheum.* **18**, 198–224 (1989)
- 48.174 B.M. Craven: Pseudosymmetry in cholesterol monohydrate, *Acta Cryst. B* **35**, 1123–1128 (1979)
- 48.175 N.T. Saraswathi, F.D. Gnanam: Effect of medicinal plants on the crystallization of cholesterol, *J. Cryst. Growth* **179**, 611–617 (1997)
- 48.176 M. Ashok, S. Narayana Kalkura, V.J. Kennedy, A. Markwitz, V. Jayanthi, K.G.M. Nair, V. Vijayan: Trace element analysis of South Indian gallstones by PIXE, *Int. J. PIXE* **12**, 137–144 (2002)
- 48.177 M. Ashok, T.R. Rautray, P.K. Nayak, V. Vijayan, V. Jayanthi, S. Narayana Kalkura: Energy dispersive x-ray fluorescence analyses of gallstones, *J. Radioanal. Nucl. Chem.* **25**, 333–335 (2003)
- 48.178 M. Ashok, D.N. Reddy, V. Jayanthi, S.N. Kalkura, V. Vijayan, S. Gokulakrishnan, K.G.M. Nair: Regional differences in constituents of gallstones, *Trop. Gastroenterol.* **26**, 73–75 (2005)
- 48.179 R.P. Bonar-Law, A.P. Davis: Cholic acid as an architectural component in biomimetic/molecular recognition chemistry: synthesis of the first “cholaphanes”, *Tetrahedron* **49**, 9855 (1993)
- 48.180 J.T. Velardo: *The Endocrinology of Reproduction* (Oxford Univ. Press, New York 1958)
- 48.181 L. Fieser, M. Fieser: *Steroids* (Reinhold, New York 1959)

- 48.182 J. Geevarghese: *Calcific Pancreatitis: Causes and Mechanisms in the Tropics Compared to the Sub-tropics* (J. Varghese, Bombay 1976)
- 48.183 A.C. Schulz, P.B. Moore, P.J. Geevarghese, C.S. Pitchumoni: X-ray diffraction studies of pancreatic calculi associated with nutritional pancreatitis, *Dig. Dis. Sci.* **31**, 476–480 (1986)
- 48.184 K.V. Narasimhulu, N.O. Gopal, J. Lakshmana Rao, N. Vijayalakshmi, S. Natarajan, R. Surendran, V. Mohan: Structural studies of the biomineralized species of calcified pancreatic stones in patients suffering from chronic pancreatitis, *Biophys. Chem.* **114**, 137–147 (2005)
- 48.185 S.R. Kamhi: On the structure of vaterite CaCO_3 , *Acta Cryst.* **16**, 770–772 (1963)
- 48.186 H.G. Beger, A.L. Warshaw, D.L. Carr-Locke, J.P. Neoptolemos, C. Russell, M.G. Sarr: *The Pancreas* (Blackwell Scientific, London 1998)

49. Crystal Growth and Ion Exchange in Titanium Silicates

Aaron J. Celestian, John B. Parise, Abraham Clearfield

In situ experiments, whether carried out in-house or at synchrotron sources, can provide valuable information on the nucleation and subsequent growth of crystals and on the mechanism of growth as well as mechanisms of phase changes and ion-exchange phenomena. This chapter describes the types of x-ray detectors, in situ cells, and detectors used in such studies. The procedures are illustrated by a study of the preparation of a tunnel-structured sodium titanium silicate, the partially niobium framework phase, and the mechanism of ion exchange as revealed by time-resolved x-ray data.

49.1 X-Ray Methods	1637
49.1.1 X-Rays and Diffraction Theory	1638
49.1.2 Neutron Diffraction Theory	1640
49.2 Equipment for Time-Resolved Experiments	1642
49.2.1 In-House X-Ray Sources	1642
49.2.2 Synchrotron Radiation Sources	1642
49.3 Detectors	1642
49.3.1 Image Plates	1642
49.3.2 Charge-Coupled Devices	1643
49.3.3 Position-Sensitive Detectors (PSD)	1643
49.3.4 Energy-Dispersive Detectors	1643
49.3.5 Silicon Strip Detector	1644
49.3.6 Other Considerations	1644
49.4 Software	1644
49.5 Types of In Situ Cells	1645
49.5.1 SECeTS Cell	1646
49.5.2 Polyimide Environmental Cell	1647
49.5.3 High-Pressure Cells	1647
49.5.4 Hydrothermal Steel Autoclave-Type Cell	1647
49.5.5 Neutron Diffraction Cell	1648
49.6 In-Situ Studies of Titanium Silicates (Na-TS) with Sitinakite Topology	1649
49.6.1 Introduction to the Problem	1649
49.6.2 Synthesis and Structure of Sodium Titanium Silicate (Na-TS)	1649
49.6.3 Synthesis Problems and In Situ Hydrothermal Study ...	1650
49.6.4 Ion Exchange of Cs ⁺ into Na-TS	1652
49.6.5 Cesium Ion Exchange into H-TS	1654
49.6.6 Sodium Niobium Titanosilicate (Nb-TS)	1655
49.6.7 In Situ Synthesis of Na-NbTS	1655
49.6.8 In Situ Ion Exchange of Cesium Ion Exchange in Na-NbTS	1656
49.6.9 Cesium Ion Exchange into H-NbTS	1656
49.7 Discussion of In Situ Studies	1658
49.7.1 Synthesis of Na-TS and Na-NbTS ..	1658
49.7.2 Exchange Mechanisms	1659
49.8 Summary	1660
References	1660

49.1 X-Ray Methods

Hydrothermal techniques for the synthesis of new materials and for crystal growth have been used extensively since the 1950s, and this has increased substantially over the last decade. The use of in situ studies in many cases is desirable since the data collection and analysis

methods do not disrupt the chemical reaction or process. In the ex situ hydrothermal process, especially when new materials are the goal, the experimentalist usually has control over the time/temperature/pressure conditions and reactant ratios of the synthesis. What is

missing in these *ex situ* processes is knowledge of what takes place as the reaction proceeds. It is possible that the phase(s) formed at elevated temperatures may revert to a more stable phase on cooling. Furthermore, several phase transformations, or metastable intermediates, may occur during the synthesis procedure that would otherwise go undetected in a typical *cook-and-look* experiment. Nucleation and crystal growth, mechanisms of phase changes, and ion-exchange processes are readily studied using *in situ* x-ray diffraction as the major experimental tool [49.1–3]. If the reaction is relatively slow and the resolution required is moderate, the *in situ* study can be carried out in an in-house x-ray facility or at a neutron facility. New detectors and more powerful x-ray and neutron sources are enabling new experimental techniques that allow routine data collection from *in situ* experiments. Compared with conventional sealed-tube x-ray sources, synchrotron radiation is 10^4 – 10^{12} times brighter. At the advanced photon source (APS), Argonne National Laboratory and the newly renovated facility at Brookhaven National Laboratory, National Synchrotron Light Source (NSLS) x-ray powder patterns can be recorded in seconds and with excellent resolution. In what follows, we will describe the types of facilities and provide several examples of how *in situ* studies are performed at synchrotron and neutron user facilities.

There are compromises involved in the collection and interpretation of time-resolved data. The data quality is affected chiefly by the poorer signal-to-noise discrimination, compared with data collected over longer time frames and high-quality *ex situ* data. However, by combining data collected in a *static* manner, on materials representing the beginning and end or the reaction pathway, for example, with time-resolved data, a more complete picture of the mechanism emerges; for example structural models of the kinetics of zeolite synthesis [49.4–6], ion exchange in their various cation-exchanged forms [49.5, 7, 8], in their dehydrated and hydrated states [49.9, 10], and with and without sorbents, are important to rationalizing their mode of operation. Monitoring these structural changes *in situ* and as a function of time allows the mechanism of transformation to be followed. Several case studies involving this approach are given below.

The quality and types of data required to uncover mechanisms depends on the information being sought. The optimization of synthetic conditions only requires identification of the phases and the pressure–temperature–composition conditions over which they

are stable, and many of these can be carried out in the laboratory setting, particularly since the wider availability of area detectors. Powder diffraction data suitable for Rietveld refinement require:

1. Access to brighter x-ray beams at second- and third-generation synchrotron storage rings
2. Versatile high-pressure/temperature and hydrothermal cells designs.

49.1.1 X-Rays and Diffraction Theory

A crystal may be defined as a solid composed of atoms, ions or molecules arranged in a pattern that is periodic in three-dimensional space. The smallest repeating pattern containing all elements and symmetry operations is termed the *unit cell*, and is constructed by three non-coplanar vectors **a**, **b**, **c**, where *a*, *b*, and *c* are the axial lengths of the unit cell, and three angles α , β , γ , where α , β , and γ are the angles between the axes. It is convenient to focus on the geometry of the periodic array. The crystal is then represented as a three-dimensional array of points, each of which has identical surroundings. There exist 14 such lattices, the Bravais lattices, that describe the geometry of crystals. The lattices are infinite in extent and it is possible to construct many sets of parallel planes that pass through the points. The perpendicular distance between any set of such planes is known as the *d*-spacing.

When a beam of monochromatic x-rays is passed through a crystal, diffraction occurs because the wavelength of the x-rays and the distances between atoms, or the sets of planes, are of the same order of magnitude. Diffraction only occurs when the waves being diffracted constructively interfere, and therefore not all *d*-spacing diffraction occurs at the same time. The Bragg equation defines the conditions for diffraction to occur

$$\sin \theta = \frac{n\lambda}{2d}, \quad (49.1)$$

where λ is the x-ray wavelength, θ is the angle of diffraction, and *n* is an integer, which for our purposes may be set to unity. From knowledge of the *d*-spacings it is possible to obtain the values of the unit cell constants. The orientation of a plane in space relative to an axial system may be given in terms of the intercepts of the plane with respect to the axes, or the vector from the origin of the axial system that is perpendicular to the plane. This latter distance is *d* and the intercepts are designated by *hkl*, where *hkl*, are integers that are the reciprocals of the intercepts; for example, if the plane

cuts the a -axis at $\frac{1}{2}a$ then

$$h = \frac{a}{\frac{1}{2}a} = 2.$$

Similarly, k and ℓ are the reciprocals of the intercepts along the b - and c -axis, respectively. There are six axial systems by which unit cells and lattices are described, or seven if we separate trigonal from hexagonal. For each axial system there is an equation relating d with hkl . For the cubic system there is only one unknown as all the unit cell dimensions are equal and the angles are all 90° , then

$$d = \frac{a}{[h^2 + k^2 + \ell^2]^{1/2}}. \quad (49.2)$$

In single-crystal studies it is possible to align each set of parallel planes at their respective Bragg angle to the x-ray beam and record all the d -spacings in three-dimensional space. For in situ synthesis studies this method would be time consuming, and most starting materials used in hydrothermal crystallization experiments are not single crystals, but rather solutions, gels or powders. It is advantageous to use the powder diffraction method to record a large number of d -spacings in one or two dimensions quickly.

The powder method is predicated on the fact that the powder will have an equal number of crystallites in all possible orientations to the x-ray beam, and all diffraction from the sets of d -spacings will be generated simultaneously [49.12]. The angle between the incident beam and the diffracted beam is always 2θ (Fig. 49.1). The detector travels about a circle of fixed radius with the sample at the center of the circle. The x-ray powder diffraction pattern (XRPD) is recorded as the diffracted intensities as a function of 2θ , and is a one-dimensional pattern. For complex structures or mixtures, the diffracted intensities may

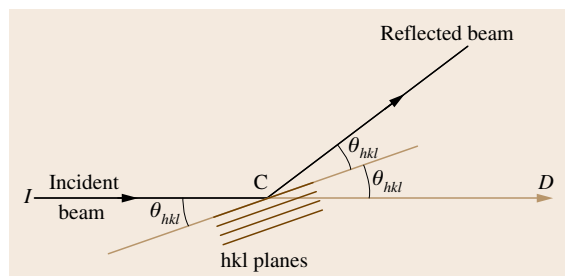


Fig. 49.1 Bragg reflection from a set of lattice planes showing that the angle between the incident beam and the reflected beam is always 2θ

overlap, and extracting the intensities of overlapping features becomes increasingly difficult with increasing number of crystalline phases. Therefore the resolving power of the diffractometer becomes an important feature in planning in situ studies. Resolution afforded by synchrotron-based diffraction is much greater than that of in-house powder diffraction techniques. The breadth of an x-ray diffracted peak is measured as the width of the peak at half-height, designated the full-width at half-maximum (FWHM). For medium-resolution powder diffractometer at a synchrotron storage ring the FWHM is $\approx 0.01^\circ$, as compared with 0.1 – 0.5° for the K_α doublet of Cu radiation from an in-house powder diffractometer. Another point to consider is that x-ray diffraction features generally broaden with increasing 2θ values, so that overlap of peaks at high 2θ values also increases.

X-ray scattering arises from the interaction of electrons with the electromagnetic field of the collimated and coherent x-ray beam. As an element's atomic number increase, so does the total number electrons around the atom, and as the number of electrons of the atom

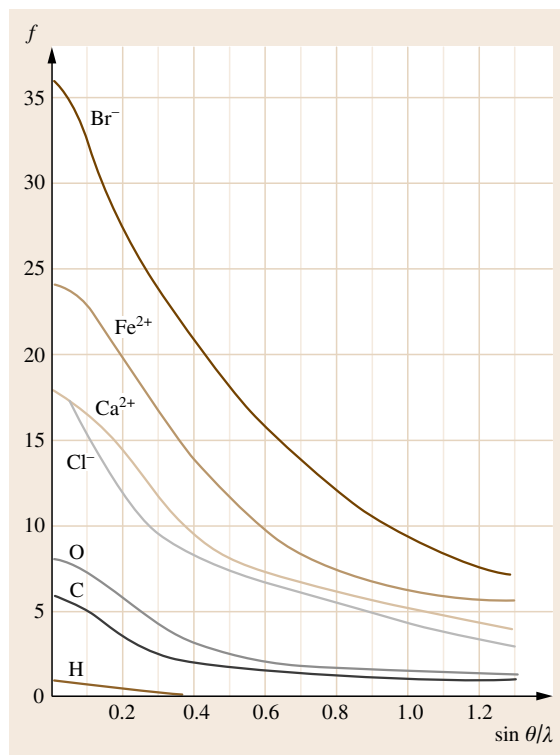


Fig. 49.2 Variation of the atomic scattering factor as a function of $\sin \theta / \lambda$ (after [49.11])

increases, so does the total x-ray scattering power. As a consequence, distinguishing between the scattering power of near neighbors in the periodic table, such as Al and Si, is often difficult because their electron configurations are similar. Also, the atomic scattering factors are angle dependent and fall off with increasing $\sin \theta$, as shown in Fig. 49.2 [49.11]. This dependence decreases the intensities of high-angle reflections. All these factors of x-ray diffraction require the use of high-intensity, well-collimated, narrow-beam radiation available at synchrotron sources. Nevertheless, in-house studies have the advantage of unlimited access where preliminary experimentation data collection may be obtained. The results from in-house data are valuable for determining experimental design, temperature ranges for synthesis, and synthesis times to optimize time spent at remote beam facilities, where access to the most desirable and well-conditioned x-ray and neutron beams is limited.

49.1.2 Neutron Diffraction Theory

Neutrons primarily interact with nuclei of atoms, leading to scattering and diffraction phenomena. According to the de Broglie equation, a beam of particles of mass M and velocity v generates a plane wave of length

$$\lambda = \frac{h}{Mv}, \quad (49.3)$$

where λ is the generated wavelength, v is the velocity, M is the mass of neutron, and h is Planck's constant. At a velocity of 4 km/s,

$$\begin{aligned} \lambda &= \frac{6.625 \times 10^{-27} \text{ g cm}^2/\text{s}}{1.67 \times 10^{-24} \text{ g} \times 4 \times 10^5 \text{ cm/s}} \\ &= 0.992 \times 10^{-8} \text{ cm}. \end{aligned}$$

This simple calculation shows that it is possible to have neutrons whose associated wavelengths are in the range to diffract from crystals or to be scattered by amorphous materials. The characteristics of neutrons provide certain advantages not obtainable with x-rays:

1. The coherent neutron scattering length (b) analogous to the x-ray atomic scattering factors for elements, does not increase with atomic number but fluctuates from element to element, and can be zero [49.13]. Thus, scattering from light elements may be as intense as that from heavy elements.
2. As a consequence of the nature of atomic scattering lengths the differences in scattering of neighboring

elements in the periodic may differ greatly, making it easy to distinguish one from the other. Isotopes also have different scattering lengths, making it possible to distinguish H from D, for example.

3. Because the nuclei are point scatterers, the value of the scattering factor (more properly, the scattering length factor) does not change with increasing values of θ . As a result, the intensity of diffracted radiation does not decrease with increased θ as is the case for x-rays.
4. Many materials exhibit low absorption values for neutrons. This fact allows the use of thicker walled vessels for high-temperature/pressure studies. Further elements (vanadium), or alloys (Ti-Zr) with $b = 0$, are exceedingly useful as null-scattering sample containers. There is no equivalent to this application for x-ray studies, where even amorphous glass adds considerable parasitic scattering to the powder diffraction pattern.
5. Magnetic behavior arises from the presence of unpaired electrons in atoms. Because neutrons possess a magnetic dipole moment, they interact with unpaired electrons. This gives rise to an additional scattering effect that results in the appearance of weak peaks in the diffraction pattern. These extra peaks can be indexed as a superlattice of the x-ray lattice and reveals the magnetic ordering of the unpaired electrons. Thus neutron diffraction can be utilized to study ferro-, ferri-, and antiferromagnetic phenomena not readily accessible to x-ray methodology.

Neutron beams can be obtained from nuclear (steady-state) reactors, where they are typically monochromated by means of curved germanium or silicon crystals (Fig. 49.3).

A second method of neutron generation is through a process termed *spallation*. A heavy-metal target, such as uranium, mercury or tungsten, is bombarded with 450 MeV protons in short uniform bursts which separate the neutrons from the target nucleus. The released neutrons are at high kinetic energy levels and must be thermalized, moderated or cooled (slowed) to be in the 0.2–5.0 Å wavelength range for suitable diffraction studies. This is accomplished by bringing epithermal neutrons into thermal equilibrium with hydrogen-rich moderators such as polyethylene and liquid methane that reduce the velocity of the neutrons. Hydrogen, being about the same mass as the neutron, is most efficient for this process. Because of the high flux of this neutron beam and its range of neutron energies, it is advanta-

geous to use the energy-dispersive method (Fig. 49.3). The Spallation Neutron Source at Oak Ridge National Laboratory uses a time-of-flight methodology. The sample is held at the center of a large ring (source-to-sample distance is 20 m) with banks of detectors held at specific angles to the incident beam, $\pm 30^\circ$, $\pm 90^\circ$, and $\pm 120^\circ$. Use of multiple detector banks increases the total collected intensities, which is necessary because the neutron beam seldom interacts with the sample. In the time-of-flight method, the time for a diffracted beam to reach the detector is measured. Combining the Bragg equation (49.1) in the form of d and substituting for λ the value given by the de Broglie equation

yields

$$d = \frac{n\lambda}{2 \sin \theta} = \frac{ht}{2ML \cdot \sin \theta}, \quad (49.4)$$

where $v = L/t$. Here we utilize the definition of velocity as length L divided by time. Because h , O , M , and L are fixed quantities the d -spacing is proportional to time. The larger the d -spacing, the longer the time for the diffracted radiation to reach the detector. Thus the powder pattern plot of I versus time inverts the normal order of the powder pattern. The smallest d -spacings are recorded at short times and the largest d -spacing is the last peak in the pattern.

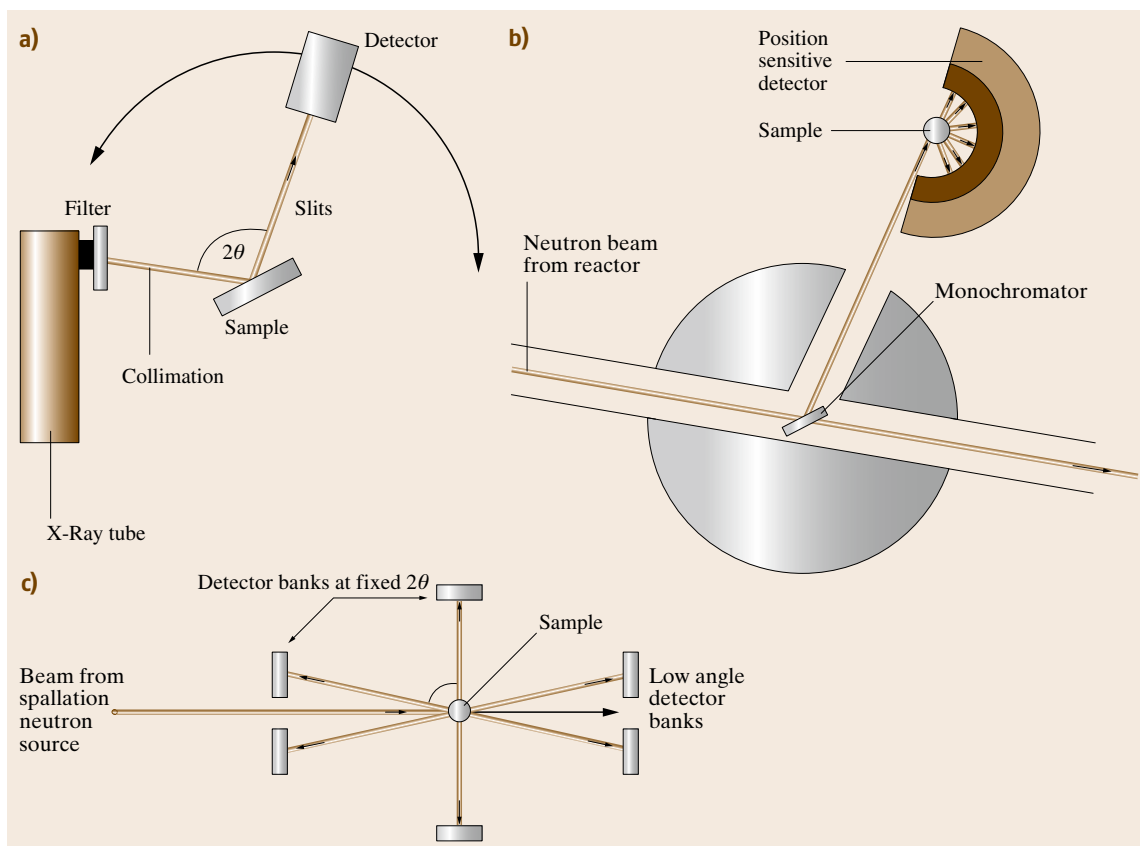


Fig. 49.3a-c Comparison of typical geometries for (a) a laboratory-based x-ray source, and for powder diffractometers found at (b) reactor and (c) spallation neutron sources. In (a) the incident x-ray beam of characteristic radiation is selected by the use of a filter (e.g., Ni filter for Cu- K_α radiation) while at a steady-state (reactor) source a single-crystal monochromator selects the desired, narrow, wavelength range from the Maxwellian distribution of neutron energies emerging from the reactor. The scattering from the sample is detected in a position-sensitive detector. In (a), at a spallation (pulsed) neutron source the energies of the neutrons scattered at fixed 2θ are determined according to their time of flight along the flight path relative to the origin of the neutron pulse. This is analogous to the use of energy-dispersive x-ray techniques (see text)

49.2 Equipment for Time-Resolved Experiments

49.2.1 In-House X-Ray Sources

For time-resolved studies the experimenter needs to record a large number of powder diffraction patterns rapidly to capture time-dependent chemical reactions, and therefore a high-intensity source of x-rays is required. A standard sealed-tube x-ray tube may provide a power of 2 kW or 40 mA at 50 kV. Special sealed tubes may be rated as high as 3 kW. The power limit is controlled by the rate at which heat can be conducted away from the anode, and x-ray intensities are directly proportional to the power. About 98% of the energy of a sealed tube is converted to heat, which would soon melt the target unless otherwise cooled. Therefore a constant stream of cold water flows across the back of the anode to conduct the heat away. Sealed-tube x-ray intensities may also be increased by the use of optical fibers. Each fiber consists of a large number of hollow glass capillaries. These capillaries act as waveguides in which the x-rays undergo total reflection from the capillary surfaces and are led to the sample with little loss of intensity.

For more powerful in-house units a rotating-anode generator may be used. In a rotating-anode x-ray generator, the anode is rotated rapidly to always supply a relatively cool metal target for the bombarding

electrons. The anode is connected to a shaft that rotates through vacuum-tight seals in the tube housing. Such units come in two power models: 12 and 18 kW. Some of the new models of rotating anodes approach the x-ray flux observed at second-generation synchrotrons.

49.2.2 Synchrotron Radiation Sources

Synchrotron radiation [49.14] is produced by the acceleration of electrons moving at near the speed of light. The charged particles move in circular orbits within an evacuated chamber termed a *storage ring*. Magnetic fields are used to alter the trajectory of the particles, and this acceleration causes them to radiate energy tangential to the ring. This radiation is then made available to the experimenter via a beamline pipe containing suitable optical components under vacuum. Compared with conventional sealed-tube sources, synchrotron radiation has a flux 10^4 – 10^{12} times brighter. Other advantages of synchrotron radiation are the broad spectral range produced and small radiation divergence, which have the advantage of wavelength selection (typically 0.4 and 1.5 Å at a bending magnet), narrow beam collimation (typically 0.01–0.6 mm), and very low beam divergence.

49.3 Detectors

To obtain a diffraction pattern suitable for structure refinement from in situ diffraction studies, a large portion of the powder pattern must be recorded in a short period of time. Typically monochromatic radiation is used with a detector such as an image plate, position-sensitive detectors, or charge-coupled device (CCD) or using energy-dispersive radiation and a multichannel analyzer. Only the most common types of detectors are discussed below.

49.3.1 Image Plates

Image plates (IP) consist of a thick layer of x-ray-sensitive phosphor on an optically transparent backing. When the x-rays strike the plate, the phosphor grains ionize. The released electrons are trapped at F-centers, which are point defects of the phosphor solid. The plate is then scanned with a small-diameter laser beam that liberates the trapped electrons, which recombine with

the ions from which they were liberated. This transition produces light that is collected in a photomultiplier that amplifies the signal. The amount of light emitted is proportional to the x-ray intensity. Any residual image can be erased by exposing the film to a light source and reused, and the IP is usually read and erased online during the experiment.

The main advantage of using an IP for data collection is the size. The IP represents one of the largest detectors for the collection of diffracted x-ray intensities, with sizes up to and exceeding 34.5 cm. Using a large detector allows data to be collected to approximately 0.8 Å depending on wavelength choice and sample-detector distance. Another advantage of using this type of area detector is that the entire Debye–Scherrer ring can be collected. During in situ crystallization studies, the material may not form in abundance to produce smooth diffraction rings. These rings will often appear spotty and incomplete con-

tributing to the problems associated with small cells that produce small quantities of crystallites. An area detector can overcome this problem as it collects data in two-dimensional space as opposed to point detectors and position-sensitive detectors. The disadvantage of **IP** detectors is the readout time. The **IP** must be digitally scanned and then erased before the next exposure can begin. The process of reading and erasing can take up to 2.5 min, during which time no data is being collected from the experiment. Although this *gap* in data collection appears to be problematic, the advantages of obtaining high-resolution diffraction data in one exposure outweigh those disadvantages.

49.3.2 Charge-Coupled Devices

A charge-coupled device (**CCD**) is simply a semiconductor chip where one side of the chip is subdivided into rectangular sections (pixels) that are approximately 10 μm on edge. Between the x-rays and the **CCD** are a phosphor and a photodiode that convert the incoming light into electrons. Depending on where the light strikes the phosphor, the electrons build in number and are trapped in the rectangular pixel on the **CCD** semiconductor surface. After a complete exposure, the **CCD** is then read using analogue-to-digital conversion, which counts the amount of electrons on each pixel, where the number of electrons is proportional to the original light intensity. In this process, it is possible to have rapid data collection and readout time with little delay between exposures.

However, there are caveats to using a **CCD** for x-ray diffraction studies. For example, if a pixel fills with electrons before the exposure is over, those excess electrons will *spill* into the surrounding wells. This can cause problems when trying to read the detector after x-ray exposure, and may be visible on the processed image as a vertical, or horizontal, streak across the entire image. Another problem is that most **CCD** chips are quite small, typical ranging in size from 512 \times 512 to 2048 \times 2048 pixels. Therefore, such small chips are made usable by having a large phosphor front plate, \approx 15 cm in size, and a fiber-optic taper that reduces the image down to the **CCD** chip, which is \approx 2 cm in size. Naturally, information will be lost during the image size reduction, and care must also be taken to remove the distortion in the fiber-optic taper prior to data reduction. The construction of larger **CCD** chips will eventually lead to the removal of the fiber-optic taper and thus produce a distortion-free raw image.

49.3.3 Position-Sensitive Detectors (PSD)

A **PSD** is a proportional counter that is position sensitive. The proportional counter consists of a tube filled with a noble gas such as xenon. A thin tungsten wire runs down the center of the tube and is positively charged. A thin window of low-absorbing glass allows the x-ray photons to enter the tube and ionize the xenon, which releases a cloud of electrons. The released electrons are drawn to the positively charged wire, giving rise to a charge pulse. The size of the pulse is proportional to the energy of the incident photon, which allows x-rays of different wavelengths to be distinguished. In a **PSD**, the wire can be long and curved to coincide with the diffractometer circle. The **PSD** is placed so as to intercept any x-rays diffracted by the sample within the angular range of the wire. The x-ray beam strikes the wire at particular 2θ values dictated by diffraction from the powder sample. The time of travel taken for the pulse to reach the end of the tungsten wire fixes the position or 2θ value. A multichannel analyzer is able to sort out all the times and amplitudes into digital form and the output is that of a conventional powder pattern.

PSDs are available in a range of sizes starting from $\approx 4^\circ$ to 120° in 2θ . All the reflections within this range are recorded simultaneously. By choosing a smaller wavelength it is possible to record the entire usable range of diffraction data in a single exposure using a 30° or 60° **PSD**. The advantage of a **PSD** is their readout time, which far exceeds that of the **IP**, and allows near-continuous diffraction patterns to be collected without interruption. Most **PSDs** are linear, thus only one-dimensional diffraction data can be obtained, which may result in diffracted intensities being missed because of incomplete Debye–Scherrer rings from non-ideal powder samples.

49.3.4 Energy-Dispersive Detectors

At a synchrotron source, a broad range of x-ray energies can be produced. The peak of the energy distribution depends on the ring characteristics, including the energy of the charged particles within the ring and the strength of the magnets used to bend particles around the ring. A beam of well-defined energy is produced for monochromatic studies by intercepting this *white* radiation with a single-crystal monochromator. Alternatively, if the powder sample is held at a specific angle and the incident beam contains a broad spectrum of wavelengths, a particular set of planes of fixed *d*-spacing will diffract only that wavelength that satisfies Bragg's

law for that value of d . Thus, all the different wavelengths which satisfy this condition for all the planes in the sample will enter the detector and be sorted out by the multichannel analyzer. The entire pattern may be recorded in less than 1 min. The main advantage of using white radiation is the intensity of the beam. The high flux, and hard x-rays, have a higher penetration depth and can pass steel environmental cells. One disadvantage of the energy-dispersive detector is that its peak resolution is poorer compared with monochromatic beams.

49.3.5 Silicon Strip Detector

A new detector, offered by Brucker Corporation, contains 192 strips of silicon which act as 192 individual detectors. This results in an almost 200 times increase in intensity. This detector together with fiber optics may open many opportunities for in situ studies in-house.

49.3.6 Other Considerations

There are several disadvantages when area detectors are used without collimation, some of which are due to the nondiscriminating nature of both imaging plates and charge-coupled devices. The synchrotron beam inevitably excites fluorescence within the hutch and care must be taken to shield these devices from stray radiation. The difficulty in designing slits for these devices also decreases the signal-to-noise discrimination since scattering from sample containers, or environmental chambers, often contaminates the pattern. Although this

can be eliminated using subtraction [49.15, 16], another possibility when powder averaging is not a problem and angular resolution can be relaxed ($\Gamma \approx 0.03^\circ$), is to use an energy-discriminating PSD fitted with a slit. While most commercial PSDs operate in the so-called *streaming mode*, proportional counting and energy discrimination are possible with these devices.

The highest possible time resolution is afforded by energy-dispersive diffraction. Since the whole pattern is recorded at once, this resolution is determined by the brightness of the beam and the readout time of the multichannel analyzer. Quantitative interpretation of crystal structure is hampered by systematic errors such as energy-dependent absorption corrections, absorption edges, and definition of the intensity versus energy curve. Reliable results have been obtained, however, and the software and method to enable structure determination using the Rietveld method are now well established [49.16, 17]. The energy-dispersive x-ray technique does have distinct advantages. The experiment allows for straightforward collimation and data collection at fixed angles, which makes it easier to discriminate parasitic scattering from sample containers.

In general, for phase identification and determination of unit cell parameters, energy-dispersive x-ray diffraction data are suitable and offer distinct advantages in terms of spatial and time resolution. In those cases where accurate determination of structural parameters is the objective, monochromatic data are preferred. Many beamlines are capable of changing between these two modes of operation, and a description of such a setup is given in two recent reviews [49.18, 19].

49.4 Software

Collection of either x-ray or neutron diffraction data with ever-increasing time resolution, as is envisioned at third-generation synchrotrons, will inevitably lead to data glut. While visual inspection, to identify the appearance of one phase or the disappearance of another, may be sufficient in some studies, an unbiased method which can be automated to provide some real-time feedback on the course of a reaction is desirable. Such a method might provide information on systematic errors as well as the appearance of new phases and the disappearance of others. It should also provide visual queues to allow the choice of a manageable number (3–5) of diffraction patterns to analyze out of the hundreds collected. One example in situ XRD

investigation, ion exchange in porous titanium silicates, is discussed below and employs iterative target transform factor analysis (ITTFa) [49.20], an unbiased mathematical treatment of the diffraction data that looks for changes as a function of time. From this processing, kinetic information and clues as to which patterns to use first for Rietveld refinement were obtained. Problems and questions such as which patterns to explore, whether measurable changes are occurring, and determining if the reaction has completed are vital for efficiently managing the ever-increasing quantities of data. Also general structure analysis software (GSAS), Fullprof+winplotr, and Power3D are freeware that are capable of handling large sets

of one-dimensional diffraction data. Since new software is continuously appearing on the Internet, the authors cannot give a detailed software overview. How-

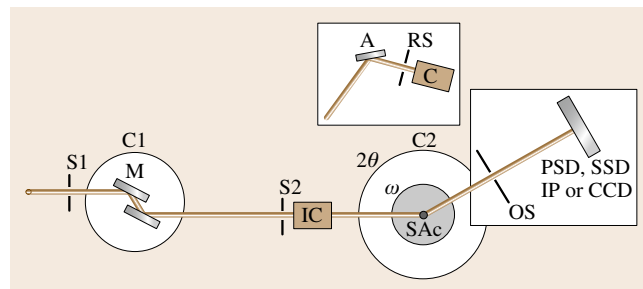
ever, the CCP14 website contains a vast collection of software that is useful in interpreting time-resolved data [49.21].

49.5 Types of In Situ Cells

Fig. 49.4 Beamline geometry suitable for time-resolved synchrotron powder diffraction in monochromatic mode. A double-crystal monochromator (M) is used to select the incident energy that is focused on the sample, capillary or flat plate holder (SAC), and recorded on a position-sensitive detector (PSD), image plate (IP) or charge-coupled device (CCD). An incident-beam monitor (IC) is needed to normalize the data to the same relative intensity scale because the synchrotron beam decays with time (after [49.22]) ►

A schematic diagram of the beamline geometry suitable for time-resolved synchrotron diffraction is shown in Fig. 49.4 [49.22]. For in situ studies where structural studies are to be performed monochromatic radiation is preferred. The beam passes through an incident beam monitor ion chamber (IC) to record the intensity of the incident beam during the entire run. Monitoring the incident beam is necessary because the synchrotron beam decays with time, and therefore the total intensity of the diffraction pattern also decreases with time. If a synchrotron runs in the so-called top-off injection mode, where electrons are continuously supplied to the storage ring, an IC is still required because the storage ring is usually not topped off to a constant value. The monitored data is then used to normalize the data to the same intensity scale.

Our own interests are twofold: to grow crystals from gels that possess ion-exchange properties and then to study the mechanism of ion exchange. The crystal growth is done to temperatures of 150–250 °C but the ion exchange may be carried out at room temperature and at ≈ 60 °C. Two different reaction cells are used for these purposes. The crystal growth experiments are carried out hydrothermally, requiring elevated pressures. A quartz capillary reaction cell introduced by Norby [49.23] is shown in Fig. 49.5. The capillary is closed at one end (A) and is held in place with a Swagelok fitting (B) mounted on a modified goniometer head. Heating can be effected by heating plates placed above and below the capillary tube so as not to obstruct the path of the x-ray beam, or by using an air blower heater. A small amount of gel to be crystallized is placed into



the capillary and fixed into the Swagelok fitting, and a pressure of N₂ is applied through the fitting. The detector is an imaging plate of which only a portion is exposed to the x-rays. This is done by placing two lead shields (D) over the IP, exposing a portion of the plate to the x-rays. At the end of each cycle the IP film is moved to expose a fresh surface. A cycle consisted of

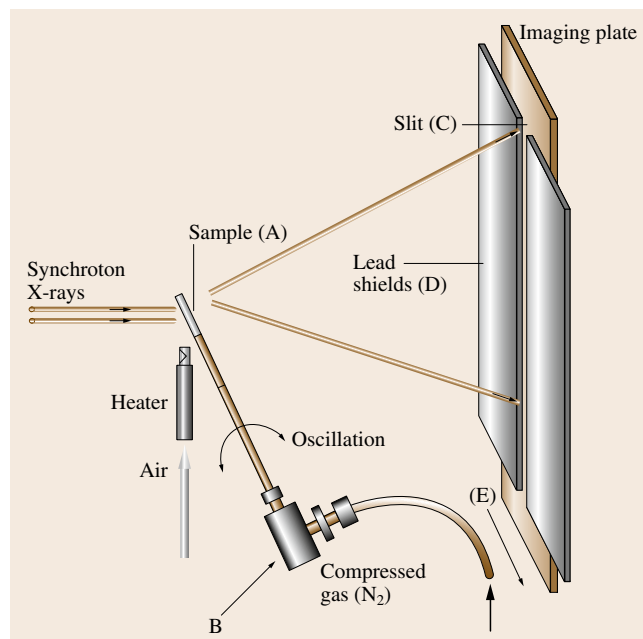


Fig. 49.5 The capillary reaction cell and translating imaging-plate detection system as used at the NSLS

a 60 s exposure and erasure, and exposing a new IP surface required 1.5 min for data processing or 2.5 min per cycle. Recent improvements in the storage ring at the NSLS Brookhaven National Laboratory and detection system have now reduced the time per cycle to seconds. This cell has been widely used by many investigators [49.3].

49.5.1 SECeRTS Cell

A somewhat different type of cell was used for the ion-exchange studies, and is also easily adaptable to synthesis studies. The design of a small environmental cell for real-time studies (SECeRTS) [49.24] is shown in Fig. 49.6. A quartz, or sapphire, capillary (0.3–1 mm OD) tube (A), open at both ends is mounted in a Swagelock tee (B) using a Vespel ferrule. A pressure can be applied, through the connected tube (C), to the surface of the reaction mixture in the capillary. For titration synthesis studies, injection takes place through a 0.3 mm quartz capillary (A) that goes through the tee and into the 1 mm capillary. This 0.3 mm capillary

is mounted between a Swagelock elbow and tee with Vespel ferrules, all of which are mounted on a modified goniometer head (E). Injection under pressure through the elbow (A) is possible via a gas-chromatography syringe (not shown) mounted on an aluminum holder. A screw connected to the piston of the syringe ensures pressurization. By turning the screw, the piston is depressed and a controlled volume can be injected into the 1 mm capillary through the 0.3 mm capillary. Alternatively, the position of the sample capillary (A) can be plugged, and the assembly can be extended to expose the injection capillary location in the x-ray beam. Ports D and C then become the supply and exhaust lines, respectively, for flow-through ion-exchange experiments or solid/gas-phase reactions.

It is important to note that completely sealed capillaries pose a significant risk to experimentalists and equipment. The pressure generated during hydrothermal reactions is difficult to control in small-diameter capillaries, and they could burst at any time during the heating of the cell. Having an open end where an overpressure of inert gas is applied is a safety feature to

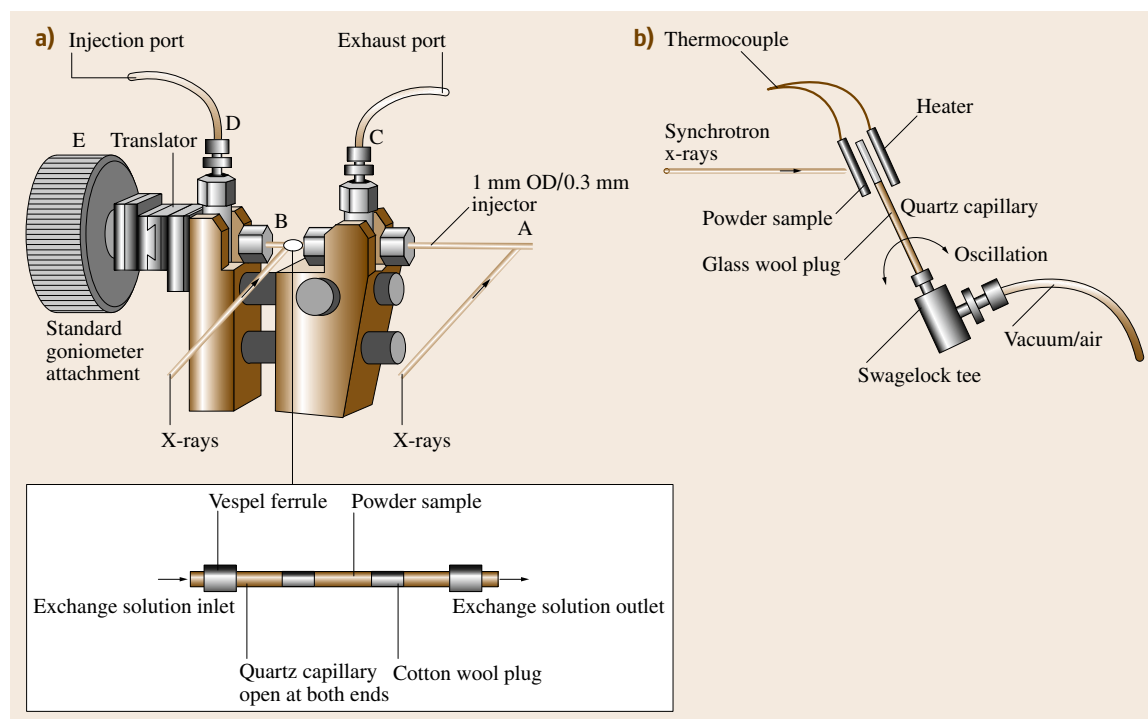


Fig. 49.6a,b View of the capillary-type small environmental cell for real-time studies (SECeRTS). (a) In situ hydrothermal titration cell and (b) simplified quartz or sapphire hydrothermal cell (courtesy of John Parise and coworkers, Stony Brook)

prevent the cell from exploding while still maintaining hydrothermal conditions.

49.5.2 Polyimide Environmental Cell

The polyimide environmental cell (PEC) was designed to alleviate the problems and safety issues associated with quartz capillaries and gas-driven solutions. Initially designed for flow-through experiments [49.26], the PEC is easily adaptable to in situ synthesis experiments by simply sealing one end and applying an overpressure of nitrogen to the other. Polyimide tubing was chosen to replace the quartz/sapphire capillaries based on multiple criteria. The tubing is flexible, thin walled, and x-ray transparent (within the radiation range of 0.1–1.54 Å) in the wide-angle region. Controlled solution flow through a larger-inner-diameter tube is easier to maintain and reproduce. Tube breakage is no longer a problem during sample loading or during the experiment because of the flexibility of polyimide. Tube transparency in the wide-angle region ($2\theta > 2^\circ$) means only x-ray scattering from the sample and solution contributes, with no parasitic scattering from the polyimide cell, to the diffraction patterns in that region. Thin walls (typically < 0.01 mm for a 0.8 mm OD tube) allows more sample in the beam and increases peak-to-background ratios.

49.5.3 High-Pressure Cells

High-pressure cells commonly in use can often be adapted with slight modification for use in in situ studies at a synchrotron. For example, the large-volume high-pressure device originally designed for diamond growth (DIA) has been successfully interfaced to a synchrotron at the Photon Factory, Japan [49.13]. Similar installations were constructed at the NSLS Brookhaven, the advanced photon source (APS) Argonne, and at Deutsches Elektronen Synchrotron (DESY) in Germany. They are utilized in the study of materials at high pressure and temperature using mainly energy-dispersive diffraction. In some cases the use of monochromatic radiation together with the IP was more effective. An example is the partitioning of Fe in a mixture of olivine and the β -phase (Fe,Mg)₂SiO₄ [49.16] using an IP and monochromatic radiation resulted in considerably better time resolution, and the mechanism of the transformation from the olivine structure to the spinel structure was observed [49.27].

Other sample cells, such as furnaces and diamond-anvil cells, are also easily transferred. Similarly, steel

hydrothermal reaction vessels can be transferred from the laboratory to the synchrotron.

49.5.4 Hydrothermal Steel Autoclave-Type Cell

Evans et al. [49.25] introduced a hydrothermal autoclave reaction vessel (Fig. 49.7) that has been extensively used in many studies [49.28]. The cell consists of a modified Parr reaction vessel (25 ml) with a section of the wall milled down to a thickness of 0.4 mm. This thinner portion of the wall permits transmission of white x-radiation and has a maximum operating temperature of 230 °C. Higher operating temperature is possible with thicker-walled cells. However they require the focusing optics available at a third-generation source [49.29]. Attached to the top of the cell is a head consisting of a pressure transducer, a safety relief valve, and an injection reservoir (2 ml). This reservoir consists of a remotely placed gate valve that permits injection of a second solution into the cell at

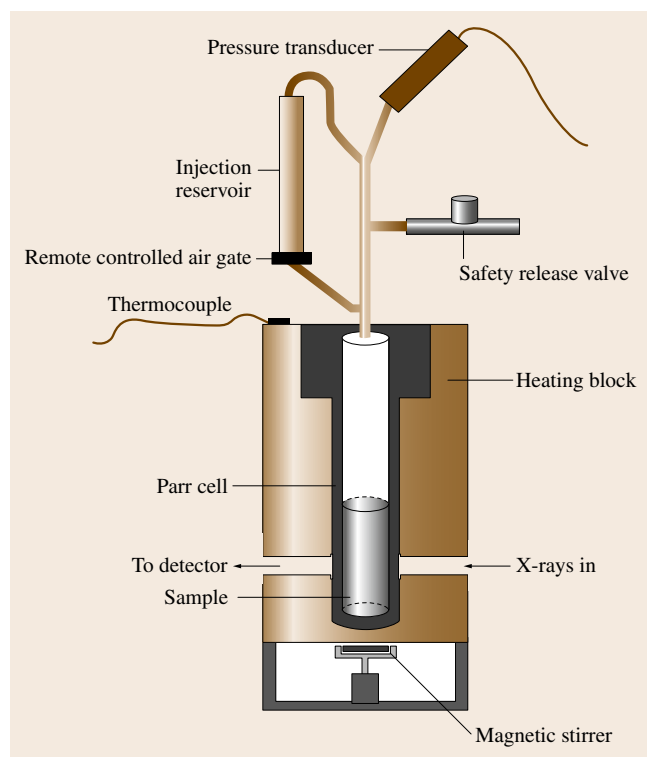


Fig. 49.7 The hydrothermal autoclave-type reaction cell due to Evans et al. [49.25]. Walls are milled down to allow x-ray transmission while permitting a maximum operating temperature of 300 °C

controlled time and temperature conditions. Temperature control of the cell is done via a resistance-heated aluminum block and is monitored with K-type thermocouples in contact with the outside of the reaction vessel.

49.5.5 Neutron Diffraction Cell

For neutron diffraction studies, a vanadium (V) tube is used instead of polyimide, quartz or sapphire. The coherent neutron scattering length of vanadium is

small, $b = -0.5$ fm, compared with that of oxygen, which is 5.8 fm, making it an ideal sample container since it contributes primarily to the incoherent background and not to the Bragg diffraction in a powder pattern (Fig. 49.3b). Also, the V-tube is much larger in diameter (6.5 mm) to allow more powder to be used (Fig. 49.8). The low absorption cross-section of neutrons allows the use of larger samples, which perhaps will be more representative of the situation when using titanium silicate (TS) (see below) in the field.

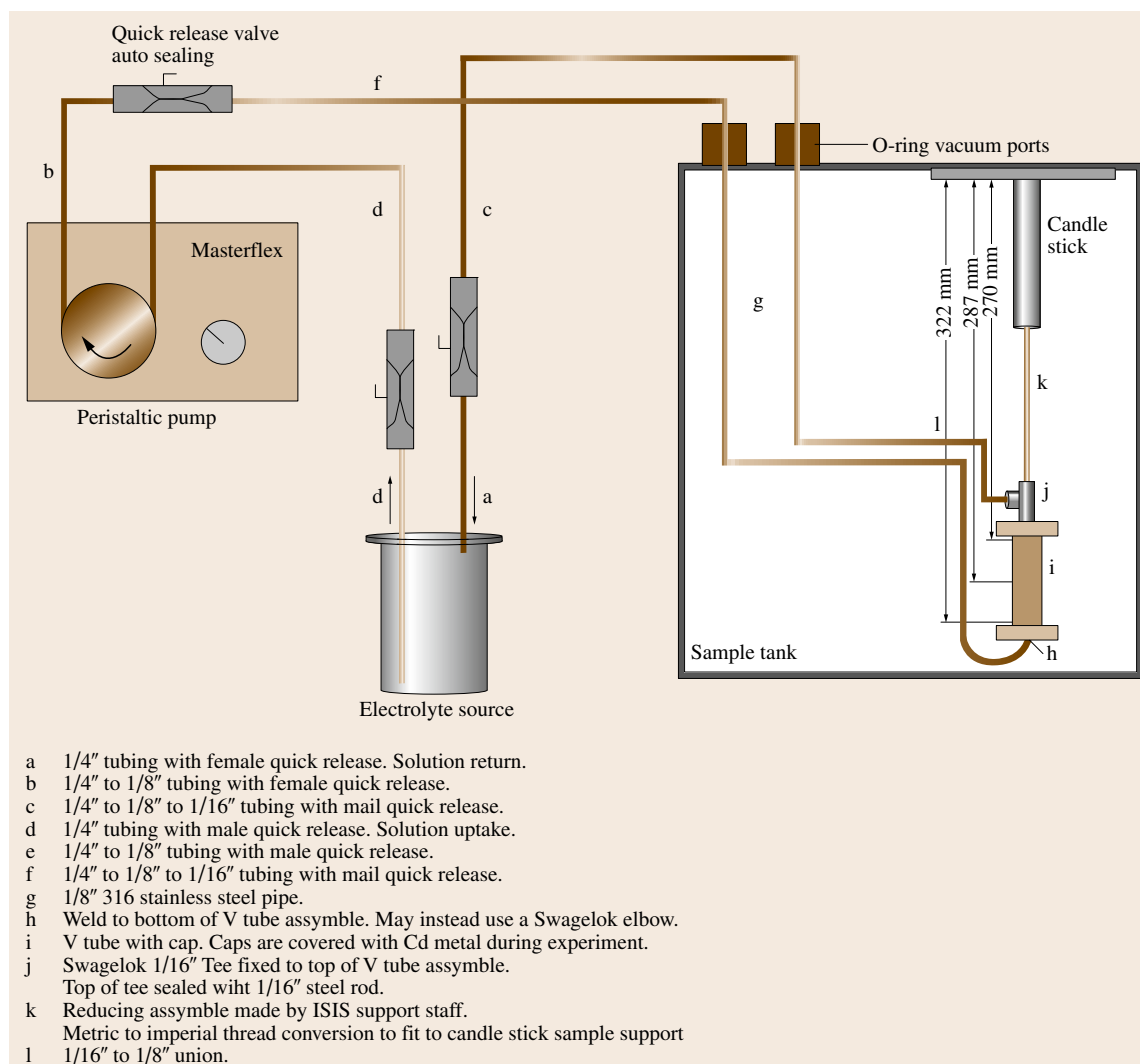


Fig. 49.8 Diagram of vanadium can assembly for flow-through studies

49.6 In-Situ Studies of Titanium Silicates (Na-TS) with Sitinakite Topology

49.6.1 Introduction to the Problem

Large quantities of nuclear waste were generated as a byproduct of the US nuclear weapons programs. The waste is held in large, underground steel tanks at both the Hanford and Savannah River sites. A search for efficient, cost-effective methods of removing cesium, strontium, and actinides from the waste solutions is an ongoing project of the Department of Energy. A sodium titanium silicate (Na-TS) was found to be highly selective for Cs^+ and Sr^{2+} in moderately alkaline solutions. When the Na-TS material was immersed in the highly alkaline wastes its selectivity for Cs^+ was low, but in a partially Nb-substituted form (Na-NbTS) the material was highly effective at removing Cs^+ [49.30]. Several problems are attendant to the use of these titanium silicates for separation of high-level waste.

The nuclear waste is a highly basic solution containing 1–3 M NaOH. It also has high sodium ion concentration, 5–7 M, and contains a variety of other ionic species. The ions that are the highest γ -emitters are the highly radioactive ^{137}Cs and ^{90}Sr , with 30 years half-lives. In addition, small amounts of Pu and Np also need to be removed from the mass of waste. This high-level waste (HLW) would be sealed in a special glass and stored in steel tanks below ground. The remaining low-level waste (LLW) would be taken up in a grout and stored aboveground.

The questions are: what are the structural and/or chemical properties of sodium titanium silicate that display such high uptake of Cs^+ in neutral to mildly basic solution, but not in the waste solutions? Also, what effect does the substitution of Nb for some Ti have on the increased selectivity toward Cs^+ ? In short, what is the origin of the high ion selectivity in these compounds? In addition, the hydrothermal syntheses by which these titanium silicates are prepared are often accompanied by the appearance of impurity phases. What are these impurities, and how can they be eliminated from the synthesis [49.5, 6]?

49.6.2 Synthesis and Structure of Sodium Titanium Silicate (Na-TS)

The ideal composition of this titanosilicate is $\text{Na}_2\text{Ti}_2\text{O}_3\text{SiO}_4 \cdot 2\text{H}_2\text{O}$. However, hydrolysis occurs in water to yield a composition of $\text{Na}_{1.64}\text{H}_{0.36}\text{Ti}_2\text{O}_3\text{SiO}_4 \cdot 1.8\text{H}_2\text{O}$ [49.31]. The crystal structure of the sodium

ion phase and the partially exchanged Cs^+ phase were determined from powder x-ray studies [49.31].

The crystals are tetragonal, with $a = 7.8082(2) \text{ \AA}$, $c = 11.9735(4) \text{ \AA}$, space group $P4_2/mcm$, and $Z = 4$. The titanium atoms occur in clusters of four grouped about a 4_2 axis, two up and two down, rotated by 90° . Each titanium is octahedrally coordinated, sharing edges in such a way that an inner core or four oxygens and four Ti atoms form a distorted cubane-like structure (Fig. 49.9).

These cubane-type structures are bridged to each other through silicate groups along the a - and b -axis directions. The titanium–oxygen clusters are 7.81 \AA apart in both the a - and b -axis directions, with the Si atoms at $c = \frac{1}{4}, \frac{3}{4}$. The c -axis is $\approx 12 \text{ \AA}$ long, which is twice the distance from the center of one cubane-like cluster to its neighbor in the c -axis direction. Two views of the framework are shown in Figs. 49.10 and 49.11. The net result of this framework arrangement is that one-dimensional tunnels are formed along the c -axis di-

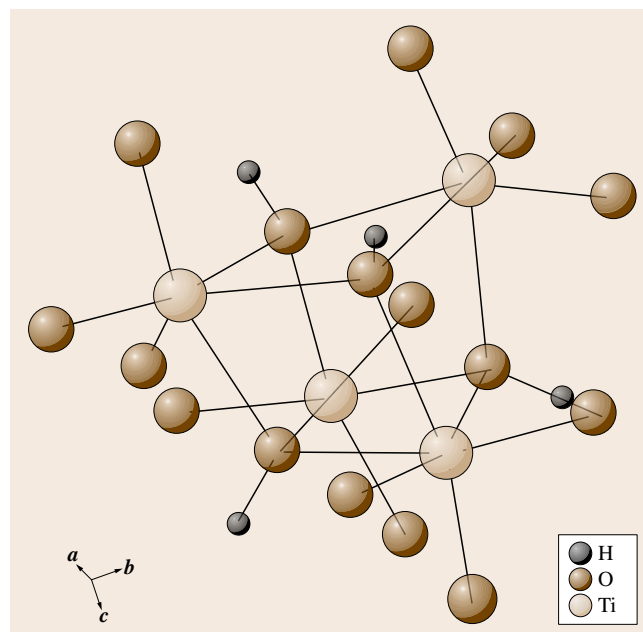


Fig. 49.9 A portion of the titanosilicate structure showing the cluster of four titanium–oxygen octahedra sharing edges to form the cubane-like Ti_4O_4 group. The oxygens within the cubane group are each bonded to a proton making them hydroxo groups. The Ti atoms are light brown, oxygens are dark brown, and hydrogens are black

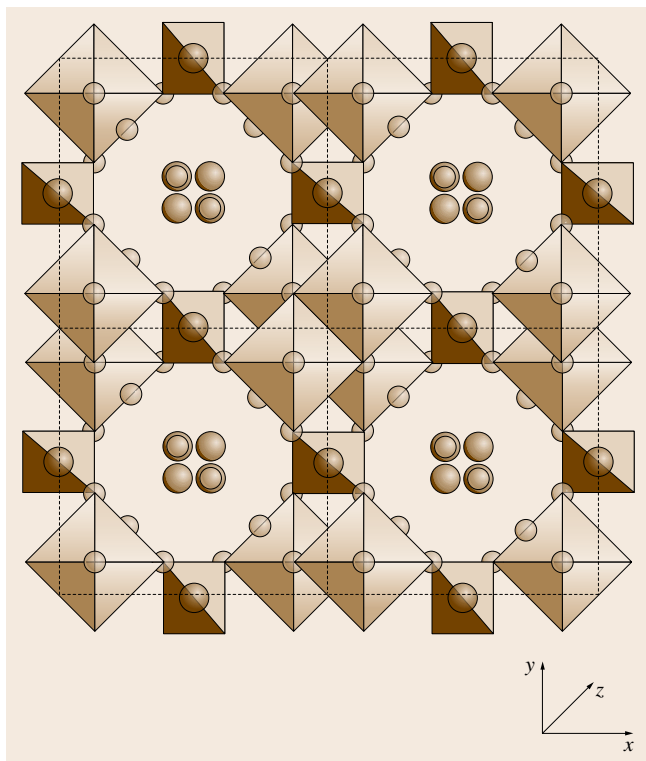


Fig. 49.10 Top view (down the c -axis) of sodium titanium silicate showing the clusters of four TiO_6 octahedra bridged by silicate groups. The tunnels are filled with Na^+ and water molecules. The Na^+ on top of the tetrahedra symbolizes the Na^+ ions sandwiched between silicate groups within the framework. Refer to Fig. 49.11 for color legend

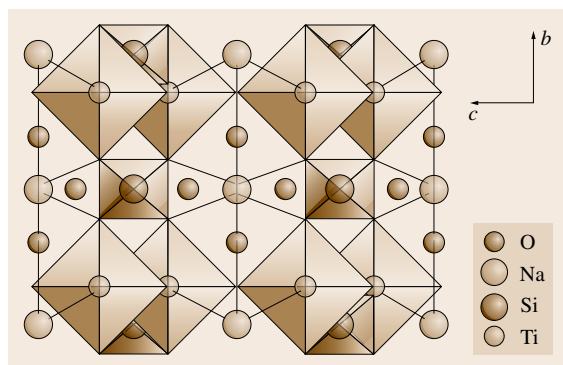


Fig. 49.11 Polyhedral representation of Na-TS structure as viewed down the a -axis, showing the hexagonal-shaped framework cavities in which half the Na^+ reside. The water molecules reside within the 8MR tunnels

rection. Perpendicular to the tunnels are vacancies in the faces, or four sides, of the tunnels. These cavities are large enough to enclose sodium ions. Four silicate oxygens bond to the sodium ion at a distance of $2.414(5) \text{ \AA}$ (Fig. 49.11). The sodium ion coordination is completed by bonding to two water molecules in the tunnels at a Na-O bond distance of $2.765(1) \text{ \AA}$. Half the sodium ions are thus accounted for in the framework sites as there are sodiums in each face at $c = 0, \frac{1}{2}$ over one c -axis cell length for a total of four out of the eight required per unit cell. The remaining sodium ions reside within the tunnels along with the water molecules. As a historical note, these compounds were originally misnamed as crystalline silico titanate (CST). However, they are silicates, so their preferred nomenclature is as a titanium silicate M-TS, where M is the exchangeable ion.

The Na-O bond distances within the tunnels are longer than the sum of the ionic radii (2.42 \AA) [49.32] at $2.76(1) \text{ \AA}$. This bond distance measurement was made with only 64% of the sodium ion sites occupied. The deficiency of sodium arises from hydrolysis during washing so that the actual formula was $\text{Na}_{1.64}\text{H}_{0.36}\text{Ti}_2\text{O}_3(\text{SiO}_4) \cdot 1.8\text{H}_2\text{O}$. Because of the deficiency of Na^+ , the sodium ion positions were found to be disordered with partial occupancy by water molecules. It is possible to obtain the fully occupied sodium phase by not washing the product of the hydrothermal reaction with water, or washing with strong NaNO_3 solution.

On exchanging Cs^+ for Na^+ by a flow-through procedure in near-neutral CsCl solution, a composition of $\text{Na}_{1.49}\text{Cs}_{0.2}\text{H}_{0.31}\text{Ti}_2\text{O}_3\text{SiO}_4 \cdot \text{H}_2\text{O}$ was obtained [49.31]. The Cs^+ occupied two positions within the large tunnel. Site one (Cs1) is located at the center of the eight-membered ring (8MR) window at $\frac{1}{4}c, \frac{3}{4}c$, and Cs2 is located at approximately $0.13c$ and $0.63c$ off from the 8MR window. Cs1 has eightfold bonding coordination to eight oxygens of the framework, four above and four below the Cs, with bond lengths of 3.18 \AA . Cs2 has fourfold bonding coordination to the framework oxygens and twofold coordination to the interstitial water with bond lengths of 3.06 and 2.95 \AA , respectively. The bulk of the Cs^+ was in site 1 and about 20% in site 2.

49.6.3 Synthesis Problems and In Situ Hydrothermal Study

A problem arose in the actual sol-gel synthesis of the Na-TS crystals. Often an impurity began to form

that on further investigation was determined to be a sodium titanium silicate of composition $\text{Na}_2\text{TiSiO}_5$ referred to as sodium titanium oxide silicate (STOS). In ex situ hydrothermal studies it was found that the amount of STOS in the mixture increased with the alkalinity of the starting gel. In contrast, the conditions for favorable Na-TS formation required a lower Na_2O content as well as lower pH. Based on this ex situ study we prepared two gels, one designed to yield pure STOS and the other to yield pure Na-TS [49.6]. The gel composition for Na-TS had the composition $1.0\text{TiO}_2 : 1.98\text{SiO}_2 : 6.77\text{Na}_2\text{O} : 218\text{H}_2\text{O}$. In situ experiments were carried out at the Brookhaven synchrotron. The source of Ti was titanium isopropoxide, to which was added NaOH and silica dissolved in NaOH. The apparatus used is that shown in Fig. 49.5, and the results are provided in Fig. 49.12. Figure 49.12 shows a three-dimensional plot of the x-ray diffraction pattern as a function of time during the TS gel heating. As can be seen from the figure, the process starts with the formation of a phase having a broad peak at about $9.5\text{--}10\text{ \AA}$. This phase was identified as sodium nonatitanate (SNT) $\text{Na}_4\text{Ti}_9\text{O}_{20}$, a semicrystalline compound that is highly selective for Sr^{2+} in alkaline solution [49.33, 34]. It starts forming at an

early stage of reaction, as confirmed by the collection of x-ray powder diffraction patterns of the dried starting gel. The intensity of the (001) SNT reflection does not change as the reaction progresses until the growth of the TS phase begins. The process of transformation of the SNT phase to the TS phase started after 1 h of constant heating at 220°C , with rapid decrease of the intensity of the SNT peaks and in-growth of the TS peaks (Fig. 49.13). The whole process of transformation lasted approximately 45 min. During the period following the transformation to TS, no significant changes occurred, except a minor increase in the TS peak intensities. No other phases were observed in this experiment.

Interestingly the highly alkaline base gel in ex situ experiments also crystallized as the SNT phase first, as shown in Fig. 49.14. After about 12 h at 200°C it is converted to the highly crystalline STOS phase in an additional 15 h. Thus, it appears that in gels of different composition and alkalinity the SNT phase forms initially. Then the sodium silicate that remains converts the SNT phase to the Na-TS phase at low sodium content and moderate alkalinity, while at higher sodium content and higher alkalinity the STOS phase prevails. Several avenues of synthesis are now open. The SNT phase is

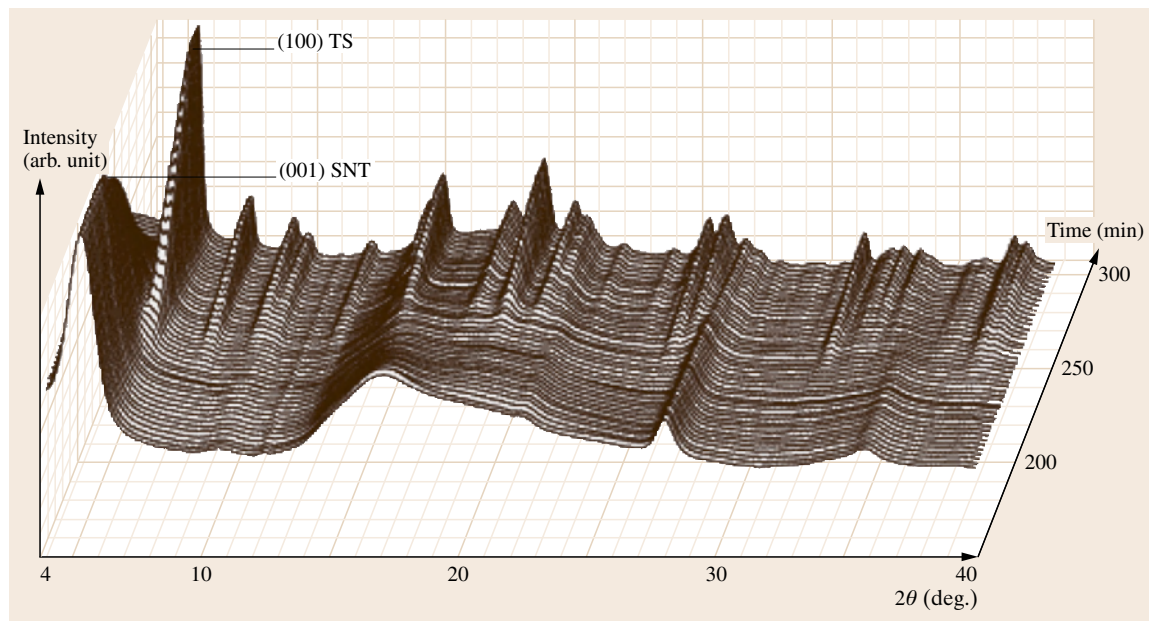


Fig. 49.12 Time-resolved x-ray powder diffraction spectra of SNT-TS transformation for the gel with composition $1.0\text{TiO}_2 : 1.98\text{SiO}_2 : 6.77\text{Na}_2\text{O} : 218\text{H}_2\text{O}$. Powder patterns are collected in 2.5 min intervals

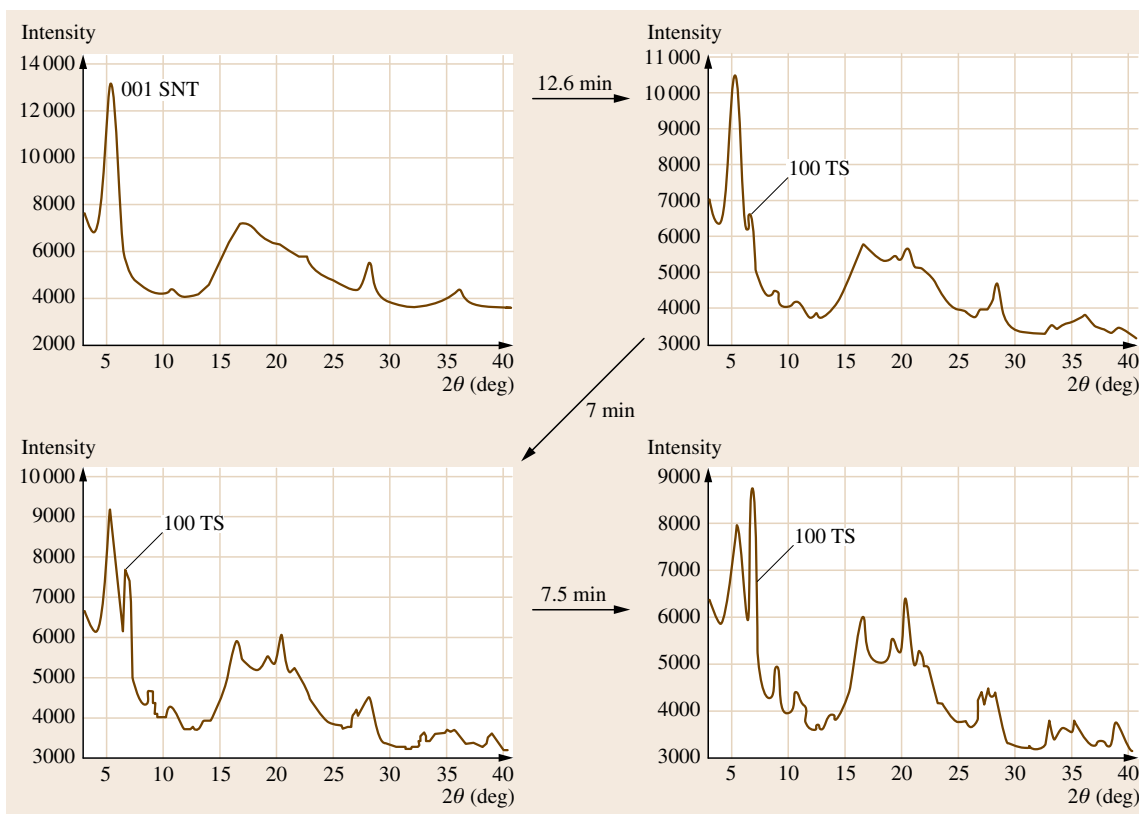


Fig. 49.13 XRD patterns of SNT (upper right) and its transformation with time to the TS phase at 220 °C. The pattern in the upper right-hand corner is that of pure SNT

readily prepared from a mixture of titanium isopropoxide and NaOH. By adding the correct balance of silica dissolved in NaOH it is possible to avoid the presence of the STOS impurity. Furthermore, by proper control of the reaction it may be possible to prepare a mixture of Na-TS and SNT, such as to remove Cs^+ and Sr^{2+} in a simple one-step process.

49.6.4 Ion Exchange of Cs^+ into Na-TS

The ion-exchange experiments were carried out at the X7B beamline of the National Synchrotron Light Source. The open-capillary SECRéTS cell was used (Fig. 49.6). Exchange of Cs^+ from a 1 mM solution of CsCl was used for the Na-TS phase and a 10 μM solution for the exchange with the protonated H-TS phase. The lower-concentration solution was necessary to slow the rate of exchange to fully observe the changes occurring in the H-TS phase. Diffracted intensities were recorded on a MAR345 imaging plate. Each diffraction

pattern was collected for 1 min with a 1.5 min lag time to read and erase the IP.

As the Cs^+ was exchanged for Na^+ in Na-TS, the unit cell volume increased from 728.8 to 732.4 \AA^3 [49.26]. The unit cell parameters a and b showed a continuous increase from 7.8060(1) to 7.8435(1) \AA and the c -axis decreased from 11.9599(2) to 11.9054(4) \AA . The ion exchange occurred in two steps. The first step, from minutes 0 to 245, involved occupancy of Cs^+ in the Cs2 site to a fractional occupancy of 0.116(5). Simultaneous with the increased occupancy of site Cs2, the water site OW2 began to decrease in occupancy (Fig. 49.15). Figure 49.15 also shows a concomitant loss of Na^+ as the Cs^+ was taken up. The second step of the ion exchange from minutes 245 to 375 was initiated when site OW2 had zero occupancy (minute 245) and involved the rapid filling of site Cs1 (Fig. 49.15). During minutes 245 to 275 the occupancy of Cs2 increases and reaches a maximum occupancy of 0.136(7). The maximum occupancy for

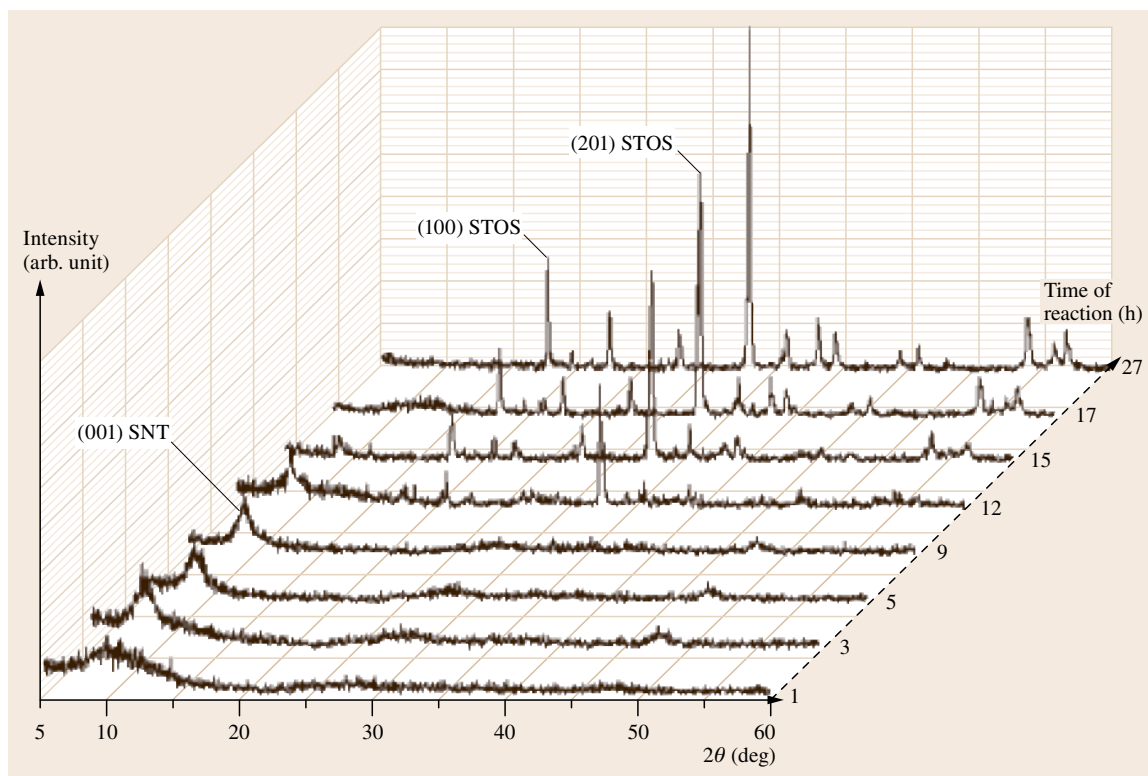


Fig. 49.14 Dynamic XRD spectra of the evolution of the STOS phase obtained in ex situ experiments from the gel of composition $1.0\text{TiO}_2 : 1.98\text{SiO}_2 : 10.53\text{Na}_2\text{O} : 218\text{H}_2\text{O}$, $T = 200^\circ\text{C}$

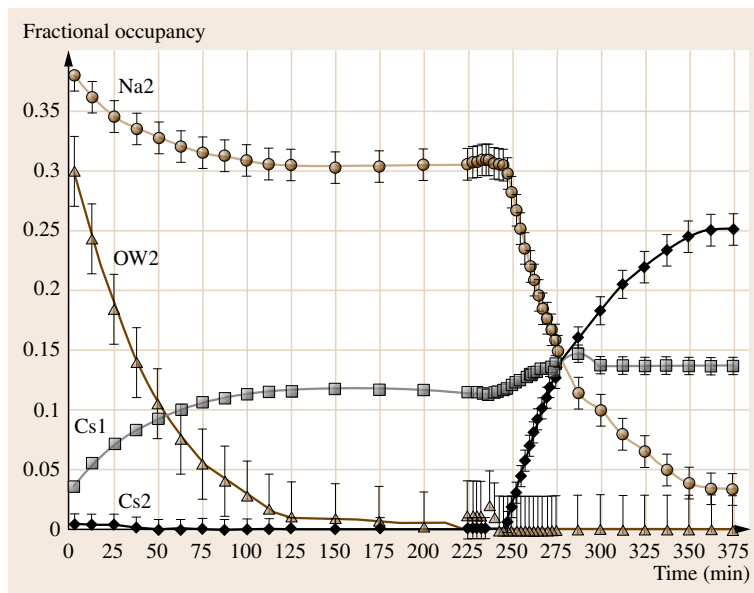


Fig. 49.15 Results of fractional occupancy refinements for Na₂, OW₂, Cs₂, and Cs₁ during the Cs⁺ ion exchange into Na-TS

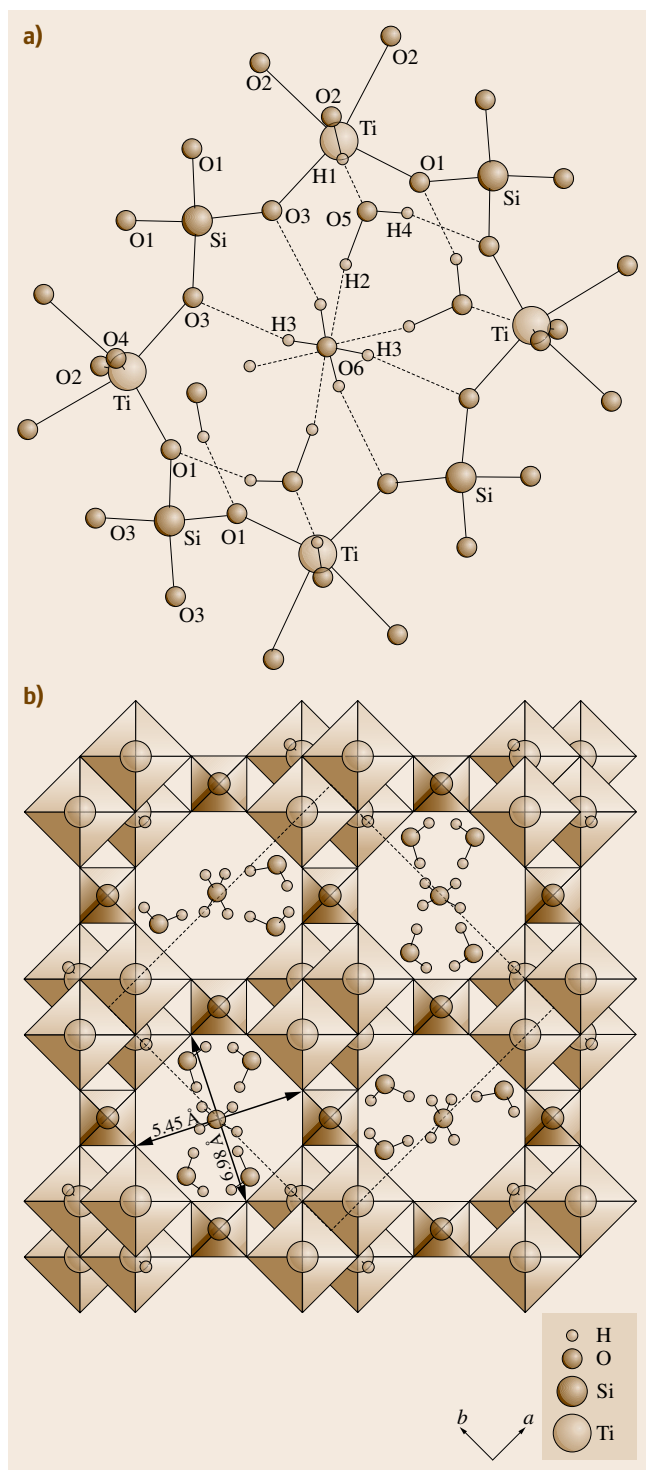


Fig. 49.16a,b Ball-and-stick representation of a portion of the proton phase $\text{H}_2\text{Ti}_2\text{O}_3(\text{SiO}_4)_4 \cdot 1.5\text{H}_2\text{O}$ as viewed down the c -axis, showing the hydrogen bonding scheme between the acid proton and the water molecules O₅ and water–water and water–framework oxygens (a) and a polyhedral representation showing the elliptical nature of the tunnel along the c -axis direction and the new unit cell (bold line) along the diagonals of the Na-TS unit cell ◀

the Cs1 site was 0.25. These values yield a formula of $\text{Na}_{1.06}\text{Cs}_{0.26}\text{H}_{0.68}\text{Ti}_2\text{O}_3\text{SiO}_4 \cdot \text{H}_2\text{O}$. The proton content was due to hydrolysis and the amount was calculated to balance the charge. Almost all the Na^+ in the tunnel was lost to hydrolysis and exchange for Cs^+ . The maximum amount, or fraction, of Cs^+ that can be exchanged into the TS phase is 0.5. This has been shown by titration with CsOH [49.35, 36] and from ex situ structural studies. The Cs^+ is too large to occupy the Na1 framework sites and for the same reason can only occupy half the tunnel sites.

49.6.5 Cesium Ion Exchange into H-TS

There is a major difference between Cs^+ ion-exchange pathways in Na-TS and H-TS. Replacement of the sodium ions by protons is accompanied by a space group change from $P4_2/mcm$ to $P4_2/mbc$ and unit cell dimensions [49.35, 37] of $a, b = 11.039(5) \text{ \AA}$, $c = 11.880(5) \text{ \AA}$. The protons are covalently bonded to the cubane oxygens and hydrogen bond to water molecules in the tunnel. The reason for the change is that the a, b axes transition from 7.806 \AA to the larger value (actually the ab square diagonal), and the symmetrical eight-membered ring perimeter of the tunnel is distorted into an elliptical shape (Fig. 49.16). The ratio of the length to the width of the tunnel is now 1.2. A very fast exchange of Cs^+ into the Cs2 site (six-coordinate site) occurs in the first 10 min of exchange, as shown in Fig. 49.17 [49.5]. The structure then reverts back to the $P4_2/mcm$ space group, restoring the symmetrical tunnel shape. At this point the Cs1 site begins to fill up, occurring simultaneously with the space group transformation. The diffraction patterns contained both phases to the end of the experiment. After 20 min, both sites continued to fill until a final composition of $\text{Cs}_{0.36}\text{H}_{1.64}\text{Ti}_2\text{O}_3\text{SiO}_4$. Since complete filling with Cs^+ would have the Cs fractional content of 0.5, the exchange was 72% complete. This value is quite high considering how dilute the exchange solution was initially.

49.6.6 Sodium Niobium Titanosilicate (Nb-TS)

Niobium forms a solid solution with the sodium titanium silicate Na-TS up to about 25% replacement of Ti by Nb. This phase, of ideal composition $\text{Na}_{1.5}\text{Ti}_{1.5}\text{Nb}_{0.5}\text{O}_3\text{SiO}_4 \cdot 2\text{H}_2\text{O}$, has a higher selectivity for Cs^+ in highly basic solutions containing higher levels of Na^+ than does the non-niobium-containing phase. As a first step in determining why this phase possesses such a high selectivity for Cs^+ , the crystal structure of the cesium ion phase was determined [49.38]. The presence of Nb^{5+} is statistically distributed over the titanium sites and reduces the sodium ion occupancy in the tunnel by half. However, in this phase considerable hydrolysis occurs, so that the tunnel contains almost no Na^+ but only water [49.38]. This lack of competing ions in the tunnel changes the coordination number of Cs^+ in the tunnel to 12. That is, there are eight water molecules per unit cell in the tunnel and two Cs^+ . With no Na^+ in the tunnel all the water molecules bond to Cs^+ at a bond distance of 3.13 Å, compared with 3.26 Å for the eight framework oxygens. This increase in coordination number apparently greatly decreases the free energy of exchange as Cs^+ changes from a weak coordination in the aqueous phase to very high coordination within the tunnel.

49.6.7 In Situ Synthesis of Na-NbTS

The preparation of the niobium Na-TS phase is often plagued with an impurity that is probably a polymeric Keggin ion, referred to as Na-IPX. A gel was prepared from Nb_2O_5 , titanium isopropoxide, silicon tetraethoxide, and 3.3 M NaOH. The ratio of constituents was $1.0\text{TiO}_2:0.167\text{Nb}_2\text{O}_5:1.33\text{SiO}_2:6.9\text{Na}_2\text{O}:228\text{H}_2\text{O}$. This gel was heated in a Teflon-lined pressure vessel at 200 °C for 4 days. The resultant Na-NbTS was highly crystalline but contained a small amount of Na-IPX. A similar gel was prepared for the in situ study at the X7B beamline of the National Synchrotron Light Source, Brookhaven National Laboratory. The wavelength used was 0.9223 Å and an external N_2 gas pressure of 250 psi was applied to the sapphire capillary. A sapphire capillary was used because silica is solubilized at the high-pH conditions of the starting gel and would weaken the integrity of the capillary. The gel was heated to 210 °C in 2 min and x-ray diffraction patterns were recorded every 2.5 min.

The initial pattern of the gel exhibited two broad peaks centered at 17.6° and 24.5° in 2θ . The results

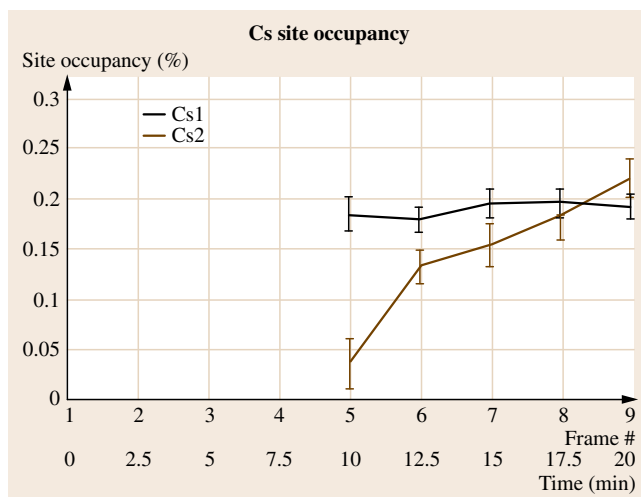


Fig. 49.17 In situ time-resolved x-ray diffraction showing the onset of Cs^+ for H^+ ion exchange to be a site-selective process. The Cs2 position first filled to $\approx 20\%$. After Cs2 filled, Cs1 began to fill the channels along the [001] direction and completed at $\approx 20\%$. The mechanism of exchange is seen as an opening of the [001] channels as Cs2 bonds to the Ti—O—Si polyhedra linkages, allowing Cs1 to fill the center of the eight-membered ring

are shown in Fig. 49.18. Between minutes 0 and 65, the broad features began to diminish. Simultaneously a third broad feature developed at $\approx 5.1^\circ 2\theta$, associated with the crystalline ordering of the Na-IPX phase. From minutes 65 to 75, the reflections from the impurity phase began to increase in intensity, with the strongest peak arising from the broad feature at $\approx 5.1^\circ$ (Fig. 49.18). From minute 75 to the end of the experiment, the impurity phase ceased to increase in intensity as the Na-NbTS phase began to crystallize. The Na-NbTS phase continued to grow for 25 min, and after 100 min no further changes in the diffraction pattern were observed.

Unit cell refinements of Na-TS during crystallization showed an initial increase in the a - and b -axes and a decrease in the c -axis in a brief span of 5 min from minute 75 to 80 (Fig. 49.19). After the initial anomalous expansion, the unit cell volume and unit cell parameters increased until the end of the experiment. The unit cell volume increased from 743 to 745 Å³ from minute 75 to the completion of the run. By slight adjustments of the gel composition it was possible to achieve phase purity by elimination of Na-IPX formation, as illustrated by this in situ study.

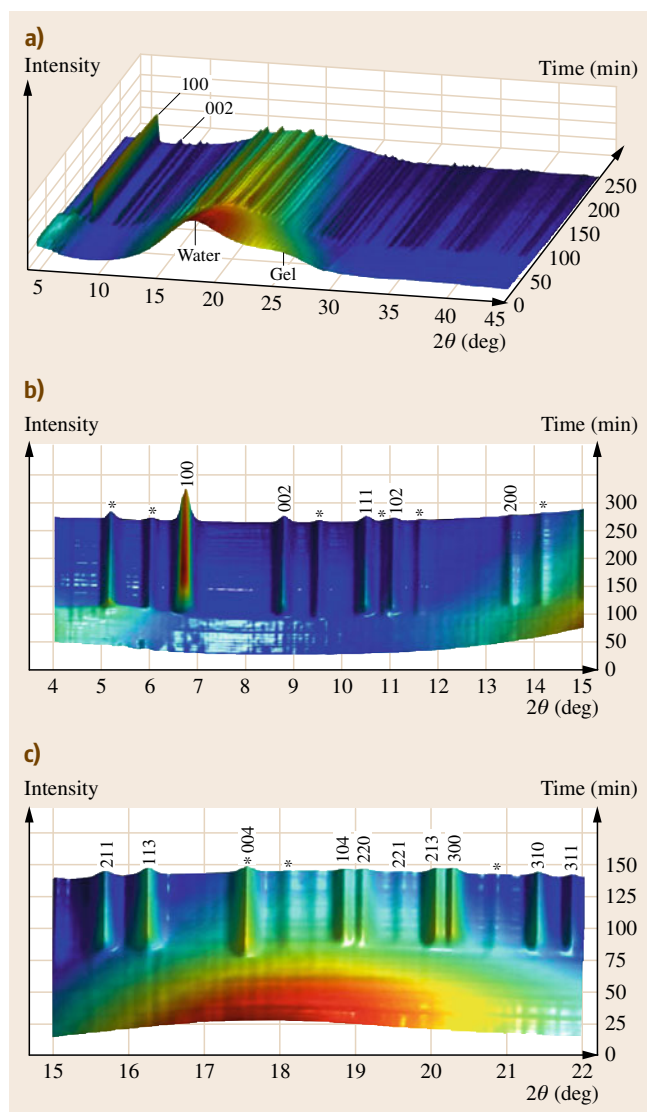


Fig. 49.18a–c Three-dimensional (3-D) time-resolved XRD plots. (a) The entire range of the acquired diffraction pattern, showing the main Na-NbCTS, water, and gel signals contributing to the pattern. (b) Zoomed plot showing the main Na-NbCTS phase index and peaks from the impurity phases (marked). (c) Zoomed plot of higher-angle diffraction data. Asterisk denotes the presence of an unidentified phase

49.6.8 In Situ Ion Exchange of Cesium Ion Exchange in Na-NbTS

The time-resolved x-ray patterns collected during Cs^+/Na^+ exchange [49.26] are shown in Fig. 49.20.

Refinements of the cell parameters during the exchange process indicated that no structural transformation had occurred during exchange. The space group remained $P4_2/mcm$ and the eight-membered ring (8MR) of the tunnel remained circular. The changes in unit cell dimensions as exchange proceeded are provided in Fig. 49.21. The a - and b -axes increased from 7.8470(5) Å to 7.8535(5) Å while the c -axis decreased from 11.980(1) Å to 11.963(1) Å. However, after an initial increase in unit cell volume due to the more rapid increase in the a , b parameters, the unit cell volume was very nearly the same at the end of the Cs^+ uptake as for the original Na-NbTS. This exchange process was interpreted as continuous filling of sites Cs1 and Cs2 with little structural distortion, which contrasts with the exchange studies in the Na-TS and H-TS forms. The break in the curves of Fig. 49.21 was due to filling of the storage ring when no x-rays were available.

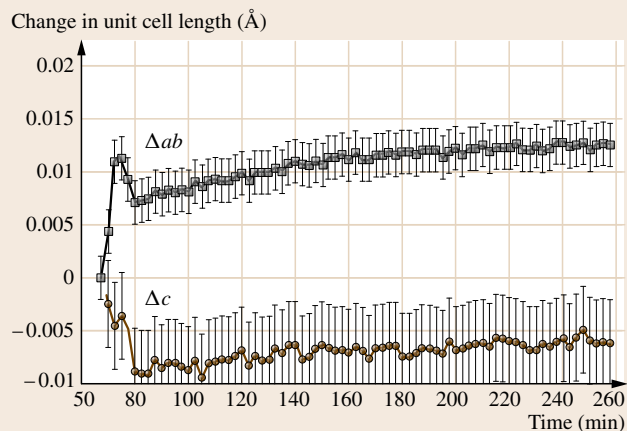
49.6.9 Cesium Ion Exchange into H-NbTS

A major difference between the Na-NbTS phase and the Na-TS phase is that no space group change occurred when the Na^+ was replaced by H^+ . The Ti/Nb fractional occupancies refined to 0.77(3) and 0.23(3), respectively, and were fixed to a ratio of 0.75/0.25 based on previous compositional studies [49.38, 39]. No Na^+ was detected by microprobe analysis. Thus, the formula, both by elemental analysis and x-ray refinement, was fixed at $\text{H}_{1.5}\text{Nb}_{0.5}\text{Ti}_{1.5}\text{SiO}_7 \cdot 2\text{H}_2\text{O}$. The proton parameters could not be determined by the x-ray refinement, but it was assumed that they are covalently bonded to the cubane oxygen sites in a similar fashion as seen in the H-TS structure. The water molecules were also distributed in crystallographic sites analogous to Na-TS. Water (OW1) is located near the walls of the 8MR and the intersection of the 6MR, i.e., those cavities where the Na^+ in the framework is located. Water (OW2) is located near the center of the channel along the c -axis, but not on the 4_2 -screw special position. This offset from the screw axis results in the partial occupancy of the OW2 site where its maximal allowed occupancy is 1/2 due to positional disorder.

No structural change was observed in the exchange reaction since all peaks in the diffraction patterns could be indexed on the basis of a single unit cell (Fig. 49.22). The unit cell dimensions initially increased to minute 70, then showed a continuous volume decrease as the a - and b -axes decreased from 7.837(1) to 7.828(1) Å and the c -axis decreased from 11.921(2) to 11.912(2) Å (Fig. 49.23). Rietveld refinement of the

Fig. 49.19 Results of the unit cell refinements of Na-NbTS during crystallization. Initial cell lengths were $a, b = 7.844(2) \text{ \AA}$, $c = 12.073(4) \text{ \AA}$ and final cell lengths were $a, b = 7.857(2) \text{ \AA}$, $c = 12.067(4) \text{ \AA}$ ►

occupancies of the sites populated by Cs^+ and water indicated that ion exchange occurred in two distinct steps (Fig. 49.24). The first occurred from minutes 0 to 197.5 and involved a gradual increase in Cs^+ uptake from 0 to 0.115(6) fractional occupancy at site 1. After the initial Cs^+ uptake, at minute 197.5, H_2O at site OW2 decreased in fractional occupancy from 0.51 to 0.24(3) within 1 min, amounting to slightly more than 0.5 mol H_2O . From minute 200 to the end of the experiment, the fractional occupancy of H_2O at site OW2 remained constant at 0.24(3). The second step of the exchange begins at minute 197.5, during which the Cs^+ uptake increased to 0.339(7) fractional occupancy at the end of the experiment (700 min). The



final formula as obtained from the x-ray data was $\text{H}_{1.33}\text{Cs}_{0.17}\text{Nb}_{0.5}\text{Ti}_{1.5}\text{SiO}_7 \cdot 1.5\text{H}_2\text{O}$.

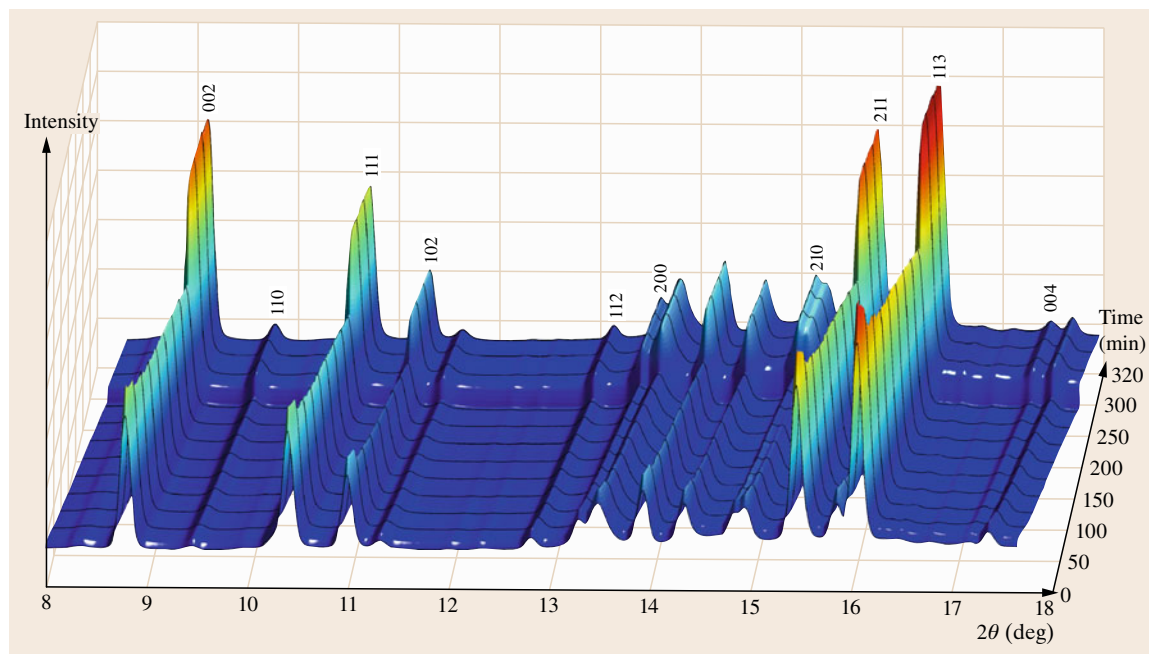


Fig. 49.20 Zoomed 3-D display of the time-resolved XRD data collected during Cs^+ exchange into Na-NbTS. Peaks from the Na-NbTS phase are indexed. Diffraction patterns are highlighted (black) every 25 min. Optimization of beam path flight tube resulted in an increase of overall intensity near minute 275

49.7 Discussion of In Situ Studies

49.7.1 Synthesis of Na-TS and Na-NbTS

Both the Na-TS and Na-NbTS are formed in a very narrow window of gel composition and alkalinity. An excess of silica relative to titanium is necessary to form Na-TS, generally a 2 : 1 ratio. The critical factor in crystallizing a pure TS compound is the

amount and concentration of NaOH in the initial gel. At high molar ratios and concentrations of NaOH, substantial amounts of STOS are obtained. At a concentration of 3.3 M and a ratio of 6.67Na₂O : 1.0TiO₂ a pure Na-TS phase is obtained. However, even with higher ratios and concentrations of NaOH, sodium nonatitanate is found to form first and then is converted to STOS, Na₂TiSiO₅, a synthetic analogue of the mineral natisite. Since the nonatitanate has a high affinity for Sr²⁺ in alkaline solution [49.40, 41], it may be possible to provide a combination of Na-TS and the nonatitanate to remove much of the high-level waste, ¹³⁷Cs and ⁹⁰Sr, from weapons-type nuclear waste with a combination of Na-TS and SNT. Time-resolved synthesis experiments and optimized synthesis procedures can be used to tailor the Na-TS : SNT ratios for a specified removal capacity

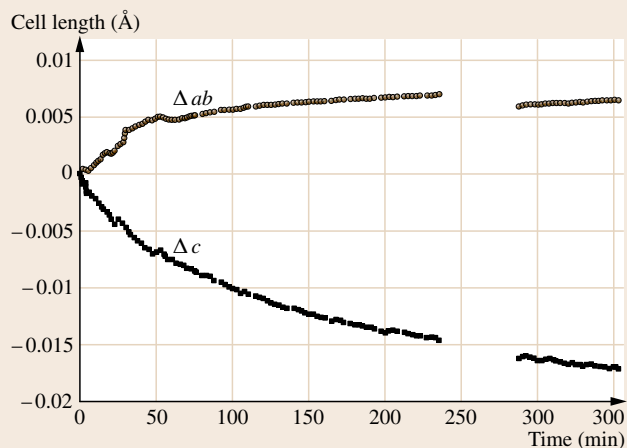


Fig. 49.21 Results of the unit cell refinements for data collected during Cs⁺ exchange into Na-NbTS. Unit cell lengths changed from $a, b = 7.8470(5) \text{ \AA}$, $c = 11.980(1) \text{ \AA}$ at minute 0 to $a, b = 7.8535(5) \text{ \AA}$, $c = 11.963(1) \text{ \AA}$ at minute 355.5. The gap in data is when no x-ray beam was available. Error bars are smaller than plot points ◀

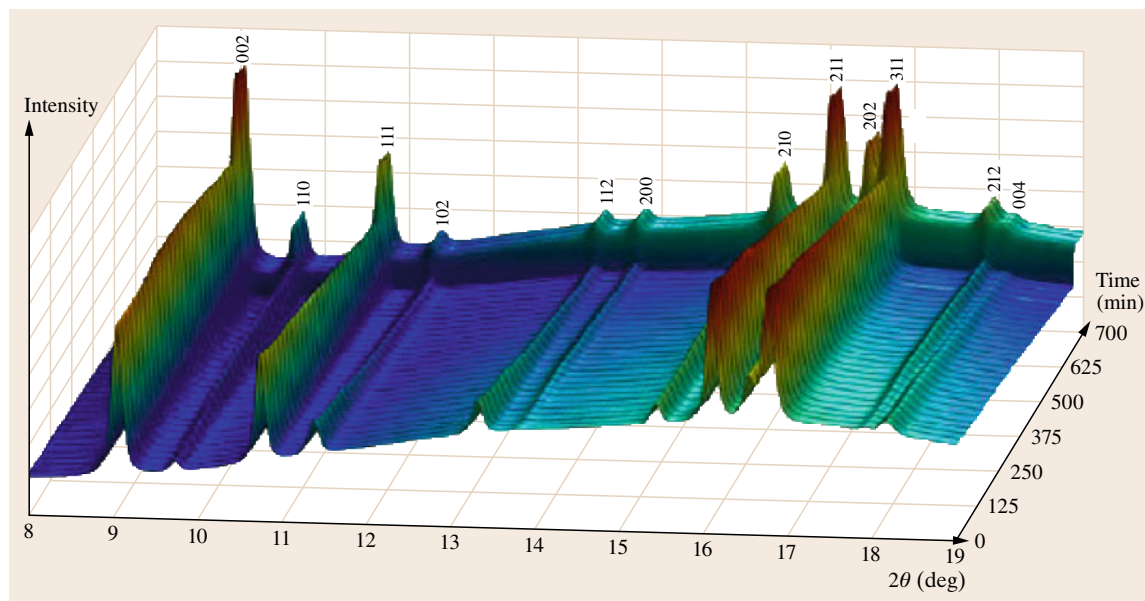


Fig. 49.22 Zoomed 3-D time-resolved XRD display for the Cs⁺ exchange into H-NbTS experiment. No impurity phases were present in the diffraction patterns. Diffraction patterns are highlighted (black) every 25 min. Optimization of beam path flight tube resulted in an increase of overall intensity near minute 625

of ^{137}Cs and ^{90}Sr , respectively, without waste of ion-exchange product.

Addition of Nb to the Na-TS reactant mix suppresses the formation of SNT but tends to form Na-IPX [49.42] as an impurity phase. A systematic study is required to determine which conditions give rise to the impurity phase to prevent its occurrence. The broad feature at $2\theta = 24.5^\circ$ in the in situ study of Na-NbTS may result from scattering by amorphous solids that are formed by hydrolysis of the alkoxides during heating to the temperature of the reactant mix. In the case of the gels prepared for synthesis of Na-TS, H_2O_2 was added so all the oxides dissolved in basic solution. The lack of solubility of TiO_2 in alkaline solution may have been responsible for the absence of any crystallization in the first 60 min of the in situ study for Na-NbTS.

49.7.2 Exchange Mechanisms

The results of Cs^+ exchange into H-NbTS indicated that the Cs1 site was the only site filled by Cs^+ . The uptake of Cs^+ in this exchanger was slow relative to exchange in H-TS. Only 0.115 fractional occupancy was achieved in the first 200 min of exchange into H-NbTS. This represents just 0.23 Cs^+ on average per unit cell, compared with an exchange capacity of two Cs^+ per unit cell. There are four water molecules per unit cell, and half of them are lost when Cs^+ has an occupancy of 0.23. After this occupancy, site Cs1 continues to increase in occupancy. This is a significantly different uptake pathway than any other TS, or NbTS, phase where the filling of one Cs site resulted in structural transition allowing a second Cs site occupancy. One might expect that, as the Cs^+ enters the tunnel, a proton coordinately bonded to a cubane oxygen would form a hydronium ion and leave the unit cell. Thus, for each Cs^+ exchanged, a water molecule as a hydronium ion would leave the solid phase. This evidently does not occur in the H-NbTS phase. Rather it might be speculated that the proton follows a hopping mechanism, traversing from lattice oxygen to water to lattice oxygen. As the Cs^+ diffuses into a unit cell the protons leave that unit cell to maintain charge balance. At the surface, the proton hops to a water molecule on the interface of the unit cell, and then leaves the solid phase.

The exchange of Cs^+ into the H-TS and H-NbTS involves different mechanisms. In H-TS there is a rapid uptake of Cs^+ into the Cs2 site. Only when sufficient cesium is present in this site does the 8MR change from its elliptical shape, with length-to-width ratio $L:S = 1.53$, to the circular geometry with $L:S = 1$. Thereafter

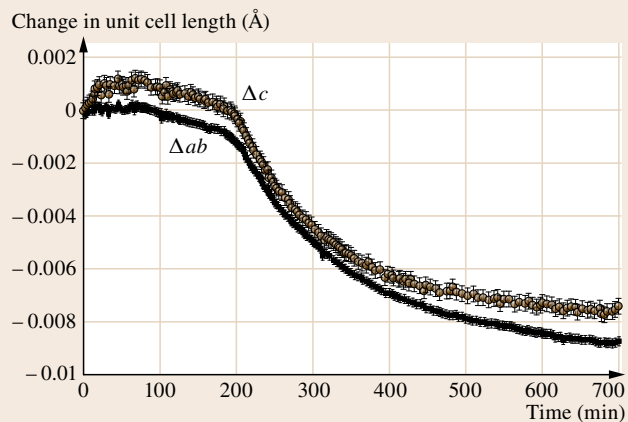


Fig. 49.23 Changes in unit cell parameters of the H-NbTS structure as Cs^+ exchanged for H^+ . The two-step process is seen between minutes 0–200 and 200–700. Unit cell lengths at minute 0 were $a, b = 7.837(1) \text{ \AA}$, $c = 11.919(3) \text{ \AA}$, and at minute 700 were $a, b = 7.828(1) \text{ \AA}$, $c = 11.912(3) \text{ \AA}$

continued diffusion takes place with the filling of the Cs1 site while the occupancy of the Cs2 site remains static.

The results of the time-resolved x-ray diffraction study of Cs^+ exchange into Na-TS illustrated a crystallographic-site-dependent process. Cesium first occupies site Cs2, located outside of the 8MR, dur-

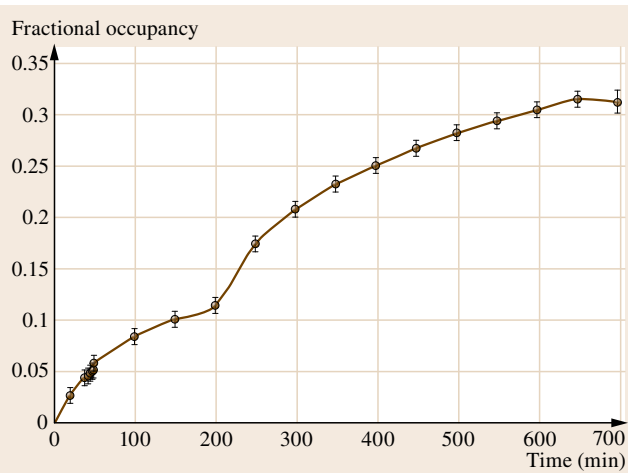


Fig. 49.24 Occupancy refinement of the Cs^+ sites Cs1 and Cs2. Cs2 is not shown because the refinements were 0.00(1) occupancy. The two-step process of Cs occupancy corresponds with the unit cell trends (Fig. 49.22). Cs^+ fractional occupancy at minute 200 was 0.115(6) and at minute 700 was 0.339(7)

ing which time water occupancy at site OW2 decreased rapidly. The process of loading site Cs2 occurred within 250 min, and was much slower in comparison with Cs^+ exchange into H-TS. When OW2 occupancy had reached zero, Cs^+ exchanged into site Cs1 located at the center of the 8MR. The reduction in water occupancy in the center of the 8MR during Cs^+ exchange for Na^+ may be caused by spatial restrictions due to the incorporation of the large Cs^+ ionic radius at site Cs2, and indirectly forces water to migrate out of the channels. This suggests that direct replacement of Cs^+ for Na^+ was favored, and the disruption of the water-hydroxyl bond network in the center of the 8MR was not favored. Once the OW2 occupancy reached zero, the Cs1 site became available and dominated the exchange process.

Although structure refinements of Cs^+ exchange into Na-NbCST could not be preformed, a possible scenario of the exchange process may be inferred in conjunction with previous static exchange studies [49.34] and these time-resolved studies. Starting

with the unit cell parameters (Fig. 49.18) as a basis for the argument, the ion exchange may have proceeded in two distinct steps. The first step was Cs^+ uptake into site Cs1, where no H_2O occupied the center of the circular 8MR. This was indicated by a nonlinear increase in the *a*- and *b*-axes lengths and a decrease in the *c*-axis length. Incorporation of Cs^+ at site Cs1 would have continued for at least 235 min along the continuous unit cell lengths trajectories. Between minutes 235 and 287 no x-ray beam was available, but a decrease in the *a* and *b* cell lengths occurred, while the *c*-axis maintained a decreasing trajectory. The decrease in the *a* and *b* cell lengths would be the onset of the second step, and at this point, site Cs^+ would have started to fill site Cs2. The availability of site Cs2 would have been initiated by a decrease in OW2 occupancy. Similar exchange mechanisms were observed in the case of Cs^+ into Na-TS, where the Cs2 site filled first to force OW2 out of the structure, and once OW2 achieved a fractional occupancy of ≈ 0.1 , Cs^+ began to fill site Cs1.

49.8 Summary

An understanding of the time-dependent nature of chemical reactions and processes is essential for the quantitative description of synthesis processes and ion-exchange mechanisms. Current time-resolved diffraction techniques do not have enough resolution to be used as the sole method for modeling complex crystallographic relationships. With current technologies and techniques, in situ diffraction studies must also be complemented by ex situ diffraction studies of the end-member phases. The kinetics of material synthesis observed here can be described as a series of compound precursor phases that eventually lead to the desired product as a result of changing gel compositions from precipitating phases. Only using in situ techniques can these cursory phases be described in the four-dimensional space of time, temperature, pressure, and composition. In addition, the intermediate precursor phases may themselves be important materials that

would normally go unnoticed during ex situ synthesis. In any case, the crystallographic and chemical make-up of the cursory phases will elucidate the mechanisms of crystal growth.

In situ ion-exchange studies illustrate the complex mobility of ion and water mobility within the voids of crystalline phase, and the time and structure dependency of the ion-exchange pathway. These types of in situ time-resolved diffraction studies can be extremely useful in understanding the selectivity and fundamental mechanisms of the ion-exchange process in open-framework materials.

While we have concentrated on the latest results from our own in situ studies, it should be recognized that many other techniques are used as in situ time-resolved procedures, particularly for crystal growth studies. A representative few are listed [49.43–48] to illustrate the extent and power of in situ methods.

References

- 49.1 P. Norby, C. Cahill, C. Koleda, J.B. Parise: A reaction cell for in situ studies of hydrothermal titration, *Mater. Sci. Forum* **31**, 481–483 (1998)
- 49.2 P. Norby: In-situ time resolved synchrotron powder diffraction studies of syntheses and chemical reactions, *Mater. Sci. Forum* **228–231**, 147–152 (1996)

- 49.3 J.B. Parise, C.L. Cahill, Y. Lee: Dynamic powder crystallography with synchrotron x-ray sources, *Can. Mineral.* **38**, 777–800 (2000)
- 49.4 C.L. Cahill, Y.H. Ko, J.C. Hanson, K.M. Tan, J.B. Parise: Structure of microporous QUI-MnGS-1 and in situ studies of its formation using time-resolved synchrotron x-ray powder diffraction, *Chem. Mater.* **10**, 1453 (1998)
- 49.5 A.J. Celestian, D.G. Medvedev, A. Tripathi, J.B. Parise, A. Clearfield: Optimizing synthesis of $\text{Na}_2\text{Ti}_2\text{SiO}_7 \cdot 2\text{H}_2\text{O}$ (Na-CST) and ion exchange pathways for $\text{Cs}_{0.4}\text{H}_{1.6}\text{Ti}_2\text{SiO}_7 \cdot \text{H}_2\text{O}$ (Cs-CST) determined from in-situ synchrotron x-ray powder diffraction, *Nucl. Instrum. Methods Phys. Res.* **238**, 61–69 (2005)
- 49.6 D.G. Medvedev, A. Tripathi, A. Clearfield, A.J. Celestian, J.B. Parise, J. Hanson: Crystallization of sodium titanium silicate with sitinakite topology: Evolution from the sodium nonatitanate phase, *Chem. Mater.* **16**, 3659–3666 (2004)
- 49.7 A.J. Celestian, J.B. Parise, C. Goodell, A. Tripathi, J. Hanson: Time-resolved diffraction studies of ion exchange: K^+ and Na^+ exchange into (Al,Ge) gismondine $\text{Na}_{24}\text{Al}_{26}\text{Ge}_{24}\text{O}_{96} \cdot 40\text{H}_2\text{O}$ and $\text{K}_8\text{Al}_8\text{Ge}_8\text{O}_{32} \cdot 8\text{H}_2\text{O}$, *Chem. Mater.* **16**, 2244–2254 (2004)
- 49.8 Y. Lee, B.A. Reisner, J.C. Hanson, G.A. Jones, J.B. Parise, D.R. Corbin, B.H. Toby, A. Freitag, J.Z. Larese: New insight into cation relocations within the pores of zeolite rho: In situ synchrotron x-ray and neutron powder diffraction studies of Pb- and Cd-exchanged rho, *Phys. Chem. B* **105**(30), 7188–7199 (2001)
- 49.9 J.B. Parise, T.E. Gier, D.R. Corbin, D.E. Cox: Structural changes occurring upon dehydration of zeolite-rho – A study using neutron powder diffraction and distance-least-squares structural modeling, *J. Phys. Chem.* **88**, 1635–1640 (1984)
- 49.10 Y. Lee, T. Vogt, J.A. Hriljac, J.B. Parise, G. Artioli: Pressure-induced volume expansion of zeolites in the natrolite family, *J. Am. Chem. Soc.* **124**, 5466–5475 (2002)
- 49.11 J.P. Glusker, K.N. Trueblood: *Crystal Structure Analysis: A Primer*, 2nd edn. (Oxford Univ. Press, New York 1985)
- 49.12 B.D. Cullity, S.R. Stock: *Elements of X-ray Diffraction*, 3rd edn. (Prentice Hall, Upper Saddle River 2001), Chap. 2
- 49.13 G.E. Bacon: *Neutron Diffraction*, 1st edn. (Clarendon, London 1962)
- 49.14 P. Coppens (Ed.): *Synchrotron Radiation Crystallography* (Academic, London 1992)
- 49.15 J.H. Chen, R. Li, J.B. Parise, D.J. Weidner: Pressure-induced ordering in $(\text{Ni,Mg})_2\text{SiO}_4$ olivine, *Am. Mineral.* **81**, 1519 (1996)
- 49.16 J.H. Chen, D.J. Weidner: X-ray diffraction study of iron partitioning between alpha and gamma phases of the $(\text{Mg,Fe})_2\text{SiO}_4$ system, *Physica A* **239**, 78–86 (1997)
- 49.17 Y.S. Zhao, R.B. VonDreele, T.J. Shankland, D.J. Weidner, J.Z. Zhang, Y.B. Wang, T. Gasparik: Thermoelectric equation of state of jadeite $\text{NaAlSi}_2\text{O}_6$: An energy-dispersive Rietveld refinement study of low symmetry and multiple phases diffraction, *Geophys. Res. Lett.* **24**, 5–8 (1997)
- 49.18 J.B. Parise, J. Chen: Studies of crystalline solids at high pressure and temperature using the DIA multi-anvil apparatus, *Eur. J. Solid State Inorg. Chem.* **34**, 809–821 (1997)
- 49.19 J.B. Parise, D.J. Weidner, J. Chen, R.C. Liebermann, G. Chen: In situ studies of the properties of materials under high-pressure and temperature conditions using multi-anvil apparatus and synchrotron x-rays, *Annu. Rev. Mater. Sci.* **28**, 349–374 (1998)
- 49.20 X. Liang, J.E. Andrews, J.A. Haseth: Resolution of mixture components by target transformation factor analysis and determinant analysis for the selection of targets, *Anal. Chem.* **68**, 378–385 (1996)
- 49.21 CCP14: Collaborative Computational Project No. 14, <http://www.ccp14.ac.uk/index.html> (last accessed September 18, 2009)
- 49.22 D.E. Cox, B.H. Toby, M.M. Eddy: Acquisition of powder diffraction data with synchrotron radiation, *Aust. J. Phys.* **41**, 117–131 (1988)
- 49.23 P. Norby: Hydrothermal conversion of zeolites: an in-situ synchrotron x-ray powder diffraction study, *J. Am. Chem. Soc.* **119**, 5215–5221 (1997)
- 49.24 P. Norby, C. Cahill, C. Koleda, J.B. Parise: A reaction cell for in situ studies of hydrothermal titration, *J. Appl. Crystallogr.* **31**, 481–483 (1998)
- 49.25 J.S.O. Evans, R.J. Francis, D. O'Hare, S.J. Price, S.M. Clark, J. Gordon, A. Nield, C.C. Tang: An apparatus for the study of the kinetics and mechanism of hydrothermal reactions by in-situ energy dispersive x-ray diffraction, *Rev. Sci. Instrum.* **66**, 2442–2445 (1994)
- 49.26 A.J. Celestian: Time-resolved structural characterization of microporous silicotitanates and niobium silicotitanates. Ph.D. Thesis (Stony Brook Univ., Stony Brook 2006)
- 49.27 J. Chen, D.J. Weidner, M.T. Vaughan, R. Li, J.B. Parise, C.C. Koleda, K.J. Baldwin: Time-resolved diffraction measurements with an imaging plate at high pressure and temperature, *Rev. High Press Sci. Technol.* **7**, 272–274 (1998)
- 49.28 R.J. Francis, D. O'Hare: The kinetics and mechanisms of the crystallization of microporous materials, *J. Chem. Soc. Dalton Trans.*, 3133–3148 (1998)
- 49.29 S. Shaw, S.M. Clark, C.M.B. Henderson: Hydrothermal formation of the calcium silicate hydrates, tobermorite $(\text{Ca}_5\text{Si}_6\text{O}_{16}(\text{OH})_2 \cdot 4\text{H}_2\text{O})$ and xonotlite

- ($\text{Ca}_6\text{Si}_6\text{O}_{17}(\text{OH})_2$): An in situ synchrotron study, *Chem. Geol.* **167**, 129–140 (2000)
- 49.30 I.A. Bray, K.J. Carson, R.J. Ellorich: *Initial Evaluation of Sandia National Laboratory Prepared Crystalline Silico-Titanates for Recovery of Cesium* (Pacific Northwest National Laboratory, Richland 1993), WA. PNL-8847
- 49.31 D.M. Poojary, R.A. Cahill, A. Clearfield: Synthesis, crystal-structures, and ion-exchange properties of a novel porous titanosilicate, *Chem. Mater.* **6**, 2364–2368 (1994)
- 49.32 C.T. Prewitt, R.D. Shannon: Use of radii as an aid to understanding the crystal chemistry of high pressure phases, *Trans. Am. Crystallogr. Assoc.* **5**, 51–60 (1969)
- 49.33 A. Clearfield, J. Lehto: Preparation, structure, and ion-exchange properties of $\text{Na}_4\text{Ti}_9\text{O}_{20} \cdot x\text{H}_2\text{O}$, *J. Solid State Chem.* **73**, 98–106 (1988)
- 49.34 J. Lehto, A. Clearfield: The ion-exchange of strontium on sodium titanate $\text{Na}_4\text{Ti}_9\text{O}_{20} \cdot x\text{H}_2\text{O}$, *J. Radioanal. Nucl. Chem.* **118**, 1–13 (1987)
- 49.35 D.M. Poojary, A.I. Bortun, L.N. Bortun, A. Clearfield: Structural studies on the ion-exchanged phases of a porous titanosilicate, $\text{Na}_2\text{Ti}_2\text{O}_3\text{SiO}_4 \cdot 2\text{H}_2\text{O}$, *Inorg. Chem.* **35**, 6131–6139 (1996)
- 49.36 A. Clearfield: Structure and ion exchange properties of tunnel type titanium silicates, *Solid State Sci.* **3**, 103–112 (2001)
- 49.37 P. Perterra, M.A. Salvado, S. Garcia-Granda, A.I. Bortun, A. Clearfield: Neutron powder diffraction study of $\text{Ti}_2(\text{OH})_2\text{OSiO}_4 \cdot 1.5\text{H}_2\text{O}$, *Inorg. Chem.* **38**, 2563–2566 (1999)
- 49.38 A. Tripathi, D.G. Medvedev, M. Nyman, A. Clearfield: Selectivity for Cs and Sr in Nb-substituted titanosilicate with sitinikite topology, *J. Solid State Chem.* **175**, 72–83 (2003)
- 49.39 V. Luca, J.V. Hanna, M.E. Smith, M. James, D.R.G. Mitchell, J.R. Bartlett: Nb-substitution and Cs^+ ion-exchange in the titanosilicate sitinakite, *Microporous Mesoporous Mater.* **55**, 1–13 (2002)
- 49.40 P. Sylvester, E.A. Behrens, G.M. Graziano, A. Clearfield: An assessment of inorganic ion-exchange materials for the removal of strontium from simulated Hanford tank wastes, *Sep. Sci. Technol.* **34**, 1981–1992 (1999)
- 49.41 E.A. Behrens, P. Sylvester, A. Clearfield: An assessment of a sodium nonatitanate and pharmacosiderite-type ion exchangers for strontium and cesium removal from DOE waste simulants, *Environ. Sci. Technol.* **32**, 101–107 (1998)
- 49.42 M. Nyman, F. Bonhomme, T.M. Alam, M.A. Rodriguez, B.R. Cherry, J.L. Krumhansl, T.M. Nenoff, A.M. Sattler: A general synthetic procedure for heteropolyniobates, *Science* **297**, 996–998 (2002)
- 49.43 S. Hermes, T. Witte, T. Hikov, D. Zacher, S. Bahnmüller, G. Langstein, K. Huber, R.A. Fischer: Trapping metal-organic framework nanocrystals: An in-situ time-resolved light scattering study on the crystal growth of MOF-5 in solution, *J. Am. Chem. Soc.* **129**, 5324–5325 (2007)
- 49.44 G. Cao, M.J. Shah: In situ monitoring of zeolite crystallization by electrical conductivity measurement: New insight into zeolite crystallization mechanism, *Microporous Mesoporous Mater.* **101**, 19–23 (2007)
- 49.45 W. Fan, M. Ogura, G. Sanker, T. Okubo: In-situ small-angle and wide-angle x-ray scattering investigation on nucleation and crystal growth of nanosized zeolite A, *Chem. Mater.* **19**, 1906–1917 (2007)
- 49.46 H. Lee, S.W. Yoon, E.J. Kim, J. Park: In-situ growth of copper sulfide nanocrystals on multiwalled carbon nanotubes and their application as novel solar cell and amperometric glucose sensor materials, *Nano Lett.* **7**(3), 778–784 (2007)
- 49.47 J. Schörmann, S. Potthast, D.J. As, K. Lischka: In-situ growth regime characterization of cubic GaN using reflection high energy electron diffraction, *Appl. Phys. Lett.* **90**, 041918/1–041918/3 (2007)
- 49.48 C.-H. Cheng, G. Juttu, S.F. Mitchell, D.F. Shantz: Synthesis, characterization and growth rates of aluminum- and Ge,Al-substituted silicalite-1 materials grown from clear solutions, *J. Phys. Chem. B* **110**(45), 22488–22495 (2006)

50. Single-Crystal Scintillation Materials

Martin Nikl, Anna Vedda, Valentin V. Laguta

Scintillation materials are employed to detect x-ray and γ -ray photons or accelerated particles. Wide-bandgap semiconductor or insulator materials with a high degree of structural perfection are suitable for this purpose. They must accomplish fast and efficient transformation of incoming high-energy photon/particles to a number of electron-hole pairs collected in the conduction and valence bands, respectively, and their radiative recombination at suitable luminescence centers in the material. Generated ultraviolet (UV) or visible light can then be detected at high sensitivity by conventional solid-state semiconductor- or photomultiplier-based photodetectors, which are an indispensable part of scintillation detectors.

An insight into this field will be provided for a wider scientific audience and at the same time we will point out some current hot topics. After reviewing the historical issues and fundamental physical processes of the x(γ)-to-visible light transformation occurring in scintillators, practically important material parameters, characteristics, and related measurement principles will be summarized. An overview of selected modern single-crystal and optical ceramic materials will be given. Particular attention will be paid to the relation between the manufacturing technology used and the occurrence of material defects and imperfections. The study and understanding of related trapping states in the forbidden gap and their role in the energy transfer and storage processes in the

50.1 Background	1663
50.1.1 Historical Aspects	1664
50.1.2 Fundamentals	1664
50.1.3 Material Characteristics	1665
50.1.4 Characterization Methods	1668
50.2 Scintillation Materials	1670
50.2.1 Lead Tungstate (PbWO ₄) Single Crystals	1670
50.2.2 Aluminum Perovskite XAlO ₃ :Ce (X = Y, Lu, Y/Lu)-Based Scintillators	1673
50.2.3 Aluminum Garnet X ₃ Al ₅ O ₁₂ :Ce (X = Y, Lu, Y/Lu)-Based Scintillators	1677
50.2.4 Ce-Doped Silicate Single Crystals	1681
50.2.5 Ce-Doped Rare-Earth Halide Single Crystals	1684
50.2.6 Optical Ceramics and Microstructured Materials	1687
50.3 Future Prospects	1689
50.4 Conclusions	1691
References	1691

material will be shown to be of paramount importance for material optimization. Correlated experiments of time-resolved luminescence spectroscopy, wavelength-resolved thermally stimulated luminescence, and electron paramagnetic resonance offer a powerful tool for this purpose. Future prospects and directions for activity in the field will be briefly mentioned as well.

50.1 Background

In the introductory part of this chapter, the history of scintillator material development will be briefly reviewed. Fundamental aspects of x(γ)-ray transformation to ultraviolet/visible photons will be explained and

practical scintillation parameters will be listed, which will aid in the quantitative evaluation of candidate materials. Preparation techniques, occurrence of defects, and their role will be discussed. Finally, experimen-

tal techniques suitable for correlated characterization of physical phenomena in scintillators will be described.

50.1.1 Historical Aspects

In November 1895 Wilhelm Conrad Röntgen noticed the glow of a barium platinocyanide screen placed next to his operating discharge tube, thus discovering a new invisible and penetrating radiation [50.1, 2], named *x-rays* in English or *Röntgen radiation* in some other languages. For *x-ray* registration, simple photographic film was found to be rather inefficient and the search for materials able to convert *x-to-visible* started immediately in order to couple with sensitive photographic-film-based detectors. Pupin introduced CaWO_4 powder, which was used for this purpose for more than 75 years. Together with ZnS -based powders introduced later by Crookes and Regener, CaWO_4 powder is the oldest phosphor material employed for detection of *x-rays*.

In early 1896, the natural radioactivity (spontaneously released high-energy radiation) of uranium was discovered by *Henri Becquerel* [50.3] and followed by pioneering works of *Marie Curie Skłodowska* and her husband *Pierre Curie*, which led to the discovery of the strongly radioactive elements polonium and radium [50.4, 5]. This kind of radiation is commonly named *gamma rays* and its energy is higher than the above-mentioned *x-rays*. Among the various methods for the detection of *gamma radiation*, scintillator-based detectors have been widely employed. It is also interesting to note that, in 1897, the cathode ray tube was invented by Braun, in which the energy of an accel-

erated electron beam is converted into visible light (in a process called *cathodoluminescence*) by a phosphor material. The mechanism of this conversion is quite similar [50.6] to that functioning in the case of *x-ray* conversion. Thus, at the end of the 19th century, two energetic (photon and particle) radiations were available, together with *gamma rays* generated by natural radioactive elements. Their enormous application potential was realized especially during World War I, which stimulated the development of phosphor and scintillator materials necessary for their practical exploitation.

The history of single-crystal scintillators begins in the late 1940s with the introduction of NaI:Tl and CsI:Tl scintillators by *Hofstadter* [50.7, 8]. Since that time a number of material systems have been reported, see Fig. 50.1 and [50.9] for an overview. The above two materials and $\text{Bi}_4\text{Ge}_3\text{O}_{12}$ (BGO), introduced by *Weber* and *Monchamp* [50.10], became widespread scintillator materials and are often used as *standard samples* to evaluate newly developed materials. Within the last 15 years there has been considerable activity in this field, triggered mainly by the needs of high-energy physics and advanced imaging applications in science, medicine, and industry. This has led to a considerable number of articles in the literature dealing mostly with Ce^{3+} -doped materials, due to the fast decay time of the $5d-4f$ radiative transition of the Ce^{3+} center (typically 20–60 ns) and its high quantum efficiency (close to 1) at room temperature (RT). For reviews see [50.11, 12].

Due to the great practical importance and relatively long history of this field, there already exists a large amount of published information on the topic. Let us mention the superb recent survey of luminescent materials by *Blasse* and *Grabmaier* [50.13], the overview of methodology in use in the radiation measurement by *Knoll* [50.14], the monograph devoted to scintillator materials from *Rodnyi* [50.15], and the useful phosphor handbook written by *Shionoya* and *Yen* [50.16]. Numerous featured review papers on phosphor and scintillator materials and their applications exist in the scientific literature as well, for instance [50.17–22].

50.1.2 Fundamentals

Wide-bandgap materials are employed for transformation of the $x(\gamma)$ -ray to ultraviolet/visible photons; see the sketch in Fig. 50.1. Consistent phenomenological descriptions of the scintillation conversion process, efficiency criteria, etc., were developed already in the 1970s [50.23] and later further refined [50.24]. Scintillation conversion is a relatively complicated pro-

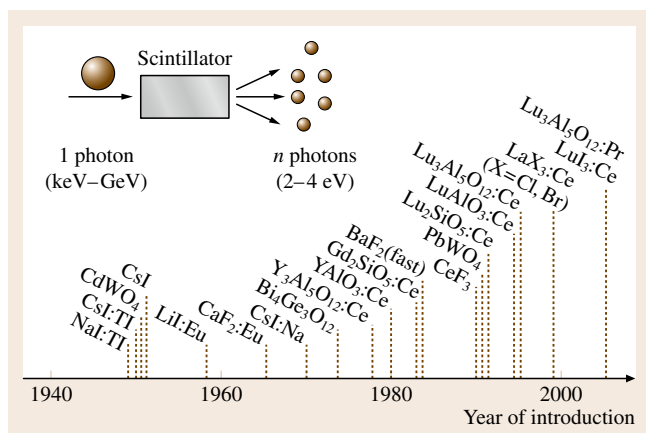


Fig. 50.1 Sketch of the scintillator principle and a timeline of single-crystal scintillators

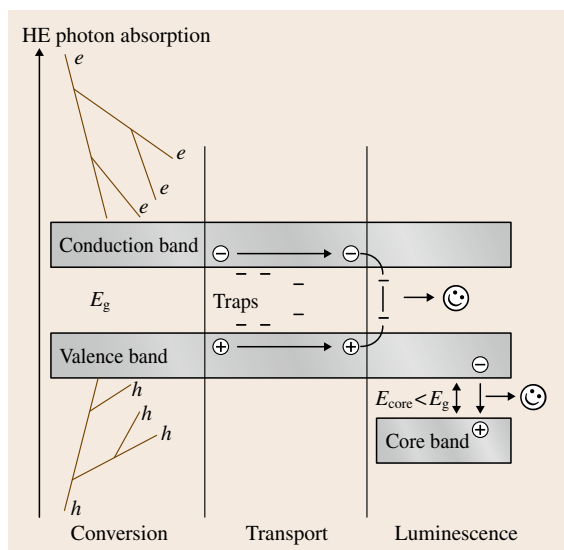


Fig. 50.2 Sketch of scintillator conversion of a high-energy (HE) photon

cess, which can be divided into three consecutive subprocesses: *conversion*, *transport*, and *luminescence* (Fig. 50.2). During the initial conversion a multistep interaction of a high-energy photon with the lattice of the scintillator material occurs through the photoelectric effect, Compton scattering effect, and pair production; for photon energies below 100 keV the first of these is of major importance. Many electron-hole pairs are created and thermalized in the conduction and valence bands, respectively. This first stage is concluded within less than 1 ps. More detailed considerations about the conversion processes have been published in [50.25, 26]. In the transport process electrons and holes (eventually created excitons) migrate through the material, repeated trapping at defects may occur, energy losses are probable due to nonradiative recombinations, etc. Considerable delay in the migration can be introduced due to this charge-carrier recapture at trapping levels in the material forbidden gap. This stage is the least predictable, as point defects, flaws, surfaces, and interfaces can introduce energy levels into the forbidden gap and strongly modify/degrade otherwise high intrinsic scintillation performance. These phenomena are strongly dependent upon manufacturing technology [50.27]. During the final stage, luminescence consists of consecutive trapping of the electron and hole at the luminescent center and their radiative recombination. Nonradiative energy transfer towards the emission center via exciton-based state is also possible. In a particular group of mater-

ials the light generation occurs in radiative transitions between the valence and first core bands (sketched in Fig. 50.2); these are so-called cross-luminescence scintillators [50.15]. The latter mechanism enables very fast, even subnanosecond, scintillation response, which is, however, usually accompanied by much slower exciton-related luminescence. This phenomenon is reported in the literature mainly for BaF₂ and other halide single crystals [50.28]. The physics of luminescent centers is usually well understood due to advanced experimental methods available for their selective and time-resolved study; see, e.g., [50.13, 14].

50.1.3 Material Characteristics

As mentioned above, in the early days of x-ray usage, just phosphor powders in the form of thin screens were employed for their registration, coupled together with a photographic film [50.17]. Later, due to the need to additionally detect and monitor higher-energy x- or γ -rays, scintillator materials were introduced in the form of single crystals (Fig. 50.1).

Despite the fact that the underlying physics is identical, scientific communities working on phosphors and scintillators have been partially separated, mainly due to the different demands of related applications and different preparation technologies employed [50.16–18]. Commonly, materials are called phosphors when used in applications using photon-integrating (steady-state) mode detection, while scintillators are employed in the (x- or γ -ray) photon-counting regime. Today, the separation between phosphor (powders) and scintillator (solid state) materials is somewhat diminished as some materials are used in both detection modes, in powder, bulk or other forms, depending on the application [50.21].

Scintillation Parameters

In the case of scintillators, x(γ)-ray photon counting consists of accumulating the generated light arriving soon after the initial conversion stage is accomplished (Fig. 50.2), as the scintillator works as a high-energy photon counter. Strongly delayed light, e.g., due to retrapping processes mentioned above cannot be technically exploited in the counting mode. Also x(γ)-ray photons of different energy should be resolved for some applications. The most important characteristics of scintillation materials for detectors are as follows:

1. Light yield (LY)
2. X(γ)-ray stopping power

3. Scintillation response – decay time
4. Spectral matching between the scintillator emission spectrum and photodetector
5. Chemical stability and radiation resistance
6. Linearity of light response with the incident $x(\gamma)$ -ray photon energy – energy resolution.

The overall scintillation efficiency of $x(\gamma)$ -ray-to-light conversion is determined by both intrinsic and extrinsic material characteristics. The number of UV/visible photons N_{ph} produced in the scintillation conversion per energy E of incoming $x(\gamma)$ -ray photon can be expressed as [50.23–25]

$$N_{\text{ph}} = [E/(\beta E_g)]SQ, \quad (50.1)$$

where E_g represents the forbidden gap of the material, S and Q are the quantum efficiencies of the transport and luminescence stages, respectively, and β is a phenomenological parameter which is typically found to be 2–3 for most materials. The relative efficiency can then be obtained as

$$\eta = E_{\text{vis}}N_{\text{ph}}/E, \quad (50.2)$$

where E_{vis} is the energy of generated UV/vis photons. The most efficient material among the phosphors and scintillators today is ZnS:Ag with $\eta \approx 0.2$. If we consider that the bandgap of the scintillator materials discussed herein is higher than that of ZnS (≈ 3 eV), then even more efficient materials could be found within those with yet narrower bandgap.

The LY of a scintillator is always an inferior value in terms of (50.1) as it represents the fraction of generated visible photons that arrived at the photodetector within a certain time gate after the high-energy photon absorption; typical values of such a time gate are in practice set between 100 ns and 10 μ s.

The $x(\gamma)$ -ray stopping power (attenuation coefficient) for a material of given thickness depends on its density ρ and its effective atomic number Z_{eff} (for the calculation of Z_{eff} ; see, e.g., [50.18]). Considering only interaction through the photoelectric effect, the stopping power is proportional to $\rho Z_{\text{eff}}^{3-4}$ [50.20].

The kinetics of the light response of a scintillator are governed by the characteristics of the transport and luminescence stages in Fig. 50.2, as they are far slower than the initial conversion. The decay rate of the luminescence center itself is defined by its transition dipole moment from the excited to ground state and can be further enhanced by additional nonradiative quenching or energy transfer processes away from the excited state. Such quenching or energy transfer, however, results in

the decrease of parameter Q in (50.1), and the overall conversion efficiency is also decreased. In the most simple case of exponential decay, the emission intensity $I(t)$ is

$$I(t) \approx \exp(-t/\tau), \quad (50.3)$$

where τ is the decay time. While decay times of the parity and/or spin-forbidden transitions for most rare-earth ions are typically of the order of several tens of μ s up to ms, in the case of allowed 5d–4f transitions of Ce^{3+} and Pr^{3+} the values scale down to tens of nanoseconds, and fully allowed singlet–singlet transition in organic molecules is still about ten times faster [50.29]. The fastest emission transitions are offered by the radiative decay of Wannier excitons in direct-gap semiconductors, where subnanosecond values have been reported for compounds such as ZnO, CuX, CsPbX_3 ($X = \text{Cl}, \text{Br}$), PbI_2 , and HgI_2 [50.30]. The emission rate is enabled by the coherent nature of the exciton state spread over a (large) number of elementary cells [50.31]. However, a serious disadvantage of the latter group of materials is the lower binding energy of their excitonic state, which results in partial ionization and consequently quenching of the exciton-related emission at RT. In bulk materials, further efficiency decrease follows from the small Stokes shift, which leads to noticeable reabsorption losses [50.32].

Due to the aforementioned re trapping processes during the transport stage sketched in Fig. 50.2, the light emission response of a material under high-energy excitation is often further complicated by slower non-exponential components. These processes are currently quantified by the afterglow (sometimes called a persistence), which is defined like a residual light intensity at some time (from a few ms to min) after the excitation is cut off [50.27]. The delayed radiative recombination will contribute to slow scintillator response, lower LY values, and worse signal-to-background ratio [50.33]. In some studies, a parameter α has been introduced to provide a comparative measure for the occurrence of delayed radiative recombination within tens to hundreds of μ s. Due to the repetitive nature of the measurement, they are reflected in the signal level before the rising edge of the decay curve [50.33, 34], as illustrated in Fig. 50.3. In practical evaluation of both phosphors and scintillators, sometimes simple 1/e or 1/10 decay times are provided, which are defined as the time when the light intensity decreases to 1/e or 1/10 of its initial intensity after a flash excitation, or the so-called mean decay time can be calculated [50.22].

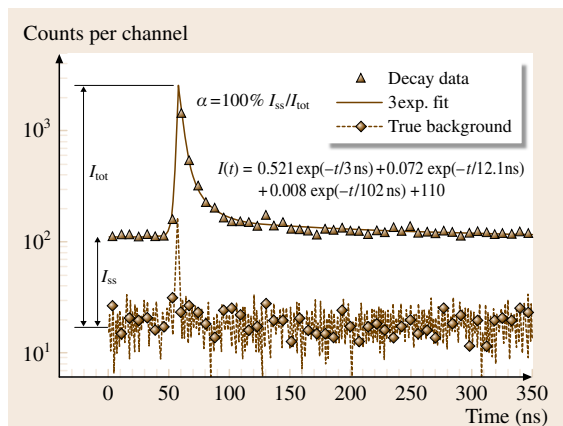


Fig. 50.3 Spectrally unresolved scintillation decay of undoped PbWO_4 , fitted by three exponential functions, $I(t)$, convoluted with the instrumental response (solid line). The true background level is displayed as well. Background enhancement in the repetitive decay measurement is reflected in I_{ss} , the superslow decay component amplitude which comes from preceding excitations and is evaluated using the coefficient α

Spectral matching between the scintillator emission band and the photodetector spectral sensitivity dependence is an obvious requirement. Classical criteria were defined some time ago as near-UV/blue emission is optimum for a photomultiplier detector, while for a photodiode the green–red spectral region was considered best. In recent years enormous development of semiconductor photodetectors has occurred and the latest generation of back-illuminated charge-coupled devices (CCDs) show enhanced sensitivity down to 200 nm.

Chemical stability concerns mainly the hygroscopicity of materials, which in some cases severely limits their long-time operation in the open air (NaI:Tl , CsI:Na , and $\text{LaX}_3\text{:Ce}$ with $\text{X} = \text{Cl, Br}$).

Radiation resistance of materials regards mainly the performance changes and instabilities due to the induced absorption resulting from material irradiation and creation of color centers. It is a matter of concern mainly in bulk scintillation materials [50.22]. In the case of overlap between induced absorption and the emission spectrum, reabsorption losses occur with resulting loss of overall efficiency and LY. An example of this behavior is shown in Fig. 50.4. While this parameter has been considered mainly in research into scintillators for high-energy physics, it should be noted that it has importance also in several medical imaging techniques [50.20] and in the case of industrial flaw de-

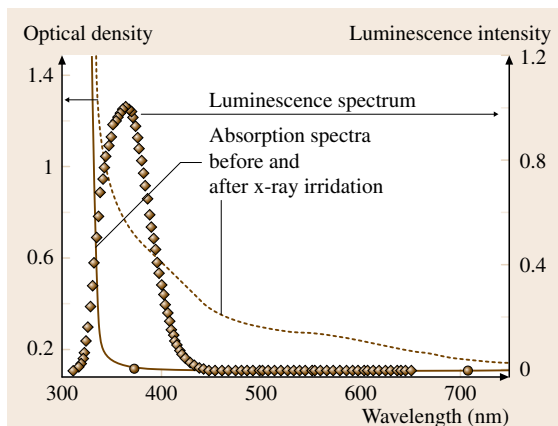


Fig. 50.4 Absorption spectra of 2 cm-thick $\text{YAlO}_3\text{:Ce}^{3+}$ single crystal before and after γ -ray irradiation (^{60}Co , 500 Gy dose) at RT. Overlap of the irradiation-induced absorption with luminescence spectrum of the material is demonstrated

tection or synchrotron beam diagnostics applications as well.

The linearity of light response with incident $x(\gamma)$ -ray photon energy in scintillators can be monitored through the dependence of LY on the incident photon energy. The value for LY is energy dependent, partly due to abrupt changes of the attenuation coefficient around the K and L edges of the elements constituting the compound, but also due to the nonequal conversion efficiency of the photoelectric and Compton scattering effects, which become progressively more important with increasing energy of incoming $x(\gamma)$ -rays. As a result the energy resolution of a scintillator material is degraded with respect to the intrinsic limits based purely on statistical grounds [50.35].

The methodology of radiation detection is described in [50.14]. To quantify the characteristics and parameters described above, the set of usually used routine methods is described in [50.21].

Preparation Technology and Material Defects

Single-crystal scintillators are readily manufactured using crystal growth from the melt, i. e., by Czochralski, Bridgman or similar techniques. Though such techniques are well established and large crystals can be grown [50.36], point or extended defects are present in these artificial materials and often limit their performance. In recent years, the micropulling down growth technique has become frequently reported in the literature [50.37]. Enabling synthesis of circular or shaped

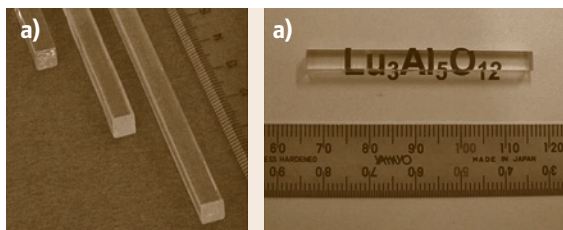


Fig. 50.5a,b Single crystal with square rod shape grown by the micropulling-down method: **(a)** sapphire single crystals and **(b)** LuAG single crystal (after [50.38])

single-crystal fibers of diameter up to several millimeters (Fig. 50.5) grown from the melt and of very good structural quality, this is a fast and economic research tool in the search for new scintillator materials [50.38] or in producing *device-size* crystal elements without the need for extensive cutting and polishing procedures.

The transport stage of scintillator conversion (sketched in Fig. 50.2) was mentioned as a critical and unpredictable period, during which the material performance can be degraded due to defects and flaws arising in the manufacturing process. In all materials, intrinsic point defects arise (e.g., cation and anion vacancies, interstitial atoms) as a result of general thermodynamic conditions and are further accompanied by extrinsic point (accidental impurities) or extended (dislocations, grain and domain interfaces) defects. In many cases, such defects introduce energy levels in the forbidden gap, which can be involved in the capture of migrating charge carriers. In the process of material optimization it is necessary to diminish or deactivate such defects to increase the material performance to its intrinsic/theoretical limit. In the case of accidental impurities or extended structural defects, the solution consists of material purification and optimization of the technological process to improve material purity and structure. However, in case of intrinsic defects, alterna-

tive solutions are pursued such as codoping the material by aliovalent ion(s) that do not participate in the energy transfer and storage processes. Due to the different charge state of the dopant ion (with respect to the original substituted lattice ion) the Coulombic equilibrium of the lattice is changed and this usually induces changes in the concentration of intrinsic point defects. Examples are the optimization of PbWO_4 by doping or codoping with trivalent ions at the Pb^{2+} site [50.22], the codoping with Zr^{4+} in $\text{YAlO}_3\text{:Ce}$ [50.39] or the recent discovery of positive influence of Eu^{2+} codoping in CsI:Tl to reduce its afterglow [50.40].

50.1.4 Characterization Methods

To understand the relation between material defects and the occurrence of traps in the material forbidden gap, their involvement in energy capture and storage, and interconnection with the production technology, a set of specific characterization methods must be used in close coordination with the manufacturing technology. Correlated experiments using time-resolved luminescence spectroscopy, wavelength-resolved thermally stimulated luminescence, and electron spin resonance in an extended temperature interval (10–300 K at least) are very powerful tools for this purpose.

Time-resolved UV/visible emission spectroscopy enables detailed understanding of the luminescence center itself, its intracenter transitions, and eventual nonradiative quenching pathways [50.13, 41]. At the same time its interconnection with the host lattice environment via energy transfer processes can be monitored. Selective pulse excitation in the vacuum ultraviolet (VUV)/UV/visible spectral region completed with x-ray or single-photon gamma-ray excitations is used for this purpose.

Thermally stimulated luminescence (TSL) or thermoluminescence allows the study of point defects giving rise to localized energy levels (traps) in a material forbidden gap. A TSL measurement is a two-stage process, which involves at least one electron trap and one hole trap. A highly simplified scheme is proposed in Fig. 50.6; see [50.42, 43] for a systematic description of these phenomena and measurement schemes. During irradiation at a given temperature (RT or cryogenic) free carriers are trapped at electron or hole centers. A subsequent heating cycle allows the carriers in shallow traps to be released and to recombine radiatively with carriers of the opposite sign stably localized at recombination centers. In the example scheme illustrated, electron traps are emptied while hole traps act as re-

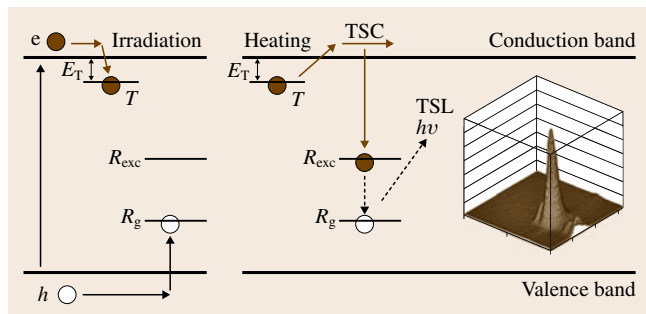


Fig. 50.6 Sketch of the TSL process

combination centers. The emitted light as a function of temperature (glow curve) displays a peak at a characteristic temperature related to the trap structure. If, before recombination, electrons are transferred to the conduction band, a thermally stimulated conductivity (TSC) signal can also be measured. In the simplest first-order kinetics model [50.42, 43] the intensity $I(t)$ of emitted photons is

$$I(T) = sn_0 \exp\left(-\frac{E_T}{k_B T}\right) \times \exp\left[-\frac{s}{\beta} \int_{T_0}^T \exp\left(-\frac{E_T}{k_B T'}\right) dT'\right], \quad (50.4)$$

where n_0 (cm^{-3}) is the number of traps filled by irradiation, s (s^{-1}) is a frequency factor, β is the heating rate, and E_T (eV) is the trap depth. In the same simplified model, if instead of being heated the sample is held at a constant temperature after irradiation, the mean time spent by carriers in the trap before recombination is

$$\tau = \frac{1}{s} \exp\left(\frac{E_T}{k_B T}\right). \quad (50.5)$$

This time governs the phosphorescence which can be spontaneously emitted at constant temperature. According to trap parameters, τ can vary in a very wide interval from ns– μs to hundreds or thousands of years. In suitable cases a detailed analysis of (50.4) or of more general ones by numerical methods [50.42, 43] results in the determination of the trap parameters (E_T , s). The mean time τ at RT can thus be evaluated, allowing direct comparison with slow components in time-resolved scintillation measurements or correlation with LY. Spatial correlation between traps and recombination centers can also sometimes be elucidated. Moreover, more detailed information can be obtained by measuring the wavelength spectrum of the emitted light (see the example in Fig. 50.6). So, whereas temperature resolution can separate different trapping processes, measurement of the TSL emission spectrum can evidence different recombination processes when several centers act simultaneously.

The nature and local structure of the defects, traps, and recombination centers mentioned above can be studied in a detailed manner by electron spin resonance (ESR) and related methods such as electron nuclear double resonance (ENDOR) and optically detected magnetic resonance (ODMR) [50.44, 45]. All of these methods are so-called local methods and exploit the interaction of the magnetic moment of the

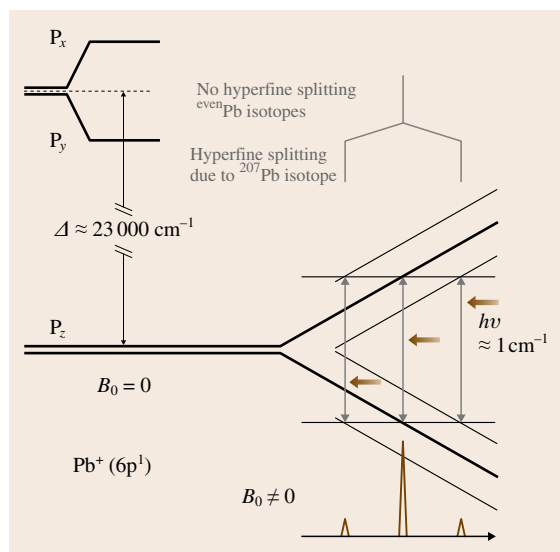


Fig. 50.7 ESR measurement principle

unpaired electron(s) or hole(s) and of the nuclei in a defect with each other and with external magnetic fields.

In a magnetic resonance experiment, the position of the resonance lines reflects both local symmetry and degree of lattice distortion around paramagnetic particle. In addition, the electron–nuclear interaction can give direct evidence for the nuclear (thus also the chemical) species coupled to the paramagnetic particle. This can be illustrated in Fig. 50.7 with an example related to the Pb^+ center in a PbWO_4 crystal [50.46] where an electron is localized at the Pb^+ p_z orbital around an oxygen vacancy. With the application of an external magnetic field B_0 the lowest energy level of Pb^+ splits nearly linearly with field strength. The microwave energy is absorbed by the sample when the frequency of the irradiation is in resonance with the energy splitting. For lead ions with nonzero nuclear spin there is an additional splitting of the energy levels (hyperfine splitting) due to the interaction of electron and nuclear magnetic moments, which gives rise to low-intensity satellites around the main resonance. Detection of hyperfine satellites in many cases allows unambiguous determination of the local structure of defects.

In favorable cases one can thus gain the following information from ESR experiments:

1. Symmetry of a defect
2. Concentration of defects

- 3. Identification of nuclei (atoms) constituting a defect
- 4. Charge state of paramagnetic ion(s) involved
- 5. Change of defect charge state under external influences (irradiation, temperature, etc.)
- 6. Dynamic properties of a defect, e.g., decay or growth of the concentration of defects after the irradiation is switched on (off).

The last item allows the direct determination of the energy of the local electronic level of a defect created by irradiation and thus can be correlated with TSL characteristics.

Further refinement of the electronic structure of absorption or luminescence centers can be obtained using the technique of optically detected ESR via magnetic circular dichroism (MCD) [50.45]. This technique provides a direct correlation between ESR and MCD by the *tagged MCD* method, when one keeps the magnetic field constant on one of the resonance positions and changes the wavelength at which the optical absorption or luminescence is detected. Therefore, ODMR offers the most compelling interrelation between atomic-scale defects and the related optical absorption or luminescence bands.

50.2 Scintillation Materials

Due to the wide variety of applications, about 20 candidate scintillator systems have been systematically studied, their manufacturing industrialized, and most of them also successfully commercialized to be used in scintillation detectors (Fig. 50.1). Parameters of selected materials are given in Table 50.1. In this section, an overview of several material systems introduced and/or intensively researched and optimized within the last 10–15 years will be given. Specifically, manufacturing technology aspects will be mentioned and essential luminescence characteristics will be described together with the materials’ scintillation performance. Further emphasis will be placed on the description of point defects, which are typical for each material group, and to their role in the processes of energy transfer and

capture in a scintillator. Correlated use of several experimental techniques and well-defined samples is vital to gain necessary insight into the underlying complex physical phenomena at the atomistic level. The optimization of scintillation materials toward their intrinsic limits can then be guided by knowledge gained about the limitations in the scintillator conversion and their relation to the manufacturing technology.

50.2.1 Lead Tungstate (PbWO₄) Single Crystals

Single crystals of PbWO₄ (PWO) were the subject of increased interest for scintillation detection in the early 1990s because of their potential use in electromag-

Table 50.1 Survey of characteristics of selected single-crystal scintillators (for those based on rare-earth halides, see Table 50.2). Light yield values are spectrally corrected

Crystal	Density (g/cm ³)	Light yield (phot/MeV)	Dominant scint. decay time (ns)	Emission maximum (nm)	$\Delta E/E$ at 662 keV (%)
CsI:Tl	4.51	61 000	800	550	6.6
NaI:Tl	3.67	41 000	230	410	5.6
BaF ₂ (only crosslumin.)	4.88	1500	0.6–0.8	180–220	7.7
Bi ₄ Ge ₃ O ₁₂	7.1	8600	300	480	9.0
PbWO ₄	8.28	300	3	410	30–40
CdWO ₄	7.9	20 000	5000	495	6.8
YAlO ₃ : Ce	5.6	21 000	20–30	360	4.6
LuAlO ₃ : Ce	8.34	12 000	18	365	8–10
Y ₃ Al ₅ O ₁₂ : Ce	4.56	24 000	90–120	550	7.3
Lu ₃ Al ₅ O ₁₂ : Ce	6.67	12 500	55	530	11
Lu ₃ Al ₅ O ₁₂ : Pr	6.67	19 000	20	308	5–6
Gd ₂ SiO ₅ : Ce	6.7	12 500	60	420	7.8
Lu ₂ SiO ₅ : Ce	7.4	26 000	35	390	7.9

netic calorimeters – the inner parts of huge detectors used in high-energy physics accelerators. The essential luminescence characteristics of **PWO** had already been studied by the 1970s [50.47–49] and the growth of tungstate and molybdate single-crystal systems was also reported in the literature [50.50]. However, the first systematic scintillation-oriented reports appeared in 1992 [50.51, 52], showing the favorable characteristics of **PWO** for the above-mentioned applications.

PWO melts congruently at 1123 °C. It shows an exceptionally high density (8.28 g/cm³) when compared with other scintillators. It exists in several structural modifications, but only the scheelite structure characterized by the tetragonal space group *I41/a* or *C4h* can be obtained using the high-temperature melt-based methods. Both Czochralski [50.53] and Bridgman [50.54] methods have been widely employed, and industrial size crystals up to about 30 cm length and 7–10 cm diameter were grown [50.55, 56]. The stoichiometry of the melt [50.57, 58], atmosphere of the growth, and postgrowth annealing [50.59] were widely studied to optimize the scintillation performance. Once the growth process was optimized, the doping of PbWO₄ by selected trivalent ions was employed as another efficient tool to further increase the figure of merit of this scintillator. See [50.22, 55, 56] for reviews of reported results.

It is well established that the **PWO** emission spectrum consists of two dominant components. The blue component, peaking at ≈ 420 nm (2.9 eV), was ascribed to the regular lattice center, namely the (WO₄)^{2−} group [50.47, 48], and identified later as the self-trapped exciton (**STE**). At higher temperatures, however, this component originates from various localized exciton states, because the **STE** is thermally disintegrated around 150 K [50.60, 61]. The green component, peaking at 480–520 nm (≈ 2.5 eV), was ascribed to a defect center (WO₃) [50.49]. Moreover, a Mo impurity (i. e., the (MoO₄)^{2−} group) was also found to give rise to an emission component at 520 nm [50.62, 63]. Temperature dependencies and temporal characteristics of these two green emissions were studied in detail and compared in a number of different **PWO** crystals [50.64]. Photoluminescence of **PWO** is heavily quenched at **RT**; this is the reason why its scintillation response is dominated by a decay time of a few ns only and its **LY** is very low (Table 50.1).

The decay kinetics of the blue and green emission components has been reported already in [50.47, 48]. Very slow nonexponential components have been observed in the 10^{−6}–10^{−4} s time scale even under selective excitation within the lowest absorption peak

of **PWO** above 180 K [50.65, 66], or in the scintillation decays excited by the 511 keV photons of ²²Na radioisotope [50.34, 67]. The thermally induced decomposition of the **STE** and excited green emission centers above 150 and 200 K, respectively [50.61, 68], establishes an intrinsic equilibrium between the localized and free electron–hole states at higher temperatures. This explains the coexistence of the first- and second-order decay mechanisms due to the prompt and delayed radiative recombination processes, respectively, observed clearly in the decay at **RT** [50.66] (Fig. 50.8). Undesirable slowing of the luminescence response was observed especially in **PWO** samples containing the WO₃ green emission centers [50.64].

Because of the mentioned thermal disintegration of the excited emission centers, any shallow trap states in the **PWO** lattice taking part in carrier capture processes become important. They modify the migration characteristics of free charge carriers through retrapping. Consequently, the speed of their delayed radiation recombination is altered. Monitoring such trap states by **TSL** measurements was reported some time ago [50.69], and more recent measurements confirm the rather rich variety of such shallow trap states in the **PWO** lattice [50.66, 70, 71], which are strongly dependent upon synthesis route. Simultaneous use of **TSL** and **ESR** experiments was applied efficiently to gain understanding about the nature of traps and details about the energy storage in **PWO** lattice. Specifically, electron self-trapping at the (WO₄)^{2−} complex anion was revealed by **ESR** [50.72]. The related paramag-

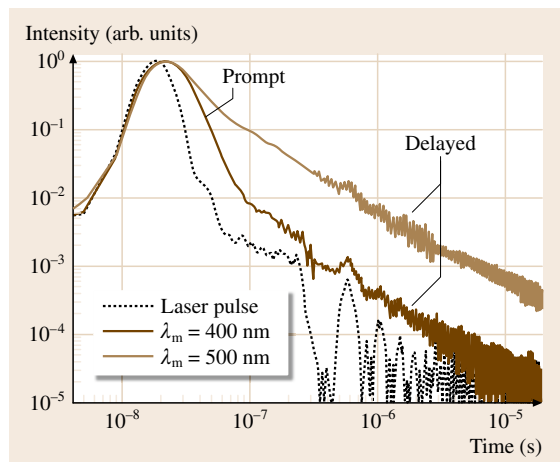


Fig. 50.8 Photoluminescence decay kinetics at **RT** of Mo-doped (160 ppm) **PWO**. $\lambda_{\text{ex}} = 308$ nm (XeCl excimer laser)

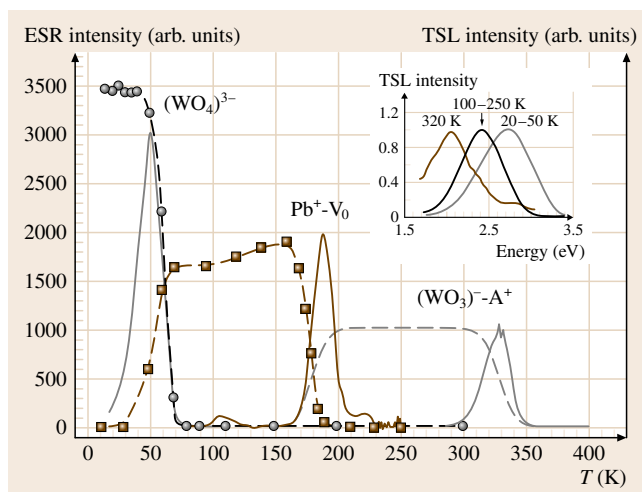


Fig. 50.9 Temperature dependence of ESR (dashed line) and TSL (solid line) signals related to $(\text{WO}_4)^{3-}$, $\text{Pb}^+-\text{V}_\text{O}$, and $(\text{WO}_3)^--\text{A}^+$ electron centers. In the inset the TSL emission spectra within the given temperature intervals are shown

netic $(\text{WO}_4)^{3-}$ center can survive up to about 50 K and its thermal disintegration is accompanied by a TSL peak (Fig. 50.9) [50.73]. In undoped PbWO_4 , a fraction of released electrons is stored in deeper $\text{Pb}^+-\text{V}_\text{O}$ traps [50.46, 74, 75], i.e., at the Pb^+ p-orbital around an isolated oxygen vacancy V_O , creating an F^+ center. This center is stable up to about 190 K and during its thermal disintegration again a TSL peak appears (Fig. 50.9). Similar to the situation at ≈ 50 K, a fraction of the released electrons are stored at still deeper traps, namely the oxygen-deficient $(\text{WO}_3)^--\text{A}^+$ complex (A^+ is a monovalent impurity or possibly a cation vacancy at a Pb position). Thermal destruction of this center occurs around 320–330 K and is again accompanied by a TSL peak [50.76]. It is worth noting that TSL emission spectra of the peaks at ≈ 50 , 190, and 320 K show maxima at different energies (inset of Fig. 50.9), pointing to the existence of three different hole traps. However, no detailed information about them could be obtained since no related hole centers have been detected by ESR thus far.

A significant change in the concentration of TSL-monitored trapping states was observed in PWO samples doped with large and stable trivalent A^{3+} ions ($\text{A}^{3+} = \text{La}^{3+}$, Y^{3+} , Lu^{3+} , and Gd^{3+}) [50.77–79]. Similar effects were obtained by using any of these dopants. Traps and related TSL peaks above 150 K were practically eliminated. La doping completely removes electron traps associated with oxygen vacancies and

stabilizes the self-trapped electron in its vicinity up to about 90–100 K [50.80]. New insight into the effect of La doping was recently gained in the study of doubly doped $\text{PbWO}_4:\text{Mo},\text{La}$ [50.81]. The Mo^{6+} ion is an efficient electron trap and the resulting $(\text{MoO}_4)^{3-}$ center is stable up to about 240–250 K [50.82]. Codoping with La resulted in a considerable increase of $(\text{MoO}_4)^{3-}$ center concentration, which was detected even without prior irradiation of the samples. Moreover, electrical conductivity above RT appeared and is governed by the same activation energy as that obtained from thermally induced disintegration of the $(\text{MoO}_4)^{3-}$ center. From these measurements, it was concluded that La^{3+} at Pb^{2+} sites introduces free electrons in the PbWO_4 conduction band, i.e., La^{3+} behaves as a donor impurity in a semiconductor. At the same time, a noticeable decrease of TSL signal related to $(\text{MoO}_4)^{3-}$ thermal disintegration around 240–250 K was found in doubly doped $\text{PbWO}_4:\text{Mo},\text{Y}$ [50.83]. To explain the increase of electron centers observed by ESR and the decrease of related TSL signal in trivalent-ion-codoped $\text{PbWO}_4:\text{Mo}$, the suppression of related hole traps must be considered. Hence, the effect of trivalent-ion doping has been understood, consisting of simultaneous suppression of oxygen vacancies and some of the hole traps. Furthermore, free excess electrons generated in the conduction band can fill electron traps of any kind. Such effects lower the capacity of the PbWO_4 lattice to trap and store generated charge carriers after x- or γ -irradiation. Consistently, the faster scintillation and photoluminescence decays are obtained [50.77, 84] and also the transmission [50.77, 84] and especially radiation resistance [50.78, 85] characteristics are noticeably improved (Fig. 50.10). Theoretical calculations established the energy levels of the defects based especially on vacancies and clarified further the effect of the La doping [50.86]. They are consistent with the experimental findings with the exception of the $\text{Pb}^+-\text{V}_\text{O}$ center, which was not found in the calculations.

For heavily A^{3+} -doped samples (above a few hundred molar ppm in the crystal), a decrease of LY was observed; this was explained by the possible creation of new nonradiative recombination traps related to La dimers/small aggregates [50.77]. Surprisingly, a very large concentration of trivalent ions could be accommodated in the PWO structure (even more than 10% of La) without significant loss of transmittance or radiation hardness. Due to extremely low LY, such heavily A^{3+} -doped PWO-based scintillators were proposed as a Cherenkov radiator [50.87]. Coulombic compensation of the excess charge of trivalent ions in such samples

was proposed as a self-compensation process in which a part of the La ions can reside at the W site [50.88]. Introduction of an interstitial oxygen was considered by the same authors as well [50.89]. Recent theoretical calculations favor the latter possibility [50.90].

Radiation damage processes and the nature of related defects were of special interest, because the resulting loss of transmission, instability of LY or even induced changes in the scintillation mechanism can strictly limit the applicability of PWO as a scintillator material in the severe radiation environments of planned detectors. Related deep traps must be stable enough at RT so that they are reflected in TSL glow curves above RT [50.91]. An attempt was made to decompose the induced absorption spectrum (inset of Fig. 50.10, curve *a*) into a sum of Gaussians, which should belong to particular color centers [50.91]. Based on correlated decomposition of irradiation-induced, high-temperature-annealing-induced, and as-grown undoped PWO absorption spectra, four bands were identified, peaking at 3.5, 2.9, 2.4, and 1.8 eV. Two components were found to contribute to the 3.5 eV band [50.92]. Ascription of these and other bands, extracted from absorption spectra, was attempted by several research groups [50.90–95]. However, none of these suggestions was supported by more conclusive methods such as ESR. An interesting suggestion about the physical origin of coloration of PbWO₄ was recently formulated [50.96], taking into account the variation of

tungsten valence in oxygen-deficient clusters, which can be created or destroyed by an appropriate post-growth annealing. In general, deep traps associated with radiation-damage-induced defects are expected to be rather complex, taking into account that the (WO₃)[−]-A⁺ electron trap responsible for the 300–330 K TSL peaks includes an oxygen vacancy and another defect nearby [50.76].

Recently, an effort has been made to increase the LY of PbWO₄ [50.97], which could allow its application outside of high-energy physics. Such a possibility is worth attempting since the thermal quenching of PbWO₄ emission is not due to intracenter quenching, but rather due to a nonradiative electron–hole recombination over the material bandgap [50.68] or around other defects [50.60]. If such thermally released electrons and holes can be efficiently and quickly radiatively recombined at an additional center, integral scintillation efficiency would rise. Doubly doped crystals (Mo, A³⁺) were reported, in which the LY value was increased about 3–4 times with respect to undoped material, while scintillation response was kept reasonably fast [50.98–100]. The effect of PbWO₄ nonstoichiometry on the LY value was studied as well [50.101]. Recently, another strategy was introduced, namely fluorine doping [50.102]. A common problem in all of these studies is that additional emission centers frequently give rise to additional shallow traps, which delay radiative recombination and keep the LY below ≈ 10% of BGO even if the integral scintillation efficiency could be increased up to a level comparable to BGO, i.e., about 25 times that of undoped PbWO₄ [50.103].

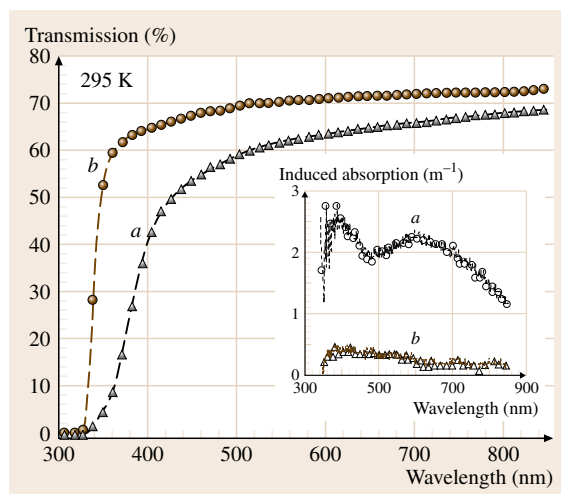


Fig. 50.10 Initial transmission and irradiation (⁶⁰Co radioisotope, 10 Gy dose) induced absorption of equivalently grown undoped (*a*) and La-doped (*b*) PbWO₄ single crystals (after [50.78])

50.2.2 Aluminum Perovskite XAlO₃:Ce (X = Y, Lu, Y/Lu)-Based Scintillators

Ce doping has provided scintillators with the highest figure of merit in this group of materials so far. Fast and efficient luminescence and scintillation is achieved due to the parity- and spin-allowed 5d–4f transition of Ce³⁺, which gives rise to the emission band at 360–370 nm (Fig. 50.11). Moreover, it is free from thermally induced nonradiative quenching at least up to 500 K. Luminescence of YAlO₃:Ce (YAP:Ce) was reported by Weber [50.104] and favorable properties of this material for scintillation applications were described later by Takeda et al. [50.105] and Atrata et al. [50.106]. A review paper devoted also to this group of scintillation materials has been published recently [50.22, 107].

Yttrium aluminate YAlO₃ has an orthorhombically distorted perovskite structure with space group *Pbnm*.

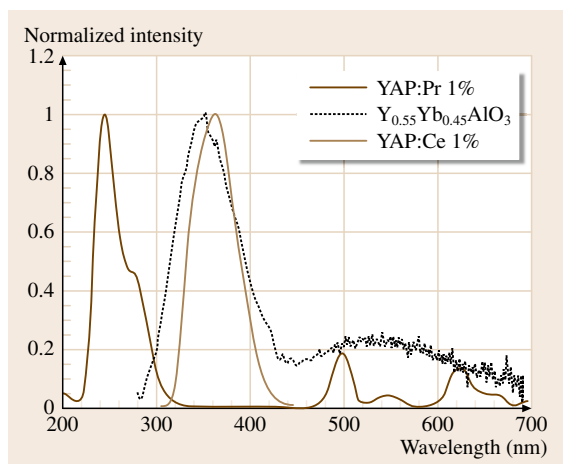


Fig. 50.11 Normalized radioluminescence spectra of doped YAlO_3 (see the legend) at RT

Crystals are grown from nonstoichiometric melt at temperatures of 1835–1875 °C [50.108], in which the 1 : 1 melt composition ($\text{Y}_2\text{O}_3:\text{Al}_2\text{O}_3$) is stable. In the case of LuAP this temperature region is shifted up by about 80 K. The nearly congruent growth of aluminum perovskites from high-temperature melt is further troubled by twin formation [50.109, 110]. Presence of light scattering centers was also reported [50.111]. The growth process is usually performed in Ar, Ar + H_2 or N_2 atmospheres or even under vacuum [50.108–112]. Optimized $\text{YAP}:\text{Ce}$ single crystals with Ce concentration up to 0.6 at.% in the crystal can be grown in boules up to about \varnothing 5 cm \times 15 cm in length in CRYTUR Ltd., Turnov, Czech Republic (Fig. 50.12). The boules of



Fig. 50.12 Zr-codoped $\text{YAP}:\text{Ce}$ single crystal (45 mm diameter and 125 mm length)

$\text{LuAP}:\text{Ce}$ grown by the Bridgman method [50.113] approach dimensions of about \varnothing 1.2 cm \times 6 cm in length with similar Ce concentrations. Due to the difficulties associated with the growth of pure LuAP single crystals (instability of perovskite phase and frequent appearance of the garnet one), attempts were made to grow mixed $\text{Y}_{1-x}\text{Lu}_x\text{AP}:\text{Ce}$ crystals ($x \leq 0.3$) [50.114]. Mixed $\text{Y}_{1-x}\text{Lu}_x\text{AP}:\text{Ce}$ ($0.15 \leq x \leq 0.8$) crystals were grown also by vertical Bridgman method [50.115]. Mixed (Y/Lu) $\text{AP}:\text{Ce}$ crystal growths, $x = 0.6$ –0.7, using Czochralski method, have been already mastered by a few industrial producers [50.116].

Five bands in the 180–300 nm region were clearly distinguished in the excitation spectrum [50.117] of the 370 nm emission of Ce^{3+} , in good agreement with the expected splitting of the 5d Ce^{3+} excited-state level due to the low Y^{3+} site symmetry. The 370 nm emission band shows a single-exponential fast photoluminescence decay (about 17 ns decay time) and slightly slower scintillation decay governed by decay time between 22 and 38 ns followed by a minor slow component of a few hundred ns [50.118, 119]. The latter component can be explained by delayed recombination of charge carriers at Ce^{3+} centers (similar to the recombination decay components in PbWO_4). The scintillation response of pure $\text{LuAP}:\text{Ce}$ is dominated ($\approx 80\%$ of the overall intensity) by the fast decay component of about 17–19 ns, and the rest of the intensity is released with a decay time of 160–180 ns. In the case of Lu-rich mixed ($x = 0.65$ –0.7) crystals, the intensity of the fast component is lowered considerably (40–54%) and accordingly the second slower component of about 190 ns decay time is more intense [50.116]. The origin of this degrading phenomenon has not yet been understood. High LY of $\text{YAP}:\text{Ce}$, up to 20 000–22 000 phot/MeV, was reported by several laboratories [50.120] (Table 50.1), decreasing with the admixture of Lu down to ≈ 12 000 phot/MeV in $\text{LuAP}:\text{Ce}$. In the process of energy transfer towards the Ce emission centers the excitonic mechanism was evidenced [50.117], but sequential capture of holes and electrons at Ce centers seems to be more important due to low efficiency of lattice exciton creation by hot electrons in the process of initial energy conversion in the YAP and LuAP lattices [50.121].

Doping aluminum perovskites by Pr^{3+} and Yb^{3+} was accomplished as well to obtain scintillators with still faster response with respect to the Ce^{3+} -doped ones; related radioluminescence spectra are shown in Fig. 50.11. The 5d–4f transition of Pr^{3+} provides a ≈ 1.5 eV high energy shifted and faster emission

with respect to the Ce^{3+} center in the host matrices with medium–strong crystal field, where the lowest 5d state is shifted below the $^1\text{S}_0$ level of Pr^{3+} . Both YAP:Pr [50.122] and LuAP:Pr [50.123] showed at least two times shorter dominant decay time with respect to the Ce-doped hosts. However, the reported LY is 2–4 times lower, so that their figure of merit is significantly degraded. The reason for the latter phenomenon is not clear as the RT quantum efficiency of Pr^{3+} luminescence center in YAP was found to be close to unity [50.124]. Cross-relaxation among Pr^{3+} ions [50.123] and lower efficiency of the energy transfer from the host to Pr^{3+} [50.124] were tentatively proposed as explanations.

Yb^{3+} doping gives rise to the charge transfer luminescence extending over near-UV and visible regions in a YAP host (Fig. 50.11). This luminescence mechanism became of renewed interest, as in the case of Yb^{3+} this kind of radiative transition is parity and spin allowed [50.125, 126] and the luminescence lifetime is typically below 100 ns. However, in most hosts it shows onset of thermal quenching well below RT, so that relatively low radioluminescence intensity and extremely fast, subnanosecond scintillation decay have been reported in $\text{Y}_{1-x}\text{Yb}_x\text{AlO}_3$ [50.127]. The highest radioluminescence intensity is obtained for $x = 0.3\text{--}0.4$. Favorably high Yb concentration is allowed due to limited concentration quenching in this system [50.128].

If one compares the results from different laboratories, the Ce^{3+} emission data in the YAP and LuYAP matrices exhibit slightly different shapes and position shifts. Several inequivalent Ce^{3+} positions were found also in ESR measurements [50.129]. The presence of stable Ce^{4+} ions is indicated in [50.130], and Ce^{4+} -related absorption transitions are ascribed to the parasitic absorption overlaying the region of the Ce^{3+} emission. Detailed studies of the temperature dependence of the LY below RT indicated the importance of shallow traps in the process of energy transfer in the YAP matrix; correlations between LY, TSL intensity, and scintillation decay were found and explained by a model based on the participation of trapping state(s) in the processes of electron transfer to trapped holes at Ce^{3+} sites [50.131]. However, no interpretation of the nature of the defects involved was proposed. Deeper electron traps related to TSL peaks at about 50 °C, 100–130 °C, 175 °C, and 225 °C in YAP:Ce and (Lu/Y)AP:Ce were ascribed to oxygen-vacancy-related defects; a thermally assisted tunneling process with the nearby lying Ce^{4+} hole center could

explain the calculated trap depth and frequency factors of these traps [50.132]. It is worth noting that in an early study [50.133] antisite defects (Y at Al site and vice versa) were considered for the stabilization of F or O^- centers, and their relation to various absorption bands in the 290–760 nm region was hypothetically assumed. The occurrence of color centers is a frequent problem in YAP and there are numerous studies in the literature dealing with this problem, [50.134, and references therein]. The induced absorption after γ -irradiation (radiation damage) of YAP:Ce was also reported [50.135] (Fig. 50.4), and bands peaking at 2.2–2.9 eV, ≈ 3.3 eV, and ≈ 3.89 eV were obtained by decomposition of the induced absorption spectra into Gaussian components. Deviation from stoichiometry, presence of transition-metal and rare-earth impurity ions, and temperature conditions during growth process strongly influence the presence and concentration of defects and color centers in as-grown crystals. Postgrowth annealing is frequently employed to decrease parasitic absorptions of the crystals in UV/visible spectral regions.

Literature information on intrinsic paramagnetic active defects in YAP crystals is rather limited. The autolocalization of holes in the form of O^- -bound small polarons was evidenced in YAP some time ago using ESR and optical techniques [50.136]. Recent ESR measurements of lightly (50 ppm) Ce-doped YAP have shown at least four different O^- center configurations caused by site inequivalence of the oxygen ions in the lattice. They are progressively transforming within themselves with increasing temperature as shown in Fig. 50.13. At the same time thermally induced decay

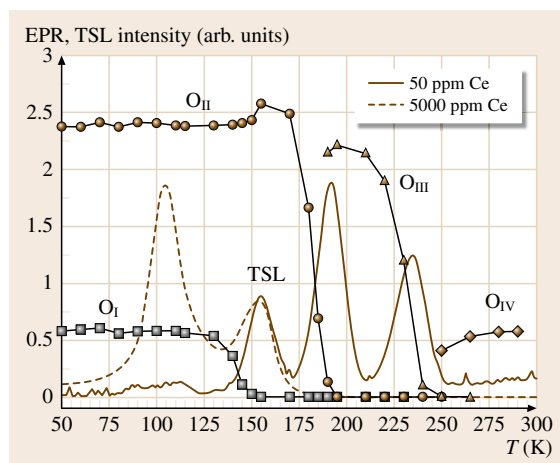


Fig. 50.13 Correlation between EPR intensity of O^- centers and corresponding TSL peaks in YAP crystals

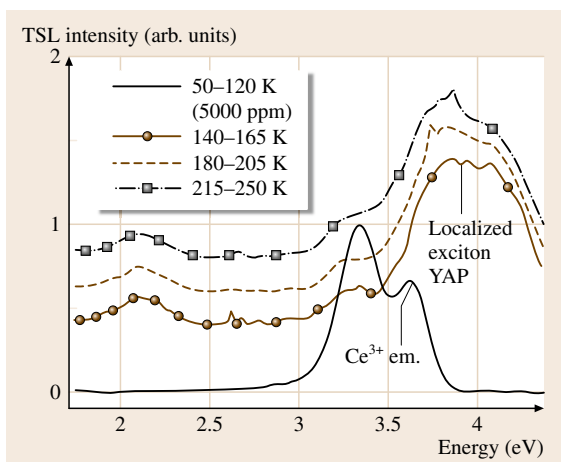


Fig. 50.14 TSL spectra in the temperature range indicated in the legend and related to glow curves in Fig. 50.6. Curves for temperatures above 140 K refer to 50 ppm Ce. Curves are vertically shifted for clarity

of each O^- center is accompanied by a TSL peak. This means that, when a hole is liberated from an O^- center, it is either captured at a deeper hole trap or migrates until a localized electron is met and such electron–hole pair radiatively recombines giving rise to a TSL glow curve peak.

The site of the just mentioned radiative-recombination process was revealed from TSL emission spectra within the glow curve peaks (Fig. 50.14). Dominant glow curve peaks related to O_I – O_{III} annihilation show the emission at 3.5–4.0 eV ascribed to a localized exciton luminescence. Localization of excitons was assumed to be close to F or F^+ centers [50.137]. In undoped YAP, also time-resolved luminescence of F^+ and F centers themselves was reported at 350 nm and 440 nm, respectively [50.138].

The above hypothesis is further confirmed by finding F_A^+ centers in the same sample by ESR measurements [50.139]. They are also found in several configurations with gradually increasing stability within the range 200–300 K, which enables the radiative recombination suggested from TSL. The F_A^+ centers are attributed to the charged oxygen vacancy near the antisite yttrium ion where, however, electron density is essentially shifted to this antisite ion. Such a defect can be described to the Al^{3+} – V_O – $Y^{2+}(Al)$ complex. In a heavily Ce-doped sample, only the self-trapped hole O_I center survives and holes are dominantly trapped at Ce^{3+} ions, as evidenced in TSL spectra (Fig. 50.14). The TSL glow curve is dominated by another electron-

trap-related peak at 100–105 K, the origin of which is still unknown. Based on the recent finding in YAG:Ce that the TSL peak at 92 K is related to an electron trap around the Y_{Al} antisite defect [50.140] and taking into account the structural and chemical similarity of such a defect in both aluminum perovskite and garnet structure ($(Y_{Al}O_6)^{9-}$ octahedron) one can tentatively suggest a similar interpretation for the 100–105 K peak in YAP:Ce.

Impurity-related centers can come either from the raw materials or due to the particular synthesis technology used. In the former case, mainly iron [50.108] and titanium ions in YAP and furthermore Yb ions in (Lu/Y)AP were evidenced by ESR. In the latter case molybdenum ions were evidenced coming from the crucible used for the growth of bulk crystals [50.108, 112]. Mo^{3+} centers in YAP were described in detail with the help of ESR [50.141]. Being transition-metal elements with easily variable charge state they can be ionized and/or serve as nonradiative recombination centers.

The above-described color centers and impurity ions in YAP crystals give rise to local electronic levels in the forbidden gap, as presented in Fig. 50.15. The Ce^{3+} impurity ion is exploited as a fast and efficient radiative recombination center in YAP:Ce scintillator. In parallel, Mo and Ti impurities serve as ionization centers which produce free electrons and holes under irradiation with energy lower than the bandgap. The position of the Ti^{3+} level is about 4.2 eV above the valence band (VB) edge [50.142]. The Mo^{4+} level is somewhat lower as 330 nm UV irradiation is already enough to excite electrons from the VB to the Mo^{4+} ions, which become Mo^{3+} . The ionization energy of Ce^{3+} ions is at least 5.5 eV [50.143]. Migrating holes can be trapped or self-trapped by the O sublattice in the form of O^- -like

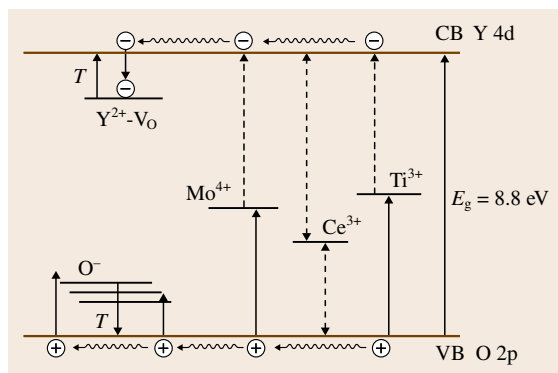


Fig. 50.15 scheme of local electronic levels of different defects in the forbidden gap of YAP

centers. The Y antisite ions give rise to the $Y_{Al}^{2+}-V_O$ defects acting as electron traps.

All the above-mentioned possibilities for hole and electron trapping can deteriorate scintillation performance of the crystal because they compete with or delay the radiative recombination at Ce^{3+} ions. In $YAP:Ce$, it has been proposed [50.131] that only 25% of the electrons generated by the ionizing photon/particle are transferred promptly to the Ce ion. The rest become trapped in three discrete sites. Consequently, there is considerable room for material optimization, particularly if the existence of these traps can be avoided. Such attempts have already been made by codoping with an aliovalent ion, which can change the Coulombic equilibrium and therefore the overall defect concentrations. Namely, Zr^{4+} codoping was used in $YAP:Ce$ [50.39, 144], which resulted in a dramatic decrease of deep oxygen-vacancy-related electron traps monitored by TSL above RT (Fig. 50.16). It is worth noting that recent atomistic calculations of Stanek et al. [50.145] dealt systematically with defect reaction energies in rare-earth aluminum perovskites and the above effect was explained considering the Frenkel recombination of Zr-induced oxygen interstitials with oxygen vacancies. Moreover, it has been shown [50.145, 146] that the relative importance of antisite and Schottky (vacancy) defects varies strongly with the cation size. While Schottky defects are of major importance in YAP , antisite defects might play a major role in $LuAP$. Such

a difference may be of some importance to explain the decreasing LY in $LuAP:Ce$. Combination of mentioned computer simulations and systematic experiments together with electronic structure calculations can provide a tool for deeper understanding of these scintillation materials and the possible technological approaches leading to their optimization.

50.2.3 Aluminum Garnet $X_3Al_5O_{12}:Ce$ ($X = Y, Lu, Y/Lu$)-Based Scintillators

Single crystals of $Y_3Al_5O_{12}$ (YAG) were among the first oxide materials grown by Czochralski technique during the 1960s [50.147]. Their development was stimulated mainly by the application for solid-state (Nd-doped) lasers, but soon the potential of Ce^{3+} -doped YAG single crystal for fast scintillators was realized as well [50.148]. The first comprehensive description of $YAG:Ce$ scintillator characteristics was reported by Moszynski et al. [50.149], who included this material among the high-figure-of-merit oxide scintillators. Isostructural $LuAG$ has a higher density (6.67 g/cm^3) than YAG (4.56 g/cm^3), which is advantageous in the case of hard x- and γ -ray detection (see the definition of stopping power in Sect. 50.1). $LuAG:Ce$ scintillator became of interest relatively recently [50.150, 151]. An early study of the Ce^{3+} and Pr^{3+} photoluminescence decay kinetics in YAG host [50.152] revealed the absence of nonradiative thermal quenching up to about 550 and 250 K, respectively. Consequently, at RT the 5d–4f transition of Ce^{3+} center can be exploited for fast and efficient scintillation in both YAG and $LuAG$ matrices.

The growth of YAG or $LuAG$ crystals by Czochralski technique provides large and high-quality crystals (Fig. 50.17), but also the micropulling down technique has been successful in growing single-crystal rods of comparable structural quality (Fig. 50.5). The former is usually accomplished using either an iridium crucible in an inert atmosphere (N_2) with small addition of oxygen [50.153], or a molybdenum crucible in a reducing ($Ar + H_2$) atmosphere [50.154]. Isostructural cubic garnet structures of YAG and $LuAG$ form a solid solution and any intermediate mixed composition can be grown. The solidification points of mixed compositions range between 2010°C ($LuAG$) and 1930°C (YAG) [50.153]. The garnet structure appears very flexible for cation substitution; such substitution was used to prepare materials with tailored lattice constants [50.155] and can, in principle, be used for the preparation of highly substituted crystals with homo-

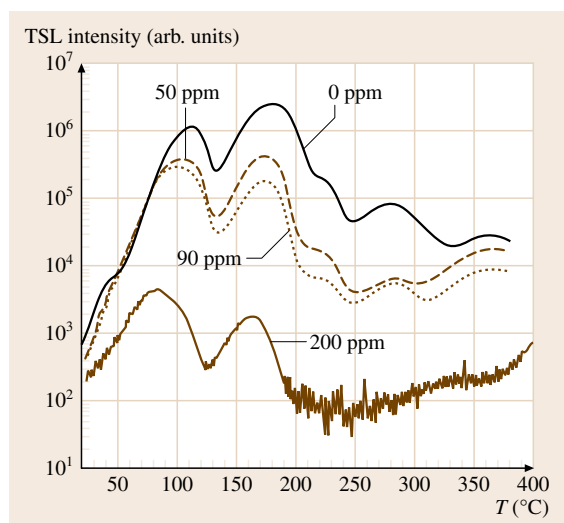


Fig. 50.16 TSL glow curves of $YAP:Ce$ after irradiation at RT. Concentration of Zr in the sample is indicated on the curves, see also [50.39, 144]

geneous composition. However, at the same time this readiness of solid-solution formation in the garnet structure points to a relative ease of compositional defect formation. Ce^{3+} predominantly substitutes for the Y (Lu) cation, but a small fraction can be found at the anti-site (Al) position as well. The segregation coefficient of Ce^{3+} in YAG and especially in LuAG host is relatively small (less than 0.1), which is an obstacle to obtaining homogeneous doping profile in large crystals.

Due to high crystal field at the dodecahedral Y (Lu) site, the 5d states of Ce^{3+} are shifted to lower energy in garnet with respect to perovskite host. The lowest $4f-5d_1$ absorption and emission bands peak around 450–460 nm and in the green–yellow part of the spectra, respectively (Fig. 50.18). With the help of photoionization threshold and excited-state absorption measurements [50.156] it was established that the lowest $5d_1$ relaxed state is placed about 1.2 eV below the conduction band of YAG, which is enough to completely inhibit undesired ionization of Ce^{3+} relaxed excited state around RT. In a LuAG host, Ce^{3+} emission is high energy shifted by about 0.1 eV with respect to YAG, pointing to a somewhat weaker crystalline field and/or covalent bonding at the Lu site. Consistently, a slightly shorter Ce^{3+} photoluminescence decay time (≈ 55 ns) is obtained at RT in LuAG with respect to YAG (≈ 62 ns) host.

While the steady-state scintillator efficiency (radio-luminescence intensity) of both YAG:Ce and LuAG:Ce of high (5–6N) purity can reach up to 700–800% of that of BGO [50.33, 157], their LY is considerably lower. Namely, values up to 300 and 150% of

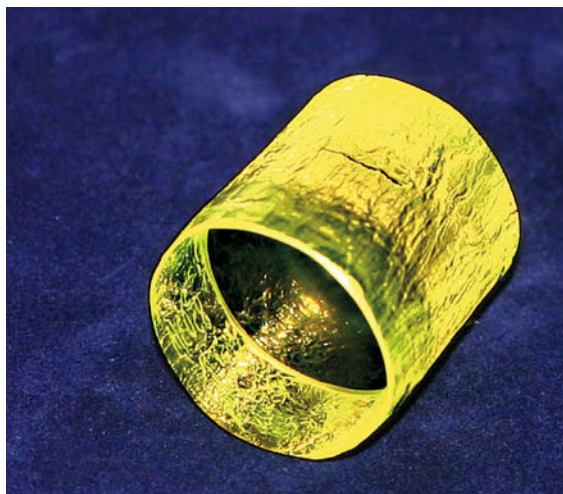


Fig. 50.17 LuAG:Ce crystal, $\varnothing 20 \times 30$ mm

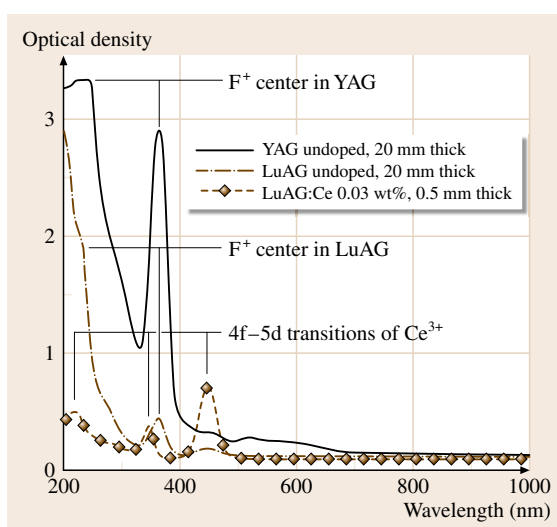


Fig. 50.18 Absorption spectra of YAG and LuAG crystals at RT

BGO were reported for YAG:Ce and LuAG:Ce, respectively [50.120]. This points to a considerable amount of *slow scintillation light* in both materials. Very slow components are reflected in the *increased background* before the rising edge of the LuAG:Ce scintillation decay, which can be quantified by the already mentioned α coefficient (Fig. 50.3). It is worth noting that the *background* level is systematically higher in LuAG:Ce than in YAG:Ce of comparable doping level, quality, and purity [50.33] in agreement with the trend in their LY values. The scintillation decay of LuAG:Ce can be approximated by a two-exponential fit with decay times of about 55–60 ns and 300–1000 ns. A recent study of LuAG:Ce [50.158] has shown that the consecutive capture of a hole and an electron at Ce^{3+} centers is the dominant energy transfer pathway in the scintillation mechanism. More than 65% of the light in the LuAG:Ce scintillation decay is released in the above-mentioned slower decay component, which appears due to delayed radiative recombination at Ce^{3+} ions. The occurrence of slow decay components over an extended time scale suggests the existence of several traps with different thermal depths, which participate in charge-carrier trapping processes.

Scintillation decay characteristics of Pr^{3+} -doped YAG were reported for the first time in 1992 [50.122] and became of renewed interest recently [50.159] when, despite partially quenched emission of the Pr^{3+} center itself, spectrally uncorrected LY values of about 300% with respect to BGO and leading to a scintillation decay

component below 20 ns were measured in high-quality single crystals. Similar to Ce^{3+} , the $5d_1$ – $4f$ emission of Pr^{3+} at the dodecahedral Y site is low energy shifted with respect to perovskite host and shows the double peak band at $318 + 375$ nm. Pr^{3+} -doped LuAG scintillator characteristics were reported only very recently [50.160]. The $5d_1$ – $4f$ emission of Pr^{3+} is high energy shifted by about 0.12 eV and the onset of thermal quenching is shifted to noticeably higher temperatures (above 350 K) with respect to YAG:Pr. At RT, the photoluminescence and leading scintillation decay times are very similar (20 ns). The integral of the radioluminescence spectra in LuAG:Pr is 1.4–1.5 times higher than in LuAG:Ce, suggesting higher intrinsic scintillation efficiency. A spectrally uncorrected LY obtained in optimized Czochralski-grown crystal exceeds 300% that of BGO [50.161]. Another advantage consists in the negligible intensity of slower $4f$ – $4f$ emission lines in radioluminescence spectra in the 450–700 nm range for any Pr concentration, contrary to the situation found in YAG, YAP or LuAP matrices [50.122, 159, 160].

Among the point defects and extrinsic impurities studied in aluminum garnets it is worth mentioning the so-called *antisite* defects, F and F^+ centers (two and one electron in an oxygen vacancy, respectively), and iron impurity ions. Furthermore, recently in LuAG single crystals, the presence of Yb^{3+} was reported. Due to the variable charge state of iron ($\text{Fe}^{2+} \leftrightarrow \text{Fe}^{3+}$) it can easily participate in charge-carrier capture and give rise to a competing energy loss pathway. At higher concentrations (above 0.1%) Fe^{3+} is evidenced by a characteristic absorption doublet at 407 + 415 nm and a luminescence band around 800 nm [50.162]. At trace Fe concentrations, the lattice distortions due to embedding Fe^{3+} at the Al site were studied in detail by ESR. Presence of Fe^{3+} in the YAG lattice is also manifested through the charge transfer transition resulting in a wide absorption band at 255 nm [50.163] (Fig. 50.18). Also a Yb^{3+} ion can introduce additional nonradiative losses in LuAG:Ce scintillator as its charge transfer luminescence (similar in shape and about 0.14 eV high energy shifted with respect to that of YAP:Yb; Fig. 50.11) is heavily quenched at RT [50.164]. Fe and Yb ions come from the Al_2O_3 and Lu_2O_3 raw materials, and can be effectively detected by ESR [50.163, 165]. The paramagnetic Ce^{3+} ion in YAG was studied via ESR as early as the 1960s [50.166]. However, only very recently has the occurrence of Ce^{3+} ions at Al sites and possible space correlation between the regular Ce_{Lu} and Lu_{Al} antisite defect been reported in LuAG host [50.167, 168].

Oxygen-vacancy-based color centers are typical defects in aluminum garnets, because of the inert or even reducing atmosphere used during crystal growth. Such atmosphere is necessary to suppress the oxidation of the Ce^{3+} ion, which can decrease scintillator performance. Oxygen vacancies form deep electron traps; they can also effectively lower the scintillation efficiency of Ce-doped aluminum garnets. F^+ centers in YAG host show absorption bands at 235 and 300 nm (Fig. 50.18) and under excitation within these bands, F^+ luminescence was reported at ≈ 400 nm. Evaluation of polarization of this luminescence led to the proposal that F^+ centers might be perturbed by an adjacent Y_{Al} antisite defect [50.169]. Absorption bands at 240 and 200 nm were ascribed to F centers; excitation within these bands yields luminescence band at 460 nm [50.170]. The most studied defect in $\text{A}_3\text{B}_5\text{O}_{12}$ garnet structure (where A and B are trivalent cations), however, is the antisite defect created by an A cation occupying a B site and vice versa (Fig. 50.19). Such defects arise due to the presence of two equally charged cations and high growth temperature, which induces thermodynamical lattice disorder. In Ce (Pr)-doped aluminum garnets the A_{Al} ($\text{A} = \text{Y}, \text{Lu}$) one is of special importance (Fig. 50.19) as it gives rise to: (i) slower emission centers in the UV region, peaking at RT within 300–350 nm, which create an unwanted competitive de-excitation pathway in addition to Ce^{3+} (Pr^{3+}); (ii) shallow electron traps, which effectively delay the radiative recombination at the fast emission center and strongly degrade scintillator timing characteristics and LY value. These defects were detected by the existence of satellite $4f$ – $4f$ emission lines of RE^{3+} ions (Er^{3+} , Nd^{3+}) revealing an octahedral (rather than dodecahedral) emission site symmetry [50.171, 172]. Systematic study of characteristics of the mentioned UV emission has been published recently using time-resolved emission spectroscopy under synchrotron excitation [50.173, 174]. Direct comparison of the bulk single crystals with single-crystalline films grown by liquid-phase epitaxy (LPE) was made. Such films are grown at substantially lower temperature ($\approx 1000^\circ\text{C}$) and therefore are free of such defects. Moreover, it was shown in aluminum garnet structure that doping by trivalent ions of strongly different radius with respect to original cations, either at the dodecahedral or octahedral sites, induces new UV emission bands, i.e., an effect analogous to process (i). La or Sc doping are some of the most studied cases [50.175, 176]. Despite the easy doping and high overall scintillator efficiency achieved in the latter case, long decay times of this lumines-

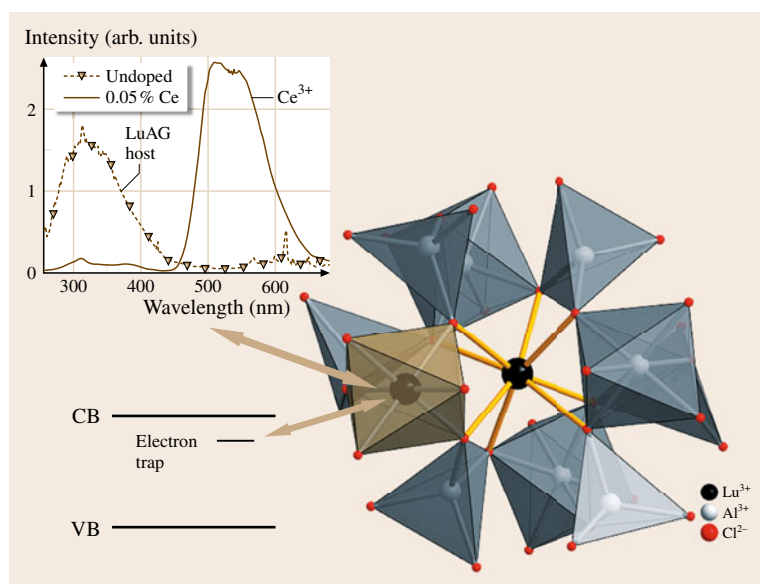


Fig. 50.19 The Lu_{Al} antisite defect in the LuAG structure. The resulting electron trap in the material forbidden gap is sketched on the left. The emission band within the range 300–350 nm due to the antisite defect and its competition with that of the Ce^{3+} center can be derived from radioluminescence spectra at RT (upper left). Emission lines around 312 nm and 615 nm in the undoped sample are due to Gd^{3+} and Eu^{3+} accidental impurities, respectively

cence (600–800 ns at RT) prevent practical application of such materials as fast scintillators.

It is worth noting, however, that in optimized YAG:Ce and LuAG:Ce bulk single crystals the residual UV emission contributes only a few percent to the total scintillation intensity, and no substantial energy transfer from the UV to Ce^{3+} band was found [50.158], so that the slowing of the scintillation response mentioned above is mainly due to the mechanism (ii), i.e., electron trapping at the antisite defect-related shallow traps before their radiative recombination at Ce^{3+} centers. In YAG:Ce, the TSL peak at 92 K was ascribed to such a trap, taking advantage of the comparison between a bulk single crystal and optical ceramics [50.140, 178]. In LuAG:Ce a comparison was made between a bulk single crystal and LPE-grown films [50.177]; the TSL structure within the 120–200 K interval was ascribed to such a trap (Fig. 50.20). Strong support for this ascription was obtained from TSL measurements of LuAG:Pr [50.179], where the glow curve below 250 K is found to be closely similar to that of LuAG:Ce, while TSL spectra are different, featuring the Pr^{3+} and Ce^{3+} emission spectra, respectively. Using the partial cleaning method, the thermal depth of the 92 K peak in YAG:Ce was calculated to be about 0.18 eV, while the triple TSL structure with peaks at 147, 169, and 187 K in LuAG:Ce was characterized by the energy values of 0.29, 0.40, and 0.47 eV, respectively. Deeper electron traps around the antisite defect and presumably higher concentration of these defects in LuAG with respect to

YAG result in a more severe delay in energy delivery to the Ce^{3+} centers in LuAG host and can thus explain the more severe LY degradation in the Lu-based garnet structure.

An interesting and technologically feasible possibility to decrease substantially trapping phenomena related to antisite defects in bulk crystals was recently announced. In mixed $\text{Lu}_3\text{Ga}_2\text{Al}_3\text{O}_{12}:\text{Pr}$ single crystal the TSL peaks in the 100–200 K temperature interval were completely suppressed, UV luminescence of the host disappeared at RT, and slower components and the

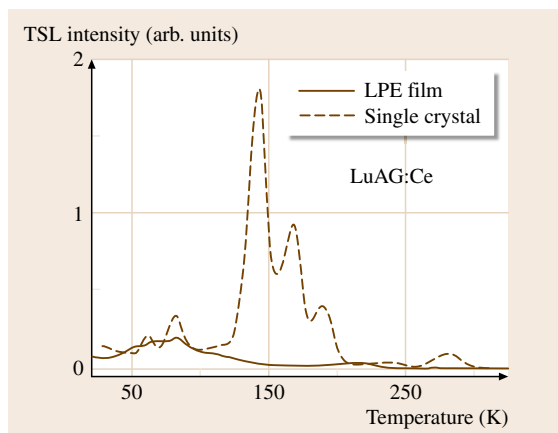


Fig. 50.20 TSL glow curves after x-irradiation at 10 K: comparison of LuAG:Ce LPE film and single crystal, see also [50.177]

α coefficient of scintillation decay were substantially lowered [50.179]. Even if the exact explanation of this effect has yet to be found, selective embedding of Ga^{3+} ions at octahedral lattice sites and related modification of the bottom of the conduction band due to lower-lying Ga-related energy levels [50.180] might be responsible for the observed effect.

Optimization of YAG- or LuAG-based fast scintillators by aliovalent ion codoping has not succeeded thus far. An attempt to codope LuAG:Ce with Zr^{4+} did not result in suppression of deep traps, at variance with what occurs in YAP:Ce [50.39, 144]. Deep traps related to 80 and 280 °C TSL peaks were markedly increased and only TSL peaks above 300 °C were suppressed [50.181]. It is interesting to note that recent atomistic simulations of defect creation in $\text{RE}_3\text{Al}_5\text{O}_{12}$ [50.182] point to a different response of the garnet lattice to tetravalent ion doping with respect to perovskite lattice [50.145, 146]. While in the latter case the production of interstitial oxygen was found as the least energy-requiring reaction, in the former case the production of RE cation vacancies seems to be the most energetically favorable process. Such a result may indicate that a different technological approach must be taken to improve aluminum garnet scintillators further.

50.2.4 Ce-Doped Silicate Single Crystals

The scintillation characteristics of Ce-doped rare-earth (RE) oxyorthosilicates were reported for the first time more than 20 years ago. After the first study, which revealed the promising properties of $\text{Gd}_2\text{SiO}_5\text{:Ce}$ (GSO) [50.183], numerous investigations were devoted to several other compounds of this material series, such as $\text{Lu}_2\text{SiO}_5\text{:Ce}$ (LSO), $\text{Y}_2\text{SiO}_5\text{:Ce}$ (YSO), $(\text{Y}_2)\text{-Lu}_2\text{Si}_2\text{O}_7\text{:Ce}$ (YPS and LPS), and several mixed compounds (most notably $(\text{Gd})_{2-x}\text{-Lu}_{2-x}\text{Y}_x\text{SiO}_5\text{:Ce}$; GYSO and LYSO, respectively). Single crystals were predominantly grown by Czochralski technique using an iridium crucible, which is necessary due to the very high melting point of these compounds (in the range $\approx 1950\text{--}2150$ °C). Radiofrequency (RF) induction heating was used in order to decrease the formation of polycrystalline regions, voids, and cracks [50.184, 185]. The optimization of all the manufacturing process enabled the growth of large single crystals (approximately 70–80 mm diameter and 200 mm length) with very good and reproducible scintillation performance [50.186–189]. Furthermore, material preparation in bulk, powders, and thin-film forms was pursued by other routes such as the pulling-

down technique [50.190], the sol–gel method [50.191, 192], and pulsed laser deposition [50.193]. In all cases promising scintillation characteristics were reported.

GSO possesses the monoclinic $P2_1/c$ crystal structure, while LSO and YSO possess the monoclinic $C2/c$ structure [50.194, 195]. The LSO structure is depicted in Fig. 50.21: it features SiO_4 tetrahedra and non-Si-bonded O atoms surrounded by four Lu atoms in a distorted tetrahedron. Band-structure and density-of-states calculations on YSO and YPS were recently performed [50.196].

In undoped crystals, in addition to intrinsic emission bands, further emission is clearly detected in the 250–400 nm region and interpreted as due to self-trapped excitons and holes [50.197]. Optical studies of Ce-doped samples showed two Ce^{3+} emission bands related to two different Ce^{3+} crystallographic sites in GSO, LSO, and YSO [50.198]. Due to its higher scintillation efficiency LSO was more thoroughly investigated; its PL spectra at 11 K are reported in Fig. 50.22 [50.199]. The doublet emission peaking at 393 and 427 nm was ascribed to Ce_1 whose luminescence is not quenched up to RT. On the other hand,

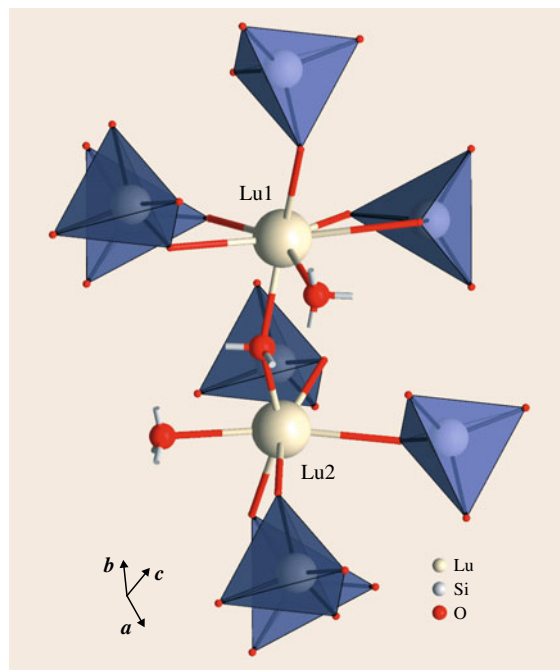


Fig. 50.21 The structure of LSO, with two Lu sites displayed and surrounding SiO_4 tetrahedra. Three oxygen ions with cut bonds form OLu_4 tetrahedra and do not participate in Si–O bonds

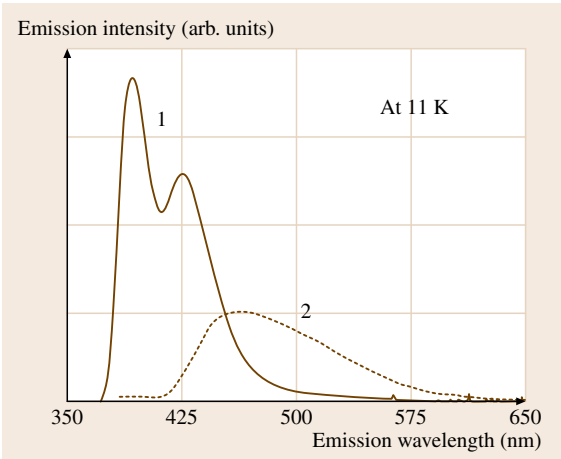


Fig. 50.22 Emission spectra of LSO at 11 K. The two emission spectra have excitation wavelength of 356 nm (solid line) and 376 nm (dashed line). Curves 1 and 2 refer to Ce_1 and Ce_2 centers, respectively (after [50.199])

the composite emission peaking at 460 nm, detected well only below 80 K, was ascribed to the Ce_2 center. The ionization processes of excited Ce^{3+} energy levels were studied by means of parallel photoconductivity and photoluminescence excitation–emission experiments [50.200], and by the microwave resonator technique [50.201], revealing three different delocalization processes of direct photoionization, tunneling, and thermal ionization of the lowest relaxed $5d_1$ level, found 0.45 eV below the conduction band.

The presence of two distinct Ce^{3+} emissions is in accordance with the existence of two Lu^{3+} crystallographic sites and with the substitutional incorporation of Ce for Lu.

Detailed information about incorporation of Ce^{3+} ions into Lu_2SiO_5 was obtained from ESR studies [50.202]. The g -value of a rare-earth ion is closely related to the wavefunction of its electronic ground state and therefore strongly depends on the point symmetry of the crystallographic site. Therefore ESR is indeed a good tool to investigate Ce^{3+} site symmetry and occupancy in crystal lattice.

Lu ions reside at two crystallographic sites with low (C_1) symmetry, Lu_1 and Lu_2 , with seven and six oxygen neighbors, respectively. Ce^{3+} ions are expected to substitute only for Lu^{3+} ions due to their similar ionic radii (Ce^{3+} : 0.103 nm; Lu^{3+} : 0.085 nm; Si^{4+} : 0.026 nm). ESR measurements support this assumption since Ce^{3+} ions are found at both lutetium sites. As the ESR intensity is directly linked to the concentration of para-

magnetic ions, the relative Ce^{3+} concentration in each site could be determined. The values are: $Ce_1 = 95\%$ and $Ce_2 = 5\%$. The most substituted site is attributed to the larger Lu_1 site with 6 + 1 oxygen neighbors. ESR spectra of LSO showing two Ce^{3+} resonance lines are shown in Fig. 50.23b. Moreover, in Fig. 50.23a the ESR spectrum of lutetium pyrosilicate ($Lu_2Si_2O_7$, LPS, with space group $C2/m$; see [50.203]) is also shown. In this case only one resonance signal is detected due to Ce^{3+} substituting for Lu^{3+} ion at the lone C_2 symmetry site.

In the $(RE)_2SiO_5$ material group, LSO presents the best figure of merit due to its highest density (7.4 g/cm³), short decay time (about 40 ns), high light output (about 3.5–4 times that of BGO), and satisfactory energy resolution (7.75%) [50.187]. Another important advantage is the absence of shallow traps, as indicated by the very low TSL intensity below RT [50.204], which is consistent with the absence of slower components in scintillation decay. On account of these characteristics, LSO found large-scale application, substituting for BGO in medical positron emission tomography (PET) systems [50.205]. Yttrium-admixed (several percent) LSO (LYSO) is an interesting alter-

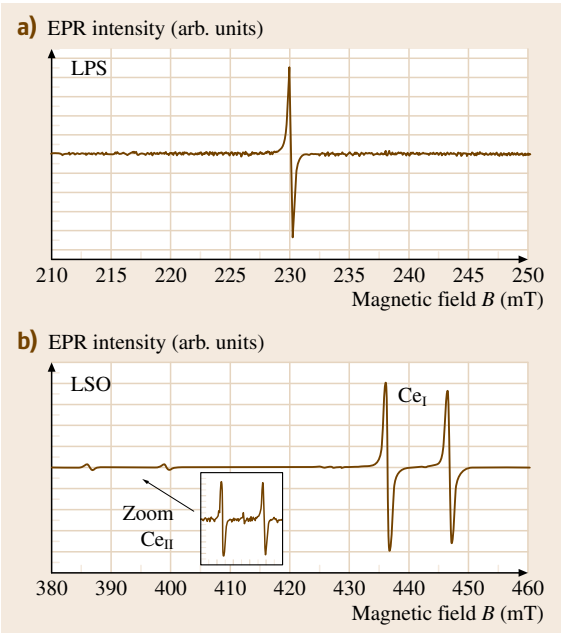


Fig. 50.23a,b ESR spectra at 12 K of Ce^{3+} in (a) LPS and (b) LSO crystals with the magnetic field B parallel to the a -axis (after [50.102]) ($\pm 5\%$). The spectra were recorded at 9.5 GHz with a microwave power of 20 mW; modulation amplitude was 1 mT (after [50.202])

native to LSO because of its more favorable growth properties due to a lower melting point, lower formation of inclusions, lower cost of starting materials, and comparable or even better scintillation performance [50.186]. GSO has clearly inferior light output (Table 50.1) and scintillation decay also shows slower components. Recently, a positive effect of Zr codoping was reported, which increases its LY by about 20% [50.206]. Due to the lower density (6.7 g/cm^3) its attenuation length is 40% longer than that of LSO. However, its application in PET cameras is being considered as well [50.207].

In the case of LSO, it was soon recognized that it exhibits a fairly strong afterglow [50.209]. It consists of a light-emission signal which decreases exponentially following the end of an excitation pulse, and that can persist for several minutes up to hours at RT. This is a detrimental property of the crystal, since it causes background instability during repeated measurements.

Fundamental studies aimed at the comprehension of the microscopic physical mechanism governing afterglow were thus carried out in order to find possible technological solutions. The activation energy of the process was found to be approximately 1 eV [50.209]; the is in accordance with the calculated trap depth of a TSL peak at 375 K (using a heating rate of 6 K/s) so that afterglow appears to be due to RT carrier detrapping from the trap responsible for this peak followed by radiative recombination at Ce^{3+} luminescent centers. Actually the 375 K peak is the first of a series of as many as six peaks observed in the glow curve above RT, whose spectral emission coincides with the Ce^{3+} 5d–4f transition [50.209]. Annealing experiments in reducing or oxidizing atmosphere led to the suggestion that traps could be related to oxygen vacancies [50.210]. The presence of oxygen-related defects following irradiation was suggested from optical absorption measurements [50.211]; oxygen vacancies, together with STEs and STHs, were proposed to be responsible for TSL peaks below RT [50.197,212]. A very nice confirmation of the intrinsic origin of traps was the finding that all oxyorthosilicates possessing C2/c structure (YSO, LSO, YbSO, ErSO) are characterized by similar TSL glow curves above RT, irrespective of their doping [50.208, 211], so that crystal structure seems to play an important role in trap properties. In Fig. 50.24 the glow curves of LSO, LSO:Ce, YSO:Ce, and YbSO:Ce are compared. The favorable absence of afterglow in LPS, accompanied by the lack of TSL glow peaks close to RT [50.213], can thus be explained in terms of its different C2/m structure, leading to different

Ce^{3+} –oxygen (and thus oxygen vacancy) configurations and distances.

It is interesting to note that Pr^{3+} doping was also attempted in order to obtain a faster scintillation response of LSO-based scintillator. Fast Pr^{3+} 5d–4f photoluminescence has a maximum at 273 nm and decay time of about 6–7 ns at RT [50.214]. However, significant ionization of the 5d₁ relaxed excited state occurs at RT, because the 5d₁ level was found to be closer to the conduction band (0.28 eV) compared with the Ce^{3+}

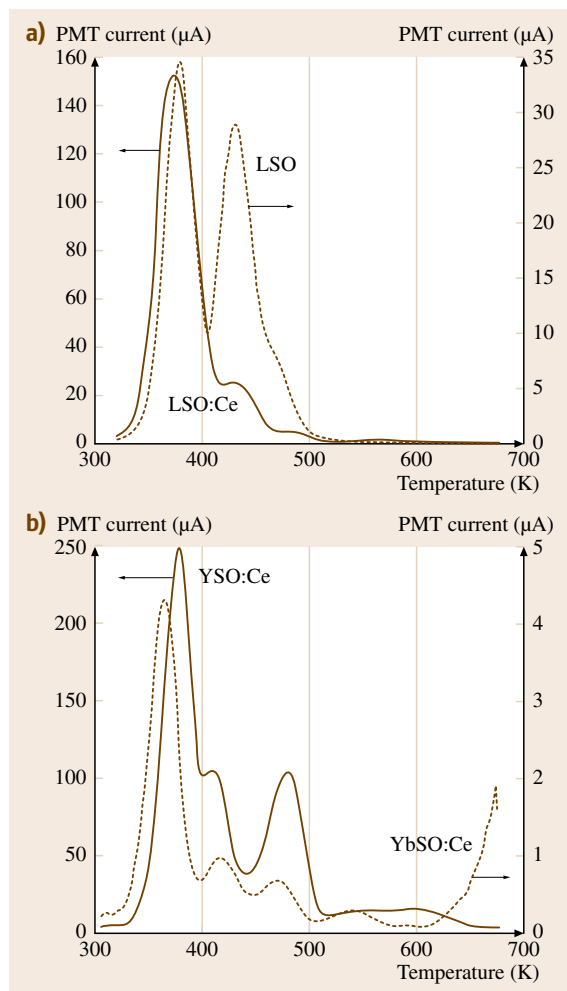


Fig. 50.24 (a) X-ray induced TSL glow curves of undoped and Ce-doped LSO taken by heating the samples at 5°C/s . (b) X-ray-induced TSL glow curves of YSO:Ce and YbSO:Ce. The sharp upturn above 650°C for the weak YbSO:Ce TSL is due to black-body radiation emanating from the silver sample holder (after [50.208])

center (0.45 eV). This ionization process significantly degrades **LY** values of LSO:Pr and prevents its practical application.

In conclusion, Ce-doped LSO, LYSO, and GSO proved to have excellent scintillating performances and are presently key materials for medical diagnostic **PET** applications; their further improvement should be based on better control of intrinsic point defects, especially those including oxygen vacancies.

50.2.5 Ce-Doped Rare-Earth Halide Single Crystals

During the last decade research on fast and efficient scintillators has found new very interesting candidates in the family of rare-earth (mostly La and Lu) halides. These are Ce-doped bromides, chlorides, and iodides

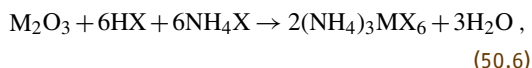
such as LaX₃:Ce and LuX₃:Ce, where X = Cl, Br or I. Some of their characteristics are listed in Table 50.2 where scintillation time decay, **LY**, and energy resolution are given for a specific Ce concentration.

Single crystals of Ce-doped rare-earth (**RE**) halides are usually obtained by vertical Bridgman growth technique using binary **RE** halides as starting materials. These starting materials can be prepared by several different routes [50.217, 223, 224]; for example, the preparation of **RE** iodides is performed by direct sealing of the metal with slight excess of iodine under vacuum in a silica ampoule, and heating up to the iodine melting point. On the other hand, the so-called *ammonium halide route* can be employed for the preparation of rare-earth chlorides and bromides. This process consists of two main steps. First, the dissolution of **RE** oxides in HCl or HBr with the addition of ammonium halide is

Table 50.2 Structural and optical characteristics of Ce-doped **RE** halides. Numbers in parenthesis in the scintillation decay time column represent the percentage of total intensity governed by the indicated decay time, while slower components characterize the decay of the remaining intensity. Times in parenthesis in the **LY** column represent the time gates with which the **LY** was evaluated. Original references are shown in square brackets

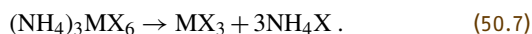
Crystal	Space group	Density (g/cm ³)	Band gap (eV)	Ce 5d–4f em. (nm)	Ce 4f–5d abs. (nm)	Ce conc. (mol%)	Scintillation decay time (ns)	LY (10 ³ phot/MeV)	Energy res. (%)
LaCl ₃ :Ce	Hexagonal <i>P</i> 6 ₃ / <i>m</i> (C ² _{6h}) [50.215]	3.86 [50.215]	7 [50.216]	337, 358 [50.215]	243, 250, 263, 274, 281 [50.215]	10	24 (60%) [50.217]	50 [50.217]	3.1 [50.217]
LaBr ₃ :Ce	Hexagonal <i>P</i> 6 ₃ / <i>m</i> (C ² _{6h}) [50.215]	5.29 [50.218]	5.6 [50.219]	355, 390 [50.219]	260, 270, 284, 299, 308 [50.219]	5	16 (100%) [50.217]	70 [50.217]	2.6 [50.217]
LaI ₃ :Ce	PuBr ₃ <i>Cmcm</i> [50.215]	5.614 [50.220]	3.3 [50.220]	452, 502 [50.220]	420 [50.219]	0.5	19 (<i>T</i> < 150 K) [50.220]	≈ 0 (RT) [50.220] 16 (<i>T</i> < 100 K)	–
LuCl ₃ :Ce	Monoclinic <i>C</i> 2/ <i>m</i> [50.215]	4.00 [50.215]		374, 400 [50.215]	215, 235 [50.215]	0.45	50 (25%) [50.215]	1.3 (0.5 μs) 5.7 (10 μs) [50.215]	16 [50.215]
LuBr ₃ :Ce	Rombohedral <i>R</i> –3 [50.215]	5.17 [50.215]		408, 448 [50.215]	310–400, 230 [50.215]	0.76	32 (10%) [50.215]	10 (0.5 μs) [50.215] 24 (10 μs)	5 [50.215]
LuI ₃ :Ce	Hexagonal <i>R</i> –3 [50.222]	5.6 [50.221]		475, 520 [50.221]	≈ 300, 390, 419 [50.221]	0.5	< 50 ns (50%) [50.222]	42 (0.5 μs) [50.222] 51 (10 μs) 58 (0.5 μs) [50.222]	4.7 [50.222]
						2		71 (10 μs)	–

achieved



where M stands for the RE element (for instance La or Lu) and X stands for Cl or Br.

Subsequently, the ternary salt is heated under vacuum (typically up to 400 °C) and decomposed to obtain the final RE halide



Purification of the binary halides by sublimation under high vacuum is finally performed, allowing oxyhalides to be separated as involatile residues. The obtained powders can be used as starting materials for Bridgman growth. The crystals grown are highly hygroscopic. They must be sealed in appropriate ampoules for handling and characterization. Recently, Bridgman growth from commercially available anhydrous binary halide powders was performed and crystals with very good optical and scintillation characteristics were obtained [50.224].

While Pr^{3+} and Nd^{3+} doping of RE halides were considered for laser applications [50.226,227], only the Ce^{3+} ion appears to be suitable as a dopant of these

matrices to obtain fast and efficient scintillators. The radioluminescence spectra of Ce-doped samples are dominated by an intense 5d–4f Ce^{3+} emission. Other emissions related to the host crystal were detected as well. The assignment of such bands to specific centers and the study of their role in the energy transfer processes towards Ce^{3+} were soon the subject of systematic investigations. In this respect the most detailed study was performed on $\text{LaCl}_3:\text{Ce}$ [50.215, 216, 219, 225, 228, 229]. Figure 50.25 displays the x-ray excited emission of $\text{LaCl}_3:\text{Ce}^{3+}$ at different Ce^{3+} concentrations [50.225]. Apart from the Ce^{3+} doublet peaking at 337 and 358 nm, a shoulder attributed to STE emission is observed at about 400 nm. The excitonic nature of the 400 nm emission was established by an optically detected magnetic resonance investigation which revealed the existence of two excited triplet states attributed to *out-of-plane* STEs [50.230], one peaking at about 310 nm (superimposed to the Ce^{3+} emission) and the second at about 420 nm, similar to the shoulder seen in Fig. 50.25. On the other hand, no stable self-trapped holes (V_k centers) were found due to their immediate recombination with an electron from the conduction band resulting in STE state creation.

The mutual intensities of the Ce^{3+} and STE emissions are found to change with temperature (Fig. 50.26).

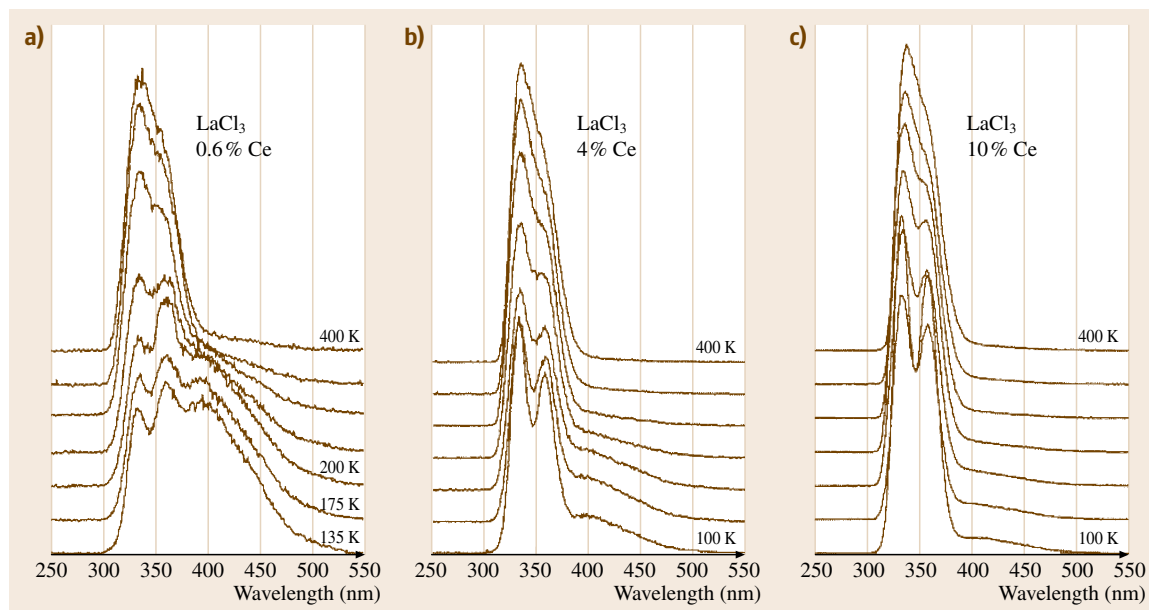


Fig. 50.25a–c X-ray excited emission in $\text{LaCl}_3:\text{Ce}$ as a function of temperature and Ce concentration: panel (a) 0.06% Ce; panel (b) 4% Ce; panel (c) 10% Ce. Unless otherwise indicated spectra are separated by 50 K temperature intervals (after [50.225])

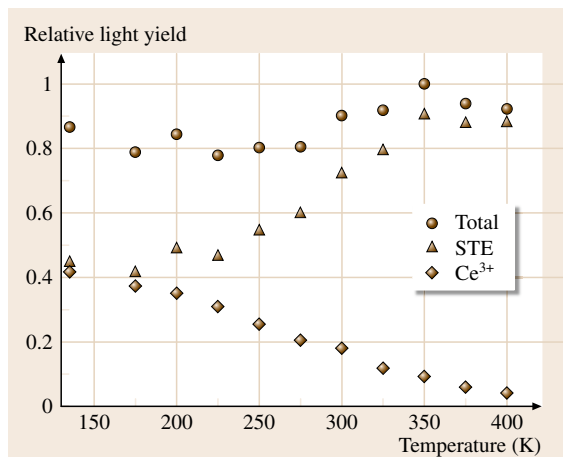


Fig. 50.26 Temperature dependence of the Ce^{3+} , STE, and total luminescence in $\text{LaCl}_3:0.57\% \text{Ce}$, derived from x-ray-induced emission spectra. The error bars are comparable with the dimensions of the data points (after [50.215])

Namely, STE emission decreases for $T > 200 \text{ K}$, while an opposite dependence is detected for the Ce^{3+} 5d–4f transition. The anticorrelation between STE and Ce^{3+} luminescence was interpreted by assuming the occurrence of energy transfer towards Ce^{3+} ions through STE diffusion. Specifically, soon after irradiation, thermalized electrons and holes form STEs, which can migrate and be trapped at Ce sites before their radiative de-excitation. STE mobility increases with increasing temperature in accordance with the observed temperature dependences in Fig. 50.26 [50.229]. The nonexponential character of the Ce^{3+} scintillation time decay [50.215, 229] was interpreted as due to the existence of two energy localization mechanisms at Ce^{3+} sites, namely (i) prompt trapping of holes and electrons by cerium ions, leading to a fast decay component determined by the intrinsic cerium 5d–4f emission lifetime, and (ii) the above-mentioned thermally assisted energy transfer from STE to cerium ions, leading to a slow scintillation decay governed by STE lifetime in the microsecond timescale. Room-temperature STE lifetime ($3.5 \mu\text{s}$) was derived from the scintillation time decay of an undoped LaCl_3 sample [50.229]. Moreover, a possible role of defects acting as trap levels in the slow scintillation decay processes was taken into account. Such trap levels were investigated in a few TSL studies [50.231, 232]. These studies showed the presence of several TSL peaks in LaCl_3 and LaBr_3 both below and above RT. However, TSL properties have not yet been clearly correlated with slow decay components.

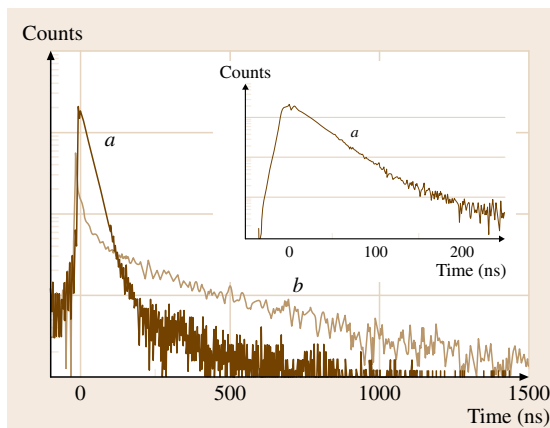


Fig. 50.27 Scintillation decay time spectra of (a) $\text{LaBr}_3:0.5\%\text{Ce}$ and (b) pure LaBr_3 at RT under ^{137}Cs γ -ray excitation. The decay of the doped sample is approximately single-exponential with decay time of 30 ns. The faster component in the decay of pure LaBr_3 is probably due to Ce^{3+} trace impurities; the longer component is due to STE luminescence. The inset shows the spectrum of $\text{LaBr}_3:0.5\%\text{Ce}$ on a shorter time scale (after [50.233])

The best scintillation performances in terms of LY, decay time, and energy resolution are displayed by $\text{LaBr}_3:\text{Ce}$ [50.218, 233, 234]. In Fig. 50.27 scintillation time decay spectra of $\text{LaBr}_3:\text{Ce}$ are shown, which feature a fast and approximately single exponential component. In this crystal, efficient direct energy localization at Ce^{3+} ions occurs and an intermediary role of STE migration processes seems to be not relevant, probably due to the shorter STE decay time and higher STE migration rate evidenced in bromides with respect to chlorides [50.219]. Moreover, a higher number of electron–hole pairs are generated with respect to LaCl_3 due to a smaller bandgap (Table 50.2), resulting in a very high LY of 70 000 phot/MeV.

Even smaller bandgap, shorter STE decay time, and higher STE migration rate characterize the heaviest iodides [50.219]. However, other drawbacks arise in the case of $\text{LaI}_3:\text{Ce}$. For example, the small bandgap value and the small energy difference (0.1–0.2 eV) between the position of the Ce 5d level and the bottom of the conduction band seem to be responsible for its very poor scintillation properties at RT [50.220]. At $T > 120 \text{ K}$ 5d electrons can be thermally activated to the conduction band and luminescence becomes quenched. A more favorable situation is encountered in the case of LuI_3 [50.221, 222, 235] due to the slightly higher bandgap value and longer emission wavelength, so that

the energy difference between the Ce^{3+} 5d level and the conduction band is greater. Thermally activated transition into the conduction band does not occur and a quite high LY (70 000 phot/MeV, Table 50.1) was reported. Optimization of $\text{LuI}_3\text{:Ce}$ is still needed as it presently shows intense slow decay components; moreover crystal inhomogeneities were also reported [50.222].

In conclusion, Ce-doped RE halides constitute a very interesting material group in which scintillation properties vary strongly due to slightly different microscopic properties. At the present time $\text{LaBr}_3\text{:Ce}$ possesses the best scintillator performances, due to a favorable combination of STE lifetime, STE migration rate, bandgap value, and position of Ce^{3+} energy levels in the forbidden bandgap.

50.2.6 Optical Ceramics and Microstructured Materials

Optical ceramics are transparent or translucent materials constituted by tight aggregating crystallite micrograins, each randomly oriented with respect to its neighbors. They have been under development as an alternative to single-crystal materials to provide bulk optical elements in the case where single crystals cannot form or when ceramic materials show superior properties, for example, in terms of achievable concentration or homogeneity of the dopant. The associated technology has developed greatly, mainly within the last two decades; in the case of cubic material, technological progress enabled bulk elements that were visually indistinguishable from single crystals and in terms of some parameters (doping profile) even clearly superior. Among the developed materials, mainly YAG:Nd and $\text{Y}_2\text{O}_3\text{:Nd}$ reached the highest degree of perfection; their primary application is in the field of solid-state lasers [50.236, 237]. The size of the single-crystal grains is on the order of a few tens of microns, interface thickness is reported to be only about 1–2 nm, and the residual volume of pores is several ppm.

It is worth noting that the application demands are clearly higher in the case of scintillators compared with laser optical ceramics. In the latter case the scattering losses due to pores (voids) and grain interfaces limit the material performance. The already achieved reduction of the pore volume down to a few ppm and interface thickness to a few nm reported in [50.236, 237] is enough to make them fully comparable to their single-crystal analogs. However, in the case of scintillators, even point defects at the atomic scale can seriously limit material performance due to the introduction of

trapping levels in the material forbidden gap. If we consider a grain size on the order of a few tens of μm and thickness of the interface layer of 1–2 nm, the expected concentration of the interface-related (trapping) states may easily reach several hundred ppm. Such a concentration can noticeably influence the characteristics of the transport stage due to retrapping of the migrating carriers or even the introduction of nonradiative traps, which can seriously degrade the scintillation response and/or overall efficiency parameters.

Development of optical ceramics for scintillator applications was triggered by the needs of computer tomography (CT) medical imaging. A review of the results achieved, mainly for the manufacturing and characterization of $(\text{Y,Gd})_2\text{O}_3\text{:Eu}$, $\text{Gd}_2\text{O}_2\text{S:Pr,Ce,F}$, and $\text{Gd}_3\text{Ga}_5\text{O}_{12}\text{:Cr,Ce}$ ceramics, was reported by Greskovich and Duclos [50.238]; see also [50.239–241] for more details about the particular materials. In the latter two materials, codoping with Ce^{3+} is used to reduce the afterglow through the capture of holes at Ce ions, $\text{Ce}^{3+} \rightarrow \text{Ce}^{4+}$ conversion, and subsequent nonradiative recombination with migrating electrons and/or temporary Eu^{2+} centers. Moreover, codoping of $(\text{Y,Gd})_2\text{O}_3\text{:Eu}$ [50.242] with Pr^{3+} appeared to be an efficient tool to reduce the afterglow (by a mechanism similar to that of the Ce ions above). Annealing in a controlled atmosphere can further diminish or passivate trapping states in the forbidden gap related to the grain interfaces. Eu^{3+} - or Tb^{3+} -doped Lu_2O_3 are worth mentioning among new optical ceramics suggested for scintillator applications and based on the slow 4f–4f transitions of rare-earth ions. True optical ceramic $\text{Lu}_2\text{O}_3\text{:Eu}$ samples were synthesized, their performance was tested in comparison with CsI:Tl , and a large-area scintillation screen was prepared [50.243, 244]. While providing 60% of the emission intensity of CsI:Tl , a better match to the CCD photodetector sensitivity was concluded. Unfortunately, $\text{Lu}_2\text{O}_3\text{:Eu}$ was found to suffer of noticeable afterglow for times longer than 6 ms [50.245].

Recently, fast and potentially less expensive optical ceramics based on Ce-doped YAG have been reported in the literature [50.246]. Nowadays, Ce-doped YAG optical ceramics are available from Baikowski, Japan Ltd., the production technology of which should be analogous to that of YAG:Nd described in [50.236]. Figure 50.28a,b shows a comparison of radioluminescence and scintillation decay characteristics in equally shaped samples ($\varnothing 15 \times 1$ mm) of an industrial standard-quality single-crystal YAG:Ce produced by CRYTUR, Ltd., Czech Republic and the aforementioned opti-

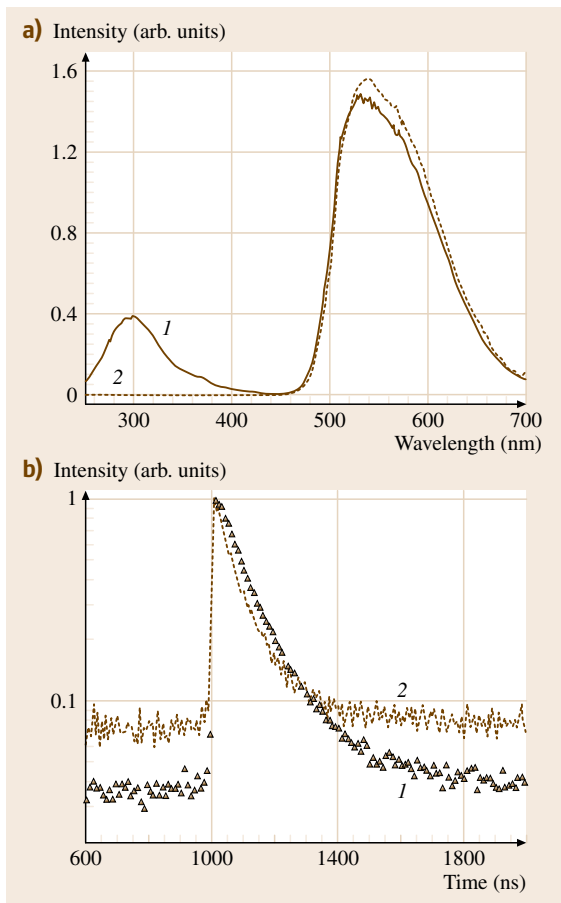


Fig. 50.28 (a) Radioluminescence spectra (Mo cathode, 35 kV) of **YAG:Ce** single-crystal (1) and ceramic (2) scintillators at room temperature. (b) Spectrally unresolved scintillation decay of **YAG:Ce** single-crystal (1) and ceramic (2) scintillators at RT, with excitation by 511 keV photons of ^{22}Na radioisotope. Approximation by a sum of exponentials yields decay time of 119 ns (1) and 85 ns (2) for the dominant component

cal ceramics [50.140]. While the radioluminescence intensity in the Ce^{3+} band at 550 nm is comparable in both samples (Fig. 50.28a), the host 300–350 nm band is absent in the ceramic sample. This UV emission is ascribed to a luminescence center based on an antisite Y_{Al} defect (Sect. 50.2.3) and its formation is crucially dependent on the preparation temperature. As the preparation temperatures of **YAG**-based optical ceramics are noticeably lower with respect to the single crystal [50.236], it can be concluded that the Y_{Al} anti-

site defects are absent in the former system. Normalized scintillation decays are shown in Fig. 50.28b. The ceramic material shows faster decay in its initial part, the decay time of which is closer to the photoluminescence lifetime of the Ce^{3+} center (about 60–65 ns). This can be explained by a higher Ce concentration and the absence of Y_{Al} antisite defects. However, a higher content of very slow scintillation components is reflected in lower amplitude-to-background ratio. The presence of such very slow decay components is usually related to traps monitored by TSL measurements somewhat below RT. Indeed, the ceramic system shows higher TSL intensity above approximately 190 K [50.140], possibly due to the presence of traps at the grain interfaces. Recently, also **LuAG:Ce** optical ceramics were prepared by a coprecipitation route [50.247] (Fig. 50.29) and the scintillation performance was compared with that of **LuAG:Ce** single crystal [50.248]. Similar to

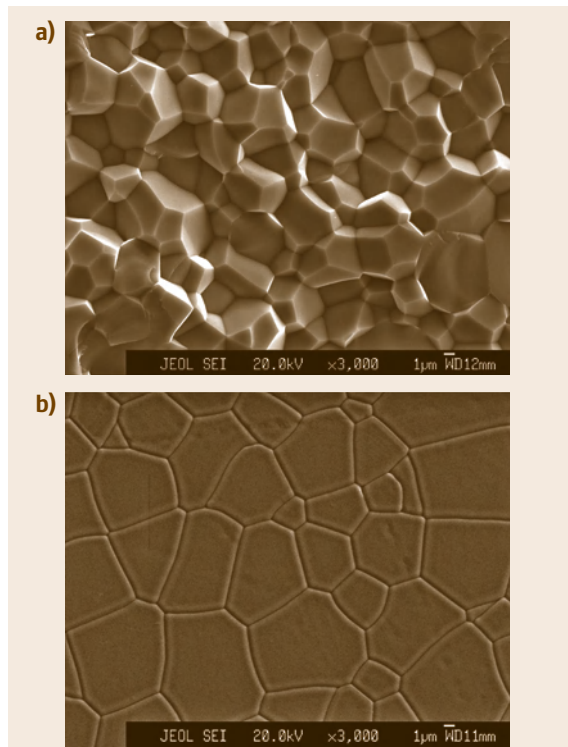


Fig. 50.29a,b Scanning electron microscopy (SEM) photographs of **LuAG:Ce** ceramics sintered at 1800 °C for 10 h under vacuum: (a) the fracture surface; (b) the polished surface after thermal etching at 1400 °C for 1.5 h [50.247] (courtesy of Xue-Jian Liu, Shanghai Institute of Ceramics)

YAG:Ce optical ceramics, high radioluminescence efficiency was found. However, noticeably lower **LY** and the presence of more intense slow components in the scintillation decay point to retrapping phenomena at the grain interfaces, which is supported also by measured **TSL** characteristics.

Microstructured materials can be classified as single-crystal-based systems grown with tailored spatial morphology. These materials were developed to meet the demand of increased x-ray absorption, while keeping high spatial resolution in the x-ray imaging screens. Few scintillation materials, namely **CsBr:Tl** [50.249], **CsI:Na** [50.250], and **CsI:Tl** [50.251–253], can be prepared by vacuum evaporation in the form of long (up to 1–2 mm) and thin (several μm diameter) needles, which are densely packed and optically isolated (Fig. 50.30). A needle layer can be directly deposited on the photodetector and, due to the light-guiding effect in the needles, the high spatial resolution is preserved with increased layer thickness, ensuring higher x-ray absorption. While this concept has been used for a long time for **CsI:Na** in image intensifiers [50.254], where the **CsI:Na** is at the inner side of the photocathode, i.e., in vacuum, it could not be used in the open atmosphere due to its extreme hygroscopicity. Only the development of this growth morphology for much less hygroscopic **CsI:Tl**, and the availability of large-

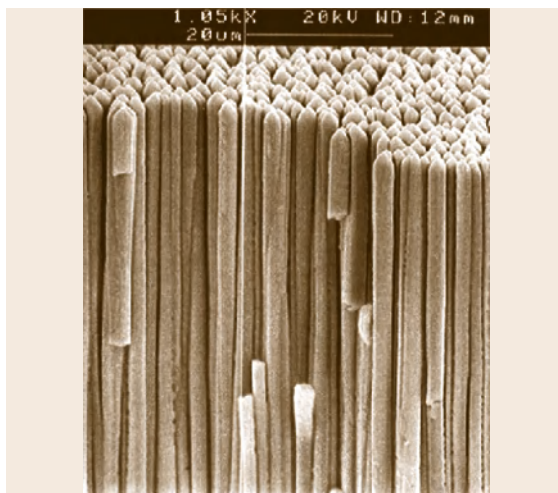


Fig. 50.30 Vapor-deposited column-shaped **CsI:Tl** scintillation crystals of very smooth structure. Diameter $\approx 3 \mu\text{m}$, length $> 0.5 \text{ mm}$; see also [50.20] (courtesy of Philips Research Laboratories, Aachen)

area position-sensitive semiconductor detectors (**CCD**, **a-Si:H** panels) enabled the construction of a new generation of flat-panel detectors, which provide a qualitative upgrade in many kinds of medical, industrial, and scientific imaging systems [50.255].

50.3 Future Prospects

Acceleration of research and development in the field of scintillation materials over the last 20 years has been motivated mainly by new demanding applications in the medical, industrial, scientific, and security imaging sectors. Further development and exploitation of powerful x-ray sources, e.g., synchrotron radiation, the availability of new radiopharmaceuticals significantly enhancing **PET** imaging capability in oncology [50.256], and the wider exploitation/monitoring of radioisotopes in different branches of human activity continue to contribute to increasing interest in fast and efficient scintillators.

Currently, there is a need for high-density, fast, and high-light-yield scintillators for **PET**. While **LSO:Ce** and **GSO:Ce** were successfully introduced and are replacing the previously used **BGO** [50.205–207] the search for a second material to be used in combined **PET** detectors to correct for the depth-of-interaction error continues [50.257]. Furthermore, in **PET** detectors

sufficiently fast and bright **Ce-** or **Pr-doped** materials enable evaluation of time-of-flight information related to the coincidence detection of two 511 keV photons from the rising edge of the scintillation decay. Such information can limit the number of random coincidences and increase the signal-to-noise ratio [50.258]. The candidates are **(Lu/Y)AP:Ce** or **LuAG-based** scintillators, which are under intense investigation. Undoubtedly, all of these materials could be further improved since the nature of defects participating in the scintillation conversion and degrading their performance is not yet fully understood.

As the majority of applications use x-ray sources with energies below 150 keV, there is significant market potential for very high light yield, medium density, fast scintillators, where the latest developments led to the discovery of the group of **Ce-doped rare-earth halides**. Also in this case, understanding of material point defects is at the early stages and improve-

ments in crystal quality are expected in the near future.

The rapidly developing field of optical ceramics may bring completely new material systems into consideration, which cannot be prepared in the form of single crystals. The recent success of slow scintillation ceramics based on Tb^{3+} -, Eu^{3+} - or Pr^{3+} -doped materials in CT medical imaging has clearly shown the potential of this manufacturing technology. Even in the case of YAG:Ce or LuAG:Ce materials, which can be relatively easily grown in single-crystal form, optical ceramics may offer an interesting alternative due to the absence of specific (e.g., antisite) defects, which degrade scintillation performance of the single crystal. On the other hand, one should keep in mind that grain boundaries and interfaces in the ceramics introduce other trapping states with undesirable consequences as described in Sect. 50.2.6.

It is interesting to mention recent literature reports dealing with phosphors prepared from materials of smaller bandgap (sulfides, selenides, tellurides) due to their expected higher conversion efficiency. In these materials the emission center can be based on an exciton localized close to a suitable doped impurity ion. Very high efficiency and decay time of about 1 μs at RT were reported for ZnTe:O [50.259]. Apart from the powder form, these materials can be prepared in the form of thin films as well using a novel sol-gel technology, which offers better controlled synthesis conditions and more perfect microcrystal grain surfaces. Thin-film scintillators were developed for special applications requiring high two-dimensional (2-D) resolution in monitoring tiny objects. High-quality single-crystalline films can be grown by liquid-phase epitaxy technique, which was demonstrated in the case of YAG and LuAG-based scintillators [50.260, 261] or ZnO [50.262].

Renewed interest in the scintillation characteristics of direct-bandgap semiconductors based on ZnO or other binary compounds has arisen recently [50.30, 31, 263] due to their superfast emission with decay times below 1 ns. Emission in these materials is due to Wannier excitons, free or localized at defects/doped ions. In the latter case it shows a low energy shift and still faster decay times of the order of tens of picoseconds.

Donor-acceptor recombination luminescence in suitably doped systems was also reported [50.264]. Such materials can show an unbeatable combination of superfast scintillation response and (intrinsically) high light yield. The problem of low Stokes shift and en-

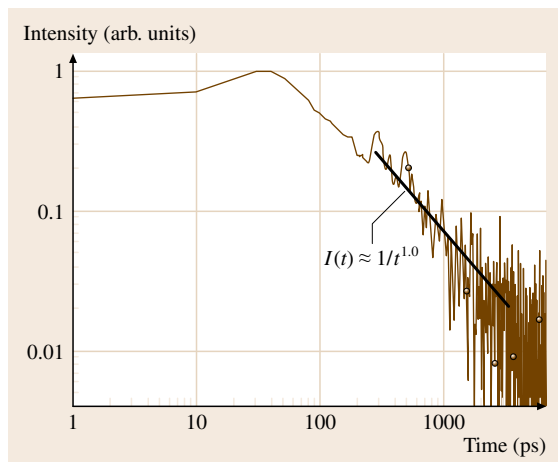


Fig. 50.31 RT photoluminescence decay of ZnO:In, Li liquid-phase epitaxy grown film. $\lambda_{\text{exc}} = 260$ nm, 150 fs laser pulse, $\lambda_{\text{em}} = 420\text{--}430$ nm. The solid line shows the $I(t)$ dependence proportional to inverse time typical of donor-acceptor pair recombination luminescence

hanced emission reabsorption in bulk elements might be solved by the aforementioned exciton localization or exploitation of fast donor-acceptor recombination luminescence (Fig. 50.31) [50.32]. A new class of so-called *quantum scintillators* based on quantum dots (nanostructures) of direct-gap semiconductors embedded in a suitable host was announced recently [50.265, 266]. These materials exploit a quantum size effect in free exciton emission, which can enhance the efficiency and luminescence speed in such nanostructured materials with respect to the bulk analogues.

A separate group of scintillation materials is under development for neutron detection. These materials must contain elements with high cross-sections for neutron capture (^6Li , ^{10}B , $^{155,157}\text{Gd}$) and ideally should have a low effective Z-number, rendering them insensitivity to γ -rays. These constraints substantially limit the number of candidate material compositions [50.267]. Such scintillation detectors are needed in new safety precautions to be employed at airports, seaports, and country borders to defend against terrorist activities and to detect illicit trafficking or inadvertent circulation of nuclear materials or radioactive sources and chemical warfare agents. Development of such monitoring portals is conditional on the availability of sufficiently intense portable neutron sources, which are under development as well.

50.4 Conclusions

In this chapter the broad field of scintillation materials has been introduced, albeit limited to selected single-crystal groups, optical ceramics, and microstructured materials. The variety of materials considered or currently under development is due to the range of demands of the ever-growing number of practical applications and the need to tailor scintillation materials to each of them.

Attention was paid not only to listing the materials and their scintillation characteristics, but also to addressing the issue of specific material defects and their relationship with the manufacturing technology used. Material defects and irregularities often give rise to energy levels in the host forbidden gap. Such energy levels can constitute trapping states, which serve as centers of nonradiative recombination or simply as delaying ele-

ments in the process of energy transport to the emission centers. Consequently, both the scintillator efficiency and timing characteristics are degraded. Understanding the underlying physical mechanisms of energy transfer and storage and the role of particular material defects is of crucial importance for bringing material performance close to the intrinsic limits. The necessity to use correlated experiments based on time-resolved spectroscopy, thermoluminescence, and magnetic resonance to understand the nature of defects has been demonstrated in several examples.

Finally, it is worth noting that another area of progress in the realization of advanced detector design concerns the rapid development of the field of semiconductor photodetectors, which are an indispensable part of scintillation detectors.

References

- 50.1 W.C. Röntgen: Über eine neue Art von Strahlen, Sitz Ber. Phys. Med. Ges. Würzb **9**, 132–141 (1895), in German
- 50.2 W.C. Röntgen: On a new kind of rays, *Science* **3**, 227–231 (1896)
- 50.3 H. Becquerel: Sur les radiations invisibles émises par les corps phosphorescents, Com. Rend. **122**, 501–503 (1896), in French
- 50.4 M. Curie: Rayons émises par les composés de l'uranium et du thorium, Com. Rend. **126**, 1101–1103 (1898), in French
- 50.5 P. Curie, M. Curie: Sur une substance nouvelle radio-active, continue dans la pechblende, Com. Rend. **127**, 175–178 (1898), in French
- 50.6 L. Ozawa, M. Itoh: Cathode ray tube phosphors, Chem. Rev. **103**, 3835–3855 (2003)
- 50.7 R. Hofstätter: The detection of gamma-rays with thallium-activated sodium iodide crystals, Phys. Rev. **75**, 796–810 (1949)
- 50.8 W. Van Sciver, R. Hofstätter: Scintillations in thallium-activated CaI_2 and CsI , Phys. Rev. **84**, 1062–1063 (1951)
- 50.9 M.J. Weber: Inorganic scintillators: today and tomorrow, J. Lumin. **100**, 35–45 (2002)
- 50.10 M.J. Weber, R.R. Monchamp: Luminescence of $\text{Bi}_4\text{Ge}_3\text{O}_{12}$: spectral and decay properties, J. Appl. Phys. **44**, 5495–5499 (1973)
- 50.11 C.W.E. van Eijk, J. Andriessen, P. Dorenbos, R. Visser: Ce^{3+} doped inorganic scintillators, Nucl. Instrum. Methods Phys. Res. A **348**, 546–550 (1994)
- 50.12 C.W.E. van Eijk: Inorganic-scintillator development, Nucl. Instrum. Methods Phys. Res. A **460**, 1–14 (2001)
- 50.13 G. Blasse, B.C. Grabmaier: *Luminescent Materials* (Springer, Berlin 1994)
- 50.14 G.F. Knoll: *Radiation Detection and Measurement* (Wiley, New York 2000)
- 50.15 P.A. Rodnyi: *Physical Processes in Inorganic Scintillators* (CRC, Boca Raton 1997)
- 50.16 S. Shionoya, W.M. Yen (Eds.): *Phosphor Handbook* (CRC, Boca Raton 1998)
- 50.17 L.H. Brixner: New x-ray phosphors, Mater. Chem. Phys. **16**, 253–281 (1987)
- 50.18 M. Ishii, M. Kobayashi: Single crystals for radiation detectors, Prog. Cryst. Growth Charact. Mater. **23**, 245–311 (1992)
- 50.19 A.J. Wojtowicz: Rare-earth-activated wide band-gap materials for scintillators, Nucl. Instrum. Methods Phys. Res. A **486**, 201–207 (2002)
- 50.20 C.W.E. van Eijk: Inorganic scintillators in medical imaging, Phys. Med. Biol. **47**, R85–R106 (2002)
- 50.21 M. Nikl: Scintillation detectors for x-rays, Meas. Sci. Technol. **17**, R37–R54 (2006)
- 50.22 M. Nikl: Wide band gap scintillation materials: Progress in the technology and material understanding, Phys. Status Solidi (a) **178**, 595–620 (2000)
- 50.23 D.J. Robbins: On predicting the maximum efficiency of phosphor systems excited by ionizing radiation, J. Electrochem. Soc. **127**, 2694–2702 (1980)
- 50.24 A. Lempicki, A.J. Wojtowicz, E. Berman: Fundamental limits of scintillator performance, Nucl. Instrum. Methods Phys. Res. A **333**, 304–311 (1993)
- 50.25 P.A. Rodnyi, P. Dorenbos, C.W.E. van Eijk: Energy loss in inorganic scintillators, Phys. Status Solidi (b) **187**, 15–29 (1995)

- 50.26 A.N. Vasil'ev: Polarization approximation for electron cascade in insulators after high-energy excitation, *Nucl. Instrum. Methods Phys. Res. B* **107**, 165–171 (1996)
- 50.27 J.A. Shepherd, S.M. Gruner, M.W. Tate, M. Tecotzky: Study of afterglow in x-ray phosphors for use on fast-framing charge-coupled device detectors, *Opt. Eng.* **36**, 3212–3222 (1997)
- 50.28 S. Kubota, J. Ruan, M. Itoh, S. Hashimoto, S. Sakuragi: A new type of luminescence mechanism in large band-gap insulators: Proposal for fast scintillation materials, *Nucl. Instrum. Methods Phys. Res. A* **289**, 253–260 (1990)
- 50.29 M. Nikl, N. Solovieva, K. Apperson, D.J.S. Birch, A. Voloshinovskii: Scintillators based on aromatic dye molecules doped in a sol-gel glass host, *Appl. Phys. Lett.* **86**, 101914 (2005)
- 50.30 S.E. Derenzo, M.J. Weber, M.K. Klintonberg: Temperature dependence of the fast, near-band-edge scintillation from CuI, HgI₂, PbI₂, ZnO:Ga and CdS:In, *Nucl. Instrum. Methods Phys. Res. A* **486**, 214–219 (2002)
- 50.31 J. Wilkinson, K.B. Ucer, R.T. Williams: Picosecond excitonic luminescence in ZnO and other wide-gap semiconductors, *Radiat. Meas.* **38**, 501–505 (2004)
- 50.32 D. Ehrentraut, H. Sato, Y. Kagamitani, A. Yoshikawa, T. Fukuda, J. Pejchal, K. Polak, M. Nikl, H. Odaka, K. Hatanaka, H. Fukumura: Fabrication and luminescence properties of single-crystalline, homoepitaxial zinc oxide films doped with tri- and tetravalent cations prepared by liquid phase epitaxy, *J. Mater. Chem.* **16**, 3369–3374 (2006)
- 50.33 M. Nikl: Energy transfer phenomena in the luminescence of wide band-gap scintillators, *Phys. Status Solidi (a)* **202**, 201–206 (2005)
- 50.34 M. Nikl, K. Nitsch, K. Polak, E. Mihóková, I. Dafinei, E. Auffray, P. Lecoq, P. Reiche, R. Uecker: Slow components in the photoluminescence and scintillation decays of PbWO₄ single crystals, *Phys. Status Solidi (b)* **195**, 311–323 (1996)
- 50.35 P. Dorenbos, J.P.M. de Haas, C.W.E. van Eijk: Non-proportionality in the scintillation response and the energy resolution obtainable with scintillation crystals, *IEEE Trans. Nucl. Sci.* **42**, 2190–2202 (1995)
- 50.36 C.D. Brandle: Czochralski growth of oxides, *J. Cryst. Growth* **264**, 593–604 (2004)
- 50.37 T. Fukuda, R. Rudolph, S. Uda: *Fiber Crystal Growth from the Melt* (Springer, Berlin 2004)
- 50.38 A. Yoshikawa, M. Nikl, G. Boulon, T. Fukuda: Challenge and study for developing of novel single-crystalline optical materials using micro-pulling down method, *Opt. Mater.* **30**, 6–10 (2007)
- 50.39 M. Nikl, J.A. Mareš, J. Chval, E. Mihóková, N. Solovieva, M. Martini, A. Vedda, K. Blažek, P. Maly, K. Nejezchleb, P. Fabeni, G.P. Pazzi, V. Babin, K. Kalder, A. Krasnikov, S. Zazubovich, C. D'Ambrosio: An effect of Zr⁴⁺ co-doping of YAP:Ce scintillator, *Nucl. Instrum. Methods Phys. Res. A* **486**, 250–253 (2002)
- 50.40 C. Brecher, A. Lempicki, S.R. Miller, J. Glodo, E.E. Ovechkina, V. Gaysinskiy, V.V. Nagarkar, R.H. Bartram: Suppression of afterglow in CsI:TI by codoping with Eu²⁺ – I: Experimental, *Nucl. Instrum. Methods Phys. Res. A* **558**, 450–457 (2006)
- 50.41 J. Hlinka, E. Mihóková, M. Nikl, K. Polak, J. Rosa: Energy transfer between A_T and A_X minima in KBr:TI, *Phys. Status Solidi (b)* **175**, 523–540 (1993)
- 50.42 S.W.S. McKeever: *Thermoluminescence of Solids* (Cambridge University Press, Cambridge 1985)
- 50.43 R. Chen, S.W.S. McKeever: *Theory of Thermoluminescence and Related Phenomena* (World Scientific, Singapore 1997)
- 50.44 J.A. Weil, J.R. Bolton, J.E. Wertz: *Electron Paramagnetic Resonance: Elementary Theory and Practical Applications* (Wiley, New York 1994)
- 50.45 J.-M. Spaeth, J.R. Niklas, R.H. Bartram: *Structural Analysis of Point Defects in Solids: An Introduction to Multiple Magnetic Resonance Spectroscopy* (Springer, Berlin 1992)
- 50.46 V.V. Laguta, M. Martini, A. Vedda, M. Nikl, E. Mihóková, P. Boháček, J. Rosa, A. Hofstaetter, B.K. Meyer, Y. Usuki: Photoinduced Pb²⁺ center in PbWO₄: Electron spin resonance and thermally stimulated luminescence study, *Phys. Rev. B* **64**, 165102 (2001)
- 50.47 W. van Loo: Luminescence of lead molybdate and lead tungstate. I. Experimental, *Phys. Status Solidi (a)* **27**, 565–574 (1979)
- 50.48 W. van Loo: Luminescence of lead molybdate and lead tungstate. II. Discussion, *Phys. Status Solidi (a)* **28**, 227–235 (1979)
- 50.49 J.A. Groening, G. Blasse: Some new observations on the luminescence of PbMoO₄ and PbWO₄, *J. Solid State Chem.* **32**, 9–20 (1980)
- 50.50 R. Öder, A. Scharmann, D. Schwabe, B. Vitt: Growth and properties of PbWO₄ and Pb(WO₄)_{1-x}(MoO₄)_x mixed crystals, *J. Cryst. Growth* **43**, 537–540 (1978)
- 50.51 V.G. Baryshevsky, M.V. Korzhik, V.I. Moroz, V.B. Pavlenko, A.S. Lobko, A.A. Fyodorov, V.A. Kachanov, V.L. Solovjanov, B.I. Zadneprovsky, V.A. Nefyodov, P.V. Nefyodov, B.A. Dorogovin, L.L. Nagornaja: Single crystals of tungsten compounds as promising materials for the total absorption detectors of the e.m. calorimeters, *Nucl. Instrum. Methods Phys. Res. A* **322**, 231–234 (1992)
- 50.52 M. Kobayashi, M. Ishii, Y. Usuki, H. Yahagi: Scintillation characteristics of PbWO₄ single crystals at room temperature, *Nucl. Instrum. Methods Phys. Res. A* **333**, 429–433 (1993)
- 50.53 K. Nitsch, M. Nikl, S. Ganschow, P. Reiche, R. Uecker: Growth of lead tungstate single crystal scintillators, *J. Cryst. Growth* **165**, 163–165 (1996)

- 50.54 K. Tanji, M. Ishii, Y. Usuki, M. Kobayashi, K. Hara, H. Takano, N. Senguttuvan: Crystal growth of PbWO_4 by the vertical Bridgman method: Effect of crucible thickness and melt composition, *J. Cryst. Growth* **204**, 505–511 (1999)
- 50.55 A.A. Annenkov, M.V. Korzhik, P. Lecoq: Lead tungstate scintillation material, *Nucl. Instrum. Methods Phys. Res. A* **490**, 30–50 (2002)
- 50.56 R. Mao, J. Chen, D. Shen, Z. Yin: Growth and uniformity improvement of PbWO_4 crystal with yttrium doping, *J. Cryst. Growth* **265**, 518–524 (2004)
- 50.57 A.N. Annenkov, E. Auffray, R. Chipaux, G.Y. Drobyshev, A.A. Fedorov, M. Géléoc, N.A. Golubev, M.V. Korzhik, P. Lecoq, A.A. Lednev, A.B. Ligon, O.V. Mishevitch, V.B. Pavlenko, J.-P. Peigneux, A.V. Singovski: Systematic study of the short-term instability of PbWO_4 scintillator parameters under irradiation, *Radiat. Meas.* **29**, 27–38 (1998)
- 50.58 P. Boháček, M. Nikl, J. Novak, Z. Malkova, B. Trunda, J. Rysavy, S. Baccaro, A. Cecilia, I. Dafinei, M. Diemoz, K. Jurek: Congruent composition of PbWO_4 single crystals, *J. Electr. Eng.* **50(2/s)**, 38–40 (1999)
- 50.59 N. Lei, B. Han, X.Q. Feng, G. Hu, Y. Zhang, Z. Yin: La^{3+} distribution and annealing effects in La:PbWO_4 crystal, *Phys. Status Solidi (a)* **170**, 37–45 (1998)
- 50.60 A. Krasnikov, M. Nikl, S. Zazubovich: Localized excitons and defects in PbWO_4 single crystals: A luminescence and photo-thermally stimulated disintegration study, *Phys. Status Solidi (b)* **243**, 1727–1743 (2006)
- 50.61 V. Murk, M. Nikl, E. Mihókova, K. Nitsch: A study of electron excitations in CaWO_4 and PbWO_4 single crystals, *J. Phys. Cond. Matter* **9**, 249–256 (1997)
- 50.62 M. Kobayashi, M. Ishii, K. Harada, Y. Usuki, H. Okuno, H. Shimizu, T. Yazawa: Scintillation and phosphorescence of PbWO_4 crystals, *Nucl. Instrum. Methods Phys. Res. A* **373**, 333–346 (1996)
- 50.63 M. Böhm, A.E. Borisevich, G.Y. Drobyshev, G.Y. Drobyshev, A. Hofstaetter, O.V. Kondratiev, M.V. Korzhik, M. Luh, B.K. Meyer, J.P. Peigneux, A. Scharmann: Influence of Mo impurity on the spectroscopic and scintillation properties of PbWO_4 crystals, *Phys. Status Solidi (a)* **167**, 243–252 (1998)
- 50.64 V. Babin, P. Boháček, A. Krasnikov, M. Nikl, A. Stolovits, S. Zazubovich: Origin of green luminescence in PbWO_4 crystals, *J. Lumin.* **124**, 113–119 (2007)
- 50.65 G.P. Pazzi, P. Fabeni, M. Nikl, P. Bohacek, E. Mihokova, A. Vedda, M. Martini, M. Kobayashi, Y. Usuki: Delayed recombination luminescence in lead tungstate (PWO) scintillating crystals, *J. Luminesc.* **102/103**, 791–796 (2003)
- 50.66 M. Martini, G. Spinolo, A. Vedda, M. Nikl, K. Nitsch, V. Hamplova, P. Fabeni, G.P. Pazzi, I. Dafinei, P. Lecoq: Trap levels in PbWO_4 crystals: Correlation with luminescence decay kinetics, *Chem. Phys. Lett.* **260**, 418–422 (1996)
- 50.67 A.N. Annenkov, E. Auffray, A.E. Borisevich, G.Y. Drobyshev, A.A. Fedorov, O.V. Kondratiev, M.V. Korzhik, P. Lecoq: Slow components and afterglow in PWO crystal scintillations, *Nucl. Instrum. Methods Phys. Res. A* **403**, 302–312 (1998)
- 50.68 E. Mihókova, M. Nikl, P. Boháček, V. Babin, A. Krasnikov, A. Stolovich, S. Zazubovich, A. Vedda, M. Martini, T. Grabowski: Decay kinetics of the green emission in $\text{PbWO}_4\text{:Mo}$, *J. Lumin.* **102–103**, 618–622 (2003)
- 50.69 A. Hofstaetter, A. Scharmann, D. Schwabe, B. Vitt: EPR of radiation induced MoO_4^{3-} centres in lead tungstate, *Z. Phys. B* **30**, 305–311 (1978)
- 50.70 E. Auffray, I. Dafinei, P. Lecoq, M. Schneegans: Local trap centres in PbWO_4 crystals, *Radiat. Eff. Defects Solids* **135**, 841–845 (1995)
- 50.71 M. Springis, V. Tale, I. Tale: Nature of the blue luminescence bands in PbWO_4 , *J. Lumin.* **72–74**, 784–785 (1997)
- 50.72 V.V. Laguta, J. Rosa, M.I. Zaritskii, M. Nikl, Y. Usuki: Polaronic $(\text{WO}_4)^{3-}$ centres in PbWO_4 single crystals, *J. Phys. Cond. Matter* **10**, 7293–7302 (1998)
- 50.73 M. Martini, G. Spinolo, A. Vedda, M. Nikl, Y. Usuki: Shallow traps in PbWO_4 studied by wavelength-resolved thermally stimulated luminescence, *Phys. Rev. B* **60**, 4653–4658 (1999)
- 50.74 V.V. Laguta, M. Martini, A. Vedda, E. Rosetta, M. Nikl, E. Mihokova, P. Boháček, J. Rosa, A. Hofstatter, B.K. Meyer, Y. Usuki: Photoinduced oxygen-vacancy related centers in PbWO_4 : Electron spin resonance and thermally stimulated luminescence study, *Radiat. Eff. Defects Solids* **157**, 1025–1031 (2002)
- 50.75 A. Hofstaetter, M.V. Korzhik, V.V. Laguta, B.K. Meyer, V. Nagirnyi, R. Novotny: The role of defect states in the creation of intrinsic $(\text{WO}_4)^{3-}$ centers in PbWO_4 by sub-bandgap excitation, *Radiat. Meas.* **33**, 533–536 (2001)
- 50.76 V.V. Laguta, M. Martini, A. Vedda, E. Rosetta, M. Nikl, E. Mihókova, J. Rosa, Y. Usuki: Electron traps related to oxygen vacancies in PbWO_4 , *Phys. Rev. B* **67**, 205102 (2003)
- 50.77 M. Nikl, P. Boháček, K. Nitsch, E. Mihokova, M. Martini, A. Vedda, S. Crocci, G.P. Pazzi, P. Fabeni, S. Baccaro, B. Borgia, I. Dafinei, M. Diemoz, G. Organtini, E. Auffray, P. Lecoq, M. Kobayashi, M. Ishii, Y. Usuki: Decay kinetics and thermoluminescence $\text{PbWO}_4\text{:La}^{3+}$, *Appl. Phys. Lett.* **71**, 3755–3757 (1997)
- 50.78 S. Baccaro, P. Boháček, B. Borgia, A. Cecilia, I. Dafinei, M. Diemoz, M. Ishii, O. Jarolimek, M. Kobayashi, M. Martini, M. Montecchi, M. Nikl, K. Nitsch, Y. Usuki, A. Vedda: Influence of La^{3+} -doping on radiation hardness and

- thermoluminescence characteristics of PbWO_4 , Phys. Status Solidi (a) **160**, R5–R6 (1997)
- 50.79 S. Baccaro, P. Boháček, A. Cecilia, S. Croci, I. Dafinei, M. Diemoz, P. Fabeni, M. Ishii, O. Jarolimek, M. Kobayashi, M. Martini, M. Montecchi, M. Nikl, G. Organtini, G.P. Pazzi, J. Rosa, Y. Usuki, A. Vedda: The influence of defect states on scintillation characteristics of PbWO_4 , Radiat. Eff. Defects Solids **150**, 15–19 (1999)
- 50.80 V.V. Laguta, M. Martini, F. Meinardi, A. Vedda, A. Hofstaetter, B.K. Mayer, M. Nikl, E. Mihóková, J. Rosa, Y. Usuki: Photoinduced $(\text{WO}_4)^{3-}-\text{La}^{3+}$ center in PbWO_4 : Electron spin resonance and thermally stimulated luminescence study, Phys. Rev. B **62**, 10109–10114 (2000)
- 50.81 V.V. Laguta, A. Vedda, D. Di Martino, M. Martini, M. Nikl, E. Mihóková, J. Rosa, Y. Usuki: Electron capture in $\text{PbWO}_4:\text{Mo}$ and $\text{PbWO}_4:\text{Mo},\text{La}$ single crystals: ESR and TSL study, Phys. Rev. B **71**, 235108 (2005)
- 50.82 A. Hofstaetter, R. Öder, A. Scharman, D. Schwabe, B. Vitt: Paramagnetic resonance and thermoluminescence of the $\text{PbWO}_4/\text{PbMoO}_4$ mixed crystal system, Phys. Status Solidi (b) **89**, 375–380 (1978)
- 50.83 M. Nikl, P. Boháček, E. Mihóková, N. Solovieva, A. Vedda, M. Martini, G.P. Pazzi, P. Fabeni, M. Kobayashi: Complete characterization of doubly doped $\text{PbWO}_4:\text{Mo},\text{Y}$ scintillators, J. Appl. Phys. **91**, 2791–2797 (2002)
- 50.84 M. Kobayashi, Y. Usuki, M. Ishii, T. Yazawa, K. Hara, M. Tanaka, M. Nikl, K. Nitsch: Improvement in transmittance and decay time of PbWO_4 scintillating crystals by La-doping, Nucl. Instrum. Methods Phys. Res. A **399**, 261–268 (1997)
- 50.85 M. Kobayashi, Y. Usuki, M. Ishii, T. Yazawa, K. Hara, M. Tanaka, M. Nikl, S. Baccaro, A. Cecilia, M. Diemoz, I. Dafinei: Improvement of radiation hardness of PbWO_4 scintillating crystals by La-doping, Nucl. Instrum. Methods Phys. Res. A **404**, 149–156 (1998)
- 50.86 Y.B. Abraham, N.A.W. Holzwarth, R.T. Williams, G.E. Matthews, A.R. Tackett: Electronic structure of oxygen-related defects in PbWO_4 and CaMoO_4 crystals, Phys. Rev. B **64**, 245109 (2001)
- 50.87 M. Kobayashi, S. Sugimoto, Y. Yoshimura, Y. Usuki, M. Ishii, N. Senguttuvan, K. Tanji, M. Nikl: A new heavy and radiation-hard Cherenkov radiator based on PbWO_4 , Nucl. Instrum. Methods Phys. Res. A **459**, 482–493 (2001)
- 50.88 Y.L. Huang, W.L. Zhu, X.Q. Feng, Z.Y. Man: The effects of La^{3+} doping on luminescence properties of PbWO_4 single crystal, J. Solid State Chem. **172**, 188–193 (2003)
- 50.89 W. Li, X.Q. Feng, Y. Huang: Characteristics of the optical absorption edge and defect structures of La^{3+} -doped PbWO_4 crystals, J. Phys. Cond. Matter **16**, 1325–1333 (2004)
- 50.90 T. Chen, T.Y. Liu, Q.R. Zhang, F.F. Li, D.S. Tian, X.Y. Zhang: First principles study of the La^{3+} doping PbWO_4 crystal for different doping concentrations, Phys. Lett. A **363**, 477–481 (2007)
- 50.91 M. Nikl, K. Nitsch, S. Baccaro, A. Cecilia, M. Montecchi, B. Borgia, I. Dafinei, M. Diemoz, M. Martini, E. Rosetta, G. Spinolo, A. Vedda, M. Kobayashi, M. Ishii, Y. Usuki, O. Jarolimek, R. Uecker: Radiation induced formation of color centres in PbWO_4 single crystals, J. Appl. Phys. **82**, 5758–5762 (1997)
- 50.92 T. Liu, Q. Zhang, X. Mi, X.Q. Feng: A new absorption band and the decomposition of the 350 nm absorption band of PbWO_4 , Phys. Status Solidi (a) **184**, 341–348 (2001)
- 50.93 A. Annenkov, E. Auffray, M. Korzhik, P. Lecoq, J.P. Peigneux: On the origin of the transmission damage in lead tungstate crystals under irradiation, Phys. Status Solidi (a) **170**, 47–62 (1998)
- 50.94 Q. Lin, X.Q. Feng, Z. Man, Y. Zhang, Z. Yin, Q. Zhang: Origin of the radiation-induced 420 nm color center absorption band in PbWO_4 crystals, Solid State Commun. **118**, 221–223 (2001)
- 50.95 Q. Deng, Z. Yin, R.Y. Zhu: Radiation-induced color centers in La-doped PbWO_4 crystals, Nucl. Instrum. Methods Phys. Res. A **438**, 415–420 (1999)
- 50.96 S. Burachas, Y. Saveliev, M. Ippolitov, V. Manko, V. Lomonosov, A. Vasiliev, A. Apanasenko, A. Vasiliev, A. Uzunian, G. Tamulaitis: Physical origin of coloration and radiation hardness of lead tungstate scintillation crystals, J. Cryst. Growth **293**, 62–67 (2006)
- 50.97 M. Kobayashi, Y. Usuki, M. Ishii, M. Itoh, M. Nikl: Further study on different dopings into PbWO_4 single crystals to increase the scintillation light yield, Nucl. Instrum. Methods Phys. Res. A **540**, 381–394 (2005)
- 50.98 M. Nikl, P. Boháček, A. Vedda, M. Martini, G.P. Pazzi, P. Fabeni, M. Kobayashi: Efficient medium-speed $\text{PbWO}_4:\text{Mo},\text{Y}$ scintillator, Phys. Status Solidi (a) **182**, R3–R5 (2000)
- 50.99 A. Annenkov, A. Borisevitch, A. Hofstaetter, M. Korzhik, V. Ligun, P. Lecoq, O. Missevitch, R. Novotny, J.P. Peigneux: Improved light yield of lead tungstate scintillators, Nucl. Instrum. Methods Phys. Res. A **450**, 71–74 (2000)
- 50.100 M. Nikl, P. Boháček, E. Mihóková, N. Solovieva, A. Vedda, M. Martini, G.P. Pazzi, P. Fabeni, M. Kobayashi: Complete characterization of doubly doped $\text{PbWO}_4:\text{Mo},\text{Y}$ scintillators, J. Appl. Phys. **91**, 2791–2797 (2002)
- 50.101 J.A. Mareš, A. Beitlerova, P. Boháček, M. Nikl, N. Solovieva, C. D'Ambrosio: Influence of non-stoichiometry and doping on scintillating response of PbWO_4 crystals, Phys. Status Solidi (c) **2**, 73–76 (2005)
- 50.102 X. Liu, G. Hu, X. Feng, Y. Huang, Y. Zhang: Influence of PbF_2 doping on scintillation properties of PbWO_4

- single crystals, *Phys. Status Solidi (a)* **190**, R1–R3 (2002)
- 50.103 M. Nikl, P. Boháček, E. Mihóková, N. Solovieva, A. Vedda, M. Martini, G.P. Pazzi, P. Fabeni, M. Ishii: Enhanced efficiency of $\text{PbWO}_4\text{:Mo,Nb}$ scintillator, *J. Appl. Phys.* **91**, 5041–5044 (2002)
- 50.104 M.J. Weber: Optical spectra of Ce^{3+} and Ce^{3+} -sensitized fluorescence in YAlO_3 , *J. Appl. Phys.* **44**, 3205–3208 (1973)
- 50.105 T. Takeda, T. Miyata, F. Muramatsu, T. Tomiki: Fast decay UV phosphor- $\text{YAlO}_3\text{:Ce}$, *J. Electrochem. Soc.* **127**, 438–444 (1980)
- 50.106 E. Autrata, P. Schauer, J. Kvapil, J. Kvapil: A single crystal of $\text{YAlO}_3\text{:Ce}^{3+}$ as a fast scintillator in SEM, *Scanning* **5**, 91–96 (1983)
- 50.107 M. Nikl, A. Vedda, V.V. Laguta: Energy transfer and storage processes in scintillators: The role and nature of defects, *Radiat. Meas.* **42**, 509–514 (2007)
- 50.108 J. Kvapil, J. Kvapil, J. Kubelka, R. Autrata: The role of iron ions in YAG and YAP, *Cryst. Res. Technol.* **18**, 127–131 (1983)
- 50.109 G.-S. Li, X.-B. Guo, J. Lu, Z.-Z. Shi, J.-H. Wu, Y. Chen, J.-F. Chen: Application of several new procedures to improve the quality of Czochralski grown $\text{Nd}^{3+}\text{:YAlO}_3$ crystals, *J. Cryst. Growth* **118**, 371–376 (1992)
- 50.110 D.I. Savytskii, L.O. Vasylychko, A.O. Matkovskii, I.M. Solskii, A. Suchocki, D.Y. Sugak, F. Wallrafen: Growth and properties of $\text{YAlO}_3\text{:Nd}$ single crystals, *J. Cryst. Growth* **209**, 874–882 (2000)
- 50.111 G.-S. Li, Z.-Z. Shi, J.-H. Wu, Y. Chen, J.-F. Chen, H. Yang: Growth of large size yttrium aluminum perovskite (YAP) laser crystals without light scattering centers, *J. Cryst. Growth* **119**, 363–367 (1992)
- 50.112 J. Kvapil, B. Manek, B. Perner, J. Kvapil, R. Becker, G. Ringel: The role of argon in yttrium aluminates, *Cryst. Res. Technol.* **23**, 549–554 (1988)
- 50.113 A.G. Petrosyan, G.O. Shirinyan, C. Pédrini, C. Dujardin, K.L. Ovanesyan, R.G. Manucharyan, T.I. Butaeva, M.V. Derzyan: Bridgman growth and characterization of $\text{LuAlO}_3\text{-Ce}^{3+}$ scintillator crystals, *Cryst. Res. Technol.* **33**, 241–248 (1998)
- 50.114 J.A. Mareš, N. Cechova, M. Nikl, J. Kvapil, R. Kratky, J. Pospisil: Cerium-doped $\text{RE}^{3+}\text{AlO}_3$ perovskite scintillators: spectroscopy and radiation induced defects, *J. Alloy. Comp.* **275–277**, 200–204 (1998)
- 50.115 A.G. Petrosyan, G.O. Shyrinyan, K.L. Ovanesyan, C. Pédrini, C. Dujardin: Bridgman single crystal growth of Ce-doped $(\text{Lu}_{1-x}\text{Y}_x)\text{AlO}_3$, *J. Cryst. Growth* **198–199**, 492–496 (1999)
- 50.116 J. Trummer, E. Auffray, P. Lecoq, A.G. Petrosyan, P. Sempere-Roldan: Comparison of LuAP and LuYAP crystal properties from statistically significant batches produced with two different growth methods, *Nucl. Instrum. Methods Phys. Res. A* **551**, 339–351 (2005)
- 50.117 T. Tomiki, H. Ishikawa, T. Tashiro, M. Katsuren, A. Yonesu, T. Hotta, T. Yabiku, M. Akamine, T. Futemma, T. Nakaoka, I. Miyazato: Ce^{3+} centres in YAlO_3 (YAP) single crystals, *J. Phys. Soc. Jpn.* **64**, 4442–4449 (1995)
- 50.118 V.G. Baryshevsky, M.V. Korzhik, V.I. Moroz, V.B. Pavlenko, A.A. Fyodorov, S.A. Smirnova, O.A. Egorycheva, V.A. Kachanov: $\text{YAlO}_3\text{:Ce}$ -fast-acting scintillators for detection of ionizing radiation, *Nucl. Instrum. Methods Phys. Res. B* **58**, 291–293 (1991)
- 50.119 S.I. Ziegler, J.G. Rogers, V. Selivanov, I. Sinitzin: Characteristics of the new $\text{YAlO}_3\text{:Ce}$ compared with BGO and GSO, *IEEE Trans. Nucl. Sci.* **40**, 194–197 (1993)
- 50.120 J.A. Mareš, A. Beitlerova, M. Nikl, N. Solovieva, C. D'Ambrosio, K. Blažek, P. Maly, K. Nejezchle, F. de Notaristefani: Scintillation response of Ce-doped or intrinsic scintillating crystals in the range up to 1 MeV, *Radiat. Meas.* **38**, 353–357 (2004)
- 50.121 C. Dujardin, C. Pédrini, J.C. Gacon, A.G. Petrosyan, A.N. Belsky, A.N. Vasil'ev: Luminescence properties and scintillation mechanisms of cerium- and praseodymium-doped lutetium orthoaluminate, *J. Phys. Cond. Matter* **9**, 5229–5243 (1997)
- 50.122 E.G. Gumanskaya, M.V. Korzhik, S.A. Smirnova, V.B. Pavlenko, A.A. Fedorov: Interconfiguration luminescence of Pr^{3+} ions in $\text{Y}_3\text{Al}_5\text{O}_{12}$ and YAlO_3 single crystals, *Opt. Spectrosc.* **72**, 155–159 (1992), in Russian
- 50.123 W. Drozdowski, A.J. Wojtowicz, D. Wisniewski, T. Lukasiewicz, J. Kisielewski: Scintillation properties of Pr-activated LuAlO_3 , *Opt. Mater.* **28**, 102–105 (2006)
- 50.124 M. Zhuravleva, A. Novoselov, A. Yoshikawa, J. Pejchal, M. Nikl, T. Fukuda: Crystal growth and scintillation properties of Pr-doped YAlO_3 , *Opt. Mater.* **30**, 171–173 (2007)
- 50.125 L. van Pieterse, M. Heeroma, E. de Heer, A. Meijerink: Charge transfer luminescence of Yb^{3+} , *J. Lumin.* **91**, 177–193 (2000)
- 50.126 M. Nikl, A. Yoshikawa, T. Fukuda: Charge transfer luminescence in Yb^{3+} -containing compounds, *Opt. Mater.* **26**, 545–549 (2004)
- 50.127 M. Nikl, N. Solovieva, J. Pejchal, J.B. Shim, A. Yoshikawa, T. Fukuda, A. Vedda, M. Martini, D.H. Yoon: Very fast $\text{Yb}_x\text{Y}_{1-x}\text{AlO}_3$ single crystal scintillators, *Appl. Phys. Lett.* **84**, 882–884 (2004)
- 50.128 J.B. Shim, A. Yoshikawa, T. Fukuda, J. Pejchal, M. Nikl, N. Sarukura, D.H. Yoon: Growth and charge transfer luminescence of Yb^{3+} -doped YAlO_3 single crystals, *J. Appl. Phys.* **95**, 3063–3068 (2004)
- 50.129 H.R. Asatryan, J. Rosa, J.A. Mareš: EPR studies of Er^{3+} , Nd^{3+} and Ce^{3+} in YAlO_3 single crystals, *Solid State Commun.* **104**, 5–9 (1997)

- 50.130 C. Dujardin, C. Pedrini, W. Blanc, J.C. Gâcon, J.C. van't Spijker, O.W.V. Frijns, C.W.E. van Eijk, P. Dorenbos, R. Chen, A. Fremout, F. Tallouf, S. Tavernier, P. Bruyndonckx, A.G. Petrosyan: Optical and scintillation properties of large $\text{LuAlO}_3\text{:Ce}^{3+}$ crystals, *J. Phys. Condens. Matter* **10**, 3061–3073 (1998)
- 50.131 A.J. Wojtowicz, J. Glodo, A. Lempicki, C. Brecher: Recombination and scintillation processes in $\text{YAlO}_3\text{:Ce}$, *J. Phys. Cond. Matter* **10**, 8401–8415 (1998)
- 50.132 A. Vedda, M. Martini, F. Meinardi, J.A. Mareš, E. Mihóková, J. Chval, M. Dusek, M. Nikl: Tunnelling process in thermally stimulated luminescence of mixed $\text{Lu}_x\text{Y}_{1-x}\text{AlO}_3\text{:Ce}$ crystals, *Phys. Rev. B* **61**, 8081–8086 (2000)
- 50.133 J. Kvapil, Jos. Kvapil, B. Perner, B. Manek, K. Blažek, Z. Hendrich: Nonstoichiometric defects in YAG and YAP, *Cryst. Res. Technol.* **20**, 473–478 (1985)
- 50.134 D. Sugak, A. Matkovskii, D. Savitskii, A. Durygin, A. Suchocki, Y. Zhydashchevskii, I. Solskii, I. Stefaniuk, F. Wallrafen: Growth and induced color centers in $\text{YAlO}_3\text{--Nd}$ single crystals, *Phys. Status Solidi (a)* **184**, 239–250 (2001)
- 50.135 J.A. Mareš, M. Nikl, E. Mihóková, N. Solovieva, K. Blažek, K. Nejezchleb, P. Maly, J. Pejchal, V. Mucka, M. Pospisil, A. Vedda, M. Martini, S. Baccaro: Radiation induced absorption color centers and damage in $\text{YAlO}_3\text{:Ce}$ and $\text{YAlO}_3\text{:Ce,Zr}$ scintillators, *Radiat. Eff. Defects Solids* **157**, 677–681 (2002)
- 50.136 O.F. Schirmer, K.W. Blazey, W. Berlinger, R. Diehl: ESR and optical absorption of bound-small polarons in YAlO_3 , *Phys. Rev. B* **11**, 4201–4218 (1975)
- 50.137 V.Y. Zorenko, A.S. Voloshinovskii, I.V. Konstantkevych, G.B. Striganyuk, V.I. Gorbenco: Exciton luminescence of YAlO_3 single crystals and single-crystal films, *Opt. Spectrosc.* **98**, 555–558 (2005)
- 50.138 V.Y. Zorenko, A.S. Voloshinovskii, I.V. Konstantkevych: Luminescence of F^{+} and F centers in YAlO_3 , *Opt. Spectrosc.* **96**, 532–537 (2004)
- 50.139 V.V. Laguta, M. Nikl, A. Vedda, E. Mihokova, J. Rosa, K. Blazek: The hole and electron traps in the YAlO_3 single crystal scintillator, *Phys. Rev. B* **80**, 045114 (2009)
- 50.140 E. Mihóková, M. Nikl, J.A. Mareš, A. Beitlerová, A. Vedda, K. Nejezchleb, K. Blažek, C. D'Ambrosio: Luminescence and scintillation properties of YAG:Ce single crystal and optical ceramics, *J. Lumin.* **126**, 77–80 (2006)
- 50.141 V.V. Laguta, A.M. Slipenyuk, J. Rosa, M. Nikl, A. Vedda, K. Nejezchleb, K. Blažek: Electron spin resonance study of Mo^{3+} centers in YAlO_3 , *Radiat. Meas.* **38**, 735–738 (2004)
- 50.142 S.A. Basun, T. Danger, A.A. Kaplyanskii, D.S. McClure, K. Petermann, W.C. Wong: Optical and photoelectrical studies of charge-transfer processes in $\text{YAlO}_3\text{:Ti}$ crystals, *Phys. Rev. B* **54**, 6141–6149 (1996)
- 50.143 K. Blažek, A. Krasnikov, K. Nejezchleb, M. Nikl, T. Savikhina, S. Zazubovich: Luminescence and defect creation in Ce^{3+} -doped YAlO_3 and $\text{Lu}_{0.3}\text{Y}_{0.7}\text{AlO}_3$ crystals, *Phys. Status Solidi (b)* **242**, 1315–1323 (2005)
- 50.144 M. Nikl, E. Mihokova, V. Laguta, J. Pejchal, S. Baccaro, A. Vedda: Radiation damage processes in complex-oxide scintillators, *Eur. Symp. Opt. Optoelectron. Damage VUV, EUV, X-ray Opt.*, ed. by L. Juha, R.H. Sobierajski, H. Wabnitz (2007)
- 50.145 C.R. Stanek, M.R. Levy, K.J. McClellan, B.P. Uberuaga, R.W. Grimes: Defect structure of ZrO_2 -doped rare earth perovskite scintillators, *Phys. Status Solidi (b)* **242**, R113–R115 (2005)
- 50.146 C.R. Stanek, K.J. McClellan, M.R. Levy, R.W. Grimes: Defect behavior in rare earth REAlO_3 scintillators, *J. Appl. Phys.* **99**, 113518 (2006)
- 50.147 M. Kokta: Growth of oxide laser crystals, *Opt. Mater.* **30**, 1–5 (2007)
- 50.148 R. Autrata, P. Schauer, Jos. Kvapil, J. Kvapil: A single crystal of YAG – New fast scintillator in SEM, *J. Phys. E* **11**, 707–708 (1978)
- 50.149 M. Moszynski, T. Ludziewski, D. Wolski, W. Klamra, L.O. Norlin: Properties of the YAG:Ce scintillator, *Nucl. Instrum. Methods Phys. Res. A* **345**, 461–467 (1994)
- 50.150 A. Lempicki, M.H. Randles, D. Wisniewski, M. Balcerzyk, C. Brecher, A.J. Wojtowicz: $\text{LuAlO}_3\text{:Ce}$ and other aluminate scintillators, *IEEE Trans. Nucl. Sci.* **42**, 280–284 (1995)
- 50.151 M. Nikl, E. Mihóková, J.A. Mareš, A. Vedda, M. Martini, K. Nejezchleb, K. Blažek: Traps and timing characteristics of LuAg:Ce^{3+} scintillator, *Phys. Status Solidi (b)* **181**, R10–R12 (2000)
- 50.152 M.J. Weber: Nonradiative decay from 5d states of rare earths in crystals, *Solid State Commun.* **12**, 741–744 (1973)
- 50.153 Y. Kuwano, K. Suda, N. Ishizawa, T. Yamada: Crystal growth and properties of $(\text{Lu,Y})_3\text{Al}_5\text{O}_{12}$, *J. Cryst. Growth* **260**, 159–165 (2004)
- 50.154 J. Kvapil, Jos. Kvapil, B. Manek, B. Perner: Czochralski growth of YAG:Ce in a reducing protective atmosphere, *J. Cryst. Growth* **52**, 542–545 (1981)
- 50.155 D. Mateika, E. Volkel, J. Haisma: Lattice-constant-adaptable crystallographics. II. Czochralski growth from multicomponent melts of homogeneous mixed-garnet crystals, *J. Cryst. Growth* **102**, 994–1013 (1990)
- 50.156 D.S. Hamilton, S.K. Gayen, G.J. Pogatshnik, R.D. Ghen, W.J. Miniscalco: Optical absorption and photoionization measurements from the excited states of $\text{Ce}^{3+}\text{:Y}_3\text{Al}_5\text{O}_{12}$, *Phys. Rev. B* **39**, 8807–8815 (1989)
- 50.157 M. Nikl, V.V. Laguta, A. Vedda: Energy transfer and charge carrier capture processes in wide-

- band-gap scintillators, *Phys. Status Solidi (a)* **204**, 683–689 (2007)
- 50.158 M. Nikl, J.A. Mareš, N. Solovieva, J. Hybler, A. Voloshinovskii, K. Nejezchleb, K. Blažek: Energy transfer to the Ce^{3+} centers in $\text{Lu}_3\text{Al}_5\text{O}_{12}:\text{Ce}$ scintillator, *Phys. Status Solidi (a)* **201**, R41–R44 (2004)
- 50.159 W. Drozdowski, T. Lukasiewicz, A.J. Wojtowicz, D. Wisniewski, J. Kisielewski: Thermoluminescence and scintillation of praseodymium-activated $\text{Y}_3\text{Al}_5\text{O}_{12}$ and LuAlO_3 crystals, *J. Cryst. Growth* **275**, e709–e714 (2005)
- 50.160 M. Nikl, H. Ogino, A. Krasnikov, A. Beitlerova, A. Yoshikawa, T. Fukuda: Photo- and radioluminescence of Pr-doped $\text{Lu}_3\text{Al}_5\text{O}_{12}$ single crystal, *Phys. Status Solidi (a)* **202**, R4–R6 (2005)
- 50.161 H. Ogino, A. Yoshikawa, M. Nikl, K. Kamada, T. Fukuda: Scintillation characteristics of Pr-doped $\text{Lu}_3\text{Al}_5\text{O}_{12}$ single crystals, *J. Cryst. Growth* **292**, 239–242 (2006)
- 50.162 S.R. Rotman, C. Warde, H.L. Tuller, J. Haggerty: Defect property correlations in garnet crystals. V. Energy transfer in luminescent yttrium aluminum-yttrium iron garnet solid solutions, *J. Appl. Phys.* **66**, 3207–3210 (1989)
- 50.163 C.Y. Chen, G.J. Pogatschnik, Y. Chen, M.R. Kokta: Optical and electron paramagnetic resonance studies of Fe impurities in yttrium aluminum garnet crystals, *Phys. Rev. B* **38**, 8555–8561 (1988)
- 50.164 I. Kamenskikh, C. Dujardin, N. Garnier, N. Guerasimova, G. Ledoux, V. Mikhailin, C. Pedrini, A. Petrosyan, A. Vasil'ev: Temperature dependence of the charge transfer and f–f luminescence of Yb^{3+} in garnets and YAP, *J. Phys. Condens. Matter* **17**, 5587–5594 (2005)
- 50.165 V.V. Laguta, A.M. Slipenyuk, M.D. Glinchuk, M. Nikl, J. Rosa, A. Vedda, K. Nejezchleb: Paramagnetic impurity defects in LuAG and LuAG:Sc single crystals, *Opt. Mater.* **30**, 79–81 (2007)
- 50.166 H.R. Lewis: Paramagnetic resonance of Ce^{3+} in YAG, *J. Appl. Phys.* **37**, 739–741 (1966)
- 50.167 V.V. Laguta, A.M. Slipenyuk, M.D. Glinchuk, I.P. Bykov, Y. Zorenko, M. Nikl, J. Rosa: Paramagnetic impurity defects in LuAG:Ce thick film scintillators, *Radiat. Meas.* **42**, 835–838 (2007)
- 50.168 C.R. Stanek, K.J. McClellan, M.R. Levy, C. Milanese, R.W. Grimes: The effect of intrinsic defects on $\text{RE}_3\text{Al}_5\text{O}_{12}$ garnet scintillator performance, *Nucl. Instrum. Methods Phys. Res. A* **579**, 27–30 (2007)
- 50.169 M. Springis, A. Pujats, J. Valbis: Polarization of luminescence of colour centres in YAG crystals, *J. Phys. Cond. Matter* **3**, 5457–5461 (1991)
- 50.170 A. Pujats, M. Springis: The F-type centres in YAG crystals, *Radiat. Eff. Defects Solids* **155**, 65–69 (2001)
- 50.171 M.K. Ashurov, Y.K. Voronko, V.V. Osiko, A.A. Sobol, M.I. Timoshechkin: Spectroscopic study of stoichiometric deviation in crystals with garnet structure, *Phys. Status Solidi (a)* **42**, 101–110 (1977)
- 50.172 V. Lupei, A. Lupei, C. Tiseanu, S. Georgescu, C. Stoicescu, P.M. Nanau: High resolution optical spectroscopy of YAG:Nd: A test for structural and distribution models, *Phys. Rev. B* **51**, 8–17 (1995)
- 50.173 Y. Zorenko, V. Gorbenko, I. Konstankevych, A. Voloshinovskii, G. Stryganyuk, V. Mikhailin, V. Kolobanov, D. Spassky: Single-crystalline films of Ce-doped YAG and LuAG phosphors: advantages over bulk crystals analogues, *J. Lumin.* **114**, 85–94 (2005)
- 50.174 Y. Zorenko, V. Gorbenko, A. Voloshinovskii, G. Stryganyuk, V. Mikhailin, V. Kolobanov, D. Spassky, M. Nikl, K. Blažek: Exciton-related luminescence in LuAG:Ce single crystals and single crystalline films, *Phys. Status Solidi (a)* **202**, 1113–1119 (2005)
- 50.175 V. Murk, N. Yaroshevich: Exciton and recombination processes in YAG crystals, *J. Phys. Cond. Matter* **7**, 5857–5864 (1995)
- 50.176 N.N. Ryskin, P. Dorenbos, C.W.E. van Eijk, S.K. Batygov: Scintillation properties of $\text{Lu}_3\text{Al}_{5-x}\text{Sc}_x\text{O}_{12}$ crystals, *J. Phys. Cond. Matter* **6**, 10423–10434 (1994)
- 50.177 M. Nikl, E. Mihóková, J. Pejchal, A. Vedda, Y. Zorenko, K. Nejezchleb: The antisite Lu_{Al} defect-related trap in $\text{Lu}_3\text{Al}_5\text{O}_{12}:\text{Ce}$ single crystal, *Phys. Status Solidi (b)* **242**, R119–R121 (2005)
- 50.178 M. Nikl, E. Mihokova, J. Pejchal, A. Vedda, M. Fasoli, I. Fontana, V.V. Laguta, V. Babin, K. Nejezchleb, A. Yoshikawa, H. Ogino, G. Ren: Scintillator materials achievements, opportunities, and puzzles, *IEEE Trans. Nucl. Sci.* **55**, 1035–1041 (2008)
- 50.179 M. Nikl, J. Pejchal, E. Mihóková, J.A. Mareš, H. Ogino, A. Yoshikawa, T. Fukuda, A. Vedda, C. D'Ambrosio: Antisite defect-free $\text{Lu}_3(\text{Ga}_x\text{Al}_{1-x})_5\text{O}_{12}:\text{Pr}$ scintillator, *Appl. Phys. Lett.* **88**, 141916 (2006)
- 50.180 Y.-N. Xu, W.Y. Ching, B.K. Briceen: Electronic structure and bonding in garnet crystals $\text{Gd}_3\text{Sc}_2\text{Ga}_3\text{O}_{12}$, $\text{Gd}_3\text{Sc}_2\text{Al}_3\text{O}_{12}$, and $\text{Gd}_3\text{Ga}_3\text{O}_{12}$ compared to $\text{Y}_3\text{Al}_5\text{O}_{12}$, *Phys. Rev. B* **61**, 1817–1824 (2000)
- 50.181 A. Vedda, D. Di Martino, M. Martini, V.V. Laguta, M. Nikl, E. Mihóková, J. Rosa, K. Nejezchleb, K. Blažek: Thermoluminescence of Zr-codoped $\text{Lu}_3\text{Al}_5\text{O}_{12}:\text{Ce}$ crystals, *Phys. Status Solidi (a)* **195**, R1–R3 (2003)
- 50.182 C.R. Stanek, K.J. McClellan, M.R. Levy, R.W. Grimes: Extrinsic defect structure of $\text{RE}_3\text{Al}_5\text{O}_{12}$ garnets, *Phys. Status Solidi (b)* **243**, R75–R77 (2006)
- 50.183 K. Takagi, T. Fukazawa: Cerium-activated Gd_2SiO_5 single crystal scintillator, *Appl. Phys. Lett.* **42**, 43–45 (1983)
- 50.184 T. Utsu, S. Akiyama: Growth and applications of $\text{Gd}_2\text{SiO}_5:\text{Ce}$ scintillators, *J. Cryst. Growth* **109**, 385–391 (1991)
- 50.185 C.L. Melcher, R.A. Manente, C.A. Peterson, J.S. Schweizer: Czochralski growth of rare earth oxyorthosilicate single crystals, *J. Cryst. Growth* **128**, 1001–1005 (1993)

- 50.186 D.W. Cooke, K.J. McClellan, B.L. Bennett, J.M. Roper, M.T. Whittaker, R.E. Münchhausen, R.C. Sze: Crystal growth and optical characterization of cerium-doped $\text{Lu}_{1.8}\text{Y}_{0.2}\text{SiO}_5$, *J. Appl. Phys.* **88**, 7360–7362 (2000)
- 50.187 C.L. Melcher, M.A. Spurrier, L. Eriksson, M. Eriksson, M. Schmand, G. Givens, R. Terry, T. Homant, R. Nutt: Advances in the scintillation performances of $\text{LSO}:\text{Ce}$ single crystals, *IEEE Trans. Nucl. Sci.* **50**, 762–766 (2003)
- 50.188 M. Jie, G. Zhao, X. Zeng, L. Su, H. Pang, X. He, J. Xu: Crystal growth and optical properties of $\text{Gd}_{1.99-x}\text{Y}_x\text{Ce}_{0.01}\text{SiO}_5$ single crystals, *J. Cryst. Growth* **277**, 175–180 (2005)
- 50.189 J.D. Zavartsev, S.A. Koutovoi, A.I. Zagumennyi: Czochralski growth and characterization of large $\text{Ce}^{3+}:\text{Lu}_2\text{SiO}_5$ single crystals co-doped with Mg^{2+} or Ca^{2+} or Tb^{3+} for scintillators, *J. Cryst. Growth* **275**, e2167–e2171 (2005)
- 50.190 B. Hautefeuille, K. Lebbou, C. Dujardin, J.M. Fourmigue, L. Grosvalet, O. Tillement, C. Pédrini: Shaped crystal growth of Ce^{3+} -doped $\text{Lu}_{2(1-x)}\text{Y}_x\text{SiO}_5$ oxyorthosilicate for scintillator applications by pulling-down technique, *J. Cryst. Growth* **289**, 172–177 (2006)
- 50.191 C. Mansuy, R. Mahiou, J.–M. Nedelec: A new sol-gel route to Lu_2SiO_5 (LSO) scintillator: Powders and thin films, *Chem. Mater.* **15**, 3242–3244 (2003)
- 50.192 C. Mansuy, J.–M. Nedelec, R. Mahiou: Molecular design of inorganic scintillators: From alcoxides to scintillating materials, *J. Mater. Chem.* **14**, 3274–3280 (2004)
- 50.193 J.–K. Lee, R.E. Münchhausen, J.–S. Lee, Q.X. Jia, M. Nastasi, J.A. Valdez, B.L. Bennett, D.W. Cooke, S.Y. Lee: Structure and optical properties of $\text{Lu}_2\text{SiO}_5:\text{Ce}$ phosphor thin films, *Appl. Phys. Lett.* **89**, 101905 (2006)
- 50.194 J. Felsche: Rare earth silicates of the type $\text{RE}_2[\text{SiO}_4]\text{O}$, *Naturwissenschaften* **11**, 565–566 (1971)
- 50.195 T. Gustafsson, M. Klintenberg, S.E. Derenzo, M.J. Weber, J.O. Thomas: Lu_2SiO_5 by single-crystal x-ray and neutron diffraction, *Acta Crystallogr. C* **57**, 668–669 (2001)
- 50.196 W.Y. Ching, L. Ouyang, Y.–N. Xu: Electronic and optical properties of Y_2SiO_5 and $\text{Y}_2\text{Si}_2\text{O}_7$ with comparison to $\alpha\text{-SiO}_2$ and Y_2O_3 , *Phys. Rev. B* **67**, 245108 (2003)
- 50.197 D.W. Cooke, B.L. Bennett, R.E. Münchhausen, J.–K. Lee, M.A. Nastasi: Intrinsic ultraviolet luminescence from Lu_2O_3 , Lu_2SiO_5 and $\text{Lu}_2\text{SiO}_5:\text{Ce}^{3+}$, *J. Lumin.* **106**, 125–132 (2004)
- 50.198 H. Suzuki, T.A. Tombrello, C.L. Melcher, J.S. Schweizer: UV and gamma-ray excited luminescence of cerium-doped rare-earth oxyorthosilicates, *Nucl. Instrum. Methods Phys. Res. A* **320**, 263–272 (1992)
- 50.199 H. Suzuki, T.A. Tombrello, C.L. Melcher, J.S. Schweizer: Light emission mechanism of $\text{Lu}_2(\text{SiO}_4)\text{O}:\text{Ce}$, *IEEE Trans. Nucl. Sci.* **40**, 380–383 (1993)
- 50.200 E. van der Kolk, S.A. Basun, G.F. Imbush, W.M. Yen: Temperature dependent spectroscopic studies of the electron delocalization dynamics of excited Ce ions in the wide band gap insulator, Lu_2SiO_5 , *Appl. Phys. Lett.* **83**, 1740–1742 (2003)
- 50.201 M.–F. Joubert, S.A. Kazanskii, Y. Guyot, J.–C. Gâcon, C. Pédrini: Microwave study of photoconductivity induced by laser pulses in rare-earth-doped dielectric crystals, *Phys. Rev. B* **69**, 165217 (2004)
- 50.202 L. Pidol, O. Guillot-Noël, A. Kahn-Harari, B. Viana, D. Pelenc, D. Gourier: EPR study of Ce^{3+} ions in lutetium silicate scintillators $\text{Lu}_2\text{Si}_2\text{O}_7$ and Lu_2SiO_5 , *J. Phys. Chem. Solids* **67**, 643–650 (2006)
- 50.203 F. Brethean-Raynal, M. Lance, P. Charpin: Crystal data for $\text{Lu}_2\text{Si}_2\text{O}_7$, *J. Appl. Cryst.* **14**, 349–350 (1981)
- 50.204 P. Szupryczynski, C.L. Melcher, M.A. Spurrier, M.P. Maskarinec, A.A. Carey, A.J. Wojtowicz, W. Drozdowski, D. Wisniewski, R. Nutt: Thermoluminescence and scintillation properties of rare earth oxyorthosilicate scintillators, *IEEE Trans. Nucl. Sci.* **51**, 1103–1110 (2004)
- 50.205 W.W. Moses: Trends in PET imaging, *Nucl. Instrum. Methods Phys. Res. A* **471**, 209–214 (2001)
- 50.206 N. Shimura, M. Kamada, A. Gunji, S. Yamana, T. Usui, K. Kurashige, H. Ishibashi, N. Senguttuvan, S. Shimizu, K. Sumiya, H. Murayama: Zr-doped $\text{GSO}:\text{Ce}$ single crystals and their scintillation performance, *IEEE Trans. Nucl. Sci.* **53**, 2519–2522 (2006)
- 50.207 S. Yamamoto, K. Matsumoto, M. Senda: Development of a GSO positron/single-photon imaging detector, *Phys. Med. Biol.* **51**, 457–469 (2006)
- 50.208 D.W. Cooke, B.L. Bennett, K.J. McClellan, J.M. Roper, M.T. Whittaker: Similarities in glow peak positions and kinetics parameters of oxyorthosilicates: evidence for unique intrinsic trapping sites, *J. Lumin.* **92**, 83–89 (2001)
- 50.209 P. Dorenbos, C.W.W. van Eijk, A.J.J. Bos, C.L. Melcher: Afterglow and thermoluminescence properties of $\text{Lu}_2\text{SiO}_5:\text{Ce}$ scintillation crystals, *J. Phys. Cond. Matter* **6**, 4167–4180 (1994)
- 50.210 R. Visser, C.L. Melcher, J.S. Schweizer, H. Suzuki, T.A. Tombrello: Photostimulated luminescence and thermoluminescence of LSO scintillators, *IEEE Trans. Nucl. Sci.* **41**, 689–693 (1994)
- 50.211 D.W. Cooke, B.L. Bennett, R.E. Münchhausen, K.J. McClellan, J.M. Roper, M.T. Whittaker: Intrinsic trapping sites in rare-earth and yttrium oxyorthosilicates, *J. Appl. Phys.* **86**, 5308–5310 (1999)
- 50.212 D.W. Cooke, B.L. Bennett, K.J. McClellan, R.E. Münchhausen, J.R. Tesmer, C.J. Wetteland: Luminescence, emission spectra and hydrogen content of crystalline $\text{Lu}_2\text{SiO}_5:\text{Ce}^{3+}$, *Philos. Mag. B* **82**, 1659–1670 (2002)

- 50.213 L. Pidol, A. Kahn-Harari, B. Viana, B. Ferrand, P. Dorenbos, J.T.M. de Haas, C.W.E. van Eijk, E. Virey: Scintillation properties of $\text{Lu}_2\text{Si}_2\text{O}_7:\text{Ce}^{3+}$, a fast and efficient scintillator crystal, *J. Phys. Cond. Matter* **15**, 2091–2102 (2003)
- 50.214 M. Nikl, H. Ogino, A. Yoshikawa, E. Mihókóvá, J. Peřchal, A. Beitlerova, A. Novoselov, T. Fukuda: Fast 5d–4f luminescence of Pr^{3+} in Lu_2SiO_5 single crystal host, *Chem. Phys. Lett.* **410**, 218–221 (2005)
- 50.215 O. Guillot-Noël, J.T.M. De Haas, P. Dorenbos, C.W.E. Van Eijk, K. Krämer, H.U. Güdel: Optical and scintillation properties of cerium-doped LaCl_3 , LuBr_3 and LuCl_3 , *J. Lumin.* **85**, 21–35 (1999)
- 50.216 J. Andriessen, O.T. Antonyak, P. Dorenbos, P.A. Rodnyi, G.B. Stryganyuk, C.W.E. van Eijk, A.S. Voloshinovskii: Experimental and theoretical study of the spectroscopic properties of Ce^{3+} doped LaCl_3 single crystals, *Opt. Comm.* **178**, 355–363 (2000)
- 50.217 K.W. Krämer, P. Dorenbos, H.U. Güdel, C.W.E. van Eijk: Development and characterization of highly efficient new cerium doped rare earth halide scintillator materials, *J. Mater. Chem.* **16**, 2773–2780 (2006)
- 50.218 E.V.D. Van Loef, P. Dorenbos, C.W.E. van Eijk: High energy resolution scintillator: Ce^{3+} activated LaBr_3 , *Appl. Phys. Lett.* **79**, 1573–1575 (2001)
- 50.219 E.V.D. Van Loef, P. Dorenbos, C.W.E. van Eijk, K. Krämer, H.U. Güdel: Influence of the anion on the spectroscopy and scintillation mechanism in pure and Ce^{3+} -doped K_2LaX_5 and LaX_3 ($\text{X} = \text{Cl}, \text{Br}, \text{I}$), *Phys. Rev. B* **68**, 045108 (2003)
- 50.220 A. Bessiere, P. Dorenbos, C.W.E. van Eijk, K.W. Krämer, H.U. Güdel, C. de Mello Donega, A. Meijerink: Luminescence and scintillation properties of the small band gap compound $\text{LaI}_3:\text{Ce}^{3+}$, *Nucl. Instrum. Methods Phys. Res. A* **537**, 22–26 (2005)
- 50.221 J. Glodo, K.S. Shah, M. Klugerman, P. Wong, B. Higgins, P. Dorenbos: Scintillation properties of $\text{LuI}_3:\text{Ce}$, *Nucl. Instrum. Methods Phys. Res. A* **537**, 279–281 (2005)
- 50.222 M.D. Birowosuto, P. Dorenbos, C.W.E. van Eijk: Scintillation properties of $\text{LuI}_3:\text{Ce}^{3+}$ —high light yield scintillators, *IEEE Trans. Nucl. Sci.* **52**, 1114–1118 (2005)
- 50.223 G. Meyer: The ammonium chloride route to anhydrous rare earth chlorides – The example of YCl_3 , *Inorg. Synth.* **25**, 146–150 (1989)
- 50.224 W.M. Higgins, J. Glodo, E. Van Loef, M. Klugerman, T. Gupta, L. Cirignano, P. Wong, K.S. Shah: Bridgman growth of $\text{LaBr}_3:\text{Ce}$ and $\text{LaCl}_3:\text{Ce}$ crystals for high-resolution gamma ray spectrometers, *J. Cryst. Growth* **287**, 239–242 (2006)
- 50.225 P. Dorenbos: Scintillation mechanism in Ce^{3+} doped halide scintillators, *Phys. Status Solidi (a)* **202**, 195–200 (2005)
- 50.226 J.S. Chivian, W.E. Case, D.D. Eden: The photon avalanche: A new phenomenon in Pr^{3+} -based quantum counters, *Appl. Phys. Lett.* **35**, 124 (1979)
- 50.227 N. Pelletier-Allard, R. Pelletier: Multiphoton excitations in neodymium chlorides, *Phys. Rev. B* **36**, 4425 (1987)
- 50.228 E.V.D. Van Loef, P. Dorenbos, C.W.E. van Eijk, K. Krämer, H.U. Güdel: Scintillation properties of $\text{LaCl}_3:\text{Ce}^{3+}$ crystals: Fast, efficient, and high energy resolution scintillators, *IEEE Trans. Nucl. Sci.* **48**, 341–345 (2001)
- 50.229 E.V.D. Van Loef, P. Dorenbos, C.W.E. van Eijk: The scintillation mechanism in $\text{LaCl}_3:\text{Ce}^{3+}$, *J. Phys. Cond. Matter* **15**, 1367–1375 (2003)
- 50.230 U. Rogulis, S. Schweizer, J.-M. Spaeth, E.V.D. Van Loef, P. Dorenbos, C.W.E. van Eijk, K.W. Krämer, H.U. Güdel: Magnetic resonance investigations of $\text{LaCl}_3:\text{Ce}^{3+}$ scintillators, *Radiat. Eff. Defects Solids* **157**, 951–955 (2002)
- 50.231 S.M. Kuzakov: Electron-hole traps and thermoluminescence of the $\text{LaCl}_3:\text{TR}$ single crystals, *Rad. Prot. Dosim.* **33**, 115–117 (1990)
- 50.232 J. Glodo, K.S. Shah, M. Klugerman, P. Wong, B. Higgins: Thermoluminescence of LaBr_3 crystals, *Nucl. Instrum. Methods Phys. Res. A* **537**, 93–96 (2005)
- 50.233 E.V.D. Van Loef, P. Dorenbos, C.W.E. van Eijk, K. Krämer, H.U. Güdel: Scintillation properties of $\text{LaBr}_3:\text{Ce}^{3+}$ crystals: fast, efficient and high-energy-resolution scintillators, *Nucl. Instrum. Methods Phys. Res. A* **486**, 254–258 (2002)
- 50.234 P. Dorenbos, E.V.D. Van Loef, A.P. Vink, E. van der Kolk, C.W.E. van Eijk, K.W. Krämer, H.U. Güdel, W.M. Higgins, K.S. Shah: Level location and spectroscopy of Ce^{3+} , Pr^{3+} , Er^{3+} , and Eu^{2+} in LaBr_3 , *J. Lumin.* **117**, 147–155 (2006)
- 50.235 K.S. Shah, J. Glodo, M. Klugerman, W. Higgins, T. Gupta, P. Wong, W.W. Moses, S.E. Derenzo, M.J. Weber, P. Dorenbos: $\text{LuI}_3:\text{Ce}$ – a new scintillator for gamma ray spectroscopy, *IEEE Trans. Nucl. Sci.* **51**, 2302–2305 (2004)
- 50.236 J. Lu, K. Ueda, H. Yagi, T. Yanagitani, Y. Akiyama, A.A. Kaminskii: Neodymium doped yttrium aluminum garnet $\text{Y}_3\text{Al}_5\text{O}_{12}$ nanocrystalline ceramics – a new generation of solid state laser and optical materials, *J. Alloy. Compd.* **341**, 220–225 (2002)
- 50.237 V. Lupei, A. Lupei, A. Ikesue: Single crystal and transparent ceramic Nd-doped oxide laser materials: a comparative spectroscopic investigation, *J. Alloy. Compd.* **380**, 61–70 (2004)
- 50.238 C. Greskovich, S. Duclos: Ceramic scintillators, *Ann. Rev. Mater. Sci.* **27**, 69–88 (1997)
- 50.239 B.C. Grabmaier, W. Rossner: New scintillators for x-ray computed tomography, *Nucl. Tracks Rad. Meas.* **21**, 43–45 (1993)

- 50.240 W. Rossner, M. Ostertag, F. Jermann: Properties and applications of gadolinium oxysulfide based ceramic scintillators. In: *Physics and Chemistry of Luminescent Materials: Proc. 7th Int. Symp.*, Vol. 98–24, ed. by C.W. Struck, K.C. Mishra, B. DiBartolo (Electrochemical Society, Pennington 1998), 187–194
- 50.241 R. Hupke, C. Doubrava: The new UFC-detector for CT-imaging, *Phys. Medica* **XV**, 315–318 (1999)
- 50.242 S.J. Duclos, C.D. Greskovich, R.J. Lyons, J.S. Vartuli, D.M. Hoffman, R.J. Riedner, M.J. Lynch: Development of the HiLight scintillator for computed tomography medical imaging, *Nucl. Instrum. Methods Phys. Res. A* **505**, 68–71 (2003)
- 50.243 A. Lempicki, C. Brecher, P. Szupryczynski, H. Lingertat, V.V. Nagarkar, S.V. Tipnis, S.R. Miller: A new lutetia-based ceramic scintillator for x-ray imaging, *Nucl. Instrum. Methods Phys. Res. A* **488**, 579–590 (2002)
- 50.244 V.V. Nagarkar, S.R. Miller, S.V. Tipnis, A. Lempicki, A. Brecher, H. Lingertat: A new large area scintillator screen for x-ray imaging, *Nucl. Instrum. Methods Phys. Res. B* **213**, 250–254 (2004)
- 50.245 C. Brecher, R.H. Bartram, A. Lempicki: Hole traps in $\text{Lu}_2\text{O}_3\text{:Eu}$ ceramic scintillators. I. Persistent afterglow, *J. Lumin.* **106**, 159–168 (2004)
- 50.246 E. Zych, C. Brecher, A.J. Wojtowicz, H. Lingertat: Luminescence properties of Ce-activated YAG optical ceramic scintillator materials, *J. Lumin.* **75**, 193 (1997)
- 50.247 H.-L. Li, X.-J. Liu, R.-J. Xie, Y. Zeng, L.-P. Huang: Fabrication of transparent cerium-doped lutetium aluminum garnet ceramics by Co-precipitation routes, *J. Am. Ceram. Soc.* **89**, 2356 (2006)
- 50.248 M. Nikl, J.A. Mareš, N. Solovieva, H. Li, X. Liu, L. Huang, I. Fontana, M. Fasoli, A. Vedda, C. D'Ambrosio: Scintillation characteristics of $\text{Lu}_3\text{Al}_5\text{O}_{12}\text{:Ce}$ optical ceramics, *J. Appl. Phys.* **101**, 033515 (2007)
- 50.249 B. Schmitt, M. Fuchs, E. Hell, W. Knupfer, P. Hackenschmied, A. Winnacker: Structured alkali halides for medical applications, *Nucl. Instrum. Methods Phys. Res. B* **191**, 800–804 (2002)
- 50.250 K. Oba, M. Ito, M. Yamaguchi, M. Tanaka: A CsI(Na) scintillation plate with high spatial-resolution, *Adv. Electron. Electron. Phys.* **74**, 247–255 (1988)
- 50.251 H. Washida, T. Sonoda: High resolution phosphor screen for x-ray image intensifier, *Adv. Electron. Electron. Phys.* **52**, 201–207 (1979)
- 50.252 C.M. Castelli, N.M. Allinson, K.J. Moon, D.L. Watson: High spatial resolution scintillator screens coupled to CCD detectors for x-ray imaging applications, *Nucl. Instrum. Methods Phys. Res. A* **348**, 649–653 (1994)
- 50.253 V.V. Nagarkar, T.K. Gupta, S.R. Miller, Y. Klugerman, M.R. Squillante, G. Entine: Structured CsI(Tl) scintillators for x-ray imaging applications, *IEEE Trans. Nucl. Sci.* **45**, 492–496 (1988)
- 50.254 C.B. Johnson, L.D. Owen: Image tube intensified electronic imaging. In: *Handbook of Optics*, Vol. 1 (McGraw-Hill, New York 1995) pp. 21.1–21.32
- 50.255 J.-P. Moy: Recent developments in x-ray imaging detectors, *Nucl. Instrum. Methods Phys. Res. A* **442**, 26–37 (2000)
- 50.256 P. Olivier: Nuclear oncology, a fast growing field of nuclear medicine, *Nucl. Instrum. Methods Phys. Res. A* **527**, 4–8 (2004)
- 50.257 T.F. Budinger, K.M. Brennun, W.W. Moses, S.E. Derenzo: Advances in positron tomography for oncology, *Nucl. Med. Biol.* **23**, 659–667 (1996)
- 50.258 W.W. Moses, S.E. Derenzo: Prospects for time-of-flight PET using LSO scintillator, *IEEE Trans. Nucl. Sci.* **46**, 474–478 (1999)
- 50.259 Z.T. Kang, C.J. Summers, H. Menkar, B.K. Wagner, R. Durst, Y. Diawara, G. Mednikova, T. Thorson: ZnTe:O phosphor development for x-ray imaging applications, *Appl. Phys. Lett.* **88**, 111904 (2006)
- 50.260 A. Koch, C. Raven, P. Spanne, A. Snigirev: X-ray imaging with submicrometer resolution employing transparent luminescent screens, *J. Opt. Soc. Am. A* **15**, 1940–1951 (1998)
- 50.261 Y. Zorenko, I. Konstankevych, M. Globus, B. Grinyov, V. Lyubinskiy: New scintillation detectors based on oxide single crystal films for biological microtomography, *Nucl. Instrum. Methods Phys. Res. A* **505**, 93–96 (2003)
- 50.262 D. Ehrentraut, H. Sato, M. Miyamoto, T. Fukuda, M. Nikl, K. Maeda, I. Niikura: Fabrication of homoepitaxial ZnO films by low-temperature liquid-phase epitaxy, *J. Cryst. Growth* **287**, 367–371 (2006)
- 50.263 J.S. Neal, L.A. Boatner, N.C. Giles, L.E. Halliburton, S.E. Derenzo, E.D. Bourret-Courchesne: Comparative investigation of the performance of ZnO -based scintillators for use as α -particle detectors, *Nucl. Instrum. Methods Phys. Res. A* **568**, 803–809 (2006)
- 50.264 B.K. Meyer, J. Sann, A. Zeuner: Lithium and sodium acceptors in ZnO , *Superlattices Microstr.* **38**, 344–348 (2005)
- 50.265 A. Kaplan, A. Sajwani, Z.Y. Li, R.E. Palmer, J.P. Wilcoxon: Efficient vacuum ultraviolet light frequency downconversion by thin films of CdSe quantum dots, *Appl. Phys. Lett.* **88**, 171105 (2006)
- 50.266 K. Shibuya, M. Koshimizu, H. Murakami, Y. Muroya, Y. Katsumura, K. Asai: Development of ultra-fast semiconducting scintillators using quantum confinement effect, *Jpn. J. Appl. Phys.* **43**, L1333–L1336 (2004)
- 50.267 C.W.E. van Eijk: Inorganic scintillators for thermal neutron detection, *Radiat. Meas.* **38**, 337–342 (2004)

Silicon Solar

51. Silicon Solar Cells: Materials, Devices, and Manufacturing

Mohan Narayanan, Ted Ciszek

The phenomenal growth of the silicon photovoltaic industry over the past decade is based on many years of technological development in silicon materials, crystal growth, solar cell device structures, and the accompanying characterization techniques that support the materials and device advances. This chapter chronicles those developments and serves as an up-to-date guide to silicon photovoltaic technology. Following an introduction to the technology in Sect. 51.1, an in-depth discussion of the current approaches to silicon material crystal growth methods for generating solar cell substrates is presented in Sect. 51.2. Section 51.3 reviews the current manufacturing techniques for solar cell devices and also presents the latest advances in device structures that achieve higher efficiency. Finally, a perspective on the technology and what might be expected in the future is summarized in Sect. 51.4.

51.1 Silicon Photovoltaics	1701
51.1.1 Physics of a Solar Cell	1701
51.1.2 The Photovoltaic Value Chain	1703
51.1.3 The Photovoltaic Module	1703
51.1.4 Commercial PV Technologies	1704
51.2 Crystal Growth Technologies for Silicon Photovoltaics	1704
51.2.1 Silicon Photovoltaics	1704
51.2.2 Single-Crystal Ingot Growth (CZ and FZ)	1705
51.2.3 Multicrystalline Ingot Growth	1707
51.2.4 Silicon Ribbon or Sheet Growth	1709
51.2.5 PV Silicon Crystal Growth Approaches	1711
51.3 Cell Fabrication Technologies	1711
51.3.1 Homojunction Devices	1711
51.3.2 Enhancing Solar Cell Performance ..	1714
51.3.3 Advanced Commercial Solar Cell Concepts	1714
51.4 Summary and Discussion	1715
References	1716

51.1 Silicon Photovoltaics

Solar cells convert sunlight into electricity via the photovoltaic effect. The photovoltaic (PV) effect was first reported in 1839 by Becquerel when he observed a light-dependent voltage between electrodes immersed in an electrolyte. However, nearly a century later in 1941, the effect was reported in silicon. In 1954, the first working solar cell module was announced. The photovoltaic industry has grown from producing a few kW in the 1960s to a multi-GW production in this decade. The success of the industry is mainly due to its ability to supply reliable and modular power, cost effectively, from a few W to multi-MW. With the market growing by nearly 20% per year for the past 10 years, the amount of silicon used in the PV industry is poised to be

significantly more than that used in the semiconductor industry in this decade.

51.1.1 Physics of a Solar Cell

When incident sunlight (photon) is absorbed by a semiconductor, photon energy is transferred to the material. If the absorbed photon has sufficient energy, interband transition occurs and an electron is excited from the valance band into the conduction band. The valance state vacated by the electron is called a hole. The free electrons generated flow freely inside the material and can be drawn to the external world to be used as electricity.

The solar radiation spectrum can be broadly divided into three portions: (1) infrared, (2) visible, and (3) ultraviolet. The long-wavelength, infrared portion of the sun spectrum does not have the threshold energy needed to free electrons from silicon atoms and passes through the cell without interacting. The material is transparent to these long wavelengths. The ultraviolet (short-wavelength) portion of the sun spectrum has more than enough energy to create the electron-hole pairs. In the case of silicon, with a bandgap of 1.1 eV at room temperature, only photons with energy greater than 1.1 eV will exhibit the PV effect. The excess energy transferred to the charge carriers is dissipated as heat. Hence, only about 40% of the incident light energy is effectively used. The irradiance spectrum is an important consideration in designing solar cells, as solar cells respond differently to photons of different energy. The spectrum of sunlight changes continually as a function of time of the day, weather, and location. Solar cells are exposed to different spectra and hence need to operate under a variety of irradiances.

The solar cell is a p-n junction, like a large-area diode with metal contacts on either side, as illustrated by Fig. 51.1. The n-type portion (typically near the front of the device) has a high density of electrons and few

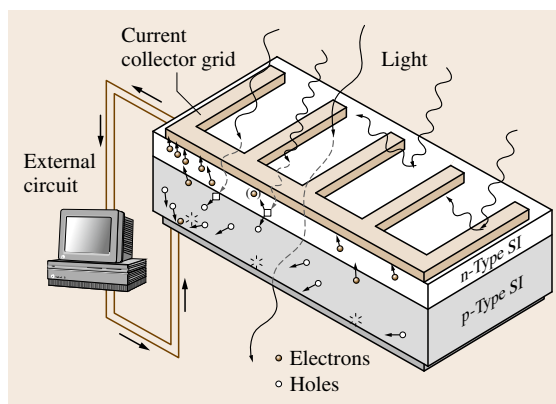


Fig. 51.1 Operation of a silicon solar cell (after [51.1])

holes, so generated electrons can travel easily in this region. The opposite is true in the p-type region, where holes travel easily. The built-in electric field near this junction of n- and p-type silicon causes photogenerated excess electrons to wander toward the grid on the front surface, while the holes wander toward the back contact. The electrons generated far away from the junction in the bulk tend to diffuse towards the junction if they are within the influence of this built-in electric field.

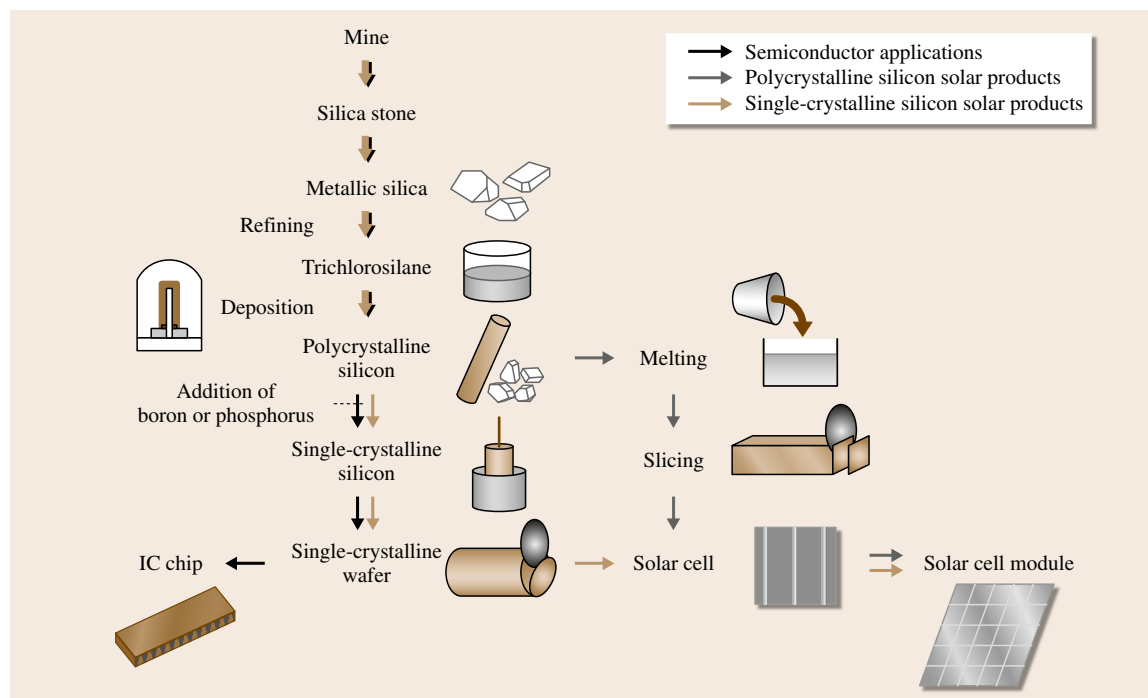


Fig. 51.2 PV silicon value stream (after [51.2])

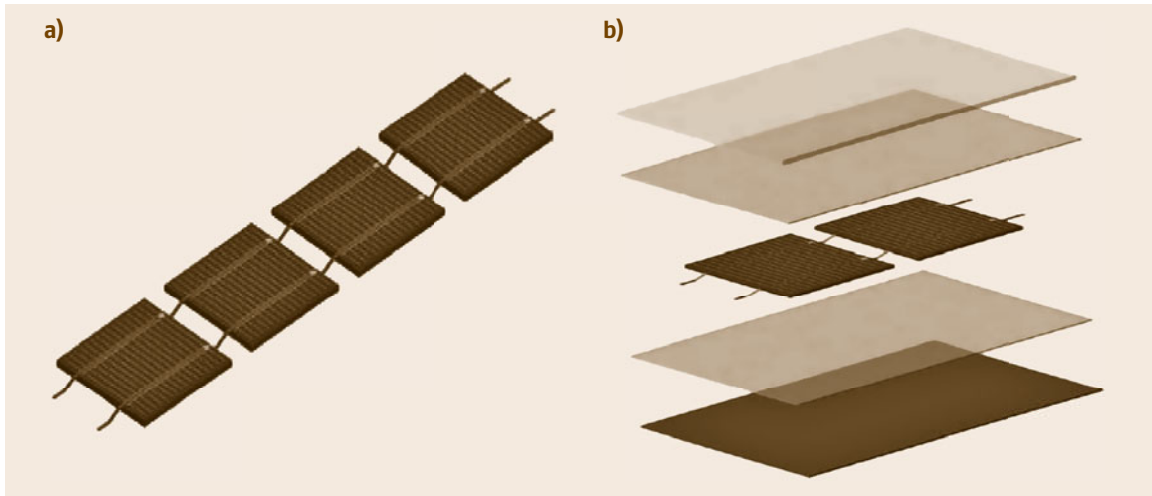


Fig. 51.3 (a) Series connection of solar cells. (b) Components of the PV module (after [51.7])

If the electrons survive their trip across the cell thickness, without recombining at defects or impurities, they are collected at the grid. Then they flow through an external circuit as current that can operate an electronic instrument or appliance. After that, they reenter the solar cell at the back contact to recombine with holes and the process repeats [51.3–6].

51.1.2 The Photovoltaic Value Chain

More than 80% of manufactured solar cells are based on a crystalline silicon (single-crystalline or multicrystalline) substrate. The value stream of the photovoltaic industry is shown in Fig. 51.2 [51.2].

High-purity polysilicon (produced by the conventional Siemens polysilicon process or by a fluidized bed process) along with recycled silicon is the dominant feedstock for the PV industry. Due to increased demand for PV systems, several programs to upgrade metallurgical-grade silicon are also being actively pursued. The feedstock is then converted into silicon wafers by casting or crystal growth followed by a wire-sawing process. Details of this process step are described in Sect. 51.2. The silicon substrate is converted into solar cells using technologies based on semiconductor device processing and surface-mount technology (SMT). The cell process technology (Sect. 51.4) mainly consists of wafer surface etching, junction formation, antireflection coating deposition, and metal contact formation. The individual solar cells are connected and assembled into the finished product: PV modules, which are integrated with system components, inverters, charge

conditioners, batteries etc. and then installed at the site.

The crystalline silicon wafer accounts for about 40% of the cost of a PV module. There have been ongoing efforts to reduce the cost of PV modules: the use of thinner substrates to save the cost of silicon used, device research to increase the conversion efficiency of the module, high-volume manufacturing with inline process control to reduce the cost of manufacturing, etc.

51.1.3 The Photovoltaic Module

The PV module is designed to generate electricity for many years (usually more than 25 years). It has to operate over a wide range of daily and seasonal variations of sunlight and weather. It must be mechanically rigid to provide a means for mounting the module into its service structure. It must be dielectrically rigid in order to protect living beings from coming into contact with dangerous electrical voltages, as well as to prevent system failure through short circuit.

The photovoltaic module (as shown in Fig. 51.3a,b) consists of a number of solar cells electrically connected to each other with metal interconnects and supported by a rigid superstrate. The interconnected cells are encapsulated by one or more layers of polymeric materials like ethyl vinyl acetate (EVA) and Tedlar, which provide electrical insulation. The encapsulation provides mechanical rigidity to the brittle cells and the flexible interconnection. In addition, it offers chemical protection as a moisture barrier. The encapsulated cell

assembly, called a laminate, is then attached to a tempered, low-iron glass superstrate. An electrical junction box is provided at the rear of the module to harness the electricity generated by the module.

51.1.4 Commercial PV Technologies

The commercial success of PV is largely due to the proven reliability and long lifetime (> 25 years) of crystalline silicon modules. Accelerated environmental testing, based on correlation of the specific failure mechanism with outdoor field test results, is used to certify the module performance in the field. If the module passes the environmental tests it will likely perform reliably for more than 20 years.

More than 85% of all modules sold today are based on crystalline-silicon solar cells. Several factors have

contributed to the choice of crystalline silicon: high cell conversion efficiencies of 15–20%; availability of commercial equipment from the semiconductor and SMT industries; extensive volume of knowledge on silicon device physics, established feedstock technologies, abundant supply of the source material (sand), etc. Other PV technologies include devices based on amorphous silicon (a-Si), cadmium telluride (CdTe), copper indium diselenide (CIS), and gallium arsenide (GaAs). While a-Si-based devices suffer from lower efficiencies, devices based on GaAs and CdTe have shown high conversion efficiencies. However, the high cost of the material, scarce raw material availability, and toxic nature of the process and material are major challenges facing these technologies for multi-GW manufacturing. Here, only silicon-based PV issues will be discussed in detail.

51.2 Crystal Growth Technologies for Silicon Photovoltaics

51.2.1 Silicon Photovoltaics

The history of crystalline and multicrystalline silicon growth for PV applications starts with, and is closely aligned with, the methods utilized in the semiconductor industry. From the first solar cell produced at Bell Labs in 1954 [51.8] on Czochralski (CZ)-grown silicon through to the development of modern high-efficiency cells, the prominent integrated circuit (IC) industry crystal growth methods have served the PV industry well. The highest-efficiency PV cells and modules commercially available today continue to use the CZ method and, to a lesser extent, the float-zone (FZ) method.

Early in IC development, it was realized that elimination of ingot wafering held many advantages, including simplified surface preparation, thinner wafers, and improved feedstock utilization. The dendritic web Si ribbon growth method, originated in 1962 [51.9], was briefly explored commercially by Dow Corning Corporation in the mid 1960s with an eye toward IC use as well as applications in the fledgling PV industry. Despite more than 30 years of development for PV use, largely by Westinghouse, the web method ultimately proved nonviable for PV production throughput needs in the rapidly growing PV industry. When Tyco Laboratories announced the growth of shaped sapphire crystals by the edge-defined film-fed (EFG) method in 1971 [51.10], Dow Corning researchers quickly realized that this method might also be useful for PV and

they published the first growth of silicon ribbons by EFG, using graphite capillary dies, in 1972 [51.11]. A few years later, in 1975, researchers at IBM published the first growth of silicon tubes by EFG [51.12] for potential application as the active, internally cooled, PV receiver in linear parabolic concentrators. The closed tubular shape eliminates edge instability problems and is easier to grow than ribbons. The later, larger, hybrid consisting of a closed tubular shape, but with multiple flat walls, is the current EFG production method for PV wafers. The wafer blanks are laser-cut from the flat tube walls. While dendritic web growth produces single-crystal ribbon surfaces, EFG growth yields multicrystalline wafers.

The dendritic web method, in a sense, spawned another multicrystalline ribbon growth method in which foreign filaments replace the continuously propagating edge dendrites. This simplifies thermal control considerably. The method was introduced as edge-supported pulling (ESP) [51.13] in 1980, using carbon-based edge filaments incorporated into the growing ribbon. After many years of dormancy, it was resurrected by Evergreen Solar as string ribbon. The string ribbon and flat-sided tubular EFG growth methods are in use today and have made strides in improving throughput by effectively increasing the width of material grown in a single apparatus through multiple wide faces (EFG) and multiple ribbons (string ribbon). This was not possible with the more complex dendritic web growth

method. Another class of silicon sheet growth methods that we will include in this discussion, although there is currently no large commercial application, is that in which the sheet moves rapidly in a direction orthogonal to the direction of heat removal. This class of growth methods has shown remarkable throughput potential (more than 40 MW of PV wafer material per machine per year), but so far has suffered from relatively large sheet thickness, small grain size, high impurity content, and low cell efficiencies.

Casting of multicrystalline silicon shapes has been conducted for over 80 years. In the mid 1970s, attention was turned to this method as a way of producing PV wafer material. Fischer and Pschunder reported casting of silicon into graphite molds for PV applications [51.15] in 1976. The technique of melting and then resolidifying silicon in the same graphite container (thermal expansion-matched to silicon), with bottom seeding, was introduced in 1979 [51.16]. Multicrystalline ingot growth has become the dominant method for PV wafer production and is most often conducted by melting and then directionally solidifying (DS) the Si material in the same silicon-nitride-coated, silica-based, square crucible with small height-to-width aspect ratio. This allows more columnar growth than taller crucibles. One semicontinuous multicrystalline ingot casting method introduced in 1985 [51.17,18] uses electromagnetic repulsion to keep silicon from adhering to water-cooled metal finger walls. Electromagnetic casting (EMC) currently produces > 2000 kg silicon ingots at a much higher throughput rate than conventional directional solidification in silica crucibles.

We will consider the above silicon growth methods that are presently in use for PV wafer manufacturing in the following sections. The categories include single-crystal ingots, multicrystalline ingots, and multicrystalline ribbons or sheets.

51.2.2 Single-Crystal Ingot Growth (CZ and FZ)

Since CZ growth is the main silicon growth method of the IC industry, it is quite well documented in other literature, and we need not go into it in detail here. A basic schematic of the process is shown in Fig. 51.4, along with one for FZ growth. Here we will focus primarily on the aspects of growth pertinent to PV applications. CZ and FZ ingots are round, so the active area of a module relative to the total area is lower than for cast or ribbon wafers, unless the ingots are trimmed to a square or rounded-square cross-section. For optimum perfor-

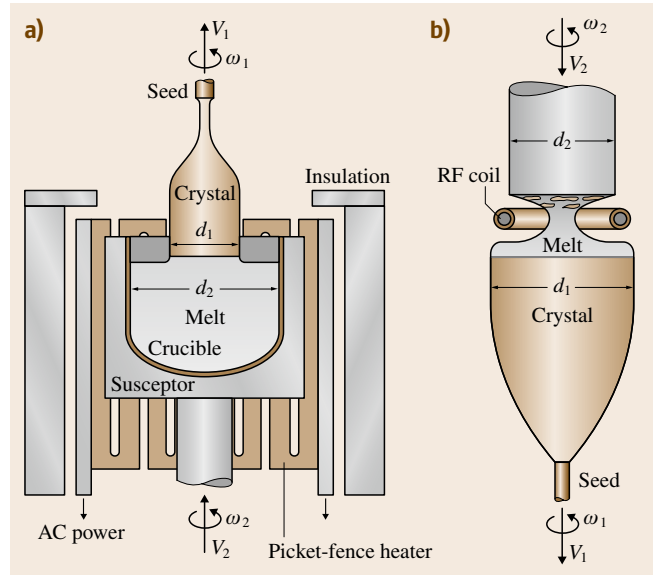


Fig. 51.4a,b Schematic of CZ (a) and FZ (b) crystal growth (after (a) [51.14], (b) [51.1])

mance, the ingots must be both single crystalline and dislocation free. Multicrystalline CZ or FZ ingots are more highly stressed than cast multicrystalline ingots, and the grain boundaries are more electrically active, resulting in poorer cell efficiency. If ingot growth is initiated single crystalline but not dislocation free, the ingots soon become multicrystalline (an exception is the special case of using a tricrystalline seed [51.19]). The requirement for dislocation-free growth means that care must be taken to avoid particulate matter, high impurity levels, sudden thermal changes, and other perturbations that could disrupt dislocation-free growth. Impurities in CZ growth (and in directional solidification of multicrystalline ingots) obey the normal freezing equation, $C/C_0 = k(1 - f)^{k_0 - 1}$, if there is thorough mixing in the liquid. C is the impurity concentration in the ingot where a fraction f of the melt has been solidified, and k is the effective segregation coefficient of the impurity (always less than the ideal segregation coefficient k_0); C_0 is the initial average impurity concentration in the melt before solidification commences. Impurity segregation is quite effective in the early-grown portion of the ingot where $C \approx kC_0$, but impurity concentrations rise monotonically to levels $> C_0$ near the termination of growth, as shown in Fig. 51.5. Boron hardly segregates at all, since $k \approx 0.9$. This is advantageous for giving a flat doping profile along the ingot, but it also dictates that no excess boron can be present in the feed-

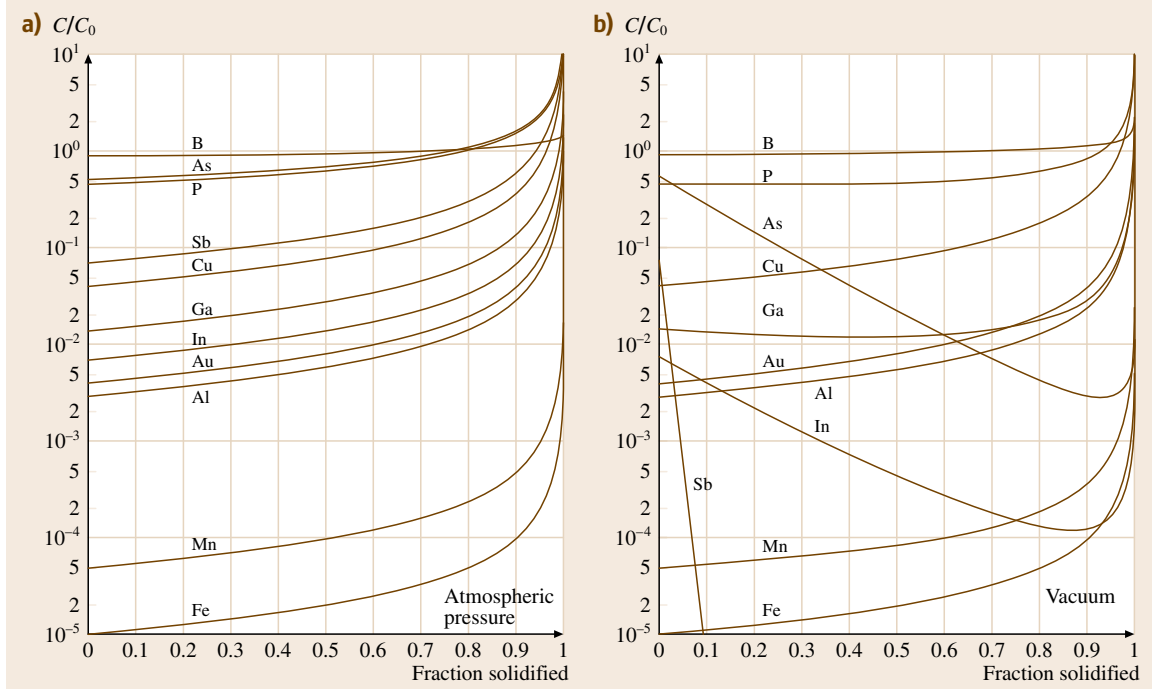


Fig. 51.5a,b Distribution of selected impurities as a function of ingot fraction solidified for CZ or directional solidification carried out in near-atmospheric pressure (a) and in vacuum (b) (after [51.14])

stock, since it cannot be removed by segregation during growth.

The vapor pressure and hence the effective evaporation coefficient of a particular impurity also can affect the observed impurity distribution in the ingot. The evaporation of an impurity depends on the growth rate and exposed melt surface area [51.20]. The approximate effect for selected impurities is shown graphically on the right-hand side of Fig. 51.5 for growth in a vacuum. By selecting an appropriate partial vacuum level, the distribution of dopants such as P or Ga can be made nearly uniform along most of the ingot length. The importance of a vacuum for reduction of P content in the material is also evident, although the magnitude of such reduction is small.

In FZ growth, or other semicontinuous growth processes, the impurity distribution, given by Peizulaev's equation [51.21], is more complex, especially if both effective segregation k and effective evaporation g coefficients are incorporated and if more than one growth pass is made on the silicon rod

$$\frac{C_n(x)}{C_0} = \left[\frac{k}{(k+g)} \right]^n \left[1 - (1-k-g)Z_n e^{-(k+g)x} \right],$$

where

$$\begin{aligned} Z_n &= n - \sum_{s=1}^{n-1} (n-s)(k+g)^{s-1} \\ &\times e^{-s(k+g)} \left[\frac{(s+x)^{s-2}}{s!} \right] \\ &\times \{(s-1)x + (s+x)[1 - (k+g)x]\}, \end{aligned}$$

where n is the number of times the ingot is zone-melted, and $C_n(x)$ is the impurity concentration at position x along the ingot (x is in units of melt zone length) after n solidification passes. Here, C_0 is the initial concentration of the impurity in the feed rod (assumed uniform).

Figure 51.6, analogous to Fig. 51.5 for CZ growth, gives the distributions of selected impurities as a function of position along a FZ ingot or other semicontinuously grown silicon form where continuous melt replenishment is used. A total length equivalent to 20 melt zones is depicted.

Note that the characteristic shape of the impurity profiles differs from the CZ case. However, judicious use of a partial vacuum can again allow flatter profiles for impurities that evaporate, and can allow phosphorus removal to some extent.

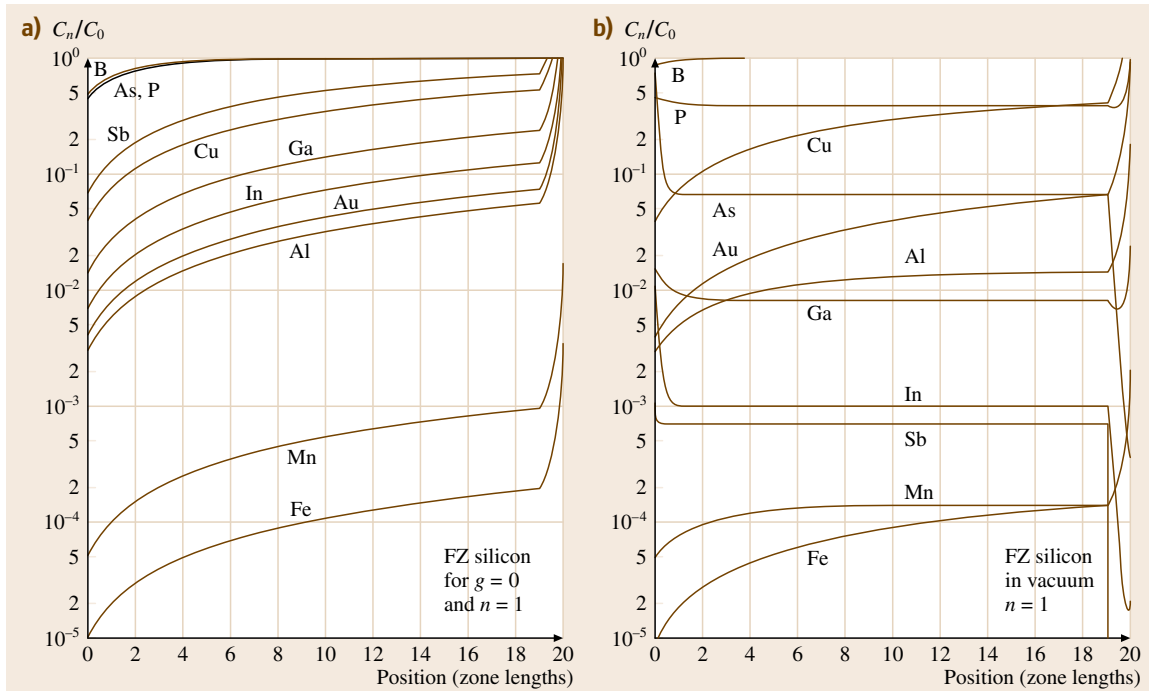


Fig. 51.6a,b Distribution of selected impurities as a function of position along ingot for FZ or other semicontinuous solidification processes with continuous melt replenishment carried out in near-atmospheric pressure (a) and in vacuum (b) (after [51.20])

For CZ growth near atmospheric pressure, the flat-test doping profiles that can be attained are those shown in Fig. 51.5, where all dopant is mixed into the initial melt volume. On the other hand, for FZ growth and other semicontinuous processes, if the dopant has a small segregation coefficient (Ga for example), there is an advantage to inserting the dopant in the first melt zone rather than having it uniformly distributed along the feed rod. This is called pill doping and results in a flat doping profile. Impurities with large segregations coefficients (B, P) must be added continuously with consumption of the feed rod.

Typically, CZ growth is conducted with an argon or argon/partial vacuum ambient and the gas flows down over the seed and melt interface, then over the rim of the crucible and down toward the bottom of the growth furnace. In this way, the copious amounts of SiO_x that form from dissolution of the quartz crucible are swept away from the growth region. FZ growth is typically conducted in a slight overpressure of argon. While growth can be done in a vacuum, some evaporation of silicon will result and cause growth disruption problems if solid Si deposits flake off the chamber or

radiofrequency (RF) coil surfaces and fall into the melt zone.

51.2.3 Multicrystalline Ingot Growth

Using a container to shape the growing ingot instead of manipulation of the solid–liquid–vapor boundary greatly simplifies control of the growth process, allows much larger ingots, and allows ingots to have a square cross-section. All of these factors improve productivity. A schematic diagram of the directional solidification (DS) or casting process is shown in Fig. 51.7. Silicon can be melted in the same container in which it is solidified, eliminating the top vessel in Fig. 51.7, which is designated directional solidification. Alternatively, it can be melted in one container and poured into a second container for solidification, as implied in the figure. This might properly be called casting with directional solidification. However, the terms DS and casting tend to be used interchangeably for either process.

Either induction (shown in the figure) or resistance heating can be used. The heat source, insulation, and heat sink are designed to provide a nearly unidirectional

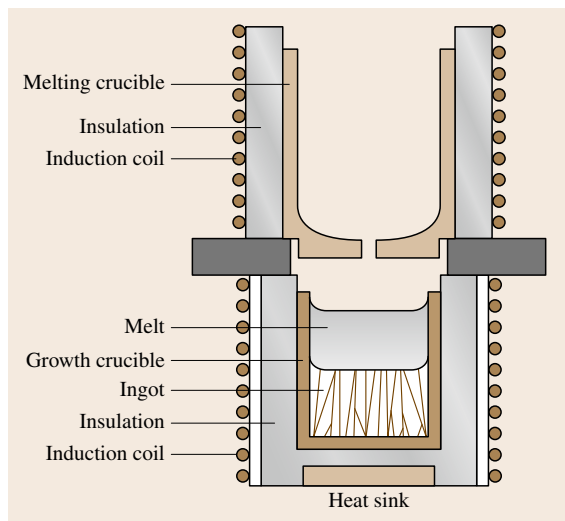


Fig. 51.7 Schematic diagram of the directional solidification process for multicrystalline silicon (after [51.22])

temperature gradient to drive columnar growth, and some relative motion may be imparted to components as growth progresses. Square-cross-section, flat-bottomed silica crucibles contain the liquid silicon. They are coated with silicon nitride to minimize sticking of the ingot to the crucible, and are a one-use item. Because of the crucible–ingot contact, single-crystal growth is not generally achieved, although some attempts at seeding have been reported, as mentioned earlier.

The same impurity distribution equation applies here as for CZ growth, and the general impurity profiles

follow those in Fig. 51.5 (melt residence time and melt surface area exposed to the ambient modify the details of the profiles in the case of a vacuum ambient). There are additional impurity phenomena to contend with in this process that are not present for CZ growth. Because the melt and the grown ingot are in contact with the container for an extended period of time, impurities can both dissolve and diffuse into the melt and later diffuse into the sides and bottom of the ingot from the crucible. Metallic impurities in the melt are strongly segregated to the last layer to freeze at the top of the ingot. During cool down of the massive ingot, these impurities can diffuse back into the top region of the ingot. These phenomena, along with small grain sizes at the ingot bottom and sides, require that a portion of the bottom, sides, and top of the ingot be cropped away because the minority charge carrier there is too low for adequate PV performance.

In the electromagnetic casting process (EMC) method, container walls comprised of water-cooled, electrically conductive *fingers* provide the sidewall melt confinement during a semicontinuous casting process. Silicon is prevented from making substantial contact with these walls by Biot–Savart law repulsion between the fingers and the melt. This is visualized in Fig. 51.8a, where a helical induction coil, a cylindrical array of fingers, and the Si melt are depicted in a top sectional view. The current directions at one instant in the RF cycle are shown. The induced currents in the fingers and in the melt are in opposite directions, giving rise to the repulsive force. In PV ingot production, a square array of fingers is used and new material is fed into the top of

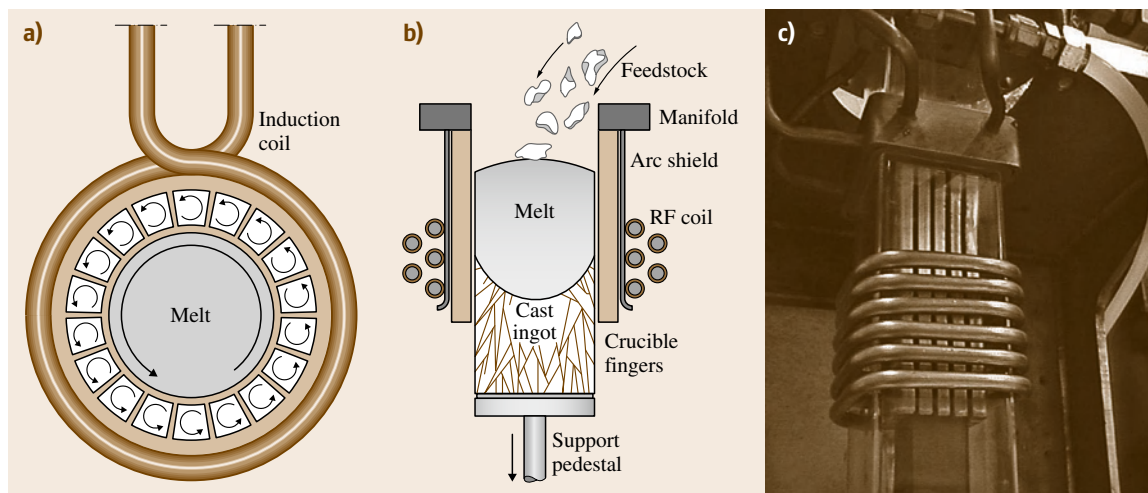


Fig. 51.8 (a) Biot–Savart repulsion [51.23], (b) EMC schematic [51.22], (c) EMC laboratory apparatus

the container while the ingot is continuously withdrawn from the bottom. A schematic of the process is shown in Fig. 51.8b, and a small, laboratory-scale apparatus is shown in Fig. 51.8c.

The impurity distribution profiles in EMC ingots follow the Peizulaev equation, since the configuration is essentially like float zoning, and the curves of Fig. 51.6 apply. Again, the details of the profiles under vacuum will depend on melt residence time and melt surface area exposed to the ambient.

In current production, ingots weighing 1 metric ton are grown with a $35 \times 35 \text{ cm}^2$ cross-section and length of $\approx 4 \text{ m}$, at a throughput (with sawing) of $500 \text{ m}^2/\text{day}$ – approximately seven times faster than any other ingot growth method. The ingots are generally cleaner than DS ingots, but have smaller grain size, with the PV conversion efficiency being about the same.

51.2.4 Silicon Ribbon or Sheet Growth

Many approaches to ribbon or sheet growth of silicon have been made over the years. Only two are in large-scale use at the time of this writing. They are the EFG and string ribbon methods mentioned in the introduction. Other methods that had been pursued until recently are dendritic web growth and a form of horizontal ribbon growth on substrate (RGS) where melt is solidified on a moving substrate that is later detached for reuse. There are indications that RGS growth may reemerge on the PV scene, so this section will summarize the EFG, string ribbon, and RGS techniques.

The EFG technique utilizes a die that is wetted by liquid silicon. The liquid rises up capillary channels in the die to reach the die top, and connects to a seed. As the seed is pulled upward, the top portion of the liquid meniscus continually solidifies, adding growth to the seed. The bottom of the meniscus spreads to the outer edges of the die top and is pinned there. The rising of liquid up the capillary channel is governed by Laplace's equation, which relates the pressure difference Δp across a liquid surface to the two principal radii of curvature of the surface R_1 and R_2 , and the surface tension γ as $\Delta p = \gamma(1/R_1 + 1/R_2) = \rho gh$. The liquid will rise vertically to a height h ; ρ is the liquid density, and g is the acceleration due to gravity. For capillary channels comprised of plates or annular tubes, one radius of curvature R_2 is approximately infinite and the other is $R_1 = s/2 \cos \theta$, where s is the plate or tube separation and θ is the wetting angle, so $h = (2\gamma/\rho gs) \cos \theta$. For silicon in graphite dies, $\theta \sim 0$ and $h \sim 2\gamma/\rho gs$.

Heights of several centimeters to 10 cm could be used, but for a number of practical reasons the height is kept quite small (impurity segregation is improved because back-mixing of the rejected impurities is better, the meniscus is higher and there is less susceptible to freeze-out to the die, the meniscus is more stable, and pick up of SiC particles on the ribbon surface is reduced).

A schematic of EFG growth using an annular die is shown in Fig. 51.9a. EFG wafer growth for PV use is similar, with the tube having eight flat faces. Sections of octagonal tubes with 10 and 12.5 cm faces are shown in Fig. 51.9b. After growth, the tubes are transported to a laser-cutting station, which removes rectangular cell blanks from the tube faces.

Typically, induction heating is used and the tubes grow in an argon ambient at about 2 cm/min linear pulling speed. FZ-type impurity profile equations apply, since the process is continuous with melt replenishment.

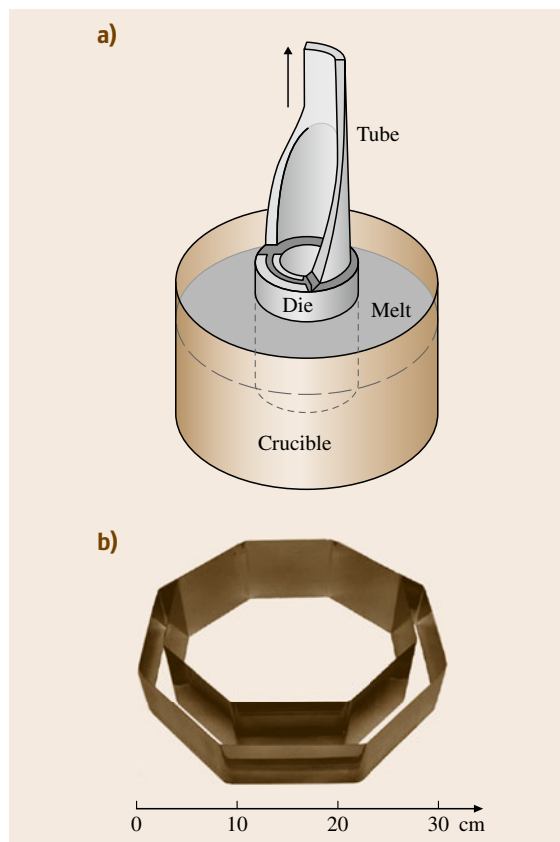


Fig. 51.9a,b Schematic of EFG tube growth (a); 10 and 12.5 cm face octagonal tube sections (b) [51.12]

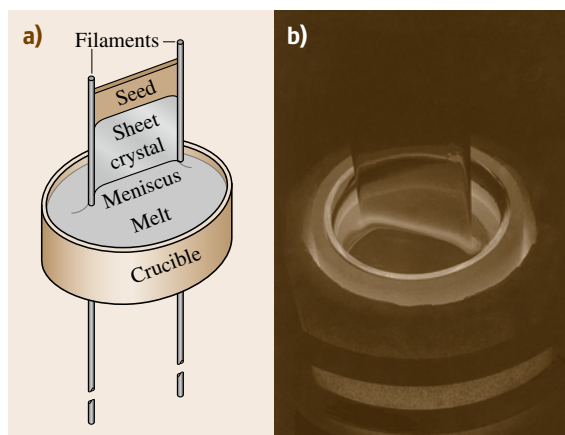


Fig. 51.10a,b Schematic of string ribbon growth (a) and (b) a growing ribbon [51.24]

However, the effective *zone length* is extremely large. Also, the fast pulling speed, lack of rotation, and capillary die restriction of back-mixing of impurities rejected at the solid–liquid interface back into the melt all reduce the effective segregation.

The string ribbon growth process is shown schematically in Fig. 51.10, along with its original ESP implementation using a quartz crucible and graphite filament *strings*. Two thin filaments enter the bottom of the crucible through small openings, pass upward through the melt, and are bridged above the melt by a seed plate. A liquid meniscus rises up to the seed plate and contin-

ually solidifies onto it as the string–seed plate assembly is moved upward at about 2 cm/min.

Carbon-based strings are typically used. They are easily wetted by the liquid silicon, and become an integral, imbedded part of the ribbon, but have the disadvantage of nucleating many small grains near the ribbon edges. The central portion of the ribbon, however, is reasonably large-grained. Other string materials (based, e.g., on alumina or quartz) can be used and nucleate much fewer grains at the edge [51.24], but the contact to the ribbon is less definite and the thermal-expansion mismatch causes them to partially or totally break away from the ribbon edge during cooling. Figure 51.11 shows the development of grain structure for graphite filaments and a graphite *seed* plate, as well as the lack of grain nucleation at the edge when quartz filaments are used. Graphite can be used for the crucible, as well as quartz.

A drawback of both EFG and string ribbon growth is the slow areal throughput. EFG addresses this by effectively growing eight ribbons simultaneously via the eight-sided tube structure. In modern string ribbon production [51.26], a long and narrow graphite mesa crucible is used to retain the continuously replenished melt by capillarity on its top surface. The long edges of the mesa are close and parallel to the ribbons, and the edges define the base of the meniscus from which the ribbons grow. Multiple pairs of strings (four in the present *quad* growth system) are used to delineate the edges of the ribbons. The mesa crucible thus plays a similar role to the die in EFG growth, the main difference being that the melt is replenished directly onto a region of the mesa top and flows laterally along it rather than arriving via distributed capillary channels as in EFG. The small volume of the melt zone reduces heater power requirements and hot-zone material requirements for growth, and the close proximity of the mesa edges to the ribbon helps to stabilize flat ribbon growth.

Impurity and dopant distribution in this system is basically governed by the same equation as for FZ growth, with some ribbon-to-ribbon variations in concentrations due to the path length differences from the replenishment point to each ribbon.

Large-area solid–liquid interface growth with heat removal perpendicular to the pulling direction has the potential to be the highest throughput silicon sheet growth method. A number of variants of the process have been tried in the past, but none are currently in large-scale commercial production. A representative schematic, in this case of the ribbon growth on sub-

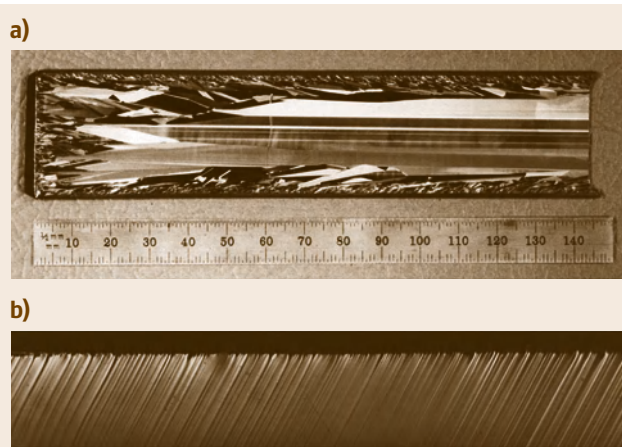


Fig. 51.11 (a) Development of grain structure in a 32 mm wide ribbon grown with graphite filaments and *seed* plate [51.25]. **(b)** A 10 mm long portion of the edge of a 20 mm wide ribbon grown with quartz filaments, showing no grain nucleation [51.24]

strate (RGS) process, is shown in Fig. 51.12. Some approaches utilize a moving substrate that is reusable. Others attempt to grow the ribbon off of the free melt surface in a crucible. The important aspect is that the length of the melt zone b be much greater than the sheet thickness t . Then fast pulling speeds can be achieved according to the equation

$$V_s = \frac{4\alpha K_m b}{(2K_m - \alpha t)tL\rho_m} \Delta T,$$

where α is the effective coefficient of heat transfer, ΔT is the temperature gradient between melt and substrate (or free surface, if no substrate is used), L is latent heat of fusion, ρ_m is the density at the melting temperature, and K_m is the thermal conductivity at the melting temperature [51.27]. The equation predicts a 6 m/min growth rate at $\Delta T = 160^\circ\text{C}$, and experimental pulling speeds near that value have been realized (Fig. 51.13). Horizontal growth of this type can be hundreds of times faster than vertical ribbon pulling, particularly if b and ΔT are maximized.

51.2.5 PV Silicon Crystal Growth Approaches

Of the many approaches that have been tried for PV silicon growth, only six are currently in commercial use. The traditional CZ method (and to a lesser extent, the FZ method) produces single-crystal silicon ingots that yield the highest-efficiency silicon solar cells. The DS and EMC multicrystalline ingot methods offer simpler operation and higher throughput (especially EMC) but a somewhat lower cell efficiencies. Ribbon growth eliminates the need for wafering and hence provides better feedstock utilization. The two methods in current use are EFG and string ribbon growth. They provide cell efficiencies similar to that of multicrystalline ingot. The family of horizontal, large solid-liquid interface

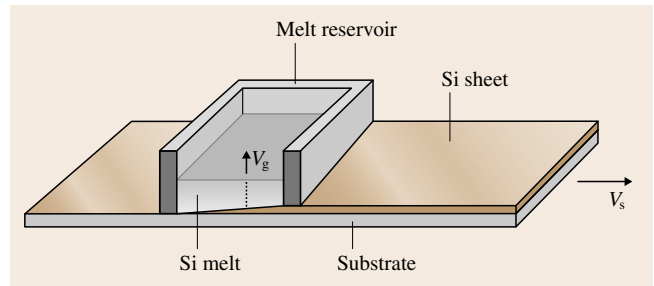


Fig. 51.12 Schematic of the RGS sheet growth process (after [51.22])



Fig. 51.13 Wide silicon sheet growing at 3 m/min (AstroPower, 2002)

techniques provides much faster sheet growth, but so far these have not been viable commercially, with cell performance limited by small grain size and high impurity content. Passivation of multiple, small grains has also proved difficult in thin-film silicon growth on substrates, and no commercially viable silicon thin-film growth approaches have been found yet.

51.3 Cell Fabrication Technologies

The main challenge of PV fabrication technologies is developing ways to cost-effectively mass-produce high-performing devices with the highest yield, reliability, and consistency. Capital efficiency, equipment efficiency, cost of production, and device performance have to be optimized to achieve these goals. In this section, in addition to the commercial cell fabrication technologies, a brief review of the advances in the silicon solar cell technologies currently being pursued by

various researchers will be discussed. The basic device structure will be discussed and the commercial production tools and process will be highlighted.

51.3.1 Homojunction Devices

Solar cells manufactured by nine out of the top ten PV cell companies in 2005 were based on homojunction devices. In this structure, only one type of semiconductor

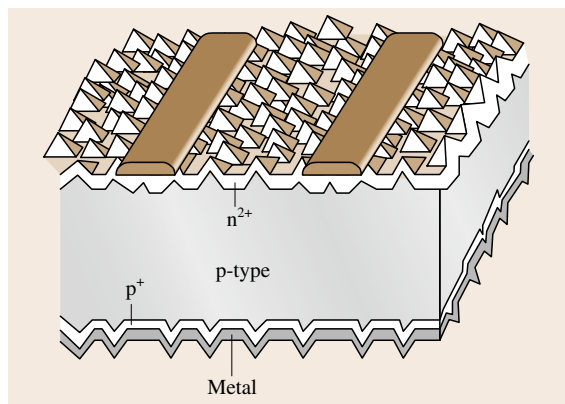


Fig. 51.14 Cross-section of a commercial silicon solar cell (after [51.28])

material, crystalline silicon, is used on both sides of the junction. The device structure is shown in Fig. 51.14.

A p-type crystalline silicon wafer (typically $225\ \mu\text{m}$ thick and $156\ \text{mm} \times 156\ \text{mm}$ in size) is used as the base substrate. After cleaning and/or texturing the front surface, n-type emitter is formed by a diffusion process (junction depth of about $0.3\ \mu\text{m}$). The front and back side are isolated by plasma or chemical etching or laser scribing. An antireflection coating of silicon nitride (about $75\ \text{nm}$ thick and refractive index of about 2.10) is deposited using plasma-enhanced chemical vapor deposition, low-pressure chemical vapor deposition, or sputtering. The front (silver) and rear contacts (aluminum and silver) are screen-printed with metallic inks and subsequently fired to make good mechanical and electrical contact. The front metal coverage is typically 8%. The completed cells are then tested and classified according to the cell parameters. The commercial efficiencies of solar cells based on multi- and monocrystalline silicon are in the range 14.5–15.5 and 16.0–17.0%, respectively. The efficiency ranges are due to the material quality, cell design, and process tools. The efficiency of monocrystalline solar cells is higher as they can be more effectively surface-textured and the electronic quality of the material is better than that of multicrystalline silicon. In the following section, each of the process steps used in commercial cell sequence and the improvement techniques being evaluated will be described [51.29, 30].

Surface Damage Removal and Texturing

In this step, the surface damage resulting from sawing is etched off using hot, concentrated (10–30%) sodium hydroxide (NaOH) solution. Approximately $10\ \mu\text{m}$ of

silicon is removed during the process. About 200 wafers are etched in a batch process. Monocrystalline silicon substrates are subsequently textured using a low-concentration etch containing 2% sodium hydroxide and isopropyl alcohol (IPA). The (100) crystal planes are etched relatively faster than other planes. This results in the intersection of (111) planes and the exposed surface forms with tiny pyramids, about $3\text{--}5\ \mu\text{m}$ in size. This process removes an additional $10\ \mu\text{m}$ of silicon.

For the past 5 years, a new technique, isochemical texturing, has been commercialized for saw-damage removal and texturing for multicrystalline wafers. The process involves use of an acid-based etch solution [hydrofluoric (HF) and nitric acid (HNO_3)] which is a standard etch in semiconductor wafer preparation. The main difference is that the etch solution is kept at a constant temperature, below $10\ ^\circ\text{C}$. Only about $10\ \mu\text{m}$ of silicon is removed, resulting in a substantial saving in raw material. Texturing of multicrystalline silicon wafers increases the conversion efficiency of the cells by reducing reflection and enabling advanced cell design parameters. A special feature of the process is that it can be performed as an inline process, hence enabling the use of thinner silicon substrates.

Emitter Formation

The semiconductor junction is formed by phosphorus diffusion across the entire front surface. The process is carried out in a tube furnace using POCl_3 as the dopant source. Inline belt furnace diffusion (using phosphoric acid solution as the dopant source) is increasingly being used to enable thin wafer processing. The semiconductor junction of the majority of commercial solar cells is about $0.3\text{--}0.5\ \mu\text{m}$ and the surface concentration is about $5 \times 10^{20}\ \text{cm}^{-3}$. The sheet resistivity (a measure of lateral resistance in the n-type doped layer) of the commercial cells is about $50\ \Omega/\text{square}$. The diffusion of dopant from a nearly infinite source into silicon at high temperature $> 860\ ^\circ\text{C}$ results in a complementary error function (erfc) or similar distribution of phosphorus (as shown in Fig. 51.15).

Excess phosphorus beyond the solid solubility limit is precipitated as inactive phosphorus in a silicon region called the *dead layer*. In this region the minority-carrier lifetime is significantly reduced or the generated carriers are recombined instantly. The high surface concentration of phosphorus and low sheet resistivity are not optimum conditions for maximizing the generation of carriers. However, widespread use of this approach is due to its compatibility with high-volume manufacturing tools such as screen-printing metallization practiced

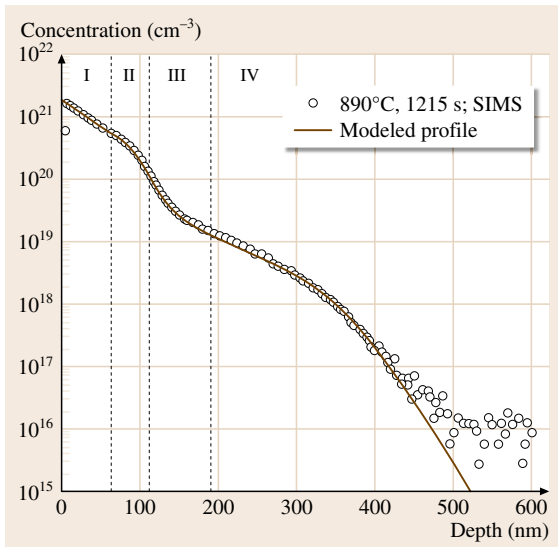


Fig. 51.15 Diffusion profile of the silicon surface (after [51.31]) (SIMS – secondary ion mass spectroscopy)

in the surface-mount assembly industry. There are several approaches being actively investigated to enhance the performance of solar cells by reducing the dead layer and developing screen-printing paste compatible with higher sheet resistivity and lower surface concentration of phosphorus [51.31].

Junction Isolation

During the diffusion step, the edge and the rear of the wafers also gets diffused. Hence, to prevent leakage paths, the front and the rear need to be isolated. There are several techniques used to achieve this in commercial solar cell manufacturing. One of the widely used techniques is a plasma etch by which the edges of coin-stacked wafers are etched. However, due to the textured surface of the wafer, some active area of the cell in the front surface is also etched. Another technique involves the use of a laser system, where the edges of the wafers (front or rear) are trenced or cleaved. During the past 3 years, a new technique has been commercialized, enabling thin wafer processing. This technique is based on chemically etching off the rear phosphorus junction without etching the front [51.33].

Phosphorus Glass Removal

In this step, the phosphorus glass formed during the diffusion step is removed using a dilute hydrofluoric acid etch. The glass is very thick (20–40 nm) and would affect the effectiveness of the antireflection layer that will

be deposited later in the process. This step can be done as a batch or inline process.

Antireflection Coating Deposition

The goal of this step is to minimize the reflection of incident light, thereby increasing PV efficiency. The weighted average of reflected sunlight from a bare silicon surface is about 30%. Under glass in the encapsulated stage, this value can be reduced to about 15%. By texturing the surface the reflection can be reduced to 10%. In order to further decrease the reflectance, an antireflection (AR) coating is applied to solar cells. By selecting an appropriate film thickness and refractive index (RI) of the AR coating, the reflection can be reduced to below 4%. Apart from ability to reduce reflection, the AR coating must be transparent, i.e., it should not absorb incident sunlight.

The most widely used antireflection coating is a silicon nitride film (about 75 nm thick with RI of about 2.10), deposited by plasma-enhanced chemical vapor deposition (PECVD). In addition to providing the antireflection properties, the silicon nitride deposition process introduces hydrogen which diffuses into bulk silicon. This hydrogenation improves the electronic quality of surface and bulk silicon by means of passivation [51.34].

Metallization and Contact Sintering

In this step, both top and rear contacts are printed and sintered. A typical front pattern is shown in Fig. 51.16.

The most widely used technique to deposit metal paste is screen printing. The top contact is a paste containing silver with organic and glass binders. On the



Fig. 51.16 Front contact metallization of a solar cell with antireflection coating [51.32]

rear, an aluminum paste is printed in all areas except where silver paste is applied to make contacts for the external circuit. The aluminum paste after sintering provides a p^+ surface (back surface field) and additional gettering of impurities in the bulk silicon. The pastes are applied sequentially with a drying step between each printing step. The printed wafers are then fired to make contact with the silicon. The front paste fires through the silicon nitride layer and makes contact to the n-type layer. If the sintering step is very aggressive (higher temperature, longer duration), the metal will make contact to the p-type bulk silicon, resulting in electrical shorting. On the other hand, if the paste is not sintered adequately the strength of the bond to the interconnection between two solar cells will be weak and will not have the required chemical and mechanical contact properties. Hence the selection of the paste, printing height, and the firing conditions are very important in determining the performance of the cell. This step determines many of the cell parameters and long-term performance of the solar cell. The strength of the interconnection between the contacts and the tabbing ribbon is affected by the paste/sintering characteristics and the soldering process [51.35].

Testing and Binning

In this last step, the solar cell is measured using a sun simulator at standard testing conditions (STC), i.e., irradiance of 1000 W/m^2 with an air mass 1.5 spectrum (AM 1.5) at 25°C . STC is selected as it is easy to reproduce in the laboratory. The cell is tested against a calibrated cell. Cell performance in air will be different from its performance under encapsulated conditions due to the difference in optical coupling and the increased series resistance. The cells are sorted and binned according to their electrical performance and various mechanical and visual defects such as cosmetics, color nonuniformity, edge chips etc. The finished cells are packed for further processing into modules. The modules will operate at conditions other than STC, hence the module manufacturer provides temperature coefficients of voltage and current as well as predicted performance as a function of irradiance.

51.3.2 Enhancing Solar Cell Performance

The gap between the efficiency of laboratory cells and commercial cells is decreasing with the commercialization of several high-efficiency techniques. Efficient solar cell design involves maximization of carrier generation and carrier collection. The generation of carriers

in a silicon solar cell depends on the electronic quality of substrates (minority-carrier lifetime), the active area (the area not covered by metal contact lines), spectral response, absence of dead layer, etc. The collection of carriers depends on bulk and surface passivation and the lateral and contact resistance.

The performance of conventional commercial cells is limited by the requirement of the metal pastes, the capability of the printing equipment, and surface recombination of the generated carriers. The front metal paste requires heavier phosphorus diffusion and increased surface concentration of phosphorus. This requirement affects current generation and current collection. The use of fine line-printing techniques, better screens, and better metal pastes reduces the shading losses due to metal coverage. The development of new pastes compatible with lower surface concentration of phosphorus and higher sheet resistivity will increase the current generation capability. The incorporation of a surface passivation layer will enhance the beneficial effects of cells with higher emitter sheet resistivity and thin cells. In addition, thin cells (less than $150 \mu\text{m}$) require a back surface field which does not bow the cells. All of these topics are being actively pursued by several paste manufacturers in collaboration with cell technologists.

51.3.3 Advanced Commercial Solar Cell Concepts

In this section, a few of the commercial sequences which are not based on conventional screen-printing technology are presented. These sequences are applicable to limited types of substrates. However, several research institutions and PV companies are trying to incorporate some of the concepts of these cells into conventional screen-printing sequences.

Buried-Contact Cells

The buried-contact solar cell sequence is one approach which has been commercialized to overcome the limitation of screen printing. Cell efficiencies up to 18% (laboratory efficiency 22.7% record cell) have been demonstrated on monocrystalline (CZ) wafers [51.36]. In this sequence the grooves are formed on the top surface into which metal contacts are plated (Fig. 51.17).

Additional high-efficiency concepts incorporated in this sequence are surface passivation and a shallow emitter with deep diffusion under the contacts. In addition to an increased number of steps, the sequence involves several high-temperature steps. Hence it re-

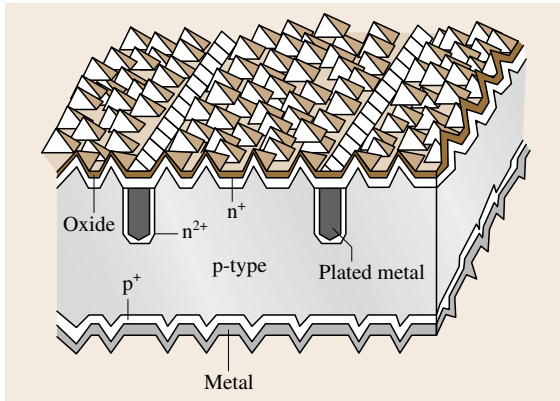


Fig. 51.17 Cross-section of a buried-contact solar cell (after [51.28])

quires monocrystalline silicon wafers with low oxygen content. This limits the widespread commercialization of buried-contact solar cells.

Back-Contact Cells

A back-contact (interdigitated contact) cell sequence has been commercialized for high-lifetime n-type wafers. Cell efficiencies up to 22.2% have been demonstrated in large-scale production [51.38]. The sequence includes a textured front surface with antireflection coating, well-passivated surfaces, and screen-printed metal contacts on the rear. The special feature of the cell (shown in Fig. 51.18) is that all the contacts are on the rear, thereby reducing the shading losses and improving the cosmetic appearance of the cells.

HIT Cells

The heterojunction with intrinsic thin layer (HIT) cell sequence has been commercialized. Efficiencies of HIT cells up to 21.8% have been reported on n-type substrates (as shown in Fig. 51.19). The unique feature of

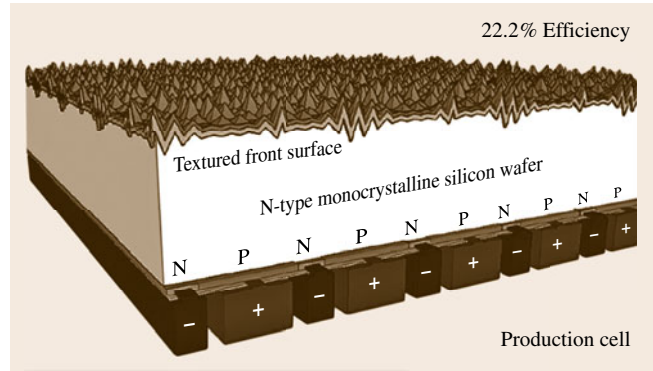


Fig. 51.18 Back-contact solar cell [51.37]

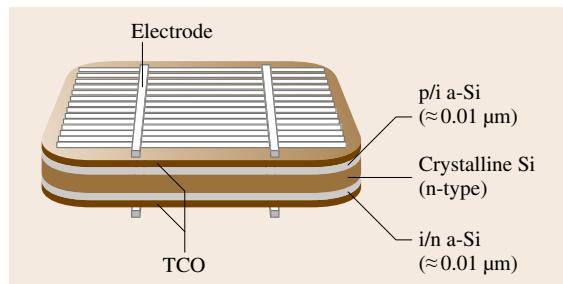


Fig. 51.19 HIT cell structure [51.37]

this sequence is the incorporation of a thin amorphous silicon layer on both surfaces of the solar cell [51.39]. These layers provide high-quality surface passivation to achieve a very low surface recombination velocity. An additional advantage of this design is that the cell can be bifacial, thereby converting backscattered light into useful power output. TCO in Fig. 51.19 refers to a thin-film conducting oxide.

It is exciting that many of these advanced cell concepts, once only achievable in laboratory-scale devices, are now being used successfully in manufacturing.

51.4 Summary and Discussion

The silicon photovoltaic industry has been on a rapid growth path over the past decade – on the order of 30–40% per year. As of 2007, the consumption of high-purity silicon for solar cells has exceeded the amount used for all other electronic applications. The rapid growth has presented challenges in all segments of the PV value chain (Fig. 51.2). However, as these challenges are met and the industry benefits from economies of scale, the technology becomes ever stronger and

closer to meeting the cost and performance milestones that will establish it as a viable source of a significant portion of world energy needs.

The well-established technology base and ready availability, proven performance, and salubrity of silicon, coupled with economies of scale in larger factories, will likely allow Si to remain the dominant PV material for the foreseeable future. The rapidly increasing demand for polycrystalline silicon feedstock for PV

use has caused a disruption in the demand/supply ratio, but this is not a fundamental problem, nor does it represent a fundamental shortage. It is, rather, a planning/forecasting issue which was exacerbated by: (1) investor caution resulting from the economic and high-technology downturn around the year 2000, and (2) investor skepticism of the viability and continued growth projections of silicon photovoltaic technology. Part of this investor reluctance results from uncertainties about whether there will be a future role of compound semiconductor thin films in photovoltaics. The performance and costs of the thin-film approaches have not so far been competitive with silicon. Furthermore, the Earth's crust contains 27.7% Si, in contrast to 0.00002% Cd, 0.00001% In, 0.000009% Se, and 0.0000002% Te (commonly used thin-film elements). So it is difficult to see how improved costs for thin-film PV can come to fruition despite the fact that they use a thinner layer of semiconductor material. The temporary shortage of polycrystalline feedstock has instigated numerous metallurgical approaches to the purification of silicon, in the hope that adequate purity for solar cells can be achieved at a lower cost than that of the Siemens process. However, this is a difficult challenge because 99.9999% or six-9s pure silicon is required for PV.

In single-crystal CZ ingot growth, we are likely to see increased effort to make hot zones more energy efficient, to grow larger diameters, and to achieve continuously melt-replenished long growth runs. There will be continuing effort to achieve more wafers per length of ingot, and to take advantage of potentially higher cell efficiencies afforded by thinner wafers when back surface fields are used in the cell design. Despite the potential advantages of FZ material, it is unlikely that its role in PV will increase significantly because of higher costs for the crack-free, long cylindrical feedstock it requires and the difficulty in producing the larger FZ diameters. Multicrystalline casting, directional solid-

ification, and electromagnetic casting command the largest share of the Si PV market. This trend is likely to continue because the processes and equipment are simpler and the throughputs are higher (especially for electromagnetic casting) by a factor of 5–20.

Even though ribbon and sheet growth technologies have the advantage of minimal silicon consumption and elimination of wafering, it is difficult for them to compete effectively with the higher throughput of ingot technologies. Their challenge will be to increase areal throughput via wider ribbons, multiple ribbons or other approaches. The effective areal throughputs of ingot growth range between 30 m²/day and 600 m²/day per machine. By contrast, a capillary die octagon tube growth machine produces about 20 m²/day and string-supported ribbon machines produce about 8–9 m²/day. We will probably see continued progress in horizontally pulled, large-area solid-liquid interface sheets by some variant of the horizontal growth method because the throughput potential is enormous and one growth furnace could easily generate material for 35 MW/a or more of solar cell production.

The future is expected to bring continued exploration of thin-layer Si growth approaches, in search of ones that have significant economic advantages over the best ingot and sheet techniques. Successful ones will have fast deposition rates, large grain sizes, high efficiencies (at least 14% production efficiency), compatibility with low-cost substrates, and amenability to low-cost cell fabrication schemes. It is not likely that production of thin-layer Si PV modules will account for a significant fraction of the mainstream PV market for at least 10 years, although they, like the ingot and sheet approaches, would have substantial advantages over many other thin-film PV approaches. These include the simple chemistry, the relative abundance of the Si starting material, compatibility with SiO₂ surface passivation, and relative lack of toxicity.

References

- 51.1 T.F. Cizsek: Silicon for solar cells. In: *Crystal Growth of Electronic Materials*, ed. by E. Kaldis (Elsevier Science, Amsterdam 1985) pp.185–210
- 51.2 J.W. Pichel, M. Yang: 2005 Solar Year-end Review and 2006 Solar Industry Forecast Renewable Energy World (2006) <http://www.renewableenergyworld.com/real/news/infocus/story?id=41508> (last accessed October 8, 2007)
- 51.3 H.J. Möller: *Semiconductor for Solar Cells* (Artech House, London 1993)
- 51.4 M.A. Green: *Solar Cells* (Prentice Hall, Englewood Cliffs 1982)
- 51.5 A. Rohatgi: Road to cost-effective crystalline silicon photovoltaics, Proc. 3rd World Conf. Photovolt. Energy Convers., Osaka (2003)
- 51.6 S. Narayanan, J. Wohlgemuth: Cost-benefit analysis of high-efficiency cast polycrystalline silicon solar cell sequences, Prog. Photovolt. 2(2), 121–128 (1994)
- 51.7 P.C. de Jong: PV Module Technology, Energy Research Centre of the Netherlands,

- <http://www.ecn.nl/en/zon/rd-programme/pv-module-technology/> (last accessed October 8, 2007)
- 51.8 G.L. Pearson, C.S. Fuller, D.M. Chapin: A new silicon p-n junction photocell for converting solar radiation into electrical power, *J. Appl. Phys.* **25**, 676 (1954)
 - 51.9 S.N. Dermatis, J.W. Faust: Process for producing an elongated unitary body of semiconductor material crystallizing in the diamond cubic lattice structure and the product so produced, US Patent 3129061 (1964)
 - 51.10 H.E. LaBelle Jr.: Growth of controlled profile crystals from the melt, part II: edge-defined, film-fed growth, *Mater. Res. Bull.* **6**, 581 (1971)
 - 51.11 T.F. Cizek: Edge-defined, film-fed growth of silicon ribbons, *Mater. Res. Bull.* **7**, 731-737 (1972)
 - 51.12 T.F. Cizek: Melt growth of crystalline silicon tubes by a capillary action shaping technique, *Phys. Status Solidi (a)* **32**, 521-527 (1975)
 - 51.13 T.F. Cizek, J.L. Hurd: Melt growth of silicon sheets by edge-supported pulling. In: *Proc. Symposia on Electronic and Optical Properties of Polycrystalline or Impure Semiconductors and Novel Silicon Growth Methods*, ed. by K.V. Ravi, B. O'Mara. St. Louis, 1980, *Electrochem. Soc. Proc.* **80**(5), 213-222 (1980)
 - 51.14 T.F. Cizek: Electromagnetic and float-zone methods for high-purity silicon solidification. In: *Containerless Processing Techniques and Applications*, ed. by W.F. Hofmeister, R. Schiffman (The Minerals, Metals & Materials Society, Warrendale 1993) pp. 139-146
 - 51.15 H. Fischer, W. Pschunder: Low cost solar cells based on large area unconventional silicon, *IEEE 12th Photovolt. Spec. Conf. Rec. (IEEE, New York 1976)* pp. 86-92
 - 51.16 T.F. Cizek, G.H. Schwuttke, K.H. Yang: Directionally solidified solar-grade silicon using carbon crucibles, *J. Cryst. Growth* **46**, 527-533 (1979)
 - 51.17 T.F. Cizek: Some applications of cold crucible technology for silicon photovoltaic material preparation, *J. Electrochem. Soc.* **132**, 963-968 (1985)
 - 51.18 T.F. Cizek: Method and Apparatus for Casting Conductive and Semiconductive Materials, US Patent 4572812 (1986)
 - 51.19 A. Endros, G. Martinelli: Silicon Semiconductor Wafer Solar Cell and Process for Producing Said Wafer, US Patent 5702538 (1997)
 - 51.20 T.F. Cizek: A graphical treatment of combined evaporation and segregation contributions to impurity profiles for zone-refining in vacuum, *J. Cryst. Growth* **75**, 61-66 (1986)
 - 51.21 S. Peizulaev: Segregation and evaporation of impurities during zone refining, *Inorgan. Mater.* **3**, 1329 (1967)
 - 51.22 T.F. Cizek: Silicon crystal growth for photovoltaics. In: *Crystal Growth Technology*, ed. by H.J. Scheel, T. Fukuda (Wiley, Sussex 2003) pp. 267-289
 - 51.23 T.F. Cizek: Some applications of cold crucible technology for silicon photovoltaic material preparation, *J. Electrochem. Soc.* **132**, 963 (1985)
 - 51.24 T.F. Cizek, J.L. Hurd, M. Schietzelt: Filament materials for edge-supported pulling of silicon sheet crystals, *J. Electrochem. Soc.* **129**, 2838-2843 (1982)
 - 51.25 J.L. Hurd, T.F. Cizek: Semicontinuous edge-supported pulling of silicon sheets, *J. Cryst. Growth* **59**, 499 (1982)
 - 51.26 E.M. Sachs: Method and Apparatus for Crystal Growth, US Patent 20060249071 (2006)
 - 51.27 H. Lange, I.A. Schwirtlich: Ribbon growth on substrate (RGS) - A new approach to high speed growth of silicon ribbons for photovoltaics, *J. Cryst. Growth* **104**, 108-112 (1990)
 - 51.28 M.A. Green: *Crystalline Silicon Solar Cells* (World Scientific, New York 2001), http://www.worldscibooks.com/phy_etextbook/p139/p139_chap4.pdf
 - 51.29 P. Manshanden, A.R. Burgers, A.W. Weeber: Wafer thickness, texture and performance of multicrystalline silicon solar cells, *Solar Energy Mater. Solar Cell.* **90**, 3165-3173 (2006)
 - 51.30 B. González-Díaz, R. Guerrero-Lemus, D. Borchert, C. Hernández-Rodríguez, J.M. Martínez-Duart: Low-porosity porous silicon nanostructures on monocrystalline silicon solar cells, *Physica E* **38**, 215-218 (2007)
 - 51.31 A. Bentzen, J.S. Christensen, B.G. Svensson, A. Holt: Understanding phosphorus emitter diffusion in silicon solar cell processing, *Proc. 21st Eur. Photovolt. Sol. Energy Conf., Dresden (2006)* pp. 1388-1391
 - 51.32 US Department of Energy, http://www1.eere.energy.gov/solar/pv_systems.html (last accessed August 17, 2005)
 - 51.33 D. Kray, S. Hopman, A. Spiegel, B. Richerzhagen, G.P. Willeke: Study on the edge isolation of industrial silicon solar cells with waterjet-guided laser, *Sol. Energy Mater. Sol. Cell.* **91**, 1638-1644 (2007)
 - 51.34 A.G. Aberle: Surface passivation of crystalline silicon solar cells: a review, *Prog. Photovolt. Res. Appl.* **8**(5), 473-487 (2000)
 - 51.35 M. Edwards, J. Bocking, J.E. Cotter, N. Bennett: Screen-print selective diffusions for high-efficiency industrial silicon solar cells, *Prog. Photovolt. Res. Appl.* **16**(1), 31-45 (2008)
 - 51.36 J. Zhao: Recent advances of high-efficiency single-crystalline silicon solar cells in processing technologies and substrate materials, *Sol. Energy Mater. Sol. Cell.* **82**, 53-64 (2004)
 - 51.37 R.M. Swanson: Photovoltaics: The path from niche to mainstream supplier of clean energy, *Sol. Power 2006 Conf. (2006)*, <http://www.tvworldwide.com/events/eqtv/061016/ppt/Swanson.pdf>
 - 51.38 K.R. McIntosh, M.J. Cudzinovic, D.D. Smith, W.P. Mulligan, R.M. Swanson: The choice of silicon wafer for the production of low-cost rear-contact

	solar cells, 3rd World Conf. Photovolt. Energy Convers., Osaka (2003) pp.11–18	conversion efficiency and commercialization of highest performance HIT modules, Proc. 3rd World Conf. Photovolt. Energy Convers., Osaka (2003) pp. 955–958
51.39	M. Tanaka, S. Okamoto, S. Tsuge, S. Kiyama: Development of HIT solar cells with more than 21%	

52. Wafer Manufacturing and Slicing Using Wiresaw

Imin Kao, Chunhui Chung, Roosevelt Moreno Rodriguez

Wafer manufacturing (or wafer production) refers to a series of modern manufacturing processes of producing single-crystalline or poly-crystalline wafers from crystal ingot (or boules) of different sizes and materials. The majority of wafers are single-crystalline silicon wafers used in microelectronics fabrication although there is increasing importance in slicing poly-crystalline photovoltaic (PV) silicon wafers as well as wafers of different materials such as aluminum oxide, lithium niobate, quartz, sapphire, III–V and II–VI compounds, and others. Slicing is the first major post crystal growth manufacturing process toward wafer production. The modern wiresaw has emerged as the technology for slicing various types of wafers, especially for large silicon wafers, gradually replacing the ID saw which has been the technology for wafer slicing in the last 30 years of the 20th century. Modern slurry wiresaw has been deployed to slice wafers from small to large diameters with varying wafer thickness characterized by minimum kerf loss and high surface quality. The needs for slicing large crystal ingots (300 mm in diameter or larger) effectively with minimum kerf losses and high surface quality have made it indispensable to employ the modern slurry wiresaw as the preferred tool for slicing. In this chapter, advances in technology and research on the modern slurry wiresaw manufacturing machines and technology are reviewed. Fundamental research in modeling and control of modern wiresaw manufacturing process are required in order to understand the cutting mechanism and to make it relevant for improving industrial processes. To this end, investigation and research have been conducted for the modeling,

52.1 From Crystal Ingots to Prime Wafers	1721
52.1.1 Semiconductor Single-Crystalline Wafers	1721
52.1.2 Alternative Wafer Production Processes	1722
52.1.3 Substrate Manufacturing with a System-Oriented Approach ..	1723
52.2 Slicing: The First Postgrowth Process in Wafer Manufacturing	1726
52.2.1 ID Saws	1726
52.2.2 The Modern Wiresaw	1727
52.2.3 Saws with Diamond-Impregnated Wires ..	1727
52.2.4 Others.....	1728
52.2.5 Comparison of Slicing Technology...	1728
52.2.6 Wafer Manufacturing for Large Wafers	1729
52.3 Modern Wiresaw in Wafer Slicing	1730
52.3.1 Definition of Modern Wiresaw	1730
52.3.2 Modern Wiresaw Technology	1731
52.3.3 Modeling and Control of the Modern Wiresawing Process ..	1731
52.4 Conclusions and Further Reading	1733
References	1733

characterization, metrology, and control of the modern wiresaw manufacturing processes to meet the stringent precision requirements of the semiconductor industry. Research results in mathematical modeling, numerical simulation, experiments, and composition of slurry versus wafer quality are presented. Summary and further reading are also provided.

Wafer manufacturing (or *wafer production*) refers to a modern process of producing single- or polycrystalline wafers from crystal ingots (or *boules*) of different

sizes and materials. The majority of wafers are single-crystalline silicon wafers used in microelectronics fabrication. Due to the increasing importance of the pho-

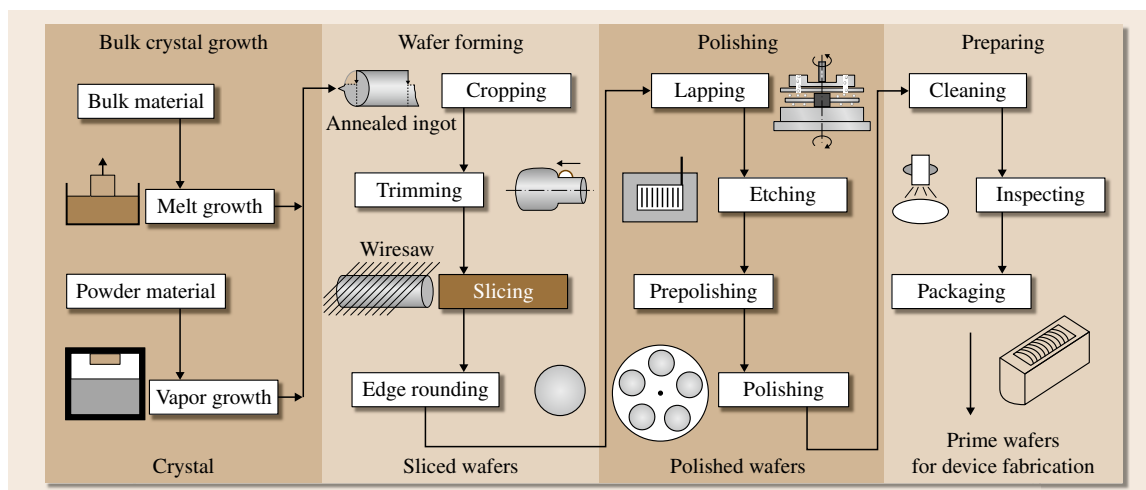


Fig. 52.1 Wafer manufacturing: from crystal ingots to prime wafers. Four categories of manufacturing operations are illustrated: bulk crystal growth, wafer forming from crystalline ingot, wafer polishing to produce prime wafers, and wafer preparing. Each category includes several operations

to voltaic (PV) industry, polycrystalline silicon wafers (although some PV wafers are single-crystalline silicon) are being produced in increased volumes. Wafers of different materials such as aluminum oxide, lithium niobate, quartz, and others have also been produced.

The health of the wafer manufacturing industry has become a good economic indicator in this microelectronics and information age; for example, when the economy suffered a downturn in the USA around 2001, the wafer production industry also suffered a drop in production due to lower demands. On the other hand, when the economy was picking up a few years afterwards, demand for wafer production heralded this recovery before it happened. With greater reliance on microelectronics, computers, and information worldwide in the 21st century, this trend is expected to become stronger than ever.

Wafer manufacturing includes a series of processes, beginning with crystal growth and ending with prime wafers, as illustrated in Fig. 52.1, in which a process flow of wafer manufacturing with various categories of operations is shown [52.1]. Slicing is the first major postgrowth wafer-forming process, and is primarily accomplished using various technologies, discussed in Sect. 52.2. The first modern wiresaws were designed and built by HCT. The first generation of industrial wiresaws were employed to slice polysilicon photovoltaic (PV) wafers. Since the introduction of the technology of the slurry wiresaw in the early 1990s, this approach has seen a dramatic increase in usage

in the USA and worldwide, replacing thousands of inner-diameter (ID) saws, primarily for the following reasons:

- Acceptance of slurry wiresaws for the slicing of silicon wafers, especially for single-crystalline silicon wafers in the microelectronics industry at the turn of the century.
- In contrast to ID sawing, wiresaw slicing results in higher throughput and can slice large wafers of different crystal materials.
- Recent research advances in slurry wiresaw and slicing manufacturing processes [52.1–78] have made significant contributions to the understanding of fundamental manufacturing process modeling, promoted research and development (R&D), and provided insights into parameter optimization and process control.
- The versatility of wiresaws to slice wafers of various sizes made of different materials.

When the single-crystalline silicon wafer manufacturing industry finally adopted the wiresaw as the main slicing tool towards the end of the 1990s, it prompted a wholesale replacement of thousands of inner diameter (ID) saws which had been the only slicing tool for decades until then. Many wiresaw equipment producers also appeared on the horizon, as well as ancillary industries for the supply of consumables such as saw wire, abrasive grits, carrier fluid,

etc. In addition to the silicon industry, wiresaws have also been employed to slice crystal wafers such as LiNbO_3 , SiC , InP , quartz, sapphire, aluminum oxide, and others.

As slurry wiresaw technology continues to become more mature and widely employed, applications in other areas also arise. A case in point is the development in the application of wiresaw reported in July 2005 [52.59]: a special-purpose wiresaw designed by HCT for Corning Inc., which weighs 50 t with a height

of 8 m (much bigger than regular industrial wiresaws), used for slicing fused silica for the production of liquid-crystal display (LCD) image mask blanks, used in the process by which makers of liquid-crystal displays imprint a pattern of electrical circuits onto the *mother glass* for computer and television displays. This example illustrates the potential of modern wiresaws in a variety of applications in the future due to the unique capability, configuration, and nature of the manufacturing process.

52.1 From Crystal Ingots to Prime Wafers

Modern *wafer manufacturing* (also called *wafer production*) includes a plethora of manufacturing operations by which prime wafers are produced from crystal ingots [52.1, 79]. For example, semiconductor devices are built on high-quality substrates and economics demands thin wafers (500–900 μm thick) of large area. Quality requirements of prime wafers include a high degree of crystalline perfection, low defect, low microstructure and subsurface damage, global surface planarization, uniform thickness, and very low residual stresses. Only when these demands are met can the full potential of the various semiconductors be realized. Figure 52.1 illustrates a flow of various processes and categories associated with the production of prime wafers from crystalline ingots.

The technology to produce semiconductor wafers is driven by many factors. New materials result in new applications that, in turn, inspire the design and engineering of new and higher-quality materials, new processing technologies, and special equipment. Broader applications of these wafers and economics demand continuous reduction in costs, improvements in quality, and innovations in materials and manufacturing technology. For example, both the size and quality of silicon substrates have been constantly increasing, and 400 mm-diameter wafer has already been used, although 300 mm wafers are the most well established today. The 400 mm silicon wafer has gradually become the standard in today's microfabrication industry, and will eventually replace 300 mm fab lines. In a similar way, the reduction in silicon wafer costs can spur exponential growth in the consumer market of solar cells.

In the following subsections, the process and operations of wafer production will be discussed.

52.1.1 Semiconductor Single-Crystalline Wafers

Typical semiconductor materials, such as silicon, lithium niobate, III–V compounds, II–VI compounds, and others, are hard and brittle. Silicon constitutes more than 90% of the total consumption of semiconductor materials, and has been extensively used in electronic and photovoltaic (PV) industries. The wafer manufacturing processes from ingot to prime wafers are illustrated in Fig. 52.1. As shown in the figure, slicing is the first major postgrowth process in wafer manufacturing. Recently, wiresaw slicing has emerged as a leading technology of wafer preparation in the semiconductor industry, especially for PV and large silicon wafers due to its capability of cutting ingots of large diameter (e.g., 300 mm and up) with small kerf loss and high yield. Nevertheless, the trend of using large wafers (with diameter of 300 mm or higher) as the future standard in microelectronic fabrication, projected by National Technology Roadmap for Semiconductors (NTRS), Semiconductor Industry Association (SIA), and Semiconductor Manufacturing Technology consortium (SEMATECH) [52.80–83], has virtually eliminated the conventional ID saw as a slicing tool, making the wiresaw an indispensable tool for wafer forming.

The importance of manufacture of silicon in the USA is illustrated by the statistics showing that in 1993 the US\$ 3 billion silicon resulted in an average of US\$ 6.67 billion device market per month and a total of US\$ 700 billion electronic equipment [52.80]. This figure has increased to sales of US\$ 10.97 billion device in 1998 [52.82] – a 65% increase over 6 years. Apart from the increase in quantity, quality requirements have also increased. Growing demand in chip surface area

produced annually is expected with the expansion of microelectronics, telecommunication, microelectromechanical systems (MEMS), and medical applications. Accompanied by the increase in wafer diameter, there is an increasing degree of integration of components and a decreasing structural width.

The objective of wafer manufacturing (or *wafer production*) for semiconductor industry is to produce prime wafers ready for microelectronics or PV solar cell fabrication, from single- and polycrystalline ingots. Four categories are outlined in Fig. 52.1 and described in the following. For the fabrication of PV solar cells, wafers are often processed as-sliced, without going through the rigorous process in Fig. 52.1, which is typically used for the production of microelectronic-scale silicon prime wafers.

Crystal Growth

Silicon ingots are grown using various techniques of crystal growth as presented in the earlier chapters of this Handbook, including bulk melt growth, powder vapor growth, and others, as illustrated in Fig. 52.1. A casting process is often employed for polysilicon ingots, normally in square shape, for PV wafers. Typical single-crystalline silicon ingots assume a cylindrical shape when grown, up to many feet tall, depending on the process.

Once the crystal ingot is grown it is processed to form wafers and substrates. The processes can be broken into three main categories, as described in the following.

Wafer Forming

The second group of manufacturing operations, also called *wafer forming* as shown in Fig. 52.1, forms the shape of thin wafers. It includes the following operations:

- Cropping both ends of the ingot (especially the tail end, which tends to have higher impurity)
- Trimming it to have a cylindrical shape with consistent cross-sectional area, followed by grinding of the orientation flat or notch to identify the crystalline orientation
- Slicing the ingot into slices of wafers
- Edge-rounding to smooth and remove tiny fractures which may have been formed along the edges of the wafer during the forming operations

Wafer Polishing

The objectives of this group of manufacturing operations are (1) to remove surface waviness and subsur-

face damage from the forming operations, and (2) to polish wafers to high precision (submicron surface roughness) with a mirror surface finish. It includes a series of operations as follows:

- *Lapping*: This is typically the first post-slicing process, based on the mechanical free abrasive machining (FAM) process to remove the surface waviness after slicing. This involves abrasives suspended in slurry to perform the mechanical process of removing the surface roughness and subsurface damage. An initial global planarization is achieved after this process.
- *Grinding*: As the size of silicon wafers becomes larger (300 mm or larger), and slicing is performed by slurry wiresaws, there are increasing demands on the grinding of the surface after slicing operations. One of the main reasons for the employment of the grinding operation is the removal of the surface waviness produced by the slicing process. Grinding using diamond tools is a faster operation than lapping. Often the demands of double-sided wafers also require grinding to be performed with consideration of elimination of the elastic spring-back effect that has commonly been found in lapping of large wafers. The ground wafers can be subject to subsequent lapping and polishing processes.
- *Polishing*: This is the final process in this category, to render well-polished wafers ready for photolithography and microelectronics fabrication to produce microelectronic chips. The standard process at this stage is chemical–mechanical polishing (CMP). Wafers at this stage are called prime wafers.

Wafer Preparing

The category of *wafer preparing* refers to steps through which the prime wafers are cleaned, inspected for defects to assure quality, and packaged in a boat ready to be shipped.

52.1.2 Alternative Wafer Production Processes

While the wafer manufacturing process outlined in Fig. 52.1 represents the general operations in wafer production, different operations in this production process may be skipped, simplified or augmented, depending on the substrate type and the requirements on surface finish. For example, the generic process can be slightly altered with epitaxial growth of a thin

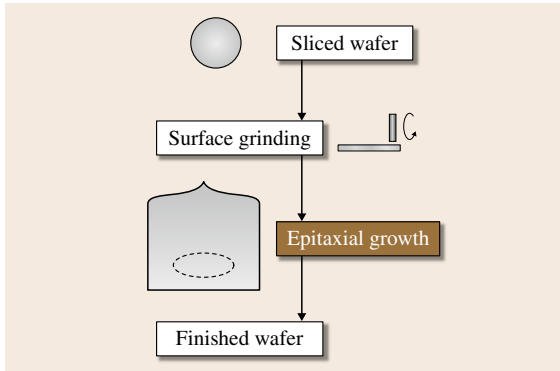


Fig. 52.2 Sliced wafers with epitaxial growth of thin layer of silicon for device fabrication. The sliced wafer is subject to surface grinding using a diamond grinding wheel, followed by the epitaxial growth process to render a finished wafer for device fabrication

layer (5–60 μm) of silicon. By so doing, the etching and CMP process can be bypassed to yield a finished wafer directly. An illustration of such a process is shown in Fig. 52.2. Certain logic gates and devices have been fabricated using these types of epitaxial wafers.

Another example is the processing of photovoltaic (PV) wafer. PV wafers are often employed as-sliced without further polishing after slicing.

52.1.3 Substrate Manufacturing with a System-Oriented Approach

The key processes and challenges in wafer manufacturing are summarized in Fig. 52.3, which shows the flow of operations discussed above. The values after each box represent typical surface roughness. Various issues related to each category of manufacturing operations are summarized in the figure for the manufacturing operations ranging from slicing, lapping, and polishing to inspecting, cleaning, and packaging.

Wafer Forming and Polishing Challenges

Tables 52.1 to 52.5 outline various important issues for consideration at every stage of the wafer production. In Table 52.1, the applications and corresponding issues in wafer forming and slicing are identified, along with research methodology. Table 52.2 outlines different applications in grinding, lapping, and polishing and relevant issues with some possible research approaches, including also considerations of materials and process control.

Wafer Preparing Challenges

Current cleaning, inspection, and metrology techniques used by industry were developed 10–20 years ago. Many recent innovations in metrology and laser-based methodology can satisfy modern demands and be

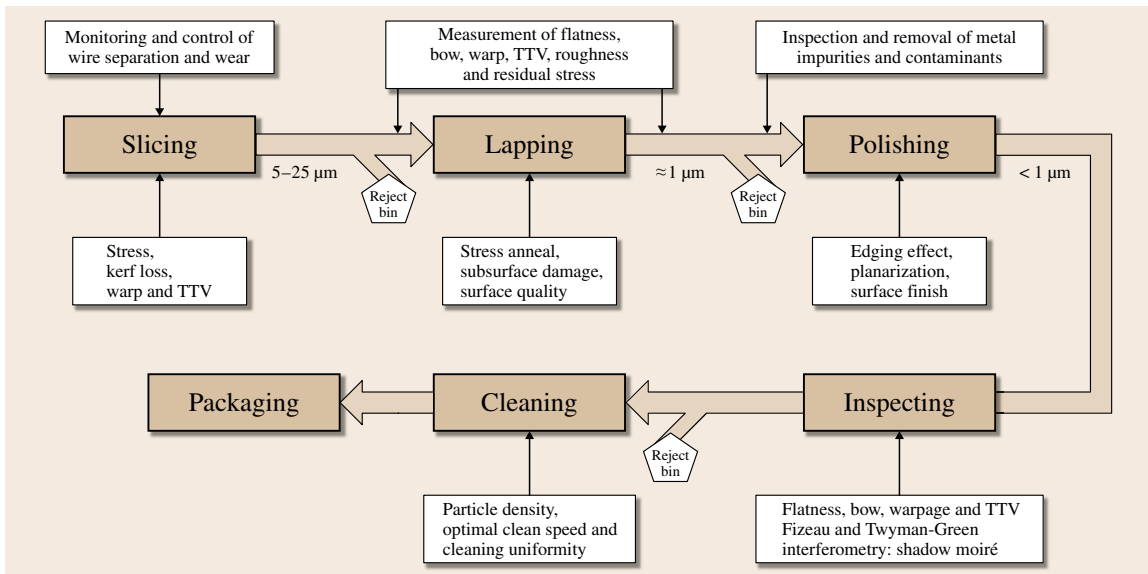


Fig. 52.3 Challenge and important process parameters in the wafer manufacturing, illustrated with typical scales of surface finish after each operation, as well as issues and challenges associated in each operation and process flow

Table 52.1 Wafer forming: potential applications and issues of consideration, as well as research approaches and methodology. Some items represent future considerations

Potential applications	Issues	Research methodology
Large-diameter substrate	Residual stress, warpage, TTV , kerf loss, dynamics, vibration	Solid and fracture mechanics modeling, stiffness control, stress relaxation, finite element method (FEM), subsurface damage
Apply cutting Si to other crystals	Different properties, process	Model-driven design, flexible manufacturing, optimized automation
Moderate number of slices (10–50): no current technology, cost-effective	Flexibility and versatility on number of slices	Model-based versatile design and fabrication in research and development
Cost reduction	Consumable, kerf loss, materials loss during forming process	Interconnected growth process control for more uniform crystal to reduce crop/trim loss; reduce kerf loss
Brittle, ductile, and very hard materials	Abrasive, wire speed, surface quality	Material- and size-independent substrate manufacturing strategies and equipment

Table 52.2 Applications and issues of consideration for lapping, grinding, and polishing in the wafer production process

Potential applications	Issues	Research methodology
Large-diameter substrate	Residual stress, warpage, TTV , kerf loss, dynamics, vibration	Modeling of stress influence, chemical versus mechanical reactions, requirements (0.35–0.13 μm), high level
Prime wafers of large diameter/size	Global planarization, parallelism of surfaces of wafers, quick removal of initial surface waviness and roughness	Geometry analysis, elastic analysis in grinding, double-sided grinding
Different materials, e.g., ultrahard materials	Abrasive, lapping speed, micro-cracks, defects, contaminants	Control strategies, holder design, expert system, experimental validation
Alternative processes for polishing, e.g., epitaxial growth	Process control, surface finish, orientation tolerance, flatness tolerance	Model-driven design, Taguchi methods, statistical process control (SPC), total quality management (TQM)

Table 52.3 Wafer preparation: the identification of potential applications as well as issues at hand with research approaches

Potential applications	Issues	Research methodology
Nonintrusive, online, multistaged, full-field, whole-wafer inspection	Warp, bow, TTV , size, methods, resolution of measurements	Capacitive probes, moiré, interferometry, and optical metrology
Next-generation cleaning tools	Clean, contaminants removal	Laser-assisted method, gas cluster ion-beam processor, superheated gas chamber

applied in the preparation of substrates. Table 52.3 outlines some issues identified and related research approaches.

Metrology, Inspection, and Quality Control
Technology’s simultaneous move towards smaller devices and larger wafer size has created new challenges

Table 52.4 Wafer manufacturing with a system-oriented approach: integrated issues with suggested research approaches and methodologies

System-oriented manufacturing	Important issues in the future	Research approaches and methodology
Real-time sensing and control of wiresaw manufacturing	Kerf loss, wire thinning and breakage, control, quality assurance	Modeling, dynamics, vibration, thermal and residual stresses, and high-level control strategies. Sensor fusion and metrology systems. Short-pulsed high-intensity laser-assisted cleaning
Integrated computer-based control systems and manufacturing automation	Interconnected processes with surface resolution from 0.5 to 0.18 μm slicing, lapping, CMP, cleaning, metrology, quality, SPC, TQM, reduce cost	Integrated engineering system. Size and material index. Substrate manufacturing systems. Implementation of optimized automation strategy manufacturing management, and expert system. Advanced control strategies, artificial neural network (ANN)
Experimental validation and benchmarking	Lab testing and new industrial equipment development. Yields and cost reduction	Taguchi experimental design. Interconnected methodology from modeling, simulation, to experiments
Industrial technology development in partnership with academics	Leadership and core competence	Industrial manufacturing leadership and knowledge base. Dissemination of research results and information database

for metrology, as desired levels of accuracy cannot be achieved by simply extending current technologies. A suite of new metrological techniques is thus required. Currently metrology is employed mostly in an offline fashion. To reach the technological goals set by NTRS, the role of metrology has to be redirected from offline sampling to inline and in situ control [52.4, 9, 12, 17, 53, 84]. The future research effort in metrology should emphasize inline or in situ measurement for quick process feedback and quality control. Table 52.4 presents system-oriented wafer manufacturing and identifies important issues of research for the future,

along with possible methodology for solutions. Table 52.5 shows the identified metrology issues in wafer manufacturing and suggests several plausible research methodologies. The specific topics can include, but are not limited to, nonintrusive, inline, full-field wafer inspection; optical methods such as Moiré, Fizeau, and Twyman–Green interferometry can provide nonintrusive, inline, full-field measurement of flatness, bow, warpage, and total thickness variation (TTV). Using these techniques, measurement throughput will be significantly increased over current technologies, which translates into cost savings. Also, measurement accu-

Table 52.5 Identified metrology issues in wafer manufacturing and plausible research methodology

Metrology issues	Research methodology
Nonintrusive, inline, full-field flatness, bow, warpage, and TTV measurement	Shadow Moiré, reflective Moiré, Fizeau and Twyman–Green interferometry
Inline residual stress measurement	Moiré interferometry and others
Real-time wire separation inspection	Moiré interferometry and others
Real-time wire thinning inspection	Laser diffraction
Inline metal impurities and contamination inspection	Fiber-optic sensors based on photoluminescence, Raman scattering, photon correlation spectroscopy, and evanescent-wavefield technique

racy, repeatability, and reproducibility can be improved by eliminating scanning by performing measurements on an entire piece simultaneously. In addition, laser speckle technology and fiber-optic sensors can also provide inline and rapid measurement of surface roughness after slicing and lapping, which is important for process feedback and control.

Real-Time Inspection of Wiresaw Operations

Practitioners in the industry of wafer production using wiresawing to slice ingots are often faced with challenges of understanding and optimizing process parameters to improve accuracy and efficiency. From the process monitoring and control point of view, two issues have been identified as having a critical impact on the quality of sliced wafers: uneven separation of wires, and wire thinning during operation. To this end, moiré interferometry and laser diffraction methods, to name but two, can be used to measure these two parameters, which can be fed back to correct the wiresaw operation in real time [52.27, 39, 85].

Inline Residual Stress Measurement

During both crystal growth and wafer production, residual stresses are created that result in warpage (i. e., the

potato chip effect) of the wafer slice. These stresses can be quantified by using the moiré method to measure the wafer warpage before and after the wafer annealing step that relieves the residual stress. This information can then be used to adjust, optimize, and improve the previous steps.

Inline Metal Impurities and Contamination Inspection

Integrated fiber-optic sensors can be designed to remotely sense metal impurities and contamination on the wafers. Material composition can be determined from the spectral response based on photoluminescence. The concentration of various species in a mix can be measured through Raman scattering, while the size of submicron particle contaminants (3–3000 nm) can be measured using photon correlation spectroscopy. A concentration of heavy metal ions as low as 1 ppb in processing baths can be estimated through absorption measurements using evanescent-wavefield sensors. Fiber-optic-based sensors can provide both characterization and feedback during various stages of high-quality wafer producing. Early detection and removal of contaminants will increase yield and reduce downtime.

52.2 Slicing: The First Postgrowth Process in Wafer Manufacturing

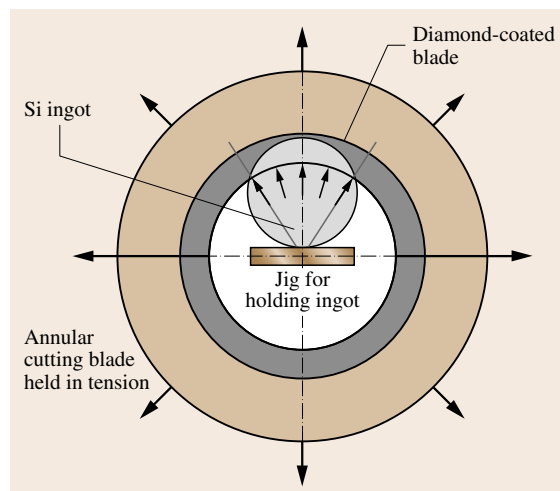
Slicing is the first postgrowth process in wafer manufacturing for wafer forming from a crystalline ingot. Different slicing technologies and equipment are discussed in the following.

52.2.1 ID Saws

In the early days of wafer production, inner diameter (ID) saws were employed. An ID saw utilizes the edge of its inner hole to slice through an ingot, as shown schematically in Fig. 52.4. As shown in Fig. 52.4, a thin annular steel blade with a round hole in the middle is coated along the ID edge with industrial diamond abrasive grits, and is stretched with very high tension to

keep the blade surface taut. The ingot to be sliced is fed through the inner-diameter hole, held by the jig shown in the figure. As the ID blade traverses down, a slice of wafer is obtained when the blade slices through the

Fig. 52.4 Schematic of inner diameter (ID) saw for wafer slicing. The ingot, held by the jig, is fed through the inner opening of the ID saw with the inner edge coated by diamond abrasive grits. The annular steel blade is stretched with very high tension and rotates at high speed to slice through the ingot, as shown, by way of a fixed abrasive ploughing machining process ►



ingot. Industrial motion control is employed for the operation and control to generate each slice of wafer.

As the diameter of the wafers in microelectronics application becomes larger, the inner diameter of the hole needs to be enlarged in order to accommodate the ingot and the jig. ID saws are practical for wafers up to 8 inches in diameter. For ingots of larger diameters, vibration becomes excessive, along with limitations of other practical issues, making ID saws unsuitable for wafer slicing.

52.2.2 The Modern Wiresaw

The modern slurry-based wiresaw has emerged as the slicing technology for semiconductor wafer production industry, as well as the preferred tool for slicing of ingots made of various materials. Since a century ago, wire has been utilized as a cutting tool to slice through stones and other materials. However, the literature on slicing using wiresaw in patent disclosures (for example [52.55, 57, 58, 62, 64, 71, 72, 86–89]) and research has only appeared in the last decade. Employed to slice single- and polycrystalline ingots to produce very thin (as thin as 200 μm) and thick wafers, the modern wiresaw is subjected to more stringent requirements to produce wafers with low total thickness variation (TTV), low warp, and low residual stresses.

A schematic of the modern wiresaw is illustrated in Fig. 52.5. A single steel wire is drawn from a supply spool and wound over three or four grooved cylindrical wire guides (four wire guides are illustrated in Fig. 52.5), to form the *wire web* surface on which the crystal ingot mounted on a holding jig is fed, with abrasive slurry manifolds feeding slurry with abrasive grits. As the wire moves with high speed, the ingot on the web is fed downward for slicing. Several hundred slices of wafers are produced simultaneously when the ingot traverses through the wire web to finish the slicing operation. More details of this modern wiresaw will be introduced in Sect. 52.3.

The modern wiresaw has sophisticated control of various parameters for successful precision operation, including control of wire tension [typical industrial proportional–integral–differential (PID) control], slurry temperature, wire speed, duty cycle of wire feed, ingot feed rate onto the wire web, and others. This is done through a computer-based monitoring and control unit to give operators greater flexibility and the ability to control and optimize the process parameters.

In addition, the wiresaw is capable of cutting much harder materials such as some III–V compounds and

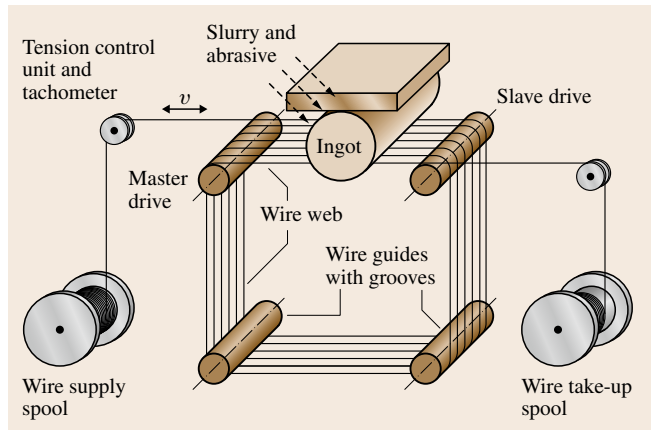


Fig. 52.5 Schematic of a modern wiresaw for wafer slicing. The schematic shows a wire supply spool with a single wire, winding over four grooved wire guides, collected by the take-up spool. The winding procedure provides wire webs as a surface of equally spaced wire segments onto which the ingot is fed to be sliced into wafers. Manifolds on both sides of the ingot pour abrasive slurry continuously onto the wire web surface

ceramics with proper abrasive grits and carrier. It has also been shown to work well for highly anisotropic materials such as lithium niobate.

52.2.3 Saws with Diamond-Impregnated Wires

Saws with diamond-impregnated wires are designed for slicing operation with different configuration and mechanisms [52.62, 90–93]. Such saws rely on the abrasives (typically industrial diamond) impregnated along the circumferential surface of a wire for slicing. The saws can be classified into rotary or reciprocating (linear) motions. Conceptually, this type of saws is akin to the ID saw because the diamond-impregnated wiresaw is essentially an ID saw with a linear instead of an annular cutting edge.

Fundamentally, however, the manufacturing process model of such saws is entirely different from that of the slurry wiresaw. This type of saw with diamond-impregnated wires removes materials by means of a ploughing process – a more brutal machining process than the rolling-indenting free abrasive machining process of the slurry wiresaw. In addition, the abrasive grits on the surface of a wire can be easily stripped off, leading to the loss of the ability for the wire to perform further slicing operations.

52.2.4 Others

As mentioned earlier in Sect. 52.1.2, as-sliced wafers can be ground first, followed by epitaxial growth process to produce wafers ready for device fabrication. In other cases, circular saws with the circumferential outer edge coated with diamond abrasive grits are also employed in slicing. This type of slicing tool is normally used for small samples, and typically is subject to a large degree of vibration and inaccuracy of surface finish.

52.2.5 Comparison of Slicing Technology

Modern wiresaw manufacturing is based on the so-called *free abrasive machining* (FAM) process with rolling-indenting, which removes materials via third-party free abrasives in slurry [52.1]. In contrast, the conventional inner diameter (ID) saw is based on the *ploughing machining* process which is characterized by the removal of materials with forceful media attached to the tool. The two schematics in Figs. 52.4 and 52.5 contrast these two manufacturing processes and arrangements.

The conventional ID saw in Fig. 52.4 cuts through the ingot to obtain one slice of wafer each time with an annular cutting blade stretched and held in high tension. The blade rotates at very high speed while feeding onto the ingot to cut through ingot with its diamond-coated inner edge. Analysis of stress and vibration in the ID saw with annular blades has been presented [52.75, 76, 94].

As shown in Fig. 52.5, and later in Fig. 52.9, the wiresaw consists of one wire moving either unidirectionally or bidirectionally on the surface of crystal ingot.

The single wire is wound carefully on the wire guides with grooves of constant pitch to form a *wire web*, as shown in Fig. 52.5. The wire guides are rotated by a pair of master-slave drives, causing the entire wire web to move at high speed while carrying the abrasive slurry to remove material from the surface of ingot. The ingot is fed in the downward direction perpendicular to the wire web as shown in Fig. 52.5. The wire is maintained at constant tension during the cutting process. A spool of cold-drawn steel wire is used to continuously supply the wire necessary for cutting.

Depending upon the process control, parallel wire marks may be visible on the wafer surface after they are sliced. Typical surface of a wafer sliced by wire-saw resembles that of a lapped wafer. The wiresaw is capable of slicing wafers of large diameter as long as the distance between the wire guides is larger than the diameter of the ingot. With a wire web consisting of 200–400 strands of wound wire, a total of 200–400 wafers are produced simultaneously once the wire has finished traversing through the ingot. Typical kerf loss is the sum of the diameter of the wire, size of abrasives, and vibration amplitude of wire. The thickness of the wafer is controlled by the pitch of the grooves on the wire guides.

Comparison Between Modern Wiresaw and ID Saw

Comparisons of various properties between the modern wiresaw and ID saw are offered in Table 52.6. From the table, it is clear that the wiresaw has much higher throughput and yield with less kerf loss and surface damage. The wiresaw has found gradually increasing usage in slicing 200 mm and 300 mm single-crystalline silicon wafers and various shapes of polycrystalline

Table 52.6 Comparisons of various properties between the modern slurry wiresaw and ID saw. The comparison suggests that the wiresaw is a more favorable tool for slicing of large quantities of wafers with better surface quality than the ID saw

Property	Wiresaw	ID saw
Manufacturing process model	FAM/lapping	Ploughing/grinding
Typical cut surface features	Parallel wire marks	Chipping and fracture
Depth of damage	Uniform, 5–15 μm	Variable, 20–30 μm
Productivity (typical)	110–220 cm ² /h	10–30 cm ² /h
Total time per run	5–8 h (depending on ingot size)	About 15 min for each slice
Wafers per run	200–400 wafers	One wafer
Kerf loss	180–210 μm	300–500 μm
Minimum thickness of wafer	200 μm (typical)	350 μm
Maximum ingot diameter	300 mm or higher	Up to 200 mm

Table 52.7 Comparisons between the modern slurry wiresaw and the saw with diamond-impregnated wires. The comparison suggests that wiresaw is a more favorable tool for most slicing operations, while the saw with diamond-impregnated wires can be quite effective for slicing very hard wafers with small size

Property	Slurry wiresaw	Saw with diamond-impregnated wires
Manufacturing process model	FAM with rolling-indenting	Ploughing
Abrasive grits	Free abrasive; rejoin cutting proc.	Lost forever once stripped off surface
Depth of damage	Uniform, 5–15 μm	Variable, 20–30 μm
Cost of consumables	Lower (per wafer)	Higher (per wafer)
Slicing very hard wafers	Not very effective	Very effective
Kerf loss	180–210 μm	250–400 μm

wafers with thickness as small as 200 μm for photovoltaic applications. The wiresaw can also be employed to slice highly anisotropic crystals and other materials such as alumina (Al_2O_3) and quartz.

Comparison Between Modern Wiresaw and Saw with Diamond-Impregnated Wires

It is important to note that the modern slurry wiresaw is entirely different from the saw with diamond-impregnated wires in which the diamond grits coated on the surface of wire are used to remove the materials by the shear-dominated process similar to the orthogonal machining process [52.90, 91]. Table 52.7 contrasts the wiresaw and saws with diamond-impregnated wires, showing that the wiresaw is suitable for general slicing operations, while saws with diamond-impregnated wires can be effective in slicing very hard or specialized wafers with small sizes.

52.2.6 Wafer Manufacturing for Large Wafers

After slicing wafers by wiresaw, the subsequent process is flattening to achieve a higher degree of parallelism and flatness of the wafer [52.2, 10, 19, 57, 74]. Both grinding and lapping are conventionally used for this process. Polishing is the next process to obtain a smoother wafer surface.

For the production of large, 300 mm silicon prime wafers using modern wiresaw for electronics fabrication, however, a special challenge with surface waviness of different wavelengths, known as the *nanotopography*, warrants special consideration. Such waviness across the surface of the large wafer is not easily dealt with using the conventional lapping operation because of the elasticity of the large wafer, causing the waviness to be flattened as the lapping tool is applied. Surface grinding, therefore, has become an attractive alterna-

tive for the initial removal of such surface waviness and roughness after slicing.

The nanotopography is illustrated in Fig. 52.6, as defined by SEMATECH. In the figure, different ranges of surface features are identified and categorized for the sake of distinguishing one from the other. Nevertheless, nanotopography and waviness, with amplitudes of surface roughness and wavelengths of waviness shown in Fig. 52.6, are typically found in large wafers.

Grinding in Wafer Manufacturing

After wafers are sliced by wiresaw, grinding is often employed for large wafers for flattening [52.66, 95, 96]. The advantages of grinding over lapping are (1) fully automatic cassette-to-cassette operation, (2) use of a fixed abrasive grinding wheel rather than loose abrasive slurry so the cost of consumables per wafer may be lower, and (3) higher throughput. However, the grinding process cannot entirely remove the waviness induced by wiresaw slicing, which is why grinding cannot totally replace the lapping process.

The grinding operation cannot remove the waviness as effectively as the lapping operation because of elas-

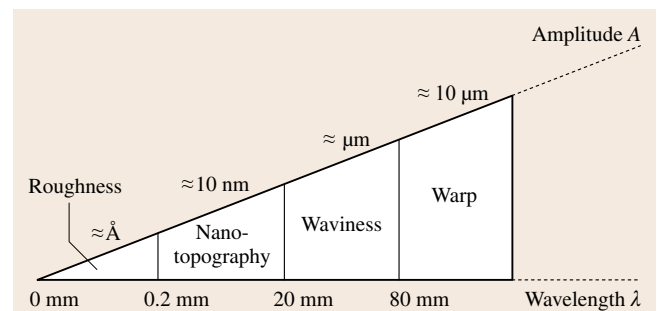


Fig. 52.6 Illustration of surface roughness classified as the *nanotopography* by SEMATECH. Nanotopography and waviness are typically found in large wafers

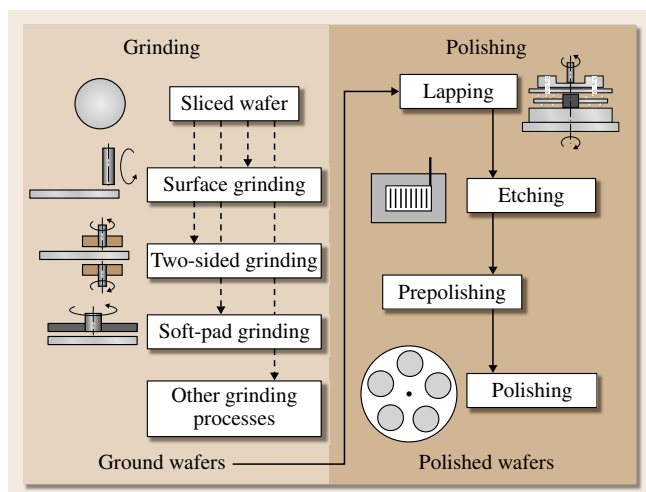


Fig. 52.7 Illustration of revised wafer manufacturing process with the insertion of the grinding operation, especially for very large silicon wafers (Fig. 52.1)

tic deformation of the wafer. When the same total force is applied on a wafer, the elastic deformation of the wafer in lapping is much smaller than that in grinding, resulting in a less pronounced spring-back effect in lapping. The amount of deformation in lapping is only 1/55 to 1/36 of that in grinding [52.77,78,97,98]. In order to improve the removal of surface waviness in grinding operation, several methods have been proposed, including:

1. Wafer grinding followed by a lapping
2. Wax mounting to reduce the effect of elasticity
3. Reduced vacuum
4. Use of a soft pad to avoid elastic spring-back after the grinding operation

A revised wafer production flow is shown in Fig. 52.7 in which the grinding operation follows the slicing operation, followed by the lapping/polishing operations.

52.3 Modern Wiresaw in Wafer Slicing

In the following subsections, the technology of modern slurry wiresaw is introduced with discussions of various topics involved in the technology and research of modern slurry wiresaws.

52.3.1 Definition of Modern Wiresaw

The term *wiresaw* or *modern wiresaw* has been used throughout this chapter to refer to the equipment for slicing crystalline ingots using a bare wire (typically cold-drawn steel wire) pressing onto the ingot with the continuous supply of abrasive slurry at the cutting interface. This is to distinguish them from saws that cut into materials with diamond-impregnated wires under various arrangements such as rotary or prismatic reciprocating motions. In a typical arrangement of a slurry wiresaw, a wire web is formed with a single bare steel wire drawn from a supply spool by winding it along grooved cylindrical wire guides, as illustrated in Fig. 52.5. Although the alternative name *multiwire saw* is also used in the literature, this is potentially misleading because modern wiresaw equipment actually operates on a *single* wire wound on grooved cylindrical guides. In addition, multiple wires are often used in diamond-impregnated reciprocating saw, which could be more appropriately called a *multiwire saw*. Since

separating materials with wire under a similar principle is a century-old technology when wire was used to slab stones in the 19th century, the term *modern wiresaw* has been adopted in this chapter and used interchange-



Fig. 52.8 Picture of a HCT wiresaw. The circled region indicates the wire web formed by the single wire winding over the grooved wire guides. To the upper right of this region is the ingot mounted on the jig, which is controlled to move downwards for slicing operation (source: HCT Inc., and GT Equipment Inc.)

Table 52.8 Operating parameters and their ranges and/or values for wiresawing

Parameter	Values and ranges
Speed of wire	5–15 m/s
Duty cycle of wire	Continuous feeding or reciprocating
Wire tension	25–35 N
Diameter of wire	150–175 μm
Wire bow angle	2–5 $^{\circ}\text{C}$
Kerf loss	180–210 μm (typically)
Slurry, carrier fluid	Water soluble or oil based
Slurry, abrasive grits	Silicon carbide (usually)
Feed rate of ingot	100–300 $\mu\text{m}/\text{min}$
Consumables	Wire and slurry

ably with *wiresaw*. The modern wiresawing is a much more rigorous process than the stone-slabbing operation using wire, and also is subject to more stringent requirements on surface finish for typical applications.

A typical industrial wiresaw is shown in Fig. 52.8, in which four wire guides are shown with a wire web face circled in the figure. A silicon ingot is shown to be fed top-down onto the top horizontal face of the wire web for slicing. To the left are the control console of the wiresaw and the wire management unit which controls the tension of the wire and manages the supply, feeding, tension, and speed of the wire.

52.3.2 Modern Wiresaw Technology

The *modern wiresaw* and associated technology discussed in this chapter utilizes a steel wire with abrasive slurry, consisting of abrasive grits suspended in carrier fluid, for the purpose of slicing crystals. Wire saws had been used in the 19th century in Europe to slab stones. Modern wiresaws, however, are employed to produce wafers with more stringent requirements of surface quality (Fig. 52.3). A typical modern wiresaw, as shown in Fig. 52.8, consists of three main components:

1. Wire management unit
2. Control and program console
3. The slicing compartment, where the ingot is sliced by feeding it onto the wire web

The slicing process of the modern slurry wiresaw belongs to the category of *free abrasive machining (FAM)*. Modern wiresaws utilize a steel wire, under high tension, moving at high speed on the surface of

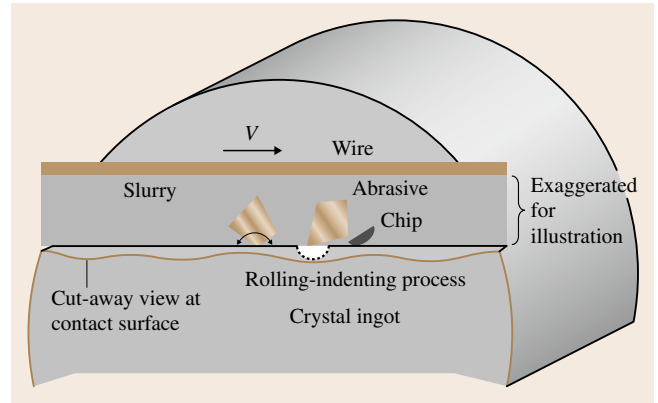


Fig. 52.9 Three-dimensional illustration of the rolling-indenting process in the wiresaw slicing process in which abrasive grits rolls and indents on the contact interface to remove materials from the substrate surface. This body abrasion process is also called *free abrasive machining (FAM)*

the substrate submerged in abrasive slurry. The wire maintains a bow angle with the cutting surface, applying a normal load along the direction of cutting. Typical parameters of wiresaw and operating parameters are summarized in Table 52.8. A schematic drawing of the modern wiresaw is shown in Fig. 52.5 with the *rolling-indenting* process shown in Fig. 52.9. The *FAM* process of wiresaw slicing with slurry is theoretically less brutal than cutting with fixed abrasive grinding processes [52.90, 91], under the condition of the same energy input, because of the inherent cutting mechanism of rolling and indenting. The cutting interface in Fig. 52.9 is exaggerated for the illustration of free abrasive grits interacting with the substrate surface in rolling and indenting due to the speed differential within the film of fluid trapped between the wire and the substrate surface. Chips are removed from the surface of the work material as a result of repeated rolling-indenting with typical micro- and nanoindentation effects.

52.3.3 Modeling and Control of the Modern Wiresawing Process

Research and studies of the modern wiresaw slicing process started to appear in the 1990s, first in patent disclosures followed by academic and industrial research. Academic-industrial-governmental synergy is characteristic of such research due to the very nature of process modeling for the wiresaw process, which requires a high degree of collaboration in order to make research results

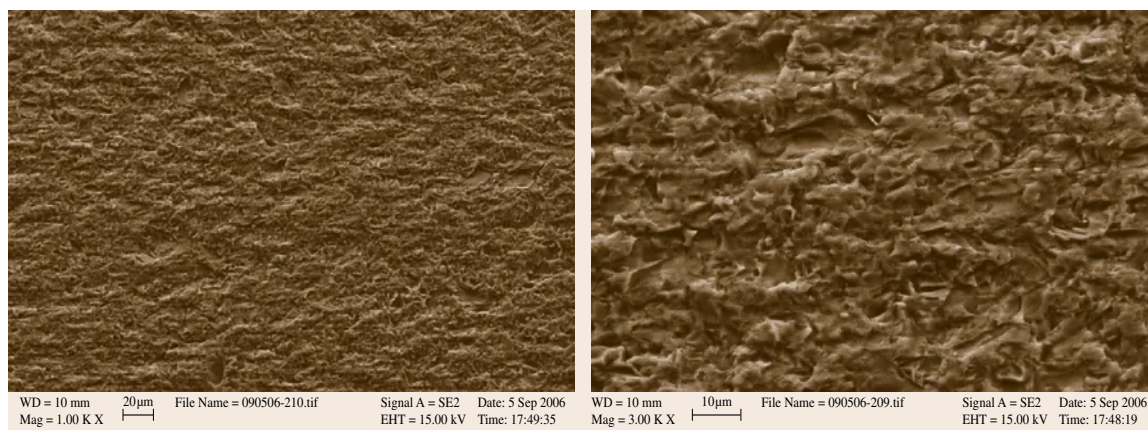


Fig. 52.10 SEM micrographs at scales of $10\ \mu\text{m}$ and $20\ \mu\text{m}$ illustrating the typical surface of an as-sliced wafer. The wafer surface shown here is from a polysilicon material sliced by an industrial wiresaw. The surface is full of random pits resulting from the rolling-indenting manufacturing process. Such a surface is very representative of wafers sliced by wiresaw under normal operating conditions

relevant. In the following subsections, a brief survey of various aspects of research and studies in wiresaw manufacturing processes is presented. Readers are referred to the bibliography at the end of this chapter for further reading.

SEM Study of Surface Characteristics of Wiresawn Wafers

Figure 52.10 shows a typical surface of an as-sliced wafer cut by an industrial wiresaw. The material of the wafer is polysilicon with rectangular surface area, to be used as a PV cell. As can be observed in the scanning electron microscopy (SEM) photo to the left with the scale bar of $20\ \mu\text{m}$, the surface is covered with a random pattern of pits caused by the rolling-indenting process. The abrasive grits used are silicon carbide 400 with an average grit size of $17\ \mu\text{m}$. A more detailed photo on the right with a scale bar of $10\ \mu\text{m}$ shows magnified patterns of random pits, with very little or nearly no fracture, as opposed to typical surface of wafers sliced by ID saws which are populated with more visible fractures on the surface.

The Rolling-Indenting Process Model

Figure 52.10 illustrates the *rolling-indenting* manufacturing process model for slicing using a wiresaw. A three-dimensional (3-D) illustration of the rolling-indenting process associated with free abrasive machining is shown in Fig. 52.9. For more details on the rolling-indenting model, readers are referred to [52.1, 13, 23, 48].

Hydrodynamic and Elastohydrodynamic Interaction

It is known that even in a lubricated wire drawing manufacturing process, the hydrodynamic effect is present. In the wiresaw machining process, the wire moving with high speed (Table 52.8) in a slurry-rich environment will induce not only the hydrodynamic effect but also elastic interaction with the steel wire. The intertwined effects result in the elastohydrodynamic phenomenon common in the modern wiresaw process. In the initial study of such phenomena [52.23], hydrodynamic process modeling and computer simulation were implemented with realistic process parameters. Later, other work also addressed and advanced this topic [52.21, 24, 39, 40]. The hydrodynamic film between the wire and substrate surface supports and suspends the normal force applied to the ingot. The contact interface through the hydrodynamic film generally supports the free abrasive machining with abrasive grits rolling and indenting on the surface of substrate. In some areas, there may be intermittent direct contact made due to the thickness of the slurry film. In [52.50], the author suggested that direct contact may be a more regular occurrence.

Vibration of the Wire in Slicing Using a Wiresaw

Vibration analysis of a stationary wire is a century-old problem with well-known solution (for example, in a stringed musical instrument). The eigenvalue problem and solution of the analysis of vibration of a moving string, however, was only solved in the early 1990s, although the differential equation of motion was first

proposed around 1970. Excessive vibration of the wire during slicing will increase the kerf – an undesirable effect. The application of eigenvalue problems of the moving wire in the wiresawing process has been presented in [52.7, 9, 20, 22, 31, 40].

Consumables in Wiresawing Process

The consumables of wiresawing process include the abrasive grits, carrier fluid, and wire. In recent years, recovery and regeneration of abrasive grits have received considerable attention due to environmental concerns. Several pieces of equipment that recycle abrasive grits have been constructed to recover a large percentage of grits. The carrier fluid has typically become water soluble instead of oil based. Wire used in wiresawing process is made of steel in a cold-drawn process, and is rather inexpensive with very consistent quality. Wires are typically discarded after each slicing operation. In

the future, it is expected that more attention will be paid to the management of these consumables due to environmental concerns.

Material-Related Subjects and Thermal Issues

Wafer slicing also depends on the materials of the crystalline ingots. It may generally be fine to assume isotropy for consideration of slicing materials such as polysilicon; however, highly anisotropic materials such as lithium niobate will display specific behavior based on its anisotropy. Even single-crystalline silicon is anisotropic, although not to the extent seen in lithium niobate. Some recent work with consideration of materials properties can be found in, e.g., [52.38, 42, 43].

Thermal issues and correlation to the surface waviness of large wafers sliced by wiresaw have attracted much attention. Studies have been performed, resulting in disclosures such as [52.51, 52, 69].

52.4 Conclusions and Further Reading

The advent of the modern wiresaw as a generic wafer slicing tool has brought about a revolution in the wafer manufacturing industry, particularly in the silicon wafering industry. As a result of the versatility and capabilities of the modern wiresaw, it has entirely replaced the ID saw technology that from the 1970s to 1990s was the primary slicing tools for wafer production. Equipped with better control and monitoring of industrial processes and research knowledge base of wiresaw process modeling and control, today's industrial wiresaws are gradually becoming the primary tool of choice for slicing.

In this chapter, modern wafer manufacturing and wafering process was discussed and illustrated. Wafer production, based on the collection of operations shown in Fig. 52.1, produces prime wafers from crystalline ingots. Slicing is the first postgrowth wafer-forming

process. Several technologies of slicing were discussed with historical perspectives. The modern slurry wiresaw and its technological development with research in process modeling to improve understanding and control of the process were also presented. Surveys of various topics in wiresaw processing and research include: modeling and control of modern wiresawing process, SEM study of surface characteristics of wiresawn wafers, the rolling-indenting process model, hydrodynamic and elastohydrodynamic interaction, vibration of wire in slicing using wiresaw, consumables in the wiresawing process, and material-related subjects and thermal issues.

Various references to research literature and patents are cited throughout the chapter. The list of references provides readers with suggestions for further reading on topics of their interests.

References

- 52.1 I. Kao: Technology and research of slurry wiresaw manufacturing systems in wafer slicing with free abrasive machining, *Int. J. Adv. Manuf. Syst.* **7**(2), 7–20 (2004)
- 52.2 I. Kao, V. Prasad, J. Li, M. Bhagavat, S. Wei, J. Talbott, K. Gupta: Modern wiresaw technology for large crystals, *Proc. ACCG/least-97* (Atlantic City 1997)
- 52.3 I. Kao, V. Prasad, J. Li, M. Bhagavat: Wafer slicing and wire saw manufacturing technology, *NSF Grantees Conf.* (Seattle 1997) pp.239–240
- 52.4 S. Wu, S. Wei, I. Kao, F.P. Chiang: Wafer surface measurements using shadow moiré with Talbot effect, *Proc. ASME IMECE'97* (ASME, Dallas 1997) pp.369–376

- 52.5 J. Li, I. Kao, V. Prasad: Modeling stresses of contacts in wiresaw slicing of polycrystalline and crystalline ingots: application to silicon wafer production, Proc. ASME IMECE '97 (ASME, Dallas 1997) pp. 439–446
- 52.6 M. Bhagavat, F. Yang, I. Kao: Elasto-plastic finite element analysis of indentations in free abrasive machining, Proc. Manuf. Eng. Div. IMECE'98 (ASME, 1998) pp. 819–824
- 52.7 S. Wei, I. Kao: Analysis of stiffness control and vibration of wire in wiresaw manufacturing process, Proc. Manuf. Eng. Div. IMECE'98 (ASME, 1998) pp. 813–818
- 52.8 I. Kao, M. Bhagavat, V. Prasad: Integrated modeling of wiresaw in wafer slicing, NSF Des. Manuf. Grantees Conf. (Monterey, 1998) pp. 425–426
- 52.9 I. Kao, S. Wei, F.-P. Chiang: Vibration of wiresaw manufacturing processes and wafer surface measurement, NSF Des. Manuf. Grantees Conf. (Monterey, 1998) pp. 427–428
- 52.10 I. Kao, V. Prasad, F.P. Chiang, M. Bhagavat, S. Wei, M. Chandra, M. Costantini, P. Leyvraz, J. Talbott, K. Gupta: Modeling and experiments on wiresaw for large silicon wafer manufacturing, 8th Int. Symp. Silicon Mater. Sci. Technol. (San Diego 1998) p. 320
- 52.11 F.P. Chiang, M.L. Du, I. Kao: Some new applications on in-plane, shadow and reflection moiré methods, Int. Conf. Appl. Optic. Metrol. (Hungary 1998)
- 52.12 S. Wei, S. Wu, I. Kao, F.P. Chiang: Wafer surface measurements using shadow moiré with Talbot effect, J. Electron. Packag. **120**(2), 166–170 (1998)
- 52.13 J. Li, I. Kao, V. Prasad: Modeling stresses of contacts in wiresaw slicing of polycrystalline and crystalline ingots: Application to silicon wafer production, J. Electron. Packag. **120**(2), 123–128 (1998)
- 52.14 F. Yang, I. Kao: Free abrasive machining in slicing brittle materials with wiresaw, Tech. Rep. TR99-03 (SUNY at Stony Brook Department of Mechanical Engineering, New York 1999)
- 52.15 F. Yang, J.C.M. Li, I. Kao: Interaction between ingot and wire in wiresaw process, Proc. IMECE'99: Electron. Manuf. Iss., Vol. 104, ed. by C. Sahay, B. Sammakia, I. Kao, D. Baldwin (ASME, New York 1999) pp. 3–8
- 52.16 M. Bhagavat, I. Kao: Computational model for free abrasive machining of brittle silicon using a wiresaw, Proc. IMECE'99: Electron. Manuf. Iss., Vol. 104, ed. by C. Sahay, B. Sammakia, I. Kao, D. Baldwin (ASME, New York 1999) pp. 21–30
- 52.17 S. Wei, I. Kao: High-resolution wafer surface topology measurement using phase-shifting shadow moiré technique, Proc. IMECE'99: Electron. Manuf. Iss., Vol. 104, ed. by C. Sahay, B. Sammakia, I. Kao, D. Baldwin (ASME, New York 1999) pp. 15–20
- 52.18 F. Yang, I. Kao: Interior stress for axisymmetric abrasive indentation in the free abrasive machining process: slicing silicon wafers with modern wiresaw, J. Electron. Packag. **121**(3), 191–195 (1999)
- 52.19 M. Chandra, P. Leyvraz, J.A. Talbott, K. Gupta, I. Kao, V. Prasad: Challenges in slicing large diameter silicon wafers using slurry wiresaw, Proc. Manuf. Eng. Div. IMECE'98 (ASME, 1998) pp. 807–811
- 52.20 S. Wei, I. Kao: Free vibration analysis for thin wire of modern wiresaw between sliced wafers in wafer manufacturing processes, Proc. IMECE'00: Packag. Electron. Photon. Dev., Vol. 28 (ASME, Orlando 2000) pp. 213–219
- 52.21 L. Zhu, M. Bhagavat, I. Kao: Analysis of the interaction between thin-film fluid hydrodynamics and wire vibration in wafer manufacturing using wiresaw, Proc. IMECE'00: Packag. Electron. Photon. Dev., Vol. 28 (ASME, Orlando 2000) pp. 233–241
- 52.22 S. Wei, I. Kao: Vibration analysis of wire and frequency response in the modern wiresaw manufacturing process, J. Sound Vib. **231**(5), 1383–1395 (2000)
- 52.23 M. Bhagavat, V. Prasad, I. Kao: Elasto-hydrodynamic interaction in the free abrasive wafer slicing using a wiresaw: modeling and finite element analysis, J. Tribol. **122**(2), 394–404 (2000)
- 52.24 L. Zhu, I. Kao: Equilibrium elastohydrodynamic interaction analysis in wafer slicing process using wiresaw, Proc. IMECE'01: EEP, Vol. 1 (New York 2001), pp. 123–128
- 52.25 F. Yang, I. Kao: Free abrasive machining in slicing brittle materials with wiresaw, J. Electron. Packag. **123**, 254–259 (2001)
- 52.26 I. Kao: The technology of modern wiresaw in silicon wafer slicing for solar cells, Invited talk at the 12th Workshop Cryst. Silicon Sol. Cell Mater. Process. (Breckenridge 2002)
- 52.27 I. Kao, F.-P. Chiang: Research on modern wiresaw for wafer slicing and on-line real-time metrology, Proc. NSF Des. Serv. Manuf. Grantees Res. Conf. (San Juan 2002)
- 52.28 I. Kao, L. Zhu: Computer simulation in back-lapping of wiresaw sliced semiconductor wafers, Proc. Des. Serv. Manuf. Grantees Res. Conf. (Birmingham 2003)
- 52.29 S. Bhagavat, I. Kao: Nanoindentation studies on a non-centrosymmetric crystal: lithium niobate, Invited talk at the High Press. Phase Transf. Workshop NSF Focus. Res. Group (FRG) (North Carolina State University, Raleigh 2004)
- 52.30 S. Bhagavat, I. Kao: Nanoindentation studies on a non-centrosymmetric crystal: lithium niobate, High Press. Phase Transf. Workshop, NSF Focus. Res. Group (FRG) (North Carolina State University, Raleigh 2004)
- 52.31 S. Wei, I. Kao: Stiffness analysis in wiresaw manufacturing systems for applications in wafer slicing, Int. J. Adv. Manuf. Sys. **7**(2), 57–64 (2004)
- 52.32 M. Bhagavat, F. Yang, I. Kao: Elasto-plastic finite element analysis of indentations in free abra-

- sive machining, Proc. Manuf. Eng. Div. Int. Mech. Eng. Congr. Expo. 1998 (IMECE'98), Anaheim, Vol. 8 (ASME, 1998) pp. 807–811
- 52.33 L. Zhu, I. Kao: On-line and real-time monitoring of moving wire with dynamic consideration in wiresaw slicing processes, Technical Report TR010–2005 (Department of Mechanical Engineering, Stony Brook University 2005)
- 52.34 S. Bhagavat, J. Liberato, I. Kao: Effects of mixed abrasive slurries on free abrasive machining processes, Proc. 2005 ASPE Conf. (ASPE, 2005)
- 52.35 S. Bhagavat, I. Kao: Ultra-low load indentation response of materials: in purview of free abrasive machining processes, High Press. Phase Transf. Workshop, NSF Focus. Res. Group (FRG) (2005)
- 52.36 I. Kao: Experiments of nanoindentation on non-centrosymmetric crystal and study of their implication in wafer manufacturing processes, Invited talk at the US–Africa Workshop Mater. Mech. (Cape Town 2005)
- 52.37 I. Kao: Experiments of nanoindentation on non-centrosymmetric crystal and study of their implication in wafer manufacturing processes, Invited talk at the US–Africa Workshop Mater. Mech. (Cape Town 2005)
- 52.38 S. Bhagavat, I. Kao: Nanoindentation of lithium niobate: hardness anisotropy and pop-in phenomenon, Mater. Sci. Eng. A **393**, 327–331 (2005)
- 52.39 L. Zhu, I. Kao: Computational model for the steady-state elasto-hydrodynamic interaction in wafer slicing process using wiresaw, Int. J. Manuf. Technol. Manag. **7**(5/6), 407–429 (2005)
- 52.40 L. Zhu, I. Kao: Galerkin-based modal analysis on the vibration of wire-slurry system in wafer slicing using wiresaw, J. Sound Vib. **283**(3–5), 589–620 (2005)
- 52.41 A. Gouldstone, I. Kao: Wafer slicing using slurry wiresaw and relevance of nanoindentation in its analysis, High Press. Phase Transf. (HPPT) Workshop (Kalamazoo 2006)
- 52.42 S. Bhagavat, I. Kao: Ultra-low load multiple indentation response of materials: in purview of wiresaw slicing and other free abrasive machining (FAM) processes, Int. J. Mach. Tools Manuf. **46**(5), 531–541 (2006)
- 52.43 S. Bhagavat, I. Kao: Theoretical analysis on the effects of crystal anisotropy on wiresawing process and application to wafer slicing, Int. J. Mach. Tools Manuf. **46**, 531–541 (2006)
- 52.44 S. Bhagavat, I. Kao: A finite element analysis of temperature variation in silicon wafers during wiresaw slicing, Int. J. Mach. Tools Manuf. **48**(1), 95–106 (2007)
- 52.45 I. Kao, S. Bhagavat: Single-crystalline silicon wafer production using wire saw for wafer slicing. In: *Semiconductor Machining at the Micro-Nano Scale*, ed. by J. Yan, J. Patten (Transworld Research Network, Kerala 2007) pp. 243–270
- 52.46 C. Chung, I. Kao: Damped vibration response at different speeds of wire in slurry wiresaw manufacturing operations, Proc. Int. Manuf. Sci. Eng. Conf. (MSEC 2008) (ASME, 2008), paper number MSEC2008-72213
- 52.47 C. Chung, I. Kao: Comparison of free abrasive machining processes in wafer manufacturing, Proc. Int. Manuf. Sci. Eng. Conf. (MSEC 2008) (ASME, 2008), paper number MSEC2008-72213
- 52.48 H.J. Möller: Basic mechanisms and models of multi-wire sawing, Adv. Eng. Mater. **6**(7), 501–513 (2004)
- 52.49 H.J. Möller, C. Funke, M. Rinio, S. Scholz: Multi-crystalline silicon for solar cells, Thin Solid Films **487**(1–2), 179–187 (2005)
- 52.50 H.J. Möller: Wafering of silicon crystals, Phys. Stat. Sol. A **203**(4), 659–669 (2006)
- 52.51 Y. Ariga: Wiresaw and cutting method, US Patent 6652356 (2003)
- 52.52 M. Bhagavat, D. Witte, S. Kimbel, D. Sager, J. Peyton: Method and apparatus for slicing semiconductor wafers, US Patent 2003170948 (2003)
- 52.53 U. Bismayer, E. Brinksmeier, B. Guttler, H. Seibt, C. Menz: Measurement of subsurface damage in silicon wafers, Prec. Eng. **16**(2), 139–144 (1994)
- 52.54 Y. Chang, M. Hashimura, D. Dornfeld: An investigation of material removal mechanisms in lapping with grain size transition, J. Manuf. Sci. Eng. Trans. ASME **122**(3), 413–419 (2000)
- 52.55 G.L. Contardi: Wire saw beads. Economic production, Indust. Diam. Rev. **53**(558), 256–260 (1993)
- 52.56 C. Hauser: Wire sawing device, US Patent 5910203 (1999)
- 52.57 R. Wells: Wire saw slicing of large diameter crystals, Solid State Technol. **30**(9), 63–65 (1987)
- 52.58 R.C. Wells: Wire saw, US Patent 4494523 (1985)
- 52.59 Corning Inc.: Corning to acquire world's largest multi-wire saw for manufacturing of image mask blanks (2005) http://www.corning.com/news_center/news_releases/2005/2005071201.aspx
- 52.60 A. Jindal, S. Hegde, S. Babu: Chemical mechanical polishing using mixed abrasive slurries, Electrochem. Solid State Lett. **5**(7), G48–G50 (2002)
- 52.61 O. Konunchuk, G. Preece: Apparatus and method for reducing bow and warp in silicon wafers sliced by a wire saw, US Patent 6352071 (2002)
- 52.62 A. le Scanff: New wire saw machine, Indust. Diam. Rev. **48**(527), 168 (1988)
- 52.63 H. Olkrug, H. Lundt, C. Andrae, J. Frumm: Process and device for producing a cylindrical single crystal and process for cutting semiconductor wafers, US Patent 6159284 (2000)
- 52.64 H. Shimizu: Wire-saw, US Patent 3942508 (1976)
- 52.65 G. E. Technologies: Advanced wiresaw for photovoltaic wafers, Technical Report, GT Equipment Technologies, Inc. (1998)
- 52.66 H.K. Tönshoff, B. Karpuschewski, M. Hartmann, C. Spengler: Grinding and slicing technique as

- an advanced technology for silicon wafer slicing, *Mach. Sci. Technol.* **1**, 33–47 (1997)
- 52.67 K. Toyama, K. Hayakawa, E. Kiuchi: Method of slicing semiconductor single crystal ingot, EU Patent 0798092 (1997)
- 52.68 J. Verhey, U. Bismayer, B. Guttler, H. Lundt: The surface of machined silicon wafers, *Semiconduct. Sci. Technol.* **9**, 404–408 (1994)
- 52.69 T. Yamada, M. Fukunaga, T. Ichikawa, K. Furno, K. Makino, A. Yokoyama: Prediction of warping in silicon wafer slicing with wire saw, *Theor. Appl. Mech.* **51**, 251–258 (2002)
- 52.70 M. Yoshioka, J. Hagiwara: Simulation of time-dependent distribution of abrasive grain size in lapping, *Jpn. Prec. Eng.* **61**(9), 1270–1274 (1995)
- 52.71 S. Herbert: UK's biggest wire saw contract, *Indust. Diam. Rev.* **49**(534), 206–207 (1989)
- 52.72 M. Kojima, A. Tomizawa, J. Takase: Development of new wafer slicing equipment (unidirectional multi wire-saw), *Sumitomo Met. Ind.* **42**(4), 218–224 (1990)
- 52.73 Y. Xie, B. Bhushan: Effects of particle size, polishing pad and contact pressure in free abrasive polishing, *Wear* **200**(1–2), 281–295 (1996)
- 52.74 G. Wenski, T. Altmann, W. Winkler, G. Heier, G. Holker: Doubleside polishing – a technology mandatory for 300 mm wafer manufacturing, *Mater. Sci. Semiconduct. Proc.* **5**(4–5), 375–380 (2002)
- 52.75 S. Chonan, Z.W. Jiang, Y. Yuki: Stress analysis of a silicon-wafer slicer cutting the crystal ingot, *J. Mech. Des.* **115**, 711–717 (1993)
- 52.76 S. Chonan, Z.W. Jiang, Y. Yuki: Vibration and deflection of a silicon-wafer slicer cutting the crystal ingot, *J. Vib. Acoust.* **115**, 529–534 (1993)
- 52.77 W. Liu, Z. J. Pei, X. J. Xin: Finite element analysis for grinding and lapping of wire-sawn silicon wafers, *J. Mater. Proc. Technol.* **129**(1–3) 2–9 (2002)
- 52.78 X.J. Xin, Z.J. Pei, W. Liu: Finite element analysis on soft-pad grinding of wire-sawn silicon wafers, *ASME J. Electron. Packag.* **126**, 177–185 (2004)
- 52.79 P. Gise, R. Blanchard: *Modern Semiconductor Fabrication Technology* (Prentice Hall, New Jersey 1986)
- 52.80 Semiconductor Industry Association (SIA): Microelectronics: vision for the 21st century, Technical Report (1994)
- 52.81 Semiconductor Industry Association (SIA): National technology roadmap for semiconductor, Technical Report (1994)
- 52.82 Semiconductor Industry Association (SIA): Published data of Semiconductor Industry Association by P.S. Peercy, Technical Report (Semiconductor Industry Association/SEMATECH 1998)
- 52.83 SEMATECH: I. Project, assorted publications and web pages of sematech.org and i300i.org, Technical Report (SEMATECH and International 300 mm Initiative 1994–1998)
- 52.84 J.A. Slotwinski, N.N. Hsu, G.V. Blessing: Ultrasonic measurement of surface and subsurface structure in ceramics. In: *Machining of Advanced Materials*, ed. by National Institute of Science and Technology (NIST) (US Government Printing Office, Washington 1993), Special Pub. 847
- 52.85 I. Kao: Research towards the next-generation reconfigurable wiresaw for wafer slicing and on-line real-time metrology, *Proc. 2001 NSF Des., Serv. Manuf. Grantees Res. Conf.* (Tempe 2001)
- 52.86 H.W. Mech: Machine and method for cutting brittle materials using a reciprocating cutting wire, US Patent 3831576 (1974)
- 52.87 D. Hayes: Demolition – the modern method, *Indust. Diam. Rev.* **50**(537), 69 (1990)
- 52.88 W. Weiland: Railway bridge cut in two, *Indust. Diam. Rev.* **50**(537), 65–66 (1990)
- 52.89 HCT Shaping Systems SA: World leader in wire saw technology, Technical Report (1995)
- 52.90 W. Clark, A. Shih, C. Hardin, R. Lemaster, S. McSpadden: Fixed abrasive diamond wire machining – part i: process monitoring and wire tension force, *Int. J. Mach. Tools Manuf.* **43**(5), 523–532 (2003)
- 52.91 W. Clark, A. Shih, R. Lemaster, S. McSpadden: Fixed abrasive diamond wire machining – part ii: experiments design and results, *Int. J. Mach. Tools Manuf.* **43**(5), 533–542 (2003)
- 52.92 D. Hayes: Japanese granite trade embraces diamond wiresaw, *Indust. Diam. Rev.* **49**, 67–69 (1989)
- 52.93 T. Chang, T. Ueng, W. Lee: Study of mechanism of diamond wiresaw, *Min. Metall.* **37**, 73 (1993)
- 52.94 S. Chonan, T. Hayase: Stress analysis of a spinning annular disk to a stationary distributed, in-plane edge load, *J. Vib. Acoust. Stress Reliab. Des.* **107**, 277–282 (1987)
- 52.95 P. Moulik, H. Yang, S. Chandrasekar: Simulation of thermal stresses during grinding, *Int. J. Mech. Sci.* **43**, 831–851 (2001)
- 52.96 Z. Zhong, V.C. Venkatesh: Surface integrity studies on the grinding, lapping and polishing processes for optical products, *J. Mater. Process. Technol.* **44**, 179–186 (1994)
- 52.97 Z. Pei, X. Xin, W. Liu: Finite element analysis for grinding of wire-sawn silicon wafers: a designed experiment, *Int. J. Mach. Tools Manuf.* **43**(1), 7–16 (2003)
- 52.98 X. Sun, Z.J. Pei, X.J. Xin, M. Fouts: Waviness removal in grinding of wire-saw silicon wafers: 3d finite element analysis with designed experiments, *Int. J. Mach. Tools Manuf.* **44**, 11–19 (2004)

Acknowledgements

A.1 Crystal Growth Techniques and Characterization: An Overview by Govindhan Dhanaraj, Kullaiiah Byrappa, Vishwanath (Vish) Prasad, Michael Dudley

The authors would like to thank Dr. Kedar Gupta and Dr. Rick Schwerdtfeger for their generous support and encouragement during the preparation of this manuscript.

We also wish to acknowledge the help rendered by Ms. K. Namratha, Dept. of Geology, University of Mysore, Mysore, India in preparing this chapter.

A.4 Generation and Propagation of Defects During Crystal Growth by Helmut Klapper

The author is indebted to J. Thar and R.A. Becker (Institut für Kristallographie, RWTH Aachen University) for the preparation of the figures.

A.6 Defect Formation During Crystal Growth from the Melt by Peter Rudolph

The author is indebted to his long-term co-workers Dr. M. Neubert, Dr. F.-M. Kießling, Dr. C. Frank-Rotsch, Dr. U. Juda, M. Czupalla, P. Lange, O. Root, U. Kupfer, M. Ziem, T. Wurche, M. Imming, U. Rehse, W. Miller (all from IKZ Berlin), and the director of IKZ Prof. R. Fornari for helpful discussions, and experimental work essentially contributing to the present chapter. He is also grateful for long-term stimulating cooperations with Dr. M. Jurisch, Dr. B. Weinert, and Dr. S. Eichler from Freiburger Compound Materials GmbH. Special thanks go to D. Bliss from the Air Force Res. Lab. (USA) for critical reading and helpful comments for manuscript revision.

B.7 Indium Phosphide: Crystal Growth and Defect Control by Applying Steady Magnetic Fields by David F. Bliss

The author would like to thank Prof. Michael Dudley for helpful guidance in x-ray topography and

crystallographic analysis, G.G. Bryant and R. Lancto for their skilled assistance in crystal growth and data acquisition, and Dr. G. Iseler for many discussions. Topography was carried out at the Stony Brook Synchrotron Topography Facility, beamline X19C, at the National Synchrotron Light Source, at Brookhaven National Laboratory, which is supported by the US Department of Energy. This research effort was supported by the US Air Force Office of Scientific Research.

B.9 Czochralski Growth of Oxide Photorefractive Crystals by Ernesto Diéguez, Jose Luis Plaza, Mohan D. Aggarwal, Ashok K. Batra

The authors gratefully acknowledge the support of the present work through NSF RISE grant # HRD-0531183. Special thanks are due to Mr. G. Sharp for fabrication of crystal growth system components. One of the authors (M.D.A.) would like to acknowledge support from NASA Administrator's Fellowship Program (NAFP) through United Negro College Fund Special Program (UNCFSP) Corporation under their contract #NNG06GC58A.

B.11 Growth and Characterization of Antimony-Based Narrow-Bandgap III-V Semiconductor Crystals for Infrared Detector Applications by Vijay K. Dixit, Handady L. Bhat

The authors are grateful to the collaborators: B. Bansal and V. Venkataraman, Departments of Physics Indian Institute of Science, Bangalore; and B.M. Arora and K.S. Chandrasekaran, Solid State Group, TIFR Mumbai. The authors are also grateful to the many authors whose work is included in this review.

B.13 Laser-Heated Pedestal Growth of Oxide Fibers by Marcello R.B. Andreetta, Antonio Carlos Hernandez

The authors would like to thank the Brazilian agencies CNPq, FAPESP, and CAPES for financial support

and also all the editors and journals that kindly allowed the reproduction of the figures that illustrate this chapter.

B.14 Synthesis of Refractory Materials by Skull Melting Technique

*by Vyacheslav V. Osiko, Mikhail A. Borik,
Elena E. Lomonova*

We wish to thank the following for help in the preparation of this chapter: Dr. O. M. Borik, Dr. V. A. Panov, and S. Semyova.

C.17 Bulk Single Crystals Grown from Solution on Earth and in Microgravity

*by Mohan D. Aggarwal, Ashok K. Batra,
Ravindra B. Lal, Benjamin G. Penn,
Donald O. Frazier*

The authors are grateful for helpful discussions with a number of graduate students and other physics faculty in the Department of Physics at Alabama A&M University. Authors are thankful to Garland Sharp for his expert machining work and Jerry Johnson for his glass-blowing jobs in the design of various crystal growth systems described in this work. Spacelab-3 and IML-1 work was supported by NASA contracts. The optical holography work for these experiments was developed in collaboration of Dr. James Trolinger of MetroLaser, Inc. This work was partially supported under NSF-HBCU RISE program HRD-0531183 and US Army Space and Missile Defense Command, Contract W9113M-04-C-0005. Two of the authors (M.D.A. and R.B.L.) would like to acknowledge support from NASA Administrator's Fellowship Program (NAFP) through United Negro College Fund Special Programs (UNCFSP) Corporation under their Contract No. NNG06GC58A.

C.18 Hydrothermal Growth of Polyscale Crystals

by Kullaiah Byrappa

The author wishes to acknowledge Prof. M. Yoshimura (Tokyo Institute of Technology, Japan), Prof. Richard E. Riman (Rutgers University, USA), Prof. Yan Li (Tsinghua University, China), Prof. T. Adschiri, and Prof. Dirk Ehrentauf (Tohoku University, Japan) for providing photographs of crystals synthesized by them and also some fruitful discussion. Thanks are also due to my group members Prof. B. Basavalingu,

Prof. K.M. Lokanatha Rai, and Prof. S. Ananda of Mysore University, India, for their assistance in preparing this chapter. The author acknowledges the help of Prof. Xu Haiyan, Anhui Institute of Architecture and Industry, Hefei, China, for providing some of the latest literature on solution processing of materials, and also for careful reading and constructive comments on this chapter. Also the authors acknowledge the help rendered by Dr. Jürgen Riegler, Tohoku University, Japan, in reading this manuscript and useful comments.

C.19 Hydrothermal and Ammonothermal Growth of ZnO and GaN

by Michael J. Callahan, Qi-Sheng Chen

The authors acknowledge collaborators whose work either influenced or was explicitly incorporated into this article. Special thanks are due to Govindhan Dhanaraj (SUNY-Stony Brook) who provided expertise on synchrotron white-beam x-ray topographs and to Dr. Buguo Wang (Solid State Sciences Corporation), Dr. Michael Alexander, Dr. David Bliss, and Michael Suscavage (Air Force Research Laboratory) for their expertise and many discussions with the authors on ammonothermal and hydrothermal research.

Finally, we thank the Air Force Office of Scientific Research (Drs. Jerry Witt, Dan Johnstone, Todd Steiner, and Don Silversmith) and the Naval Research Lab (Dr. Colin Wood) for their past and current support of research on wide-bandgap semiconductors.

C.20 Stoichiometry and Domain Structure of KTP-Type Nonlinear Optical Crystals

by Michael Roth

The author is grateful to Dr. N. Angert and Dr. M. Tseitlin for their long-term collaboration and numerous discussions on the science and technology of KTP-type crystals as well as for providing some crystal and domain photographs.

C.21 High-Temperature Solution Growth: Application to Laser and Nonlinear Optical Crystals

*by Joan J. Carvajal, Maria Cinta Pujol,
Francesc Díaz*

The authors thank to our colleague Prof. Magdalena Aguiló for her relevant contribution specially in structural and crystallographic aspects. This work was

supported by the Spanish Government under projects MAT2008-06729-C02-02/NAN and the Catalan Authority under project 2009SGR235. J.J. Carvajal and M.C. Pujol are supported by the Education and Science Ministry of Spain and European Social Fund under the Ramon y Cajal program, RYC2006-858.

C.22 Growth and Characterization of KDP and Its Analogs

by Sheng-Lai Wang, Xun Sun, Xu-Tang Tao

We wish to thank the following for help in the preparation of this chapter and for helpful discussions: Bing Liu, Xiao-Min Mu, Bo Wang, Yong-Qiang Lu, Liang Li, Prof. Chang-Shui Fang, Prof. Xin-Guang Xu (Shandong Univ., Jinan, China), Dr. Natalia Zaitseva, and Dr. Jim De Yoreo (LLNL). The authors also wish to thank Dr. Govindhan Dhanaraj for critically reading the manuscript and helpful discussion.

D.24 AlN Bulk Crystal Growth by Physical Vapor Transport

by Rafael Dalmau, Zlatko Sitar

This work was supported by the DoD Multidisciplinary University Research Initiative (MURI) administered by the Office of Naval Research (ONR) under grant N00014-01-1-0716, monitored by Dr. C.E. Wood.

D.26 Growth of III-Nitrides with Halide Vapor Phase Epitaxy (HVPE)

by Carl Hemmingsson, Bo Monemar, Yoshinao Kumagai, Akinori Koukitu

The authors gratefully acknowledge contributions from P.P. Paskov, T. Paskova, and V. Darakchieva, concerning new data cited and some illustrations. Our collaboration with the Epigress/Aixtron company (F. Wischmeyer, M. Heuken) in development of HVPE growth procedures and related equipment has been most helpful. We also have benefiting from a collaboration with A. Usui at Furukawa KK.

D.27 Growth of Semiconductor Single Crystals from Vapor Phase

by Ramasamy Dhanasekaran

The author is highly grateful to his research co-workers Dr. O. Senthil Kumar, Dr. S. Soundeswaran, Dr. M. J. Tafreshi, Dr. E. Varadarajan, Dr. P. Prabukanthan, and K. Senthilkumar for useful discussions and

support in understanding the concepts presented in this chapter. Thanks are also due to Dr. B. Vengatesan and Dr. K. Balakrishnan, who initiated the vapor growth activities at Crystal Growth Centre, Anna University. The help rendered by R. Arunkumar, G. Bhagyaraj, T. Shabi, and M. Senthil Kumar in preparing this manuscript is duly acknowledged.

E.28 Epitaxial Growth of Silicon Carbide by Chemical Vapor Deposition

by Ishwara B. Bhat

The author would like to thank Canhua Li and Rongjun Wang for carrying out a major portion of the work described herein as part of their Ph.D. theses. Financial supports from DARPA contract #DAAD19-02-1-026 and the ERC program of the NSF are acknowledged.

E.30 Epitaxial Lateral Overgrowth of Semiconductors

by Zbigniew R. Zytkiewicz

The author thanks Dr. D. Dobosz for her assistance in the LPE growth of the ELO structures, Dr. E. Papis and K. Babska for the photolithography and processing of the substrates, and Dr. J. Domagala for XRD analysis of the samples. Contributions of Prof. T. Tuomi, Prof. P. McNally, Dr. R. Rantamaki, and Dr. D. Danilewsky to synchrotron x-ray topography experiments and Dr. A. Rocher to TEM studies of the GaAs structures are highly appreciated. The author is also very grateful to Prof. S. Dost for his valuable comments and feedback. This work was carried out with partial financial support from the Polish Committee for Scientific Research under grant 3T08A 021 26. Partial support from the Natural Sciences and Engineering Research Council of Canada (NSERC) is also gratefully acknowledged.

F.37 Vapor Growth of III Nitrides

by Dang Cai, Lili Zheng, Hui Zhang

This work was supported by the DOD Multidisciplinary University Research Initiative (MURI) program administered by the Office of Naval Research under Grant N00014-01-1-1-0716 monitored by Dr. Colin E. Wood. We would like to express our gratitude to Drs. Williams Mecouch and Zlatko Sitar from North Carolina State University for providing experimental data.

H.47 Protein Crystal Growth Methods

*by Andrea E. Gutiérrez-Quezada,
Roberto Arreguín-Espinosa, Abel Moreno*

One of the authors (Abel Moreno) thanks CONACYT (Mexico) project No. 82888 for sponsorship. Roberto Arreguín-Espinosa acknowledges financial support from the project DGAPA-UNAM, No. IN210007. Andrea E. Gutiérrez-Quezada acknowledges scholarship from SNI-CONACYT.

H.48 Crystallization from Gels

by S. Narayana Kalkura, Subramanian Natarajan

The authors wish to thank Dr. E.K. Girija, S.A. Martin Britto Dhas (Madurai Kamaraj University, India), Dr. George Varghese (St. Berchmans College, Mahatma Gandhi University, India), and Dr. V. Jayanthi (Stanley Medical College, Chennai, India) for all their help in preparing this chapter. S.N.K. thanks AICTE and UGC, India for financial assistance for carrying out majority of the work reported in the review. S.N. thanks the UGC for the SAP funding to his Institution.

H.49 Crystal Growth and Ion Exchange in Titanium Silicates

*by Aaron J. Celestian, John B. Parise,
Abraham Clearfield*

Support for this work was provided by NSF-CHE-0221934 (CEMS) and DMR-051050 to John B. Parise and NSF-EAR programs. A. Clearfield would like to acknowledge the Department of Energy (DOE) through DE-FG07-01ER63300 and Westinghouse Savannah River Technology Center. We acknowledge the support of the Advanced Photon Source, Argonne National Laboratory, the National Synchrotron Light Source, Brookhaven National Lab-

oratory, the National Institute of Standards and Technology, U.W. Department of Commerce, and the ISIS facility at the Rutherford Appleton Laboratory in providing the neutron research facilities used in this work.

H.50 Single-Crystal Scintillation Materials

by Martin Nikl, Anna Vedda, Valentin V. Laguta

Authors are indebted to K. Nejezchleb, C. W. E. van Eijk and Xue-Jian Liu for providing material for Figs. 50.12, 50.17, 50.29 and 50.30, respectively, M. Dusek for preparation of figures of material structures, P. Bohacek, K. Nejezchleb, N. Senguttuvan, and A. Novoselov for information about crystal growth, E. Jurkova for the help in manuscript preparation, and C. R. Stanek for useful comments and linguistic corrections. Financial support of Czech GACR 202/05/2471, GA AV S100100506, KAN300100802 and Italian Cariplo foundation projects is gratefully acknowledged.

H.52 Wafer Manufacturing and Slicing Using Wiresaw

*by Imin Kao, Chunhui Chung,
Roosevelt Moreno Rodriguez*

The authors wish to thank Professor Vish Prasad, who has been instrumental in the collaboration of this research on wiresaw slicing and wafer manufacturing. His enthusiasm has always been an inspiration. Several industrial collaborators include Dr. Kedar Gupta, John Talbott, and others. The lead author would also like to thank his previous students who work in wiresaw manufacturing: Drs. Milind Bhagavat, Songbin Wei, Liqun Zhu, and Sumeet Bhagavat, and Mr. Abhiram Govindaraju. The research has been supported by various National Science Foundation (NSF) grants and the United States Department of Energy (DoE) grants.

About the Authors



Francesco Abbona

Università degli Studi di Torino
Dipartimento di Scienze Mineralogiche
e Petrologiche
Torino, Italy
francesco.abbona@unito.it

Chapter A.3

Professor Francesco Abbona received the MSc in Chemistry from the University of Torino, where he is now Full Professor of Mineralogy. His first research was devoted to minerals of the Alps, then he has done research mainly on the relationship between crystal morphology and crystal structure and nucleation and evolution of crystals from aqueous solutions. He is also interested in historical crystallography.

Mohan D. Aggarwal

Alabama A&M University
Department of Physics
Normal, AL, USA
mohan.aggarwal@aamu.edu



Chapters B.9, C.17

Mohan Aggarwal is a Professor and Chair of the Physics Department at Alabama A&M University. He earned his PhD degree in physics from Calcutta University in 1974 and did his post doctoral work at Pennsylvania State University. He has extensive experience in the bulk crystal growth and characterization of a variety of organic and inorganic nonlinear optical crystals, piezoelectric materials and scintillator materials using the solution and melt growth techniques. He is the author or coauthor of more than 204 publications including a few book chapters.

Marcello R.B. Andreeta

University of São Paulo
Crystal Growth
and Ceramic Materials Laboratory,
Institute of Physics of São Carlos
São Carlos, SP, Brazil
marcello@ifsc.usp.br



Chapter B.13

Marcello R.B. Andreeta received his PhD in Materials Science and Engineering from Universidade de São Paulo, Brazil (2001). His research interests include crystal growth, solid-state lasers, Raman and AFM microscopy. Currently he develops new crystalline compounds for optical devices using laser-heated pedestal growth technique at the Crystal Growth and Ceramic Materials Laboratory (IFSC-USP), São Carlos, SP, Brazil.



Dino Aquilano

Università degli Studi di Torino
Facoltà di Scienze Matematiche,
Fisiche e Naturali
Torino, Italy
dino.aquilano@unito.it

Chapter A.3

Professor Dino Aquilano graduated in Physics from Torino University in 1963. From 1974 to 1976 he enjoyed a CNR-NATO fellowship at the CRMC2-CNRS, Univ. Aix-Marseille III. Since 1980 he was an Associated Professor of Mineralogy at the Faculty of Sciences of Torino University. He retired at the end of 2007 and is now a Professor under 3-years contract at the Faculty of Science of Torino University. He has published more than 100 papers on the theoretical and experimental aspects of crystal growth with particular attention to surface microtopography of flat crystal faces, twinning and polytypism as growth phenomena, growth kinetics of crystal faces from pure and impure solutions, and relationships between morphology (equilibrium and growth) and crystal structure.



Roberto Arreguín-Espinosa

Universidad Nacional Autónoma
de México
Instituto de Química
Mexico City, Mexico
arrespin@unam.mx

Chapter H.47

Roberto Arreguín-Espinosa received the Laurea degree in Biology, the MS degree in Marine Biology and the PhD in Biochemistry at Universidad Nacional Autónoma de México. His research activities include the analyses of tridimensional structure of macromolecules with biological interest by means of x-ray, circular dichroism, dynamic light scattering and NMR techniques. He is member of the Protein Society and Mexican Academy of Science since 2002.

Jie Bai

Intel Corporation
Hillsboro, OR, USA
jie.bai@intel.com



Chapter [G.44](#)

Jie Bai received her PhD degree in materials science and engineering from Stony Brook University in 2006. She joined Amberwave Systems the same year. Her research focused on structural characterization and study of semiconductor epitaxial films. Currently, she works as a failure analysis engineer at Intel.

Stefan Balint

West University of Timisoara
Department of Computer Science
Timisoara, Romania
balint@math.uvt.ro



Chapter [F.40](#)

Stefan Balint obtained his PhD in Mathematics in 1976 and is currently a full Professor at the Faculty of Mathematics and Computer Science of the West University of Timisoara, Romania. His research interests include nonlinear dynamics, stability and control with applications in fluid dynamics, material science, aircraft dynamics and artificial neural networks.

Ashok K. Batra

Alabama A&M University
Department of Physics
Normal, AL, USA
ashok.batra@aamu.edu



Chapters [B.9](#), [C.17](#)

Ashok Batra received MTech and PhD degrees from Indian Institute of Technology, Delhi. Currently, he is a faculty member in the Department of Physics at Alabama A&M University. He was a co-investigator on a solution crystal-growth experiment flown aboard NASA-IML-1 space shuttle mission. His research interests include crystal growth, organic solar cells, ferroelectric, pyroelectric, piezoelectric materials and their applications, nano-composites, and nanostructured chemical sensors. He has published more than 80 publications.

Handady L. Bhat

Indian Institute of Science
Department of Physics
Bangalore, India
hlbhat@physics.iisc.ernet.in



Chapter [B.11](#)

Handady L. Bhat obtained his BSc from Mysore University and both MSc and PhD from Sardar Patel University, Gujarat, India. He joined the Physics Department of the Indian Institute of Science, Bangalore as a Research Associate in 1973, and progressed steadily to become a professor in 1993. He was the chairman of this department during 2002-2006. During 2006-2008 he was a CSIR emeritus Scientist and is currently a visiting faculty. He is also a visiting professor at Centre for Liquid Crystal Research, Bangalore. His research interests include crystal growth and physics with special reference to ferroelectric, nonlinear optical, semiconductor and magnetic materials. He has over 200 research publications and is currently the Joint Secretary of Materials Research Society of India.

Ishwara B. Bhat

Rensselaer Polytechnic Institute
Electrical Computer
and Systems Engineering Department
Troy, NY, USA
bhati@rpi.edu



Chapter [E.28](#)

Ishwara B. Bhat is a Professor of Electrical, Computer and Systems Engineering Department at Rensselaer Polytechnic Institute (RPI). He received his BSEE from Indian Institute of Technology, India and his MS and PhD degrees from Electrical Engineering RPI. Bhat joined Rensselaer in 1985 as a research associate and was promoted to full professor in 2000. His research focus is on the epitaxial growth and characterization of several II–VI, III–V, and IV–IV semiconductors. He has published over 100 articles in refereed journals and has served as a member of the program committee of several national and international conferences.

David F. Bliss

US Air Force Research Laboratory
Sensors Directorate Optoelectronic
Technology Branch
Hanscom AFB, MA, USA
david.bliss@hanscom.af.mil

**Chapter B.7**

Dr. David Bliss has been the Program Manager for crystal growth at the Air Force Sensors Directorate's Hanscom Research Site for the past 20 years. He received an SM degree in Materials Science and Engineering from MIT and a PhD from SUNY Stony Brook. He has written over fifty papers for journals and conferences and holds 10 patents. Most recently he has been leading a US Air Force-funded project to develop bulk gallium nitride substrates for GaN lasers and electronics. He is the past president of the American Association for Crystal Growth, and is involved in many aspects of novel crystal development in the US and abroad.

Mikhail A. Borik

Russian Academy of Sciences
Laser Materials
and Technology Research Center,
A.M. Prokhorov General Physics Institute
Moscow, Russia
borik@lst.gpi.ru

**Chapter B.14**

Mikhail A. Borik received the PhD degree in technology of Electronic Materials from the Lebedev Physics Institute of the USSR Academy of Sciences in 1985. He is currently Senior Research Scientist at the Laser Materials and Technology Research Center of A.M. Prokhorov General Physics Institute Russian Academy of Sciences. His scientific interests are in the field of crystal growth of high-temperature oxides, skull melting technique, and the technology of high-temperature glasses.

Liliana Braescu

West University of Timisoara
Department of Computer Science
Timisoara, Romania
lilianabraescu@balint1.math.uvt.ro

**Chapter F.40**

Liliana Braescu obtained her PhD in Mathematics in 2002 and is currently an Associate Professor at the Faculty of Mathematics and Computer Science of the West University of Timisoara, Romania. Her research interests include control theory, stability and domains of attractions with applicability in modelling of the crystal growth processes, blood coagulation, and dental endosteal implantation.

Kullaiah Byrappa

University of Mysore
Department of Geology
Mysore, India
kbyrappa@gmail.com

**Chapters A.1, C.18**

Prof. Byrappa graduated from the University of Mysore, India, with Ranks and Gold Medals. Then he left India during 1977 to pursue PhD work at the Moscow State University, Russia. He is specialized in Crystal Growth and Material Processing using the hydrothermal technique. He has published over 180 research papers in the International Journals, and also authored and edited several. He is the member of the International Commission on Crystal Growth and Characterization of Materials; International Commission on Mineral Synthesis and Interface Processes; Council Member of the Asian Association for Crystallography, Council Member of the Indian National Science Academy Crystallography Association. Prof. Byrappa is a recipient of Sir C.V. Raman Award for 1998 in Physical Sciences, two times recipient of the Golden Jubilee Award of the University of Mysore for the years 1986 and 1992. During 2005, he was awarded the Materials Research Society of India Medal. He is a Fellow of the World Academy of Ceramics. He is leading a hydrothermal research laboratory.

Dang Cai

CVD Equipment Corporation
Ronkonkoma, NY, USA
dcai@cvdequipment.com

**Chapter F.37**

Dr. Dang Cai is an expert in the field of process modeling and equipment design for vapor growth systems. He received his PhD from the Stony Brook University in Mechanical Engineering. Dr. Cai is currently working as a project manager at CVD equipment Corporation, NY, USA. His research interests include III nitrides vapor growth and solar cell related thin film coatings on glass.

**Michael J. Callahan**

Chapter C.19

GreenTech Solutions
Hanson, MA, USA
mjcal37@yahoo.com

Michael Callahan was employed by the United States Air Force Research Laboratory in 1999 and was the Principal Investigator of the High-Pressure Solution Growth Facility located at Hansom AFB, USA from 2004-2008. Mr. Callahan received a MS degree in Electrical Engineering from Western New England College. His research interests include solution growth of large single crystals particularly gallium nitride and multifunctional oxides. He is currently a member of the MRS and SPIE and is active proponent of solvothermal and hydrothermal crystal growth research.

**Joan J. Carvajal**

Chapter C.21

Universitat Rovira i Virgili (URV)
Department of Physics
and Crystallography of Materials
and Nanomaterials (FICMA-FICNA)
Tarragona, Spain
joanjosep.carvajal@urv.cat

Joan J. Carvajal graduated in Chemistry (1997) and received his PhD in Chemistry (2003) from the Universitat Rovira i Virgili. Currently he is Ramon y Cajal Researcher at the same university. He is author of more than 30 ISI papers, and 5 book chapters. His research interests cover synthesis and crystal growth of optical and semiconductor materials at the micro- and nanoscale for photonic applications.

Aaron J. Celestian

Western Kentucky University
Department of Geography and Geology
Bowling Green, KY, USA
aaron.celestian@wku.edu



Chapter H.49

Dr. Aaron Celestian is an Assistant Professor of Mineralogy at Western Kentucky University. He completed his Geology BSc at the University of Arizona, and then finished his MSc and PhD at Stony Brook University. His research interests are in time-resolved molecular-scale characterization of microporous Earth materials and synthetic analogues, with application to the Earth and sciences and industry.

Qi-Sheng Chen

Chinese Academy of Sciences
Institute of Mechanics
Beijing, China
qschen@imech.ac.cn



Chapter C.19

Qi-Sheng Chen graduated and obtained the MS degree both at Department of Mechanics, Peking University and received the PhD degree from the Institute of Mechanics, Chinese Academy of Sciences in 1997. Chen was Faculty administrator and coordinator at the Department of Mechanical Engineering, Florida International University in 2001. Since 2002, Chen has been Research Professor at the Institute of Mechanics, Chinese Academy of Sciences. His research activities include computational fluid dynamics and crystal-growth process modeling.

**Chunhui Chung**

Chapter H.52

Stony Brook University
Department of Mechanical Engineering
Stony Brook, NY, USA
chuchung@ic.sunysb.edu

Mr. Chunhui Chung received his MS degree from the Department of Mechanical Engineering, National Cheng Kung University, Tainan, Taiwan in 2004. He is a PhD candidate in the Department of Mechanical Engineering, Stony Brook University, New York, USA. His research focuses on the wafer manufacturing processes including the wiresaw slicing, lapping, and other relevant topics.

**Ted Ciszek**

Chapter H.51

Geolite/Siliconsultant
Evergreen, CO, USA
ted_ciszek@siliconsultant.com

T.F. (Ted) Ciszek is an experimental physicist with an emphasis on silicon crystal growth and materials science for photovoltaics. He is a retired Principal Scientist at the DOE National Renewable Energy Laboratory (NREL), now operating an independent consulting business, Siliconsultant, a division of Geolite. He holds 25 issued patents with several others pending, and 170 technical journal and proceedings publications.

Abraham Clearfield

Texas A&M University
Distinguished Professor of Chemistry
College Station, TX, USA
clearfield@chem.tamu.edu



Chapter H.49

Abraham Clearfield is a Distinguished Professor of Chemistry at Texas A&M University. He has been awarded both the Southwest and the Northeast Regional ACS awards and received an honorary PhD from Oviedo University, Spain. He discovered the major zirconium phosphate phases that involved him in major contributions to the field of inorganic ion exchange materials and its use in nuclear waste programs.

Hanna A. Dabkowska

Brockhouse Institute
for Materials Research
Department of Physics and Astronomy
Hamilton, Ontario, Canada
dabkoh@mcmaster.ca



Chapter B.12

Hanna Dabkowska received the MS degree in Chemistry from Warsaw University and the PhD degree in Physics from the Institute of Physics Polish Academy of Science in 1983. In 1990 she joined McMaster University as a Research Scientist. Her research interests include crystal growth of oxide materials by different methods. She is a Chair of the Commission of Crystal Growth and Characterization in the International Union of Crystallography and a Member of the Executive Committee of the International Organization for Crystal Growth. She is in author and co-author of more than 91 research papers.

Antoni B. Dabkowski

McMaster University, BIMR
Brockhouse Institute
for Materials Research,
Department of Physics and Astronomy
Hamilton, Ontario, Canada
dabko@mcmaster.ca

Chapter B.12

Antoni Dabkowski has extensive experience in crystal growth of oxide materials with expertise in design, construction, and computerization of crystal growth equipment. He works with techniques such as liquid-phase epitaxy (magnetic garnets, thin films), the Czochralski method and top seeding, growth from high-temperature solutions, directional solidification and Bridgman, as well as optical floating zone. Since recently he has been interested in piezo- and ferroelectric perovskites, thin films of electrically conductive oxides as well as in the influence of substrates on epitaxial film properties. He is author and co-author of more than 45 research papers.

Rafael Dalmau

HexaTech Inc.
Morrisville, NC, USA
rdalmau@hexatechinc.com

Chapter D.24

Rafael Dalmau received the PhD degree in Materials Science and Engineering from North Carolina State University. His research interests are in bulk crystal growth, metalorganic vapor phase epitaxy, and characterization of wide band gap nitride semiconductors. He is currently developing aluminium nitride substrate technology at HexaTech Inc.

Govindhan Dhanaraj

ARC Energy
Nashua, NH, USA
ghanaraj@arc-energy.com



Chapters A.1, D.23, G.42

Dr. Govindhan Dhanaraj is a Chief Scientist and Manager of Crystal Growth Technologies at ARC Energy, Nashua, NH. He was a research faculty at the Department of Materials Science and Engineering, Stony Brook University, NY from 2000 to 2007. He served as a research Assistant Professor at Hampton University, VA until 1999 and specialized in crystal growth of semiconductors and optical materials, epitaxial films and defect evaluation. Dr. Dhanaraj earned a PhD degree from the Indian Institute of Science (Bangalore) and then joined the Rajaramanna Center for Advanced Technology in India as a senior scientist. Based on his accomplishments, he was awarded with the prestigious Extraordinary Ability Category O1 VISA status by the United States BCIS. He is a co-organizer of the Industrial Growth Symposium under the American Crystal Growth Conference in 2009.

Ramasamy Dhanasekaran

Anna University Chennai
Crystal Growth Centre
Chennai, India
rdhanasekaran@annauniv.edu;
rdcgc@yahoo.com



Chapter D.27

Dr. Dhanasekaran is a Professor in Crystal Growth Centre at the Anna University Chennai, India and is working there for the past thirty one years. He obtained his PhD degree in 1986 and did extensive research at Stanford University, USA and University of Nijmegen, The Netherlands. He is the recipient of TANSA award in 2004 and IACG National award-2006. His research interests include nucleation and theories of crystal growth, growth of III–V, II–VI and I–III–VI₂ compounds, NLO and relaxor-ferroelectric single crystals. He has successfully completed several National/International sponsored research projects in the field of crystal growth.

**Ernesto Diéguez**

Universidad Autónoma de Madrid
Department Física de Materiales
Madrid, Spain
ernesto.dieguez@uam.es

Chapter B.9

Ernesto Diéguez (PhD 1983, Madrid) is a Professor of Physics in the Department of Physics of Materials, and Head of the Crystal Growth Lab. His research interest is mainly in crystal growth processes and technology of bulk crystals and thin films. He is currently (2006-2010) Director of the Department of Physics of Materials.

**Vijay K. Dixit**

Raja Ramanna Center
for Advance Technology
Semiconductor Laser Section,
Solid State Laser Division
Indore, India
dixit@rrcat.gov.in

Chapter B.11

Vijay Kumar Dixit obtained his BSc and MSc degrees in Physics from Kanpur University, Uttar Pradesh (UP), India. He obtained his PhD degree from the Department of Physics, Indian Institute of Science, Bangalore, India in 2004. He is working at Raja Ramanna Centre for Advanced Technology Indore, India as a scientist since 2002. During 2008-2009 he was a 21st century Global Center of Excellence (GCOE) fellow at the Department of Materials Science and Engineering, Tohoku University, Japan. His research interests include mainly semiconductor materials science and technology with special reference to photodetector, laser and nanostructures. He has over 30 journal publications and is a member of many professional bodies.

Sadik Dost

University of Victoria
Crystal Growth Laboratory
Victoria, BC, Canada
sdost@me.uvic.ca



Chapter E.29

Dr. Dost is Professor and Canada Research Chair in Semiconductor Crystal Growth, and Director of the Crystal Growth Laboratory at the University of Victoria. He has served as Founding Director of the University Centre for Advanced Materials and Related Technology (CAMTEC) for five years, and also as Chair of the Department of Mechanical Engineering for seven years. His current research combines experimental and theoretical study of crystal growth of semiconducting single crystals. He is well known internationally for his work on liquid-phase electroepitaxy.

Michael Dudley

Stony Brook University
Department of Materials Science
and Engineering
Stony Brook, NY, USA
mdudley@notes.cc.sunysb.edu



Chapters A.1, D.23, G.42, G.44

Dr. Michael Dudley is a Professor of Materials Science & Engineering at Stony Brook University. He obtained his PhD in Engineering from Warwick University, UK in 1982 and then worked as a PostDoc at Strathclyde University, UK. He is an expert in the synchrotron x-ray topography characterization of defects in single crystal materials with a view to understanding their origins.

**Partha S. Dutta**

Chapter B.10

Rensselaer Polytechnic Institute
Department of Electrical, Computer
and Systems Engineering
Troy, NY, USA
duttap@rpi.edu

Dr. Partha S. Dutta is a Professor of Electrical, Computer and Systems Engineering at Rensselaer Polytechnic Institute, Troy, New York. His research interests include semiconductor bulk crystal growth, materials for solid state lighting, photovoltaics, terahertz and nonlinear optical applications, optoelectronic device fabrication and free space optical communication systems. He is a co-founder of Auterra Inc., a company specializing in nanoscale materials.

**Francesc Díaz**

Chapter C.21

Universitat Rovira i Virgili (URV)
Department of Physics
and Crystallography of Materials
and Nanomaterials (FiCMA-FiCNA)
Tarragona, Spain
f.diaz@urv.cat

Francesc Díaz is Full Professor of Applied Physics. Since its foundation in 1996, he has been Coordinator of the Physics and Crystallography of Materials (FiCMA) research group. He is author of 180 ISI papers, 4 books, 3 patents and more than 40 chapters of books. He is currently focussed on nanostructuring of optical materials, spectroscopy and lasing of rare-earth ions in crystalline hosts.

Paul F. Fewster

PANalytical Research Centre,
The Sussex Innovation Centre
Research Department
Brighton, UK
paul.fewster@panalytical.com



Chapter G.41

Paul Fewster has a PhD and DSc from London University, the Paterson Medal from the Institute of Physics, the Industrial Crystallography Award from the British Crystallographic Association, where he is an Honorary Member. He worked in Philips Research from 1981-2002 until he became Head of Research for PANalytical (formerly Philips Analytical). His research interests are in x-ray scattering, including simulation, the influence of the instrument and the reliability of interpretation, for perfect crystalline, distorted layer structures and polycrystalline materials.

Donald O. Frazier

NASA Marshall Space Flight Center
Engineering Technology Management
Office
Huntsville, AL, USA
donald.o.frazier@nasa.gov



Chapter C.17

Donald O. Frazier received his undergraduate degree from Wayne State University and PhD in Physical Chemistry from Rutgers University. He is Chief Scientist for Physical Chemistry at the NASA Marshall Space Flight Center in Huntsville, AL. His research interests include molecular spectroscopy, physical chemistry of solutions, crystal growth, and photonic device materials. He recently co-edited the book "Nonlinear Optics and Applications".

**James W. Garland**

Chapter E.32

EPIR Technologies, Inc.
Bolingbrook, IL, USA
jgarland@epir.com

Dr. Garland received his Physics PhD from the University of Chicago. He was Assistant Professor at the University of California at Berkeley 1954-1958 and Associate Professor 1958-1960 and Professor 1960-1994 at the University of Illinois at Chicago. He has held National Science Foundation and Sloan Foundation fellowships. He joined EPIR in 2005 where his primary interest is II-VI single-crystal multijunction solar cells.

**Thomas F. George**

Chapter F.40

University of Missouri–St. Louis
Center for Nanoscience,
Department of Chemistry
and Biochemistry,
Department of Physics and Astronomy
St. Louis, MO, USA
tfgeorge@umsl.edu

Professor Thomas F. George received his Ph.D. in Chemistry from Yale University, followed by postdoctoral appointments at MIT and the UC-Berkeley. He then had the following positions: Professor of Chemistry at the University of Rochester, Dean of Science at SUNY-Buffalo, Provost at Washington State University, Chancellor at the University of Wisconsin-Stevens Point, and currently Chancellor at the University of Missouri-St. Louis along with an appointment as Professor of Chemistry and Physics. His research in chemical/laser/materials/nanophysics has led to 700 papers, 5 authored books and 16 edited books. He was elected as a foreign member of the Korean Academy of Science and Technology in 2004 and received an honorary doctorate in physics (“honoris causa”) from the University of Szeged in Hungary in 2008.

Andrea E. Gutiérrez-Quezada

Chapter H.47

Universidad Nacional Autónoma
de México
Instituto de Química
Mexico City, Mexico
30111390@escolar.unam.mx



Andrea Gutiérrez-Quezada completed her BSc of Chemistry at the Universidad Nacional Autónoma de México (UNAM) in 2008 supervised by Professor Abel Moreno. Her research interests include protein evolution studies and biomineralization processes.

Carl Hemmingsson

Chapter D.26

Linköping University
Department of Physics, Chemistry
and Biology (IFM)
Linköping, Sweden
cah@ifm.liu.se



Carl Hemmingsson received the MS and PhD degree from Linköping University in 1991 and 1998, respectively. From 1999 to 2001 he was developing growth of SiC using HTCVD at Okmetic AB. In 2003, he joined the Materials Science Group at Linköping University as a senior researcher and since then, his main interest has been growth of bulk GaN using HVPE.

Antonio Carlos Hernandez

Chapter B.13



University of São Paulo
Crystal Growth
and Ceramic Materials Laboratory,
Institute of Physics of São Carlos
São Carlos, SP, Brazil
hernandes@ifsc.usp.br

Antonio Carlos Hernandez received his PhD in Applied Physics from University of São Paulo (USP) in 1993. He is currently a Full Professor at the Institute of Physics of São Carlos (USP), Brazil. His research interests are mainly in crystal growth, physical properties, dielectric and ferroelectric ceramics, non-crystalline materials and nanostructured materials. He is a researcher of National Council for Scientific and Technological Development (CNPq).

Koichi Kakimoto

Chapter B.8



Kyushu University
Research Institute for Applied Mechanics
Fukuoka, Japan
kakimoto@riam.kyushu-u.ac.jp

Koichi Kakimoto is a Deputy Director and a Professor of the Institute of Applied Mechanics of Kyushu University. He received his PhD in Engineering in 1955 from the Graduate School of Electronic Engineering, University of Tokyo. Previous positions included Researcher at NEC Fundamental Research Laboratories (1985), Visiting Researcher of Université Catholique des Louvain in Belgium (1989), Prof. Kakimoto's research focuses on the effects of external fields on melt flow and crystallization.

Imin Kao

Chapter H.52

State University of New York
at Stony Brook
Department of Mechanical Engineering
Stony Brook, NY, USA
imin.kao@stonybrook.edu



Being the Director of the Manufacturing Automation Laboratory (MAL) at SUNY Stony Brook, Professor Kao conducts research in robotics and manufacturing, MEMS, modeling and diagnosis of manufacturing processes, free abrasive machining, and wafer manufacturing. A member of ASME and IEEE, he also served as an associate editor of IEEE Transactions on Robotics and Automation and Journal of Advanced Manufacturing Systems.

John J. Kelly

Utrecht University,
Debye Institute for Nanomaterials
Science
Department of Chemistry
Utrecht, The Netherlands
j.j.kelly@uu.nl



Chapter G.43

John Kelly received his PhD degree from University College Dublin, Ireland in 1970. He was a research scientist at Philips Research Laboratories in Eindhoven and Hamburg. Since 1987 he has been a Professor of Chemistry at Utrecht University. His interests within the Debye Institute for Nanomaterials Science include surface chemistry, materials science and electrochemistry of metals and semiconductors.

Jeonggoo Kim

Neocera, LLC
Beltsville, MD, USA
kim@neocera.com



Chapter E.35

Dr. Jeonggoo Kim is a scientist with a research background in pulsed-energy deposition processes. He received the DSc degree in Department of Mechanical & Aerospace Engineering from the George Washington University and worked in Naval Research Laboratory in DC. He has extensive experience in oxides and biomedical materials with thin film technologies, especially in multilayer processes including superlattice, combinatorial and large area depositions.

Helmut Klapper

Institut für Kristallographie
Aachen, Germany
klapper@xtal.rwth-aachen.de;
helmut-klapper@web.de



Chapter A.4

Dr. Helmut Klapper is a retired Professor of Crystallography and Crystal Physics. His main research activities are: crystal growth from solutions and melts (the latter mainly organic crystals), studies of crystal defects with imaging methods (mainly x-ray topography) and investigations of phase transitions, twins and domains structure by x-ray topography and optical methods. He has been chairman of the “Commission of Crystal Growth and Characterization of Materials” of the “International Union of Crystallography” (1993-1999).

Christine F. Klemenz Rivenbark

Krystal Engineering LLC
General Manager and Technical Director
Titusville, FL, USA
ckr@krystalengineering.com



Chapter E.31

Dr. Christine K. Rivenbark has a Chemical Engineering degree from Switzerland and a PhD degree in Electronic Engineering from the University of Tokyo, Japan. After working as a Research Engineer at the Swiss Federal Institute of Technology in Lausanne (EPFL), she became Assistant Professor at the University of Central Florida in Orlando, FL. She is co-founder and Managing Director of Krystal Engineering LLC, a company specialized in the development of LPE films and bulk crystals of oxides and semiconductors. She is an elected member of the Crystal Growth Commission of the IUCr and a program committee member of IEEE FCS.

Christian Kloc

Nanyang Technological University
School of Materials Science
and Engineering
Singapore
ckloc@ntu.edu.sg



Chapter D.25

Christian Kloc is a University Professor at the School of Materials Science and Engineering, Nanyang Technological University in Singapore. He received his higher education in chemistry, and earned his PhD in physics from Polish Academy of Sciences. At first in Poland, and later in the University of Konstanz, Germany, he focused on crystal growth of semiconductors. Later in Bell Labs, NJ, USA, and currently in Singapore, his research interests are on technology of new materials.

**Solomon H. Kolagani**

Chapter E.35

Neocera LLC
Beltsville, MD, USA
harsh@neocera.com

Dr. Kolagani is an acknowledged expert in pulsed energy deposition processes and has 20 years experience in several thin film deposition technologies. He has managed over 25 government-funded programs related to complex metal oxides. He received his PhD degree from the Indian Institute of Technology, New Delhi, (1983); he was faculty at the Indian Institute of Science (1983-1990); then he worked at Bellcore (1990-1992) and joined Neocera in 1992. He has more than 50 research publications and holds 7 US Patents.

**Akinori Koukitu**

Chapter D.26

Tokyo University of Agriculture
and Technology (TUAT)
Department of Applied Chemistry
Tokyo, Japan
koukitu@cc.tuat.ac.jp

Akinori Koukitu received his Doctor degree from the Tohoku University in 1981, with Prof. J. Nishizawa. He was a visiting scientist at Max-Planck Institute between 1986 and 1987. He became Associate Professor and Professor of TUAT in 1988 and 2000, respectively. He has worked on vapor phase epitaxy growth of III-V semiconductors, in situ monitoring of crystal growth from vapor, and thermodynamic analysis of semiconductor alloys.

Milind S. Kulkarni

MEMC Electronic Materials
Polysilicon and Quantitative Silicon
Research
St. Peters, MO, USA
mkulkarni@memc.com



Chapter F.38

Dr. Milind Kulkarni is Vice President of Polysilicon and Quantitative Silicon Research, at MEMC Electronic Materials. He holds a doctorate in Chemical Engineering and a master's degree in business administration, both from Washington University in Saint Louis. His interests span various fields of science and engineering relevant in upstream semiconductor and solar silicon processing, along with finance, operations and manufacturing management.

Yoshinao Kumagai

Tokyo University of Agriculture
and Technology
Department of Applied Chemistry
Tokyo, Japan
4470kuma@cc.tuat.ac.jp



Chapter D.26

Yoshinao Kumagai received the Dr. Eng. from the University of Tsukuba in 1996. He was researcher of Texas Instruments Inc. from 1996 to 1999. Then, he moved to Tokyo University of Agriculture and Technology. Since 2004, he has been Associate Professor in the Department of Applied Chemistry. His research interest is mainly crystal growth from the vapor phase.

**Valentin V. Laguta**

Chapter H.50

Institute of Physics of the ASCR
Department of Optical Materials
Prague, Czech Republic
laguta@fzu.cz

Valentin Laguta received the MS degree from Kiev State University, then received the CSc and DrSc degrees (Physics and Mathematics) from the Institute for Problems of Materials Science of the Ukrainian National Academy of Science in 1988 and 2006, respectively. Since 2006, he is the leading senior scientist in the Institute of Physics of the AS CR, Prague. Research activities include defects and radiation-induced phenomena in solids, physical properties of magnetoelectric materials.

**Ravindra B. Lal**

Chapter C.17

Alabama Agricultural
and Mechanical University
Physics Department
Normal, AL, USA
rbal@comcast.net

Dr. Ravindra B. Lal received his MS and PhD degrees in Physics from University of Agra, India in 1958 and 1962 respectively. He is presently an Emeritus Professor of Physics at Alabama A&M University. He has extensive experience of growing crystals from solution, both on ground and in space for infrared detectors and frequency doubling materials. He was the principal investigator of two space shuttle experiments on Spacelab-3 and the First International Microgravity Laboratory in 1985 and 1992 respectively.

Chung-Wen Lan

National Taiwan University
Department of Chemical Engineering
Taipei, Taiwan
cwlan@ntu.edu.tw



Chapter F.36

Dr. Chung-wen Lan is Distinguished Professor of Chemical Engineering at National Taiwan University and General Director of Photovoltaics Technology Center at Industrial Technology Research Institute. He is also Chairman of Taiwan Photovoltaic Industry Association. He obtained his PhD degree in Materials Science from the University of Wisconsin at Madison in 1991. He received several awards including the Distinguished Research Awards from the National Science Council of Taiwan and Research Contribution Awards from National Taiwan University for his research contribution to industry. His research interests include crystal growth, photovoltaics, transport phenomena, and computer simulation.

Hongjun Li

Chinese Academy of Sciences
R & D Center of Synthetic Crystals,
Shanghai Institute of Ceramics
Shanghai, China
lh_li@mail.sic.ac.cn



Chapter B.15

Hongjun Li received PhD degree in Materials Science from Shanghai Institute of Optics and Fine Mechanics (SIOM), Chinese Academy of Sciences (CAS). He is currently an Associate Researcher at the Shanghai Institute of Ceramics (SIC), CAS. His research interests are mainly in analysis of crystal defects, numerical simulation of crystal growth systems and optimization of crystal growth techniques.

Elena E. Lomonova

Chapter B.14



Russian Academy of Sciences
Laser Materials
and Technology Research Center,
A.M. Prokhorov General Physics Institute
Moscow, Russia
lomonova@lst.gpi.ru

Elena E. Lomonova received the PhD degree in Technology of Electronic Materials from the Lebedev Physics Institute of the USSR Academy of Sciences in 1980 and a Doctorate in Technology of Electronic Materials from the General Physics Institute of Russian Academy of Sciences in 2001. She was given the Prize of the USSR Council of Ministers in 1991. She is currently Head of Laboratory at the Laser Materials and Technology Research Center of A.M. Prokhorov General Physics Institute Russian Academy of Sciences. Her scientific interests are in the field of crystal growth of high-temperature oxides, skull melting technique, investigation of chemical, physical and mechanical properties of refractory oxides.

Ivan V. Markov

Chapter A.2



Bulgarian Academy of Sciences
Institute of Physical Chemistry
Sofia, Bulgaria
imarkov@ipc.bas.bg

Professor Ivan Markov obtained his PhD degree in Electrochemical Nucleation of Metals in the Institute of Physical Chemistry of the Bulgarian Academy of Sciences, Sofia, where he is at present a Research Professor. From 1992 to 1994 he was with the Department of Materials Science of the National Tsing Hua University, Taiwan, in 1998 with the Department of Condensed Matter Physics of the Universidad Autónoma de Madrid, and in 2004 with the Department of Physics of the Hong Kong University. His research interests are concerned primarily with nucleation and epitaxy. He is author of the textbook "Crystal Growth for Beginners".

Bo Monemar

Chapter D.26

Linköping University
Department of Physics,
Chemistry and Biology
Linköping, Sweden
bom@ifm.liu.se



Bo Monemar obtained his PhD from Lund University in 1971. He was appointed Professor and Head of the Materials Science Division at Linköping University in 1983. He was a member of the IUPAP Semiconductor Commission 1987-1993, and then its secretary 1993-1999. His research covers semiconducting materials, recently mostly III-nitrides. Monemar has published about 1110 papers internationally.

Abel Moreno

Universidad Nacional Autónoma
de México
Instituto de Química
Mexico City, Mexico
carcamo@unam.mx



Chapter H.47

Abel Moreno obtained the BSc in Chemistry at the “Bene meritis” Autonomous University of Puebla (BUAP, Mexico) and the PhD in Chemistry from the University of Granada (Spain). His research activities include crystallogenes, crystallochemistry, biomineralization, and protein crystallography by x-ray diffraction techniques. He has been Professor of Biological Chemistry from 2005 and member of the Mexican Academy of Sciences since 1998.

**Roosevelt Moreno Rodriguez**

State University of New York
at Stony Brook
Department of Mechanical Engineering
Stony Brook, NY, USA
roosevelt@dove.eng.sunysb.edu

Chapter H.52

Roosevelt Moreno Rodriguez is a Fulbright scholar at Stony Brook University, where he is currently a PhD student. His research interests include fingerprint analysis, mathematical modeling of time-frequency analysis, wavelets, intelligent fault detection and diagnostic (FDD) as applied in manufacturing processes. He is a member of the Institute of Electrical and Electronics Engineers (IEEE).

**S. Narayana Kalkura**

Anna University Chennai
Crystal Growth Centre
Chennai, India
kalkura@annauniv.edu

Chapter H.48

Dr. S. Narayana Kalkura is a Professor at the Crystal Growth Centre of Anna University Chennai. He received the MSc and PhD degrees in Physics from the University of Kerala. He joined Anna University as a faculty in 1991. He is an expert in the crystallization of compounds that cause crystal deposition diseases. He was a STA fellow at the National Institute of Biosciences and Human Technology, Tsukuba, Japan (1996-1997) and a staff scientist at the University of Hamburg (2001-2004), specializing in crystallization and structural analysis of biomolecules. His current research interests are on biomineralization and synthesis of nanomaterials for tissue engineering and drug delivery applications.

Mohan Narayanan

Reliance Industries Limited
Gaithersburg, MD, USA
mohan.narayanan@ril.com



Chapter H.51

Srinivasamohan (Mohan) Narayanan joined Reliance Industries Limited as Chief Technology Officer, Solar. Prior to joining RIL, he was the Vice President Technology of Trina Solar based in China and has worked for 17 years at BP Solar, an integrated global PV company. He received his PhD in 1990 from the University of New South Wales, Australia and MS in Materials Science from Case Western Reserve University, Cleveland, USA. He has more than 70 publications and holds a number of patents.

Subramanian Natarajan

Madurai Kamaraj University
School of Physics
Madurai, India
s_natarajan50@yahoo.com



Chapter H.48

Subramanian Natarajan obtained BSc and MSc degrees in Physics from the University of Madras and PhD (1979) from the Madurai Kamaraj University, India. Joining as a Lecturer in the School of Physics of the Madurai Kamaraj University in 1976, he is presently (2008) a Senior Professor and the Chairperson. His major fields of interest are crystallization of small molecules of biological and non-linear optical materials and the crystallography of small molecules.

**Martin Nikl**

Academy of Sciences
of the Czech Republic (ASCR)
Department of Optical Crystals,
Institute of Physics
Prague, Czech Republic
nikl@fzu.cz

Chapter H.50

Martin Nikl graduated in 1982 from Faculty of Nuclear Science and Physical Engineering, Czech Technical University and obtained his PhD in 1986 from the Institute of Physics, Czech Academy of Sciences. Currently, he serves as the Department Head of the Institute of Physics, Academy of Sciences CR. His research interests include luminescence and scintillation mechanism in wide band-gap solids, energy transfer processes and role of material defects in them.

**Vyacheslav V. Osiko**

Chapter B.14

Russian Academy of Sciences
Laser Materials
and Technology Research Center,
A.M. Prokhorov General Physics Institute
Moscow, Russia
osiko@lst.gpi.ru

Vyachslav V. Osiko is Academician, Professor, and Director of the Laser Materials and Technology Research Center of the A.M. Prokhorov General Physics Institute Russian Academy of Sciences. He received the Lenin Prize (1980), the Prize of the USSR Council of Ministers (1991) and R. Laudise Prize from the International Organization of Crystal Growth (1992). He is a member of the Russian Optical Society and a Fellow of the Materials Research Society. His scientific interests are in the field of solid-state physics and technology of materials.

John B. Parise

Chapter H.49

Stony Brook University
Chemistry Department
and Department of Geosciences
Stony Brook, NY, USA
john.parise@stonybrook.edu



Dr. John B. Parise is a joint-Professor in Chemistry and in Geosciences. His expertise is in the area of crystallography and solid-state chemistry. Special interests include the synthesis of novel materials using high-pressure routes, and the characterization of mineral transformation as a function of p , T and time using crystallographic tools on powders and single crystals at synchrotron x-ray and neutron sources.

Srinivas Pendurti

Chapter F.39

ASE Technologies Inc.
Cincinnati, OH, USA
spendurti@asetech.com



Srinivas Pendurti obtained his PhD in 2003 from Stony Brook University, New York. His main research interests are in computational materials science and fluid mechanics. Presently he is based in Cincinnati, USA and works in the gas turbine industry.

**Benjamin G. Penn**

Chapter C.17

NASA/George C. Marshall Space Flight
Center
ISHM and Sensors Branch
Huntsville, AL, USA
benjamin.g.penn@nasa.gov

Benjamin Penn received the PhD in Fiber and Polymer Science from North Carolina State University. He is currently a polymer scientist in the ISHM and Sensors Branch at the NASA/ George C. Marshall Space Flight Center. His research interests include the development of sensors for the detection of chemical agents and structural health monitoring.

**Jens Pflaum**

Chapter D.25

Julius-Maximilians Universität Würzburg
Institute of Experimental Physics VI
Würzburg, Germany
jpflaum@physik.uni-wuerzburg.de

Professor Jens Pflaum is an expert for molecular solid-state physics. He received his PhD from Bochum University in 1999 followed by a postdoctoral fellowship at Princeton University. He continued research on transport phenomena in organic crystals at Stuttgart University 2001-2008. In 2008 he became Professor at Würzburg University and group leader of the Organic Photovoltaics and Electronics division at the ZAE Bayern with focus on molecular optoelectronics.

Jose Luis Plaza

Chapter B.9

Universidad Autónoma de Madrid
Facultad de Ciencias,
Departamento de Física de Materiales
Madrid, Spain
joseluis.plaza@uam.es



Dr. Jose Luis Plaza graduated in Physics at the University Autónoma of Madrid in 1996. He got his PhD in 2000 for his work on GaSb crystal growth. He obtained a postdoc position at the University of Birmingham at the Nanoscale Physics Research Laboratory studying the fabrication of gold nanowires by e-beam lithography. In 2004 he got a Ramon y Cajal Research Position at the Universidad Autónoma de Madrid. Currently his field of research involves oxide and semiconductor crystal growth and nanostructuring surfaces by low energy argon ions.

Udo W. Pohl

Technische Universität Berlin
Institut für Festkörperphysik EW5-1
Berlin, Germany
pohl@physik.tu-berlin.de

Chapter [E.33](#)

Udo W. Pohl studied Physics in Aachen and Berlin, Germany. He obtained his PhD and Venia Legendi from Berlin Institute of Technology, where he is presently COO of the Center for Nanophotonics at the Institute of Solid State Physics. Since 2009 he has been Adjunct Professor of Experimental Physics at Berlin Institute of Technology. He has authored about 200 scientific publications including eight book contributions and two patents. His research focuses mainly on low-dimensional semiconductor epitaxy and spectroscopy.

**Vishwanath (Vish) Prasad**

University of North Texas
Denton, TX, USA
vish.prasad@unt.edu

Chapters [A.1](#), [F.39](#)

Vishwanath “Vish” Prasad is the Vice President for Research and Economic Development at the University of North Texas (UNT). He received his PhD from the University of Delaware, his Master of Technology from the Indian Institute of Technology, Kanpur, and his BT from Patna University in India – all in Mechanical Engineering. Dr. Prasad’s research interests include thermofluid sciences, energy systems, electronic materials, and micro-electronics. He has published over 200 refereed articles and edited/co-edited several books. Dr. Prasad is an elected Fellow of the American Society of Mechanical Engineers (ASME). He has received many special recognitions such as the Educator of the Year (2007) award from HENAAC and the LACCEI Medal from the Latin American and Caribbean Consortium of Engineering Institutions (LACCEI).

**Maria Cinta Pujol**

Universitat Rovira i Virgili
Department of Physics
and Crystallography of Materials
and Nanomaterials (FiCMA-FiCNA)
Tarragona, Spain
mariacinta.pujol@urv.cat

Chapter [C.21](#)

M.C. Pujol received the PhD in Chemistry from University Rovira i Virgili (2001) for work on the growth and characterization of lanthanide doped monoclinic double tungstates. Since 2004 she belongs to the group FiCMA (Physics and Crystallography of Materials). She is focussed on the growth of bulk and nanocrystals of lanthanide doped materials, and their crystal-physical and spectroscopic characterization.

Balaji Raghothamachar

Stony Brook University
Department of Materials Science
and Engineering
Stony Brook, NY, USA
braghoth@notes.cc.sunysb.edu

Chapters [D.23](#), [G.42](#)

Balaji Raghothamachar (Stony Brook University, PhD 2001) is Research Professor at the Department of Materials Science & Engineering, Stony Brook University and leading scientist for x-ray topography at the National Synchrotron Light Source (NSLS), Brookhaven National Laboratory, where he is involved in materials science engineering strategic planning for NSLS and NSLS-II. Research activities include x-ray topography, bulk and nanocrystal growth of semiconductor materials, high resolution x-ray diffraction and electron microscopy. He is an active member of MRS and AACG.

Michael Roth

The Hebrew University of Jerusalem
Department of Applied Physics
Jerusalem, Israel
mroth@vms.huji.ac.il

Chapter [C.20](#)

Michael Roth received the MSc degree in Physics from the University of Latvia (Riga, 1969) and the PhD degree in Physics from the Hebrew University of Jerusalem (1977). He joined the Hebrew University of Jerusalem as a faculty staff member in 1982 and is a Professor of Applied Physics there. His research interests include crystal physics, crystal growth, defect structure and properties of electronic materials. He is the President of the Israel Association for Crystal Growth and an Associate Editor of the Journal of Crystal Growth.

**Peter Rudolph**

Chapter A.6

Leibniz Institute for Crystal Growth
Technology Development
Berlin, Germany
rudolph@ikz-berlin.de

Professor Peter Rudolph is employed at the Leibniz Institute for Crystal Growth. He obtained the PhD in Solid State Physics from the Technical University of Lvov in 1972 and the Professor position at the Humboldt University of Berlin in 1985. From 1993-1994 he was Guest Professor at the Tohoku University in Sendai. His research includes all aspects of crystal growth. He is associate editor of J. Crystal Growth, president of the German Society of Crystal Growth and member of the IOCG executive committee. He received innovation prizes in 2001 and 2008.

**Akira Sakai**

Chapter E.34

Osaka University
Department of Systems Innovation
Osaka, Japan
sakai@ee.es.osaka-u.ac.jp

Professor Akira Sakai received the Master's degree in Engineering in 1986 and the doctorate in 1996 from Nagoya University. In 1986, he joined Fundamental Research Laboratory, NEC Corp. He became Associate Professor at the Graduate School of Engineering in Nagoya University in 1999 and Professor at the Graduate School of Engineering Science in Osaka University in 2007. His research interests include semiconductor epitaxial growth, defect and strain engineering, and characterization of materials on the micro- and nanometer scale. He is Member of the Japan Society of Applied Physics, the Electrochemical Society, and the Materials Research Society.

Yasuhiro Shiraki

Tokyo City University
Advanced Research Laboratories,
Musashi Institute of Technology
Tokyo, Japan
yshiraki@tcu.ac.jp



Chapter E.34

Yasuhiro Shiraki received the master's degree in applied physics in 1967 and the doctorate in 1975 from the University of Tokyo. In 1969, he joined the Central Research Laboratory, Hitachi, Ltd. He became Associate Professor at the Research Center for Advanced Science and Technology of the University of Tokyo in 1987 and Professor at the Department of Applied Physics in 1991. In 2004, he retired from the University of Tokyo and became Professor and Director of Advanced Research Laboratories, Musashi Institute of Technology. He currently serves as Vice-President of Tokyo City University which is the new name of the institute. He is Emeritus Professor of the University of Tokyo, Fellow of Institute of Physics, Fellow and Vice-President of the Japan Society of Applied Physics, and Member of Science Council of Japan.

Theo Siegrist

Florida State University
Department of Chemical
and Biomedical Engineering
Tallahassee, FL, USA
siegrist@eng.fsu.edu



Chapter D.25

Theo Siegrist is Professor in the Chemical and Biomedical Engineering Department at Florida State University. Previously, he was a Member of Technical Staff at Bell Laboratories, Alcatel-Lucent, where he was active in research on single-crystal organic semiconductors studying structure-property relationships in acene systems.

**Zlatko Sitar**

Chapter D.24

North Carolina State University
Materials Science and Engineering
Raleigh, NC, USA
sitar@ncsu.edu

Zlatko Sitar is Distinguished Kobe Steel Professor of Materials Science and Engineering at North Carolina State University. His research is concerned with crystal and thin-film growth and characterization of and device development in III-nitrides and carbon materials (GaN, AlN, InN, diamond, nanotubes), and study and formation of heterogeneous interfaces.

**Sivalingam Sivananthan**

Chapter E.32

University of Illinois at Chicago
Department of Physics
Chicago, IL, USA
siva@uic.edu; siva@epir.com

Dr. Sivananthan is Liberal Arts and Sciences Distinguished Professor of Physics, and Microphysics Laboratory Director at the University of Illinois at Chicago. He founded and is CEO of EPIR Technologies, Inc. and Sivananthan Laboratories, Inc. He pioneered the MBE growth of CdTe/Si and of HgCdTe on CdZnTe and CdTe/Si. His other primary interest is II–VI high-efficiency single-crystal multijunction solar cells.

Mikhail D. Strikovski

Chapter E.35

Neocera LLC
Beltsville, MD, USA
strikovski@neocera.com



Mikhail D. Strikovski is Senior Scientist at Neocera since 2000. He received his PhD from the Institute of Applied Physics, Russia (1985), and worked at the Texas Center for Superconductivity from 1996 to 2000. His main interests are physics and applications of plasma fluxes generated by pulsed-laser and electron beams. He is active in design of a variety of instrumentation for the pulsed plasma thin-film deposition technology.

Xun Sun

Chapter C.22

Shandong University
Institute of Crystal Materials
Jinan, China
sunxun@icm.sdu.edu.cn



Xun Sun is a Professor in the Institute of Crystal Materials, Shandong University, China. He received his PhD in Materials Science in 2002 from Shandong University. Dr. Sun's current research interests are functional crystal materials, especially the growth and properties of KDP (DKDP) crystals.

Ichiro Sunagawa

Chapter A.5



University Tohoku University (Emeritus)
Tokyo, Japan
i.sunagawa@nifty.com

Professor Ichiro Sunagawa graduated from Tohoku University in 1947 and received his DSc in 1957 and a Doc. Honoris Causa (France) in 1982. From 1948 to 1971 he was a mineralogist in the Geological Survey of Japan (GSJ) of the Agency of Industrial Science and Technology (old AIST) now National Institute of Advanced Industrial Science and Technology (new AIST). From 1971 to 1988 he was Professor of Mineralogy at Tohoku University, and from 1989 to 2007 Principal of the Yamanashi Institute of Gemmology and Jewellery Arts. His main interests are crystal growth fundamentals, mineralogy, and gemmology. He published many books and papers on these topics.

Xu-Tang Tao

Chapter C.22



Shandong University
State Key Laboratory of Crystal Materials
Jinan, China
txt@sdu.edu.cn

Xu-Tang Tao is a Professor of Functional Materials at the Institute of Crystal Materials and the State Key Laboratory of Crystal Materials, Shandong University. His research interests include organic and organic-inorganic hybrid photonic materials, laser and nonlinear optical crystal materials. He has published over 160 original papers and obtained several honors due to his studies.

Vitali A. Tatartchenko

Chapter B.16

Puteaux, France
vitali.tatartchenko@orange.fr



Vitali Tatartchenko graduated as an Engineer – Physicist from Leningrad Polytechnic University, received his PhD degree in 1970, Doctor of Sciences degree in 1977, and Professor rank in 1985. At famous institutions of the Soviet Union, Italy, Bulgaria, USA and France, he has had 50 years of unique experience of activity in all aspects of crystal growth: theory, experiments, installation design, and industrial technologies development. Dozens of his pupils have been active scientists in the field of crystal growth.

Filip Tuomisto

Helsinki University of Technology
Department of Applied Physics
Espoo, TKK, Finland
filip.tuomisto@tkk.fi



Chapter G.46

Filip Tuomisto received his Doctor of Science in Technology from the Department of Engineering Physics and Mathematics, Helsinki University of Technology (TKK) in 2005. He is currently an Academy Research Fellow at TKK, where he leads the positron research group. His research interests include physics of positrons in matter, defect spectroscopy of semiconductors and metals, and semiconductor optoelectronics.

Anna Vedda

University of Milano-Bicocca
Department of Materials Science
Milano, Italy
anna.vedda@unimib.it

Chapter H.50

Anna Vedda received the Laurea degree in Physics from the University of Milano in 1981, and she is currently Associate Professor at the University of Milano-Bicocca. Her principal fields of interest include the optical and structural properties of scintillating crystals and glasses for medical and high-energy physics applications, materials for radiation dosimetry, and insulating layers for microelectronics devices.

Lu-Min Wang

University of Michigan
Department of Nuclear Engineering
and Radiological Sciences
Ann Arbor, MI, USA
lmwang@umich.edu

Chapter G.44

Professor Lu-Min Wang has a Diploma in Metallic Materials Engineering from Beijing Polytechnic University (1982), an MS and holds a PhD in Materials Science, University of Wisconsin-Madison (1984, 1988). His primary research interests involve transmission electron microscopy (TEM) studies of microstructure evolution of solids during irradiation of energetic particles and particle beam modification of materials for engineering applications. He is seeking for a better understanding and control of the irradiation induced microstructure evolution. Lumin also has a strong interest in understanding the leaching processes of nuclear waste forms by cross-sectional TEM analysis. His most recent research effort focuses on ion beam modification of materials and irradiation induced nanostructures.

Sheng-Lai Wang

Shandong University
Institute of Crystal Materials,
State Key Laboratory of Crystal Materials
Jinan, Shandong, China
slwang@icm.sdu.edu.cn



Chapter C.22

Sheng-Lai Wang received the MS degree in Physics and the PhD degree in Materials Science from Shandong University in 1992 and 2000, respectively. Since 2005, he has been Professor at the Institute of Crystal Material (ICM) and The State Key Laboratory of Crystal Materials, Shandong University. His research interests are functional and ceramic materials mainly in KDP type crystal growth and related functional studies.

Shixin Wang

Micron Technology Inc.
TEM Laboratory
Boise, ID, USA
shixinwang@micron.com



Chapter G.44

Shixin Wang is a Senior Engineer at Micron Technology, Inc. He received his PhD degree from the University of New Mexico in 1997 and BS degree at Beijing Polytechnic University in 1986. His research interests are in radiation effects, electron optics, transmission electron microscopy, electron energy loss, and electron tomography.

Jan L. Weyher

Polish Academy of Sciences Warsaw
Institute of High Pressure Physics
Warsaw, Poland
weyher@unipress.waw.pl

Chapter G.43

Jan Weyher graduated as Mechanical Engineer and obtained MSc degree at Warsaw Technical University and PhD degree at Military Academy of Technology in Warsaw. He received DSc (habilitation) at University of Montpellier. His research activities are focused on studying defects in semiconductors, especially compound materials (GaAs, InP, GaN, SiC) using selective etching and complementary methods.



Jun Xu

Chinese Academy of Sciences
Shanghai Institute of Ceramics
Shanghai, China
xujun@mail.shcnc.ac.cn

Chapter [B.15](#)

Dr. Jun Xu is a Professor of Materials Science and Condensed Physics and research project leader at the Shanghai Institute of Ceramics, the Chinese Academy of Sciences (SIC,CAS). He has developed on optical single crystals, especially laser and opto-electronic functional crystals for more than 20 years. He was the winner of “China Youth Science and Technology Innovation Award”, awarded by All-China Youth Federation. He was also the winner of National Science Fund for Distinguished Young Scholars in 2005.

Hui Zhang

Tsinghua University
Department of Engineering Physics
Beijing, China
zhhui@tsinghua.edu.cn



Chapter [F.37](#)

Dr. Hui Zhang is a Professor of Engineering Physics at the Center for Public Safety Research at Tsinghua University in China. He received his PhD degree in Polytechnic University at Brooklyn in 1994 and worked as assistant professor and then an Associate Professor at the State University of New York at Stony Brook. His research interests include thermal system design, process modeling, computational fluid mechanics, and disaster modeling and mitigation.

Lili Zheng

Tsinghua University
School of Aerospace
Beijing, China
zhenglili@tsinghua.edu.cn



Chapter [F.37](#)

Dr. Lili Zheng is a Professor of Aerospace at Tsinghua University in China. She received her PhD degree in Cambridge University in 1994 and worked as Assistant Professor and then an Associate Professor at the State University of New York at Stony Brook. Her research interests include physically based modeling, engineering thermophysics, process control, and animation.



Mary E. Zvanut

University of Alabama at Birmingham
Department of Physics
Birmingham, AL, USA
mezvanut@uab.edu

Chapter [G.45](#)

Dr. Zvanut received her PhD in Physics from Lehigh University and studied transport at University of North Carolina and electronic materials at NRL. Dr. Zvanut joined the Physics Department at University of Alabama at Birmingham in September, 1992, and spent a sabbatical studying Si SiC at Wright Patterson AFB. Recent work focuses on the interactions of point defects in SrTiO₃ and the effect of oxidation and graphitization of SiC.



Zbigniew R. Zytkeiwicz

Polish Academy of Sciences
Institute of Physics
Warszawa, Poland
zytkie@ifpan.edu.pl

Chapter [E.30](#)

Zbigniew R. Zytkeiwicz received his PhD degree and then habilitation in Physics from the Institute of Physics of the Polish Academy of Sciences (IP PAS) in Warsaw. He is currently Professor at the IP PAS. His research interests include all aspects of physics and technology of epitaxial growth and defect engineering in semiconductor heteroepitaxial structures.

Detailed Contents

List of Abbreviations	XXXI
------------------------------------	------

Part A Fundamentals of Crystal Growth and Defect Formation

1 Crystal Growth Techniques and Characterization: An Overview

Govindhan Dhanaraj, Kullaiah Byrappa, Vishwanath (Vish) Prasad,

<i>Michael Dudley</i>	3
1.1 Historical Developments	3
1.2 Theories of Crystal Growth	4
1.2.1 Surface Energy Theory	5
1.2.2 Diffusion Theory	5
1.2.3 Adsorption Layer Theory	6
1.2.4 Screw Dislocation Theory	6
1.3 Crystal Growth Techniques	6
1.3.1 Solid Growth	7
1.3.2 Solution Growth	8
1.3.3 Crystal Growth from Melt	9
1.3.4 Vapor-Phase Growth	10
1.4 Crystal Defects and Characterization	11
1.4.1 Defects in Crystals	11
1.4.2 Observation of Crystal Defects	12
References	15

2 Nucleation at Surfaces

<i>Ivan V. Markov</i>	17
2.1 Equilibrium Crystal-Ambient Phase	18
2.1.1 Equilibrium of Infinitely Large Phases	18
2.1.2 Equilibrium of Small Crystal with the Ambient Phase	20
2.1.3 Equilibrium Shape of Crystals	22
2.2 Work for Nucleus Formation	24
2.2.1 General Definition	24
2.2.2 Formation of 3-D Nuclei on Unlike Substrates	25
2.2.3 Work of Formation of 2-D Crystalline Nuclei on Unlike and Like Substrates	27
2.3 Rate of Nucleation	28
2.3.1 General Formulation	28
2.3.2 Rate of Nucleation on Single-Crystal Surfaces	30
2.3.3 Equilibrium Size Distribution of Clusters	31
2.3.4 Rate of Nucleation	32
2.4 Saturation Nucleus Density	35
2.5 Second-Layer Nucleation in Homoepitaxy	38

2.6 Mechanism of Clustering in Heteroepitaxy 43

2.7 Effect of Surfactants on Nucleation 45

2.8 Conclusions and Outlook 48

References 48

3 Morphology of Crystals Grown from Solutions

Francesco Abbona, Dino Aquilano 53

3.1 Equilibrium Shape 55

 3.1.1 The Atomistic Approach:
 The Kossel Crystal and the Kink Site 55

 3.1.2 Surface Sites and Character of the Faces 55

 3.1.3 The Equilibrium Crystal – Mother Phase:
 The Atomistic Point of View 57

 3.1.4 The Equilibrium Shape of a Crystal on a Solid Substrate ... 58

 3.1.5 The Stranski–Kaischew Criterion
 to Calculate the Equilibrium Shape 60

3.2 The Theoretical Growth Shape 64

 3.2.1 The Structural Approach 64

 3.2.2 Crystal Structure and Bond Energy:
 The Hartman–Perdok Theory 64

 3.2.3 The Effect of Foreign Adsorption on the Theoretical
 Growth Shape 66

3.3 Factors Influencing the Crystal Habit 71

3.4 Surface Structure 72

 3.4.1 The α -Factor and the Roughening Transition 72

 3.4.2 Kinetic Roughening 72

 3.4.3 Polar Crystals 72

 3.4.4 Looking at Surfaces with AFM 73

3.5 Crystal Defects 73

3.6 Supersaturation – Growth Kinetics 73

 3.6.1 Growth Laws 74

 3.6.2 Some Experimental Results 74

3.7 Solvent 75

 3.7.1 Choice of Solvent 76

 3.7.2 Change of Solvent 76

 3.7.3 Solvent–Solute 77

 3.7.4 Solvent–Crystal Surface 77

 3.7.5 Mechanisms of Action 77

3.8 Impurities 78

 3.8.1 The Main Factors 78

 3.8.2 Kinetic Models 78

 3.8.3 Adsorption Sites 80

 3.8.4 Effect of Impurity Concentration and Supersaturation 80

 3.8.5 Effect of Impurity Size 82

 3.8.6 Composition of the Solution: pH 83

3.9	Other Factors	84
3.9.1	Temperature	84
3.9.2	Magnetic Field	85
3.9.3	Hydrodynamics	85
3.10	Evolution of Crystal Habit	85
3.11	A Short Conclusion	86
3.A	Appendix	86
3.A.1	The Equilibrium Pressure of an Infinite Monoatomic Crystal with Its Own Vapor	86
References	87
4	Generation and Propagation of Defects During Crystal Growth	
	<i>Helmut Klapper</i>	93
4.1	Overview	94
4.2	Inclusions	95
4.2.1	Foreign Particles	95
4.2.2	Solvent Inclusions	96
4.2.3	Solute Precipitates	99
4.3	Striations and Growth Sectors	101
4.3.1	Striations	101
4.3.2	Growth Sectors	102
4.3.3	Vicinal Sectors	103
4.3.4	Facet Sectors	104
4.3.5	Optical Anomalies of Growth Sectors	105
4.3.6	Growth–Sector Boundaries and Relative Growth Rates	105
4.4	Dislocations	107
4.4.1	Growth Dislocations and Postgrowth Dislocations	107
4.4.2	Sources of Growth Dislocations	107
4.4.3	Burgers Vectors, Dislocation Dipoles	109
4.4.4	Propagation of Growth Dislocations	110
4.4.5	Postgrowth Movement and Reactions of Dislocations	116
4.4.6	Postgrowth Dislocations	118
4.4.7	The Growth–Promoting Role of <i>Edge</i> Dislocations	119
4.5	Twinning	120
4.5.1	Introductory Notes	120
4.5.2	Twin Boundaries	121
4.5.3	Formation of Twins During Growth	122
4.5.4	Growth–Promoting Effect of Twin Boundaries	124
4.5.5	Formation of Twins after Growth	125
4.6	Perfection of Crystals Grown Rapidly from Solution	125
References	127
5	Single Crystals Grown Under Unconstrained Conditions	
	<i>Ichiro Sunagawa</i>	133
5.1	Background	134
5.2	Smooth and Rough Interfaces: Growth Mechanism and Morphology	136
5.3	Surface Microtopography	139

5.4	Growth Forms of Polyhedral Crystals	143
5.5	Internal Morphology	146
5.6	Perfection of Single Crystals	152
	References	156
6	Defect Formation During Crystal Growth from the Melt	
	<i>Peter Rudolph</i>	159
6.1	Overview	159
6.1.1	Defect Classification	160
6.1.2	Consequences of Crystal Defects for Devices	161
6.2	Point Defects	163
6.2.1	Native Point Defect Generation	163
6.2.2	Extrinsic Point Defect Incorporation	170
6.2.3	Constitutional Supercooling – Morphological Instability ...	175
6.3	Dislocations	176
6.3.1	Dislocation Types and Analysis	177
6.3.2	Dislocation Dynamics	178
6.3.3	Dislocation Engineering	187
6.4	Second-Phase Particles	188
6.4.1	Precipitates	189
6.4.2	Inclusions	190
6.5	Faceting	191
6.6	Twinning	193
6.7	Summary	194
	References	195

Part B Crystal Growth from Melt Techniques

7	Indium Phosphide: Crystal Growth and Defect Control by Applying Steady Magnetic Fields	
	<i>David F. Bliss</i>	205
7.1	Historical Overview	205
7.2	Magnetic Liquid-Encapsulated Growth	206
7.2.1	Evolution of Crystal Growth Under Applied Magnetic Fields	206
7.2.2	Crystal Shaping Measures	207
7.2.3	Apparatus for Magnetically Stabilized Crystal Growth	209
7.3	Magnetic Field Interactions with the Melt	209
7.3.1	Hydrodynamic Principle	209
7.3.2	Effect of Magnetic Field on Crystal Twinning	210
7.4	Dislocation Density	216
7.4.1	Dislocation Reduction During Seeding	217
7.4.2	Analysis of Dislocations	219
7.5	Magnetic Field Effects on Impurity Segregation	220
7.5.1	Compensation Mechanism of InP:Fe	221
7.5.2	The Role of Hydrogen	222
7.5.3	Annealing Experiments	222

7.6	Optical Characterization of InP:Fe	224
7.7	Summary	226
	References	227

8 Czochralski Silicon Single Crystals for Semiconductor and Solar Cell Applications

	<i>Koichi Kakimoto</i>	231
8.1	Silicon Single Crystals for LSIs and Solar Applications	232
8.1.1	Conventional Czochralski Silicon	232
8.1.2	Magnetic Czochralski (MCZ) Silicon	235
8.2	Control of Crystal Defects in Czochralski Silicon	237
8.2.1	Criterion for Characteristic Defect Formation	237
8.2.2	Effect of Pulling Rate and Temperature Gradient	238
8.3	Growth and Characterization of Silicon Multicrystal for Solar Cell Applications	239
8.3.1	Recent Development of Crystalline Silicon for Solar Cells ...	240
8.4	Summary	240
	References	241

9 Czochralski Growth of Oxide Photorefractive Crystals

	<i>Ernesto Diéguez, Jose Luis Plaza, Mohan D. Aggarwal, Ashok K. Batra</i>	245
9.1	Background	246
9.2	Crystal Growth	246
9.2.1	Czochralski Method of Crystal Growth	246
9.3	Design and Development of Czochralski Growth System	247
9.3.1	Furnace Construction	247
9.3.2	Heating Methods	247
9.3.3	Temperature Control Techniques	248
9.3.4	Common Crucible Materials	249
9.3.5	Crystal Rotation and Pulling Arrangement	249
9.3.6	The Czochralski Crystal Growth System	249
9.3.7	Automatic Diameter Control for Czochralski Crystal Growth Technique	251
9.4	Growth of Lithium Niobate Crystals and Its Characteristics	252
9.4.1	Crystal Growth of Lithium Niobate	252
9.4.2	Mold-Pushing Melt-Supply Double-Crucible Czochralski Apparatus	255
9.4.3	Congruent Lithium Niobate Crystal Growth by Automatic Diameter Control Method	255
9.4.4	Poling of Lithium Niobate	257
9.4.5	Periodically Poled Lithium Niobate Structures	258
9.4.6	Doped Lithium Niobate Crystals	260
9.4.7	Relevant Properties and Characteristics	261
9.5	Other Oxide Photorefractive Crystals	262
9.6	Growth of Sillenite Crystals and Its Characteristics	264
9.6.1	Growth of Bulk Sillenite Crystals	264
9.6.2	Solid-Liquid Interface	266

9.6.3	Core Effect	267
9.6.4	Morphology and Faceting	268
9.6.5	Other Growth Defects	269
9.6.6	Doping of Sillenites	270
9.6.7	Relevant Properties	271
9.6.8	Growth of Photorefractive Bismuth Silicon Oxide Crystals ..	272
9.7	Conclusions	273
	References	273

10 Bulk Crystal Growth of Ternary III–V Semiconductors

	<i>Partha S. Dutta</i>	281
10.1	III–V Ternary Semiconductors	282
10.2	Need for Ternary Substrates	283
10.3	Criteria for Device-Grade Ternary Substrates	284
10.4	Introduction to Bridgman Crystal Growth Techniques	286
10.4.1	Bridgman Techniques	286
10.4.2	Gradient Freezing Techniques	288
10.4.3	Seed Generation for New Materials	289
10.4.4	The Seeding Process	290
10.4.5	Growth Rate Determination Methods	290
10.5	Overview of III–V Binary Crystal Growth Technologies	292
10.5.1	Phase Equilibria for Binary Compounds	292
10.5.2	Binary Compound Synthesis	293
10.5.3	Single-Crystal Growth Processes	297
10.5.4	Cleaning Procedures for Growth Chamber, Crucible, and Charge	299
10.6	Phase Equilibria for Ternary Compounds	300
10.6.1	Pseudobinary Phase Diagram	300
10.6.2	Ternary Phase Diagram	300
10.6.3	Quaternary Phase Diagram	301
10.7	Alloy Segregation in Ternary Semiconductors	302
10.8	Crack Formation in Ternary Crystals	304
10.8.1	Phenomena of Crack Formation	304
10.8.2	Elimination of Cracks	306
10.8.3	Crystal Growth Rate for Crack-Free Ternary Crystals	308
10.9	Single-Crystalline Ternary Seed Generation Processes	308
10.9.1	Bootstrapping Method	308
10.9.2	Directional Solidification by Normal Freezing	309
10.9.3	Directional Solidification by Solute Diffusion and Precipitation	310
10.9.4	Growth of Lattice-Mismatched Ternary on Binary Using Quaternary Grading	311
10.10	Solute Feeding Processes for Homogeneous Alloy Growth	311
10.10.1	Growth from Large-Volume Melts	311
10.10.2	Solute Feeding Using Double-Crucible Configuration	312
10.10.3	Solute Feeding in the Vertical Bridgman Method	313
10.10.4	Solute Feeding by Crucible Oscillation	314

10.10.5 Growth Using Compositionally Graded Feed	315
10.10.6 Periodic Solute Feeding Process	315
10.11 Role of Melt–Solid Interface Shapes	318
10.12 Conclusion	321
References	321

11 Growth and Characterization of Antimony–Based Narrow–Bandgap III–V Semiconductor Crystals for Infrared Detector Applications

<i>Vijay K. Dixit, Handady L. Bhat</i>	327
11.1 Importance of Antimony–Based Semiconductors	329
11.2 Phase Diagrams	330
11.2.1 InSb	330
11.2.2 InAs _x Sb _{1–x}	330
11.2.3 InBi _x Sb _{1–x}	331
11.3 Crystal Structure and Bonding	331
11.3.1 Crystal Structure and Bonding of InSb	331
11.3.2 Structural Properties of InAs _x Sb _{1–x}	332
11.3.3 Crystal Chemical Aspect of Bi Substitution in InSb	333
11.4 Material Synthesis and Purification	333
11.4.1 Volatilization	333
11.4.2 Zone Refining	333
11.5 Bulk Growth of InSb	334
11.5.1 Zone Melting	334
11.5.2 Vertical and Horizontal Bridgman Methods	334
11.5.3 Bulk Growth of InAs _x Sb _{1–x}	335
11.5.4 Bulk Growth of InBi _x Sb _{1–x}	337
11.5.5 Growth of Thick Layers of InSb, InAs _x Sb _{1–x} , and InBi _x Sb _{1–x} , by Liquid–Phase Epitaxy	337
11.6 Structural Properties of InSb, InAs _x Sb _{1–x} , and InBi _x Sb _{1–x}	340
11.6.1 InSb	340
11.6.2 InAs _x Sb _{1–x}	342
11.6.3 InBi _x Sb _{1–x}	344
11.6.4 InSb, InAs _x Sb _{1–x} , and InBi _x Sb _{1–x} Grown on GaAs	345
11.7 Physical Properties of InSb, InAs _x Sb _{1–x} , and InBi _x Sb _{1–x}	346
11.7.1 Band Structure of InSb, InAs _x Sb _{1–x} , and InBi _x Sb _{1–x}	346
11.7.2 Transport Properties of InSb, InAs _x Sb _{1–x} , and InBi _x Sb _{1–x} ..	347
11.7.3 Optical Properties of InSb, InAs _x Sb _{1–x} , and InBi _x Sb _{1–x}	352
11.7.4 Thermal Properties of InSb and Its Alloys	356
11.8 Applications	357
11.9 Concluding Remarks and Future Outlook	359
References	360

12 Crystal Growth of Oxides by Optical Floating Zone Technique

<i>Hanna A. Dabkowska, Antoni B. Dabkowski</i>	367
12.1 Historical Notes	367
12.2 Optical Floating Zone Technique – Application for Oxides	368

12.3	Optical Floating Zone and Traveling Solvent Crystal Growth Techniques	369
12.4	Advantages and Limitations of the Floating Zone Techniques	370
12.5	Optical Floating Zone Furnaces	371
12.6	Experimental Details of Ceramics and Rod Preparation for OFZT	372
12.7	Stable Growth of Congruently and Incongruently Melting Oxides	373
12.8	Constitutional Supercooling and Crystallization Front Stability	375
12.9	Crystal Growth Termination and Cooling	377
12.10	Characterization of Crystals Grown by the OFZ Technique	377
12.11	Determination of Defects in Crystals – The Experimental Approach	380
12.12	Details of Conditions for Growth of Selected Oxide Single Crystals by OFZ and TSFZ Methods	383
12.13	Conclusions	386
	References	386
13	Laser-Heated Pedestal Growth of Oxide Fibers	
	<i>Marcello R.B. Andreetta, Antonio Carlos Hernandez</i>	393
13.1	Fiber-Pulling Research	394
13.2	The Laser-Heated Pedestal Growth Technique	399
	13.2.1 Source Preparation and Seeding	400
	13.2.2 Automatic Diameter Control Applied to LHPG	401
13.3	Fundamentals	402
	13.3.1 Conservation of Mass	402
	13.3.2 Balance of Heat Transfer	403
	13.3.3 Mechanical Stability	404
	13.3.4 Growth Under Controlled Atmosphere	405
	13.3.5 Dopant Distribution	406
	13.3.6 Pulling Crystalline Fibers Under Electric Field	407
13.4	Fiber Growth Aspects	409
	13.4.1 Congruent Melting Fibers: The Search for Stoichiometry	409
	13.4.2 Incongruently Melting and Evaporating Fibers	416
	13.4.3 Eutectic Fibers	416
13.5	Conclusions	418
	References	419
14	Synthesis of Refractory Materials by Skull Melting Technique	
	<i>Vyacheslav V. Osiko, Mikhail A. Borik, Elena E. Lomonova</i>	433
14.1	Overview	433
14.2	Techniques for Growth of Single Crystals in a Cold Crucible	435
	14.2.1 Directional Crystallization of the Melt	437
	14.2.2 Crystal Growth by Pulling on a Seed from the Melt in a Cold Crucible	441
14.3	Growth of Single Crystals Based on Zirconium Dioxide	443
	14.3.1 Crystal Structure of Zirconium Dioxide	445
	14.3.2 Phase Diagrams of the ZrO_2 – Y_2O_3 System	445
	14.3.3 Stabilization of Cubic and Tetragonal Structures in Zirconia-Based Materials	447

14.3.4	Cubic Zirconia Crystals (Fianits)	448
14.3.5	Growth, Properties, and Application of PSZ Crystals	459
14.4	Glass Synthesis by Skull Melting in a Cold Crucible	465
14.4.1	Refractory Glasses of the $R_2O_3-Al_2O_3-SiO_2$ ($R = Y, La$, Rare-Earth Element) Systems	467
14.4.2	Immobilization of Radioactive Waste in Stable Solid Blocks	468
14.5	Conclusion	469
	References	469

15 Crystal Growth of Laser Host Fluorides and Oxides

	<i>Hongjun Li, Jun Xu</i>	479
15.1	Crystal Growth of Laser Fluorides and Oxides from Melt	479
15.1.1	Laser Crystal Growth from the Melt	480
15.1.2	Czochralski Technique (CZ)	480
15.1.3	Temperature Gradient Technique (TGT)	482
15.1.4	Heat-Exchanger Method (HEM)	483
15.1.5	Vertical Bridgman Technique (VBT)	484
15.1.6	Horizontal Bridgman Technique (HBT)	485
15.1.7	Laser-Heated Pedestal Growth Method (LHPG)	486
15.1.8	Flux Technique (FT)	487
15.2	Laser Crystal Defects	487
15.2.1	Ti:sapphire	487
15.2.2	Nd-Doped Laser Crystals	489
15.2.3	Yb-Doped Laser Crystals	492
15.2.4	Other Activator-Doped Laser Crystals	498
15.3	Crystal Growth Techniques Characterization	501
15.3.1	Czochralski (CZ) Process	501
15.3.2	Temperature Gradient (TGT)	501
15.3.3	Heat-Exchanger Method (HEM)	502
15.3.4	Vertical Bridgman Technique (VBT)	502
15.3.5	Horizontal Bridgman Technique (HBT)	502
15.3.6	Laser-Heated Pedestal Growth (LHPG)	503
15.3.7	Flux Technique (FT)	503
	References	503

16 Shaped Crystal Growth

	<i>Vitali A. Tatartchenko</i>	509
16.1	Definitions and Scope of Discussion: SCG by CST	510
16.2	DSC – Basis of SCG by CST	512
16.2.1	Lyapunov Set of Equations	513
16.2.2	Capillary Problem – Common Approach	514
16.2.3	The Equation of Crystal Dimension Change Rate	515
16.2.4	The Equation of the Crystallization Front Displacement Rate	516
16.2.5	SA in a System with Two Degrees of Freedom	516

16.3	SA and SCG by CZT	517
16.3.1	Capillary Problem	517
16.3.2	Temperature Distribution in the Crystal–Melt System	517
16.3.3	SA and Crystal Growth	519
16.4	SA and SCG by VT	519
16.4.1	Practical Results of the Theoretic Analysis	519
16.4.2	SA–Based Automation of VT	521
16.5	SA and SCG by FZT	522
16.6	TPS Capillary Shaping	522
16.6.1	Capillary Boundary Problem	522
16.6.2	Stability Analysis	529
16.6.3	Experimental Tests of the Capillary Shaping Statements ...	530
16.6.4	Impurity Distribution	534
16.6.5	TPS Definition	537
16.6.6	TPS Brief History	537
16.7	TPS Sapphire Growth	539
16.7.1	Modifications of TPS	540
16.7.2	Crystal Defects	541
16.7.3	Applications	545
16.8	TPS Silicon Growth	546
16.8.1	Shaped Silicon Structure	546
16.8.2	Local Electronic Properties of Shaped Silicon	549
16.8.3	TPS Silicon Growth	551
16.9	TPS Metals Growth	551
16.10	TPS Peculiarities	552
	References	552

Part C Solution Growth of Crystals

17 Bulk Single Crystals Grown from Solution on Earth and in Microgravity

	<i>Mohan D. Aggarwal, Ashok K. Batra, Ravindra B. Lal, Benjamin G. Penn, Donald O. Frazier</i>	559
17.1	Crystallization: Nucleation and Growth Kinetics	561
17.1.1	Expression for Supersaturation	561
17.1.2	Effects of Convection in Solution Growth	563
17.1.3	Effect of Impurities	564
17.2	Low-Temperature Solution Growth	566
17.2.1	Solution Growth Methods	566
17.3	Solution Growth by Temperature Lowering	567
17.3.1	Solvent Selection and Solubility	567
17.3.2	Design of a Crystallizer	569
17.3.3	Solution Preparation and Starting a Growth Run	573
17.4	Triglycine Sulfate Crystal Growth: A Case Study	574
17.4.1	Growth of Single Crystals of Triglycine Sulfate	574
17.4.2	Growth Kinetics and Habit Modification	576

17.5	Solution Growth of Triglycine Sulfate Crystals in Microgravity	582
17.5.1	Rationale for Solution Crystal Growth in Space	583
17.5.2	Solution Crystal Growth Method in Space	583
17.5.3	Results and Discussion	588
17.6	Protein Crystal Growth	592
17.6.1	Protein Crystal Growth Methods	592
17.6.2	Protein Crystal Growth Mechanisms	593
17.6.3	Protein Crystal Growth in Microgravity	593
17.7	Concluding Remarks	594
	References	594

18 Hydrothermal Growth of Polyscale Crystals

	<i>Kullaiah Byrappa</i>	599
18.1	History of Hydrothermal Growth of Crystals	603
18.2	Thermodynamic Basis of the Hydrothermal Growth of Crystals	606
18.2.1	Hydrodynamic Principles of the Hydrothermal Growth of Crystals	606
18.2.2	Thermodynamic Modeling of the Hydrothermal Growth of Crystals	608
18.2.3	Solutions, Solubility, and Kinetics of Crystallization under Hydrothermal Conditions	610
18.3	Apparatus Used in the Hydrothermal Growth of Crystals	615
18.3.1	Morey Autoclave	617
18.3.2	Tuttle–Roy Cold–Cone Seal Autoclaves	617
18.3.3	General–Purpose Autoclaves and Others	618
18.4	Hydrothermal Growth of Some Selected Crystals	620
18.4.1	Quartz	620
18.4.2	Aluminum and Gallium Berlinites	625
18.4.3	Calcite	628
18.4.4	Gemstones	629
18.4.5	Rare–Earth Vanadates	633
18.5	Hydrothermal Growth of Fine Crystals	634
18.6	Hydrothermal Growth of Nanocrystals	637
18.7	Concluding Remarks	640
18.A	Appendix	641
	References	646

19 Hydrothermal and Ammonothermal Growth of ZnO and GaN

	<i>Michael J. Callahan, Qi–Sheng Chen</i>	655
19.1	Overview of Hydrothermal and Ammonothermal Growth of Large Crystals	657
19.1.1	Comparison of Ammonia and Water as Solvents	657
19.1.2	Growth of Large Crystals by the Transport Growth Model ..	659

19.2	Requirements for Growth of Large, Low-Defect Crystals	661
19.2.1	Thermodynamics: Solubility and Phase Stability	661
19.2.2	Environmental Effects on Growth Kinetics and Structure Perfection (Extended and Point Defects)	664
19.2.3	Doping and Alloying	665
19.3	Physical and Mathematical Models	666
19.3.1	Flow and Heat Transfer	666
19.3.2	Porous-Media-Based Transport Model	666
19.3.3	Numerical Scheme	667
19.4	Process Simulations	669
19.4.1	Typical Flow Pattern and Growth Mechanism	669
19.4.2	Effect of Permeability on the Porous Bed	670
19.4.3	Baffle Design Effect on Flow and Temperature Patterns ...	670
19.4.4	Effect of Porous Bed Height on the Flow Pattern	672
19.4.5	Simulation of Reverse-Grade Soluble Systems	672
19.5	Hydrothermal Growth of ZnO Crystals	674
19.5.1	Growth Kinetics and Morphology	674
19.5.2	Structural Perfection – Extended Imperfections (Dislocations, Voids, etc.)	676
19.5.3	Impurities, Doping, and Electrical Properties	678
19.5.4	Optical Properties	679
19.6	Ammonothermal GaN	681
19.6.1	Alkaline Seeded Growth	681
19.6.2	Acidic Seeded Growth	683
19.6.3	Doping, Alloying, and Challenges	684
19.7	Conclusion	685
	References	685
20	Stoichiometry and Domain Structure of KTP-Type Nonlinear Optical Crystals	
	<i>Michael Roth</i>	691
20.1	Background	691
20.1.1	KTP Crystal Structure	692
20.1.2	Crystal Growth	694
20.2	Stoichiometry and Ferroelectric Phase Transitions	697
20.2.1	KTiOPO ₄ Crystals	697
20.2.2	RbTiOPO ₄ Crystals	700
20.2.3	Other KTP Isomorphs	702
20.3	Growth-Induced Ferroelectric Domains	703
20.3.1	Domains in Top-Seeded Solution-Grown KTP	704
20.3.2	Domain Boundaries	705
20.3.3	Summary of Ferroelectric Domain Structures	707
20.3.4	Single-Domain Growth	707
20.4	Artificial Domain Structures	708
20.4.1	Electric Field Poling	708
20.4.2	As-Grown Periodic Domain Structure	711

20.5	Nonlinear Optical Crystals	713
20.5.1	Optical Nonuniformity	713
20.5.2	Gray Tracks	715
References	716

21 High-Temperature Solution Growth: Application to Laser and Nonlinear Optical Crystals

<i>Joan J. Carvajal, Maria Cinta Pujol, Francesc Díaz</i>	725
21.1 Basics	726
21.1.1 Historical Background and Overview	726
21.1.2 Most Important Families of Laser and Nonlinear Optical Materials	727
21.2 High-Temperature Solution Growth	731
21.2.1 Top-Seeded Solution Growth (TSSG)	732
21.2.2 Liquid-Phase Epitaxy (LPE)	734
21.3 Growth of Bulk Laser and NLO Single Crystals by the TSSG Method ...	736
21.3.1 Crystal Growth from Low-Viscosity Solutions: Fluorides, Tungstates, and Vanadates	736
21.3.2 Crystal Growth from High-Viscosity Solutions: Phosphates and Borates	739
21.4 Liquid-Phase Epitaxy: Growth of Epitaxial Films of Laser and NLO Materials	746
21.4.1 Epitaxial Films of Laser Materials: Lanthanide-Doped KLuW on KLuW Substrates	746
21.4.2 Epitaxies Within the Structural Field of KTP	748
References	752

22 Growth and Characterization of KDP and Its Analogs

<i>Sheng-Lai Wang, Xun Sun, Xu-Tang Tao</i>	759
22.1 Background	759
22.2 Mechanism and Kinetics of Crystallization	761
22.2.1 Studies of KDP Crystal Surfaces	761
22.2.2 Nucleation Studies in Supersaturated Solution	763
22.2.3 Dislocation Mechanism	765
22.2.4 Growth on Two-Dimensional Nuclei	767
22.2.5 Growth from Crystal Edges	767
22.3 Growth Techniques for Single Crystals	769
22.3.1 Parameters Affecting Growth Rate	769
22.3.2 Stability of Solution	770
22.3.3 Conventional Methods	771
22.3.4 Rapid Growth from a Point Seed	773
22.4 Effect of Growth Conditions on Defects of Crystals	776
22.4.1 Impurity Effect	776
22.4.2 Supersaturation	779
22.4.3 Filtration	780
22.4.4 Hydrodynamic Effects	781

22.5 Investigations on Crystal Quality 783

22.5.1 Spectroscopic Studies 783

22.5.2 Homogeneity 784

22.5.3 Laser Damage Threshold 787

References 789

Part D Crystal Growth from Vapor

23 Growth and Characterization of Silicon Carbide Crystals

Govindhan Dhanaraj, Balaji Raghothamachar, Michael Dudley 797

23.1 Silicon Carbide – Background and History 797

23.1.1 Applications of SiC 798

23.1.2 Historical Development of SiC Crystal Growth 798

23.2 Vapor Growth 799

23.2.1 Acheson Method 799

23.2.2 Lely Method 799

23.2.3 Modified Lely Method 800

23.2.4 Sublimation Sandwich Method 800

23.2.5 Chemical Vapor Deposition 800

23.3 High-Temperature Solution Growth 801

23.3.1 Bulk Growth 801

23.3.2 Liquid-Phase Epitaxy 802

23.4 Industrial Bulk Growth by Seed Sublimation 802

23.4.1 Growth System 803

23.4.2 Seeding and Growth Process 804

23.5 Structural Defects and Their Configurations 805

23.5.1 Micropipes and Closed-Core Screw Dislocations 806

23.5.2 Basal Plane Dislocations in 4H-SiC 809

23.5.3 Threading Edge Dislocations (TEDs) in 4H-SiC 814

23.6 Concluding Remarks 816

References 817

24 AlN Bulk Crystal Growth by Physical Vapor Transport

Rafael Dalmau, Zlatko Sitar 821

24.1 PVT Crystal Growth 822

24.2 High-Temperature Materials Compatibility 825

24.3 Self-Seeded Growth of AlN Bulk Crystals 827

24.4 Seeded Growth of AlN Bulk Crystals 829

24.4.1 Growth on SiC Seeds 829

24.4.2 Growth on AlN Seeds 831

24.5 Characterization of High-Quality Bulk Crystals 832

24.5.1 Structural Properties 832

24.5.2 Fundamental Optical Properties of AlN 835

24.5.3 Impurities 838

24.6 Conclusions and Outlook 839

References 839

25 Growth of Single-Crystal Organic Semiconductors

<i>Christian Kloc, Theo Siegrist, Jens Pflaum</i>	845
25.1 Basics	845
25.2 Theory of Nucleation and Crystal Growth	847
25.2.1 Stability Criteria for Nuclei	847
25.2.2 Thermodynamic Considerations of Crystal Growth	847
25.2.3 Growth Morphology in Relation to Symmetry	848
25.2.4 Structural Defects	848
25.3 Organic Materials of Interest for Semiconducting Single Crystals	848
25.4 Pregrowth Purification	850
25.4.1 Zone Refinement	851
25.4.2 Sublimation and Its Modifications	852
25.5 Crystal Growth	854
25.5.1 Melt Growth	855
25.5.2 Growth from the Gas Phase	857
25.5.3 Solvent-Based Growth Methods	862
25.6 Quality of Organic Semiconducting Single Crystals	862
25.7 Organic Single-Crystalline Field-Effect Transistors	863
25.8 Conclusions	864
References	865

26 Growth of III-Nitrides with Halide Vapor Phase Epitaxy (HVPE)

<i>Carl Hemmingsson, Bo Monemar, Yoshinao Kumagai, Akinori Koukitu</i>	869
26.1 Growth Chemistry and Thermodynamics	869
26.2 HVPE Growth Equipment	872
26.3 Substrates and Templates for Bulk GaN Growth	875
26.3.1 Sapphire	875
26.3.2 Silicon Carbide	876
26.3.3 GaAs	876
26.3.4 Lattice-Matched Substrates	877
26.3.5 Growth on Templates	877
26.3.6 Basic 1S-ELO Structures	877
26.3.7 2S-ELO	878
26.4 Substrate Removal Techniques	879
26.4.1 Laser Lift-Off	879
26.4.2 Self-Separation	880
26.4.3 Mechanical Polishing	881
26.4.4 Plasma Etching	881
26.4.5 Chemical Etching and Spontaneous Self-Separation	881
26.5 Doping Techniques for GaN in HVPE	882
26.5.1 n-Type Doping of GaN	882
26.5.2 p-Type Doping of GaN	882
26.6 Defect Densities, Dislocations, and Residual Impurities	883
26.7 Some Important Properties of HVPE-Grown Bulk GaN Material	887
26.8 Growth of AlN by HVPE: Some Preliminary Results	888
26.9 Growth of InN by HVPE: Some Preliminary Results	890
References	891

27 Growth of Semiconductor Single Crystals from Vapor Phase	
<i>Ramasamy Dhanasekaran</i>	897
27.1 Classifications of Vapor Growth	899
27.2 Chemical Vapor Transport – Transport Kinetics	901
27.2.1 Transport Models	901
27.2.2 Physical Chemistry of Chemical Transport Reactions	902
27.2.3 Factors Affecting the CVT Reaction	903
27.2.4 Choice of Transporting Agents	904
27.2.5 Advantages and Limitations of CVT Method	904
27.3 Thermodynamic Considerations	905
27.3.1 Estimation of Optimum Growth Parameters for the ZnSe–I ₂ System by CVT	905
27.3.2 Fluctuations in the Transport Rates	906
27.3.3 Supersaturation Ratios in the ZnS _x Se _{1-x} System	908
27.4 Growth of II–VI Compound Semiconductors by CVT	912
27.4.1 Apparatus	912
27.4.2 Preparation of Starting Materials	913
27.4.3 Growth of ZnSe Single Crystals	914
27.4.4 Growth of CdS Single Crystals	915
27.5 Growth of Nanomaterial from Vapor Phase	916
27.6 Growth of I–III–VI ₂ Compounds	917
27.6.1 Growth of Undoped and Doped Crystals of CuAlS ₂	918
27.6.2 Growth of Undoped and Doped Crystals of CuAlSe ₂	919
27.6.3 Growth of CuGaS ₂ –Based Single Crystals	921
27.6.4 Growth of AgGaS ₂ and AgGaSe ₂ Single Crystals	923
27.7 Growth of GaN by VPE	925
27.7.1 Vapor–Phase Epitaxy (VPE)	925
27.7.2 VPE GaN Film Growth	925
27.7.3 Strength of HVPE Method	926
27.7.4 Development of VPE System for the Growth of GaN	926
27.7.5 Growth of GaN by HVPE	927
27.7.6 Characterization of GaN Films	928
27.8 Conclusion	929
References	930

Part E Epitaxial Growth and Thin Films

28 Epitaxial Growth of Silicon Carbide by Chemical Vapor Deposition	
<i>Ishwara B. Bhat</i>	939
28.1 Polytypes of Silicon Carbide	941
28.2 Defects in SiC	942
28.2.1 Micropipes	942
28.2.2 Screw Dislocations	942
28.2.3 Growth Pits and Triangular Inclusions	943

28.3	Epitaxial Growth of Silicon Carbide	944
28.3.1	Substrates for Silicon Carbide Growth	944
28.3.2	How to Control the Polytypes in SiC Homoepitaxy	945
28.3.3	SiC Epitaxial Growth Techniques	946
28.3.4	Chemical Vapor Deposition	946
28.4	Epitaxial Growth on Patterned Substrates	952
28.4.1	Selective Epitaxial Growth	953
28.4.2	Selective Epitaxial Growth of 4H-SiC Using TaC Mask	954
28.4.3	Orientation Dependence of SiC Selective Growth	956
28.4.4	Effects of Mask-to-Window Ratio ($M : W$) on SiC Selective Growth	957
28.4.5	Effects of C/Si Ratio on SiC Selective Growth	959
28.4.6	Mechanism of Selective Etching and Effect of Atomic Hydrogen	960
28.4.7	Fabrication of 4H-SiC p-n Junction Diodes Using Selective Growth	960
28.5	Conclusions	961
	References	961

29 Liquid-Phase Electroepitaxy of Semiconductors

	<i>Sadik Dost</i>	967
29.1	Background	967
29.1.1	Liquid-Phase Electroepitaxy	968
29.1.2	Natural Convection	970
29.1.3	Applied Magnetic Fields	970
29.1.4	Observation of Growth Rate	970
29.2	Early Theoretical and Modeling Studies	971
29.2.1	Peltier-Induced Growth Kinetics: Electromigration Mechanism	971
29.2.2	A One-Dimensional Model	973
29.2.3	Source-Current-Controlled (SCC) Growth	975
29.3	Two-Dimensional Continuum Models	977
29.4	LPEE Growth Under a Stationary Magnetic Field	978
29.4.1	Experiments	979
29.5	Three-Dimensional Simulations	981
29.5.1	Simulation Model	982
29.5.2	Numerical Method	983
29.5.3	Effect of Magnetic Field Strength	984
29.5.4	Evolution of Interfaces	989
29.5.5	Effect of High Electric and Magnetic Field Levels	990
29.6	High Growth Rates in LPEE: Electromagnetic Mobility	992
29.6.1	Estimation of the Electromagnetic Mobility Value	993
29.6.2	Simulations of High Growth Rates in a GaAs System	994
	References	996

30 Epitaxial Lateral Overgrowth of Semiconductors

<i>Zbigniew R. Zytkeiwicz</i>	999
30.1 Overview	1000
30.2 Mechanism of Epitaxial Lateral Overgrowth from the Liquid Phase ..	1002
30.2.1 Choice of Substrate Geometry for Growth of ELO Layers	1004
30.2.2 Optimization of Liquid-Phase Lateral Overgrowth Procedure	1007
30.3 Dislocations in ELO Layers	1011
30.3.1 Filtration of Substrate Dislocations in ELO	1011
30.3.2 Structural Perfection of Coalescence Front in Fully Overgrown ELO Structures	1014
30.4 Strain in ELO Layers	1016
30.4.1 Mask-Induced Strain in Homoepitaxial ELO Layers	1017
30.4.2 Thermal Strain in ELO Layers	1024
30.5 Recent Progress in Lateral Overgrowth of Semiconductor Structures ..	1026
30.5.1 Developments in Liquid-Phase ELO Growth	1027
30.5.2 New Concepts of ELO Growth	1030
30.6 Concluding Remarks	1034
References	1035

31 Liquid-Phase Epitaxy of Advanced Materials

<i>Christine F. Klemenz Rivenbark</i>	1041
31.1 Historical Development of LPE	1042
31.2 Fundamentals of LPE and Solution Growth	1042
31.3 Requirements for Liquid-Phase Epitaxy	1044
31.4 Developing New Materials: On the Choice of the Epitaxial Deposition Method	1044
31.5 LPE of High-Temperature Superconductors	1046
31.5.1 Phase Relations, Solvent System, and Solubility Curves	1046
31.5.2 Heat of Solution	1048
31.5.3 Supersaturation and Driving Force for LPE	1048
31.5.4 Substrates and Epitaxial Relationship	1049
31.5.5 LPE Growth System and Film Growth Procedure	1051
31.5.6 Growth Mechanisms and Growth Parameters: Theory Versus Experiment	1052
31.6 LPE of Calcium Gallium Germanates	1055
31.6.1 Solvent System	1055
31.6.2 Substrates for Homoepitaxial LGT LPE Film Growth	1056
31.6.3 LPE growth of LGS, LGT, and LGN	1057
31.6.4 Structural and Chemical Characterization of Doped LGT LPE Films	1057
31.7 Liquid-Phase Epitaxy of Nitrides	1059
31.7.1 Developments and Trends in LPE of GaN and AlN	1060
31.7.2 Substrates for Epitaxy of Nitrides	1061

31.7.3	Growth System and Optimization	1062
31.7.4	Morphological Evolution of LPE-Grown Nitride Films	1062
31.8	Conclusions	1063
	References	1064

32 Molecular-Beam Epitaxial Growth of HgCdTe

	<i>James W. Garland, Sivalingam Sivananthan</i>	1069
32.1	Overview	1070
32.1.1	Why HgCdTe Is Important	1071
32.1.2	Why MBE Is the Preferred Method of Growth for HgCdTe IR Detectors and Imagers	1072
32.1.3	General Description of the MBE Growth Technique	1072
32.2	Theory of MBE Growth	1073
32.2.1	Pseudo-Equilibrium Theories	1074
32.2.2	Kinetic Theories	1075
32.3	Substrate Materials	1076
32.3.1	Substrate Orientation	1077
32.3.2	CdZnTe Substrates	1077
32.3.3	Si-Based Substrates	1084
32.3.4	Other Substrates	1087
32.4	Design of the Growth Hardware	1088
32.4.1	Mounting of the Substrate	1088
32.4.2	Valving of the Effusion Cells	1089
32.5	In situ Characterization Tools for Monitoring and Controlling the Growth	1090
32.5.1	Spectroscopic Ellipsometry (SE): Basic Theory and Experimental Setup	1090
32.5.2	SE Data Analysis	1092
32.5.3	SE Study of Hg Absorption and Adsorption on CdTe	1098
32.5.4	Correlation Between the Quality of MBE-Grown HgCdTe and the Depolarization and Surface Roughness Coefficients Measured by in situ SE	1099
32.5.5	Surface Characterization by in situ RHEED	1100
32.5.6	Other in situ Tools for Controlling the Growth	1101
32.6	Nucleation and Growth Procedure	1101
32.6.1	Nucleation and Growth of CdTe or ZnTe on Si	1101
32.6.2	Substrate Preparation and Growth of HgCdTe	1102
32.7	Dopants and Dopant Activation	1104
32.7.1	Extrinsic n-Type Doping	1104
32.7.2	Extrinsic p-Type Doping	1105
32.7.3	In situ Group I Dopant Incorporation	1106
32.7.4	In situ Group V Dopant Incorporation	1106
32.7.5	As Activation	1106
32.8	Properties of HgCdTe Epilayers Grown by MBE	1107
32.8.1	Electrical and Optical Properties	1107
32.8.2	Structural Properties	1110
32.8.3	Surface Defects	1110

32.9	HgTe/CdTe Superlattices	1112
32.9.1	Theoretical Properties	1113
32.9.2	Growth	1114
32.9.3	Experimentally Observed Properties	1114
32.10	Architectures of Advanced IR Detectors	1115
32.10.1	Reduction of Internal Detector Noise	1116
32.10.2	Increasing Detector Response	1116
32.10.3	High-Speed IR Detectors	1117
32.10.4	High-Operating-Temperature (HOT) IR Detectors	1118
32.11	IR Focal-Plane Arrays (FPAs)	1118
32.12	Conclusions	1119
	References	1121

33 Metalorganic Vapor-Phase Epitaxy of Diluted Nitrides and Arsenide Quantum Dots

	<i>Udo W. Pohl</i>	1133
33.1	Principle of MOVPE	1133
33.1.1	MOVPE Precursors	1133
33.1.2	Growth Process	1135
33.2	Diluted Nitride InGaAsN Quantum Wells	1137
33.2.1	Nitrogen Precursors	1138
33.2.2	Structural and Electronic Properties of InGaAsN	1139
33.2.3	Dilute Nitride Quantum Well Lasers	1141
33.3	InAs/GaAs Quantum Dots	1142
33.3.1	The Stranski-Krastanow 2-D-3-D Transition	1142
33.3.2	MOVPE of InAs Quantum Dots	1144
33.3.3	Quantum Dot Lasers	1147
33.4	Concluding Remarks	1148
	References	1148

34 Formation of SiGe Heterostructures and Their Properties

	<i>Yasuhiro Shiraki, Akira Sakai</i>	1153
34.1	Background	1153
34.2	Band Structures of Si/Ge Heterostructures	1154
34.3	Growth Technologies	1156
34.3.1	Molecular-Beam Epitaxy	1156
34.3.2	Chemical Vapor Deposition	1157
34.4	Surface Segregation	1157
34.5	Critical Thickness	1161
34.6	Mechanism of Strain Relaxation	1163
34.7	Formation of Relaxed SiGe Layers	1165
34.7.1	Graded Buffer	1165
34.7.2	Low-Temperature Method	1166
34.7.3	Chemical-Mechanical Polishing Method	1167
34.7.4	Ion Implantation Method	1168
34.7.5	Ge Condensation Method	1169

34.7.6	Dislocation Engineering for Buffer Layers	1170
34.7.7	Formation of SiGeC Alloys	1172
34.8	Formation of Quantum Wells, Superlattices, and Quantum Wires	1173
34.9	Dot Formation	1177
34.10	Concluding Remarks and Future Prospects	1184
References		1184

35 Plasma Energetics in Pulsed Laser and Pulsed Electron Deposition

<i>Mikhail D. Strikovski, Jeonggoo Kim, Solomon H. Kolagani</i>		1193
35.1	Energetic Condensation in Thin Film Deposition	1193
35.2	PLD and PED Techniques	1194
35.3	Transformations of Atomic Energy in PLD and PED	1195
35.3.1	Plasma Formation of Vaporized Material	1196
35.3.2	Plasma Formation in PED	1198
35.3.3	Expansion of Plasma and Particle Acceleration	1199
35.3.4	Deceleration of Plasma in Background Gas	1202
35.4	Optimization of Plasma Flux for Film Growth	1204
35.4.1	Ion Current of Plasma Propagating in Ambient Gas	1205
35.4.2	Optimization of Growth of GaN Films – A Materials Example	1206
35.5	Conclusions	1208
References		1209

Part F Modeling in Crystal Growth and Defects

36 Convection and Control in Melt Growth of Bulk Crystals

<i>Chung-Wen Lan</i>		1215
36.1	Physical Laws for Transport Processes	1217
36.1.1	Conservation Equations	1217
36.1.2	Boundary Conditions	1218
36.2	Flow Structures in the Melt	1219
36.2.1	ZM Configuration	1219
36.2.2	Bridgman Configuration	1225
36.3	Flow Control by External Forces	1228
36.3.1	Steady Magnetic Field	1229
36.3.2	Rotation	1233
36.3.3	Vibration	1237
36.4	Outlook	1238
References		1238

37 Vapor Growth of III Nitrides

<i>Dang Cai, Lili Zheng, Hui Zhang</i>		1243
37.1	Overview of Vapor Growth of III Nitrides	1244
37.1.1	Various GaN/AlN Vapor-Growth Systems	1244
37.1.2	Modeling of AlN/GaN Vapor Deposition	1246

37.2	Mathematical Models for AlN/GaN Vapor Deposition	1248
37.2.1	Transport Equations	1248
37.2.2	Growth Kinetics	1249
37.2.3	Numerical Solution	1251
37.3	Characteristics of AlN/GaN Vapor Deposition	1251
37.3.1	Theoretical Analysis of Heat and Mass Transfer	1251
37.3.2	Thermodynamic and Kinetic Analysis of Chemical Reactions	1254
37.4	Modeling of GaN IVPE Growth – A Case Study	1258
37.4.1	Scaling Analysis	1258
37.4.2	Computational Issues	1258
37.4.3	Gas-Phase and Surface Reactions Analysis	1259
37.4.4	Geometrical and Operational Conditions Optimization	1264
37.4.5	Effect of Total Gas Flow Rate on Substrate Temperature ...	1264
37.4.6	Effect of Substrate Rotation on Deposition Rate and Deposition Uniformity	1269
37.4.7	Quasi-equilibrium Model for Deposition Rate Prediction ..	1270
37.4.8	Kinetic Deposition Model	1271
37.5	Surface Evolution of GaN/AlN Film Growth from Vapor	1274
37.6	Concluding Remarks	1275
	References	1276

**38 Continuum-Scale Quantitative Defect Dynamics
in Growing Czochralski Silicon Crystals**

<i>Milind S. Kulkarni</i>		1281
38.1	The Discovery of Microdefects	1283
38.2	Defect Dynamics in the Absence of Impurities	1284
38.2.1	The Theory of the Initial Incorporation of Intrinsic Point Defects	1284
38.2.2	The Quantification of the Microdefect Formation	1290
38.3	Czochralski Defect Dynamics in the Presence of Oxygen	1304
38.3.1	Reactions in Growing CZ Crystals	1304
38.3.2	The Model	1305
38.3.3	Defect Dynamics in One-Dimensional Crystal Growth	1308
38.3.4	Defect Dynamics in Two-Dimensional Crystal Growth	1310
38.4	Czochralski Defect Dynamics in the Presence of Nitrogen	1313
38.4.1	The Model	1313
38.4.2	CZ Defect Dynamics in One-Dimensional Crystal Growth ...	1316
38.4.3	CZ Defect Dynamics in Two-Dimensional Crystal Growth ...	1318
38.5	The Lateral Incorporation of Vacancies in Czochralski Silicon Crystals	1321
38.5.1	General Defect Dynamics: A Brief Revisit	1322
38.5.2	Defect Dynamics Under Highly Vacancy-Rich Conditions ...	1323
38.5.3	Defect Dynamics Near the Critical Condition	1324

38.6	Conclusions	1328
38.6.1	CZ Defect Dynamics in the Absence of Impurities	1329
38.6.2	CZ Defect Dynamics in the Presence of Oxygen	1330
38.6.3	CZ Defect Dynamics in the Presence of Nitrogen	1330
38.6.4	The Lateral Incorporation of Vacancies	1331
References	1332

39 Models for Stress and Dislocation Generation in Melt Based Compound Crystal Growth

<i>Vishwanath (Vish) Prasad, Srinivas Pendurti</i>	1335
39.1	Overview	1335
39.2	Crystal Growth Processes	1336
39.2.1	Czochralski Technique	1336
39.3	Dislocations in Semiconductors Materials	1337
39.3.1	Deleterious Effects of Dislocations	1337
39.3.2	Origin of Dislocations	1338
39.4	Models for Dislocation Generation	1339
39.4.1	CRSS-Based Elastic Models	1340
39.4.2	Viscoplastic Models	1342
39.5	Diamond Structure of the Crystal	1343
39.6	Deformation Behavior of Semiconductors	1346
39.6.1	Stage of Upper and Lower Yield Points	1347
39.7	Application of the Haasen Model to Crystal Growth	1350
39.8	An Alternative Model	1351
39.8.1	Different Types of Dislocations	1351
39.8.2	Dislocation Glide Velocity	1352
39.8.3	Dislocation Multiplication	1355
39.8.4	Work Hardening	1357
39.8.5	The Initial Dislocation Density	1358
39.9	Model Summary and Numerical Implementation	1360
39.9.1	Summary of the Model	1360
39.9.2	Numerical Implementation	1361
39.10	Numerical Results	1362
39.10.1	Strength of Convection in the Melt and Gas	1362
39.10.2	Temperature Boundary Condition	1362
39.10.3	A Sample Case	1363
39.10.4	Effect of Gas Convection and Radiation	1368
39.10.5	Melt Convection and Rotation Reynolds Numbers	1369
39.10.6	Control of Encapsulation Height	1371
39.10.7	The Cool-Down Period	1371
39.10.8	The $[1\bar{1}1]$ Growth Axis	1372
39.10.9	Summary of the Calculations and Some Comparisons	1373
39.11	Summary	1374
References	1375

40 Mass and Heat Transport in BS and EFG Systems

<i>Thomas F. George, Stefan Balint, Liliana Braescu</i>	1379
40.1 Model-Based Prediction of the Impurity Distribution – Vertical BS System	1380
40.1.1 Burton–Prim–Slichter Uniform–Diffusion–Layer Model (UDLM)	1380
40.1.2 Chang–Brown Quasi–Steady–State Model (QSSM)	1381
40.1.3 Adornato–Brown Pseudo–Steady–State Model (PSSM)	1383
40.1.4 Nonstationary Model (NSM)	1384
40.1.5 Modified Quasi–Steady–State Model (MQSSM) and Modified Nonstationary Model (MNSM)	1386
40.1.6 Larson–Zhang–Zheng Thermal–Diffusion Model (TDM)	1387
40.2 Model-Based Prediction of the Impurity Distribution – EFG System	1389
40.2.1 The Uniform–Diffusion–Layer Model (UDLM)	1389
40.2.2 Tatarchenko Steady–State Model (TSSM)	1389
40.2.3 Melt Replenishment Model (MRM)	1390
40.2.4 Melt Without Replenishment Model (MWRM)	1397
References	1400

Part G Defects Characterization and Techniques**41 Crystalline Layer Structures with X-Ray Diffractometry**

<i>Paul F. Fewster</i>	1405
41.1 X-Ray Diffractometry	1406
41.2 Basic Direct X-Ray Diffraction Analysis from Layered Structures	1407
41.2.1 Theory	1407
41.2.2 Interpretation of Data Collected from Planes Parallel to the Surface – the ω – 2θ Scan – an Example	1409
41.2.3 Interpretation of Data Collected from Several Reflections – The Reciprocal Space Map – An Example	1411
41.3 Instrumental and Theoretical Considerations	1412
41.3.1 The Instrument for Collecting X-Ray Diffraction Patterns ..	1412
41.3.2 Interpreting the Scattering by Simulation	1412
41.4 Examples of Analysis from Low to High Complexity	1413
41.4.1 Established Methods	1413
41.4.2 New Methods and New Analyses	1416
41.5 Rapid Analysis	1419
41.6 Wafer Micromapping	1420
41.7 The Future	1421
References	1422

42 X-Ray Topography Techniques for Defect Characterization of Crystals

<i>Balaji Raghothamachar, Michael Dudley, Govindhan Dhanaraj</i>	1425
42.1 Basic Principles of X-Ray Topography	1426
42.1.1 Contrast	1426
42.1.2 Resolution	1427

42.2	Historical Development of the X-Ray Topography Technique	1428
42.3	X-Ray Topography Techniques and Geometry	1430
42.3.1	Conventional X-Ray Topography Techniques	1430
42.3.2	Synchrotron-Radiation-Based X-Ray Topography Techniques	1431
42.3.3	Recording Geometries	1435
42.4	Theoretical Background for X-Ray Topography	1435
42.4.1	Limitation of Kinematical Theory of X-Ray Diffraction	1436
42.4.2	Dynamical Theory of X-Ray Diffraction	1436
42.5	Mechanisms for Contrast on X-Ray Topographs	1440
42.5.1	Orientation Contrast from Subgrains and Twins	1440
42.5.2	Extinction Contrast	1441
42.6	Analysis of Defects on X-Ray Topographs	1445
42.6.1	Basic Dislocation Analysis	1445
42.6.2	Contrast from Inclusions	1446
42.6.3	Contrast Associated with Cracks	1448
42.7	Current Application Status and Development	1449
	References	1450

43 Defect-Selective Etching of Semiconductors

	<i>Jan L. Weyher, John J. Kelly</i>	1453
43.1	Wet Etching of Semiconductors: Mechanisms	1454
43.1.1	Chemical Etching	1454
43.1.2	Electrochemical Etching	1454
43.1.3	Electroless Etching	1456
43.1.4	Photogalvanic Etching	1458
43.2	Wet Etching of Semiconductors: Morphology and Defect Selectivity	1459
43.2.1	Chemical Etching	1459
43.2.2	Electrochemical Etching	1459
43.2.3	Electroless Etching	1460
43.2.4	Photogalvanic Etching	1461
43.3	Defect-Selective Etching Methods	1461
43.3.1	Orthodox Etching for Revealing Dislocations	1461
43.3.2	Electroless Etching for Revealing Defects	1469
	References	1473

44 Transmission Electron Microscopy Characterization of Crystals

	<i>Jie Bai, Shixin Wang, Lu-Min Wang, Michael Dudley</i>	1477
44.1	Theoretical Basis of TEM Characterization of Defects	1477
44.1.1	Imaging of Crystal Defects Using Diffraction Contrast	1478
44.1.2	Phase-Contrast High-Resolution Transmission Electron Microscopy (HRTEM)	1482
44.1.3	Diffraction Techniques	1484
44.1.4	STEM, EELS, and EFTEM in Microanalysis	1489
44.1.5	FIB for TEM Sample Preparation	1493

44.2 Selected Examples of Application of TEM to Semiconductor Systems 1493

44.2.1 Studies of Conventional Heteroepitaxial Semiconductor Systems 1494

44.2.2 TEM Studies of Large-Mismatch Heteroepitaxial Systems .. 1500

44.2.3 Application of STEM, EELS, and EFTEM 1509

44.3 Concluding Remarks: Current Application Status and Development . 1514

References 1515

45 **Electron Paramagnetic Resonance Characterization of Point Defects**

Mary E. Zvanut..... 1521

45.1 Electronic Paramagnetic Resonance 1522

45.2 EPR Analysis 1524

45.2.1 Zeeman Effect 1524

45.2.2 Nuclear Hyperfine Interaction 1526

45.2.3 Interactions Involving More than One Electron 1529

45.2.4 Total Number of Spins 1533

45.3 Scope of EPR Technique 1534

45.3.1 Defects in a Thin Film on a Substrate 1534

45.3.2 Defects at an Interface 1535

45.3.3 Defects at Surfaces 1536

45.3.4 Nondilute Systems 1537

45.4 Supplementary Instrumentation and Supportive Techniques 1538

45.4.1 Photo-EPR 1539

45.4.2 Correlation with Electrically Detected Trapping Centers and Defect Levels 1541

45.4.3 Heat Treatment and EPR 1543

45.5 Summary and Final Thoughts 1545

References 1546

46 **Defect Characterization in Semiconductors with Positron Annihilation Spectroscopy**

Filip Tuomisto 1551

46.1 Positron Annihilation Spectroscopy 1552

46.1.1 Positron Implantation and Diffusion in Solids 1552

46.1.2 Positron States and Annihilation Characteristics 1553

46.1.3 Positron Trapping at Point Defects 1556

46.1.4 Experimental Techniques 1557

46.2 Identification of Point Defects and Their Charge States 1560

46.2.1 Vacancies in Si: Impurity Decoration 1560

46.2.2 Vacancies in ZnO: Sublattice and Charge State 1562

46.2.3 Negative Ions as Shallow Positron Traps in GaN 1564

46.3 Defects, Doping, and Electrical Compensation 1565

46.3.1 Formation of Vacancy-Donor Complexes in Highly n-Type Si 1566

46.3.2 Vacancies as Dominant Compensating Centers in n-Type GaN 1568

46.4	Point Defects and Growth Conditions	1569
46.4.1	Growth Stoichiometry: GaN Versus InN	1570
46.4.2	GaN: Effects of Growth Polarity	1572
46.4.3	Bulk Growth of ZnO	1573
46.5	Summary	1576
	References	1576

Part H Special Topics in Crystal Growth

47 Protein Crystal Growth Methods

	<i>Andrea E. Gutiérrez-Quezada, Roberto Arreguín-Espinosa, Abel Moreno ...</i>	1583
47.1	Properties of Biomacromolecular Solutions	1584
47.2	Transport Phenomena and Crystallization	1587
47.3	Classic Methods of Crystal Growth	1587
47.4	Protein Crystallization by Diffusion-Controlled Methods	1588
47.4.1	Crystallization in Microgravity Environments	1588
47.4.2	Crystallization in Gels	1589
47.4.3	Crystallization in Capillary Tubes	1590
47.5	New Trends in Crystal Growth (Crystal Quality Enhancement)	1591
47.5.1	Crystallization Under Electric Fields	1591
47.5.2	Crystallization Under Magnetic Fields	1592
47.5.3	Combining Electric and Magnetic Fields	1593
47.5.4	Robotics and High-Throughput Protein Crystallization	1593
47.6	2-D Characterization via Atomic Force Microscopy (Case Study)	1595
47.6.1	General Overview	1595
47.6.2	Coupling AFM and Electrochemistry for Protein Crystal Growth	1596
47.6.3	AFM Characterization by Protein Immobilization by Means of Polypyrrole Films Deposited on Different Electrodes (HOPG and ITO)	1597
47.7	3-D Characterization via X-Ray Diffraction and Related Methods	1598
	References	1599

48 Crystallization from Gels

	<i>S. Narayana Kalkura, Subramanian Natarajan</i>	1607
48.1	Gel Growth in Crystal Deposition Diseases	1608
48.1.1	Gel Growth of Crystals	1608
48.1.2	Types of Gels	1608
48.1.3	Mechanism of Gelling	1609
48.2	Experimental Methods	1609
48.2.1	Chemical Reaction	1609
48.2.2	Complex Dilution	1609
48.2.3	Solubility Reduction	1610
48.2.4	Chemical Reduction	1610
48.2.5	Electrochemical/Electrolysis	1610
48.2.6	Crystal Growth in the Presence of a Magnetic Field	1610
48.2.7	Nucleation Control	1610

48.3	Pattern Formation in Gel Systems	1610
48.4	Crystals Grown Using Gel Technique	1611
48.4.1	Advantages of Crystallization in Gels	1613
48.5	Application in Crystal Deposition Diseases	1614
48.5.1	Crystal Deposition Diseases	1614
48.5.2	Significance of In Vitro Crystallization	1614
48.5.3	Crystallization of the Constituents of Crystal Deposits	1616
48.6	Crystal-Deposition-Related Diseases	1616
48.6.1	Urinary Stone Disease	1616
48.6.2	Theories of Urinary Stone Formation	1616
48.6.3	Role of Trace Elements in Urinary Stone Formation	1617
48.7	Calcium Oxalate	1617
48.7.1	Crystallization of Calcium Oxalate	1617
48.7.2	Effect of Trace Elements	1618
48.7.3	Effect of Tartaric and Citric Acids	1618
48.7.4	Effect of the Extracts of Cereals, Plants, and Fruits	1618
48.8	Calcium Phosphates	1619
48.9	Hydroxyapatite (HAP)	1620
48.10	Dicalcium Phosphate Dihydrate (DCPD)	1620
48.10.1	Effect of Additives on Crystallization of Calcium Phosphates	1620
48.10.2	Effect of Some Extracts of Cereals, Plants, and Fruits and Tartaric Acid	1622
48.10.3	Calcium Hydrogen Phosphate Pentahydrate (Octacalcium Phosphate, OCP)	1622
48.10.4	Magnesium Ammonium Phosphate Hexahydrate (MAP) and Magnesium Hydrogen Phosphate Trihydrate (MHP) ...	1622
48.11	Calcium Sulfate	1623
48.12	Uric Acid and Monosodium Urate Monohydrate	1623
48.13	L-Cystine	1624
48.14	L-Tyrosine, Hippuric Acid, and Ciprofloxacin	1625
48.15	Atherosclerosis and Gallstones	1625
48.15.1	Crystal Growth in Bile	1625
48.15.2	Cholesterol and Related Steroids	1626
48.15.3	Cholic Acid	1627
48.16	Crystallization of Hormones: Progesterone and Testosterone	1628
48.17	Pancreatitis	1628
48.17.1	Calcium Carbonate	1629
48.18	Conclusions	1629
	References	1630
 49 Crystal Growth and Ion Exchange in Titanium Silicates		
	<i>Aaron J. Celestian, John B. Parise, Abraham Clearfield</i>	1637
49.1	X-Ray Methods	1637
49.1.1	X-Rays and Diffraction Theory	1638
49.1.2	Neutron Diffraction Theory	1640

49.2	Equipment for Time-Resolved Experiments	1642
49.2.1	In-House X-Ray Sources	1642
49.2.2	Synchrotron Radiation Sources	1642
49.3	Detectors	1642
49.3.1	Image Plates	1642
49.3.2	Charge-Coupled Devices	1643
49.3.3	Position-Sensitive Detectors (PSD)	1643
49.3.4	Energy-Dispersive Detectors	1643
49.3.5	Silicon Strip Detector	1644
49.3.6	Other Considerations	1644
49.4	Software	1644
49.5	Types of In Situ Cells	1645
49.5.1	SECeTS Cell	1646
49.5.2	Polyimide Environmental Cell	1647
49.5.3	High-Pressure Cells	1647
49.5.4	Hydrothermal Steel Autoclave-Type Cell	1647
49.5.5	Neutron Diffraction Cell	1648
49.6	In-Situ Studies of Titanium Silicates (Na-TS) with Sitinakite Topology	1649
49.6.1	Introduction to the Problem	1649
49.6.2	Synthesis and Structure of Sodium Titanium Silicate (Na-TS)	1649
49.6.3	Synthesis Problems and In Situ Hydrothermal Study	1650
49.6.4	Ion Exchange of Cs^+ into Na-TS	1652
49.6.5	Cesium Ion Exchange into H-TS	1654
49.6.6	Sodium Niobium Titanosilicate (Nb-TS)	1655
49.6.7	In Situ Synthesis of Na-NbTS	1655
49.6.8	In Situ Ion Exchange of Cesium Ion Exchange in Na-NbTS ..	1656
49.6.9	Cesium Ion Exchange into H-NbTS	1656
49.7	Discussion of In Situ Studies	1658
49.7.1	Synthesis of Na-TS and Na-NbTS	1658
49.7.2	Exchange Mechanisms	1659
49.8	Summary	1660
	References	1660

50 Single-Crystal Scintillation Materials

	<i>Martin Nikl, Anna Vedda, Valentin V. Laguta</i>	1663
50.1	Background	1663
50.1.1	Historical Aspects	1664
50.1.2	Fundamentals	1664
50.1.3	Material Characteristics	1665
50.1.4	Characterization Methods	1668
50.2	Scintillation Materials	1670
50.2.1	Lead Tungstate (PbWO_4) Single Crystals	1670
50.2.2	Aluminum Perovskite $\text{XAlO}_3\text{:Ce}$ ($\text{X} = \text{Y, Lu, Y/Lu}$)-Based Scintillators	1673

50.2.3	Aluminum Garnet $X_3Al_5O_{12}:Ce$ ($X = Y, Lu, Y/Lu$)–Based Scintillators	1677
50.2.4	Ce–Doped Silicate Single Crystals	1681
50.2.5	Ce–Doped Rare–Earth Halide Single Crystals	1684
50.2.6	Optical Ceramics and Microstructured Materials	1687
50.3	Future Prospects	1689
50.4	Conclusions	1691
	References	1691

51 Silicon Solar Cells: Materials, Devices, and Manufacturing

	<i>Mohan Narayanan, Ted Cizsek</i>	1701
51.1	Silicon Photovoltaics	1701
51.1.1	Physics of a Solar Cell	1701
51.1.2	The Photovoltaic Value Chain	1703
51.1.3	The Photovoltaic Module	1703
51.1.4	Commercial PV Technologies	1704
51.2	Crystal Growth Technologies for Silicon Photovoltaics	1704
51.2.1	Silicon Photovoltaics	1704
51.2.2	Single–Crystal Ingot Growth (CZ and FZ)	1705
51.2.3	Multicrystalline Ingot Growth	1707
51.2.4	Silicon Ribbon or Sheet Growth	1709
51.2.5	PV Silicon Crystal Growth Approaches	1711
51.3	Cell Fabrication Technologies	1711
51.3.1	Homojunction Devices	1711
51.3.2	Enhancing Solar Cell Performance	1714
51.3.3	Advanced Commercial Solar Cell Concepts	1714
51.4	Summary and Discussion	1715
	References	1716

52 Wafer Manufacturing and Slicing Using Wiresaw

	<i>Imin Kao, Chunhui Chung, Roosevelt Moreno Rodriguez</i>	1719
52.1	From Crystal Ingots to Prime Wafers	1721
52.1.1	Semiconductor Single–Crystalline Wafers	1721
52.1.2	Alternative Wafer Production Processes	1722
52.1.3	Substrate Manufacturing with a System–Oriented Approach	1723
52.2	Slicing: The First Postgrowth Process in Wafer Manufacturing	1726
52.2.1	ID Saws	1726
52.2.2	The Modern Wiresaw	1727
52.2.3	Saws with Diamond–Impregnated Wires	1727
52.2.4	Others	1728
52.2.5	Comparison of Slicing Technology	1728
52.2.6	Wafer Manufacturing for Large Wafers	1729

52.3	Modern Wiresaw in Wafer Slicing	1730
52.3.1	Definition of Modern Wiresaw	1730
52.3.2	Modern Wiresaw Technology	1731
52.3.3	Modeling and Control of the Modern Wiresawing Process ..	1731
52.4	Conclusions and Further Reading	1733
	References	1733
	Acknowledgements	1737
	About the Authors	1741
	Detailed Contents	1759
	Subject Index	1791

Subject Index

- I_1 type step 1504
 ξ anisotropy factor 67
 α and β dislocation 1345
 α -factor 67, 72
 β -BaB₂O₄ (BBO) 746
 β -BaB₂O₄ (β -BBO) 730
 β -sitosterol 1626
 γ -lithium aluminum oxide (LiAlO₂) 877
 30° and 60°
 – dislocation 178
 60°
 – dislocation 1344
 I–III–VI₂ compound 917
 – growth parameter 917
 2,2-diphenyl-1-picrylhydrazyl (DPPH) 1533
 II–VI compound semiconductor 912
 2-D–3-D transformation
 – in Stranski–Krastanov growth 44
 – in Volmer–Weber growth 44
 2-adamantylamino-5-nitropyridine (AANP) 398
 2-methyl-4-nitroaniline (MNA) 569
 III nitride 1244
 300 mm large wafer 1731
 III–V binary crystal growth technology 292
 III–V compound 193
 III–V material 328
 4H-SiC 954
 – p–n junction 960
 – wafer 812
- ### A
- A defect 1283, 1292, 1322
 ab initio method 1246
 abrasive grit 1733
 abrasive slurry 1730
 absorption at laser Wavelength 499
 absorption coefficient (α) 352
 absorption edge 352
 – spectroscopy (ABES) 1089
 accelerated crucible rotation technique (ACRT) 175, 307, 316, 318, 334, 336, 734, 739
 acceptance angle 714
 acceptor activation 1541
 acceptor passivation 1541
 Acheson
 – method 799
 – process 798
 acidic seeded growth 683
 acoustooptic (AO) 162
 activation energy 1273, 1352
 active inhomogeneity 1471
 additional absorption (AA) 495
 additive decomposition of strain tensor 1342
 adhesion energy 59
 adhesive growth 1596
 adhesive-type growth mechanism 136
 Adornato–Brown pseudo-steady-state model (PSSM) 1383
 ADP
 – rapid growth 126
 adsorbed species 1257
 adsorption
 – isotherm 80
 – of impurity 580
 – process 581
 – site 565
 adsorption isotherm
 – Frumkin–Fowler adsorption 62
 – Henry adsorption 62
 – Langmuir adsorption 62
 adsorption–desorption balance 62
 advanced IR detector 1115
 advanced photon source (APS) 1638, 1647
 advanced protein crystallization facility (APCF) 594
 advantage
 – chemical vapor transport 904
 – crystallization in gels 1613
 AFM characterization 1597
 afterheater 382, 396
 agar 1608
 agar-agar 1618
 AgGaS₂ 731
 AgGaSe₂ 731
 – single crystal 923
 agglomeration of point defects 1338
 Al source instability 828
 Al₂O₃ 442
 Al₂O₃:Cr 395
 Al₂O₃–ZrO₂ 418
 Al₂O₃/GdAlO₃ 417
 Al₂O₃–ZrO₂(Y₂O₃) (ZA) 416
 Albon and Dunning model 79
 Alexander–Haasen model 1351
 alkaline halide flux 741
 alkaline seeded growth 681
 alkyl precursor 1134
 alloy disorder 1109
 alloy segregation in ternary semiconductor 302
 alloying 665, 684
 AlN
 – bandgap 835
 – bulk crystal 827
 etch pit density 834
 etching 827, 834
 growth 821
 prismatic glide 834
 seeded growth 829
 – by HVPE 888
 – cracking 830
 – fundamental optical property 835
 – growth habit 828
 – growth rate 823
 – powder sintering 838
 – seed 831
 AlN/GaN
 – vapor deposition
 characteristic 1251
 mathematical model 1248
 alternative model 1351
 alternative wafer production process 1724
 Aluminum garnet X₃Al₅O₁₂:Ce (X = Y, Lu, Y/Lu)-based scintillators 1677
 aluminum nitride (AlN) 821
 aluminum vapor pressure 823
 ambipolar conduction 347
 amelogenin 1622
 ammonia (NH₃) 1138
 ammonium chloride (NH₄Cl) 873
 ammonium dihydrogen phosphate (ADP) 96
 ammonothermal
 – GaN 681
 – growth system 666
 – solvents 663
 amorphous layer 1492
 analog-to-digital converter (ADC) 1558
 analysis

– dislocation 219
 – gas flow 1251
 – of defects on x-ray topographs 1445
 analytical analysis of heat and mass transfer 1252
 angle fixation 525
 – boundary condition 523
 angular vibration technique (AVT) 1237
 anionic impurity 776
 anisotropic material 1735
 anisotropy 1735
 – of properties 1464
 annealing 190, 438, 466
 – experiment 222
 annihilation 1557
 – characteristic 1553
 annular capillary channel (ACC) 1391
 annular dark field (ADF) 1490
 anomalous birefringence 785
 antimonide-based compounds 294
 antimony (Sb) 328
 antiphase boundary (APB) 944
 antireflection (AR) 1715
 antisite 167
 aperiodic poled LN (APPLN) 258
 apparatus 912
 application 545, 713
 – in crystal deposition diseases 1614
 – of STEM, EELS, and EFTEM 1509
 applied magnetic field 970
 applying steady magnetic field 205
 arbitrary Lagrangian Eulerian (ALE) 1397
 arsenide
 – activation 1106
 – implantation 1105
 – incorporation 1105
 – indiffusion 1105
 – monolayer 1087
 – precursor 1102
 – quantum dot 1133
 arsenide-based compound 296
 arthritis 1619
 as-grown 711
 – SiC crystal 806
 – single crystal 922
 aspect ratio trapping (ART) 1500
 asymmetric reflection 341
 atherosclerosis and gallstones 1625
 atmosphere 406
 atmospheric pressure (AP) 1157

atomic
 – ordering 1485
 – structure 762
 atomic absorption spectroscopy (AAS) 1083
 atomic energy 1195
 atomic force microscopy (AFM) 15, 135, 140, 340, 765, 766, 827, 1081, 1083, 1595
 – step velocity 779
 atomic layer epitaxy (ALE) 1044
 atomistic
 – approach 55
 – point of view 57
 – theory of nucleation
 equilibrium size distribution of clusters 31
 – view of equilibrium 62
 attachment energy 56, 65
 Auger electron spectroscopy (AES) 1083
 Auger recombination 1107, 1108, 1112
 autoclave-type cell 1647
 automatic diameter control (ADC) 247, 399–402
 – for Czochralski crystal growth 251
 – of crystal 249
 automation of VT 521
 avalanche photodiode (APD) 1117
 axial field growth 211
 axial temperature gradient 266
 axisymmetrical problem 523

B

B defect 1283, 1292
 Ba_{0.77}Ca_{0.23}TiO₃ (BCT) 405
 BaB₂O₄ (BBO) 691
 back-contact cell 1717
 background gas 1202
 back-reflection 806
 – SWBXT image 807
 – topograph 806, 810
 baffle design 670
 balance of heat transfer 403
 band anticrossing (BAC) 1140
 – model 360
 band structure 346, 1154
 Bardeen–Herring mechanism 179
 barium rare-earth fluoride (BaREF) 728
 barium titanate 246
 basal dislocation 14
 basal plane 811
 – dislocation (BPD) 15, 806, 810, 1466
 – stacking fault (BSF) 1501
 basal slip 488
 basic dislocation analysis 1445
 basic principle
 – x-ray topography 1426
 BaTiO₃ 410, 411
 BCF (Burton–Cabrera–Frank) 6
 – equation 74
 benzil 100
 benzophenone 99
 Bi₁₂GeO₂₀ (BGO) 270, 442
 Bi₁₂Si₁₂O₂₀ (BSO) 270
 Bi₁₂SiO₂₀ (BSO) 404
 Bi₁₂TiO₂₀ (BTO) 270, 416
 Bi₂₀SiO₂₀ (BSO) 264
 BiB₃O₆ (BIBO) 731
 bidomain 705, 708
 – structure 704
 bile 1626
 binary compound synthesis 293
 binding energy 342, 563
 biological macromolecules
 – nucleic acid 1583
 – polysaccharide 1583
 – protein 1583
 biomacromolecular solution
 – property 1584
 biomimetic recognition 1627
 bioseparation process 592
 Biot 403
 biotechnology 582
 bipolar transistor (BPT) 162
 bipyramidal 1625
 birefringence 161, 692, 1092
 bismuth sillenite Bi₁₂MO₂₀ (BMO) 264
 Bi–Sr–Ca–Cu–O 411
 bleaching impurity 268
 blocker type additive 70
 bootstrapping method 308
 borate 730, 739, 743
 Born approximation (BA) 1413
 boron nitride (BN) 825
 Borrmann effect 1438
 bound exciton (BE) 887
 boundary
 – classification 705
 – condition 515, 1218, 1362
 – layer model 1137
 boundary condition
 – capillary 525
 bow angle 1733
 BOX (buried oxide) 1169
 BPD (basal plane dislocation) 809

- Bragg
 – angle 14
 – line 1488
 – reflection 1486
 – relation 1407
 Bravais law 54
 Bravais–Friedel 137
 Bravais–Friedel–Donnay–Harker (BFDH) law 64
 breaking strain 403
 bridge layer 1031
 Bridgman
 – crystal growth technique 286
 – method 263
 – technique 10, 286, 335
 Bridgman autoclave 618
 Bridgman–Stockbarger (BS) 1379
 – technique 437
 bright field (BF) 1477, 1478
 – image 344
 brittle state 116
 BSCCO 399, 408
 bubble 191
 – precipitation 99
 bubbler 1135
 buffer layer 1083–1085, 1170
 buffered oxide etch (BOE) 960
 building unit (BU) 64
 built-in electric field 704, 705
 bulk
 – crystal growth of ternary III–V semiconductor 281
 – GaN growth 875
 – laser crystal 736
 – species 1257
 bulk growth 801
 – $\text{InAs}_x\text{Sb}_{1-x}$ 335
 – $\text{InBi}_x\text{Sb}_{1-x}$ 337
 – of InSb 334
 bunched growth step 141
 Burgers vector 109, 114, 219, 766, 806, 1446, 1480
 – determination of 114
 – direction 1445
 – magnitude 1446
 – sense 1446
 buried-contact cell 1716
 bursitis 1619
 Burton–Cabrera–Frank (BCF) 54, 577
 – theory 119
 Burton–Prim–Slichter (BPS) 134, 303
 – relation 175
 – theory 416
 – uniform-diffusion-layer model (UDLM) 1380
C
 C/Si ratio 959
 $\text{Ca}_{1-x}\text{Sr}_x\text{MoO}_3$ (CSMO) 406
 $\text{Ca}_2\text{FeMoO}_6$ (CFMO) 406
 cadmium (Cd) 333, 1617
 CaF_2 162, 163, 412
 CaF_2 –MgO 418
 calcification 1629
 calcite 628
 calcium
 – carbonate 1629
 – gallium germanate, $\text{Ca}_3\text{Ga}_2\text{Ge}_4\text{O}_{14}$ (CGG) 1055
 – hydrogen phosphate pentahydrate (octacalcium phosphate, OCP) 1622
 – phosphate 1619
 – phosphate dihydrate 1615
 – sulfate 1623
 – tartrate 1610
 calcium oxalate 1617
 – crystallization 1617
 – dihydrate (COD) 1615, 1617
 – monohydrate (COM) 1615, 1617
 calculation of phase diagram (CALPHAD) 447
 calibration of etching 1467
 calorimetry curve 343
 CaMoO_4 (CMO) 400, 405, 412
 CaO – ZrO_2 418
 capacitance–voltage (C–V) 960, 1541
 capillary
 – boundary condition 525
 – boundary problem for TPS 522
 – boundary problem solution 527
 – problem 517
 – problem – common approach 514
 – shaping technique (CST) 509
 capillary shaping technique (CST) 510
 capping 96
 carrier gas 872, 1260
 carrier lifetime 357
 $\text{CaSrCu}_2\text{O}_4$ 401
 catching boundary condition 523, 525, 526
 cathode luminescence (CL) tomography 149
 cathode-ray luminescence (CL) 135
 cathodoluminescence (CL) 680, 835, 884, 1453, 1467
 CCD (charge-coupled device) 1642
 CdS single crystal 915
 CdTe 162, 168, 171, 184–186, 190, 191
 – growth 1101
 – growth nucleation 1101
 CdTe/GaAs substrate 1077
 CdTe/Si substrate 1076, 1077
 CdZnTe substrate 1076, 1077
 – characterization 1082
 – screening 1082
 Ce-doped rare-earth halide single-crystal 1684
 Ce-doped silicate single crystal 1681
 cell
 – formation 183
 – pattern 181
 – patterning 182, 188
 – size 184
 – structure 182
 cellular
 – growth 376
 – interface 176
 – structure 162, 456, 457
 central capillary channel (CCC) 1391
 cesium ion exchange 1654, 1656
 chalcopyrite 731
 challenges 684
 Chang–Brown quasi-steady-state model (QSSM) 1381
 change of the face character 82
 Chapman–Enskog formula 902
 character of the face 55
 characteristic configuration of growth dislocation 110
 characteristics of CVD process 1248
 characterization 239, 832, 1405
 – method 1668
 – of crystals 377
 – tool 1090
 charge dislocation 351
 charge state 1560, 1562
 charge-coupled device (CCD) 236, 1449, 1643
 chemical
 – characterization 1057
 – etching 340, 806, 881, 1454, 1459
 – inhomogeneity 1339
 – potential 1136
 – reaction 1254
 – reduction 1610
 – transport reaction 902

- chemical vapor deposition (CVD)
800, 899, 900, 939, 946, 1044,
1157, 1206
- chemical vapor transport
– advantage 904
- chemical vapor transport (CVT)
135, 897, 899–901
– technique 1573
– transport kinetics 901
- chemomechanical polishing (CMP)
827, 1167, 1724
– method 1167
- Chernov mechanism
– direct integration 74
- chloride VPE (Cl-VPE) 926
- choice and change of solvent 76
- cholesterol 1626, 1627
- cholesteryl acetate 1627
- cholic acid 1627
- ciprofloxacin 1625
- circular cone shaper wall 523
- circular or polygonal spiral 140
- circumferential stress component
1367
- citric acid 1618
- classical nucleation theory 1291
- cleaning 1725
- cleaning procedures for growth
chamber, crucible, and charge
299
- climb 1350
- close-core screw dislocation 806
- cluster 562
– balance 1301
- clustering in heteroepitaxy 43
- Cl-VPE gallium trichloride (GaCl_3)
926
- CO_2 laser 395
- coalescence front 1014
- cobalt 1621
- cobble texture of quartz (0001) face
104
- coefficient of thermal expansion
(CTE) 500
- coercive field 709
- coherent
– x-ray source 1417
- coincidence lattice 1501
- cold crucible (CC) 437, 441, 442,
466
- cold crucible (CC) 434, 436
- cold-cone seal autoclave 617
- cold-drawn steel wire 1730
- collagen gel 1620
- colony 462
- color center 494
- colored quartz 632
- combining electric and magnetic
fields 1593
- commercial solar cell concept 1716
- common crucible material 249
- comparison of ammonia and water as
solvents 657
- compensating center
– dominant 1568
- compensating defect 1542
- compensation mechanism 221
- compensation ratio 226
- complex dilution 1609
- complexity 1413
- composition 698, 910, 1488
– amplitude 175
– profile 340
– sensitivity 1414
– variation 1420
- compound 165
– semiconductor 8
- computational fluid dynamics (CFD)
1361
- computational issue 1258
- computer tomography (CT) 1687
- concave interface 267
- concentration sensor 774
- concentric ring 1611
- conductivity 349
- congruent
– composition 269
– lithium niobate 254
– lithium niobate crystal 255
– melting 373, 409
– melting fibers – the search for
stoichiometry 409
– melting point 253
- connected net analysis 69
- conoscopic pattern 12
- conservation
– equation 1217
– law of Burgers vectors 109
– of mass 402
- constant-strain-rate compression test
1346
- constitutional supercooling 176,
188, 375, 457
- construction ceramics 444
- consumables in wiresawing process
1735
- contact plane 121
- contact sintering 1715
- contactless chemical vapor transport
technique (CCVT) 1573
- continuous feeding during growth
745
- continuous filtration 781, 788
– system (CFS) 771
- continuous wave (CW) 260
- continuum model 977
- continuum-scale quantitative defect
dynamics in growing Czochralski
silicon crystal 1281
- contrast 1426, 1448
– associated with cracks 1448
– from inclusions 1446
– transfer function (CTF) 1482
- contrast on x-ray topographs 1440
- controlling the growth 1090
- convection 1215
– diffusion (CD) 1398
– flow 144
– in the melt 1362
– pattern 407
- convective stirring 439
- convective frequency 175
- conventional method 771
- convergent-beam electron diffraction
(CBED) 1478, 1486
- cool-down period 1371, 1372
- cooled sting assembly 584
- cooled sting technique 583
- cooperating spiral 119
- coordinate measuring machine
(CMM) 781
- copper gallium diselenide (CuGaSe_2)
898
- copper indium diselenide (CuInSe_2)
898
- copper indium disulfide (CuInS_2)
898
- core 268
– effect 267
– energy of dislocation 113
- correlation with electrically detected
trapping centers and defect levels
1541
- corrosion 567
- corundum 630
- Cottrell atmosphere 1462
- counterdiffusion method 1590
- counterelectrode (CE) 1454, 1455
- covalent state 332
- CP analysis 1097
- crack 1448
- crack formation 304
- crack formation in ternary crystal
304
- cracker cell 1090
- creep curve 1349
- criterion for characteristic defect
formation 237

- critical condition 1324
- critical condition for radiation dominance 1248
- critical layer thickness of dot nucleation 1143
- critical point (CP) model 1095
- critical supersaturation 75
- critical thickness 1161, 1497
- critical-point (CP) energy 1091
- critical-resolved shear stress (CRSS) 177, 179, 1340
- CrO₃/HF/H₂O in the dark 1469
- cross-slip 178, 1350
- CRSS-based elastic model 1340
- crucible free 393
- crucible material 249, 825, 826
- crystal 691
 - characterization 11
 - chemical aspect of Bi substitution in InSb 333
 - cooling 377
 - defect 11, 73, 541, 1478
 - observation 12
 - density 251
 - edge 767, 768
 - grown under unconstrained condition 133
 - habit 565, 578
 - originated particle (COP) 188
 - potential 347
 - rotation and pulling arrangement 249
 - seed holder 572
 - shaping measure 207
 - structure 445
 - structure and bonding 331
 - structure and bonding of InSb 331
 - surface 761
 - truncation rod (CTR) 762
 - twin 213
- crystal deposition
 - disease 1614
 - related disease 1616
- crystal face
 - atomically rough 1002
 - imperfect singular 1002
 - perfect singular 1002
- crystal growth 4, 574, 854, 1335, 1724
 - and ion exchange in titanium silicates 1637
 - classic method 1587
 - control of crystal defects 237
 - from low-viscosity solutions 736
 - Haasen model 1350
 - high-viscous solution 739
 - history 394
 - hydrodynamic effect 781
 - in bile 1625
 - in space 583
 - in the presence of a magnetic field 1610
 - limitation 375
 - new trend 1591
 - nucleation 847
 - of laser fluorides and oxides from melt 479
 - of lithium niobate 252
 - process 1336
 - classification 7
 - rate for crack-free ternary crystal 308
 - SiC 798
 - system 1380
 - technique 6
 - traveling solvent 369
 - termination 377
 - theory 4
- crystal orientation
 - nonstandard 951
- crystal quality 783, 1592
 - enhancement 1591
 - spectroscopic study 783
- crystalline
 - defect 1079
 - fiber 407
 - imperfection 805
 - layer structure 1405
 - quality 13
 - SiC 799
 - silico titanate (CST) 1650
 - silicon 240
- crystallization 452, 561, 1587
 - capillary tube 1590
 - electric field 1591
 - energy 65
 - front 516
 - front instability 376
 - gel 1589
 - high-throughput 1594
 - in gels 1613
 - magnetic field 1592
 - microgravity environment 1588
 - of calcium oxalate 1617
 - of hormones 1628
 - of hormones: progesterone and testosterone 1628
 - of the constituents of crystal deposits 1616
- crystallizer 569
- reciprocating motion 575
- crystallographic
 - orientation 454
 - plane 694
 - shape 768
- crystallography
 - law 54
- crystal–melt system 517
- CsTiOAsO₄ (CTA) 692
- CuAlSe₂ crystal 919
- cubic solid solution 444
- cubic zirconia 435
- CuGaS₂ 922
 - based single crystal 921
- CuInTe₂ crystal 920
- Curie temperature 697–699, 701, 702, 705
- Curie–Weiss law 697
- cusped field growth 212
- CVD (chemical vapor deposition) 798
 - epitaxial film 801
 - reactor configuration 947
- CVT
 - reaction 903
 - ZnSe–I₂ system 905
- CVT growth
 - chemical parameter 903
- CVT growth of crystals 904
- geometrical parameter 904
- CVT method
 - advantage 904
 - limitation 904
- cystinosis 1624
- cystinuria 1624
- cytochrome c 1598, 1599
- CZ defect dynamics 1291, 1316, 1318, 1330
 - absence of impurity 1329
 - lumped model 1297
 - the quantification 1299
- Czochralski (CZ) 312, 501, 1215, 1281, 1706
 - crystal growth system 249
 - defect dynamics 1304, 1313
- Czochralski growth 192, 335, 713
 - of organic crystal 99
- Czochralski growth system
 - design 247
 - development 247
- Czochralski method 9
 - of crystal growth 246
- Czochralski silicon 232
- conventional 232
- crystal
 - vacancy 1321
- Czochralski technique 1336

Czochralski technique (CZT) 441,
480, 509

D

D defect 1283, 1322
dark field (DF) 1477, 1478
Dash seeding 216, 218
Davey and Mullin model 79
dead zone 76, 80, 81, 780
Debye–Waller factor 1487
deceleration of plasma 1202
decomplexation 1613
decomposition of nitrogen precursor
1138
decorated dislocation 15
deep positron state 1554
deep-level transient spectroscopy
(DLTS) 950, 1539, 1541, 1542
defect 1565
– at an interface 1535
– characterization 1551
– control 205
– density 15, 883
– formation energy 165
– impurity effect 776
– in AlN/GaN films originating from
SiC substrate steps 1503
– in crystal 380
– in SiC 942
– level 1541, 1543
– mapping 225
– of crystal 776
– passivation 1087
– selectivity 1459
– site 35
defect dynamics 1284, 1310, 1324
– general 1322
– in one-dimensional crystal growth
1308
defects
– in a thin film on a substrate 1534
defects at surfaces 1536
defect-selective etching (DSE)
1453, 1461
deformation
– behavior of semiconductor 1346
– plastic 156, 183
– potential (b) 356
– stage 1347
degenerate 346
degeneration 453
– crystal orientation 453
– crystal size 453
– geometric selection 453
deionized (DI) water 299

deleterious effects of dislocation
1337
density 733
dental calculus 1619
depolarization 1091, 1093, 1099,
1100
deposition rate 1269
– expression 1272
– prediction 1270
deposition uniformity 1269
desolvation at surface site 76
detectivity (D^*) 357, 590
detector 1642
– noise 590
– response 1116
determination of Burgers vector
– direction 1445
– sense and magnitude 1446
determination of line direction 1445
detrapping 1557
deuterated KDP crystal 786
deuterated potassium dihydrogen
phosphate (DKDP) 96
deuterated triglycine sulfate (DTGS)
575, 579
developing new material 1044
developments in liquid-phase ELO
growth 1027
deviation from calculated direction
113
deviation from stoichiometry 165
device-grade ternary substrate 284
dewetting 265
diameter control 401
diamond 149
– abrasive grit 1728
– cubic 1485
– growth (DIA) 1647
– impregnated wire 1731
– structure of the crystal 1343
dicalcium phosphate
– (DCP) monetite 1619
– dihydrate (DCPD) 1615, 1620
dichlorosilane (SiH_2Cl_2) 882
dielectric function library
1092–1095
differential interference contrast
– (DIC) 1464
– microscopy (DICM) 135
differential scanning calorimetry
(DSC) 261
differential thermal analysis (DTA)
331, 370, 373
diffraction
– contrast 1478
– contrast imaging 1479

– efficiency 259
– image 589
– technique 1484
– theory 1638
diffuse scattering 1416
diffuse scattering of x-ray 333
diffuser plate 1088, 1089
diffusion 166, 800, 1003
– coefficient 583, 902
– in solids 1552
– layer 375
– theory 5
diffusion-controlled
– crystallization apparatus for
microgravity (DCAM) 594
– method 1588
– process 591
diglycine sulfate (DGS) 578
dilute nitride quantum well laser
1141
diluted nitrides 1133
diluted Sirtl with light (DSL) 175,
1460
dimensionless group 1251
dimethylhydrazine ($(\text{CH}_3)_2\text{NNH}_2$)
1138
dipole of dislocations 178
direct current (DC) 408
direct dislocation image 1442
directional crystallization 437, 440,
450, 454
directional solidification (DS) 1707,
1709
– by normal freezing 309
– by solute diffusion and
precipitation 310
discrete lattice structure 113
discrete rate equation 1299
disilane (Si_2H_6) 882
dislocation 107, 160, 161, 176, 340,
497, 543, 566, 588, 676, 883, 1086,
1110, 1409, 1469
– 30° and 60° 178
– 60° 1344
– analysis 177, 1488
– bunching 185, 186
– bundle 181, 187
– core observation 1483
– density 12, 179, 216, 344, 404,
785, 1085, 1365
– different types 1351
– dipole 109
– dynamics 178
– dynamics (DD) 177
– edge dislocation 109
– engineering 187, 1170

- free mechanism 767
- generation 152, 155, 1335
- geometrical position 1465
- glide 184
- glide velocity 1352, 1355
- in ELO layers 1011
- in semiconductor material 1337
- in SiC 1466
- jungle 182
- lineage 181
- loop 168, 180
- loop–hole configuration 813
- mechanism 765
- misfit 1417
- multiplication 180, 1338, 1355, 1356
- nucleation 1338
- pivot 812
- redirection in AlN/sapphire
 - epilayer driven by growth mode modification 1507
- reduction during seeding 217
- screw dislocation 109
- slip 220
- threading 1417
- type 177
- wall 187
- disorientation angle 181
- dispersion surface 1437
- displacement
 - rate 516
 - reaction 1623
 - reaction method 1609
- dissipative structuring 184
- dissolution 151
- distinction between natural and synthetic gemstones 155
- distorted-wave Born approximation (DWBA) 1413
- distributed Bragg reflector (DBR) 1176
- distribution coefficient 170, 333, 456, 460, 738
- distribution of dislocation density 1366
- distribution of impurity 778
- domain 704
 - boundary 705, 706
 - formation 704
 - kinetics 704
 - polarization 257
 - switching 252
- domain structure 258, 462, 463, 691
 - artificial 708
 - ferroelectric 691
- Donnay–Harker 137

- donor concentration 348
- donor defect EL2 173
- dopant
 - activation 1104
 - concentration 1059
 - distribution 406
 - recharging 173
 - solubility 171
- doped crystal 918
 - of CuAlS₂ 918
 - of CuAlSe₂ 919
- doped LGT LPE film 1057
- doped lithium niobate crystal 260
- doped TGS 580
- doping 665, 678, 684, 1355, 1565
 - extrinsic 1104
 - incorporation technology 949
 - n-type 1104
 - of sillenite 270
 - p-type 1104, 1105
 - technique for GaN in HVPE 882
- Doppler broadening 1553
 - spectroscopy 1559
- DOS (density of states) 789
- dot formation 1177
- dot-in-a-well (DWELL) 1147
- double crucible in the CZ (DCCZ) 254
- double diffusion 1612, 1613
- double layer ELO (2S-ELO) 878
- double tungstate 736, 737
- double-crucible Czochralski (DCCZ) 255
- double-crucible technique 443
- driving force 136
- drug design 592
- DSE of InP 1464
- DSL system 1470
- Dupré's formula 58
- dyeing of crystal 103
- dynamic polygonization 183, 185
- dynamic reflectance spectroscopy (DRS) 1089
- dynamic stability of crystallization (DSC) 509
- dynamical image 1443
- dynamical theory 1413
 - of x-ray diffraction 1436
- dynamical x-ray theory 215

E

- Eagle–Picher (EP) 1573
- early theoretical and modeling study 971
- eccentricity of spiral steps 154

- EDAX spectrum 344
- edge defined film fed growth (EFG) 538
- edge dislocation 6, 119, 178, 219, 342
 - growth-promoting 119
- edge facet 213
- edge ring 1322
- edge-defined film fed growth (EFG) 394, 1379, 1389, 1706
- edge-ring 1327
- edge-supported pulling (ESP) 1706
- EELS 1509
 - application 1509
 - application in microanalysis 1509
 - elemental analysis 1491
 - fine edge to study interface material 1509
 - spectrum 1491
 - study of Mn diffusion 1509
- E-etch 1463
- effect of additives on crystallization of calcium phosphates 1620
- effect of convection in solution growth 563
- effect of decoration and composition 1465
- effect of dislocation 785
- effect of flow rate on substrate temperature 1266
- effect of impurities 564
- effect of impurities on TGS crystal growth 579
- effect of impurity concentration and supersaturation 80
- effect of magnetic field on crystal twinning 210
- effect of magnetic field strength 984
- effect of seed 142, 145
 - crystal 577
- effect of tartaric and citric acids 1618
- effective diffusion length 1274
- effective distribution coefficient 149, 407, 409, 712
- effective mass 346
- effective medium approximation (EMA) 1099
- effective nonlinear coefficient 709
- effective segregation coefficient 172
- effective stress 1357
- effusion cell 1089
- EFTEM 1509
 - to enhance contrast 1512
 - to map elemental distributions 1512

- to reduce diffraction contrast 1512
- Ehrlich–Schwoebel barrier 39
- eight-membered ring (8MR) 1650
- EL2 defect 167
- elastic energy of dislocations 1466
- (elastic) stress response 1342
- elastohydrodynamic interaction 1734
- electric field 407
- poling 708
- electric level 990
- electrical assisted laser floating zone technique (EALFZ) 408
- electrical compensation 1565
- electrical conductivity 261
- electrically active inhomogeneity 1471
- electrically detected magnetic resonance (EDMR) 1546
- electrically detected trapping 1541
- electrochemical etching 1454, 1459
- electrochemical/electrolysis 1610
- electroless etching 1456, 1460
- electroless etching for revealing defects 1469
- electroless etching in the dark 1457, 1460
- electroless photoetching 1457, 1460
- electromagnetic (EM) 207
- electromagnetic casting (EMC) 1707
- electromagnetic Czochralski (EMCZ) 1238
- electromagnetic mobility 992
- electromigration 971, 1028
- electron beam (EB) 1181
- interaction 1199
- plasma generator 1199
- electron cyclotron resonance (ECR) 1087
- electron energy-loss spectroscopy (EELS) 380, 1478, 1486, 1489
- electron ionization 271
- electron microprobe analysis (EPMA) 380
- electron nuclear double resonance (ENDOR) 1546, 1669
- electron paramagnetic resonance (EPR) 15, 495, 680, 695, 1521
- electron spin resonance (ESR) 1521, 1669
- electron trap center 716
- electron-beam induced current (EBIC) 549, 944, 1453
- electronegativity 359
- electronic balance 249
- electron-nuclear double resonance (ENDOR) 715
- electrooptic (EO) 262, 691
- effect 271
- element partitioning 134, 147, 149
- in different growth sectors 150
- elemental spiral 141, 153
- elimination of crack 306
- ellipsoidal mirror 369
- ellipsometer design 1091
- ELO
- choice of growth technique 1004
- filtration of dislocation 1001
- filtration of dislocations 1011–1014
- growth anisotropy 1005
- growth enhanced by dislocation 1006, 1008, 1025
- growth retarded by doping 1009, 1010
- mask-induced strain 1017–1024
- perfection of coalescence front 1014–1016
- surface supersaturation in LPE 1007
- thermal strain 1024
- ELO growth
- new concept 1030
- emerald 141, 631
- emissivity of the liquid surface 272
- emitter formation 1714
- encapsulation height 1371
- end chain energy (ECE) 67
- energetic condensation 1193
- energy factor of dislocation 111
- energy gap 329
- energy minimization 405
- energy-dispersive detectors 1643
- energy-dispersive x-ray analysis (EDAX) 340, 380
- energy-dispersive x-ray spectroscopy (EDS) 1478
- energy-dispersive x-ray spectroscopy (TEM-EDS) 1486
- energy-filtered transmission electron microscopy (EFTEM) 1478, 1490, 1515
- energy-loss near-edge structure (ELNES) 1492
- enthalpy 164
- entropy 164
- of fusion 192
- environmental concern 1735
- environmental effect 664
- epilayer
- InAs_xSb_{1-x} 338, 355
- InBi_xSb_{1-x} 339, 355
- InSb 337, 355
- epilayer uniformity 1108, 1109
- EPiR Technologies 1102
- epitaxial film 746, 802
- of laser material 746
- epitaxial lateral overgrowth (ELO) 113, 877, 999, 1000, 1002, 1042
- of semiconductors 999
- epitaxial relationship 1049
- epitaxy 593
- GaN/AlN/SiC 1506
- epitaxy of nitride
- substrate 1061
- epitaxy within the structural field of KTP 748
- EPR analysis 1524
- EPR technique 1534
- equation
- conservation 1217
- equilibrium
- concentration of clusters 29
- crystal 57
- crystal–ambient phase 18
- curve 1585
- distribution 170
- form 137
- of infinitely large phase 18
- of small crystal with the ambient phase 20
- phase diagram 330, 331
- shape (ES) 55, 60, 66
- shape crystal 58
- shape of crystals 22
- surface profile 66
- thermodynamics 1075
- vapor pressure 1260
- equipment for time-resolved experiments 1642
- error function (erfc) 1714
- estimation of the electromagnetic mobility value 993
- etch pit density (EPD) 177, 188, 334, 1077, 1083, 1341, 1461
- etch pit pattern 340
- etchant composition 1464
- etching anisotropy 215
- etching in the dark 1457
- etching of multilayer laser structures 1468
- etching of semiconductors 1453
- ethyl alcohol 575
- ethyl vinyl acetate (EVA) 1705
- ethylene dithiotetrathiafulvalene (CH₂NH₂)₂C₂H₄O₆ (EDT) 569

EuAlO₃ 412
 eutectic 411
 – fiber 416
 – solidification 383
 evaporating fiber 416
 evolution of crystal growth under
 applied magnetic field 206
 evolution of crystal habit 85
 evolution of interfaces 989
 evolution of internal variables and
 plastic strain 1342
 evolution with growth 1099
 Ewald sphere 1486
 excess shear stress 1341
 exchange mechanisms 1659
 expansion of plasma 1199
 experimental details of ceramics
 preparation for OFZT 372
 experimental simulation study 733
 experimental tests of the capillary
 shaping statement 530
 expression system
 – membrane protein 1594
 extended atomic distance mismatch
 (EADM) 1502
 extended imperfection 676
 external force 1228
 extinction contrast 1441
 extract
 – cereal 1618
 – fruit 1618
 – plant 1618
 extrinsic atom 172
 extrinsic point defect 170

F

F (flat) face 138
 face character 66
 faces of TGS 578
 facet 160, 191, 192, 490, 544
 – formation 193
 – interface 191
 – sector 104
 faceting of rounded surfaces 96
 factor affecting growth form 143
 factors influencing morphology of
 pits 1462
 factors influencing the crystal habit
 71
 fast Fourier transform (FFT) 1506
 fault
 – Shockley 813
 feed rod 369
 femtosecond laser irradiation (FSLI)
 1591

fermentation process 592
 Fermi level 353, 1355
 – effect 171
 ferritin 1599
 ferroelastic switching 125
 ferroelectric
 – domain 700, 703, 707
 – material 273
 – phase transition 697
 FFT (fast Fourier transform) 1506
 fiber growth 409
 fiber pulling 394
 field effect transistor (FET) 860,
 863, 968, 1153
 figure of merit (FOM) 483
 film growth 1204
 filtration 780
 – of substrate dislocations in ELO
 1011
 fingerprinting of cut stones 155
 finite crystal 57
 finite element 1361
 fitting to a library 1097
 flame fusion technique 9
 flat 562
 – bottomed etch pit (F-type) 139
 – face (F-face) 55
 – interface 263
 flight crystal growth cell 586
 flight hardware 584
 flight optical system 586
 floating zone (FZ) 367, 394, 509,
 583, 1281, 1304, 1706
 – advantage 370
 – limitation 370
 – temperature gradient 370
 flow
 – control 1228
 – pattern 669, 670, 672
 – simulation 872
 – structure 1219
 flow and heat transfer 666
 fluctuation of growth conditions
 143
 fluctuation of growth conditions
 (growth accidents) 96
 fluid experiments system (FES) 584
 fluid field 585
 fluids experiment system (FES) 586
 fluorescence quenching 496
 fluoride 728, 738
 flux 375
 – growth 9, 725
 – technique (FT) 487, 503
 focal-plane array (FPA) 1069, 1118
 focused ion beam (FIB) 1467, 1493

foggy inclusion 776
 Fokker–Planck equation (FPE)
 1290, 1299, 1301
 forced convection 266, 564
 foreign adsorption 61
 foreign particle 95, 1339
 foreign substrate 1275
 forest dislocation 1358
 formation of 3-D nuclei on unlike
 substrate 25
 formation of quantum wells,
 superlattices, and quantum wire
 1173
 fourfold symmetry 1341, 1366
 Fourier-transform infrared
 spectroscopy (FTIR) 261, 1079,
 1083, 1089, 1108
 Frank fault 813
 Frank partial dislocation 807
 Frank's conservation law 109
 Frank–Read mechanism 178
 Frank–Read source 812
 Frank–van der Merwe growth 20
 Frank–van der Merwe growth mode
 1073
 free abrasive machining (FAM)
 1724, 1730, 1733
 free carrier absorption (FCA) 354
 free convection 266
 free energy 562
 Frenkel
 – defect 166
 – reaction 1304
 – reaction dynamics 1284
 frequency conversion 760
 frequency doubling 692, 710
 friction coefficient 464
 from crystal ingot to prime wafer
 1723
 front stability 375
 full width at half maximum (FWHM)
 12, 830, 886, 1077, 1079, 1082,
 1110, 1409, 1558, 1639
 fully overgrown ELO structure
 1014
 fundamental dislocation theory 816
 fundamentals
 – LPE 1042
 furnace construction 247

G

GaAs 162, 166, 169–171, 175, 179,
 182, 183, 186, 190, 231, 350, 355,
 876
 – system 994

- wafer 181
- gallbladder 1626
- gallium
 - berlinite 625
 - evaporation 1262
 - iodine vapor growth 1245
 - monochloride (GaCl) 926
- galvanomagnetic application 358
- galvanomagnetic device 358
- GaN 655, 663, 1410
 - by HVPE 927
 - by VPE 925
 - deposition rate 1271
 - film growth 925
- GaN film 928
 - characterization 928
- GaN IVPE growth
 - modeling 1258
- GaN/AlN
 - film growth 1274
 - vapor-growth system 1244
- GaN/AlN/SiC epitaxy 1506
- GaP 170
- gas convection 1368, 1373
- gas mixing process 1267
- gas phase 1256
- gas-phase reaction 1256
 - analysis 1259
- gas-source MBE (GSMBE) 946, 1141, 1160, 1177
- Gaussian reflector 397
- Gd₂SiO₅:Ce (GSO) 1681
- Ge condensation method 1169
- Ge substrate 1088
- Ge_{1-x}Si_x 163
- gel
 - acupuncture method (GAME) 1590
 - method 560
 - system
 - pattern formation 1610
 - technique 1611
- gel growth 566
 - of crystals 1608
- gelling 1609
- gemstone 629
- general
 - defect dynamics 1322
- general formulation 28
- general purpose autoclave 618
- generation
 - of defects 93
 - of micropipes 804
 - of point defect 1345
- genomics 1584
- geometric factor 343
- geometric partial misfit dislocation (GPMD) 1503
- geometrical partial misfit dislocation (GPMD) 1506
- geometrical position of dislocations with respect to the surface 1465
- geometrically necessary boundary (GNB) 182
- geometry optimization 1268
- Ge-on-insulator (GOI) 1170
- GeTe 168
- g-factor 329
- Gibbs free energy equation 1586
- Gibbs–Thomson effect 1004, 1008, 1030
- Gibbs–Thomson equation 5
- g-jitter 584
- glacial acetic acid (CH₃COOH) 299
- glancing incidence 345
- glass synthesis by skull melting 465
- glass-forming melt 438
- glass-forming region 467
- glide dislocation 1344
- global modeling 184
- globular cell morphology 183
- glow discharge mass spectrometry (GDMS) 211, 839, 1522
- glow discharge mass spectroscopy (GDMS) 222
- governing equation 1305, 1314
- graded buffer 1165, 1498
 - and insertion of strained layers 1498
- graded double layer heterojunction (DLHJ) 1116
- graded layer 1414
- gradient freezing technique 288
- grain boundary 160, 162, 184, 464
- grain expansion 831
- grain-free growth 185
- graphite component 803
- graphitization of SiC 805
- Grashof number 564
- gravitational force 588
- gray track 691, 700, 715
 - center 715
 - formation 716
- grazing incidence
 - imaging 807
 - small-angle scattering 1418
 - SWBXT 808
 - XRT 815
- green-radiation-induced infrared absorption (GRIIRA) 716
- grinding 1724, 1731
- grooved cylindrical wire guide 1732
- ground-based cooled sting apparatus 585
- group I dopant 1106
 - diffusion 1106
 - incorporation 1106
- group III nitride 821
- group V dopant incorporation 1106
- growing CZ crystal
 - reactions 1304
- growth 239, 1027, 1711
 - angle 515
 - angle certainty 530
 - axis 1372
 - band 151
 - banding 146
 - chemistry 869
 - condition 152, 776, 1569
 - control 1101
 - defect 269
 - dislocation 107, 805, 1358
 - facet 460
 - from melt 9
 - habit 577
 - hardware 1088
 - hillock 103, 114
 - history 147
 - interface (G) 306
 - interruption (GRI) 1145
 - law 74
 - mechanism 582, 970, 1052
 - parameter 1052
 - period 1365
 - pit 943
 - polarity 1572
 - procedure 1101
 - process 1135
 - spiral 806
 - stoichiometry 1570
 - striae 456
 - striation 213, 455
 - surface evolution 1274
 - technology for silicon photovoltaics 1706
 - temperature 578, 910
 - twin 121
 - under controlled atmosphere 405
 - unit 164
 - using compositionally graded feed 315
- growth form 137, 143
 - of polyhedral crystals 143
- growth from
 - crystal edge 767
 - large-volume melt 311

- supercooled melt 99
- growth history and internal morphology 148
- growth kinetics 73, 561, 577, 664, 1249
- of CVD process 1250
- growth of
 - AgGaS₂ 923
 - bulk crystals 1215
 - bulk sillenite crystal 264
 - compounds 8
 - GaN films 1206
 - III-nitrides with halide vapor-phase epitaxy (HVPE) 869
 - lattice-mismatched ternary on binary using quaternary grading 311
 - lithium niobate crystal 252
 - organic semiconductor 846
 - photorefractive bismuth silicon oxide crystal 272
 - silicon crystals of semiconductor grade by Czochralski (CZ) technique 232
 - sillenite crystals and its characteristic 264
 - single crystals based on zirconium dioxide 443
 - thick layer 337
- growth of CZ crystal 449
 - equipment 449
 - flowsheet 450
 - impurity 451
 - melt formation 450
 - melt propagation 451
 - melting 449
 - mode of melting 451
 - raw material 449
- growth on
 - spheres 96
 - templates 877
 - two-dimensional nucleus 767
- growth rate 5, 306, 457, 805, 970, 994
 - anisotropy 376
 - determination method 290
 - dispersion 106
 - in LPEE 992
 - linear 712
 - parameter 769
- growth sector (GS) 101, 102, 146, 147, 677, 700, 701, 706
 - boundary 101, 102, 105
- growth shape 66
 - structural and bond-energy approach 64

- growth system 1062
 - and optimization 1062
- growth technique 134, 769
- for single crystals 769
- growth unit (GU) 64
- gypsum 1623

H

- habit change 69
 - with supersaturation 75
- habit modification 576
- habitus 144
- Hagen–Strunk mechanism 1494
- hair inclusion 98
- hairlike inclusion 780
- hairpin dislocation 119
- half-crystal position 19
- half-loop array (HLA) 811
- halide vapor-phase epitaxy (HVPE) 869, 1245
- Hall effect 1107, 1108
- Hall factor 348
- hanging drop method 592
- Hartman–Perdok theory 64
- heat and mass transfer 1251, 1252
- heat shield 439
- heat transfer 563
- heat treatment 1543
- heat-exchanger method (HEM) 480, 483, 502
- heating method 247
- helical Liesegang ring 1611
- hematite 141
- heteroepitaxial semiconductor system 1494
- heterogeneous nucleation 58, 910
- heteropolar crystal 6
- heterostructure bipolar transistor (HBT) 162, 1153
- hexagonal dislocation loop 1351
- hexamethyldisilane (HMDS) 947
- Hg absorption 1098
- Hg adsorption 1098
- (Hg,Cd)Te 175
- HgCdTe 1069, 1071, 1072
- HgCdTe (MCT) 328
- HgCdTe growth 1078, 1079, 1102, 1103
- HgTe/CdTe superlattice (SL) 1112
 - Auger recombination 1113
 - energy gap 1113, 1114
 - experimentally observed property 1114
 - growth 1114
 - growth quality 1115
- interdiffusion 1113
- interfacial roughness 1115
- inverted band 1113
- optical absorption 1113
- theoretical property 1113
- high nitrogen pressure (HNP) 1564
- high resolution x-ray diffraction (HRXRD) 929
- high speed IR detector 1117
- high-angle annular dark field (HAADF) 1490
- high-angle annular dark field in scanning transmission electron microscope (HAADF-STEM) 380
- high-angle annular dark-field scanning TEM (HAADF-STEM) 1484
- high-density protein crystal growth system (HDPG) 594
- high-electron-mobility transistor (HEMT) 968, 1059, 1172
- higher-order Laue zone (HOLZ) 1486, 1488, 1496
- high-frequency device 798
- high-frequency heating 248
- high-index surface 1077
- high-level waste (HLW) 1649
- highly n-type Si 1566
- highly oriented pyrolytic graphite electrode (HOPG) 1597
- highly vacancy-rich condition 1323
- high-operating-temperature (HOT) 1118
- high-potassium KTP 710
- high-power device 798
- high-power electron beam 1199
- high-pressure ammonothermal technique (HPAT) 684
- high-pressure cells 1647
- high-quality bulk crystal
 - characterization 832
 - structural property 832
- high-quality crystal 1584
- high-resolution multiple-crystal diffractometer 1412
- high-resolution transmission electron microscopy (HRTEM) 177, 380, 1478, 1482
- high-resolution x-ray diffraction 1406
- high-resolution x-ray diffraction (HRXRD) 340, 833
- high-temperature
 - CVD (HTCVD) 801
 - glass 465

- growth 560
 - materials compatibility 825
 - solution (HTS) 9, 731
 - solution growth 725, 799
 - bulk growth 801
 - superconductor (HTSC) 373, 1042, 1046
 - hillock 704
 - hippuric acid 1625
 - historical development of LPE 1042
 - HIT cell 1717
 - hollow core (micropipe) 806
 - hollow morphology 1625
 - hologram thermal fixing 261
 - holographic
 - image 260
 - interferometry 586
 - optical element (HOE) 587, 589
 - tomography 584
 - HOLZ line 1488
 - homoepitaxial ELO layer 1017
 - homoepitaxial layer 811
 - homoepitaxial LGT LPE film growth 1056
 - homoeptitaxy 1056
 - homogeneity 133, 784, 1421
 - homogeneous nucleation 909
 - homogenization 466
 - homojunction device 1713
 - homopolar crystal 6
 - horizontal Bridgman (HB) 169, 1216
 - crystal 287
 - technique (HBT) 485, 502
 - horizontal gradient freezing (HGF) 288
 - horizontal ZM (HZM) 1216, 1223
 - hot-wall CVD 801
 - hot-wall Czochralski (HWC) 170
 - hourglass inclusion 97
 - hydrazine (H_2NNH_2) 1138
 - hydride vapor-phase epitaxy (HVPE) 656, 681, 899, 925, 926, 1001, 1564, 1568, 1572
 - hydrochloric (HCl) 299
 - hydrodynamic
 - condition 782
 - effect 781
 - film and hydrodynamic interaction 1734
 - principle 209
 - hydrodynamics 85, 98
 - of the solution 733
 - hydrofluoric acid (HF) 299
 - hydrogen ion concentration (pH) 1609
 - hydrogen passivation of defects 1087
 - hydrogen passivation of Si surface 1101
 - hydrogen–vacancy complex 223
 - hydrothermal (HT) 1573
 - condition 610
 - method 8
 - steel autoclave-type cell 1647
 - hydrothermal growth 599
 - apparatus 615
 - growth kinetics 674
 - hydrodynamic principle 606
 - morphology 674
 - of fine crystals 634
 - thermodynamic basis 606
 - thermodynamic modeling 608
 - ZnO crystals 674
 - Hydrothermal ZnO 674
 - hydroxyapatite (HAP) 608, 1615, 1620
-
- ID saw 1730
 - identification flat (IF) 1463
 - idler 714
 - image force 110
 - image plates (IP) 1642
 - imaging 1478
 - immersion-seeded KTP 694
 - immobilization 468
 - impact ionization 1117
 - imperfect layer 1408
 - imperfect structure 1413
 - imperfection 566, 590
 - impurity 160, 458, 577, 580, 678, 699, 838, 1284
 - concentration 11, 770, 777
 - decoration 1560
 - distribution 534, 1380, 1389
 - effect 144, 776
 - effectiveness 80
 - getter region 268
 - incorporation 711, 839
 - segregation 220
 - impurity adsorption 78
 - theoretical growth 69
 - In bump connector 1119
 - in situ
 - cell 1645
 - control 169, 170, 1727
 - ion exchange 1656
 - studies of titanium silicates 1649
 - study 1658
 - synthesis of Na-NbTS 1655
 - x-ray experiment 1419
 - InAs/GaAs
 - quantum dot 1142
 - $\text{InAs}_x\text{Sb}_{1-x}$ 342, 345, 349, 350, 352, 353
 - transmission spectra 353
 - $\text{InAs}_x\text{Sb}_{1-x}$ 330
 - $\text{InBi}_x\text{Sb}_{1-x}$ 331, 344, 345, 350, 352, 355
 - InBiSb 347
 - incandescent heating 367
 - incidental dislocation boundary (IDB) 182
 - inclusion 95, 160, 163, 186, 255, 456, 458, 491
 - incorporation 190
 - primary 95
 - secondary 95
 - trapping 191
 - zonal 97
 - incongruent melting 370, 416, 726
 - incongruently melting 373
 - incorporation coefficient 172
 - indirect laser-heated pedestal growth (ILHPG) 397
 - indium (In) 328
 - bismuth (InBi) 328
 - bismuth arsenic antimonide ($\text{InBi}_x\text{As}_y\text{Sb}_{1-x-y}$) 329
 - phosphide (InP) 205, 231
 - tin oxide electrodes (ITO) 1597
 - induction
 - furnace 272, 803
 - heater 253
 - heating 247
 - heating system 249
 - period 764
 - industrial
 - bulk growth 802
 - crystallization 77
 - production 435
 - inertial confinement fusion (ICF) 759
 - infinite crystal 57
 - infrared (IR) 15, 162, 283, 328
 - absorption 224, 488, 716
 - active lattice mode 355
 - detector 1118
 - laser scattering tomography 189
 - photodetector 357
 - InGaAsN
 - electronic property 1139
 - nitrogen precursor 1139
 - quantum wells 1137
 - valence band offset 1140
 - inhibitor 1465, 1616

- inhomogeneity of impurity 544
 inhomogeneous 337
 initial dislocation density 1358
 initial incorporation 1285
 InN by HVPE 890
 inner diameter (ID) saw 1728
 inner-diameter (ID) 1722
 InP 180, 185, 194
 in-plane scattering 1418
 InSb 191, 192, 330, 340, 350, 352
 – wafer 342, 352
 InSb substrate 1088
 inspection 1726
 integrated circuit (IC) 1706
 interaction between dislocations 1356
 interaction coefficient 1358
 interface 359, 1501
 – defect 1543
 – diffusion 167
 – growth kinetics 268
 – kinetics 193
 – of epitaxial systems 1483
 – processing 1193
 – roughness 1415
 interface type
 – castellated 1416
 – fractal 1416
 – staircase 1416
 interference-contrast microscope (DICM) 140
 interferogram 591
 intermediary image 1444
 internal detector noise 1116
 internal morphology 146
 internal stress 543
 International Microgravity Laboratory (IML-1) 582, 583
 intersecting stacking fault 1506
 interstitial 167
 interstitial atom 160
 intrasectorial sector 146
 intrinsic
 – carrier concentration 349
 – defect 260
 – point defect 172, 1284
 – point defect balance 1285
 – point defect property 1327
 inversion domain (ID) 1464, 1472
 – boundary (IDB) 1501
 inverted temperature gradient method 832, 839
 in vitro crystallization 1614
 iodine
 – gallium reaction 1261
 – vapor pressure 1260
 – vapor-phase epitaxy (IVPE) 1243, 1245
 ion acceleration 1200
 ion beam etching (IBE) 625
 ion chamber (IC) 1645
 ion current 1205
 – of plasma propagating in ambient gas 1205
 ion energy 1200
 – spectrum 1201
 ion exchange 708, 1652
 – of Cs⁺ into Na-TS 1652
 ion implantation 1105
 – method 1168
 ion-beam-assisted deposition (IBAD) 1204
 ionic conductivity 694, 710
 ionized impurity scattering 351
 ion-scattering spectroscopy (ISS) 1087
 island
 – formation 1074, 1075, 1103, 1104
 – growth 1596
 – morphology 338
 – structure 461
 isopropyl alcohol (IPA) 1714
 isothermal evaporation 575
 isotropic thermal strain response 1343
 iterative target transform factor analysis (ITTFA) 1644
-
- J**
 Jackson factor 167, 192
 jewelery 4
 jog 1356
 joint density of states (JDS) 1094, 1096
 Jones matrix 1091
 junction FET (JFET) 940
 junction isolation 1715
-
- K**
 K₆P₄O₁₃ 751
 K(D_xH_{1-x})₂PO₄ (DKDP) 759
 K(Gd_{0.5}Nd_{0.5})(PO₃)₄ 732
 K(Ta_xNb_{1-x})O₃ (KTN) 162
 K₂W₂O₇ 737
 K₆P₄O₁₃ 749
 KDP
 – rapid growth 126
 kerf loss 1730
 KGd(PO₃)₄ (KGdP) 742
 KGd(WO₄)₂ 738
 KGdW 737
 KH₂PO₄ (KDP) 730
 KH₂W 738
 Kikuchi line 1488
 Kim model 1095–1098
 kinematic viscosity 564
 kinematical theory 1413
 – of x-ray diffraction 1436
 kinetic
 – deposition model 1271
 – Monte Carlo method 1246
 – of crystallization 610, 614, 761
 – related conditions 1461
 – roughening 72, 593
 – step coefficient 168
 – theory 1075
 – trapping model 1556
 kinetic model
 – Bliznakow mechanism 78
 – Cabrera–Vermilyea (CV) mechanism 79
 kinetic modeling 1256
 – of surface reaction 1257
 kinetically limited growth 1136
 kink 55, 562, 581, 1354
 kinked face (K-face) 57
 KLiYF₅ (KLYF) 738
 KLuW 737
 KNbO₃ (KN) 730
 KNd(PO₃)₄ (KNP) 742
 knife-edge 587
 Knoop microhardness 1617
 Knudsen cell (K-cell) 1156
 Kossel crystal 55
 KREW 732, 737, 746
 KTA crystal 702
 KTi_{1-x}Sn_xOPO₄ 749
 KTi_{1-x}Ge_xOPO₄ 750
 KTi_{1-x}Ge_xOPO₄ 751
 KTiOAs_xP_{1-x}O₄ 749
 KTiOAsO₄ (KTA) 692
 KTiOPO₄ (KTP) 740, 746
 KTiOPO₄ (KTP) 691, 692
 KTiOPO₄ crystal 697
 KTiOPO₄ (KTP) 730, 746
 KTP 714, 739, 742, 751
 KTP crystal 702
 KTP crystal growth 694
 KTP crystal structure 692
 KTP hydrothermal growth 694
 KTP isomorph 702, 710
 KTP-type 691
 Kubota and Mullin model 79
 KYbW 737
 KYF₄ (KYF) 738

L

- $\text{La}_{0.67}\text{Ca}_{0.33}\text{MnO}_3$ 410
 $\text{La}_3\text{Ga}_{5.5}\text{Nb}_{0.5}\text{O}_{14}$ (LGN) 1055
 $\text{La}_3\text{Ga}_{5.5}\text{Ta}_{0.5}\text{O}_{14}$ (LGT) 1055
 $\text{La}_3\text{Ga}_5\text{SiO}_{14}$ (LGS) 1055
 LaAlO_3 402
 labile zone 562
 laboratory instrument 1419
 LaGaO_3 (LGO) 1049
 L-alanine doped triglycine
 sulfo-phosphate (ATGSP) 579
 Landau level spacing 351
 Lang projection technique 1430
 Lang technique 13
 Langmuir isotherm 79
 lanthanide 746
 lapping 1724, 1725, 1731
 large crystal 659
 large-angle convergent-beam electron
 diffraction (LACBED) 1478,
 1488
 large-angle grain boundary 185
 large-eddy simulation (LES) 1216
 large-mismatch heteroepitaxial
 system 1500
 large-mismatch interface 1502
 L-arginine phosphate (LAP) 569
 L-arginine phosphate monohydrate
 (LAP) 568
 L-arginine tetrafluoroborate (LAFB)
 569
 laser 4, 161
 – and nonlinear optical material
 727
 – beam scanning (LBS) 135
 – beam scanning microscope
 (LBSM) 140
 – beam tomography (LBT) 135
 – conditioning 789
 – crystal defect 487
 – crystal growth 480
 – damage threshold 787
 – diffraction 1728
 – diode (LD) 162, 879, 898, 1059,
 1244
 – emission microanalysis (LEM)
 535
 – gas breakdown 1198
 – heated 393
 – heated pedestal growth (LHPG)
 174, 393, 395, 399, 486, 503
 – heated pedestal growth method
 (LHPG) 480
 – host fluoride 479
 – induced damage (LID) 789
 – induced damage threshold (LDT)
 787
 – ion source 1197
 – lift-off process (LLO) 879
 – material 727, 746
 – plasma ion source 1200
 – plasma range 1203
 – scattering tomography (LST)
 177, 181, 1453
 lateral epitaxial overgrowth (LEO)
 953, 1086
 lateral incorporation of vacancies
 1331
 lateral incorporation of vacancy
 1321
 lateral overgrowth 1026
 lattice
 – constant 693
 – distortion 493
 – matched substrate 877
 – mismatch 1110
 – near-coincidence 1502
 lattice parameter 344, 446, 1411,
 1488
 – InAsSb 332
 – InBiSb 332
 Laue pattern 340
 Laue photograph 379
 Lawrence Livermore National
 Laboratory (LLNL) 760, 775
 layer-by-layer growth 167
 LBO 743, 744
 L-cystine 1624
 lead tungstate 1670
 lead zirconium titanate (PZT) 608,
 634
 ledge 562
 Lely method 798, 799
 – modified 800
 Lely platelet 800
 L-histidine tetrafluoroborate 573
 L-histidine tetrafluoroborate (LHFB)
 569
 LHPG system 397
 Li_2O 416
 $\text{Li}(\text{Nb}, \text{Ta})\text{O}_3$ 410
 LiAlO_2 (LAO) 1060
 LiB_3O_5 (LBO) 691
 LiBO_3 (LBO) 730
 Liesegang ring 1608
 LiGaO_2 (LGO) 1060
 light- and heavy-hole effective mass
 350
 light scattering 458
 light-beam induced current (LBIC)
 549
 light-emitting diode (LED) 162,
 328, 798, 898, 1059, 1244
 – performance 802
 LiIO_3 731
 limitation of chemical vapor transport
 904
 limitation of kinematical theory
 1436
 LiNbO_3 (LN) 162, 168, 192, 252,
 401, 404, 406, 413, 415, 416, 708,
 729
 line defect 11
 line direction 1445
 lineage 187
 liquid and solid phase 561
 liquid encapsulated Czochralski
 (LEC) 163, 188, 206, 289, 1465
 liquid inclusion 96
 liquid phase 402, 1002
 – diffusion (LPD) 979
 – electroepitaxy (LPEE) 338, 967,
 968, 1028
 – electroepitaxy of semiconductors
 967
 – ELO 1027
 – epitaxy (LPE) 9, 283, 328, 337,
 725, 732, 734, 735, 746, 748, 751,
 802, 946, 975, 1001, 1041, 1072,
 1679
 requirement 1044
 – epitaxy (LPE) of nitride 1059
 – lateral overgrowth 1007
 liquid-crystal display (LCD) 1723
 liquid–solid interface 337
 LiTaO_3 413
 lithium
 – gallate (LiGaO_2) 877
 – niobate (LiNbO_3) 273
 – strontium aluminum fluoride
 (LiSAF) 728
 lithium niobate
 – near-stoichiometric 252, 255
 lithium niobate (LiNbO_3) 246
 – crystal 253
 LiYF_4 (YLF) 738
 load cell 249
 local electronic properties of shaped
 silicon 549
 local lattice distortion 270
 local shaping technique (LST) 540
 local vibrational mode (LVM) 222
 locking stress 1342, 1354
 Lomer–Cottrell mechanism 187
 long-range stress 114
 long-wavelength infrared (LWIR)
 358, 1105

Lothe theorem 111
 low pressure (LP) 1157
 low to high complexity 1413
 low-angle grain boundary (LAGB)
 181, 185, 543, 1060
 low-defect crystal 661
 low-energy electron-beam irradiation
 (LEEBI) 882, 1060
 lower yield stress 1348
 low-level waste (LLW) 1649
 low-temperature growth 560
 low-temperature method 1166
 low-temperature poling 710
 low-temperature-grown GaN
 (LT-GaN) 876
 low-thermal gradient 1374
 low-viscosity melt 695
 L-pyroglutamic acid crystal 573
 L-tyrosine 1625
 $\text{Lu}_2\text{SiO}_5\text{:Ce}$ (LSO) 1681
 LY 1666
 Lyapunov equation 513
 lysozyme 593

M

macroscopic motion of the fluid
 563
 macrosegregation 172
 magnesium 1618
 magnesium ammonium phosphate
 (MAP) 1615, 1617, 1622
 magnetic circular dichroism (MCD)
 1670
 magnetic Czochralski (MCZ) silicon
 235
 magnetic field 85, 175, 194, 970,
 1374
 – effect 220
 – interaction with the melt 209
 – level 990
 magnetic liquid encapsulated
 Czochralski growth (MLEC) 205
 magnetic liquid encapsulated
 Kyropoulos growth (MLEK)
 205, 208
 magnetic liquid-encapsulated
 Czochralski growth (MLEC) 207
 magnetite (Fe_3O_4) single crystal
 441
 magnetoresistive random-access
 memory (MRAM) 1509
 majority-carrier reaction 1454,
 1459
 malformed form 144
 malic acid 1621
 Marangoni convection 370
 Marangoni number (Ma) 1391
 mask width 958
 mask width-to-window width ratio
 958
 mask-induced strain 1017
 mass thickness contrast 1478
 master equation for equilibrium
 57
 material synthesis and purification
 333
 materials compatibility 825
 Maxwell–Jeffries-formula 1386
 MBE growth
 – technique 1072
 – theory 1073
 mean escape depth 343
 mean lattice site 55
 mean separation work 22
 mean size of crystals 454
 mechanical characteristics 468
 mechanical polishing 881
 mechanical stability 404
 mechanical stirring of the solution
 745
 melt 437, 480, 1219
 – based compound 1335
 – convection 1369
 – density 251
 – epitaxy (ME) 328, 339
 – growth 9, 855
 – replenishment (MR) 1390
 – replenishment model (MRM)
 1390
 melt meniscus 515
 – shaping condition 514
 melting point (mp) 370, 393
 melt–solid (M–S) 319
 – equilibrium 436
 – interface 452
 – interface shapes on radial
 uniformity of ternary crystal 318
 membrane protein 1594
 meniscus instability 192
 meniscus surface equation 514
 meniscus wetting 273
 merohedral twin 121
 metabolic stone 1620
 metal impurity 1728
 metal ion complex 580
 metal wire 394
 metallization 1715
 metalorganic chemical vapor
 deposition (MOCVD) 829, 899,
 901, 1044, 1072, 1133, 1245, 1541,
 1569
 metalorganic MBE (MOMBE)
 1072, 1141
 metalorganic vapor-phase epitaxy
 (MOVPE) 10, 113, 283, 328,
 869, 890, 901, 925, 1001, 1072,
 1133
 metal–oxide–semiconductor (MOS)
 162, 1154
 metal–oxide–semiconductor
 field-effect transistor (MOSFET)
 940, 1165, 1541
 metal-semiconductor field effect
 transistor (MESFET) 163
 metamorphic rock 152
 metaphosphate concentration 777
 metastable condition 331
 metastable phase boundary 330
 metastable zone 561, 764
 methyl-(2,4-dinitrophenyl)-
 aminopropanoate (MAP)
 569
 methyltrichlorosilane (MTS) 949
 metrology 1726
 microanalysis 1489, 1509
 micro-area x-ray fluorescence
 (MXRF) 135
 microdefect 1283, 1286
 microelectronics (ME) 162, 1721
 microfaceting 376
 microgravity 265, 335, 582
 – condition 8
 – diffusion-controlled crystallization
 594
 – environment crystallization 1588
 – grown TGS crystal 589
 – handheld protein crystallization
 apparatus 594
 – protein crystallization apparatus
 (PCAM) 594
 microinhomogeneity 174
 Microphysics Laboratory (MPL)
 1089, 1095, 1102, 1103
 micropipe (MP) 98, 802, 806, 942
 – density 805
 micro-pulling-down method (μ -PD)
 480
 microsegregation 172
 microstructure 461
 microstructured material 1687
 microtwin 1110
 microtwinning 1079
 microvoid 168
 mid-wave IR (MWIR) 1105
 mineral 133
 minimum-energy theorem 110
 minority-carrier

– lifetime 1083
 – reaction 1456, 1460
 – recombination lifetime 1107, 1108
 miscut 1077
 misfit dislocation 186, 1494
 mismatch between the substrate and the film 751
 mismatch heteroepitaxy 359
 mismatched epitaxy 355
 Mn diffusion 1509
 mobility 1087
 – ratio 348
 model for dislocation generation 1339
 model-based prediction 1380, 1389
 modeling 434
 modeling of AlN/GaN vapor deposition 1246
 modern wiresaw 1729, 1730, 1732, 1735
 modifications of TPS 540
 modified non-stationary model (MNSM) 1386
 modified quasi-steady-state model (MQSSM) 1386
 modulation-doped field-effect transistor (MODFET) 1165
 moiré fringe 1502
 moiré interferometry 1727
 mold-pushing melt-supplying (MPMS) 255
 molecular dynamics (MD) 76
 molecular-beam epitaxy (MBE) 10, 18, 283, 328, 605, 869, 890, 946, 1004, 1044, 1069, 1070, 1133, 1156, 1162, 1206, 1245, 1567, 1569
 mollusk 1614
 molten zone profile 405
 monitoring 1090
 monoatomic crystal 86
 monochromatic beam 1434
 monochromator 1645
 monoclinic (m) 445, 574
 – phase 764
 monodomain crystal 257
 monohalide (GaCl) 926
 monolayer (ML) 1172
 monolithic microwave integrated circuit (MMIC) 162, 216
 monosilicic acid 1609
 monosodium urate monohydrate (MSUM) 1615, 1623
 Monte Carlo simulation 69, 73
 Morey autoclave 617

morphodrome 70, 82
 morphological evolution 136, 1062
 morphological habit 701
 morphological importance (MI) 64
 morphological instability 136, 173, 175, 781
 morphological shape 706
 morphology 133, 136, 578, 848, 1459
 – and faceting 268
 – of growth spiral 140
 – of pits 1462, 1465
 – of sillenite crystal 268
 mosaic block 1409
 Moss–Burstein effect 353
 mother phase 57
 mounting of the substrate 1088
 MOVPE of InAs quantum dot 1144
 MOVPE precursor 1133
 Mueller matrix 1091
 multicarrier conduction 350
 multicrystalline (MC) 162
 – ingot growth 1709
 multidomain
 – crystal 698
 multilayer model 1092
 multiple quantum well (MQW) 1469
 multiple reflection 353
 multiple-beam interferometry (MBI) 135, 140
 multiple-exposure holography 585
 multiplication rate 1348
 multiwire saw 1732

N

Na-NbTS
 – cesium ion exchange 1656
 – in situ synthesis 1655
 nanocrystal 637
 nanomaterial 916
 nanostructure 463
 nanotopography 1731
 National Aeronautics and Space Administration (NASA) 583
 National Ignition Facility (NIF) 761, 774
 National Institute of Standards and Technology (NIST) 588
 National Physical Laboratory (NPL) 301
 National Renewable Energy Laboratory (NREL) 898
 National Synchrotron Light Source (NSLS) 1431, 1638
 native point defect concentration 165
 natural and synthetic diamond 150
 natural and synthetic quartz 142, 145
 natural convection 563, 970
 natural crystallization 135
 natural diamond 151
 Navier–Stokes (NS) 1397
 Nb₂O₅ 413
 Nd₃Ga₅O₁₂ 443
 Nd:YAG 399
 NdBa₂Cu₃O_{7-x} (NdBCO) 1046
 Nd-doped congruent LN (Nd:CLN) 252
 Nd-doped laser crystal 489
 NdGaO₃ (NGO) 1049
 near-band-edge (NBE) 838
 near-coincidence
 – lattice 1502
 near-stoichiometric
 – lithium niobate (nSLN) 252, 255
 necking 382, 1359
 – of seed crystal 256
 needle defect 1082
 negative ion 1564
 neighboring confinement structure (NCS) 1175
 neutron diffraction 380
 – cell 1648
 – theory 1640
 newberyite 1622
 Newton–Raphson 1361
 niobate 729
 nitric acid (HNO₃) 299
 nitride 1059
 nitrogen (N₂) 822
 nitrogen precursor 1138
 NLO single crystal 736
 Nomarski image 218
 noncentrosymmetric 271
 noncongruent melt 176
 nonconservative system 173
 noncritical phase matching (NCPM) 692, 714
 nondilute system 1537
 nonflat interface 269
 nonintrusive wafer inspection 1727
 nonlinear coefficient 708, 713
 nonlinear optical (NLO) 162, 691, 1625
 – crystal 691
 – material 726, 728
 nonmerohedral twin 121
 nonmetabolic stone 1620
 nonpolar layer 1572

nonstationary model (NSM) 1384
 nonstoichiometry 171, 189, 699
 nonuniform composition 1080
 normal growth rate 65
 n-type doping of GaN 882
 nuclear hyperfine interaction 1526
 nuclear magnetic resonance (NMR) 693, 1522, 1592
 nucleation 45, 192, 339, 452, 565, 735, 763, 808, 1101
 – at surface 17
 – calculation 908
 – control 1610
 – exclusion zone 35
 – of intrinsic point defects 1304
 – phenomenon 1586
 – study 763
 nucleus (N) 1462
 numerical
 – implementation 1360, 1361
 – method 983
 – model for vapor growth systems 1247
 – modeling of GaN IVPE growth 1258
 – modelling of CVD process 1246
 – result 1362
 – scheme 667
 – simulation 179
 – solution 1251

O

observation of dislocations 1500
 observation of growth rate 970
 O-cluster 1306, 1309
 octacalcium phosphate 1618
 off-centered Czochralski system 258
 one-dimensional
 – crystal growth 1316
 – initial incorporation 1288
 – model 973
 – nucleation 27
 one-step ELO structure (1S-ELO) 877
 operational condition 1264
 OPO interaction 714
 opposite domain LN (ODLN) 258
 optical
 – absorptivity 1108
 – afterheater 397
 – anomaly of growth sectors 105
 – breakdown of gases 1198
 – ceramic 1687
 – characterization 224

– cutoff 1112
 – dielectric function 1091
 – glass 465
 – material 726
 – nonuniformity 713
 – parametric oscillation (OPO) 691
 – phonon occupancy 354
 – plasmatron 1198
 – property 679
 – pyrometer 249
 – pyrometry 1089
 – transmittance 1108
 – uniformity 458
 optical absorption 1112
 – spectrum 784
 optical floating zone (OFZ) 368
 – application for oxides 368
 – composition evolution 374
 – crack 382
 – furnace 371
 – high pressure 371
 – inclusion 382
 – modelling 370
 – overheating 370
 – self-flux 375
 – technique 368, 369
 optically detected magnetic resonance (ODMR) 1546, 1669
 optimization 1007, 1062, 1264
 optimization of growth of GaN films
 – a materials example 1206
 optimization of liquid-phase lateral overgrowth procedure 1007
 optimization of plasma flux for film growth 1204
 optimum growth parameter 905
 optoelectronic devices and integrated circuit (OEIC) 968
 optoelectronic integrated circuit (OEIC) 216, 1153
 optoelectronics 1336
 ordinary differential equation (ODE) 1361
 organic additive 778, 1622
 organic light-emitting diode (OLED) 865
 organic semiconducting single crystal 862
 organic semiconductor
 – Bridgman technique 856
 – Czochralski technique 857
 – gas phase growth 857
 – single-crystal 845
 organometallic crystal 1612
 organometallic vapor-phase epitaxy (OMVPE) 901

orientation
 – contrast 1440
 – dependence 956
 – determination 340
 – flat (OF) 1463
 – state 121
 oriented film 338
 origin of dislocation 1338
 origin of screw dislocation 808
 Orowan relation 180, 1347
 orthodox etching 1461, 1468
 orthophosphate 692
 Ostwald ripening 189, 1143
 Ostwald's step rule 86
 overheating 194, 436
 oxidation-induced stacking fault (OSF) 168, 1284
 oxide 393, 479, 728
 – crystal 433, 434
 – glass 433
 – photorefractive crystal 262
 oxygen
 – contamination 824
 – redistribution 463
 – stoichiometry 441
 – vacancy 715

P

packaging 1725
 pancreatic stone protein (PSP) 1629
 parabolic band 349
 partial differential equation (PDE) 1397
 partial dislocation 1344, 1497
 partial pressure 1135
 particle acceleration 1199
 particle diagnostics 586
 particle imaging 586
 partly stabilized zirconium dioxide (PSZ) 444
 passivation 1086
 pathological biomineralization 1614
 pattern formation in gel systems 1610
 patterned domain 257
 patterned substrate 952, 1086
 PbMoO₄ 170
 PbTe 168, 185
 pearl 1614
 PED technique 1194
 Peierls
 – barrier 1343
 – energy 113
 – potential 178, 1346

- Peltier interface demarcation (PD) 291
- Peltier-effect 1028
- Peltier-induced growth kinetic 971
- Pendellösung fringes (PF) 1444
- pendeo-epitaxy (PE) 1031
 - of GaN 1032
- penetration twin 122
- perfection 133, 152
 - limit 164
 - of crystals grown rapidly from solution 125
 - of single crystal 152
- periodic bond chain (PBC) 54, 64, 137
- periodic domain 259
 - structure (PDS) 708, 711, 713
- periodic modulation 259
- periodic poled LN (PPLN) 258
- periodic poling lithium niobate (PPLN) 398
- periodic solute feeding process 315
- periodically poled KTP (PPKTP) 691, 708
- periodically poled lithium niobate structure 258
- peripheral ring 1322, 1327
- peritectic decomposition 374
- peritectic transformation 373
- permeability 670
- perturbation frequency 175
- pH of solution 577, 579
- phase
 - composition 460
 - contrast microscopy (PCM) 135, 140
 - extent 165, 169
 - modulator 273
 - relation 1046
 - stability 661
 - transformation 448
 - transition 125, 446
- phase conjugated optical waveguide 273
- phase diagram 330
 - of the $\text{ZrO}_2\text{--Y}_2\text{O}_3$ system 445
- phase equilibrium 663
 - for binary compound 292
 - for ternary compound 300
 - of ZnO 662
- phases with different composition 270
- phase-shifting interferometry (PSI) 135, 140
- phase-shifting microscopy (PSM) 135, 140
- phlogopite 141
- phosphate 730, 739
 - flux 740
 - solution 748
- phosphide-based compound 296
- phospholipid lecithin 1626
- phosphorus glass removal 1715
- photo-assisted MBE (PAMBE) 1072, 1107
- photochromic property 271
- photoconductive-decay lifetime 1082
- photoconductivity 260
- photoconductor (PC) 358, 1116
- photodiode (PD) 162, 357
- photo-EPR 1539
- photoetching 1470
- photogalvanic etching 1458, 1461, 1471
- photoionization cross section 343
- photoluminescence (PL) 15, 683, 835, 918, 1082, 1158, 1207
 - mapping 1083
- photorefractive (PR) 252
 - crystal 264
 - damage 258, 261
 - gain 221
 - oxide material 246
- photovoltaic (PV) 898, 1703, 1722, 1723
 - efficiency (PVE) 162
 - module 1705
 - value chain 1705
- physical laws for transport processes 1217
- physical property 346
- physical vapor deposition (PVD) 135, 900
- physical vapor transport (PVT) 135, 800, 821, 899, 900, 946, 953
- physicochemical properties of the solution 733
- piezoelectric 262, 264, 703
- planar defect 11
- planar doping 1107
- plasma 1202
 - acceleration 1197
 - energetics 1193
 - enhanced chemical vapor deposition (PECVD) 1715
 - etching 881
 - expansion 1197
 - flux 1204
 - formation 1198
- formation in PED 1198
- formation of vaporized material 1196
- processing 1193
- propagation in gas 1203
- plastic
 - deformation 156, 183
- plastic relaxation 178, 180, 184
- plastic state 116
- plate shaped crystal 521
- PLD technique 1194
- ploughing 1730
- plume range 1203
- Pockels cell 760
- point defect 11, 160, 161, 163, 1556, 1569
 - characterization 1521
 - concentration 164
 - engineering 168
 - generation 163
 - identification 1560
 - kinetics 167
- point group symmetry 697
- point seed 773
- point-bottomed (P-type) etch pit 139
- polar growth 1572
- polar surface 72
- polarity 1463, 1479, 1484, 1486
 - of III–V material 1464
 - of twinning 214, 215
- polarizer 4
- poling of crystal 252
- poling of lithium niobate 257
- polishing 1725
- polyacrylamide 1629
- polycrystal 192
- polycrystalline SiC 804
- polyelectrolyte 82
- polyethylene oxide (PEO) 1609
- polygonal or circular spiral 141
- polyhedral crystal 138, 143
- polyhedral seed 572
- polyimide environmental cell (PEC) 1647
- polymorphic transition 726
- polypyrrole (ppy) 1597
- polyscale crystal 599
 - growth 4
- polytype formation 805
- polyvinyl alcohol (PVA) 1609
- porous bed 670
 - height 672
- position-sensitive detector (PSD) 1643
- positron

– annihilation spectroscopy 1551, 1552
 – density at a vacancy 1555
 – emission tomography (PET) 1682
 – implantation 1552
 – lifetime 1553
 – lifetime spectroscopy 1557
 – state 1553
 – trapping 1556
 – trapping rate 1556
 – wavefunction 1553
 postgrowth dislocation 107, 118
 postgrowth movement of dislocations 116
 postgrowth treatment 788
 potassium amide (KNH_2) 664
 potassium azide (KN_3) 664
 potassium dihydrogen phosphate, KH_2PO_4 (KDP) 96, 560, 568, 569, 759
 potassium double tungstate (KREW) 728
 potassium iodide (KI) 664
 potassium niobium tantalate (KTN) 398
 potassium stoichiometry 716
 potassium titanyl phosphate (KTP) 691
 potassium vacancy 700
 power rectifier 798
 practical results of the theoretic analysis 519
 Prandtl number 734
 precipitate 160, 163, 189, 1339
 precipitation 376
 precursor
 – decomposition 1135
 – for SiC CVD epitaxial growth 946
 – ligand 1134
 – vapor pressure 1134
 predicting the growth morphology 65
 prediction 1254
 pregrowth purification 850
 primary agglomeration 1616
 primary crystallization field (PCF) 1046
 primary nucleation 763
 prime wafer 1723
 prismatic stacking fault (PSF) 1501, 1504, 1508
 prismatic zone 577
 probabilistic model of second-layer nucleation 42
 process simulation 669
 processed seed 572
 profile of growth spirals 150
 progesterone 1628
 propagation
 – of growth dislocation 110
 – of twin boundary 123
 propagation of defects 93
 properties of CZ crystal 455
 proportional–integral–derivative (PID) 251
 proportional–integral–differential (PID) 248, 286
 proportional–integral–differential (PID) controller 913
 protein crystal growth 592
 – AFM 1596
 – electrochemistry 1596
 – facility (PCF) 594
 – in microgravity 593
 – mechanism 593
 – method 592
 protein crystallization 1588
 – high throughput 1593
 protein immobilization 1597
 proteomics 1584
 pseudobinary phase diagram 300
 pseudodielectric function 1091
 pseudo-equilibrium theory 1074
 pseudohexagonal twin 124
 pseudosemicoherent interface 1501
 PSZ crystal 459
 – composition 459
 – cooling rate 459
 – phase transformation 459
 Pt wire 400
 p-type doping of GaN 882
 pulling 407, 441
 – on a seed 443
 – rate and temperature gradient 238
 – rate of crystal 247
 pulsed electron beam source (PEBS) 1196
 pulsed electron deposition (PED) 1193, 1194
 pulsed laser deposition (PLD) 1193, 1194, 1206
 pure and doped lithium niobate crystal 256
 purification 913
 purity 163
 PV technology 1706
 PVT crystal growth 822
 pyroelectric 703
 – effect 262
 pyrolytic boron nitride (pBN) 291, 296

Q

Q-switch 273
 qualify control 1726
 quality variation 1420
 quantification of the microdefect formation 1290
 quantitative estimation of dopant concentration 1059
 quantum dielectric theory (QDT) 355
 quantum dot (QD) 1142
 – arsenide 1133
 – buried 1417
 – growth interruption 1145
 – InAs/GaAs 1142
 – laser 1147
 – multimodal size distribution 1146
 – ripening 1146
 – strain energy 1143
 – structural property 1147
 – subensemble 1146
 – surface 1417
 quantum efficiency (QE) 1116
 quantum well (QW) 1160, 1173
 quantum wire 1418
 quartz 149, 620
 quasi-equilibrium deposition model 1270
 quasi-equilibrium model 1270
 quasi-phase-matched (QPM) 691
 quasi-phase-matching (QPM) 708
 quaternary phase diagram 301
 quenching 336

R

$\text{R}_2\text{O}_3\text{--Al}_2\text{O}_3\text{--SiO}_2$ system 467
 radial morphology 263
 radial temperature gradient 1364
 radiation 1368
 – detector 4
 – model selection criterium 1249
 radiative recombination 1107, 1108
 radioactive waste 468
 radiofrequency (RF) 248, 251, 367, 435, 831, 1044
 – generator 248
 Raman 693
 – peak 355
 – spectrum 783
 ramping mode 256
 random alloy scattering 350
 rapid analysis 1419
 rapid growth 773
 – method 73

– of ADP 126
 – of KDP 126
 rapid-thermal annealing (RTA) 1567
 rapid-thermal chemical vapor deposition (RTCVD) 1162
 rare earth (RE) 259, 262, 368, 1681
 – lithium fluoride (RELf) 728
 – vanadate (REVO₄) 633, 728
 rate equations approach 36
 rate of nucleation 28, 32
 – on single-crystal surface 30
 rate-dependent 1342
 ray-tracing simulation 807
 Rb_xK_{1-x}TiOPO₄ 751
 RbTiOAsO₄ (RTA) 692
 RbTiOPO₄ (RTP) 740
 RbTiOPO₄ (RTP) 691, 692
 RbTiOPO₄ crystal 700
 RbTiOPO₄ (RTP) 741
 RCA passivation of Si surface 1101
 reaction free energy 1263
 reaction in growing CZ crystals 1314
 reaction involving no aggregation 1304
 reaction of dislocations 116
 reactive ion etching (RIE) 881
 reactor geometry 872
 readout integrated circuit (ROIC) 1118
 real-time inspection 1728
 reciprocal space 1407
 – map (RSM) 833, 1082, 1411
 reciprocating motion 572
 recombination 1082, 1107
 – enhanced dislocation glide (REDG) 810
 – of electrons and holes on dislocations 1470, 1471
 recording geometry 1435
 – back reflection 1435
 – transmission 1435
 recovery process 150
 reduced pressure (RP) 1157
 reference electrode (RE) 1454, 1455
 reflexicon 398
 reflection high-energy electron diffraction (RHEED) 1072, 1083, 1089, 1099, 1100, 1102
 reflection topograph 342
 reflectometry 1413
 refraction of dislocation lines 110
 refractive index (RI) 587, 698, 713, 714, 1715
 refractory 434
 – material 433
 – melt 440
 regeneration 768, 774
 relation of Dupré 20
 relative growth rate 105
 relaxed SiGe layer 1165
 replenishment model (RM) 1397
 reported model 1502
 residual impurity 883
 residual strain 356
 residual stress 1728
 – measurement 1728
 resistance 358
 resistivity 711
 responsivity 591
 retardance 1091
 retrofitting the MBE chamber 1092
 reverse current (RC) 408
 reverse diffusion 1628
 Reynolds number 564, 734
 RF (radiofrequency) 1709
 RGS (ribbon growth on substrate) 1712
 ribbon-to-ribbon (RTR) 522
 RMS (root-mean-square) 1167
 robotics 1593
 rocking curve 341, 379, 1058
 – measurement 1058
 rod preparation for OFZT 372
 rolling-indenting
 – model 1730
 – process model 1734
 room temperature (RT) 350, 1664
 – photoluminescence (RTPL) 1207
 rotating analyzer ellipsometer (RAE) 1091, 1092
 rotating compensator ellipsometer (RCE) 1091, 1092
 rotating disc technique 574
 rotating magnetic field 191
 rotating thermal field 745
 rotation 1233
 – of crucible 1370
 – of crystal 1370
 – Reynolds numbers 1369
 rotatory Bridgman method (RBM) 328, 336
 rough interface 136
 roughening transition 72
 round cylindrical crystal 519
 RTA crystal 702
 RTP 742
 – crystal 702
 ruby 630
 Rutherford scattering 1490

S

salol 102
 sapphire (Al₂O₃) 630, 656, 875, 899
 – fiber 396
 saturation
 – nucleus density 35
 – temperature 575, 576
 scaling analysis 1258
 – of a CVD reactor 1258
 scaling exponent in diffusion 37
 scanning Auger microprobe (SAM) 829
 scanning electron microscopy (SEM) 15, 331, 340, 346, 380, 929, 1006, 1079, 1162
 scanning force microscopy (SFM) 259
 scanning photoconductivity 225
 scanning photocurrent (sPC) 224
 scanning transmission electron microscopy (STEM) 1163, 1489
 scanning tunneling microscopy (STM) 135, 140, 1163
 scattering 491, 1412
 – amplitude 1407
 Scheil equation 173
 Scherzer point resolution 1483
 schlieren system 587
 Schmidt contour 186
 Schottky defect 166
 Schwutke technique 1429
 Scientific Production Company (SPC) 1574
 scintillation material 1663, 1670
 scintillation parameter 1665
 scintillator
 – aluminum perovskite 1673
 – device 264
 screw dislocation (SD) 6, 15, 178, 180, 219, 806, 942, 1352, 1466
 – mechanism 769
 – theory 6
 screw-oriented BPD 813
 SE data analysis 1092
 SECeRTS cell 1646
 secondary agglomeration 1616
 secondary ion mass spectrometry (SIMS) 1564
 secondary nucleation 765
 secondary Peierls potential 1354
 secondary-ion mass spectrometry (SIMS) 259, 681, 682, 785, 787, 829, 1059, 1083, 1157, 1415, 1522, 1572

- second-harmonic generation (SHG) 691, 697, 729, 775
- second-layer nucleation in
 homoeptitaxy 38
- second-phase particle 189
- sector boundary 786
- Seebeck 408
- seed 146, 152, 382, 441
 – crystal 573, 804
 – generation for new material 289
 – length 251
 – orientation 570
 – rod 369
 – rotation mechanism 571
 – sublimation 802
 – temperature 800
- seeded
 – growth 822
 – sublimation growth 800
- seeding 400
 – process 263, 290
- segregation 172, 270
 – coefficient 171, 172, 337, 375
- selected area diffraction (SAD) 829, 1478, 1484
 – pattern 345
- selective epitaxial growth (SEG) 953, 1181
- selective-area growth 1086
- self-assembly of islands 1074
- self-flux 695, 750
- self-seeded growth 822, 827
- self-separation 880
- self-trapped exciton (STE) 1671
- Sellmeier equations 715
- semiconductor 967, 1459, 1551
 – alloy 1485
 – grade 232
 – grade silicon 802
 – single crystal 897
 – single-crystalline wafer 1723
 – structure 1026
 – substrate 661
 – wet etching 1459
 – zincblende structure 1485
- sense of screw dislocation 807
- separation work 55
- sequential etching 1468
- sex hormone 1628
- shaded area 209
- shallow positron
 – state at negative ions 1555
 – trap 1564
- Shanghai Institute of Optics and Fine Mechanics (SIOM) 482
- shaped
 – crystal 517, 519
 – crystal by FZT 522
 – crystal growth (SCG) 509
 – silicon structure 546
- shear modulus 806
- shear stress 178, 184
- shield gas flow rate 1266
- Shockley
 – fault 813
 – partial 178, 1497
 – partial dislocation 809
- Shockley–Read–Hall (SRH) 1085, 1107
 – recombination 1108
- shoulder facet 214
- shoulder zone 266
- shuffle dislocation 1344
- Si substrate 1076
- Si/Ge
 – growth technology 1156
 – heterostructure 1154
- Si₃N₄ powder 802
- Si-based compliant substrate 1086
- Si-based substrate 1084
- SiC 141
 – Acheson method 153
 – based device 798
 – based device technology 816
 – boule 805, 816
 – bulk growth 802
 – epitaxial growth technique 946
 – growth system 803
 – homoeptitaxy 945
 – Lely method 153
 – polytype 805
 – seed 829
 – selective growth 956, 959
- Si-face epilayer 811
- SiGe heterostructure 1153
- SiGeC structure 1415
- SiGe-on-insulator (SGOI) 1169
- signal-to-noise ratio (SNR) 1118
- silane (SiH₄) 800, 882
- silica gel 1608
- silica nozzle angle 1268
- silicon (Si) 166, 231, 358
 – multicrystal 239
 – on cloth (SOC) 551
 – on insulator (SOI) 944, 1086, 1169
 – photovoltaics 1703, 1706
 – ribbon growth 1711
 – solar cell 1703
 – strip detector 1644
 – wafer 1722
- silicon carbide (SiC) 656, 797, 876, 939, 1734
 – growth 944
 – polytype 941
 – substrate 944
- silicon crystal 232
 – semiconductor grade 232
- sillinite 266
- simulation 1412
 – model 789, 982
 – of LID 789
- single crystal 4, 152, 334, 769, 923
 – by OFZ 383
 – fiber (SCF) 393
 – growth 1707
 – growth process 297
 – organic semiconducting 862
 – perfection 152
 – ternary seed generation process 308
- single diffusion 1612
- single slip 1346
- single-domain
 – crystal 698
 – growth 707
- single-ended pinning point 813
- Sirtl-type etchant 1460
- site stability and adsorption 63
- sitnakite topology 1649
- sitting drop method 593
- sixfold defect distribution 1341
- sixfold symmetry 1372
- size of pits 1467
- skull melting (SM) 433, 434
- slice energy 56, 65
- slicing 1725, 1728
 – technology 1730
- slip
 – band 834
 – dislocation 1359
 – system 341, 1340
- slow cooling (SC) 9
 – bottom growth (SCBG) 9
- small environmental cell for real-time studies (SECeRTS) 1646
- smooth interface 136
- SnTe 168
- sodium
 – azide (NaN₃) 664
 – metasilicate 1609
 – niobium titanosilicate (Nb-TS) 1655
 – nitrate (NaNO₃) 1219
 – nonatitanate (SNT) 1651
 – titanium oxide silicate (STOS) 1651

- titanium silicate (Na-TS) 1649
- urate monohydrate 1624
- software 1644
- solar cell 240, 1703
- application 239
- binning 1716
- fabrication 1713
- performance 1716
- testing 1716
- solid solution 330
- solid–liquid interface (SLI) 136, 253, 265–267, 735, 762
- solid-state
 - electrochemistry 1597
 - laser (SSL) 726, 727
- solidus 331
- solubility 567, 610, 613, 661, 696, 1585
 - curve 561, 1046, 1047
 - determination 568
 - gradient 567
 - of ammonothermal GaN 663
 - of berlinite 613
 - of gallium orthophosphate 614
 - of hydrothermal ZnO 662
 - of quartz 613
 - parameter 568
 - plot 1585
 - reduction 1610, 1613
- soluble system
 - reverse-grade 672
- solute boundary layer 172
- solute feeding
 - crucible oscillation 314
 - homogeneous alloy growth 311
 - in vertical Bridgman method 313
 - using double-crucible 312
- solute precipitate 99
- solute trail 99
- solution
 - circulating method 771
 - flow 154
 - grown KTP 704
 - inclusion 782
 - preparation 573
 - stirring (SS) 1591
 - temperature 737
- solution growth 1042
 - chemical/gel method 567
 - crystallizer 570
 - high temperature 696
 - high-temperature 731
 - low temperature 566
 - method 566
 - of triglycine sulfate 582
 - slow cooling method 566
- slow evaporation 566
- temperature gradient method 567
- temperature lowering 567
- top-seeded 696, 732
- solvent 568
 - adsorption on crystal surface 77
 - based growth method 862
 - effect on the crystal habit 75
 - inclusion 96
 - selection 567
 - system 1046, 1047, 1055
- solvent–solute interaction 77
- Soret effect 1388
- source preparation 400
- source-current-controlled (SCC) 975
- space group 332
- space grown TGS crystal 591
- space-charge electric field 254
- space-charge grating 221
- Spacelab-3 (SL-3) 583
- spatial instability 437
- spatially resolved x-ray diffraction (SRXRD) 1019
- spectroscopic ellipsometry (SE) 1072, 1089, 1090
 - calibration 1093
 - composition determination 1094
 - temperature determination 1094, 1098
- spectroscopic library 398
- sphalerite structure 1487
- spherulite 1621
- spinning disc growth 576
- spin–orbit splitting 347
- spintronics 4
- spiral growth 136, 1596
 - linear and parabolic growth rate 74
- spiral morphology 141
- splitting energy 356
- spontaneous nucleation 770
- spontaneous polarization 704, 709
- spontaneous self-separation 881
- spreading resistance (SR) 549
- spring plate 1089
- sputtering (SP) 1206
- Sr₂RuO₄ 414, 416
- SrMoO₄ 400
- stability
 - criterion for nuclei 847
 - of a crystal site 61
 - of crystallization 512
 - of solution 770
- stability analysis (SA) 509, 516, 529
- and crystal growth 519
- stable growth 373
- stacking fault (SF) 178, 810, 814, 885, 944, 1466, 1479, 1489, 1497
- and partial dislocations 1497
- energy 193
- stacking mismatch boundary (SMB) 1501, 1506
- stacking sequence rule 813
- staining of crystal 102
- standard testing conditions (STC) 1716
- start melting 435
- starting compound 914
- starting material 913
- state at negative ions
 - shallow positron 1555
- static stability 515
- stationary magnetic field 978
- stationary state 1349
- stationary temperature profile (STP) 900, 918
- steady magnetic field 1229
- STEM 1509
 - imaging 1490
- step flow 813
- growth 1074, 1075, 1110
- step separation 140
- step source
 - longitudinal 120
 - transverse 120
- stepped 562
 - face (S-face) 57
- steroid 1610, 1626
- hormone 1628
- sticking probability 1273
- stimulated Raman scattering (SRS) 728
- Stockbarger method 9
- stoichiometric crystal 254
- stoichiometric LN (SLN) 252
- stoichiometry 170, 188, 409, 691, 697
 - potassium 691
- strain 785, 787, 1488
 - in ELO layers 1016
 - measurement 1489
 - reducing layer (SRL) 1147
 - relaxation 1163
- strained layer 1498
- Stranski–Kaischew criterion of the mean separation work 60
- Stranski–Krastanov
 - growth 20, 1104
 - growth mode 1073, 1074
- Stranski–Krastanow

– 2-D–3-D transition 1142
 strength property 463
 striation 101, 174, 383, 489, 711
 strontium
 – barium niobate (SBN) 396
 – carbonate 1611
 – tartrate 1610
 structural
 – characterization 1057
 – coherence 345
 – defect 848, 1110
 – dynamics 341
 – form 137
 – instability 70
 structural perfection 676, 1014
 – of coalescence front in fully
 overgrown ELO structures 1014
 structural property 340, 1139
 – HgCdTe 1110
 – InAs_xSb_{1–x} 332
 structure of small clusters 32
 structure perfection 664
 structure–properties relationship
 713
 struvite 1622
 subgrain 1440
 sublattice 1562
 sublimation 852
 – growth 802, 1274
 – sandwich method (SSM) 800
 submerged heater method (SHM)
 320
 substrate 875, 1083, 1087
 – dislocation in ELO 1011
 – epitaxial relationship 1049
 – for epitaxy of nitride 1061
 – for homoepitaxial LGT LPE film
 growth 1056
 – impurity 1080
 – manufacturing with
 system-oriented approach 1725
 – material 1076
 – orientation 1077
 – preparation 1101, 1102
 – removal technique 879
 – rotation 1269
 – rotation effect 1269
 – roughness 1081
 – surface curvature 1082
 – temperature 1264
 substrate–nozzle distance 1269
 succinonitrile (SCN) 1223
 sulfate-containing flux 741
 supercooling 4, 192, 194, 338
 supercritical fluid technology (SCF)
 619

superheated aqueous solution 8
 superheating 185, 186
 superlattice 1410
 supersaturated solution 763
 supersaturation 5, 6, 21, 73, 339,
 561, 578, 735, 779, 804, 908, 1273,
 1586
 – and driving force for LPE 1048
 – ratio 57, 561, 908
 – relative 561
 surface
 – acoustic wave (SAW) 657, 1059
 – anisotropy 1091
 – attachment 735
 – characterization 1100
 – damage 1339
 – damage removal 1714
 – energy 5, 137, 194, 405
 – energy theory 5
 – microtopography 134, 139
 – modification 1193
 – morphology 339, 461
 – nonstoichiometry and
 contamination 1082
 – reaction 1255–1257, 1272
 – reaction analysis 1259, 1262,
 1263
 – reconstruction 69
 – relief of the growth face 114
 – roughness 67, 1093, 1099, 1725
 – segregation 1157
 – site 55
 – structure 72
 – tension 58, 733
 surface defect 1110
 – crater 1111
 – cross-hatching 1112
 – flake 1111, 1112
 – hillock 1112
 – microvoid 1111
 – needle defect 1112
 – roughness 1112
 – triangle defect 1111
 – void 1111
 surface-mount technology (SMT)
 1705
 surfactant 45
 – efficiency 46
 – mediated growth (SMG) 1160
 SWBXT back-reflection image 806
 symmetry 848, 1373, 1462
 – of growth spiral 141
 synchrotron radiation 13
 – source 1642
 – topographic study 341
 synchrotron topography (ST) 181

synchrotron white beam x-ray
 topography (SWBXT) 209, 677,
 806, 827, 1359
 synchrotron x-radiation diffraction
 588
 synchrotron x-ray topography
 (SXRT) 1019, 1021
 synovial fluid 1623
 synthesis
 – of Na-TS and Na-NbTS 1658
 synthesis problem 1650

T

TaC mask 954
 tailor-made additive 70, 83
 tangled dislocation 181, 186
 tantalum carbide (TaC) 826
 tartaric acid 1618, 1622
 Tatarchenko steady-state model
 (TSSM) 1389
 Te monolayer 1087
 Te precipitate 1080, 1082
 technique
 – surface characterization 1595
 technique of pulling from shaper
 (TPS) 509
 TEM
 – application 1493
 – CL observation of prismatic
 stacking faults 1508
 – EDS (energy-dispersive x-ray
 spectroscopy) 1486
 – study of dislocations 1467
 temperature 1362
 – control technique 248
 – dependent Hall measurement
 (TDH) 1541
 – distribution 438, 517
 – effect on adsorption 84
 – effect on crystal habit 84
 – field 1363
 – gradient technique (TGT) 403,
 404, 439, 480, 482, 501
 – gradient zone melting (TGZM)
 335
 – oscillation 712
 – pattern 670
 – ramping 1089
 – reduction method (TRM) 771,
 773
 template 875
 ternary phase diagram 300
 ternary substrate 283
 terrace 563
 – of growing faces 581

- tertiarybutylhydrazine
 (C_4H_9)(H)NNH₂ 1138
 testosterone 1628
 tetragonal (t) 445
 – DKDP crystal 772
 – phase (TZP) 444
 tetragonal–monoclinic phase
 transition 772
 tetramethoxysilane (TMOS) 1609
 texturing 1714
 theorem of Herring 96
 theoretical calculations of hyperfine
 1528
 theories of urinary stone formation
 1616
 theory of preferred direction 110
 thermal
 – annealing 788
 – condition 440
 – conductivity 733, 1078
 – cycling 1085
 – diffusion model (TDM) 1387
 – expansion coefficient 467
 – fluctuation in slicing 1735
 – gradient 396
 – lensing 711
 – mismatch 1110
 – property of InSb 356
 – shock 1364, 1373
 – stimulated conductivity (TSC)
 1669
 – stimulated luminescence (TSL)
 1668
 – strain 1350
 – strain in ELO layers 1024
 – stress 499, 813, 1339
 – treatment 699
 thermocouple 248, 1089
 thermocouple calibration 1103
 thermodynamic 163, 869
 – analysis of gas-phase 1254
 – approach 61
 – consideration 847, 905
 – factor 1466
 – kinetic analysis 1254
 – potential 164
 – prediction 1255
 – prediction of surface reactions
 1255
 – property 1265
 – supersaturation 57
 thermoelastic stress 179
 thermoelectric effect 969
 thermophysical 583
 – characteristics 468
 thermoplastic relaxation 177
 thickness determination 1486
 thin film 1534
 – deposition 1193
 thiophene ($\text{C}_4\text{H}_4\text{S}$) 854
 third harmonic-generation (THG)
 775
 Thomson–Gibbs
 – equation 21, 22
 – formula 58
 Thomson–Gibbs–Wulff equation
 (TGW) 59
 threading dislocation (TD) 875,
 899, 1060, 1110
 threading edge dislocation (TED)
 811
 three-dimensional (3-D) 18, 20,
 232, 1172, 1222
 – characterization 1598
 – generalization 1352
 – simulation 981
 threefold symmetry 1372
 three-phase boundary (TPB) 193,
 210, 214
 three-vessel solution circulating
 method (TVM) 772
 Ti:Al₂O₃ 406
 Ti:sapphire 487
 Tiller criterion 176
 tilt variation 1420
 time of flight 1201
 time varying temperature profile
 (TVTP) 918
 time-resolved experiment 1642
 time-varying temperature profile
 (TVTP) 900
 TiO₂ 414
 titanium oxide 703
 titanium silicate 1649
 Tm-doped epitaxial layer 748
 Tm-doped KLuW 747
 Tokyo Denpa (TD) 1574
 top-seeded solution growth (TSSG)
 9, 487, 691, 725, 732, 734, 1042
 total gas flow rate 1264
 total number of spins 1533
 total thickness variation (TTV)
 1727, 1729
 TPS (technique of pulling from
 shaper)
 – brief history 537
 – capillary shaping 522
 – definition 537
 – metal growth 551
 – peculiarity 552
 – sapphire growth 539
 – silicon growth 546, 551
 trace element 1617, 1618
 tracht 144
 transducer 4
 transformation
 – hardening 444
 – of atomic energy in PLD and PED
 1195
 – twin 125
 transition
 – metal 252
 – stress 1353
 transmission 352
 – electron microscopy (TEM) 15,
 189, 340, 380, 462, 829, 1006,
 1079, 1162, 1426, 1453, 1477
 – spectrum 354, 783
 – topograph 218, 810, 813
 transmitted wavefront (TWF) 786
 transparent spectrum 783
 transport
 – agent 904
 – equation 1248
 – growth model 659
 – kinetics 901
 – limited growth 1136
 – model 666, 901
 – phenomena 1587
 – property 347
 – rate 906
 transverse magnetic field 231
 – applied Czochralski (TMCZ)
 method 235
 transverse magnetoresistance 346
 transverse optic (TO) 1158
 trapiche ruby 151
 trapping 1557
 – center 1541
 – coefficient 1556, 1567
 traveling heater method (THM)
 174, 315, 335
 traveling solvent floating zone
 (TSFZ) 367, 368
 – self-flux 373, 374
 traveling solvent zone (TSZ) 9, 373
 triamterene 1625
 triangular inclusion 943
 tribotechnical property 464
 tricalcium phosphate (TCP)
 whitlockite 1619
 trichloroethylene (TCE) 927
 triglycine sulfate
 – crystal growth 574
 – single crystal 574
 triglycine sulfate
 ($\text{NH}_2\text{CH}_2\text{COOH}$)₃H₂SO₄ (TGS)
 569, 574

TSSG (top-seeded solution growth) 708
 tube shaped crystal 520
 tungstate
 – flux 740, 741, 750
 – melt 741
 – solution 748, 750
 tunneling current 1112
 twin 160, 544, 1440, 1485
 twin boundary 121
 – growth-promoting effect 124
 – propagation 123
 twin formation
 – after growth 125
 – by inclusions 123
 – by nucleation 122
 – during growth 122
 twin law 120
 twinning 120, 193, 194, 334, 341
 – dislocation 121
 twin-plane reentrant-edge effect (TPRE) 124
 two shaping elements technique (TSET) 551
 two-dimensional (2-D) 18
 – characterization 1595
 – crystal growth 1310, 1318
 – epitaxial adsorption layer 71
 – epitaxy 82
 – equilibrium shape 61
 – mechanism 74
 – nucleation 167, 767
 – nucleation growth (2DNG) 136
 – nucleus 767
 type I diamond 156
 type II diamond 156
 types of gels 1608
 types of in situ cells 1645
 TZM vessel 618

U

ultrahigh pressure high temperature (UHPHT) 155
 – metamorphic rock 155
 ultrahigh vacuum (UHV) 398, 1156
 ultralarge-scale integrated circuit (ULSI) 231
 ultraviolet (UV) 162, 728, 888
 undercooling 712
 undoped crystal of CuAlS_2 918
 undoped crystal of CuAlSe_2 919
 UNi_2Al_3 398
 universal compliant (UC) 944
 upper yield stress 1348

Urbach tail energy 1109
 uric acid 1623
 urinary stone disease 1616
 urinary stone formation 1616, 1617
 – theory 1616
 use of a defective seed 1339

V

V/III ratio 1267
 vacancy 160, 167, 694
 – concentration 1567
 – condensation 190
 – in Si 1560
 – in ZnO 1562
 – potassium 699
 – related complex 1575
 vacancy defect 1554
 vacancy–donor complexes 1566
 valence band (VB) 1457, 1676
 valved cell 1090
 van der Pauw (vdP) 358
 van der Waals force 6
 vanadate 739
 vapor composition 805
 vapor condensation 798
 vapor diffusion apparatus (VDA) 1589
 vapor growth 799
 – classification 899
 – of III nitride 1244
 vapor phase (VP) 897, 898, 1573
 – epitaxy (VPE) 11, 901, 925, 926, 954, 1001, 1041, 1046, 1206
 – growth 10
 vapor pressure 5
 – controlled Czochralski (VCz) 169, 170, 188, 190
 vapor–liquid–solid (VLS) 138, 193
 – mechanism 138, 146
 Vegard's law 332
 Verdet constant 468
 Verneuil
 – method 9
 – technique (VT) 509
 vertical and horizontal Bridgman method 334
 vertical Bridgman (VB) 169, 1216, 1227
 – crystal 286
 – technique (VBT) 480, 484, 502
 vertical gradient freeze (VGF) 169, 188, 288
 vertical magnetic field applied Czochralski method (VMCZ) 235

vertical-cavity surface-emitting laser (VCSEL) 1414
 very large-scale integrated circuit (VLSI) 939, 1153
 vibration 1237
 – of wire 1734
 vicinal
 – facet 103
 – plane 703
 – pyramid 103, 114
 – sector 103
 – sectorality 786
 Vicker's microhardness 1617
 virtual interface approximation 1092
 virtual-crystal approximation (VCA) 350
 viscoplastic model 1342
 viscosity 568, 733
 – melt 695
 void-assisted separation (VAS) 881
 voids 676
 volatility 567
 volatilization 333
 Volmer–Weber growth 20
 – mode 1073
 volume and surface diffusion 76
 volume defect 12
 von Mises contour 180
 von Mises invariant 179
 VPE system 926

W

wafer
 – annealing 190
 – bowing 880
 – characteristics 1734
 – forming 1724, 1725
 – micromapping 1420
 – polishing 1724
 – preparing 1724
 – slicing 1722, 1732
 wafer manufacturing 1721, 1722
 – and slicing using wiresaw 1721
 warp 1727, 1731
 warpage 1728
 waste recycling 469
 waviness 1731, 1735
 weak beam dark field (WBDF) 1479
 welded closure 618
 wet-etching of semiconductor 1459
 – mechanism 1454
 wetting 59
 – angle hysteresis 525

- condition 523
- function 24
- to-catching condition transition 523
- whisker 146
- white-beam x-ray topography 1431
- wide-bandgap semiconductor 821
- Wilson plot 1589
- window retardation 1092
- window width (W) 958
- wire web 1730
- wiresaw 1721, 1722
- operation 1728
- process parameter 1733
- work for nucleus formation
- general definition 24
- work hardening 1347, 1357
- work of formation of 2-D crystalline nuclei on unlike and like substrate 27
- working electrode (WE) 1454, 1455
- Wulff
- plot 137
- theorem 96
- Wulff–Kaischew theorem 23
- wurtzite 832
- structure 1487

X

- xanthine 1615
- x-ray
- and diffraction theory 1638
- anomalous scattering 215
- crystallography 1599
- diffractometry 1405, 1406
- method 12, 1637
- photoelectron spectroscopy (XPS) 342, 1083, 1087, 1158
- powder diffraction 379
- powder diffraction pattern (XRPD) 1639

- refractive index 1408
- x-ray diffraction (XRD) 12, 341, 829, 885, 889, 1017, 1057, 1084, 1110, 1405, 1436, 1598
- analysis 1407
- dynamical theory 1436
- kinematical theory 1436
- limitation 1436
- pattern
- instrument 1412
- x-ray scattering
- established method 1413
- new method 1416
- rapid analysis 1419
- x-ray topograph 766, 810, 1440, 1445
- analysis of defects 1445
- image 781
- x-ray topography (XRT) 13, 14, 135, 805
- basic principle 1426
- Berg–Barrett topography 1430
- conventional 1430
- Lang 1430
- monochromatic-beam 1434
- synchrotron-radiation-based 1431
- technique 1430, 1431
- theoretical background 1435
- white-beam 1431

Y

- $Y_3Al_5O_{12}$ (YAG) 162
- $(Y_2)-Lu_2Si_2O_7:Ce$ (YPS and LPS) 1681
- $Y_2SiO_5:Ce$ (YSO) 1681
- YAG 414
- $YBa_2Cu_3O_{7-x}$ (YBCO) 1044
- Y–Ba–Cu–O 415
- Yb-doped KLuW 747
- Yb-doped laser crystal 492
- yellow luminescence (YL) 887
- Young's relation 59

- yttrium aluminum garnet (YAG) 728
- yttrium aluminum perovskite (YAP) 728
- yttrium iron garnet (YIG) 1042

Z

- Z-contrast STEM 1509
- Zeeman effect 1524
- Zeldovich factor 29
- zeolite 8
- zero-force theorem 110
- zero-loss peak (ZLP) 1491
- zinc 1617
- oxide (ZnO) 655, 1446
- zirconia 433
- zirconia crystal 448
- cubic 448
- cubic lattice 447
- ion radius 447
- mechanism of stabilization 448
- stabilization 447
- tetragonal 448
- zirconium dioxide 445
- ZM configuration 1219
- $ZnGeP_2$ 731
- ZnO
- bulk growth 1573
- electrical properties 678
- ZnS_xSe_{1-x} single crystal 908
- ZnS_xSe_{1-x} system 908
- ZnSe single crystal 914
- ZnTe buffer 1102
- ZnTe growth nucleation 1101
- ZnTe on Si 1101
- zoisite 633
- zonal inclusion 97
- zone
- melting (ZM) 173, 334, 1216
- refinement 851
- refining 333
- ZrO_2 417
- ZrO_2 – Y_2O_3 phase diagram 446